TRANSACTIONS

VOLUME 48

USING THE EARTH TO SAVE THE EARTH

2024 Geothermal Rising Conference

GEOTHERMAL RISING
301 N Palm Canyon Drive, Suite 103
Palm Springs, CA 92262 • USA

GRC *TRANSACTIONS*, VOLUME 48

Using the Earth to Save the Earth

2024 GEOTHERMAL RISING CONFERENCE

GEOTHERMAL RISING
301 N Palm Canyon Drive,
Suite 103
Palm Springs, CA 92262 · USA

Copyright © 2024 Geothermal Rising
Printed in the United States of America

Notice

All views and conclusions in this publication are those of the individual authors of the papers in which they are contained, and should not be interpreted as necessarily representing the official policies and/or views/recommendations of Geothermal Rising (GR). Draft papers were reviewed by the GRC 2024 Technical Program Committee. Final paper submissions were not reviewed for scientific and/or editorial correctness prior to publication. The papers presented in this publication are reproduced as faithfully as possible by Geothermal Rising. The contents of papers in this volume, however, are solely the responsibility of the authors.

ISSN: 0193-5933
ISBN: 0-934412-30-8

Table of Contents

Closed Loop / Advanced Geothermal Systems **1**

Dayo Akindipe et al.

Thermal and Well Flow Performance of Closed-Loop Geothermal in the Wattenberg Area 2

Mohammad Aljubran et al.

Techno-Economic Viability of Flexible Dispatch of Unconventional Geothermal Systems 22

Corey Dufrene, Elizabeth Cambre, Joe Hill

Unlocking Geothermal Potential: Investigating Vacuum Insulated Tubulars for Improved K-Value Accuracy 43

Raquel S.P. Hakes et al.

Influence of Reservoir Convection on Heat Extraction with Closed-Loop Geothermal Systems 56

Orkhan Khankishiyev et al.

Evaluation of Multilateral Well Design and sCO2 for Closed Loop Geothermal Systems 72

Richard Lein et al.

Field Design Optimization for Horizontal Directional Drilled Ground Heat Exchangers 96

Liangping Lia et al.

Optimization of Borehole Thermal Energy Storage Systems 118

Nakao Yoshinobu et al.

A Case Study on Geothermal Power Generation Systemby Semi-open Loop Carbon Dioxide Circulation 128

Anna Rogers et al.

In-Situ Stress Review for a Closed-Loop Geothermal Project in Geretsried, Germany 144

Junyuan Zhang, Erick Burns, Hongbin Zhan

The Advantages of Electric-grade Heat Storage in Long Closed-loop Wells 156

Ali Zidane and Danylo Oryshchyn

Optimizing Geothermal Borehole Number and Positioning through a Simulated Annealing Algorithm 169

Diversity, Equity, Inclusion, and Belonging 186

Diana Acero-Allard et al.

Geothermal Collegiate Competition: Evolution and Impact 187

Brandy Brazell Obvintseva

Strengths-Based Bridges: Fostering Diversity, Inclusion, and Innovation in the Geothermal Industry 205

Alison Thompson, London Hillyer

Canadian Policy Opportunities for the Geothermal Energy Industry (August 2024) 213

Simon Webbison et al.

Ormat Technical Career Path Development and Implementation 230

Jon Weers et al.

GeoBridge: Connecting Communities to Geothermal Information and Opportunities 243

Downhole Logging **254**

Garry Andrews, Mark Satre

Innovative E-line Intervention Solutions for Geothermal Wells 255

Gawan Berentelg, Stefan Dietze, Veit Hagenmeyer

inliSAMP, a Modularly Designed Fluid Downhole Sampler for Deep Geothermal Applications - Proof of Concept 268

Jorge Alberto Rangel-Arista et al.

Temperature and Pressure Transient Analysis: Pre and Post-Deflagration Assessment 294

Michael Richter et al.

Utilization & Testing of Advanced Wireline Conveyed Subsurface Tools in Vapor Dominated Reservoirs – The Geysers 308

Melanie B. Schneider et al.

Chloride-based Wireline Tool for Measuring Fracture Inflow in Enhanced Geothermal Systems (EGS) Wells: Field Deployment Updates 327

Sigit Suryanto et al.

Fracture Characterization using Borehole Image Log, A Single Well Case Study from an Exploration Well at Tompaso Geothermal Field, North Sulawesi, Indonesia 354

Naveen Velmurugan et al.

Preventing Downhole Tool Failure During Geothermal Well Construction Using a Hybrid Real-Time Temperature Management Advisory System 367

Andrew Wright

Long-term High Temperature High Pressure Cable for Geothermal Logging Tools 382

Andrew Wright et al.

300 Degree Celsius Electronic Component Packaging for Geothermal Tools 388

Drilling **400**

Michael Adams and Reza Fard

Extending Drilling Tool Life in Geothermal Wells with Recent Advances in Low Thermal Conductivity Coatings 401

Andrew Barry et al.

Well Control Considerations for a Global Geothermal Industry: A Historical Review and an Assessment of Current and Future Requirements 411

Joven John Cayao and Alger Danielle Ballon

Revolutionising Geothermal Well Design and Operations with High-Temperature Metal Expandable Packer Technology: A Novel Approach in Drilling and Workover 426

John Clegg et al.

Breaking the 200°C Barrier – Development of an Integrated High Temperature Directional Drilling System 432

Veerabhadra S Denduluri, Maria Juenger, Eric van Oort

Severe Lost Circulation Mitigation using Temperature Activated Materials 443

Joshua Gossanyi et al.

Driving Down Exploration Costs in Geothermal Through Core Drilling 454

Meng Meng et al.

Mechanical Evaluation of a Novel Cement Formulation used for Thermal Energy Storage Wells 471

Anthony LeBaron et al.

High Temperature Characterization and Drilling Simulation of rock from Utah FORGE 485

Chong Lin, Arash Dahi Taleghani

A Coupled Simulation of Fracture Sealing of Lost Circulation Materials at Elevated Temperatures 498

Liam Lines et al.

Enhanced Weight on Bit Application in Hard Rock Drilling Through Innovative Anchoring Technology 514

Dionne Mayibeki et al.

Effect of Hydrostatic Pressure on Mechanical Specific Energy and Interfacial Friction Angle in Hard Rock Drilling 526

Komang Wisnu Murti et al.

Drilling Ultra High Temp Geothermal Well Using Standard Temperature Drilling Tools 541

Panurach Dumrongthai et al.

Enhancing Geothermal Drilling Performance: A Stuck-Pipe Risk Advisor Leveraging Causal-AI and Semantic Web for Explainable Decision Support 550

Conner Richardson et al.

Optimizing Hard Rock Geothermal Drilling Efficiency With PDC Bits: A Comprehensive Study 568

Ningyu Wang, Pradeepkumar Ashok, Eric van Oort

Managed Temperature Drilling: Real-Time Damage Monitoring of Insulated Drill Pipes and an Automatic Controller to Mitigate Effects of Subsequent Temperature Increase 587

Ariatama Yustisia et al.

Drilling Innovation Enables Faster Delivery of Geothermal Wells in Indonesia 598

Economics **606**

Dayo Akindipe et al.

Geothermal Power Systems Analysis: Outcome of Industry Stakeholders Workshop 607

Luke P. Frash

Whispers of a New Frontier for Safe and Profitable Geothermal Anywhere 619

Stephen E. Gardner and D. D. Faulder

Geothermal Reserves Standards: A Study of the Applicability of the SPE Petroleum Resources Management System, a Proposed Classification Framework for Geothermal Reserves and Resources 633

Jonathan L. Ho, Juliet Simpson, Anne Barlas

Assessing the Economic Value of Underground Thermal Storage for Hybrid Geothermal Power 647

Patrick Mays et al.

An Economic Evaluation of Parasitic Losses and the Impact of Conformance Control on Parasitic Losses in an EGS Horizontal Well 657

Andrew Pauli et al.

Collaboration and Continuous Improvement Makes Utah Geothermal Project Economic and Successful 682

Kotaro Shinozaki et al.

A Questionnaire Survey and An Agent-based Simulation as to Consensus Building on Geothermal Development in Japan 696

Greg Ussher, Aimee Calibugan, Julian McDowell

Probability of Discovery as a Useful Concept for Communicating Exploration Drilling Uncertainty 706

Energy Conversion / Utilization **715**

Reza Agahi

Geothermal Power for Green Hydrogen Production 716

Joseph Bonafin, Queenie Lam, Peter Marsters

Integration of ORC Technology with EGS Systems to Meet the Demands of Future Grids 723

Brianna Byrd and Brett Bauer

High-Pressure Pelton Turbines: A Simple yet Effective Means of Scaling the Energy Storage and Geothermal Industry 735

Ximena Guardia et al.

Design and Performance Analysis of a Supersonic Ejector Prototype for Connecting High and Low-Pressure Geothermal Wells 744

John Klaerner, Lev Ring

An Overview of the Performance Testing of a Supercritical CO2 Geothermal Turbine 761

Leanne Komaromi, Roman Shor, Harris Switzman

Techno-economic Feasibility of Deep Geothermal Systems in a Low-Enthalpy Reservoir, Western Canada Sedimentary Basin 778

Isaias Marroquin et al.

Grid Resilience Analysis on Geothermal District Heating and Cooling Implementation Alongside Four Existing Oil and Gas Wells in Tuttle, Oklahoma 793

Meng Meng et al.

Mechanical Evaluation of a Novel Cement Formulation used for Thermal Energy Storage Wells 806

John R. Muir, Andrew J. Van Horn

The Third Electric Energy Transition Calls for Geothermal Energy Assurance 820

Nyawir Erique Otienoh, Omenda Peter Ayodo, Varet Jacques

Maximizing the Kenyan Rift Geothermal Energy - The Otutu Rift Segment Case 838

R. Roundtree et al.

Monetizing Low-Moderate Enthalpy Geothermal Reservoirs: Lessons Learned 855

Lokesh Kumar Sekar, Mohammad Aljubran, Esuru Rita Okoroafor

Optimizing Flexible Geothermal Energy Generation: A Techno-Economic Analysis Using FGEM For EGS Huff-N-Puff 864

P. Siratovich et al.

Generating Value from Geothermal Non-Condensable Gas Emissions 876

Ian Richardson, Simon Webbison

Greenhouse Gas Emissions Reduction: Global Geothermal Power Plant Catalog 887

Enhanced / Engineered Geothermal Systems 904

Christian Akhilome, Sushobhan Pradhan, Prem Kumar Bikkina

Experimental Investigation of the Flow Behavior of Ionic Liquids for use as Working Fluids in Enhanced Geothermal Systems 905

Koenraad F. Beckers et al.

EGS Reservoir Modeling for Developing Geothermal District Heating at Cornell University 919

Sharat Chandrasekhar et al.

Scaling and Thermal Penetration Depth in Enhanced Geothermal Energy Production 936

Branko Damjanac et al.

Interpretation of Stimulated Permeability by Model Calibration with Data from Circulation Program at FORGE 963

Katrine J. M. Hareland et al.

Experimental Analysis of Fluid Hydraulics in Enhanced Geothermal Systems 976

Abdul Muqtadir Khan et al.

Integrated Lifecycle Simulation for Utah FORGE: Part I – Fracture Geometry Calibration 988

Olga Kresse et al.

A Review of Enhanced Geothermal Systems Subsurface Life Cycle Optimization 1012

Yunxing Lu et al.

Understanding Impact of Complex Fracture Patterns in EGS In-Situ Stress Estimations Through Post-Peak Pressure Analysis from High-Temperature True-Triaxial Block Fracturing Experiments 1034

Peter M. Meier et al.

Learning Curve of Seismic Risk Mitigation for EGS Since Basel 2006 to Utah FORGE 2024 from the Perspective of a Project Developer 1046

Mauricio A. Rivas et al.

Geopressured Geothermal Systems: An Efficient and Sustainable Heat Extraction Method 1058

John C. Stormont et al.

High-temperature Polymers to Modify Fracture Permeability 1076

Yuan Tian, Roland Horne

Influence of Hydraulic Fracturing on Induced Seismicity Based on a Combined Flow and Geomechanical Model 1086

Zhi Ye1, Ahmad Ghassemi

Analysis of the Stimulated Volume and Seismicity Migration in Utah FORGE Stimulations 1103

Qitao Zhang, Arash Dahi Taleghani

Operation Strategy to Avoid Thermal Short-circuit in EGSs with Horizontal Wells 1116

Geochemistry **1128**

Jacob DeAngelo, Erick R. Burns, Stanley P. Mordensky

Predicting Hydrothermal Reservoir Depth from Chemical Geothermometers Using a Three-Dimensional Temperature Model in the Great Basin, USA 1129

Steve DeOreo, Melinda Wright

Stable Isotope Characterization of the High-Temperature Steam Reservoir of the Northwest Geysers: Review of Data Acquired During Step Out Drilling Program and Integration into 3D Geological Model 1140

Tianlong Jiang et al.

Development of a New Screening Method for Low Silica Adhesion Resin Materials Based on the Ab Initio Quantum Chemical Approach 1153

Ram Kumar et al.

Development of Reactive Transport Models for Very High Temperature Heat Aquifer Storage (VESTA) at a Pilot Site in Germany 1168

Fritz Earwin Monterozo

Inhibition of Iron Sulfide to Prevent Brine Pump Capacity Decline 1184

Yuya Nakashima et al.

Development of Carbon-based Coating to Suppress Silica Scale Accumulation on the Inner Surface of Pipes 1193

Claire J Newton et al.

A Simple Predictive Tool for Geothermal Amorphous Aluminosilicate Scales: Correlation with Field Examples 1208

Jeanne Vidal et al.

How Important Is the Hydrothermal Alteration in the Upper Rhine Graben for Geothermal Lithium Assessment? 1229

Geology **1239**

James E. Faulds et al.

Structural Setting and Geothermal Potential of Northeastern Reese River Valley, North-Central Nevada: Highly Prospective Detailed Study Site for the INGENIOUS Project 1240

Emilie Gentry, Joe Batir

Geothermal Resource and Opportunities Assessment of Colorado 1258

Kellen Gunderson, Christian Hardwick

Characterizing Sedimentary Geothermal Reservoirs: Case Study from the Great Salt Lake Basin 1273

Nicole R. Hart-Wagoner et al.

Exploring Geothermal Potential of Great Basin Sub-Regions 1291

Nicholas H. Hinz et al.

Geological Mapping Standards for Developing Geothermal Resource Conceptual Models; Survey Design, Applications, Pitfalls and Remedies 1310

Shari Kelley

Evaluation of the Geothermal Potential of the Southern San Luis Basin, Taos County, New Mexico 1337

Kurt O. Kraal, Paul C. Schwering

Remote Sensing Case Studies for Detection and Interpretation of Geothermal Surface Materials for Geothermal Exploration in the Basin and Range, Nevada, USA 1353

Nicole Lautze et al.

Final Results of the Hawai‘i Play Fairway Project 1373

Bridget Y. Lynne, Eylem Kaya, Alex Morriss

Characterisation of Core from a New Zealand Geothermal Field and its Potential Reaction to Receiving CO2-rich Injection Fluids 1379

Kevin McCarthy, Will Pettitt, Rich Priem

Geothermal Play Fairway Analysis (GPFA) - Part II: Texas/Gulf Coast Mechanisms of Heat Generation 1398

Sarah D. Milicich et al.

Fracture Permeability in Basement Greywacke for Supercritical Geothermal Drilling Planning 1418

Guy Oliver et al.

Mount Augustine: Exploring For A New Geothermal Resource In South-central Alaska 1435

Tito Satria Putra Perdana et al.

Characterizing Subsurface Structures and Determining In-Situ Stress Orientations: A Case Study from the Tuchang Geothermal Prospect Area, Northeastern Taiwan 1463

Imam M. Prasetyo, Teguh Prabowo, R.M. Tofan Sastranegara

Discrete Reservoir Characteristics Within Lahendong Geothermal System 1481

Drew Spake et al.

Conceptual Model of the Puna Geothermal System 1487

J. Eric Stautberg, Steven A. Sonnenberg

Identifying Sedimentary Geothermal Play Types in the Cretaceous Strata of South Texas Through High-Resolution Temperature-Depth Mapping Based on Corrected Bottom-Hole Temperature Measurements 1508

Jesse Turk et al.

Alteration Assemblages and Paragenesis at the Sorik Marapi Geothermal Prospect, Sumatra, Indonesia 1520

Jeanne Vidal et al.

A Comprehensive Exploration and Modeling Approach for Heat and Geothermal Lithium Extraction in the Upper Rhine Graben 1540

J. Vidal et al.

Towards a Conceptual Model of Deep Circulations in Cerro Pabellón Geothermal System (Andean Cordillera, Northern Chile) 1552

Maxwell Wilmarth, Drew Siler

Evolution of Shallow Temperature Surveys 1566

Ming-Yu Wu et al.

Implication of Geothermal Conduits with the Relationship Between Fracture Intensity and Fault Distribution in the Central Mountain Area of Taiwan 1577

Geophysics **1597**

Ahmed Alhani et al.

Exploration of Deep Hot Sedimentary Aquifer Geothermal Systems in The Midyan Basin of Saudi Arabia by ENOWA-NEOM 1598

Jacob Anderson et al.

Preliminary Ground and Airborne-based Geophysical Mapping and Modelling of an Active Hydrothermal System at Mammoth Lakes, California 1613

Muhammad Tajul Arifin, Aditya Abdurrahman Juanda, Mulyanto

Base of Clay Cap Temperature Characterization in Sumatra Island, Study Case in PGE Fields 1640

Racine Basant, Graham Ryan, Oshaine Blake

Meso-scale Geophysical Characterization of the Geothermal System in Montserrat, W.I. 1651

Joseph Batir, Jerjes Porlles, Emilie Gentry

Buffalo Valley and Surrounding Temperature Data: Heat Flow Calculation and Implications for Geothermal Exploration 1661

Sireesh Dadi et al.

Microseismic Monitoring During a Next Generation Enhanced Geothermal System at Cape Modern, Utah 1673

Tait Earney et al.

Geophysical Modeling of a Possible Blind Geothermal System Near Battle Mountain, NV 1699

Jeffrey Eppink et al.

Reducing Costs and Mitigating Risk for Geothermal Energy with Permeable Fracture Imaging 1720

Inusa P Fauzi et al.

Sibayak Geothermal Field: New Insights from Updated MT Model 1747

Matthew Folsom et al.

A Direct Comparison of Resistivity Models from Helicopter Transient Electromagnetic and Magnetotelluric Datasets Collected over a Blind Geothermal System in East Hawthorne, Nevada, USA 1762

Jonathan M.G. Glen, Tait Earney

The Influence of Pre-existing Structures on Geothermal Springs: Inferences from Potential Field Mapping in Surprise Valley, CA and Other Sites in the Northwestern Great Basin 1786

Zeming Hu et al.

Mitigating Induced Seismicity in Geothermal Energy Production: The Application of the Traffic Light System (TLS) and Global Case Studies 1801

Joël Le Calvez, Takashi Mizuno, Pierre Bettinelli

Integrating Geophysics Into Geothermal Workflows: Example of DAS-Acquired Microseismic Monitoring and a Few Other Fiber Optic-Based Applications 1816

Yohei Morifuji et al.

Repeat Microgravity Measurements in Beppu Geothermal Area, Japan 1822

Zach Reynolds et al.

Detailed Airborne Magnetic Survey of the Puna Geothermal Venture and the Lower East Rift Zone, Island of Hawai‘i 1835

Friedemann Samrock et al.

Geological Causes for Deep Electrical Conductors under Volcanic High-Enthalpy Geothermal Systems 1849

Anya Seward et al.

Aerial Thermal Infrared to Assess Surface Heat Loss at High Temperature Geothermal Fields, Taupo Volcanic Zone, New Zealand 1865

Low-Temperature / Direct Use **1882**

Arlene Anderson, Alexis McKittrick, Lindsay Morse

U.S. DOE Community Geothermal Heating and Cooling Design and Deployment Status 1883

Fady Anees et al.

A Preliminary Investigation on the Performance of a Dual-Source Heat Pump using both the Air and the Ground 1892

Trevor Atkinson et al.

Galleries-to-Calories (G2C): An International Collaboration Evaluating Thermal Energy Storage in Abandoned Mines for District Heating 1905

Carl Belmonte

Technical Feasibility of a Novel Geothermal-Solar Thermal Hybrid Plant 1915

Estefanny Davalos Elizondo, Nicole Taverna, Abra Gold.

Low-Temperature Geothermal Play Fairway Analysis for the Denver Basin 1931

Christine Doughty et al.

Shallow Geothermal Resources for Cooling Applications at the University of Hawai‘i 1956

Jay Egg

How 5th Generation Energy Networks Can Be The Source Of Energy To Supply High Temperature Water to Decarbonize Buildings Using High Temperature Distribution Loops 1979

Nicholas Fry et al.

City-scale Thermal Energy Network Design for Utility Decision Makers 1988

Nicholas Fry et al.

Developing Geothermal District Heating in Lakeview, Oregon 2003

Carson Gemmill et al.

Advancing District Energy Geoexchange Solutions in Single Family Home and Mixed-Use Communities: Strategies and Real-World Insights 2014

Heimir Hjartarson, Egill Maron Thorbergsson and Thráinn Fridriksson

Rangárveita - Small District Heating in the South Part of Iceland - Future Master Plan 2030

Jonathan Ho et al.

Grid Value Analysis of Geothermal Systems for End-Use Applications 2043

Carter Johnson, Justin Mariniak

Exploring the Open Loop Geothermal Potential of the Penn South Neighborhood, NY, Using Numerical Modeling 2058

Zeyneb Magavi, Angie Alberto-Escobar, Isabel Varela

A Definitional Taxonomy for (Geo)Thermal Energy Networks 2089

Hannah Pauling, Slater Podgorny, Dayo Akindipe

Development and Preliminary Analysis of a U.S. Geothermal Heat Pump Installation Database 2111

Juliet G. Simpson et al.

National Modeling of Geothermal District Energy Systems with Ambient-Temperature Loops Using dGeo 2118

Isabel Varela, Zeyneb Magavi

The First Open-Source Database for Geothermal Networks 2132

Bissett Young et al.

Towards Accurate Geothermal Mapping: Analyzing BHT Correction Approaches and Impact on Project Economics 2160

Haiyan Zhou et al.

Case Studies of Borehole Thermal Energy Storage System Design and Operating Schedules 2175

Machine Learning / Computing **2188**

Paul Michael B. Abrasaldo, Sadiq J. Zarrouk1, Andreas W. Kempa-Liehr

Unsupervised Machine Learning For Assessing Geothermal Heat Exchanger Performance 2189

Ahmed G. Almetwally, Mary F. Wheeler, Robert K. Podgorney

FORGE Geothermal Project Modeling using Phase Field Finite-Element 2204

Pascal D. Caraccioli et al.

Separating Signals in Elevation Data Improves Supervised Machine Learning Predictions for Hydrothermal Favorability 2217

Shaolin Jahan Eidee et al.

Hard Rock Drilling Efficiency Mapping Using Machine Learning 2237

Magnus Thor Jonsson, Lilja Magnusdottir

Predicting Steam Production in Water-Dominant Geothermal Reservoirs affected by Reinjection rate Using Recurrent Neural Networks 2255

Shunsuke Kaneko, Shigemi Naganawa, Elvar K. Bjarkason

Development of Artificial Neural Networks for Estimating Static Formation Temperature 2268

Nicole Taverna et al.

Fostering Geothermal Machine Learning Success: Elevating Big Data Accessibility and Automated Data Standardization in the Geothermal Data Repository 2279

Jon Weers et al.

Empowering Geothermal Research: The Geothermal Data Repository's New AI Research Assistant 2292

Pengju Xing et al.

Prediction of Formation Properties Based on Drilling Data from Multiple Wells at Utah FORGE Site Using Machine Learning 2303

Mineral Extraction **2323**

Shaily Gupta, Margaret M. Busse

Quantifying the Impact of Water Needs for Lithium Production from Geothermal Brines in the Salton Sea KGRA 2324

Richard Holt, William Rickard, Mary Mann

Initial Simulations of Lithium Production from Geothermal Brines 2337

Kim Mohler

What's in Your Brine - a Case for Critical Minerals Co-production from Geothermal Brines 2344

Esty Mustika Suud, Suryantini, Herbert Lubis

Review of Lithium Extraction Suitable for Indonesia Geothermal Brine 2359

Non-Technical **2377**

Laura Chiaramonte et al.

Advancing Understanding of Geothermal Representation in the Power Sector to Accelerate Deployment 2378

Mike Kaleikini, Erica Freese, Alissa Sanchez

Navigating Geothermal Permitting under HEPA: The PGV Repower Project 2396

Kristina Hagström Ilievska

Creating a Universal Pitch for Geothermal: A Declaration of Communication 2402

Catherine Lambert, Dominic Balog-Way, Katherine McComas

A Social Science of the Subsurface: Advances in EGS Communication and Engagement Research 2414

Rose Mathenge

Embracing a Circular Model in the Management of Cooling Tower Fill Packs. A Case Study of a Pilot Project Rolled out in Partnership Between Kengen and 'Jua Kali' Entrepreneurs 2435

Regional Updates **2442**

Ysaline Bacon et al.

The Deep Geothermal Energy Potential of Baker Lake (Nunavut, Canada): Initial Resource Assessment from Monte Carlos Analysis 2443

Joseph Batir, Emilie Gentry, Michael Jones

Fort Wainwright Army Installation Geothermal Prototype Initiative: Initial Results 2466

Catherine Hickson, Brian Fairbank

Canadian Expertise and Financing in Global Geothermal Exploration and Development 2476

Katherine Huang, Catherine Hickson

Geothermal Energy Technology Solutions Based on Canada's Geological Provinces 2481

John W. Lund, Gerald W. Huttrer, Aniko N. Toth

Geothermal Development and Use, 1995-2024 2496

Orhan Mertoglu et al.

Exploring the Past, Present, and Future: Geothermal Energy on the 100th Anniversary of the Turkish Republic 2508

Michaël Thibault et al.

Evaluation of the Precambrian Basement Temperature Below Four South Slave Communities, Northwest Territories, Canada 2517

Paul Thomsen, Kayla Dowty

Geothermal Resource and Transmission Planning in the Western United States: A Review of Recent Results and a Roadmap for Continued Expansion 2545

Aniko N. Toth, David K. Fenerty, Orsolya L.Sztermen

How Can the EU's Post-Communist Countries Use Geothermal to Achieve Energy Independence? 2570

Whitney Trainor-Guitton et al.

Improving Geothermal Representation in Energy Analysis Tools to Quantify Geothermal's Role in Decarbonization 2586

Reservoir / Production **2604**

Fathan Hamim Abdurachman et al.

Temporal Evolution of Kamojang Reservoir Pressure: Unraveling Upflow Dynamics in a Dry Steam Geothermal System Through Multidisciplinary Analysis 2605

John Akerley et al.

Mammoth Casa Diablo IV: A Case Study for Cooperative Baseline Analysis to Mitigate Environmental Impacts 2619

Baojun Bai et al.

Development and Evaluation of Preformed Particle Gels for Preferential Fluid Flow Control in Geothermal Reservoirs 2641

Naura T. Fadjar et al.

Enhancing Reservoir Performance Insight: A Comprehensive Monitoring Approach with Steam Allocation Lumut Balai (SALB) Application 2657

Sven K. Hartvig et al.

Characterization of Flow in Induced Fractured Networks Using Tracers in Enhanced Geothermal Systems 2674

Magnus Thor Jonsson

A Wellbore Model Approach for Scaling Prediction and Condition Assessment 2688

Orkhan Khankishiyev et al.

Gas Lift Production Optimization in Liquid-dominated Geothermal Wells 2701

Kunhwi Kim et al.

Updates of Numerical Reservoir Model for Sorik Marapi Geothermal Field 2719

Rebecca Kreuzer et al.

Hot Springs and Geysers: Exploring Historical and Modern Impacts of Geothermal Energy Production on Surface Thermal Features and Standardizing Management Practices 2731

Rochelle Longval et al.

Improving Geothermal Well Production through Scale Removal: A Lakeview, Oregon Case Study 2745

Arkaitz Manterola Donoso et al.

Optimizing Geothermal Resource Management: Insights from Stock Reservoir Modeling Analysis in Icelandic Fields 2750

John Murphy et al.

Permeability and Numerical Modeling of the Puna Geothermal Venture 2768

Nicholas Prina et al.

Puna Geothermal Venture Flow Testing: Facility Design Upgrades and Results 2785

Santiago Rocha et al.

Conceptual Hydrothermal Model of the Salton Sea KGRA 2803

Yuan Tian et al.

Power Outputs from the Field Tests of Thermoelectric Generators at Different Temperatures 2825

H. Tounsi et al.

Dynamic Modeling of Fracture Networks to Optimize Geothermal Reservoir Performance 2838

Minh Tran et al.

Coupled Multi-Segment Wellbore and Thermal Modeling in a Deep Sedimentary Geothermal Field -- a Case Study for the DEEP Geothermal Project, Saskatchewan, Canada 2853

Cesar Vivas, Zeming Hu, Saeed Salehi

Textural Analysis of Sedimentary Rocks: Implications for Geothermal Reservoir Characterization 2865

Ahmed S. Zakaria

Unlocking the Full Production Potential of Geothermal Wells in Indonesia using a Novel In-situ Generated Acid Fluid Technology 2879

Super-Hot Geothermal **2889**

Greg Asher, Sriram Vasantharajan

An Integrated Asset Management Model for Superhot Rock Enhanced Geothermal Systems 2890

Isabelle Chambefort et al.

The Superhot Opportunity for New Zealand- Joining the Ends Together 2910

Daniel W. Dichter

Ideal Thermal-Hydraulic Performance of Geothermal Power Systems Above 300 °C 2922

Jenna Hill et al.

Optimizing Energy Production for Large Scale Superhot Rock Geothermal 2951

Gunnar Skúlason Kaldal, Steinþór Níelsson, Þorri Jökull Þorsteinsson

Increased Structural Integrity of Casings of High-Temperature Geothermal Wells using Novel Technologies 2963

Bjarni Pálsson

Superhot Geothermal - Experience and Outlook in Iceland 2974

Transition from Oil & Gas **2984**

Moones Alamooti1, Olusegun Stanley Tomomewo

Modeling a Hybrid Renewable Energy System for Bowman County, North Dakota: Assessing the Feasibility of Transitioning from Coal to Wind, Solar, and Geothermal Power 2985

Stian Engebretsen, Taha Taha, Mohammed Abd-Allah

Optimizing Design and Operation of Closed Loop Geothermal Wells with Integrated Asset Simulation 3005

Kagan Kutun, Abra Gold, Koenraad Beckers

Geothermal Reservoir Simulation Analysis in Support of Electricity Co-Production Feasibility Study at the Blackburn Oil Field, Nevada 3019

Alfred Lacazette et al.

Geothermal Prospecting in Existing Oil and Gas Basins 3038

Hyunjun Oh et al.

Impact of Geothermal District Heating System on Flexibility of Microgrid in Tuttle, Oklahoma 3056

Eva Schill et al.

DeepStor - District Heating From High-Temperature Heat Storage In A Depleted Hydrocarbon Reservoir In The Upper Rhine Graben 3066

Tribal Communities **3076**

A. Blair et al.

Indigenous Participation in Geothermal Projects: Learnings from Aotearoa New Zealand 3077

A. Blair et al.

The Waiwhatu Project: Developing Shared Language (English-Te Reo Māori) for Communicating Geothermal Scientific Terms 3098

Alex Hessinger et al.

Why Does Geothermal Matter for Tribal Land? The Geothermal Journey of the Pawnee Nation 3111

Alice Kim, Nicole C. Lautze, Donald M. Thomas

Empowering the Lānaʻi Island Community with Groundwater and Geothermal Resources 3121

Vagif Mammadzada et al.

Geothermal Direct-Use Application for Greenhouse Heating: Case Study of Osage Tribal Nation 3131

Well Construction & Completion **3154**

Jorge Andres Alvarez Escobar et al.

Zonal Isolation Concept for FORGE Geothermal Wells 3155

Alfred Eustes et al.

A Summary of the FORGE Project for the Development of Multi-Stage Fracturing System and Wellbore Tractor to Enable Zonal Isolation During Stimulation and EGS Operations in Horizontal Wellbores 3168

Neil Glover, Geoffrey Garrison, Steve Glidewell et al.

Development and Qualification of an Elastomer Based Retrievable Packer for Effective Annular Isolation in Enhanced Geothermal Systems 3185

Gatra Kusuma et al.

Integration Well Construction, Value to Reduce Overall West Java Geothermal Development Cost 3202

Tatiana Pyatina, Toshifumi Sugama

Alkali-Activated Gibbsite Cement for Use in CO2-rich Geothermal Wells 3216

Kayode Sanni et al.

Comparative Analysis of Casing-Cement Interfacial Bonding Shear Strength Using Class G and Class H Cement at Room and Elevated Temperatures 3228

Closed Loop / Advanced Geothermal Systems

Thermal and Well Flow Performance of Closed-Loop Geothermal in the Wattenberg Area

Dayo Akindipe, Abra Gold, Geoffrey Kiptoo Mibei, Adam Ketchum and Koenraad Beckers

National Renewable Energy Laboratory

Keywords

Closed-loop geothermal, slender body theory, Wattenberg anomaly, techno-economic analysis

ABSTRACT

Closed-loop geothermal systems provide an alternative to resource-constrained hydrothermal systems and stimulation-intensive enhanced geothermal systems. In this work, we apply the slender-body theory (SBT) model, to simulate the well flow and heat transfer performance of U-loop well designs in the Wattenberg area of the Denver-Julesburg Basin. Three U-loop well patterns are investigated, including a single-, double-, and multi-lateral design. The subsurface within the area of interest is characterized by deep, hot (> 200°C) igneous/metamorphic basement rock underlying multiple sedimentary formations. The lateral section(s) of the U-loop lie(s) within a target depth of 6 km, where temperatures are estimated to approach 300°C. As a base case, conduction-only heat transfer is investigated through simulations with the SBT model within U-loops with open-hole laterals that exchange heat directly with the hot, dry rock using water as a working fluid. The utilization of supercritical CO_2 as a heat transfer fluid is also considered. For each scenario, the system performance in terms of annual heat production and temperature profile over a 20-year project lifetime are assessed. Also, the levelized costs of heat and electricity (LCOH and LCOE) are determined using a top-down techno-economic analysis model. The results show that the performance- and cost-optimized U-loop design is one having an injection-production well spacing of 1,000 meters with ten 50-meter-spaced laterals that traverse a subsurface system with a temperature gradient of 60°C/km. By injecting 20°C-water at a rate of 60 kg/s through this loop, an average heat production of 19 MW_{th} (i.e., 2.2 MW_e net plant output) can be achieved, resulting in an LCOE and LCOH of \$136/MWh_e and \$1.53/GJ, respectively, over a 20-year project life.

1. Introduction

A first-of-a-kind geothermal drilling project in Colorado, titled the Geothermal Limitless Approach to Drilling Efficiencies (GLADE), has been funded by the Geothermal Technologies Office (GTO) of the U.S. Department of Energy (DOE). The project aims to significantly improve

drilling rates by combining proven and novel drilling technology and analytics to safely drill twin high-temperature wells in the Wattenberg area of the Denver-Julesburg (D-J or Denver) Basin (Figure 1). The D-J Basin is a structural basin with a large asymmetric syncline comprising Paleozoic, Mesozoic, and Cenozoic sedimentary rock layers underlain by a Precambrian basement with igneous and metamorphic lithology (Curtis, 1988). The local vertical depth to the basement is expected to be in the range ~3,000 to ~3,800 m (Porro et al., 2012). A representative cross section along the line A-A' of Figure 1 is shown in Figure 2. The sedimentary layers are dominated by subaerial deposits, with minimal carbonates (Abbott & Noe, 2004). Oil and gas production occurs from several formations in the basin, including the Pierre shale, lower Cretaceous formations, and the Lyons sandstone (Nelson & Santus, 2011; Crowell et al., 2012). Using aeromagnetic surveys and cross-correlation with exposed bedrocks in the Front Range, Sims et al. (2001) interpreted bedrocks through Colorado and established that, for the study area, the expected basement lithology consists of either Paleoproterozoic gneiss or Paleoproterozoic granite (Sims et al., 2001).

The Greater Wattenberg area is associated with a thermal anomaly characterized by higher geothermal gradients than the surrounding area (Weimer, 1996). The youngest rocks observed are predominantly sedimentary, devoid of indications of recent volcanism. The heat source for the observed anomalous geothermal gradients is not well understood, because the deepest wells in the Denver Basin penetrate only to about 2,700 m in depth (Higley & Cox, 2007). The complex structure in the deep basin (reverse faults associated with brittle deformation and basin buckling), underlain by conductive minerals in the basement rock are factors that could concentrate heat in the region. This model for anomalous heat flow in a sedimentary basin is consistent with geothermal "play types" that develop in the foreland basin of a conduction-dominated orogenic belts (Moeck, 2014; Davalos-Elizondo et al., 2023). Thermal replenishment has been hypothesized to be supported by either deep-seated magmatic intrusions, an upflow zone of a deep hot water system facilitated by faults, or a deep conductive zone created by mineralization of highly conductive minerals associated with the Colorado Mineral Belt (Eaton, 2023). Geological data from planned deep wells may help shed light on heat and fluid sources in the Wattenberg area.

Using bottom hole measurement data from 6,181 oil and gas wells drilled in the area, Lacazette et al. (2024) developed isotherms around the major hot spot in the Wattenberg area. Their map revealed a thermal gradient between 40°C/km and 60°C/km in the hot spot (Lacazette et al., 2024). The target vertical depth of the proposed twin wells is on the order of 6.1 km, significantly surpassing the Phanerozoic sedimentary layers and into the Precambrian basement. There, it is anticipated that temperatures at the target depth could be between 240°C and 360°C. At these temperatures the thermal energy from the subsurface could be primarily harnessed for geothermal power with next-generation geothermal technologies, including closed-loop geothermal (CLG) and enhanced geothermal systems (EGS). With a CLG/EGS development in a conduction-only reservoir, heat extraction typically proceeds faster than natural replenishment rates, resulting in a long-term decline of reservoir and production temperature (Fox et al., 2013). Heat transfer in low-thermal conductivity basement rocks, such as those in the Wattenberg area, is presumed to proceed at slow rates requiring significant time for thermal replenishment in the target reservoir after depletion.

In this work, we apply the slender-body theory (SBT) model to simulate the well flow and heat transfer performance of possible closed-loop (U-loop) well designs drilled in the Wattenberg area

of the Denver Basin. Three U-loop designs are investigated, including a (a) single-lateral, (b) double-lateral, and (c) multi-lateral design. We have also compared the performance of both water and carbon dioxide (CO_2) as working fluids for the closed-loop heat transfer process. Finally, we determine and compare the cost of each design option to determine the most feasible design for electricity generation and heating applications.

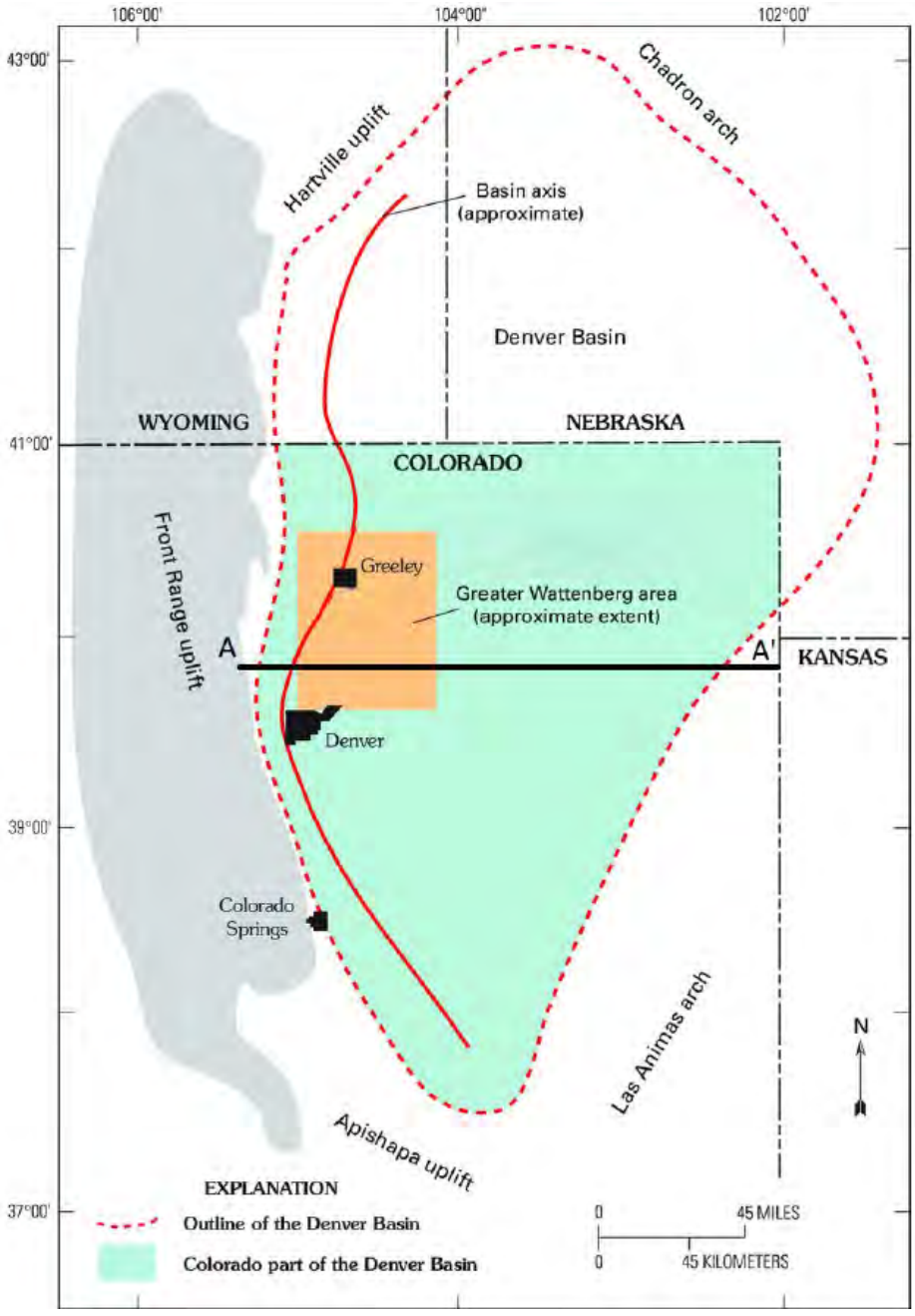

Figure 1: Greater Wattenberg area (orange rectangle) in the Denver Basin (approximate extent shown with red dashed line). The A-A' cross section is shown in Figure 2. The figure was modified from Roberts (2007).

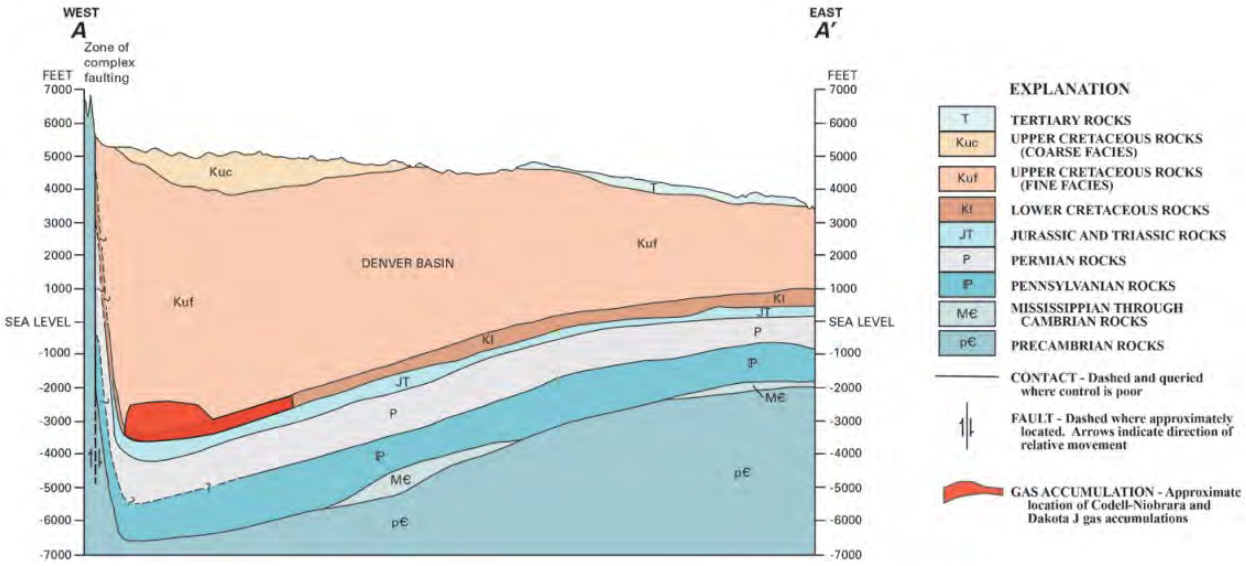

Figure 2: Representative cross section for the Denver Basin along the line A-A' in Figure 1. The Denver Basin is a large asymmetric syncline with a deepest point about 3,900 m below surface. The figure is from Nelson and Santus (2011).

2. Slender Body Theory (SBT) Modeling for Closed-Loop Well Designs

The SBT model is a MATLAB-based tool used for wellbore simulation that effectively models heat exchange, fluid profiles, and pressure profiles for closed-loop geothermal systems without high computational demand (Beckers & Johnston, 2022). By asymptotically matching a three-dimensional infinite cylinder to a one-dimensional finite line source, the model solves for temperature and pressure at each tubing element along the wellbore that is undergoing conductive heat transfer with the rock. Further information about the theory and the model implementation is found in (Beckers et al., 2015; Beckers & Johnston, 2022). The SBT is applicable to this study because the vertical distance covered by the loop is so large that the vertical and lateral geometry can be approximated as a slender, one-dimensional track. Therefore, we have applied this model to simulate the effects of altering different wellbore geometric parameters, reservoir fluid properties, and material and flow conditions in a closed-loop geothermal system to determine an optimal design from a standard base case within a conductive subsurface domain.

2.1 Closed-Loop Wellbore Geometry

We have designed twin wells based on a synthetic wellbore trajectory. The system envisioned consists of two parallel wells with a total vertical depth of 6.1 km and connected at the bottom by one or multiple laterals, depending on the investigated scenario. It is important to state that the designed well patterns are not representative of the actual well plan for the GLADE project, which is still under development.

2.1.1 Base Case

First, we implemented a base case scenario in the SBT tool, with the geometry shown in Figure 3. Both injection and productions wells have a straight vertical section down to a depth of 3,100 m,

followed by an inclined section with an angle of 12 degrees down to a vertical depth of about 6.1 km. The base case geometric properties are as described below:

- Two laterals were simulated in the Y-dimension between the production and injection wells at depth.
- Injection and production wells reached a vertical depth of 6.1 km.
- The vertical injection and production wellbore radius was 0.108 m (radius = 4.25 in; diameter = 8.5 in) and was uniform in both wells.
- The lateral wellbore radius was 0.108 m (radius = 4.25 in; diameter = 8.5 in).
- The pipe internal wall roughness was 1×10^{-6} m.
- The lateral length horizontally connecting the injection and production wells was 100 m in the Y-dimension.
- The distance between laterals was 25 m in the X-dimension.

In this and other simulation cases, all wellbores (injection, production, and laterals) along the heat exchanger path were assumed to be open hole with a negligible rock permeability at the well-formation interface. Conduction-only heat transfer between the rock and fluid was simulated, and all simulations were run on a basis of a 20-year operational lifetime. The well designs do not account for wellbore curvature; consequently, laterals are 90 degrees from the vertical direction. Going from 90 degrees to actual curvature would only slightly change total heat exchanger length (and heat transfer area). Therefore, having no curvature is expected to have negligible effect on heat extraction.

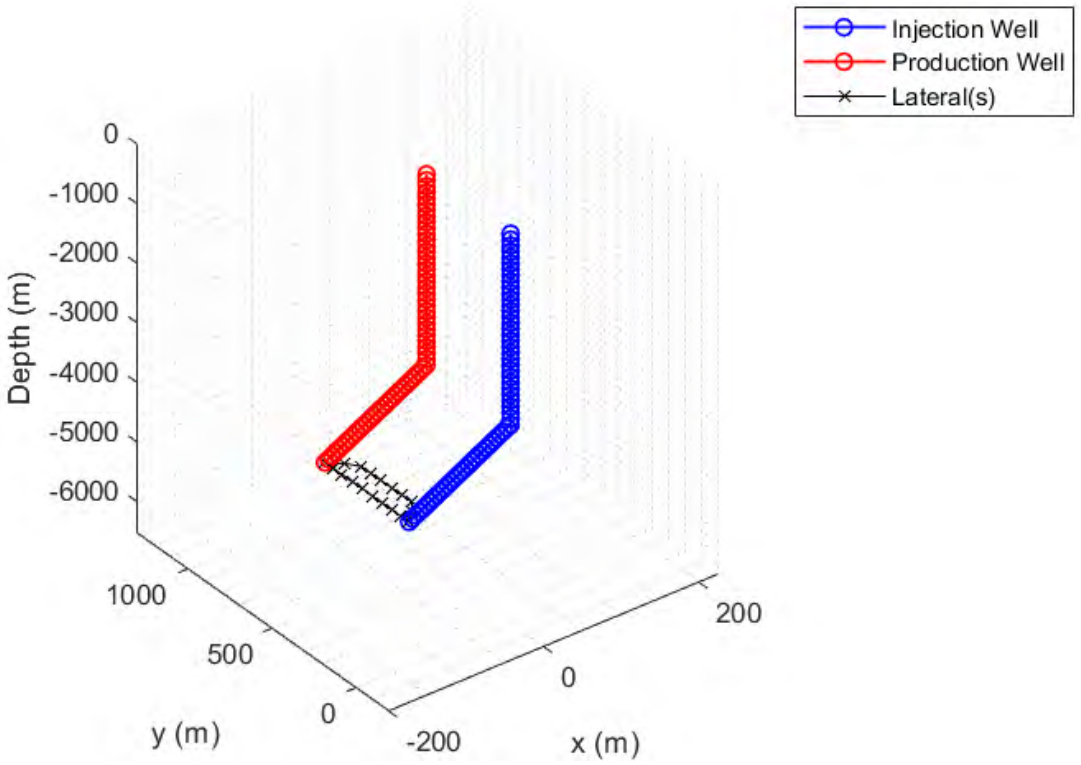

Figure 3: Well geometry schematic for the base case scenario showing the well track notated by colored circles as described in the legend on the right. Lateral length in the Y-dimension has been exaggerated to 500 m for visualization purposes (the original base case lateral length in the Y-dimension is 100 m).

2.1.2 Other Simulation Scenarios

Beyond the base case, we ran multiple simulation scenarios by varying the input parameters relating to the (a) well geometry, (b) flow boundary conditions, and (c) rock and fluid materials to determine the effect of parameter variability on the heat production from the closed-loop system. Table 1 shows the 15 scenarios and the input parameters that were varied in each simulation.

Table 1: The 15 simulation scenarios that were investigated in this work.

Simulation Scenarios	Number of laterals	Lateral spacing (X-direction), m	Well spacing (Y-direction), m	Injection rate, kg/s	Injection temp., °C	Thermal Gradient, °C /km	Rock type	Working fluid
Scenario A (Base case)	2	25	100	40	20	50	Granite	Water
Scenario B	1	25	100	40	20	50	Granite	Water
Scenario C	10	25	100	40	20	50	Granite	Water
Scenario D	2	10	100	40	20	50	Granite	Water
Scenario E	2	50	100	40	20	50	Granite	Water
Scenario F	2	25	500	40	20	50	Granite	Water
Scenario G	2	25	1000	40	20	50	Granite	Water
Scenario H	2	25	100	20	20	50	Granite	Water
Scenario I	2	25	100	60	20	50	Granite	Water
Scenario J	2	25	100	40	40	50	Granite	Water
Scenario K	2	25	100	40	60	50	Granite	Water
Scenario L	2	25	100	40	20	40	Granite	Water
Scenario M	2	25	100	40	20	60	Granite	Water
Scenario N	2	25	100	40	20	50	Gneiss	Water
Scenario O	2	25	100	40	20	50	Granite	CO_2

2.2 Fluid and Rock Thermophysical Properties

We simulated water and CO_2 as working fluids. Variable fluid properties were employed, allowing pressure and temperature to affect the density, specific heat capacity, thermal conductivity, and dynamic viscosity of both fluids. Granite and gneiss (Table 2) were used in two simulated cases. It is noteworthy that the subsurface geology in the study area is not homogeneous. There is a high uncertainty in the lithology of the basement rock in the Wattenberg area due to the unavailability of well data at the target depth. To account for the effect of the overburden sedimentary lithology, we have used the same depth-scaled averages for the rock properties and considered only one representative lithology (i.e., granite or gneiss) for the reservoir rock.

Table 2: Thermophysical properties of the two rock types studied in this work.

Lithology	Density, kgm^{-3}	Heat capacity, $Jkg^{-1}K^{-1}$	Thermal Conductivity, $Wm^{-1}K^{-1}$
Gneiss	2,570	1,080	2.9
Granite	2,540	1,185	3.1

3. System Performance

The base case is the control scenario. This case simulated a production and injection well that was 6.1 km deep with a 0.108-m radius. Two laterals were simulated that connected the production and injection wells. These laterals were approximately 100-m long and spaced approximately 25 m apart (Figure 3). Granite was the reservoir rock, and a constant ground surface temperature was selected at 20°C. The results of the base case simulation presented in Table 3 reveal an average production temperature, final temperature, and heat production of 56.1°C, 53.3°C, and 6 MW_{th}, respectively. In the remainder of this section, we probe the effect of well geometry, boundary conditions, and rock and fluid characteristics on the system performance.

Table 3: Output variables of average temperature, final temperature, and heat production for the 15 scenarios after a 20-year simulation.

Simulation Scenarios	Avg. Production Temperature, °C	Final Temperature, °C	Avg. Heat Production, MW_{th}
Scenario A (Base case)	56.1	53.3	6.00
Scenario B	55.4	52.7	5.88
Scenario C	64.7	60.8	7.44
Scenario D	55.4	52.7	5.90
Scenario E	56.3	53.5	6.03
Scenario F	59.7	56.6	6.61
Scenario G	64.3	60.6	7.38
Scenario H	83.0	78.9	5.26
Scenario I	45.3	43.3	6.27
Scenario J	71.2	68.9	5.21
Scenario K	86.4	84.4	4.42
Scenario L	48.9	46.7	4.80
Scenario M	63.3	60.0	7.21
Scenario N	54.0	51.4	5.70
Scenario O	68.2	64.7	4.40

3.1 Effect of U-Loop Geometry

3.1.1 Number of Laterals

The number of laterals in the U-loop varied from one, two (base case), and 10 laterals. All other geometry specifications, boundary conditions, and material properties were as in the base case. The general heat production and output temperature trend is an initial high heat production rate (and temperature) followed by a steep decline within the first few weeks of production towards a steady state. This is typical for closed-loop systems with a single (constant) flow rate. It is apparent that 10 laterals offer an elevated average heat production over 20 years (7.44 MW_{th}) compared to both single and double laterals (5.88 and 6.0 MW_{th}, respectively; Figure 4). Scenario C with 10 laterals also results in an elevated outlet temperature compared to Scenarios A and B.

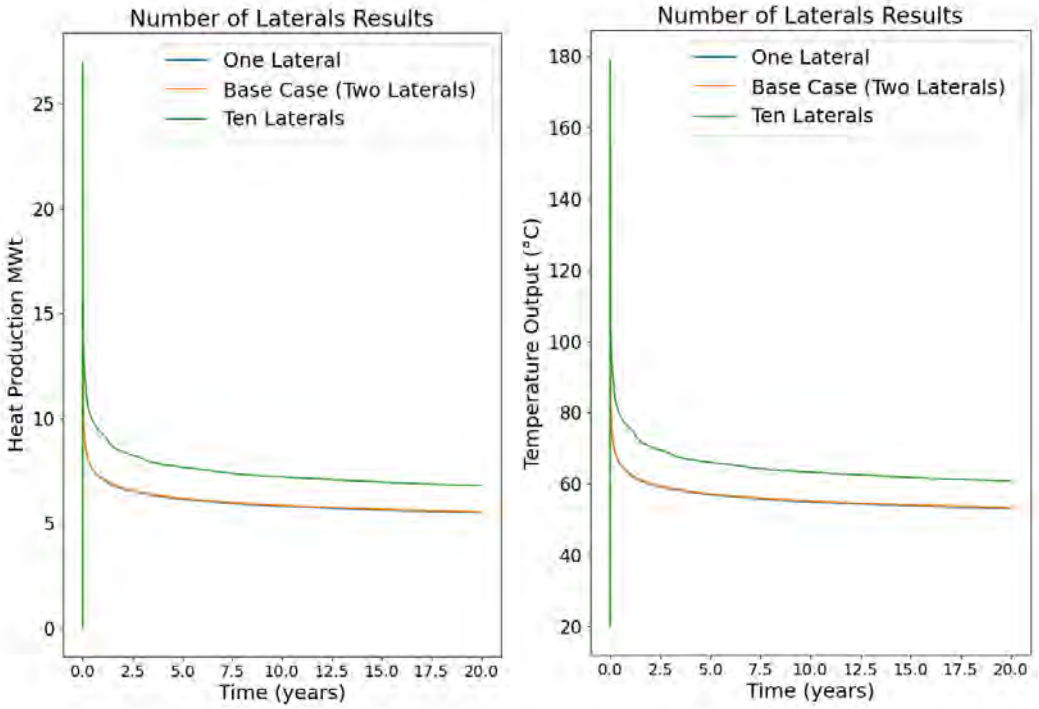

Figure 4: Heat production (MW_{th}) and temperature (°C) output over 20 years for one, two, and 10 laterals. The one- and two-lateral cases overlap due to similar heat production and output temperatures.

3.1.2 Lateral Spacing

Next, 10-m, 25-m (base case), and 50-m lateral spacings in the X-direction were simulated. All other geometry specifications, boundary conditions, and material properties were base case. Simulation results showed that a larger spacing in the X-direction between the laterals increases the outlet temperature by less than 1°C and the average heat production by less than 150 kW (Table 3). This is because, for this well design, thermal interference between laterals is minimal above the 10-m spacing. Therefore, a lateral spacing of 25 m was used as the default to minimize losses due to interference between the laterals.

3.1.3 Well Spacing

The spacing between the injection and production well in the Y-direction was modified from 100 m (base case) to 500 m and 1,000 m in Scenarios F and G, respectively. All other geometry specifications, boundary conditions, and material properties were base case. Extending the well spacing in the Y-direction between the injection and production wells yields an elevated heat production and outlet temperature output (Figure 5).

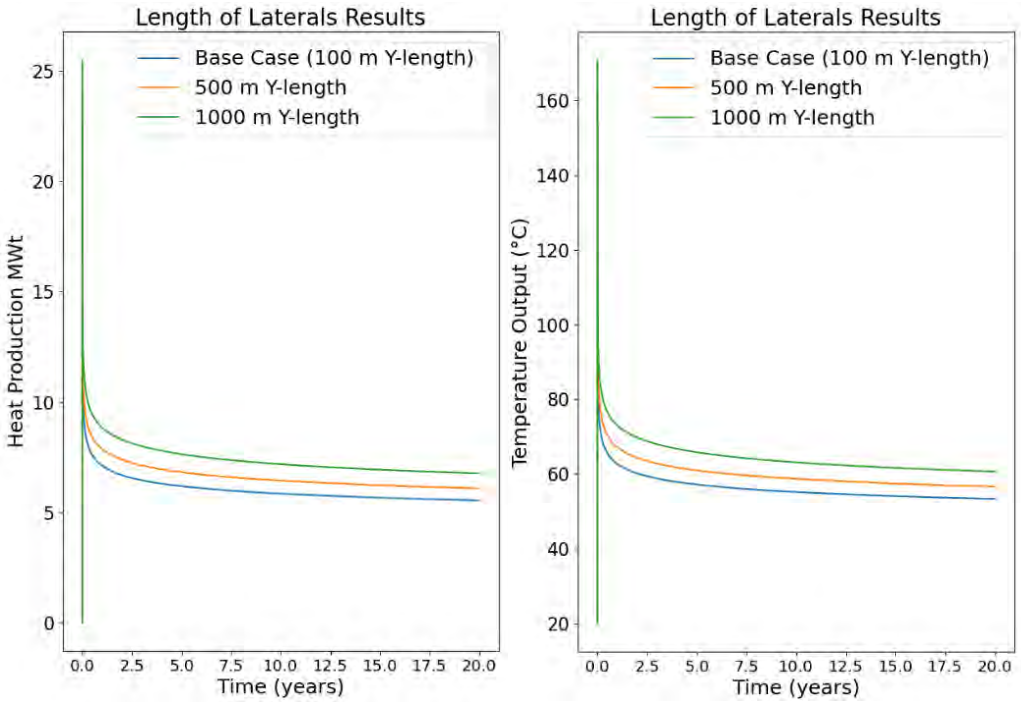

Figure 5: Heat production (MW_{th}) and temperature (°C) output over 20 years for 100-m, 500-m, and 1,000-m length laterals.

3.2 Effect of Boundary Conditions

3.2.1 Injection Rate

The system performance for multiple injection rates of 20 kg/s (Scenario H), 40 kg/s (base case), and 60 kg/s (Scenario I) were compared. All other geometry specifications, boundary conditions, and material properties were the same as the base case. Lower injection rates facilitated lower heat production over time compared to higher injection rate (Figure 6). The opposite trend was observed for outlet temperatures, where lower injection rate had higher output temperature compared to higher injection rates. This is in line with previous observations by Beckers et al. (2022), who reported that decreasing flow rate will decrease heat output, but increase outlet temperature in both co-axial and U-loop systems. This is because the reduction in mass flow is more significant than the slight rise in temperature (due to longer residence time) resulting in a combined effect of lower heat production. This observation suggests that a lower injection rate allows for better outlet temperature control and would benefit applications that need to meet this requirement. For systems that aim to maximize power output, a higher flow rate is necessary.

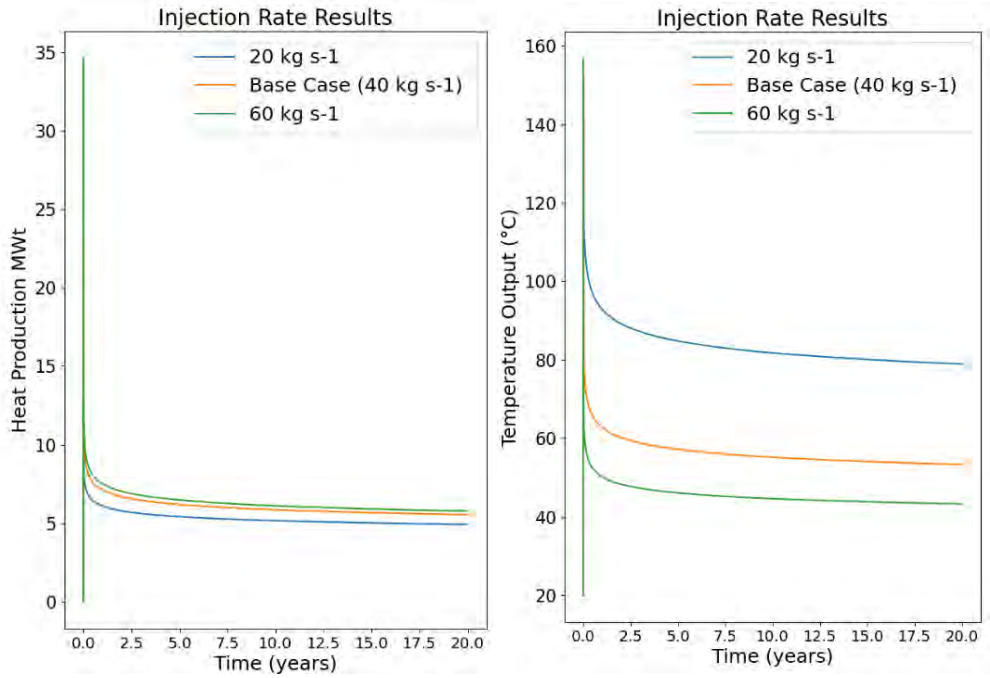

Figure 6: Heat production (MW_{th}) and temperature (°C) output over 20 years for injection rates of 20, 40, and 60 kg/s.

3.2.2 Injection Temperature

To understand the effect of the injection temperature on system performance, we ran simulations for Scenario J (injection temperature = 40°C) and Scenario K (injection temperature = 60°C). The results were compared to the base case with an injection temperature of 20°C. As shown in Figure 7, the higher injection temperatures were characterized by a lower heat production over the project life. The resulting average heat production was 5.21 MW_{th} and 4.42 MW_{th} for Scenario J and Scenario K, respectively. On the other hand, higher injection rates enabled a higher production temperature (Figure 7). Similar to results reported in prior work, increasing injection temperature results in a reduction in the extractable energy (a function of the difference between the reservoir temperature and the injection temperature), which in turn result in a lower heat production (Beckers et al., 2022).

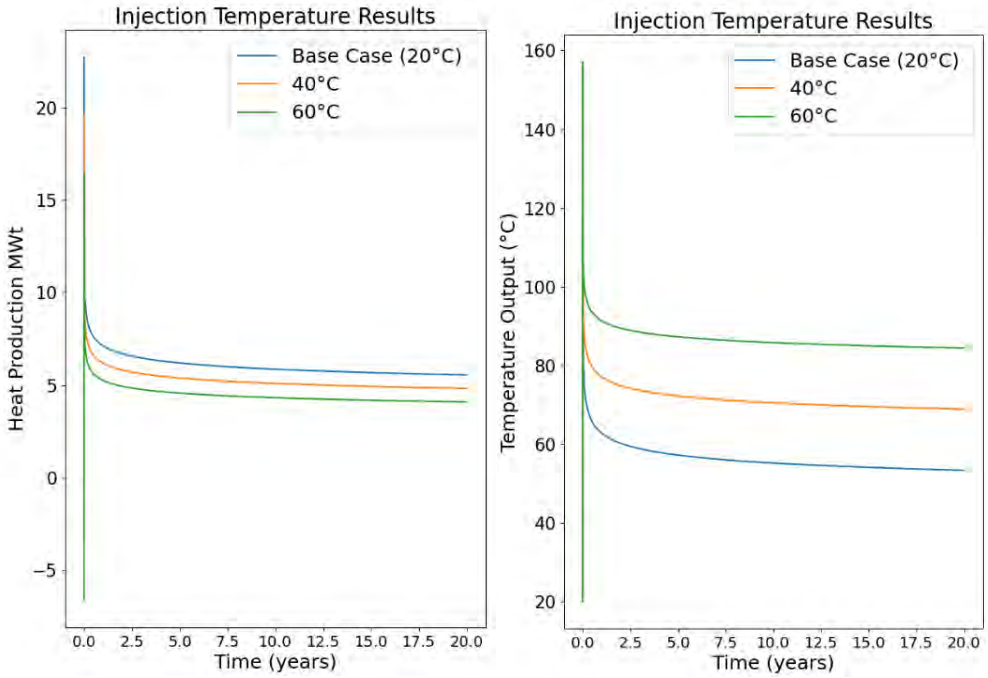

Figure 7: Heat production (MW_{th}) and temperature (°C) output over 20 years for inlet temperatures of 20°C, 40°C, and 60°C.

3.2.3 Geothermal Gradient

Variations of the subsurface geothermal gradient were employed as 40°C/km (Scenario L), 50°C/km (base case), and 60°C/km (Scenario M). All other geometry specifications, boundary conditions, and material properties were base case. Overall, it is apparent that higher heat production and outlet temperature throughout the project life are directly correlated to the magnitude of the geothermal gradient (Figure 8).

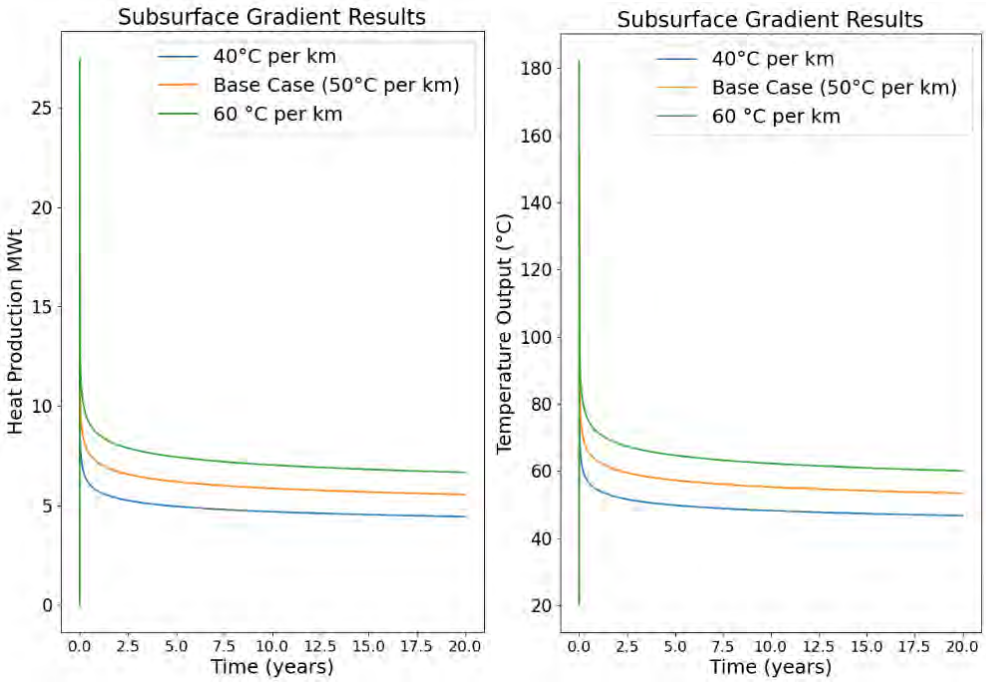

Figure 8: Heat production (MW_{th}) and temperature (°C) output over 20 years for 40°C/km, 50°C/km, and 60°C/km.

3.3 Effect of Rock and Fluid Types

3.3.1 Rock Type

To understand and quantify the uncertainty in the lithology of the basement rock and its effect on thermal performance, we completed simulations for the two end cases, i.e., the base case with granite and Scenario N with gneiss. The results in Table 3 show that a gneiss basement lithology results in lower output temperature and heat production over the project life. This arises from a combination of a higher thermal conductivity and heat capacity for the same volume of granite compared to gneiss.

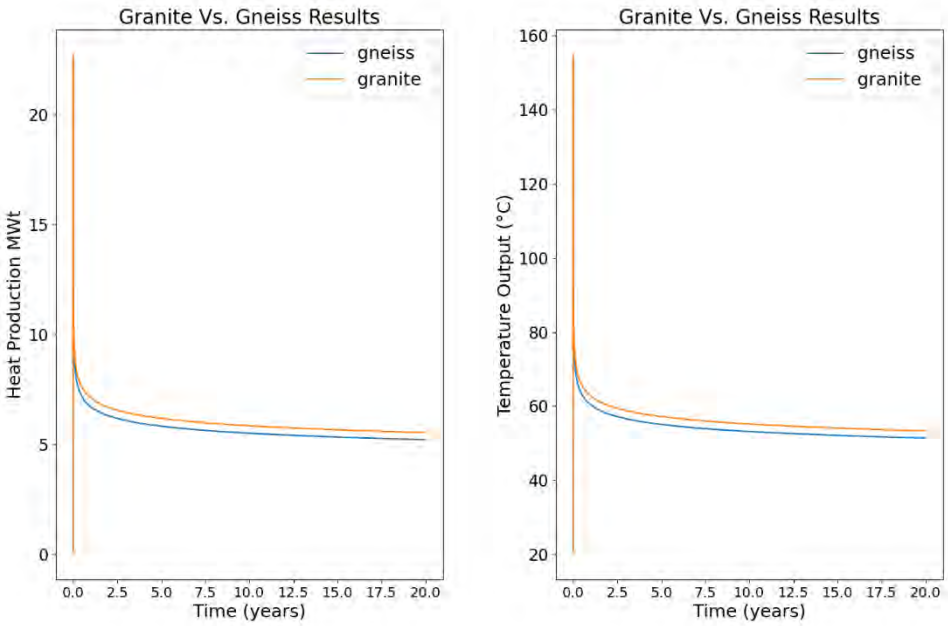

Figure 9: Heat production (MW_{th}) and temperature (°C) output over 20 years for gneiss versus granite.

3.3.2 Working Fluid

The thermal property and composition of the working fluid in a closed-loop system are important factors that influence performance. In this study, water and CO_2 were compared. At a constant injection wellhead pressure of 100 bar, the CO_2 is supercritical within the closed loop system as it traverses the reservoir domain and the production well. As displayed in Figure 10, the average production temperature for a CO_2-based U-loop was elevated compared to water, yet the opposite was evident for average heat production. Water shows an elevated average heat production (6.0 MW_{th}) compared to CO_2 (4.4 MW_{th}). The higher heat production is mainly due to the higher specific heat capacity of water compared to CO_2 (4.2 versus 0.84 J kg^{-1} K^{-1}). However, the higher outlet temperatures for CO_2 arises from the lower rate of reservoir thermal depletion (due to less heat extracted).

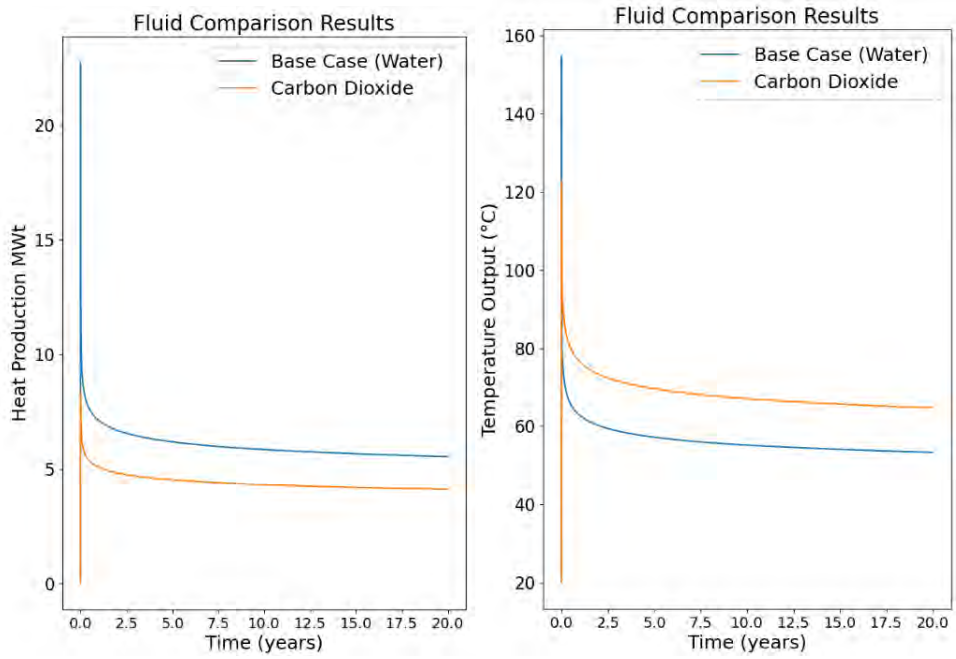

Figure 10: Heat production (MW_{th}) and temperature (°C) output over 20 years for CO_2 and water.

3.4 Optimal Well Design

An optimal well design scenario for both heat production and outlet temperature maximization has been developed based on the observed parameters and their effects over a 20-year lifetime. This scenario includes a production and injection well that was 6.1 km deep with a 0.108-m radius. Connecting the two wells are 10 laterals with radii of 0.108 m, 50-m spacing between each of the ten laterals in the X-dimension, and a well spacing of 1,000 m in the Y-dimension (Figure 11). To maximize heat production, the injection temperature is held constant at 20°C, with a constant injection rate of 60 kg/s, and flow divided evenly over the 10 laterals. The reservoir rock is granite, with an average thermal conductivity of 3.1 W m^{-1} K^{-1}, average heat capacity of 1,185 J kg^{-1} K^{-1}, and a density of 2,540 kg m^{-3}. A constant ground surface temperature was selected at 20°C and the geothermal gradient through the subsurface was 60°C/km. Water was the utilized working fluid. The pressure at the injection wellhead was 100 bar. Outputs of the system are summarized in Table 4. The trends in heat production and outlet temperature over time are summarized and compared to the base case in Figure 12. It is important to highlight that this is the performance-optimized design. The techno-economic feasibility of drilling and developing such a system is discussed in Section 4.

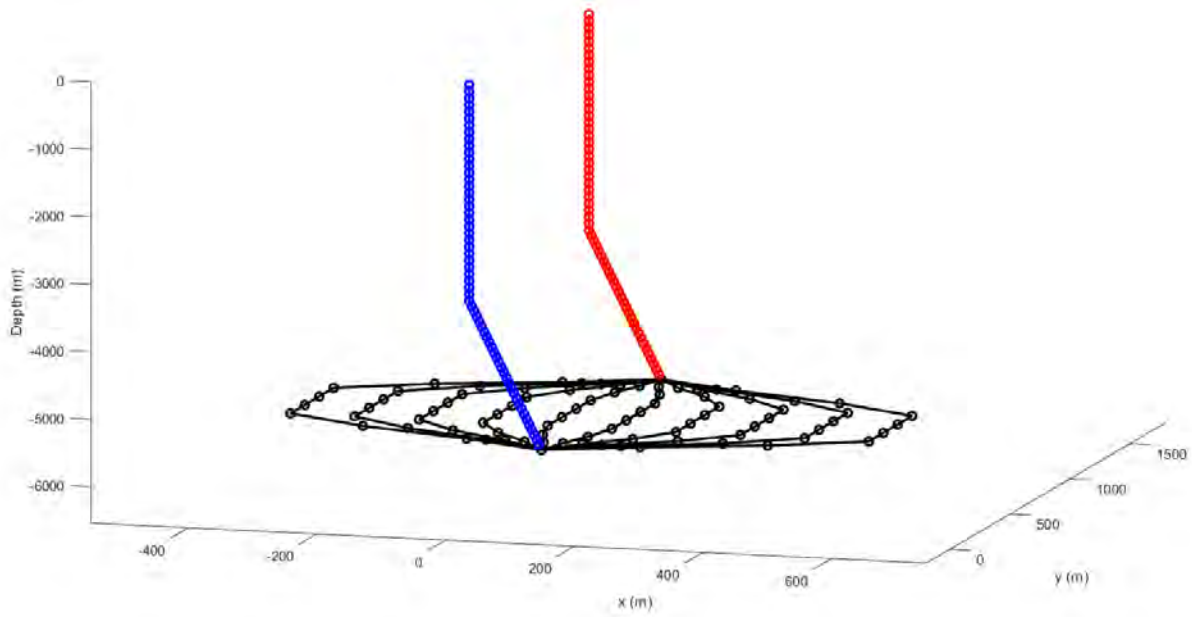

Figure 11: Optimized geometry schematic developed from observed outputs of prior scenarios.

Table 4: Inputs and outputs parameters for the optimized heat production case scenario for water after a 20-year simulation.

Parameter	**Unit**	**Value**
Input		
Injection Rate	kg/s	60
Injection Temperature	°C	20
Geothermal Gradient	°C/km	60
Number of laterals		10
Lateral Length	m	1000
Well Spacing	m	50
Rock Type		Granite
Output		
Average outlet temperature	°C	95.7
Average heat production	MW_{th}	19
Final temperature	°C	88.8

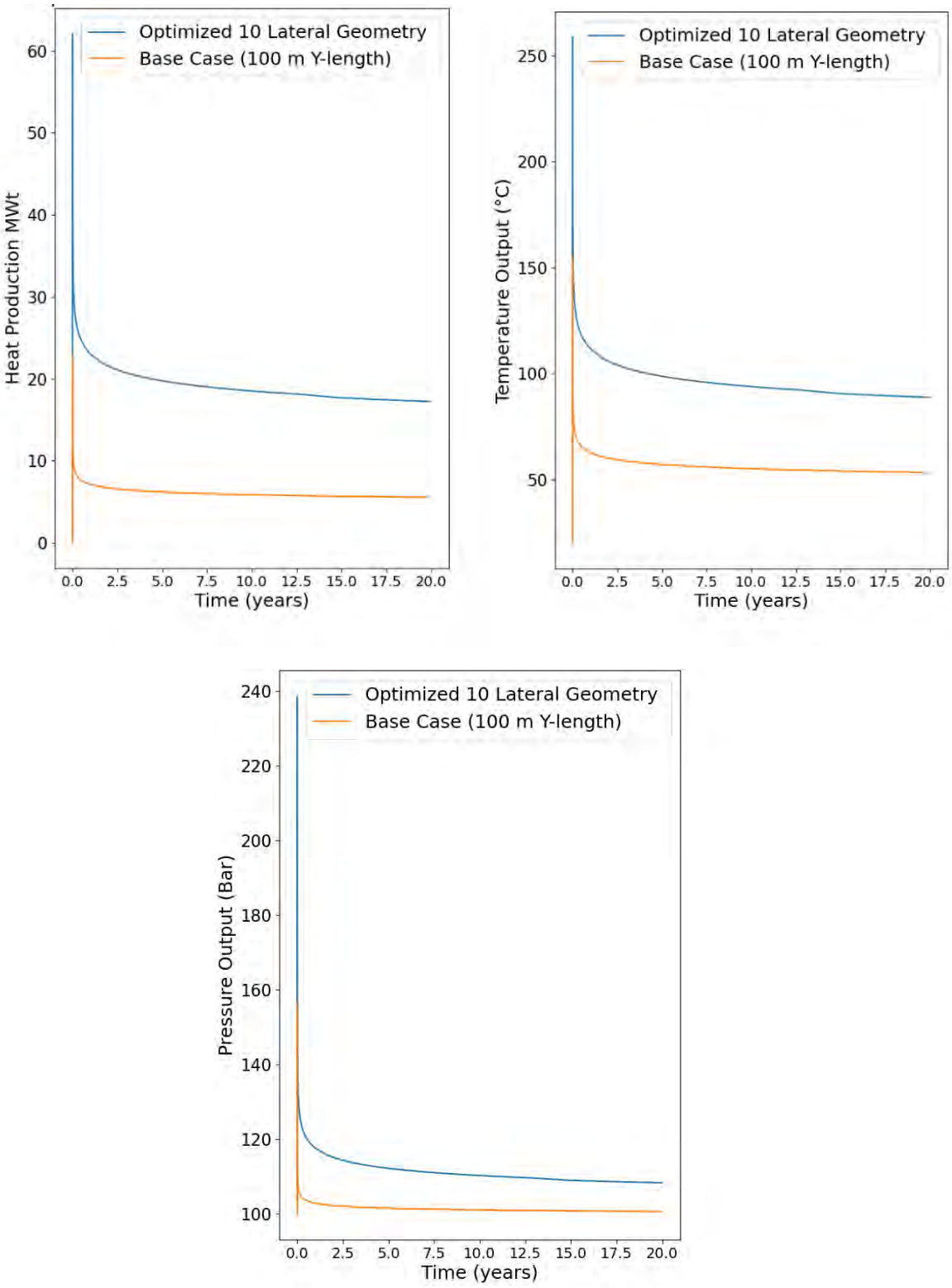

Figure 12. Optimized versus base case heat production, temperature output, and outlet pressure over 20 years for maximized heat production.

4. Techno-Economic Assessment

We have developed a simplified techno-economic assessment (TEA) model to estimate the lifecycle costs of the performance-optimized U-loop system. The TEA is a top-down Excel-based model that estimates the capital cost, operation and maintenance (O&M) costs, and the levelized costs of energy (electricity or heat). The input assumptions used in the model are listed in Table 5. These assumptions cover unit costs for the surface plant (for electricity generation only) installation and directional drilling. The model does not include the cost of project financing and does not account for tax credits or other incentives that can improve project economics.

Table 5: Input assumptions for parameters in the TEA model.

Parameters	**Baseline Value**	**Parameter Variability**	**References**
Power conversion factor, %	12%	10-15%	Beckers and Johnston (2022)
Plant availability, %	95%	-	Beckers and Johnston (2022)
Lateral cost per meter, $/m	600	400-800	Beckers and Johnston (2022)
Vertical cost per well, $	7,500,000	-	Beckers and Johnston (2022)
Power plant installation cost, $/kW	2,500	-	Beckers and Johnston (2022)
Heat exchanger cost, $	1,250,000	-	Beckers and Johnston (2022)
O&M as percent of capital cost, %	1.5% (electricity) 1% (heat)	-	Beckers and Johnston (2022)
Plant lifetime, yr.	20	-	
Discount rate, %	7%	5-9%	Beckers and Johnston (2022)

To determine the performance- and cost-optimized system, we executed the TEA model using the baseline input assumptions (Column 2 in Table 5) and the optimal values of the U-loop design parameters identified in Section 3 and listed in Table 4. The resulting levelized cost of electricity (LCOE) and levelized cost of heat (LCOH) were \$136/MWh$_e$ and \$1.53/GJ, respectively. Additionally, to account for uncertainty in the TEA parameters we considered six other optimal cases with variability in power plant conversion factor, lateral drilling cost, and discount rate. The results are shown in Table 6. These show that the LCOE can be further improved with higher efficiency power conversion systems while the LCOH benefits from lower discount rates. Drilling costs are important for both electricity and heating use cases with a larger degree of impact in the heating case.

Table 6: Output from the TEA modeling for both electricity and heating use cases for the optimal closed-loop design.

Parameter	Unit	Optimal I	Optimal II	Optimal III	Optimal IV	Optimal V	Optimal VI	Optimal VII
Power Conversion Factor	%	12	10	15	12	12	12	12
Lateral Cost per m	$/m	600	600	600	400	800	600	600
Discount Rate	%	7	7	7	7	7	5	9
Plant power output (electric)	kW_e	2,166	1,805	2,708	2,166	2,166	2,166	2,166
Plant power output (heat)	kW_{th}	18,050	18,050	18,050	18,050	18,050	18,050	18,050
Capital cost (electric)	$/$kW_e$	13,164.82	15,297.78	11,031.86	13,072.48	13,257.16	13,164.82	13,164.82
Annual O&M cost (electric)	$/$kW_e$-yr	197.47	229.47	165.48	196.09	198.86	197.47	197.47
Capital cost (heat)	$/$kW_{th}$	1,349.03	1,349.03	1,349.03	1,337.95	1,360.11	1,849.63	1,349.03
Annual O&M cost (heat)	$/$kW_{th}$-yr	13.49	13.49	13.49	13.38	13.60	18.50	13.49
20-yr LCOE	$/$MWh_e$	135.69	156.58	114.80	125.74	145.64	115.99	156.79
20-yr LCOH	$/GJ	1.53	1.53	1.53	1.39	1.66	1.30	1.77

4. Conclusion

In this paper, we have implemented the SBT model to investigate the thermal profiles and well production performance of a U-loop well drilled into the Wattenberg area of the Denver-Julesburg Basin. A scenario-based assessment of the effect of input variables, categories as the well geometry, boundary conditions, and rock and fluid properties, on heat transfer and well production performance was implemented. This model-enabled assessment revealed that a U-loop design characterized by an injection to production well spacing of 1,000 m with ten 50-m-spaced laterals that traverse a conductive subsurface system with a temperature gradient of 60°C/km maximizes thermal energy production. Specifically, injecting 20°C-water at a rate of 60 kg/s through the optimized U-loop, an average heat production of 19 MW_{th} (i.e., 2.2 MW_e net plant output) was achieved, resulting in an LCOE and LCOH of \$136/MWh_e and \$1.53/GJ, respectively.

Acknowledgement

This work was authored by the National Renewable Energy Laboratory, operated by Alliance for Sustainable Energy, LLC, for the U.S. Department of Energy (DOE) under Contract No. DE-AC36-08GO28308. Funding was provided by the U.S. Department of Energy Office of Energy Efficiency and Renewable Energy (EERE) Geothermal Technologies Office (GTO). The views expressed in the article do not necessarily represent the views of the DOE or the U.S. Government.

REFERENCES

Abbott, D. M., Jr., & Noe, D. C. (2004). The consequences of living with geology: A model field trip for the general public (second edition). In E. P. Nelson & E. A. Erslev (Eds.), *Field Trips in the Southern Rocky Mountains, USA* (Vol. 5, p. 0). Geological Society of America. https://doi.org/10.1130/0-8137-0005-1.185

Barrett, J. K., & Pearl, R. H. (1978). *Bulletin 39—An Appraisal of Colorado's Geothermal Resources* [Bulletin]. Colorado Geological Survey, Department of Natural Resources. https://coloradogeologicalsurvey.org/publications/geothermal-resources-colorado-2/

Beckers, K. F., & Johnston, H. E. (2022). *Techno-Economic Performance of Eavor Loop 2.0* (NREL/CP-5700-81887). Stanford, CA: Stanford University. https://www.osti.gov/biblio/1972816

Beckers, K. F., Koch, D. L., & Tester, J. W. (2015). Slender-body theory for transient heat conduction: Theoretical basis, numerical implementation and case studies. *Proceedings of the Royal Society A: Mathematical, Physical and Engineering Sciences*, *471*(2184), 20150494. https://doi.org/10.1098/rspa.2015.0494

Beckers, K. F., Rangel-Jurado, N., Chandrasekar, H., Hawkins, A. J., Fulton, P. M., & Tester, J. W. (2022). Techno-Economic Performance of Closed-Loop Geothermal Systems for Heat Production and Electricity Generation. *Geothermics*, *100*, 102318. https://doi.org/10.1016/j.geothermics.2021.102318

Crowell, A. M., Ochsner, A. T., & Gosnold, W. (2012). Correcting Bottom-Hole Temperatures in the Denver Basin: Colorado and Nebraska. *GRC Transactions*, *36*, 201–206.

Curtis, B. F. (1988). Sedimentary rocks of the Denver basin. In L. L. Sloss (Ed.), *Sedimentary Cover—North American Craton: U.S.: Vol. D-2* (pp. 182–196). Geological Society of America. https://doi.org/10.1130/DNAG-GNA-D2

Davalos-Elizondo, E., Kolker, A., Taverna, N., & Holt, E. (2023). *Assessing Low-Temperature Geothermal Play Types: Relevant Data and Play Fairway Analysis Methods* (NREL/TP-5700-87259). National Renewable Energy Laboratory (NREL), Golden, CO (United States). https://doi.org/10.2172/2001118

Eaton, M. (2023). *Causes of Geothermal Temperature Anomalies In the Denver Basin: With Application to Petroleum and Geothermal Energy*. MUTDOC Consortium - Spring 2023 Sponsor Meeting, Golden, Colorado. https://protected.mines.edu/mudtoc/wp-content/uploads/sites/18/2023/05/Eaton_Spring2023.pdf

Fox, D. B., Sutter, D., Beckers, K. F., Lukawski, M. Z., Koch, D. L., Anderson, B. J., & Tester, J. W. (2013). Sustainable heat farming: Modeling extraction and recovery in discretely fractured geothermal reservoirs. *Geothermics*, *46*, 42–54. https://doi.org/10.1016/j.geothermics.2012.09.001

Higley, D. K., & Cox, D. O. (2007). Oil and Gas Exploration and Development along the Front Range in the Denver Basin of Colorado, Nebraska, and Wyoming. In D. K. Higley (Ed.), *Petroleum Systems and Assessment of Undiscovered Oil and Gas in the Denver Basin Province, Colorado, Kansas, Nebraska, South Dakota, and Wyoming—USGS Province 39* (p.

41). U.S. Geological Survey. https://pubs.usgs.gov/dds/dds-069/dds-069-p/REPORTS/69_P_CH_2.pdf

Lacazette, A., Cumell, S. P., Matt, V. J., Cottrel, M. G., Karimi, S., Marsh, B. D., & Chmela, W. R. (2024, February 12). Using Petroleum Industry Data to Locate, Characterize, and Simulate a Hot Sedimentary Aquifer Geothermal Prospect. *Proceedings*. 49th Workshop on Geothermal Reservoir Engineering, Stanford University, Stanford, California. https://geothermal.tech/wp-content/uploads/2024/02/Lacazette-et-al-2024-Stanford-Geothermal-rev-.pdf

Moeck, I. S. (2014). Catalog of geothermal play types based on geologic controls. *Renewable and Sustainable Energy Reviews*, *37*, 867–882. https://doi.org/10.1016/j.rser.2014.05.032

Nelson, P. H., & Santus, S. L. (2011). Gas, oil, and water production from Wattenberg Field in the Denver Basin, Colorado. In *Open-File Report* (2011–1175). U.S. Geological Survey. https://doi.org/10.3133/ofr20111175

Porro, C., Esposito, A., Augustine, C., & Roberts, B. (2012). An Estimate of the Geothermal Energy Resource in the Major Sedimentary Basins in the United States. *GRC Transactions*, *36*, 1359–1370.

Roberts, S. B. (2007). Coal in the Front Range Urban Corridor—An Overview of Coal Geology, Coal Production, and CoalBed Methane Potential in Selected Areas of the Denver Basin, Colorado, and the Potential Effects of Historical Coal Mining on Development and Land-Use Planning. In D. K. Higley (Ed.), *Petroleum Systems and Assessment of Undiscovered Oil and Gas in the Denver Basin Province, Colorado, Kansas, Nebraska, South Dakota, and Wyoming—USGS Province 39* (p. 45). U.S. Geological Survey. https://pubs.usgs.gov/dds/dds-069/dds-069-p/REPORTS/69_P_CH_3.pdf

Sims, P. K., Bankey, V., & Finn, C. A. (2001). Preliminary Precambrian basement map of Colorado – A geologic interpretation of the aeromagnetic anomaly map. In *Open-File Report* (2001–364). U.S. Geological Survey. https://doi.org/10.3133/ofr01364

Weimer, R. J. (1996). *Guide to the Petroleum Geology and Laramide Orogeny, Denver Basin and Front Range, Colorado* (Buletin 51). Colorado Geological Survey, Department of Natural Resources. https://doi.org/10.58783/cgs.b51.bsvl1261

Techno-Economic Viability of Flexible Dispatch of Unconventional Geothermal Systems

Mohammad Aljubran,[1] Koenraad Beckers,[2] Geoffrey Mibei,[2] and Roland Horne[1]

Stanford University[1] and National Renewable Energy Laboratory[2]

Keywords

Flexible geothermal; Techno-economics; Unconventional systems

ABSTRACT

Flexible geothermal operations could boost project returns through the allocation of improved power purchase agreements and/or exploitation of power price arbitrage opportunities. In this study, we investigated the techno-economic feasibility of variable flow rate control and time-of-day pricing in closed-loop geothermal systems. We considered U-shaped multilateral system configurations and modeled a variety of technical system parameters. These designs were simulated using a slender-body theory (SBT) model for transient heat transfer and fluid flow. This subsurface model was integrated into the flexible geothermal economic model (FGEM) tool to evaluate the overall flexible geothermal system techno-economics. Future hourly ambient temperature conditions were based on the Sup3rCC dataset. Published datasets were used for future hourly wholesale electricity prices. We analyzed four operating strategies: 1) baseload operation, 2) seasonal dispatch (high flow rate during summer and nominal flow rate during the rest of the year), 3) net generation maximization by varying flow rate to maximize net power output, and 4) revenue maximization by varying flow rate to maximize revenue. We ran all four scenarios for a multiloop configuration with 12 lateral passes, 7-km vertical depth and 87-km total drilling length. Furthermore, we assumed a 60°C/km geothermal gradient and ambient temperature and wholesale electricity prices for New Mexico as a typical state location. The nominal flow rate was set to 80 kg/s. When considering drilling costs of $1,000/m and a discount rate of 7%, the generation maximization scenario resulted in the lowest levelized cost of electricity (LCOE) of ~$150/MWh. When considering project return on investment (ROI), defined as lifetime net income divided by upfront capital costs, all flexible operation scenarios performed better than the base case scenario. The highest ROI of 80% was obtained with the revenue maximization scenario. With drilling costs of $200/m and a discount rate of 5%, the generation maximization scenario resulted in LCOE of $49/MWh.

1. Introduction

1.1 Closed-Loop Geothermal Systems

Closed-loop geothermal systems, sometimes referred to as advanced geothermal systems or next-generation geothermal systems, are proposed to use a heat transfer fluid circulating in a closed-loop configuration through a co-axial ("pipe-in-pipe") or U-loop-type subsurface heat exchanger to produce reservoir heat to the surface, as seen in Figure 1. The heat transfer fluid does not penetrate the rock but stays within the heat exchanger. These systems have recently received significant attention and investment, with several companies proposing to develop and commercialize this technological concept. Postulated benefits include not requiring reservoir permeability, limited need for exploration, easier handling of heat transfer fluid (e.g., clean water) at the surface, and relatively easy design and prediction of production temperatures. A key challenge is the limited thermal performance in conduction-only systems, requiring deep and hot reservoirs and/or extremely long drilling lengths to produce multi-megawatt power systems.

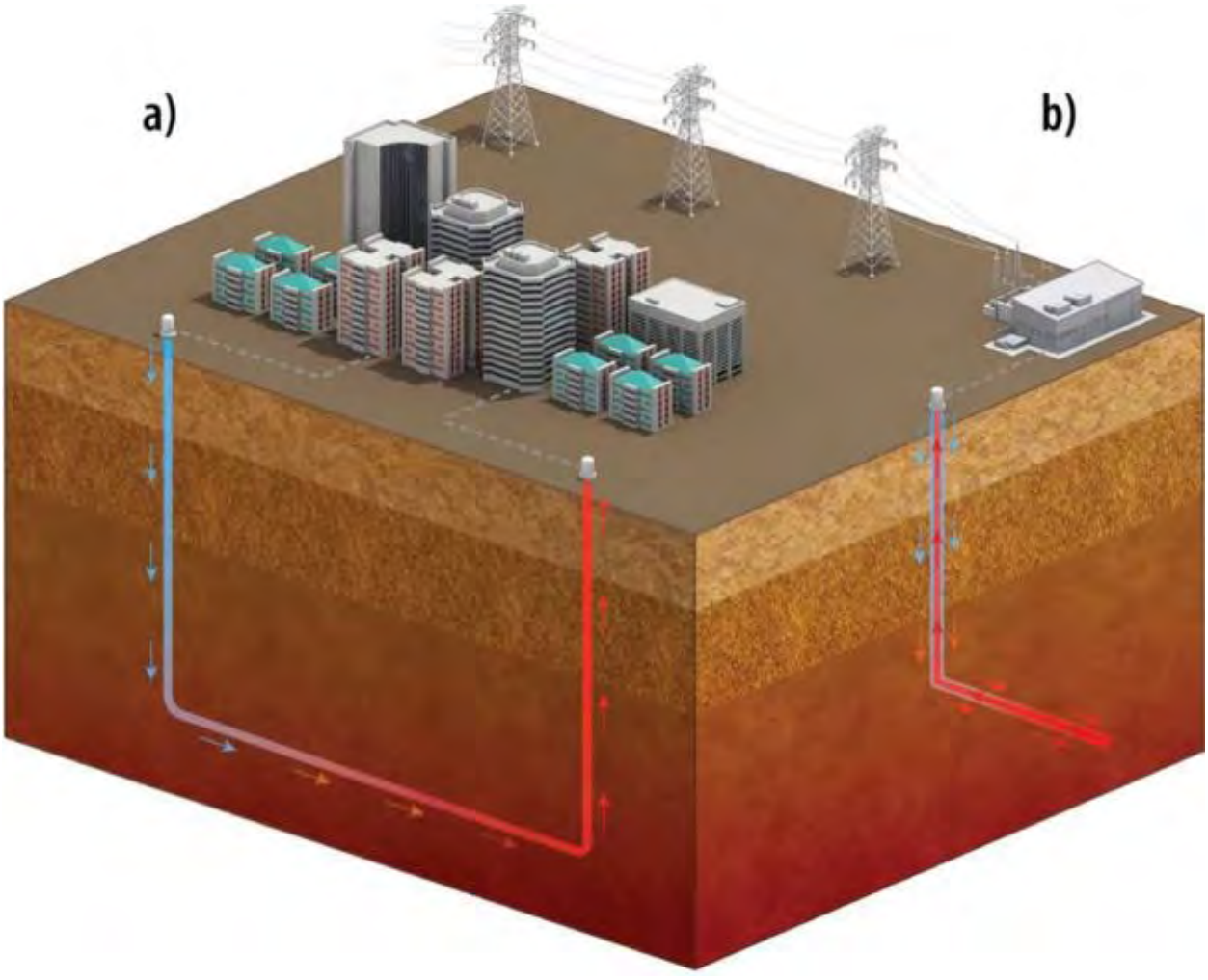

Figure 1.: Conceptual diagram of two types of closed-loop geothermal: (a) U-loop and (b) co-axial.

Various studies have been conducted to investigate the techno-economic performance of closed-loop geothermal systems. Beckers et al. (2022) studied levelized cost of heat and electricity for several co-axial and U-loop designs for a range of subsurface and operation conditions (i.e., different injection temperatures, flow rates, heat transfer fluids, depths, and geothermal gradients). Beckers and Johnston (2022) studied the performance of a multiloop design for a low- and high-geothermal gradient scenario, which forms the basis of subsurface design in this paper. Multiple studies were undertaken by the closed-loop geothermal working group (CLGWG), a U.S. Department of Energy (DOE)-funded multilaboratory and university research effort investigating the performance of various closed-loop geothermal systems. These studies include a general feasibility study by White et al. (2023); developing a database of precalculated reservoir simulations of multiple closed-loop designs (Beckers et al. 2023) used in a web-based closed-loop geothermal simulation tool—the GeoCluster tool (CLGWG 2023); investigating the heat transfer performance of closed-loop geothermal systems with thermally conductive enhancements (Beckers et al. 2024); and assessing the impact of convection on the performance of closed-loop systems (Hakes et al. 2024).

1.2 Flexible Geothermal Operations

Geothermal power has emerged as a key contender in the transition toward a greener and more resilient energy landscape, given its ability to provide consistent “baseload” power: a constant, reliable, and steady supply of electricity always (Tester et al. 2021). Geothermal power is often operated under power purchase agreements (PPAs), where an operator typically earns a fixed nominal price per energy unit generated (Moradpoor et al. 2023). By signing PPAs, geothermal operators limit revenue uncertainties associated with trading in the open and volatile electricity market, especially in decarbonized grids that are significantly penetrated by intermittent resources, e.g., solar and wind (Aljubran and Horne 2023a). On the other hand, load-serving entities often sign geothermal PPAs because they come with continuous power availability, high capacity factors, long lifespans and stability, and environmental benefits.

However, the high penetration of intermittent resources caused an increase in the value for dispatchable geothermal generation that would fill in the diurnal and seasonal gaps. Researchers and engineers worldwide have used various strategies to achieve dispatchable geothermal operations. Considering both economic viability and technical factors is essential to achieve dispatchable operations. Aljubran and Horne (2024a) categorize these operations into four main types: wellhead throttling, steam vent-off, turbine bypass, and storage. Considering conventional geothermal systems hybridized with lithium-ion battery units in a highly volatile electricity market (e.g., California), researchers found diurnal flexible operations resulted in up to 28% improvement in project profitability per unit energy generated (Aljubran and Horne 2023a). Whereas adding battery units involves significant upfront costs, another study considered wellhead throttling and turbine bypassing in enhanced geothermal systems and concluded an additional 11% of geothermal power can be realized across the United States through flexible operations (Aljubran and Horne 2024b). Other efforts investigated the value of hydrogen coproduction as a means of flexible geothermal operations in New Zealand to alleviate the hydropower supply uncertainty associated with the frequent droughts (Marsh et al. 2023).

1.3. Problem Statement

Past studies on the techno-economic performance of closed-loop geothermal systems generally focus on baseload operation with constant flow rate and injection temperature of the heat transfer fluid, a constant ambient temperature, and a constant PPA price. In this project, we investigated the techno-economic performance of flexible closed-loop geothermal operation. For example, operating a closed-loop geothermal system in a load-following capacity ("dispatchable geothermal") may allow boosting power output at times of high electricity prices and obtain a better PPA price. Lowering the flow rate during times of low electricity prices may allow the rock temperature to partially recover thermally, which may increase the longevity of the system. In this project, we investigated net present value and LCOE for flexible operation of a closed-loop system under various scenarios.

2. Methodology

2.1 System Design

We selected a multiloop design for the subsurface closed-loop system in this project, based on a previous study by Beckers and Johnston (2022). This design assumes 12 lateral passes with total vertical depth of 7 km and total drilling length of about 87 km, as seen in Figure 2. The spacing between the laterals is 500 m. We considered the scenario with a geothermal gradient of 60°C/km. The nominal flow rate is 80 kg/s, corresponding to an average production temperature of approximately 210°C.

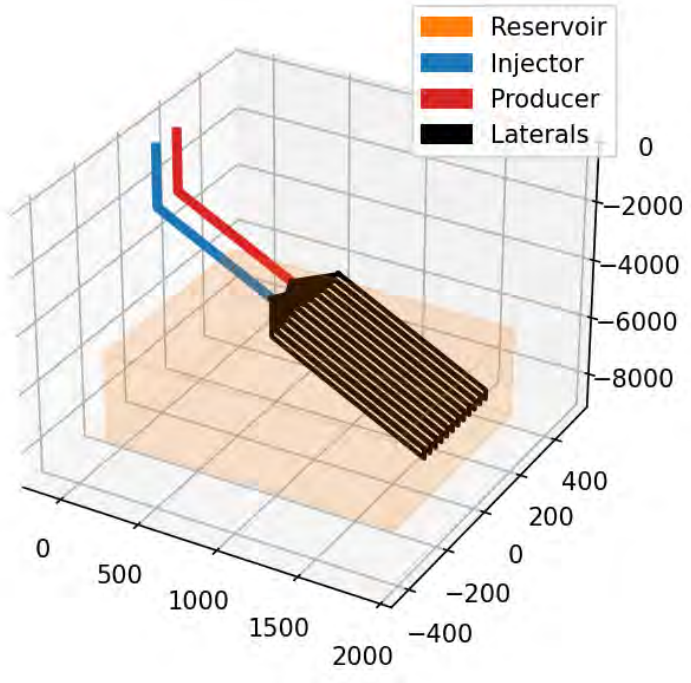

Figure 2: Subsurface configuration of the multiloop system.

2.2 Slender-Body Theory Model

We simulated the closed-loop subsurface heat extraction with the slender-body theory (SBT) model for transient heat conduction, developed by Beckers et al. (2015; 2022). The SBT model is a computationally fast heat transfer model using analytical equations (Green's functions) to simulate heat transfer between the heat exchanger and surrounding rock, requiring only a one-dimensional spatial discretization of the exchanger instead of a full three-dimensional domain discretization with traditional numerical simulators. A double integration (over space and time) is still required to simulate the impact of all past heat exchange at every element; however, simplifications in time and space domains are implemented in the SBT model to speed up that step, as seen in Figure 3. The SBT model can simulate only reservoir heat conduction with constant reservoir thermophysical properties but allows for varying fluid injection temperature and flow rate. As part of this study, a Python version of the SBT model has been coupled with FGEM and set up to simulate hourly heat extraction over the system lifetime.

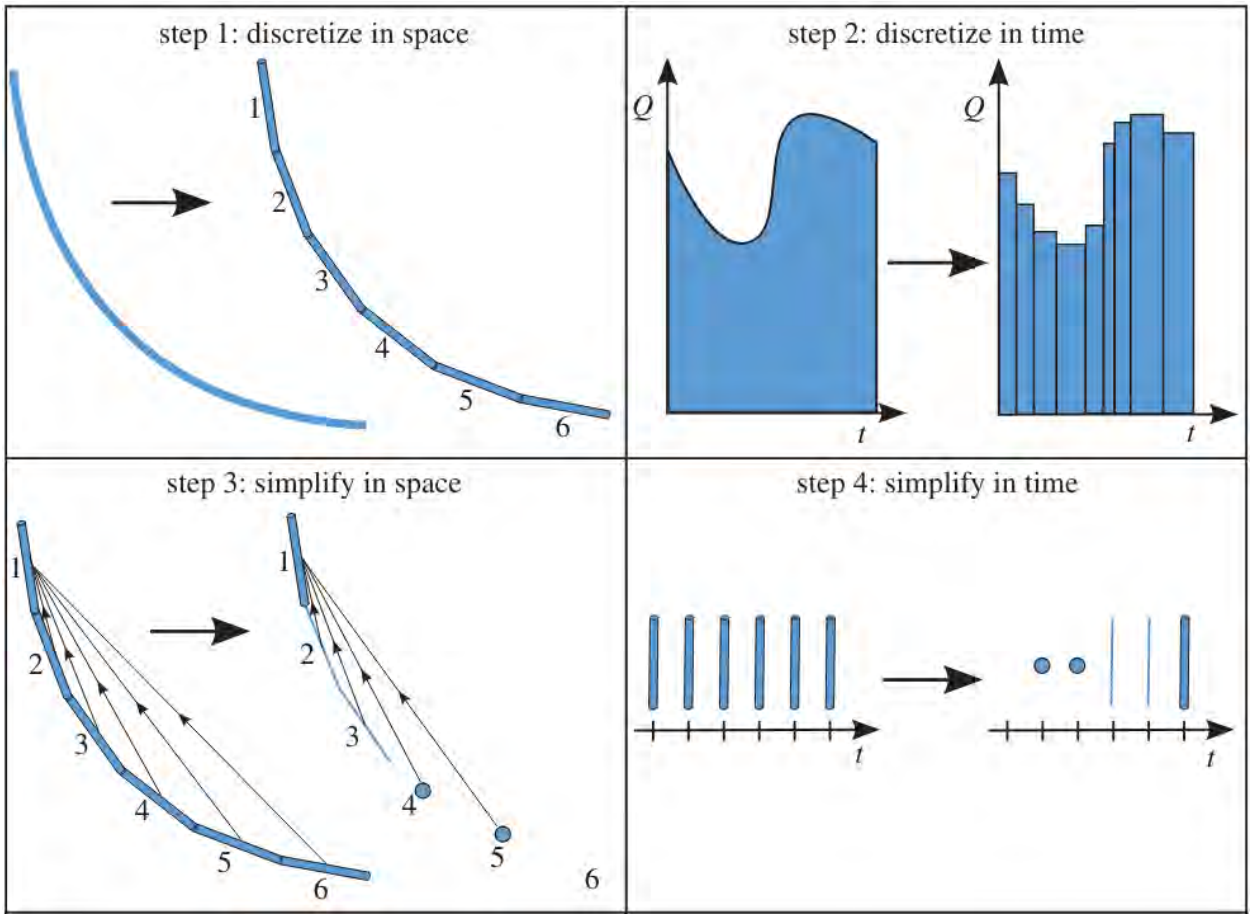

Figure 3: SBT model represents numerical implementation of using Green's functions to simulate heat transfer between fluid in heat exchanger and surrounding rock. The heat exchanger is discretized in space with "pipe elements," allowing the use of analytical equations (i.e., point source, line source, cylindrical source) to rapidly calculate heat exchange.

2.3 Binary Power Plants

There exist several types of power plants, such as dry steam, single-and multi-flash steam, organic Rankine cycle (ORC) or binary cycle plants, and combined cycle power plants (DiPippo 2012). Other than one triple-flash plant constructed in 2011, all geothermal capacity additions across the United States from 2000 through 2020 have been binary plants (Robins et al. 2021). Several key factors have driven this dominating trend. An ORC plant can operate efficiently with low-enthalpy geothermal resources; hence, it is suitable for a larger number of geothermal resources (Kagel et al. 2005). Binary power plants are closed systems, which minimizes emissions and environmental impact, unlike flash plants, which could release toxic and greenhouse gases such as hydrogen sulfide and carbon dioxide (Bonalumi et al. 2017). This is key for complying with increasingly strict environmental regulations and meeting increasing demand for clean energy. In addition, binary plants are modular and scalable, allowing incremental capacity additions and easier adaptation to varying resource conditions (DiPippo 1999). Thus, the research of this study focused on the use of ORC power plants.

Practically, power plants never operate under fixed conditions, where ambient temperature fluctuates, production temperature declines, and geofluid mass flow rate is adjusted. Thus, power output would be overestimated if a plant were assumed to always operate under on-design conditions. Hence, it is necessary to model and optimize power plants for off-design conditions. In this study, an ORC power plant was modeled and optimized across operating conditions to accommodate the variable operational settings over the geothermal project lifetime.

Seen in Figures 4 and 5, the main components of an air-cooled geothermal subcritical ORC binary power plant are the turbine, generator, condenser, feed pump, preheater, and evaporator. Three fluids are involved in the heat exchange process: geofluid, working fluid, and air. The geofluid is produced at point (a) under the wellhead pressure and temperature, then passes through the evaporator to the design pinch-point conditions at point (b) and finally through the preheater to exit at reinjection conditions at point (c) to the injection well. The high-pressure, vaporized working fluid enters the turbine at point (1) and expands through the turbine, converting thermal energy into mechanical energy, which drives the power generator. The low-pressure vapor exits the turbine at point (2) and enters the condenser, where it releases its remaining heat as a two-phase fluid at point (g) and eventually exits at point (3). The fluid is then pumped through point (4) to the preheater where it is heated to the saturation point (5) and eventually evaporated (and superheated, if needed) to point (1), completing the ORC cycle. Air is used to cool the working fluid in the condenser, entering at ambient conditions at point (x), through the condenser pinch-point conditions at point (f), and exiting at a higher temperature at point (y). The thermodynamic processes of the working fluid are shown in the pressure-enthalpy diagram of Figure 5. The system components were analyzed based on established thermodynamic laws most often used for refrigeration and air conditioning cycles (DiPippo 2012). The cycle thermal efficiency was estimated based on the first law of thermodynamics whereas net power output was then computed by subtracting the parasitic losses because of working fluid pumping and air fan cooling from the gross power generation.

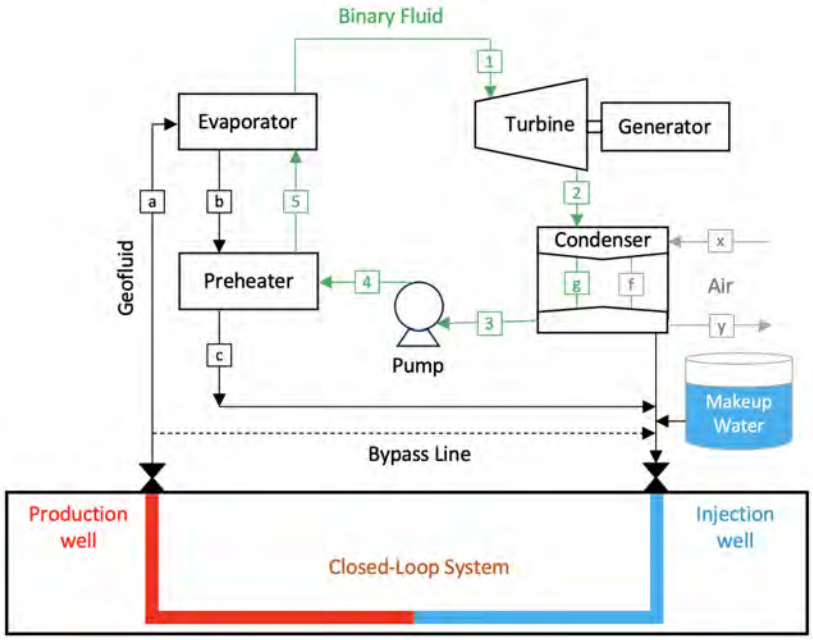

Figure 4: Schematic of the ORC binary power plant model components with emphasis on the flow paths of the geofluid (black), binary fluid (green), and cooling air (gray).

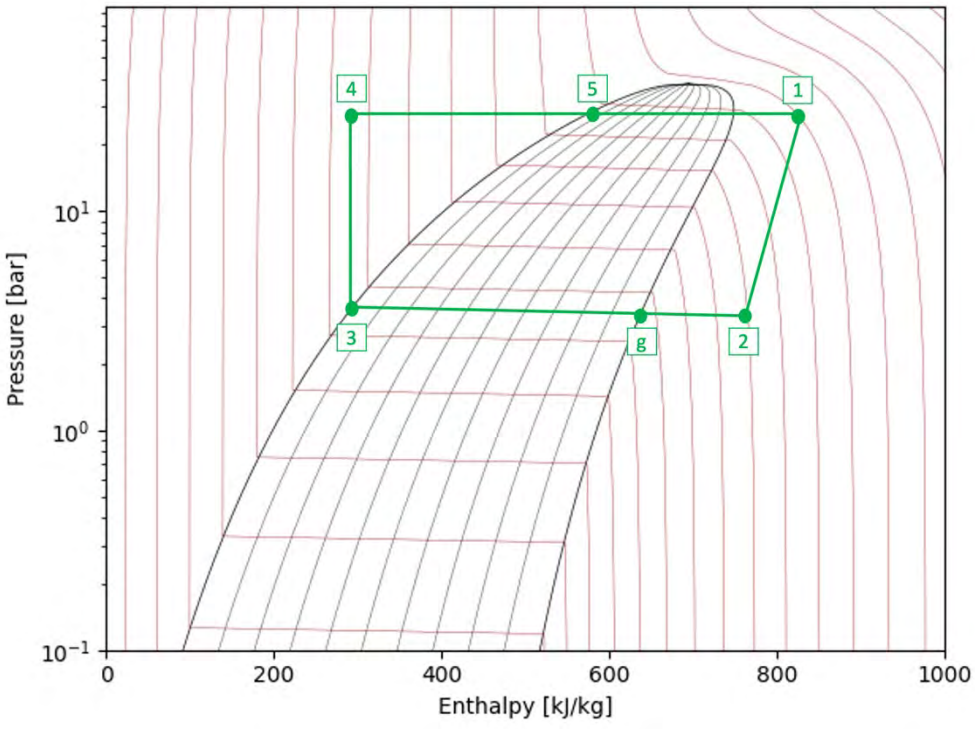

Figure 5: Example binary fluid pressure-enthalpy diagram with fluid undergoing heat-to-electricity-conversion cycle corresponding to Figure 4.

The proposed model was used in an optimization framework to design power plants optimally. Usual parameters were set across simulations, with butane as the binary working fluid, reinjection temperature of 60°C, heat exchanger pinch-point of 5.8°C, and condenser pinch-point of 3.0°C

(DiPippo 2012). The optimization objective was to maximize net power output by controlling the turbine inlet temperature, inlet pressure, and outlet pressure. Bound constraints were set to ensure subcritical conditions while allowing superheating of the working fluid, positive system pressure differential to prevent moisture from contaminating the working fluid, and operational conditions below the working fluid critical pressure. Inequality constraints were set to guarantee mass and energy balance across fluid cycles, a minimum of 2-bar positive differential pressure across the turbine, pinch-point constraints, no temperature profile crossing within the heat exchanger train and condenser, and 95% working fluid vapor quality at the turbine outlet. Adaptive particle swarm optimization (Zhan et al. 2009) was used to optimize this single-objective problem. The resulting operational conditions and power output represent the optimal on-design power plant performance. In addition, the on-design preheater, evaporator, and condenser surfaces areas were computed accordingly.

This model was developed in Python and verified by comparing against two air-cooled geothermal ORC binary power plants developed using the IPSEpro software (Beckers et al. 2022) with a similar power plant configuration. Both validation scenarios involved geofluid mass flow rate of 80 kg/s, ambient temperature of 15°C, and reinjection temperature of 60°C. The first verification scenario was based on a low-enthalpy geothermal resource producing saturated liquid at 125°C, with propane as a working fluid. Compared to the IPSEpro model net power output of 2.25 MWe, the proposed Python model yielded 2.30 MWe (2.2% difference). The second verification scenario was based on a high-enthalpy geothermal resource producing saturated liquid at 210°C, with butane as a working fluid. Compared to the IPSEpro model net power output of 8.40 MWe, the proposed Python model yielded 8.82 MWe (4.9% difference). Hence, it was concluded the proposed model was suitable to evaluate power output performance across scenarios.

The on-design ORC power plant modeling and optimization framework was then compared to the GEOPHIRES power plant correlations, a geothermal techno-economics simulator (Beckers and McCabe 2019). The GEOPHIRES expressed the net power output and reinjection temperature as functions of the geofluid production temperature and ambient temperature alone, with no correspondence to the geofluid flow rate. They also assumed the most optimal power output across an array of working fluids. In addition, these correlations were limited to production temperatures of 100–200°C, ambient temperature of 5–25°C. As seen in Figure 6, using a fixed ambient temperature of 15°C and mass flow rate of 80 kg/s, the proposed air-cooled ORC power plant model was used to evaluate the optimal on-design net specific power output across various combinations of geofluid production temperature and binary working fluids. Note how the results closely matched the on-design GEOPHIRES ORC power plant correlations between 100°C and 200°C with small differences attributed to the use of liquid water cooling and recuperator in the GEOPHIRES correlations. Most importantly, extrapolating the GEOPHIRES correlations beyond their design range of 100–200°C resulted in significantly overestimating the net power output. This on-design comparison further verified and emphasized the necessity for using the proposed ORC power plant model and optimization framework.

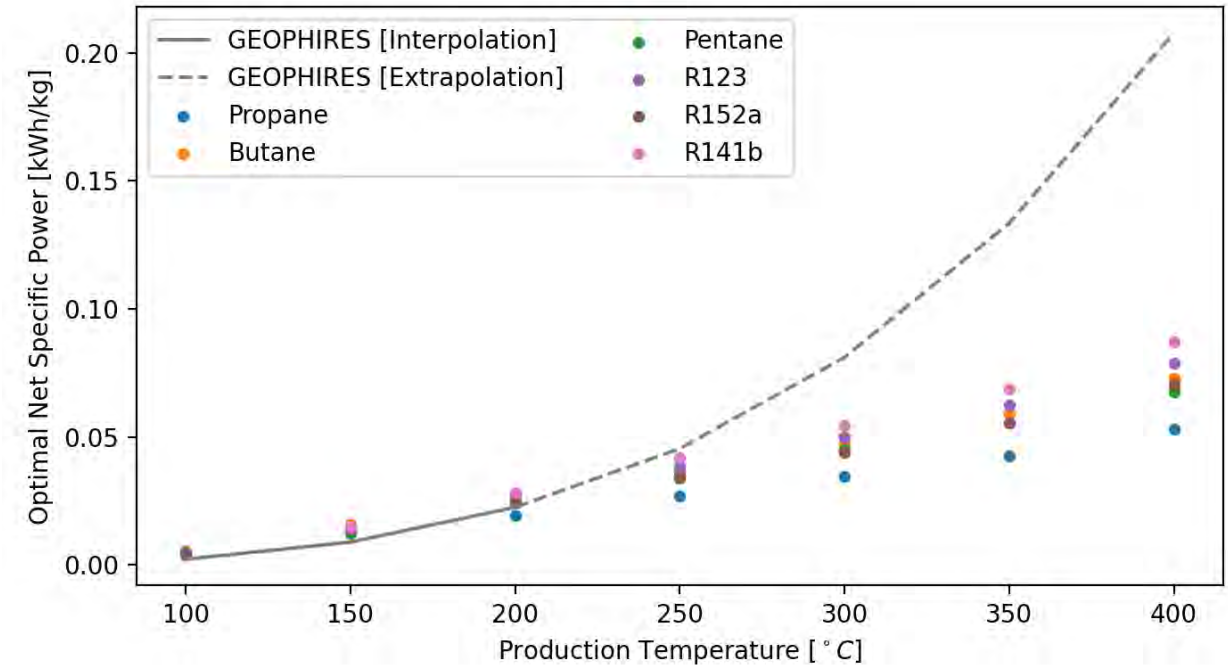

Figure 6: Comparison of the proposed ORC power plant versus the GEOPHIRES correlations in modeling the net optimal power output across a range of geofluid production temperatures and binary working fluids.

Although optimized for on-design operational conditions, the same power plant should also be reoptimized when operational conditions change. This task is called off-design optimization. In off-design settings, the optimization objective was to simultaneously maximize net power output and reinjection temperature by controlling the turbine inlet temperature, turbine inlet pressure, turbine outlet pressure, working fluid mass flow rate, and difference between working fluid temperature at the condenser outlet and ambient temperature. In addition to bound constraints, 16 inequality constraints and 7 equality constraints were used. Inequality constraints were identical to the on-design optimization setup. Equality constraints were set to ensure mass and energy balance across the system components and constrain the off-design solution to the on-design surface areas of the preheater, evaporator, and condenser. The degradation in the turbine isentropic efficiency because changing the working fluid mass flow rate off-design was also modeled as a second-degree parabola following (Beckers 2022). In this process, the nondominating sorting genetic algorithm (Deb et al. 2002) was used to optimize this dual-objective problem.

Integrating the optimization framework into this study directly would be computationally expensive. To avoid this difficulty, on- and off-design simulations were conducted across a range of conditions. Seen in Figure 6, butane was found to be among the most efficient binary fluids for the range of interest. A total of 387,475 off-design optimization runs were conducted for production temperature, ambient temperature, and geofluid mass flow rate ranges of 125–400°C, -40–40°C, and 20–200 kg/s, respectively. For each on-design setting, third-degree polynomial fits were generated to map the off-design production temperature, ambient temperature, and geofluid mass flow rates to net power output and reinjection temperature, achieving mean absolute errors of 1.5 MWe and 1.1°C, respectively. Figures 7 and 8 show the variation in net power output and reinjection temperature across off-design parameters for an on-design configuration with production temperature, ambient temperature, and geofluid mass flow rate of 150°C, 20°C, and 80

kg/s, respectively. Net power output increases with increasing off-design geofluid production temperature and mass flow rate. Meanwhile, the variation in net power output was not monotonic with ambient temperature where changing the latter off-design required significant adjustments to the mass flow rates of the working fluid; hence, the isentropic turbine efficiency would degrade accordingly. Meanwhile, Figure 8 shows operating with relatively low geofluid mass flow rates resulted in cases with excessive parasitic losses at the feed-in pump and air fan; hence, the ORC binary power plant could not be operated with positive net power output given the thermodynamic constraints of the system.

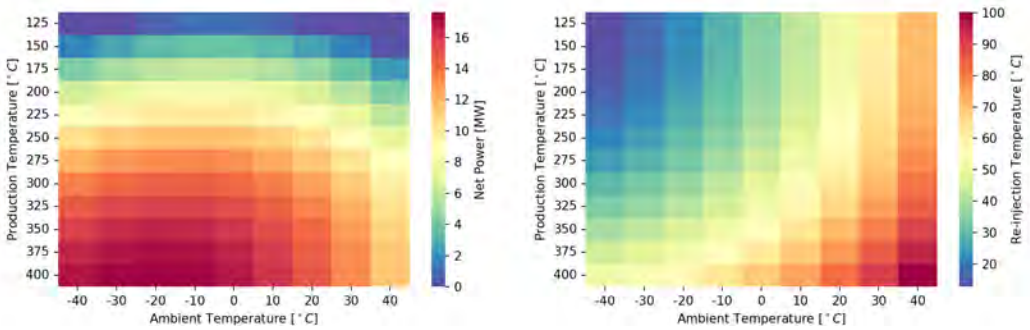

Figure 7: Off-design net power output and reinjection temperature at a constant off-design geofluid mass flow rate of 80 kg/s, optimized for an on-design configuration with production temperature, ambient temperature, and geofluid mass flow rate of 150°C, 20°C, and 80 kg/s, respectively.

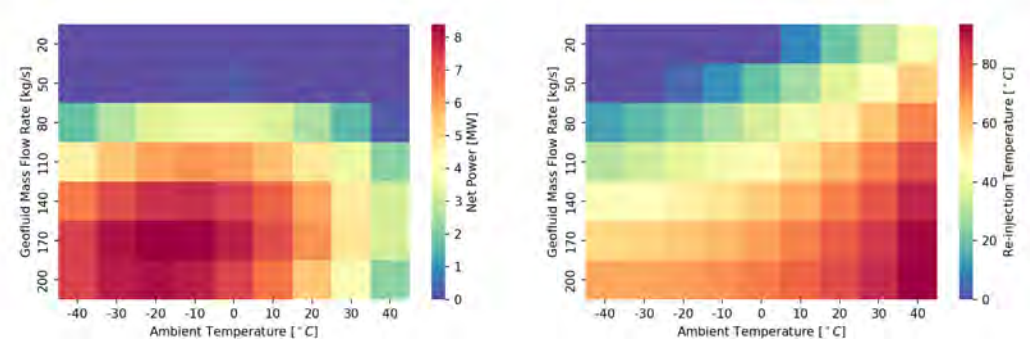

Figure 8: Off-design net power output and reinjection temperature at a constant off-design production temperature of 150°C, optimized for an on-design configuration with production temperature, ambient temperature, and geofluid mass flow rate of 150°C, 20°C, and 80 kg/s, respectively.

2.4 FGEM Model

We used the Flexible Geothermal Economics Model (FGEM) to evaluate the techno-economics of geothermal systems with various operational strategies, such as baseload and flexible operation (Aljubran and Horne 2024a). FGEM couples technical, economic, and market modules at either high- or low-frequency time frames and incorporates a diverse array of parameters, from geothermal resource and plant design to operational dispatch strategies and power market dynamics. This unique integration yields valuable insights into the viability of flexible geothermal power systems and their harmonization within the existing energy landscape.

The FGEM workflow requires several user inputs, including a configuration file, data files, and a dispatch strategy. Upon input validation, FGEM then performs sequential modeling through

distinct modules, each modeling the techno-economic aspects of specific components within the system. These modules include the subsurface reservoir, single-phase wellbore flow dynamics and heat transfer, weather patterns, power plant performance (single-flash or binary systems), energy storage units (e.g., thermal and/or electrochemical energy storage technologies), and power market dynamics (e.g., wholesale, capacity, green energy credits, PPA). For various flash and binary power plant types, FGEM captures the effect of hourly variations in ambient temperature, which govern power plant efficiency and injection fluid temperature.

We incorporated the SBT subsurface model of the multiloop well design with test location nearby the Lightning Dock geothermal power plant, New Mexico. We used hourly time stepping to emulate changes in ambient temperature, which was forecasted at hourly resolution using the Sup3rCC model (Buster et al. 2024). In addition, we integrated our newly developed off-design ORC power plant model into FGEM, which allows capturing variations in power generation and reinjection temperatures. We used FGEM's financial models to estimate project capital expenditures (CAPEX), operating expenses (OPEX), and LCOE with a discount rate of 7% and investment tax credit (ITC) of 30%. In FGEM, we adopted spatially variant transmission line costs based on $2/mile-kW (Aljubran and Horne 2024c). Various drilling rates were considered in this work to evaluate the viability of the system in consideration across scenarios.

To evaluate the value of flexibility in closed-loop systems in the absence of a PPA, it was required to attain power market forecasts. We adopted the 2022 NREL Cambium dataset for the state of New Mexico, which provides forecasts spanning 2024–2050 (Gagnon et al. 2021). Considering 30-year-lifetime geothermal power plants constructed in 2024, there was a need to extrapolate these forecasts beyond 2050. Thus, we extrapolated the Cambium market forecasts linearly based on yearly growth/decline to cover the desired period of 2024–2055. Note Cambium comes with four forecast scenarios: MidCase, MidCase95By2050, HighRECost, and LowRECost. MidCase is a BAU scenario where no nascent technologies are considered while production tax credits and ITCs from the Inflation Reduction Act do not phase out. MidCase95By2050 is like MidCase, except it considers a constraint that enforces 95% decarbonization by 2050 and includes nascent technologies. HighRECost and LowRECost are also like MidCase, except with high and low renewable energy costs, respectively. Meanwhile, because Cambium does not offer projections for the renewable energy credits (RECs) markets, we adopted publicly available forecasts provided by Energy and Environmental Economics, Inc. (E3 Inc. 2022). These are based on an open-source avoided-cost calculator developed for the California trading hub NP15. Particularly, we assumed these RECs forecasts provide reasonable projections across power markets in the United States.

3. Results and Discussion

To understand the potential benefits of flexible power generation to closed-loop systems, we considered four operational strategies: baseload, seasonal, generation maximization, and revenue maximization. In baseload operations, the production flow rates were held constant at 80 kg/s throughout the project lifetime. Seasonal dispatch involved production flow rates of 125 kg/s during July–October and 80 kg/s otherwise, with the premise of increasing generation during the summer when demand for electricity is greater. Generation maximization involved a dynamic controller that attempts to maximize power generation by changing the production mass flow rate within the range of 10–125 kg/s. Revenue maximization involved varying mass flow rates to follow the wholesale energy price of the MidCase Cambium scenario. Prices were rescaled to

resemble mass flow rates with the range of 10–125 kg/s. Meanwhile, all other time-series parameters (e.g., geothermal production temperature, ambient temperature, power plant performance, power market pricing) were allowed to change across scenarios. We considered a 7-MW ORC power plant at a cost of $2,442/kW. Based on proximity to the nearest transmission line, interconnection cost was at a rate of $130/kW. Because of the thermosiphon effect, no injection or production pumps were required. As a baseline, we assumed a drilling cost of $1,000/m; hence, the total system drilling cost was $87 million. In addition, 15% contingency cost was introduced to account for unplanned expenditure. Figure 9 shows the CAPEX breakdown, which was dominated by drilling costs because of the significant drilling lengths required to achieve the system in consideration. Optimistically, we assumed this system was associated with zero water losses to the rock in the subsurface, self-flowing with no pumping requirements, and run independently with negligeable labor needs at the wellsite and power plant. Hence, the system in consideration was assumed to have zero OPEX.

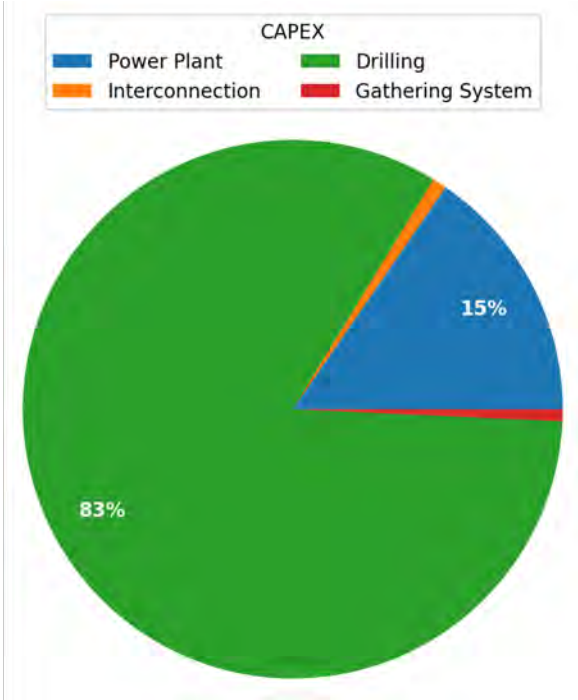

Figure 9: Breakdown of CAPEX costs for the project considered in this study.

Figure 10 shows several operational parameters throughout the 30-year project lifetime for the baseload scenario. Though the field (i.e., total) production mass flow rate was held constant, changes were driven by the diurnal and seasonal oscillations of the ambient temperature and the decline in production temperature. Following the decline in the production temperature, power generation started at the installed nameplate capacity of 7 MW and eventually converged to approximately 3 MW, on average. Reinjection temperatures started at about 100°C and eventually converged to about 50°C. Elevated ambient temperatures in the summer resulted in a drop in power generation, because of the decrease in power plant thermal efficiency, and an increase in reinjection temperatures.

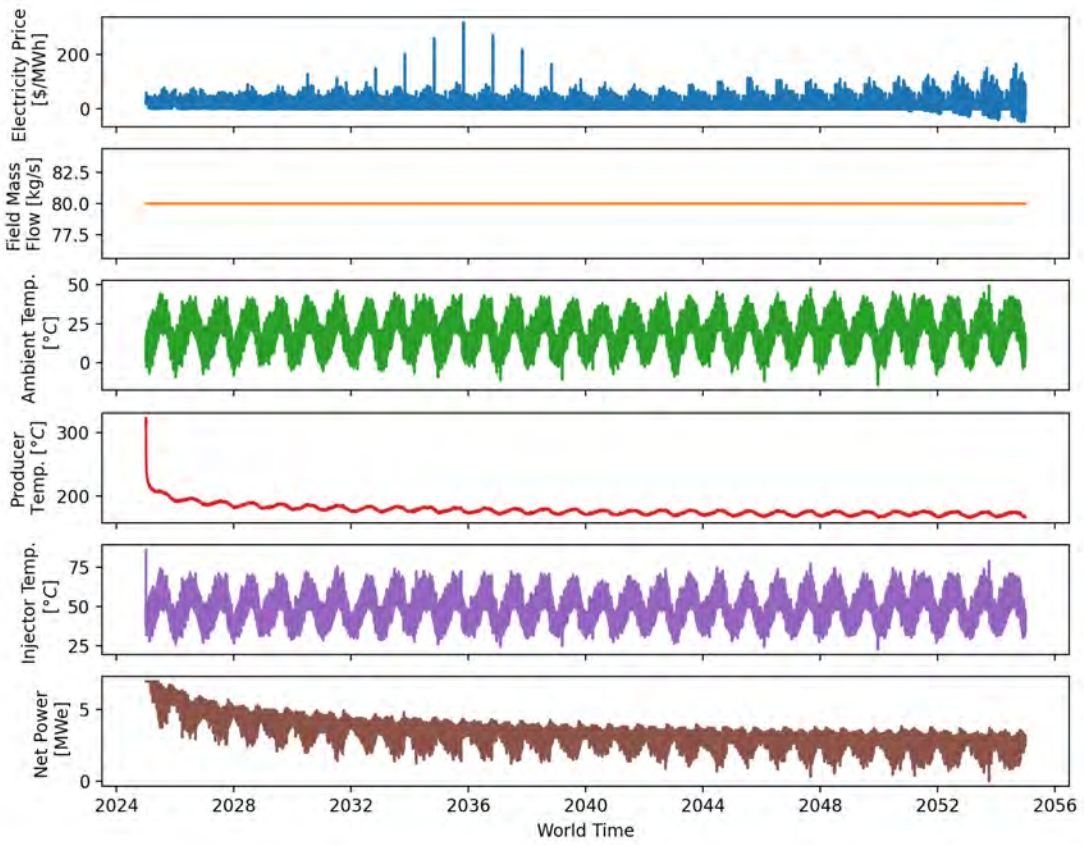

Figure 10: Operational parameters of the baseload strategy over the lifetime of the closed-loop project in consideration.

Figure 11 illustrates several operational parameters over the 30-year project lifetime operated with the seasonal dispatch strategy. The field production mass flow rate varied seasonally, which allowed the closed-loop system to recharge and achieve power output of nearly 5 MW even at later stages of the project lifetime. It is important to note the closed-loop system was rapidly responsive to changes in the production mass flow rates, allowing quick charge and discharge of conductively transferred heat. Despite these adjustments, the annual decline in production temperature is evident, starting around 300°C and steadily decreasing over the project duration. Reinjection temperatures oscillated seasonally, starting near 100°C and stabilizing around 60°C, on average—slightly higher than the baseload scenario. Net power output fluctuated more dynamically compared to the baseload scenario, reflecting the variable mass flow rates and ambient temperature impacts on the system's thermal efficiency. This strategy highlights the potential for optimizing geothermal power generation by aligning production with market demand and seasonal thermal efficiency variations.

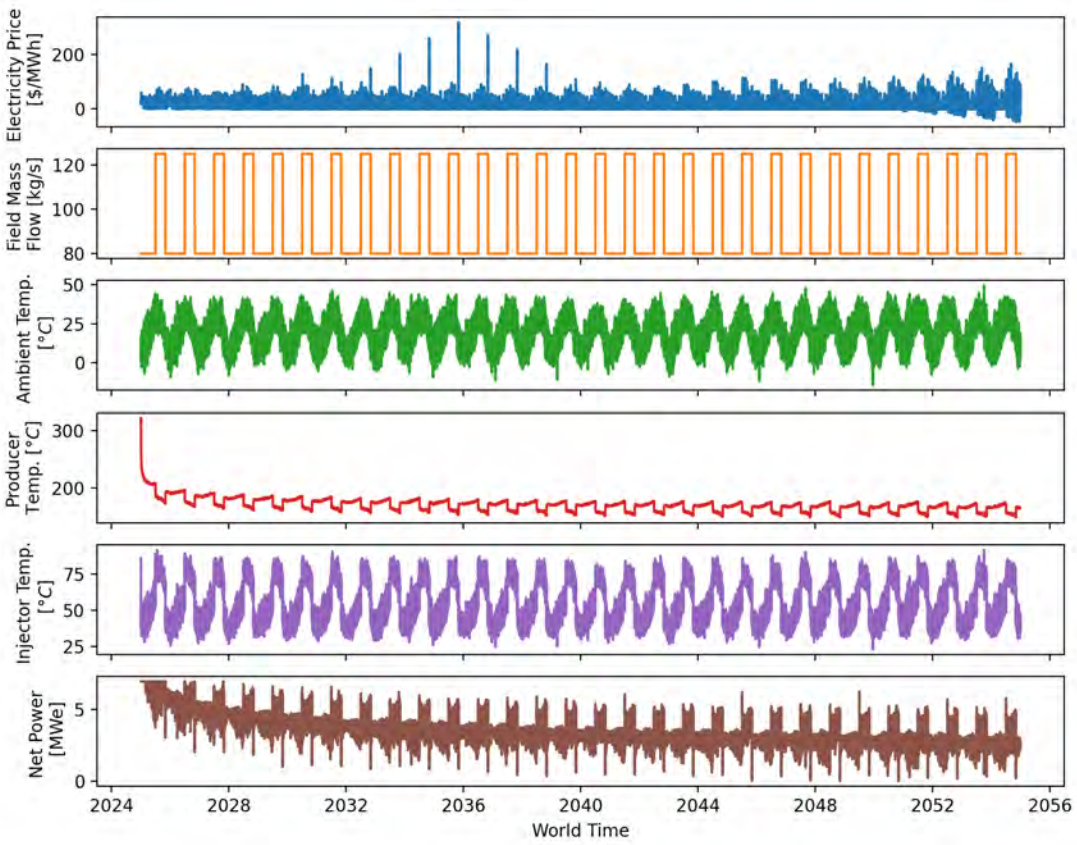

Figure 11: Operational parameters of the seasonal strategy over the lifetime of the closed-loop project in consideration.

Figure 12 shows several operational parameters over the 30-year project lifetime operated with the generation maximization dispatch strategy. During the first year of operations, when the reservoir temperature was still high, this strategy elected to reduce the mass flow rate while still operating at the nameplate power capacity of 7 MW. As the geothermal production temperature declined, the dynamic controller elected to increase the mass flow rates to the maximum allowable value of 125 kg/s with the objective of maintaining the power plant output at its nameplate capacity. However, this was found to have a counterproductive effect where higher mass flow rates would conductively cause the subsurface resource temperature to deplete even further with a quick response time. With 125 kg/s flow rates, the reservoir temperature stabilized at around 180°C at quasi-steady conditions. Reinjection temperatures oscillate seasonally, starting near 100°C and stabilizing around 70°C, on average, slightly higher than the baseload and seasonal scenarios. Net power output fluctuated around an average of 4 MW.

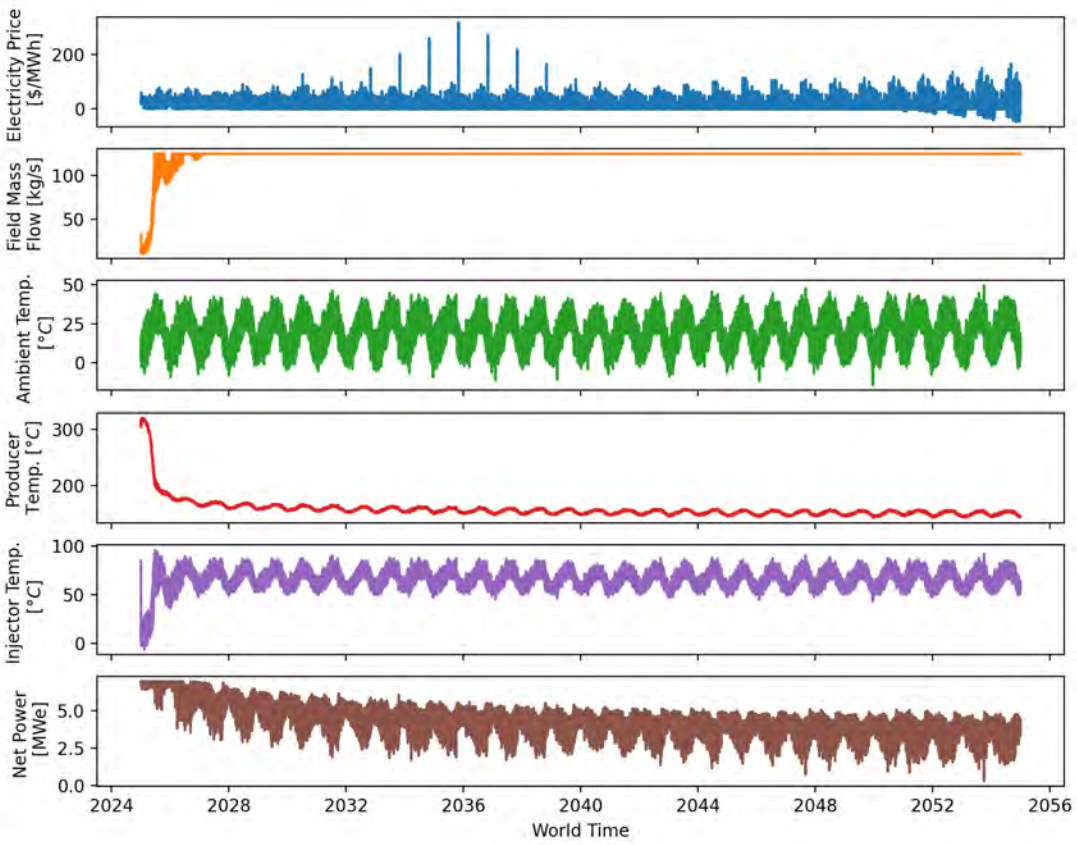

Figure 12: Operational parameters of the generation maximization strategy over the lifetime of the closed-loop project in consideration.

Figure 13 shows several operational parameters over the first year of operations under the revenue maximization dispatch strategy. Production mass flow rates had the same frequency as the wholesale energy market price while being limited to a range of 80–125 kg/s. This had the benefit of boosting generation during hours of the year when the wholesale market energy prices were higher. This approach resulted in a quasi-steady reservoir temperature of around 210°C and reinjection temperature of nearly 50°C, on average. This approach allowed the net power output to oscillate between near-zero and the power plant nameplate capacity of 7 MW even at latter stages of the project lifetime.

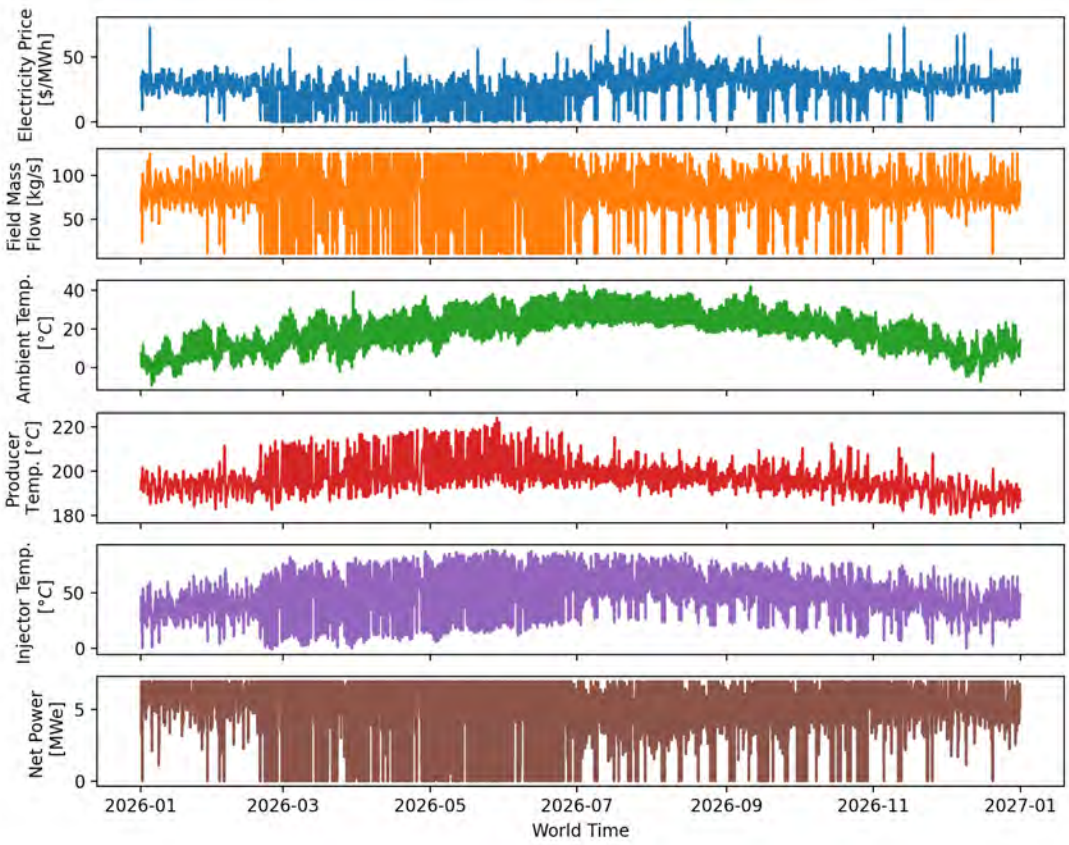

Figure 13: Operational parameters of the revenue maximization strategy over the first year of the closed-loop project in consideration. We chose to zoom in on the first year of operations for visual convenience.

Figure 14 compares the economic performance of the different strategies in terms of LCOE and return on investment (ROI). ROI here is defined as project lifetime net income divided by upfront capital costs. Baseload, seasonal, generation maximization, and revenue maximization had LCOE of $191, $180, $155, and $216/MWh, respectively. Both generation maximization and seasonal dispatch resulted in reduced LCOE compared to the BAU baseload strategy because they were associated with greater net power output, on average, as seen in Figure 15. However, despite the significant improvement in LCOE, at $1,000/m drilling costs, flexible generation still had LCOEs significantly higher than the 2035 target LCOE of $45/MWh set by DOE for geothermal projects. In addition, all these projects were unprofitable (ROI < 100%) when operated under the MidCase scenario of the 2022 Cambium forecasts. Nevertheless, we observed all flexible generation strategies yielded improved ROI, with revenue maximization ranking on top.

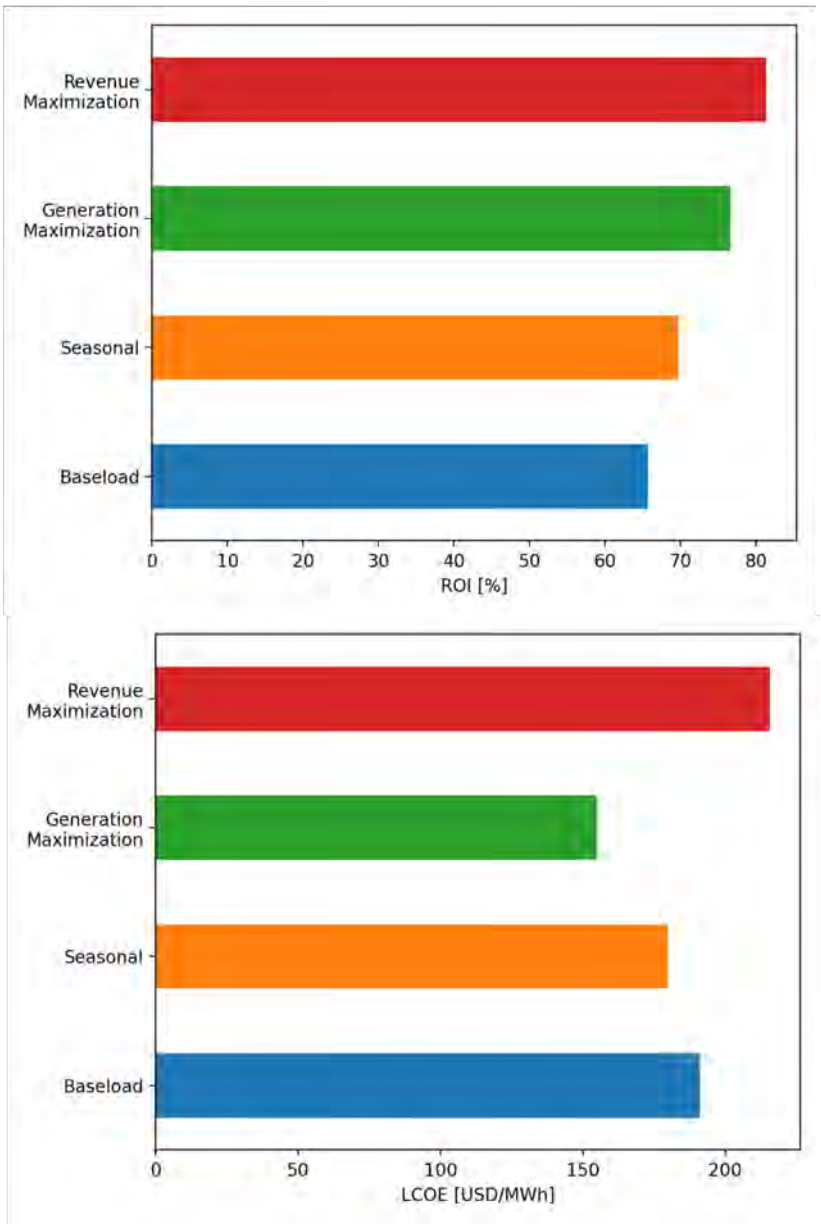

Figure 14: Bar charts showing ROI (top) and LCOE (bottom) across the different dispatch strategies of the closed-loop system in consideration.

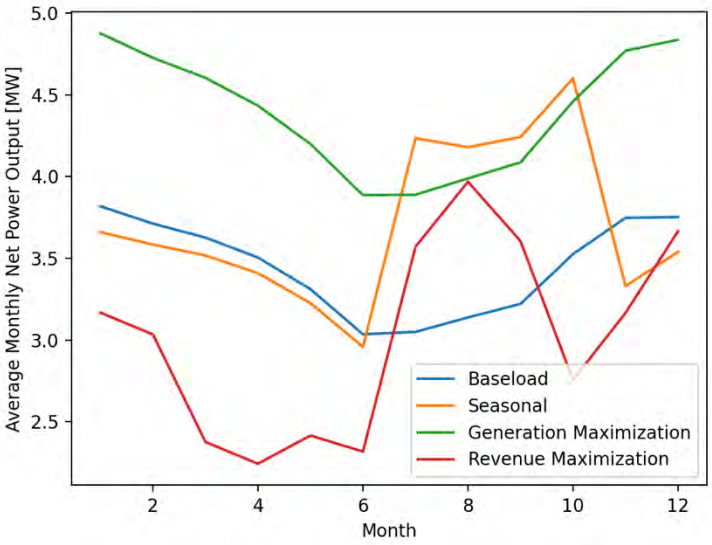

Figure 15: Average monthly net power output under different operational strategies of the closed-loop system in consideration.

With a drilling cost of $1,000/m and discount rate of 7%, closed-loop geothermal systems with flexible operation have high LCOE in the range of $150–220/MWh (Figure 14). We explored the impact of drilling and discount rates on LCOE in the case of baseload and generation maximization dispatch operations (Figure 16). Under the highly optimistic scenario of $200/m drilling cost and 5% discount rate, operating the closed-loop system in consideration under baseload and generation maximization dispatch strategies resulted in LCOE values of $60 and $49/MWh, respectively.

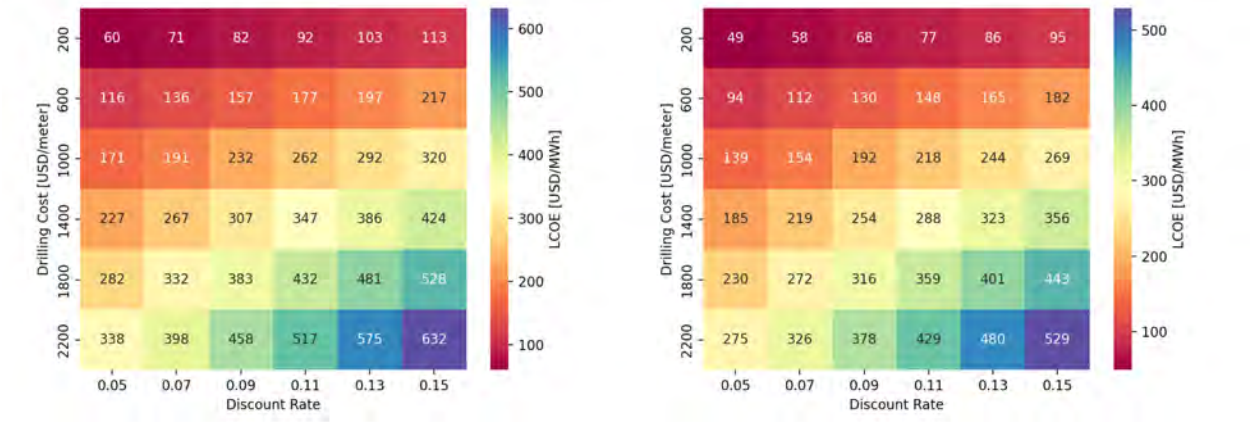

Figure 16: Sensitivity analysis of LCOE with respect to drilling and discount rates of the baseload (left) and generation maximization (right) dispatch strategies.

4. Conclusions

In this project, we coupled FGEM with the SBT model to investigate the techno-economic performance of the flexible operation of closed-loop geothermal systems. We modeled a multiloop system with 12 lateral passes, 7-km vertical depth and total drilling length of approximately 87

km. The geothermal gradient was set to 60°C/km, and hourly ambient temperature conditions were assumed for New Mexico based on the Sup3rCC future weather dataset. Future market electricity prices for New Mexico were based on the Cambium dataset.

We simulated four scenarios with hourly time stepping: 1) baseload scenario with nominal flow rate of 80 kg/s, 2) seasonal dispatch scenario with summer flow rate of 125 kg/s and 80 kg/s the rest of the year, 3) generation maximization scenario where a dynamic controller attempts to maximize net power output by adjusting the flow rate (within a range of 10–125 kg/s), and 4) revenue maximization scenario where a dynamic controller adjusts flow rate (within a range of 10–125 kg/s) to maximize net revenue considering Cambium MidCase wholesale electricity prices.

Considering $1,000/m drilling cost and 7% discount rate, the maximum generation scenario resulted in the lowest LCOE of approximately $150/MWh. The highest ROI was for the revenue maximization scenario, with an ROI of 80% (based on lifetime income and cost). Obtaining LCOE below $70/MWh requires a very low drilling cost and low discount rate. For, example, when drilling at $200/m (about 5 times lower than current drilling costs) and with a discount rate of 5%, the LCOE for the base case scenario is $60/MWh and for the generation maximization scenario is $49/MWh.

Acknowledgment

We would like to thank Stanford University and the Stanford Research Computing Center for providing computational resources and support that contributed to these research results. This work was authored in part by the National Renewable Energy Laboratory, operated by Alliance for Sustainable Energy, LLC, for the U.S. Department of Energy (DOE) under Contract No. DE-AC36-08GO28308. Funding provided by the U.S. Department of Energy Office of Energy Efficiency and Renewable Energy Geothermal Technologies Office. The views expressed herein do not necessarily represent the views of the DOE or the U.S. Government. The U.S. Government retains and the publisher, by accepting the article for publication, acknowledges that the U.S. Government retains a nonexclusive, paid-up, irrevocable, worldwide license to publish or reproduce the published form of this work, or allow others to do so, for U.S. Government purposes.

REFERENCES

Aljubran, M. J. and Horne, R. N. “FGEM: Flexible Geothermal Economics Modeling tool.” *Applied Energy* 353 (2024a): 122125.

Aljubran, M. J. and Horne, R. N. “Supply Characterization of Baseload and Flexible Geothermal.” *Nature Scientific Reports*, in prep. (2024b).

Aljubran, M. J., and Horne, R. N. “Techno-economics of Enhanced Geothermal Systems Across the United States Using Novel Temperature-at-Depth Maps.” Proceedings, 49th Stanford Workshop on Geothermal Reservoir Engineering, Stanford University, Stanford, CA (2024c).

Aljubran, M. J., Volkov, O., and Horne, R. N. “Techno-economic modeling and optimization of flexible geothermal operations coupled with energy storage.” Proceedings, 48th Stanford Workshop on Geothermal Reservoir Engineering, Stanford University, Stanford, CA (2023a).

Beckers, K., Ketchum, A., and Augustine, C., 2024. *Evaluating Heat Extraction Performance of Closed-Loop Geothermal Systems with Thermally Conductive Enhancements in Conduction-Only Reservoirs*. Golden, CO: National Renewable Energy Laboratory. NREL/CP-5700-88557.

Beckers, K., Vasyliv, Y., Bran-Anleu, G. A., Martinez, M., Augustine, C., and White, M., “Tabulated Database of Closed-Loop Geothermal Systems Performance for Cloud-Based Technical and Economic Modeling of Heat Production and Electricity Generation.” Proceedings: 48th Workshop on Geothermal Reservoir Engineering, Stanford University, Stanford, CA (2023).

Beckers, K. F. and Johnston, H. E., 2022, February. “Techno-economic performance of Eavor-Loop 2.0.” In Proceedings 47th workshop on geothermal reservoir engineering, Stanford, California.

Beckers, K. F., Koch, D. L., and Tester, J. W., 2015. “Slender-body theory for transient heat conduction: theoretical basis, numerical implementation and case studies.” Proceedings of the Royal Society A: Mathematical, Physical and Engineering Sciences, 471(2184), p. 20150494.

Beckers, K. F., Rangel-Jurado, N., Chandrasekar, H., Hawkins, A. J., Fulton, P. M., and Tester, J. W., 2022. “Techno-economic performance of closed-loop geothermal systems for heat production and electricity generation.” *Geothermics* 100, p. 102318.

Beckers, Koenraad F. and Kevin McCabe. “GEOPHIRES v2. 0: updated geothermal techno-economic simulation tool.” *Geothermal Energy* 7 (2019): 1–28.

Bonalumi, D., Bombarda, P., and Invernizzi, C. “Potential performance of environmental friendly application of ORC and Flash technology in geothermal power plants.” *Energy Procedia* 129, 621–628 (2017).

Buster, Grant, Brandon N. Benton, Andrew Glaws, and Ryan N. King. “High-resolution meteorology with climate change impacts from global climate model data using generative machine learning.” *Nature Energy* (2024): 1–13.

DiPippo, R. *Geothermal power plants: principles, applications, case studies and environmental impact*. Butterworth-Heinemann (2012).

DiPippo, R. “Small geothermal power plants: design, performance and economics.” *GHC bulletin* (1999).

E3 Inc. “Avoided Cost Calculator for Distributed Energy Resources (DER).” Retrieved from: https://www.ethree.com/public_proceedings/energy-efficiency-calculator/ (2022).

Gagnon, P., Cowiestoll, B., and Schwarz, M. 2023. *Cambium 2022 scenario descriptions and documentation*. Golden, CO: National Renewable Energy Laboratory. NREL/TP-6A40-84916.

Hakes, R. S. P., Bozinoski, R., Beckers, K. F., and Ketchum, A., “Influence of Reservoir Convection on Heat Extraction with Closed-Loop Geothermal Systems.” *GRC Transactions*, Vol. 48 (2024).

Kagel, A., Bates, D., and Gawell, K. *A guide to geothermal energy and the environment* (2005).

Marsh, A., Aljubran, M. J., Konstantopoulos, I., and Newton, M. “Flexible geothermal application within the New Zealand electricity market.” World Geothermal Congress (2023).

Moradpoor, I, Syri, S., and Santasalo-Aarnio, A. “Green hydrogen production for oil refining–Finnish case.” *Renewable and Sustainable Energy Reviews* 175 (2023): 113159.

Robins, J. C., Kolker, A., Flores-Espino, F., Pettitt, W., Schmidt, B., Beckers, K., Pauling, H., and Anderson, B. 2021. *2021 U.S. geothermal power production and district heating market report*. Golden, CO: National Renewable Energy Laboratory. NREL/TP-5700-78291.

Tester, Jefferson W., Koenraad F. Beckers, Adam J. Hawkins, and Maciej Z. Lukawski. “The evolving role of geothermal energy for decarbonizing the United States.” *Energy & environmental science* 14, no. 12 (2021): 6211–6241.

White, M., Vasyliv, Y., Beckers, K., Martinez, M., Balestra, P., Parisi, C., Augustine, C., Bran-Anleu, G., Horne, R., Pauley, L., Bettin, G., Marshall, T., and Bernat, A. “Numerical investigation of closed-loop geothermal systems in deep geothermal reservoirs.” *Geothermics* 116 (2024).

Zhan, Z. H., Zhang, J., Li, Y., and Chung, H. S. H. “Adaptive particle swarm optimization.” *IEEE Transactions on Systems, Man, and Cybernetics, Part B (Cybernetics)* 39(6), 1362–1381 (2009).

Unlocking Geothermal Potential: Investigating Vacuum Insulated Tubulars for Improved K-Value Accuracy

Corey Dufrene, Elizabeth Cambre, Joe Hill

Vallourec

Keywords

Advanced Geothermal Systems, AGS, VIT, Closed loop, Insulated tubing, k value

ABSTRACT

Vacuum Insulated Tubulars (VITs) have emerged as a promising technology for enhancing the efficiency of Advanced Geothermal Systems (AGS). By significantly reducing heat transfer between the cold fluid injected through the annulus and the hot fluid produced through the VIT, these vacuum-insulated designs ensure minimal heat loss from the geothermal fluid as it travels from the reservoir to the surface, thereby maximizing energy extraction efficiency. The performance of VITs is evaluated using the K-value metric, where lower K-values indicate superior insulation properties and reduced heat transfer through the tubular walls.

Accurately determining the overall K-values of VITs involves addressing numerous uncertainties stemming from complex heat transfer mechanisms influenced by factors such as gas composition within the vacuum space, material properties, and construction quality. Experimental testing using an R&D VIT test bench allows for comprehensive assessment under various conditions by simulating expected downhole environments with varying temperatures, flow rates, and working fluids. This research outlines laboratory investigations conducted to analyze the K-values of two joints of VITs in a controlled geothermal setup, aiming to optimize VIT design for AGS applications and ultimately enhance energy efficiency and cost-effectiveness in geothermal systems.

1. Introduction

The concept of vacuum insulated tubulars (VIT) in the oil and gas industry dates to the 1980s, driven by the need to enhance thermal efficiency in the production and transportation of hydrocarbons, particularly in challenging environments such as the deepwater Gulf of Mexico, Arctic regions, and areas with permafrost. During this period, the industry began to recognize the potential benefits of VITs for thermal insulation. The initial applications were primarily in offshore drilling and production, where maintaining the temperature of the produced fluids was crucial to prevent hydrate formation and wax deposition. These early VITs were essentially just double-

walled pipes with a vacuum in the annular space, providing a barrier to conductive and convective heat transfer.

During the 1990s, significant advancements in VIT technology were driven by the increasing complexity of oil and gas extraction projects. Improved manufacturing techniques and materials enhanced the durability and efficiency of VITs. The VIT offering described in this paper introduced several innovations, including the use of multilayer insulation (MLI) within the vacuum space and advanced getters to maintain the vacuum over extended periods. These improvements enabled more extensive use in high-temperature and high-pressure (HTHP) environments.

In the 2000s, the application of VITs expanded beyond offshore drilling to onshore and Arctic operations [5]. The industry began to focus on optimizing the design and installation of VITs to maximize thermal performance while minimizing costs. Computational modeling and simulation tools became essential in designing VIT systems, predicting thermal behavior, and optimizing the insulation performance for specific field conditions. The use of VITs in steam-assisted gravity drainage (SAGD) operations for heavy oil recovery became particularly prominent. VITs helped maintain the steam temperature in injection wells, improving the efficiency of the SAGD process and reducing energy consumption.

By the 2010s, VIT technology had matured, with several oil and gas companies adopting standardized VIT designs for various applications. The focus shifted towards enhancing the reliability and ease of installation of VITs. Modular and pre-fabricated VIT systems became more prevalent, significantly reducing installation time and costs. Additionally, advancements in non-destructive testing (NDT) techniques enabled better quality control during both the manufacturing and installation processes.

The utilization of VITs in geothermal applications, particularly in AGS, leverages these decades of technological evolution to address specific challenges associated with heat transfer and energy efficiency. Experimental VIT testing plays a critical role in this context by enabling engineers to simulate expected downhole environments and assess performance under varying conditions. The R&D VIT test bench, for instance, allows for the measurement of K-values not only under ambient conditions but also across a range of temperatures and flow rates, providing a more accurate and comprehensive understanding of system performance. This capability is crucial for refining VIT designs to meet specific performance goals, whether maximizing production temperatures and heat extraction or optimizing the levelized cost of energy (LCOE) and installation costs.

Addressing the uncertainties in accurately determining K-values necessitates comprehensive modeling approaches, rigorous experimental validation, and ongoing refinement of testing methodologies. Factors such as gas composition within the vacuum space, material properties, construction quality, and dynamic operating conditions must be meticulously considered to ensure reliable K-value determinations. Through such dedicated research efforts, the efficiency and performance of closed-loop geothermal systems can be significantly optimized, contributing to the sustainable development and utilization of geothermal energy resources.

This paper aims to outline laboratory research conducted to analyze the k-values of two joints of a VIT in a geothermal setup within a lab environment. Both cold and hot fluids will flow through the VIT system in a coaxial design to mimic an AGS closed loop system, with temperatures

measured throughout the system to model and determine the K-values. This VIT test bench used for this testing has two main advantages:

1. K-values can be measured not only under ambient conditions but also at various temperatures and flow rates, allowing for greater accuracy of the entire system.

2. The test bench enables the assessment of new products (such as connections and insulators) in simulated working conditions during the design phase, providing a more accurate prediction of thermal performance and overall, well efficiency.

In conclusion, the investigation into vacuum insulated tubulars (VITs) for Advanced Geothermal Systems (AGS) represents a crucial step toward realizing the full potential of geothermal energy. The use of VITs in geothermal wells offers significant benefits, including reduced heat loss and enhanced energy extraction efficiency. Accurately determining K-values, not only through general experimental data but through project-specific testing, is essential for optimizing VIT design, as it directly impacts thermal performance, energy efficiency, and cost-effectiveness. The complexities and uncertainties in determining K-values highlight the need for rigorous research and experimentation. By addressing these challenges through comprehensive modeling, experimental validation, and refinement of testing methodologies, we can ensure reliable K-value determination and optimize the efficiency and performance of closed-loop geothermal systems. This paper underscores the importance of ongoing research efforts aimed at analyzing and improving the thermal properties of VITs, ultimately contributing to the sustainable development of geothermal energy resources.

2. VIT and Geothermal Applications

High quality Vacuum Insulated Tubulars (VITs) play a crucial role in coaxial closed-loop geothermal systems by maintaining the thermal integrity of the geothermal fluid as it circulates between the surface and the subsurface. In these systems, VITs are used to minimize heat loss during the transport of heated fluid from deep underground reservoirs to the surface. The vacuum insulation within the tubulars significantly reduces conductive and convective heat transfer, ensuring that the fluid retains its high temperature throughout the journey from the subsurface to the surface. This efficiency is vital for maximizing the energy extraction from the geothermal source and improving the overall system performance.

Moreover, VITs contribute to the structural integrity and reliability of coaxial closed-loop geothermal systems. These tubulars are designed to withstand the high-pressure and high-temperature conditions typical of geothermal environments. Their durable construction and advanced insulation properties allow for consistent and long-term operation, reducing the need for frequent maintenance or replacement. Additionally, the use of VITs in these systems helps to prevent thermal degradation of the surrounding geological formations, further enhancing the sustainability and environmental friendliness of geothermal energy extraction. Overall, VITs are integral to the success of coaxial closed-loop geothermal systems, offering both thermal efficiency and durability.

2.1 VIT Performance Parameters and Challenges for Geothermal Applications

VITs in geothermal applications must maintain their insulating properties over long periods, often a 30-year time frame, without significant degradation. This involves using materials and construction methods that ensure long-term vacuum stability and resistance to corrosion from geothermal fluids.

Over time, maintaining the vacuum within VITs can be difficult due to potential leaks and material outgassing. Even small breaches can lead to a loss of vacuum and reduced insulation efficiency, necessitating regular monitoring and maintenance. The quality of VIT manufacturing and the use of highly optimized materials and processes significantly extend the life expectancy of vacuums in severe environments.

In summary, while vacuum insulated tubulars offer significant performance benefits for geothermal applications, they also present several challenges that need to be addressed. Overcoming these challenges requires advances in materials science, manufacturing techniques, and installation practices to ensure the long-term viability and efficiency of VITs in geothermal energy production.

3. VIT k-value calculation

The overall calculation of thermal conductivity (k value) for VITs involves the combination of several factors. The thermal conductivity for most of the pipe, denoted as k_{pipe}, is primarily controlled by the vacuum. This value, which is measured during manufacturing, typically ranges between 0.004 and 0.006 W/m·K, reflecting the high insulation performance of the vacuum annulus within the pipe body. The most critical factor for overall VIT performance, however, is the thermal conductivity of the connections on the extremity of the pipe, referred to as $k_{connection}$ and illustrated in Figure 1 below. It is estimated that heat losses in the connection are responsible for over 75% of the overall heat loss of the entire VIT string [4]. One of the objectives of this testing program will be to confirm the overall impact of the connection on VIT thermal performance.

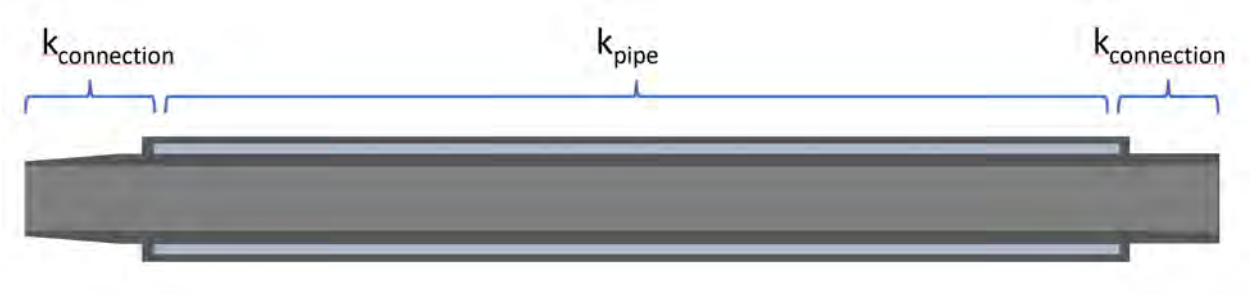

Figure 1: Thermal conductivities (k values) of VIT

During VIT production, the vacuum is tested and confirmed, but the overall thermal performance of the entire joint is not measured. There are heat losses at the extremities of the pipe where there is no vacuum, and these sections heavily contribute to the overall thermal performance of the VIT. There are multiple effects to be considered:

- Conduction between inner and outer pipe at weld joint
- Flow pattern convective effects at the change in OD profile [2]
- Non metallic insulating sleeves to lower heat transfer from connection

Figure 2: Thermal conductivities (k values) of VIT in made-up condition

3.1 VIT k-value modeling

When assessing geothermal applications for VIT, current state-of-the-art analysis is with Wellcat™ software, an oil and gas standard software developed by Halliburton. Wellcat™ is a very capable tool, and provides a basic option for VIT modeling. However, the software has limitations for inputs of k-value and the impact of k-value with flowrate and flow state.

Vallourec has developed an in-house, web-based program specifically aimed at coaxial closed loop analysis. This program provides accurate analysis of fluid temperatures for a multitude of input variables (well dimensions, temperature gradients, flow rates, fluid types, formation heat transfer, etc.). The figure below shows an example of the temperature outputs, and also highlights the importance of insulated tubing in closed loop systems.

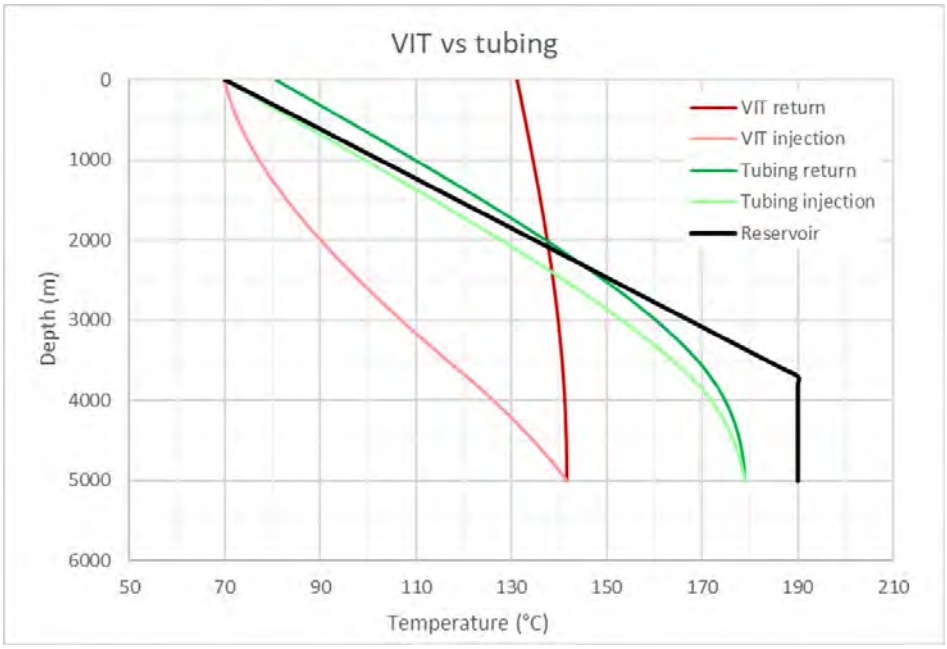

Figure 3: Example of closed loop results, VIT (red) vs non VIT (green) tubing in a closed loop system

In this example of a closed loop system, the use of standard non-insulated tubing (represented by the green lines in Figure 3) shows only a marginal heating of the production fluid from surface injection to return. By comparison, the use of vacuum insulated tubing (in red) shows how much heat is retained on the return from bottomhole to surface, allowing for more thermal energy potential [3]. For easier comparison, all variables between the two situations are fixed (flowrate, well geometry, etc).

All computational software benefits from having field and/or experimental data to corroborate the calculations. The aim of the VIT test bench will be to improve the predictive accuracy of modeling software and allow for subsurface and surface equipment optimization.

4. Test bench setup, parameters

The fundamental principle of this VIT test bench is straightforward: to accurately measure the thermal efficiency of an entire VIT joint. This is done by enclosing the VIT joint within a casing, circulating hot oil inside the VIT, and measuring the heat transferred to the water flowing over the VIT.

The VIT test bench comprises a full-length R3 (~40ft) 4.5” x 3.5” L80 VIT pipe. To test heat transfer within the VIT, hot oil is circulated inside the inner pipe annulus. An external oil reservoir is wrapped with an induction heater and then the oil is pumped into the VIT. To improve the even distribution of heat to the inner diameter (ID) of the VIT, oil flows along a rotating shaft with impellers, rather than simply flowing through the system. The goal is to achieve a steady-state temperature where the heated oil flows consistently, and the inlet and outlet temperatures of the oil are stable. Additionally, the oil temperatures are measured at multiple points within the system to ensure proper temperature distribution.

To measure the thermal conductivity of the VIT, water is circulated in the annular space between the VIT and the outer casing. Upon entering and exiting the system, the water temperature is precisely measured. The temperature delta represents the amount of heat loss from the VIT, and is calculated.

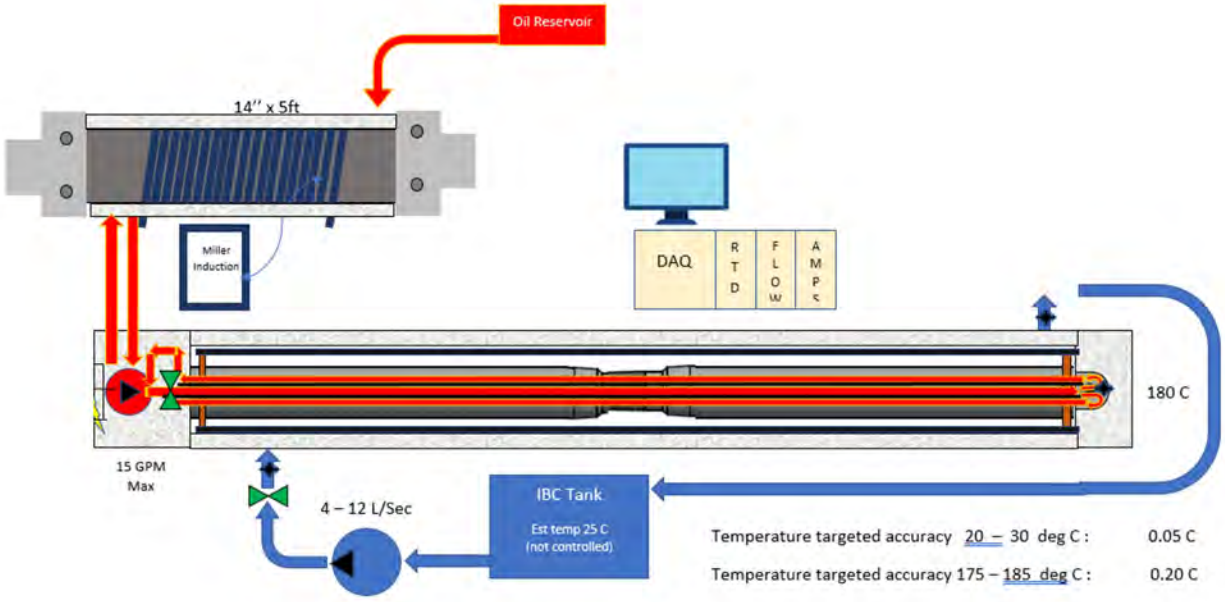

Figure 4: VIT test bench schematic

The VIT is placed inside an outer casing, composed of 7" x 0.540" pipe. Therefore, the annular space for water flow around the VIT is calculated as follows:

$$Area = \frac{\pi}{4}(D_o^2\text{-}D_i^2)$$

$$D_o = 7.0" - 2*0.54 = 5.92"$$

$$D_i = 4.50"$$

$$= \frac{\pi}{4}(D_o^2\text{-}D_i^2) = 11.62in^2$$

with a radial gap of:

$$D_o - D_i = 5.92" - 4.50" = {}^{1.42"}/_{2} = 0.71"$$

The oil is circulated inside the 4.5" x 3.5" VIT, with an ID of 2.992", equating to an internal area of:

$$Area = \frac{\pi}{4}D_{\square}^2 = 7.03 \text{ in}^2$$

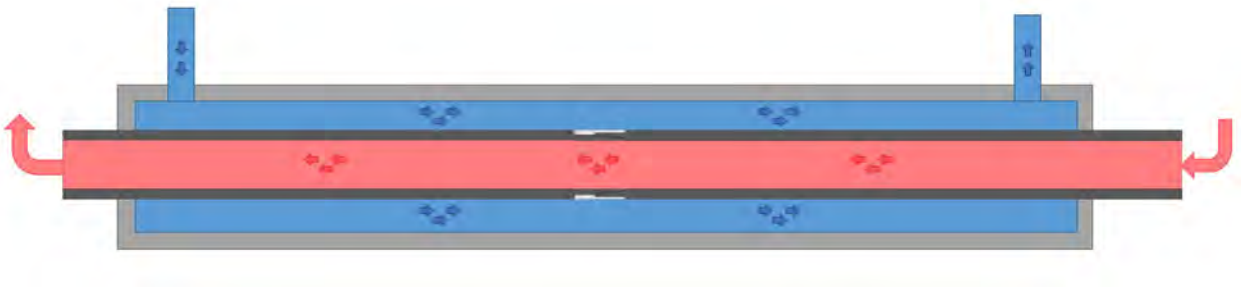

Figure 5: Flow direction for VIT test bench

To verify the performance of the VIT, the heat transfer from the inner medium to the outer medium is measured. The outer fluid flows in the opposite, coaxial direction to the inner fluid, and the flow rate can be precisely adjusted to accurately emulate downhole conditions.

5. Initial testing results

Tests were initially conducted to establish a baseline for a common VIT size with available field data. A 4.5” x 3.5” VIT with a premium thread was selected for this initial test.

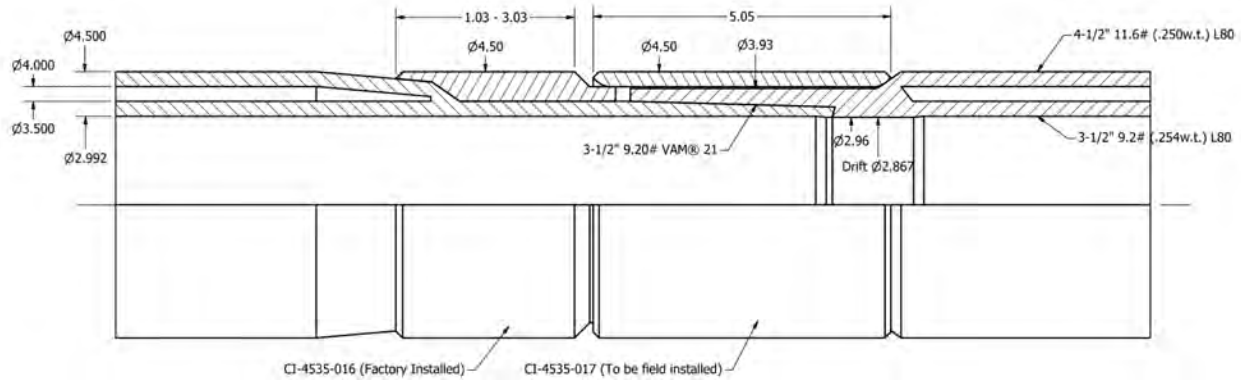

Figure 6: 4.5” x 3.5” VIT with premium threads

The testing program includes tests with the annular fluid flow at four different flow rates (20 gpm, 30 gpm, 40 gpm, and 50 gpm). The flow rate is adjusted after the working fluid stabilized at a set temperature of 180°C. The temperature of the annular fluid (water) was measured at the system's inlet and outlet over a period of 2 hours. After this testing period, the flow rate was adjusted, the oil temperature was re-stabilized, and the test was repeated at the next flow rate. This procedure was repeated multiple times to ensure data consistency.

As shown in the graph below, the temperature difference between the inlet and outlet decreases as the flow rate increases. This predictable trend occurs because higher flow rates allow less time for the fluid to interact with the hotter elements of the VIT. Additionally, the consistent temperature of the VIT working fluid oil (shown in Figure 8) demonstrates that the VIT is in a steady-state

condition. Thus, any change in the temperature of the annular water fluid is due to heat transfer, not external sources.

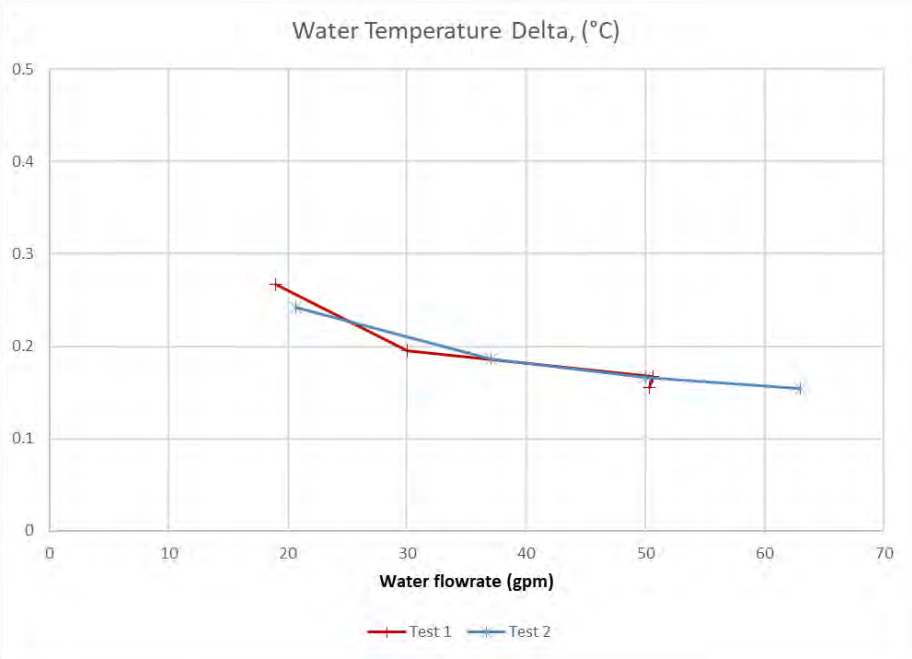

Figure 7: Test results with coupling insulator

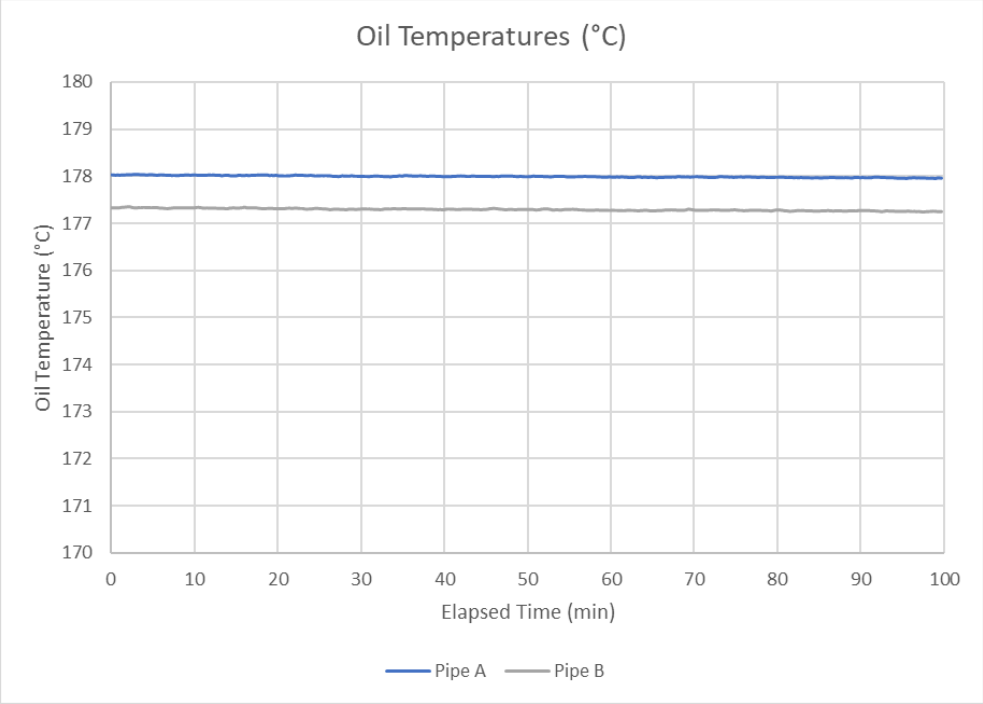

Figure 8: Example of oil temperature measured inside the VIT for the duration of a test (20gpm with insulator)

To calculate the k-value based on these results, the temperature differential between the inlet and outlet temperature of the water is compared to the stabilized oil temperature inside the inner pipe of the VIT.

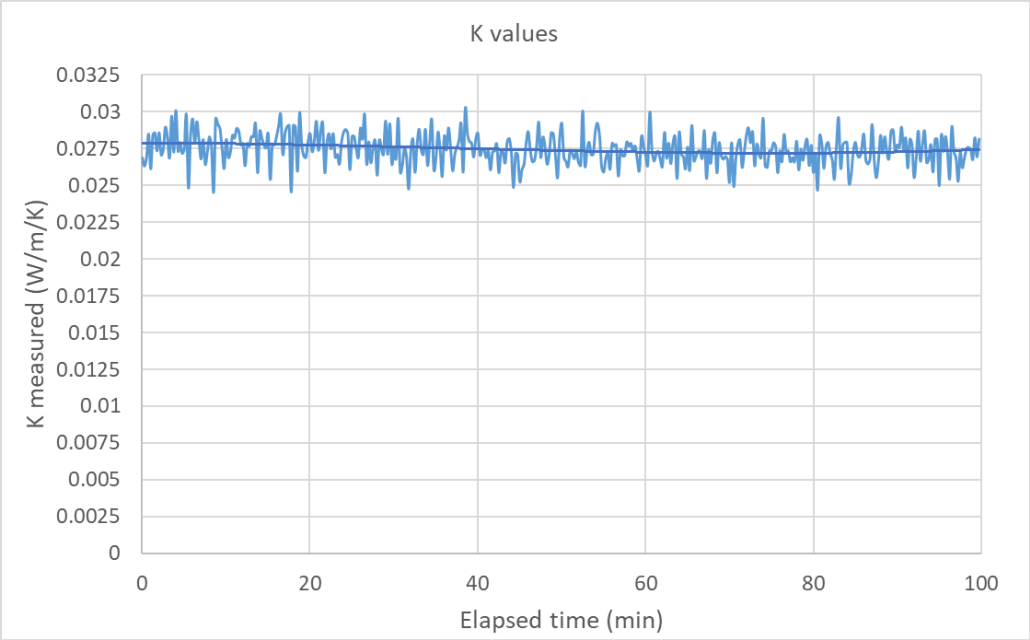

Figure 9: K-value result stability over duration of test (50gpm test with insulator)

As shown in the chart below, the k value is calculated and plotted for the multiple tests at each flowrate. The proximity of these k values indicate that the 1) VIT test bench is consistent and repeatable and 2) the k value slightly changes with an increase of flow rate.

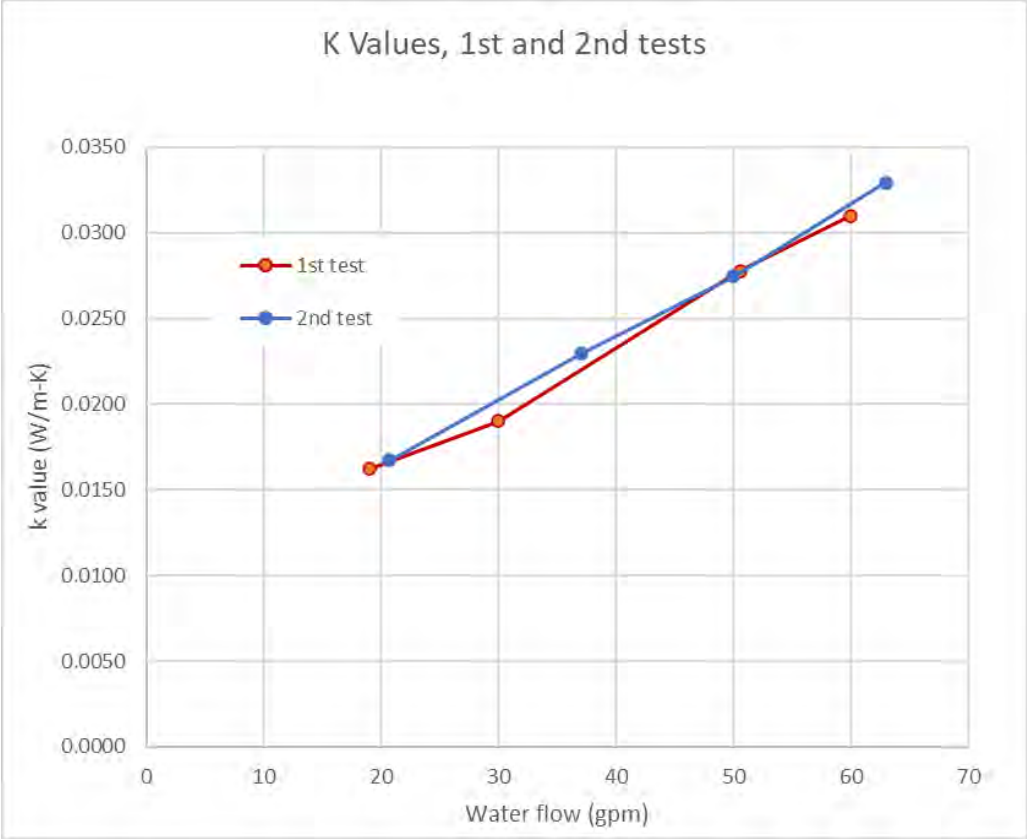

Figure 10: K-value results at different flow rates

6. Additional testing

Following this initial testing condition, additional tests are ongoing to further correlate the testing data to known, measured data.

The initial test configuration featured a 4.5” x 3.5” VIT with a connection insulator, tested to 4 different water flowrates. The next planned test will repeat the same temperatures and flowrates with the same VIT, but the coupling insulator surrounding the connection will be removed. This test (denoted in Figure 11 as “Test 2”) will determine the increase in thermal conductivity with the removal of the coupling insulator. The final test in the program (Test 3) will repeat the same flowrates with the same configuration of VIT, but will only include the vacuumed pipe without a connection. This test will provide a baseline and comparison to the thermal conductivity of the vacuumed pipe, which is directly measured during the manufacturing process.

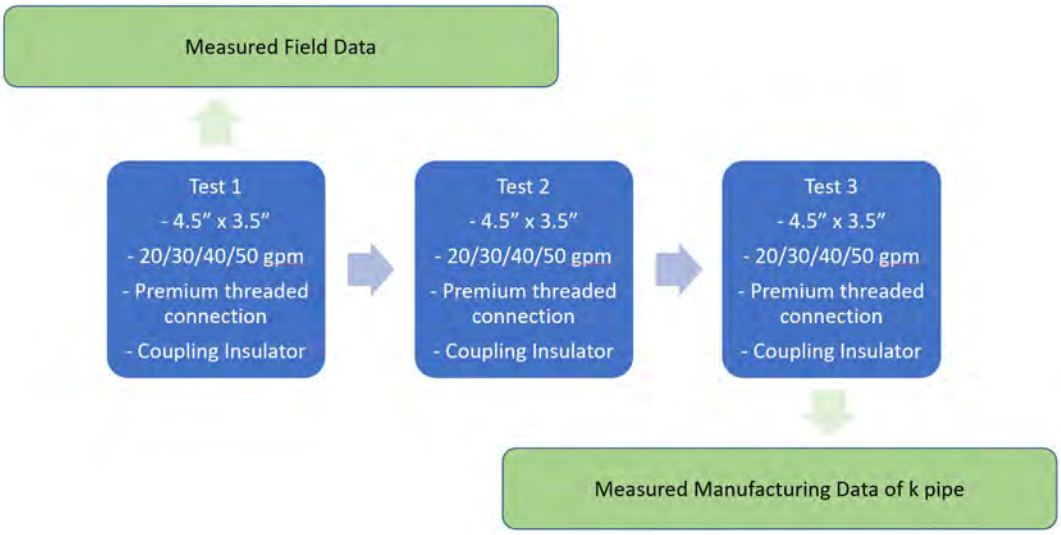

Figure 11: Test program details and objectives

7. Data application

The testing conducted with the VIT test bench provides significantly more accurate k-value measurements of VIT systems, better simulating downhole environments. Moreover, the results have been used to enhance the accuracy of VIT and geothermal predictive modeling. Upcoming field tests, scheduled for completion by the end of 2024, will allow for further comparison and fine-tuning, providing more precise simulations for potential geothermal applications.

This improvement in accuracy also allows for better VIT optimization in wells, which can be achieved in several ways. Firstly, the overall string length can be adjusted to ensure the optimum surface temperature for either heat generation or direct use. The increased confidence in VIT performance reduces the margin of error, thereby minimizing resource wastage. Additionally, improved k-value accuracy and VIT predictive modeling can identify new sectors of the geothermal market that could benefit from insulated pipes. The performance model is directly linked to techno-economic analysis, offering more precise and appealing LCOE and ROI figures for potential users. The VIT test bench enables dynamic k-value testing, verifying thermal conductivity at various temperatures and flow rates, a first for the industry. This further enhances the accuracy of predictive modeling and optimization under specific operating conditions.

8. Next steps

Following the benchmark testing performed on the 4.5" x 3.5" premium connection VIT for proper calibration and tuning, the VIT test bench has numerous applications. Firstly, the bench can be adapted to emulate specific user conditions, enabling physical validation and qualification testing of VITs before field deployment. This not only provides end users with confidence in the product's performance but also enhances the accuracy of predictive modeling.

Additional testing is planned for Vallourec's super-hot rock VIT connection, designed for use at temperatures up to 400°C. This connection offers premium insulative properties without the need for a thermoplastic (PTFE) coupling insulator, which currently lowers the overall temperature rating to 250°C.

REFERENCES

1. Higgins, B., Muir, J., et al. "GreenFire Energy Closed-Loop Geothermal Demonstration at the Coso Geothermal Field." *GRC Transactions, Vol. 43, 2019*, Geothermal Rising Conference, 2019.
2. Kolo, I., Brown, C.S., et al. "A comprehensive review of deep borehole heat exchangers (DBHEs): subsurface modelling studies and applications." *Geothermal Energy*, (2024, 12-19).
3. Śliwa, T., Kruszewski, M., et al. "The application of vacuum insulated tubing in deep borehole heat exchangers." *AGH Drilling Oil Gas*, 2017.
4. Ceyhan, I., Vasantharajan, S., et al. "Novel Experimental Method to Determine the Performance of Vacuum Insulated Tubing VIT for Deepwater Applications." *Offshore Technology Conference*, 2021. OTC-31260-MS
5. Smith, B.G., Williams, T. "Vacuum Insulated Tubing got Enhanced Thermal Performance in Deepwater and Arctic Environments." *Offshore Technology Conference*, 2012.

Influence of Reservoir Convection on Heat Extraction with Closed-Loop Geothermal Systems

Raquel S.P. Hakes[1], Radoslav Bozinoski[1], Koenraad F. Beckers[2], Adam Ketchum[2]

[1]Sandia National Laboratories*, Livermore, CA, USA

[2]National Renewable Energy Laboratory†, Golden, CO, USA

Keywords

Closed-loop geothermal, advanced geothermal systems, next-generation geothermal, reservoir simulations, reservoir convection

ABSTRACT

Over the past few years, advancements in closed-loop geothermal systems (CLGS), also called advanced geothermal systems (AGS), have sparked a renewed interest in these types of designs. CLGS have certain advantages over traditional and enhanced geothermal systems (EGS), including not requiring in-situ reservoir permeability, conservation of the circulating fluid, and allowing for different fluids, including working fluids directly driving a turbine at the surface. CLGS may be attractive in environments where water resources are limited, rock contaminants must be avoided, and stimulation treatments are not available (e.g., due to regulatory or technical reasons). Despite these advantages, CLGS have some challenges, including limited surface area for heat transfer and requiring long wellbores and laterals to obtain multi-MW output in conduction-only reservoirs.

CLGS have been investigated in conduction-only systems. In this paper, we explore the impact of both forced and natural convection on the levels of heat extraction with a CLGS deployed in a hot wet rock reservoir. We bound potential benefits of convection by investigating liquid reservoirs over a range of natural and forced convective coefficients. Additionally, we investigate the effects of permeability, porosity, and geothermal temperature gradient in the reservoir on CLGS outputs. Reservoir simulations indicate that reservoir permeabilities of at least ~100 mD are required for natural convection to increase the heat output with respect to a conduction-only scenario. The

*Sandia National Laboratories is a multimission laboratory managed and operated by National Technology and Engineering Solutions of Sandia, LLC., a wholly owned subsidiary of Honeywell International, Inc., for the U.S. Department of Energy National Nuclear Security Administration under DE-NA0003525. SAND2024-07551C.

†This work was authored in part by the National Renewable Energy Laboratory, operated by Alliance for Sustainable Energy, LLC, for the U.S. Department of Energy (DOE) under Contract No. DE-AC36-08GO28308.

impact increases with increasing reservoir temperature. When subject to a forced convection flow field, Darcy velocities of at least 10^{-7} m/s are required to obtain an increase in heat output.

1. Introduction

In this paper, we present numerical reservoir simulation results exploring the impact of natural and forced convection on closed-loop geothermal heat extraction. Closed-loop geothermal systems (CLGS), also known as advanced geothermal systems (AGS), rely on subsurface heat extraction through a pipe-in-pipe (coaxial) or U-loop type heat exchanger with the heat transfer fluid staying within the heat exchanger and not entering the surrounding reservoir rocks. These designs have recently gained increased interest and investment as a "geothermal anywhere" technology as they do not require in-situ reservoir permeability or fluid pathways—they can be designed for drilling into impermeable reservoirs or can target permeable, convection-dominated reservoirs. However, by constraining the fluid within the heat exchanger, the heat transfer area is limited, which impacts the thermal performance of the system.

When evaluating the performance of CLGS, the focus is often on systems located in conduction-only media (e.g., White et al. 2024; Beckers et al. 2022; Beckers and Johnston 2022; Beckers et al. 2023). Here, we simulate a porous medium instead of impermeable dry rock and investigate how much heat extraction increases with the presence of water flow through the porous medium. We conducted a range of simulations and explored the impact of porosity, permeability, and reservoir temperature on overall heat extraction through both natural and forced convection. Natural convection is driven by temperature gradients in the hot wet rock, while forced convection represents the situation when there is a natural background flow in the porous medium. While forced convection is not common, there are some geothermal reservoirs where these conditions may occur.

Two prior studies investigated CLGS in a porous medium subject to natural convection. Oldenburg et al. (2016) considered a U-loop design with one 1.1-km-long lateral at 2.5 km depth and bottom-hole temperature of 250°C. CO_2 as heat transfer fluid was injected at the surface at 60 kg/s and 75°C. The scenario with negligible permeability (heat conduction-only) resulted in a long-term heat production of about 1.5 MW_{th}. The scenario with a permeable zone (permeability of 10^{-10} m^2 or about 100 D) of 40 m thick around the lateral resulted in long-term heat production of about 3.5 MW_{th}. Similarly, White et al. (2024) simulated a U-loop configuration with a 4-km-long lateral at 2.5 km depth and bottom-hole temperature of 190°C. Water was injected at 30°C and 15 kg/s. Available power (i.e., net exergy production) after 25 years of operation in a heat conduction-only reservoir is about 290 kW_e. When simulated in a porous medium allowing for natural convection, the available power increases with increasing permeability. For a permeability of 50 mD, the available power after 25 years is about 295 kW_e, while for a permeability of 500 mD, it increases to about 530 kW_e.

We chose a subset of possible convection conditions to explore here: a U-tube configuration for a hot wet rock reservoir with liquid water between an impermeable overburden and underburden. Liquid reservoirs are common. We did not simulate a specific location. Instead, we assumed a simplified reservoir with uniform matrix porosity and permeability, most similar to a sedimentary basin. However, geothermal wells can be deployed in a variety of systems, including steam reservoirs and magmatic reservoirs.

The paper consists of five sections including this introduction section. Section 2 presents our research methods and discusses the models developed using two simulation codes, Sierra Thermal/Fluids: Aria, a generalized Galerkin finite element method code (Notz et al. 2016) and COMSOL (COMSOL 2019). Natural convection and forced convection results are presented in Sections 3 and 4, respectively. Overall conclusions are provided in Section 5.

2. Simulation Methods

Simulations exploring the impact of convection were conducted in both Aria and COMSOL. A U-tube configuration was chosen, as it was anticipated that natural convection will have the largest impact on a horizontal well, and we aimed to bound the potential impacts of convection. The Aria simulations explored reservoir heat extraction through a full U-tube configuration. The COMSOL simulations focused on a 100-m-long section of a lateral of a U-tube configuration. The different codes were used to explore different conditions in the parameter space, then compared for two analogous configurations. Using the two codes allows us to compare the independently developed models with one another to see how well they agree with one another. A good agreement in this benchmarking gives us confidence that we can trust the results to have broader applicability.

2.1 Aria Simulations

The impact of natural convection on a U-loop configuration was investigated. The computational domain is made up of two 2.5-km vertical wells that are modeled as hot dry rock (conduction-only). These connect to a 1-km horizontal section of hot wet rock (conduction and convection) that is made up of permeable layers. The impermeable domain is modeled as 2D axisymmetric with a radius of 150 m. The permeable domain is investigated through a 3D numerical simulation and measures 1 km × 250 m × 250 m. Relatively higher permeability hot wet rock is 125 m thick (white and yellow blocks in Figure 1) sandwiched between an overburden and underburden of lower permeability hot dry rock. The permeable and impermeable sections are decoupled from each other, except through the heat exchanger, which runs the entire length of the domain and has a diameter of 44.45 cm (17.5 in.), a standard large well size.

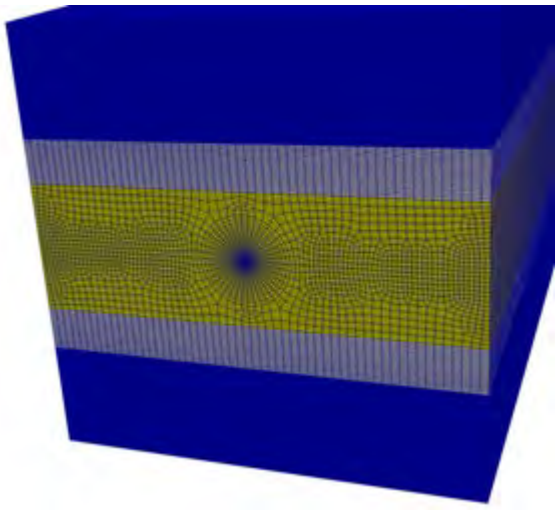

Figure 1: Computational domain in Aria for the permeable reservoir

The mass and heat flow in the hot wet rock are modeled as single-phase Darcy flow with the formation fluid modeled as pure liquid water. The variation of fluid density with temperature due to the heat exchanger gives rise to buoyantly-driven convection currents, drawing warmer water to the heat exchanger and allowing cooled water to pool below the heat exchanger. The domain is initially at hydrostatic pressure, and the initial formation temperature is set according to the depth and geothermal gradient. The vertical sides are impervious to heat and mass flow and can be considered symmetry planes. The top and bottom surfaces are maintained at the initial temperatures.

The working fluid for the heat exchanger was liquid water and was injected into the borehole at 30°C. Parameters that were studied include the mass flow rate of the working fluid (2 and 10 kg/s), porosity of the rock (1%-25%), permeability of the rock (1 mD-20 D), and the geothermal gradient within the rock (30°C/km, 60°C/km, and 90°C/km). The lower porosities are consistent with typical deep geothermal reservoirs and the higher (10%-25%) were chosen to match what was investigated by Oldenburg et al. (2016). The lower end of the permeability range was selected to match what is seen in various well locations. The upper values were chosen to evaluate what conditions are necessary to see a significant impact from convection. The geothermal gradient values are consistent with typical values found within the first few kilometers' depth of the crust. We simulated heat extraction over 20 years and compared output temperature over time and heat output at the 20-year mark for the different porosities, permeabilities, and geothermal gradients.

2.2 COMSOL Simulations

2.2.1 Natural Convection

We developed models in COMSOL to explore the impact of natural convection on heat extraction with water flowing through a pipe in a porous medium (Figure 2). The heat exchanger has a length of 100 m and diameter of 6 in. (15.2 cm) and is placed at the center of the porous medium, with dimensions of 250 m × 100 m × 250 m. The porous medium was placed at a depth of 3.5 km (center of the block). A 62.5-m-thick impermeable layer of overburden and underburden is placed on top and below the porous medium, respectively. We simulated three temperature gradients: 30°C/km, 60°C/km, and 90°C/km, which correspond to temperatures of, respectively, 130°C, 235°C and 340°C at 3.5 km depth (assuming 25°C at the surface). Water is injected in the pipe at 30°C and 2 kg/s. We imposed a temperature-dependent density function for the water in the porous medium to induce a pressure gradient (due to changes in temperature), resulting in natural convection currents. We also specified a temperature-dependent viscosity correlation for the water in the porous medium. The water in the pipe and porous medium is assumed to have a constant specific heat capacity of 4,200 J/kg/K. The rock has a dry thermal conductivity of 2.83 W/m/K. The flow boundary is set to a no-flow boundary condition for all exterior surfaces. The temperature at the top (x = 187.5 m), bottom (x = -187.5 m), left (y = -125 m) and right (y = 125 m) boundary is set to a constant boundary temperature condition (equal to the initial rock temperature). The other surfaces are set to a no-heat flux boundary condition (i.e., at the front (z = -50 m) and back (z = 50 m) domain boundaries). No fluid can enter or leave the porous medium. We simulated heat extraction over 20 years and compared heat output at the 20-year mark for different temperature gradients, permeabilities and porosities.

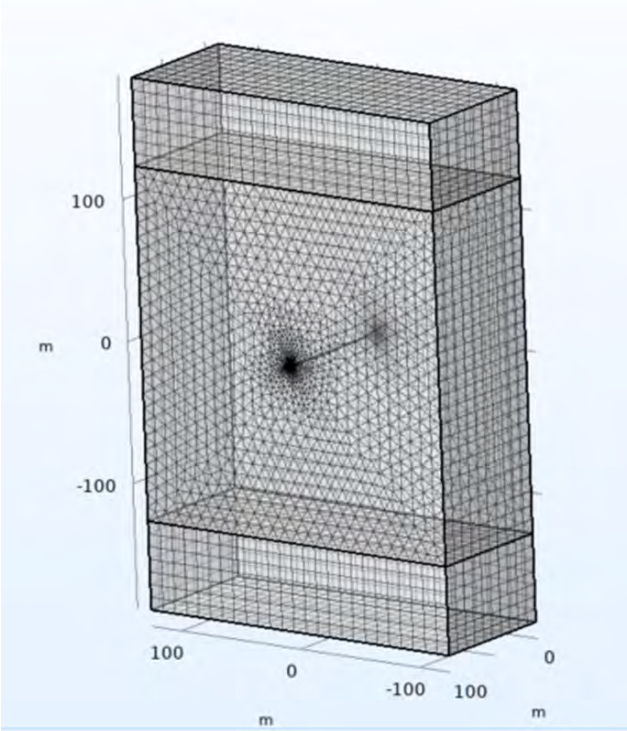

Figure 2: Computational domain in COMSOL for studying natural convection

2.2.2 Forced Convection

Forced convection represents the scenario where a natural background flow exists in the reservoir. In some reservoirs, pressure differentials can naturally occur, forcing in-situ water to flow through the reservoir. We developed a model in COMSOL to investigate the impact of a forced convection flow field on the heat extraction with water flow through a pipe placed in a porous medium (Figure 3). The heat exchanger has a length of 100 m and diameter of 6 in. (15.2 cm) and is placed at the center of a 100 m × 100 m × 50 m porous medium block. The porous medium is initially at a uniform temperature of 100°C. Water is injected in the pipe at 50°C and 2 kg/s. A uniform and constant Darcy flow is imposed through the porous medium entering on one end (at a constant 100°C) and leaving the domain at the other end. A uniform flow field is a highly simplified assumption but nonetheless can provide insights on the level of water flow needed to see an impact. The water in the pipe and porous medium is assumed to have constant properties with density of 1,000 kg/m^3 and specific heat capacity of 4,200 J/kg/K. The rock has a dry thermal conductivity of 2.83 W/m/K. We simulated heat extraction over 20 years and compared the heat output for different Darcy fluid flow velocities.

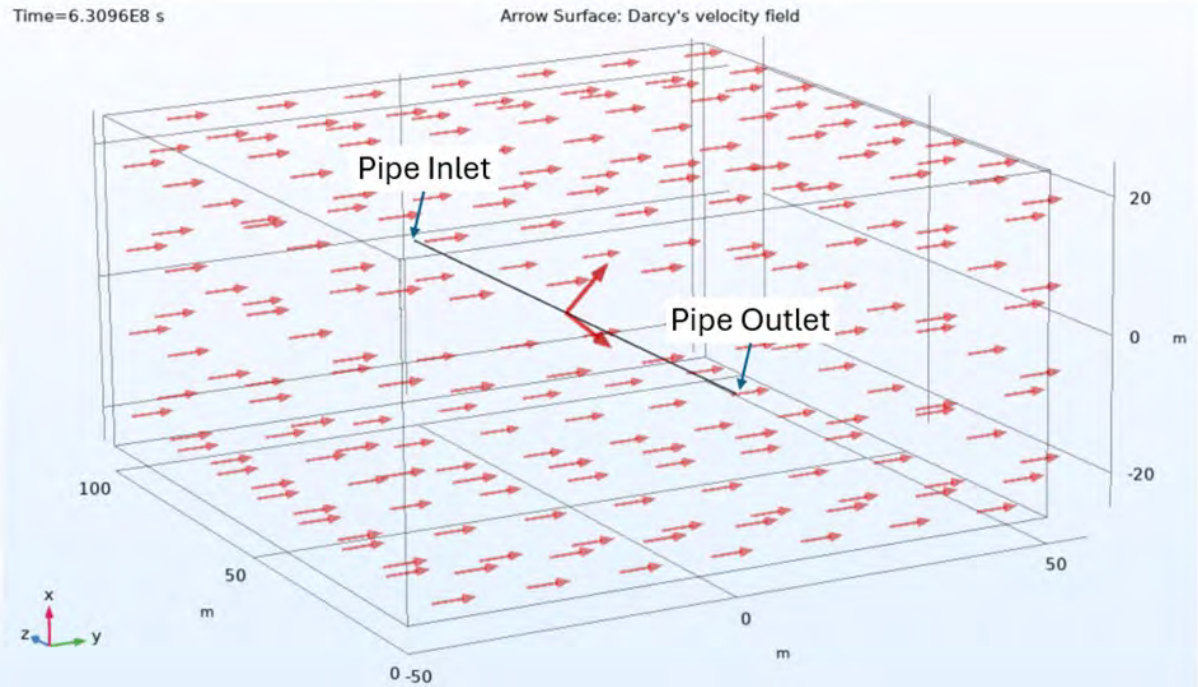

Figure 3: Computational domain in COMSOL for studying forced convection

3. Natural Convection Results

3.1 Aria Results

Qualitative indication of convection can be seen by visualizing the flow field within the permeable hot wet rock (shown in Figure 4). Variation in fluid density due to temperature causes cooler water to flow downward, as warmer water is drawn up to the heat exchanger. This density difference gives rise to a pair of counter-rotating, buoyantly-driven convection cells on either side of the tube. The strength of these vortices varies with the different convective conditions (primarily affected by permeability and temperature gradient) and drives the temperatures produced by the heat exchanger.

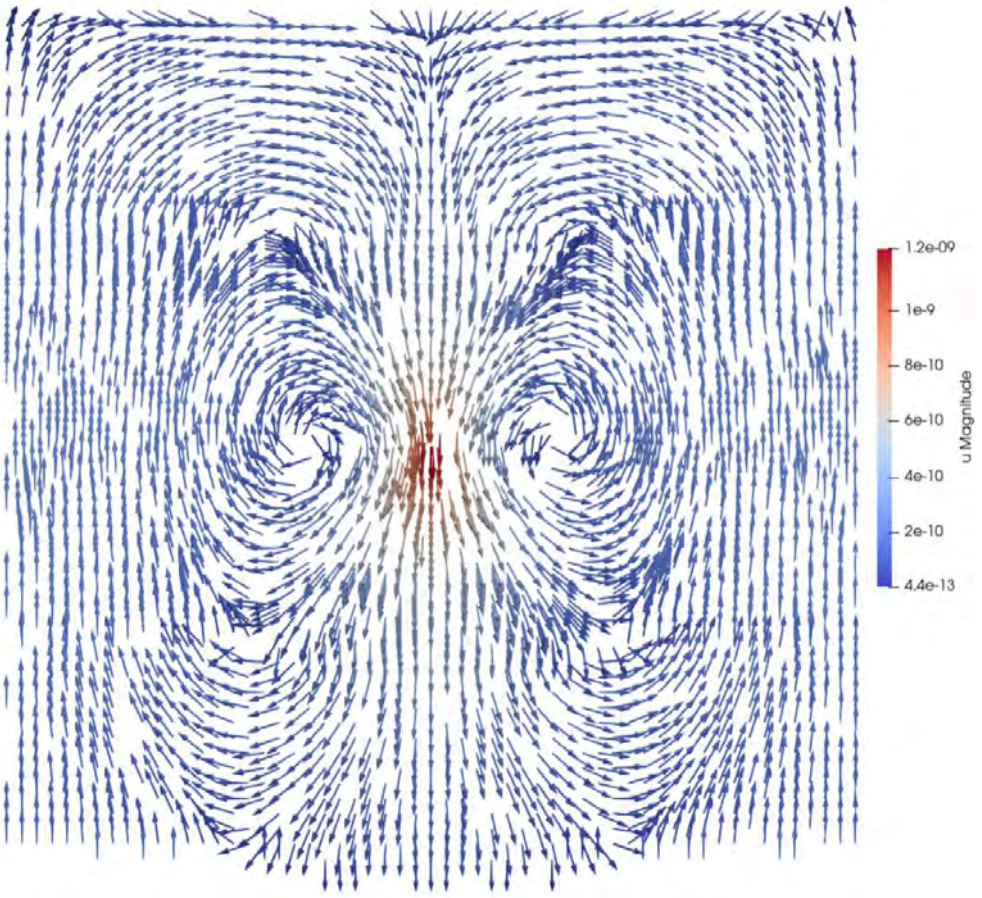

Figure 4: Cooled, denser formation water induces a downward flow near the closed-loop heat exchanger, giving rise to a pair of counter-rotating, buoyantly-driven convection cells on either side of the tube. Heat exchanger (not shown) is in the center of the velocity field, into/out of the page.

We explored the qualitative and quantitative impact of convection on (1) the steady 20-year heat output of the well and (2) the production temperature over the lifespan of the well. Both were compared to a conduction-only case to indicate the potential benefit of convection for different conditions. Figure 5 shows the increase in heat output from convection compared to conduction for varying permeability and two mass flow rates. At low permeability, there is no increase in heat output over conduction. At 500 mD, there is a low increase (<10% increase in heat output). At 1 D and above, heat output increases with increasing permeability. Notably, the higher mass flow rate of 10 kg/s increases the impact of convection over conduction on heat output. We explore these differences further by investigating the production temperature over the lifespan of the well.

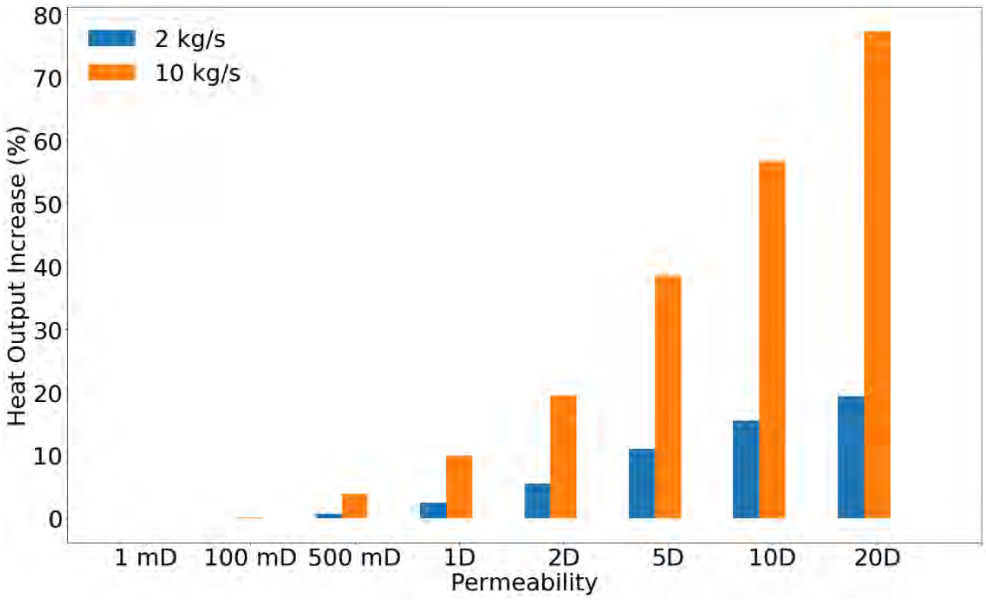

Figure 5: Increase in heat output due to natural convection versus the heat conduction-only scenario for 30 C/km geothermal gradient and 1% rock porosity at working fluid mass flow rates of 2 and 10 kg/s

Figure 6 shows the production temperature over time for the 10 kg/s case shown in Figure 5. As before, we see a minor increase in temperature at 500 mD and higher production temperatures as we increase the permeability. The 10 kg/s flow rate experiences a spike in production temperature that subsequently decreases over the lifespan of the well. The 2 kg/s flow rate (not shown) experiences a similar trend with permeability. The lower flow rate produces higher production temperatures; however, the higher flow rate sees a greater relative impact of convection on production temperature with permeability. These results are consistent with the differences we see with flow rate on the heat output increases.

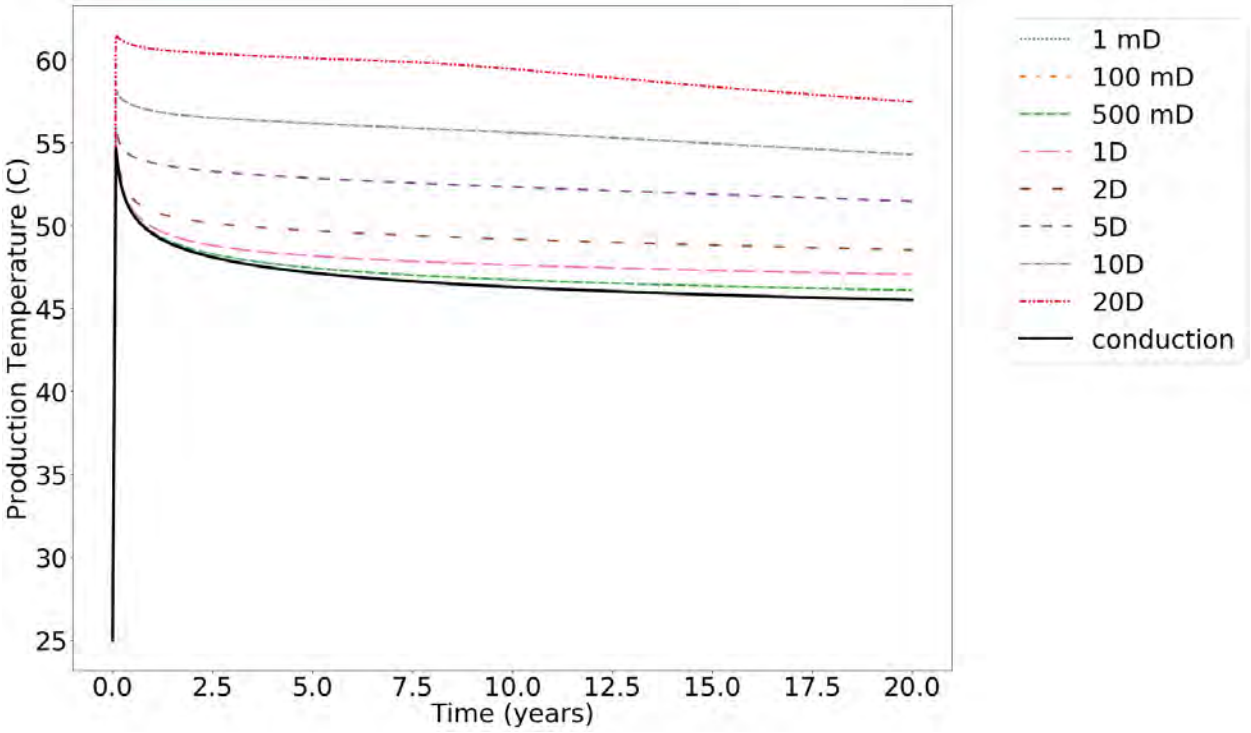

Figure 6: Comparison of production temperatures for varying permeability at 1% rock porosity and a 30 C/km geothermal gradient. Results are shown for a working fluid with a mass flow rate of 10 kg/s. Permeability begins to have a clear impact at approximately 1 D.

Results shown thus far were kept at a constant rock porosity and geothermal gradient. Porosity (increased at a constant permeability) had a negligible impact on production temperatures and heat output; increasing porosity above 1% did not show an increase in production temperature for either mass flow rate at a permeability of 1 D. We also varied the geothermal gradient, which impacted the temperature experienced by the lateral portion of the well in the hot wet rock as well as the vertical portions of the well in the hot dry rock. Figure 7 shows the impact of geothermal gradient on production temperature. Geothermal gradient has the largest impact on production temperature for both conduction and convection cases of any parameters we varied. This is anticipated, as a higher gradient results in a larger temperature difference to drive the convection in the porous rock.

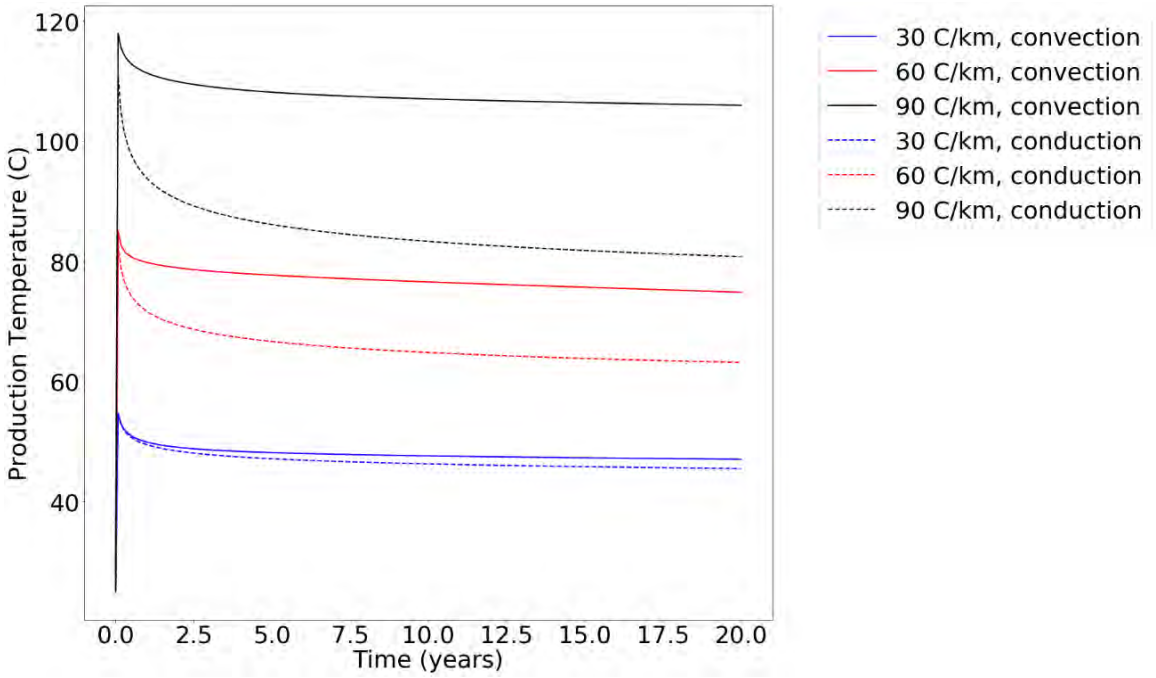

Figure 7: Effects of geothermal gradients for 1 D permeability and 10% porosity for 10 kg/s working fluid mass flow rate. Solid lines indicate the convection cases, while dashed lines indicate the conduction cases.

Both flow rates indicate that convection has a larger benefit when the geothermal gradient is higher. For the 10 kg/s cases, we see production temperatures increases of 1˚C, 12˚C, and 25˚C for 30 ˚C/km, 60 ˚C/km, and 90˚C/km, respectively. We see a similar trend at 2 kg/s, but the benefit of convection for each geothermal gradient is higher for the higher mass flow rate.

3.2 COMSOL Results

Figure 8 presents the long-term increase in heat production relative to the conduction-only scenario for porous medium permeabilities ranging from 1 µD to 1 D (approximately 10^{-18} m^2 to 10^{-12} m^2) and three temperature gradients. An increase of 100% means the heat production has doubled. The results suggest that for this scenario, a minimum permeability of 10 to 100 mD for the higher gradient cases and more than 100 mD for the lower gradient case is required to obtain an increase in heat output with respect to the conduction-only scenario. The boost in heat output increases with higher rock temperatures, a result of the larger density-driven driving force and lower viscosity at higher temperatures. Figure 9 presents the simulation results for different porosities but constant permeability (100 mD) and geothermal gradient (60°C/km). For all porosities considered, the heat output was about 37% higher than the scenario with heat conduction only. Increasing the porosity slightly decreased the boost in thermal output (i.e., increase of 37.6% for 1% porosity vs. increase of 37.2% for 20% porosity).

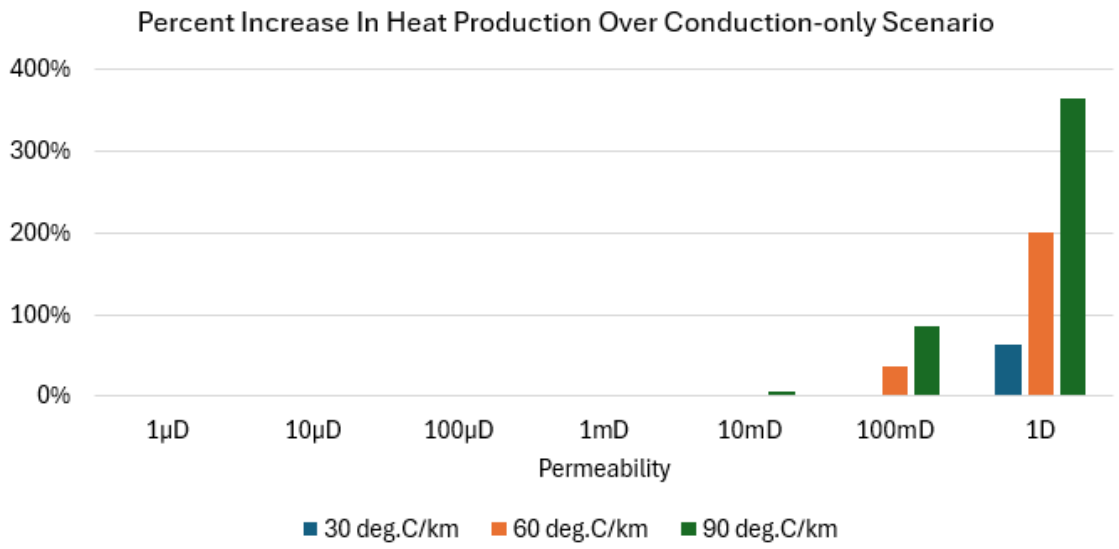

Figure 8: Increase in heat output due to natural convection versus the heat conduction-only scenario for three different geothermal gradients and a range in permeabilities

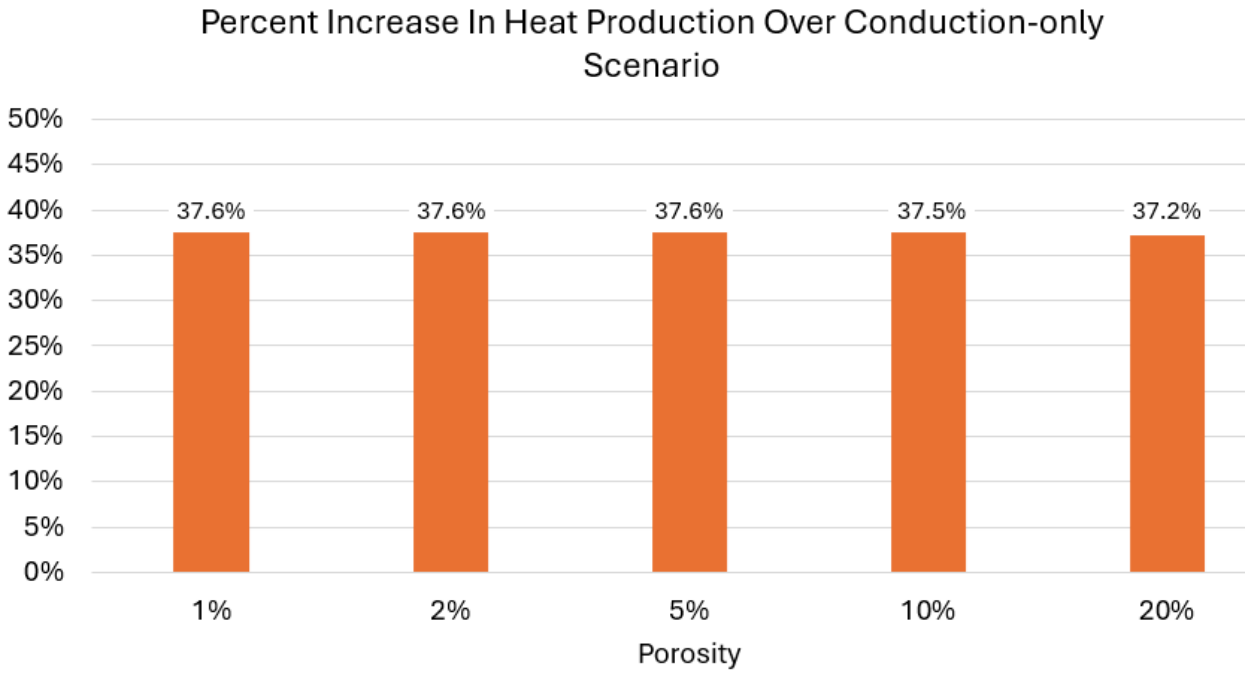

Figure 9: Increase in heat output due to natural convection versus the heat conduction-only scenario for a porosity in the range 1 to 20%. For all scenarios, the geothermal gradient is 60°C/km and the porous medium permeability is 100 mD.

3.3 Comparison Between Aria and COMSOL Simulations

We ran simulations with both Aria and COMSOL to verify the two codes against each other, to determine that results were not dependent on the code used. To confirm the applicability of the results between the two simulation codes, verification cases were run at permeabilities representing low convection (50 mD) and high convection (500 mD). Note that the comparatively high convection case is lower than previously presented results; here, the goal was to investigate code comparisons for realistic rock permeabilities. In Aria, we ran a full U-tube configuration with 2.5 km vertical wellbore lengths and a 1-km lateral length. In COMSOL, we ran the first 100 m of the lateral at a depth of 2.5 km (i.e. the temperatures are consistent with that depth for the geothermal gradient used in the Aria simulation). The difference in domain arose because Aria was run on HPC, while COMSOL was run locally. The production temperature presented from *both* simulations is the temperature 100 m into the lateral. Cases were run with 1 kg/s flow rate of working fluid (water). Because the Aria simulation is a full U-tube configuration, conduction was set to be negligible in the vertical wells; temperatures at the start of the lateral (where the COMSOL simulation begins) varied by less than 1˚C.

Figure 10 shows the results comparing Aria and COMSOL. Models agree well with each other at both permeabilities. At 500 mD, we see a difference of several degrees Celsius, corresponding to a difference of about 10% in heat output. At 50 mD, the predicted temperature difference is negligible. A few differences exist between the Aria and COMSOL model, likely explaining the discrepancy in production temperature for the 500 mD case. Two key differences include: (1) COMSOL only simulates the water density and viscosity as a function of temperature while Area simulates all water properties as a function of both temperature and pressure, and (2) the COMSOL model has about 20,000 mesh elements (and runs on a local computer) while Aria has over 800,000 elements (and runs on high-performance computing machines). The small difference in thermal output at higher permeabilities is deemed acceptable in this study as we investigate high-level trends such as permeability required for natural convection to cause an impact and order of magnitude increase in heat output due to natural convection.

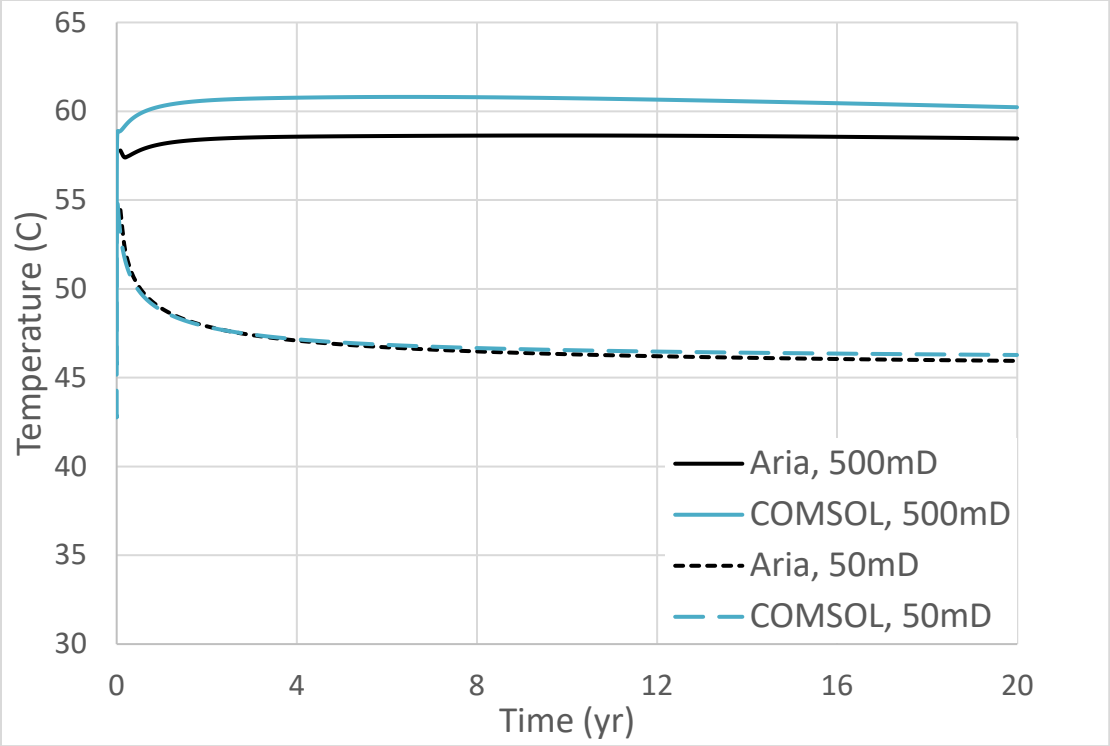

Figure 10: Comparison of Aria and COMSOL results for production temperature for an analogous case. Heat production estimated with both tools agrees within a few percent.

4. Forced Convection Results

Figure 11 presents the increase in thermal output after 20 years of operation (expressed as thermal output with convection versus thermal output without convection) for Darcy flow velocities ranging from 10^{-10} to 10^{-5} m/s. The results indicate that a minimum Darcy velocity of 10^{-7} m/s is required to impact thermal output with heat extraction increasing rapidly with increasing Darcy velocity. A Darcy velocity of 10^{-7} m/s corresponds to a water mass flux of about 10^{-4} kg/s/m^2. Equivalently, water flowing at a Darcy velocity of 10^{-7} m/s will have migrated about 3.15 m after 1 year.

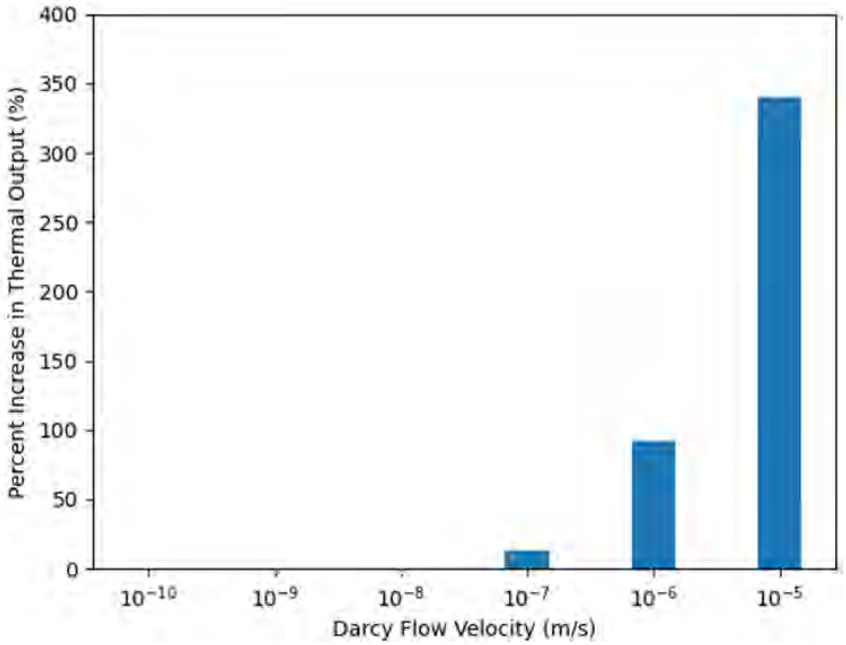

Figure 11: Percentage increase in thermal output with forced convection as a function of Darcy flow velocity. A Darcy velocity of at least 10^{-7} m/s is required to obtain an increase in heat production with convection.

5. Conclusions

In this work, we applied two simulation codes, Aria and COMSOL, to explore the impact of forced and natural convection on production temperature and heat output with closed-loop heat exchangers. At sufficiently high Darcy velocities (either due to an imposed field with forced convection or as a result of buoyancy-driven convection cells with natural convection), the water flow in the reservoir replenishes the removed heat around the heat exchanger, resulting in a boost in production temperature and heat output with respect to the conduction-only scenario.

For studying natural convection, we explored the impact for a range of permeabilities (1 μD to 20 D), porosities (1% to 25%) and geothermal gradients (30 to 90°C/km). We focused on U-loop designs with the horizontal lateral(s) located in a porous medium. Simulation results with both simulation codes indicate an increase in heat output is obtained due to natural convection with a permeability of at least ~100 mD. For higher permeabilities (1 D and larger), the production temperature and heat output rapidly increase with increasing permeability. An increase in reservoir temperature increased the impact of natural convection, while porosity only had a minor effect. Typical permeabilities at 2 km depth in the continental crust are on the order of 1 mD, several orders of magnitude smaller than the permeabilities required for natural convection to have a significant impact on thermal output. Overall, results were very sensitive to natural permeability; thus, the simulation results suggest that the most impact on heat extraction is through higher permeability reservoirs.

In this work, we made several choices to constrain possible range of convection. For example, all simulations considered a permeable hot wet rock section sandwiched between an impermeable overburden and underburden. A single case investigating the removal of the overburden and underburden found negligible differences between the two cases. Thus, one was investigated to constrain the impacts of convection. However, other design and geologic systems are feasible and

warrant further investigation. Additionally, the focus of this work was on water reservoirs. Additional cases in steam reservoirs could be investigated.

Acknowledgement

The authors would like to acknowledge Yaro Vasyliv for model development assistance and Gabriela Bran Anleu for discussions and input, as well as their previous work developing conduction-only models in Aria. Funding provided by the U.S. Department of Energy Office of Energy Efficiency and Renewable Energy Geothermal Technologies Office. This work was authored in part by the National Renewable Energy Laboratory, operated by Alliance for Sustainable Energy, LLC, for the U.S. Department of Energy (DOE) under Contract No. DE-AC36-08GO28308. This paper describes objective technical results and analysis. Any subjective views or opinions that might be expressed in this paper do not necessarily represent the views of the U.S. Department of Energy or the United States Government. The U.S. Government retains and the publisher, by accepting the article for publication, acknowledges that the U.S. Government retains a nonexclusive, paid-up, irrevocable, worldwide license to publish or reproduce the published form of this work, or allow others to do so, for U.S. Government purposes.

REFERENCES

Beckers, K., Vasyliv, Y., Bran-Anleu, G. A., Martinez, M., Augustine, C., and White, M. “Tabulated Database of Closed-Loop Geothermal Systems Performance for Cloud-Based Technical and Economic Modeling of Heat Production and Electricity Generation.” *Proceedings: 48th Workshop on Geothermal Reservoir Engineering*, Stanford University, Stanford, CA (2023).

Beckers, Koenraad F., Nicolás Rangel-Jurado, Harish Chandrasekar, Adam J. Hawkins, Patrick M. Fulton, and Jefferson W. Tester. "Techno-economic performance of closed-loop geothermal systems for heat production and electricity generation." Geothermics 100 (2022): 102318.

Beckers, Koenraad F., and Henry E. Johnston. "Techno-economic performance of Eavor-Loop 2.0." In Proceedings 47th workshop on geothermal reservoir engineering, Stanford, California. 2022.

COMSOL - COMSOL Multiphysics Reference Manual, Comsol, Inc., Burlington, MA, United States (2019) Available at: https://doc.comsol.com/5.5/doc/com.comsol.help.comsol/COMSOL_ReferenceManual.pdf

Notz, P.K., et al. (2016) SIERRA Multimechanics Module: Aria User Manual. Tech. rep. Albuquerque, NM: Sandia National Laboratories.

Oldenburg, C., Pan, L., Muir, M., Eastman, A. and Higgins, B. “Numerical simulation of critical factors controlling heat extraction from geothermal systems using a closed-loop heat exchange method.” *Proceedings: 41st Workshop on Geothermal Reservoir Engineering*, Stanford University, Stanford, California, (2016).

White, M., Vasyliv, Y., Beckers, K., Martinez, M., Balestra, P., Parisi, C., Augustine, C., Bran-Anleu, G., Horne, R., Pauley, L., Bettin, G., Marshall, T., and Bernat, A. “Numerical investigation of closed-loop geothermal systems in deep geothermal reservoirs.” *Geothermics,* 116 (2024).

GRC Transactions, Vol. 48, 2024

Evaluation of Multilateral Well Design and sCO2 for Closed Loop Geothermal Systems

Orkhan Khankishiyev[1], Gurban Hasanov[1], Elvin Ismayilov[1], Yuxing Wu[1], Hamidreza Karami[1], Saeed Salehi[2]

[1]Well Construction Technology Center, University of Oklahoma, Norman, OK, USA

[2]Lyle School of Engineering, Southern Methodist University, Dallas, TX, USA

Keywords: *CLGS, multilateral, geothermal, supercritical CO2, thermal, flow, model*

Abstract

The super-hot enhanced geothermal systems were simulated to generate remarkably high megawatts of electricity per well, while in practice, the extreme underground conditions proved to be challenging for long-term production operations. This paper presents a comprehensive investigation into Multilateral Closed Loop Geothermal Systems (CLGS) using water and supercritical CO2, targeting enhanced power generation in high-temperature geothermal environments up to 350°C, while eliminating production issues such as heavy corrosion and scale formation.

Focused on optimizing system performance and ensuring well integrity, the study employs advanced flow and thermal models alongside mechanical simulation models to investigate the heat production performance of CLGS under different well design and production settings and examine the behavior of casing and cement under the subsurface temperatures. By exploring multilateral well completion techniques and varying operational parameters such as the number of laterals, injection pressure, and mass flow rate, the research identifies strategies to maximize energy recovery and minimize the levelized cost of electricity.

Significant enhancements in power generation are demonstrated, particularly with the use of supercritical CO2, which despite its lower specific heat capacity, achieves higher temperature outputs at increased resource temperatures, effectively lowering electricity costs. Sensitivity analyses highlight the critical impact of well design on system efficiency, revealing optimal flow rates and the importance of insulated tubing to prevent heat loss. Structural modeling results further indicate potential failure risks due to stress concentrations at crucial lateral junctions in the well architecture. Key findings include a production temperature decline of 15-20°C after 20 years and significant economic benefits from increasing resource temperatures and the number of lateral sections. The paper underscores the potential of CLGS to significantly improve the economic and operational sustainability of geothermal power generation, offering robust insights into the strategic deployment of these systems in challenging geothermal environments.

1. Introduction

The demand for sustainable energy is increasing with the rising population and growing global economy. Fossil fuel-generated energy has the highest consumption records over the last century, significantly impacting the manmade release of carbon dioxide into the atmosphere (Ritchie et al., 2024). Despite its potential as a cost-effective source of energy production, geothermal energy utilization remains notably low, comprising a mere 0.24% of the global energy consumption in 2022 (IEA, 2023). The theory and calculations on paper indicate that the planet Earth has an enormous amount of sustainable and recoverable geothermal energy that is capable of supplying heat and electricity to humanity for a long time (Tester et al., 2006). Special emphasis should be placed on the term “recoverable” which heavily relies on the existence of sophisticated technology. The enthalpy recovery efficiency of the existing geothermal production wells decreases over time due to limited well depth and technology (Soltani et al., 2019).

Multilateral closed-loop geothermal systems, also known as Advanced Geothermal Systems (AGS), offer a promising approach for heat extraction from low-permeability formations, which are more common than highly permeable hydrothermal systems. These systems operate by circulating fluids through a closed-loop wellbore system, exchanging heat with the surrounding rock without permeating the reservoir. While CLGS has been proposed for nearly a century, recent attention and commercial investment have revitalized interest in their potential. Proponents highlight advantages such as minimal need for reservoir stimulation, reduced risk of induced seismicity, and the ability to repurpose abandoned wells or extract heat without producing reservoir fluids. However, challenges remain, including ensuring sufficient contact area with the rock for effective heat extraction and managing the costs associated with drilling and connecting multiple loops of horizontal wells. Given the significant debate surrounding the feasibility, performance, and cost-competitiveness of CLGS, a comprehensive and independent evaluation of their techno-economic performance is essential in guiding future investments and developments in closed-loop geothermal technology.

There are several sophisticated multilateral CLGS designs proposed by various companies around the world but most of them rely on the further development of the already advanced technologies to enable the realization of concepts such as U-shaped well drilling and application of exotic materials. This study investigates the feasibility of closed-loop geothermal systems completed with tried and tested multilateral well technologies using structural, fluid flow/thermal, and techno-economic models. In the subsequent sections, detailed descriptions of the models employed in this study are provided, including the finite-element structural model, dynamic multiphase flow/thermal model, and techno-economic model. Next, the results are presented, and their implications are discussed accordingly. Specifically, the well integrity aspects are analyzed, flow and thermal performance are studied, and economic evaluation is conducted. Sensitivity analyses are provided to study the impact of well design, number of lateral sections, and subsurface temperature. Finally, conclusions are drawn based on the findings in the last section.

2. Literature Review

2.1 Geothermal energy resources

Geothermal energy, stemming from the Earth's internal heat content, presents diverse resources for power generation (Cheng, 1979). This internal heat originates from both residual heat from planetary accretion and the ongoing radioactive decay of isotopes within the Earth's crust (Turcotte

& Schubert, 2002). The Earth's mantle, exhibiting plastic behavior due to high temperatures and pressures, facilitates convective movements, leading to varying temperature gradients. Typically, the geothermal gradient through the crust ranges between 25 to 30 °C per km of depth in most of the world. The conductive heat flux averages 0.1 MW/km². These values are much higher near tectonic plate boundaries where the crust is thinner (Pollack et al., 1993). They may be further augmented by combinations of fluid circulation, either through magma conduits, hot springs, or hydrothermal circulation. Earth's interior temperature and pressure are high enough to cause some rock to melt and the solid mantle to behave plastically. Parts of the mantle flow upward since it is lighter than the surrounding rock. Temperatures at the core-mantle boundary can reach over 4000 °C (7200 °F) (Lay et al., 2008).

The Geovision report by the U.S. DOE (2019) provides a detailed classification of geothermal resources and applications accordingly. Hydrothermal systems are natural reservoirs of hot water or steam located beneath the Earth's surface. These systems occur when water percolates deep into the Earth's crust, heats up, and then rises to the surface through fractures and faults, forming hot springs, geysers, and fumaroles (Browne, 1978). Enhanced Geothermal Systems (EGS), on the other hand, involve engineering techniques to create or enhance geothermal reservoirs where natural conditions are not optimal. This typically involves drilling deep into the Earth's crust and fracturing the rock to create pathways for fluid circulation. Water is injected into the fractured rock, where it heats up by the surrounding heat sources, and then extracted to the surface to generate electricity (Olasolo et al., 2016). Distinct from the systems mentioned above, the Closed Loop Geothermal Systems (CLGS) utilize heat exchange technology to transfer heat between the Earth and a closed-loop fluid circulation system. These systems typically involve drilling boreholes into the ground, circulating a heat transfer fluid through underground pipes, and then transferring the heat to a heat exchanger at the surface to generate electricity or provide heating and cooling for buildings (Tester & Smith, 1977). The CLGS provides full isolation of the working fluid from contacting the surrounding formations or reservoir fluids, only allowing the heat transfer to occur from the formation through the well cement and casing to the working fluid (Hecht-Méndez et al., 2013).

2.2 Types of geothermal power plants

Geothermal power plants are used to convert thermal energy into electrical energy using steam turbines (DiPippo, 2012). There are three main types of geothermal power plants (See Figure 1), and they employ different technologies based on subsurface fluid characteristics and temperatures (U.S. DOE, 2019). Dry steam, flash steam, and binary cycle power plants are the primary types utilized. Dry steam power plants directly utilize high-temperature hydrothermal fluids, primarily composed of steam, to drive turbines and generate electricity (Zarrouk & Moon, 2014). Flash steam plants, the most prevalent, exploit high-pressure fluids from underground reservoirs, inducing rapid vaporization in the flash tank and sending the vapor to drive turbines (Mosaffa & Zareei, 2018). Binary-cycle power plants, capable of utilizing lower temperature resources, employ a secondary fluid with a lower boiling point than water. This fluid, heated by geothermal fluids through a heat exchanger, undergoes vaporization to drive turbines and produce electricity (Ghasemi et al., 2013).

While conventional and closed-loop geothermal technologies offer avenues for thermal and electric energy production, they face significant limitations in accessing the vast potential of geothermal resources. Research indicates that only a small fraction, approximately 2%, of the

Earth's geothermal resources are accessible through conventional means, primarily due to the limited availability of permeable regions conducive to traditional geothermal technologies (Geiser et al., 2016; Khankishiyev et al., 2023a). Consequently, a substantial portion of geothermal energy remains untapped, particularly within the hot dry rock formations lying beneath impermeable layers. For instance, a comprehensive study in 2006 highlighted that the identified geothermal capacity in the United States stood at 2.8 GW, whereas an additional 25 GW of resources were identified, with an estimated 90 GW more suspected to be available (Tester et al., 2006). Despite these vast opportunities, technological advancements are imperative to harness this potential effectively (Khankishiyev, 2024). As of the end of 2023, global installed geothermal power generation capacity across 24 countries stood at 16.1 GW, with the United States alone accounting for 3.8 GW (Ediger & Akar, 2023). However, with projects planned or under development, geothermal energy could potentially become accessible in up to 82 countries, indicating a growing global interest and potential for expansion in the geothermal energy sector (Lund et al., 2022).

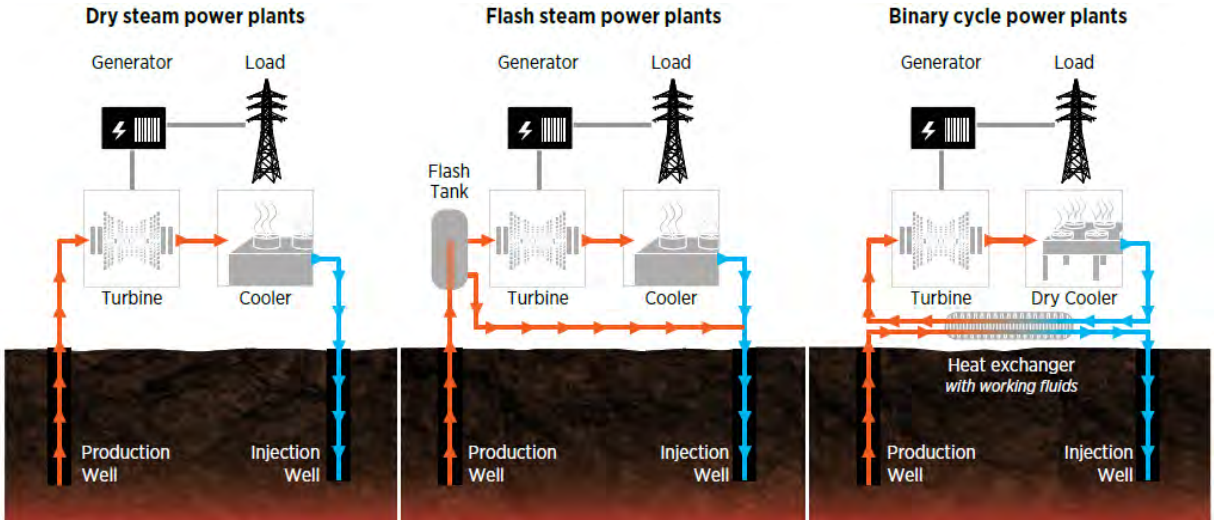

Figure 1: Geothermal power-plant configurations employed based on subsurface fluid characteristics and temperatures: dry steam, flash steam, and binary cycle. Although the illustration uses the production and injection well that is typical for the EGS, these power plant configurations are being used for hydrothermal and CLGS applications as well. (U.S. DOE, 2019)

2.3 Problems associated with the Hydrothermal and Enhanced Geothermal Systems

Geothermal energy has long been recognized as a sustainable power source, yet its development is not without significant challenges and costs (Khankishiyev & Salehi, 2023; Vivas et al., 2020). Operational difficulties extend beyond technical complexities to encompass political, cultural, and environmental concerns. The chemical composition of geothermal fluids poses a considerable risk to well integrity due to potential scaling and corrosion issues, which are prevalent in geothermal utilization (Khankishiyev et al., 2024 (a)). Kruszewski and Wittig (2018) conducted a comprehensive analysis of failure modes in 20 high-enthalpy geothermal wells worldwide, including locations in Iceland, Italy, and Japan. Geothermal wells encounter various production problems that impact efficiency and output. Scaling and mineral deposition reduce fluid flow and heat transfer efficiency, while corrosion of steel components compromises well integrity (Karlsdóttir & Thorbjornsson, 2012; Klapper et al., 2019). Erosion of casing and tubing due to high-velocity fluid flow leads to maintenance needs and reduced well integrity, with erosion-corrosion accounting for significant damages in geothermal systems (Kurata et al., 1992; Nogara & Zarrouk, 2018). Wellbore leaks resulting from casing corrosion or faulty connections can have

severe impacts, including dangerous steam eruptions, highlighting the importance of prompt detection and mitigation (Kalvenes, 2017; Phi et al., 2019). Moreover, reservoir decline over time presents a significant challenge to sustained energy production, necessitating effective reservoir management techniques (Beckers et al., 2017; Zais & Bodvarsson, 1980). The lack of permeability and reservoir fluid is another main limiting factor for the development of EGS in high-potential super-hot dry rock geothermal resources, which can be eliminated by the application of multilateral CLGS (Chen & Jiang, 2015; Hu et al., 2024; Khankishiyev et al., 2023b).

2.4 Multilateral CLGS concepts

Multilateral Closed Loop Geothermal Systems (CLGS) adapt concepts from the oil and gas industry, allowing for the drilling and completion of multiple lateral boreholes within a single main bore (Nalla & Shook, 2004). These systems offer alternative well-construction strategies for vertical, inclined, horizontal, and extended-reach wells, aiding in reducing both capital and operational expenditures while enhancing production. In super-hot deep geothermal wells where costs are high, multilateral designs offer significant economic efficiencies, aligning with the goals of reducing overall project expenses and increasing productivity (Stimac et al., 2010). The Technology Advancement of Multilaterals (TAML) provides a classification system for multilateral junctions, facilitating comparisons between different designs based on support and hydraulic integrity. There are six recognized multilateral completion levels in the industry with higher TAML levels indicating increased complexity and cost (Hogg, 1997). These completion levels can be applied in various well geometries. Figure 2 shows some of the geometries for the multilateral well completions, while there are even more complex designs such as U-shaped wells proposed by several companies (Toews et al., 2020; Vany et al., 2020).

Multilateral CLGS functions by utilizing a circulating fluid inside the laterals to absorb heat stored underground, which is then transported to the surface via the production string and discharged through a heat exchanger (Wang et al., 2020). A greater number of laterals and extended lateral sections provide a higher surface area for better heat exchange. This heat can be utilized for various purposes, including the production of electrical energy or direct applications like district heating or greenhouse heating. To generate power, the extracted heat is typically transferred to a binary process, such as an Organic Rankine Cycle (ORC) or Kalina cycle, especially suited for the expected low to medium fluid temperatures recovered from the geothermal reservoir (Hecht-Méndez et al., 2013). Since the system is isolated from the formation, different types of working fluids such as chemically treated water and supercritical CO2 can be applied to increase the enthalpy recovery efficiency from the rocks (Hu et al., 2020).

2.6 Feasibility of multilateral CLGS

Multilateral CLGS wells offer several advantages over other geothermal technologies. Firstly, they are geographically and geologically independent, as they do not rely on specific hot fluid flow rates or frackable hot rock zones underground. This independence simplifies planning processes and reduces the risk of encountering limiting factors associated with location (Yuan et al., 2021). Secondly, CLGS operates without physical interaction between the circulating fluid and surrounding formations, minimizing environmental impact and eliminating technical issues such as severe corrosion and scale formation (Hu et al., 2020). Lastly, the placement of maintenance-intensive components at the surface ensures reliable long-term operation predictions, with some estimates suggesting operational lifetimes of up to 30 years or more (Beckers et al., 2022).

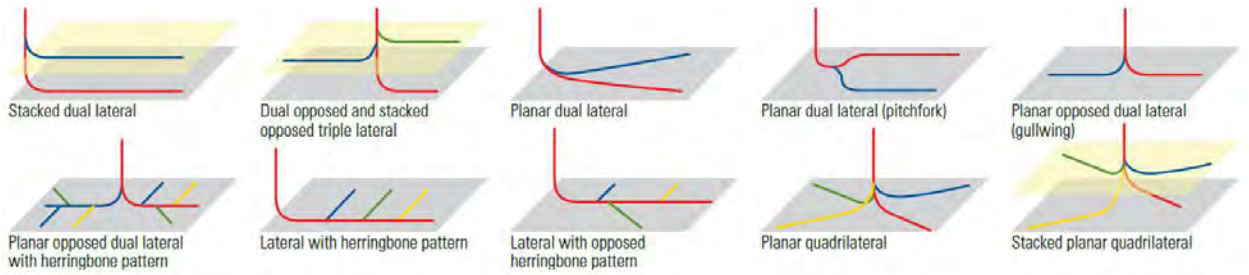

Figure 2: The geometry of a multilateral well is intricately shaped by the production targets, considering their depths and lateral extents. These wells can feature laterals on the same horizontal plane or follow the same vertical direction but at different depths, offering a versatile configuration for targeting multiple zones within a single reservoir. (SLB, 2021)

In a particular modeling study, Song et al. (2018) used numerical methods to carry out CLGS heat production performance for a U-shaped well where two wells are connected underground and one of them is used to inject cold water, while the other is used to produce the hot water. The study revealed that CLGS exhibits a stable production region with the potential for electricity generation, with outlet temperature and thermal power remaining nearly constant in this region. Additionally, inlet temperature significantly influences heat extraction performance, suggesting an optimal range of 30°C to 40°C, while the wellbore diameter has minimal impact on heat production, indicating that larger diameters are unnecessary for CLGS applications, helping to reduce drilling costs. Figure 3 illustrates the model results after 20 years of production. With 3500 m true vertical depth, 6000 m long horizontal section, and 130°C subsurface temperature at depth, 63°C outlet temperature was simulated when the inlet temperature was 40°C.

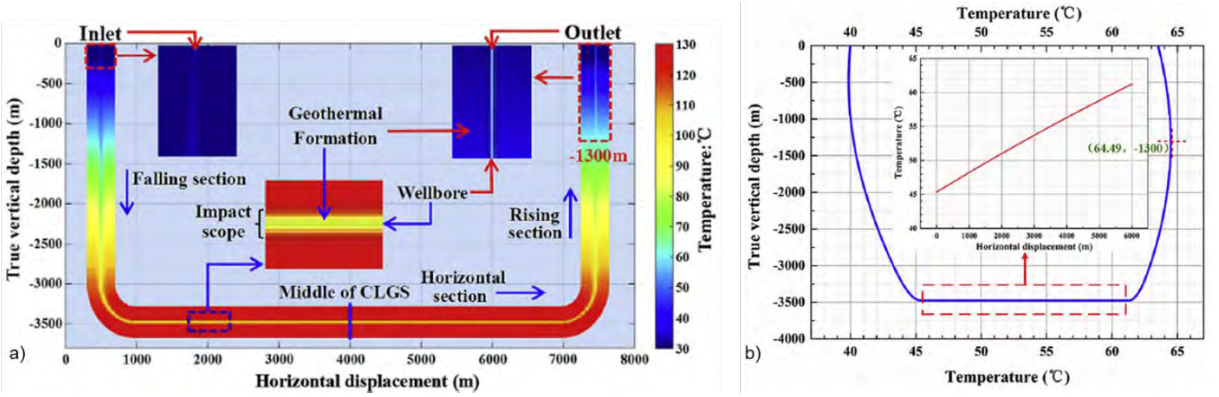

Figure 3: Numerical CLGS model results after 20 years of production: a) Temperature contours of the U-shaped CLGS wellbore and near-wellbore formation; b) Temperature profile of the working fluid inside the descending, horizontal section, and ascending sections. The subsurface temperature at the horizontal section is 130°C (Song et al., 2018)

Sun et al. (2018) used the same numerical model but changed the circulation fluid to CO2 to measure the impact. The outlet temperature was estimated to be as high as 96°C when 6°C CO2 was injected into the loop with a 4 kg/s flow rate. It was also observed that increasing the flow rate to 14 kg/s decreased the outlet temperature by about 50%. One of the important observations from the application of CO2 as a working fluid was that the relationship between outlet CO2 temperature and inlet pressure exhibited a discontinuous or contrary behavior, with outlet temperature initially increasing with inlet pressure up to 28 MPa before decreasing, attributed to the Equal-Enthalpy

theory, indicating the presence of an optimal inlet pressure for achieving the highest outlet fluid temperature.

Wang et al. (2021) conducted a numerical modeling of multilateral CLGS using a co-axial well design as shown in Figure 4 over 30 years. Energy ratio results indicated that with a reservoir temperature of 250°C, the total energy output increased by 77.43% compared to a reservoir temperature of 150°C. Increasing the number of lateral wellbores significantly enhanced the total energy output, with the maximum increase range reaching 119.11% when comparing 6 lateral wellbores to 2 lateral wellbores. The maximum outlet temperature change due to varying wellbore size was only 1.49°C, indicating minor effects on the system's performance.

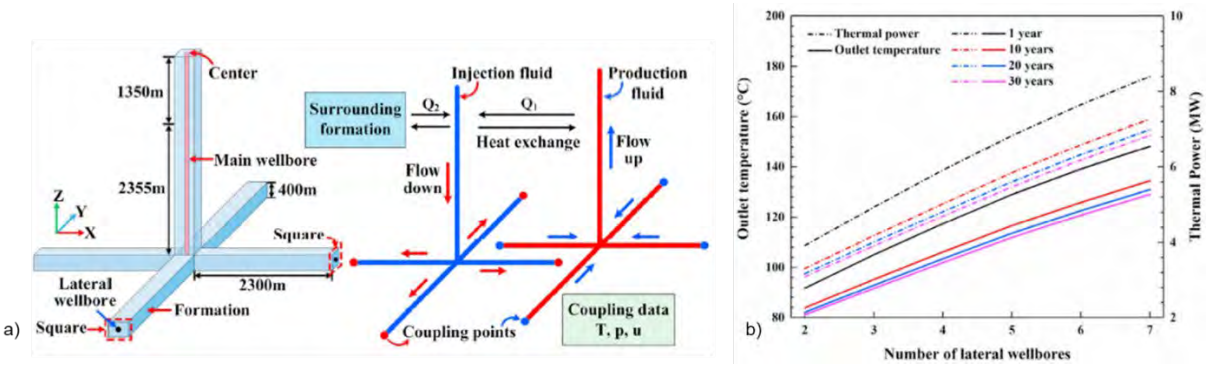

Figure 4: Numerical CLGS modeling using co-axial well design: a) Schematic of the computational model with 4 lateral sections; b) Outlet temperature and thermal power profiles vs. the number of lateral sections over 30 years of production.

In another comprehensive study, Beckers et al. (2022)showed that average heat production rates ranged from about 2 to 15 GWh per year for co-axial designs and from 9 to 67 GWh per year for U-loop designs. Levelized cost of heat estimates varied from approximately $20 to $110 per MWh for greenfield co-axial systems and $10 to $70 per MWh for U-loop systems, while electricity production ranged from 0.12 to 7.5 GWh per year with levelized costs ranging from $83 to $2,200 per MWh. Overall, the findings highlight the importance of minimizing drilling costs to make closed-loop geothermal systems economically viable, especially for electricity production.

3. Model Description

This section describes the models developed to explore the potential of the CLGS systems and carry out sensitivity analysis for multiple design factors. In general, three models are developed: the dynamic flow model, the techno-economic model, and the finite-element structural model. The use option of the extracted hot fluid in this model is the electricity generation using the Organic Rankine Cycle (ORC). Overall, the CLGS model is composed of surface facilities such as high-pressure high-flow rate pumps and heat exchangers and a subsurface component which is a multilateral well with three horizontal sections.

3.1 Dynamic Flow and Thermal Model

The dynamic flow model is developed in a commercially available steady-state multiphase flow simulator (SLB, 2024). The schematic diagram of the multilateral well is illustrated in Figure 5 below. For most of the analysis, a multilateral well with three horizontal sections is used while single and dual lateral sections are also simulated. The well deviation survey, rock temperature, and thermal conductivity are given in Table 1 below. The true vertical depth of all three horizontal

sections is 2500 m. The well has three parts: a vertical section (0-2134 m MD), a build-up section (2134-2987 m MD), and three 1220 m long horizontal sections (2987-4207 m MD). The horizontal sections are placed 120 degrees apart from each other to ensure minimum interference of the heat transfer medium in near-well formation. The ground temperature at the surface is 15°C and the ambient temperature at 2500 m TVD is 150°C. The average thermal gradient is 0.054 °C/meter for the whole interval. The rock-specific heat capacity is set to 840 J/(kg.K) for the whole interval. The thermal conductivity of the rock is set to 3 W/(m.K) from the surface to 1600 m TVD and 3.6 W/(m.K) to 2500 m TVD, which is close to the thermal conductivity of granite.

Table 2 shows the dimensions of the casings, liner, and tubing, including setting depth and diameters. The thermal conductivity of the carbon steel casings and liner are set to 48 W/(m.K). The fluid is pumped through the annulus and produced through the insulated tubing that has a thermal conductivity of 0.01 W/(m.K). There are several commercially available vacuum-insulated tubing (VIT) products provided by different manufacturers with this level of thermal conductivity. The cement around the surface and intermediate casing is two inches thick while it is set to one inch for the liner. The thermal conductivity value for the cement is set to 1.557 W/(m.K) according to the commonly used H and G class cements in well construction. Since cement has higher thermal conductivity than water and drilling mud, the annulus between casings is filled with cement up to the surface.

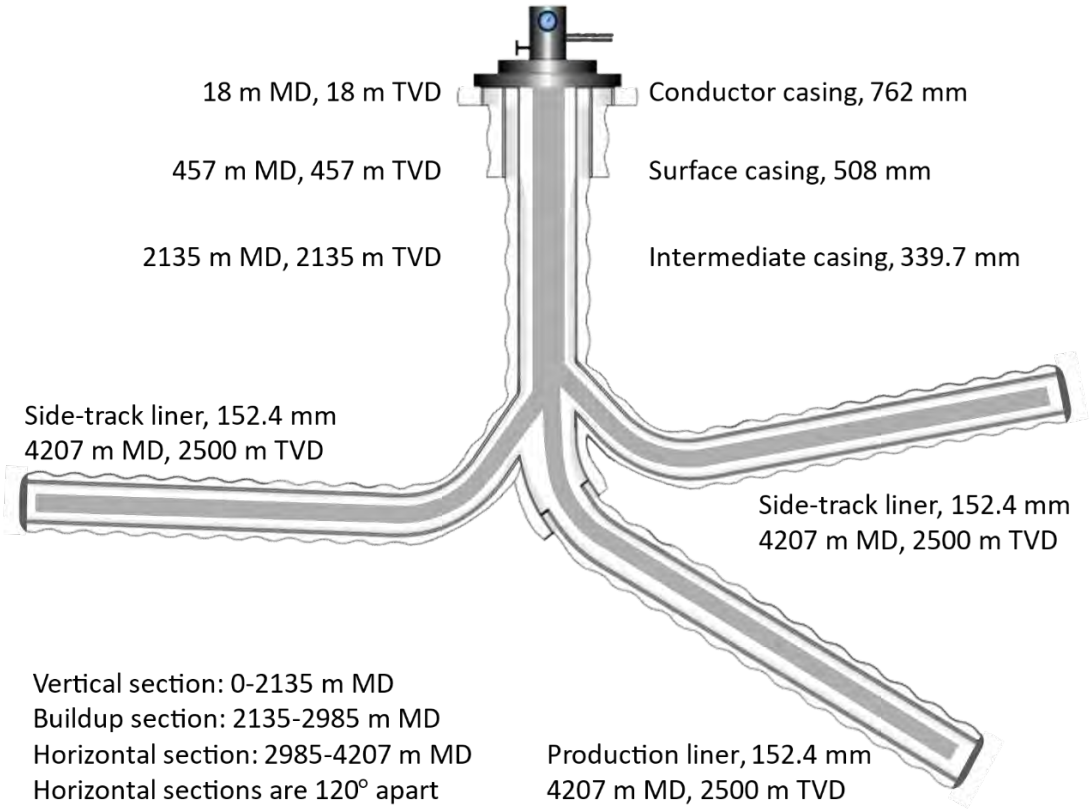

Figure 5: Schematic diagram of the multilateral well developed in steady-state flow simulator

Table 1: Well deviation survey, subsurface temperature, and rock thermal conductivity. The data on the last row of the table is the same for all three lateral sections.

MD, m	TVD, m	Horizontal section, m	Angle, deg	Rock temperature, °C	Rock thermal conductivity W/(m.K)
0	0	0	0	15	3
1000	1000	0	0	69	3
1600	1600	0	0	101	3
2134	2134	0	0	130	3.6
2198	2195	20	17	134	3.6
2271	2256	60	34	137	3.6
2365	2316	132	50	140	3.6
2484	2384	230	56	144	3.6
2682	2454	416	69	148	3.6
2987	2500	717	81	150	3.6
4207	2500	1220	90	150	3.6

Table 2: Dimensions and thermal conductivity of the casing and tubing.

Section type	From MD, m	To MD, m	ID, mm	OD, mm	Roughness, mm	Thermal conductivity, W/(m.K)
Conductor	0	18	736.6	762.0	0.0254	48
Surface Casing	0	457	485.7	508.0	0.0254	48
Intermediate Casing	0	2135	320.4	339.7	0.0254	48
Production Liner	2110	4207	131.8	152.4	0.0254	48
Production Tubing	0	4205	76.2	101.6	0.0254	0.01

Water and supercritical CO2 are the two fluid types used in the simulations at different injection flow rates and pressures. The thermal conductivity and specific heat capacity of the water are 0.6055 W/(m.K) and 4185 J/(kg.K) respectively. The thermal properties of sCO2 change with increasing pressure and temperature which is continuously calculated by the compositional fluid during simulations. For example, at 100°C temperature and 15 MPa pressure, sCO2 has around 0.045 W/(kg.K) thermal conductivity and 1600 J/(kg.K) specific heat capacity at 20 MPa pressure and 35°C temperature. To keep the CO2 under supercritical conditions, pressure and temperature at the surface facilities are kept above 7.5 MPa and 35°C.

The steady-state multiphase flow simulator incorporates a wide variety of industry-standard multiphase flow correlations that have been developed through decades of research, as well as industrial data collection and analysis. The model enables the calculation of pressure losses, flow

velocities, and flow regimes at any node given in the system. The heat transfer modeling part of the simulator provides an accurate estimation of the heat transfer from the rock to the circulating fluid through cement and casing. The model recalculates the temperature and pressure-dependent fluid properties during the simulation at any given depth in the well to achieve accurate flow and thermal modeling. The simulator carries out comprehensive energy-balance calculations accounting for convection, conduction, Joule-Thomson cooling and heating, and frictional heating.

3.2 Finite-element Structural Model

One of the best advantages of the closed-loop geothermal system is the isolation of the wellbore from the surrounding formation. The circulating fluid does not encounter the surrounding rock and formation fluid, thus preventing challenges such as corrosion and scale precipitation. However, the integrity of the wellbore and stress distribution around it is still as important as it is for other geothermal systems and has been investigated through several numerical studies (Wu et al., 2021). In this research, stress regimes around the multilateral junction are modeled to study the stress distribution in the casing-cement-formation medium using a finite-element mechanical modeler (ANSYS, 2024). Three types of cylinder stresses (radial, hoop, and axial) are critical for assessing different failure mechanisms around the wellbore (Kang et al., 2022). Radial stress is a normal stress that acts either towards or away from the well central axis. Hoop stress is defined as normal stress that occurs in the tangential direction around the wellbore. Axial stress refers to a normal stress that runs parallel to the well central axis, influencing its longitudinal stability.

The temperature around the formation is 130°C. The stress and pressure data are sourced from the Utah FORGE geothermal project database (Ye et al., 2022). The schematic of the 2D finite element model is given in Figure 6 below. It shows the side view of the junction section and the top view of the cross-sections 1 and 2. The angle between the main and lateral wellbore is 15 degrees and the distance between the cross-sections is 0.5 m.

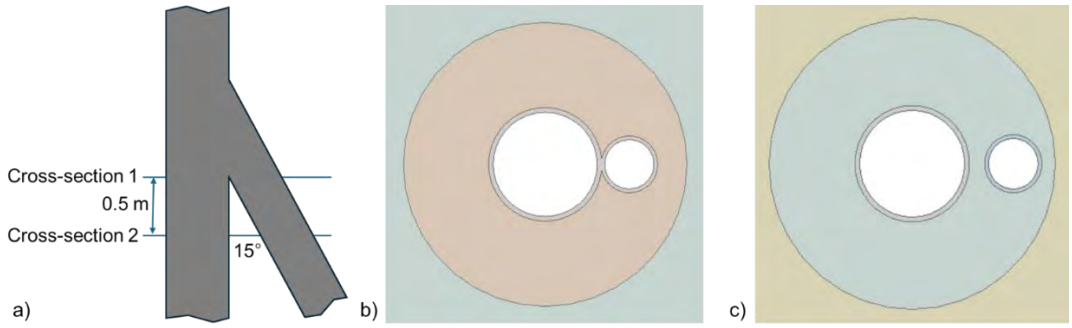

Figure 6: Schematic diagram of the structural model developed in finite-element simulator. a) The side view of the multilateral window interval, b) Cross-section 1, c) Cross-section 2

The details of the structural model are as follows:

- Main bore casing: OD 339.7 mm and ID 320.4 mm
- Lateral bore liner: OD 152.4 mm and ID 131.8 mm
- Cement thickness: 50 mm
- Formation with and length: 7 meters (it must be at least 10 times bigger than the cement outer diameter to avoid boundary effect during simulation)
- Formation temperature: 130°C
- Depth: 2134 m
- Minimum horizontal stress gradient: 14 kPa/m

- Maximum horizontal stress gradient: 17.4 kPa/m
- Pore pressure gradient: 0.43 psi/ft

Table 3: Material properties of steel casing, cement sheath, and formation for the structural model. The thermal properties are taken from Bu et al. (2017) and Olmeda et al. (2013). The formation rock properties are taken from the Branch and Balmer (1953).

Model Component	Parameter	Value
Steel casing	Young's modulus, E_s (GPa)	200
	Poisson's ratio, v_s	0.3
	Thermal expansion coefficient, α_s (10^{-6}/K)	11.43
	Thermal conductivity, K_s (W/m.K)	45
Cement sheath	Young's modulus, E (GPa)	12.5
	Poisson's ratio, v_c	0.34
	Thermal expansion coefficient, α_c (10^{-6}/K)	9.4
	Thermal conductivity, K_c (W/m.K)	0.3
Formation	Young's modulus, E_f (GPa)	68.9
	Poisson's ratio, v_f	0.26
	Thermal expansion coefficient, α_f (10^{-6}/K)	8
	Thermal conductivity, K_f (W/m.K)	2.9

3.3 Techno-economic Model

The levelized cost of electricity is estimated using a techno-economic model developed in an open-source geothermal simulator (Beckers & Ross, 2023; NREL, 2024). The model combines the reservoir, surface plant, and economic models together using empirical relationships. In this study, however, the results of the flow and thermal model are used as an input for the techno-economic model. The end use of the temperature is set to the generation of electricity through ORC that uses low-boiling point working fluid. The heat extracted from the CLGS using water or sCO2 is transferred to this working in the heat exchanger. The techno-economic tool uses equations developed by Augustine (2009) to convert heat into electricity using thermal efficiency correlations.

Capital costs and operation and maintenance (O&M) costs are estimated using basic cost correlations. For calculating the overall capital costs of the system, drilling costs and surface plant expenses are evaluated. Drilling expenses are derived by multiplying the total drilling depth by a standard cost per meter, which is typically set at $1,000/m, due to the unique aspects of closed-loop well designs, such as lengthy open-hole laterals, and the potential for greater than typical drilling depths (Beckers et al., 2023). The costs of the surface plant are determined by the capacity of the plant, with specific cost metrics derived from the research of Beckers and Johnston (2022) and Beckers and McCabe (2019). A default value of $3,000/kWe is used for calculating the cost of electricity generation infrastructure. O&M costs are computed as a percentage of the investment in surface plant infrastructure, set at 1.5% by default, as identified in studies by Beckers and

Johnston (2022). Due to the closed-loop nature of the system, which prevents fluid exposure to the environment, issues related to scaling and corrosion are not expected, thus eliminating wellfield maintenance expenses. Pumping costs for direct use are included, calculated based on specified electricity rates. For power generation, the required pumping power is deducted from the total electrical output of the plant. Costs related to exploration, potential well redrilling, well field maintenance, or land leasing are excluded from capital and O&M cost considerations (Beckers and McCabe, 2019).

Table 4: Values of some parameters for the techno-economic model

Parameter	Value
Well Configuration	CLGS with three multilateral sections
Number of wells	Two production wells, $1000/m
Heat transfer fluid	Water and sCO2
End-use	Electricity
Temperature, flow rate, and pressure	Imputed from flow and thermal models
System Lifetime	20 years
Power plant cost	$3,000/kWe
Total O&M cost	$44k/year
Total capital cost	$32.4M

4. Results and Discussion

4.1 Production forecast over 20 years

The flow and thermal and thermal model simulations were run for sCO2 and water at 10-40 kg/s mass flow rates. The model provides the temperature of the fluid along multiple nodes in the closed-loop system. Figure 7 shows the flowing water temperature profile along the annulus in the descending and horizontal sections of the CLGS and inside the tubing along the horizontal and ascending sections at the start of the production. The simulation results for the sCO2 at the beginning of production are given in Figure 8. The injection temperature for both fluids is 35°C while the injection pressure is calculated by the model based on the system pressure loss dominated by the friction to achieve system outlet pressure of 0.5 MPa for water and 20 MPa for sCO2. Both plots show that the heat transfer to the circulating fluid starts at around 600 m down in the annulus. At lower flow rates, the fluid heats up in the descending section of the well more than at higher flow rates. However, the main heating occurs in the horizontal sections of the well. Once the fluid enters the insulated tubing at higher flow rates (30-40 kg/s), the fluid temperature remains relatively constant as it travels through the tubing in horizontal and ascending sections. Whereas at lower flow rates (10-20 kg/s), the fluid temperature decreases by 5-15°C because of heat loss from the hotter fluid in the tubing to the colder fluid in the annulus since low flow rates give more time for the heat transfer to occur. Despite the reservoir temperature of 150°C, the water reaches a maximum of 141°C at 10 kg/s rate and 99°C at 40 kg/s. On the other hand, sCO2 reaches a maximum of 147°C at 10 kg/s and 125 at 40 kg/s. The reason is that sCO2 has a smaller specific heat capacity compared to water. The same reason also causes the sCO2 to lose heat by 25-35°C as it travels through the tubing in horizontal and ascending sections. Overall, the water temperature at the wellhead was estimated to be higher when the water was used (98-130°C) compared to sCO2 (90-118°C).

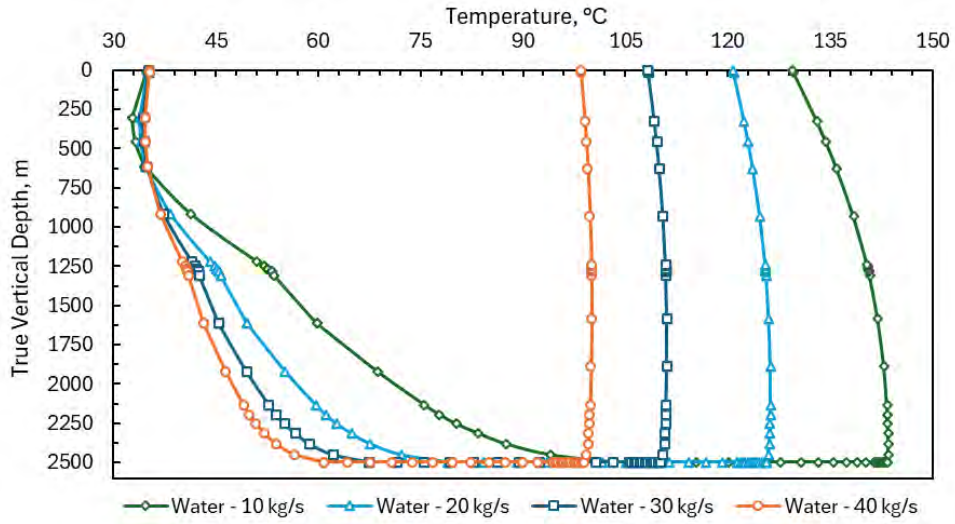

Figure 7: Flowing water temperature profile along the flow path at the start of production

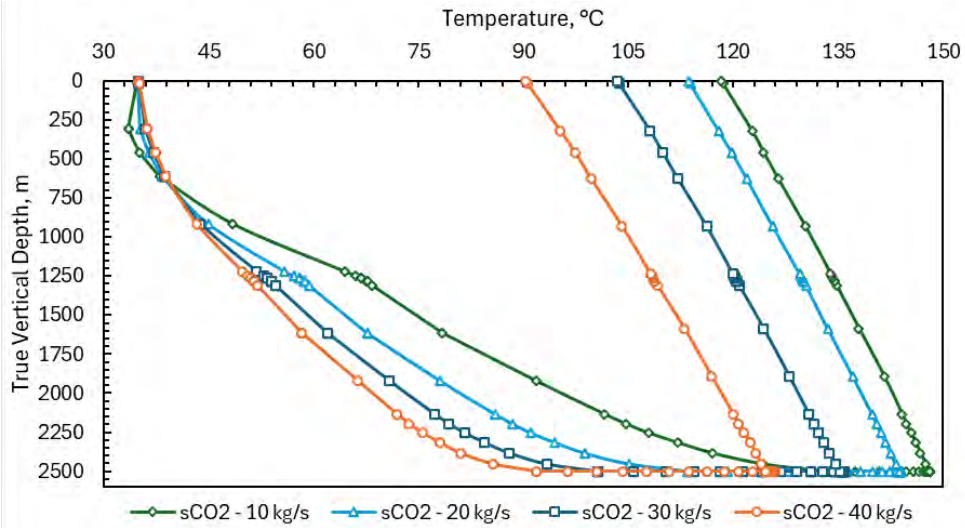

Figure 8: Flowing sCO2 temperature profile along the flow path at the start of production

The simulation was carried out for 20 years of production using both fluid types. The outlet temperature versus time for 10-40 kg/s water and sCO2 flow rate over is shown in Figure 9. After 20 years of production, production temperature at the wellhead decreased by 15-20°C for both fluid types and all flow rates. A rapid decline occurred within the 6 months of production, while it was slower for the rest of the years. It can be explained by the low thermal conductivity of the formation. The heat transfer from the formation to the circulating fluid is limited to conduction only in closed-loop systems. Although geothermal energy is renewable, heat extraction is faster than heat recovery in the near-wellbore formation. Also, heat transfer happens faster when the differential temperature between near-wellbore formation and circulating fluid is higher. Compared to continuous production, the intermitted production during the most demanding hours of the day would enable the temperature of the formation around the wellbore to increase back to the initial temperature. After 20 years, the produced water temperature was still higher than the sCO2 temperature (84-109°C for water and 73-96°C for sCO2).

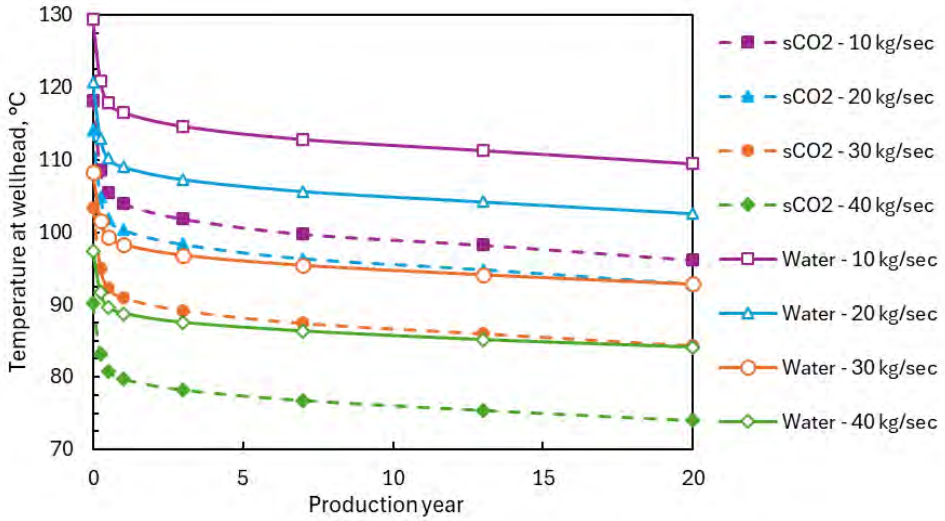

Figure 9: Temperature of the water and sCO2 at the wellhead over 20 years of production forecast

4.2 Impact of resource temperature

One of the most important factors to consider in order to achieve more affordable geothermal energy is drilling into hotter formations at lower cost. In this section, the depth and design of the multilateral well were kept the same while the resource temperature was increased from 150°C to 350°C at 2500 m TVD. The geothermal gradient from the surface to 2500 m TVD is kept constant. The mass flow rate was set to 40 kg/s for water and sCO2. The results in Figure 10 show that outlet water temperature increased from 99°C to 213°C. This increase was even higher for sCO2 (from 91°C to 261°C). Above 175°C resource temperature, the sCO2 outlet temperature was above water temperature, whereas the produced heat of water was still above that of sCO2 since water has higher specific heat capacity. The techno-economic model results showed that the levelized cost of electricity would decrease from 29.7 cents/kWh to 14.2 cents/kWh using water when the rock temperature was 350°C. Similarly, the cost was estimated to drop from 49.7 cents/kWh at 150°C to 17.5 cents/kWh at 350°C.

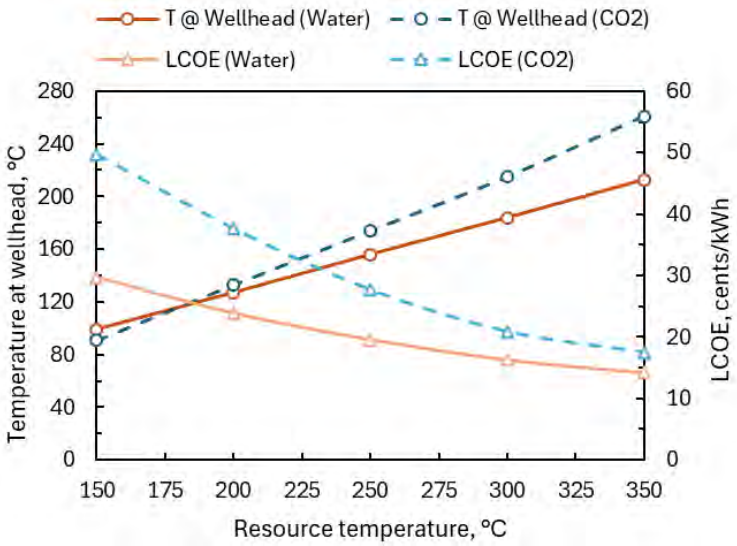

Figure 10: Impact of resource temperature on fluid temperature at the well outlet and LCOE

4.3 Impact of injection rate

The mass injection rate of the circulating fluid has a direct impact on how much heat will be produced from the closed-loop system. Therefore, the mass flow rate of water and sCO2 from 1 kg/s to 80 kg/s were used in the flow and thermal model to estimate the outlet temperature and system pressure loss. The system pressure loss shows how much pumping pressure will be required to create circulation in the closed-loop system. Higher pressure loss means more pumping power is needed, which increases the cost of the operations. The formation temperature at 2500 m TVD was 150°C and injection pressure was set to 20 MPa. The impact of injection mass flow rate on outlet temperature and system pressure loss for water and sCO2 is plotted in Figure 11 below. The outlet temperature reached the highest value of 129°C and 114°C for water and sCO2 accordingly at a 10 kg/s rate and gradually fell to around 75°C as the flow rate increased up to 80 kg/s. Meanwhile, the system pressure loss was negative or close to zero at flow rates up to 20 kg/s. Up to this rate, the pressure increase due to the volumetric expansion of the circulating fluid was bigger than the frictional pressure loss. Increasing the flow rate up to 80 kg/s frictional pressure loss resulted in system pressure loss rising up to 28 MPa for water and 24 MPa for sCO2. Overall, the outlet temperature and system pressure loss for sCO2 application was smaller than that of water.

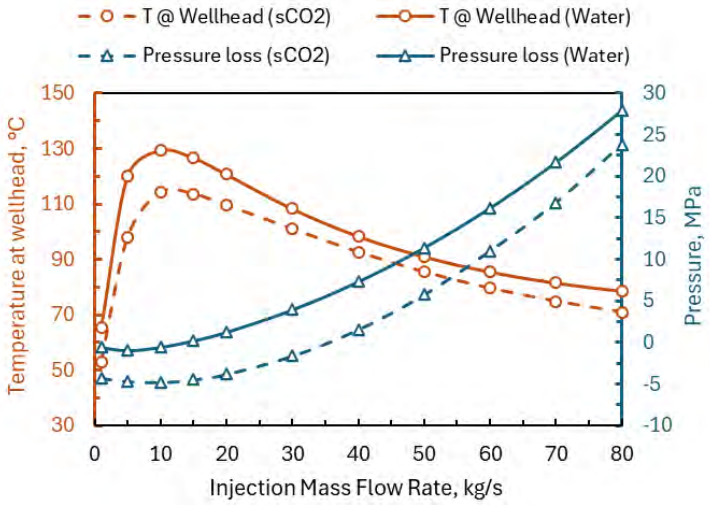

Figure 11: Impact of injection mass flow rate on outlet temperature and system pressure loss

Although the 10 kg/s injection rate yielded the highest temperature for water and sCO2, it is not the optimal flow rate when the overall heat production and LCOE are considered. According to Figure 12, the highest heat production of 5.6 MW is achieved at around 40 kg/s water flow rate when the LCOE was estimated to be the lowest at around 27 cents/kWh. Above 40 kg/s of water rate, the produced heat gradually decreased and LCOE slightly increased (4.6 MW and 32.8 cents/kWh at 80 kg/s). The heat production using sCO2, on the other hand, kept rising to 2.7 MW at an 80 kg/s mass flow rate, which also caused LCOE to increase to 61 cents/kWh. The optimal mass flow rate of sCO2 can be identified by looking at the LCOE trend, which is 40 kg/s providing 45 cents/kWh electricity. In general, water recovered three times more energy from the closed-loop system and resulted in 40% cheaper electricity generation compared to the application of sCO2. It was shown in the previous section that this difference was much smaller when the CLGS was developed at high subsurface temperatures.

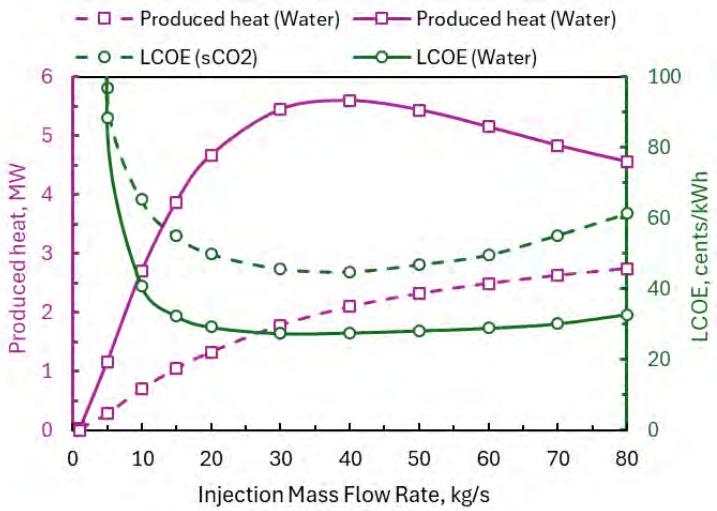

Figure 12: Impact of injection mass flow rate on produced heat and levelized cost of electricity

4.4 Impact of injection pressure

Simulations showed that injection pressure has no impact on the heat extraction from the well when the water is used. The thermal properties of the water stayed constant under the given injection pressures. However, the thermal properties of the supercritical CO2 changed as the injection pressure increased from 12 MPa to 24 MPa. In all four cases, the resource temperature was 150°C and the mass flow rate was set to 40 kg/s. It was observed that at higher injection pressures, the temperature of the sCO2 in the horizontal section annulus reached bigger values and less heat loss occurred as the fluid traveled upward through the tubing. For example, at 12 MPa injection pressure, the fluid reached to maximum of 111°C at the end of the horizontal section and decreased to 62°C (49°C heat loss) at the wellhead, whereas at 24 MPa, a maximum of 127°C at the end of the horizontal section and fall to 95°C (32°C heat loss) at the wellhead.

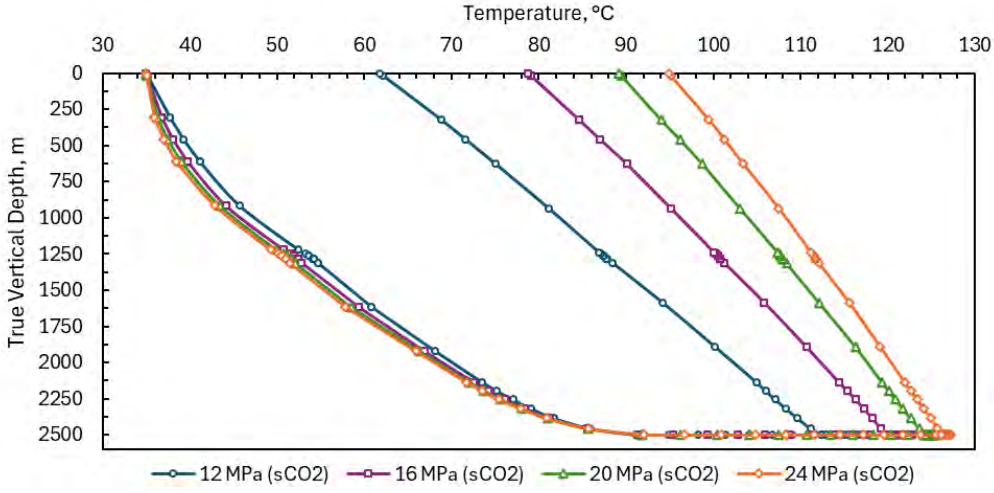

Figure 13: Impact of sCO2 injection pressure on outlet temperature

4.5 Impact of the number of lateral sections

Since the heat transfer in closed-loop systems occurs through conduction only, the total surface area around the lateral wellbore section is very important to recover more heat from the surrounding rock. Therefore, the number of horizontal sections from one to three was modeled keeping the injection temperature and mass flow rate at 35°C and 40 kg/s accordingly. The system

outlet pressure was set to 0.5 MPa for water and 20 MPa for supercritical CO2. The simulation result for the temperature profile along the wellbore is plotted in Figure 14. It shows that for the case of one 1220-meter horizontal section, the temperature of the water rises to 75°C before entering the insulated tubing and stays relatively constant as it is produced. And for sCO2 this value is 104°C before entering the tubing and 74°C at the wellhead. For the case of three 1220-meter lateral sections, circulating water reached a maximum temperature of 100°C before entering the insulated tubing and dropped to 98°C as it is produced at the wellhead. Similarly, the sCO2 temperature increased up to 126°C before entering the insulated tubing and produced at 90°C at the wellhead. The simulation showed that a longer total length of the horizontal section results in more heat transfer to the fluid and higher producing temperature. Although increasing the number of laterals increased the well construction cost from $8 million to $15 million, the LCOE dropped from 51 cents/kWh to 27 cents/kWh. As mentioned earlier, the positive contribution of higher production temperatures to the LCOE outweighs the increasing capital expenditure due to high well development costs.

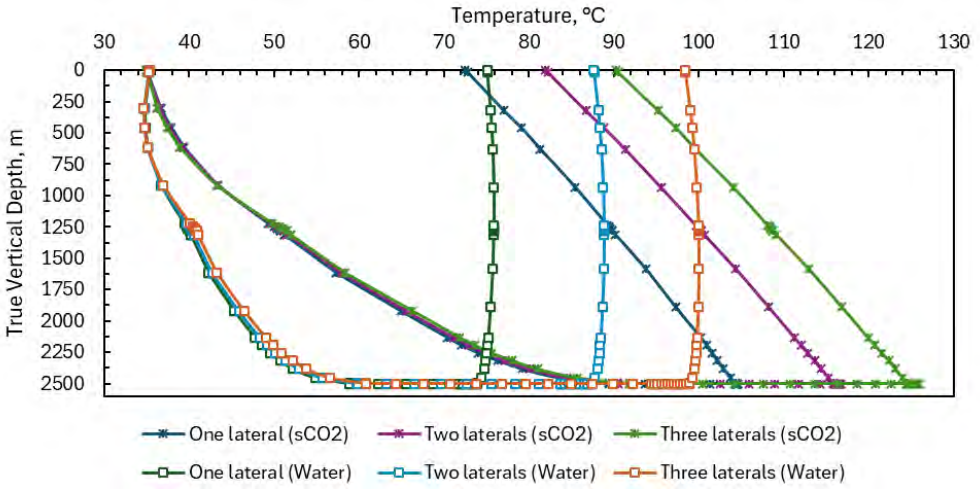

Figure 14: Impact of the number of laterals on temperature profiles along the well

4.6 Impact of casing and tubing size

To evaluate the impact of casing and tubing size on outlet temperature, three well designs were developed, only changing the size of the liner and tubing installed in the lateral sections as given in Table 5 below. From Case 1 to Case 3, the lateral sections become bigger in terms of diameter, creating more surface area for heat transfer and less obstruction for the fluid flow.

Table 5: Three cases with different liner and tubing sizes to evaluate the impact on the outlet temperature and system pressure loss

Design #	Liner OD, mm	Liner ID, mm	Tubing OD, mm	Tubing ID, mm
Case 1	136.8	114.7	89.5	71.7
Case 2	154.0	131.9	101.7	83.9
Case 3	180.5	158.4	120.5	102.7

Since the sCO2 thermal properties are impacted by the system pressure, water is used as a circulation fluid for the simulation of these three cases. The resource temperature was 150°C. Water injection temperature and pressure were fixed at 35°C and 7.5 MPa respectively. The

resulting outlet temperature profiles against injection mass flow rate are provided in Figure 14. It was confirmed through simulations that a bigger wellbore size results in slightly better heat recovery from the formation. For example, by changing the wellbore size from Case 1 to Case 3, the temperature at the wellhead increased from 85°C to 95°C at a 40 kg/s injection rate. Another advantage of a bigger wellbore was proved to be the smaller injection pressure. As shown in Figure 15, changing the design from Case 1 to Case 3 dropped the system pressure loss from 11 MPa to negative 3MPa, which means thermal expansion of the fluid provides more pressure support than frictional pressure loss. The difference becomes much bigger as higher injection mass flow rates are applied. At 80 kg/s, Case 1 resulted in around 10 times bigger pressure loss compared to Case 3 well design.

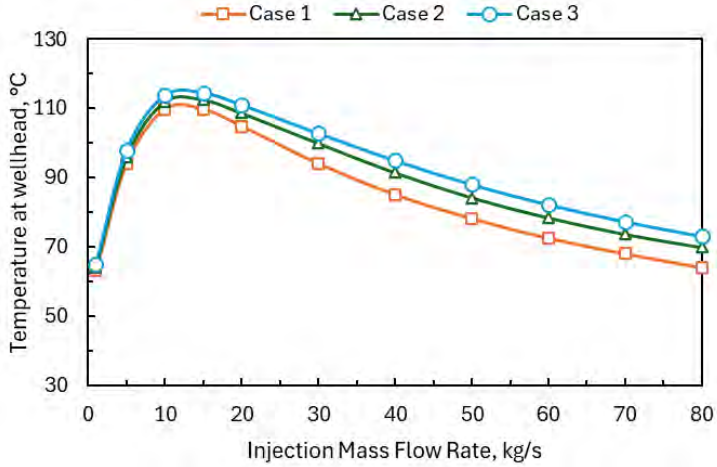

Figure 15: Impact of casing and tubing size on water outlet temperature

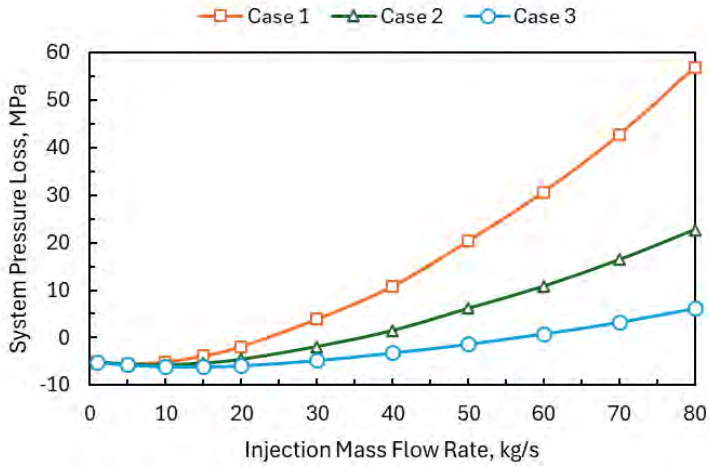

Figure 16: Impact of casing and tubing size on system pressure loss

4.7 Impact of tubing insulation

To prevent the heat of the fluid inside the production tubing from transferring to the colder fluid circulating in the annulus, production tubing must be insulated. The most common carbon steel material used for tubing manufacturing has a thermal conductivity value of around 48 W/(m.K). For comparison, granite rock has a thermal conductivity of around 2.99 W/(m.K) with a high porosity and 3.62 W/(m.K) for ones with a low porosity. That means, if the tubing is not insulated, the heat would be lost to colder fluid in the annulus faster than it was gained from the hot formation.

Therefore, insulated tubing with overall thermal conductivity ranging from 0.01 W/(m.K) to 10 W/(m.K) was tested in the simulation models using water as a circulating fluid. The injection temperature was set to 35°C and production pressure was set to 0.5 MPa while the rock temperature was 150°C at 2500 m TVD. As expected, production temperature decreased significantly as the thermal conductivity increased. Compared to the most conductive tubing, the production temperature was at least two times bigger with the least thermally conductive tubing. For example, at a 40 kg/s water injection rate, the produced water temperature was 98°C when the tubing with 0.01 W/(m.K) thermal conductivity was used, while it was 49°C when the thermal conductivity was increased to 10 W/(m.K).

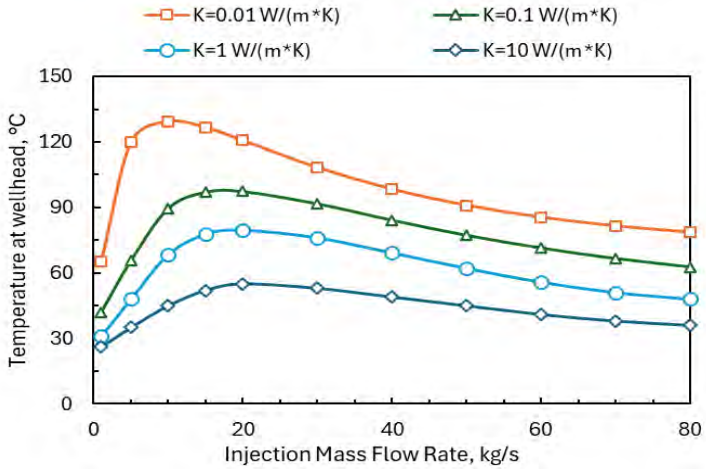

Figure 17: Impact of tubing insulation on water outlet temperature

4.8 Structural modeling results

In the structural modeling results section, an analysis of the equivalent stress distribution within the cement sheath is presented, focusing specifically on cross-sections 1 and 2, as depicted in Figure 18. A considerable disparity in stress levels is observed, with the equivalent stress at the top cross-section found to be 23% higher than at the bottom cross-section. Despite the minimal vertical distance of 0.5 meters between these two sections, the strength of the rock at both locations is assumed to be consistent. This assumption leads to the conclusion that a heightened risk of failure is exhibited by the top section, which experiences higher stress. Importantly, the intersection between the main and lateral bores is identified as the critical zone for potential failure. This analysis highlights the importance of careful stress distribution assessment and proactive failure risk management in junction zones of the multilateral well designs.

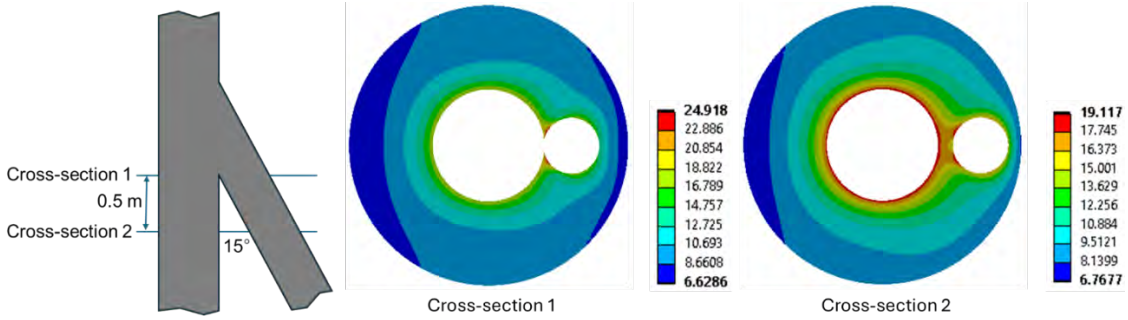

Figure 18: Equivalent stress distribution within the cement sheath for cross-sections 1 and 2. The unit of the color bar is MPa.

Conclusion

In summary, this study provides a comprehensive analysis of Multilateral Closed Loop Geothermal Systems (CLGS) using both water and supercritical CO2 as a circulation fluid, demonstrating substantial potential for enhancing power generation while eliminating issues related to corrosion and scale formation. Notably, the use of supercritical CO2, despite its lower specific heat capacity compared to water, contributes to higher temperature outputs in scenarios involving higher resource temperatures, reducing the levelized cost of electricity effectively. Moreover, the findings underscore the critical importance of optimal design parameters, including the number of lateral sections and the size of casing and tubing, which significantly influence heat transfer and system efficiency. The study also explores the necessity of insulation in production tubing to prevent heat loss, ensuring more sustainable energy production. Additionally, structural modeling results indicate significant stress challenges, especially at critical junctions within the well architecture, which could impact long-term operational integrity. Key findings from the study include:

- The simulation results demonstrate that lower flow rates allow for greater heating in the descending section of the well, but the most significant heating occurs in the horizontal sections, where higher flow rates (30-40 kg/s) maintain relatively stable fluid temperatures as they travel through insulated tubing.
- Optimal flow rates for both water and sCO2 were identified to be 40 kg/s considering the heat production and levelized cost of electricity.
- After 20 years of operation, a production temperature decline of 15-20°C was observed for both fluid types across all flow rates, reflecting the slow thermal recovery rates of the surrounding formations.
- Increasing the resource temperature from 150°C to 350°C resulted in outlet temperatures for water rising from 99°C to 213°C and for sCO2 from 91°C to 261°C. This enhancement also led to a significant drop in the levelized cost of electricity from 29.7 cents/kWh to 14.2 cents/kWh using water.
- Increasing the number of laterals and their length increases the well construction cost.
- The addition of lateral sections, from one to three, not only increased the heat recovery from 75°C to 100°C for water but also decreased the levelized cost of electricity (LCOE) from 51 cents/kWh to 27 cents/kWh, despite increasing well construction costs from $8 million to $15 million.
- Utilizing insulated tubing with a thermal conductivity of 0.01 W/(m.K) significantly maintained higher fluid temperatures (98°C for water at a 40 kg/s injection rate), compared to 49°C when the conductivity was increased to 10 W/(m.K).
- The equivalent stress at the top cross-section of the cement sheath is found to be 23% higher than at the bottom, highlighting a higher risk of failure at the top section due to the stress concentration near the junctions between the main and lateral bores.

These findings demonstrate the technical viability and economic potential of CLGS, especially when designed with consideration for optimal flow rates, insulation, resource temperatures, and structural integrity at critical junctions.

Acknowledgements
The first author would like to thank all the co-authors for their contribution to this study. Special thanks to the University of Oklahoma for providing simulation software and to GreenPath Systems for funding that made the research and conference attendance possible.

Declaration of Competing Interest
The authors declare that they have no known competing financial interests or personal relationships that could have appeared to influence the work reported in this paper.

Data Availability
The model files, well design data and simulation results can be provided upon request to the corresponding author at orkhan@ou.edu.

References
ANSYS. (2024). Ansys Simulation Software. In: https://www.ansys.com/company-information/ansys-simulation-software.

Augustine, C. R. (2009). *Hydrothermal spallation drilling and advanced energy conversion technologies for engineered geothermal systems* Massachusetts Institute of Technology].

Beckers, K., Vasyliv, Y., Bran-Anleu, G. A., Martinez, M., Augustine, C., & White, M. (2023). *Tabulated Database of Closed-Loop Geothermal Systems Performance for Cloud-Based Technical and Economic Modeling of Heat Production and Electricity Generation*.

Beckers, K. F., & Johnston, H. E. (2022). Techno-economic performance of Eavor-Loop 2.0. Proceedings 47th workshop on geothermal reservoir engineering, Stanford, California,

Beckers, K. F., & McCabe, K. (2019). GEOPHIRES v2. 0: updated geothermal techno-economic simulation tool. *Geothermal Energy*, *7*, 1-28.

Beckers, K. F., Rangel-Jurado, N., Chandrasekar, H., Hawkins, A. J., Fulton, P. M., & Tester, J. W. (2022). Techno-economic performance of closed-loop geothermal systems for heat production and electricity generation. *Geothermics*, *100*, 102318.

Beckers, K. F., & Ross, M. I. (2023). *Utilizing GEOPHIRES-X Beyond Electricity*.

Beckers, K. J., Young, K. R., Johnston, H., & Snyder, D. M. (2017). Analysis of Geothermal Reservoir and Well Operational Conditions using Monthly Production Reports from Nevada and California. *Geothermal Resources Council 41st Annual Meeting*.

Branch, U. S. B. o. R. E. L., & Balmer, G. G. (1953). *Physical properties of some typical foundation rocks*. Commissioner's Office.

Browne, P. (1978). Hydrothermal alteration in active geothermal fields. *Annual review of earth and planetary sciences*, *6*(1), 229-248.

Bu, Y., Chang, Z., Du, J., & Liu, D. (2017). Experimental study on the thermal expansion property and mechanical performance of oil well cement with carbonaceous admixtures. *RSC advances*, *7*(46), 29240-29254.

Chen, J., & Jiang, F. (2015). Designing multi-well layout for enhanced geothermal system to better exploit hot dry rock geothermal energy. *Renewable Energy*, *74*, 37-48.

Cheng, P. (1979). Heat transfer in geothermal systems. In *Advances in heat transfer* (Vol. 14, pp. 1-105). Elsevier.

DiPippo, R. (2012). *Geothermal power plants: principles, applications, case studies and environmental impact*. Butterworth-Heinemann.
Ediger, V. S., & Akar, S. (2023). *Historical Pattern Analysis of Global Geothermal Power Capacity Development*.
Geiser, P. A., Marsh, B. D., & Hilpert, M. (2016). Geothermal: The Marginalization of Earth's Largest and Greenest Energy Source.
Ghasemi, H., Paci, M., Tizzanini, A., & Mitsos, A. (2013). Modeling and optimization of a binary geothermal power plant. *Energy*, *50*, 412-428.
Hecht-Méndez, J., Paly, M. d., Beck, M., & Bayer, P. (2013). Optimization of energy extraction for vertical closed-loop geothermal systems considering groundwater flow. *Energy Conversion and Management*, *66*, 1-10.
Hogg, C. (1997). Comparison of multilateral completion scenarios and their application. SPE Offshore Europe Conference and Exhibition,
Hu, Z., Vivas, C., Salehi, S., & Khankishiyev, O. (2024). Machine Learning-Based Rock Facies Prediction Using Geothermal Data: A Comparative Analysis of Algorithms.
Hu, Z., Xu, T., Feng, B., Yuan, Y., Li, F., Feng, G., & Jiang, Z. (2020). Thermal and fluid processes in a closed-loop geothermal system using CO2 as a working fluid. *Renewable Energy*, *154*, 351-367.
IEA. (2023). *World Energy Outlook* https://www.iea.org/reports/world-energy-outlook-2023
Kalvenes, K. L. (2017). Investigation of Corrosion in Geothermal Wells - A Qualitative Risk Assessment.
Kang, Y., Samuel, R., & Kumar, V. (2022). Casing Failures in High Temperature Geothermal Wells: An Analytical Study. *Day 1 Mon, October 03, 2022*.
Karlsdóttir, S. N., & Thorbjornsson, I. O. (2012). Hydrogen Embrittlement And Corrosion In High Temperature Geothermal Well. *Corrosion*.
Khankishiyev, O. (2024). *Design And Construction Of A Novel Drilling Rig For The Investigation Of Hard Rock Drilling For Super-Hot Enhanced Geothermal System Development* University of Oklahoma]. United States.
Khankishiyev, O., & Salehi, S. (2023). Technology Review and Techno-Economic Analysis of Super-Hot EGS Development in Hard Rock Formations. *Geothermal Resources Council Transactions*, *47*, 2979-2997.
Khankishiyev, O., Salehi, S., Hasanov, G., & Hu, Z. (2024 (a)). Application of Distributed Temperature Sensing (DTS) in Geothermal Wells. *PROCEEDINGS, 49th Workshop on Geothermal Reservoir Engineering*, *49*.
Khankishiyev, O., Salehi, S., Vivas, C., Nygaard, R., & Rehg, D. (2023a). Geothermal Energy in Sedimentary Basins: Assessing Techno-economic Viability for Sustainable Development. *Geothermal Resources Council Transactions*, *47*, 2470-2484.
Khankishiyev, O., Salehi, S., Vivas, C., Nygaard, R., & Rehg, D. (2023b). Techno-Economic Investigation of Geothermal Development in Sedimentary Basins. *ASME Open Journal of Engineering*.
Klapper, H., Schorling, P., Lause, B., Mok, W. M., Zonneveld, W. v., Castricum, A., & Moeller, M. (2019). Addressing Integrity Issues in Downhole Equipment by Corrosion Inhibition in Sweet Geothermal Brines. *Corrosion*.
Kruszewski, M., & Wittig, V. (2018). Review of failure modes in supercritical geothermal drilling projects. *Geothermal Energy*, *6*, 1-29.

Kurata, Y., Sanada, N., Nanjo, H., & Ikeuchi, J. (1992). Material damages in geothermal power plants. *Proceedings of the 14th New Zealand geothermal workshop*, *1*, 159-164.

Lay, T., Hernlund, J., & Buffett, B. A. (2008). Core–mantle boundary heat flow. *Nature Geoscience*, *1*(1), 25-32. https://doi.org/10.1038/ngeo.2007.44

Lund, J. W., Huttrer, G. W., & Toth, A. N. (2022). Characteristics and trends in geothermal development and use, 1995 to 2020. *Geothermics*, *105*, 102522.

Mosaffa, A., & Zareei, A. (2018). Proposal and thermoeconomic analysis of geothermal flash binary power plants utilizing different types of organic flash cycle. *Geothermics*, *72*, 47-63.

Nalla, G., & Shook, G. M. (2004). Engineered geothermal systems using advanced well technology. *Geothermal Resources Council Transactions*, *28*, 117-123.

Nogara, J. B., & Zarrouk, S. J. (2018). Corrosion in geothermal environment: Part 1: Fluids and their impact. *Renewable & Sustainable Energy Reviews*, *82*, 1333-1346.

NREL. (2024). *GEOPHIRES-X*. https://github.com/NREL/GEOPHIRES-X

Olasolo, P., Juárez, M. C., Morales, M. P., D´Amico, S., & Liarte, I. A. (2016). Enhanced geothermal systems (EGS): A review. *Renewable & Sustainable Energy Reviews*, *56*, 133-144.

Olmeda, J., De Rojas, M. S., Frías, M., Donatello, S., & Cheeseman, C. (2013). Effect of petroleum (pet) coke addition on the density and thermal conductivity of cement pastes and mortars. *Fuel*, *107*, 138-146.

Phi, T. H., Elgaddafi, R., Ramadan, M., Ahmed, R., & Teodoriu, C. (2019). Well Integrity Issues: Extreme High-Pressure High-Temperature Wells and Geothermal Wells a Review.

Pollack, H. N., Hurter, S. J., & Johnson, J. R. (1993). Heat flow from the Earth's interior: Analysis of the global data set. *Reviews of Geophysics*, *31*(3), 267-280. https://doi.org/https://doi.org/10.1029/93RG01249

Ritchie, H., Rosado, P., & Roser, M. (2024). *Global Energy Production and Consumption* https://ourworldindata.org/energy-production-consumption

SLB. (2021). *The Defining Series: Multilateral Wells* (R. v. Flatern, Ed.). SLB. https://www.slb.com/resource-library/oilfield-review/defining-series/defining-multilateral-wells

SLB. (2024). Pipesim steady-state Multiphase flow simulator. In: https://www.software.slb.com/products/pipesim.

Soltani, M., Moradi Kashkooli, F., Dehghani-Sanij, A. R., Nokhosteen, A., Ahmadi-Joughi, A., Gharali, K., Mahbaz, S. B., & Dusseault, M. B. (2019). A comprehensive review of geothermal energy evolution and development. *International Journal of Green Energy*, *16*(13), 971-1009. https://doi.org/10.1080/15435075.2019.1650047

Song, X., Shi, Y., Li, G., Shen, Z., Hu, X., Lyu, Z., Zheng, R., & Wang, G. (2018). Numerical analysis of the heat production performance of a closed loop geothermal system. *Renewable Energy*, *120*, 365-378.

Stimac, J., Baroek, M., Pazziuagan, D., & Vicedo, R. (2010). Multilateral Geothermal Wells in Volcanic-hosted Reservoirs–Objectives, Challenges and Results. Proceedings, World Geothermal Congress, Bali, Indonesia,

Sun, F., Yao, Y., Li, G., & Li, X. (2018). Geothermal energy development by circulating CO2 in a U-shaped closed loop geothermal system. *Energy Conversion and Management*, *174*, 971-982.

Tester, J., & Smith, M. (1977). *Energy extraction characteristics of hot dry rock geothermal systems*.
Tester, J. W., Anderson, B. J., Batchelor, A. S., Blackwell, D. D., DiPippo, R., & Drake, E. M. (2006). The Future of Geothermal Energy: Impact of Enhanced Geothermal Systems (EGS) on the United States in the 21st Century.
Toews, M., Riddell, D., Vany, J., & Schwarz, B. (2020). Case study of a multilateral closed-loop geothermal system. Proceedings world geothermal congress, Reykjavik, Iceland, April,
Turcotte, D. L., & Schubert, G. (2002). *Geodynamics* (2 ed.). Cambridge University Press. https://doi.org/10.1017/CBO9780511807442
U.S. DOE. (2019). *GeoVision: Harnessing the heat beneath our feet* https://www.energy.gov/eere/geothermal/geovision
Vany, J., Hirschmiller, J., & Toews, M. (2020). Subsurface characterization methods for multilateral closed loop geothermal systems. Case study of field scale technology demonstration project in Alberta, Canada. *GRC Trans*, *44*(December), 1360-1361.
Vivas, C., Salehi, S., Tuttle, J. D., & Rickard, B. (2020). Challenges and opportunities of geothermal drilling for renewable energy generation. *Geothermal Resources Council Transactions*, *44*, 904-918.
Wang, G., Song, X., Shi, Y., Yang, R., Yulong, F., Zheng, R., & Li, J. (2021). Heat extraction analysis of a novel multilateral-well coaxial closed-loop geothermal system. *Renewable Energy*, *163*, 974-986.
Wang, G., Song, X., Shi, Y., Yulong, F., Yang, R., & Li, J. (2020). Comparison of production characteristics of various coaxial closed-loop geothermal systems. *Energy Conversion and Management*, *225*, 113437.
Wu, Y., Patel, H., & Salehi, S. (2021). Parametric Study of Mechanical Stresses within Cement Sheath in Geothermal Wells. *Geothermics*, *90*, 102000.
Ye, Z., Fang, Y., Ghassemi, A., & McLennan, J. (2022). A Preliminary Wellbore In-situ Stress Model for Utah FORGE. ARMA US Rock Mechanics/Geomechanics Symposium,
Yuan, W., Chen, Z., Grasby, S. E., & Little, E. (2021). Closed-loop geothermal energy recovery from deep high enthalpy systems. *Renewable Energy*, *177*, 976-991.
Zais, E. J., & Bodvarsson, G. (1980). Analysis of production decline in geothermal reservoirs. *Lawrence Berkeley National Laboratory*.
Zarrouk, S. J., & Moon, H. (2014). Efficiency of geothermal power plants: A worldwide review. *Geothermics*, *51*, 142-153.

Field Design Optimization for Horizontal Directional Drilled Ground Heat Exchangers

Richard Lein[1], Hikari Fujii[1], Saeid Mohammadzadeh Bina[1], Hiroyuki Kosukegawa[1], Retsu Harada[2]

[1]Akita University, [2]Biotex Inc.

Keywords

Ground Source Heat Pumps, Horizontal Directional Drilling, FEFLOW, Numerical Simulation, Thermal Response Test

ABSTRACT

Ground Heat Exchangers (GHEs) drilled using Horizontal Directional Drilling (HDD) technology have been proven to be a cost-efficient way of installing ground source heat pump systems (GSHP). They can also be installed in places where conventional horizontal ground heat exchangers (HGHE) would not be possible e.g., due to lack of land.

For the purpose of this research a two-day thermal response test has been conducted on a GHE installed in a double layered horizontal borehole in Saga City, Japan in March 2022. The two boreholes have a length of 59 m and 56 m, respectively. The maximum depth reached was 5 m for the upper borehole and 9.5 m for the lower borehole. Based on the installed GHEs dimensions and the geology of the test side a numerical model was developed in the numerical simulation software Finite Element subsurface FLOW system (FEFLOW) and validated with the temperatures of the heat medium at the return point and the outlet of the GHE measured during the Thermal Response Test (TRT).

After validation, the model was used to carry out a sensitivity analysis for different field layouts for HDD GHEs. The study investigated the optimum design for several layouts. The layouts chosen to utilize 2 to 4 GHEs either connected parallel or in series and simulate their performance. To compare the different layouts and find the optimum design at the location, a gym next to the installed GHE in Saga was used. Based on the gym's heating loads and an assumed coefficient of performance (COP) of 5.5 for cooling and 3.5 for heating the performance was compared. Lastly long-term simulations were carried out to compare the performance of several layouts over a long time period and investigate the influence on the ground.

1. Introduction

For the year 2019, the residential sector in Japan accounts for 159 million tons of CO2 emission, 74.3 million tons of this can be accounted for heating, cooling and hot water supply. To reduce this amount, Japan plans to continue to develop technology that reduces carbon emissions, and increase the use of renewable energies as power sources. This is necessary to achieve the goals of the Japanese government, formulated as the long-term strategy under the Paris Agreement, which aims to reduce greenhouse gas emissions by 46% in 2030 and to net zero until the year 2050 (The Government of Japan (2021).

A reliable system used worldwide, that can provide a solution to reduce greenhouse emissions caused by heating and cooling in residential buildings, are GSHP systems. In 2019, a total of 2662 facilities have been equipped with GSHP systems in Japan. Combined these GSHP have an installed capacity of 163 megawatts (MW), out of which 44% are used in residential buildings (Yasukawa et al. 2020). Even though installation in residential housing makes up for the majority of projects, bigger scale projects are also a common worldwide, and in Japan can be found, for example, in Tokyo Sky Tree (Bina et al. 2020).

GSHP systems are commonly installed either in boreholes or in shallow trenches. Both methods have their advantages and disadvantages and depending on the situation can be the preferred method. In Japan, GSHP systems installed in boreholes come with the problem of high drilling costs in comparison to America, other Asian countries, or Europe. HGHE, which are installed in trenches dug by excavators to remove the soil, are cheaper to install than boreholes (Bina et al. 2020). However, the large land requirement is, in a country like Japan, is another problem. To solve this problem alternative installations of HGHE have been investigated. Fujii et al. (2012) and Fujii et al. (2013) investigated the use of Slinky-Coil HGHE. They developed a model using FEFLOW, which takes into account the energy balance at the land surface. Based on this modeling and field tests they conducted a long-term cooling and heating test and showed that double-layer slinky coils could increase the heat exchange capacity remarkably. They also optimized the design by investigating the installation depth, the direction of circulation and the influence of the reflectance of the surface. Pu et al. (2018) investigated the effect of pipe arrangement, pipe spacing, buried depth and bending number of the pipes. They revealed that the difference between an in-line arrangement and a staggered arrangement is depending on the offset displacement and that for small offsets in-line arrangements showed better results. They also showed that the main factor affecting the thermal efficiency of HGHE is the thermal interference between adjacent pipes. Shi et al. (2022) looked into the performance of HGHE in four different configurations based on a 3D numerical model that considers atmosphere-soil interactions. They studied the effects on the thermal performance as well as the economic efficiency. Their results showed that from the investigated arrangement, serial connected tubes outperformed tiled-tube, spiral-tube and slinky coil HGHE under the tested conditions. They also showed that increased tube spacing can greatly increase performance due to lower thermal interference. Another way to improve performance was examined by Saeidi et al. (2023) by attaching fins to a HGHE for cooling operations. They investigated the effect of different materials used for the fins, position of fins, and the length and diameter of fins. They found that copper was best suited for heat transfer and larger diameter fins increase heat transfer, whereas longer fins beyond 1 m length do not further increase performance. They also found that fins are more favorable when installed on HGHE instead of vertical GHE. While a lot of research focused on improving HGHE, other researchers tried to combine HGHE with existing technologies to further increase usage. Léveillée-Dallaire et al. (2023) installed

Slinky-Coil HGHE under a greenhouse in Canada and showed the use of HGHE with limited space. The results of their study showed how much percent of the greenhouses heating and cooling could be covered. They also found that when installed under a greenhouse, the heating performance increases, while cooling becomes less effective. Further approaches to combine HGHE with other technologies have been conducted by Dacquay et al. (2020) who combined GHE with sewage pipes. Their study showed that the system has a profitable lifespan of 25 years and highlighted key parameters affecting the system. Further results included that the installation depth and that the thermal properties of the high-density polyethylene pipe used do not influence the performance. It was also shown that for a sustainable behavior the sewage pipe capacity was at 50% and 75%. Another way to improve HGHE suggested by Bottarelli et al. (2022) was the use of phase change materials in the backfilling. The results showed that these could help deal with peak loads in harsh weather and therefore recommend the use in climates with hot summers and cold winters. However, they found that the main effect can be observed in summer, while in lower temperatures in winter water was as suitable as the phase change material. A good summary of the majority of the recent GSHP studies is provided by Rashid et al. (2023). However, it is evident from this overview that conventional vertical GSHP and HGHE are the subject of the majority of studies.

A third way to install GHE is the use of HDD technology. In Japan this technology has first been introduced by Hamada et al. (2007). HDD is a drilling method used to install pipes or cables which does not require to disturb the surface by digging a trench. The drilling is launched from equipment at the surface and follows a pre-defined path. It is a highly flexible method which can reduce drilling cost by reducing work time needed for construction and reducing land surface requirements. Furthermore, it is also capable of drilling very varying boreholes that can be adapted to many locations' requirements. HDD drilling is commonly known for its use in the installation of pipes and cables under obstacles such as roads, railroads, or rivers.

In North America HDD is already frequently used to install GHEs either by inserting a U-Tube or by drilling large U-shaped boreholes. Grupp and Fortunato (2014) describe a system installed on the American West Coast, where several U-Tubes were inserted into HDD boreholes and field test conducted. They described the biggest challenge faced during trials was the missing regulations for this kind of technology and under sizing of the installed GHE. Dacquay, Lohrenz, and Fujii (2022) utilized an HDD drilled HGHEs in two layers to develop and evaluate a software and hardware package that calculates future ground hear exchanger temperatures to avoid thermal imbalance. The installation method used allowed for the use of a bigger diameter by inserting a single pipe into the borehole. Similar, Bina et al. (2020) investigated and simulated a HDD HGHE installed in Saga, Japan. By utilizing their model, they investigated the influence of nominal diameter, horizontal length, installation depth, and groundwater flow on the system. They also compared the results of an economic analysis with a regular vertical GSHP system to show the cost efficiency of HDD drilled HGHE. However, by just installing a single layered system, they found that a lot of energy got wasted returning the heat medium to the inlet above ground, due to the length of the borehole. On the same project location Tsuya et al. (2021) conducted test to determine the influence of the flowrate and flow-direction in the HGHE. They conducted a TRT on the HGHE and showed its applicability to this kind of system. During the testing the flow direction was reversed and showed a declining heat exchange rate. After testing they conducted sensitivity studies to show the influence of the flow rate on the heat exchange capacity and determined the optimum flowrate for the field test area. Their research also showed that for pipes with larger diameters higher flowrates are required to maintain a good performance. The same test

site has been used in a modified state by Lein et al. (2024). In their research the test site was expanded to a double layered HDD drilled HGHE. This was done based on previous research that showed layering HGHE can improve the performance (Fujii et al. 2012). The authors investigated the applicability of water injection into the boreholes to improve performance. This has been proven effective in vertical GHE (Inoue et al. 2014) and as HDD drilled HGHE combine the properties of HGHE and vertical GHE, they can benefit from layering and water injection both. The study considered several parameters for water injection, like injection rate, injection temperature, injection place, and permeability of the underground. The results showed improvement of heat exchange rates for higher injections rates up to 2 L/min. They also showed the influence of the geology and injection place that can alter result significantly when the ground is impermeable and water injection occurs in all boreholes.

A lot of research conducted is done by utilizing simulations. When simulating HGHE it is important to consider the interaction between ground surface and the atmosphere, especially the heat flow. The heat flow is influenced by many parameters, like atmospheric temperature, solar radiation, and others. Tang and Nowamooz (2020) showed the importance of this interaction in their simulations by conducting them when considering the interaction between atmosphere and soil and without it. For this they developed a model that considers the energy water balance on the land surface. Nam and Chae (2014) coupled models for ground heat transfer, ground surface heat and ground heat exchanger to predict the heat exchange rate in case studies. The investigated ground heat exchanger was installed in the foundation of a building, with the goal of creating a design tool for HGHE. With this they achieved good results for heating, however cooling operations need more input data due to factors like heat emissions of mechanical equipment not being considered. To consider the interaction between surface and atmosphere this paper will use the approach by Fujii et al. (2019) using the Sol-Air temperature (SAT). The SAT uses several parameters and combines them into a new variable that was used as a new input for their simulations. Using the SAT led to good results in the analysis they conducted in the same area as this study.

The literature study does point out several gaps in the overall research on HDD drilled HGHE. Design analysis have been frequently carried out in many studies as shown in literature research, but mainly focusing on HGHEs. Especially the interaction and performance of several HDD drilled HGHE has not been well investigated yet. This is where this paper aims to fill the knowledge gap and help improve design decisions for HDD HGHE systems. On the base of a field test conducted in Saga, Japan on a double layered HDD HGHE and an adjacent gym, several designs for HDD HGHE have been tested and compared as the main objective of this paper. Following a TRT, the measurement results were utilized to build and validate a numerical model in FEFLOW. This model was then adapted to investigate five different designs. These include the original system installed, ring shaped HGHE, two parallel HGHEs, angled HGHEs, serial connected HGHE and two double layered HGHE in a staggered arrangement. To investigate their performance a gym next to the original installed HDD HGHE was used as reference. After calculating the required heating and cooling loads for one year and the necessary heat exchange rate, each design was compared with each other. For the parallel system and the angled system sensitivity studies have been carried out to determine suitable distance and angles respectively, to achieve optimal performance for the location. Lastly long-term simulations have been carried out over a span of 10 years for the same systems to determine long-term performance, influences on the ground and sustainability of the system.

2. Field Test and Numerical Modelling

On the southern island of Kyushu in Japan, in the city of Saga, a double layered HDD drilled HGHE was constructed. The drilling and connection of the HGHE, seen in Figure 1, were done under the parking lot of Biotex Co. Ltd. in two U-shaped boreholes. The upper and lower boreholes have a length of 59 meter (m) horizontally and a depth of 5 m and 56 m and a depth of 9.5 m respectively. Inside the borehole high density polyethylene pipes with an outer diameter of 60 mm and an inner diameter of 52 millimeter (mm), and a thermal conductivity of 0.42 watt per meter-kelvin (W/m/K) was installed. The annular space of the borehole with a diameter of 114.3 mm was naturally filled and eliminates the need for grouting or casing.

Figure 1 Drilling and connection of the boreholes

On its path, seen in Figure 2 the borehole crosses through the different geological layers at the location which consist of clay and sand, shown in Figure 3. At a depth of 3.8 m clay is interrupted by a thin sand layer before reaching a depth of 7 m, and being replaced with sand. Laboratory measurements carried out on samples from the location have given a thermal conductivity of 0.951 W/m/K for clay and 1.261 W/m/K for sand in water-saturated conditions. The groundwater level at the test site was measured at a depth of -0.98 m.

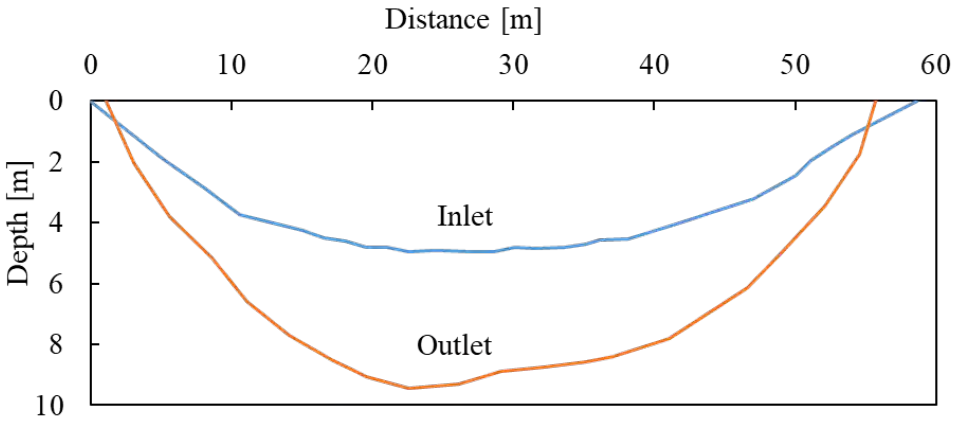

Figure 2 Drill path of the boreholes

The test field's location is situated in the temperate climate zone with no dry season and hot summer (Cfa) according to the Köppen climate classification (Kottek et al. 2006). The weather in Kyushu is characterized by hot summers with high precipitation and moderately cold winters with low precipitation.

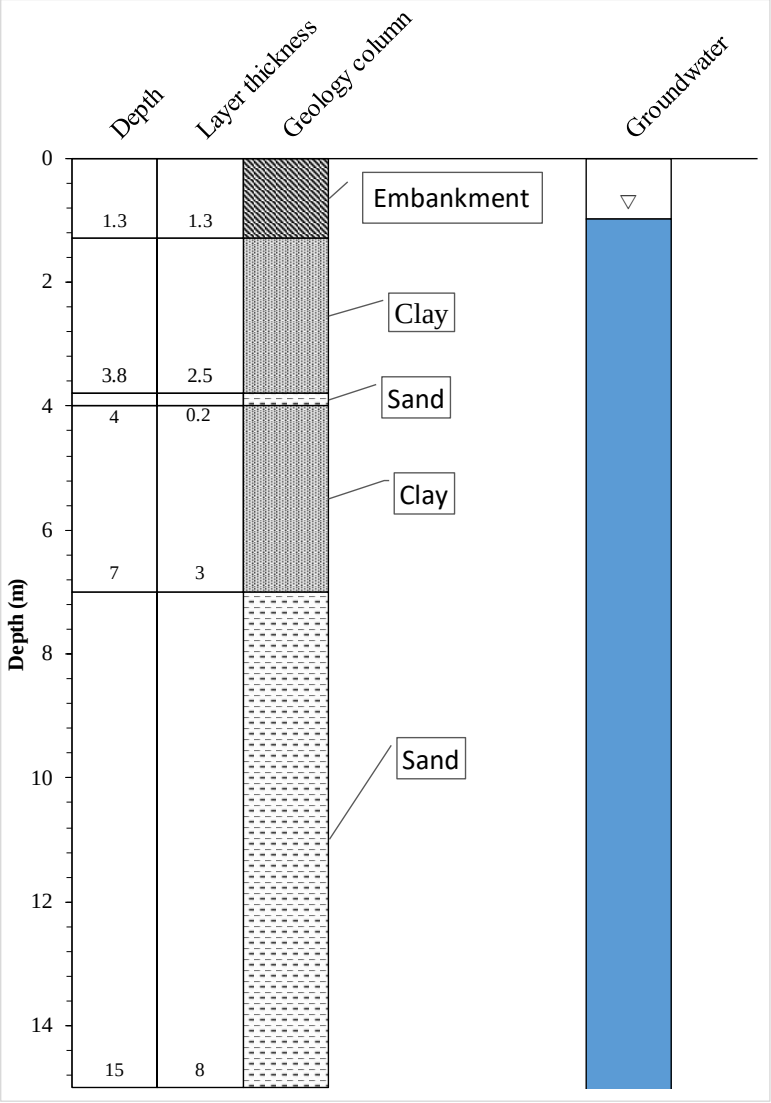

Figure 3 Geological column of the test area

2.1 Results of the Field Test

In spring of 2022, a field test took place. From March 24 to March 26 a TRT was conducted using the testing equipment of Akita University shown in Figure 4. The apparatus has a total capacity of 10-kilowatt (kW) heating, which is split to two heaters with a capacity of 6 kW and 4 kW respectively.

Figure 4 Testing equipment of Akita University

For the TRT, a constant heat load of 5 kW with a flow rate of 20 liter per minute (L/min) was applied on the system. As a heat medium water was utilized. One benefit of installing the double-layer HGHE is that inlet and outlet are now located close to each other, which eliminates heat losses occurring when installing a single-layer HGHE where the heat medium is transported back above ground. During the TRT several parameters have been measured and can be seen in Figure 5. The temperature was measured at three points, the inlet, the turn-point and the outlet. Furthermore, the flowrate and ambient temperature were recorded and the average heat exchange rate was calculated to be at around 5.21 kW (43.79 watt per meter (W/m)). During the last quarter of testing rain started, which decreased the temperature in all three points measured. The total amount of rainfall of 59 mm was observed at the local weather station in Saga City. Due to the HGHE not being fully completed and thus allowing the inflow of water, this behavior can be explained. Another factor that explains this behavior is the installation method itself. Due to the drilling being shallow in the beginning and having a low angle a sizeable amount of the GHE is closer to the surface than normal HGHEs and can be influenced by rain faster.

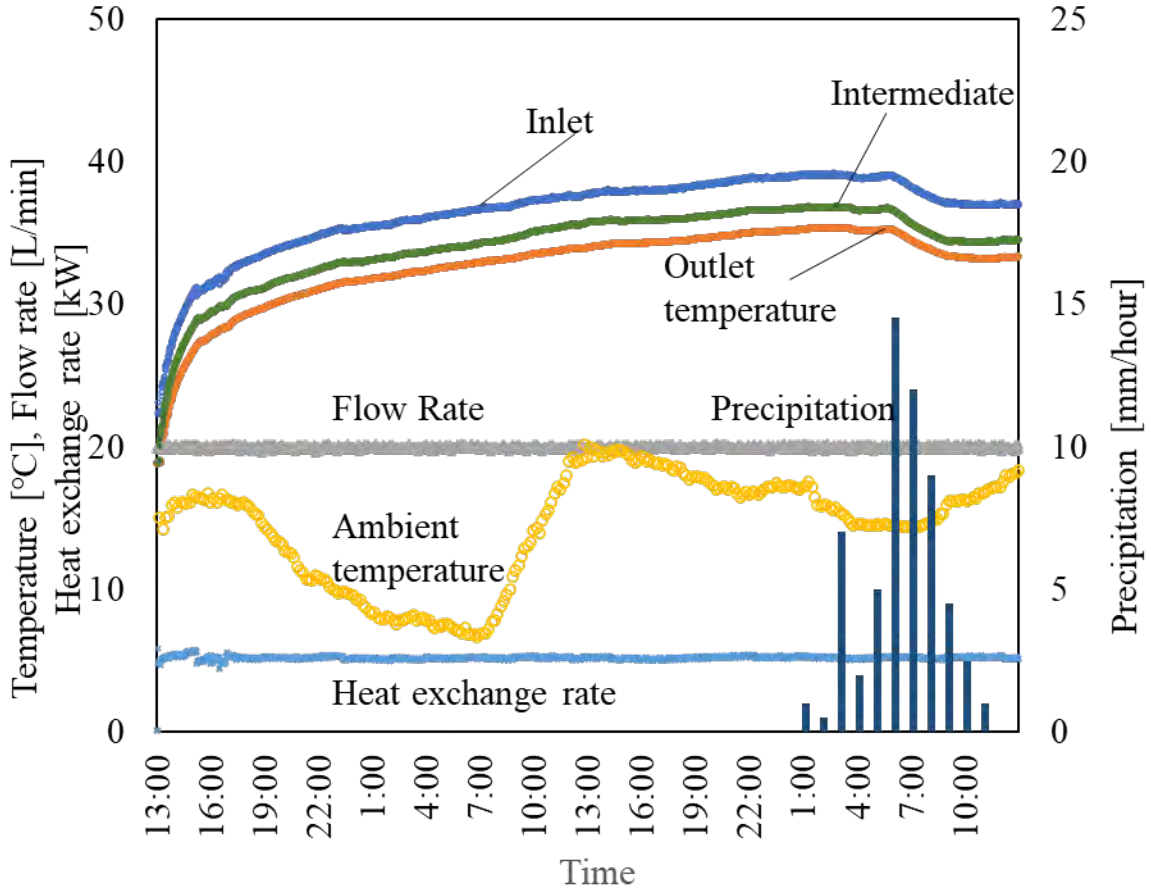

Figure 5 Result of the Thermal Response Test

2.2 Numerical Modeling

Using FEFLOW 8.1 (Diersch 2013) as software, a numerical was created to simulate the problem. FEFLOW uses the following three equations to simulate mass and heat transport:

$$\frac{\partial}{\partial t}(\varepsilon_\alpha \rho^\alpha) + \frac{\partial}{\partial x_i}(\varepsilon_\alpha \rho^\alpha v_i^\alpha) = \varepsilon_\alpha \rho^\alpha Q_\rho^\alpha \quad (1)$$

$$v_i^\alpha + \frac{k_{ij}^\alpha}{\varepsilon_\alpha \mu_\alpha}\left(\frac{\partial p^\alpha}{\partial x_j} - \rho^\alpha g_j\right) = 0 \quad (2)$$

$$\frac{\partial}{\partial t}(\varepsilon_\alpha \rho^\alpha E^\alpha) + \frac{\partial}{\partial x_i}(\varepsilon_\alpha \rho^\alpha v_i^\alpha E^\alpha) + \frac{\partial}{\partial x_i}(j_{iT}^\alpha) = \varepsilon_\alpha \rho^\alpha Q_T^\alpha \quad (3)$$

Mass conservation, Momentum conservation, and Energy conservation are expressed by the Equations 1 to 3 respectively. With ε being the porosity, α the ground thermal diffusivity in square meter per second ($m^2 s^{-1}$), ρ the gas density in kilogram per cubic meter (kg m^{-3}), v_i the vector of pore velocity in meter per second (m s^{-1}), Q_ρ the fluid mass sink/source in per second (s^{-1}), $k_{ij}$the permeability tensor in square meter (m^2), μ the dynamic viscosity of gas in kilogram per meter per second (kg $m^{-1} s^{-1}$), p the gas pressure in pascal (Pa), g_j the gravitational vector in meter per

second squared (m s^{-2}), E the internal thermal energy density in square meter per second squared (m^2 s^{-2}), x_i the cartesian coordinates (m), j_{iT}^{α} the Fourier's heat flux vector in kilogram per cubic second (kg s^{-3}), and Q_T the source of heat (kg $m^{-1}s^{-1}$).

Figure 6 shows the dimensions of the model. To create the model, the well path was imported using an Auto CAD file and the map function of FEFLOW.

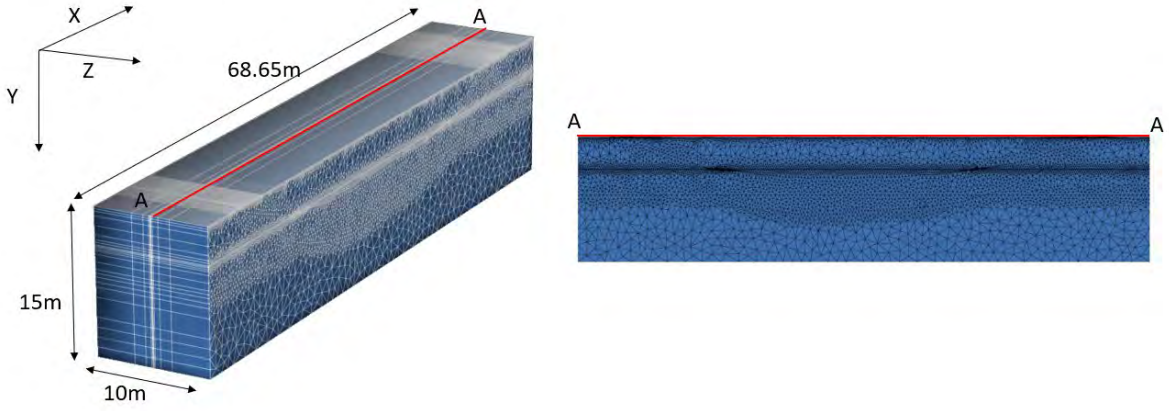

Figure 6: Dimensions of the model

The mesh of the model consists of a total of 162,252 elements which were refined and defined in a way around the HGHE to have at least 5 m of blank mesh existing to prevent any influence from any boundary conditions. The boundary conditions of the model are displayed in Table 1.

Table 1: Boundary Conditions	
Fluid Flux:	No inflow from the bottom or the sides of the model, inflow from the top according to rainfall observed
Hydraulic Head:	No groundwater flow
Boundary Condition:	Adiabatic at peripheral boundaries 19.7°C at the bottom boundary of 15 m (average of SAT) SAT from the surface
Soil:	
Thermal Conductivity:	Clay: 0.951 W/m/K, Sand: 1.261 W/m/K
Heat Capacity:	2.52 Megajoule per cubic meter kelvin ($MJ/m^3/K$)
Pipe:	
Thermal Conductivity:	0.42 W/m/K

To obtain the initial conditions of the ground temperature at the start of the TRT, a 2.5-year long simulation was used utilizing the SAT, as no temperature measurements of the underground were taken. With the data of this simulation Equation 4 was created and imported into the model:

$$T=-0.00388092*y^3-0.15539878*y^2-2.04325121*y+10.91131541 \quad (4)$$

With T being the temperature (°C) and y the depth.

The SAT was used for the as the temperature input on the surface of the simulations to consider the influence of the atmosphere. This method was been proven as accurate based on previous studies in the same location utilizing this method. The SAT is used in the simulations instead of the air temperature as an input and considers more parameters as shown in Equation 5:

$$SAT=\theta_0+1/\alpha_0((1-\alpha_s)*J-\varepsilon*J_{eh} \quad (5)$$

With θ_0 being the ambient temperature (°C) and J the solar radiation in watt per square meter (W/m²). Both were derived from the local weather station in Saga City. α_0 and α_s are the coefficients for heat transfer between air and soil in watt per square meter kelvin (W/m²/K) and the Albedo (0.3 for soil), respectively. Lastly, ε is the dimensionless factor for long wave emission and J_{eh} the effective emission (W/m²).

To validate the model the inlet temperature measured during the TRT was used as input data to simulate the turning point and outlet temperature. Figure 7 shows the result of the history matching using the two temperatures simulated, which both show a good match throughout the whole time of the TRT. The average errors for the turning point temperature are 0.17°C and 0.09°C for the outlet temperature.

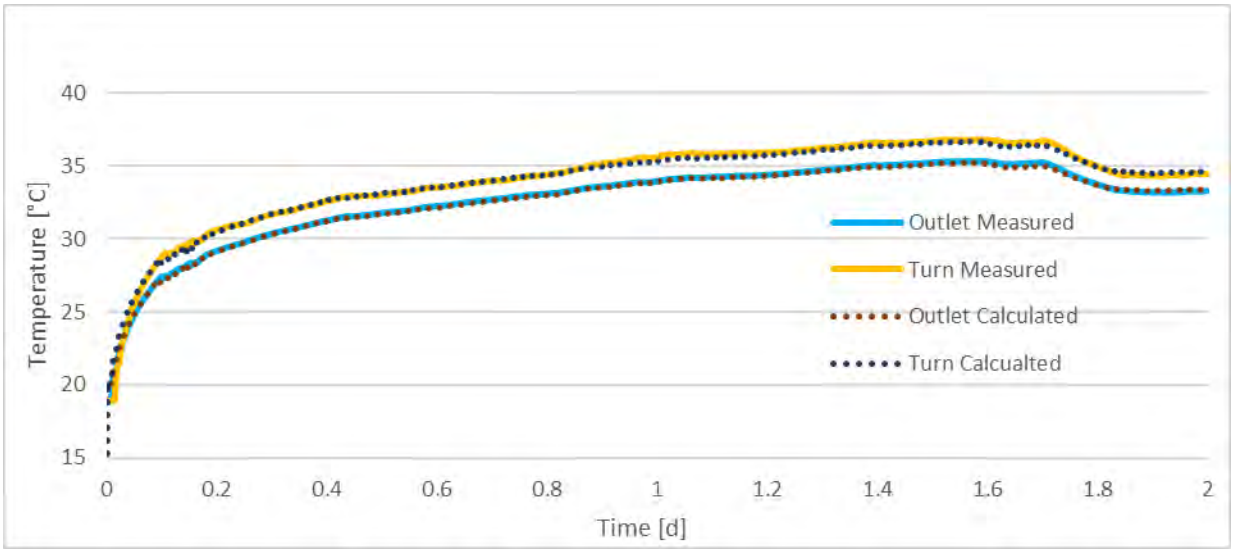

Figure 7: Results of history matching

3. Design Boundary Conditions and Input Data

3.1 Input Parameters

To simulate the performance of the different designs, the heat loads required for a gym next to the originally installed HGHE will be used. The outline of the gym can be seen in Figure 8. The gym covers a total surface area of 1027.35 m² and a roof area of 328.76 m².

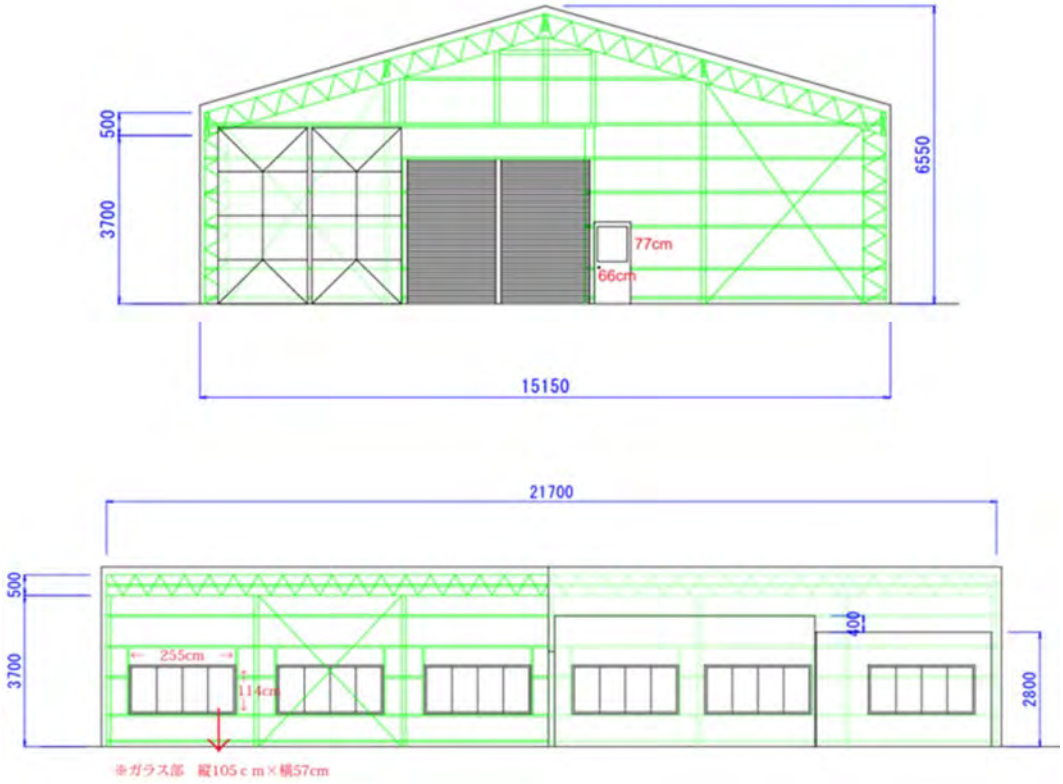

Figure 8: Geometry of the gym

To calculate the heat loads for the gym the Equations 6 and 7 have been used.

$$Q_h = \frac{U*A_e(T_i - T_o)}{A_f} - \frac{I*\eta}{A_f} \quad (6)$$

$$Q_c = \frac{U*A_e(T_o - T_i)}{A_f} + \frac{I*\eta}{A_f} \quad (7)$$

Where Q_h and Q_c are the heating and cooling heat loads (W/m²), U the average heat transfer coefficient (0.87 in the case of Saga City), A_e the surface area of the building (m²), A_f the roof area of the building (m²), T_i the target room temperature (°C), T_o the outside Temperature, I the solar radiation (W/m²) and η the average solar heat gain rate. The weather data for the calculations have been taken from the local weather station in Saga City. The required heat exchange rate for the gym can be seen in Figure 9. For the calculations a constant coefficient of performance (COP) of 5.5 for cooling and 3.5 for heating was assumed.

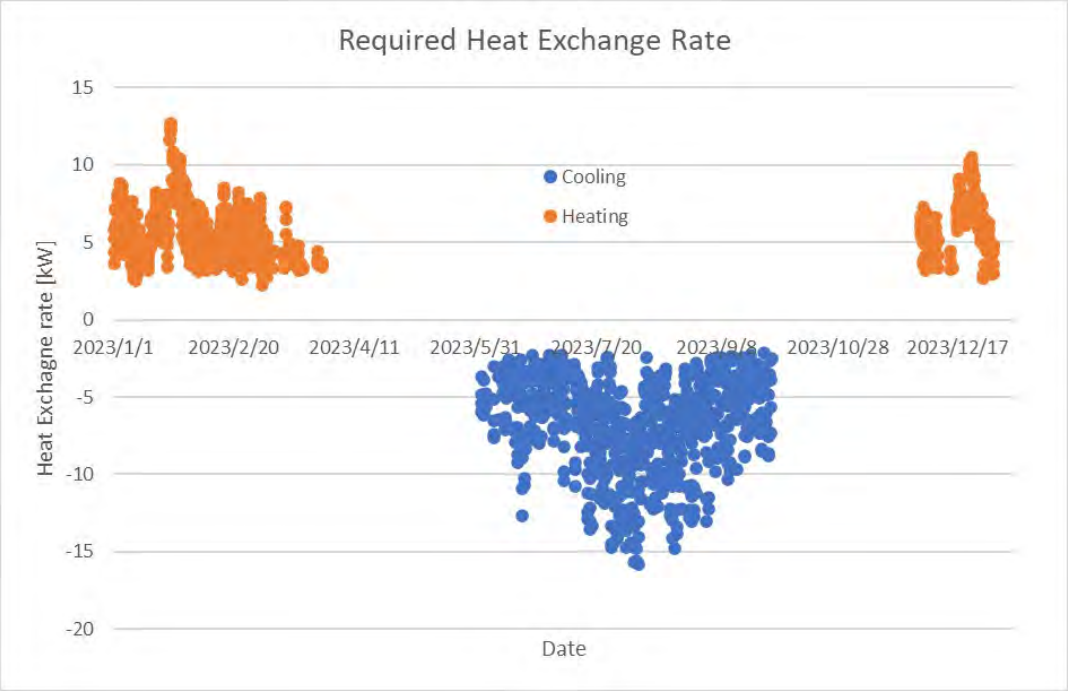

Figure 9: Required Heat Exchange Rate for the gym

Afterwards Equation 8 was used to calculate the required heat exchange in the GHE for a set flowrate:

$$q=\dot{Q}*Cp*\rho*\Delta T \quad (8)$$

Where q is the amount of heat transfer (W), $\dot{Q}$ is the volumetric flowrate in cubic meter per second (m^3/s), Cp the specific heat of the heat exchange fluid in kilojoule per kilogram kelvin (kJ/kg*K), ρ the density of the fluid (kg/m^3) and ΔT the temperature difference between inlet and outlet.

As input on the surface the SAT based on weather data from the year 2023 was used. This data was measured at the local weather station and the SAT was calculated by using Equation 5.

3.2 Boundary Conditions

To guarantee comparability of design the following boundary conditions have been set as seen in Table 2.

Table 2: Boundary Conditions	
Heat Load:	According to gym calculations
COP:	Heating: 3.5 Cooling: 5.5
Target Room temperature:	Heating: 20°C Cooling: 24°C
Daily Operation Time:	15:00-19:00
Flowrate:	30 L/min
Pipe length:	120 m and 240 m
Surface:	SAT
Heat Medium:	Water

For the case studies the simulation time will be set to 1 year to cover the heating and cooling period. Heating was done from December to March and cooling operations occurred from June to September. The operation time was set from 15:00 to 19:00 according to the usual usage for the gym. Furthermore, the total land area covered by the GHE was limited to a size of 1 hectare. The geology of the model will be based on the original geology in Saga as well as the size and properties of the GHE.

4. Sensitivity Studies

To evaluate different designs the following section will cover a sensitivity analysis to show the influence of the designs chosen. In total six different designs with two pipe lengths have been investigated, which are displayed in Table 3 and Table 4:

Table 3: Total Pipe length 120m

Straight:		Original HGHE installed in Saga
Ring:	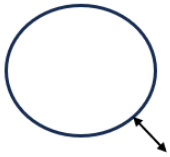	Total pipe length of about 120 m with a radius of 20 m

Table 4: Total Pipe length 240 m

Parallel arrangement:	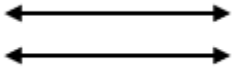	2 layers 120 m pipe length in each system 60 m per layer
Staggered arrangement:	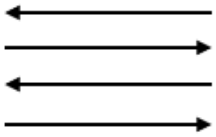	1 layer 120 m pipe length in each system 60 m length per pipe
Series arrangement:		2 layers 120 m each 60 m per layer
Angled arrangement:	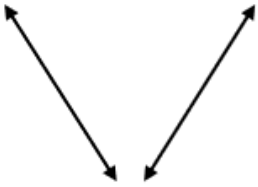	2 Layers 120 m pipe length in each system 60 m per layer

For some of the designs, sensitivity analysis have been carried out to determine ideal design parameters.

4.1 120 m Pipe Length

To achieve comparability the performance of the originally in Saga installed system was simulated using the boundary conditions for the gym described in the previous chapter. The result of this simulation can be seen in Figure 10.

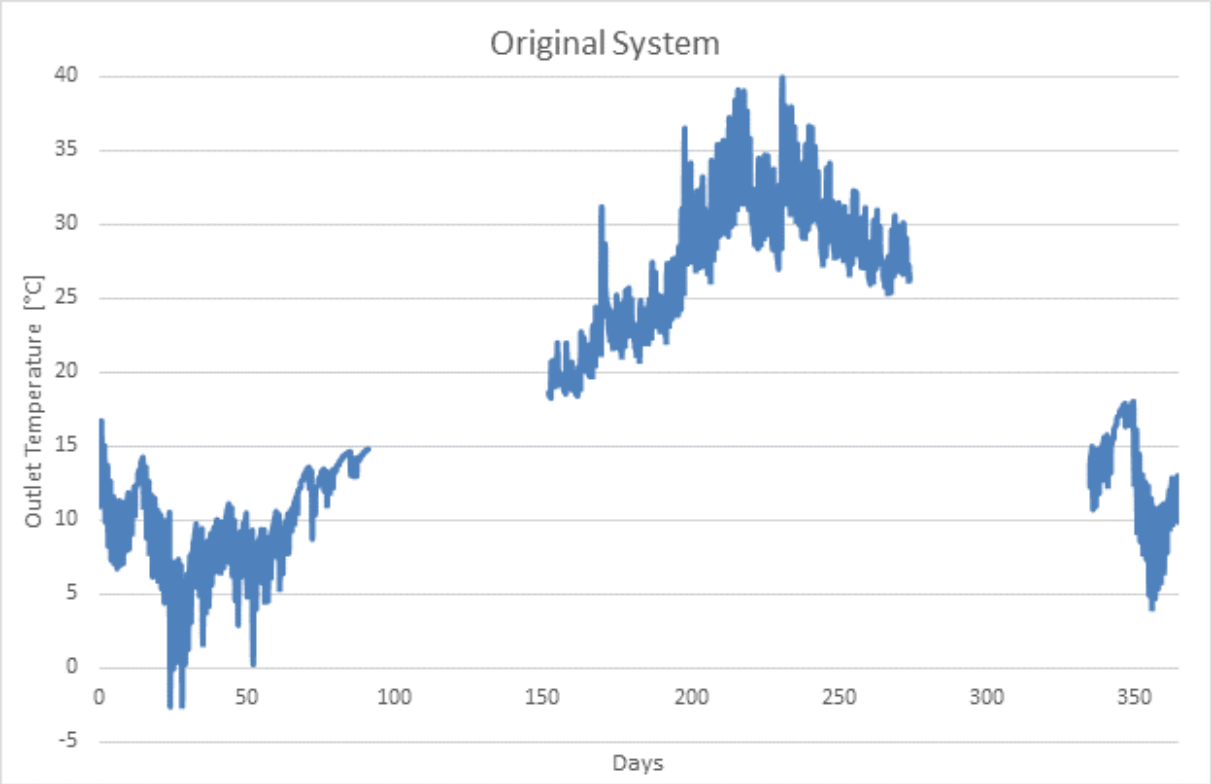

Figure 10: Performance of the original system

The data from this simulation will mainly be used as a comparison to other designs, however it is already visible that this system reaches negative degrees for the outlet temperature in winter and up to 40°C in the summer which is usually undesirable, therefore it was concluded that a larger system is more desirable.

The second sensitivity study conducted with a pipe length of 120 m was an HDD HGHE in the shape of a ring. It was chosen to conduct it with this pipe length as this was, according to the installing company, the smallest drilling radius possible. Figure 11 shows the performance of the ring shaped GHE, installed at a depth of 5 m, compared to the original system. Comparison of the two arrangements shows only small differences in the performance. This difference can be explained by the installation depth of the system. While the straight arrangement is a double-layer installation, the ring was only installed in one layer. If installed at the same depth as the upper layer (5 m), the performance will be slightly worse for the ring, caused by the better performance of deeper installed HGHE. Similar behavior is observed when the HGHE is installed at a depth of 10 m, equivalent to the deeper borehole, which leads to slightly better performance than a system with a straight arrangement. However, no further testing on this shape has been conducted, as a field test utilizing this design is currently being planned.

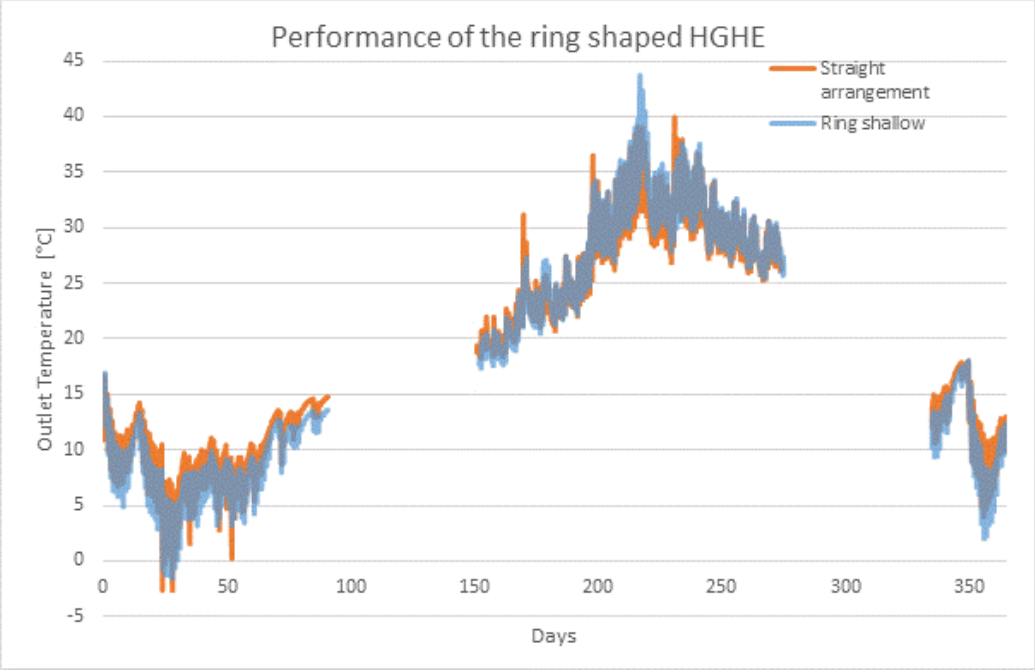

Figure 11: Performance of the ring-shaped HDD HGHE

4.2 240 m Pipe Length

For a pipe length of 240 m the performance of four different systems has been investigated. Beforehand for the 2 parallel Systems and the Angled System the influence of the distance between the systems and the angle has been investigated. For this a constant heat load of 10 kW and a flow rate of 30 L/min was applied to the system over the course of 30 days. The result for the 2 parallel systems can be seen in Figure 12.

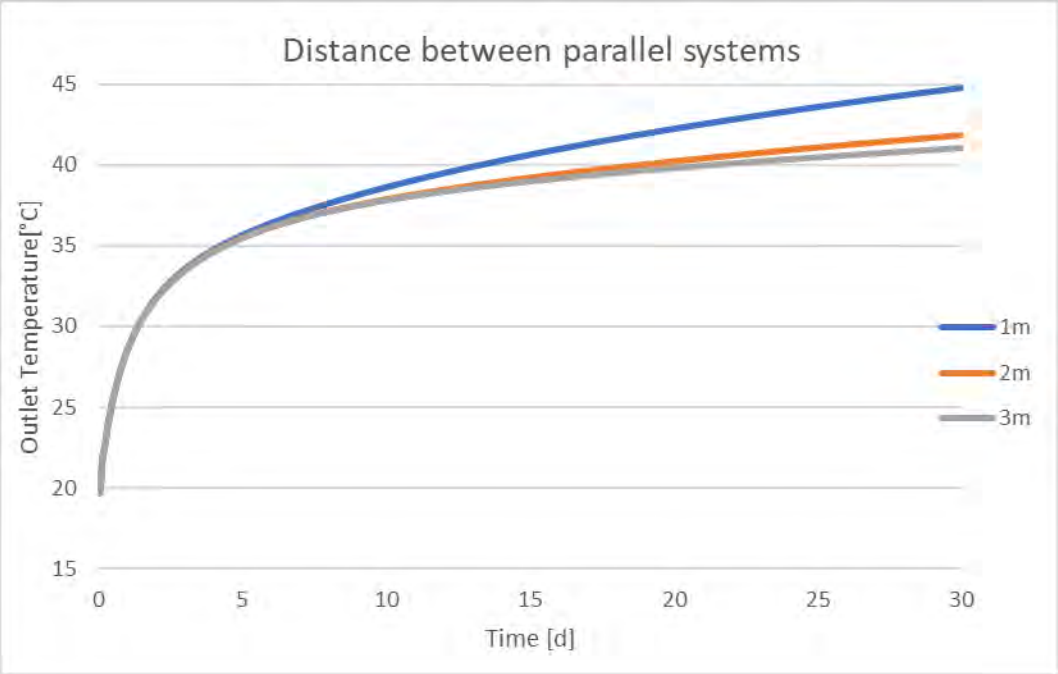

Figure 12: Distance between parallel systems

The simulation shows that for this kind of arrangement a wider spacing between the systems is preferable. As the interference on each other becomes noticeable smaller with increasing spacing a distance of 3 m has been chosen for the analysis to use the available space as efficiently as possible. For the angled arrangement angles of 15°, 30° and 45° between the pipes have been investigated, which can be seen in Figure 13.

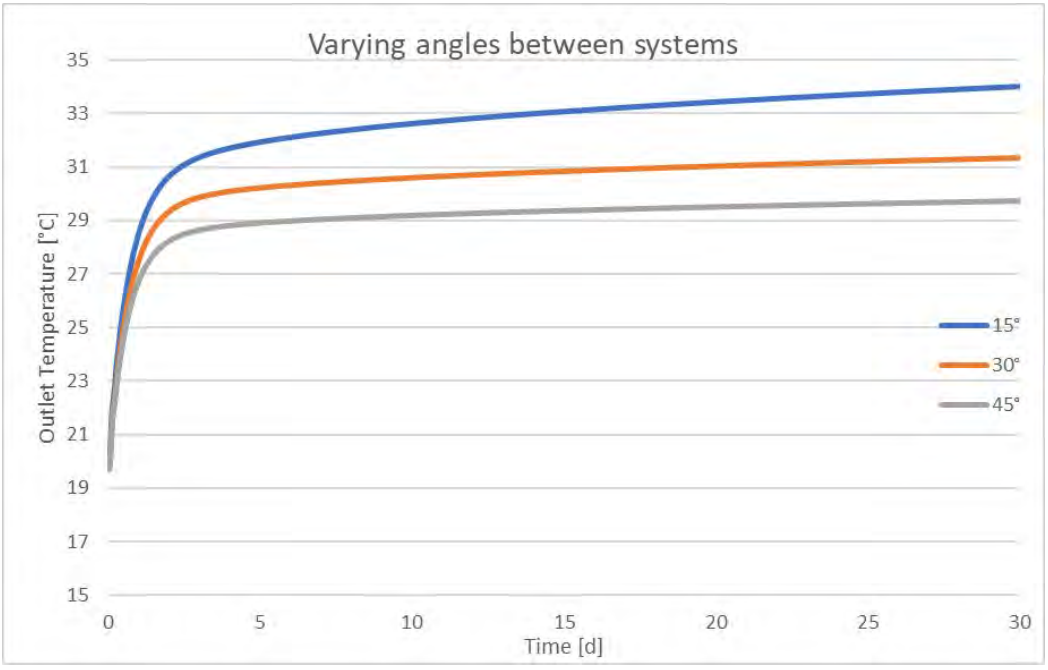

Figure 13: Comparison of varying angles

Larger angles in this design mean a large increase in land usage. This behavior can be seen in Figure 14, where that distance between the turning point of the systems increases by about 34.6 m when comparing an angle of 15° and 45° between the pipes. This design was tested with the idea of drilling several boreholes from one starting point in a circular pattern. Based on this idea, and the results from the simulation an angle of 30° was chosen for the sensitivity study. While an angle of 45° would result in a better performance when just utilizing two or three systems, choosing an angle of 30° between the systems would allow the installation of 4 more systems when installing them in a full 360° circle.

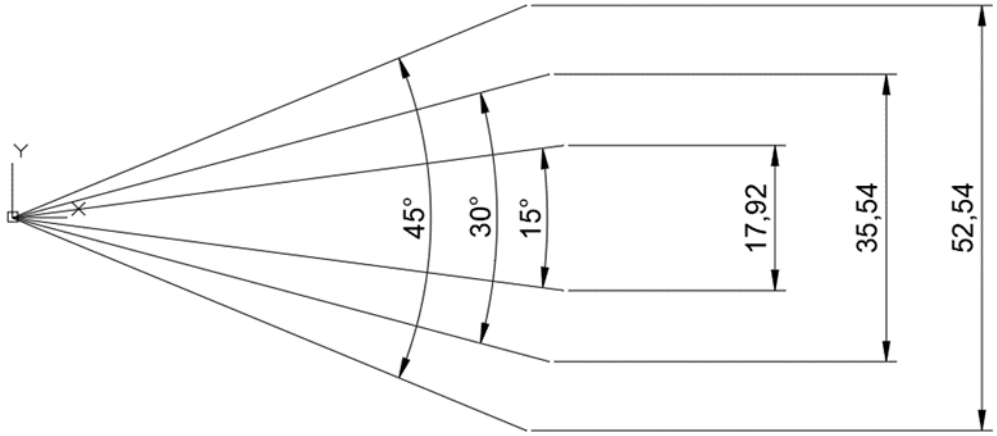

Figure 14: Distance between the turning point for different angles

The results of the comparison of the systems utilized for the gym in Saga can be seen in Figure 15. The first thing to notice is that a system with a pipe length of 240 m is much more suitable for the gym compared to a system with 120 m pipe length. During peak loads the outlet temperature does not surpass 33°C for cooling or fell below a temperature of 5°C in heating. When comparing the performance of the systems, it can be seen that the angled system has the best performance. This can be explained with the wide spacing between the pipes and therefore lower thermal interference between the systems. However, the much larger land requirement of this kind of system mean consideration has to be taken when using more than two systems like in the study. Surprisingly there is only a very small difference between two parallel systems and a serial connection of two systems, with the later one having a slightly better performance. This shows that for the chosen parameters the thermal interference was only minimal and a design can be selected based on land availability. The results also agree with previous research done on conventional HGHE, where series connections had a better performance, compared to other designs. This means that serial connected designs, that would e.g. surround a house, can be a promising way of installing HDD HGHE, which would not require a lot of additional land. The performance of the staggered system was very comparable to the parallel system, however, when peak loads occurred it performed much worse. This can be explained by former observations in research that showed that certain staggered arrangements of pipes might perform worse than in line arrangements like in the parallel system. As only one type of staggered arrangement has been tested in this research, more work needs to be conducted to get more reliable results.

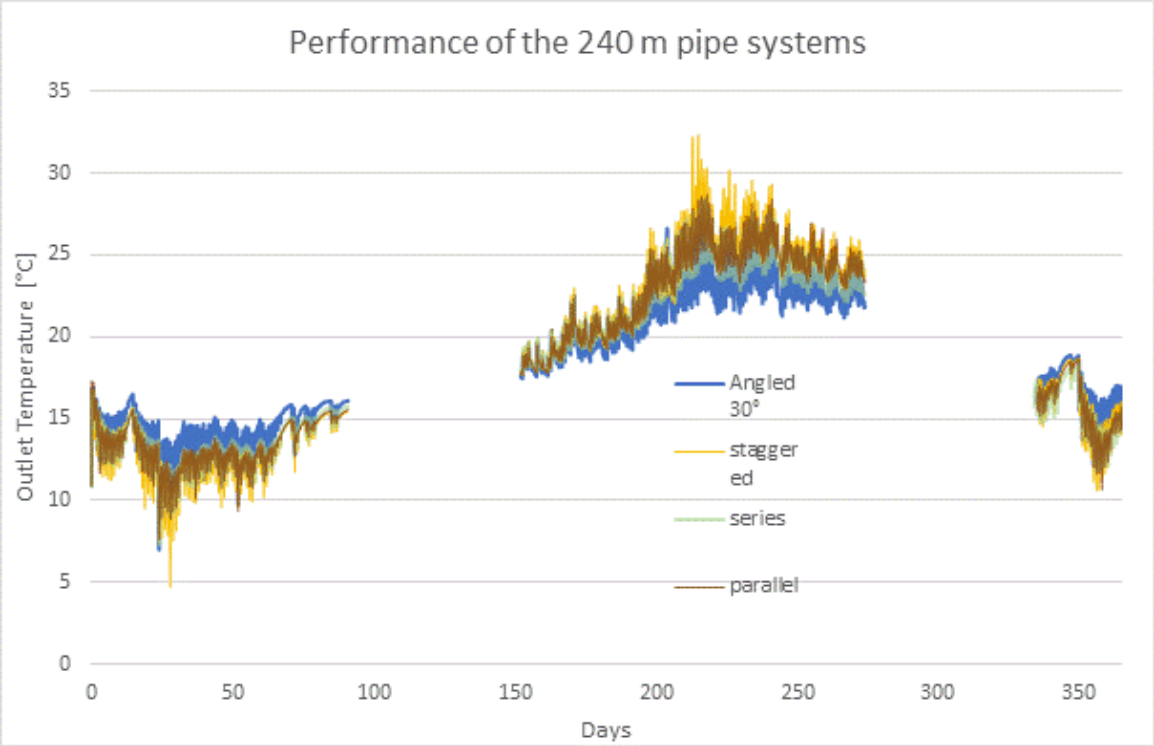

Figure 15: Comparison of results with 240 m pipe length

5. Long Term Simulations

The last chapter of this paper will focus on long-term simulations to analyze the impact on the ground and long-term sustainability. Results of the first three years of the 10-year simulations can be seen in Figure 16. Exemplary the performance of the angled system was shown, as the best performing system. The first thing to notice is that all simulations show the same behavior in year two, where outlet temperatures are much higher than in the first year. The reason for this is the difference in temperatures in different years. For the simulations weather data based on 2023 has been used. However, the initial conditions are set at the start of the year 2023, which makes them influenced by weather data from the year 2022, which was a lot colder than the following year. However, after one year this effect disappears. The two peaks appearing in summer and winter can be explained by the use of the data from the gym for repeated years, which had two peaks each, during cooling and heating operations.

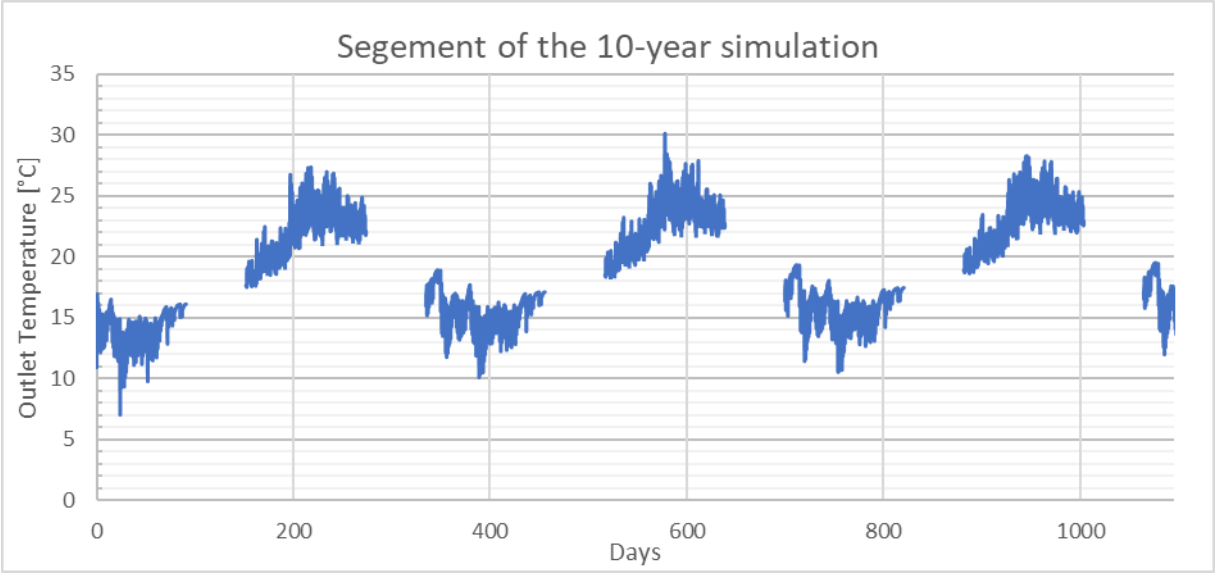

Figure 16: Segment of the 10-year simulation

Something that can be noted overall is that over the course of ten years there is a slight increase in average outlet temperature. This can be observed in all systems tested to a certain degree, ranging from 1.5°C to 3°C. In the smaller systems this development is stronger and in general shows an energy imbalance and the fact that the ground cannot recover enough during the rest periods. This energy imbalance can also be seen in the required heat and cooling loads, with 4.73 MW for cooling and 3.48 MW for heating. For long-term performance this will mean a drop in efficiency of the system. A slight increase in temperature of the ground can also been seen in Figure 17. While the changes have a very small magnitude, especially around the lower pipe they are clearly visible.

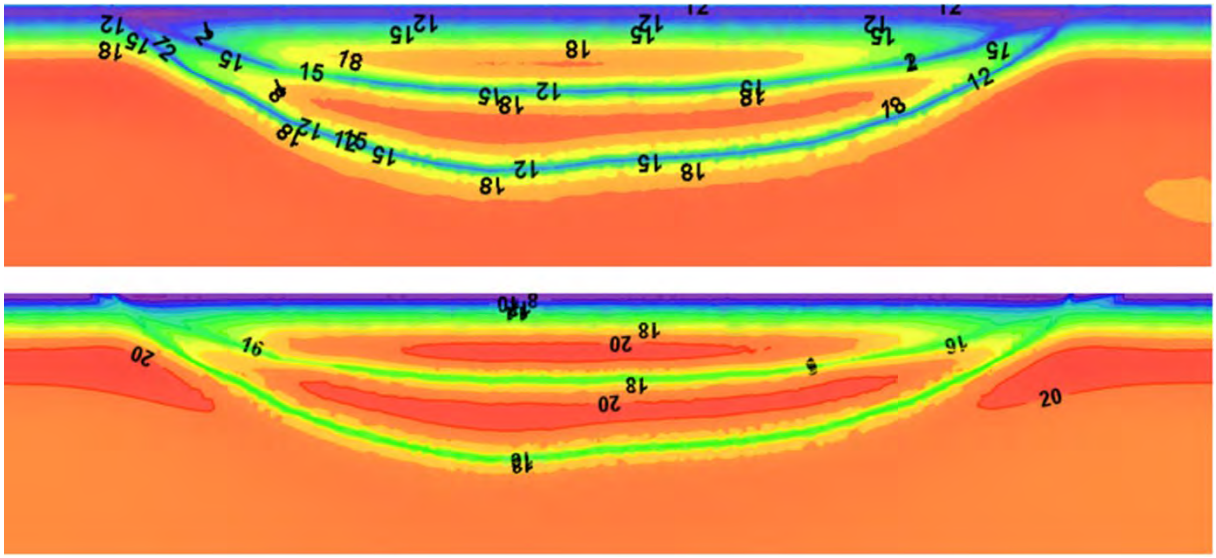

Figure 17: Temperature development in February of year 5 and 10

6. Conclusions

In this study, a field test and numerical simulations were done to optimize field design for HDD drilled HGHE. A TRT was performed on an HGHE installed in Saga City, Japan, in March 2022. The HGHE consisted of two boreholes with a diameter of 114.3 mm at a depth of 5 m and 9.5 m and a length of 59 m and 56 m, respectively.

Based on this the field test, geology and the wells a numerical model was related in FEFLOW and validated using history matching of the turn point temperature and the outlet temperature measured during the TRT. The model was then used to evaluate several installation designs based on heat load calculations for a building and their long-term performance. The evaluated shapes were, the original system, a ring-shaped system, a parallel system, a serial connected system, a staggered system and an angled system. The building used for the calculations was a gym adjacent to the original project in Saga City. Based on the usage hours and the design of the gym the required heat load for the year was calculated and afterwards used in the simulations as input. The results can be summarized in the following points:

- The ring shape has a similar performance like the straight system and will be further investigated in following studies. The performance depends strongly on the installation depth of the ring, and is better when installed at a deeper depth.
- The other arrangements performed in the following order: angled > series > parallel > staggered. With the difference between the performance of series and parallel arrangement being minimal.
- Different arrangements still can be preferable over better performing arrangements due to the large space requirements for e.g. the angled arrangement
- Long-term performance has shown an energy imbalance in the system that would lead to a temperature increase of 1.5°C to 3 °C, depending on the system.

Overall, it was shown that the high flexibility of HDD drilling allows for the installation of different designs that can be adapted to the situation needed. Future research should focus on the field testing of designs, the large-scale application of designs, and the additional testing for certain arrangements, like the staggered arrangement tested.

REFERENCES

Bina, Saeid Mohammadzadeh, Hikari Fujii, Shunsuke Tsuya, Hiroyuki Kosukegawa, Shigemi Naganawa, and Retsu Harada. "Evaluation of utilizing horizontal directional drilling technology for ground source heat pumps." *Geothermics* 85 (2020). 101769.

Bottarelli, Michele, Eleonora Baccega, Silvia Cesari, and Giuseppe Emmi. "Role of phase change materials in backfilling of flat-panels ground heat exchanger." *Renewable Energy* 189 (2022). 1324-1336.

Dacquay, Connor, Hartmut M Holländer, Miroslava Kavgic, Pooneh Maghoul, Hongwei Liu, and Hikari Fujii. "Evaluation of an integrated sewage pipe with ground heat exchanger for long-term efficiency estimation." *Geothermics* 86 (2020). 101796.

Dacquay, Connor, Ed Lohrenz, and Hikari Fujii. "Ground heat exchanger thermal imbalance prevention using dynamic long-term ground temperature predictions." *International Journal of Green Energy* 19 (9) (2022). 977-985.

Diersch, Hans-Jörg G. *FEFLOW: finite element modeling of flow, mass and heat transport in porous and fractured media*. Springer Science & Business Media. (2013).

Fujii, Hikari, Keita Nishi, Yoshihito Komaniwa, and Naokatsu Chou. "Numerical modeling of slinky-coil horizontal ground heat exchangers." *Geothermics* 41 (2012). 55-62.

Fujii, Hikari, Shunsuke Tsuya, Retsu Harada, and Hiroyuki Kosukegawa. "Field test of horizontal ground heat exchangers installed using horizontal directional drilling technology." Proceedings of the 44th Workshop on Geothermal Reservoir Engineering. Stanford (2019).

Fujii, Hikari, Shohei Yamasaki, Takahiro Maehara, Takashi Ishikami, and Naokatsu Chou. "Numerical simulation and sensitivity study of double-layer Slinky-coil horizontal ground heat exchangers." *Geothermics* 47 (2013). 61-68.

Grupp, David, and Paul Fortunato. *Directional-Bore Ground Source Heat Pump Field Report.* Western Cooling Efficiency Center, University of California (California) (2014).

Hamada, Yasuhiro, Makoto Nakamura, Hisashi Saitoh, Hideki Kubota, and Kiyoshi Ochifuji. "Improved underground heat exchanger by using no-dig method for space heating and cooling." *Renewable energy* 32 (3) (2007). 480-495.

Inoue, Yohei, Ryuichi Itoi, Naokatsu Chou, Hiroaki Okubo, and Hikari Fujii. "Enhancement of heat exchange capacity of ground heat exchangers by injecting water into wells." Proceedings, Thirty-ninth Work. Geotherm. Reserv. Eng. (2014).

The Government of Japan "Long-Term Strategy under the Paris Agreement." (2021).

Kottek, Markus, Jürgen Grieser, Christoph Beck, Bruno Rudolf, and Franz Rubel. "World map of the Köppen-Geiger climate classification updated." (2006).

Lein, Richard, Hikari Fujii, Rino Ikeda, Saeid Mohammadzadeh Bina, Retsu Harada, and Hiroyuki Kosukegawa. "Optimization of double layered horizontal directional drilled ground heat exchangers by water injection into the borehole." *Geothermics* 118 (2024). 102913.

Léveillée-Dallaire, Xavier, Jasmin Raymond, Jónas Þór Snæbjörnsson, Hikari Fujii, and Hubert Langevin. "Performance Assessment of Horizontal Ground Heat Exchangers under a Greenhouse in Quebec, Canada." *Energies* 16 (15) (2023). 5596.

Nam, Yujin, and Ho-Byung Chae. "Numerical simulation for the optimum design of ground source heat pump system using building foundation as horizontal heat exchanger." *Energy* 73 (2014). 933-942.

Pu, Liang, Lingling Xu, Di Qi, and Yanzhong Li. "Structure optimization for horizontal ground heat exchanger." *Applied Thermal Engineering* 136 (2018). 131-140.

Rashid, Farhan Lafta, Nabeel S Dhaidan, Ahmed Kadhim Hussein, Fadhel Noraldeen Al-Mousawi, and Obai Younis. "Ground heat exchanger in different configuration: Review of recent advances and development." *Geoenergy Science and Engineering* (2023). 211879.

Saeidi, Reza, Younes Noorollahi, Soowon Chang, and Hossein Yousefi. "A comprehensive study of Fin-Assisted horizontal ground heat exchanger for enhancing the heat transfer performance." *Energy Conversion and Management: X* 18 (2023). 100359.

Shi, Yu, Qiliang Cui, Xianzhi Song, Fuqiang Xu, and Guofeng Song. "Study on thermal performances of a horizontal ground heat exchanger geothermal system with different configurations and arrangements." *Renewable Energy* 193 (2022). 448-463.

Tang, Fujiao, and Hossein Nowamooz. "Outlet temperatures of a slinky-type horizontal ground heat exchanger with the atmosphere-soil interaction." *Renewable Energy* 146 (2020). 705-718.

Tsuya, Shunsuke, Hikari Fujii, Hiroyuki Kosukegawa, Bina Saeid Mohammadzadeh, and Retsu Harada. "Field Test and Numerical Simulation of Single-Tube Horizontal Ground HeatExchangers Installed Using Horizontal Directional Drilling Method." *Journal of the Geothermal Research Society of Japan* 43 (1) (2021). 7-17.

Yasukawa, Kasumi, Nobuyasu Nishikawa, Masakatsu Sasada, and Tadahiko Okumura. "Country update of Japan." Proceedings World Geothermal Congress (2020).

Optimization of Borehole Thermal Energy Storage Systems

Liangping Lia[1], Michael Tetteh[1], Matthew Minnick[2], Haiyan Zhou[2]

[1]Department of Geology and Geological Engineering, South Dakota School of Mines and Technology, Rapid City, 57701, USA

[2]Energy Group, RESPEC Inc., Rapid City, SD 57703, USA

Keywords

Genetic algorithm, Optimization, Borehole thermal energy storage, Recovery efficiency

ABSTRACT

Borehole Thermal Energy Storage (BTES) represents an advanced technology tapping into the Earth's sub- surface to store and extract thermal energy for both heating and cooling purposes. The performance of BTES systems hinges greatly on selecting the right operational parameters. Among these parameters, the flow rates during charging and discharging phases play a pivotal role in determining the system's efficiency in recovering heat. In this research, we introduce the application of a Genetic Algorithm as a tool for optimizing these operational parameters within a baseline BTES model. The model itself was developed using FEFLOW and was subjected to simulation over a 3-year period. Following each 3-year simulation, the Genetic Algorithm iteratively adjusted the operational parameters to achieve the optimal configuration, maximizing heat recovery from the BTES system. Additionally, sensitivity analysis was carried out to examine the influence of BTES system size and borehole spacing on heat recovery efficiency. The results demonstrate that the Genetic Algorithm successfully optimized parameters, resulting in improved heat recovery efficiency. Furthermore, the sensitivity analysis revealed that a closer borehole spacing is associated with higher recovery efficiency.

1. Introduction

Historically, non-renewable energy sources like fossil fuels have dominated the global energy landscape. However, increasing reliance on renewable energy is crucial for reducing carbon emissions. Thermal energy storage (TES) emerges as a promising solution, allowing excess energy to be stored and utilized during peak demand periods (Lanahan and Tabares-Velasco, 2017). Underground thermal energy storage (UTES) utilizes subsurface reservoirs to store thermal energy. Two primary methods include aquifer thermal energy storage (ATES) and borehole thermal energy storage (BTES). While ATES systems face challenges due to hydrogeologic conditions,

BTES systems offer a viable alternative (Akta¸s and Kir¸ci¸cek, 2021; Shi et al., 2023). BTES systems store heat in soil or rock environments during peak heat periods and extract it when the heat is needed, contributing to grid stability and reducing energy demand fluctuations (Pourahmadiyan et al., 2023).

Despite the potential of BTES systems, optimizing their efficiency, particularly in terms of recovery efficiency, remains a significant challenge (Wo-loszyn, 2018; Casasso and Sethi, 2014). Manual calibration of parameters is common but time-consuming and uncertain (Zhang, 2016). To address this, modern optimization techniques like particle swarm optimization (PSO), simulated annealing (SA), and genetic algorithms (GA) are proposed (Kennedy and Eberhart, 1995; Press and Teukolsky, 1991). PSO mimics the collective behavior of birds and fish but struggles with complex datasets (Eltamaly et al., 2020). SA, inspired by metallurgical annealing, excels at identifying global optima but may get trapped in local extrema (Delahaye et al., 2019; Eren et al., 2017). GA, inspired by natural selection, offers versatility and parallelism, making it suitable for multidimensional optimization problems (Slowik and Kwasnicka, 2020; Yang, 2021).

In this study, GA was employed to optimize two critical operational parameters—charging and discharging flow rates for BTES systems (Pourahmadiyan et al., 2023). This optimization aims to maximize energy storage and recovery while minimizing losses, operational costs, and greenhouse gas emissions (Zhang, 2016; Possemiers et al., 2014). By utilizing GA, the study seeks to contribute to the advancement of sustainable energy solutions and address the challenges associated with manual calibration methods (Wo-loszyn, 2018; Casasso and Sethi, 2014).

2. Methodology

2.1 Finite element model

The FEFLOW software, which is a finite element modeling tool, was employed to simulate and compute temperature variations in the subsurface while transferring heat during charging and discharging. The temperature changes in the ground around the borehole can be expressed through the following equation:

$$\rho \cdot c \cdot \frac{\partial T}{\partial t} = \nabla \cdot (k \cdot \nabla T) + Q$$

where ρ (kg/m^3) is the density of the ground, c ($J/(kg * K)$ is the specific heat capacity of the ground, and T (^0C) is the temperature, t is time, k ($W/(m * K)$) is the thermal conductivity of the ground, Q (J/s) is the heat source and sink in the system.

The study considered a BTES system with a circular configuration, primarily because the favorable packing density it provides for boreholes within a designated area. This allows for the efficient installation of more boreholes in a given space, thereby optimizing the overall thermal energy storage capacity of the system. To streamline our model, we focused on one quadrant of the circular BTES system, as shown in Figure 1b.

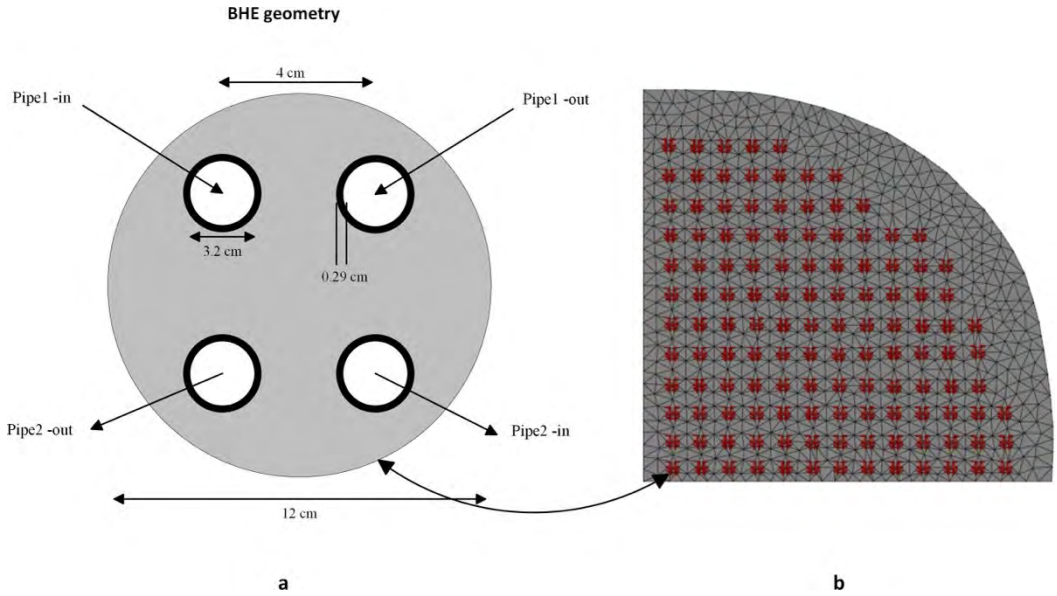

Figure 1: Finite element model grid for this study

The FEM model employed is a homogeneous system with a depth of 30 m, comprising 6 layers and a vertical discretization of 5 m. The modeling of BHEs utilizes a quasi-stationary analytical model based on work by Eskilson and Claesson (1988). The model considers the configuration of double U-shaped BHEs connected in parallel. The borehole diameter is 12 cm, with a pipe separation of 4 cm between each U-shaped BHE. The pipes have a diameter of 3.2 cm, and the thickness of the pipe walls is 0.29 cm. Figure 1a shows the cross-section of the borehole heat exchanger.

2.2 Finite element model

The optimization procedure is detailed in Algorithm 1. Specifically, this study employs a genetic algorithm as the optimization method.

Algorithm 1: Optimization of Parameters Using Genetic Algorithm and FEFLOW

Model Set: N_w = Number of parameters
Set: N_{pop} = Number of population
Set: N_{gen} = Number of generations
begin
  Generate new population, **New$_{pop}$** = (N_{pop}, N_w)
  for *generation* = 1, 2, ⋯ , N_{gen} **do**
    Implement the fitness function
    for i = 1, 2, ⋯ , N_{pop} **do**
      Insert parameters into the Feflow model
      Run Feflow model and calculate recovery efficiency (RE)
    Select the best chromosomes in the current population to join the mating pool:
    for i = 1, 2, ⋯ , N_{pop} **do**
      Eliminate the chromosome with the least *RE*
    Replace it with the chromosome with the highest *RE*
    parent = (N_{pop}, N_w)
    Generate next generation using the crossover function:
    offspring = (N_{pop}, N_w)
    Add variation to the offspring using the mutation function:
    New$_{pop}$ = (N_{pop}, N_w)
  end

In this study, a genetic algorithm is employed to regulate two operational parameters (charging and discharging flow rate), while the grout thermal conductivity and the thermal conductivity of the ground remains fixed. The objective of this optimization process is to obtain an optimum recovery efficiency (RE). The RE is computed on a yearly bases, such that for each year cycle, the first half of the year computes the quantity of heat stored and the second half of the year computes the amount of heat retrieved from the BTES system, Figure 2.

$$RE = \frac{\nabla \mathrm{H}_{recovered}}{\nabla \mathrm{H}_{stored}} \times 100\%$$

This study considered two BHE spacings, a 2.5 m spacing and a 10 m spacing. The genetic algorithm ran for 30 generations because, following a pilot experiment, there was a considerable reduction in recovery efficiency differences from the 25th generation to the 30th generation. The objective was to explore the efficacy of mathematical algorithms in obtaining optimal parameters for a BTES system design. Algorithm 1 shows the process of implementing the optimization. During the optimization process, three scenarios were considered, as shown in Table 1. These scenarios are presented to analyze the impact of the number of boreholes and their spacing on the overall heat recovery efficiency. The implementation of the genetic algorithm for the optimization process is illustrated in algorithm 1.

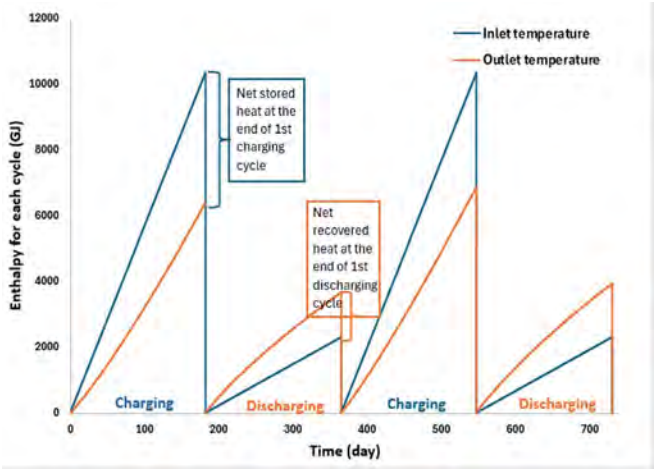

Figure 2: Recovery efficiency calculation

Table 1: Scenarios studies.

Scenarios	BHE spacing (m)	Number of BHEs
1	2.5	127
2	2.5	37
3	10	13

2.3. Results

2.3.1. Optimization for 2.5 m BHE spacing

The optimization procedure for BTES with a 2.5 m BHE spacing considered two distinct scenarios. In the first scenario, a substantial number of BHEs, approximately 127, were deployed, as indicated in scenario 1 of the table. The second scenario involved fewer BHEs, approximately 37, as depicted in scenario 2. The outcomes of the optimization process for these two scenarios are depicted in Figures 3 and 4.

For scenario 1, after 30 generations, the optimal recovery efficiency reached approximately 65% by the 28th generation. At this juncture, the charging and discharging flow rates were approximately 18 m^3/day and 39 m^3/day, respectively. Scenario 2, with fewer BHEs, achieved an approximate recovery efficiency of 52.9% by the 29th generation. The charging and discharging flow rates were approximately 20.5 m^3/day and 36.9 m^3/day, respectively. The results of the analysis provide compelling evidence indicating a direct relationship between the increase in discharging flow rates and the corresponding rise in recovery efficiency. Upon closer examination of Figure 3, a discernible trend emerges wherein successive generations witness a notable uptick in both discharging flow rates and recovery efficiency. This suggests a positive correlation between these variables over time.

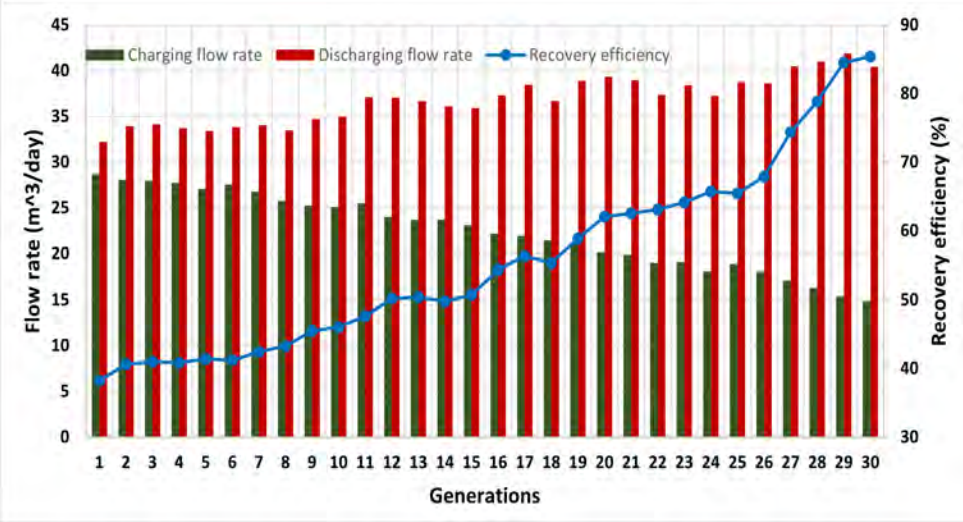

Figure 3: Optimal parameters and recovery efficiency for scenario 1

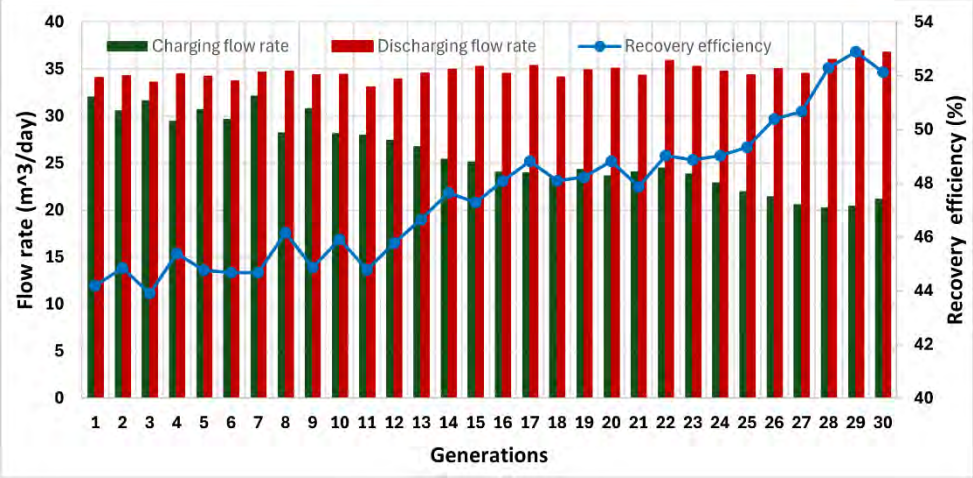

Figure 4: Optimal parameters and recovery efficiency for scenario 2

Furthermore, Figure 4 further bolsters this observation by highlighting instances where the algorithm generates higher discharging flow rates, coinciding with significant spikes in recovery efficiency. These findings underscore the importance of monitoring and optimizing discharging flow rates as a crucial factor in enhancing overall recovery efficiency within our operational processes. By comprehending and harnessing this relationship, we can effectively enhance our process performance and achieve greater efficiency.

2.3.2. Optimization for 10 m BHE spacing

This optimization procedure was conducted with a 10 m BHE spacing, as illustrated in scenario 3. After 30 generations, the optimal recovery efficiency reached approximately 14.9% in the 30th generation (Figure 5). The charging and discharging flow rates were 24.8 m^3/day and 36.2 m^3/day, respectively. Throughout the optimization process, there was minimal improvement in the overall recovery efficiency. This becomes particularly apparent when analyzing the trends in both charging and discharging flow rates. Across successive generations, there were negligible changes (either increase or decrease) between the previous parameters of charging and discharging

flow rates and the subsequent ones generated. However, an interesting pattern emerges when there's a notable disparity between the discharging and charging flow rates, particularly when the former exceeds the latter. In such instances, a significant increase in recovery efficiency was observed. Moreover, a stark contrast in the flow rate dynamics between this scenario and scenarios 1 and 2 is noteworthy. Here, both the charging and discharging flow rates appear to be relatively high. This deviation from the previous scenarios, where the charging flow rates were notably lower compared to discharging flow rates, can be attributed to the larger distances between the BHEs. The greater distance between the BHEs necessitates a higher flow rate to effectively circulate heat through the system and extract it efficiently. Consequently, the requirement for higher flow rates in this scenario underscores the intricate interplay between system design parameters, such as BHE spacing, and operational variables like flow rates, all of which impact the overall efficiency and effectiveness of the system.

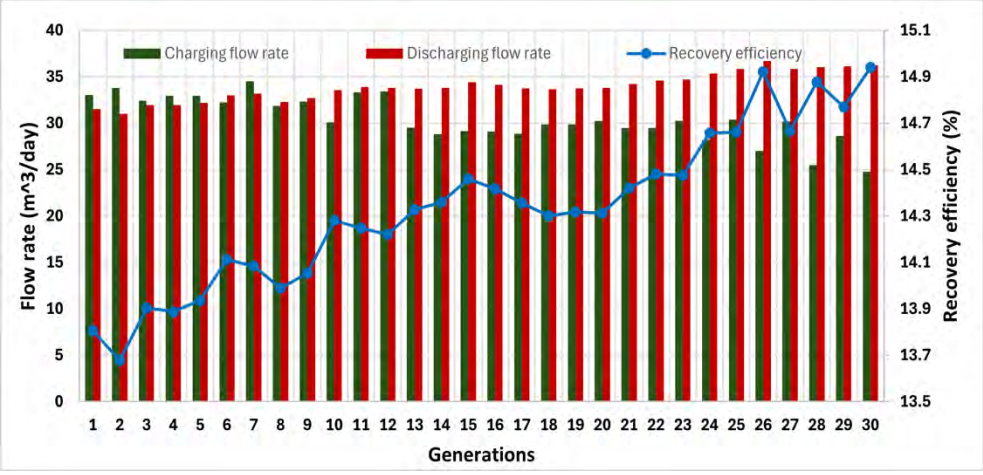

Figure 5: Optimum parameters and recovery efficiency for scenario 3

The recovery efficiency for a 3-year cycle is depicted in Figure 6 for both 2.5 m (scenario 1) and 10 m spacings. The difference in recovery efficiency between the two BHE spacings widens with each successive year, indicating that the 2.5 m spacing will continue to recover more heat than the 10m spacing in additional cycles.

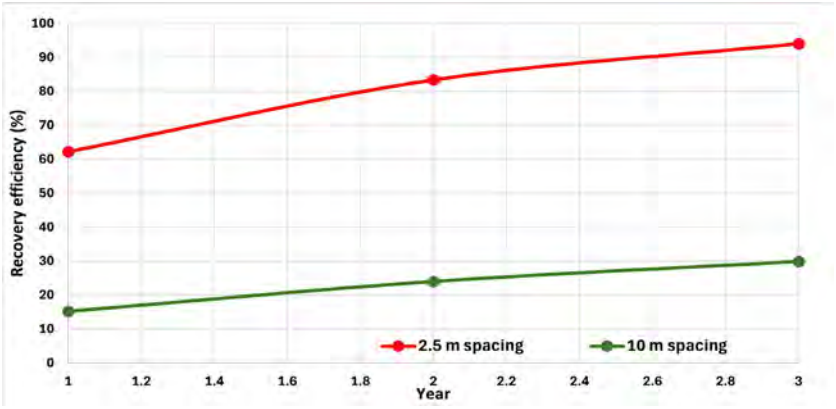

Figure 6: Recovery efficiency for a 3-year cycle

2.3.3. Base case vs optimum case

In scenario 1, the BTES system underwent a six-year simulation cycle to conduct a comparative analysis between a base case scenario, characterized by a charging and discharging flow rate of 20 m^3/day, and the optimized configuration of scenario 1. Throughout this simulation, the dynamic interaction between charging and discharging cycles and their subsequent impact on outlet temperature variations emphasized the crucial significance of optimizing operational parameters to achieve optimal system performance.

Figure 7 offers a comparative overview of the recovery efficiency between the base and optimized scenarios. In the initial year, the base case achieved a recovery efficiency of 34.1%, while the optimized scenario demonstrated a significantly higher efficiency of 62.2%. This disparity in recovery efficiency indicates that a larger portion of the injected energy is recovered during the discharging phase in the optimized scenario, thus enhancing the energy efficiency and cost-effectiveness of the BTES system. Moreover, it suggests a reduced environmental impact, as the system operates more efficiently, minimizing energy wastage.

To comprehensively assess the long-term effectiveness of the BTES system, it is essential to examine the recovery rates across multiple cycles. Over the course of the six-year cycle, the base case peaked at a recovery efficiency of 60.6%, whereas the optimized scenario consistently surpassed this, achieving a significantly higher recovery efficiency of 96.5%. The widening disparity in recovery efficiency between the optimized and base scenarios with each successive cycle underscores the optimized scenario's ability to extract more heat per cycle compared to the base scenario, indicating sustained superior performance over time.

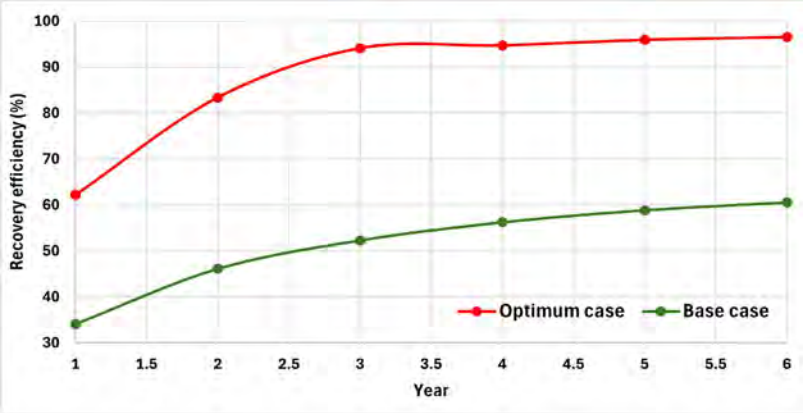

Figure 7: Recovery efficiency of base case and optimum case

3. Conclusion

This research study aimed to regulate the operation of BTES systems by utilizing a genetic algorithm to search for appropriate parameters for maximizing energy recovery. The study focused on design, operational, and geological parameters. Design parameters included thermal conductivity of the grout and BHE spacing, with two spacing configurations considered. The geological parameter was the subsurface's thermal conductivity, of which both the subsurface's thermal conductivity and the grout thermal conductivity were held constant. The optimization algorithm focused on

operational parameters, such as charging and discharging flow rates. The recovery efficiency was computed at the end of of each year of simulation.

The results highlighted the intricate relationship between recovery efficiency, BHE spacing, and the volumetric charging and discharging flow rates within the BTES system. It was evident that smaller BHE spacing correlated with higher recovery rates, while, within a specific BHE spacing, higher discharging flow rates contributed to enhanced recovery efficiency. However, an interesting observation emerged regarding the interplay between BHE spacing and flow rates during charging. It was noted that when the BHE spacing was smaller, the flow rate during charging tended to be lower compared to configurations with larger BHE spacing. This suggests a trade-off between BHE spacing and flow rates during charging, indicating the need for careful consideration when optimizing these parameters. Moreover, an optimal BTES model was developed and compared against the base case. The findings revealed that the optimal model achieved an impressive recovery efficiency of 96.5% over a simulated six-year period. This highlights the effectiveness of optimizing system parameters in maximizing energy recovery and overall system performance.

By delving into the impact of various parameters on system performance, this study contributes to the use of mathematical algorithms for obtaining optimal parameters, ultimately enhancing the efficient design and operation of BTES systems.

Acknowledgement

This work has been supported through a grant from the National Science Foundation (OIA-1833069).

REFERENCES

Akta¸s, A., Kir¸ci¸cek, Y., 2021. Chapter 6 - solar thermal systems and thermal storage, in: Akta¸s, A., Kir¸ci¸cek, Y. (Eds.), Solar Hybrid Systems. Academic Press, pp. 127–137.

Casasso, A., Sethi, R., 2014. Sensitivity analysis on the performance of a ground source heat pump equipped with a double u-pipe borehole heat exchanger. Energy Procedia 59, 301–308. European Geosciences Union General Assembly 2014, EGU Division Energy, Resources the Environment (ERE).

Delahaye, D., Chaimatanan, S., Mongeau, M., 2019. Simulated annealing: From basics to applications, in: Gendreau, M., Potvin, J.Y. (Eds.), Handbook of Metaheuristics. Springer. volume 272 of *International Series in Operations Research & Management Science (ISOR)*, pp. 1–35.ISBN 978–3–319–91085–7.

Eltamaly, A.M., Al-Saud, M., Abokhalil, A.G., Farh, H.M., 2020. Simulation and experimental validation of fast adaptive particle swarm optimization strategy for photovoltaic global peak tracker under dynamic partial shading. Renewable and Sustainable Energy Reviews 124, 109719.

Eren, Y., İbrahim B. Küçükdemiral, İlker Üstoğlu, 2017. Chapter 2 - introduction to optimization, in: Erdinç, O. (Ed.), Optimization in Renewable Energy Systems. Butterworth-Heinemann, Boston, pp. 27–74.

Eskilson, P., Claesson, J., 1988. Simulation model for thermally interacting heat extraction boreholes. Numerical heat transfer 13, 149–165.

Kennedy, J., Eberhart, R., 1995. Particle swarm optimization, in: Proceedings of ICNN'95 – International Conference on Neural Networks, pp. 1942–1948 vol.4.

Lanahan, M., Tabares-Velasco, P.C., 2017. Seasonal thermal-energy storage: A critical review on btes systems, modeling, and system design for higher system efficiency. Energies 10.

Possemiers, M., Huysmans, M., Batelaan, O., 2014. Influence of aquifer thermal energy storage on groundwater quality: A review illustrated by seven case studies from belgium. Journal of Hydrology: Regional Studies 2, 20–34.

Pourahmadiyan, A., Sadi, M., Arabkoohsar, A., 2023. 6 - seasonal thermal energy storage, in: Arabkoohsar, A. (Ed.), Future Grid-Scale Energy Storage Solutions. Academic Press, pp. 215–267.

Press, W.H., Teukolsky, S.A., 1991. Simulated Annealing Optimization over Continuous Spaces. Computer in Physics 5, 426–4290.

Shi, Y., Cui, Q., Song, X., Liu, S., Yang, Z., Peng, J., Wang, L., Guo, Y., 2023. Thermal performance of the aquifer thermal energy storage system considering vertical heat losses through aquitards. Renewable Energy 207, 447–460.

Slowik, A., Kwasnicka, H., 2020. Evolutionary algorithms and their applications to engineering problems. Neural Computing and Applications 32, 12363–12379.

Wo-loszyn, J., 2018. Global sensitivity analysis of borehole thermal energy storage efficiency on the heat exchanger arrangement. Energy Convers Manag 166, 106–119.

Yang, X.S., 2021. Chapter 6 - genetic algorithms, in: Yang, X.S. (Ed.), Nature-Inspired Optimization Algorithms (Second Edition). second edition ed.. Academic Press, pp. 91–100.

Zhang, Y., 2016. Research of thermal energy storage technology in the solar thermodynamic power. Journal of Power and Energy Engineering 4, 42

A Case Study on Geothermal Power Generation System by Semi-open Loop Carbon Dioxide Circulation

NAKAO Yoshinobu[1], SUENAGA Hiroshi[1], FUKADA Toshiaki[1], MASUOKA Kentaro[2], GOTO Ryota[2], OHSATO Kazumi[3] and TERAI Amane[4]

[1]Central Research Institute of Electric Power Industry

[2]TAISEI CORPORATION

[3]Geothermal Energy Research and Development Co., Ltd

[4]Japan Organization for Metals and Energy Security

Keywords

Carbon dioxide, Geothermal Power, Numerical simulation, Feasibility study

ABSTRACT

Much of Japan's geothermal resources cannot yet be economically exploited, although geothermal energy is potentially a very valuable domestic energy source for Japan. Therefore, many industries and research institutes in Japan have been researching and developing technologies to utilize geothermal energy.

Since 2020, we have been studying the development of a geothermal power generation system using supercritical carbon dioxide (sCO_2) circulation, sCO_2 geothermal power system. It is expected that the thermal efficiency of a geothermal power system can be improved and that the environmental impact of installing the system can be reduced by using sCO_2 as the working fluid.

We have conducted laboratory experiments to simulate the closed loop system by sCO_2 circulation and demonstrated thermosiphon phenomena in which sCO_2 could spontaneously circulate in the U-shaped closed loop system due to its density difference with temperature. In addition, we constructed a numerical simulation model to calculate the sCO_2 flow in the U-shaped closed loop system and estimated the amount of electricity generated by the system. In addition, the numerical simulation model was used to find the appropriate power generation cycle and conditions for the sCO_2 geothermal power system to achieve maximum power output.

In the past fiscal year, we have conducted numerical simulation studies on the heat extraction efficiency of the sCO_2 geothermal power system in a geothermal reservoir with hot water using

TOUGH3 (ECO2N V2.0). And we have estimated the sustainable amount of electricity generated by an semi-open loop sCO_2 geothermal power system based on the results of reservoir simulations. We found that power output increases with higher reservoir temperature, deeper injection wells, and lower injection temperatures, and that a development targeting a 1 km^2 geothermal reservoir at a depth of 4,000 m and a temperature of 300℃ is expected to generate approximately 10 MWe of power.

1. Introduction

In October 2020, Japan declared its intention to achieve carbon neutrality by 2050[1]. In the Sixth Strategic Energy Plan, which was revised in 2021[2], the share of renewable energy in the electricity mix in 2030 was significantly revised upward significantly from 22-24% to 36-38%, and the introduction of renewable energy is expected to be accelerated in the future. The target for geothermal power generation has been set at the same level as in the Fifth Strategic Energy Plan, and it is considered necessary to step up efforts to further increase the amount of installed geothermal power generation. And the Strategic Energy Plan mentions the development of technology to increase and stabilize the amount of steam available for geothermal power generation by artificially injecting water from the ground as an example. Therefore, the development and implementation of enhanced geothermal system (EGS) technology is an urgent issue in Japan (Kaieda, 2015).

Since 2020, the authors have started research on the development of technology for EGS using sCO_2 as a heat extraction medium by utilizing high-temperature underground rocks. In EGS using sCO_2 as a working fluid, the thermosiphon phenomenon has been proposed (e.g., Atrens et al., 2009), in which sCO_2 circulates naturally without requiring a driving force for the fluid. This is a phenomenon in which sCO_2 in a closed loop is heated in the hot reservoir rock after injection, becomes low density due to the large change in density relative to the change in temperature of the sCO_2, rises to the surface due to buoyancy, cools as power is generated above ground, and then becomes high density and flows down to the underground due to gravity (Higgins and Oldenburg, 2016). In addition, the following effects can also be expected.

- Because sCO_2 has a low viscosity, it can be injected at high pressure to create finer fracture surfaces with high heat exchange efficiency.
- The high density and compressibility of sCO_2 is also expected to improve the efficiency of heat extraction in production wells.
- CO_2 that does not contribute to circulation is sequestered underground as minerals, which is expected to prevent CO_2 leakage from CCS reservoir.
- Utilizing high-temperature sCO_2 reduces the required flow rates for achieving the same power output, enabling turbines and other equipment to be smaller in size.

[1] https://www.meti.go.jp/english/policy/energy_environment/global_warming/ggs2050/index.html

[2] https://www.meti.go.jp/english/press/2021/1022_002.html

Thus, a sCO_2 geothermal power system has many advantages, including the expansion of geothermal power generation sites, including deep underground areas that have not yet been utilized, dramatic increase in the amount of geothermal power generated, effective utilization of abandoned geothermal wells where hot water cannot be obtained, cost reduction and scenic enhancement due to compact surface facilities, etc. However, there are no examples of sCO_2 geothermal power systems being developed in Japan, and demonstrations of such systems have only just begun in the United States and other countries (Alvarado, 2023, Chandrasekar, 2023, Kerr, 2023, and Klenner, 2023). In addition, because of the complex geological structure of the bedrock in Japan, it is necessary to develop a unique sCO_2 geothermal power system that is compatible with this geological structure, and consistent research and development from system design to on-site demonstration is required.

A sCO_2 circulation experimental apparatus was constructed at Central Research Institute of Electric Power Industry (CRIEPI) as part of the New Energy and Industrial Technology Development Organization (NEDO) project "Development of a carbon dioxide circulation geothermal power generation system" in order to demonstrate the thermosiphon phenomenon, which has been shown theoretically but not yet verified, through laboratory experiments and to clarify the conditions under which the phenomenon can occur (NEDO, 2022).

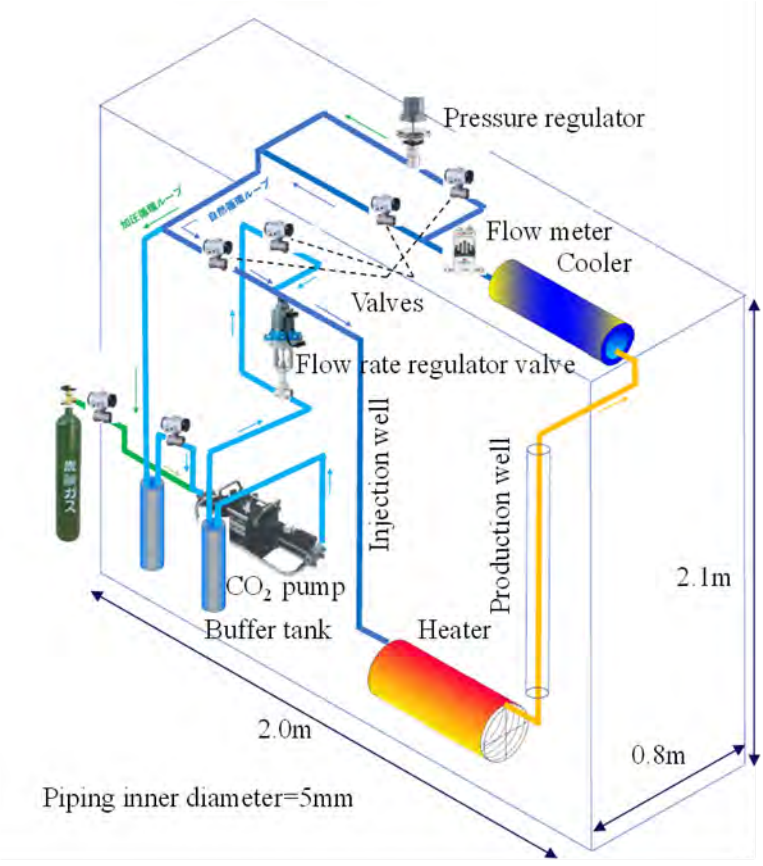

Figure 1: Closed loop sCO2 circulation experimental apparatus conceptual diagram (NEDO, 2022)

The purpose of this study is to conduct a feasibility study of the sCO_2 geothermal power system in the preliminary stage of technology demonstration, and to identify the elementary technologies required for the demonstration. We have conducted laboratory experiments to simulate the closed loop system by sCO_2 circulation and demonstrated thermosiphon phenomena in which sCO_2 could spontaneously circulate in the U-shaped closed loop system caused by its density difference with temperature. In addition, we have constructed a numerical simulation model to calculate the sCO_2 flow in the U-shaped closed loop and estimate the amount of electricity generated by the system (Nakao et al., 2023). And now we have started numerical simulations for semi-open loop systems through sCO_2 circulation.

2. Plant simulation for semi-open loop sCO_2 geothermal power system

In this project, JOGMEC has developed an innovative geothermal power generation technology that does not rely on hydrothermal resources by injecting sCO_2 into geothermal reservoirs and extracting heat from geothermal resources. We have conducted wellbore simulation and thermal efficiency analysis for a closed loop sCO_2 geothermal power system consisting of a sCO_2 injection well, a production well, and multiple lateral wells connecting the wellbores, and reported the results at GRC2023 (Nakao et al., 2023).

In this report, geothermal reservoir simulation and plant simulation (wellbore simulation and thermal efficiency analysis) were conducted for an semi-open loop sCO_2 geothermal power system, as shown in Figure 1, which consists of a sCO_2 injection well, a production well, and a reservoir constructed by hydraulic fracturing (EGS reservoir). The calculation flow of the plant simulation is shown below.

i. Reservoir simulation: The coupled transport of groundwater and injected sCO_2 between the injection and production wells was simulated using a planar two-dimensional five-spot model which was based on a model by Pruess (Pruess, 2006). TOUGH3[3] developed by LBNL, was used as the numerical code to calculate the temperature, pressure, and flow rate of circulating sCO_2 at the bottom of the injection and production wells.

ii. Plant simulation: Using a wellbore simulator developed by CRIEPI, the temperature, pressure, and flow rate of circulating sCO_2 (assumed to be pure CO_2 in this report) at the injection and production wellheads were calculated based on the circulating sCO_2 conditions at the bottom of the injection and production wells. Then, the power output of the sCO_2 geothermal power system was calculated using EnergyWin (Koda 1999, Takahashi 2007, Nakao 2011), a general-purpose analysis software developed by CRIEPI, by converging the temperature and pressure conditions at the power generation plant so that the sCO_2 conditions to be returned to the injection well were equal to the sCO_2 conditions set in the wellbore simulation. The relationship between the thermodynamic state and fluid properties of sCO_2 is based on the database of REFPROP 10 (NIST, 2022).

[3] https://tough.lbl.gov/software/tough3/

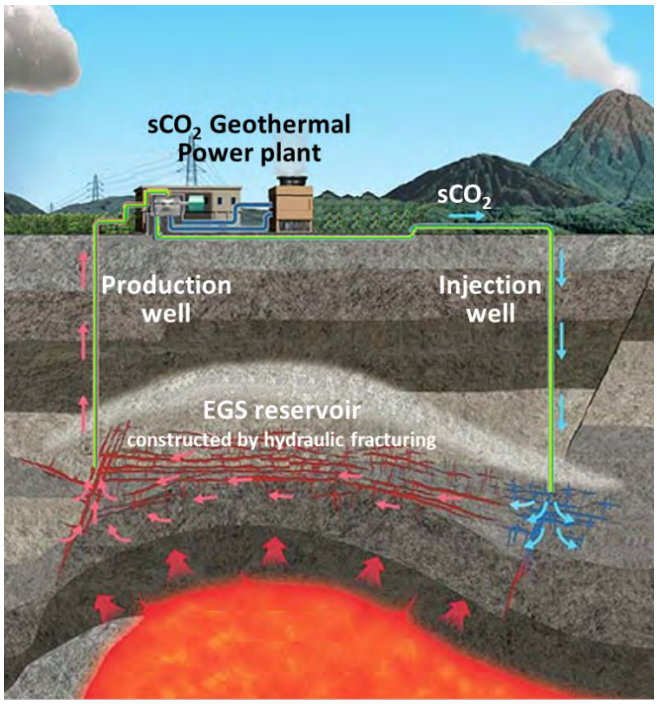

Taken form the JOGMEC website: https://www.jogmec.go.jp/publish/plus_vol13.html
Additions were made to the figure.

Figure 1: Conceptual model of semi-open loop sCO_2 geothermal power system

2. Geothermal reservoir simulation

2.1 Numerical simulation model

To investigate the heat extraction of the sCO_2 geothermal power system in a geothermal reservoir with hot water, numerical simulations were conducted using a planar two-dimensional five-spot model. When injection and production wells are arranged as staggered, it is possible to model only part of the target area due to symmetry. This five-spot modeling has been used in many previous studies. In reality, it may be difficult to construct as many wells as in the 5-spot model due to economic reason and so on. Injected fluid loss could be caused by many reasons, if the number of wells is not enough as 5-spot model. As a result, CO_2 suppletory could be required at the surface continuously. So, in reality, there are many problems to consider, but in this study, we focus to evaluate plant simulation simply. Thus, we created 5-spot model based on a five-spot model by Pruess (2006) using a distance of 707.1 m between injection and production wells (Figure 2). Matrix-fracture heat exchange was modeled using the “multiple interacting continua” (MINC) method (Pruess et al., 1982,1985) with subgridding of matrix blocks into five continua. This means highly idealized and homogenous reservoir conditions as illustrated in Table 1. Injection and production wells were given as fixed temperature and pressure grids. The other conditions of the model are shown in Table 1. In this study, chemical reaction was not considered in order to avoid the complexity of calculations as this first step study, but we plan to consider interaction with CO_2 and rock in the future work.

Table 2 shows the simulation cases of this heat extraction study. It can be classified into 3 cases of initial reservoir temperatures (300, 250 and 200 °C). In each case, calculations were performed

in 16 different initial conditions: 4 patterns of initial reservoir pressures (10, 20, 30 and 40 MPaA) multiplied by 4 patterns of injected sCO_2 temperatures at the bottom of the injection well (80, 100, 120 and 140 °C[4]). A numerical code, TOUGH3, which is a numerical simulator of non-isothermal flows of multi-component, multi-phase fluids in three-dimensional porous and fractured media, was used. The ECO2N V2.0 EOS module was used, which allows the thermal-hydraulic calculation of sCO_2 in a temperature range from 10 to 300 °C and a pressure up to 60 MPaA.

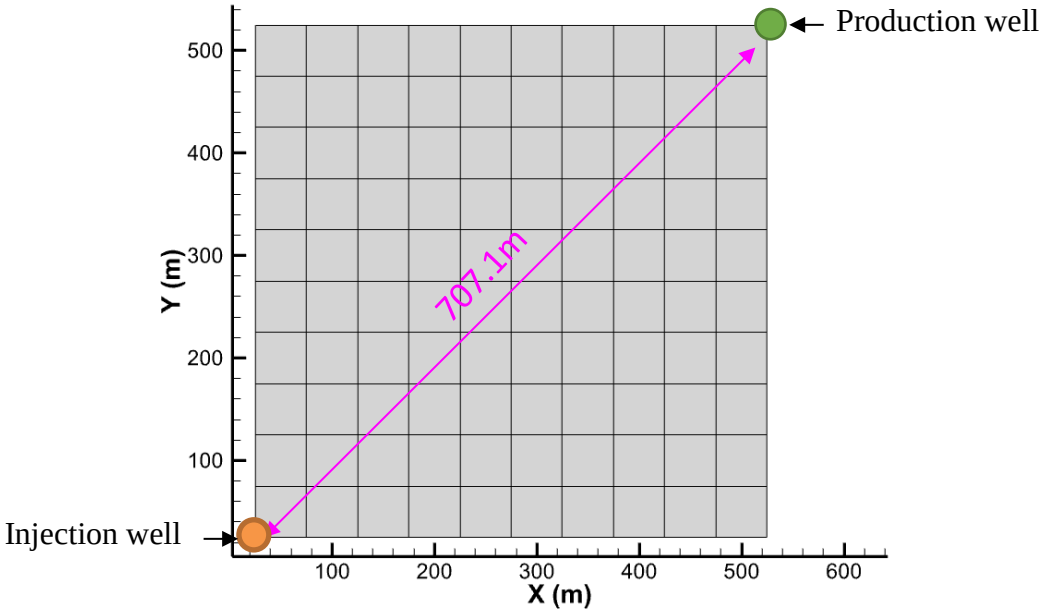

Figure 2: Schematic diagram of a planar two-dimensional five-spot model in this study. Side boundary condition is Neuman type, zero flux boundary here.

Table 1: Model parameters used in this heat extraction study.

Reservoir	Value	Unit
Thickness	305	m
Fracture spacing	50	m
Fracture volume fraction	2	%
Permeability in fracture domain	5.0×10^{-14}	m^2
Porosity in fracture domain	50	%
Permeability in matrix domain	5.0×10^{-18}	m^2
Porosity in matrix domain	15	%

[4] In this paper, the temperature of injected sCO_2 is used as a parameter to compare and verify the effect of natural circulation due to density difference of sCO_2 and the effect of increasing sCO_2 temperature at the production wellhead by injecting sCO_2 at high temperature. Note that these temperatures are those at the bottom of the injection well, which are below 40°C at the injection wellhead depending on the conditions.

Rock grain density	2650	kg/m^3
Rock specific heat	1000	J/kg/°C
Rock thermal conductivity	2.1	W/m/°C
Production/Injection	Value	Unit
Pattern area (1 unit area in a symmetrical well arrangement)	1	km^2
Injector-producer distance	707.1	m
Pressure at injection well grid	Initial reservoir pressure plus 1MPa	
Pressure at production well grid	Initial reservoir pressure minus 1MPa	

Table 2: List of numerical simulation cases for this heat extraction efficiency study.

	Case 1	Case 2	Case 3
Initial reservoir temperature of the model (°C)	300	250	200
Initial reservoir pressure of the model (MPaA)	10, 20, 30 and 40		
Injected sCO_2 temperature (°C)	80, 100, 120 and 140		

2.2 Results of geothermal reservoir simulation

The production gas (almost exclusively CO_2) mass flow rate, pressure, and temperature at the bottom of the production well in each case are shown in Figure 3 through 5, respectively. The pressure at the bottom of the production well was estimated by a radial model, which was run separately using the pressure and mass flow rate results from these five-spot model studies. The internal diameter of the production well was assumed to 8.5 inches. The sCO_2 injection temperature on the horizontal axis is the temperature calculated from the conditions at the bottom of the production well based on wellbore simulation described in Section 3.1 below.

The mass flow rate of the production gas is the average value for the period when CO_2 reaches (breakthrough) the production well and the flow rate and the temperature are stable (10 to 20 years after the start of sCO_2 injection, referring Figure 6). In the five-spot model, all side, upper and lower face boundaries are Neumann boundary, therefore no fluid and heat flux towards into or outward the model which means the leak-off is zero in the model. That is, the only flow into and out of the model is through the arbitrary specified well grid. It is clear that within the scope of this study, the higher the pressure or the lower the initial reservoir temperature, the higher the produced gas mass flow rate tends to be. The pressure at the bottom of the production well showed almost no difference due to the initial reservoir temperature. The temperature at the bottom of the production well showed almost no difference due to the sCO_2 injection temperature. There was no temperature drop in the production well 10 to 20 years after the start of injection, and the initial reservoir temperature was maintained.

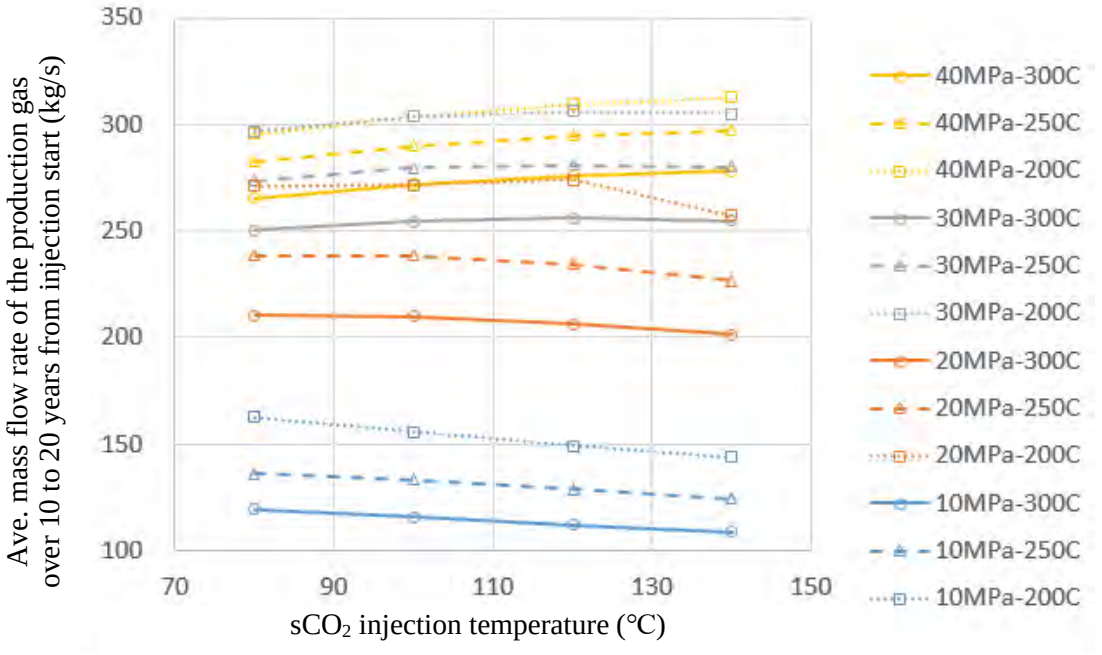

Figure 3: Mass flow rate of the production gas at the bottom of the production well. Each value is averaged over 10 to 20 years from the start of sCO_2 injection. In the left side indicates the initial reservoir pressure, and right side indicates the initial reservoir temperature.

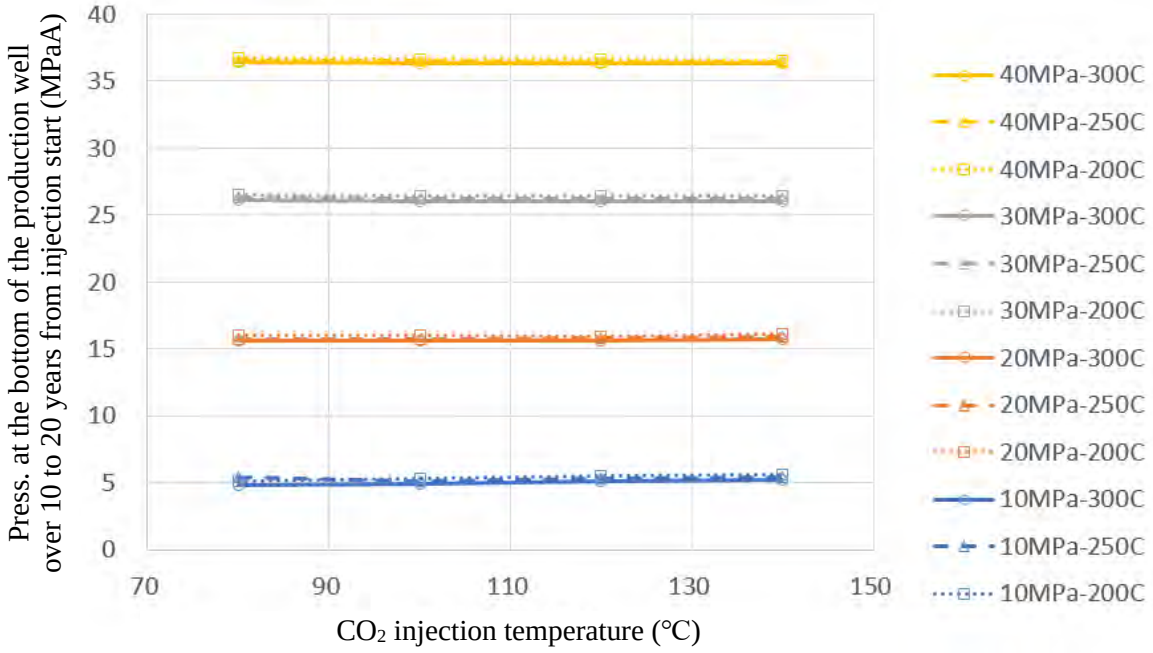

Figure 4: Pressure at the bottom of the production well. Each value is averaged over 10 to 20 years from the start of sCO_2 injection start time. In the left side indicates the initial reservoir pressure, and right side indicates the initial reservoir temperature.

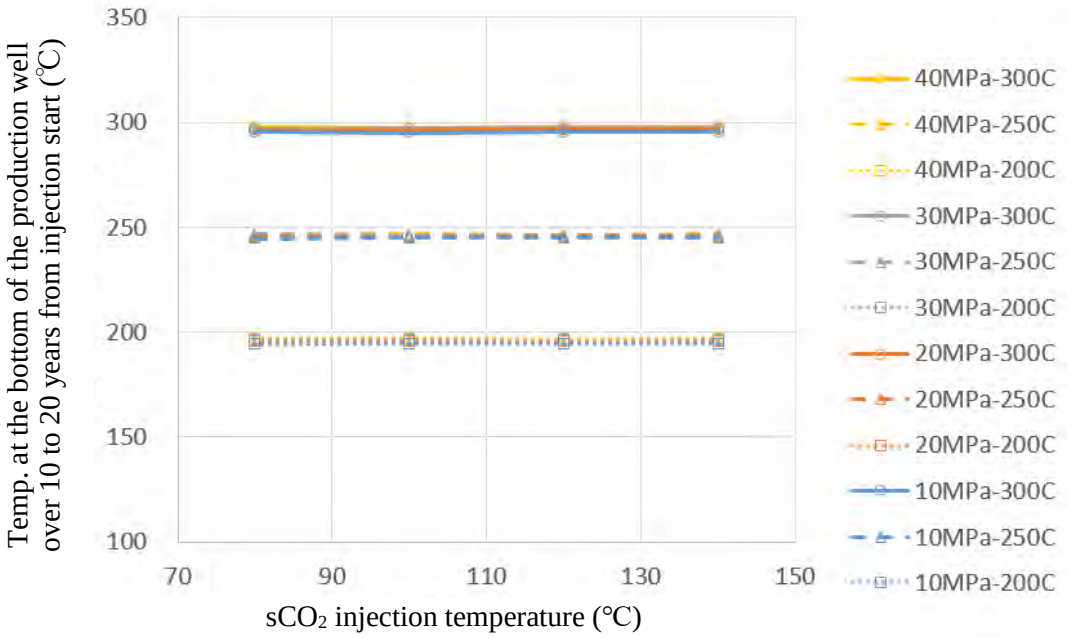

Figure 5: Temperature at the bottom of the production well. Each value is averaged over 10 to 20 years from the start of sCO_2 injection. In the left side indicates the initial reservoir pressure, and right side indicates the initial reservoir temperature.

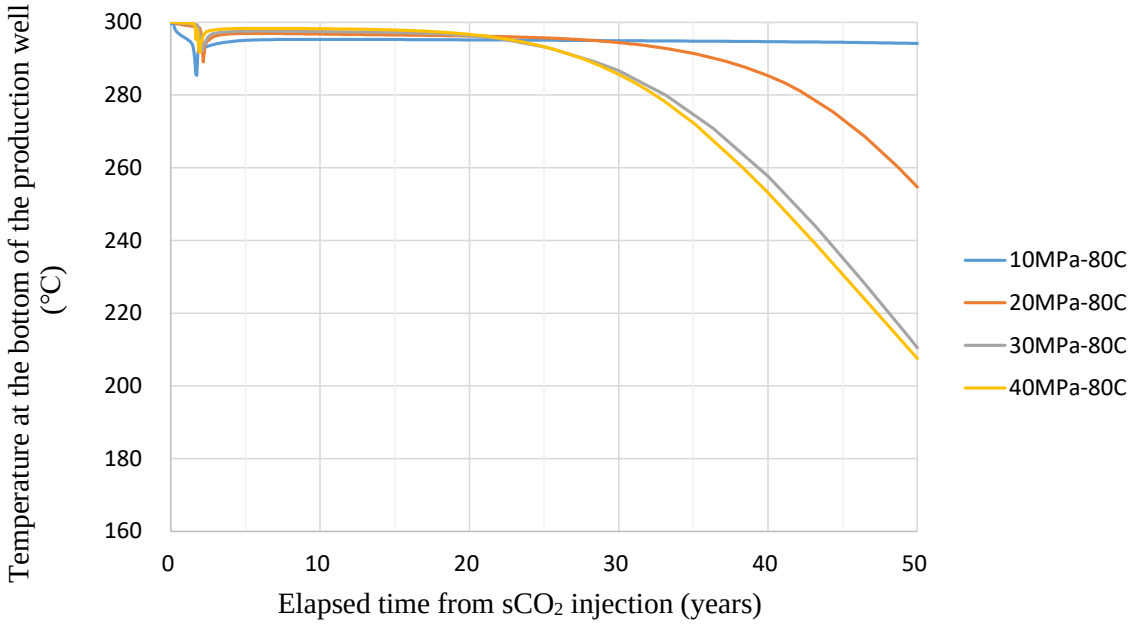

Figure 6 Temperature variations at the bottom of the production well in some cases in which the initial reservoir temperature is 300 ℃ and injection sCO_2 temperature is 80 ℃. The value in the legend indicates the initial reservoir pressure.

3. Plant simulation

3.1 Wellbore simulation method and conditions

The wellbore simulations were conducted using the same methods as in the previous report (Nakao et al., 2023). The flow path of the wellbore simulation is shown in Figure 7. Both the injection and production wells were drilled vertically. The heat exchange between the rock and the working fluid (sCO_2) is governed solely by heat conduction, and there is no CO_2 leakage from either well.

The temperature, pressure, and flow rate of the circulating sCO_2 at the bottom of the injection and production wells are based on the results of the reservoir simulation described above. However, the results of the five-spot model analysis for a 1 km square area showed that the flow rate of circulating sCO_2 was over 100 kg/s, which is fairly large flow rate for a well with a normal well diameter and would cause a large pressure loss. Therefore, in this wellbore simulation, the circulating flow rate per well is used as 1/4 of the reservoir simulation results.

Based on these numerical conditions, the temperature and pressure changes from the bottom of the injection well to the injection wellhead and from the bottom of the production well to the production wellhead are calculated using a wellbore simulator when sCO_2 is flowing in the well as the circulating medium. However, the internal diameter of the well is assumed to be constant, and the flow is assumed to be steady and one-dimensional.

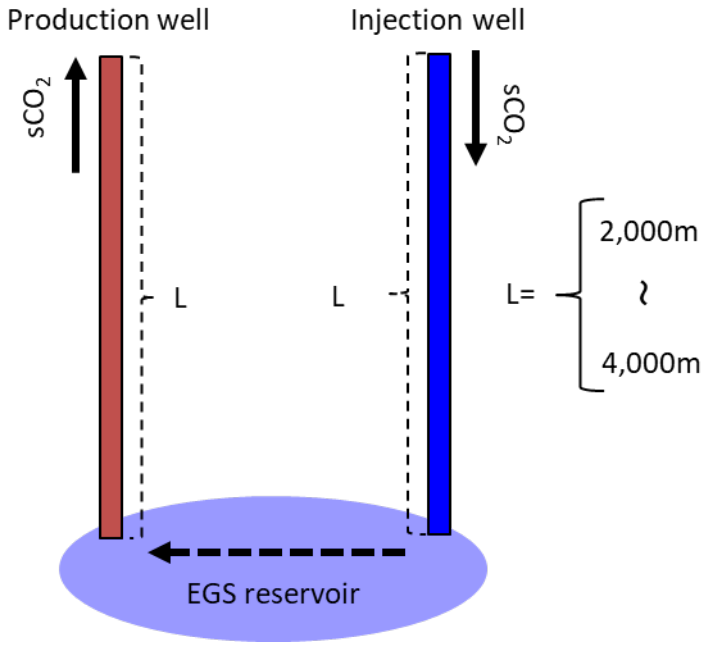

Figure 7: Flow path of the wellbore simulation

Table 3 shows the numerical conditions for wellbore simulation. In this study, as mentioned above, the results corresponding to approximately 15 years after the start of sCO_2 injection are used for the estimation the power generation potential at the time when a relatively stable circulation state is reached after the start of sCO_2 injection.

Table 3: Numerical conditions for wellbore simulation

Parameter	Value	Unit
Depth of injection and production wells	2,000 3,000 4,000	m
Inner diameter of flow path	0.216	m
Roughness of the flow path	4.57×10^{-5}	m
Temperature at ground	15	℃
Temperature of reservoir	200 300	℃
Thermal conductivity of rock	2.1	W/m/K
Specific heat of rock	1,000	J/kg/K
Density of rock	2,500	kg/m^3
Time from initial state of the EGS reservoir	15	years

3.2 Thermal efficiency analysis method and conditions

Through the wellbore simulation mentioned above, differences in sCO_2 conditions at the injection and production wellheads, in other words, turbine differential pressures and enthalpy differences between the injection and production wellheads, can be determined. Therefore, in the thermal efficiency analysis, plants that can sufficiently recover these turbine differential pressures and enthalpy differences were assumed for each analysis condition, and the power generation output was estimated.

Figures 8 and 9 show the configuration of the thermal efficiency analysis model and T-s diagram for sCO_2 geothermal power system constructed by EnergyWin. Based on the results of thermal efficiency analyses of six different power generation cycle models conducted in previous studies, the recuperation power generation cycle was selected as the simplest and most efficient power generation cycle (Nakao et al., 2023). This cycle is basically the thermodynamic Brayton cycle in which sCO_2 extracted from the production well is directly fed to a CO_2 turbine and expanded to near injection wellhead pressure to generate electricity, everything happens in the supercritical region. However, since the sCO_2 is still at a high temperature at the turbine outlet, the sCO_2 is returned to the subsurface through the injection well after heat recovery in the regenerative heat exchanger before being returned to the subsurface. A cooler and a CO_2 compressor are installed after the regenerative heat exchanger to adjust the sCO_2 pressure at the outlet of the CO_2 turbine and the sCO_2 conditions at the injection wellhead. Then, Table 2 shows the numerical conditions for the thermal efficiency analysis.

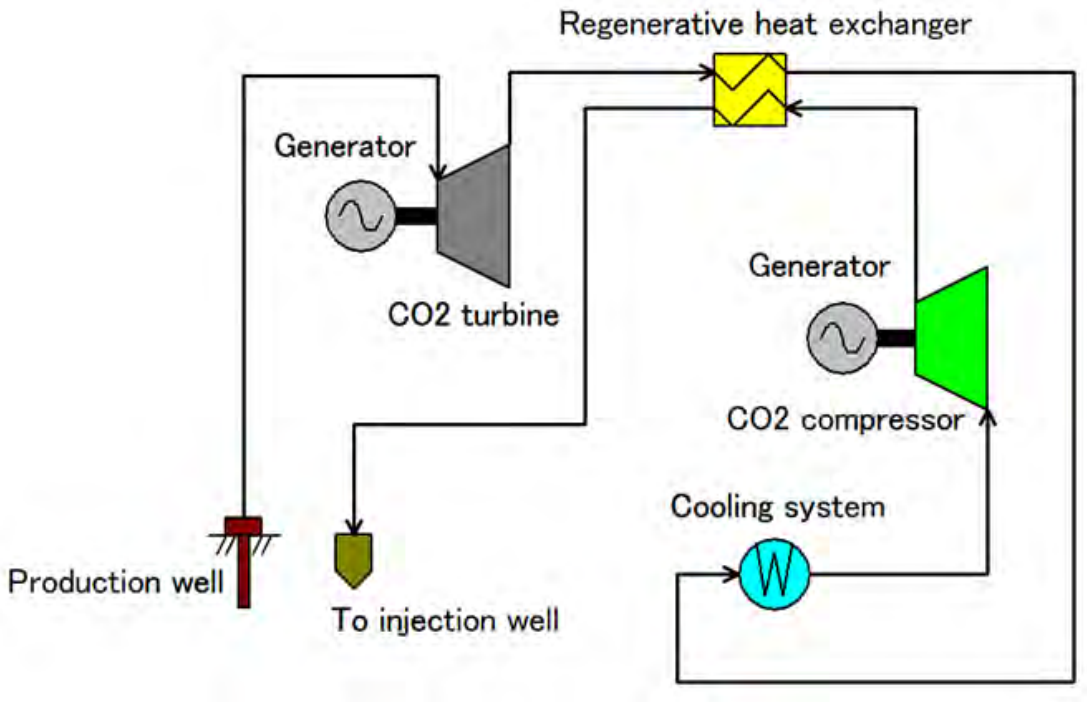

Figure 8: Configuration of thermal efficiency analysis model, Recuperation power generation cycle

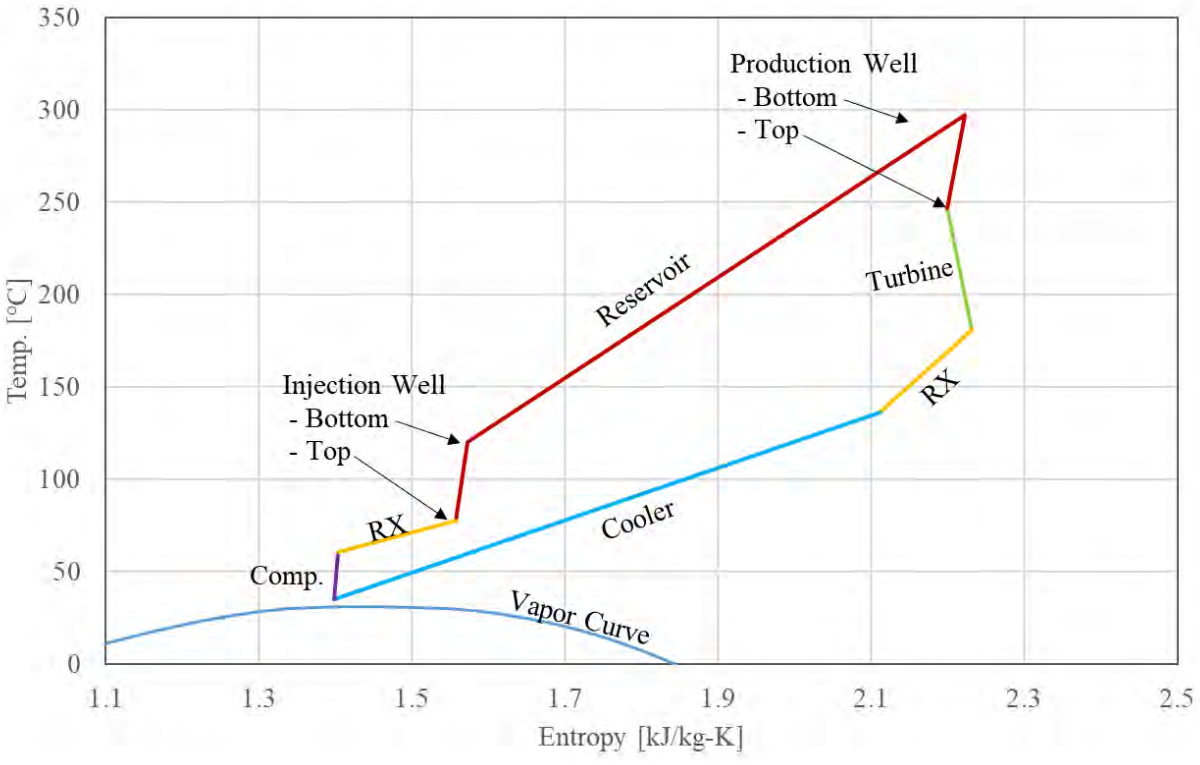

Figure 9: Example of T-s diagram of semi-open loop sCO_2 geothermal power system

Table 4: Numerical conditions for thermal efficiency analysis

Component		Property	Value	Unit
CO_2 turbine		Adiabatic efficiency	77.2	%
Generator		Mechanical efficiency	95	%
Regenerative heat exchanger		Temperature efficiency	90 or less	%
		Minimum ΔT	5 or more	℃
		Pressure loss	0.1	MPa
CO_2 compressor		Adiabatic efficiency	88	%
Cooling system	Cooler	Minimum ΔT	5 or more	℃
		Pressure loss	0.1	MPa
	Cooling tower	ΔT of coolant	5	℃
		Fan power supply	Based on actual data	kW
	Pump	Pump efficiency	80	%

3.3 Analysis results of plant simulation

In the plant simulation of the semi-open loop sCO_2 geothermal power system, the conditions for maximum net power generation output were obtained by taking the conditions of the bottom of the injection and production wells. The conditions that maximize the net power generation output of the power generation cycle were obtained by varying the regenerative heat exchanger outlet temperature and pressure of the cycle as parameters.

Figure 10 shows the net power generation output and gross power generation output of the system for each wellbore condition. However, since the sCO_2 flow rate used in the plant simulation is 1/4 of the flow rate from the reservoir simulation performed considering a two-dimensional five-spot production-injection problem for a 1 km square area, as described above, this figure shows the analytical results for the power generation output multiplied by four.

Higher reservoir temperatures result in higher sCO_2 temperatures and pressures at the production wellhead, resulting in higher power output from the power generation cycle. The deeper the well, the lower the sCO_2 temperature at the production wellhead, but the higher the pressure and the higher the expansion ratio of the turbine, the higher the power output of the power generation cycle. The higher the wellhead temperature of the injection well, the higher the gross power output of the cycle, while the net power output was lower. This is because the higher temperature at the injection wellhead results in a lower density of sCO_2, which requires a higher pressure at the injection wellhead. Since there is little difference in temperature and pressure at the production wellhead regardless of the temperature and pressure at the injection wellhead, and since more heat can be recovered from the waste heat at the turbine outlet by injected sCO_2, the gross power generation output is almost the same when expanded to the same pressure level. However, if a higher pressure is required at the injection wellhead, the net power generation is lower because of the greater

compression power required to raise the pressure to the injection pressure. For example, with a reservoir temperature of 300°C and a well depth of 4,000 m, increasing the injection temperature from 40°C to 90°C increases the CO_2 turbine power by approximately 2,100 kW, while the boosting power of the injected sCO_2 increases from approximately 1,200 kW to 4,800 kW, resulting in a decrease of approximately 1,700 kW in the net power generation output.

In this study, the maximum net power generation output was estimated to be approximately 10.5 MW for the case where the reservoir temperature is 300°C, the well depth is 4,000 m, the injection wellhead temperature is 54.4°C, and the injection wellhead pressure is 15.1 MPaA.

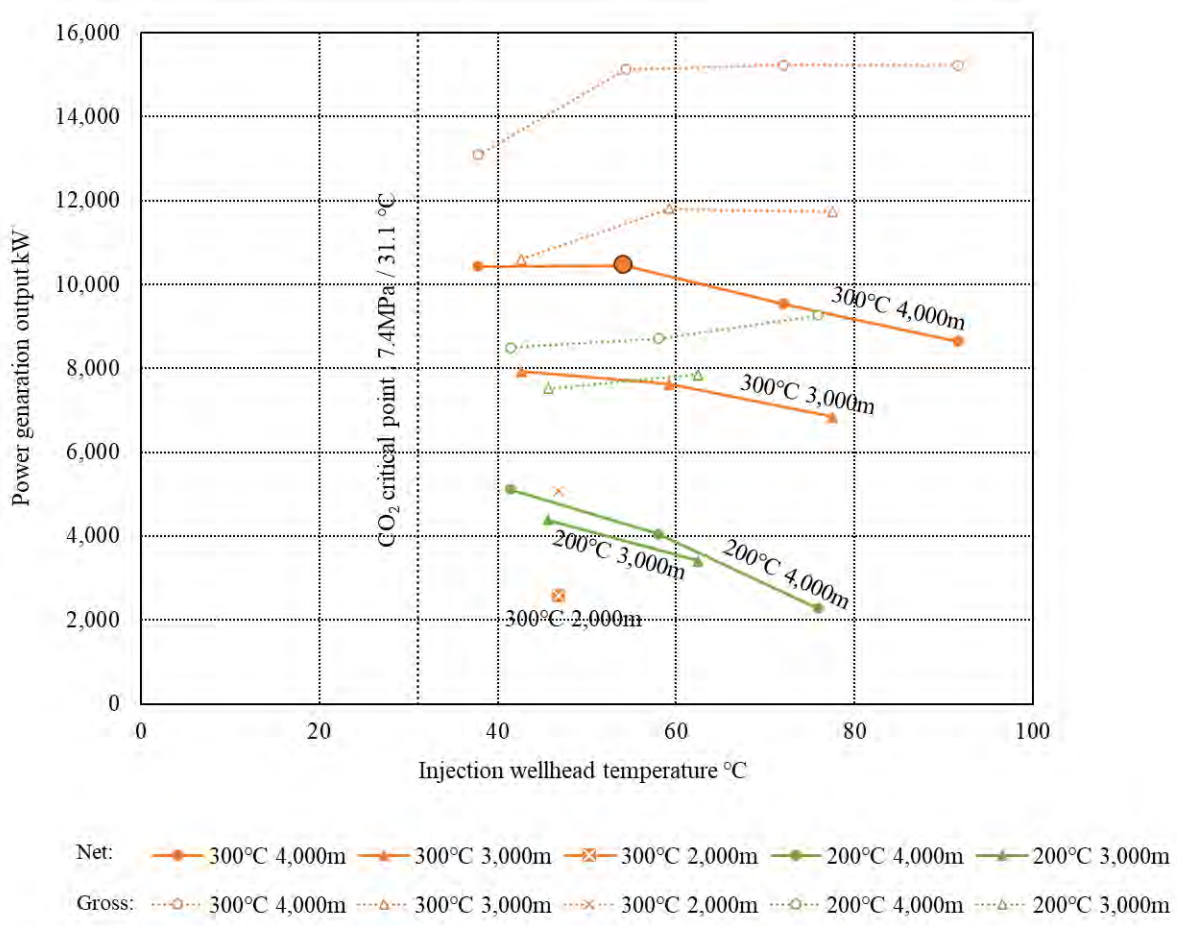

Figure 10: Relationship between the injection wellhead temperature and gross/net power generation output of the semi-open loop sCO_2 geothermal power system

4. Conclusion

We have estimated the sustainable amount of electricity generated by an idealized semi-open loop sCO_2 geothermal power system based on the results of reservoir and plant simulations. And we found that net power generation output increases with higher reservoir temperature, deeper injection wells, and lower injection temperatures, and that a development targeting a 1 km square geothermal reservoir at a depth of 4,000 m and a temperature of 300°C is expected to generate approximately 10 MW. However, under these conditions in this paper, the waste heat above 150°C

at the outlet of the CO_2 turbine cannot be fully regenerated, and much heat is discharged outside the system. In the future, further improvement is needed, such as considering a combined-cycle power generation system using a binary power generation system as a bottoming cycle.

In this study, the production gas was assumed to be pure CO_2 during the period when CO_2 reaches (breakthrough) the production well and the flow rate is stable (10 to 20 years after the start of sCO_2 injection). However, if we are considering that the transition from a water-bearing reservoir to a CO_2-dominated reservoir, it may pose some geochemical challenges, such as generation of acidic fluids and precipitation of mineral phases within the reservoir that might reduce flow rates of circulating sCO_2. Furthermore, catastrophic damage to the power generation facilities may occur. Therefore, it is necessary to evaluate the geochemical effects of sCO_2 injection on water-bearing reservoirs in the next phase of this project.

Our future goal is to estimate the geothermal development potential of the sCO_2 geothermal power system when applied in Japan, after conducting a cost and economic analysis.

Acknowledgement

Most of the presented work was supported by JOGMEC program. We would like to thank JOGMEC for their support with our project and discussions on the results.

REFERENCES

Alvarado, R., Molina, S., Chandrasekar, H., Amaya, A., and Scherer, J. (2023): Residual Heat Extraction from Depleted Heavy-Oil Wells in Thermal EOR, GRC Transactions, Vol. 47, Reno, Nevada, October 1-4.

Atrens, A.D., Gurgenci, H., and Rudolph, V. (2009): CO_2 Thermosiphon for Competitive Geothermal Power Generation, Energy and Fuels, 23, 553-557.

Chandrasekar, H., Sonnenthal, E., Amaya, A., Rutqvist, J., Oldenburg, C., Golla, G., Manuel, F., Klenner, R., Ng, A., Ellis, S., Gilbert, B., and Scherer, J. (2023): Coupled Thermal Hydraulic Mechanical and Chemical (THMC) Modeling of the GreenLoop system in the Southeast Geysers, California, GRC Transactions, Vol. 47, Reno, Nevada, October 1-4.

Higgins, B. S. and Oldenburg, C. M. (2016): PROCESS MODELING OF A CLOSED-LOOP SCO_2 GEOTHERMAL POWER CYCLE, The 5th International Supercritical CO_2 Power Cycles Symposium, Texas, March 29-31.

Kaieda H. (2015): Current Status and Issues in Technology Development of Enhanced Geothermal System (EGS), CIREPI Report, N14017.

Kerr, T., Klaerner, J., Nielson, J., and Weiss, N. (2023): Innovations in Geothermal Power based on the Commissioning and Testing Results of Sage Geosystems' sCO2 Prototype Turbine, GRC Transactions, Vol. 47, Reno, Nevada, October 1-4.

Klenner, R., Angolano, J., Long, T., Rich, P., Antle, R., Amaya, A., Chandrasekar, H., Golla, G., Murtland, C., Bordenave, R., Hill, J., and Roussie, G. (2023): Constructing a Test Facility to

Demonstrate and Commercially Scale Geothermal Technologies, GRC Transactions, Vol. 47, Reno, Nevada, October 1-4.

Koda E. (1999): Study on High Performance CAES Power Generation System Applying the Advanced Combined Cycle Technology, Proceedings of International Gas Turbine Congress, Kobe, Japan, November 14-19.

Nakao Y., Suenaga H., Fukada T., Ohsato K., and Terai A. (2023): Feasibility study on geothermal power generation system by carbon dioxide circulation, GRC Transactions, Vol. 47, Reno, Nevada, October 1-4.

Nakao Y., Takahashi T., and Watanabe Y. (2011): DEVELOPMENT OF PLANT PERFORMANCE ANALYSIS SYSTEM FOR GEOTHERMAL POWER PLANT, Proceedings of the ASME 2011 Power Conference, Denver, Colorado, July 12-14.

National institute of standards and technology (NIST) (2022): https://www.nist.gov/srd/refprop

New Energy and Industrial Technology Development Organization (NEDO) (2022): Feasibility Study Program “Geothermal power system by carbon dioxide circulation”, Fiscal year of 2020-2021 report.

Pruess, K. (2006): Enhanced Geothermal Systems (EGS) Using CO2 as Working Fluid - A Novel

Approach for Generating Renewable Energy with Simultaneous Sequestration of Carbon,

Geothermics, Vol. 35, No. 4, pp. 351–367, August.

Pruess, K., and T.N. Narasimhan. (1982): On Fluid Reserves and the Production of Superheated Steam from Fractured, Vapor-Dominated Geothermal Reservoirs, J. Geophys. Res., Vol. 87, No. B11, PP. 9329-pp. 9339.

Pruess, K., and T.N. Narasimhan. (1985): A Practical Method for Modeling Fluid and Heat Flow in Fractured Porous Media, Soc. Pet. Eng. J., Vol. 25, No. 1, pp. 14 – pp. 26, February.

Takahashi T., Nakao Y., and Koda E. (2007): Analysis and evaluation about Advanced humid air turbine system, International Conference on Power Engineering-2007, Hangzhou, China, October 23-27.

In-Situ Stress Review for a Closed-Loop Geothermal Project in Geretsried, Germany

Anna Rogers[1], Ulf Boeker[2], Stephen Longfield[1], and Carsten Reinhold[2]

[1]Eavor Technologies Inc., [2]Eavor GmbH

Keywords

Geomechanics, In-Situ Stress Estimate, Closed-Loop Geothermal, Germany

ABSTRACT

Eavor Technologies Inc. (Eavor™) is currently drilling a complex, multi-lateral closed-loop geothermal system (an "Eavor-Loop™") in the Geretsried area, Bavarian Molasse Basin, southern Germany. A total of four Eavor-Loops are planned for the location, and spud for Loop 1 was in July 2023. The target for the Eavor-Loop development is the Jurassic Malm carbonate formation.

Geomechanics, including in-situ stress estimation, is important in Eavor-Loop designs to evaluate wellbore stability, mud weights, operating pressures, and to optimize well orientations. GEN-1 and GEN-1ST-A1 are nearby offset wells and were used to constrain the geomechanical model pre-drill. However, within the academic community, there is considerable uncertainty over the stress regime in the Bavarian Molasse Basin. Normal faulting, strike slip and reverse faulting regimes have all been predicted in relatively close proximity.

As part of the completion of the first loop, a series of Formation Integrity Tests (FITs) were completed by Eavor. These data points provide new insights into the possible stress regime. This paper will present the pre-drill and current estimates for the stress regime for the Geretsried area, and the planned future data collection. The understanding of the stress regime will impact the chosen mud weights while drilling, and the optimal drilling direction for future loops, to reduce the likelihood of wellbore instability.

Introduction

Eavor Technologies Inc. (Eavor™) is a closed-loop geothermal energy company founded in Calgary, Alberta, Canada in 2017. An Eavor-Loop™ is an innovative geothermal solution for power generation and district heating. The key technical differentiator is the use of a subsurface multilateral closed-loop system that relies only on conductive heat transfer, as opposed to convection or fluid flow like in a conventional geothermal system. A full-scale prototype of the first-generation closed-loop system was successfully built and tested at the Eavor-Lite™ facility in 2019, in sedimentary rock in Alberta.

In 2023, Eavor spudded its first commercial scale project in Geretsried, Germany. This project is an Eavor-Loop 1.0 design, in the Jurassic Malm carbonate formation. To complete the Eavor-Loop, two wells (here named GEL-A1 and GEL-B1) are drilled to a depth of ~4.5 km and landed at a ~90° inclination in the Malm. The wellbores are cased and cemented into the Malm formation. GEL-A1 was landed slightly higher than GEL-B1, and these wells will become the sidetrack points for the multilateral sections of the loop. This analysis was performed at the time of completion of the landing of the main wellbores (Q1 2024).

A series of multilateral sidetracks are planned to be drilled ~3 km from the mainbores, with each associated well from GEL-B1 and GEL-A1 connected at the toes to complete the closed-loop system. Further geoscience data and image logging are planned to be collected in both the vertical and lateral wells. An example schematic demonstrating an operating Eavor-Loop 1.0 design, as compared to the proto-type Eavor-Lite, is shown in Figure 1.

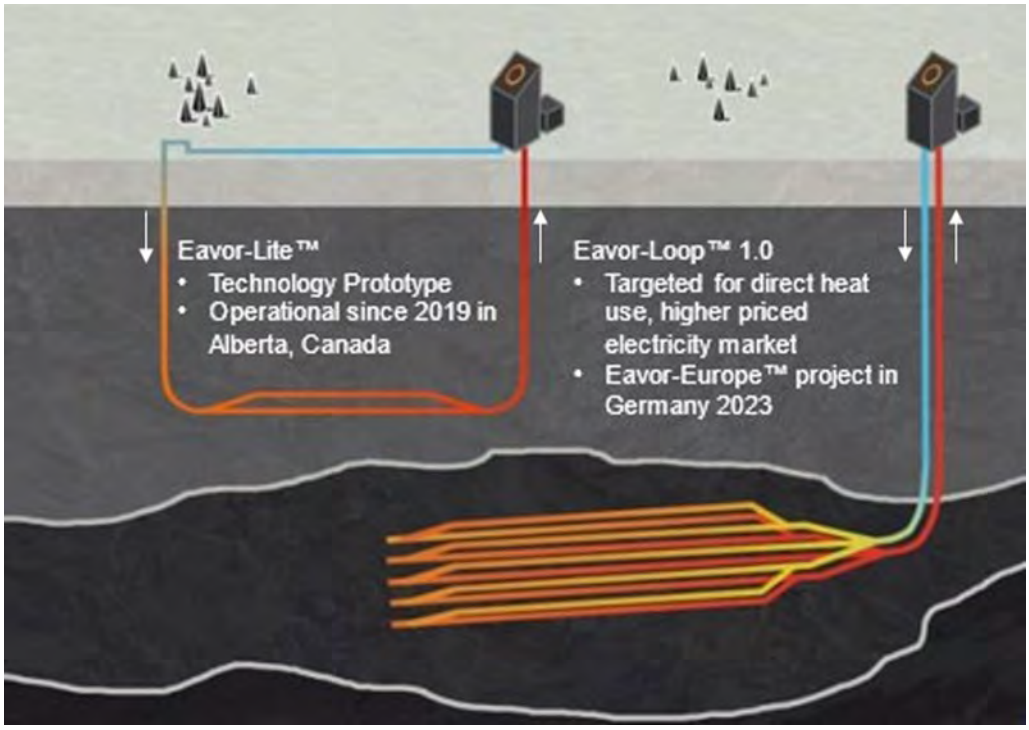

Figure 1: Schematic comparison of Eavor-Lite and Eavor-Loop 1.0 design. Note that this is for visualization purposes and does not display the final well plans or relative sizes of the loops at Geretsried.

GEN-1 and GEN-1ST-A1 are offset wells, drilled from the same pad as GEL-A1 and adjacent to GEL-B1, which were used to constrain the geomechanical model. GEN-1 and GEN-1ST-A1 were intended to be conventional geothermal wells but failed to find sufficient permeability (Backers et al., 2022). They were drilled in 2013 and 2017, respectively, and useful data were collected to refine the in-situ stress estimates. There are a few other further offset wells that have had relevant data collection, including the Unterhaching Gt 1, Hofolding 1, and Grambach 1 (Figure 2).

Figure 2: Surface locations of the Eavor-Loop and offset wells GEN-1 (and 1ST-A1), Unterhaching Gt 1, Hofolding 1, Grambach 1 (Google Earth). Geretsried is located directly north of the Alps, and the Eavor-Loop is targeting the Jurassic Malm carbonate formation in the Bavarian Molasse Basin.

Understanding the in-situ stress tensor, which includes the three principal stresses and their orientations, plays an important role in wellbore stability prediction, trajectory optimization, drilling pressure limits, and cement program design. Since there is no salt or active faulting here, it is reasonable to assume that one of the principal stresses is near-vertical and is referred to as the overburden stress (S_v; Moos and Zoback, 1990). The other two principal stresses are perpendicular horizontal stresses, a minimum (S_{hmin}) and a maximum (S_{Hmax}).

Both the magnitude and azimuth of the in-situ stresses can vary laterally and with depth, making the task of estimating the stress tensor notoriously difficult. In addition to this, there is uncertainty over the stress regime in the Bavarian Molasse Basin, as normal faulting, strike slip and reverse faulting regimes have all been predicted in the areas adjacent to Geretsried. The Bavarian Molasse Basin is located directly north of the Alps and is a classic foreland basin (Reinecker et al., 2010), which has implications on the present-day stress regime at Geretsried.

This paper will focus on a discussion of the stress estimate for the Eavor-Loop 1.0 project in Geretsried, Germany, based on the learnings from the recent Formation Integrity Tests (FITs).

Literature Review

Within the academic community there is considerable uncertainty over the stress regime in the Bavarian Molasse Basin, which has been reviewed in Reinecker et al. (2010), Drews et al. (2019), Ziegler & Heidbach (2020), Backers et al. (2022), and Ahlers et al. (2022). There are numerous other publications which cover this topic, but a detailed review of these is out of scope for this paper. Instead, the cited papers are used to demonstrate the wide variability in stress approximations. Normal faulting ($S_{hmin} < S_{Hmax} < S_v$), strike slip ($S_{hmin} < S_v < S_{Hmax}$) and reverse faulting ($S_v < S_{hmin} < S_{Hmax}$) regimes have all been predicted within a relatively small geographic area. Here, the focus of this review was on the Bavarian Molasse Basin and more locally on the Geretsried area.

As presented by Reinecker et al. (2010), four-arm caliper and image logs were analyzed in 137 wells with a depth of investigation that ranged from surface to 6000 mTVD. A total of 1348 borehole breakouts and 59 drilling-induced fractures were observed in 98 wells in the Bavarian Molasse Basin. The breakouts were often observed to have large angular widths (> 60°) and high eccentricities (> 50% more than bit size). They occurred at shallow depths; less than 600 mTVD in 27 wells, and with some breakouts observed at less than 100 mTVD. The observation of breakouts at shallow depths suggests that the horizontal stress magnitudes (or, at least S_{Hmax} magnitude) are high in the Bavarian Molasse Basin. Based on these observations, Reinecker et al. (2010) speculated that a strike slip or thrust faulting stress regime presently exists in the shallow Bavarian Molasse Basin.

In Drews et al. (2019), leak-off tests (LOT), FIT and cementation pressure data were analyzed and the implications on the present-day stress regime in the Bavarian Molasse Basin were discussed. The primary case study used in this paper was a LOT completed at 825 mTVD at the Unterhaching Gt 1 well (Figure 2) in a shale unit. The authors showed that all values obtained from the LOT are significantly lower than the estimated S_v (i.e., fracture propagation pressure of ~1.58 SG), implying that either a normal faulting or strike slip stress regime is present at this well location. Additionally, they stated that using a coefficient of sliding friction (μ_s) of 0.6 in the critically stressed crust equation results in a strike slip stress regime assumption. However, by using $\mu_s = 0.4$, the critically stressed crust equation indicates a normal faulting stress regime. The authors argued that the correct lithological context has not been considered before this study, and that a $\mu_s = 0.4$ is more representative for the shale. Based on this, they suggested that a normal faulting regime may be present in the shallow Bavarian Molasse Basin.

Ziegler & Heidbach (2020) generated a high-resolution 3D stress model of the Bavarian Molasse Basin. The resulting uncertainty in the modelled stress state was due to variability in the stress magnitude data records used for calibration. As a result, there were larger uncertainties in the modelled S_{Hmax} magnitude and significantly smaller uncertainties in the S_{hmin} magnitude, since S_{hmin} is typically easier to quantify. From the Ziegler & Heidbach 3D stress model, the principal stresses were extracted in the project area. At the closest modelled depth to the Eavor-Loop target interval (4,443 mTVD), which is presumed to be associated with the Malm, Ziegler & Heidbach predict a strike slip regime with $S_v = 2.50$, $S_{Hmax} = 4.65 \pm 1.13$ SG, and $S_{hmin} = 1.79 \pm 0.18$ SG. Ziegler & Heidbach also contemplated the existence of a transtensional regime ($S_{hmin} < S_{Hmax} \sim S_v$) but based on evidence from FIT data they suggested that a strike slip regime was more likely.

Backers et al. (2022) estimated the Geretsried Malm stress field as part of the ZoKrateS project. The ZoKrateS project was a multistage hydraulic fracture stimulation of the Malm in GEN-1ST-A1 in 2021 (LIAG, 2021). The GEN-1ST-A1 well was initially drilled in 2017 and re-entered 4 years after the initial drill, and it was found to be stable and in good hole condition. Backers et al. (2022) referenced an internal report which suggested a strike slip faulting regime, with S_v = 2.48 SG, S_{Hmax} = 2.72 SG, and S_{hmin} = 1.63 – 2.15 SG. Similar to Drews et al. (2019), they suggested that μ_s may be lower than 0.6 since a clay rich filling of the discontinuities should be assumed.

Ahlers et al. (2022) provided a continuous finite element prediction of the crustal stress with focus on the sedimentary basins in Germany. The study by Ahlers et al. (2022) included a larger area as compared to Ziegler & Heidbach (2020), which may lead to higher uncertainty in the Bavarian Molasse Basin. The 3D model was calibrated with minimum expected values for both S_{hmin} and S_{Hmax} magnitudes. Internally at Eavor, the X, Y, Z stress data was extracted over the project area, and a python code was then written to calculate S_v, S_{Hmax}, S_{hmin} at this location, using eigenvectors for stress direction and eigenvalues for principal stress magnitude. At the closest depth to the target interval (4,366 mTVD), which is presumed to be associated with the Malm, they predict a normal faulting regime with S_{hmin} = 1.40 SG, S_{Hmax} = 1.78 SG, S_v = 2.40 SG. However, Ahlers et al. (2022) stated that the Bavarian Molasse Basin results are very inconsistent compared to the rest of Germany. Below 1000 mTVD, S_{Hmax} predictions appear to split into two groups with both normal faulting and strike slip results.

Table 1 summarizes the in-situ stress states identified by Ziegler & Heidbach (2020), Backers et al. (2022) and Ahlers et al. (2022), for the Malm target interval in the Bavarian Molasse Basin.

Table 1: In-situ Stress Estimates in the Malm, Geretsried (Bavarian Molasse Basin) from recent studies.

Study	S_{hmin} (SG)	S_v (SG)	S_{Hmax} (SG)	Regime
Ziegler & Heidbach (2020)	1.79 ± 0.18	2.50	4.65 ± 1.13	Strike Slip
Backers et al. (2022)	1.63 – 2.15	2.48	2.72	Strike Slip
Ahlers et al. (2022)	1.40	2.40	1.78	Normal

Based on the most recent publications, it appeared that normal and strike slip faulting were more likely for the Geretsried area, with the possibility of stress changes with depth. These were the two most likely stress regimes carried in the pre-drill analysis. However, a reverse faulting regime also can't be ruled out at this point due to the high uncertainty identified by Reinecker et al. (2010).

While there is significant uncertainty in the stress magnitudes at Geretsried, the S_{Hmax} azimuth prediction is consistent. This can be seen in the World Stress Map (Heidbach et al., 2018) data points from borehole breakout and drilling induced tensile failure (Figure 3). Most indicators point to a N/S azimuth. The S_{Hmax} azimuth is expected to be highly uniform here (Reinecker et al., 2010).

Figure 3: World Stress Map over the Geretsried area (Heidbach et al., 2018). All indicators in the area are from drilling induced fractures or borehole breakouts and suggest a S_{Hmax} azimuth close to N/S. Project site is indicated by the star.

Offset Well Data

The overburden stress can be calculated from the density of the rock formations in the subsurface. There were no density logs collected in the GEN-1 and GEN-1ST-A1 wells due to regulatory restrictions, washouts, and a lean acquisition program. Instead, Gardner's equation was used to calculate density from sonic data in the offset wells GEN-1, GEN-1ST-A1, Grambach-1, and Hofolding-1 (Figure 2). A moving average of 30 m was applied before integrating the different density profiles to obtain a range of S_v profiles of which the minimum and maximum were deemed representative for the uncertainty range. The maximum calculated S_v may still be on the low side because of washouts on the offset log readings. At the top of the Malm, the S_v was calculated to be 2.44 – 2.52 SG. There is more consistency in the S_v prediction in literature (Table 1) as compared to the horizontal stress values, so the overburden stress evaluation will not be the focus of this paper. For the pre-drill modelling, S_v = 2.45 ± 0.1 SG was carried.

Several successful FITs were completed in the GEN-1 well and were provided by the prior drilling operator Enex Power Germany GmbH (Enex). A FIT can represent a minimum value for the minimum stress estimates. The data points, which are summarized in Table 2, can be used to constrain the horizontal stress evaluation. These FITs were completed in preparation for the suspected high pore pressure zone deeper in the well.

Table 2: FIT data from the GEN-1 well; EMW = test result in equivalent mud weight units. Provided by Enex.

#	Well	Depth (mTVD)	FIT EMW (SG)	Formation	Lithology
FIT 1	GEN-1	2,925	1.45	Chattian Sands	Sandstone/Marl
FIT 2	GEN-1	2,941	1.85	Chattian Sands	Sandstone/Marl

Geretsried Eavor-Loop Data

A series of FITs were completed in both GEL-A1 and GEL-B1 wells. The equivalent mud weight value (EMW) of the planned FITs were chosen based on the required mud weights to complete the subsequent wellbore section. There is a known very high pore pressure located at Geretsried at ~3250 mTVD (Drews et al., 2020), so relatively high FITs were needed to ensure the well could achieve a safe mud weight for drilling.

FITs were conducted at drill out of the casing shoe, exposing ~5 m of open hole. The well was then pressured up to a desired EMW by pumping at a low and constant rate. No leak-off was observed for any of these FITs and pressure held for ~10 minutes. The results are in Table 3. When no leak-off is observed, it can be assumed that the pressure has not reached the fracture gradient, and therefore is likely lower than the minimum stress.

Table 3: FIT data from GEL-A1/B1; EMW = test result in equivalent mud weight units.

#	Well	Depth (mTVD)	FIT EMW (SG)	Formation	Lithology
FIT A	GEL-A1	767	1.70	Neuhofener Beds	Marl
FIT B	GEL-B1	769	1.74	Neuhofener Beds	Marl
FIT C	GEL-A1	2,905	2.15	Chattian Sands	Sandstone/Marl
FIT D	GEL-B1	2,899	2.15	Chattian Sands	Marl
FIT E	GEL-B1	4,163	1.85	Rupel-Tonmergel	Limestone
FIT F	GEL-A1	4,480	1.45	Malm	Limestone/Dolomite

2.15 SG is a notably high FIT value, but confidence is added since both wells were able to reach this without leak-off. S_V at this depth (~2,900 mTVD) is estimated to be ~2.35 SG, which implies that the minimum stress is approaching the overburden stress.

A lower FIT value was chosen for the Malm since the operations team did not want to risk fracturing the target interval for the Eavor-Loop. However, there were additional indications that the minimum stress may be quite high in the deeper sections of Geretsried, below the high pore pressure zone. For the cement job for the 11-7/8” shoe at 4,137 mTVD, accounting for both the mud and the cement, a very high equivalent circulating density was reached which resulted in a downhole pressure of approximately 1.97 SG EMW. Additionally, a cement squeeze was completed and a downhole pressure of 2.14 SG EMW was achieved. However, it is not certain whether this squeeze was connected to any fresh formation. No losses were observed in the cement job or squeeze, which suggests that these pressures are below the fracture gradient, and therefore below the minimum stress. This cement data can be used as a low confidence minimum stress indicator but not as conclusive data points.

Discussion

The objective of this paper is to reflect on how the newly acquired FIT data in the Geretsried area may affect the understanding of the in-situ effective stresses, and the stress regime. This is valid as of Q1 2024, as further data is planned to be collected, and the geomechanical model is continuously being refined while drilling.

No new material information was collected for S_v, so this estimate remained the same. The pore pressure (P_p) estimate was refined in two ways. There is currently uncertainty in the pore pressure trends, and both of the following cases are currently considered to be likely. S_v and both P_p estimates are displayed in Figure 4.

P_p Case 1 was determined from a review of the mud weights used in GEL-A1 and GEL-B1 and any influxes/losses that were observed while drilling the vertical section. However, there are no direct measurements of pore pressure in the field so an alternative pore pressure case from literature was also considered. P_p Case 2 was estimated based on the findings of Drews et al. (2020). The authors generated a 3D basin model which suggested that pressure likely already starts to build in the Chattian Sands. This early pressure build was not observed in either in GEL-A1 or GEL-B1, and the Chattian Sands section was successfully drilled with near hydrostatic (~1.1 SG) mud weights. However, the Chattian Sands are very low permeability so any high pore pressure likely would not be detected during drilling (Drews et al., 2020).

To generate preliminary lower bounds on the minimum stress curves, S_{hmin} was anchored to the highest FIT data point (2.15 SG at ~2,900 mTVD in both GEL-A1 and GEL-B1). The Effective Stress Ratio (ESR, Zoback, 2010) was used to calculate a continuous profile of S_{hmin}, using S_v and both pore pressure estimates (Equation 1). The ESR from P_p Case 1 was calculated to be ~0.83, and ~0.67 for P_p Case 2. Minimum S_{hmin} cases resulting from Equation 1 are shown in Figure 4.

Equation 1: Effective Stress Ratio (ESR)

$$ESR = \frac{S_{hmin} - P_p}{S_v - P_p}$$

Uncertainty remains for the S_{Hmax} approximation, and consequently also for the stress regime. The GEL-A1 and GEL-B1 FIT values at ~2,900 mTVD were very high relative to S_v, and it is known that an increased pore pressure can lead to a higher fracture gradient and minimum stress. Based on the uncertainty in the pore pressure at this interval, it is currently possible that the ~2,900 mTVD FITs were high from pore pressure related effects, or from regional stress effects. However, since the fracture gradient is approaching S_v, it appears unlikely that strong normal faulting is present at this depth. This would suggest at least an isotropic ($S_{hmin} \sim S_{Hmax} \sim S_v$), combined strike slip/reverse ($S_{hmin} \sim S_v < S_{Hmax}$), or reverse faulting regime ($S_v < S_{hmin} < S_{Hmax}$) at the depth of ~2,900 mTVD. Further data would need to be collected to refine the S_{Hmax} approximation.

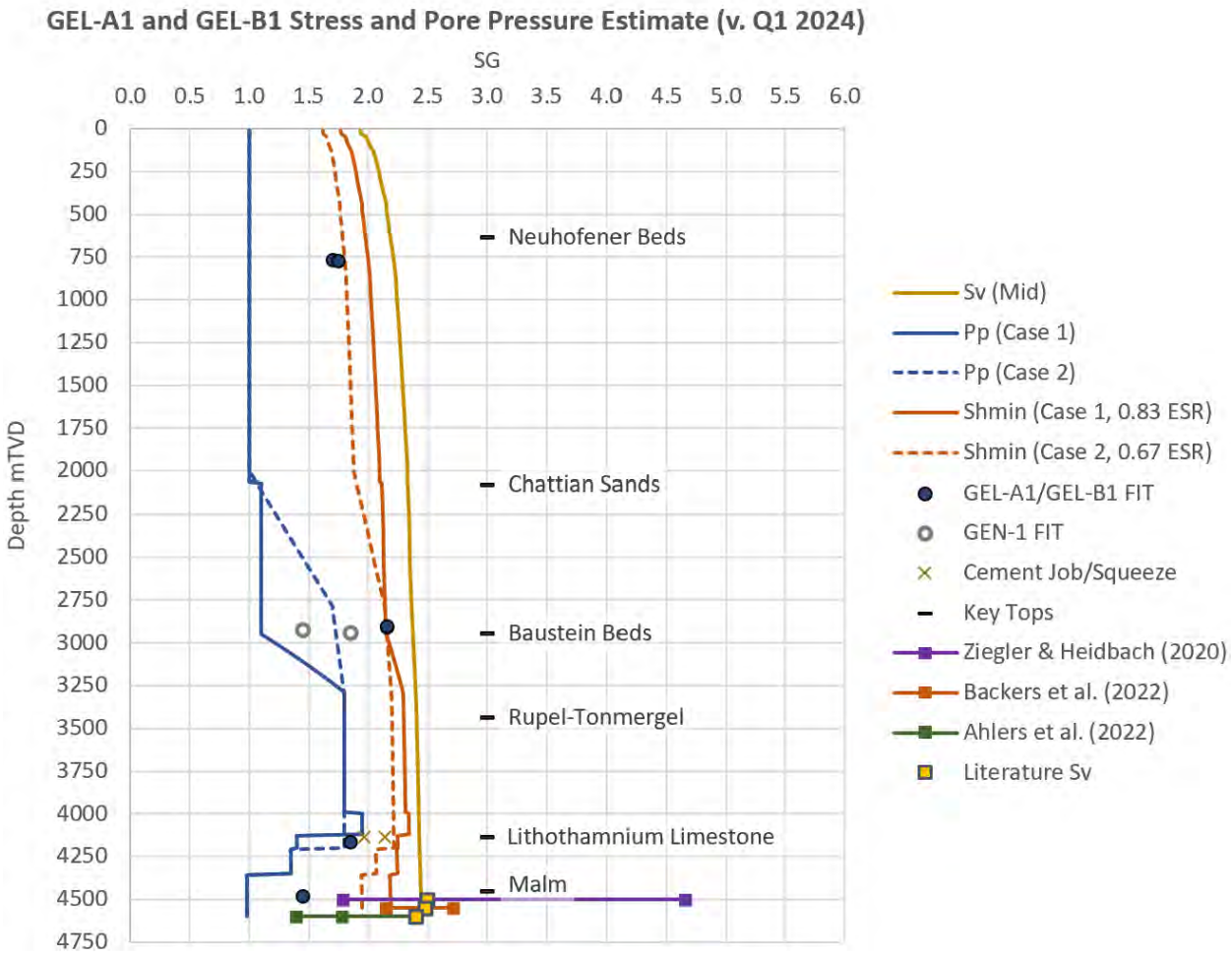

Figure 4: GEL-A1 and GEL-B1 Stress and Pore Pressure Estimates as of Q1 2024. FIT (high confidence) and cement data (low confidence) are shown, compared to literature Malm stress approximations by Ziegler & Heidbach (2020), Backers et al. (2022) and Ahlers et al. (2022) (Table 1). The S_{hmin} (ESR) curves are estimated from the ~2,900 mTVD GEL-A1 and GEL-B1 FITs, paired with the pore pressure cases.

To optimize the drilling of the Eavor-Loop, it is a priority to understand the in-situ stress in the Malm (~4,500 mTVD). The Malm is known to be underpressure (Drews et al., 2020), which affects the S_{hmin} estimate. As discussed, a lower bound S_{hmin} estimate was extrapolated to the Malm from an ESR (Equation 1, Figure 4). S_{hmin} Case 1 results in a generally higher minimum stress estimate than S_{hmin} Case 2. This method is one way of estimating the minimum S_{hmin} in the Malm, however there is uncertainty whether there could be a stress change with depth, where the ESR method would no longer apply.

Other than a difference in pore pressure between the Chattian Sands and the Malm, there are two explanations for why the minimum stress in the Malm at ~4,500 mTVD may be less than the FIT at 2,900 mTVD. The ESR approximation may be invalid if there is either active faulting between the Baustein Beds and the Malm, or a significant change in mechanical properties and stiffness which is affecting the stress distribution. There is limited tectonic activity that has been recorded near Geretsried, but blind thrusts in the area have been mapped on seismic by Shipilin et al. (2020).

As Loop 1 is drilled, more data will be collected to better understand the stress state and rock properties. Continued mudlogging and image logging are planned to be collected in both the vertical and lateral wells. If breakouts or tensile failure are observed in either the vertical or horizontal wells, this could help to refine the stress estimate. However, if the stress regime is reverse faulting, it would be challenging to refine all three stress magnitudes in the stress tensor, since the minimum stress would be S_v.

Additionally, it is possible that the FITs do not represent the lower bound of the minimum stress. If the formations have a high breakdown pressure, and have a high tensile strength, the FIT could overestimate the minimum stress (Zoback, 2010). If the stress uncertainty persists, an extended leak-off test (XLOT) should be considered while balancing the risk of operationally high pressures that would be required at these depths.

From the FIT data, an isotropic, combined strike slip/reverse or reverse faulting seems plausible in the Geretsried area at ~2,900 mTVD. At this depth, strong normal faulting would appear to be unlikely. However, a predominantly normal faulting regime in the Malm cannot be ruled out at this point, leaving open the possibility of a stress change at the depth of the Malm target interval (~4,500 mTVD). Geomechanical models must be continuously revised as a well is drilled. As Loop 1 progresses and the team learns more about the wellbore stability and stress state in the laterals, the drilling fluid can be updated to the optimized mud weight.

Summary

There is uncertainty in the stress regime in the area adjacent to the Geretsried Eavor-Loop project. Normal faulting ($S_{hmin} < S_{Hmax} < S_v$), strike slip ($S_{hmin} < S_v < S_{Hmax}$) and reverse faulting ($S_v < S_{hmin} < S_{Hmax}$) regimes have all been predicted within a relatively small geographic area (Reinecker et al., 2010; Drews et al., 2019; Ziegler & Heidbach, 2020; Backers et al., 2022; Ahlers et al., 2022). Prior to drilling the Geretsried Eavor-Loop, it was thought that normal faulting or strike slip faulting regimes would be more likely.

High FIT data points were collected in the GEL-A1 and GEL-B1 mainbores. At ~2,900 mTVD, FIT values of 2.15 SG were reached, approaching the expected S_v value (~2.35 SG). The FIT was repeatable in GEL-A1 and GEL-B1 with no leak-off observed. Due to this, it seems unlikely that the Geretsried area has a strong normal faulting stress regime at this depth, and it appears more plausible this interval is in either an isotropic ($S_{hmin} \sim S_{Hmax} \sim S_v$), combined strike slip/reverse ($S_{hmin} \sim S_v < S_{Hmax}$), or reverse faulting regime ($S_v < S_{hmin} < S_{Hmax}$). These FITs have provided new insights into the stress regime, as they are much higher than what is normally achieved in the Bavarian Molasse Basin.

However, in the deeper Malm there is still uncertainty in the stress. It is possible that the stresses change at the depth of the Malm, which could be due to either pore pressure affects, active faulting between the Baustein Beds and the Malm, or a significant change in mechanical properties and stiffness which is affecting the stress distribution. This remaining uncertainty highlights the importance of collecting stress information at multiple depths, and the requirement to characterize the target interval specifically. Further data collection is planned in the Eavor-Loop, including image logging in both the vertical and horizontal wells, which could potentially refine the stress state in the Malm. As drilling progresses in Geretsried, the stress environment will be continuously evaluated and refined to optimize the drilling program and future Loop 2-4 placement.

References

Ahlers, S., Röckel, L., Hergert, T., Reiter, K., Heidbach, O., Henk, A., Müller, B., Morawietz, S., Scheck-Wenderoth, M., & Anikiev, D. (2022). The crustal stress field of Germany: A refined prediction. Geothermal Energy. https://doi.org/10.1186/s40517-022-00222-6

Ahlers, S., Henk, A., Hergert, T., Reiter, K., Müller, B., Röckel, L., Heidbach, O., Morawietz, S., Scheck-Wenderoth, M., & Anikiev, D. (2022). The crustal stress state of Germany – Results of a 3D geomechanical model v2.0. TUdatalib. https://tudatalib.ulb.tu-darmstadt.de/handle/tudatalib/2624.5. https://doi.org/10.48328/tudatalib-437.5

Backers, T., Kahnt, R. & Stockinger, G. (2022). Structural dominated geothermal reservoir reaction during proppant emplacement in Geretsried, Bavaria. Geomechanics and Tunnelling. 15. 58-64. 10.1002/geot.202100091

Drews, M., Seithel, R., Savvatis, A., Kohl, T., & Stollhofen, H. (2019). A normal-faulting stress regime in the Bavarian Foreland Bavarian Molasse Basin? New evidence from detailed analysis of leak-off and formation integrity tests in the greater Munich area, SE-Germany. Tectonophysics. https://doi.org/10.1016/j.tecto.2019.02.011

Drews, M. C., Hofstetter, P., Zosseder, K., Shipilin, V., & Stollhofen, H. (2020). Predictability and controlling factors of overpressure in the North Alpine Foreland Basin, SE Germany: an interdisciplinary post-drill analysis of the Geretsried GEN-1 deep geothermal well. Geothermal Energy, 8(1). https://doi.org/10.1186/s40517-020-00175-8

Google Earth. (2024). Germany. Satellite image. Retrieved from https://earth.google.com/. Accessed May 26, 2023

Heidbach, O., Rajabi, M., Cui, X., Fuchs, K., Müller, B., Reinecker, J., Reiter, K., Tingay, M., Wenzel, F., Xie, F., Ziegler, M. O., Zoback, M.-L., & Zoback, M. D. (2018). The World Stress Map database release 2016: Crustal stress pattern across scales. Tectonophysics, 744, 484-498. https://doi.org/10.1016/j.tecto.2018.07.007

Heidbach, O., Rajabi, M., Reiter, K., Ziegler, M. O., & WSM Team. (2016). World Stress Map Database Release 2016. GFZ Data Services. https://doi.org/10.5880/WSM.2016.001

Leibniz Institute of Applied Geophysics (LIAG). (2020). ZoKrateS: A demonstration and pilot project for geothermal utilization. LIAG Website. https://www.leibniz-liag.de/en/research/projects/third-party-funded-projects/zokrates.html. Accessed June 16, 2024

Reinecker, J., Tingay, M., Müller, B., & Heidbach, O. (2010). Present-day stress orientation in the Bavarian Molasse Basin. Tectonophysics, 482, 129–138

Shipilin, V., Tanner, D., Hartmann, H., & Moeck, I. (2020). Multiphase, decoupled faulting in the southern German Bavarian Molasse Basin – Evidence from 3-D seismic data. Solid Earth, 11, 2097-2114. https://doi.org/10.5194/se-11-2097-2020

Simpson, R. (1997). Quantifying Anderson's Fault Types. Journal of Geophysical Research, 102(B8), 17909-17919

Ziegler, M., & Heidbach, O. (2020). The 3D stress state from geomechanical–numerical modelling and its uncertainties: A case study in the Bavarian Molasse Basin. Geothermal Energy, 8(1). https://doi.org/10.1186/s40517-020-00162-z

Zoback, M. D. (2010). Reservoir Geomechanics. Cambridge University Press

The Advantages of Electric-grade Heat Storage in Long Closed-loop Wells

Junyuan Zhang[1], Erick Burns[2], and Hongbin Zhan[1]

[1]Department of Geology and Geophysics, Texas A&M University

[2]U.S. Geological Survey

Keywords

closed-loop; long well geothermal; semi-analytical solution; periodic source; modeling

ABSTRACT

Though long (e.g., tens of kilometers) closed-loop geothermal wells are under consideration for the extraction of subsurface heat, these wells might also serve as an efficient energy storage mechanism for electricity generation. Using a semi-analytic model solution, the potential for electric-grade heat storage as a function of ambient temperature (e.g., corresponds to depth of loop), well length, well diameter, and flow rate is evaluated. The following simplified cases for comparison of standard closed loop operation with energy storage operation were considered: [1] constant flow rate and constant temperature (90 °C) injection to represent the standard closed-loop base-case; and [2] constant flow rate and annual cycle sinusoidal temperature (90-150 °C) to represent seasonal (summer) charging while solar resources are peak. Initial temperatures for all scenarios considered herein are a uniform 175 °C. Electric-grade heat is assumed to be delivered whenever temperatures at the extraction point exceed 90 °C. For calculation purposes only, if temperature falls below 100 °C, it is assumed that heat delivered is sub-economic, so no electricity would be produced. For all scenarios, temperatures at the extraction well asymptotically approach the flow-weighted average injection temperature, but energy storage scenarios exhibited a damped time-varying signal that diminishes in magnitude with length of the loop. The asymptotic approach depends on initial temperatures in the rock and the heat extraction rate (a function of well diameter and flowrate). This analysis demonstrates that shorter closed loops can produce more electricity over time than longer closed-loops previously proposed for electricity production over typical engineering design lifetimes (e.g., 30 years). Although only a high-temperature scenario is considered herein, rock that is initially below boiling temperature would not host a standard closed-loop resource, but injection of hot water seasonally would asymptotically heat this low-temperature system to temperatures capable of electricity production. In other words, regardless of initial temperatures, closed loops could be used to store electricity with no critical minerals in the geothermal battery.

1. Introduction

In recent years, increased attention has been paid to renewable energy to reduce global warming and dependence on fossil energy. Geothermal energy has been proposed as one of the most important components of renewable energy due to its reliability, availability, and potential to supply baseload power (Zarrouk & Moon, 2014). A complementary technology to traditional geothermal resources is to store surplus energy from episodic renewables (e.g., wind and solar) for later use. Storage is often done with electrochemical batteries, but a potential alternative is underground thermal energy storage (UTES) which is technically feasible (c.f., Burns et al., 2020), and proven applications generally target low temperatures (< 90 °C, but often near local ambient air temperature). Methods like aquifer thermal energy storage (ATES) can store energy by injecting heated water into the aquifer (Burns et al., 2020; Qi et al., 2023); however, temperatures significantly above ambient background can cause rapid adverse geochemical changes, affecting structural stability and/or potentially leading to plugging and loss of permeability due to dissolution or precipitation of minerals.

Herein, we evaluate the potential to store and recover moderate-to-high-temperature fluid (>90 °C and >150 °C, respectively) in closed-loop systems. Closed loop systems that have been proposed for extraction of heat must be deep and long to access high temperatures and provide sufficient surface area to allow for long-duration delivery of electricity because radial conduction of heat to a well is an inefficient process (e.g., White et al., 2023). If heat is periodically injected, electricity production can be improved and could allow for the use of shorter length loops than is required for heat extraction only. As part of this research, the effect of time-varying injection temperature on heat delivered at the outflow for conversion to electricity is examined by comparing it to a base-case representing standard closed-loop operations. In particular, temperature and electric-grade energy at the outflow corresponding to different length loops is documented.

2. Method

A semi-analytic solution representing standard closed-loop heat extraction and periodic heat storage are used to solve the time varying heat flow problem in the Laplace domain (e.g., Arfken & Weber, 1995), and the solution is numerically integrated for the inverse Laplace transform (c.f., Zhou et al., 2022). We compare a simple sinusoidal input temperature to a constant input temperature, both at constant flow, then predict the delivered temperature and heat at distance along the loop to understand how heat would be delivered as a function of length of loop.

2.1 Conceptual Model

The conceptual model (Fig. 1) is used to illustrate the mathematical representation of the fluid and heat transport process within and near a horizontal long closed well (i.e., the loop) in a heat extraction or storage horizon. Vertical sections of the loop are assumed to be insulated to prevent heat exchange between colder shallower rocks and the loop. The surrounding rock is a conduction-only region that is assumed to be thick enough to avoid other impacts (e.g., heat exchange with other layers or hydrothermal systems), so mathematically, this region is assumed to be a semi-infinite system. The thermal property of the rock is assumed to be homogeneous with a uniform initial temperature (175 °C for all simulations herein). Water at a prescribed temperature is injected on one end of the well (left side in Fig. 1) and heat is advected towards the other with a constant flow rate (right side in Fig. 1). The analytic solution allows for variable temperature injection, and

two cases are compared herein: constant 90 °C for the standard closed-loop base-case, and sinusoidally varying 90-150 °C representing seasonal storage (i.e., period is yearly). The hypothesis is that seasonal charging with heat will maintain higher temperatures at the end of loops, allowing the production of more electric-grade heat with shorter loops. Water within the pipe is assumed to be well-mixed, and heat is exchanged with the surrounding rock through conduction in the radial direction perpendicular to the axis of the pipe. Because steel has higher thermal conductivity than rock, and pipes are comparatively thin, heat conduction through the pipe wall is not limiting, so the pipe is not explicitly represented. Thermal properties of materials filling the annular space between the loop and the rock are assumed to be the same as for the rock. The coordinate system is set as follows: the origin is at the center of the left end of the well. The *x-axis* is horizontal, pointing to the right; *r* is the radial coordinate in a vertical cross-section, pointing away from the center of the well; *R* is the radius of the well [L], *T* is temperature [Θ], *c*, *ρ,* and *k* are specific heat capacity [$L^2T^{-2}\Theta^{-1}$], density [ML^{-3}], and thermal conductivity [$MLT^{-3}\Theta^{-1}$] of the material. Notation *f* means flow property inside the well, and notation *b* means material property of the rock outside the well.

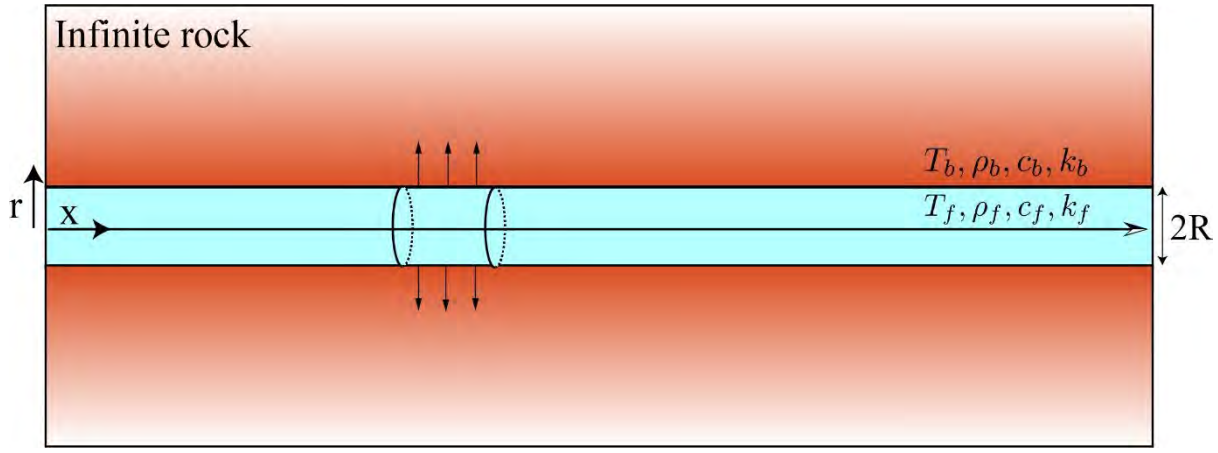

Figure 1: The 3D conceptual model of the closed loop long well system. The well is a cylinder that allows heat exchange radially with an arbitrarily large domain (assumed to be infinite for the solution). Water is injected on the left at a constant rate and variable temperature. As water flows in the direction x, the variations in temperature are damped, and over time as the borehole and surrounding rock are heated, temperature will asymptotically approach the average injection temperature for large distances.

Compared to traditional proposed use of closed-loops, which only extract heat, we postulate that periodic heat injection into closed loops is a way to store periodic excess energy in a system where geochemical plugging concerns are negligible (i.e., pipes). For instance, during summer, batteries are charged by electricity generated using solar panels or other intermittent sources of renewable energy for delivery hours or days later, but electric batteries cannot store energy for as long as geological thermal energy storage systems (e.g., weeks to years). While solar may seem an obvious choice, electricity from wind is also seasonal, and if some excess from the wind or solar glut periods could be stored long-term in high-temperature loops, this provides an option that does not depend on critical minerals used for chemical batteries.

Standard or literature supported values are selected for material properties and engineered system rates and sizes. Burns et al. (2024) indicated that effective bulk thermal conductivities for the Great Basin of the southwestern United States, where many geothermal systems have been identified, range from 2.4 to 3 W m^{-1} K^{-1}. Therefore, 2.6 W m^{-1} K^{-1} is used to represent the rock thermal

conductivity for all analyses herein. The density of granite is assumed to be 2,750 kg/m^3 and specific heat capacity is 790 J kg^{-1} K^{-1}. Using these three terms, one can calculate the thermal diffusivity as 37.75 m^2 per year. For estimates, we assume that after electric-grade heat is extracted, the colder water is injected at 90 °C (which gives our constant temperature for injection of the base case). For heat storage, it is assumed that heat can be extracted down to 90 °C, so heat added (stored) via the sine wave periodic heat source, is the heat corresponding to the difference between injected temperature and 90 °C. Thirty years is selected as the modeling time to correspond to a 30-year engineering lifetime of the facility.

Loop lengths of 15-20 km have been postulated for closed-loop systems, so herein the analyses consider 2, 5, 10, and 20 km. The injection rate is selected to be 0.1 m^3/s for a well radius of 0.2 m (White et al., 2023). For comparison, rates of ½ and twice this value (i.e., 0.05 and 0.2 m^3/s, respectively) are simulated.

2.2 Mathematical Model

Although the fluid flow rate is assumed to be constant, an annual sine wave heat source is used to represent periods of heat addition and extraction. If neglecting horizontal heat conduction inside the well, i.e., only considering a horizontally advective transport system, one has the following governing equation (described by notation *f*):

$$\frac{\partial T_f}{\partial t} = -\frac{Q}{\pi R^2}\frac{\partial T_f}{\partial x} - q \tag{1}$$

where Q is the volumetric flux of fluid inside the well [L^3T^{-1}], q is a heat sink term describing the heat loss to the rock through conduction [ΘT^{-1}], and it can be described by the following Eq. (2). The boundary condition on the left is described in Eq. (3), and the initial condition is in Eq. (4):

$$q = -\frac{2k_b}{\rho_b c_b R}\frac{\partial T_b}{\partial r}\Big|_{r=R} \tag{2}$$

$$T_f(x=0,t) = M\sin(\alpha t) + T_m \tag{3}$$

$$T_f(x,t=0) = T_0 \tag{4}$$

where T_m is the average injection temperature [Θ], M is the magnitude of the variation from mean injection temperature [-], α is the frequency [T^{-1}], and T_0 is the initial temperature inside the well [Θ].

For the rock outside the well (described by notation *b*), we only consider the heat conduction, and the related governing equation is:

$$\frac{\partial T_b}{\partial t} = \frac{k_b}{\rho_b c_b}\frac{1}{r}\frac{\partial}{\partial r}\left(r\frac{\partial T_b}{\partial r}\right) \tag{5}$$

where at the shell of the well ($r = R$), the temperature in bulk (T_b) equals to the temperature in the well (T_f), which is described in Eq. (6). Assuming that the rock has the same temperature as the well at the beginning, the temperature of the infinite long distance from the well will not change. The infinite radial boundary condition is described in Eq. (8), and the initial condition is in Eq. (7).

$$T_b(x,t,r=R) = T_f(x,t) \tag{6}$$

$$T_b(x,t=0,r) = T_0 \tag{7}$$

$$T_b(x,t,r=\infty) = T_0 \tag{8}$$

Using Laplace transform and Green's function of the modified Helmholtz equation (Arfken & Weber, 1995, Table 8.5) on Eqs. (1)-(8), one can solve the governing equations in Laplace space:

$$\overline{T_{f1}} = \left(M\frac{\alpha}{p^2+\alpha^2} + \frac{T_m - T_0}{p}\right)\exp\left[-\frac{\pi R^2}{Q}\left(p + \frac{2D_b}{R}\frac{\mathrm{K_1}\left(\sqrt{\frac{\mathrm{p}}{\mathrm{D_b}}}\mathrm{R}\right)}{\mathrm{K_0}\left(\sqrt{\frac{\mathrm{p}}{\mathrm{D_b}}}\mathrm{R}\right)}\sqrt{\frac{\mathrm{p}}{\mathrm{D_b}}}\right)x\right] \tag{9}$$

where T_{f1} is the temperature change inside the well [Θ] and defined as $T_f = T_{f1}+T_0$, the overbar symbol means the variable is in Laplace space, p is the Laplace transform operator, thermal diffusivity D is defined as $k/\rho c$ to represent heat conduct in fluid and rock, respectively [L^2T^{-1}], K_n is the second kind modified Bessel function with order n (n=0,1 in this research). By using the numerical inverse Laplace transform, one can get the final solution in the time domain as:

$$T_f = L^{-1}\left\{\left(M\frac{\alpha}{p^2+\alpha^2} + \frac{T_m - T_0}{p}\right)\exp\left[-\frac{\pi R^2}{Q}\left(p + \frac{2D_b}{R}\frac{\mathrm{K_1}\left(\sqrt{\frac{\mathrm{p}}{\mathrm{D_b}}}\mathrm{R}\right)}{\mathrm{K_0}\left(\sqrt{\frac{\mathrm{p}}{\mathrm{D_b}}}\mathrm{R}\right)}\sqrt{\frac{\mathrm{p}}{\mathrm{D_b}}}\right)x\right]\right\} + T_0 \tag{10}$$

By using the same method, one can obtain the semi-analytical solution with constant temperature boundary as:

$$T_f = L^{-1}\left\{\left(\frac{T_m - T_0}{p}\right)\exp\left[-\frac{\pi R^2}{Q}\left(p + \frac{2D_b}{R}\frac{\mathrm{K_1}\left(\sqrt{\frac{\mathrm{p}}{\mathrm{D_b}}}\mathrm{R}\right)}{\mathrm{K_0}\left(\sqrt{\frac{\mathrm{p}}{\mathrm{D_b}}}\mathrm{R}\right)}\sqrt{\frac{\mathrm{p}}{\mathrm{D_b}}}\right)x\right]\right\} + T_0 \tag{11}$$

Furthermore, the analytical solution in this study is in Laplace space and needs a numerical method to implement the numerical inverse Laplace transform (Zhou et al., 2022). The numerical inverse method used in this research is called the Gaver-Stehfest method. It is a discrete approximation of the Widder-Post inversion algorithm (Stehfest, 1970) and is implemented in Python with the mpmath package (The mpmath development team, 2023). (Verification of this model is provided in the supplementary material)

2.3 Energy Delivered Calculation

To estimate heat delivered, for each distance (x; corresponding to loop length), the difference between the extracted temperature and 90 °C is calculated. To convert this to thermal energy, multiply the temperature difference with injection rate (Q), density of water (ρ_f = 993.18 kg/m^3) and thermal capacity of water (c_f = 4181 J kg^{-1} K^{-1}), yielding electric-grade thermal energy extracted from the system. This thermal energy could be converted to electricity, but herein, a conversion efficiency was not assumed, so all comparisons are in terms of heat. It is recognized that a minimum temperature differential (above 90 °C) would be required to be economic, so for comparison purposes here, 10 °C (i.e., we assume electricity production stops if temperature drops below 100 °C) is used.

To evaluate total usable electric-grade heat over the life of the project (30-years), the heat flux is integrated over time (only when extraction is >100 °C), calculating the accumulated energy (AE) produced by the geothermal system as:

$$AE = \int_0^{t_{end}} Q c_f \rho_f T_{m,dif} dt \quad (12)$$

where t_{end} is the time interval to calculate the AE value [T]; $T_{m,dif}$ is the modified temperature difference calculated by the extracted temperature minus 90°C [Θ] and modified means the $T_{m,dif}$ will be set to zero if the difference is lower than 10 °C (because no energy will be extracted from the system).

3. Results and Discussion

Fig. 2 shows the extracted temperature change for the standard closed-loop heat-extraction only scenario at all four loop lengths for all three test injection rates. The dashed green line corresponds to the 100 ºC limit, the assumed limit where electricity production would cease because it is not economic. As postulated by other researchers (e.g., White et al., 2023), long loop lengths are required to allow continued electricity production for the full 30 years. From the 0.1m^3/s injection rate base-case, the model indicates that well length exceeding 10 km will have economically beneficial thermal production for the full 30 years. If using a higher injection rate, only an extremely long well (at least 20 km) will be economically beneficial for the duration. If the flow rate is slower, a well length greater than 5 km will produce heat beneficially.

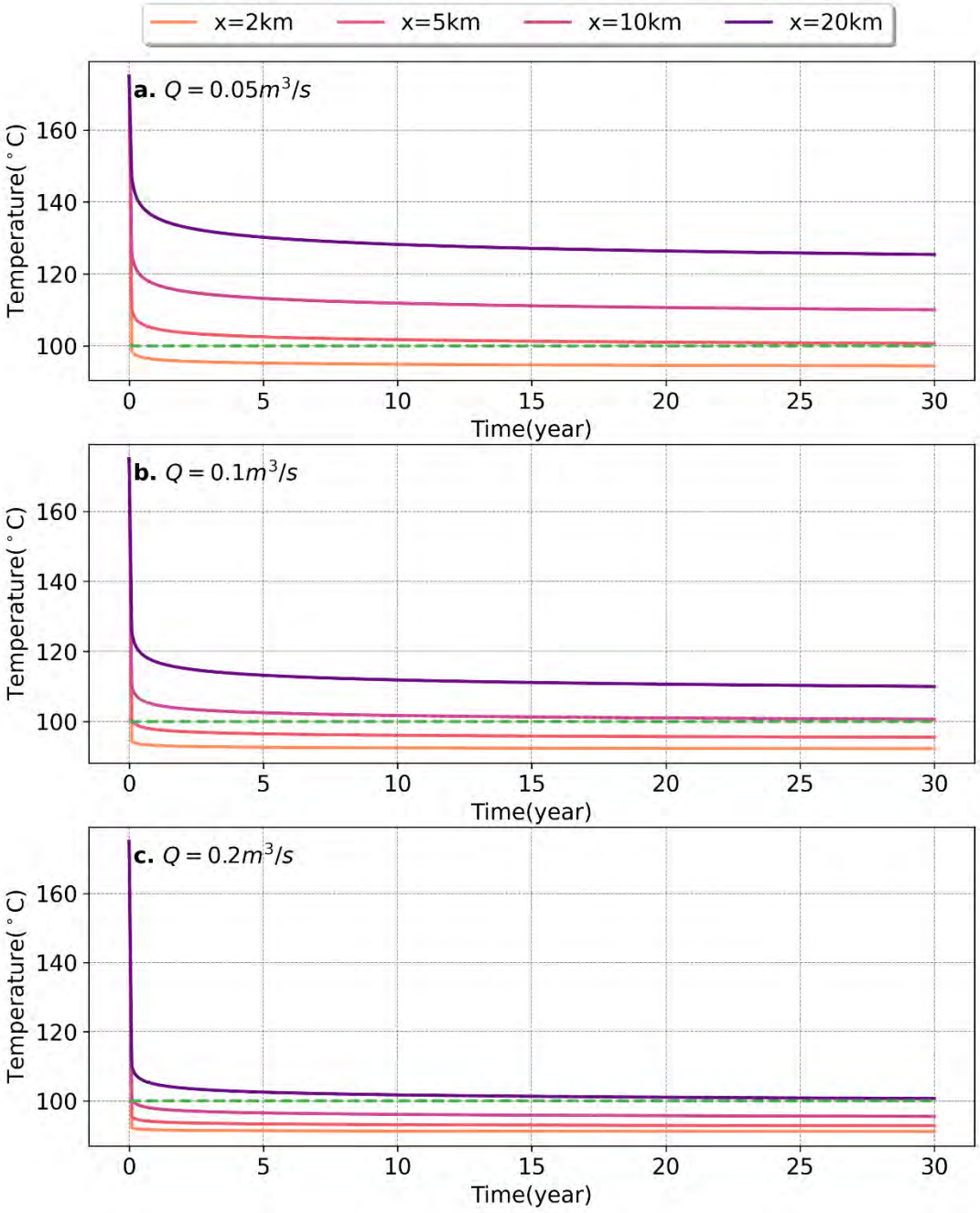

Figure 2. Extracted temperature change with different injection rate and well length under constant source condition. The green dashed line indicates the temperature at 100 °C.

Fig. 3 is analogous to Fig. 2, with the only change being the seasonal storage of heat. Unlike the extraction only case, all loop lengths could produce electricity in all of the 30 years of operation, but shorter loops and higher flow rates have some part of the year where electricity could not be produced.

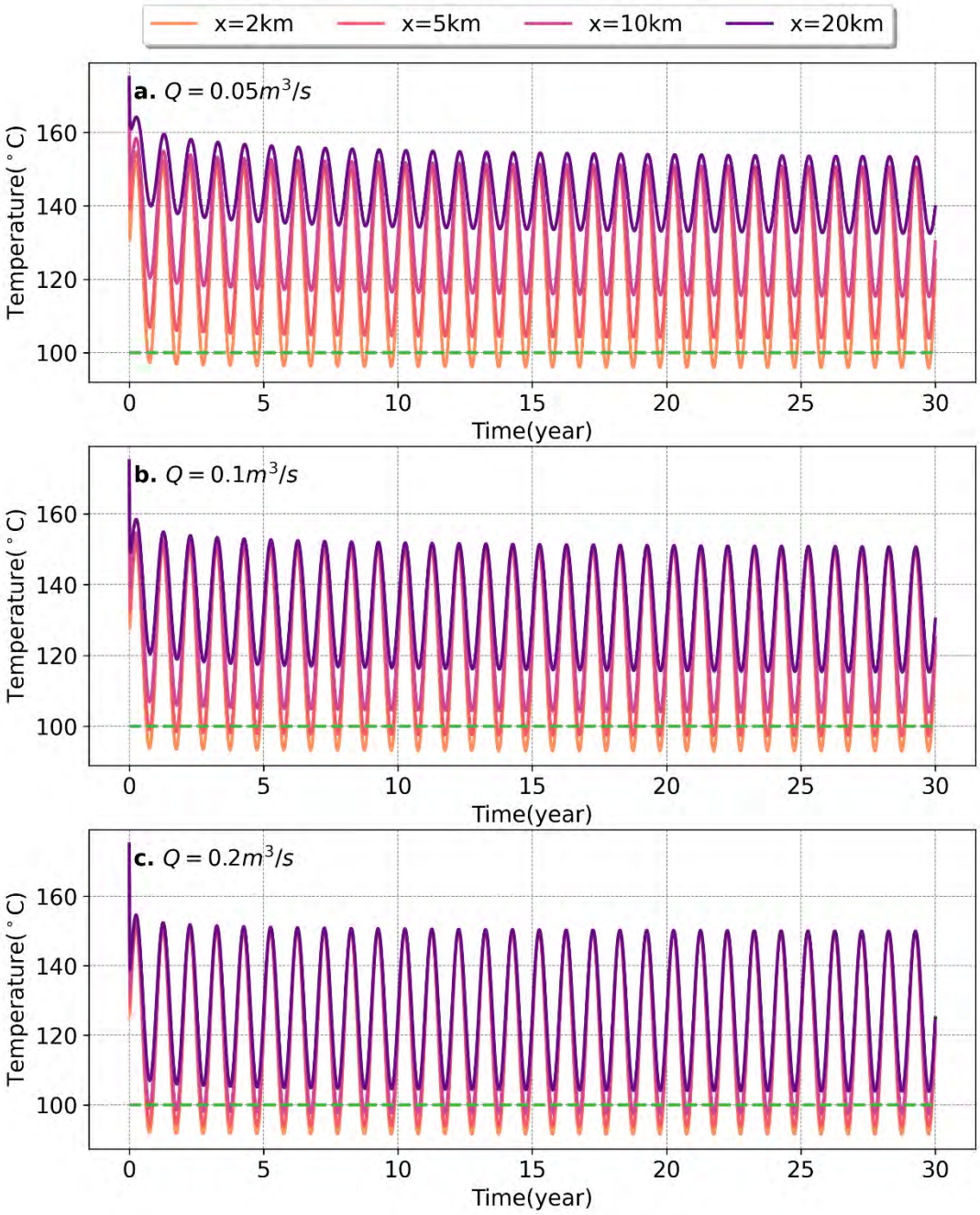

Figure 3. Extracted temperature change with different injection rate and well length under sine wave source condition. The green dashed line indicates the temperature at 100 °C.

A close examination of Fig. 3 reveals that the peaks and troughs shift a small amount in time for longer lengths, demonstrating that there is injection lag seen at the outflow with more lag for longer pipes, but the lag is still comparatively small (e.g., days to a few weeks) due to the high rate of flow through the pipe. A more pronounced effect is the damping of the range of oscillations with distance. Also, asymptotically, the sine wave for every profile will go to 120 °C on average (i.e., the average of the sine wave input), so examination of Fig. 3 also gives sense of longevity of the system.

Fig. 4 shows cumulative electric-grade energy delivered for all scenarios in Figs. 2 and 3, demonstrating that even with shorter pipes, periodic heat injection greatly increases long term heat delivery. With a careful comparison of Fig. 4 with Fig. 2-3; the following observations can be made: (1) Although a slower injection rate can lead to a higher extracted temperature, a higher injection rate results in a higher AE (i.e., there is an optimal flow rate that can be estimated); (2) For a standard injection rate, even a 5-km well with a periodic injection source can produce substantially more energy than a 20-km well with a constant source (i.e., with much lower drilling cost for a shorter loop, more energy can be supplied at a pseudo-steady rate); (3) As the injection rate increases, compared with the heat storage scenarios, the extracted AE with the constant source strategy shows minimal change (i.e., heat extraction from storage scenarios may be sensitive to storage and extraction choices, which cannot be evaluated using analytic solutions for long-loop extraction only scenarios).

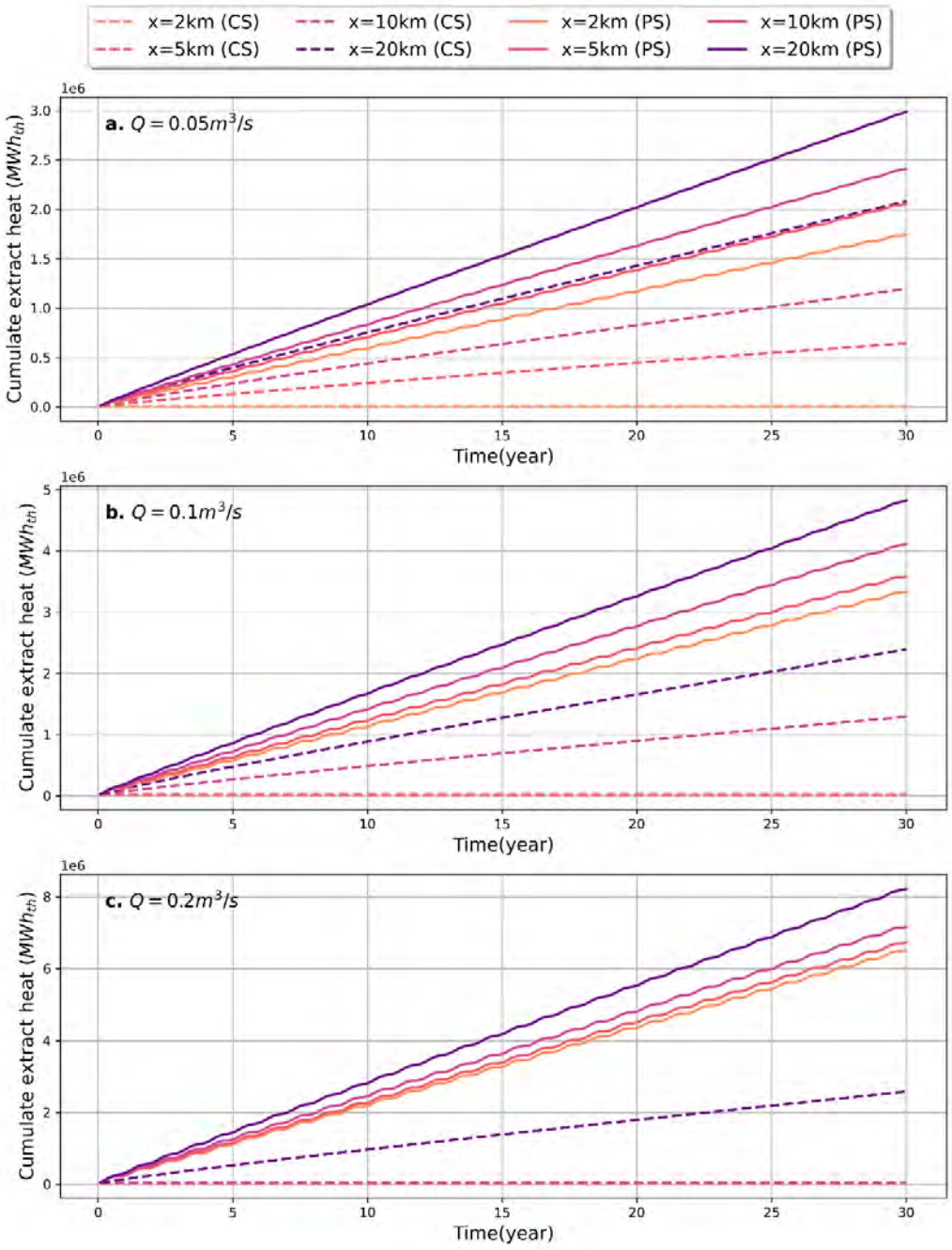

Figure 4. Accumulated extract heat energy change with different injection rates and well lengths under constant source conditions (solid line) and periodic (sine-wave) source conditions (dash line). In the legend, CS means constant source, and PS means periodic source. Cases that cannot produce economic beneficial energy are removed from the figure.

Although the horizontal well assumption simplified the boundary conditions and allowed comparison with loops for heat extraction only, for heat storage scenarios, temperature near the loop will be dominated by long-term average injected temperature. Because initial temperature becomes less important over time, loop depth and orientation can be flexible, so expensive horizontal wells might be replaced with less expensive configurations, including possibly coaxial designs.

4. Summary

This study uses a semi-analytical model to evaluate the potential of closed-loop geothermal long wells for heat extraction. An analytical solution to the radial advective-conductive unsteady heat transfer equation with heat injection and extraction was obtained in Laplace space derived using Green's function and Laplace transform. Numerical methods are applied to transform the solution in Laplace space to the time domain. By comparing the closed-loop long well systems under different conditions meant to compare standard long closed-loop operations with energy storage in closed-loops, the primary conclusions of this research are:

(1) Shorter loops can produce electric-grade energy at higher rates if surplus heat is periodically injected (stored).
(2) Injection rates can be optimized to produce more energy over the lifetime of the facility.
(3) With cost savings of drilling, periodic injection of heat could be more economically beneficial than a constant source well.

Acknowledgements

We thank Dasong Gao (MIT) for improving the numerical inverse Laplace transform code used in this research. We also want to thank the reviewers, Dr. Kewei Chen and Dr. Justin Birdwell, whose suggestions improved this paper. Portions of this research were conducted with the advanced computing resources provided by Texas A&M High Performance Research. Funding for Erick Burns was provided by the U.S. Geological Survey Energy Resources Program. Any use of trade, firm, or product names is for descriptive purposes only and does not imply endorsement by the U.S. Government.

Notation

Parameter	Definition
C	Specific heat capacity [$L^2T^{-2}\Theta^{-1}$].
D	Thermal diffusivity, defined as $D = k/c\rho$ [L^2T^{-1}].
K	Thermal conductivity [$MLT^{-3}\Theta^{-1}$].
K_n	Second kind modified Bessel function with order n (n=0,1 in this research).
M	Magnitude of the variation from mean injection temperature [-].
P	Laplace transform operator.
Q	Volumetric flux of fluid inside the well [L^3T^{-1}].
Q	heat sink term describing the heat loss to the rock through conduction [ΘT^{-1}].
t_{end}	Time interval to calculate the AE value [T].
T	Temperature [Θ].
T_m	Average injection temperature [Θ].
T_0	Initial temperature inside the well [Θ].
T_{f1}	Temperature change inside the well [Θ] and defined as $T_f = T_{f1}+T_0$.

$T_{m,dif}$	Modified temperature difference calculated by the extracted temperature minus 90°C [Θ] and modified means the $T_{m,dif}$ will be set to zero if the difference is lower than 10 °C.
A	Frequency [T^{-1}].
P	Density [ML^{-3}].
AE	Accumulated energy [L^2MT^{-2}], defined by $AE = \int_0^{t_{end}} Q c_f \rho_f T_{m,dif} dt$.
Subscript f	Flow property inside the well.
Subscript b	Material property of the rock outside the well.

REFERENCES

Arfken, G.B., & Weber, H.J. Mathematical Methods For Physicists (4th ed.). Elsevier. (1995).

Barbier, E. Geothermal energy technology and current status: an overview. *Renewable and Sustainable Energy Reviews*, 6(1), (2002). 3-65. https://doi.org/10.1016/S1364-0321(02)00002-3

Burns, E., Bershaw, J., Williams, C., Wells, R., Uddenberg, M., Scanlon, D., Cladouhos, T., & Houten, B. Using saline or brackish aquifers as reservoirs for thermal energy storage, with example calculations for direct-use heating in the Portland Basin, Oregon, USA. *Geothermics*, 88, (2020). 101877. https://doi.org/10.1016/j.geothermics.2020.101877

Burns, E., DeAngelo, J., & Williams, C. F. Updated three-dimensional temperature maps for the Great Basin, USA. In Proceedings of the 49th Workshop on Geothermal Reservoir Engineering, Stanford University, Stanford, California, February 12-14, (2024)

Oldham, K., Myland, J., & Spanier, J. An Atlas of Functions: with Equator, the Atlas Function Calculator (2nd ed.). Springer New York, NY. (2009). https://doi.org/10.1007/978-0-387-48807-3

Qi, C., Zhou, R., & Zhan, H. Analysis of heat transfer in an aquifer thermal energy storage system: On the role of two-dimensional thermal conduction. *Renewable Energy*, 217, (2023). 119156. https://doi.org/10.1016/j.renene.2023.119156

Stehfest, H. Algorithm 368: Numerical inversion of Laplace transforms [D5]. *Communications of the ACM*, 13(1), (1970). 47–49. https://doi.org/10.1145/361953.361969

The mpmath development team. mpmath: a Python library for arbitrary-precision floating-point arithmetic (version 1.3.0), (2023). http://mpmath.org/

White, M., Martinez, M., Vasyliv, Y., Beckers, K., Bran-Anleu, G., Parisi, C., Balestra, P., Horne, R., Augustine, C., Pauley, L., Bettin, G., Marshall, T., & Closed Loop Geothermal Working Group. Closed-loop geothermal working group study - Understanding thermal performance and economic forecasts via numerical simulation. In Proceedings of the 48th Workshop on Geothermal Reservoir Engineering. Stanford University, Stanford, California, February 6-8, (2023)

Zarrouk, S. J., & Moon, H. Efficiency of geothermal power plants: A worldwide review. *Geothermics*, 51, (2014). 142-153. https://doi.org/10.1016/j.geothermics.2013.11.001

Zhou, R., Wang, Q., & Qi, C. Heat transfer in a fracture embedded in a finite matrix: On the role of geometries and thermal dispersivity in the fracture. *International Journal of Thermal Sciences*, 178, (2022). 107602. https://doi.org/10.1016/j.ijthermalsci.2022.107602

Optimizing Geothermal Borehole Number and Positioning through a Simulated Annealing Algorithm

Ali Zidane[1,2] and Danylo Oryshchyn[3]

[1]National Energy Technology Laboratory, 3610 Collins Ferry Road, Morgantown, WV 26505, USA
[2]NETL Support Contractor, 3610 Collins Ferry Road, Morgantown WV 26505, USA
[3]National Energy Technology Laboratory, 1450 Queen Avenue SW, Albany, Oregon 97321, USA

Keywords

Geothermal Energy; Borehole Optimization; Simulated Annealing; Sustainable; Energy; Geothermal Reservoirs

ABSTRACT

As the demand for sustainable energy sources intensifies, geothermal energy stands out as a promising solution. Efficient utilization of geothermal reservoirs relies on optimal borehole placement and density, a complex optimization problem. This paper introduces a novel algorithm leveraging simulated annealing to address the challenges associated with optimizing both the total number of boreholes and their spatial distribution in geothermal applications.

The proposed algorithm employs simulated annealing, inspired by the annealing process in metallurgy, to iteratively explore and refine the solution space. By systematically adjusting the temperature parameter, the algorithm balances exploration and exploitation, allowing it to escape local minima and converge towards a globally optimal solution. The objective is to minimize the total number of boreholes while maximizing their effectiveness in harnessing geothermal energy.

The algorithm's performance is evaluated through simulations on various geothermal reservoir scenarios. Results demonstrate its ability to adapt to diverse geological conditions and provide solutions that optimize the utilization of geothermal resources. This paper concludes with a discussion of the algorithm's potential applications, scalability, and contributions to advancing sustainable geothermal energy solutions.

1. Introduction

The gradual shift from fossil fuels to clean, affordable, and dependable energy sources necessitates the adoption of low-carbon technologies capable of meeting extensive commercial demands across all energy sectors (Piiponen et al., 2022). Geothermal energy originates from the Earth's core, approximately 2900 km beneath the surface, (Williams, 2024). This form of thermal energy is renewable, as it stems from temperatures surpassing those of the sun's surface, sustained by the ongoing radiogenic decay of natural isotopes. Borehole heat exchanger (BHE) and Ground Source Heat Pump (GSHP) systems harness geothermal energy, offering an eco-friendly alternative to traditional heating and cooling methods (Capozza et al., 2012; Yuan et al., 2016).

Geothermal heat offers a promising energy source with significantly reduced CO_2 emissions compared to conventional fossil fuels. Shallow geothermal systems are increasingly harnessed for heating and cooling applications in buildings and greenhouses (Lund and Toth, 2021). The capital investment and risk of the resource being less productive than hoped motivate development of data and tools to de-risk geothermal installations (CORDIS, 2023; Ireland Department for the Environment, Climate and Communications, 2023). To strengthen the competitive stance of geothermal energy in the renewable market, engineers need access to precise, adaptable, and efficient computational tools for effective system design and analysis.

Over the last four decades, geothermal systems have been analyzed through analytical, semi-analytical, and numerical modeling, dating back to works by Horne (1980) and Eskilson and Claesson (1988). Li and Lai (2015) and Zhao et al. (2020) have reviewed numerous models in this regard. Analytical models offer the advantage of computational speed, whereas numerical models can more easily accommodate complex geometries and boundary conditions, (Piipponen et al., 2022). In recent times, there has been a growing emphasis on optimizing the design and sizing of ground-source systems to elevate their environmental and operational efficiency (Alavy et al., 2013; Javed, 2012l Javed and Spitler, 2017; Kavanaugh and Rafferty, 2014; Ozbek et al., 2015; Rees, 2016). Engineers can consult established engineering guidelines (Kavanaugh and Rafferty, 1997; Stauffer et al., 2013), or standard planning software to determine the appropriate borehole length for a given energy demand. Still, research continues for optimization to further enhance the expected capacity of an installation. Current research efforts predominantly focus on enhancing the accuracy of design inputs (Claesson and Javed, 2018; Fujii et al., 2009), developing computationally efficient design methodologies (e.g., He et al., 2011; Javed and Claesson, 2011; Fossa et al., 2024), and determining optimal ground loop lengths (Cui et al., 2015; Hackel and Pertzborn, 2011).

Geothermal energy sources exhibit varying depths, ranging from shallow levels of tens to hundreds of meters, to intermediate depths extending several kilometers, and deeper levels where molten rocks generate exceptionally high temperatures (Al-Khoury, 2012). In a study by Piipponen et al. (2022), the influence of geological and engineering factors on the heat output of medium-deep geothermal boreholes was explored using the finite element method in COMSOL Multiphysics. By simulating various engineering parameters, the study employed a performance simulation approach to develop models of borehole heat exchangers (BHEs).

In Jain et al. (2015), the long-term response of operated engineered geothermal system (EGS) reservoirs was examined based on numerical stimulation of an optimized heat extraction process, (Clauser, 2003). They systematically varied parameters such as flow rate and well separation in

the subsurface, investigating various EGS configurations and their sustainability. The finite-difference method was employed to solve the transient coupled equations of fluid flow and heat transfer in a fluid-saturated porous medium, as implemented in the forward modeling code, SHEMAT (Clauser, 2003).

Schulte et al. (2016) presented an approach for the simulation and optimization of medium-deep borehole thermal energy storage (MD-BTES) systems. To optimize the design of an MD-BTES system, they evaluated numerous configurations representative of the range of variability in the design parameters. The seasonal operation was numerically simulated for each configuration to predict the thermal behavior of the MD-BTES system. The simulation of the operation of an MD-BTES system was based on the application of the standard Galerkin method, implemented in an adapted MATLAB® environment for finite elements. In their work, the algorithm is designed to assess hundreds of parameter combinations to reach an optimal solution. It halts only when the score of the best individual cannot be enhanced beyond a set fitness function tolerance after a specified number of stall iterations. Evaluating each configuration against the constraint demands substantial computational effort. Depending on the model size, a single numerical simulation can span from several days to weeks. To address this challenge, they employ a proxy model derived from a considerably smaller set of numerical training simulations using arbitrary polynomial chaos expansion.

Javed et al. (2019) presented a systematic and comprehensive investigation into sizing the ground-source heating and cooling system for a newly constructed kindergarten building in Oslo, Norway. One of the study's objectives was to examine the potential for optimizing the borehole system design by adjusting the building's envelope characteristics to balance the ground heating and cooling loads. The final phase involved conducting a sensitivity analysis on the proposed design to evaluate the influence of uncertainties in the design parameters. All design simulations were conducted using the Superposition Borehole Model, SBM (Eskilson, 1986).

Bayer et al. (2014) introduced a mathematical procedure for the optimization of BHE fields. The optimization approach aims to enhance efficiency by examining the overall underground temperature variations within the BHE field. For a specified energy demand, optimal efficiency is attained when minimizing the maximum temperature change. They presented a simulation technique that utilizes temporally and spatially superimposed line source equations. Additionally, a sensitivity analysis is conducted to ascertain the maximum temperature changes in the ground and to assess potential improvements through individual BHE workload optimization.

In Li et al. (2017) the effects of load optimization and geometric arrangement on BHE fields were investigated. The outlet fluid temperature served as the optimization target to examine how load distribution and geometric arrangement influence the performance of BHE fields. The authors presented four different borehole arrangements in one application. However, they did not provide specific justification for these arrangements over numerous others for the same application. Instead, they analyzed the outcomes of these arrangements in relation to the objective function.

Liu and Han (2023) utilized simulated annealing to optimize the length of a section of tunnel wall fitted with fluid loops for extracting heat from the surrounding rock. Their algorithm perturbs a COMSOL® 3D model of the tunnel domain and heat exchanger to select an optimal section length within predefined location constraints. The chosen section length must not exceed the length of the tunnel, and heat extraction must occur only where heat is available in the tunnel. Flow rate and

inlet temperature for the heat transfer fluid are kept constant, and the minimum length meeting the heating requirement is considered the optimum length.

The RowWise algorithm by Spitler et al. (2022) adjusts borehole spacing to determine the minimum number of boreholes needed to satisfy a user-specified load. Boreholes are arranged in rows, with the flexibility to rotate the orientation of the rows to evenly distribute them across a given land-space if necessary. Users can also define the perimeter of the space to comprise evenly spaced boreholes, potentially reducing the number of bores required in the field interior. The g-function is applied to the resulting array to compute the required borehole depth. As of 2022, the authors of Spitler et al. were working on methods to reduce calculation time for this approach. They also noted that finding a true global optimum for large fields is currently impractical. Global optimization methods capable of optimizing the placement of hundreds of boreholes are an active area of research, with potential applications in GHE design expected in the near future.

The work presented in this paper is part of The GeoCoHorT project, for which the National Energy Technology Laboratory (NETL) is building an in-ground heat exchanger design and simulation tool, which will be applied to the preliminary design and business case development for a transaction-controlled heating district in Limerick, Ireland. This application poses some special challenges. When considering urban applications of GSHP, available space for borehole arrays will be variable. Considering a transaction-controlled heating district (Hosseinnezhad et al., 2021; Maurer et al., 2023; O'Regan, et al., 2021), the design of the borehole array needs to enable useful energy storage and extraction for district thermal balance and efficiency.

The following study presents a novel algorithm that employs simulated annealing to address the challenges of optimizing both the total number of boreholes and their spatial distribution in geothermal applications. Inspired by the metallurgical annealing process, the algorithm iteratively explores and refines the solution space. To the best of our knowledge, such an algorithm has not been documented in the existing literature. Through systematic adjustment of the temperature parameter, the algorithm strikes a balance between exploration and exploitation, enabling it to avoid local minima and converge towards a globally optimal solution. The objective is to minimize the total number of boreholes while maximizing their efficiency in harnessing geothermal energy.

2. Methodology

2.1 Governing Equations

Global optimization presents significant computational challenges, and exact methods often face limitations when dealing with large instances. Simulated annealing is a probabilistic meta-heuristic known for its ability to escape local minima. Originating from the Metropolis algorithm, it was initially introduced in the realm of combinatorial optimization, (Kirkpatrick et al., 1983), where the objective function is defined within a discrete domain. Initially introduced for solving discrete optimization problems, SA has since been extended to continuous domains – for example, optimization of multimodal functions in a continuous domain (Corana et al., 1987; Zidane, 2022). Its notable advantage over other solution techniques has established SA as a practical approach for addressing complex optimization problems. The selection of cooling schedule and the subsequent candidate distribution are crucial factors in defining a simulated annealing algorithm, (Miki et al., 2002). In this study, SA is tailored to optimize both the total number and locations of boreholes within a specific field.

The heat transfer equation governing the ground under conditions of low Peclet number groundwater flow is provided as follows:

$$\left(\rho c_p\right)_{eff}\frac{\partial T}{\partial t} - k_{eff}\nabla.(\nabla T) + Q_b = 0 \quad (1)$$

The terms $\left(\rho c_p\right)_{eff}$ and k_{eff} represent the effective volumetric heat capacity (J/m^3·K) and effective thermal conductivity (W/m·K) of the ground, respectively, calculated using:

$$\left(\rho c_p\right)_{eff} = \varphi\rho_w c_{p,w} + (1-\varphi)\rho_s c_{p,s} \quad (2)$$

and

$$k_{eff} = \varphi k_w + (1-\varphi)k_s \quad (3)$$

where φ is the porosity, $\rho_w c_{p,w}$, k_w, $\rho_s c_{p,s}$, and k_s are the volumetric heat capacity and thermal conductivity for both water and soil respectively. Q_b is the energy introduced into the ground from the boreholes installed in the field.

2.2 Optimization Scheme

Given a field's dimensions, the proposed approach seeks to optimize the total number and configuration of boreholes to maximize the total energy extraction. The optimization adheres to the following constraints provided as input:

- The maximum allowable depth for borehole installation.
- The minimum distance allowed between two boreholes along the x-axis.
- The minimum distance allowed between two boreholes along the y-axis.
- The input and output fluid temperatures.
- The properties of the borehole material.

Therefore, the objective function for building-heat rejection to the ground could be written as:

$$\arg\max\left(Q_{b,x,y,t}\right) \quad \forall(x,y), t \in \Omega, \tau \quad (4)$$

where Ω and τ represent the computational domain and simulation time respectively.

The proposed algorithm simulates the random placement of a variable number of boreholes, leading to an energy change. If this change results in a positive energy difference, the new configuration with the higher energy state is accepted. Conversely, if the energy change is negative and lowers the energy state, the new configuration might still be accepted based on the Boltzmann probability factor (P) as shown below (eq. 5)

$$P = \exp\left(\frac{-\Delta E}{\Delta E_{ave} T_a}\right) \quad (5)$$

where ΔE is the cost difference between the current design and the previous one; ΔE_{ave} is the running average value of ΔE, it normalizes the change in the objective, and T_a is the "annealing

temperature" in SA; it correlates with the mobility of the optimization process to accept a higher-cost design.

3. Examples

This section provides three numerical simulation examples to showcase the capabilities of our model. The first example examines a homogeneous domain with 50 potential borehole installation locations. The second example addresses the same issue but with heterogeneous ground thermal properties. The third example presents a more complex scenario involving the potential installation of 264 boreholes.

3.1 Example 1

In a 100 m x 50 m domain (Figure 1), a minimum distance of 10 m is maintained between two boreholes along both the x and y axes, allowing for the potential installation of 50 boreholes, as illustrated in Figure 1. Each borehole is assumed to have a diameter of 15 cm and a thermal resistance of 0.05 mK/W. The maximum allowable depth for installation is 70 m. The soil is characterized by a uniform porosity of 0.2 and a water saturation level of 30%. The inlet and outlet liquid temperatures are set at 23.89 °C (75 °F) and 21.12 °C (70 °F), respectively. The soil temperature is assumed to increase linearly with depth, starting at 283 K at the surface and reaching a maximum of 293 K. This temperature is averaged over the length of the borehole depth.

In this example, the objective is to determine the optimal number and locations of boreholes from the available 50 sites to maximize the total injected energy over a one-year period. Given the vast number of potential combinations, exhaustively modeling all possibilities is impractical. For instance, selecting just 10 boreholes out of the 50 sites results in over 10 billion potential configurations. Figure 2 depicts two configurations of borehole selection – 15 and 24, respectively.

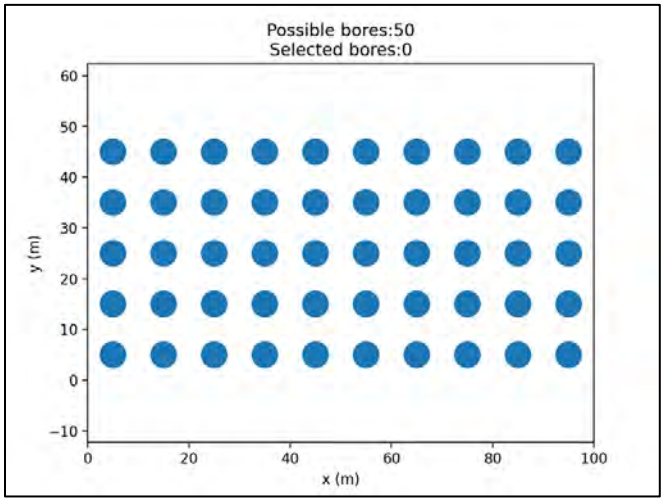

Figure 1: Domain showing the possible locations of 50 boreholes: Example 1.

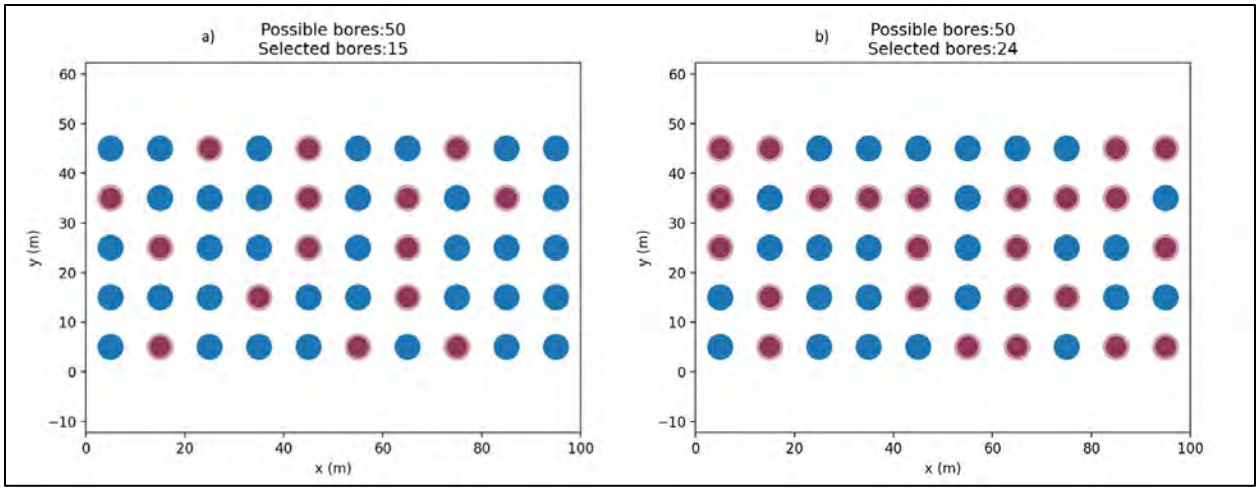

Figure 2: One case, selecting 15 (a) and 24 (b) boreholes to be installed from 50 possible locations: Example 1.

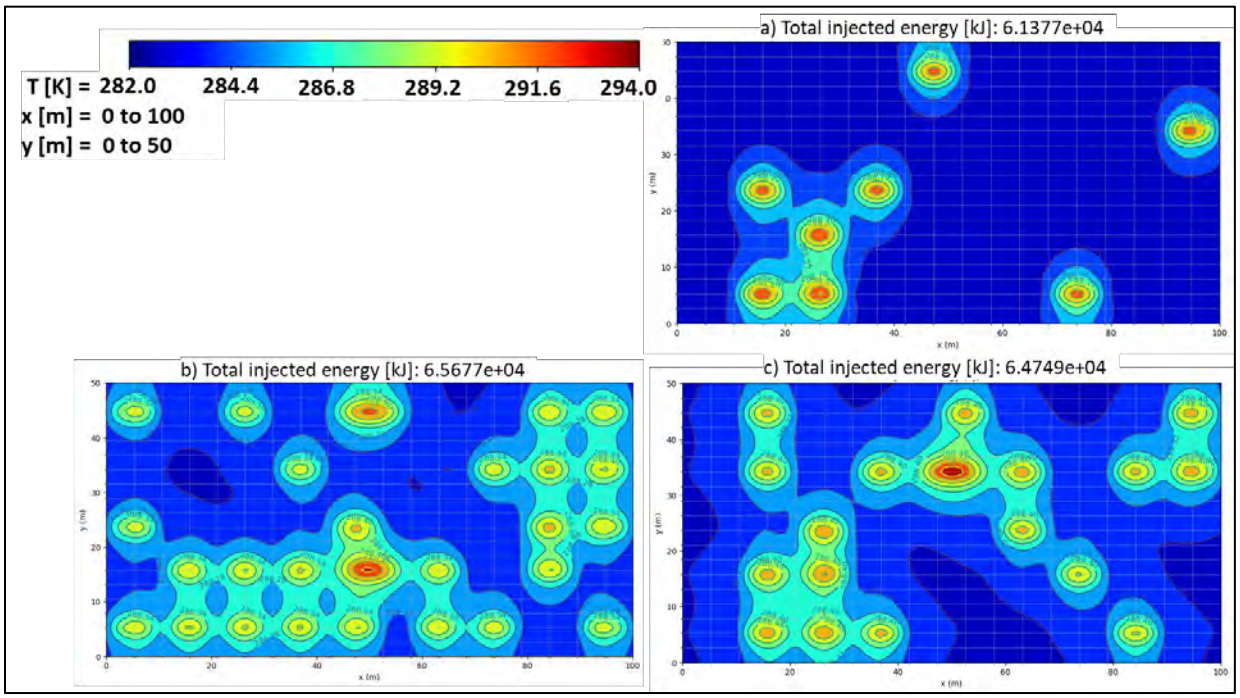

Figure 3: Temperature distribution [K] with three different configurations with 8 (a), 29 (b), and 19 (c) boreholes: Example 1.

The algorithm operates as follows: The minimum distance on the *x* and *y* axes between two boreholes determines the maximum number of boreholes that can be installed. The optimization goal is to maximize the total injected energy and to determine the number and distribution of boreholes that achieve this maximum. It's important to note that the optimal number and distribution may not be unique for a given problem.

The algorithm begins by randomly selecting a number of boreholes from the total possible combinations. Then, it generates a random distribution of these boreholes. At this point, the

algorithm has both the number of boreholes to be installed (N) and their distribution (D), both chosen randomly. The next step is to calculate the total injected energy (E) based on the selected N and D, and this energy value is stored.

The algorithm then repeats the process, generating a new set of borehole numbers and distribution $(N, D)_{new}$, which are used to calculate a new total injected energy $(E)_{new}$. If E_{new} is greater than the previously calculated energy (E), the new solution is considered better. If it's not, it still has a chance of being in the direction of a better solution. This acceptance probability is calculated using Boltzmann's probability distribution. A given optimization run conducted 30 annealing cycles, each comprising 20 trials.

An accepted distribution is determined by the Boltzmann probability, as explained in the previous section. Figure 3 displays the temperature distribution for three borehole configurations accepted by the algorithm during its progress to identifying the optimum. These occur at iteration 8, 19, and 29 as shown in Figure 4.

Figure 4 illustrates the relationship between the total injected energy in the field and the number of boreholes across all 30 annealing cycles. The results demonstrate an increasing trend in the injected load with each iteration, suggesting that the model converges towards maximizing the total injected energy. This ensures the selection of an optimal borehole number and geometric distribution for maximization.

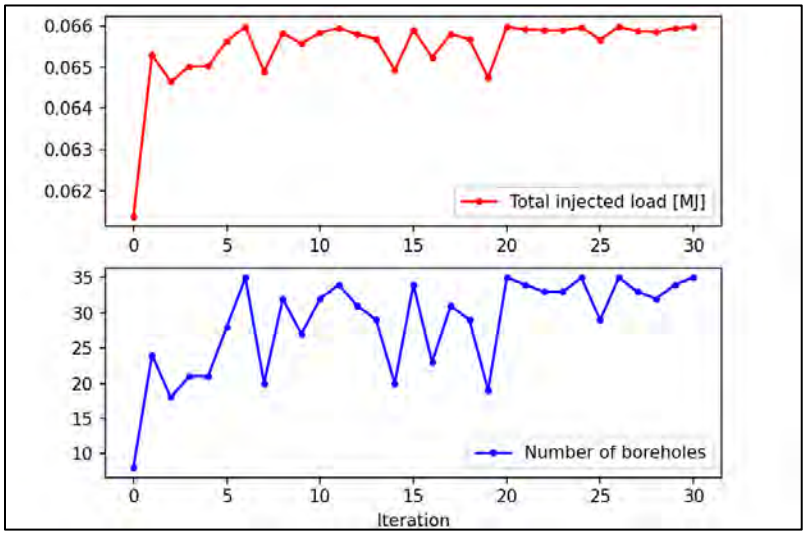

Figure 4: Variation in the injected load and the number of boreholes over the 30 annealing cycles: Example 1.

Figure 5 displays the optimal number and locations of selected boreholes that maximize the injected load in the field.

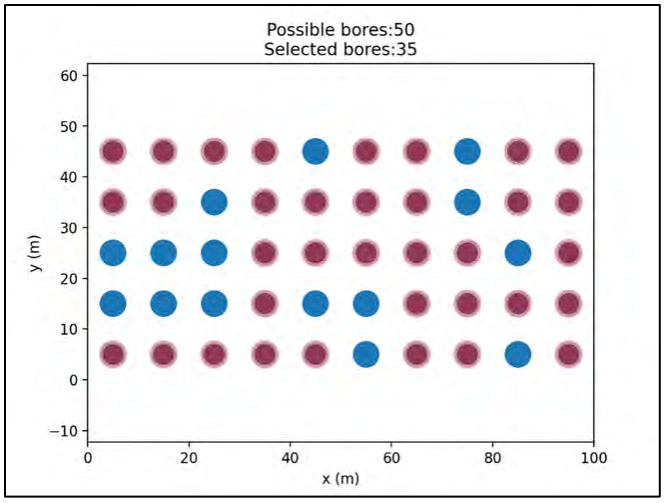

Figure 5: Locations and quantity of chosen boreholes optimizing the injected load: Example 1.

3.2 Example 2

This example retains the setup from the previous case but introduces a modification by incorporating a heterogeneous domain. The distributions of porosity and water saturation can be seen in Figure 6. Changes in these parameters influence the temperature distribution by impacting heat capacity, thermal conductivity, and the heat diffusion coefficient.

The domain's heterogeneity influenced the total injected energy compared to the homogeneous scenario. In the homogeneous case, the energy was 0.066 MJ, whereas it is now 0.063 MJ. Although the optimal number of boreholes remains 35, consistent with the homogeneous case, their arrangement differs, as illustrated in Figure 7. The fluctuation of injected energy and the total borehole count across annealing cycles is depicted in Figure 8. For reference, the temperature distribution of the configuration that maximizes the injected load is presented in Figure 9.

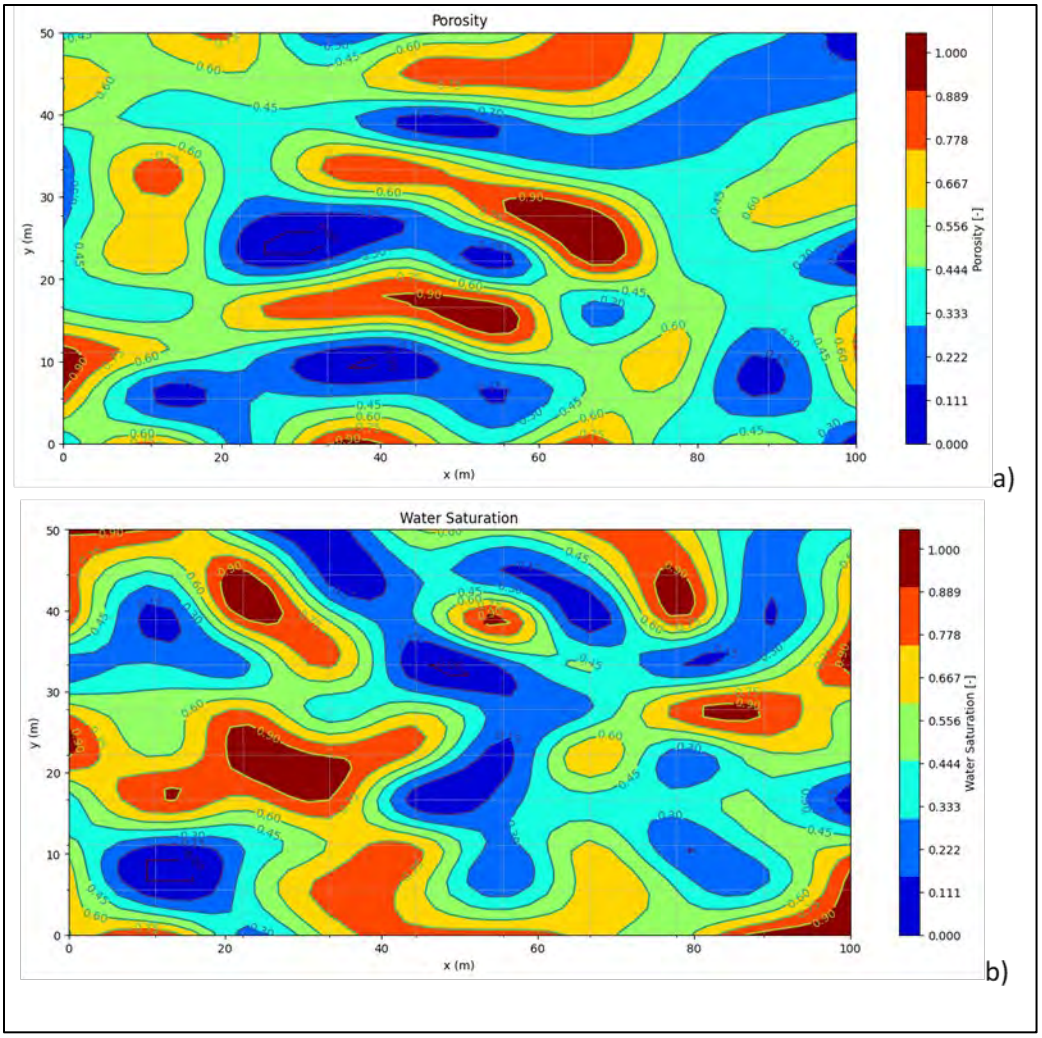

Figure 6: Porosity (a) and water saturation (b) distribution: Example 2.

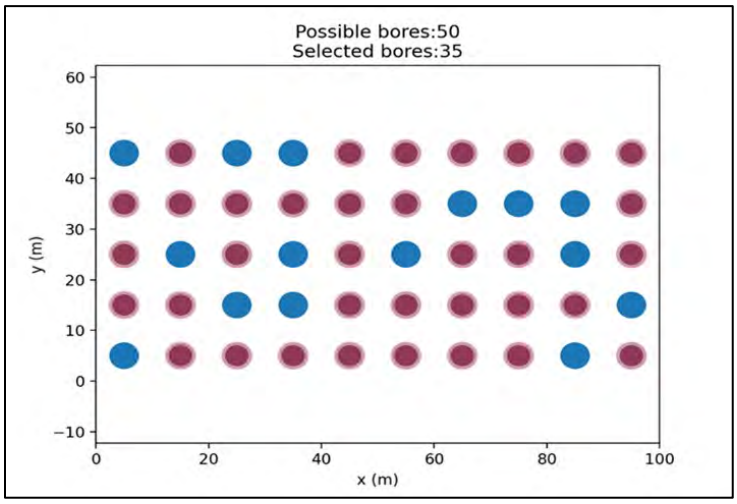

Figure 7: Locations and quantity of chosen boreholes optimizing the injected load: Example 2.

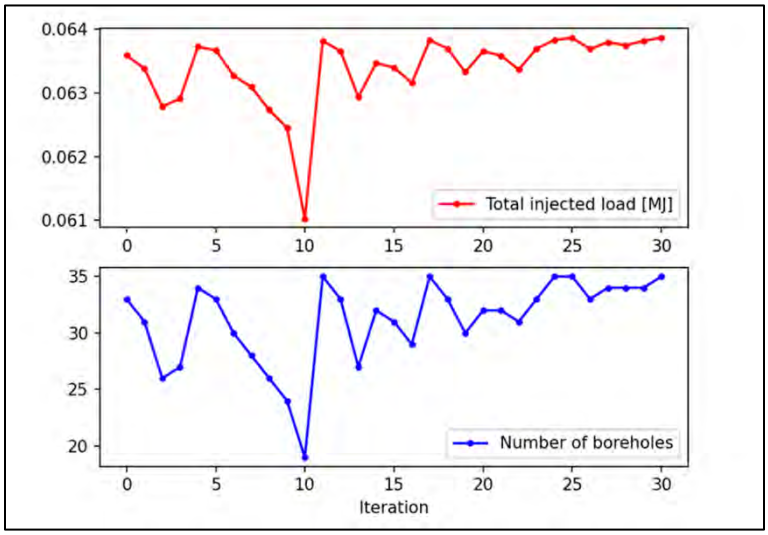

Figure 8: Variation in the injected load and the number of boreholes over the 30 annealing cycles: Example 2.

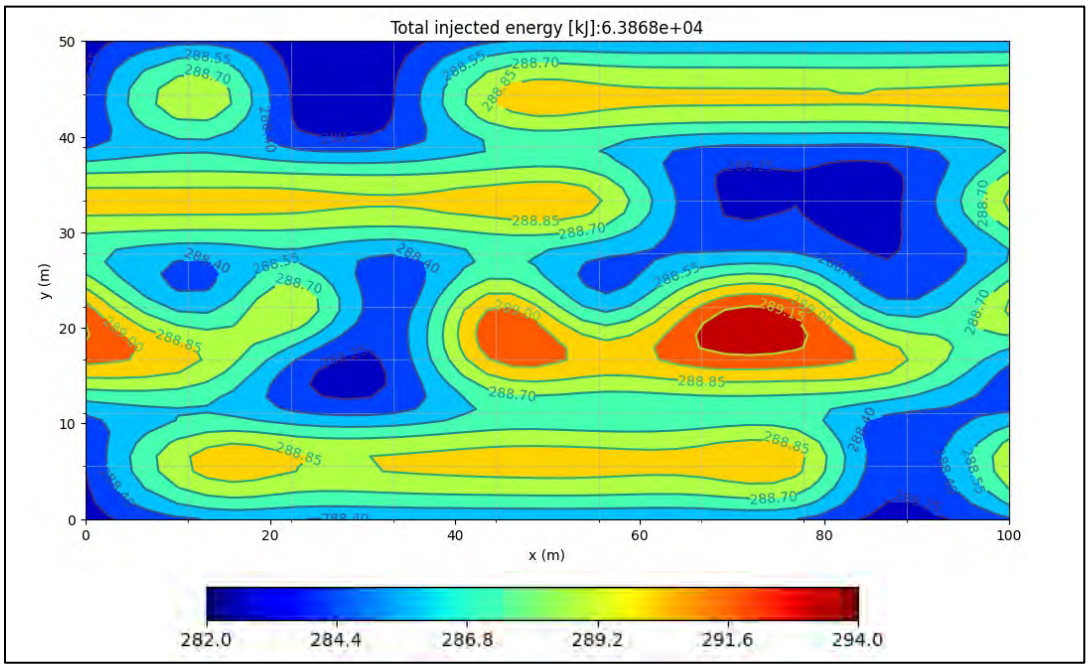

Figure 9: Temperature distribution of the configuration that maximizes the injected load: Example 2.

3.3 Example 3

In the final example examines a larger domain with a reduced separation distance between the boreholes on the x and y axes, set at 6 m. With a total domain length of 200 m and a height of 50 m, this allows for the installation of 33 boreholes along the x-axis and 8 boreholes along the y-

axis. This results in a potential total of 264 boreholes that could be installed, as illustrated in Figure 10. The properties of the domain are consistent with those in Example 1.

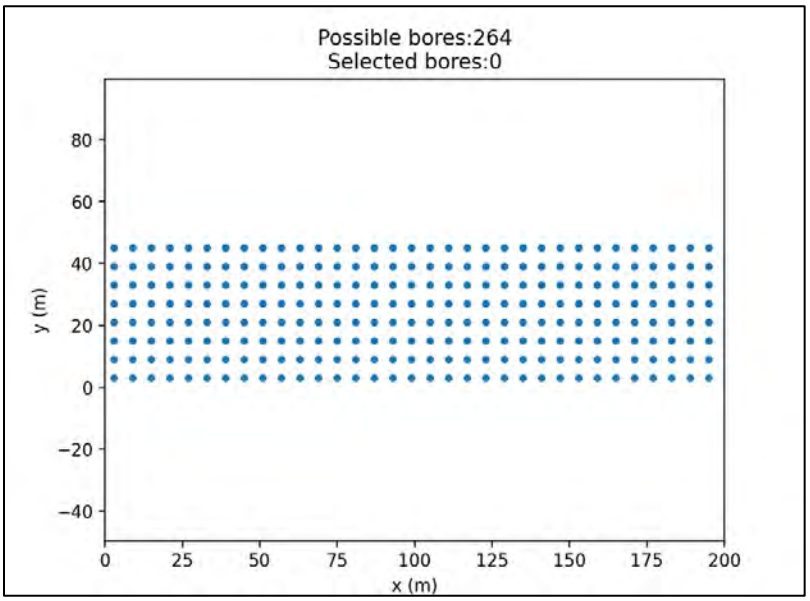

Figure 10: Domain illustrating the 264 potential locations for borehole installations: Example 3.

Investigating the variation of the total injected load and the number of boreholes during the annealing cycles, a significant difference from the previous examples is observed: an increasing injected load is accompanied by a decreasing total number of installed boreholes (Figure 11). This behavior arises because the high density of borehole installations hinders the dissipation of heat from the injected load. The maximum injected load is achieved by limiting the total installed boreholes to fewer than 70. Specifically, the maximum injected load of 0.067 MJ is attained with 63 boreholes installed.

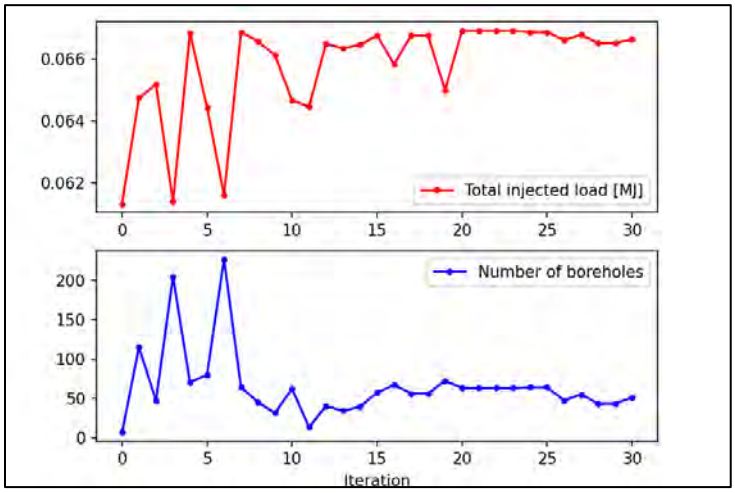

Figure 11: Variation in the injected load and the number of boreholes over the 30 annealing cycles: Example3.

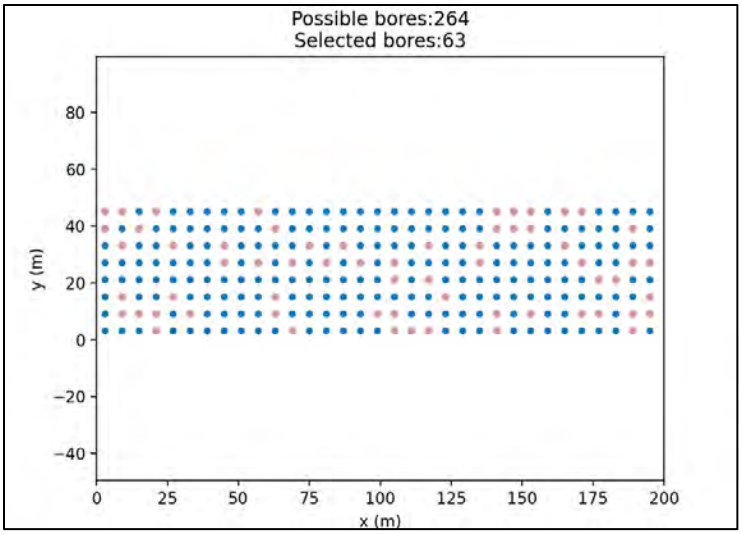

Figure 12: Locations and quantity of chosen boreholes optimizing the injected load: Example 3.

The locations of the 63 boreholes that maximize the injected load are shown in Figure 12. For reference, the temperature distribution with the optimal configuration is shown in Figure 13.

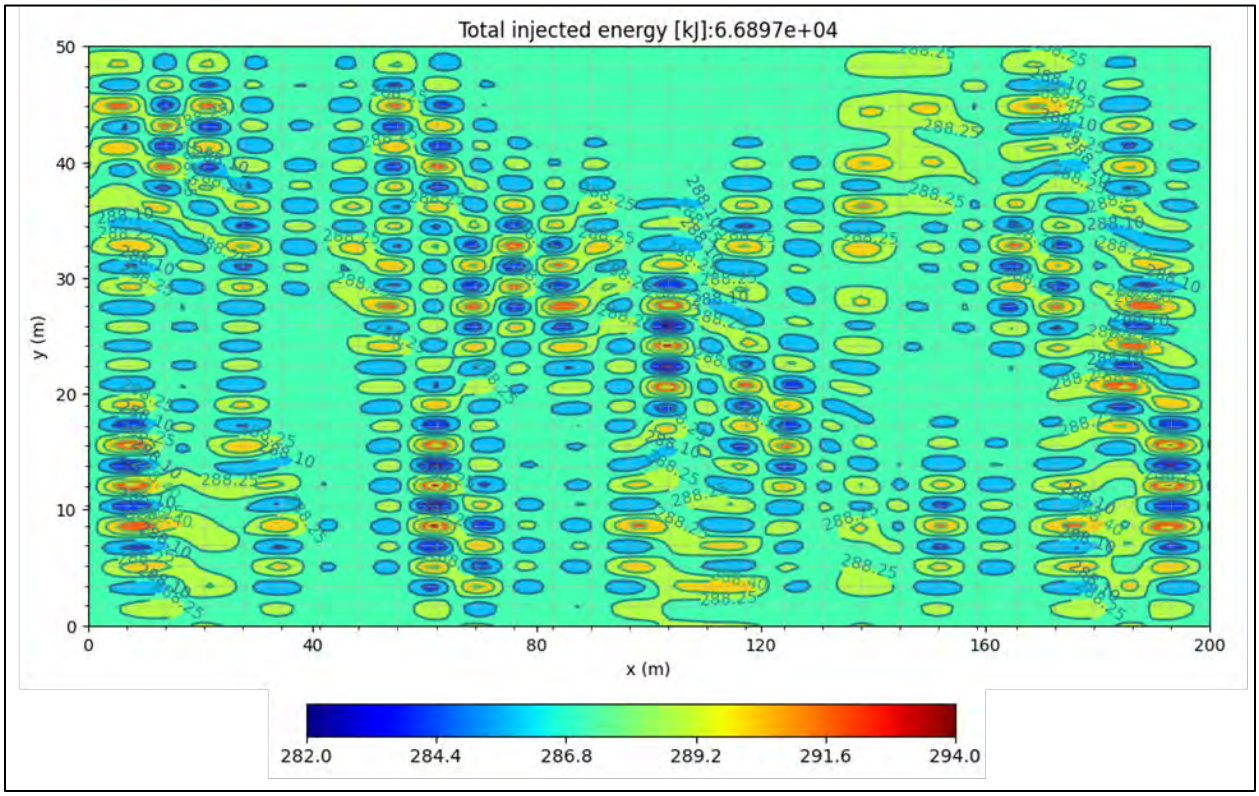

Figure 13: Temperature distribution of the configuration that maximizes the injected load: Example 3.

3. Summary and Future Work

This paper introduces a novel algorithm that utilizes simulated annealing to address the complexities of optimizing both the total number of boreholes and their spatial distribution in geothermal systems. The algorithm's efficacy was demonstrated through simulations across various geothermal reservoir scenarios, encompassing both homogeneous and heterogeneous conditions. It effectively determines the optimal configuration of boreholes in terms of number and placement to maximize the total injected load. This optimization task, due to its vast possible borehole location combinations, is otherwise daunting to solve. Notably, all simulations were completed within a few minutes on a standard PC. The study focuses on low Peclet numbers in the subsurface, assuming stagnant water with potential variations in saturation across the domain. Future work will incorporate groundwater flow effects to further examine its influence on borehole numbers and distribution. Objective functions to consider heating modes can be applied to design for optimal placement of boreholes for heating and cooling modes both occurring across the desired time domain.

Disclaimer

This project was funded by the United States Department of Energy, Geothermal Technologies Office, and executed at the National Energy Technology Laboratory, in part, through a site support contract. Neither the United States Government nor any agency thereof, nor any of their employees, nor the support contractor, nor any of their employees, makes any warranty, express or implied, or assumes any legal liability or responsibility for the accuracy, completeness, or usefulness of any information, apparatus, product, or process disclosed, or represents that its use would not infringe privately owned rights. Reference herein to any specific commercial product, process, or service by trade name, trademark, manufacturer, or otherwise does not necessarily constitute or imply its endorsement, recommendation, or favoring by the United States Government or any agency thereof. The views and opinions of authors expressed herein do not necessarily state or reflect those of the United States Government or any agency thereof.

Nomenclature

c_p	specific heat at constant pressure, ($J/kg \cdot K$)
E	energy
ΔE	difference in cost between the current design and the previous one
ΔE_{ave}	average value of the change in ΔE
D	distribution of boreholes
k	thermal conductivity, ($W/m \cdot K$)
N	number of boreholes to be installed
P	probability
Q	thermal energy, (J)
T	temperature, (K)
t	time, (s)
T_a	annealing temperature
x	distance, (m)
y	distance, (m)
ρ	density, (kg/m^3)
τ	simulation time
φ	porosity
Ω	computational domain

Subscripts	
b	borehole
w	water
s	soil
eff	effective

Math Symbols	
arg max	$\arg\max(f)$ is the set of values, a, for which $f(\alpha)$ is a maximum
exp	$exp(\alpha) = e^{\alpha}$
$\in$	belongs to/is element of (set membership)
$\forall$	for all (Universal Quantifier)

REFERENCES

Alavy, M., Nguyen, H. V., Leong, W. H., and Dworkin, S. B., "A methodology and computerized approach for optimizing hybrid ground source heat pump system design." *Renewable Energy*, 57, (2013), 404–412.

Al-Khoury, R., "Computational Modeling of Shallow Geothermal Systems". ISBN10-0415596270: CRC Press (2012), 1877-0274.

Bayer, P., de Paly, M., and Beck, M., "Strategic optimization of borehole heat exchanger field for seasonal geothermal heating and cooling." *Applied Energy*, 136, (2014), 445-453.

Capozza, A., Carli, M. D., and Zarrella, A., "Design of borehole heat exchangers for ground-source heat pumps: A literature review, methodology comparison and analysis on the penalty temperature." *Energy and Buildings*, 55, (2012), 369–379.

Claesson, J., and Javed, S., "Explicit Multipole Formulas for Calculating thermal resistance of single U-tube ground heat Exchangers." *Energies*, 11(1), 214. (2018).

Clauser C. (ed), "Numerical simulation of reactive flow in hot aquifers: SHEMAT and processing SHEMAT." *Springer Verlag*, Heidelberg-Berlin, (2003).

Cordis – EU research results, "Why can't we use geothermal everywhere?" *Publication Office of the European Union*, (2023), https://cordis.europa.eu/article/id/442835-why-can-t-we-use-geothermal-everywhere#:~:text=Putting%20geothermal%20everywhere%20does%20run,boreholes%20drilled%20into%20the%20ground.

Corona, A., Marchesi, M., Martini, C., and Ridella, S. "Minimizing multimodal functions of continuous variables with the simulated annealing algorithm." ACM Transactions on Mathematical Software, 13(3), (1987), 262-280.

Cui, W., Zhou, S., and Liu, X. "Optimization of design and operation parameters for hybrid ground-source heat pump assisted with cooling tower." *Energy and Buildings*, 99, (2015), 253–262.

Department of the Environment, Climate and Communications., "Policy Statement on Geothermal Energy for a Circular Economy." *Government of Ireland*, (2023).

Eskilson, P., and Claesson, J., "Simulation model for thermally interacting heat extraction boreholes." *Numerical Heat Transfer*, 13, (1988), 149–65.

Fossa, M., Morchio, S., Antonella, P., and Memme, S., “Accurate design of BHE fields for geothermal heat pump systems: The ASHRAE-Tp8 method compared to non-aggregated schemes applied to different European test cases.” *Energy and Buildings*, 303, (2024).

Fujii, H., Okubo, H., Nishi, K., Itoi, R., Ohyama, K., and Shibata, K., “An improved thermal response test for U-tube ground heat exchanger based on optical fiber thermometers.” *Geothermics*, 38(4), (2009), 399–406.

Hackel, S., and Pertzborn, A., “Effective design and operation of hybrid ground-source heat pumps: Three case studies.” *Energy and Buildings*, 43(12), (2011), 3497–3504.

He, M., Rees, S., and Shao, L., “Simulation of a domestic ground source heat pump system using a three-dimensional numerical borehole heat exchanger model.” *Journal of Building Performance Simulation*, 4(2), (2011), 141–155.

Horne, RN., “Design considerations of a down-hole coaxial geothermal heat exchanger.” *Transactions - Geothermal Resource Council*, 4, (1980), 569–72.

Hosseinnezhad, V., Hayes, B., O'Regan, B., and Siano, P., “Practical Instights to Design a Blockchain-Based Energy Trading Platform.” *IEEE Power and Energy Society Section*, 9, (2021), 154827-154844.

Jain, C., Vogt, C. and Clauser, C., “Maximum potential for geothermal power in Germany based on engineered geothermal systems.” *Geothermal Energy*, 3, 15, (2015).

Javed, S., and Claesson, J., “New analytical and numerical solutions for the short-term analysis of vertical ground heat exchangers.” *ASHRAE Transactions*, 117(1), (2011), 3–12.

Javed, S., and Spitler, J., “Accuracy of borehole thermal resistance calculation methods for grouted single U-tube ground heat exchangers.” *Applied Energy*, 187, (2017), 790–806.

Javed, S., Ørnes, I. R., Myrup, M., and Dokka, T. H., “Design optimization of the borehole system for a plus-Energy kindergarten in Oslo, Norway.” *Architectural Engineering and Design Management*, 15(3), (2019), 181–195.

Kavanaugh, S. P., and Rafferty, K. D., “Geothermal heating and cooling: Design of ground-source heat pump systems.” Atlanta: *ASHRAE*, (2014).

Kavanaugh SP, and Rafferty KD. “Ground-source heat pumps: design of geothermal systems for commercial and institutional buildings.” *American Society of Heating, Refrigerating and Air-Conditioning Engineers*, (1997).

Kirkpatrick, S., Gelatt, C. D. and Vecchi, M. P., “Optimization by simulated annealing.” *Science* 220, (1983), 671–680.

Li, C., Mao, J., Zhang, H., Li, Y., Xing, Z., and Zhu, G., “Effects of load optimization and geometric arrangement on the thermal performance of borehole heat exchanger fields.” *Sustainable Cities and Society*, 35, (2017), 25-35.

Li M, and Lai ACK., “Review of analytical models for heat transfer by vertical ground heat exchangers (GHEs): a perspective of time and space scales.” *Applied Energy*,151, (2015), 178–91.

Liu, J., and Han, C., “Design and optimization of heat extraction section in energy tunnel using simulated annealing algorithm.” *Renewable Energy*, 213, (2023), 218–232.

Lund, J. W., and Toth, A.,N. “Direct Utilization of Geothermal Energy 2020 Worldwide Review.” *Proceedings: World Geothermal Congress 2020+1*, Reykjavik, Iceland (2021).

Maurer, J., Tschuch, N., Krebs, S., Bhattacharya, K., and Cañizares, C., “Toward transactive control of coupled electric power and district heating networks.” *Applied Energy*, 332, (2023).

Miki, M., Hiroyasu, T. and Ono, K., “Simulated annealing with advanced adaptive neighborhood.” *Proceedings: Second international workshop on Intelligent systems design and application*, Dynamic Publishers, Inc., (2002), 113–118.

O'Regan, B., Rodrigues da Silva, F., O'Leidhin, E., Tahir, F., Mould, K., Hayes, B. P., “Lyons, P. P2P, CSC and TE: A Survey on Hardware, Software and Data.” *Energies,* 14(3851), (2021).

Ozbek, M., Yavuzturk, C., and Pinder, G., “Optimal ground source heat pump system design. *Technical Report: DOE Project Number DE-EE002801,* (2015).

Piipponen, K., Martinkauppi, A., Korhonen, K. et al., “The deeper the better? A thermogeological analysis of medium-deep borehole heat exchangers in low-enthalpy crystalline rocks.” *Geothermal Energy* 10, 12, (2022).

Rees, S. (ed.)., “Advances in ground-source heat pump systems.” Oxford, *Woodhead Publishing*, (2016).

Stauffer F, Bayer P, Blum P, Molina-Giraldo N, and Kinzelbach W., “Thermal use of shallow groundwater.” *CRC Press*, (2013).

Schulte, D.O., Rühaak, W., Oladyshkin, S., Welsch, B., and Sass, I., “Optimization of medium-deep borehole thermal energy storage systems.” *Energy Technology* 4(1), (2016), 104–113.

Spitler, J,D., West, T., and Liu, X., “Ground Heat Exchanger Design Tool with RowWise Placement of Boreholes.” *Proceedings: International Ground Source Heat Pump Association Research Track*, Las Vegas, NV, (2022).

Williams, D.R., “Earth Fact Sheet.” *NASA*, (2024, January 11), Retrieved June 10, 2024, from https://nssdc.gsfc.nasa.gov/planetary/factsheet/earthfact.html

Yuan, Y., Cao, X., Wang, J., and Sun, L., “Thermal interaction of multiple ground heat exchangers under different intermittent ratio and separation distance.” *Applied Thermal Engineering*, 108, (2016), 277–286.

Zhao Y, Pang Z, Huang Y, and Ma Z., “An efficient hybrid model for thermal analysis of deep borehole heat exchangers.” *Geothermal Energy*, 8(1), (2020).

Zidane, A., “Multiphase Unified Flash Analysis and Stability Algorithm (MUFASA): An Open-Source Software.” *arXiv*, 2211.15373, (2022).

Diversity, Equity, Inclusion, and Belonging

Geothermal Collegiate Competition: Evolution and Impact

Diana Acero-Allard[1], Elisabet Metcalfe[2], Estefanny Davalos Elizondo[1], Rebecca Mitchell[1], Daniel Zimny-Schmitt[1]

[1]National Renewable Energy Laboratory, Golden, CO

[2]U.S Department of Energy, Geothermal Technologies Office

Keywords

Geothermal Collegiate Competition, Geothermal Technology, Students, Workforce, Outreach

ABSTRACT

In 2010, the U.S. Department of Energy (DOE) announced the launch of its inaugural National Geothermal Student Competition. The competition was open to all colleges, universities, and other post-secondary institutions in the United States, and was labeled as the first-ever to address geothermal education. The GeoVision, published in 2019 by the Geothermal Technologies Office (GTO), stated that improving geothermal energy education and outreach is critical in reducing risks and costs of geothermal technology deployment. The key actions included improving public education and outreach about geothermal energy and providing resources intended to attract and inform a skilled geothermal workforce. Student competitions in particular have the ability to increase awareness of renewable energy fields by engaging multi-disciplinary students in compelling design challenges to prepare them for careers in renewable energy.

GTO, in partnership with an administration team at the National Renewable Energy Laboratory (NREL), currently supports the Geothermal Collegiate Competition (GCC), with the main objective of advancing and cultivating collegiate student knowledge and career interest in geothermal energy. The administrating team works toward growing the number of students and collegiate institutions engaged, as well as diversifying the scope of the student design challenges. The main intentions of this publication are documenting the competition's evolution, setting a baseline for future GCC impact analysis and serving as a guide to other students' competition design committees looking for ideas to capture and increase the interest of students in collegiate competitions.

1. Introduction

The Geothermal Collegiate Competition (GCC) is part of the DOE funded competitions for students providing competitors the opportunity to get involve with a clean energy competition to help jumpstart a clean energy career. Through the GCC the DOE Geothermal Technologies Office

(GTO) encourages students to develop innovative solutions for geothermal energy application challenges and build career skills for the clean energy workforce.

In 2019, GTO published the GeoVision Report. The report highlights a general lack of awareness and understanding of geothermal energy's potential to contribute to the development of a clean energy future amongst policy makers and society-at-large. (DOE, 2019). The GCC helps to address this awareness gap by engaging multi-disciplinary collegiate students, faculty, industry mentors and communities into geothermal challenges.

Student competitors in the GCC gain experience solving relevant industry challenges that prepare them for careers in geothermal and related energy fields, while benefiting from mentorship, training, and collaboration. The GCC supports DOE's ongoing work to help grow the domestic geothermal industry and address employment gaps through experiential learning.

Ongoing goals of the competition include advancing and growing collegiate student knowledge and career interest in geothermal energy by increasing the number of students and collegiate institutions engaged, diversifying the scope of the challenges, engaging industry representatives in partnership roles, and raising the profile and outreach of the competition to a broader audience.

The information used in this publication was extracted from the competition's publicly available promotional material and press releases. The statistics were obtained from reports submitted to DOE by the competition administrators. Some competitions have incomplete or non-existent records, particularly the earliest years. All information about the competitions is open to revision.

2. History of the Geothermal Collegiate Competition

The GCC has origins going back over a decade. Since 2010, a total of 11 geothermal competitions targeting students to solve challenges relevant to technical and non-technical barriers for geothermal energy have been completed. Table 1 summarizes the geothermal student competitions from 2010 to 2023. The competition was not carried out in 2017 and 2018.

Notice the name of the competition has changed from 2011 through 2014 it was titled as the *National Geothermal Student Competition*, for competitions in 2016 and 2019 it was called the *Geothermal Design Challenge* and from 2020 to present is known as the *Geothermal Collegiate Competition*.

2.1 National Geothermal Student Competition 2011

GTO and NREL launched the National Geothermal Student Competition (NGSC) with 11 participant collegiate teams selected (Figure 1) after several U.S. colleges, universities, and postsecondary educational institutions participated in a competitive process. The NGSC was dubbed a first-of-its kind intercollegiate contest challenging students to conduct a comprehensive assessment of the geothermal energy potential of the Rio Grande Rift geologic province in southeastern Colorado and northeastern New Mexico. The competition objectives were to develop students' geothermal awareness and research skills, and expose participants to real world challenges (NREL, 2011). Detailed documentation about deliverables, evaluation process, winning teams and prizes was not found for this competition.

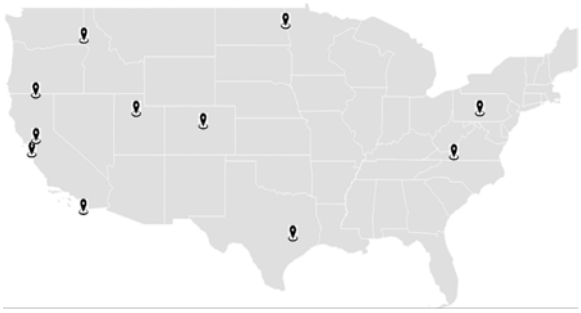

Figure 1: U.S. map showing 11 selected collegiate institutions for the NGSC 2011 (Colorado School of Mines, Oregon Institute of Technology, San Diego State University, Stanford University, Texas A&M University College Station, Pennsylvania State University, University of Utah, University of California Davis, University of Idaho, University of North Dakota, Virginia Polytechnic Institute and State University)

2.2 National Geothermal Student Competition 2012

This competition challenged undergraduate and graduate student teams to conduct a high-quality assessment of the Snake River Plain site in Idaho using innovative exploration technologies such as: geophysics, geochemistry, remote sensing, and geology. With eight teams as finalists, DOE announced Idaho State University as the winner of its NSGC 2012 with the project, "Development of an integrated, testable conceptual model of blind geothermal resources in the eastern Snake River Plain: application to the Newdale geothermal prospect" (ISU, 2012). Boise State University won second place, and Southern Methodist University Geothermal Laboratory finished third (Figure 2). Detailed documentation about deliverables, evaluation process, and prizes was not found for this competition.

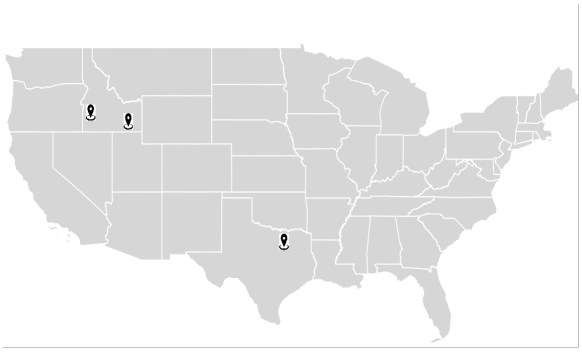

Figure 2: U.S. map showing three winning collegiate institutions of NGSC 2012 (Idaho State University, Boise State University, Southern Methodist University)

2.3 National Geothermal Student Competition 2013

In early May 2013, DOE announced the selection of four semi-finalists to advance to the final round (Figure 3) of the NGSC 2013. The competition challenged student teams to develop a business white paper on geothermal energy production and commercialization. Student teams submitted a concept paper containing technical analysis, budget plan and policy analysis sections

to compete. The evaluation criteria included completeness, clarity of project approach and methodology, technical viability, commercial viability and impact. The four semi-finalist teams received an award of $5,000 to complete their business plans, and $500 to be used to startup a geothermal club on their college campuses (UTRGV, 2013). Detailed documentation about deliverables and winning teams was not found for this competition.

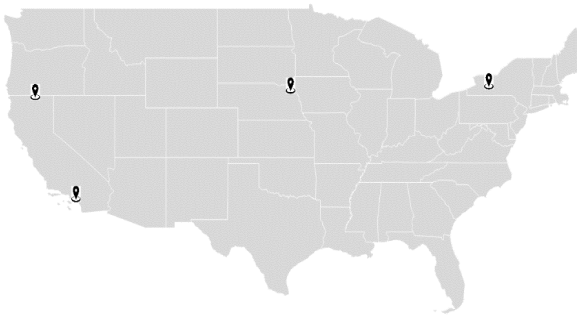

Figure 3: U.S. map showing four semi-finalist collegiate institutions of NGSC 2013 (University of Rochester; Oregon Institute of Technology; University of South Dakota – LTEC; California State Polytechnic University, Pomona)

2.4 National Geothermal Student Competition 2014

NGSC launched in 2014 with the title GeoEnergy Is Beautiful. The competition sought students interested in building and showcasing scientific research, communication and leadership skills to convey the role of geothermal energy as an important contributor to the nation's clean energy future via posters and visual aids.

The relative invisibility of geothermal energy renders it difficult to explain to a broad public audience. Graphics and infographics are frequently necessary to convey large quantities of data and complex information to facilitate insight, comprehend patterns, and understand complex messages while keeping text to a minimum.

Participating teams were asked to develop a powerful, robust, high-quality infographic explaining an aspect of geothermal power production and a communication and outreach strategy to disseminate the infographic to the public for maximum impact. Teams were required to have up to three students from graduate, undergraduate, and/or high school senior level, as well as a team sponsor such as professor, faculty member, post-doctorate or a teaching fellow. Teams could include additional sponsors from non-academic organizations.

The competition was comprised of two rounds. In round one, all participating teams were asked to submit the communications and outreach strategy and a mockup of their infographic; five applications were selected at the end of round one. In round two, the selected teams developed a full packet containing their final infographic and a final communications and outreach strategy.

Each team received a total award of $2,500, where $2,000 was expected to be used as stipend and $500 for the implementation of a component of their outreach strategy. The five teams were invited with paid expenses to the Geothermal Resources Council annual meeting 2014 to present their

infographic and meet geothermal stakeholders. During the meeting the top three teams were announced (Figure 4). DOE recognized Truckee Meadows Community College as the winner of first place, University of Texas Pan American (today part of University of Texas Rio Grande Valley) in second place, and University of Mississippi in third place (DOE, 2014).

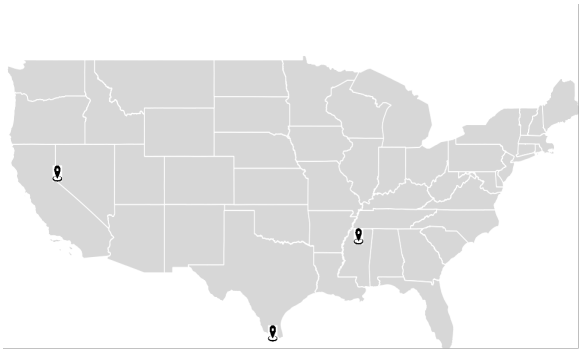

Figure 4: U.S. map showing three collegiate institution winning teams of NGSC 2014 (Truckee Meadows Community College, University of Texas Pan American, University of Mississippi)

2.5 Geothermal Design Challenge 2016

At the end of 2015, the competition launched another infographic challenge and trademark as the Geothermal Design Challenge. Students were invited to answer the question, "What is the future of geothermal energy and how will it impact you?". Five topics were recommended: History of Geothermal Energy, Workforce and Education, Science and Technology, Environmental Impacts, and Economics.

Students from high schools and universities were asked to form teams of two or three members and encouraged to find a team sponsor. For those students interested in participating but could not find the right team members, the competition provided an email contact to help their search for a matching team (INL, 2015).

The competition opened in December 2015, lasted eight months and contained three rounds. In round one, teams were asked to create a first draft of an infographic, and after a down select, round two teams refined and finalized their infographic. During the second round, teams received a one-on-one mentoring in geothermal energy and graphics arts. In the third and final round, teams selected, developed, and executed a social media campaign to promote their final infographics.

A team comprised of three students from Carnegie Mellon University's School of Design received the grand prize. They received $2,500 and an all-expenses paid trip to the Geothermal Resources Council annual meeting 2016 to showcase their work (CMU, 2016). Detailed documentation about deliverables, and finalist teams was not found for this competition.

2.6 Geothermal Design Challenge 2019

The 2019 Geothermal Design Challenge began in early January and concluded mid-April of the same year. The challenge asked teams to use actual data collected from the Frontier Observatory for Research in Geothermal Energy (FORGE) site in Milford, Utah, to create data visualization portfolios that answered the question, "Where do you target your next production well to maximize geothermal reservoir performance?". Specific datasets located in the Geothermal Data Repository (GDR) were provided for the challenge, including maps and well, drilling, temperature, surface, and reservoir testing data.

Teams from colleges and high schools were asked to imagine themselves as members of the FORGE project team tasked with placing a new geothermal well that would help researchers better understand Enhanced Geothermal Systems (EGS). Through data visualization techniques of their choosing and the data provided, teams were instructed to communicate an ideal subsurface location within the FORGE area to create a sustainable subsurface heat exchanger with minimal environmental consequences (FORGE, 2019).

The competition obtained 15 final submissions that were reviewed thoroughly by a panel of professionals. Three winning teams were selected: in first place, a joint team from DePaul University and Georgia Institute of Technology with the submission, "EGS Site Selection Using GIS and Machine Learning," was awarded $5,000; in second place, a team from Colorado School of Mines with the submission, "Open-Source Approach to 3D Communication," was awarded $3,500; and in third place, a team from Stanford University with the submission, "Want to Explore FORGE Data?," was awarded $2,500 (Figure 5).

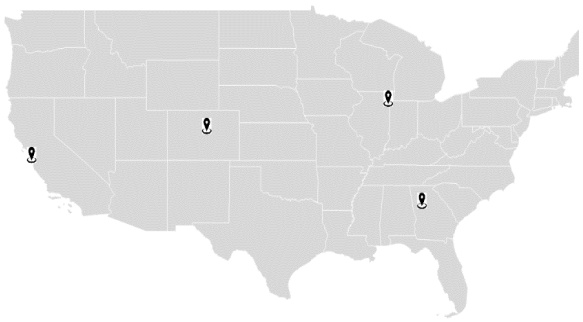

Figure 5: U.S. map showing four collegiate institution winners of Geothermal Design Challenge 2019 (DePaul University/Georgia Institute, Colorado School of Mines, Stanford University)

2.7 Geothermal Design Challenge Spring 2020

In 2020 the Geothermal Design Challenge Geographic Information System (GIS) Mapping competition focused on fostering understanding and sharing the benefits of geothermal technologies. Student teams were asked to research data, interpret information, and create a map (digital interactive or static print) showing how GIS could best communicate the benefits of geothermal technology. Through this deliverable, teams were asked to address the challenging questions, "How can geospatial mapping increase our understanding of this important renewable

energy resource? How can GIS improve how we visualize and communicate about geothermal energy?"

Registration for the Geothermal Design Challenge opened in January 2020, and submissions for the compliance review were due approximately three months later. Teams were required to pass an initial compliance review to advance to the final round of the competition. Some of the map requirements included that geothermal energy must be the primary theme, the analyzed data must be cited, it must include at least one dataset sourced from the Geothermal Data Repository (GDR), it should be technically accurate, and educational sponsor information should be included.

The challenge had a total of 78 registered students across 42 teams, including 31 from universities and 11 from high schools. Teams registered were in 25 U.S. states. The winning digital team, UW Cart Lab from University of Wisconsin-Madison titled, "The Rise of Geothermal," received a grand prize of $5,000. The winning print team, Flying Squirrels from Northern Virginia Community College titled, "Where to Tap Low-Temp Enhanced Geothermal Energy," also received $5,000 (INL, 2020). Five additional finalists were reported from Reykjavik University Iceland School of Energy (not shown in Figure 6), University of Alaska Anchorage, University of Montana, Stanford University and Bar Ilan University (not shown in Figure 6), and University of Maryland College Park (Figure 6).

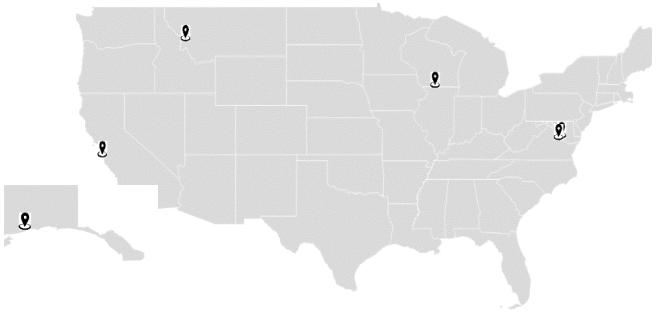

Figure 6: U.S map showing six collegiate institution finalists of Geothermal Design Challenge Spring 2020 (University of Alaska Anchorage, University of Montana, Stanford University, University of Maryland College Park, University of Wisconsin-Madison, Northern Virginia Community College)

2.8 Geothermal Design Challenge Fall 2020

GTO and NREL launched the Geothermal Design Challenge Fall 2020, where multidisciplinary teams of undergraduate and graduate students created robust, high-quality infographics illustrating aspects of geothermal energy production that were backed by technical data and accompanied by communications and outreach strategies to maximize impact.

The final deliverable package consisted of an executive summary, the infographic, communications or outreach strategy and a data appendix. The infographic should be innovative with a unique and compelling theme, be creative, be clear, contain relevant visual information and propose a relevant message. The communications and outreach strategy were evaluated for a clear approach and methodology, feasibility and impact with a broad audience.

The deliverables were submitted by participants in two phases via the HeroX platform, beginning with a progress concept submission followed by a final entry. Nine submissions were received from Antelope Valley College, Colorado School of Mines, Michigan Tech, Montgomery College, Texas A&M Corpus Christi, Tuskegee College, University of California Irvine, University of California Santa Cruz, and University of North Dakota (Figure 7).

The winning teams were: the first-place team Thermal Vision from University of North Dakota with the submission, "Geothermal Applications for the World," the second-place team Geo Slugs from University of California Santa Cruz with the submission, "Green & Unseen: The Future of Geothermal Power," and the third-place team from Antelope Valley College with the submission, "The Heat Beneath Our Feet." The competition did not provide monetary prizes (DOE, 2020).

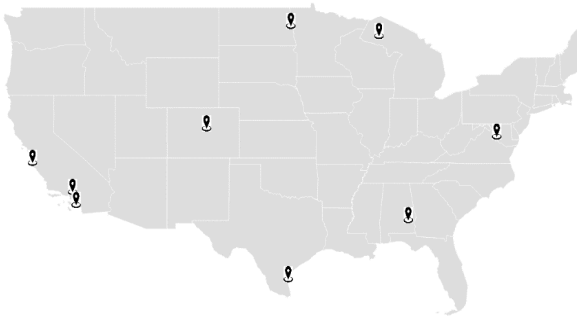

Figure 7: U.S. map showing nine collegiate institution finalists of Geothermal Design Challenge Fall 2020 (Antelope Valley College, Colorado School of Mines, Michigan Tech, Montgomery College, Texas A&M Corpus Christi, Tuskegee College, University of California Irvine, University of California Santa Cruz, University of North Dakota)

2.9 Geothermal Collegiate Competition Spring 2021

During the spring of 2021, GTO and NREL launched the Geothermal Collegiate Competition. This competition challenged students to identify a community or campus site to implement a direct-use geothermal energy system and conduct an initial resource assessment, load and usage determination, and preliminary economic feasibility analysis.

Additionally, teams were challenged to identify and interview relevant stakeholders for selected site to develop a stakeholder engagement strategy document. The strategy should contain key findings from interviews, materials to educate stakeholders about geothermal energy, a visual aid or tool to engage and educate local stakeholders about geothermal direct use case in their communities and a plan for sharing the tool more broadly.

Cash prizes of $1,000, $750, and $500 were awarded for first-, second-, and third-place winners, respectively. Honorable mentions were also awarded, with $250 for a well-done geoscience component and for an outstanding stakeholder engagement strategy.

Registered teams were required to submit deliverables in two phases: a mandatory progress submission and a final submission. The final submission was comprised of five scored sections: site identification, resource assessment, usage assessment, preliminary economic feasibility analysis, and stakeholder engagement strategy. The progress submission contained a subset of these sections.

The competition received 15 final submissions from 17 collegiate institutions (Figure 8). The winning teams were: University of North Dakota in first place, University of Oklahoma in second place, and Cornell University in third place. Additionally, the University of California Berkeley and Rutgers University received the honorable mention for their stakeholder engagement strategy and Colorado School of Mines for the geoscience's component (DOE, 2021).

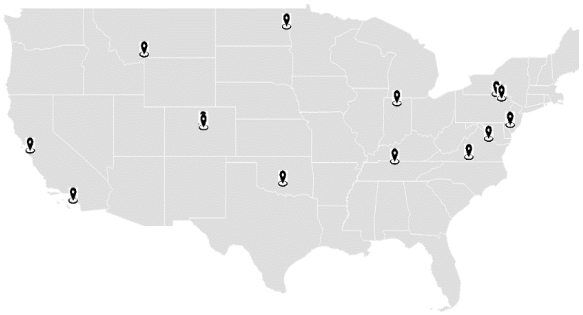

Figure 8: U.S. map showing 16 collegiate institution finalists of Geothermal Collegiate Competition Spring 2021 (Binghamton University, Colorado School of Mines, Cornell University, Cypress College, Liberty University, Montana State University, Northern Virginia Community College, Rutgers University, SUNY Broome, Temple University, UC Berkeley, University of Colorado, University of North Dakota, University of Notre Dame, University of Oklahoma, Western Kentucky University)

2.10 Geothermal Collegiate Competition Fall 2021 - Spring 2022

In its first full academic year version from fall 2021 to spring 2022, the Geothermal Collegiate Competition asked collegiate student teams to analyze geothermal technologies for a district energy application. The use case consisted of one or more commercial or multifamily buildings or an industrial or agricultural process with property access rights to geothermal resources. Student teams, required to be comprised of at least three students, developed a geothermal concept for an identified site working with real-world parameters, including actual energy load, utility rates, and subsurface data while designing their district-use project. Input from community stakeholders was required to obtain realistic project constraints and considerations.

As part of the competition strategy to support students, a series of training sessions were organized by NREL with topics from geothermal 101, technoeconomic analysis tools, 3D modeling software, systems design, and responsible stakeholder engagement. The videos were publicly posted and are available at the YouTube NREL Learning channel.

Main submission deliverables required the teams to include site identification, resource assessment, usage assessment, economic feasibility analysis, environmental impact analysis, stakeholder engagement strategy, and a stakeholder engagement event plan. Additionally, teams had to select two out of the following elective modules: curriculum supplement, conceptual geologic model, engineering design, and project development and solicitation.

The stakeholder engagement deliverables should include a list of stakeholders relevant to the project, a summary of engagements, a description of the possible community engagement event, and a letter of commitment from the prospective host of the event. The winning teams were required to execute the stakeholder event proposed in their projects. Additional funds were provided to the winning teams to execute the event within the following months after the winners' announcement.

Cash prizes were awarded for first place ($10,000), second place ($5,000), and third place ($2,500). The collegiate institutions of the first-, second-, and third-place teams each received a $10,000 University Support Cash Prize to be used in planning and implementing a local stakeholder engagement event.

Five full final submissions were received (Figure 9), including teams from Temple University, University of Colorado-Boulder, University of North Dakota and Reykjavik University, and University of Oklahoma (two teams). First place was awarded to the University of Oklahoma, second place to the University of North Dakota and Reykjavik University (not showing in figure), and third place to the University of Colorado Boulder (DOE, 2022).

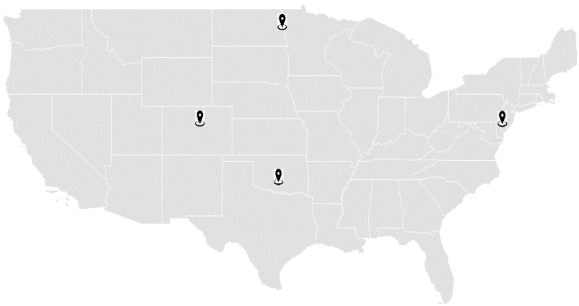

Figure 9: U.S. map of four collegiate institution finalists of Geothermal Collegiate Competition Fall 2021-Spring 2022 (Temple University, University of Colorado-Boulder, University of North Dakota, University of Oklahoma (two teams))

2.11 Geothermal Collegiate Competition 2023

The Fall 2023 Geothermal Collegiate Competition engaged student teams to develop and analyze forward-thinking geothermal heating and cooling concepts for a community or campus. Students were asked to assume the role of developer of a geothermal heating and cooling system for a district-scale application. In the interest of increasing diversity of disciplines, institutions, and applications, two types of tracks were designed for this competition cycle: the Technical Track and the Policy Track.

For the Technical Track, teams were asked to present a qualitative justification for deploying a geothermal district heating and cooling (GDHC) system in their proposed district (community or campus) and a conceptual design of a geothermal system based upon community needs, available resources, and prospective benefits to that community. Teams in the Policy Track were asked to present a qualitative justification for deploying a GDHC system in their proposed district including an analysis of the regulatory environment, financial incentives, and an economic assessment (DOE, 2023).

Three office hours sessions and two informational webinars were held for the competition. Teams were offered the option of registering early and being paired with an industry mentor, who supported their navigation of the competition; 19 teams took advantage of this offer.

Registration broke records. A total of 117 students formed 33 teams from 24 different collegiate institutions to propose innovative geothermal heating and cooling solutions for their communities. The competition engaged students from 14 states from a variety of disciplines, including mechanical and petroleum engineering, environmental policy, economy, finances, biology, city planning, architecture, dietetics, occupational therapy, supply chain management, and others.

For the final submission deadline, the competition received a total of 22 submissions from 18 collegiate institutions (Figure 10). Projects were comprised of diverse types of communities, such as campuses, low- and mixed-income residential buildings, and recreational infrastructure, the majority of which were located in rural areas.

The winners were announced via a live webinar on February 15, 2024. First- and second-place prizes were awarded in each track with $10,000 and $6,000 in cash prizes, respectively. Each first-place team also received $9,000 in additional funds for the purpose of planning and executing a stakeholder event in their project community. The first- and second-place winners of the Technical Track were awarded to the University of Oklahoma and the University of Tulsa, respectively. For the Policy Track, first place went to the Princeton University and Columbia University team, while second place went to the University of California, San Diego team.

Figure 10: U.S. map showing 18 collegiate institution finalists of Geothermal Collegiate Competition Fall 2023 (Aims Community College, California State University Bakersfield, Colorado School of Mines, Duke University, Massachusetts Institute of Technology, Norwich University, Princeton University and Columbia University, Smith College, Texas A&M University, University of California Davis, University of California San Diego, University of Colorado-Boulder, University of Michigan - Ann Arbor, University of Oklahoma, University of Tulsa, University of Wisconsin – Madison, West Virginia University)

Table 1. Summary of geothermal student competitions sponsored by DOE from 2010 to 2023. NGSC=National Geothermal Student Competition, GDC=Geothermal Design Challenge, GCC=Geothermal Collegiate Competition. NREL=National Renewable Energy Laboratory, ORISE= Oak Ridge Institute for Sciences and Education, INL=Idaho National Laboratory.

Title	Year/Term	Administrator	General Topic	Number of Finalist Teams
NGSC	2011	NREL	Assessment of geothermal resources at the Rio Grande Rift	11
NGSC	2012	ORISE	Assessment of geothermal resources at the Snake River Plain	8
NGSC	2013	ORISE	Development of a business white paper on geothermal energy production and commercialization	4
NGSC	2014	ORISE	GeoEnergy is Beautiful 2014 Infographics	5
GDC	2016	INL	GeoEnergy is Beautiful 2016 Infographics	Not reported
GDC	2019	INL	Data Visualization: FORGE	15
GDC	2020 Spring	INL	Geospatial Mapping	7
GDC	2020 Fall	NREL	Infographics	9
GCC	2021 Spring	NREL	Community Geothermal	15
GCC	2021 Fall-2022 Spring	NREL	District Energy Systems using Geothermal Resources	5
GCC	2023	NREL	Geothermal District Heating and Cooling Systems	22

3. Impact

More than 300 students participated in the geothermal competition from 2010 to 2023 as part of at least 101 finalist teams. Due to their professional expertise in the geothermal field, some GCC alumni are still involved as mentors or reviewers of current competitions.

A total number of 56 domestic collegiate institutions (Figure 11) from 30 states and two international universities have submitted entries to the competition. In the early years of the competition, when high schools were eligible to participate, about 11 institutions of that level registered to compete.

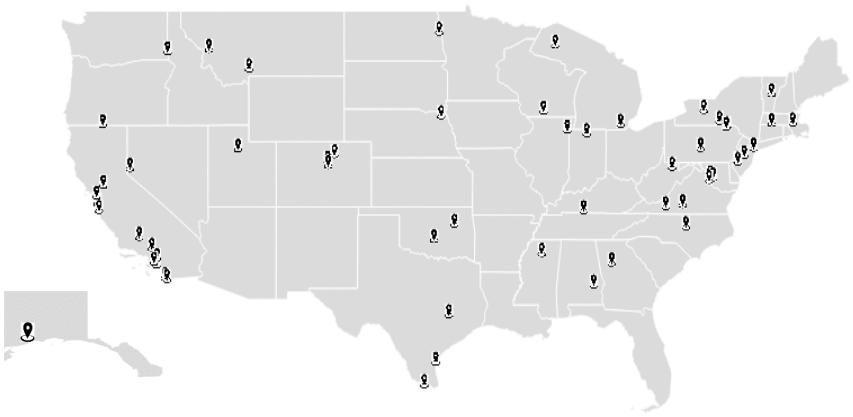

Figure 11: U.S. map showing 56 collegiate institution finalists of Geothermal Collegiate Competition since 2010

Out of the 56 collegiate institutions participating, eight are categorized as Asian American and Native American Pacific Islander Serving Institutions (AANAPISI), six as AANAPISI and Hispanic-Serving Institutions (HSI), five as HSI, one Historically Black Colleges and Universities (HBCU) and one Native American-Serving Non-Tribal Institutions (NASNTI) (Figure 12). All these categories are part of the Minority Serving Institutions (MSI) program.

Although community college participation has been low in the competition, it should be noted they had remarkable achievements. Truckee Meadows Community College won first place in 2014 for their infographic, and Northern Virginia Community College won first place in spring 2020 for the print-version GIS map titled, “Where to Tap Low-Temp Enhanced Geothermal Energy.”

Only five teams have participated in the competition including students from more than one institution. The competition reassures collaboration through encouragement of multidisciplinary teams as well as participants with various backgrounds to compete.

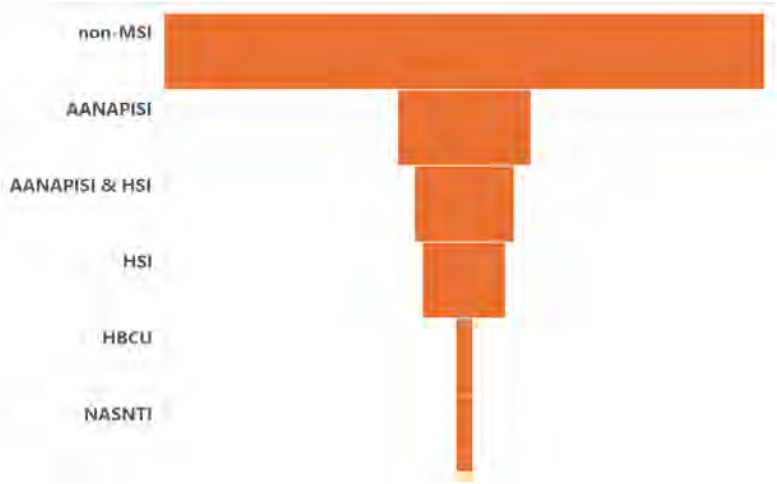

Figure 12: Distribution of non-MSI and MSI collegiate institutions in GCC from 2010 to 2023. MSI=Minority Serving Institutions (MSI), AANAPISI=Asian American and Native American Pacific Islander Serving Institutions, HSI=Hispanic-Serving Institutions, HBCU=Historically Black Colleges and Universities, NASNTI=Native American-Serving Non-Tribal Institutions

Historically the competition has targeted colleges with geothermal-related technical programs, such as geosciences and engineering. The addition of a new track with a policy focus in 2023, intended to increase participation amongst schools with policy, economics, and social programs. During registration for the 2023 competition, students were asked to list their major discipline; additional to the expected majors as geosciences and engineers, disciplines like: Finances, Business, City Planning, Architecture, Economics and Statistics, Energy Management, Industrial Technology, Public Affairs, International Relations, Social Sciences, and Supply Chain Management were listed. For the ongoing 2024 competition, the policy track is being offered again.

Currently, teams are not required to have a faculty advisor to participate in the competition; however, it is encouraged to connect with one. Over the years of the competition, it has been seen that teams accompanied by faculty are highly motivated to participate and win the competition. This might relate to the extra technical support an experienced faculty member can provide to the students. Some faculty make the competition challenge part of their class projects for their students. As an example, six teams from the same institution participated in the 2023 competition as the professor from their heat transfer class recommended the competition challenge as part of the fall semester program.

As part of the competition strategy to provide technical support to the students, a series of training sessions were recorded in 2021. The videos were publicly posted and are available at the YouTube NREL Learning channel.

Additional technical support and industry engagement has increased during the decade of the competition. Since 2020, the company Seequent has provided free student licenses and training for Leapfrog Energy®, a commercial software to evaluate geothermal resources. Another well-received initiative by the students was the mentor-team pairing, which started in the 2023 competition. Several geothermal experts were recruited from industry, academia, and national

laboratories to support student teams during the competition. Mentors' commitments included meeting with the student team regularly, discussing the progress of the project, and providing expert feedback.

The total cash prize has varied according to the recognition levels, sometimes by additional honorable mentions or supplementary prizes like paid attendance at key professional events, and funds to plan community stakeholder events. In figure 13, cumulative cash prizes are shown. Note for GCC 2022 the cash prizes were increased considerably; the injection of funds was made by DOE based on direct student feedback. Non-tangible prizes, like recognition on DOE and national laboratories' media channels, have been added to allow students and schools to promote their achievements publicly.

Figure 13. Cumulative cash prize pools and teams participating for the Geothermal Collegiate Competition from 2010 to 2023. Cash Prizes in thousands of dollars. Additional prizes, such as conference expenses paid, scholarships, and event funds, are not included. S=Spring. F=Fall

Since the spring 2021 competition, the technical topic has related to geothermal district heating and cooling for communities within the U.S. These types of projects have been proposed by the students on college campuses, tribal communities, low- and mixed-income communities, and community buildings such as school districts, local government offices, and federal facilities. Some exemplary applications for tribal communities were:

- The winning team of 2021-2022 created a prospect on gas well recompletion for geothermal district heating in Mandaree, North Dakota, located on the Fort Berthold Indian Reservation in the Mandan and Arikara nation. The project would generate heat as well as food through an integration of a direct-heated greenhouse. Judges praised this team for their exhaustive evaluation of the potential for geothermal direct heat using abandoned oil and gas wells.

- In fall 2022, the winning team designed and analyzed a system repurposing six abandoned oil and gas wells in Shawnee, Oklahoma to provide clean, renewable geothermal energy for more than 730,449 square feet of educational and municipal buildings, including sites within the Absentee Shawnee Tribe and Potawatomi Nation.

- For the GCC 2023, the newly introduced Policy Track winning team developed a proposal for a geothermal district heating and cooling system in Elim, an Alaska Native community on the Seward Peninsula. The team received the highest score due to their clarity and thorough research on applicable permitting and approval requirements, cost estimates based on well-sourced costs, and potential incentive options.

As previously mentioned, teams competing from 2021 were asked to develop a community engagement strategy including a stakeholder event plan. The goal of having student teams planning a stakeholder event was to get them involved with the communities benefitted and impacted by their proposed projects. Winners from the competitions of fall 2021-spring 2022 and 2023 have executed four stakeholder events with community participation and a variety of attendee backgrounds. For the sponsor and administrator teams, these events are currently the only in-person interaction opportunity with the student teams during the competition. The feedback received from the students, college personnel, community members, and participants about the events has been positive. It is noticeable that students put a significant amount of effort on the execution of the event.

4. Conclusions

The Geothermal Collegiate Competition challenges students to scale up geothermal technologies in a way that prioritizes the unique needs of individual stakeholder groups and communities. GCC's student competitors gain experience in solving real-world challenges while benefiting from mentorship, training, and collaboration. The GCC supports GTO's ongoing efforts to grow the domestic geothermal industry and address employment gaps through experiential learning.

From the beginning of the competition in 2010, more than 300 students have proposed innovative ideas for real-world problems with real-world solutions that benefit a diverse range of communities. In every version of the geothermal competition, GTO and administrators found innovative approaches to increase participation and to inspire students across the country to overcome real barriers of the geothermal industry. A few of many examples include creating non-technical tracks to motivate diverse disciplines, forming mentoring programs, providing free technical software access, creating elective modules, and increasing the national recognition of winning teams.

The maintenance of student competitions and a broad outreach beyond the typical disciplines from the geothermal field are critical to sustain a diverse pipeline for the sector's future workforce. Strategies to increase retention of current participating institutions and targeting minority serving institutions (MSI) are vital to reach the diverse backgrounds anticipated.

Based on participants' feedback, large cash prizes have a positive response from students considering participating in a collegiate competition. Additional prizes, such as attending professional conferences to present their projects, scholarships for short training programs, or certifications, are also worth evaluating as part of the prizes pool.

One of the goals of the competitions is to expose students to a hands-on learning experience and support them in getting skills applicable in an entry-level job. There is a great opportunity to increase the two-way interest between industry and students. Current geothermal internship programs vary largely; therefore, looking for a direct collaboration between student competitions and internship programs within the industry seems to be an interesting path to analyze in the short term.

Acknowledgement

This work was authored by the National Renewable Energy Laboratory, operated by Alliance for Sustainable Energy, LLC, for the U.S. Department of Energy (DOE) under Contract No. DE-AC36-08GO28308. Funding was provided by the U.S. Department of Energy Geothermal Technologies Office. The views expressed in the article do not necessarily represent the views of the DOE or the U.S. Government. The U.S. Government retains and the publisher, by accepting the article for publication, acknowledges that the U.S. Government retains a nonexclusive, paid-up, irrevocable, worldwide license to publish or reproduce the published form of this work, or allow others to do so, for U.S. Government purposes.

Multiple stakeholders are deeply involved during the implementation of the geothermal competition, including faculty, mentors, and communities. The authors of this publication want to thank all of them for their continuous engagement.

REFERENCES

CMU. 2016. “Students Win Geothermal Design Challenge” Accessed July 2024. https://www.cmu.edu/news/stories/archives/2016/august/geothermal-challenge.html

DOE. 2014. “National Geothermal Student Competition.” Accessed July 2024. https://www.energy.gov/eere/geothermal/national-geothermal-student-competition

DOE. 2019. *GeoVision: Harnessing the Heat Beneath Our Feet*. Washington, D.C. DOE/EE-1306. https://www.energy.gov/eere/geothermal/downloads/geovision-harnessing-heat-beneath-our-feet

DOE. 2020. “Geothermal Design Challenge Fall 2020 Winners.” Accessed July 2024. https://www.energy.gov/eere/geothermal/articles/geothermal-design-challenge-fall-2020-winners

DOE. 2021. “Geothermal Collegiate Competition Spring 2021 Winners.” Accessed July 2024. https://www.energy.gov/eere/geothermal/geothermal-collegiate-competition-spring-2021-winners

DOE. 2022. “DOE Announces Winners of the 2022 Geothermal Collegiate Competition.” Accessed July 2024. https://www.energy.gov/eere/articles/doe-announces-winners-2022-geothermal-collegiate-competition

DOE. 2023. “Geothermal Collegiate Competition.” Accessed July 2024. https://www.energy.gov/eere/geothermal/geothermal-collegiate-competition

FORGE. 2019. “Student Competition.” Accessed July 2024. https://utahforge.com/studentcomp/

INL. 2015. “GeoEnergy is Beautiful 2016 Student Competition, Project Plan.” Internal report. INL/PRO-15-35957.

INL. 2020. “2020 Geothermal Design Challenge Overview.” Internal report. INL/MIS-20-58786.

ISU. 2012. “Idaho State University wins U.S. Department of Energy’s National Student Geothermal Competition.” Accessed July 2024. Idaho State University wins U.S. Department of Energy’s National Student Geothermal Competition | Idaho State University (isu.edu)

NREL. 2011. “National Geothermal Student Competition.” Accessed July 2024. https://www.nrel.gov/docs/gen/fy11/51862.pdf

UTRGV. 2013. “2013 National Geothermal Student Competition.” Accessed July 2024. https://www.utrgv.edu/cstem/_files/documents/geothermal-technologies-program.pdf

Strengths-Based Bridges: Fostering Diversity, Inclusion, and Innovation in the Geothermal Industry

Brandy Brazell Obvintseva[1]

[1] Principal Strategist, Gallant Culture; Certified StrengthsCoach® Gallup

Keywords:

Diversity, Inclusion, Geothermal Energy, CliftonStrengths, Cross-Sector Collaboration, Renewable Energy, Cultural Integration, Gallup.

ABSTRACT

The advancement of the geothermal energy sector represents a critical frontier in the global shift toward renewable energy sources. A significant challenge in this endeavor is the integration of diverse industrial cultures, specifically those of the traditional oil and gas industry and the burgeoning environmental energy sector. This paper explores the hypothetical application of Gallup's CliftonStrengths framework to bridge this cultural divide, positing that leveraging individual and collective strengths can facilitate a celebration of diversity, inclusion, and varied perspectives. This examination proposes that understanding and applying these disparate sectors' inherent talents and strengths can enhance collaboration, innovation, and progress in geothermal energy development. By adopting the CliftonStrengths approach, the paper hypothesizes a scenario where the unique contributions of everyone are recognized and valued, fostering a more inclusive and productive dialogue between the traditional energy and environmental sustainability communities. This strengths-based strategy not only aims to accelerate the practical advances in geothermal technology and project execution but also seeks to establish a model for cross-sector cooperation rooted in mutual respect and shared objectives. Through theoretical analysis, this study illustrates the potential of the CliftonStrengths framework to act as a catalyst for uniting diverse groups, thereby contributing to the faster realization of geothermal energy's potential in the renewable energy landscape.

1. Introduction

The geothermal industry is at the forefront of the transition to renewable energy. Yet, it faces significant challenges in integrating the diverse industrial cultures of traditional oil and gas sectors with the emerging renewable energy community. The historical dominance of fossil fuel-based energy production has led to deeply entrenched practices and cultures that may not align with the values of the renewable energy sector. Diversity and inclusion (D&I) have been recognized as crucial for fostering innovation, enhancing problem-solving capabilities, and driving sustainable development in this sector.

1.1 Importance of Diversity and Inclusion

Diversity brings a variety of perspectives that can drive innovation and lead to more effective problem-solving. In geothermal energy, where technological challenges and environmental considerations are paramount, diverse teams are better equipped to develop innovative solutions. Inclusion ensures that all voices are heard and valued; creating a collaborative environment that leverages human potential. The integration of diverse perspectives not only leads to more robust solutions but also fosters a culture of mutual respect and understanding, which is essential for the long-term success of any organization.

1.2 Objective and Scope of the Paper

This paper investigates the potential application of Gallup's CliftonStrengths framework to bridge cultural divides and foster a more inclusive and collaborative environment in the geothermal industry. It explores how strengths-based approaches can enhance team performance, foster innovation, and promote a culture of inclusion. The focus is on integrating insights from traditional energy sectors and the growing renewable energy sector to create a cohesive strategy for advancing geothermal energy development. By examining the foundational principles of the CliftonStrengths framework and its application in various organizational settings, this paper aims to provide actionable insights for industry leaders.

2. Literature Review

2.1 Gallup's CliftonStrengths Framework

Gallup's CliftonStrengths framework emphasizes identifying and leveraging individual strengths to enhance team performance and organizational success. This framework is based on the premise that focusing on strengths leads to greater engagement, improved performance, and a more positive workplace culture. According to Gallup, organizations that adopt a strengths-based approach can significantly increase employee productivity and retention.

2.1.1 Basic Tenets of CliftonStrengths

The CliftonStrengths framework is founded on several key tenets:

- Strengths Identification: Recognizing that each individual has unique talents that can be harnessed for personal and organizational success.
- Strengths Development: Focusing on developing these strengths rather than solely addressing weaknesses.
- Strengths Utilization: Aligning tasks and roles with individuals' strengths to maximize efficiency and job satisfaction.
- Strengths Integration: Encouraging teams to leverage each member's strengths to foster collaboration and achieve collective goals.

2.1.2 Application in Organizational Settings

In organizational settings, the CliftonStrengths framework can be used to identify employees' unique strengths and align them with roles and responsibilities that maximize their potential. This approach fosters a culture of recognition and appreciation, where individuals feel valued for their contributions. It also encourages collaboration by highlighting complementary strengths within teams. These results in a more engaged and motivated workforce better equipped to tackle complex challenges and drive innovation.

2.2 Diversity in the Energy Sector

The energy sector, including geothermal energy, has historically struggled with diversity. According to a recent Boston Consulting Group (BCG) report, the energy industry is at risk of falling behind in terms of gender diversity, with women significantly underrepresented in technical and leadership roles. This lack of diversity can hinder innovation and limit the industry's ability to attract and retain top talent.

2.2.1 Gender and Ethnic Diversity Challenges

The BCG report highlights that the underrepresentation of women and ethnic minorities in the energy sector is a significant barrier to achieving a diverse and inclusive workforce. Women make up only 22% of the workforce in the traditional energy sector, and ethnic minorities are similarly underrepresented. These disparities are even more pronounced in leadership positions, where women and minorities often face additional barriers to advancement.

2.2.2 Benefits of Diversity

Diverse teams bring various perspectives that can lead to more innovative solutions. Studies have shown that companies with higher levels of diversity are more likely to outperform their peers regarding financial performance and innovation. In the energy sector, where complex technical challenges are common, diverse teams are better equipped to develop effective solutions and drive industry advancements. Moreover, team diversity enhances creativity and the ability to solve problems by providing a broader array of ideas and approaches to address issues.

2.3 Current State of Diversity in Geothermal

The 2022 GR DEI Paper highlights the efforts of Geothermal Rising to promote diversity, equity, and inclusion within the geothermal community. The paper discusses baseline demographic data and outlines strategies for increasing diversity and fostering an inclusive environment.

2.3.1 Demographic Data and DEI Initiatives

The 2022 GR DEI Paper presents demographic data from surveys conducted within the geothermal community. These surveys reveal significant diversity gaps, particularly in gender and ethnic representation. Geothermal Rising has implemented a range of DEI initiatives to address these disparities, including mentorship programs, diversity training, and targeted recruitment efforts.

2.3.2 Impact of DEI Efforts

The impact of these DEI efforts has been significant, with increased representation of women and ethnic minorities in the geothermal workforce. Geothermal Rising's initiatives have also led to a more inclusive workplace culture where employees feel valued and respected for their

contributions. This has contributed to higher levels of employee engagement and satisfaction and improved organizational performance.

3. Methodology

This whitepaper integrates qualitative and quantitative data from various sources to provide a comprehensive overview of the current state of diversity in the geothermal industry. Data were gathered from Gallup reports, industry publications, and internal surveys conducted within the geothermal sector. The analysis focuses on the potential application of the CliftonStrengths framework to enhance collaboration and innovation through a strengths-based approach.

3.1 Data Collection

Data were collected from various sources, including Gallup's workplace studies, industry reports from the Boston Consulting Group (BCG), and internal surveys conducted by Geothermal Rising. These sources provided a comprehensive overview of the current state of diversity in the energy sector and the impact of DEI initiatives on organizational performance.

3.2 Analysis Techniques

The analysis involved a combination of qualitative and quantitative techniques. Qualitative data were analyzed using thematic analysis to identify key themes and patterns related to diversity and inclusion. Quantitative data were analyzed using statistical methods to examine trends and correlations between diversity and organizational performance. The findings were then integrated to provide a holistic view of the current diversity in the geothermal sector and the potential benefits of a strengths-based approach.

3.3 Integration of Gallup's Framework

Gallup's CliftonStrengths framework was integrated into the analysis to explore how a strengths-based approach could enhance diversity and inclusion in the geothermal sector. This involved examining the alignment between individual strengths and organizational roles and identifying opportunities for leveraging strengths to drive innovation and collaboration.

4. Findings

4.1 Diversity in the Geothermal Industry

Like many sectors within the energy industry, the geothermal industry faces significant diversity challenges. The US Workforce Diversity Data report indicates that the energy workforce is predominantly male and lacks representation from minority groups. In the geothermal sector specifically, women and racial minorities are underrepresented, with significant disparities in leadership roles.

4.1.1 Gender and Ethnic Representation

According to the US Workforce Diversity Data, women make up only 25% of the workforce in the geothermal industry (up 3% since a 2022 paper was published by Geothermal Rising (see citation), and ethnic minorities are similarly underrepresented. These disparities are particularly

pronounced in technical and leadership roles, where women and minorities face additional barriers to advancement.

4.1.2 Barriers to Diversity

Barriers to diversity in the geothermal industry include unconscious bias, lack of mentorship opportunities, and limited access to networks and resources. These barriers can prevent women and minorities from advancing in their careers and contributing fully to the industry. Addressing these barriers requires targeted efforts to promote diversity and inclusion, including mentorship programs, diversity training, and recruitment initiatives.

4.2 Benefits of a Strengths-Based Approach

Gallup's CliftonStrengths framework enhances diversity and inclusion within the geothermal industry. Organizations can foster a more inclusive environment that values diverse perspectives and skills by focusing on individual strengths. This approach has been shown to improve team dynamics, increase innovation, and drive organizational success.

4.2.1 Enhancing Team Dynamics

A strengths-based approach can enhance team dynamics by encouraging collaboration and recognizing the unique contributions of each team member. By focusing on strengths, organizations can create a more positive and inclusive workplace culture where employees feel valued and motivated to contribute to their full potential.

4.2.2 Driving Innovation

Diverse teams that leverage individual strengths are more likely to develop innovative solutions to complex challenges. A strengths-based approach can drive innovation and accelerate progress in the geothermal industry, where technological advancements are crucial for sustainable energy production.

4.3 Case Studies and Examples

The State of the Global Workplace 2024 report provides several case studies highlighting successful diversity and inclusion initiatives in the energy sector. These case studies illustrate the positive impact of a strengths-based approach on employee engagement and organizational performance. Geothermal Rising's DEI initiatives serve as a model for organizations looking to enhance diversity and inclusion within their sectors.

4.3.1 Case Study: Geothermal Rising

Geothermal Rising has implemented a range of DEI initiatives to increase diversity and foster an inclusive workplace culture. These initiatives include mentorship programs, diversity training, and targeted recruitment efforts. As a result, Geothermal Rising has seen an increase in the representation of women and minorities in its workforce and higher levels of employee engagement and satisfaction.

4.3.2 Case Study: Global Energy Corporation

Global Energy Corporation, a leading energy company, has adopted Gallup's CliftonStrengths framework to enhance diversity and inclusion within its workforce. By focusing on individual strengths, the company has created a more inclusive environment that values diverse perspectives and encourages collaboration. This approach has led to higher levels of innovation and improved organizational performance.

5. Discussion

5.1 Challenges and Opportunities

The geothermal industry faces unique challenges in integrating a diverse workforce. However, these challenges also present opportunities for growth and innovation. A strengths-based approach can help overcome cultural barriers and foster a more inclusive environment that values the contributions of all employees.

5.1.1 Addressing Unconscious Bias

Unconscious bias is a significant barrier to diversity and inclusion in the geothermal industry. By promoting awareness of unconscious bias and implementing training programs, organizations can create a more inclusive workplace where all employees feel valued and respected.

5.1.2 Leveraging Diversity for Innovation

Diverse teams bring various perspectives that can drive innovation and lead to more effective problem-solving. By leveraging the unique strengths of each team member, organizations can develop innovative solutions to complex challenges and enhance their competitive advantage.

5.2 Implications for Policy and Practice

To achieve greater diversity and inclusion, the geothermal industry must adopt policies that support a strengths-based approach to workforce development. This includes providing training and development opportunities focusing on individual strengths and implementing policies promoting diversity and inclusion at all levels of the organization.

5.2.1 Policy Recommendations

Policy recommendations for promoting diversity and inclusion in the geothermal industry include:

- Implementing mentorship programs to support the career development of women and minorities.
- Providing diversity training to raise awareness of unconscious bias and promote inclusive behaviors.
- Establishing recruitment targets to increase the representation of women and minorities in technical and leadership roles.

5.2.2 Best Practices for Organizations

Best practices for organizations include:

- Conducting regular diversity audits to assess the representation of women and minorities in the workforce.
- Offering flexible work arrangements to support work-life balance and attract diverse talent.
- Creating employee resource groups to provide support and networking opportunities for underrepresented groups.

5.3 Future Directions

Future research should explore the long-term impact of strengths-based approaches on diversity and inclusion within the geothermal industry. Additionally, continued efforts are needed to develop and implement policies that support a diverse and inclusive workforce and measure the effectiveness of these initiatives over time.

5.3.1 Areas for Future Research

Areas for future research include:

- Examining the impact of strengths-based approaches on employee engagement and retention in the geothermal industry.
- Investigating the role of leadership in promoting diversity and inclusion within the geothermal sector.
- Assessing the effectiveness of diversity training programs in reducing unconscious bias and promoting inclusive behaviors.

5.3.2 Long-Term Impact of Diversity Initiatives

Future research should focus on the long-term impact of diversity initiatives on organizational performance and innovation. By measuring the outcomes of these initiatives over time, organizations can identify best practices and develop strategies for sustaining diversity and inclusion in the geothermal industry.

6. Conclusion

Integrating Gallup's CliftonStrengths framework can bridge cultural divides and foster a more inclusive and innovative environment in the geothermal industry. By focusing on individual and collective strengths, the geothermal sector can enhance collaboration, drive innovation, and accelerate the transition to renewable energy. The findings suggest that a strengths-based approach can play a crucial role in promoting diversity and inclusion, leading to a more sustainable and successful industry.

Acknowledgements

We would like to thank all contributors and sources of data and insights, including Gallup, Geothermal Rising, and the authors of the referenced reports.

REFERENCES

Eric Gregoire, Boston Consulting Group. *"Energy Sector Risks Falling Behind in Gender Diversity."* Retrieved from https://www.bcg.com/press/18september2023-energy-sector-risks-falling-behind-gender-diversity (2023).

Jim Harter, Gallup. *"Why Build a Strengths-Based Culture."* Retrieved from https://www.gallup.com/workplace/470621/why-build-strengths-based-culture (2023).

Gallup. *"Nuances of Coaching CliftonStrengths in the DEI Space."* Retrieved from https://www.gallup.com/cliftonstrengths/en/393410/nuances-coaching-cliftonstrengths-dei-space.aspx (2023).

Bailey Nelson, Gallup. *"Ways CliftonStrengths Promotes an Inclusive Workplace."* Retrieved from https://www.gallup.com/cliftonstrengths/en/354185/ways-cliftonstrengths-promotes-inclusive-workplace.aspx (2023).

Gallup. *"State of the Global Workplace."* Retrieved from State of the Global Workplace 2024 Report (2024).

Gallup. *"Advancing DEI Initiatives: A Guide for Organizational Leaders."* Retrieved from DEI Perspective Paper (2022).

Geothermal Rising. *"Diversity, Equity, and Inclusion in the Geothermal Community."* Retrieved from GR DEI Paper (2022).

NASEO and BW Research Partnership. *"US Workforce Diversity Data Findings."* Retrieved from US Workforce Diversity Data Findings (2021).

Canadian Policy Opportunities for the Geothermal Energy Industry (August 2024)

Alison Thompson; London Hillyer

The Canadian Geothermal Energy Association (CanGEA)

Keywords

Policy; Canada; Alberta; British Columbia; Geothermal; Incentives; Risk Mitigation; Regulatory; Permitting

ABSTRACT

Geothermal energy, despite its availability, has been largely untapped in Canada thus far. The industry has struggled to gain traction due to a lack of foundational support and strategic policy frameworks. This paper explores the existing federal and provincial policy landscapes to identify gaps and propose actionable recommendations to stimulate the geothermal sector. With strategic policy support and targeted investments, Canada has the potential to unleash its geothermal resources.

At the federal level, the promising Clean Technology Investment Tax Credit (ITC), now inclusive of geothermal heat and electricity, provides up to a 30% refundable tax credit. Further policy opportunities for the federal government to play its part to lay the foundation of the industry may include Heat Price Swapping Agreements (HPSAs) and establishing a clear framework for geothermal carbon offset projects and Carbon Contracts for Difference (CCFD). Further, a risk mitigation drilling fund would support geothermal developers by compensating unsuccessful projects and recycling funds from successful ones, thereby reducing financial risks and encouraging private sector investment.

In Alberta, targeted projects to fuel-switch industrial processes to geothermal heat can significantly reduce emissions while developing new energy sources. These demonstrations would prove the economic and technical feasibility of geothermal energy. Similar to existing incentives for petrochemicals and carbon capture, a dedicated geothermal incentive program would attract investment and accelerate industry development. On the regulatory side, extending surface access rights, addressing urban drilling regulations, ensuring exclusive rights to pore space, and considering electricity market reforms are areas for further policy reforms to catalyze the geothermal energy industry.

In British Columbia, introducing geothermal tax incentives similar to established mining and heat pump tax credits can attract investment and reduce the financial burden on developers. Introducing a geothermal portfolio standard in the CleanBC Industry Fund and as part of BC Hydro’s Integrated Resource Plan can facilitate the development of geothermal heating and electricity systems. Encouraging geothermal offset projects through the Fuel Switch Offset Protocol, reconsidering well classifications, exempting waste heat from regulation, and streamlining the permitting process can further remove barriers and expedite geothermal project development in the province.

Introduction

Canada represents a virtually new frontier for geothermal energy development with significant market and moderate resource potential. In our view, geothermal development has stalled because there has been an over-focus on electrification, as in the mid-2010s federal funding targeted electricity-generation, thus overlooking the foundations of the industry– direct-use of geothermal heat. Provinces on the other hand, have simply had other priorities, or have not been sufficiently educated or persuaded to recognize the potential and benefits of geothermal energy; however, this is beginning to change – as indicated by recent announcements such as the Alberta Drilling Accelerator.

The entire supply chain stands to benefit from industry-enabling legislation and regulations including developers, drillers, financiers, scientists and consultants, supply and service providers etc. Policy work has the potential to save millions ($) and save years on geothermal energy projects, enabling more projects to commence and finish, creating more sure and swift returns for developers and financiers. With a world-class energy sector and professionals to match, tapping into and commercializing geothermal resources in Canada could unfold rapidly with the right investments and policy shifts.

This paper will review the existing frameworks at the federal level, Alberta, and in British Columbia (BC) to recommend policy proposals from the perspective of geothermal energy stakeholders. There may be opportunities in other provinces as well, though this paper emphasizes Alberta and BC given that the bulk of geothermal industry stakeholders currently are developing projects and exploring potential projects in these two provinces, given the availability of Canada's highest quality resources in relation to market opportunities.

1. Federal

In Canada, geothermal permitting, leasing, project approvals and tenure is primarily handled at the provincial level, not the federal level. At the federal level, policy opportunities relate primarily to financial incentives and risk mitigation, as geothermal projects are not likely to be affected by proposed federal regulatory legislation, such as the Impact Assessment Act, which was initially struck down by the Supreme Court for encroaching on provincial jurisdiction (Killoran et al., 2023). Natural Resources Canada, a federal agency, funds various programs related to natural resource development, and under the current government, prioritizes clean resources, technologies, and emissions-reducing projects.

1.1 Investment Tax Credits (ITCs)

<u>The Clean Technology ITC</u>

This ITC represents not a policy gap, but a policy win. The 2022 Fall Economic Statement introduced the initial details of the Clean Technology ITC. Mentioned eligible clean technology equipment included systems relating to storage, heat pumps, nuclear, and solar—notably absent was geothermal energy. Immediately, CanGEA began a campaign to ensure geothermal energy systems would be included in legislative drafts of the Clean Technology ITC. After a series of half-a-dozen meetings with both sides of the aisle and dozens more communications beginning in late 2022, in the Spring of 2023, Environment Minister Guilbeault announced the expanded

eligibility of the Clean Technology ITC to include geothermal energy systems, as is also contained in Budget 2023.

The Clean Technology ITC is a refundable tax credit of up to 30% of investments in eligible property acquired on or after March 28, 2023. Eligible equipment includes, *"(v)equipment used exclusively for the purpose of generating electrical energy or heat energy, or a combination of electrical energy and heat energy, solely from geothermal energy, that is described in subparagraph (d)(vii) of Class 43.1 in Schedule II to the Income Tax Regulations, but excluding any equipment that is part of a system that extracts fossil fuel for sale"* (Parliament of Canada, 2023). If labour requirements (prevailing wage and apprenticeship conditions) are not satisfied, the tax credit rate would drop by 10 percentage points.

This ITC was introduced in the House of Commons on November 30, 2023, as part of a broader package (C-59) to implement provisions of the Fall Economic Statement and as of summer 2024, is available to claim in an updated Schedule 31 ITC form for corporations.

CCUS Investment Tax Credit Parity and Hydrocarbon Co-production:

Our industry may receive up to 30% via the Clean Technology ITC, whereas the CCUS Investment Tax Credit provides up to 60%. We are grateful for geothermal energy's eligibility under the Clean Technology ITC, though 60% would of course be preferred over 30%.

Hydrocarbon Co-production:

Furthermore, the ITC legislation specifies that— *"equipment used for geothermal energy projects that will co-produce oil, gas or other fossil fuels would not be eligible for the [Clean Technology Investment Tax] credit."* Geothermal projects that may co-produce hydrocarbons will still reduce net emissions and should not be excluded from the Clean Technology ITC.

Conclusion

Although there are still ways to improve the Clean Technology ITC for geothermal energy, such as raising the percentage points to match CCUS and accommodating for hydrocarbon co-production, we commend the Government for their forward-thinking approach to our energy future and would encourage energy developers across Canada, and abroad, to consider adding Canadian geothermal projects to their portfolio, considering this new incentive to develop geothermal energy.

1.2 Renewable Heating Portfolio Standard (RHPS) and Heat Price Swapping Agreements (HPSAs)

Although the Federal Government in Canada cannot mandate a Renewable Portfolio Standard (RPS) for public utilities (which would fall into provincial jurisdiction), they can mandate a RPS for federal agencies. RPS mandates in the U.S., such as Executive Order 13514 and 13693, have led to the power purchase agreements (PPAs) of geothermal energy by federal departments, such as by the Department of Defense (DoD).

Although PPAs are well established and proven effective, the geothermal industry is not yet at the maturity level in Canada to generate electricity in a competitive market – thus PPAs would need

to be adjusted to pay premiums for baseload renewable energy. A more necessary (and novel) policy market mechanism at this time would be the idea of Heat Price Swapping Agreements (HPSAs), given that direct-use of geothermal heat is the low hanging fruit of the industry, and will serve as its foundation. Heat cannot be dispatched onto a grid, and it loses energy rapidly if it is transported across even small distances; therefore, at the federal level in Canada, to enable government buildings and/or agencies to purchase geothermal heat, the government could implement a HPSA Program to meet the targets of a Renewable Heating Portfolio Standard (RHPS).

The Government of Canada is the single largest building owner in Canada (Efficiency Canada, 2024). Under the HPSA Program, a government building customer would swap the price they pay for heat (natural gas) with a customer located near a geothermal heat resource. The government customer would continue to receive their existing heating source but pays the price for geothermal heat. Meanwhile, the customer near the geothermal resource would receive geothermal heat but pay the usual price of the government customer's conventional heat. By purchasing geothermal heat in place of natural gas, carbon emissions would be reduced, local air quality would improve, and energy security would be enhanced.

The Canadian Gas Association (CGA) has likewise proposed procurement of renewable natural gas (RNG) for the heating of the federal buildings, which calls for a 5% and 25% blend of RNG by 2025 and 2030 respectively (Canadian Gas Association, 2021). However, opting for geothermal heating instead would enable the Federal Government to eliminate virtually all GHG emissions from these buildings rather than only by 110,000 tonnes/year by switching to RNG. This will help to reduce the Government of Canada's 11.2 million GJ/yr of natural gas reliance, either directly or through renewable heat credits, which is equivalent to taking 124,500 homes/year from fossil fuels (Canadian Geothermal Energy Association, 2021).

The cost of RNG quoted at $18/GJ by the CGA is a premium over the current natural gas rate. Once established, geothermal heat prices are extremely economic, competitive, virtually immune to commodity price fluctuations, and would likely be much lower than the price of RNG. Locking in geothermal heat at a fair price over a long-fixed period would not only help the federal government reduce GHG emissions but would secure a sustainable rate for these buildings. Additionally, while a geothermal power facility would create approximately 17 times as many full-time jobs as a comparable natural gas facility, CanGEA (2014) posits that would be a comparable ratio to a geothermal heating system versus a natural gas burning system.

An HPSA Program could lead to a cascading effect of geothermal heating sites across Canada, as waste heat from an initial industrial customer can then feed into nearby district heating infrastructure. As the Federal Government invests in building greater geothermal heating infrastructure, further growth within other communities through greater knowledge capacity will be enabled. Moreover, the infrastructure created for geothermal projects has a long-life cycle and is extremely resilient relative to conventional combustion heating infrastructure, enhancing energy security.

A white paper may be necessary to explore the feasibility of the HPSA Program. The paper would determine the capability and outcomes of acquiring geothermal heat for hundreds of Government of Canada federal buildings. As well, the project will develop a deeper understanding of the implications of an RHPS policy in Canada and how creating a renewable heating credit trading

system would assist the Federal Government in the procurement of geothermal heating for their federal buildings and to meet GHG reduction goals. The HPSA Program would promote a stable foundation for the geothermal industry and establish its infrastructure and supply chains.

1.3 A Clear Framework for Geothermal Carbon Offset Projects and Geothermal Carbon Contracts for Difference (CCFD)

The proposed federal regulations to cap emissions in the oil and gas sector present a substantial opportunity for the geothermal energy industry. Establishing a clear framework for geothermal carbon offset projects can maximize this opportunity, ensuring that the benefits persist regardless of political changes. This framework should include Carbon Contracts for Difference (CCFD) specific to geothermal projects, providing the financial certainty necessary for long-term investments.

Additionally, the framework should facilitate credit trading among emitters and enable collaboration on offset and emission-reducing projects, including projects that would switch from combustion fuels to direct-use geothermal heat. Emitters contributing to emission-reducing projects offsite should still receive credits for these reductions, even if their own emissions are not directly decreased. This approach encourages investments in emissions reductions wherever they can be most effectively achieved, promoting national solutions over localized ones, and recognizing contributions to broader emissions reduction goals.

The Federal Government should establish a comprehensive framework that would accommodate geothermal energy Carbon Contracts for Difference (CCFD). Although some individual CCFD deals have been signed with specific companies in other industries (Department of Finance Canada, 2023), there is no broad framework in place. CCFDs guarantee the future price of carbon, offering financial stability for geothermal energy investments. Without a robust CCFD framework, the future of large-scale geothermal projects could be jeopardized if political support wanes after the upcoming federal election. Establishing this framework would provide certainty and encourage sustained investment in geothermal projects, securing their role in Canada's clean energy future.

1.4 Geothermal Exploration Risk Mitigation Drilling Fund

Heat customers with existing assets who are interested in switching to geothermal heat face significant financial and technical risks in making the transition. Developers aiming to sell electricity also confront drilling risks and the potential challenges of not finding quality resources at economic costs or lacking sufficient capital to develop resources that are cooler or more difficult to access. A risk mitigation insurance program, where unsuccessful projects are compensated and successful ones pay back premiums to the program, would minimize risks for both the government and the private sector. This government-backed initiative would encourage private sector participation by providing a safety net for developers, reducing the financial risks associated with geothermal projects.

A revolving risk mitigation drilling fund would be immensely beneficial for the geothermal industry. Access to this fund would likely be competitive, with bids evaluated based on project feasibility and potential impact. Initial funding allotments would be awarded to kick-start projects, with subsequent disbursements provided on a milestone basis. This phased approach ensures that funds are allocated efficiently, and projects are monitored for progress and viability.

Successful developers would repay the investment, effectively recycling the funds back into the program. Conversely, unsuccessful developers would be forgiven and have no obligation to repay, thereby minimizing financial risks for both developers and the government. Thus, the program provides grants (forgiven loans) as well as loans that are eventually repaid. This model ensures that successful projects offset the costs of unsuccessful ones, maintaining a balanced and effective risk management strategy, and ensuring the sustainability of the fund and continuous support for new projects.

Key features of the proposed risk mitigation program:

- Projects would compete for initial funding based on their feasibility and potential impact.
- Initial allotments to start projects, with subsequent disbursements contingent on meeting specific milestones.
- Successful developers repay the loans, recycling funds back into the program for future projects.
- Unsuccessful developers are forgiven, reducing financial risks for all parties involved.
- The program supports all geothermal technologies, both for electricity generation and direct-use heat applications, excluding ground source heat pumps.

This structured and balanced approach to risk mitigation and funding would significantly reduce the barriers to entry for geothermal projects. The program could also be replicated and proposed at the provincial level.

2. Alberta

Alberta represents a virtually new frontier for geothermal energy development with significant market and moderate resource potential. Hydrothermal resources are immediately accessible for relatively low-risk development with already existing and mature technologies, not necessarily for power generation, but more readily for direct-use, which will in turn access and collect critical data from deep aquifers, de-risking them for later electricity generation.

With more than 600,000 oil and gas wells already drilled in Alberta, we have enough data to determine that approximately 4,000 of them may be geothermally interesting (CanGEA, 2023). Critical to achieving the emissions reduction and energy resilience goals of Alberta, is the utilization of every readily available energy resource. It is geothermal heat that is readily and immediately available, and this heat happens to be baseload, abundant, renewable, and low-emitting.

With a world class energy sector and professionals to match, tapping into and commercializing geothermal resources in Alberta could come to fruition rapidly with the right strategy, investments, and policy developments.

2.1 Fiscal: Industrial Fuel-switching to Direct-use of Geothermal Heat Demonstration Projects

There is a great fit between the heat demand of Alberta's industries (large final emitters) and Alberta's geothermal potential to supply— a few projects are already in the early stages of

development, such as the Canfor Geothermal Wood Kilns Project near Whitecourt and the Latitude 53 Project near Hinton. The development of our geothermal energy resources for direct-use of heat could reduce emissions by about ⅔ in our heavy industry sectors, or 18.9 MT/year (Borealis Geothermal, 2023). In addition, land impacts are extremely minimal and do not disrupt natural water cycles or ecosystems. The ideal geothermal temperatures needed to satisfy the demand for heat in industrial processes such as food processing, pulp and paper manufacturing, vegetable dehydration, dairy and sugar processing, aquaculture, and greenhouses etc. exist in Alberta. Processes such as these cannot be fully or efficiently electrified, thus renewable thermal energy is the only way to sustainably decarbonize these energy intensive essential industries. Crucially, many of these operations are already proximate to accessible geothermal resources. There is an additional economic opportunity to harness the cascading or waste geothermal heat from these industrial customers to feed into municipalities for district heating.

To stress the efficiency of direct-use, the direct transfer of geothermal heat avoids the inefficiencies and energy losses associated with generating and transmitting electricity and then converting electricity into heat. Furthermore, geothermal resources maintain a nearly constant temperature throughout the year, providing a reliable and stable heat supply that is not subject to weather variations nor requires combustion. Geothermal installations are also characterized by their long operational lifespan, typically ranging from 25 to 50 years, with minimal degradation in performance. Finally, maintenance and operational costs are low – virtually unmatched in the subsurface energy industry.

Critical to the rapid development and commercialization of geothermal direct-use is the existing technical and drilling expertise, infrastructure, and supply chains that exist in Alberta's world class energy workforce. These jobs are highly transferrable to the geothermal industry and would require little-to-no retraining. More broadly speaking, a developed geothermal industry could create tens of thousands of jobs including temporary and construction jobs (Borealis Geothermal, 2023). Additionally, it would protect 73,000 existing heavy industry jobs that may be threatened by federal emissions reduction strategies (Borealis Geothermal, 2023).

Although the risk of accessing the geothermal resource is low, potential industrial customers of direct-use (large final emitters) are wary of the risks associated with retrofitting/replacing their combustion systems with geothermal energy systems. Heat customers with existing assets that are interested in switching to geothermal heat have to somehow justify the financial and technical risks of making the switch. A risk mitigation insurance program where unsuccessful projects are compensated, and successful ones pay back premiums to the program would minimize risk for both the government and the public sector. The private sector would also be emboldened by government sponsorship of the initiative.

2.2 Fiscal: Geothermal Incentive Program

Following the establishment of the foundation of the industry with direct-use pioneer projects, to further catch the eye of investors, fruition of a 12% geothermal incentive program akin to the

Alberta Petrochemicals Incentive Program and the Alberta Carbon Capture Incentive Program, as directed in the mandate letter to the Energy and Minerals Minister to catalyze the industry will rapidly scale the industry to the next level of maturity. Broadened eligibility to include geothermal-hydrocarbon co-production would partially compensate for the omission of such projects from the Federal Clean Technology ITC.

2.3 Fiscal: Expanded Scope of the Alberta Drilling Accelerator (ADA) to Include Subsurface Data Collection

The ADA represents a massive public policy win and opportunity for the geothermal industry, given that the "geothermal component" of the accelerator has been given priority order. However, the current focus of the ADA is to advance and accelerate drilling technology, as per the geothermal policy mandate from the Alberta Emissions Reduction and Energy Development Plan. As a result, the scope of the project includes only limited reservoir testing (e.g. wireline logging to determine the lithology, fluid and porosity of the strata from the base of the surface casing to total well depth, as mandated by the regulations); completions are not considered as part of the initiative.

After the geothermal drilling component, later stages of the ADA would assess the integration of other drilling techniques for industries such as CCUS, helium, and rare earth minerals. In Alberta, these emerging industries are generally interested in targeting a similar pore space – deep basal sediments in the Western Canada Sedimentary Basin. Unfortunately, there is a dearth of information associated with these deep basal sediments because most information of Alberta's subsurface comes from decades of data collected from oil and gas reservoirs that are found in shallower formations. Further understanding of the characteristics of these poorly tested reservoirs would be extremely helpful for advancing emerging subsurface industries, including geothermal.

While advances in drilling are important components for accelerating the aforementioned industries, there is an opportunity to leverage the ADA initiative and include funding support for reservoir testing. Drilling through the basal sediments could test both basal sediments and the basement itself, collecting critical data for emerging subsurface industries in the province, including geothermal. It is in the interest of the geothermal industry to socialize this opportunity with stakeholders, the public, and the Governments of Canada and Alberta, to ensure that the ADA is fully leveraged and expanded to catalyze evolving subsurface industries within the province.

The reservoir testing aspect of the ADA could include:

- Core samples and permeability/porosity measurements.
- Drill Stem Tests (DST), H_2S measurements, water samples.
- Wireline logs (including standard gamma ray, resistivity, sonic, and neutron/density logs as well as detailed temperature measurements).
- Injection/production tests (when possible).
- Diagnostic Fracture Injection Test (DFIT) to determine formation pressure, permeability, and fracture closure pressure.

To get the most value out of the data collected during the testing program it is imperative that locations of high geothermal/lithium/helium/CCUS potential are targeted as test drilling locations

by the ADA. Furthermore, the selected drilling contractor must be equipped to properly execute the testing program.

2.4 Regulatory: Surface Access Rights

The Surface Rights Act allows oil and gas developers to appeal to access land in cases where developers and landowners cannot reach an agreement. Section 2.3 of AER Directive 089 expressly excludes geothermal from the same right-of-entry mechanisms under the Surface Rights Act. Given that most geothermal development is likely to occur on private land, this creates a significant barrier to geothermal resource development, as landowners can simply refuse access and geothermal has no recourse, presenting complexities, costs, and risks for geothermal developers and investors that do not exist in other provinces—namely BC and Saskatchewan which do provide equitable surface access rights to geothermal.

In Alberta, there exists political sensitivities with respect to landowner rights; as such, a reasonable compromise to protect landowners may entail a public interest test by restricting geothermal surface rights to locations that matter—aligning with provincial objectives to responsibly develop resources and cut red tape. For a geothermal project to be eligible for surface access, criteria may be set such as a minimum emissions reduction threshold, job creation and retention, and demonstration of good faith efforts to fairly compensate and negotiate with landowners.

2.5 Regulatory: Urban Drilling in the Presence of sour gas (H_2S)

In collaboration with the private sector, regulator, and the relevant ministries, it is critical we find a safe regulatory solution to enable geothermal drilling in the presence of sour gas (H_2S) near communities. Current H_2S regulations (Directive 56) require drilling to be distant from population centres. This might not be a problem for hydrocarbons, but for geothermal, it makes sense to be near the heat customer. There are also other rules pertaining to rigs, drilling mud, backup equipment, and training that may be unnecessarily stringent for our industry. The actual hazard presented by drilling through H_2S reservoirs, on the way to sweet geothermal reservoirs, has largely been managed without incident for decades now. This necessitates changing the regulations to reflect geothermal drilling and production.

2.6 Regulatory: Exclusive Rights to Pore Space

Pertaining to pore space hierarchy, it is critical that where geothermal and other subsurface rights coexist, geothermal projects are ensured to commence first with exclusive pore space rights, to access the resource before it is sterilized by other subsurface developments. This will significantly increase investor confidence in geothermal projects.

2.7 Regulatory: Electricity Market Reform

Alberta is known for its longstanding energy-only market, in which electricity generators are only paid for the power they provide to the market. As a longer-term objective to scale up the electricity market share of geothermal sources by assuring developers of a profitable price for geothermal electricity that is well worth the risk, it would be necessary to make common sense reforms to the Alberta electricity market.

In response to rising strains on the grid, Alberta's Premier has been calling for the need for reliable sources of baseload power, openly criticizing the unreliability of Alberta's intermittent renewable resources. In late 2023, a grid alert came in the wake of a "deep freeze," in which increased demand took most of the blame for the shortage. A later alert on April 5, 2024, cannot be blamed solely on increased demand, rather, intermittent resources were generating at very low capacities and many gas generators were not running that morning (Doering, 2024). It has also become increasingly discussed that providers may be shutting down generation to inflate and manipulate the price. Perhaps an overhaul of Alberta's energy market is past due.

The government has touted its commitment to *"protecting Alberta's grid and ensuring our province continues to generate reliable baseload power both now and in the future."* It is becoming increasingly apparent that market measures are needed to lay the groundwork for the public and private sectors to work together to unleash baseload geothermal megawatts onto Alberta's grid. Such measures may be a capacity market that pays for both energy and the baseload capacity (availability) of geothermal, as AESO recommended in a 2016 report. Another option would be for Alberta to encourage geothermal power by creating a public utility that pays a premium for baseload dispatchable power, similar to a first-of-its-kind Clean Transition Tariff (CTT) that Google and a Nevada public utility introduced to enable private sector giant customers to pay a higher rate for clean baseload power.

2.8 Regulatory: Update Directive 060 to Mandate the Utilization of Geothermal Waste Heat

Alberta's AER Directive 060: *Upstream Petroleum Industry Flaring, Incinerating, and Venting* provides guidelines and requirements for the flaring, incinerating, and venting of gas in Alberta's upstream petroleum industry. The directive requires industry to harness flare gas, implementing practices to reduce flaring and venting volumes through conservation, utilization, and minimizing gas releases. Operators must monitor flaring, incinerating, and venting activities and report data to the AER, enabling effective oversight and enforcement of regulations. An additional provision of the directive to mandate the utilization of geothermal waste heat from oil and gas operations could be developed.

Co-produced wastewater from oil and gas operations is sometimes hot enough to be used for power generation in binary geothermal power plants. If able to be produced, this electricity can be used to decarbonize the oil and gas operation and/or provide clean energy to the grid. More significantly, co-produced wastewater from oil and gas operations is nearly always hot enough for direct-use heating. In theory, co-produced water with temperatures as low as 40°C could be used to economically heat a greenhouse. District energy systems used for space heating and commercial activities are viable options for communities and entrepreneurs in the areas surrounding oil and gas operations.

Many oil and gas wells may produce approximately less than 10% hydrocarbons and greater than 90% water –co-produced (Kemp, 2014). Co-produced water, at a minimum temperature and volumetric threshold, should be mandated to be used for economic and environmental benefit in much the same way that the AER Directive 060 has mandated the utilization of flare gas. A co-produced water analogue to AER Directive 060 would result in the maximization of the utility of the drilled well and the associated land disturbance. Furthermore, the implementation of a co-produced water analogue to AER Directive 060 will reduce the costs and risks associated with geothermal energy development by using already existing infrastructure such as roads, well pads,

and electrical connections, thereby encouraging the growth of Alberta's nascent geothermal industry.

3. British Columbia

The Province of British Columbia boasts some of the highest quality geothermal resources available in Canada. British Columbia has the resource, market, and political conditions to follow the pathway to geothermal development set by states such as California, as there are notable parallels. Although GHG reduction policies set by the BC government are encouraging the search for clean power sources, permitting red tape, regulatory disparities, and lack of up-front targeted capital, are inhibiting the initial takeoff of geothermal energy projects within the province.

3.1 Fiscal: Tax Incentives

Parity with existing mining tax credits.

The BC Government has established the 20% Mining Flow-Through Share (MFTS) tax credit, and a 20-30% the B.C. Mining Exploration Tax Credit (METC), to encourage investment in critical resources. Eligible expenses may include prospecting, geological surveys, and drilling. Given BC's clean electricity and GHG reduction goals, a similar Geothermal Energy Tax Credit for electricity generation and direct-use would be in line with provincial objectives.

Carbon Tax Credits for Direct-use Geothermal Investments.

To build out the foundations of the geothermal industry, it is logical to go after the low hanging fruit—namely hydrothermal resources for direct-use applications—and tailor initial incentive policies around this opportunity. Geoscience BC's 2016 report titled *Direct-Use Geothermal Resources in British Columbia* featured a tax incentive proposal called the Carbon Tax Credits for Direct-Use Geothermal Investments. Incentivizing the use of geothermal would equate to reduced electricity and natural gas demand, which is exactly what the province is looking for.

3.2 Fiscal: Funding Parity

Carve-out for geothermal energy in the Clean BC Industry Fund.

Currently, as standalone greenfield projects, geothermal energy projects do not fall under any eligibility stream of CleanBC funding, unless a geothermal developer partners with a large emitter. An additional stream to fund greenfield clean energy projects, including geothermal, would enable fuel-switching away from emitting fuels, thus contributing to the goals and purpose of CleanBC programs. For example, geothermally heated greenhouse projects, whether new projects or retrofit projects, should be included as an eligible project type under the CleanBC Building Innovation (CBBI) Fund. Also, a geothermal portfolio standard could be paired with the Fund whereby a portion of funding would be dedicated to a minimum threshold of geothermal heat as the carbon offset mechanism.

Direct public investments into geothermal district heating.

BC has recently announced an investment of up to $151 million toward the Federal Oil to Heat Pump Affordability (OHPA) program. Additionally, The CleanBC Better Homes program provides incentives for homeowners to install a heat pump for cooling and air filtration.

Geothermal heat can also be used directly to heat and cool municipal districts even more efficiently than heat pumps or natural gas, and thus should receive equivalent public investment or eligibility under existing heat pump funding streams. District heating systems could also provide the infrastructure needed to hook up geothermal stoves – which could be paired or consolidated with the existing Community Wood Smoke Reduction Program.

3.3 Regulatory: Encouraging Geothermal Offset Projects

The Fuel Switch Offset Protocol (FSOP) in British Columbia, established in 2018, enables offset projects that reduce emissions through energy conservation, energy efficiency, and switching to lower-carbon fuels. The FSOP is currently under review to assess its alignment with the Greenhouse Gas Industrial Reporting and Control Act (GGIRCA) and ensure it continues to deliver real, quantifiable, verifiable, permanent, and incremental emissions reductions. Given the potential of geothermal energy to significantly reduce greenhouse gas emissions, it is an opportune time to advocate for its inclusion and consideration in the revised FSOP, to ensure that geothermal development is encouraged as an offset project option for developers and emitters seeking to meet GHG reduction mandates. Additionally, consideration and flexibility of geothermal as offset projects in connection to BC's developing new Output-based Pricing System and Net-zero New Industry policies would be helpful to raise awareness of the geothermal opportunity in connection with these various GHG reduction policies and initiatives in BC.

3.4 Regulatory: Reconsider Geothermal Well Classifications

Currently, the Geothermal Resources Act serves to regulate all activities associated with the exploration for and production of geothermal resources above 80 °C. While the Geothermal Resources Act lends itself well to regulating Hot Sedimentary Aquifers (HSA) geothermal resources, it is not optimized to regulate the development of fault controlled geothermal resources that require exploration – the vast proportion of BC's geothermal resource portfolio. Geothermal well classifications should be reconsidered under the Geothermal Resources Act. In particular, the BC Government should reconsider the creation of a well classification for 'Thermal Gradient Wells' for fault-controlled resources under the Geothermal Resources Act, built to the standards of Geotechnical Wells licensed under the Water Sustainability Act.

3.5 Regulatory: Exempt Waste Heat from BCUC Regulation

We recommend that heat as a by-product <u>not</u> be regulated by the BC Utilities Commission and/or be granted an exemption from regulation. As illustrated in Figure 2, below, an individual geothermal energy application often uses only a portion of the available energy. As such, a portion of the energy remains and can be used in other applications (i.e. cascading energy use) such as greenhousing, aquaculture and crop drying. It is this by-product heat, also known as 'waste heat,' that should not be regulated. This recommendation would increase investor confidence and aligns with one of BC's clean energy objectives, "to reduce waste by encouraging the use of waste heat," as stated in the Clean Energy Act.

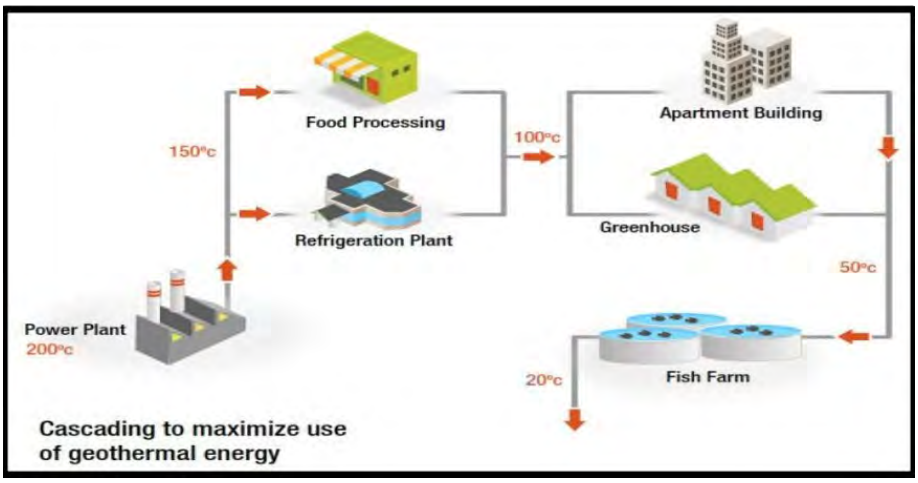

Figure 1: An example of cascaded energy use

3.6 Regulatory: Streamlined Geothermal Permitting

There are a series of measures that could be observed to smooth out the geothermal permitting process in BC.

1. Increasing the number of available geothermal permits to encourage more players to enter the market, sparking competition and innovation. BC is falling behind Alberta in this regard, as BC has only issued one permit to Alberta's 32 in the same time period, as measured by the Canadian Geothermal Energy Association (CanGEA).
2. A redesigned and simplified geothermal-specific permit application portal. Currently, geothermal developers have to apply through a non-tailored application management system, which is arduous and unintuitive. The portal could be redeveloped to be more user-friendly and tailored to the unique needs and characteristics of geothermal energy projects, as Alberta has done, making it less time-consuming and more cost-effective for new and existing geothermal energy providers.
3. That BC budget greater resources to the Energy Policy and Regulation Branch to enable increased staff to accelerate geothermal permit and lease processing.

<u>Cost Recovery</u>

In the United States, proposed federal permitting reform legislation has been complemented with cost-recovery provisions, namely in H.B. 7422 and S. 4753 In the United States, legislative cost recovery provisions would authorize the Bureau of Land Management to charge developers for the cost of streamlined permit processing to ensure the agency possesses the staffing resources needed to complete reviews.

In BC, the equivalent agency is the BC Energy Regulator (BCER), and we likewise propose a compromise of a balanced legislative package to streamline permit processing inclusive of a cost recovery provision to bolster the staffing capabilities of the Regulator. Staff who process geothermal applications should have a minimum technical knowledge of the industry necessary to understand the nuances and risks (or lack thereof) of an application. It may also be necessary for

the Regulator to create or reform training materials necessary to bolster staff knowledge of geothermal energy and streamline application processing.

We would like to see cost recovery as a temporary measure until both the Regulator and applicants have established a repeatable process with clear expectations and consistently streamlined outcomes. The key to any cost recovery is the determination of what is a reasonable cost. For instance, lawyers splitting hairs for the sake of it may be great for their billable hours but may not be fully recoverable or efficient. In other instances, it may be advisable for the Regulator to bring in consultants from developer companies. These personnel may advise on regulatory design – but not on specific project approvals—to avoid a conflict of interest.

Cost-recovery could also be launched in Alberta to likewise bolster the permitting capacity of the Alberta Energy Regulator.

3.7 Regulatory: A Geothermal-Procurement Standard

When Regulators identify new technologies, or generation sources that will improve service quality, e.g., improvements of reliability and cleanliness, the Regulator can order utilities to acquire certain types of energy or install certain technologies (BCUC, 2019). BC Hydro is already directed to seek out approximately 3,000 GWh/year of additional clean energy as early as late fall 2028 (BC Hydro, 2024). Although it would be unreasonable to mandate a public utility to purchase geothermal power from generators that is not yet available, setting a minimum standard or goal for geothermal power acquisition as part of BC Hydro's Integrated Resource Plan would compel the BCER to accelerate permit approvals and the Minister to create incentives for energy developers to add geothermal projects to their portfolios.

3.8 Regulatory: Periodic Legislated Reviews of Geothermal-related Legislation

From the perspective of members of the Canadian Geothermal Energy Association (CanGEA), there are series of potential legislative reforms in the BC Geothermal Resources Act that would improve the development landscape for geothermal energy projects, either for direct-use or power generation. Furthermore, as the industry develops, qualms and issues which have not yet arisen are nearly certain to arise. It is critical that legislation be flexible to the needs of the evolving industry. For example, BC's Environmental Assessment Act (EAA) requires a mandatory review and industry stakeholder engagement every four years. It would be in the interest of the geothermal industry that the Geothermal Resources Act (and Alberta's Geothermal Resource Development Act) also be subject to periodic mandatory review and industry consultation.

A few areas for potential review in the BC EAA are outlined below:

<u>Timeline Certainty:</u>

Currently, it is unclear when developers can expect a decision to be made on their permit applications. Timeline certainty is needed to reduce cost, risk, and investor uncertainty in geothermal projects in the province of BC. Lack of deadlines for the BC Energy Regulator (BCER) to finalize assessments represents a gap in the Geothermal Resources Act.

Decision Appeals:

Section 5(1) of the Act states, *"The minister may issue or refuse to issue a permit, whether or not the requirements of this Act have been complied with, and the refusal is final."* CanGEA proposes that an appeal mechanism instead be put in place, which represents a protection of public rights and interest.

Grounds for Refusal:

Section 12(1) states, *"Subject to the regulations, the regulator may issue, subject to conditions, restrictions and stipulations considered necessary or desirable, or may refuse to issue, a well authorization."* It would reduce uncertainty for industry and investors for the Legislator and/or Regulator to clarify grounds and criteria for refusing a well authorization.

Conclusion

Geothermal energy holds immense potential for transforming Canada's energy landscape, providing a stable, renewable, and low-emission source of power and heat. However, the industry has faced significant challenges due to policy gaps and lack of targeted support. By addressing these challenges through strategic policy and legislative reforms at both federal and provincial levels, Canada can unlock the full potential of its geothermal resources.

Federally, introducing clear frameworks for carbon offset projects, enhancing tax credits, and establishing supportive market mechanisms such as Carbon Contracts for Difference (CCFD) can provide the necessary financial stability and incentives for geothermal development. Additionally, a risk mitigation drilling fund would reduce the financial and technical risks for developers, encouraging more investments in geothermal projects.

In Alberta, the opportunity lies in leveraging existing resources and expertise to develop direct-use geothermal heat projects. Fiscal incentives, such as a dedicated geothermal incentive program and demonstration projects, can stimulate initial development. Regulatory reforms, including granting surface access rights and addressing urban drilling regulations, are essential to create a favourable environment for geothermal exploration and production.

British Columbia, with its high-quality geothermal resources, requires targeted fiscal incentives and funding parity to attract investments. Regulatory adjustments, such as encouraging geothermal offset projects, reconsidering well classifications, and streamlining the permitting process, can remove barriers and accelerate the deployment of geothermal technologies.

REFERENCES

AESO. "Alberta's Wholesale Electricity Market Transition Recommendation." 2016.

BC Energy, Mines and Low Carbon Innovation. "Expanded Heat Pump Program Helps British Columbians Save on Home-Energy Costs." 2014. https://news.gov.bc.ca/releases/2024EMLI0023-000739.

BC Environment and Climate Change Strategy. "Greenhouse Gas Industrial Reporting and Control Act Bulletin 028." 2023. https://www2.gov.bc.ca/assets/gov/environment/climate-change/ind/reporting-emissions/2023/ggirca-bulletin-028.pdf.

BC Hydro. "2024 Call for Power." 2024. https://www.bchydro.com/work-with-us/selling-clean-energy/2024-call-for-power.html?utm_source=direct&utm_medium=redirect&utm_content=2024callforpower

BCUC. "British Columbia Utilities Commission – Indigenous Utilities Regulation Inquiry – Project No. 1598998 Scott Hempling – Utility Regulation Report" 2019. https://docs.bcuc.com/documents/proceedings/2019/doc_54078_a-8-hempling-utility-regulation-report.pdf

Borealis Geothermal. "HOT Portfolio." 2023.

Canadian Gas Association. "CGA By the Numbers: The Renewable Natural Gas Opportunity in Federal Buildings." 2021. https://www.cga.ca/wp-content/uploads/2021/09/CGA-By-the-Numbers_The-Renewable-Natural-Gas-Opportunity-in-Federal-Buildings-1.pdf.

Canadian Geothermal Energy Association. "Geothermal Energy: The Renewable and Cost-Effective Alternative to Site C." 2014, pp. 6-7, 26.

Canadian Geothermal Energy Association. "Greening of Federal Buildings through Geothermal Heat." 2021.

Canadian Geothermal Energy Association. "British Columbia Budget Consultation 2021 Submission." 2020. https://www.leg.bc.ca/content/CommitteeDocuments/41st-parliament/5th-session/fgs/submissions/1036-11250.pdf.

Coso Operating Company. "Project Information." Retrieved in 2024. https://cosoenergy.com/who-we-are/.

Department of Finance Canada. "Budget 2024: Fairness for Every Generation." 2024. https://budget.canada.ca/2024/home-accueil-en.html.

Department of Finance Canada. "Deputy Prime Minister Welcomes the Canada Growth Fund's First Carbon Contract for Difference." 2023. https://www.canada.ca/en/department-finance/news/2023/12/deputy-prime-minister-welcomes-the-canada-growth-funds-first-carbon-contract-for-difference.html.

Department of Finance Canada. "Fall Economic Statement 2022." 2022. https://www.budget.canada.ca/fes-eea/2022/report-rapport/FES-EEA-2022-en.pdf.

Doering, Jason. "Apr 5, 2024 Alberta Supply Shortfall Event – The Facts." 2024. https://jasondoering.substack.com/p/apr-5-2024-alberta-supply-shortfall.

Efficiency Canada. "Advancing Mandatory Building Performance Standards in Canada: A Call for Federal Leadership." 2024, p. 5. https://www.efficiencycanada.org/wp-content/uploads/2024/01/Advancing-Mandatory-Building-Performance-Standards-in-Canada-%E2%80%94-Policy-Brief.pdf.

Emissions Reduction Alberta. "Geothermal Lumber Drying Kilns." Accessed 2024. https://www.eralberta.ca/projects/details/geothermal-lumber-drying-kilns/.

Geoscience BC. "Direct-Use Geothermal Resources in British Columbia." 2016. https://cdn.geosciencebc.com/project_data/GBCReport2016-07/GBC%20Report2016-07_SectionA_Summary.pdf.

Government of Alberta. "Making Alberta a Geothermal Energy Leader." 2024. https://www.alberta.ca/release.cfm?xID=90261DBAEA3AF-CE21-DFF5-D6DD88B135AD45E2.

Government of BC, King's Printer. "Clean Energy Act." Accessed 2024. https://www.bclaws.gov.bc.ca/civix/document/id/complete/statreg/10022_01.

Government of Canada. "T2 Corporation – Income Tax Guide – Chapter 7: Page 8 of the T2 Return." Accessed June 2024. https://www.canada.ca/en/revenue-agency/services/forms-publications/publications/t4012/t2-corporation-income-tax-guide-chapter-7-page-8-t2-return.html#P3284_246737.

Kemp, John. "Water is the Biggest Output of U.S. Oil and Gas Wells." Reuters, 2014. https://www.reuters.com/article/idUSKCN0J223O/.

Killoran, Maureen, Duncanson, Sander, Sutherland, Sean, and Noga, Brodie. "Supreme Court of Canada Finds the Federal Impact Assessment Act Unconstitutional." 2023. Osler. https://www.osler.com/en/insights/updates/supreme-court-of-canada-finds-the-federal-impact-assessment-act-unconstitutional/#:~:.

Parliament of Canada. "C-59: An Act to Implement Certain Provisions of the Fall Economic Statement Tabled in Parliament on November 21, 2023 and Certain Provisions of the Budget Tabled in Parliament on March 28, 2023." 2023. https://www.parl.ca/LegisInfo/en/bill/44-1/C-59.

Province of Alberta. Alberta King's Printer. "Surface Rights Act." Accessed 2024. https://kings-printer.alberta.ca/1266.cfm?page=S24.cfm&leg_type=Acts&isbncln=9780779847662.

Sightline Climate. "Google’s New Tariff for Clean Firm Power." 2024. https://www.ctvc.co/googles-new-tariff-for-clean-firm-power-201/?ref=ctvc-by-sightline-climate-newsletter.

Smith, Danielle. Office of the Premier. "Mandate Letter - Energy and Minerals." 2023. https://open.alberta.ca/dataset/bf7f9a42-a807-49b3-8ba3-451ae3bc2d2f/resource/c87b60b4-217e-4d60-98be-1bbd2f538353/download/em-mandate-letter-energy-and-minerals.pdf.

Smith, Danielle. 2024. https://x.com/ABDanielleSmith/status/1776283193408409659

Ormat Technical Career Path Development and Implementation

Simon Webbison, Robin Zuza, John Murphy, Charles Triola, John Akerley, Adam Johnson, Josh Nordquist, Brent Proulx, Bryan Ott, Kelly Blake, Fikri Dermawan, Brian Canning and Ben Fry

Ormat Technologies Inc, Reno NV, USA

Keywords

Ormat, Technical Career Path

ABSTRACT

Ormat Technologies Inc (Ormat) has recently developed and deployed a geothermal-specific Technical Career Path, covering the roles of Geology, Geophysics, Geochemistry, Reservoir Engineering, Reservoir Modeling and Drilling Engineering.

This paper will discuss the: development process, considerations and challenges that went into the Technical Career Path, the deployment process, key learnings, and, future considerations. Twelve categories were developed and new job titles determined, and the requirements of each will be shared in full in this paper to enable other organizations to benefit from this work.

1. Introduction

Ormat has one of the largest geothermal resource teams globally with over forty scientists and engineers. This paper discusses the development and deployment of a Technical Career Path for the resource team. Benefits of a department-specific Technical Career Path includes attracting talent, encouraging professional development, boosting job satisfaction, strengthening competitive advantage, and supporting succession planning. All these benefits have the benefit of improving the geothermal industry's ability to attract and maintain a strong technical workforce. It was determined to publish a paper on this process to assist other organizations in implementation of a Technical Career Path, and to assist with standardization of job titles within the industry.

2. Development of a Technical Career Path

At Ormat, prior to commencing the development of a Technical Career Path existing titles used (but not limited to) included: Chief Discipline (e.g. Chief Geologist), Principal Discipline (e.g. Principal Reservoir Engineer), Senior Discipline (e.g. Senior Geologist), Staff Discipline (e.g.

Staff Geophysicist), Discipline (e.g. Geochemist), with Staff Discipline and Discipline interchangeable depending on the technical function.

The Technical Career Path was initially developed to cover the main Geothermal Resource technical disciplines of Geology, Geophysics, Geochemistry, Reservoir Engineering, Reservoir Modeling and Drilling Engineering.

The following sections discuss the development process of the Technical Career Path.

2.1 Initial Feedback

The idea to improve the promotion process and implement a technical career path came after increasing feedback channels between management and the technical staff. Feedback channels included monthly 1-on-1's with feedback forms and anonymous surveys. Key items that came out of feedback from both 1-on-1's and a team engagement survey were:

- There was a desire to have a Technical Career promotion process
- There was a lack of clarity on the way that people are promoted, with perceptions that those closest to management were preferentially treated or those that pushed hard for themselves
- There was a lack of clarity on titles, in particular what does "Staff" mean and "Resource Engineer", and what is the relevancy of job titles to associated industries (mining, oil and gas)
- That promotion and performance needs to be linked to all the key areas in the technical career path
- The singularity of the Chief title is perceived to cap an individual's possible development
- There was a lack of clarity regarding roles/responsibilities for particular titles (i.e. expectations and accountabilities)
- Technical authorities (higher level technical roles) haven't had clear sign-off or decision-making delegation of authority.
- The expectation of coaching/mentoring between experience levels was unclear and not aligned.
- Higher level technical roles haven't been expected to help improve systems
- There was a lack of incentives or motivation to align technical roles with business objectives specifically around driving excellence or advancing workflows
- Overall we need to formalize expectations

Key items that came from feedback acquired through collaboration with other geothermal operators or professionals associated with previous major geothermal operators:

- Any technical career path needs to be specific enough to enable development planning, but not specific that it limits or achieves the wrong overall outcomes
- There is a need to prevent box-ticking that goes against the intention of wholesome development of individuals
- Recommended incentivization of specialization for individuals that delivers good team outcomes. For example, filling capability gaps within the team and not having everyone specialize in one space

- We need to ensure consistency across assessments for promotion, which is best done as a panel of technical managers to prevent inconsistencies across the team or misinterpretations
- It is important to give feedback to individuals out of assessments to give guidance for where there needs to be continued development
- Managers need to ensure they don't set expectations of promotions, to prevent false-hope and to prevent undermining the technical career assessment panel
- Ahead of getting to Senior, it is recommended to consider 3 levels to acknowledge the required progression. Having two levels prior to senior can result in a feeling of stagnation early in ones career
- Implementing a career path should be paired with a positive team-culture to prevent hierarchy becoming an issue within the group and getting in the way of collaboration and team outcomes
- There is a need to ensure collaboration, team building, coaching/coachability etc. are part of the technical career path
- Wherever possible align the technical career path with established company processes, such as training and technical career processes, however care needs to be made to ensure company processes do not work against the intent of technical development

2.2 Forward Progress

A selected group (the "foundation group") was assigned to determine a path forward to develop a Technical Career Path based on collected feedback. This group included all the functional managers and group managers across the technical disciplines of Geology, Geophysics, Geochemistry, Reservoir Engineering, Reservoir Modeling and Drilling Engineering, as well as representation from Human Resources.

Key items to determine for the group were:

- Working out how to consult with the wider team and when feedback would be sought, and how to both act on, and close-out, that feedback
- Determining the Categories/Areas that we wished to define parameters within a career path
- Determining the number of levels in the Technical Career Path
- Determining the titles that go with each level in the Technical Career Path
- Working out how and who to consult within upper management across these disciplines and Human Resources.

2.3 Development of Categories

Evaluation of other Technical Career Paths that were shared from within the geothermal industry and from associated industries, such as oil and gas, resulted in the following categories to create a comprehensive and balanced career path.

A general concept was established early that technical development alone is insufficient to capture all elements required for career development and career advancement and that other areas needed to be measured. These included 'soft-skills' and the recognition of the impact that soft-skills have on career growth, personal development, team culture, and business impacts. The resulting categories are shown in Table 1.

Table 1: Categories with specific Breakdowns for the Technical Career Path

Categories	Breakdown areas
Behaviors	• Level of Initiative & Latitude • Problem Solving • Elevating Culture
Technical	• Breadth of Knowledge • Depth of Knowledge (core competencies) • Accuracy & Relevant Application
Interpersonal Skills	• Leadership • Coaching, Mentoring & Training • Communication
Impacts	• Sphere of Influence • Business Alignment & Relevancy • Systems & Processes

2.5 Development of Levels and High-Level Measures

By being a global company it was noted that there are variabilities across some countries (whereby some cultures value a title change itself very importantly) and that some smaller start-up type companies have less issues with providing title changes (less system-impact concerns). There were concerns that to customize a system for one country that it could cause issues elsewhere that we needed to be considerate of. As the majority of our technical staffing is based in the United States of America, it was determined that the framework should be structured primarily for this market and made to have slight adjustments to factor in cultural considerations for our technical team in Indonesia.

Factoring in feedback, it was determined we would have three levels prior to Senior with a purpose of enabling development steps and measuring progress at a reasonable timeframe. This was the primary driver, however a consideration was made to prevent risk of overt hierarchy and that perhaps the external facing title would stay similar.

As part of the determination of the levels, the foundation group worked to develop simplified high-level measures which are noted in Table 2.

Consideration was made if there was a need to have either one or two levels above Senior, and in the end it was determined to have two. This was for two reasons:

1) There were already Principal and Chief titles within the organization, thereby to some level there was already establishment of two levels above Senior
2) Feedback from other companies felt that if there is only one level above Senior, then the obtaining of Senior may be challenging and perception related to other companies or industries that the granting of the title will be late. This increased the risk of staff turnover if this was to occur.

Table 2: Levels of the Technical Career Path with simplified High-Level Measures

Level	High Level Measures
7	• *Industry title level of Chief, Head, Advisor or Senior Advisor etc* • Regarded as absolute industry-leader across broader geothermal and discipline • Significant track record of mentoring, training, adding significant business value, guiding business strategy
6	• *Industry title level of Principal* • Limited routine project work, or significantly reduced levels. Major focus on mentoring, processes, reviewing etc, and special projects • Regarded industry-wide, internal technical leadership group
5	• *Industry title level of Senior* • Can lead a joint-venture or acquisition process from a technical perspective factoring in business and cultural considerations • Mentoring others consistently occurring, wide-ranging influence in business • Fully developed capability across all core disciplines
4	• Sphere of influence increasing • Within company regarded for specialization within a core competency of the discipline, continued advancements of all core competencies and broader knowledge across all disciplines
3	• Technical knowledge and ability across all core competencies has developed, broadening knowledge across all associated disciplines • Given projects to be primary on without extensive oversight
2	• Entry level for roles from University (or early career), even with Masters or PhD, extensive mentoring and direction provided • Developing core competencies, developing broad knowledge across all disciplines
1	• Entry level for fixed-term internships

It was important to also note internships, which at this stage have not been factored into the matrix to-date as it is relatively self-explanatory.

2.5 Development of Titles

Titles were initially proposed as per Table 3, which was to use the existing titles wherever possible and to try a new title in place of Chief to remove the association with this being a singular title.

One of the existing titles within Ormat was the title of Staff (e.g. “Staff Geologist”) which was beneath the Senior title and was used for some technical disciplines and not others. Within associated industries and within Ormat, the title of Staff had different feelings associated with it. In some cases, it sat beneath a straight discipline title, and sometimes it sat above Senior. Therefore, it was noted that the title of Staff was confusing in-particular when advertising for recruitment purposes. A more appropriate title was proposed, and this was the title of “Project”. This was felt to be more relevant, as we have numerous operational and exploration projects.

In consultation on moving the title from Chief to Advisor, it became apparent that the title of Advisor has a connotation with sitting outside a team to a certain level and that this role isn’t so much within the workflows and only provides advice. Therefore, the existing title of Chief was retained and there was a re-definition that the title is not intended to limit to one individual per discipline. As a part of the implementation, a promotion was made within one of the disciplines that resulted in the appointment of a second Chief which further reinforced the lack of singularity. It should be noted that not every discipline has a Chief, and that the integrity of the Technical Career Path matrix takes precedence over desires of titles through guiding and informing progression within the framework.

Table 3: Connection of Technical Career Path Levels with the Titles

Level	Titles as Initially Consulted	Titles Implemented
7	Advisor	Chief
6	Principal	Principal
5	Senior	Senior
4	Staff II	Project II (external facing - “Project”)
3	Staff I	Project I (external facing - “Project”)
2	Discipline	Discipline
1	Intern	Intern

One of the other items that was changed was that all “Resource Engineers” had a job title to “Reservoir Engineer” to align with external companies and associated industries. It was felt that this change would increase the relevancy of job advertisements and the likelihood of getting suitable candidates.

2.6 Development of Matrix

A matrix was developed that is in the Tables and Pages that follow this section. Key components of the development of this matrix were:

- The matrix was initially put together by one member of the foundation group and then there were multiple sessions to review this by the whole group, whereby the initial member didn’t participate in the initial review. This was to get alignment and ownership by the rest of the group and to enable a meaningful review.
- That there needed to be a continuum and evolution through the levels. For example, under “Level of Initiative & Latitude” was going from received direct guidance, detailed review

and supervision (Discipline) through to having significant autonomy to ensure the team and company is a world leader in its work and outcomes (Chief). This is consistent with good people management approaches around Autonomy as covered in Pink (2009).

- There was a need to balance the level specificity with broad outcomes to prevent box-ticking activities whereby people chase a promotion and not necessarily the development itself.
- At the Discipline and Project levels there is a general focus on: investing in your own development; achieving positive results; showing improvements and closing gaps; and, aligning behaviors with expectations.
- At the Senior, Principal and Chief levels there is a general focus on: investing in other team members development and growth; supporting achievement of the company's goals; growing standards and ways of working; and, being a role model for behaviors to all team members.
- It was acknowledged that improvements would be made to the matrix over time after each promotion review round factoring in feedback from the review group.

		Level - Title					
	Category	**2 - Discipline**	**3 – Project I**	**4 – Project II**	**5 - Senior**	**6 - Principal**	**7 - Chief**
Behaviors	Level of Initiative & Latitude	- Receives guidance and detailed review on many aspects of work - Requires mentoring and supervision of work products - Ensures completion of work assignments consistent with basic knowledge - Initiates routine procedures and seeks out mentors as needed for progress	- Receives moderate guidance from mentor(s) and peers - Capable of being the Project lead and will proactively check in with technical mentor(s) - Proceeds on own initiative or judgement with occasional supplementary coaching and progress reviews	- Complete assignments based on general objectives - Proactively proceeds on work with complete ownership - Responsibilities requires high dependability for being on-top of all elements of work and delivering work outputs, without follow-up being required - Utilizes resources, stakeholders, and technical mentors appropriately and proactively	- Demonstrates consistency in providing information and data - Ensures team and direct management are well informed - Deliverables include strong and accurate technical recommendations - Takes the initiative to organize technical work for appropriate distribution to all stakeholders	- Consistently proactive, with a high level of initiative to independently determine work objectives for self and team - Focuses effort of self and team for accuracy of impact	- Autonomy to ensure the team and Company is a world leader in its work and outcomes
	Problem Solving	- Capable of supporting others with working through problems - Can provide and process data/information that supports the team or objective	- Capable of defining problem statement and putting together a proposed method to approach problem - Able to identify resources required and their availability and actively seeks these resources as-required	- Capable of complex problem solving - Demonstrates creativity in managing problems to reach a solution	- Robust in using first principal approaches when problem solving - Utilizes both internal and external resources as appropriate - Introduces external best-practices based on industry knowledge and standards	- Guides wider team(s) to correct problem solving approaches and tools - Conducts problem solving for highly complex problems with high-impact - Develops solutions to problems where few precedents exist	- Track record of problem solving with high-impact across the Company
	Elevating Culture	- Maintains a learning mindset - Able to give and receive feedback in a constructive manner - Must be a consistent collaborative member of their team - Contributes to harmonious team culture	- Actively participates and contributes to team discussions - Develops and engages in understanding international cultures that facilitates teamwork and partnership - Cultivates a positive team environment in all situations - Actively interested in others work and how their work affects others	- Is consistently highly proactive - Delivers outcomes and results consistently	- Maintains team standards and consistently provides timely, specific and constructive feedback to others - Leads conversations within team settings, no matter the composition of the team - Supports onboarding new staff - Celebrates success and provides appropriate recognition	- Complete awareness of team-wide work activity and culture - Comes in at the right time and level with an appropriate style for the situation - Sets and maintains high team standards	- Presence on staff is highly-regarded industry-wide and is favorable for recruitment of employees

		Level - Title					
	Category	**2 - Discipline**	**3 – Project I**	**4 – Project II**	**5 - Senior**	**6 - Principal**	**7 - Chief**
Technical	Breadth of Knowledge	- Learning company ways and fundamentals of the industry - Training in the use and application of basic principles, techniques, and tools as assigned - Developing proficiency with appropriate software applications, computing tools, and other tools associated with the role - Clearly understands the role & responsibility of others and their importance to add value and achieve company objectives	- Maintains and expands technical knowledge through practical application - Able to compile, organize, and interpret data - Familiarity with Project management frameworks (e.g. PMI – PMBOK) - Clear understanding of roles and responsibilities and interface with business partners and stakeholders	- Capable of being relied upon as part of any due diligence activities within their technical area - Broad knowledge of all associated disciplines - Has conducted basic project management training and now possess a high familiarity with Project frameworks and operates seamlessly within this framework	- In-depth knowledge of key components of all associated disciplines - Experience across the full value chain of geothermal (exploration, development, and operations) - Capable of leading a multi-disciplinary team for any due diligence or joint-venture activities - Capable of handling work or assignments that are not part of one's normal work routine - Solid understanding and practice of project management, able to produce PM documentation, e.g., business cases, work programs, project summary presentations and project lookbacks	- Deep understanding of more than one geographic area (with significant working experience) - Functional experience working across multiple geothermal reservoir types - Wide understanding of all geothermal reservoir types and intimate knowledge on how that impacts ones own discipline as well as broad knowledge on impacts on other discipline areas	- In-depth global knowledge of geothermal resources across all geological types - Knowledge of all disciplines associated with Geothermal
	Depth of Knowledge	- Maps out core competencies to address gaps for development and learning plan - Commences taking proactive steps to learn and develop core competencies - Converts data into information under supervision	- Has developed understanding of core competencies and demonstrates ability to operate independently within own discipline, with frequent check-ins and feedback from technical mentors - Clearly understands limitations of current knowledge of core competencies	- Continued development of core competencies - Increased trust and reliance on the delivery of technical work - Has developed specialization of at least one core competency that is regarded as being company and industry leading	- Full development of all core competencies - Able to teach and train core competencies either internally or externally (e.g. to new staff)	- Ensures the correct methodologies are applied for analysis within the team - Creates new tools and methods as required to develop a world class team - Considered industry expert within discipline	- Develops innovative tools and methods to ensure Company deliverables when no other approaches are known
	Accuracy & Relevant Application	- Dependable and uses sound judgement in all activities - Discusses approach in-advance and consistently checks in on it	- Utilizes technical knowledge to achieve measurable and relevant outcomes	- Delivers quality work and high throughput - Recognizes and captures uncertainty and risk in work	- Successfully leads work activities that are multi-disciplinary in nature - Applies knowledge that results in meaningful value to the Company	- Consistently demonstrates results with innovative application of knowledge, resulting in exceptional value to the Company	- Recognized internally & externally for ensuring analysis or problem solving is always conducted with world-leading approach

		Level - Title					
	Category	**2 - Discipline**	**3 – Project I**	**4 – Project II**	**5 - Senior**	**6 - Principal**	**7 - Chief**
Interpersonal Skills	Leadership	- At all times represents the company positively in alignment with company values - Working towards taking on primary roles on projects	- Has responsibility on specific projects as a technical project lead - Organizes and achieves progress on projects that are under their responsibility	- Leads members of other disciplines and departments towards project outcomes - Proactively works with peers to achieve objectives on projects as a team, even if not within own direct responsibility	- Demonstrates leadership in creating new projects and business opportunities - Resolves and manages technical conflict amongst peers - Acts in an ethical manner and delivers a presence of professionalism and role modeling	- Leads major technological advancements with significant added impact - Prioritizes time availability for the benefit of others - Changes approach and style to the situation successfully - Reviews technical work in a timely, appropriate, and proactive manner - Inspires and holds team accountable for technical standards and outcomes - Consistently acts as a leader no matter the setting	- Cultivates relationships and ensures a highly ethical team relationship - Highly respectful relationships in all settings, based on style and track-record - Seen internally and externally as a true leader for their track-record in lifting both the Company and Industry
	Coaching, Mentoring, & Training	- Willingly works with more senior technical peers to receive coaching, mentoring and training - Proactively participates and works through internal training opportunities - Able to give and receive feedback in a constructive manner	- Seen to be significantly improving in all aspects through actively engaging with coaching, mentoring & training.	- Capable of providing formal training in a particular areas of expertise - Recognizes opportunities to train and mentor, and acts upon them - Can oversee interns successfully	- Motivates and develops team utilizing effective training & mentoring - Prioritizes team development and learning over providing the direct answer themselves	- Major focus on targeted & efficient broader team training - Works with management to develop training plans within the team - Trains and develops other stakeholders to achieve business objectives - High awareness of team and individual competencies to identify gaps and to rectify these	- Ultimately provides confidence to upper management that the capability of the team is world-class, through ensuring appropriate coaching, mentoring & training is conducted within the wider team across all competencies
	Communication	- Can prepare technical insights in a suitable communication method - Can prepare and deliver an effective presentation - Asks insightful questions - Correctly utilizes company templates for communication	- Able to provide clear recommendations in a suitable communication method for the audience - Ensures details are correct in any communication method - Can prepare and deliver logical, well-supported presentations to peers, management and immediate stakeholders - Consistently professional in all communication channels - Communicates to the right stakeholders consistently	- Consistently utilizes the right communication channel and approach for the situation in a timely manner to achieve an outcome - Capable of writing conference-level technical papers and reports	- Ability to communicate complex technical matters to general audiences and influence thinking - Reviews others work and provides impactful feedback to improve communication - Ensures transparency through timely and appropriate communication by self and to the team	- Continued development in ability to communicate highly technical matters to appropriate audience - Able to provide board-level communication (e.g. papers and presentations) - Capable of writing journal-level technical papers	- Commands clear communication and presentations to any audience type or level (e.g. general population, board, highly technical forum etc.)

		Level - Title					
	Category	**2 - Discipline**	**3 – Project I**	**4 – Project II**	**5 - Senior**	**6 - Principal**	**7 - Chief**
Impacts	Sphere of influence	- Limited to manager and immediate work group	- Sphere of influence expands to peers in other work groups within technical realm - Acts as a primary point person for projects to other business units (e.g. Business Development or Operations)	- Sphere of influence internally increasing wider to key stakeholders	- Influence extends to industry and relevant professional bodies - Regularly represents the Company at industry or stakeholder meetings	- Regarded highly by industry and professional bodies - Well known and respected by executive management internally with a track record of performance and results	- Known and highly respected by other major geothermal operators - Proven track record that commands respect instantly both internally and externally
	Business alignment & relevancy	- General awareness of business drivers - Basic understanding of economics and financial drivers	- Applies basic economic/risk analysis to projects. Can produce a simple economic analysis - Possess basic knowledge of projects and power plant operations, - Understands the impacts of own work on project schedule, cost and quality - Prioritizes work to align with Company objectives	- Can produce economic calculations - Factors in risk and uncertainty consistently into work conducted - Understands impacts of own discipline to other projects, power plant operations, Business Development, etc; and vice-versa	- Work and projects fully consider risk and uncertainty - Utilizes economic calculations factoring in risk/uncertainty to prioritize work - Driving decisions to optimize project schedule, cost and quality	- Utilizes economic calculations, factoring in risk/uncertainty, to align Company objectives with opportunities identified - Understands how new and evolving technologies impact business unit and Company objectives	- Consistently drives business strategies in the right direction - Consistently drives industry, education organizations, agencies and others towards business objectives
	Systems & processes	- Gains knowledge of business systems & processes	- Uses business systems & processes (including tools) consistently and correctly - Identifies areas for improvement within own business unit's systems & processes	- Drives improvements of systems & processes within own business unit - Ensures engagement to deliver results in a high-quality manner	- Accountable for the use of systems & processes correctly - Technical authority within certain processes (e.g. drilling) that requires accuracy and relevance - Innovates to improve and build tools to improve business systems & processes, with reason and logic - Documents processes & systems clearly in a high-quality manner	- Proactively benchmarks systems & processes used against other geothermal companies and related industries to ensure Company is world-class with foresight to upcoming trends and implications to Company - Takes ownership within group of particular systems & processes and ensures continued relevancy	- Track record of consistent delivery implementing systems & processes that result in meaningful impacts

2.7 Technical Career Path – Promotion Review Process

A promotion review process occurs twice per year. Some key components to note are:

- The technical review group is made up of all the functional managers of the disciplines, even if no nominations have been made for their specific function/discipline
- Observing the process, and ultimately signing off on the outcomes are the Vice President(s) of the two groups: Exploration & Resource Management; Drilling.
- Nominations would be made by managers ahead of the review process
- Nominations can be made by any manager of any individual within the process, to prevent bias against any particular individuals
- An in-person review process is held, and discussion is made on each individual throughout the matrix. Consideration is made for comparisons to others throughout this process to ensure consistency in application. This review process has been found to take at least half a workday of time.
- Active debate is encouraged within the technical review group, as this group is there to balance bias that is overly critical or overly generous. Oversight from the Vice President(s) helps ensure the process is consistent and biases are not in-play.
- There needed to be achievement of all twelve categories of the Technical Career Path Matrix to enable promotion to occur.
- Notes are captured to enable development conversations for those who do not achieve a promotion, and feedback is then provided afterwards to the individual. This is to be fed back into the individuals development plan.

A key learning has been the need to have 6-monthly reviews to prevent bias towards providing a promotion for the lower levels in the Technical Career Path. In addition, one promotion round should be conducted around the company annual review process. Considerations for higher roles such as Senior, Principal and Chief should realistically only be done around the annual review process.

3. Learnings and Future Considerations

As a high-level sign of success, the following year's engagement survey resulted in no comments related to the Technical Career Path, with focus on other items instead. This is considered a success.

Key learnings include:

- It is important to get organizational buy-in to the deployment of a Technical Career Path. As part of this, having the need clearly articulated through something such as an engagement survey assists in achieving buy-in.
- The development, deployment, and on-going utility of a Technical Career Path takes significant effort and drive, and that the easy path is to not do it. There is a balance point whereby the size of the team covered by this makes the effort worthwhile.

- Review processes need to be 6-monthly to prevent bias towards providing a promotion for the lower levels in the Technical Career Path
- Changes to job titles, with the removal of Staff and the implementation of Project has worked well. The movement from Resource Engineer to Reservoir Engineer has also resulted in more relevant applicants during hiring processes.
- Attempting to keep the Project title external facing and to behind the scenes track Project I and Project II has been difficult with issues throughout the HR systems, job descriptions, pay benchmarking etc.
- Updating of job descriptions with inputs from the Technical Career Path is essential to ensure full alignment of expectations for each level.

Future considerations include:

- Improve how to determine when someone is ready for consideration for promotion, i.e. should there be a self-evaluation of readiness, or should nominations only come from management? Ideally we would have some form of 360˚ evaluation.
- Adding specific training requirements, which can be conducted within your organization to the matrix is important. An example is that there has recently been deployment within the company of things such as: the Project Management Institute's project management processes and associated PMP® or CAPM® qualifications; and, the Blanchards SLII® leadership model.
- Not all technical disciplines within the business, such as engineering, have a structure such as this, and there are abilities to widen the scope in a more meaningful company-wide manner.
- A need to align Behaviors and Interpersonal Skills with a company-wide competency model, with provision for learning and training options.
- There is a need to widen the scope of the Technical Career Path for other disciplines, such as technician roles or smaller disciplines such as Artificial Lift.

Acknowledgement

The authors would like to thank all those involved in the process of consultation and deployment of the Technical Career Path, with special thanks internally to Shimon Hatzir, Liza Tavori and Nidia Rivera for their support and sponsorship. Lauren Riemenschnitter was instrumental in enabling this work. Thanks also go to those who were available for industry history of Technical Career Ladders or Paths from other companies, in particular to Bill Cumming, Lutfhie Azwar and Ian Richardson.

REFERENCES

Pink, Daniel H. Drive: (2009) The Surprising Truth About What Motivates Us. Riverhead Books, New York, New York

GeoBridge: Connecting Communities to Geothermal Information and Opportunities

Jon Weers[1], Austin Venhuizen[1], Tara Wertz[1], Faith Smith[1], Elisabet Metcalfe[2] and Sean Porse[2]

[1] National Renewable Energy Laboratory (NREL)

15013 Denver West Parkway

Golden, CO 80401-3305

[2] U.S. Department of Energy (DOE)

1000 Independence Ave. SW

Washington D.C. 20004

Keywords

Geothermal, community, bridge, engagement, resources, information, opportunities, open, access, OpenEI, DOE, NREL, discoverability, usability, accessibility, innovation, connection

ABSTRACT

The geothermal community is well established with long-standing events, organizations, and tools that are known across the geothermal community. But many of these tools and resources are located behind pay walls, require memberships, or are otherwise difficult to find, especially for people looking to join the geothermal community. These barriers to access can prevent outsiders from discovering valuable geothermal resources, limiting the geothermal community's potential for collaboration with other communities, such as clean energy entrepreneurs looking to expand into geothermal energy. The Department of Energy's (DOE) GeoBridge serves to bring these communities together by acting as a single, publicly accessible, searchable portal that facilitates easy access to available geothermal knowledge and information. It works to expand and diversify the pool of geothermal stakeholders by providing in-roads to geothermal information and community resources. It helps build a stronger geothermal community; one inclusive of individuals and groups from a variety of different backgrounds, including potential investors and start-up companies looking to accelerate innovation in geothermal technologies.

By linking communities to geothermal information, analysis and expertise, GeoBridge serves as a launch point, directing interested parties to existing data and tools, events, educational resources,

STEM programs, permitting and regulatory information, and other resources that can be used to evaluate, promote, and discover geothermal opportunities.

1. Introduction

Geothermal technologies such as Enhanced Geothermal Systems (EGS) and Ground Source Heat Pumps (GSHPs) have been gaining national attention over the last several years, boosted in part by high-profile projects like Google's project with Fervo Energy (McDermott 2023). As more people become interested in geothermal, many of them, especially those in professions adjacent to geothermal technologies or in other industries, are finding it challenging to get connected to the resources they need to join the geothermal community.

The National Renewable Energy Laboratory (NREL), working with the Department of Energy (DOE) and an advisory board comprised of geothermal experts from many different segments of the geothermal community, have identified the need for an aggregate information portal to address gaps in information that are making it difficult for some communities to get started in geothermal. A cursory analysis identified 9 user communities facing notable information gaps. In some cases, the information they seek is simply not available, while in others, it is hidden behind membership or pay walls, invisible to search engines, or otherwise undiscoverable.

DOE's GeoBridge facilitates easier access to geothermal knowledge and information by making it universally accessible to all, and by bridging knowledge gaps that exist between the established geothermal community and the 9 user communities identified below. (GeoBridge 2024).

GeoBridge works to expand and diversify the pool of geothermal stakeholders to help build a stronger geothermal community; one inclusive of individuals and groups not traditionally linked to geothermal research and analysis, including potential investors, municipalities interested in geothermal and start-up companies looking to accelerate innovation in geothermal technologies.

2. Origins of GeoBridge

An early example of the need for GeoBridge came from the DOE Geothermal Data Repository (GDR), which provides free, universal access to geothermal data. Each dataset on the GDR has a primary Point of Contact (POC) listed to allow users to ask detailed questions about the data contained with the dataset, such as the conditions and methods used to acquire the data, any assumptions made, or other questions critical to understanding the data. The GDR also has links that allow users to "Contact GDR Help" to ask questions about the GDR platform itself or request technical assistance with data submission (Weers et al 2022). However, recent inquires to both these communication channels have illuminated potential gaps in information that could be making it challenging for outsiders to join the geothermal community. The GDR Help team along with numerous dataset POCs and other geothermal subject matter experts have reported fielding a growing number of questions unrelated to their established communication channels.

GDR Help, for example, has recently been receiving questions such as, *"What colleges or universities should I be considering if I want to have a career in geothermal energy?"* and *"What events should I attend to meet geothermal professionals or learn more about emerging geothermal technologies?"*

While the answers may seem obvious to many, it's important to recognize that the geothermal community is well established with long-standing events that require little-to-no advertisement to garner participation. Events like the Geothermal Rising Conference (GRC) and the Stanford Geothermal Workshop are well known to those already in the community. Their cadence and locations are stable, predictable, and familiar to those that have been before. However, these events and others are not easily discoverable through conventional means, including internet searches. This is but one example of an information gap identified by the GeoBridge team. Additional gaps are listed in *Section 3: Identified Information Gaps*.

2.1 Information Accessibility and Discoverability

It is important to fully recognize and appreciate the likely journey an information seeker has undertaken prior to emailing the GDR Help team. On the road to answers, people asking questions like those above do not start with an email to the GDR Help team. More likely, they begin their journey at a search engine or by asking their question to an Artificially Intelligent (AI) chat bot; in both cases expecting an instant response. Yet, at some point in their search, these information seekers are arriving at the GDR, finding the GDR Help email (located under the Help menu or in the footer of each page), opening an email program, typing their question in an email to an unfamiliar recipient and then awaiting a response. This is not an efficient way to get information in the modern world. Sending an email to GDR Help is often a last resort, the (presumably) final attempt of a desperate information seeker.

The questions above, and many more like them, are indicative of larger gaps in the availability of relevant geothermal information. Whatever the answers may be, we can assume that they are not easily discoverable through conventional means.

2.2 Community Engagement

The GeoBridge team reached out to geothermal subject matter experts across the geothermal community to identify information gaps. Many of the experts had recently fielded similar queries from students, job seekers, startup companies, regulators, utilities and more. The people in these communities were clearly struggling to find answers to their questions and were otherwise unable to engage the geothermal community.

The primary objective of GeoBridge is to bring these communities together to improve diversity in geothermal energy and bridge the gap between established geothermal communities, emerging startups, and the next generation of the geothermal workforce. To fulfill that objective, the GeoBridge team established an Advisory Group consisting of experts and representatives of many different aspects of the geothermal community.

2.2.1 Formation of the GeoBridge Advisory Group

The GeoBridge Advisory Group was formed in early 2024 and contains members from industry, non-profit organizations, universities, DOE, national labs, international associations, installers, state energy offices, and the Women In Geothermal (WING) network. The group is also representative of the many aspects of geothermal technologies, with experts in EGS, GSHPs, direct use, low temp, analysis, policy, and development. The GeoBridge Advisory Group was selected to be representative of the geothermal community at large and tasked with assisting the GeoBridge team with the identification information gaps and the prioritization of efforts to address those gaps.

3. Identified Information Gaps

The following information gaps have been identified and prioritized by the GeoBridge team through conversations with the GeoBridge Advisory Group and interviews with industry professionals, geothermal experts, and other stakeholders. These gaps are organized by community along with examples of their respective needs and described in the sections below:

Section	Community
3.1	**Entrepreneurs** looking to introduce their technology into the geothermal space
3.2	**Professionals** looking to find and build a career in geothermal including work force development and training for the next generation of geothermal workers
3.3	**Homeowners and Businesses** interested in learning how heat pumps can save them money
3.4	**Students** looking for studies programs that will set them up for a career in geothermal
3.5	**Organizations** looking to generate more interest in geothermal projects and job openings
3.6	**Teachers** looking to integrate geothermal learning into their lesson plans
3.7	**Policy Makers** looking to introduce geothermal into their communities and educate their constituents
3.8	**Utilities** looking for guidance on how to incorporate geothermal energy into their future plans
3.9	**Regulators** looking for assistance and best practices for approving and monitoring geothermal systems

Table 1. Identified information gaps organized by communities and their respective needs.

3.1 Entrepreneurs looking to introduce their technology into the geothermal space.

DOE initiatives such as GEODE (DOE GTO 2024) are helping to address technology and knowledge gaps in geothermal through the transfer of technology, expertise, and best practices from the oil and gas industry. Many other efforts already bridge the gap between geothermal and oil and gas, however there are numerous other industries, both established and emerging, with geothermally relevant technologies that are struggling to make a connection. The GDR Help email has received inquiries from startup companies specializing in high temperature electronics, special cements, and advanced sensing technologies such as Distributed Acoustic Sensing (DAS), each looking to expand into geothermal energy, but unsure of who to talk to, what events to attend, or how to get connected with geothermal experts.

3.2 Professionals looking to find and build a career in geothermal

It is difficult for outsiders with geothermal-relevant skills to discover opportunities in the geothermal industry. This is especially relevant to GSHP companies who are struggling to find certified installers and technicians (IGSHPA 2024). Many people aren't aware that their existing skills are applicable to geothermal technologies while others are searching for ways to advance their careers in geothermal. Increasing awareness of training and certification programs can help with workforce development. Additionally, links to prominent geothermal employers and their job boards can provide additional pathways for others to advance their geothermal careers.

3.3 Homeowners and Businesses interested in learning how heat pumps can save them money

Interest in GSHPs has grown considerably in recent months. Searches for GSHP incentive programs, average costs and the feasibility of installation by region have increased by as much as 1,200% in the last two years (Google Trends 2024). However, an in-depth analysis of the search terms used and the resources available indicated that homeowners and businesses alike were failing to find the unbiased information they need to make informed decisions. The GeoBridge team found that members of these communities are often turning to Reddit forums, friends, neighbors, and other unvetted sources to find answers to their questions. Furthermore, incentive programs for GSHPs can be difficult to find as they often toe the line between energy efficiency and green building programs and will appear inconsistently in lists of one or the other depending on region and funding source.

3.4 Students looking for studies programs that will set them up for a career in geothermal

Many of the inquiries received by the GDR Help team were from high school students and undergraduates interested in a career in geothermal, wanting to know which schools are the most involved in the geothermal community and which degree programs are most likely to be valued by hiring organizations.

3.5 Organizations looking to generate more interest in geothermal projects and job openings

Geothermal organizations frequently share their progress, project updates, and job openings during popular geothermal events, but these announcements often do not reach beyond the established geothermal community. GeoBridge is built upon OpenEI's wiki making it easy for others to contribute to topics and provide additional information. Users can leverage this structure to advertise their projects and successes to a broader network and connect with new audiences and communities to help fill open positions.

3.6 Teachers and educators looking to integrate geothermal learning into their lesson plans

Energy education is critical for the adoption and acceptance of new and innovative technologies. However, geothermal is typically only a small piece of renewable energy education. While geothermal energy appears to be easily understood within the confines of a textbook, it is difficult to illustrate in hands-on activities. GeoBridge includes a variety of resources for teachers and educators such as hands-on activities and lesson plans broken down by appropriate grade level, with examples of standards and corresponding materials (e.g., Next Generation Science Standards).

3.7 Policy Makers looking to introduce geothermal into their communities and educate their constituents

Policy makers, including state and local energy offices, are struggling to find the information they need to affect long term changes in their energy grid, including the adoption of geothermal technologies. Even in communities where there is considerable motivation to adopt geothermal technologies, community leaders still need assistance crafting effective policies and regulations, and educating their constituents on the benefits, economics, and potential job opportunities of geothermal technologies.

3.8 Utilities looking for guidance on how to incorporate geothermal energy into their future plans

Utilities interested in geothermal energy are struggling to find the information they need to make informed decisions. They are finding it difficult to sort through the multitude of tools and resources available, to identify information that is current and relevant to their service territories.

3.9 Regulators looking for assistance and best practices for approving geothermal systems

The classification of GSHPs varies from state to state, with some states classifying them as water wells, requiring additional permits and restricting proposed locations. The approval of new geothermal projects in these areas often depends on the limitations of outdated or potentially unrelated regulations, and in some areas can prevent GSHP wells from existing beneath residential structures (Gergely et al 2023). The regulations, best practices and lessons learned from communities with high GSHP adoption rates could help expedite the adoption of geothermal technologies in other areas.

Similarly, as EGS technologies begin to expand to other regions across the country, states less familiar with regulating geothermal technologies are seeking technical assistance and information on regulatory best practices.

4. Bridging the Gaps

GeoBridge is working to bring these communities together by acting as a single, publicly accessible, searchable portal that facilitates easy access to available geothermal knowledge and information.

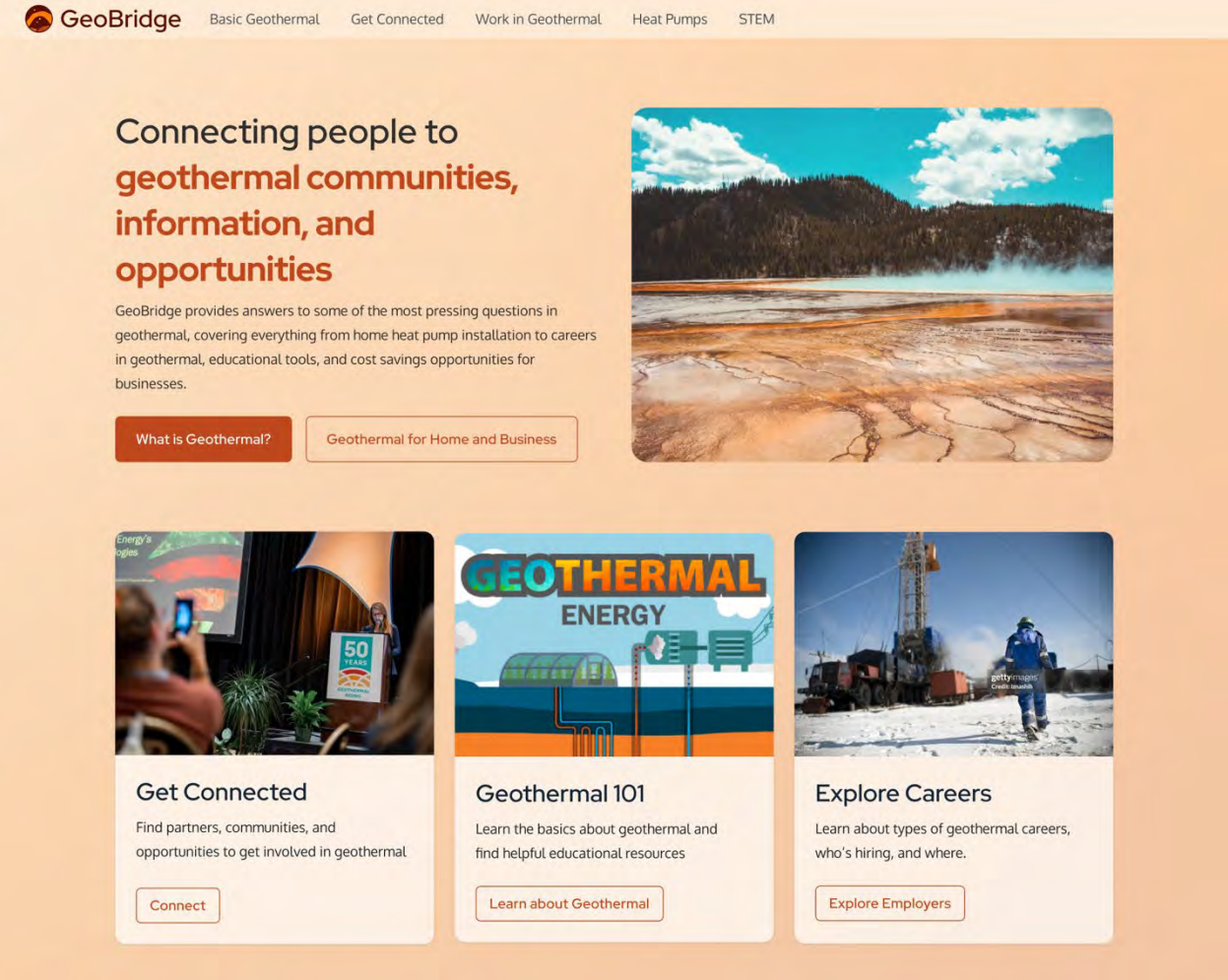

Figure 1 GeoBridge home page and main site navigation.

The GeoBridge site has been organized around the needs of the communities and information gaps identified in Table 1. The collective needs of these communities were clustered into common themes, which formed the basis for the main navigation. Additional pathways to information are featured in tiles on the homepage (Figure 1), which have been designed to align with common questions about geothermal pulled from recent inquiries to the GDR team and an analysis of search terms being used on major search engines.

In addition to the homepage and main navigation, GeoBridge features focus pages tailored to information from each of the common themes identified across the target communities. For example, a page on how to get connected within the geothermal industry (Figure 2) helps entrepreneurs, businesses, students, and aspiring professionals find the events, resources and connections they need. These content pages were prioritized by the GeoBridge team and the Advisory Group based on community engagement and outreach efforts and are designed to maximize the impact of GeoBridge's efforts to bridge the information gaps identified above.

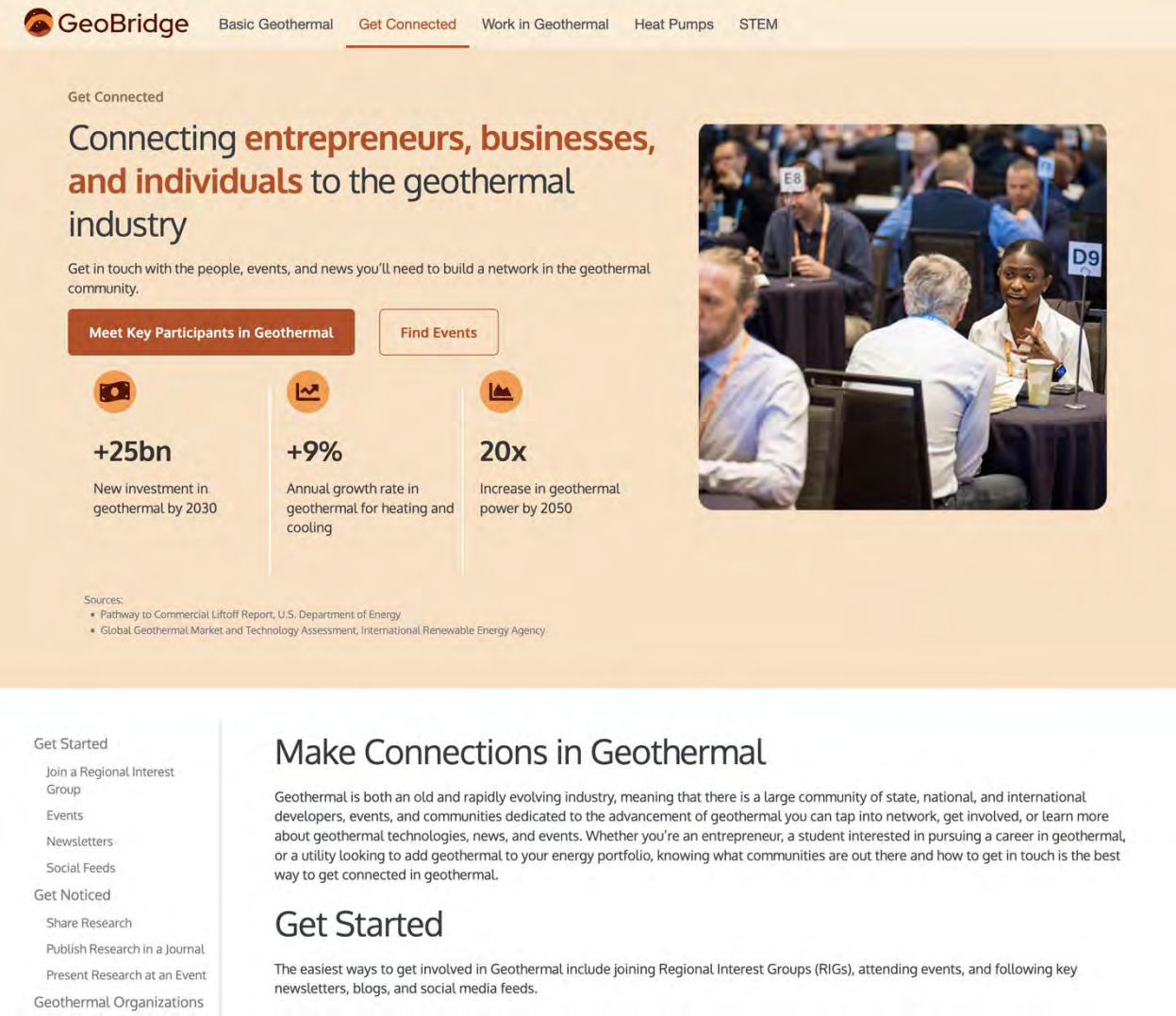

Figure 2 GeoBridge focus page for entrepreneurs, businesses, students, and aspiring professionals looking to make connections in the geothermal industry.

4.1 Content Roadmap

Content development and organization activities included in the initial launch of GeoBridge were outlined in a Content Roadmap developed from the gap analysis and prioritization efforts of the GeoBridge team, DOE, and the Advisory Group. The Content Roadmap also outlines future development efforts planned for Federal Fiscal Year 2025 (FY25), which include providing additional information and resources for:

1) Entrepreneurs looking to accelerate the development of their technologies, seek additional funding, or collaborate on new projects with existing geothermal teams.
2) Homeowners and businesses interested in GSHPs looking for an impartial, reliable source for information on the cost and feasibility of GSHPs in their local area.

3) Professionals seeking careers in geothermal or looking to apply their skills toward geothermal ventures.
4) Students interested in geothermal-relevant graduate programs.
5) Teachers looking for resources and experiences outside of the classroom such as geothermal field trips.
6) Work force development resources and additional information on training and certifications needed to become GSHP installers, technicians, and other supporting trades.

4.2 Built on OpenEI: Open Energy Information

GeoBridge has been developed in the OpenEI wiki, enabling quick and easy content updates and allowing the geothermal community to assist in keeping resources and links up to date. OpenEI uses a Semantic Mediawiki hosted in a secure cloud environment to provide universal access to energy information. Launched in 2009 as part of the White House Open Government Initiative (Brodt-Giles 2009), information on OpenEI is freely available and is accessible online through web browsers and numerous Application Programming Interfaces (APIs), making it a powerful and effective information dissemination engine. It is currently home to over 50,000 content pages and more than a dozen energy-related data and analysis applications.

By leveraging the OpenEI platform, GeoBridge content is easily discovered by search engines and is automatically disseminated to dozens of other sites.

4.3 Avoiding Duplication of Effort

GeoBridge helps users find the information they need without generating duplicative content. In cases where pertinent information already exists online, GeoBridge points to the best sources for that information. For resources with difficult to discover information, such as information behind membership or pay walls, GeoBridge acts as a guide providing users with the additional context needed to access the information they seek.

The GeoBridge team coordinates closely with the GeoBridge Advisory Group, which includes operators of other geothermal information portals, who help ensure that GeoBridge efforts are complimentary to the ongoing and future efforts of other sites. The GeoBridge team is working closely with Geothermal Rising, IGSHPA, and state energy offices to address these gaps across the geothermal information space and to serve the needs of the communities identified above without being duplicative.

5. Conclusion

Users of GeoBridge are able to answer their questions, make connections, and find useful inroads into the established geothermal community through links to existing knowledge hubs, databases, and websites from a variety of sources, including other national labs, energy.gov, Geothermal Rising, the International Geothermal Association (IGA), state and local geothermal hubs, and more.

GeoBridge creates pathways to information not currently available or easily discoverable and makes it easier for outsiders to find information and opportunities within the geothermal industry. It helps to expand and diversify the larger geothermal community by bridging gaps to geothermal

information and community resources. As a result, it helps build a stronger geothermal community; one inclusive of individuals and groups from a variety of different backgrounds, including potential investors, clients interested in geothermal and start-up companies looking to accelerate innovation in geothermal technologies.

Acknowledgements

This work was authored in part by the National Renewable Energy Laboratory (NREL), operated by Alliance for Sustainable Energy, LLC, for the U.S. Department of Energy (DOE) under Contract No. DE-AC36-08GO28308 with funding provided by U.S. Department of Energy Office of Energy Efficiency and Renewable Energy (EERE) Geothermal Technologies Office (GTO). The views expressed in the article do not necessarily represent the views of the DOE or the United States Government. The United States Government retains and the publisher, by accepting the article for publication, acknowledges that the United States Government retains a nonexclusive, paid-up, irrevocable, worldwide license to publish or reproduce the published form of this work, or allow others to do so, for United States Government purposes.

The authors of this paper would like to acknowledge Sandy Lee, Jay Huggins, Hanna Fields, and the rest of the OpenEI team for their work supporting the design, development and underlying architecture of GeoBridge. Additionally, we would like to thank Amanda Kolker for her guidance and expertise.

REFERENCES

Brodt-Giles, D. “Open Energy Information.” White House Open Government Initiative, White House Archives. 20 September 2009. Web. https://obamawhitehouse.archives.gov/open/innovations/OpenEnergyInformation

DOE GTO. “Geothermal Energy from Oil and Gas Demonstrated Engineering (GEODE) Funding Opportunity Quick Guide”. U.S. Department of Energy, Office of Energy Efficiency and Renewable Energy, Geothermal Technologies Office (DOE GTO. 13 June 2024. Web. https://www.energy.gov/eere/geothermal/geothermal-energy-oil-and-gas-demonstrated-engineering-geode-funding-opportunity

GeoBridge. “GeoBridge.” OpenEI: Open Energy Information. National Renewable Energy Laboratory (NREL), 13 June 2024. Web. https://openei.org/wiki/GeoBridge

Gergely, R., Bevacqua, A., Barry, R. C. “New Jersey Ground Source Heat Pump Baseline Report.” New Jersey Department of Environmental Protection, Bureau of Climate Change and Clean Energy. December 2023. Web. https://dep.nj.gov/wp-content/uploads/cleanenergy/new-jersey-ground-source-heat-pump-baseline-report_final.pdf

Google. “Google Trends.” Alphabet, Inc., 15 May 2024. Web. https://trends.google.com/trends/

GTO. “$13 Million in Funding Available for Community Geothermal Heating and Cooling.” Geothermal Technologies Office (GTO), Office of Energy Efficiency & Renewable Energy (EERE), U.S. Department of Energy (DOE). 17 July 2023. Web.

https://www.energy.gov/eere/geothermal/articles/13-million-funding-available-community-geothermal-heating-and-cooling.

IGSHPA. “IGSHPA workforce development plan.” Internation Ground Source Heat Pump Association (IGSHPA). 16 May 2024. Web. https://igshpa.org/wp-content/uploads/Workforce-development-plan-2024-May.pdf

McDermott, J. “New Google geothermal electricity project could be a milestone for clean energy.” Climate, Associated Press, 28 November 2023. Web. https://apnews.com/article/geothermal-energy-heat-renewable-power-climate-5c97f86e62263d3a63d7c92c40f1330d

Weers, J., Anderson, A., and Taverna, N. “The Geothermal Data Repository: Ten Years of Supporting the Geothermal Industry with Open Access to Geothermal Data” *GRC Transactions*, Vol. 46, 2022.

Downhole Logging

Innovative E-line Intervention Solutions for Geothermal Wells

Garry Andrews, Mark Satre

Welltec

Keywords

E-line interventions, wellbore remediation, mechanical interventions, well integrity, wellbore clean-out

ABSTRACT

E-line interventions play a crucial role in maximizing the productivity and lifespan of geothermal wells. Geothermal energy is an important renewable energy source with significant potential for global energy sustainability. However, geothermal wells present various challenges, including scaling, corrosion, and mechanical issues which necessitate periodic interventions to maintain or restore their optimal performance. E-line interventions offer a versatile and efficient method for diagnosing, evaluating, and resolving these issues.

The main E-line intervention categories can be categorized into two main approaches: logging, and mechanical interventions. Logging interventions involve the deployment of various tools to acquire real-time data on well conditions to diagnose and evaluate well performance and assist in decision-making for subsequent interventions. Mechanical interventions, on the other hand, employ e-line conveyed tools to directly address issues in the wellbore such as wellbore clean-out, scale removal, casing repair, pipe recovery, and fishing operations, thus contributing to enhanced well performance and prolonged lifespan. A description of the mechanical intervention solutions will be detailed in the paper with the objective of broadening knowledge of the extensive applications.

1. Introduction

With its ability to provide a constant and reliable energy supply, geothermal energy is increasingly becoming a focal point for energy sustainability initiatives worldwide. However, the operational efficiency and longevity of geothermal wells are often compromised by challenges such as scaling, corrosion, mechanical failures, and reservoir depletion. Addressing these challenges necessitates periodic well interventions.

E-line intervention solutions have emerged as a pivotal technology in maintaining and enhancing the productivity of geothermal wells. By leveraging advanced diagnostic and mechanical intervention tools, e-line technology offers a robust and efficient approach to tackle the myriad of issues that can afflict geothermal wells. This paper delves into the specifics of e-line intervention methodologies, with a particular focus on mechanical interventions, illustrating their applications and benefits in the context of geothermal energy production.

2. E-line Intervention Methodologies

E-line interventions are broadly categorized into two primary methodologies: logging interventions, and mechanical interventions. Each serves a distinct purpose in the maintenance and enhancement of geothermal well performance.

2.1. Logging Interventions

Logging interventions involve the use of various diagnostic tools deployed via an electric line to gather real-time data on well conditions. These tools provide critical insights into the well's performance, enabling operators to make informed decisions about necessary interventions.

Common logging tools include:

- Temperature and Pressure Gauges: Monitor real-time well conditions
- Caliper Logs: Measure the diameter of the wellbore to identify restrictions
- Corrosion Logs: Measure the extent of corrosion in downhole tubulars
- Cement Bond Logs: Assess the quality of cement around the casing
- Flow Meters: Evaluate the flow rate and distribution within the well

2.2. Mechanical Interventions

Mechanical interventions utilize e-line conveyed tools to address and rectify physical issues within the wellbore. These interventions are essential for maintaining the well's structural integrity and operational efficiency. Common mechanical interventions in oil and gas wells that can be applied in the geothermal setting include:

- Wellbore clean-out and scale removal
- Casing repair
- Fishing operations
- Annulus leak repair
- Workover and abandonments

3. Benefits of E-Line Interventions vs Other Intervention Methods

Electric line (E-line) mechanical interventions offer several distinct advantages over coiled tubing and slickline operations in oil and gas wells, and one of the primary benefits is the precision and control afforded by the technology. E-line tools can deliver real-time data and feedback, enabling operators to perform highly accurate and targeted interventions. This real-time capability allows for immediate adjustments and optimization of downhole operations, which can significantly reduce intervention times and enhance overall efficiency. Additionally, E-line interventions are

typically less invasive and produce a smaller footprint from equipment compared to coiled tubing, making them more suitable for operations in constrained or complex environments. Unlike slickline, which lacks the capability to transmit real-time data, E-line can power and communicate with sophisticated downhole tools, enabling a wider range of mechanical tasks such as milling, high-force actuating for fishing or swaging, and tubular punching and cutting with greater precision. Furthermore, the ability to deploy advanced robotic and electric-powered tools on E-line can lead to more effective problem resolution, reduced non-productive time (NPT), and enhanced safety by minimizing the need for heavy mechanical operations. Overall, the versatility, precision, and efficiency of E-line mechanical interventions make them a highly valuable option for maintaining and optimizing well performance.

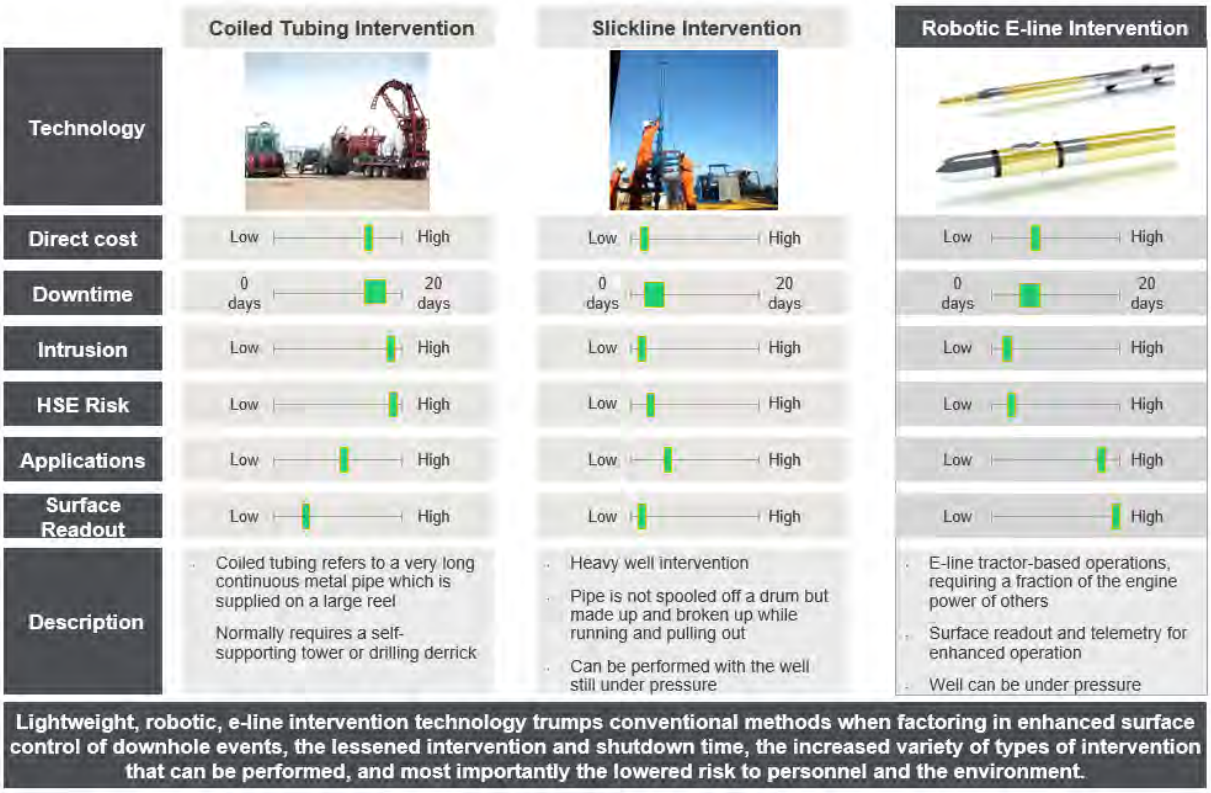

Figure 1: Comparison of coiled tubing, slickline, and e-line intervention methods (ref. SPE-203064-MS)

4. Overview of E-line Bottom Hole Assemblies – Standard BHA

A standard BHA for an e-line mechanical will include the following tools and configurations:

- Cable head with mechanical weakpoint – backup means of releasing from a stuck BHA with fishing neck for later retrieval.
- Surface command release device – primary means of release from a stuck BHA with fishing neck for later retrieval.
    - Multiple surface command release devices can be run in the BHA
- Correlation device – CCL or GR/CCL
- E-line tractor (optional) – for conveyance in deviated or horizontal wells or for providing weight on bit for milling operations.

- Principal objective tools
  - Downhole actuator for fishing or casing repair
  - Suction tool for the removal of loose debris
  - Milling tool for the removal of scale, cement, or consolidated deposits
  - Mechanical, non-explosive cutting and punching tools

Figure 2: Example e-line mechanical intervention BHA showing individual components.

5. Electric Line Mechanical Interventions Solutions

5.1. Wellbore Clean-out

E-line suction tools are highly effective for wellbore clean-out operations in geothermal wells, offering a sophisticated solution for removing debris and obstructions that can impair well performance. These tools are deployed via an electric line, allowing precise placement at the target depth where they create a powerful vacuum to extract loose debris such as sand, and other particulates. The ability to operate efficiently under the high-temperature conditions of geothermal wells makes e-line suction tools particularly advantageous. Real-time data transmission and surface control capabilities enable operators to monitor and adjust the clean-out process dynamically, ensuring thorough debris removal without causing damage to the wellbore. This method not only enhances the efficiency and productivity of geothermal wells but also minimizes downtime and reduces the need for more invasive and costly intervention techniques.

These tools operate by means of downhole electric motor driving a hydraulic pump creating a differential pressure and suction. This suction pulls both the wellbore fluid and debris into bailer sections, with the fluid then passing through filters and back out to the wellbore.

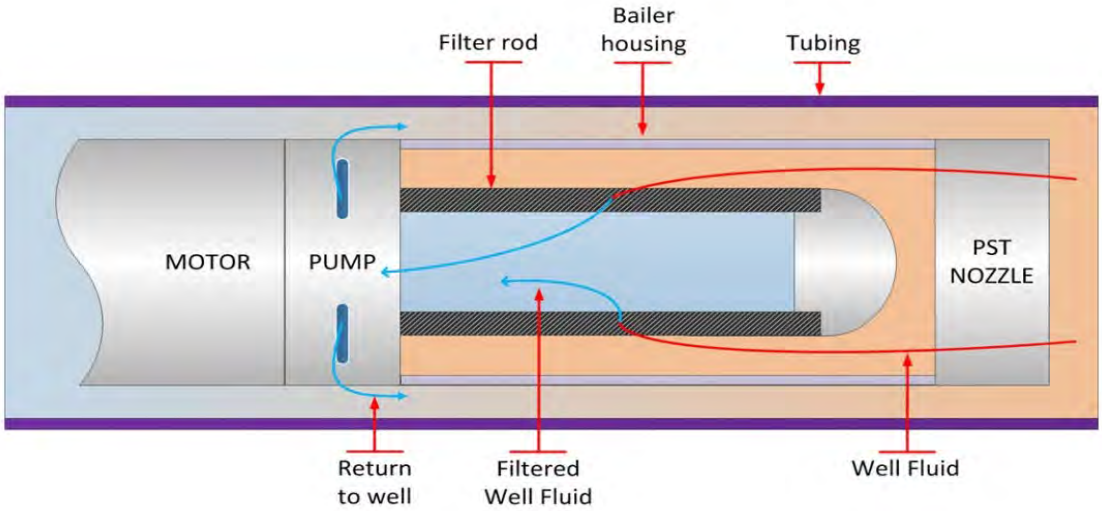

Figure 3: Diagram of e-line suction tool cross section showing fluid and debris paths.

5.1.1. Wellbore Clean-out Capabilities

Several sizes of tools are available for applications in different wellbore sizes with 2.125”, 3.125” and 4.25” outer diameter (OD) tools. These base tool sizes can then be configured with varying ODs of bailers for increased debris recovery e.g. the 3.125” tool can be run with 3.125”, 3.5” or 4” OD bailers. The maximum possible recovery is with the 4.25” tool is 21gal per run when the tool is configured with seven bailers.

5.1.2. Wellbore Clean-out Considerations

As with most of the e-line tools mentioned in this paper, the temperature and pressure limitations are 300°F and 20,000psi. respectively. Some of the solutions mentioned here do have the ability to run in 350°F and 25,000psi.

Expected debris also needs to be taken into consideration ensuring that the correct filters and nozzles are utilized ensuring maximum recovery possible per run. If the debris makeup is unknown, these configurable parts can be changed between runs refining the clean-out approach when a debris sample is collected.

5.1.3. Wellbore clean-out Case Story

An Australian operator wanted to explore options for wireline conveyed sand bailing in one of their offshore platform gas producing wells. The objective was to remove twenty-six meters of sand fill inside the 9.625" production casing, with an internal diameter (ID) of 8.681". Due to the landing nipple at the end of the tubing, the minimum run-in-hole restriction of the production tubing string was 3.987".

To limit the number of clean-out runs, the latest technology in e-line deployed suction tools with a 4.25" OD was chosen, which provided increased recovery volume over its smaller cousins, plus real-time surface control and monitoring. Because of the tool's overall diameter, the landing nipple also required milling to allow access. Therefore, a specially designed 4.412" mill bit was manufactured and run on a milling tool – a tool requiring tractor conveyance to provide weight-on-bit and counter the reactive torque.

As the well had low deviation, the subsequent clean-out toolstring was run standalone (without tractor). One of the key factors governing the feasibility of conducting this operation on e-line was the overall toolstring lengths, where the lubricator height was limited to approximately 16 meters.

The e-line deployed milling technology – which produces a grinding action rather than cutting – successfully milled through the landing nipple and a ball catcher in four runs, thus increasing the ID sufficiently to allow access for the clean-out toolstring. A well fluid column of approximately 7 bar is required to enable operation of the suction tool. The clean-out tool was configured with three bailer sections (seven max) for the first run, to determine sand recovery optimization. Three different sizes of micron bailer filters are provided; prior knowledge of debris particle size is therefore advantageous. In this case, a slickline bailing sand sample had been recovered, which immediately aided filter choice. Seventeen bailing runs were conducted over five days (with the number of bailer sections increased to six), successfully recovering a total of 918 liters of sand,

equating to about 2.4 tons. Ultimately, the process enabled perforation of two additional gas zones to increase production.

The e-line toolstring, consisting of six different sensors and robotic tools, made this a more controllable and inherently safer operation than coiled tubing methods, as well as having a smaller footprint with reduced environmental impact.

5.2. Scale Removal

E-line milling tools are a viable option for addressing the prevalent issue of mineral scale buildup that can obstruct fluid flow and reduce well efficiency in geothermal wells. These tools, deployed via an electric line, allow for precise navigation and positioning at the site of scale deposits. Once in place, the milling tools utilize high strength cutting elements to grind and remove the hardened scale, restoring the wellbore's ID and enhancing fluid conductivity. The E-line deployment provides continuous power and real-time data transmission, enabling operators to closely monitor the milling process and make necessary adjustments to ensure thorough scale removal. By using these advanced tools, operators can significantly improve the operational efficiency and longevity of geothermal wells, minimizing downtime and maintenance costs.

5.2.1. Scale Milling Capabilities

Two options of milling tool are available for the removal of scale: one being tools with milling *only* capability, the other being those with combined milling and suction capability. The milling and suction option can be applied when there is no flow path in the well, with the tool itself creating a fluid circulation for the movement and collection of cuttings. The milling only tool requires either fluid production or bullheading to move the cuttings produced. With both options, a tractor is required to be run above the milling tool to both provide weight on bit and to hold back torque from the rotating head.

The evolution of milling technology has also increased the parameters in which scale can now be milled out to with BHA's allowing up to 8.5" OD milling bits to be deployed on e-line.

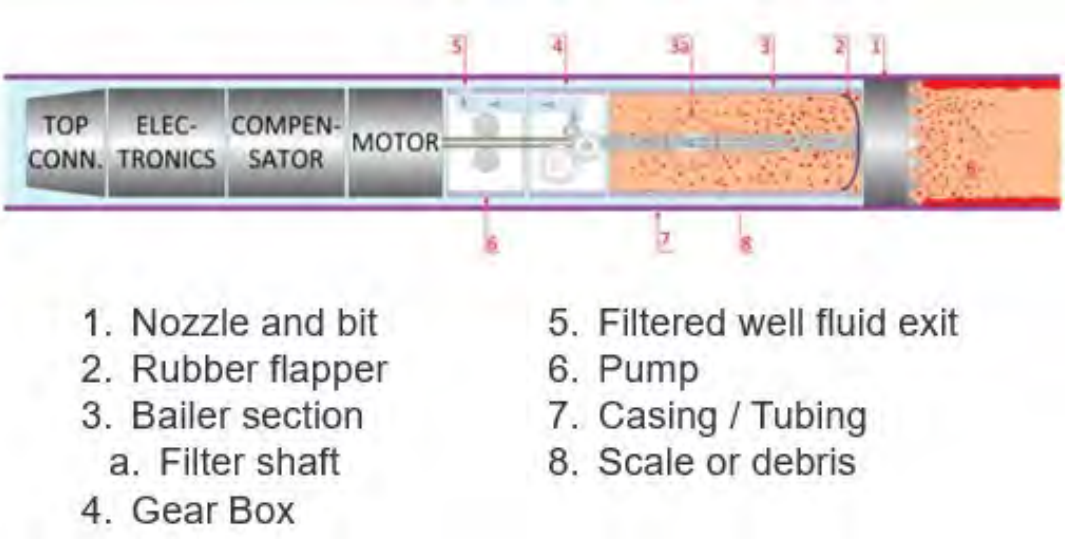

Figure 4: Diagram of e-line milling and suction tool cross section.

5.2.2. Scale Milling Considerations

When planning a scale milling operation, the main considerations to ensure a successful operation are expected scaling interval, expected scaling extent (as to whether the flowpath is fully closed or only restricted) and required (resulting) wellbore ID (dependent on if the original wellbore ID is required or only a sufficient ID for subsequent well operations).

If the scale interval is expected to be long but there is still a flow path, the preferred method is with the milling only tool. In a geothermal application, fluid bullheading is recommended as this will both move the cuttings from the bit face but also quench the well allowing for more favorable operating conditions. The wellbore sump then must be factored in to ensure there is sufficient volume below the milling interval for the cuttings generated. These will be forced to the toe of the well to later be produced or removed via further e-line runs.

5.2.3. Scale Milling Case Story

A dual completion oil producer offshore Malaysia had been having CaCO3 scale buildup problems since it was put on production in 2004. By mid-2008, the scale had accumulated severely in the short string of the well, almost choking oil production. The 3-1/2” x 9.2 lbs/ft tubing internal diameter had been reduced from 2.992” to approximately 1.50” all the way to the end of tubing. Due to the scale, Q oil from the short string had been reduced from an average of 2,000 bbl/day to almost 70 bbl/day.

Mechanical milling of the scale by coiled tubing was not an option due to the limited deck space and crane capacity on the platform. The operator chose milling on electric wireline utilizing a combination of the e-line tractor and miller with a customized 2.70” outer diameter scale milling bit because of a permanent minimum restriction of 2.813” in the well.

During the scale milling operation, the well was being flowed with a choke size of 22/64 equivalent to a flow rate of approximately 120 bbl/day to flow the debris to surface as well as for heat dissipation purpose at the mill bit.

The operation achievements include:

- A total of 5,350 ft CaCO3 scale interval was milled (vertical scrapping and rotational milling)
- Total time from rig up-rig down: 14 hours
- Time savings: approx. 4 days (compared to coiled tubing)
- A path with an internal diameter of 2.70” was obtained
- Increased oil production: 36 bbl/day (Immediate additional gain post scale milling)

The open path enabled further slickline operations such as tubing broaching to scrap remaining scale in the tubing or maintain the open path for the remaining production life of the well followed by changing out the gas lift valve. Q oil is expected to be further increased by another 300 bbl/day after changing out the gas lift valve.

5.3. Casing Repair

E-line mechanical intervention technology is highly effective for performing casing repairs, addressing issues such as deformation and buckling that can compromise well integrity and ultimately production. Using tools like an e-line stroker and swaging tools, these interventions can be precisely deployed to the damaged section of the casing via an electric line, which provides both conveyance and power. The stroker tool applies controlled mechanical forces to realign and stabilize the casing, while the swaging tool presses against the casing walls, reshaping and reinforcing them to restore their structural integrity. This process is monitored in real-time through continuous data transmission, allowing for immediate adjustments to optimize the repair. This approach not only extends the operational life of the well but also minimizes downtime and avoids the need for more invasive and costly repair methods.

Figure 5: Casing swage shown connected to the bottom of an e-line stroker

5.3.1. Casing Repair Capabilities

With the increase in downhole tool capabilities and new e-line stroker tools now being able to push / pull 100klbs (3.5” OD) and 28klbs (2.125” OD), this allows these surface-controlled tools to be applied to more operation types normally the remit of heavier intervention methods like coiled tubing or snubbing. With 100klbs of force available at depth, swaging is now possible via e-line with these operations being considered standard for collapsed or buckled intervals up to 10ft in length. A surface command release device will be run between the stroker and swage as a backup means to release in the vent the swage become stuck.

5.3.2. Casing Repair Considerations

A caliper is always recommended prior to performing a swage operation, to understand the extent and length of collapse. This would then inform planning on the well specific approach when it comes to swage size and swage OD step up per run.

An SIT is always recommended for any tubulars not yet swaged with one of the SIT objectives being to record tool surface readout, force required and planned swage OD approach. These parameters would then be used during the operation as a guide for completing the objective.

5.3.3. Casing Repair Case Story

A US land operator scheduled intervention work on an existing well to retrieve a packer with sand screen assembly. A casing collapse above and below salt formations in three intervals prevented the retrieval of the packer. The 7" 32# P110 casing deformation ranged from 5.67" ID to 5.8" ID, with lengths ranging from 3' to 6' with the packer having a 5.875" OD and 7.6' length. An SIT was performed with the well-specific casing showing the e-line stroker and swage as a viable option to recover casing ID.

An intervention was then planned based on the results of the SIT, with the objective of enlarging the area/s with casing restrictions enough to allow packer retrieval. The e-line stroker with 100klbs force 312 expanded the three restrictions in a single run with a 5.9" OD swage. A subsequent run with caliper data confirmed a baseline ID of 5.85" – 5.9" ID throughout the Charles salt formation section of the well. Swaging was performed in a single day (daylight operations) with the operator ultimately being able to successfully retrieve the packer and return the well to production. The application of e-line mechanical tools also meant the avoidance of a heavier and costlier intervention method, such as coiled tubing.

5.4. Fishing Operations

E-line stroking tools are essential for efficient downhole fishing operations and can be applied to geothermal applications. These tools are conveyed via an electric line and once correlated on depth will use sophisticated mechanical actions, such as surface command gripping and latching combined with high force stroking, up and down, to effectively dislodge and retrieve the stuck or stubborn items. The electric line system provides continuous power and real-time data transmission, allowing operators to monitor the fishing process closely and make real-time adjustments to optimize the operation. These adjustments can be an increase in pulling force or release and relatch mid-run. This capability not only minimizes operational downtime and reduces the risk of further damage to the wellbore but also enhances the overall efficiency and safety of fishing operations. By utilizing these advanced tools, operators can achieve successful fishing interventions, ensuring the continued productivity and longevity of geothermal wells.

Figure 6: Example E-line Fishing BHA with Surface Command Latch Tool and 100klbs Force

5.4.1. Fishing Capabilities

With the ever-increasing force of e-line stroker tools, these e-line options are now becoming the first choice for fishing operations. Downhole forces now available are 28klbs for slimhole, and 100klbs available for larger completions and casing. These forces are bi-directional, controllable from surface and can be stepped up and down in 500lb increments. The surface readout and surface control mean what is happening downhole is being monitored real-time at surface and the approach can be changed on the fly based on what is happening downhole.

The high force tools in combination with surface-controlled latching tools adds another level of capability over conventional fishing methods, where a fishing can be latched and unlatched multiple times in one run. This ability can be used to incrementally increase the latch area allowing for higher overpull.

Whilst the bi-directional stroker tools and surface command latching tools provide the primary and secondary means of release from a fish which cannot be retrieved, a surface command release device can also be included in the string as a tertiary means to recover the e-line BHA to surface.

5.4.2. Fishing Considerations

Surveillance runs should be performed in advance of any fishing run to confirm the fishing neck or fish stickup is clear from any debris or absent of damage. These can take the form of LIB, camera or gauge runs.

E-line specifications should also be planned for to ensure the tensile strength of the cable is sufficient for the recovered fish. Along those same lines, if pressure control equipment is required, the lubricator section should be of sufficient length to both hold the main BHA *and* items retrieved from the wellbore.

5.4.3. Fishing Case Story

A strong offshore oil producer well was shut down after an unsuccessful slickline plug-retrieval operation, which led to the slickline toolstring and isolation plug becoming stuck at a shallow depth. Heavy-duty fishing was performed using electric wireline self-anchoring hydraulic stroking tool. While pulling, 100Klbs of force was applied to free the slickline toolstring from the plug. This paper is written to share the experience gained while planning, preparing, and executing this high-profile job.

After reviewing all available options, it was decided to use the high-capacity version of the electric wireline hydraulic stroking tool, rated to 100,000 lbs. The approach to the job was to retrieve the slickline toolstring either as one piece or break it into parts by applying maximum force and retrieving via multiple runs. After fish retrieval, a further plan was to retrieve the isolation plug using slickline. The preparation phase included a function test at the base with full reconstruction of the well situation to confirm the approach as correct.

The base function test was performed to determine if the high level of force from the electric wireline hydraulic stroking tool would break the slickline toolstring or release it from the plug. For the test, the exact fish components, including the plug, were set up in a horizontal tubing. A long overshot was designed to swallow the jars in the slickline toolstring. It took five upward strokes, up to 100,000 lbs, to release the slickline toolstring from the plug's fishing neck. The ring of the fishing neck sheared from isolation plug.

Following the base function test, equipment was mobilized offshore. The heavy duty overshot was installed on the fish using Slickline. The electric wireline hydraulic stroking tool was then rigged up on, run-in-hole, and latched onto the overshot. After two strokes of up to 100,000 lbs, the slickline toolstring released cleanly from the fishing neck of the plug (similar to the base function test).

The plug was successfully retrieved and the well was brought back onto production. Using the electric wireline hydraulic stroking tool allowed a rigless intervention, in a cost-effective, safe and time-controlled manner.

5.5. Workover and Abandonments

The advent of non-explosive pipe cutting and pipe punching tools has revolutionized e-line mechanical intervention services, particularly in high-risk environments like geothermal wells. These advanced tools provide a safer, more controlled alternative to traditional explosive methods, significantly reducing the risk of accidental detonation and subsequent damage to the wellbore or surrounding formations. By eliminating the need for explosives, non-explosive tools enhance operational safety and simplify logistics, as there are fewer regulatory hurdles and transportation restrictions. Additionally, the precision of non-explosive cutting and punching tools ensures cleaner cuts and more accurate perforations, which are crucial for subsequent intervention tasks such as casing repairs, fluid circulation, and pressure equalization. The ability to deploy these tools via an electric line allows for real-time monitoring and dynamic adjustments, further improving the efficiency and success rate of intervention operations. Overall, the integration of non-explosive technologies in e-line mechanical interventions has led to safer, more efficient, and environmentally friendly well maintenance and repair processes.

5.5.1. Workover and Abandonment Capabilities

The introduction of e-line non-explosive pipe punching and cutting intervention tools allows the operator to have real-time confirmation of a successful cut and/or punch. The e-line cutters with tool ranges from 3.5” to 9 5/8” tubulars produce a beveled cut which does not require subsequent dressing. These cuts can also reliably be performed in compression with no impact on cutting time. Reach of the cutting arms can also be limited to protect tubulars outside of the target pipe.

The e-line non-explosive punchers also provide a real-time confirmation of successful punch, a known flow path area, a limit to the punch depth of penetration and do not leave burrs on the OD of tubing or casing. The current tools available can punch from 2.825” tubing out to 10.75” casing. Punch direction can be oriented to punch on the high side or provide full coverage holes.

The above tools can be combined allowing a one run cut and punch solution, further saving rig time.

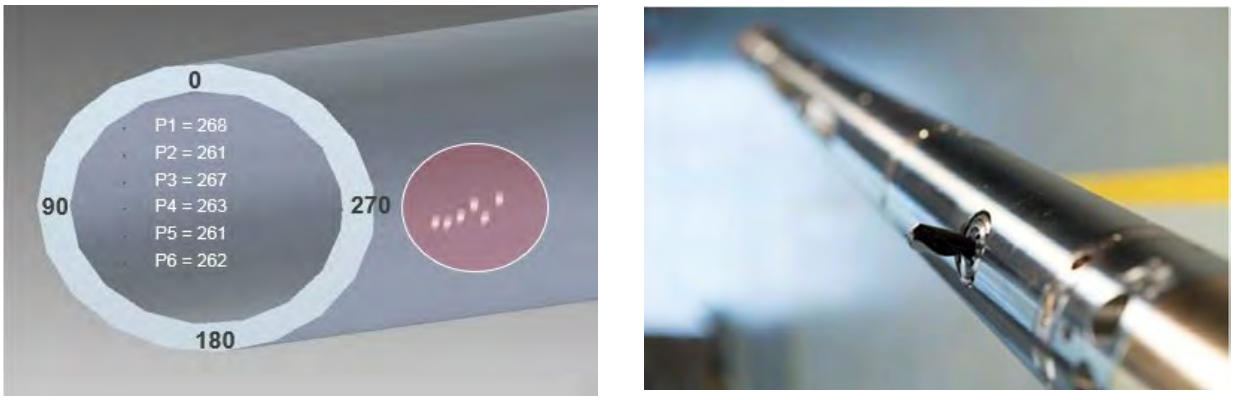

Figure 7: Example of tubing punch operation with the orientation defined for the e-line mechanical puncher.

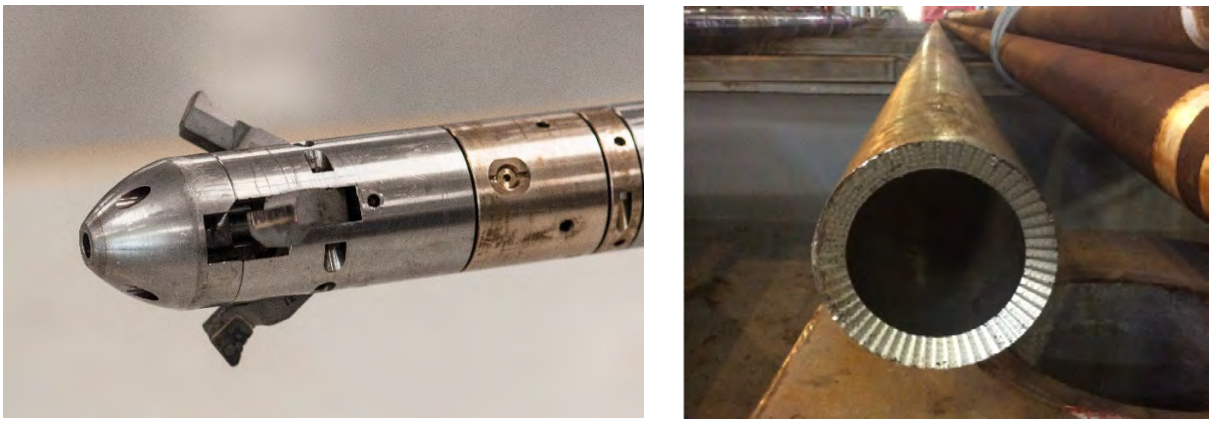

Figure 8: Example of pipe cutting operation showing a clean cut performed in compression on heavy walled tubing.

5.5.2. Workover and Abandonment Considerations

For the utilization of either the e-line mechanical puncher or cutter, there has to be confirmation of previously cutting the tubing or casing. If the target pipe has not been cut or punched, an SIT must be performed to confirm toolstring setup. The surface readout recorded in the SIT will then be utilized in the operation as a guide. Again, for either tool, the limiter for the cutting arm reach, or puncher bit reach, has to be predetermined as this involves the installation of a mechanical stop/no-go.

5.5.3. Workover and Abandonment Case Story

During a subsea remote-operated vehicle survey in a North Sea field, an operator discovered that three wells had leaks in their horizontal Christmas trees. It was therefore imperative to undertake workover interventions to remedy these leaks as soon as possible. The operator evaluated the need for replacing the Christmas trees, as well as the upper completion, in each well. As part of the work scope, it was necessary to punch and cut the 7”, 32 ppf tubing just above the production packer.

The selection criteria for the cutter tool included the following parameters:

- Tool must run on electric line (e-line).
- Tool must be able to cut tubing in compression.
- Tool must not cause damage to the outer casing.
- Tool must leave a clean, beveled edge after the cut, allowing for safer entry in the lower part of the completion on subsequent runs.

The operator found a precision tool that satisfied the above criteria: an electrohydraulic e-line pipe-cutting tool.

Unforeseen challenges emerged, however, when a ballistic puncher was used prior to cutting. The first attempt to punch made by the ballistic puncher failed to achieve fluid circulation. Luckily, the operator also mobilized a recently developed electrohydraulic pipe-punching tool run on e-line as a contingency. This tool can be oriented such that it drills holes sideways, maximizing the potential for successful fluid circulation. The electrohydraulic puncher tool was given a green light. It drilled 16 holes, performing as expected. It was followed by the e-line cutting tool, which made a clean

cut. Thus, all operational objectives were met. The well was recompleted successfully, and two more wells followed.

6. Conclusion

E-line intervention solutions represent a transformative approach to addressing the complex challenges faced by geothermal wells, ensuring their operational efficiency, and extending their productive lifespan. By utilizing proven advanced diagnostic and mechanical intervention tools, e-line technology offers precise, safe, and efficient methods to mitigate issues such as scaling, corrosion, and mechanical failures. This paper has explored the specific methodologies and applications of e-line mechanical interventions, highlighting their significant benefits in maintaining and enhancing geothermal energy production. As the global focus on energy sustainability intensifies, the role of e-line interventions in optimizing geothermal wells will become increasingly crucial, supporting the broader adoption and reliability of geothermal energy as a sustainable power source.

NOMENCLATURE

E-line	-	electric line
BHA	-	bottom hole assembly
NPT	-	non-productive time
OD	-	outer diameter
ID	-	inner diameter
SIT	-	systems integration test
PPF	-	pound per foot

REFERENCES

Timofey Yakovlev, Hani Sagr, and Sultan Al Harthi, Welltec; Fahmi Aulia, Saudi Aramco “Wireline Conveyed Robotic Intervention for Obstruction Cleaning and Sampling in Horizontal Wells Completed with Open Hole – Worldwide First Job Experience” SPE-*203064-MS*

David Field, Welltec “Sand Fill Clean-Out on Wireline Enables Access to Additional Perforation Zones in Gas Well Producer *IPTC-23048-EA*

F.S. Lam and J.P. Collins "Production Enhancement Through E-Line Tractor Technology” - *OSEA2008 111108*

Sudesh Prabhakaran, Mamoun Khogali, Juan Jose Nobile Blanco, Alexander Delos Santos Santos, Chirag Harish Rathod, and Steven Rajesh Sequeira, Welltec Oilfield Services Doha LLC - “World's First Fishing Operation on Wireline, Where 100,000 Lbs of Pull Force Was Applied: A Case Story” *SPE-209043-MS*

M.C. Benguergoura, Welltec, J. Bergem, Aker BP "Precision Surgery for Well Workover: An Innovation in Well Intervention” - *SPE-195635-MS*

inliSAMP, a Modularly Designed Fluid Downhole Sampler for Deep Geothermal Applications - Proof of Concept

Gawan Berentelg, Stefan Dietze and Veit Hagenmeyer

Institute for Applied Computer Science IAI

Karlsruhe Institute of Technology KIT

Keywords

downhole fluid sampler, geothermal borehole logging, in situ temperature and pressure, monitor and record

ABSTRACT

The fluid sampler inliSAMP is being developed for remote controlled downhole sampling in deep geothermal boreholes. inliSAMP is designed based on the system platform for downhole tools hotToolKIT. It is a follow-up development to the inliCAM. Thus, both probes are built up from modular components of the construction kit. A new sampling and storage concept is developed and realized in a functional demonstrator (sampling volume 480 cm^3). The sampling process was tested and proven to work under laboratory conditions up to 90 bars. The demonstrator sampling system is remotely controlled via wireline using real time data. Temperature, pressure in different locations of the sample chamber, and electronic components are permanently monitored and recorded. In the design, most electronic components such as a highly efficient power supply, motor drivers and control units are placed inside a supply probe Dewar flask. The in-situ storage of the monophasic sample is being realized by an adaptive hydraulic and heating control system. The hydraulic components are developed for high dynamic loads and small installation spaces. Furthermore, the functional demonstrator fulfils the requirements of the design standard downhole logging tools (T = 200 °C, p = 60 MPa, harsh and corrosive fluids). Currently, the mechanic units such as the sample chamber, sensors, and hydraulic power pack are mounted on a socket in a demonstrator housing and are tested under realistic conditions on a test rig at the Karlsruhe Institute of Technology (KIT) in preparation for a borehole deployment. The functional tests of the sample procedure include descent of the probe, the sample intake, maintenance of sample temperature, and dispensing at changing ambient temperatures on a test rig. The focus of the research is on temperature monitoring, control, and operation management of in situ downhole sampler. This paper gives an overview over commercially available fluid sampler, the development process, a test rig for fluid samplers, explains the technical details of the complete system and presents the results of the proof of concept and the quality measure of sample temperature and pressure.

1. Introduction

This paper presents a novel fluid sampling concept for remote in-situ downhole sampling, the design of the inliSAMP probe and a proof of concept on a test rig. inliSAMP stands for "in situ live sampler". It is designed for remote-controlled sampling in deep boreholes and was developed at the Karlsruhe Institute of Technology. It is a modular build up tool based on the system platform for downhole tools hotToolKIT (Holbein et al., 2018) and a follow-up development of the video inspection probe inliCAM (in situ live camera). As a conventional downhole sampling probe, inliSAMP is lowered on a wireline in the completed borehole, and it collects a fluid sample from the borehole fluid at formation conditions. The probe stores and maintains the fluid sample nearly in situ conditions until it is transferred to a transport container at the surface.

Providing insights to downhole fluids are a crucial for the evaluation and exploitation of underground resources such hot water, crude oil, CO2 storage, and shale gas (Hsieh et al., 2021). The increasing number of projects in exploitation of geothermal energy from a reservoir or carbon storage injection of supercritical CO2 “require accurate geochemical analyses of formation water and gas samples for chemical characterization and monitoring purposes” (Wolff-Boenisch and Evans, 2014), (Lund et al., 2022), and (Ayliffe, 2022). Merely representative downhole fluid samples provide important information for aqueous chemistry, isotopic composition, and gas characterization analyses as “the physical and chemical properties of geothermal water that is at or close to equilibrium with host rocks in water-dominated reservoirs change from their initial state to the surface sampling condition during the up flow of the fluid along the wellbore” (Akın and Kargı, 2019).

The data of a downhole sample and its dissolved gases are important information for geothermal use, exploitation and research, e.g. the assessment of the operation conditions, the heat transfer and mineral scaling (Hsieh et al., 2021) and (Wolff-Boenisch and Evans, 2014). In application of mineral carbon storage, a representative sample of injection conditions is needed to evaluate the hydro-geochemical pattern and proportions of *CO*2 mineralization of the aquifer (Alfredsson et al., 2016). In another application, "dissolved gas concentrations in groundwater are useful environmental tracers that can be used to determine groundwater residence times, understand geochemical processes, monitor contamination plumes, and identify mineral, oil, and gas reserves" (Eddie W. Banks et al., 2017). Further, in the oil and gas industry, representative formation fluid analyses are essential as precipitates of paraffins and asphaltenes are examined. In groundwater studies, which also detect volatile tracers such as SF6 in samples (Wolff-Boenisch and Evans, 2014).

"The main processes that change the reservoir water chemistry in the wellbore are the boiling of water, degassing of dissolved gases and the consequences of adiabatic cooling and mineral scaling. The combined effects of the increase in dissolved species concentration (boiling), decrease in temperature, rise in pH (degassing) and redistribution of bulk compositions among species (speciation) cause mineral scaling in the wellbore" (Akın and Kargı, 2019). These effects appear due to change in the formation pressure and temperature, as the mineral saturation is further dependent on temperature (Lowenstern et al., 2012). Precipitation occurs in the sample chamber with at alterations of its environmental conditions such as pH, temperature, and pressure changes (Wolff-Boenisch and Evans, 2014).

Obtaining a representative water sample, means to preserve technically the physical conditions of the downhole reservoir in the water sample, ongoing the time the sample is collected, during transport out of the borehole until it is transferred to a transport container at the surface.

Well sampling techniques distinguish between downhole (in-situ) and uphole (ex-situ) sampling. Today, available commercial downhole samplers and specific field-tested samplers are lowered to the target depth in the borehole. A positive displacement sampler (PDS) are systems, which is described in (Wolff-Boenisch and Evans, 2014) and still state of the art, for example the Single-Phase Reservoir Sampler of Schlumberger (Schlumberger, 2020). Other in situ technologies as vacuum and flow through samplers are here not considered, as they have no pressurization of the collected sample (Conaway et al., 2016). A PDS consists in principle of a housing with cable head connected to a wireline, a sample chamber and a time-controlled valve. It works with a prefilled pressurized displacement fluid that first exerts a piston on the closure and second, when a timer sets the valve open, it controls a slow displacement while existing differential pressure to the formation. A pressurized gas such as Nitrogen can be used to keep in the sample above reservoir pressure, while cooled from outside down during uplift and transportation. "Deployment of a PDS or keeping the well over pressurised can produce a single-phase fluid, which requires the sample extraction line to be operated under overpressure with respect to the formation or the bubble point and the introduction of a well-defined sampling loop to acquire a representative sub-sample."(Wolff-Boenisch and Evans, 2014)

The following state-of-the-art examples show the variety and current usage cases: The Positive Displacement Sampler PDSshort provided by Leutert for example has a sample capacity of 600 cm^3, an operating temperature of 180 °C and a sample pressure of 1035 bars. With a preloaded pressurized chamber, it retrieves a representative sample in a single-phase condition to the surface (Leutert, 2021). The sampling of deep geothermal wells and CO_2 reservoirs with the Leutert positive displacement sampler (PDS) is well documented in many publications, for example in (Kampman et al., 2013) and (Regenspurg et al., 2010). The Armada® SPS-A Single-Phase Sampler by Halliburton operates at similar conditions and has the additional feature to preload scavenger fluid. Further, the sample chamber material is designed for detection of trace elements such as H_2S (Halliburton, 2022).

The GTFSampler is composed of a shut-in valve, maximum thermometer, a filter, check valve and a sampling cylinder with noble gas as Nitrogen. It is designed for temperatures up to 200 °C and pressures up to 77 to 226 bars. It is made for the retrieval of geothermal fluids (water, vapor, and gas) with a sampling volume of 500 cm^3 (Hsieh et al., 2021). The Multi-Temperature Fluid sampler (MTFS) is designed for fluid sample 1000 cm^3 with operation temperatures up to 190 °C, non-gas tight and to connect different probes in a row in the Deep Sea Drilling Project Hole 504B. It uses a syringe style design of the sample chamber and a "mechanical trigger that utilizes the thermal-response properties of a shape memory alloy (SMA)" (Wheat et al., 2020). The MTFS can be deployed with the elevated temperature borehole sensor (ETBS) tool in the borehole (International Ocean Discovery Program, 2022).

The downhole sampler of the project SECURe-Subsurface Evaluation of Carbon capture and storage and unconventional Risks is made for retrieval of integer fluid samples (water, oil, gas) with any contamination and leakage to the surface. The analyzation of geochemical composition of the fluid sample is done in a laboratory on site. The probe transmits measured data via the wire line (Ricroch et al.). The variation in the products is the quality of the fluid sample as pressurization

sample while intake, storage, the product specification and fluid sample volume. Most of the probes have a countdown timer to open the inlet valve and use a pressurized displacement fluid and gas. Furthermore, most probes do not transmit real-time data about the status of the sample, temperature and pressure, as they operate purely mechanically. Findings from current research projects are the need of more downhole data of the sampling process (Ricroch et al.), sample pressurization and verification further reservoir information to the taken sample such as downhole pressure and temperature.

Commercially available samplers today only partially have remote control and monitoring of the sampling process as well as active control of the samples taken. This issue is to be addressed by developing a remotely controllable and monitorable sampling probe. To improve the integrity of a representative fluid sample, it is crucial to log the full sampling process. The quality of the fluid sample can be enhanced with a remotely operated opening and closing unit. Further, an adaptive control and monitor system is used to maintain the formation pressure and temperature inside the sample chamber. The quantity of samples can be increased with a shorted preparation time at the surface and faster sampling, as well as by multiple sampling at different depths. How is an automatic sampler downhole probe designed, and how is the procedure to remotely controlled collect and retrieve a fluid sample from a deep borehole at nearly in situ conditions?

The novel inliSAMP probe has remote controlled actors and sensors for intake, storage, and retrieval of the sample. A steerable hydraulic unit and a resistance heater are used as actuators for an adaptive pressure and heating system. With the developed sampling procedure, a fluid sample can be stored and maintained under nearly in situ conditions, without the need of a displacement fluid and pressurized nitrogen. The mission of the downhole fluid sampler inliSAMP is to take a sample larger than 450 cm^3 from the borehole at an arbitrary depth and retrieve a single-phase sample to the surface at in situ downhole conditions with logging data. In this research, a novel sampling procedure is being developed and implemented in a demonstrator probe inliSAMP. The demonstrator is a simplified hardware version of the borehole probe. This involves the experimental investigation of the sampling process, the temperature distribution in the sample chamber and the sample pressure during the process.

The main focus of the research is to develop a solution for keeping the sample temperature and pressure constant during the ascent at a changing ambient temperature. For this purpose, a constructive solution, extended sampling procedures and the use of a temperature control with limited heating power are combined. The demonstrator with the sampling procedure is tested on a test bench. Chemical analysis and measurement of dissolved and undissolved gases in the sample are not performed.

Moreover, inliSAMP is specially designed to meet the requirements of most geothermal boreholes in Central Europe. The main requirements are an operating temperature of 200 °C, a maximum thermal water pressure of 60 MPa, and resistance against very corrosive and harsh environments (Spatafora et al., 2019). The specifications are consolidated in the so-called hotToolKIT requirements. At the Karlsruhe Institute of Technology, within the workgroup Geothermal Energy at the Institute for Automation and Applied Informatics was developed an open-source platform for geothermal borehole tools and probes to enhance and innovate the information quality and integrity of deep geothermal applications. The hotToolKIT platform is the renaming and commercialization of the ZWERG modular system and the two downhole probes inliCAM (working title GeoKAM) and inliSAMP (working title WASAM) (Holbein et al., 2018).

hotToolKIT links the requirements of deep boreholes, electronic hard- and software, a design construction kit. Standardized testing is applied for variable uses such as a video inspection system GeoKam (Spatafora et al., 2019), a permanent cooling system (Holbein, 2019) and a new downhole sampling system (Isele et al., 2015b) and (Berentelg et al., 2020).

2. Novel fluid sampling method for deep boreholes

HotToolKIT is a modular system for design, construction, and operation of downhole tools and high-temperature applications. The general operating parameters of the environment condition for all probes are listed in Table 1. The tool and technology development are structured by applying a repetitive modular design. Development costs and the risk of errors are thus significantly minimized (Holbein et al., 2017).

The module-based probes consist of universal modules and task-specific application modules. The universal modules include all components such as a housing and thermal insulation, which each type of probe requires. The application module is developed task-specific and is made of assemblies, actuators, and sensors. Special electromechanical couplings enable the individual modules to be connected and combined (Isele et al., 2015b).

The sampling probe inliSAMP structure is build up from standards of the hottoolKIT. inliSAMP is composed of an application module: the sampling unit and various universal modules such as a hydraulic power pack, insulation, power supply unit, and a communication board. The probe consists of two sections, a high-temperature section with the sample unit and hydraulic power pack with a coupling (Holbein et al., 2017) and an insulated section for temperature sensitive electrical components. A suitable Dewar tube from hotToolKIT is used for the thermal insulation of the electronic components. Control circuits boards, as HiTES, communication electronics, and power electronics are installed to operate and monitor the probe (Dietze, 2020). The module groups are each protected by a stable housing tube which is screwed to the coupling (Spatafora et al., 2016).

The sampling unit, the application module for the task of downhole sampling and fluid storage, is a new development. It consists, in principle, of an insulated and heated pressure vessel named the sample chamber attached to a hydraulic cylinder (Berentelg et al., 2020). The hydraulic cylinder is actuated by a hydraulic power unit. The container is closed by two axially movable pistons which are directed over a rod. The distance between the pistons corresponds to the volume of the sample to be taken up in the so-called sample chamber.

The developed fluid sampling procedure is simplified by a five-phase principle: descending the probe, sample taking, closing, pressurization, temperature control, and sample dispensing. The phases are illustrated in Figure 1 showing a Pressure vessel with an Inlet hole, Heating, mechanical Stops, and a Sample piston and Valve piston. The sampling concept is based on the function of a syringe and a valve. Each piston, shown, has seals on both sides and can only be shifted axially by fluid pressure or the piston rod force:

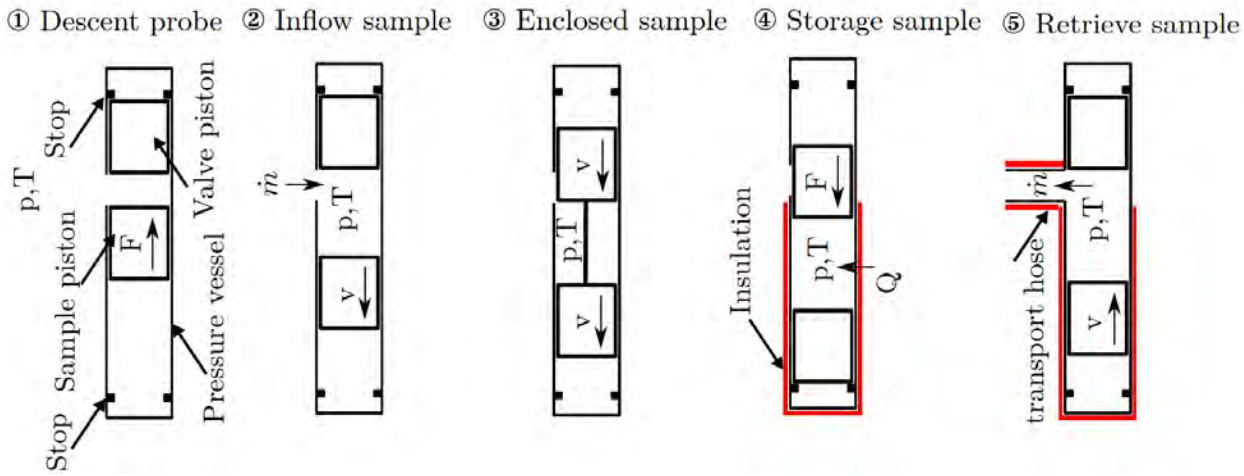

Figure 1: fluid sample principle in five phases: ①descent probe: The probe is submerged into the borehole to a selected depth. The Sample piston is held in place as the sample container closure is open. The Valve piston pushes against a Stop. The sensor system measures temperatures outside and inside and the pressure. ② As the Sample piston is released, the fluid enters the sample chamber. ③ the defined sample volume in the sample container is enclosed by the two pistons, and everything is moved until the Valve piston closes the inlet. Then the sample is sealed. ④During emergence and at the surface, the sample pressure is controlled by the Valve piston force and the sample temperature is controlled by an electric heater. ⑤When dispensing via a hose, the Sample piston presses the Valve piston against the upper Stop and the sample is transferred to a transport container with minimal loss.

①*Descent probe*

The probe is submerged into the fluid-filled borehole to a selected depth via the wireline. The rising pressure pushes the Valve piston constantly against a Stop, and rising temperature heats up the probe slowly. The Sample piston is held in place by the piston rod force *F* as the sample container closure is open. The sensor system measures temperatures inside *T_in* and outside *T_out* and the ambient pressure *p*.

②*Inflow sample*

At the selected depth, the piston retention force is set lower than the force on the piston. As a result, the piston moves and fluid flows into the sample vessel. The inflow velocity is determined by the velocity of the piston rod.

③*Enclose sample*

The stroke of the piston rod determines the volume of the fluid sample. The collected sample is shuttled between the Sample piston and the Valve piston, and thus the system is in a state of equilibrium. Piston force is used to move the system until the Valve piston closes the inlet. Then the sample is sealed yet can still be moved axially in one direction.

④*Storage sample*

The temperature *T_in* and pressure *p* of the sealed sample are kept constant by an adaptive control of piston force and heating power. During emergence and at the surface, the ambient temperatures are lower than in the sample and the sample chamber. The sample pressure *p* is dependent on the true sample temperature and can be manually controlled by the Valve piston force.

⑤*Retrieve sample*

When dispensing via a hose, the Sample piston presses the Valve piston against the upper Stop and the sample is transferred to a transport container with minimal loss. To avoid a drop in temperature in the out flowing sample, the fittings, hose, and transport cylinder are preheated up to sample temperature.

Table 1: Environment condition and requirements for sampler and downhole probes, taken from (Spatafora et al., 2019)

Borehole depth	5 km
Diameter open hole	approx. 220 mm / 8 ½ inch
Diameter Housing tube	<95 mm
Ambient Temperature	<200 °C
Ambient pressure	<600 bar, 60 MPa
Sample Volume	> 450 cm3
Pressure keeping & record	+20 bar
Temperature maintain & record	± 5 K
single phase sample, CO2, *uGT*	slow sampling, heat control

2.1 Enhancement of temperature control

In the sampling principle, the sample chamber temperature is assumed to be equal to the ambient temperature at all times downhole. Thermal inertia, heat transfer, temperature stratification in the sample and in the sample chamber is neglected. In reality, there are temperature differences between the outside and inside the probe, as the deployment time is reduced. Generally, these differences are summarized by the Φ-factor. The Φ-factor or thermal inertia is the ratio of the mass times the heat capacity of the sample to the sample container. The closer this is to value 1, the more representative the sample is (Ekkehard, 2020). For a more representative sample in the sampler, the following procedures are recommended: Preheat the sample chamber to ambient temperature with a dummy sample. The heat transfer across the shell surface is reduced by an insulating layer. Furthermore, by forcing natural convection in the sealed fluid sample, temperature stratification is avoided.

3. Design demonstrator probe inliSAMP and sampling procedures

3.1 Design and layout of mechanical components inliSAMP

The proof of concept demonstrated the implementation of the novel sampling method, illustrated in Figure 1. The inliSAMP probe was engineered and constructed as a demonstrator for this purpose. A specific sampling procedure was developed for inliSAMP, which was then deployed

on a borehole test rig under laboratory conditions. The sampling procedure was successfully tested with the demonstrator. The demonstrator inliSAMP is built according to the hottoolKIT standards. It consists of two high-temperature modules: the task specific sampling unit and a universal hydraulic power pack. The two modules are built up and installed in a housing tube, see Figure 2. The electronics boards required for the remote operation of the demonstrator are outside the housing tube and are supplied by laboratory power supplies. The setup is shown schematically in yellow on Figure 3. Components and assemblies used from the modular system and new designed parts for the borehole probes, are at different stages of product readiness and have different material requirements. For the sample unit, mainly stainless steel 1.4313 QT900, 1.4307, and 2.468 (Inconel® Alloy 718) were selected.

3.1.1 Hydraulic power pack

The hydraulic power pack is a module from the construction kit (Holbein et al., 2017) for down-hole tools. The hydraulic power pack consists of a 4-3-way valve, a high temperature pump, a high temperature motor, an oil tank and a lowering brake valve on the secondary side. Table 2 lists all purchased parts that were used. Figure 3 shows the hydraulic circuit diagram.

Table 2: Used purchased parts in the demonstrator inliSAMP

Item	Product	Producer
Electric Motor	EC-4pole 32 brushless 480 Watt | Heavy Duty	Maxon motor AG
Motor control board	EPOS4 CoMPact 50/8 CAN	Maxon motor AG
Fixed displacement micropumps	PB33	Hydro Leduc
4/3 Directional spool valve solenoid operated	WK06E-01	Tries GmbH & Co. KG
Lowering brake valve	SJ 00 G	HAWE Hydraulik SE
Heating mat	RS Pro Silicon Heater Mat, 80 W, 200 x 400mm, 12 V dc	RS Components GmbH
Pressure sensor	Series 7 LHP Inconel®Alloy 718	KELLER AG
Temperature sensor	PT 1000 Class B 1.0 x 3.0 mm	Farnell GmbH
Temperature sensor	PT 1000 Class B 1.7 x 1.7 mm	RS Components GmbH
Hydraulic fluid (fire resistant)	AeroShell Fluid 31	Shell Deutschland GmbH

3.1.2 Sampling unit

The sampling module comprises a sample chamber and two double-acting hydraulic cylinders arranged in tandem, as shown in enlargement in Figure 2. Connecting the hydraulic cylinders in parallel increases the piston rod force for both extension and retraction strokes. Both cylinders are equipped with a pressure sensor to monitor the force transmission over the piston rod. Pressure sensor P 3 measures the extension pressure (PUSH) and P 2 measures the retraction pressure (PULL) refers to Figure 3. The hydraulic fluid pressure data is crucial to operate and control the

sampling process remotely. The measured pressure rise in the cylinder tube is important information for determining the piston position in the sample chamber.

The sample chamber is a heatable pressure vessel insulated over the circumferential surface, see Figure 2. The connection between the housing tube and the sample chamber is implemented with a small inlet flange and bushing. This is radially connected to an axially and radially movable sleeve, which is around the inlet bore of the sample chamber (Berentelg et al., 2020). The sample chamber tube has an inner diameter of 55 mm and a stroke of 305 mm; thus, the sample volume is approximately 480 cm^3. The sample volume can be easily increased by using a longer stroke and longer tubes. The piston rod diameter is 20 mm in the sample chamber and 22 mm in the hydraulic cylinder due to buckling. Standard fine pitch threads of M20 X 1.5 are used for coupling and end stop. The assemblies are connected by a special gland and a multi-part piston rod.

As shown in the concept in Figure 1, the water sample is taken between the Sample piston and the Valve piston. In the design shown in Figure 2, both pistons are axially mounted movable on a piston rod. The piston movement is controlled between both stops. They are equipped with O-rings (material Fluorocarbon (FKM)), back-up rings (material Polytetrafluoroethylene (PTFE)) and guide rings (material PTFE with bronze) on the piston seal and rod seal. The sealing clearance between the tube and the piston is approximately 2/10 mm.

Technical cleanliness in the sample chamber is provided through the design, preparation, and the sampling process. At the beginning of sampling, when the cleaned probe is lowered, the two pistons are in contact on the face and the inlet port is filled with demineralized water. Due to the vertical position of the hole of the inlet and length and small diameter of the pipe, little substance exchange takes place through the water inside and outside. This could be further reduced by the use of a push-off cap. Due to the small axial stroke of 65 mm at sample termination, it is feasible to equip the moving piston with a pressure sensor and a short and a long resistance temperature sensor probe using flexible, high temperature pre-bent wires. The pressure sensor records the ambient pressure in the borehole and, after closure, the sample pressure in the sample chamber. Two immersion temperature sensors measure the temperatures in the sample chamber. A longer temperature sensor (immersion depth 20 mm) measures the sample temperature, defined *T1*. while the short sensor (immersion depth 1 mm) measures the boundary layer temperature between sample and piston, defined *T2*. Furthermore, the borehole temperature and the outside temperature are recorded with an external temperature sensor, defined as T inlet flange *T_IF* on the nose of the probe. When the probe is lowered downhole (descent probe), the water pressure pushes the Sample piston (lower piston) on the piston rod against a Nut, the lower Stop. The upper Stop for the Valve piston is a short, thick-walled pipe. The hydraulic valve is closed, and the pump is at a standstill, hence the retention force from the Sample piston is transferred to the hydraulic cylinder via the piston rod.

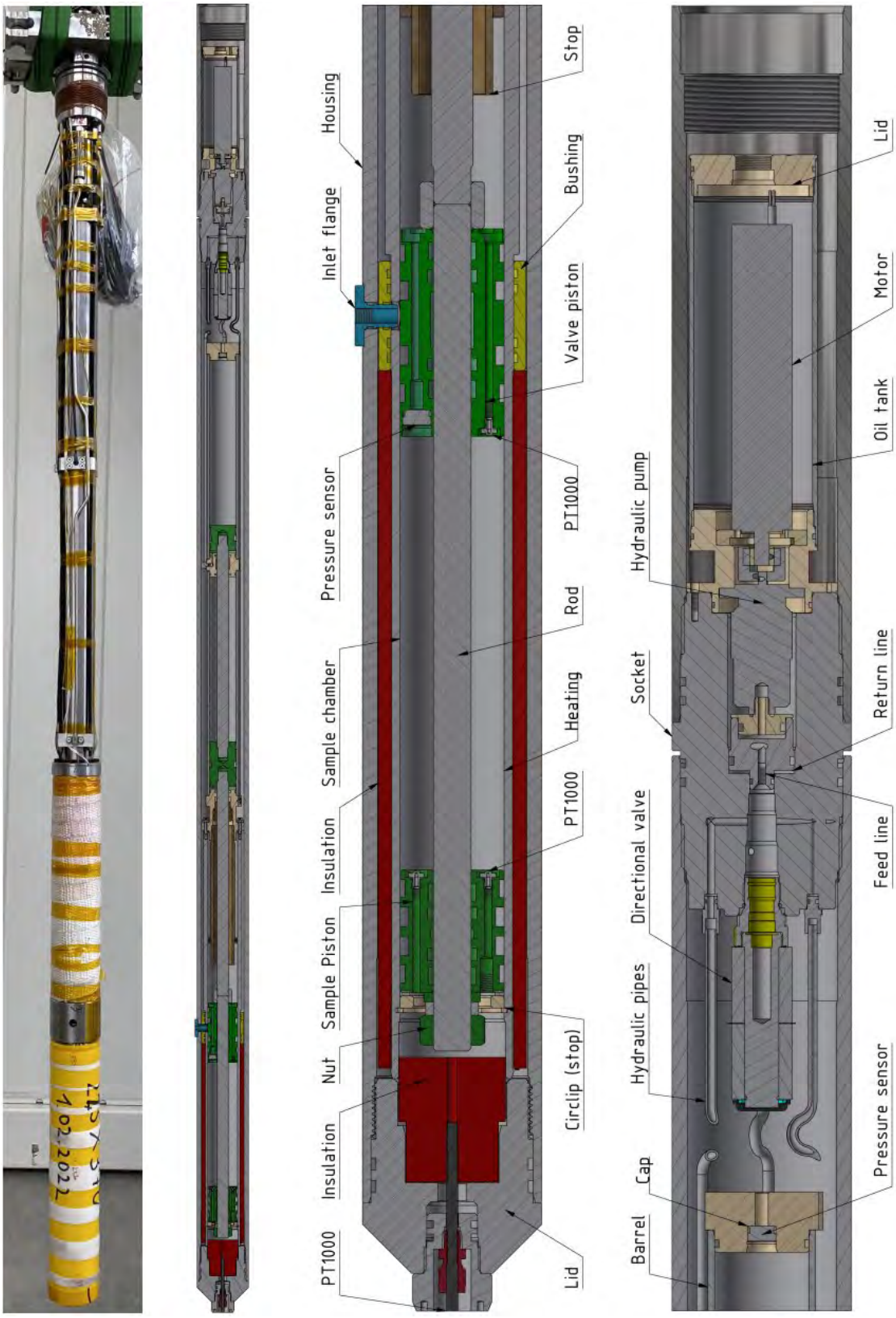

Figure 2: Left to right: photo of demonstrator inliSAMP used in test rig, CAD model borehole probe inliSAMP, enlargement: sample chamber, hydraulic power pack.

To initiate the inflow sample under load (inflow sample), the valve opens the retraction cylinder and hydraulic oil flows through a lowering brake valve to the tank. The lowering brake valve enables a set constant flow rate, largely disengaged of the load, and is used to adjust the sampling time according to the application requirements. Simultaneously, the pump transports oil on the extension side without back pressure. The process is terminated by contact between the Valve piston and the collar on the tie rod at the end of the stroke. A force equilibrium (enclosed sample) is created, and the movement of the Sample piston stops immediately. Thus, only little fluid power is required to move the Sample piston, the fluid sample and the Valve piston to the lower Stop, a heavy retaining ring. The retaining ring is seated in a groove in the pressure vessel tube and the exact position is adjusted by spacers.

The sample is sealed when the lower O-ring of the Valve piston has passed over the inlet bore. This initiates the storage phase, in which pressure and temperature are kept constant. The pressure in the sealed hot sample is temperature-dependent and must not fall below the borehole pressure. The pressure can be increased or decreased by changing the heating power, or more precisely, changing the global sample chamber temperature.

In case of leakage, deviation, or temperature drops, the sample pressure can be manually increased as required by fluid power through the piston rod and the Valve piston without changing the sample temperature. The heating of the sample chamber carries out three functions, heating the sample chamber and dummy sample before sampling in a hotter environment, keeping the temperature of the sample constant at colder outside temperature and to avoid shrinkage of assemblies. The resistance heating mat is glued onto the sample chamber up to the bushing and insulated towards the outside (see Figure 2 left). During storage phase, the outside temperatures are below the sample temperature and required heating power depends on the outside temperature.

The heating and insulation design of the sample unit is adapted from everyday objects such as an electric kettle. During storage phase, the heat source is at the bottom and the heat sink, the coldest point, is at the top. Thus, the different density of the fluid creates a static buoyancy. Natural convection leads to a homogeneous permeability and temperature distribution in the sample chamber. Before sample dispensing (retrieve sample), the inlet flange and outer housing is heated externally with a heating jacket (Leutert, 2021). In addition, the lower Nut on the piston rod must be manually readjusted. This reduces the pressure drop during sample dispensing.

3.2 Wireline power supply unit, control and communication board

3.2.1 Power supply requirements and layout for inliSAMP

The probe is powered by a DC power supply. Unlike the inspection tools such as the inliCAM probe, the expected consumption of the probe is much higher (Dietze, 2020). The embedded system and the communication systems are using about 10 W. The expected power consumption for the heat and motor control is approximately 400 W. In addition, the valves require 10 watts, and the maximum power is calculated as 420 W. It is recommended to use the theoretical maximum power transfer at the impedance matching point, where the output voltage is the same as the voltage over the cable and thus the probe voltage is half of the supply. For the coax cable of inliCAM, about 4.2 km long, and including a higher cable resistance to heat, a power supply with 520 Volt DC is needed. When less power is needed, nearly the maximal voltage applies to the entrance of the DC-DC converters at the probe. Therefore, special DC-DC converters operating at

high volt are needed. For inliSAMP an additional circuit converter for use of long cables and storage functionality was invented. It operates in a Dewar flask with cooling reservoir (Dietze, 2020). Alternatively, a larger cable diameter with more copper can be used, but this will increase the weight and require larger winding equipment. A coaxial cable is usually very heavy in itself. The maximum length should be short enough with a reserve, before tearing itself off from weight. For example, the inliCAM cable weighs 1125.6 kg (in air), which is about 25% of the cable strength. Holding a probe with additional 150 kg is acceptable in water (RochesterWireCable., 2012).

3.2.2 Communication and embedded system

Communication, modems, and processing system were designed and developed for a universal use in borehole probes (Holbein et al., 2018). The main board of the embedded system, High Temperature Embedded System (HiTES), has as main chip a Field Programming Array (FPGA), which allows an implementation of algorithms for data modulation and demodulation in a suitable flexible way.

The wireline cable communication system was developed by an external partner and is presented in (Schubert et al., 2015) The communication system consists of plug & play software and hardware and further a Softcore-CPU for control and monitoring. The whole communication system is the same as the one successfully used for the inliCAM project, including the filter amplifier boards. The host modem, which is connected to the host PC via Ethernet, is a HiTES - system too, identical as for all wireline connected probes.

3.2.3 Electronics for measurement and control technology

To get access to the peripheral sensor and actors of inliSAMP, an IO-plugon-Board for HiTES has been developed, handling several measurement inputs and digital outputs. A motor control board for the hydraulic motor with a suitable size for the probe Dewar (Spatafora et al., 2016) was obtainable from Maxon™ (EPOS4 CoMPact 50/8 CAN, see Table 2). A Power IO board (PIO), which enables control of valves and heaters, as well as inputs for temperature sensors (Resistance thermometer, PT1000) and pressure sensors (piezoresistive pressure transducers), was built and installed. The layout of the circuit fits the mounting bars of the main board in the Dewar tube.

3.2.4 Information management

The host-PC software from hotToolKIT (Isele et al., 2015a), named “GeoGUI” is a workbench where forms can be composed with gadgets, which are connected to values to the probe or sending commands. InliSAMP has several forms and is designed with a GUI for full live control of the system. GeoGUI is connected to an SQL database and for example has the ability to replay a session at different speeds. Additional database export features were implemented for InliSAMP: Sensor data, valve position, motor control values, please refer to Figure 3.

3.2.4 *Control and monitoring of pressure and temperature in the sample chamber*

For the operation, partly automatized procedures have been implemented to HiTES Firmware to make remote control easier: To handle pressure, a "Wait-until-P_set-raise" and "maintain-P_set", where P_set is selectable out of the measured pressures in the inliSAMP. The procedures compare the measured P_set with a demand pressure and, if necessary, drives the motor of the hydraulic

pump with a demand velocity. Heating of the probe is done by supplying the heat mat with 28 Volt and up to 18 Ampere.

Table 3: Sampling procedure: actions, monitoring, and measurements as positions of sensors are in Figure 3 and Figure 4.

operation	Phase principle	environment borehole test rig	Function for the probe operator or computer	Monitoring Measuring data in the probe
descent	①descent probe	p increase TIF increase	valve CLOSED preheat sample chamber motor 0 rpm.	P1 increase TIF; T1 increase P2, P3 = 1 bar
dummyIN	②inflow probe	p const TIF const	valve Port PUSH (B) heat sample chamber motor 4500 rpm	P1 const T1 increase P2 increase, as a braking element
dummyOUT	⑤outflow probe	p const TIF const	valve Port PULL (A) heat sample chamber motor 2500 rpm	P1 const T1 const P2 increase
sampleIN	②inflow probe	p const TIF const	valve Port PUSH (B) keep heat sample chamber motor 4500 rpm	P1 const T1 const P2 increase, as a braking element
enclose	③enclose probe	p const TIF const	valve Port PUSH (B) control heat sample chamber motor 2500 rpm	P1 const T1 const P2 and P3, decrease to balance
storage	④storage sample	p decrease TIF decrease	valve Port PUSH (B) control heat sample chamber motor 1500 rpm	P1 const T1 const P3 increase
sampleOUT	⑤retrieve sample	p = 1 bar T air = 14 °C	valve Port PULL (A) control heat sample chamber motor 2500 rpm	P1 const T1 const P2 increase

The use of a software of pulse-width modulation (PWM) with a cycle of two seconds and a minimal time slot of 20 milli seconds results in a demand of X % PWM of the maximal power of 504 watts. To heat up the sample chamber (demand temperature T_{demand} increase of the water sample), the nominal power is approximately 400 watts, this is defined for 100 % PWM heating power. For temperature control, a PI-Algorithm is provided with a cycle period of 100 milli seconds: The bias X of demand and curing temperature T_{cur} is calculated in Equation 1.

$$x_d(t) = T_{demand} - T_{cur}(t) \qquad (Equation\ 1)$$

$$x_{sum}(t) = k_{s0}x_{sum}(t-1) + k_{s1}x_d(t) \qquad (Equation\ 2)$$

$$y(t) = k_p x_d(t) + k_i x_{sum}(t) \qquad (Equation\ 3)$$

The sum for integral part is done in Equation 2. But additionally, because of the lack of negative output, there is no cooling possible, the integral sum is kept positive or set to zero. The vanish

factor k_{s0} should be greater than zero and less than 1.0. Equation 3 shows the addition of the P- and the I-Part creating the output y. For example, the P-factor k_p is default set to 5.9. With ignoring the I-Part the maximum y = 100 % PWM is then reached when $T_{cur} < T_{demand} - 17$ K and defines a linear working range of 17 K below the demand temperature.

3.3 Sampling procedure

The sampling procedures are the sequences of operations the operator or the program runs through. It includes 7 operations steps and is listed in Table 3. These are the execution of the 5 different fluid sample principles, see Figure 1. The function at system level is not explained. It involves the operation of the control elements in sequence as given in the Table 3 and observation of the measurement data by the operator or a program. Below are listed the controls and measuring sensors for the execution and monitoring of the fluid sampling. The positions of the sensors and actuators are shown in Figure 3 and Figure 4.

- Control element:
  - hydraulic directional valve, status flow: Port PULL (A); CLOSED; Port PUSH (B)
  - electric motor rpm, user selectable: 1500 to 6000 rpm
  - heating, user selectable or controller max. 400 watts: 0 to 100 % PWM heat power
- Monitoring system
  - sample chamber temperature, Valve piston: T1, T2; Sample piston: T3.
  - borehole environment temperature outside inliSAMP: TIF
  - sample pressure: P1; pressure hydraulic pull; P2 pressure hydraulic push: P3.

The sampling procedure listed in Table 3 and actions are started and ended by predefined measured values and predefined states. Before sampling or testing, the preparation includes a surface pressure test, use of clean and rinsed equipment, connection check, and power supply review. At "**descent**" of the probe in the borehole the ambient pressure P1 and temperatures TIF, T1 increases with depth, the sample chamber is empty and heated up in accordance to TIF. The valve is at status CLOSED and motor on stop. At planned depth, temperature, formation pressure or some other point, the operation **dummyIN** starts, the hydraulic valve opens Port PUSH (B) and the motor set to 4500 rpm. It is finished when P2 decreases. Then the full sample chamber with T1 is heated up to TIF. In the next operation **dummyOUT** the hydraulic valve opens Port PULL (A) and the motor set to 2500 rpm, and it dispenses the dummy sample. It is finished when P1 rises up. The sample chamber temperature T1 is kept constant at TIF using the heating. At sampleIN the hydraulic valve opens Port PUSH (B) and the motor set to 4500 rpm. The sample is taken and the chamber temperature T1 is heated up again to TIF if necessary. It is finished when P2 decreases. To enclose the fluid sample, the hydraulic valve again opens Port PUSH (B) and the motor set to 2500 rpm. It is finished when P1 rises a little up the hydraulic cylinder are in equilibrium as the sample is confined between Sample valve and Piston valve. The sample chamber temperature is kept to T1. To store the fluid sample, the hydraulic valve opens Port PUSH (B) and the motor set intermittent to 1500 rpm and finished when P1 rises up a little in a hysteresis loop. The control of the chamber temperature and pressure is achieved via the T1 control. This may be used as an alternative method. At surface conditions, the sample dispensed "sampleOUT" with hydraulic valve opens Port PULL (A) and the motor set to 2500 rpm. At first, the system is in balance, hence only small force is required. When the sample chamber is connected to the transport cylinder, the full mechanic load has to be applied. The heat control heats the sample chamber to T1. The operation is completed

when P1 rises up. The procedure was carried out in the proof of concept experiment in section 5. A detailed protocol of the experimental demonstration can be sent on request.

4. Setup test environment demonstrator inliSAMP

4.1 Test rig characteristics for fluid sampling

The functioning of sampling procedure and quality of measurements outputs of the demonstrator inliSAMP are evaluated on a test rig under laboratory conditions. The test rig simulates the environmental conditions in the borehole at a specific depth. Only demineralized water in the liquid state is used as downhole fluid. By varying the parameters of pressure and temperature of the water, different virtual depths can be reached. Heating and cooling sequences simulate the descent and ascent of the probe. This is essential for mapping the heating and cooling processes inside the probe. The test rig delivers a flow of water at a constant temperature and pressure. The sample is taken from a heated pressure vessel (preheater). In a real downhole application, the sample from the borehole is dispensed into a transport cylinder (Leutert, 2021). In this test rig, the sample is returned to the preheater at the end of the sampling procedure. The probe mechanism sets the flow rate. To maintain the aggregate condition of the water, the design of the test rig has to be failure safe. To fulfil the boundary conditions of taking samples up to 200 °C, all components have to be temperature rated. For safety measures, the sample pressure is scaled from 600 bars to 60 bars. This is possible as the isobars are adequately close to each other in the liquid state (Huber et al.). Demineralized water is used to prevent rust.

4.2 Test environment for hot water deep borehole

The test rig is shown in Figure 3 for the execution and monitoring of the fluid sampling procedure described in subsection 3.3. The demonstrator inliSAMP stands upright on a support and is permanently connected to the test rig. The test rig consists of a commercial standard hydraulic double-acting cylinder (DAC) with fastenings, a heatable pressure vessel (preheater) and a heating hose. The DAC is grabbed by a lifting hook at the head. Test weights (2.1 t) equivalent to 88 bars are attached to the rod of DAC. The retracting port of the DAC is connected with a hose via a check ball valve to the lower port of the preheater. A commercial flexible heating hose connects the upper port of the preheater to the inlet flange of the demonstrator inliSAMP. The demonstrator inliSAMP and the preheater are mounted vertically to obtain convection in the vessels. Tap water is used to cool the outer housing tube of the demonstrator. A pressure gauge and transmitter, and a lower and upper thermocouples type K monitor the pressure. Pressure *P* 4 and temperature, *T_Ph* and *T_IF* are logged by a computer. All hot hoses and connections are insulated and heated externally. The laboratory power supply units for the heaters are regulated manually. For testing, the demonstrator inliSAMP is equipped with additional temperature sensors that provide information about the operation of the probe and help gain a better understanding of the sampling processes and effects in the probe. For easier handling in test operation, the lower lid is also not used, see Figure 4. Hence, temperature *T_Ph* and *T_IF* represents the borehole temperature in the test rig. The outer temperature sensor *T_IF* is mounted on the inlet flange to the sample

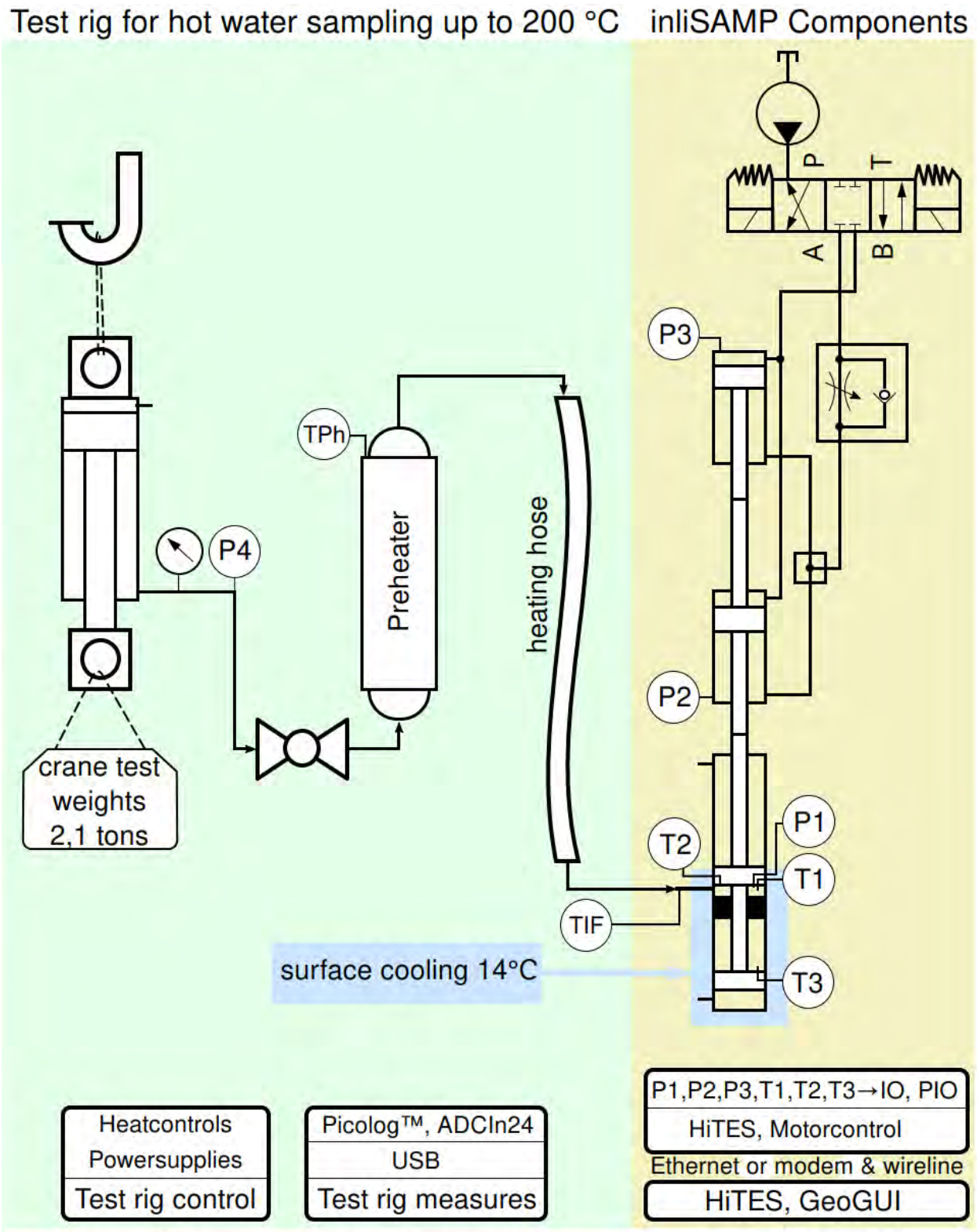

Figure 3: green: Test rig for hot water sampling up to 200 °C; yellow: hydraulic circuit diagram of fluid demonstrator inliSAMP.

chamber and important during the **descent** and **storage** operations as well while dispensing the sample. On the probe *T_HM* is on the internal heating mat. It monitors the maximum heating temperature placed on the tube at a lower heat flux. *T_SC*2 is positioned in the centre of the sample chamber tube and provides information about the heat transfer to the housing and the sample chamber. *T_SC*2 is near the inlet flange and bushing, it monitors the heat flux over the thermal bridge of the demonstrator. The immersion temperature sensor *T*3 in the Sample piston, together with temperature sensors *T*1 and *T2*, monitors the temperature stratification in the fluid sample over the height of the sample chamber.

4.3 Test run fluid sampling procedures

The planned tests involve going through the full sampling procedure (see Table 3) using the test rig and the demonstrator inliSAMP. The objective is to test the sampling process applied with the demonstrator and evaluate the temperature curves and pressure maintenance over the full sampling procedure. The sampling history data are proof for the quality of the water sample. In addition, the following issues are to be answered by the experiment: Required heating power during different operations and in transition, heat up and temperature regulation in a cold environment, stability of pressure and temperature of the sealed sample, temperature stratification and natural convection in the sample, behaviour of the temperature curve, during sample taking and dispensing.

5. Results proof of concept demonstrator

5.1 Test execution Sampling procedure

In the **descent** probe operation, the probe housing tube was heated up to 200 °C with a detachable heating band, as well as the test rig components such as the water-filled preheater, and the heating hose. Inside, the PWM heating power preheated the empty sample chamber to 200 °C. The sample pressure was set by the ambient pressure at approximately 88 bars (see Figure 4). A heated fluid sample was taken in the sample chamber. After **dummyIN** operation, the dummy sample was deliberately overheated by the PWM heating power up to 204 °C, to avoid a temperature drop in the next operation. The other temperatures were manually controlled to be constant at about 200 °C. While dispensing the dummy sample at **dummyOUT** the PWM heating power was maintained in the sample chamber temperature. After short stabilization of the reference temperature, at **sampleIN** the final sample was taken at 200 °C. During **enclose** the sample was enclosed by the moving Sample piston and Valve piston and was heated up with the PWM heating power to 200 °C. Briefly, after sealing the sample at **storage**, the external heaters are switched off and only the PWM heating power was used to maintain the sample temperature. The heating hose is removed. The housing tube and the inlet flange are cooled down to 14 °C with faucet water. The PWM heating power is used to maintain the sample temperature and pressure remotely. The hydraulic system was being additionally used to manually increase the pressure. For the retrieval of the sample into the preheater at **sampleOUT**, the heating hose was reconnected to the inlet flange and the heating band heats up the housing tube. The PWM heating power was reduced to avoid overheating and overpressure while heating from outside. At constant temperatures at the inner and outer vessels, the sample is dispensed to the preheater.

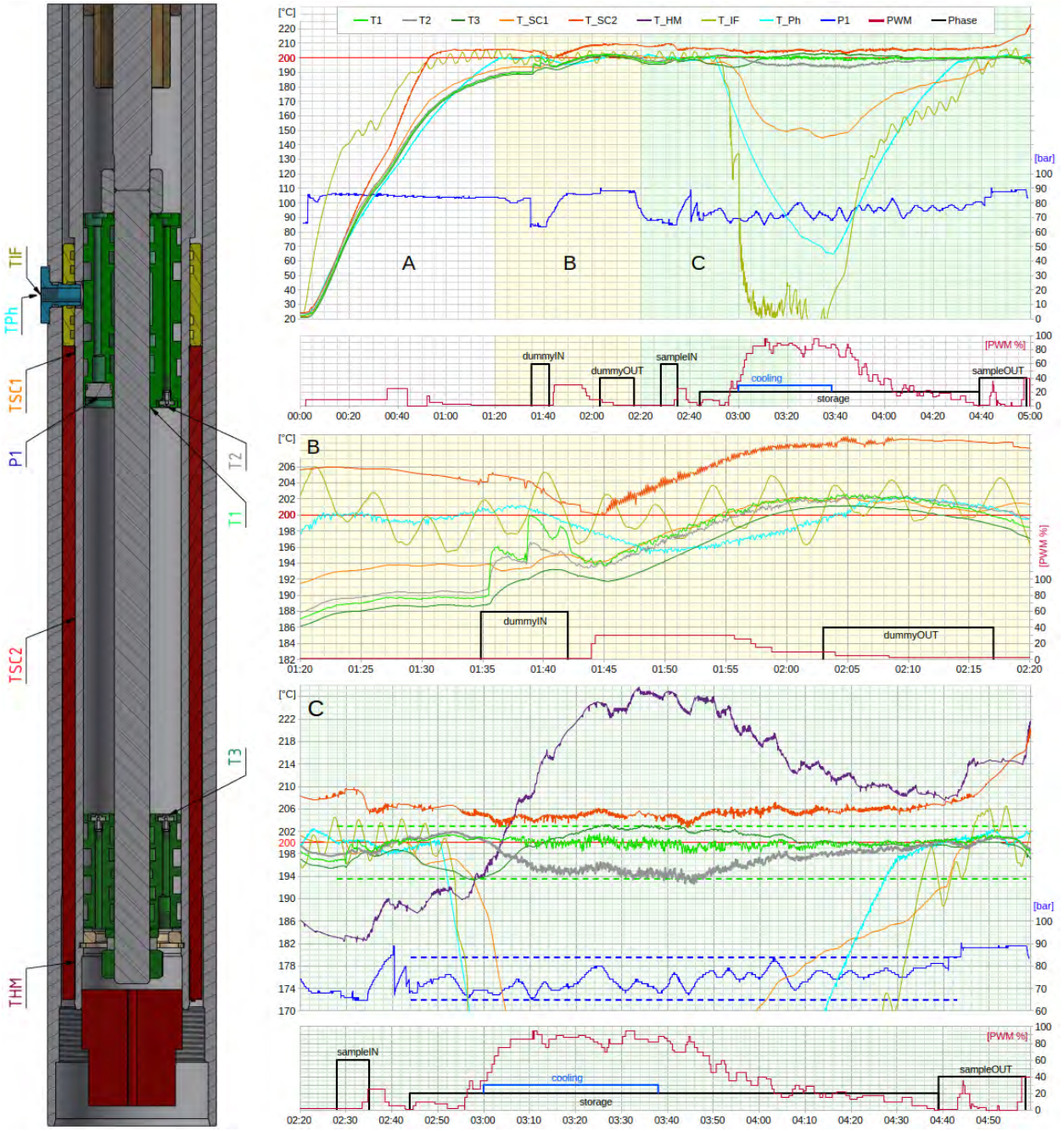

Figure 4: Left: sample chamber with temperature measuring points and pressure sensor (P1). Right: Data of test run with a dummy sample and representative water sample. The upper diagram is an overview of all measured values and operations. Section B shows dummy sample inflow (dummyIN), heat up and stabilize, dummy sample output (dummyOUT), Section C shows sample inflow (sampleIN), heat up and stabilize, sample output retrieval (sampleOUT).

5.2 Results and data of the demonstration run

The measured values of the sensors from the test are shown in Figure 4. The upper section is the overview of all data and performed operations over a demonstration run. The temperature data is shown on the left ordinate and the pressure data is shown on the right ordinate. On the abscissa,

the time of experiment and additionally the steps of sampling procedure and PWM heating power of heating are listed. Section B shows the intake, heat up and dispensing of the dummy sample, and section C shows the intake, storage and dispensing of the representative sample in greatly enlarged form. The accurate representation of the data is intended to facilitate the presentation of thermodynamic effects of the different operations and to show the quality of the equipment.

5.2.1 Result descent probe: heat up and pressure monitor in Figure 4 section A

During heat up, the temperatures *T1, T*2, *T*3 and *T_SC*1 increased slower than the middle outer sample chamber temperature *T_SC*2. At 01:00 *T_SC*2 stabilized with 205 °C, at a utilization rate of 14% PWM heating power, illustrated in the upper Figure 4 section A. At the end of this operation the curve of *T1, T*2, *T*3 and *T_SC*1 flattened, and they have reached a plateau at 190 °C, the temperature difference is 3 K. Temperatures *T_IF* and *T_Ph* showed oscillations and were on average about 200 °C hot. As the fluid sample was open until the **storage** operation, the surrounding pressure was dependent on the test rig. First, the surrounding pressure *P*1 was above 65 bars. During the heating period, the pressure increased to 88 bars due to thermal expansion and the resulting static friction forces in the cylinder. These can be explained by the design of the test setup. The temperature data showed that the heat transfer from the outer housing tube to the sample chamber varies in vertical (axial) direction. In the area from the inlet flange the heat transfer is high, and at the lower part of the sample chamber vessel to the piston it is low. It is limited by the maximum operation temperature of the heating mat and sealing. It is monitored with *T _HM* in section C. Therefore, the empty sample chamber can only be slowly preheated from the outside and inside.

5.2.2 Result dummy sample: inflow, heat up and outflow in Figure 4 section B

During the inflow of the hot sample (*T_Ph*=201 °C), temperatures *T1, T*2, and *T3* increased immediately at 01:35 shown in Figure 4 section B. After taking the sample, *T_SC*2 decreased from 205 to 200 °C at 01:45 evenly. Due to thermal inertia and thermal gradients, the taken sample temperature *T1, T*2, was 194 °C, 5 K below the reference temperature of 200 °C. The reference temperature *T_Ph* decreased after the sampling as cold-water flows into the preheater, this does not affect the demonstration. With 30% PWM heating power from 1:45 to 1:55, the dummy sample was overheated *T_SC*2 at 210 °C, so fluid temperatures *T1, T*2 increased to 202 °C, with *T3* reached only 201 °C at 02:05. After dispensing the dummy sample, *T1* decreased to 197 °C, whereas *T2* was approximately 1 K above. Temperature *T*3 decreased to 195 °C at 2:20. Despite minimal PWM heating power, *T_SC*2 remained at 210 °C.

As a finding, the 200 °C hot water dummy sample from the preheater heats up the upper part of the sample chamber and the pistons. In summary, the fluid sample becomes slightly colder, as the heat is distributed in the probe. Due to the increased heat transfer in a fluid loaded sample chamber, the system can be PWM power heated more homogeneously and faster to reach equilibrium with the reference temperature.

5.2.3 Results sample: inflow, heat up, storage and retrieval, sampleOUT in Figure 4 section C

After preheating with the dummy sample at 2:20, the temperatures at the different temperature measuring points are much closer to each other. At the beginning of the operation Temperatures **sampleIN** at 2:30 *T3, T1, T2* were at 196 °C to 198 °C represented in the Figure 4 section C. The

PWM heating power with 10 to 20% was used to maintain the taken sample *T1* and *T2* at 200 °C at 02:40, however, temperature *T3* did not increase consider-ably. Before the sample is drawn and enclosed the heating controller starts maintaining the sample temperature, represented by a dashed green line in Figure 4 section C. Since the pressure in the sample *P* 1 was dependent on the total fluid temperature, it also ramps up until 90 bars.

At 02:44 after the **enclose** operation the fluid sample was sealed and thus the sample probe is disconnected from the test rig. The operation **storage** has been started and can be controlled by the operator. From this moment, the fluid sample in the sample chamber was separated from the pressure compensation of the test rig. Due to the closed sample chamber, the pressure *P*1 was directly dependent on the actual temperature. This state is marked by a dashed blue line. Furthermore, the dashed line blue and green represent the range of minimum and maximum values of pressure and temperature in the **storage** operation. Small temperature changes of the inert mass of fluid sample and sample chamber result in large pressure changes, as the pressure values went up and down. It had the lower boundary at inlet pressure 65 bars and upper boundary at 83 bars (blue dashed line), as the given procedure allows only positive elevations.

At 02:50 all external heaters were disabled, and *T_Ph* began to decrease slowly to 65 °C. The housing tube and inlet hole *T_IF* were cooled below 20 °C, first with air and then with faucet water. Hence, the temperature at the inlet flange *T_SC*1 decreased to 145 °C, simultaneously *T1, T*2 decreased and stabilized at 201 °C at 02:56. Temperature *T3* dropped to 194 °C, the lower boundary of the temperature range.

Next, the PWM heating power was ramped-up to 90% to maintain *T1* at a constant value. At 02:58 at temperature lines intersection point the lower piston temperature *T3* and *T_SC*1 started to rise and stabilized to 203 °C at 03:26 the upper boundary value. Concurrent *T2* over time decrease to 194°C with small aberration. As well, *T1* wobbled around the target temperature with ± 1 K difference.

During the **storage** operation and extensive *cooling*, temperature *T_SC*2 decrease evenly to a minimum of 204 °C, although the PWM heating load was at peak. Further, the curve *T_HM* showed a maximum temperature of 227 °C at 03:40, indicating the activity of the internal heat mat. At 03:40 the detachable heating band, preheater and heating hose were set back and heated up to a reference temperature of 200 °C of the test rig. The PWM heating power was reduced accordingly. The fluid sample temperatures *T1, T*2, and *T3* slowly converge nearly to 200 °C, beginning at 03:45 until 04:39. When the sample was half retrieved *T1, T*2 rose to 201 °C. After sample dispensing *sampleOUT*, the *T1, T*2, *T*3 dropped to a minimum of 198 °C, while *T_IF* and *T_Ph* fluctuated slightly. During sample dispensing, the pressure increases to 88 bars to overcome the frictional forces in the cylinders.

The results and data show that after dispensing the dummy sample, temperatures in the sample chamber dropped 2 K because of cooling effects in the sample chamber. This small value indicates that the temperature is evenly distributed. Next, the incoming hotter sample heats up slightly the sample chamber, as *T*1 and *T2* rose. After the additional heating with the PWM heating of the chamber, there was subsequently a temperature stratification due to cooling processes and an inhomogeneous temperature distribution in the sample chamber. During the **storage** operation and cooling stage, the top of the sample chamber and inlet flange is colder as the bottom (see design of the probe Figure 2). As shown in the measurement data applying the heating power to the lower

part of the sample chamber, leads to a reversal of the thermodynamic system and the temperature stratification dissolved (follow *T3* from 2:56 to 3:35). This result is an inversion of the temperatures. At the lower Sample piston, the highest temperatures are measured, and at the boundary layer at the Valve piston the lowest. The temperature *T1* immersed in the fluid remained approximately constant but gets many small jumps. In addition, the sample chamber wall temperature *T_SC*2 decreased while heating power is high. The effect can be explained by the occurrence of natural convection, as the chamber is cooled at the top and heated at the bottom. The coincident heating and cooling of the sample chamber leads to vertically different temperatures in the fluid sample. Thus, a flow is created by different temperatures of layers, which affects the density. This leads to a steady temperature exchange, increased cooling of the sample chamber tube, and mixing of the sample.

After the water cooling was disabled, the heating power was reduced accordingly. Simultaneously, the vertical temperature difference in the sample decreased. Due to the homogeneous temperature distribution in the sample chamber and the successful mixing of the sample, the temperatures converged towards 200 °C.

As the experiment shows, an electrical heating power of 400 watts, insulation and good design of the sample chamber is sufficient to maintain the temperature in the sample chamber permanently. Furthermore, the seals (O-ring) kept the pressure in the sampling process without leakage on the demonstration run. Materials FKM and FFKM were used. The experience with these materials under the given conditions at 200 °C and 60 to 100 bars is the failure of the O-ring after passing through the radial inlet bore several times. A revision of the design is necessary here.

Furthermore, the housing tube of the demonstrator housing is made of steel. A housing tube of the same dimension made of Inconel® Alloy 718 has a lower thermal conductivity, and the system would be cooled and heated more slowly by the environment.

6. Discussion

The findings from the experiment show that, under laboratory conditions, a fluid sample can be taken, stored and dispensed using the demonstrator inliSAMP in the test rig. The quantitative results from the experiment show that with the execution of the fluid sampling procedure, the sample temperature and pressure in the sample chamber deviates only slightly from reference fluid in the preheater. Thus, proof of concept has shown that a fluid sample can be collected and stored in the inliSAMP demonstrator under nearly in-situ conditions.

First, a water dummy sample with 200 °C and 65 bars was taken from the preheater. In the cold sample chamber inside the probe, it was heated up to the target temperature of 200 °C and dispensed back in the preheater. Second, the actual sample was taken from the preheater and stored in a clean, warmed-up sample chamber. When the sample was stored in the demonstrator, the heating hose was disconnected. The outer housing was cooled down to 14 °C. The sample temperature and pressure were maintained by the sample chamber heater control and hydraulic piston force. Only small pressure overshoots were allowed. Natural convection is used to keep a homogeneous sample. At the end, the sample was dispensed into the preheater at nearly 200 °C and 88 bars.

The inliSAMP demonstrator consists of a stable housing with the sample unit and a hydraulic power pack and electric supply. The parts are developed accordance to the HottoolKIT standards and taken from the modular system. The sample unit was developed for undisturbed and pressure-constant sample collection, storage, and dispensing. The high-performance hydraulic unit was engineered for high temperature operation and for usage in very small, round installation spaces. The associated communication and power supply was provided via a high temperature circuit board HiTES and power supply units in the laboratory.

The sampling procedure was developed for the inliSAMP demonstrator with the aim of obtaining a representative fluid. A key feature is the preheating of the sample chamber by a dummy sample, mixing and adaptive temperature control of the sealed sample during uplift and transportation. The test rig provides preheated water with a permanent pressure control. Also heating jackets and a heating band for thermal simulation of a borehole environment. The total power consumption of the demonstrator was also derived from the experiment. The power requirement is approximately 470 Watts for inliSAMP (see section 3.2), 400 Watts for heating at an ambient temperature of 14 °C in water, 50 Watts for the electric hydraulic motor, 10 Watts for the alternately powered valve and 10 Watts for permanent power for embedded and communication. Thus, for industrial available cables, the maximum cable length or operation depth can be calculated. A coax cable of 5 km length and 500 V DC capable, with a bit thicker wire than the cable of video probe inliCAM is required.

The quality of the fluid sample taken with the demonstrator has been assured by various technical measures such as the use of an adaptive intake and sealing mechanism, temperature controllers and temperature monitoring. Sample temperature and pressure, and sample status can be directly monitored and logged. Before the storage operation the temperature can be increased manually by the operator. The sample pressure can be increased manually as often and as high as desired during storage.

The temperature distribution in the sample is monitored at three measuring points and adjusted by an internal heating control according to the predefined procedure. The temperature gap between the sample chamber and the borehole is reduced by preheating. With a dummy sample, the temperature difference is reduced to 6 K at 200 °C during 3 hr testing. Convection dissolves the temperature stratification and permanently mixes the sample in the storage operation. Processes such as over heating, cooling, degassing, mineral perception which result in an alteration of the sample are suppressed by these measures. The pressure in the sample chamber is identical to the formation pressure until sealing. Moreover, the sample is collected slowly, independent of the load. Due to the simple sealing mechanism, the formation pressure or a higher adjustable sample pressure is in the sample chamber. Hence, there are no pressure differences and processes such as flashing and adiabatic cooling does not occur. The overpressure is to ensure no alteration of the sample, the maximum range value is 20 bars plus, due to thermal expansion.

Similar temperatures to the test bed and demonstrator at 190 – 197.5 °C were measured downhole in geothermal wells using the GTFSampler (Hsieh et al., 2021). After the probe has cooled down to about 20 °C, the sample pressure is 25 bars, The aqueous composition of the sample is verified by a simulation and the geochemical characteristics provides knowledge about the geothermal reservoir. Hence, downhole procedure of full pressurization at formation pressure and pressurization above dissolved gas pressure should be further investigated. A similar result is provided by the in-situ sampling (150 °C, 45 MPa) in Groß Schönebeck, Germany with the Leutert

system (Regenspurg et al., 2010) from the borehole. Here, no results of the measurement of pressure and temperature at the surface are measured, as only downhole fluid from the borehole analysis is existent. In addition, the inliSAMP demonstrator could provide temperature and pressure data over the wireline.

The integrity of the fluid sampler inliSAMP demonstrator is maintained by a representative fluid sample, a measurement log of the entire sample process history, real-time monitoring and remote control. The log contains data from the sample chamber (fluid temperature and pressure), borehole temperature, and operating data from the hydraulic power pack. The operating data provides important information about the status of every operation of the sampling procedure, the sampling time and the success of the sampling. In the SECURe project the sampler provides temperature and pressure data from downhole and volume. In the deployment, a pressure of 41.5 to 42 bars is measured, which is in the same magnitude to the experiment. Temperature and pressure are not maintained, so that no data is available during uplift to the measuring station (Ricroch et al.). However, it would be interesting to compare the sensor data accuracy and sample function with the inliSAMP demonstrator, as both probes can transfer real time data to the operator.

The inliSAMP demonstrator reduces the sampling time in the borehole, since no displacement fluid and pressurization fluid are required. Furthermore, repeatability of the sampling procedure is easily possible with the electrical and mechanical components. In the future, this will also include sampling with several probes or sample chambers. As preparation at site, a rinsing of the sample camber, check of the functions and filling of demineralized water is required. To obtain a representative sample from the borehole, the following fundamental requirements for temperature and pressure management as well as cleanliness of the sampling procedure and design were met. The experimental results and findings on the behaviour of the developed sampling procedure and inliSAMP demonstrator show progress in the field of in situ sampling tool development.

7. Conclusion

Extensive investigations have been carried out for the development of a novel sampling procedure, the sample chamber design and the implementation of a sampling module in the inliSAMP demonstrator. The overall objective was to develop a sample unit with controls and actors to retrieve a representative sample from downhole to surface with monitoring and control in real time data. The sampling module was mounted in a demonstrator housing and the developed sampling procedure was performed on a test bed under laboratory conditions. The investigations were mainly focused on design calculations of the sample chamber, the sample intake, and closing mechanism plus the sampling procedure with a minor temperature distribution in the sampler and a permanent pressure maintenance. Standards, experience with materials, and component developments were adopted and/or further enhanced from the hotToolKIT construction kit.

The main investigations and results of the proof of concept test showed:

- With the sampling procedure the fluid sample is taken, stored and delivered near in-situ downhole conditions.
- With a two-piston mechanism and operation hydraulic force, the sample is taken up without flashing, sealed without pressure change, recompressed if required and released again. Pressure change occurs during the storage and dispensing of the sample.

- In the sample chamber, the temperature distribution in the sample is monitored and logged over time at three positions. A tube heating mat is used to preheat the sample chamber, maintaining the temperature of the fluid sample and mix the sample due convection flows. Small deviations occur when the sample is let in and out.
- The inliSAMP demonstrator is monitored, supplied and operated with real time data via the wireline. Thus, a free choice of operations is possible. Additional operations could be performed such as sampling repetition, dispensing of any fluid downhole, multiple sampling and extended measurements.

During the proof of concept demonstration run and previous runs of the test rig, the pressure range is plus 20 bars in the storage operation during uplift and the temperature range is about 6 K during the sample intake in a preheated sample chamber. Thus, the in-situ conditions of the formation fluid a nearly maintained. The pressure increase could be reduced by improved automatized control of the temperature. For each process operation, a controller should also be developed to simplify remote operation by the operator and to partially automate sampling. A further test would be of importance with brine including dissolved gases in the test rig and a subsequent fluid and gas analysis. Furthermore, a revision of the design of the inlet hole and the seal is necessary to increase the lifetime of the sealings. For deployment of a prototype probe in the borehole, electronic components such as a power management system and power supply are under development. Many existing solutions such as the Dewar tube, cold reservoir and communication unit can be adopted from the inliCAM. This research on the inliSAMP probe has focused intensively on the sampling process and the maintenance of in situ downhole conditions in the sample chamber, as well as the enhancement of the integrity of the sampling data.

Acknowledgement

I extend my warmest greetings to my colleagues at the institute, the workshop leader and all the suppliers. Thank you for the collaboration.

REFERENCES

Akın, T., Kargı, H., 2019. Modelling the geochemical evolution of fluids in geothermal wells and its implication for sustainable energy production. Geothermics 77, 115–129. doi:10.1016/j.geothermics. 2018.09.003.

Alfredsson, H.A., Mesfin, K.G., Wolff-Boenisch, D., 2016. The syringe sampler: An inexpensive alternative borehole sampling technique for co 2 -rich fluids during mineral carbon storage. Greenhouse Gases: Science and Technology 6, 167–177. doi:10.1002/ghg.1543.

Ayliffe, C., 2022. 25.5.2022 Geothermal Energy Production Utilisation. ThinkGeoEnergy URL: https://www.thinkgeoenergy.com/geothermal/geothermal-energy-production-utilisation/.

Berentelg, G., Spatafora, L., Hagenmeyer, V., 2020. Wasam, a modularly designed fluid downhole sampler for deep geothermal applications. Geothermal Resources Council (GRC) doi:10.5445/IR/ 1000127866.

Conaway, C.H., Thordsen, J.J., Manning, M.A., Cook, P.J., Trautz, R.C., Thomas, B., Kharaka, Y.K., 2016. Comparison of geochemical data obtained using four brine sampling methods at

the secarb phase iii anthropogenic test co2 injection site, citronelle oil field, alabama. International Journal of Coal Geology 162, 85–95. doi:10.1016/j.coal.2016.06.001.

Dietze, S., 2020. Control and communication technologies of cable-based borehole probe - final GRC Transactions, Vol. 44. URL: https://publikationen.bibliothek.kit.edu/1000131541.

Eddie W. Banks, Stanley D. Smith, Michael Hatch, Lawrence Burk, and Axel Suckow, 2017. Sampling Dissolved Gases in Groundwater at in Situ Pressure: A Simple Method for Reducing Uncertainty in Hydrogeological Studies of Coal Seam Gas Exploration. doi:10.1021/acs.estlett.7b00457.s001.

Ekkehard, F., 2020. 16/08/2022. AN 134_VariPhi The Patented Immersion Heater Thermal Runaway Tests URL: https://analyzing-testing.netzsch.com/_Resources/Persistent/0/4/3/a/043ad64fd7dd71a1ea0ca5764f5359e9acb70b65/AN%20134_VariPhi%20The%20Patented%20Immersion%20Heater%20Thermal%20Runaway%20Tests.pdf.

Halliburton, 2022. Armada®sps-a single-phase sampler: Downhole collection of reservoir fluid samples for pressure-volume-temperature (pvt) analysis
URL: https://cdn.brandfolder.io/G1R8FA5S/as/q5uwqk-1jkrs0-5z1vcv/H012196-ArmadaSPSA.pdf.

Holbein, B., 2019. Theoretische und Experimentelle Kältemittel- und Dichtungsauswahl und Komponentenentwicklung zur Langzeitkühlung von Elektronik in Untertagewerkzeugen. Karlsruher Institut für Technologie (KIT). doi:10.5445/IR/1000094597.

Holbein, B., Dietze, S., Hurst, F., Isele, J., Spatafora, L., Wiegel, F., Hagenmeyer, V., 2018. Quality management and improvement for geothermal energy projects using the platform-based tool development technology - ZWERG. Geothermics 71, 320–330. doi:10.1016/j.geothermics.2017.10.010.

Holbein, B., Isele, J., Spatafora, L., 2017. New downhole tool designs for EGS based on platform development approach, in: Geothermal Resources Council Annual Meeting and GEA GeoExpo+, Salt Lake City, Utah, October 1-4, 2017, Geothermal Research Council. pp. 2453–2469. URL: https://publikationen.bibliothek.kit.edu/1000075690.

Hsieh, P.S., Lin, C.K., Chang, Y.T., Lu, H.Y., Yang, T.F., 2021. The gtfsampler: A new downhole equipment for geothermal fluid sampling and its testing results in the chingshiu geothermal field, ilan, taiwan. Geothermics 94, 102077. doi:10.1016/j.geothermics.2021.102077.

Huber, M., Harvey, A., Lemmon, E., Hardin, G., Bell, I., McLinden, M., . Nist reference fluid thermodynamic and transport properties database (refprop) version 10 - srd 23. doi:10.18434/T4/ 1502528.

International Ocean Discovery Program, 2022. 10.08.2022. iodp jrso • downhole logging tools. URL: https://iodp.tamu.edu/tools/logging/index.html.

Isele, J., Bauer, C., Dietze, S., Holbein, B., Spatafora, L., 2015a. The zwerg project: a platform for innovative logging tools, in: Proceedings of the World Geothermal Congress 2015, Melbourne, Australia. URL: https://publikationen.bibliothek.kit.edu/170100882.

Isele, J., Spatafora, L., Wiegel, F., Holbein, B., 2015b. Kamerainspektionssystem für tiefe Geothermie Brunnen (GeoKAM): Abschlussbericht: Forschungsvorhaben: 0325580. Karlsruhe Institute of Technology.

Kampman, N., Maskell, A., Bickle, M.J., Evans, J.P., Schaller, M., Purser, G., Zhou, Z., Gattacceca, J., Peitre, E.S., Rochelle, C.A., 2013. Scientific drilling and downhole fluid sampling of a natural co 2 reservoir, green river, Utah. Scientific Drilling 16, 33–43. doi:10.5194/sd-16-33-2013.

Leutert, 2021. Fluid sampling, in: Kuchuk, F.J., Ramakrishnan, T.S., Onur, M. (Eds.), Wireline Formation Testing: Hardware, Pressure Transient Testing, Interpretation and Sampling. Society of Petroleum EngineersRichardson, Texas, USA, pp. 347–364. URL: https://www.leutert.com/media/oilgas/downloads/sampling/datasheet_downhole-fluid-sampler_en_screen.pdf, doi:10.2118/9781613998434-17.

Lowenstern, J.B., Bergfeld, D., Evans, W.C., Hurwitz, S., 2012. Generation and evolution of hydrothermal fluids at Yellowstone: Insights from the heart lake geyser basin. Geochemistry, Geophysics, Geosystems 13, n/a–n/a. doi:10.1029/2011GC003835.

Lund, J.W., Huttrer, G.W., Toth, A.N., 2022. Characteristics and trends in geothermal development and use, 1995 to 2020. Geothermics 105, 102522. doi:10.1016/j.geothermics.2022.102522.

Regenspurg, S., Wiersberg, T., Brandt, W., Huenges, E., Saadat, A., Schmidt, K., Zimmermann, G., 2010. Geochemical properties of saline geothermal fluids from the in-situ geothermal laboratory Groß Schönebeck (Germany). Geochemistry 70, 3–12. doi:10.1016/j.chemer.2010.05.002.

Ricroch, P., Estublier, A., Guelard, J., Noirez, S., Martin, F., Mougin, P., Karimi, A., . Development of a downhole sampler and an integrated analysis system for in situ deep fluids analysis. URL: https://www.securegeoenergy.eu/sites/default/files/SECURe_D4.8_Final.pdf.

RochesterWireCable., 2012. Signal transmission cable, code: Sc0010162co01.

Schlumberger, 2020. Single-phase reservoir sampler URL: https://www.slb.com/-/media/files/testing-services/product-sheet/single-phase-reservoir-sampler-ps.pdf.

Schubert, B., Flöter, M., Kühne, T., Keusgen, W., 2015. GeoKam Abschlussbericht: Konzeptionierung eines Kabelmodems für ein Kamerainspektionssystem. Fraunhofer Institut für Nachrichtentechnik Heinrich Hertz Institut.

Spatafora, L., Isele, J., Holbein, B., 2016. The GeoKAM - a tool for video inspections in hot deep geothermal boreholes. 41st Workshop on Geothermal Reservoir Engineering, Stanford, CA URL: https://publikationen.bibliothek.kit.edu/1000054080.

Spatafora, L., Isele, J., Ritzhaupt-Kleissl, H.J., Hagenmeyer, V., Aktaa, J., 2019. Avoiding thermal-stress-induced failures by design optimization when brazing perlucor *Iconel* 718 components. Journal of ceramic science and technology 10, 1. doi:10.4416/JCST2019-00011.

Wheat, C.G., Kitts, C., Webb, C., Stolzman, R., McGuire, A., Fournier, T., Pettigrew, T., Jannasch, H., 2020. A new high-temperature borehole fluid sampler: the multi-temperature fluid sampler. Scientific Drilling 28, 43–48. doi:10.5194/sd-28-43-2020.

Wolff-Boenisch, D., Evans, K., 2014. Review of available fluid sampling tools and sample recovery techniques for groundwater and unconventional geothermal research as well as carbon storage in deep sedimentary aquifers. Journal of Hydrology 513, 68–80. doi:10.1016/j.jhydrol.2014.03.032.

Temperature and Pressure Transient Analysis: Pre and Post-Deflagration Assessment

Jorge Alberto Rangel-Arista[1*], Sadiq J. Zarrouk[1], Eylem Kaya[1], and Katie McLean[2]

[1] Department of Engineering Science, University of Auckland, Private Bag 90210, Auckland, New Zealand.

[2] Contact Energy Ltd, Wairakei Power Station, Taupo, New Zealand.

Keywords

Geothermal well testing, deflagration, temperature transient analysis, pressure transient analysis, temperature derivative.

ABSTRACT

Geothermal well test analysis is an essential tool for understanding reservoir behaviour and determining the parameters of fluid flow dynamics such as reservoir permeability, skin effect, wellbore storage and reservoir boundaries. Traditionally, only the pressure transients are analysed, while temperature transients are often overlooked despite their sensitivity to the changes in the wellbore and reservoir conditions. This work presents the temperature and pressure transient analysis conducted during the pre and post-deflagration testing of well BR064 in the Ohaaki geothermal field, New Zealand. The study uses a novel numerical framework to investigate temperature and pressure data resulting from the well-testing, matching them with their respective derivatives (temperature and pressure). Analysing temperature gives additional information about the reservoir and enhances the conventional pressure transient analysis. Through the temperature derivatives, it is possible to understand the complex heat transfer phenomena in the wellbore and obtain further information from existing well test data that are typically not considered.

1. Introduction

Deflagration is a stimulation method that uses subsonic high-pressure gas generated through an explosive charge that cleans the perforated linear and enhances the skin zone permeability of the wellbore (Zarrouk and McLean, 2019). The deflagration method has been used in different geothermal fields to improve well performance without conclusive results (Ohren et al., 2011; Sigurdsson, 2015; Bixley et al., 2016; McLean et al., 2016). Bixley et al. (2016) pointed out that an increase in the production flow rate indicates that deflagration was successful. However, this can take several months because the temperature, fractures, and well flow need to stabilise.

Completion well testing is usually carried out to assess the deflagration efficacy, which typically examines pressure and flow rate data (pressure transient analysis, PTA) to estimate reservoir, skin zone and wellbore properties such as permeability, skin factor and boundaries/faults (Zarrouk and McLean, 2019). The completion well testing involves the injection of cold water into the

geothermal well employing different rates, whilst the pressure, temperature, and spinner (PTS) sensor tool records the changes along the geothermal well.

Conventional analytical PTA considers constant fluid temperature (isothermal conditions) (Sidorova et al., 2014). However, this approach can prompt inaccurate results because it neglects the effects of temperature (Benson and Bodvarsson, 1986; Zarrouk and McLean, 2019). Nowadays, the numerical PTA methods can account for non-isothermal conditions, but they are not yet widely incorporated into the analysis.

The temperature transient analysis (TTA) investigates the temperature data from well testing under transient thermal conditions (Rangel-Arista et al., 2023). Therefore, TTA is an ideal complement to PTA, providing further insights (Ramazanov et al., 2010; Palabiyik et al., 2016).

Several works have investigated the supplementary application of TTA alongside PTA approaches. For instance, Palabiyik et al. (2013) developed a non-isothermal reservoir simulator for single-phase liquid-dominated geothermal systems. Onur and Palabiyik (2015) presented an analytical model to compute temperature and pressure at the sandface during constant-rate production tests. Panini and Onur (2018) proposed a TTA-PTA analytical model for a vertical oil well in a radial composite reservoir. Rangel-Arista et al. (2022) updated McLean and Zarrouk's (2017) geothermal framework for numerical pressure analysis, incorporating temperature conditions. Rangel-Arista et al. (2023) utilised Rangel-Arista et al.'s (2022) updated framework to investigate the non-isothermal effects of downflow in the Well CHI-8A (El Salvador) during pressure falloff.

The previous works investigated the deflagration process only by analysing the pressure response (Ohren et al., 2011; Sigurdsson, 2015; Bixley et al., 2016; McLean et al., 2016). Meanwhile, the works involving the temperature response analysis focused on wells without deflagration (Palabiyik et al., 2013; Onur and Palabiyik, 2015; Panini and Onur, 2018; Rangel-Arista et al., 2022; Rangel-Arista et al., 2023).

Therefore, we selected the BR64 dataset for this work to evaluate the effectiveness of deflagration through both temperature (TTA) and pressure (PTA) analysis, using data from injection tests performed pre and post deflagration.

2. Case Study: BR064

Figure 1 shows the casing profile of geothermal well BR064, a single-phase (only liquid) wellbore in the Ohaaki geothermal field, New Zealand. The well has a total depth of 2057 m, with a reservoir thickness of 864.5 m. Based on pressure, temperature, and spinner (PTS) sensor tool data, a pay zone of 400 m is estimated, with the remaining reservoir thickness composed of impermeable rock.

Figure 2 shows BR064 well testing parameters, pre (Pre-D), during and post (Post-D) deflagration: pressure, temperature, sensor tool depth, and injection flow rate. During Pre-D phase, water injection causes wellbore cooling (Figure 2) for approximately 123633 s (34.34 hours) from the beginning to point A. Prior to reaching Point A, pressure and temperature fluctuations occur because the PTS sensor tool travels up and down along the wellbore (Figure 2). Before point A, the injection flow rate experiences incremental increases in three steps: 10, 21 and 31.7 kg/s.

Moments before point A in the Pre-D (Figure 2), the sensor tool reaches the target depth, leading to a decrease in flow rate from 31.7 kg/s to 2.91 kg/s, commencing a non-zero pressure falloff (Zarrouk and McLean, 2019) for the Pre-D period (A-B). During this time, temperature buildups from 67.3°C to 137.85°C (ΔT∼70.55°C), whilst pressure falls off from 129.72 to 121.91 bar (ΔP∼7.81 bar). The pressure falloff period lasts for 36,301 s (10.08 hours).

Once the Pre-D falloff period is over (Figure 2, A-B), the PTS tool travels to the bottom of the well (B-D). Then, the injection flow rate increases (C-D) to 29.16 kg/s for additional wellbore cooling. Next, the flow rate drops (E-F). During period D-G (Figure 2), deflagration occurs as the downhole PTS sensor is removed from the wellbore. At point G, the PTS sensor tool re-enters the well, travelling downward to the target depth. Afterwards, the PTS tool travels up and down the well to identify loss zones (Zarrouk and McLean, 2019) (G-H), prompting temperature and pressure peaks (Figure 2). Simultaneously, the injection flow rate exhibits two incremental increases (G-H): 21 and 32.16 kg/s. Before point H, the sensor tool returns to the target depth (Figure 2).

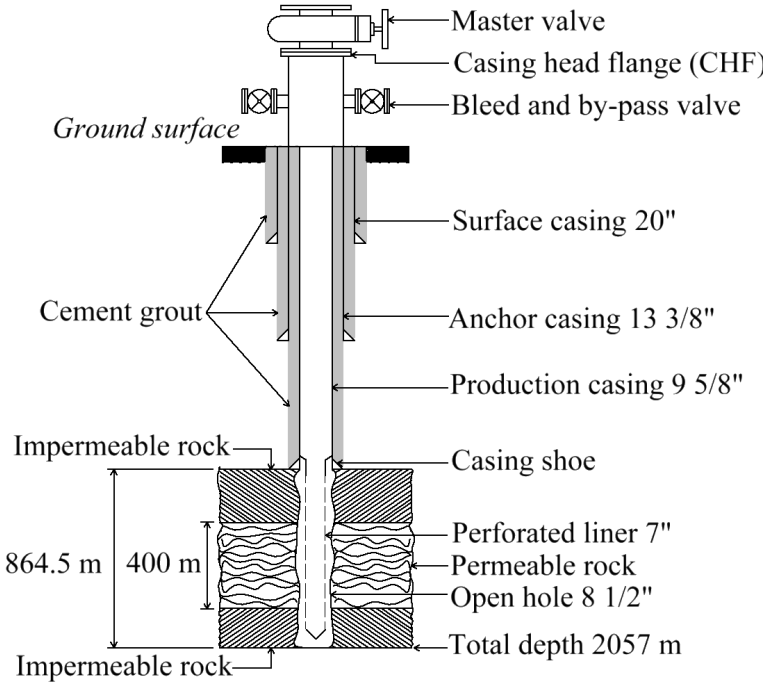

Figure 1: Well BR064 casing diagram.

At point H (Figure 2), the injection flow rate drops (2.91 kg/s), prompting the Post-D non-zero pressure falloff period (H-I), which lasts 31,771 s (8.82 hours). During this time, the temperature increases from 60.74°C to 127.86°C (ΔT∼67.12°C), whereas the pressure decreases from 135.23 bar to 122.43 bar (ΔP∼12.8 bar).

Figure 3 shows the pressure and temperature responses during pressure falloff for Pre-D and Post-D. The pressure responses remain transient without reaching full equilibrium (Figure 3), although the falloff period lasted more than 8 hours for both cases. This can indicate a low reservoir permeability with possible damage in the near wellbore zone.

The temperature increases rapidly during the first moments because of the drop in the injection flow rate (Figure 3). The cooling effect diminishes as the flow rate declines, prompting the sudden temperature increase until the new injection flow step stabilises. The temperature rises gradually after the rapid growth (Figure 3) because of the cooling effect induced by the low injection flow rate (2.91 kg/s). The rapid pressure fall and temperature rise seen in Post-D indicate a stronger (enhanced) connection between the wellbore and reservoir.

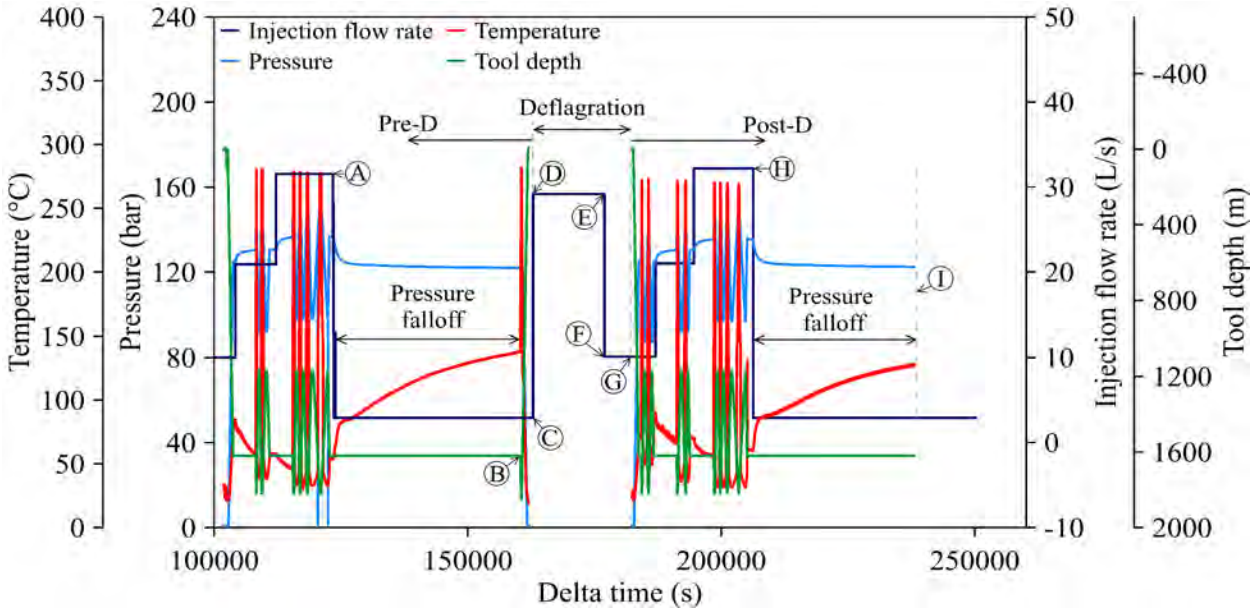

Figure 2: Pre (Pre-D) and post (Post-D) deflagration well testing.

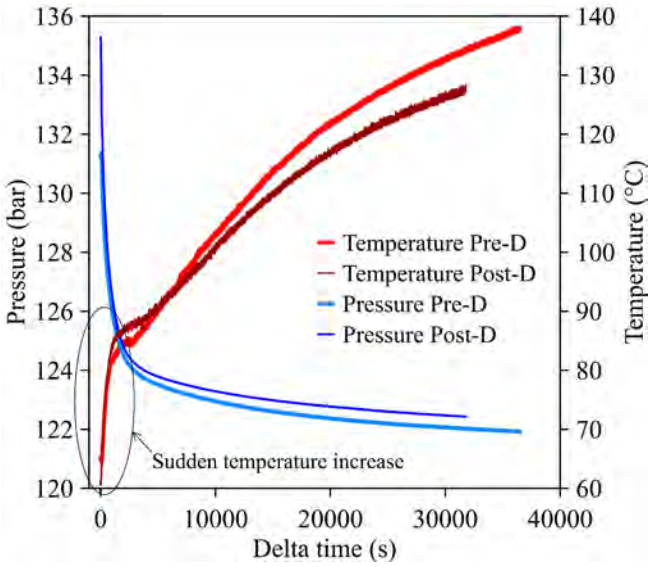

Figure 3: Temperature and pressure during pressure falloff, pre (Pre-D) and post (Post-D) deflagration.

Figure 4 shows the pressure difference ($dP = P_i - P$) and pressure derivative (dP') for Pre-D and Post-D. The duration of the wellbore storage effect (unity slope straight line response) is shorter

during Post-D than Pre-D. This shows improvement in the connection between the wellbore and the reservoir post-deflagration.

Then the transient effect prompts a large hump (Figure 4), indicating damage in the skin zone (positive skin). After the skin effect, a 0.4 unit slope appears, probably indicating the presence of a boundary.

Figure 5 shows the temperature difference ($dT = T_i - T$) and temperature derivative (dT') for Pre-D and Post-D. Multiple prominent peaks appear at the beginning (1st zone) and middle (2nd zone) because of the small temperature changes. Some peaks are more significant, indicating that almost constant temperature occurred, prompting the temperature derivative to tend to zero (Rangel-Arista et al., 2023). Two flattening zones appear for both derivatives, containing peaks with slight changes (Figure 5).

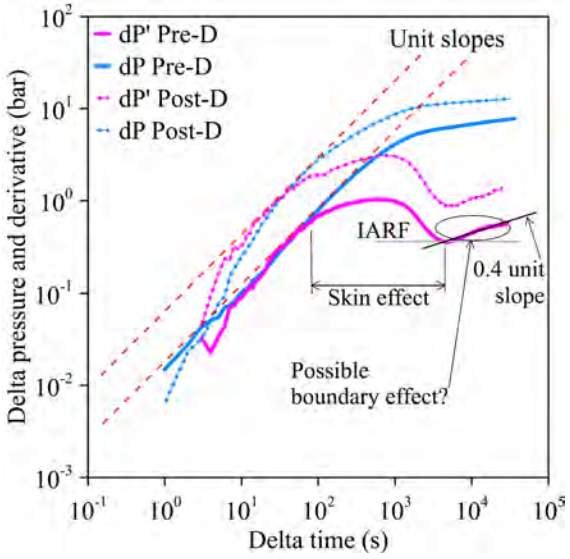

Figure 4: Pressure derivative, pre (Pre-D) and post (Post-D) deflagration.

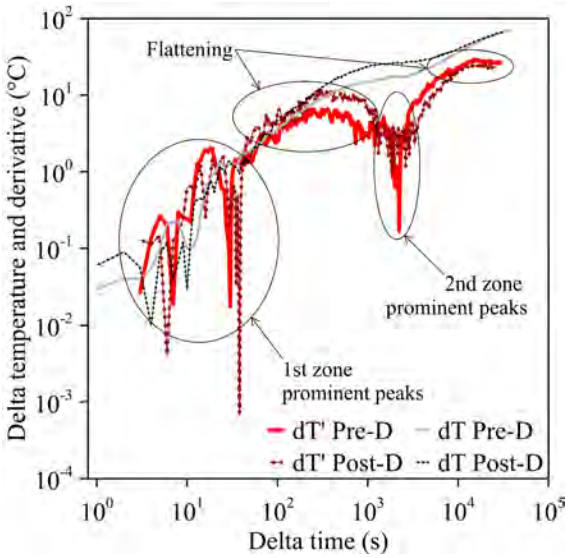

Figure 5: Temperature derivative during pressure falloff, pre (dT' Pre-D) and post (dT' Post-D) deflagration.

3. Well Test Framework Set Up

We used Rangel-Arista et al.'s (2022) numerical modelling framework, which updated McLean and Zarrouk's (2017) numerical framework for analysing the transient pressure to include the transient temperature. Rangel-Arista et al. (2022) demonstrated that matching the TTA along the PTA will result in a more accurate reservoir parameter estimations while unlocking additional information about the reservoir.

Rangel-Arista et al.'s (2022) framework employs AUTOUGH2 and PyTOUGH. AUTOUGH2 is a reservoir simulator based on TOUGH2 (Pruess et al., 1999), a general-purpose simulator to model subsurface fluid and heat flow in geothermal reservoirs. PyTOUGH manages AUTOUGH2, handling grid construction, data files, plotting and analysis of results, as well as the implementation of initial and boundary conditions and physical parameters (Croucher, 2020).

The framework uses a grid geometry that consists of three radial layers with multiple blocks in the radial direction to capture the changes in temperature in the vertical and radial directions more efficiently (Figure 6) (Rangel-Arista et al., 2022). The blocks are spaced logarithmically, representing the wellbore, skin zone and reservoir. The central cylinder blocks represent the wellbore, while skin zone blocks extend from the wellbore radius up to 5 m. Reservoir blocks extend from the skin zone to 20000 m. The pay zone, 400 m thick, is represented (Figure 1) by three layers, each 133.33 m thick.

3.1. Numerical Modeling Framework: Pressure Response

The pressure response was analysed according to McLean and Zarrouk's (2017) framework, which employs the fractional dimension model (Zarrouk and McLean, 2019) to represent the fractured reservoir in dynamic conditions (Barker, 1988). This method simulates complex fractured reservoirs better without explicitly considering rock mechanics (Zarrouk et al., 2007).

The fractional dimension theory considers assigning a number that ranges from one to three, typically involving non-integer values (fractional numbers). Number one represents a linear flow along a plane (fracture wall). Two represents radial flow converging in the well, forming a round disc. Three represents flow from all directions converging in the well, creating a spherical flow (Zarrouk and McLean, 2019).

3.2. Numerical Modeling Framework: Temperature Response

The underground heat transfer involves conduction, convection and advection processes, occurring simultaneously (Zarrouk and McLean, 2019). The new PTA and TTA modelling framework (Rangel-Arista et al., 2022) simplifies the heat transfer mechanism by assuming that only conduction (thermal diffusion only) takes place, achieved by artificially changing the Péclet number.

This simplification is necessary due to the complex heat transfer between the wellbore and reservoir throughout the feed zones, where hot and cold fluids enter and leave the well through a complex network of fractures within the reservoir. The full representation of this process would require a detailed mapping of all the feed zones with multiple sensors along these areas, which is impractical due to the cost and high temperatures involved.

In our approach, we assumed that the Péclet number averages conduction, convection, and advection within the wellbore and skin blocks, changing for each step to match the temperature response. A Péclet number close to one reflects that most heat transfer is due to conduction. Higher Péclet numbers denote dominant convection, meaning a more significant interaction between the injection flow (cold) and hot fluid (from the reservoir and feed zones).

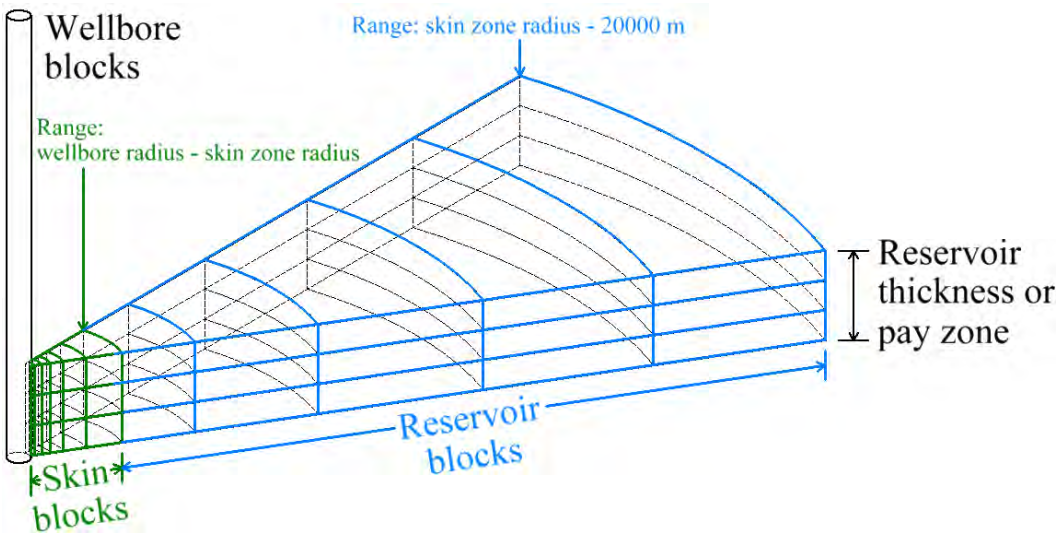

Figure 6: Grid geometry.

3.3. Numerical Modeling Framework: Parameters and Solution

Table 1 shows the parameters used to set up the geothermal numerical framework. Wellbore volume, pay zone, and wellbore radius correspond to the actual dimensions of well BR064. We utilised 40 and 60 blocks per layer for the skin zone and reservoir, respectively (based on our experiments to calibrate the geothermal TTA-PTA framework).

The modelling time is divided into multiple steps to match the temperature and pressure responses. The Péclet number and fractional dimension are the only parameters changing in each step. The remaining factors related to the wellbore, skin zone, and reservoir maintained the same values throughout the simulation.

Table 1: The geothermal well testing framework sets up initial parameters for Well BR064.

Model parameters	Input
Well volume (m^3)	75
Pay zone (m)	400
Well radius: r_w (m)	0.10795
Model radial extent (km)	20
Number of layers	3
Layer thickness	133.33
Skin zone blocks per layer	40
Reservoir blocks per layer	60
Injectate temperature (°C)	67
Reservoir porosity (dimensionless)	0.1

Reservoir permeability: $k \times 10^{-15}$ (m^2)	10
Reservoir temperature (°C)	290
Skin zone radius: r_s (m)	4
Skin factor: s (dimensionless)	6
Skin zone permeability: $k_s \times 10^{-15}$ (m^2)	3.76

4. Results

Figure 7 shows the temperature and pressure history matches between field data and models for the Pre-D (Figure 7a) and Post-D (Figure 7b). Both show very good matches between the model and field data.

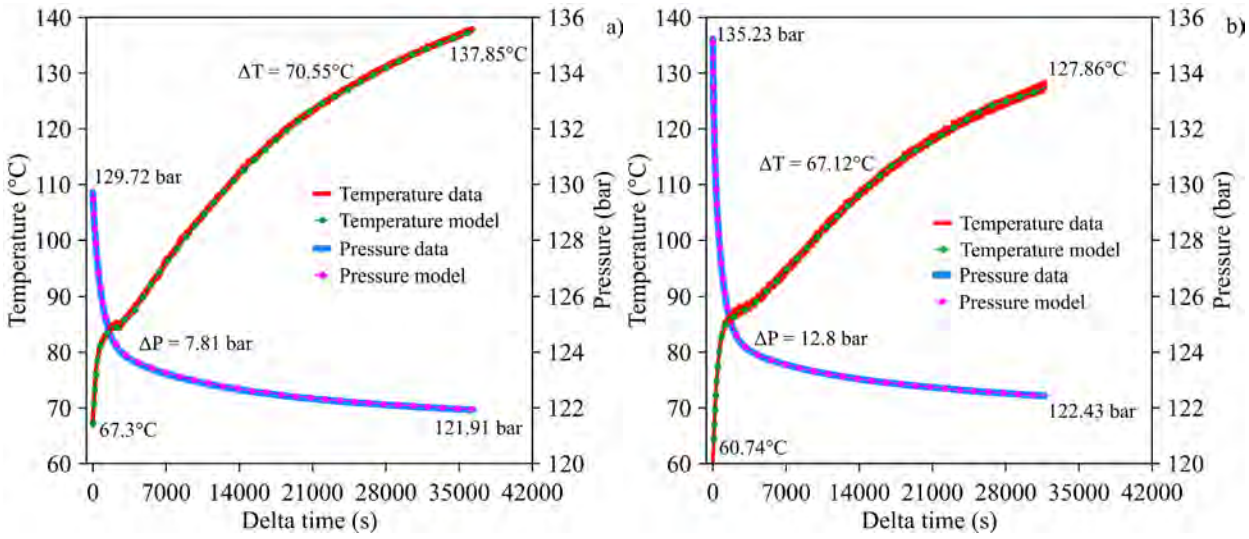

Figure 7: Temperature and pressure matches, a) pre and b) post deflagration.

Figure 8 shows the Péclet number changes needed to match the temperature response for Pre-D and Post-D. During period A (Figure 8), the Péclet number starts with high values, gradually decreasing over time because the last injection flow step effects (31.52 kg/s) are still present but diminishing for both Pre-D (Figure 8a) and Post-D (Figure 8b). This indicates a transition from convection to conduction because the amount of injection fluid is less (the cooling effect of the injection diminishes), prompting the sharp temperature rise for both periods (Pre-D and Post-D). Simultaneously, although hot fluid comes from the reservoir, its impact on the wellbore and skin zone is smaller than the cooling effect caused by the last injection step.

The Péclet number (Figure 8) rises during period B for both cases (Pre-D and Post-D). The increase is more noticeable for Pre-D (Figure 8a), where the heat transfer occurs mainly in the wellbore and skin zones (indicating lower permeability or connection with the reservoir). For the Post-D (Figure 8b), the reservoir zone interacts slightly more (more permeability or connections with the reservoir), reflecting a less significant increment.

The effects of the new injection period (2.91 kg/s) at the end of period B (Figure 8) are less noticeable than the last injection period (31.52 kg/s), prompting the lowest Péclet number. This indicates that convection decreases, tending to conduction, although convection prevails.

The new injection flow rate (2.91 kg/s) is entirely stable at the beginning of period C (Figure 8). Simultaneously, the hot fluid from the reservoir 'kicks in' according to the new injection flow rate (2.91 kg/s), increasing the Péclet number for Pre-D (Figure 8a) and Post-D (Figure 8b). Then, it stabilises for both cases (Pre-D and Post-D), with slight variations up to the period C end. The Péclet number is slightly more significant for the Post-D case (Figure 8b) along period C, indicating that more hot fluid comes from the reservoir (permeability increase), creating a considerable temperature rise rate for Post-D (Figure 7b) than for Pre-D (Figure 7a).

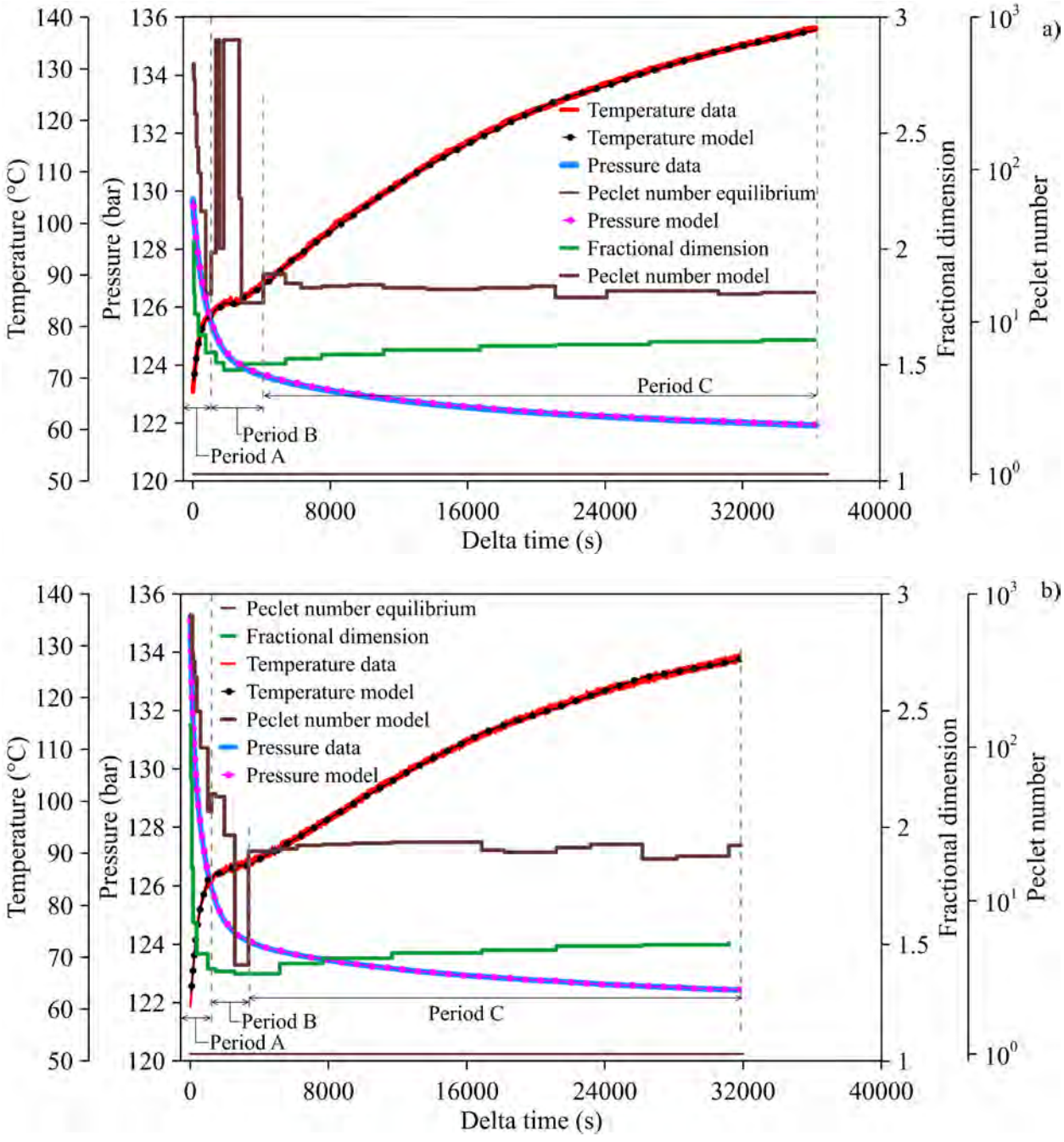

Figure 8: Temperature match and Péclet number, a) pre and b) post-deflagration period.

Figure 9 shows the pressure derivate match for Pre-D and Post-D. Both cases show a smooth match along the falloff during the wellbore storage effect, skin zone (transient zone) and reservoir response. We are unable to discuss the possible presence of the boundary (Figure 9) because of the lack of field information.

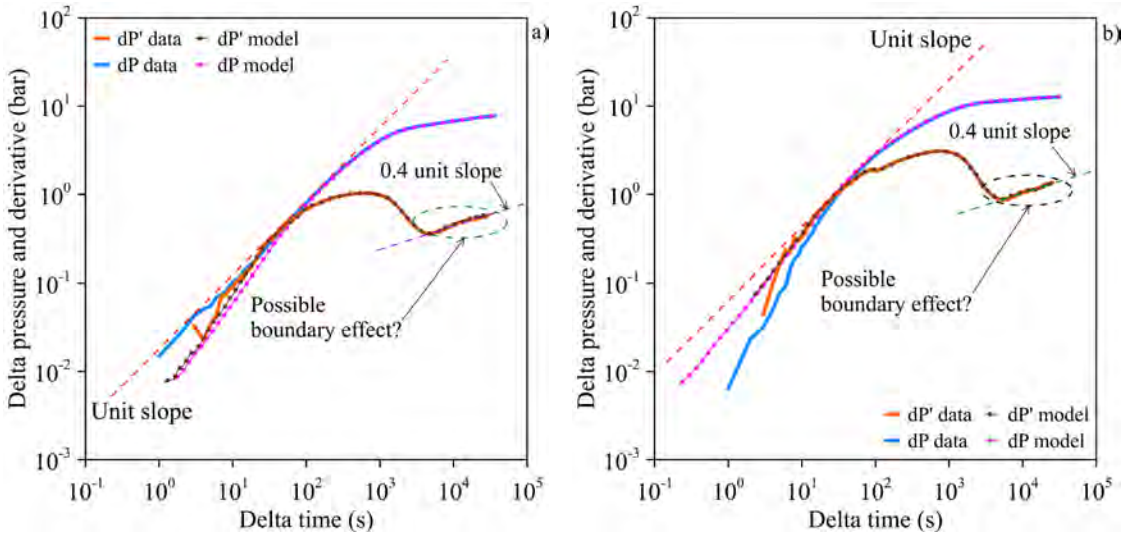

Figure 9: Delta pressure (dP) and pressure derivative (dP') match, a) pre and b) post deflagration period.

Figure 10 shows the temperature derivative match for the Pre-D and Post-D, displaying the same periods as the temperature match (Figure 8). Prominent downward peaks appear at the beginning of Period A (Figure 10) before the flattening. The peaks represent less notable temperature changes that almost reach constant Temperature, prompting the derivative to tend to zero.

After these initial peaks (Figure 10), the trend flattens in period A, accompanied by slight oscillations in the temperature derivative, reflecting the water injection process. Next, in period B (Figure 10), the last injection step (31.52 kg/s) effects vanish entirely. Simultaneously, the new injection flow step (2.91 kg/s) starts producing effects, and the hot fluid from the reservoir rises. At the end of period B (Figure 10), the new injection flow rate (2.91 kg/s) is fully developed.

The Pre-D case (Figure 10a) shows the temperature stabilisation point (Period B), where an almost constant temperature is reached, prompting the derivative to tend to zero. Then, hot fluid 'kicks in' according to the new injection flow step (2.91 kg/s).

During period B, in the Post-D case (Figure 10b), a temperature stabilisation zone appears instead of the temperature stabilisation point (Figure 10a). This indicates that the temperature changes are more significant in Post-D than for Pre-D, suggesting a connection improvement between the wellbore and reservoir. In Pre-D, slight temperature changes almost reach constant temperature, prompting the temperature derivative to approach zero (Figure 10a). In Post-D, more considerable temperature variations occur, resulting in the absence of a constant temperature and preventing the temperature derivative from approaching zero (Figure 10b).

During Period C (Figure 10), the temperature derivative rise reflects the temperature increase, which is almost similar for Pre-D (Figure 10a) and Post-D (Figure 10b). Flattening occurs at the

end of Period C because of the injection flow step effect for Pre-D (Figure 10a) and Post-D (Figure 10b).

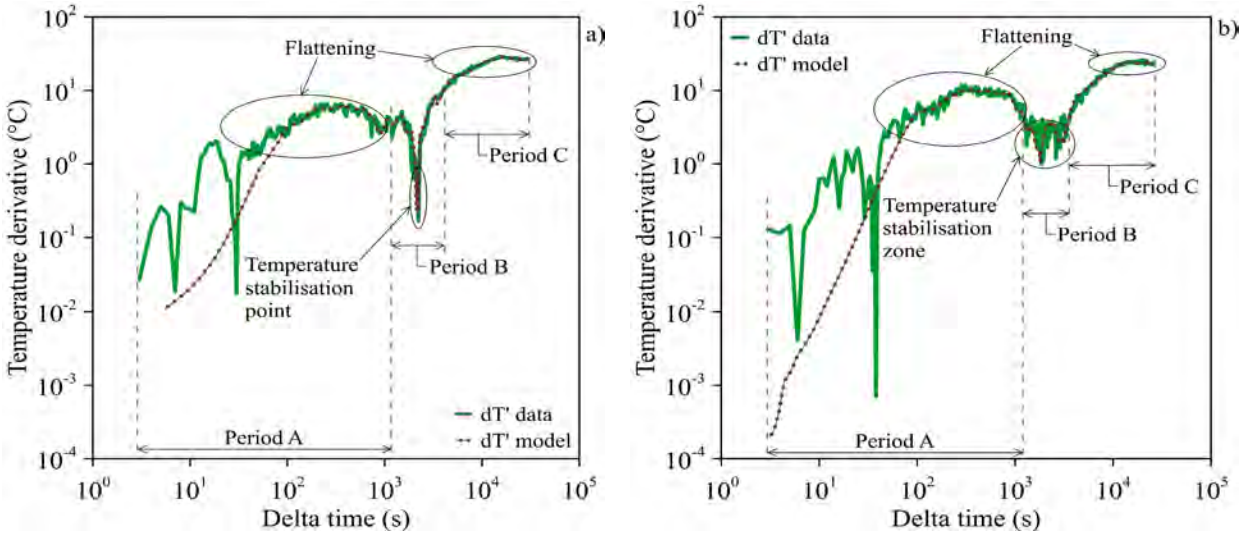

Figure 10: Temperature derivative (dT') match, a) pre and b) post deflagration period.

Table 2 shows the changes observed in the Pre-D and Post-D cases. The remaining parameters maintained the same values as shown in Table 1. A slight permeability rise occurs at the skin zone, increasing by 4.62 mD. The skin factor decreased by one unit, indicating that the damaged area improved because of deflagration, enhancing the connection between the wellbore and reservoir.

Table 2: Parameters affected by deflagration.

Parameters	Pre deflagration	Post deflagration
Skin factor: *s* (dimensionless)	6	5
Skin zone permeability: $k_s \times 10^{-15}$ (m^2)	3.76	8.38

5. Conclusions

The deflagration process resulted in a minor improvement in the skin zone permeability and a reduction in the skin factor. This confirms the findings of previous studies indicating that deflagration has a limited impact on the well performance as it only improves the near wellbore part of the reservoir. Despite the improvements, the skin zone in well BR64 remains positive Post-Deflagration, indicating that the skin damage still exists in this well. The cause of skin damage can be further investigated, and other solutions, such as chemical treatment, can be put in place to stimulate the well.

The temperature transient analysis proved to be helpful in interpreting the well-testing data. In this case, the effects of deflagration caused an improvement in the wellbore-reservoir connection, displaying a faster temperature rise Post-D compared to Pre-D. This is evident in the temperature derivatives at period B. The temperature stabilisation zone is less noticeable for Post-D compared

to Pre-D, indicating a quicker stabilisation following the transition between injection flow steps and the influx of hot fluid from the reservoir after deflagration.

Our analysis captured the complex heat transfer dynamics by accounting for thermal diffusion and Péclet number, providing insight into the multiple interactions between the injection flow steps and hot fluid flow from the reservoir.

Our study demonstrates that the temperature derivative is a sufficiently sensitive tool to show various complex heat transfer interactions, allowing the identification of distinct zones corresponding to the multiple interactions. This capability enhances the interpretation of temperature data, providing an additional layer of understanding of the heat transfer process occurring within the well.

Acknowledgements

The first author thanks the National Council of Humanities, Science and Technology of Mexico (CONAHCYT) for kindly providing the PhD scholarship to study at the University of Auckland.

This work was possible through the New Zealand Ministry of Business, Innovation and Employment (MBIE) through the Reversing Carbon Emissions in Geothermal Energy Industry – Template for Emissions – Intensive Industries project funds (UOAX2211).

NOMENCLATURE

k	Reservoir permeability (m^2)
k_s	Skin zone permeability (m^2)
P	Pressure at time t or pressure (bar)
P_i	Initial pressure (bar)
T	Temperature at time t or Temperature (°C)
T_i	Initial temperature (°C)
r_w	Well radius (m)
r_s	Skin zone radius (m)
s	Skin factor (dimensionless)

Acronyms

Post-D	Post deflagration
Pre-D	Pre deflagration
PTA	Pressure transient analysis

PTS Pressure, Temperature and spinner sensor

TTA Temperature transient analysis

REFERENCES

Barker, J. A. "A generalised radial flow model for hydraulic tests in fractured rock." *Water Resources Research,* 24, (1988), 1796-1804.

Benson, S. M., and Bodvarsson, G. S. "Non-isothermal effects during injection and falloff tests." *SPE Formation Evaluation,* 1, (1986), 53-63.

Bixley, P., Mclean, K., Lim, Y. W., and Wilson, D. "Assessing the effectiveness of declaration in multiple-feedzone wells." *Proceedings the 38th New Zealand Geothermal Workshop,* Auckland, New Zealand (2016).

Croucher, A. E. "PyTOUGH user's guide." *Department of Engineering Science, University of Auckland,* (2020).

McLean, K., and Zarrouk, S. J. "Pressure transient analysis of geothermal wells: A framework for numerical modelling." *Renewable Energy,* 101, (2017), 737-746.

McLean, K., Zarrouk, S. J., and Wilson, D. "Application of numerical methods for geothermal pressure transient analysis: A deflagration case study from new zealand." *Proceedings of Stanford Geothermal Workshop,* California, USA (2016).

Ohren, M., Benoit, D., Kumataka, M., and Morrison, M. "Permeability recovery and enhancements in the soda lake geothermal field, fallon, nevada." *Transactions - Geothermal Resources Council,* 35, (2011), 493-497.

Onur, M., and Palabiyik, Y. "Nonlinear parameter estimation based on history matching of temperature measurements for single-phase liquid-water geothermal reservoirs." *World Geothermal Congress,* Melbourne, Australia (2015).

Palabiyik, Y., Onur, M., Tureyen, O. I., and Cinar, M. "Transient temperature behavior and analysis of single-phase liquid-water geothermal reservoirs during drawdown and buildup tests: Part I. theory, new analytical and approximate solutions." *Journal of Petroleum Science and Engineering,* 146, (2016), 637-656.

Palabiyik, Y., Tureyen, O. I., Onur, M., and Paker Deniz, M. "Pressure and temperature behaviors of single-phase water geothermal reservoirs under various production/injection schemes." *38th Workshop on Geothermal Reservoir Engineering,* California, USA (2013).

Panini, F., and Onur, M. "Parameter estimation from sandface drawdown temperature transient data in the presence of a skin zone near the wellbore." *SPE Europec Featured at 80th EAGE Conference and Exhibition,* Copenhagen, Denmark (2018).

Pruess, K., Oldenburg, C. M., and Moridis, G. J. "TOUGH2 user's guide version 2." *Earth Sciences Division, Lawrence Berkeley National Laboratory,* (1999).

Ramazanov, A. S. S., Valiullin, R. A., Sadretdinov, A. A., Shako, V. V., Pimenov, V. P., Fedorov, V. N., and Belov, K. V. "Thermal modeling for characterisation of near wellbore zone and

zonal allocation." *SPE Russian Oil and Gas Conference and Exhibition*, Moscow, Russia (2010).

Rangel-Arista, J. A., Zarrouk, S. J., Kaya, E., and McLean, K. "Exploring the use of temperature transient analysis during pressure falloff testing in geothermal wells." *Proceedings 44th New Zealand Geothermal Workshop*, Auckland, New Zealand (2022).

Rangel-Arista, J. A., Zarrouk, S. J., Kaya, E., and Pacheco, R. E. R. "Geothermal temperature and pressure transient analyses of well CHI-8A, el salvador during pressure falloff." *Proceedings 45th New Zealand Geothermal Workshop*, Auckland, New Zealand (2023).

Sidorova, M., Theuveny, B., Pimenov, V., Shako, V., and Guzman-Garcia, A. G. "Do not let temperature transients hinder your buildup pressure interpretation – proper gauge placement in highly productive reservoirs in well testing operations." - *SPE Annual Caspian Technical Conference and Exhibition*, Astana, Kazakhstan (2014).

Sigurdsson, O. "Experimenting with deflagration for stimulating geothermal wells." *Proceedings, World Geothermal Congress*, Melbourne, Australia (2015).

Zarrouk, S., and McLean, K. "Geothermal well test analysis: Fundamentals, applications and advanced techniques." *Elsevier*, (2019).

Zarrouk, S., O'Sullivan, M., Croucher, A., and Mannington, W. "Numerical modelling of production from the poihipi dry steam zone: Wairakei geothermal system, new zealand." *Geothermics*, 36, (2007), 289-303.

Utilization & Testing of Advanced Wireline Conveyed Subsurface Tools in Vapor Dominated Reservoirs – The Geysers

Michael Richter, John Jacobson, Jeffrey Johnston, Reza Khastoo, Javier Serrano

Calpine Corporation

Kaldera, LLC

Rapid Prototypes, LLC

Scientific Drilling International

Keywords

Calpine – The Geysers, wellbore integrity, wireline, downhole logging, XY caliper, bi-directional, casing inspection, multi-finger caliper, subsurface tool testing, high temperature

ABSTRACT

The exploration and exploitation of vapor dominated geothermal reservoirs present unique challenges due to their complex subsurface dynamics and elusive fluid behaviors. This abstract proposes a novel approach of utilizing and testing of advanced high temperature and high-pressure subsurface wireline conveyed tooling to enhance the characterization and understanding of such reservoirs and the wellbore environment. Traditional techniques often struggle to accurately capture these properties, leading to suboptimal resource utilization and operational inefficiencies. In response, this testing study advocates for the integration of cutting-edge subsurface tool testing methodologies and leveraging state-of-the-art technologies to provide comprehensive insights into reservoir characterization.

Through the development of advanced downhole tools equipped with high-resolution sensors and high-temperature mitigation techniques, new approaches to sub-surface wireline conveyed cased hole and open hole logging aim to capture data including temperature gradients, pressure differentials, steam flow profiles, feed-zone identifications, and wellbore integrity. By obtaining and analyzing this data in conjunction with existing reservoir models and geological data, geologists, reservoir engineers, and seismologists can optimize feed-zone characterization models, refine placement strategies, and improve reservoir management practices. Furthermore, the

continuous monitoring enabled by these tools facilitates early detection of reservoir and wellbore anomalies and enhances the efficiency of reservoir surveillance programs.

The continued development of this technology offers significant potential for the geothermal industry by enabling more informed decision-making processes, reducing operational risks, limiting operational non-productive times, and maximizing resource recovery. Furthermore, the insights gained from these tests can contribute to the advancement of geothermal energy as a sustainable and reliable source of clean energy, thus supporting global efforts towards mitigating climate change and transitioning towards a low-carbon future.

1. Introduction

Located in Lake and Sonoma County, California, The Geysers Geothermal Steamfield epitomizes humanity's quest for sustainable energy sources and the formidable power of Earth's geological dynamics. Encompassing over 44 square miles, this expansive complex of steam vents, hot springs, and bubbling pools stands as the world's single largest geothermal electrical operation. Beyond its natural allure, it serves as a crucial energy resource powering millions of homes and businesses while minimizing environmental impact. Exploring the depths of The Geysers reveals not only the intricacies of geothermal energy production but also the delicate equilibrium between harnessing Earth's resources and conserving its natural splendor for future generations.

With 316 active production wells and 53 active injection wells spread across the vast steamfield, each requires subsurface maintenance and monitoring to meet regulatory standards, ensure wellbore integrity, and sustain steamflow reliability. Essential to these efforts are advanced wireline tools and equipment, including Pressure, Temperature, and Spinner tools (PTS), 15-arm Kinley Casing Calipers, "bridge busters" for chisel broaching, and downhole cameras. Engineered to thrive in the challenging conditions typical of The Geysers, where reservoir temperatures average 371ºF, these tools are designed for durability and optimal performance.

As drilling technology continues to advance and wells within the geothermal field deepen, temperatures in the wellbores are expected to rise. This progression underscores the critical need for ongoing enhancement and innovation in subsurface tools and equipment capable of withstanding escalating environmental demands. Calpine is actively evaluating newly developed tools suitable for the rigorous geothermal environment. These collaborations also offer invaluable insights to tool developers and manufacturers, who rigorously test tools in diverse environments over extended periods, focusing on durability, precision in data collection, and operational efficiency.

2. Kaldera PTS-XY Bi-Directional Caliper Logging Tool Testing

The Kaldera, LLC. founders have been manufacturing and supplying tools specifically designed for geothermal fields for over three decades. During this time, they have observed a growing need for devices that enhance operational efficiency to reduce costs.

High-temperature logging tools that can record well pressure, temperature, and flow rates (PTS tools) have been crucial in helping geothermal fields maintain high production levels. However, these tools do not provide information on changes to the internal diameter caused by natural scale buildup over time.

In the oil and gas industry, XY Caliper logging tools have long been a standard part of an operator's toolbox. Unfortunately, typical temperatures in geothermal operations are roughly double those in oil and gas, making the temperature rating of XY Calipers designed for oil and gas unsuitable for most hot geothermal wells, which usually exceed the tool's nominal 350 degrees Fahrenheit rating.

The lack of a suitable XY Caliper tool for geothermal operations left operators with a few options. They could lower multiple gauge rings of different diameters to various depths to get a rough idea of the internal diameter, a time-consuming and costly process. Alternatively, they could cool the well and then use a lower-temperature XY Caliper tool designed for oil and gas. However, cooling the well may be both costly and risky.

Even when using an XY Caliper tool designed for higher temperatures, the ability to simultaneously record pressure, temperature, and flow allows operators to save time by eliminating the need of an additional PTS survey run.

Due to the required length of both an XY Caliper and a PTS tool, coupling the two together presents a challenge for wireline operators, who must source a sufficiently long lubricator and crane.

Kaldera decided to integrate the PTS sensors and a high-temperature geothermal XY Caliper into a single tool with a single electronic section. This integration reduces the total length compared to combining two tools in one run, thus lowering operational costs.

PTS/XY Caliper tools have been sold and operated in Central America and Asia. These tools help eliminate the need for running multiple gauge rings before logging services, record the full profile of scale buildup in the internal diameter of the casing and liner, and better understand calcite buildup. This information helps determine the chemical dosage required during the maintenance of geothermal wells. Kaldera's patented PTS-X/Y combination tool is the only tool designed for the geothermal market that records inside diameter, pressure, flow, and temperature.

2.1 General Specifications & Basic Theory

2.1.1 Tool Specifications

Characteristics	**Specifications**
Pressure Range	Up to 8,500 psi
Pressure Accuracy	0.05% FS
Temperature Range	325ºC/617ºF (Caliper) 350ºC/660ºF (PTS)
Temperature Accuracy	±0.15ºC
X-Y Caliper Range	2.75" to 13 3/8" Casing
X-Y Caliper Accuracy	±0.25"
Tool Length	121.5"
Tool Weight	80 lbs
Spinner Range	10 to 20,000 rpm
Sampling Frequency	Up to 8 Hz (Adjustable)

Figure 1: Image of a Fully Assembled Kaldera PTS-XY Caliper tool in combination.

2.1.2 Basic Tool Theory

The tool incorporates high-temperature electronics and a vacuum flask for electronic protection, alongside modular and proprietary sensors for detecting mechanical diameter changes. It consists of four main sections. Firstly, the Electronics Section comprises a vacuum flask, serving as a heat shield to safeguard all electronics. The Pressure and Temperature Sub-Assembly follows, crucial for monitoring external temperature and pressure to assess well conditions accurately. Next, the XY Caliper features four naturally open arms equipped with roller wheels, ensuring constant contact with the well's inside diameter. Fully closed, the tool maintains an outside diameter of 2.75 inches, enabling passage through 3-inch restrictions and measurement of casing diameters up to 13-3/8 inches, facilitating versatile use across a wide range of geothermal wells. Finally, the Spinner, situated at the tool's bottom, measures flow rate, delivering essential data on well performance.

2.2 Kaldera XY Caliper Durability Testing

Kaldera collaborated with Calpine to assess the XY Caliper's resilience in the open hole segment of a wellbore. This partnership aimed to enhance steam flow calculations for Calpine’s reservoir engineers and gain insights into formation anomalies, all while minimizing wireline operational time. The test's primary objective was to evaluate the tool's functionality and durability in the demanding open hole environment. Although no electronic measurements were taken during the test, the X-Y Bi-Directional Caliper, equipped with roller wheels, was designed to hover above the casing or open hole surface. Its spring-loaded arms offered flexibility to navigate obstructions or narrow holes while ensuring contact with the wall surface for accurate diameter measurements.

While starting to run in the well, the Wireline Operator monitored the tension meter for any deviations. The X-Y Caliper performed admirably, with tension deflections occurring as anticipated at specific depths, including the crossover points between different casing strings and through the milled window. The tool exhibited smooth movement within both the casing and open hole sections, meeting expectations regarding its performance and detecting tension changes indicative of varying hole sizes.

Upon retrieval, the caliper showed significant wear, with most roller wheels worn down by at least half and missing pins that held the upper arm together. Scratches and abrasions adorned the arms, despite the drilling of a 10 5/8” hole size. Some arms displayed substantial wear, nearly compromising the integrity of the keep pin holding them together.

Despite the wear and tear experienced during the open hole run, the Kaldera X-Y Casing Caliper Tool performed admirably, fulfilling its intended purpose of casing ID measurements. While the test revealed wear and damage, the tool endured without failure, marking the test as a success overall.

2.3 Kaldera XY Caliper Full Function Field Testing

The XY Caliper underwent comprehensive field testing at The Geysers geothermal resource in Northern California. This resulted in the successful execution of the inaugural downhole field trial for the fully assembled Kaldera geothermal PTS/XY Caliper, representing a pivotal moment in affirming the functionality and deployment viability of this cutting-edge technology. The trial served as a testament to the robustness and effectiveness of the Kaldera PTS/XY tool, showcasing its ability to meet the demands of real-world geothermal operations.

Figure 2: Figure of the Kaldera PTS-XY Caliper Tool being removed after the completion of the test at The Geysers.

The field test was conducted within a well comprising both 11 ¾” and 13 3/8” casings, presenting a relatively simple and controlled geological environment. Notably, the instrumentation exhibited impeccable functionality, evincing a conspicuous absence of discernible physical anomalies during its traverse within the wellbore casing. Furthermore, the casing caliper adeptly captured and meticulously documented bi-directional data, as vividly depicted in the accompanying graphical representation. Noteworthy achievements include the accurate identification of pivotal

transitions, such as the 13 3/8” to 11 ¾” crossover, alongside the discernment of numerous casing collars and rugosity dispersed throughout the spatially intricate wellbore environment.

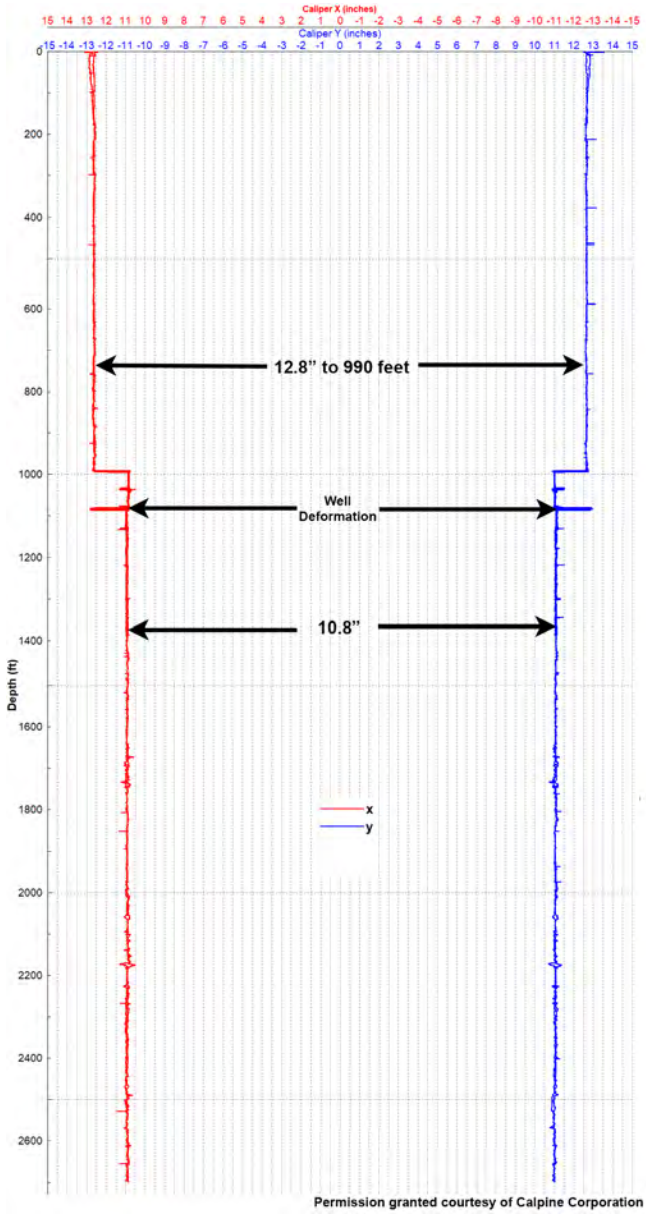

Figure 3: Figure showing the graphical results of the of the Kaldera PTS-XY Caliper Tool full functional field test clearly indicating the 11 ¾” & 13 3/8” crossover.

3. Rapid Prototypes, LLC Ultra-High Temperature Logging Tool (UHTLT)

The Ultra-High Temperature Logging Tool (UHTLT) was developed as part of the Department of Energy’s HeroX design challenge, sponsored by the Geothermal Technologies Office. This challenge aimed to showcase the potential of additive manufacturing to advance the geothermal industry.

The logging tool relies on additive manufacturing (AM) as a core manufacturing capability that allows for optimal geometric design to reduce thermal conductivity and radiative heat transfer between the electronics and the geothermal reservoir (well). By reducing heat transfer flux from the outside of the tool to the sensitive electronics equipment in the center, increased exposure times at higher temperatures can be achieved without the need for expensive and complex ultra-high temperature electronics.

In this approach, the prolonged and costly avenue of researching and developing 400°C electronic modules has been bypassed. Instead, the team utilized well-documented and field-proven 200°C electronic components from the Oil and Gas industry and created a more effective packaging system through AM.

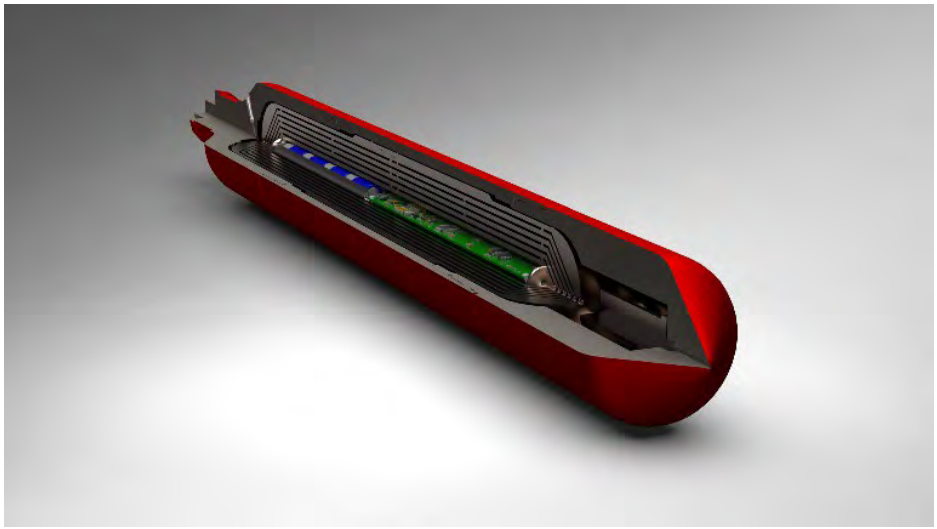

Figure 4: Computer Rendering of the cross-section view of the UHTLT design concept.

The heat sink was manufactured using Powder Bed Laser Fusion (PBLF). The Oak Ridge National Lab (ORNL) team, supported by the HeroX voucher, underwent four iterations to manufacture the internal components shown on the right side of Figure 5. These iterations were necessary to ensure adequate support for internal components and geometric features, and to optimize the powder application and removal processes. Following manufacturing, the AM components were removed from the build plate and forwarded to the team for machining and assembly.

Figure 5: Final components of UHTLT.

Internally, the Ultra-High Temperature Logging tool electronics were designed for operation up to 200°C with a safety margin of 10°C. Passive components were selected in accordance with high

temperature design considerations and overrated in terms of power, voltage, etc., to provide an additional safety margin.

The PCB implemented for the field trial was tested to 210°C. With continued testing, the expected maximum temperature is approximately 220°C.

The design of the printed circuit board (PCB) was based upon industry standards for downhole, high temperature circuit board design with the following design choices made to mitigate the risks of high temperature exposure.

Partial & final assembly is shown in Figure 7 & Figure 8.

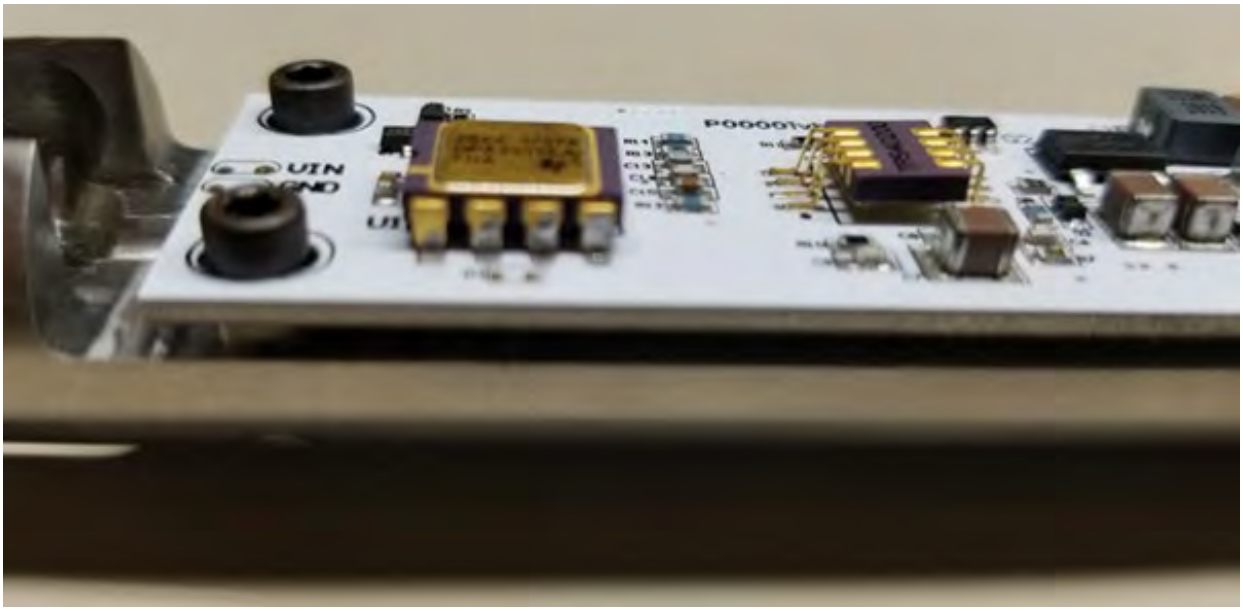

Figure 6: Image of the electrical components indicating optimization of materials selection, component orientation, mounting & traces.

Figure 7: Partially assembled tool with housing removed to show internal heat sink.

Figure 8: Fully assembled tool.

3.1 General Specifications & Basic Theory

3.1.1 Tool Specifications

Operational Description	**Specification**
Tool OD	4.5” / 114.3mm
Max Tool Length	15ft / 4.57m (prototype is 40 inches)
Max Temperature	400°C / 752°F
Max Pressure	15,000PSI / 1034Bar
Max Time at Temperature	10 hours
Well Fluid Compatibility	2% H_2S, HCl, 20% NaCl Brine, pH≥2
Measurements	Well Temperature, Well Pressure, Inclination, Orientation, Electronic Temperature
Electrical Description	**Specification**
Max Temperature	200°C / 392°F
Max PCB Width	0.71” / 18mm
Max PCB Length (incl batteries)	3.28ft / 1m
Pressure Measurement Range	0 – 15,000PSI / 0 – 1207Bar
Pressure Measurement Accuracy	10PSI / 0.69Bar
Pressure Measurement Resolution	1PSI / 0.07Bar
Temperature Measurement Range	-55 - 450°C / -67 - 842°F
Temperature Measurement Accuracy	1°C / 1.8°F
Temperature Measurement Resolution	0.1°C / 0.18°F
Inclination / Orientation Accuracy	2°
Inclination / Orientation Resolution	0.5°
Sampling Frequency	Programmable | <10Hz
Data Storage	Onboard – non-volatile
Data Recovery	Serial retrieval
Mechanical Description	**Specification**
Tool OD	4.5” / 114.3mm
Max Tool Length	15ft / 4.57m (prototype is 40 inches)
Cable Connection	1-1/16 – 10 UN
Max tensile strength	20,000lbsf / 89,000N
Max compression strength	20,000lbsf / 89,000N

3.1.2 Basic Tool Theory

In the development of the UHLTL, several geometric and material combinations were investigated. The optimal design uses a series of annual spaces fabricated with stainless steel and vacuum sealed. The combined effect of mitigating conductivity and radiation heat transfer leads to a tool of >32 hours at <200C for the electronics package, as shown in Figure 9.

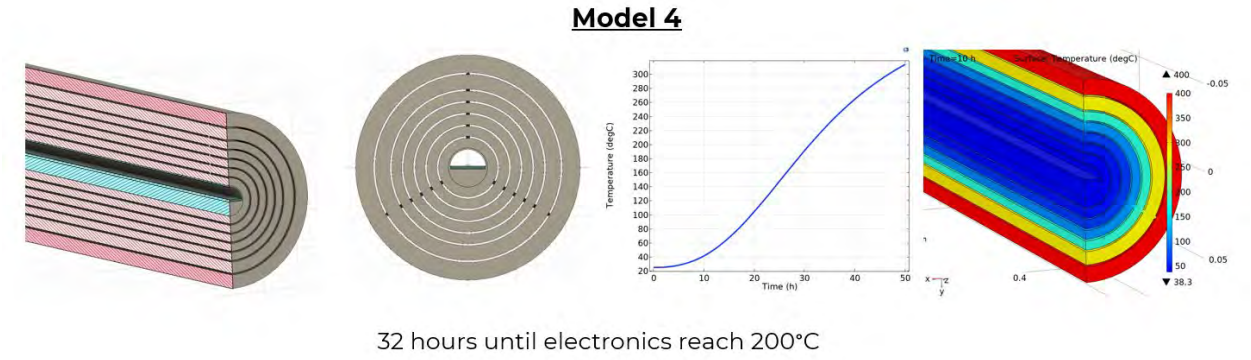

Figure 9: Modeled mitigation of conductivity and radiation heat transfer.

As the thermal energy is absorbed in the tool pressure housing, the temperature of the pressure housing quickly reaches the temperature of the surrounding fluid. This thermal energy is then transferred to the outermost concentric layer of the heat sink via radiation and conduction. The thermal energy transfer from layer to layer is driven primarily by radiative heat transfer since both conductive and convective modes have been minimized in the design of the tool. The time it takes to increase the temperature of the concentric layers is determined by the rate of thermal energy transfer driven primarily by the surface emissivity and specific heat capacity of each layer.

3.2 Performance Testing in Geothermal Wellbore Conditions at The Geysers

The testing in the well was instrumental in testing the performance of the tool in a real-world scenario. This provided conditions that were not attainable in the lab such as well fluid heat capacity, humidity and fluid flow as the tests were conducted in a live well.

Four tests were conducted in this well and are described below:

3.2.1 Test #1

Test 1 was conducted on August 1, 2023. The objective of Test 1 was to deploy the UHTLT into the well for a guaranteed safe duration. The bottom hole temperature of the well was unknown as the last attempt to log the well failed due to wireline and tool failure.

The maximum external temperature the electronic module observed downhole was 216°C while the maximum internal temperature only reached 155°C. The log file of the recorded temperature data from Test 1 as recorded by the UHTLT is shown in Figure 10.

During Test 1, the tool was set to begin logging when the electronic module reached 70°C.

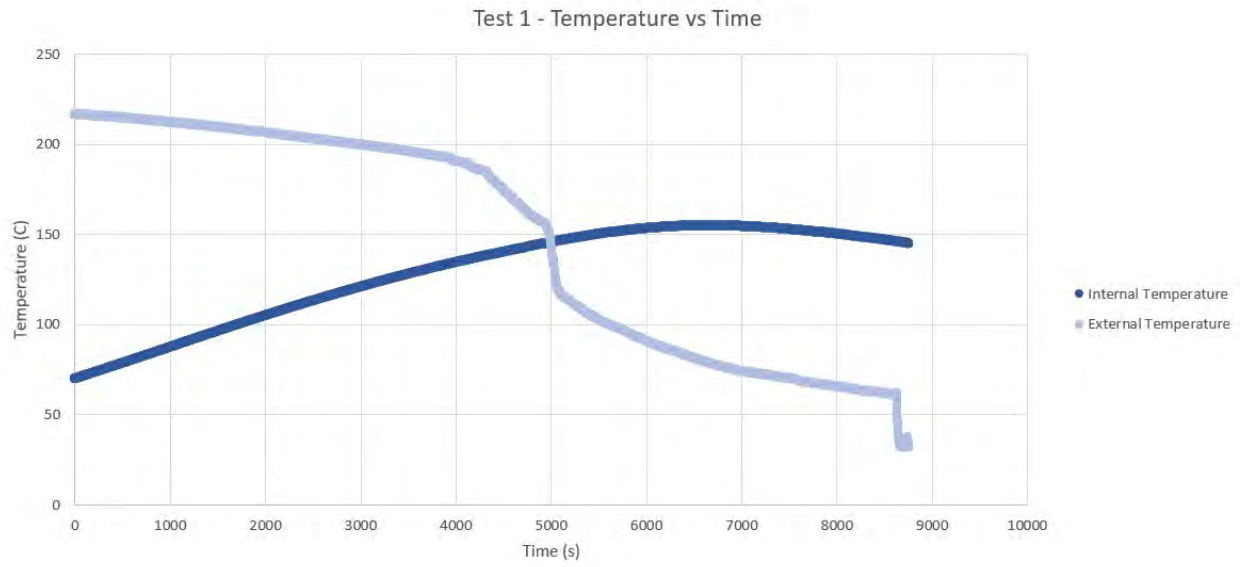

Figure 10: Test 1 data.

As seen in Figure 10, the tool was POOH when the logging began indicating that the tool was in the well for over 60 minutes before the internal temperature reached 70°C. It is also noteworthy that the internal temperature continued to rise after the tool was removed from the well, as highlighted by the rapid decrease in external temperature. This behavior was anticipated.

3.2.1.1 Test Parameters

Characteristics	Specifications
Run-In-Hole Speed	100 ft/min
Total Depth	4500 ft
Pull-Out-Of-Hole Speed	50 ft/min
Dwell Time at Depth	15 minutes
Total Time in Well	2.5 hours

3.2.2 Test #2

Test 2 was conducted on August 2, 2023. The objective of Test 2 was to deploy the UHTLT into the well for an increased dwell time to validate the model generated during the SNL test while still maintaining a safety margin to prevent approaching the temperature limit of the battery pack. The test plan for August 2, 2023 was to perform 2 runs during the day which is more representative of the operational requirements for Calpine to have an interest in the UHTLT as a commercially viable product.

During Test 2, the UHTLT was assembled and prepared for the runs ”on-site” using the tailgate of the rental pickup as a mobile workbench. This was used to highlight the field operational maturity of the tool; i.e. the tool does not need to be assembled by a team of highly trained personnel in a clean lab which would not be commercially ideal any wireline operator.

The tool firmware was also updated to begin logging after the internal temperature of the tool reached 50°C for 10 minutes, a decrease from the previous 70°C threshold. This was implemented to capture more data while downhole as it was observed from Test 1 that the UHTLT did not begin logging until the tool was being POOH and at an approximate depth of 2900ft. With the increased dwell time as well as the decreased internal temperature threshold, the UHTLT began logging earlier in the run and at TD.

The log file of the recorded temperature data as recorded by the UHTLT for Test 2 is shown in Figure 11.

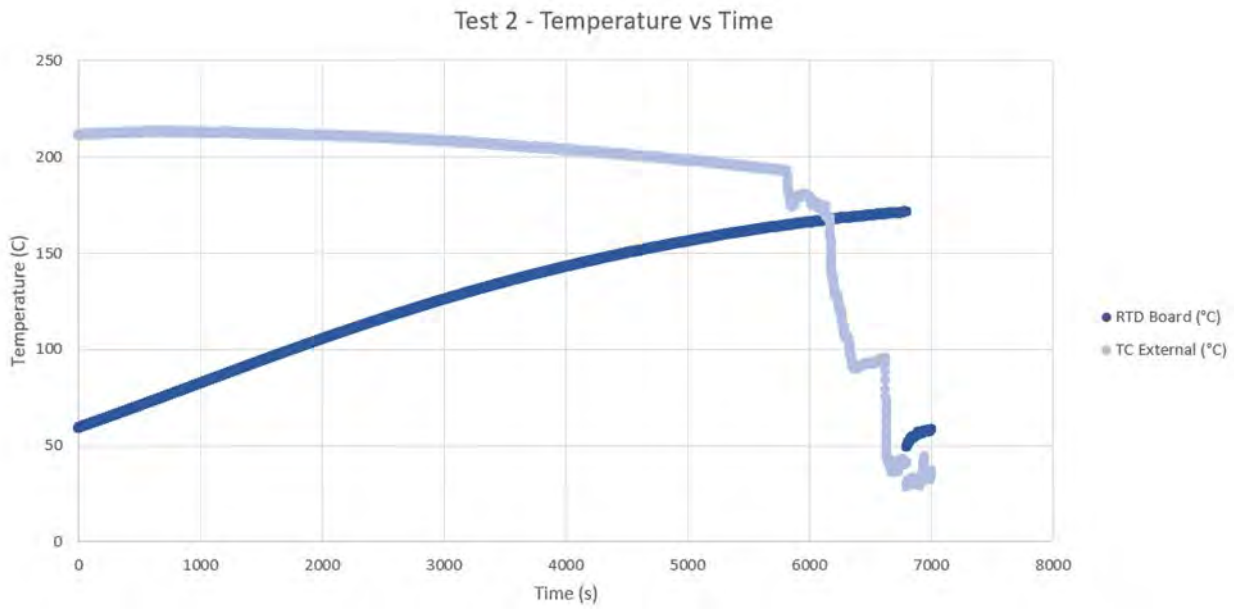

Figure 11: Test 2 data.

As seen in Figure 43, the maximum external temperature of the UHTLT was measured after the tool began logging in contrast to Test 1 where the UHTLT began logging with a decreasing external temperature. The downhole temperature of the Prati-4 well was measured at 213°C.

It can also be seen from Figure 43 that the internal temperature reached a maximum temperature of 171°C and decreased dramatically. This was due to a new procedure to cool the tool which was implemented during Test 2. The tool was rigged down and placed on a bed of ice to rapidly cool the external housing of the tool to allow for safe handling temperatures to be reached within minutes.

3.2.2.1 Test Parameters

Characteristics	Specifications
Run-In-Hole Speed	100 ft/min
Total Depth	4500 ft
Pull-Out-Of-Hole Speed	50 ft/min
Dwell Time at Depth	30 minutes
Total Time in Well	2.75 hours

3.2.3 Test #3

Test 3 was also conducted on August 2, 2023 with Test 2. The objective of Test 3 was to deploy the UHTLT into the Prati-4 well at a high rate of speed to test the vibration resilience of the tool while under real temperatures and pressures.

As previously stated, a secondary objective was to perform 2 runs during the day to showcase the ability of the UHTLT to maintain the wireline deployment schedule setup by Calpine.

During Test 3, the tool began the operational run at an elevated temperature due to the heat sink temperature being cooled to 50°C after Test 2. This allowed the UHTLT to begin logging during the pre-run vacuum. This allowed the well temperature to be captured while RIH as well as POOH.

The log file of the recorded temperature data as recorded by the UHTLT for Test 3 is shown in Figure 12.

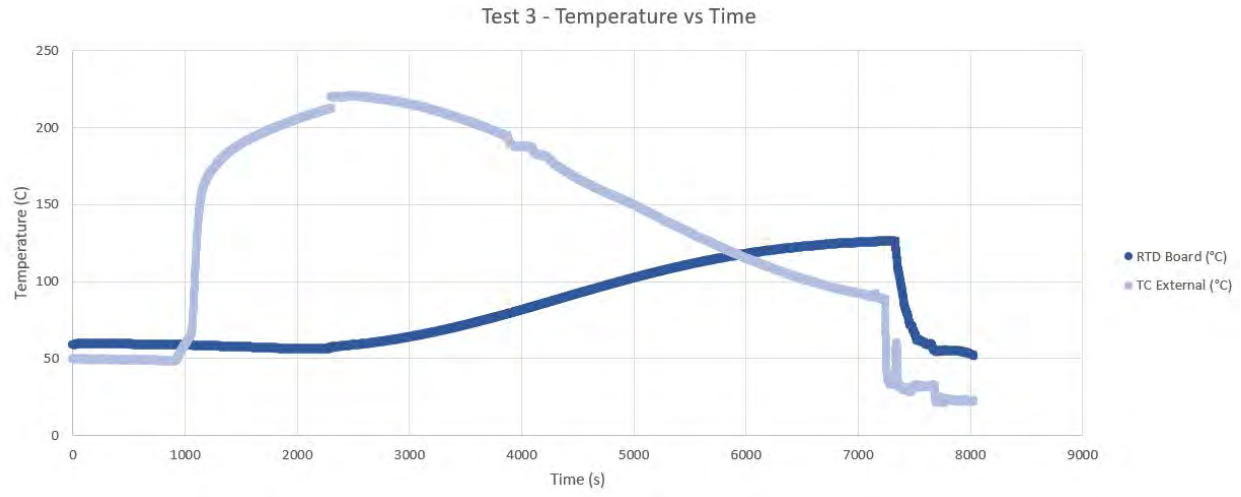

Figure 12: Test 3 data.

As seen in Figure 12, the internal temperature of the UHTLT continued to cool for approximately 20 minutes after the tool was inserted into the steam flow of the Prati-4 well. The rapid increase in temperature highlights the high temperatures measured not only at TD, but throughout the well as the steam temperature decreases by a small amount between TD and exiting the well into the steam collection system.

As this run was RIH and POOH very quickly, coupled with a short dwell time, the maximum internal temperature was very low at only 126°C. The maximum external temperature measured during Test 3 was 220°C. Contrary to Test 2, the UHTLT was placed in the back of the rental pickup and driven to the wireline workshop while still on and cooling. The tool was removed from the well at approximately 4000 seconds in Figure 12 as indicated by the temperature transient. At the time the UHTLT was removed from the well, the internal temperature was measured to be 82°C.

Test 3 was an important test for the UHTLT as it highlighted a different use case of the UHTLT. Currently the main objective of the UHTLT was an increased dwell time at 400°C. The use case

discussed with Calpine at the close of Test 3 was to use the UHTLT as a TD temperature measurement tool when RIH and POOH quickly using low temperature batteries to negate the delay in the logging data capture. With this test, it can be shown that by using low temperature batteries such as low-cost AA alkaline batteries, pre-cooling the heat sinks to -20°C and having a minimum dwell time at TD, the UHTLT can be used to go into a well of any temperature as long as the mechanical integrity of the tool is not diminished.

3.2.3.1 Test Parameters

Characteristics	Specifications
Run-In-Hole Speed	200 ft/min
Total Depth	4500 ft
Pull-Out-Of-Hole Speed	200 ft/min
Dwell Time at Depth	10 minutes
Total Time in Well	55 minutes

3.2.4 Test #4

Test 4 was conducted on August 3, 2023. The objective of Test 4 was to test the control heat sink in a comparison run with Test 2. This would allow the effects of the ultra-high polished internal layers to be tested in a real-world environment.

Test 4 took over 2 hours to prepare for vacuum, approximately 4 times longer than using the UHTLT with the nominal heat sink. The UHTLT was prepared in the wireline workshop and would not be able to be assembled in the field as had been done during Test 2 and Test 3. It is noteworthy to highlight that due to a mechanical interference fit issue, the ceramic balls used to separate the external layers with the housing of the UHTLT were removed which would decrease the dwell time of the UHTLT with the control heat sink.

The log file of the recorded temperature data as recorded by the UHTLT for Test 4 is shown in Figure 13.

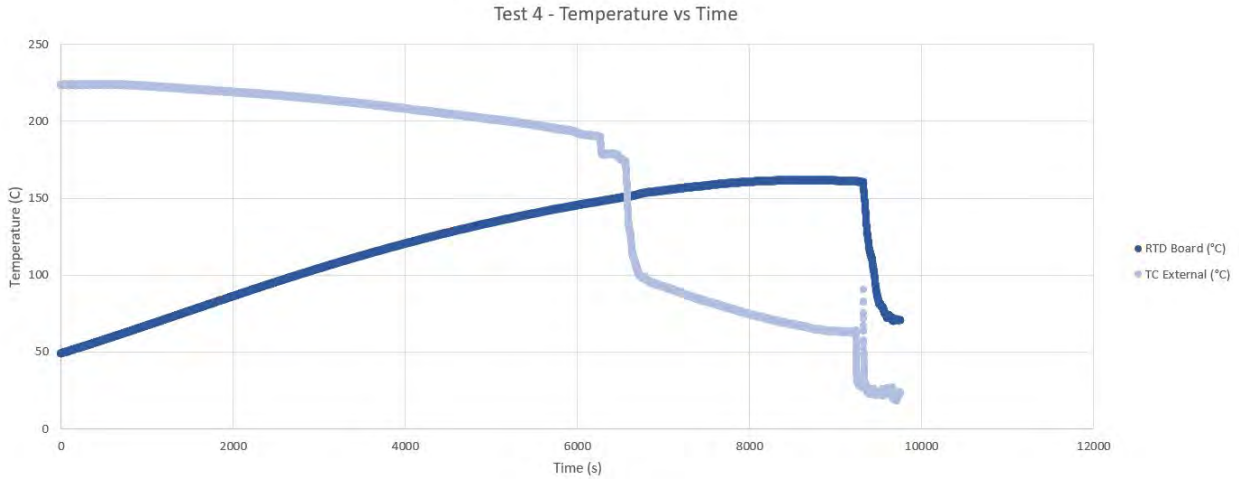

Figure 13: Test 4 data.

As seen in Figure 50, the UHTLT began logging after the maximum temperature had passed indicating that the tool was being POOH when the tool began acquiring data. The maximum internal temperature measured during Test 4 was 161°C, and the maximum external temperature measured was 224°C.

After the UHTLT was rigged down, the tool was placed in the back of the rental pickup truck and transported back to the wireline workshop for disassembly.

3.2.4.1 Test Parameters

Characteristics	Specifications
Run-In-Hole Speed	100 ft/min
Total Depth	4500 ft
Pull-Out-Of-Hole Speed	50 ft/min
Dwell Time at Depth	30 minutes
Total Time in Well	55 minutes

3.2.5 Comparison of Test #2 & Test #4

As seen in Figure 50, the UHTLT was exposed to a slightly higher external temperature in Test 4 at 224°C in comparison with the maximum external temperature of Test 2 at 213°C. The maximum internal temperature of the UHTLT during Test 4 was measured at 161°C while the maximum internal temperature of the UHTLT during Test 2 was measured at 171°C. Given the similarity of the test in terms of RIH speed, dwell time and POOH speed, the test showed a marginal improvement of the control heat sink. Therefore, the additively manufactured heat sink will not require a high degree of internal polishing to perform, however a path to polishing the AM heat sink will be continued in 2024 to gain performance.

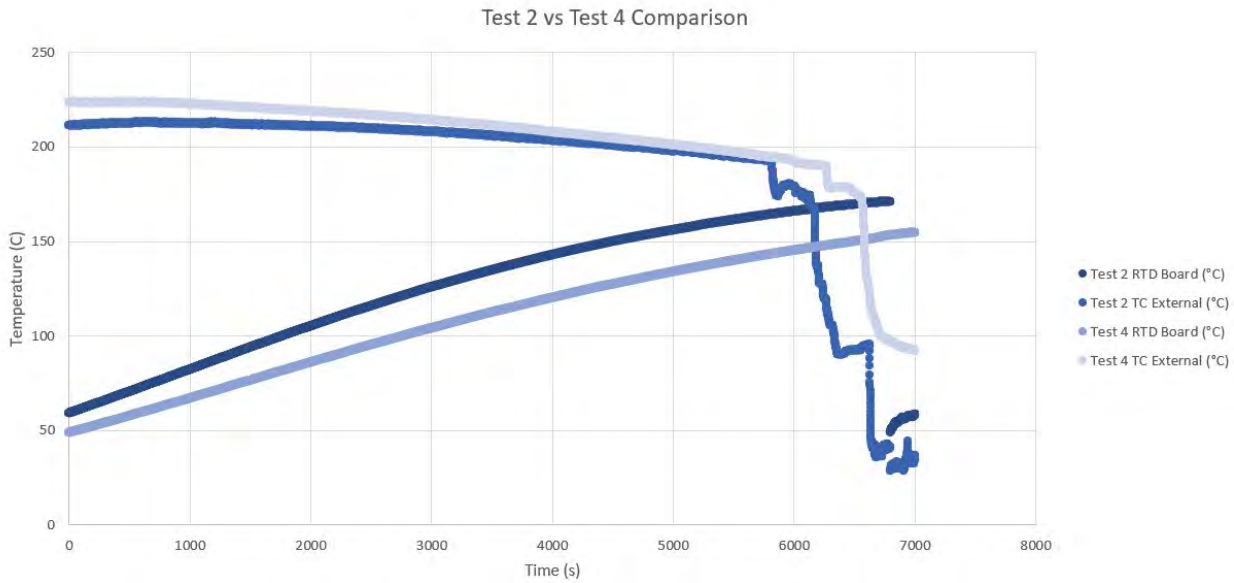

Figure 14: Test 2 & Test 4 data.

3.3 Post-Field Testing Developmental Tool Improvements

Rapid Prototypes, LLC plans to continue developing the tool with low-temperature, lower-cost electronics and battery requirements in preparation for additional testing as a "screening tool". By eliminating expensive electronics, they aim to significantly reduce the tool's cost and enhance its usability for customers, thereby improving operational efficiency. Additionally, they intend to investigate the impact of vacuum versus non-vacuum tools to streamline operator assembly and preparation time.

The ultimate objective is to design a tool that field crews can set up, test, operate, and download data from in an efficient and straightforward manner, thereby reducing operational costs and minimizing training requirements for technicians.

Due to the tool's simplicity and durability, there is perceived market potential as a rapid screening tool capable of measuring bottom hole temperatures up to 650°C. Through pre-run cooling procedures, it is anticipated that the tool can operate in wells with higher temperatures than any other currently available tool, provided that runs are kept under 1-2 hours.

4. Future Field Verification of Scientific Drilling International’s MFT-40 Casing Caliper at the Geysers

Scientific Drilling International (SDI) has stood as a cornerstone of the oil & gas industry since the mid-1970s, continually evolving through acquisitions, expansions, and achievements. Over the years, SDI's commitment to innovation has extended beyond oil & gas, benefiting the geothermal sector, particularly in drilling and subsurface wellbore assessment. Among the array of casing calipers tested at The Geysers, the MFT-24 stands out, initially tailored for oil & gas applications.

However, the MFT-40 emerges as a testament to SDI's dedication to progress, stemming from the MFT-24 but reimagined for the demanding environments of geothermal wellbores. This evolution showcases enhanced mechanics, electronics, and software).

Already validated and operational across diverse global locales, from southern California to Europe and the Far East, the MFT-40 now faces the distinct challenge posed by The Geysers. Conducting field verification within the intricate wells of The Geysers steamfield, the MFT-40 must prove its mettle in varying conditions while capable of seamless integration with non-conductive wireline systems, all while ensuring steadfast reliability amidst fluctuating temperature ranges.

4.1 Tool Specifications

Characteristics	Specifications
Tool Length	Caliper – 5.58’ Centralizer (2) – 3.19’ Total – 11.98’
Weight	215 lbs
Measurement Range	5.5” – 15.5”
Maximum Temperature	343ºC (650ºF)
Measurement Sample Rate	50 samples/sec
Horizontal Accuracy/Resolution	Radially ±0.02”/0.001”
Vertical Resolution	0.12”
Inclinometer/High-Side Resolution	± (5-355º) rotation & inclination
Maximum Pressure	12,000 psi
Construction Materials	Corrosion resistant throughout

Figure 15: Image of the SDI MFT-40 Casing Caliper with caliper arms retracted prior to running in the well.

4.2 Field Verification Calpine Benefits

The Vulcan™ MFT 40 is equipped with advanced features specifically designed to streamline casing inspection processes. Featuring a finger sensor positioned every 9°, high-speed electronics, and generous memory capacity, it boasts a sampling rate of 50 times per second, thereby yielding detailed results within a matter of hours rather than days. Its capability to log multiple casing sizes in a single operational pass minimizes production interruption, eliminating the need for multiple runs. Functioning optimally at ultra-high temperatures of up to 650°F/343°C, it facilitates rapid decision-making with prompt data turnaround. Its innovative design facilitates on-site maintenance, while its robust electronics package ensures reliable logging even in high-temperature environments. Additionally, the Vulcan™ MFT 40 provides comprehensive data delivery, including reports featuring statistical joint-by-joint analysis, logs of finger radii raw and centered, cross-sections, and selected 3D images, thus enhancing overall operational efficiency and decision-making processes.

4.3 Proposed MFT-40 Field Verification at The Geysers

The thorough validation regimen of the MFT-40 spans across five separate wellbores within the Geysers, serving as a methodical examination of its precision, dependability, and resilience for sustained operational deployment. These wellbores, comprising four designated for production and one allocated for injection purposes, present a diverse array of challenges that scrutinize the MFT-40's capabilities. These challenges encompass a gamut of complexities, ranging from navigating intricate casing profiles, inclusive of scab liners, to withstanding the severe conditions prevalent in high-temperature wellbores, where temperatures exceed 500°F. Moreover, the prospect of encountering casing deformations or damage further underscores the necessity to evaluate the MFT-40's resilience in authentic operational scenarios. Its extensive array of caliper arms and its ability to curtail lost production time could position it as an indispensable asset in the perpetual upkeep and oversight of geothermal wells within the field, thus ensuring sustained operational efficacy and reliability in the long term.

5. Conclusion

The successful field trials and operational deployments of these advanced tools underscore their role in optimizing operational efficiencies, curbing expenditures, and enhancing the precision of data acquisition. Moreover, the collaborative synergy between technology developers and operational partners like Calpine operations at The Geysers underscores a proactive strategy aimed at surmounting challenges and pushing the boundaries of what is feasible in geothermal exploration and production. In the future, sustained research and development endeavors will be pivotal in further refining these tools and broadening their capacities to meet the dynamic demands of the geothermal sector.

Disclaimer:

The views expressed in this paper are those of the author(s) and do not necessarily reflect the views of Calpine Corporation or its affiliates. Any opinions, findings, conclusions, or recommendations expressed in this paper are solely those of the author(s) and do not represent the opinions or policies of Calpine Corporation or its affiliates.

All intellectual property rights related to the content of this paper, including but not limited to data, text, graphics, images, and other materials, are owned by Calpine Corporation. No part of this paper may be used, reproduced, distributed, relied upon, or transmitted in any form or by any means without the prior written permission of Calpine Corporation.

REFERENCES

Geysers. (2022). Geysers By The Numbers. Retrieved from https://geysers.com/The-Geysers/Geysers-By-The-Numbers.

Sledz, D., Johnson, A., Pollock, S., Fraser, A., & Khastoo, R. (2020). Design Features of an Emerging Casing Inspection Technology and its implication for Geothermal Well Quenching. Retrieved from https://www.geothermal-library.org/index.php?mode=pubs&action=view&record=1034314.

Chloride-based Wireline Tool for Measuring Fracture Inflow in Enhanced Geothermal Systems (EGS) Wells: Field Deployment Updates

Melanie B. Schneider[1], Sarah Sausan[2], Marshall Hartung[2], Roland Horne[2], Alfred H. Cochrane[1], Jiann-cherng Su[1], Andrew A. Wright[1], Taylor Myers[1], Joseph Pope[1], Joshua Tafoya[1]

[1]Sandia National Laboratories

[2]Stanford University

Keywords
Chloride concentration, Fracture Inflows, Utah FORGE, EGS, Chloride, Single-Phase

ABSTRACT

This paper presents the ongoing development of a chloride-based wireline tool designed to detect and quantify inflows from feed zones in geothermal wells. The tool aims to characterize stimulation events in EGS wells at Utah FORGE (Frontier Observatory for Research in Geothermal Energy) and other EGS sites. Successful development of the chloride tool would greatly improve production monitoring of the fractures and enable proactive prescription of additional stimulations over the life of the field, thus helping to improve EGS commercial feasibility.

The recent developments of the chloride tool have focused on preparing for and conducting the field deployment at the Utah FORGE site. The field-scale tool assembly features a FORGE sensor package housing the Ion Selective Electrode (ISE), a pH electrode, and a reference electrode, as well as a Mitco PTS sensor package for secondary downhole measurements. A high-temperature logging tool has been developed and tested to capture and transmit data from the chemical sensors to the surface through a 7-conductor wireline cable. Alongside the development of the field-scale tool, flow experiments were carried out in the artificial well system at the Stanford Geothermal Lab. These experiments provided crucial insights into how the chemical tool responds to different variables, including the chloride concentration in the feed zone, its vertical positioning relative to the feed zone, and the presence of other chemical species in the feed zone fluid. The results highlight the tool's sensitivity to various parameters, underscoring the potential of using chloride concentration measurements as a method for inferring feed zone inflow rates in geothermal wells. The tool was successfully deployed at the Utah FORGE site using a wireline truck in the vertical well 58-32 and the directional production well 16B(78)-32.

1. Introduction

Enhanced Geothermal Systems (EGS) use artificial fractures to increase fluid extraction in less permeable geothermal reservoirs (Huenges, 2016). Artificial fractures are created through hydraulic stimulation and may close over time, reducing the productivity of the EGS wells (Fei et al., 2023). By monitoring the productivity of artificial fractures, operators can prescribe mitigation techniques such as restimulation. Timely interventions can help to keep the fractures open and flowing throughout the geothermal plant's lifetime, which typically lasts between 30 and 50 years (Sullivan et al., 2010).

The pressure-temperature-spinner (PTS) tool is commonly used to measure inflow rates from feed zones, with the spinner part determining the flow rate (Sisler et al., 2015). PTS tools show limitations in wells with low fluid velocity, low enthalpy, and large diameters (Acuña and Arcedera, 2005). The study found that there was an overestimation of the inflow rate in the vertical section compared to the nonvertical section of the well. Furthermore, changes in hole diameter outside of slotted liners will influence spinner rotation, which could be misinterpreted as an actual change in flow rate.

A geochemistry-based alternative to the PTS tool has been developed by Sandia National Laboratory and the Stanford Geothermal Program as part of the Utah Frontier Observatory for Research in Geothermal Energy (FORGE) project. This tool uses an ion-selective electrode to measure chloride concentration in the well fluid via electrical voltage between a sensor formed from a combination of pressed AgS and AgCl powder and a reference electrode formed from pressed AgCl powder (Hess et al., 2014). Chloride concentration readings around the feed zone can be used to calculate the feed zone inflow rate. In this paper, this tool is referred to as the "chloride tool", the tool assembly is shown in Figure 1-1. A major advantage of the chloride tool is that it does not require knowledge of the hole diameter, which is a limitation of PTS tools.

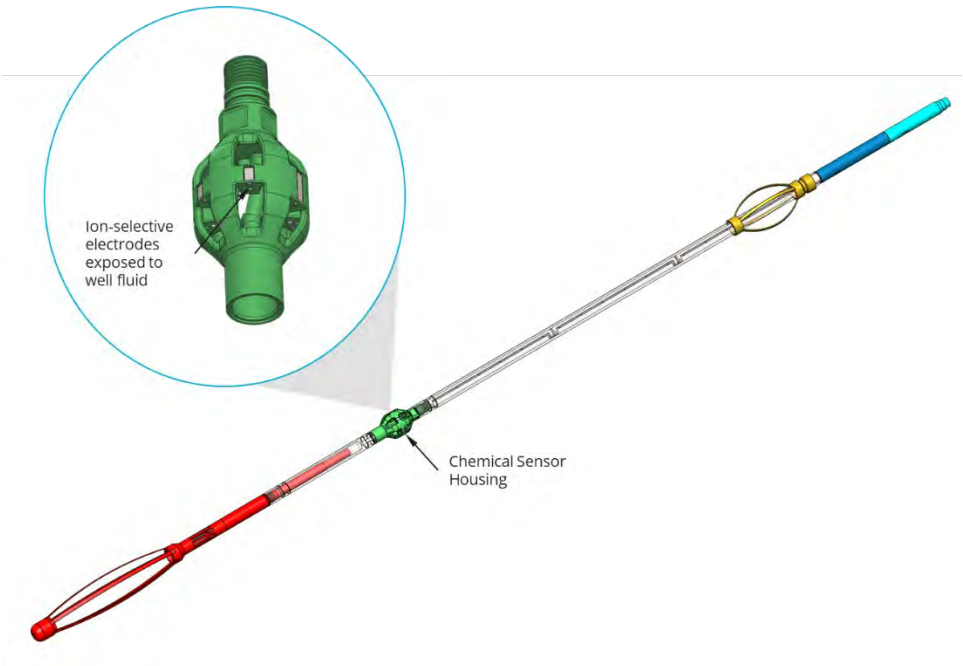

Figure 1-1: Field-deployable chloride tool assembly with close up of chemical sensor housing.

This study expanded on a previous investigation by Gao et al. (2017), which used a similar chloride tool prototype developed by Sandia National Laboratory (Cieslewski et al., 2016; Corbin et al., 2017). In the preliminary study, the team used measurements from the ion-selective electrode to estimate the enthalpy of the feed zone. They targeted chloride concentrations because chloride is consistently present in the liquid phase of geothermal reservoirs. (Sausan, 2023). Building upon that previous research, the current study aimed to develop a field-deployable version of the chloride tool to be used at the Utah FORGE project, which features EGS wells with single-phase fluid and multiple feed zones. This study focused on estimating the feed zone inflow rate, specifically in single-phase flow conditions, rather than enthalpy. The ultimate goal is to leverage insights from the Utah FORGE field trial for broader applications across various EGS sites. More importantly, this study explored a wider role of geochemistry, indicated by the chloride species concentration change, in determining fluid flow patterns in geothermal wells. Typically, the practical application of geochemistry in the geothermal industry revolves around estimating enthalpy or using tracer studies. However, this wider use of geochemistry could enhance our comprehension of the behavior of geothermal wells and fields.

This study employed a multifaceted approach, integrating analytical methods, numerical simulations, laboratory experiments, data science techniques, and field trials. Previously reported progress can be found at Sausan et al. (2021**,** 2023) and Judawisastra et al. (2022, 2023). This paper highlights the latest progress involving field-scale tool fabrication and testing, laboratory setup improvements, and numerical simulations involving the field-scale tool housing and at Utah FORGE temperature and pressure operating conditions. Finally, the successful deployment of the tool at the Utah FORGE site is described.

2. Tool Development and Assembly

2.1 Chloride Tool Assembly

The field-deployable chemical tool assembly incorporates the Mitco PTS sensor package and a tip centralizer at the leading edge of the tool. This is used for secondary downhole measurements to compare the geochemistry-based alternative method to the commonly used PTS measurements. A wire guide component was developed to adapt the PTS tool to the FORGE chemical sensor housing. The sensor wires from both the Mitco PTS tool and the chemical sensors pass through a wire feedthrough in the chemical sensor housing to the high-temperature logging tool in the electronics housing. The electronics housing connects to the wireline via a 4-conductor feedthrough that is adapted to a 7-pin conductor feedthrough that matches the wireline connection. The full assembly schematic is shown in Figure 2-1.

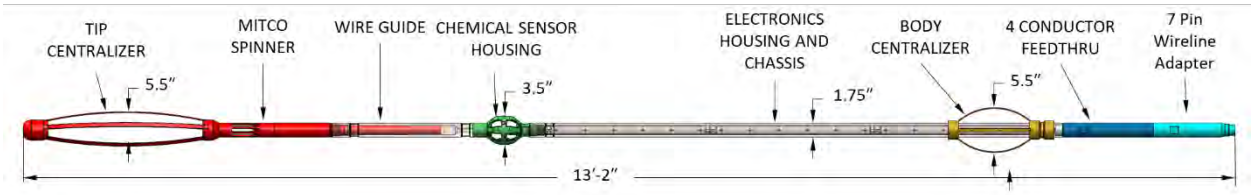

Figure 2-1: Field-deployable chloride tool schematics, including an existing PTS tool adapted to the chloride-based wireline tool and high-temperature developed by Sandia National Laboratory.

2.2 Chemical Sensor Fabrication and Testing

The chloride tool developed by Sandia National Laboratory consists of an ion-specific electrode coupled with a reference electrode. The constituent materials used to develop the ion-selective electrode and reference depend on the ion of interest. The ion-specific electrode probe generates a voltage proportional to the chloride concentration in the fluid, while the reference electrode provides the reference potential for the pair.

The Ion-Specific Electrodes (ISE) probe consists of a pellet formed from an equal part by a mass mixture of Silver Sulfide powder and Silver Chloride (AgS/AgCl) powder. The powder is weighed and transferred to a ¼" diameter die press and compressed to 4000 lbs. and held at constant pressure for 15 minutes. The pellet is then transferred to a preheated oven at 200°C for one hour and then cooled to room temperature.

A CuAg plated pellet wire adapter was fabricated to centralize a high-temperature nickel-plated copper wire on a conductive surface. The CuAg plated pellet wire adapter was attached to the pellets using a high temperature conductive epoxy and cured in a mold to keep the wire adapter centralized on the pellet. The assembled pellets and wire adapters are shown in Figure 2-2. The assembled sensors were then coated with Gagekote #1, a protective coating rated up to 455°C. This configuration of sensor design can then be sealed in the tool assembly using a commercial compression seal feedthrough bulkhead (rated up to 870°C and 10ksi) and allow for multiple sensors to be tested in the same tool.

Figure 2-2: ISE and reference sensor assemblies before application of Gagekote.

To demonstrate the ruggedness of the chemical sensors under High-Pressure, High-Temperature (HPHT) conditions, a laboratory test was conducted using the Sandia autoclave. The sensors and

bulkhead connection design were submerged in 225°C brine at 5000 psi for 24 hours and showed stable measurements. This provided confidence that the chemical sensor design could survive at the Utah FORGE conditions.

To demonstrate the capability of the sensor performance in the chemical composition of the brine at Utah FORGE, samples of flowback water from Utah FORGE Well 16A (78)-32 and 16B(78)-32 were collected and tested using the ISE electrode sensors. The chemical composition of the samples is shown in Table 2-1. Figure 2-3 shows the calibration fit of the well samples in comparison to various molarities of Potassium Chloride (KCl) in distilled water. The voltage measurements of the samples from the flowback in both wells are in good agreement with the measurements of the KCl solution, with lower correlation to the fit line at the lowest chloride concentrations.

Table 2-1: Chemical composition of well samples from Utah FORGE Wells 16A(78)-32 and 16B(78)-32

DATE TIME	LOCATION	Major (mg/l)									
		pH	Na	K	Ca	Mg	B	SiO_2	Cl	SO_4	HCO_3
7/19/2023 20:00	16A(78)-32 Utah FORGE	7.43	621	80.2	92.3	4.13	2.07	167	1300	162	105
7/20/2023 7:50	16B(78)-32 Utah FORGE	6.69	2871	319	44	0.07	9.05	81	4384	239	383
7/20/2023 15:00	16B(78)-32 Utah FORGE	6.64	81	7	109	3.48	0.32	78	122	115	276

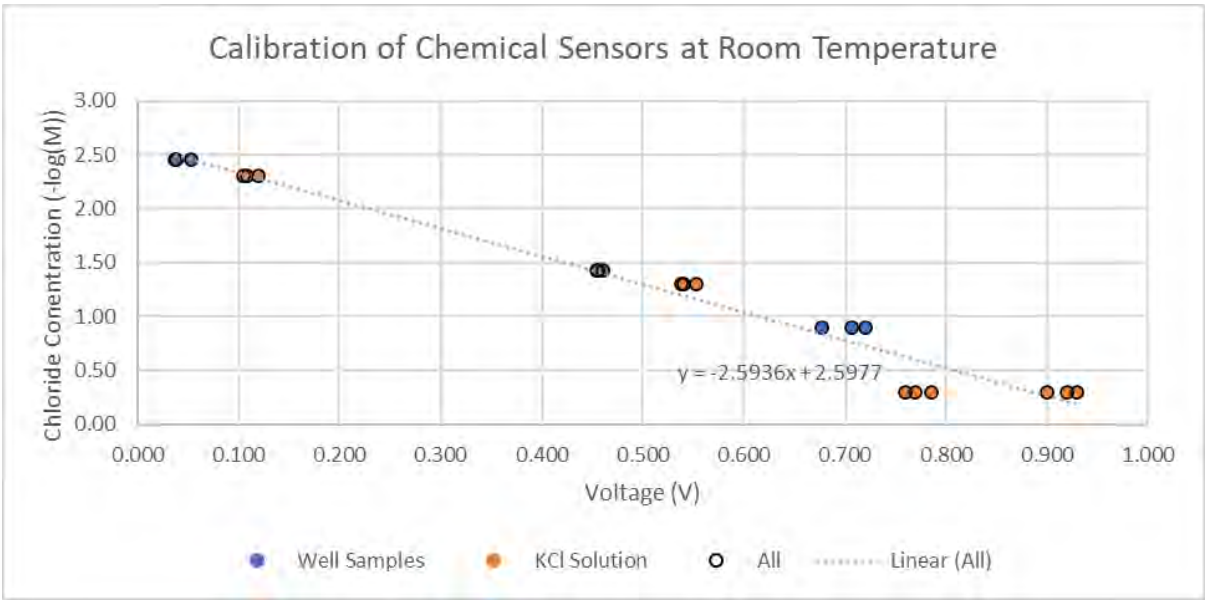

Figure 2-3: Calibration of chloride sensors in KCl solution and samples from wells 16A and 16B for sensors deployed in Utah FORGE Well 16B.

2.2.2 Chemical Sensor Housing

The chemical sensor housing has been designed and developed to enclose the ion-selective chemical sensors, pH Sensor, and the reference electrode sensor. The sensor housing was designed to allow flow to pass through the housing and interact with the chemical sensors uniformly. The housing includes retainer slots to incorporate three Ion-Selective Electrode (ISE) sensors, one reference electrode sensor, and two pH sensors. The sensors are routed through a wire feed-through and sealed using a Conax Compression Seal Fitting. In the current setup, the Conax Compression Seal Fitting can hold up to four wires, this allows for two ISE sensors, one pH sensor, and one reference electrode, the remaining retainer slots are left empty. The housing also includes a wire feed-thru to accommodate the downstream Mitco PTS sensor used for secondary measurements. The unique feature combinations (internal tube, pellet slots) are enabled through metal additive manufacturing. Three sensor housings were manufacture and tested to ensure they are pressure safe and leak resistant. A sensor housing with installed sensors is shown in Figure 2-4.

Figure 2-4: Fabricated sensor housing populated with installed sensors and bulkhead fitting.

2.3 High Temperature Logging Tool

Two versions of the High-Temperature (HT) Logging Tool have been developed and assembled to capture and transmit data from the chloride sensors and PTS spinner tool through the wireline to the surface. The primary version incorporates a modified and previously deployed and tested HT electronics package. The system is composed of three main boards: 1) a digital board featuring a Honeywell HT HT83C51 microcontroller, a Sandia custom high-temperature Application-specific Integrated Circuit (ASIC), and memory, 2) an analog board equipped with an analog to digital converter (ADC), multiplexer, and operation amplifies for the pressure and temperature inputs, and 3) a buffer board that includes a Chemical Buffer Amplifier (CBA) designed to convert the chemical sensor's high input impedance to low impedance. Two full assemblies of the primary HT logging tools have been assembled and tested to confirm operation (see Figure 2-5). The secondary logging tool was constructed to serve as a backup for contingency in the field. This electronic system uses the EV-HT-200CDAQ1 High-Temperature Data Acquisition Reference Design Platform from Analog Devices Inc as an alternative to the digital and analog board in the first system. All three logging tools have been tested to confirm they can accurately capture readings from the chloride and pH sensors, record measurements from the Mitco PTS module, and relay the information through the wireline cable.

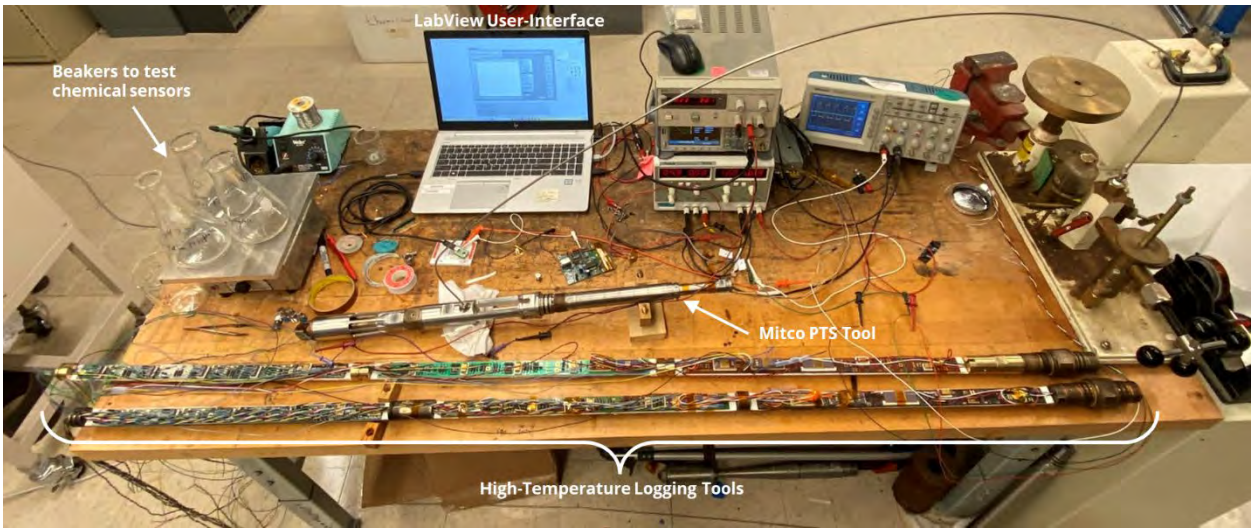

Figure 2-5: Primary High-Temperature Logging Tools being tested to confirm operation in benchtop test.

A LabView user interface has been developed (shown in Figure 2-6) to efficiently handle serial data from the tool, offering real-time data display and recording capabilities on a PC. The interface is designed for compatibility with both the primary and secondary High-Temperature Logging tools. This streamlined field operations for each tool configuration.

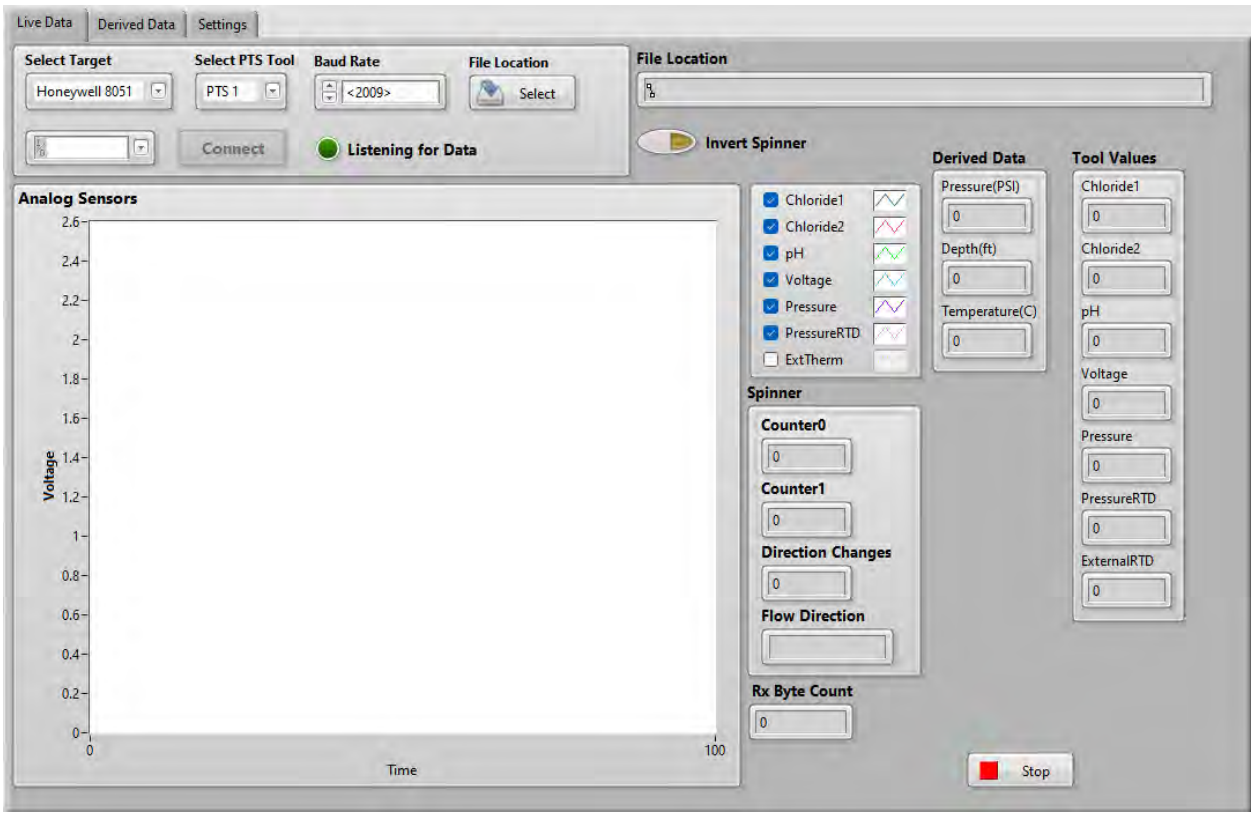

Figure 2-6: LabView User Interface for Field-Scale Chloride Tool

3. Laboratory Experiments

The new iteration of the chloride tool housed two ISE probes, known as ISE probe #2 and ISE probe #3. A calibration was performed to determine an empirical relationship between the voltage readings of the ISE probes and the chloride concentration of the surrounding fluid. The calibration curves for both ISE probes, provided in Equation 3.1 and Equation 3.2, exhibited strong linear relationships ($R^2 = 0.975$ and $R^2 = 0.961$) between their voltage readings and the negative common logarithm of chloride concentration in mol/L.

$$-\log_{10}(\mathrm{M}) = -20.64 * \mathrm{V} + 0.596 \quad (3.1)$$

$$-\log_{10}(\mathrm{M}) = -35.31 * \mathrm{V} + 0.550 \quad (3.2)$$

Using the calibration curves, the voltage readings from both ISE probes could be converted into chloride concentration values. Flow experiments in the artificial well system in the Stanford Geothermal Laboratory were conducted. The first set of experiments involved the chloride tool being held in a static vertical position in the artificial wellbore while a series of two one-minute feed zone flows occurred. These experiments granted insight into the behavior of the chloride tool in response to varying the parameters needed to infer the feed zone inflow rate in geothermal wells.

The first variables tested were the chloride concentration of the feed zone fluid and the vertical location of the chloride tool relative to the feed zone jet. The results of these experiments are shown in Figure 3-1 and Figure 3-2 for ISE probe #2 and ISE probe #3 respectively.

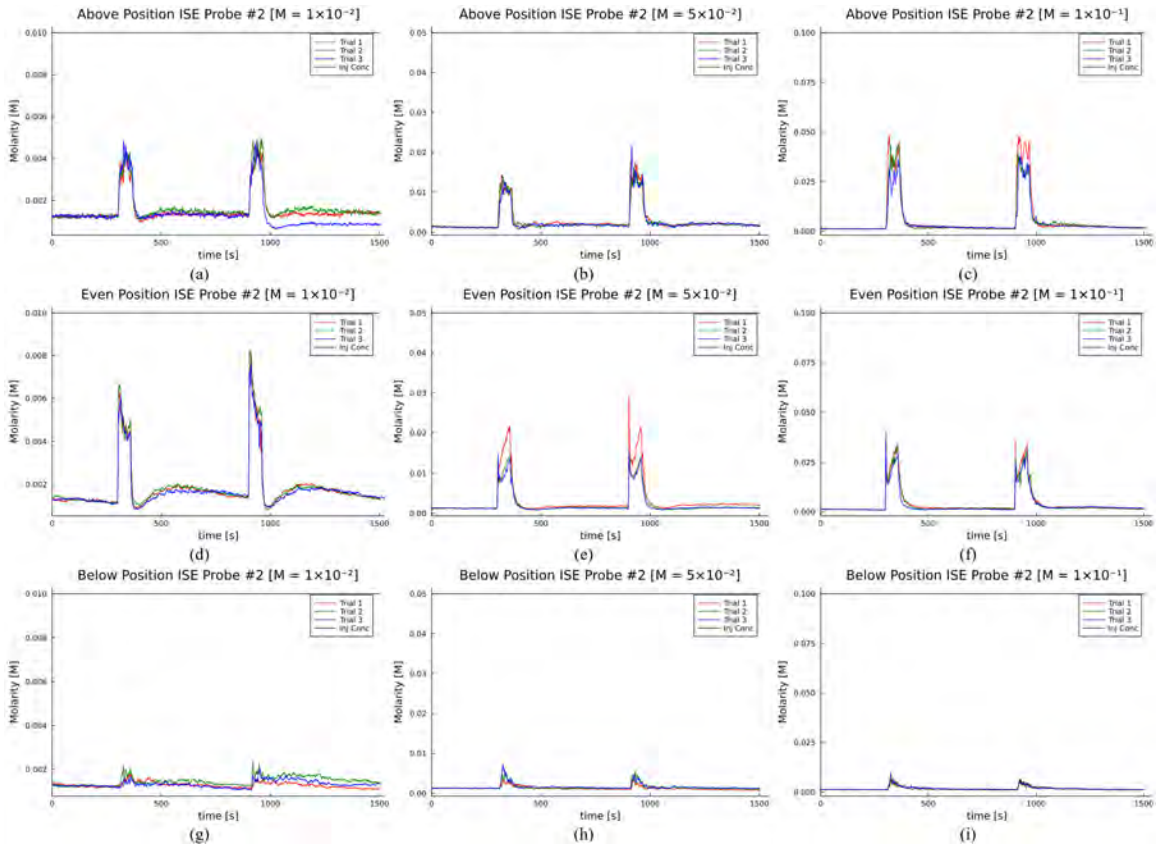

Figure 3-1: Molarity time series for ISE probe #2 in the above, even, and below positions for chloride concentrations of (a, d, and g) 1×10^{-2} mol/L, (b, e, and h) 5×10^{-2} mol/L, and (c, f, and i) 1×10^{-1} mol/L

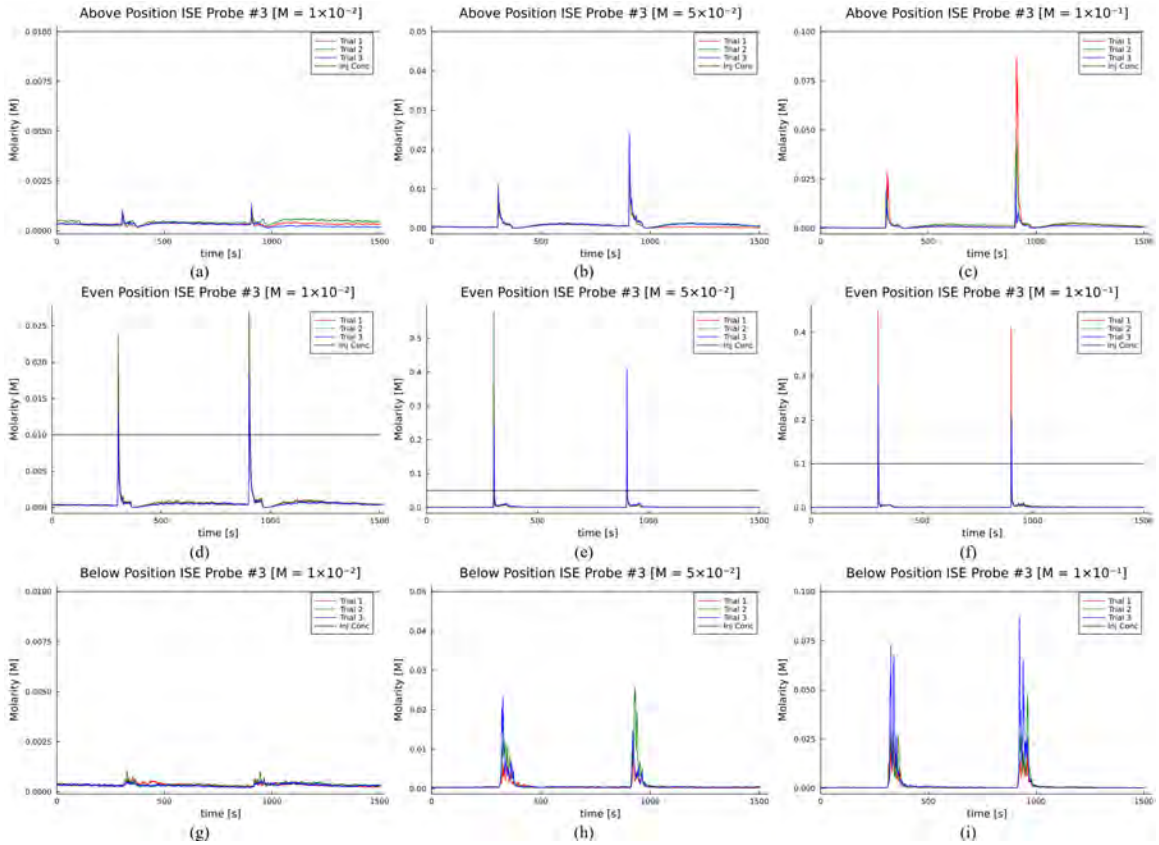

Figure 3-2: Molarity time series for ISE probe #3 in the above, even, and below positions for chloride concentrations of (a, d, and g) 1×10^{-2} mol/L, (b, e, and h) 5×10^{-2} mol/L, and (c, f, and i) 1×10^{-1} mol/L

The most notable result seen in Figure 3-1 and Figure 3-2 was the different behavior of the ISE probes when the chloride concentration of the surrounding fluid changed. Specifically, ISE sensor #2 exhibited smooth and gradual changes to its molarity readings that then plateaued. In contrast, the molarity readings of ISE probe #3 spiked immediately when the chloride concentration of the surrounding fluid changed. Then, the molarity readings of ISE probe #3 decreased, even though no changes to the surrounding fluid occurred. Additionally, these experiments suggested that higher feed zone chloride concentrations produced the most accurate and repeatable responses for both ISE probes.

Additional static experiments with the chloride tool were conducted to determine the effect of varying the feed zone inflow rate and the presence of additional chemical species in the feed zone fluid. The first set of additional experiments found that higher feed zone inflow rates led to higher accuracy when inferring the chloride concentration of the feed zone. The second set of experiments suggested that a significant amount of interference occurred when bromide, and to a lesser extent sulfate, were present in the feed zone fluid. This finding aligns with the literature, which indicates that ion-selective electrodes are imperfectly selective and particularly susceptible to interference from ions such as bromide, iodide, cyanide, silver, and sulfide due to their selectivity coefficients (Baker et al., 1980; Rhodes & Buck, 1980). The interference resulted in the ISE probes massively overestimating the concentration of the individual ions. However, the presence of bromide and

sulfate ions stabilized the readings of the chloride tool when compared to a feed zone fluid containing only bromide, chloride, or sulfate ions. These findings for ISE probe #2 are shown in Figure 3-3.

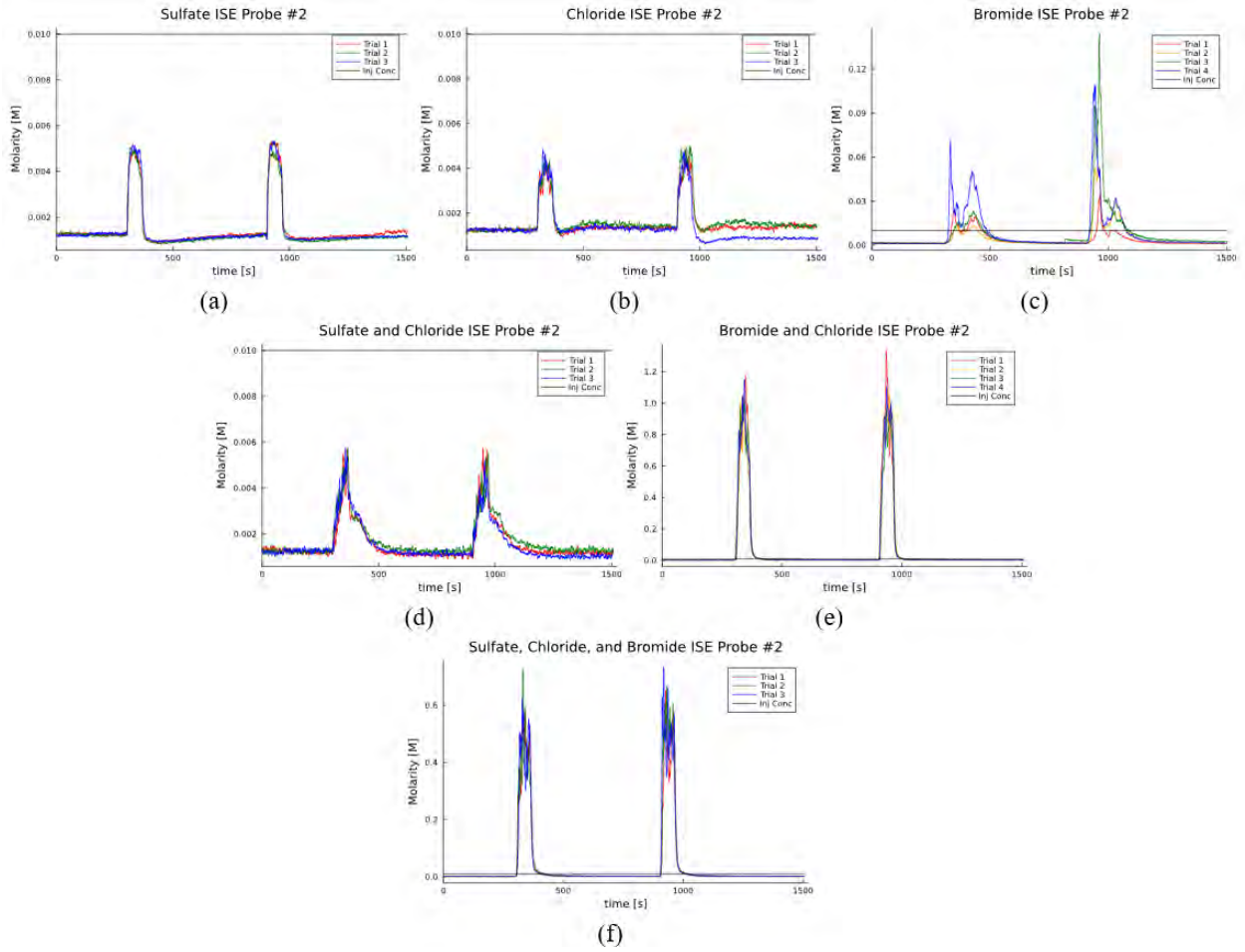

Figure 3-3: Molarity time series for ISE probe #2 for feed zone fluid containing 1×10^{-2} mol/L solutions of (a) sulfate, (b) chloride, (c) bromide, (d) sulfate and chloride, (e) bromide and chloride, and (f) sulfate, chloride, and bromide.

To better imitate field operations, laboratory experiments in which the chloride tool was moved vertically in both directions to measure the chloride concentration across the depth of the artificial wellbore were conducted. These dynamic experiments provided insight into the performance of the chloride tool as it was actuated in the run-in hole (RIH) and pull-out of hole (POOH) directions. The molarity measurements were then used with the analytical solution derived by Sausan et al. (2022) to estimate the mass inflow rate for a single feed zone.

The first series of dynamic experiments tested various chloride concentrations of the feed zone fluid and the direction of motion of the chloride tool. These experiments found that feed zone fluids with higher chloride concentrations resulted in the most accurate feed zone inflow rate inferences. However, these accurate inferences were seen only for ISE probe #3 in the POOH direction. This is likely because the behavior of ISE sensor #3 caused it to best capture the rapid

changes in chloride concentration when the chloride tool moved through the feed zone jet. The results of these experiments are shown in Figure 3-4 and Figure 3-5 for ISE probe #2 and ISE probe #3 respectively. Additionally, Table 3-1 shows the estimates of mass inflow rate $\dot{m}_{in}$ for a single feed zone averaged across the three trials and the percentage error between the actual and inferred inflow rates.

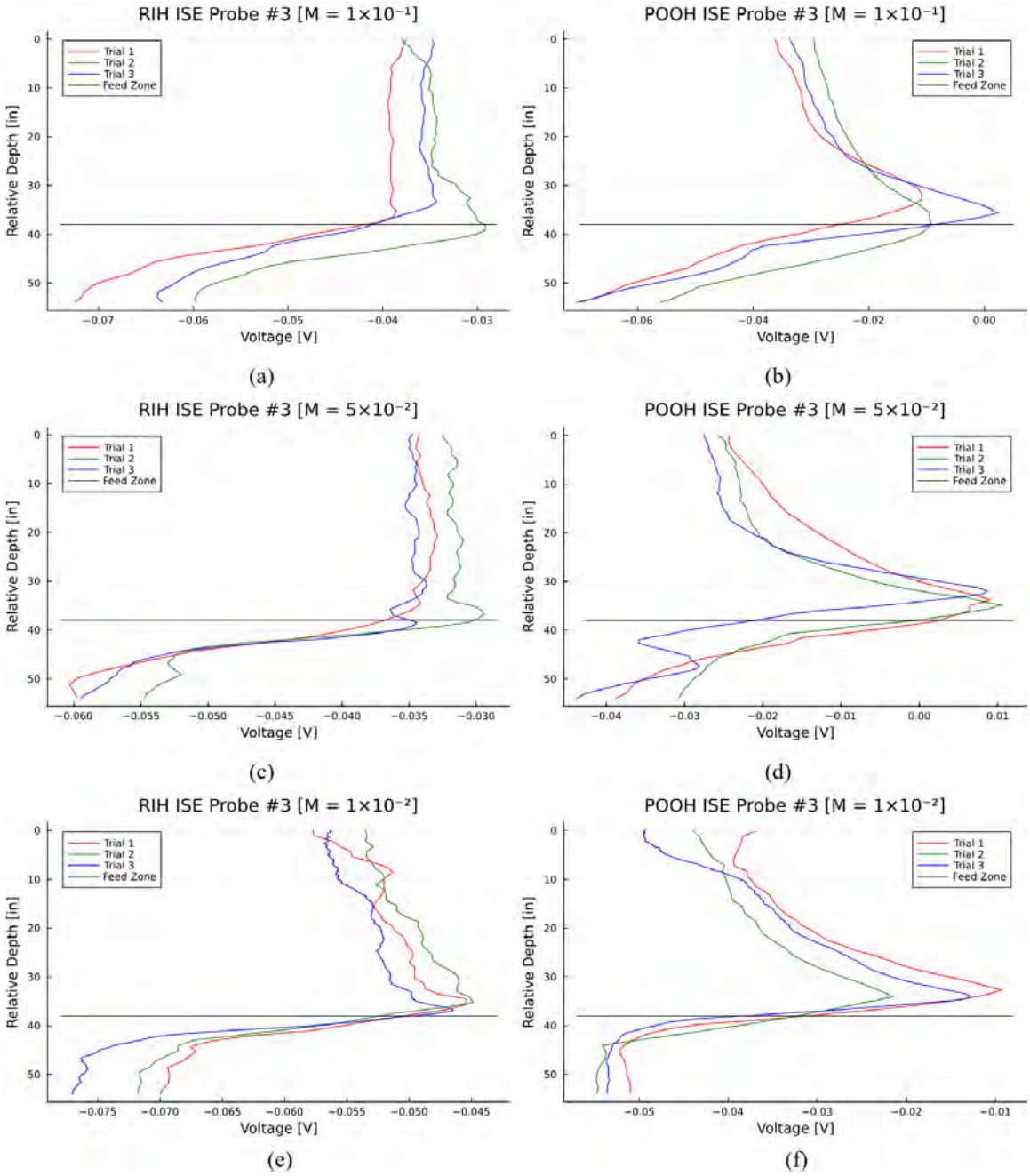

Figure 3-4: Molarity vs. Depth for ISE probe #2 in the RIH and POOH directions for feed zone fluids with chloride concentrations of (a and b) 1×10^{-1} mol/L, (c and d) 5×10^{-2} mol/L, and (e and f) 1×10^{-2} mol/L

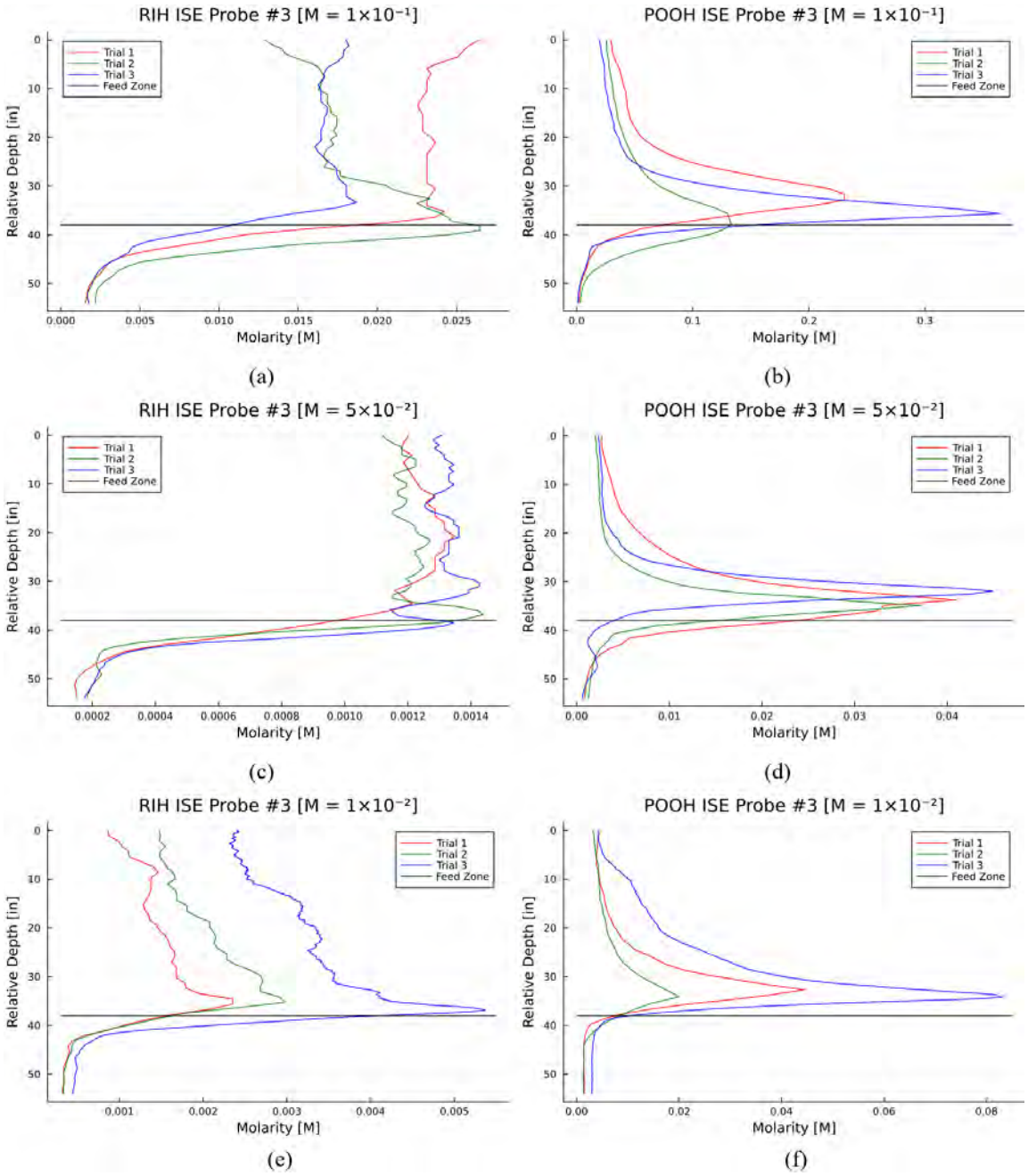

Figure 3-5: Molarity vs. Depth for ISE probe #3 in the RIH and POOH directions for feed zone fluids with chloride concentrations of (a and b) 1×10^{-1} mol/L, (c and d) 5×10^{-2} mol/L, and (e and f) 1×10^{-2} mol/L

Table 3-1: Average inferred feed zone inflow rates and percentage error for the various scenarios at different chloride concentrations of the feed zone fluid

Feed Zone Chloride Concentration	Scenario	ISE Probe	Average Inferred Flow Rate (kg/s)	Percentage Error
1×10^{-1} mol/L	RIH	#2	1.256	993%
1×10^{-1} mol/L	POOH	#2	1.010	778%
1×10^{-1} mol/L	RIH	#3	0.730	535%
1×10^{-1} mol/L	POOH	#3	0.109	-5%
5×10^{-2} mol/L	RIH	#2	1.131	884%
5×10^{-2} mol/L	POOH	#2	0.877	662%
5×10^{-2} mol/L	RIH	#3	0.773	572%
5×10^{-2} mol/L	POOH	#3	0.031	-73%
1×10^{-2} mol/L	RIH	#2	0.866	653%
1×10^{-2} mol/L	POOH	#2	0.886	670%
1×10^{-2} mol/L	RIH	#3	0.393	242%
1×10^{-2} mol/L	POOH	#3	0.078	-33%

Further experiments were conducted to test the following independent variables: the angular position of the chloride tool, the feed zone inflow rate, and the presence of additional ions in the feed zone fluid. These experiments found that the chloride tool underestimated the feed zone inflow rate when the ISE sensors and the feed zone jet were on opposing sides of the well. Additionally, when the feed zone inflow rate was varied, no significant changes to the accuracy of the inferred feed zone inflow rates were seen. Finally, when bromide was present in the feed zone fluid, the magnitudes of the molarity readings were significantly greater than other experiments. However, the relative changes to the measured concentration still provided accurate estimations of the feed zone inflow rate. In contrast, the presence of sulfate ions in the feed zone fluid did not affect the chloride concentration readings of the ISE sensors nor the ability of the chloride tool to infer feed zone inflow rates.

These findings highlight the sensitivity of the chloride tool to multiple parameters that characterize geothermal wells. Overall, these laboratory experiments yielded promising results when measuring a vertical series of chloride concentrations in the artificial geothermal well. As such, the method of inferring feed zone inflow rates in a geothermal well using chloride concentration measurements, albeit on a relative rather than absolute scale, holds promise.

4. Field Testing

The field-deployable chloride tool was deployed in FORGE Wells 58-32, a vertical monitoring well with a total depth of 7,536 ft, and Well 16B(78)-32, a deviated production well drilled to a total depth of 10,947 ft. For 58-32, the weight of the tool was sufficient to lower the tool with gravity; however, in 16B(78)-32, a wireline roller was needed to help convey the tool through the well deviation. Figure 4-1 shows the wells on the Utah FORGE site and Table 4-1 provides an overview of the two FORGE wells and the deployment techniques in each.

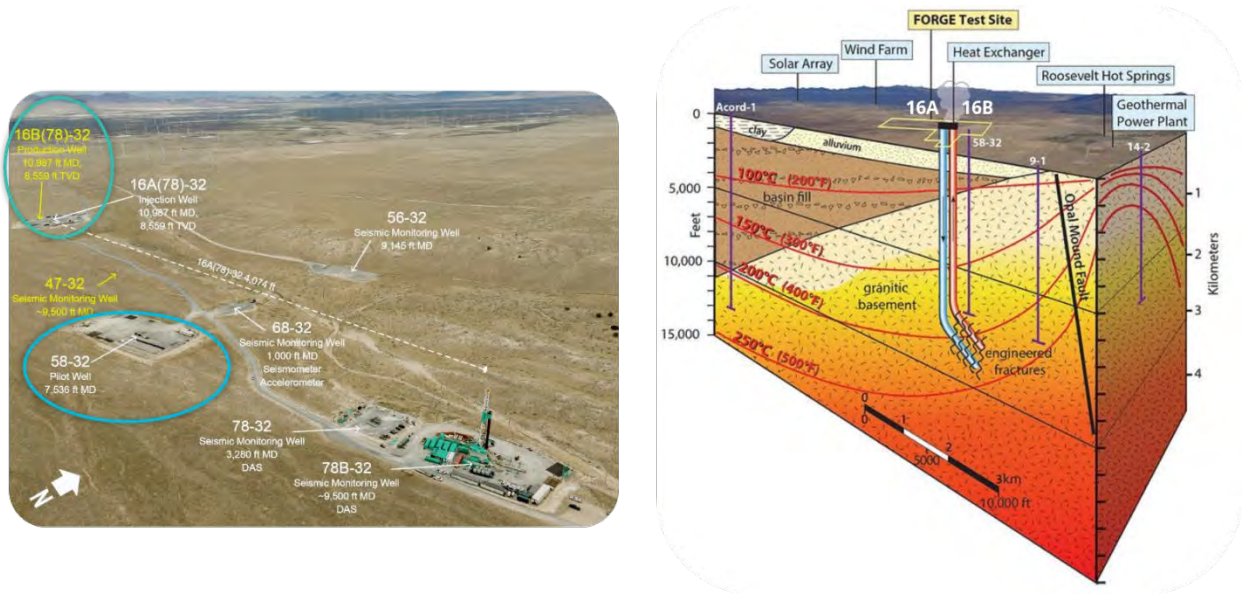

Figure 4.1: Utah FORGE site with planned deployment wells circled (left) and geological and heat model of the Utah FORGE site (right) (source: Utah FORGE)

Table 4-1: Overview of tool deployment scenarios in Utah FORGE wells 58-32 and 16B(78)-32.

FORGE Well	Well Type	Curve Profile	Total Depth	Deployment Technique
58-32	Vertical Pilot Well	N/A	7,536 ft	Tool deployed on Sandia wireline with weight of tool
16B(78)-32	Directional Production Well	5˚/100 ft	10,947 ft	Tool deployed through wireline service company with conveyance rollers to assist with well deviation

4.2 FORGE Well 58-32 Deployment

The first deployment was executed June 12-14, 2024, at Utah FORGE Well 58-32, an open and vertical pilot well. Three tool assemblies were prepared for contingency in the field. The Sandia wireline truck was used to deploy the tool into the well and a tip and body centralizer were used to centralize the tool within the 7” casing. The tool was deployed to five test locations shown in Figure 4-2, above, below, and within the cased and perforated zones to test the capability of the ion-selective electrodes to measure chloride concentration readings around the feed zone and determine if these measurements can be used to calculate the feed zone inflow rate.

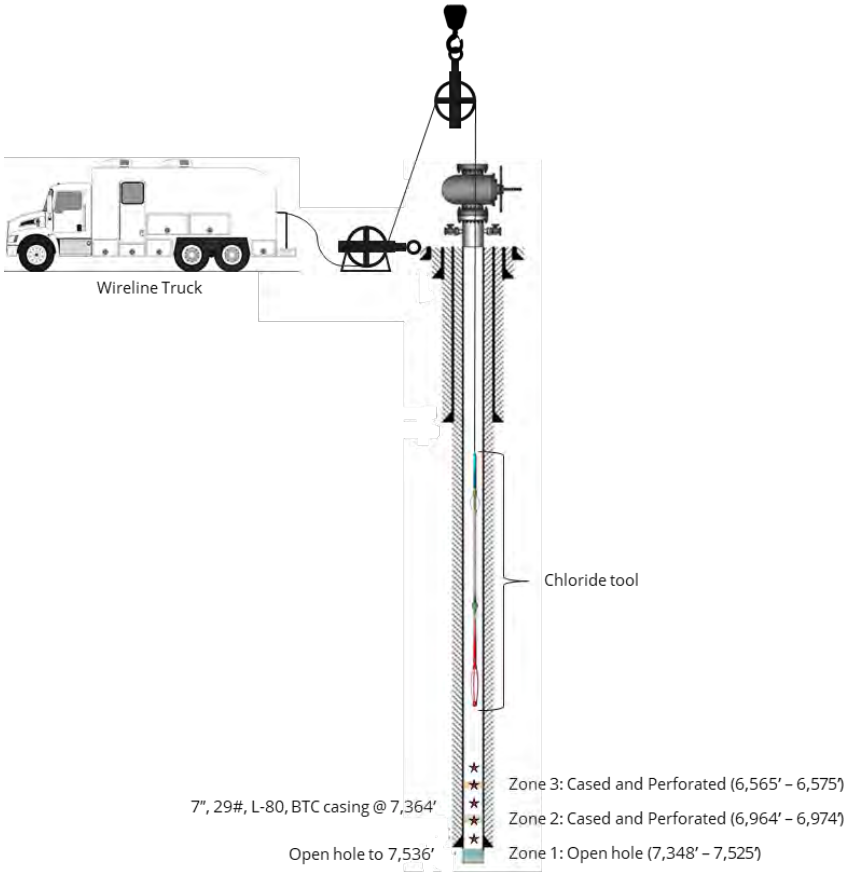

Figure 4-2: Illustration of tool deployment plan for Utah FORGE Well 58-32.

The two primary tools experienced issues during deployment and were pulled out the hole before collecting data. The secondary tool was successfully deployed to 7,168 ft MD with a maximum measured temperature of 190˚C. Measurements were recorded at each test location during the run-in hole (RIH) and pull-out-of-hole (POOH), with noticeably better during the POOH run in comparison to the RIH run. The measurements suggest that there were no internal flows in the well during the logging, which was not unexpected as the well was not producing at the time. Figure 4-3 shows the deployment of the tool into Utah FORGE well 58-32 using the Sandia wireline truck.

Figure 4-3: Deployment at Utah FORGE Well 58-32.

The logging results are shown in Figure 4-4 for the run-in hole (RIH) and Figure 4-5 for the pull-out of the hole (POOH). The first two columns display data from two chemical sensors, while the following two columns show temperature data from the PTS and CPU. The CPU temperature data is considered to be more accurate in magnitude for this particular run, despite the lag in heating up caused by its position inside the electronics component rather than in direct contact with the fluid. The last three columns represent the flow data from the PTS sensor. The perforated zones are marked with yellow regions; the short interval creates the appearance of a line.

A decrease in voltage (i.e., a spike to the left) would correlate with an increase in chloride concentration, indicating inflow presence. If accompanied by a temperature spike coming from geofluid entering the wellbore, the voltage spike will strongly indicate inflow presence. The RIH data shows no strong indication of such a spike around Zone 2 and 3. Meanwhile, spikes in both directions are observed in the chloride voltage columns near Zone 1, which also correlates with a temperature increase. However, the PTS counter did not increase, even with a location pause. Thus, the interval is not interpreted as flowing or experiencing notable internal flow.

The POOH run provides much cleaner data than the RIH run, which was expected as the laboratory experiments have indicated the same behavior. However, chemical sensor voltage data from the shallower part of the POOH, as indicated in Figure 4-5, is erroneous and cannot be used for interpretation. Similar to RIH, spikes are seen near Zone 1 but are not interpreted as flow because

the PTS counter did not change at all. There seems to be a voltage spike near Zone 3, which is also accompanied by a temperature spike. However, the spike was only caused by one data point; again, no corresponding counter or direction change from PTS was present. Thus, it is concluded that the logged interval did not indicate the presence of any inflow. If there were any internal flow happening, it could occur within the open hole section, which was below the maximum depth of our runs as it was considered undesirable to run the tool below the casing shoe.

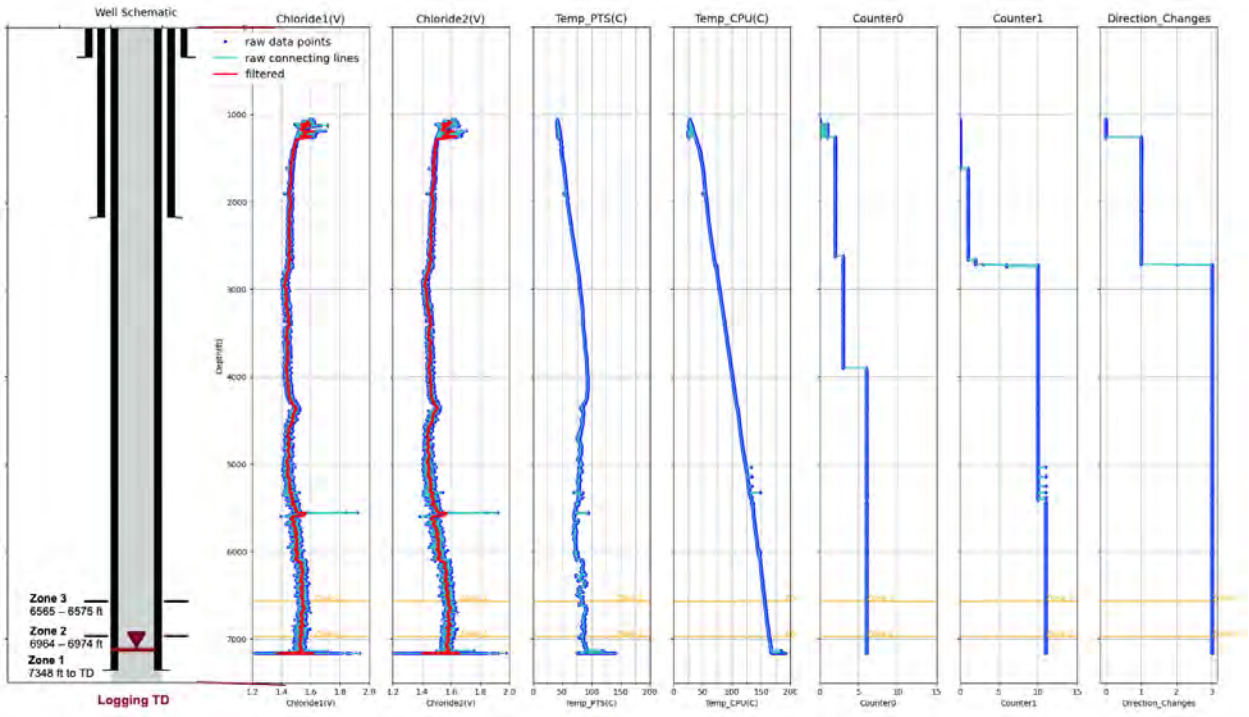

Figure 4-4: logging results during Run in Hole (RIH) at well 58-32.

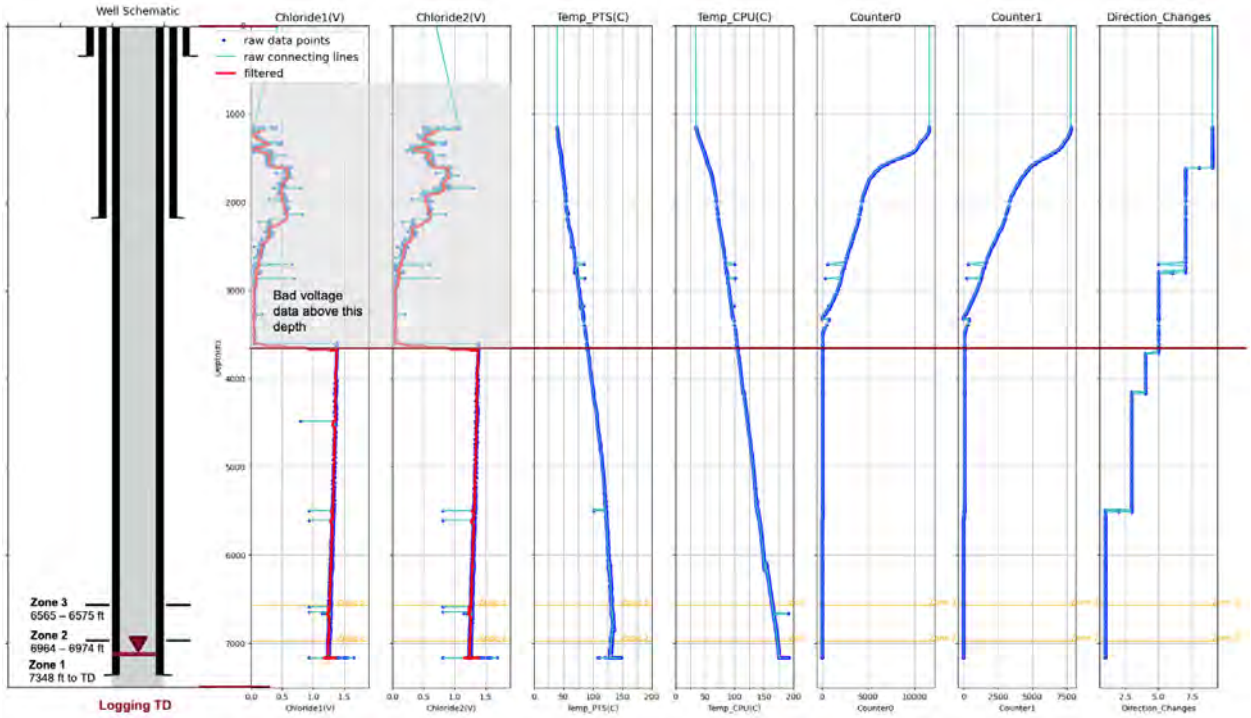

Figure 4-5: logging results during Pull Out of Hole (POOH) at well 58-32.

The voltage signals from the two chemical sensors appear to resemble each other. Thus, the readings from the first sensor were used to evaluate converting the chemical sensor voltage into chloride concentration. Calibration for the field tool used at 58-32 was performed with KCl solution in distilled water and fluid samples from well 16A(78)-32 and 16B(78)-32. The molarity result using the best available calibration curve is shown in Figure 4-6, showing a range of around 0.2 for RIH data and between 0.25 to 0.75 M for POOH data. However, this calibration curve is unreliable due to a discrepancy in the third tool bench calibration after acquisition.

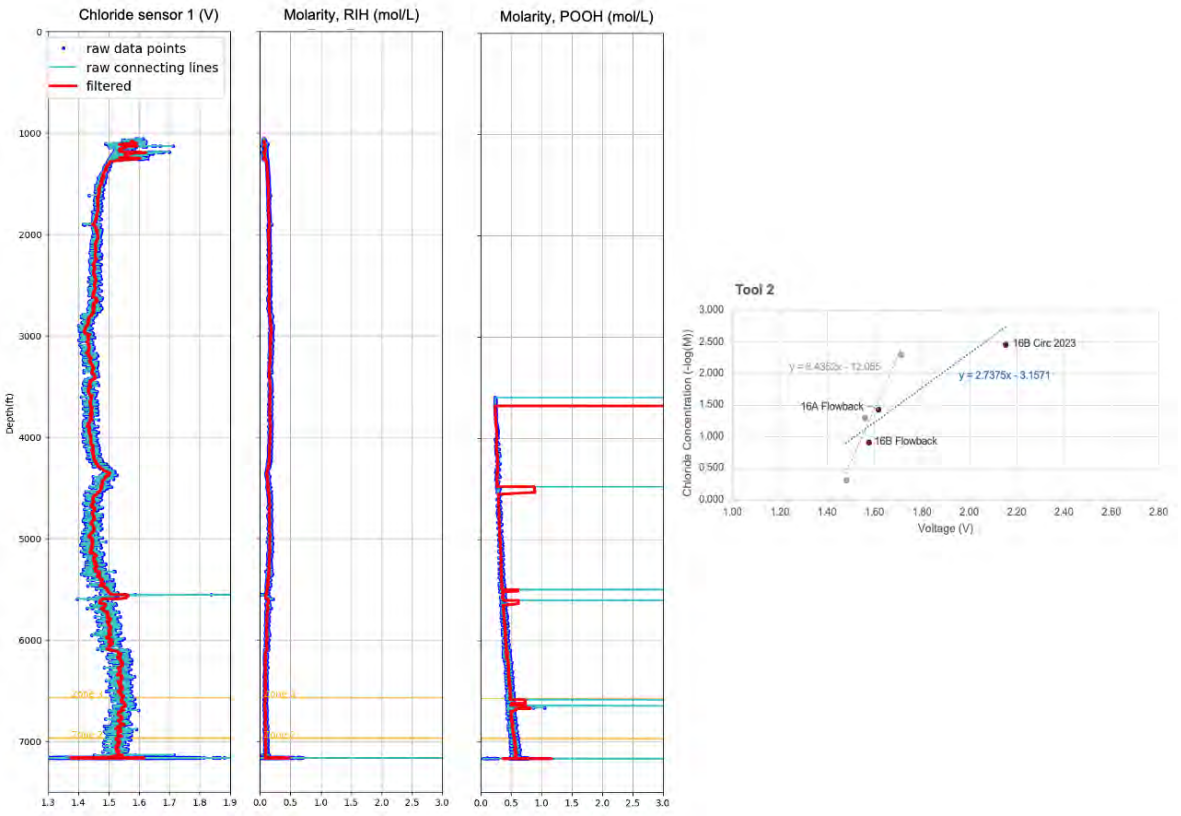

Figure 4-6: converted molarity from the chemical sensor 1 voltage data during RIH and POOH using Tool 2 calibration curve (blue line)

In Table 4-2, the sum of the molarity of relevant chemical species ranges from 0.0046 to 0.12 M. Recent laboratory experiments have shown that in addition to chloride, the ISE is sensitive to bromide (B) and, to a lesser extent, sulfate (SO4), as discussed in Section 3. While chloride is more common in brine water and often determines the molarity, the ISE reacts to bromide and sulfate to varying degrees. The logging results overestimate the chloride concentration compared to available samples, albeit not from well 58-32 itself. Additionally, the RIH data shows a lower concentration than the POOH data, which is closer to the truth. Consequently, improvements will be made to the chemical sensor to ensure more accurate readings for the follow-up test at 16B(78)-32.

Table 4-2; Relevant chemical species of well samples from Utah FORGE Wells 16A(78)-32 and 16B(78)-32

DATE & TIME		WELL	Concentration (mg/l)			Molarity (mol/l)			Sum of molarity (mol/l)
			B	Cl	SO4	B	Cl	SO4	
7/19/2023 20:00		16A(78)-32	2.07	1300	162	2.59E-05	3.66E-02	12.2.4.69E-03	0.0383
7/20/2023, 7:50		16B(78)-32	9.05	4384	239	1.13E-04	1.23E-01	2.49E-03	0.1261
7/20/2023, 15:00		16B(78)-32	0.32	122	115	4.01E-06	3.44E-03	1.20E-03	0.0046

4.3 FORGE Well 16B Deployment

The second deployment was conducted August 19, 2024, at Utah FORGE Well 16B(78)-32 during a 30-day circulation test. Two chemical tool assemblies were prepared for contingency in the field. The tool was deployed using an SLB wireline truck, weight bars, and Petromac rollers to assist in conveying the tool through the flowing and deviated well. This test was conducted to test the feasibility of the geochemistry-based approach to map fractures and quantify feed zone inflow rates in a flowing well. Well 16B has five stages, each with 3-5 guns, this provided the opportunity to map up to 20 fractures. For this deployment, ten test locations were planned, to target measurement at and between perforations. For each test location, the tool was held to allow for a stationary measurement of the chloride sensors and PTS tool. The logging between each test location would provide a blind “fly by” measurement to determine the feasibility of mapping fractures using a running log. Figure 4-7 illustrates the deployment plan, with the measurement locations shown as stars and Table 4-3 summarizes the measured depth of the perforation stages and planned and executed test locations during the RIH and POOH logs.

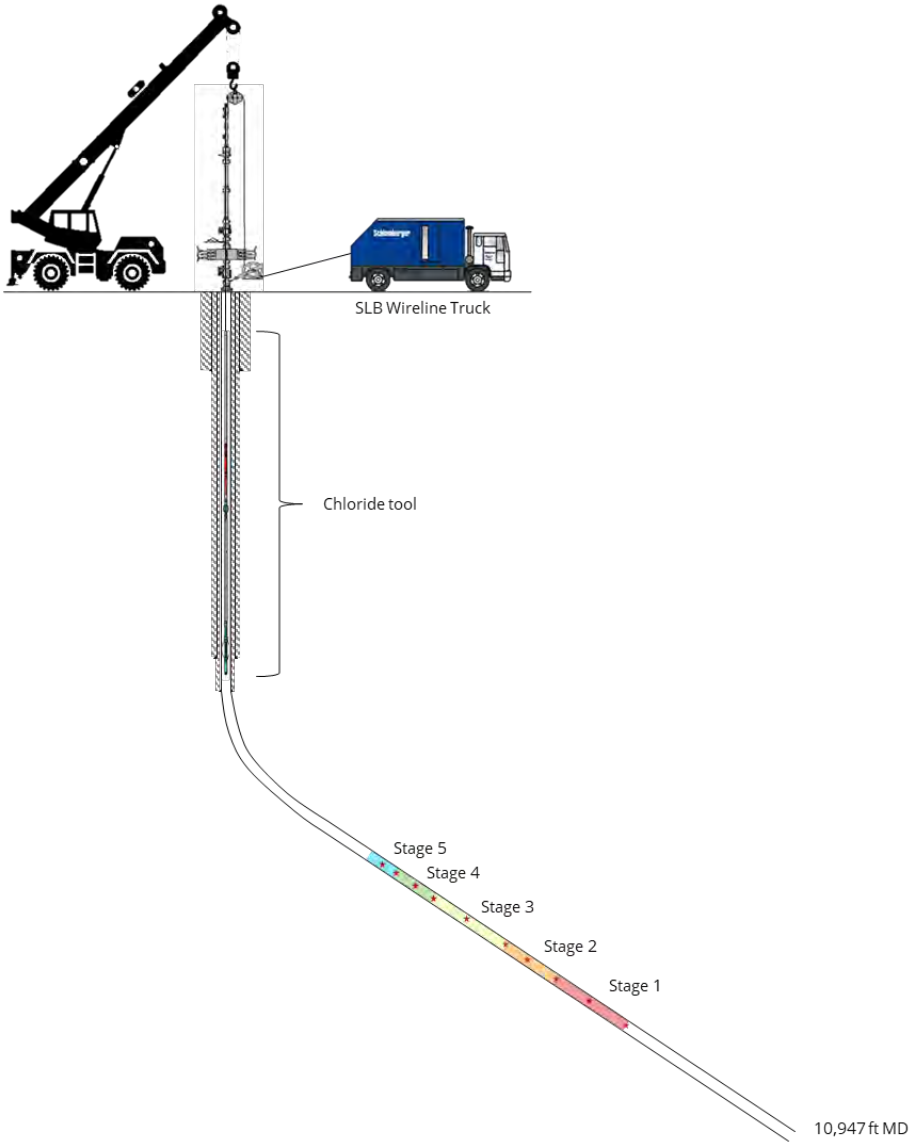

Figure 4-7: Illustration of tool deployment plan for Utah FORGE Well 16B(78)-32. Perforation stages shown in highlighted zones and planned test locations shown as red stars.

Table 4-3: Measured Depth of perforation stages and planned and actual test locations.

	Measured Depth (ft)							
	Gun 1	**Gun 2**	**Gun 3**	**Gun 4**	**Gun 5**	**Planned Test Location**	**Actual RIH Test Location**	**Actual POOH Test Location**
Stage 5	8500 - 8806	8806 - 8855	8855 - 8876	8876- 8920		8865	8865	8865
						8920	8920	8920
Stage 4	8920 - 8978	8978 - 9013	9013 - 9042	9042 - 9155		9030	9030	9030
						9155	9155	9155
Stage 3	9155 - 9306	9306 - 9368	9368 - 9407			9388	9388	9388
						9407	-	-
Stage 2	9407 - 9440	9440 - 9455	9455 - 9469	9469 - 9495	9495 - 9600	9462	-	-
						9600	-	-
Stage 1	9600 - 9720	9720 - 9753	9753 - 9765	9765 - 9800		9759	-	-
						9800	-	-

The tool was successfully deployed to approximately 9,480 ft with a maximum measured temperature on the tool of 210°C. Figure 4-8 shows the fully assembled tool being loaded into the lubricator by the SLB team and Figure 4-9 shows the Utah FORGE Well 16B test site during the logging. The monitor wellhead pressure, flowline temperature, and separator liquid discharge flow during the log were 260-263 psi, 180°C, and 294-330 gpm, respectively. Measurements were recorded through Stage 3, at which point the log began to show potential issues. The wireline operator noted the tool had stopped moving at approximately 9,480 ft. After recovering tension in the line, the tool was brought back up the well for the POOH log to record measurements in Stage 4 and 5. The measurements in the RIH log were of noticeably better quality than the POOH log, potentially indicating damage to the tool. The measurement results indicate a change in chloride concentration in the perforation zones, suggesting the chemical tool is capable of mapping fractures in a flowing well.

Figure 4-8: Full chemical tool assembly attached to weight bars and being loaded into lubricators.

Figure 4-9: Utah FORGE Well 16B test site with lubricator stacks for chemical tool.

5. Conclusion

The latest updates on the chloride tool development have focused on the deployment of the field-scale tool at the Utah FORGE site. Three assembled field-scale tools were constructed and tested in the lab, testing different iterations of the sensor pellet, tool housing, data electronics package, and assembly, and confirming operation of the tool on the wireline. The tool assembly features a Mitco PTS sensor package for secondary measurements, a wire guide component, chemical sensor housing, and HTHP electronics for data transmission through a 7-conductor feedthrough to the wireline. The sensor housing was fabricated using metal additive manufacturing, and was designed to integrate with the logging tool, accommodating Ion-selective Electrode (ISE) sensors, reference sensors, and pH sensors to be exposed to the flow in the well.

Concurrent with the development of the field-scale tool, flow experiments were conducted in the artificial well system at the Stanford Geothermal Lab. These laboratory experiments provided insights into the chemical tool's response to varying parameters, including chloride concentration in the feed zone, the tool's vertical position relative to the feed zone, and the presence of additional chemical species in the feed zone fluid. The findings demonstrated the chemical tool's sensitivity to multiple parameters, suggesting that using chloride concentration measurements to infer feed zone inflow rates in geothermal wells is a promising method.

The tool was successfully deployed at FORGE Well 58-32 an open, vertical well in June 2024, and FORGE Well 16B(78)-32, a pressurized and flowing deviated well in August 2024. Both deployments demonstrated the capability of the tool to withstand Utah FORGE conditions, and the feasibility of a geochemistry-based approach to map fractures in a flowing well (16B), with no false positives in a nonflowing well (58-32).

ACKNOWLEDGMENTS

This work is part of the Utah FORGE project under award number 3-2418 as a collaborative project between Stanford University and Sandia National Laboratory, supported by the U.S. Department of Energy. Sandia National Laboratories is a multimission laboratory managed and operated by National Technology & Engineering Solutions of Sandia, LLC, a wholly owned subsidiary of Honeywell International Inc., for the U.S. Department of Energy’s National Nuclear Security Administration under contract DE-NA0003525. This paper describes objective technical results and analysis. Any subjective views or opinions that might be expressed in the paper do not necessarily represent the views of the U.S. Department of Energy or the United States Government. Paper registration ID: SAND2024-11132C.

The authors would also like to extend their gratitude to SLB and the Utah FORGE team for their invaluable support in the field deployment effort.

REFERENCES

Acuña, J. A. and. Arcedera B. A.: Two-Phase Flow Behavior and Spinner Data Analysis in Geothermal Wells, Proceedings 13th Workshop on Geothermal Reservoir Engineering, Stanford University, Stanford, California (2005).

Baker, C. Kahn, S.E., Bermes, E.W.: Effect of Bromide and Iodide on Chloride Methodologies in Plasma or Serum. Annals of Clinical and Laboratory Science, Vol. 10, No. 6 (1980).

Chen, Y.; Selvadurai, A. P. S.; Zhao, Z. Modeling of Flow Characteristics in 3D Rough Rock Fracture with Geometry Changes under Confining Stresses. Computers and Geotechnics 130, 103910 (2021).

Co, C..,Pollard, D., Horne, R. Towards a Better Understanding of the Impact of Fracture Roughness on Permeability-Stress Relationships Using First Principles. Proceedings 42nd Workshop on Geothermal Reservoir Engineering, Stanford University, Stanford, California (2017).

Fei, F., Lu, Y., Bunger, A. P., & Cusini, M.: Experimental and Numerical Study of Hydraulic Fracturing in Enhanced Geothermal Systems (EGS), Proceedings 48th Workshop on Geothermal Reservoir Engineering, Stanford University, Stanford, California (2023).

Fu, P., Schoenball, M., Morris, J., Ajo-Franklin, J., Knox, H., Kneafsey, T., Burghardt, J., White, M.: Microseismic Signatures of Hydraulic Fracturing: A Preliminary Interpretation of Intermediate-Scale Data from the EGS Collab Experiment. Proceedings 44th Workshop on Geothermal Reservoir Engineering, Stanford University, Stanford, California (2019).

Gao, X., Egan, S., Corbin, W.C., Hess, R.F., Cieslewski, G., Cashion, A.T., and Horne, R.N.: Analytical and Experimental Study of Measuring Enthalpy in Geothermal Reservoirs with a Downhole Tool, GRC Transactions, Vol.41(2017).

Hess, R., Boyle, T., Limmer, S., Yelton, W., Bingham, S., Stillman, G., Cieslewski, G.: Real-Time Downhole Measurement of Ionic Tracer Concentration and pH in Geothermal Reservoirs, GRC Transactions, Vol. 38 (2014).

Huenges, E.: 25 - Enhanced geothermal systems: Review and status of research and development, Geothermal Power Generation, Woodhead Publishing, Pages 743-761, (2016).

Ishibashi, T., Watanabe, N., Hirano, N., Okamoto, A., and Tsuchiya, N.: Upgrading of Aperture Model based on Surface Geometry of Natural Fracture for Evaluating Channeling Flow, GRC Transactions, 36, (2012), 481-486.

Judawisastra, L. H., Sausan, S., Cherng-Su, J., Horne, R. N.: Development Update on Chloride-based Inflow Measurement in Fractured Enhanced Geothermal Systems (EGS) Wells, Proceedings 48th Workshop on Geothermal Reservoir Engineering, Stanford University, Stanford, California (2023).

Judawisastra, L. H., Sausan, S., Horne, R. N.: Analytical, Experimental and Numerical Development Update on Inflow Measurement in Geothermal Wells from Chloride Concentration. Proceedings, 8th Indonesia International Geothermal Convention & Exhibition, (2022).

Rhodes, R. K., Buck, R. P.: Competitive Ion-Exchange Evaluation of the Bromide Interference on Anodized Silver/Silver Chloride Electrodes, Analytica Chimica Acta, Volume 113, Issue 1, (1980).

Sausan, S., Judawisastra, L. H., Horne, R. N.: Development of Downhole Measurement to Detect Inflow in Fractured Enhanced Geothermal Systems (EGS) Wells, Proceedings 47th Workshop on Geothermal Reservoir Engineering, Stanford University, Stanford, California (2022).

Sausan, S., Judawisastra, L. H., Cherng-Su, J., Horne, R. N.: Chloride-based Wireline Tool for Measuring Feed Zone Inflow in Enhanced Geothermal Systems (EGS) Wells: Experimental, Numerical, and Data-driven Updates, Geothermal Resources Committee Transactions Vol 47 (2023), pg. 841-863.

Sausan, S., Hartung M. B., Cherng-Su, J., Schneider, M., Wright, A. A., Horne, R.: Updates on the Development of Chloride-based Wireline Tool for Measuring Feed Zone Inflow in Enhanced Geothermal Systems (EGS) Wells, Proceedings 48th Workshop on Geothermal Reservoir Engineering, Stanford University, Stanford, California (2024).

Sausan, Sarah: Investigating Fluid Flow Behavior in Enhanced Geothermal System (EGS) Wells: Numerical and Data-Driven Approaches, MS Thesis, Energy Resources Engineering Department, Stanford University (2023).

Sisler, J., Zarrouk, S. J., Adams, R.: Improving the Performance of Geothermal Pressure, Temperature and Spinner (PTS) Tools Used in Down-Hole Measurements. Proceedings, World Geothermal Congress 2015, Melbourne, Australia (2015).

Sullivan, J.L., Clark, C.E., Han, J., Wang, M.: Life-Cycle Analysis Results of Geothermal Systems in Comparison to Other Power Systems, Argonne National Laboratory ANL/ESD/10-5 (2010)

Xiao, F., Shang, J., Wanniarachchi, A., Zhao, Z.: Assessing Fluid Flow in Rough Rock Fractures Based on Machine Learning and Electrical Circuit Model. Journal of Petroleum Science and Engineering, 206, 109126 (2021).

Zhang, Y., Chai, J.: Effect of Surface Morphology on Fluid Flow in Rough Fractures: A Review. Journal of Natural Gas Science and Engineering 79, 103343 (2020).

Fracture Characterization using Borehole Image Log, A Single Well Case Study from An Exploration Well at Tompaso Geothermal Field, North Sulawesi, Indonesia

Sigit Suryanto*, Sonny Wiyoga, Syayidu Guntur Maarif*, David P. Timisela*, Jayanti Anggraini*, Dedi Juandi**, Rudi Hartanto****

***PT Pertamina Geothermal Energy, ** SLB**

Keywords

Borehole Image, Fracture, Matrix, Permeabiliy, Feed Zone

ABSTRACT

An electrical borehole image log was recorded using freshwater mud in one of an exploration well at Tompaso geothermal field, Minahasa Regency, North Sulawesi Province with well deviation up to 25 degree. The log penetrated volcanic rocks in 2 runs within 12.25inch (1129m length) and 9.875inch (829m length) hole sizes. The objective of this study is to understand the fracture distribution and permeability characteristic of the Tompaso geothermal field by integrating borehole image with mud log, side wall core, petrographic analysis and spinner log to better locate the permeable zone and assessing the potential of this field.

A total of eleven lithotypes were classified. The 12.25-inch section is predominantly composed of volcanic breccia and coarse-grained pyroclastics, with thin lava layers observed at various depths. While lava is more prevalent in the 9.875-inch section, volcanic breccia and pyroclastics remain the dominant lithotypes. There were eleven fracture zones can be divided based on the fracture orientation, density, and lithotype association which later can be correlated with the spinner data to determine the feed zones.

Integration of borehole image data, sidewall cores, and surface geological mapping reveals that high permeability zones within the depth interval of 1023 mMD to 2167 mMD are predominantly controlled by matrix permeability of pyroclastic rocks, lithological contacts, and NE-SW striking fracture zones dipping southeast. This fracture zone likely correlates with the damage zone of the Tompaso fault. In contrast, permeability within the deeper interval of 2167 mMD to 3003 mMD is primarily influenced by E-W striking fractures and faults dipping south, likely associated with the Riendengan Caldera Rim. By targeting specific fracture orientations and lithology, it can enhance the probability of encountering productive zones and maximizing geothermal resource exploitation in the Tompaso field.

1. Introduction

Pertamina Geothermal Energy drilled an exploration well at Tompaso geothermal field, Minahasa Regency, North Sulawesi Province. Borehole image log penetrated volcanic rocks in 2 runs within 12.25in (1129m length) and 9.875in (829m length) hole sizes in the TPS-X well. (Figure 1). The area is part of a complex fault system with various fault patterns, including the NE-SW pattern and the NW-SE pattern that influenced by the NE-SW compressional tectonic regime (modification from Suryanto et al., 2020). There is almost no ENE-striking displacement in the area between instead of the NE-striking lineament such Panasen Fault. Therefore, we believe these volcanoes caldera and crater wall has faked the tectonic lineament which misleads the interpretation of the active left-lateral strike-slip Soputan Fault in the previous literature (Ikhwan et al., 2021). Knowing the fracture characteristic and their relation to the flow zone, therefore it is very important to understand the reservoir behavior with regards to the complexity of the field.

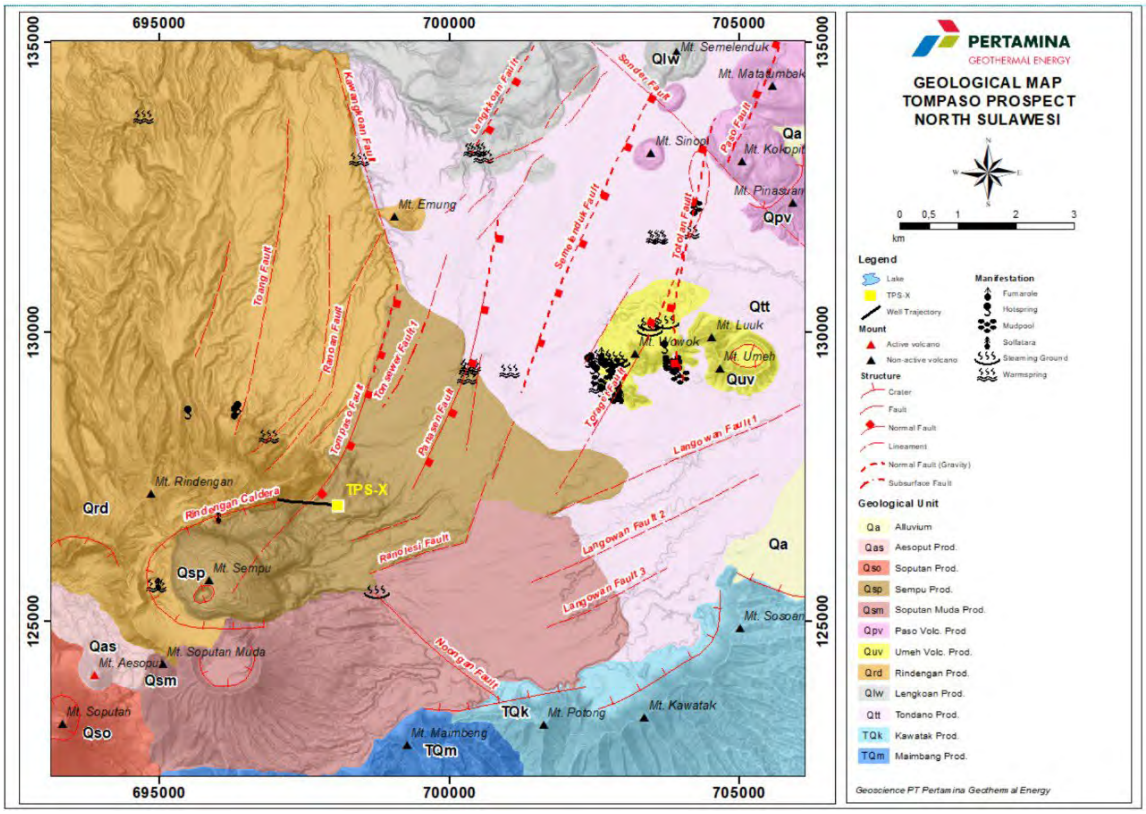

Figure 1: Geological map and geothermal manifestation distribution in Tompaso Field (modification from Suryanto, 2020)

The objectives of the study were to perform borehole image logs analysis including lithotype interpretation, manual dip picking, dips classification, structural analysis, fracture computation, and fracture zonation. Integration with other measurements and their advanced analysis will lead to better locate the permeable zone and assessing the potential of this field.

2. Method

The primary data source for this study was borehole image logs, with gamma-ray and mud logs added to refine lithology characterization. A workflow (Figure 2) was developed, integrating these

datasets to interpret permeable zones. Independent image log interpretation was followed by the use of spinner logs to confirm the presence of flow-contributing fractures. Meanwhile, core data and petrographic analysis confirmed lithotypes identified through image and log analysis, shedding light on the type of permeability sources within the TPS-X well.

The image log was processed to get static and dynamic images, afterward structural features were manually picked by fitting sinusoids to planar or sub-planar features that cut the borehole. Structural features such as fractures and faults were identified as planes that cut across bedding (e.g. fractures and faults). Fractures were further classified as conductive (considered as being open / filled by conductive minerals) and resistive (considered to be healed). While litho-type is defined as distinct combinations of lithology, texture, and structure of a rock (also known as facies). In fracture analysis, lithotype, structural analysis, and fracture computation were used as bases to classify the fracture zonation based on their relation and association. Spinner log, core data, and thin sections are also used to be integrated with the fracture interpretation from the borehole image to identify the location of feed zone.

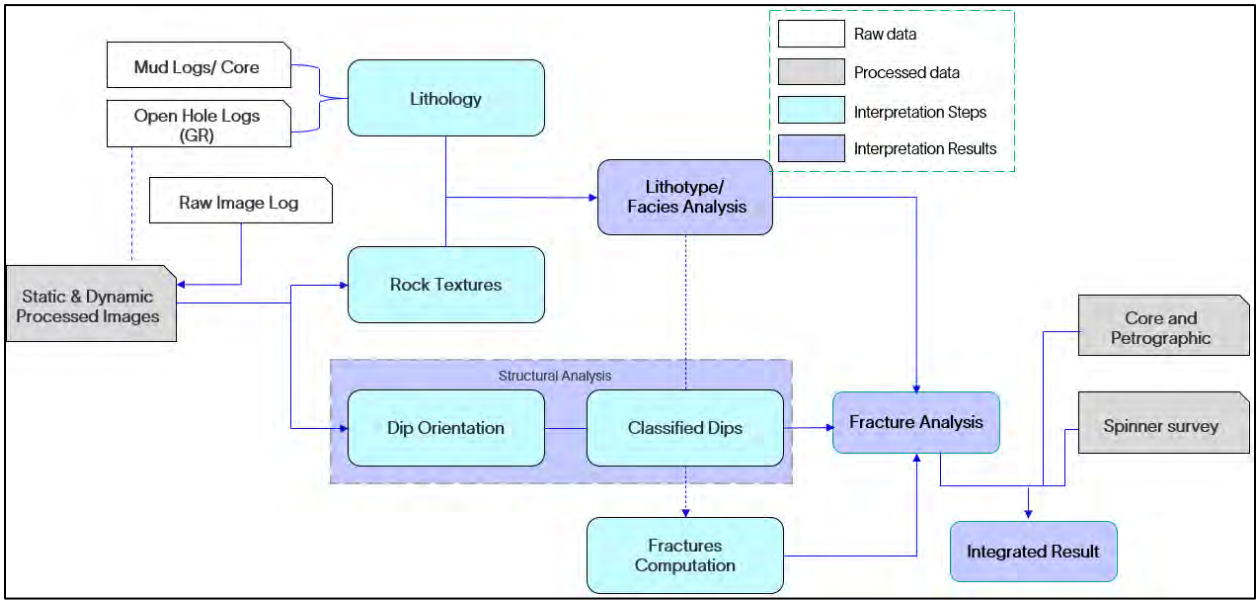

Figure 2: The general workflow of borehole image interpretation in well TPS-X.

3. Borehole Image Interpretation

3.1 Lithotype Interpretation

The lithology was derived and interpreted from the integration of mud logs and conventional log interpretations. Following lithology interpretation, texture and structure were inferred from visual inspection of borehole image appearance (Figure 3).

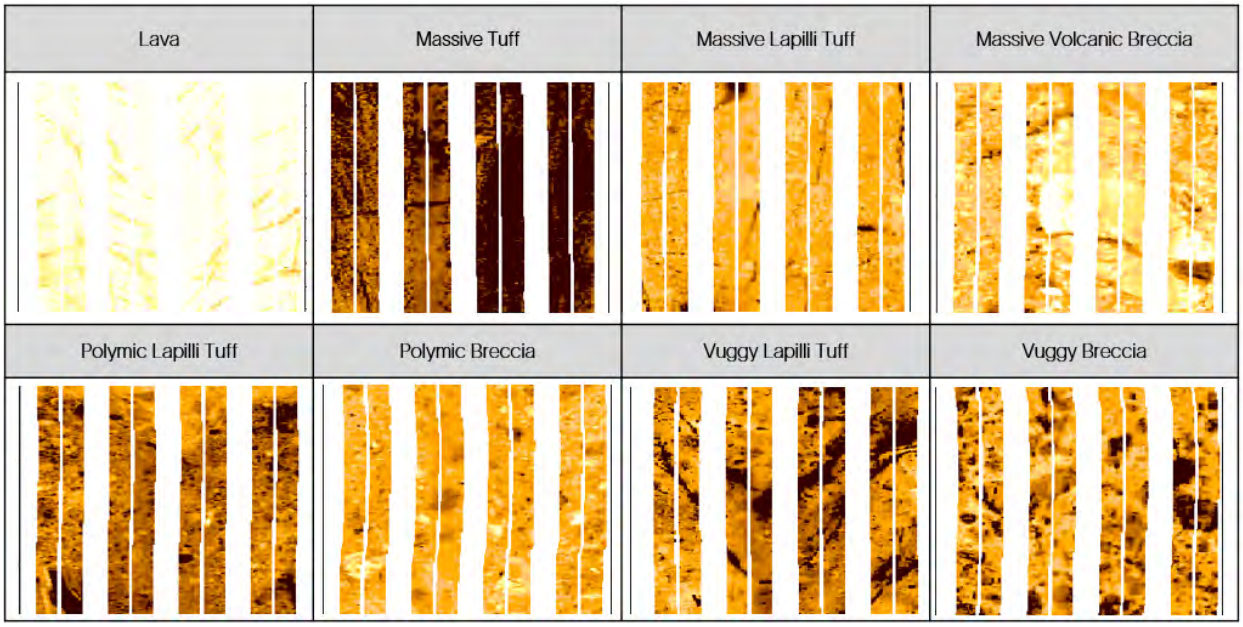

Figure 3: Borehole image textural/ structural features catalog in well TPS-X.

In the TPS-X well, a total of eleven lithotypes were classified (Table 1). In this study, lithotype is defined as distinct combinations of lithology, texture, and structure of a rock (also known as facies).

Symbol	Facies	Descriptions
	Lava	Relatively bright image appearance with massive texture
	Massive Tuff	Relatively dark image appearance with fine apparent texture and structure-less
	Bedded Tuff	Relatively dark image appearance with fine apparent texture and development of beddings
	Massive Lapilli Tuff	Relatively dark image appearance with medium apparent fragment size and structure-less
	Bedded Lapilli Tuff	Relatively dark image appearance with medium apparent texture and development of beddings

Symbol	Facies	Descriptions
	Massive Volcanic Breccia	Relatively dark image appearance with large apparent fragment size and structure-less
	Bedded Volcanic Breccia	Relatively dark image appearance with large apparent texture and development of beddings
	Polymic Lapilli Tuff	Lapilli tuff with mix of medium size resistive and conductive spots interpreted as fragments and relatively high GR
	Polymic Breccia	Breccia with mix of large size edgy resistive and conductive spots interpreted as fragments and relatively high GR
	Vuggy Lapilli Tuff	Breccia with large size resistive and conductive spots interpreted as vugs with relatively low GR
	Vuggy Breccia	Breccia with predominant large size edgy conductive and minor resistive spots interpreted as vugs with relatively low GR

Table 1: Borehole image* textural/ structural features catalog in well TPS-X.

The 12.25-inch section is predominantly composed of volcanic breccia and coarse-grained pyroclastics, with thin lava layers observed at various depths. While lava is more prevalent in the 9.875-inch section, volcanic breccia and pyroclastics remain the dominant lithotypes (Figure 4).

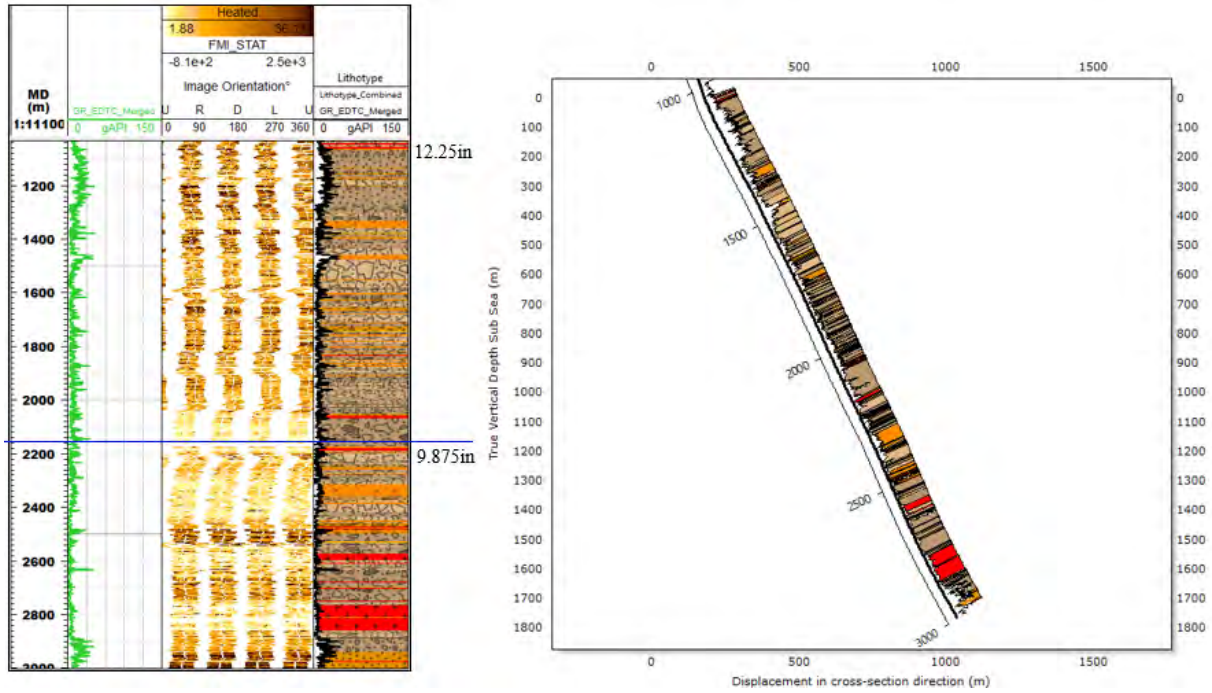

Figure 4: A total of eleven lithotypes were classified in well TPS-X.

3.1 Dip Classification and Structural Interpretation

Planar features intersecting the borehole, such as fractures and faults, were manually identified and analyzed. This process entailed fitting sinusoids to the traces of these features as they intersected the borehole. The dip azimuth is defined by the location of the lowest point on the sinusoid trough, while the dip magnitude is determined by the amplitude of the sinusoid. Fractures were classified as conductive (considered as being open / filled by conductive minerals) and resistive (considered to be healed). Resistive fractures are considered to be healed by resistive minerals such as quartz or calcite (Brata et al., 2014).

Faults are similar in appearance to fractures but show a sense of displacement or associated deformation. Joints are uniform low/moderate/high angle features which are commonly developed in lava lithotype. These joints look similar to fractures, but they are generally occurring in distinct sets.

Structural interpretation involves identifying and characterizing geological features formed by tectonic processes, such as bedding planes, fractures, and faults. This includes determining their orientations to understand the deformational history of the rocks. Additionally, analysis of drilling-induced features can provide insights into the present-day tectonic stress field.

In well TPS-X, the 9.875-inch section has a higher frequency of conductive fractures, possible faults, and joints, which are usually associated with permeable zones. In contrast, the 12.25-inch section has fewer of these features, with bedding planes and resistive fractures being more common (Table 2). Lithological contacts within layered lithotypes can also act as permeable zones. This layering is most evident in the 9.875-inch section, observed as interbeds of volcanic breccia, lapilli tuff, and vuggy breccia.

Section	Number of classification & Orientation	Bedding	Conductive Fractures	Disc. Conductive Fractures	Possible Faults	Resistive Fracture	Joints
12.25 inch	n	47	56	557	2	133	15
	main orientation	NNW	NE-SW	NE-SW	NE-SW & E-W	NNW-SSE	NE-SW
9.875 inch	n	19	146	1560	16	44	275
	main orientation	WNW	N-S	N-S	NNW-SSE	NW-SE	NE-SW

Table 2: Summary table of dip picked over 12.25 in and 9.875 in the well TPS-X.

3.2 Fracture Properties

The electrical image response to fractures is a function of the fracture geometry, the flushed zone resistivity, and the mud resistivity. Quantifying fracture properties can be invaluable in assess the presence of fracture which potentially contributes as permeable zone. Fracture computation was conducted to calculate fracture density, define as number of fractures in window divided by window length (1/m). Conductive fractures, discontinuous conductive fractures, possible faults, and joint and resistive fractures are dip features included in the calculation for the entire logged intervals.

In the 12.25-inch section, a relatively high density of discontinuous conductive fractures is observed in the uppermost and lowermost intervals, predominantly associated with lava lithotypes. Conversely, low to medium fracture densities characterize approximately 80% of this section, primarily within breccia-dominated intervals. The 9.875-inch, display higher overall fracture density compared to the 12.25-inch sections. This elevated fracture density in the 9.875-inch section appears to be correlated with the increased presence of lava lithologies. This suggests that lithological variations play a crucial role in fracture development within the whole study interval. The lava, potentially due to its inherent mechanical properties or emplacement mechanisms, may be more susceptible to fracturing compared to the breccia.

4. Integrated Fracture Interpretation

Integrated Fracture Characterization (IFC) was performed on well TPS-X to assess its fracture development and productivity. This detailed integration provides valuable insights into the well's fracture network, aiding in understanding its production behavior and optimizing future development strategies.

4.1 Integration of Borehole Image and Well Log Data

The logged interval was initially divided into distinct zones based on fracture orientation, density, and lithotype association. This approach identified 11 fracture zones across the 12.25-inch and 9.875-inch hole sections (Figures 5&6). The dips that are considered in defining these zones include conductive fracture (CF), discontinuous conductive fracture (DCF), possible fault (PF), resistive fracture (RF) and join (JT).

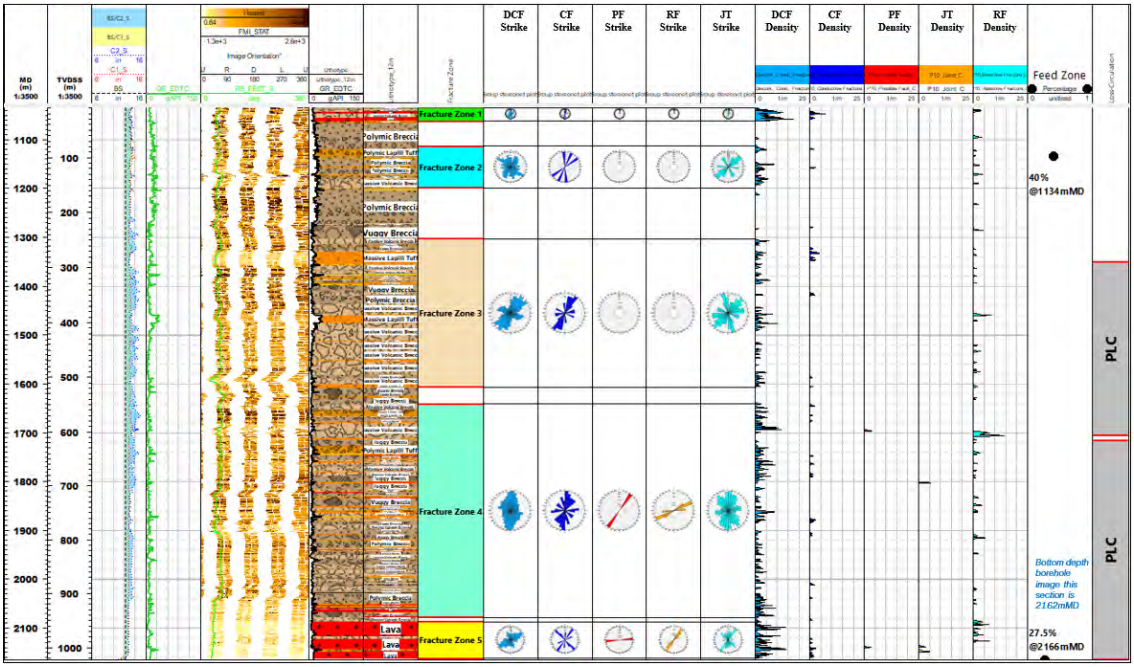

Figure 5: Fracture zone based on fracture orientation, density, and lithotype association in 12.25 inch.

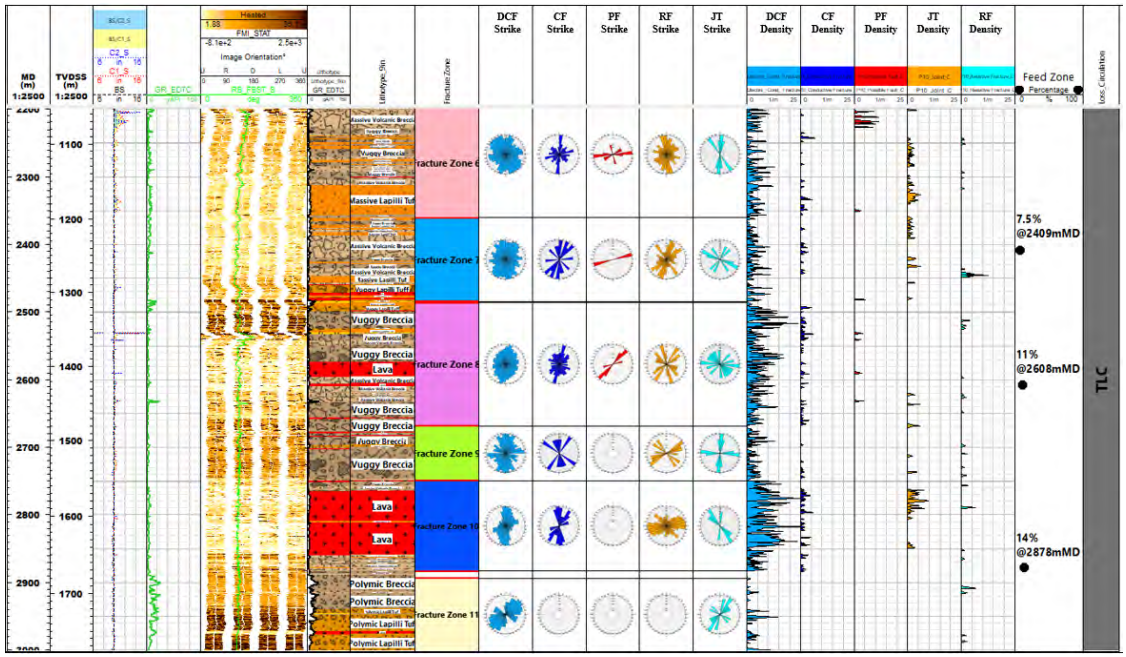

Figure 6: Fracture zone based on fracture orientation, density, and lithotype association in 9.875 inch.

These fracture zones are subsequently integrated with circulation data acquired during drilling and permeability contributions derived from spinner survey data. Notably, in this well, partial losses were observed in the 12.25-inch section, commencing within fracture zone 3 and persisting until fracture zone 5. Subsequently, the well experienced total losses throughout the remainder of the

interval until the end of 9.875-inch section. Table 3 summarizes all fracture zones and their characteristics using all of the previously mentioned criteria.

Section	Fracture Zone	Interval (mMD)	Main Direction					Associate Lithotype	Remarks
			DCF (n)	CF (n)	PF (n)	JT (n)	RF (n)		
12.25 inch	Fracture Zone 1	1035 – 1062	NE-SW (89)	N-S (6)	-	-	NW-SE (5)	Interbedded lava and volcanic breccia capped by polymic breccia.	No loss circulation
	Fracture Zone 2	1113 – 1199	NW-SE (60)	NE-SW (3)	-	-	NW-SE (10)	Volcanic breccia overlain by interbedded polymic breccia and polymic lapilli tuff	No loss circulation
	Fracture Zone 3	1303 – 1607	NE-SW (94)	NNE-SSW (15)	-	-	NNW-SSE & NE-SW (22)	Interbedded of volcanic breccia, lapilli tuff and vuggy breccia with minor lava, tuff and polymic lapilli tuff	Partial loss 2-12.7 BPM
	Fracture Zone 4	1641 – 2078	N-S (222)	NNE-SSW (21)	NE-SW (1)	ENE-WSW (5)	N-S & NW-SE (59)	Interbedded of polymic breccia, vuggy breccia, volcanic breccia, lapilli tuff, vuggy lapilli tuff, polymic lapilli tuff with minor lava.	Partial loss 2-16.5 BPM
	Fracture Zone 5	2087 – 2162	NE-SW (86)	NE-SW & NW-SE (9)	E-W (1)	NE-SW (10)	NE-SW & NW-SE (28)	Interbedded of polymic breccia, vuggy breccia, volcanic breccia, lapilli tuff, vuggy lapilli tuff, polymic lapilli tuff with minor lava.	Partial loss 4-9.4 BPM
9.875 inch	Fracture Zone 6	2173 – 2360	NNW-SSE (265)	N-S (28)	E-W (8)	NNW-SSE (101)	N-S & NW-SE (6)	Interbedded of lapilli tuff, volcanic breccia, vuggy breccia and lava.	Total loss
	Fracture Zone 7	2360 – 2484	NNE-SSW (147)	NNE-SSW (11)	ENE-WSW (1)	NNE-SSW (47)	WNW-ESE (6)	Interbedded of lapilli tuff, vuggy lapilli tuff, volcanic breccia, vuggy breccia and lava.	Total loss
	Fracture Zone 8	2486 – 2668	NNE-SSW (476)	NNE-SSW (58)	NE-SW (7)	NNW-SSE & NNE-SSW (13)	E-W (10)	Interbedded vuggy breccia with volcanic breccia, lapilli tuff, vuggy lapilli tuff and lava	Total loss
	Fracture Zone 9	2668 – 2750	NNE-SSW (109)	NE-SW & NW-SE (8)	-	NE-SW (14)	N-S & E-W (7)	Dominated by vuggy breccia with minor vuggy lapilli tuff and lava	Total loss
	Fracture Zone 10	2750 – 2883	N-S (519)	N-S (40)	-	ENE-WSW (100)	NW-SE (5)	Dominated by lava with interbedded volcanic breccia, vuggy breccia and minor lapilli tuff	Total loss
	Fracture Zone 11	2894 – 3001	NE-SW (44)	-	-	-	NE-SW (10)	Polymic lapilli tuff overlain by polymic breccia with minor lava and volcanic breccia	Total loss

Table 3: Summary of fracture zones based on on fracture orientation, density, and lithotype association.

To better understand the complex relationship between fracture characteristics and permeability contribution, a ranking system was created. This ranking system prioritizes the total average density per square meter of Conductive Fractures (CF) and Possible Faults, excluding Discontinuous Conductive Fractures (DCF) due to their partially closed/healed nature. This ranking is then integrated with pertinent information regarding associated loss circulation events to enhance our understanding of their interrelationships (Table 4).

A key finding from this analysis is that a high total average density of fractures within a zone does not necessarily translate to a proportionally high contribution to permeability. In well TPS-X, the zone with the highest fracture density (rank 1), which is primarily composed of volcanic vuggy breccia with lava, contributes only 11% of permeability. The zone with the highest permeability contribution based on spinner data (fracture zone 2, rank 10) has much less fracture density compare to the highest-ranked zone and is primarily composed of polymic breccia. Notably, fracture zone 2 had no circulation loss during drilling.

Rank	Fracture Zone	Interval (mMD)	DCF 1/m	CF 1/m	PF 1/m	JT 1/m	RF 1/m	Total CC+PF 1/m	Feed Zone (Spinner log)
1	Fracture Zone 8	2486 – 2668	4.96	0.53	0.11	0.08	0.08	**0.64**	11% @2608mMD
2	Fracture Zone 6	2173 – 2360	2.91	0.27	0.32	0.59	0.05	**0.59**	
3	Fracture Zone 10	2750 – 2883	7.77	0.54	0	0.84	0.13	**0.54**	14% @2878mMD
4	Fracture Zone 1	1035 – 1062	6.06	0.48	0	0	0.3	**0.48**	
5	Fracture Zone 5	2087 – 2162	2.63	0.16	0.04	0.14	0.6	**0.2**	27.5% @2166mMD
6	Fracture Zone 7	2360 – 2484	2.26	0.15	0.04	0.43	0.23	**0.19**	7.5% @2409mMD
7	Fracture Zone 9	2668 – 2750	2.32	0.14	0	0.21	0.15	**0.14**	
8	Fracture Zone 3	1303 – 1607	0.55	0.09	0	0	0.14	**0.09**	
9	Fracture Zone 4	1641 – 2078	0.97	0.07	0.01	0.01	0.26	**0.08**	
10	Fracture Zone 2	1113 – 1199	1.14	0.05	0	0	0.19	**0.05**	40% @1134mMD
11	Fracture Zone 11	2894 – 3001	0.93	0	0	0	0.16	**0**	

Table 4: Zone rank summary based on the average density of DCF, CF and PF.

These findings suggest that within this study interval, the dominant contribution to permeability may not be derived from secondary permeability structures like fractures or faults. Instead, primary permeability factors, such as matrix permeability or lithological contacts, may play a more significant role in fluid flow. To confirm lithological interpretations and gain further insights into the permeability characteristics from each lithology and core analysis were conducted. This detailed analysis provides valuable information for assessing the quality and permeability potential of the identified lithologies.

4.2 Integration of Core data and Borehole image

In the well TPS-X, pressure and temperature (P/T) were acquired under static conditions and pressure, temperature, spinner (PTS) were acquired under flowing conditions. Static temperature readings revealed high temperatures, reaching approximately 280°C at 1100 mMD. Spinner data identified several feed zones, with notable contributions at 1134 mMD (40%), 2166 mMD (27.5%), 2409 mMD (7.5%), 2608 mMD (11%), and 2878 mMD (14%) (Figure 7 & 8).

The largest production contribution in well TPS-X originates from 1134 mMD, located within pyroclastic tuff with low fracture density (Figure 8.a). This suggests permeability at this depth is primarily controlled by matrix permeability within the pyroclastic rock or lithological contacts. In contrast, the remaining feed zones at 2166 mMD, 2409 mMD, 2608 mMD, and 2878 mMD are situated within altered andesite and altered andesite breccia, and their permeability is predominantly controlled by fractures and faults striking NE-SW and E-W.

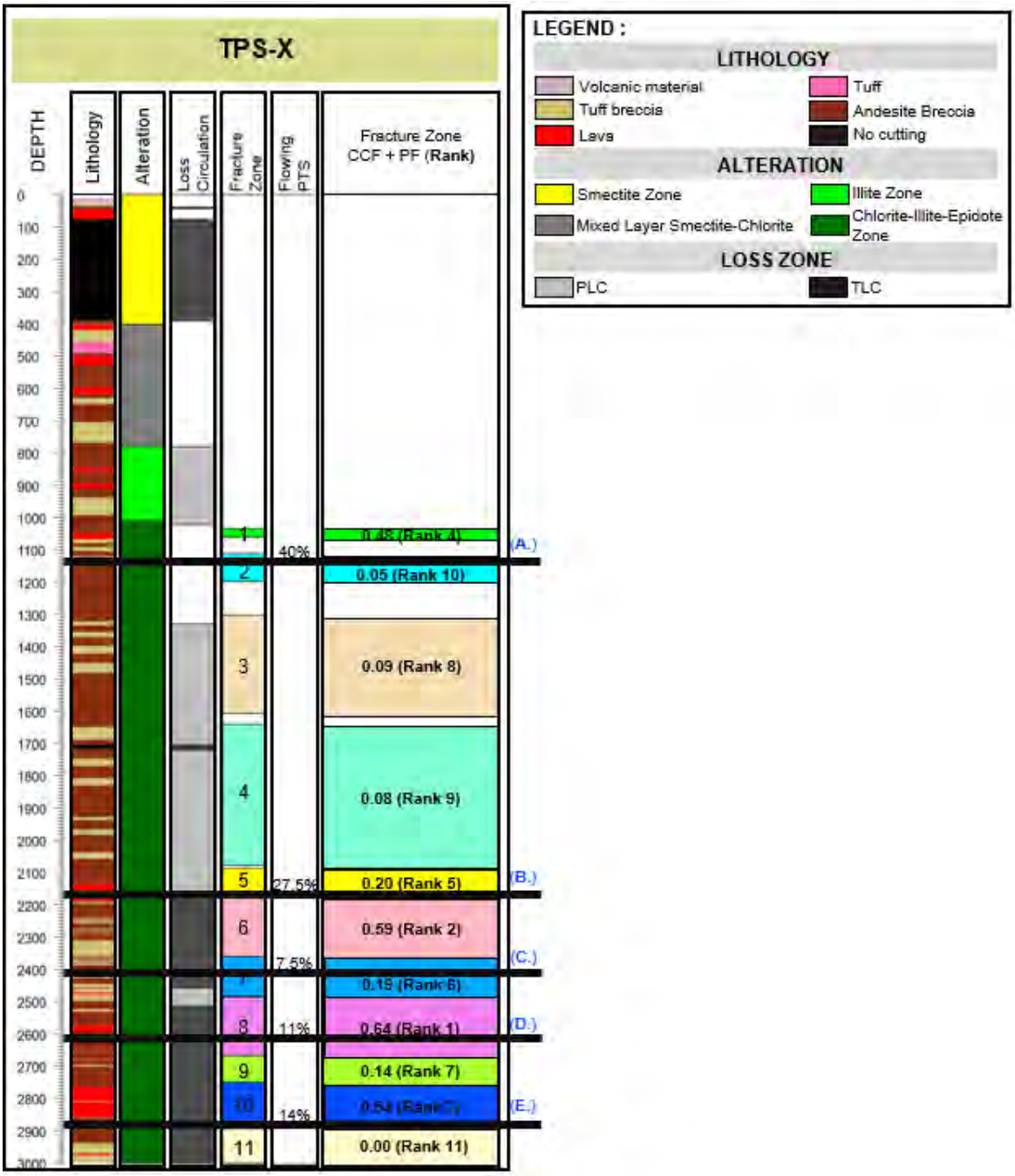

Figure 7: Fracture zone and their association with lithology from core data, alteration zone along with loss zone and feed zone from spinner data.

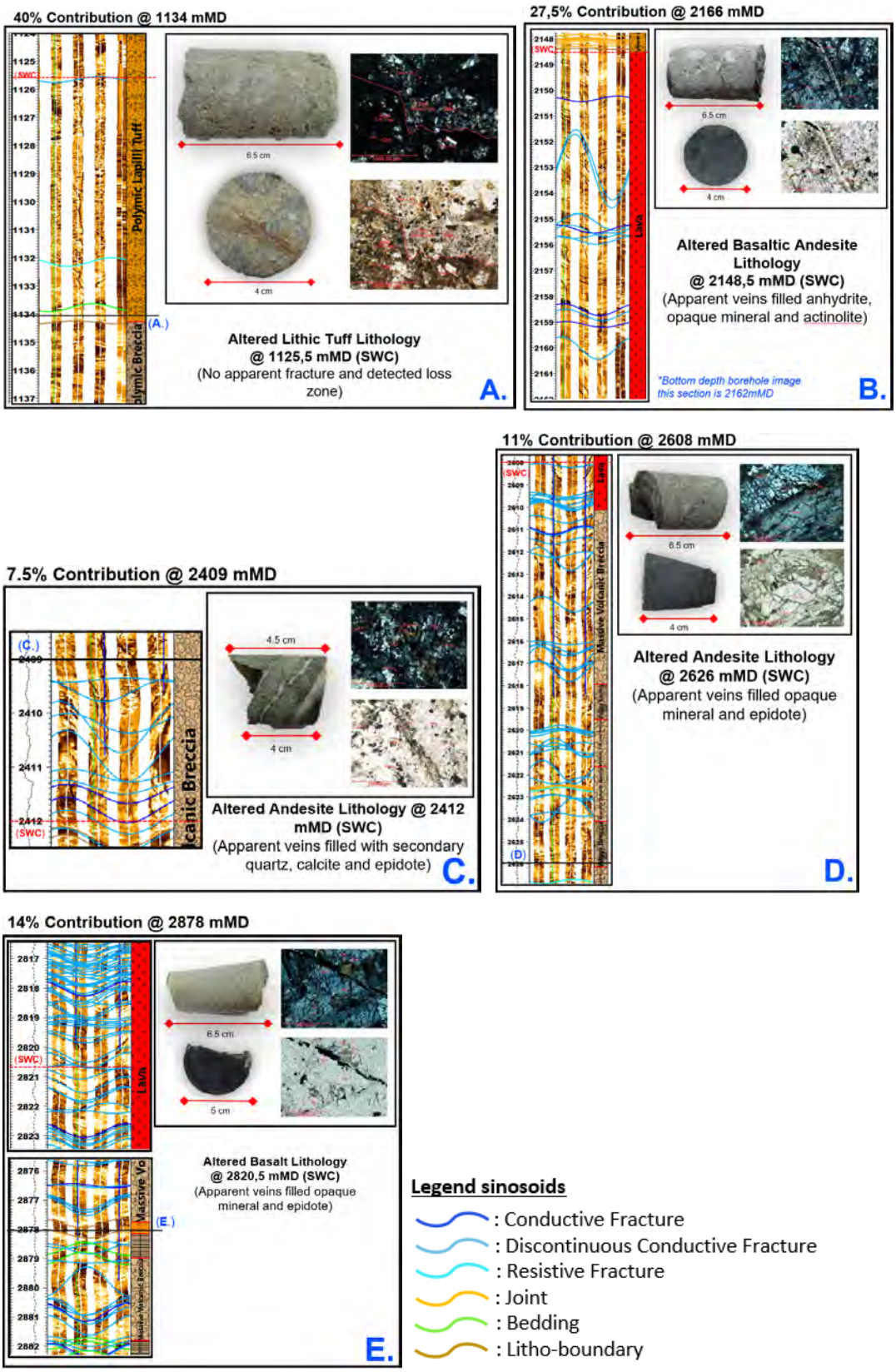

Figure 8: Core data is compared with lithology independently define from borehole image. Feedzone is ploted to see the association. The largest production from 1134 mMD and within pyroclastic tuff (8.A).

Integration of borehole image data, sidewall cores, and surface geological mapping reveals that high permeability zones within the depth interval of 1023 mMD to 2167 mMD are predominantly controlled by matrix permeability of pyroclastic rocks, lithological contacts, and NE-SW striking fracture zones dipping southeast. This fracture zone likely correlates with the damage zone of the Tompaso fault, a primary drilling target in well TPS-X. In contrast, permeability within the deeper interval of 2167 mMD to 3003 mMD is primarily influenced by E-W striking fractures and faults dipping south, likely associated with the Riendengan Caldera Rim. The higher density of conductive fractures and possible faults observed near the Riendengan Caldera Rim (Figure 9) compared to the Tompaso fault region suggests their role as significant permeability pathways.

The drilling of well TPS-X confirms the presence of both the Tompaso fault and Riendengan Caldera Rim. Future drilling efforts can strategically target the NE-SW trending alignment of the Tompaso fault and the E-W trending Riendengan Caldera Rim to optimize geothermal resource exploitation.

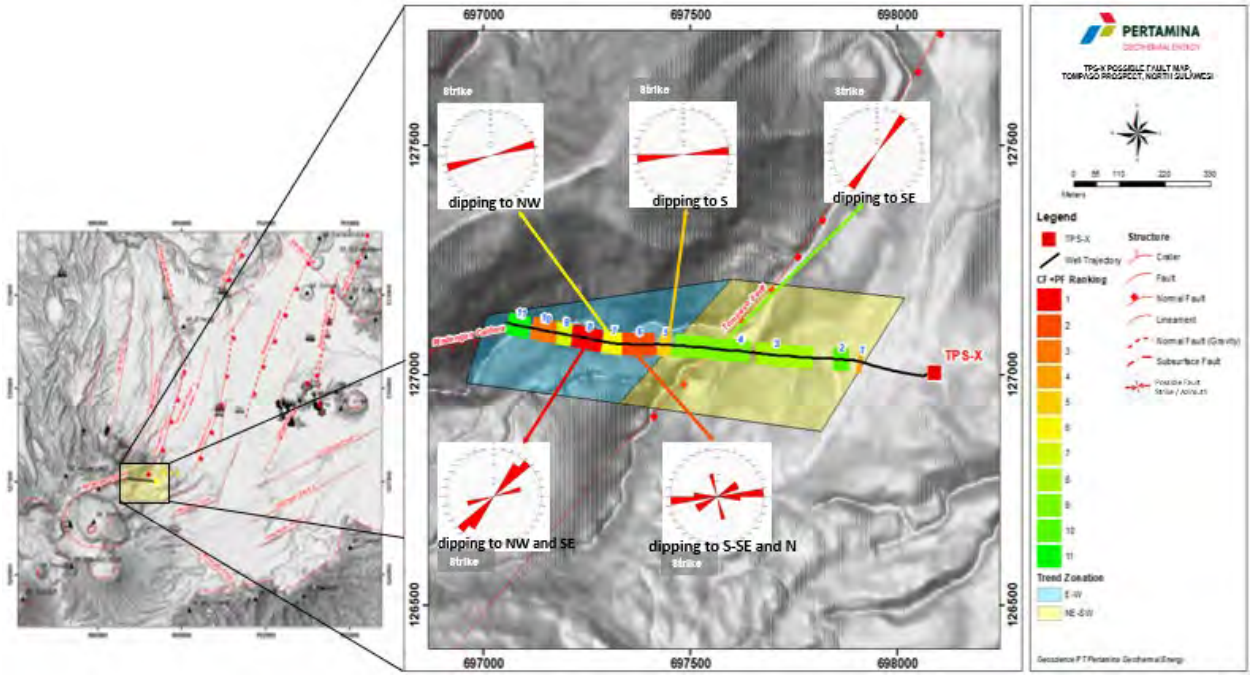

Figure 9: Geological structure map of Tompaso Field, North Sulawesi, Indonesia. The higher density of conductive fractures and possible faults observed near the Riendengan Caldera Rim.

5. Conclusion

The comprehensive analysis of borehole image logs, integrated with geological and wellbore data, has provided valuable insights into the fracture network and permeability characteristics of the Tompaso geothermal field. Eleven distinct fracture zones were identified, with varying orientations, densities, and lithological associations. Contrary to initial expectations, high fracture density did not always correlate with high permeability contribution. Instead, matrix permeability within pyroclastic and lithological contacts played a significant role, particularly in the upper part of 12.25-inch. Notably, the largest production contribution (40%) in well TPS-X originates from

a depth of 1134 mMD, situated within pyroclastic tuff, highlighting the importance of matrix permeability in this specific zone. Deeper intervals (9.875-inch) exhibited permeability dominated by E-W striking fractures and faults with minor direction toward NE-SW, potentially associated with the Riendengan Caldera Rim, respectively.

The findings of this study underscore the importance of integrating multiple data sources in geothermal reservoir characterization. The complex interplay between lithology and fracture properties highlights the need for a nuanced approach to permeability assessment. By targeting specific fracture orientations and lithology, it can enhance the probability of encountering productive zones and maximizing geothermal resource exploitation in the Tompaso field. The identification of the Tompaso fault and Riendengan Caldera Rim as key structural controls on permeability provides valuable guidance for future drilling strategies. Moreover, the presence of pyroclastic tuff in the upper part of the 12.25-inch section, significantly contributes to permeability, further highlighting the importance of understanding lithological controls on reservoir productivity.

Acknowledgement

The authors would extend their sincere appreciation to Pertamina Geothermal Energy for granting permission to publish this paper. We also gratefully acknowledge the valuable assistance and expertise provided by Pasca Siburian and the SLB D&I team throughout the interpretation process.

REFERENCES

Brata, R., Prasetyo, I., Boubakeur, I., Pokhriyal, K., Lilasari, L. "Fracture Segregation Approach in Geothermal Reservoir Evaluation a Case Study from Indonesia." Proceeding: Indonesia International Geothermal Convention & Exhibition (2014).

Ikhwan, M., Thamrin, M.H., Mochamad., Raharjo, I.B. "A Revised Tectonic Model of Minahasa District Based on LiDAR, Image Log and Fracture Stability Analysis in Tompaso." Proceedings: 43rd New Zealand Geothermal Workshop, (2021).

Pertamina Geothermal Energy (PGE).: Fracture Study of Well TPS-X based on Borehole Resistivity Imaging: Pertamina Geothermal Energy Internal Report (2024).

Pertamina Geothermal Energy (PGE).: Petrographic Analysis of Well TPS-X based on Side Wall Core Data: Pertamina Geothermal Energy Internal Report (2023).

Pertamina Geothermal Energy (PGE).: Final Well Report of Well TPS-X: Pertamina Geothermal Energy Internal Report (2024).

Suryanto, S., Sastranegara, Tofan., Untoro, Antonius., Afif, Nanda., Effendi, Ristio., Raharjo, Imam., and Suryantini. "Integrated Geoscience Data to Identify Heat Source Beneath Umeh Volcanic Complex in Tompaso Geothermal Fiedl." ITB International Geothermal Workshop (2020).

Preventing Downhole Tool Failure During Geothermal Well Construction Using a Hybrid Real-Time Temperature Management Advisory System

Naveen Velmurugan and Sadjad Naderi

Virgil Dynamics SAS

Pradeepkumar Ashok and Michael Yi

Intellicess, Inc.

Keywords

Geothermal wells, Drilling, Hydrothermal model, Real-time prediction

ABSTRACT

Drilling cost-efficient, safe, and deep wellbores is key to scaling geothermal energy. However, the elevated costs associated with high non-productive and invisible loss times (NPT/ILT) are taxing on the operators, acting as a severe bottleneck in utilizing geothermal energy. In deep geothermal wells, the leading contributors to NPT/ILT are the failure of downhole tools and/or absence of their measurements.

Continuous downhole parameter measurements are often hindered by mud circulation interruptions or downhole tool failures caused by high operating temperatures. During drilling operations, the mud temperature fluctuates due to its thermal interaction with the surrounding environment, which is typically hotter. This variability is particularly pronounced during activities such as connection and tripping, when mud circulation and downhole measurements are unavailable. Estimating temperature distribution along the wellbore before deploying costly downhole tools is critical to mitigate the risk of failure. Furthermore, developing an effective strategy to cool the mud relies on factors including circulation rate, duration, and inlet mud temperature.

In this study, we introduce an approach that combines physics-based modeling and machine learning techniques to achieve real-time prediction of mud temperature distribution. This method aims to enable precise and continuous estimate of mud temperature along the wellbore, facilitating more efficient well thermal management. An automated calibration system tailored for adjusting parameters within the physics-based hydrothermal model was also developed. This calibration process is designed to enhance the accuracy of the model and further improve the performance of the monitoring system. The calibration system is smartly triggered by Discrete Event Simulation (DES) technique as and when operational conditions change on the rig. The advisory system synergizes with the monitoring system to suggest optimal mud circulation durations and flow rates.

These recommendations are tailored to the inlet mud temperature, thereby ensuring precise control over the targeted temperature profile within the wellbore.

Our approach has been validated using select cases from the Utah FORGE dataset for which wellbore temperature measurements were available. Our real-time monitoring system was able to estimate the mud temperature profile along the wellbore after prolonged stagnation of mud inside the wellbore due to other operations like connection and tripping when bottom hole mud temperature measurements were absent. The automatic calibration technique proved efficient in updating uncertain model parameters to provide improved predictions. Ultimately this approach can drastically improve temperature monitoring and management during the construction of a geothermal well and reduce tool failure.

1. Introduction

Geothermal energy is one of the leading candidates for providing a clean energy infrastructure. However, drilling deep wells to extract necessary heat energy poses a distinctive challenge: the intense temperatures encountered during the exploration of deep underground reservoirs. During the drilling process, drilling mud – an engineered fluid – is circulated through the drill string and up to the surface through the annulus. Drilling mud is essential to maintain pressure inside the wellbore, removal of rock cutting and lubrification, among others. They also act as a conduit for mud pulse telemetry (MPT) for data transmission while drilling from the expensive downhole tools. However, the elevated temperatures encountered in geothermal wellbores lead to increasing wear and tear of downhole tools (Mitchell & Miska, 2011) and thus elevating the risk of tool failure (Kruszewski & Wittig, 2018) leading to lack of critical wellbore information for an efficient drilling operation.

Estimating bottom hole temperature is paramount in geothermal wellbore construction and numerical simulations using finite element models (FEMs) and finite difference methods (FDMs) can be utilized, but their computational burdens often limit their real-time application (Chen & Novotny, 2003). Reduced order models such as analytical models (Hasan & Jang, 2021) and semi-analytical models (Polat, 2022) offer reduced computation effort but compromises on accuracy due to simplifying assumptions that overlook crucial factors like complex wellbore geometries and transient thermal behaviors. Data-driven machine learning (ML) models pose certain drawbacks such as heavy reliance on data quality that are generally lacking and their transferability to new scenarios can be challenging (Kshirsagar & Sanghavi, 2022). An improved approach is necessary to overcome the current approaches requiring static input requirements rendering them impractical for real-time decision-making during a dynamic drilling operation (Gonzalez Angarita, 2020) where the rig states and operational parameters (mud flow rate, drill string rotation, location of bit with respect to hole depth, etc.) change quite frequently. In this study, a Physics-Informed Machine Learning (PIML) model is proposed offering a combination of physics-based FDM model (Hasan, Kabir, & Sarica, 2018) with real-time data suitable for predicting mud temperature distribution along the wellbore.

The strength of using FDM models in simulating heat transfer within wellbores lies in discretizing the wellbore geometry into a grid, allowing for the precise evaluation of heat conduction, convection, and radiation across each individual point (Holmes & Swift, 1970) by considering influencing factors like fluid flow dynamics, formation properties, and frictional heating (Zhang, Xiong, & Guo, 2018). The resulting temperature profiles offer detailed insights into the thermal

landscape within a wellbore (Zhou, 2013). However, FDM models rely heavily on accurate input parameters, including rock and material thermal properties, fluid rheology (Merlo, Maglione, & Piatti, 1995), and wellbore geometry (Hasan, Kabir, & Wang, 2009). In reality, the input parameters come with significant uncertainties due to limited downhole measurements and indirect measurements from historical drilling operations, introducing potential discrepancies between the model predictions and real-world temperature profiles. Although computationally expensive, calibrating these models is necessary, commonly based on iterative trail-and-error approaches, until the simulated temperature profiles match the measured values at certain locations, like mud temperature at the wellbore outlet (Tekin, 2010). In this work, a calibration technique suitable for geothermal wellbore temperature estimation that is computationally efficient for real-time applications is utilized. The hydrothermal model presented in the next section was introduced in Naderi et al., 2024 and repeated here for improved readability.

2. Hydrothermal model

2.1 Governing equations

The borehole is modeled to capture thermal interactions between the wellbore and the surrounding rocks. The model is built on the following key assumptions: (i) the drilling fluid is treated as incompressible, maintaining constant density, specific heat capacity, and thermal conductivity; and (ii) the velocity of the drilling fluid inside the drill string and annulus is considered solely in the axial direction, while the radial velocity is disregarded. Governing equations (1) to (5) describe the heat flow in the fluid inside the drill string, the drill string pipe, the fluid in the annular space, the first layer of casing, and the casing/cement/surrounding formation, respectively and are detailed in the literature (Zhang, Xiong, & Guo, 2018).

$$-\frac{\partial(\rho_1 c_1 v_p T_1)}{\partial z}+\frac{2h_1(T_2-T_1)}{r_1}+\frac{q_p}{\pi r_1^2}=\frac{\partial(\rho_1 c_1 T_1)}{\partial t} \tag{1}$$

$$\frac{\partial}{\partial z}\left(\frac{\lambda_p \partial T_2}{\partial z}\right)+\frac{2h_2(T_3-T_2)r_2}{r_2^2-r_1^2}-\frac{2h_1(T_2-T_1)r_1}{r_2^2-r_1^2}=\frac{\partial(\rho_2 c_2 T_2)}{\partial t} \tag{2}$$

$$\frac{\partial(\rho_3 v_a c_3 T_3)}{\partial z}+\frac{2h_3(T_4-T_3)r_3}{r_3^2-r_2^2}-\frac{2h_2(T_3-T_2)r_2}{r_3^2-r_2^2}+\frac{q_a}{\pi(r_3^2-r_2^2)}=\frac{\partial(\rho_3 c_3 T_3)}{\partial t} \tag{3}$$

$$\frac{\partial}{\partial z}\left(\lambda_4\frac{\partial T_4}{\partial z}\right)+\frac{2h_3(T_5-T_4)}{r_4^2-r_3^2}-\frac{2h_3(T_4-T_3)r_3}{r_4^2-r_3^2}=\frac{\partial(\rho_4 c_4 T_4)}{\partial t} \tag{4}$$

$$\frac{\partial}{\partial z}\left(\lambda_i\frac{\partial T_i}{\partial z}\right)+\frac{1}{r}\frac{\partial}{\partial r}\left(\lambda_{effective}^{i,\,i+1} r\frac{\partial T}{\partial r}\right)=\frac{\partial(\rho_i c_i T_i)}{\partial t} \tag{5}$$

Here, r and z denote radial and axial coordinates, respectively. In Equations (1) to (4), the subscript numbers follow the layer order illustrated in Figure 1a, while the subscript i in Equation (5) denotes the layer number in casing/cement/surrounding formation. While a constant spacing is considered in the axial direction, a gradually increasing mesh is considered in the radial direction, whose schematic is shown in Figure 1b.

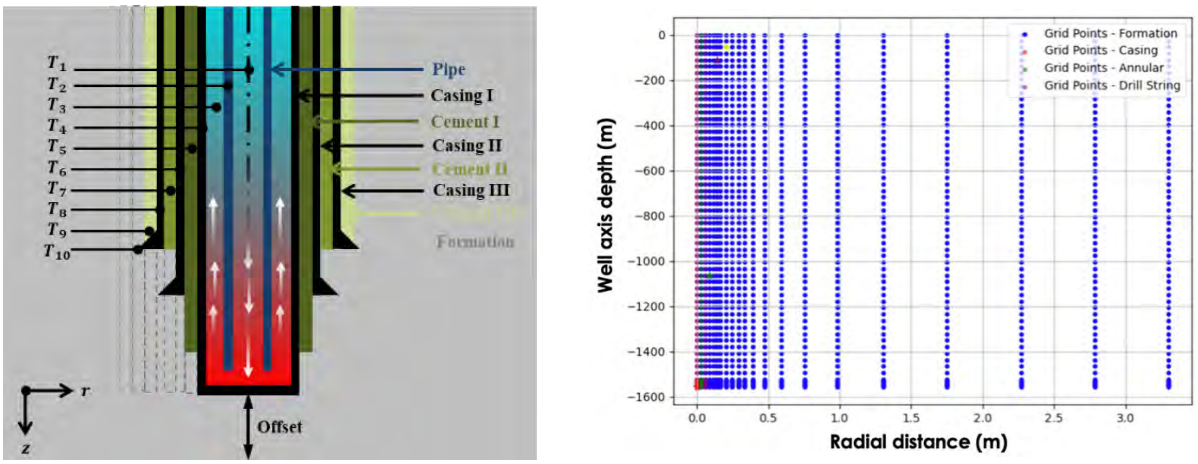

(a) (b)

Figure 1: (a) 2D schematic of a coaxial borehole heat exchanger, and (b) schematic of a 2D cross section through 3D model of the discretization of FDM grid. (Adapted from Naderi et al., 2024.)

In the context of the equations, T, h, λ, c and ρ represent temperature, convective heat transfer coefficient, thermal conductivity, specific heat capacity, and density, respectively. The conductivity coefficient between layer i and $i+1$, denoted as $\lambda_{effective}^{i,i+1}$, is calculated using the thermal-electrical analogy (Brown, Cassidy, Egan, & Griffiths, 2021), employing the following formulation:

$$R_{effective} = \frac{1}{\lambda_{effective}}, \quad R_{effective} = R_i + R_{i+1} = \frac{1}{\lambda_i} + \frac{1}{\lambda_{i+1}} \tag{6}$$

This expression signifies that the thermal resistivity of the effective layers can be considered analogous to electrical resistivity in series. The next section details the calculation of q_p and q_a, representing friction-induced heat source in drilling pipe and annular, respectively.

2.2 Source terms

The calculation of the friction-induced heat source involves considerations of fluid dynamics within the drilling pipe and the annulus (Zhang, Xiong, & Guo, 2018). Numerous empirical and analytical models exist for this purpose. Here, the Reynolds number (Re) as a crucial parameter is defined as (Durst & Arnold, 2008):

$$Re = \frac{\rho v D_h}{\mu} \tag{7}$$

where μ is the dynamic viscosity of the mud, and D_h and v are the hydraulic diameter and fluid velocity respectively. It should be noted that for the annular flow, $D_h = 4\,(d_3^2 - d_2^2)/(d_3 + d_2)$, where d_3 represents the diameter of the wellbore, and d_2 is the outer diameter of the drill string. For laminar flow ($Re \leq 2000$), the coefficient of friction resistance (f) is calculated as:

$$f = \frac{16}{Re} \tag{8}$$

In turbulent flow ($Re > 2000$), f is determined using the empirical Darcy friction factor equation:

$$\frac{1}{\sqrt{f}} = 4\log\left(Re\sqrt{f}\right) - 03.95 \quad (9)$$

The frictional resistance pressure drop in the drill string is then computed using:

$$\frac{\Delta P}{\Delta L} = \frac{2f\rho v_p^2}{d_1} \quad (10)$$

where L denotes the flow distance of drilling fluid. Similarly, in the annular region, the pressure drop is determined by:

$$\frac{\Delta P}{\Delta L} = \frac{2f\rho v_a^2}{d_3 - d_2} \quad (11)$$

Finally, the heat source term (q) in Equations **(1)** and **(3)** is quantified by:

$$q = \frac{\Delta P Q}{\Delta L} \quad (12)$$

where Q is the volumetric flow rate of drilling fluid.

2.3 Boundary and initial conditions

The initial temperature in the formation is determined by a linearly increasing geothermal gradient (G). Although a linear, continuous relationship is assumed, adjustments like including stepwise changing G can be made in the assimilation process, as discussed later in the following sections.

The inlet temperature is known and can be measured directly on the ground:

$$T_1(z = 0, t) = T_{in} \quad (13)$$

At the bottom of the well, the annulus drilling fluid temperature is equal to the drilling fluid temperature inside the drill string and the drill string temperature:

$$T_1(z = z_f, t) = T_2(z = z_f, t) = T_3(z = z_f, t) \quad (14)$$

where z_f is the vertical depth at the bottom of the well. There is no heat exchange between the formation and the atmosphere at the surface:

$$\frac{\partial T}{\partial z}\Big|_{z=0} = 0 \quad (15)$$

The formation temperature far away from the wellbore is undisturbed and is equal to the initial formation temperature. This condition is described at r_f, the end of the rock domain in the radial direction:

$$\frac{\partial T}{\partial r}\Big|_{r \to r_f} = 0 \quad (16)$$

2.4 Numerical solution

An implicit numerical method is implemented for the FDM employed in this work. Details of the implementation are adapted from (Zhang, Xiong, & Guo, 2018). This in contrast with the authors' earlier work (Naderi et al., 2024) where an explicit numerical scheme was implemented. The current approach is preferred for issues related to numerical stability while handling the real time data – streaming from the electronic drilling recorder (EDR) and/or the mud logging units. The FDM employed in this work for solving the governing equations utilizes a first-order forward difference scheme for temporal discretization and a central difference scheme for spatial discretization.

2.5 Sensitivity and observability

The primary objective of this work is to estimate the bottom hole temperature during geothermal drilling operations to better protect the downhole tools from thermal failures. The aforementioned hydrothermal model is dependent on several input parameters with high uncertainties and their perturbations can cause large impact on the estimation of bottom hole temperature. Thus, a preliminary sensitivity analysis is carried out. Since, geothermal gradient is not accurately known a priori to drilling a well, its sensitivity is numerically studied through trail-and-error approach. Two different scenarios are considered in this study: short circulation duration of about 3 hours (see Figure 2) and long circulation duration of about 2 days (see Figure 3). In addition, during the short circulation scenario, the geothermal gradient was changed at half-time, i.e., from 0.02 to 0.4 at 1.5 hours of circulation. The simulation parameters for this analysis are provided in Table 1. In all scenarios, the following observations hold:

1. The wellbore temperature profile is strongly dependent on the initial geothermal gradient. Any nominal variations in the gradient does not affect the bottom hole temperature estimation. Thus, initial model calibration when the required information is available or extracted from the real time data plays a crucial role in utilization of the hydrothermal model for temperature management system.
2. For a given variation in the geothermal gradient, changes in the outlet mud temperature were insignificant and changes in the bottom hole temperature were only slightly better. This leads to our hypothesis that geothermal gradient is not *observable* when only surface temperature is considered as the system measurement and bottom hole temperature is a necessary measurement during the calibration process.

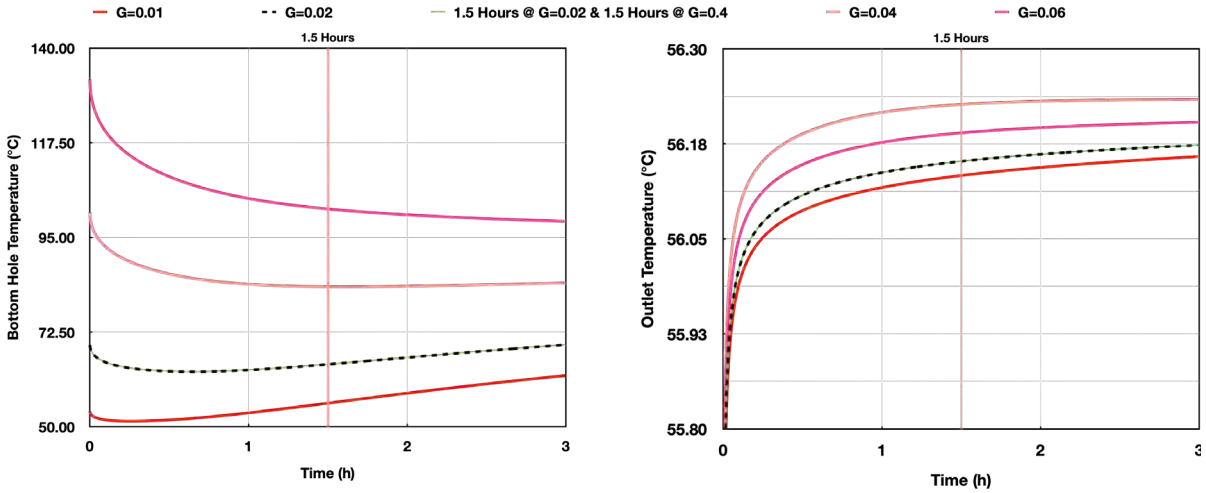

(a) (b)

Figure 2. Evolution of the bottom hole temperature (a) and the mud outlet temperature at the surface (b) during a short circulation scenario of 3 hours, for various geothermal temperature gradients (G). Changing G from 0.02 to 0.4 at 1.5 hours of circulation time shows no variation in the temperature evolution for both the parameters.

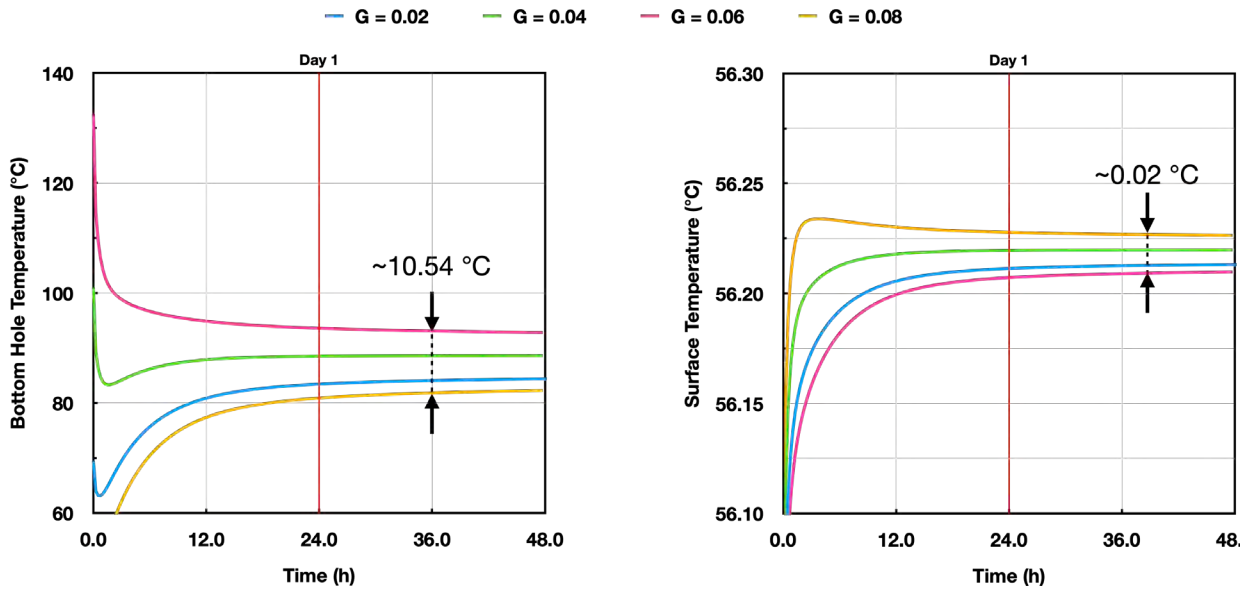

(a) (b)

Figure 3. Evolution of the bottom hole temperature (a) and the mud outlet temperature at the surface (b) during a long circulation scenario of 2 days, for various geothermal temperature gradients.

3. Model validation using UTAH Forge dataset

3.1 Data handling and calibration technique

As schematically illustrated in Figure 4, this engine comprises two distinct compositions, as already introduced in Naderi et al., 2024.:

1. **Static Data-Based Model:** This model component provides the initial condition to the dynamic model. When necessary, steady state solution can be utilized to transit to the transient simulation of the wellbore thermal dynamics. Since this segment is independent of considering input data in real-time, the choices for simulation time-step and techniques like implicit or explicit approach are open but must be suitably chosen to align with the thermal system's overall dynamics.

2. **Dynamic Data-Based Model:** Starting from the static-data based model simulation results as its initial condition, this model segment integrates live measurements into its simulation. Data assimilation, a critical process fusing observations with model predictions is operational to integrate real-time measurements and dynamics. The time step for this dynamic model aligns directly with the data frequency (here, 1 second) of the thermal-hydro model, ensuring continuous synchronization with real-time conditions.

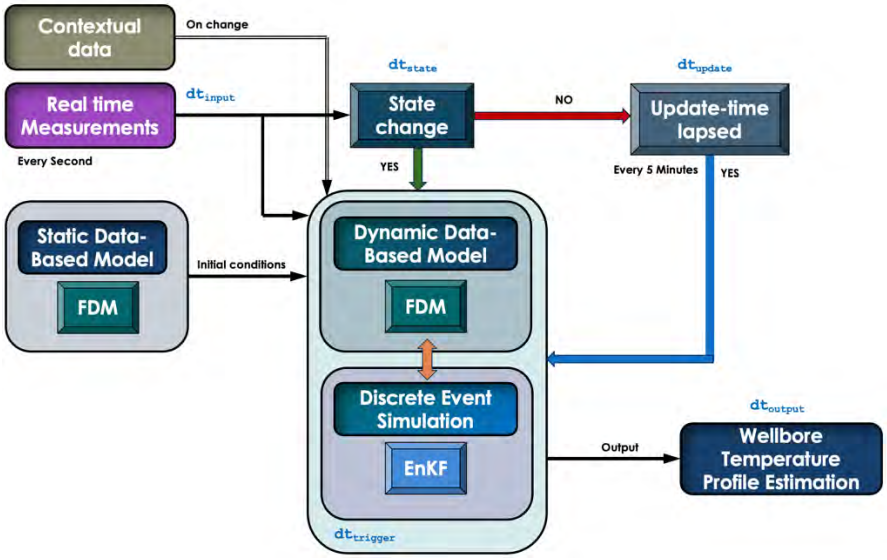

Figure 4: Schematic representation of the integrated framework, illustrating the dynamic assimilation of real-time data into the forward-marching explicit numerical solution. (Adapted from Naderi et al., 2024.)

Discrete Event Simulation (DES) stands as a computational modeling approach designed to analyze and comprehend the intricate dynamics of complex systems. Unlike continuous simulations, where changes unfold continuously over time, DES focuses on events that occur at distinct points in time, capturing the discrete nature of operations and interactions within a system. This is particularly relevant in well construction where rig state change and operational parameter

changes constitute discrete events. For further details on DES in this context, please refer to Naderi et al., 2024.

3.2 Utah FORGE Wellbore sections

This framework was applied to a simulation considering a coaxial well represented by concentric cylinders in 3D with mud flowing through the drill string and rising to the surface through the annular region between drill pipe and casing. The drill string components and casing program for sections using BHA 9 and BHA 18 referencing wellbore 16A(78)-32 are detailed in Table 1. The simulation encompasses a directional well trajectory, incorporating both vertical and horizontal sections.

Table 1: Basic data of drill string and casing program for wellbore 16A(78)-32.

Parameter	Inner diameter (mm)	Outer Diameter (mm)	Depth (m)
Drill Pipe	110	127	Variable
First Casing	220	240	1062.5
Second Casing	320	340	116.4
Third Casing	480	510	39.3

In configuring the model for evaluation and calibration using the Utah FORGE dataset, the static segment of the framework was defined from the surface down to the section corresponding to BHA 9 and 18 separately – the regions chosen for assimilation performance assessment. The raw data were trimmed and processed to enhance data quality and provide distinct case of continuous drilling operation for simplicity in model validation. Later, all operations in the respective BHA sections were considered. The time windows considered for sections BHA 9 and BHA 18 are clearly marked in Figure 5(a) and 6(a), respectively. As noted in the earlier sections, correct estimation of the initial conditions, i.e., the static model is important in simulating the temperature evolution through the dynamic model. This is reflected in the simulation results for BHA 9 and BHA 18. It can be noted from Figure 5(a) that by manipulating the initial estimate of geothermal gradient allowing for least error between the simulated and measured temperature profiles at the simulation start, the temperature dynamics follows the measurements. However, this is not the case when the input parameters are erratic as can be seen from Figure 5(b); although the initial conditions were manipulated in order to track the temperature dynamics at the later stage, there exists significant differences in the predicted and measured temperature in some regions. The initial state calibration was carried out through trial-and-error approach in this study but can be extended to an automatic calibration technique with ease. Similar observations can be noted for simulations in section BHA 18 as reflected in the Figure 6.

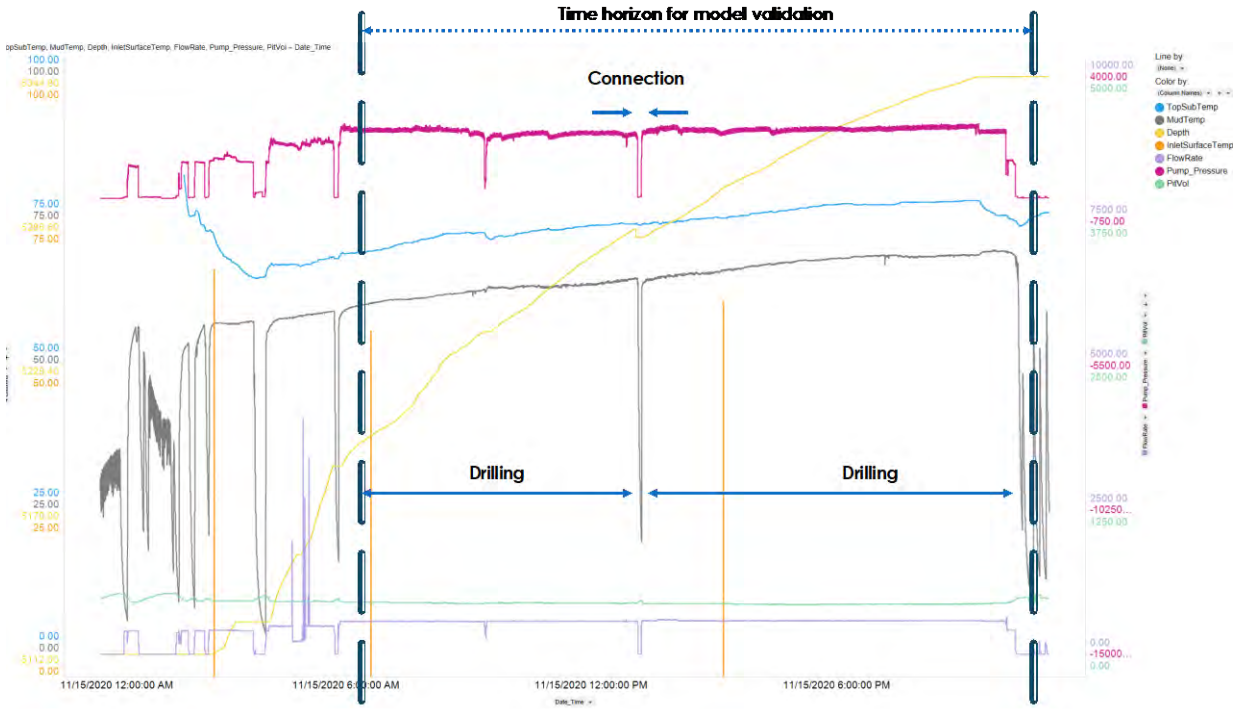

(a)

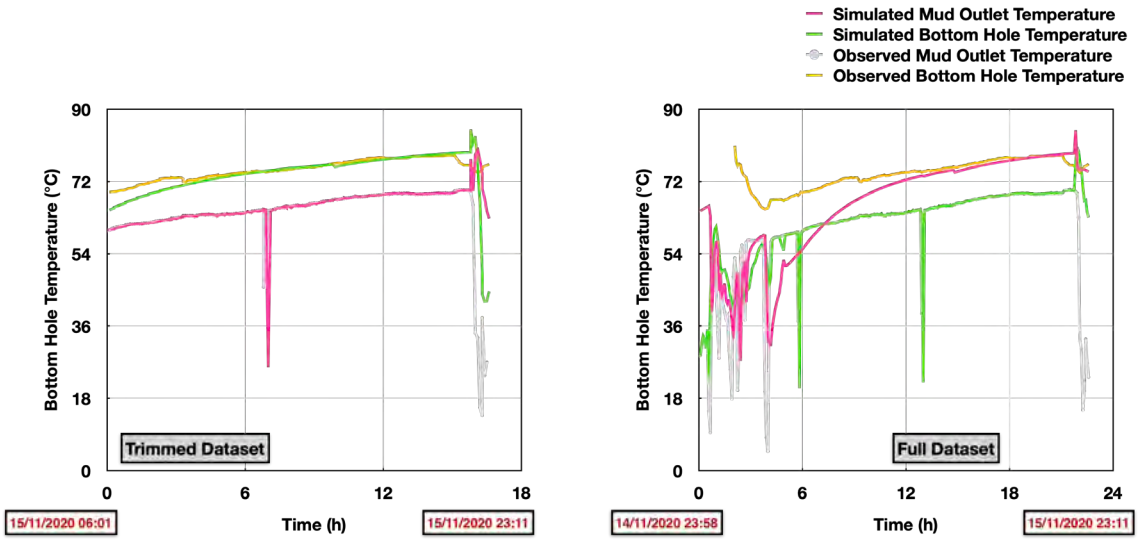

(b) (c)

Figure 5. (a) A selection of timeseries data from BHA 9 section of well 16A(78)-32 in Utah FORGE dataset; (b) Comparison of the time evolution of simulated and measured temperatures for a trimmed dataset for the section; and (c) Comparison of the time evolution of simulated and measured temperatures for full dataset for the section.

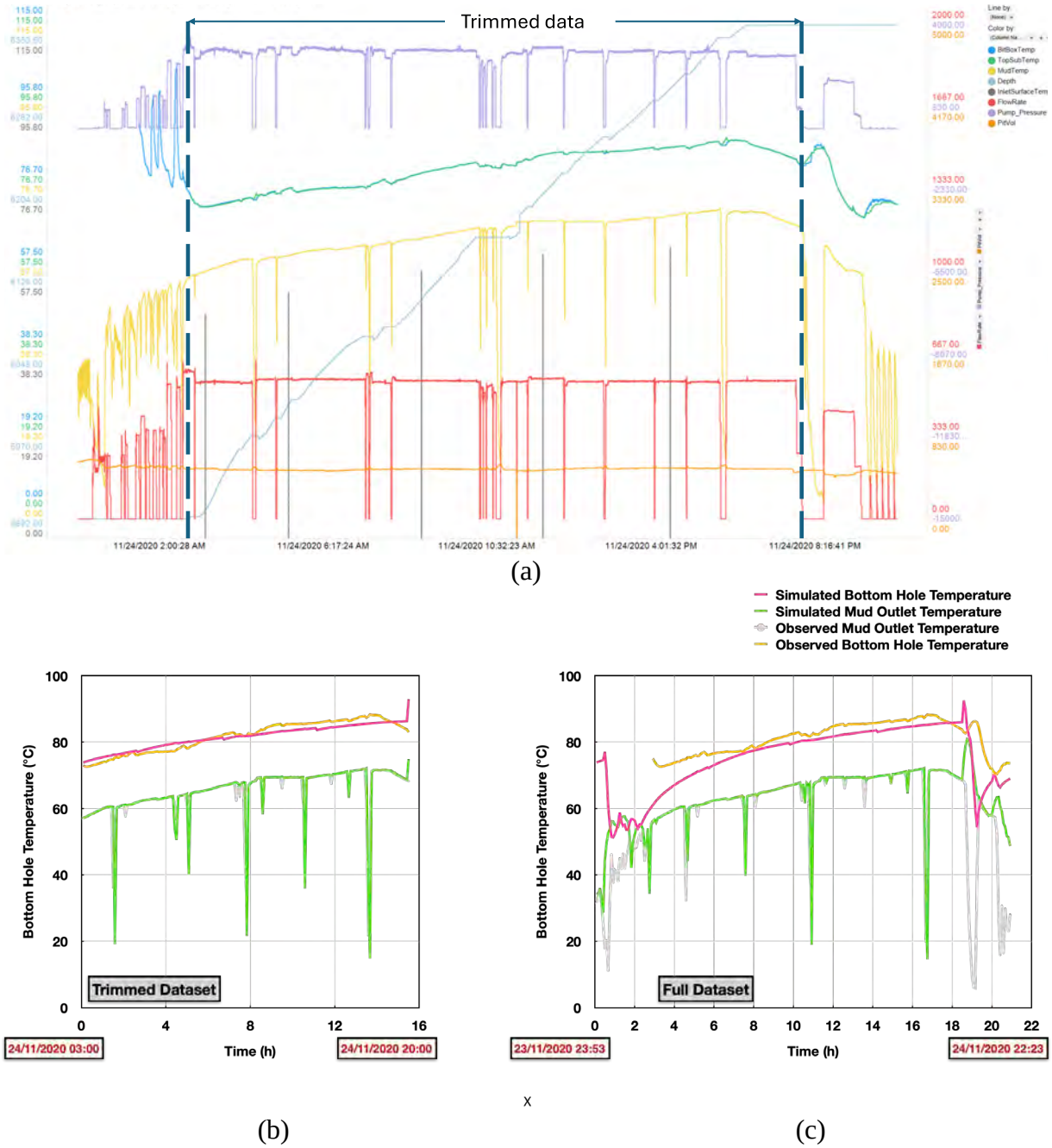

Figure 6. (a) A selection of timeseries data from BHA 18 section of well 16A(78)-32 in Utah FORGE dataset; (b) Comparison of the time evolution of simulated and measured temperatures for a trimmed dataset for the section; and (c) Comparison of the time evolution of simulated and measured temperatures for full dataset for the section.

4. Wellbore thermal management system

A hydrothermal simulator is an important tool for drilling geothermal wells offers important insights into the temperature distribution along the wellbore. It can be noted in the considered cases that the maximum temperature encountered in the wellbore are not always necessarily at the bottom. This is shown in the Figure 7 for two sections: nearly vertical BHA 9 and deviated BHA

18. The considered system generates the temperature profile along the wellbore depth at set time intervals, say every 5 minutes and provides information on the maximum temperature and the depth at which it is experienced. Given the computationally efficient model considered in this study, circulation rate and timing can be iterated over a certain interval to manage the wellbore temperature distribution accordingly. This information is crucial in cases like tripping in with downhole tools wherein they experience temperatures higher than their operational limit before they reach the bit is on-bottom. Thermal management becomes important to extend the operational lifetime of such tools and in avoiding significant NPT/ ILT due to downhole tool failures.

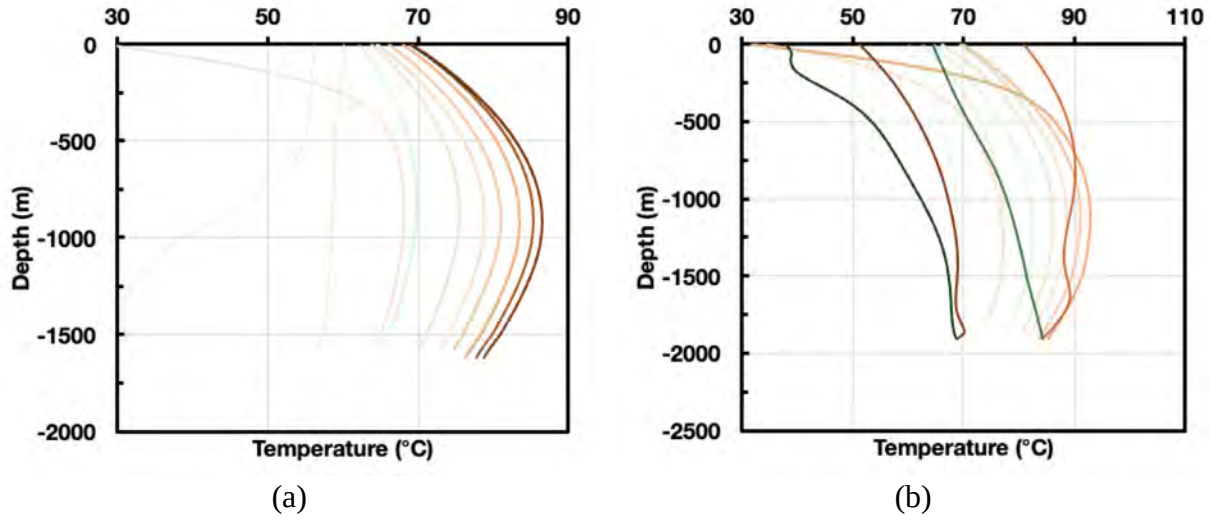

(a) (b)

Figure 7. Time evolution (light to dark) of the temperature profile for the full dataset along the measured depth of the well for sections BHA 9 and BHA 18 of Utah FORGE well. Green line represents the temperature profile of mud inside drill string and brown the mud in annulus.

5. Conclusions

In this work, a computationally efficient hydrothermal model was developed to estimate the temperature distribution along the wellbore. The model has been updated from the authors' previous work to ensure numerical stability while handling real time data from the mud logging unit. The sensitivity analysis shows that the initial estimate of the geothermal gradient is important to follow the temperature dynamics of the system and that the gradient is not observable from the surface temperature as a measurement alone. Thus, bottom hole temperature measurements are necessary to calibrate the model through ML methods to accommodate the model uncertainties. The DES triggers the model to simulate temperature profile on system changes and the maximum temperature region is identified to inform on the mud circulation rate and time to allow for the downhole tool operations.

To build an automated thermal management system, further analysis of the controllability and the observability of the hydrothermal system is necessary. This shall pave way to designing an efficient controller for real time recommendation of the circulation rate and the circulation time for an optimized wellbore temperature profile.

Nomenclature

Abbreviations

BHA	Bottom Hole Assembly
DES	Discrete Event Simulation
FEM	Finite Element Model
FDM	Finite Difference Method
ML	Machine Learning
MPT	Mud Pulse Telemetry
NPT	Non-Productive Time
PIML	Physics-Informed Machine
3D	3 Dimensional
1D	1 Dimensional

Variables

R	Analogical thermal-electrical
h	Convective heat transfer
ρ	Density
Z	Depth
d	Diameter
f	Friction resistance coefficient
ΔP	Frictional resistance pressure
G	Geothermal gradient
q	Heat source term
D_h	Hydraulic diameter
r	Radius
Re	Reynolds number
c	Specific heat capacity
T	Temperature
λ	Thermal conductivity
t	Time
dt	Timestep
ν	Viscosity

Units

°C	Degree Celsius
K	Kelvin
kg	Kilogram
m	Meter
mm	Millimeter
Pa	Pascal
s	Second

Acknowledgement

The authors acknowledge the Utah FORGE project for the open dataset used in this study. The authors would like to thank Virgil Dynamics and Intellicess for granting permission to publish the results of their collaborative project in enhancing drilling performances in the geothermal industry.

REFERENCES

Chen, Z., & Novotny, R. J. (2003). Accurate prediction wellbore transient temperature profile under multiple temperature gradients: finite difference approach and case history. *SPE Annual Technical Conference and Exhibition.* (pp. SPE-84583) SPE .

Mitchell, R. F., & Miska, S. (2011). *Fundamentals of drilling engineering.*

Hasan, A. R., & Jang, M. (2021). An analytic model for computing the countercurrent flow of heat in tubing and annulus system and its application: Jet pump. *Journal of Petroleum Science and Engineering*, 203, 108492.

Polat, C. (2022). A semi-analytical solution technique for predicting circulating mud temperatures. *Journal of Natural Gas Science and Engineering*, 106, 104754.

Kshirsagar, A., & Sanghavi, P. (2022). Geothermal, oil and gas well subsurface temperature prediction employing machine learning. *47th workshop on geothermal reservoir engineering.*

Gonzalez Angarita, J. C. (2020). *Integrated Modelling and Simulation of Wellbore Heat Transfer Processes through High-level Programming, Sensitivity Analysis and Initial Approach with Machine Learning Predictive Models.* Norway: University of Stavanger.

Hasan, A. R., Kabir, C. S., & Sarica, C. (2018). *Fluid flow and heat transfer in wellbores.* Richardson, Texas, Richardson, Texas: Society of Petroleum Engineers.

Holmes, C. S., & Swift, S. C. (1970). Calculation of circulating mud temperatures . *Journal of petroleum technology*, 22(06), 670-674.

Zhang, Z., Xiong, Y., & Guo, F. (2018). Analysis of wellbore temperature distribution and influencing factors during drilling horizontal wells. *Journal of Energy Resources Technology*, 140(9), 092901.

Zhou, F. (2013). *Research on heat transfer in geothermal wellbore and surroundings.* Berlin.

Hasan, A. R., Kabir, C. S., & Wang, X. (2009). A robust steady-state model for flowing-fluid temperature in complex wells. *SPE Production & Operations*, 24(02), 269-276.

Merlo, A., Maglione, R., & Piatti, C. (1995). An innovative model for drilling fluid hydraulics. *SPE Asia Pacific Oil and Gas Conference and Exhibition* (pp. pp. SPE-29259). SPE.

Tekin, S. (2010). *Estimation of the formation temperature from the inlet and outlet mud temperatures while drilling geothermal formations* . Master's thesis, Middle East Technical University.

Brown, C. S., Cassidy, N. J., Egan, S. S., & Griffiths, D. (2021). Numerical modelling of deep coaxial borehole heat exchangers in the Cheshire Basin, UK. *Comuters & Geosciences*, 152, 104752.

Durst, F., & Arnold, I. (2008). *Fluid mechanics: an introduction to the theory of fluid flows.* Berlin: Springer.

Naderi, S., Velmurugan, N., Nannapaneni, P., Yi, M., & Ashok, P. An Integrated Data and Physics-based Temperature Model for Real-time Estimation of Bottomhole Temperature for Downhole Tool Failure Prevention.

Moura, C. A., & Kubrusly, C. S. (2012). *The Courant-Friedrichs-Lewy (CFL) condition: 80 years after its discovery.* . Basel: Birkhäuser.

Budgaga, W., Malensek, M., Pallickara, S., Harvey, N., Breidt, F. J., & Pallickara, S. (2016). Predictive analytics using statistical, learning, and ensemble methods to support real-time exploration of discrete event simulations. *Future Generation Computer Systems*, 56, 360-374.

Lang, S., Kuetgens, M., Reichardt, P., & Reggelin, T. (2021). Modeling production scheduling problems as reinforcement learning environments based on discrete-event simulation and openai gym. *IFAC* (pp. 54(1), 793-798). IFAC-PapersOnLine.

Kruszewski, M., & Wittig, V. (2018). Review of failure modes in supercritical geothermal drilling projects. *Geothermal Energy*, 6(1), 28.

Long-term High Temperature High Pressure Cable for Geothermal Logging Tools

Andrew Wright

Sandia National Laboratories

Keywords

Geothermal, Long-term, High Temperature, High Pressure, Cable, Logging Tools, 300°C

ABSTRACT

Downhole logging tools are commonly used to characterize multi-thousand-foot geothermal wells. The elevated temperatures, pressures, and harsh chemical environments present significant challenges for the long-term operation of these tools, especially when real-time data transmission to the surface is required via data cable lines. Teflon-based single or multi-conductor cables with grease-filled cable heads are typically used for downhole tools. However, over extended periods of operation, the grease used to seal the conductors can slowly dissolve into the well fluid, creating electrical shorts and disabling data transmission. Additionally, when temperatures exceed 260 °C, Teflon can soften, potentially allowing parallel conductors to make contact and cause shorts. Between 2009 and 2015, Draka Cableteq USA, now part of the Prysmian Group, developed a multi-conductor/fiber cable and a four-conductor cable capable of operating above 300 °C. While a full study was conducted on the conductor/fiber cable, the evaluation of the four-conductor cable remained incomplete. With the increasing need for long-term high-temperature (HT) operation of logging tools, Sandia National Laboratories is now completing the evaluation of the four-conductor cable. The four-conductor cable has two major novel aspects. Firstly, its glass braid insulation can operate above 300 °C, eliminating the potential for shorts. Secondly, the insulated conductors are encased in metal tubing along the full length of the cable, creating a high-pressure seal between the cable and the tool. This metal tubing eliminates the need for a grease seal, a major limiting factor in the operation time of common cable lines. Sandia National Laboratories will conduct multiple tests to characterize the cable at temperatures above 300 °C and pressures up to 5,000 psi. This cable would enable tools to operate continuously at elevated temperatures, pressures, and in harsh fluids for extended periods, potentially lasting months.

1. Introduction

Evaluating a geothermal well is essential for assessing well integrity, reservoir formation, and overall characterization. Various subsurface instrumentation tools are used to collect different data

sets depending on the type of well, temperature and pressure profile, and well conditions. Most commonly, instrumentation tools with local energy storage and memory store all the data locally, referred to as memory tools. These memory tools are lowered into multi-thousand-foot wells, continuously storing data until they are either brought back to the surface, the energy storage is depleted, or the memory is full. Memory tools are an economical approach for short-term (<24 hours), low data rate, non-real-time measurements (i.e. temperature, pressure, and fluid chemistry).

For applications requiring long-term (>24 hours), high-speed data rates, or real-time measurements, instrumentation with a data line is necessary, as illustrated in Fig. 1. Most current instrumentation tools use single or multi-conductor cables with Polytetrafluoroethylene (PTFE) insulation surrounded by a metal wire rope due to their cost-effectiveness and rated temperature range (up to 260 °C for short-term operation). These cables transition to the instrumentation tool through a 'cable head.' Since the cables use wire rope, the cable head is filled with high-temperature grease to prevent fluid from contacting the exposed conductors. However, over hours of operation in the well's harsh environment, the grease erodes away, eventually causing electrical shorts and disabling the tool's functionality. Additionally, when the cable reaches temperatures above 260 °C, the PTFE insulation begins to soften, potentially causing shorts between parallel conductors.

With the growing need for long-term measurements, especially for enhanced geothermal system (EGS), it is becoming essential to develop data cables that can sustain temperatures from 250 °C to 320 °C, while being exposed to pressures reaching 5,000 psi and the harsh fluids of the well for durations ranging from one day to several months.

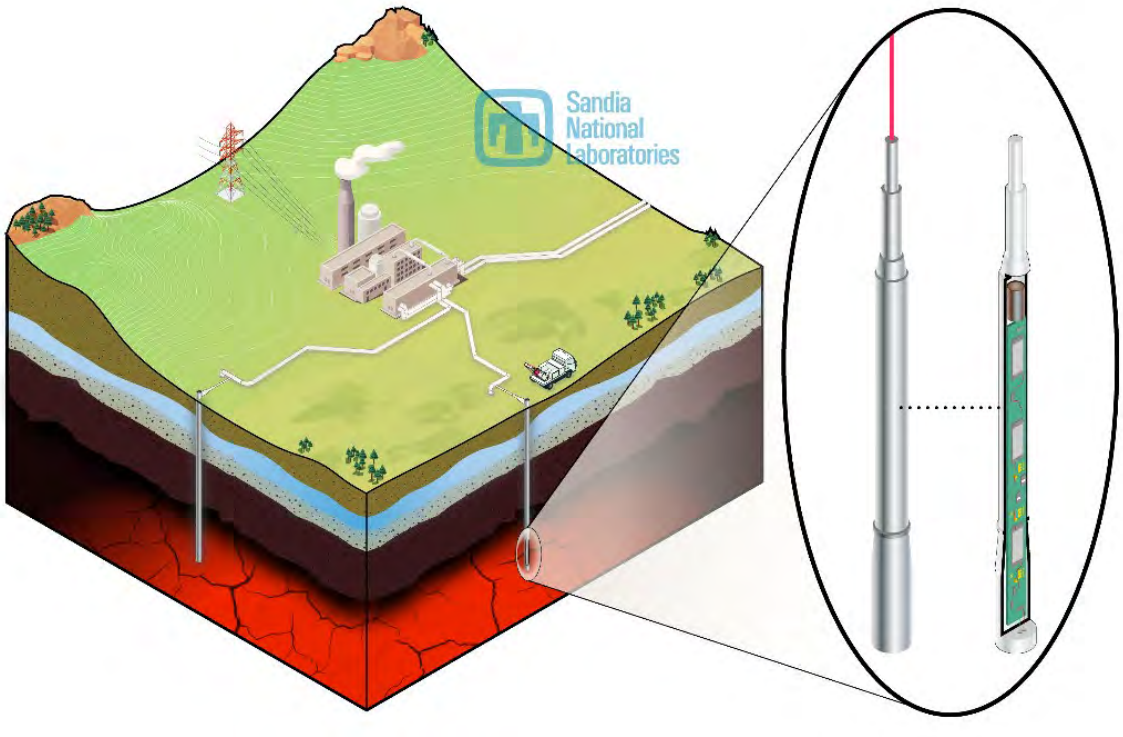

Figure 1: Illustration of the instrumentation tool lowered into a multi-thousand foot well with communications between the tool and wireline truck.

One such solution for a long-term, reliable data cable has been developed by the Prysmian Group. Under an American Recovery and Reinvestment Act (ARRA) grant in 2009, Draka Cableteq USA, now part of the Prysmian Group, was awarded funding to develop a high-temperature cable for EGS applications. Prysmian developed two types of cables: one with conductors and optical fiber surrounded by high-temperature epoxy as the dielectric[1], and a second cable with four conductors but with glass braid insulation. This paper focuses on the second cable, which consists solely of conductors.

The cable comprises four 18 AWG 2% nickel conductors with mica tape and glass braid insulation. Surrounding the conductors and dielectric is an Incoloy-825 tubing with a 0.25” outer diameter and a 0.028” wall thickness. The braid surrounding the tubing is made of 0.040” Incoloy-825 to support the weight of the instrumentation tool. Swagelok fittings are used at the end of the tubing to create a high-pressure seal with the instrumentation tool. Sandia has access to 5,000 – 8,500 feet of this cable. Prysmian's goal for this cable is to achieve continuous operation at 374 °C. An image of the four-conductor cable is shown in Fig. 2. Sandia has been evaluating the four-conductor cable at elevated temperatures and pressures to confirm its functionality.

Figure 2: Spool with 5,000 to 8,500 feet of cable from Prysmian. Consists of four 18 AWG 2% nickel conductors with mica tape and glass braid insulation. Surrounding the conductors and dielectric is an Incoloy-825, 0.25” outer-diameter, 0.028” wall thickness tubing. Braid surrounding the tubing is made with 0.040” Incoloy-825 to support the weight of the instrumentation tool. Swagelok is used at the end of the tubing to create a high-pressure seal with the instrumentation tool.

2. Cable Evaluation

The first experiment for the cable involves evaluating its performance at temperatures reaching 300 °C. Initially, it is expected that the binder within the glass braid will degrade, potentially affecting the electrical isolation between conductors at elevated temperatures. However, this issue can be mitigated by baking the binder at the elevated temperature for an extended period. To monitor for the effect of the glass braid's resistance over time at elevated temperatures, the four conductors were connected to an ohm meter data acquisition (DAQ) system capable of measuring up to 90 MΩ.

Figure 3: Ten feet of Prysmian cable to go under evaluation in an oven set to 300 °C.

The four conductors were referenced to the metal tubing of the cable. A ten-foot section of the cable was cut from the spool and placed in the oven, connected to the DAQ system. The cable was baked at 300 °C for approximately 17 hours. As shown in the data in Figure 4, the resistance between the conductors and the tubing initially dropped rapidly from an unmeasurable level down to about 5-6 MΩ. After 1-2 hours, the resistance began to increase and continued to rise over the next 15 hours.

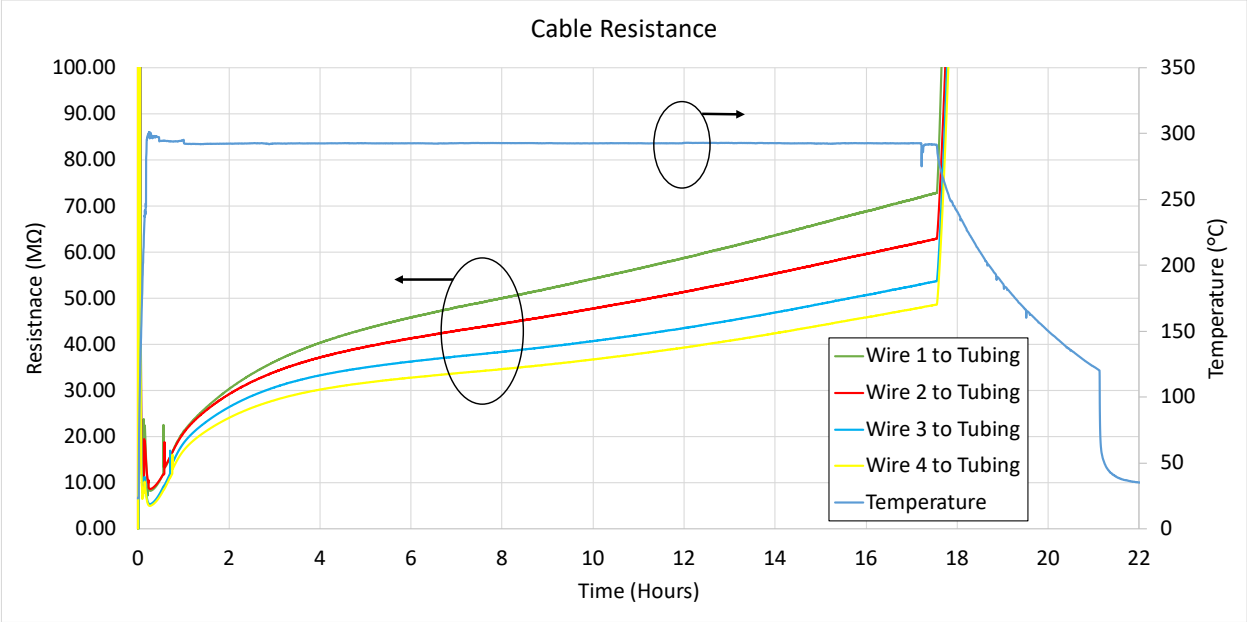

Figure 4: Recorded cable resistance of each of the four conductors in reference to the Incoloy-825 tubing while in the oven at a temperature of 300 °C.

At room temperature, the resistance between the conductors and the metal tubing across the >5,000 ft length of the cable is 50-70 kΩ, while the resistance between conductors is 100-120 kΩ. The resistance of the conductor from one end to the other is approximately 73 ohms. Without baking out the binder, the cable would not function properly at elevated temperatures. However, after the

baking process, the cable performs as expected at both room temperature and 300 °C. From the results, it would take close to 24 hours to bake out the binder.

Next, the cable was evaluated in a 300 °C, 5000 psi autoclave. The cable was fed through the lid port and sealed with a 0.25” Conax fitting with a Lava seal rated to handle the elevated conditions. Inside the autoclave, a Swagelok cap was used to seal the tip of the cable tubing, while the wires on the other end were exposed to the environment. This test aimed to determine if the Swagelok seal would fail under these conditions. Figure 5 shows the cable seal to the autoclave lid along with the Swagelok cap end. The autoclave was filled with tap water that contains a pH of 9. The cable exhibited no observable leaks with the autoclave set to 300 °C and 5000 psi for 27 hours. Future testing with real geothermal fluid is necessary to accurately mimic the corrosive behavior of the well. Though these initial tests indicate that the cable is suitable for the harsh temperatures and pressures of a geothermal wells.

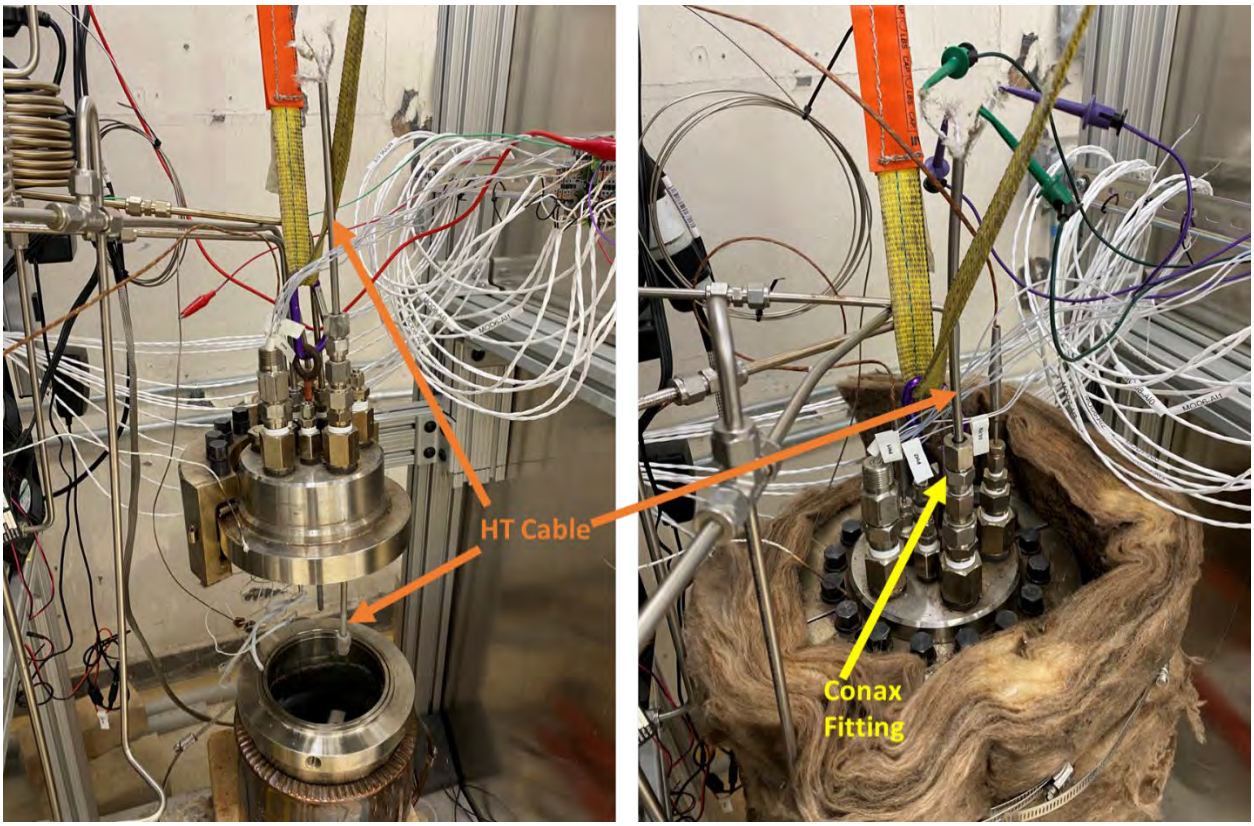

Figure 5: Prysmian cable under evaluation in the autoclave under conditions of 300 °C and 5,000 psi.

The final test Sandia will conduct involves baking the entire >5,000 ft length of Prysmian cable at 300 °C. The cable will be unspooled from the reel and placed within a steel container, allowing it to expand at high temperatures and mitigating potential damage. This setup will enable us to evaluate changes in resistance and measure the spectral response (RF frequencies that can propagate through the cable) at elevated temperatures. Spectral response measurements will be taken before, during, and after the baking process to assess the cable's communication performance. This experiment will be conducted soon at Sandia, with the results to be presented in a final report.

3. Conclusion

In conclusion, Prysmian Group has developed a cable specifically designed for geothermal applications. Engineered to function at 300 °C and 5,000 psi, this cable is ideal for both short-term exposure to temperatures above 260 °C and long-term applications. Its ability to seal directly to the cable without the need for high-temperature grease significantly reduces the risk of leakage over extended periods. This study found that the cable can sustain temperatures reaching 300 °C with high parallel cable resistance once the binder has been baked out. Additionally, the cable was tested at 300 °C and 5,000 psi, showing no signs of leaks after 27 hours of continuous operation. This technology is critical for effectively evaluating enhanced geothermal systems where logging tools must operate continuously at elevated temperatures. It will enable the industry to measure formations, assess well integrity, and monitor changes in fluid flow.

Acknowledgement

Sandia National Laboratories is a multi-mission laboratory managed and operated by National Technology & Engineering Solutions of Sandia, LLC (NTESS), a wholly owned subsidiary of Honeywell International Inc., for the U.S. Department of Energy's National Nuclear Security Administration (DOE/NNSA) under contract DE-NA0003525. This written work is authored by an employee of NTESS. The employee, not NTESS, owns the right, title and interest in and to the written work and is responsible for its contents. Any subjective views or opinions that might be expressed in the written work do not necessarily represent the views of the U.S. Government. The publisher acknowledges that the U.S. Government retains a non-exclusive, paid-up, irrevocable, world-wide license to publish or reproduce the published form of this written work or allow others to do so, for U.S. Government purposes. The DOE will provide public access to results of federally sponsored research in accordance with the DOE Public Access Plan.

Sandia would like to acknowledge Kendall Waterman from Prysmian for his contributions to the research on the four-conductor high-temperature cable, which have significantly expanded our understanding of its capabilities. We also extend our gratitude to Taylor Myers for his dedicated efforts in evaluating the high-temperature cable. Finally, we would like to thank Joe Henfling for his guidance and providing the historical context of the cable.

REFERENCES

[1] Pastouret, A., Gooijer, F., Overton, B., Jonker, J., Curley, J., Constantine, W., and Waterman, Kendall M. "Complete Fiber/Copper Cable Solution for Long-Term Temperature and Pressure Measurement in Supercritical Reservoirs and EGS Wells." United States: N. p., 2015. Web. doi:10.2172/1225845.

[2] Henfling, J., and Norman, R. "Dewarless Logging Tool – 1st Generation." SAND2000-1680, Sandia National Laboratories, Albuquerque, NM (2000).

[3] Henfling, J., Normann, R. "High Temperature Downhole Reservoir Monitoring System." Proceedings Twenty-Ninth Workshop on Geothermal Reservoir Engineering, Stanford University, California (2004).

300 Degree Celsius Electronic Component Packaging for Geothermal Tools

Andrew Wright, Manuel Montano, Joshua Larson, Deborah Hagen, and Steven Larson

Sandia National Laboratories

Keywords

Geothermal, High Temperature, Packaging, Ceramic, Gold-Tin, Wire bonding

ABSTRACT

Downhole logging tools embedded with various sensors are commonly deployed into multi-thousand-foot geothermal wells to gain a deeper understanding of the well's characteristics. One of the significant challenges in evaluating geothermal wells is that formation temperatures can exceed 200 °C and commonly reach up to 320 °C. A common technique for logging tools involves using low-temperature electronic components, which can operate at high speeds and provide high resolution, housed inside a specialized enclosure known as a vacuum flask. These flasks are designed to mitigate heat transfer to the components, allowing the tool to operate at elevated temperatures for several hours. However, when a logging tool is required to operate at 250 °C for long-term periods, the vacuum flask is not a viable solution. With the increasing need for fracture formation detection and well integrity characterization in enhanced geothermal systems (EGS), tools must operate in harsh environments for durations ranging from 24 hours to 6 months. Using a geothermal downhole tool for these extended periods at temperatures above 200 °C necessitates that all components are rated for such high temperatures. Sandia National Laboratories is developing methods to improve the reliability of embedded electronic systems to operate at temperatures reaching 300 °C. By utilizing off-the-shelf high-temperature (HT) integrated circuits (ICs), the ICs will be either gold-tin bonded or wire bonded (depending on the device format) onto a ceramic printed circuit board (PCB). Unlike other PCB materials, ceramic PCBs do not degrade at 300 °C. In addition to these bonding methods, Sandia will explore various epoxies with similar thermal coefficients of expansion to conformally coat the ICs, further enhancing reliability under vibration and mechanical shock. Employing these techniques will enable long-term operation of geothermal subsurface instrumentation at temperatures reaching 300 °C.

1. Introduction

Evaluating geothermal wells using electronic systems presents a unique set of challenges primarily due to the extreme environmental conditions encountered deep underground. One of the foremost

issues is the high temperature, often ranging between 200–300 °C, which can severely impact the performance and reliability of electronic components. Most commercially available electronics are not designed to operate at such elevated temperatures, leading to potential failures or degraded performance. This necessitates the development and use of specialized high-temperature electronics that can withstand these harsh conditions. Additionally, the high-pressure environment, coupled with the presence of corrosive fluids, further complicates the design and deployment of electronic systems, requiring robust packaging and protective measures to ensure long-term functionality.

Another significant challenge is the transmission of data from subsurface sensors to the surface. The low analog signals generated by state-of-the-art subsurface sensors degrade significantly as they travel through the 5,000–10,000+ feet of cable required to reach the surface. This degradation can cause the signals to fall below the noise floor, making them difficult to distinguish and analyze. To address this, real-time data acquisition systems must convert these low analog signals into digitized signals using embedded electronic systems (EES) positioned near the sensors. These EES units, which include microcontrollers and other components for local signal processing, must also be qualified for high-temperature operation. However, the limited availability of commercially viable components that can reliably function above 200 °C poses a significant hurdle. Overcoming these challenges requires innovative solutions in high-temperature electronics, advanced packaging techniques, and robust data transmission methods to ensure accurate and reliable evaluation of geothermal wells.

Sandia National Laboratories are evaluating methods to package EES that would be capable of operating at temperatures up to 300 °C. Recently, Sandia completed a study using RelChip's RC10001 microcontroller in a surface-mount device (SMD) configuration, which is the only modern microcontroller on the market that can function at 300 °C. Several challenges were identified when using standard packaging techniques for 300 °C operation. This evaluation focuses on four high-temperature packaging techniques; ceramic printed circuit boards (PCB), gold-tin soldering, wire bonding, and conformal coatings; to address the issues observed with SMD packaging. If successful, these techniques will enable the EES to operate reliably for long-term characterization of deeper and hotter wells at temperatures up to 300 °C.

2. Surface Mount Device Packaging Challenges

Integrated circuits (ICs) can be constructed using various packaging techniques, including thru-hole devices, surface-mount devices (SMDs), and dies. Thru-hole devices are designed with leads that pass-through holes on a printed circuit board (PCB) and are soldered on the opposite side, providing strong mechanical bonds and reliable connections, making them suitable for high-stress environments. Surface-mount devices (SMDs), on the other hand, are mounted directly onto the surface of the PCB, offering a smaller footprint and enabling higher component density, which reduces the overall size and cost of electronic systems. This makes SMDs particularly advantageous for compact and cost-sensitive applications. Dies, which are diced wafers containing the circuit before being placed in a thru-hole or SMD package, represent the most basic form of ICs. They are often used in custom or high-performance applications where direct bonding to a substrate is required, allowing for optimized thermal and electrical performance. Each packaging technique has its own set of advantages and is chosen based on the specific requirements of the application, such as mechanical strength, space constraints, and thermal management.

To achieve the goal of operating electronic systems at 300 °C while minimizing the cost of the tool, we aim to use SMD and die components. However, we have identified three significant challenges for SMD ICs at temperatures reaching 300 °C:

Challenge 1: Typical PCBs, such as Roger materials (e.g., RO3003, RO4003) and polyimides (e.g., Arlon85N), have decomposition temperatures around 260 °C. Consequently, these PCBs have a limited operating time at 300 °C. The material begins to decompose, leading to both dielectric-to-metal and dielectric-to-dielectric delamination (Fig. 1), which strains the electrical connection between the PCB and the SMD IC.

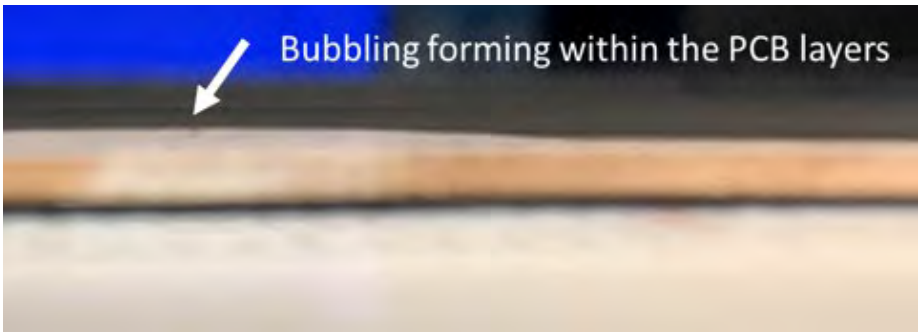

Figure 1: Rogers4003 PCB cross-section, showing a bubble forming between the multilayer board after baking at 300 °C.

Challenge 2: High-temperature (HT) solder, such as 93.5Pb/5Sn/1.5Ag, which has a melting point of 301 °C, interacts with the gold plating on the pins of off-the-shelf SMD ICs at elevated temperatures. Gold tends to diffuse into the solder, degrading the solder joint and weakening the electrical and mechanical connection between the SMD and the PCB. Gold plating is necessary on HT SMDs because gold does not oxidize under high-temperature conditions. Degradation of the solder is evident in Fig. 2.

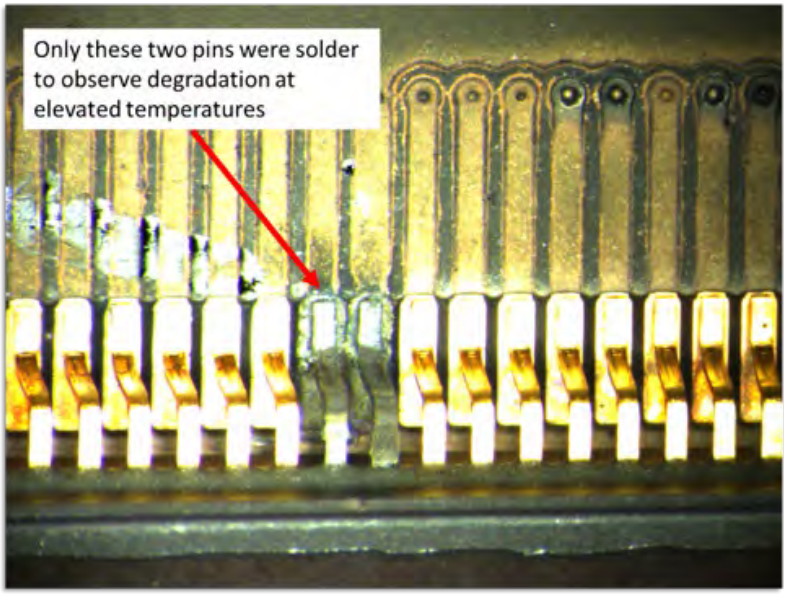

Figure 2: Two pins of the IC had been soldered with observation of the gold wicked into the HT solder .

Challenge 3: Every material has a temperature-dependent coefficient of thermal expansion (CTE). When the CTE of the IC materials differs from that of the PCB materials, the PCB may expand more quickly than the IC, leading to strain between the IC and the PCB.

The combination of these challenges can cause the SMD to debond from the PCB, thereby diminishing or completely halting the functionality of the embedded electronic system (EES). Geothermal tools must operate reliably under harsh well conditions for extended periods, often hours at a time. Additionally, these tools require minimal maintenance to keep the costs of each geothermal evaluation low. To address these issues, we are exploring alternative materials and packaging techniques for SMD and die ICs.

3. Surface Mount Device Packaging Techniques

To enhance the reliability of off-the-shelf ICs packaged onto PCBs for operation at 300 °C, our team is investigating following key factors: the PCB material, the electrical connection between the IC and PCB, and the conformal coating over the IC and electrical connections to protect them from the harsh high-temperature environment and strengthen the mechanical bond. Specifically, Sandia is exploring the use of ceramic for the PCB, gold-tin (Au/Sn) solder, wire bonding, and high-temperature epoxy for the conformal coating.

3.1 Ceramic Printed Circuit Boards

Ceramics can operate effectively at temperatures well above 300 °C and are commonly used in power electronic applications, where ICs generate excessive heat. Given its widespread use in power electronics, ceramic is readily available for industrial manufacturing. In this study, Sandia has been evaluating alumina (Al_2O_3) ceramic (Fig. 3) for packaging the ICs.

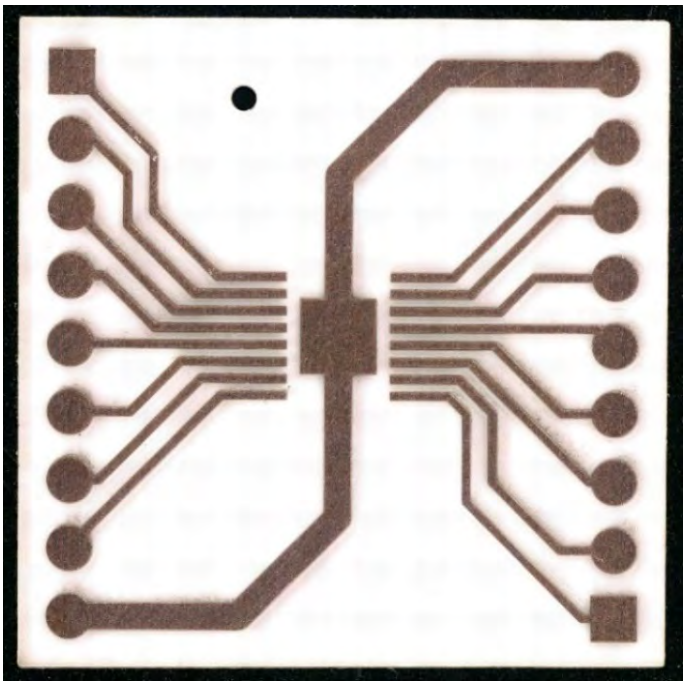

Figure 3: PCB circuit etched onto Al_2O_3 with a thickness of 0.020". The copper is attached via a titanium seed layer to improve adhesion of the copper to the ceramic.

We selected the electroless-nickel electroless-palladium immersion-gold (ENEPIG) plating pattern, commonly used for wire bonding die ICs, with the following targeted thicknesses: Ti/Cu/Nickel (Ni)/Palladium (Pd)/Gold (Au) at 150/750/250/250/250 nm, respectively. Thin Au coatings have been employed for many years in sputtering and electroplating to control corrosion and oxidation of underlying films. However, this simple mitigation strategy can be compromised by the diffusion of both species: Au moving into the base coating and the base coating migrating through the Au. This diffusion depends on the physical and chemical properties of the metals and the temperature. A common material system that exhibits this issue is a Cu coating capped with Au, where a thicker Cu layer is protected from oxidation by Au. While this approach works in the short term at room temperature, over a few months, the Cu will slowly migrate to the surface and form copper oxides. If the coating is exposed to elevated temperatures, this transformation can occur in minutes rather than months. These oxides reduce conductivity and eliminate wettability for soldering. With sufficient diffusion, the entire coating can oxidize.

The common solution to this issue is the addition of a barrier material between the Cu and Au. Many materials have proven effective as diffusion barriers, including Ni, Ti, Pt, Pd, W, and others. For this study, the industry standard ENEPIG stack was initially chosen and adapted for sputter deposition. The ENEPIG stack uses a bulk Cu layer followed by Ni as the main diffusion barrier. Two capping layers are then applied: Pd, which further acts as a diffusion barrier and reduces the total amount of Au needed, and Au as the final capping layer. A titanium adhesion layer was added to improve the adhesion of the stack to an oxide substrate.

The standard ENEPIG stack was evaluated at 300 °C, and after a couple of weeks, the Au surface oxidized, indicating the diffusion of Cu. By a fortunate accident, another ceramic sample with the metal stack was missing the Cu due to a fabrication error. It was discovered to be missing the Cu because the gold plating did not oxidize after baking at 300 °C for a full month. This serendipitous finding revealed that the lifetime operation of the metal stack is significantly improved simply by removing the Cu. To compensate for the lack of Cu, the Ni layer will be made thicker to enhance electric current flow.

For our lab experiments, a circuit was etched onto the board using laser machining. The laser needed to etch through a metal stack thickness ranging from 900 to 1650 nm. We utilized an LPKF Protolaser R4 picosecond laser with a wavelength of 515 nm for this purpose. This compact tool is primarily intended for rapid PCB prototyping (typically on FR4 substrates) and short production runs, but it is versatile enough to process a wide variety of designs and materials. We found that the tool effectively minimizes the heat-affected zone due to its short-duration pulses and produces highly accurate, well-defined parts, as shown in Fig. 3. The material was placed on the tool stage (vacuum chuck) and aligned with the digital circuit design. A sequence of routines was used to process the circuit board, including isolation, hatching, and cutting.

First, the traces were defined and isolated using an isolation routine with the following laser parameters:

- Laser Power: 3.65 watts
- Laser Frequency: 150 kHz
- Routing speed: 600 mm/s
- Number of laser repetition paths: 20

The isolation routine, typically used on laminated substrates to facilitate subsequent processing, may be omitted in the future. We found it might be unnecessary for good trace definition on the non-laminated substrate and could remove an excessive amount of material.

Next, the hatching routine removed the areas of thin film remaining between the traces. For non-laminated substrates, total ablation is necessary. This step used the following laser parameters:

- Laser Power: 7.3 watts
- Laser Frequency: 300 kHz
- Routing speed: 1900 mm/s
- Number of laser repetition paths: 2

Finally, the cutting routine defined the board outline and the vias. Each of these features required slightly different parameters due to their size. Small features like the vias experience a much higher level of laser interaction compared to the larger board outline, thus requiring fewer repetitions to fully remove the part.

Via:

- Laser Power: 8 watts
- Laser Frequency: 200 kHz
- Routing speed: 300 mm/s
- Number of laser repetition paths: 750

Board Outline:

- Laser Power: 8 watts
- Laser Frequency: 200 kHz
- Routing speed: 300 mm/s
- Number of laser repetition paths: 500
- Analyses of ENEPIG degradation

With the finalized PCB featuring a lack of copper ENEPIG stack up and a laser-machined circuit pattern, minimal degradation was observed after 700 hours at 300 °C. The traces remained strongly bonded to the ceramic substrate, with only slight discoloration of the gold (Au).

3.2 Gold-Tin Solder

Having demonstrated a non-degrading PCB at elevated temperatures, we proceeded to evaluate the electrical bonding of the IC using gold-tin (Au/Sn) solder. We employed Mitsubishi Materials USA gold-tin (Au78/Sn22) solder with specific particle sizes (5-16 µm), flux type (AS1), viscosity (90 Pa-s), and solidus/liquidus states (278 °C / 301 °C, respectively) to bond the SMD to the PCB. A four-stage Sikama oven, running a temperature profile as shown in Fig. 4, was used to properly process the gold-tin solder while minimizing the time the IC was exposed to elevated temperatures.

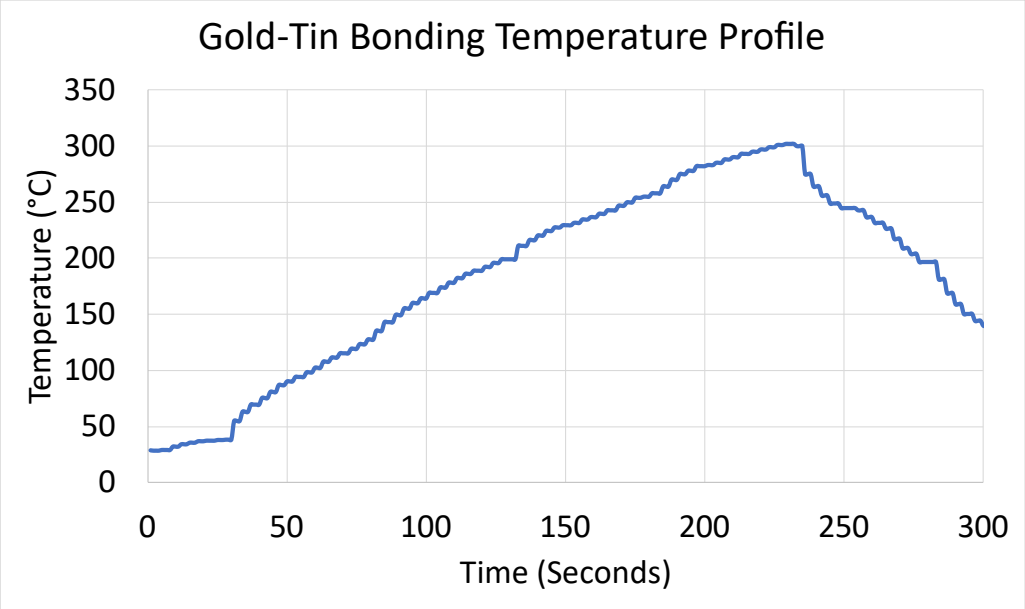

Figure 4: Four-stage Sikama oven temperature profile for the Au78/Sn22 solder. In this profile, the temperature max was 300 °C, but sometimes the temperature may reach up to 320 °C.

A Cissoid CHT-RIGEL voltage regulator was bonded to the ceramic PCB using gold-tin solder (Fig. 5). The sample was subjected to a constant temperature of 300 °C for 170 hours. The regulator remained functional up to 270 °C, after which the thermal protection deactivated the device at 300 °C. While no delamination of the SMD IC from the PCB was observed, the Au traces blackened, as shown in Fig. 5, due to the presence of Cu in the ENEPIG stack. This sample was tested before discovering that the absence of Cu in the metal stack significantly improves performance. Despite the oxidation of the Au, a strong bond was maintained between the IC and the traces. The images also show that the gold-tin solder mitigated the oxidation of the traces near the pins. Moving forward, we plan to test the packaged PCB under vibration at 300 °C to determine whether the gold-tin is entering a liquidus state and/or whether fusion of the deposited metal layer causes degradation of the solder joint.

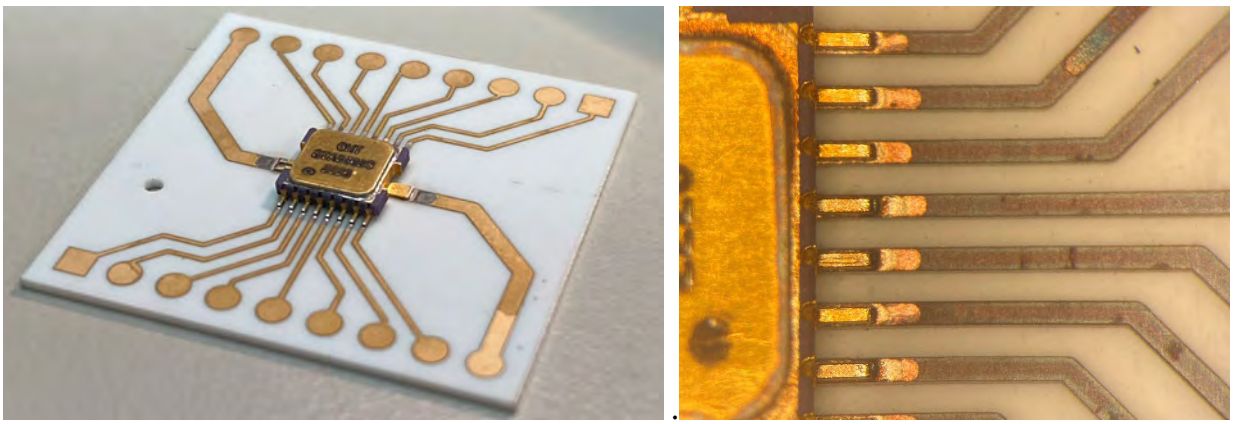

Figure 5: (Left) Al_2O_3 with ENEPIG plated circuit with a gold-tin bonded CHT-RIGEL IC. This ENEPIG stack up contained Cu. The lack of Cu improve, was discovered after this evaluation. (Right) A strong bond remained on the Au/Sn even the oxidation observed on the gold traces.

3.3 Chip-on-Board Wire Bonding

As an alternative to Au/Sn bonding, an unpackaged IC in die format can be directly attached to the ceramic PCB using conductive curable paste and wire bonding. This approach offers the advantage of wire bonds acting as strain relief for the electrical connection in the event of a CTE mismatch between the IC and the PCB. However, there are some disadvantages: only a limited number of industrially produced HT ICs are available in die format, and the die is significantly more fragile than an SMD IC, making it more susceptible to damage during packaging.

The die attach material must meet both processing and operational constraints. Key requirements include a strong bond between the die and the alumina substrate, survivability at temperatures up to 300 °C, electrical conductivity, and resistance to corrosion. Additionally, die attach materials must have very low unbound ionics, typically less than 25 ppm for each ion. Ions such as sulfur, sodium, and lithium are known to promote corrosion.

Typical die attach epoxies are unsuitable for environments at 300 °C because the polymers degrade at such high temperatures. Eutectic solders are often used to attach dies to ceramics, especially for ceramic packages. However, the processing temperatures for solders such as Sn/Pb eutectic solders and no-lead tin-based solders like SAC305 are below the operating temperature of 300 °C. Brazing materials, on the other hand, have processing temperatures that are too high for silicon dies.

For this application, sintered silver die attach was selected. Sintered silver die attach materials contain very small silver fillers mixed into polymers and solvents, which can be dispensed as a paste. The high surface area to volume ratio of the silver particles allows them to sinter, or fuse together, during curing at approximately 200 °C. The fused silver forms a metallurgical bond with the back of the silicon die and the gold on the alumina substrate. During curing, the solvents evaporate, leaving very little polymer behind. The strength of the bond between the die and the substrate is achieved through the metallurgical joining facilitated by the silver.

Abelstik ICP 9000 (hybrid sinter silver) was selected to electrically attach a Cissoid CHT-RIGEL voltage regulator in die format to the PCB. A thermogravimetric analysis (TGA) was conducted on the sintered silver to measure mass loss at elevated temperatures. The results from the TGA are shown in Fig. 6.

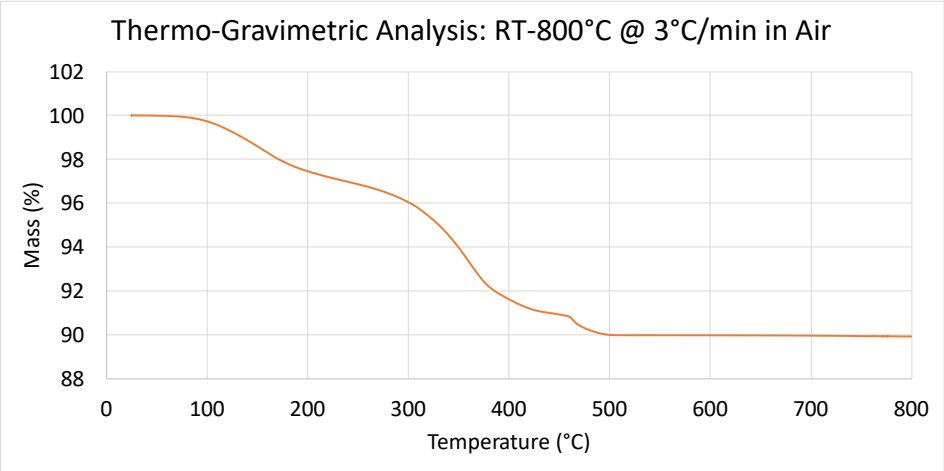

Figure 6: Thermo-gravimetric analysis of the Abelstick ICP 9000 hybrid sintered silver.

After attaching the IC die to the PCB, 0.001" wire was ball-bonded between the die and PCB to establish the electrical connection. The packaged device is shown in Fig. 7. The device was then evaluated in an oven at 300 °C. In die format, we were able to deactivate the thermal protection and observed voltage regulation at 300 °C, but only for a short period before the device failed. After failure, the input voltage matched the output voltage at 250 °C and dropped to 0.4 V at 300 °C. Despite this, since a voltage was still observable, the test continued. The device was baked at 300 °C for 300 hours, during which the wire bonds remained strong and the voltage remained consistent. As shown in the right image of Fig. 7, the gold discolored after the extended baking process, but the wire bond remained intact. In this ENEPIG stack up, there was no Cu.

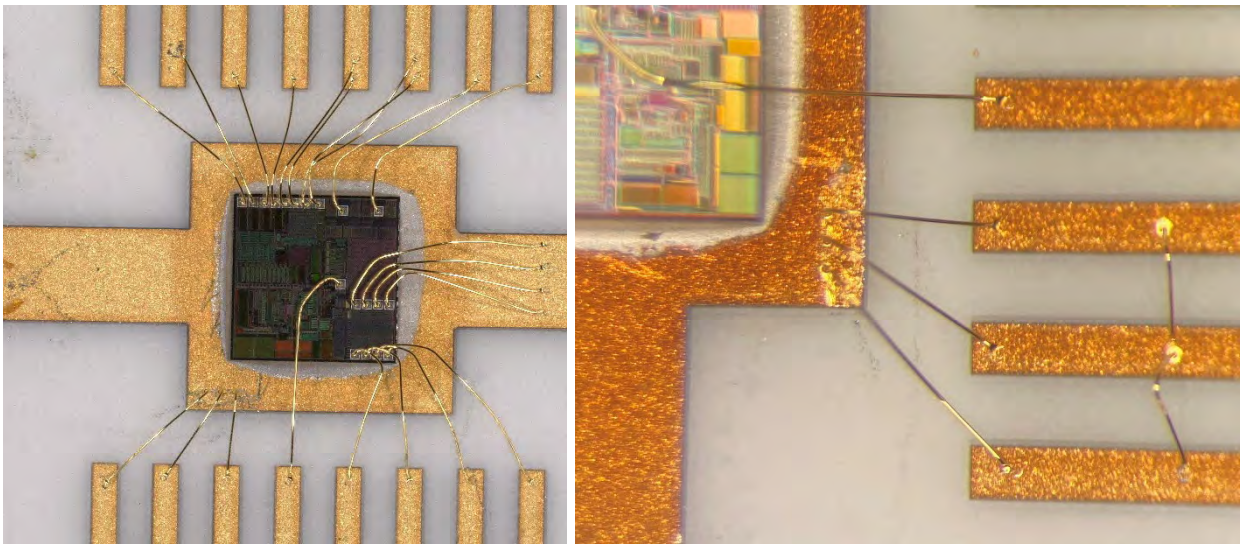

Figure 7: CHT-RIGEL in a die format epoxied to the gold pad on the ceramic PCB (Left) before baking and (Right) after baking at 300 °C for 300 hours.

3.4 Conformal Coating

We hypothesized that applying a conformal coating over the electrical connections could strengthen the mechanical bond between the IC and PCB. To test this hypothesis, we evaluated several off-the-shelf high-temperature (HT) epoxies from multiple companies. We established three criteria for a desirable epoxy: (1) low viscosity to allow for the application of a thin layer over the structures, (2) suitability for HT operation, and (3) a coefficient of thermal expansion (CTE) like that of the ceramic PCB (6–9 ppm/˚C). Ultimately, we selected Micro Measurements' 800 °C line of ceramic epoxies: WC-16 (CTE 7.2 ppm/°C), HG-1 (10.8 ppm/°C), and NCC-3 (12.6 ppm/°C). Due to its close CTE match, we expected WC-16 to be the most promising candidate.

The epoxy was applied to the wire-bonded device reviewed in section 3.3, with an image of the epoxied device shown in Fig. 8. The device was re-evaluated at 300 °C for another 300 hours. Further analysis is required for this approach, as the output voltage dropped and high current was observed on the input. The connection could not be visually inspected due to the opaque color of the ceramic epoxy. It is predicted that the high current draw is due to further degradation of the IC, as the ceramic epoxy remained dielectric and did not produce conductivity. Additional experiments were conducted on the WC-16 epoxy applied to wire bonds between two traces on

the PCB. After 500 hours at 300 °C, an electrical connection was still observed through the wire bonds, indicating the wire bond survived.

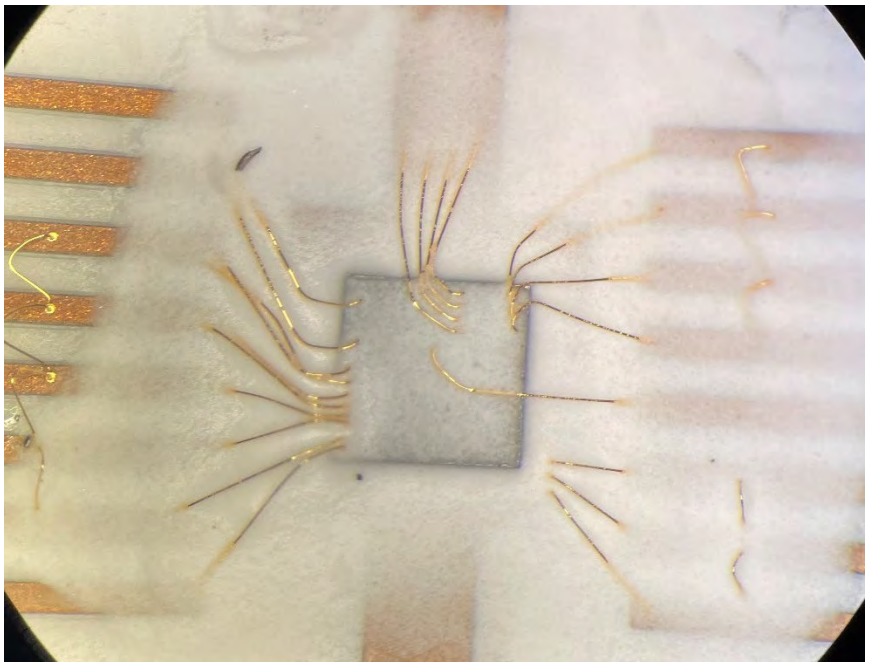

Figure 8: Wire bonded CHT-RIGEL on a ceramic PCB that has been conformal coated with WC-16 ceramic epoxy.

4. Conclusion

Sandia's preliminary experiments indicate that ceramic PCBs with altered ENEPIG stack up, gold-tin soldering, wire bonding, and high-temperature conformal coatings all hold significant potential for enhancing the performance and reliability of embedded electronic systems exposed to temperatures of 300 °C and above for extended periods. However, further testing is necessary to evaluate yield and confirm performance under vibration conditions. One major concern is the possibility of gold-tin solder reaching a liquidus state at 300 °C, although the conformal coating may provide mechanical support to mitigate this issue. These techniques represent a promising advancement in the development of HT electronics, particularly for long-duration geothermal hardware applications.

In the second year of this effort, Sandia will use these techniques to develop and evaluate a data link capable of operating at 300 °C. Initial evaluations have identified some essential components that can survive at 300 °C for a short period before failure. Proposed future research will require the focus on the development of silicon carbide (SiC) ICs that are rated to operate continuously at 300 °C and greater, further advancing the field of high-temperature electronics.

Acknowledgement

Sandia National Laboratories is a multi-mission laboratory managed and operated by National Technology & Engineering Solutions of Sandia, LLC (NTESS), a wholly owned subsidiary of Honeywell International Inc., for the U.S. Department of Energy's National Nuclear Security

Administration (DOE/NNSA) under contract DE-NA0003525. This written work is authored by an employee of NTESS. The employee, not NTESS, owns the right, title and interest in and to the written work and is responsible for its contents. Any subjective views or opinions that might be expressed in the written work do not necessarily represent the views of the U.S. Government. The publisher acknowledges that the U.S. Government retains a non-exclusive, paid-up, irrevocable, world-wide license to publish or reproduce the published form of this written work or allow others to do so, for U.S. Government purposes. The DOE will provide public access to results of federally sponsored research in accordance with the DOE Public Access Plan.

Sandia would like to also acknowledge Adrian Casias, Michael Dirnberger, Ken Coombes, Connor Healey, Frances Lucero, and Tipphachane Jennings for their work on the fabrication of the PCB, die bonding, wire bonding, or die testing.

REFERENCES

Demeus, L., Delatte, P., Dessard, V., Adriaensen, S., Viviani, A., Renaux, C., and Flandre, D. “The Art of High Temperature FD-SOI CMOS.” IEEE (1999).

Henfling, J., and Norman, R. “Dewarless Logging Tool – 1st Generation.” SAND2000-1680, Sandia National Laboratories, Albuquerque, NM (2000).

Henfling, J., Normann, R. “High Temperature Downhole Reservoir Monitoring System.” Proceedings Twenty-Ninth Workshop on Geothermal Reservoir Engineering, Stanford University, California (2004).

Rogers, J., Ohme, B., and Normann, R. “New Paradigm in Electronics Needed to Take the Heat of Deep Gas Drilling.” The American Oil & Gas Reporter (2005).

Swenson, G., and Ohme, B. “HTMOS™: Affordable High Temperature Product Line.” Aerospace Honeywell.

Reed, L. “A 250˚C ASIC Technology” HiTEN (2013).

Normann, R., and Glowka, D. “Designing Logging Tools for Future High Entropy Geothermal Power.” GRC Transactions, Vol. 38 (2014).

Zheng, W. et al. “A frequency domain scheme for high speed telemetry down hole wire line communication.” Int. Conf. Instrum. Meas. Comput. Commun. Control 1413–1417 (2015).

Tran, T., Sun, W., Zeng, J. & Wiecek, B. “High-bitrate downhole telemetry system.” 2015 IEEE Int. Symp. Power Line Commun. Its Appl. ISPLC 2015 280–284 (2015).

Liyanage, M. et al. “Evolution of Wireline Telemetry and its Impact on Formation Evaluation.” 22nd Form. Eval. Symp. Japan 22, (2016).

Cheng, L., Jinfeng, C., Shangchun, F. & Jun, Y. “Analyzing the validity of a DFT-based improved acoustic OFDM transmission along rotating simulated drillstring.” Mech. Syst. Signal Process. 81, 447–460 (2016).

Middlestead, R. W. “Digital Communications with Emphasis on Data Modems.” (Wiley, 2017).

Cieslewski, G., and Cashion, A. “High Temperature Quadrature Amplitude Modulation of Orthogonal Frequency Division Multiplexing.” Volume 2017, Hiten (2017).

Soares, M., Durham, W., and Behbahani, A. “A 0.15um SOI High Temperature ARM Microcontroller for Local Control Nodes: Status of the Next Step.” AIAA Propulsion and Energy Forum, Cincinnati, Ohio (2018).

Wright, A., Cashion, A., and Tiong, F. “Evaluation of High Temperature Microcontrollers and Memory Chips for Geothermal Applications.” GRC2022 Conference, Reno, Nevada (2022).

Wright, A., and Cashion, A. “High Temperature High Speed Data Transfer (Data Link).” GRC2022 Conference, Reno, Nevada (2022).

Wayne, J., and Bozack, M., “Thermosonic Gold Wire Bonding to Palladium Finishes on Laminate Substrates.” 1998 International Conference on Multichip Modules and High Density Packaging

Burla, R., Chen, L., Zorman, C., and Mehregany, M., “Development of Nickel Wire Bonding for High-Temperature Packaging of SiC Devices.” IEEE Transactions on Advanced Packaging, (June 2009)

Yu, F., Johnson W., and Hamilton, W., “Pressureless Sintering of Microscale Silver Paste for 300 °C Applications.” IEEE Transactions on Components, Packaging and Manufacturing Technology, Volume: 5, Issue: 9, (September 2015)

Hagler, P., Henson, P., and Johnson, W., “Packaging Technology for Electronic Applications in Harsh High-Temperature Environments.” IEEE Transactions on Industrial Electronics, Volume: 58, Issue: 7, (July 2011)

Zhang, R., Johnson, R. W., Tilak, V., Zhang, T., & Shaddock, D. (2010). “Characterization of thick film technology for 300 C packaging.” Additional Papers and Presentations, 2010(HITEC), 000097-000107.

Fang, K., Isaacs-Smith, T., Johnson, R. W., Vert, A., Zhang, T., & Shaddock, D. (2012). “Recent progress in thin film multichip packaging for high temperature digital electronics.” Additional Papers and Presentations, 2012(HITEC), 000407-000412.

Wright, A., and Montano, M., “300 Degree Celsius Electronic Component Packaging.” Additional Papers and Presentations, 2024(HITEN)

Drilling

Extending Drilling Tool Life in Geothermal Wells with Recent Advances in Low Thermal Conductivity Coatings

Michael Adams and Reza Fard

Tuboscope NOV

Keywords

Geothermal drilling, Enhanced geothermal systems, thermal conductivity, insulated coating

ABSTRACT

Drilling into geothermal reservoirs challenges the reliability and long-term operability of drilling tools in the bottomhole assembly (BHA). The sensitive electronics in many downhole tools often fail at high temperatures, which drives up drilling costs by adding downtime to pull the string and replace failed components in the BHA.

This paper presents a novel solution: an internal insulating drill pipe coating that helps keep drilling fluids and the BHA below a certain temperature threshold to extend tool life downhole. The solution builds on coating advances originally developed to protect tubulars in aggressive oil and gas environments from corrosion, wear, and deposit buildup while improving hydraulic efficiencies to reduce pumping horsepower.

It also includes components that reduce heat transfer rates through the drill string and keep the fluid cooler. The new coating has a thermal conductivity of $k = 0.1808\ W/mK$, nearly 250 times lower than the conductivity of steel pipe, which vastly increases the thermal insulation of the pipe.

In the field, the insulated coating helped keep mud temperatures below 115°C (239°F), well under the standard 150°C (302°F) threshold for most geothermal operations.

The insulated, coated drill pipe is being successfully deployed at several geothermal and oil gas projects globally, with operators placing new orders.

1. Introduction

Of the many renewable energy sources currently driving the energy transition, geothermal offers a vast, sustainable, and essentially inexhaustible energy source that could produce clean, reliable, baseload-level power at scale. It is also the only renewable energy source that naturally produces heat. Because large-scale heating and cooling applications contribute an estimated 40% of all

carbon emissions worldwide (Lund & Toth, 2021), geothermal is also viewed as a viable option for resolving a significant share of human-produced carbon emissions.

However, despite its potential as a reliable, carbon-free energy source, conventional geothermal power production capacity worldwide currently stands at roughly 16 gigawatts, equivalent to just 0.5% of electricity generation capacity from renewable sources (International Renewable Energy Agency, 2023).

Global interest in geothermal energy is growing thanks to its promise of abundant, reliable, and carbon-free heat and baseload power. Other factors spurring greater interest in geothermal energy include technological advancements, societal demand for sustainable energy, and bipartisan governmental support for renewable energy projects that promise long-term job growth. Rystad Energy predicts that by 2030, the anticipated global installed capacity for geothermal power generation will reach nearly 32 gigawatts (Rystad Energy, 2023), roughly double what it is today.

To deliver this anticipated capacity, project developers have realized that conventional geothermal systems are not the answer. Traditional geothermal systems tap into naturally occurring hot water sources in relatively shallow and lower-temperature reservoirs, many of which are found in only certain locations around the world.

Enhanced geothermal systems (EGS) are being developed at a faster pace due to the higher energy production and location flexibility they provide compared to conventional geothermal. Rather than relying on natural underground water sources, most EGS projects in development are closed-loop systems comprising multiple wells—at least one injector and one or more production wells (Figure 1). These projects pump water from the surface into the injection well, deep into dry rock formations at temperatures of 200^{o}C (392^{o}F) or higher. The injected water becomes superheated as it migrates through the hot rock before traveling back to the surface through a production well. As a result, EGS creates a continual loop of water injection and superheated water production, without an underground water source, to expand geothermal’s reach to many more places around the globe.

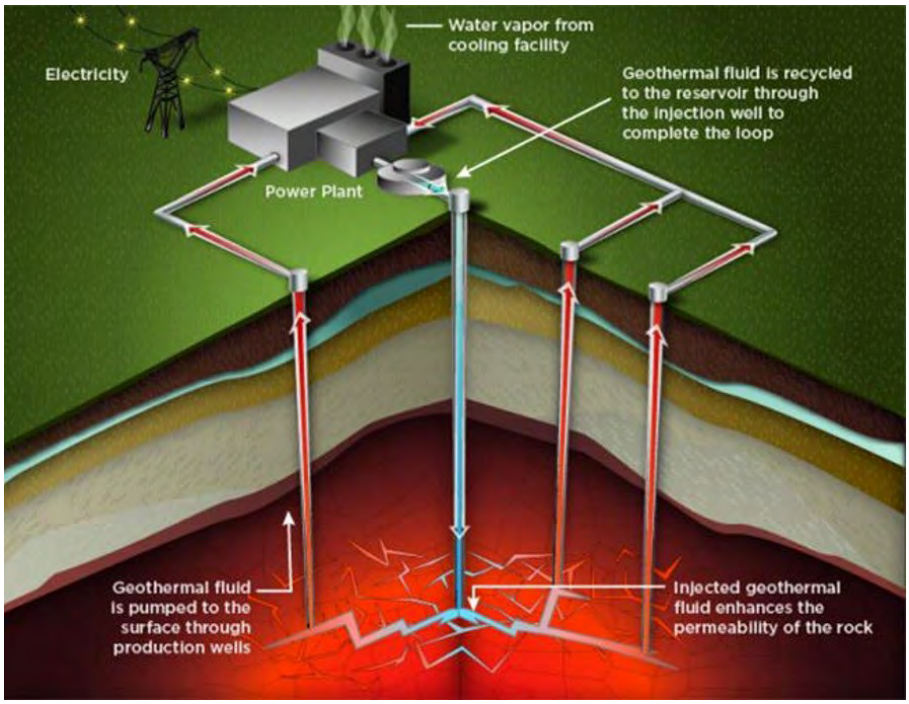

Figure 1: General layout of an enhanced geothermal system, with one injector well and three producing wells. Source: US Department of Energy (2013)

Constructing a closed-loop EGS requires drilling injection and production wells deep into hot-rock reservoirs (typically two miles [3.2 km] or greater beneath the surface). It also requires drilling multiple lateral sections that connect the injectors and producers to help achieve sufficient heat transfer surface area to collect geothermal heat in quantities required to make the project economically viable.

Creating the multilateral sections requires directional and measurement-while-drilling (MWD) tools in the bottomhole assembly (BHA). These tools help steer the drill bit during drilling so that the bit stays in the geothermal zone of interest and effectively intersects the wellbore.

Such tools were developed initially and used successfully in oil and gas drilling operations. However, the higher reservoir temperatures in EGS drilling exceed the maximum operating temperature limit of many typical BHAs and the sensitive electronics in MWD sensors, which are currently rated to 150°C-175°C (302°F-347°F). The drill string and the BHA tools are exposed to these high reservoir temperatures for extended periods while drilling long multilaterals. This essentially guarantees a high risk of tool failures and results in a “drilling blind” scenario in which the drilling team continues building out the multilateral without the necessary downhole data to make informed directional drilling decisions.

One option to improve drilling performance in EGS reservoirs is to redesign the BHA components and MWD tools to operate reliably at higher temperatures. While such developments are being investigated, they require significant time, effort, and investment to re-engineer key components and will delay the widespread adoption of geothermal production at scale.

A faster and more economical option calls for developing solutions that keep existing tools cooler while drilling. This paper examines one such solution: insulated pipe coatings that lower the

thermal conductivity of drill pipe to reduce heat exchange between drilling fluids inside the pipe and in the annular space between the reservoir and pipe. By keeping drilling fluids cooler, such a solution would reduce bottomhole temperatures at the BHA and help protect sensitive electronics to make directional drilling possible. This paper includes work presented by the authors previously (Adams & Fard, 2023), but with additional discussions on the thermal conductivity, corrosion, and chemical resistance testing performed to confirm a coating candidate's performance in the aggressive, high-temperature environments of EGS reservoirs.

2. Thermal Conductivity Control Holds the Key to Temperature Control

The thermal conductivity of a material is a measure of its ability to conduct heat (Figure 2). Thermal conductivity is typically calculated from the defining equation for Fourier's Law for heat conduction (Bird, Stewart, and Lightfoot, 2006):

$$q = -k * \frac{T2-T1}{L} \qquad (1)$$

Where q is the heat flux (W/m^2), k is the thermal conductivity (W/mK), T2 and T1 are the two temperatures on either side of the conducting material (in K), and L is the separation distance (in m).

For geothermal drilling applications, the lower the thermal conductivity, the better. Low thermal conductivity translates to lower heat transfer rates through the drill string, keeping the drilling fluid cooler to minimize the temperature impact on BHA tools and retaining more high-energy heat in the pipe on its way to the surface.

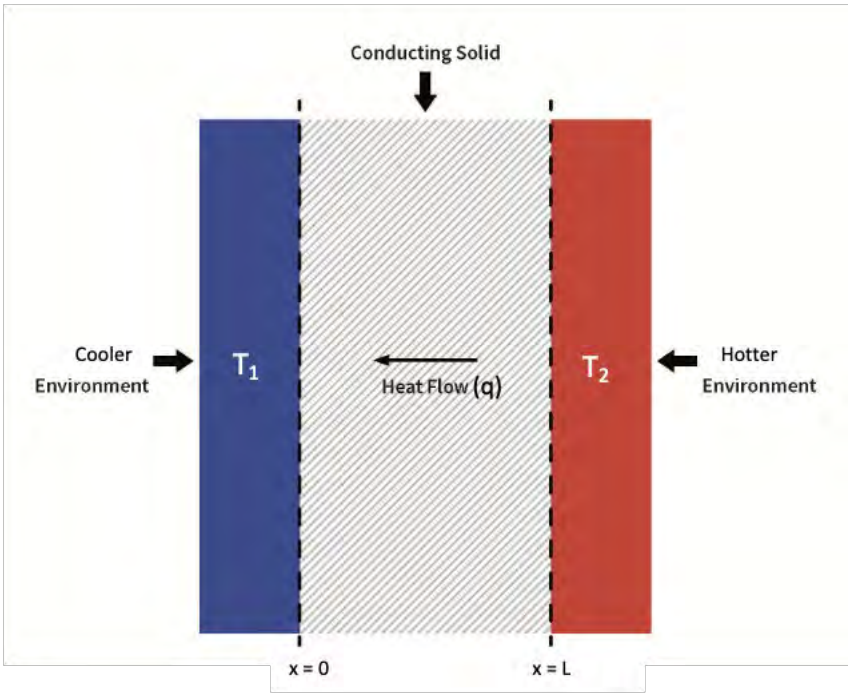

Figure 2: The thermal conductivity of a solid material (of a given thickness L) can be easily defined in terms of the heat flow (q) across a temperature difference (T_2-T_1).

Discussions with geothermal operators guided the target thermal conductivity value of the drill string to protect sensitive BHA electronics. While many tools are rated to 150°C or above, operators want to keep drilling fluids below 120°C (248°F) to provide extra precaution against damage to the BHA components. To stay below this temperature threshold, a drill string with a thermal conductivity of 0.5 W/mK or lower was required.

Carbon steel is the most commonly used drill string material in most drilling applications due to its relatively low cost (compared to other alloys) and proven history of performance over decades. However, the thermal conductivity of unprotected carbon steel is 45 W/mK, two orders of magnitude higher than the required thermal conductivity value (Table 1).

Table 1: Thermal conductivity values of various materials

Material	Thermal Conductivity (W/mK)
Diamond	1,000
Copper	401
Aluminum	237
Carbon steel	45
Water	0.5918
Polyurethane foam	0.03

Rather than begin a lengthy research project to find an entirely different starting material for drill pipe that provided the desired thermal conductivity, the focus shifted to developing an insulating coating material for carbon steel with a thermal conductivity of 0.5 W/mK or less.

Internal plastic coatings have been applied to tubular goods and drill pipes for more than 70 years to provide long-term corrosion control, improve hydraulic efficiency by reducing surface roughness and friction, and prevent deposit buildup on the pipe surface (Lauer, 2007). However, until recently, the insulating properties of such coatings were not an essential requirement or consideration.

Tuboscope embarked on a project to develop a low-conductivity coating for geothermal drilling applications, using its own proven drill pipe coatings for oil and gas applications as a starting point. The development plan was as follows:

- Establish the thermal conductivity and properties of current oil and gas drill pipe coatings
- Adjust the coating formulation to decrease thermal conductivity to 0.5 W/mK or lower, as needed
- Verify that the new coating maintains the required chemical and corrosion performance required in drilling applications

3. Testing Methodology

3.1. Thermal Conductivity Testing of Drill Pipe Coatings

The ASTM E1530-19 test method (ASTM, 2019) was used to measure the thermal conductivity of various coating materials. This test is the primary measurement method for solids such as metals, polymers, composites, and paste less than 25 mm thick and under controlled conditions.

This steady-state measurement of thermal resistance represents the full sample thickness and mature heat transfer properties of test materials. Thermal conductivity is calculated from the thermal resistance measurements and is considered the most accurate method of testing the true thermal conductivity of heterogeneous materials.

3.2. Measuring Physical Properties and Chemical/Corrosion Resistance of Coating Candidates

Researchers conducted additional tests to ensure that the formulation modifications to produce a low-conductivity coating did not alter or negatively impact the coating's ability to improve hydraulic efficiencies and mitigate corrosion in the drill pipe.

Chemical and corrosion performance testing was performed in autoclave and immersion tests. The autoclave tests were designed to measure the integrity of coating materials under elevated temperature and pressure in both sweet (CO_2) and sour (H_2S) environments. Varying degrees of sour testing can be achieved up to 15% H_2S by volume.

Immersion tests on coatings subject the material to extended exposure to various corrosive solutions. These tests can be carried out at elevated temperatures in clear reaction vessels to study the degradation of the material.

A range of physical property tests were conducted to evaluate the coating's ability to withstand high flow rates of drilling fluids in the presence of solid particulates that may enter the drill pipe as contaminants from the drilling process. These tests include Taber abrasion tests that measure coating loss (in mils [thousandths of an inch] or microns), impact resistance (both direct and reverse), and flexibility (both ring crush and mandrel bend testing). The surface roughness of the applied coating was also measured to ensure that the new coating maintained the desired level of hydraulic efficiency and steady flow of drilling fluids through the pipe.

4. Laboratory Testing Identifies Suitable Coating Candidate

Per the ASTM E1530-19 test method, the current coating class had an average thermal conductivity of 0.8360 W/mK, much lower than carbon steel alone (45 W/mK) but still higher than the operator's target value. Through iterative formulation adjustments, researchers arrived at a coating formulation with an average conductivity of just 0.1808 W/mK, well below the conventional coating value and the operator's target (Figure 3).

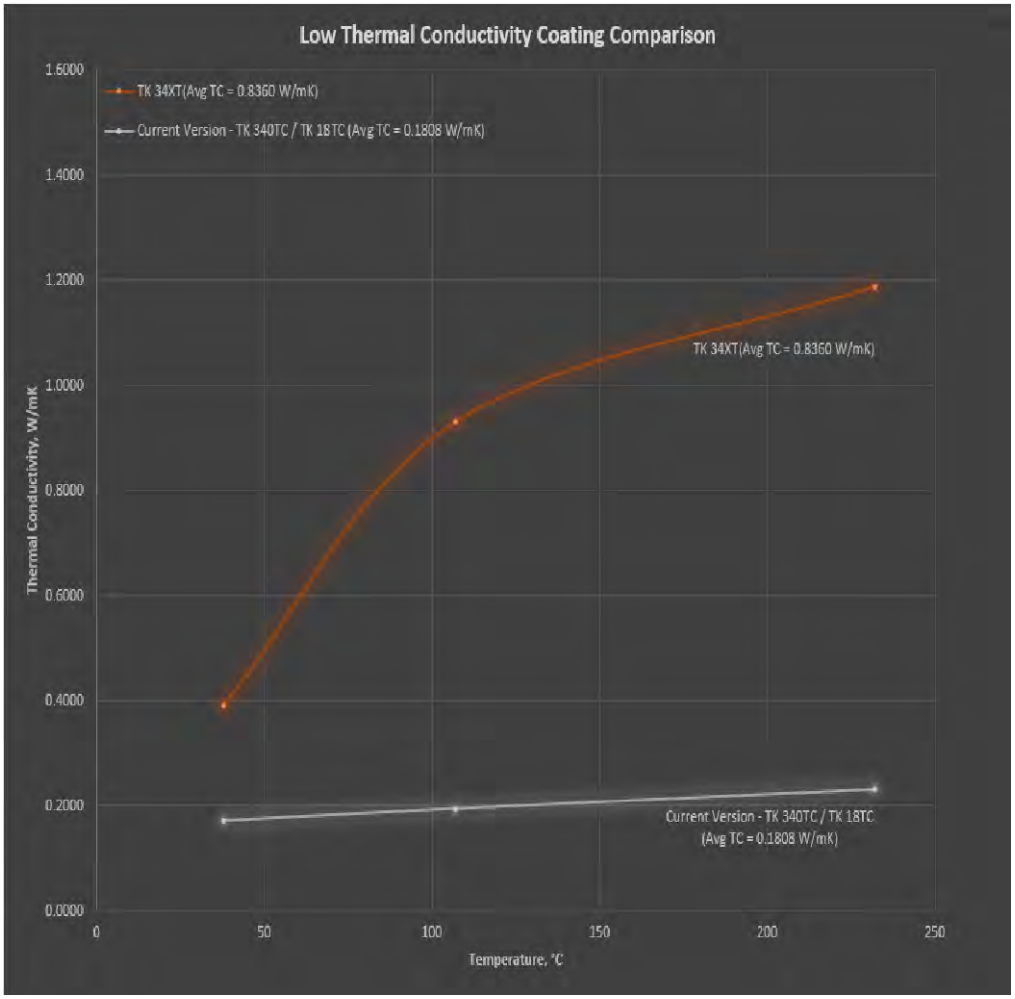

Figure 3: Compared to the conventional coating (red curve), the insulated coating (white curve) delivered far lower thermal conductivities across a wide temperature range.

Additional testing of the new formulation's physical properties showed the same level of reliable downhole performance as the previous generation of coatings (Table 2). The insulated coating demonstrated superior impact, chemical, and abrasion resistance as well as excellent corrosion mitigation properties—all of which helped verify the coating's robustness in harsh geothermal drilling environments.

The coating applies evenly and smoothly to minimize surface roughness and increase hydraulic efficiencies. A smooth coating surface will help prevent the buildup of scale and other solid deposits while promoting the laminar flow of drilling fluids in the pipe. This optimizes mud pumping efficiencies at the surface and provides additional cooling benefits to the BHA downhole.

Table 2: Summary of thermal conductivity and physical properties, comparing the incumbent conventional coating with the optimized, low-conductivity coating

	Conventional coating	Low-conductivity coating
Type	Liquid epoxy phenolic	Powder modified Novolac
Applied thickness	5-9 mils (127-229 microns)	20-30 mils (508-762 microns)
Abrasion resistance (Taber Thickness Loss, mils/1000 Cycles)	0.6	0.32
Surface Roughness (Rz µm)	11.97	2.43
Thermal Conductivity (w/mK)	0.8360	0.1808
Ring crush, mils of deflection	50	108
Reverse impact (in*lb)	51	185
Direct impact (in*lb)	80	88

5. Proving Its Potential in The Field

A geothermal operator evaluated the new insulating coating on drill pipe as part of an EGS development project in New Mexico, USA. The operation called for drilling a single well, with a sidetrack, more than 5 km (3.1 mi) deep in granite with rock temperatures of ~250°C (482°F). Local geothermal gradients in the region can exceed 50 °C (122°F) per km. The operator selected the single well and sidetrack design to replicate one half (either the injector or a producer) of a commercial closed-loop EGS project.

The new insulating coating was applied to the inside of a 5.5-in. base pipe at a thickness of 20-30 mils. In addition to temperature measurements from MWD tools, the operator placed temperature sensors along various parts of the drill string to record annular fluid temperatures and validate a transient thermodynamic drilling model.

The well was drilled a total of 18,000 ft (5.5 km) into the reservoir at temperatures up to 250°C. With the coated drill pipe in the hole, the mud temperature never exceeded 95°C (203°F), well below the operator's target temperature of 120 °C to prevent BHA damage. After drilling, an examination of the coated drill pipe showed that the insulated coating withstood the high torque and tensile loads and maintained high integrity to enable drilling at depths of 5.5 km or greater.

Based on these test results, the operator purchased an additional string of insulated, coated drill pipe for a commercial geothermal project planned in Europe.

Other geothermal applications for the insulated drill pipe await as operators secure funding and regulatory approvals. In the meantime, the coated pipe is catching the attention of oil and gas operators who face similar drilling challenges in high-temperature reservoirs of 150°C or higher.

6. Conclusions

- Thermal conductivity is key to optimizing geothermal drilling. Drill strings with low thermal conductivity keep drilling fluid and tools cooler for longer.

- Low conductivity coatings initially developed for oil & gas can be easily modified/refined for drilling long multilaterals in deeper, hotter geothermal reservoirs.
- Thorough testing and refinement of coatings delivered a low TC coating (<0.5 W/mK target) that maintained superior corrosion, chemical, and hydraulic performance.
- Field testing confirmed that the new coating kept mud below the 120°C threshold to protect BHA tools while drilling an 18,000-ft geothermal well.
- Encouraged by early successes, operators are placing more insulated drill pipe orders to continue field trials.

Acknowledgments

The authors thank our oil, gas, and geothermal customers who continue evaluating low thermal conductivity, insulated drill pipe in their extreme temperature drilling operations. Thanks to NOV for their support and efforts in advancing alternate energy developments like geothermal. Moreover, thanks to NOV's scientists, laboratory technicians, and manufacturing centers for consistently designing and delivering low TC coatings that meet the demands of deeper, hotter reservoirs.

REFERENCES

Adams, Michael and Fard, Reza. "Optimizing geothermal's potential with advanced insulative coating technology." *Think GeoEnergy*, December 5, 2023. https://www.thinkgeoenergy.com/optimizing-geothermals-potential-with-advanced-insulative-coating-technology. Accessed July 9, 2024.

ASTM International. ASTM E1330-19. "Standard Test Method for Evaluating the Resistance to Thermal Transmission by the Guarded Heat Flow Meter Technique." February 18, 2019. https://www.astm.org/e1530-19.html. Accessed June 8, 2024.

Bird, R.B., Stewart, W.E., and Lightfoot, E.N. *Transport Phenomena*. Vol. 1, Wiley (2006). ISBN 978-0-470-11539-8.

International Renewable Energy Agency and International Geothermal Association. "Global Geothermal Market and Technology Assessment." Abu Dhabi, UAE (February 2023). https://www.irena.org/Publications/2023/Feb/Global-geothermal-market-and-technology-assessment#:~:text=Electricity%20generation%20from%20geothermal%20energy,(GWe)%20in%202021. Accessed June 6, 2024.

Lauer, R.S. "The Use of High-Performance Polymeric Coatings to Mitigate Corrosion and Deposit Formation in Pipeline Applications." *Corrosion*. (2007). https://api.semanticscholar.org/CorpusID:136581316. Accessed June 6, 2024.

Lund, J.W., and Toth, A.N. "Direct Utilization of Geothermal Energy 2020 Worldwide Review." *Proceedings World Geothermal Congress 2020+1*, Reykjavik, Iceland (October 2021).

Rystad Energy. "Energy Transition Report: Geothermal Market Outlook." Oslo, Norway (May 2023. https://sf-asset-manager.s3.amazonaws.com/97637/616/3933.pdf. Accessed June 6, 2024.

US Department of Energy, Office of Energy Efficiency & Renewable Energy. (October 23, 2013). *Diagram showing how electricity is produced using enhanced geothermal systems* [graphic]. Retrieved from https://www.energy.gov/eere/articles/geothermal-energy-glance-back-and-leap-forward.

Well Control Considerations for a Global Geothermal Industry: A Historical Review and an Assessment of Current and Future Requirements

Andrew Barry and Mohamed Amer, Wild Well Control, and Julmar Shaun S. Toralde and Robby L. Darby, Weatherford

Keywords

Well control, blowout, geothermal

ABSTRACT

Geothermal well blowouts pose a significant financial and reputational risk to companies exploring for or developing geothermal energy resources. The potential catastrophic impact of a major geothermal blowout can tarnish in the arena of public opinion the recent gains of the geothermal renaissance that the nascent and fast-growing global geothermal industry is experiencing.

Given the increasing geological and geographical distribution of geothermal projects, the introduction of new well architectures and advanced drilling technologies and the drive towards hotter supercritical geothermal reservoirs to achieve greater global energy contribution and scale, a comprehensive assessment of the well control and blowout contingency considerations unique to the geothermal industry is needed.

With this in mind, a thorough historical review of available well-control-related information, publication and events will be conducted. This will provide a solid foundation for the determination of the current and future well control risks and blowout contingency requirements of the geothermal industry. The paper also intends to cover the issues involved with the direct application of conventional oil and gas well control techniques and methods in the geothermal industry and to raise relevant concerns about what the geothermal industry is doing and identify possible pitfalls in the direction that the industry is headed.

1. Introduction

Geothermal formations are comprised of reservoirs of hot water that naturally occur or are man-made at varying temperatures and depths below the earth's surface. As defined by Naturally occurring geothermal formations (with heat, water, permeability) that have historically been developed for heating and electricity generation purposes are usually classified as of the hydrothermal type (US Department of Energy, Office of Energy Efficiency and Renewable Energy, 2024), but other types such as geopressured-geothermal systems, which contain water with somewhat elevated temperatures and with pressures well above hydrostatic for their depth, as

well as magmatic systems, with temperature ranging from 600°C to 1400°C also exist. Man-made geothermal systems usually target Hot Dry Rock (HDR) geothermal resources, with ideal temperatures from 200°C to 350°C, and are usually referred to as enhanced geothermal systems (EGS) or advanced geothermal systems (AGS) or advanced closed loop (ACL), depending on the technologies being used to develop the resource. Rock types are typically granite, granodiorite, quartzite, greywacke, basalt, or volcanic tuffs but geothermal reservoirs in sedimentary rock types are also possible.

Because geothermal formations are usually under pressured (pore pressure less than fluid pressure in a full wellbore), influx into the wellbore is rare. Geothermal well control considerations, as described by Wild Well Control (2024), are primarily due to these two causes for loss of control:

- An unexpectedly hot formation is encountered at a shallow depth where the annulus pressure is insufficient to keep the drilling fluid or the formation fluid from flashing to steam.
- Lost circulation causes the fluid level and the pressure in the wellbore to suddenly fall far enough for the same thing to happen.

If complete control is not lost, simply pumping cold water into the wellbore can usually kill the well.

Like in oil and gas drilling settings, the apparatus that controls a geothermal kick and potential outflow at the wellhead is called the blowout preventer (BOP) or blowout prevention equipment (BOPE). According to the Handbook of Best Practices for Geothermal Drilling published by Sandia National Laboratories, the geothermal BOP stack comprises five types of device to shut off the wellbore and prevent fluid flow out of it: rotating control devices (RCD) or rotating heads, annular preventers, pipe rams, blind rams, and shear rams. The basic function of each is to shut off the wellbore, but they operate in slightly different ways. Below the BOP stack, there is a drilling spool with two valved lines (called the choke and kill lines) connected to the drilling spool so that fluids can be either released from or pumped into the wellbore as part of the well-control process. (Finger & Blankenship, 2010) (Weatherford, 2024)

Compared to the sedimentary formations of most oil/gas reservoirs, hydrothermal geothermal formations are, by definition:

- Hot (production intervals from 160°C to above 300°C)
- Often hard (240+ MPa compressive strength), abrasive (quartz content above 50%)
- Highly fractured (fracture apertures of centimeters)
- Under pressured
- Often contain corrosive fluids
- Some formation fluids have very high solids content [total dissolved solids (TDS) in some brines it can be above 250,000 ppm]

Purba et al. highlight that the fundamental differences between petroleum and geothermal environment systems lie in reservoir and fluid temperatures, rock permeability and pressure and the heterogeneity of the rock-forming systems. (Purba, et al., 2022).

Purba et al. also emphasizes that the generalization of well control methods and blowout preventer (BOP) designs between petroleum and geothermal can be dangerous because generally well control methods and equipment in the petroleum industry are designed to anticipate pressure. It adds that geothermal is likely to face a well control situation that is influenced by temperature, and that the availability of a continuous supply of cold water, the ability and reliability of the pump on the rig, and an adequate BOP temperature rating are the main factors that must be considered.

Finger and Blankenship (2010) highlight that though pressures in geothermal drilling are almost always lower than those encountered in oil and gas drilling, the key to control is having adequate casing setting depths, which will permit shutting the well if a kick is detected in the early stages. They warn that unexpected steam flow in a permeable formation that is not completely sealed by casing is particularly dangerous; because steam can begin to flow up the outside of the previous casing string ("underground blowout") and eventually destroy the casing's integrity and often causes loss of the drill rig.

The geothermal well control incidents in the following section highlight these hazards and emphasizes the fact that geothermal well blowouts pose a significant financial and reputational risk to companies exploring for or developing geothermal energy resources. Though most of the well control case studies featured in this paper are from historical geothermal development projects involving hydrothermal resources, the risks involved and lessons learned will have a high degree of applicability to the new technologies being tested or piloted involving enhanced and advanced geothermal systems (EGS / AGS / ACL) that are receiving a lot of recent attention from the global energy community.

Adaptations that might be required from a well control standpoint to accommodate these new geothermal technologies and methods that have the potential to bring geothermal anywhere and everywhere are presented in the section following the case studies.

2. Geothermal Well Control Incidents and Statistics

With the rapidly evolving and expanding geothermal energy industry future in mind, a historical review of publicly available well-control-related information, publication and events was conducted as part this paper. It is intended to provide a solid foundation for the determination of the current and future well control risks and blowout contingency requirements of the geothermal industry.

So in terms of risk, how does geothermal energy systems compare to other energy sources and which what is the level of risk involved with well blowouts? A paper published on "Comparative accident risk assessment with focus on deep geothermal energy systems in the Organization for Economic Co-operation and Development (OECD) countries" provides some insights on the matter. The paper concludes that the drilling and stimulation phases of deep geothermal energy development are considered the riskier due to the potential of blowouts or release of drilling muds and stimulation fluids during these operations. Within the drilling phase, blowout accident risk is significantly higher than the transportation, storage and use of caustic soda. In both the stimulation phase and drilling phase of geothermal operation blowouts are among the highest risks. This is related to the fact that if a blowout happens the effect can be catastrophic not only for the deep geothermal project itself, but for the workers in the area. It is interesting to note that blowouts in the drilling phase are higher with respect to the stimulation phase. This could be possibly due to

the fact that during a stimulation phase the bore should have been stabilized in terms of pressures, while during the drilling phase, kicks from different gasses, i.e. natural gas, hydrogen sulfide, could still happen in an unpredictable way, leading to an increased risk. (Spada, Sutra, & Burgherr, 2021)

It is interesting to note that the study also developed and compared deep geothermal cases (best and worst) against fossil, hydrogen and selected renewable technologies, in terms of expected accident risk. The lowest fatality rate, i.e., expected risk, was found for the deep geothermal energy best case. The deep geothermal energy worst case is similar to wind offshore and performs better than the fossil, hydrogen, hydropower and biogas energy chains. In contrast, in terms of extreme accident risk, maximum consequences, i.e., extreme risk, for both deep geothermal energy scenarios were similarly low as for other renewables, implying that they are substantially less prone to high-consequence events than fossil, hydrogen, and hydropower energy chains.

Going further into the details of geothermal well blowout incidents and risks, the table below lists down by country and by approximate year the instances of the same available in published literature and in the worldwide web, using the search terms “blowout” or “well control” in the publication title or in the Internet or AI Chatbot search query. Snippets of the incidents found (in chronological order) are provided in the paper but the complete list of sources (including links to available geothermal blowout videos) are also provided in the References section.

Table 1. Geothermal Well Control Incidents by Location and Year (tallied from incidents with publicly available information cited in this paper)

	Country								
Year	**HUN**	**IND**	**IDN**	**JPN**	**NZL**	**PHP**	**TUR**	**USA**	**Total**
1958					1				1
1960					2				2
1976								1	1
1983								2	2
1989								1	1
1991				1				1	2
2003						1			1
2010	1			1			1		3
2014						1			1
2016			3						3
2018			1						1
2019			1						1
2020			1						1
2022		1							1
2023				1					1
Total	1	1	6	3	3	2	1	5	22

Legend: Complete Country Names: HUN – Hungary; IND – India; IDN – Indonesia; JPN – Japan; NZL – New Zealand; PHP – Philippines; TRK – Turkey; USA – United States of America.

2.1 New Zealand – 1958 and 1960

This article published in the Geothermics journal describes three blowouts that have occurred in Wairakei: at bore WK26 which blew out early in 1960, at bore WK204 later the same year, and bore WK201, which happened in 1958. The paper mentions that the location of two of these is still marked by large craters (WK201, 204), while the situation at the third (WK26) was recovered and there is now little evidence of the events that took place. None of the blowouts resulted in loss of life, but all provided learning experiences and had a substantial influence on subsequent geothermal drilling practices at Wairakei and elsewhere in New Zealand. (Bolton, Hunt, King, & Thompson, 2009)

A Ministry of Works video on WK204, the 'Rogue Bore' of the Wairakei Geothermal Field has been uploaded by user DamageIncNZ and is available on YouTube, the link to which is provided in the References. (DamageIncNZ, 2015)

2.2 USA - California - 1976

The effects of the blowout of Union Oil Company geothermal well "G.D.C." 65-28 are described, photographed, and diagrammed in this paper. Attempts to control the well are also described. This well, like over 50 percent of the wells drilled at The Geysers, was sited on a Quaternary landslide, according to the authors, and an attempt was made to determine whether or not the well blew out as a result of renewed movements on the old slide. (Bacon, 1976)

2.3 USA – California - 1983

This paper describes the drilling of a relief well Thermal 15 in the Thermal Shallow Reservoir in the Geysers, which was drilled in November, 1983, to a total depth of 700 feet. A steam entry encountered at 490 feet was found to communicate with the high permeability upflow zone of the Thermal Shallow Reservoir. A low-flowrate, higher-pressure steam entry at 600 feet was not detected while drilling but was indicated during a subsequent spinner survey. The pressure, flowrate, and enthalpy of the five wells completed in the upflow zone, including the Thermal 4 blowout, were monitored and recorded over a four month period before, during and after Thermal 15 was drilled. It was found that the Thermal 4 blowout communicates with the upper flow zone of the Thermal Shallow Reservoir, the Thermal 4 flowrate is controlled by the shallow reservoir pressure, and the high permeability of the upflow zone allows such strong interference effects that three of the four commercial production wells will maximize production from this reservoir. (Mogen & Maney, 1985)

2.4 USA - Utah - 1983

This GRC Transactions paper describes the capping of a geothermal blowout near Cove Fort, Utah. The blowout occurred on October 24, 1983, and was considered uncontrollable after four days of attempts by the drilling crew to cool and cement the well. Well control specialists arrived on October 29th, 1983 to establish procedures for containment of the blowout. Upon arrival to the rig site, it was estimated that the flow rate through the 20" conductor casing was 800 ft/sec, with an estimated minimum of 100 ppm hydrogen sulfide. Attempts had been made to measure the temperature of the 97% steam and H2S mixture, with the result being the destruction of a 400 F temperature probe. Steam temperature was estimated to be between 400°F and 600°F. The initial step, in order to control the well, was the removal of the drilling rig, followed by putting in place

surface casing support for the installation of blowout prevention equipment. Wellbore stability was then established followed by the cementing and plugging of the well. (Gray & Gass, 1984)

2.5 USA - Nevada - 1989

This publication focuses on Ormat's 14-6 well that blew out near Fallon, Nevada, on January 1989. The well was drilled using the same drilling program followed on other field wells. However, an unexpected fault caused severe lost circulation, and eventually, the well blew out. The nature of the problems required a combination of surface and subsurface well control techniques. Time was important because the well was flowing 5,000 gpm of 350°F geothermally heated water. (Adams & Thomson, 1989)

2.6 USA - Hawaii - 1991

In June 1991, a high-pressure high-temperature geothermal well, KS-8, being drilled by the Puna Geothermal Venture located in Hawaii kicked and unloaded at 3,476 ft (1,059 m). This well was estimated to have a possible bottomhole temperature of 650°F (343°C) and a reservoir pressure approaching 2,300 psi (15,858 kPa). (Rickard, et al., 1995)

After the well blew out, Hawaii state officials ordered a halt to all drilling. The incident routed 75 people from their homes on the island of Hawaii. The state Department of Health and the county ordered the company to stop drilling while the incident was investigated. (Essoyan, 1991)

Immediate attempts to kill the well were unsuccessful, and the long process of well control was started. Several attempts to kill the well over the next 2 weeks were unsuccessful. The volume of water required to cool the well necessitated drilling a water well. Specialists in the area of well control began transporting snubbing equipment and personnel to Hawaii and their snubbing operation was critical in the final kill operation. (Rickard, et al., 1995)

2.7 Philippines - 2003

This paper describes a blowout that occurred on PNOC-EDC Well 5R-12D, which was drilled as a reinjection well in pad 5R4 of the Malitbog sector to augment the injection capacity of the 231 MW Malitbog Visayan Geothermal Power Corporation (VGPC) power plant. The well was spudded on July 19, 2003 and its 610 mm surface casing was set at 110m. Drilling of the 533 mm hole proceeded normally until partial and subsequently total circulation loss (TLC) was encountered, and blind drilling using water was performed until 450 m. After pullout of the string to 106 m, the well kicked. The annular preventer was closed while the excess pressure was bled off through the bleed line. Water was then pumped through the string at 37 li/s but apparently this was insufficient to quench the well. After a few minutes, steam was noticed coming up in the cellar area. Additional water was pumped in the annulus through the connected cementing lines at 26 li/s. The steam discharge intensified, forming a mushroom-like cloud that rose some 50 m above the well, and thereafter, spewing mud, soil and rocks. A crater structure soon developed around the concrete cellar area that made the whole rig fall on its side after 8 hours of continuous and uncontrolled discharge. (Herras, Caranto, & Palma, 2004)

Another paper on a related topic documents how PNOC-EDC drilled Well 5R-13D, the first geothermal relief well in the Philippines. Well 5R-13D is probably the only relief well in the geothermal industry drilled using a single shot directional survey system. This well was designed

to relieve the pressure of the uncompleted Well 5R-12D that blew out and toppled down the drilling rig on top of it after encountering a shallow pressurized two-phase zone at 450m estimated at about 4 MPa. Early completion of Well 5R-13D was very important to control the environmental, social and economic impact brought about by the continuous discharge. In spite of the various drilling constraints like the proximity of the drilling pad against the main geologic fault prompting a revised welltrack, the non-utilization of MWD tools and time constraints, Well 5R-13D successfully intersected and quenched Well 5R-12D. As an added bonus, the completion test results suggest that this well can even be utilized as a production well. To fully seal off the formerly discharging Well 5R-12D at surface, a series of cement plugs were set through its cut-off casing. (Jumawan, Mendita, Aguilar, Belista, & Retuya, 2005)

2.8 Hungary - 2010

This paper describes the existence of a high temperature and highly over-pressured geothermal reservoir that was proven during a steam blowout in Fabiansebestyen, South-eastern Hungary. The pressure balance of the drilling mud broke down during an incorrect drilling operation. An intensive inflow took place from a fractured dolomite reservoir at 3880m depth. The pressure of the reservoir was 73.1 MPa, its temperature was 199.6°C. The abrupt pressure increase pushed the drill collar to the blowout preventer, seriously damaging the safety valve. The blowout displaced the mud from the borehole and in a very short time it developed into a steam blowout. The blowout held constant for 46 days until staff succeeded in sealing the well. The mathematical model of the blowout is also presented in the paper. (Toth, 2010)

2.9 Japan - 2010

The Onikobe single-flash steam turbine geothermal power plant in Japan has been supplying electricity to the grid for 36 years. Numerous natural geothermal manifestations were present in the field prior to development. New fumaroles accompanied by hot liquid discharges spontaneously appeared near Well 128 on 8 September 2010. The new features were monitored carefully – the manifestations intensified abruptly on 8 October, and engulfed Well 128 the same day. The fumaroles continued to grow until a large scale steam explosion occurred on 17 October 2010. A crater-lake formed and the Well 128 wellhead became submerged in hot water. After the steam explosion, steam and water continued flowing from the crater-lake. Fluid sampling was performed using a radio-controlled helicopter, and results of the chemical analysis of the fluid showed that the fluid in the crater was identical to production well 128 fluid. This suggests that Well 128 was damaged by the steam explosion incident, and that the residual flow from the crater-lake afterwards could be due to a casing failure in Well 128. This paper describes the sequence of crater-lake events and relief well drilling which finally succeeded in killing and plugging Well 128. (Takizawa, et al., 2013)

2.10 Turkey - 2010

Alasehir is the most important geothermal site in western part of Turkey. Many geothermal wells have been drilled in Alasehir Plain to produce the geothermal fluid from the deep reservoir in the last 10 years. A blowout accident happened during a geothermal well drilling operation in Alasehir Plain, and significant amount of geothermal fluid surfaced out along the fault zone in three locations. When drilling string entered the reservoir rock about 1000 m, blowout occurred. As the well head preventer system was closed because of the blowout, high-pressure fluid surfaced out

along the fault zone cutting the Neogene formation. In order to understand the geothermal fluid effects on groundwater chemistry, physical and chemical compositions of local cold groundwater were monitored from May 2012 to September 2014 in the study area. The geothermal fluid was found to be of Na–HCO3 water type, and especially, arsenic and boron concentrations reached levels as high as 3 and 127 mg/L, respectively. The concentrations of arsenic and boron in the geothermal fluid and groundwater exceeded the maximum allowable limits given in the national and international standards for drinking water quality. (Rabet, Simsek, Baba, & Murathan, 2016) Another related study by Timur intended to determine contaminated area in Alesehir by using magnetic susceptibility measurements for the surface and VLF-R method for underground layers. (Timur, 2013)

2.11 USA - Nevada - 2010

This news article mentioned that a legislative audit in Nevada mentioned that there was a 2010 incident where geothermal fluids and steam temporarily flowed uncontrollably on the surface. No one was hurt during the incident. The audit also provided information on oil and geothermal production in Nevada. In 2012, 2.4 million megawatt hours of electricity were provided by Nevada geothermal wells, mostly found in Churchill and Washoe counties, enough to power 219,000 homes. (Vogel, 2014)

2.12 USA - California - 2014

This news article reported that an Ormat geothermal well north of Brawley blew out in May 2014. It was described as a blown well head at the Ormat geothermal plant north of Brawley and it was still shooting into the air uncontrolled when the article was published by the local news outlet. It did not appear that anyone was injured. (Imperial Valley Press, 2014)

2.13 Indonesia - 2016

This technical paper documents capping job activities in three geothermal wells that were done successfully in Indonesia, at a PT. Pertamina Geothermal Energy (PGE) location in Cluster-A Hululais Field. A landslide in Bukit Beriti 2 km away from the location of Hululais-A had damaged three production wells that broke all of the wellheads. In order to prevent more severe effects, immediate and effective well control action was taken. Before the capping job was conducted, clearing work was done, and an appropriate well control method was then selected based on the actual condition of each well, before the capping job was successfully carried out using the BOP method. (Toni, et al., 2017)

2.14 Indonesia - 2018-2019

Wayang Windu geothermal field in Indonesia completed a drilling campaign in 2020 in order to maintain full generation of unit 1 and unit 2 at 277 MW. Four new makeup wells were drilled from two different pads, MBA pad and MBD pad, with two wells drilled in each pad. Two of the four wells drilled had well control events that occurred in different wells and pads. The sequence of well control events were recorded and documented clearly from initial condition until well is safely secured, through combination of down hole pressure and temperature sensors installed in Measure While Drilling (MWD) tool as well as surface pressure, temperature and flow sensors installed in surface line. Some of takeaways from well control events are as follows: (1) In total losses condition, well control events can be grouped into two conditions, steam flow from above and

below the head liquid column; (2) Steam flow from above the head liquid column may occur due to the hydrostatic column drops below steam feed zone that allows saturation condition to occur and fluids flashing into steam; (3) Steam flow from below the head liquid column may occur due to the wellbore hydrostatic pressure drops significantly that leads to an underbalanced condition relative to the formation pressure. This allows hot fluid circulation from deeper depth and flashing at surface; (4) Continuous water supply is safeguard for well control risk and water supply shall be tested prior to spud in and maintain back up water storage full all the time. (Souvanir, Putra, & Darmawan, 2021)

2.15 Indonesia - 2020

This news article from ThinkGeoEnergy mentions that PT Medco Energi has shared details on a recent well steam kick out at its Blawan Ijen geothermal project in East Java, Indonesia. The incident occured on April 24, 2020 and has since been contained and the well is under control again. PT Medco Cahaya Geothermal (MCG) is a joint venture company between of PT Medco Power Indonesia and PT Ormat Geothermal Power informed that there has been a steam kick during the drilling of IJN 6-1 well at IJEN PLTP project located in Blawan Ijen, East Java. This steam kick occurred during the time of drilling at IJN 6-1 entering a shallow depth high temperature steam reservoir at 630 m.The BOP functioned properly during the incident, however due to the increase of the pressure and temperature of the well, steam flowed to the surface. AS of publication, MCG is still working to manage the steam kick and stabilizing the well by pumping heavy drilling mud and it is expected the situation will be stabilized soon. The incident has been reported and coordinated with the related government body, local authorities and socialized with local communities. (Richter, 2020)

2.16 India 2022

This news article by the DownToEarth website mentions that the Oil and Natural Gas Corporation Energy Centre (OECT) and the Iceland Geosurvey (ISOR), which have signed a memorandum of understanding (MoU) for developing a geothermal plant in Puga, Ladakh, have termed a recent accident at the site as a ‘freak incident’ and that they have also said the geothermal fluid that leaked from the ground and flowed into the Puga nullah, a tributary of the Indus, was benign. (Patil, 2022)

The article also mentions that Ravi, the director-general of OECT, told media in Leh August 31, 2022 that the team at the site had encountered a shallow reservoir at a high temperature of 120-130 degrees Celsius while drilling between August 4 and 9. The team immediately stopped the drilling at a depth of 39 metres depth. Further drilling required cooling the shallow reservoir. Due to heavy rain on August 16, the power supply from the grid needed for cooling failed. There was a delay of 20 minutes in restoring the power supply and this is when a blowout occurred. The ONGC has now closed the borehole and is all set to conduct further exploratory drilling at a different location on the same 5 hectares of land in the Puga hot spring area that has been granted wildlife clearance by the state board for wildlife. (Patil, 2022)

A video of a ground report by ThePrint's Simrin Sirur & Praveen Jain tracks the Ladakh renewable energy project's challenges & prospects. The link to the video is provided in References. (ThePrint, 2022)

2.17 Japan 2023

This news article from Kyodo News mentions that four people have so far complained of illness in a town near Hokkaido's Niseko mountain resort after steam erupted during drilling for a geothermal energy development project, Mitsui Oil Exploration Co. said. Hydrogen sulfide at the site in Rankoshi and a high level of arsenic in water collected in a nearby area were detected. Mitsui Oil began drilling on June 25 to survey the potential resource, and the steam erupted four days later. According to the company and the town, the arsenic level detected from the nearby water was 1,590 times higher than the standard for drinking water and 318 times higher than that for water for agricultural use. Mitsui Oil has been disposing of water accumulated at the site of the steam eruption by dumping it in an area approximately 500 meters away from a pond known for being a tourist site, according to a company official. At a press conference in Rankoshi, Mitsui Oil President Hidenori Harada stated that the Hokkaido government has instructed the company to cease dumping water outside the site. However, it is expected to take approximately two weeks to construct a pipeline that will redirect the accumulated water to a well about 1 kilometer away. (Kyodo News, 2023) (Kombrink, 2023)

3. Well Control Considerations for Future Geothermal Development

Given the increasing geological and geographical distribution of geothermal projects, the introduction of new well architectures and advanced drilling technologies and the drive towards hotter supercritical geothermal reservoirs to achieve greater global energy contribution and scale, an assessment of the well control and blowout contingency considerations unique to the geothermal industry is needed.

3.1 Hydrothermal

3.1.1 BOPE for Mining Drilling Equipment Used Geothermal Drilling Operations

All drilling operations inside the geothermal environment, including mining drilling, have the same risk on the well control side. Well control equipment is normally not required in mineral/mining drilling exploration, but for some mineral coring operation that intersect a geothermal area, high temperature of water/steam and/or gases could be encountered during the drilling operation. Irwansyah et al (2021) stipulates that in order to safely conduct drilling, we need to consider the use of well control equipment for mineral/mining drilling operations in geothermal areas. For the application of the geothermal well control to mining drilling operations, the mining well schematic should be modified. There are two additional sections that have to be drilled with 9-1/2” and 6-1/2” IADC bits. Those additional sections will support the installation of a 7-1/16” diverter, thus ensuring the safety of the mining drilling operation. Then the mining drilling can be continued for the rest of the section by installing IPI (inflatable packer). (Irwansyah, Gilang, Augustino, Adityatama, & Wiharlan, 2021)

3.1.2 Kick Detection and Temperature Management

The Sandia Handbook of Best Practices for Geothermal Drilling mentions that better methods for inflow and returns metering are available, and if well control is expected to be an issue, these methods should be investigated. Other indicators of impending flow from the well are the influx of gas, rapid rise in the temperature of returning fluids and encountering rapid drilling, particularly if associated with a loss of returns. It adds that as in many contexts, prevention of a problem is

more efficient than a cure and a number of methods are available to estimate the wellbore temperature profile and warn that a problem may be near: comparison of drilling fluid inflow and outflow temperatures; maximum-reading thermometers either run just above the bit or lowered through the drill pipe on a wireline; or onboard logging tools that can transmit temperature data in real time, as it is always important to know as much as possible about the downhole environment. (Finger & Blankenship, 2010) Technologies for early kick detection and inflow and returns flow and temperature measurement have already been partly deployed in geothermal settings through managed pressure drilling (MPD) methods. (Weatherford, 2024)

3.2 Enhanced and Advanced Geothermal Systems

3.2.1 BOPE for Big-Bore Wells

Deeper and hotter plays and requirements for bigger wellbores to be able to increase the commercial viability of geothermal development projects. Well architectures associated with new geothermal technologies are increasingly requiring larger BOP equipment to be able to deliver the volumes of steam required while drilling fewer wells for their projects. However, BOP systems available in inventory that are mostly geared towards oil and gas applications do not usually go as large as those that are required by the geothermal big-bore designs (17-1/2" or larger), thereby possibly putting a constraint on implementing future EGS / AGS / ACL projects because of the very limited number of larger BOP systems available, unless more of these BOP systems will be manufactured by BOP systems providers.

3.3 Oil and Gas Well Conversion to Geothermal

3.3.1 Well Control Considerations for Both Geothermal / Oil & Gas

Finger and Blankenship (2010) mention that there are geothermal fields (such as Cooper Basin, in South Australia) in which hydrocarbon resources are also found and that this, of course, means that well control procedures and equipment must be capable of handing the somewhat different characteristics of both drilling environments. With the advent of "geothermal everywhere", and initiatives to be able to convert legacy oil and gas assets into geothermal systems, especially in existing petroleum basins, it is important that both the geothermal and oil and gas aspects of well control be properly taken into consideration when planning operations in these hybrid environments.

3.4 Supercritical Geothermal Systems

3.4.1 BOPE Elastomer Seals Good For 260°C

The Sandia Handbook of Best Practices for Geothermal Drilling states that though there will usually be detailed local regulatory requirements for the BOPE the critical factors are to make sure that the BOP pressure rating is adequate and that all the elastomer seals in the equipment are qualified for high temperature. It mentions that most BOPE are dressed with the normal temperature rubbers, which have a working temperature limit of 121°C, because of the high cost and limited availability of high temperature BOP rubbers. It adds that even dressing the BOP's with high temperature rubbers may not provide adequate safety, as they have a working temperature limit of 177°C and as pressures increase when circulating out a high temperature kick, even these higher temperatures can be exceeded. For this reason, a cooling line should be

connected below the pipe rams to pump cool water down through the inside of the BOP and out the choke line during a kill operation, if the temperature might exceed the working temperature of the BOPE. (Finger & Blankenship, 2010)

The high temperature capability of elastomeric sealing elements used in ram type blowout preventers was being addressed by a research project described in a paper by Parker (1995) that require that they must be capable of operating in steam and brine up to 500°F (260°C). Typical well drilling equipment used for oil and gas drilling is designed to operate up to 250°F and under special conditions up to 350°F. The paper reports on the final phase of a joint development project in which high temperature elastomers were tested in ram type BOPs under geothermal conditions. Tests were conducted at ENECs Secolo #1 geothermal well near Larderello, Italy in the period from November 1990 to April 1991. The final phase testing demonstrated improved high temperature elastomer compounds and specially designed ram packer plates would permit operation at 425°F and 1800 psi for significantly longer periods of time than the test goal of 54 hours. (Parker, 1995)

4. Conclusion

The incident case studies and considerations for future development highlight that geothermal well control can be a complex topic, but it is clearly critical to a successful geothermal drilling operation so a holistic approach to well control should be adopted. As such, well-control engineering and procedures and risk management should be part of well planning, so that the proper casing design is developed during the planning stage. Careful planning, modeling and execution of geothermal projects should also comprise a robust well control contingency plan. Sound engineering, multi-disciplinary engineering design, and analysis will ensure a successful outcome. It is essential that proper well control preparations be established and crews will be familiar with them when drilling begins so that rig crews be trained to react quickly and appropriately to an unexpected event that might jeopardize the well.

Given the rapidly increasing volume of geothermal wells being drilled globally of the natural and man-made reservoir type as well as the intention of geothermal operating companies to drill larger, deeper and hotter wells to improve the commercial viability of geothermal energy, it is important that the industry be made aware of the potential catastrophic impact of a major geothermal blowout and mitigate against or prepare for it. Failure to do so might squander the immense gains of the global renaissance that the resurgent and expanding geothermal industry is experiencing.

REFERENCES

Adams, N., & Thomson, J. (1989, June 1). How a geothermal blowout was controlled. *Environmental Science, Engineering, Geology*.

Bacon, C. F. (1976, January 1). Blowout of a geothermal well. The Geysers Geothermal Field, Sonoma County, California. *Calif. Geol.*

Bolton, R. S., Hunt, T. M., King, T. R., & Thompson, G. E. (2009, March). Dramatic incidents during drilling at Wairakei Geothermal Field, New Zealand. *Geothermics, 38*(1), 40-47. doi:https://doi.org/10.1016/j.geothermics.2008.12.002

DamageIncNZ. (2015, June 7). *Wairakei Rogue Bore WK204 Well Blowout.* Retrieved August 19, 2024, from YouTube: https://youtu.be/ZfhXgIm-mMs?si=ZhagSxslzAMpWqcb

Essoyan, S. (1991, June 15). *Blowout Shuts Geothermal Unit in Hawaii*. Retrieved August 19, 2024, from Los Angeles Times: https://www.latimes.com/archives/la-xpm-1991-06-15-mn-503-story.html

Finger, J., & Blankenship, D. (2010). *Handbook of Best Practices for Geothermal Drilling.* Albuquerque: Sandia National Laboratories.

Gray, J., & Gass, D. W. (1984). Capping of a Geothermal Blowout. *Geothermal Resources Council, Transaction. 8.* Geothermal Resources Council.

Herras, E. B., Caranto, J. A., & Palma, R. R. (2004). A Geoscientific Approach in the Design and Success of the First Relief Well at the Leyte Geothermal Production Field. *Geothermal Resources Council Transactions. 28.* Geothermal Resources Council.

Imperial Valley Press. (2014, May 1). *Brawley geothermal well blows, still not under control.* Retrieved August 19, 2024, from Imperial Valley Press Online: https://www.ivpressonline.com/quicknews/brawley-geothermal-well-blows-still-not-under-control/article_93bd5aa8-d186-11e3-8fd1-0017a43b2370.html

Irwansyah, D., Gilang, R., Augustino, V., Adityatama, D., & Wiharlan, H. (2021). Geothermal Well Control Equipment Application for Mining Drilling in Geothermal Environment. *Proceedings 43rd New Zealand Geothermal Workshop.* Wellington, New Zealand.

Jumawan, J. E., Mendita, F. E., Aguilar, M. Z., Belista, B. B., & Retuya, R. E. (2005). The Philippines' First Geothermal Relief Well. *Proceedings World Geothermal Congress 2005.* Antalya, Turkey: World Geothermal Congress.

Kombrink, H. (2023, June 30). *A geothermal blowout in Japan*. Retrieved August 19, 2024, from GEOExpro: https://geoexpro.com/a-geothermal-blowout-in-japan/

Kyodo News. (2023, July 8). *4 complain of illness after steam eruption near Hokkaido's Niseko*. Retrieved August 19, 2024, from Kyodo News: https://english.kyodonews.net/news/2023/07/414284ea9955-4-complain-of-illness-after-steam-eruption-near-hokkaidos-niseko.html#:~:text=Four%20people%20have%20so%20far%20complained%20of%20illness,water%20collected%20in%20a%20nearby%20area%20were%20detected.

Mogen, P., & Maney, J. (1985). The Thermal 15 Relief Well and Production Performance of the Thermal Shallow Reservoir. *Proceedings, Tenth Workshop on Geothermal Reservoir Engineering.* Stanford, California, USA: Stanford University.

Parker, B. G. (1995). Development of Geothermal Capable Elastomers for Use in Ram Type Blowout Preventers Phase IV Testing at Geothermal Wellsite. *Geothermal Resources Council Transactions. 19.* Geothermal Resources Council.

Patil, N. (2022, September 02). *'Freak incident': ONGC, ISOR downplay geothermal fluid discharge into Ladakh's Puga nullah.* Retrieved August 19, 2024, from DownToEarth: https://www.downtoearth.org.in/pollution/-freak-incident-ongc-isor-downplay-geothermal-fluid-discharge-into-ladakh-s-puga-nullah-

84703#:~:text=Due%20to%20heavy%20rain%20on%20August%2016%2C%20the,threw%20up%20muck%20from%20the%20geothermal%20drill%20hole.

Purba, D., Adityatama, D. W., Fadhillah, F. R., Al-Asyari, M., Gumelar, P., Gunawan, A., & Nugraha, R. P. (2022). A Discussion on Petroleum and Geothermal Subsurface Characteristic Differences and Its Impact to Well Control Methods During Drilling. *Proceedings, 47th Workshop on Geothermal Reservoir Engineering.* Stanford, California: Stanford University.

Rabet, R. S., Simsek, C., Baba, A., & Murathan, A. (2016, December 31). Blowout mechanism of Alasehir (Turkey) geothermal field and its effects on groundwater chemistry. *Environmental Earth Sciences, 76*.

Richter, A. (2020, May 3). *Steam kick from geothermal exploration well at Blawan Ijen geothermal project.* Retrieved August 19, 2024, from ThikGeoenergy: https://www.thinkgeoenergy.com/steam-kick-from-geothermal-exploration-well-at-blawan-ijen-geothermal-project/

Rickard, B., Livesay, B., Teplow, B., Winters, S., Evanoff, J., & Howard, W. (1995). Control of Well KS-8 in the Kilauea Lower East Rift Zone. *World Geothermal Congress.* Florence, Italy: World Geothermal Congress.

Souvanir, T., Putra, R. B., & Darmawan, D. (2021). Example Case of Geothermal Well Control Event. *Proceedings World Geothermal Congress 2020+1*. Reykjavik, Iceland: World Geothermal Congress.

Spada, M., Sutra, E., & Burgherr, P. (2021). Comparative accident risk assessment with focus on deep geothermal energy systems in the Organization for Economic Co-operation and Development (OECD) countries. *Geothermics, 95*. doi:https://doi.org/10.1016/j.geothermics.2021.102142

Takizawa, K., Iwasaki, O., Todaka, N., Shimizu, I., Tezuka, S., & Nakanishi, S. (2013). Geothermal Relief Well at the Onikobe Geothermal Power Station. *GRC Transactions. 37.* GRC.

ThePrint. (2022, September 8). *After 'freak incident' it's full steam ahead for India's 1st geothermal power project in Ladakh.* Retrieved August 19, 2024, from YouTube: https://www.youtube.com/watch?v=fuMvVxiQ76U

Timur, E. (2013). Determination of the contaminated area after the blowouts in Alasehir (Manisa/Turkey) Geothermal Area using geophysical methods. *EGU General Assembly 2013.* Vienna.

Toni, A., Irawan, T., Prasetyo, A. D., Andika, F. A., Prasetyo, I. M., & Saputra, M. B. (2017). Success Story Handling the Blowout of Three Wells in Hululais Geothermal Field with Capping Method. *GRC Transaction. 41.* GRC.

Toth, A. (2010). Steam Blowout from an Over Pressured Geothermal Reservoir in Hungary. *GRC Transactions* (pp. 211-214). Geothermal Resources Council.

US Department of Energy, Office of Energy Efficiency and Renewable Energy. (2024). *Geothermal Basics*. Retrieved from US Department of Energy, Office of Energy Efficiency and Renewable Energy: https://www.energy.gov/eere/geothermal/geothermal-basics

Vogel, E. (2014, January 7). *Audit: Nevada inspects oil, geothermal wells infrequently*. Retrieved August 19, 2024, from Las Vegas Review - Journal Capital Bureau: https://www.reviewjournal.com/news/audit-nevada-inspects-oil-geothermal-wells-infrequently/

Weatherford. (2024). *Geothermal Energy Solutions*. Retrieved from Weatherford: https://www.weatherford.com/new-energy-solutions/geothermal-energy-solutions/

Weatherford. (2024). *Rotating Control Devices*. Retrieved from Weatherford: https://www.weatherford.com/products-and-services/drilling-and-evaluation/managed-pressure-drilling/rotating-control-devices/

Wild Well Control. (2024). *Geothermal*. Retrieved August 19, 2024, from Wild Well Control: https://www.wildwell.com/ccus/geothermal

Revolutionising Geothermal Well Design and Operations with High-Temperature Metal Expandable Packer Technology: A Novel Approach in Drilling and Workover

Joven John Cayao[1] and Alger Danielle Ballon[2]

Welltec A/S[1] and Geological Society of the Philippines[2]

Keywords

Metal Expandable Packer (MEP), relining, tieback, low-pH wells

ABSTRACT

The unique differences between geothermal and oil and gas wells require a tailored approach to well design, aimed at extending the lifespan of geothermal wells and addressing the critical challenges of operating mature geothermal fields. Oftentimes, geothermal wells have to intersect faults and other complex lithologies to maximize production. As a result, partial to massive losses lead to uncertainties in cementing operations and cement quality.

In some cases, channeling, development of micro-annulus, and cement degradation result in compromised well integrity and declining production. To address these integrity issues that shorten the effective life-of-well, a workover must be executed in a cost-effective way while ensuring that wells remain safe, efficient, and profitable to operate.

Welltec and a geothermal operator in the Philippines have worked together to address these challenges in four geothermal production wells in need of workover due to collapsed and parted casing within the 13-3/8” casing. A conventional workover by which wells are relined using a bridge plug was deemed unsuitable as drilling out the plug and chasing the debris to bottom could cause further damage to the liners subjected to low pH fluids. Furthermore, the risk of trapped fluid could lead to another casing failure. Thus, the solution requires a certain degree of cementing and control to achieve casing integrity.

This paper presents a solution design featuring high-temperature Metal Expandable Packer (MEP) technology and second stage cementing collar/s, and its application in case studies involving a geothermal production field in Leyte, Philippines. The study focuses on how MEP technology enables the reinstatement of well integrity without the need for a drill-out run.

By applying the learnings from previous deployments, the improved MEP facilitates long-string tieback and relining to ~1,300 meters, which was previously deemed unfeasible due to collapse issues, limiting deployment to depths of ~700 meters.

Designs for upcoming new corrosion-resistant-alloy (CRA) wells have been reviewed and evaluated to overcome very acidic environments.

These wells require immediate relining of production casings as part of the improvements from previously drilled CRA wells in the same sector and would utilize the MEP to avoid damaging the CRA casings during drill out of plugs.

This new design and strategy to include MEP technology in workover and drilling situations can be adapted to mitigate integrity issues resulting in premature failure, and extend the effective life of geothermal wells. This innovative drilling technology designed specifically for geothermal wells provides a pathway to greater repeatability, safety, and control to effectively harness geothermal resources.

1. Introduction

Channeling, development of micro-annulus, and cement degradation result in compromised well integrity and declining production (Jimenez, 2022). Challenges in maintaining the integrity of the wells in one of the major fields of a geothermal operator in the Philippines were related to having poor casing cementing jobs (i.e. channeling and the development of micro-annulus) and the extreme temperature cycles (i.e. cement degradation and casing collapse/break due to cyclic loading). These challenges, coupled with the low pH reservoir fluids, made the conventional relining method through the use of a bridge plug unsuitable as drilling out the bridge plug and chasing the debris to the bottom through the perforated/slotted production liners could cause further damage to the liners that were embrittled by the low pH reservoir fluids.

The objective of this paper is to illustrate the method in conducting long relining operations on wells with compromised well integrity due to shallow collapsed casing and casing breaks within the 13-⅜" production casing interval, with deep production casing setting depths (i.e. 1,400 meters and deeper) using Metal Expandable Packer (MEP) and port collar.

The long relining concept, utilizing the MEP and port collar, was developed to address the challenge of relining deep production casings. This approach reduces the installation costs of corrosion-resistant alloy liners by allowing them to be set conventionally with three liner joints overlapping the production casing shoe, rather than using the current design that requires a long composite casing string with the top-of-liner at a depth of 700 to 800 meters. However, this solution also brought forth challenges, mainly pertaining to having a good reline cementing job. The high temperature delta from the MEP setting depth, the high pumping pressure of cement volumes that pose risks to the casing integrity in terms of the burst and collapse rating, as well as the capacity of the MEP needs to be addressed to make this concept viable for operation.

2. Methods, Design and Technology

2.1 Well Design

Relining with cementing is usually undertaken to address casing problems in the 9-5⁄8" production casing in instances of regular-sized holes and 13-⅜" casing in instances of big holes. The conventional practice is to run a bridge plug and set it just above the top-of-liner to isolate the production casing during the relining/tieback casing-cementing operation. Since the traditional bridge plug is not retrievable, this would entail drilling out the plug and chasing the debris to the bottom of the perforated liners.

The minimum reline setting depth is determined by the expected reservoir pressure. However, the current workover design on low pH wells is venturing on long relines to ensure that the whole production casing will be repaired.

2.2 Design Approach

Driven by the increasing associated costs of drilling a new well and the risk of compromising the integrity of the well while conducting a workover, the geothermal industry has always tried to optimize the design and strategy in repairing geothermal wells. Due to the extreme conditions, such as high temperature cycling whereby a well can be cooled down to ~40 °C and heated up to ~350 °C during production, a proper cement job is deemed critical to ensure that there will be no trapped fluid that could result in annular pressure build up and casing collapse. An innovative MEP technology has been designed and engineered specifically for geothermal well construction and workover applications.

This MEP provides enhanced integrity via a metal expansion sleeve mounted onto the liner / casing, set hydraulically to create an annular seal within minutes. The technology, with its design, also allows rotation during deployment, making it easier to reach the target depth without the risk of prematurely setting the packer.

Being utilized in oil and gas for more than a decade, the MEP can function not only as an independent barrier, but also in conjunction with cement as a supplementary annular barrier proven by successful deployments in the past with the same operator utilizing a high-temperature MEP.

However, this has been limited to shallow relining whereby setting depths were not more than ~780mMD. This improved approach to geothermal relining will pave the way to a workover program that will make long relining feasible. These optimizations can be achieved by introducing a thermally robust MEP technology with the ability to withstand high temperature and highly corrosive fluids while providing a V0 qualified seal.

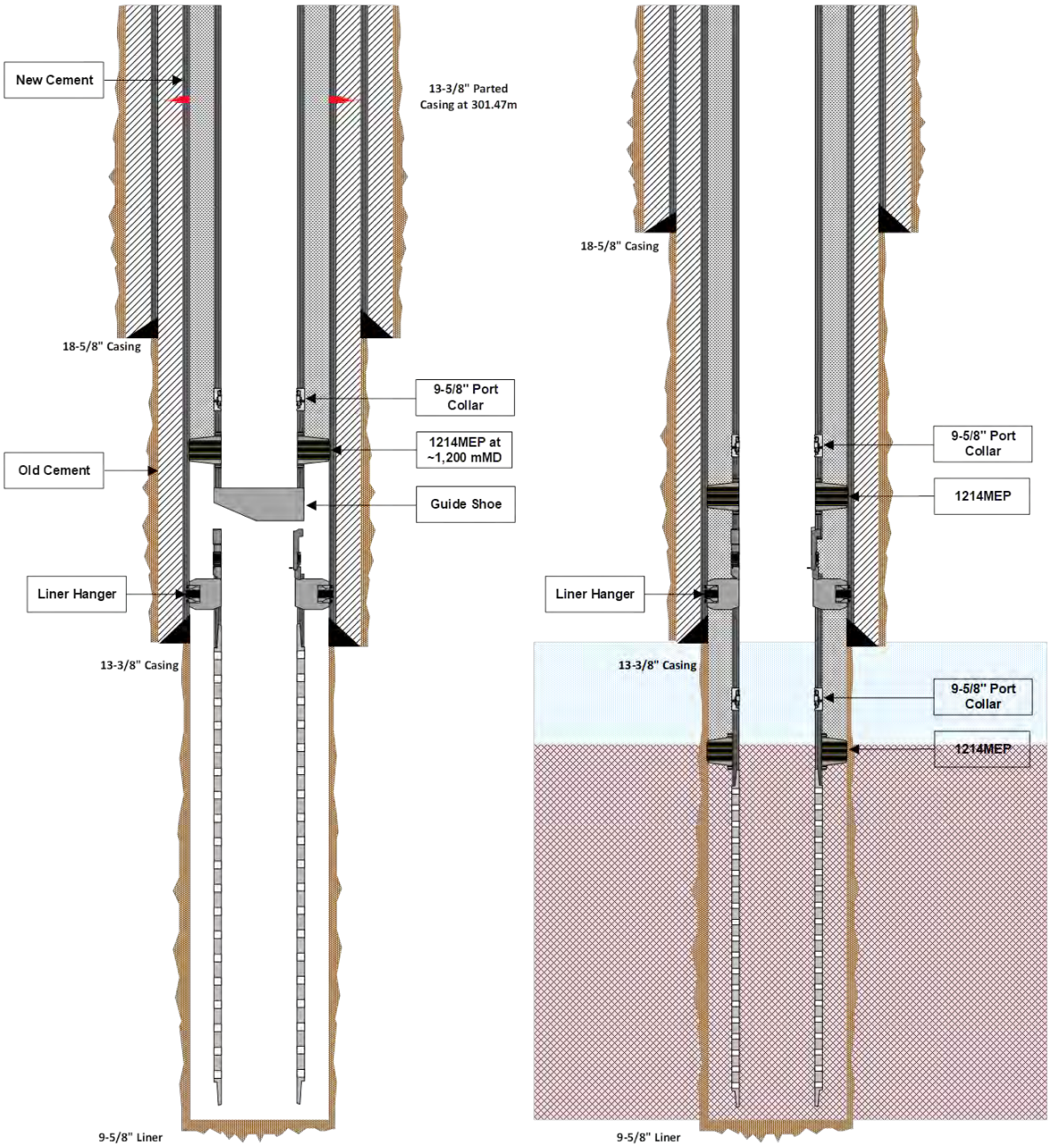

Figure 1 (Left): Well configuration using the MEP and port collar for Workover Operations.
Figure 2 (Right): Well configuration using the MEP and port collar for Drilling Operations.

All these improvements in eliminating the dedicated drill-out run during well relining can be achieved by introducing thermally robust MEP technology with the ability to withstand temperatures in excess of 300°C – this technology provides a reliable, high-integrity zonal isolation element to function as a fixed part of the well construction. A two-stage cement port collar also needs to be utilized and positioned above the MEP for cementing operations.

Simulations during the design phase showed that there is a risk of trapped fluid between the cement port collar and the MEP. Despite the MEP being rated at 6,000 psi differential pressure, the trapped fluid poses a risk to the reline casing between the two tools. To mitigate this risk, rupture disks, which serve as a pressure relief device, are incorporated in the design, and installed between the MEP and the cement port collar. This allows greater control of the well ensuring better efficiency throughout its life.

A valve block system is incorporated in the design of the MEP enabling higher differential pressure rating. In addition to this, and to complement the two burst disks installed, a rupture disk was also incorporated in the valve block system to relieve any fluid that may be trapped between the base

pipe and the MEP expansion sleeve.

With the ability of the MEP to hold the aforementioned differential pressure and the design optimization implemented, a long relining with depths ranging from ~1,000mTVD to ~2,200mTVD are deemed feasible.

2.3 Initial Operations Planning

As the design is flexible enough to address issues in both new and old wells, careful and detailed planning must be done to address the issues of each.

For wells where casing integrity is almost absolute, like newly drilled ones, tieback or casing relining can immediately proceed without conducting any diagnostics. However, in instances where wells are challenged with abrasive or extremely acidic fluids such as in low pH wells, it is recommended to perform caliper logging to ensure that the MEP will be set in a competent casing.

An MEP can be set in an open or cased hole with and have the ability to conform with the shape of the hole it is being set in. However, in the event that the casing is extremely compromised leaving channeling behind, a caliper log coupled with pressure-temperature spinner survey to detect leaks and diagnose the well will help in ensuring the objective is met.

Furthermore, in cases where a cold zone is identified and cannot be cased off by the previous casing, the same MEP configuration can also be set in an open hole and seal off the cold zone preventing the production of the well to be compromised.

3. Conclusion

For decades, the geothermal drilling industry has relied on drillable plug in addressing the relining requirements of the wells. Until recently, the strategic options of drilling and well engineers were limited to drillable solutions that often resulted in further damage and reduced life-of-well.

As this paper demonstrates, the novel MEP features an innovative and flexible design enabling it to be used in drilling and workover applications for both open and cased hole while addressing the risks associated with cementing. The MEP, which serves as a pressure-tight base to prevent cement contamination, and the cement port collar for stage cementing, brought about a solution design that completely eliminates the dedicated drill out run after a cement job, thereby reinstating well integrity while delivering rig time savings and the ability to accelerate the production.

The rupture disks combined with the unique valve block system facilitate long relining requirements without the need to use multiple packers and cement port collars allowing flexibility during the initial well construction, providing an efficient and economical solution.

Despite the thermal cycles adding extra strain and the challenging well conditions, the varied range of seals and valve block configurations that can be utilized make the MEP one of the primary options in relining and tieback applications, especially for low pH geothermal wells. The robust nature of MEP technology and its anchoring capability at high temperature makes it ideal for geothermal applications.

With the understanding of the criticality to maintain the integrity and prolong the life of geothermal wells, this new design and strategy in the workover and drilling of new wells can be adapted to mitigate well integrity issues otherwise resulting in premature failure and shorter effective life-of-well. Furthermore, this innovative drilling technology designed specifically for geothermal wells provides a pathway to greater repeatability, safety, and control to allow the operators to effectively harness geothermal resources.

The actual deployment of this solution is scheduled for H2 of 2024.

REFERENCES

Hallundbæk, S., and Gutteress, F. "Improving Geothermal Well Design for Optimal Performance." (2022).

Jimenez, K. B. "Characterization of annulus well cement quality to estimate the leakage potential in cement well barriers." University of Stavanger, Stavanger, Norway. (2022).

Jolie, E., Scott, S., Faulds, J., Chambefort, I., Axelsson, G., Gutierrez-Negrin, L.C., Ziegler, B., Richter, A., Zemedkun, M. T. "Geological Controls on Geothermal Resources for Power Generation." Nat Rev Earth Environ 2, 324–339. *https://doi.org/10.1038/s43017-021-00154-y*. (2021)

Breaking the 200°C Barrier – Development of an Integrated High Temperature Directional Drilling System

John Clegg, Peter Harvey, Steve Krase and Matthew White

Hephae Energy Technology Corp

Keywords

EGS, AGS, unconventional, high temperature, electronics, cooling, MWD, RSS.

ABSTRACT

So-called “unconventional” geothermal wells, also known as “EGS” (Enhanced Geothermal System) and “AGS” (Advanced Geothermal System) wells, are increasingly being funded and are starting to be drilled in large numbers. For understandable reasons, initial projects have been drilled at temperatures similar to those found in hotter oil and gas wells – initial EGS and AGS projects have been drilled at temperatures below 175°C in order to take advantage of existing oil and gas drilling technologies that have been developed to operate under those conditions.

However, because unconventional geothermal wells are drilled for heat, not hydrocarbons, an arbitrary temperature limit based on what was an appropriate specification for a different industry makes no sense. This is particularly true because, as will be demonstrated in the paper, there is a strong correlation between temperature of the reservoir and economic performance of an asset.

Further, although we cannot yet be certain which of the many proposed designs for EGS and/or AGS will ultimately prevail, almost without exception the pilots being drilled and the projects being proposed rely for their performance on accurately drilled horizontal wells, often pairs or multiples of wells drilled closely together, sometimes at a given offset and sometimes even intersecting. This requires a high degree of accuracy and control when drilling and therefore strongly suggests that the technologies used for drilling horizontal and extended reach wells has a place in geothermal drilling – if only it could be made to work reliably at higher temperatures. Ideally the temperatures limits of those technologies could be increased to beyond 200°C and ultimately as high as 300°C.

Unfortunately, although the oil and gas industry has made great strides over the years in getting the operating temperature of downhole electronics from below 100°C to 175°C, and, even on rare

occasions, to 200°C, the approaches taken in oil and gas tools do not lend themselves to getting to the even higher temperatures that unconventional geothermal will need.

This paper describes a unique, blank sheet of paper, approach to the design and packaging of electronics and sensors, to create a brand-new tool that combines the functions of Measurement While Drilling (MWD) and Rotary Steerable Systems (RSS) and which will be able to break that 200°C barrier.

It describes the design decisions made and modelling done to ensure enhanced thermal performance without sacrificing any of the resistance to shock and vibration that oil and gas tools have acquired over the years – shock and vibration being significant in the hard, high friction basement formations that EGS and AGS will most likely inhabit.

It will show the results of thermal testing and lessons learned along the way and demonstrate the viability of a fully working integrated MWD/RSS system capable of operating in the previously "forbidden" region above 200°C.

1. Introduction

As noted above, EGS and AGS pilot wells have tended to be drilled at temperatures below 200°C, and it would appear to be more than just coincidence that this is the technical limit of the directional drilling and measurement tools that have been developed over the years for the oil and gas industry. Some of the unconventional geothermal pioneers have publicly stated their desire to drill deeper and at much higher temperatures, for example Eavor (Lowdon & Hodder, 2024).

Research using the US Department of Energy Geothermal Electricity Technology Evaluation Model (GETEM) reveals the significant leverage of temperature over the economics of geothermal wells, as seen in Figure 1 below.

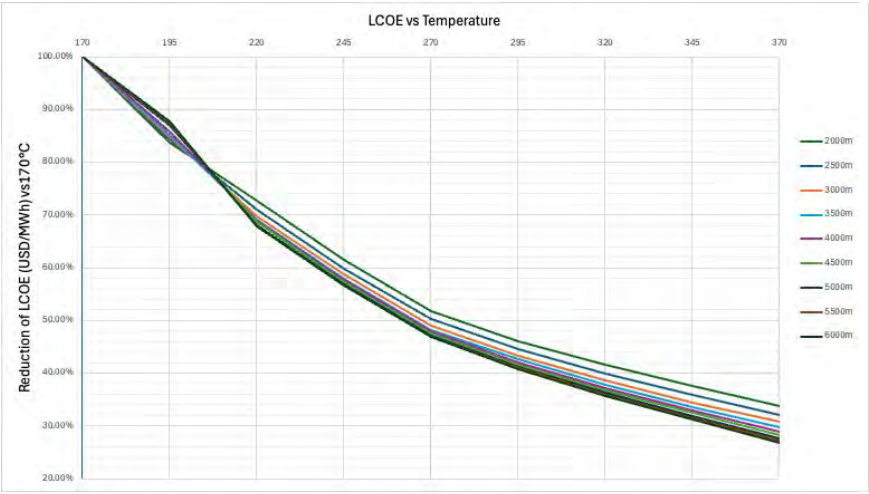

Figure 1: LCOE as a function of reservoir temperature.

Figure 1 results from modelling multiple scenarios and then normalizing for the levelized cost of electricity (LCOE) produced. What is clear is that the normalized curves follow a very consistent pattern. They show a substantial decline in LCOE as a result of temperature for the EGS systems

that we modelled using GETEM. Although the results are not shown here, increasing temperature has a similar impact on AGS system economics.

Compared with 170°C, increasing the reservoir temperature to 210°C will reduce the LCOE by approximately 25%. Increasing the reservoir temperature further to 300°C reduces LCOE by 65-75%. This reveals very powerful economic value that could be realised by drilling deeper and hotter wells.

2. The growth, and then stall, of drilling temperature capability

If we step back to the last century, when MWD tools were first introduced, the temperature ratings were driven by the rating of commercially available electronic components. In 1978, the first commercial MWD system was introduced with a temperature rating of 85°C. By 1996 a commercial MWD had been released with a temperature rating of 175°C, and others followed by 2001. So, in less than 20 years, the industry gained 90°C of capability and the ability to drill the majority of oil and gas reservoirs.

In a Journal of Petroleum Technology article written by Robin Beckwith in 2013, Baker Hughes' Robert Estes stated that 200°C is the new target: "high temperatures in the oil field seem to go in jumps of 25°C and these jumps may take 10 years". However it's been more than 10 years since that article was written and we haven't seen a 25°C jump yet.

Effectively, progress seems to have stalled since the turn of the century.

Even the apparent temperature capability of the tools that the oil and gas industry has got used to using are not necessarily all that they seem. Research based on operations in a high temperature field in North America shows that while MWD failures show a correlation with temperature, they tend to occur a long way below the 175°C temperature rating of the tools.

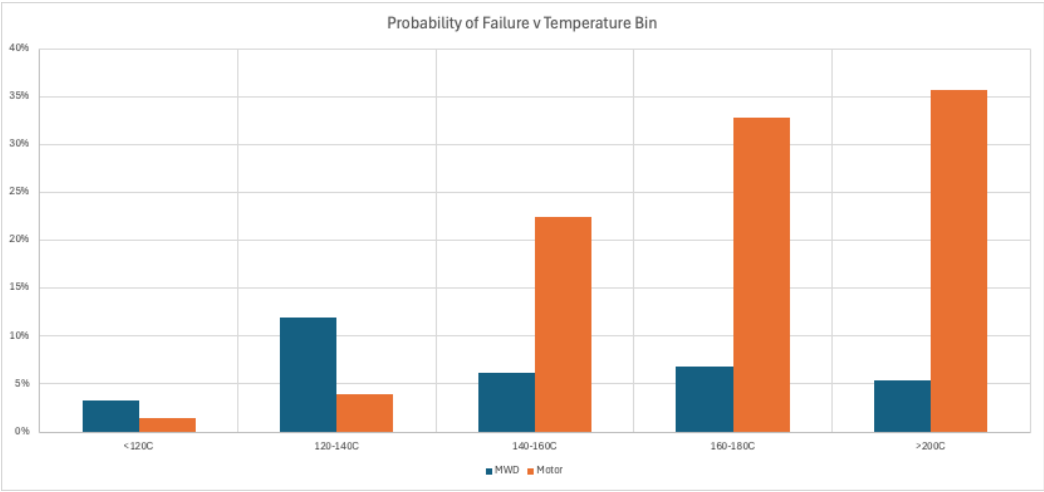

Figure 2: Probability of run terminating failure as a functional temperature.

It can be seen from figure 2 that MWD failures pick up between 120°C and 140°C. They appear to fall away above 140°C, but the reason for this is because the motors used to drill these wells, having significant elastomeric content, tend to fail in this range. These motor failures then mask MWD failures because the data plotted is based on the reason for pulling out of hole. Therefore, a

rapid motor failure could hide an incipient MWD failure. This strongly suggests that the electronics used in existing MWD and RSS tools for oil and gas drilling is going to be difficult to apply to the higher temperatures required for unconventional geothermal.

3. What about mitigating technologies?

Of course, there is a difference between the circulating temperature to which drilling tools are normally exposed and the reservoir temperature. This is because drilling mud coming from the surface tends to be cooler and picks up a limited amount of heat on its way downhole. In theory, this means that drilling equipment can be protected from the worst temperature excesses of the downhole environment.

Innovations including coated drill pipe, insulated drill pipe, and mud chillers on the surface, can enhance this effect further. Chillers can reduce the temperature of the fluid being introduced to the well and the insulated pipe can keep it colder for longer. However, there is a growing recognition that these complementary technologies are not a complete solution to high temperature drilling. A recent report produced for the Clean Air Task Force suggested that a hybrid solution incorporating mud chilling, insulated or possibly just coated pipe, and high temperature electronics would be the best way forward. This is partly because this combination will allow drilling tools rated up to 300°C to work in much deeper, super-hot reservoirs. It is also in no small part because, at risk of stating the obvious, because cooling fluids that are colder than the reservoir temperature will only keep tools cool while the mud is flowing.

Figure 3 shows mathematical modelling of the heating and cooling of an MWD tool in a high temperature well during and after a connection. The exact values have been redacted for confidentiality reasons, but the pattern is clear. During the six minutes it takes to make a connection, a tool will gain significant heat and its temperature will rise. It is possible to protect a tool against temperature rise during a connection, but any mitigation that is put in place will likely involve insulation, and the same insulation then traps the heat gained inside the tool after the connection is completed. Once circulation recommences, the rate of temperature loss is much lower than the rate at which the tool gained temperature, and it can take perhaps twenty minutes for the tool to recover to the circulating temperature. This makes it very difficult for cool mud and drill pipe installation to protect tools in deeper, hotter wells.

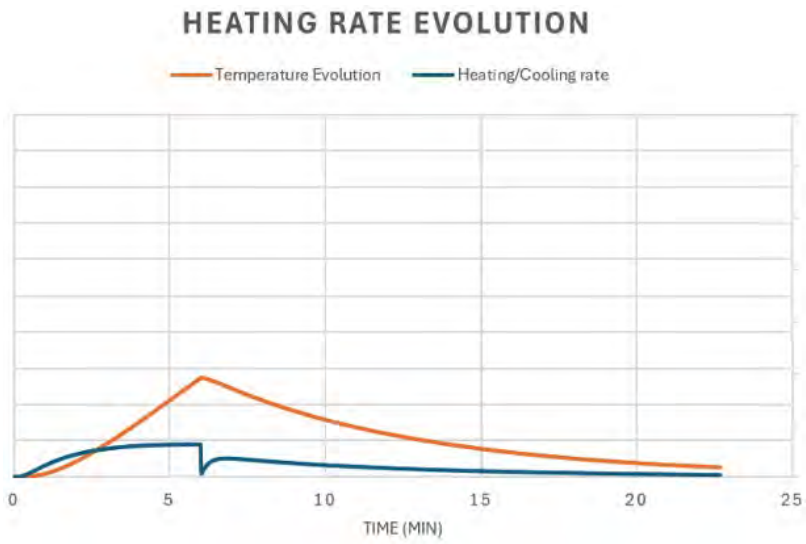

Figure 3: Temperature evolution during a connection.

A second problem is encountered when running into a hot well to get the drill bit and the bottom hole assembly (BHA) to the bottom of the hole. There is no circulation while running in hole and so any tool in the drilling assembly will be exposed to mud which has likely been heated to reservoir temperature. It is possible to mitigate this using a technique known as staging (see for example Javay *et a*l, 2020), whereby a tool is run into the hole until it approaches its temperature limit, and then fluid is temporarily circulated in order to decrease the bottom hole temperature and to cool the tool down. This process then repeats until the tool gets to bottom. It is not unusual for this to add as much as a day to operations when running into deep, hot wells. Increasing the survival temperature for the electronics and sensors on board the drilling tool would significantly reduce the amount of staging required.

Insulation of downhole tools combined with cooling has also been tried, but generally for entire systems.

One case history is DESCRAMBLE, or “DEep Super CRitical AMBients of continentaL Europe”. (Vedum et al, 2017) This project was funded by the European Union and managed by SINTEF in Oslo, Norway. It built a logging tool specified to 450°C using components rated between 200°C and 300°C in addition to a dewar type heat shield. But it was only rated for eight hours operation. It was tested in a 250°C geothermal well in Lardarello, Italy and yielded some useful insight into the behaviour of the electronic components we will need at high temperature.

Another is a logging while drilling (LWD) tool created for the IDDP-2 well in Iceland. In 2018, Stefánsson *et al* described a 300°C system which included a relatively standard, 175°C capable MWD that was put into a flask and kept cool using phase change materials. The requirement here was for 50 hours operation. There is no published record of the tool being used downhole, but the reference describes successful laboratory test results.

Both examples just shown illustrate the use of insulation and cooling systems to protect electronics. As we push for higher and higher operating temperatures, it is likely that some type of cooling will be necessary. However, it might not be necessary to cool the entire tool, as was attempted here, and the paper will return to this.

4. High temperature electronics technologies

As far as the oil and gas drilling industry is concerned, the approach to high temperature electronics has traditionally been one of screening and selection (Beckwith, 2013), whereby components that might not be rated to the operating temperature of the tool are screened to see which, and how many, of any design will survive at higher temperature. The evidence would seem to suggest that this approach cannot get us reliably beyond 200°C .

A few oil and gas manufacturers have managed to get drilling tools close to this temperature, for example Weatherford's 200°C rated logging while drilling (LWD) tool.

To get to this temperature, designers have used application specific integrated circuits (ASICs) or multi-chip modules (MCMs). These technologies can certainly help, for example MCMs offer high density for improved electrical performance with a reduced amount of substrate material. The significantly reduced size and aspect ratio of these components can also make them very effective in high shock and vibration environments.

Unfortunately this design approach can be expensive with very high non-recurring engineering (NRE) charges. This can make it hard to use them for projects where there is likely to be a low volume, for example, high temperature MWD and RSS tools.

A better approach in the short term is likely to use discrete components either selected for the temperature resistance or protected from the temperature, as this is a much more economical way of building small quantities of tools.

Materials science and pressure from other industries (notably aerospace and deep space) are driving demand for higher temperature components. Most notably, see NASA's Venus Rover program and its specification of 480°C! In the future we might expect to see fully depleted Silicon on Oxide (FD-SOI) substrates become available. This technology will lower parasitic capacitance and will significantly reduce leakage currents, and is expected to be good to 300°C with only small changes to existing manufacturing processes. It has a high Technology Readiness Level (TRL) but has historically been difficult to get in small quantities. As the industry grows, it might be possible to interest manufacturers, but this is not a solution for the next few years.

Group III to V semiconductors (based on alloys containing elements from group III and V in the periodic table) will potentially work to 500°C but these are years away from being ready for prime time.

5. A new approach to downhole, high temperature electronics

This paper will now describe a different approach to high temperature electronics.

The approach is based on three key requirements:

- Protect the assembly from the external borehole temperature
- Protect components from themselves and efficiently and quickly remove the heat that the components generate internally
- Take the rejected heat from the components to a place where it will do no harm.

Dewar, or Thermos, flasks can be used to provide protection from the external environment but can be problematic in that they prevent the internal heat from escaping. So, they must be used with care. Heat needs to be removed as well as repelled. Components do not just have to be protected from the environment – they also must be protected from themselves and the heat they generate.

A lot of thought must go into how to get heat away from the components quickly and into places where the heat will do no harm. For lower temperatures, this can be as simple as conducting it into the drilling mud flowing past the tool. For higher temperatures, other strategies may be required including cooling technologies. A board design and mounting scheme is needed that can work in either case.

Figure 4 shows a new generation, high temperature circuit board. Unlike the boards used in almost all RSS, MWD and LWD tools, it is not a long, thin rectangular shape designed to run the length of an electronics chassis or insert.

Instead, it is relatively small, and circular, and surrounded by a thermally conductive ring which serves to take the heat away rapidly as part of a “thermal superhighway”. This affords significant advantages. It means that no individual component is far from the “superhighway”. It allows for optimisation of the axial and radial location of components in the assembly. The shape of the boards promotes radial transport of heat as the effective thermal resistance reduces as the heat flows from the centre of the board.

This arrangement also means that boards can be combined in a modular architecture for thermal management (see below). And the resonant frequency of the resulting board is very high, much higher than conventional RSS/MWD/LWD boards, which will be of use in the high shock and vibration environments expected in deep geothermal wells.

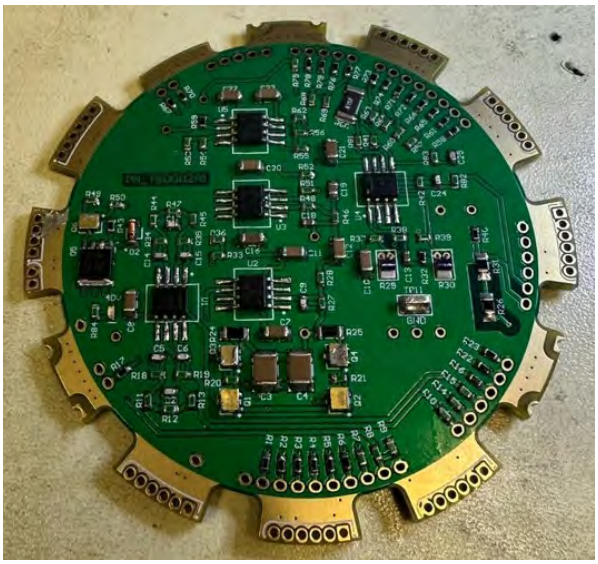

Figure 4: High temperature printed circuit board.

Individual circular boards are stacked together, a bit like potato chips in a tube, to create subassemblies of a handful of boards. The subassemblies are connected by steel rings which form the “superhighway”. Figure 5 shows how this is achieved.

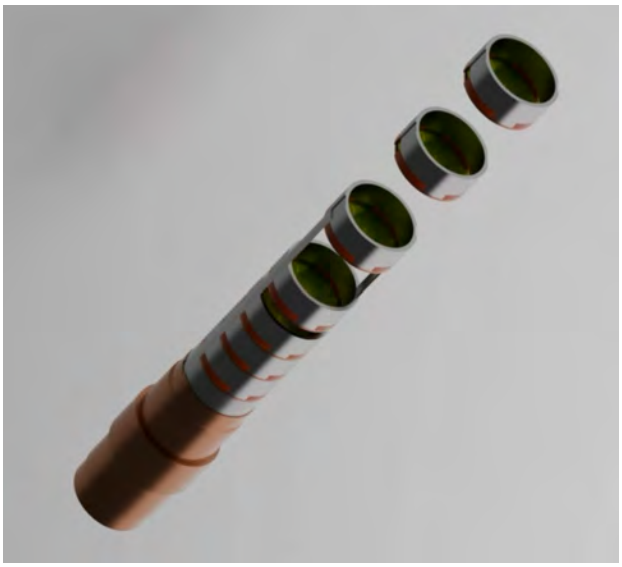

Figure 5: Stack of circular boards surrounded by "thermal superhighway".

And Figure 6 shows a close-up of an individual board with its corresponding ring element.

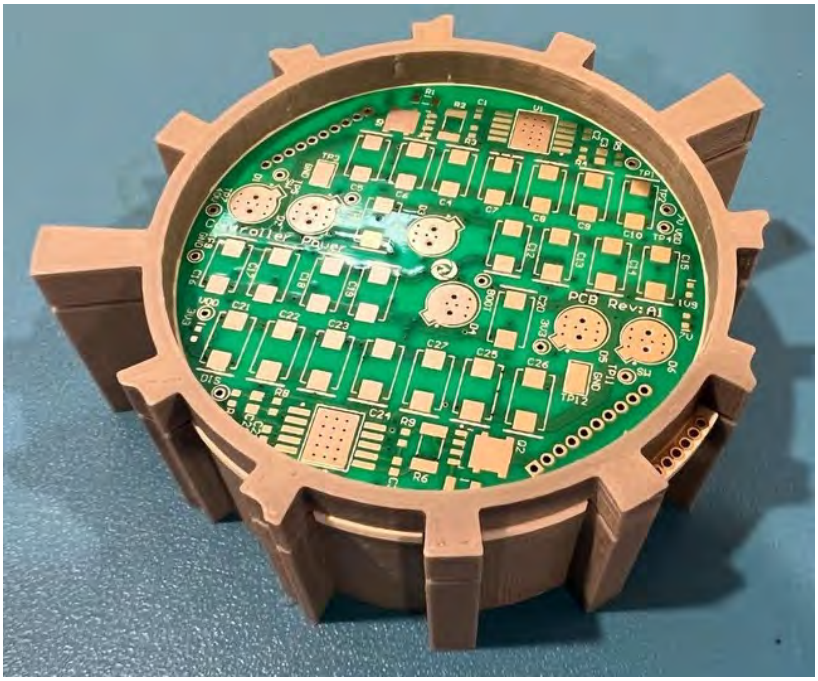

Figure 6: Individual circular board with "superhighway" ring element.

The combination of board design, materials selection and ring element design has been optimised through thermal modelling. The combination has been shown to manage the temperature of components at the centre of the board very effectively, keeping them within 2°C or less of the surrounding environment. It is worth remembering here that components have to be protected from themselves and the heat they generate. For this reason, the best that can be achieved is to get them to the same temperature as whatever medium is being used to cool them.

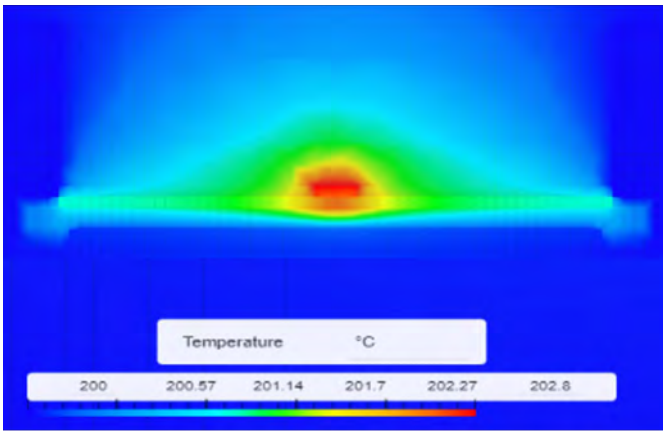

Figure 7: Thermal modelling of circuit board.

For a 210°C MWD tool, drilling mud cooling will be sufficient. Most electronic components to be used are already manufacturer rated to 210°C and the rest have successfully been repackaged in ceramic to work at higher temperatures. Test results are described in the next section.

For higher temperatures, some form of cooling will be needed. This could be by using phase change, or heat sinks, for example, but in every case the heat must be effectively transported from the board to the cooling device. The board stack described above has been designed to do this – heat generated on any board can very effectively be rejected to cooling.

Thermoelectric devices may also play a part. Thermoelectric coolers are based on a phenomenon known as the Peltier-Seebeck effect. Using this effect, heat can be removed when current is driven through a thermocouple junction. Miniature thermoelectric coolers can be placed in intimate contact with electronic devices to selectively move heat away. Currently, the reliability of commercially available devices falls off significantly at temperatures between 200°C and 220°C. Fortunately, materials developed for the space program have allowed thermoelectric devices to operate at temperatures as high as 500°C in deep space probes, which means that they could be available to us in the future.

In order for systems to remain cost effective, cooling must be used selectively. Previous projects described above have attempted to cool the whole assembly to the minimum capability of any individual component. This can work for short periods of time, however this approach can be very expensive and power hungry. An alternative approach is to build a series of small chambers and cool each to an appropriate temperature for the weakest component therein. This will avoid cooling a lot of components that do not need it and is much more efficient than maintaining the whole tool at a low temperature. The modular design described above was created with modular cooling and small chambers in mind.

6. Initial test results

Initial testing has focused on proving “the physics” for a 210°C MWD tool – that is, heat testing components and boards temperatures between 220°C and 230°C for extended periods to make sure that there are no fundamental issues there will prevent components from working – such as leakage or capacitance issues. This testing has proved successful, with components, prototype boards and downhole ready boards heat soaked at these high temperatures for over 500 hours.

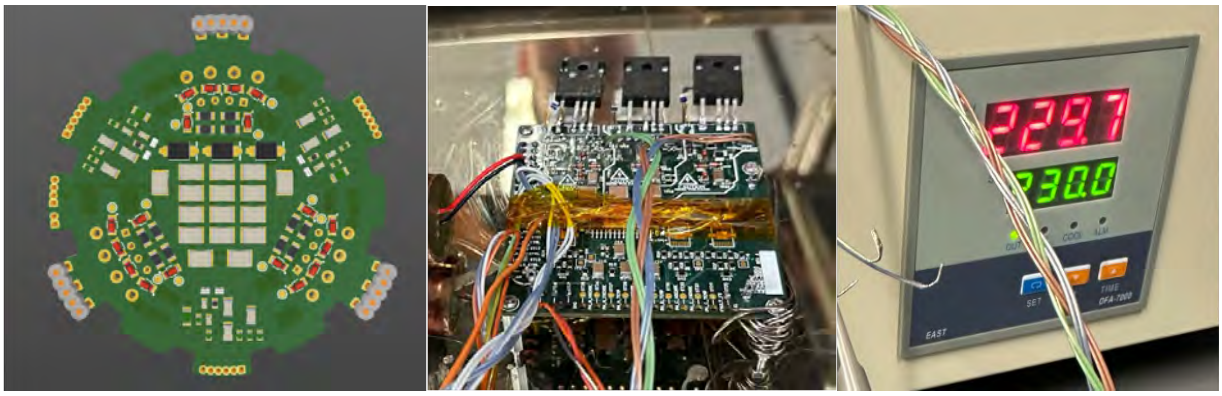

Figure 8: Three phase inverter PCB: downhole design; prototype and temperature measurement.

At the time of writing, this testing will be followed by highly accelerated life testing (HALT) of subassemblies and modules, combining temperature with shock and vibration. It will be no surprise if some issues arise during these tests, but the key point is that solving these problems is simply engineering. It doesn't require new laws of physics. Getting to reliable high temperature electronics is now simply an engineering task.

7. Conclusions

Although AGS and EGS wells have initially been drilled at wells below 200°C, developers are looking to drill much deeper and hotter, driven by substantial reductions in LCOE and improvements in economics that come with increasing temperature.

To drill the well profiles needed, the geothermal industry will need MWD and RSS tools with the ability to operate at these higher temperatures.

The temperature capability of MWD tools used in oil and gas wells grew rapidly from 85°C to 175°C at the end of the last century, but has struggled to grow since then.

Mitigating technologies like insulated drill pipe can help, but only when drilling mud is circulating. When mud circulation stops, MWD tools will heat up rapidly.

To protect electronics at high temperature, three issues need to be addressed:

- Protect the assembly from the external temperature
- Protect components from themselves by efficiently and quickly removing the internally generated heat
- Take the rejected heat to a place where it will do no harm.

A new generation of circular PCBs arranged in a stack with carefully designed thermal conductivity can address all three of these issues.

Cooling may be required for operation at high temperatures, but it is not necessary to cool the entire tool – only those components that need it.

Testing has demonstrated the ability to operate at temperatures up to and above 210°C without cooling.

Acknowledgement

The authors would like to thank the team at Hephae Energy Technology for their support and inspiration.

REFERENCES

Beckwith, R. “Downhole Electronic Components: Achieving Performance Reliability.” *Journal of Petroleum Technology*, (2013).

Brady, J. and Galley, T. “Development of the First Commercial Hot Hole MWD System.” *SPE-36432-MS* presented at the SPE Annual Technical Conference and Exhibition, Denver, CO (1996).

Department of Energy, Geothermal Technologies Office “Geothermal Electricity Technology Evaluation Model.” (2016).

Griffin, W. and Keith, F. “MWD North Sea Field Use.” *Journal of Petroleum Technology*, (1982), 2888-2898.

Hache, J. and Till, P. “New-Generation Retrievable MWD Tool Delivers Superior Performance in Harsh Drilling Environments.” *SPE-67718-MS* presented at the SPE/IADC Drilling Conference, Amsterdam, Netherlands (2001).

Javay, A. *et al.* “Mud Cooler and Chiller Packages in High-Temperature Deep Horizontal Gas Wells: A Case Study from Saudi Arabia.” *SPE-203260-MS* prepared for presentation at the Abu Dhabi International Petroleum Exhibition & Conference, Abu Dhabi, UAE (2020).

Keast, C. *et al*. “Fully Depleted Silicon-on-Insulator (FDSOI) CMOS Technology Optimized for Enhanced Geothermal System Temperature Operation” *Geothermal Resources Council Transactions Volume 46*, Reno, NV (2022) 373-379.

Kleawyothatis, T., Pruimboom, J., Dendandome, S., Pisarnbut, N., and Thipmongkolsilp, P. “Thailand Joint Development Project Delivers 200°C M/LWD Triple Combo: Eliminating Wireline, Driving World Class Efficiency and Slashing Days Per Well.” *IADC/SPE-191054-MS* presented at the IADC/SPE Asia Pacific Drilling Technology Conference, Bangkok, Thailand (2018).

Lowdon, R. and Hodder, M. “Directional & Surveying Challenges in Geothermal Well Construction.” *SLB Geothermal Webinar Series*, (2024).

NASA, “NASA Glenn Demonstrates Electronics for Longer Venus Surface Missions.” (2017).

Pink, T., Pearce, R. and Bour, D. “Bridging the Gaps: A Survey of Methods, Challenges, and Pathways Forward for Superhot Rock Drilling.” Clean Air Task Force. (2024).

Stefánsson, A. *et al* “A 300 Degree Celsius Directional Drilling System” *IADC/SPE-189677-MS* presented at the SPE/IADC Drilling Conference, Fort Worth, TX (2018).

Vedum, J., Røed, M., Kolberg, S., Hjelstuen, M., Liverud, A. and Stamnes, Ø. “Development of a Novel Logging Tool for 450°C Geothermal Wells” *Conference & Exhibition on High Temperature Electronics Network (HiTEN)* Cambridge, UK (2017).

Severe Lost Circulation Mitigation using Temperature Activated Materials

Veerabhadra S Denduluri, Maria Juenger, and Eric van Oort

The University of Texas at Austin

Keywords

Lost Circulation, Geothermal Wells, Fractures, Vugs, Viscosity, Sandstone

ABSTRACT

This paper demonstrates the effectiveness of thermally activated materials (TAMs) in managing severe to total fluid losses during geothermal (GT) well construction. The objective is to address lost circulation challenges in scenarios where conventional methods, such as the use of lost circulation pills and cement squeezes, fail to provide a satisfactory solution.

During GT drilling, severe lost circulation events frequently occur when the drilling fluid infiltrates fractured or vugular formations. The lost fluid experiences a temperature increase in the fractures and vugs due to the exposure to higher in-situ formation temperature with invasion depth. This temperature rise can be strategically utilized to seal the fractures or vugs. If TAMs are inherently present in the lost fluid, they can alter the viscosity, increasing it and making the fluid harder to displace, thereby preventing further fluid losses. This study examines the inclusion of TAMs in fluid formulations for use in targeted cement squeeze jobs.

Several types of TAMs have been identified and evaluated in different fluid formulations. To validate the effectiveness of TAMs, fracture plugging tests were conducted. Fluid formulations with TAMs were circulated through the sample, and their plugging behavior was observed and quantified. The resulting samples were then visualized using CT scans. These tests demonstrated that TAMs effectively sealed the fractures, providing robust evidence of their ability to mitigate fluid losses and the efficacy of the thermal activation mechanism. TAMs are novel materials that can be engineered to mitigate severe losses in GT wells, where lost circulation is one of the crucial challenges.

1. Introduction

High-temperature geothermal (GT) wells are being constructed more frequently due to their ability to provide reliable and sustainable energy. However, lost circulation remains one of the key factors contributing to non-productive time (NPT) in the GT well construction (Blankenship et al., 2005). When lost circulation events occur, GT drilling companies must address them before resuming drilling, which significantly increases well construction costs. These events represent up to 10 to 20% of well construction costs and sometimes even exceed 20% for exploration wells (Finger and Blankenship, 2010). The selection of remediation techniques in managing fluid losses is mostly based on trial and error (Alsaba et al., 2014) and this approach may not be ideal for GT wells due to the currently small number of wells being drilled, making it essential to get it right the first time. For example, a study conducted on fifteen GT wells in Japan revealed no clear trend between the success or failure rates of lost circulation materials with respect to depth and temperature (Hyodo et al., 2000). This lack of a definitive pattern leaves significant room for assumptions and highlights the need for a more systematic approach to address lost circulation.

In GT wells, cement squeeze jobs are commonly employed to address severe fluid losses in the formation. However, these jobs have a high failure rate, reaching up to 80% (Cole et al., 2017). Multiple squeeze jobs are typically needed to seal fractures effectively, yet the overall probability of success remains below 50% (Magzoub et al., 2020). This emphasizes the need for a more reliable method with a higher likelihood of success. Traditional lost circulation materials, including fibrous (e.g., mica, cellulose), granular (e.g., nut shells), and flake (e.g., cellophane) types, are commonly used to manage lost circulation (Alsaba et al., 2014). Although effective in some situations, their performance in GT wells is inconsistent due to the presence of high-temperature conditions. These materials eventually lose their structural integrity, failing to properly seal fractures or vugs (Magzoub et al., 2020).

Several researchers have investigated epoxy and polyester-based resins to determine their effectiveness in establishing a durable seal that is capable of withstanding thermal stresses. However, these resins lose their sealing capability once they encounter 200°F (Saleh et al., 2020; Loeppke et al., 1990), making them unsuitable for higher temperatures. Thus, developing a tailored solution for lost circulation control is essential for the economic GT well construction, especially to tackle severe losses.

This paper will demonstrate how thermally activated materials (TAMs) are suitable for managing severe lost circulation events in GT wells. The fluid formulations are designed to take advantage of the temperature difference between the wellbore and the fractures or vugs. By leveraging this temperature variation, we aim to show how TAMs can effectively seal fractures or vugs and control fluid losses.

2. Materials and Experimental Methods

2.1 Cementitious Materials

Two types of cementitious materials were utilized in this study to develop fluid formulations: Ordinary Portland Cement (OPC) and Class F Fly Ash (FA). The oxide compositions of these materials, expressed as mass percentages, are shown in **Table 1**. The OPC and FA were obtained from Texas Lehigh Cement Company and SEFA Group, respectively.

Table 1: Chemical composition of cementitious materials used in this study.

Material	Content (%)								
	Al_2O_3	SiO_2	Fe_2O_3	CaO	MgO	SO_3	Na_2O	K_2O	Loss on ignition
OPC	5.30	20.80	6.33	61.70	1.30	2.60	0.57	0.50	0.90
FA	27.40	54.10	9.62	1.70	1.00	0.20	2.35	2.51	1.12

2.2 TAMs

Four distinct types of TAMs were identified and used in this study, as shown in **Table 2**. These belong to the categories of polymers, salts, and non-polar materials. For the OPC-based fluid formulations, which were prepared with a water-to-solid ratio of 0.385, TAMs were incorporated. For the FA-based fluid formulations, different alkaline activators were added to create geopolymers or alkali-activated materials, with a water-to-solid ratio of 0.35.

Table 2: TAMs and their properties.

Material	Family	Color and State	Specific Gravity
TAM 1	Polymer	Opaque brown liquid	1.012
TAM 2		Clear liquid	1.005
TAM 3	Non-polar material	Brown liquid	1.019
TAM 4	Salt	White powder	1.200

2.3 Rheology and Mechanical Properties

The rheological profiles of fluid formulations are critical in assessing the effectiveness of TAMs. For temperatures below 200°F, a rotational viscometer was employed to obtain these profiles. At temperatures exceeding 200°F, a High-Pressure High-Temperature (HPHT) Consistometer was used to evaluate the fluid consistency profile, which is related to the fluid's rheology. Compressive

and tensile strength tests were conducted to evaluate the mechanical behavior of TAMs once they enter fractures or vugs.

2.3.1 Rheology and Consistency

Rheological profiles as a function of temperature were obtained using a Couette coaxial cylinder rotational oilfield viscometer, following the guidelines of API RP 10B-2 (2010). The fluid was subjected to a constant shear rate of 150 rpm and the temperature was gradually increased from surface temperature (73°F) to 200°F.

Fluid consistency tests were performed using an HPHT Consistometer, where the temperature was gradually increased from 73°F to 350°F over 90 minutes. The pressure was initially set at 1000 psi and progressively increased to 3000 psi during this period. The fluid was subjected to a constant shear rate of 150 rpm throughout the test. When the fluid achieves a Bearden consistency (Bc) value of 70, it is considered non-displaceable, indicating its ability to mitigate further fluid losses.

2.3.2 Compressive and Tensile Strength

Three cylindrical samples (4 inches in length and 2 inches in diameter) of the fluid formulations were cured for one day at the temperature expected in the fractures. Compressive strength was estimated using Equation 1, following ASTM C39/C39M (2021), with a ramp rate set at 48 psi/sec. Tensile strength was calculated using Equation 2, with a ramp rate set at 12 psi/sec, following ASTM C496/C496M (2017).

$$Compressive\ strength(psi) = \frac{F}{A} \quad \text{..... (1)}$$

$$Tensile\ strength\ (psi) = \frac{2F}{\pi LD} \quad \text{..... (2)}$$

F represents the load at failure (lbf), A is the cross-sectional area (in^2), L is the length of the sample (in), and D is the diameter of the sample (in).

2.3.3 Fracture Plugging Tests and CT Scans

The fracture plugging tests were conducted using the setup illustrated in **Figure 1**. A cylindrical sandstone sample with a fracture size of 0.25 inches / 0.63 cm was used, and it was equipped with a heating jacket to provide the necessary heat. After incorporating the TAMs into the fluid formulations (at temperature T1), the fluids were circulated through the fracture in the pre-heated sandstone sample, which was heated to match the temperature (T2) that the fluid would encounter in a GT well fracture. A collector was placed beneath the sandstone sample to gather any passing fluid. If a significant amount of fluid was collected, the formulation was considered ineffective for plugging the fractures. On the other hand, if only a minimal amount of fluid was collected, the formulation was considered highly effective at sealing the fractures. The sandstone samples were then examined using CT scans to visualize the plugging behavior of the formulations.

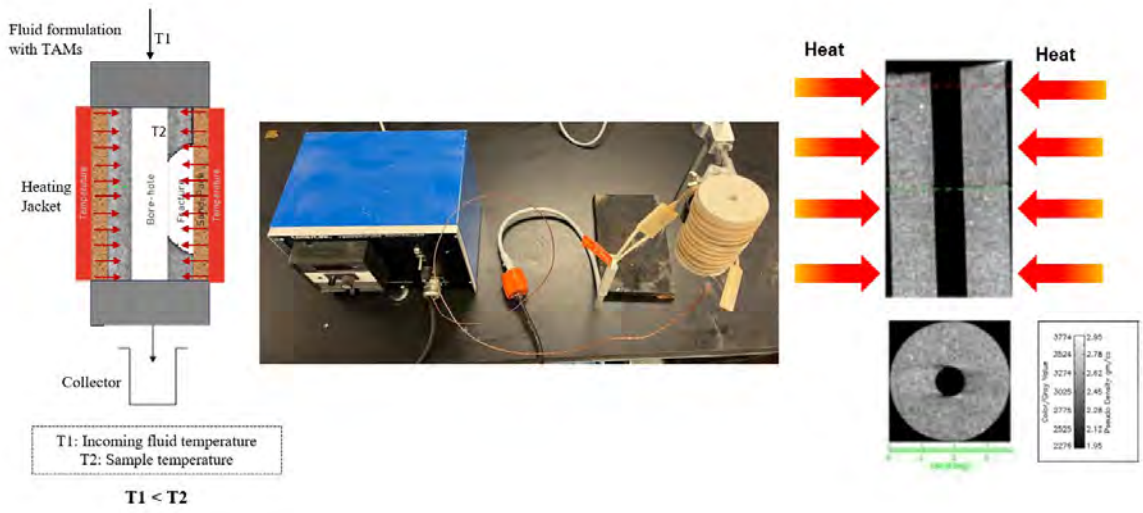

Figure 1: Fracture Plugging Test Setup. All sandstone samples were heated to the target temperature and allowed to equilibrate for 30 minutes before initiating fluid circulation.

3. Experimental Results and Discussion

During circulation, drilling mud or cement formulations encounter the bottom hole circulating temperature (BHCT) in the wellbore. However, once entering fractures or vugs, the formulations quickly experience the bottom hole static temperature (BHST), which is higher than the BHCT due to the natural GT gradient. This temperature contrast is exploited in this study which can help seal the fractures or vugs in GT wells. Denduluri et al. (2024) demonstrated this effect using a thermo-hydraulic simulation in a Utah Forge GT well, where the BHST of 315°F contrasts sharply with a BHCT as low as 200°F. The core idea is that when TAMs are incorporated into the fluid formulations, the mixture remains in a liquid state in the near wellbore region. However, upon entering the fractures or vugs, it undergoes a phase change, becoming highly viscous or solid, effectively sealing the fractures. These temperature conditions are crucial for understanding and designing TAMs for different GT wells.

Low and Medium-Temperature Plugging Solution

TAMs 1, 2, 3, and 4 were incorporated into the OPC fluid formulations and tested for viscosity as a function of temperature, as shown in **Figures 2 and 3**. The results were compared to the viscosity of the OPC fluid formulation (without TAMs), the standard choice for cement squeeze operations in GT wells. The viscosities of formulations with TAMs 1, 2, 3, and 4 displayed a sharp increase at various temperatures known as trigger temperatures. For example, 5% TAM 1 demonstrated an increase in viscosity at 184°F. In contrast, the viscosity of the OPC formulation remained steady without significant changes, highlighting why many cement squeeze jobs fail. The viscosity increases caused by TAMs upon entering fractures can be highly effective in mitigating fluid

losses. By adjusting the concentration of TAMs in the fluid formulations, the trigger temperatures can be effectively modified, which is beneficial for developing solutions tailored to a variety of GT wells. These formulations are particularly suitable for shallow GT wells where the temperatures encountered are not extremely high.

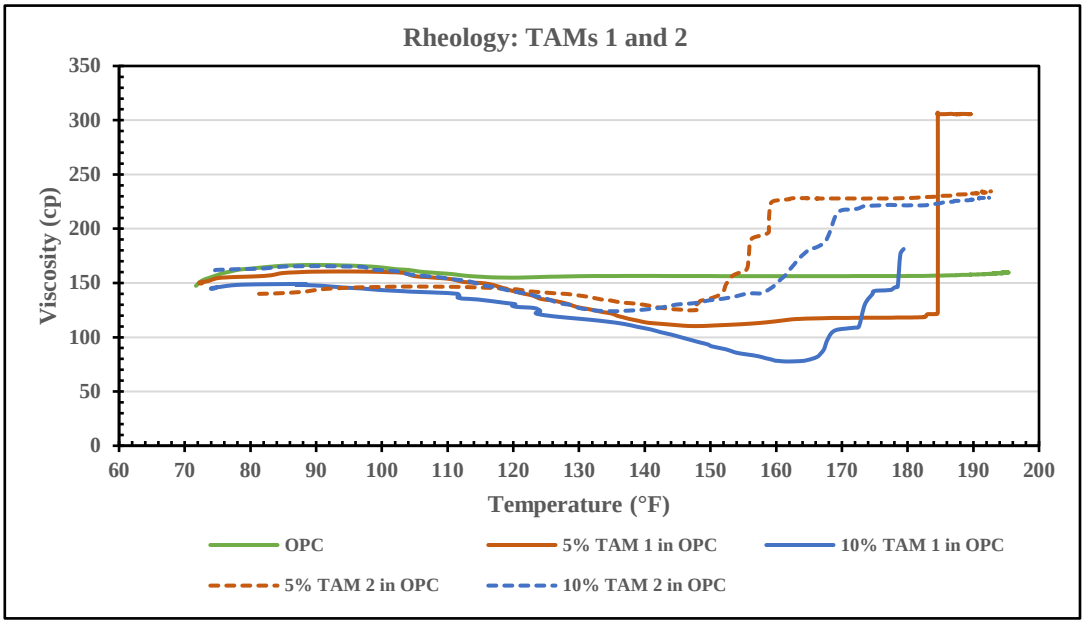

Figure 2: Rheology profiles of fluid formulations with TAMs 1 and 2. When viscosity increases and flatlines after reaching the trigger temperature, the formulation is no longer pumpable.

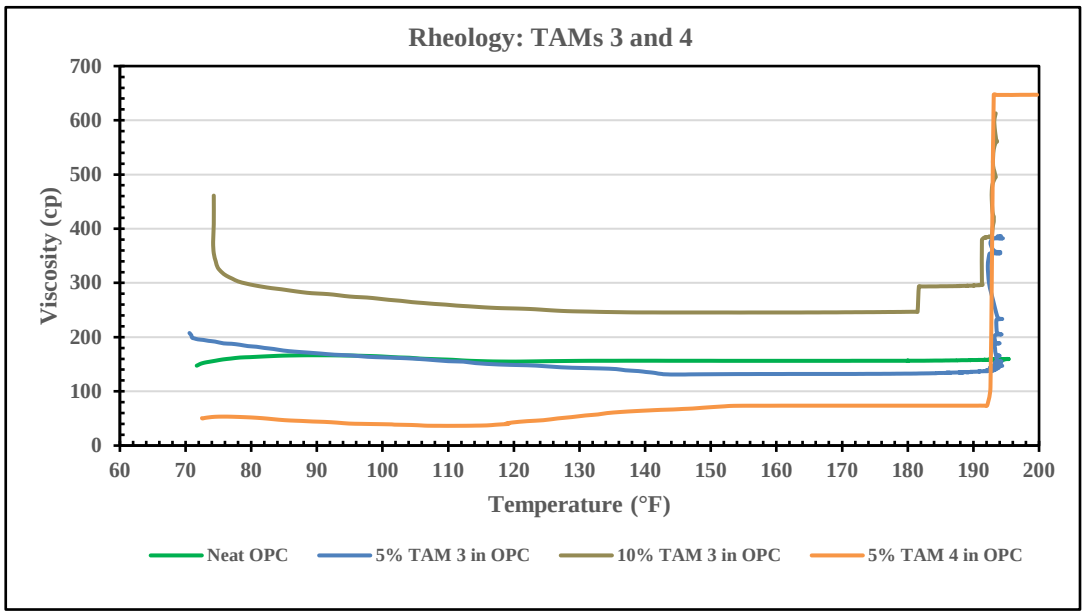

Figure 3: Rheology profiles of fluid formulations with TAMs 3 and 4. When viscosity increases and flatlines after reaching the trigger temperature, the formulation is no longer pumpable.

High-Temperature Plugging Solution

A high-temperature plugging solution for GT wells can be found in the geopolymer family. Unlike OPC, which is susceptible to acid gases such as CO_2 and H_2S commonly encountered in high-temperature GT wells, geopolymers provide high resistance to these gases (Khalifeh et al., 2018). Thus, geopolymers can be explored for lost circulation control purposes in GT wells. Geopolymers have been researched for their application as a high-temperature cementing material, displaying excellent thermal stability and superior casing-cement bond strength (Denduluri et al., 2023; Ogienagbon et al., 2023). In this study, FA was used as a cementitious material (aluminosilicate source), and different alkaline activators were utilized to create the geopolymer formulations. HPHT consistometer was used to evaluate the consistency of the formulation as a function of temperature, as shown in **Figure 4**. Two high-temperature plugging systems were developed, displaying trigger temperatures of 262°F and 362°F, respectively. These fluid formulations become effectively non-pumpable or non-displaceable at temperatures exceeding 262°F and 362°F, making them highly suitable for deep GT wells.

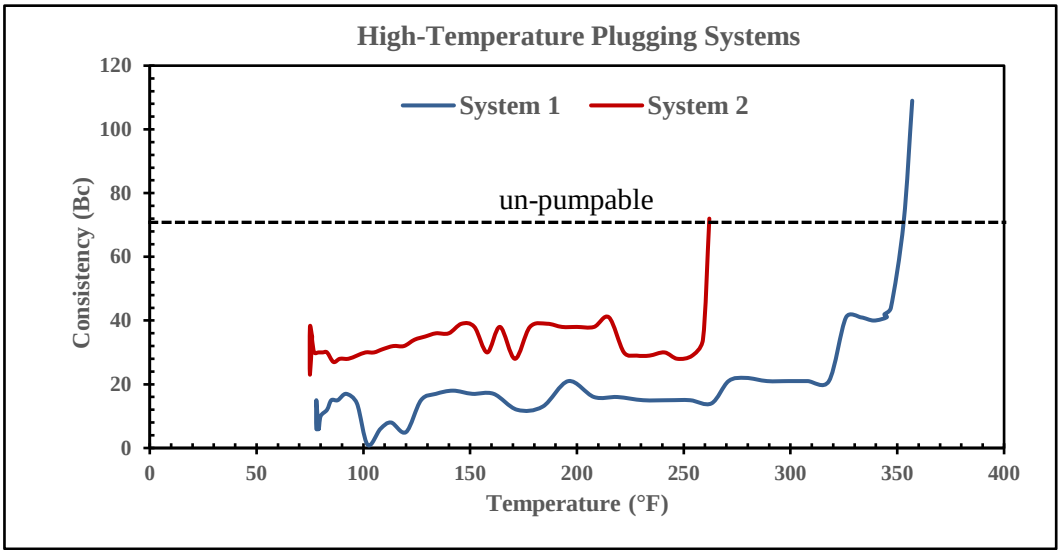

Figure 4: High-temperature plugging systems for lost circulation control in GT wells. The formulation is considered no longer pumpable once the consistency reaches a value of 70 Bc.

Mechanical Properties

The compressive and tensile strength values of fluid formulations with TAMs 1, 2, 3, and 4 are presented in **Figure 5**. These formulations were cured at 180°F for one day to estimate their strength. This information provides insight into the appropriate timing for resuming GT drilling operations to avoid further fluid losses after a cement squeeze job. The lost fluid needs substantial compressive and tensile strength to maintain mechanical integrity within the fractures or vugs. The values in Figure 5 demonstrate that the mechanical integrity of the fluid formulations developed in this study will be well-preserved, which ultimately helps in controlling fluid losses. On the other

hand, traditional materials, such as cellulosic/fibrous materials used for controlling lost circulation exhibit poor mechanical performance (Lin et al., 2024).

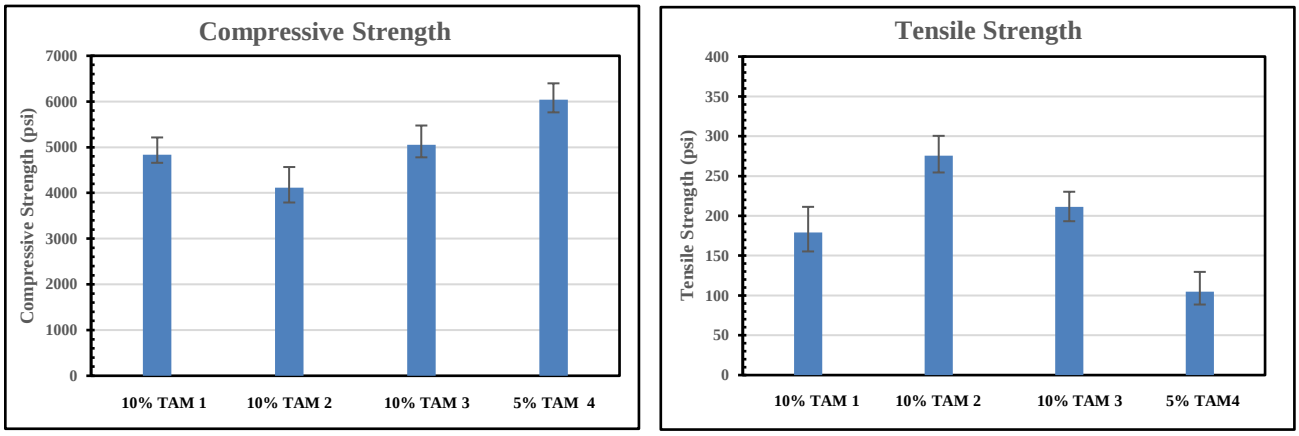

Figure 5: Mechanical properties of the fluid formulations with TAMs.

Fracture Plugging Test and CT Scans

The sandstone sample was pre-heated to the trigger temperatures indicated in Figures 2 and 3, after which the fluid formulations with TAMs were circulated through the borehole. When the OPC fluid formulation (conventional formulation used in GT wells) was circulated, 80% of the fluid was collected in the bottom collector. In contrast, for the OPC fluid formulations with TAMs 1, 2, 3, and 4, no fluid was collected at the bottom. This indicates that the fluid completely plugged the borehole in the sandstone sample, demonstrating the thermal activation mechanism of TAMs 1, 2, 3, and 4. Following these tests, CT scans of the sandstone samples revealed that the borehole was predominantly plugged, with invasion depths illustrated in **Figure 6**. TAMs can be utilized for cement squeeze jobs to effectively seal fractures or vugs in different formations within GT wells.

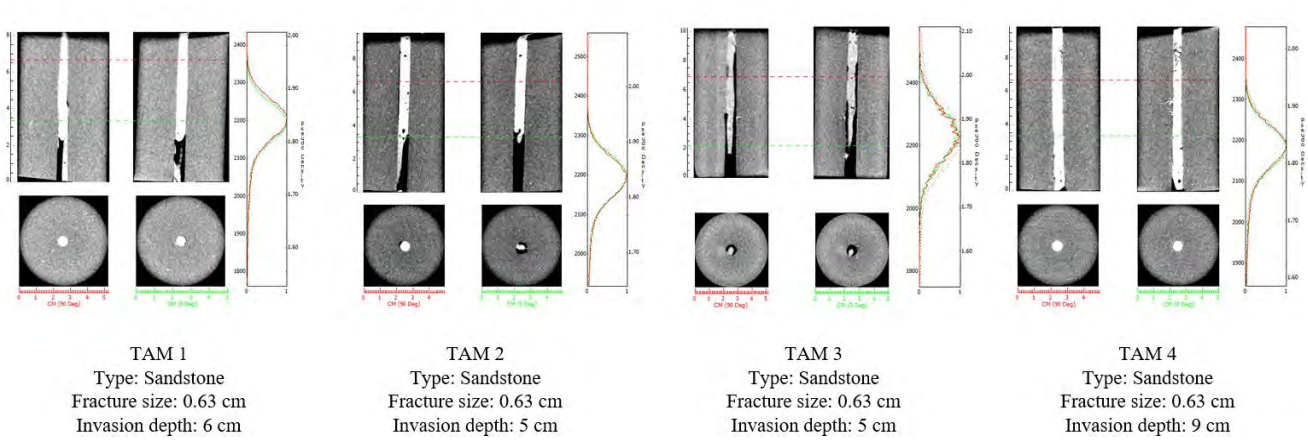

Figure 6: CT scans of sandstone samples circulated with fluid formulations containing TAMs 1, 2, 3, and 4 show that the borehole is effectively plugged, arresting further fluid losses.

4. Conclusions

This paper showcases the feasibility of using TAMs to address lost circulation challenges in GT wells. By leveraging the temperature contrast between the wellbore and fractures or vugs, fluid formulations with TAMs are designed to undergo a phase change, becoming highly viscous or solid, effectively sealing the fractures or vugs. This approach heavily relies on precise temperature modeling, which is essential for developing tailored solutions for different wells. Fluid formulations can be customized for different geological formations and GT gradients or depths. The compressive and tensile strengths of TAMs demonstrate their ability to maintain structural integrity within fractures or vugs. Fracture plugging tests and post-test CT scans also confirmed the effectiveness of TAMs in sealing fractures. Implementing TAMs in fluid formulations offers a promising solution for reducing well construction costs and NPT associated with lost circulation in GT wells.

Acknowledgments

We are very thankful to the members of the Rig Automation and Performance Improvement in Drilling (RAPID) research consortium for their guidance and financial support. We also extend our thanks to Akshay Thombare and Munir Aldin for their support.

REFERENCES

Alsaba, M., Nygaard, R., Saasen, A., and Nes, O.M. Laboratory evaluation of sealing wide fractures using conventional lost circulation materials. SPE Annual Technical Conference and Exhibition, Amsterdam, The Netherlands. (2014).

Alsaba, M., Nygaard, R., Hareland, G., and Contreras, O. Review of lost circulation materials and treatments with an updated classification. In AADE National Technical Conference and Exhibition, Houston, TX, USA. (2014).

API RP 10B-2. Recommended practices for testing well cements. American Petroleum Institute. (2010).

Arshad, U., Jain, B., Ramzan, M., Alward, W., Diaz L., Hasan, I., Aliyev, A., and Riji, C. Engineered solution to reduce the impact of lost circulation during drilling and cementing in Rumaila Field, Iraq. International Petroleum Technology Conference, Doha, Qatar. (2015).

ASTM C39/C39M. Standard test method for compressive strength of cylindrical concrete specimens. American Society for Testing and Materials, West Conshohocken, Pennsylvania, USA. (2021).

ASTM C496/C496M. Standard test method for splitting tensile strength of cylindrical concrete specimens. American Society for Testing and Materials, West Conshohocken, Pennsylvania, USA. (2017).

Blankenship, D.A., Wise, J.L., Bauer, S.J., Mansure, A.J., Normann, R.A., Raymond, D.W., and LaSala, R.J. Research efforts to reduce the cost of well development for geothermal power generation. In Proceedings of the ARMA US Rock Mechanics/Geomechanics Symposium, Anchorage, Alaska, USA. (2005).

Cole, P., Young, K., Doke, C., Duncan, N., and Eustes, B. Geothermal drilling: A baseline study of nonproductive time related to lost circulation. In Proceedings of the 42nd Workshop on Geothermal Reservoir Engineering, Stanford University, California, USA. (2017).

Denduluri, V., Thombare, A., Aldin, M., Juenger, M., and van Oort, E. Thermally activated lost circulation mitigation of severe losses in fractured and vugular Formations. SPE/IADC International Drilling Conference and Exhibition, Galveston, Texas, USA. (2024).

Denduluri, V., Ulerio II, George., Genedy, Moneeb., Juenger, Maria., and van Oort, E. Experimental investigation of geopolymers for application in high-temperature and geothermal well cementing. SPE/IADC International Drilling Conference and Exhibition, Stavanger, Norway. (2023).

Finger, J., and Blankenship, D. Handbook of best practices for geothermal drilling. Sandia National Laboratories, Albuquerque, NM, USA. (2010).

Hyodo, M., Kitao, K., and Furukawa, T. Development of database system for lost circulation and analysis of the data. World Geothermal Congress, Japan. (2000).

Khalifeh, M., Hodne, H., Saasen, A., Dziekonski, M., and Brown, C. Bond strength between different casing materials and cement. SPE Norway One Day Seminar, Bergen, Norway. (2018).

Lin, C., Xu, Q., Han, L., Li, G., He, H., Zhou, H., and She, J. Fracture sealing performance of granular lost circulation materials at elevated temperature: A theoretical and coupled CFD-DEM simulation study. *Petroleum Science* **21** (1): 567-581. (2024).

Loeppke, G. E., Glowka, D. A., and Wright, E. K. Design and evaluation of lost-circulation materials for severe environments. Journal of Petroleum Technology, 42(3), 328-337. (1990).

Magzoub, M. I., Salehi, S., Hussein, I. A., and Nasser, M.S. Loss circulation in drilling and well construction: The significance of applications of crosslinked polymers in wellbore strengthening: A review. *Journal of Petroleum Science and Engineering*, 185, 106653. (2020)

Ogienagbon, A., Korsnes, R. I., Khalifeh, M., Wu, Y., and Salehi, S. Performance of geopolymers in geothermal wells. 57th U.S. Rock Mechanics/Geomechanics Symposium, Atlanta, Georgia, USA. (2023).

Saleh, F., Teodoriu, C., and Ezeakacha, C. Geothermal drilling: A review of drilling challenges with mud design and lost circulation problem. 45th Workshop on Geothermal Reservoir Engineering, Stanford University, California, USA (2020).

Driving Down Exploration Costs in Geothermal Through Core Drilling

Joshua Gossanyi[1], Steve Schneider[2], John Tuttle[3], Robin Zuza[1], Bryan Ott[1], Drew Spake[1], Emma-Katherine Kluge[1], Adrian Wiggins[1], Shaun Fleming[2], Josh Nordquist[1], Simon Webbison[1]

[1]Ormat Technologies Inc.

[2]Major Drilling Group International, [3]Sinclair Well Products and Services

Keywords

Core, drilling, coring, slim-hole, performance, learning, curve, reduction, cost, days vs depth, campaign

ABSTRACT

Exploration drilling is key to answering critical resource questions. Projects can appear uneconomic before a resource is understood if sunk exploration costs are too high, thus low-cost exploration is key to growth. The importance of reducing early exposure is becoming more relevant as the data set from extensive drilling campaigns in the 1970's and 1980's has been consumed. Available levers to reduce exploration cost typically require a compromise in scope.

The utilization of small diameter drilling, primarily using mining technology has been attempted in the past by multiple operators where this technique has traditionally failed to significantly reduce cost while delivering adequate scope. A recent drilling campaign has demonstrated an 85% campaign cost reduction utilizing wireline coring on a mining rig, resulting in significant reduction in total exploration spend. This campaign has reached a technical limit with high reliability and low non-productive time (NPT) forcing the team to investigate more novel ways of working to drive further gains. Sufficient subsurface information has been obtained to de-risk prospects while reducing environmental impact. Key methods to achieve these savings are discussed and are comprised of the following elements. Firstly, a robust performance improvement process that started with focusing on building reliable repeatable operations, followed by a plan/monitor/review/feedback loop to continuously learn. Secondly, a project-based way of working was utilized to empower team members, push decision making to the appropriate level and set the project up for scaling by ensuring a common group was working each prospect. Thirdly, project scope was reduced to the lowest practical level. Lastly, the overall operating

model leveraged expert knowledge with a focus on learning together and building vendor relationships. This paper summarizes the success of the campaign with a learning curve showing dramatic well on well reductions that are comparable to learning curves published from the Oil and Gas (O&G) industry. Additionally, the impact of moving from field to field is highlighted showing that most of the learnings were transferable.

1. Introduction

Ormat Technologies Inc (Ormat) operates the largest number of geothermal resources generating electricity globally, with operations across six countries. They have seen steady growth over the last 25 years with a large portion through exploration and development. More than 40 prospects have been explored most of which are centered in the Great Basin located in the United States within Nevada and California. With continued demand for new geothermal electricity, they have focused their efforts towards increasing exploration activity to meet this demand and to fill new power purchase agreements (Ormat 2024). A core drilling campaign was recently undertaken showing large performance gains with a high level of technical information provided.

Reducing exploration costs is the key to opening additional resource for two reasons. Firstly, lower exploration costs reduce project sunk costs, resulting in better returns on successful projects and reducing expenses writing-off unsuccessful projects. Secondly, reduced exploration costs allow higher risk prospects to be drilled, proving more prospects and while drilling to test the upside of a project.

Classically, slim hole drilling has been used to de-risk resources using small conventional drilling equipment and hole sizes down to six inches. Ever increasing competition from Oil and Gas has made it difficult to acquire and contract rigs in a cost-effective manner. Figure 1 shows the operator's Exploration and Development Workflow. Risks, time, and costs are considered when it comes to the Exploration Drilling stage, whereby projects move through slim hole drilling to full size drilling. However, if the cost differential between slim hole and full size is too small, projects are incentivized to move directly to full size drilling, where a successful well may be commercially utilized for either production or injection. For this reason, reducing slim hole drilling cost can simplify decision making and reduce early exposure by introducing data early on a project's viability.

Due to costs associated with classic slim hole drilling rigs, a mineral exploration rig was sourced for a slim hole campaign with bottom hole sizes near 4 inches. Because of the limited footprint mineral exploration rigs also enable the ability to drill wells prior to an Exploration Environmental Assessment (EA) being completed, making use of Categorical-Exclusion provisions, resulting in a reduced project development timeframe by allowing full-size drilling upon receipt of an approved EA.

Between July 2022 and June 2024, the campaign has drilled 18 wells with significant learnings throughout. The small hole diameter has presented challenges requiring in-depth review of operations to drive reliability. Once proven reliable the team focused on improving performance with an overall 85% reduction in well cost from the first to last well.

Detailed analysis of drilling performance has yielded several key insights that can be used when planning future campaigns.

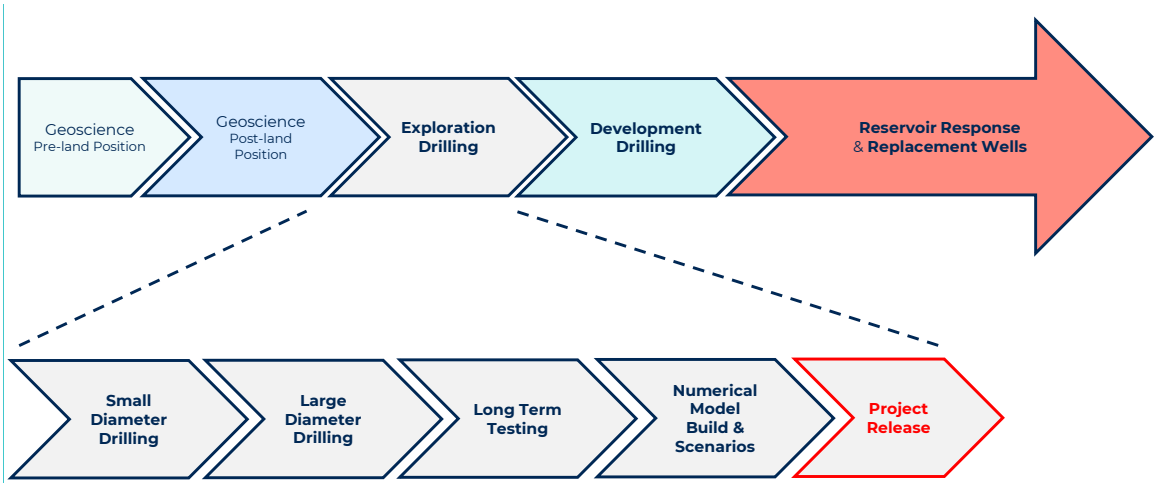

Figure 1: Operator Exploration and Development Workflow

The following definitions apply in this paper. Campaign refers to the entire coring campaign over 18 wells. Prospects refers to individual prospects or operating areas and wells refers to each well drilled. Operations refers to the process of constructing a well from initial pad construction to drilling to TD and cementing all casing strings.

2. Competitive Market for Slim-hole Rigs

Slim-hole drilling generally provides a significant capital reduction due to the smaller footprint, less manpower, and reduced infrastructure required. The merits of slim-hole drilling and the frequency of past campaigns are evident and summarized by Mackenzie et al (2017). Typical slim-hole campaigns have utilized hole diameters greater than 6 inches and utilize smaller conventional drilling equipment. With hole sizes greater than 6 inches slim-hole drilling has proven effective and provides data on-par with full size drilling at a reduced cost, however these well sizes typically aren't suitable for commercial production or injection use.

Recently the number of smaller conventional rigs has reduced, especially in the Western United States. The driving forces behind this reduction in the market have been large shifts in the Oil and Gas industry, predominantly in California where most geothermal drilling equipment is sourced. Additionally, the United States has a large rig fleet operating in the unconventional Oil and Gas industry, this draws suitable rigs away from the Geothermal industry where long-term contracts may be available. This creates an environment where the geothermal industry can't effectively compete for rigs.

Core drilling has been intermittently used within the operator over the last 25 years, with the last major campaign taking place a decade ago. Due to this and based off historical experience the operator sourced a rig from the mineral exploration industry. An LF230 built by Boart Longyear is being utilized to continuously wireline core wells. This approach helps isolate the campaign from the market influence coming from Oil and Gas.

3. Core Drilling Overview

Slim hole drilling is generally defined as wells ending with a hole size near six inches. This is the lower limit for most drilling equipment utilized in the geothermal and O&G industries. Smaller than 6 inches requires less common drill strings, smaller motors and presents unique challenges for most equipment. In the mineral extraction industry small diameter drilling has been done with wireline core rigs for decades. This process involves drilling with thin-walled core rods hoisted and driven by a rig. The bottom hole assembly (BHA) consists of a hollow drill bit and a stationary core tube. As the rock is drilled core moves into the core tube and is retrieved by a wireline overshot every 10'. The core retrieved can be evaluated to determine what formations are present.

This process has several unique advantages compared to conventional slim hole drilling. Less formation is removed by the drill bit reducing the power required reducing overall rig size. Pad sizes, water consumption and manpower requirements are dramatically reduced when compared to a typical drilling rig, reducing environmental impact as well as simplifying permitting in certain jurisdictions. Thin-walled flush joint core rods can be sized to nest inside one another. Common sizes are PQ, HQ and NQ with diameters of 2.75", 3.50" and 4.625" respectively as shown in Figure 2. By similarly sizing all components smaller sizes fit into larger sizes allowing holes to continue if a string gets stuck without the need to pull the stuck string from the well.

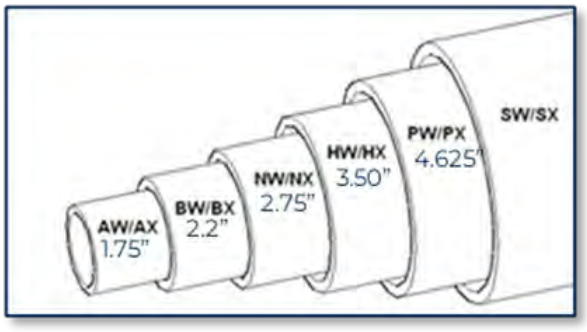

Figure 2: Common Core Rod Sizes

The advantages of core drilling aren't without drawbacks limiting the scope where this technology can be utilized. Typical coring open hole and rod sizes limit the effectiveness of cementation. A typical PQ hole is drilled with a 4.9" bit with 4.5" casing installed. Small annular clearances dramatically decrease the casing standoff, reducing the likelihood that a adequate cement job can be accomplished. Reduced power available from the drilling rigs and reduced strength of the thin wall core rods limits the depth that can be drilled and increases the risk of parting a tool string in tough hole conditions. Typical mineral exploration rigs are not equipped with blow out prevention equipment as this technology is not a default requirement.

An additional advantage of a core rig set up and associated lower-foot print, is the ability to permit core wells as Categorical Exclusions. Under the Geothermal Steam Act of 1970, a categorical exclusion may be used for activities that pose no significant risk to the quality of human environment. When approved, drilling core wells as temperature gradient wells above the reservoir still maintains high value and can mitigate preparing an environmental assessment prior to resource mapping. Figure 3 shows the small footprint of the LF230 rig utilized in this campaign.

Figure 3: Boart Longyear LF230 Core Rig

4. Core Well Utility

Core wells differ from traditional slim-hole wells largely because the final hole diameters are reduced from ~6 inches to <4 inches. This introduces many challenges for data acquisition and has an impact on the available well objectives that can be achieved.

Prior to starting the campaign, the operator sought to characterize the core itself, temperature log the entire well, image log the final hole section and where possible obtain permeability data where permits allow. If all these pieces of data could be obtained core wells could be used to fully supplement early exploration drilling.

During the campaign, cores were logged and many image logs were obtained. Additionally, substantial temperature data has been used to detail trends within the prospects. Permeability data has proven challenging for multiple reasons related to the small hole size. Well objectives were modified to rely on qualitative permeability data vs quantitative. This result wasn't a surprise due to the high frictions present in small holes, resulting in minimal change to the overall campaign plan.

5. Core Campaign Overview

The core drilling campaign has been ongoing across Nevada since the third quarter of 2022. The rig is currently drilling the 19th well over a total of 5 prospects as of June 2024.

When pre-planning the campaign historical well designs were used as the starting point. The current standard core well design is shown in Figure 4 and includes:

- 7” conductor set in 9-7/8” hole, this section is drilled with a 6-1/4” rotary bit and opened to 9-7/8” to reduce the total power requirements
- 4-1/2” surface casing set in 6-1/4” hole, this section is drilled with a PQ core bit to 4.9” and opened to 6-1/4” to allow space for an adequate cement job.
- HQ hole drilled at 3.83” to well total depth (TD), if required this section can be extended by stepping down to NQ hole drilled at 2.9”, 3.5” casing or HQ rods are used to keep the hole open when extending.
- The well is completed with slotted 2-1/16” liner. The installation of a liner allows for future function of the well for temperature gradient or monitoring purposes without risk of hole collapse.

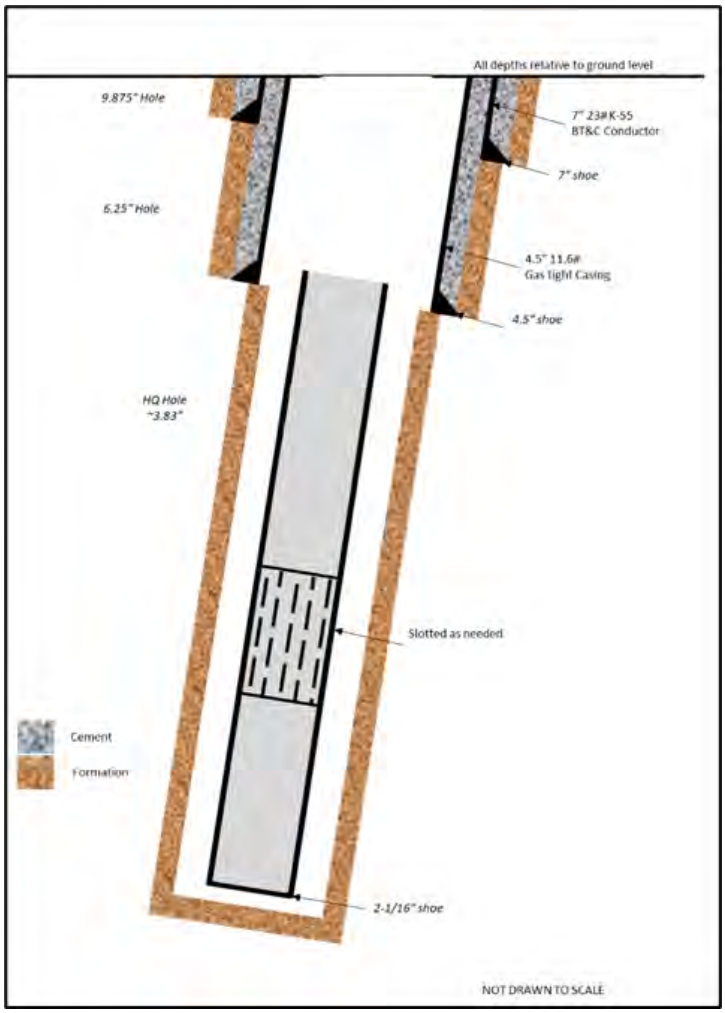

Figure 4: Typical core Well Design

6. Core Campaign Performance Journey

The operator has seen a continuous core drilling campaign as an avenue to continue portfolio growth and to find new hydrothermal systems projects to develop. Due to the length of the campaign the performance improvement has been a unique journey and consists of challenges and learnings not seen in many other Geothermal campaigns. The core campaign success can be attributed to a focus on reliability, project-based workflow, reducing project scope and working closely with vendors.

6.1 Reliability Before Performance

The first two wells in the campaign were constructed at nearly two times the proposed budget. An after-action review was put together that highlighted many inconsistencies in operational procedures, damaged equipment and a lack of supervision. To ensure the poor performance wasn't duplicated the campaign was paused and a project wide workshop was performed to identify issues and solutions. This process was done over the course of two days.

Members of the rig team, onsite supervision, engineering and any other staff involved were invited. The workshop was loosely based off the standard hazard identification (HAZID) process where the drilling process was broken into more than 50 steps. Each step was reviewed in detail before risks and mitigations were identified. If mitigations had not been implemented an owner was assigned to ensure implementation. At the close of the workshop 73 actions were identified with 10 having a high ranking for immediate implementation. These 10 actions could result in loss of a well if the risk associated with it was realized.

70% of the action items were resolved on the subsequent two wells yielding a reduction in well construction time by approximately 50%. To ensure ongoing mitigation of issues a new format for the drilling program was built which included specific activities with responsible parties. These items are checked off during each operation to mitigate complacency. The new drilling program was rolled out with the assistance of the drill site managers and contractor supervisors to ensure onsite buy in, alleviating any concerns of excess micromanagement.

Additionally, a detailed project risk register was developed. The risk register was broken into sections where risks that were common to every operation were part of the standard drilling program and risks unique to each location were covered as needed.

To ensure the activities in the drilling program and risks in the risk register were addressed the drilling program was used as the basis of the drill the well on paper (DWOP) exercise with no additional preparation of materials. This ensured that onsite personnel, engineering staff and subsurface staff were familiar with the program and the risks embedded within it. This also confirmed buy in from all levels of the project team before the start of operations.

6.2 Removing Excess Oversight: Project Based Workflow

Core drilling was used as the basis for updating the working team structure within the operators organization, whereby a matrix organization was developed. In this new organization a project manager (PM) became responsible for delivery of all aspects of well construction with each discipline reporting via a dotted line to the PM. The project team was empowered to make decisions and mature the project inline with project or well objectives. This reduced the ability of

a specific function to drive decisions. For example, a well wasn't drilled to the maximum depth to prove it was feasible, instead wells were drilled to minimum TD to satisfy data collection requirements. Another example would be choosing a suboptimal directional plan that still delivers 90% of the technical data but allows the project to utilize core drilling.

The project-based workflow forced the project team to identify clear well objectives. These objectives were used to design wells with the minimum technical scope. Operations were performed with the objectives in mind and excess was removed from the system as it was clear what was required to meet the objectives.

6.3 Avoiding Excess Complexity by Limiting Scope

During the after-action review, it became evident that the project had experienced scope creep from its initial inception. Complex bottom hole targets with multiple intercepts were included on the second well. The after-action review found that core drilling in un-stabilized hole either due to washouts or open cavities will likely damage the drilling rods. This is due to the high fatigue experienced at coring revolutions per minute (RPM's) in over gauge hole. In mineral extraction, targets like this are avoided. Geothermal has a unique requirement that wells target open fractures and often times drill through clay rich zones above these fractures. To ensure future wells had the best chance of reaching the required depth, complex targets were removed in favor of drilling two wells in environments with multiple targets. This ensured that the worst well issues were encountered at a point where total depth could be called early, and most data had been obtained. The eventual low cost per well facilitated this shift to simple targets with increasing well count.

Additionally, it was confirmed that core wells supply high quality temperature and image log data and typically can only provide qualitative permeability data. This is due to the high friction when flowing into or out of the small diameters in core wells. Limited infrastructure and shallow casing shoes further exacerbate this issue. Based off this learning project workflows and objectives were updated whereby core wells were only used to provide qualitative permeability data. In many cases due to the permits utilized for drilling of the core wells, injection testing was not employed due to being permitted under categorical exclusion provisions. It was possible to conduct injection testing if wells are permitted as a Geothermal Drilling Permit (GDP) which can only occur once an environmental assessment is in place.

As the campaign progressed significant learnings were realized. The project team has ensured that project scope has not increased and that stakeholders were aware of what core wells could and couldn't do. This has ensured that the expectations from prospect to prospect remain constant and that all wells can be drilled following a common methodology. This is key for ensuring learnings can be captured and passed from well to well.

6.4 Creating a Team: Vendor Partnerships

The after-action review highlighted multiple technical and procedural gaps between conventional mineral extraction drilling and geothermal drilling. Due to this a focus was placed on integrating vendor and operator knowledge to ensure a high level of integration. The rig supplier was relied upon as the expert in operating coring equipment and the operator understood the unique subsurface risks in conventional geothermal reservoirs. It was confirmed that resolving many of the issues found in the after-action review wouldn't be possible without a continuous operational

campaign. For this reason, the campaign was not stopped in favor of starting again after procedures were updated.

The rig provider in a close partnership with the operator developed several new ways of working including heightened pipe inspection criteria, batch cement mixing, consistent rig layouts, minimal civil engineering criteria, and staffing models to support the high workload. This was especially critical as the campaign accelerated and the project team had little time to rework prospect to prospect.

Other major service providers for drilling fluids and civils work were integrated into the project team as well. This ensured that objectives were clear and that providers gave input early in the project maturation.

The mud provider worked closely with the operator to formulate a mud program that could apply to most core drilling situations. This program evolved over the first 5 wells in the campaign with a full-time mud engineer on site. As the process became repeatable the mud engineer was removed in favor of having the rig manage drilling fluids.

The after-action review showed gaps in supervision, as a result the level of staffing during operations was tailored to support the unique scope of work. The operator deployed 24-hour supervision and the rig provider added an additional supervisor to cover 24 hour operations. This ensured sufficient staffing onsite to confirm the quality of each step in the process.

7. Learning Curve Analysis

Throughout the campaign a learning curve was experienced. As of June 2024, 18 wells have been drilled across Nevada in six separate prospects. Throughout the campaign performance has been tracked on multiple metrics including dollars/ft, days/100’ and dollars for the first 1000’. All metrics show the same general trend with some differences later in the campaign.

7.1 Evaluating the Learning Curve

Below is a summary of all wells drilled to date. 3 of the wells were drilled in two operations showing 21 operations total. Well names have been replaced with a prospect and well identifier whereby the first digit identifies the prospect, and the second digit identifies the well within that prospect. The third digit denotes wells that were deepened through a separate event.

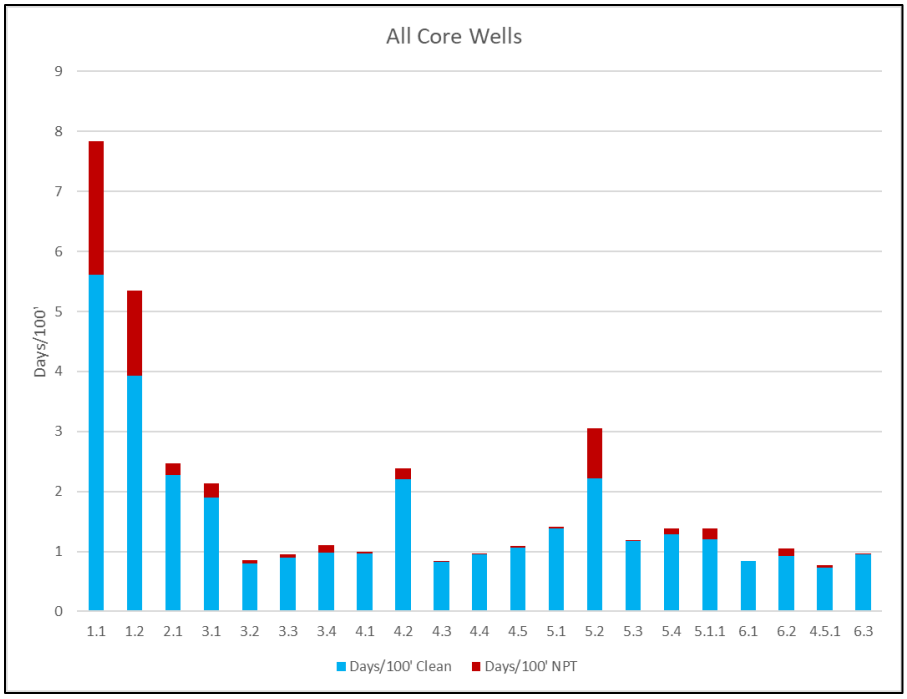

Figure 5: Whole Campaign Performance days/100'

Figure 5 shows that significant learnings over the campaign were realized. It also highlights that the full well set is too diverse to compare as the trends vary later in the campaign due to non-drilling impacts, masking performance changes.

Plotting the data from Figure 5 for the first 1000' in each well gives the most representative data set to highlight learnings as all wells would have shared the same operational steps up to this point including drilling and setting conductor, drilling and setting surface casing, installing and testing Blowout prevention equipment (BOPE) and drilling HQ hole.

This breakdown is required as 3 wells were deepened in separate well entries. They don't carry the higher capital and time expenditure to cement surface and conductor strings. It also normalizes the unique challenges encountered in wells drilling deeper than 3000' where hard rock and the diversity in permitting limitations impacts the well construction durations. Examples include temperature limitations, directional limitations, or TD restrictions. This data set also doesn't account for differences in planned vs NPT activities as NPT activities were part of the process to construct those wells. Figure 6 shows the performance of all wells drilled to 1000'.

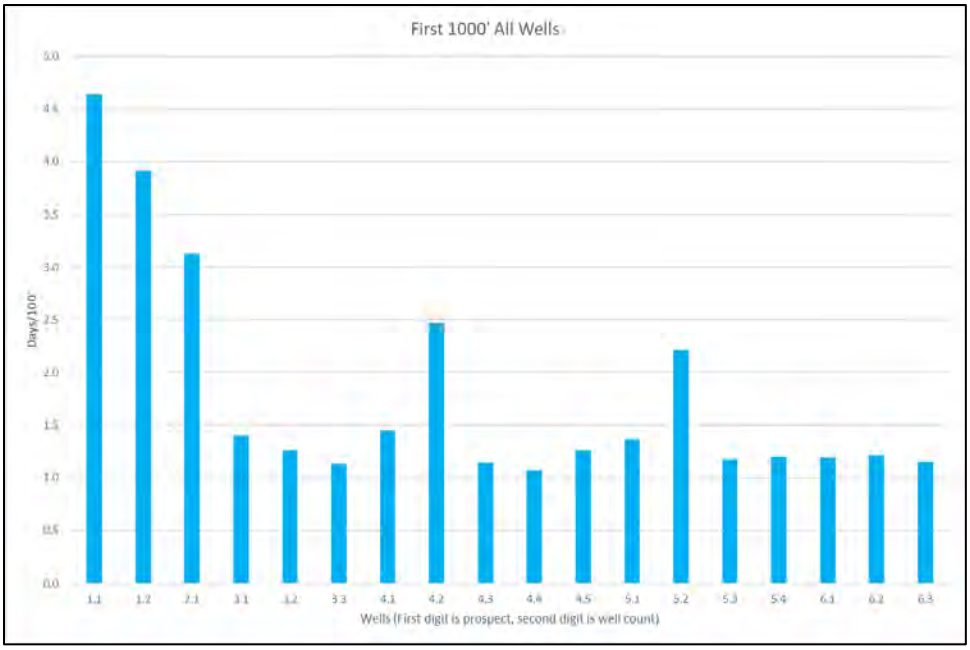

Figure 6: All wells to 1000' days/100'

Wells in prospect 5 had significantly deeper surface casing than all other campaigns, due to this, durations for that section were normalized by truncating the drilling duration to match the average of all other wells. The deeper surface casing is considered a technical step change making the wells distinctly different as equipment and procedural changes took place to accomplish those wells. Figure 7 shows the results of truncating wells in prospect 5.

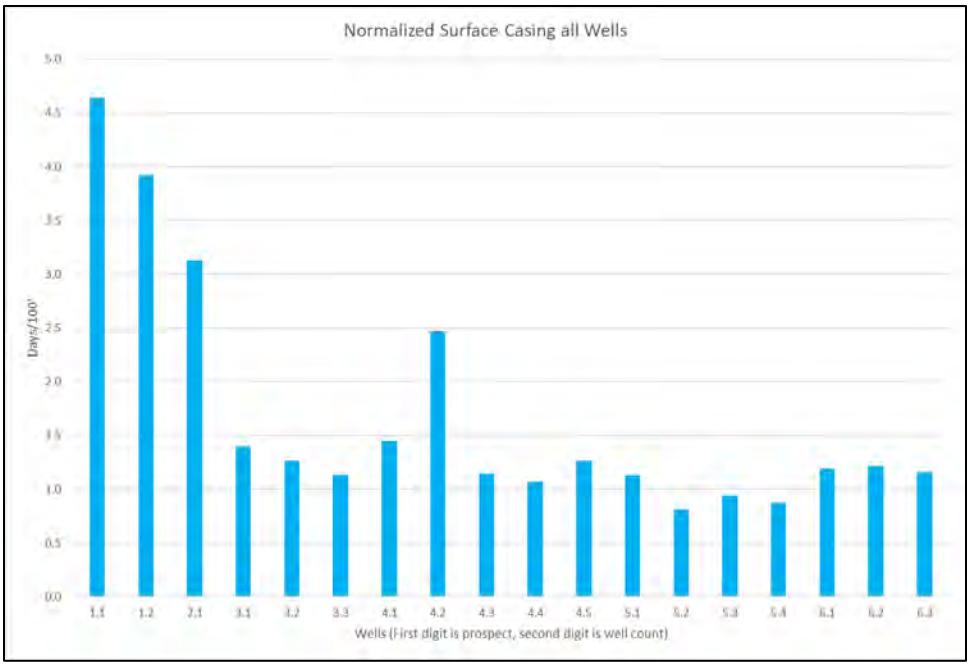

Figure 7: All wells with normalized for surface casing to 1000', plotted in days/100'

Figure 7 contains the scope of work where >70% of campaign expenditure has occurred. Reducing durations and cost on this scope of work will yield the biggest campaign impacts at this time.

7.2 Learning Curve Insights

7.2.1 Reliability First: After Action Review Process

An in-depth after-action review and integrated workshop yielded results on the third and fourth wells that were immediately evident as shown in Figure 5. The biggest cumulative impact from the workshop was a reduction in NPT from ~40% to ~9% by the third well. Reducing NPT and increasing reliability of operations allowed the team to move from immediate problem solving to performance engineering. Both macro and micro drilling key performance indicators ("KPI's") could be tracked more easily because the data wasn't masked by high NPT. From this data the team could analyze all operations in a well and focus on improvements on an operation-by-operation basis. A continuous feedback loop was created and utilized to further drive performance and capture learnings. This feedback loop is shown in Figure 8.

Figure 8: Continuous performance feedback loop

7.2.2 Days vs Depth Curves: A way to quickly share information

KPI's evolved over the campaign from macro to micro. Macro KPI's include; gross drilling time, section rate of penetration (ROP), gross move duration. Micro KPI's include; a detailed time for each section of a well (13 sections total), BOPE rig up and testing time, wellhead installation time, on bottom ROP, circulating time and wait on cement time. As more data was collected the KPI's were used for planning cost and time estimates on future wells, where subsurface expectations were broken into 3 well types and projected to the proposed well depths. Days vs Depth ("DvD") curves of all wells were used to compare estimates and communicate to stakeholders real time

performance. Figure 9 gives an example of the estimating process mid campaign. The green DvD curve is the estimate produced by analyzing the other wells in the data set, the overall drilling duration is prolonged due to applied contingency. This can be seen in the rightward shift of the estimate and reduced slope when compared to the other wells.

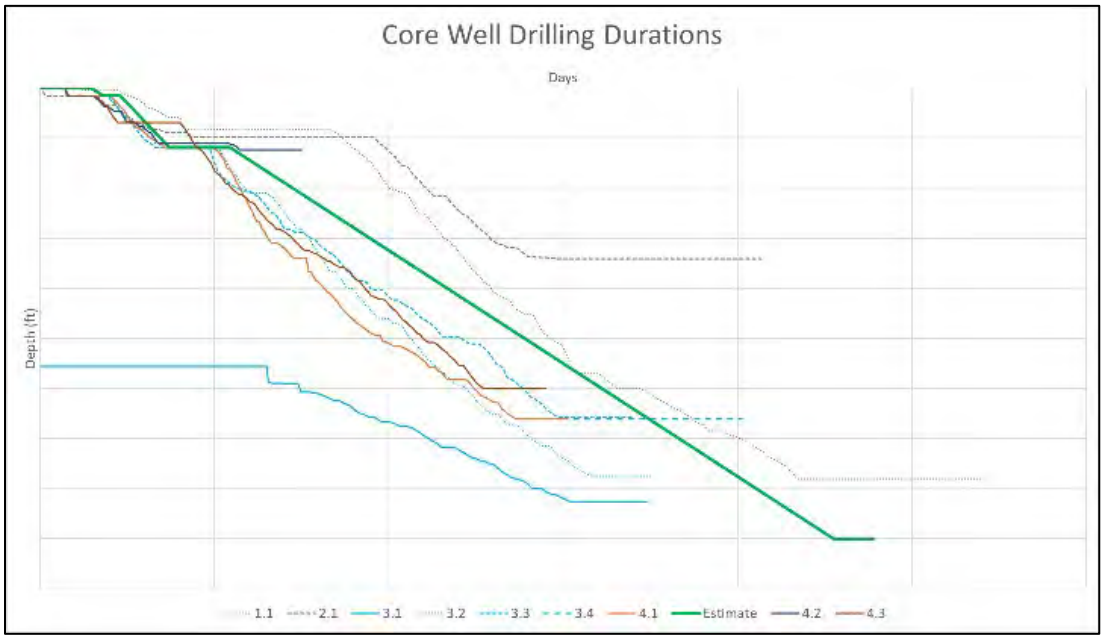

Figure 9: Days vs depth estimating example

A dashboard was developed to track real time well performance real time and uses the DvD curve as the basis for showing where a current well is vs plan. Figure 10 shows a sample of an early dashboard that was adopted.

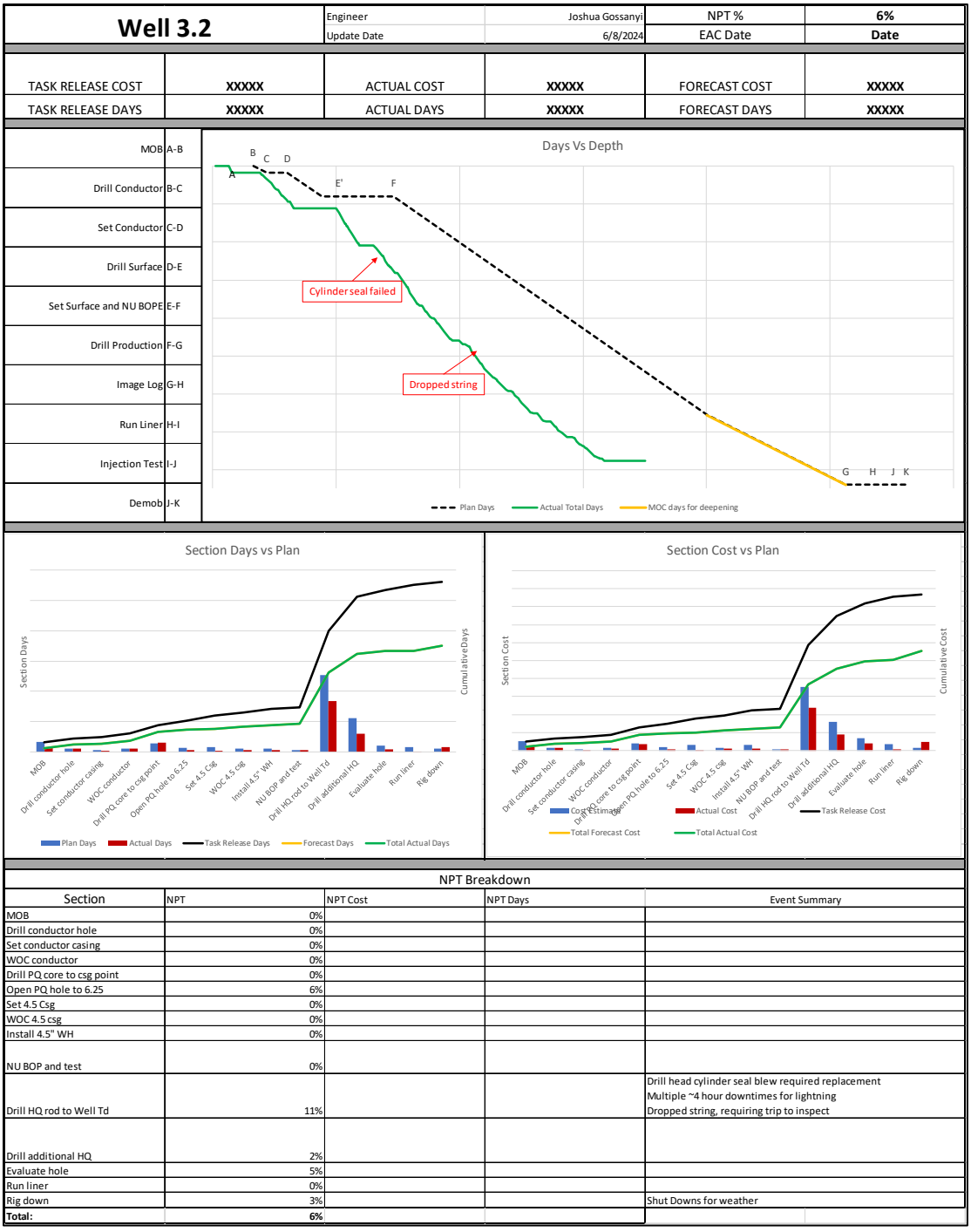

NPT Breakdown

Section	NPT	NPT Cost	NPT Days	Event Summary
MOB	0%			
Drill conductor hole	0%			
Set conductor casing	0%			
WOC conductor	0%			
Drill PQ core to csg point	0%			
Open PQ hole to 6.25	6%			
Set 4.5 Csg	0%			
WOC 4.5 csg	0%			
Install 4.5" WH	0%			
NU BOP and test	0%			
Drill HQ rod to Well Td	11%			Drill head cylinder seal blew required replacement Multiple ~4 hour downtimes for lightning Dropped string, requiring trip to inspect
Drill additional HQ	2%			
Evaluate hole	5%			
Run liner	0%			
Rig down	3%			Shut Downs for weather
Total:	**6%**			

Figure 10: Well performance dashboard

The dashboard in Figure 10 was manually updated and tracked through excel. As the campaign matured and interest within the company grew to monitor performance an automated dashboard was built to update from the operators well data system via a Microsoft Power BI application. The new dashboard uses a similar layout and gives users an immediate progress update.

7.2.3 Practice Makes Perfect: Continuous Campaign Advantage

A continuous campaign has allowed the team to implement the performance loop effectively. This would not be possible in a non-continuous campaign typically seen in conventional geothermal with a small well count split into several drilling events.

The campaign has reached a technical limit, the point at which existing tools and procedures are fully optimized. Further improvements are only possible by implementing new ways of working, new technologies, new procedures, or other new novel approaches. Continuing to utilize the existing ways of working and technology is unlikely to produce significant performance improvements. To move the technical limit the team has worked up multiple bespoke tools that will reduce well construction time. To ensure these items are implemented a performance waterfall was built and used to get stakeholder buy in when investing in new approaches. Items are broken up into three categories:

1. Changes in procedures such as a reduction in required wait on cement time by utilizing different blends.
2. New technology deployment such as a unique wellhead installation technique.
3. Procurement updates such as reducing the support or oversight of a particular vendor.

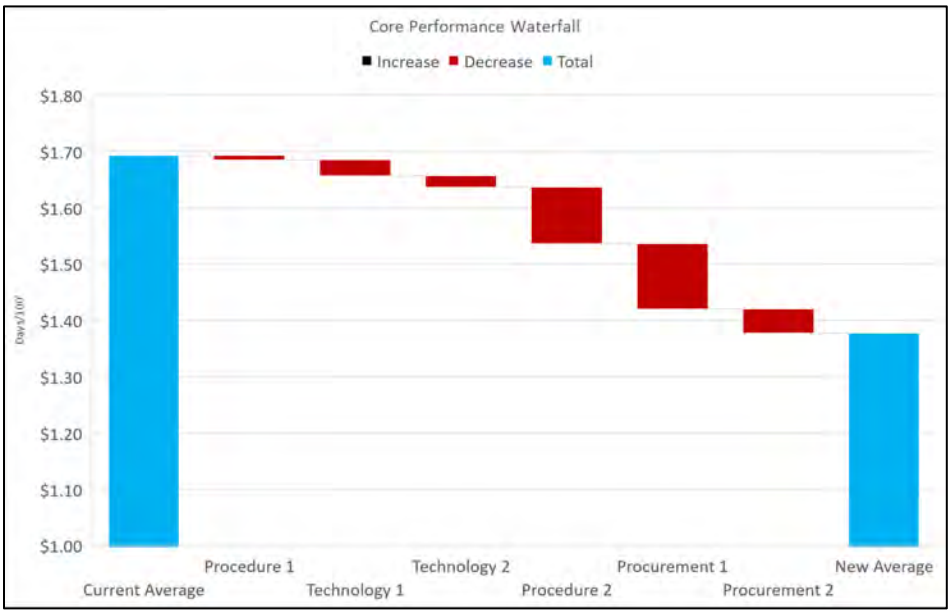

Figure 11: Performance Improvement Staircase

Figure 11 shows the relative impact on days/100' when converted from the total dollar amount of initiatives that are being matured. At the time of writing ~30% of the improvements identified in this waterfall have been implemented or will be implemented on the next well with all planned for implementation by the end of 2024.

Safety performance was improved and maintained because of continuous operations. The operator and the major service providers focused on ensuring crews involved in the campaign were consistent. This allowed many safe working procedures to be specialized for the unique operations. No lost time incidents occurred during the campaign and first aid cases reduced as

safe work practices were updated. The stability of crews has also provided a strong training base for new employees joining the team where short service employee percentages are low.

7.2.4 Large Campaign Decisions Matter: Assess Impacts When Planning

Larger campaign strategy has an impact on performance. Wells in campaign 5 occurred during the winter months in a remote high elevation location. The risk that was realized during this campaign was inadequately characterized before starting and resulted in many wells coming in over budget. The mischaracterization was largely due to confidence gained during previous campaigns with low NPT and quick learnings. This is evident in Figure 6. The highest contribution in that campaign to NPT was poor road conditions limiting the ability to move water. That contribution was most strongly seen in the deep drilling sections where a high loss rate required large volumes of water, which was trucked in. In comparison campaigns 3 and 4 occurred in good weather and were co-located in the same general area. This allowed learnings to be more directly carried from one campaign to the other. Early campaign planning now incorporates these learnings and will seek to reduce winter exposure as well as co-locate prospects as much as possible.

7.2.5 Moving to New Locations Can be Hard: New Prospects Require Focus

Figure 6 shows the campaign sees an uptick in drilling duration every time the rig moves to a new prospect. Each time the rig is broken down for a long move it requires time to get it back up and running effectively. This is commonly known as shake-down time and is a result of ensuring equipment has been re-assembled correctly. Additionally, each prospect introduces new subsurface challenges. When drilling in a new area the crew may intentionally slow down to limit the likelihood of issues occurring. Changes from prospect to prospect also occurred due to differences in basement depth, alluvium depth, rock composition and remoteness.

The coring campaign has been effective at reducing the impact of moving from prospect to prospect. Limiting project scope and adhering to the same procedures at each prospect has reduced the NPT encountered when moving to an acceptable level. Due to this, prospects can be broken into smaller well counts allowing the subsurface teams to glean as much information from early wells before making decisions on future wells.

8. Conclusion

Core drilling has proven a valuable process in the operators exploration toolbox. Overall drilling costs in the campaign have been reduced by 85% between the first well and the most recent well. The process has become repeatable with accurate estimates being used to release well budgets. The low costs have increased flexibility within new prospects to allow ever more challenging resources to be explored.

The team has worked very hard to first reduce NPT and make operations repeatable. This allowed a focus on KPI’s to drive further performance. To ensure continued improvements going forward an improvement staircase was developed and is being implemented.

The 85% reduction in well cost has come at very little loss in well utility whereby wells are still regularly logged and qualitative permeable data is obtained.

A learning curve in Figure 5 was realized and confirms the lessons in this paper as well as validates the ways of working used within the core project team.

The large reduction in cost has allowed the program to function independently of full-size drilling giving flexibility and accountability to the project team to either move exploration prospects to full size drilling or release the projects that aren't viable.

Acknowledgement

I appreciate the support of all authors and members of the team early-on, specifically Rob Selwood, Chris Gates, Daniel Lawrie and CJ Triola. Thank you goes to all vendors who have worked so hard to support this core hole drilling campaign. Thanks to Ormat for allowing publishing of this paper.

REFERENCES

Mackenzie K.., Ussher G., Libbey R., Quinlivan P., Dacanay KJ., Bogie I., Use of Deep Slimhole Drilling for Geothermal Exploration, Proceedings the 5th Indonesia International Geothermal Convention & Exhibition 2017

Ormat (2024) https://s1.q4cdn.com/231465352/files/doc_presentations/2024/Jun/20/Ormat-AD-Final-for-printing.pdf

Mechanical Evaluation of a Novel Cement Formulation used for Thermal Energy Storage Wells

Meng Meng[1], Tatiana Pyatina[2], Luke Frash[1], Bijay KC[1], Uwaila Iyare[1], Yerkezhan Madenova[1]

[1] Los Alamos National Laboratory

[2] Brookhaven National Laboratory

Keywords: Triaxial compression, thermal cycling, mechanical modeling, safe operating envelope

ABSTRACT

High Temperature Reservoir Thermal Energy Storage (HT-RTES) is a promising solution for large-scale energy storage that can stabilize the electric grid, increase its flexibility, and provide energy on demand. Despite its advantages, the HT-RTES wells require a higher standard for cement integrity due to higher temperatures and thermo-mechanical stresses during injection and production. In this study, we provided a thorough mechanical investigation on the hydrophobic fly ash cenospheres (FCS) incorporated calcium aluminate cement, which exhibits a lower thermal conductivity compared to conventional oil and gas well cement to prevent heat losses. The cement was treated with superhydrophobic polymethylhydrosiloxane (PMHS). The compression tests were conducted under in situ high pressure high temperatures, with pressure reaching up to 10 MPa and temperature up to 180 °C. The findings revealed that the PMHS-treated specimens, after undergoing simulated thermo-mechanical stresses, showed an increase in cement compressive strength from 4.6-30 MPa to 6.1-33 MPa, an improvement in elastic modulus from 0.34-1.37 GPa to 1.1-3.3 GPa, and an enhancement in Poisson's ratio from 0.07-0.15 to 0.1-0.33. Therefore, lightweight calcium-aluminate cement formulations with PMHS treated FCS could preserve its mechanical performance after subjecting to thermal shock. We further incorporated the measured properties into a fully coupled thermoporoelastic model for wellbore integrity analysis. Results show that the novel PMHS treated FCS could resist large range of pressure and temperature perturbations during heat injection and production. Overall, this novel formulation could be a promising solution to the durability of the HT-RTES wells.

1. Introduction

In a thermal storage site, hot fluid is injected into a subsurface reservoir, where the formation rock absorbs and retains the heat energy from the injected fluid. When the heat energy is needed, those hot liquid will be produced to the surface. The cyclic injection and production occur daily, seasonally, or even longer durations based on specific applications. To achieve the long-term

effective thermal storage, safe wellbores are essential, and cement integrity is one of the primary concerns for the wellbore durability. A proper cement system needs to have the following characteristics: (1) good resistance to thermal shock and thermal cycling over large temperature ranges; (2) low thermal conductivity to minimize the thermal loss during the repeating injection and production across the wellbore; (3) low modulus to withstand severe pressure and temperature perturbations caused by injection and production; and (4) low density to avoid fracturing the weak, unconsolidated, or naturally fractured rock formations.

Ordinary Portland cement (OPC) is known for its poor performance in thermal shock resistance. Temperatures between 200-300 ℃ could cause micro-cracking propagation (Boquera et al., 2021). The dihydroxylation of portlandite happens in OPC at temperatures ≥ 500 ℃, leading to free lime formation that converts to highly expansive hydration products (Sugama et al., 2018). In contrast, Calcium aluminate cement (CAC) is capable to withstand thermal shock at temperatures over 500-600 ℃ (Sugama et al., 2018; Boquera et al., 2021). The usage of fly ash and silica flour improved cement performance at elevated temperatures.

The thermal conductivity of OPC depends on the water saturation content, density and porosity. It varies between 0.3 and 1.3 $Wm^{-1}K^{-1}$ (Wolterbeek et al., 2023). According to Fourier's law of heat conduction, the heat loss due to conduction is linearly related to material thermal conductivity. Zhou et al. (2023) developed a chemical-induced nitrogen-filled foam cement with low thermal conductivity of 0.3 $Wm^{-1}K^{-1}$ that achieved a 11.77 °C higher temperature at the wellhead compared to adjacent wells using fly-ash low density cement.

The elastic modulus of OPC can go up to over 40 GPa, and the oilwell cement has an elastic modulus between 1 and 10 GPa (Nelson, 2006). The geothermal cement has been found with similar elastic modulus as oil well cement (Philippacopoulos and Berndt, 2001; Pyatina, 2018). Higher elastic modulus up to 15 GPa has been reported under specific testing conditions and formulations (Pang et al., 2021; Meng et al., 2023). Well integrity modeling analysis have shown that elastic modulus is more important than compressive strength in maintaining well safety (Lavrov and Torsæter, 2016; Meng et al., 2021).

Cement density ranges from 1400 kg/m^3 to 2400 kg/m^3 depending on specific applications. Density can be adjusted by using heavyweight additives (Barite, Hematite, Ilmenite) or lightweight additives (gas, bentonite, microspheres). For the geothermal well, the formation might be naturally fractured, and a lightweight cement is beneficial to avoid fracturing the formation.

To achieve the preferred properties of geothermal cement, one type of PMHS treated FCS incorporated calcium aluminate cement has been created (Simerjeet, 2012; Sugama et al., 2018; Sugama and Pyatina, 2021). Its mechanical properties under uniaxial compression conditions, thermal conductivity, water-repellent property, phase identification, and microstructures have been quantified (Sugama and Pyatina, 2021). However, the mechanical properties under triaxial conditions have not been evaluated. In this paper, we have conducted triaxial compression tests under high temperature high pressure conditions, with pressures up to 10 MPa and temperatures up to 180 °C. Our results have demonstrated the good performance of PMHS-treated cement in thermal resistance under simulated wellbore conditions.

2. Methods

2.1 Experiments

The materials used to prepare the PMHS-treated alkali-activated calcium aluminate cement with Class F fly ash have been described in detail by Sugama and Pyatina (2018) and their description will not be repeated here. The preparation procedures, however, are as follows.

1) Pouring cement slurry into the test mold, followed by 24 hours curing at room temperature;
2) Removing the mold and curing the samples at 99±1% relative humidity for 24 hours at 85 ˚C;
3) Autoclaving the samples for 24 hours at 250 ˚C.

For each formulation, we evaluated their mechanical performance before and after undergoing thermal shock. The thermal shock is performed by three-cycle of 200 °C heating for 24h, followed by old water quenching for 30 minutes. The detailed experimental matrix is shown in Table 1.

Table 1 Experimental matrix

Specimens	Thermal Shock	Testing Conditions
1	No	Uniaxial compression test
2		Uniaxial compression test
3		Uniaxial compression test
4		10 MPa confining pressure
5		180 °C, no confining pressure
6		180 °C, 10 MPa confining pressure
7	Yes	Uniaxial compression test
8		Uniaxial compression test
9		Uniaxial compression test
10		10 MPa confining pressure
11		180 °C, no confining pressure
12		180 °C, 10 MPa confining pressure

We utilized our high-temperature and high-pressure triaxial compression equipment (Figure 1) to measure the mechanical properties of cement. The equipment can withstand temperatures up to 200 °C and provides a confining pressure range from 0 to 70 MPa. The load capacity of the equipment is 1000 kN. Axial and radial deformations were monitored using high temperature linear variable differential transformer rated up to 200 °C. Throughout the compression tests, we maintained the strain rate at approximately 10^{-6} /s. For high temperature high pressure experiments, a customized rubber is required to tolerate the harsh environment and avoid fluid communication between the sample and the silicone confining oil.

This facility shown in Figure 1 is capable to control and monitor pore pressure as well. However, the pore pressure was not applied in our experiments because cement typically has low permeability, and it takes a long time for pore pressure to stabilize. Thies PMHS treated cement has a low permeability of 0.1-0.15 micro-Darcy (Bauer et al., 2020). During the high temperature test without confining pressure, we left the pore pressure line open to the atmosphere to allow free water evaporation. This was necessary to prevent thermal induced pore pressure from building up and potentially breaking the rubber in the absence of confining pressure. As to the high temperature high pressure tests, it is recommended to increase the confining pressure to at least 2 MPa before raising the temperature. The water boiling point at 2 MPa is over 212.5 °C, which avoids

significant thermal induced pore pressure. If the sample is brittle, the confining pressure can go directly to the designed value. Since the cement samples seem to be ductile, it is better to elevate the pressure to 10 MPa after temperature reached 180 °C. During the heating stage, a continuously constant confining pressure control was maintained with self-designed software.

Figure 1: Triaxial compression equipment with sample setup

2.2 Modeling

The measured parameters have been implemented into one thermoporoelastic analytical model. The model development and details have been described in our previous publications (Meng et al., 2021, 2023; Zhang et al., 2022). The model demonstrates how the cement performs under pressure and temperature perturbations during fluid injection and production.

3. Results

3.1 Mechanical properties of cement before thermal shock

Three uniaxial compression tests have been conducted, and their mechanical properties are close to each other with small variance (Figures 2 to 4). The compressive strengths are 4.7 MPa, 4.6 MPa, and 5.1 MPa, respectively. The elastic modulus is (1.15 ± 0.05) GPa, (1 ± 0.03) GPa, and (1.2 ± 0.1) GPa. Poisson's ratios were recorded at 0.14 ± 0.1 for the first two tests, and 0.10 ± 0.1 for the third test. The stress strain curves in Figures 2 to 4 indicate plastic deformation near the peak strength values. For instance, in Figure 3, axial strain increases from 0.4% to 0.6% as axial stress approaches the maximum value of 4.6 MPa, and continues to increase to 1.2% as axial stress drops to 2 MPa. This demonstrates the strong ductility of the cement, which is not typical for brittle Class G cement. In our previous experiments, the axial deformation for Class G cement with silica flour is around 0.4% at the maximum axial stress point and the stress dropped quickly after that (Meng et al., 2023). Additional evidence of ductility was observed in the triaxial compression test under 10 MPa confining pressure, where axial strain exceeded 10% as the axial stress continued to rise (Figure 5).

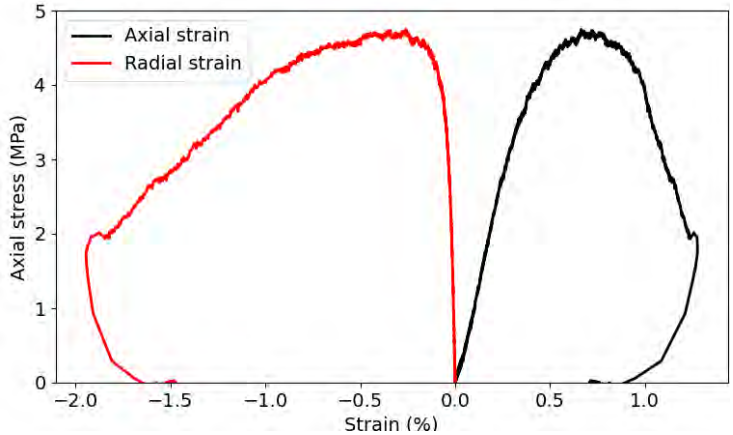

Figure 2: Stress - strain curve of the first uniaxial compression testing before thermal shock

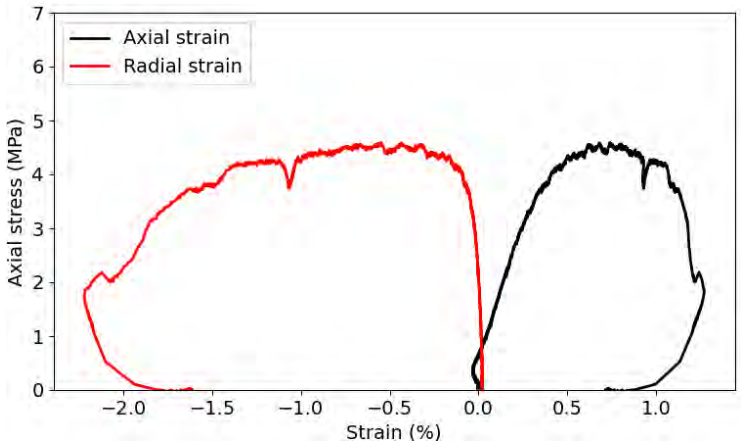

Figure 3: Stress-strain curve of the second uniaxial compression testing before thermal shock

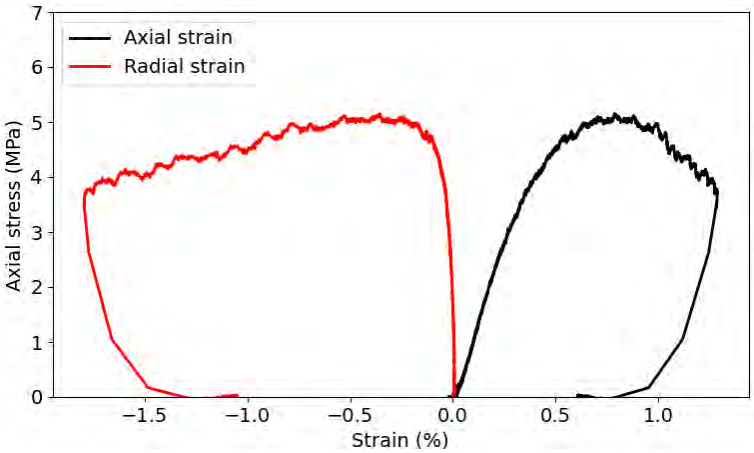

Figure 4: Stress-strain curve of third uniaxial compression testing before thermal shock

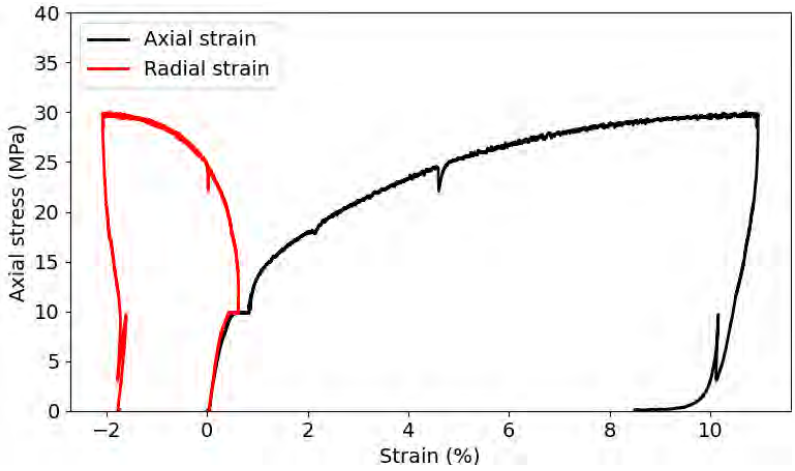

Figure 5: Stress-strain curve under 10 MPa confining pressure before thermal shock

In the following 10 MPa, 180 °C triaxial test, the stress-strain curve shows more complex behavior compared to the test conducted under high confining pressure alone (compare Figure 6 with Figure 5). Figure 7 shows the process of the progressively increasing pressure, temperature, and compression stress. Initially, the confining stress was raised to 10 MPa, during which the axial strain increased from 0 to 2%, and radial strain from 0 to 0.7%. With the confining pressure held constant at 10 MPa, the temperature was then raised to 180 °C. During this stage, the axial strain further increased to 6%, while the radial strain sensor failed. After temperature reached to 180 °C, the axial strain was still increasing under a slower rate. To save time and avoid axial strain sensor out of range, the specimen started to be compressed. This strong ductile performance creates challenges to our measurement.

There are two ways to improve the future testing performance. Firstly, as mentioned in the Experiments section, initially setting the confining pressure to a lower value of 2 MPa before elevating the temperature might help mitigate deformation during the temperature elevation, though it would not prevent the deformation after 10 MPa is applied. Secondly, curing the specimen under 10 MPa and 180 °C during the specimen preparation stage might prove beneficial. The cement sample was prepared under ambient pressure conditions, which is expected to be less consolidated than high pressure curing. If the curing conditions were maintained the same to the testing conditions, the specimen might show less plastic deformation.

For uniaxial compression test under 180 °C, the specimen shows stronger deformation compared to uniaxial compression tests under room temperature. Axial strain is 1.4% when reaching the peak value for the 180 °C, while the ambient tests showed only ~0.6% axial deformation at the peak stress point.

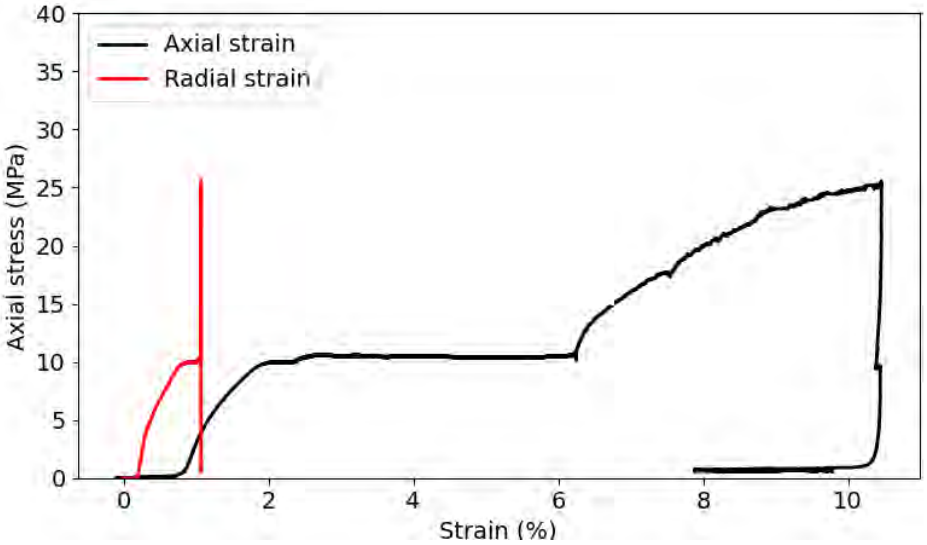

Figure 6: Stress-strain curve under 10 MPa confining pressure and 180 °C before thermal shock

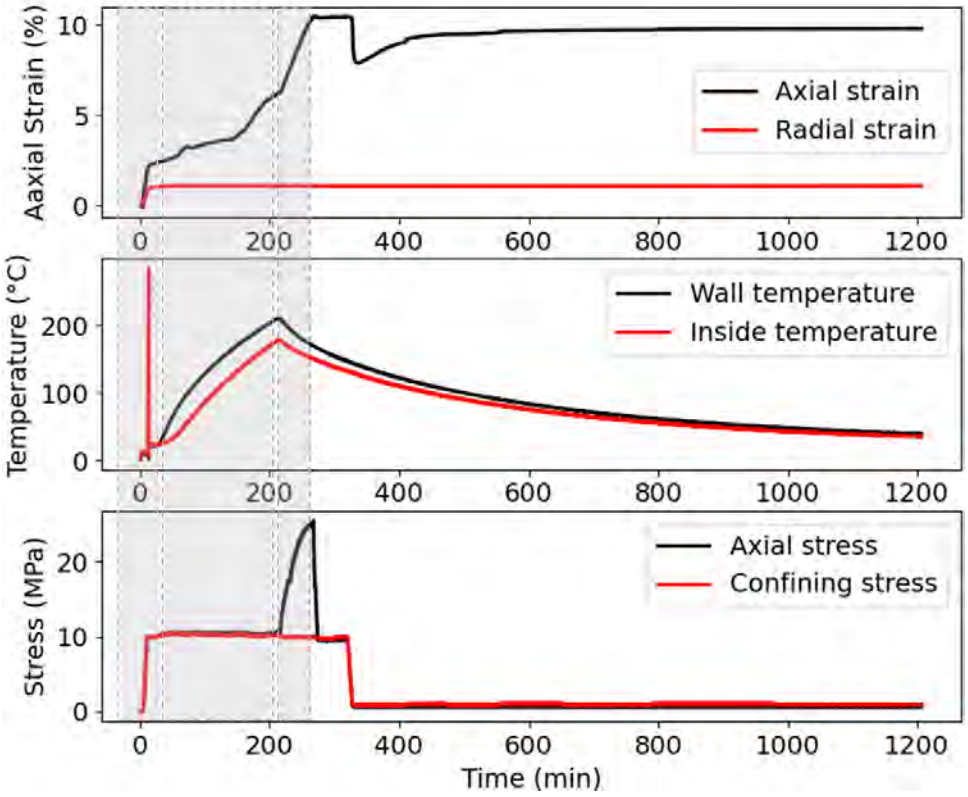

Figure 7: Triaxial compression testing under 10 MPa confining pressure and 180 °C. The first grey area shows that this cement has strong deformation during confining pressure application. The second grey area shows that the deformation continues during the heating stage. The third grey area shows the compression stage.

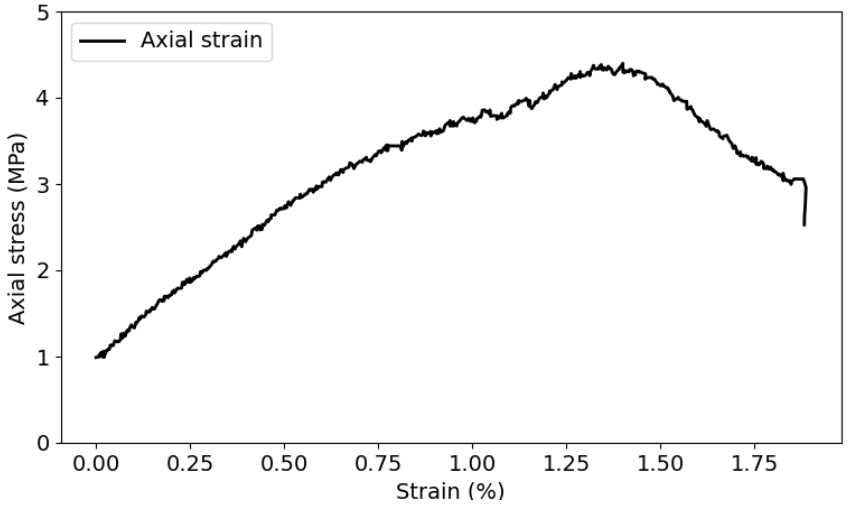

Figure 8: Stress-strain curve under 180 °C before thermal shock

3.1 Mechanical properties of cement after thermal shock

The same types of experiments were conducted on the specimens after undergoing thermal shock. The detailed stress-strain curves are shown from Figures 9 to 14, and the mechanical properties are summarized in Table 2. After experiencing thermal shock, the compressive strength of the specimens increased to 7.6 MPa, 6.14 MPa, and 6.7 MPa, representing a 42% increase compared to the samples without thermal shock. The elastic modulus also increased to (1.75 ± 0.15) GPa, (1.15 ± 0.05) GPa, and (1.6 ± 0.1) GPa, demonstrating an increase of 34%.

In the 10 MPa confining pressure compression test, the compressive strength increased slightly from 30 MPa to 32 MPa, while modulus increased from (1.7 ± 0.2) GPa to (2.5 ± 0.4) GPa. Comparing the shapes of the stress-strain curves in Figures 5 and 12, the specimen subjected to thermal shock reached near peak strength at just 4% axial strain, whereas the stress for the non-thermal shock specimen continued to climb until reaching 10% axial strain. This behavior indicates that the thermal shock reduces the ductility of the cement.

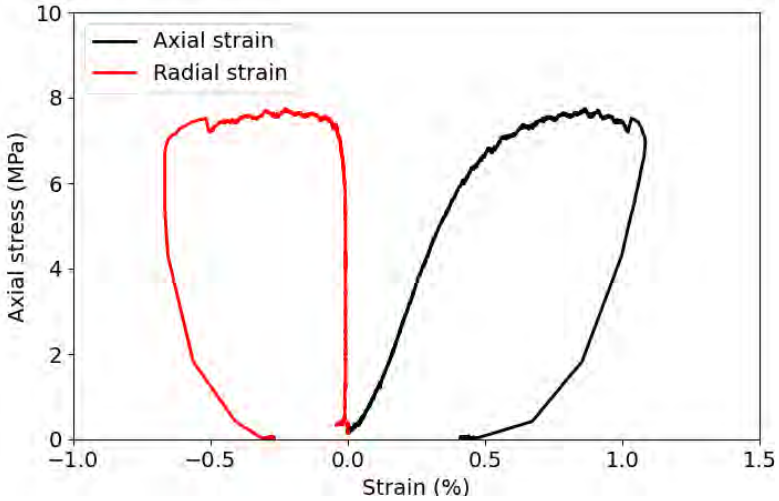

Figure 9: Stress-strain curve of the first uniaxial compression testing before thermal shock

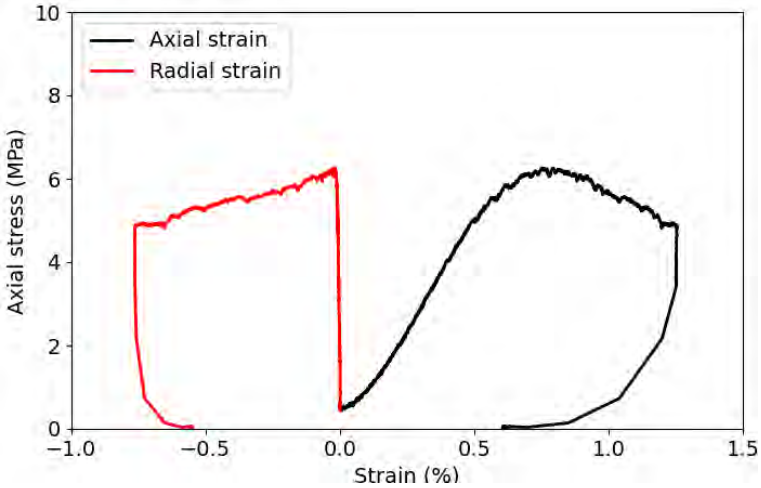

Figure 10: Stress-strain curve of the second uniaxial compression test after thermal shock

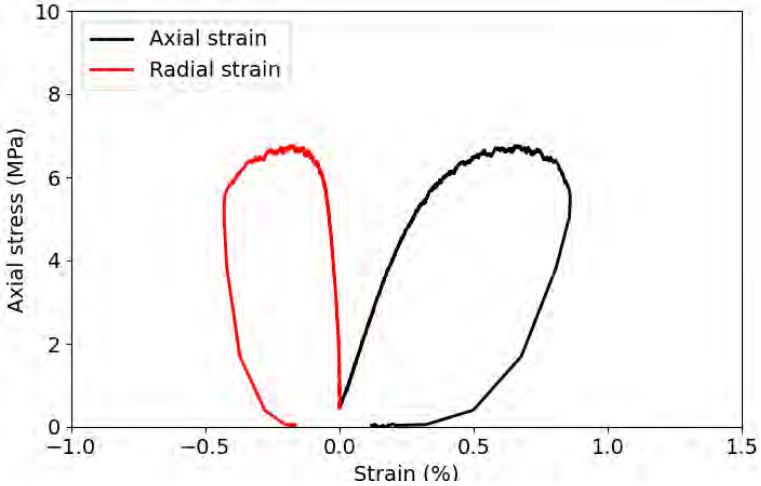

Figure 11: Stress-strain curve of the third uniaxial compression test after thermal shock

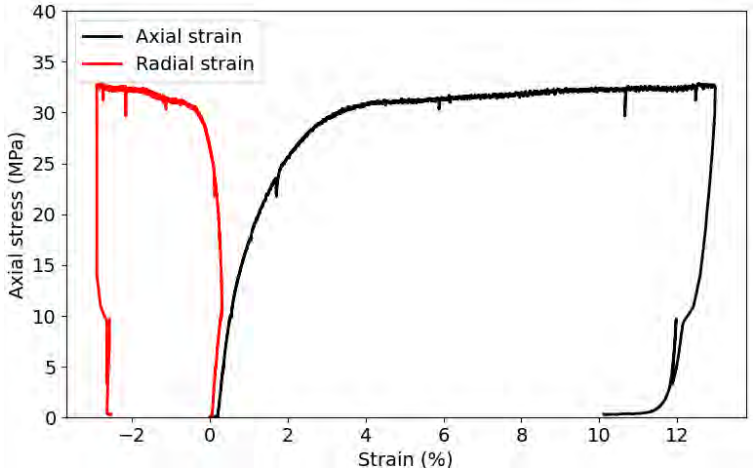

Figure 12: Stress-strain curve under 10 MPa confining pressure after thermal shock

Similar behavior was observed in the compression tests conducted under 180 °C and 10 MPa confining pressure, as shown in Figures 6 and 13. After undergoing thermal shock, the compressive strength increased from 25 MPa to 32.3 MPa, and the elastic modulus increased from (1.33 ± 0.05) GPa to (3.15 ± 0.15) GPa. At near maximum axial stress, the axial strain recorded was only 3% for the specimen that had undergone thermal shock, in contrast to the continuing increase in stress beyond 10% axial strain observed in the specimen without thermal shock.

The results of uniaxial compression tests under 180 °C further confirmed this pattern of increased compressive strength coupled with reduced ductility, as shown by comparisons between Figure 14 and Figure 8.

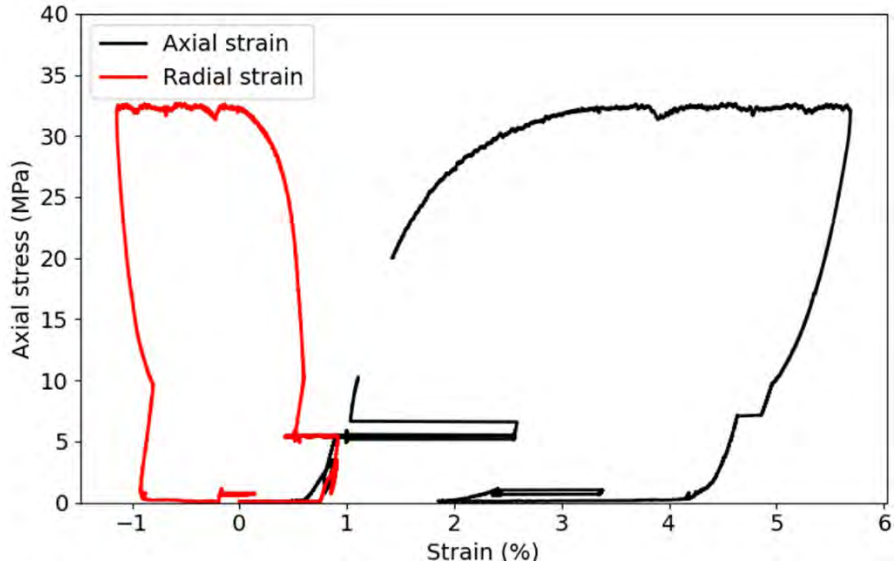

Figure 13: Stress-strain curve under 10 MPa confining pressure and 180 °C before thermal shock. Axial strain data was lost in the middle of the test, resulting in the disconnection of the black curve.

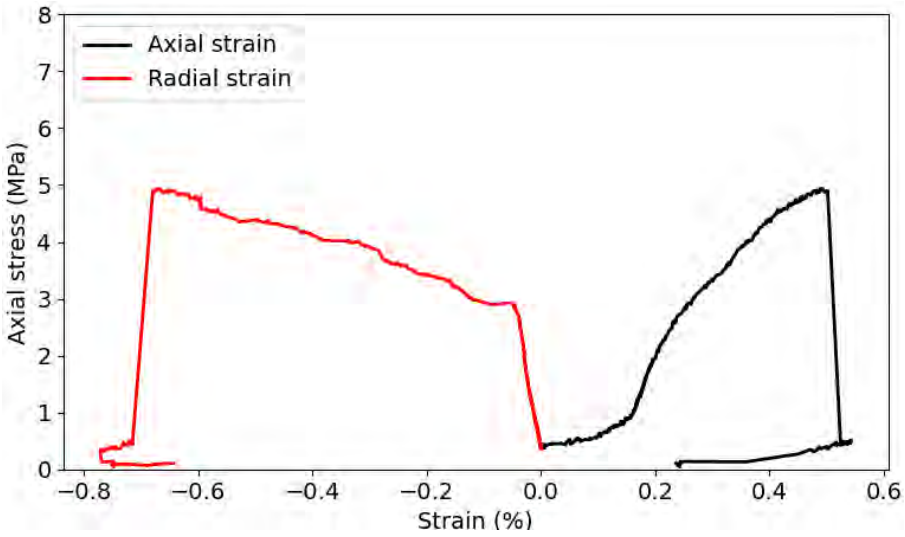

Figure 14: Stress-strain curve under 180 °C after thermal shock

Table 2 Mechanical properties of the PMHS treated cement before and after undergoing thermal shock.

PMHS treated Cement	Before Thermal Shock			After thermal shock		
	Strength (MPa)	Modulus (GPa)	Poisson's ratio	Strength (MPa)	Modulus (GPa)	Poisson's ratio
UCS 1	4.7	1.15 ± 0.05	0.14 ± 0.01	7.6	1.75 ± 0.15	--
UCS 2	4.6	1 ± 0.03	0.14 ± 0.01	6.14	1.15 ± 0.05	--
UCS 3	5.1	1.2 ± 0.1	0.1 ± 0.01	6.7	1.6 ± 0.1	--
UCS average	4.8	1.12 ± 0.06	0.08 ± 0.01	6.8	1.5 ± 0.1	0.04 ± 0.01
10 MPa	30	1.7 ± 0.2	0.09± 0.02	32	2.5 ± 0.4	0.13 ± 0.02
180 C	4.34	0.35 ± 0.01	--	4.9	1.9 ± 0.3	0.3 ± 0.02
10 MPa 180 C	25	1.33 ± 0.05	--	32.3	3.15 ± 0.15	0.17 ± 0.02

The above experimental results show the promising performance of this PMHS treated FCS incorporated calcium aluminate cement after undergoing thermal shock. The fundamental mechanisms have been explained by Sugama and Pyatina (2008), which were summarized here:

(1) Cenospheres + sodium metasilicate → silanol and sluminol groups on the surface

(2) Silanol and sluminol groups + PMHS → siloxane oxygen-linked M-FCS

(3) At high temperatures of 175 °C or 250 °C → depolymerization at the FCS surface

(4) Siloxane → low crosslinked silicon-like polymer after repolymerization

(5) The repolymerization-induced product protects FCS from pozzolanic reactions

3.2 Modeling results

Using the data obtained from our triaxial compression tests, we applied a thermoporoelasitc model to determine the safe operating envelope for this cement. Figure 15 shows that this cement has a wide range of safe applications. No failures were observed in the normal range of pressure and temperature perturbations. The temperature drawing down by 50 °C is an aggressive change that typically challenges regular brittle cement. The main reason for this wide envelope is due to low modulus of this cement.

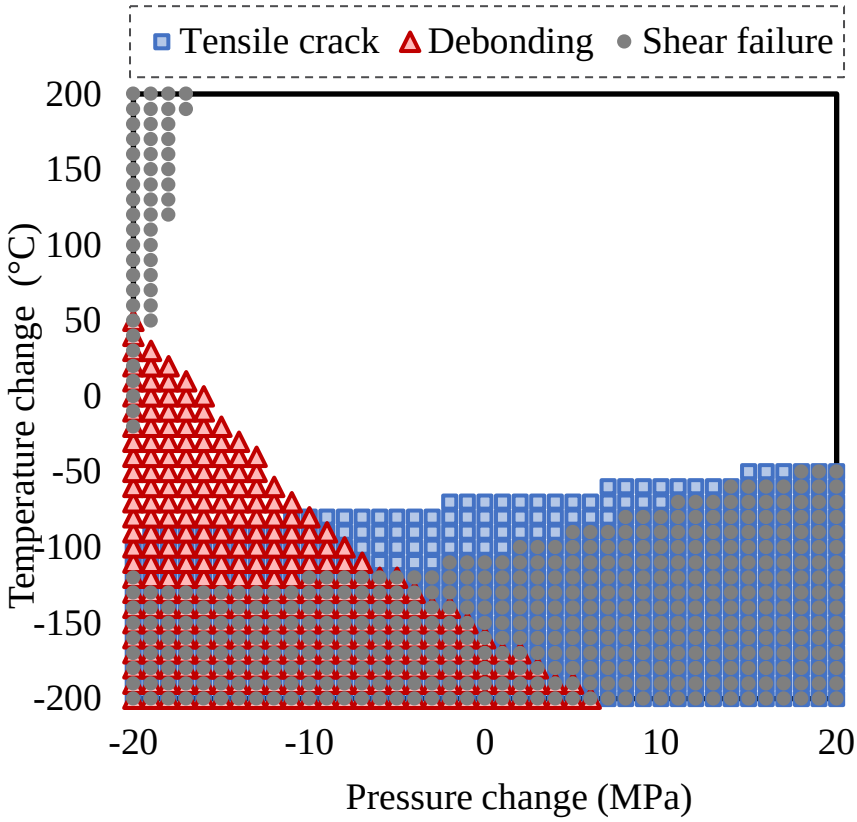

Figure 15: Safe operating envelope for the PMHS treated cement

4. Conclusions

Our study focused on PMHS-treated alkali-activated calcium aluminate cement with Class F fly ash, subjecting it to thermal cycling and measuring their mechanical properties through triaxial compression tests under high pressure and high temperatures. The key insights are summarized as follows:

1. This novel cement formulation demonstrates robust performance in resisting thermal shock. Instead of mechanical degradation, both the strength and modulus of the cement increased after exposure to thermal shock.

2. PMHS induced the dehydrogenation, depolymerization, and repolymerization processes, resulting in the formation of polymers that protects the FCS from pozzolanic reactions. This explains the cement's capability to maintain its mechanical performance under thermal shock.

3. The low modulus of this cement contributes to a broad safe operating envelope, as shown by modeling analysis. This highlights the cement's capability to effectively handle variations in pressure and temperature, offering significant advantages for its use in harsh environments.

Acknowledgement

Financial support for this work is gratefully acknowledged from the U. S. Department of Energy (DOE) Office of Energy Efficiency & Renewable Energy's Geothermal Technologies Office for "Cements and a modeling tool to calculate their viability under various exploitation conditions of HT RTES systems" with award number of DE-LC-0000016. We also gratefully acknowledge support from the U.S. Department of Energy (DOE) Office of Basic Energy Sciences for "Center for Coupled Chemo-Mechanics of Cementitious Composites for EGS (C4M)" and U. S. DOE Geothermal Technologies Office (GTO) funded project – Geothermal Limitless Approach to Drilling Efficiencies (GLADE; DE-EE0010444) led by Oxy USA, Inc.

REFERENCES

Boquera, L., Castro, J. R., Pisello, A. L., Fabiani, C., D'Alessandro, A., Ubertini, F., & Cabeza, L. F. Thermal and mechanical performance of cement paste under high temperature thermal cycles. *Solar Energy Materials and Solar Cells*, 231, (2021), 111333.

Meng, M., Pyatina, T., Solovyov, V., Bijay, K. C., & Frash, L. (2023). Evaluation of Cement Mechanical Performance in Thermal Storage Wells. In 2023 Geothermal Rising Conference: Using the Earth to Save the Earth, GRC 2023 (pp. 889-900).

Meng, M., Frash, L., Carey, J. W., Niu, Z., Zhang, W., Guy, N., ... & Welch, N. (2021). Predicting cement-sheath integrity with consideration of initial state of stress and thermoporoelastic effects. SPE Journal, 26(06), 3505-3528.

Lavrov, A., & Torsæter, M. (2016). Physics and mechanics of primary well cementing.

Pang, X., Qin, J., Sun, L., Zhang, G., & Wang, H. (2021). Long-term strength retrogression of silica-enriched oil well cement: A comprehensive multi-approach analysis. Cement and Concrete Research, 144, 106424.

Philippacopoulos, A. J., & Berndt, M. L. (2001). Mechanical property issues for geothermal well cements. *Transactions-Geothermal Resources Council*, 119-124.

Sugama, T., & Pyatina, T. (2018). Alkali-activated cement composites for high temperature geothermal wells. Scientific Research Publishing, Inc. USA.

Sugama, T., & Pyatina, T. (2021). Hydrophobic Lightweight Cement with Thermal Shock Resistance and Thermal Insulating Properties for Energy-Storage Geothermal Well Systems. Materials, 14(21), 6679.

Pyatina, T., & Sugama, T. (2018). Cements for high-temperature geothermal wells. *Cement based Materials*, 221-235.

Bauer, S. J., Barrow, P. C., Pyatina, T., & Sugama, T. (2020). Thermal expansion fluid flow and thermal shock of cement and a cement/steel interface at elevated pressure and temperature. Paper presented at 45th Workshop on Geothermal Reservoir Engineering, Stanford, 2020.

Wolterbeek, T. K. T., & Hangx, S. J. T. (2023). The thermal properties of set Portland cements–a literature review in the context of CO_2 injection well integrity. *International Journal of Greenhouse Gas Control*, 126, 103909.

Zhang, W., Eckert, A., Hilgedick, S., Goodman, H., & Meng, M. (2022). Wellbore Integrity: An Integrated Experimental and Numerical Study to Investigate Pore Pressure Variation during Cement Hardening under Downhole Conditions. *SPE Journal*, 27, (2022), 488-503.

Zhou, W., Wang, C., Meng, R., Chen, Z., Lu, H., & Chi, J. (2023). Study on thermal insulation cement and its thermal insulation characteristics for geothermal wells. *Scientific Reports*, 13(1), 4157.

High Temperature Characterization and Drilling Simulation of rock from Utah FORGE

Anthony LeBaron[1], Xiaoge Gan[1], John McLennan[2], Jim Marquardt [2], Dan Belnap[1], Yi Fang[1]

[1]SLB

[2]University of Utah

Keywords

Rock mechanics, triaxial tests, high-temperature rock, PDC bits, Discrete Element Modeling

ABSTRACT

Deep drilling through hard rock is a significant economic obstacle to the widespread adoption of enhanced geothermal systems (EGS). Decreasing drilling costs with polycrystalline diamond bits is a high priority for the geothermal industry. Therefore, it is important to characterize the mechanical behavior of rock in high-pressure, high-temperature environments and develop predictive rock cutting simulations for further optimization of drilling.

In this paper, we utilize laboratory compression tests up to 200° C to characterize rock cores from the Utah FORGE site. Two rocks were studied: A granodiorite from well 16A(78)-32 at a depth of approximately 5900 ft MD, and a gneiss from well 78B-32 at a depth of approximately 8500 ft MD. Triaxial compression tests were performed on these samples at several confining pressures up to 6,000 psi, and at temperatures up to 200° C.

After laboratory testing, a discrete element model was developed using the PFC3D software package. The model was tuned to match rock properties at room temperature and at elevated temperature through a series of triaxial compressive simulations. Then, single cutter scraping experiments were modeled. Cutting forces from the model were compared to cutting forces from single cutter rock scraping experiments, showing that the model can be used to predict and further optimize cutting performance.

1. Introduction

When drilling hard rock for enhanced geothermal systems (EGS), mechanical properties of the rock are critical to understanding drilling mechanics and reservoir stimulation. While rock recovered from the Utah FORGE site has been studied extensively at room temperature (e.g. LeBaron et al, 2023; FORGE, 2022), rock mechanical properties at high temperatures have not been studied. With reservoir rock at Utah FORGE reaching temperatures of 230° C, it is important to understand whether the rock behaves differently in situ than at room temperature.

With increasing interest in EGS, many scholars have studied the effects of temperature on igneous rocks associated with EGS. Ma et al (2020) and Yin et al (2021) both studied triaxial compression in granite at temperatures up to 400° C and confining pressure up to 60 MPa. Ma et al (2020) found that peak strength increased until the rock reached a critical temperature of 200°-300° C, and then decreased. Yin et al (2021) found that Young's modulus increases slightly up to a threshold temperature of 300°-350° C, and then decreases. Zhao et al (2017) performed triaxial tests on granite at temperatures up to 600° C and pressures up to 25 MPa. They found that Young's modulus decreased with increasing temperature, and that at 400° C and 25 MPa confinement the rock did not fail but exhibited ideal plastic flow, a different phenomenon than that observed at room temperature. Zhou et al (2024) tested a gneiss granite at 25° and 200° C, finding that strength decreased at 200° C while there was no trend in elastic modulus.

In this paper, we evaluate two rock types from the Utah FORGE site using triaxial compression tests at temperatures up to 200° C and confining pressure up to 41 MPa. We then perform a rock cutting simulation with a discrete element model calibrated to the granodiorite samples and discuss the effects of rock temperature on drilling mechanics.

2. Experimental Procedure

Tests were performed using a high-temperature load frame. The test matrix is shown in Table 1. From each rock type, 6 axially aligned plugs were made and subjected to triaxial testing: 3 at room temperature (nominally 25° C), and 3 at 93° C.

For high temperature samples, a nominal confining pressure (around 2 MPa) was applied. Then, the sample was heated and held at temperature overnight. Next, confining pressure was increased to its target value, the rock was held at this target pressure for an hour, and then axial load was applied to fail the sample.

Specimens measuring 25.4mm in diameter and 50.8mm in length were plugged from the original cores. Sample images of granodiorite and gneiss specimens are shown in Figure 1.

Table 1: Triaxial Test Matrix

Rock Type	Temperature	Confining Pressure (MPa)
Granodiorite Well 16A(78)-32 Approx. 5,800ft MD	25° C	10.3, 20.7, 41.4
	93° C	10.3, 20.7, 41.4
Gneiss Well 78B-32 Approx. 5,800ft MD	25° C	10.3, 20.7, 41.4
	93° C	10.3, 20.7, 41.4

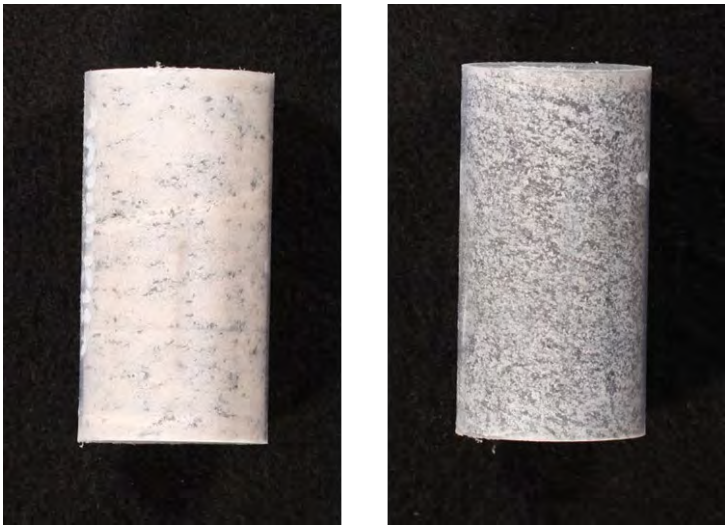

Figure 1: Granodiorite (left) and gneiss (right) plugs before testing

3. Experimental Results

3.1 Peak Strength

Peak axial stress results are shown in Figure 2. For both rock types, there was no consistent increase or decrease in strength with temperature. For the gneiss, there was almost no difference between the low temperature and high temperature tests. For the granodiorite, there was more variability but no clear trend with temperature.

3.2 Static Young's Modulus

Static Young's modulus was higher in the granodiorite than in the gneiss, with unconfined values around 55 GPa and 30 GPa, respectively. While the granodiorite showed on average no change in Young's modulus with increasing temperature, the gneiss showed slightly higher modulus at high temperature (Figure 3). However, the sample size is not adequate to draw any significant conclusions.

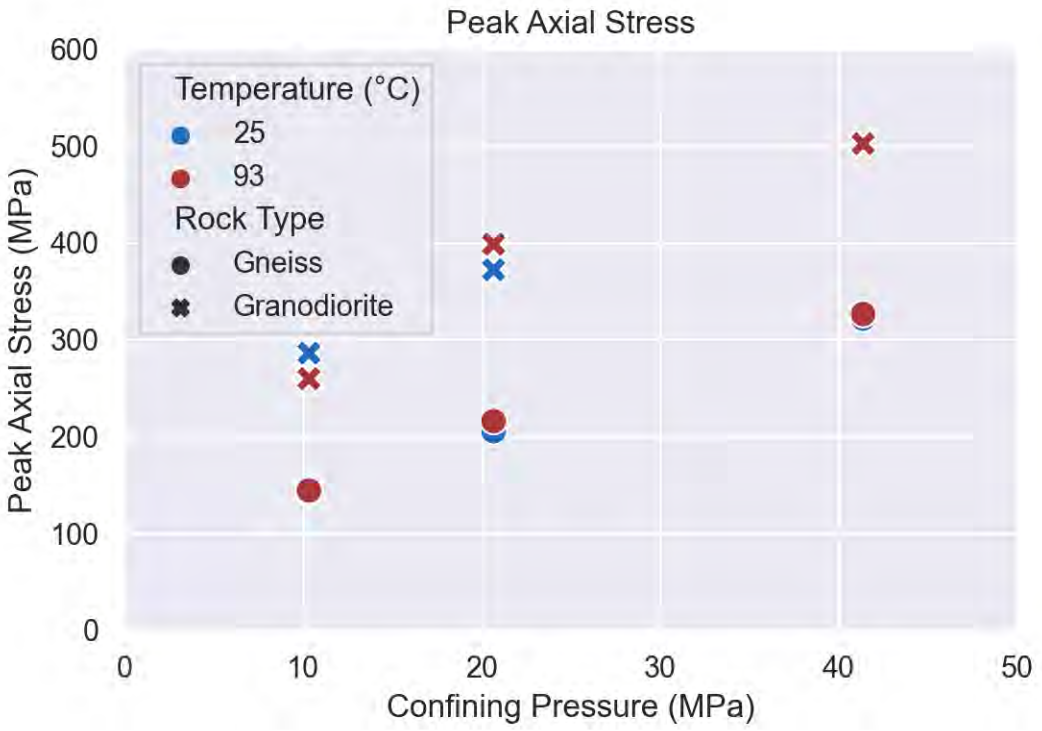

Figure 2: Peak Axial Stress for both rock types at both temperatures

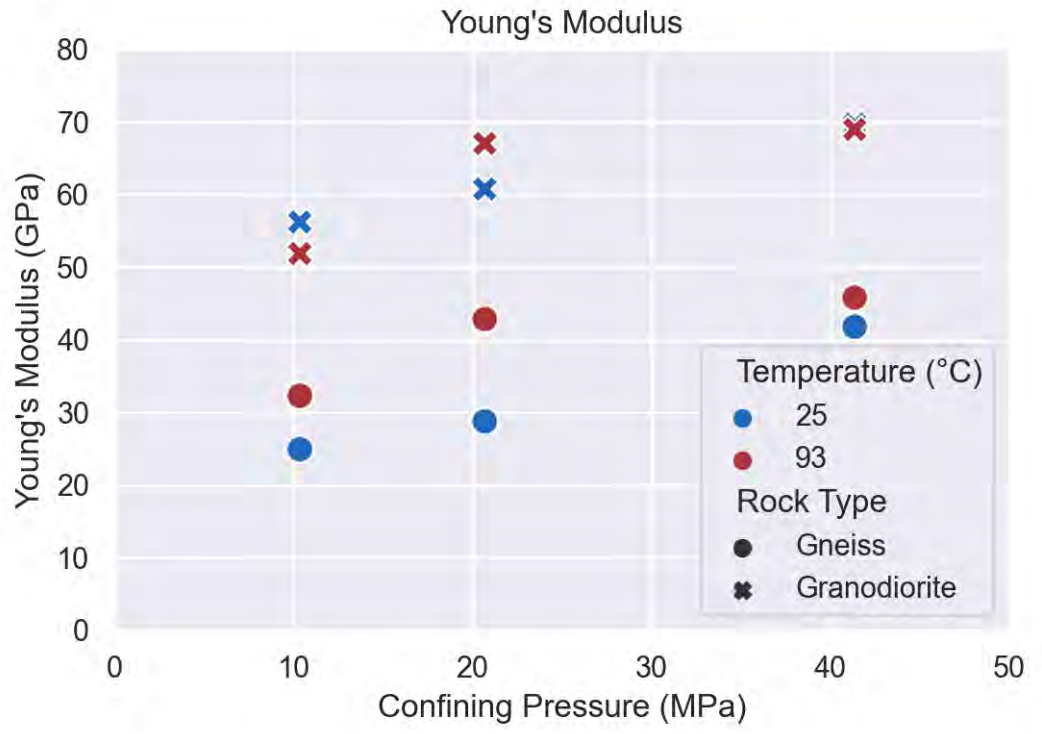

Figure 3: Static Young's modulus as measured during triaxial tests

3.3 Yield Stress

Stress at yield was determined using the Point of Positive Dilation (PPD) method; i.e. the stress at which volumetric strain changed from decreasing to increasing was taken as the yield stress of the material. As expected, yield stress consistently increased with increasing confining pressure (Figure 4). However, there was no correlation between temperature and yield stress.

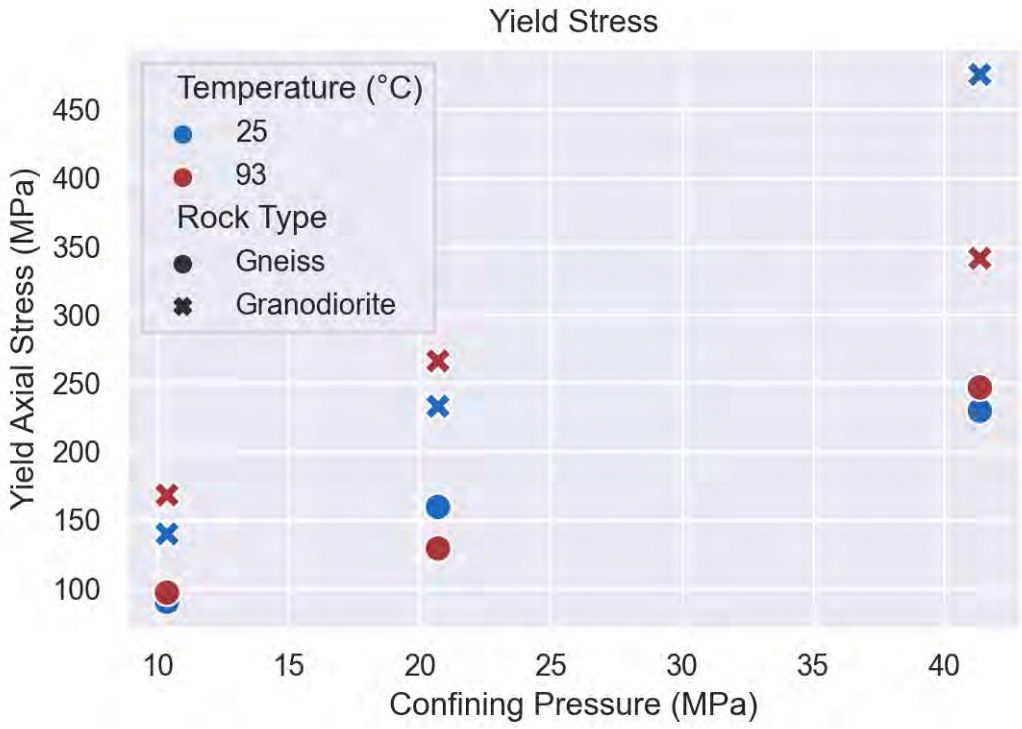

Figure 4: Yield Stress

3.4 Tests at 200° C

An additional set of paired tests was performed at room temperature and 200° C under 0.7 MPa (100 psi) of confining pressure. These pseudo-UCS tests are part of a planned series of tests at 200° C, and more results will be given in a future publication. In the data presented here, one sample of each rock type was tested at room temperature and one sample of each rock type was tested at 200° C. Axial strength for the granodiorite drops from 261 MPa at room temperature to 217 MPa at 200° C, a 17% decrease (Figure 5). Given the inherent variability of rock and the small sample size, we cannot make any broad conclusions about the strength of the granodiorite at high temperature. The gneiss showed a 4% increase in strength at 200° C, which we interpret as negligible given the inherent variability in rock.

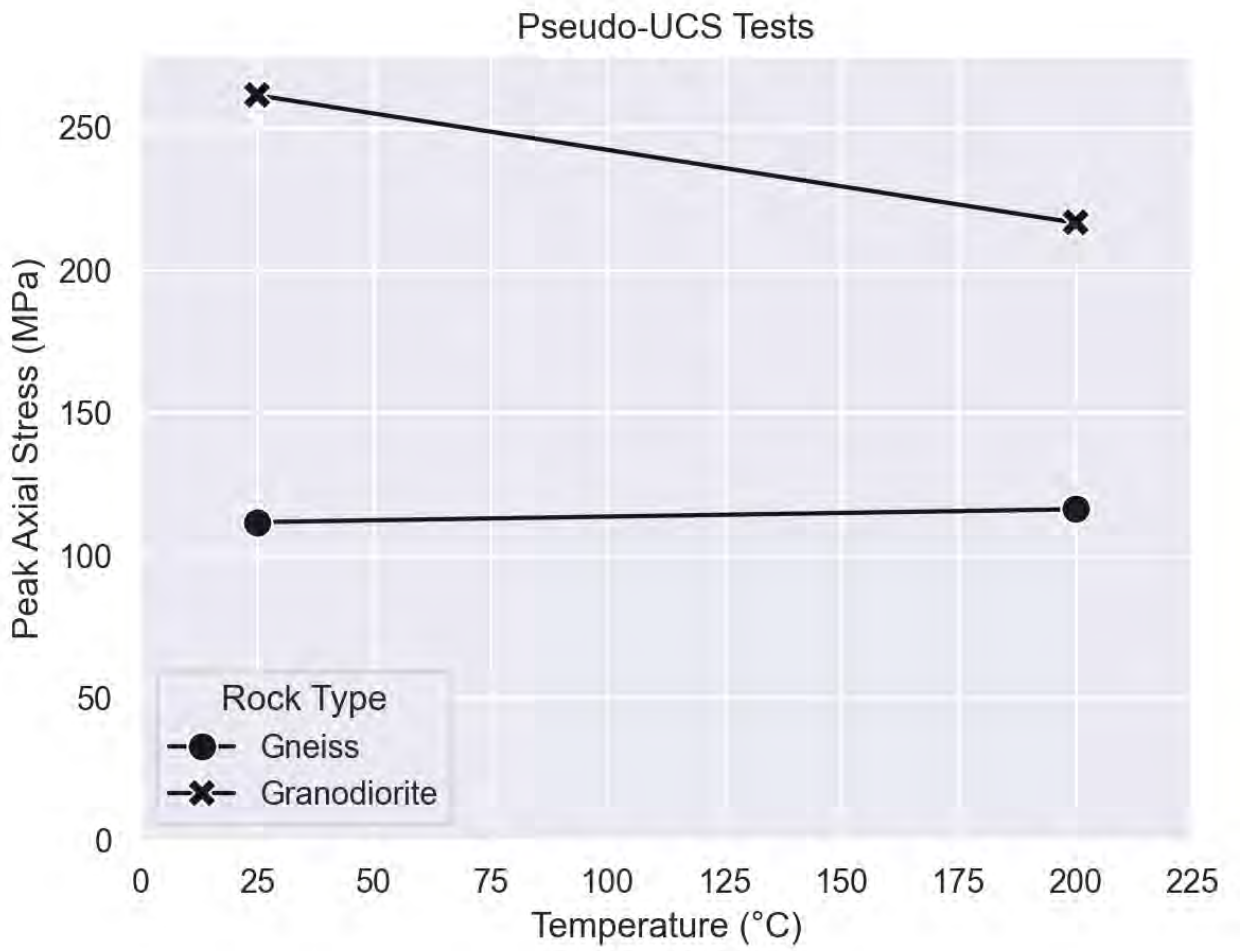

Figure 5: Axial Strength under 0.7 MPa confining pressure

4. Rock Cutting Simulation

4.1 Description of Method

Discrete Element Modeling (DEM) is a non-continuum explicit modeling technique that has been widely applied to rock cutting (e.g. Ledgerwood, 2013; Kalogeropoulos and Michalakopoulos, 2023). In DEM, rock is represented as a densely packed network of particles, typically spheres. These particles are connected by bonds that can transmit forces and moments until their strength is exceeded. We used the commercial package Particle Flow Code 3D (PFC3D) to simulate rock cutting in the granodiorite. The simulations represented rock as a random packing of rigid balls connected by deformable bonds. Then, a rigid body representing a polycrystalline diamond cutter was moved through the rock at a constant velocity and fixed depth of cut.

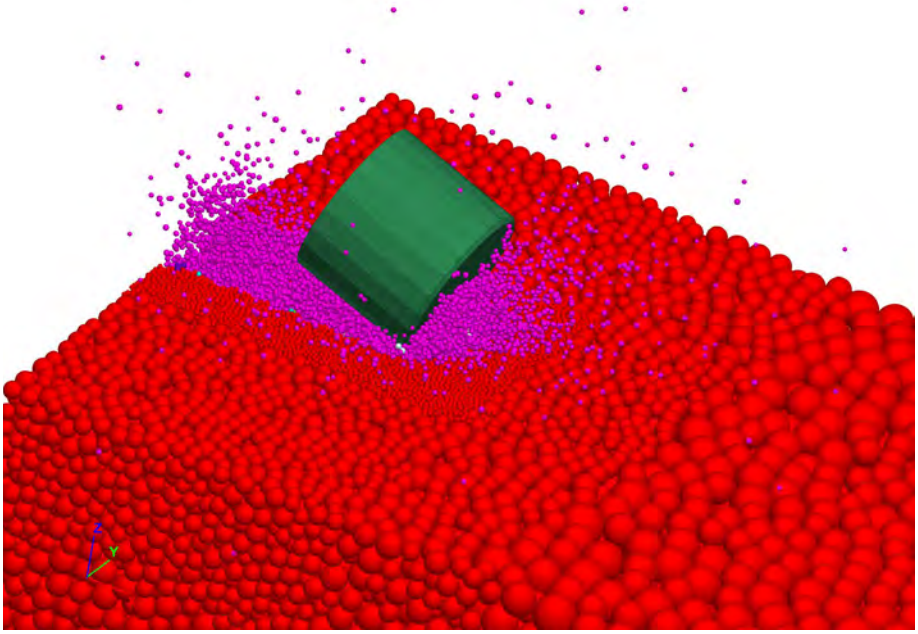

Figure 6: Screenshot of rock cutting in PFC3D at 0.060" depth of cut and 20° backrake.

In PFC3D, ball-ball interactions are governed by the parallel bond model. When intact, a parallel bond can transmit force and moment between balls. If the bond is broken by being loaded to failure, it can only transmit compressive forces and frictional shear force (Figure 7). The bond is given a tensile strength value and a shear strength envelope. If either is exceeded, the bond is considered failed and transformed into the unbonded state. The failure envelope for the parallel bond is illustrated in Figure 8. For more details on the parallel bond model, see Itasca (2021).

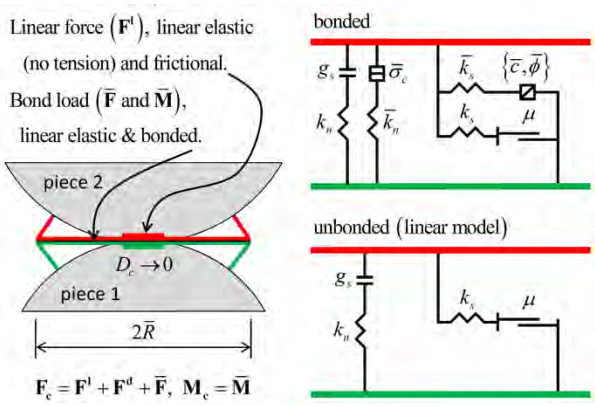

Figure 7: Schematic of the linear parallel bond model. From Itasca (2021)

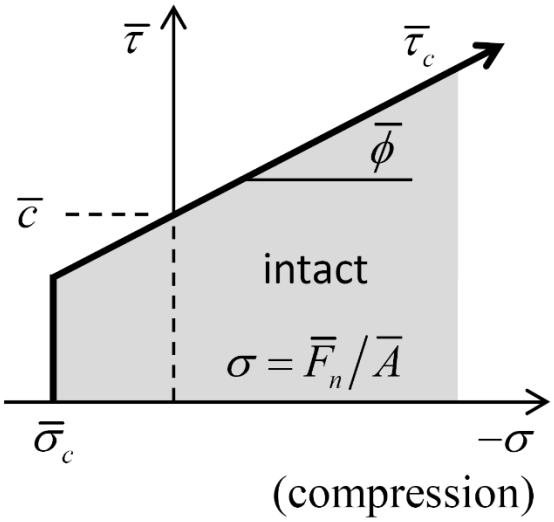

Figure 8: Failure envelope for a single linear parallel bond. From Itasca (2021).

The synthetic rock was assembled as a graded distribution of randomly packed balls. The balls that underwent cutting were the smallest, while balls furthest from the cutting zone were the largest (Figure 6). The graded arrangement permits high-fidelity simulation in the cutting zone and a realistic far-field elastic response while minimizing computational cost. Numerical damping was used to create a quasi-static rock cutting model. Damping force is applied to ball *i* as:

$$F_i + F_i^d = M_i A_i \tag{1}$$

Where F_i is the sum of physical forces applied to the ball, F_i^d is the non-physical damping force, and M_i and A_i are the mass and acceleration of the ball. The non-physical damping force is

$$F_i^d = -\alpha\, |F_i| sign(V_i) \tag{2}$$

Note that the negative sign in Eq. (2) ensures that the magnitude of velocity is always decreasing. In this study, $\alpha = 0.7$ to implement a quasi-static condition.

4.2 Model Parameters

A synthetic rock material was calibrated to match the triaxial compressive strength of the granodiorite from this study. Models were set up to generate cylindrical rock samples 12.5mm in diameter by 25mm long. For the uniaxial compressive test, the rock material was compressed axially between displacement-controlled rigid walls. For triaxial compressive tests, an outer wall simulating an elastic membrane was applied to the rock sample and pressure was applied until the desired confining pressure was reached. Then, the displacement-controlled rigid walls were applied to produce axial stress. Figure 9 shows a sample after failure from a confined compression test. Displacement in the vertical (z) direction shows a shear band running from top right to bottom left of the specimen, mimicking the actual failure mode of rock compressed axially under high confining pressure.

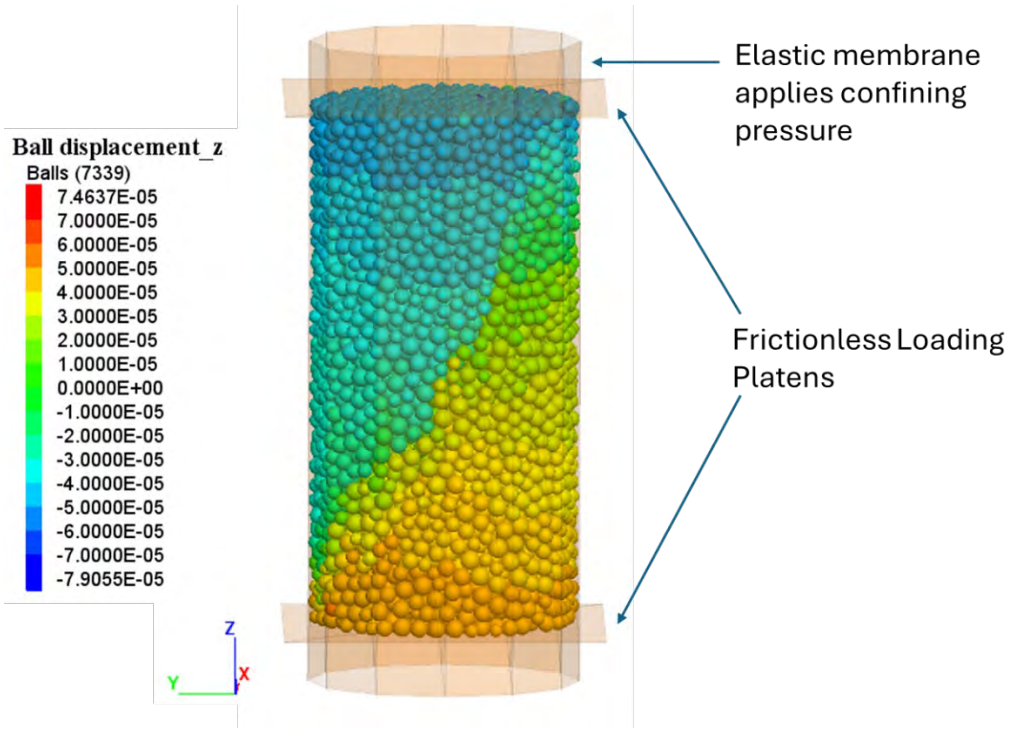

Figure 9: Ball displacement after failure in a triaxial compression test. A shear band runs from bottom left to top right.

Bond and ball micro-parameters are given in Table 2. While most properties were assigned as constants, ball diameter and bond strength were assigned randomly for each ball and bond. The value was chosen by randomly sampling a distribution. For ball diameter, a uniform distribution between 0.4 and 0.6 mm was used. For bond tensile strength and cohesion, a Gaussian distribution was used based on the mean and standard deviation given in Table 2

Table 2: Micro-parameters for granodiorite

Parameter	**Value**
Bulk Density	2600 kg/m^3
Ball Minimum Diameter	0.4 mm
Ball Maximum Diameter	0.6 mm
Bond Elastic Modulus	29 GPa
Bond shear modulus $\overline{k_s}$	9.1 GPa
Ball-Ball Friction Coefficient μ	0.5
Parallel Bond Installation Gap	7E-5 m
Parallel Bond Tensile Strength $\bar{\sigma_c}$	120 MPa mean, 24 MPa Standard Deviation
Parallel Bond Cohesion $\bar{c}$	120 MPa mean, 24 MPa Standard Deviation
Parallel Bond Friction Angle $\bar{\phi}$	60°

These model parameters reproduced the peak strength of the rock under triaxial compression well (Figure 10), especially at higher confining pressure. Note that unlike real rock, the parallel bond model does not recreate the increased elastic modulus observed at high confining pressure. The discrete element model also fails to replicate the residual strength and post-peak softening seen in

the laboratory tests. Instead, stress drops quickly after reaching peak strength, with none of the models showing notable softening. Nonetheless, the parallel bond model can predict the forces associated with rock cutting.

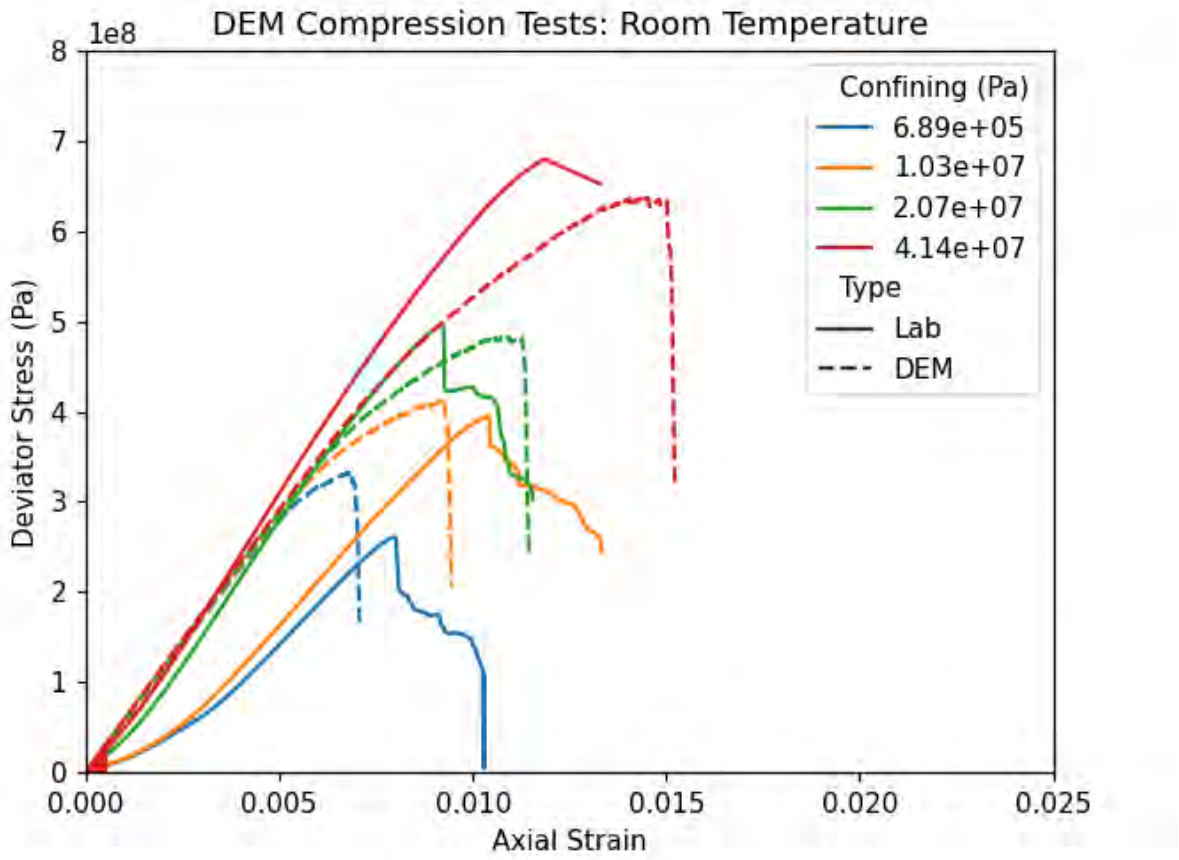

Figure 10: Stress-strain response of DEM and laboratory experiments for unconfined and confined compression.

4.3 Rock Cutting Model

After the model was calibrated via unconfined compression and triaxial compression, a graded rockmass was generated using the micro-parameters from the calibration. The discrete element model was evaluated at 0.5, 1.0mm and 1.5mm depth of cut. Cutting force results were compared to laboratory results reported by LeBaron et al (2023) for the granodiorite at these same DOC.

At all depths of cut, the model showed a good match with mean cutting force and the standard deviation of cutting force (Figure 11). While many rock cutting modelers report a correlation between peak forces (e.g. Qianqian et al, 2015) or mean force (e.g. LeBaron et al, 2023), the model presented here shows a good reproduction of the mean force and peak force.

Peak forces are the highest forces experienced by the cutter and are the forces associated with rock chipping. In these models, peak forces, taken here to be the 95th percentile of forces recorded during cutting, matched well at all three depths of cut (Figure 12).

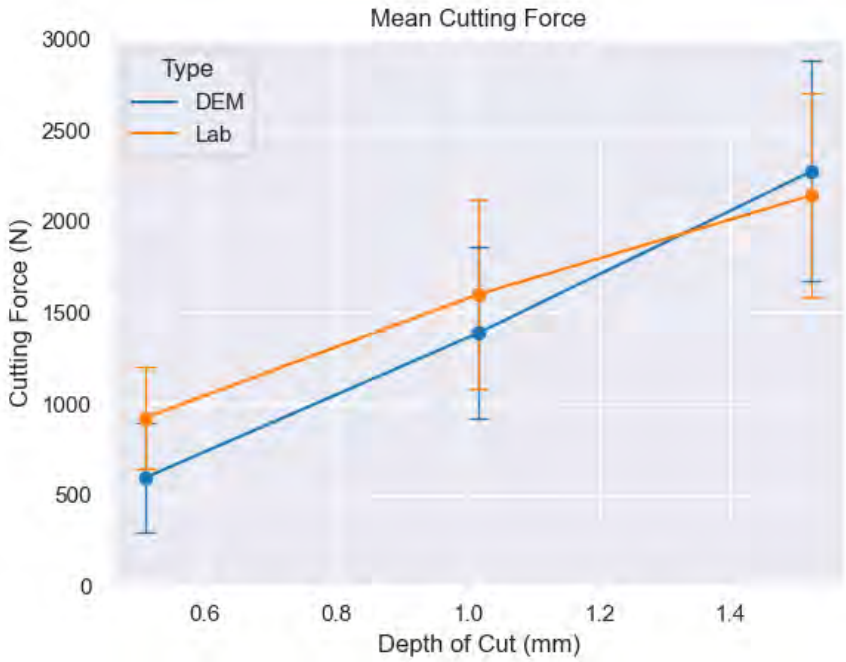

Figure 11: Mean Cutting force at various depth of cut. Error bars represent one standard deviation.

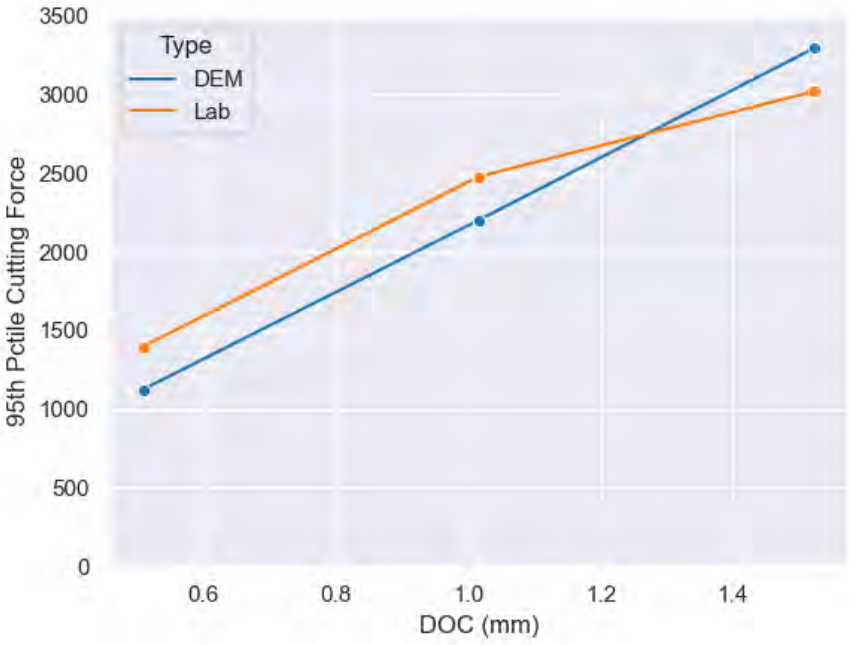

Figure 12: 95th percentile cutting force for all three DOC.

5. Conclusions

With drilling as one of the key challenges in EGS, it is critical to understand the in-situ mechanical behavior of dry hard rock to optimize cutter and drill bit design and operating parameters. The

granodiorite and gneiss presented here are two of the major rock types encountered during drilling at the Utah FORGE site. The high temperature tests shown here do not support the conclusion that rock mechanical properties are inherently different at 93° C than they are at room temperature. However, the preliminary tests shown at 200° C may show an effect of decreasing strength and increasing Young's modulus at high temperature. Further results will help to clarify the trend.

Discrete element models implemented in PFC3D, are a promising tool to predict rock cutting efficiency. The parallel bond model, one of the simpler bonded particle models available in PFC3D, appears adequate to predict rock cutting forces as validated by laboratory tests at multiple depths of cut. The rock cutting forces discussed here show a good match of not only mean force, but the overall distribution of forces experienced by the cutter during rock cutting. By knowing the full range of force fluctuation that the cutter undergoes, it may be possible to use this tool to predict cutter fatigue life or even vibrations at the rock-cutter interface.

REFERENCES

Chen, Y.L., Wang, S.R., Ni, J., Azzam, R., and Fernandez-Steeger, T.M. "An experimental study of the mechanical properties of granite after high temperature exposure based on mineral characteristics." *Engineering Geology*, 220, (2017), 234-242.

DuPriest, F. and Noynaert, S. "Continued Advances in Performance in Geothermal Operations at FORGE Through Limiter-Redesign Drilling Practices." *IADC/SPE International Drilling Conference and Exhibition.* Galveston, USA (2024).

El-Said, K., Gierke, B., Howard, E., and Gradl, C. "Review of Drilling Performance in a Horizontal EGS Development." *49th Workshop on Geothermal Reservoir Engineering*. Stanford, USA (2024)

FORGE. "Mechanical Properties Well 16A(78)-32 and Well 78B-32." (2022)

Itasca Consulting Group, Inc. "PFC – Particle Flow Code, Ver. 7.0." (2021) Minneapolis: Itasca

LeBaron, A., McClennan, J., Marquardt, J., Gan, X., Jones, C., Belnap, D., Fang, Y., Panayirci, M. and Moore, J. "Numerical Simulation of Rock Cutting for the Utah FORGE Geothermal Project." *Geothermal Rising Conference Transactions*. Reno, USA (2023)

Ma, X., Wang, G., Hu, D., Liu, Y., Zhou, H., and Liu, F., "Mechanical properties of granite under real-time high temperature and three-dimensional stress." *International Journal of Rock Mechanics and Mining Sciences*, 136, (2020)

Qianqian, Z., Zhennan, H., Mengqi, Z., and Jianguang, Z. "Prediction of tool forces in rock cutting using discrete element method." *Electronic Journal of Geotechnical Engineering*, 20 (2015) 1607-1625.

Yin, W., Feng, Z., and Zhao, Y. "Effect of Grain Size on the Mechanical Behaviour of Granite Under High Temperature and Triaxial Stress." *Rock Mechanics and Rock Engineering*, 54 (2021), 745-758.

Zhao, Y.S., Wan, Z.J., Feng, Z.J., Xu, Z.H., and Lian, W.G. "Evolution of mechanical properties of granite at high temperature and high pressure." *Geomechanics and Geophysics for Geo-energy and Geo-resources*, 3, (2017), 199-210.

Zhou, H., Liu, Z., Liu, F., Shao, J., and Li, G. “Anisotropic strength, deformation and failure of gneiss granite under high stress and temperature coupled true triaxial compression.” *Journal of Rock Mechanics and Geotechnical Engineering*, 16, (2024), 860-876.

Zou, J., Yang, W., and Han, J. “Discrete Element Modeling of the Effects of Cutting Parameters and Rock Properties on Rock Fragmentation.” *IEEE Access*, 8, (2020), 136393-136408.

A Coupled Simulation of Fracture Sealing of Lost Circulation Materials at Elevated Temperatures

Chong Lin, Arash Dahi Taleghani*

Department of Energy and Mineral Engineering, Pennsylvania State University, State College, 16801, USA

Email address: aud440@psu.edu

Keywords

Geothermal well drilling; HTHP formation; lost circulation material; CFD-DEM; fracture sealing.

ABSTRACT

Lost circulation is one of the major problems encountered in drilling geothermal and HTHP (high temperature and high pressure) formations. A part of these problems can be attributed to the high temperature and presence of hard and fractured rocks. Consequences and treatment of these lost circulation events can be extremely costly. Underbalanced drilling and LCMs (lost circulation materials) are the two most common methods to address the lost circulation problem. However, some LCMs have proved to be unsuccessful due to the unpredictable nature of fractures, complicated dynamics of LCM, as well as the change of mechanical properties of LCMs under high-temperature conditions. Long-distance circulations in high-temperature environments usually lead to the decline of size, strength, and friction coefficient of LCMs in parallel to the reduction of drilling fluid viscosity, and eventually failure in sealing fractures. In this paper, we developed a coupled CFD-DEM by combining computational fluid dynamics with discrete element methods to simulate the fracture sealing process by LCMs. The viscosity of drilling fluid, particle size, Young's Modulus, Poisson's ratio, and friction coefficient of LCMs were determined to represent possible variations under geothermal conditions. A series of sensitivity studies were conducted to further understand the fracture sealing efficiency of LCMs at elevated temperatures. The results show that a reduction in particle size, friction coefficient, and Young's modulus lowers bridging's probability, and slows down bridging initiation, but deepens the sealing depth, and tighter but the result is an unstable sealing zone. We noticed that the bridging mechanism changes from single-particle bridging to dual-particle bridging as particle size reduces. Also, the reduction of drilling fluid viscosity makes the sealing zone form faster and shallower.

1. Introduction

Geothermal energy is an important renewable energy resource especially for off-grid locations. It has received increasing attention in recent decades because it is an almost renewable, clean, low-carbon, safe, and ubiquitous resource. Therefore, geothermal energy can be an alternative to traditional fossil energy and a supplement for the growing energy consumption worldwide. The

geothermal well has been the most effective technique to get geothermal energy from underground to the surface. Drilling the well is the primary element in the cost of geothermal energy application, however, due to high temperatures (160~300+ °C), hard formation rocks (240+ MPa compressive strength), highly fractured (fracture apertures in the order of centimeters) and under-pressured situations, lost circulation has been one of the major in increasing the costs for drilling and completion in geothermal wells. Lost circulation treatments may represent possibly 15% of the total well cost (Finger and Blankenship, 2010). Lost circulation may also lead to troublesome, unsafe and costly consequences, such as drilling fluid loss, significant down times, stuck pipe, wellbore instability, well kick, incomplete primary cement job and in severe case well abandonment. The treatment for these issues can be very challenging and costly (Pierce and Livesay, 1994).

Lost circulation materials (LCMs), cementing, blind drilling and underbalanced drilling are the most common methods to address the lost circulation problem during geothermal drilling and completion. LCMs are routinely added to the drilling fluid to prevent lost circulation and primarily used when lost circulation is encountered. Unfortunately, most of the LCMs developed and used in oil and gas drilling have proved to be little or no use due to the unpredictive nature of the fractures (with the width in the order of centimeters), the complicated motion of LCM particles, as well as the change of mechanical properties of LCMs at elevated temperatures (Loeppke et al. 1990; Visser et al. 2018). However, using LCMs is still the first choice of drillers to treat lost circulation problems because it takes up very little time and minimum equipment and is reasonably inexpensive if successful. Using LCMs is also a better choice for temporary sealing of production zones rather than permanent sealing by cement (Finger and Blankenship, 2010). It is noteworthy that LCMs can be added to the cement slurry to cure severe lost circulation events induced by large fractures.

Three typical LCMs are used in geothermal drilling: fibrous, flaky and granular. Fibrous and flaky LCMs bridge the fracture to change the fracture into a porous structure and catch the following LCMs. Granular LCMs form a porous bridge, which gradually reduces the permeability of the sealing zone (Nugroho et al., 2017). Loss of circulation due to induced or natural fractures is best remedied by Mica flakes which have proven to function adequately, whereas conventional LCM materials used in drilling muds should be avoided (Visser et al., 2018). Unfortunately, although the application of LCMs is not satisfactory, the underlying mechanisms for the failure of LCMs to seal fracture are still unclear. This paper develops a CFD-DEM model to simulate the fracture sealing process by LCMs. The viscosity of drilling fluid, particle size, Young’s Modulus, Poisson's ratio, and friction coefficient of LCMs were determined to represent a possible variation range under the geothermal temperature range. A series of sensitivity analyses were conducted to further understand the sealing efficiency of LCMs in fractures for temperatures rising up to 300 °C. Through this, we are trying to understand the mechanisms behind the failure of conventional LCMs in sealing fractures in geothermal environments.

2. Effect of elevated temperature on basic properties of LCMs and drilling fluid

Temperature heavily influences the viscosity of the drilling fluid. Regardless of the base fluid, AV (apparent viscosity) of the drilling fluid generally decreases with an increase in temperature. However, PV (plastic viscosity) of drilling fluid is found to decrease initially, and then slightly increases with an increase in temperature (Wang et al. 2012; Garcõâ et al. 2001; Amani and Al-

jubouri 2012; Sheng-ying et al. 2008). Table 1 gives the viscosity variation of different drilling fluids at elevated temperatures. We can see that the viscosity of the drilling fluid can decrease from nearly 300 mPa·s to 1 mPa·s as temperature raises over 200 ℃. The lowest viscosity of drilling fluid is 0.25 mPa·s at high temperatures (Garcõâ et al., 2001).

Table 1 Viscosity variation of drilling fluid at elevated temperatures.

Drilling Fluid	Density (g/cm^3)	T (℃)	AV (mPa·s)	PV (mPa·s)	Reference
Fresh water-based	2.2	50~220	320~63	312~51	Wang et al. (2012)
Brine-based	2.2	50~220	117.5~44.5~55	110~34~65.5	
Geothermal spring water-based	1.031	15~150	(11.2~19.7)~(1.9~8.6)	(6.0~10.7)~(2.3~6.7)	Avci and Mert (2019)
2# Diesel-based	1.32	23.9~204.4	(53~167)~(6~17)	(43~144)~(3~12)	Yan and Zhao (2003)
Mentor26 mineral oil-based	1.32	23.9~204.4	(80~217)~(12~29)	(58~167)~(7~18)	

When LCMs are pumped and circulated from the ground to the thief zone, they will experience a series of environmental changes as well as physical and chemical reactions such as increases in temperature and pressure, or drilling fluid immersion, high-speed shearing, collision between particles and flow boundaries and collision between particles. Then the abrasion of LCMs can be promoted by thermal, mechanical, and chemical interactions occurring during the transport process. Experimental studies have shown that walnut shell, graphite, marble granules, calcium carbonate, and other common LCMs experienced a significant reduction of particle size under a specific shear rate in the drilling fluid at high temperatures for a one-half to a complete day (Scott et al. 2012; Yang 2015; Valsecchi 2014; Grant 2016). Kang et al. (2019) showed through experiments that size degradation of granular calcium carbonate by abrasion is slightly sensitive to the fluid temperature (80~160 °C). Their later work shows that walnut shell and millimeter-scale granular calcium carbonate experience both quality and size loss after heating to 180 °C in the oil-based drilling fluid (Kang et al. 2019). Decreasing fluid viscosity can result in a higher size degradation rate (Kumar et al., 2013). Therefore, size degradation of LCMs may aggravate at elevated temperatures due to the viscosity of the fluid decreases.

Table 2 Size degradation of LCM particle at elevated temperatures

LCM	Rotation speed (rpm)	t (min)	Fluid	T (°C)	D_{90} (μm)	Size degradation rate (%)	References
Calcium carbonate	1000	30	Water-based fluid	80	44.153	35.80	Kang et al. (2019)
				100	44.153	35.37	
				120	44.153	34.40	
				120	16.435	10.57	
				120	27.765	28.75	
				120	201.431	45.05	
				120	510.447	59.46	
				140	44.153	33.40	
				160	44.153	33.54	
Calcium carbonate	4000	30		49	300~1400	5~80	Kumar et al. (2013)

Graphitic carbon	Xanthan viscosifier	700~1250	14~17
Walnut	solution	900	1

Mechanical properties of geomaterials are reported to be sensitive to temperature. The most critical and typical mechanical properties of LCMs are their compressive strength, Young's modulus, Poisson's ratio and friction coefficient. The experimental results of carbonatite (limestone and marble) show that compressive strength, elastic modulus, and Poisson's ratio generally decrease at elevated temperatures (Fig. 1). The uniaxial compressive strength can reduce from 120 MPa to 86MPa after heating up to 300 °C, the elastic modulus can reduce from 22 GPa to 7 GPa after heating at 300 °C, and the Poisson's ratio can reduce from 0.3 to 0.1 after heating at 300 °C (Brotóns et al. 2013; Zhang et al. 2009). Kang et al. (2019) found that the friction coefficient of walnut shell and calcium carbonate reduces to 28% and 1% of the original value after heating to 180 °C, respectively. The carbonatite is the natural source of calcium carbonate, which is the most popular LCM used in drilling operations. In other words, the compressive strength, elastic modulus, Poisson's ratio and friction coefficient of LCMs generally decrease as temperature increases.

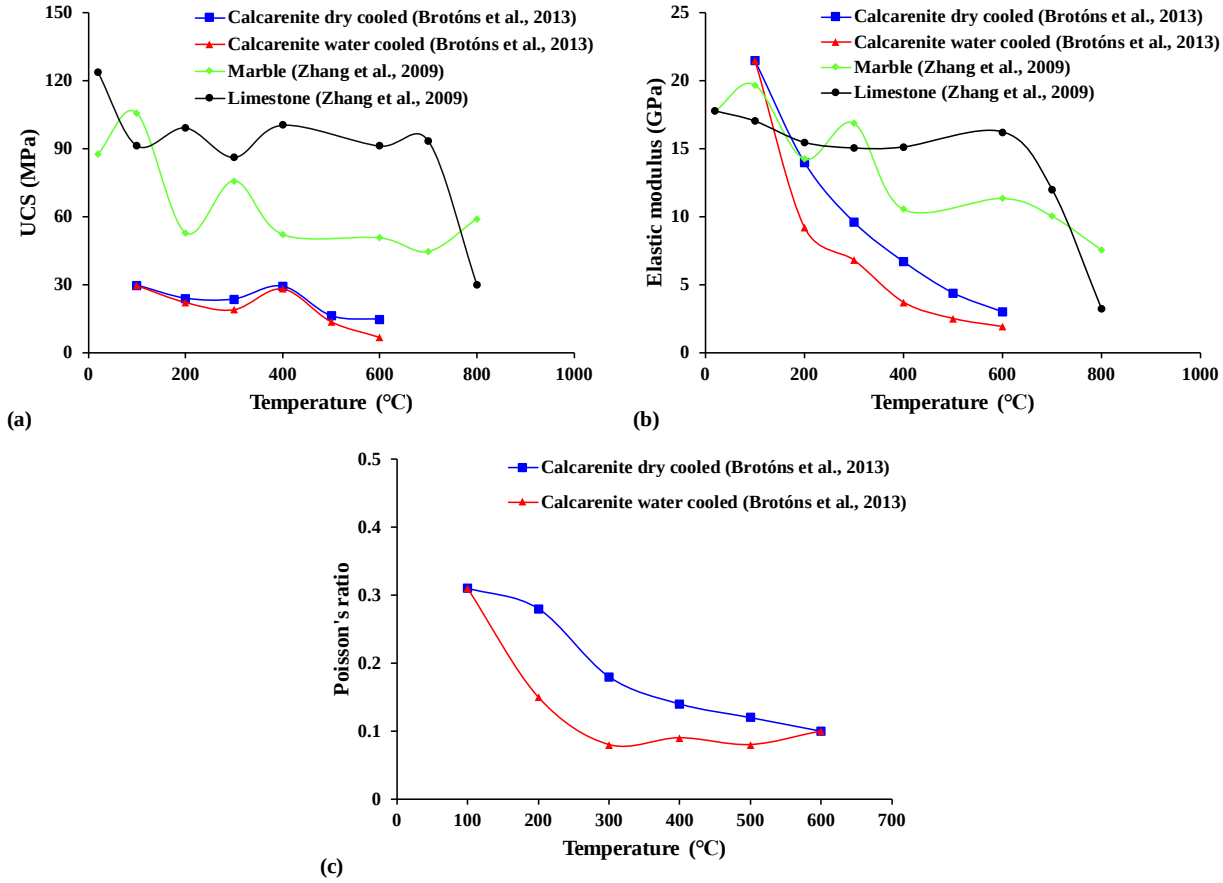

Fig.1 Mechanical properties of carbonatite change at elevated temperatures, e.g. (a) uniaxial compression strength (UCS) ; (b) Elastic modulus; and (c) Poisson's ratio.

3. Methodology

The goal is to simulate the flow of LCM laden drilling fluid and the sealing process driven by bridging of LCM particles in a vertical fracture. We mainly investigate the effect of variations in mechanical properties at elevated temperatures on the sealing process. The fracture geometry used here is a vertical wedge shown in Fig. 2. The modelled fracture has a length of 100 mm, a height of 25.4 mm, and width varying gradually from 1 mm to 0.33 mm from the inlet to the outlet (the fracture inlet width, W_{fi}=1mm). We assumed that formation is very stiff so the fracture walls are assumed to be rigid smooth surfaces, although the fracture roughness may help the bridging process. Hence, this model can be a simplified representation of a part or whole of the real fracture in the subsurface.

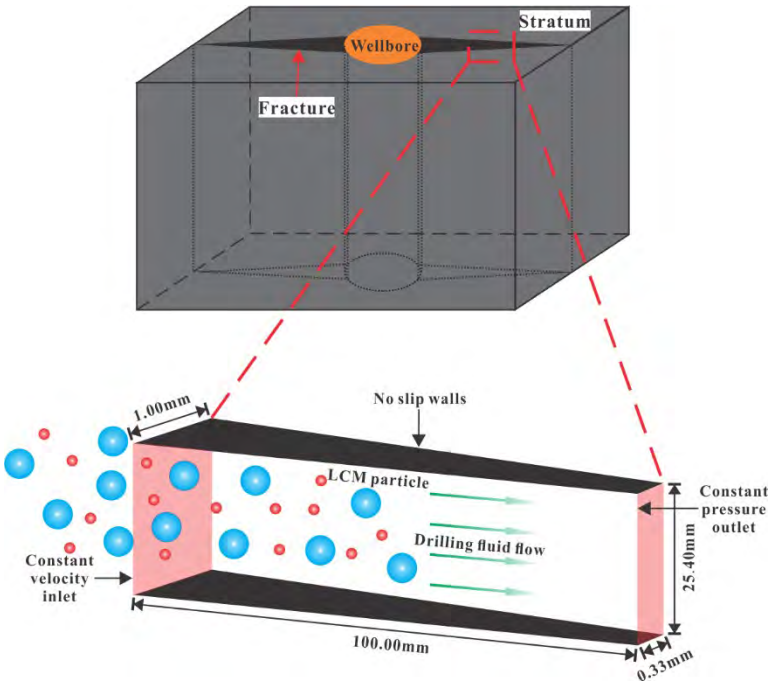

Fig. 2 A schematic diagram of fracture geometry used in the simulation.

The coupled CFD-DEM model of fracture sealing by LCMs is developed based on the open source CFDEM®coupling (Kloss et al. 2012; Hager et al. 2018). The number of particles used in the simulation is about 100, 000, the unresolved CFD-DEM method (Hager, 2014) is utilized to simulate the considerable number of particles' involved in the fracture sealing process. In the CFD-DEM, the fluid phase is assumed to be a continuum and its meso-scale motion is described by the volume-averaged Navier-Stokes equation, while the micro-scale motion of the solid phase is described by Newton's and Euler's second laws. The motion of an incompressible-fluid phase in the presence of a secondary particulate phase is governed by the volume-averaged Navier–Stokes equations (Zhou et al. 2010)

The DEM used here is a Lagrangian method. The trajectory of each particle is calculated under the consideration of influences by other particles, walls or present forces. The motion of a particle consists of a rotational component and a translational component. The translational and angular accelerations of a sphere are based on the corresponding momentum balances.

The CFD domain is gridded into hexahedral mesh cell with size of 2mm×2mm×(0.34~1)mm. The characterized length of a single cell is at least 3 times larger than particle diameter, which can obtain accurate and convergent results (Peng et al., 2015). Besides, this size also ensures the porosity changes gently. A constant injection rate, constant pressure and a no-slip wall were set as the boundary conditions at the inlet, outlet and fracture walls, respectively. A linear velocity of 1m/s along the fracture direction is the initial velocity condition at the inlet. The pressure at the outlet is considered to be zero. The gravity is 9.81 m/s^2 in the direction of fracture height. Other field data will be calculated based on these velocity and pressure field data. The solver cfdemSolverPiso provided by CFDEM® coupling for handling unresolved CFD-DEM problems is used to solve the governing equations. The implementation of the solvers is based on OpenFOAM's pisoFoam. The Reynolds Number (*Re*) is a non-dimensional parameter which indicates whether the flow follows the laminar or turbulent regime. According to the Reynolds number of the non-circular duct calculated by the hydraulic diameter, the Reynolds Number in our study remains less than 100, which indicates a laminar flow inside the fracture. Although drilling fluids are typically non-Newtonian fluids, the shear thinning behavior can be approximated as Newtonian fluid due to the relatively low flow rate in this problem. Thus, the drilling fluid flow is treated as a laminar flow of incompressible Newtonian fluid, here. After a comprehensive consideration of Courant number for CFD calculation, Rayleigh time, Hertz time and particle relaxation time for DEM calculations, and response time of fluid and particle, the time step of CFD and DEM was chosen 10^{-5} and 10^{-7}s, respectively. Therefore, the coupling time steps are every 100 DEM time steps.

For the next sections, we have designed a series of numerical experiments to understand the effect of mechanical property variations at elevated temperatures on the fracture sealing process. The basic parameters used in the simulation are shown in Table 3.

Table 3. Parameters of the fluid phase and solid phase used in the simulation

Phase	Property parameter	Value
Fluid	Density, kg/cm^3	1700
	Dynamic viscosity, Pa·s	0.0001/0.01/0.05/0.1/0.15
Solid	Density, kg/cm^3	2700
	Diameter, mm	0.1/0.2/0.33/0.4/0.5/0.6/0.7/0.8/0.9/1.0
	Young's modulus, GPa	0.1/1/10/30/50/70/100
	Poisons ratio	0.1/0.2/0.3/0.4/0.5
	Restitution coefficient	0.5
	The friction coefficient of particles	0/0.2/0.4/0.6/0.8/1.0
	The friction coefficient of particle and fracture surface	0/0.2/0.4/0.6/0.8/1.0

4 Results and Discussion

4.1 Effect of thermally reduced viscosity of drilling fluid on fracture sealing

Fig. 3 to Fig.4 show that the formation of a sealing zone by LCMs can be significantly influenced by the reduction of drilling fluid viscosity at elevated temperatures. The volume concentration of the LCMs is 10% in all simulations. A sealing situation is when particles stop and accumulate in a cross-section of the fracture, and the pressure of the fracture inlet builds up simultaneously. First of all, any reduction of the drilling fluid viscosity changes the velocity of LCM particles at high

temperatures. In low-viscosity drilling fluid, LCM particles move faster but with a lower local concentration compared to that in the high-viscosity drilling fluid. LCM particles move further and bridge faster at low viscosity (Fig. 3). However, the settlement of particles in the fracture is inconspicuous because of the insertion velocity, fracture length and particle concentration. Reduction of the drilling fluid viscosity has significantly shortened the sealing zone depth, in other words, sealing occurs earlier inside the fracture. When the viscosity of drilling fluid drops from 150 to 0.1 mPa·s, the sealing zone depth decreases initially and then changes little after 10 mPa·s (Fig. 4). Results of μ=0.1 and 1 mPa·s are similar while results of μ=10, 50, 100 and 150 mPa·s are similar. It is notable that the viscosity of the particle-laden fluid cannot change with various volume fractions of particles in the unresolved CFD–DEM model (Blais et al., 2016). Therefore, the viscosity here is only the viscosity of the pure fluid phase.

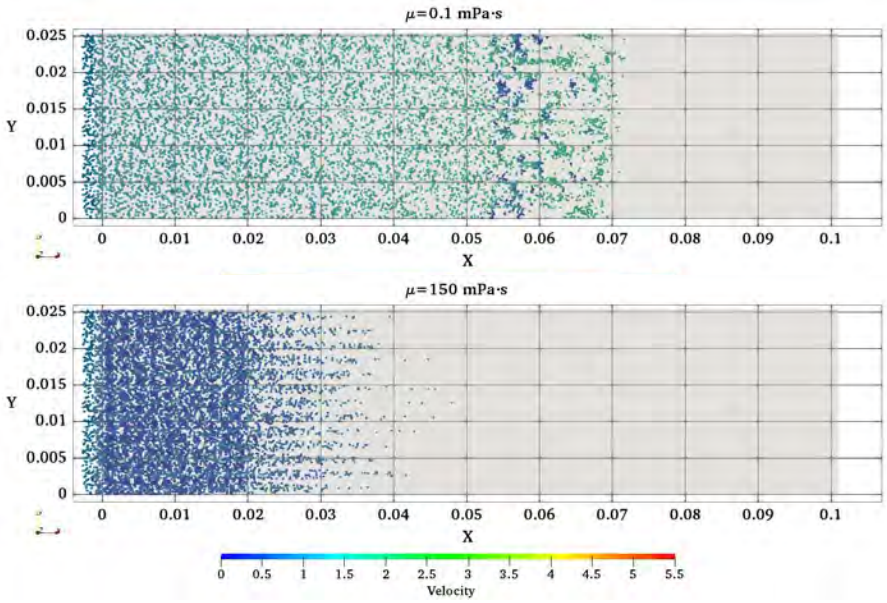

Fig. 3 Snapshots of LCM particles in motion under various drilling fluid viscosity after 0.6~0.8 $V_{fracture}$ drilling fluid is moved through the fracture. LCM particles moves along the fracture length direction with few particle bridges in low viscosity drilling fluid. The color means the velocity magnitude of the particle, which reflects the movement state of particles. The velocity increases gradually as color changes from blue to red.

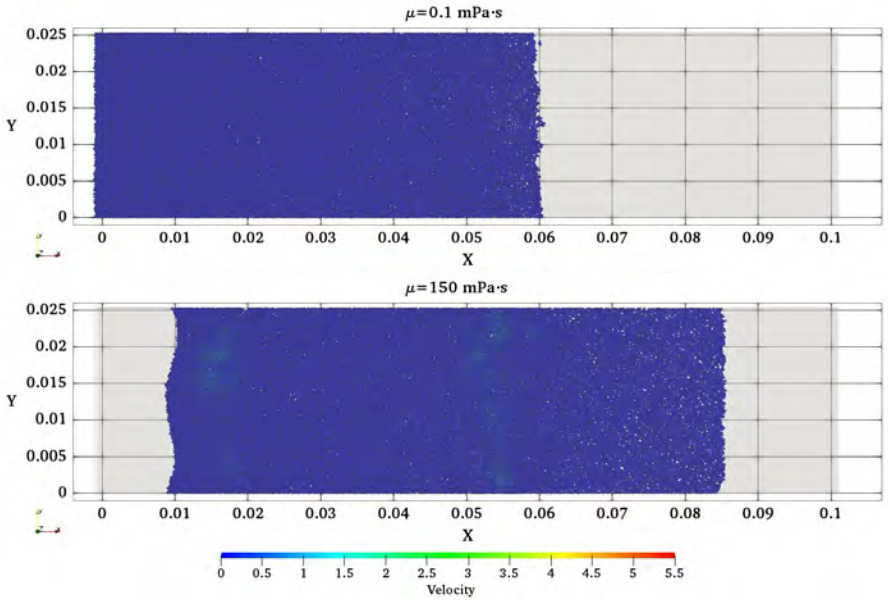

Fig. 4 Final fracture sealing state of LCMs under various drilling fluid viscosity after about 10 $V_{fracture}$ drilling fluid is moved through the fracture. The dark blue color means all particles in the figure has been immobile under drilling fluid flow, which indicates a seal.

In addition to changes in the location of the formation of the sealing zone, a reduction of drilling fluid viscosity also affects the quality of the formed seal. Fig. 5a shows that both the maximum and the stable pressure difference between the inlet and outlet of the fracture decreases as the viscosity of the drilling fluid reduces. The pressure difference is 33 MPa at the viscosity of 150 mPa·s while it reduces to 0.17 MPa at the viscosity of 0.1 mPa·s. According to the Kozeny-Carman equation (Carrier, 2003), the pressure difference of a laminar and steady-state fluid flow through a random packing is directly proportional to the viscosity of the fluid. However, the ratio of pressure difference is not equal to that of the corresponding viscosity. It means that the pressure difference variation is also impacted by other factors except for viscosity variation. Simulation results show that the porosity of the sealing zone under decreasing drilling fluid viscosity is 0.461, 0.469, 0.481, 0.489, 0.477 and 0.475, respectively. Porosity increases as viscosity reduces from 150 to 10 mPa·s and decreases as viscosity reduces from 10 to 0.1 mPa·s. In other words, the sealing zone becomes looser as viscosity drops. The flowrate at the fracture outlet continuously decreases from 2.50×10^{-5} to 1.16×10^{-5} m^3/s as the viscosity of drilling fluid reduces from 150 to 0.1 mPa·s (Fig. 5b). The cumulative drilling fluid volume passing through the fracture before sealing initially decreases and then slightly increases as viscosity of drilling fluid reduces. The smallest lost, *i.e.* lowest cumulative drilling fluid volume, is obtained by the drilling fluid with a viscosity of 10 mPa·s (Fig. 5c). This trend is consistent with that of the porosity of the sealing zone. It is noticeable that the major change in pressure difference, flow rate, and cumulative fluid loss volume occurs when the viscosity of the drilling fluid drops from 150 to 100 mPa·s. Below this limit, these three parameters change slightly by viscosity changes (Fig. 5d), as the viscosity of 150 mPa·s is high enough to continually destroy the initially formed sealing zone and push them back into deeper position until a stable seal forms. Therefore, the flow rate at the outlet and cumulative fluid loss are much higher than in the other cases. The large pressure difference is the result of combining the effect of the highest viscosity and flow rate of drilling fluid and the lowest porosity of the sealing zone.

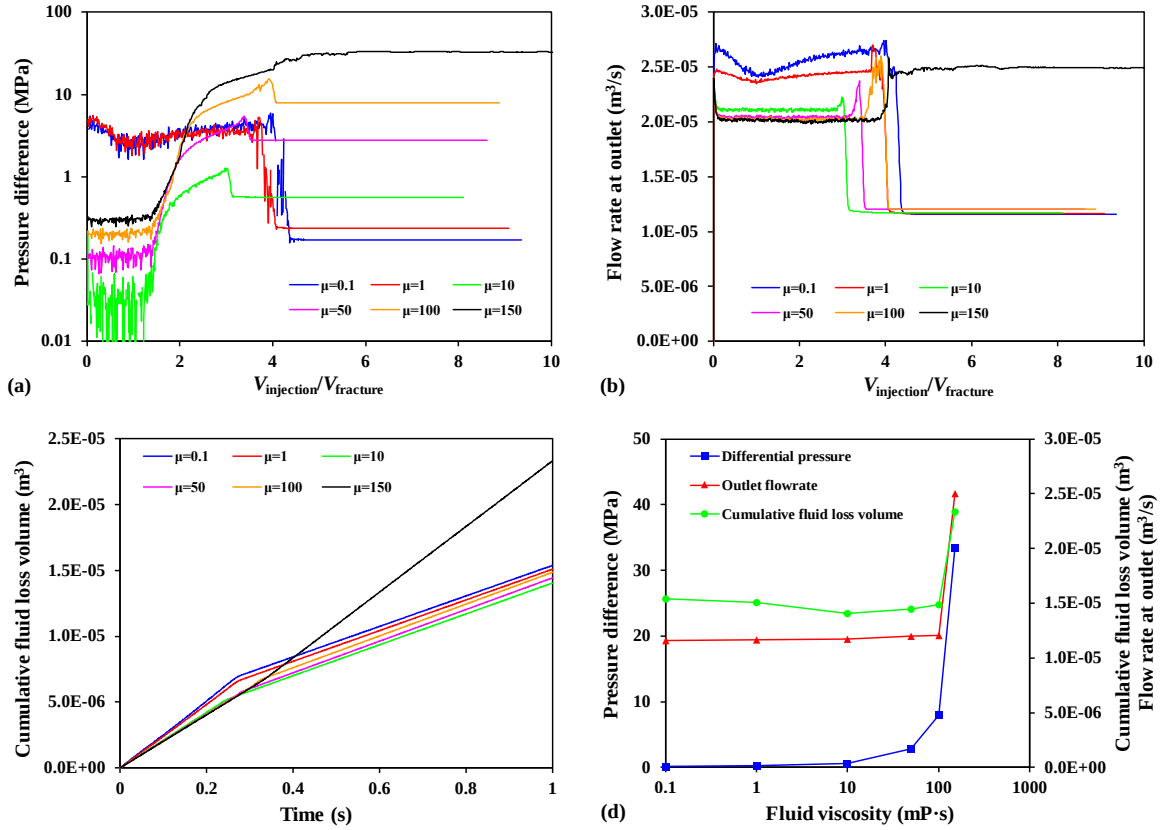

Fig. 5 Variation of the flowing parameter inside the fracture at various viscosities of the drilling fluid: (a) pressure difference; (b) flow rate at the outlet; (c) cumulative drilling fluid loss volume; (d) flowing parameter at the final state.

According to the simulation results, it is evident that as the temperature rises, the viscosity of the drilling fluid reduces affecting fracture sealing by LCM. LCM particles bridge faster and form a shallower sealing zone with less fluid loss and lower pressure difference in the fracture. The low viscosity of drilling fluid means low resistance for a particle moving. The particle can move faster to reach a suitable position to bridge in low viscous drilling fluid than higher ones. Reduction of drilling fluid viscosity seems to be positive for a rapid formation of the sealing zone. However, low viscous drilling fluids lead to more settlement of LCM particles in the bottom of the fracture. It is unfavorable for fracture sealing if the concentration of LCMs is lower than the critical value.

4.2 Effect of thermally induced particle size degradation on fracture sealing

Particle size is one of the essential properties of LCM design for sealing a fracture. Size degradation of LCM particles, which is driven by thermal expansion rupture and thermal abrasion (Scott *et al*. 2012; Grant 2016; Kang *et al*. 2019), has a significant impact on fracture sealing efficiency. Particle size can reduce to 20% of its original value in a downhole elevated temperatures circulation environment. As shown in Fig. 6 (the last two figures), in the size of

1.0~0.6 W_{fi}, the formation process of the sealing zone is dominated by the single-particle bridging mechanism. For particle diameter, D=1.0 W_{fi}, LCM particles seal outside the inlet due to wedge shape and size of fracture. For D=0.6 W_{fi}, LCM particles seal inside the fracture, which is similar to that of D=0.7, 0.8 and 0.9 W_{fi}. As particle size decreases from 1.0 to 0.6 W_{fi}, both bridging initiation time and bridging depth increase. For D=0.4 and 0.5 W_{fi}, the sealing process is dominated by a dual-particle bridging mechanism in the near field and a single-particle bridging mechanism in the far field. The LCM particles bridge at a short distance from the inlet by the dual-particle bridging mechanism and the escaping particles bridge again at a deeper position by the single-particle bridging mechanism, leaving a space between these two sealing zones (Fig. 6, the middle figure). However, the stability of the sealing zone formed by the dual-particle bridging mechanism is weaker than the one formed by the single-particle bridging mechanism. The initial bridging zone may crush in the middle (Fig. 7). It may be because particles can easily bridge at the top and bottom of the fracture, where three walls provide a sort of confinement for the particle flow. The later-coming particles pack at the previous bridge and extend to the middle gradually. Therefore, in the initial stage of the formation of the sealing zone, the middle part is the weakest part. For LCM particle size less than 0.3 W_{fi}, the process of the sealing formation is dominated by a dual-particle bridging mechanism (Fig. 6, the first two figures). However, when the particle sizes are smaller than 0.2 W_{fi}, the LCM particles cannot seal the fracture through the whole fracture height at this concentration. Moreover, the formed incomplete sealing zone will crash eventually. Besides, when the dual-particle bridging mechanism begins to work in the size range of 0.5~0.2 W_{fi}, both dual-particle bridging initiation time and bridging depth increase as the particle size decreases. Since the outlet width of the fracture is 0.34mm, LCM particles with a size smaller than 0.17 W_{fi} can barely bridge to seal the fracture.

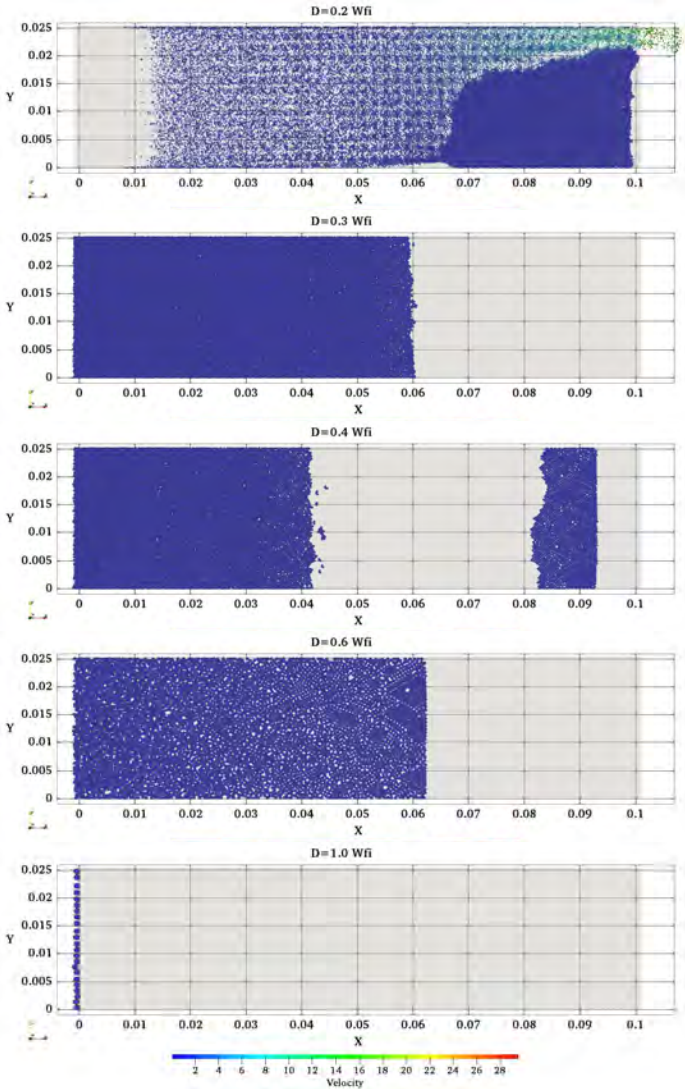

Fig. 6 Final fracture sealing states by LCMs under conditions defined by various ratios of LCM particle diameters to the width of fracture inlet after about 10 $V_{fracture}$ drilling fluid is injected.

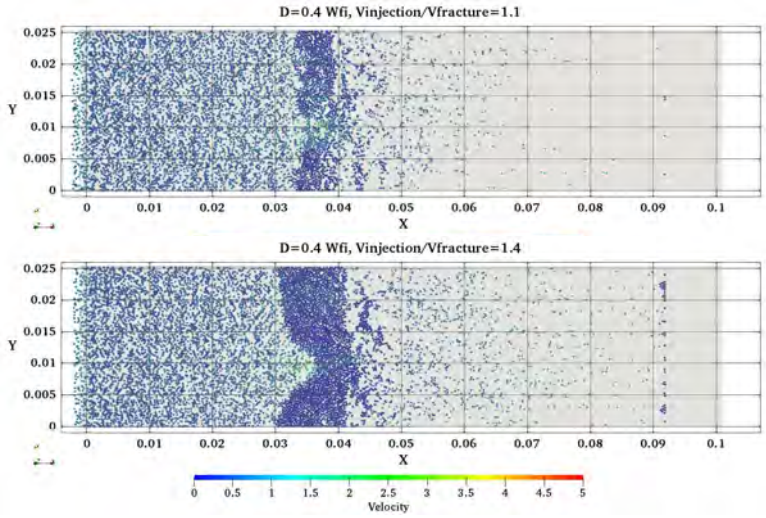

Fig. 7 Evolution of sealing zone by LCMs particle with size D=0.4 W_{fi}.

The quality of the sealing zone is also significantly affected by the particle size (Fig. 8). As particle size reduces from 1 W_{fi} to 0.3 W_{fi}, the pressure difference gradually increases except for D=0.5 W_{fi}. This is because particle with D=0.5 W_{fi} forms two thin sealing zones compared to the other particle sizes, which results in a lower differential pressure. Considering the fact that the injection rate is kept constant in our simulations, the pressure difference can be an indicator of the permeability of the sealing zone, which means that finer particles can form a tighter sealing zone. The final flow rate and cumulative fluid loss volume change slightly as particle size varies. However, D=0.2 W_{fi} and D=1.0 W_{fi} obtain larger flow rate and cumulative fluid loss than the other particle sizes, as no complete sealing zone formed.

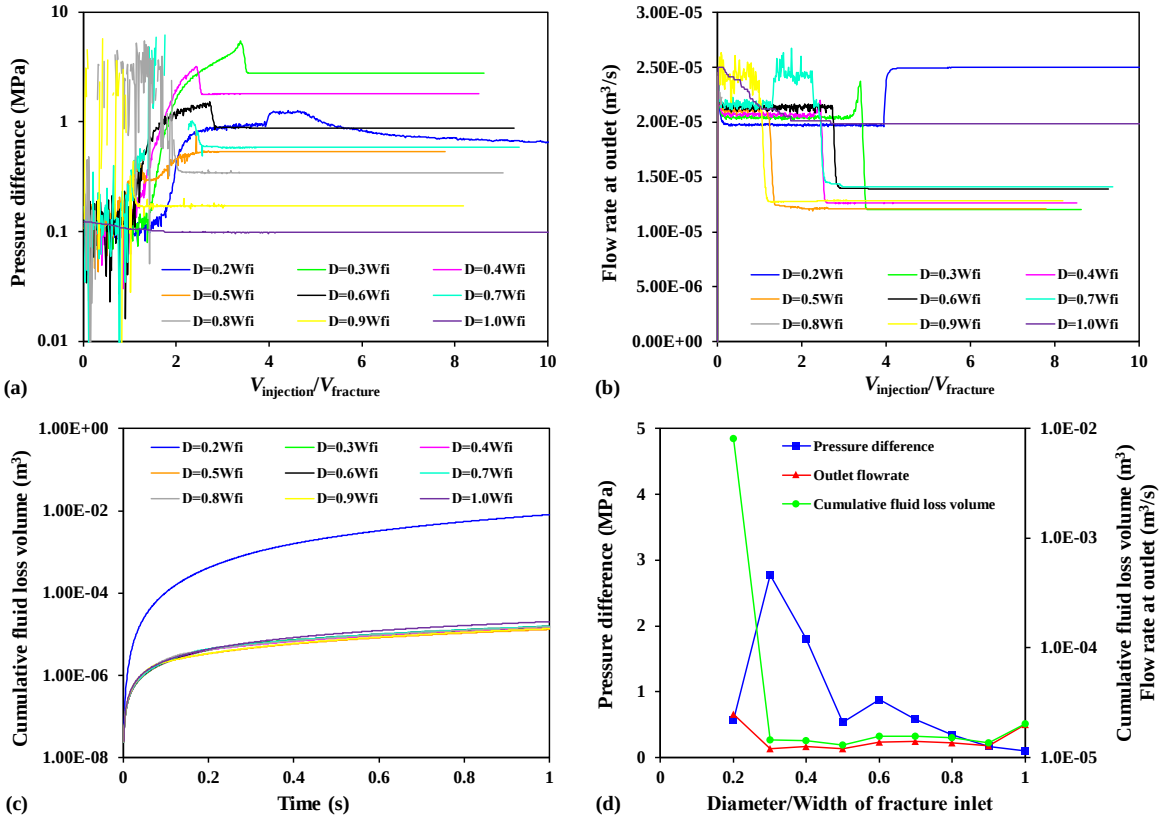

Fig. 8 Variation of different flow parameters for various ratios of LCM diameter to the inlet width of the fracture is shown, these parameters are (a) pressure difference; (b) flow rate at the outlet; (c) cumulative drilling fluid loss volume; (d) flowing parameter at the final state.

Therefore, the reduced particle size due to the thermal degradation can increase the bridging time and the bridging depth. Moreover, the bridging mechanism also switches from a single-particle bridging mechanism to a dual-particle bridging mechanism. However, the reduced particle size can form a tighter sealing zone.

5. Conclusions

A coupled CFD-DEM model is developed to simulate the sealing process of LCM particles in wedge-shaped fractures. Variations of drilling fluids and LCMs at elevated temperatures is summarized. Simulation of the fracture sealing process by LCMs particles is conducted using various parameters of drilling fluid and LCMs.

The elevated temperature usually leads to the decline of size, strength and friction coefficient of LCMs and reduction of drilling fluid viscosity. The bridging mechanism also changes from single-particle bridging to dual-particle bridging as particle size reduces. As a result of the combining effect of variations in drilling fluid and LCM properties at elevated temperatures, a successful fracture sealing case by conventional LCMs may become unstable and even completely fail at elevated temperatures.

Acknowledgment
Chong Lin acknowledges the China Scholarship Council (CSC No. 201808510204) for a joint Ph.D. fellowship, and the Energy Institute of the Pennsylvania State University for hosting and supporting his visiting.

References

Abrams, A., 1977. Mud design to minimize rock impairment due to particle invasion. J. Pet. Technol. 29, 586–592. https://doi.org/10.2118/5713-PA

Amani, M., Al-jubouri, M., 2012. An Experimental Investigation of the Effects of Ultra-High Pressure and Temperature on the Rheological Properties of Water-Based Drilling Fluids, in: SPE/APPEA International Conference on Health, Safety, and Environment in Oil and Gas Exploration and Production. SPE/APPEA International Conference on Health, Safety, and Environment in Oil and Gas Exploration and Production, Perth. https://doi.org/10.2118/157219-MS

Avci, E., Mert, B.A., 2019. The Rheology and Performance of Geothermal Spring Water-Based Drilling Fluids. Geofluid 2019. https://doi.org/10.1155/2019/3786293

Blais, B., Lassaigne, M., Goniva, C., Fradette, L., Bertrand, F., 2016. Development of an unresolved CFD–DEM model for the flow of viscous suspensions and its application to solid–liquid mixing. J. Comput. Phys. 318, 201–221. https://doi.org/10.1016/j.jcp.2016.05.008

Brotóns, V., Tomás, R., Ivorra, S., Alarcón, J.C., 2013. Temperature influence on the physical and mechanical properties of a porous rock: San Julian's calcarenite. Eng. Geol. 167, 117–127. https://doi.org/10.1016/j.enggeo.2013.10.012

Chakraborti, R.K., Kaur, J., 2014. Noninvasive Measurement of Particle-Settling Velocity and Comparison with Stokes' Law. J. Environ. Eng. 140, 4013008. https://doi.org/10.1061/(ASCE)EE.1943-7870.0000790

Concha, A.F., 2009. Settling velocities of particulate systems. Kona Powder Part. J. 27, 18–37. https://doi.org/10.14356/kona.2009006

Crowe, C.T., Schwarzkopf, J.D., Sommerfeld, M., Tsuji, Y., 2011. Multiphase Flows with Droplets and Particles (Second Edition). CRC Press, Boca Raton. https://doi.org/10.1201/b11103

Di Felice, R., 1994. The voidage function for fluid-particle interaction systems. Int. J. Multiph. Flow 20, 153–159. https://doi.org/10.1016/0301-9322(94)90011-6

Dick, M.A., Heinz, T.J., Svoboda, C.F., Aston, M., 2000. Optimizing the Selection of Bridging Particles for Reservoir Drilling Fluids, in: 2000 SPE International Symposium on Formation Damage. Society of Petroleum Engineers, Lafayette. https://doi.org/10.2118/58793-MS

Ergun, S., 1952. Fluid flow through packed columns. Chem. Eng. Prog. 48, 89–94.

Finger, J., Blankenship, D., 2010. Handbook of Best Practices for Geothermal Drilling, Sandia National Laboratories. Albuquerque.

Garcõâ, A., Espinosa, G., Moya, S.L., 2001. Rheological property measurement of drilling fuids used in geothermal wells. Appl. Therm. Eng. 21, 283–302. https://doi.org/10.1016/S1359-4311(00)00003-X

Grant, P., Lassus, L., Savari, S., Whitfill, D.L., 2016. Size Degradation Studies of Lost Circulation Materials in a Flow Loop, in: IADC/SPE Drilling Conference and Exhibition. IADC/SPE Drilling Conference and Exhibition, Fort Worth. https://doi.org/10.2118/178774-MS

Hager, A., 2014. CFD-DEM on Multiple Scales - An Extensive Investigation of Particle-Fluid Interactions. Johannes Kepler University Linz.

Hager, A., Kloss, C., Goniva, C., 2018. Combining Open Source and Easy Access in the field of DEM and coupled CFD-DEM: LIGGGHTS®, CFDEM®coupling and CFDEM®workbench, in: 28th European Symposium on Computer Aided Process Engineering. Elsevier, Graz, pp. 1699–1704. https://doi.org/10.1016/B978-0-444-64235-6.50296-5

Hands, N., Kowbel, K., Maikranz, S., Nouris, R., 1998. Drill-in fluid reduces formation damage, increases production rates. Oil Gas J. 96, 65–69.

Kang, Y., Tan, Q., You, L., Zhang, X., Xu, C., Lin, C., 2019. Experimental investigation on size degradation of bridging material in drilling fluids. Powder Technol. 342, 54–66. https://doi.org/10.1016/j.powtec.2018.09.086

Kang Yili, Kaicheng, W., Chengyuan, X., Lijun, Y., Wang Limin, Ning, L., Li Jiaxue, 2019. High-temperature aging property evaluation of lost circulation materials in deep and ultra-deep well drilling. Acta Pet. Sin. 40, 215–223. https://doi.org/10.7623/syxb201902010

Kloss, C., Goniva, C., Hager, A., Amberger, S., Pirker, S., 2012. Models, algorithms and validation for opensource DEM and CFD–DEM. Prog. Comput. Fluid Dyn. 12, 140–152. https://doi.org/10.1504/PCFD.2012.047457

Kumar, A., Chellappah, K., Aston, M., Bulgachev, R., 2013. Quality Control of Particle Size Distributions, in: SPE European Formation Damage Conference and Exhibition. Society of Petroleum Engineers, Noordwijk. https://doi.org/10.2118/165150-MS

Lapple, C.E., Shepherd, C.B., 1940. Calculation of particle trajectories. Ind. Eng. Chem. 32, 605–617.

Loeppke, G.E., Glowka, D.A., Wright, E.K., 1990. Design and evaluation of lost-circulation materials for severe environments. J. Pet. Technol. 42, 328–337. https://doi.org/10.2118/18022-PA

Luo, X., Luo, P., 1992. Study on the application of shielding temporary plugging technique in reservoir protection. Drill. Fluid Complet. Fluid 9, 19–27.

Norouzi, H.R., Zarghami, R., Sotudeh-Gharebagh, R., Mostoufi, N., 2016. Coupled CFD-DEM Modeling: Formulation, Implementation and Application to Multiphase Flows. John Wiley & Sons, Ltd First, Chichester, UK.

Nugroho, W.A., Hermawan, S., Lazuardi, B.H., Mirza, R., 2017. Drilling Problems Mitigation in Geothermal Environment, Case Studies of Stuck Pipe and Lost Circulation, in: SPE/IATMI Asia Pacific Oil & Gas Conference and Exhibition. Society of Petroleum Engineers, Jakarta. https://doi.org/10.2118/186922-ms

Peng, Z., Elham Doroodchi, Luo, C., Behdad Moghtaderi, 2015. Influence of Void Fraction Calculation on Fidelity of CFD-DEM Simulation of Gas-Solid Bubbling Fluidized Beds. AICHE J. 61, 857–866. https://doi.org/10.1002/aic

Pierce, K.G., Livesay, B.J., 1994. A Study of Geothermal Drilling and the Production of Electricity from Geothermal Energy. Albuquerque.

Poła, J., Bancewicz, M., Koza, Z., Poła, J., Bancewicz, M., Koza, Z., 2017. Is Magnus effect relevant for proppant settling in narrow fractures? Energy Procedia 125, 443–449. https://doi.org/10.1016/j.egypro.2017.08.097

Rushd, S., Hassan, I., Sultan, R.A., Kelessidis, V.C., Rahman, A., Hasan, H.S., Hasan, A., 2018. Terminal settling velocity of a single sphere in drilling fluid. Part. Sci. Technol. 1–10. https://doi.org/10.1080/02726351.2018.1472162

Scott, P.D., Beardmore, D.H., Wade, Z.L., Evans, E., Franks, K.D., 2012. Size degradation of granular lost circulation materials, in: IADC/SPE Drilling Conference and Exhibition. Society of Petroleum Engineers, San Diego. https://doi.org/10.2118/151227-MS

Shengying, Z., Jienian, Y., Yong, S., Hongxia, Z., 2008. Rheological properties of oil-based drilling fluids at high temperature and high pressure. J. Cent. South Univ. 15, 457–461. https://doi.org/10.1007/s11771−008−399−7

Sun, Z., Balhoff, M.T., Espinoza, D.N., 2018. Fluid Injection Induced Fracture Initiation Based on a Resolved CFD-DEM Approach.

Valsecchi, P., 2014. On the Shear Degradation of Lost Circulation Materials. SPE Drill. Complet. 29, 323–328. https://doi.org/10.2118/163512-PA

Visser, C.F., III, A.W.E., Baker, W., Tucker, J., Quick, R., Nagle, T., Bell, J., Bell, S., Bolton, D., Nagandran, U., 2018. Geothermal Drilling and Completions: Petroleum Practices Technology Transfer. National Renewable Energy Laboratory, Golden. https://doi.org/10.2172/1490999

W. David Carrier, III, F.A., 2003. Goodbye, Hazen; Hello, Kozeny-Carman. J. Geotech. Geoenvironmental Eng. 129, 1054–1056. https://doi.org/10.1061/(ASCE)1090-0241(2003)129:11(1054)

Wang, F., Tan, X., Wang, R., Sun, M., Wang, L., Liu, J., 2012. High temperature and high pressure rheological properties of high-density water-based drilling fluids for deep wells. Pet. Sci. 9, 354–362. https://doi.org/10.1007/s12182-012-0219-4

Wellmann, C., Lillie, C., Wriggers, P., 2008. Comparison of the macroscopic behavior of granular materials modeled by different constitutive equations on the microscale. Finite Elem. Anal. Des. 44, 259–271. https://doi.org/10.1016/j.finel.2007.11.007

Xu, C., Yan, X., Kang, Y., You, L., You, Z., Zhang, H., Zhang, J., 2019a. Friction coefficient: A significant parameter for lost circulation control and material selection in naturally fractured reservoir. Energy 174, 1012–1025. https://doi.org/10.1016/j.energy.2019.03.017

Xu, C., Zhang, J., Kang, Y., You, L., Yan, X., Cui, K., Lin, C., 2019b. Investigation on the Transport and Capture Behaviours of Lost Circulation Material in Fracture with Rough Surface, in: International

Petroleum Technology Conference. International Petroleum Technology Conference, Beijing. https://doi.org/10.2523/IPTC-19571-MS

Yan, J., Zhao, X., 2003. Rheological properties of polymer-gel drilling fluids at high temperature and pressure. Acta Pet. Sin. 24, 104–109. https://doi.org/10.1007/s10553-013-0394-z

Yang, L., 2015. Comparative Analysis of Lost Circulation Material Particle Size and Degradation in Drilling Fluids. The University of Texas at Austin.

Zhang, L., Mao, X., Lu, A., 2009. Experimental study on the mechanical properties of rocks at high temperature. Sci. China, Ser. E Technol. Sci. 52, 641–646. https://doi.org/10.1007/s11431-009-0063-y

Zhou, Z.Y., Kuang, S.B., Chu, K.W., Yu, A.B., 2010. Discrete particle simulation of particle–fluid flow: model formulations and their applicability. J. Fluid Mech. 661, 482–510. https://doi.org/10.1017/S002211201000306X

Enhanced Weight on Bit Application in Hard Rock Drilling Through Innovative Anchoring Technology

Liam Lines[1], Matus Gajdos[2], William Murray[1], Mark Webb[3], Graham Watson[3], Monika Chmelikova[2], Igor Kocis[2], and Tomas Kristofic[2]

[1] GA Drilling, LLC, 4201 Main St, Ste. 200 – 189, Houston, TX 77002, United States

[2] GA Drilling, a. s., Technology Center, Vapenka 4, 841 07 Bratislava, Slovakia

[3] GA Drilling Ltd., Broad Quay House, Prince Street, BS1 4DJ Bristol, United Kingdom

Keywords:

hard rock drilling, downhole anchoring, long horizontal wells

ABSTRACT

An increasing number of geothermal projects require long horizontal well sections to be drilled through hard rock formations. Among these projects are those from well-known industry frontrunners that drill sets of inclined or horizontal wells to form downhole heat exchangers (closed loop Advanced Geothermal Systems – AGS) or Enhanced Geothermal Systems (EGS). These, and many other geothermal drilling scenarios, suffer from dysfunctions like insufficient transfer of weight on bit (WOB), drillstring buckling, and stick-slip that significantly impact cost and, ultimately, the feasibility of the project.

An innovative Downhole Anchoring and Drive (DAD) system will tackle the challenges associated with drilling long wells through hard rock and enhance especially those with long highly inclined sections. The DAD system grips the wellbore in close proximity to the drill bit and is designed to reduce damaging and inefficient drilling dysfunctions. The system includes smart control and actuation systems along with sensor feedback to autonomously drive the drilling process at the drill bit rather than at the surface. Moreover, it has the capability of applying significant axial push and pull forces to the drilling assembly and drillstring which enables additional WOB (essential for efficient drilling in hard rock) and dynamically optimizes it to dramatically improve drill bit and drill motor life and performance.

The first version of the tool was tested in Q2/2023 in a shallow test well of a leading rig contractor in Houston, TX. This paper summarizes the development and testing activities undertaken in 2024.

1. Introduction

The emerging concepts of AGS or EGS require drilling a significant quantity of long inclined or horizontal sections through challenging environments resulting from a combination of their high vertical depth (between 10,000 to 20,000 ft), hard crystalline rock formations with high friction factors (high drillstring torque and drag), and high formation temperature (a reliability challenge for downhole tools). The length of the horizontal section currently ranges from 5,000 (El-Sadi, 2024) to 9,000 ft (Longfield, 2022). The ability to drill long(er) horizontal sections cost effectively is essential for project economics (White, 2023). However, in practice, this is difficult to achieve because of the drilling dysfunctions that result when using conventional drilling technologies and processes in these applications.

The Downhole Anchoring and Drive (DAD) system currently under development will be a key component of future hard rock drilling systems and will eliminate and/or overcome the common drilling dysfunctions plaguing the cost-effective drilling of hard rock. It will reduce geothermal well construction costs through the application of significant and optimized downhole thrust force to the drill bit and allow faster and/or longer wells to be drilled than currently possible with today's conventional technologies. What follows is an overview of the problems typically encountered while drilling hard rock, what the DAD system is, how it eliminates these, and ultimately how it is a key enabler to future Autonomous Reeled Drilling Systems (ARDS).

2. Challenges related to geothermal well construction

Challenges related to well construction of long horizontal sections include drilling dysfunctions which consume significant amounts of energy that could otherwise be used to drill rock faster. They take many forms but ultimately increase drilling cost and risk through elevated downhole tool wear and damage, reduced Rate of Penetration (ROP), increased number of trips in and out of the hole, and potentially, in the case of lost in-hole event, the loss of a well.

A typical example of dysfunction is torsional vibration – large fluctuations, usually periodic, in the drill-bit rotation rate despite a constant rotation rate at the surface. Torsional vibration ultimately stems from the inverse relationship between drilling torque and the rotation speed of the now ubiquitous PDC drill bit. This results in negative damping and a tendency for the drill bit's rotary speed (and the drillstring connected to it) to oscillate when perturbed (Richard, 2007).

Another example of dynamic dysfunction is lateral vibration whereby the lateral stabilization of the drilling assembly and/or the engagement of the drill bit with the rock (a large component of drill bit lateral stability is the result of PDC cutter force balancing that relies on sufficient cutter engagement with the rock face) is insufficient to constrain lateral force instability or acceleration of the drill bit or other components within the drilling assembly. Not only can this form of dysfunction result in damage to downhole tools, but it can also cause significant irregularity in the wellbore path (tortuosity) that can then result in poor weight transfer to the drill bit (and further lateral vibration issues) as drilling progresses (Dupriest, 2013). Two common types of lateral vibration are forward whirl – typically occurs with limber drillpipe/collars that process in the same direction and similar frequency to drillstring rotation – and backward whirl – typically occurs on the drill bit and stabilizers whereby the rotation of the component within the wellbore is in the opposite direction to drillstring/bit rotation and at much higher frequency (Stroud, 2011). Both

result in high-impact shock and vibration damage along with rapid accumulation of bending fatigue (especially in the case of backward whirl).

Dynamic stability plots show the relationship of the above dysfunctions to drilling parameters (Figure 1). For maximum performance, it's desirable to work toward the upper right of the stability plot using the highest WOB along with the highest RPM while avoiding adverse dynamics – staying in the optimum zone. Watson (2013) confirmed through fundamental cutter testing that PDC drill bit ROP and life are maximized in hard rock by drilling at high WOBs.

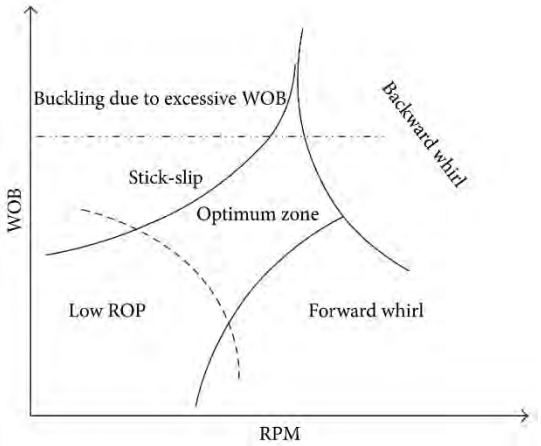

Figure 1: Typical Stability Diagram for Drilling (Wu, et al. 2010)

Avoidance and/or mitigation of dysfunction is challenging. Typically, the cause of the dysfunction is at the bottom end of the drilling assembly (for instance, the PDC drill bit) whereas the control and actuation system is many kilometers away on the top side. This results in a severely underactuated drilling system that can be very challenging to control (Krstic, 2022 & Auriol, 2022).

Figure 2 shows a drillstring drag analysis for the longest 3D granite well drilled in Thailand (Thai, 2022). This well reached a Total Depth (TD) of 22,200 ft with a circa 11,480 ft horizontal section. The cumulative drag at TD at 0 rpm (sliding) was predicted at 185,200 lbs. with approximately 25 lb./m rate of increase in the horizontal section. The DAD system can apply up to 60,000 lbs. of extra WOB in this hole size. In this well, that would have resulted in an extra 7,874 ft or 77% more horizontal footage before the same drillstring drag and levels of buckling would have been encountered.

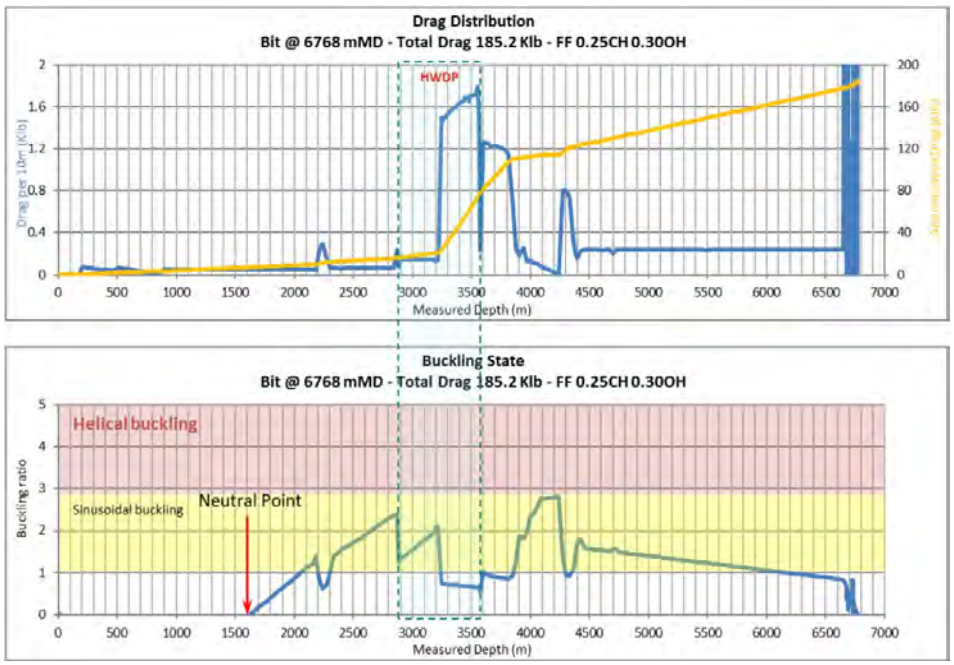

Figure 2: Drag Plot for Long Granite Well in Thailand (Thai, 2022)

What if the control and actuation system responsible for the drilling process were placed downhole in proximity (within 100 ft) of the source of instability e.g., the drill bit? What if it could apply significant and controlled downhole WOB to counteract the inverse bit torque to rotary speed relationship/negative damping and keep the drill bit cutters consistently engaged with the rock face to improve lateral stability and cutter life? What if this system could apply a significant WOB downhole directly to the drill bit to eliminate drillstring buckling and maximize reach? The answer is a more efficient drilling system that can drill both further and faster than the incumbent technology and ultimately reduces well construction cost and risk. This is what the DAD system offers the global drilling industry.

3. Downhole Anchoring and Drive (DAD) System

The DAD system is positioned within the bottom hole assembly (BHA) and contains hydraulically actuated gripping elements that anchor the BHA to the borehole wall and allow torsional and/or axial load to be reacted directly into the borehole rather than conveyed many thousands of feet above. The system contains a hydraulic thrusting unit that can apply significant and controlled thrust to the drill bit to both drill faster and actively reduce drilling dysfunction. The drilling process is controlled from the bottom of the hole with real-time sensor feedback to aid in optimization and includes many of the control modes that Drillers are accustomed to with the latest surface-based Automatic Drillers (ROP, WOB, Torque, etc.).

Dupriest and Noynaert (2022) showed that high WOB combined with more aggressive PDC cutters reduced drill bit wear rates and increased footage drilled in hard and abrasive formations. However, the same paper showed that this set-up generated stick-slip, an abrupt change in drill bit rotation rate, which had a very negative impact on the drill bit.

The resulting stability plot with the DAD system in the BHA can be seen in Figure 3. The threshold for buckling has shifted upward resulting from the ability of the DAD system to apply WOB

downhole and require less compression in the drillstring above (compression causes buckling). The stability resulting from local gripping of the wellbore has eliminated forward whirl and the ability to increase WOB and drill bit cutter engagement with the rock reduces the tendency to backward whirl. Ultimately, this extends the optimum zone, allowing higher WOBs and higher RPMs to be used, resulting in faster ROPs with fewer occurrences of damaging dynamics and adverse PDC cutter wear.

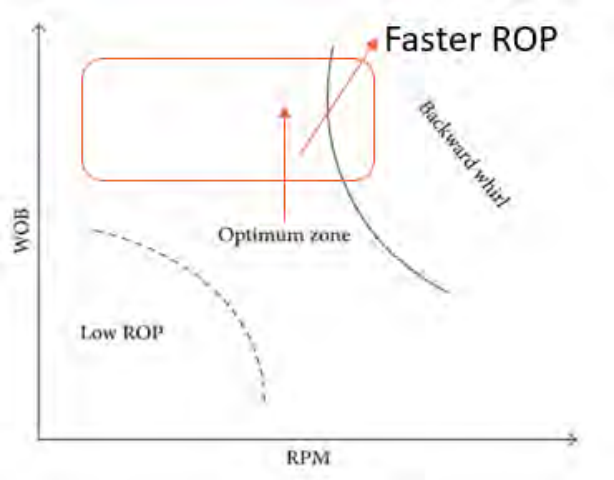

Figure 3 Modified Stability Plot Showing the Impact of the DAD System

3.1 Testing of the Anchoring Functionality

The predecessor to the DAD system focused on mechanically isolating the drill bit from the 'spring' of the drillstring to provide a rigid torsional anchor point above the drill bit to react with the torque output from the drilling motor/drill bit and allows maximum weight to be applied without triggering stick-slip.

The Concept Prototype (CP) utilized hydraulic oil to energize gripper pistons. The gripper pistons extended to grip the wellbore wall and transmit torque. The tool comprised two anchoring units connected via a closed hydraulic circuit. This hydraulic circuit synchronized the movement of the two anchors such that while one was gripping the wellbore the other unit was resetting position to take over from the gripping unit when it reached the end of its travel. The target was to continuously react torque to the formation via the grippers up to the maximum ROP – 70 ft/hr. for the CP.

The CP tool had no means of applying thrust to the drill bit and relied on it being applied by conventional means – heavy weight or drill collars in the BHA and the Driller controlling hook load/slack off weight to apply force to the drill bit. This CP was tested at the facility of a major drilling contractor in Houston, Texas, where they drilled a shallow cased hole filled with cement. The specifics of the test and results are described in Gajdos (2024). The shake-down test was successfully concluded with two main achievements:

1. The CP tool reliably gripped the wellbore while drilling and the movement of the two anchoring units was sufficiently synchronized (via the closed hydraulic circuit connecting them) to ensure continuous gripping during the test. The CP achieved the

required 70 ft/hr. with testing not able to reach the maximum limit of the tool´s capability.

2. Downhole drilling dynamic subs located above and below the downhole motor detected vibrations reduced by up to 35% when compared to drilling without the CP in the drillstring.

Despite the successes, there were two notable challenges faced by the CP tool:

1. On the trip out of hole one, one of the hoses connecting the tool's hydraulic circuits to the surface hydraulic power pack – the CP tool relied on surface-based equipment for hydraulic power – was damaged. This damage allowed cement and casing debris to enter the tool's hydraulic circuits (see Figure 4) and this required a full disassembly of the tool to remove prior to rebuild. Additional filtration was placed on the hydraulic circuits to prevent the spread and migration of debris throughout the system, in the case of infiltration, although the commercial version of the tool was not envisaged to require hydraulic lines to be run between the tool and surface and hence this particular failure mechanism – debris ingress through damaged hydraulic hose – would not exist.

Figure 4: Collected Cuttings

2. Figure 5 shows edge damage to the carbide gripping surface on the anchoring pistons. Minor surface damage was reported after interaction with hard rock (Gajdos, 2024). There is also the situation when the grippers interact with steel casing. The damage to the grippers after such a situation can be seen in Figure 5.

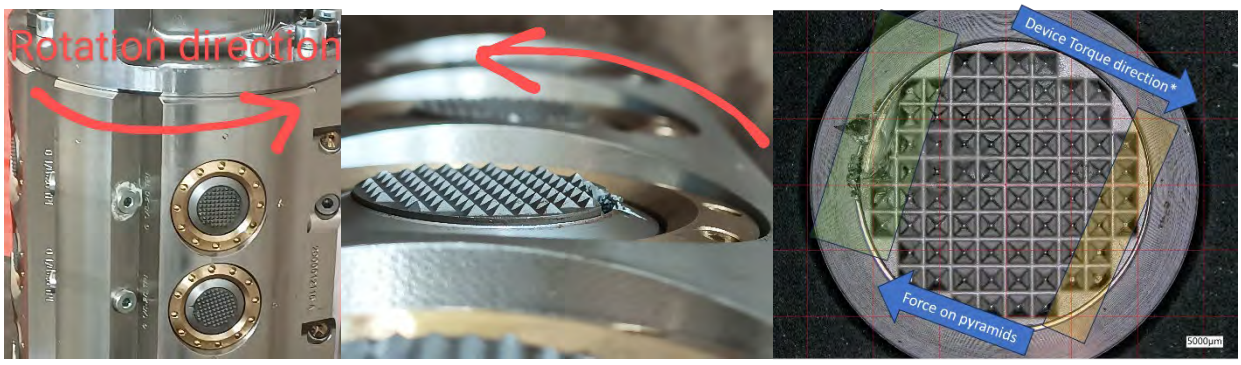

Figure 5: Damage on the Grippers after the Testing of Gripping in Steel Casing and Increasing Torque until the Tool Starts to Slip (left and center); Microscopy View on the Gripper with Highlighted Sections of Damage (at right).

The grippers were analyzed and several interesting conclusions were made:

1. Most damage occurs on one side of the gripper (green rectangle in Figure 5 right and Figure 6). These are brittle fractures in the case of the carbide gripper element. Subsequent damage to the piston body from the carbide fragments can be seen as a scratch in the direction of rotation/forces acting on the gripper piston.
2. The fractures were identified to be caused dominantly by tensile stresses because of one or more of the following:
   a. The carbide inserts do not conform to the inside of the casing/borehole (the gripper is planar vs. curved) – the edge stressed by tension fractured down to the brazed interface. The edge stressed in compression was found to have blunted gripper tips (in these materials, the tensile strength limit is several times lower than compressive).
   b. Incomplete circumferential mechanical support of gripper pad in the gripper pistons – the braze filler sits sub-flush to the top surface of the counterbore in the piston. This results in poor load transfer from the gripper pad into the piston and results in increased tensile loading.

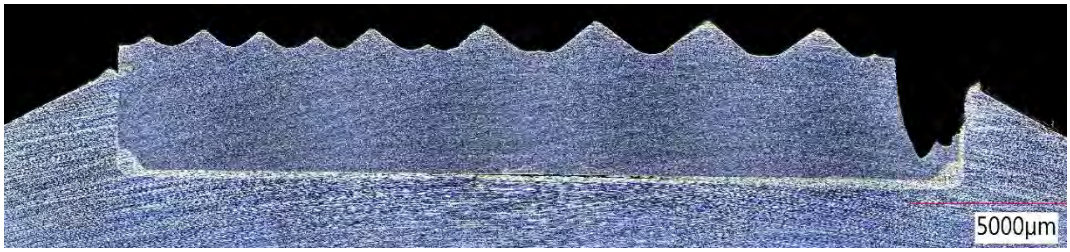

Figure 6: Cross Section of the Gripper Top with Visible Damage on the Right-hand Side

Based on this testing, it was concluded that the gripper elements must be curved to more closely conform to the shape of the casing's inside surface. This improvement will also benefit gripping in hard rock, although the small amount of deformation, penetration, and/or crushing that occurs between the gripper element and the rock reduces the susceptibility to this issue and helps more evenly distribute the stress in the gripper.

3.2 DAD Design and Configuration

A requirement for the original anchoring concept was for a purely hydro-mechanical tool with no electrical or electronic systems. This resulted from the desire for ultra-high temperature operations (350°C) for geothermal applications. As a drive to simplify the hydromechanical controls and modularize the design, it was decided to 'electrify' the anchoring tool with the addition of electronic actuation and control and, at the same time, add extra capabilities such as the application of controlled axial thrust/WOB to the drilling assembly and implementation of autonomous control loops similar to those in today´s cutting-edge automated drilling systems – these enhancements resulted in the DAD system as shown in Figure 7.

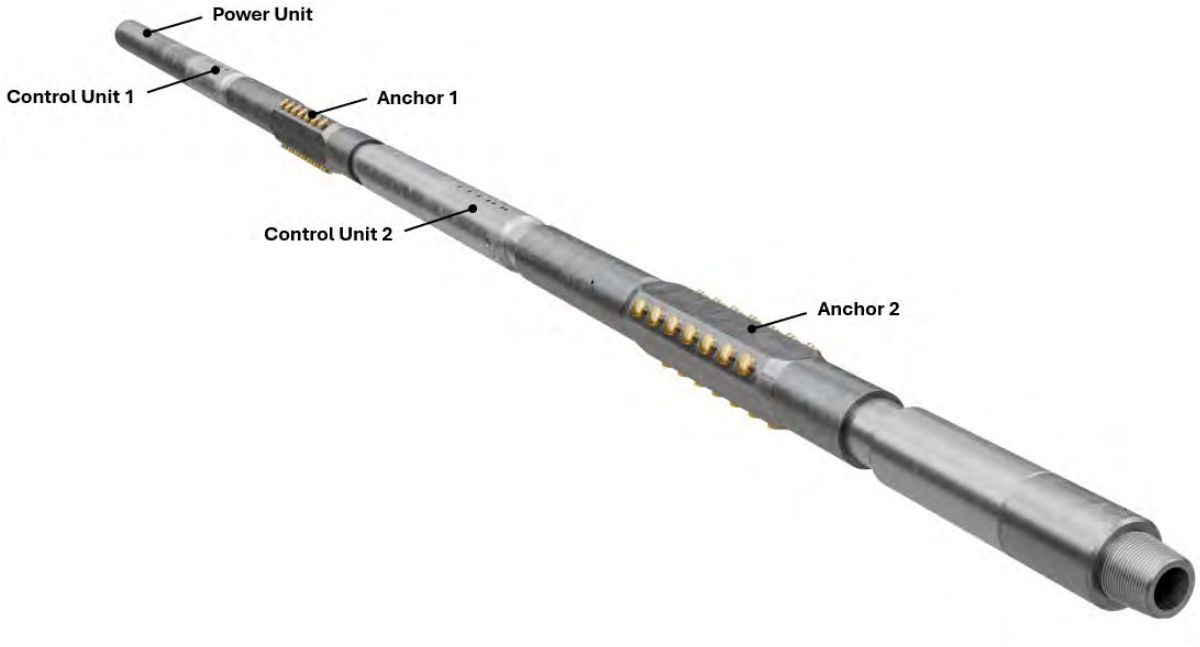

Figure 7: Visualization of the Downhole Anchoring and Drive (DAD) system

A summary of the enhancements of the DAD system over the CP tested at the drilling contractor's facility in Houston:

1. It incorporates an electronic/electrical control and actuation system to allow enhanced active control mechanisms to optimize the drilling process and reduce dysfunction.
2. Allows the drillstring to be rotated through the anchors to minimize drillstring drag and allow the use of conventional directional drilling motors and processes (e.g., slide and rotate).
3. Includes a comprehensive set of sensors and diagnostic data – e.g., pressure, torque, WOB, temperature, RPM, shock, and vibration.
4. Utilizes pressurized drilling fluid to reduce tool complexity and cost and will follow a similar design ethos to the most commercially successful RSS tools.
5. It includes an axial push/pull capability which can be used to apply additional WOB to improve ROP through higher depth of cut and/or reduced drillstring buckling/drag.
6. The modular design allows multiple anchors and thrusting units to be stacked in series should higher forces be required.
7. Utilizes a common electrical architecture that facilitates power and communications exchange between multiple modules and other third-party tools in the BHA creating the potential for a true integrated and autonomous drilling system.

The DAD System has two main tool configurations:

1. Axial anchoring only allows the central shaft to rotate through the anchoring modules and for true "plug and play" into conventional bent motors and jointed-pipe applications without the need for extra tools in the drillstring. The system utilizes modulation of axial thrust to mitigate stick-slip (and other dysfunctions).

2. Axial and Torsional anchoring – Torsionally locks the central shaft running through the system to the anchors such that when the anchors engage the borehole wall the drillstring above the DAD system cannot be rotated. Drilling motor torque reacts into the borehole wall (via the anchors) rather than into the drillstring. Allows high torque and extended reach drilling with coil tubing.

The DAD system comes equipped with the following control modes:

1. ROP Mode – This mode utilizes anchor traverse speed to control ROP, allowing for much more consistent drilling, eliminating common dysfunctions (e.g., axial stick-slip), and well control issues.
2. Bit Torque Mode – Utilizes torque feedback to stabilize drilling torque, significantly improving motor and drill-bit life and allowing motors to be run closer to maximum power (faster ROP) without risk of damage.
3. WOB Mode – This mode utilizes feedback from the WOB sensor to control axial thrust to stabilize WOB for a more consistent drilling process.

The commercial tool is undergoing development and testing for planned deployments towards the end of 2025.

4. Autonomous Reeled Drilling System (ARDS)

In addition to optimization of the drilling process through the proximity of the DAD system to the drill bit and its advanced control and actuation system, its ability to react torque and axial force into the formation is a critical enabler for drilling large diameter, hard rock wells with reeled pipe and/or coiled tubing. Coiled tubing is typically used for small diameter, low-cost well intervention and workover operations which require low torque and pull/weight capacity (compared to conventional jointed pipe in drilling applications). The ability to drill large hole diameter holes through hard rock with coiled tubing offers immense cost savings over conventional jointed pipe operations:

1. Smaller, lower-cost drilling rig due to reduced derrick capacity and tubular handling requirements.
2. Faster drilling and tripping times due to not needing to make/break rotary connections and pick-up/rack-back pipe (typically 3-4x the tripping speed compared to conventional jointed pipe).
3. Improved well control through the ability to continuously circulate while tripping in/out of the hole.
4. Reduced workplace hazards due to the elimination of rotary-shouldered connections made/broken on the rig floor.
5. Improved command and control of the downhole tools through a continuous data link to the surface via wireline.

A schematic overview of the ARDS with the DAD system can be seen in Figure 8.

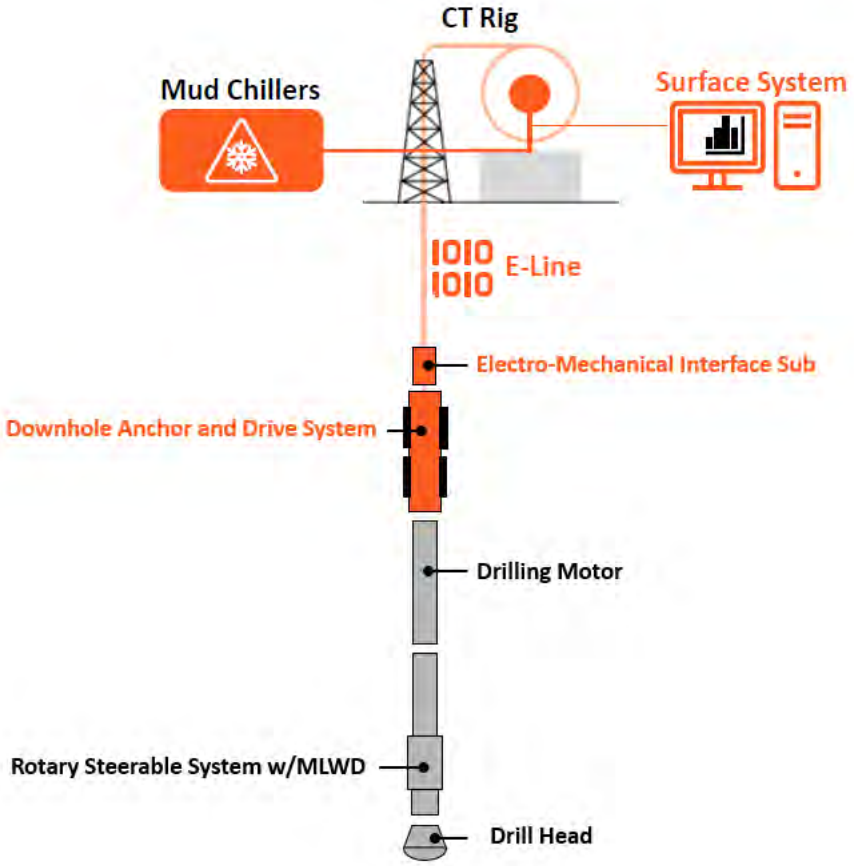

Figure 8: The Main Components of ARDS

The components of the Autonomous Reeled Drilling System are as follows:

1. Drill Head – conventional PDC, roller cone, or alternative rock destruction methods e.g., plasma.
2. Directional Drilling Assembly – allows steering of wellbore along with navigational and petrophysical logging measurements. Pictured above with Rotary Steerable System (RSS).
3. Drilling Motor – converts hydraulic energy in drilling fluid into mechanical energy for rotating the drilling assembly.
4. DAD System – the anchoring system reacts to the drilling motor torque into the formation to avoid damage and twisting of the coiled tubing string. The 700 series DAD can react to the stall torque of the heaviest duty 7-in OD drilling motors (for drilling 8.5-in to 8.75-in nominal hole size).
5. Coiled Tubing Interface – electromechanical connection of DAD system and BHA to coil tubing.
6. Coiled Tubing – customized coil tubing with improved fatigue properties and mechanical/hydraulic capacities.
7. E-Line – provides power and communications conduit between surface and downhole tools.
8. Rig – standard CT/intervention rig.

9. Surface System – this system allows data visualization, bidirectional communications, and control of the DAD system. It is also possible to receive MWD and LWD data.

5. Conclusion

This paper describes the innovative new Downhole Anchoring and Drive System proposed for hard rock drilling in geothermal applications. Typical forms of drilling dysfunction are discussed, along with the ability of the DAD system to mitigate these along with its ability to extend drilling distances through the application of downhole thrust. The DAD system will be commercially deployed in 2025 for geothermal applications. DAD system is also presented as the critical enabler of an Autonomous Reeled Drilling System, introducing a complete paradigm change in geothermal well construction.

REFERENCES

Auriol, J., Boussaada, I., Shor, R., Mounier, Hugues., Niculescu, Silviu-Iulian., 2022. "Comparing Advanced Control Strategies to Eliminate Stick-Slip Oscillations in Drillstrings," IEEE Access volume 10, pp. 10949-10969, 2022, doi: 10.1109/ACCESS.2022.3144644.

Dupriest, F. 2013, "Thus, The Lowly Stabilizer," Presentation Given at International Association of Directional Drilling, July Meeting, 2013.

Dupriest, F. and Noynaert, S., 2022, "Drilling Practices and Workflows for Geothermal Operations," Proceedings of the IADC/SPE International Drilling Conference and Exhibition, Galveston, Texas, USA. https://doi.org/10.2118/208798-MS

El-Sadi, K., Gierke, B., Howard, E., Gradl, C., 2024, "Review Of Drilling Performance in a Horizontal EGS Development," Proceedings of the Stanford Geothermal Workshop 2024, Stanford University, USA.

Gajdos, M., Watson, G., Webb, M., Glover, D., Kristofic, T., Kocis, I., Lines, L., Murray, W., Codazzi, D. and Jeffryes, B., 2024, "Progress in Development and Testing of Anchoring Technology for Hard and Abrasive Drilling Conditions," Proceedings of the Stanford Geothermal Workshop 2024, Stanford University, USA.

Krstic, M., 2022 "Control of Drill String and Flow Instabilities by PDE Backstepping" Proceedings of the Fifth International Colloquium on Nonlinear Dynamics and Control of Deep Drilling Systems, pp. 13-14, University of Maryland, USA.

Longfield, S., Schwarz, B., Hodder, M., Stuebing, T., Holmes, M., Vany, J., Mölk, D., 2022. "Eavor Loop™ Commercial Project at Geretsried, Molasse Basin, Germany," Proceedings of the European Geothermal Congress 2022, Berlin, Germany.

Richard, T., Germay, C., Detournay, E., 2007, "A simplified model to explore the root cause of stick-slip vibrations in drilling systems with drag bits," Journal of Sound and Vibration, Volume 305, Issue 3, 2007, Pages 432-456, ISSN 0022-460X, https://doi.org/10.1016/j.jsv.2007.04.015

Stroud, D. R., Lines, L. A., and D. J. Minett-Smith., 2011, "Analytical and Experimental Backward Whirl Simulations for Rotary Steerable Bottom Hole Assemblies." Paper presented at the

SPE/IADC Drilling Conference and Exhibition, Amsterdam, The Netherlands, March 2011. doi: https://doi.org/10.2118/140011-MS

Thai, L., Nguyen, N., Blackwell, G., and Minh D., 2022, "Longest 3D Horizontal Granitic Basement Section Record Drilled in Vietnam Using Friction Reduction Technology and Real-Time Torque & Drag Management." Paper presented at the IADC/SPE Asia Pacific Drilling Technology Conference and Exhibition, Bangkok, Thailand. doi: https://doi.org/10.2118/209915-MS

Watson. G., 2013, "Effect of Drilling Parameters on PDC Cutter Wear," Hard Rock Drilling Workshop, International Research Institute of Stavanger (2013).

White, M., Martinez, M., Vasyliv, Y., Beckers, K., Bran-Anleu, G., Parisi, C., Balestra, P., Horne, R., Augustine, C., Pauley, L., Bettin, G., Marshall, T., 2023. "Closed-loop Geothermal Working Group Study – Understanding Thermal Performance and Economic Forecasts via Numerical Simulation," Proceedings of the Stanford Geothermal Workshop 2023, Stanford University, USA.

Wu, S. X, Paez, L., Partin, U. Agnihotri, M., 2010, "Decoupling stick-slip and whirl to achieve breakthrough in drilling performance," Proceedings of the IADC/SPE Drilling Conference and Exhibition, pp. 966–978, New Orleans, USA. https://doi.org/10.2118/128767-MS

Effect of Hydrostatic Pressure on Mechanical Specific Energy and Interfacial Friction Angle in Hard Rock Drilling

Dionne Mayibeki, Shaolin Jahan Eidee, Geir Hareland and Mohammed F. Al Dushaishi

Oklahoma State University

Keywords

Confining pressure, Mechanical specific energy, Interfacial friction angle, Hard rock drilling, Geothermal

ABSTRACT

Interfacial Friction Angle (IFA) is the frictional resistance experienced at the interface between the PDC cutters and the formation. Mechanical specific energy (MSE) is the energy required to remove a unit volume of rock during drilling. IFA is affected by normal and drag forces, including depth of cut (DOC) and rate of penetration (ROP), which also impacts MSE. Accurate interpretation of IFA and MSE in hard rock is crucial and can be used to optimize hard rock and geothermal drilling. This study used an in-house rig to test two 3¾" PDC bits (4 and 5-blade designs) to characterize IFA and MSE under hydrostatic pressures of 0 psi, 1000 psi, and 2000 psi. Tests were conducted in Sierra White Granite (SWG) using water as the drilling fluid at constant rotational speeds of 80 and 150 RPM, and the weight on bit (WOB) was incrementally increased while ROP and bit torque (T) were recorded. Results showed that the impact of hydrostatic pressure on MSE becomes distinctly evident at WOB values greater than 4000 lbs for both bits. Beyond this threshold, the effect on MSE is decreased for the tests under confinement, suggesting a change in rock failure criteria from elastic to more plastic deformation. The MSE for the unconfined tests (0 psi) decreases substantially after 4000 lbs, whereas this decrease is not observed in the tests under confinement (1000 psi and 2000 psi). The unconfined tests showed a more apparent decrease in MSE in Phase 2 (the efficient drilling phase) with increasing WOB, where the most effective drilling is seen when MSE values approach the rock's unconfined compressive strength (UCS). The values for MSE at a given confinement show the same trend for MSE but with a different low limit, indicating a distinctly different failure mode criterion. Results also showed that IFA becomes nearly constant in the efficient cutting phase of the drilling process. It was observed that increased confinement increases IFA during Phase 2 of the drilling process. During the inefficient phase of drilling (Phase 1), a higher IFA was observed due to insufficient WOB.

1. Introduction

When drilling in impermeable formations, hydrostatic pressure from the weight of the drilling fluid acts as confining pressure by uniformly applying force to the rock being penetrated at the bottom of the wellbore (Rampersad et al., 1994). Enhanced or deep geothermal wells are characterized by hard abrasive impermeable rock without formation fluids. This study assumes hydrostatic pressure as the confining pressure without considering pore pressure. Understanding the impact of confining pressure (i.e., hydrostatic pressure from the drilling fluid column) on IFA and MSE is crucial for optimizing drilling efficiency and reducing overall costs.

1.1 Mechanical Specific Energy (MSE)

Mechanical Specific Energy (MSE) is simplified as the energy required to cut a volume of rock, as depicted by Equation 1.

$$\text{MSE} = \frac{\text{Work done in cutting action}}{\text{Volume of rock removed}} \quad (1)$$

MSE has been widely used to measure drilling efficiency and maximize rate of penetration (ROP). While previous literature discusses the effects of MSE on drilling performance under atmospheric conditions, very little information is provided on the effects of confining pressure on MSE and its impact on drilling efficiency. Models have been established to calculate the specific energy required to remove a specific volume of rock. Teale (1965) proposed a model for calculating MSE in rotary drilling, which uses measurements of torque, weight on bit (WOB), and rotational speed (RPM). Teale's studies also demonstrated that maximum drilling efficiency occurs when MSE equals the unconfined compressive strength (UCS) of the formation being drilled; therefore, MSE can be used to identify optimal drilling efficiency. By comparing MSE to the formation's UCS in real-time, drilling performance can be evaluated, and drilling parameters can be adjusted accordingly to achieve the best results.

Pessier and Fear (1992) modified Teale's (1965) model and provided a way to calculate torque at the bit without reliable torque measurements where torque is calculated from the weight on bit (WOB). Even though Pessier and Fear's (1992) model uses WOB to calculate torque, the WOB is still based on surface measurements. Wellbore friction and inclination in directional drilling greatly influence WOB and torque values. This causes a deviation in the surface read WOB and torque values from actual downhole values. This limitation is not accounted for in Teale's (1965) and Pessier and Fear (1992) models. Dupriest and Koederitz (2005) later proposed an MSE model based on Teale's (1965) model incorporating mechanical bit efficiency. Dupriest and Koederitz (2005) assumed a mechanical bit efficiency of 35%. However, researchers (Hammoutene and Bits, 2012; Amadi and Iyalla, 2012) argued that the mechanical bit efficiency is bit specific and also differs based on the formation being drilled, which poses limitations on Dupriest and Koederitz's (2005) model.

Researchers have since sought to incorporate hydraulic energy into the MSE function to account for bit cleaning and removing cuttings from the hole (Mohan et al. 2009). Rajabov et al. (2012) studied the effects of back rake and side rake angles on the MSE of single PDC cutters with selected rocks at varying depths of cut (DOC) and confining pressures. It was found that the MSE decreases with increasing DOC up to 0.08" under both atmospheric and confining pressures in

Carthage Marble, Mancos Shale, and Torrey Buff Sandstone and then starts to increase slightly at DOC above 0.08". Rajabov et al. (2012) results suggested that the MSE increases significantly at low confining pressures and that the cutting mechanism changes at high confining pressures. Tests conducted by Rajabov et al. (2012) also showed that increasing confining pressure from 250 psi to 500 psi did not affect the MSE as opposed to increasing from atmospheric pressure to 250 psi, which indicates that most of the increase in MSE and decrease in cutting efficiency occurs at low confining pressures.

1.2 Interfacial friction angle (IFA)

The interaction between the rock and the cutter generates a frictional force at the cutter interface, which is characterized by the Interfacial Friction Angle (IFA). This angle represents the resistance encountered by the cutter as it penetrates and shears the rock, influencing the efficiency and effectiveness of the drilling process. IFA significantly affects the cutter's horizontal and vertical force components. Figure 1 shows the forces acting on a sharp cutter as reported by Detournay and Defourny (1992), where F_n is the normal force, F_d is the drag force, θ is the back rake angle, and ψ is the IFA. The IFA interaction between the rock and drill bit cutters plays a key role in the bit's response and overall performance.

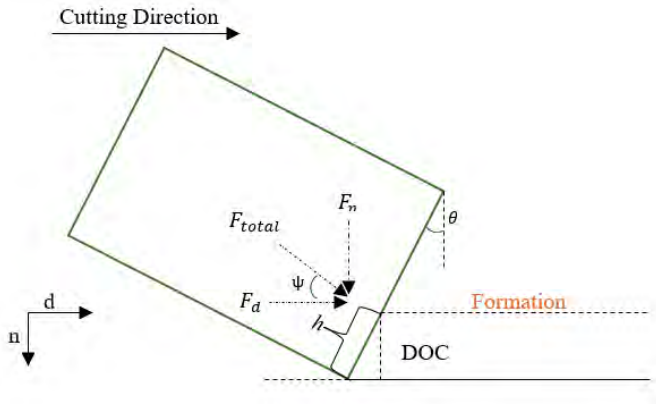

Figure 1: Force balance for sharp cutters (Detournay and Defourny, 1992)

IFA models derived from single cutter analysis are used with ROP models to improve ROP estimation and aid in drilling efficiency, improving overall drilling costs. The complexity of the cutting mechanism involving hard formations at high confining pressures is one of the primary sources of inaccurate ROP predictions in hard rock drilling; therefore, it is essential to estimate IFA as accurately as possible to optimize ROP successfully. Atashnezhad et al. (2020) developed an empirical model for PDC cutter rock IFA estimation to estimate different phases of drilling using a Differential Evolution Algorithm (DEA) where single cutter analysis was used. The IFA model includes the cutter velocity, PDC cutter back rake, rock's unconfined compressive strength (UCS), PDC cutter diameter, and DOC. Figure 2 shows an example of the IFA general trend for hard and soft rocks with increasing DOC, where two distinct drilling phases can be seen. IFA values are higher in Phase 1 and decrease as DOC is increased significantly for hard rock until Phase 2 is reached. At this point, the decrease in IFA becomes less steep, and the effect of DOC is

minimal. A horizontal trend is observed for soft rocks, signifying little to no effect on IFA with increasing DOC.

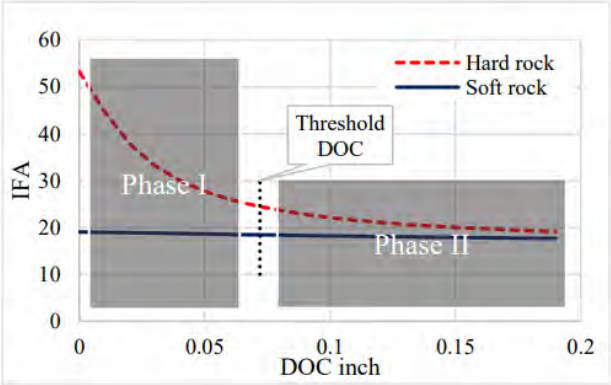

Figure 2: IFA trend for hard and soft rocks showing two phases of drilling (Atashnezhad et al., 2020)

This paper aims to analyze the direct effect of hydrostatic pressure from the drilling fluid at the bottom of the wellbore while drilling on MSE and IFA in Sierra White Granite (SWG) and discuss the impact of MSE and IFA on drilling efficiency in hard rock drilling.

2. Methodology and Testing

2.1 Bit Information

Two polycrystalline diamond compact (PDC) bits, 4-bladed and 5-bladed, each with a diameter of 3¾ inches, were used for laboratory testing. The front and side profiles of the 4-bladed and 5-bladed bits are shown in Figures 3 and 4, respectively. The properties of these bits are detailed in Table 1.

Figure 3: Bit 1- Four Bladed PDC bit front and side profile

Figure 4: Bit 2- Five Bladed PDC bit front and side profile

Table 1: Bit Properties

	Bit 1	Bit 2
Bit Diameter (inch)	3-¾	3-¾
Number of Face Cutters	11	19
Number of Blades	4	5
Cutter Diameter (mm)	13	11

2.2 Experimental

An indoor drilling rig, designed to simulate typical field conditions under both atmospheric and confining pressures was employed for testing. The experimental procedure followed was consistent with the methodology reported by Mayibeki et al., 2023. The experiments were performed at atmospheric and confining pressures of 1000 and 2000 psi. The tests were performed at 80 and 150 RPM rotational speeds, with the weight on bit (WOB) gradually increasing to approximately 6500 lbf. Sierra White Granite (SWG) was used with an unconfined compressive strength (UCS) of 28,000 psi, bulk density of 165.4 lb/ft^{-3}, and Young's Modulus of 6×10^{6} psi. The permeability and porosity of the granite were assumed to be negligible.

The indoor rig features a drill string powered by hydraulic energy. The WOB is electronically controlled, while the torque necessary for rotating the drill string is generated by a belt drive system connected to an electric motor, which is also hydraulically powered. The drilling fluid used in the testing was water, maintained at a flow rate of 100 gallons per minute and a constant temperature of 60 °F.

The rock sample was lowered into a confinement cell, which was pressurized using water to conduct the confinement testing. A back pressure regulator adjusted the pressure setting for a specific test. Sensors were placed at the drill string to monitor ROP, WOB, and rotational speed, where the sampling rate of the measured data was set to 100 Hz for the tests under atmospheric conditions and 2000 Hz for the tests under confinement.

3. Results and Discussion

3.1 MSE Analysis

MSE was calculated using Teale's (1965) model, as shown in Equation 2. In this model, WOB is measured in pound-force (lbf), the bit area (Ab) is measured in square inches (in²), RPM is measured in revolutions per minute (rev/min), the torque generated at the bit (T) is measured in foot-pound-force (ft-lbf), and ROP is measured in feet per hour (ft/hr).

$$\mathrm{MSE} = \left(\frac{\mathrm{WOB}}{\mathrm{Ab}}\right) + \frac{120\pi\times\mathrm{RPM}\times\mathrm{T}}{\mathrm{Ab}\times\mathrm{ROP}} \quad (2)$$

3.1.1 Four-Bladed Bit MSE Analysis

MSE results were initially analyzed as a function of the applied WOB to observe how MSE changes when the WOB is gradually increased from 2 klbf to 6.5 klbf at confining pressures of 0, 1000, and 2000 psi. Figures 5a and 5b illustrate the effect of incremental WOB on MSE at rotational speeds of 80 and 150 RPM, respectively.

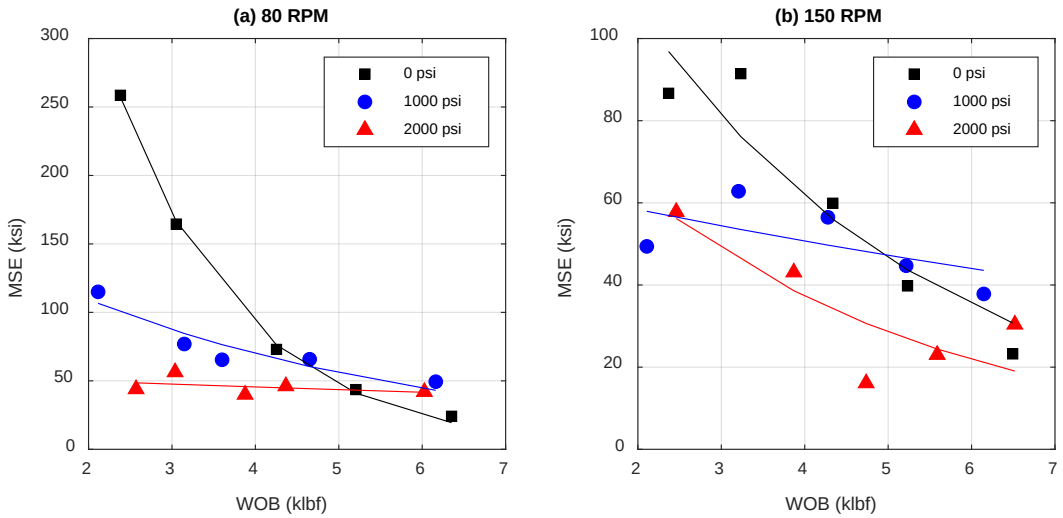

Figure 5: MSE as a Function of WOB Under Confining Pressures of 0, 1000, and 2000 psi at (a) 80 RPM and (b) 150 RPM

At lower WOB or during Phase 1 of drilling, the 0 psi tests exhibit higher MSE values than those under confinement. In the absence of confining pressure at lower WOB, fractures can propagate uncontrollably and irregularly due to the lack of external pressure. Confining pressure helps to maintain stress concentration around the drill bit cutters, enhancing its efficiency. Additionally, confining pressure contributes to the stability of the rock, creating a more localized stress concentration that ensures the applied energy is used effectively to remove a volume of rock. Without confinement, applied stress is more likely to disperse, reducing the efficiency of the rock-breaking process. This means more energy is required to achieve the same penetration rate compared to confined conditions. However, as WOB values exceed 4 klbf, the MSE for the 0 psi tests continues to decrease significantly, while the tests under confinement show nearly constant MSE values with a slight increase for the tests at 2000 psi.

At higher confining pressures, the rock failure mechanism appears to shift from brittle to ductile failure. Tests conducted by (He & Xu, 2015) reported a critical depth (i.e., hydrostatic pressure) beyond which the rock shifts from brittle to ductile failure. This transitional phase occurs at higher confining pressures, causing MSE to remain nearly constant or increase slightly for tests under confinement. This makes it more challenging to determine the most efficient drilling conditions at high confining pressures. Under confinement, the MSE requirement is more consistent and sustained due to the continuous shearing process. Because the rock has more of a ductile cutting action at high confining pressures, the energy required in the drilling process remains stable and does not fluctuate as much. Unlike brittle failure, where energy spikes might be observed, ductile deformation requires a constant energy supply, as observed in He and Xu's (2015) experiments.

As a result of the consistent and sustained MSE requirement, achieving the most efficient drilling parameters becomes more challenging. When drilling with higher weight on bit (WOB) at high confining pressures, the rock becomes harder due to increased stress, requiring more energy to drill it. Hydrostatic or confining pressure inhibits the formation of macro cracks and increases the rock's strength (Liu et al., 2021). As a result, the MSE also increases, especially in the tests conducted at 2000 psi confining pressure. However, the tests with 1000 psi confinement display a higher average MSE than the 2000 psi test, suggesting that the transition from brittle to ductile rock failure mode may occur around 1000 psi, increasing energy requirements at this pressure. Rajabov et al. (2012) observed a similar behavior where most of the MSE increase and energy consumption was seen at lower confining pressures.

Additional optimization techniques must be explored to achieve efficient drilling in hard rock under high confining pressures to reduce MSE. A higher RPM can lower MSE values due to the faster cutting action from the bit's rotation. However, real-time optimization methods are crucial for monitoring key parameters such as WOB, RPM, ROP, torque, and MSE to ensure an efficient and cost-effective drilling operation without excessively wearing the bit. The effect of confining pressure on MSE was also analyzed for constant WOB values of 2, 4, and 6 klbf to observe how MSE changes under varying confining pressures while maintaining constant WOB. Results are displayed in Figures 6a and 6b, illustrating the findings at (a) 80 RPM and (b) 150 RPM.

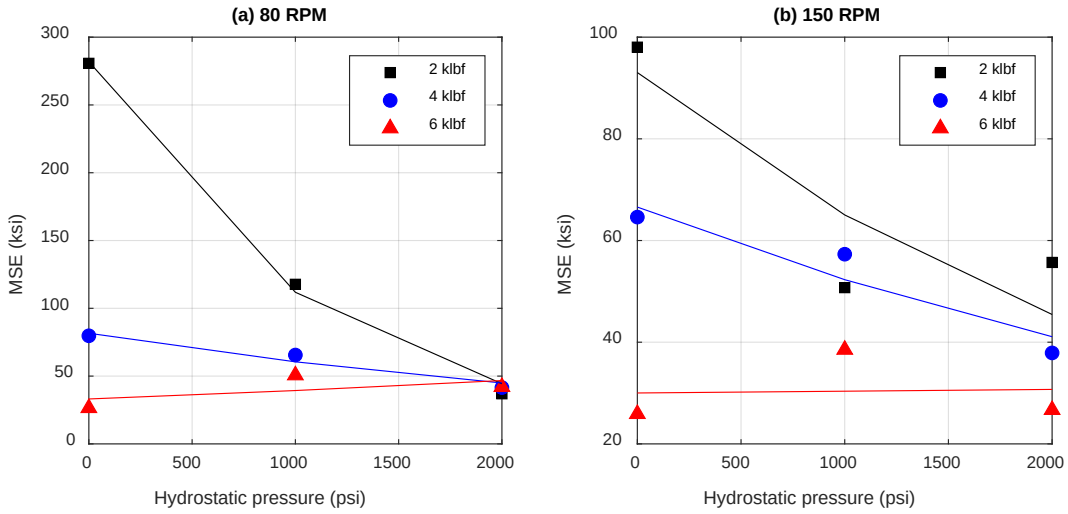

Figure 6: MSE vs Confining Pressure for a Constant WOB at (a) 80 RPM and (b) 150 RPM

The tests with the highest WOB show the lowest overall MSE at atmospheric pressure and under confinement, except for the test at 80 RPM and 2000 psi, where the lowest WOB shows the lowest MSE. A higher WOB ensures improved bit-rock contact, better cutter engagement, consistent cutting action, and enhanced energy transfer and utilization. These factors collectively reduce the MSE required to drill the rock, improving drilling efficiency. Drilling with a lower WOB is inefficient for hard rock at high confining pressures. An optimum WOB is necessary to lower MSE without excessively wearing out the bit.

The effect of confining pressure on MSE was also analyzed for constant DOC values of 0.01, 0.03, 0.06, and 0.1 inches/rev to observe how DOC influences MSE under varying confining pressures.

DOC (inches/rev) was calculated using Equation 3, where ROP (ft/hr) represents the penetration rate and RPM signifies revolutions per minute. Figures 7a and 7b show the effect of confining pressure on MSE based on DOC for 80 and 150 RPM, respectively.

$$\mathrm{DOC} = \frac{\mathrm{ROP}}{\mathrm{RPM}} \tag{3}$$

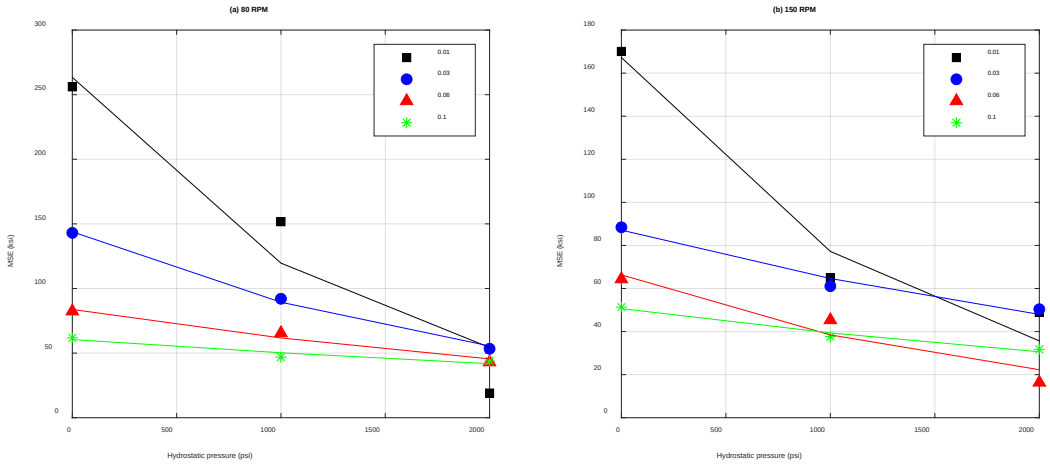

Figure 7: MSE vs Confining Pressure for a Constant DOC at (a) 80 RPM and (b) 150 RPM

Higher MSE values are observed at lower DOC and lower confining pressures due to reduced cutting efficiency and poor bit-rock interaction. When confining pressure exceeds 1000 psi, MSE significantly decreases for the test conducted at 0.01 inches/rev DOC and 80 RPM. At higher confining pressures, lower MSE values are observed at lower DOC values and 80 RPM due to the rock deforming plastically and undergoing shear failure. This suggests that a lower DOC facilitates more efficient drilling than a higher DOC when drilling hard rock under high confining pressures and low RPM.

However, a lower DOC and low RPM can result in lower ROP, making optimization techniques crucial for effective drilling. When drilling with a higher RPM, a higher DOC of 0.06 inches/rev is preferred, resulting in the lowest MSE, as shown in Figure 7b. A higher DOC tends to have lower MSE values at lower confining pressures due to increased penetration and easier fracture propagation from the brittle failure mechanism. In contrast, lower DOC values are more effective at higher confining pressures, where ductile failure dominates, as Richard et al. (1999) and He and Xu (2015) reported.

3.1.2 Five-Bladed Bit MSE Analysis

Results for MSE versus confining pressure at incremental WOB were analyzed for the 5-bladed bit. The WOB was gradually increased from 2 klbf to 6.5 klbf at (a) 80 RPM and (b) 150 RPM under confining pressures of 0, 1000, and 2000 psi. Figures 8a and 8b display the results at 80 RPM and 150 RPM, respectively.

Similar to the 4-bladed bit, tests with a lower WOB observed higher MSE at lower confining pressures, except for the test at 2000 psi and 80 RPM, which showed a continuous increase in MSE (Figure 8a). At higher confining pressures where plastic behavior is prevalent, the rock absorbs more energy as the rock deforms continuously without fracturing (He & Xu, 2015). At WOB values greater than 4 klbf, the MSE for the 0 psi test continues to decrease significantly, a trend not observed in the other tests. An increase in MSE is seen for the test under 2000 psi at 80 RPM, as more energy is required to break the rock at higher confining pressures. The increased pressure compresses the rock more tightly around the drill bit, requiring more energy to achieve effective penetration. Consequently, higher confining pressures demand a more significant input of energy to overcome the rock's increased resistance, resulting in higher MSE values. The increased confining pressure and plastic deformation increase the overall energy demand, leading to higher MSE values.

Increasing WOB can achieve Minimum MSE at a lower value in unconfined conditions. However, reaching the minimum MSE requires a greater WOB under higher confining pressures. This indicates that the MSE and energy consumption in drilling vary with confining pressure, with optimal drilling efficiency being easier to achieve in unconfined environments. As confining pressure increases, the rock's resistance to drilling also increases, necessitating higher WOB to attain the minimum MSE. Moreover, this trend suggests that there is a point beyond which further increases in WOB might not significantly reduce MSE or may even increase it due to the complexities of rock deformation and failure mechanisms under high pressure, as observed in the tests at 2000 psi and 80 RPM for both bits. This emphasizes optimizing WOB based on the specific confining pressure conditions to achieve the most efficient drilling performance.

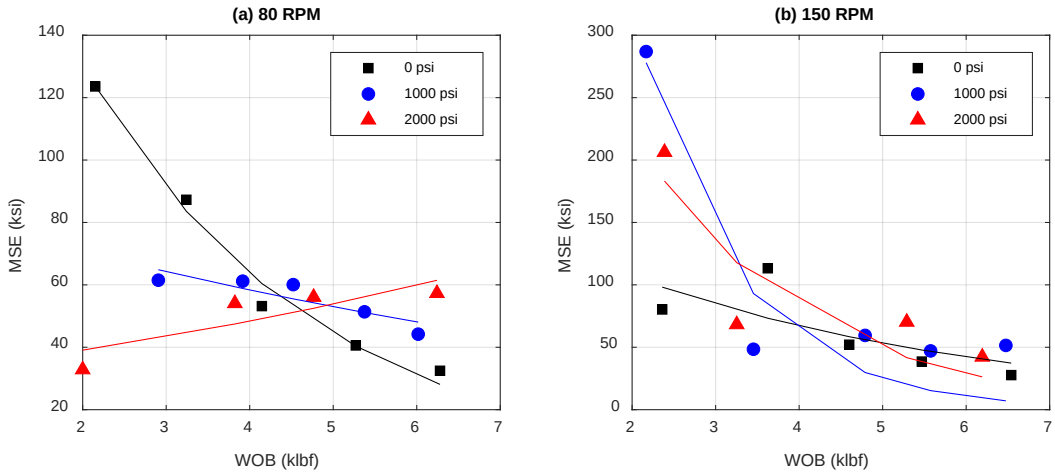

Figure 8: MSE as a Function of WOB Under Confining Pressures of 0, 1000, and 2000 psi at (a) 80 RPM and (b) 150 RPM for the 5-bladed PDC bit

Figures 9a and 9b illustrate the effect of confining pressure on MSE under constant WOB values of 2, 4, and 6 klbf at (a) 80 RPM and (b) 150 RPM. Unlike the 4-bladed bit, tests at higher WOB values exhibit the lowest MSE, only up to 1000 psi for the tests conducted at 80 RPM. The MSE for the 2 klbf test shows a continuous decrease in MSE, a trend not observed in the other tests. This observation suggests that for the 5-bladed bit, drilling with a lower WOB and a lower RPM under high confining pressures might be optimal for efficient drilling, but this will result in reduced

ROP and increased rotating time. However, tests conducted with higher WOB at higher RPM achieved the lowest MSE, as shown in Figure 9b. Drilling with a high RPM can cause vibrations and stability issues, therefore, a higher WOB may be necessary to maintain bit stability, reduce vibrations, and ensure a smoother drilling process.

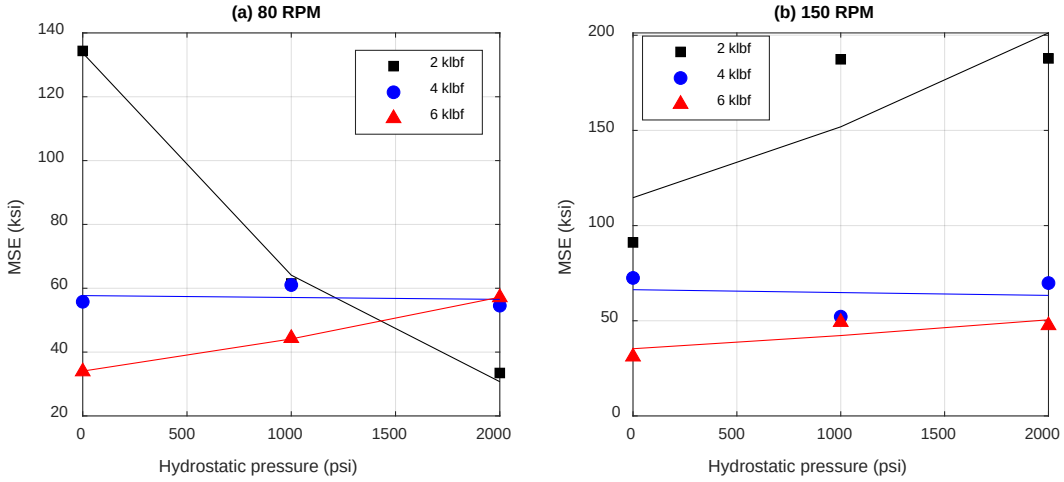

Figure 9: MSE vs Confining Pressure for a Constant WOB at (a) 80 RPM and (b) 150 RPM

The effect of confining pressure on MSE at different DOC was also analyzed at 80 and 150 RPM for the 5-bladed bit. Figures 10a and 10b present the results at 80 and 150 RPM, respectively.

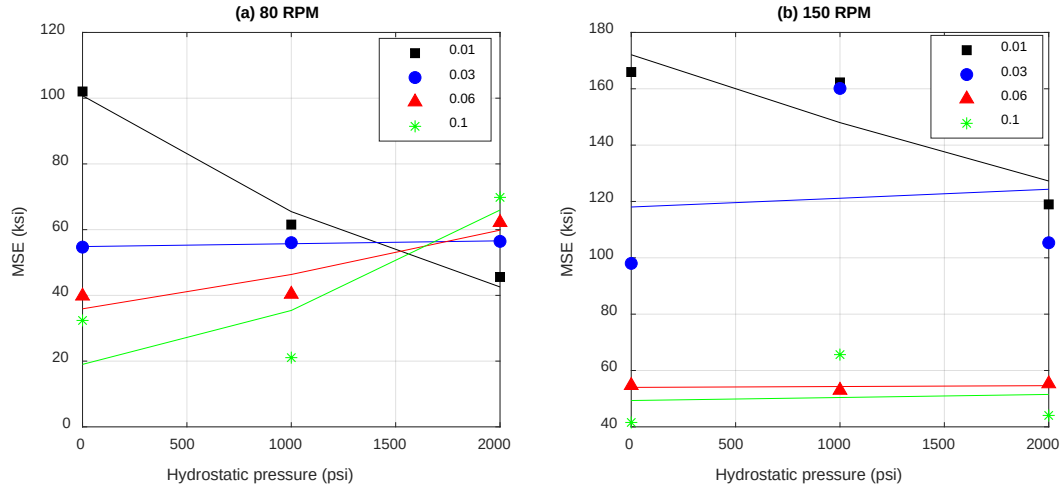

Figure 10: MSE vs Confining Pressure for a Constant DOC at (a) 80 RPM and (b) 150 RPM

Similar to the 4-bladed bit, tests with a lower DOC exhibit higher MSE values at lower confining pressures due to poor bit-rock interaction. At 80 RPM, as confining pressure increases, the MSE for the test with the lowest DOC of 0.01 inches/rev continues to decrease significantly, while the other tests show a steady increase in MSE. This observation further reinforces that a lower RPM and DOC of 0.01 inches/rev are optimal for drilling hard rock at high confining pressures. However, at 150 RPM, tests with a higher DOC demonstrate the lowest MSE, indicating that

drilling with a higher DOC is most effective at higher rotational speeds, as observed with the 4-bladed bit.

3.2 IFA Analysis

Principles from Detournay and Defourny's (1992) IFA model were used to create a correlation shown in Equation 7, to calculate the equivalent bit IFA values. Hareland & Rampersad's (1994) equivalent radius concept was also used to calculate the drag force on a cutter (DFOC). In Equation 7, ψ denotes the IFA (deg), WOC is the weight on cutter (klbf), DFOC is the drag force generated at the cutter (klbf), and BR is the cutter back rake (deg). WOC and DFOC can be calculated from Equations 4 and 5 respectively. The equivalent bit radius (Re) measured in inches can be calculated from Equation 6.

$$\mathrm{WOC} = \frac{\mathrm{WOB}}{\mathrm{Nc}} \tag{4}$$

$$DFOC = \frac{\frac{\text{Measured Torque}}{\mathrm{Re}}}{\mathrm{Nc}} \tag{5}$$

$$\mathrm{Re} = \frac{\mathrm{Db}}{\sqrt[2]{2}} \tag{6}$$

$$\psi = \mathrm{Tan}^{-1}\left(\frac{\mathrm{WOC}}{\mathrm{DFOC}}\right) - \mathrm{BR} \tag{7}$$

3.2.1 Four-Bladed Bit IFA Analysis

Figures 11a and 11b illustrate the effect of confining pressure on IFA as a function of the applied WOB and RPM. For a constant WOB, increasing confining pressure results in a higher IFA at both rotational speeds. This is mainly due to the increased normal forces at the contact interface between the drill bit and the rock, which results in greater frictional resistance. The lower WOB tests show the highest average IFA at both rotational speeds. Lower WOB results in decreased penetration rates, causing the drill bit to remain in contact with the rock for a longer duration. This extended contact increases the likelihood of higher frictional resistance, leading to a higher observed IFA.

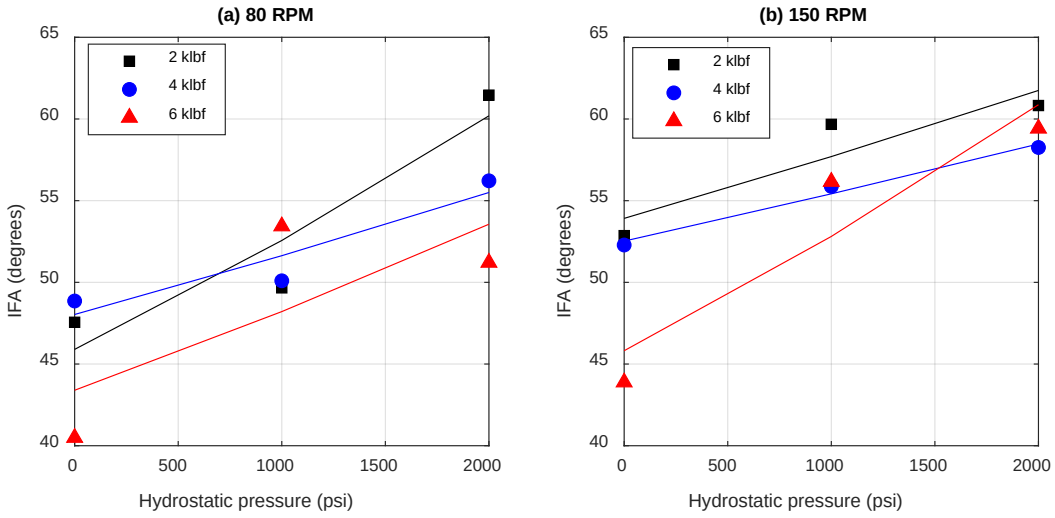

Figure 11: IFA vs Confining pressure for a constant WOB at (a) 80 RPM and (b) 150 RPM

The relationship between specific energy and drilling strength is given by the ratio shown in Equation 8 where E is the specific energy (lb/in^2), S is the drilling strength (lb/in^2), Fn is the normal force (lbf), Fd is the drag force (lbf), θ is the back rake angle (deg) and ψ is the IFA (deg)

$$E \cdot S = \frac{F_n}{F_d} = \tan(\theta + \psi) \tag{8}$$

The ratio of the normal force to the drag force changes with varying angles, affecting the efficiency and mode of drilling. Consequently, the normal force to drag force ratio also affects the IFA. As seen from the results, drilling at higher confinement requires more WOB to overcome the rock's resistance to fracture. While WOB increased with higher confinement, the required torque did not increase proportionally and decreased in some cases. The observed increase in WOB without a proportional increase in torque under higher confining pressures implies a transition in the cutting mode. During this transitional phase, spikes in IFA can be observed in some tests. This suggests that higher normal forces are needed to initiate and sustain cutting in more ductile conditions where plastic flow occurs more smoothly compared to brittle failure mode. Brittle failure results in rough fracture surfaces, causing spikes in IFA when the rock fractures and breaks away. However, in ductile mode, where the rock tends to flow and deform plastically, lower IFA values are observed.

The transition from brittle to plastic cutting modes highlights the need to adjust WOB and monitor torque to maintain drilling efficiency. Optimization of drilling parameters for different confining pressure conditions is necessary to improve rock penetration and drilling efficiency.

3.2.2 Five-Bladed Bit IFA Analysis

The effect of confining pressure on IFA for the 5-bladed bit is illustrated in Figures 12a and 12b, for rotational speeds of 80 RPM and 150 RPM, respectively. The 5-bladed bit generally exhibits lower average IFA values at higher confining pressures when compared to the 4-bladed bit. This is due to the improved weight distribution and reduced stress concentration resulting from the

increased contact area with the rock formation. At a constant WOB and 80 RPM, the IFA steadily increases from 0 to 1000 psi across all WOB levels. However, when confining pressure is increased from 1000 to 2000 psi, the 2 klbf test shows a slight decrease in IFA due to lower contact pressure and less friction. For the tests under 150 RPM, the IFA shows an increase in the 2 klbf and 6 klbf tests when the confining pressure is increased from 0 to 1000 psi and a decrease in the 4 klbf test. Again, this decrease can also be attributed to the change in rock failure mechanism from brittle to ductile experienced at higher confining pressures. Plastic deformation experienced in ductile mode results in smoother surfaces and reduced resistance at the interface between the drill bit and the rock. This can cause a decrease in IFA values at higher confining pressures.

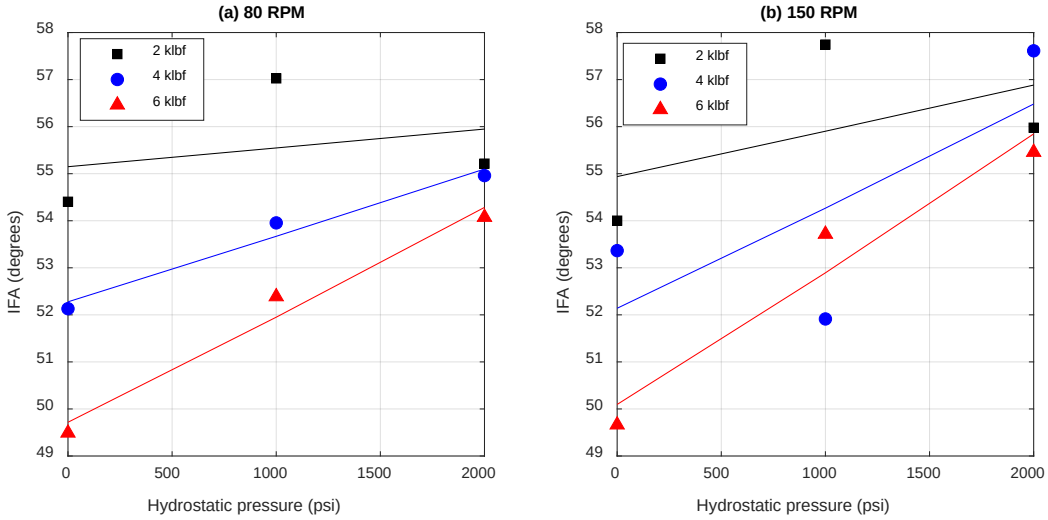

Figure 12: IFA vs Confining pressure for a Constant WOB at (a) 80 RPM and (b) 150 RPM

4. Conclusions

- Higher confining pressures significantly enhance the rock's strength by increasing its resistance to fracturing. This means that more energy and WOB are required to achieve the same rate of penetration or depth of cut, impacting drilling costs and operational efficiency. Optimizing drilling parameters becomes crucial to balance MSE and ensure an economical drilling operation.
- The results from the presented drill bit testing agree with previous studies that show that as confining pressure increases, a transition in rock failure modes occurs in hard rock. At lower confining pressures, brittle failure is dominant and involves sudden fracturing and higher specific energies. In comparison, at higher confining pressures, ductile failure dominates and requires sustained energy input due to gradual deformation. This transition complicates drilling efficiency, necessitating adjustments in drilling parameters to achieve drilling efficiency.
- Drilling with a higher WOB typically yields the lowest MSE, indicating efficient rock removal. However, tests at 2000 psi confining pressure and 80 RPM reveal that using a lower WOB achieves the lowest MSE, highlighting a subtle relationship influenced by confining pressure and RPM. This variability further proves the need to tailor drilling

parameters to specific operational contexts, particularly under high confining pressures, for optimal efficiency and performance.

- Tests conducted at 1000 psi and 80 RPM with a 0.01 inches/rev DOC show a significant decrease in MSE, suggesting that lower DOC values are more efficient under high confining pressures. This means that energy consumption is reduced at lower DOC, and penetration rates are improved due to the rock's plastic deformation and shear failure characteristics.
- The Interfacial Friction Angle (IFA) increases with increasing confining pressure for a given WOB due to higher normal forces at the drill bit-rock interface, resulting in greater frictional resistance. During the transition from brittle to ductile failure modes, spikes in IFA occur due to rougher fracture surfaces in brittle failure. In contrast, ductile deformation leads to lower IFA values as the rock undergoes plastic flow. Understanding these dynamics enables informed decision-making in drilling operations, enhancing overall efficiency and performance.

Acknowledgement

This study was partly supported by the U.S. Department of Energy, DOE EERE –Geothermal Technologies Program under Award Number EE0008603.

REFERENCES

Amadi, K., and I. Iyalla. "Application of Mechanical Specific Energy Techniques in Reducing Drilling Cost in Deepwater Development." *Paper presented at the SPE Deepwater Drilling and Completions Conference*, 2012.

Atashnezhad, A., S. Akhtarmanesh, S. Sleeper, S. Hellvik, and G. Hareland. "Developing an Empirical Model for PDC Cutter Rock Interfacial Friction Angle Estimation Using Differential Evolution Algorithm." *Paper presented at the ARMA US Rock Mechanics/Geomechanics Symposium*, 2020.

Detournay, E., and P. Defourny. "A Phenomenological Model for the Drilling Action of Drag Bits." *Paper presented at the International Journal of Rock Mechanics and Mining Sciences & Geomechanics Abstracts*, 1992.

Dupriest, F. E., and W. L. Koederitz. "Maximizing Drill Rates with Real-Time Surveillance of Mechanical Specific Energy." *Paper presented at the SPE/IADC Drilling Conference and Exhibition*, 2005.

Hammoutene, C., and S. Bits. "FEA Modelled MSE/UCS Values Optimise PDC Design for Entire Hole Section." *Paper presented at the North Africa Technical Conference and Exhibition*, 2012.

Hareland, G., and P. R. Rampersad. "Drag - Bit Model Including Wear." *Paper presented at the SPE Latin America/Caribbean Petroleum Engineering Conference*, Buenos Aires, Argentina, April 1994.

He, X., and C. Xu. "Discrete Element Modelling of Rock Cutting: From Ductile to Brittle Transition." *International Journal for Numerical and Analytical Methods in Geomechanics*, vol. 39, no. 12, 2015, pp. 1331-1351.

Liu, W., X. Zhu, Y. Lv, and H. Tong. "On the Mechanism of Thermally Induced Micro-Cracking Assisted Rock Cutting in Hard Formation." *Journal of Petroleum Science and Engineering*, vol. 196, 2021, article 107666.

Mayibeki, D., G. Hareland, M. Al Dushaishi, and S. Blaylock. "The Effect of Confinement on Rate of Penetration (ROP) in Hard Rock." *Paper presented at the 57th U.S. Rock Mechanics/Geomechanics Symposium*, 25 June 2023.

Mohan, K., F. Adil, and R. Samuel. "Tracking Drilling Efficiency Using Hydro-Mechanical Specific Energy." *Paper presented at the SPE/IADC Drilling Conference and Exhibition*, 2009.

Pessier, R., and M. Fear. "Quantitative Common Drilling Problems with Mechanical Specific Energy and Bit-Specific Coefficient of Sliding Friction." *Paper presented at the 67th Annual Technical Conference and Exhibition*, Washington, DC, October 4, 1992. Paper SPE 24584.

Rajabov, V., S. Miska, L. Mortimer, M. Yu, and E. Ozbayoglu. "The Effects of Back Rake and Side Rake Angles on Mechanical Specific Energy of Single PDC Cutters with Selected Rocks at Varying Depth of Cuts and Confining Pressures." *Paper presented at the SPE/IADC Drilling Conference and Exhibition*, 2012.

Rampersad, P. R., G. Hareland, and P. Boonyapaluk. "Drilling Optimization Using Drilling Data and Available Technology." *SPE Latin America/Caribbean Petroleum Engineering Conference*, 27 Apr. 1994.

Richard, T., E. Detournay, A. Drescher, P. Nicodeme, and D. Fourmaintraux. "The Scratch Test As A Means To Measure Strength of Sedimentary Rocks." *Paper presented at the SPE/ISRM Rock Mechanics in Petroleum Engineering*, 8 July 1998.

Teale, R. "The Concept of Specific Energy in Rock Drilling." *Paper presented at the International Journal of Rock Mechanics and Mining Sciences & Geomechanics Abstracts*, 1965.

Zhang, Zong-Xian. "Chapter 6 - Environmental Effects on Rock Fracture." *Rock Fracture and Blasting*, edited by Zong-Xian Zhang, Butterworth-Heinemann, 2016, pp. 135-153. ISBN 9780128026885.

Drilling Ultra High Temp Geothermal Well Using Standard Temperature Drilling Tools

Komang Wisnu Murti[1], Gatra Kusuma[1], Hargi Kurniawidana[1], and Edyson Purba[2]

[1]SLB Oilfield Services

[2]Pertamina Geothermal Energy

Keywords

Geothermal, Drilling, High Temperature, Standard Drilling Tools, Drilling

ABSTRACT

Geothermal drilling has become more and more attractive as an option in the search for new green-energy exploration and production. This activity has been driven by the demand for new energy and the existence of technological advances. However geothermal drilling operations have unique challenges, which need to be carefully addressed. These environments will challenge the equipment to be exposed to high downhole temperatures which will exceeds the standard temperature equipment and tool ratings, risking burning the drilling tools which result in costly equipment damage and non-productive drilling time.

The effort of designing and developing equipment to be operated in high temperature conditions continually happen. However, this effort will increase the production cost and limit the availability of equipment deployment to operate in another environment. As alternative, drilling through high temperature volcanic formations up to 250°C using standard temperature tools (150°C rating) will requires specific drilling practices to keep the tools survive and reduce the risk of failures. To overcome the associated challenges, field experience introduces a flexible engineered approach to avoid any non-productive time (NPT) that is associated due to tools failure.

This paper will present a systematic approach to overcome volcanic geothermal drilling challenges associated with high temperatures. Hence the goal is to have an optimum, safe, efficient drilling operations and emphasize in drilling practice with standard temperature tools (150°C rating) in formation temperatures up to 250°C.All the paragraphs of the paper are set in <Normal Style>. The paragraphs should not have line breaks between them – the GRC Normal Style will space the paragraphs automatically. Please be very careful to use styles throughout the document, so that all the papers will have a similar appearance.

1. Introduction

Indonesia is renowned for its significant geothermal potential, boasting an estimated 29,000 MW of geothermal resources, making it one of the top geothermal energy reserves in the world. Positioned on the Pacific Ring of Fire, Indonesia benefits from abundant geothermal activity due to its numerous volcanoes, offering a substantial and largely untapped energy resource.

As of 2024, Indonesia's installed geothermal capacity stands at approximately 2,133 MW, which is about 7% of its total potential. This positions Indonesia as the second-largest producer of geothermal energy globally, after the United States. The current utilization of this resource, however, represents only a fraction of what is feasible, highlighting a significant opportunity for expansion.

The Indonesian government has set ambitious goals to increase the country's geothermal capacity as part of its broader strategy to transition to renewable energy sources. By 2030, the government aims to boost the installed geothermal capacity to 8,000 MW. This plan is part of Indonesia’s commitment to reduce greenhouse gas emissions and decrease reliance on fossil fuels, thereby promoting a sustainable energy future.

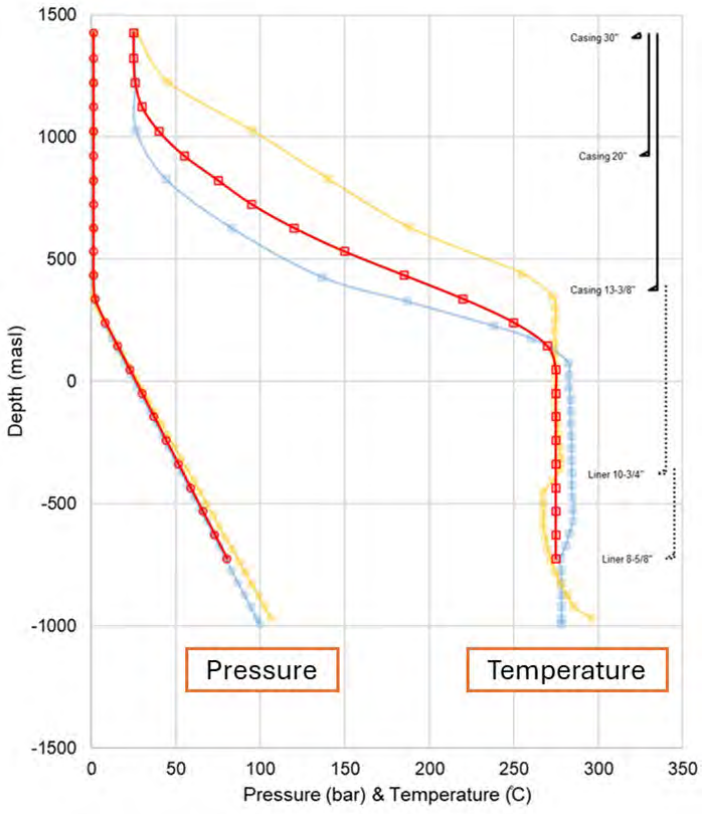

Figure 1. Temperature and pressure prediction.

Geothermal drilling in Indonesia, unlike conventional oil and gas drilling, involves penetrating through volcanic formations characterized by extremely high temperatures. Standard drilling equipment is typically rated for temperatures up to 150°C, but geothermal formations can reach temperatures of 250°C or higher as shown at Figure 1. This disparity presents a risk of equipment

failure, leading to costly downtime and equipment replacement. The challenge is to conduct efficient and safe drilling operations while minimizing risks associated with high-temperature environments.

2. Methodology

Geothermal drilling in Indonesia is particularly challenging due to the high-temperature reservoirs found throughout the country's geothermal fields. These fields are located in diverse geological settings, each presenting unique difficulties for drilling operations. The key geothermal fields span from North Sumatra to East Java, and their reservoir temperatures can reach up to 250°C.

Specific Challenges in High-Temperature Reservoirs

1. Equipment Durability and Performance
    a. High-Temperature Exposure: Standard drilling tools are typically rated for temperatures up to 150°C. However, the reservoir temperatures in many Indonesian geothermal fields can exceed this limit, reaching up to 250°C as shown at Figure 2. Prolonged exposure to such high temperatures can cause thermal degradation of drilling tools, leading to frequent failures and costly replacements.

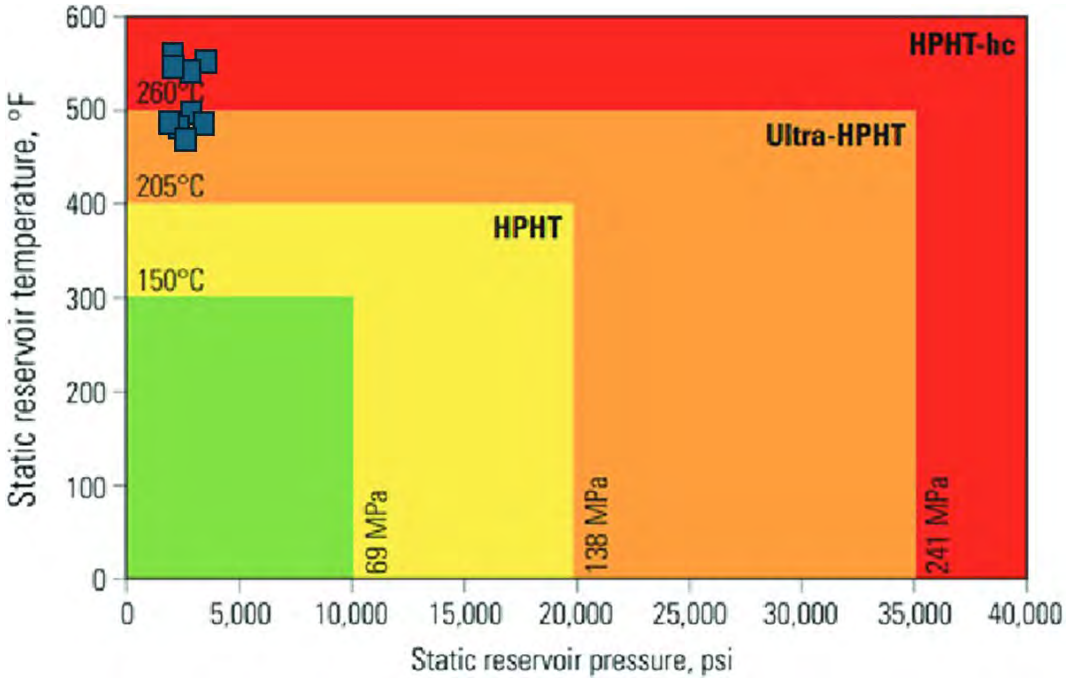

Figure 2. High temperature low pressure geothermal in Indonesia.

    b. Corrosion and Erosion: The geothermal fluids in these high-temperature reservoirs are often corrosive, containing dissolved gases like CO_2 and H_2S, which can corrode metal components of the drilling tools and equipment. Additionally, the abrasive nature of geothermal fluids can cause erosion, further reducing the lifespan of drilling tools.
2. Operational Efficiency

a. Non-Productive Time (NPT): Equipment failures due to high temperatures and corrosion can lead to significant non-productive time (NPT), where drilling operations are halted for tool replacement or repair. This not only increases operational costs but also delays project timelines.
b. Cooling Requirements: Managing the high downhole temperatures requires effective cooling strategies, such as optimizing mud circulation rates and using cooling fluids. These measures are essential to maintain the integrity of the drilling tools but can complicate the drilling process and increase operational complexity.

3. Safety Concerns
   a. High-Pressure Steam Zones: Many geothermal fields have high-pressure steam zones, which pose significant safety risks. Blowouts and uncontrolled releases of steam can endanger the safety of the drilling crew and equipment.

Figure 3. Equipment damage after exposed to steam kick

   b. Acidic Fluids: The presence of acidic fluids in some geothermal reservoirs requires the use of specialized materials and coatings to protect the drilling tools and equipment. Failure to adequately address these conditions can result in rapid deterioration of the drilling infrastructure.

4. Cost Implications
   a. High-Cost Equipment: The development and deployment of high-temperature-resistant tools are expensive, increasing the overall cost of geothermal drilling projects. This cost factor is a major consideration, especially for projects with limited budgets.
   b. Maintenance and Replacement: Frequent maintenance and replacement of drilling tools due to high-temperature exposure and corrosion add to the operational costs. Ensuring a steady supply of spare parts and maintaining an efficient maintenance schedule are critical for managing these expenses.

2.1 Conventional approach, using High Temp Tools

Given above challenges in drilling high temperature reservoir, the conventional approach will be

Pros of Using High-Temperature Tools

- Reliability: High-temperature tools are engineered specifically for the harsh conditions of geothermal drilling, ensuring better performance and reduced risk of failure.

- Durability: These tools are made from materials that can endure prolonged exposure to high temperatures, resulting in longer operational life.

Cons of Using High-Temperature Tools

- Cost: High-temperature tools are significantly more expensive to manufacture and procure.
- Limited Availability: Due to their specialized nature, these tools are not as readily available as standard temperature tools, potentially leading to delays in operations.
- Increased Production Costs: The cost of designing, developing, and deploying these tools increases the overall production costs, making the operation less economically viable.

Alternative Approach: Using Standard Temperature Tools

Given the high costs and limited availability of high-temperature tools, an alternative approach is to use standard temperature tools (rated up to 150°C) with specific drilling practices designed to mitigate the risks associated with high-temperature environments.

Pros of Using Standard Temperature Tools

- Cost-Effective: Standard temperature tools are less expensive and more readily available.
- Flexibility: These tools can be deployed in a variety of drilling environments, not just high-temperature geothermal formations.
- Cons of Using Standard Temperature Tools
- Risk of Failure: Standard tools are not designed for high-temperature conditions, increasing the risk of equipment failure.
- Operational Challenges: Using standard tools in high-temperature environments requires careful planning and execution to avoid non-productive time (NPT).

Drilling Practice and Risk Mitigation Using Standard Temperature Tools

To successfully use standard temperature tools in high-temperature environments, specific drilling practices must be implemented. These practices include:

- Circulation Management: Maintaining an optimal mud circulation rate to cool down the drill bit and other downhole tools.
- Heat Dissipation: Utilizing techniques such as intermittent drilling to allow the equipment to cool down.
- Monitoring: Continuous monitoring of downhole temperatures and tool conditions to anticipate and address potential failures before they occur.
- Adaptive Strategies: Implementing flexible drilling strategies that can be adjusted based on real-time data from the drilling operation.

3. Results and Discussion

3.1 Prediction VS Simulation Circulating Temperature Profile

The simulation data derived from prognostic profiles and optimized using offset well data provides a detailed circulation temperature profile during drilling operations, as illustrated in Figure 4.

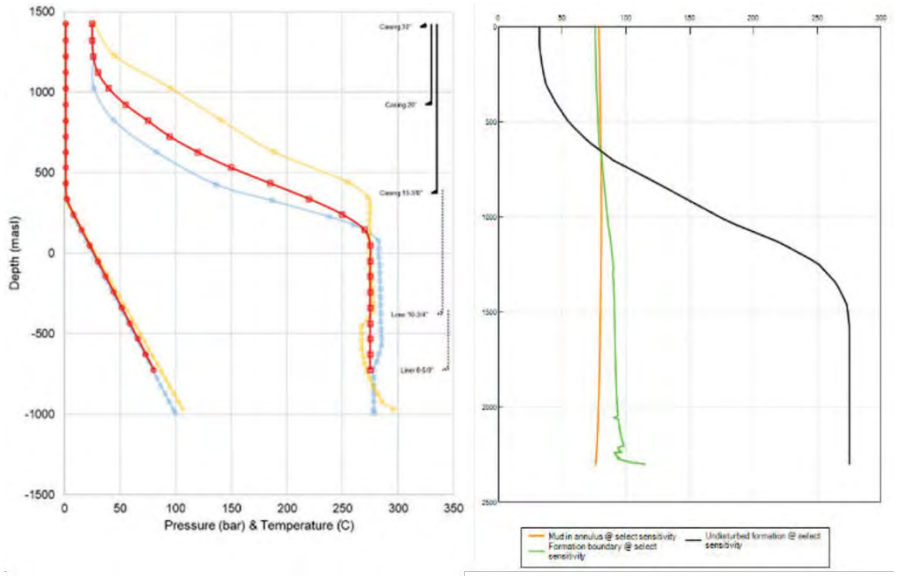

Figure 4. Prediction and simulation temperature profile.

Accurate simulation outcomes play a crucial role in assessing the feasibility of tool selection and funding allocation for successful geothermal drilling operations. By leveraging advanced modeling techniques, such as those integrating historical data from offset wells, stakeholders can make informed decisions that mitigate risks and optimize operational efficiency.

Furthermore, these precise simulations not only enhance operational planning but also contribute to cost-effectiveness and project viability. They enable stakeholders to anticipate challenges and adjust strategies preemptively, thereby improving overall project outcomes. This proactive approach not only instills confidence in investors and partners but also positions the project favorably for securing future funding and expanding its operational footprint. As the industry continues to evolve, the integration of robust simulation methodologies remains essential for driving innovation and achieving sustainable success in geothermal drilling.

3.2 Actual Circulating Temperature Profile

Field data shows that maintaining an optimal circulating temperature profile is crucial for the success of geothermal drilling operations as shown at Figure 5.

By carefully managing the circulation rate, combination on pump rate of Mud and Air it is possible to keep the temperature of the drilling fluid within a range that is safe for standard temperature tools. This practice helps in preventing overheating and potential steam kick.

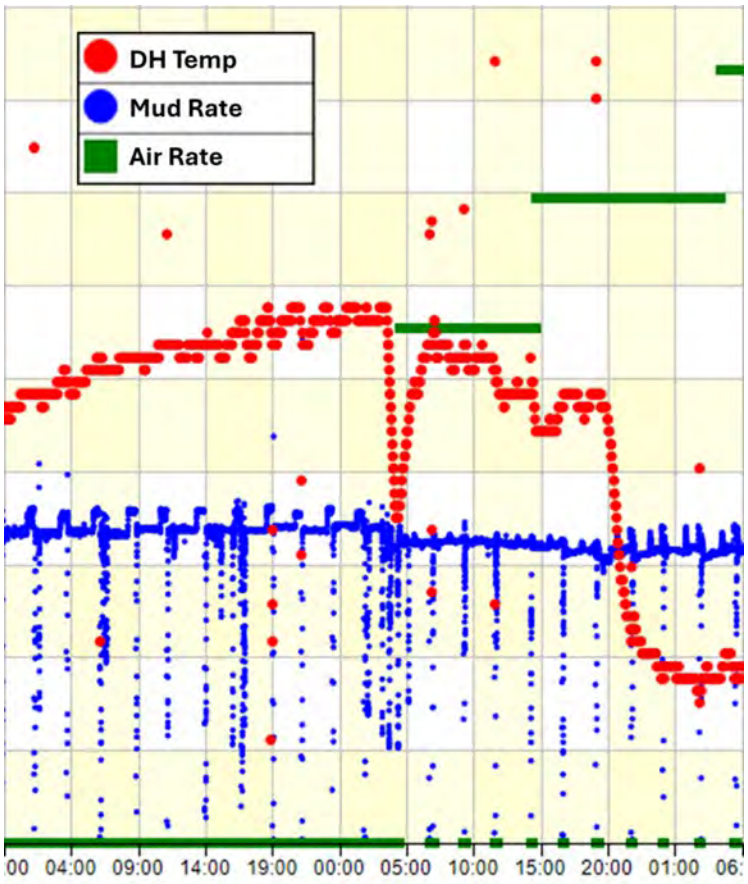

Figure 5. Managing down hole temperature.

3.3 Drilling Strategies in Hot Reservoir Sections

Effective drilling strategies are essential when operating in hot reservoir sections. One approach is to use a combination of high-viscosity drilling mud and cooling fluids to protect the drilling tools. Another strategy involves intermittent drilling, where the operation is paused periodically to allow the tools to cool down, thereby extending their operational life.

Key strategy in drilling ultra high temperature section with standard temperature equipment.

- Bottom Hole Assembly Selection
  Start from trajectory planning and decide either smart tools required to drill the section or rotary with dumb irons will be sufficient.
- Staging In and Out Procedure
  Prior to tripping into the hot reservoir zone, frequent temperature check is required and circulate if the temperature is close to 90% of equipment temperature ratings.
- High Temp Connection Practice
  Minimize static time without pumping in the hot reservoir zone, E-Mag MWD with fast surveying method is an advantage.
- Air to Fluid Ratio Management
  Balancing the ratio is crucial, too high on one side could lead to overheating or steam kick.

- Water Supply Management
  Continuous water supply is mandatory when drilling the hot zone. Whenever there is indication of shortage water supply, the bottom hole assembly need to be secured in safe zone.

3.4 Contract Requirements as Supporting Operation

To ensure smooth and efficient drilling operations, it is essential to have clear contract requirements that support the use of standard temperature tools in high-temperature environments. These requirements should include provisions for:

- Tool Replacement: Agreements on rapid replacement of tools in case of failure.
- Operational Flexibility: Allowances for adaptive drilling strategies based on real-time data.
- Risk Sharing: Clear delineation of responsibilities and risk-sharing between the operator and the drilling contractor.

4. Discussion and Conclusion

Drilling Ultra High Temperature Geothermal using Alternative Approach, standard temperature rating tools, has advantages in reducing overall drilling cost. This approach is proven to be successful in Indonesia geothermal wells. Over the years geothermal drilling cost in Indonesia become more efficient, where the equipment selection is one of the key contributors.

Risk of using standard temperature can be managed with proper drilling practice. If the drilling practice is not followed, it will be result in equipment damage that can increase the well cost by 20%. Project briefing to address the strategy need to involve all stakeholder to ensure smooth and safe operation execution.

Drilling with standard temperature tools unlock the opportunity for further understanding of geothermal reservoir, by potentially using the Logging While Drilling equipment where it has broad selection in standard temperature rating. At the moment the reservoir characterization mainly done with only Pressure and Temperature Logging. Some of the wells can be logged with quenching method to obtain Image and Sonic data, however if the wells is too hot and quenching method not successful, the logging attempt will be canceled.

Geothermal drilling in high-temperature volcanic formations presents unique challenges that require innovative approaches and robust risk mitigation strategies. While high-temperature tools offer reliability, their high cost and limited availability necessitate the exploration of alternative methods. Using standard temperature tools with specific drilling practices provides a viable solution, enabling efficient and safe operations while controlling costs. By adopting a flexible, engineered approach and implementing comprehensive risk mitigation strategies, it is possible to overcome the challenges of geothermal drilling and unlock the vast potential of geothermal energy.

REFERENCES

EBTKE Team, Guideline for Geothermal Drilling Cost Efficiency. Indonesia. 2022

Elder, W.A. Drilling Into Magma and The Implications of The Iceland Deep Drilling Project (IDDP) for High Temperature Geothermal Systems Worldwide. California. 2014

Finger John, Handbook of Best Practice Geothermal Drilling. California. 2010

Kurnia, Agus Ziyad. Collaborative Directional Drilling Method For Geothermal Wells In North Sumatra. Jakarta. 2017

Purwanto, Eko Hari. An Updated Statistic Evaluation of Drilling Performance Drilling Cost and Well Capacity of Geothermal Fields in Indonesia. World Geothermal Congress. 2021

Ryo, Ando. Simulating Effect Of Insulated Drillpipe On Downhole Temperature In Supercritical Geothermal Well Drilling. New Zealand.2020

Yudi, Indrinanto. A Collaborative Engineering Approach To Achieve Success In Geothermal Drilling Application. Bandung. 2017

Enhancing Geothermal Drilling Performance: A Stuck-Pipe Risk Advisor Leveraging Causal-AI and Semantic Web for Explainable Decision Support

Panurach Dumrongthai, Kenneth Lee Riedel*, Michael John Williams, Maria Fernanda Vargas Izquierdo, Syed Aaquib Hussain, Ni Made Wilasari, Maharani Devira Pramita, Fitria Anindita**

***Star Energy Geothermal; ****SLB**

Keywords

Geothermal, Drilling, Stuck Pipe Risk Advisor, Causal AI, Semantic Web, Machine Learning

ABSTRACT

Geothermal drilling operations face inherent challenges, with stuck-pipe incidents posing significant risks to both safety and project success. In this paper, we introduce a groundbreaking stuck-pipe risk advisor (SPRA) that integrates causal artificial intelligence (AI) and semantic web technologies to provide explainable real-time decision support and enhance drilling performance.

Our causal-AI model uses advanced machine-learning algorithms to analyze historical drilling data, identifying complex relationships and potential risk factors which may lead to stuck-pipe incidents. By leveraging causal relationships, the SPRA can proactively assess the likelihood of a stuck-pipe occurrence based on current drilling conditions.

To enhance transparency and trust in the decision-making process, our system incorporates semantic web technologies to generate explainable outputs. The SPRA generates detailed explanations of its predictions, using semantic annotations to link specific risk factors through causal relationships. This not only aids drilling operators in understanding the basis of the system's reported risk levels but also facilitates continuous learning and improvement of drilling practices.

In addition, the SPRA has a flow-diagram-based interface for drilling operators that shows risk factors, possible solutions, and interactive explanations in real time. By empowering operators with actionable insights, the SPRA aims to support the wellsite team in reducing the frequency of stuck-pipe incidents, enhancing drilling efficiency, and ultimately contributing to the overall safety and success of geothermal drilling projects.

We present the development, validation, and practical application of the SPRA, demonstrating its potential to revolutionize geothermal drilling performance through causal AI and semantic web technologies.

1. Introduction

Indonesia is located among three active tectonic plates and has more than 80 active volcanoes, contributing to Indonesia's wealth of geothermal potential (Nasruddin et al. 2016). Improving the efficiency of geothermal well drilling is viewed as a key enabler for continued development of this potential. Several challenges have been identified in geothermal drilling; for example, the lithology is predominantly igneous rock, which is hard and abrasive. Geothermal facies are dominated by a wide and complex range of fractures and faults, which act as primary drilling targets but also cause lost circulation, which is a common issue in geothermal drilling. The lithology encountered in geothermal drilling also includes paleosols rich in smectite and illite, along with tuffaceous siltstones, which bring the added challenge of swelling or reactive clays. These conditions can lead to wellbore instability and severe hole problems during drilling.

Negotiating the combined challenges of lost circulation, swelling clays, and unstable formations is recognized in Star Energy Geothermal (SEG) as fundamental to avoiding stuck pipe incidents. Stuck pipe refers to a situation in drilling where the drill string cannot rotate, move up, or move down. There are several types of stuck pipe based on a variety of root causes: mechanical sticking, differential sticking, and hole geometry. In geothermal, the most common cause of stuck pipe is mechanical sticking, resulting from combinations of factors such as hole cleaning, unconsolidated formations, fractured-faulted formations, and reactive clays.

Current SEG drilling practice involves post-job studies of previous stuck pipe incidents, identification of subsurface hazards from offset well analysis, and continuous monitoring of drilling parameters by wellsite geologists and drilling engineers in a Real-Time Decision Center (RTDC). When situations and conditions indicate increased risk of stuck pipe, appropriate mitigating practices are implemented.

Our delivered solution augments, streamlines, and automates the SEG approach through detection of key decision points, an automated population of questionnaires, AI-accelerated identification of root causes and the explanations for them, and the gathering of the relevant related scenarios for review. This review is examined by the SEG decision makers, who direct a mitigation response if one is warranted.

As an example, through this raised level of automation, SEG's knowledge of subsurface hazards is supported by real-time detection of fractures encountered during drilling. Since SEG's previous wells information and experience have been used to fine-tune the AI, and each example is also available for direct comparison to the generated explanation for the current situation, the system provides a consistent and repeatable high level of process adherence, analysis, and best practice.

All steps in the deliberate, review and collate sequence are automated using causal artificial intelligence (casual AI) (for an introduction to causal AI see Hurwitz and Thompson, 2023). Within the workflow, the geologist and engineers interact with the system following a RACI (Responsible, Accountable, Consulted, Informed) matrix and operational sequence.

To develop the causal-AI, extensive workshops involving well engineers and geologists conducted iterative reviews between engineering and AI interpretation definitions of stuck pipe incident events. A semantic web risk ontology encodes this mapping between human and machine-readable statements that are causally consistent; the causal network is built by inferring interconnections in a guided causal discovery (Pfaff-Kastner et al., 2024). Questionnaires covering geological, well

engineering, and drilling practice encompass the complete system, including aspects where real-time sensors do not yet provide the input. Where real-time sensor data and machine learning can provide an answer, the system can accept it (autofill). Taking this “whole problem” approach, automating a system that supports the full engineering requirements rather than trying to extract information from the more limited set of things that are already available as data streams, differentiates our approach.

The estimated risk is reported relative to both the current state on the ground and uncertainty around it. Review of historical cases and possible future scenarios train and fine-tune the causal network, extending a consistent collaborative framework from desktop to Edge Internet of Things (IoT).

Estimating the risk of stuck pipe comprises an analysis of drilling parameters, real-time measurements, and domain knowledge from geologists and engineers. Additionally, understanding the causal path of stuck pipe events in geothermal wells helps to trace a direct line between the potential event and the preventative and mitigation measures. All these aspects are addressed in the solution that we propose.

2. Challenge of stuck pipe in Geothermal Drilling operation

Generally, stuck pipe events have been one of the biggest problems impacting geothermal drilling operations worldwide. Particularly for geothermal drilling in Indonesia, factors that enhance the risk of stuck pipe in geothermal wells include drilling fluid losses and the presence of reactive clays.

Severe fluid losses ranging from partial to total losses cause problems removing the cuttings from the wellbore. The use of aerated fluid drilling is a common mitigation practice in these areas. When total fluid losses are encountered, there is no knowledge of drill cutting behavior within the borehole. In the presence of fractured formations, the cuttings could move into the formation, but also the cuttings could accumulate near the bottom hole assembly (BHA) and create restrictions in the annular space. This can lead to stuck pipe events due to the presence of solids in the borehole.

As mentioned before, aerated drilling is a common practice in geothermal well drilling. This practice brings complexities in the management of pressures in the system, the control of solids, and the modeling of the hydraulics. Those elements increase the complexity of stuck pipe prevention management.

Furthermore, geological hazards such as reactive clays and tuffaceous siltstones can cause hole instability due to the clays' reaction with water, which worsens over time. Reactive clays can also cause sticky conditions, leading to stuck pipe events. Another risk aspect of geothermal reservoirs is the presence of naturally unconsolidated formations. Those formations can cause caving into the annulus and, together with cuttings, increase the number of solids in the borehole.

2.1 Risk of Stuck pipe in Geothermal Drilling

Drilling geothermal wells presents a unique challenge due to the inherent risk of encountering fractured formations with low reservoir pressures. When the drill bit intersects these fractures, the wellbore fluid pressure can exceed the reservoir pressure. Aerated mud drilling addresses this issue by injecting air into the drilling fluid to lighten the fluid column. However, this technique comes with its own drawbacks. The drill cuttings may not effectively circulate out, accumulating in the wellbore or within the fractures themselves. This accumulation of cuttings, along with the inherent friction of the drill pipe against the wellbore, makes it difficult to accurately predict torque and drag. As a result, the increased drag caused by the cuttings can lead to situations where the drill pipe becomes stuck.

2.1.1 Formation-related Risks in Geothermal Drilling through Volcanic Rock

For geothermal applications, drilling through volcanic rock presents several formation-related risks that can significantly impact wellbore stability and drilling efficiency. Here is a breakdown and illustration of several key risks (Figure 1):

1. **Clay Swelling:** Volcanic formations often contain highly reactive clays, notably paleosols and tuffaceous siltstones. These clays can absorb water from water-based drilling muds, causing them to swell and potentially stick the drill pipe. Prolonged exposure to drilling fluids can exacerbate this issue, making it critical to manage drilling times and potentially use alternative mud systems that are less likely to cause swelling.
2. **Unconsolidated Formations:** Certain volcanic rock formations, particularly ash deposits or breccia, may be poorly consolidated or unconsolidated. This means the rock lacks sufficient cohesion and can crumble easily during drilling. The resulting loose gravel and rock fragments can significantly increase the number of cuttings generated within the wellbore. Excessive cuttings can hinder circulation, impede accurate torque and drag calculations, and ultimately lead to stuck pipe incidents.
3. **Drilling near Faults and Fractures:** Faults and natural fractures frequently litter volcanic landscapes. When drilling close to these geological features, especially in the direction of maximum stress, the wellbore can encounter zones of weakness. These weak zones can collapse or cave in during drilling, potentially trapping the drill pipe and causing significant wellbore instability. Careful wellbore planning and monitoring are essential to mitigate the risks associated with drilling near faults and fractures.

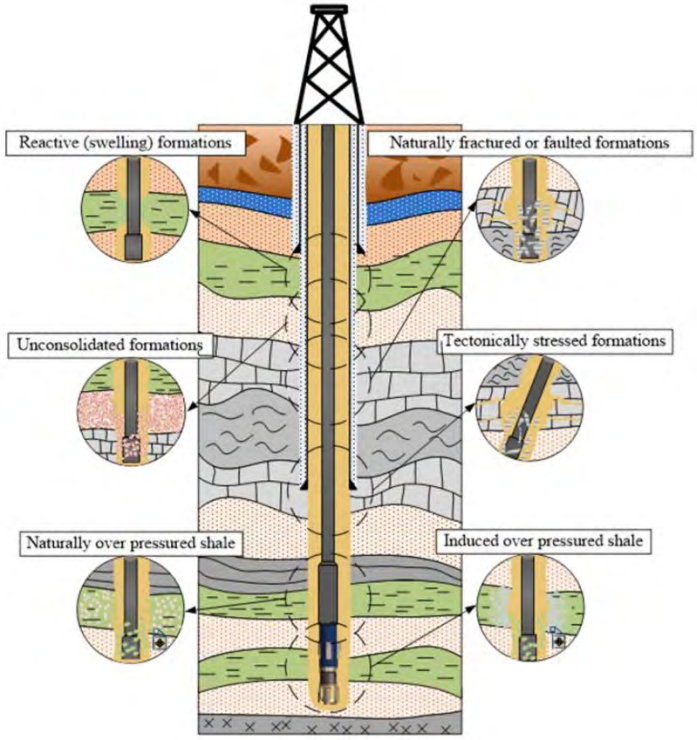

Figure 1: Clay Swelling formation and Unconsolidated Formation can be potential of geothermal hydrothermal system stuck pipe. (Pašić, 2020)

2.1.2 Stuck Pipe Risk from Downward Annular Flow in Geothermal Drilling

Encountering natural fractures while drilling geothermal wells presents a significant risk of stuck pipe due to a phenomenon that results in downward annular flow. In normal drilling scenarios, circulation ensures fluid travels down the drill pipe and returns upwards through the annulus, carrying cuttings out of the wellbore. However, when the drill bit intersects a natural fracture, the pressure dynamics change. Following is a description and illustration of this phenomenon (Figures 2 and 3):

1. **Pressure Differential:** Natural fractures within geothermal formations often possess much lower pressure compared to the pressurized drilling fluid circulating in the wellbore. This creates a pressure imbalance.
2. **Fluid Loss and Downward Movement:** When a fracture occurs, the annulus may divert some or all of the pressurized drilling fluid and the suspended cuttings into it. This loss of fluid disrupts the normal upward flow in the annulus.
3. **Downward Annular Flow and Cutting Accumulation:** In some situations, the pressure differential can be so significant that it can cause a reversal of flow within the annulus. The drilling fluid and cuttings, instead of traveling upwards can flow downwards due to the pressure differential. This downward movement of solids can lead to a situation where cuttings accumulate or pack off around the stabilizers and bottom hole assembly (BHA).
4. **Increased Friction and Stuck Pipe:** The stabilizers on the BHA are critical for maintaining the wellbore condition and directional control. However, a buildup of cuttings around the stabilizers due to downward flow significantly increases friction between the

drill string and the wellbore wall. This increased friction can lead to the drill pipe becoming stuck, potentially requiring complex and expensive operations to free it.

In conclusion, natural fractures encountered during geothermal drilling require a proactive approach to reduce the risk of stuck pipe due to downward annular flow. Real-time monitoring of drilling parameters and adjustments to drilling practices, such as reducing pump pressure, can help prevent this issue and ensure smooth wellbore completion.

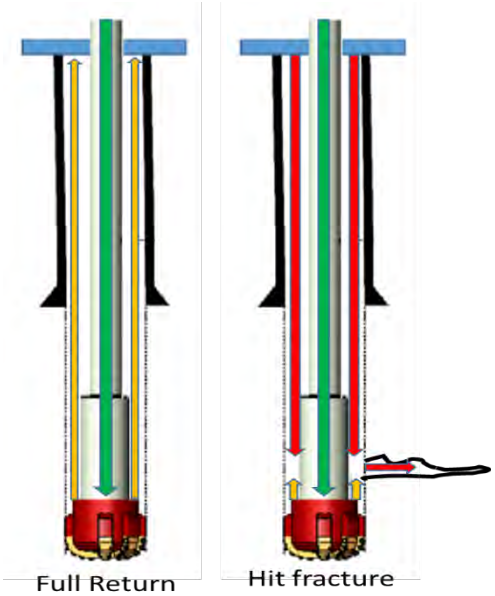

Figure 2. Drilling with full return can cause solids to rise, but impact fractures can cause fluid in the annulus to go downward and any solid that remains in the annulus can obstruct the stabilizer.

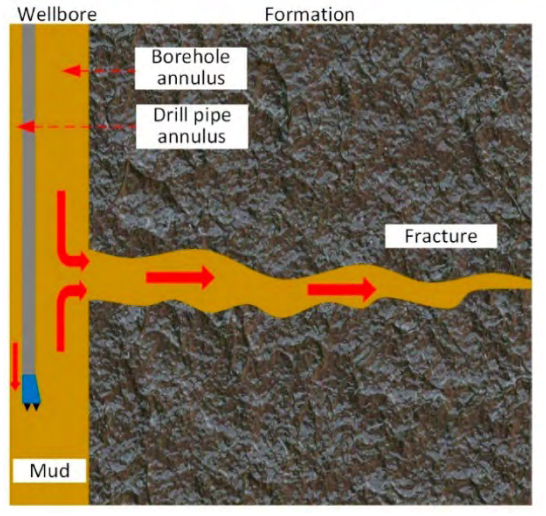

Figure 3: Drilling fluid losses. (Yi, 2018)

2.1.3 Stuck Pipe Risk due to cutting size, well inclination and aerated drilling to hole cleaning

Ensuring proper hole cleaning becomes a paramount concern during geothermal drilling when encountering natural fractures. The drill bit and the Bottom Hole Assembly (BHA) can shear larger cuttings. Large cutting presence necessitates a high annular velocity to overcome the settling velocity of the cuttings and prevent them from accumulating in the wellbore. However, achieving this optimal velocity presents a challenge.

Hole cleaning issues can significantly increase the risk of stuck pipe, and the carrying capacity of drilling fluid is reduced by aerated drilling. Drilling naturally fractured geothermal formations commonly employs this strategy, which involves injecting air into the drilling fluid to reduce its density. While this technique helps maintain circulation, the increased air content significantly reduces the fluid's carrying capacity for cuttings. This creates a trade-off: maintaining circulation while potentially compromising the ability to remove cuttings effectively (Figure 4).

Impact of Wellbore Inclination: Hole cleaning efficiency is further complicated by wellbore inclination. In deviated wells, particularly those with high inclination angles, cuttings tend to settle on the low side of the wellbore due to gravity. This can create a layer of cuttings that hinders circulation and increases the risk of pack-off, a situation where cuttings become lodged and prevent further drilling progress (Figure 4).

Friction Build-up and Stuck Pipe: The combined effects of reduced carrying capacity and hindered cuttings removal due to inclination can lead to a risky buildup of cuttings in the wellbore. This accumulation increases friction between the drill string and the wellbore wall. When this friction becomes excessive, the drill pipe can become stuck, requiring complex and costly operations to free it (Figure 5).

Therefore, meticulous hole cleaning practices are crucial in geothermal drilling, particularly in fractured zones. Balancing pressure control with proper fluid rheology and optimizing drilling parameters based on wellbore inclination are vital to ensure efficient cutting removal and minimize the risk of stuck pipe incidents (Figure 4).

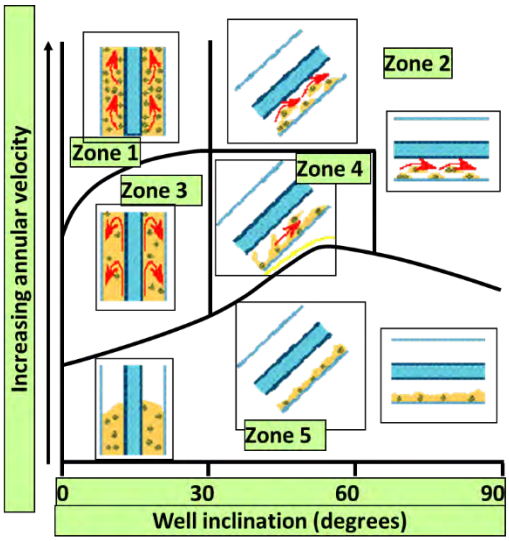

Figure 4: Cuttings distribution based on annular velocity and well inclination. (SLB)

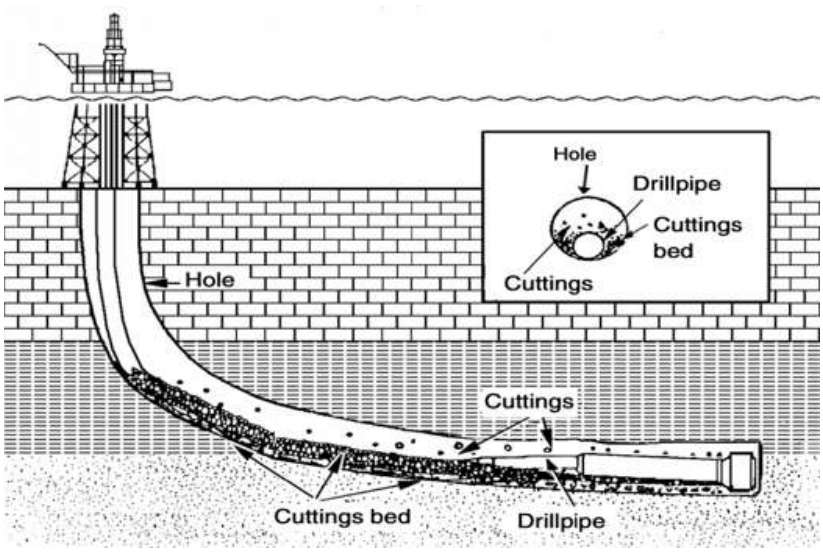

Figure 5: Cuttings build up in directional drilling. (Sanchez, et al., 1997)

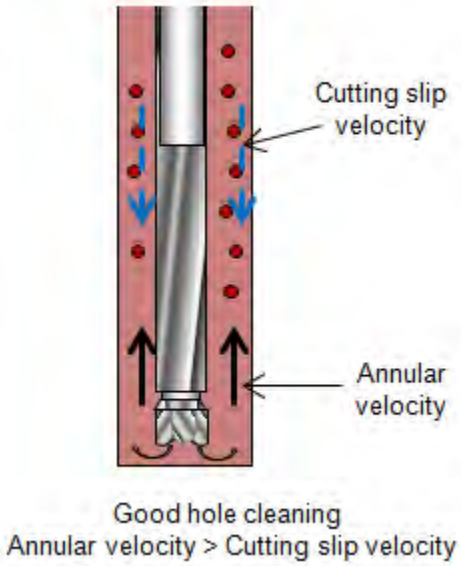

Figure 6: Hole Cleaning. (Zhou, 2011)

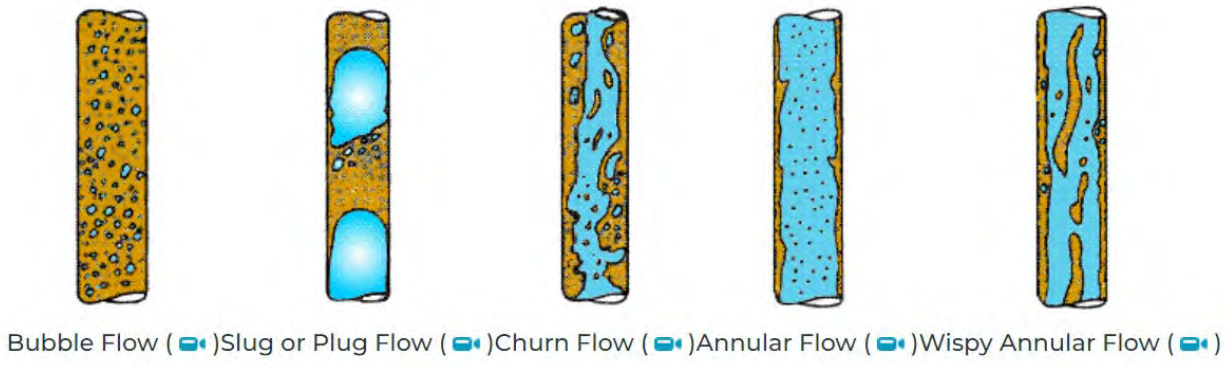

Figure 7: Aerated drilling requires close control to maintain circulation and solids removal under varying flow regimes (Thermopedia).

3. Solution

The significant benefits of reducing the frequency of stuck pipe incidents have inspired the creation of an innovative early detection system and risk advisor, specifically designed to enhance geothermal drilling applications. This system will leverage a robust knowledge base constructed upon causal relationships and historical drilling data. Employing causal AI through a powerful probabilistic graphical model, this system will perform real-time analysis and risk assessment during drilling operations. By implementing this intelligent system, geothermal drilling can benefit from several key advantages:

- **Early Warnings for Natural Fractures:** Natural fractures encountered during drilling are a leading cause of stuck pipes. The knowledge base, built upon historical data and expert knowledge, will identify key indicators and patterns associated with encountering fractures. The causal framework will then analyze real-time drilling parameters, such as pump pressure, flow rate, and drilling vibrations, and provide early warnings before the drill bit hits a major fracture. This allows for proactive adjustments to drilling practices, potentially mitigating stuck pipe incidents altogether.
- **Improved Decision-Making:** The system's real-time risk assessment capabilities will empower drilling personnel to make informed decisions throughout the drilling process. By quantifying the likelihood of encountering stuck pipe based on current drilling conditions, the system can recommend adjustments to drilling parameters, such as reducing pump pressure or modifying drilling fluid properties. This data-driven approach fosters proactive risk management, leading to safer and more efficient drilling operations.
- **Knowledge Capture and Continuous Improvement:** We designed the developed system to continuously learn and improve its risk assessment capabilities. The integration of new drilling data into the semantic web knowledge base refines the causal model, resulting in a more accurate and reliable prediction of stuck pipe risks. This continuous learning process ensures the system remains effective over time, adapting to changing geological conditions and evolving drilling practices.

This knowledge-based early warning system, powered by causal-AI, presents a promising solution for mitigating stuck pipe risk in geothermal drilling. By providing early warnings and facilitating informed decision-making, this system can significantly improve the safety and efficiency of geothermal well development.

The development of the stuck-pipe risk advisor (SPRA) is being implemented through a collaborative effort between Star Energy and SLB, as follows:

3.1 Causal-AI Concept

Causal artificial intelligence addresses an issue in machine learning, namely that identifying and understanding causal relationships is a barrier for correlation-based systems (Pearl, 2009). Our method uses a Shapes Constraint Language-based semantic web reasoner (see Pareti & Konstantinidis, 2021) to make sure that the causal relationships found in geological and well engineering contexts are fully consistent across a knowledge graph representation. The relationships form a directed acyclic graph (DAG), identifying each node with a concept and representing a cause-to-effect relationship between a pair of nodes through each directed edge. In addition to nodes in the Bayesian sense (observable properties, latent variables, unknown parameters, or hypotheses), we additionally represent actions. In terms of cause-effect relationships, we recognize both that actions may be interventions (Pearl, 2009); our actions can be recognized as those of temporal AI planning, which may also require certain preconditions to be met before taking action (e.g., Fox & Long, 2003). This offers a pathway to autonomous operations (Liu et al., 2024) and dynamic configuration, which are the key enabling technologies for the real-time use case proposed here.

Within the network, a risk may be assessed using the well-known techniques of belief propagation (Pearl, 1982); with the role of actions handled using the do-calculus (Pearl, 2009; Pearl & Mackenzie, 2018).

One recognized advantage of both semantic web technologies and causal AI directed graphs is their capability to inform explanations (Clinciu et al., 2021). We combine these explainable artificial intelligence (XAI) techniques with the well-known capabilities of knowledge graph-led search for semantic web technologies (Dong et al. 2009) to provide enhanced validation, digital reporting, and offset well analysis.

Our explainable AI causal network (XAI-CN) system represents a neuro-symbolic artificial intelligence system (Sarker et al., 2022) which can organically develop and extend its automation capabilities as the digital well-site operations mature.

3.2 Alarm System Concept

The dynamic configuration and automated execution provided by XAI-CN empower the network to be seamlessly triggered by a data-driven ML agent. Automatic detection of fractures, using the

signature of increasing ROP and flowrate combined with a drop in pump pressure, will generate a fracture alarm that the smart system will swiftly and efficiently identify.

In the use case of geothermal stuck-pipe, SEG Well Engineers have identified a “golden window” in the drilling process that is key to the timing of stuck-pipe risk evaluation. We will develop a data-driven ML agent to identify the "golden window" from time-series data in real-time, which will then initiate a server call to the XAI-CN system, triggering the full risk assessment process.

3.3 Autofill (Time Series) Concept

A unique aspect of XAI-CN is the ability to dynamically configure to accept real-time inputs as an alternative to having human experts answer questions within the questionnaire. When a full risk assessment is triggered, the XAI-CN system will explore the available “auto-fill” agents to gain as much information as possible; a reduced form questionnaire is then presented to the Well Engineer. The autofill feature will automatically populate the indicators for fracture, which include a bump in ROP and a loss in flowrate due to a decrease in pump pressure. Drilling parameters response [Standpipe pressure trend, ROP trend, WOB trend, ROP range, and RPM range], depth from last fracture, and mud flow rate range will also be auto filled based on sensor information parsed with proprietary SLB algorithms.

3.4 Deployment

The sensors on the drilling rig stream real-time drilling data to the company's drilling platform. Evaluating risks using a causal knowledge graph that captures well engineering domain knowledge and experience. Explanation for the estimated risk level, including preliminary root-cause suggestions. User will have immediate access to comprehensive information that captures risks from similar jobs. Forecasting scenarios enables the evaluation of potential mitigation methods.

4. Result and Discussion

The tool itself contains two software products: Drilling log monitoring for automatically detecting potential risk zones early and an AI-based semantic web to analyze the risk in each potential risk zone more deeply using a causal AI network.

4.1. Real-time delivery system

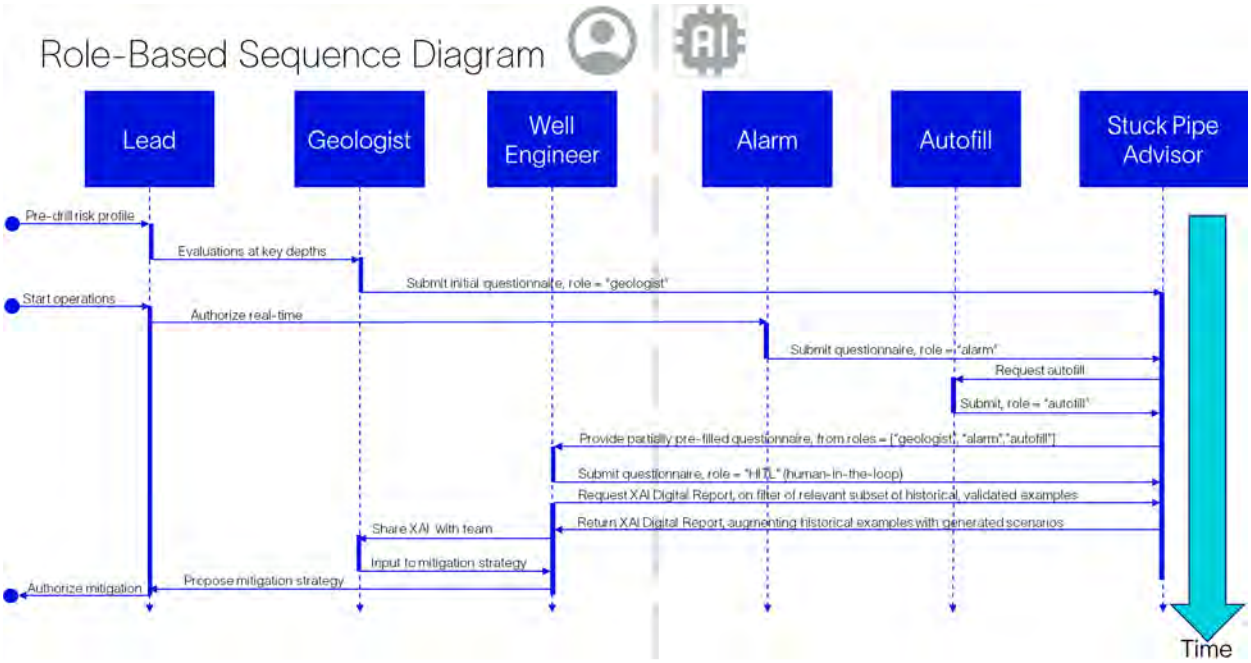

Figure 8 Example operations sequence diagram.

We recognize the roles of three (3) nominal team members: the team lead, the geologist, and the well engineer. This team collaborates with XAI-CN (designated as Stuck Pipe Advisor) and the AI/ML alarm and autofill. We recognize that some information is available ahead of on-bottom drilling; in particular, the expectations around geology may be pre-populated. When drilling commences, the alarm is continually monitoring the real-time signals to detect fractures and identify the "golden window." On recognizing this "golden window", the autofill elements are triggered to provide automated supporting information before the well engineer and geologist are presented with the partially filled questionnaire. The review and update of the questionnaire by the well engineer and geologist allows the system to operate with an up-to-date information set. The XAI-CN can then provide the root-cause analysis and off-set well analysis that informs the whole team, enabling the team lead to make their decisions on prevention and mitigation (Figure 8).

The presentation of the digital results combines the current risk profile, its explanation, and the relevant offset well information. Figure 9 shows an example flow chart, where the system has identified five (5) primary features that contribute to the assessment that there is currently a risk of stuck pipe due to wellbore geometry. Four of the identified key contributors are observations, and one is an action, namely that the BHA had to be changed, which, combined with recent observations of tight spots when pulling out of a hole (POOH), and previous albeit minor sticking, raises awareness of potential risk. A hole caliper measurement, the path shown in yellow in Figure 9, was the primary contributor to this understanding of risk, but the context is provided by the rest of the diagram. Importantly, this allows the search to share a set of nearby cases with similar risks, which the team can further filter to match the field and hole size, just as in conventional offset well analysis. These nearby cases may include suggestions for preventive or mitigation measures. It is

this access to combined knowledge at the time of decision-making that enables the team to make informed choices, ultimately avoiding stuck pipe incidents.

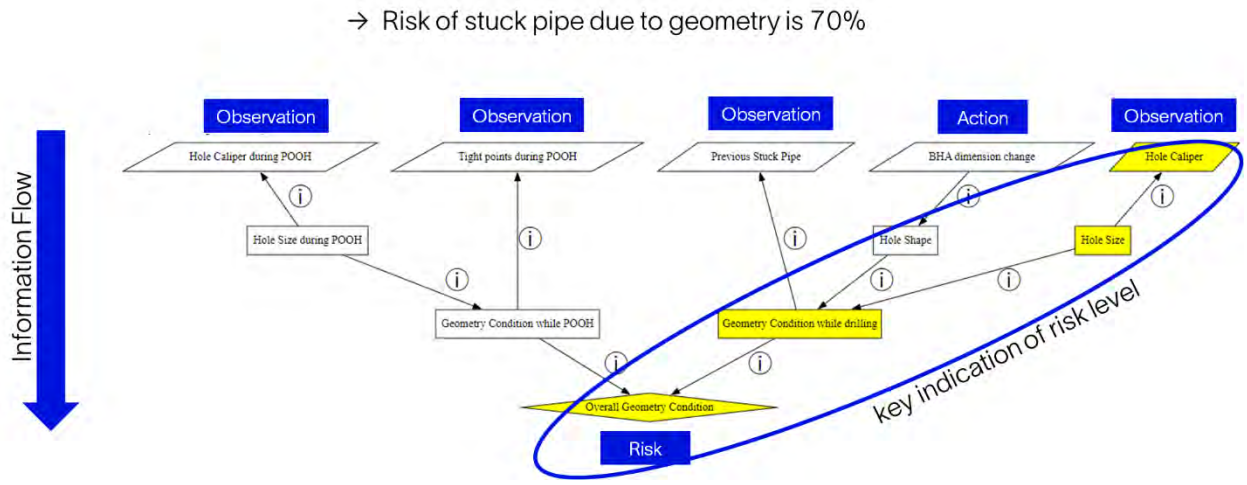

Figure 9. An example explanation flow chart.

4.2 Early Detection system

4.2.1 Automated Potential Risk Zone Detection

In geothermal drilling operations, the early detection of fracture zones is crucial for mitigating the risks associated with stuck pipe, a common challenge that can lead to significant operational delays and increased costs. As described previously, fracture zones can cause partial or total loss of circulation, leading to hole cleaning problems and cuttings pack-off. These zones, if not identified and managed promptly, can cause the drill string to become stuck, necessitating costly retrieval operations or even abandonment of the well.

Real-time monitoring systems, developed to address this challenge, enhance the predictive capabilities and operational safety of drilling in geothermal fields. The inclusion of a traffic light flagging system in these monitoring solutions represents a significant advancement in risk management. This system employs a color-coded alert mechanism to indicate the proximity to potential feed zones, thus enabling on-site engineers to take timely preventative actions.

The flagging system utilizes real-time data from drilling parameters such as measured depth, bit depth, rate of penetration (ROP), standpipe pressure (SPP), and weight on bit (WOB). We closely monitor these parameters for specific changes that signal approaching fracture zones, also known as the "golden window". Based on the data collected from several wells across multiple fields, the system classifies the level of potential risk into five color codes: Red indicates a very high risk where ROP increases sharply and SPP drops rapidly; orange signifies a high risk with moderate changes in ROP or SPP; blue represents a medium risk with moderate changes in both parameters; yellow and green denote lower risks with gradual changes.

This system's effectiveness in geothermal drilling lies in its ability to provide a clear, real-time visualization of risk levels through an intuitive color-coded scheme. By enabling better

anticipation of feed zones, the system aids in proactive decision-making and risk mitigation. Additionally, a semantic web interface enhances the system during medium- to high-risk scenarios, providing a transparent analysis of the risks within the golden window. This technological integration not only improves safety, but it also optimizes drilling efficiency by reducing non-productive time due to stuck pipe incidents. We enhance the real-time monitoring of drilling logs by incorporating a traffic light flagging system into the mud log data time series. This system alerts us whenever a potential risk zone, also known as the "golden window," approaches.

Oil and gas companies have explored time-series-based identification of open fractures (Al-Adwani et al., 2012), in this project, we defined a completely new identifier for the 'golden window' based on several drilling parameters. We create flagging based on changes in values over the last 2 hours for several drilling parameters, such as measured depth, bit depth, rate of penetration (ROP), standpipe pressure (SPP), and weight on bit (WOB), which closely correlate to the potential risk of stuck pipe.

There are basically five color codes in the traffic light (Figure 10), depending on the level or potential risk. Red for very high potential risk when ROP is highly increasing and SPP is rapidly dropping. Orange for high potential risk, when either ROP is moderately increasing or SPP is slightly dropping, and the other one is changing extremely. Blue for medium potential risk when both ROP is moderately increasing or SPP is slightly dropping. Yellow and green for low potential risk, when both ROP is slowly increasing and SPP is slowly dropping.

We set up cut-off values as boundaries for each of the categories based on the existing value on the dataset. There are thousands of time series drilling log data from hundreds of wells covering three geothermal fields as the dataset that we used for observation for creating the cut-off logic of color codes mentioned above. Therefore, these color codes help on-site engineers identify an upcoming potential risk zone for risk mitigation before it happens. In addition, starting with blue code, orange code, and red code will trigger the system to show up the semantic web for transparent risk analysis within the golden window.

Overall, the traffic light flagging system represents a transformative approach to managing drilling risks in geothermal operations, underscoring the importance of technological innovation in the pursuit of energy resource extraction.

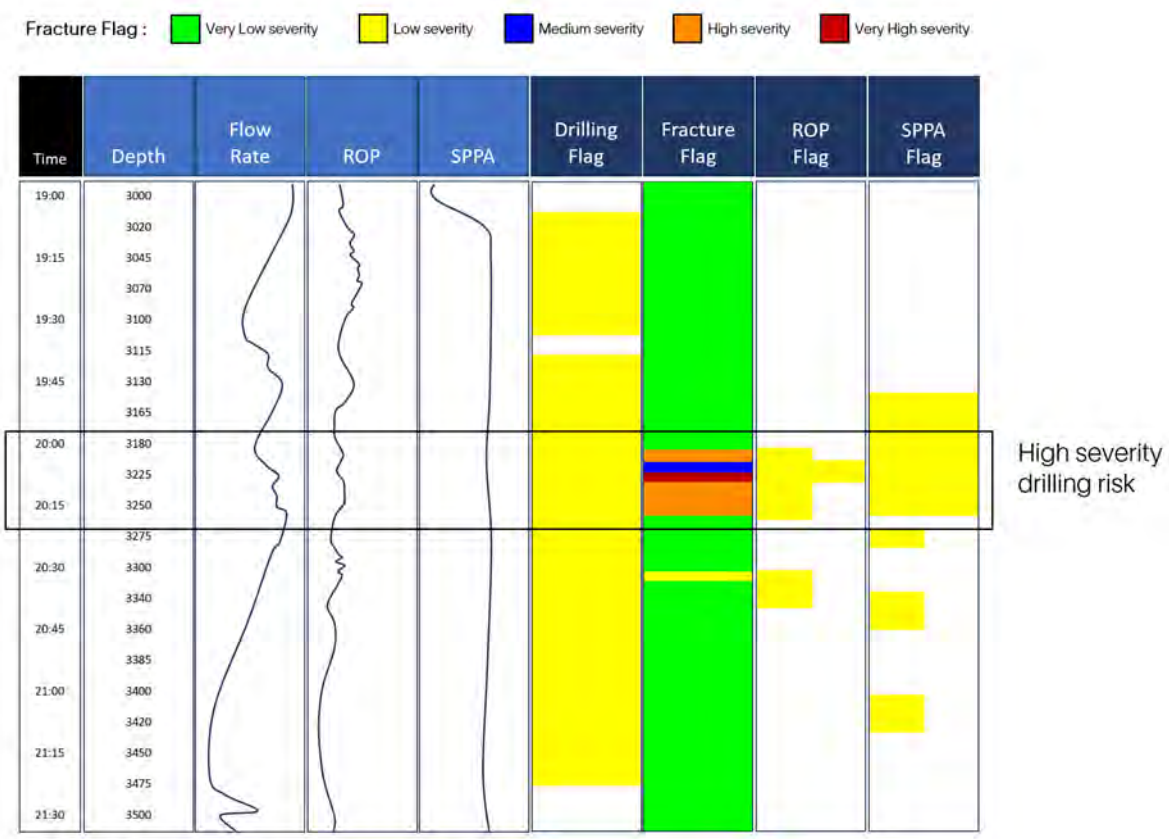

Figure 10. Sample of fracture risk "golden window" flagging

4.2.2 Semantic Web Risk Ontology

Our semantic web risk ontology provides transparent and trustworthy inferences about risk relationships (Figure 11). We have a core set of relationships that support application development by combining publicly available ontologies for sensors (Janowicz et al., 2019) with internally developed ontologies, which we will detail in a future paper[1] .

The relationships play two key roles in the system: firstly, after the AI has identified the key relationships that explain the current risk, the machine representation needs to be mapped to natural language and diagrams that the team facing the decision-making can explore.

In mapping to a machine representation, a causal reasoner continually checks the latest information for circularity (cause-effect reasoning errors) and missing or duplicate nodes. Subject matter experts' flag and debate and review the knowledge to resolve flagged inconsistencies or omissions.

To establish the explanation, we first perform a calculation step that uses an information criterion to identify the most significant paths through the knowledge graph. This is achieved by combining a mutual information entropy measure (Kjærulff & Madsen, 2012) Using a shortest path algorithm,

[1] Pers. Comm. Peter Gregory

we extract the graph's subsection using the do-calculus approach (Pearl, 2009). We then translate this machine-readable output into an explanation flow chart (Clinciu et al., 2021) described by semantic web relationships (Figure 11), which in turn can be translated into human-readable text using an LLM, which is known to outperform solutions relying on LLM alone (Allemang and Sequeda, 2024).

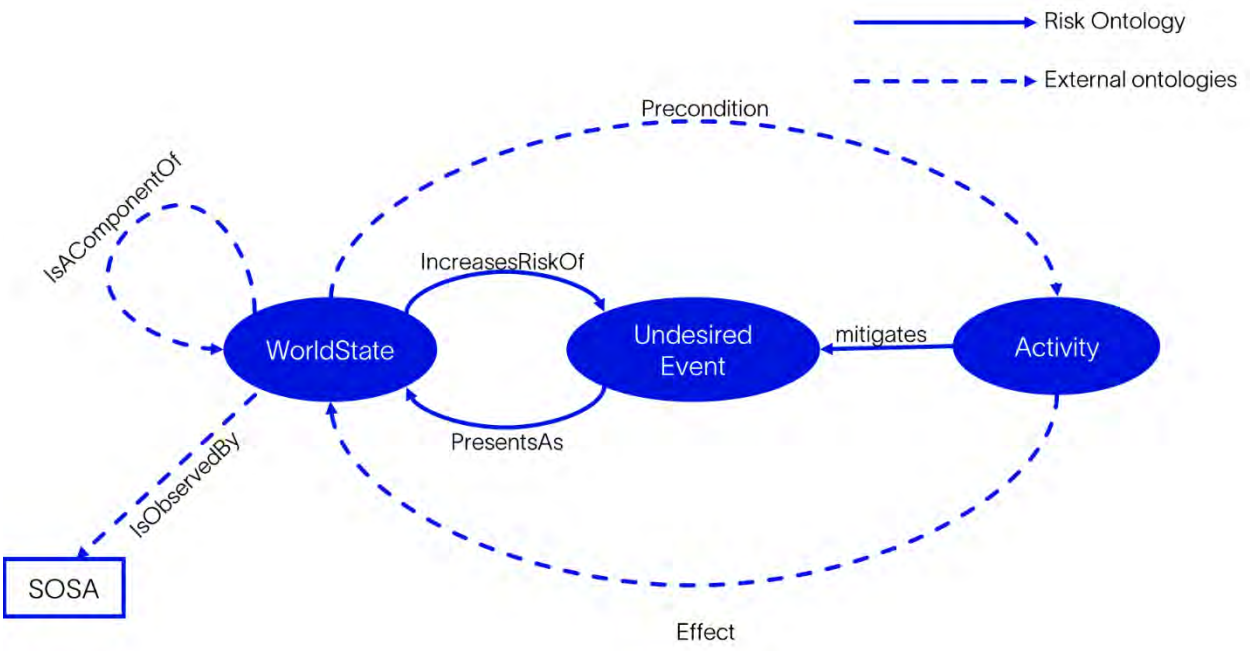

Figure 11 The risk ontology (personal communication from P. Gregory)

Our causal AI model uses advanced machine-learning algorithms to analyze historical drilling data, identifying complex relationships and potential risk factors leading to stuck-pipe incidents. By leveraging causal relationships, the SPRA can proactively assess the likelihood of a stuck-pipe occurrence based on current drilling conditions.

The SPRA generates detailed explanations of its predictions, using semantic annotations to link specific risk factors and causal relationships. This not only assists drilling operators in understanding the basis of the system's reported risk levels, but also facilitates continuous learning and improvement of drilling practices. In addition, the SPRA has a flow-diagram-based interface for drilling operators that shows risk factors, possible solutions, and interactive explanations in real time.

5. Conclusions

Because stuck pipes directly affect the total cost of drilling a well, prevention and mitigation are essential. For a long time, the stuck pipe problem has been a major issue in the industry. Traditional procedures for predicting stuck pipe incidents, on the other hand, leave room for digital innovation because most current methods are susceptible to human bias.

The artificial intelligence process has the potential to drastically reduce the problem of stuck pipes. We can construct the AI from historical occurrences to predict downhole issues in advance, giving the operation crew ample time to take preventative and mitigation measures. This can significantly reduce the consequences of NPT and other failures in wells. Furthermore, AI workflows can limit human error in interpretation.

Causal AI powers this knowledge-based early warning system, providing a viable solution to mitigate the risk of stuck pipes in geothermal drilling. This method has the potential to dramatically improve the safety and efficiency of geothermal well development by providing early warnings and allowing informed decision-making.

REFERENCES

Al-Adwani, T., Singh, S., Khan, B., Dashti, J., Ferroni, G., Martocchia, A., Estarabadi, J., "Real Time Advanced Surface Flow Analysis for Detection of Open Fractures", presented at the SPE Europec/EAGE Annual Conference, Copenhagen, Denmark (2012).

Allemang, D., Sequeda J, Increasing the LLM Accuracy for Question Answering: Ontologies to the Rescue!, https://arxiv.org/abs/2405.11706

Clinciu, M., Lau, H., Williams, M.J. Explainable Bayesian Networks via Natural Language Explanations and Interactive Visualization (2021) Caltech Explainable AI Virtual Workshop.

Dong H., Hussain F. K., Chang E., A survey in semantic search technology, (2008) 2nd IEEE International Conference on Digital Ecosystems and Technologies.

Dorman Purba, et al. "Integrated Stuck-Pipe-Prevention Campaign in Geothermal Drilling Project in Indonesia: A Proactive Approach" Proceeding *World Geothermal Congress*, Reykjavik, Iceland (2021).

Fox, M. & Long, D., PDDL2.1: An Extension to PDDL for Expressing Temporal Planning Domains, (2003), Journal Artificial Intelligence Research. 20, p. 60-124.

Hurwitz, J.S., & Thompson J.K., Causal Artificial Intelligence: The Next Step in Effective Business AI (2023), John Wiley & Sons, ISBN 978-139-418-4156.

Janowicz, K., Haller A., Cox S. D. J., Le Phuoc D., Lefrancois M., SOSA: A lightweight ontology for sensors, observations, samples, and actuators (2019), Journal of Web Semantics, v56, p1-10.

Kjærulff, U. B., Madsen, A. L.. Bayesian Networks and Influence Diagrams: a Guide to Construction and Analysis, Springer, (2012).

Liu, K., Ba, S., Goel, P., Kim, J., Continuous feedback loop between surface and downhole for autonomously drilling a section, SPE 218117 (2024).

Nasruddin, M., Alhamid I., Daud Y., Surachman A., Sugiyono A., Aditya H.B., Mahlia T.M.I., Potential of geothermal energy for electricity generation in Indonesia: A review (2016), *Renewable and Sustainable Energy Reviews*, v53, p733-740.

Pareti, P, and Konstantinidis, A review of SHACL: from data validation to schema reasoning for RDF Graphs, https://arxiv.org/abs/2112.01441

Pašić, B.; Gaurina-Međimurec, N.; Mijić, P.; Medved, I. Experimental research of shale pellet swelling in nano-based drilling muds. Energies 2020, 13, 6246.

Pearl J., Reverend Bayes on inference engines: a distributed hierarchical approach (1982), AAAI-82 Proceedings, p133- 136.

Pearl, J., Causality: models, reasoning and inference, Cambridge University Press (2009) ISBN 978-0521895606.

Pearl, J., Mackenzie, D (2018). The Book of Why: The New Science of Cause and Effect. Basic Books. ISBN 9780465097616.

Pfaff-Kastner M. M., Wenzel K., Ihlenfeldt S., Concept Paper for a Digital Expert: Systematic Derivation of (Causal) Bayesian Networks Based on Ontologies for Knowledge-Based Production Steps (2024), Mach. Learn. Knowl. Extr. v6(2), p898-916.

Sarker, M.K., Zhou L., Eberhart A., Hiztler P., Neuro-symbolic artificial intelligence (2021), *AI Communications*. **34** (3): 197–209.

Thermopedia, Gas-Liquid Flow, thermopedia.com

Yi Feng 1,Gao Li 1,Yingfeng Meng 1, and Boyun Guo, A Novel Approach to Investigating Transport of Lost Circulation Materials in Rough Fracture, Energies 2018, 11(10), 2572; https://doi.org/10.3390/en11102572

Thermopedia, Gas-Liquid Flow, thermopedia.com

Optimizing Hard Rock Geothermal Drilling Efficiency With PDC Bits: A Comprehensive Study

Conner Richardson-Fervo Energy; Elliot Howard-Fervo Energy; Jordan Self-Ulterra Drilling Technologies; Shana Larson-Ulterra Drilling Technologies; Charles Douglas-Ulterra Drilling Technologies; David Cormier-Ulterra Drilling Technologies; William Dubose-Ulterra Drilling Technologies

Keywords

Fervro Energy, Ulterra Drilling Technologies, Geothermal, Horizontal, Granite, PDC Drill Bit

ABSTRACT

This paper presents a comprehensive analysis of the application of Polycrystalline Diamond Compact (PDC) bits in geothermal drilling operations, aiming to enhance overall drilling efficiency and geothermal wellbore performance when drilling hard and abrasive granite. Additionally, it explores the unique challenges associated with geothermal drilling in granite and evaluates the suitability of PDC bits in addressing these challenges.

Key aspects covered in the paper include the engineering, design, and optimization of PDC drill bits tailored for hard and abrasive rock in geothermal environments, with a focus on factors such as cutter geometry, cutting structure design and bit body material composition.

This paper provides insights into the implementation of PDC bits in geothermal projects that drill hard and abrasive granite lateral intervals. Learnings from traditional oil and gas drilling methods shed light on the potential advantages, such as increased penetration rates, increased run lengths and reduced drilling costs.

The findings of this study contribute valuable knowledge to the geothermal drilling community, offering a roadmap for optimizing drilling practices through the utilization of advanced PDC bit technology. This paper concludes with recommendations for future research directions and the continued advancement of geothermal drilling techniques to support the sustainable development of clean, renewable geothermal energy resources.

Unlocking geothermal energy from some of the most challenging geologic production zones below the Earth’s surface utilizing the latest technologies and drilling techniques has proven to demonstrate the economic viability of this type of clean energy extraction. These innovations can be used as building blocks for future innovations and technologies to unlock the Earth’s geothermal potential even more efficiently.

1. Introduction

Geothermal drilling is a means of harnessing clean, renewable energy from the Earth which is available 24 hours per day, 7 days per week. Tungsten carbide (TCI) and milled tooth (MT) roller cone drill bits, while effective, have certain limitations, such as higher wear rates, seal or bearing related failures, slower penetration rates (ROP) and increased downtime for trips related to the cutting structure degradation or seal/bearing related issues. The adoption of PDC drill bits presents an opportunity to address these challenges and achieve substantial cost savings in geothermal drilling projects.

PDC drill bits feature a fixed cutting structure (no moving components) equipped with synthetic diamond cutters, providing improved hardness, thermal and abrasion resistance. These features enable faster penetration rates through various geological formations, reducing the overall drilling time and well construction cost. The enhanced drilling efficiency of PDC bits directly translates to cost savings by minimizing rig operational costs and accelerating project timelines.

This paper includes a case study highlighting the successful application of PDC drill bits in a geothermal drilling project in southwest Utah. This case study highlights specific instances where cost savings were realized through improved drilling efficiency, reduced downtime, and extended bit life.

The implementation of PDC drill bits in geothermal drilling operations offers a reliable solution for achieving cost savings. Enhanced drilling efficiency, reduced downtime, and extended bit life contribute to overall project economics, making PDC drill bits one of the key technologies in the pursuit of clean, sustainable geothermal energy extraction.

With the introduction of PDC bits along with subsequent improvements to the bit design, PDC cutter technology, bit body materials changes along with increased gauge pad length the performance in the 8.75” lateral section (±30ksi granite) of the geothermal wells has increased performance from 1,172’ to 2,911’ drilled with a single bit (148%). The respective ROP followed suit with an 11% increase.

The foundation of the overall success of innovative new projects is the working partnership between the service companies and the operators executing the drilling campaign.

Application Definition

- Rock Properties and Challenges
- Drive Type (Top Drive, PDM)
- Rig Capabilities

Bit Design Selection and Criteria

- Blade Count, Cutter Size, Cutter Technology, CFD
- Bit Body Material (Steel or Matrix)

Field Test Trials

- Drill Bit Performance (EDR Data Analysis)
- Dull Bit Evaluation

2. The Value of Partnership Between Operator and Service Provider

A good partnership between an operator and a service provider involves clear communication, mutual trust, and shared goals. The operator relies on the service provider for specialized expertise and equipment, while the service provider relies on the operator for detailed information and clear feedback to efficiently deliver services or products that meet the operator's objectives. Both parties work collaboratively to optimize operations. Regular feedback and performance evaluations help maintain the partnership's effectiveness and drive continuous improvement. When operators and service providers form a solid partnership through mutual sharing of knowledge and expertise, significant benefits and advantages are realized by both parties. By working closely with the operator, the service provider gains access to a higher level of detail regarding the operator's specific needs, challenges, and operational requirements. This deeper understanding allows the service provider to tailor more effective solutions in a timelier manner. The operator can then realize more frequent and more significant step changes in performance.

Partnering with a service provider enables the operator to engage in more meaningful interactions throughout the project lifecycle. With regular interaction, time spent with a service provider becomes more valuable with less time required for each interaction. The operator achieves better results in less time. This close collaboration fosters a dynamic feedback loop wherein the service provider can quickly iterate on their solutions based on real-time feedback from the operator and detailed historical understanding. By maintaining open lines of communication and actively soliciting input from the operator, the service provider can ensure that their solutions remain aligned with ever-evolving needs and priorities, delivering greater value for the operator. Trust between the two parties must be established as well because data shared from either side may be sensitive. An understanding of allowed and disallowed uses of shared information must be determined and understood. However, the sharing of this detailed information from both parties is vital to maximize the speed and effectiveness of solutions.

Optimizing drill bit design for hard rock drilling in an effective and timely matter required significant communication, data-sharing, and feedback between the operator and the drill bit company. It required a trusting partnership. Initially, the drill bit company shared lessons learned and expertise from previous hard rock applications such as the Utah FORGE project. The operator trusted the bit company with proprietary access to their specific geology, wellbore geometry, bottom-hole assemblies (BHA), and drilling parameters. The drill bit company and operator used the data to understand differences and similarities leading to initial bit designs selected and agreed upon for trial.

After initial trials with the service provider's bit, the iterative process of improvement began. The drill bit company was able to review drilling parameters and dull conditions of the bits with the operator and apply their suggestion for improvement in design. The operator was able to express honest and constructive feedback on performance. The drill bit company trusted the operator with proprietary details on proposed drill bit cutting structure design and bit material changes that could be made to increase performance. The operator was able to express their opinion and expertise to mold and shift recommendations to better fit their operational goals and requirements. Each drill bit run was a learning opportunity for the partnership to better understand and overcome the limiting factors together to iterate and improve. The partnership improved the operator's performance from expecting less than 1,000-ft per bit run to achieving multiple single-bit runs

over 2,000-ft, reducing the number of bits/BHA's required per well and reducing the overall cost while reducing NPT time.

3. PDC Drill Bit Design

An 8.75", 7 bladed-13mm cutter matrix body PDC bit (**Bit-A**) was initially designed to drill the challenging granite formation in Utah – specifically for the Fervo Energy Cape Station project in Milford, Utah. The interval of interest was the 4,500' to 5000' lateral section in the ±30ksi compressive strength abrasive granite. The formation TVD is ±8700'. Over a 7-month period several design and materials changes were implemented to improve the drilling efficiency and dull condition of the drill bit which resulted in a new PDC bit product line (**Bit-B**). **Figure 1** below shows the baseline bit alongside the modifications made after the first field trials. Modifications including an increased gauge pad length, cutter geometry shape change and matrix body materials change.

Figure 1: Bit-A (7 blades, 13mm cutters), Bit-B (7 blades, 13mm cutter)

PDC drill bits feature diamond-enhanced cutters that are highly resistant to wear and abrasion. Granite's hardness is well-suited for PDC bits, allowing them to maintain their cutting effectiveness over extended drilling periods.

The inherent hardness of PDC bits enables efficient penetration through granite formations. The PDC drill bits provide a continuous and consistent cutting action, resulting in faster drilling rates compared to conventional roller cone bits. **Figure 2** below shows the drilling mechanics of a roller cone insert versus a PDC cutter.

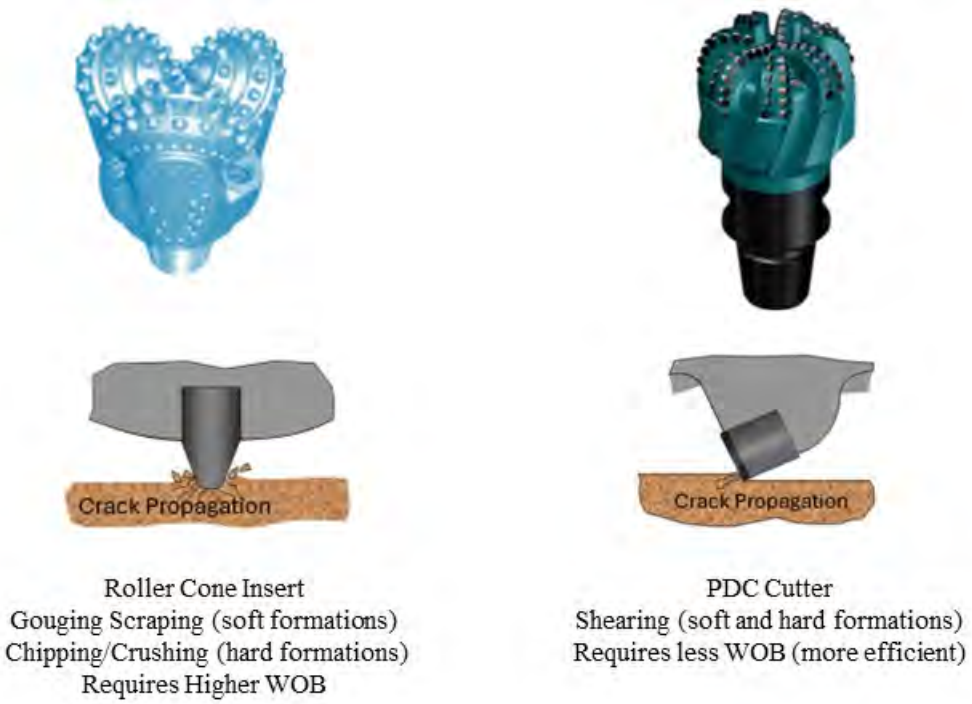

Figure 2: Roller cone insert vs PDC cutter Rock Mechanics

PDC bits contribute to reduced cycle time as they withstand the abrasive nature of granite, minimizing the need for frequent bit changes. This characteristic enhances operational efficiency and reduces overall drilling costs. The robust design of PDC bits leads to an extended lifespan in granite drilling applications. This longevity not only reduces the frequency of bit replacements but also contributes to cost savings by minimizing equipment mobilization and demobilization.

Adjusting drilling parameters, such as weight on bit (WOB) and rotational speed (RPM), can further optimize the performance of PDC bits in granite formations. Proper drilling practices ensure maximum efficiency and longevity of the bits.

Granite drilling generates significant heat at the rock and cutter interface, therefore adequate cooling mechanisms must be implemented to prevent overheating of PDC bits. The bottom hole temperature in the Cape Station project ranges between 400°-425°F. The temperature does not pose a significant challenge for the PDC bits as proper fluid circulation helps dissipate heat and maintains optimal drilling conditions. Although elevated temperature environments can affect downhole tool life, the high downhole temperature has been proven to not drastically affect PDC bit performance.

PDC cutting structure changes are generally made after dull trends are identified on the drill bit. It generally takes between three to five runs on a cutting structure to identify dull trends if all the other variables are held constant (WOB, RPM, flow rate, geology). Materials changes (matrix body, cutters) can be made after one run if an undesirable dull condition exists such as bit body erosion and/or impact/thermal/abrasive wear on cutters.

In summary, PDC drill bits paired with a drilling rig with adequate capabilities are well-suited for drilling granite due to their hardness, thermal and abrasion resistance, and efficient cutting action. Implementing PDC technology in granite drilling operations enhances overall drilling performance, reduces downtime, and contributes to cost-effective and successful projects.

4. PDC Cutter Development

Before the release/commercialization of any new PDC cutters to the field, there is extensive and time-consuming collaboration with the vendors' engineers. Prior to a cutter making it to the field, extensive lab cutter tests are performed to ensure the best product is ready for field trials. After the new cutter designs pass the rigorous field tests and evaluation (performance and dull condition) the cutters then progress to commercialization or, if required are sent back to the vendors' development teams for modifications. Each cutter being tested undergoes extensive post run evaluation to understand the observed dull conditions for future design improvements.

The first step, prior to any modification to the bit design, was to investigate and test new cutter technology. The transition from traditional round PDC cutters to multi-dimensional shaped PDC cutters to improve the cutting efficiency was made after the initial field trials. Scribe cutters (**Figure 3**) are the embodiment of a force multiplier. Like a knife-edge, they feature a prominent cutting edge that reduces the exposed cut face by 36% to improve the cut-crush ratio while drilling. The result is a cutter that focuses the maximum available weight transfer into challenging formations. The same force is applied across a smaller area, increasing the load per unit area (PSI).

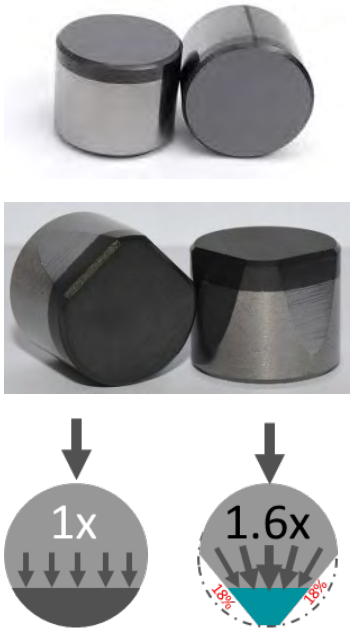

Figure 3: Round Cutters and Scribe Cutters

When selecting a scribe cutter attention must be paid to how "sharp" the cutting tip is. Small tip widths generally increase drilling efficiency but may result in a reduction in durability. A "blunter" tip results in a reduction in drilling efficiency but increases in durability.

When drilling at a moderate to high depth of cut the PDC cutters oftentimes get buried to >0.100" depth of cut (DOC). The high depth of cut places a force surface on the cutting edge, resulting in a gradient of loads and forces on the cutting face. This gradient of forces places a moment arm on the cutter, a compressive force on the tip and a neutral state away from the edge, putting a tensile load on the diamond table. Hard composite materials such as PDC cutters perform better in compression than tension.

PDC cutters are comprised of two primary materials, synthetic diamond and a tungsten carbide substrate. The synthetic diamond must be engineered to withstand the application that it is targeting. The key considerations for the selection of the diamond include impact resistance, wear resistance and thermal resistance. Most applications around the world require the proper balance of these three material properties based on the rock properties/lithology, drive system and drilling fluid. The tungsten carbide substrate is the supporting structure for the diamond table and is needed to attach the cutters to the PDC bit body with the use of a braze material. The tungsten carbide substrate is also a component that is modified/engineered to increase its erosion and corrosion resistance. **Figure 4** below shows the diamond grit, tungsten carbide substrate, HTHP cubic press and resulting PDC cutter.

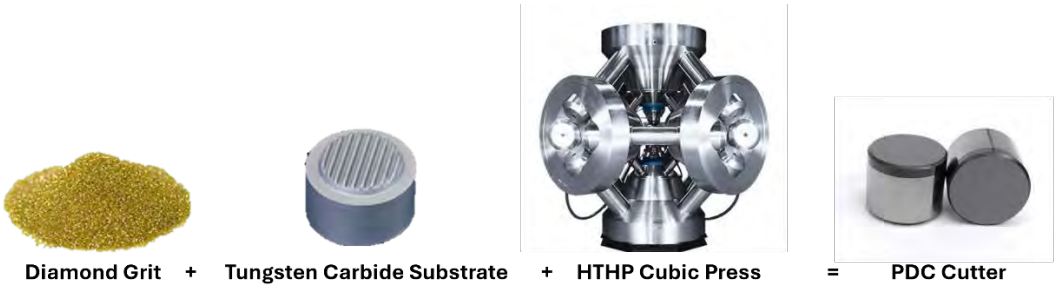

Figure 4: PDC Cutter (synthetic diamond and tungsten carbide substrate)

The system that is a PDC cutter must balance the various parameters and components that go into its creation. The crux of a PDC cutter is internal stresses, both mechanical and thermal. Interface patterns must distribute the internal compression/tension stresses efficiently to mitigate stress risers (failure initiation points). Lower interface heights result in higher thermal stability but results in lower strength of the compact. Tall interfaces enable higher strength but interferes with the maximum leach depth and braze thermal stability.

Higher pressure sintering allows for higher diamond packing density but creates a more fragile crack-prone diamond table. Higher density diamond also limits the leach ability of diamond, which can limit the effective thermal stability of the PDC cutter.

Lab development of PDC cutters typically revolves around milling granite, which for general geothermal environments is a similar pairing versus "producing" formations. The typical UCS of the granite used on the Vertical Turret Lathe (VTL) tests is around 20-25ksi. Parameters can be adjusted on the VTL to simulate downhole dysfunction, such as vibration. Through iterative tests evaluating single variable changes, the engineers can develop trade-off curves on development levers. It is critical that the rock of the VTL remain consistent to ensure like-like development comparisons.

Since drilling is a multimodal loading and failure mechanism environment, PDC cutters must be designed to service the primary modes of failure. Abrasion is caused by conventional shearing of formation. Thermal degradation by the bearing surface and friction caused by the shearing mechanism. Impact by either the formation (chert, dolomite, anhydride, etc.) or by parameter selection leading to vibration (axial or horizontal) or tangentially (stick-slip, HFTO). Because of these multi-modal loading scenarios, cutters must be designed to be off-center balanced, otherwise any one of these failure modes can exploit the designed product weakness.

5. PDC Gauge Pad Length Change

Gauge pad length was increased to improve tracking capabilities in the lateral interval, which inherently improves borehole quality, thereby reducing cycle time. The initial field trial was done with bits equipped with 3.0” gauge pad lengths (**Bit-A**), which transitioned over the project to bits re-designed with 6.0” gauge pad lengths (**Bit-B**). The transition to the longer gauge bit was on the third well on the Cape Station project and was set as the standard gauge pad length for all subsequent 8.75” designs. **Figure 5** shows the 7 bladed – 13mm cutter bit with different gauge pad lengths.

Figure 5: 8.75” Bit-A with 3.0” Gauge Pad on the Left and 8.75” Bit-B with 6.0” Gauge Pad on the Right

6. Matrix Bit Body Materials Development

A new matrix body material (tungsten carbide and binder) was incorporated to survive the erosion in the abrasive granite formation/environment encountered when drilling in this area in Utah. The abrasive nature of the granite had a negative effect on the matrix bit body of the PDC bit resulting in non-rerunnable bits due to erosion/abrasion on the bit body near the bit/rock interface. As the footage drilled over the span of the project increased due to drilling efficiency and drill bit improvements (cutter shape and design changes), the number of hours on bottom has also increased, exposing the limitation of the standard matrix powder used. Knowing that limitation on erosion/abrasion resistance was going to result in bit bodies being damaged beyond repair, a new matrix powder was deployed on all future bits manufactured for the application. **Figure 6** below shows the reduction in erosion/abrasion on the blades by moving to new matrix powder.

Some of the material properties of the matrix powder are listed below:

60% Increase in TRS (Base Strength)

50% Increase in fatigue life

25% Increase in thermal resistance

95% Increase in abrasion resistance

Figure 6: Original Matrix Powder (left) vs New Matrix Powder (right)

7. Dull PDC Bit Study

The dull photos in **Figure 7** are from the original design with standard round cutters, the original bit body matrix powder and the original 3.0” gauge pad length. The longest run on that frame was 1,172’ and it had an ROP of 44 feet/hour. **Figure 8** is the modified bit design with shaped cutters, new more erosion resistant matrix powder and was equipped with a 6.0” gauge pad length. This

bit drilled 2,911’ and it had an ROP of 49 feet/hour. This represents an increase in footage drilled of over 148% with an ROP increase of 11%. Although the dull state of the bit is worse than the previous best run on the original bit, the performance trade-off was substantial. This performance significantly improved upon the prior performance of the competitor PDC bits that on average drilled 531’ at an ROP of 55 feet/hour.

Figure 7: Bit-A, PDC1, MP1 (1,172’ @ 33.0 fph)

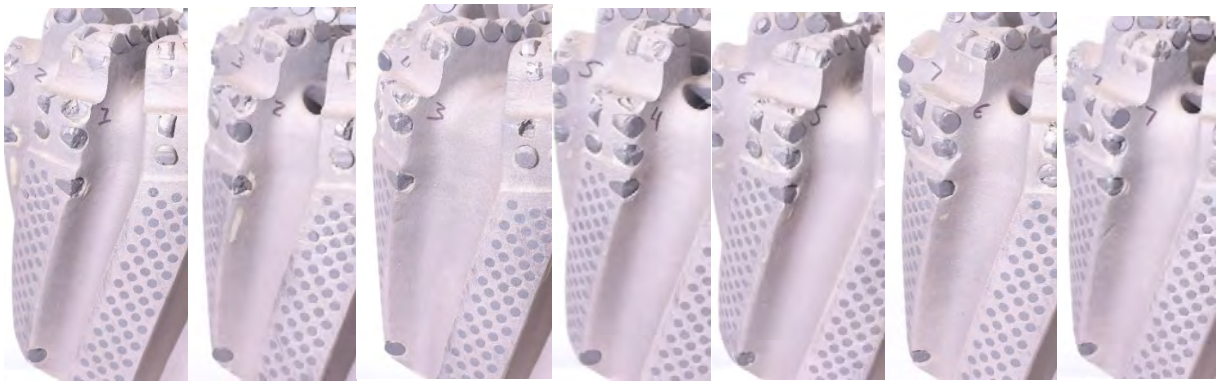

Figure 8: Bit-B, PDC2, MP2, GPL2 (2,911’ @ 37.0 fph)

8. PDC Drill Bit Design Changes

After initial PDC bit and PDC cutter field trials, each dull bit underwent dull evaluation by both the local applications engineers, Cutter R&D engineers as well as other PDC experts in the organization to identify where design and/or cutter improvements could be made to enhance the drill bit performance (footage and/or ROP) and dull condition.

Figure 9 shows design changes regarding the bits profile to address a dull characteristic limiting the performance of the original field trial PDC bit. In this case, the profile and back rakes were changed to lower the amount of work each cutter saw starting at the nose location on bit profile.

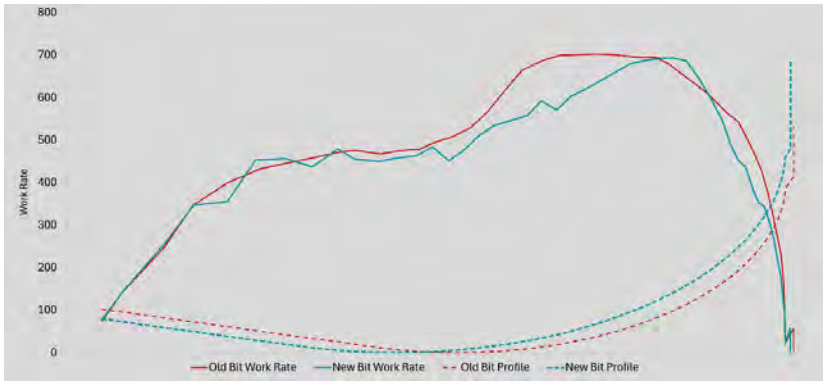

Work Rate Curve – Bit Profile

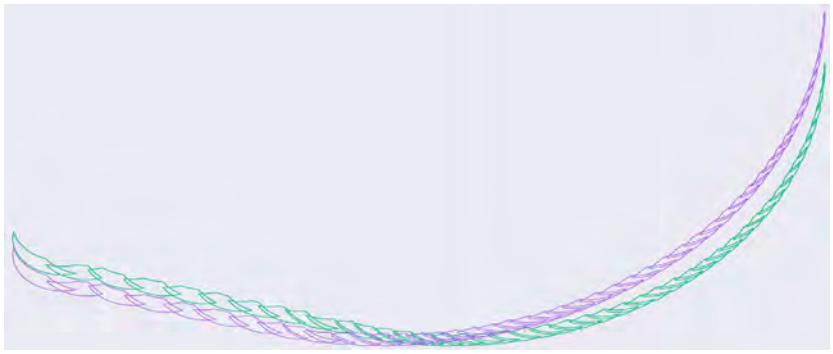

Cut Shape Round Cutters

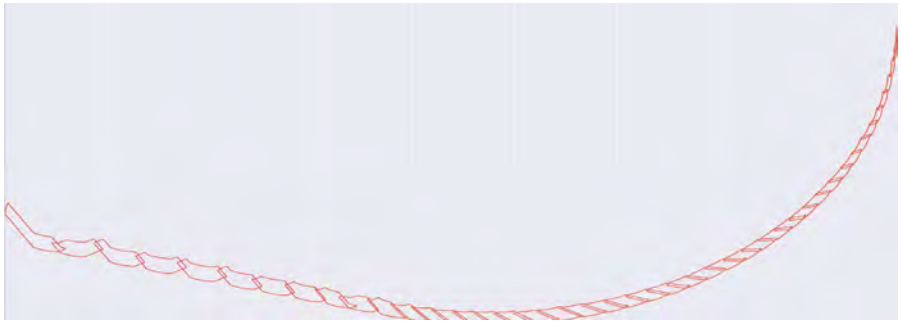

Cut Shape Scribe Cutters

Figure 9: Examples of PDC Profile Changes, Work Rate and Cut Shape

9. Improved Drilling Efficiency in The Lateral: 6 Well Case Study

The graph below (Figure 10) shows all the 8.75” bit runs in the lateral section. Both Ulterra (bit provider-A) and competitor bits are included. Although the scope of this paper is focused on the design and materials changes to the PDC bit itself, there were drilling efficiency gains made by changes to the bottom hole assembly and operating parameter optimization. The bits in the lateral section were all run on steerable PDM’s (Positive Displacement Motors). Run parameter changes were made based on the previous wells and bit dulls analyzing the EDR Data (Electronic Drilling Recorder Data) and adjusting the WOB, RPM and Flow Rate accordingly to improve both footage drilled and ROP.

- Well #1: 9 PDC bits used in the lateral (364 hours + Trips)
- Well #6: 2 PDC bits used in the lateral (144 hours + Trips)
- Reduced well time in the lateral by 9 days over the span of 6 wells (a 7 month time period)
- 78% decrease in bit runs – 60% decrease in drilling time in the lateral

Figure 10: Days vs Depth Chart

The graph below (**Figure 11**) represents the six subject horizontal wells and the drilling efficiency gains in footage and ROP in the lateral interval. The graph clearly shows the increased footage drilled per bit over the initial six wells of the drilling program. The wells are listed in chronological order from left to right on the graph.

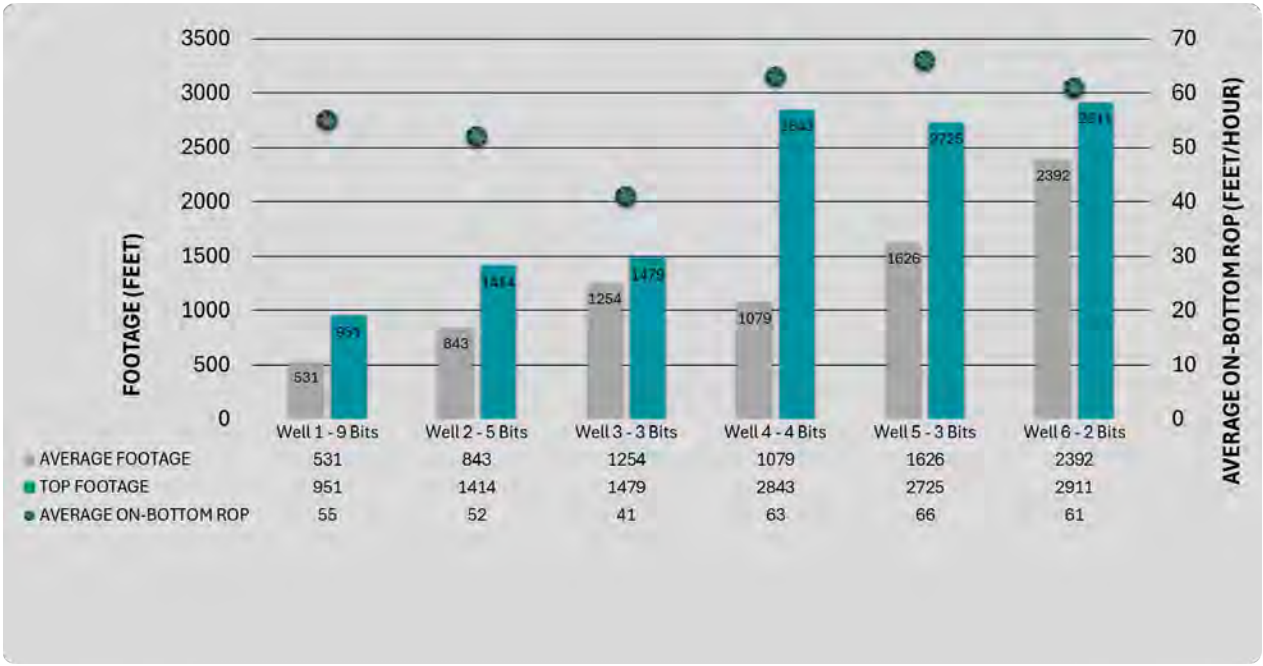

Figure 11: Metrics (Average Footage and Average om-bottom ROP) by Well – Lateral Interval

The table below (**Figure 12**) only represents bit povider-A's PDC runs shown on the chart above (**Figure 11**). The changes to the PDC Bit include cutting structure changes, PDC cutter changes, matrix powder changes and gauge pad length changes.

Well	Depth In	Depth Out	Footage	On Bottom ROP	Dull Condition	Run Date	PDC Bit Changes			
							Design	Cutter	Powder	Gauge
WELL 1	7037	7470	433	51	2-1-WT-S-IN-CT-DTF	08/23	BIT 1	PDC 1	MP1	GPL1
WELL 1	7470	7914	444	48	8-3-RO-S-IN-CT-PR	08/23	BIT 1	PDC 1	MP1	GPL1
WELL 2	7094	7756	662	62	4-2-RO-C-IN-WT-TD	09/23	BIT 1	PDC 2	MP1	GPL1
WELL 3	7646	8000	354	56	1-2-CT-S-IN-NO-BHA	10/23	BIT 1	PDC 2	MP1	GPL1
WELL 3	9838	11010	1172	44	2-4-BT-S-IN-CT-PR	10/23	BIT 1	PDC 1	MP1	GPL1
WELL 3	12122	13601	1479	62	8-3-CR-C-1-BT-TD	11/23	BIT 2	PDC 2	MP1	GPL2
WELL 4	6800	7721	921	60	4-3-CT-A-IN-WT-BHA	11/23	BIT 1	PDC 2	MP1	GPL1
WELL 4	8970	9110	140	55	0-1-CT-G-IN-NO-DTF	11/23	BIT 1	PDC 2	MP1	GPL1
WELL 4	9110	9547	437	44	1-1-CT-G-IN-BT-PR	11/23	BIT 1	PDC 2	MP1	GPL1
WELL 4	9547	12390	2843	56	3-6-WT-S-IN-ER-PR	11/23	BIT 2	PDC 2	MP1	GPL2
WELL 4	12390	13288	898	95	1-1-BT-G-IN-CT-TD	11/23	BIT 2	PDC 2	MP1	GPL2
WELL 5	6560	8307	1747	63	3-5-BT-A-1-WT-BHA	12/23	BIT 2	PDC 2	MP2	GPL2
WELL 5	9070	10384	1314	62	3-5-BT-A-1-WT-DMF	12/23	BIT 2	PDC 2	MP2	GPL2
WELL 5	10384	13109	2725	72	7-3-CR-C-2-WT-DMF	12/23	BIT 2	PDC 2	MP1	GPL2
WELL 5	13109	13949	840	51	4-5-BT-A-3-CT-TD	12/23	BIT 2	PDC 2	MP1	GPL2
WELL 6	8950	11861	2911	49	2-5-RO-S-2-BT-PR	01/24	BIT 2	PDC 2	MP2	GPL2
WELL 6	11861	13734	1873	78	3-1-CR-C-1-BT-TD	01/24	BIT 2	PDC 2	MP2	GPL2

Figure 12: 8.75" PDC Runs

10. Wellbore Design and Geometry

The Cape Station wells in Beaver County, Utah in this study all consist of wellbores that include a lateral section of around ±5000’ at a true vertical depth (TVD) around ±8700’. The heat map scale on the right side of the plot shows the on bottom ROP (**Figure 13**).

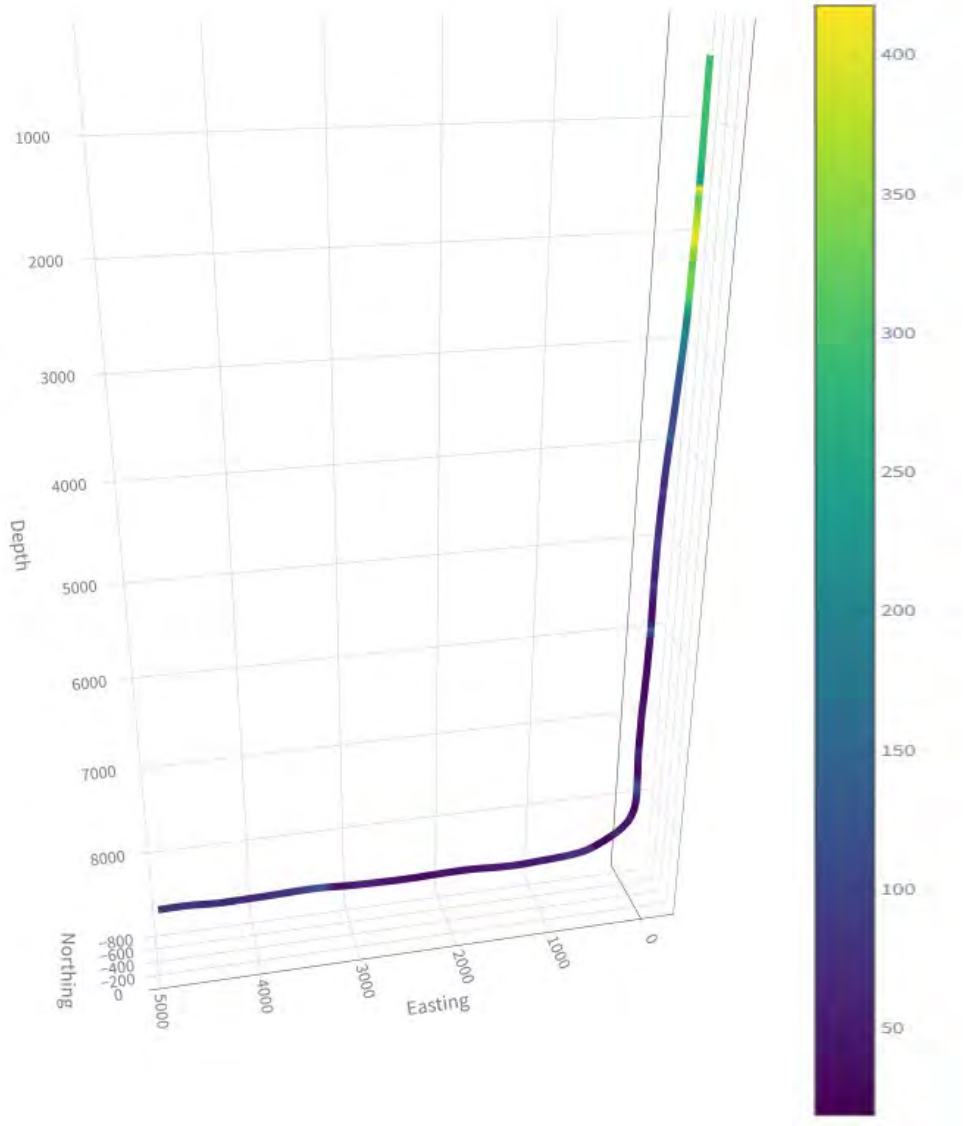

Figure 13: W3P Sample Geothermal Wellbore Trajectory with ROP

11. Present and Future Geothermal Opportunities

Although there is potential to drill Geothermal wells in many areas of the United States, this paper is focused on geothermal activity in Beaver County, Utah. This is one of the more challenging areas/formations in the United States to extract the energy from the earth due to the lithology (granite) being drilled in the lateral section. **Figure 14** below shows the location of the Cape Station project in Utah.

Figure 14: Cape Station: Beaver County, Utah Geothermal Location

The map below (**Figure 15**) shows the proximity of the Utah FORGE geothermal project relative to the Cape Station project.

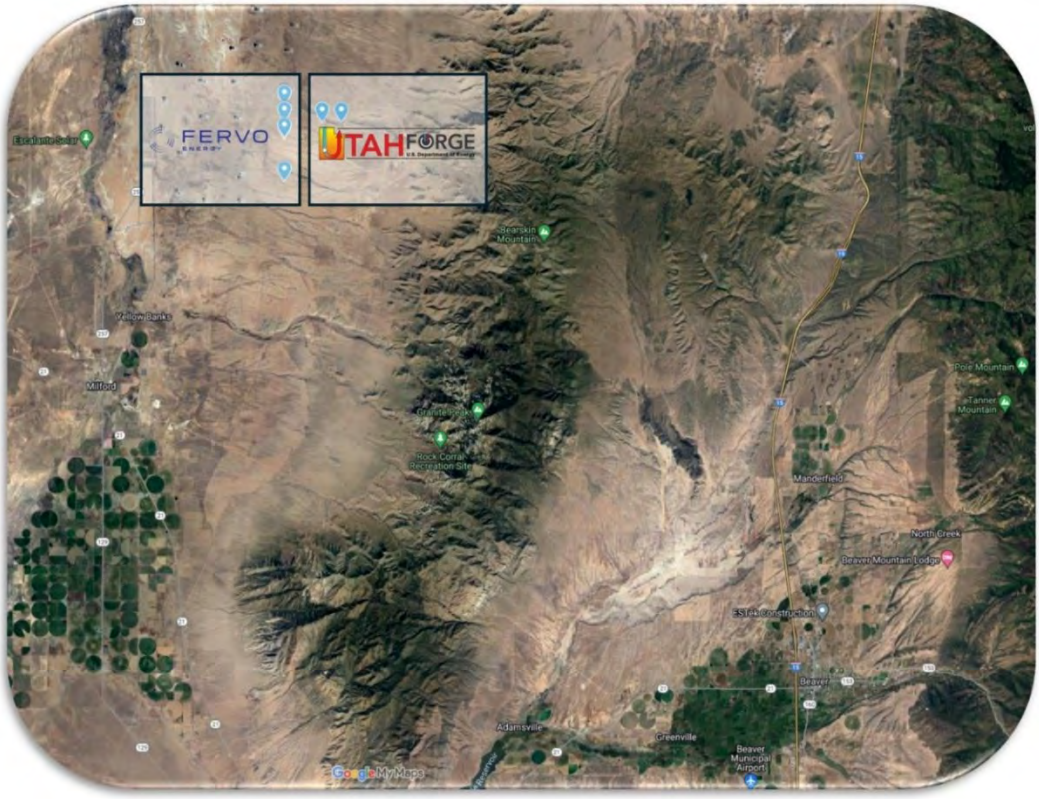

Figure 15: Cape Station and Utah FORGE Geothermal Well Locations

Figure 16 shows the areas in the United States and potential areas for future geothermal projects. The state of Utah is highlighted as it is the current focus of this paper and PDC development for the hard rock (granite) being drilled in the lateral.

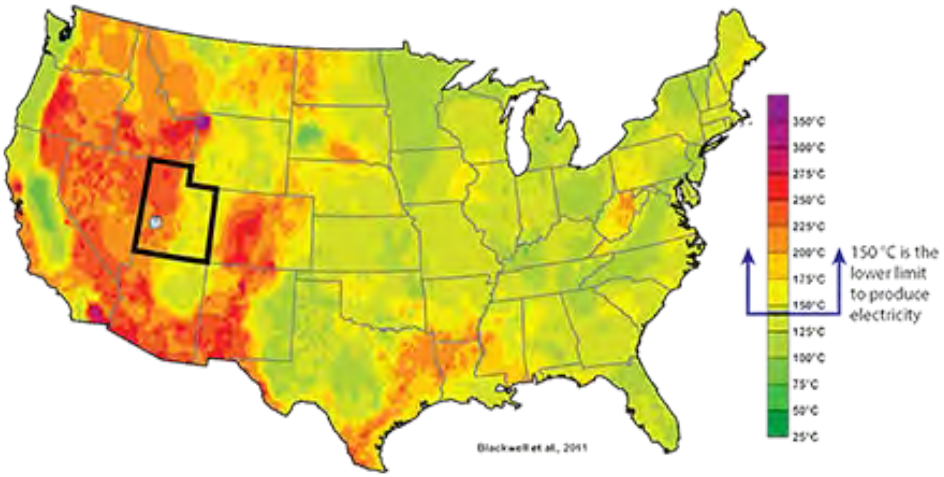

Figure 16: Potential Future Geothermal Operations (Blackwell et al., 2011)

12. Formation Characteristics

Most granite is a medium to coarsely crystalline igneous rock. Its color and texture depends largely on the relative abundance of quarts,feldspar (a family of rock-forming minerals), and mica.

Granite, one of the hardest, least brittle rocks on the planet (on the Mohs scale of mineral hardness, it generally falls between about 6 and 7). This translates into 25 to 30ksi unconfined compressive strength rock ('unconfined' is how the equivalent measure is presented in the drill bit industry, developing bits for the oil and gas industry).

Granite's density is high when compared to other, similarly drilled rock such as limestone or shale. Its density can range from 2.63 to 2.75 g/cm³ – which contributes heavily to its strength and durability.

Pore spaces make rock more vulnerable to substances penetrating it by capillary attraction or macroscopic flow. Granite'sporosity is so low that it is almost completely immune to water absorption and weathering.

Granites great stength can be attributed to it's granular texture. This quality is invariable due to granite being formed via interlocking, mineral crystals.

These specific properties might not apply to all granite formations in Utah. That depends on geological conditions and the mineral content of the rock. Very specific properties of granite in certain locations in Utah will have to be investigated on-site. The properties of the rock can also be tested off-site through the use of core samples that can be sent out to a lab for detailed testing of the mechanical properties. In fact, samples of the granite formation from the adjacent Utah FORGE project were sent out for analysis and the information gatherered is available on their website. The compressive strength of the rock can also be calculted utilizing electronic log data (such as gamma ray and sonic) and a mathematical model.

Figure 17 below shows properties of rock material in terms of unconfined compressive strenght (UCS) in kpsi.

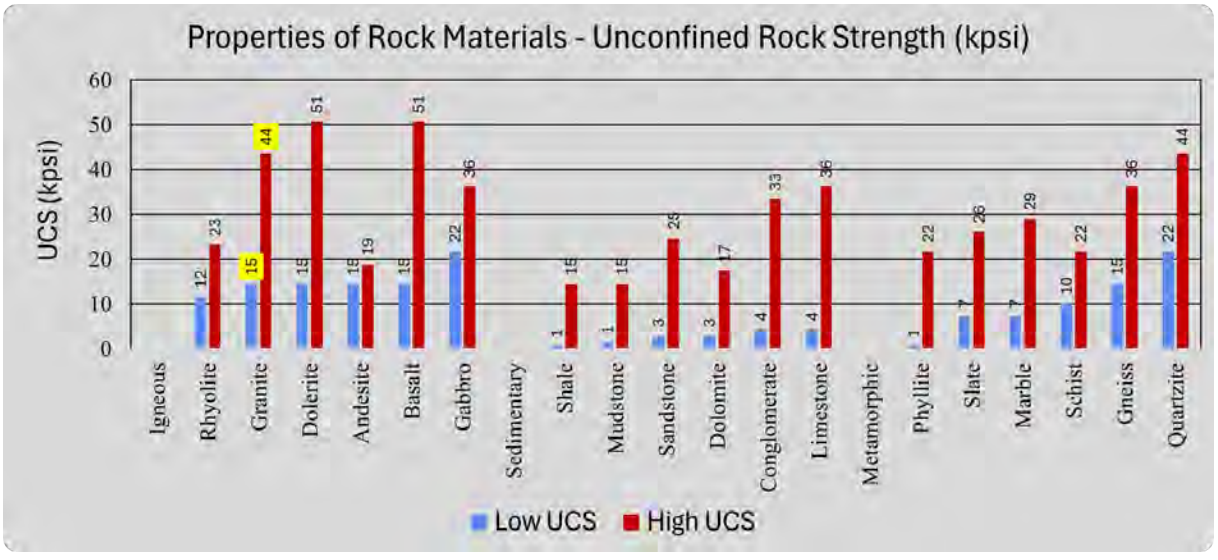

Figure 17: Unconfined Compress Strength of Various Rock Types

13. Conclusion

Our mission and the primary goal of these types of conference is to collaborate on technologies and techniques that allow us to produce clean and affordable energy.

One of the primary goals is to increase drilling efficiency that enables operators to tap into energy sources in the least amount of time and capital. Drilling efficiency gains alone, reduces the overall “unavoidable” carbon footprint of tapping into these energy sources.

The PDC bit manufacturers contribution is small in stature, a PDC drill bit measures around one foot in height, but monumental on the overall efficiency.

The Operator is currently drilling a 100 well project in Beaver County, Utah with the end goal of producing 400 MW of 24/7 carbon-free energy. At the time of writing this paper the team has already reduced the time in the ±5000’ lateral section from 15 days to 6 days and from 9 bit runs to 2 bits runs.

To put this into perspective, in 7 months, the team has reduced the drilling time in the lateral section alone from 1500 days to 600 days (extrapolated over the 100 well drilling program). This translates into a 60% reduction in time in the lateral section.

The geothermal community can further minimize its carbon footprint by its individual and group efforts to increase efficiency through collaboration.

Future development in the Utah geothermal application will include further development of PDC cutting structures, PDC cutters as well as parameter roadmaps. Other drilling related practices that affect PDC bit performance (such as connection and off bottom practices) are continually being reviewed and optimized by the operator.

Acknowledgements

We would like to acknowledge the great people involved in the Cape Station geothermal project in Utah, both in the office and in the field. The entire team on H&P 492, including all onsite service providers, all played a major role on the project. There are so many support people behind the scenes that contribute to the success of these types of projects it is hard to name them all. So, to those people, we offer our sincere gratitude to those that put their fingerprint on the success that all of us enjoy due to your commitment and contribution to being the best at what you do daily.

REFERENCES

Utah Forge (Frontier Observatory for Research in Geothermal Energy), https://openei.org/wiki/UtahFORGE

Redshaw, J., Scotchman, A., Laing, R., Dwyer, J., Trichel, K. 2007. “Achieving Superior Application Engineering. Proven Holistic Approach Disseminated to a Wider Community Key to Success”. SPE 109839 paper presented at SPE Annual Technical Conference and Exhibition, 11-4 November, Anaheim, California.

Thomas, S., Aljezany, M., Klink, Z., Scott, D. 2004. “Expanding Application of PDC into Harder, More Abrasive Formations: Performance Step Change in Saidu Arabia”. SPE 92435 paper presented at the SPE/IADC Drilling Conference, 2-4 March, Dallas, Texas.

Dupriest, F., Sowers, S. 2009. “Maintaining Steerability While Extending Gauge Length to Manage Whirl”. SPE/IADC 119625 paper presented at SPE/IADC Drilling Conference and Exhibition, 17-19 March 2009, The Netherlands.

Alienikoff, J.N., Nielson, D.L., Hedge, C.E., and Evans, S.H., 1987, Geochronology of Precambrian and Tertiary rocks in the Mineral Mountains, south-central Utah. US Geological Survey Bulletin 1622, p. 1-12.

Massachusetts Institute of Technology, “The Future of Geothermal Energy”, https://www1.eere.energy.gov/geothermal/pdfs/future_geo_energy.pdf

Abbreviations

BIT 1 = Cutting Structure 1

BIT 2 = Cutting Structure 2

CFD = Computational Fluid Dynamics

DOC = Depth of Cut

EDR = Electronic Drilling Recorder Data

GP1 = Gauge Pad Length 1 = 3” Gauge Pad Length

GP2 = Gauge Pad Length 2 = 6” Gauge Pad Length

MD = Measured Depth (feet)

MT = Milled Tooth

MP1 = Standard Matrix Powder

MP2 = Matrix Powder with better material properties for erosion resistance

PDC Bit = Polycrystalline Diamond Compact Bit

PDC1 = PDC Cutter 1 = Tradition 13mm Round Cutter

PDC2 = PDC Cutter 2 = Scribe Shaped 13mm Cutter

PDM = Positive Displacement Motor

ROP = Rate of Penetration (feet/hour)

TCI = Tungsten Carbide Insert

TVD = True Vertical Depth (feet)

UCS = Unconfined Compressive Strength

Managed Temperature Drilling: Real-Time Damage Monitoring of Insulated Drill Pipes and an Automatic Controller to Mitigate Effects of Subsequent Temperature Increase

Ningyu Wang[1,2], Pradeepkumar Ashok[2], Eric van Oort[2]

[1] Tsinghua University; [2] The University of Texas at Austin

Keywords

Managed Temperature Drilling, Insulated Drill Pipes, Automatic Temperature Controller

ABSTRACT

Drill pipe insulation is an effective method for downhole temperature management in high-temperature wells. Of late, the most popular pipe insulation method has been the application of a coating of low thermal conductivity to the inner wall of the drill pipe. When the coating is damaged, the insulation is also partially breached, leading to temperature management disruptions and higher downhole temperature.

Detection and prediction of coating damage is thus pivotal to successful downhole temperature management. There is currently no approach for the evaluation and detection of insulation coating damage. In this paper, we first propose a method to estimate drill pipe insulation integrity and then describe an automatic controller to account for the negative effects.

The insulation coating integrity evaluation workflow involves first using an advanced thermo-hydraulics model of the well to perform simulations of the planned drilling operations. From the simulation results, the relation between the bottom hole circulating temperature (BHCT) (and the surface temperature) and the drill pipe's average apparent thermal conductivity is established. We then use this relationship and compare it to the relationship between BHCT and surface temperature during actual drilling operations to determine damage (this is reflected as a change in the apparent thermal conductivity).

Next, to control the well's bottomhole temperature, a feedforward proportional, integral, derivative (PID) controller is used. In this study, the surface inlet temperature and the pump flow rate are used as the control inputs. Data from high-temperature land wells in the US using insulated drill pipes were used for the study. The effect of peeling and thinning of the insulation (the two prominent types of insulation damage) and its negative temperature effects were investigated.

This is the first study that demonstrates an approach to estimate the integrity of the drill pipe coating during actual drilling operation. In addition, a controller is suggested to automatically control /recommend flow rate and inlet temperature changes.

1. Introduction

When drilling geothermal wells, the high downhole temperature is a critical issue that lowers the life of the drilling tools, alters the fluid properties, and increases drilling risks and costs (van Oort et al., 2021). The development of high-temperature tools, drilling fluids, and cements have enabled drilling in extreme downhole conditions, but the increased cost from applying these advanced tools impair the profitability of many geothermal projects.

The fundamental premise behind managed temperature drilling (MTD) is to optimize the drilling plan and operation to maintain the downhole temperature within the working limit of the drilling tools and the drilling fluid. It aims to balance the capability of all components in the drilling system to optimize the drilling cost and performance in extreme downhole temperature conditions. By utilizing MTD, the drillable formation temperature of the drilling system can be expanded beyond the limits of each of the components in the drilling system.

One approach to keeping the downhole temperature within limits is to constrain the temperature increase of the drilling mud pumped into the drill pipe until it reaches the bottom of the hole. The mud traveling through the drill pipe is typically cooler than the mud in the annulus returning to the surface. The steel which is between the mud in the drill pipe (DP) and the annulus has a high thermal conductivity of 45 W/m/K. Under normal circumstances, the thermal energy flows from the annulus to the inside of the drill pipe, heating the mud, and in effect reducing the mud's ability to cool the bottomhole assembly. To suppress the heat transfer across the drill pipe, the drill pipe may be insulated. Among the MTD tools, insulated drill pipes are shown to be particularly effective, especially in deeper wells. Simulations show that drill pipe insulation is very effective for temperature management at depth, while the impact of surface mud cooling on the downhole temperature decreases in deeper wells (Khaled et al., 2023).

Tubing and pipeline insulation have been studied in the past with respect to heavy oil production and transportation (Lombard et al., 2008; Bell et al., 2021). To mobilize the heavy oil, hot steam is injected into the reservoir to heat the oil and thus decrease its viscosity. To keep the steam's high temperature and preserve the thermal energy carried by the steam, the steam is injected through insulated tubings. Once the heavy oil is produced and pumped into the transmission pipeline, pipeline insulation is used to suppress the heat dissipation from the oil to the environment to maintain the temperature and viscosity of the crude oil. In general, two types of insulation technology have been applied in the field, including insulation layers made of low-thermal-conductivity materials (Bell et al., 2021), and vacuum insulation (Singh et al., 2007).

Compared to production tubing and the transmission pipeline, DP works under more dynamic conditions. The alternating torques, the ever-changing axial load and the vibrations along with the impact forces challenge the robustness of the insulation structure. Furthermore, the thickness of the DP is strictly limited to allow more mud to flow through the DP and the annulus.

Between the two most popular DP insulation approaches, vacuum insulation is expensive and prone to damages by downhole impact and vibration, while the low-conductivity coating insulation

has a much lower installation cost and is less sensitive to impact and vibration. These advantages made insulative coating the prevailing DP insulation technology. However these insulations also fail, and there is as yet, no research on the real-time diagnosis and evaluation of the health of the DP insulation coating.

In this paper, we propose a method and procedure to diagnose the health of the insulation coating during drilling and introduce an automatic controller for downhole temperature maintenance in case of insulation failure. In the proposed method, a thermo-hydraulic model of the well is established and the relation between the circulating temperature and the coating health is first acquired. Then, using the measured surface and downhole temperature, the insulation health can be determined, and the remaining lifespan of the coating estimated. A PID controller is developed to maintain the downhole temperature when the insulation coating fails. The proposed procedure and the controller are demonstrated using simulated case studies.

2. Insulation Health Diagnosis

During drilling, the bottomhole circulating temperature (BHCT) and the surface temperature of the returning mud in the annulus are functions of formation properties, wellbore geometry, operational parameters, drillstring geometry, and drillstring properties including the DP apparent thermal conductivity. Assuming other parameters are unchanged, the BHCT and the surface temperature are functions of the DP apparent radial thermal conductivity k_{app}.

To get the relation between the mud circulating temperature and k_{app}, a thermo-hydraulic model of the well is established using the model developed by van Oort et al. (Fallah, 2021; Khaled et al., 2023; Wang et al., 2023). Based on the model, we assume the k_{app} and simulate the downhole temperature until steady state to get the BHCT. The BHCT at different assumed k_{app} is calculated and the BHCT-k_{app} curve is plotted (see Fig. 2). We will show in the case study that k_{app} is in fact a function of BHCT if the DP is sufficiently insulated.

The cross-section of the DP is a circular ring. Since the outer surface of the DP contacts the wellbore and suffers wear and impact, the insulation coating is on the inner surface to maximize the coating's life. Assuming the coating has a uniform thickness, the cross-section of the coating is also a circular ring. The k_{app} of the DP-coating system can be represented by (Bird et al., 2009)

$$k_{app} = \frac{\left(\ln\frac{r_{out}}{r_{in}}\right)_{DP+coating}}{2\pi L} \cdot \frac{1}{\frac{\left(\ln\frac{r_{out}}{r_{in}}\right)_{coating}}{2\pi L k_{coating}} + \frac{\left(\ln\frac{r_{out}}{r_{in}}\right)_{DP}}{2\pi L k_{DP}}} = \frac{\left(\ln\frac{r_{out}}{r_{in}}\right)_{DP+coating}}{\frac{\left(\ln\frac{r_{out}}{r_{in}}\right)_{coating}}{k_{coating}} + \frac{\left(\ln\frac{r_{out}}{r_{in}}\right)_{DP}}{k_{DP}}} \quad (1)$$

where r_{in} and r_{out} are the inner and outer radii of the corresponding layer, L is the unit length, k is the thermal conductivity, subscript $coating$ refers to the coating layer, and subscript DP refers to the steel part of the DP.

There are two typical damage modes for the coating: peeling, where part of the coating peels off the DP while the remaining coating keeps the thickness; thinning is when the coating is worn out uniformly. In this study, we assume that the coating damage is uniform along the drillstring, which means the coating health for each stand of DP is the same.

The DP insulation coating process is in its early stage of development and not all damage modes are properly documented. In this paper, we assume that there can be two damage modes: peeling or (and) thinning.

If peeling is the dominant coating damage mode, k_{app} is a function of the ratio of the remaining coating, α, and the thermal conductivity of the steel and the coating.

$$k_{app} = \alpha k_{steel} + (1-\alpha) k_{perfect} \tag{2}$$

$$\alpha = \frac{k_{app} - k_{perfect}}{k_{steel} - k_{perfect}} \tag{3}$$

where $k_{perfect}$ is the apparent radial thermal conductivity when there is no coating damage, and k_{steel} is the thermal conductivity of steel/non-coated DP.

If thinning is the dominant coating damage mode, we can derive the relation between the remaining ratio of coating thickness, β.

Assuming the initial thickness of the coating is $t_{coating}$, the inner radius of the coating is

$$(r_{in})_{coating} = (r_{in})_{DP} - \beta t_{coating} \tag{4}$$

Substituting Eq. (4) into Eq. (1) and expanding the log terms, we get

$$k_{app} = \frac{\ln r_{out,DP} - \ln\left(r_{in,DP} - \beta t_{coating}\right)}{\frac{\ln r_{in,DP} - \ln\left(r_{in,DP} - \beta t_{coating}\right)}{k_{coating}} + \frac{\left(\ln \frac{r_{out}}{r_{in}}\right)_{DP}}{k_{DP}}} \tag{5}$$

Eq. (5) can be rearranged to obtain the below.

$$\left(\frac{k_{app}}{k_{coating}} - 1\right) \cdot \ln\left(r_{in,DP} - \beta t_{coating}\right) = \frac{k_{app}}{k_{coating}} \ln r_{in,DP} + \frac{k_{app}}{k_{DP}} \left(\ln \frac{r_{out}}{r_{in}}\right)_{DP} - \ln r_{out,DP} \tag{6}$$

$$\beta = \frac{1}{t_{coating}} \left(r_{in,DP} - \exp\left[\frac{1}{\frac{k_{app}}{k_{coating}} - 1} \cdot \left(\left(\frac{k_{app}}{k_{coating}} - \frac{k_{app}}{k_{DP}} \right) \ln r_{in,DP} + \left(\frac{k_{app}}{k_{DP}} - 1 \right) \ln r_{out,DP} \right) \right] \right) \tag{7}$$

In practice, the k_{app} of the DP-coating system can be plotted against the BHCT. The k_{app} can then be easily looked up from the curve using the measured BHCT. Eq. (3) and Eq. (7) can also be plotted for easy reference.

In summary, the apparent thermal conductivity k_{app} is first calculated via simulation. If the dominant coating damage mode is peeling, the remaining coating area ratio α can be calculated using Eq. (3); if the dominant coating damage mode is thinning, the remaining coating thickness ratio can be calculated using Eq. (7). By monitoring and extrapolating how α and β decrease during drilling, the remaining lifespan of the insulation coating may be estimated.

3. Case Study

For the case study we use a representative L-shape horizontal well in the Haynesville basin. The well trajectory is shown in Fig. 1. The well has a true vertical depth (TVD) of 12,000 ft and the formation temperature at that depth is 385°F. A coating is painted on the inner surface of the 4.5" DP for insulation purpose.

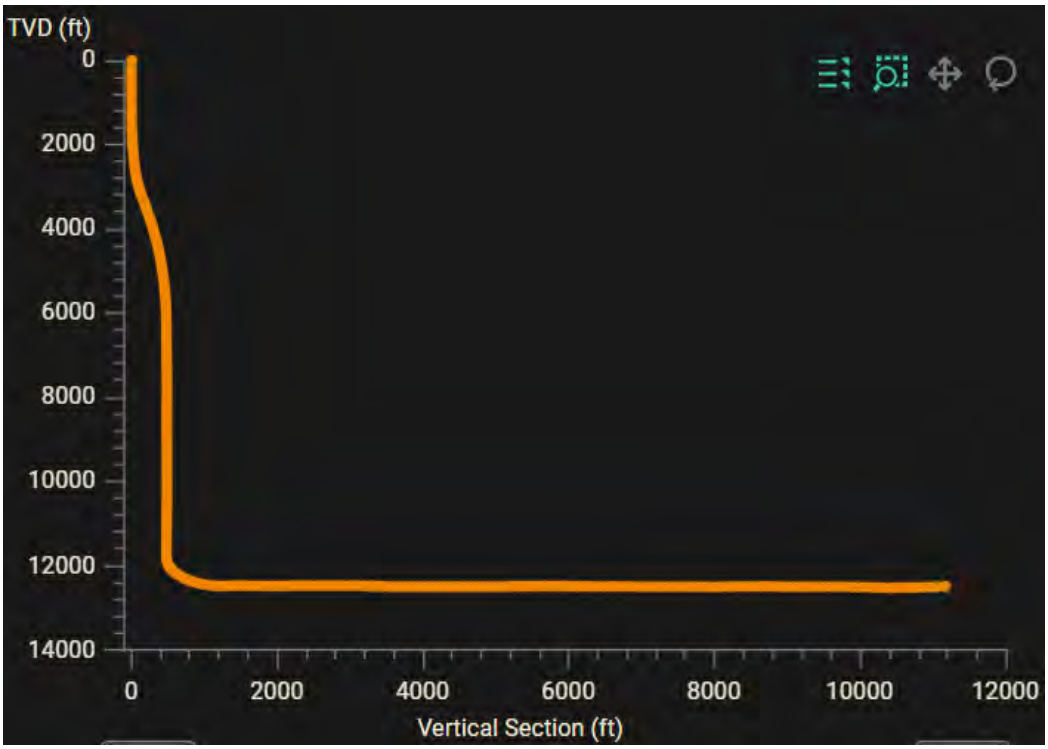

Figure 1: Case study well trajectory.

The well is modeled using the advanced hydraulics software developed by van Oort et al. (Fallah, 2021; Khaled et al., 2023; Wang et al., 2023). The DP is modeled as a uniform material of k_{app} which is calculated using Eq. 1.

Even with the mud cooler and the insulated DP, the downhole temperature became challenging for the downhole tools even before reaching the designed total depth. At measured depth (MD) 19,000 ft, which is in the middle of the lateral section, the BCHT for different k_{app} is modeled and simulated. The BHCT and mud temperature at the outlet are plotted in Fig. 2. According to Fig. 2, BHCT can be significantly decreased by as much as 100° F if k_{app} is sufficiently low. When the normalized k_{app} increases to about 30%, the BHCT is almost as high as that of using a non-insulated DP. In a field application, the BHCT can be measured and k_{app} can then be looked up using Fig. 2.

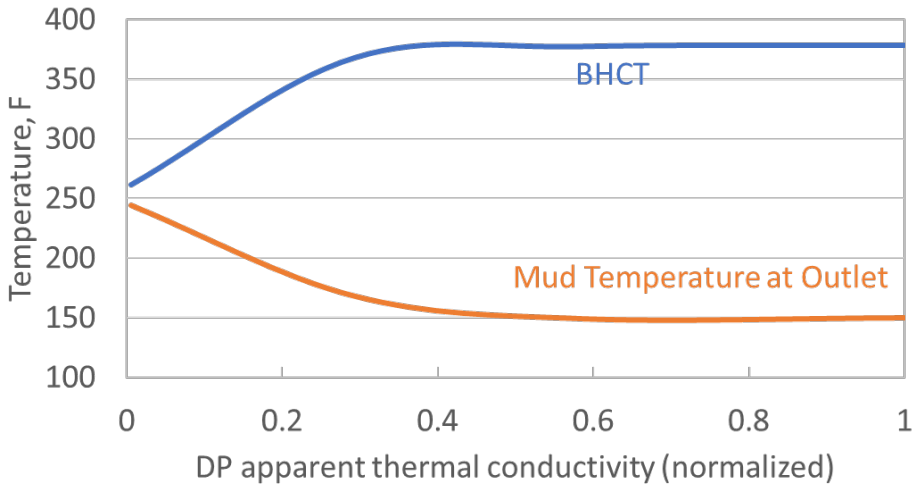

Figure 2: Relation between the mud temperature and the DP apparent thermal conductivity, k_{app}.

Fig. 3 shows the k_{app}-α curve calculated from Eq. 3. The k_{app} increases linearly as α drops. To achieve a normalized k_{app} of above 30%, the remaining coating area ratio required is $\alpha > 70\%$. Assuming peeling is the dominant damage mode of this DP, if the measured BHCT is 300 F, we look up Fig. 2 to get $k_{app} = 0.1$, and look up Fig. 3 to get $\alpha = 0.9$. By calculating α at different MD, the speed of coating damage can be calculated, and the remaining lifespan of the coating can be estimated.

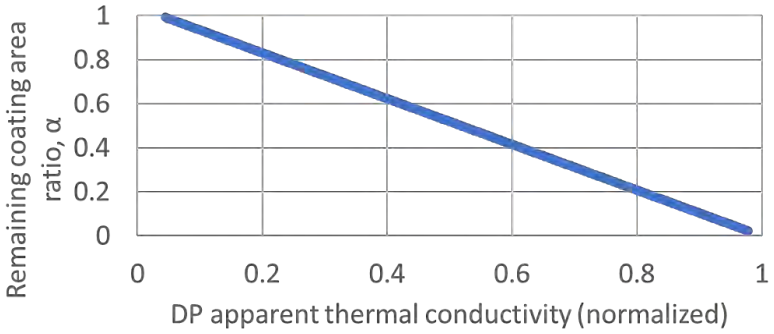

Figure 3: Relation between the remaining coating area ratio, α, and the DP apparent thermal conductivity, k_{app}.

Fig. 4 shows the k_{app}-β curve calculated using Eq. 6. Here, k_{app} grows nonlinearly as β drops. To achieve a normalized k_{app} of above 30%, the required remaining coating thickness ratio is 18% ($\beta > 18\%$). Assuming thinning is the dominant damage mode of this DP, if the measured BHCT is 300 F, we look up Fig. 2 to get $k_{app} = 0.1$, and then look up Fig. 4 to get $\beta = 0.7$. Here again, by calculating β at different MD, the speed of coating damage can be calculated, and the remaining lifespan of the coating can be estimated.

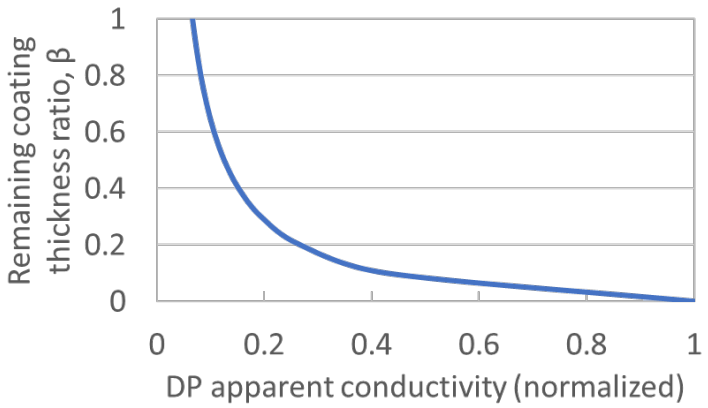

Figure 4: Relation between the remaining coating thickness ratio, β, and the DP apparent thermal conductivity, k_{app}.

The above method enables online diagnosis of the DP insulation coating without pull-out-of-hole. Based on the calculated coating damage speed and remaining coating lifespan, the driller can better plan the maintenance of the DP and decide when to switch to a new set of DPs. Figures 2-4 are based on the specific well data but can be used as a reference for general wells.

4. Automated Downhole Temperature Control System

If the insulation coating is damaged, the mud flowing through the DP receives excessive heat and may not sufficiently cool the bottom hole regions of the well. The BHCT is then increased and may lead to BHA components' accelerated aging or even sudden failure.

To mitigate the impact of the coating damage and maintain the BHCT, a feedforward PID controller is developed, as shown in Fig. 5. The controller controls the pump and the mud cooler. When the BHCT exceeds $BHCT_{max}$, the difference between $BHCT_{max}$ and BCHT is calculated and fed into the PID controller to get the control signal u_{PID}. At the same time, a feedforward block calculates the feedforward control signal u_{ff}. The total control signal u_{tot} is a weighed sum of u_{PID} and u_{ff}. The plant can be either the pump or the mud cooler. A higher pump rate and a lower inlet mud temperature will, in most cases, restore the BHCT to within the limit of the downhole tools.

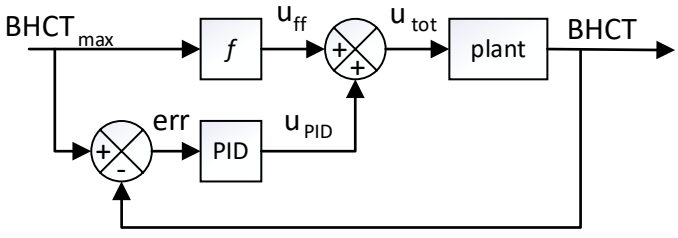

Figure 5: Feedforward PID controller.

This controller is demonstrated via a simulation based on the Utah FORGE dataset. The Utah FORGE 16A78-32 well at 5,900 ft is simulated using the model developed by van Oort et al. (Fallah, 2021; Khaled et al., 2023; Wang et al., 2023). The parameters of the well are listed in Tables 1-3. The insulation coating is assumed to be 0.02 inch thick with a thermal conductivity of 0.116 BTU/(h.ft.°F)

Table 1. Drilling fluid properties for Utah FORGE 16A78-32 well

Drilling Fluid Properties	
Fluid density (ppg)	8.9
Fluid plastic viscosity (lbf.s/100ft^2)	41771
Specific heat capacity (BTU/(lb.°F))	0.896
Thermal conductivity ((BTU.in)/(hr.ft^2.°F))	5.200

Table 2. Formation geothermal properties for Utah FORGE 16A78-32 well

Formation Geothermal Properties	
Formation surface temperature (°F)	67.85
Formation temperature gradient (°F/ft)	0.041
Rock density (ppg)	23.367
Formation specific heat capacity (BTU/(lb.°F))	0.222
Formation thermal conductivity ((BTU.in)/(hr.ft^2.°F)	16.016

Table 3. Wellbore configuration for Utah FORGE 16A78-32 well

Wellbore Configuration	
Wellbore depth (ft)	5900
Wellbore inclination (deg)	0

At the beginning of the simulation, the temperature in the well is at static equilibrium with the formation temperature. The pump is then turned on for 500 min to reach a steady state. Then, the DP apparent thermal conductivity k_{app} is increased from 4.585 BTU/(h.ft.°F) to 26.017 BTU/(h.ft.°F). The increase in k_{app} immediately increases the BHCT from 264°F to 290°F. The controller is then activated and the results for using the pump, and the mud cooler independently are shown in Figs. 6 and 7.

Fig. 6 shows the performance of the controller when only the pump rate, Q is changed. As the BHCT increases above the preset goal, the controller increases the mud pump rate from 400 gpm to 550 gpm. As a result, the BHCT decreases to below the preset limit of 290°F within a few minutes.

Fig. 7 shows the performance of the controller when controlling only the mud inlet temperature, T_{in}. As the BHCT increases above the preset goal, the controller forces the mud cooler to decrease the mud inlet temperature from 120°F to about 90°F.

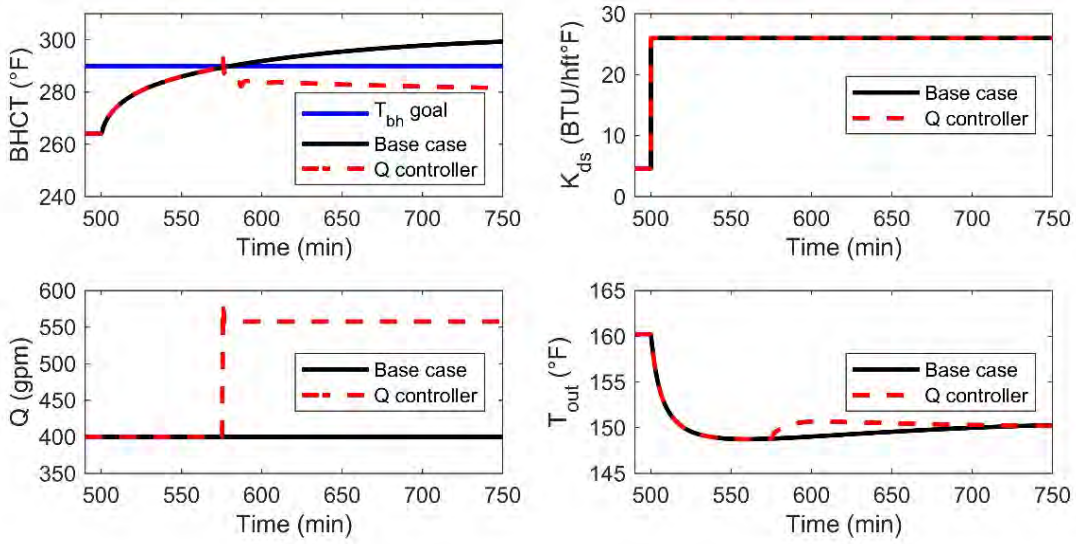

Figure 6: Performance of the controller when coating is damaged using only the pump.

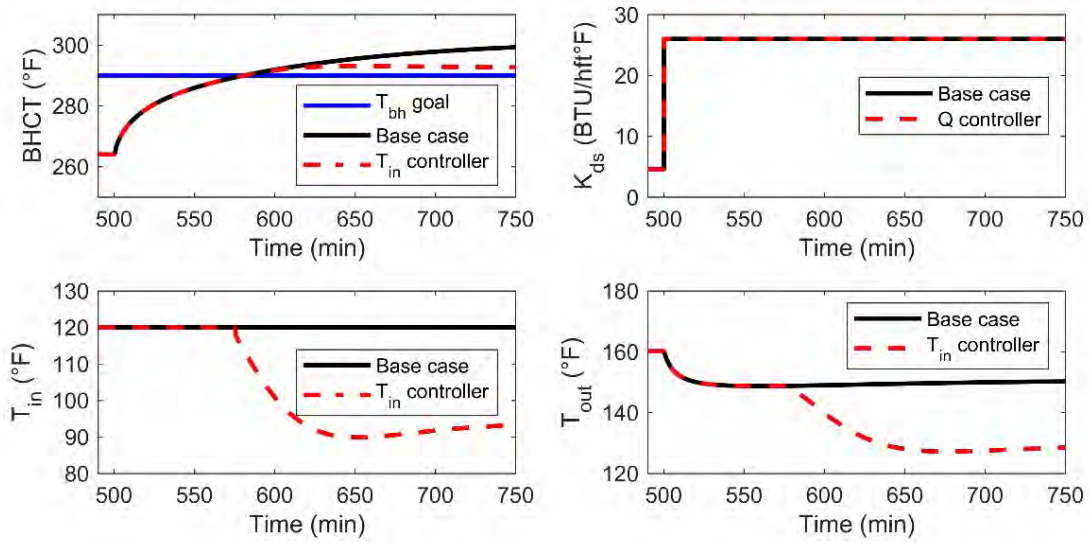

Figure 7: Performance of the controller when coating is damaged using only the mud cooler.

5. Conclusion

In this paper, we proposed a method and procedure to diagnose the insulation coating of insulated DP in real-time. To maintain the downhole temperature even when the coating is damaged, we developed a PID controller that uses the mud pump and the mud cooler to manage the downhole temperature.

(1) We used a validated thermo-hydraulic model to study the impact of apparent DP thermal conductivity on surface and downhole temperature.

(2) Assuming uniform coating damage along the drillstring, the relationship between apparent DP thermal conductivity and coating damage is derived.

(3) We proposed a method and procedure for online diagnosis of the health of DP insulation coating and showcased the method in a case study. If the dominant damage mode of the coating is peeling, the remaining coating area ratio can be determined. If the dominant damage mode of the coating is thinning, the remaining coating thickness ratio can be determined. The speed of coating damage can be calculated, and the remaining lifespan of the insulation coating can be estimated.

(4) A PID controller is developed to mitigate the impact on BHCT from sudden coating damage. The controller controls the mud pump and the mud cooler. The controller is demonstrated using a validated thermo-hydraulic model on the Utah FORGE dataset.

Glossary

k_{app}	-apparent thermal conductivity
$k_{coating}$	-insulation coating thermal conductivity
k_{steel}	-steel thermal conductivity
$k_{perfect}$	-apparent DP-coating system thermal conductivity when there is no coating damage
r_{out}	-outer radius
r_{in}	-inner radius
$t_{coating}$	-coating thickness
α	-ratio of the remaining coating if the dominant damage mode is peeling
β	-ratio of the remaining coating thickness if the dominant damage mode is thinning

Acknowledgement

The authors wish to acknowledge the financial support provided by the Rig Automation and Performance Improvement in Drilling (RAPID) Consortium at the University of Texas at Austin for this project.

REFERENCES

Bell, E., Lu, Y., Daraboina, N. and Sarica, C., 2021. Thermal methods in flow assurance: A review. *Journal of Natural Gas Science and Engineering*, 88: 103798. https://doi.org/10.1016/j.jngse.2021.103798.

Bird, R.B., Steward, W.E., Lightfoot, E.N., 2009. Transport Phenomena. 2nd Edition. Wiley Global Education. New York. 305-307.

Fallah, A., 2021. An advanced hydraulic-thermal model for drilling & control of geothermal wells. Doctoral Dissertation. The University of Texas at Austin, Austin, Texas, USA.

Khaled, M.S., Wang, N., Ashok, P., and van Oort, E., 2023. Downhole heat management for drilling shallow and ultradeep high enthalpy geothermal wells. *Geothermics*, 107.102604. https://doi.org/10.1016/j.geothermics.2022.102604.

Lombard, M.S., Lee, R., Manini, P. and Slusher, M.S., 2008, March. New advances and a historical review of insulated steam injection tubing. Presented at the SPE Western Regional Meeting, Bakersfield, California, USA, March 29. https://doi.org/10.2118/113981-MS.

Singh, P., Walker, J., Lee, H.S., Gharfeh, S., Thomason, B. and Blumer, D., 2007. An Application of Vacuum-Insulation Tubing for Wax Control in an Arctic Environment. *SPE Drilling & Completion*, 22(02): 127-136. https://doi.org/10.2118/111006-PA.

van Oort, E., Chen, D., Ashok, P., Fallah, A., 2021. Constructing deep closed-loop geothermal wells for globally scalable energy production by leveraging oil and gas erd and hpht well construction expertise. Presented at the SPE/IADC International Drilling Conference and Exhibition. Virtual. https://10.2118/204097-MS.

Wang, N., S. Khaled, M., Luu, A., Ashok, P. and Van Oort, E., 2023, October. Downhole Temperature Estimation of a Growing High-Temperature Wellbore Using a Modified Drift Flux Modeling Approach. Presented at SPE Annual Technical Conference and Exhibition, San Antonio, Texas, USA, October 2023. https://doi.org/10.2118/214836-MS.

Drilling Innovation Enables Faster Delivery of Geothermal Wells in Indonesia

Ariatama Yustisia, Mohammad Khairanto Nugroho, Roger Lee
Baker Hughes Company

Ashadi, Kiki Yustendi
KS Orka Renewables Pte. Ltd.

Keywords

Drill Bits, hybrid, volcanic

ABSTRACT

Geothermal power in Indonesia is an increasingly significant source of renewable energy as a result of its volcanic geology. A case study from Indonesia is presented on reducing drilling days on geothermal applications in North Sumatra using innovative hybrid polycrystalline diamond compact (PDC) and roller cone drill bit technology. Results of distance drilled and drilling penetration rates are compared to offsets.

The primary obstacle in the Sorik Marapi field is formation drillability. The lithology is a mixture of multiple hard volcanic formations consisting of breccia, tuff and andesite. The coarse rock fragments cemented together can damage and wear down the cutters and inserts on drill bits. And the interbedded nature of the formations create non-homogenous drilling which can also damage drill bits. The operator began working closely with a service provider to re-imagine how a well can be put on production faster in order to return value for stakeholder quicker. The continuous improvement process led to a partnership in innovation for the 17.5-in and 12.25-in. sections.

Consistent introduction of new drill bit technology has allowed this operator to complete wells faster by reducing drilling days. The solution was to deploy the hybrid drill bit which is more efficient, capable of producing higher penetration rates and smoother drilling. By combining the efficient shearing of PDCs and the crushing strength of roller cones the hybrid bit has the potential to maintain higher overall rate of penetration (ROP) for more distance than a roller cone or PDC bit could individually. The roller cone inserts pre-fracture the hard lithologies, making it easier for the PDC cutters to plow away the formation. And the combined crushing and shearing cutting structure provides improved overall stability when drilling through interbedded formations. In addition the smooth drilling nature of the hybrid bit perfectly maintained the tangent well trajectory.

This paper describes the partnership between the operator and bit service provider that led to the success in developing the optimal technology to deliver superior performance in igneous

formations. The collaboration in technology development contributed to drilling wells more efficiently and more accurately and enabling the operator to reach total depth (TD) reliably in the most challenging and complex geothermal drilling environments.

1. Geothermal Power in Indonesia

Many countries have been investing in geothermal power for decades. This is the case for the Asian Pacific countries located along the Ring of Fire. On the Indonesian island of Sumatra is a stratovolcano which is a significant source of renewable energy. The rock formations in this application are highly interbedded extrusive magma (lava) which is composed of rhyolite and andesite. Breccia, tuff, metamorphic phyllite and quartzite are also found in the lithology. The fractured nature of the formation leads to partial and total lost circulation.

An operator faced challenges while drilling the 17.5-in and 12.25-in sections of geothermal wells. The hard, abrasive and interbedded formations generate significant drilling dysfunctions (torque and vibrations) that quickly dulled PDC drill bits, leading to low ROP. For PDC bits, durability on the shoulder profile is the primary weak point. This limits the ability of PDCs to complete the section in one run, and results in higher costs from additional bits and delays from additional trips to change bits.

Figure 1 – West coast of Island of Sumatra, near capital city of Padang (black dot)
(Source: Wikipedia.org)

2. Drilling Simulation Software

The three dimensional bit drilling simulation software is the first step to creating a robust and durable cutting structure for geothermal applications in volcanic applications. A primary feature of the design methodology, the software creates advanced simulations that guide the selection, manufacture, and deployment of the optimal drill bit for specific hard and abrasive well conditions. By providing both full bit response and individual cutting element analysis, the bit drilling simulation affords more informed design decisions, shorter development cycles, and reduced need for costly lab or field testing. The value proposition for the drilling simulation software are further documented by Duffy et al, 2022 and Russell et al, 2022. The software uses a polygonal surface

mesh to accurately simulate bit-rock interactions under downhole drilling conditions and analyze the hybrid bit's PDC and TCI (tungsten carbide insert) dual-cutting mechanism together in one model. Performing design iterations to optimize these values—the software helps pinpoint a bit design that offers improved durability and higher ROP at a lower cost per foot.

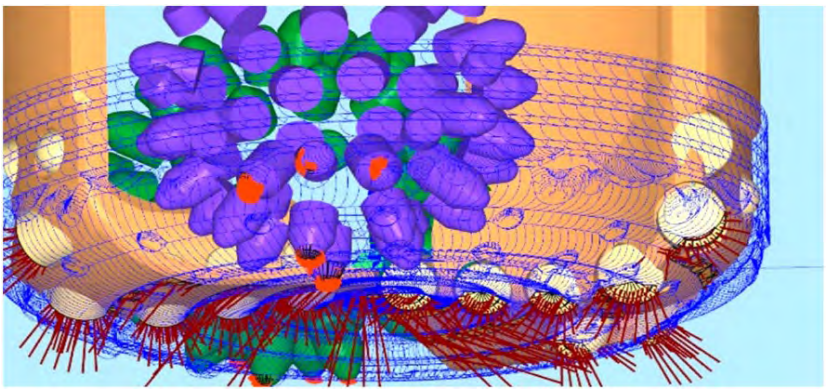

Figure 2 - Modeling drill bit-rock interactions using a polygonal surface mesh and cutter stress loading display

3. PDC & Roller Cone Hybrid Drill Bit Design

Unique drill bit solutions are needed for the most challenging applications. Since their introduction to the drilling industry in 2011, the hybrid drill bit have met this need with a dual cutting mechanism that combines the crushing action of a roller cone with the shearing action of a PDC. These designs leverage roller cone and PDC cutting elements to minimize vibrations, improve drilling efficiency and extend run length in difficult applications. In non-homogenous extrusive rocks it delivers improved drilling rates of penetration over Tricone drill bits, and is more consistent than PDC drill bits which are susceptible to impact damage. Additional case studies of hybrid performance in Asia Pacific have been documented by Lockwood et al (2021) and Wan et al (2015).

For this application, the hybrid design package featured precision balanced blade count and cone optimization, resulting in a proven performance step-change. Increased blade counts improved lateral stability while making the bit more aggressive to stand up to wear and tear. Recessed shoulder cutters increased diamond volume, which improved durability to keep the bit engaged and extend distance drilled. Sharp, dense cones further allowed improved rates of penetration. Cutter selection options included impact resistant dual-chamfer cutters specifically selected to handle increased loads of challenging drilling environments to improve drilling speed and efficiency.

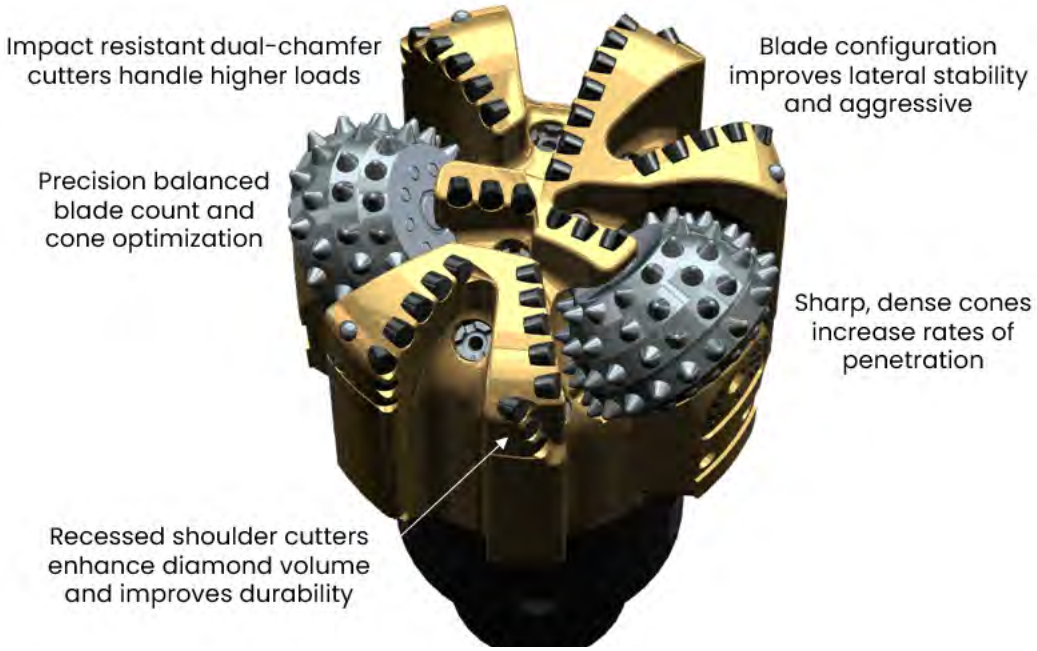

Figure 3 – Hybrid drill bit features

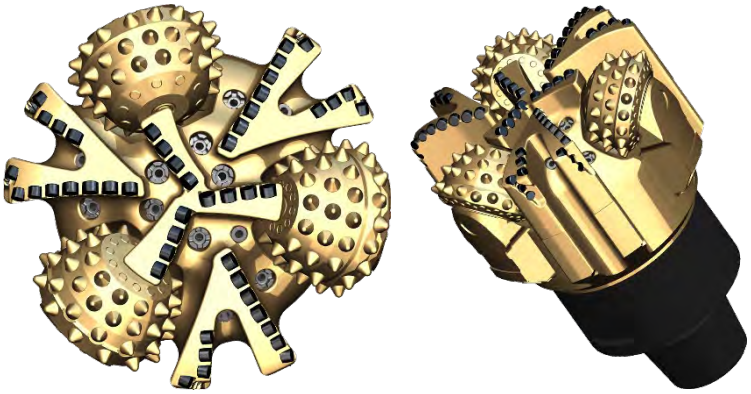

Figure 4 – 17.5-in Hybrid, 6-Blades, 3-Cones,
19mm (3/4-in) cutters, Conic Inserts for Aggressiveness

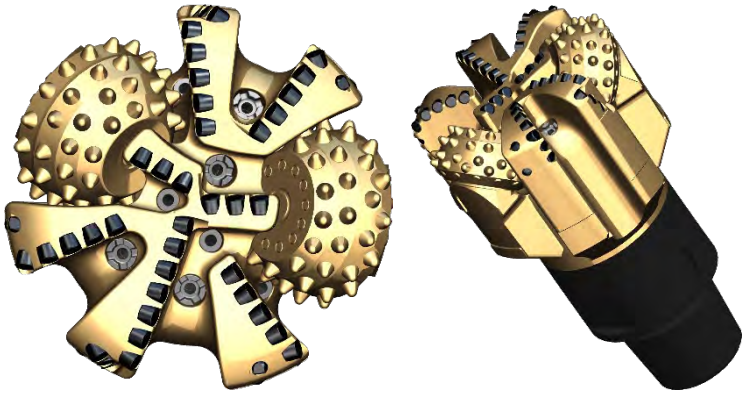

Figure 5 – 12.25-in Hybrid, 5-Blades, 2-Cones,
16mm (5/8-in) cutters, Conic Inserts for Aggressiveness

4. General Performance Results

Data from over forty wells were analyzed. In the 17.5-in section, the hybrid (designated as KM in graph) delivered 27% improvement in distance drilled and 74% improvement in ROP over roller cones. In the 12.25-in section, the hybrid delivered 105% improvement in distance drilled and 45% improvement in ROP over roller cones.

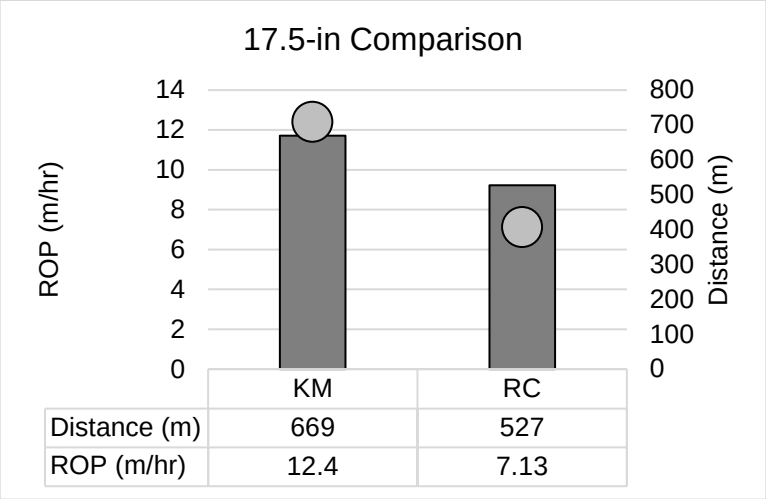

Figure 6 – Performance comparison for 17.5-in sections: 27% improvement in distance drilled (bars), 74% improvement in penetration rate (circles).

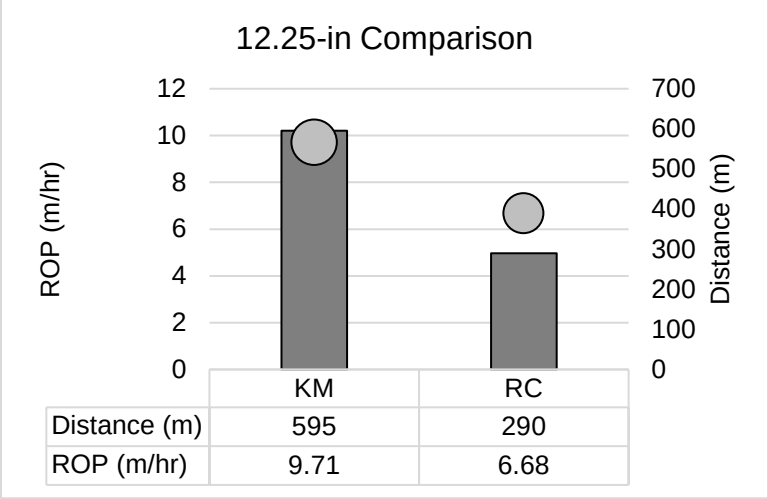

Figure 7 – Performance comparison for 12.25-in sections: 105% improvement in distance drilled (bars), 45% improvement in penetration rate (circle).

5. Detailed Performance from 17.5-in Section

The 17.5-in section is drilled with one bit to section total depth (TD). The average hybrid distance drilled of 669 meters is 27% farther than the average roller cone distance drilled of 527 meters. The hybrid achieved a maximum distance drilled of 876 meters in one run. The average ROP of 12.40 m/hr is 74% faster than the average roller cone ROP of 7.13 m/hr. The hybrid achieved a maximum ROP of 15.36 m/hr in one run. The hybrid averages 56 hours of drilling, with maximum of 82 hours.

The 17.5-in hybrid are comprised of 6-Blades, 3-Cones, with 19mm (3/4-in) PDC cutters. The 17.5-in roller cones are classified as IADC 435 – 515.

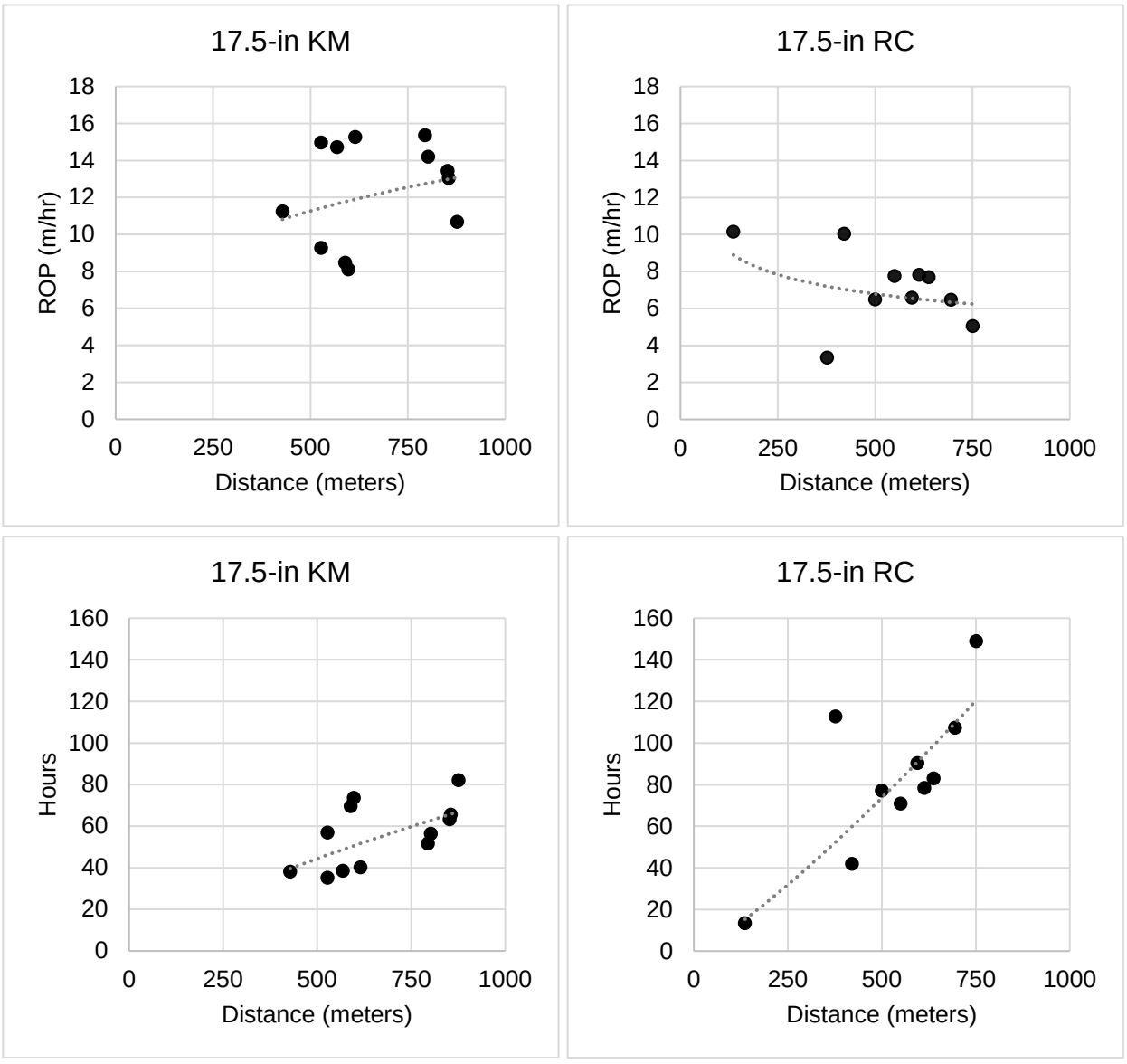

Figure 8 – Detailed performance comparison for 17.5-in sections

6. Detailed Performance from 12.25-in Section

The 12.25-in section is drilled with one bit to section TD. The average hybrid distance drilled of 595 meters is 105% farther than the average roller cone distance drilled of 290 meter. The average ROP of 9.71 m/hr is 45% faster than the average roller cone ROP of 6.68 m/hr. The hybrid achieved a maximum ROP of 14.98 m/hr in one run. The hybrid achieved a maximum distance drilled of 1030 meters in one run. The hybrid averages 63.6 hours of drilling, with maximum 87 hours.

The 12.25-in hybrid are comprised of 5-Blades, 2-Cones with 16mm (5/8-in) PDC cutters. The 12.25-in roller cones are classified as IADC 437 – 537.

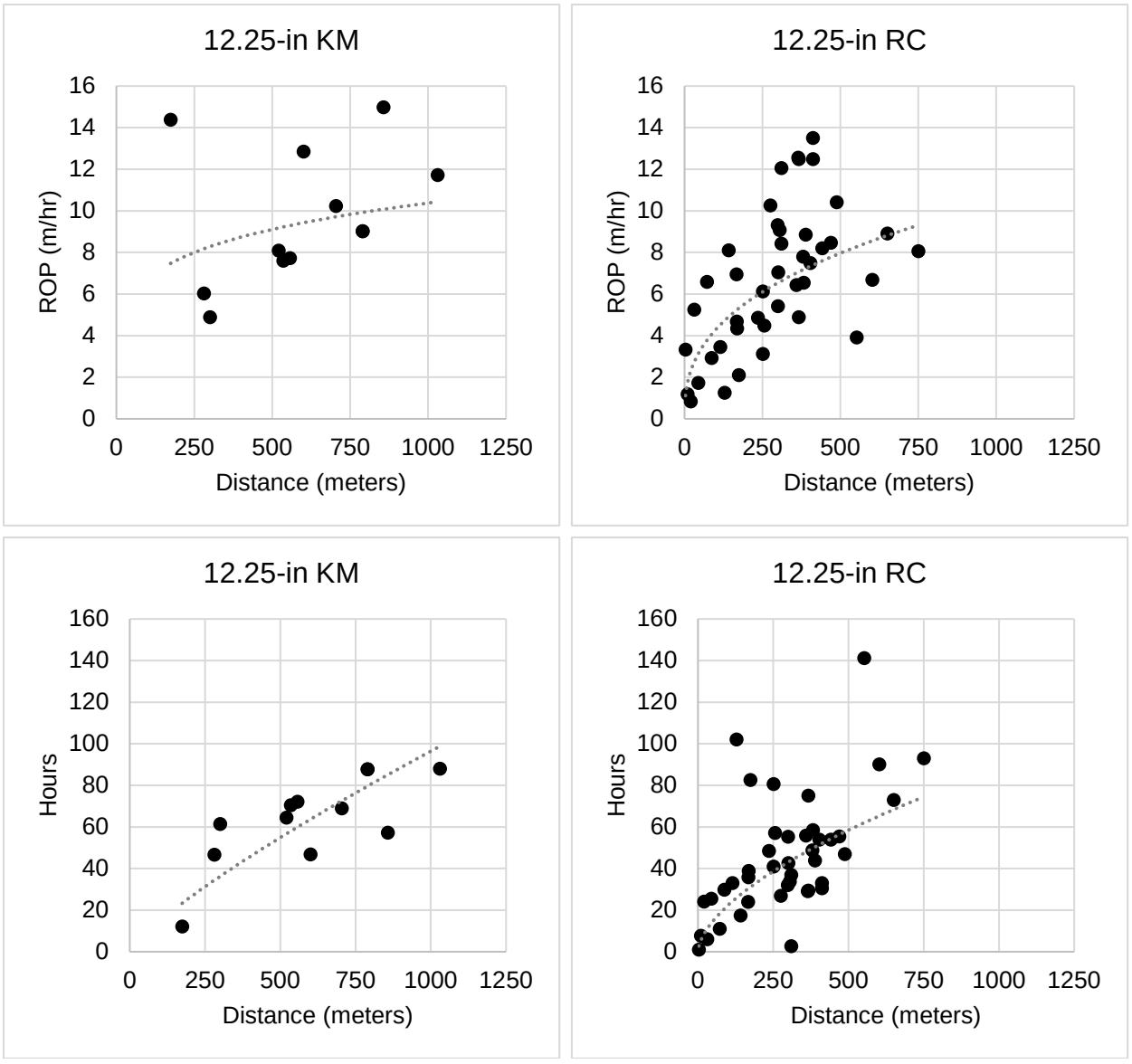

Figure 9 – Detailed performance comparison for 12.25-in sections

7. Conclusions

For decades, legacy roller cone drill bits have been used to drill geothermal wells at slow penetration rates. The learnings from this Indonesia application are chartering a new path of exceptional drilling performance utilizing hybrid drill bits. As stated by Oueslati et al in 2019, the transfer of innovation and best practices from the established oil & gas industry is key to reducing the risk and cost of geothermal projects. The application of this technology is enabling faster delivery of geothermal wells in Indonesia.

Acknowledgement

The authors would like to recognize KS Orka and PT Sorik Marapi Geothermal Power for their partnership and collaboration in bringing innovative drill bit technologies to the geothermal industry.

The authors would like to thank the management of Baker Hughes for permission to publish this manuscript with contents pertaining to:

Vulcanix™ geothermal drill bit solutions

Vulcanix™ geothermal Tricone

Vulcanix™ geothermal hybrid Kymera

Tetrahedron™ 3D bit drilling simulation software

Stabilis™ dual-chamfer cutters

REFERENCES

Lockwood N. and Wasuthalainunt N. "Hybrid Drill Bits Double Drilling Efficiency in Geothermal Wells in Japan." *GRC Transactions* (2021) Vol. 45.

Oueslati H., Passuello B., Lehr J., Nurzad D., Mattie T., Vaccaro M., Alfani A. "Learning from the Oil & Gas Industry: Leveraging Innovation and Integration to Reduce the Risk and Cost of Geothermal Projects." *European Geothermal Congress*, Den Haag, The Netherlands (2019).

Wan J., Lan Z., Guo H., Gao C., Sheng S., Valbuena F., Zeng J. "New Generation Cutter Boost Hybrid Bit Performance in Volcanic Basement in Northeast China." *SPE/IATMI Asia Pacific Oil & Gas Conference and Exhibition*, Bali, Indonesia (2015).

Duffy S., Wasuthalainunt N., Wongnang C. "Improved Drilling Performance in Asia Pacific Formations Through Digitally Augmented Design Process for Shaped Cutter Drill Bits." *Offshore Technology Conference Asia*, Kuala Lumpur, Malaysia (2022) OTC-31346-MS.

Russell, S., Duffy. S., Matthews, O., "Shaped Cutter Performance Optimization Through Advanced Drilling Simulations." *IADC/SPE International Drilling Conference and Exhibition in Galveston*, Texas USA (2022) SPE-208681-MS.

Economics

Geothermal Power Systems Analysis: Outcome of Industry Stakeholders Workshop

Dayo Akindipe, Erik Witter, Matthew Prilliman, Brian Mirletz, Jonathan Ho, Whitney Trainor-Guitton, Paul Pinchuk and Travis Williams

National Renewable Energy Laboratory

Keywords

Techno-economic analysis, GETEM, Annual Technology Baseline, geothermal power, ReEDS

ABSTRACT

Geothermal cost and performance evaluation implemented via techno-economic assessment (TEA) modeling is critical for the U.S. Department of Energy (DOE) and other geothermal industry stakeholders in assessing the current state of geothermal technologies and to identify existing hurdles to commercially viable geothermal development. The Geothermal Electricity Technology Evaluation Model (GETEM) is a major TEA tool used in estimating the economic feasibility and levelized cost of energy (LCOE) of conventional hydrothermal systems and enhanced geothermal systems (EGS). Since 2021, GETEM has been transitioning from an intricate spreadsheet model to a user-friendly tool within the System Advisor Model (SAM) developed by the National Renewable Energy Laboratory (NREL). Apart from enabling an expanded visibility of the geothermal model among other renewable resources, having GETEM in SAM has the advantage of simulation automation, better usability, updates tracking, active user inputs/feedback, and extended financial modeling. GETEM is used in developing supply curves for NREL's Annual Technology Baseline (ATB), which provides inputs to the Renewable Energy Potential (reV) and the Regional Energy Deployment System (ReEDS) models. The geothermal module in NREL's reV model assesses the geothermal energy potential in the conterminous United States by defining the geospatial intersection of geothermal resources with existing grid infrastructure within the constraint of land use characteristics. The ReEDS model is a capacity expansion model used for simulating the long-term build-out and operation of the U.S. generation and transmission system based on current energy costs and policies. To ensure enhanced representation of current industry trends in our model transitions and development, we organized a two-day virtual workshop to elicit geothermal industry stakeholder input and recommendations on our current approaches and assumptions on techno-economic, resource assessment, and deployment scenarios modeling of geothermal technologies. Participants included developers, operators, investors, regulatory agencies, system modelers, national laboratory researchers, consultants, and other stakeholders. In this workshop, we gained stakeholder insights on current geothermal plant performance (i.e., capacity factors), updated drilling costs and learning curves, and next-generation technologies such as closed-loop and superhot rock geothermal. Other outcomes from this workshop and its impact on future geothermal development feasibility, resource availability, and capacity expansion studies are compiled and discussed.

This report is available at no cost from the National Renewable Energy Laboratory (NREL) at www.nrel.gov/publications.

1. Introduction

The geothermal energy industry in the United States has seen a significant increase in technology advancements and public and private sector interests in recent years. Substantial investments in next-generation geothermal technologies have been reported, with an estimated $396 million invested in next-generation companies between 2021 and 2023 (DOE, 2024a). These have translated to a record number of power purchase agreements (PPAs) since 2020 (Robins et al., 2021; DOE, 2024a). Simultaneously, technological improvements are being made in multiple phases of geothermal power development such as drilling and completion, power plant design, and optimization. These innovations are being accelerated by technology demonstration projects like FORGE and the EGS Pilot Demonstrations specifically targeted at de-risking next-generation geothermal technologies.

The National Renewable Energy Laboratory (NREL) has supported the U.S. Department of Energy's (DOE's) effort in de-risking geothermal power projects. Through its Geothermal Technologies Office (GTO), the DOE previously engaged NREL in developing the GeoVision report. The GeoVison report describes a pathways and scenarios for technology advancement (DOE, 2019). Other efforts such as the Geothermal Earthshot analysis have been used to determine the pathway to get to low-cost enhanced geothermal systems development (Augustine et al., 2023). In these studies, NREL has provided business as usual and scenario-based analyses to the DOE using a defined methodology. First, base cases for resource (e.g., hydrothermal or EGS) and technology (flash or binary) pairs are determined using the Geothermal Electricity Technology Evaluation Model (GETEM) (DOE, 2016). This bottom-up techno-economic assessment (TEA) model estimates the lifecycle performance and cost of a geothermal project based on predefined assumptions for each project development phase. The outputs from this model are used to develop supply curves (i.e., cost versus cumulative resource capacity plots) that can be used for future deployment planning. GETEM is the primary model used in the geothermal technology representation in NREL's Annual Technology Baseline (ATB) that defines the current and future costs and performance levels for multiple renewable energy technologies (NREL, 2024). Supply curves developed primarily with GETEM are used in ReEDS for capacity expansion modeling of geothermal deployments into the future relative to other electricity generation technologies, policies, decarbonization goals, and other constraints (Gagnon et al., 2024). Figure 1 illustrates the interrelationship between GETEM, the ATB, and ReEDS. Recently, GETEM has been transitioning from an Excel-based workbook to a user-friendly model within NREL's System Advisor Model (SAM) tool. This transition is at its last stage of model alignment. GETEM in SAM is available both as a module in the Graphic User Interface (GUI)-enabled SAM model and the Python code-based PySAM available on GitHub. Having GETEM in SAM will enable a wider outreach beyond traditional users, incorporation of other geothermal next-generation technologies (including closed-loop and superhot rock geothermal), comparability with other renewable energy technologies, and a robust financial modeling capability (*System Advisor Model (SAM)*, 2022).

This report is available at no cost from the National Renewable Energy Laboratory (NREL) at www.nrel.gov/publications.

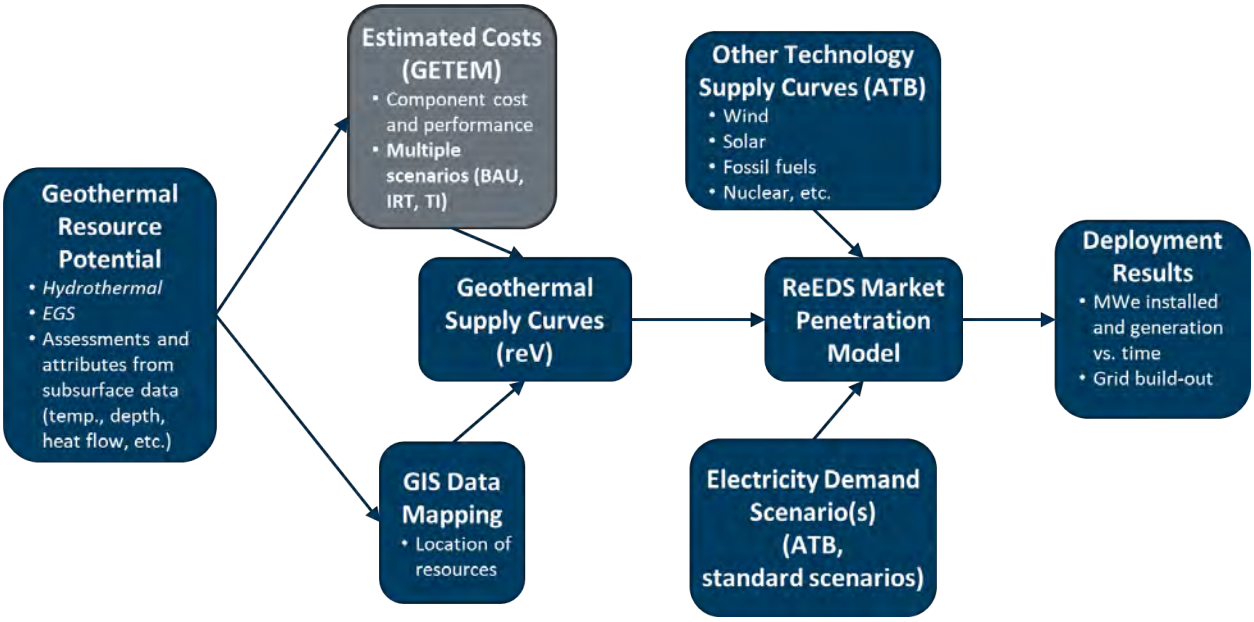

Figure 1: The interrelationship between GETEM, the ATB, reV, and ReEDS in determining future technology deployment scenarios. BAU= Business As Usual, IRT = Improve Regulatory Timeline, TI = Technology Improvement scenarios used in the GeoVision study (DOE, 2019)

The Renewable Energy Potential (reV) model is another NREL tool that has been recently adapted with capabilities to estimate and geospatially represent, with multiple levels of uncertainty, the available geothermal resources in the conterminous United States (Pinchuk et al., 2023). In developing these estimates, the reV model uses geospatial datasets, including heat flow and temperature at depth maps, grid infrastructure data, and geographical constraints (e.g., land use characteristics) to determine geothermal resource availability down to a 1-km^2 spatial resolution (Pinchuk et al., 2023). The model also takes in installation cost inputs from PySAM and in-built spur line transmission (or grid connection) cost model to develop supply curves for both hydrothermal and EGS technologies. The model methodology is shown in Figure 2.

On January 9-10, 2024, NREL gathered 66 geothermal industry stakeholders from around the country to discuss progress made in making our models more representative of the state-of-the-art and future expectations of the geothermal industry. This virtual workshop was titled the "NREL Geothermal Power Systems Analysis Workshop." Participants represented geothermal developers, operators, state agencies, non-profit organizations, investors, power system modelers, subject matter experts, the DOE-GTO, and national laboratories. Over the two days, NREL presented ongoing work in GETEM, SAM, reV and ReEDS and their anticipated impacts on future ATB and capacity expansion and scenario modeling. Breakout sessions also gave room for participants to identify and discuss gaps in our model assumptions and methods to ensure better representation of the performance, cost, and value of geothermal power systems. In this article, we summarize the major takeaways from the workshop discussions.

This report is available at no cost from the National Renewable Energy Laboratory (NREL) at www.nrel.gov/publications.

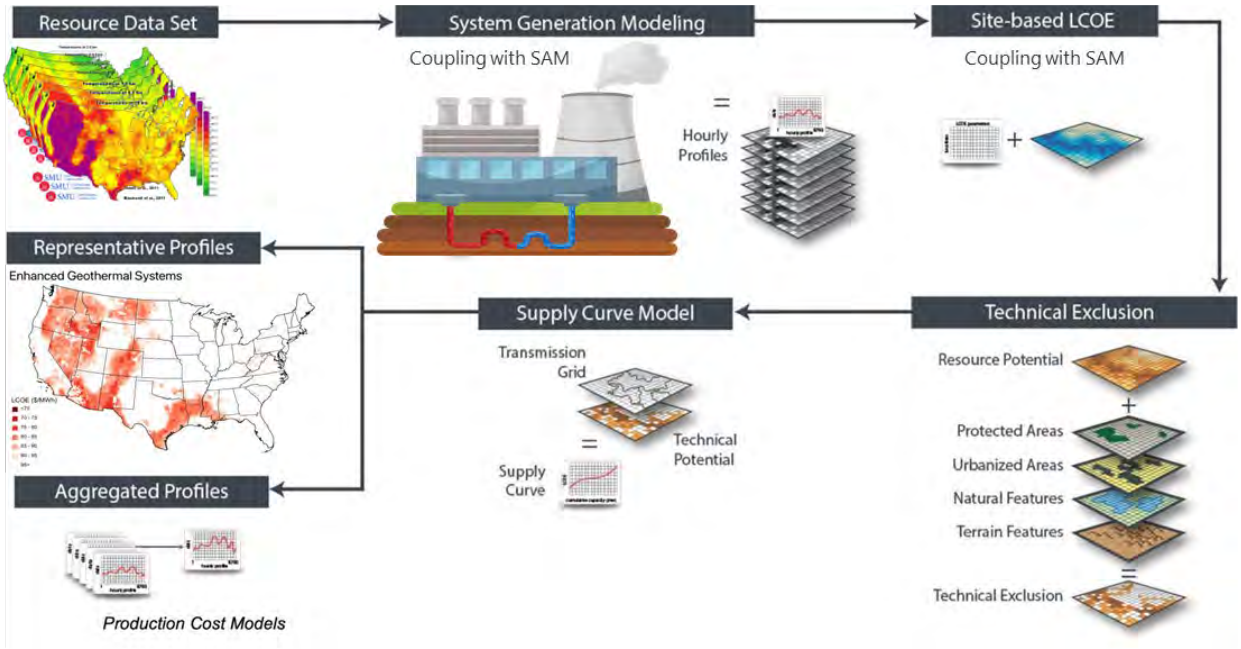

Figure 2: The reV model methodology implemented to estimate resource potential and generate geospatially-distributed cost profiles

2. Workshop Discussions

The NREL Geothermal Power Systems Analysis Workshop discussions were centered on four main topics:

- GETEM and SAM model updates
- The ATB process and geothermal representation in the ATB
- Geothermal representation in ReEDS
- Geothermal resource potential estimation with reV

The following subsections describe the major talking points around the highlighted topics.

2.1 GETEM and SAM Model Updates

2.1.1 Resource Temperature Limit on Binary Cycles

A major technical consideration that was discussed is how the GETEM model implements binary plant operations. The Excel-based GETEM model intrinsically assumes that binary plants do not operate beyond 200°C (G. L. Mines, 2016). Hence, once a system specification greater than 200°C is imputed into the model, it assumes a flash-based power cycle. According to Mines (2016), the reason for this restriction is that downhole production pump technology at the time GETEM was developed had a 200°C operational limit (G. L. Mines, 2016). GETEM assumes that flash plants have sufficient reservoir pressure and do not require production pumps. Also, the temperature-based correlations for the binary plant cost estimation in GETEM has this same 200°C limit. This temperature-based partitioning between flash and binary cycles is not an actual physical constraint. Multiple plants worldwide run on organic Rankine cycles (ORCs) that utilize geothermal energy resources above 200°C. Therefore, Excel-GETEM appears to characteristically underestimate the

This report is available at no cost from the National Renewable Energy Laboratory (NREL) at www.nrel.gov/publications.

potential of binary cycles at high temperatures. The GETEM in SAM model accommodates simulations of binary power plants with resource temperatures above 200°C. It also accommodates flash plant operations at temperatures below this threshold. However, since it is inherently based on GETEM, there is a need to update the plant cost correlations in SAM to accommodate higher resource temperatures.

2.1.2 Exploration Drilling Success Rates

Hydrothermal resource exploration comes with its inherent resource confirmation uncertainty. In the western U.S, a vast number of convection-dominated hydrothermal plays that can be traced back to surface expressions (e.g., geysers, fumaroles, and hot springs) have been discovered. Hence, to increase the potential for resource discovery, drilling for "blind" resources is set to become the norm in future hydrothermal exploration, just as in the oil and gas industry today. This comes with an increased requirement for exploration (geological, geochemical, and geophysical) data acquisition that culminates in a test drilling phase where full-size wells are drilled to confirm resource availability (heat, permeability, and suitable reservoir fluid volume) and productivity. Generally, for hydrothermal systems, the global average historical success rate for the first full-size well has been reported as 50%, increasing to 59% for the first five wells (Allen et al., 2013). GETEM currently defaults to a 50% success rate (53% was used in the 2023 ATB). Wells are deemed unsuccessful for several reasons, including drilling dry holes, loss of mechanical integrity during drilling, inadequate pressure and temperature, low productivity, and geochemical considerations (corrosion and scaling tendencies) (Allen et al., 2013). With significant improvement in data collection before test well drilling, data-enhanced conceptual model development, and advancements in drilling technology (e.g., sidetracking), success rate estimations for hydrothermal, and by extension EGS, projects need to be revisited. Determining a representative value for exploration drilling success may require an updated study similar to Allen et al. (2013) and expert consultation on additional costs incurred to reducing well failure rates.

2.1.3 Beyond the Levelized Cost of Electricity (LCOE)

The LCOE is a metric that expresses the discounted cost to install and operate a geothermal plant over its generation life cycle. It is typically used to compare cost competitiveness from one geothermal project to another and between geothermal and other renewable energy technologies. It is also used to determine the contract electricity price for a PPA. Because it is strictly project-based, it does not account for the system value of the plant as a service provider to the electric grid (Mai et al., 2021; DOE, 2024a). Specifically, the ability of geothermal plants to offer both firm and dispatchable electricity (among other ancillary services) to the grid is not captured within the definition of the LCOE. The LCOE does not also account for avoided costs (e.g., additional generation and transmission costs) that could have been incurred to meet demand. Other metrics that have been proposed include the Levelized Value of Electricity (LVOE), Net Value of Electricity (NVOE), Net Value of Capacity (NVOC), Profitability-Adjusted LCOE, Levelized Avoided Cost of Electricity (LACE) and Cost of Valued Energy (COVE) (EIA, 2017; Simpson et al., 2020; Mai et al., 2021; Loth et al., 2022). Both NVOE and LACE account for only the system value leaving out the effect of cost. Others account for both system cost and value with varying degrees of complexity in their estimation. GETEM only considers LCOE and does not have the capability to estimate value-derived revenues. Although SAM calculates LCOE, it also has a robust financial model that can estimate cost- versus value-derived metrics such as return on investment

This report is available at no cost from the National Renewable Energy Laboratory (NREL) at www.nrel.gov/publications.

(ROI). Therefore, once a suitable metric beyond LCOE is established for geothermal, it should be implementable in SAM.

2.1.4 Other Discussion Points

We have summarized other discussion points that were raised during the GETEM in SAM session in Table 1. These relate to both performance- and cost-based parameters.

Table 1: Summary of other discussion points in the GETEM in SAM session

Discussion Point	Excel-GETEM	GETEM in SAM
Investment tax credits (ITC) and production tax credit (PTC)	Not accounted for	ITC and PTC can be included in the estimation of LCOE and in financial modeling. Other similar tax credits and incentives can be accommodated.
Reservoir modeling	No capabilities	No implicit reservoir model. However, SAM has the Gringarten model for fractured systems that can be used to determine EGS reservoir performance. Reservoir simulation results (pressure and temperature timeseries) can be imported as CSV files from other modeling software.
Ability to incorporate hybrid models e.g., solar photovoltaic (PV) /concentrating solar thermal-geothermal hybrids	No direct capabilities. Can model the geothermal part of a hybrid system	The current hybrid model just implemented in the latest SAM version is for PV-wind-battery hybrid systems. Future SAM versions could incorporate hybrid models by leveraging TEA models developed within GTO's Hybrids Portfolio.
Imputing actual reservoir performance and plant generation data	No capabilities	SAM has an additional module for a "Generic" system. In the current Geothermal module, reservoir temperature timeseries can be uploaded into SAM.
Estimating the system value of carbon emissions reduction	Determining the cost of carbon and carbon offsets is beyond the TEA scope of the model	Determining the cost of carbon and carbon offsets is beyond the TEA scope of the model. However, SAM is sufficiently flexible to accommodate financial calculations that include cashflows from carbon credits.

2.2 Geothermal Representation in the ATB

2.2.1 Next-Generation Technologies

Next-generation geothermal technologies like EGS and closed-loop geothermal (CLG) are gaining traction in terms of technology development and a defined pathway towards commercialization. Currently, the ATB accounts for conventional hydrothermal systems and next-generation EGS (as Near-Field and Deep EGS). Near-Field EGS resources are defined as brownfields that are proximal to an existing hydrothermal resource. A case in point is Fervo's EGS development in the Blue

This report is available at no cost from the National Renewable Energy Laboratory (NREL) at www.nrel.gov/publications.

Mountain Geothermal field in Nevada (Norbeck & Latimer, 2023). Deep EGS resources in the ATB are defined as greenfields that have not been previously developed and are geologically conduction-dominated plays.

CLG systems are not currently represented in the ATB. Several factors have constrained their inclusion in the ATB. The first is technology standardization. Multiple CLG system designs have been proposed and have been broadly categorized based on the loop design into coaxial/pipe-pipe/downhole heat exchanger (with or without a lateral), U-loop (single-, double-, or multi-lateral), and the Eavor Loop. Technology categorization that is strictly based on loop design may create standardization complexities as new loop designs emerge. The second factor is the definition of a representative plant size for each loop design. Can we assume similar plants sizes as in hydrothermal and EGS? A third factor is that, based on previous results from past TEA, LCOE for CLG systems could range from 2,200 $/MWh for the coaxial loop to 70 $/MWh for the Eavor Loop (Beckers et al., 2022; Beckers & Johnston, 2022). There may be a requirement to prioritize more competitive designs for representation in the ATB.

Superhot rock/supercritical geothermal, which targets resources above 375°C, is also not currently represented in the ATB. The technology is still emerging with the first-of-a-kind (FOAK) demonstration to be implemented in Newberry, Oregon as part of GTO's EGS Pilot Demonstrations portfolio (DOE, 2024b). There is presently no comprehensive TEA model for superhot systems due to the uncertainty in assessing costs for major project phases including drilling and completion, stimulation, and power plant construction. Future iterations of the ATB will accommodate superhot rock geothermal as data from the Newberry project and other pilot projects become available.

2.2.2 Effect of Plant Size

Plant size is an important factor in the estimation of lifecycle costs of a geothermal project. Generally, larger power plants tend to enjoy the benefits of economies of scale. Allowing for less intensive costs (on a per-kW basis) for leasing and permitting, project infrastructure, project financing, and operation and maintenance. From a thermodynamic perspective, larger plants could also benefit from higher energy conversion efficiency (at higher resource temperatures) and better overall plant efficiency. The economics of next-generation technologies like EGS can be improved at larger plant size deployments. The 2023 ATB assumes the following plant sizes for EGS technologies: Deep EGS = 25 MW (Binary) and 30 MW (Flash); Near-Field EGS = 30 MW (Binary) and 40 MW (Flash) based on the classification by Mines (2013). EGS developers are targeting 100-MW commercial plant build outs. Although a 100-MW plant size is used in the EGS Advanced Scenario ATB for a 2035 deployment year, it is currently too aggressive for a mid-case (Moderate) scenario. However, it may be considered in a future ATB once a FOAK 100-MW EGS plant is operational. In the 2024 ATB, we will revise the EGS plant sizes to 40 MW for both Deep and Near-Field EGS to keep pace with technology trends.

2.2.3 Capacity Factor

The capacity factor is a major plant performance indicator in the ATB and a direct input to the calculation of project capital expenditure (CAPEX). In the ATB, geothermal capacity factor is assumed to be constant throughout the project lifecycle but differs by plant technology (80% for binary for 90% for flash) (NREL, 2024). These capacity factor estimations are based on historical

This report is available at no cost from the National Renewable Energy Laboratory (NREL) at www.nrel.gov/publications.

plant data and may be heavily affected by the performance of legacy hydrothermal developments that are currently producing way below their designed plant output capacities. A revision of capacity factor estimation that takes account of improvement in air-cooled binary cycle technology and plant availability would require extensive input from geothermal plant operators. Further discussion on this topic is planned for a follow-on workshop this summer.

2.2.4 Technology Maturation

The ATB categorizes technologies as either "mature" or "nascent". Mature technologies are defined as those with a representative plant in operation or under construction in the United States in the base year (i.e., 2021 for the 2023 ATB) (NREL, 2023). Technologies outside the maturity definition are classified as nascent. Over time, hydrothermal technologies have been classified as mature while EGS are nascent. From an ATB perspective, the FOAK commercial EGS project developed in 2023 does not precisely fit the definition of mature technology in the ATB because it did not lead to the build out of a new power plant. Two horizontal wells were drilled, completed, and stimulated, and the resulting flow was tied back to an existing geothermal plant (Norbeck & Latimer, 2023). Future ATB iterations may need to account for this case by defining a mid-case technology definition as this may be the technology commercialization pathway for Near-Field EGS projects.

2.2.5 Geothermal Learning Rates

Since the 2023 ATB, we have adopted a learning curve approach to determining future costs of geothermal technology development scenarios. An explanation of this approach can be found in the ATB documentation (NREL, 2024). Essentially, a single factor learning curve that expresses the power-law relationship between cumulative capacity and cost was used to determined future capital costs beyond the base year to the full deployment year of the Moderate and Advanced scenarios (i.e., 2035). The learning rate, which determines the slope of the curve, expresses the rate at which technologies adopt learning by doing practices to increase capacity and reduce cost. The assumptions for geothermal learning rates are shown in Table 2. The 13% learning rate for the hydrothermal Moderate scenario was derived from historical drilling and completion learning rates in the unconventional oil and gas industry (Fukui et al., 2017). The EGS Moderate learning rate was derived from the low-end approximation for learning rates found in the study by Latimer & Meier (2017) that compiled at historical learning rates in both geothermal and oil and gas projects. The 30% rates for the Advanced EGS and hydrothermal are based on the high-end estimation of learning rates found in the same study (Latimer & Meier, 2017). In a recent paper by El-Sadi et al. (2024), a 35% in-project learning rate has been achieved so far in the Cape Station, Milford, Utah drilling campaign (El-Sadi et al., 2024). This in-project improvement can form a basis for reevaluating the inter-project learning rate assumptions in future ATB efforts.

Table 2: Learning rate assumptions used in the 2023 ATB

Scenario	Base Year–2035	2035–2050
Moderate Scenario	13% (hydrothermal), 18% (EGS)	0.5% annual cost reduction
Advanced Scenario	30%	0.5% annual cost reduction

This report is available at no cost from the National Renewable Energy Laboratory (NREL) at www.nrel.gov/publications.

2.3 Geothermal Representation in ReEDS

2.3.1 Classification of Geothermal Resources

The ATB classifies geothermal resources as hydrothermal, Near-Field EGS, and Deep EGS with a resource temperature dependent tie back to a binary or flash cycle. In capacity expansion modeling in ReEDS using defined standard scenarios (Gagnon et al., 2024), this classification obscures the high-value and low-cost sites on the supply curve that are competitive with other renewable technologies. Hence, a new temperature-based resource classification for geothermal in ReEDS that could elucidate these high-value sites was discussed at the workshop. Table 3 below shows the 10 resource classes. This applies to each resource type – hydrothermal, Near-Field EGS, and Deep EGS. A comment was made at the workshop on the skewness of the temperature bins towards higher temperature resources with lower site counts. Hence, it was recommended that the bin size should be proportional to the site counts or available resource count within each class.

Table 3: Temperature-based resource classes for geothermal in ReEDS

Resource Class	Bin Lower Bound (Resource Temp, °C)	Bin Upper Bound (Resource Temp, °C)
1	>325	None
2	>300	325
3	>275	300
4	>250	275
5	>225	250
6	>200	225
7	>175	200
8	>150	175
9	>125	150
10	0	125

2.5 Geothermal Resource Potential Estimation with reV

Discussions during the workshop on the reV model were limited to questions about understanding how the model works and how to improve data collection on estimating resource potential at higher geospatial resolution for both hydrothermal and EGS. For example, the reV model uses the temperature at depth and thermal conductivity data layers for both hydrothermal and EGS resources. Since hydrothermal units are more convection-dominated than EGS, this increases the uncertainty of estimating hydrothermal resource potential with reV since it is solely based on conductive heat flow. There is a need for more high-resolution convective heat flow data to characterize hydrothermal resource potential at national scale.

3. Outcomes and Future Plans

The NREL Geothermal Power Systems Analysis Workshop exposed areas for improvement in both modeling capabilities and scope. Discussions covered TEA modeling with GETEM and SAM, geothermal representation in the ATB, scenarios analysis modeling with ReEDS, and resource potential estimation and geospatial representation in the reV model. Participants at the workshop were fully engaged and provided suggestions on model improvement, especially in the

This report is available at no cost from the National Renewable Energy Laboratory (NREL) at www.nrel.gov/publications.

representation of next-generation geothermal systems, including closed-loop and superhot rock geothermal. As these next-generation technologies become mainstream, opening a new frontier in dispatchable and flexible geothermal operations, geothermal power analysis models will be required to represent crosscutting performance, cost, and value of geothermal to the electric grid. A follow-on workshop is planned for this summer with a focus on improving and updating assumptions on various phases of a geothermal project lifecycle in the GETEM in SAM model.

Acknowledgement

This work was authored by the National Renewable Energy Laboratory, operated by Alliance for Sustainable Energy, LLC, for the U.S. Department of Energy (DOE) under Contract No. DE-AC36-08GO28308. Funding was provided by the U.S. Department of Energy Office of Energy Efficiency and Renewable Energy (EERE) Geothermal Technologies Office (GTO). The views expressed in the article do not necessarily represent the views of the DOE or the U.S. Government.

REFERENCES

Allen, M., Avato, P. A., Gehringer, M., GeothermEx, Harding-Newman, T., Levin, J., Loksha, V. B., Meng, Z., Moin, S., Morrow, J., Oduolowu, A. O., Pantelias, A., & Sanyal, S. K. (2013). Success of geothermal wells: A global study (Other Environmental Study 78230). World Bank Group. https://documents1.worldbank.org/curated/en/305681468168834775/pdf/782300WP0Succe00Box0377330B0PUBLIC0.pdf

Augustine, C., Fisher, S., Ho, J., Warren, I., & Witter, E. (2023). Enhanced Geothermal Shot Analysis for the Geothermal Technologies Office (NREL/TP-5700-84822). National Renewable Energy Laboratory. https://doi.org/10.2172/1922621

Beckers, K. F., & Johnston, H. E. (2022). Techno-Economic Performance of Eavor Loop 2.0 (NREL/CP-5700-81887). Stanford, CA: Stanford University. https://www.osti.gov/biblio/1972816

Beckers, K. F., Rangel-Jurado, N., Chandrasekar, H., Hawkins, A. J., Fulton, P. M., & Tester, J. W. (2022). Techno-Economic Performance of Closed-Loop Geothermal Systems for Heat Production and Electricity Generation. Geothermics, 100, 102318. https://doi.org/10.1016/j.geothermics.2021.102318

DOE. (2016). GETEM - Geothermal Electricity Technology Evaluation Model [Computer software]. U.S. DOE. https://www.energy.gov/eere/geothermal/geothermal-electricity-technology-evaluation-model

DOE. (2019). GeoVision: Harnessing the Heat Beneath Our Feet (DOE/EE–1306). U.S. Department of Energy. https://doi.org/10.15121/1572361

DOE. (2024a). Pathways to Commercial Liftoff: Next-Generation Geothermal Power. Department of Energy. https://liftoff.energy.gov/wp-content/uploads/2024/03/LIFTOFF_DOE_NextGen_Geothermal_v14.pdf

This report is available at no cost from the National Renewable Energy Laboratory (NREL) at www.nrel.gov/publications.

DOE. (2024b, February 13). Biden- Harris Administration Invests $60 Million to Expand Clean, Renewable Geothermal Energy. Energy.Gov. https://www.energy.gov/articles/biden-harris-administration-invests-60-million-expand-clean-renewable-geothermal-energy

EIA. (2017). Levelized Cost and Levelized Avoided Cost of New Generation Resources in the Annual Energy Outlook 2017. U.S. Energy Information Administration. https://www.eia.gov/outlooks/archive/aeo17/pdf/electricity_generation.pdf

El-Sadi, K., Gierke, B., Howard, E., & Gradl, C. (2024, February 14). Review Of Drilling Performance In A Horizontal EGS Development. Proceedings, 49th Workshop on Geothermal Reservoir Engineering. Stanford Geothermal Workshop, Stanford University, Stanford, CA. https://pangea.stanford.edu/ERE/db/GeoConf/papers/SGW/2024/Elsadi.pdf

Fukui, R., Greenfield, C., Pogue, K., & van der Zwaan, B. (2017). Experience curve for natural gas production by hydraulic fracturing. Energy Policy, 105(June 2017), 263–268. https://doi.org/10.1016/j.enpol.2017.02.027

Gagnon, P., Pham, A., Cole, W., Awara, S., Barlas, A., Brown, M., Brown, P., Carag, V., Cohen, S., Hamilton, A., Ho, J., Inskeep, S., Karmakar, A., Lavin, L., Lopez, A., Mai, T., Mowers, J., Mowers, M., Murphy, C., … Williams, T. (2024). 2023 Standard Scenarios Report: A U.S. Electricity Sector Outlook (NREL/TP-6A40-87724). National Renewable Energy Laboratory. https://www.nrel.gov/docs/fy24osti/87724.pdf

Latimer, T., & Meier, P. (2017). Use of the Experience Curve to Understand Economics for At-Scale EGS Projects. Stanford University. https://pangea.stanford.edu/ERE/pdf/IGAstandard/SGW/2017/Latimer.pdf

Loth, E., Qin, C., Simpson, J. G., & Dykes, K. (2022). Why we must move beyond LCOE for renewable energy design. Advances in Applied Energy, 8, 100112. https://doi.org/10.1016/j.adapen.2022.100112

Mai, T., Mowers, M., & Eurek, K. (2021). Competitiveness Metrics for Electricity System Technologies (NREL/TP-6A20-72549). National Renewable Energy Lab. (NREL), Golden, CO (United States). https://doi.org/10.2172/1765599

Mines, G. (2013, 22). Geothermal Electricity Technology Evaluation Model (GETEM). Geothermal Technologies Office 2013 Peer Review, Washington, D.C. https://energy.gov/sites/prod/files/2014/02/f7/mines_getem_peer2013.pdf

Mines, G. L. (2016). GETEM User Manual (Manual INL/EXT-16-38751). Idaho National Laboratory. https://workingincaes.inl.gov/SiteAssets/CAES%20Files/FORGE/inl_ext-16-38751%20GETEM%20User%20Manual%20Final.pdf

Norbeck, J. H., & Latimer, T. (2023). Commercial-Scale Demonstration of a First-of-a-Kind Enhanced Geothermal System. https://eartharxiv.org/repository/view/5704/

NREL. (2023). Annual Technology Baseline - Definitions. https://atb.nrel.gov/electricity/2023/definitions

NREL. (2024). 2024 NREL Annual technology Baseline—Geothermal. Annual Technology Baseline. https://atb.nrel.gov/electricity/2024/geothermal

Pinchuk, P., Thomson, S.-M., Trainor-Guitton, W., Buster, G., & Maclaurin, G. (2023). Development of a Geothermal Module in reV: Quantifying the Geothermal Potential while

This report is available at no cost from the National Renewable Energy Laboratory (NREL) at www.nrel.gov/publications.

Accounting for the Geospatial Intersection of the Grid Infrastructure and Land Use Characteristics (NREL/CP-5700-87163). Davis, CA: Geothermal Resources Council. https://www.osti.gov/biblio/2290263

Robins, J., Kolker, A., Flores-Espino, F., Pettitt, W., Schmidt, B., Beckers, K. F., Pauling, H., & Anderson, B. (2021). 2021 U.S. Geothermal Power Production and District Heating Market Report (NREL/TP-5700-78291). National Renewable Energy Laboratory. https://dx.doi.org/10.2172/1808679

Simpson, J., Loth, E., & Dykes, K. (2020). Cost of Valued Energy for design of renewable energy systems. Renewable Energy, 153, 290–300. https://doi.org/10.1016/j.renene.2020.01.131

System Advisor Model (SAM) (Version 2022.11.21). (2022). [Computer software]. National Renewable Energy Laboratory. sam.nrel.gov

This report is available at no cost from the National Renewable Energy Laboratory (NREL) at www.nrel.gov/publications.

Whispers of a New Frontier for Safe and Profitable Geothermal Anywhere

Luke P. Frash

Los Alamos National Laboratory

Keywords

Fracture Caging, CGS, EGS, AGS, Reservoir Engineering

ABSTRACT

The potential of geothermal power to fulfill the energy needs for all nations persists, despite not yet having been achieved. To promote its development, attention is generally given to solving those challenges that are tractable and compatible with conventional thinking, such as decreasing the cost of drilling. Meanwhile, two of the most crucial problems are often bypassed due to their complexity: these being the need for prevention of induced seismicity and the need for predicting performance uncertainty. Recently, we developed a stochastic design tool to meet the challenge of uncertainty assessment and to investigate the potential of fracture caging to control the risk of induced seismicity. Here, we use this tool to investigate the feasibility of full-scale development of hot dry rock resources for clean baseload power generation. We investigate various strategies for development that include advanced, enhanced, and caged geothermal systems. We investigate economics with consideration of drilling depth, thermal gradient, and number of wells. Our work predicts that it is possible to safely and profitably develop geothermal nearly anywhere using the currently available tools. However, achieving this will require a shift in thinking.

1. Introduction

Numerous studies investigated the future of geothermal energy beyond conventional convective systems (Tester et al., 2006; Hamm et al., 2020). They predicted that deep hot dry rock resources (Duchane and Brown, 2002) can yield from 60 to 100 GW of electric power as long as the needed technologies could be developed and made affordable. The basis of this premise centered on the application of hydraulic fracturing to create sufficient surface area for economic heat extraction in any reservoir that otherwise would not be able to facilitate enough flow for production (Gringarten et al., 1975). In addition, this premise assumes that the required high-temperature tools for well drilling, stimulation, and flow control can be developed. More crucially, this premise requires the development of seismic risk mitigation technologies, that are currently limited to monitoring based approaches (Majer et al., 2012) and limits on injection volumes (McGarr, 2014). However, our

experience shows that these methods are unreliable even if they are considered best practices (Kim et al., 2018; Ellsworth, 2013).

Proposed new approaches to seismicity control include cyclic soft stimulation (Hofmann et al., 2019) and fracture caging (Frash et al., 2018; Frash et al., 2021). Cyclic soft stimulation involves injection with oscillating flow and applies only during fracture creation. It is based on the idea that fatigue, thermal effects, and poromechanical effects can aid fracture propagation to ultimately reduce the net pressure needed to grow fractures and hence reduce the likelihood of triggering a large seismic event. Fracture caging involves drilling an array of boundary wells around a target reservoir before fluid injection to then intercept and contain both fluid flow and seismicity. The method entails drilling multiple wells and is anticipated to be employed throughout the life of a geothermal system. Yet another proposed method to reduce the risk of seismicity is closed loop geothermal systems (Beckers et al., 2022), also called advanced geothermal systems, using a looped array of wells with fluid is circulated only through these wells. In this case, no fractures would be required but the drilling costs are likely to be high because radial heat transfer to wells is much slower than bi-linear heat transfer to fractures. This stems from the expectation that hot dry rock systems will be thermal conduction limited during long-term heat recovery.

In this study, the technoeconomic performance of deep hot dry rock systems is evaluated using a fast simplified-physics model named GeoDT (Frash, 2021). This tool enables Monte-Carlo ensemble modeling to better quantify uncertainty for the performance of various reservoir designs, all with the goal of seeking an optimized, reliable, and economic approach to harvest geothermal energy. Here, we investigate the techno-economics of closed-loop Advanced Geothermal Systems (AGS), sand-propped Enhanced Geothermal Systems (EGS), and new hydraulic fracture Caged Geothermal Systems (EGS). Our analysis considers varied well depths, thermal gradients, and numbers of wells. The model includes well placement, hydraulic stimulation, heat recovery, power conversion, and economics to then estimate the net present value for inter-design comparison. We will show that primary details for maximized performance include reservoir temperature, in-situ stress direction, proppant permeability, number of wells, well spacing, and number of fractures.

2. Model Setup

Geothermal Design Tool (GeoDT) is a fast simplified-physics screening tool that is intended for rapid assessment and design optimization for well and fracture dominated geothermal systems. It is not meant for modelling conventional convective geothermal systems. This study investigates the cost and performance of AGS, EGS, and CGS (Fig. 1).

GeoDT uses a sequentially coupled solver (Fig. 2) to estimate the impact of design elements, in-situ stress, natural fractures, hydraulic stimulation, fluid circulation, heat transfer, thermal-electric power conversion, and economics. Examples of the included physics are stress-dependent fracture conductivity, shear stimulation and dilation, induced seismicity, and transient heat flow from the rock to the fluid. The solver prioritizes speed over accuracy with the intent of informing decision making in a timely manner that requires minimal expertise and effort. Most simulations complete in less than 20 seconds using a generic desktop computer (Frash et al., 2023).

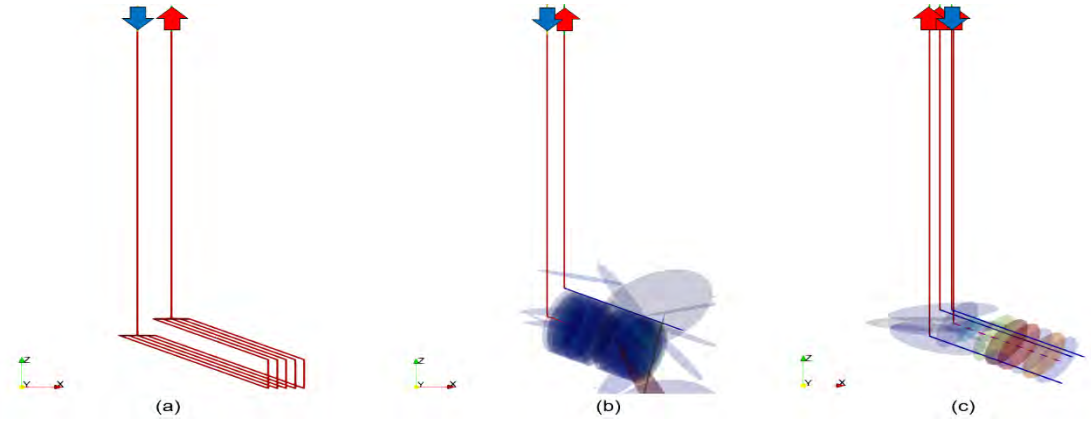

Figure 1: Model concepts for closed loop AGS, sand propped multi-stage EGS, and fracture caged CGS. The details of each design were varied to optimize performance and cost, seeking maximum net present value.

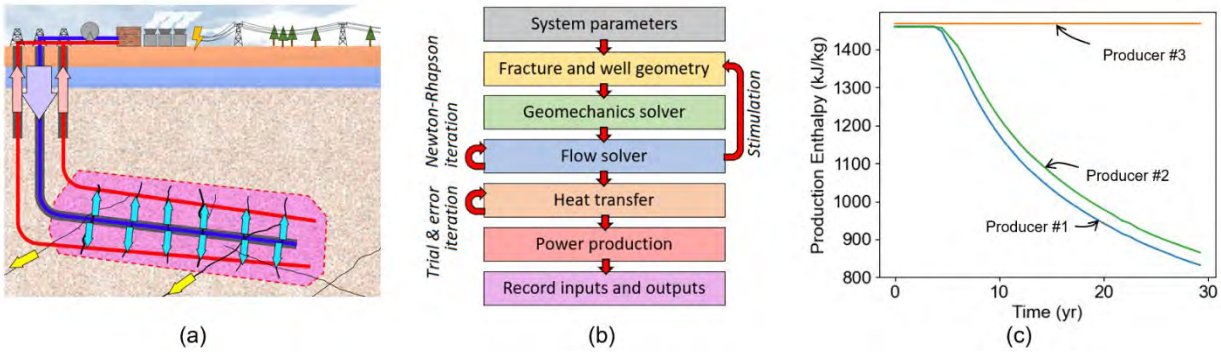

Figure 2: GeoDT solves the technoeconomic performance of AGS, EGS, and CGS using a sequentially-coupled solver (b) based on a 3D stress-dependent network of wells and fractures. Its goal is to rapidly estimate the performance curve (c) of a given design (a) in an uncertain subsurface environment.

The model parameters needed to define the wells were many (Table 1). These included number of wells, flow rates, back pressures, well diameters, lengths, depths, casing thicknesses, number of perforation clusters, perforation diameters, stimulation volume, sand concentration in the frac fluid, proppant permeability, fluid viscosity, and more. The model parameters needed to setup the reservoir were even more numerous. The included rock thermal gradient, stress regime, ambient temperature, rock density, elastic properties, fracture properties, fracture stimulation properties, and more. In comparison, the parameters for the economic model were quite simple. For our base case, we use a parameter set from an earlier study for greenfield geothermal energy development. The source of each model value is given by the references therein (Frash et al., 2024). Elaboration on the details of how GeoDT functions, its validation, and why these model parameters were selected is beyond the scope of this study but can be found in cited references. In the forthcoming sections, we combine previous findings and new results to elucidate the key reservoir parameters that control the economics of AGS, EGS, and CGS to reveal that several important and commonly held assumptions are likely to be false. This will ultimately lead to our current conclusion that a shift in thinking is needed to achieve prolific, safe, and profitable geothermal anywhere.

3. Well and Stress Orientation

One of the first studies that used GeoDT investigated the likelihood of successfully developing a reservoir using CGS without any site-specific information being known about the subsurface

(Frash, 2022). Neither AGS nor EGS had yet been implemented in this older version of GeoDT. The study completed a Monte-Carlo ensemble model of 50,000 fully random scenarios followed by 10,000 scenarios for the optimized design having 7 to 9.4 km depth, 45 to 55 °C/km gradient, injection at 0.030 to 0.046 m^3/s, 3 to 6 production wells, and wells drilled within 45° of the minimum principal stress which was set as North in this scenario set. The last detail was critical for making sense of the results and for increasing the chance of achieving high power output from

Table 1. Base model parameters (Frash et al., 2024).

Parameter	Variable	Min	Max	Unit	Parameter	Variable	Min	Max	Unit
Production Well Count	w_count	1	4	ea	Well Inclined Azimuth	w_azimuth	75	75	deg
Well Phase	w_phase	90	270	deg	Well Inclined Dip	w_dip	25	25	deg
Perforation Clusters	perf_clusters	3	48	ea	Well Inclined Proportion	w_proportion	0.8	0.8	m/m
Sand to Water Concentration	sand	0	0.044	m3/m3	Well Inclined Length	w_length	2000	2000	m
Well Intervals	w_intervals	1	16	ea	Casing Inner Radius	ra	0.1397	0.1397	m
Well Spacing	w_spacing	50	700	m	Casing Outer Radius	rb	0.1524	0.1524	m
Target Injection Rate	Qinj	0.01	1.00	m3/s	Borehole Radius	rc	0.1778	0.1778	m
Reservoir Size (Half)	size	2500	2500	m	Well Hydraulic Roughness	rgh	80	80	
Model Thermal Gradient?	gradient	TRUE	TRUE	T/F	Cement Thermal Conductivity	CemKt	2	2	W/m2
Reservoir Depth	ResDepth	6100	6100	m	Cement Specific Heat Capacity	CemSv	2000	2000	kJ/m3-K
Thermal Gradient	ResGradient	36	50	C/km	Generator Efficiency	GenEfficiency	0.85	0.85	
Rock Density	ResRho	2550	2950	kg/m3	Lifespan of Production	LifeSpan	15	15	yr
Rock Thermal Conductivity	ResKt	2.27	3.58	W/m2	Production Wellhead Pressure	p_whp	1	1	MPa
Rock Specific Heat Capacity	ResSv	0.74	1.2	kJ/kg-K	Injection Temperature	Tinj	20	90	C
Surface Temperature	AmbTempC	0	0	C	Convection Coefficient	H_ConvCoef	3	3	
Surface Pressure	AmbPres	0.101	0.101	MPa	Water Density	PoreRho	920	932	kg/m3
Rock Young's Modulus	ResE	55	62	GPa	Water Viscosity	Poremu	0.2	0.2	cP
Rock Poisson's Ratio	Resv	0.26	0.4		Proppant Pack Conductivity	kf	10	10	um2cm
Minimum Earth Stess Coef.	Ks3	0.3	0.8	Pa/Pa	Perforation Diameter	perf_dia	0.015	0.015	m
Intermediate Stress Coef.	Ks2	0.4	1.1	Pa/Pa	Perforations per Cluster	perf_per_cluste	3	3	
Minimum Stress Azimuth	s3Azn	60	90	deg	Production Well Drawdown	dPp	0	0	MPa
Azimuth's Uncertainty	s3AznVar	0.75	0.75	deg	Solver's Pressure Increment	dPi	0.02	0.02	MPa
Minimum Stress Dip	s3Dip	0	30	deg	Maximum Injection Pressure	pfinal_max	0.9	0.9	s3
Dip's Uncertainty	s3DipVar	0.75	0.75	deg	Fracture Friction Angle	phi	30	50	deg
Fracture Count Set 1	fNum	40	80		Fracture Cohesion	mcc	1	6	MPa
Fracture Count Set 2	fNum	20	40		Hydraulic Fracture Cohesion	hfphi	15	35	deg
Fracture Count Set 3	fNum	10	20		Hydraulic Fracture Friction Angle	hfmcc	0.1	0.4	MPa
Fracture Diameter	fDia	200	2000	m	Electric Sales	sales_kWh	0.1372	0.1372	$/kWh
Fracture Slip-Length Scaling	gamma	0.001	0.063	m/m	Drilling Cost	drill_m	2763.06	2763.06	$/m
Fracture Dilation-Slip Scaling	a	0	0.13	m/m	Drill Pad Cost	pad_fixed	5.90E+05	5.90E+05	$
Fracture Hydraulic-Dilation Scaling	N	0	2	m/m	Power Generation Cost	plant_kWe	2025.65	2025.65	$/kW
Fracture Compressibility	alpha	2.00E-09	1.00E-07	1/Pa	Exploration Cost (Geophysics)	explore_m	2683.41	2683.41	$/m
Proppant Compressibility	prop_alpha	2.00E-09	1.00E-07	1/Pa	Operation Cost (Maintenance)	oper_kWh	0.03648	0.03648	$/kWh
Fracture Initial Hydraulic Aperture	bh	1.00E-08	1.00E-04	m	Earthquake Penalty (Coefficient)	quake_coef	2.00E-04	2.00E-04	$/Mw
Boundary Hydraulic Aperture	bh_bound	1.00E-04	1.00E-03	m	Earthquake Penalty (Exponent)	quake_exp	5	5	$/Mw
Fracture Stranding Scale Factor	f_roughness	0.125	1	m/m					

the scenario set. Note that well orientation varied randomly from North to East and from horizontal to vertical. This covers the whole 3D range of well orientations because of geometric symmetry. For interpretation, the results were filtered and interpreted using box plots. Results from successful scenarios that achieved at least 20 MWe net power output are reproduced here (Fig. 3). More recent work builds on this foundation by assuming that a developer will measure the in-situ stresses to then drill wells parallel to the minimum principal stress. This direction will likely have uncertainty around ±20° (Fu et al., 2021; Kelley et al., 2024), but this is much better than nothing.

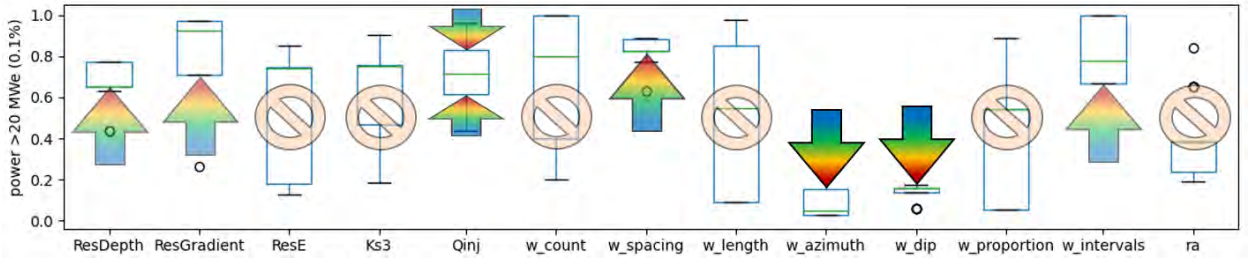

Figure 3: Boxplot showing correlations between CGS model inputs and high performance outcomes. Reservoir parameters were assumed to be unknown. The 0.1% of scenarios that achieved this performance mark showed a need for high temperatures (ResDepth and ResGradient), high injection rates (Qinj), large well spacing (w_spacing), and wells near-parallel to the minimum principal stress (w_azimuth and w_dip). Plotted values are normalized to the ranges used for model inputs (e.g., 4 km < ResDepth < 10 km). Arrows highlight trends and crosses highlight no-trends.

4. Strategy and Number of Wells

One of the top selling points for EGS is a minimized drilling effort where as few as two wells can be required to generate power. In a strong contrast, AGS proposes the opposite with maximized drilling length at depth to enhance total thermal output. In between, CGS proposes to drill a few more wells than EGS to achieve improved reservoir control and higher power output. Despite the commonly held assumptions, it is not obvious which of these three strategies will perform best. Likewise, the optimized approach for each strategy is not self-evident. Here, GeoDT is employed to investigate the optimization of each design and to compare each strategy.

To begin, let us consider a closed-loop AGS concept with a looped array of wells drilled sub-horizontally within a reservoir at 6 km depth and with 36 to 50 °C/km thermal gradient (Frash et al., 2024). This scenario is based on the greenfield GLADE geothermal drilling project near Fort Collins, CO. Next, lets fix all the well design variables except for the flow rate and the number of loops drilled into the reservoir (i.e., the number of wells). More specifically, we consider designs with 5, 13, and 25 loops (Fig. 4).

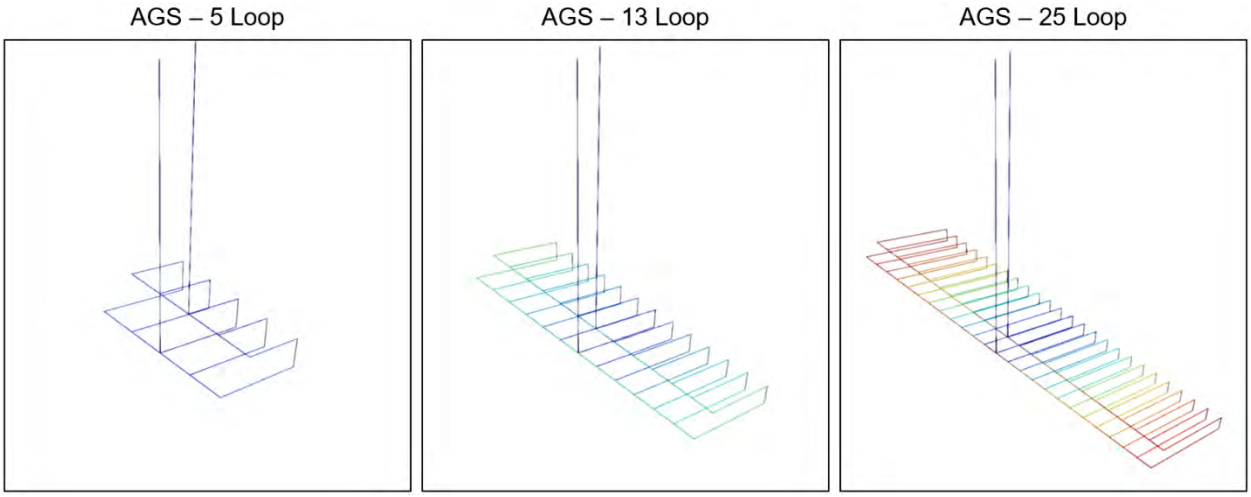

Figure 4: Closed-loop AGS designs having 5, 13, and 25 loops, 6000 m depth, and 2000 m long sub-laterals.

Each design was evaluated for 3,000 realizations to factor subsurface uncertainty into the results. These results can be displayed using color-scaled scatterplots to aid interpretation of the outputs that include timeseries data, 3D geometry, and a myriad of additional parameters (Fig. 5). Knowing that thermal performance is extremely sensitive to flow rate, these plots will all show flow on one axis. If the flow is too slow, the produced fluid will be cold by the time it reaches the surface. If the rate is increased, the fluid now becomes hot but could be uneconomic. Then if increased more, the produced fluid will cool faster over time. At the fastest rates, frictional losses become extreme so pumping power and pressures can become untenable. The optimal flow rate for peak sustained power production and peak economy will be dependent on AGS, EGS, and CGS design and the reservoir properties. In other words, a best estimate is needed to ensure that a given system performs at peak, but there will be irreducible uncertainty in this estimate. This study captures that uncertainty through its Monte-Carlo approach accompanied by design-based filtering of the results. Note that it is rarely useful to filter results by outcomes (e.g., net power production) because outcomes depend on uncontrollable rock properties. Instead, quantile statistics filtered by design decisions offer a better approach to identify promising designs (Fig. 6).

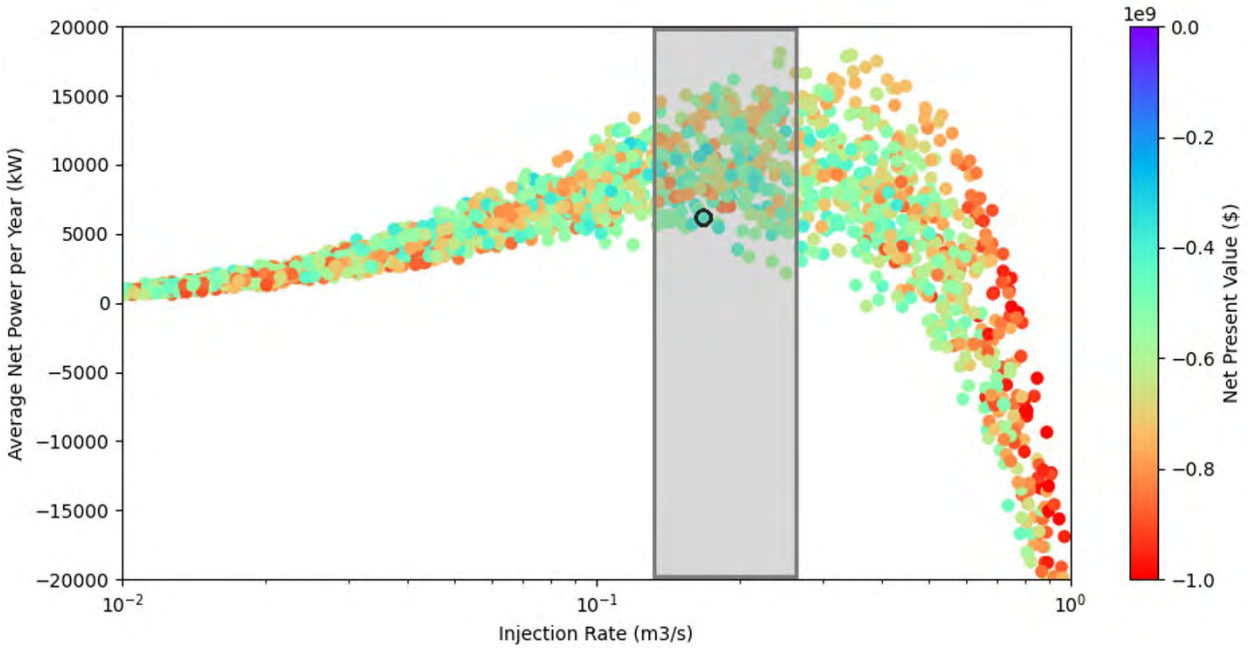

Figure 5: Example scatter plot of project net present value as a function of average net power production per year, being total generated power less pumping power over a 15 year lifespan in this example. Peak economy is achieved when the flow rate is optimized to produce the hottest fluid for the longest time at the highest rate. Optimum flow and design parameters were identified for every scenario by using model input ranges that were broad enough to assure that optima could be found.

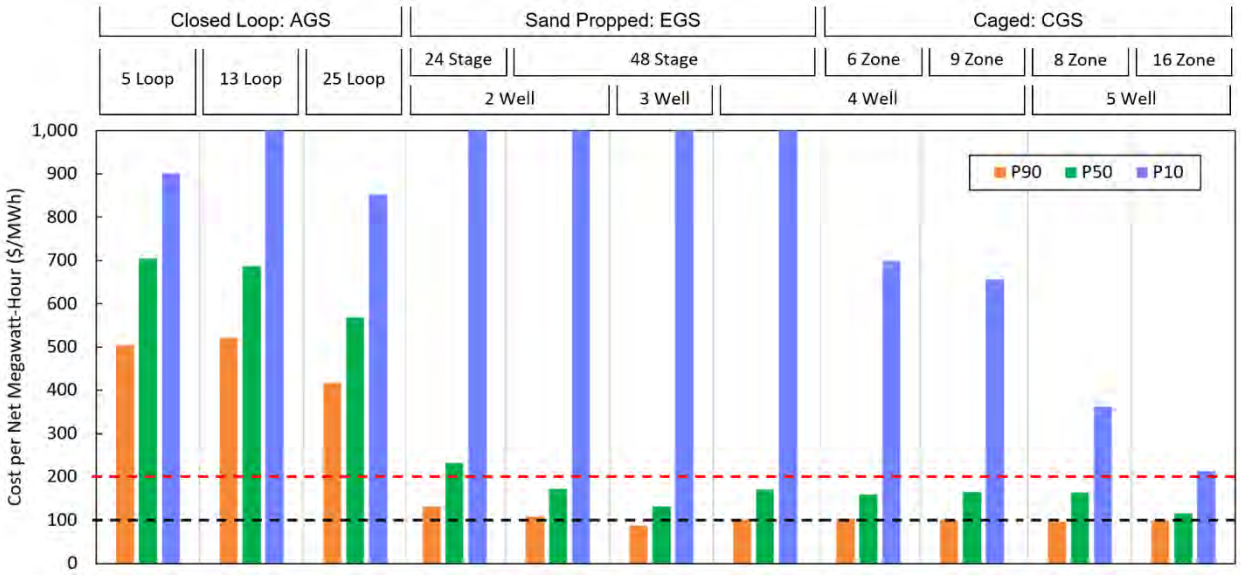

Figure 6: Comparison of the cost of electricity for AGS, EGS, and CGS with more than one design variant for each development strategy (e.g., number of wells). The lowest cost of electricity is achieved for 3-well 48-stage EGS. The most reliable and affordable cost of electricity is achieved with 5-well 16-zone CGS. The most affordable electricity from AGS is achieved with 25-loops. These quantile statistics are reaped from filtered data that isolated optimized flow rates and designs within each variant. This analysis included around 48,000 realizations, all obtained in about two weeks using GeoDT and a desktop computer. The result points a path forward to steer future high-fidelity modeling efforts by showing which development strategy is most likely to yield an economic outcome (Frash et al., 2024).

The execution of this effort yielded valuable insights regarding the potential of AGS, EGS, and CGS. At the foremost, the result shows that a minimum number of wells is not the most economic option. Instead, a low well count can actually increase the likelihood of project failure, leading to an elevated risk of the worst-case outcome. In the case of EGS, the worst-case outcome includes injection induced seismicity at larger than tolerable magnitudes. This prediction agrees with field experience where larger than tolerable earthquakes were observed in Basel, Landau, Soultz-sous-Forêts, and Pohang (Kim, 2018). Simpler models than GeoDT, such as Gringaten's, lack the ability to predict the likelihood of structural failures arising from poor fluid containment. The methods used in GeoDT permit a glimpse of these effects, but the results cannot and should not be assumed to be correct with respect to their specific values. In truth, reliable and accurate forecasts of seismic risk may never be possible because of the high uncertainty inherent to the subsurface.

Another key outcome from this effort was identification of the most promising designs for AGS, EGS, and CGS. For AGS, designs that maximized the number of loops (i.e., the length of the wells in the hot reservoir) worked best. In addition, AGS performed better when the loops were near horizontal because steeply dipping loops incur a mixture of heating and cooling effects which lowers the efficiency of the heat exchanger. However, too many loops will increase the risk of loss of access to the reservoir because a operational problems could cause damage to the vertical wells, meaning that the system has single point of failure which could result in a total loss of subsurface assets. For EGS, designs that maximized the number of stimulated fractures performed best. The models included attempts to improve flow uniformity through the fracture network using smaller casing perforations, tuned proppant permeability, and in-well zonal isolation, but these tricks came with an excessively increased pumping cost because they all required decreasing the conductivity

of the fractures. The optimized number of wells for EGS was found to be three, one injector and two producers. For CGS, four to five wells and designs that maximized the number of injection zones yield the best results. Unlike EGS, stimulation never tops in CGS so injection rates were never limited by downhole pressures. Also, unlike EGS, proppants were not injected in CGS to hold fractures open. The obvious drawback of this approach is perpetually high injection pressures and high flow rates yielding higher pumping losses, but the total achievable flow rate is higher so that makes up for the loss.

5. Depth and Thermal Gradient

Drilling for water, oil, gas, wastewater, and geothermal most often targets a specific geology at a known or estimated depth. Building on from this, it is expected that hot dry rock geothermal will do the same. However, the potential of a resource is linked to its temperature and the depth at which that temperature will be achieved may not be known, especially for greenfield resources. To investigate drilling strategy economics, we employ GeoDT to estimate the net present value of AGS, EGS, and CGS greenfield projects where the thermal gradient is unknown (Fig. 7; Fig. 8). The gradient for this analysis varies from 55 to 120 °C/km for well depths from 2 to 8 km. Results from this work reveal that flow rate and reservoir temperature have a first-order effect on economy, but well depth and geothermal gradient have a second order effect. This is intuitive in hindsight because higher temperatures are needed to achieve higher efficiency for the conversion of heat to electricity (Zarrouk and Moon, 2014). Today, only moderate drilling temperatures can be managed with a soft maximum of around 300 °C (572 °F). We note the common knowledge that elastomers tend to degrade above 200 °C and steel melts above 1300 °C, yet the model maximum temperature is 1200 °C. Thus, we can ignore results with temperatures above 300 °C for practical reasons.

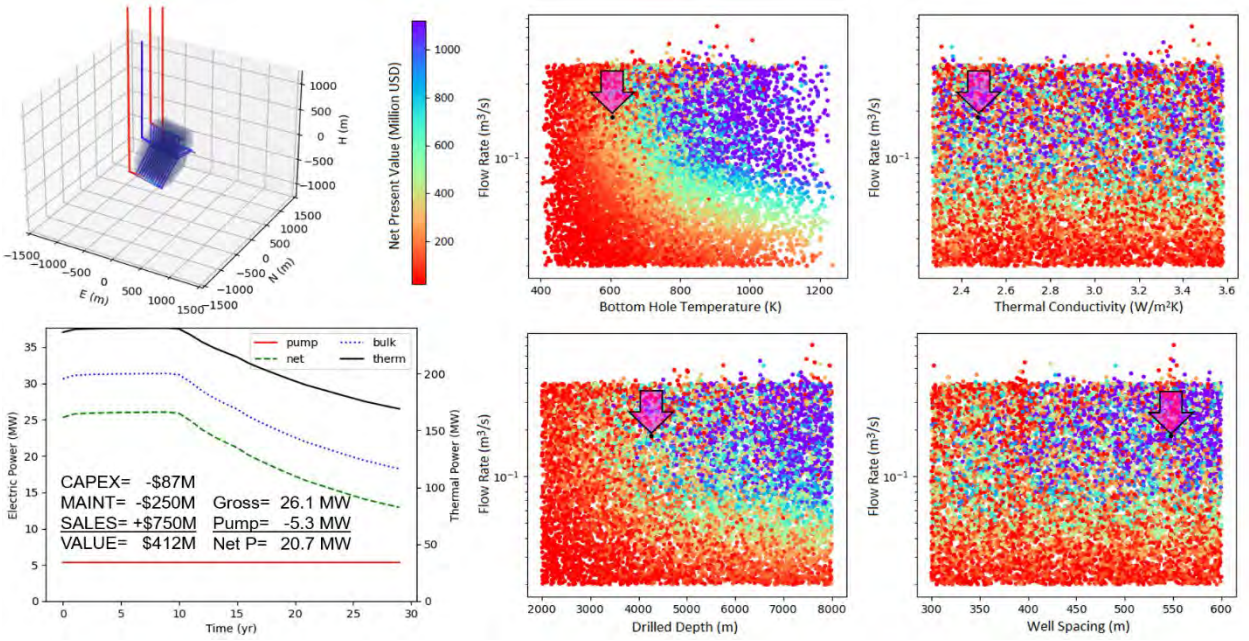

Figure 7: Net present value for 4-well 12-zone CGS showing first-order dependence on reservoir temperature and flow rate, second-order dependence on well depth, and tertiary dependence on well spacing. Thermal conductivity had no discernible effect, in part due to its low variance from 2.2 to 3.6 W/m²K.

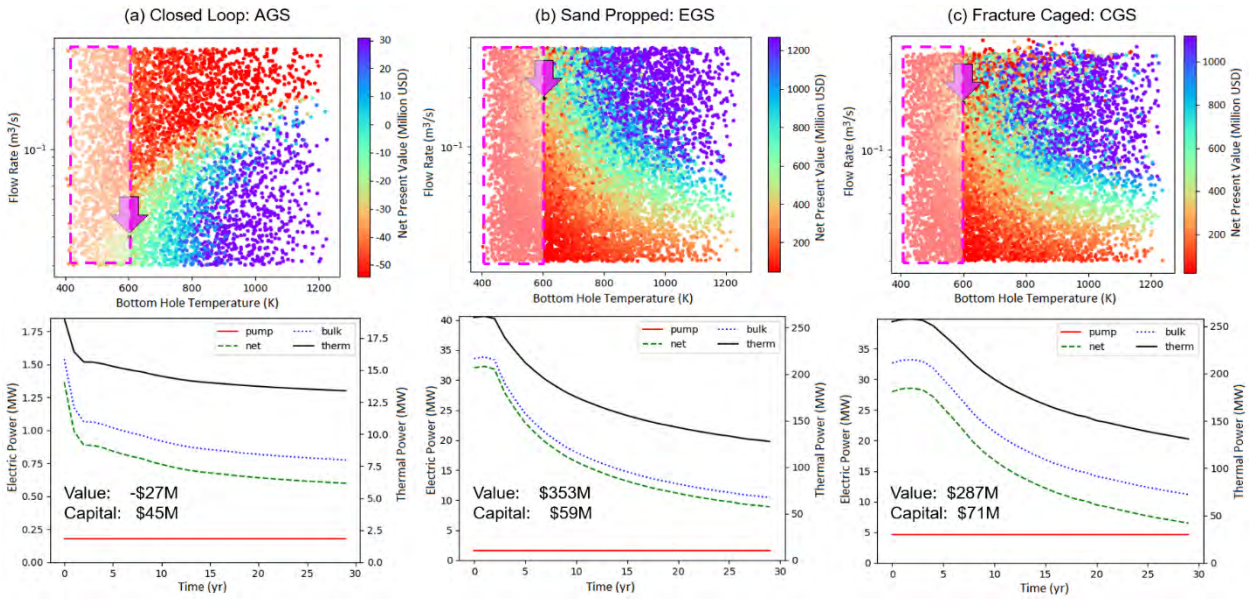

Figure 8: Net present value for optimized 13-loop AGS, 3-well 30 stage EGS, and 4-well 12-zone CGS. Higher economic flow rates for EGS and CGS is the primary reason why these systems outperform AGS. Natural shear fractures and faults were excluded from this analysis to mask their chaotic effect.

The nominal high-performance scenarios occurred with a reservoir temperature of 300 °C and at the lowest optimum flow rate. This associated with cooling over time but the increase in bulk harvestable power makes up for the losses. The lowest optimum rate helps flatten the performance curve which then simplifies the design process for surface turbomachinery. Routinely, GeoDT shows that some amount of thermal decline is favorable for peak economics because the higher temperature gradient in the conduction-dominated reservoir serves to extract heat more rapidly.

6. Natural Fractures and Seismicity

Natural fractures and faults are a source of undesirable complexity in AGS, EGS, and CGS. When drilling, these features can thief the drilling mud away from the rig, causing lost circulation and slower rates of penetration. When stimulating and circulating, these fractures can cause hydraulic fractures to coalesce. This causes premature cooling in the form of sparse flow paths (i.e., short-circuits). They can also interfere by preventing pressure buildup during well stimulation. GeoDT predicts these mechanisms with randomly placed critically stressed fractures (Fig. 9). In addition, GeoDT estimates the induced maximum seismic magnitudes as a function of fracture size, shear stress drop, and statistics (Lay and Wallace, 1995; Kanamori and Anderson, 1975; Gutenberg and Richter, 1954). This enables a first estimate of the seismic risk associated with a given geothermal reservoir design (Fig. 10).

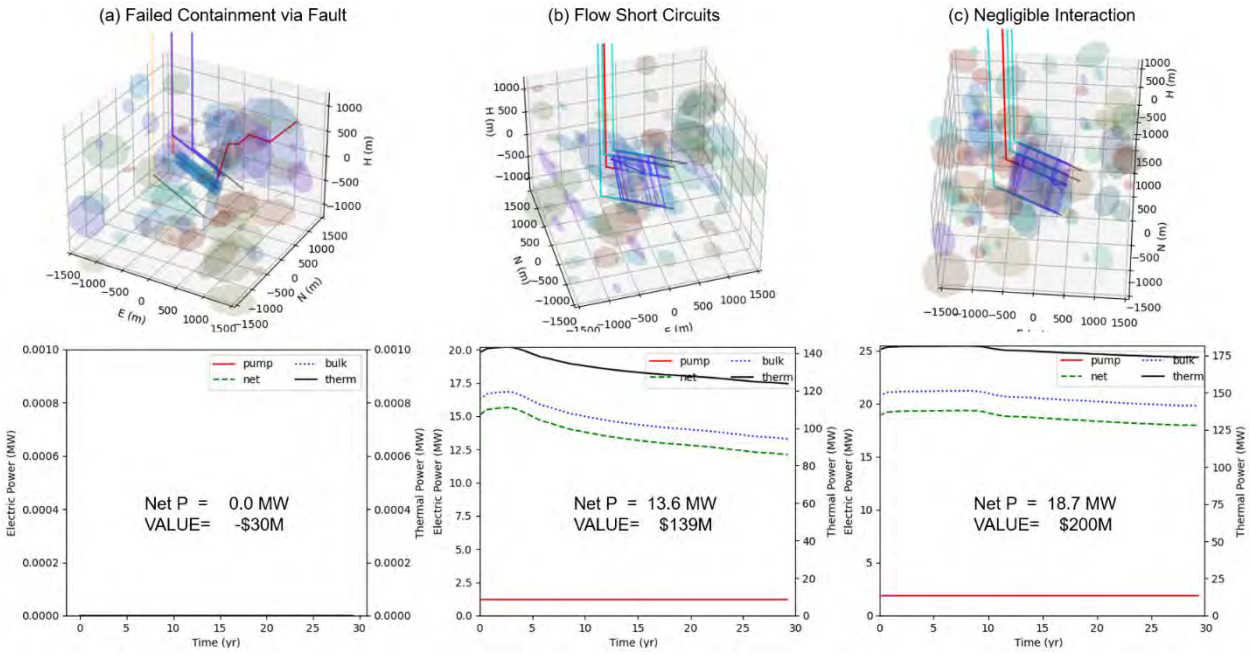

Figure 9: Faults and natural fractures introduce a mechanism for induced earthquakes and for high fluid loss. Optimized CGS designs should acknowledge that natural fractures can interfere with the system to then identify the high reliability designs that minimize the likelihood of a negative outcome.

Quantile statistics (Fig. 6) reveal the impact of design on seismics risk through a reduction in the performance uncertainty and a reduced likelihood of failure scenarios (e.g., >$300 USD/MWh for EGS and CGS). Scatterplots (Fig. 10) reveal trends in the design optimization process to identify details that should help to ensure success. A closer inspection of the results will reveal that failed containment associates with the largest magnitude seismic events for AGS, EGS, and CGS. For AGS, this will be apparent during drilling and initial fluid circulation so its diagnosis and cure (i.e., injection of cement or sealants) is straightforward. For EGS and CGS, some fluid losses should be expected during circulation and the action of faults can cause the injection and production rates to be equal despite fluid loss. This is because each well could connect to a different fracture system. Diagnosis of lost containment in EGS and CGS will require testing using methods such as tracers and microseismic monitoring. Mitigation measures could include injection of cements, gels, and diverters to clog the fast flow paths. Alternatively, additional wells could be drilled to intersect the fast flow path to then establish containment of all flow.

Unique to CGS, any natural fractures inside or interconnecting the wells are likely to have their flow contained by the fracture caging effect (Frash et al., 2021). This means that the risk of failed containment stems from the possibility of well-parallel fractures or from stimulated fractures connecting to a highly conductive fault that bypasses boundary wells (i.e., producers). Combining this process with how CGS production wells ought to be open to flow during stimulation means that a failure scenario for CGS can be identified within hours of beginning the injection. This offers an early opportunity to stop and employ seismicity mitigation measures before the fault becomes perturbed enough to trigger a large seismic event. This extra safety margin is part of what makes CGS a compelling option despite its need for more wells than the minimum EGS design. Tools such GeoDT are required to reveal these opportunities, quantify their merits, and devise mitigation options to the failure scenarios. Ultimately, the goal is to maximize the likelihood of achieving economic geothermal power.

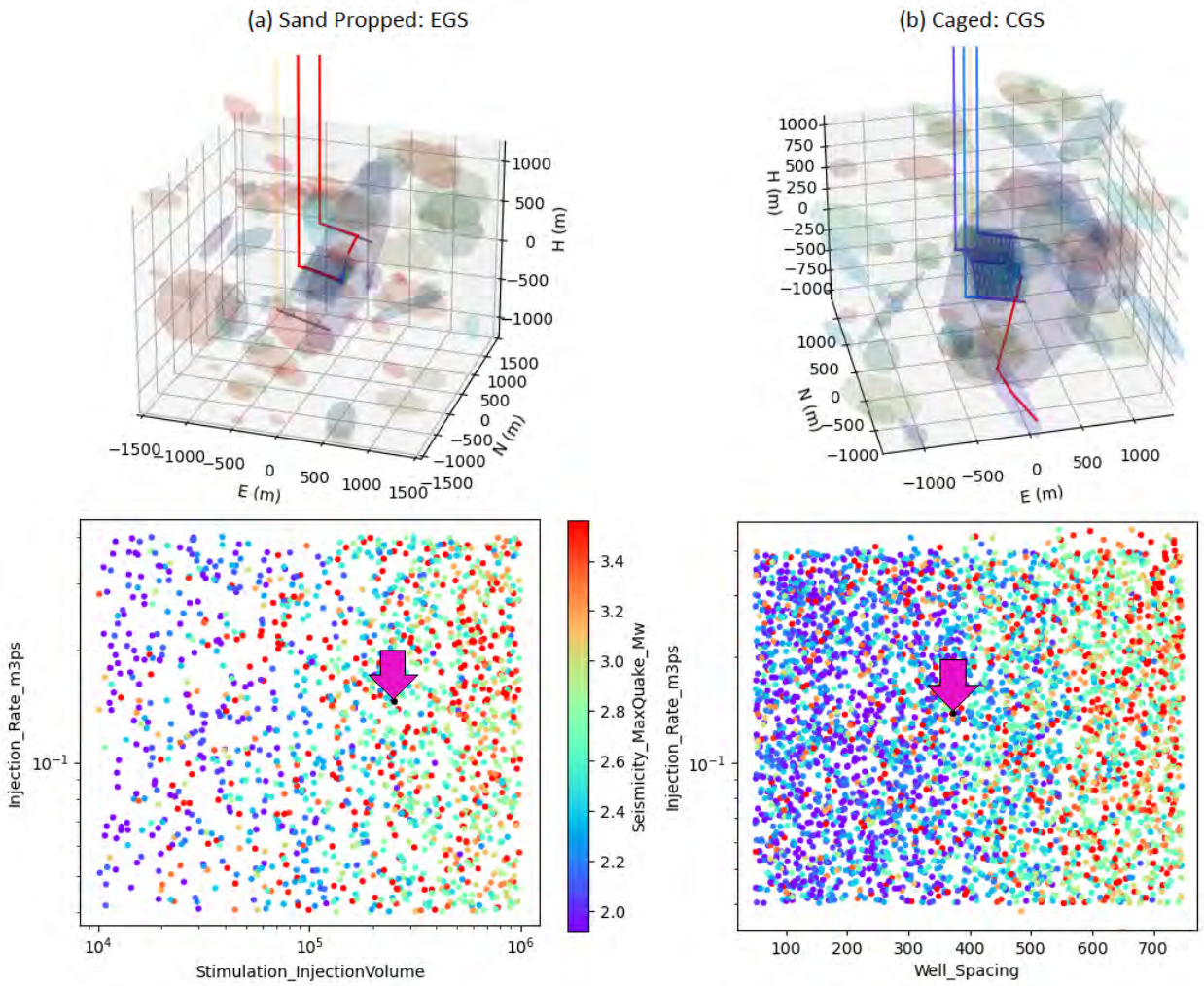

Figure 10: Maximum induced earthquake forecast by GeoDT for (a) EGS as a function of stimulation volume and (b) CGS as a function of well spacing. Mitigation measures such as the traffic-light protocol are not used in this study in order to better reveal the influence of reservoir design on seismic risk. Results from the EGS model are more sparse than for CGS because low injection volumes will fail to connect the injection well to the production well when the well spacing is too large. These failure scenarios are not shown on the plot because the circulation flow rates are too slow to plot. The same issue does not apply to CGS because the stimulation phase is the circulation stage, which never stops.

7. Economics

Recent experience drilling geothermal wells near Milford, UT and Blue Mountain, NV indicates that drilling costs could be lower than previously thought (Dupriest and Noynaert, 2022; Norbeck, et al., 2023; Lowry et al., 2017). This advancement stems from learning models, improvements in drilling methods, and the benefits of batch drilling. This information was used to update our cost model for drilling deep wells to an estimate of $1400 USD/m. This combined with the findings above leads to an updated economic estimate for the potential of CGS (Fig. 11). In short, it could be possible to generate electricity from hot dry rock at a cost point of $64 to $98 USD/MWh. This would make geothermal energy competitive to solar with energy storage at its estimated cost of $46 to $102 USD/MWh (Lazard, 2023), before government incentives.

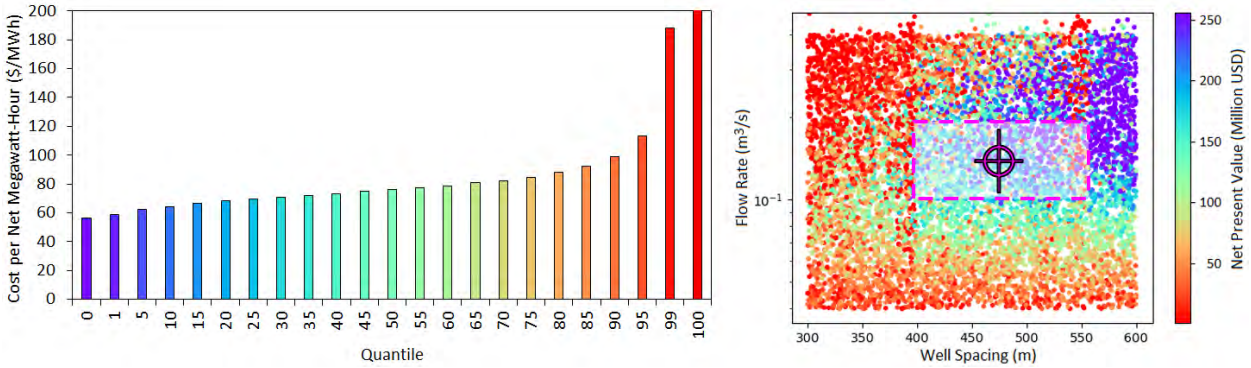

Fig. 11: Economic forecast from GeoDT for the most viable CGS design with its risk mitigation measures. The nominal cost of electricity (i.e., P50) is estimated at $75 USD/MWh.

8. Conclusions

This study investigated the technoeconomic potential of AGS, EGS, and CGS in greenfield settings where information about the subsurface is limited. The analysis is based on Monte-Carlo ensemble modeling with GeoDT to explore a large parameter space, beginning from a start scenario where no site-specific data was known. We note that GeoDT is a fast simplified physics solver that pairs measurements of complex processes, with upscaling theory, and fracture networks to estimate the energy generation and value of various geothermal reservoir designs. The analysis indicates that EGS is likely to yield the cheapest power from unconventional deep hot dry rock resources, but at a risk of triggering earthquakes. Caged Geothermal Systems (CGS) provide the next best cost at $64 to $98 USD/MWh after its initial capital investment of around $70M. AGS yields the highest cost of electricity at $275 to $560 USD/MWh and the lowest risk of induced seismicity.

Acknowledgement

This work is supported by Department of Energy (DOE) Basic Energy Sciences LANLE3W1. Additional support was provided by Los Alamos National Laboratory's Directed Research and Development – Exploratory Research program under LDRD-ER-20220175ER and the DOE Geothermal Technologies Office (GTO) funded project – Geothermal Limitless Approach to Drilling Efficiencies (GLADE; DE-EE0010444) led by Oxy USA, Inc. We are grateful for this funding provided by DOE and LANL. The views expressed herein do not necessarily represent the views of the U.S. Department of Energy of the United States Government.

REFERENCES

Beckers, K.F., Rangel-Jurado, N., Chandrasekar, H., Hawkins, A.J., Fulton, P.M., Tester, J.W. (2022). Techno-Economic Performance of Closed-Loop Geothermal Systems for Heat Production and Electricity Generation. Geothermics, 100, 102318.

Duchane, D., Brown, D. (2002). Hot Dry Rock (HDR) Geothermal Energy Research and Development at Fenton Hill, New Mexico. Geo-Heat Centre Quarterly Bulletin.

Dupreist, F., Noyanaert, S. (2022). Drilling Practices and Workflows for Geothermal Operations. In proceedings of the IADC/SPE International Drilling Conference and Exhibition, Galveston, TX, 8-10 March.

Ellsworth, W.L. (2013). Injection-induced earthquakes. Science, 341(6142), 1225942.

Frash, L.P. (2021). GeoDesignTool – GeoDT. https://github.com/GeoDesignTool/GeoDT.

Frash, L.P. (2022). Optimized Enhanced Geothermal Development Strategies with GeoDT and Fracture Caging. In proceedings of the 47th Workshop on Geothermal Reservoir Engineering, Stanford, CA, 7-9 September.

Frash, L.P., Fu, P., Morris, J., & EGS Collab Team, (2018). Fracture caging: Can we control the extent of a hydraulic fracture stimulated zone. Paper presented at 43rd Workshop on Geothermal Reservoir Engineering, Stanford University, Stanford, CA.

Frash, L.P., Fu, P., Morris, J., Gutierrez, M., Neupane, G., Hampton, J., Welch, N.J., Carey, J.W., & Kneafsey, T. (2021). Fracture caging to limit induced seismicity. Geophysical Research Letters, 48(1), e2020GL090648.

Frash, L.P., Meng, M., K C, B. (2024). Greenfield Reservoir Engineering for the Wattenberg Field with Comparison of Advanced, Enhanced, and Caged Geothermal Systems. In proceedings of the 49th Workshop on Geothermal Reservoir Engineering, Stanford, CA, 12-14 February.

Frash, L.P., Sweeney, M., Meng, M., K C, B., Iyare, U.C., Madenova, Y., Carey, J.W., Li, W. (2023). Exploring the Limitations of Fracture Caging in NextGen Enhanced Geothermal Systems. In proceedings of the 57th US Rock Mechanics / Geomechanics Symposium, Atlanta, GA, 25-28 June.

Fu, P., Schoenball, M., Ajo-Franklin, J.B., Chai, C., Maceira, M., Morris, J.P., Wu, H., Knox, H., Schwering, P.C., White, M.D, et al. (2021). Close Observation of Hydraulic Fracturing at EGS Collab Experiment 1: Fracture Trajectory, Microseismic Interpretations, and the Role of Natural Fractures. JGR Solid Earth, 126, e2020JB020840.

Gringarten, A.C., Witherspoon, P.A., Ohnishi, Y. (1975). Theory of heat extraction from fractured hot dry rock. Journal of Geophyscial Research, 80, 1120-1124.

Gutenberg B. and Richter C.F. (1954). Seismicity of the Earth and Associated Phenomena, 2nd ed. Princeton, N.J. Princeton University Press.

Hamm, S.G., Augustine, C.R., Tasca, C., & Winick, J. (2019). An Overview of the US Department of Energy's GeoVision Report. Golden, CO: National Renewable Energy Laboratory.

Hofmann, H., Zimmermann, G., Farkas, M., Huenges, E., Zang, A., Leonhardt, M., Kwiatek, G., Matrinez-Garzon, P., Bohnhoff, M., Min, K.-B., P., Fokker, R., Westaway, Bethmann, F., Meier, P., Yoon, K.S., Choi, J.W., Lee, T.J., Ki. K.Y., (2019). First field application of cyclic soft stimulation at the Pohang Enhanced Geothermal System site in Korea. Geophysical Journal International, 217, 926–949 (2019).

Kanamori H., and Anderson D.L. (1975). Theoretical basis of some empirical relations in seismology. Bulletin of Seismological Society of America, 65, 1073–1095.

Kelley, M., Raziperchikolaee, S., Likrama, F. (2024). Milestone 3.4 Report – In-Situ Measurement of Stress. Battelle.

Kim, K.H., Ree, J.H., Kim, Y., Kim, S., Kang, S.Y., & Seo, W. (2018). Assessing whether the 2017 M w 5.4 Pohang earthquake in South Korea was an induced event. Science, 360(6392), 1007-1009.

Lay T. and T. Wallace. (1995). Global Modern Seismology, Academic Press: New York.

Lowry, T.S., Finger, J.T., Carrigan, C.R., Foris, A., Kennedy, M.B., Corbet, T.F., Doughty, C.A., Pye, S., Sonnenthal, E.L. (2017). GeoVision Analysis Supporting Task Force Report: Reservoir Maintenance and Development. Sandia National Laboratories, SAND2017-9977.

Lazard. (2023). Levelized Cost of Energy+. Lazard.

Majer, E., Nelson, J., Roberson-Tait, A., Savy, J., Wong, I. (2012). Protocol for addressing induced seismicity associated with enhanced geothermal systems. US Department of Energy: Geothermal Technologies Program.

McGarr, A., Maximum magnitude earthquakes induced by fluid injection. JGR Solid Earth, 119, 1008-1019 (2014).

Norbeck, J., Latimer, T., Gradl, C., Agarwal, S., Dadi, S., Eddy, E., Fercho, S., Lang, C., McConville, E., Titov, A., Voller, K., Woitt, M. (2023). A Review of Drilling, Completion, and Stimulation of a Horizontal Geothermal Well System in North-Central Nevada. In proceedings of the 48th Workshop on Geothermal Reservoir Engineering, Stanford, CA, 6-8 February.

Tester, J., Andersen, B.J., Batchelor, A.S., Blackwell, D.D., DiPippo, R., Drake, E.M., Livesay, B., Morre, M.C., Nichols, K., Petty, S. (2006). The Future of Geothermal Energy. Massachusetts Institute of Technology, ISBN: 0-615134386.

Zarrouk, S.J., Moon, H. (2014). Efficiency of geothermal power plants: A worldwide review. Geothermics, 51, 142-153.

Geothermal Reserves Standards: A Study of the Applicability of the SPE Petroleum Resources Management System, a Proposed Classification Framework for Geothermal Reserves and Resources

Stephen E. Gardner and D. D. Faulder

Ryder Scott Company, L.P.

Keywords

Reserves, resources, geothermal resources classification framework, thermal recovery factor, SPE, PRMS, GRMS, EGS, power density

ABSTRACT

The global geothermal industry is over 100 years old and is growing as suppliers seek to meet ever-increasing energy demands in an era of de-carbonization. Yet, unlike the petroleum industry, the geothermal industry has no universally accepted set of guidelines, standards, or protocols to guide what are called '*reserves*' in financial statements and reports. Consistency in reserves and resources classifications (wherein reserves are a subset of resources), estimation methodologies, and the related disclosures is needed by investors, regulators, and corporate management teams to compare geothermal opportunities and clearly communicate the differences in terms that are well defined and understood. Another benefit of such standards is to show value added during the exploration and early development phase of a project as resources mature from one classification to another. In this study, a literature survey was conducted of existing classification standards in order to provide the backdrop for an evaluation of a geothermal resources classification framework based on the SPE Petroleum Resources Management System (SPE-PRMS). A brief review of methodologies for estimating recoverable heat was also conducted. The SPE-PRMS is a widely recognized international standard for petroleum resources, and its applicability to the formulation of a classification framework for geothermal resources was explored. Additional terminology is introduced to define geothermal reserves, resources, and associated concepts. An initial geothermal resources management system (GRMS) is presented.

1. Introduction

As many observers are aware, the geothermal industry is poised for an investment surge due to several factors. One such factor is the continued push toward de-carbonization of energy sources driven by environmental and social concerns; another is the need for growth in base-load renewable power, and a third is the emerging economic viability of Enhanced Geothermal Systems (EGS). The large resource base in the earth's crust to 4 km depth is a major driver of EGS. New geothermal projects require capital for exploration, wellfield development, and power plant construction. Total project costs can be $4 million to $6 million per developed MWe (the electrical power output from a power plant is specified in megawatts electric, or MWe), and projects may take several years to generate first revenue. The California Public Utility Commission has called for 1000 MW of new, base-load renewable power by 2028 to help supply the state's growing needs and energy transition goals, requiring $4 billion to $6 billion, or more. In Utah, Fervo Energy is developing 400 MWe of EGS power at a reported cost of $1.1 billion (Fervo 2023). These large capital projects require outside investment from financial institutions, private equity, investment banks, and other sources.

Many of these potential new investors are likely to have experience investing in the petroleum industry and are familiar with many common and shared activities with the geothermal industry, such as subsurface geoscience evaluation, well drilling and completions (including horizontal wells), and fluid production through surface pipelines and facilities. These investors may also have experience with petroleum reserves standards and have some expectation that there are similar standards and protocols for geothermal reserves. For other new investors, geothermal projects may be their first foray into subsurface assets and development. Both types of investors are likely unfamiliar with the nuances of geothermal exploration, development, power plant operations, and selling produced power to a utility or a large power purchaser (e.g., a server farm, a mine, etc.).

At this point, it is important to note that *reserves*, whether for petroleum or geothermal, are a subset of *resources*. As such, *resources* encompass the full spectrum of estimated quantities: discovered as well as undiscovered, recoverable as well as unrecoverable, commercial as well as uneconomic, and produced as well as remaining. *Reserves*, as will be further defined in section 3.3, comprise the portion of *resources* that are discovered, recoverable, commercial, and remaining as of a given date. Throughout this work, we sometimes refer to the terms *reserves and resources* together, simply for emphasis.

The geothermal industry in the United States history is blotted by projects[1,2,3,4,5] that did not meet economic expectations. While there may be many technical reasons why a project experiences commercial difficulties, the issue often revolves around a mismatch between expectations of what the asset could produce, i.e., the asset's reserves, and the associated production profile with respect

[1] Johnson, G., *Imperial Valley Project: SDG&E Pins Hopes on Geothermal Plant*, Los Angeles Times, June 20, 1985.
[2] Johnson, G., *SDG&E: to Shut Geothermal Plant" Unocal, Chevron Unit Late Drilling Wells, Utility Says,* Angeles Times, June 24, 1987.
[3] Johnson, G., *Chevron Seeks Ruling on SDG&E; Contract Liability*, Los Angeles Times, August 13, 1987.
[4] Johnson, G., *SDG&E: Files Suit Over Geothermal Contract*, Angeles Times, August 19, 1987.
[5] Johnson, G., *SDG&E: Negotiating to Sell Heber Geothermal Plant*, Angeles Times, August 19, 1987

to time, rate, pressure, and enthalpy. A review of the financial statements from domestic U.S. companies that produce geothermal energy, such as NCPA (Baker Tilly 2018-2023), Chevron (2005-2022), and Ormat (2005-2023), suggests a current capacity factor of ~52% (i.e., current electrical power production as a percentage of the initial installed plant capacity). As a project is incentivized toward profitability, the question may be asked, *why is the average project delivering only about half of its installed capacity?* At least part of the answer to that question, and others, may be found in properly understanding the uncertainty around a project's geothermal reserves and resources.

2. Literature Review

The passage of the 1970 Geothermal Steam Act by the U.S Congress, provided for the leasing of Federal lands for geothermal exploration and development. The Act defined a *known geothermal resource area* as "an area in which the geology, nearby discoveries, competitive interests, or other indicia would, in the opinion of the Secretary, engender a belief in men who are experienced in the subject matter that the prospects for extraction of geothermal steam or associated geothermal resources are good enough to warrant expenditures of money for that purpose." It should be noted that several criteria are specified: geologic favorability, subject matter experts, and commercial opportunity.

In response, the first national assessment of the domestic geothermal resource base was performed by the United States Geologic Survey, USGS (White and Williams 1975). This assessment reviewed a comprehensive catalog of hot springs and thermal features in order to estimate the size, temperature, and heat-in-place using either direct temperature measurements or inferred from geothermometry. The national assessment was updated several times by the USGS, with the last update in 2008 (Muffler 1975, 1979; Reed 1983; Williams et al. 2008). They described a volumetric methodology for calculating the usable heat-in-place above a given reject temperature using either deterministic or probabilistic methods.

These USGS studies all referred to the geothermal *resource base* as *reserves*, highlighting the differences on how to define this key term. Furthermore, the USGS did not rely on economic criteria in defining reserves, thus missing a key factor, commerciality. This is understandable, since the early years of the industry were not concerned about precise reserves definitions and protocols as the technology was still evolving, experience was being gained, and the limited number of projects worldwide were still in their infancy. This is not the case today, as the industry has matured, with over 50 U.S. domestic power projects and more than 100 globally.

2.1 An Evolution of Geothermal Reserves Classification Standards

The U.S. domestic geothermal industry experienced a number of major oil companies, new entrants, and other players leaving the space throughout the 1990s, a period characterized by industry reorganization. Serious discussion of geothermal reserves started appearing in the literature post-2000 and has advanced toward formal protocols and standards. Three stages can be discerned from the literature.

The first stage spans about 2000 to 2008, with discussion of reserves categories and estimation methods. An early paper by Sanyal et al. (2005) proposed a process for booking geothermal reserves. It provides an excellent summary of basic principles with suggested categories and a

discussion of deterministic and probabilistic reserves estimation methods. A review by Clotworthy et al. (2006) suggested reserves categories of Proven, Probable, and Inferred and included an economic test as reserves were only to be considered "that are generally accepted to be commercially extractable with existing technology and prevailing market conditions." These authors referenced the SPE/WPC guidelines for petroleum in using deterministic and probabilistic methods.

The second stage covers approximately 2008 through 2015, coinciding with the development of Enhanced Geothermal Systems (EGS) in Australia. This required Australian regulations, protocols, and standards for determining geothermal reserves for financial reporting (Australian Reporting Code Committee 2010). The code used for its conceptual basis the Joint Ore Reserves Committee (JORC) approach and was adopted with minimal changes in Canada by the Canadian Geothermal Code Committee (2010a, 2010b). These codes recommended using a thermal recovery factor of 25% based on reservoir numerical model studies or a probabilistic model with a triangular distribution of 15%, 20%, and 25% for min, median, and max. The thermal recovery factor was then used to define proven reserves for the early Australian EGS pioneers. Somewhat in contrast, Grant (2015) presented a pervasive argument that for mature hydrothermal systems, a best estimate thermal recovery factor is 8% to 10% and that the Australian Code and Lexicon overstates hydrothermal recovery factors by 75%. Since EGS developments can have lower recovery factors than traditional hydrothermal projects, the overstatement becomes even greater in those instances.

In a review of the Cooper Basin, Habanero project, Geodynamics Ltd. (2014) presents an excellent summary of said project, including geoscience and financial information with over $400 million expended. It was apparent that the *proven reserves* that were booked were an attraction for initial capital investors, based on the Australian protocols. The company was incorporated in 2000 and listed on the Australian Securities Exchange in September 2002. After extensive testing, the project demonstrated 1 MWe in October 2013. The post project study estimated capital costs of $21 million per developed MWe, which is four to six times greater than a typical 50 MWe binary power plant. One observation from this situation is that if a project is to fail financially, it is better to do so sooner than later.

The third stage started approximately 2015, with the literature providing documentation of project data from around the world. Ciriaco et al. (2020) presented an excellent summary on current methods of estimating in-place thermal resources and thermal recovery factors for over 40 fields worldwide. It is interesting to note the legacy impact of the Australian probabilistic methodology described earlier (i.e., min, median, max of 15%, 20%, and 25%), with fifteen projects using probabilistic thermal recovery factors of 20% or greater. The United Nations has published detailed classification and specifications for geothermal resources in an effort to establish an international standard (UNECE 2019, 2022). This standard has yet to gain wide use by the geothermal industry; however, it does demonstrate a maturing technical understanding and an increasing emphasis on geothermal reserves standards worldwide.

2.1 Estimation Methodologies for Geothermal Reserves

Early discussions on booking geothermal reserves included a review of existing methods conceptually based on the Society of Petroleum Engineers (SPE) and the World Petroleum Congress (WPC). Various methods including volumetric analysis, production decline curve analysis, lumped parameter modeling, numerical simulation, and the application of sophisticated

stochastic methods were reviewed. Additional authors referred to Clotworthy in 2006 for establishing a conceptual framework for geothermal reserves and sub-categories reflecting different degrees of resource confidence. They used a three-level classification system; Proven, Probable, and Inferred, based loosely on the McKelvey diagram used by SPE. A general consensus has developed since then to use proved, proved plus probable, and proved plus probable plus possible categories to represent the 90th percentile (P90), the 50th percentile or median (P50), and the 10th percentile (P10) of the cumulative probability of exceeding the reserves estimate. Deterministic methods were assumed to represent a P50 estimate.

A key difficulty in differentiating between proved and non-proved categories is the thermal recovery factor. Given a typically large heat-in-place, a small difference in the recovery factor can have a large impact on the estimated proved reserves. An excellent review of geothermal resource assessment methodologies by Ciriaco et al. (2020) summarized thermal recovery factors from the literature for a number of fields worldwide to be from 5% to 38%, with most of the fields using probabilistic methods and triangular distributions (min, median, max). This compilation included three U.S. domestic fields: Coso, Dixie Valley, and The Geysers, all very well characterized and with long production histories that exhibited thermal recovery factors of 8% to 11%. These low thermal recovery factors from large, well-managed assets with over 30 years of production history suggest that recovery factors much greater than this may be optimistic. Moreover, optimistic thermal recovery factors may be related to high porosity assumptions since they are proportional in a given analysis. Zarrouk (2013) proposed that thermal recovery factors should consider the host porosity and type of geothermal system.

Decline curve analysis (DCA) has long been used in the petroleum industry to forecast reserves from properties that are actively producing. While many geothermal fields use pumped wells at fixed rates, several geothermal fields use flowing wells and are subject to mass depletion, such as Coso and The Geysers. DCA has been used for many years at The Geysers for estimating remaining steam reserves and to estimate well flow capacity (*kh*) (Faulder 1996, 1997; Reyes 2004). In another instance, a common petroleum evaluation software was utilized to observe the historical performance trends in an established geothermal field and then apply DCA to multiple data streams, including steam and water mass, in order to forecast the future production (Ryder Scott Company 2021).

The difficulty in using strictly volumetric methods of heat-initially-in-place and a thermal recovery factor leads to considerations of how to estimate the production potential of a new prospect or a discovery without extensive geoscience and engineering data. The concept of power density has been studied by Wilmarth and Stimac (2015), Cummings (2016), Wilmarth et al. (2021), and Holmes (2024). Power density is defined as generating capacity divided by producing area. Figure 1 shows power density (MW_e/km^2) plotted vs. reservoir temperature (°C) for over a hundred fields worldwide. Distinctions were made between different tectonic environments, and an exponential regression was performed. The resulting plot showed a range of power density at each temperature, empirically representing the lognormal distribution of key underlying data, primarily area.

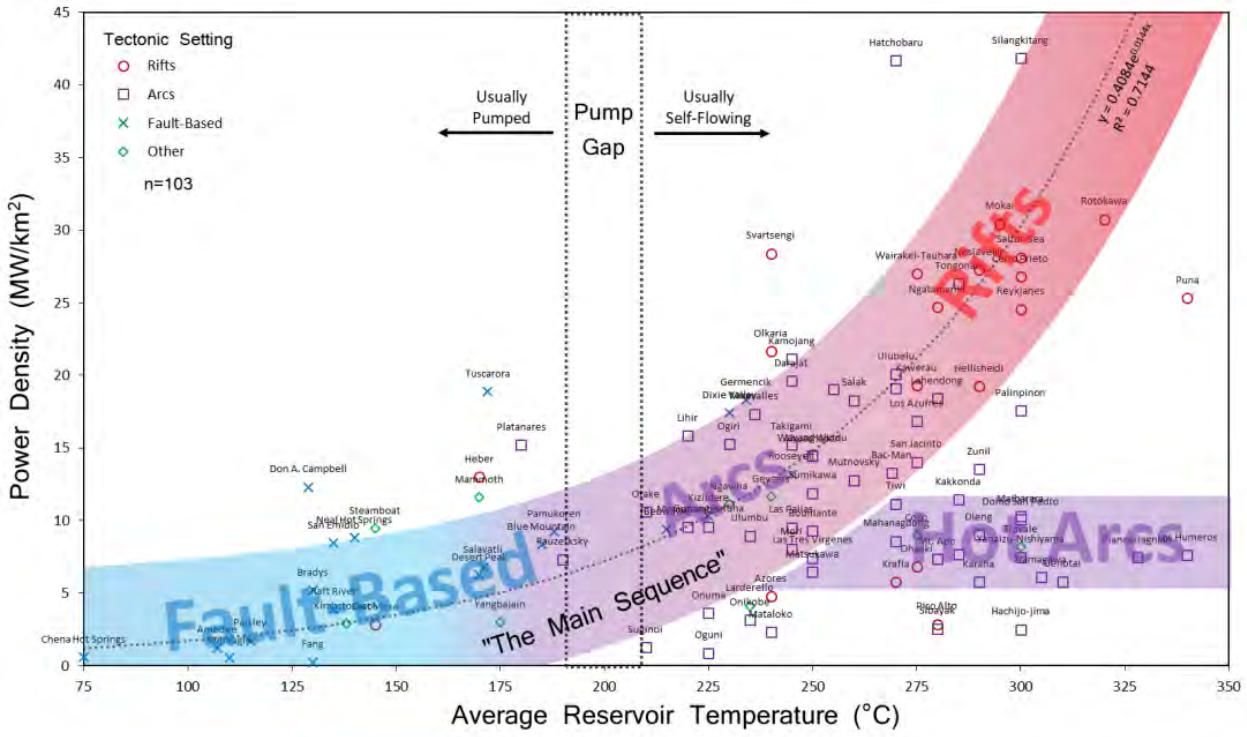

Figure 1: Power Density versus average reservoir temperature, from Wilmarth et al. (2020).

One distinct advantage of the power density method is not having to assume a thermal recovery factor, and power density increases with temperature, making intuitive sense. Another advantage is the data is based on actual operating experience for an increasing number of fields. One critique of the method is the choice of which capacity for power generation to use, the initially installed plant capacity or the actual stabilized power generation after some period of time. Another critique is the calculation of field size, since the area of the wellfield operations is dependent on the development strategy used. The power densities presented do not include a table of the underlying data used, and future work on this topic should develop a defined protocol for consistency and transparency. Yet, with refinement and an expanding data set, the power density method may provide a robust method for resource comparison using statistical methods, especially in the early appraisal stage of a project. A minimum and maximum estimated reservoir temperature can be used to bracket the power density distribution. An estimate of the defined field size multiplied by the power density provides an early estimate of the power generation potential.

A number of authors point to the evolving approach of using reservoir simulation to model the dynamic reservoir response during exploitation and to quantify heat recovery (Fang et al. 2022; Sanyal and Sarmiento 2005; Winofa et al 2020). The complex nature of modeling hydrothermal systems requires a large geoscience data set synthesized into a geologic model of the resource, such as temperature, porosity, and permeability within the structural and stratigraphic controls and open hydrologic boundaries. Mature projects typically have sufficient geologic and engineering data to construct and calibrate reservoir simulation models, and where sufficient data is available, reservoir simulation is a preferred method. To ensure their reliability, reservoir simulation models need to be regularly updated and recalibrated, taking care to understand why the forecast and actual

operations did not match, for such cases. We note that demonstrating or calculating the reliability of reservoir simulation, or any other estimation methodology, is a key criterion for assigning specific reserves categories to quantities of recoverable heat.

3. A Viable Classification Framework for Geothermal Reserves and Resources

3.1 The Need for Geothermal Reserves Standards

In general terms, reserves are the supply of a certain commodity that is available for future use, and for companies that sell commodities, reserves are a crucial measure of resource magnitude, growth (or decline), and longevity. For the energy industry, particularly for oil and natural gas, this is no exception. The establishment of standards for estimating and reporting petroleum reserves has been of great importance for many decades and is widely accepted as a critical part of carrying out business and defining the value of the company. Corporate management teams use reserves to understand their portfolio and to plan future development activities. Reserves represent an asset and are an integral part of the company's accounting to determine earnings. Regulators use reserves to plan for public energy needs and infrastructure, to predict tax revenue and inform tax incentives, and to help administer the use of natural resources. Investors use reserves to compare company performance and investment opportunities. Accordingly, reserves standards provide consistency in resource classifications, estimation methodologies, and the related disclosures. This consistency of information promotes reliable estimates and clear communication about such estimates, which then brings stability to the market place. Stakeholders are able to compare opportunities, manage portfolios, and transact with greater comprehension and confidence.

Whether for petroleum or for geothermal energy, this same reasoning and need for reserves standards applies. As discussed earlier, multiple geothermal standards have been in existence for many years (Australia, Canada, UNECE, etc.). However, a particular set of standards has yet to emerge as being widely-accepted. This reality may be at least partly due to the geothermal energy industry being something of a sleeping giant, when compared to the current mix of global energy supply. As worldwide economies continue to seek additional sources of energy to meet ever-growing demand, especially sources with a low carbon intensity, geothermal energy is positioned to become more common and to attract more investment capital. The acceptance and use of reserves standards are necessary to aid in the development and growth of geothermal energy, thus creating favorable conditions for a universal geothermal reserves standard to take hold. Yearsley (2019) discusses using the SPE framework for analyzing the transaction value of geothermal assets.

3.2 Experience from Hydrocarbons

The SPE Petroleum Resources Management System, a.k.a. SPE-PRMS or simply PRMS, is an important international standard for defining and classifying *petroleum* resources (Society of Petroleum Engineers 2018). Its principles are commonly applied to oil and gas assets around the world. Not only is the PRMS framework widespread, but many technical experts and other energy stakeholders are already highly familiar with its principles and application, having utilized it for decades. Furthermore, other standards for hydrocarbons, such as COGEH and the SEC guidelines, make reference to the PRMS. This high degree of acceptance and familiarity is important and may

help position the PRMS to be a natural bridge to a geothermal classification system, especially for stakeholders that already have some background in oil and gas.

In August of 2022, SPE issued a statement recognizing that the PRMS principles were being applied to non-hydrocarbons, including geothermal resources. SPE did not object "as long as it is made clear that while such application is outside of the PRMS, PRMS principles have been followed, while involving other subject matter expert parties as appropriate, and applied as though the extracted resources were considered as petroleum (Society of Petroleum Engineers 2022)." This statement opens the door for the acceptance and application of the principles of the PRMS for geothermal resources classification.

The technical estimation of petroleum or geothermal resources involves the assessment of quantities that have an inherent degree of uncertainty. The uncertainty in the estimates of recoverable volumes is represented by the *category* assigned to the estimates. Furthermore, these quantities are associated with exploration, appraisal, and development projects at various stages of design and implementation. The commercial aspects considered (e.g., technical, economical, regulatory, and legal) will relate the project's maturity status, or *classification*, to the chance that a technically viable project will actually be implemented. The PRMS classification framework provides a methodical approach to classify a given project according to its commercial maturity and to categorize the range of estimates according to the associated uncertainty of those estimates, for a project outcome. Since the PRMS is principles-based instead of rules-based, it inherently allows for adaptability to geothermal applications. In addition, petroleum and geothermal projects share many similarities, such as geologic and fluid flow characteristics, exploration and extraction technologies, and economic modeling. On the other hand, there are also important differences, including recovery of heat versus hydrocarbons, capital requirements and infrastructure, saleable products, and market drivers. We recognize that situations may arise requiring a departure from the PRMS as a guideline; however, our initial work has made it apparent that many reserves-related questions for geothermal energy become more straightforward by first looking for an analogy in the handling of hydrocarbon reserves. Finally, for the purposes of our discussion here, the adapted classification framework will be referred to as the Geothermal Resources Management System, or GRMS.

3.3 Important Terms and Definitions

As mentioned earlier, it is first important to distinguish between the terms *resources* and *reserves* in the context of geothermal energy. Leveraging language from the PRMS and adapting it to geothermal, the term *resources* comprises all quantities of geothermal energy, discovered and undiscovered, recoverable and unrecoverable, already produced as well as remaining, that are naturally occurring within the earth. Furthermore, Heat Initially-in-Place (HIIP) is a term that refers to a geothermal resource before any production has occurred. Again leveraging language from the PRMS, *reserves* are the portion of resources that are "commercially recoverable by application of development projects to known [sources] from a given date forward under defined conditions." Furthermore, reserves must satisfy four criteria: they must be "discovered, recoverable, commercial, and remaining based on the development project(s) applied." The exergy, or the useable portion of total energy in a system, of a geothermal project depends upon differences in temperature between the source heat and the reject, or waste, heat. Thus, the amount of geothermal reserves of a project can be different depending upon factors such as the type of

geothermal power plant, the reject temperature of the plant, or in the case of a direct heat application, whatever the minimum temperature is of the particular application.

Since geothermal reserves and resources as defined above are energy, their unit of measurement is joules, or more commonly, megawatt-hours (MWh) after the conversion to electrical energy. In the case where geothermal energy is used as direct heat, the British thermal unit (BTU) is another appropriate unit of measurement. We note that a megawatt (MW, 1 million joules per second) is a rate and is suitable to measure instantaneous energy production, such as the electrical power output from a geothermal plant, but it is not the appropriate measure for our definitions of reserves and resources. Furthermore, although geothermal energy is typically carried as heat by steam or water, which are measured in mass units such as kg or pounds-mass (lbm), the mass itself of steam or water does not represent an amount of energy nor would it qualify as geothermal reserves.

Using the PRMS as a model, we define proved, or P1, geothermal reserves as those quantities of geothermal resources that, by analysis of geoscience and engineering data, can be estimated with reasonable certainty to be commercially recoverable from a given data forward from known reservoirs and under defined economic conditions, operating methods, and government regulations. The term *reasonable certainty* means a high degree of confidence that quantities will be recovered (i.e., at least 90% probability, if probabilistic methods are used). We define probable, or P2, geothermal reserves with the same definition from the PRMS as for oil and gas: those additional reserves that analysis of geoscience and engineering data indicates are less likely to be recovered than proved reserves but more certain to be recovered than possible reserves (i.e., in a probabilistic context, there is at least 50% probability that the sum of proved plus probable (2P) reserves will be recovered). Lastly, we define possible, or P3, reserves with the same definition from the PRMS for oil and gas: those additional reserves that analysis of geoscience and engineering data indicates are less likely to be recoverable than probable reserves (i.e., in a probabilistic context, there is at least 10% probability that the sum of proved plus probable plus possible (3P) reserves will be recovered).

Beyond reserves, additional quantities of geothermal resources may be classified as contingent or prospective. Again using the PRMS as a model, we define contingent geothermal resources as those quantities estimated, as of a given date, to be potentially recoverable from known sources by application of development projects, but which are not currently considered to be commercially recoverable owing to one or more contingencies. Contingencies may include various issues, such as no available market, an operator's commitment or financial ability to proceed with development, uneconomic costs or prices, regulatory barriers, environmental opposition, etc. Similar to how the categories of reserves (i.e., proved/P1, probable/P2, and possible/P3) represent different ranges of uncertainty, contingent resources are categorized into C1, C2, and C3, where C1 corresponds to the same technical certainty as P1, C2 corresponds to P2, and C3 corresponds to P3. It is important to note that, similar to P1, P2, and P3 reserves, the terms C1, C2, and C3 are also representative of incremental quantities.

We define prospective geothermal resources as those quantities that are estimated, as of a given date, to be potentially recoverable from undiscovered sources. Prospective resources are sub-classified with the same nomenclature as the PRMS: 1U, 2U, and 3U. These categories are cumulative quantities and represent low, best, and high estimates, respectively.

As our scope with this paper is limited and the application of reserves and resources concepts to geothermal is still developing, we refer the interested reader to the current PRMS document, where additional terms and guidance are given for hydrocarbons that we believe in many instances are readily analogous to geothermal.

3.3 GRMS Classification Framework and Flowchart

As mentioned earlier, a focus of this work was to examine the suitability of adapting the PRMS to geothermal energy. The complete PRMS document is available from the Society of Petroleum Engineers. While it is beyond the scope of this paper to present every detail of our GRMS adaptation, the two figures below convey some key messages. We remind the reader that this initial GRMS may continue to evolve as more geothermal projects are encountered and evaluated.

Figure 2 below has been adapted for geothermal energy from the PRMS classification framework for hydrocarbons. The matrix shows the geothermal resource classifications and categories as were previously defined in section 3.2, the progression of commercial maturity along the y-axis, and the range of uncertainty in estimates along the x-axis. The figure allows a user to characterize where a particular project lies in terms of development maturity while simultaneously designating the uncertainty in a given estimate.

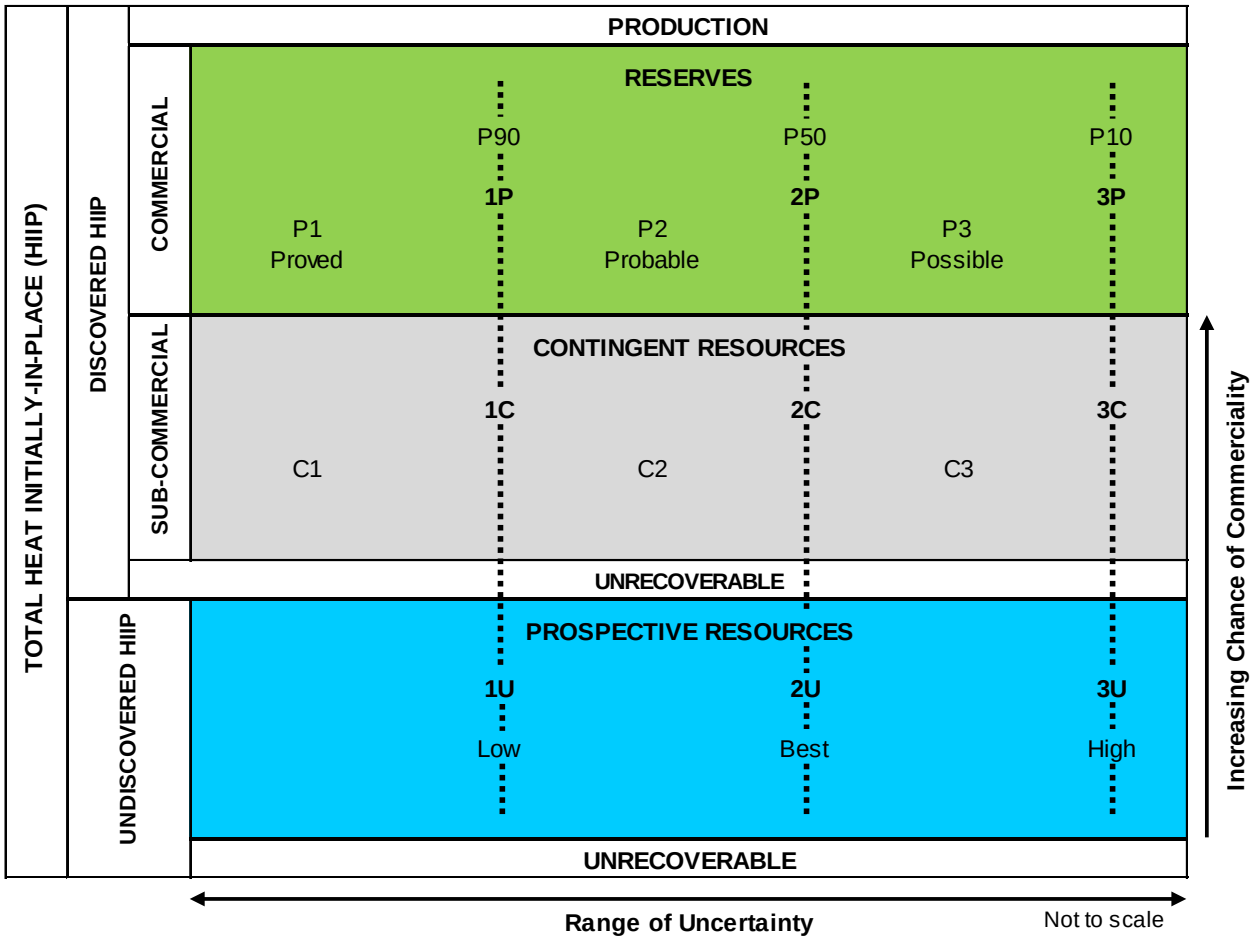

Figure 2: Geothermal resources classification framework (adapted from the SPE-PRMS, page 2).

Figure 3 is adapted for geothermal application from a concept graphic published by the Oil and Gas Climate Initiative, or OGCI (Oil and Gas Climate Initiative 2022). Based on the PRMS structure, the OGCI had originally generated the figure for application to carbon capture and storage. We have further modified it here for use with geothermal resources. The flowchart allows a user to understand and communicate the path that a project follows as it progresses, as well as what hurdles may remain to reach the next level of maturity, all the while utilizing the resource classifications and categories that were given in Figure 2.

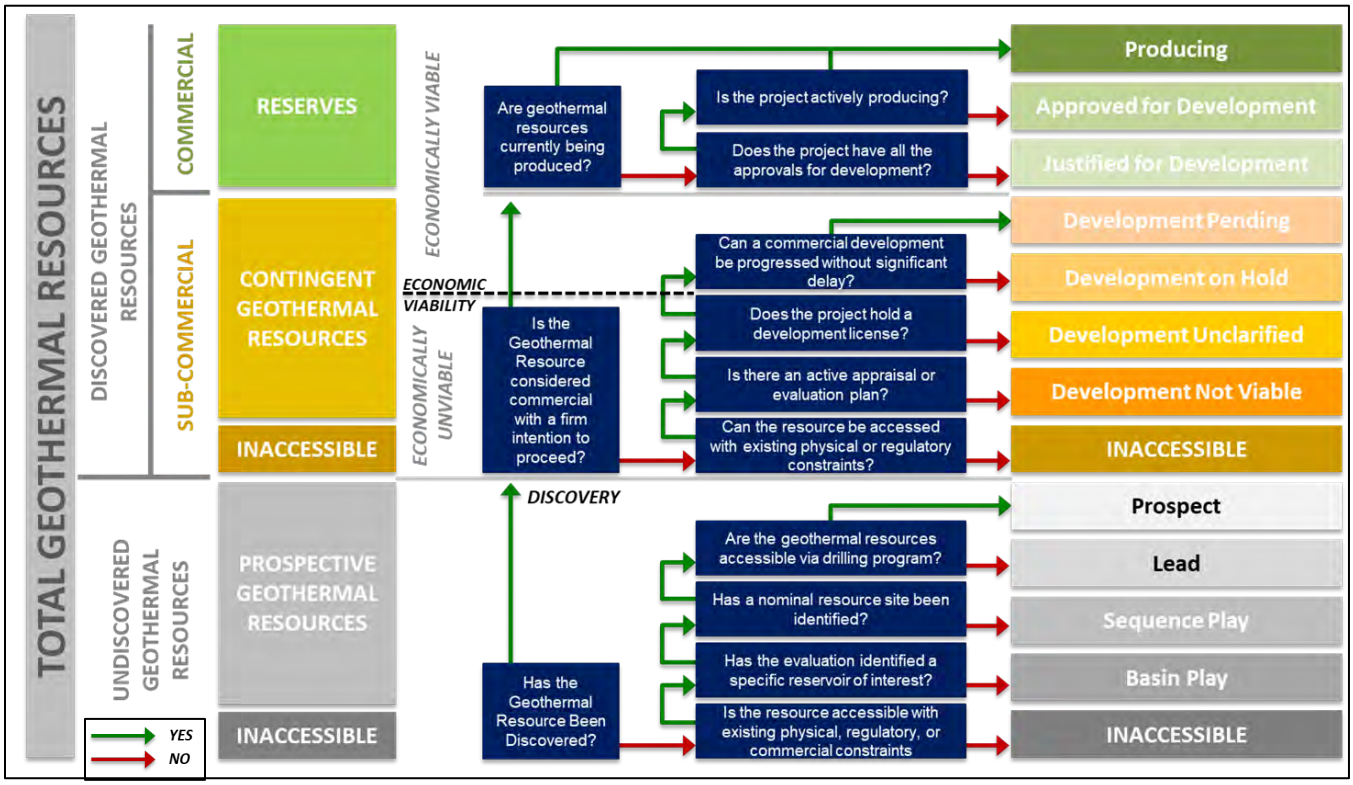

Figure 3: Flowchart for Assigning Project Sub-Classes (adapted from the OGCI CO2 Storage Resource Catalogue Cycle 3 Report, page 16).

4. Conclusions

The U.S. domestic and worldwide geothermal industries have matured with sufficient experience and data to apply formal definitions, methodologies, and protocols for estimating geothermal reserves and resources. Our literature survey and review of existing standards indicated an increasing interest and emphasis over the past two decades in the development of classification standards for geothermal reserves and resources. Yet no single set of standards has become widely accepted throughout the world. The Petroleum Resources Management System (PRMS), the common global standard for hydrocarbons, provides a good analogy for the establishment of a Geothermal Resources Management System (GRMS) and has an important advantage by being familiar to many energy stakeholders. Multiple case studies are ongoing by the authors to test the

utility of the suggested GRMS framework. Over time, additional application of the GRMS to geothermal reserves evaluations will help identify and resolve future questions or gaps in the framework.

ACKNOWLEDGEMENTS

Thank you to Ryder Scott Company, L.P. for sponsoring this work and to John Allen for his contributions early-on while working at Ryder Scott.

REFERENCES

Atkinson, P., 2012. *Proved Geothermal Reserves - Framework and Methodology,* Proc. 34th NZ Geothermal Workshop, 8 Pages.

Australian Reporting Code Committee, 2010. *The Geothermal Reporting Code, Second Edition (2010), Australian Code for Reporting of Exploration Results, Geothermal Resources and Geothermal Reserves,* 34 Pages.

Baker Tilly US, LLP, *NCPA and Associated Power Corporations, Combined Financial Statements*, 2018 through 2023 inclusive, Independent Auditors.

Benoit, D., 2013. *An Empirical Injection Limitation in Fault-Hosted Basin and Range Geothermal Systems,* GRC Trans. v37, 8 Pages.

Canadian Geothermal Code Committee, 2010a. *The Canadian Geothermal Code for Public Reporting, Reporting of Exploration Results, Geothermal Resources and Geothermal Reserves 2010 Edition,* Canadian Geothermal Energy Association, 34 Pages.

Canadian Geothermal Code Committee, 2010b. *The Canadian Geothermal Code for Public Reporting, Reporting of Exploration Results, Geothermal Resources and Geothermal Reserves 2010 Edition, Code Overview and Key Terms,* Canadian Geothermal Energy Association, 6 Pages.

Ciriaco, A.E., Zarrouk, S.J., and Zakeri, G., 2020. Geothermal resource and reserve assessment methodology: Overview, analysis and future directions, *Renewable and Sustainable Energy Reviews, 119,* 31 Pages.

Chevron, Annual Report, 2005 through 2022 inclusive.

Clotworthy, A.W., Ussher, G.N., Lawless, J.V., and Randle, J.B., 2006. *Toward an Industry Guideline for Geothermal Reserves Determination*, Proc. 28th NZ Geothermal Workshop, 10 Pages.

Cummings, W., 2016. *Resource Capacity Estimation Using Lognormal Power Density from Producing Fields and Area from Resource Conceptual Models: Advantages, Pitfalls, and Remedies*, Proc. 41st Workshop on Geothermal Reservoir Engineering, 7 Pages.

Fan, Y., Zhang, S., Huang, Y., Pang, Z., and Li, H., 2022. Determining the Recoverable Geothermal Resources Using a Numerical Thermo-Hydraulic Coupled Modeling in Geothermal Reservoirs, *Frontiers in Earth Science, v9*, 12 Pages.

Faulder, D.D., 1996. *Production Decline Curve Analysis at The Geysers, California Geothermal Field*, Colorado School of Mines, MS Thesis, 97 Pages.

Faulder, D.D., 1997. *Advanced Decline Curve Analysis in Vapor-Dominated Geothermal Reservoirs*, SPE 38763, SPE Annual Technical Conference.

Fervo Energy, 2023. Fervo Energy Breaks Ground on the World's Largest Next-gen Geothermal Project, Sep. 25, 2023, https://fervoenergy.com/fervo-energy-breaks-ground-on-the-worlds-largest-next-gen-geothermal-project/ (Accessed 7 Aug. 2024).

Geodynamics Ltd., 2014. *Habanero Geothermal Project Field Development Plan*, Document Number: COM-FN-OT-PLN-01166, Revision No: 1.0, 9 October 2014, 182 Pages.

Grant, M.A., 2015. *Resource Assessment, a Review, with Reference to the Australian Code*, Proc. World Geothermal Congress, Australia, 8 Pages.

Holmes, R.C., 2024. *Power Density Geothermal Resource Estimation Revisited*, Proc. 49th Workshop on Geothermal Reservoir Engineering, Stanford, SGP-TR-127, 9 Pages.

Muffler, L.P.J., 1979. *Assessment of Geothermal Resources of the United States-1978*, U.S. Geologic Survey Circular 790, 163 Pages.

Oil and Gas Climate Initiative, 2022. CO2 Storage Resource Catalogue Cycle 3 Report, Mar. 2022, https://www.ogci.com/wp-content/uploads/2023/04/CSRC_Cycle_3_Main_Report_Final.pdf. (Accessed 16 May 2024).

ORMAT TECHNOLOGIES, INC., United States Security and Exchange Commission, Form 10-K filings, 2005 through 2023 inclusive.

Reed, M.J., ed., 1983. Assessment of Low-Temperature Geothermal Resources of the United States, *U.S. Geologic Survey Circular 892*, 73 Pages.

Reyes, J.L.P., Li, K., Horne, R.N., 2004. *A New Decline Curve Analysis Method Applied to The Geysers*, Proc. 29th Workshop on Geothermal Reservoir Engineering, Stanford, SGP-TR-175, 8 Pages.

Ryder Scott Company, 2021. Ryder Scott Geothermal Audit in Oil and Gas Reserves Software is Newest Wrinkle, *Reservoir Solutions, July-Sept. 2021*, https://ryderscott.com/wp-content/uploads/1Rs3QJuly812.12pm.pdf (Accessed 14 August 2024).

Sanyal, S.K. and Sarmiento, Z., 2005. *Booking Geothermal Energy Reserves*, GRC Trans. v29, 8 Pages.

Society of Petroleum Engineers, 2018. Petroleum Resources Management System, Jun. 2018, https://info.specommunications.org/rs/833-LLT-087/images/PRMgmtSystem_V1.01%20Nov%2027.pdf (Accessed 14 May 2024).

Society of Petroleum Engineers, 2022. Extension of PRMS Principles to Non-Hydrocarbons, Aug. 2022, https://www.spe.org/en/industry/reserves/non-hydrocarbons/ (Accessed 9 May 2024).

UNECE, 2019. *United Nations Framework Classification for Resources Update 2019*, ECE ENERGY SERIES No. 61, 28 Pages.

UNECE, 2022. *Supplementary Specifications for the application of the United Nations Framework Classification for Resources (Update 2019) to Geothermal Energy Resources*, October 25, 2022, 26 Pages.

U.S. Congress, 1970. Geothermal Steam Act of 1970. *Public Law -1-581, December 24, 1970*, 19 Pages.

Winofa, N.C, Lesmana, A., Pratama, H.B., Saptdadji, N.M., and Ashat, A., 2020. The Application of Numerical Simulation Result for a Geothermal Financial Model with Probabilistic Approach: A Comprehensive Study, *IOP Conf. Series: Earth and Environmental Science, 417*, 13 Pages.

White, D.E., and Williams, D.L., 1975, Assessment of Geothermal Resources of the United States-1975: *U.S. Geological Survey Circular 726*, 155 Pages.

Williams, C.F., Reed, M.J., and Mariner, R.H., 2008. *A Review of Methods Applied by the U.S. Geologic Survey in the Assessment of Identified Geothermal Resources*, Open-File Report 2008-1296, 30 Pages.

Wilmarth, M., and Stimac, J., 2015. *Power Density in Geothermal Fields,* Proc. World Geothermal Congress, Melbourne, 7 Pages.

Wilmarth, M., Stimac, J., and Ganefianto, G., 2021. *Power Density in Geothermal Fields, 2020 Update*, Proc. World Geothermal Congress, Reykjavik, 2021, 8 Pages.

Yearsley, E., 2019. *Estimating Indicative Transaction Value of Geothermal Reserves Based on a Method from the Petroleum Industry*, GRC Trans. v43, 7 Pages.

Zarrouk, S.J. and Smiyu, F., 2013. *A Review of Geothermal Resource Estimation Methodology*, Proc. 35th NZ Geothermal Workshop, 8 Pages.

Assessing the Economic Value of Underground Thermal Storage for Hybrid Geothermal Power

Jonathan L. Ho, Juliet Simpson, and Anne Barlas

National Renewable Energy Laboratory

Keywords

Storage, Long Duration Storage, Capacity Expansion Model, Geothermal Hybrid, Value

ABSTRACT

Solutions are needed to address resource adequacy in the electric power system for highly decarbonized systems. The storage duration, the length of time a storage device can provide continuous output at its rated capacity, must be sufficient to receive full credit toward resource adequacy. Longer peaks and high fractions of variable renewable generation have increased the required duration to potentially seasonal durations. Underground Thermal Energy Storage (UTES) can be adapted to a hybrid storage power plant or heating and cooling applications to satisfy the need for long-duration storage. In this study, we use the Renewable Energy Deployment System (ReEDS) capacity expansion model to evaluate the increase in value for an enhanced geothermal system (EGS) resources by adding UTES. In modeled scenarios, using geothermal without storage as a baseline we compare the increase in economic value for plants with a range of storage characteristics. The added value of a hybrid storage plant changes depending on assumptions including the length of storage duration, efficiency, and ability to charge storage from the grid during periods of low energy prices. Relating proposed characteristics for geothermal UTES hybrids to the modeled economic value provides insight into economically viable costs for developing UTES as well as what combination of technology characteristics and future energy and policy assumptions drive significant value increases.

1. Introduction

As a result of rapid reductions in technology costs combined with policy support, variable renewable energy (VRE), including wind and solar, are expected to represent an increasing share of U.S. power generation. Geographic and resource diversity help address generator intermittency but have declining benefits at higher penetrations. Storage is a natural complement to VREs as it addresses energy imbalances between periods of abundance and relative resource scarcity. This paper examines the added economic value of long duration Underground Thermal Energy Storage (UTES) as part of a geothermal hybrid power plant to meet.

The increasing penetration of VRE benefits from geographic and spatial diversity, which helps mitigate uncertainty in power generation, especially when coupled with flexible transmission. Due to limitations in network topology and region spanning high net demand, there remain periods when storage or peak capacity will be utilized to ensure sufficient supply. Peaking capacity often natural gas fuels, which in highly decarbonized power systems may not be possible to operate. Ensuring sufficient supply with storage necessitates longer storage durations and the length of time storage can discharge at its rated capacity to address longer net peaks associated with increasing penetrations of VRE.

One prominent well-known challenge is the diurnal mismatch exemplified by the "duck curve," where solar generation peaks during the day resulting in low net load (demand minus variable renewable generation), as the sun sets the net peak demand reflects a steep ramp as PV generation decreases. This issue is driven by a mismatch in the timing of generation availability and the demand and can be bridged using long-duration storage to shift excess daytime generation to evening peak demand. Long-duration storage is a loosely defined term but, generally refers to storage periods exceeding four hours but less than several days or weeks. This is well suited to diurnal needs as well as periods of high net load lasting for a period under a week.

Longer periods of high net load can result from high demand for space heating and cooling with wind droughts and extended periods of low wind generation. This, combined with seasonal patterns in demand and resource availability, requires storage shifting energy by periods on a seasonal basis. Seasonal storage requires substantially longer storage durations (hundreds or thousands of hours), limiting the types of technologies that could feasibly address this need.

Existing storage technologies face scalability limitations when addressing long and seasonal durations. Batteries are highly flexible but have costs that quickly scale with longer storage durations. Pumped hydro can provide long-duration storage but is constrained by geographic limitations and is less feasible for seasonal durations. Hydrogen storage offers storage capacities at a seasonal scale but remains uncertain in terms of developing a large scale production, storage, transportation, and utilization system. In contrast, when coupled with geothermal energy, UTES presents a scalable and potentially cost-effective solution for long-duration and seasonal storage. UTES systems store thermal energy in underground reservoirs, making them suitable for extensive storage periods. When integrated with geothermal plants, UTES can enhance the flexibility of traditionally baseload geothermal plants, allowing them to store excess thermal energy and dispatch it as needed. This integration transforms geothermal plants from "use-it-or-lose-it" operations to more flexible resources. Enhanced Geothermal Systems (EGS), which are not restricted to naturally occurring subsurface permeability, can be deployed throughout the U.S., further broadening the applicability of geothermal-UTES solutions.

This paper focuses on assessing the value of geothermal energy integrated with UTES as a long-duration storage solution. By examining the scalability, cost-effectiveness, and operational benefits of geothermal-UTES systems, we aim to highlight their potential to enhance the flexibility and reliability of renewable energy systems.

1.1 Geothermal UTES Background

UTES has a proven history of being used as aquifer thermal energy storage (ATES) in Europe, particularly for district heating and cooling systems (Fleuchaus et al. 2018). The subsurface can

be used for thermal storage in multiple ways including boreholes, reservoirs, or aquifers for thermal storage, and that thermal energy can be used for direct heating, direct cooling, or improved heat pump efficiency. Using UTES for heating and cooling may be most beneficial for seasonal storage when the thermal source to charge the storage is free or nearly free. UTES for heating and cooling could significantly impact the electrical grid, both to statically reduce loads on the grid and to dynamically shift when electricity is used to meet heating and cooling loads.

Geological thermal energy storage (GeoTES) (or reservoir thermal energy storage (RTES)) creates an artificial warm subsurface reservoir via heat input from the surface that can later be extracted for use to generate electricity (or be used as heat) (McTigue et al. 2023; Wendt et al. 2019; Sharan et al. 2021; Atkinson et al. 2023). Typically, the reservoir is accessed via a doublet with two wells (one "hot" and one "cold"), operated in a push/pull fashion (McTigue et al. 2023). One example of this would be to pair a concentrating solar power plant (CSP) with GeoTES. The CSP plant would then store excess heat during the day in the subsurface for later use at night (long-duration storage) or in the winter (seasonal storage). This concept is being explored by Premier Resource Group in California (Cox 2023) but has not yet been implemented in the field. GeoTES allows for significantly longer storage durations than current thermal storage technologies (molten salt tanks, packed bed, hot water tanks, etc).

Another example of UTES is in-reservoir energy storage (IRES) for enhanced geothermal systems (EGS). IRES uses pressure-based energy storage (rather than directly using thermal) within an EGS reservoir. IRES allows for a build-up of geothermal fluid in the subsurface (via either increased injection pumping while keeping outlet pumping constant or throttled output flow while keeping injection pumping constant), increasing the mass of geothermal fluid within the reservoir and thus increasing the pressure. The system can then choose to discharge additional hot fluid at a later time or discharge it at the normal rate but using less injection pumping (and thus have a higher net power production). While the energy is stored in the form of pressure, it is utilized as heat to drive a power cycle.

IRES was first defined in Ricks et al. (2022) and is being pursued for commercialization by Fervo Energy (Temple 2023) as "FervoFlex". It is currently at a low technology readiness level, and many questions remain about its potential operation, performance, and cost.

2. Methods

2.1 ReEDS Background

The Regional Energy Deployment System (ReEDS) model is NREL's flagship capacity expansion tool designed to model the evolution of the U.S. power system (Ho et al 2021). ReEDS considers the requirements of operating a power system using existing and new investments in generation storage and transmission while minimizing total operating and investment costs. ReEDS is characterized by its granular spatial and temporal resolution. It divides the U.S. into regions that preserve transmission network topology and provide detailed insights into resource and demand diversity. ReEDS utilizes consistent weather year data (2007-2013) to capture the variability and renewable energy sources and demand, ensuring a robust grid integration and reliability analysis.

The model includes a comprehensive representation of generation technologies and significant detail in characterizing renewables such as geothermal, solar, and wind. Resource supply curve information conveys cost and energy generation potential for generation technologies, including geothermal. Specific technology and year define plant capital, operating, and finance costs, with assumptions documented in NREL's Annual Technology Baseline.

ReEDS has the option to make, if necessary, new investments to ensure all system requirements are met. When selecting an investment, the mathematical optimization considers the revenue for services provided (energy, capacity, renewable portfolio) against the investment and operating costs over an economic lifetime. Investments are only selected if revenue meets or exceeds costs. This differs from metrics like Levelized Cost of Energy or Levelized Cost of Storage, which are based on cost normalized to predetermined roles. Levelized cost metrics are not able to represent a mix of services provided (e.g., energy + capacity) and do not consider the value of those services at the time they are provided, which may significantly exceed the levelized cost.

2.2 Model Expansion

The storage available with geothermal UTES is directly linked to an in-plant energy source similar to dispatchable hydroelectric power or concentrating solar power with storage. This differs from standalone storage technologies like batteries and pumped hydro storage, where energy for storage is sourced from the grid. We developed a generalized hybrid storage plant representation based upon the existing solar PV hybrid representation.

In a geothermal context, the following parameters define the operations of a hybrid storage plant with long-duration storage:

- cap: The design capacity defined for a geothermal plant relative to the size of its geothermal field that operates electricity production in equilibrium with thermal energy.
- r: The ratio between the capacity defined by size of thermal field and the size of the turbines used to produce electricity.
- eff: The round trip efficiency of energy stored in a given time period.
- dur: The length of time that the geothermal hybrid could discharge from storage at its rated capacity.

The plant has three operating decisions:

- Gen: Electricity produced from available energy from the geothermal field.
- In: Energy from geothermal field is stored through UTES in terms of electric efficiency.
- Out: Energy withdrawn from storage and used to produce electricity.

For a geothermal hybrid, the operations are defined by the following constraints:

1) Defines available geothermal energy in each time period.

$$cap = Gen_t + In_t \quad \forall t$$

2) Electricity produced cannot exceed the rated turbine capacity in each time period.

$$Gen_t + eff * Out_t \leq \frac{cap}{r} \quad \forall t$$

These equations are coupled with overarching storage equations that enforce the maximum state of charge for energy storage, defined by multiplying the storage duration by the design capacity. The storage state of charge is tracked between subsequent time periods, allowing it to increase if plant generation is lowered to increase storage or decrease if a plant withdraws energy from storage.

The addition of storage characteristics allows modeled geothermal power plants to store energy to produce during more valuable time periods, increasing the value of a prospective plant. This can allow hybrid geothermal plants the flexibility to operate responsively to grid conditions and complement the variability of solar and wind. The higher sizing of turbines relative to a conventional geothermal design allows a plant to increase its capacity contribution towards resource adequacy requirements.

2.3 Quantifying Value

Geothermal with UTES is in an early stage of commercialization with substantial uncertainty in cost. A conventional grid analysis would begin with specified costs and associated characteristics and model the investment in new capacity. Instead, we approached this by identifying how much value is added to a plant if different storage characteristics were applied. This characterizes the cost premium compared to a geothermal plant without storage, which is economically justified. The quantified added value can be calculated specific to the location and scenario to identify how geothermal UTES could specifically be applied.

ReEDS is a linear optimization model, which, while reporting investments and operations, also provides marginal prices on constraints and reduced costs on decision variables. These are a property of the relationship between the primal form (minimization) of an optimization problem and its dual form (maximization). This relationship can be utilized to calculate a reduced cost for a decision variable, which is the amount that costs would need to decrease in order for it to become part of the optimal solution. For any decision variable that is part of the optimal solution, the reduced cost must be exactly zero; otherwise, it would be possible to improve the model solution. Decision variables that do not form part of the optimal solution have negative indicating that marginal costs exceed marginal revenue. Reduced costs can indicate whether a decision variable would enter the basis if revenue increased or costs fell.

We utilize the reduced cost on the EGS investment decision variable to identify added value from adding storage characteristics utilizing methods described in Mai et al. (2021). Varying the characteristics of storage efficiency, duration, and capacity increases the marginal revenue for prospective EGS investments. Leaving cost parameters unchanged, comparing the change in reduced cost of an EGS plant with storage against a reference plant without storage provides an added economic value associated with these characteristics.

2.4 EGS IRES Parameter Range

As compared to conventional hydrothermal resources, EGS has the potential to be implemented more widely across the United States. IRES is a unique option for energy storage with EGS that

can be sited at any EGS plant with little to no additional cost. The key to IRES is not installing new storage equipment but changing how the system operates. Though IRES may incur some additional costs from oversizing the pumping or power production equipment, it otherwise does not add capital cost to the system. Thus, IRES will be investigated for its potential impacts on the electrical grid.

The operation of an IRES system was modeled for daily load shifting in (Ricks, Norbeck, and Jenkins 2022), resulting in reported annual efficiency values. It is suspected that there is potential for hundreds of hours of seasonal storage, but the roundtrip efficiency may be significantly reduced, and this seasonal storage aspect has not been investigated in detail. To provide reasonable bounds for seasonal storage, we see that (Ricks, Norbeck, and Jenkins 2022) finds a storage duration used in one of their model runs to be 450 hours, while (Ricks et al. 2024) notes a storage duration as high as 1100 hours. Corresponding seasonal storage efficiencies are never discussed, so a large range is considered. Efficiency depends on storage pressure, shut-in time, and discharge power, among other factors. Ricks found a range of roundtrip efficiencies from 60-90% for different simulations focused on diurnal storage cycling, with an average across all studied scenarios of 81% (Ricks, Norbeck, and Jenkins 2022).

For storage power, storing/discharging an extra 10-20% above the rated power for the geothermal power plant is discussed (Ricks et al. 2024; Ricks, Norbeck, and Jenkins 2022). Additionally, overrating the power cycle compared to the geothermal field is discussed up to 60% (though details to support that level of storage within that subsurface are not provided).

2.4 Modeled Scenarios

In our analysis we modeled the added value of an EGS with UTES focused on long duration storage. Modeled configurations had up to 20 hours of storage and a round-trip storage efficiency of 90%. The ratio between the design capacity and the turbine capacity was assumed to be 83%. These properties were applied to geothermal resources in the Western Interconnection and modeled in ReEDS through 2050. These properties were applied to the existing geothermal resource supply curve utilized in ReEDS. ATB moderate costs for geothermal were used, which intentionally kept EGS costs prohibitively high for investment. This ensured that in our simulations, EGS with storage would not be built and would alter the price equilibrium of the optimal solution. However, it would allow us to compare the relative shift in reduced cost.

The need for longer durations of seasonal storage is in part a function of the fraction of variable renewables deployed. In addition to a reference policy scenario, which maintains all on the books policies we also modeled a high carbon tax scenario with $600 per metric ton in 2035.

3. Results

The western U.S. has an existing higher abundance of renewable resources relative to other regions within CONUS. Under reference policies, the share of renewable energy reaches 80%, while with a CO2 tax, this increases to 98%. Adding the storage characteristics shows a significant initial increase in the added value of the plant. The most significant component of this is a result of the rise in capacity value from the oversizing of the turbines assumed in a storage configuration.

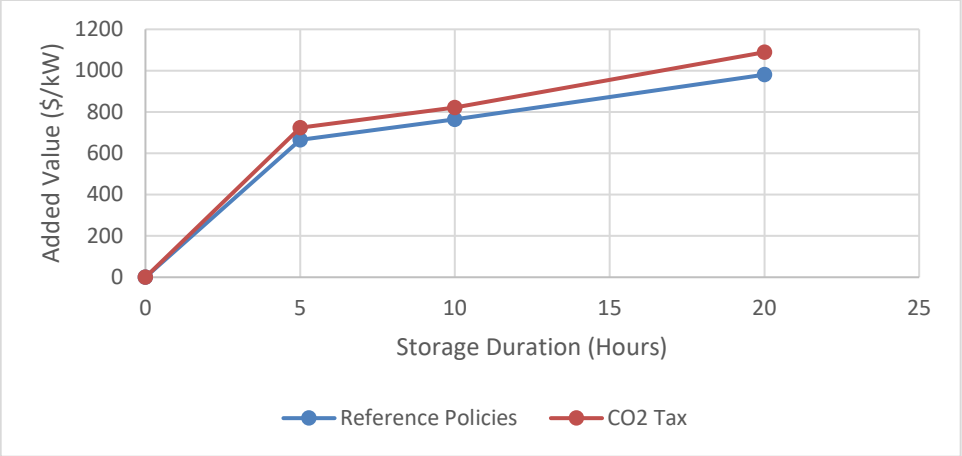

Figure 1. The average added value for EGS with UTES at different storage durations for reference policies and 100% decarbonization cases.

Increasing the storage capacity grows the plant value at a slower rate relative to the initial boost. In both cases, this increase continues through the modeled 20 hours of storage duration, suggesting that the storage duration was not saturated with 10 hours of storage duration. The gap in added value between the Reference Policies case and the CO2 Tax case increases at 20 hours of storage duration, indicating that the higher renewable penetration is associated with a greater relative need for long-duration storage.

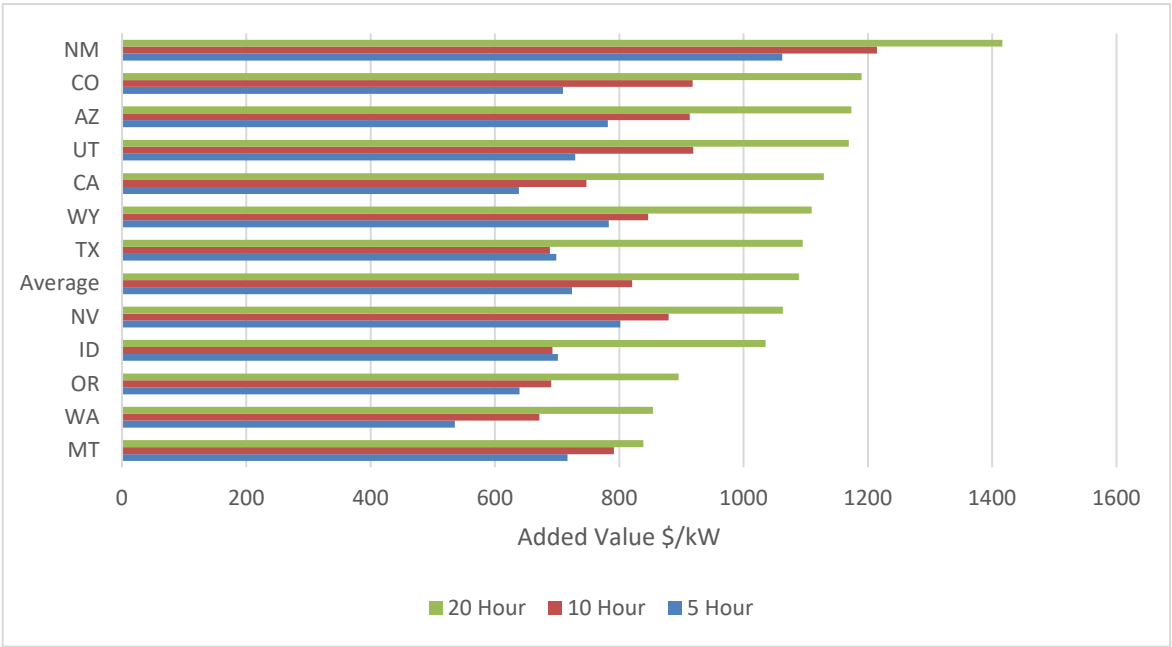

Figure 2. Average added value with by storage duration for EGS with UTES by State in CO2 Tax scenario.

The earlier west wide average added value obscures regional differences in added value for EGS with UTES. Examining the state average added value for EGS with UTES under the CO2 tax scenario reveals regional trends connected to the availability of location-specific resources. The average added value for UTES is up to 30% higher in New Mexico compared to the. Among the states, there is a north-south divide, with southern states typically recording higher added values. This is likely a combination of two effects. States below the west-wide average have significant existing hydropower capacity, while not all of this is dispatchable, with a substantial number of run-of-river hydropower plants in the Pacific Northwest, the availability of hydropower resources suppresses the economic value of UTES storage as it has significant overlap with the type of services EGS UTES could provide. Those being emissions-free storage and capacity. While regions with higher-than-average added value have hydro resources, they represent a proportionally smaller share of in-state resources.

The other factor that elevated regions with higher favorability and investment in solar PV. At 98% renewable generation, there is a limit to the load and resource diversity that can be leveraged to ensure sufficient electric power supply during periods of system stress. Low production periods can occur, requiring peaking units and energy shifting through storage, but they will occur on a more regular and predictable basis in regions with high fractions of PV due to the diurnal production cycle. For this reason, the combination of reduced dispatchable hydro and increased solar favorability form a complement with long-duration storage, increasing the value in these regions.

4. Discussion and Future Work

Using reduced costs in linear optimization to estimate the added value of adding long-duration storage characteristics to geothermal technologies offers a marked improvement over traditional metrics like LCOE and LCOS. Reduced cost metrics can directly measure the changes in revenue for hypothetical plant configurations without requiring a bottoms up calculation of construction and operating costs. The method provides insight into regional and scenario-specific revenue improvement differences for geothermal with UTES storage. While LCOE and LCOS remain useful metrics for comparing proposed technologies, they have limited insight into how a plant would operate and whether an optimal mix of services would yield a net positive value. The added value metric remains compatible with bottoms-up engineering cost analysis and can provide an economically justifiable cost premium over a more conventional design. This type of analysis scales well and allows decision-makers and designers to understand the range of grid service niches on the grid that a hypothetical UTES design could address.

Longer durations of UTES storage, less optimistic round trip efficiencies, parasitic storage losses, and larger sizing of turbines for a more rapid drawdown of stored energy are all dimensions we are interested in exploring in future analysis. Analysis of seasonal duration storage dramatically increases computation complexity but can be overcome with national scale analysis through storage with sparse chronology, linking operations in representative days to the actual days in the year to track seasonal shifts in energy. Work is being scaled up to leverage high-performance computing capabilities to extend this analysis to the national scale.

The scalability of UTES makes it a useful tool for addressing long-duration and seasonal storage needs on the grid for high-renewable and low-carbon power systems. UTES can be linked to other technologies, including Concentrating Solar Power with Geologic Thermal Energy Storage as well

as stand-alone Carnot batteries. The methods applied here to quantify added value for geothermal with UTES could be used to analyze both technologies' long and seasonal storage configurations. We are assessing the added value to CSPs of long and seasonal-duration storage using methods consistent with those discussed in this paper.

The applied methods could be implemented in other capacity expansion modeling frameworks based upon optimization with convex conditions that ensure global optimality for a solution. ReEDS is an open-source model, and the necessary metrics to calculate reduced costs for proposed technologies are built into the model. Other analysis teams could utilize this model to assess configurations and designs relevant to their design and analysis efforts.

REFERENCES

Atkinson, Trevor, Daniel Ginosar, Jakub Toman, Birendra Adhikari, and John Podgorney. 2023. "Reservoir Thermal Energy Storage Benchmarking." INL/RPT-22-69373-Rev002, 1997222. https://doi.org/10.2172/1997222.

Cox, John. 2023. "West Kern Energy Project Would Turn Depleted Oil Reservoir into Synthetic Geothermal Storage." The Bakersfield Californian, June 4, 2023. https://www.bakersfield.com/news/west-kern-energy-project-would-turn-depleted-oil-reservoir-into-synthetic-geothermal-storage/article_aa5f9646-0227-11ee-ad6e-afd238d89f1e.html.

Fleuchaus, Paul, Bas Godschalk, Ingrid Stober, and Philipp Blum. 2018. "Worldwide Application of Aquifer Thermal Energy Storage – A Review." Renewable and Sustainable Energy Reviews 94 (October):861–76. https://doi.org/10.1016/j.rser.2018.06.057.

Ho, Jonathan, Jonathon Becker, Maxwell Brown, Patrick Brown, Ilya Chernyakhovskiy, Stuart Cohen, Wesley Cole, et al. 2021. "Regional Energy Deployment System (ReEDS) Model Documentation: Version 2020". Golden, CO: National Renewable Energy Laboratory. NREL/TP-6A20-78195. https://www.nrel.gov/docs/fy21osti/78195.pdf.

Mai, Trieu, Matthew Mowers, and Kelly Eurek. 2021. "Competitiveness Metrics for Electricity System Technologies". Golden, CO: National Renewable Energy Laboratory. NREL/TP-6A20-72549. https://www.nrel.gov/docs/fy21osti/72549.pdf.

McTigue, Joshua D, Juliet G Simpson, Guangdong Zhu, Ghanashyam Neupane, and Daniel Wendt. 2023. "Design of a Geothermal Power Plant With Solar Thermal Topping Cycle." In GRC Transactions.

Mowers, M. and Mai, T., 2021. "A relative value framework: Why do different electricity system technologies have different economic value?". The Electricity Journal, 34(8), p.107007.

Ricks, Wilson, Jack Norbeck, and Jesse Jenkins. 2022. "The Value of In-Reservoir Energy Storage for Flexible Dispatch of Geothermal Power." Applied Energy 313 (November 2021). https://doi.org/10.1016/J.APENERGY.2022.118807.

Ricks, Wilson, Katharine Voller, Gerame Galban, Jack H. Norbeck, and Jesse D. Jenkins. 2024. "The Role of Flexible Geothermal Power in Decarbonized Electricity Systems." Nature Energy, January, 1–13. https://doi.org/10.1038/s41560-023-01437-y.

Sepulveda, Nestor A., Jesse D. Jenkins, Aurora Edington, Dharik S. Mallapragada, and Richard K. Lester. 2021. “The Design Space for Long-Duration Energy Storage in Decarbonized Power Systems.” Nature Energy 6 (5): 506–16. https://doi.org/10.1038/s41560-021-00796-8.

Sharan, Prashant, Kevin Kitz, Daniel Wendt, Joshua McTigue, and Guangdong Zhu. 2021. “Using Concentrating Solar Power to Create a Geological Thermal Energy Reservoir for Seasonal Storage and Flexible Power Plant Operation.” Journal of Energy Resources Technology 143 (1): 010906. https://doi.org/10.1115/1.4047970.

Temple, James. 2023. “This Geothermal Startup Showed Its Wells Can Be Used like a Giant Underground Battery.” MIT Technology Review. March 7, 2023. https://www.technologyreview.com/2023/03/07/1069437/this-geothermal-startup-showed-its-wells-can-be-used-like-a-giant-underground-battery/.

Wendt, Daniel, Hai Huang, Prashant Sharan, Kevin Kitz, Sidney Green, John McLennan, and Ghanashyam Neupane. 2019. “Flexible Geothermal Power Generation Utilizing Geologic Thermal Energy Storage.” Idaho National Laboratory.

An Economic Evaluation of Parasitic Losses and the Impact of Conformance Control on Parasitic Losses in an EGS Horizontal Well

Patrick Mays, William Fleckenstein, Hossein Kazemi, Kaveh Amini, Balnur Mindygaliyeva

GTO Technologies, Inc.

Colorado School of Mines

Keywords

Geothermal, Enhanced Geothermal Systems, EGS, Economics, Parasitic Losses

ABSTRACT

In this paper we present a mathematical model to evaluate the economic impact of parasitic losses on electrical generation opportunity costs due to frictional pressure losses and thermal losses in an EGS system. Specifically, we will evaluate the impact of rate vs. wellbore geometry (well length, casing size, number of hydraulic fracture stages, etc.) as well as doublet and triplet well systems. The analysis will quantify the economic costs of parasitic losses of the electricity generated by the facility and equipment that circulates water through the EGS. Additionally, we will evaluate the impact of conformance control measures used in oilfield waterfloods and why these techniques would not be economical in EGS.

We have presented a mathematical model to estimate the system parasitic power losses for a given flow rate. First, the frictional loss through a given pipe diameter is calculated with the Reynolds number. This method uses the Roughness of the pipe, and the pipe diameter to determine the friction pressure loss for different wellbore geometries at varying flow rates. The method then calculates the friction (or, equivalently the effective fracture permeability) in the induced fracture system. This model provides a deterministic basis of hydraulic horsepower requirements of the circulation system and the impacts of the circulating system's parasitic losses on an EGS development's economics. This evaluation includes the traditional conformance control methods of tubing, packers, and Injection Control Devices (often called Outflow Control Devices) on the energy requirements of the EGS circulation system.

This model demonstrates that the largest operating cost of an EGS system is the "Opportunity Cost" associated with using the generated carbon-free energy to run the circulating system. If this cost is not fully understood and modeled prior to deploying the EGS, the reduction of the salable

electricity could cause a significant impact to the economics. Furthermore, if traditional 'plug and perf' completion techniques do not provide the required conformance control and traditional methods of conformance control are required to manage injection, the frictional losses could be so great that the system requires more electricity than it generates.

In the paper first we examine the relative economic effects of the system circulation rates and wellbore geometric configuration on the opportunity costs of parasitic losses including the impact of post-facto conformance control, in addition to the typical operating cost estimate based on plant and field size. Second, we illustrate the need to properly model and understand parasitic losses prior to the design of the development plan for any EGS project. Third, we discuss the impact of alternative conformance control measures on the project economics.

1. Introduction

The heat within the Earth has been used to generate carbon free electricity since 1904 when the first geothermal power plant was built at the Lardorello dry steam field in Tuscany, Italy. From a humble beginning of 10 kilowatts (kW) of energy, Lardorello Geothermal Complex has grown to a capacity of 769 megawatts (MW) and currently it is the 2nd largest geothermal power plant in the world (Statista, 2024).

The current global geothermal power generation capacity is 16 gigawatts (GW), and the United States lead the world with 3.9 GW of geothermal power (Figure 1).

In the United States the Geysers Geothermal Complex is capable of producing 900 megawatts (MW) of electricity through its 18 power plants. However, even with the tremendous resources like the Salton Sea and the Geysers Fields in California, the Mean Net Generation of geothermal electricity in the United States has stagnated between 1.5 GW and 1.9 GW since 1990 (Robins, et al. 2021).

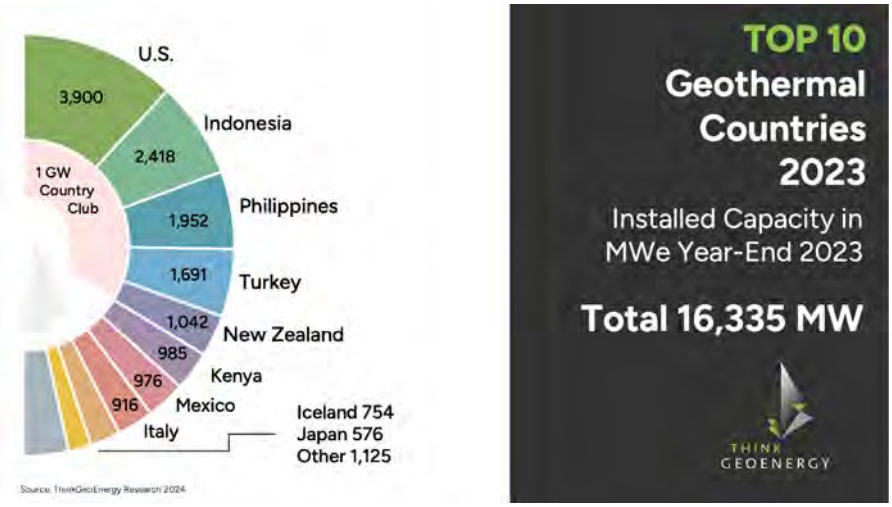

Figure 1: Top 10 geothermal countries in the world as of 2023 (ThinkGeoEnergy, January 2024).

The primary cause of this stagnation in growth is because the main source of the geothermal power in the world is from subsurface hot water reservoirs known as hydrothermal resources where the reservoirs' high temperatures and permeabilities provide natural or pumped flow of superheated

water to the surface for economical generation of electricity. Unfortunately, scarcity of hydrothermal fields and the trifling discovery of new fields that can significantly grow carbon-free power to offset current declining fields are the reasons for non-growth of hydrothermal reservoirs. It is estimated that only 2% of the geothermal resources in the world are accessible using hydrothermal technology (Geiser, Marsh and Hilpert, 2016). Between 2016 and 2021, eleven (11) plants were taken offline, removing 103.3 MW of nameplate capacity and only seven (7) new plants have gone online during this time supplying 186.3 MW of nameplate capacity (Robins, et al. 2021).

In an attempt to grow geothermal power generation beyond the limits of hydrothermal systems, there has been a great deal of research and development resulting in advances in a newer form of geothermal power generation referred to as Enhanced (or Engineered) Geothermal Systems (EGS). In contrast to the high-permeability hydrothermal systems, the EGS heat reservoirs typically consists of hot-dry-rocks with extremely low porosity, permeability; and no water is present in the limited pore spaces. This resource is referred to as Hot Dry Rock (HDR). To produce heat from an HDR, a subsurface heat exchanger must be created. Water can be injected into this subsurface heat exchanger and circulated to extract heat from the rock. Specifically, one creates an artificial link between 2 or more horizontal bore holes using hydraulic stimulation technology to allow cold water to be pumped down an "injector" well to a depth of sufficient geothermal heat. Once at depth, the water will be heated within the fracture network by the surrounding rocks to a temperature sufficient to generate electricity. The heated water will then be recovered to surface via the producer(s) and typically run through an Organic Rankin Cycle (ORC) plant to generate carbon free electricity

The key enablers to EGS are step change technology advances in extended reach, horizontal drilling and multi-stage hydraulic fracturing due to the development of shale hydrocarbon resources. Wells that with a true vertical depth (TVD) of 9,000 ft and a lateral departure of greater than 5,000 ft horizontally are now being drilled in under 25 days, in rocks that 7 years ago would have taken over 90 days to drill at 3 to 4 times the cost. In addition to drilling and stimulating the wells, the EGS systems require continuous injection of water into the target hot rock zone because of the absence of water in such systems (Mindygaliyeva, et al. 2024).

The availability of a water source for use in the EGS presents multiple challenges that must be examined for any EGS development project to be economically successful. First, access to the source and quantity of water for well stimulation (i.e., hydraulic fracturing) and fluid circulation must be established as part of project selection. Second, daily rates and volumes circulated to generate electricity to be economically viable must be understood. Third, modeling the required horsepower to run the circulation system and the potential impacts on for-sale-electricity (referred to as parasitic losses). Fourth, managing conformance control solutions (to distribute water evenly in the hydraulic fracture flow paths) and their impact on parasitic losses and thermal decline.

2. Key Variables Impacting Economics in an EGS System

Several key variables impact the economics of EGS. These variables were evaluated stochastically (Fleckenstein et al, 2023). The three dominant independent variables in EGS economics are (1) thermal decline, (2) flow rate per well, and (3) Power Purchase Agreement (PPA) pricing. It is not the intent of the current analysis to project what PPA pricing to use in economics, nor to project how long the current tax credits will last, nor whether carbon credits will enter the United States

market the same way as in the European Union. Rather, using a fixed set of assumptions for these variables, this analysis focuses on the thermal decline and flowrate per well to understand their impact on the net power production.

2.1. EGS System Heat Extraction Fundamentals

For an EGS system to successfully function, a minimum of two horizontal wellbores must be interconnected through a system of fracture stimulations. When there is one injector and one producer in a pair, the system is referred to as a "doublet" (Figure 2). It is critical that controlled water flow passed from the injection well to the production well as evenly as possible across the fracture system. As the water flows through the fracture to the production well, the geothermal energy from the Earth heats the fluid. The hot water flows up the production well and is converted into electricity at the surface using an ORC.

The alternate EGS system to the doublet is the 'triplet'. The concept of the triplet is that there is a single injector flanked on each side by a producer, creating a one injector, two producer system (Figure 3). The fractures are generated from the injector and will grow out radially in the direction of the maximum horizontal stress. If the two producers are correctly orientated on either side of the injector, perpendicular to the principal maximum stress, the fracture "wings" will intercept both producers. A properly engineered triplet system is ideal from a cost perspective, because only 1 set of stimulations from the injector can connect it to two producers, thus reducing completion costs by 50% and reducing the need to drill a second injection well.

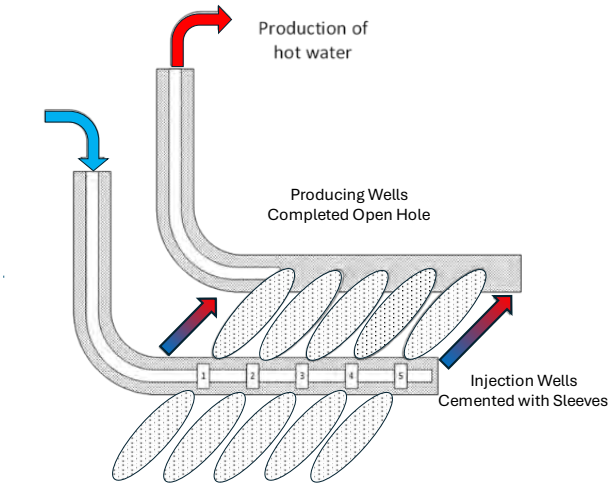

Figure 2: Doublet EGS Well System

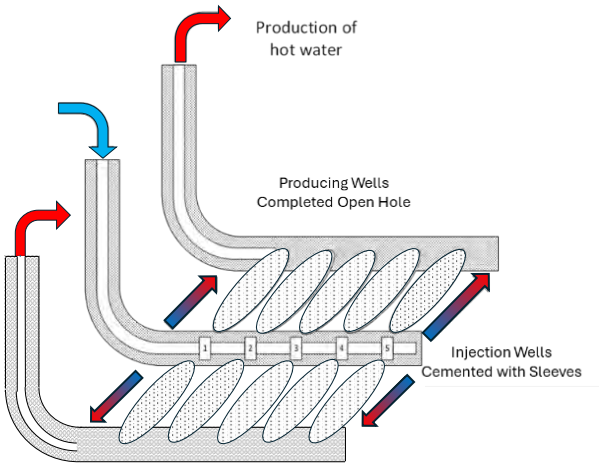

Figure 1: Triplet EGS Well System

2.2. Estimating Power Conversion and Required Flow Rate

The analysis method used starts by understanding the initial resource temperature (T_{r0}, in this analysis assumed to be the same as the plant input temperature for simplification) by drilling a regional exploration well. Once the temperature profile is understood, the required flow rate per well is calculated to design the subsurface system rate to match the power generation, in this case

the ORC. Starting with a base assumption that systems of 5 MW per doublet or 10 MW per triplet are required to be economic. Two methods were used to determine the estimated flow rate based on the resource temperature.

A common source to predict power from a binary plant (e.g., an ORC system) is to use equation 7.1 by Tester published in the 2006 MIT-led report (MIT led interdisciplinary panel 2006) where Tester extrapolated the thermal efficiency (η_{th}) based on the geofluid temperature of eight operating binary plants. Tester's linear regression resulted in the following formula for thermal efficiency (MIT led interdisciplinary panel, 2006):

$$\eta_{th} = 0.0935\,T - 2.3266 \quad (1)$$

Where,

$\eta_{th} = thermal\ efficiency,\ \%$ (For reservoir temp 90 ^{o}C - 250 ^{o}C $\Rightarrow$ 6 *to* 21%)

$T = Temperature\ of\ produced\ fluid,\ ^{o}C$

The equation for calculating electric power:

$$Q = \dot{m} c_w \Delta T \quad (2)$$

Where,

Q = electric power (J/s)

$\dot{m}$ = mass flow rate entering power generation turbine (kg/s)

c_w = specific heat of water (J/(kg·˚C)),

$$\Delta T = inlet\ T - Outlet\ T, (^{\circ}C) \quad (3)$$

Considering thermal efficiency of power plants, we can calculate the megawatt output of the plant using the following equation:

$$Q\eta_{th}/1{,}000{,}000 = plant\ power, MW \quad (4)$$

Utilizing the average plant ΔT of 73˚C (Moon et al, 2012) in plants greater than 150˚C and less than 250˚C, the required production rate to generate 5 MW can be solved for the assumed initial reservoir temperature T_{r0} of 205˚C at 60,200 BWPD per producer. Note, that the injection rate must account for formation fluid loss as documented at Blue Mountain (Norbeck and Latimer 2023). In this analysis it is assumed a fluid loss to formation of 8%.

As a validation check against Tester's formulas, the power conversions factors from Moon (Moon and Zarrouk, 2012) were evaluated for the same data set of plants greater than 150˚C and less than 250˚C. This resulted in an average power conversion factor of 4.72E-07 MW-hr / (˚C·BWPD) and a resulting rate per producer of 51,700 BWPD for 5 MW, representing a 16% difference from Tester's equation. For the Gringarten model used in this paper, the average of the two rate predictions of 56,000 BPD was used with a power conversion factor of 4.36E-07 MW-hr / (˚C·BWPD).

It is important to note that ~200˚C is recognized as a critical break over point between flash systems and binary systems. If a flash system is used, the efficiency of the plant could potentially reach 31% as documented by an MIT led interdisciplinary panel (MIT, 2006). However, this efficiency will have to be derated assuming that the cooling tower is replaced with air cooling to maintain 100% capture of the fluids for reinjection. Flashing also brings additional scaling issues for the plant depending on the water chemistry and must be evaluated on a case-by-case basis. For these reasons, all assumptions in this analysis use ORC power plants.

2.3. Modeling of a Subsurface Heat Exchanger

Modeling of subsurface heat exchanger is the same for both the 'doublet' and 'triplet'. In a typical EGS system, the wells are drilled to a formation that has a geothermal temperature of 200˚C to 260˚C. As the fluid is injected into the well it will slowly increase in temperature with depth. Once the fluid exits the wellbore the fluid is forced through the fracture where the heat from the earth will raise the temperature of the fluid to approximately the same temperature as the formation. The water will continue to the production well where it is produced back to surface for conversion to electricity. The temperature of the water will slowly decrease as it travels to the plant as a function of depth, wellbore geometry, flowrate, and ambient temperature. This can be countered through various insulation technologies in the market, such as vacuum insulated tubulars and cement with low thermal conductivity. For simplicity in this model, the bottom hole outflow temperature has been assumed as the same as the surface temperature.

The basis of modeling the heat exchanger using horizontal wells with multiple fractures in a reservoir was first developed by Gringarten, (Gringarten et al., 1975), and further advanced by Doe (Doe, McLaren and Dershowitz, 2014). Gringarten's heat extraction model was based on a set of parallel fractures with uniform properties—including fracture height (y), length (z), transmissibility (T), flow rate (q), and fracture half-spacing (xe). The length (z) represented the distance from the injector to the producer, and the total length (x) represented the horizontal length of the wellbore with the model allowing for a variable number of fractures (n) (Figure 4).

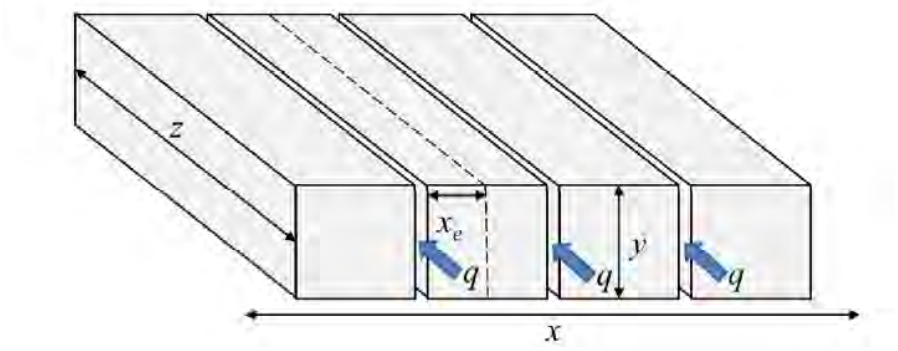

Figure 4: Gringarten et al. model, modified by Doe et al. (Augustine, 2016).

Using this model Gringarten developed a solution for thermal modeling an EGS system using dimensionless produced temperature (T_{wD}), dimensionless time (t_D), and dimensionless half-fracture spacing (X_{ED}), later simplified by Doe (Doe, McLaren and Dershowitz, 2014).

$$T_{wD} = \frac{T_{Ro} - T_w(z,t)}{T_{Ro} - T_{wo}} \tag{5}$$

Where

$T_w(z,t) =$ water temperature at z and t, ^oC
$T_{Ro} =$ intilal rock temperature at point of injection, e.g., 300^oC
$T_{wo} =$ water injection temperature, e.g., 40^oC

$$t_D = \frac{(\rho_w c_w)^2}{K_R \rho_R c_R}\left(\frac{q}{z}\right)^2 (t - \frac{z}{v}) \cong \frac{(\rho_w c_w)^2}{K_R \rho_R c_R}\left(\frac{q}{z}\right)^2 t \quad (6)$$

Where,

$q =$ volumetric flow rate per fracture per unit thickness in y direction, cm^3/s
$(e.g., 1.45 \text{ x } 10^5 cm^3/s)$
$z =$ distance above the injection point, cm
$v =$ water velocity in fracture, cm/s
$t =$ time, s
$\rho_w =$ *water* density, g/cm^3; e.g., 1.0 g/cm^3
$c_w =$ *water specific heat*, $cal/(g.^oC)$; e,g., 1.0 cal/(g.^{o}C)
$\rho_R =$ *rock* density, g/cm^3; e.g., 2.65 g/cm^3
$c_R =$ *rock specific heat*, $cal/(g.^oC)$; e,g., 0.25 cal/(g.^{o}C)
$K_R =$ *rock* thermal coductivity, cal/(cm.s.^{o}C) ; e.g., 6.2 x 10^{-3}cal/(cm.s.^{o}C)

$$x_{ED} = \frac{\rho_w c_w}{K_R}\left(\frac{q}{z}\right) x_E \quad (7)$$

Where,

$x_E =$ *fracture spacing*, *cm*; *e.g.*, $4,000$ *cm*

Using these dimensionless values and assumed uniform properties, Gringarten published these type curves for solving thermal decline based on reservoir properties and flow rates (Figure 5).

As noted by Doe, the function of thermal decline depends on the mass flow rate in the fracture vs. thermal diffusion rate from the rock matrix to the fractures (Figure 6). If the flow rate is too high within the fracture, it will travel faster than the rock matrix can supply heat to the fracture face. Alternatively, at lower flow rates, the thermal front in the matrix is better able to keep up with the rate of fluid flow in the fracture, causing a slower decline response, but steeper decline once it starts.

There must be a balance as fluid is pumped past the down hole heat exchanger to maintain the low-rate thermal front of Figure 6. Premature thermal decline from the high-rate thermal front can be caused by two events. The first event is pumping too much water down the injector compared to

the relative amount of fracture face surface area the system has, causing the entire system to prematurely decline. The second is a lack of conformance control, where the correctly calculated amount of water is pumped downhole, but it is preferentially traveling down a small subset of fractures, causing these fractures to prematurely cool, impacting the average outlet temperature's decline. This event is often referred to as '***short circuiting***'.

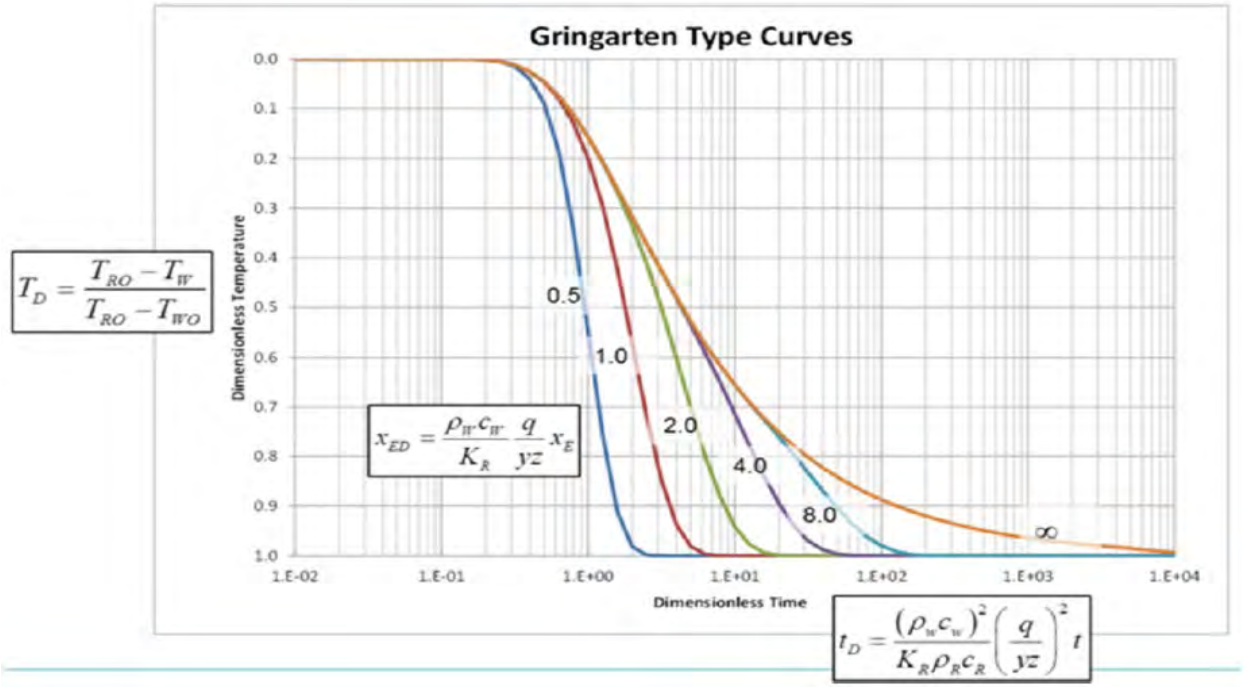

Figure 5: Gringarten type curves (Augustine, 2016).

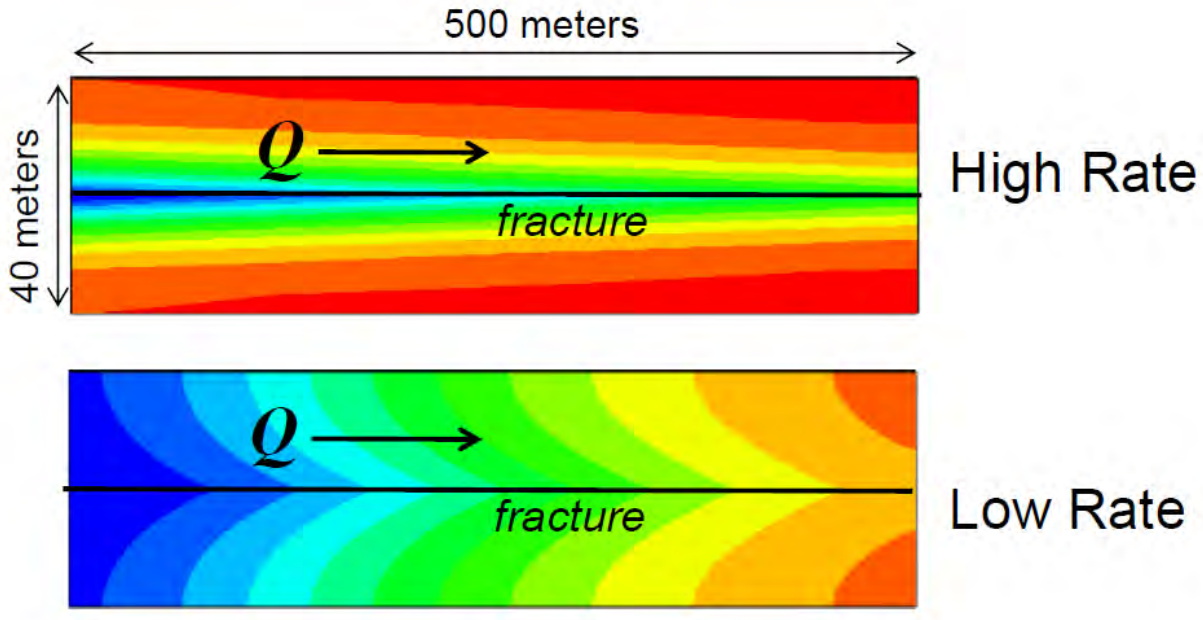

Figure 6: Diagram of thermal front vs flow rate (Doe, McLaren and Dershowitz, 2014).

Using the work established by Gringarten et al., and Doe et al. for a simplified model, a theoretical EGS was designed to model the thermal decline of a system. Using the parameters in Table 1, a "doublet" EGS system was modeled.

Table 1: EGS Parameters for Gringarten Thermal Decline

Density of Water	ρ_w	874 kg/m^3		Horizontal length	X	2414 m	7920 ft
Heat Capacity Water	c_w	4180 J/Kg˚C		spacing between horizs.	y	220 m	722 ft
Thermal Cond. Rock	K_R	3.00 J/m˙s ˚K		Frac height (penny fracs)	Z	440 m	1444 ft
Density of Rock	ρ_R	2750 kg/m^3		Total Flow Rate	q	0.103 m^3/s	56,000 BPD
Heat Capacity Rock	c_R	790 J/Kg˚C		Initial Reservoir Temp	T_{R0}	205 ˚C	478 ˚K
	C_1	2.05E+06 s/m^2		Abandonment Temp	T_w	164 ˚C	437 ˚K
	C_2	1.22E+06 s/m^2		Reinjection Temp	T_{w0}	60 ˚C	333 ˚K
				Dimensionless Outlet Tem	T_{wD}	0.28	
number of fractures	n	55		Dimensionless 1/2 space	X_{eD}	0.52	
frac 1/2 spacing	Xe	21.9 m	72 ft	Dimensionless time	t_D	0.73	
Frac spacing	2Xe	43.9 m	144 ft	Desired life	t	30 years	9.46E+08 seconds

Using the dimensionless variables, a graph of temperatures vs time was created (Figure 7); then, regression analysis was conducted to obtain Eq. 7. This equation and others were the basis for the economic model and subsequent calculations.

$$T(t) = -0.0009t^3 - 0.0279t^2 + 0.4193t + 204.06 \quad (t \text{ in years}) \tag{8}$$

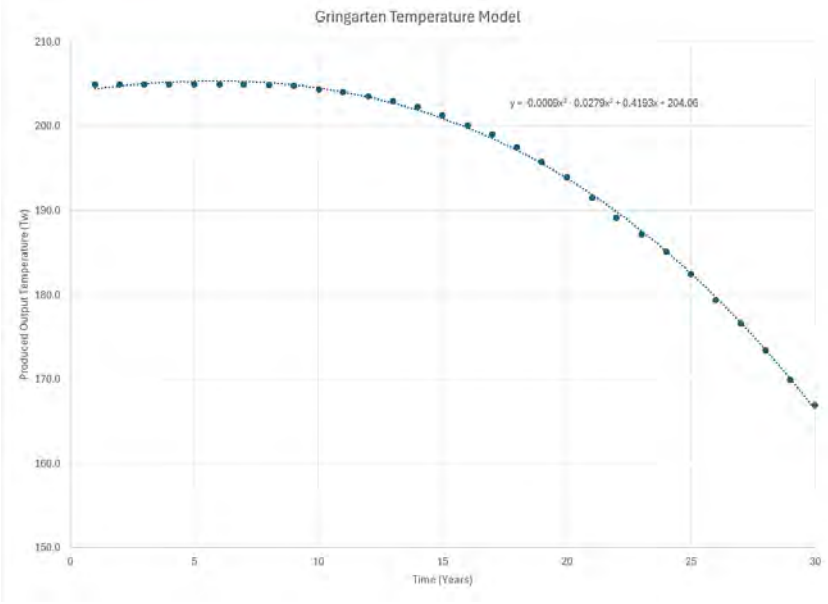

Figure 7: Thermal decline of theoretical EGS using Gringarten's model (Gringarten et. al., 1975).

There is criticality of designing an ORC to optimize the pinch point between the produced water and the working fluid. Understanding that the plant can be optimized for initial production based on the data gained in the exploration well, as the thermal decline occurs the plant efficiency will decrease, this is graphically depicted in figure 7.7 of the MIT report for flash plants. The economic model's maximum Temperature decline is 40˚C, as compared to Augustine's maximum decline (Augustine, 2011) of 32˚C. However, to account for the thermal decline and for the separation from the pinch point, the economic model assumes a linear 1.2 % loss in power generation for

every 1˚C drop in thermal decline, severely decreasing the electrical output in later years. In actual operations, similar to oil and gas fields, "infill" wells will most likely be drilled starting in year 20, to deeper, untapped resources to maintain higher heat, extending the plant life to 40+ years for a marginal cost.

2.4. Defining and Quantifying Parasitic Losses

Within the hydrothermal industry, parasitic loads are the electrical loads required to run the binary pumps, cooling tower fans, lighting, control room, and other equipment on site necessary to run the facility (DiPippo, 2016), typically around 8%. However, many economic models assume a fixed operating expense and overlook the variability of power needed (and associated costs) that EGS systems require due to the power required for the circulation of a significant amount of water. In the Gringarten model above, the required water circulation is estimated to be over 11,000 barrels of water per day (BWPD) for every MW of electricity produced at 205˚C. Previously, water circulation loads were calculated to be as high as 10% (Banks, et al., 2020) in Clarks Lake. However, this analysis was not for deep horizontal wells and considered friction loss to be insignificant. In deep, horizontal EGS systems, friction must be considered.

In this analysis, it is assumed that the resource is 9,845 ft deep, requires a horizonal lateral length of 7,920 ft, 55 frac stages, at a spacing of 144 ft between stages, with a total flow rate of 56,000 BWPD (~1,020 BWPD per frac). Later, these dimensions will be used with various wellbore architectures to demonstrate the frictional impact and resulting parasitic losses on EGS through Nodal Analysis.

Calculating the friction of the system for the parasitic losses was developed through a process of nodal analysis, using the inside diameter and the roughness of the tubulars combined with the density and viscosity of water (at temperature) and the friction within the fractures themselves. These properties were used to calculate the Reynolds numbers and Moody Friction Factors to generate the head loss in each node which was converted to psi. Six models were created for 9-5/8" 47ppf casing; 7" 35ppf casing; & 4" 11ppf tubing, each at 60˚C for injection and 205˚C for Production. These curves are identified in the appendices.

Once the friction loss models were created, the program was able to generate wellbore profiles with the following dimensions for both the producers and injectors (unless noted):

7" casing across the reservoir with 9-5/8" casing to surface

7" long string from TD to Surface

4" 'conformance string' across the reservoir with 9-5/8" casing to surface

4" 'conformance string' across the reservoir with 7" casing to surface

It is important to note that for casing burst calculations during stimulation, we required a burst strength of greater than 10,000 psi across the reservoir. Combining this requirement with the impact of thermal cycling on high strength alloys we did not evaluate 9-5/8" across the reservoir. This may be possible with special alloy tubulars.

The nodal model then calculated the frictional impact across the tubulars to the top of the reservoir, then the friction to each fracture initiation point based on the distance between stages. As the flow in the wellbore decreased at each node, the model calculated the new friction loss to the next fracture initiation point until the end of the well was reached.

To calculate the friction loss through the fractures the results from Blue Mountain were evaluated using the relationship of pressure drop/ft of fracture (modified to fracture ½ length since the project was a doublet) vs BPD fluid/ft fracture height, (Pearson, 2001). According to Titov (Titov, et al. 2023) the average fracture height was estimated at 800 ft and the average fracture half-length was estimates at 800 ft using micro seismic and fiber optic data. However, the average distance between wells was estimated at 365 ft and the effective fracture height was estimated to be 300 ft by Norbeck (Norbeck and Latimer 2023) and these numbers were used for the calculation. Using this data from Norbeck, to get the injection pressure vs rate and corresponding production rates and pressures, the model described above used nodal analysis to solve for the pressure losses in the fractures to generate Figure 8. The resulting model and regression for friction loss was history matched against Blue Mountain and found to be accurate.

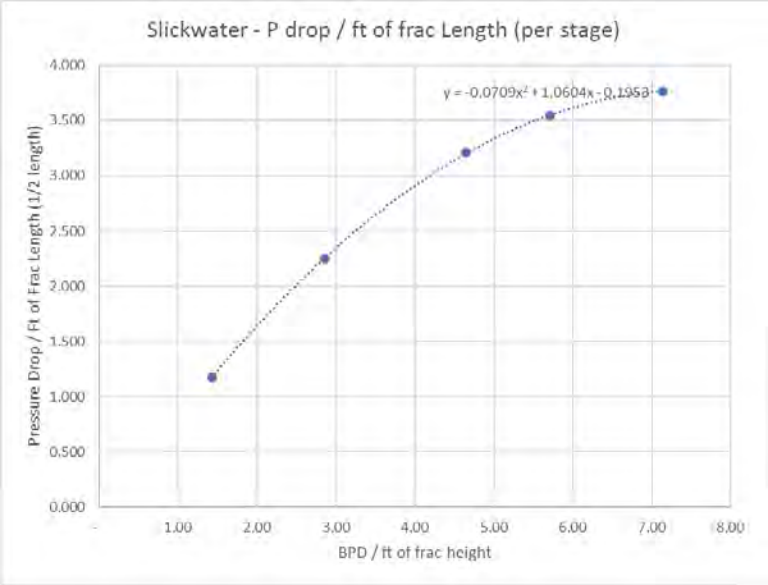

Figure 8: Calculated friction losses in the fractures of Project Red using 70/140 equivalent proppant.

Using API data, (Pearson, 2001), it is well established that the permeability of ceramic proppant, or even 30/50 Ottawa sand is significantly higher than the 70/140 equivalent sand that was pumped at Blue Mountain. At a closure stress of 5,000 psi, the API permeability of 40/70 bauxite is over 7 times greater, and 30/50 Ottawa is 2.4 times greater. One then can make a modest assumption that with improved fracturing technology the pressure losses within the fracture could be reduced by 66%. Thus, in our example with 56,000 BWPD traveling through 55 fractures, this change in proppant could have a required pressure decrease for the system of over 300 psi.

Using the same methodology outlined above for the friction losses returning up the producer, the entire pressure loss of the system can be calculated and the required HHP calculated for either a doublet or a triplet and used to define the system's parasitic losses.

Using the hypothetical doublet used in Gringarten's thermal model, and the well architecture described in Norbeck's paper (Norbeck and Latimer, 2023) on Blue Mountain, the pressure drop with a 7" long string from Surface to TD in both the injector and the producer can be calculated. Using a reservoir depth of 9,845 ft (3,000 m) and a lateral length of 7,920 ft, with 55 fractures, 144 ft between fractures and 56,000 BWPD the model can calculate the expected pressure drop in the system. In this scenario the expected pressure drop of the system is 3,104 psi.

$$HHP = \frac{P_{pump}(psi) \cdot q_{inj}(gpm)}{1714} \tag{9}$$

For example, an injection rate of 1,764 gpm and pressure drop of 3,104 psi, the required HHP to run the circulating system is 3,130 HP.

2.5. Thermal Decline

The concept of accelerated thermal decline due to "Short Circuiting" was further examined by Doe (Doe, McLaren and Dershowitz 2014). The team analyzed thermal decline using the initial Gringarten model (Gringarten, Witherspoon and Ohnishi, 1975) with 10 uniform fractures, then refined the model further by adding variations:

(a) Initial model (for direct comparison to Gringarten) :10 uniformly spaced, parallel fractures with uniform apertures.

(b) As (a), with variable fracture spacing and constant fracture transmissivity (aperture assumed based on a cubic law).

(c) As (b), Variable fracture spacing and lognormally distributed fracture transmissivity.

(d) As (c), with increased aperture coefficient of variation.

(e) As (c), with decreased aperture coefficient of variation.

(f) As (c), with fractures defined by a distribution of fracture size, orientation, and intensity based on a field case study.

The first analysis looked at 10 uniform fractures with varying fracture spacing to understand the impact on spacing assuming a total flow rate of 0.15 m3/s (81,500 bbl/day), or a rate per fracture of 0.015 m3/s (8,150 bbl/day) for 1,000 m x 1,000 m fractures (Figure 9).

Doe noted two major effects by modeling the scenarios (b) through (f) above. First, the temperature maps show that thermal interference and more rapid thermal depletion occurs in areas of great fracture density. This is independent of the aperture or fracture conductivity. The second observation was that variable apertures create variable breakthrough times or 'short circuiting' among fractures with considerably more aperture or fracture conductivity, Figure 10.

Doe found that using a variable aperture negates much of the advantage of distributing flow over multiple fractures that the Gringarten model predicts due to the second power relationship of dimensionless time to rate. This data was plotted on the familiar outlet temperature vs. time and the impact of the thermal decline from 'short circuiting' could be visualized, Figure 11.

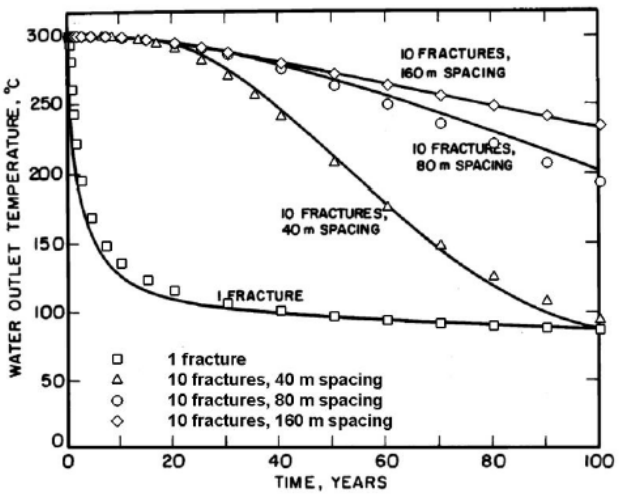

Figure 9: Water outlet temperature for Gringarten example with Frac Spacing increasing (Doe, McLaren and Dershowitz 2014).

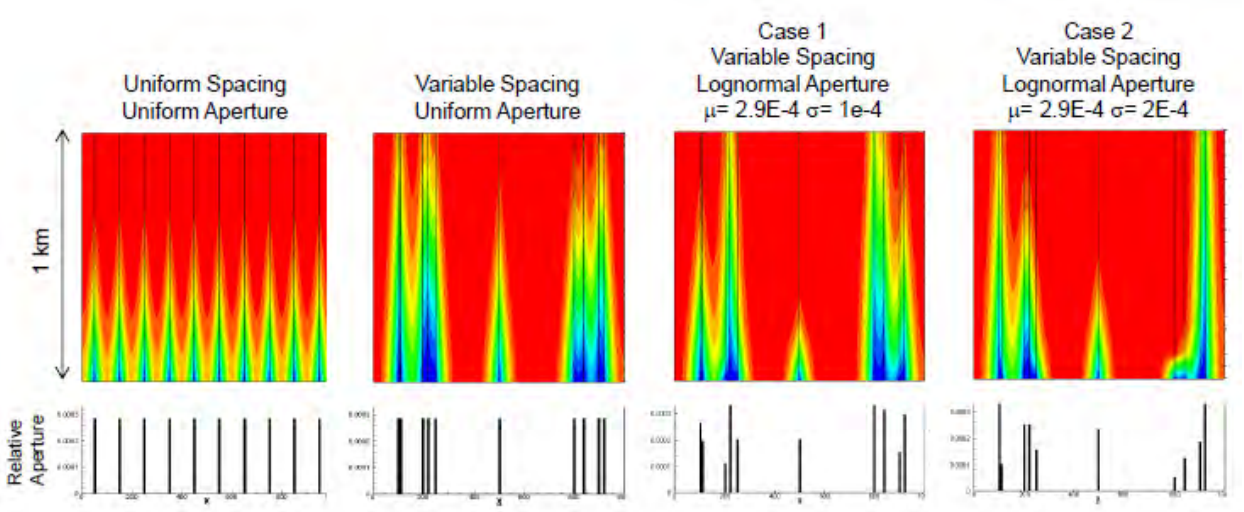

Figure 10: Heat maps for parallel fractures using variable spacing and fracture conductivity (Doe, McLaren and Dershowitz, 2014).

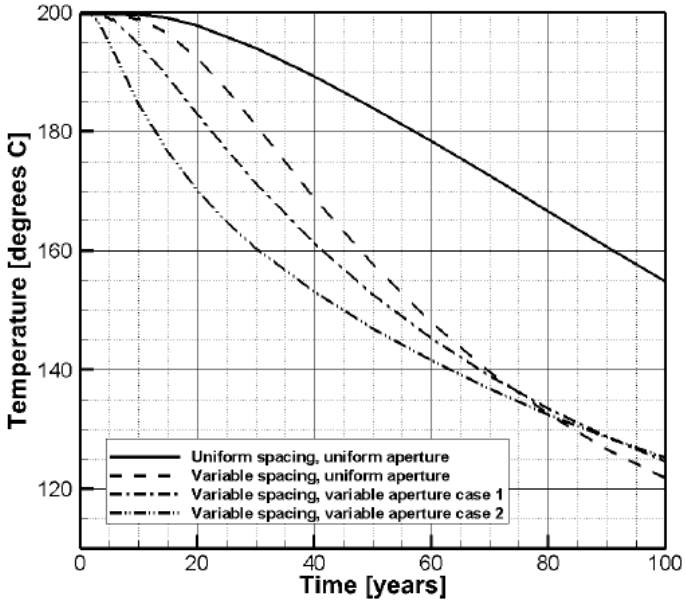

Figure 11: Impact on temperature output for variable fracture spacing and fracture conductivity (Doe, McLaren and Dershowitz, 2014).

2.6. Predicting Thermal Decline

The EGS project at Blue Mountain has fundamentally changed the EGS industry. For the first time, models created by early innovators can be compared against actual data from an EGS site that uses a horizontal injector and producer connected by multiple fracture stimulations. The two wells were drilled to a vertical depth of approximately 7,700 ft., and each had a horizontal lateral section of roughly 3,250 ft. Both wells had 7", 35 ppf, P-110 production casing run from surface to TD. The average offset spacing was 365 ft. The Injector was completed with a total of 16 stages with each stage having approximately 150 ft. All stages except stages 12 and 13 had 6 clusters per stage and 6 shots per cluster. Stages 12 & 13 had 9 clusters per stage and variable shots per cluster. The proppant was a mixture of 100 mesh and 40/70 mesh silica sand. The producer was completed in a similar technique with a total of 20 stages.

The first published injection profile from Blue Mountain showed just how different the reality of the injection profile is as compared to Gringarten's very simplified model of uniform fractures. Of approximately 18,100 BWPD of injection during the spinner survey there was a wide discrepancy of water per stage. Table 2 and Figure 12 show the stage, vs water injection allocation at Blue Mountain EGS.

Table 2: Blue Mountain Injection allocation

Stage	Approximate Injection Allocation (BWPD)
1	1,150
2	250
3	1,000
4	100
5	1,300
6	1,650
7	600
8	2,000
9	2,100
10	2,550
11	400
12	1,000
13	1,200
14	1,100
15	700
16	1,000
Total	18,100

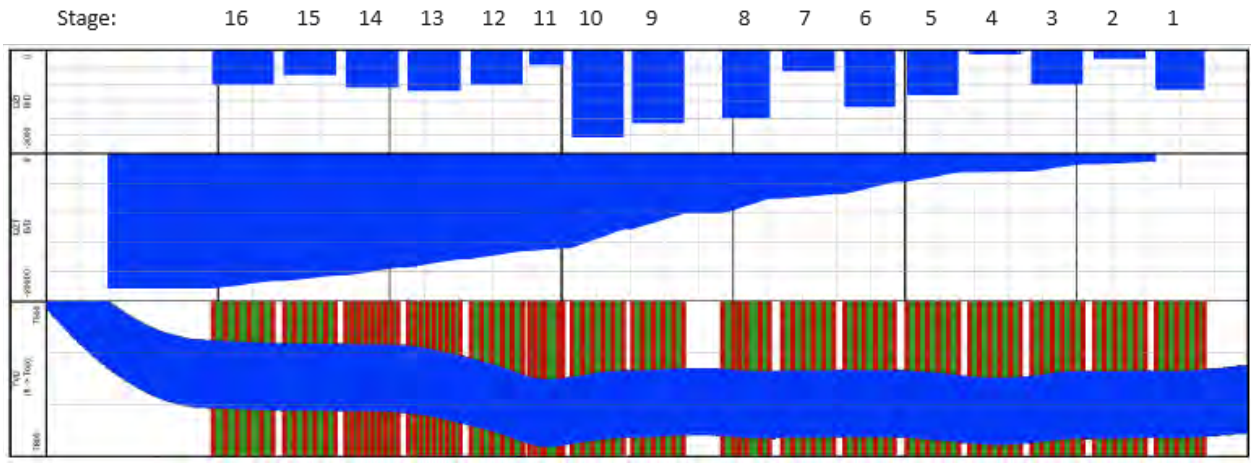

Figure 12: Blue Mountain spinner survey showing the amount of fluid allocated to each frac cluster (Norbeck and Latimer 2023).

2.7. Economic Impact from a Lack of Conformance Control

Using the data generated at the Blue Mountain site combined with the Gringarten Model, the predictions generated by Doe et al. can be evaluated and put into an economic model. The flow rates noted above were distributed into quartiles for the evaluation (Figure 13).

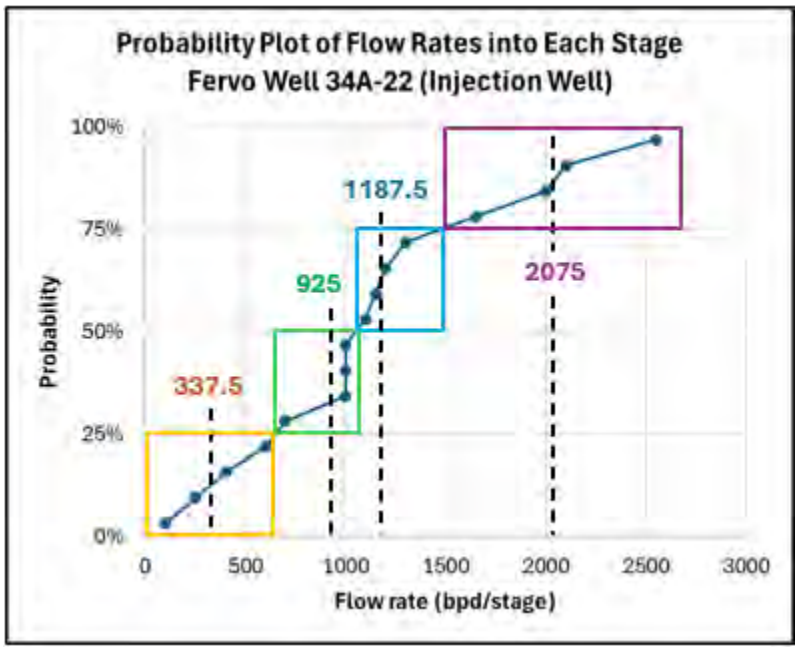

Figure 13: Flow distribution at Blue Mountain by quartiles.

Using the resulting flow rates per stage for each quartile, the flow distribution can be allocated to our theoretical well's Gringarten model using the following Table 3.

Table 3: Allocation of flow for Gringarten Model based on Blue Mountain

Flow Stream	FERVO Blue Mountain Project		This Paper
	Flow Rate (bpd/stage)	Normalized Rate (Rate/Avg. Rate)	Flow Rate (bpd/stage)
1st Quartile	338	0.298	304
2nd Quartile	925	0.818	832
3rd Quartile	1,188	1.050	1,068
4th Quartile	2,075	1.834	1,867
Average	1,131	1.000	1,018

These flow rates were then proportionally distributed into the theoretical well using Gringarten type curves. Using MATLAB, thermal decline curves were generated for each set of fracture by interpolating dimensionless time, dimensionless temperature and dimensionless half-fracture spacing. The decline for each quartile and the composite thermal decline using flow balance was plotted against the original Gringarten curve in Figure 14.

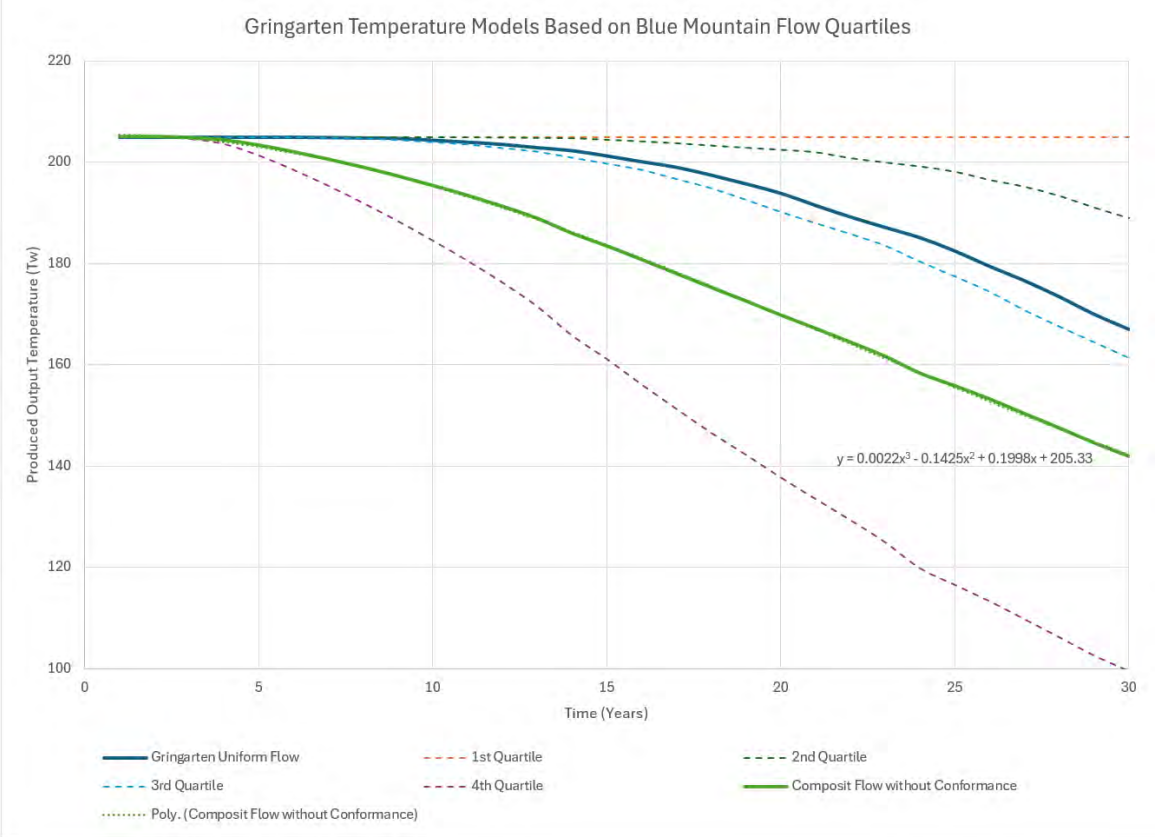

Figure 14: Gringarten temperature models based on Blue Mountain flow quartiles.

Using Figure 14, the impact of the short circuiting can be visualized with three areas that are of major concern. First, the composite decline curve for short-circuiting starts considerably earlier, in this case as early as year 3 with short-circuiting vs. year 10 with conformance control. Second, the rapid separation of the short-circuiting composite curve causes the short circuit system to reach the 25˚C decline mark 10 years earlier than conformance control curve. Third, the 1st and 2nd quartiles (50%) of the resource show limited heat harvesting in the first 20 years and essential no heat harvesting for the duration of the project in the 1st quartile.

The impact on power production follows the same trends. Figure 15 examines the Gringarten models for the system given conformance as well as short circuits. The calculations use a plant up time of 90%, the power conversion factors discussed earlier of 4.36E-07 MW-hr / (˚C·BWPD), 8% ORC plant parasitic loads, and the temperature predictions from Figure 14. The short circuit's temperature drops below the critical 3.0 MW of electricity generating capability by year 15 and generates 26% less total electricity during the 30-year life of the plant.

2.8. Introduction to "Perf and Plug" vs. Sleeves

Similar to Blue Mountain, the standard completion design for EGS has defaulted to the "Perf and Plug" technique. This has been used exclusively at Project Cape as well as all non-open hole stimulation at Forge. There are significant advantages to "Perf and Plug" that has made it a favorite among completion engineers, the largest being cost. Thanks to the advancements in the shale boom from the early 2000's through today, the cost have dropped significantly for this technique. Additionally, the reliability of the perforating guns and the plugs has improved.

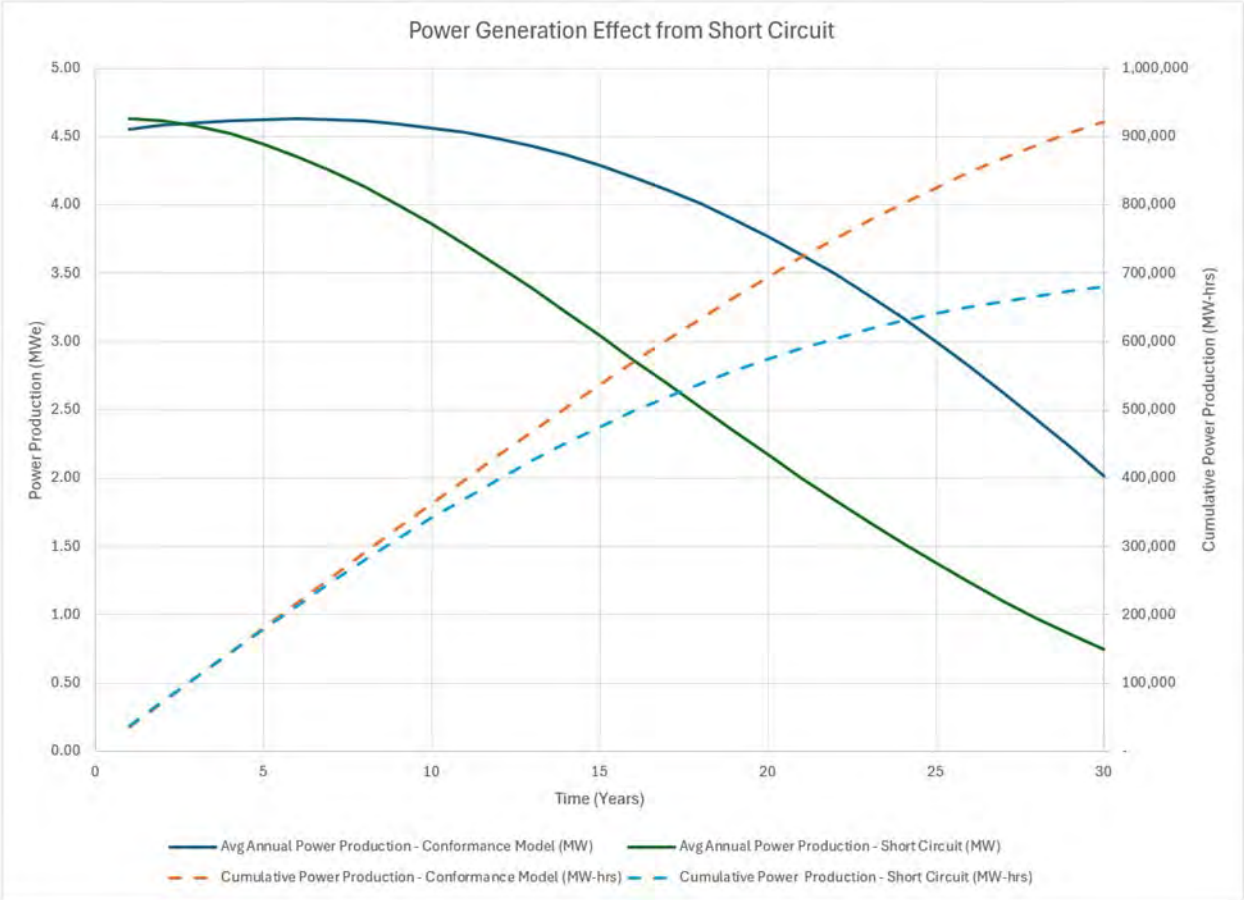

Figure 15: Power generation differences between conformance control and short circuits.

Unfortunately, "Perf and Plug" comes with a major disadvantage. Once perforations are shot through the casing and fracture stimulated, the only effective way to shut them off or slow down injection through the short circuits is to run an inner-string with multiple packers and outflow control devices (OCD). A typical conformance design using inner-string consists of the original 7" casing, perforated and stimulated in 50-150 locations down the wellbore. A 4" inner-string would be run across the injection interval using a packer to separate each stage with an OCD located between each packer to control flow into each interval where there is a short circuit.

Unfortunately, this system has two major drawbacks. First are the frictional losses described in the Nodal Analysis section increase over 17 times at injection temperatures and 1,500 gpm. Second the reliability of packers is unproven at these temperatures, compounded by the cyclic loading of cool (150˚F) injection temperature followed by 400˚F reservoir temperatures during shut in periods.

The oil and gas industry has tried to use gels, cement, and other chemicals to manage injection conformance control over the years, all with very limited success. The combination of difficulty using this technology to manage conformance in 3,000-8,000 BPD injectors at 150˚F, with the increase in difficulty of EGS requiring 60,000-120,000 BPD at temperatures in excess of 400˚F creates significant doubt in the viability of these options in EGS.

The alternative to “Perf and Plug” that is currently used in the shale market, predominately in Canada, is the frac sleeve technology. The advantage to the frac sleeve is that if the sleeve is designed properly, the sleeve and be shifted back into the closed position to shut off a short circuit without giving up internal diameter in the casing and inadvertently increasing friction pressure and parasitic losses.

Additionally, technology is being investigated that will allow for an OCD to be built directly into the sleeve allowing for a regulator position that will limit the injection into short circuits, preventing the premature cooling of the system, but still allowing for the heat to be harvested from that section of the reservoir.

2.9. Modeling the Impact of Inner-Strings on Friction

Using the same flow loop as described in the Nodal Analysis section the only realistic ability to implement conformance control in Perf and Plug is with an Inner String. Figure 16 is a graphical depiction of how a 4” Inner-String system would look in 7” casing.

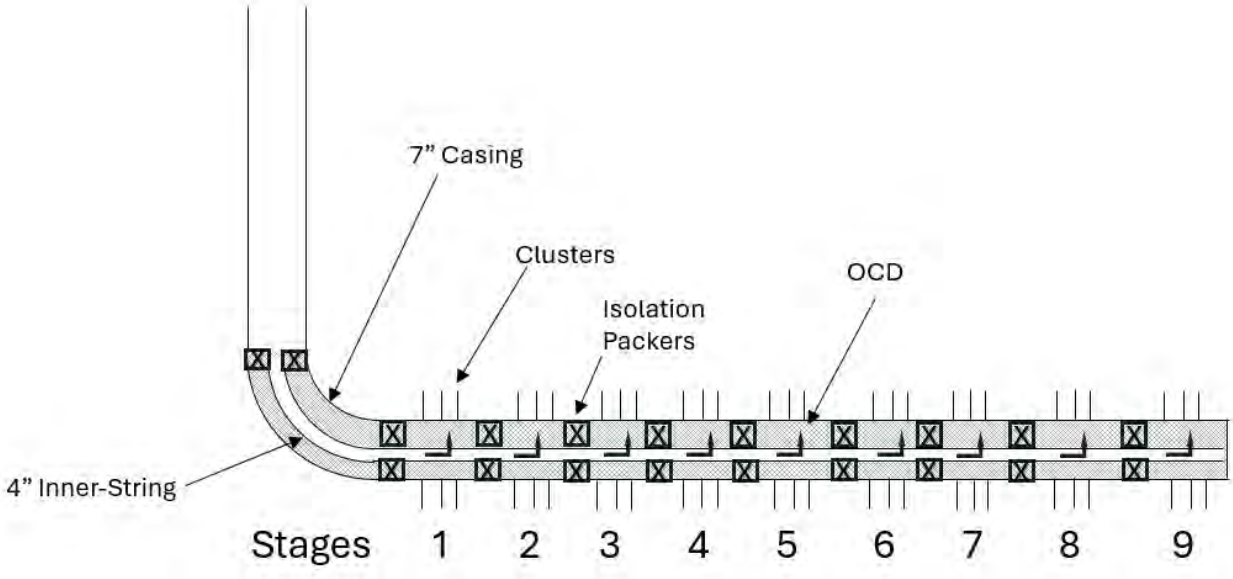

Figure 16: 4" Inner-string in 7" casing with outflow control devices.

Returning to the Nodal Analysis described earlier for the hypothetical doublet using 7” casing in both the producer and injector, 55 frac stages and 56,000 BWPD, the system required 3,130 HP. Assuming the same system, but on the injector only, there is a 4” conformance inner string run from the top of the 1st stage (10,930 ft MD) to the bottom of the well (17,765 ft MD) the power requirement to circulate the water jumps to 6,207 HP. Converting this to power with an 80% pump efficiency results in 5.8 MW, or 115% of the power produced.

$$MW_e = \frac{HHP \times 0.000745699}{\eta_{pump}} \tag{10}$$

This exercise shows quickly that if “Perf and Plug” is chosen as the completion alternative, then there is not an economic alternative for conformance control.

Alternatively, the ability to maintain full bore with the sleeves and having the ability to shut off short circuits or in the future be able to install regulator positions within the sleeves will allow for a system of conformance control without significant impact on the economics.

2.10. Parasitic Loads for Different Well Architecture

Using the same flow loop as described in the Nodal Analysis and the Impact of Inner-Strings on Friction an analysis was performed of different wellbore architectures. The reason for performing a deep dive on these variables is the theoretical EGS system that was analyzed in this paper assumed the Blue Mountain design with 7” long strings of casing in both the injector and the producer. This design indicated that to circulate 56,000 BWPD for 55 stage EGS with 144’ spacing, the system would require 3,130 HP. This is the equivalent of 2.9 MW of electricity or 58.3% of the electricity generated prior to plant parasitic losses. Table 4 examines the parasitic losses as a function of the wellbore architecture. The critical insight gained from this data is that for the required rates to generate greater than 5 MWe per well, the friction of the system becomes a dominant variable. The numbers for production and injection 7” long strings are consistent with Blue Mountain in Norbeck (Norbeck and Latimer 2023), where parasitic losses of 0.5 to 1.0MW were observed in a considerably shorter (~2,400’) injection interval and using lower rates (800 GPM or 27,000 BWPD Injected). The model used for this paper estimated 0.6 MW of parasitic losses for Blue Mountain at 800 gpm.

Table 4: Parasitic Losses as a Function of Well Design

Injector Architecture	Producer Architecture	Doublet / Triplet	Injection Rate (BWPD)	Friction Losses (psi)	Parasitic Losses (MWe)
7” Long String	7” Long String	Doublet (5MWe)	60,480 (8% fluid loss)	3,041 psi	2.9 MWe
7” Long String + 4” Inner-string	7” Long String	Doublet (5MWe)	60,480 (8% fluid loss)	6,031 psi	**5.8 MW**
9-5/8” x 7” Liner	9-5/8” x 7” Liner	Doublet (5MWe)	60,480 (8% fluid loss)	1,426 psi	1.4 MW
9-5/8” x 7” Liner + 4” Inner-string	9-5/8” x 7” Liner	Doublet (5MWe)	60,480 (8% fluid loss)	4,416 psi	4.2 MW
9-5/8” x 7” Liner	9-5/8” x 7” Liner	Triplet (10MWe)	120,960 (8% fluid loss)	2,639 psi	5.1 MW
7” Long String	7” Long String	Triplet (10MWe)	120,960 (8% fluid loss)	6,847 psi	**13.1 MW**

Critical insight gained from this modeling effort is the impact of the 7” long string as compared to using a 9-5/8” casing set above the resource with a 7” liner through the resource interval. This change in design can reduce the parasitic loads by over 50%. Additionally, without converting to

a casing / liner design or increasing bore sizes considerably to an 8-5/8” or 9-5/8” long string, the frictional impact for the triplet’s flow rate is detrimental to the economics of the project.

There are multiple reasons why casing long strings can be preferred, including operational efficiency and the ability to run fiber optics. However, all advantages of a long string over a liner must be weighed against the cost of the parasitic losses incurred with the additional friction vs. a liner.

3. Conclusions

1. Generation of geothermal electricity in the United States has stagnated between 1.5 GW and 1.9 GW since 1990. The primary cause of this stagnation is the lack of new hydrothermal reservoirs discoveries.
2. To grow geothermal power generation, geothermal power generation using Enhanced (or Engineered) Geothermal Systems (EGS) has tremendous potential. New technologies are being developed to provide economies of scale and low thermal declines needed to provide economic power generation.
3. Key variables impacting the economics of EGS power generation are the thermal decline, flowrate per well, parasitic losses and success of conformance control.
4. Parasitic losses are defined as the electricity used to power a geothermal field and power plant that does not contribute to the net electric power yield of a plant for transmission.
5. Frictional losses in the wellbore and in hydraulic fractures across various well completions geometries must be optimize for an economic EGS development.

Appendix

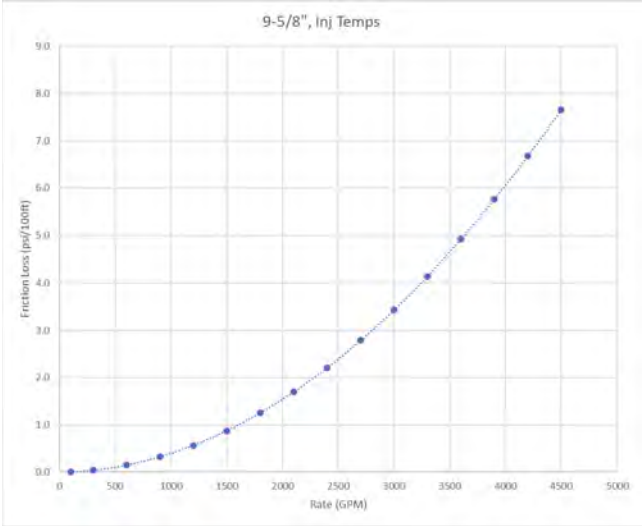
9-5/8", Inj Temps
Friction Loss (psi/100ft)
Rate (GPM)

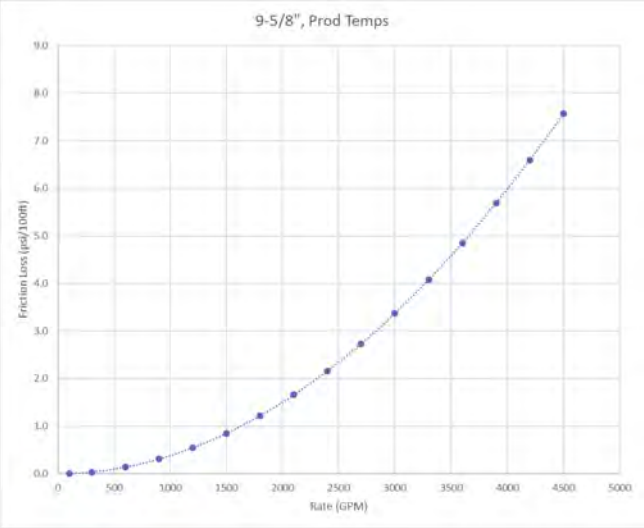
9-5/8", Prod Temps
Friction Loss (psi/100ft)
Rate (GPM)

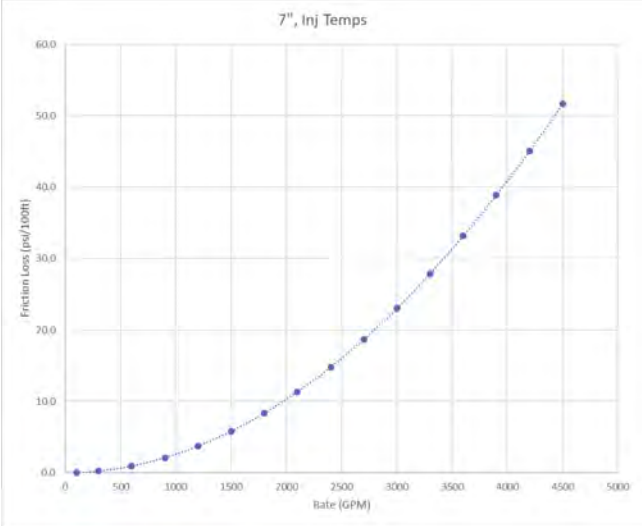
7", Inj Temps
Friction Loss (psi/100ft)
Rate (GPM)

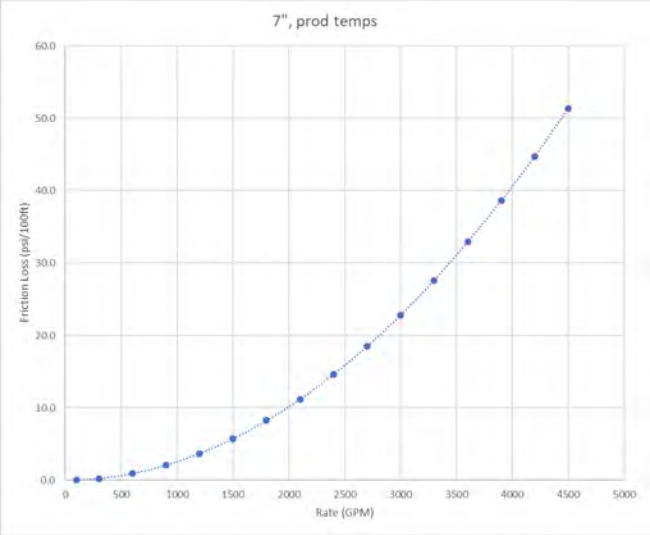
7", prod temps
Friction Loss (psi/100ft)
Rate (GPM)
0.0
10.0
20.0
30.0
40.0
50.0
60.0
0
500
1000
1500
2000
2500
3000
3500
4000
4500
5000

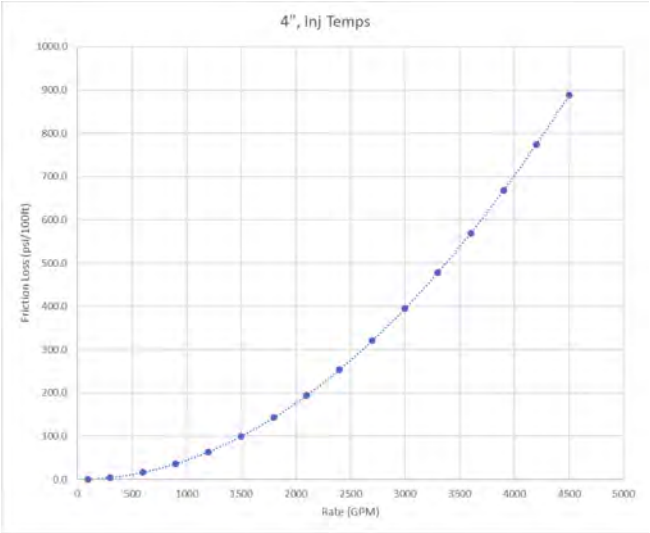
4", Inj Temps
Friction Loss (psi/100ft)
Rate (GPM)
0.0
100.0
200.0
300.0
400.0
500.0
600.0
700.0
800.0
900.0
1000.0
0
500
1000
1500
2000
2500
3000
3500
4000
4500
5000

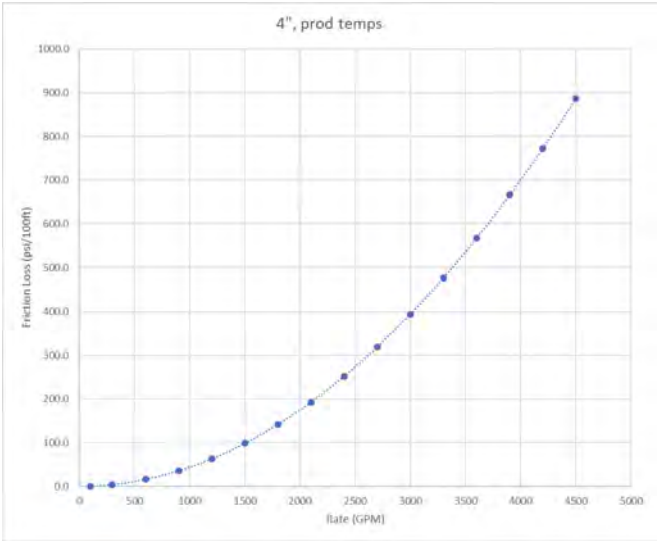
4", prod temps
Friction Loss (psi/100ft)
Rate (GPM)
0.0
100.0
200.0
300.0
400.0
500.0
600.0
700.0
800.0
900.0
1000.0
0
500
1000
1500
2000
2500
3000
3500
4000
4500
5000

Acknowledgement

This material is based upon work supported by the Department of Energy, Office of Energy Efficiency and Renewable Energy (EERE), under Award Number DE-EE0007080. This report was prepared as an account of work sponsored by an agency of the United States Government. Neither the United States Government nor any agency thereof, nor any of their employees, makes any warranty, express or implied, or assumes any legal liability or responsibility for the accuracy, completeness, or usefulness of any information, apparatus, product, or process disclosed, or represents that its use would not infringe privately owned rights. Reference herein to any specific commercial product, process, or service by trade name, trademark, manufacturer, or otherwise does not necessarily constitute or imply its endorsement, recommendation, or favoring by the United States Government or any agency thereof. The views and opinions of authors expressed herein do not necessarily state or reflect those of the United States Government or any agency thereof.

REFERENCES

Augustine, Chad. 2016. "A Methodology for Calculating EGS Electricity Generation Potential." Golden, CO: GRC Transactions, Vol. 40, 2016.

Augustine, Chad. 2011. Updated U.S. Geothermal Supply Characterization and Representation for Market Penetration Model Input. Golden, CO: National Renewable Energy Laboratory.

Banks, Jonathan, Arif Rabbani, Kabir Nadkarni, and Evan Renaud. 2020. "Estimating parasitic loads related to brine production from a hots Sedimentary aquifer geothermal project: A case study from the Clarke Lake gas field, British Columbia." (Renewable Energy, ELSEVIER) (153).

DiPippo, Ronald. 2016. Geothermal Power Plants, 4th edition. Waltham, Ma: Butterworth-Heinemann / Elsevier.

Doe, Thomas, Robert McLaren, and William Dershowitz. 2014. "Discrete Fracture Network Simulations of Enhanced Geothermal Systems." Stanford, CA: Thirty-Ninth Workshop on Geothermal Reservoir Engineering.

Fleckenstein, William, Kazemi Hossein, Royer Colby, Loff Geneva, and Zimmermann Jens. 2023. "A Stochastic Economic Analysis of An Enhanced Geothermal System." Golden Colorado: GRC Transactions, Vol. 47, 2023.

Geiser, Pater, Bruce Marsh, and Markus Hilpert. 2016. "Geothermal: The Marginalization of Earth's Largest and Greenest Energy Source." Stanford, California: 41st Workshop on Geothermal Reservoir Engineering.

Gringarten, W. A., A. P. Witherspoon, and Y. Ohnishi. 1975. "Theory of Heat Extraction from Hot Dry Rock." (Journal of Geophysical Research) 80, 1120-1124.

Mindygaliyeva, Balnur, Ozan Uzun, Kaveh Amini, Kazemi Hossein, and William Fleckenstein. 2024. "Assessment of Two Recent Hot Dry Rock Thermal Energy Production Projects." (Geothermics).

MIT led interdisciplinary panel. 2006. The Future of Geothermal Energy; Impact of Enhanced Geothermal Systems (EGS) on the United States in the 21st Century. Idaho Falls, ID: Idaho National Laboratory.

Moon, Hyungsul, and Sadiq J. Zarrouk. 2012. "EFFICIENCY OF GEOTHERMAL POWER PLANTS: A WORLDWIDE REVIEW." Auckland, New Zealand: New Zealand Geothermal Workshop 2012 Proceedings.

Norbeck, Jack H., and Timothy M. Latimer. 2023. "Commercial-Scale Demonstration of a First-of-a-Kind." Houston, TX: EarthArXiv.

Pearson, C. Mark. 2001. "Dimensionless Fracture Conductivity, Better Input Values Make Better Wells." (Journal of Petroleum Technology) (January, 2001).

Robins, Jody C., Amanda Kolker, Francisco Flores-Espino, William Pettitt, Brian Schmidt, Koenraad Beckers, Hannah Pauling, and Ben Anderson. 2021. 2012 U.S. Geothermal Power Production and District Heating Market Report. Golden, CO: National Renewable Energy Laboratory.

Titov, Aleksei, Jack Norbeck, Sireesh Dadi, Katharine Voller, Mark Woitt, Steven Fercho, Emma McConville, et al. 2023. "Case Study: Completion and Well Placement Optimization Using Distributed Fiber Optic Sensing in Next-Generation Geothermal Projects." (Unconventional Resource Technology Conference).

Collaboration and Continuous Improvement Makes Utah Geothermal Project Economic and Successful

Andrew Pauli, Baxter Whittington and Roger Lee, Baker Hughes Company
Carlos Menendez and Conner Richardson, Fervo Energy

Keywords

Drill Bits, PDC, granite, ROP

ABSTRACT

Building upon successful test wells in the Utah FORGE geothermal project, a Service Company partnered with Fervo Energy to continue production wells in the application. A case study from Utah is presented on reducing drilling days on a granite geothermal well using innovative polycrystalline diamond compact (PDC) drill bit technology.

A critical deliverable in the drilling program was to increase distance drilled with PDC bits in the 12.25-in vertical and 8.75-in curve sections. Drilling through hard and abrasive formations in the Utah application can increase cutter wear and shorten bit life. The lithology consists of igneous granite with pockets of metamorphic gneiss with rock hardness unconfined compressive strengths (UCS) of 33-40k psi. The continuous improvement process led to aggressive new product development resulting in improved dulling conditions and greater distances drilled.

Reduction in drilling days from well to well was achieved in both the vertical and curve sections. The custom PDC designs were comprised of longer profiles with extended shoulders for durability and parabolic cones for high weight on bit (WOB) operating parameters. Strategic placement of multi-dimensional shaped cutters across the cutting structure provided valuable advantages to enhancing efficiency and durability. A record run drilling 936 feet was achieved in the 12.25-in vertical section. This was a fifty percent increase in distance drilled compared to the next best offset. And a benchmark was set in the 8.75-in section with one bit completing the curve. This was an improvement over the first well which required four bits to complete the curve.

For decades, legacy roller cone drill bits have been used to drill geothermal wells at slow penetration rates. The learnings from this Utah application are chartering a new path of exceptional drilling performance utilizing PDC drill bits. The application of this technology is making the uptake of geothermal wells economic and successful.

1. Background on Drilling Geothermal Wells

Geothermal applications are diverse in terms of rock hardness, temperature and overall formation drillability. Roller cone drill bits were the first to slowly hammer away at volcanic formations. In Finland the Tricone drilled a granite with UCS of 560 megapascal (MPa), equivalent to 81 kilo pound per square inch (k psi) (Cardoe et al, 2021). And in Iceland the Tricone drilled an application where the circulating temperature was 300 degrees Celsius (Stefansson et al, 2018). Next came the Kymera hybrid drill bit which quickly became the reliable choice for drilling tough, interbedded lithologies such as those found in Turkey and the Asian Pacific Ring of Fire (Oueslati et al, 2019 and Lockwood et al, 2021). In these non-homogenous extrusive rocks the Kymera delivered improved drilling rates of penetration (ROP) over the Tricone, and was more consistent than PDC drill bits which were susceptible to impact damage. The recent push by the Utah FORGE project to drill geothermal wells faster has led to developments in PDC drill bit technology. Documentation by Dupriest et al in 2022 and 2024 details the learnings and advancements to improving drilling penetration rates in igneous granite and metamorphic gneiss. Testing focused on the physics-based, limiter-redesign workflow to address specific changes in drill bit design – such as extending the safe operating limits of bits beyond the industry's common practices, and the impacts of bit aggressiveness and ROP decline.

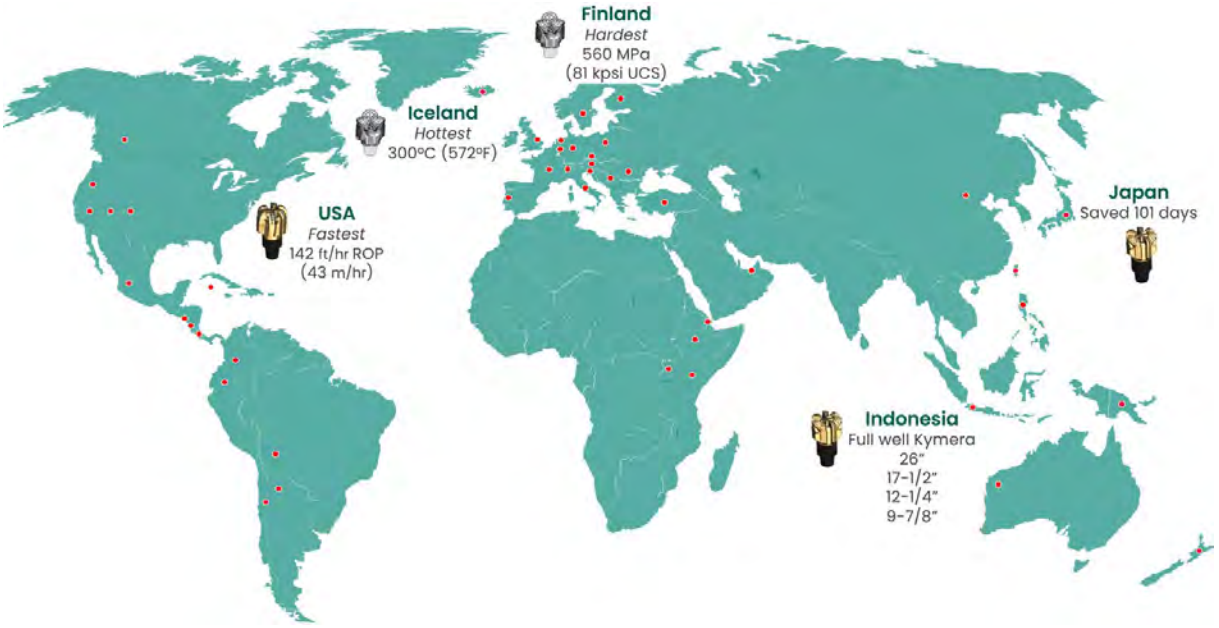

Figure 1 – Geothermal Drill Bit Solutions for diverse applications.
Red dots designate the Service Company's successful experiences in geothermal wells.

2. Learnings from Utah FORGE

Drilling efficiency was the key in the Utah FORGE project. Two important drill bit design learnings from the testing are 1) frame integrity to withstand extreme loading, and 2) efficient cutting structure to achieving faster ROP. The granite and gneiss in the Utah application are relatively homogenous and lends itself to be drilled with PDC, however the high rock strength

posed the main challenge. Simply put, a great deal of power is needed to drill hard rock, and the drill bit must stay sharp to drill faster and further.

Figure 2 – Utah FORGE core samples. Granite at left with rock strength 33-40k psi, gneiss at right. The granite formation top begins around 3,000 – 4,500 ft TVD.

In FORGE, 9.5-in PDC bits were tested on a mud motor bottomhole assembly (BHA) in a vertical and tangent well using upwards of 67k lbs of WOB and 235 rpm at the bit. By comparison, drilling a shale gas well with a similar sized PDC bit would require only half the WOB. A 3D drilling simulation software was used to optimize a cutting structure profile with strategic placement of multidimensional cutters. The 6-blades drill bit achieved a record ROP of 142 feet per hour (ft/hr). Offset runs using different drill bits yielded only 90 ft/hr – 36% slower. The reservoir static temperature of 440^{o} F (225^{o} C) at 8,000 – 9,000 feet total vertical depth (TVD) was not an issue for the PDC bit which has no moving parts. In addition the actual circulating temperature was significantly lower.

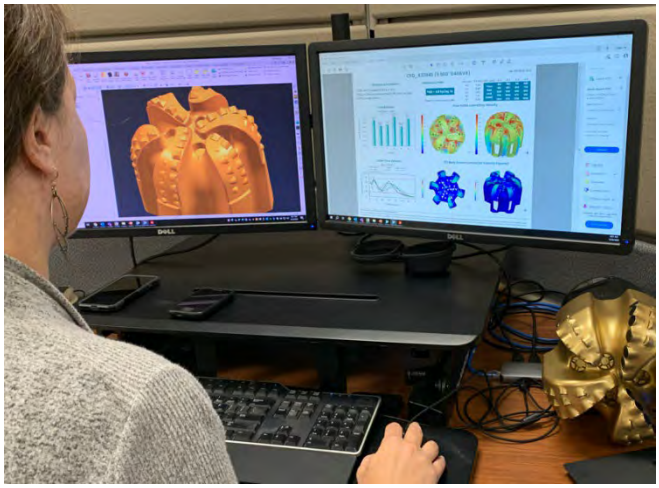

Figure 3 – Field-Based Design Engineers work closely with Operators in developing solutions. Shown on the computer screen is the original 9.5-in design from the Utah FORGE project.

Drilling Simulation Software

The 3D bit drilling simulation software is the first step to creating a robust and durable cutting structure for geothermal applications in igneous and metamorphic lithologies. A primary feature of the design methodology, the software creates advanced simulations that guide the selection, manufacture, and deployment of the optimal drill bit for specific hard and abrasive well conditions. The value proposition for the drilling simulation software are further documented by Duffy et al, 2022 and Russell et al, 2022.

The software models drill bit-rock interactions using a polygonal surface mesh that consists of connected faces to form 3D representations of the bit and rock. The polygonal mesh brings greater versatility to complex models by simulating how different bit designs and cutter layouts respond to changes in complex bit and bent motor motions, formation variations, PDC geometry, cutter size and shape, bit body changes, and diamond table thickness. The software also simulates bit performance in a range of different BHAs and drilling environments. The simulations consider drilling loads on cutters, depth-of-cut control elements, the bit body, and gauge pads. These loads are added to predict weight on bit, torque, ROP, steering force, and other operational parameters.

The full bit drilling model also incorporates a cutter overload integrity response surface model, which relies on applied pressure at the bit and cut area values to predict cutter stresses. Overload integrity risks are plotted on 3D color plots that display the predicted stresses for each cutter along the bit profile. In addition, a cutting aggressivity model characterizes the aggressiveness of different shaped cutter designs as they shear through the rock face. The software includes several grid model drilling simulations that assess how changes to cutter geometry impact drilling performance. These grid model simulations lend themselves to an iterative process that validates small changes to cutter design and layout—without the added time and cost of manufacturing and field-testing each design. By characterizing overload integrity and aggressivity—and then performing design iterations to optimize these values—the software helps pinpoint a bit design that offers improved stability and higher ROP at a lower cost per foot.

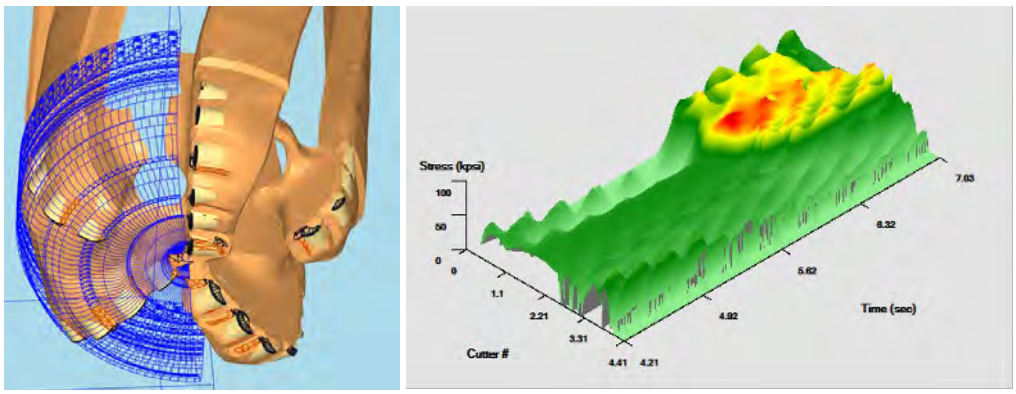

Figure 4 - Modeling drill bit-rock interactions using a polygonal surface mesh (left). A 3D cutter overload integrity risk plot highlights areas of highest cutter stress while drilling (right). With this information, the bit design team adjusts the model to minimize cutter stresses to acceptable risk levels.

Cutting Structure Profile

Stability and preventing cutter wear are primary focus for PDC bits. In high UCS applications, diamond bits can be prone to lateral or torsional instability leading to accelerated cutter wear. If the PDC cutters can remain sharp, then it will continue to achieve acceptable drilling rates of penetration whereas a dull bit will become slow and inefficient. Cutting structure profiles with a parabolic cone are preferred to distribute the high WOB forces across the inner cone and nose cutters. Longer shoulder profiles are also best suited for hardrock applications for increased durability and to prevent initial cutter wear from instability. (Hanafy et al, 2024).

Hydraulics

The higher temperatures generated when drilling hard and abrasive lithologies coupled with the inherent downhole temperatures of the formation can accelerate cutter wear. Open layout designs with maximized junkslot area and face volume improves flow while multiple nozzles maintain cooling on the outer portions of the bit.

Cutters

Strategic placement of multidimensional shaped cutters across the profile have many advantages. A durable edge cutter in the cone of the bit absorbs loading and resists breakage when high weight-on-bit is applied to drill hard formations. A chisel shaped edge placed on the nose profile improves drilling efficiency. Shaped cutters apply point loading to increase drilling rates of penetration. The shoulder of the bit which sees the largest amount of wear benefits from a cutter that is both durable and efficient.

The chisel cutters also contain a unique nonplanar diamond table geometry which reduces friction and heat generation at the rock interface which improves overall drilling efficiency. The nonplanar geometry generates 25% less heat than conventional planar cutters. This heat reduction translates to a more durable cutting edge, less cracking and spalling, and a longer drilling run life. (Russell et al, 2022).

Figure 5 – Placement of multidimensional shaped cutters across cutting structure profile. Chisel shaped edge for improved drilling efficiency.

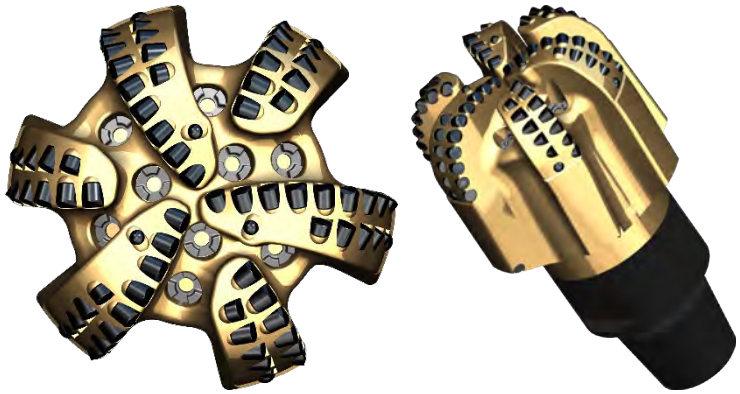

Figure 6 – 9.5-in 406 PDC Drill Bit with 6-Blades, 13mm (1/2-in) cutters, Multi-Port Hydraulics, Depth-of-Cut Control for overload protection, and secondary cutting elements for durability and wear resistance

3. Develop 1 GW of Geothermal Power by 2030

Fervo Energy began a robust drilling campaign to bring one gigawatt (GW) of power online. To achieve this, investments are directed in the categories of Drilling, Completions and Surface Facilities with 40% of the spend on Drilling. The campaign calls for steady drilling of production wells in 2024 with significant ramp up by 2026 to meet market demand. (Source: www.fervoenergy.com)

The Utah FORGE test wells were drilled as vertical and tangent ending in 9.5-in hole size. By contrast these wells are planned as vertical, tangent, curve and lateral designs with the vertical and tangent sections drilled in 12.25-in and the curve and lateral sections drilled in 8.75-in. This directional well plan along with more common 8.75-in hole size relates well with standard oil & gas applications.

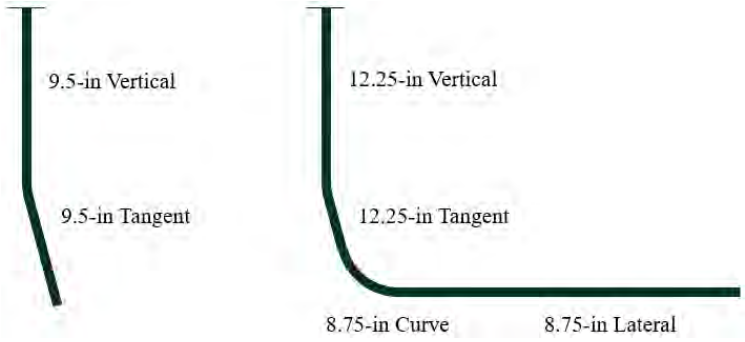

Figure 7 – Comparison of well profiles: test well at left; production well at right

4. Vertical 12.25-in Section

The performance in the 12.25-in vertical section is split into two sections based on UCS with an Upper section of low UCS, and a Lower section containing high UCS granite. PDC development was focused on the Lower granite section where drilling performance is critical for the operator's metrics. Some wells in this area had a shorter section of granite and could use aggressive bit designs while other wells needed more robust bit designs to drill over one thousand feet of granite. Based on this knowledge, three 12.25-in bit designs were selected to test using lessons learned from the Utah FORGE project. The first digit of the designation is the cutter size in fractions of an inch, and the last two digits are blade count:

- 6-blades/16mm (5/8-in) cutters – designated as 506
- 6-blades/13mm (1/2-in) cutters – designated as 406
- 7-blades/16mm (5/8-in) cutters – designated as 507

.

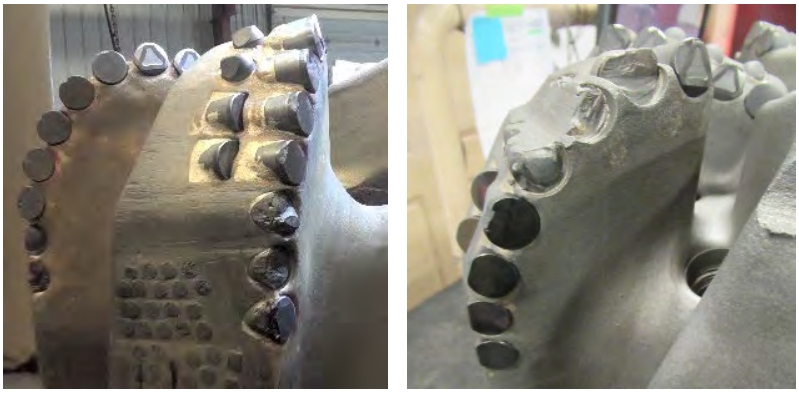

Figure 8 – Run 1 on 506 with gage cutter damage (left).
Run 2 on 506 with severe shoulder cutter damage (right).

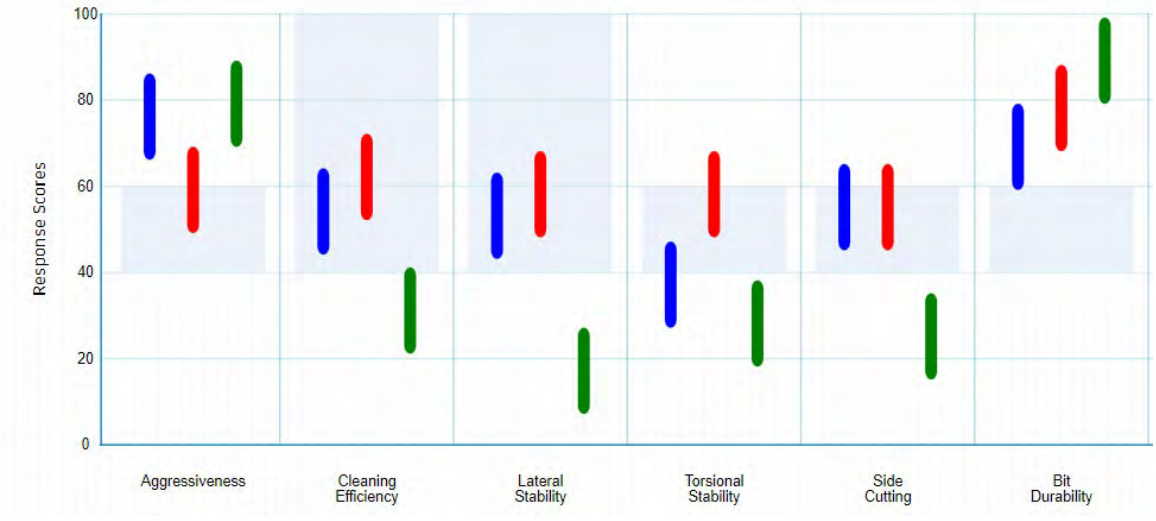

Figure 9 – Bit behavior comparison of the three 12.25-in bit designs:
506 (Blue), 406 (Red), 507 (Green)

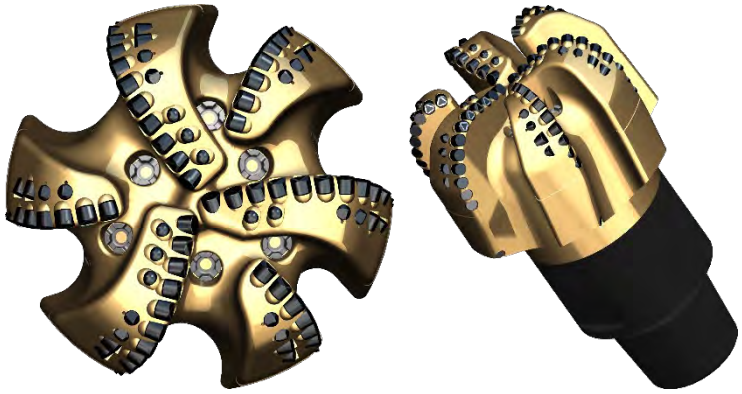

Figure 10 – 12.25-in 506 PDC Drill Bit with 6-Blades, 16mm (5/8-in) cutters, Depth-of-Cut Control for overload protection, and secondary cutting elements for durability and wear resistance

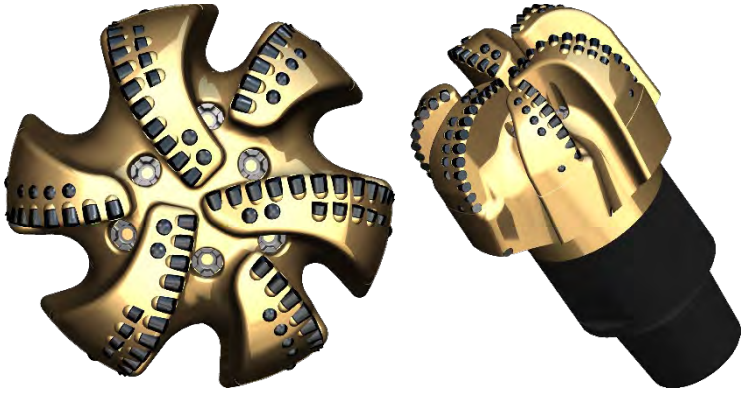

Figure 11 – 12.25-in 406 PDC Drill Bit with 6-Blades, 13mm (1/2-in) cutters, Depth-of-Cut Control for overload protection, and secondary cutting elements for durability and wear resistance

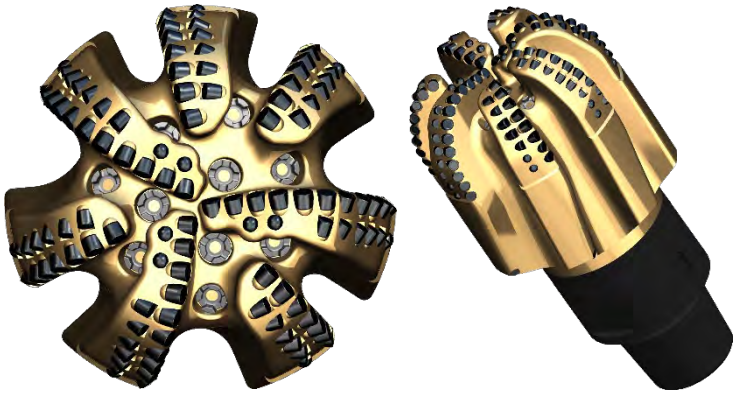

Figure 12 – 12.25-in 507 PDC Drill Bit with 7-Blades, 16mm (5/8-in) cutters, Multi-Port Hydraulics for cooling, Depth-of-Cut Control for overload protection, and secondary cutting elements for durability and wear resistance

The 506 was first to be tested with two runs in the Lower vertical. Dull analysis showed the design was not stable nor durable enough for this application. The first run drilled 1,281 feet to casing point and showed signs of lateral vibration with chipping on the gage cutters. The second run drilled 2,628 feet with surface data and dull confirming occurrence of stick-slip, leading to overloaded and broken cutters in the shoulder. See above Figure 8.

Due to future wells in this program requiring more distance to be drilled in the Lower granite section, two new designs were created to address the challenges of shoulder durability and overall bit stability that were seen on the 506. The next iteration, a 406, switched to 13mm cutters on the shoulder which increased cutter count by 15% to improve durability. It also introduced more depth of cut control for torsional stability. In addition a 507 was created to address the shoulder durability through an increase in diamond volume by adding an additional blade. Overall diamond volume increased 15% from the extra blade. A profile change increased the diamond volume in the shoulder by 52% compared to the 506 design. Figure 9 below shows the Bit Durability comparison for the three designs.

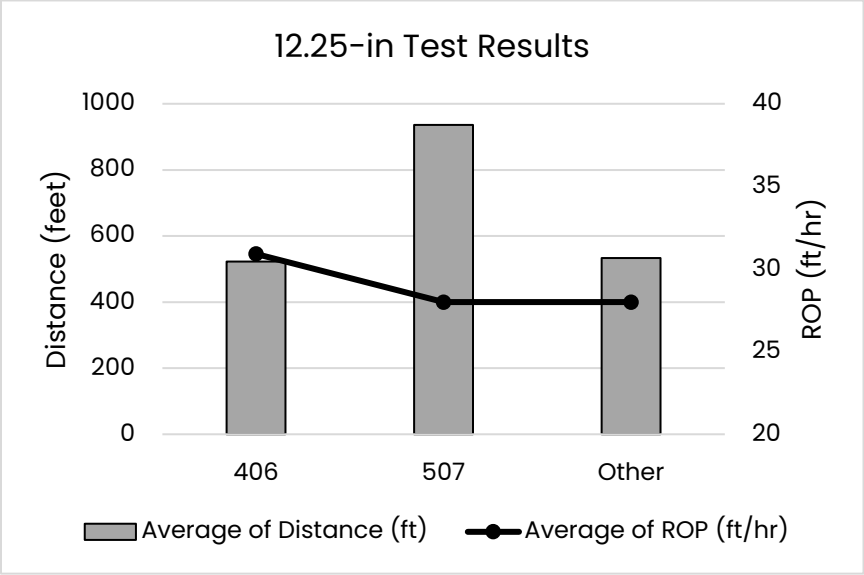

Figure 13 – Distance drilled and ROP metrics from tests on new PDC designs

Evaluation of the 406 and 507 were done in a head-to-head test against a 6-blades/13mm cutters design from another provider. The 507 produced superior performance when compared to the other two runs by increasing the distance drilled by 79% from an average of 523 feet to 936 feet.

Dull condition also showed a large improvement with the 507 when compared to the 406. The 406 was pulled for poor penetration rate with a deep ringout in the shoulder. By contrast, the more durable 507 had a few broken cutters in the nose, and minor chipping in the shoulder.

.

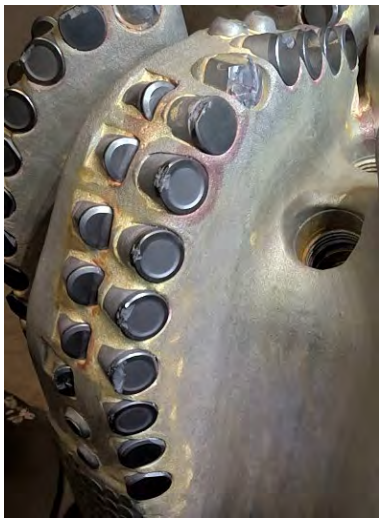

After this initial testing, seven more wells were drilled with six additional tests of the 507 along with four tests of a 7-blade/13mm cutters design from another provider. The 507 showed a 43% increase in distance drilled, and a 4% increase in rate of penetration when compared to the design from another provider.

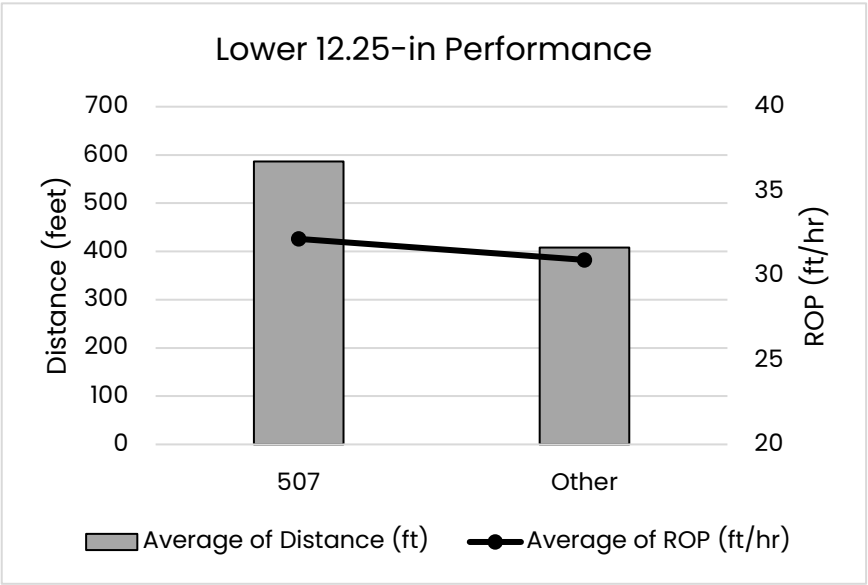

Figure 15 – Distance drilled and ROP metrics for Lower 12.25-in section

5. Curve 8.75-in Section

This drilling program was unique to this area with the goal to drill a horizontal well profile compared to the high inclination vertical wells that were drilled by Utah FORGE. The primary goal for the 8.75-in section was to drill the 1,000 feet curve in one run. The drill bit would need to build angle in the hard formation and precisely land the curve on target. Operational information for the horizontal drilling performance are documented by El-Sadi et al, 2024.

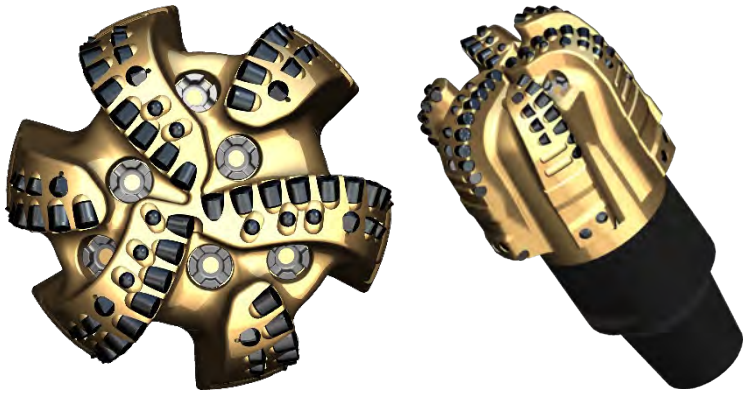

Figure 16 – 8.75-in 406 PDC Drill Bit with 6-Blades, 13mm (1/2-in) cutters, 3-in gauge pad with AntiWalk Technology for directional control, Depth-of-Cut Control for steerability, and secondary cutting elements for durability and wear resistance

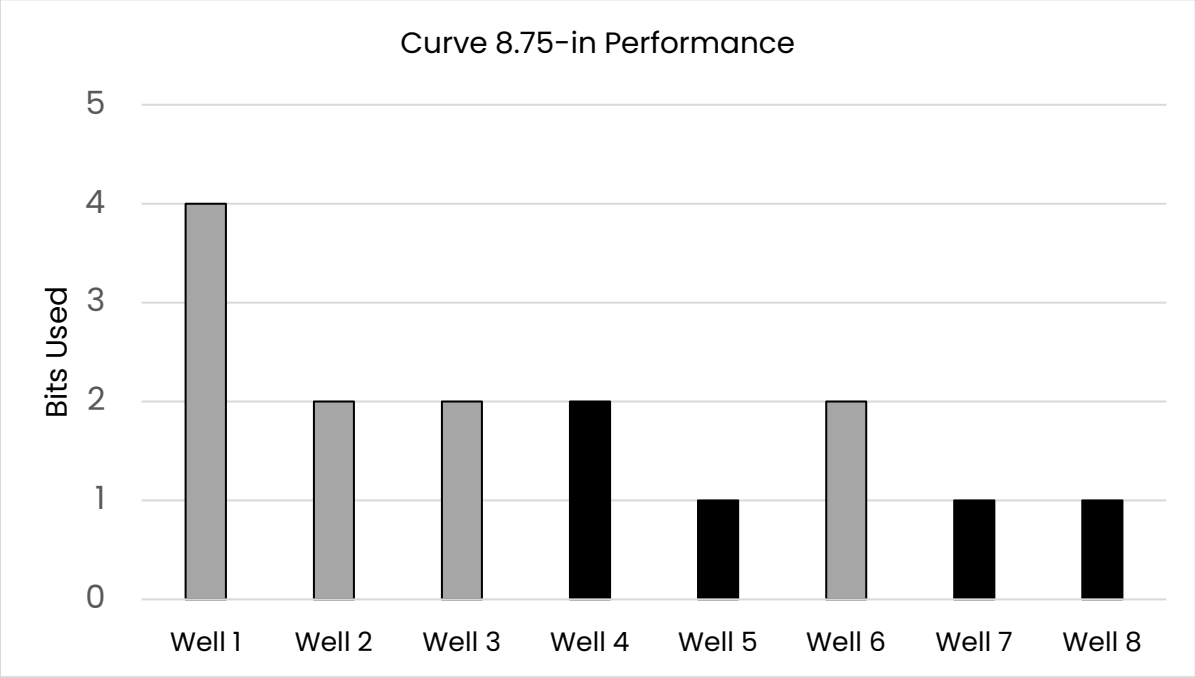

Figure 17 – Quantity of bits used in 8.75-in curve section.
The successful 406 was used on Wells 4, 5, 7 and 8 (black bars).

The first three wells in this program used PDC bits from another provider. Consequently, the first well required four bits – two PDCs and two roller cones – to complete the curve. The PDC bits from another provider were unable to properly drill the curve, resulting in low penetration rates. The PDCs were pull out of hole and roller cones were run in hole to steer the curve back on target. It was observed this highly technical section would be challenging to complete in one PDC run.

From a drill bit perspective lessons learned from oil & gas applications were applied to recommend a PDC design for this application. A successful 406 from the Permian and Anadarko Basins was chosen based on durability for drilling granite, and depth-of-cut control capability for directional toolface control. This design included a special gage configuration making it easier to steer on the directional motor assembly (Spencer et al, 2019). After the above design was introduced on well 4 a consistent one-run curve was achieved on wells 5, 7 and 8, see Figure 17. A 60% reduction in drilling days and larger scope drilling costs savings are also documented by El-Sadi et al, 2024.

6. Conclusions

By collaborating with operators and other service providers, we have optimized drilling performance in geothermal applications through advanced PDC drill bit designs. Our findings demonstrate a continuous improvement in performance, significantly reducing well costs and enhancing the economic viability of geothermal wells. Specifically, we have increased the distances drilled with PDC bits in the 12.25-in vertical and 8.75-in curve sections through software modeling and the optimization of cutting structure profiles, hydraulics, and cutters. As stated by Oueslati et al in 2019, the transfer of innovation and best practices from the established oil & gas industry is key to reducing the risk and cost of geothermal projects. This is critical to support the robust drilling campaign to bring one gigawatt of power online by 2030.

Historically, legacy roller cone drill bits have been used to drill geothermal wells at slow penetration rates. The insights gained from this Utah application are paving the way for exceptional drilling performance and establishing a foundation for the broader adoption of PDC drill bits. This engineering and technology application is making geothermal wells more economical and successful.

Acknowledgements

The authors would like to recognize the Utah FORGE project Team and Fervo Energy for their partnership and collaboration in bringing innovative drill bit technologies to the geothermal industry.

The authors would like to thank the management of Baker Hughes for permission to publish this manuscript with contents pertaining to:

Vulcanix™ geothermal drill bit solutions

Vulcanix™ geothermal Tricone

Vulcanix™ geothermal hybrid Kymera

Vulcanix™ geothermal PDC

Prism™ shaped-cutter technology

Tetrahedron™ 3D bit drilling simulation software

AntiWalk technology

REFERENCES

Cardoe J., Nygaard G., Lane C., Saarno T., Bird M. "Oil and Gas Drill Bit Technology and Drilling Application Engineering Saves 77 Drilling Days on the World's Deepest Engineered Geothermal Systems EGS Wells." *SPE/IADC International Drilling Conference and Exhibition* (2021) SPE/IADC-204121-MS.

Duffy S., Wasuthalainunt N., Wongnang C. "Improved Drilling Performance in Asia Pacific Formations Through Digitally Augmented Design Process for Shaped Cutter Drill Bits." *Offshore Technology Conference Asia*, Kuala Lumpur, Malaysia (2022) OTC-31346-MS.

Dupriest F. and Noynaert S. "Drilling Practices and Workflows for Geothermal Operations." *IADC/SPE International Drilling Conference and Exhibition*, Texas USA (2022) IADC/SPE-208798-MS, DOI 10.2118/208798-MS.

Dupriest F. and Noynaert S. "Continued Advances in Performance in Geothermal Operations at FORGE Through Limiter-Redesign Drilling Practices." *IADC/SPE International Drilling Conference and Exhibition*. Texas USA (2024) IADC/SPE-217725-MS, DOI 10.2118/217725-MS.

El-Sadi K., Gierke B., Howard E., Gradl C. "Review Of Drilling Performance In A Horizontal EGS Development." *49th Workshop on Geothermal Reservoir Engineering*, Stanford, California USA (2024) SGP-TR-227.

Hanafy A., Kueck A., Pauli A., Huang X., Bomidi J. "Case Study: Deep Insights from Downhole Sensing Unlocks Extended Bit Footage for Economic Drilling of Vibration Prone Abrasive Sandstones in Central USA." *IADC/SPE International Drilling Conference and Exhibition*, Texas USA (2024) SPE-217667-MS.

Hanafy A., Kueck A., Pauli A., Huang X., Bomidi J. "The Benefit of In-Bit Sensing for Efficienct Drilling of Deep Reach Lateral Wells in HFTO Prone Interbedded Abrasive Lithologies in North America Land." *International Petroleum Technology Conference,* Dhahran, Saudi Arabia (2024) IPTC-24120-MS.

Lockwood N. and Wasuthalainunt N. "Hybrid Drill Bits Double Drilling Efficiency in Geothermal Wells in Japan." *GRC Transactions* (2021) Vol. 45.

Oueslati H., Passuello B., Lehr J., Nurzad D., Mattie T., Vaccaro M., Alfani A. "Learning from the Oil & Gas Industry: Leveraging Innovation and Integration to Reduce the Risk and Cost of Geothermal Projects." *European Geothermal Congress,* Den Haag, The Netherlands (2019).

Russell S., Duffy. S., Matthews O., "Shaped Cutter Performance Optimization Through Advanced Drilling Simulations." *IADC/SPE International Drilling Conference and Exhibition in Galveston,* Texas USA (2022) SPE-208681-MS.

Spencer R., Pierce B., Grimes R. "Industry's First PDC Bit Gauge Design for Improved Tracking In North American Horizontal Wells." *SPE/IADC International Drilling Conference and Exhibition,* The Hague, The Netherlands (2019) SPE-194150-MS.

Stefansson A., Duerholt R., Schroder J., Macpherson J., Hohl C., Kruspe T., Eriksen, T. "300 Degree Celsius Directional Drilling System." *IADC/SPE Drilling Conference and Exhibition,* Texas USA (2018) IADC/SPE-189677-MS.

A Questionnaire Survey and An Agent-based Simulation as to Consensus Building on Geothermal Development in Japan

Kotaro Shinozaki[1], Jun Nishijima[2], and Tatsuya Wakeyama[3]

[1]Department of Earth Resources Engineering, Graduate School of Engineering, Kyushu University, Fukuoka 819-0395, Japan

[2]Faculty of Engineering, Kyushu University, Fukuoka 819-0395, Japan

[3]School of Environment and Society, Tokyo Institute of Technology, Tokyo 152-8550, Japan

Keywords Geothermal, Social Acceptance, Consensus Building, Game Theory, Agent-based Simulation

ABSTRACT

Japan ranks in third globally in terms of the potential of geothermal power resources with 23.47 GW; in fact, it ranks in 10th with regard to installed capacity in the world. Among many bottlenecks which hinder the domestic development of geothermal power plants, oppositions from local hot spa owners have been a primary problem. Therefore, successful consensus building with them will be of vital importance to be achieved so as to make full use of geothermal resources throughout Japan. In light of this situation, with the aim to promote successful consensus building on geothermal development, this study first developed an agent-based simulation illustrating opinion formation processes among hot-spa owners toward geothermal development. Afterwards, this study conducted questionnaire survey for hot-spa owners in Oguni town to collect data on their opinions and behaviors. Then, this study carried out the agent-based simulation with the collected data in order to check out the validity of the simulation. Finally, discussion was done as to the applicability of the invented simulation. Further research should be continued to investigate the method to validate the simulation.

1. Introduction

Japan is blessed with third-largest amounts of geothermal resources in the world, while the installed capacity of geothermal power generation is no more than 603 MW, making Japan located in 10th globally. Although Japanese government aims to increase the installed capacity to 1.6 GW by 2030, domestic geothermal development is not speedy enough to achieve that goal for now. One of the primary reasons why the geothermal development in Japan has been stagnant is intensive oppositions from local hot spa owners. They suspect that geothermal power plants reduce the output of their hot springs since they use a lot of hot vapor and water in the underground to

generate electricity. Although little data has revealed the inverse effect of geothermal power generations on the outputs of nearby hot springs in Japan, the scientific evidence alone are not effective enough to let down guards of hot-spa owners. Therefore, consensus building with hot spa owners is one of the key elements in order to just accelerate the domestic geothermal development.

2. Previous Research and Purpose of This Research

Social acceptance is a concept which describes what conditions are required for some technology to be accepted by society (Maruyama, 2014). Previous research on consensus building of geothermal development was conducted based on this concept and aimed at finding out elements contributing to successful consensus. While it provided us with helpful findings for successful consensus building with qualitative approaches, there has been little research based on quantitative approaches. Studies with quantitative approaches are highly expected not only to help verify the findings from the qualitative research to date numerically, but also to contribute to giving new perspectives to this geothermal challenge. In addition, as a concept of evidence-based policy making, or EBPM indicates, quantitative approaches and methods are effective tools to transform existing policies to solve social challenges. This is also considered true of geothermal development, and the demands for them have been increased more than ever (Yasukawa et al., 2018).

Komori et al. (2023) is one example of a few of earlier studies applying a quantitative approach to an analysis of geothermal consensus building. The study developed a compartment model to simulate an elapsed change of the number of supporters and opponents for a geothermal project over several decades. A novel characteristic of the study is an introduction of effective susceptibility number Re, a time-varying index inspired by an effective reproduction number from an epidemiologic study. They concluded through their parametric studies the Re number could represent well the level of opinion exchanges or the frequency of dialogue and interactions in their research area. While the study exhibited one possible way to numerically model consensus building of geothermal development, as they mentioned in their paper as well, the model is lack of individual diversity, that is, it does not explain the processes of interactions among individuals with different attitudes. Moreover, it seems that the effective susceptibility number suggested in the paper requires considerable efforts and careful settings of the relating parameters for the appropriate interpretation. Although they explained the relationship of the parameter change with the social trends of the research area in their paper, the parameter alteration itself was based on their arbitrary assumptions, resulting in a sort of tautological rationale and unconvincing explanation. In order to come up with effective solutions of social acceptance of geothermal energy, it is vitally required to take diversity of each individual into consideration as well as time-varying dynamics. Therefore, this study aims to construct a simulator prototype for geothermal consensus building which can illustrate diverse behaviors of individual.

3. Research Method

3.1 Agent-based Simulation

Agent-based simulation (ABS) is a bottom-up type of simulation based on the behaviors of agents, which are defined as autonomous subjects. They follow certain rules of their behaviors and act accordingly through their interactions with the others. This simulation can visualize an overall result of them and help us understand complicated dynamics of interactions among diverse agents.

An ABS of this research was developed using Artisoc ver. 4.2.1 standard, an agent-based simulator founded by Kozo Keikaku Engineering Inc.

3.2 Simulation Setting

The ABS of this research aimed to model opinion formation processes among hot spa owners and their subsequent results of the community as a whole. It was based on Axelrod's iterated prisoners' dilemma game, where players repeated prisoners' dilemma game for a certain number of times. The ABS of this study modified a number and varieties of strategies of the Axelrod's and added opinion formation processes. It was composed of agents, strategies, and payoff matrices. The agents were defined as hot spa owners, and three different types of agents were set as neutralists, supporters, and opponents. The strategies were expressed in the form of four different integers as shown in Table 1 below.

Table 1 Value – strategy correspondence

Value	Strategy
0	Random
1	All Corporation (AllC)
2	All Defection (AllD)
3	Opportunism

Each strategy defines how agents assigned to it choose cooperation or non-cooperation in interactions with other agents. Agents with random strategy decide their actions at random: cooperation at 50% and non-cooperation at 50%. Those who follow AllC strategy always cooperate, whilst those with AllD strategy never cooperate. Opportunism agents determine their actions based on the atmosphere among overall agents. When the simulation starts, all agents are assigned to one of the three types, which is to say, neutralists, supporters, and opponents. The strategies of neutralists are determined randomly while supporters and opponents take AllC and AllD strategy respectively. Table 2 and 3 below shows the payoff matrices of cooperative (Random and AllC) and risk-aversive (AllD and opportunism) agents respectively. The agents refer to these payoff matrices according to their types and the results of their interactions in order to calculate their payoff. The left and right-side number expresses the payoff for hot spa owner 1and 2 respectively, and the numbers bolded in the tables indicate the payoff given as a result of best-response strategy to the other's one.

This simulation includes two processes agents go through, which are, an opinion formation process and a learning process. A flowchart of the opinion formation process of them is shown in Figure 1. In a timestep, each agent randomly moves around a simulation field to find another agent to interact with. When the agent bumps into another agent, they interact with each other based on their strategies, which gives each agent opinion and score values, output parameters of this simulation. The opinion parameter increases when the result (Coop, Coop) is selected, and the score parameter represents the sum of payoff. The value of the score parameter can be seen as an agent's confidence, given that it reflects successful experiences of consensus building. Their values are 0 at an initial condition, and as the agents interact, they change their values as shown in Figure 1. Repeating this process 10,000 times, this simulation can illustrate how overall opinions can be formed based on interactions among the agents. In addition to the opinion formation

process, agents have their chances to conduct their learning processes, where they transform their strategies in a trial-and-error way at every 100 timesteps to review their best strategies. The flowchart of the learning process is shown in Figure 2 below. In the learning process, an agent randomly chooses another agent to compare its score to decide whether or not it changes its strategy. In this way, agents learn to find out their best strategy in the course of time. These whole processes are repeatedly conducted 100 times in order to eliminate the influence of randomness.

Table 2 Payoff matrix of cooperative agents

Hot spa owner 1 \ Hot spa owner 2	Cooperate	Not cooperate
Cooperate	(**2**, **2**)	(-1, 0)
Not cooperate	(0, -1)	(**0**, **0**)

Table 3 Payoff matrix of risk-aversive agents

Hot spa owner 1 \ Hot spa owner 2	Cooperate	Not cooperate
Cooperate	(**0**, **0**)	(-1, **0**)
Not cooperate	(**0**, -1)	(**2**, **2**)

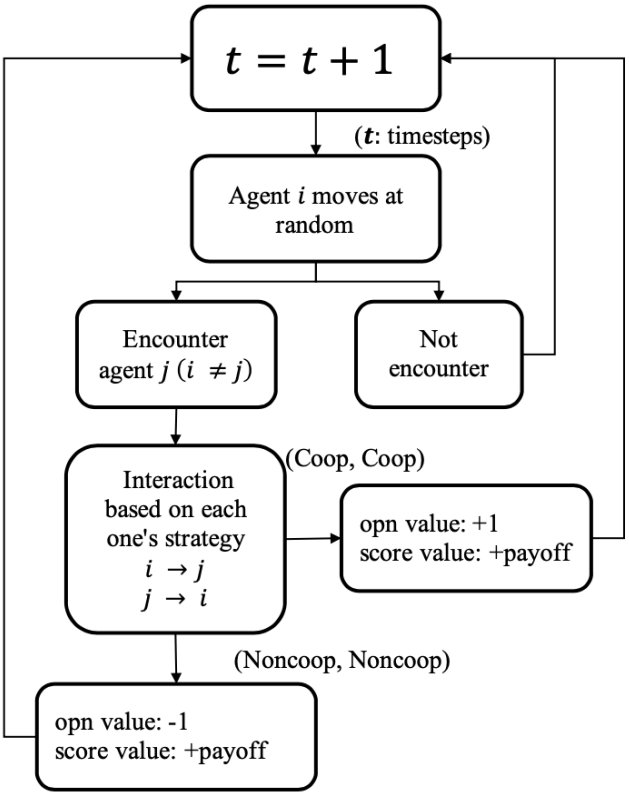

Figure 1 Flowchart of the opinion formation process

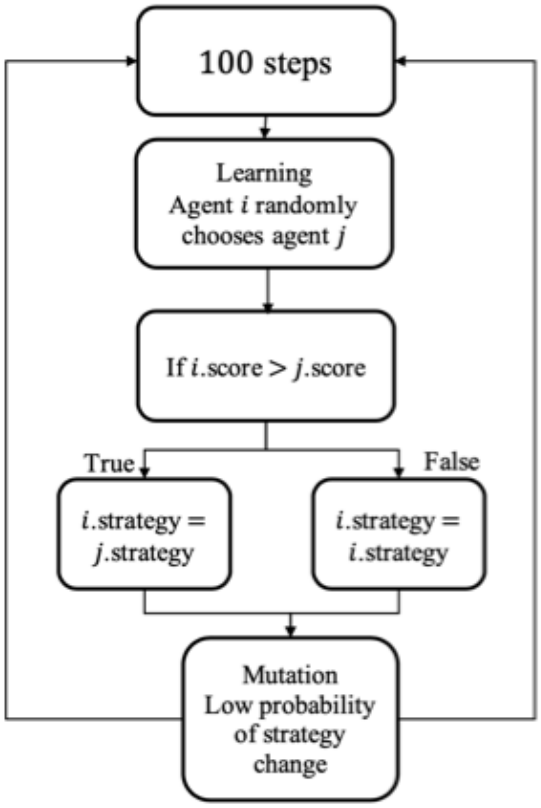

Figure 2 Flowchart of the learning process

An ABS for an analysis of an actual geothermal case has yet to be done. It is essential to put actual data into this simulation as input parameters and examine whether or not this ABS can coherently illustrate the corresponding outcome. Therefore, this study conducted questionnaire survey in Oguni town, Kumamoto Prefecture so as to collect actual data on attitudes of hot spa owners toward geothermal development and to examine the validity of the invented simulation.

4. Questionnaire Survey

The questionnaire consists of two fundamental questions which specify a respondent's residential area and its style of hot spa business, and the following fifteen questions on its basic knowledge about geothermal energy and its attitudes toward geothermal development in the research area. This survey was conducted for twenty-six hot spa owners in Oguni town between October 2nd and 13th, 2023. The questionnaire was distributed in the form of paper to each respondent and collected in person in order to increase the response rate as much as possible. As a result, 23 responses out of 26 were successfully collected and were considered enough rates to represent overall attitudes on geothermal development among hot spa owners. Questions directly related with ABS parameters settings in the questionnaire are shown in Table 4 below.

Table 4 Primary questions asked in the Oguni Town survey

Q1. What do you think about geothermal development for power generation in Oguni town in the future? 1. Strongly advance 2. Partially advance 3. Not advance very much 4. No advance at all 5. No idea Q2. As to geothermal development plans in Oguni town so far, how did you decide your attitudes toward them? Select the answer which best matches your decision-making process. 1. Never changed your opinion 2. Followed others 3. Communicated your opinion with others and did not change it in the end. 4. Communicated your opinion with others and changed it in the end. 5. Other ( ) Q3. How often do you talk about power-generation-related topics such as geothermal power generations and binary power generations with neighborhood people? 1. Seven or more times out of ten chances 2. About five times out of ten chances 3. About three times out of ten chances 4. About one time out of ten chances 5. Seldom talk about them

5. Result

Figure 3 below shows the questionnaire results with regard to questions in Table 4.

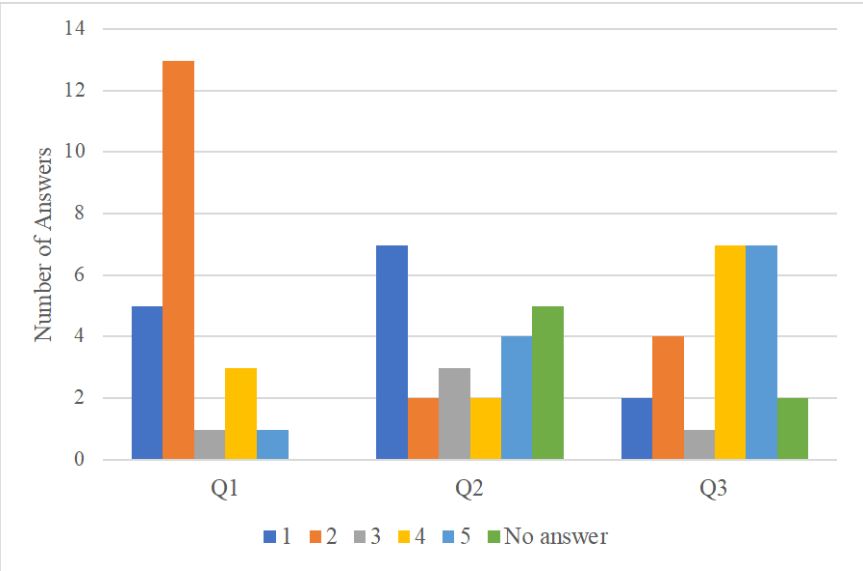

Figure 3 Questionnaire results

The ABS was modified based on this questionnaire results. There were two crucial changes made to reflect the questionnaire results to the prototype of the ABS. The first change was to modify the encounter rate of the simulation. The rate was set as about 21% based on the Q3 answer result of the questionnaire. The encounter rate was changed by coordinating the size of a simulation field as 40 × 40. The second one was about the change of agent type distribution at initial condition. This change was made so that the distribution was coherent with the Q2 result. The number of respondents who selected answer one was considered an agent without the learning processes throughout the simulation. They were allocated to either supporters or opponents based on their Q1 and Q2 answers. Those with other answers were seen as the neutralists, which follow the learning process. By customizing the behaviors of the agents this way, the simulation result is likely to reflect the geothermal development for power generation in Oguni town.

Figure 4 below displays the average strategy distribution of the agents at the end of the simulation. AllC and AllD agents are dominant strategies among the four, and AllD strategy marked the highest number of agents with 11.68, followed by AllC with 10.57. Figure 5 below shows elapsed change of average opinion and payoff value through the simulation. The average opinion value is equal to the summation of the number of agents' cooperation divided by the number of agents multiplied by timesteps. The same equation is applied to average payoff value. The average opinion value plunges down at the very early time and then remains constant at around -0.05, while the average payoff value gradually increases over time to converge to 0.59

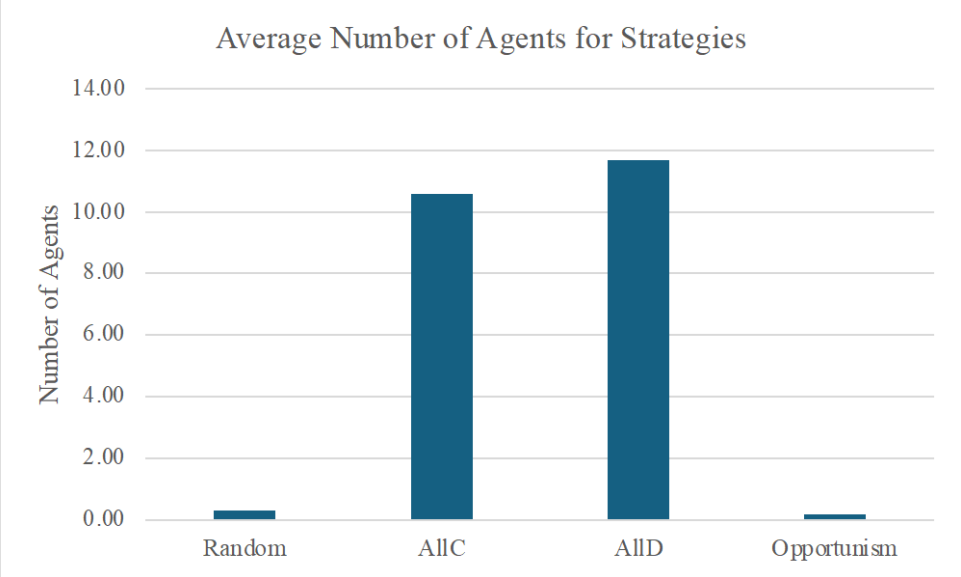

Figure 4 Simulation results about average strategy distribution of agents at the end of simulation

.

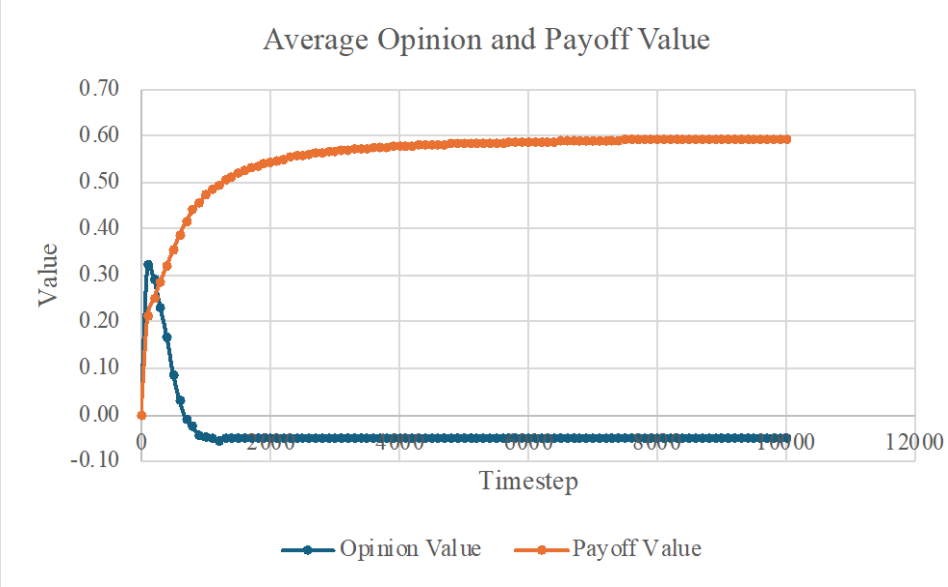

Figure 5 Simulation result on elapsed change of average opinion value and payoff value

6. Discussion

From the results in Figure 4 and 5, the invented ABS could not reproduce the opinions of hot spa owners toward geothermal development in Oguni town, given that the hot spa owners in the town are for the geothermal development as a whole. It is because the payoff matrix of risk-aversive agents, referred to by those with AllD and opportunism strategies, gives them higher payoffs than the one of cooperative agents, used by those with random and AllC strategies. As shown Table 2 and 3, cooperative payoff matrix gives the agents $2 - 1 = 1$ payoff on average while risk-aversive matrix does $2 + 0 = 2$. This difference might cause the risk-aversive agents to gain higher payoffs, which makes more agents choose not to cooperate. Another possible reason for this misfit could be an algorithm of the learning process. The learning process forces agents to suddenly change their strategies just because their payoffs are inferior to the ones of comparing agents, which might not well illustrate actual opinion formation process.

As to checking the validity of this simulation, this study found out that it was not appropriate to utilize questionnaire survey results in Oguni town. It is because the simulation result in this study shows the possible future transition of overall opinion based on the current opinion and behavior of the hot spa owners in the area, and thus there are no valid counterparts to make a comparison with now. Therefore, it is necessary to find out common facts observed in consensus building of past geothermal development for checking the validity of the simulation. The validity of the simulation can be checked out whether or not it successfully reproduces the common facts.

Although it is considered that this agent-based simulation is still halfway through to its actual application, at the same time it achieved illustration of diverse ways of thinking and behaviors among individual, which was one of the goals this study aimed at. The introduction of various types, strategies, and payoff matrices of agents enabled this simulation to illustrate diverse opinions and their complicated interactions among agents. This simulation also included time-

varying dynamics of their opinions by bringing in the opinion learning process, which could trace the change of opinions. Furthermore, there is an interesting finding to take into consideration. It is that the overall opinion might be mostly determined at very early time. The elapsed change of average opinion value in Figure 5 shows a sudden change from about 0.3 to -0.05 before 1000 timesteps, and then remains almost constant throughout the simulation. This pattern of transition may indicate the importance for geothermal developer to closely and continuously contact with hot spa owners at an early stage. In fact, the guideline for conservation of hot spring resources published by Ministry of the Environment (2024) strongly recommends that geothermal developers create a place for opinion interactions with local hot spa owners such as a council at the earliest stage of geothermal development in order to facilitate consensus building with them.

7. Conclusion

This study set out for constructing an agent-based simulation illustrating consensus building situation of geothermal development, where hot spa owners with diverse opinions and behaviors interact with one another. In order to achieve that goal, this study developed an agent-based simulation based on game theory, into which opinion formation and learning process were integrated. Diversity of the individual, which had not been realized in previous research, was introduced by setting different agent types, strategies, and payoff matrices. The combination of these elements enabled the simulation to illustrate complicated opinion formation process of consensus building on geothermal development. Adding to that, this study conducted questionnaire survey in Oguni town, Japan to utilize for validation of the invented simulation. Although the survey successfully collected actual data as to opinions and attitudes of hot spa owners toward geothermal development in the area, it was found out that it was not suitable to make use of the questionnaire results for validating the simulation. While the simulation development is not enough for application, it still indicated supportive results of activities recommended by the government for successful consensus building. Further research should focus on finding out how to check the validity of the invented simulation so that it can work as guidance for action in the future consensus building.

Acknowledgement

This work was supported by JST, the establishment of university fellowships towards the creation of science technology innovation, Grant Number JPMJFS2132 (Q-ENERGY Fellowship).

REFERENCES

Maruyama Y. "Socialization of renewable energy" *Yuhikaku*, (2014), 18,19.

Matsuda S.,Bahr K., Tsuchiya N., and Takemori T. "Agent based simulation with data driven parameterization for evaluation of social acceptance of a geothermal development: a case study in Tsuchiyu, Fukushima, Japan" *Scientific reports nature portfolio*, (2022).

Komori Y., Kioka A., and Nakagawa M. "Predictive model for history matching of social acceptance in geothermal energy projects" *Renewable Energy Focus 45*, (2023), 192–200.

Yasukawa K., Kubota H., Soma N., and Noda T. "Integration of natural and social environment in the implementation of geothermal projects", *Geothermics*, 73, (2018), 111–123.

Ministry of the Environment, "Guideline regarding conservation of hot spring resources (relating with geothermal power generation) (Revised)", last viewed 2024/08/01, https://www.env.go.jp/nature/onsen/pdf/guideline202303.pdf.

Probability of Discovery as a Useful Concept for Communicating Exploration Drilling Uncertainty

Greg Ussher[1], Aimee Calibugan[1] and Julian McDowell[2]

[1]Jacobs, New Zealand

[2]Jacobs, Canada

Keywords

UNFC, resource classification, exploration, drilling risk, success

ABSTRACT

The United Nations Framework Classification for Resources (UNFC) is a globally recognized system for classifying projects and the resources they produce and has an accompanying Geothermal Specification that has been developed by a working group of the International Geothermal Association (IGA). This is gaining traction as the only currently valid system for classifying geothermal projects and was recently applied to most of the New Zealand geothermal resource. Within the Geothermal Specification is a provision for reporting the Probability of Discovery (PoD) for a project before deep drilling. The PoD is the chance that a reasonable (or planned) exploration drilling program will succeed in finding a useful geothermal source.

PoD is similar in concept to Probability of Success (PoS) as applied in oil and gas exploration but allows for a more generalized evaluation without a defined drilling program. Increasing use of the PoS and PoD concept in geothermal recently is due to its promotion by leading practitioners but is yet to be universally accepted or understood. However, it is increasingly accepted as an important tool for conveying the uncertainty inherent in exploration drilling.

Recent adoption of the PoD concept as a tool to assist approvals for state and World Bank funded drilling in Indonesia has driven a need to better define PoD and how it is estimated. A methodology and calculation tool has been developed and is presented for further consideration by the industry.

1. Introduction

UNFC provides a globally consistent framework for assessing geothermal projects. It is a shift from the conventional geothermal characterization to a more holistic approach providing indications on the technical feasibility, economic viability, risks, and sustainability of the project.

Readers are directed to Beardsmore et al., (2021), UNECE (2022), Falcone and Beardsmore (2015), Grant and Ussher (2015) and Ussher et al., (2023) for comprehensive descriptions of the UNFC principles and its application to geothermal energy resources. In this paper, we focus on the application of the UNFC to an exploration project, in which the PoD is an important feature. Inherent in this stage of a project it is worth noting the key concepts of the UNFC as they apply.

Firstly, a '**Geothermal Energy Source'** is the energy contained in rocks, sediments and/or soils, including any fluid contained underground or naturally discharging at the ground surface, which is available for extraction and/or conversion into energy products.

Secondly is the difference between '**Known vs. Potential'.** A Known Source is classified where one or more wells/hot springs are established and a significant quantity of recoverable thermal energy established through testing/sampling logging. A Potential Source is one where there is no direct evidence (from drilling) establishing the existence of a significant quantity of recoverable thermal energy. The existence of energy is inferred from geoscientific data only.

2. Probability of Discovery (PoD)

The UNFC scheme has included the concept of probability of discovery (PoD). It refers to the probability that further exploration, drilling and well testing will result in the confirmation of a Known Geothermal Energy Source. It is required to be reported for the Potential Geothermal Energy Sources under the UNFC system.

Generally, PoD is similar in concept to Probability of Success (PoS) as applied in oil and gas exploration but allows for a more generalized evaluation of early-stage (pre-drilling) exploration projects. Beardsmore et al. (2021) highlighted the importance of clarity around whether shallow productive wells could be considered within the PoD concept to demonstrate existence of a deeper, yet to be drilled, resource. They comment that the deeper resource should still be considered unknown in the UNFC sense and highlighted that importance of acknowledging inconclusive results when considering ultimate classifications.

Recently, the PoD concept has been adopted as a tool to assist approvals for state and World Bank funded geothermal drilling projects in Indonesia. This has subsequently triggered the need to better define PoD and how it is estimated.

3. Probability of Success (PoS)

In oil and gas exploration, the total geological PoS is calculated by multiplying PoS values for segment elements (geological risk factors). The application of the PoS concept varies considerably through the oil and gas industry, with the number of factors used ranging from 4 to 19 depending on the company (Milkov, 2015, 2021). Milkov (2015) notes the risk of encountering bias and subjective judgments within the PoS concept leading to inconsistency across companies and wide range of factors. They proposed an algorithm in the form of systematic risk tables for probabilities for only six factors, with the intent of improving drilling decision and reducing bias.

In a study of 375 conventional petroleum exploration prospects/wells and 80 drilled wells, Milkov (2022) noted that the actual geological success rate (58%) was much higher than the average pre-drill probability of geological success, PoS (37%). Explorers, in general and on average, significantly overestimated geological risks before drilling and made many more discoveries than

expected. This may be because the estimation of risk factors was too conservative, or that the way they are combined was causing PoS to be too low.

We observe that an approach adopted by some geothermal teams with backgrounds in the oil and gas industry is to evaluate the probability of finding several key factors (suitable temperature, permeability and chemistry are often used) and then multiplying these together. It is possible that these may not all be entirely mutually independent and hence simple multiplication is overly conservative. It is also true that if one added more factors such as pressure (water depth), ability to drill wells or a minimum size, then this would add additional factors and inevitably reduce the PoS. So, a different approach is possibly worth considering.

4. Jacobs Probability of Discovery Tool

In an effort to enable a consistent and systematic approach for determining PoD, Jacobs has developed an excel-based tool which calculates the PoD of a given geothermal project. The concept is to break the review of factors down to manageable elements and give guidance to their evaluation to drive consistency of application. The calculation then works in a way that weights most strongly those elements which are most reliably assessed and can influence the PoD either positively or negatively.

The PoD tool considers the critical elements (Figure 1) required for a successful project which include the a) reservoir temperature, b) benign fluid chemistry, c) the physical ability of expected reservoir to produce (i.e., can wells be productive given favorable temperature and permeability, and considers the depth of water table), and d) the ability to complete wells in the desired area of the reservoir. The calculated PoD essentially represents the chance that after drilling the planned wells that a useful geothermal reservoir can be discovered.

Figure 1: Critical Elements for the PoD Calculation

5. PoD Calculations and Key Elements

The temperature expectation parameter is assessed firstly to indicate if production is realistic at all for a given prospect based on reservoir temperature and water level. The probability for temperature, permeability and chemistry and drilling are then determined.

A selection of 0 to 3 rating is provided for each sub-factor (i.e. for temperature the sub-categories relate to presence and character of springs, fumaroles, temperature gradient wells and heat source) with the logarithmic average of the sub-category ratings used to determine the probability for each category (where 0 = 1, 1 =10, 2=100 and 3=1000).

The overall project PoD is calculated using the minimum probability of the 5 categories multiplied by the average of all the sub-categories. The assumption here is that the PoD must be lower than the minimum of any main parameter, but these parameters are not all mutually independent so a simple multiplication of all the categories biases too low. The multiplication with the average of the parameters is used as an alternative to multiplying all the parameters together.

5.1 Temperature Expectation

Basically, this is a check on whether the expected reservoir temperature is adequate for the depth of reservoir "water level". If the temperature is too low and water level deep, wells cannot flow. This is further illustrated in the simple schematic in Figure 2. In the example, well A (high T, deep WL), well B (high T, shallow WL) and well D (med T, shallow WL) all sustain flow but on the other hand, well C (med T, deep WL) cannot be flowed realistically. Figure 3 shows the rating selection for temperature expectation sub-categories on reservoir temperature and depth to water level. Resources which do not have 'self-flowing' wells can still be developed with pumping, but water depth also strongly influences the viability of pumping, as parasitic power increases greatly as water depth increases. This correlation for pumped wells needs further consideration, but conceptually can, and should, be applied similarly.

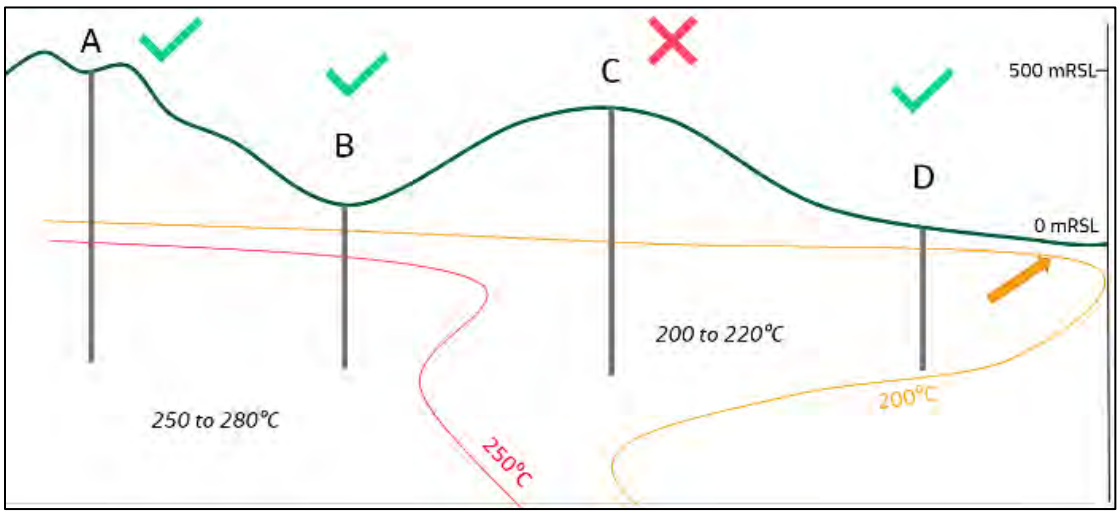

Figure 2: A simple schematic illustrating the influence of reservoir temperature and water level on the success of the well. See texts for explanation.

	0	1	2	3
Temperature expectation				
Expected reservoir temperature	Less than 210 C	210 to 230 C	230 to 260 C	More than 260 C or vapour-dominated reservoir
Water level	Near surface or overpressured or steam-dominated	150 m	300 m	deeper

Figure 3: Selection parameters for temperature expectation.

5.2 Temperature Probability

Considerations for temperature probability include the following: a) presence of high flowrate chloride springs indicated to be coming direct from reservoir which typically provide best geothermometry, b) presence of fumarole activity which is a strong indicator of an active systems and can provide good isotope geothermometry, c) shallow temperature wells that demonstrate temperature gradients within the cap of the system and are consistent with expected gradients within the clay cap and d) age of volcanics/heat source or deep structures and indicators of high heat flow. Figure 4 shows the selection parameters for temperature.

Note that these are not necessarily determining presence of a high temperature, rather the confidence that the temperature that *you expect and need for useful production* will be found. This is apparent in the selection and weighting of the sub-factors we have defined, which are all about the *confidence* that we have about the temperature indications.

Temperature probability	0	1	2	3
High flowrate springs	No springs discharging primary reservoir water	Weak, distant or dilute springs	One or two low flow springs (<1 l/s) with geothermal water content	Several low flow or one high flow springs with clear geothermal content
Presence of fumaroles	No fumaroles or steaming ground	Steaming ground	Weak fumarole activity, probably depositing sulphur	Strong fumaroles with pressurised steam - steamflows noisy
Temperature gradient wells	No TG wells	TG wells with inconslusive results or not deep enough	TG wells that support inferred temperature gradients and at least 70% of target reservoir temperature (in deg C)	TG wells achive closer to reservoir temperature or at least top of reservoir temperature
Heat source indicators	Volcanics older than Quarternary or no indicators of high heat flow region	Volcanics 0.5 to 2 Ma or indicators of deep faulted system	Volcanics 0.2 to 0.5 Ma or strong indicators of deep structural system	Younger volcanism nearby or majjor structure system, with springs on structure

Figure 4: Selection parameters for temperature.

5.3 Permeability Probability

Permeability takes into consideration the lateral outflows, fault permeability and nature of the clay cap in the system (Figure 5). Major lateral outflows indicate good permeability in liquid-dominated systems. These may be indicated by spring flows combined with geophysics. Steam-dominated systems or steam caps may have bicarbonate waters indicating boiling and high heat flow. Fault permeability is also evaluated including whether faulting is clearly providing permeability in the system, with indicators like springs or fumaroles along well-defined structures. Clay cap up-doming and thickness is another indicator for permeability. Systems with good permeability tend

to have good buoyancy above the upflow area and hence have an up-domed base of the clay cap (typically defined by geophysics; magneto-telluric signatures). The clay cap (< 10 ohm.m) also tends to be thinnest where isotherms in reservoir dome upwards. There should be caution though with up-doming of the MT conductor within a volcanic system as these may be volcanic-induced alteration. Figure 5 shows the selection parameters for permeability.

Permeability probability	0	1	2	3
Lateral Outflows from system	Limited or no outflows	Some outflows indicated with primary fluids, distal springs with small flows	Moderate outflows, distal or near springs with significant flows of primary water or bicrbonate fluids from above a boiling or steam dominated system	Strong indications of major outflows, high volume springs of primary water, bicarbonate flows off a steam dominated reservoir, or strong indicators of being a steam dominated system.
Fault permeability	There is no clearly defined faulting and no evidence that faulting is providing permeability	Some faulting is present but no evidence it is likely controlling permeability	Faulting is clearly defined and of a type that could provide permeability	Faulting is clearly defined and thermal discharges are associated with the faulting
Clay cap : up-doming and thickness	Clay cap is not well defined, is generally > 10 Ohm.m, or is very thick (> 1.5 thick in area to be drilled)	Clay cap is 0.7 to 1.5 km thick	Clay cap is less than 700 m thick with limited updoming	Clay cap is less than 700m thick and showing some updoming

Figure 5: Selection parameters permeability.

5.4 Chemistry Probability

The key considerations for chemistry assessment include a) presence of neutral, alkali chloride fluids as evidenced by spring flows is a positive indicator of having reasonably benign fluids in reservoir, b) presence of magmatic gases, highly acid-chloride springs or isotopes indicating magmatic origins raises risk that fluids may be acidic at least in places in the system and c) gas content of the fluids can cause a system to be uneconomic to develop. Figure 6 shows the selection parameters for chemistry.

Chemistry probability	0	1	2	3
Neutral reservoir fluids	There are no springs from the system to indicate reservoir chemistry	Springs indicate possible presence of acidic fluids, such as high sulphate, low pH	Springs indicate minor risk of acidic fluids	High flow springs probably of primary waters have neutral pH and no indicators of sulpate or other risk parameters.
Presence of magmatic fluids	Strong indicators of magmatic fluids (e.g., HCl, HF or SO2), or acid chloride springs and no indicatons of neutral fluids in system	Strong indicators of magmatic fluids but also evidence of neutral fluids in same system	Minor indications of magmatic fluids near system, but other indications of nuetral fluids	No magmatic indications and postive indications of neutral fluids as evidence by high flow springs
Gas content	High gas content in fumaroles > 15%	Medium content of gas in fumaroles or steaming ground (5-15%), or abundant bicarbonate ground water flows from system	Small gas content (2-5%) from fumaroles. or limited bicarbonate groundwater flows	Low has content on fumaroles or steaming ground (<2%) or not other indicators of significant gas content

Figure 6: Selection parameters for chemistry.

5.5 Drilling Probability

The drilling category focuses on the targeting of favourable area, technical risks and capability, and the organization capability (Figure 7). The overall success of the project will depend heavily on the ability to drill in the favourable part of the system as represented by the temperature, permeability conditions referenced in the earlier discussions, and that the planned well depth is sufficient to test the expected reservoir. In terms of technical risks, the target depth is at limits of rig capability, geological risks such as difficult formations, shallow thermal activity, and significant depth to the top of reservoir can all increase the risk that target depth is not reached and contribute to inconclusive drilling results. Lastly is the capability of the developer/owners' technical team, drilling contractor, contract arrangements and service company with drilling in similar conditions, which will also impact drilling success. **Error! Reference source not found.** illustrates the key characteristics of systems with favourable PoD in contrast to low PoD systems.

Drilling probability	0	1	2	3
Targeting of favourable area	Wells cannot be located in the main high probability or P50 area or not deep enough to confidently test the reservoir	Some wells are located outside the P50 area and none in high probability area or are only marginally deep enough to test the expected reservoir	All wells are located in the P50 area and wells are deep enough to test the expected reservoir	Wells are all located in high probability area and deep enough to definitively test the expected reservoir
Technical risks and capability	There are multiple concerns on geology, thermal activity, depth to top of reservoir or limits of planned well depth	Some identified concern about 2 or more factors	Minor concerns about one of the risk factors	There are no particular risk concerns identified
Organisational capability	Owner's team and drilling contractors have NO relevant experience on geothermal drilling	Owner's team and drilling contractors have worked on at least 1 geothermal well drilling.	At least key individuals in owner's team have relevent experience completing geothermal drilling and drilling contractor has relevent experience with planned drilling rig.	Owner's team (as a team) and main contractors have prior experience completing drilling on similar geothermal campaigns

Figure 7: Selection parameters for drilling.

Probability of Discovery (PoD)	Productivity check	Pre-Exploration Drilling Indicators			
	Temperature and Water Level	Temperature	Permeability	Chemistry	Drilling
Favourable PoD	Temperature high Shallow water level	Presence of fumaroles, High temperature, high flow hot springs Good quality geothermometry temperatures Younger volcanism nearby as possible heat source Presence of major structure system, with spring on structures TG wells indicating hot temperatures	Presence of several faults (extensional faults) Alignment of thermal features with the identified faults Lateral outflows Domed clay cap and thinning cap over the up-dome	Presence of alkali chloride springs No volcanic gases Stable isotope indicating predominantly heated meteoric water origin No indications of high gas content	Exploration wells are located in high probability area and deep enough to definitively test the reservoir No risk concerns identified Owner's team and drilling contractors have relevant geothermal drilling experience
Limited / low PoD	Lower temperature Deep water level	Absence of fumaroles or hot springs Low geothermometry temperatures Mixed or partially equilibrated waters Absence of alkali chloride springs (for geothermometry analysis) TG wells indicating low temperatures or no TG wells	Associated with tight structures Minimal geologic structures identified Limited outflows if a liquid system	Absence of neutral-pH alkali chloride waters Presence of volcanic gases Stable isotope indicating magmatic origin	Exploration wells cannot be located in P50 or high probability area and/or not deep enough to test the reservoir Multiple risk concerns identified Owner's team and drilling contractors have no relevant geothermal drilling experience

Figure 8: A summary of key characteristics of geothermal systems with favorable PoD vs low PoD.

6. Case Study Applications

To test if the PoD tool works with actual geothermal projects, we have applied it retrospectively on ten projects across Indonesia which have all moved to at least the exploration drilling phase. Care was taken to use the information that was available pre-drilling to calculate each PoD. Table 1 summarizes the results of the case studies which shows a good correlation between the calculated pre-drilling PoD and the post-drilling results. In this study, PoD results of <50% correlated with projects which failed to demonstrate useful geothermal resource, while all projects with >50% succeeded with the realization of installed power capacity. This demonstrates that the PoD tool, in its current state, can be effectively utilized to assess the possible outcome of a geothermal project.

Table 1: A comparison of pre-drilling PoD and the post drilling results of actual geothermal projects in Indonesia.

Project	PoD (Pre-Drilling)	Post-Drilling Results
A	89%	Success – 271 MW installed capacity
B	78%	Success – 220 MW installed capacity
C	83%	Success – 330 MW installed capacity
D	80%	Success – 140 MW installed capacity
E	59%	Success – 170 MW installed capacity
F	32%	Fail – poor permeability, 200 ºC at 2800 m
G	47%	Fail – Poor permeability, Tmax of 156 ºC at 920 m; may not have been deep enough
H	18%	Fail – 4 deep wells drilled with depths of 1800-1900 m; 2 of the wells had poor permeability; 2 wells had 140 ºC and 213 ºC discharge fluids, respectively.
I	44%	Fail – 71 ºC at 605 m; thermal gradient at 7ºC/100 m; good permeability
J	15%	Fail - Deep well had no productivity and modest temperatures

7. Conclusions

The PoD is the chance that a reasonable (or planned) exploration drilling program will succeed in finding a useful geothermal source. This represents an important concept to qualify and quantify in a systematic way such that the allocation of funds for geothermal project exploration can be considered using with a suitable and justifiable screening tool.

Recent adoption of the PoD concept as a tool to assist approvals for state and World Bank funded drilling in Indonesia has driven a need to better define PoD and how it is estimated. A methodology and calculation tool has been developed and is presented for further consideration by the industry.

A study of 10 geothermal project in Indonesia has demonstrated that the PoD tool, in its current state, can be effectively utilized to assess the possible outcome of a geothermal project. We encourage the industry to use this approach, to facilitate further development of this type of tool and refine it over time. We also encourage consideration the application of the broader UNFC system for classifying geothermal projects and fairly representing their development status.

Acknowledgements

Jacobs thanks those at UNECE, IGA, and the dedicated professionals in the wider industry who continue to support the development and use of the UNFC for geothermal resources.

REFERENCES

Beardsmore, G., Ali, A., Brommer, M., Chen, H., Conti, P., Falcone, G., Fridriksson, T., Hogarth, R., Mijnlieff, H., Rumberg, G., and Ussher, G. "UNFC Resource Classification Applied to Real World Geothermal Projects: Outcomes from an Education and Implementation Pilot Program." *Proceedings World Geothermal Congress 2020+1*, Reykjavik, Iceland, (2021).

Grant, M.A. and Ussher. G.N.U. "UNFC-2009 and Geothermal Resource Classification." *Proceedings 37th New Zealand Geothermal Workshop* (2015).

Milkov, A.V. "Pre-drill Assessments and Drilling Outcomes in Mexico in 2018–2022 and Historical Experience from Norway and the Netherlands: Lessons Learned and Recommendations for Future Petroleum Exploration". *Nat Resour Res* 31, (2022), 2483–2504.

Milkov, A.V. "Reporting the expected exploration outcome: When, why and how the probability of geological success and success-case volumes for the well differ from those for the prospect." *Journal of Petroleum Science and Engineering*, Volume 204, (2021).

Milkov, A.V. "Risk tables for less biased and more consistent estimation of probability of geological success (PoS) for segments with conventional oil and gas prospective resources." *Earth-Science Reviews*, Volume 150, (2015).

UNECE. "Supplementary Specifications for the application of the United Nations Framework Classification for Resources (Update 2019) to Geothermal Energy Resources." *UNECE Publication.* United Nations Framework Classification for Resources Ad Hoc Committee of the International Geothermal Association (2022).

Ussher, G.N.H., Lebe, J.L., Calibugan, A., Brotheridge, J., Quinao, J., Hendri, R., and McLeod, J. "Application of the United Nations Framework Classification for Geothermal Projects in the Waikato Region." *Proceeding 45th New Zealand Geothermal Workshop* (2023).

Energy Conversion / Utilization

Geothermal Power for Green Hydrogen Production

Reza Agahi, Ph.D.

Nikkiso Clean Energy & Industrial Gases

Keywords

Geothermal ORC Power Plant, Green Hydrogen, Hydrogen Liquefaction, Electrolyzer, Proton Exchange Membrane

ABSTRACT

Investment in and development of geothermal power projects have been going through feast and famine cycles during the last few decades. Capital expenditure, private or institutional, are rushed into geothermal power plant development as soon as governments enact some form of incentive for renewable energy and there are no activities as soon as the incentive terms expires.

The worldwide campaign for reduction and elimination of environmental pollution and using hydrogen as the preferred fuel is well underway and being sponsored by almost all countries. Hydrogen production in general and green hydrogen in particular is rapidly increasing. Total investment in net zero emission projects that was projected at $3,000 billion for 2021-2025 will exceed $4,300 billion by 2030.

Green hydrogen is defined as the hydrogen that is produced by splitting water by electrolysis. Electrolyzers that are powered by electricity from a geothermal power plant produce green hydrogen. Utilizing a renewable source energy that generates no polluting emissions into the atmosphere produces the most sustainable and cleanest hydrogen.

The fast growth of demand for green hydrogen is an excellent opportunity for investment and development of geothermal power plants. In this paper, the authors present a brief description of green hydrogen production and liquefaction facilities. There is also a short reference to oxygen liquefaction as a byproduct of an electrolyzer. The paper continues with a simulated evaluation of green hydrogen production and liquefaction from a 15 MW geothermal ORC power plant. The simulation is configured to demonstrate green hydrogen production as an energy storage option for the period of low demand for electrical power.

1. Introduction

Geothermal power plants cost more than other thermal power plants in the regions where geothermal resources are available. In most cases the return on investment for a geothermal power

plant is longer than other types and hence there is less tendency in development and investment in geothermal power plant. The inherent uncertainties about the geothermal resource quality and quantity complicate the decision-making process.

On the other hand, the electricity produced by a geothermal power plant is in the category of renewable energy and considered as the base load. The latter characteristics are the motivations for a few countries on the ring of fire to introduce some form of short-term incentives for electricity produced by the geothermal power plants. The incentives come as tax credit, guaranteed power purchase agreement at a rate higher than conventional electricity, government sponsored interest free loans and the like.

The above referenced government-initiated incentives are normally for a limited term, i.e., 20 years. The geothermal power plant revenue drops after the sunset of the incentives and the power plants management should resort to some measures to optimize their income by reducing their losses. Capacity reduction during off peak demand, selling steam as a commodity during low demand periods and energy storage during low price power sale are some options available to the power producers.

2. Green Hydrogen Production

The worldwide campaign for reduction and elimination of environmental pollution and using hydrogen as the preferred fuel is well underway and being sponsored by almost all countries. Hydrogen production in general and green hydrogen in particular is rapidly increasing. More than seventy countries have already developed or are preparing hydrogen strategies. There are more than twenty giga-scale green hydrogen projects in progress worldwide. Total investment in net zero emission projects that was projected at $3,000 billion for 2021-2025 will exceed $4,300 billion by 2030.

There are several hydrogen production processes and with the ongoing research that list is growing. The latter expanding range of processes and technologies are color coded depending on its carbon dioxide footprint. The color code green hydrogen is produced by electrolysis using electricity from renewable sources to split water into hydrogen and oxygen without emitting carbon dioxide.

3. Geothermal Power for Green Hydrogen Production

Unprecedented demand for green hydrogen is providing another option to sell renewable power in general and geothermal power in particular for the geothermal power plant owners/investors. Figure 1 shows the green hydrogen production process. Geothermal power is an ideal power source for production of green hydrogen. The green hydrogen production process receiving power from a geothermal power plant could operate continuously and there is not much production fluctuation due to fluctuation in the electricity availability. The electricity from all other renewable sources fluctuates between 0-100% depending on the availability of the source of renewable energy. The latter fluctuation impacts the hydrogen production and provides challenges for turndown capability of the downstream processes such as hydrogen liquefaction.

In the following sections, we present a study for utilizing electricity from a geothermal Organic Rankine Cycle (ORC) to produce high purity hydrogen and liquefy hydrogen for refueling usage

or export. A brief discussion about utilization of the side product such as liquid Oxygen is also presented.

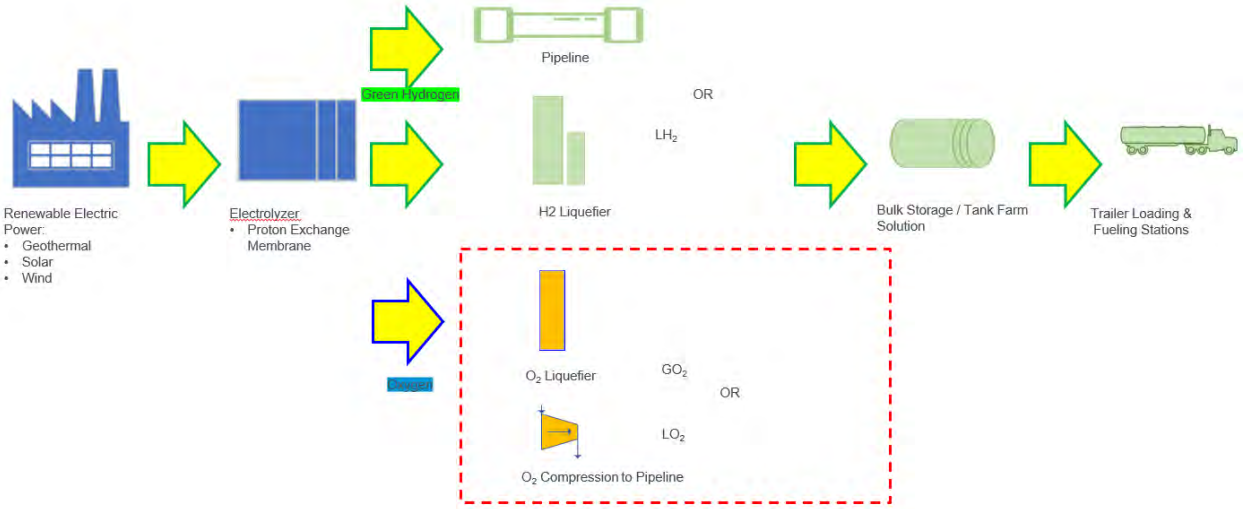

Figure 1. Green Hydrogen Production and Distribution Process

4. **Green Hydrogen Production and Liquefaction using Electricity from a Geothermal Organic Rankine Cycle (ORC) Power Plant**

The first step in green hydrogen production is electrolyzer. There are several processes to electrolyze water and each one has its own advantages and disadvantages. In this presentation we assume Proton Exchange Membrane (PEM) system, Figure 2.

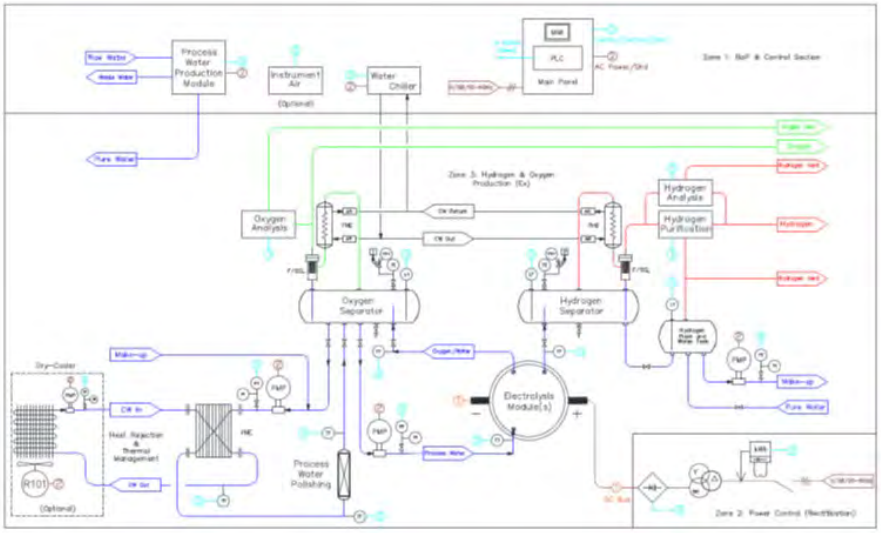

Figure 2. Proton Exchange Membrane (PEM) Electrolyzer

Figure 3. shows input to and output from the electrolyzer. It requires 340 tons per day of fresh water and 14 MW of electricity. The electrolyzer uses 46 t/d of water to produce 5 t/d of hydrogen at 10-40 bar pressure and 41 t/d of oxygen at 4 bar pressure. The balance of water, 294 t/d is discharged back into the water supply.

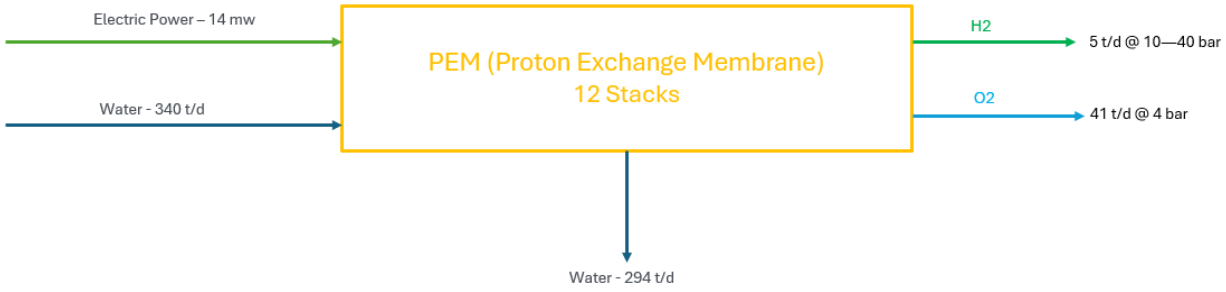

Figure 3. Electrolyzer Performance Data

There are two entirely different strategies for transportation of hydrogen for short distance, high pressure gas and low-pressure liquid. Both methods of transportation have its own advantages and disadvantages. In this study we assume that both hydrogen and oxygen products are needed, and liquefaction processes are required for transportation

Unprecedented demand for green hydrogen is providing another option to sell renewable power in general and geothermal power in particular for the geothermal power plant owners/investors. Figure 1 shows the green hydrogen production process. Geothermal power is an ideal power source for production of green hydrogen. The green hydrogen production process receiving power from a geothermal

5. Hydrogen Liquefaction

Hydrogen liquefaction requires deep cryogenic temperature and normally consists of two-step refrigeration. The preliminary refrigeration of the compressed hydrogen is normally achieved by a nitrogen cycle and the final refrigeration and liquefaction requires a deep cryogenic cycle utilizing cycle either helium or hydrogen. In this study we assume the final refrigeration cycle is a hydrogen cycle. Figure 4. Shows the hydrogen liquefaction process.

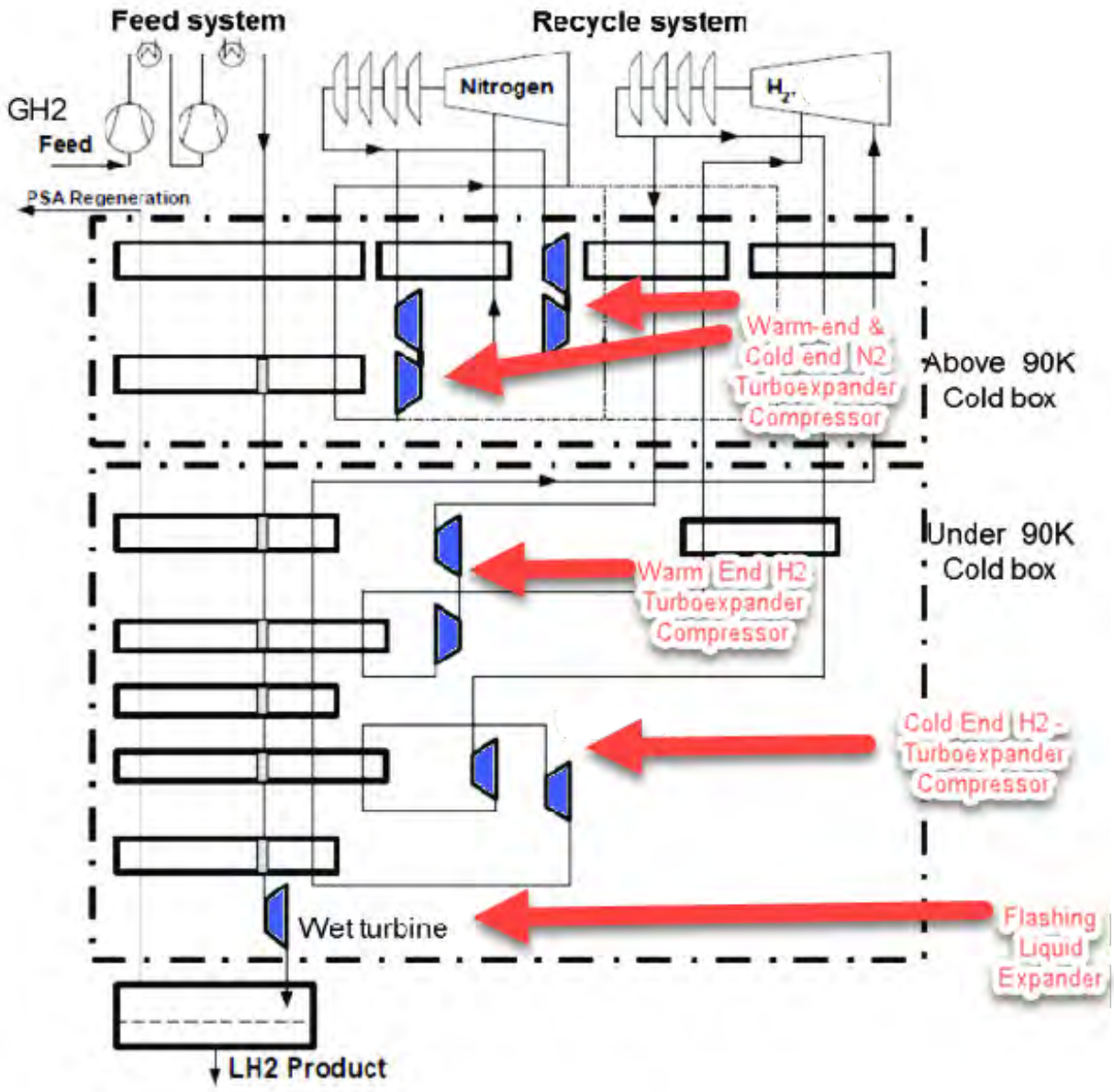

Figure 4. Hydrogen Liquefaction Schematic

Figure 5 shows the required electric power to liquefy 5 t/d of gaseous hydrogen into liquid.

Figure 5. Hydrogen liquefaction power requirements.

In this study we consider that the oxygen product will also be transported to an industrial complex by tanker truck. Figure 6 depicts the power requirements for the oxygen liquefying plant.

Figure 6. Oxygen Liquefier Data

Table 1. summarizes the performance of 5 t/d green hydrogen liquefaction plant utilizing 20 MW electricity from a geothermal ORC plant.

	PEM	LH2	LO2	Total
Electricity, MW	14	4	2	20
Fresh Water, t/d	340			
Returned Water, t/d	294			
Production, t/d		5	41	

Table 1. 20 MW Green Hydrogen Liquefaction Plant

Acknowledgement

The author wish to acknowledge support from Patrick McCalley of Neuman and Eser Company

REFERENCES

Dr. Celal Erbay, Head of Energy and Technology Policies Department, Mineral Research Agency, May 22, 2024.

5 MW PEM Electrolysis Plan for Hydrogen Production, Technology Overview (Rev.3.5) Neuman and Eser, HyPEM Electrolyzer

Integration of ORC Technology with EGS Systems to Meet the Demands of Future Grids

Joseph Bonafin[1], Queenie Lam[2] and Peter Marsters[2]

[1]Turboden

[2]Fervo Energy

Keywords

Enhanced geothermal system (EGS), Organic Rankine Cycle (ORC), ORC turbogenerator, dispatchability, modularity, power generation

ABSTRACT

The combined utilization of Organic Rankine Cycle (ORC) technology and advancements in Enhanced Geothermal Systems (EGS) hold significant promise for unlocking the full potential of geothermal resources for dispatchable power generation. Geothermal energy, with its inherent reliability and minimal carbon footprint, is the solution for sustainable electricity production. Modern drilling techniques and subsurface analytics complement ORC systems, creating a synergistic partnership that addresses key challenges in future grid management.

Future grids require firm, clean, dispatchable power to ensure reliability and sustainability. To examine this need, we took data from NREL's Cambium mid-case scenario, identified the highest emission hours per month in 2035, and then averaged net load and emissions by hour for that month. This approach allows us to pinpoint the periods within the year when emissions are at their peak, offering insights into the correlation between net load and emissions during these critical hours. The results highlight the necessity for energy resources that can ramp up production quickly and efficiently, particularly during non-solar hours. We then discuss how EGS and ORC systems enable the extraction of continuous, dispatchable, carbon-free power from geothermal resources, contributing to a more sustainable and resilient energy mix. The combination of the huge resource potential of EGS coupled with the production flexibility of ORC systems make is the key to decarbonizing future grids.

1. Introduction

Geothermal energy, with its ability to provide continuous baseload power and minimal carbon footprint, is poised to play a critical role in the global energy transition. This paper explores how Enhanced Geothermal Systems (EGS) and advanced Organic Rankine Cycle (ORC) technology combined with innovative contracting can meet the needs of future grids. Previous examples of the combination of the two technologies have been implemented by geothermal companies. At

Soultz-sous-Forêts, France, an EGS system was developed by creating artificial reservoirs in hot rock formations. Water was injected into deep wells to create fractures, allowing heat extraction. The hot water was then used to generate electricity using ORC technology. The Soultz Project demonstrated the viability of combining EGS and ORC, expanding geothermal energy's potential in non-traditional areas. Despite technical challenges, it showed how EGS can harness geothermal energy in regions without natural hydrothermal resources (Ravier et al. 2019). During the production testing of Project Red, a full-scale commercial EGS pilot, system flow rates reached up to 63 liters per second (L/s) (Norbeck and Latimer 2023). For comparison, the Soultz Project achieved a flow rate of 30 L/s (Schill et al. 2017).

1.1 Background on Fervo Energy

Fervo is a next-generation geothermal developer founded in 2017 with the mission to provide 24/7/365 firm, clean energy from geothermal resources previously considered uneconomic for geothermal power generation. Producing geothermal power requires heat, permeability, and fluid. Heat from the earth's core acts as an energy source, elevating temperatures beneath the surface. Fissures in subsurface rock provide paths for water to travel and conduct heat. As water flows through these fractures, it heats up, ultimately producing hot pressurized water that can power a thermodynamic cycle to generate electricity.

1.2. Traditional Geothermal

Traditional geothermal development targets naturally occurring fracture systems using vertical drilling. This approach presents a few significant problems. First, vertical wells intersect only a small portion of geothermal reservoirs, (Mackenzie et al. 2023). Second, in reservoirs with abundant natural fractures, drilling fluid may be lost to pores in the rock, increasing well costs (Vollmar et al. 2013). Given these challenges, roughly twenty percent of traditional geothermal wells cannot on their own support commercially viable flow rates (ESMAP 2013).

There are two primary reasons why traditional geothermal cannot meet the demands of future grids. The first is that the resource is geographically limited. Enhanced Geothermal Systems (EGS) can help expand geothermal power by more than a factor of 20, for up to 90 GW to 5 TW of clean firm power by 2050 in the U.S. (Blankenship et al. 2024) (Ricks et al. 2024). The second reason is that, as opposed to conventional geothermal, EGS can dictate its resource conditions and target specific subsurface temperatures more precisely with potentially higher values, and specify as much geothermal water flowrate as needed (and drill accordingly). Hot dry rock reservoirs, combined with horizontal drilling are order of magnitudes larger than conventional ones. This capability allows EGS to be more adaptable and scalable, addressing the temperature and resource limitations that traditional geothermal faces.

While the basic physics are comparable between traditional geothermal and EGS systems, the scalability, flexibility, and customizability of EGS systems radically change their potential contribution to future grids.

1.3 Innovative Enhanced Geothermal System

Innovative EGS uses three methods to address traditional geothermal issues: horizontal drilling, multi-zonal completion, and distributed fiber optic sensing. Precision directional drilling enables increased access to more subsurface surface area per well, cutting project costs. Multi-zone completion techniques evenly distribute the flow of injection fluids across the entire geothermal reservoir. Enhancing flow distribution dramatically extends the lifespans of enhanced geothermal systems. Finally, robust measurement and diagnostics via distributed fiber optic sensing allows thorough assessments of subsurface temperatures, pressures, and permeability with greater precision than traditional geothermal.

1.4 Background on ORC technology

ORC technology converts low to high enthalpy heat sources into electricity. ORC systems are known for their high utilization range, modular design, low maintenance needs, and minimal environmental footprint, making them ideal for geothermal applications. Organic Rankine Cycle (ORC) technology has been increasingly implemented in geothermal power generation, especially for low-to-medium enthalpy resources (100-180°C). As of recent years, ORC technology is widely used in over 20 countries, contributing significantly to geothermal capacity worldwide. The ORC process is particularly suited to locations where traditional steam turbines are not viable. It uses organic fluids with lower boiling points than water to efficiently convert geothermal heat into electricity, even at lower temperatures.

The United States, Turkey, New Zealand, Germany, the Philippines and other traditional geothermal countries are leaders in deploying ORC for geothermal applications. In the United States, ORC is extensively used in Nevada and California. New Zealand and Turkey, with its rapidly growing geothermal sector, have also adopted ORC in many of their new plants. In low enthalpy and deep geothermal basins such as Molasse Becken in Germany, ORC is the only viable option for power production.

Globally, ORC technology contributes to about 4 GWs of installed geothermal capacity (Market study by Turboden), making it a key component in the broader adoption of geothermal energy. The continued expansion of ORC technology is expected, driven by its adaptability to a wide range of geothermal conditions. Thanks to this, in the last 5 years the ORC technology has doubled its shares among other competing technologies such as single and double flash, dry steam turbines (Thinkgeoenergy 2022).

1.5 Collaboration between ORC and EGS technologies at Cape Station

Fervo Energy is developing the multi-phase Cape Station geothermal development located in Beaver County, Utah, northeast of Milford. Turboden was selected to design, procure and commission the complete ORC unit for Phase 1 of Cape Station geothermal project. This 1st phase will begin delivering around-the-clock, clean power to the grid in 2026. The turbines feature axial flow, multistage and run at 1800 rpm. The turbines are directly coupled to the electric generator and the design inlet pressure is about 29 bar and 11 bar for the high pressure and low pressure cycles respectively. The expected turbine isentropic efficiency is higher than 90% (total to static,

including all the stage losses). The axial geometry is the most suitable to achieve high efficiency in the widest range of operation; it is expected in fact a derating of the efficiency of only -3% during summer operation, and -5% during winter operation. The turbines are designed to maximize energy production according to the Cape Station site ambient conditions.

2. Overview of Future Grids

Dispatchable, air-cooled geothermal technology is essential for balancing future energy grids amid increasing fluctuations from intermittent renewable energy integration. Future grids require firm, clean, dispatchable power to ensure reliability and sustainability. To examine this need, we took data from NREL's Cambium mid-case scenario, identified the highest emission hours per month in 2035, and then averaged net load and emissions by hour for that month. This approach allows us to pinpoint the periods within the year when emissions are at their peak, offering insights into the correlation between net load and emissions during these critical hours. The results, shown in Figure 3, highlight the necessity for energy resources that can ramp up production quickly and efficiently, particularly during non-solar hours (Gagnon et al. 2023).

2.1 Grids in 2035

Projected average emission rate for in-region generation, or carbon dioxide from direct combustion in kg/MWh varies significantly across regions of the western U.S. Northern Grid West has the lowest average emission at 8 kg/MWh, while Northern Grid South has the highest average emission at 91.7 kg/MWh (Gagnon et al. 2023).

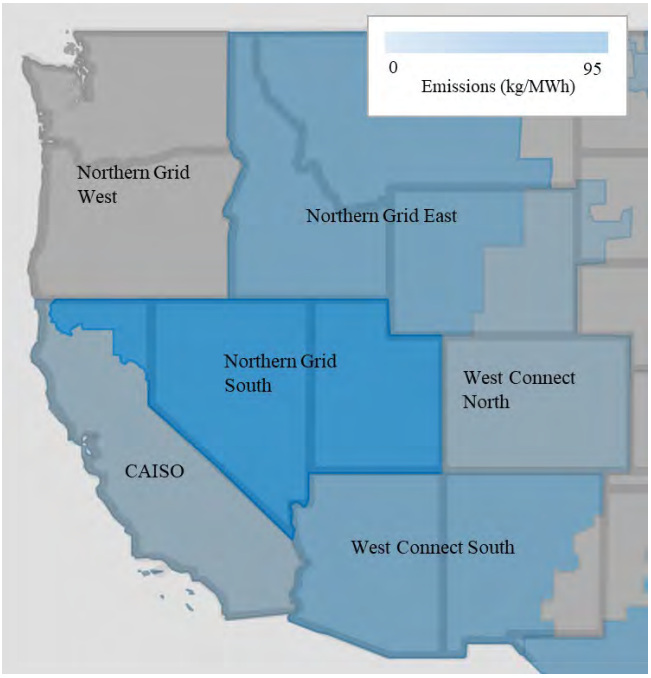

Figure 1. Heatmap of projected average emissions in 2035 in the western U.S.

In September of 2035 in the CAISO region, the load ranges from 30 GW in the morning to around 25 GW in the afternoon, and back to 55 GW in the evening, showing a ramp of 35 GW. The Northern Grid South region has a similar trend, with a net load of about 11 GW in the morning,

dropping to –2.5 GW in the afternoon, and rising to a peak of 13 GW in the evening, resulting in a ramp of 29 GW. The West Connect South shows an average net load of around 11 GW in the morning, decreasing to –0.7 GW in the midday hours, and increasing to 18 GW in the evening, resulting in a ramp of 30.4 GW.

During the month of September, all grids except for those in the Pacific Northwest and CAISO show an excess of generation during daytime hours and high emissions in the evening and morning hours. The duck curve seen so prominently in California today expands to every region across the West.

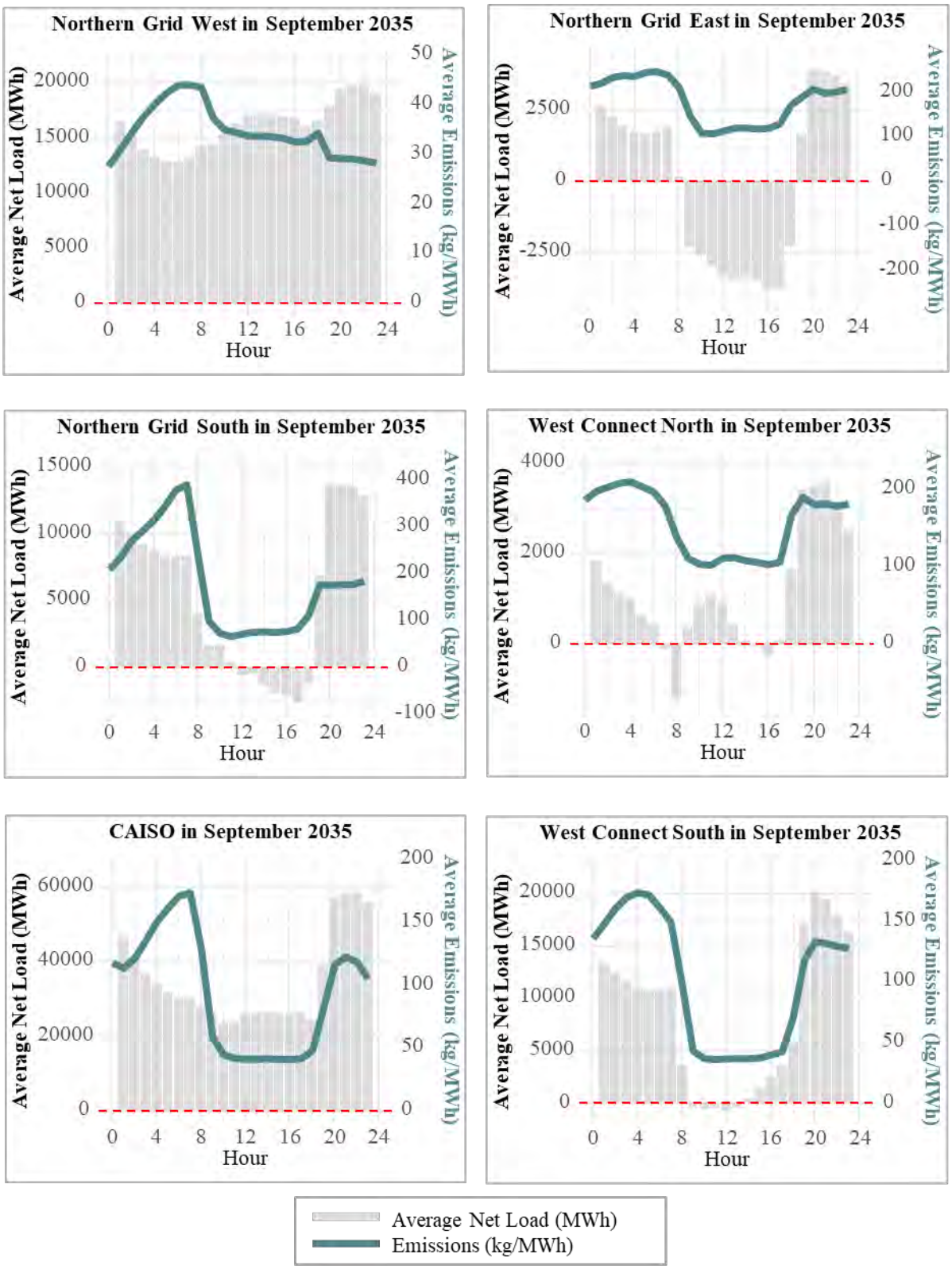

Figure 2. Emissions Versus Net Load Source: Fervo Analysis, NREL Cambium

Despite differences, all grids would be aided by a resource that is clean, flexible, and anti-correlated with solar. It must produce minimal to no greenhouse gas emissions, ramp up or down quickly to match demand fluctuations, and generate power when solar power is less available, such as during the evening or night. Dispatchable, air-cooled, geothermal is this resource.

3. Why Geothermal Works: Innovative Drilling Techniques and Coupled with ORC

Firm, clean power is not only essential for balancing future energy grids, but innovative drilling techniques and ORC technology also demonstrate technical viability for large-scale implementation.

3.1 Overview of modern drilling techniques employed by Fervo Energy

Modern drilling techniques have revolutionized geothermal well field development. These techniques, including directional drilling, hydraulic stimulation, and advanced subsurface analytics, enhance the efficiency and effectiveness of geothermal resource extraction.

Directional drilling allows for precise targeting of geothermal reservoirs, maximizing the extraction of heat from the subsurface. This technique involves drilling wells at various angles rather than just vertically, which increases the contact area with the geothermal resource and improves the overall energy yield. Hydraulic stimulation involves injecting high-pressure fluid into the well to create fractures in the rock formations. This enhances the permeability of the reservoir, allowing for greater flow of geothermal fluids and increased heat extraction. Advanced subsurface analytics, including 3D seismic imaging and real-time data monitoring, optimizes field development. These technologies provide detailed insights into subsurface geology, enabling precise well placement and efficient resource management.

These innovative drilling techniques and subsurface analytics maximize the efficiency of geothermal energy extraction, reducing costs and improving the overall performance of geothermal projects. These techniques have been applied at Cape Station and major improvements in drilling performance have been observed throughout its development (Fervo Energy 2024).

3.2 Turboden's ORC Technology

The well-known Rankine Cycle is a thermodynamic process that converts heat into work. This cycle typically employs steam as the working fluid to spin a turbine and generate power, accounting for approximately 85% of global total electricity production. In contrast, the Organic Rankine Cycle (ORC) uses an organic fluid with a lower boiling point and higher molecular mass than water, enabling it to effectively utilize lower temperature heat sources.

The ORC turbogenerator operates at slower peripheral speed and without eroding metal parts and blades. It uses low-to-high-enthalpy geothermal fluid to preheat and vaporize an organic working fluid in the evaporator. The vaporized fluid then drives a turbine directly coupled with an electric generator, producing clean and reliable electric power.

The organic exhaust vapor passes through a recuperator, heating the organic liquid upstream to the preheater, before being condensed in the condenser. The organic working fluid is then pumped back into the recuperator, preheaters and evaporator, completing the closed-cycle operation. This process is particularly well-suited for geothermal applications due to several advantages:

1. **High Utilization:** The ORC technology can effectively convert low to high-temperature heat sources into electricity (as opposed to steam plants).
2. **Modular Design:** The scalable design allows for easy integration with existing geothermal infrastructure.
3. **Low Maintenance:** ORC systems have relatively low maintenance costs and high operational reliability.
4. **Environmental Benefits:** The ORC process produces no emissions and has a minimal environmental footprint.
5. **Dispatchability:** It can provide a consistent and reliable source of electricity that can be adjusted to meet demand fluctuations.

The use of an automatic control system for the ORC turbogenerator minimizes the need for continuous monitoring. The ORC turbogenerator can operate at partial loads, self-adapting to the available thermal power or following a grid operator's load profile. This flexibility enables ORC power plants to adjust their output to match grid demand, thereby enhancing the reliability of geothermal energy as both a base load and peak load power source. As a base load source, geothermal energy provides a stable electricity supply to meet minimum demand. As a peak load source, ORC plants can, given resource conditions (available via EGS) quickly ramp up output to meet higher demand during peak hours (Turboden 2016).

4. Innovating Technology along with Contracting

While EGS and ORC power plants are technically viable for adjusting to grid demand, current contracting structures lack the flexibility needed to provide economic incentives for operators to adjust to energy market fluctuations. This section discusses current and future contracting structures.

4.1 Traditional PPAs

Traditional Power Purchase Agreements (PPAs) offer fixed pricing, quantity, and terms for electricity, ensuring financial stability and predictable revenue for a developer. They benefit EGS by providing a guaranteed level of revenue but do not adapt to real-time energy demand fluctuations. Consequently, the traditional PPA’s fixed prices offer minimal environmental benefits as they do not incentivize EGS to align production with demand variations.

4.2 Capacity Agreements

Capacity agreements involve setting a fee for available capacity, ensuring operators get paid for maintaining readiness to generate electricity, regardless of actual production. This structure provides financial stability while allowing production flexibility to meet market demands. However, the facility is not incentivized to produce Renewable Energy Credits (RECs) nor load follow.

4.3 Merchant Sales

Merchant sales electricity at fluctuating market-based prices, allowing operators to respond dynamically to real-time demand. This setup maximizes environmental benefits by incentivizing operators to supply energy during high-demand periods, reducing grid reliance on carbon-intensive

sources. Merchant agreements introduce significant financial uncertainty due to price fluctuations, making it challenging to secure financing.

While traditional contracting structures do not meet the mark, innovative contracting can combine successful aspects from different structures.

4.4 Clean Transmission Tariff

Fervo worked with Google and NV Energy in a Clean Transition Tariff (CTT) which creates long-term agreements for utilities and customers to invest in clean firm capacity, like enhanced geothermal energy, ensuring 24/7 clean energy supply. NV Energy, through a unique energy supply agreement with Google, partnered with Fervo Energy to add 115 MW of geothermal power. This collaboration offers a customizable framework for varying state regulations, enhancing clean and reliable power delivery (Corio and Kober 2024).

4.5 Hybrid Contracting Structures

Geothermal developers are also exploring hybrid contracting structures, combining merchant contracting during the day and set prices during the night to meet the grid's needs. Merchant contracting disincentivizes producing energy during hours when solar and storage capabilities meet or exceed energy demands since prices during these hours are typically low or negative. This hybrid ensures pricing certainty by contracting set prices outside hours of solar energy and storage capabilities. It also provides a degree of flexibility to meet demands during the day if prices reflect significant need for renewable energy, while also providing additional incentives to supply energy at night when carbon intensive resources are likely to be called upon.

4.6 Tolling with Time Based Brine

Another viable contracting structure is a PPA with prices shaped to market demand. During hours when renewable energy supply is high relative to demand, prices would be set low if an operator supplied electricity. During hours when renewable energy supply falls below demand, prices would be set higher to account for limited hours that the resource is called upon. This structure provides financial certainty for an operator while allowing a limited degree of flexibility to respond to energy demands.

4.7 Looking Ahead

To address the limitations of traditional contracting structures, Fervo Energy is exploring innovative and hybrid contracting concepts that combine successful aspects from different structures. These include merchant contracting for real-time demand responsiveness, capacity agreements for financial stability, and tailored pricing to reflect market demands. Collaborations like the Clean Transition Tariff (CTT) with Google and NV Energy, adding 115 MW of geothermal power, demonstrate the potential for flexible, long-term agreements to support 24/7 clean energy supply while meeting future grid demands (Corio and Kobor 2024).

5. Challenges and Development Risks

Geothermal energy development faces some challenges and risks. Drilling and stimulation involve geological uncertainties that can lead to cost overruns and delays, necessitating advanced

techniques and real-time monitoring. Induced seismicity, caused by high-pressure fluid injection, is another concern. Fervo mitigates induced seismicity risk through comprehensive seismic monitoring and an Induced Seismicity Mitigation Plan (ISMP). Reservoir maintenance and depletion also pose challenges, particularly with flexible and dispatchable operations that require careful management of pressure and temperature.

ORC is a proven and mature technology with millions of cumulative operational hours worldwide. The critical components such as the Turbines are not in contact with geothermal fluids (such as traditional flash steam Turbines), ensuring long life of the components with minimal maintenance activities. Most of the equipment is available “off-the shelf” and can be procured in a short time in case of need. In a traditional hydrothermal project, the main risk during operation is represented by the potential fouling, scaling or corrosion inside the tubes and pipes of the plant. At Cape Station it is expected minimum scaling and corrosion potential at the design temperatures of production and reinjection, with the expected levels of minerals dissolved in the water being low, due to the fact they stem from ground water and not deep mineral-rich faults.

6. Future Prospects

Flexible Enhanced Geothermal Systems hold significant potential for load-following generation and long-duration energy storage, making them a critical asset in decarbonized electricity systems. This paper evaluates the impact of operational flexibility on the long-term value and deployment potential of EGS power in the western U.S., finding that flexible EGS substantially increases optimal geothermal penetration and reduces bulk electricity supply costs compared to inflexible systems. With a potential 5 TW electric generation capacity in the U.S., EGS can complement large-scale deployment of variable renewable energy resources (Ricks et al. 2024).

6.1 Modularization

The ORC plant is designed with modular components. Turbines, generators, pumps, heat exchangers, and air-cooled condenser are based on identical modules that can be replicated to scale up with capacity. Modularity is helpful for maintainability as well, as the same spare parts can be shared for different ORC units. For Phase 1, Turboden has split the overall capacity in three generators, 62.5 MVA each, which is currently at the higher end of four-poles synchronous generators available on the market. The other components such as turbines, ORC pumps and heat exchangers, are designed to accommodate for higher flowrates and inlet temperatures, together with the minimum ambient temperatures at site, to overcome any “bottleneck” for the energy generation at off-design conditions. Other components such as the air-cooled condenser are made by modular items (bundles and fans), replicated in a number suitable for ensuring optimal condensing pressure at all times of operation.

The same modularization will be implemented at Phase 2, where it is anticipated to reach higher temperatures and capacity for each ORC module. This will further allow a decrease in capex per MW installed, thanks to the higher scale and higher efficiency effect.

6.2 Geothermal Anywhere

While this paper analyzes the Western U.S. emissions and net load in 2035, other power markets will face similar challenges due to the increasing integration of intermittent resources like solar and wind. Firm, clean energy that can function as both a baseload and peak energy source is

necessary in every market to balance and decarbonize the grid. Geothermal energy, with its capability for stable and dispatchable power, stands out as a versatile solution that can be implemented in various geographical regions.

7. Conclusion

This paper has outlined the critical advancements and collaborative efforts between EGS and ORCs in the geothermal energy sector. Innovative drilling techniques, such as horizontal drilling, multi-zonal completion, and distributed fiber optic sensing, address traditional geothermal challenges by enhancing reservoir access, improving fluid distribution, and providing precise subsurface diagnostics. These advancements significantly increase the efficiency and reliability of geothermal energy extraction. Complementing this, ORC technology efficiently converts low to high-temperature heat sources into electricity, offering high efficiency, modular design, low maintenance, environmental benefits, and dispatchability. The synergy between EGS drilling innovations and ORC systems ensures optimized energy production and operational flexibility. Together, they pioneer a new model of clean, sustainable, and reliable power generation. Their innovative contracting strategies, including carbon-based and hybrid models, further enhance the financial viability and environmental impact of geothermal projects. This collaboration exemplifies how advanced technology and strategic contracting can drive the future of geothermal energy, providing a robust solution to meet the demands of evolving energy grids.

REFERENCES

Avato, P., Success of Geothermal Wells: A Global Study (ESMAP 2013).

Bini, Bertanzi, Belotti, “COMBINED CONTROL METHOD OF AN ORGANIC RANKINE CYCLE - European Patent Office - EP 3277933 B1 (storage.googleapis.com)”

Blankenship, D., Gertler, C., Kamaludeen, Mohamed., O’Connor, M., Porse, S. “Pathways to Commercial Liftoff: Next-Generation Geothermal Power.” U.S. Department of Energy (March 2024).

Corio, A. P. and Kobor, B. “How we’re working with utilities to create a new model for clean energy.” Google (2024). https://blog.google/outreach-initiatives/sustainability/google-clean-energy-partnership/.

Fervo Energy. “Fervo energy drilling results show rapid advancement of geothermal performance.” (2024). fervoenergy.com/fervo-energy-drilling-results-show-rapid-advancement-of-geothermal-performance/.

Gagnon, P., Perez, P. A. S., Obika, K., Schwarz, M., Morris, J., Gu, J. and Eisenman, J. “Cambium 2023.” *National Renewable Energy Laboratory* (2023). https://scenarioviewer.nrel.gov.

Mackenzie, A., Datta, A., George, A. “Barriers to Next-Gen Geothermal.” Institute for Progress (November 2023). https://ifp.org/hot-rocks-part-three-barriers-to-next-gen-geothermal/.

Norbeck, J. H., and Latimer, T. M. “Commercial-Scale Demonstration of a First-of-a-Kind Enhanced Geothermal System.” Fervo Energy. (2023). https://doi.org/10.31223/X52X0B.

“ORC Systen: Organic Rankine Cycle solutions for power generation with turbogenerators.” Turboden. (n.d.). https://www.turboden.com/products/2463/orc-system.

Ravier G. et al., Towards an optimized operation of the EGS Soultz-sous-Forêts power plant (Upper Rhine Graben, France) 2019.

Ricks, W., Voller, K., Galban, G., Norbeck, J. H. and Jenkins, J. D. “The role of flexible geothermal power in decarbonized electricity systems.” *Nature Energy* (2024). https://doi.org/10.1038/s41560-023-01437-y.

Vollmar, D., Wittig, V., & Bracke, R. J. I. G. A. H. (2013). Geothermal Drilling Best Practices: The Geothermal translation of conventional drilling recommendations-main potential challenges. *International Geothermal Association: Home* (2013).

High-Pressure Pelton Turbines: A Simple yet Effective Means of Scaling the Energy Storage and Geothermal Industry

Brianna Byrd[1] and Brett Bauer[2]

[1]Sage Geosystems

[2]Canyon Hydro

Keywords

Pelton turbine, mechanical energy storage, geothermal, high pressure, high efficiency, geopressured geothermal systems

ABSTRACT

This paper presents a technological advancement in energy storage and geothermal technology with the development of a high-pressure Pelton turbine designed for deployment on the flowback cycle of deep well operations. Conventionally used at high-head hydroelectric sites, the Pelton turbine has been reimagined to harness high-pressure held in deep wells, offering a new pumped storage approach in the form of mechanical energy.

The custom-designed Pelton turbine features a 3.2MW rating across a range of pressures from 3,500 to 5,000 psi, making it a unique but robust solution for extracting energy from high-pressure energy storage or geothermal reservoirs. With efficiency on par with pumped hydro storage facilities, this turbine introduces a scalable and cost-effective solution to geothermal energy extraction. This turbine technology will increase the mechanical efficiency and decrease the cost of energy storage and geothermal facilities, making them a more likely solution for a source of energy storage or geothermal power generation.

The use of this technology in the subsurface energy storage industries marks a significant departure from traditional geothermal practices, as it now captures the abundant pressure available from pumping and flowing back water in deep wells, providing a simple yet highly efficient means of energy extraction. This has allowed companies to develop new means of energy storage technologies, lower the cost and increase the efficiency of geothermal applications, which harvests both pressure and heat, and become cost-competitive with other forms of energy storage and baseload power.

The simplicity of the high-pressure Pelton turbine offers an affordable and scalable solution, paving the way for the widespread deployment in geothermal and energy storage wells. This paper discusses the design, performance expectations, and transformative potential of this technology, positioning it as a key player in the sustainable energy landscape.

1. Introduction

The search for more sustainable and efficient energy sources has led to significant advancements in renewable energy technologies. Among these, geothermal energy stands out as a promising and consistent source of power. Most typical geothermal systems currently only harvest the heat in a geothermal reservoir, and do not consider the pressure that could be harvested, inherently increasing the efficiency of a system, which opens the geothermal industry to a new type of geothermal, called Geopressured Geothermal Systems (GGS). Unlike traditional Enhanced Geothermal Systems (EGS) or Advanced Geothermal Systems (AGS), GGS harvests not only the heat but also the inherent pressure (mechanical energy) within geothermal wells, effectively doubling the net power output of these wells.

A suite of technologies has been developed to harness geothermal energy at various heat grades and applications. The first is a mechanical subsurface storage technology, a deep but low-grade geothermal energy storage system, which utilizes the high-pressure Pelton turbine to convert mechanical energy (pressure) to electricity. This system is similar to traditional pumped storage hydro (PSH) but operates under higher pressures due to the natural geostatic forces acting upon the artificially created fractures. These fractures, created through gravity fracking, act as subterranean balloons that are filled with water. The Earth's tendency to close these fractures results in the water being expelled with significant force to the surface, which is then converted into energy using the Pelton turbine. Additionally, the previously mentioned GGS technology is similar to the mechanical subsurface energy storage technology, but at greater depths utilizes both the pressure and heat of the produced water. See Figure 1 for a typical pumped storage hydro (PSH) system.

The Pelton turbine, traditionally employed in lower-pressure PSH facilities, has been re-engineered to leverage the high pressures encountered in GGSsystems. This adaptation represents a leap in technology, as it combines the reliability and simplicity of established hydroelectric equipment with the novel application of high-pressure geothermal energy extraction. The custom-made high-pressure Pelton turbine is a testamentto innovation, cost reduction, and the rapid deployment of utility-scale and commercially viable renewable energy in the geothermal space.

This paper delves into the technical and practical aspects of thehigh-pressure Pelton turbine and its role in advancing the availability of geothermal systems. It explores the design considerations, engineering challenges, and the potential for this technology to help revolutionize the geothermal industry.

2. Background on Pelton Turbines

The Pelton turbine, also known as the Pelton wheel, is an impulse-type water turbine that was developed by the American inventor Lester Allan Pelton in the 1870s (see Figure 2). It marked a significant advancement in hydroelectric technology, extracting energy from the impulse of moving water (the kinetic energy) rather than the water’s dead weight, which was the common

method of the time. Pelton's design was revolutionary because it extracted almost all of the water's impulse energy, making it a highly efficient piece of technology.

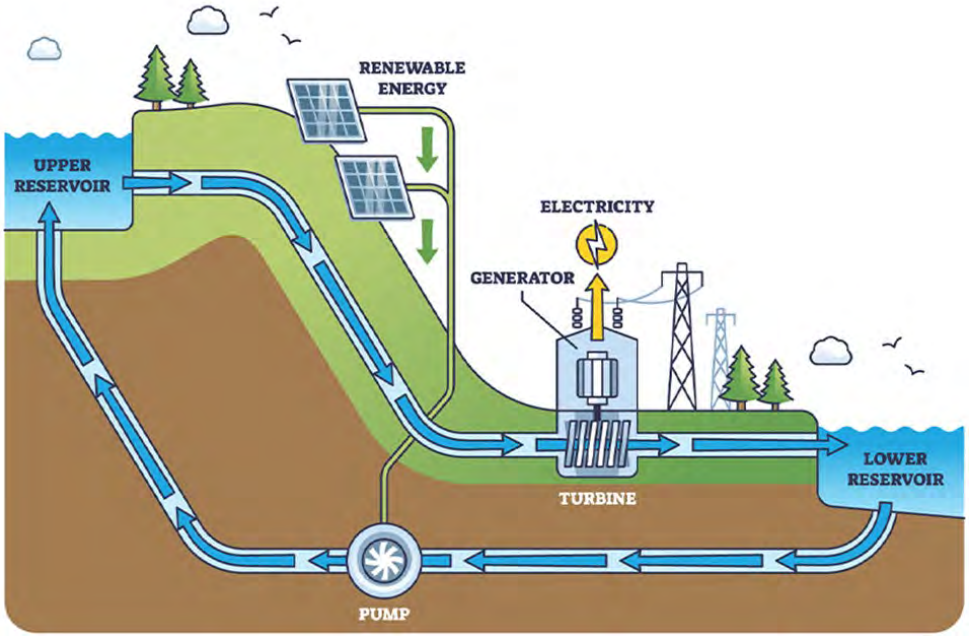

Figure 1: Setup of a closed loop pumped storage hydropower (PSH) facility (Cropley 2023).

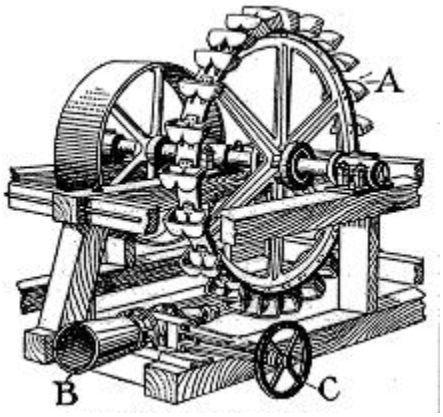

Figure 2: Pelton turbine produced by Lester A. Pelton in the 1870s from his patent, which was granted in 1889 (Vermilion History Society 2020).

Lester Allan Pelton, born in 1829, moved to California during the Gold Rush era and eventually turned his attention to the inefficiencies of water wheels used in mining operations. By the mid-1870s, Pelton had developed a wooden prototype of his new wheel, and in 1878, the first commercial model was installed at the Mayflower Mine in Nevada City, California. The efficiency advantages of Pelton's invention were quickly recognized, and it became a sought-after product for mining and later, hydroelectric power generation.

The Pelton wheel operates on the principle of capturing the kinetic energy of a high-velocity water jet. The water strikes specially designed buckets along the wheel's perimeter, which splits the

water jet and reverses its flow, effectively transferring its momentum to the wheel. This design allows for high mechanical efficiency, especially in applications where a high head of water is available, which results in more energy.

The Pelton turbine has been used in modern energy needs for PSH, which is a type of hydroelectric power generation used to balance supply and demand on the electricity grid. The system involves two reservoirs at different elevations. During periods of low electricity demand, excess electrical power is used to pump water from the lower reservoir to the upper reservoir. When there is a high demand for electricity, water is released from the upper reservoir back down to the lower reservoir, passing through turbines to generate electricity. A Pelton turbine, specifically, is used in high-head, low-flow applications within this system. The Pelton turbine operates by converting the kinetic energy of a jet of water into mechanical energy; water from the upper reservoir is directed through nozzles to strike the buckets of the Pelton wheel, causing it to spin and drive a generator. This setup is highly efficient for energy recovery in pumped storage systems due to the Pelton turbine's ability to operate efficiently at varying water flow rates and pressures.

3. Background on Long Duration Energy Storage Systems in the Subsurface

Long-duration energy storage (LDES) technologies function as underground, pumped-hydro-like mechanical energy storage systems in deep geologic structures created via a vertical fracture system in low-permeability (< 50 millidarcy) formations. The rock can be sedimentary or hard rock (igneous, granites, etc.), as long as the permeability is low. The resulting fracture system, sealed underground, acts like a reservoir for holding pressurized water.

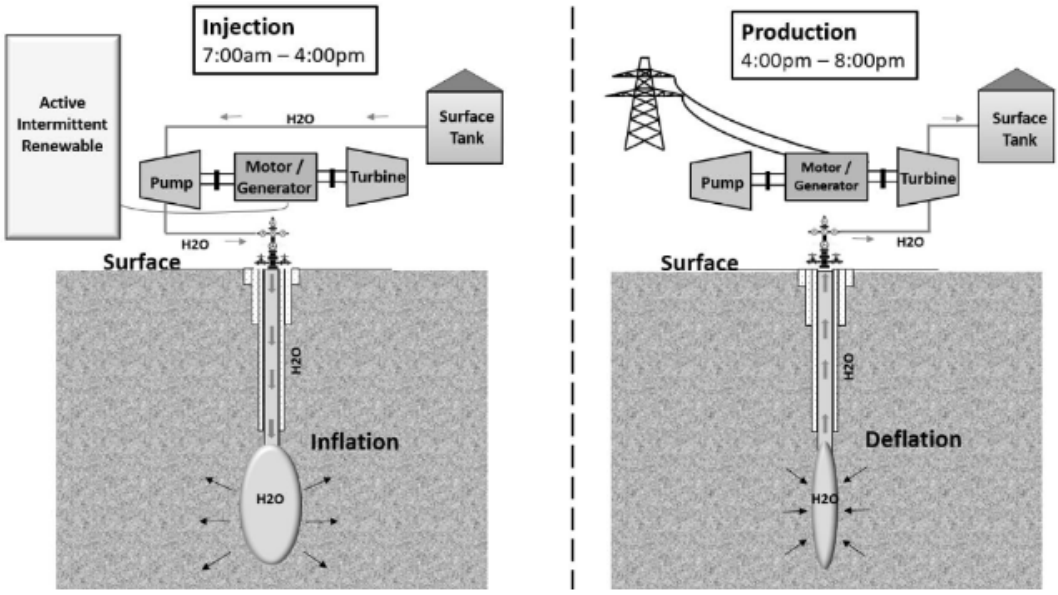

Figure 3: Schematic of a subsurface mechanical energy storage system in its two phases: the storing of energy (left) and production of energy (right) (Simpkins, et al. 2023).

For mechanical energy storage (without heat), the target geologic formations for the reservoirs are deep, typically 7,000 to 12,000 feet, where the high in-situ stresses in the rock drive the fracture closure and therefore the discharge cycle. Charging involves pumping water from a surface storage through the wellbore into the fracture network, which acts as an artificial underground reservoir,

and building pressure above hydrostatic by inflating the fracture network with a volume of water. Discharging involves turning off the pump and allowing the fracture to partially deflate and push the water back up the wellbore to the surface, where it drives a Pelton type turbine-generator. The round trip efficiency (RTE) of this system is 70-75% with a duration range of 4 to 24+ hours, and water losses less than 2% as measured during a2023 commercial pilot demonstration. These vertical fractures are operated between fracture opening and fracture extension pressure, meaning there is always a volume of water in the fracture, and only about 10% of this volume is cycled to maintain a high RTE. This technology is very flexible in that, if required, additional water can be pulled from the fracture to generate electricity with the only potential impact being lower RTE. The energy storage system produces free low-quality heat (< 100°C) that can be potentially used to power cooling and/or thermal desalination systems.

A variant of this mechanical energy storage technology involves stored subsurface water harvesting natural geothermal heat from the surrounding formation, which is used to generate electricity through a binary cycle power plant, using either a commercial Organic Rankine Cycle (ORC) or a proprietary supercritical CO2 (sCO2) power system. In this scenario, both the heat and pressure energy of the water contribute to the net electricity generation at the surface. For this geothermal energy storage technology, a formation temperature between 150 and 250°C is required.

These technologies were developed as a response to the challenges posed by intermittent renewable energy sources such as wind and solar power, which have done a great job greening the grid, but are frequently curtailed and contribute to grid instability. The variability in generation from these sources and the inability to control the time of day when the power is generated makes it difficult for electricity grids to consistently meet peak demand, particularly during periods when renewable output is low, such as nights or cloudy days. Traditional solutions like natural gas peaker plants and coal-fired power stations provide reliable energy supply but come with environmental concerns. Figure 4 shows what is called a “duck curve” that shows the electricity demand/supply throughout the day typically controlled by solar energy production between 9 AM and 6 PM.

These technologies address these challenges with a mechanical and/or thermal energy storage system designed to enhance grid stability and support renewable energy integration. These innovative technologies store energy underground in subsurface formations (see Figure 5), utilizing the natural high-pressure environment to store water under pressure and/or harvest heat. During periods of high demand or low renewable generation, the stored water is released and channeled through a Pelton turbine to convert kinetic energy into electricity. This cyclical process of water injection and extraction enables these systems to function as a sustainable energy storage solution. This energy storage can cost-effectively deliver a storage duration of 4 to 24+ hours, readily enabling time matching with any intermittent power source. Modeling of blended Levelized Cost of Energy (LCOE) for solar paired with Sage’s EarthStore is $0.05/kWh at 100+MW scale, assuming a price point of $0.02/kWh for solar. The same blended LCOE of solar paired with lithium-ion batteries is double, or $0.10/kWh.

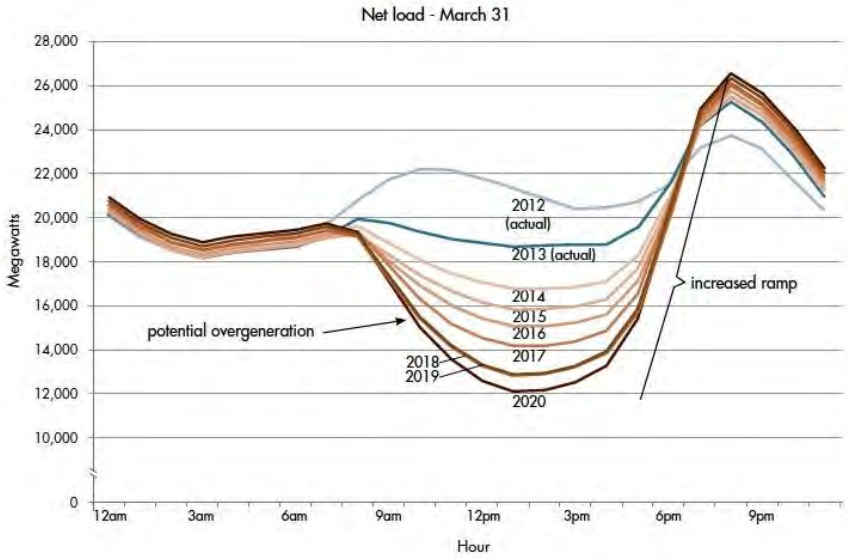

Figure 4: Energy demand "duck curve" (Jones-Albertus 2024).

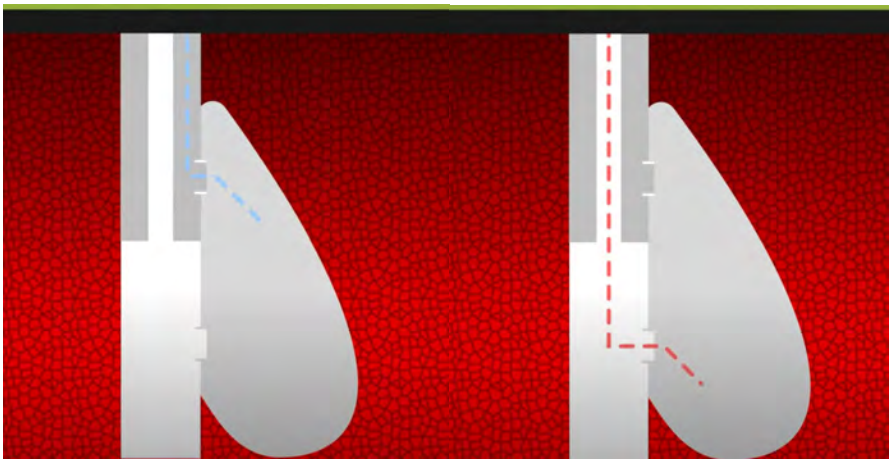

Figure 5: Sage Geosystems' pump in and flowback process (Sage Geosystems 2024).

In regions like California, where seasonal energy demands vary significantly (see Figure 6)—peaking during hot summer months—the flexibility of energy storage types like these becomes crucial. These technologies enable the energy supply to be varied throughout the year, complementing the intermittency of solar and wind power, and their own changing generation profile by season. Additionally, the capability to provide long-duration energy storage is invaluable during extreme weather events such as storms, tornadoes, hurricanes, etc. by ensuring continued energy supply to critical facilities such as hospitals, data centers, and military bases when conventional renewable sources are unavailable.

As the demand for clean energy storage solutions grows amid global efforts to reduce carbon emissions and enhance energy resilience, these technologies represent a pivotal advancement in sustainable energy technology. Their ability to integrate seamlessly with existing renewable infrastructure while mitigating the challenges of intermittency underscores their potential to support a reliable, commercially viable, and environmentally responsible energy future.

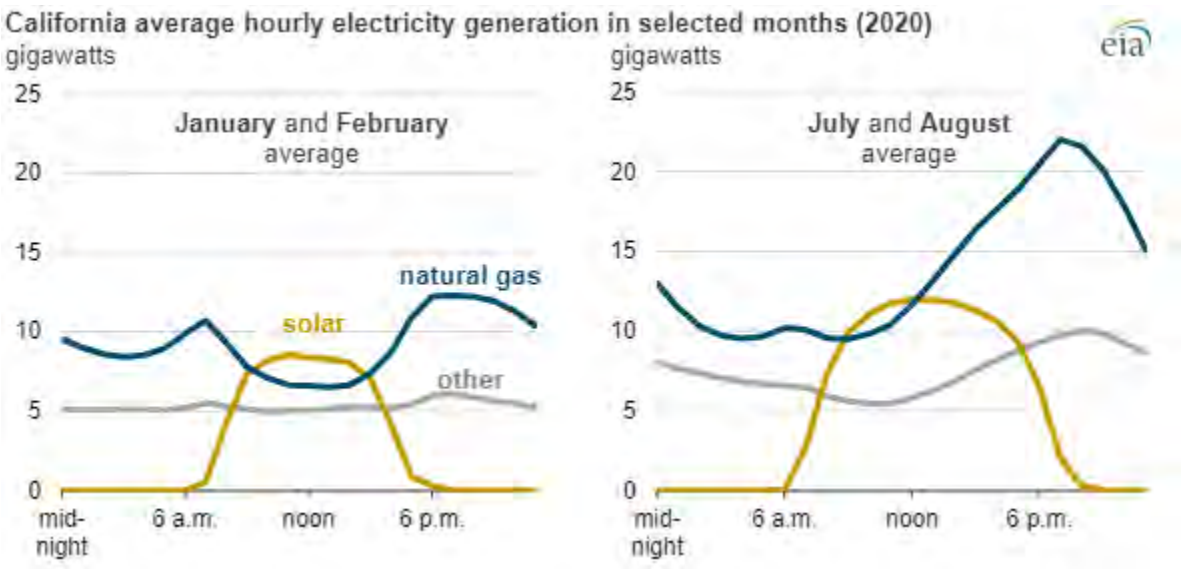

Figure 6: California solar vs. natural gas peaker supply graphs (Dyl and Comstock 2020).

4. Experimental Data from Preliminary 1MW Study

Before developing a full-scale high-pressure Pelton turbine, a preliminary study was conducted for a smaller-scale version. The parameters for this study included pressure ratings from 1,500 to 3,500 psi (pressure per square inch), a flow rate between 1.9-4.2 CFS (cubic feet per second), a target of 1 MW (megawatt) power output, and a higher limit of 95°C for the temperature of the water coming out of the well. It is important to note that the 95°C temperature limit was to ensure the fluid stays in single-phase, as Pelton turbines are not designed to handle two-phase fluids.

The biggest challenge in this study was that this would be the highest head for a Pelton turbine in history. It would require a Variable Speed Drive with the wide pressure range as well as a high speed generator capable of 180% overspeed.

Critical engineering tasks included jet formation, runner modeling and stress analysis, the variable speed mechanism, and the generator design. A significantconcern that was considered but resolved was the stress that the runner would be experiencing, especially when encountering water with higher TDS (total dissolved solids) or when sharp-shaped solids were present in the water. These dissolved solids could wear down the “cups” or “buckets” on the runner, which is the part of the Pelton turbine that is pushed by the water in order to turn. Pelton turbines already have a very robust design, and material considerations such as the addition of coatings on the runner buckets can overcome erosion concerns.

The study found it possible to design and manufacture a Pelton turbine and control system for the presented conditions.

5. Results and Discussion

In the preliminary 1MW Pelton turbine study, several critical challenges and solutions were identified and addressed. First, adapting Pelton turbines to operate at unprecedented high heads posed significant engineering hurdles, particularly regarding runner stresses and shaft speeds. With

shaft speeds typically lower in hydroelectric turbines, the high pressure Pelton's operation at 1,800 rpm necessitated advanced Computational Fluid Dynamics (CFD) and Finite Element Analysis (FEA) for runner design to withstand centrifugal forces effectively. Addressing natural frequencies also required iterative refinements to ensure structural integrity.

Second, achieving optimal jet formation at velocities up to 262 meter/second or 860 feet/second presented another pivotal challenge that was resolved. The design intricacies of the nozzles and precise jet formation were meticulously analyzed through two-phase CFD simulations. These efforts were crucial in optimizing energy transfer efficiency from the high-pressure water jets to rotational mechanical energy.

Another issue was the need for variable speed operations, which was paramount given the wide range of pressures encountered. Traditional Pelton turbines operate most efficiently within a narrower pressure band. This prompted the adoption of a variable frequency drive (VFD) for the generator. This adaptive control system dynamically adjusts turbine speed relative to inlet pressure, thereby maximizing efficiency across varying operational conditions.

Lastly, the design of a robust generator capable of up to 180% overspeed under uncontrolled load rejection conditions was pivotal. Collaboration with a company to custom-design a generator not only addressed rotor stresses at elevated speeds but also accounted for unique rotor dynamics induced by the Pelton turbine's operational characteristics. This solution ensured reliable performance and longevity of the generator amidst demanding operational scenarios.

6. Summary and Conclusion

Energy storage and geothermal energy are critical technologies needed to deliver clean power generation amidst growing concerns over climate change and energy security. The development of Geopressured Geothermal Systems (GGS) technologies, distinct from traditional Enhanced Geothermal Systems (EGS) or Advanced Geothermal Systems (AGS), enhancing energy extraction efficiencies by leveraging both heat and pressure from geothermal wells will be pivotal to the clean energy industry. The development of long duration energy storage technologies in the subsurface, utilizing the newly developed high-pressure Pelton turbine design, exemplifies a significant technical leap in renewable energy solutions, technology, and equipment development. This paper details the engineering complexities and solutions involved in adapting Pelton turbines to operate efficiently under high pressures, optimizing jet formation dynamics, implementing variable speed operation strategies, and designing resilient generators. This high-pressure Pelton turbine is pivotal in advancing the practical viability of geothermal energy as a scalable, reliable, and environmentally responsible energy source. As research and development continue, such innovations hold promise for broader adoption and integration of geothermal technologies in the global energy mix, contributing to sustainable development goals and reducing the reliance on fossil fuels.

Acknowledgement

The authors would like to thank the Sage Geosystems and Canyon Hydro teams in their collaborative effort to make this technology a reality. In particular, we would like to thank Lance

Cook, Shannon Bolton, Mike Maloney, and the engineering team at Canyon Hydro for all of their efforts and input into this project.

REFERENCES

Canyon Hydro. “Hydroelectric Turbine Systems.” Canyon Hydro - Hydroelectric Systems for Utilities and Independent Power Producers.

Cropley, John. “Closed-Loop Hydro’s Climate Impact Found Less Than Batteries.” RTO Insider, 27 Aug. 2023.

Dyl, Katie, and Owen Comstock. “In California, Natural Gas Helps Balance Changes in Electricity Demand and Solar Output.” U.S. Energy Information Administration (EIA), 11 Dec. 2020.

Jones-Albertus, Becca. “Confronting the Duck Curve: How to Address over-Generation of Solar Energy.” Office of Energy Efficiency & Renewable Energy.

Simpkins, Douglas, et al. “Energy Storage in Deep Hydraulic Fractures: Mathematical Model and Field Validation.” 2023

Vermilion Historial Society. “Lester A. Pelton.” Vermilion Historical Society, 2 Mar. 2020.

Design and Performance Analysis of a Supersonic Ejector Prototype for Connecting High and Low-Pressure Geothermal Wells

Ximena Guardia[1], Daniel Wanga Odongo[1], Gunnar Dagur Jónsson[1], Ragnar Lárusson[1], Guðrún Sævarsdóttir[1], Yonatan Afework Tesfahunegn[1], Hilmar Már Einarsson[2], María Sigríður Guðjónsdóttir[1]

[1]Department of Engineering, Reykjavik University, Reykjavik, Iceland. [2]Landsvirkjun, Reykjavik, Iceland.

Keywords

Declining geothermal wells, ejectors for geothermal, geothermal experimental work

ABSTRACT

Geothermal production wells are susceptible to pressure decline over time, which could make them unusable for power generation when their pressure drops below the plant's operating conditions. This situation could decrease the power output, necessitating drilling make-up wells at a considerable capital cost. This study looks at options for using an ejector to mitigate this problem. An ejector is a static device that can potentially be used to draw fluid from a low-pressure well using a flow from a nearby high-pressure well. In ejectors, two flows are combined in a mixing chamber, and the mixture passes through a diffuser, leaving at an intermediate outlet pressure, which could be higher than the pressure of the low-pressure well.

Although ejectors are widely utilized in industries such as oil and gas and refrigeration, their application in geothermal energy has mainly been limited to gas extraction from power plant condensers. However, the literature lacks reports of successful ejector use for inducing geothermal fluid from low-pressure wells. As part of the Geoejector project, this paper focuses on the design, development, and performance analysis of a supersonic laboratory scale ejector prototype constructed at Reykjavik University. The prototype was tested using saturated steam for primary and secondary flows under different pressure conditions.

1. Introduction

An ejector is a static device that mixes a high-pressure primary flow with a low-pressure secondary flow in a customised mixing chamber. The mixture passes through a diffuser, leaving the ejector at an intermediate outlet pressure (Villa et al., 1999).

In a supersonic ejector, the high-pressure primary fluid expands and accelerates through a converging-diverging nozzle, reaching supersonic speed. This creates a low-pressure region at the

nozzle's exit, which allows the entrainment of the low-pressure secondary fluid into the mixing chamber, where both fluids start to mix until thoroughly combined inside the constant area mixing section (CAMS). A series of shock waves are produced within the CAMS, compressing and decelerating the flow to subsonic velocities before entering the diffuser. Further fluid compression and an increase in pressure are achieved as the combined streams flow through the subsonic diffuser section of the ejector (Manoj & Lijo, 2021) (Aidoun et al., 2019).

The performance of an ejector is characterized by the pressure, temperature, and velocities of primary and secondary fluids, the dimensions of the ejector, and its back pressure. Key geometrical factors influencing the performance of the ejector include the nozzle exit position (NXP)[1] and the ratio between the CAMS and the primary nozzle area (Yan et al., 2012).

A schematic view of a typical supersonic ejector is shown in Figure 1. The numbers represent flow positions used for the supersonic ejector calculations of the analytical model developed by (Andal, 2023), where 1 is the entrance of the primary flow, 2 is the nozzle's throat position, 3 is the nozzle's exit, 4 is the primary flow at the hypothetical throat[2] position, 5 is the entrance of the secondary flow, 6 is the secondary flow at the hypothetical throat position, 7 is the CAMS, 8 is the shock wave position, and 9 is the diffuser exit.

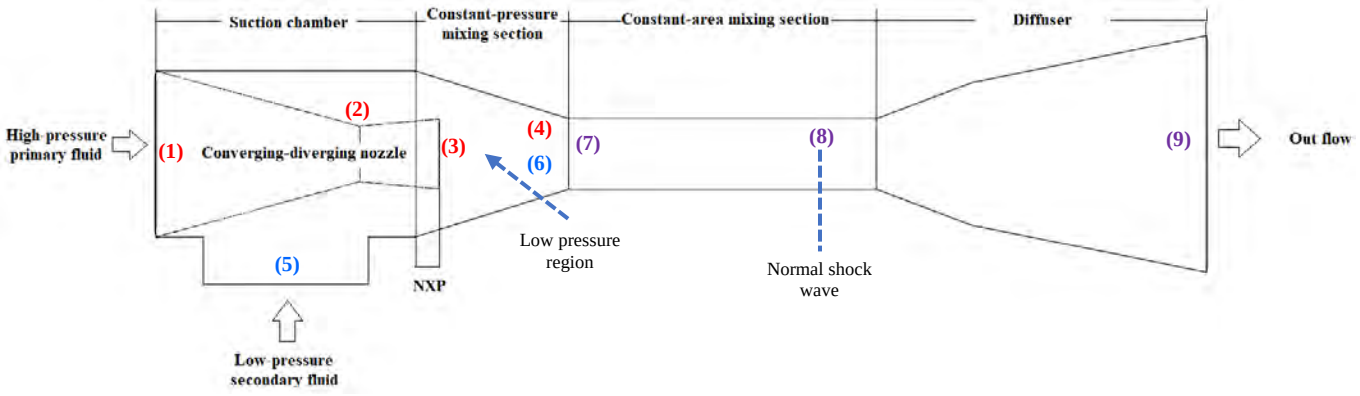

Figure 1. Schematic of a supersonic ejector adapted from (Ding et al., 2016).

In the geothermal industry, ejectors mainly extract non-condensable gases from condensers (Strušnik et al., 2016). Still, no published experimental validated information exists regarding their usage for fluid extraction from geothermal wells. A patent from 1999 (United States Patent N° 5899273, 1999) described an ejector to increase the fluid recovery from geothermal wells, but no further information on its usage was found. Also, it is known that the company Reykjavik Energy used an ejector on the Hellisheiði power plant in 2012 for managing scaling in a turbine which got high-enthalpy dry steam from a new well. The flow from that well was used in an ejector as the primary flow, and fluid from low-enthalpy two-phase wells was used as a secondary flow. This seemed to have washed the high-enthalpy steam and solved the scaling issue in the turbine (G. Kjartansson, personal communication 2023).

[1] The nozzle exit position (NXP) is defined as the distance of the primary nozzle exit from the inlet of the constant pressure mixing section (converging section) (Yan et al., 2012).
[2] The hypothetical throat is where the secondary flow is assumed to have reached sonic velocity (Huang et al., 1998).

In 2021, the power company Landsvirkjun tested a rudimentary subsonic ejector at the Theistareykir Geothermal Power Plant to use the high-pressure geothermal fluid from well ThG-11 to induce flow from the low-pressure well ThG-15. The tests showed that entrainment from the secondary flow was achieved. However, the pressure of the primary flow during the tests was kept between 12.6 and 15.4 bar-g, which is far below the nominal operating pressure of well ThG-11 (25 bar-g on average). This resulted in the pressure difference between the high- and low-pressure wells during the tests being significantly lower than in actual operation. Using an analytical model, it was estimated that an average of 20.6% pressure reduction of the primary flow occurred in the convergent nozzle used in the tests (Guardia et al., 2023). A significantly greater reduction in pressure would be needed under real operational conditions.

For that reason, the analysis developed by (Guardia et al., 2023) suggested that a supersonic ejector employing a convergent-divergent nozzle would be required to create enough under-pressure to entrain the secondary flow under normal primary pressure conditions of well ThG-11. In that sense, an analytical model was developed by (Andal, 2023), finding that a supersonic ejector could potentially increase the pressure of the fluid from well ThG-15 up to and above the working pressure of the power plant (9.5-10 bar-g), which would potentially add up to 0.8 MWe for additional power generation.

This study focuses on designing and building a laboratory-scale supersonic ejector prototype at Reykjavik University based on the analytical model developed by (Andal, 2023). The prototype was tested using saturated steam for primary and secondary flows under different pressure conditions and for different geometrical factors NXP and area ratio.

2. Methodology

2.1 Ejector design

The supersonic ejector prototype was designed for a primary flow of 0.005 kg/s entering at 7.2 bar-g and 212°C, and a secondary flow of 0.003 kg/s entering at 2.3 bar-g and 170.6°C. Table 1 shows the properties and dimensions of the ejector calculated with the analytical model (Andal, 2023) for the flow positions presented in Figure 1.

Table 1. Calculated properties and dimensions of the laboratory scale ejector

	1 **Entrance of the primary flow**	**2** **Nozzle throat**	**3** **Nozzle exit**	**4** **Primary flow at hypothetical throat**	**5** **Entrance of the secondary flow**	**6** **Secondary flow at hypothetical throat**	**7** **CAMS**	**8** **Shock wave**	**9** **Diffuser exit**
Diameter (mm)	15.7	2.4	3.4	-	20.0	3.1	4.0	4.0	20.0
Mass flow (kg/s)	0.005	0.005	0.005	0.005	0.003	0.003	0.008	0.008	0.008
Pressure (Bar-g)	7.2	3.4	0.1	0.8	2.3	0.8	0.8	1.2	2.7
Enthalpy (kJ/kg)	2866.0	2754.9	2508.2	2592.8	2803.0	2698.7	2701.6	2741.1	2841.6
Mach number	0.0	1.0	1.9	1.6	0.0	1.0	1.1	0.9	0.0

Note: The points are indicated in Figure 1.

According to the analytical model, the CAMS should have a diameter of 4.0 mm, but three additional ejectors with different CAMS diameters were made to test the performance sensitivity to this parameter: 5.0, 7.0, and 9.0 mm (see Table 2 and Figure 2).

Table 2. Dimensions of ejectors used in the laboratory experiments.

Ejector type	D1 (mm)	D2 (mm)	D3 (mm)	D4 (mm)	D5 (mm)	L1 (mm)	L2 (mm)	L3 (mm)	L4 (mm)	L5 (mm)	L6 (mm)	NXP (mm)
4.0 mm CAMS	15.7	2.4	3.4	4.0	20.0	63.0	5.6	63.2	74.9	20.9	66.5	5.4
5.0 mm CAMS	15.7	2.4	3.4	5.0	20.0	63.0	5.6	60.8	75.2	21.2	66.2	7.8
7.0 mm CAMS	15.7	2.4	3.4	7.0	20.1	63.0	5.6	65.5	77.6	19.3	65.7	3.1
9.0 mm CAMS	15.7	2.4	3.4	9.0	19.8	63.0	5.6	64.0	76.2	19.6	66.7	4.6

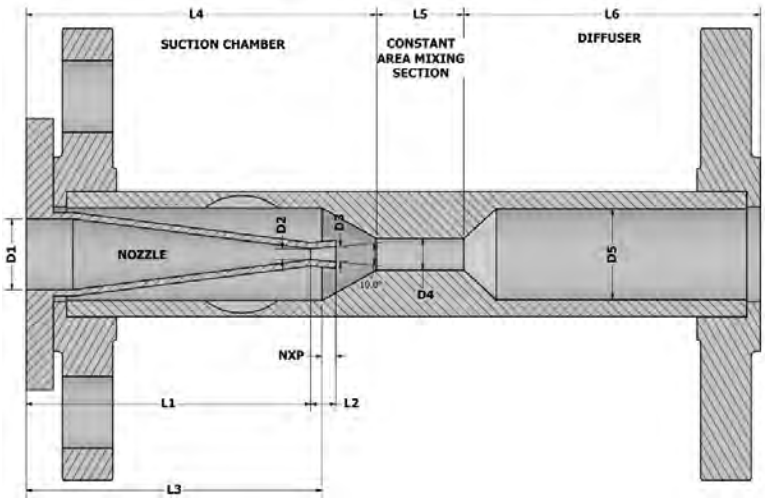

Figure 2. Drawing showing the general setup of the ejectors that were manufactured.

2.2 Ejector manufacturing

An aluminium nozzle was 3D printed to fit the dimensions in Table 2 (see Figure 3) in Tæknisetur ehf.-IceTec, using the selective laser melting printer iSLM160 (Tæknisetur ehf.-IceTec, 2024).

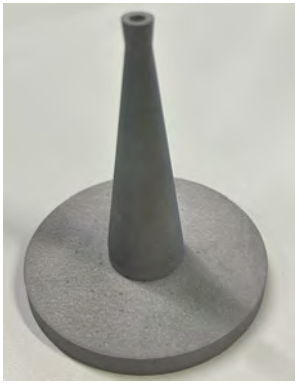

Figure 3. Aluminium nozzle printed in 3D.

The four mixing chambers were manufactured at Reykjavik University with Stainless Steel 304 using a high-precision lathe machine model TR1340VS from JESCO MACHINERY LTD. Holes of 4.3 mm were made in all mixing chambers. Then, 5 mm threads were made on them to introduce the miniature pressure sensor.

Finally, to test different NXPs, two aluminium blocks were manufactured to get 0 mm and -7.4 mm NXP, respectively (see Figure 4 and Figure 5).

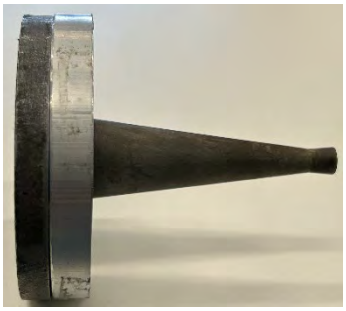

Figure 4. Nozzle with Aluminium block used for 0 mm NXP.

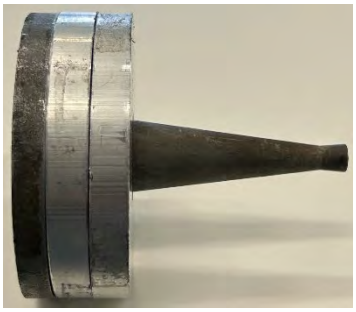

Figure 5. Nozzle with Aluminium block used for -7.4 mm NXP.

2.3 Equipment

Two boilers were used for the primary and secondary steam flow production. The boiler used for the primary flow production can produce steam at a pressure range from 7-7.2 bar-g pressure at a temperature between 212 and 215°C. In contrast, the boiler used for the secondary flow production has a pressure range from 1-10 bar-g and a working temperature from 100-185°C.

The following pressure, temperature and mass flow sensor equipment was used to obtain the data during the experiment. Their location is shown in Figure 6:

- 3 pressure sensors PCE-28/EXD type with a pressure range of 0 to 10 bar-a.
- 1 micro pressure sensor JC91 type with a pressure range of 0.7 to 10 bar-a.
- 4 temperature probes STA 206 P-type with a temperature range of -20 to 250 °C.
- 1 vortex flow meter Endress D 200 Model with a pressure range of 0 to 10 bar-a, and a temperature range of -40 to 260°C.
- 1 Pressure gauge with a pressure range of 0 to 12 bar-a.

All sensor values were recorded using a Programmable Logic Controller (PLC). Finally, two separators were used in the experiments to remove the water from the steam flow, and a heat exchanger was used to condense the total outlet flow from the system for the total mass flow measurement.

2.4 Setup

Figure 6 shows the schematic diagram of the process flow of the laboratory experiment setup, while Figure 7 shows the final setup that was implemented. The setup includes two boilers for steam generation for the primary and secondary flows and two separators to remove water residuals from the flows. Pressure sensors (PS), temperature sensors (TS), and a vortex flow meter (VFM) are used to measure pressure, temperature, and mass flow, respectively. The setup also incorporates the manufactured ejectors and a heat exchanger to condense the total mass flow, which is then measured using beakers and a scale (FM). Additionally, air pressure regulators were included to test for leakages with air before conducting the steam tests.

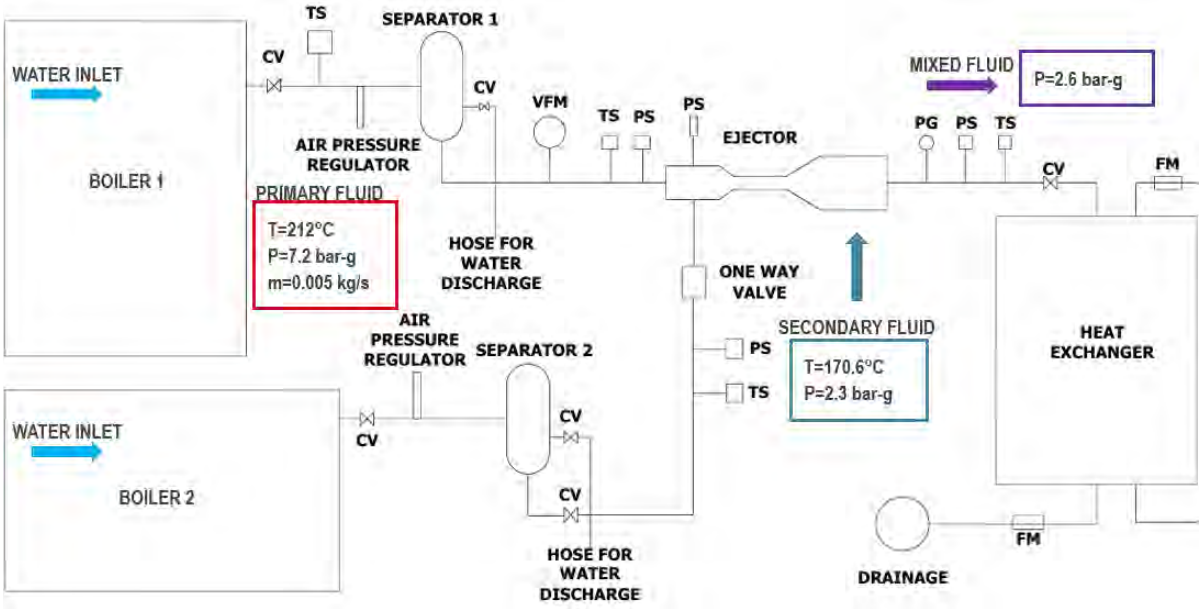

Figure 6. Schematic diagram of the laboratory experiment setup.

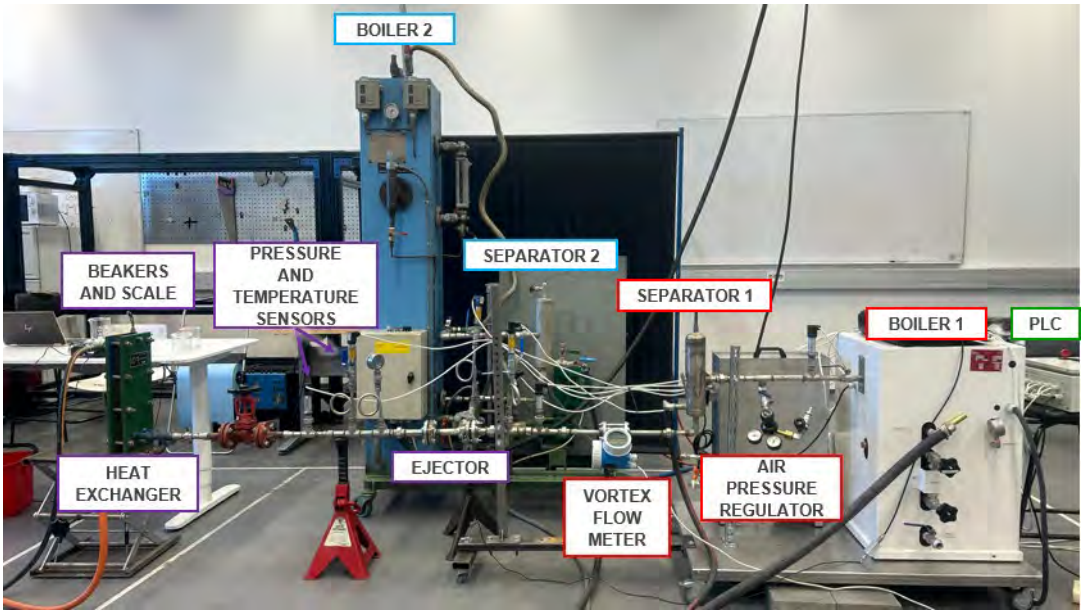

Figure 7. Final set-up laboratory experiments.

2.5 Process

The four ejectors (see Table 2) were tested using the same pressure and temperature for the primary (7.2 bar-g and 212°C) and secondary inlets (2.3 bar-g and 170.6°C), as well as the same outlet pressure or back pressure (2.6 bar-g). The analytical model suggests an outlet pressure of 2.7 bar-g; during the tests, however, a 2.6 bar-g pressure was set to have a better reading of the pressure gauge.

The outlet valve for the water separated from the primary flow was kept open until no more water was seen coming out. Then, the valve was closed and waited until a reading of 7.2 bar-g was on the primary flow boiler pressure gauge. After reaching the desired pressure in the primary flow (7.2 bar-g), we closed the outlet valve to achieve a back pressure of 2.6 bar-g.

After 2 minutes of reaching the desired outlet pressure, we started the mass flow readings at the heat exchanger outlet using a scale and three beakers until we had 12 consecutive readings (each reading after filling up one beaker of 300 mL). The primary flow was measured simultaneously with the vortex flow meter.

Boiler 2 for the secondary flow production was turned on when completing the primary flow readings. The outlet valve for the water separated from the secondary flow was kept open until no more water was seen coming out. Then, we closed the valve and waited until getting a reading of 2 bar-g on the secondary flow boiler pressure gauge. After two minutes of reaching the desired secondary flow pressure, we started the total mass flow readings at the outlet of the heat exchanger using a scale and three beakers until having 12 readings (each reading after filling up one beaker of 300 mL). The primary flow was measured simultaneously with the vortex flow meter.

3. Results

3.1 Effect of variation of area ratio

Table 3 summarizes the main results of the tests for different area ratios, which is one of the geometrical parameters that affect the ejector performance.

The area ratio here is the ratio of the CAMS area to the nozzle's throat area (see Equation 1); the gained pressure refers to the difference between the outlet pressure (or back pressure) and the secondary flow pressure (see Equation 2); and finally, the entrainment ratio is the ratio of secondary flow to the primary flow (see Equation 3).

$$Area\ ratio = \frac{CAMS\ area}{Nozzle's\ throat\ area} \tag{1}$$

$$Gained\ pressure = Back\ pressure - Secondary\ flow\ pressure \tag{2}$$

$$Entrainment\ ratio = \frac{Secondary\ flow}{Primary\ flow} \tag{3}$$

Table 3. Gained pressure, back pressure, entrainment ratio, and average pressure in the suction chamber for different area ratios.

Nozzle's throat diameter (mm)	CAMS diameter (mm)	Area ratio	Back pressure (bar-g)	Secondary flow pressure (bar-g)	Gained pressure (bar)	Entrainment ratio	Average pressure in the suction chamber (bar-g)
2.4	4.0	2.69	2.57	2.23	0.34	0.04	2.70
2.4	5.0	4.20	2.94	2.23	0.71	0.17	1.97
2.4	7.0	8.23	2.73	2.23	0.50	0.08	1.97
2.4	9.0	13.61	2.63	2.24	0.39	0.04	2.10

Figure 8 shows the pressure, temperature, and mass flow values of primary, secondary, and outlet flows during the ejector test for the 4.0 mm CAMS. The average pressure of the secondary flow (2.2 bar-g) is lower than the average pressure at the suction chamber (2.7 bar-g), preventing the entrance of the secondary flow into the system for most of the test time. This is confirmed by the low temperature recorded by the secondary flow sensor (104.4°C on average), and the total flow obtained from the test is very close to the primary flow, indicating no entrainment of the secondary flow. Therefore, the 4.0 mm CAMS ejector does not function effectively under the experimental conditions.

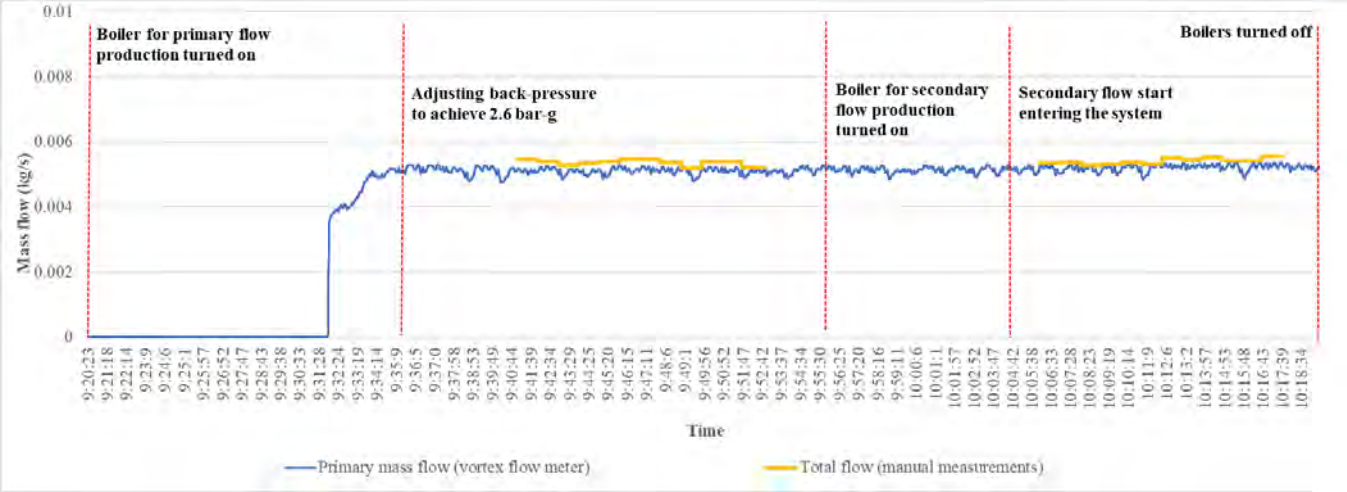

Figure 8. Results of pressure (top), temperature (middle), and mass flow (bottom) variation of primary, secondary, and outlet flows in the 4.0 mm CAMS ejector test.

In contrast, Figure 9 shows the pressure, temperature, and mass flow variation of primary, secondary, and outlet flows in the 5.0 mm CAMS ejector test. Here, the pressure of the secondary flow (2.2 bar-g) is higher on average than the pressure at the suction chamber (1.9 bar-g), allowing the entrance of the secondary flow into the system. This is confirmed by the high temperature registered in the secondary flow sensor (169.7°C on average), and the total flow obtained from the test is 16.6% higher than the primary flow, indicating the successful entrainment of the secondary flow. Therefore, the 5.0 mm CAMS ejector operates effectively under the experimental conditions.

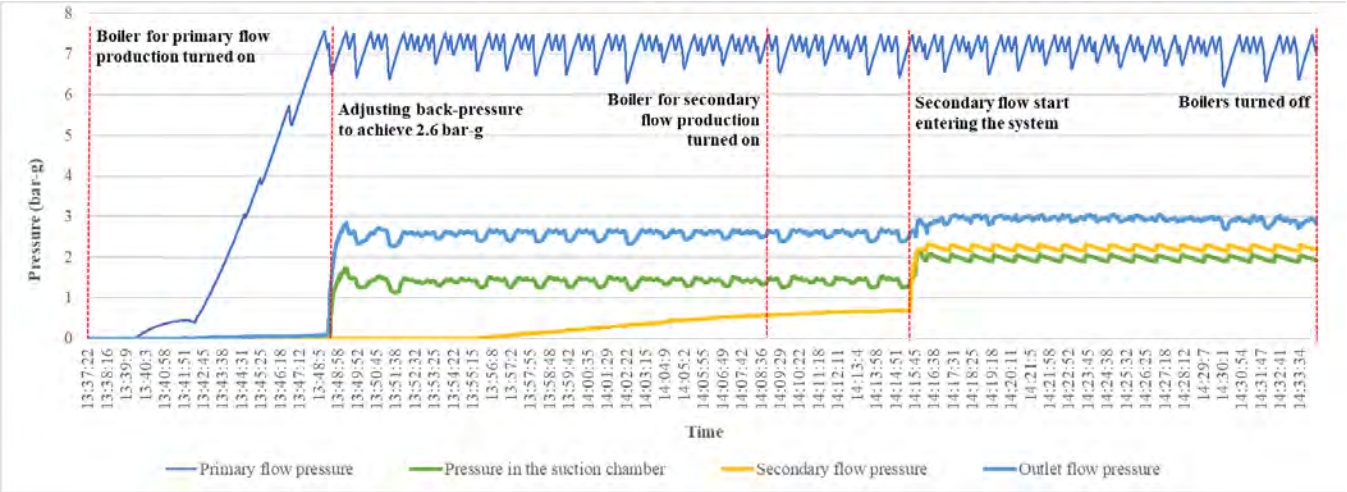

Figure 9. Results of pressure (top), temperature (middle), and mass flow (bottom) variation of primary, secondary, and outlet flows in the 5.0 mm CAMS ejector test.

Similarly, Figure 10 shows the pressure, temperature, and mass flow variation of primary, secondary, and outlet flows in the 7.0 mm CAMS ejector test. When the two flows are combined, the average pressure of the secondary flow (2.2 bar-g) is higher than the average pressure at the suction chamber (1.9 bar-g), allowing the entrance of the secondary flow into the system. This is confirmed by the high temperature recorded by the secondary flow sensor (169.8°C on average), and the total flow obtained from the test is 7.9% higher than the primary flow, indicating successful entrainment of the secondary flow. Therefore, the 7.0 mm CAMS ejector operates effectively under the experimental conditions but with less entrainment than the 5.0 mm CAMS ejector.

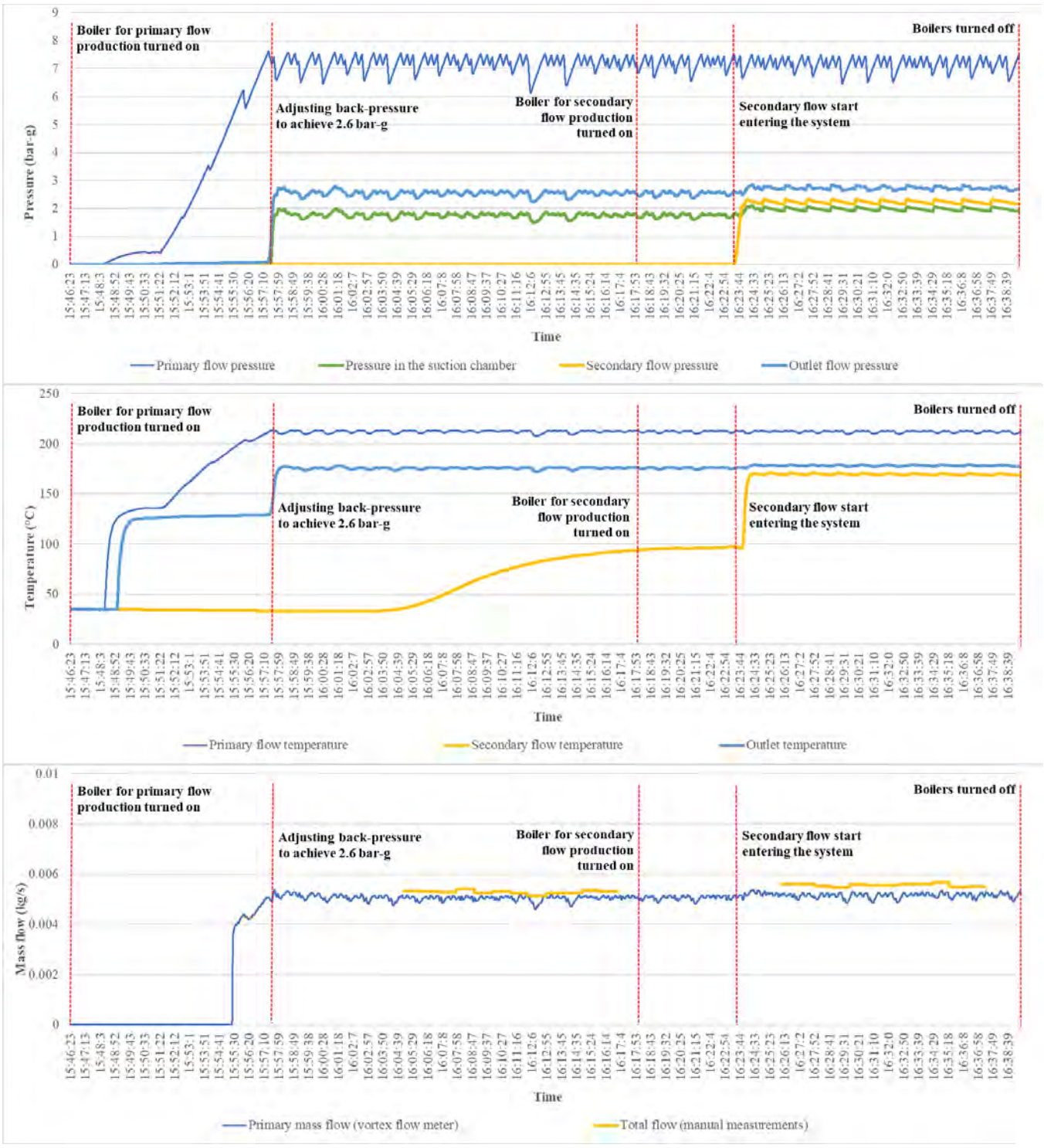

Figure 10. Results of pressure (top), temperature (middle), and mass flow (bottom) variation of primary, secondary, and outlet flows in the 7.0 mm CAMS ejector test.

Finally, Figure 11 shows the pressure, temperature, and mass flow variation of primary, secondary, and outlet flows in the 9.0 mm CAMS ejector test. The average pressure of the secondary flow (2.2 bar-g) is higher than the average pressure at the suction chamber (2.1 bar-g), allowing minimal entrance of the secondary flow into the system. This is confirmed by the high temperature recorded

by the secondary flow sensor (168.8°C on average), and the total flow obtained from the test is just 4.2% higher than the primary flow, indicating very low entrainment of the secondary flow. Therefore, the 9.0 mm CAMS ejector operates under the experimental conditions but with very low entrainment.

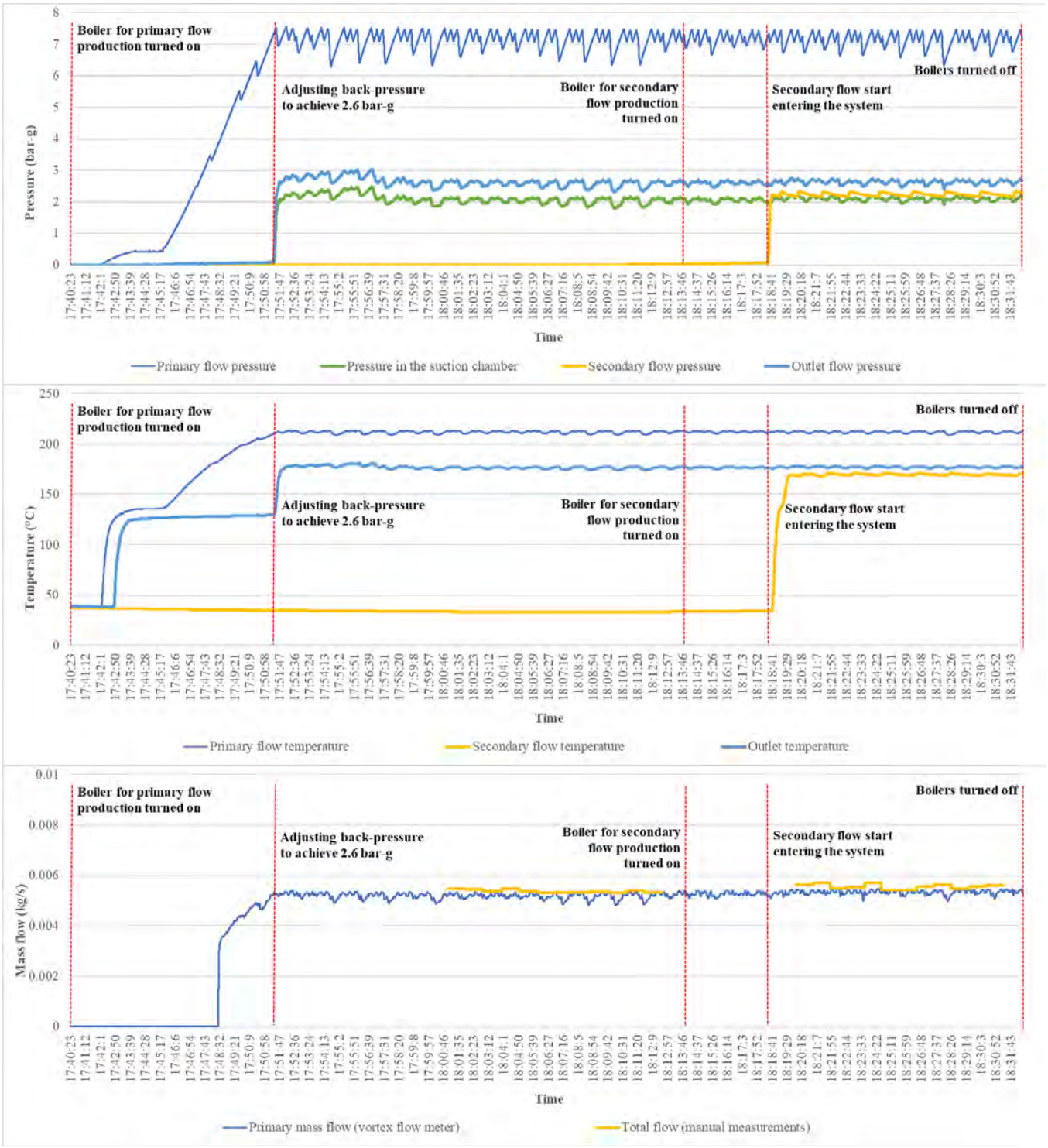

Figure 11. Results of pressure (top), temperature (middle), and mass flow (bottom) variation of primary, secondary, and outlet flows in the 9.0 mm CAMS ejector test.

Figure 12 shows the variation in the entrainment ratio for the manufactured ejectors with different area ratios. The area ratio of 4.2, corresponding to the 5.0 mm CAMS ejector, has the highest entrainment ratio, indicating the greatest entrainment of the secondary flow. This suggests that an area ratio of 4.2 is optimal for this ejector setup, as both lower and higher area ratios result in decreased entrainment.

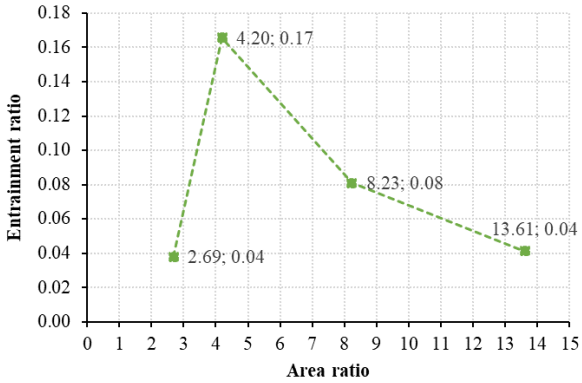

Figure 12. Entrainment ratio variation with the area ratio.

The low entrainment from the 4.0 mm CAMS ejector results from its small diameter, which prevents the combined fluid from going inside the CAMS, increasing the pressure in the suction chamber, as seen in Figure 13. On the other hand, the low entrainment in the 9.0 mm CAMS ejector results from its big diameter, which decreases the pressure in the CAMS to similar values to the secondary flow pressure, preventing a regular flow from high to low pressures.

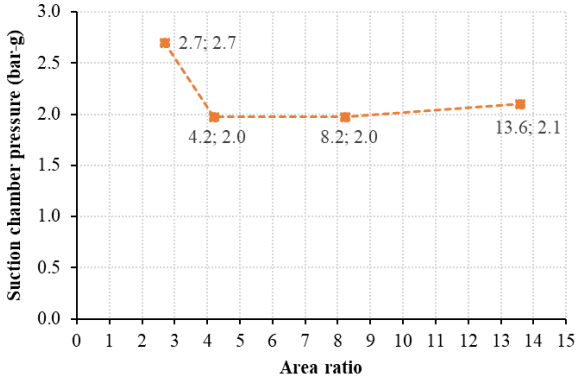

Figure 13. Suction chamber pressure variation with the area ratio.

Despite setting up the same secondary flow pressures and the same back pressure for all the tests, an increase in the final back pressure values was observed following the same behaviour as the entrainment ratio (see Figure 12), which means that the back pressure increase is a result of the entrainment of the secondary flow. The gained pressure for all the cases is presented in Figure 14.

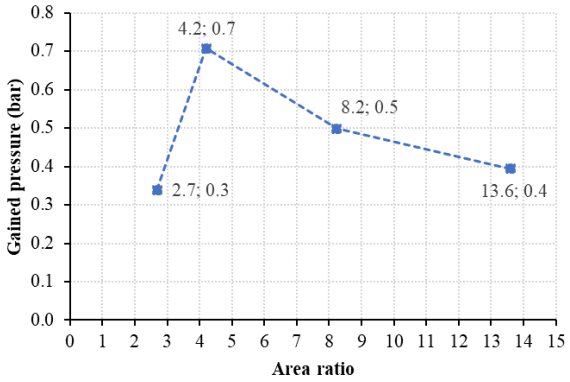

Figure 14. Gained pressure variation with the area ratio.

3.2 Effect of variation of NXP

Table 4 summarizes the main results of the NXP tests performed with the 5.0 mm CAMS ejector.

Table 4. Gained pressure, back pressure, entrainment ratio and average pressure in the suction chamber for different NXP.

NXP (mm)	Back pressure (bar-g)	Secondary flow pressure (bar-g)	Gained pressure (bar)	Entrainment ratio	Average pressure in the suction chamber (bar-g)
-7.4	2.83	2.30	0.54	0.01	2.18
-0	3.01	2.30	0.71	0.06	2.06
7.8	2.90	2.30	0.61	0.05	2.02

Table 4 and Figure 15 show that a 0 mm NXP provides the highest entrainment ratio, while the -7.4 mm NXP has the lowest, reaching even negative values (back flow). This suggests that there is more entrainment of the secondary flow when the nozzle exit goes further inside the constant pressure mixing section. Also, a slight decrease in the suction chamber pressure is seen when this happens (see Figure 16). However, when the NXP continues to increase, the entrainment ratio decreases slightly, and this could mean that part of the primary flow is lost due to the collision with the walls of the constant pressure mixing section.

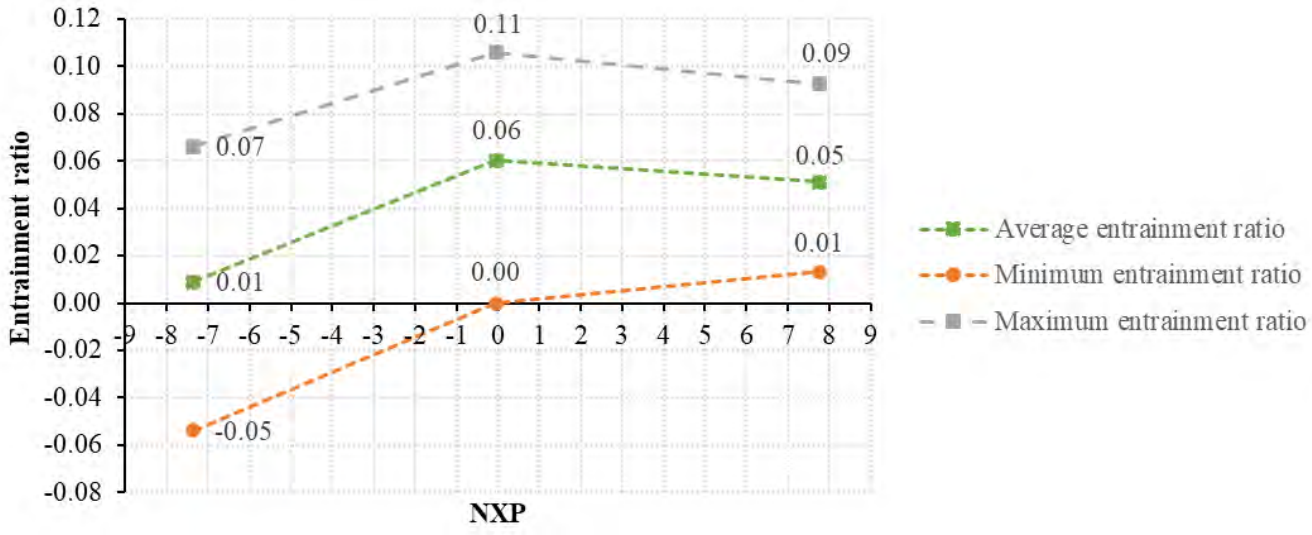

Figure 15. Entrainment ratio variation with the NXP.

For the three NXP tested, the suction chamber pressure values recorded had a standard deviation between 4.9 and 5.1% despite the greater deviation of the primary flow pressures, with standard deviations between 19.7 and 25.5%. At the same time, entrainment ratio values had a standard deviation between 2.2 and 3.3%. This means that fluctuations on the primary flow pressures have minimal effect on the values of the entrainment ratio, so the changes on the entrainment can be attributed to the variations on NXP.

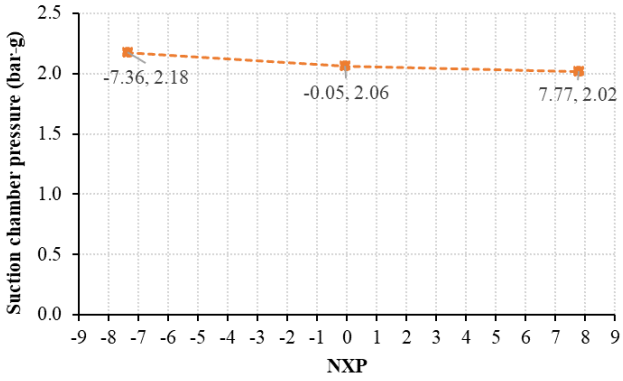

Figure 16. Average suction chamber pressure variation with the NXP.

Finally, more pressure from the secondary flow could be gained with 0 or positive NXP, as shown in Figure 17.

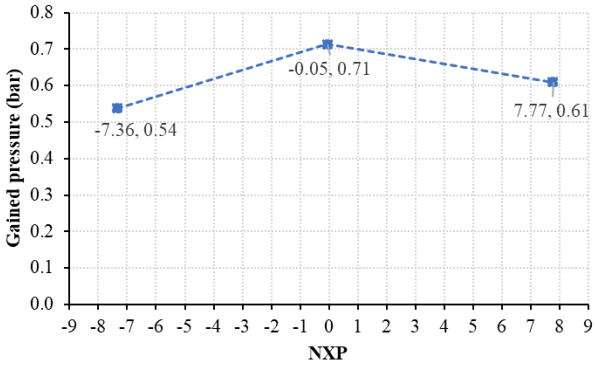

Figure 17. Average gained pressure variation with the NXP.

4. Conclusions

The supersonic ejector prototypes built at the laboratory of Reykjavik University fulfilled the ejector principle.

An area ratio of 4.20 corresponding to a 5 mm CAMS ejector was optimal for the testing conditions, showing the highest entrainment ratio and gained pressure.

An area ratio of 2.69 corresponding to a 4 mm CAMS ejector showed the worst performance due to the low CAMS diameter, which does not enable the entrance of the secondary flow and increases the pressure in the suction chamber. On the other hand, high CAMS diameters also reduce the entrainment ratio due to the decreased pressure difference between the back pressure and the secondary flow pressure.

Ejectors with zero and positive NXP provide a higher entrainment ratio and gained pressure for the ejector prototypes tested.

Further improvements in the analytical model and the development of computational fluid dynamics (CFD) models are suggested to provide a better understanding of the performance of the supersonic ejector prototypes.

Acknowledgement

This project has received funding from Rannis Technology Development Fund, Project Number 2112948-0611, VOR Reykjavik Energy Research Fund, Rannis Student Innovation Fund, Reykjavik University Equipment Fund and SIF Sustainable Institute and Forum. Their contributions are highly appreciated.

REFERENCES

Aidoun, Z., Ameur, K., Falsafioon, M., & Badache, M. (2019). Current Advances in Ejector Modeling, Experimentation and Applications for Refrigeration and Heat Pumps. Part 1: Single-Phase Ejectors. *Inventions*, 10-12.

Andal, J. (2023). *Geoejector: Extracting geothermal fluid from a low-pressure geothermal well.* Reykjavik: Reykjavik University.

Andal, J. M., Lárusson, R., Guardia Muguruza, X., Sævarsdóttir, G., Afework Tesfahunegn, Y., Júlíusson, E., Sigríður Guðjónsdóttir, M. (2023). Improvement of a Geoejector Design Using an Analytical Model and Data from Theistareykir Geothermal Field, Iceland. *Proceedings World Geothermal Congress 2023*, (pp. 1-10). Beijing, China.

Guardia Muguruza, X., Macatangay Andal, J., Lárusson, R., Sævarsdóttir, G., Afework Tesfahunegn, Y., Júlíusson, E., Guðjónsdóttir, M. (2023). Connecting high- and low-pressure geothermal wells using an ejector: Analysis of first field tests at the Theistareykir Geothermal Power Plant. *Proceedings World Geothermal Congress 2023*, (pp. 1-11). Beijing, China, April 17 – 21, 2023.

Huang, B., Chang, J., Wang, C., & Petrenko, V. (1999). A 1-D analysis of ejector performance. *International Journal of Refrigeration*, 354–364.

Jung, D. (1999). *United States Patent No. 5899273.*

Strušnik, D., Golob, M., & Avsec, J. (2016). Effect of non-condensable gas on heat transfer in steam turbine condenser and modelling of ejector pump system by controlling the gas extraction rate through extraction tubes. *Energy conversion and management*, 228-246.

Tæknisetur ehf.-IceTec. (2024, July 12). *Tæknisetur*. Retrieved from https://www.taeknisetur.is/t%C3%A6ki-og-b%C3%BAna%C3%B0ur

Villa, M., De Ghetto, G., Paone, F., Giacchetta, G., & Bevilacqua, M. (1999). Ejectors for Boosting Low-Pressure Oil Wells. *SPE Production & Facilities*, 229–234.

An Overview of the Performance Testing of a Supercritical CO_2 Geothermal Turbine

John Klaerner and Lev Ring

Southwest Research Institute and Sage Geosystems

Keywords

Supercritical CO_2 (sCO_2), sCO_2 Turbine, sCO_2 Power Cycle, Flow Loop, Geothermal

ABSTRACT

A new supercritical carbon dioxide (sCO_2) turbine has been tested to conditions anticipated for geothermal power production. The prototype machine owned by Sage Geosystems was designed by Southwest Research Institute (SwRI) for operation in a low to mid-enthalpy geothermal field at a 3 MW scale. The closed loop CO_2 system within a geothermal power plant will allow for improved conversion of heat to power by taking full advantage of the efficiency and power density of sCO_2 turbomachinery. The megawatt-scale system offers a significant reduction in overall size and cost versus other commercial heat-to-power conversion systems.

This paper will present data from the laboratory testing of the Sage Geosystems sCO_2 turbine at SwRI to show the aerodynamic performance and power output along with how the data is used to prove the models of the 3 MW setup under field conditions. Design parameters including process temperature, pressure, and speed will all be achieved throughout the test progression. The proven mechanical integrity and rotordynamics of the modular design will be discussed, along with operating procedures of turbine subsystems used for this design.

The turbine has been successfully operated at full design temperature and over 80% of the design speed at the time of this publication. Further tests are ongoing to reach full operating conditions in Summer 2024. The paper will conclude with details on the turbine startup and shutdown process to provide a better understanding of potential use cases for a similar class turbine.

1. Introduction

Geothermal energy was originally used for various heating applications. It was not until 1904 when the renewable energy source was used to produce electricity (Lund, 2004). From then on, various configurations and systems have been designed and manufactured to convert geothermal energy (or heat) to moving electrons. These systems include various steam cycles and Organic Rankine Cycles (ORCs) which run on different refrigerants in a separate closed loop system. In recent years, the revolution of supercritical carbon dioxide (sCO_2) cycles and turbomachinery have demonstrated a successful and efficient system for turning heat into mechanical energy across a vast range of temperatures (Moore et al., 2018, Nielson et al., 2022).

sCO_2 is also considered a refrigerant in power systems (e.g., R744) and is used as a baseline for comparing the global warming potential (GWP) of other cycle refrigerants over time; many of which have or are being phased out. By having a GWP orders of magnitude below other energy cycle mediums and also acting as a fire suppressant, there are many positive environmental and safety attributes about sCO_2 when compared to other refrigerant-based systems.

With a supercritical regime above 31°C and 73.8 bar (88°F and 1,071 psi), CO_2 can remain in the same phase throughout a full cycle at common geothermal conditions in comparison to the refrigerants used in ORCs, which experience a constant temperature phase change during the heat input and rejection process. When in the supercritical phase, CO_2 fluid densities can be comparable to liquids while maintaining the viscosity of a gas, allowing for very efficient energy input. The additional benefit of an sCO_2 system is the reduction in machinery size, equating to reduced overall costs in hardware and footprint. This size reduction, for the same power level, is what CO_2 turbomachinery is known for.

Improved efficiency, smaller footprint, and lower equipment cost enables CO_2 to reduce the overall costs of geothermal energy production and are all reasons Sage Geosystems (Sage) sees the merit in this cycle (Nielson, Weiss, 2022). While many CO_2 cycle components are becoming commercially available, a mid-enthalpy turbine at 3 MW power scale remains uncustomary. Based on geothermal conditions from South Texas wells, the rotating machinery team at Southwest Research Institute (SwRI) has used previous design and test experience to develop, commission, and test a 3 MW sCO_2 geothermal turbine for Sage.

The turbine and impeller configuration under test in the laboratory are designed to operate at 150°C and 158 bar (300°F and 2,300 psi), but the modularity and interchangeability features of the design allow for easy movement between wells or quick aerodynamic changes to maximize the power output at various well conditions. Overall dimensions of the turbine are approximately 3ft diameter and 4ft in length, creating a five to ten times smaller unit than other steam turbines of similar power output. Table 1 details the operating range that the turbine is intended to function. The impeller designed and installed for the laboratory test is on the lower end of the power output range due to laboratory component limits such as the heat source and sink, piping size, and the capabilities of the compressor used to supply the flow.

Table 1. Turbine Operation Range

Condition	Range
Power Output	0.5 to 3 MWe Output
Operating Speed	22,000 RPM
Inlet Pressure	22.5 MPa max
Outlet Pressure	10 MPa max
Inlet Temperature	175°C max

To date, the turbine and subsystems needed for operation have been fully commissioned and have undergone multiple laboratory tests with CO_2. This paper discusses results and achievements while also illustrating learnings from operating a high-speed overhung turbine. Further information on the test setup and operating configuration has been previously published (Kerr et al., 2023).

2. Impeller and Machinery Design

Based on the desire to have a machine configuration that could be used in a wide array of operating conditions, the turbine was designed in an overhung configuration, shown in Figure 1, allowing for reduced effort in changing critical turbine components to accommodate different flow designs. One aspect considered in machine design that plays a large role in operation is critical speed of the rotor and impeller assembly. This is the rotational speed of the rotor that matches and excites the natural frequency of the spinning shaft, potentially causing vibration issues in a machine if not well dampened. A design effort was made to keep the nominal operating speed below the rotor critical speed to reduce complexity and avoid having exclusion ranges which affect startup and shutdown scenarios. This was made possible through the design and fabrication of a lightweight titanium impeller.

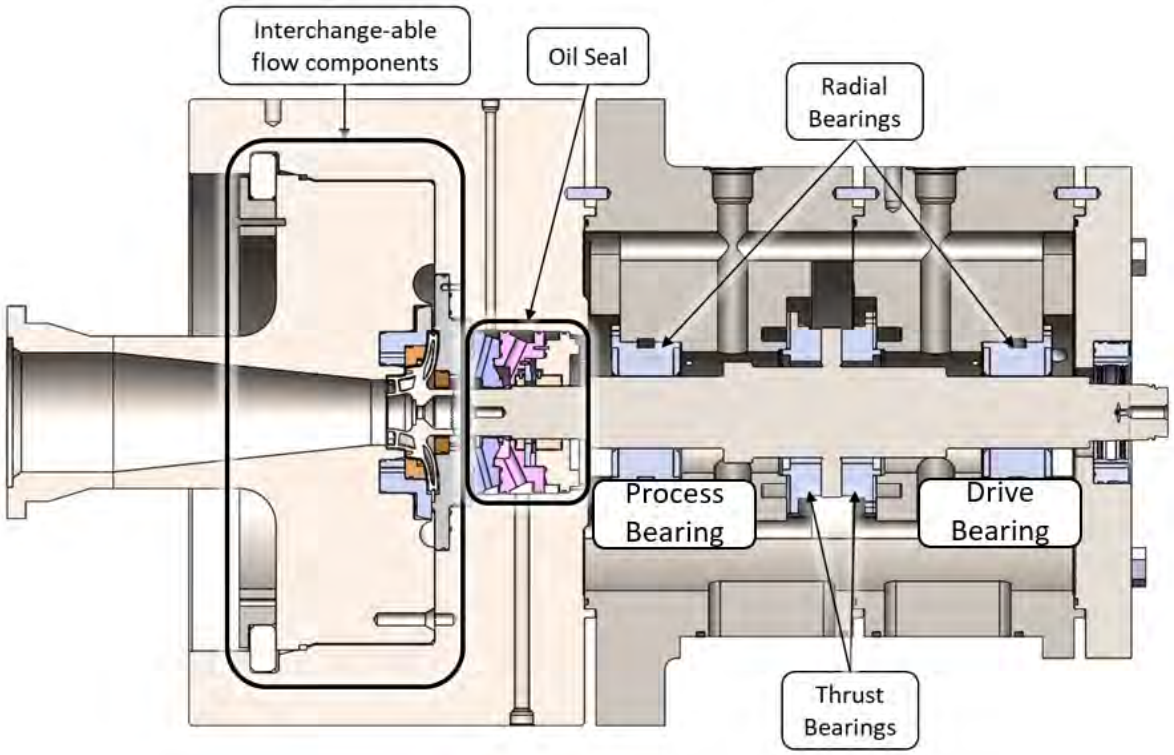

Figure 1. Turbine cross section with key components

The goal of a higher rotor critical speed also affects the design and selection process of the tilting pad radial bearings used in the turbine. Geometric parameters such as clearance ratio and preload, both illustrated in Figure 2, were set accordingly. The selected bearings had a clearance ratio of 1.5 mils per inch and a preload of 0.45, both of which are within typical manufacturer recommended bounds but also different from other tilted pad journal bearings operated at similar speeds in other SwRI designs. The selected bearings also have an integral squeeze film damper (SFD), a system that can provide increased dampening to the rotor supports at the cost of some support stiffness. This feature was intended to be locked/unused for the subcritical speed design to keep bearing stiffnesses high.

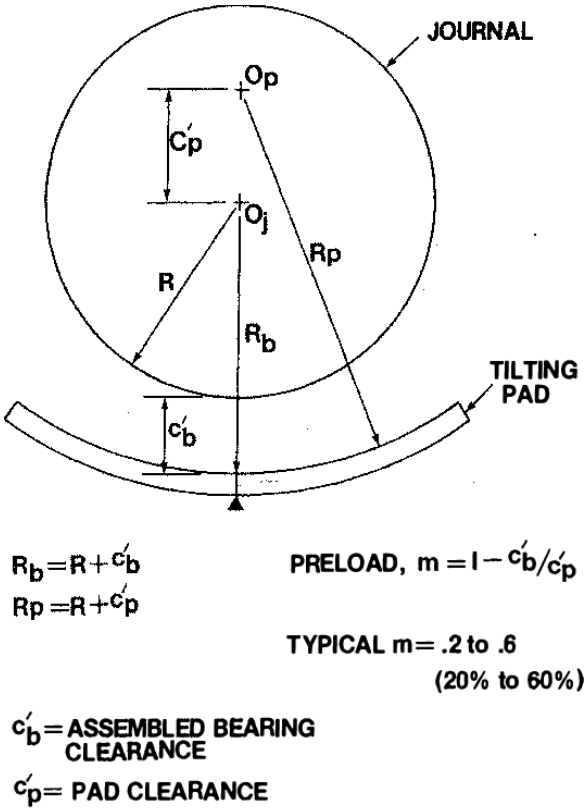

Figure 2. Tilting pad journal bearing geometry parameters (Nicholas, 1994)

The previously published spin test of the turbine using compressed air (Kerr et al., 2023) was with the titanium impeller, however, issues in the print quality and unremovable build support material in the impeller knee area compelled the team to switch to a heavier material with better printing quality experience. The new impeller, made of Inconel, provided a much cleaner finish following subsequent machining and balance efforts. In contrast, the weight increase of the overhung impeller prevented the turbine operational speed from remaining below the new rotor critical speed and required the SFDs be unlocked. This weight change altered the vibration response of the rotor and shifted the critical speed to 10,000 RPM.

Figure 3 shows the initial predictions of the shaft vibration response using the heavier Inconel impeller in conjunction with the SFD's. While the model predicted a low vibration response, the machine would need to be operated in a way to avoid the critical speed during startup and shutdown phases.

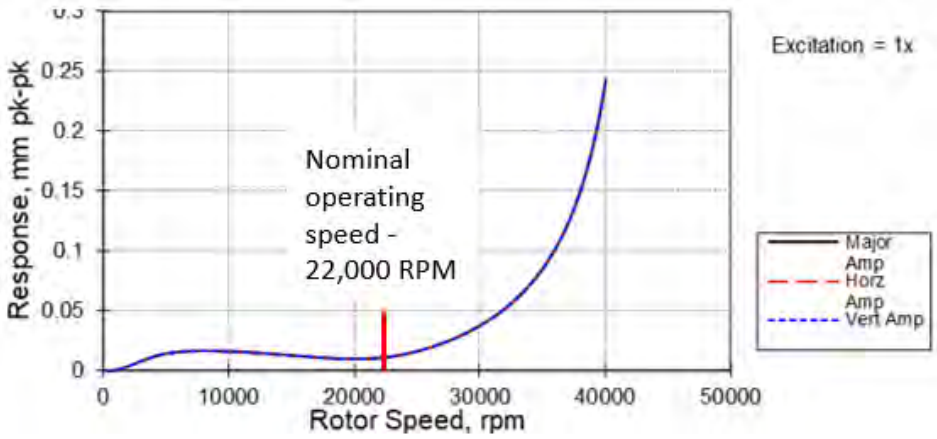

Figure 3. Model prediction of the turbine shaft vibration response

3. Test Plan

With the turbine complete and other systems ready for operation, the original test matrix was reviewed and iterated upon. While the turbine skid includes a 12.233:1 ratio gearbox and 3 MW synchronous generator for electricity production, initial uncoupled (spin) tests were needed to understand the performance of the turbine alone. This also simplified initial tests, allowing SwRI turbine operators to better understand the nuances of the turbine without the additional complexity of the full equipment train. The uncoupled test would also allow for quantifying the frictional losses in the turbine from both windage and drag forces. Following spin testing of the turbine, it will then be coupled to the gearbox and generator. Using a load bank system, the generated power output will be measured and the overall heat-to-electricity efficiency will be determined.

Milestones such as initial spin, bearing break-in, seal break-in, surpassing the critical speed, reaching full temperature, and reaching full speed all needed to be completed to validate the turbine. Each condition met on the test plan aids the SwRI turbine operators in understand how the turbine and subsystems function, and also how the compressor and turbine operate simultaneously in the test.

In the laboratory facility, a multi-stage sCO_2 compressor is used to drive the sCO_2 flow needed to operate the turbine. The SwRI-housed integrally geared compressor, fully tested in recent years (Allison et al., 2018), requires a full-time operator and takes approximately 1 hour to reach full speed from initial startup. The compressor limitations due to its dry gas seals require that compressor inlet pressures remain above 24 bar (350 psi) at full speed. This provides a minimum turbine inlet pressure of approximately 27.5 bar (400 psi) for startups. The abundance of real-time data monitored by SwRI operators, for controlling and analyzing both the compressor and turbine, is depicted in Figures 4 and 5. Over 300 data channels are being recorded in the combined operation. Additional vibration monitoring of both machines is conducted at a third control station by another SwRI test engineer.

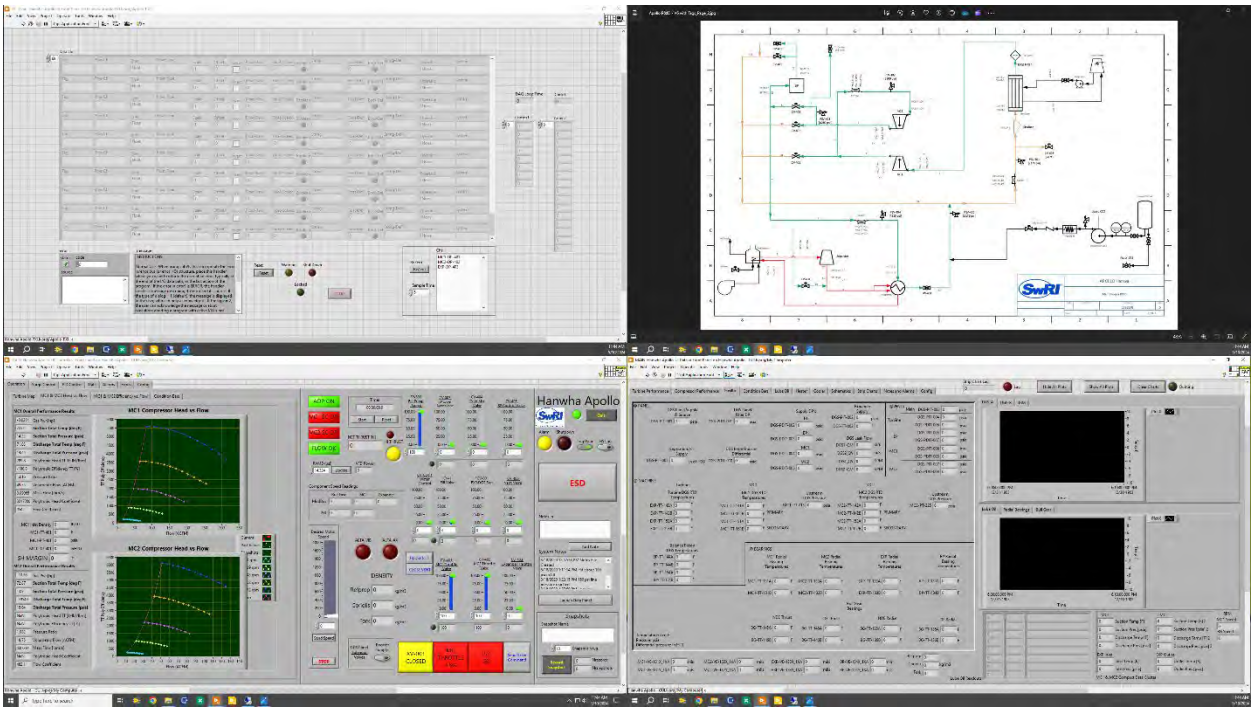

Figure 4. SwRI Operator's view of CO_2 compressor control panel and operating conditions

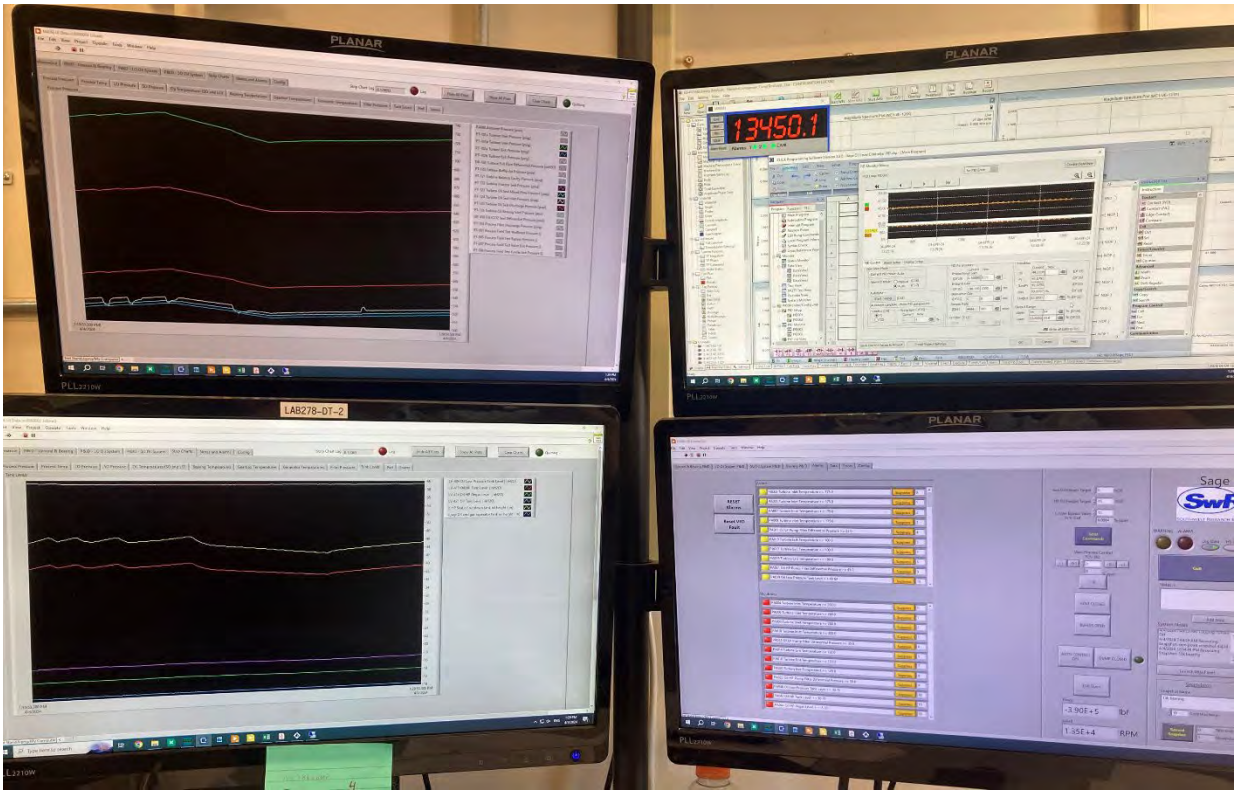

Figure 5. SwRI Operator's view of Sage Geosystems turbine control panel and operating conditions

4. First Startup

As previously published, startup procedures of purging the CO_2 loop and starting the oil seal system and lubrication system were all followed as planned. The first startup of the turbine with CO_2 went well, but operators did experience a high breakaway torque that had to be overcome. Due to the single overhung nature of the design, the pressure forces on the impeller result in a significant axial force against the opposite thrust bearing, keeping lubrication oil from getting between the surfaces. Breakaway torque requirements were estimated to be 10X that of the torque required to keep the rotor spinning after startup. These acting pressure forces can be seen in Figure 6, equating to approximately 350 lbs. per one hundred psi of pressure when stationary.

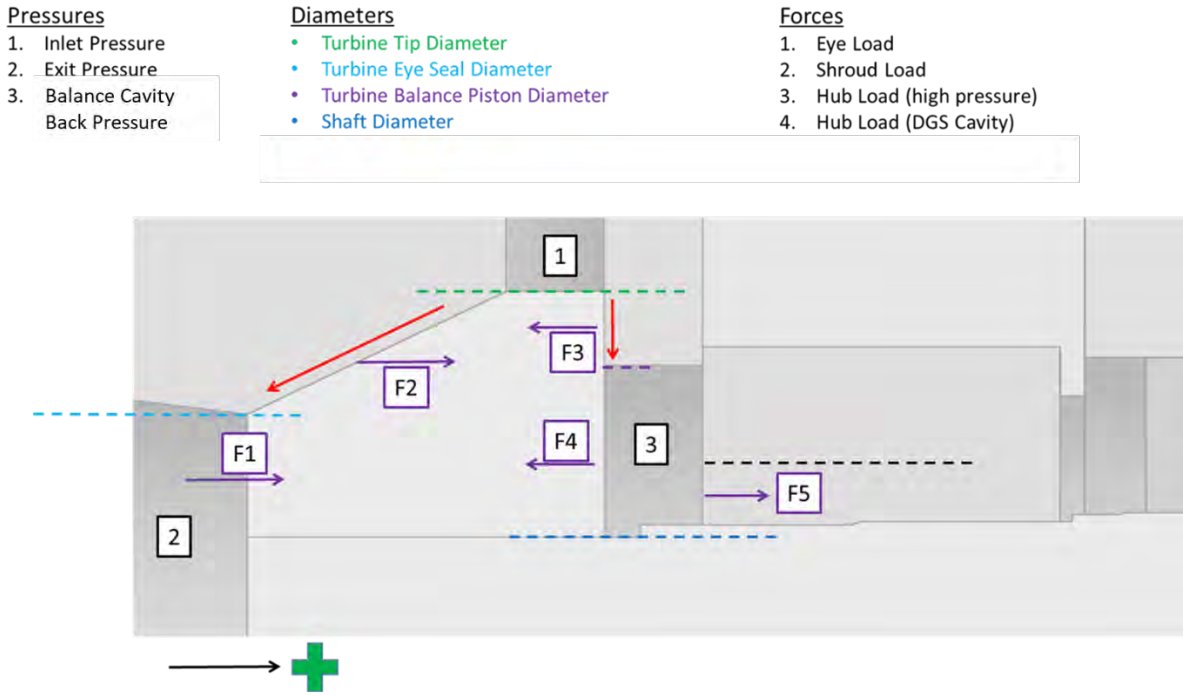

Figure 6. Map of pressure forces on the impeller adding to the thrust load at startup

To overcome the high breakaway torque, the turbine was spun by hand under no flow conditions from the disconnected shaft end. Once spinning, there was enough momentum in the machine to allow personnel to clear the area before introducing CO_2 flow to keep the machine turning.

A CO_2 flow rate of 1.5 lbm/s at 77°C and 31 bar (170°F and 450 psi) was needed to maintain a speed of 2,700 RPM as depicted in Figure 7. Due to the operating principles of hydrodynamic bearings, 2,000 RPM was selected as the lowest continuous speed. While the turbine had previously spun faster in an air spin test, the speed was not maintained long enough due to the limited air volume to achieve steady state performance of the system. The turbine was run at this low idle speed for 15 minutes to allow for bearing temperatures to stabilize while also providing time for monitoring of the oil seal and seal subsystems. Although used in various other machines for decades, this marked the first time a CO_2 machine operated with a floating ring oil seal.

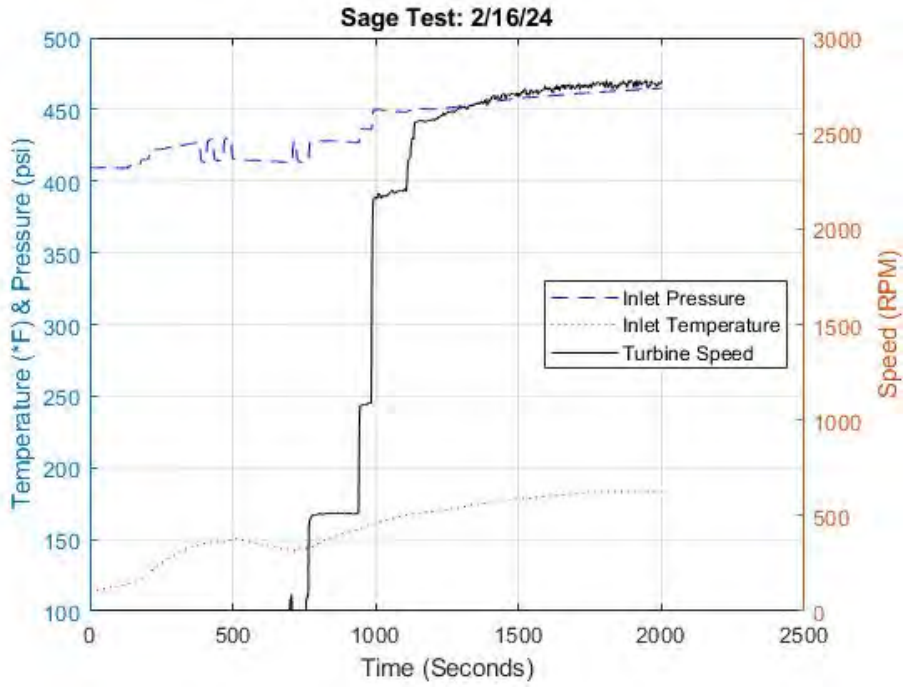

Figure 7. Graphical illustration of the turbines first spin with CO_2

Following the hold at idle speed, flow was gradually increased to speed the turbine up to 4,000 RPM, where it was again allowed to stabilize. Vibration data showed very low synchronous vibrations but did indicate the existence of a sub-synchronous vibration at approximately 40% of running speed. While not alarming at this operating condition, the vibration frequency and characteristics resembled that of floating ring oil seals in other machines (Allaire et al., 1987). Floating ring oil seal operation in other machines and rotordynamic effects have shown that there is a limit on speed at lower pressures. An example plot of this speed limit published by Dresser Rand can be seen in Figure 8.

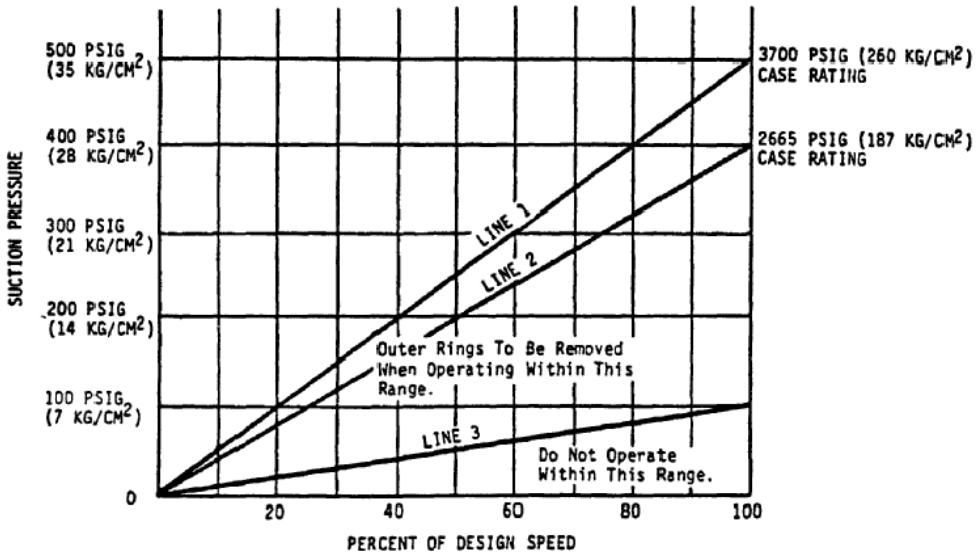

Figure 8. Minimum suggested operating speed versus pressure from literature (Wilcox, 2000)

To continue past 4,000 RPM, CO_2 was added to increase the fluid mass in the loop. This increases pressure and mass flow at a steady rate which also increases speed of the turbine. The slow acceleration (200 RPM per minute) shown in Figure 9 allowed for SwRI operators to continue monitoring of the various subsystems while managing the test.

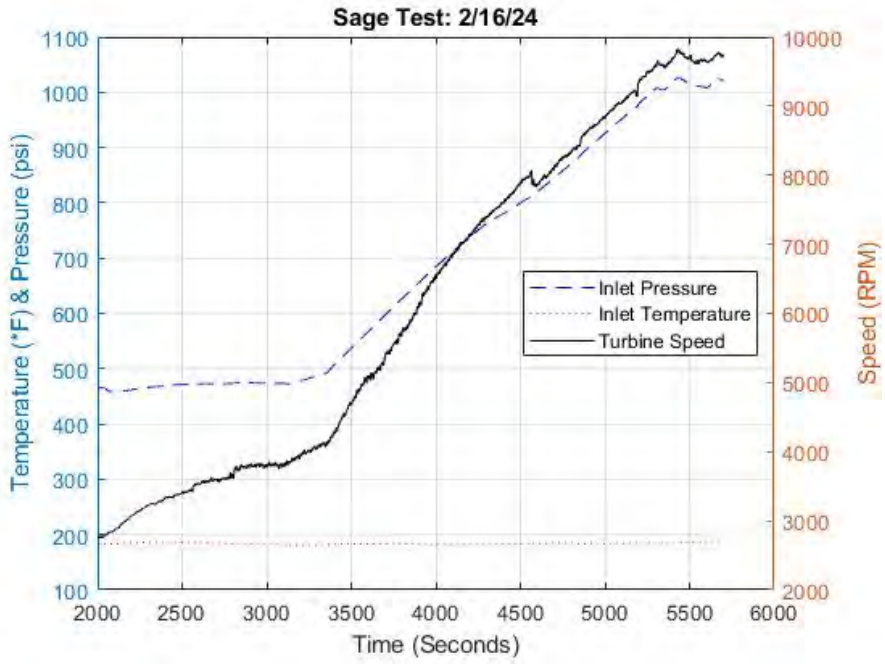

Figure 9. Adding CO_2 to the loop slowly increases pressure and turbine speed.

Upon reaching 9,500 RPM, the process side radial bearing reached a pad temperature of 107°C (225°F), a level that was not at the shutdown limit of 121°C (250°F), but still much higher than the bearings should operate; especially below half speed. To lower the bearing temperatures back to a normal operating range below 93°C (200°F), the turbine speed was reduced and held near 8,000 RPM.

As seen by the bearing temperature and speed plot in Figure 10, there were instances near 8,000 RPM when the process radial bearing temperature would fluctuate 10-15°F rapidly. These changes also correlated to speed change spikes of a few hundred RPM and the appearance and disappearance of sub-synchronous vibrations. All of these are effects of the oil seal rings shifting position which changes the load exerted on the process radial bearing. As expected, less radial load from the oil seals lowered the bearing temperature and increased the turbine speed.

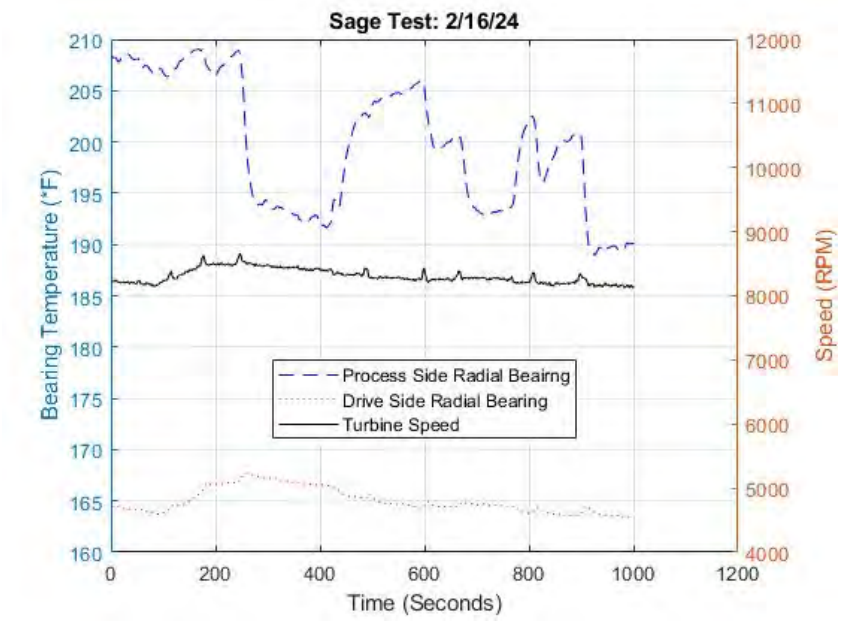

Figure 10. Plot of radial bearing temperatures and spikes in rotation speed caused by the oil seal

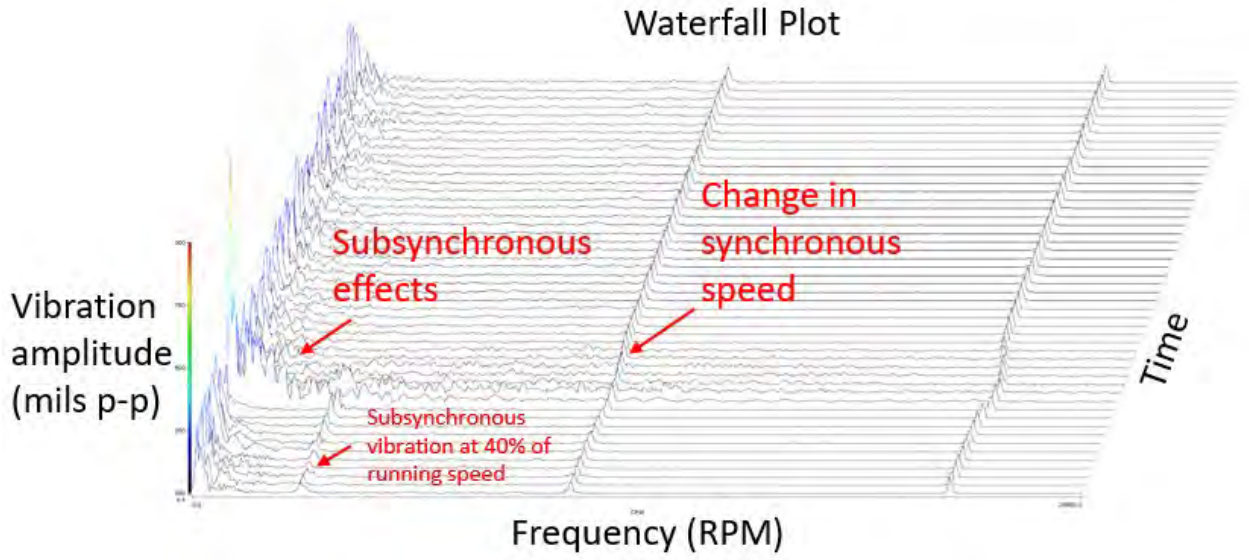

Figure 11. Waterfall plot of the various turbine vibration frequencies during operation

While the maximum speed was limited by the bearing temperatures, operation at full inlet temperature was still achieved during the test. Over a one-hour span of operation, the turbine inlet temperature was increased from 93°C to 150°C (200°F to 300°F) using the heat source, a natural gas burner blowing over an Inconel tube heat exchanger. Full temperature inlet conditions of 150°C (300°F) were maintained for a duration of the test to allow the turbine, casing, and other internal components to reach maximum equilibrium temperature. The full temperature operation also allowed for the team to ensure that the "sour" oil, a mixture of the drain from the oil seal and the process CO_2 buffer flow, was operating at a suitable temperature.

After 4 hours of turbine operation, the turbine was shut down along with the CO_2 compressor system and other subsystems. Project engineers began investigation of the root cause(s) of the high bearing temperature. Based on the data collected for the first test, the high bearing temperatures were the only abnormal condition.

5. Corrective Actions

Following a review of the test data and operating conditions, the turbine was removed from the test stand and disassembled to inspect the rotor and radial bearings. As previously mentioned, the radial bearings had a tighter clearance ratio than other SwRI designs, and while no vibration issues were noticed, the high bearing temperature pointed towards the need to increase clearance between the bearing and rotor. A check of the movement of the rotor in the journal bearing was done to confirm the as-operated clearance. This helped in finalizing further calculations to determine how much material needed to be removed from the rotor bearing journals. Figure 12 shows the directional clearances and flower-shaped support pattern expected for a tilting pad journal bearing with 4 pads.

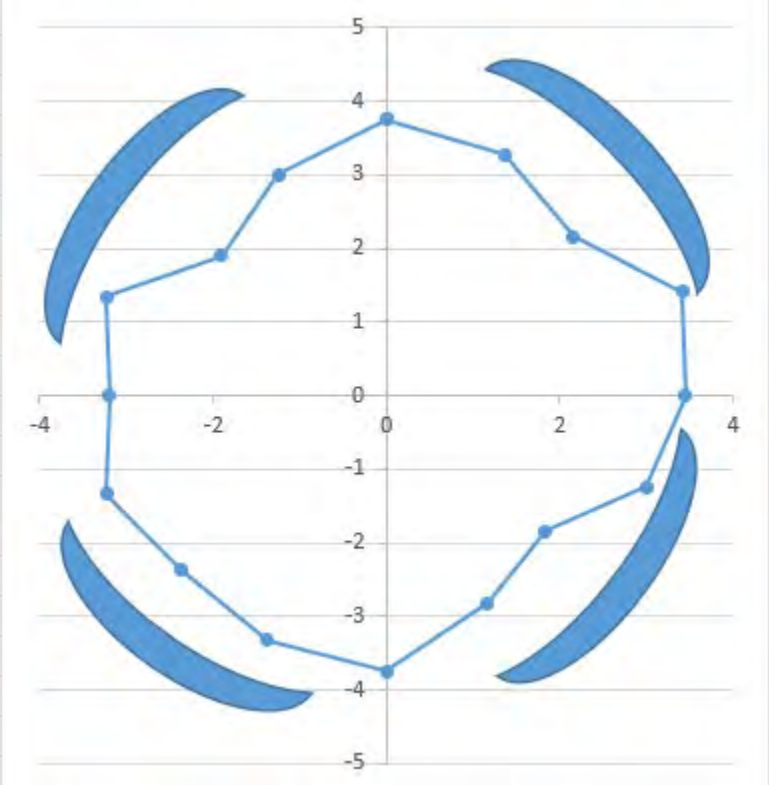

Figure 12. Depiction of process radial bearing clearance with respect to pad orientation

While the journal bearing clearances were being increased, the team evaluated other system changes that were needed. A hydrostatic oil feature was designed and added to the thrust bearing to lessen the breakaway torque mentioned. Targeted startup pressures for the turbine are desired to be above the supercritical level of 73.8 bar (1,071 psi), which would only add to the high breakaway forces from the thrust bearing. Each of the 10 pads that make up the tilting pad thrust bearing were cross-drilled and plumbed with 1/16th-inch tubing to supply high pressure oil,

creating a constant oil film between the rotor thrust disk and bearing. Figure 13 shows the distribution of the oil lines to each drilled pad.

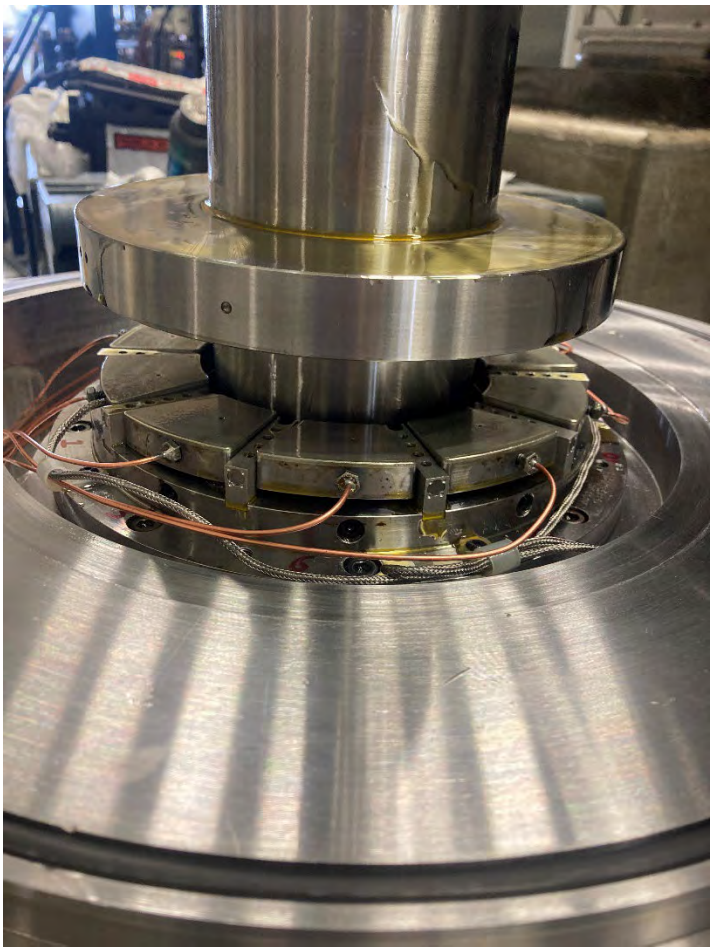

Figure 13. Lines plumbed into each thrust bearing pad to supply hydrostatic jacking oil

While working with the bearing manufacturer on rotordynamic calculations and predictions, SwRI directed the original rotor manufacturer to reduce the bearing journal diameter. This change increased the clearance ratio to 1.9 mils per inch, allowing the bearing temperatures to run at a cooler temperature while maintaining rotordynamic stability. Grinding of the rotor journals was followed by a rebalance of the shaft. The modified components were inspected upon completion, and the turbine was reassembled for further testing. Other internal components were inspected while the machine was disassembled, but no abnormalities were noted.

6. Further Testing

Startup for the second turbine test followed the process used for the first operation. The turbine oil seal system was activated prior to completing purge cycles of the loop to remove all air in the piping system. Following the third purge cycle, the system CO_2 pressure was increased to 220 psi to meet the compressor startup parameters and then further raised to 400 psi at the compressor inlet while the driver was increased to full speed.

Before the second spin of the turbine, bearing lubrication oil was confirmed to be in operational condition, followed by initiating the hydrostatic jacking oil supply to the modified thrust bearing. Figure 14 shows a before and after illustration of the rotor axial position and the approximate 2 mils in which the rotor shifted as a result of the jacking oil. This small gap filled with oil provided the decrease in resistance necessary to eliminate the high breakaway torque. Manual rotation of the turbine was performed under this condition and confirmed that the high breakaway torque was no longer an issue. By already having oil between the thrust disk and bearing pads, starting torque was now estimated at less than 2X the torque required to maintain rotation.

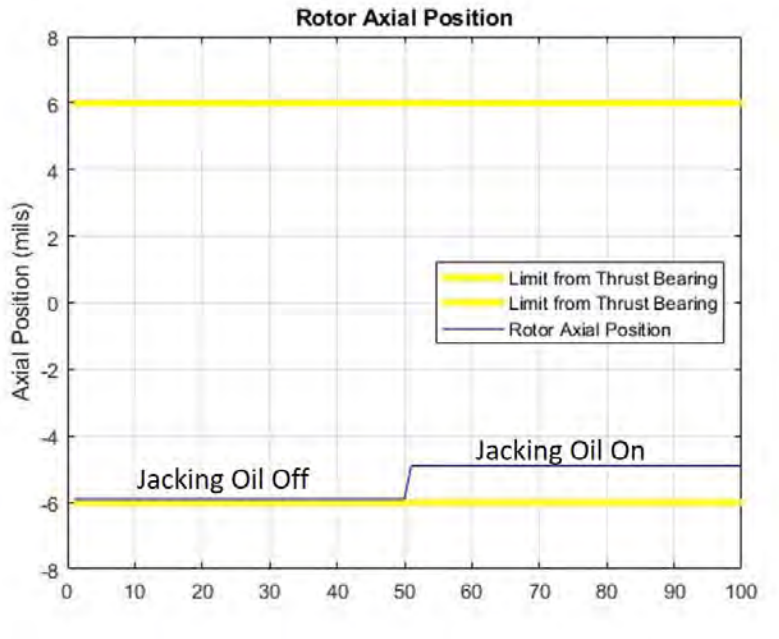

Figure 14. A blue line indicating the rotor axial position shift due to jacking oil. The yellow lines represent the nominal axial limits during operation based on the thrust bearings.

Startup of the turbine occurred at conditions similar to the previous run; turbine inlet of 77°C and 28.8 bar (170°F and 410 psi). There was no need to perform an initial spin by hand to overcome the breakaway torque for this test. Once stable rotation was established, the hydrostatic jacking oil valve was closed to prevent any undesired oil flow in either direction.

Monitoring of the turbine systems, including the bearing temperatures that limited the previous test and vibrations based on the new machine assembly, demonstrated that all operating parameters were closer to the design conditions. Upon reaching 9,500 RPM, the previous maximum speed, bearings temperatures were approximately 35-40°F lower than during previous operation. Synchronous vibrations remained extremely low, showing a good machine balance, however, the small amount of sub-synchronous movement was still present from the oil seals.

The turbine was slowed to adjust the compressor flow conditions to ensure adequate flow was available to surpass the turbine critical speed, with the intent of limiting the time in the 10,000-RPM range. Once the compressor conditions were ready, the turbine was accelerated via a position change of the turbine control valve, up to a speed of 12,000 RPM. At this point, the sub-

synchronous vibrations subsided, and the process end radial bearing temperature decreased again by 35°F as shown in Figure 15.

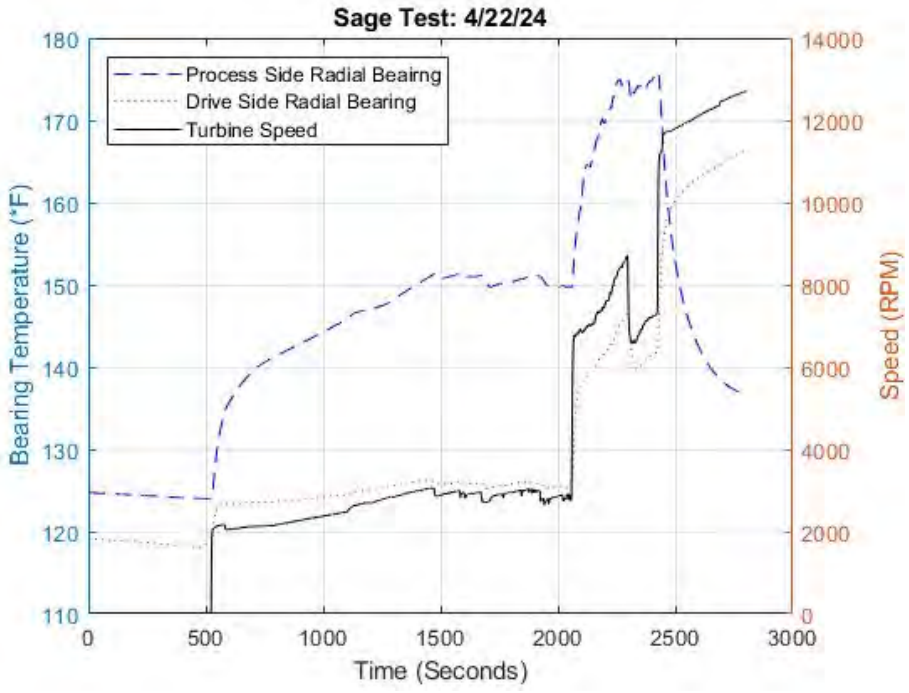

Figure 15. A significant decrease in process radial bearing temperatures occur when the oil seal rings lock in place

These effects can both be contributed to the “locking” of the oil seals in their desired location and lessening the load applied through the rotor to the nearest journal bearing. The new maximum attained speed near 12,000 RPM was held while all systems reached equilibrium. At this point in the test, the system was over half speed and reached that level in less than 40 minutes from initial turbine rotation.

A steady increase in loop pressure after this point provided a steady increase in speed. The heat source flame temperature was increased as well with the increasing flow rate to maintain a stable temperature between 135°C and 150°C (275°F and 300°F) at the turbine inlet. Turbine inlet pressures were increased to 70.7 bar (1,025 psi), resulting in a turbine speed of 18,000 RPM. Turbine discharge pressure at that time was 46.5 bar (675 psi) with all systems running steady. At that point there was a peak in sub-synchronous vibrations, again likely from the oil seal, that caused the machine to trip based on pre-programmed emergency limits set into the control and data acquisition systems.

Testing that occurred on subsequent days allowed for operations between 14,000 and 17,000 RPM but were each halted due to vibrations from the oil seal system. Based on test configurations run throughout each test, it was determined that the seals were not being supplied sufficient seal oil to stay locked at increased speeds. The subsequent achievable speed was lowered by each vibration induced shutdown, indicating that parts of the oil seal were wearing prematurely. This was also confirmed in other literature (Allaire, Kocur, 1985). Oil system modifications, exterior to the turbine, are underway at the time of this publication to ensure additional seal oil can be supplied

and better controlled based on the test learnings. The face seal of each floating ring is being re-machined to provide a better sealing surface.

The system was designed to operate with 10 psi oil pressure differential across the process oil seal. The existing oil seal rundown tank configuration limited the supply to 4.5 psi which lowered the flow through each seal, reducing the stabilizing effects. For further operations, the oil supply pressure will be based on a differential pressure measurement directly at the seal. The rundown tank will stay active for failure or emergency shutdown scenarios, but not dictate the high-pressure supply.

7. Conclusions and Next Steps

The completed operations of the Sage Turbine have been very successful from both operational and design perspectives. Each test has achieved new milestones and brings the technology closer to field-ready status. Improvements to the design include the bearing clearance adjustments as well as addition of the hydrostatic thrust bearing features. Learnings of the free-spinning characteristics and oil seal system operation aspects have been documented and small adjustments are being made to continuously improve the setup.

A final uncoupled (spin) test will be conducted to ensure the turbine is operating as intended, with the various modifications presented, to allow the turbine to reach the full design speed of 22,000 RPM. This is the final milestone before coupling the turbine to the gearbox and generator for load testing. Prior to supplying any excitation current to the generator or turning on the load banks, the full equipment train (turbine, gearbox, and generator) will be operated at full speed to observe and understand the impact of the additional load resulting from the newly-connected equipment.

The sCO_2 turbine load testing will be conducted following the most recent and proven startup procedure used during the spin testing phase. The load testing will be performed in stages to evaluate the turbine's startup performance under higher pressures and will culminate in full supercritical operations above 31°C and 73.8 bar (88°F and 1,071 psi).

Power output up to approximately 500kW is expected from the test impeller considering losses in the rotating equipment at full design conditions. This energy will be absorbed by a load bank connected to the generator and operated in load steps of 5kW. Power output will be monitored and recorded with the generator DECS-150 control system.

These tests will be used as the final data points to show the aerodynamic efficiency of the CO_2 system and how it operates under geothermal conditions. Heat-to-electricity efficiency modeling and calculations at full-scale conditions will also be performed using this data, allowing comparisons of this sCO_2 turbine system to systems in use today for geothermal power generation. Simple impeller changes based on specific well conditions remain a key feature in the modularity of Sage's efficient turbine design. These machinery design and fluid characteristics combined provide a path to lower Levelized Cost of Electricity (LCOE), making geothermal energy cost competitive with other renewable sources.

REFERENCES

Lund, John W. 2004. “100 Years of Geothermal Power Production” *GHC Bulletin, September 2004*

Moore, Jeffrey J., Stefan Cich, Meera Day-Towler, Doug Hofer, Jason Mortzheim. 2018. “Testing of a 10 Mwe Supercritical CO_2 Turbine” *Proceedings of the 47th Turbomachinery Symposium.*

Nielson, Jordan, Douglas Simpkins, Kelsi Katcher. 2022. “Techno-Economic Analysis of a Geothermal sCO_2 Thermosiphon Power Plant, *Proc. Of 7th International Supercritical CO_2 Power Cycles Symposium.*

Nielson, Jordan, Nathan Weiss. 2022. “Sage Geosystems Proprietary sC02 Turbine Flow Loop Testing” *GRC Transactions, 46(GRC1034600)*

Nicholas, John C. 1994. “Tilting Pad Bearing Design” *Proceedings of the 23rd Turbomachinery Symposium.*

Kerr, Thomas, John Klaerner, Jordan Nielson, Nathan Weiss. 2023. “Innovations in Geothermal Power based on the Commissioning and Testing Results of Sage Geosystems’ sCO_2 Prototype Turbine” *GRC Transactions, 47*

Allison, T., Pelton, R., Wilkes, J., Smith, N., Jung, S., 2018, “Experimental Validation of a Wide Range Centrifugal Compressor Stage for Supercritical CO_2 Power Cycles,” Proc. of ASME Turbo Expo 2018, Paper GT2018- 77026, June 11-15, Lillestrom, Norway

Allaire, P., Stroh, C., Flack, R., Kocur, J., and Barrett, L., 1987, “Subsynchronous Vibration Problem and Solution in a Multistage Centrifugal Compressor,” Proceedings, 16th Turbomachinery Symposium, pp. 65–73.

Wilcox, Ed. 2000. “API Centrifugal Compressor Oil Seals and Supporting Systems – Types, Selection, and Field Troubleshooting.” *Proceedings of the 29th Turbomachinery Symposium.*

Allaire, P. E.; Kocur, J. A., Jr., 1985, “Oil Seal Effects and Subsynchronous Vibrations in High-Speed Compressors,” Proc. of the Workshop on Rotordynamic Instability problems, NASA CP XXXX (available on line at NASA publications)

Techno-economic Feasibility of Deep Geothermal Systems in a Low-Enthalpy Reservoir, Western Canada Sedimentary Basin

Leanne Komaromi[1], Roman Shor[2], and Harris Switzman[3]

[1]University of Calgary, Calgary, Alberta, Canada

[2]Texas A&M University, College Station, Texas, USA

[3]The Calgary Airport Authority, Calgary, Alberta, Canada

Keywords

Low-enthalpy geothermal, direct-use heat, techno-economic assessment

ABSTRACT

This study evaluates the techno-economic feasibility of two different deep geothermal system designs for direct-use heating to meet the Calgary Airport Authority's energy demands and support net-zero carbon targets. Geological targets of interest include Upper Devonian carbonates and pre-Cambrian basement rocks, assessed for their geothermal potential and reservoir characteristics. A closed-loop geothermal system in u-loop configuration and an enhanced geothermal system were simulated to compare environmental and economic performance using the GEOPHIRES-X software. Results show that systems deployed at 4 km depth with water as the working fluid have the capacity to reduce 59% of natural gas consumption and abate approximately 396,000 tCO_2-equivalent emissions for YYC over the study period. This research demonstrates the feasibility of deep geothermal systems in low-enthalpy basins within urban centres and highlights important areas for future work to support geothermal development in these basins.

1. Introduction

The Government of Canada has set ambitious net-zero targets for 2050, which have influenced similar targets across the country by provincial governments and industry. As part of an ambitious net-zero strategy, the Calgary Airport Authority (CAA) is exploring behind-the-fence renewable energy generation to integrate with or replace current energy systems at the Calgary International Airport (YYC). YYC is the fourth busiest airport in Canada and as such, operates continuously at full-scale resulting in high energy consumption, emissions, and operating costs. Reliance on the

Alberta grid for electricity and natural gas for heating introduces uncertainty when setting sustainability strategies, in addition to other challenges related to climate risk in the region on a whole.

Calgary, Alberta is situated in a “low-enthalpy” geothermal zone, characterized by a geothermal gradient of approximately 25ºC/km depth. From the Middle Paleozoic to the Precambrian basement (approximately 2.5 to 3.8 km depth), reservoir temperatures are estimated to be 60 to 100 ºC (Majorowicz and Grasby, 2021). Advances in drilling technology and geothermal system efficiencies are increasingly making these low-enthalpy zones, specifically near urban areas, more technically favourable to geothermal development for direct-use heat or electricity generation via organic Rankine cycle turbines. As a reliable, base-load energy source, deep geothermal resource development will be a key piece in driving sustainable growth and meeting commonplace net-zero targets. This study evaluates the techno-economic feasibility of deep geothermal systems for direct-use heating under the low-enthalpy reservoir conditions estimated for YYC.

2. Background

2.1 Calgary International Airport Current Emissions and Energy Demand

On average from 2018 to 2023, the Calgary Airport Authority (CAA) emitted 13,400 tCO_2e of scope 1 emissions and 65,000 tCO_2e of scope 2 emissions (Calgary Airport Authority, 2024). Scope 1 emissions are those generated on-site from activities like burning natural gas or other fuels and scope 2 are associated with using electricity from the local grid. Over the past six years, YYC’s natural gas and electricity demand has averaged about 277,000 GJ and 111,450,000 kWh annually, respectively (Komaromi, 2024).

YYC has two main terminal buildings, the International Terminal Building (ITB) and the Domestic Terminal Building (DTB). Heating for the DTB is provided by a central utilities plant that contains three natural gas power boilers. Two of the original boilers from 1976 are still in operation and a third boiler was added in 2001. There is a combined 30 MW of thermal energy provided by this plant. There is also a geothermal field for the ITB which is currently experiencing performance issues and is not used. Recent engineering assessments found that approximately 54% of natural gas is used for heating and cooling, 5% for domestic hot water, 36% for ventilation (blowers and fans), and the remaining 5% for small equipment like cooking appliances (Komaromi, 2024). Given the current system design and allocation of natural gas, 59% could be replaced with a renewable heat source such as direct-use heat from a deep geothermal system.

The global aviation sector anticipates steady passenger growth over the next decades with an estimated two-fold increase by 2043 (Transport Canada, 2022; International Air Transport Association, 2024). As the fourth largest airport in Canada, YYC expects to experience similar growth in passenger numbers and will need to accommodate this through facility expansion. Additionally, electrification of transportation is increasing demand for electric vehicle charging infrastructure (Komaromi, 2024). YYC is facing the challenge of meeting these demands while striving for more sustainable operations and meeting net-zero by 2050 targets. Deep geothermal development is being assessed as part of a broad net-zero pathway and decarbonization roadmap which looks to integrate building efficiency upgrades with renewable energy technology to provide a secure, carbon-neutral energy supply and enhanced climate-resiliency.

2.2 Geology of the Western Canada Sedimentary Basin

The Western Canada Sedimentary Basin is a massive wedge-shaped package of sedimentary deposits extending from the Rocky Mountains to the Canadian Shield. In the deepest part of the basin along the Rocky Mountain deformation belt, it is approximately 5 km thick. The sedimentary succession of the WCSB lies unconformably on the pre-Cambrian basement. The Paleozoic to Middle Jurassic interval is primarily shallow marine deposition with carbonates, evaporites, and terrigenous shales (Mossop and Shetsen, 1994) while the Devonian succession is characterized by carbonate platforms deposited during subtropical, open-marine conditions. The Devonian succession is subdivided into four groups: the Beaverhill Lake Group, the Woodbend Group, the Winterburn Group, and the Wabamun Group (Mossop and Shetsen, 1994). Due to their geothermal potential (Weydt et al., 2018; Majorowicz and Grasby, 2021) and lateral extent below Calgary, the Woodbend Group and pre-Cambrian basement are of particular interest for this study.

The Cooking Lake Formation carbonate platform and overlying Leduc Formation reefs of the Woodbend Group have well documented potential for geothermal development. The Cooking Lake Formation forms an approximately 75 m thick platform that the Leduc Formation reefs built upon, reaching thicknesses of approximately 250 m in some areas (Mossop and Shetsen, 1994). The Leduc Formation reefs are surrounded by Duvernay, Majeau Lake, and Ireton formation shales. The reefs have an average porosity of approximately 8%, reservoir permeability of 10^{-12} to 10^{-15} m^2, and thermal conductivities ranging from 3 to 5 W/m K (Weydt et al., 2018). Hydrologically, the aquifers belong to the Upper Devonian Hydrogeological Group which consists of four aquifers, separated by laterally discontinuous aquitards. The Leduc Formation is a historic hydrocarbon reservoir in the WCSB with some of the provinces' most prolific pools and production dating back to 1947 (Chow et al., 1995).

The pre-Cambrian basement is not as well studied as the overlying sedimentary units, particularly under the deepest parts of the basin in the western part of the province where the study area is. Generally, the basement is composed of crystalline igneous and metamorphic rock types that vary spatially with evidence of deformation and recrystallization (Burwash et al., 1994).

2.3 Geothermal gradient and temperature

The Precambrian basement has significant influence over the thermal conditions and heat distribution of the WCSB (Majorowicz and Grasby, 2020). In the thickest parts of the basin, temperatures are highest and range from around 110 to 120ºC. Majorowicz and Grasby (2020) estimate maximum temperatures of approximately 170ºC in the northwest part of the province. The study area at Calgary, AB has temperatures ranging from approximately 70 to 100ºC depending on the target formation.

The geothermal gradient is a function of heat flow and thermal conductivity and varies laterally across the WCSB. The highest vertical temperature gradients, approximately 40 to 55ºC/km, occur in the sparsely populated northern part of Alberta. In the southwest where the study area is, the gradient is estimated to be about 25 to 30ºC/km (Majorowicz and Grasby, 2020).

2.4 Advances in geothermal drilling

The cost of exploration and drilling in geothermal development is a major component of capital costs of projects. Drilling often occurs under challenging conditions including borehole instability,

ultra-high strength rocks (e.g. crystalline granites), and high subsurface temperatures that can exceed temperature limits of drilling and completions tools. Recently, demonstrations by the Frontier Observatory for Research in Geothermal Energy (FORGE) and Fervo showed that enhanced geothermal systems (EGS) can successfully be drilled in hot, dry granites with significant reductions in drilling time which translates to lower capital costs (Sugiura et al., 2021; El-Sadi et al., 2024).

At the Eavor-Deep project in New Mexico, insulated drill pipe technology was field tested and demonstrated the ability to use existing bottom-hole assembly tools for drilling and completions in high-temperature rocks. The ability to apply existing drilling technology to exploit geothermal resources will enable hotter, more economically feasible configurations (Brown et al., 2023; Vetsak et al., 2024).

3. Methodology

To assess the techno-economic feasibility of deep geothermal development at the Calgary International Airport (YYC), a business-as-usual scenario was modelled to compare the energy and resulting emissions performance of deep geothermal systems. To establish estimated formation depths and reservoir rock properties, a subsurface assessment was conducted and the results were used in subsequent geothermal systems modelling (Komaromi, 2024). Data sources include internal YYC reports and documents, publicly available well logs, and other literature.

GEOPHIRES-X, a techno-economic simulator developed for geothermal system application, was used to model reservoir, wellbore, and surface plant performance and costs (Beckers, 2016; Beckers & McCabe, 2019). Two designs for direct-use heating were assessed, both using water as the working fluid: an EGS and a closed-loop geothermal system (CLGS) in u-loop configuration. The estimated geologic properties for the Leduc Formation and the pre-Cambrian granite in the WCSB were incorporated into the model for simulations run at 3 km depth and 4 km depth, respectively. Appendix tables A-1 to A-4 summarize the parameters used in the geothermal systems modelling.

4. Results

4.1 Well log analysis

Based on the well log analysis of formation tops in the study area, the Leduc formation is estimated to be approximately 200 m thick and 3000 m deep below Calgary. The basal Cambrian sandstone (BCS) overlying the pre-Cambrian basement is estimated to be 3200 m deep. There were no wells in the study area that fully penetrated the BCS so thicknesses could not be determined as part of well log analysis. However, the BCS is documented throughout the WCSB as having a thickness ranging from 40 to 80 m (Alberta Geological Survey, 2024). There was only one well in the eastern portion of the assessed area that fully penetrated the Leduc Formation, and it showed a thickness of 128.4 m. This is in line with regional thinning of sedimentary successions from west to east in the WCSB (Komaromi, 2024).

All the wells in the study area had recorded bottom-hole temperatures (BHT) that were used to estimate temperatures in the subsurface. For BHTs recorded in the Leduc Formation, temperatures range from 141ºC to 61ºC and with an average of 84.6ºC. BHTs recorded in the BCS ranged from

86ºC to 52ºC and had an average of 74.3ºC (Komaromi, 2024). It should be noted that all wells used in this study were drilled for oil and gas exploration with some dating as far back as 1951. Therefore, BHT recordings may not accurately reflect the geothermal conditions in the reservoir.

Only one well in the study area had recorded gas analysis data. Analysis was done higher up in the succession in the Wabamun Formation at an interval from 2500 m to 2520 m and shows 0.1227 ppm of hydrogen sulphide gas (Komaromi, 2024).

4.2 GEOPHIRES simulation results

Two geothermal systems were simulated at two target depths using GEOPHIRES-X based on the estimated subsurface parameters and rock properties. All systems were simulated using water as the working fluid, with a geothermal gradient of 25°C/km, and with an injection temperature of 40°C. At 3 km depth, geology-specific parameters used were based on lithological properties of dolomite: reservoir heat capacity of 920 J/kg/K, reservoir density of 2900 kg/m3, and reservoir thermal conductivity of 5.3 W/m/K. At 4 km depth, geology specific parameters were set based on lithological properties of granite: reservoir heat capacity of 790 J/kg/K, reservoir density of 2650 km/m^3, and reservoir thermal conductivity of 3.5 W/m/K. For the EGS, reservoir porosity and permeability were set at 20% and 1e-15 m^3, respectively, and with one production and one injection open hole wellbores. The CLGS was configured with two, 1 km multilaterals for a total of 2000 m of non-vertical length.

4.2.1 Enhanced geothermal system results

The EGS modelled at 3 km depth has an average heat production of 8.57 MW_{th} and an average production temperature of 76.6 °C. This is equivalent to approximately 285,000 GJ of heat provided annually. Figure 1 shows the production temperature and heat production over time for the EGS system at 3 km depth. Based on default GEOPHIRES-X parameters, the total capital cost is estimated to be $22.18M and operating costs are $1.01M annually. The results of the simulated EGS at 3 km depth are presented in Table 1.

When modelled for 4 km depth and the lithologic properties of granite, the EGS system has an average heat production of 11.78 MW_{th} and an average production temperature of 91.7 ºC, or approximately 376,000 GJ of heat annually, on average. Figure 2 shows the results of the simulated EGS over time at 4 km depth. The capital cost of this system is estimated at $31.32M with an annual operating cost of $1.4M. Table 1 provides a summary of the results for the simulated EGS at 4 km depth.

4.2.2 Closed-loop geothermal system results

The CLGS modelled at 3 km depth has an average heat production of 7.18 MW_{th} and an average production temperature of 68.0 °C. Figure 3 shows these results. The total capital cost is estimated to be $28.93M and operating costs are $0.6M/year, based on the GEOPHIRES default parameters. The results for the CLGS at 3 km depth can be found in Table 2.

At 4km depth, the CLGS has an average heat production of 7.83 MW_{th} and average production temperature of 70.7 ºC, giving approximately 224,000 GJ/ year in produced heat. Figure 4 shows these results. The estimated capital cost of this system is $40.72M while the operating cost is $0.99M/year. Table 2 summarizes the results of the CLGS at 4 km depth.

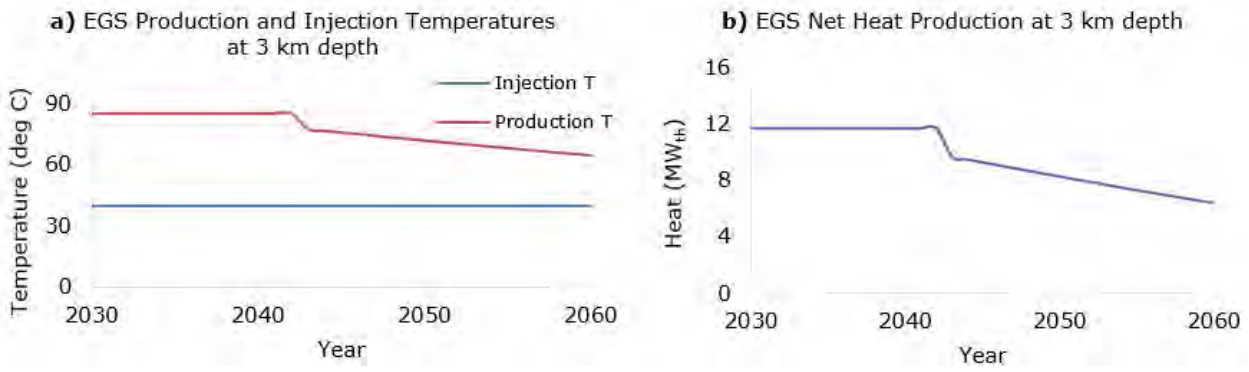

Figure 11: Simulation results for enhanced geothermal system at 3 km depth with one injection and one production wellbore. a) Production and Injection temperature results; b) Net heat production results.

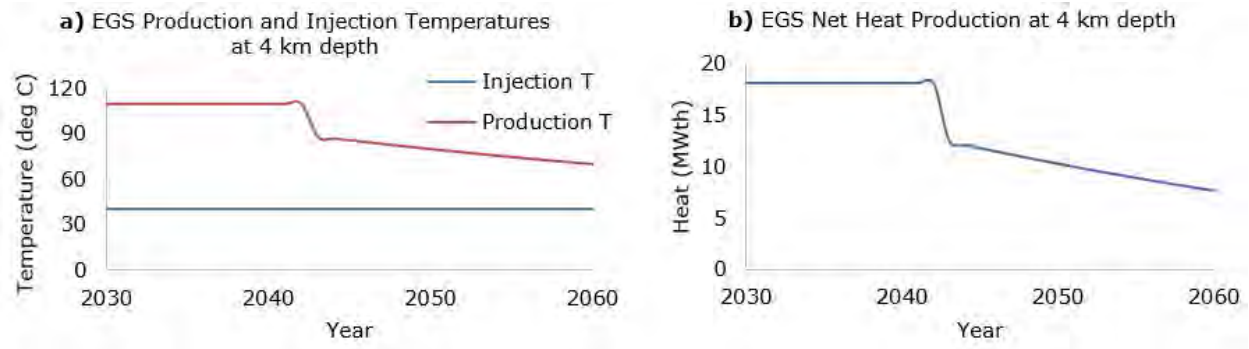

Figure 22: Simulation results for enhanced geothermal system at 4 km depth with one injection and one production wellbore. a) Production and injection temperature results; b) Net heat production results.

Table 1: Simulation results for enhanced geothermal systems at 3 km and 4 km depths.

Enhanced Geothermal System for Direct-use Heating (3 km depth)	
Average net heat production	8.57 MW_{th}
Average net annual heat provided	74.5 GWh/year
Average geofluid production temperature	76.6 ºC
Total capital costs	$22.18/M
Total annual operating costs	$1.01M/year
Levelized cost of heat	$9.91/MMBTU
Enhanced Geothermal System for Direct-use Heating (4 km depth)	
Average net heat production	11.78 MW_{th}
Average net annual heat provided	74.5 GWh/year
Average geofluid production temperature	91.6 ºC
Total capital costs	$31.32/M
Total annual operating costs	$1.4M/year
Levelized cost of heat	$9.57/MMBTU

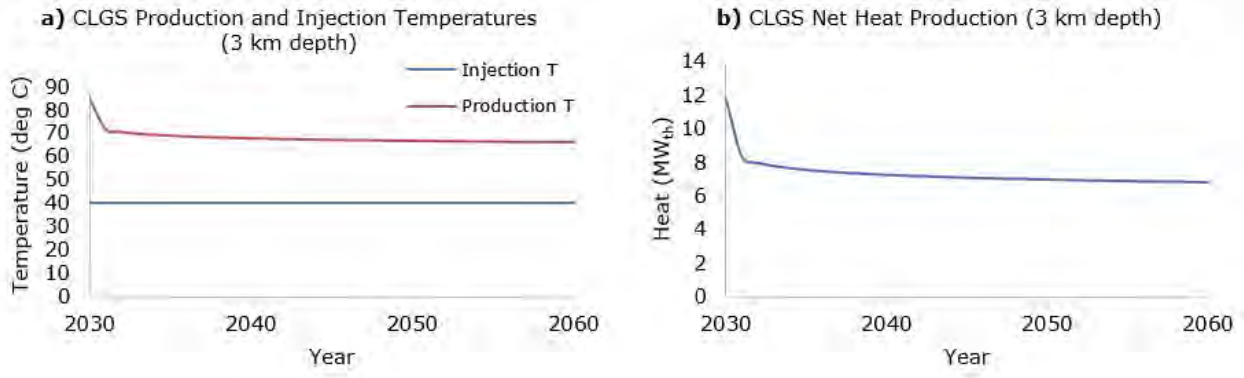

Figure 3: Simulation results for closed-loop geothermal system in u-loop configuration at 3 km depth with two, 1 km multilaterals. a) Production and Injection temperature results; b) Net heat production results.

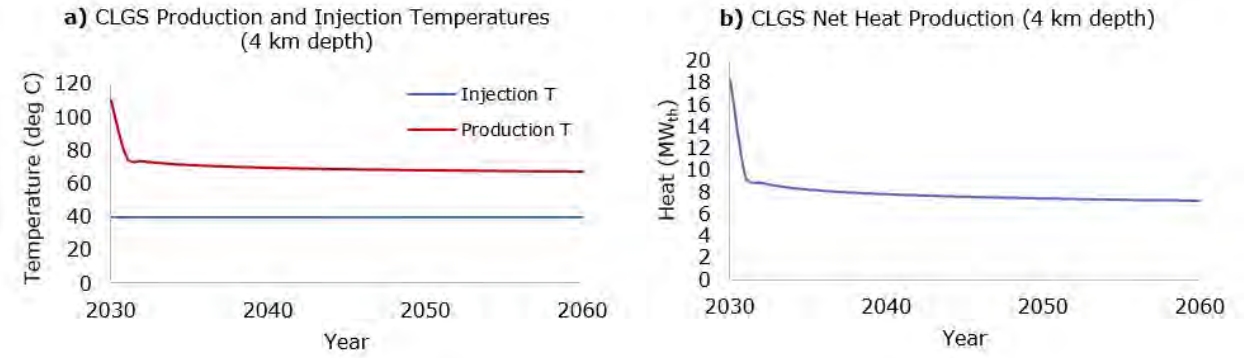

Figure 4: Simulation results for closed-loop geothermal system in u-loop configuration at 4 km depth with two, 1 km multilaterals. a) Production and Injection temperature results; b) Net heat production results.

Table 2: Simulation results for closed-loop geothermal system designs at 3 km and 4 km depths.

Closed-loop Geothermal System for Direct-use Heating (3 km depth)	
Average net heat production	7.18 MW_{th}
Average net annual heat provided	57.0 GWh/year
Average geofluid production temperature	68.0 ºC
Total capital costs	$28.93M
Total annual operating costs	$0.6M/year
Levelized cost of heat	$13.98/MMBTU
Closed-loop Geothermal System for Direct-use Heating (4 km depth)	
Average net heat production	7.83 MW_{th}
Average net annual heat provided	61.97 GWh/year
Average geofluid production temperature	70.1 ºC
Total capital costs	$40.72M
Total annual operating costs	$0.99M/year
Levelized cost of heat	$15.51/MMBTU

4.3 Energy and environmental performance

For either a CLGS or EGS at 4 km depth, the entire 59% of business-as-usual natural gas consumption for heating and domestic hot water can be replaced with direct-use heat from geothermal resources. This is equivalent to a reduction in approximately 7.8M GJ of natural gas over the entire study period from 2030 to 2060 and results in approximately 396,000 tCO_2e emissions abated.

At 3 km depth, the forecasted natural gas demand will exceed the annual heat production of the EGS around 2056 and the CLGS around 2053, by a very small margin.

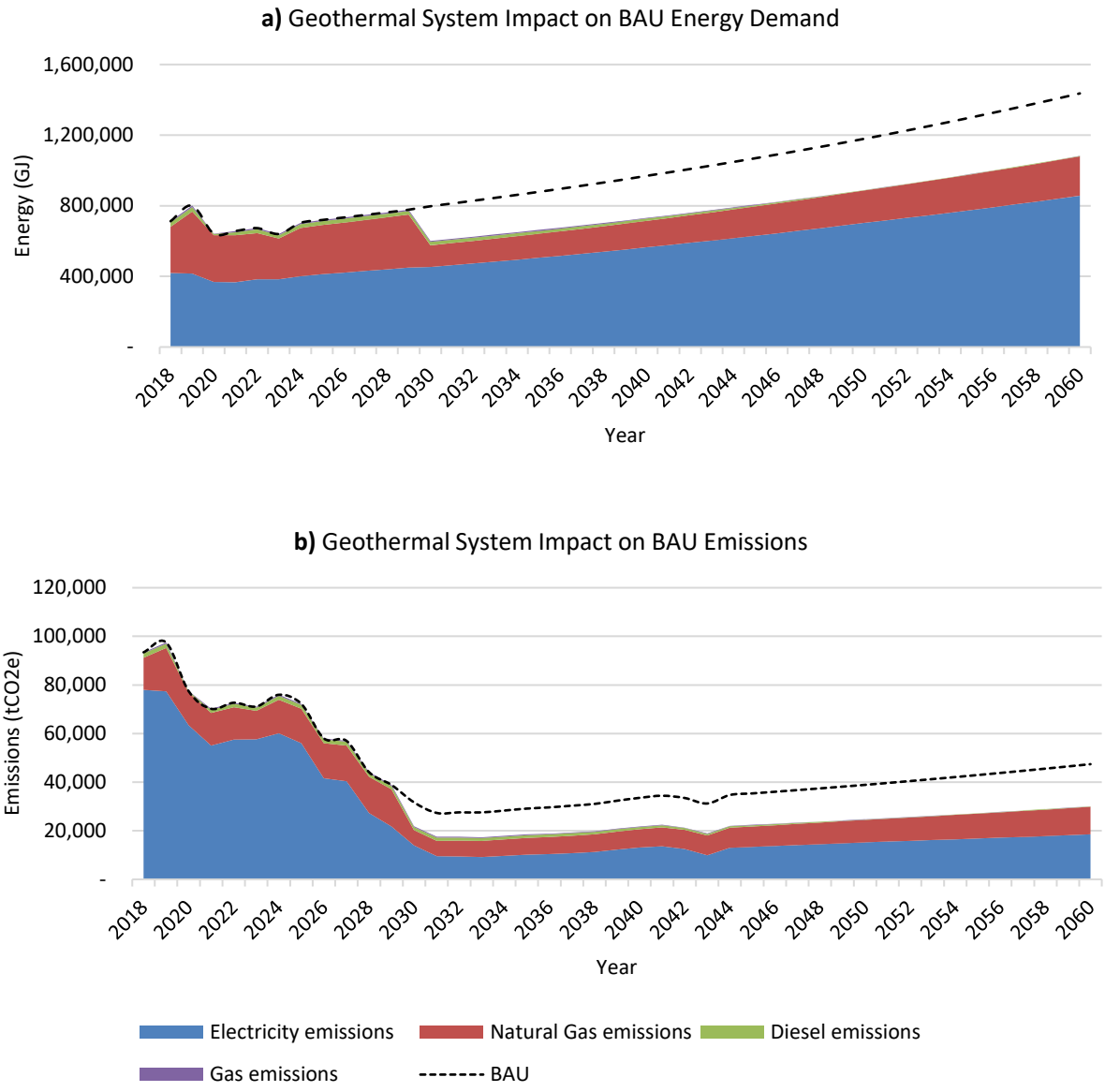

Figure 55: Energy and emissions reduction from business-as-usual forecast for either EGS or CLGS at 4 km depth. a) Reduction in natural gas consumption off business-as-usual forecasted values; b) Emissions abatement from geothermal system off business-as-usual forecast (adapted from Komaromi, 2024).

5. Discussion

Exploitation of low-enthalpy geothermal resources near urban centres could be critical for supporting net-zero carbon targets due to geothermal energy's ability to provide baseload, reliable power and replace high emitting fuels like natural gas for heating. This study assessed the techno-economic feasibility of either an enhanced geothermal system or a closed-loop geothermal system at two different target depths under the estimated reservoir conditions in Calgary, Alberta to support the net-zero targets of the Calgary International Airport (YYC). Results show that at 3 km depth, either an EGS or CLGS can meet the energy demand of YYC for the beginning of the study period, however, after about 25 years of production, thermal draw down along with increasing demand due to business growth led to a deficit in heat production.

At 3 km depth, the target sedimentary unit would be the Leduc Formation. This is a well-documented oil and gas reservoir that has been producing in the region since the late 1940s. However, spatial distribution of these hydrocarbon reservoirs is complex and there are also documented brine and water reservoirs. While co-production of geothermal fluids and hydrocarbons is technically feasible and demonstrated as commercially viable, for YYC the goal is simply decarbonization via deep geothermal system development and co-production of hydrocarbons lies outside of their interests. Additionally, the Leduc Formation and overlying sediments are known to contain hydrogen sulfide gas. Since YYC is situated within an urban area, hydrogen sulfide release would be dangerous, costly, and could have far reaching impacts beyond just the operation of the airport. Therefore, an EGS system in the Leduc Formation dolomites carries higher risk of encountering hydrocarbons or H_2S than a CLGS due to the necessary production of subsurface brines in an EGS system. These risks emphasize the importance of further exploration and research into the subsurface conditions at YYC to better characterize reservoir conditions.

By drilling to 4 km depth into the pre-Cambrian crystalline basement rocks, the risk of hydrocarbon co-production is much lower than in the Leduc Formation, however drilling becomes more challenging and costly. Additionally, stimulation at these depths for an EGS development is more technically challenging than would be in the sedimentary overlying rocks. However, heat production from either an EGS or CLGS in the pre-Cambrian basement would be more than sufficient to meet current and future energy demand of YYC.

The levelized costs of heat (LCOH) were calculated using default parameters in GEOPHIRES-X. This allows comparison on a relative scale only where the EGS systems at both 3 and 4 km depths have lower LCOH due to lower capital costs and higher heat production. However, if an EGS system were to be drilled within the Leduc Formation, additional infrastructure for mitigating co-produced gas risk would likely be required and was not accounted for here. For all systems, the cost of weatherization to protect surface equipment from the very cold winter temperatures also would need to be assessed. Additionally, further assessment of existing infrastructure at YYC and the viability of integrating with a deep geothermal system will need to be analyzed in detail to establish more certain cost figures.

Ultimately, there are risks and rewards for each chosen subsurface depth and for each design of geothermal system. Given the risk of hydrocarbon and H_2S gas in the Leduc Formation, an EGS at this interval may be the least feasible option for YYC despite sufficient heat production for at least the next 25 years, based on the models. A CLGS in the Leduc Formation would carry less

operational risk of co-produced gases but the additional cost for lower heat production, makes this a less attractive option. If capital allows, a CLGS at 4 km depth carries the lowest operational risk and will provide enough heat to meet the growing needs of YYC until at least 2060 with abated emissions significantly helping YYC to achieve their net-zero targets.

6. Conclusions

The techno-economic feasibility of deep geothermal systems at the Calgary International Airport were assessed based on the estimated subsurface conditions. Results show that economically, an EGS system at 3km depth could sufficiently meet the energy needs of YYC for the next 25 years based on business-as-usual forecasting and simulations run in GEOPHIRES-X. However, in considering operational risk due to hydrocarbons in the sedimentary units, an EGS or CLGS at 4 km depth is favourable. Subsurface conditions below YYC are not well known and this study demonstrates the need for additional research with the end-goal being a science well drilled on YYC property. Overall, a deep geothermal system to support the net-zero targets of YYC is shown to be both technically and economically feasible.

Acknowledgement

This work was supported by the Calgary Airport Authority and the Energi Simulation Centre for Geothermal Systems Research at the University of Calgary.

REFERENCES

Beckers, K. F., & McCabe, K. (2019). GEOPHIRES v2.0: updated geothermal techno-economic simulation tool. *Geothermal Energy*, *7*(1). https://doi.org/10.1186/s40517-019-0119-6

Brown, C. A., Holmes, M., Zatonski, V., & Toews, M. (2023). Enablement of High-Temperature Well Drilling for Multilateral Closed-Loop Geothermal Systems. *48th Workshop on Geothermal Reservoir Engineering*.

Burwash, R. A., McGregor, C. R., & Wilson, J. (1994, July 14). *Chapter 5 - Precambrian Basement*. Alberta Geological Survey. https://ags.aer.ca/atlas-the-western-canada-sedimentary-basin/chapter-5-precambrian-basement

Calgary Airport Authority. (2024). *Sustainability Strategy 2022-2026*. YYC Sustainability Strategy. https://www.yycsustainability.com/climate-action/#1.1

Chow, N., Wendte, J., & Stasiuk, L. D. (1995). Productivity Versus Preservation Controls on Two Organic-Rich Carbonate Facies in the Devonian of Alberta: Sedimentological and Organic Petrological Evidence. *Bulletin of Canadian Petroleum Geology*, *43*(4), 433–460. https://doi.org/10.35767/gscpgbull.43.4.433

El-Sadi, K., Gierke, B., Howard, E., & Gradl, C. (2024). Review Of Drilling Performance In A Horizontal EGS Development. *49th Workshop on Geothermal Reservoir Engineering*. 49th Workshop on Geothermal Reservoir Engineering.

International Air Transport Association. (2024). *Global Outlook for Air Transport - Deep Change*. https://www.iata.org/en/iata-repository/publications/economic-reports/global-outlook-for-air-transport-june-2024-report/

Komaromi, L. (2024). *Techno-economic feasibility study for a deep geothermal system at the Calgary International Airport*.

Majorowicz, J. A., & Grasby, S. E. (2020). Heat transition for major communities supported by geothermal energy development of the Alberta Basin, Canada. *Geothermics*, *88*, 101883. https://doi.org/10.1016/j.geothermics.2020.101883

Majorowicz, J., & Grasby, S. E. (2021). Deep Geothermal Heating Potential for the Communities of the Western Canadian Sedimentary Basin. *Energies*, *14*(3), 706. https://doi.org/10.3390/en14030706

Mossop, G., & Shetsen, I. (1994). *Geologic atlas of the Western Canada Sedimentary Basin*. Canadian Society of Petroleum Geologists and Alberta Research Council. https://ags.aer.ca/reports/atlas-western-canada-sedimentary-basin

Sugiura, J., Lopez, R. E., Borjas, F., Jones, S., McLennan, J., Winkler, D. D., Stevenson, M., & Self, J. (2021). Oil and Gas Drilling Optimization Technologies Applied Successfully to Unconventional Geothermal Well Drilling. *SPE Annual Technical Conference and Exhibition*. https://doi.org/10.2118/205965-ms

Transport Canada. (2022). *Canada's Aviation Climate Action Plan*.

Vetsak, A., Besoiu, C., Zatonski, V., Torre, A., Hodder, M., & Toews, M. (2024). The Insulated Drill Pipe - Field Experience and Thermal Model Validation. *International Drilling Conference and Exhibition*. https://doi.org/10.2118/217753-ms

Weydt, L. M., Heldmann, C.-D. J., Machel, H. G., & Sass, I. (2018). From oil field to geothermal reservoir: assessment for geothermal utilization of two regionally extensive Devonian carbonate aquifers in Alberta, Canada. *Solid Earth*, *9*(4), 953–983. https://doi.org/10.5194/se-9-953-2018

APPENDIX

Table A-1: Techno-economic assessment input parameters to GEOPHIRES-X for EGS at 3 km depth and direct-use heating end-use.

Input Parameters	Value
Reservoir Simulation	
Reservoir Model	1-Dimension Linear Heat Sweep
Reservoir Depth	3 km
Gradient	25 ºC/km
Reservoir Volume Option	Reservoir volume only
Reservoir Volume	1.00E+09
Reservoir Impedance	0.2 GPa*s/m3
Injection Temperature	40 ºC
Reservoir Heat Capacity	920 J/kg/K
Reservoir Density	2900 kg/m^3
Reservoir Thermal Conductivity	5.3 W/m/K
Reservoir Porosity	0.2
Reservoir Permeability	1.00E-15 m^2
Wellbore Simulation	
No. of Production and Injection Wells	1
Production and Injection Well Diameter	8 inches
Ramey Production Wellbore Model	False
Production Flow Rate per Well	70 kg/s
Production Wellbore Temperature Drop	5 ºC
Surface Plant Simulation	
End-Use Option	Direct-use heat
Utilization Factor	0.9
Surface Temperature	15 ºC
Plant Lifetime	40 years
Economic	
Exploration Capital Cost	$0

Table A-2: Techno-economic input parameters to GEOPHIRES-X for CLGS in u-loop configuration for direct-use heating at 3 km depth.

Input Parameters	Value
Reservoir Simulation	
Reservoir Model	1-Dimension Linear Heat Sweep
Reservoir Depth	3 km
Gradient	25 ºC/km
Reservoir Volume Option	Reservoir volume only
Reservoir Volume	1.00E+09
Reservoir Impedance	1.0e-03 GPa*s/m3
Injection Temperature	40 ºC
Reservoir Heat Capacity	920 J/kg/K
Reservoir Density	2900 kg/m^3
Reservoir Thermal Conductivity	5.3 W/m/K
Reservoir Permeability	1.00E-18 m^2
Wellbore Simulation	
Is AGS	True
Closed-loop configuration	U-loop
Total nonvertical length	2000 m
No. multilateral sections	2
Multilaterals cased	True
No. of Production and Injection Wells	1
Production and Injection Well Diameter	8 inches
Ramey Production Wellbore Model	False
Production Flow Rate per Well	70 kg/s
Production Wellbore Temperature Drop	5 ºC
Surface Plant Simulation	
End-Use Option	Direct-use heat
Utilization Factor	0.9
Surface Temperature	15 ºC
Plant Lifetime	40 years
Economic	
Exploration Capital Cost	$0
Stimulation Capital Cost	$0

Table A-3: Techno-economic assessment input parameters to GEOPHIRES-X for EGS at 4 km depth and direct-use heating end-use.

Input Parameters	Value
Reservoir Simulation	
Reservoir Model	1-Dimension Linear Heat Sweep
Reservoir Depth	4 km
Gradient	25 ºC/km
Reservoir Volume Option	Reservoir volume only
Reservoir Volume	1.00E+09
Reservoir Impedance	0.2 GPa*s/m3
Injection Temperature	40 ºC
Reservoir Heat Capacity	790 J/kg/K
Reservoir Density	2650 kg/m^3
Reservoir Thermal Conductivity	3.5 W/m/K
Reservoir Porosity	0.2
Reservoir Permeability	1.00E-15 m^2
Wellbore Simulation	
No. of Production and Injection Wells	1
Production and Injection Well Diameter	8 inches
Ramey Production Wellbore Model	False
Production Flow Rate per Well	70 kg/s
Production Wellbore Temperature Drop	5 ºC
Surface Plant Simulation	
End-Use Option	Direct-use heat
Utilization Factor	0.9
Surface Temperature	15 ºC
Plant Lifetime	40 years
Economic	
Exploration Capital Cost	$0

Table A-4: Techno-economic input parameters to GEOPHIRES-X for CLGS in u-loop configuration for direct-use heating at 4 km depth.

Input Parameters	Value
Reservoir Simulation	
Reservoir Model	1-Dimension Linear Heat Sweep
Reservoir Depth	4 km
Gradient	25 ºC/km
Reservoir Volume Option	Reservoir volume only
Reservoir Volume	1.00E+09
Reservoir Impedance	1.0e-03 GPa*s/m3
Injection Temperature	40 ºC
Reservoir Heat Capacity	790 J/kg/K
Reservoir Density	2650 kg/m^3
Reservoir Thermal Conductivity	3.5 W/m/K
Reservoir Permeability	1.00E-18 m^2
Wellbore Simulation	
Is AGS	True
Closed-loop configuration	U-loop
Well geometry configuration	U-loop
Total nonvertical length	2000 m
No. multilateral sections	2
Multilaterals cased	True
No. of Production and Injection Wells	1
Production and Injection Well Diameter	8 inches
Ramey Production Wellbore Model	False
Production Flow Rate per Well	70 kg/s
Production Wellbore Temperature Drop	5 ºC
Surface Plant Simulation	
End-Use Option	Direct-use heat
Utilization Factor	0.9
Surface Temperature	15 ºC
Plant Lifetime	40 years
Economic	
Exploration Capital Cost	$0
Stimulation Capital Cost	$0

Grid Resilience Analysis on Geothermal District Heating and Cooling Implementation Alongside Four Existing Oil and Gas Wells in Tuttle, Oklahoma

Isaias Marroquin[1], Hyunjun Oh[1], Zeming Hu[2], Saeed Salehi[2,3], and Runar Nygaard[2]

[1]National Renewable Energy Laboratory, Golden, Colorado, USA

[2]Mewbourne School of Petroleum and Geological Engineering, University of Oklahoma, Norma, Oklahoma, USA

[3]Texas A&M International University, Laredo, Texas, USA

Keywords

Resilience, REopt, Ground source heat pump, Plate heat exchanger, District heating and cooling, Oil and gas well

ABSTRACT

This study builds on the existing techno economic and environmental life cycle assessments performed for a geothermal district heating and cooling system implementation in Tuttle Oklahoma with four existing oil and gas wells. Its resilience in meeting the peak annual heating and cooling loads of the district assuming a temporary disconnection from the electrical grid is assessed both qualitatively and quantitatively. Attributes of resilience and qualitative criteria established by Kolker et al. (2022) for geothermal district heating systems are applied to the proposed case to highlight its vulnerabilities. Results indicate that increasing the redundancy and diversity in the physical configuration of the distributional piping can considerably increase the system's resilience. A quantitative assessment executed via the REopt tool predicts that the ancillary electricity required to power the geothermal system's heating and cooling can be met by an onsite emergency diesel generator during times of grid outages for over 28 days.

1. Introduction

The resilience of an energy system describes its ability to sustain normal operation and meet typical loads during and around times of disruptions induced by various forces. Disruptions are a result of system component fatigue and end of life, natural disasters, extreme weather, human error, and upstream supply chain issues. As highlighted by Kolker et al. (2022), resilience is defined differently across stakeholders such that attributes of resilience (i.e. reliability, redundancy, resourcefulness, responsiveness) are discussed to compare the resilience across energy systems that differ in primary source (e.g. natural gas, photovoltaic, wind) and physical configuration/scale (e.g. distributed energy resources, district energy system).

The potential disruptions that an energy system risks and its suitability to be resilient in a given application are geographically dependent as the environmental, political, social, and economic

context changes. For example, it is not logically sensible to compare the resilience of a concentrated solar microgrid operating in Texas, United States versus southern Chile due to the stark difference in the annual distribution of incoming solar irradiance, policy around energy (resources) and security, end-use applications and social patterns of energy consumption, and the cost to deliver energy from various primary sources. The most resilient energy system for each location would look very different because their unique risks yield an optimal solution that is impactful under the local conditions of the site.

Additionally, there is no uniformly established method of quantifying the resilience of an energy system. This makes the comparison of resilience between two different energy systems a rather qualitative exercise subject to criteria established by the analyst. The existing literature on energy system resilience is sparse, conceptual, and high level. It mainly discusses concepts and definitions related to energy resilience and proposes relevant metrics that can be analyzed and/or quantified for a comparative assessment of energy resilience. Additionally, studies on energy resilience tend to be focused on grid electricity generation rather than district heating and cooling for which geothermal as an energy source is least considered.

However, the topic of energy resilience is becoming an emerging area of study in regard to meeting energy demands in a time of increasing natural disasters and extreme weather events. Namely, heating and cooling which contributes to 35% of total end use building energy consumption is a crucial service to consistently uphold. Global average surface temperatures continue to increase at an alarming rate such that natural phenomena such as droughts and hurricanes have become stronger and witnessed more frequently. Their effects have been proven to devastate energy infrastructure, including the lives and services that are dependent on such. At the same time, energy consumption has increased due to climate change and population growth such that resilient energy systems are essential to minimize the disrupting effects of energy supply shortages to society and the economy during times of critical loads. Renewable energy presents itself as a promising solution to address one key driver (e.g. carbon emissions) of warming temperatures which in turn affects energy system functionality and energy consumption patterns. Specifically, geothermal energy is a resilient alternative to heating and cooling when compared to conventional systems due to low transportation needs in its upstream supply chain, a high capacity factor, long operational lifetimes, low operational costs, and subsurface equipment which is shielded from ambient conditions.

To address the lack in literature assessing the system resilience of geothermal energy, we consider the use of four abandoned oil and gas wells in Tuttle Oklahoma for a direct use geothermal district heating and cooling system implementation. Its resilience is evaluated relative to the existing decentralized natural gas system of boilers and furnaces in a district of 250 homes, a primary school, and a secondary school. Details on the technoeconomic feasibility and environmental life cycle impacts of such energy system transition are detailed in Oh et al. (2024) and Marroquin et al. (expected), respectively. We leverage the criteria proposed by Kolker et al (2022) as a “variety of relative resilience criteria that can be evaluated to allow more structured analysis of resilience improvements associated with a particular resilience mitigation strategy” for qualitatively measuring the resilience of geothermal district heating systems. Additionally, we configure the National Renewable Energy Laboratory’s (NREL’s) local-scale renewable energy dispatch model named REopt for a quantitative resilience analysis of the proposed geothermal system to answer two key questions. First, what is the maximum grid outage duration that the geothermal system

can withstand while meeting 100% of the heating and cooling demand of the district at a probability of at least 50% during times of peak electricity consumption by the geothermal system (i.e. during peak heating and cooling loads). Second, what is the probability distribution that the geothermal system will survive the outage while meeting its heat load as a function of outage duration? The model considers the existing natural gas fired heating system of the district such that results highlight the net energy resilience benefits of a geothermal energy system implementation.

2. Methods

Kolker et al. (2020) summarizes current energy use in Arctic countries and dives into the opportunities for increased geothermal energy as a renewable resource for electric and thermal energy supply, including cascaded use. In doing so, resilience attributes of integrated geothermal energy systems are highlighted to determine whether techno economically feasible geothermal systems would be resilient relative to the current energy practices in the Arctic. The high-level resiliency attributes of geothermal energy are leveraged to formulate a list of questions which are each attributable to one of the four pillars of resiliency (i.e. reliability, redundancy, resourcefulness, and recovery). Unique sets of resilience attributes, components, and criteria are presented for geothermal power and thermal systems, respectively. In this study, we adopt the key resilience attributes and components of thermal systems (i.e. Table 3) from Kolker et al. (2022) to qualitatively measure the resilience of the proposed geothermal district heating and cooling system for the Tuttle district.

REopt is a web-based tool that evaluates the technoeconomic feasibility of integrating renewable energy resources and more energy efficient methods into the existing power grid of a residential, commercial, or small industrial stock of buildings. The model can consider resources such as photovoltaics and geothermal heat pumps including systems with combined heat and power and battery storage. User defined inputs consist of energy goals (e.g. cost savings, clean energy), energy system technologies (e.g. wind, battery), site & utility information (e.g. site location, building floor area, heating fuel cost, utility provider), and energy load profiles (e.g. annual hourly electricity consumption, heating fuel consumption, and cooling load profiles). The model optimizes the capacity sizes and dispatch strategies of the integrated electric and thermal technologies such that the electric, heating, and cooling demands of the building stock are supplied at the site's lowest life cycle cost of energy.

For the case of this study, grid electricity, central plant water-to-water ground source heat pumps, and a diesel generator were selected in REopt as source technologies to supply the energy profiles of a primary school, secondary school, and 250 single family homes located in Tuttle Oklahoma. In the previous work of Oh et al. (2024), the representative building types of the district were modelled in EnergyPlus to simulate their energy flows and heat transfers. Outputs served as input into GeoPHIRES to estimate the potential geothermal energy that can be extracted from a nearby abandoned oil and gas well site to supply heat to the district. With an economic life cycle assessment executed in parallel, the technoeconomic feasibility of a direct-use geothermal district heating and cooling system integration in the aforementioned Tuttle district was established. From the previous work in EnergyPlus, the output heating fuel consumption and cooling load of the buildings (Figure 1) was inputted into REopt.

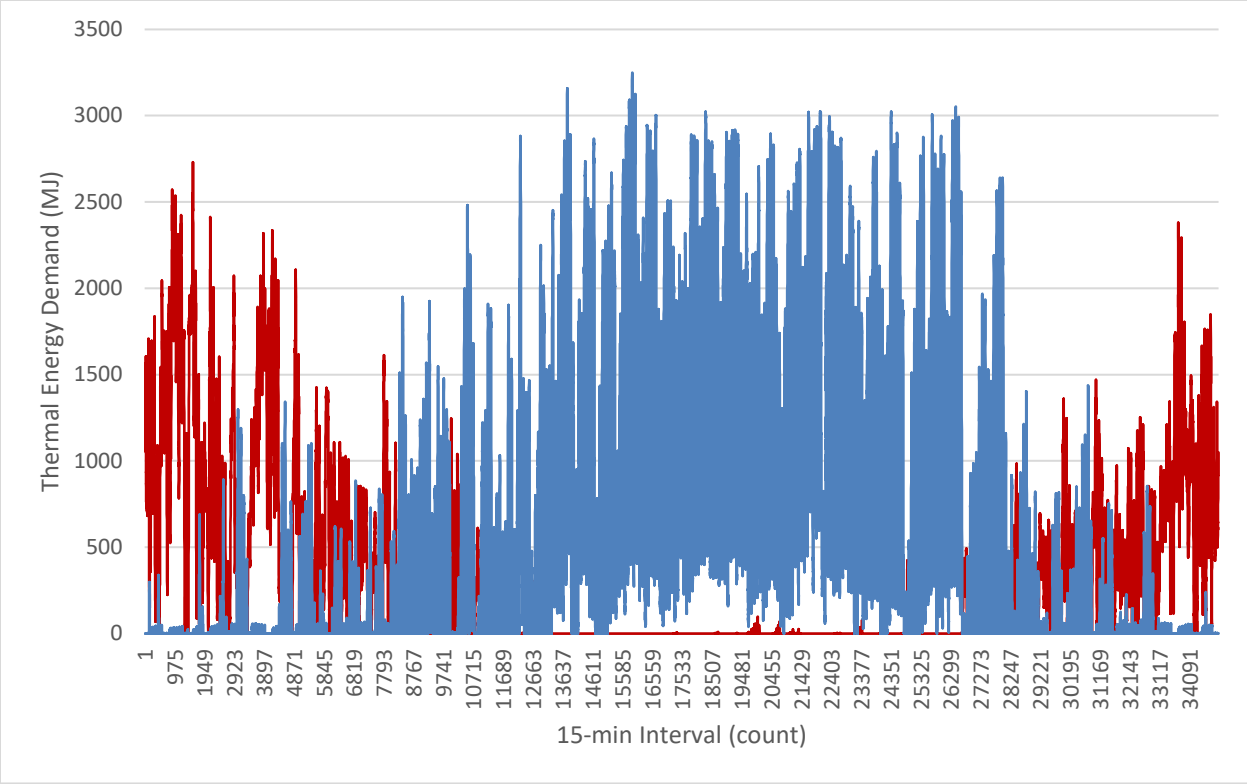

Figure 1: Heating and cooling demand of the Tuttle district as outputted by EnergyPlus based on the local weather and relevant energy performance parameters of the building stock

Although the direct-use geothermal system considers a central plate heat exchanger rather than central ground source heat pumps, a tool-based quantitative analysis of energy resilience is largely constrained to the limitations of the REopt tool. This is because no other tool with the same objective functionality exists to the knowledge of the authors at the time of this study. Geothermal capabilities within REopt are relatively new and currently have ongoing efforts to improve and expand such that the most representative energy system module within REopt to the proposed case of this study is central water-water ground source heat pumps. However, it is important to note that relevant metrics can be calculated following various approaches and equations as outlined in Das et al. (2020) whose applications are independent of the system design.

Additionally, results of Oh et al. (2024) indicated that the high electricity consumption required to power the cooling supply of the district relative to the heating supply via direct geothermal use deem the system techno economically infeasible for cooling. This is because a direct-use geothermal system must be coupled with an absorption chiller to provide cooling in addition to heating. At the same time, a chiller requires electricity as its primary source of energy to extract heat from water while a central plate heat exchanger requires electricity as ancillary energy to extract and inject subsurface geothermal fluid. The electricity consumption of the chiller is about 80% of the cooling demand while the electricity consumption of the well pumps is orders of magnitude less than the heat demand. The annual cooling demand is also greater than heating by a factor of 1.32 and a 1:1 heat exchange is assumed at the central plate heat exchanger. As a result, significantly more electricity is consumed for cooling versus heating. More electricity consumption than a conventional air-conditioning system was concluded for the direct use

geothermal system in cooling mode such that geothermal cooling is not techno economically feasible via direct use. However, the central ground source heat pump system chosen in REopt to represent the proposed case study exhibits a higher annual average coefficient of performance (COP) for cooling relative to heating. It is determined by REopt as a function of inlet and outlet temperature. Therefore, the central plant water-to-water heat pumps within REopt are selected to serve as proxy for a geothermal system implementation that is techno economically feasible of meeting the heating and cooling demand of the Tuttle district.

Furthermore, existing energy resilience analyses optimize electricity supply rather than heating and cooling. As an example, critical load within REopt is defined as the electricity demand that must be met during an outage (i.e. temporary disconnection from the electric grid) such that the probability of an off-grid energy system to meet the electric loads of a community is the metric to quantify the resilience of the system. However, a geothermal heating and cooling system is inherently tied to the electric grid. This is because delivering geothermal energy requires an ancillary electrical input to circulate fluid and upgrade the exergy of extracted geothermal energy as needed to meet a given demand. This means that during times of a grid outage, a geothermal heating and cooling system will lose functionality in addition to all other electrical appliances in a building. This also indicates that by specifying the electrical load of the district to be the total consumption at the meter as outputted by EnergyPlus (Figure 2), results of energy resilience from REopt would be optimized to meet the loads of existing electronic appliances rather than heating and cooling from geothermal energy.

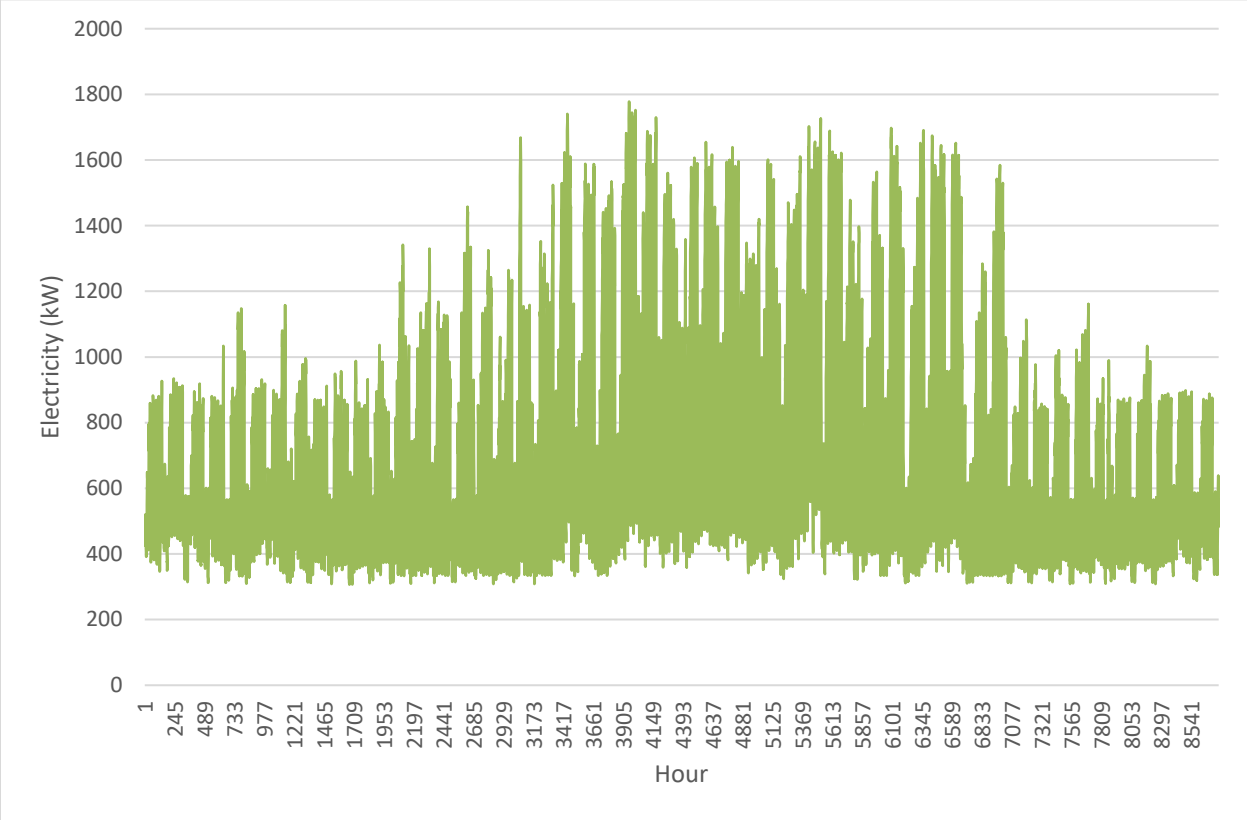

Figure 2: Electricity consumed by the district as outputted by EnergyPlus based on the local weather and relevant energy performance parameters of the building stock

Given that the objective of this study is to evaluate the resilience of a geothermal district heating and cooling system, the application of the REopt tool to assess energy resilience was strategically modified from current practice. To overcome its limitation of considering only the effect of an outage on electricity supply, REopt was executed in two sequentially dependent runs. The initial execution of REopt involved selecting only cost savings as the energy goal in order to generate and leverage cost optimal system performance dispatch information (i.e. REopt's main functionality). The energy system dispatch represents a single-year of data at the hourly level of electricity generation and/or consumption by the technologies considered in the model's optimization. Non-zero electric loads are outputted for the relevant technologies if they are deemed cost effective for installation and operation against the continuing operation of the existing grid and heating and cooling system to meet building loads. However, new technologies can be forced into the solution of the objection function which is set to minimize the life cycle cost of energy even if operating the existing system is the cost optimal solution.

The adoption of a geothermal district heating and cooling system to displace the existing natural gas boilers and electric chillers of the Tuttle district results in a negative net present value such that by default, REopt outputs zero dispatch of the geothermal system. It also indicates that loads are met entirely by the grid and existing heating and cooling systems. This is due to the high upfront cost of manufacturing and installing the various geothermal energy system components which would not be required for the existing system. The integration of the diesel generator is also neglected due to the cost of delivering diesel as a fuel for on-site electricity generation rather than purchasing from the grid. Therefore, the geothermal heat pump was manually forced to be integrated into the solution by specifying in the inputs that its purchase and installation to displace the existing heating and cooling system is a constraint that must be met. The model now considers the input heating and cooling loads to be entirely met by the new geothermal technology. As a result, dispatch results contain the required annual electrical consumption profile of the ground source heat and circulation pumps to meet the specified heating and cooling demand of the district (Figure 1).

The hourly system performance dispatch results of the pumps for heating and cooling as outputted by REopt served as the input electrical load for the second simulation. GSHP as an energy source was unselected such that the electric grid and emergency diesel generator are the two options the model must now choose from to meet the electrical demand of the district. In this run, electrical demand represents the electricity required to deliver the heating and cooling demand of the district via a central plant geothermal heat pump system. At the same time, electricity is the constraining factor to a continuous supply of heating and cooling by the geothermal system during times of grid outages such that the resilience outputs of the new REopt run can be used to infer the resiliency of the geothermal system in supplying heating and cooling. In fact, one can expect the ancillary electrical energy needed by the geothermal system to be supplied by the off-grid emergency generator during times of grid outages.

The last input parameters to be specified in REopt before initiating the second run were specific to the assessment of resilience. The "multiple outage" model was selected to consider four 2-hour outages over the course of a year whose outage periods (i.e. start date and time) are by default determined by the model to occur at seasonal energy demand peaks based on the input electricity load profile and its maximum values per season (i.e. winter, spring, summer, autumn). Mixed integer linear programming optimizes the objective function with respect to life cycle cost of

energy such that demand is supplied at the lowest cost from various sources. This applies to times of critical and non-critical load. The sizing and dispatching of energy is constrained to the technologies specified by the analyst and their limitations (e.g. operational and maintenance cost). Therefore, loads met during times of grid outages by technologies with ancillary input electricity requirements (e.g. geothermal) must rely on a generator.

3. Results

Kolker et al. (2022) expands on the four qualitative attributes of energy system resilience by developing a list of criteria to assess large scale grid connected geothermal power systems, geothermal microgrids, and geothermal district heating systems (section 6). The criteria are presented as generic then further applied to a set of case studies representing existing systems in Artic countries. In this study, we adopt the established qualitative criteria to assess the resilience of the proposed geothermal district heating and cooling system of the Tuttle district in meeting the peak thermal loads of the district at times of electric grid disruptions. As formatted in Table 9 and 10 of Kolker et al. (2022), we present the results below.

Table 1. Qualitative criteria of resilience for a geothermal district energy system as established by Kolker et al. (2022) and applied to the proposed case of Tuttle Oklahoma

Attribute	**District Energy Components**
Reliability **(How does the system perform under typical conditions?)**	**Maintenance plans** Monitor heat carrier working fluid and refrigerant levels in the heat pump-based system and water in the distributional side of the direct use geothermal system. Replenish fluids to levels required for typical operating conditions as needed. Ensure geothermal heat extraction does not exceed regulation and reinjection of fluid follows protocol.
	Performance monitoring Continuously record the production and injection temperatures of the wells including production flow and geothermal exchange rates. Monitor inputs and outputs of system components during peak thermal loads.
	Age of system/components As part of the maintenance, track the length of service each system component has acquired since the commencement of its operation. Different units have varying design lifetimes.
	Maintain outage stats Document the energy flows of the system during times of grid outages. Statistically analyze historical data to predict the

	probability distribution of future outages. Leverage results to reinforce the system to better withstand such events.
	Leakage detection system As part of the maintenance, periodic checking of pipes for deterioration and signs of potential failure. Installation of continuous pressure monitoring system to detect fluctuations that occur at pipe failure.
Redundancy **(What single points of failure does the system exhibit?)**	**Multiple heat plants** Multiple water-to-water ground source heat pumps at central plant in the geothermal heat pump-based system. A heat exchanger of multiple brazed steel plates at the central plant and a natural gas boiler in the direct use geothermal system.
	Multiple heat sources Four inactive oil and gas wells 2 km south of the district with a borehole depth of 2.1 to 3.3 km and geothermal resource temperatures of 65 to 90 deg C. Geometry of wells offer a doublet or quartet configuration with variable flow rate and heat extraction.
	Redundant workforce Electric utility would ensure a secure grid connection of the geothermal system during normal operating conditions. An on-site team dedicated to maintaining the physical components of the district heating system would involve geothermal heat pump or plate heat exchange and water pump design experts.
	Redundant pumps Submersible water pumps sit inside the boreholes, circulation pumps between the wells and the central plant, and circulation pumps between the central plant and district. To prevent system malfunction due to pump failure, auxiliary backup pumps should be installed.
Resourcefulness **(Are there diverse and flexible options to bounce back from disruption?)**	**Building level thermal resilience** Thermal performance of buildings affects the loads imposed on energy systems and therefore indirectly influences the planning strategies for system resilience. Assuming thermal loads predicted by REopt will be consistent during anticipated grid outages, the thermal performance of buildings is not further considered as a factor affecting the resilience of the proposed geothermal district heating system in this study.

	Meshed distribution systems One production and one injection pipe form a closed geothermal loop at the wellfield side of the system. The distributional side consists of a central, bi-directional, hot/cold supply/return loop that connects to the piping networks of the individual buildings. Further efforts to design a more resilient pipe network is required to ensure the delivery of thermal energy in the case of a main line failure.
	Ability to exceed design capacity in extreme hot or cold events Thermal energy equipment sizing such as central heat pumps or absorption chiller are based on the annual peak heating and cooling demands of the district. A factor of safety in the design of each system component would be required to accommodate for extreme hot or cold events that exceed the current design capacity of the proposed geothermal system.
	Thermal storage capacity The central heat pump-based system can fully meet thermal requirements without any thermal storage, given sufficient electricity to fill the exergy gap between geothermal supply and thermal demand. The central plate-based system can also fully meet thermal requirements given sufficient natural gas for peak heat and an absorption chiller for cooling. In any case, thermal storage can be utilized to store energy when geothermal supply is greater than demand and used during peak thermal loads. This would decrease the dependency on imported electricity and natural gas.
	Ability to meet multiple temperature delivery needs Delivery of thermal energy is in the form of water. Existing buildings have temperature mixing valves such that they are repurposed for the proposed geothermal system to deliver water at desired and variable end use temperatures.
	Time to recover – thermal resilience of buildings Thermal performance of buildings affects the loads imposed on energy systems and therefore indirectly influences the planning strategies for system resilience. Assuming thermal loads predicted by REopt will be consistent during anticipated grid outages, the thermal performance of buildings is not further considered as a factor affecting the resilience of the proposed geothermal district heating system in this study.
	Ease of recovery – supply chain flexibility

	Supply chain issues during critical loads are not expected as the primary source of geothermal energy is undisrupted and diesel for electricity is stored on-site.
Recovery **(Will the system return to normal operation after undergoing a disruption?)**	**Standardized parts and supplies** For all major and minor physical system components, an up-to-date list of the most readily available vendors and manufactures must be maintained. Contact information and relevant products must be documented in the database.
	Plan for recovery Replace damaged components (if any) and redirect electrical input to geothermal system from grid to emergency generator. Monitor on-site supply of diesel. Ensure diesel shortages do not occur via communication with the electric utility regarding their recovery and informing the district of excessive thermal loads.
	Spare parts inventory Each main physical system component (e.g. heat pump) with an expected lifetime of less than 30 years must have a spare stored on-site. Ancillary components such as wirings and insulation can be ordered accordingly after unforeseen events occur.
	Workforce for recovery A specialized force would be kept on standby and deployed by the central, on-site maintenance team during grid outages to ensure expected functionality of the emergency generator in replacing the grid's service at critical loads.

As expected, the electricity required to supply the heating and cooling demand of the district during grid outages (i.e. critical load) is met entirely by the emergency diesel generator. It is expected to meet 100% of the critical loads at an average probability of 98.4% for an outage duration of two hours. This corresponds to an annual total of 5162 kWh of electricity generated on site for which 1206 (i.e. 23.4%) is attributable to the winter outage, 1311 (i.e. 25.4%) to spring, 1376 (i.e. 26.7%) to summer, and 1269 kWh (i.e. 24.6%) to autumn (Figure 3). Their corresponding times of occurrences which are consistent with the seasonal thermal demand peaks are February 17 at 3pm, May 24 at 2pm, June 14 at 2pm, and September 11 at 2pm.With an assumed fuel higher heating value (HHV) of 40.7 kWh/gallon and a thermal-to-electric conversion efficiency (% HHV-basis) of 32.2%, at least 394 gallons of diesel are expected to be stored on site per year to drive the critical heating and cooling load supply. Additionally, the maximum grid outage duration that REopt's Energy Resilience Performance (ERP) post-processing tool can consider is 672 hours (i.e. 28 days). For 28 days of dysconnectivity from the grid, the geothermal system has a 53.5% chance of meeting 100% of the heating and cooling demand during those times.

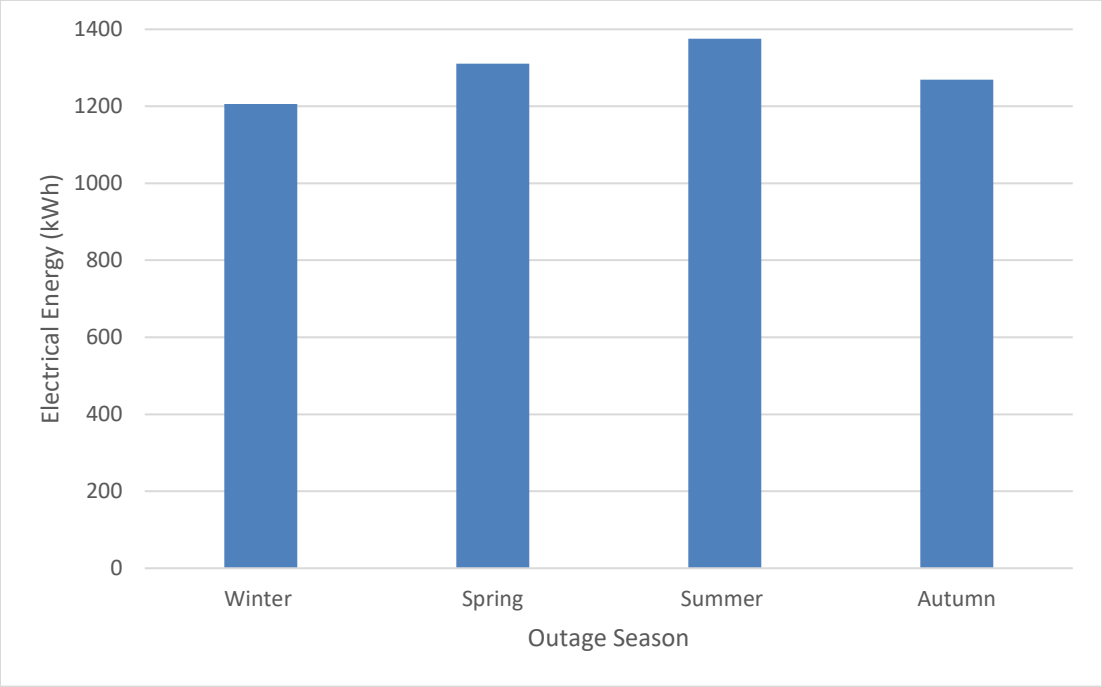

Figure 3: Electrical power supply of emergency diesel generator to geothermal heat pump system for heating and cooling during the Winter, Spring, Summer, and Autumn 2-hour grid outages occurring on February 17 at 3pm, May 24 at 2 pm, June 14 at 2pm, and September 11 at 2 pm, respectively

As the modelled outage duration increases from 1 to 672 hours, the average probability of surviving an outage starting at any time during the year steadily decreases (Figure 4). Although difficult to infer from the graph, the rate of change in probability decreases with respect to increasing outage duration. In other words, the difference in probability between surviving a 24- (i.e. 96.4%) versus 48-hour (i.e. 94.4%) outage is greater than the difference in probability between surviving a 624- (i.e. 55.9%) versus 648-hour (i.e. 54.7%) outage. This equates to a difference in probability of 2.08 versus 1.21%, respectively. The greatest rate of decrease in survival probability (i.e. 1.52%) is observed between a 0- (i.e. 100%) and a 1-hour (i.e. 98.5%) outage.

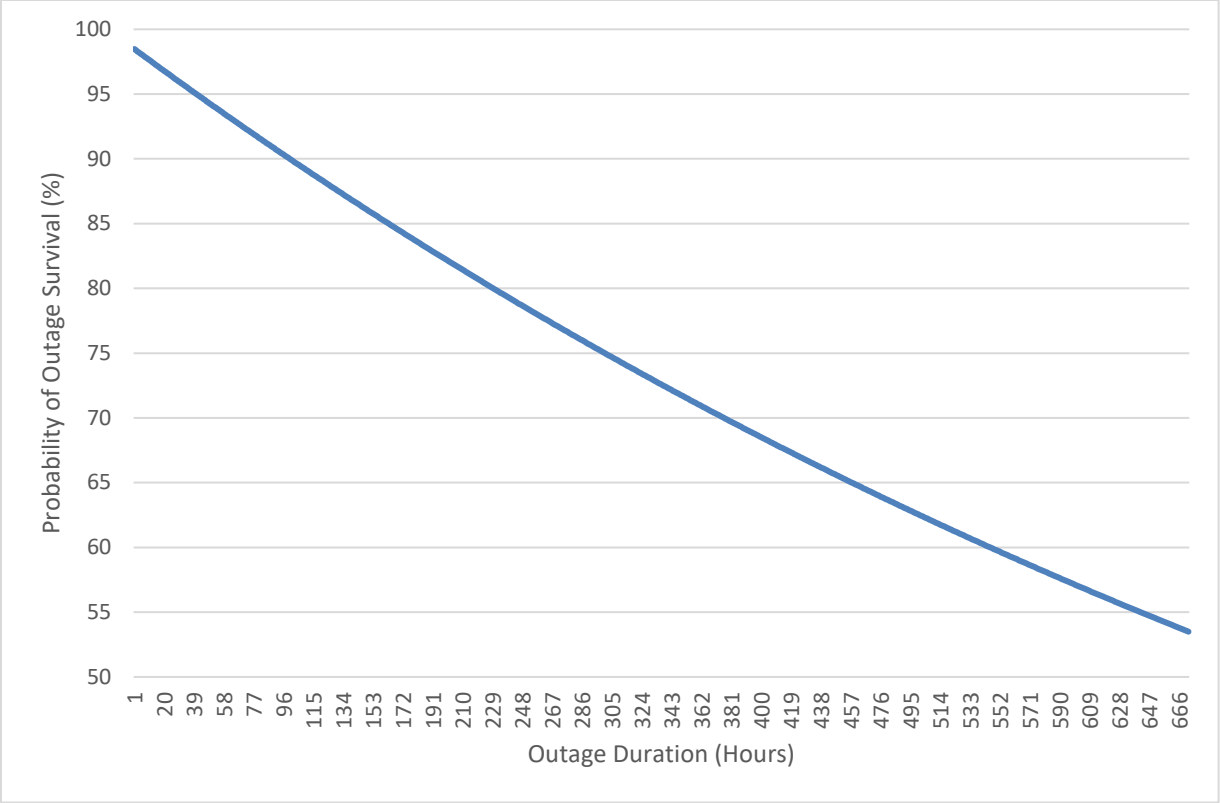

Figure 4: Probability distribution function of outage survival with respect to outage duration for the emergency diesel generator in meeting the electrical load of the geothermal district heating and cooling system

Conclusions

Literature and tools that assess the energy resilience of a geothermal district heating and cooling system are sparse in the existing domain. Additionally, the repurposing of inactive oil and gas wells for direct geothermal use is a renewable energy option that can meet the thermal loads of communities. This study adopts the qualitative framework from Kolker et al. (2022) and the quantitative assessment tool (i.e. REopt) from the National Renewable Energy Laboratory to establish the resilience of a direct-use geothermal district energy system in meeting the thermal loads of an existing community in Tuttle Oklahoma. The previous works of Oh et al. (2024) determined the technoeconomic feasibility of such an energy system implementation via life cycle cost estimations, geologic modelling, and building energy simulations for which the results served as input to this study.

The qualitative assessment performed highlights critical properties of the proposed geothermal energy system which influence its reliability, redundancy, resourcefulness, and recoverability. While it also serves as a blueprint of best practices to maximize the system's resilience in meeting the typical thermal loads of the community, the quantitative assessment estimates the system's capability in meeting the four seasonal peak thermal loads with an assumed grid outage. Although the results of this study are high level, the methods described can serve as a foundational building block to increase the available literature on the intersection of energy resilience and geothermal district systems. Additionally, results can support others' analyses.

Acknowledgement

This work was authored by the National Renewable Energy Laboratory, managed and operated by Alliance for Sustainable Energy, LLC for the U.S. Department of Energy (DOE) under Contract No. DE-AC36-08GO28308. Funding provided by the U.S. Department of Energy Geothermal Technologies Office under Contract No. DE-EE0009962. The views expressed in the article do not necessarily represent the views of the DOE or the U.S. Government. The U.S. Government retains and the publisher, by accepting the article for publication, acknowledges that the U.S. Government retains a nonexclusive, paid-up, irrevocable, worldwide license to publish or reproduce the published form of this work, or allow others to do so, for U.S. Government purposes. The authors appreciate Jennifer Kurtz, Craig Turchi, and Deanna Cook, at the National Renewable Energy Laboratory for reviewing the manuscript.

REFERENCES

Das, L., Munikoti, S., Natarajan, B., and Srinivasan, B.. "Measuring smart grid resilience: Methods, challenges and opportunities." *Renewable and Sustainable Energy Reviews*, Volume 130, 2020, 109918, ISSN 1364-0321, https://doi.org/10.1016/j.rser.2020.109918.

Kolker, A. , Slaght, R.G., Anderson, B., Reber, T., Zyatitsky, K., and Pauling, H. 2022. "Geothermal Energy and Resilience in Arctic Countries." National Renewable Energy Laboratory, Golden, CO. NREL/TP-5700-80928. https://www.nrel.gov/docs/fy22osti/80928.pdf.

Oh, H., Akar, S., Beckers, K., Bonnema, E., Vivas, C., and Salehi, S. "Techno-economic feasibility of geothermal energy production using inactive oil and gas wells for district heating and cooling systems in Tuttle, Oklahoma." *Energy Conversion and Management*, Volume 308, 2024, 118390, ISSN 0196-8904, https://doi.org/10.1016/j.enconman.2024.118390.

Mishra, S., Pohl, J., Laws, N., Cutler, D., Kwasnik, T., Becker, W., Zolan, A., Anderson, K., Olis, D., and Elgqvist, E. "Computational framework for behind-the-meter DER techno-economic modeling and optimization—REopt Lite." *Energy Systems*, 2021, https://reopt.nrel.gov/tool.

Mechanical Evaluation of a Novel Cement Formulation used for Thermal Energy Storage Wells

Meng Meng[1], Tatiana Pyatina[2], Luke Frash[1], Bijay KC[1], Uwaila Iyare[1], Yerkezhan Madenova[1]

[1] Los Alamos National Laboratory

[2] Brookhaven National Laboratory

Keywords: Triaxial compression, thermal cycling, mechanical modeling, safe operating envelope

ABSTRACT

High Temperature Reservoir Thermal Energy Storage (HT-RTES) is a promising solution for large-scale energy storage that can stabilize the electric grid, increase its flexibility, and provide energy on demand. Despite its advantages, the HT-RTES wells require a higher standard for cement integrity due to higher temperatures and thermo-mechanical stresses during injection and production. In this study, we provided a thorough mechanical investigation on the hydrophobic fly ash cenospheres (FCS) incorporated calcium aluminate cement, which exhibits a lower thermal conductivity compared to conventional oil and gas well cement to prevent heat losses. The cement was treated with superhydrophobic polymethylhydrosiloxane (PMHS). The compression tests were conducted under in situ high pressure high temperatures, with pressure reaching up to 10 MPa and temperature up to 180 °C. The findings revealed that the PMHS-treated specimens, after undergoing simulated thermo-mechanical stresses, showed an increase in cement compressive strength from 4.6-30 MPa to 6.1-33 MPa, an improvement in elastic modulus from 0.34-1.37 GPa to 1.1-3.3 GPa, and an enhancement in Poisson's ratio from 0.07-0.15 to 0.1-0.33. Therefore, lightweight calcium-aluminate cement formulations with PMHS treated FCS could preserve its mechanical performance after subjecting to thermal shock. We further incorporated the measured properties into a fully coupled thermoporoelastic model for wellbore integrity analysis. Results show that the novel PMHS treated FCS could resist large range of pressure and temperature perturbations during heat injection and production. Overall, this novel formulation could be a promising solution to the durability of the HT-RTES wells.

1. Introduction

In a thermal storage site, hot fluid is injected into a subsurface reservoir, where the formation rock absorbs and retains the heat energy from the injected fluid. When the heat energy is needed, those hot liquid will be produced to the surface. The cyclic injection and production occur daily, seasonally, or even longer durations based on specific applications. To achieve the long-term

effective thermal storage, safe wellbores are essential, and cement integrity is one of the primary concerns for the wellbore durability. A proper cement system needs to have the following characteristics: (1) good resistance to thermal shock and thermal cycling over large temperature ranges; (2) low thermal conductivity to minimize the thermal loss during the repeating injection and production across the wellbore; (3) low modulus to withstand severe pressure and temperature perturbations caused by injection and production; and (4) low density to avoid fracturing the weak, unconsolidated, or naturally fractured rock formations.

Ordinary Portland cement (OPC) is known for its poor performance in thermal shock resistance. Temperatures between 200-300 ℃ could cause micro-cracking propagation (Boquera et al., 2021). The dihydroxylation of portlandite happens in OPC at temperatures ≥ 500 ℃, leading to free lime formation that converts to highly expansive hydration products (Sugama et al., 2018). In contrast, Calcium aluminate cement (CAC) is capable to withstand thermal shock at temperatures over 500-600 ℃ (Sugama et al., 2018; Boquera et al., 2021). The usage of fly ash and silica flour improved cement performance at elevated temperatures.

The thermal conductivity of OPC depends on the water saturation content, density and porosity. It varies between 0.3 and 1.3 $Wm^{-1}K^{-1}$ (Wolterbeek et al., 2023). According to Fourier's law of heat conduction, the heat loss due to conduction is linearly related to material thermal conductivity. Zhou et al. (2023) developed a chemical-induced nitrogen-filled foam cement with low thermal conductivity of 0.3 $Wm^{-1}K^{-1}$ that achieved a 11.77 °C higher temperature at the wellhead compared to adjacent wells using fly-ash low density cement.

The elastic modulus of OPC can go up to over 40 GPa, and the oilwell cement has an elastic modulus between 1 and 10 GPa (Nelson, 2006). The geothermal cement has been found with similar elastic modulus as oil well cement (Philippacopoulos and Berndt, 2001; Pyatina, 2018). Higher elastic modulus up to 15 GPa has been reported under specific testing conditions and formulations (Pang et al., 2021; Meng et al., 2023). Well integrity modeling analysis have shown that elastic modulus is more important than compressive strength in maintaining well safety (Lavrov and Torsæter, 2016; Meng et al., 2021).

Cement density ranges from 1400 kg/m^3 to 2400 kg/m^3 depending on specific applications. Density can be adjusted by using heavyweight additives (Barite, Hematite, Ilmenite) or lightweight additives (gas, bentonite, microspheres). For the geothermal well, the formation might be naturally fractured, and a lightweight cement is beneficial to avoid fracturing the formation.

To achieve the preferred properties of geothermal cement, one type of PMHS treated FCS incorporated calcium aluminate cement has been created (Simerjeet, 2012; Sugama et al., 2018; Sugama and Pyatina, 2021). Its mechanical properties under uniaxial compression conditions, thermal conductivity, water-repellent property, phase identification, and microstructures have been quantified (Sugama and Pyatina, 2021). However, the mechanical properties under triaxial conditions have not been evaluated. In this paper, we have conducted triaxial compression tests under high temperature high pressure conditions, with pressures up to 10 MPa and temperatures up to 180 °C. Our results have demonstrated the good performance of PMHS-treated cement in thermal resistance under simulated wellbore conditions.

2. Methods

2.1 Experiments

The materials used to prepare the PMHS-treated alkali-activated calcium aluminate cement with Class F fly ash have been described in detail by Sugama and Pyatina (2018) and their description will not be repeated here. The preparation procedures, however, are as follows.

1) Pouring cement slurry into the test mold, followed by 24 hours curing at room temperature;
2) Removing the mold and curing the samples at 99±1% relative humidity for 24 hours at 85 ˚C;
3) Autoclaving the samples for 24 hours at 250 ˚C.

For each formulation, we evaluated their mechanical performance before and after undergoing thermal shock. The thermal shock is performed by three-cycle of 200 °C heating for 24h, followed by old water quenching for 30 minutes. The detailed experimental matrix is shown in Table 1.

Table 1 Experimental matrix

Specimens	Thermal Shock	Testing Conditions
1	No	Uniaxial compression test
2		Uniaxial compression test
3		Uniaxial compression test
4		10 MPa confining pressure
5		180 °C, no confining pressure
6		180 °C, 10 MPa confining pressure
7	Yes	Uniaxial compression test
8		Uniaxial compression test
9		Uniaxial compression test
10		10 MPa confining pressure
11		180 °C, no confining pressure
12		180 °C, 10 MPa confining pressure

We utilized our high-temperature and high-pressure triaxial compression equipment (Figure 1) to measure the mechanical properties of cement. The equipment can withstand temperatures up to 200 °C and provides a confining pressure range from 0 to 70 MPa. The load capacity of the equipment is 1000 kN. Axial and radial deformations were monitored using high temperature linear variable differential transformer rated up to 200 °C. Throughout the compression tests, we maintained the strain rate at approximately 10^{-6} /s. For high temperature high pressure experiments, a customized rubber is required to tolerate the harsh environment and avoid fluid communication between the sample and the silicone confining oil.

This facility shown in Figure 1 is capable to control and monitor pore pressure as well. However, the pore pressure was not applied in our experiments because cement typically has low permeability, and it takes a long time for pore pressure to stabilize. Thies PMHS treated cement has a low permeability of 0.1-0.15 micro-Darcy (Bauer et al., 2020). During the high temperature test without confining pressure, we left the pore pressure line open to the atmosphere to allow free water evaporation. This was necessary to prevent thermal induced pore pressure from building up and potentially breaking the rubber in the absence of confining pressure. As to the high temperature high pressure tests, it is recommended to increase the confining pressure to at least 2 MPa before raising the temperature. The water boiling point at 2 MPa is over 212.5 °C, which avoids

significant thermal induced pore pressure. If the sample is brittle, the confining pressure can go directly to the designed value. Since the cement samples seem to be ductile, it is better to elevate the pressure to 10 MPa after temperature reached 180 °C. During the heating stage, a continuously constant confining pressure control was maintained with self-designed software.

Figure 1: Triaxial compression equipment with sample setup

2.2 Modeling

The measured parameters have been implemented into one thermoporoelastic analytical model. The model development and details have been described in our previous publications (Meng et al., 2021, 2023; Zhang et al., 2022). The model demonstrates how the cement performs under pressure and temperature perturbations during fluid injection and production.

3. Results

3.1 Mechanical properties of cement before thermal shock

Three uniaxial compression tests have been conducted, and their mechanical properties are close to each other with small variance (Figures 2 to 4). The compressive strengths are 4.7 MPa, 4.6 MPa, and 5.1 MPa, respectively. The elastic modulus is (1.15 ± 0.05) GPa, (1 ± 0.03) GPa, and (1.2 ± 0.1) GPa. Poisson's ratios were recorded at 0.14 ± 0.1 for the first two tests, and 0.10 ± 0.1 for the third test. The stress strain curves in Figures 2 to 4 indicate plastic deformation near the peak strength values. For instance, in Figure 3, axial strain increases from 0.4% to 0.6% as axial stress approaches the maximum value of 4.6 MPa, and continues to increase to 1.2% as axial stress drops to 2 MPa. This demonstrates the strong ductility of the cement, which is not typical for brittle Class G cement. In our previous experiments, the axial deformation for Class G cement with silica flour is around 0.4% at the maximum axial stress point and the stress dropped quickly after that (Meng et al., 2023). Additional evidence of ductility was observed in the triaxial compression test under 10 MPa confining pressure, where axial strain exceeded 10% as the axial stress continued to rise (Figure 5).

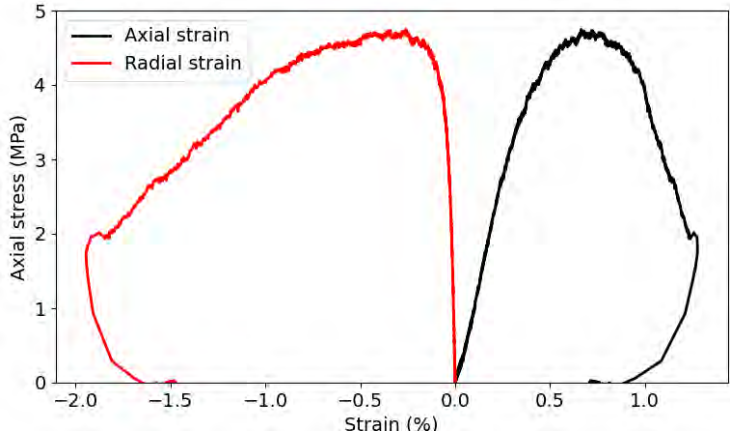

Figure 2: Stress - strain curve of the first uniaxial compression testing before thermal shock

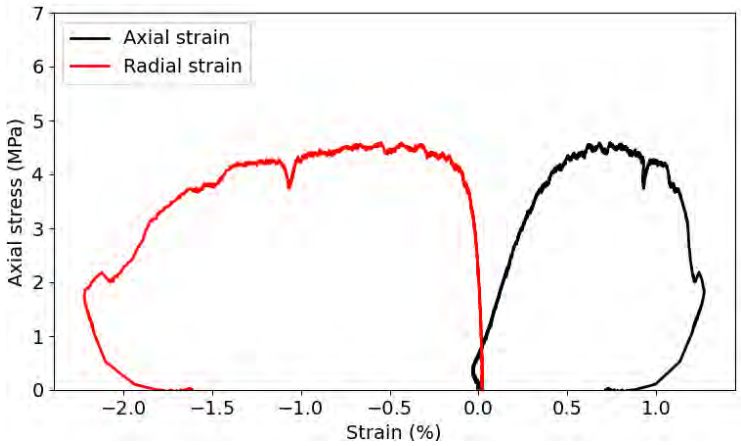

Figure 3: Stress-strain curve of the second uniaxial compression testing before thermal shock

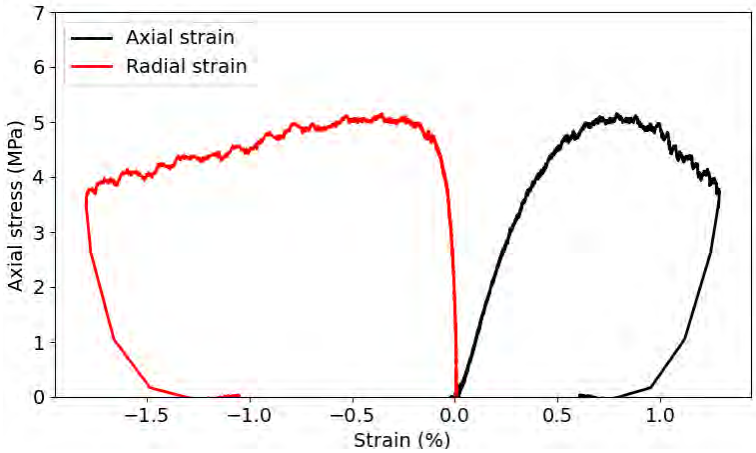

Figure 4: Stress-strain curve of third uniaxial compression testing before thermal shock

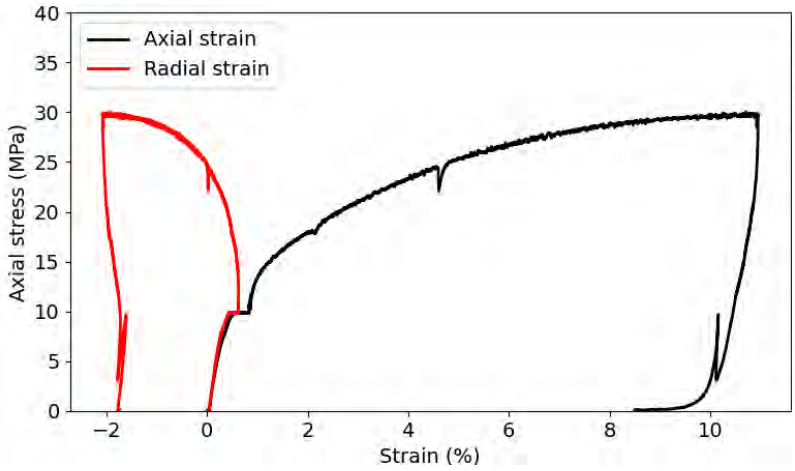

Figure 5: Stress-strain curve under 10 MPa confining pressure before thermal shock

In the following 10 MPa, 180 °C triaxial test, the stress-strain curve shows more complex behavior compared to the test conducted under high confining pressure alone (compare Figure 6 with Figure 5). Figure 7 shows the process of the progressively increasing pressure, temperature, and compression stress. Initially, the confining stress was raised to 10 MPa, during which the axial strain increased from 0 to 2%, and radial strain from 0 to 0.7%. With the confining pressure held constant at 10 MPa, the temperature was then raised to 180 °C. During this stage, the axial strain further increased to 6%, while the radial strain sensor failed. After temperature reached to 180 °C, the axial strain was still increasing under a slower rate. To save time and avoid axial strain sensor out of range, the specimen started to be compressed. This strong ductile performance creates challenges to our measurement.

There are two ways to improve the future testing performance. Firstly, as mentioned in the Experiments section, initially setting the confining pressure to a lower value of 2 MPa before elevating the temperature might help mitigate deformation during the temperature elevation, though it would not prevent the deformation after 10 MPa is applied. Secondly, curing the specimen under 10 MPa and 180 °C during the specimen preparation stage might prove beneficial. The cement sample was prepared under ambient pressure conditions, which is expected to be less consolidated than high pressure curing. If the curing conditions were maintained the same to the testing conditions, the specimen might show less plastic deformation.

For uniaxial compression test under 180 °C, the specimen shows stronger deformation compared to uniaxial compression tests under room temperature. Axial strain is 1.4% when reaching the peak value for the 180 °C, while the ambient tests showed only ~0.6% axial deformation at the peak stress point.

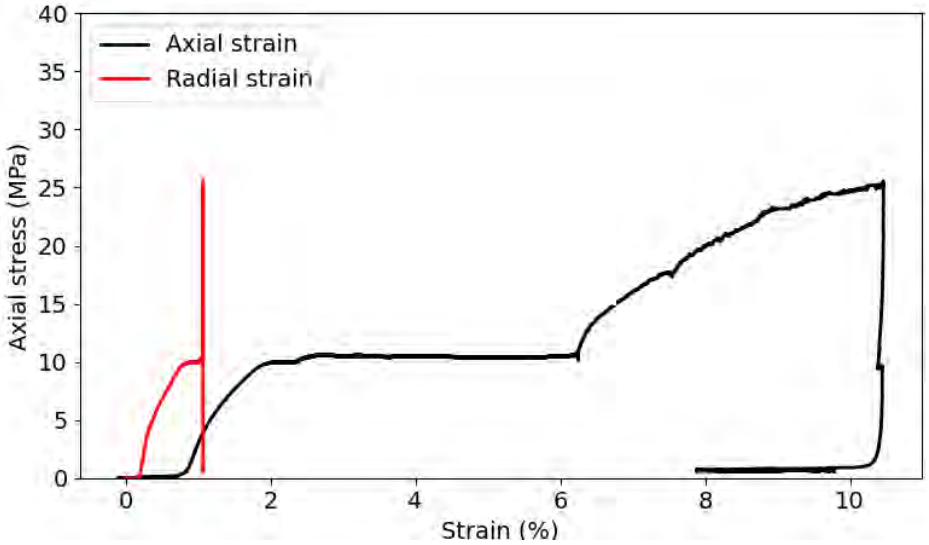

Figure 6: Stress-strain curve under 10 MPa confining pressure and 180 °C before thermal shock

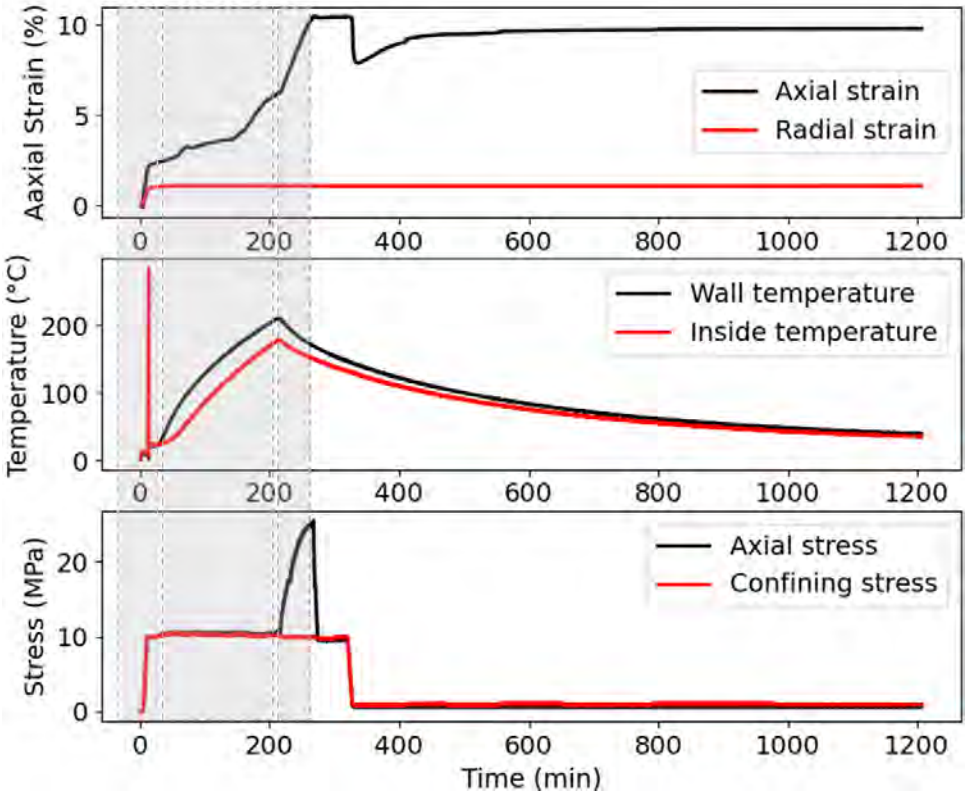

Figure 7: Triaxial compression testing under 10 MPa confining pressure and 180 °C. The first grey area shows that this cement has strong deformation during confining pressure application. The second grey area shows that the deformation continues during the heating stage. The third grey area shows the compression stage.

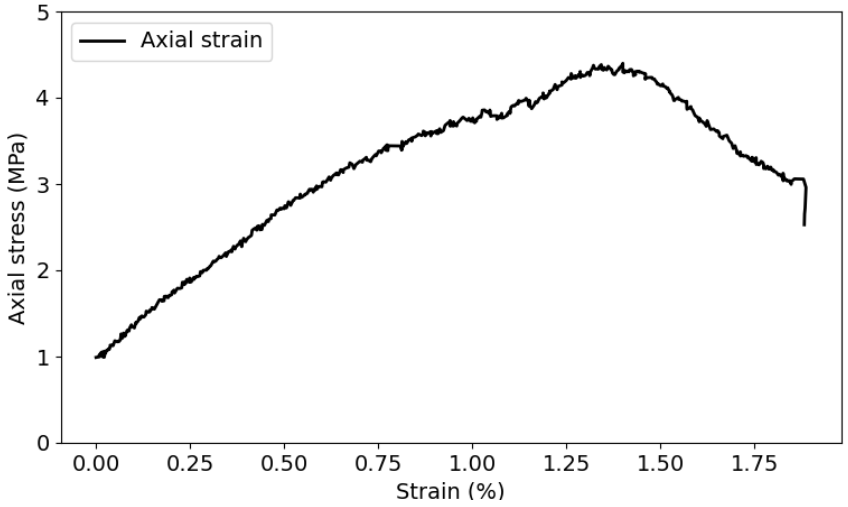

Figure 8: Stress-strain curve under 180 °C before thermal shock

3.1 Mechanical properties of cement after thermal shock

The same types of experiments were conducted on the specimens after undergoing thermal shock. The detailed stress-strain curves are shown from Figures 9 to 14, and the mechanical properties are summarized in Table 2. After experiencing thermal shock, the compressive strength of the specimens increased to 7.6 MPa, 6.14 MPa, and 6.7 MPa, representing a 42% increase compared to the samples without thermal shock. The elastic modulus also increased to (1.75 ± 0.15) GPa, (1.15 ± 0.05) GPa, and (1.6 ± 0.1) GPa, demonstrating an increase of 34%.

In the 10 MPa confining pressure compression test, the compressive strength increased slightly from 30 MPa to 32 MPa, while modulus increased from (1.7 ± 0.2) GPa to (2.5 ± 0.4) GPa. Comparing the shapes of the stress-strain curves in Figures 5 and 12, the specimen subjected to thermal shock reached near peak strength at just 4% axial strain, whereas the stress for the non-thermal shock specimen continued to climb until reaching 10% axial strain. This behavior indicates that the thermal shock reduces the ductility of the cement.

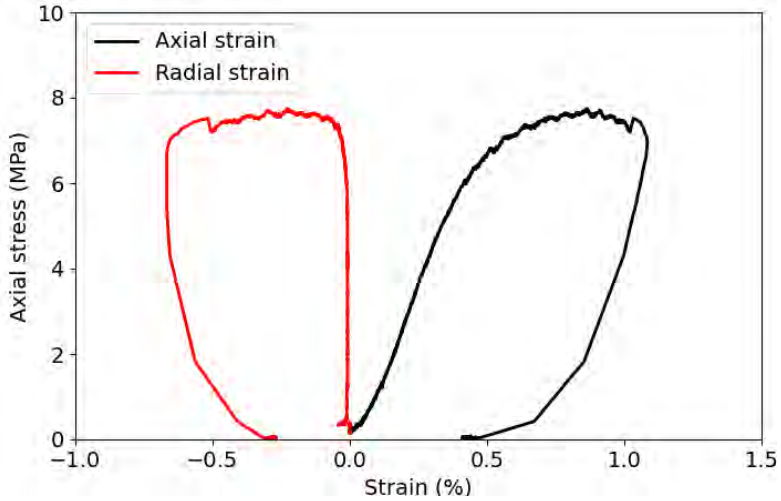

Figure 9: Stress-strain curve of the first uniaxial compression testing before thermal shock

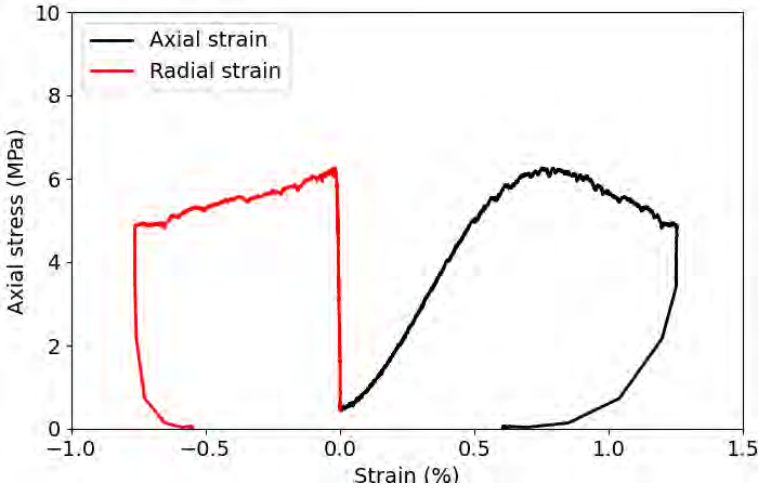

Figure 10: Stress-strain curve of the second uniaxial compression test after thermal shock

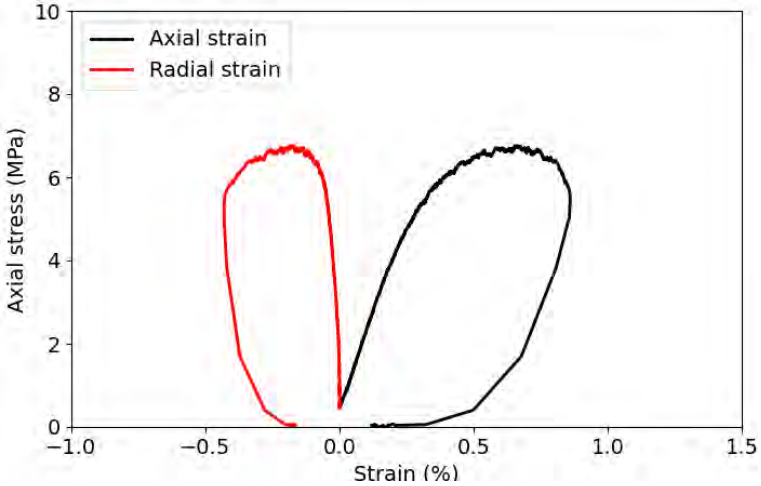

Figure 11: Stress-strain curve of the third uniaxial compression test after thermal shock

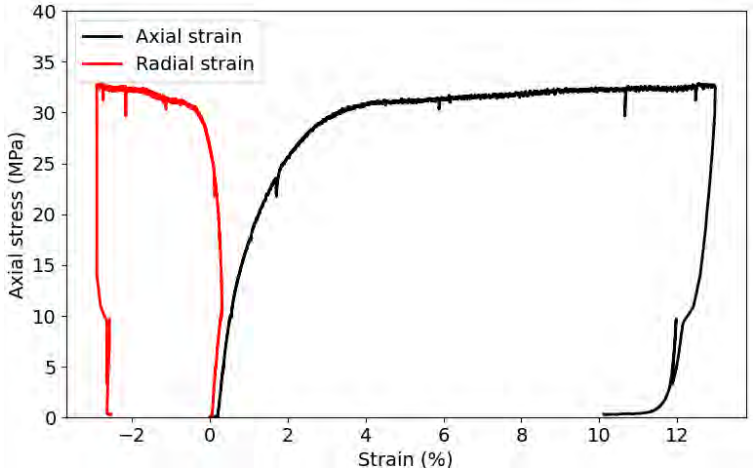

Figure 12: Stress-strain curve under 10 MPa confining pressure after thermal shock

Similar behavior was observed in the compression tests conducted under 180 °C and 10 MPa confining pressure, as shown in Figures 6 and 13. After undergoing thermal shock, the compressive strength increased from 25 MPa to 32.3 MPa, and the elastic modulus increased from (1.33 ± 0.05) GPa to (3.15 ± 0.15) GPa. At near maximum axial stress, the axial strain recorded was only 3% for the specimen that had undergone thermal shock, in contrast to the continuing increase in stress beyond 10% axial strain observed in the specimen without thermal shock.

The results of uniaxial compression tests under 180 °C further confirmed this pattern of increased compressive strength coupled with reduced ductility, as shown by comparisons between Figure 14 and Figure 8.

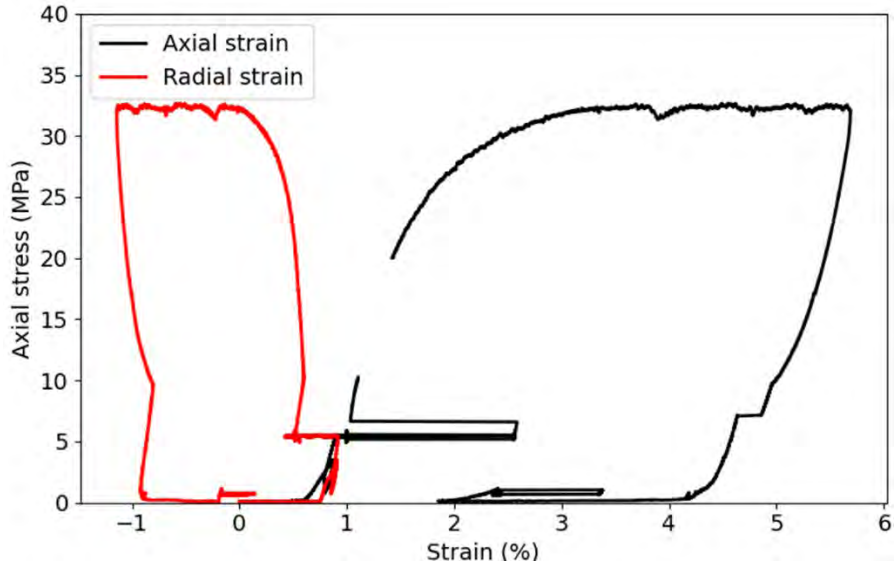

Figure 13: Stress-strain curve under 10 MPa confining pressure and 180 °C before thermal shock. Axial strain data was lost in the middle of the test, resulting in the disconnection of the black curve.

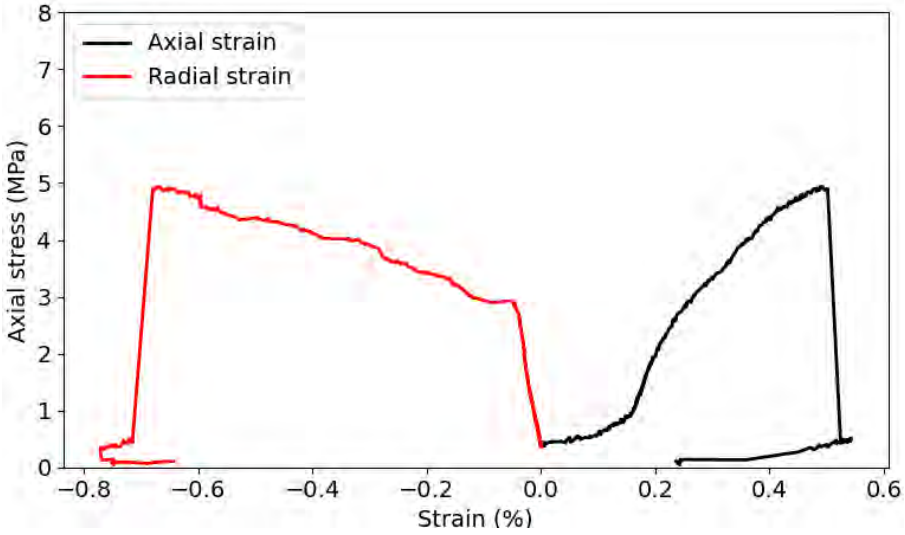

Figure 14: Stress-strain curve under 180 °C after thermal shock

Table 2 Mechanical properties of the PMHS treated cement before and after undergoing thermal shock.

PMHS treated Cement	Before Thermal Shock			After thermal shock		
	Strength (MPa)	Modulus (GPa)	Poisson's ratio	Strength (MPa)	Modulus (GPa)	Poisson's ratio
UCS 1	4.7	1.15 ± 0.05	0.14 ± 0.01	7.6	1.75 ± 0.15	--
UCS 2	4.6	1 ± 0.03	0.14 ± 0.01	6.14	1.15 ± 0.05	--
UCS 3	5.1	1.2 ± 0.1	0.1 ± 0.01	6.7	1.6 ± 0.1	--
UCS average	4.8	1.12 ± 0.06	0.08 ± 0.01	6.8	1.5 ± 0.1	0.04 ± 0.01
10 MPa	30	1.7 ± 0.2	0.09± 0.02	32	2.5 ± 0.4	0.13 ± 0.02
180 C	4.34	0.35 ± 0.01	--	4.9	1.9 ± 0.3	0.3 ± 0.02
10 MPa 180 C	25	1.33 ± 0.05	--	32.3	3.15 ± 0.15	0.17 ± 0.02

The above experimental results show the promising performance of this PMHS treated FCS incorporated calcium aluminate cement after undergoing thermal shock. The fundamental mechanisms have been explained by Sugama and Pyatina (2008), which were summarized here:

(1) Cenospheres + sodium metasilicate → silanol and sluminol groups on the surface

(2) Silanol and sluminol groups + PMHS → siloxane oxygen-linked M-FCS

(3) At high temperatures of 175 °C or 250 °C → depolymerization at the FCS surface

(4) Siloxane → low crosslinked silicon-like polymer after repolymerization

(5) The repolymerization-induced product protects FCS from pozzolanic reactions

3.2 Modeling results

Using the data obtained from our triaxial compression tests, we applied a thermoporoelasitc model to determine the safe operating envelope for this cement. Figure 15 shows that this cement has a wide range of safe applications. No failures were observed in the normal range of pressure and temperature perturbations. The temperature drawing down by 50 °C is an aggressive change that typically challenges regular brittle cement. The main reason for this wide envelope is due to low modulus of this cement.

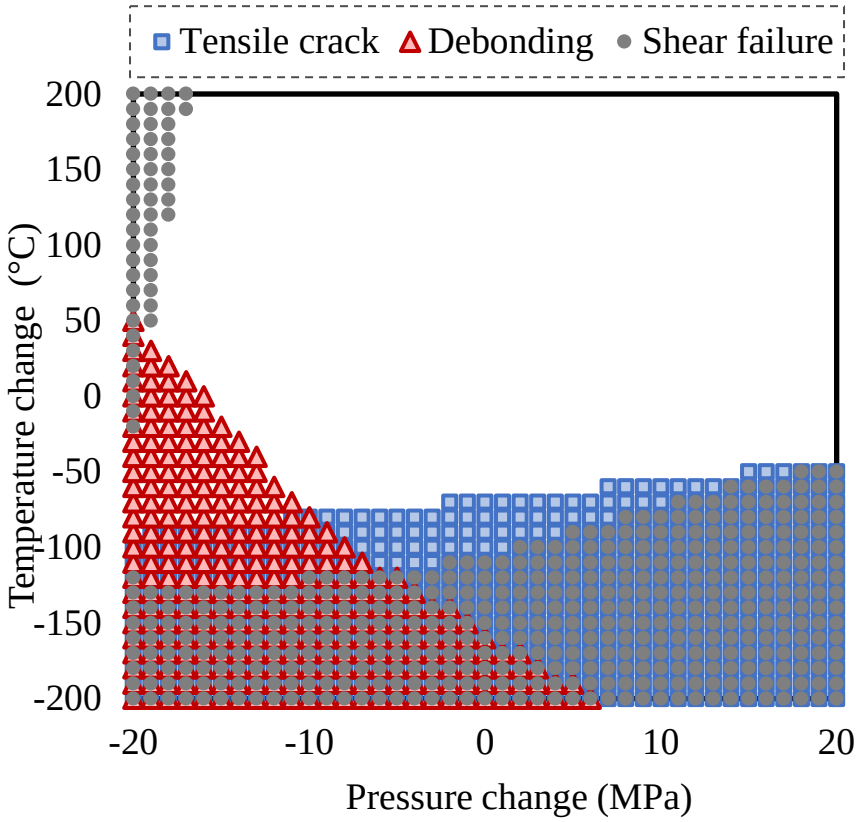

Figure 15: Safe operating envelope for the PMHS treated cement

4. Conclusions

Our study focused on PMHS-treated alkali-activated calcium aluminate cement with Class F fly ash, subjecting it to thermal cycling and measuring their mechanical properties through triaxial compression tests under high pressure and high temperatures. The key insights are summarized as follows:

1. This novel cement formulation demonstrates robust performance in resisting thermal shock. Instead of mechanical degradation, both the strength and modulus of the cement increased after exposure to thermal shock.

2. PMHS induced the dehydrogenation, depolymerization, and repolymerization processes, resulting in the formation of polymers that protects the FCS from pozzolanic reactions. This explains the cement's capability to maintain its mechanical performance under thermal shock.

3. The low modulus of this cement contributes to a broad safe operating envelope, as shown by modeling analysis. This highlights the cement's capability to effectively handle variations in pressure and temperature, offering significant advantages for its use in harsh environments.

Acknowledgement

Financial support for this work is gratefully acknowledged from the U. S. Department of Energy (DOE) Office of Energy Efficiency & Renewable Energy's Geothermal Technologies Office for "Cements and a modeling tool to calculate their viability under various exploitation conditions of HT RTES systems" with award number of DE-LC-0000016. We also gratefully acknowledge support from the U.S. Department of Energy (DOE) Office of Basic Energy Sciences for "Center for Coupled Chemo-Mechanics of Cementitious Composites for EGS (C4M)" and U. S. DOE Geothermal Technologies Office (GTO) funded project – Geothermal Limitless Approach to Drilling Efficiencies (GLADE; DE-EE0010444) led by Oxy USA, Inc.

REFERENCES

Boquera, L., Castro, J. R., Pisello, A. L., Fabiani, C., D'Alessandro, A., Ubertini, F., & Cabeza, L. F. Thermal and mechanical performance of cement paste under high temperature thermal cycles. *Solar Energy Materials and Solar Cells*, 231, (2021), 111333.

Meng, M., Pyatina, T., Solovyov, V., Bijay, K. C., & Frash, L. (2023). Evaluation of Cement Mechanical Performance in Thermal Storage Wells. In 2023 Geothermal Rising Conference: Using the Earth to Save the Earth, GRC 2023 (pp. 889-900).

Meng, M., Frash, L., Carey, J. W., Niu, Z., Zhang, W., Guy, N., ... & Welch, N. (2021). Predicting cement-sheath integrity with consideration of initial state of stress and thermoporoelastic effects. SPE Journal, 26(06), 3505-3528.

Lavrov, A., & Torsæter, M. (2016). Physics and mechanics of primary well cementing.

Pang, X., Qin, J., Sun, L., Zhang, G., & Wang, H. (2021). Long-term strength retrogression of silica-enriched oil well cement: A comprehensive multi-approach analysis. Cement and Concrete Research, 144, 106424.

Philippacopoulos, A. J., & Berndt, M. L. (2001). Mechanical property issues for geothermal well cements. *Transactions-Geothermal Resources Council*, 119-124.

Sugama, T., & Pyatina, T. (2018). Alkali-activated cement composites for high temperature geothermal wells. Scientific Research Publishing, Inc. USA.

Sugama, T., & Pyatina, T. (2021). Hydrophobic Lightweight Cement with Thermal Shock Resistance and Thermal Insulating Properties for Energy-Storage Geothermal Well Systems. Materials, 14(21), 6679.

Pyatina, T., & Sugama, T. (2018). Cements for high-temperature geothermal wells. *Cement based Materials*, 221-235.

Bauer, S. J., Barrow, P. C., Pyatina, T., & Sugama, T. (2020). Thermal expansion fluid flow and thermal shock of cement and a cement/steel interface at elevated pressure and temperature. Paper presented at 45th Workshop on Geothermal Reservoir Engineering, Stanford, 2020.

Wolterbeek, T. K. T., & Hangx, S. J. T. (2023). The thermal properties of set Portland cements–a literature review in the context of CO_2 injection well integrity. *International Journal of Greenhouse Gas Control*, 126, 103909.

Zhang, W., Eckert, A., Hilgedick, S., Goodman, H., & Meng, M. (2022). Wellbore Integrity: An Integrated Experimental and Numerical Study to Investigate Pore Pressure Variation during Cement Hardening under Downhole Conditions. *SPE Journal*, 27, (2022), 488-503.

Zhou, W., Wang, C., Meng, R., Chen, Z., Lu, H., & Chi, J. (2023). Study on thermal insulation cement and its thermal insulation characteristics for geothermal wells. *Scientific Reports*, 13(1), 4157.

The Third Electric Energy Transition Calls for Geothermal Energy Assurance

John R. Muir, Andrew J. Van Horn

GreenFire Energy, Inc., Walnut Creek, California

Keywords

The third electric energy transition, energy security, electric power, thermal energy, the U.S. electricity grid, geothermal energy, resilience, reliability, baseload power, resilient continuous power, closed-loop geothermal energy systems (CLG), enhanced geothermal systems (EGS), advanced geothermal systems (AGS), the "heat beneath our feet," green energy, clean energy microgrids, resilient community energy systems, climate change, global energy transition.

ABSTRACT

The third electric energy transition in the last one-hundred years is now underway in the United States. This major transition is challenging the "centralized grid" model of power generation and distribution, especially for large, energy intensive end-users. These consumers include manufacturing plants, data centers, metal smelters, refineries, chemical plants, military bases and emergency services that now consume about a third of all electric power.[1]

The third transition has not been a planned evolution, but instead emerged from the disruptive combination of rapidly escalating energy demand, climate change concerns, increasing volatile energy prices, and recurring U.S. regional power outages. Consequently, traditional suppliers, typified by today's electric and gas utilities, load serving entities (LSEs) and energy service providers (ESPs), are being supplemented and supplanted by new types of energy suppliers including Distributed Energy Resources (DERs), aggregators of demand responsive customers, microgrids, resilient community grids, Battery Energy Storage Systems (BESS), "prosumers," and Community Choice Aggregators (CCAs). The key driver for this transition is the need for "energy assurance" – a multi-factor concept that includes the continuous availability, reliability, resilience, scalability and price stability of energy while still meeting goals for decarbonization.

Energy assurance has also become a primary concern of large organizations that consume enormous supplies of electricity and thermal energy. These organizations realize that electric energy demand is outstripping supply and that the regulated "commodity" energy market model is incapable of responding adequately. Availability is now a top priority. But even if the regulated market could generate sufficient energy to meet market demand, the ability to deliver that energy reliably is highly suspect due to aging transmission lines, line congestion, and the prevailing vulnerability to weather related events, fire, and cyber-attacks. As a result, energy-intensive

organizations are actively seeking “behind the meter” energy solutions that enable them to assure and control their energy supply.

This “behind the meter” strategy has obvious advantages, first because it avoids some costs and risks of transmission, distribution, regulatory oversight, and wholesale market coordination, and second because self or co-located generation allows energy-intensive organizations to pay for the energy attributes that most closely correspond to their needs.

The quest for energy assurance has spurred intense interest in geothermal energy. In addition to its enormous potential magnitude, geothermal energy offers a unique combination of energy assurance attributes. Geothermal energy can provide both firm, baseload electric power and direct thermal energy that is critical in many manufacturing operations. “Behind the meter” geothermal power also offers price stability and insulation from grid outages and regulatory mandates. In short, geothermal energy is moving from being an attractive energy alternative to an indispensable component of the third electric energy transition.

Introduction

In the United States a highly regulated electricity market has evolved for over 100 years as electricity consumption became ubiquitous, transmission networks proliferated, and different fuels for power generation came into use. Because the geothermal industry has failed to actively participate in drafting and influencing the laws and regulations that have structured U.S. energy markets until very recently, funding for and investment in geothermal energy has been orders of magnitude lower than that for other energy technologies.

In order to enable geothermal energy to gain essential funding and to reduce the time for projects to come online and generate revenues, it is important for industry participants to have a better understanding of the actions, events and mandates that have enabled oil, coal, natural gas, nuclear and hydro energy supplies to dominate energy markets and more recently for solar, wind, hydrogen and batteries to compete for market share.

The following sections describe the first two U.S. electric energy transitions and discuss elements of the third energy transition now in progress. The first energy transition of the electricity grid was defined by the regional electrification architecture of large-scale projects such as the Grand Coulee and Boulder dams and the Tennessee Valley Authority that made electricity available to large numbers of homes and businesses for the first time during in the 1930s. That first model comprised capital intensive infrastructure, including generating plants powered by coal and hydro-electric dams, high-capacity regional transmission lines to transport power, and local distribution systems owned and operated by utility companies.

Figure 1 below illustrates some of the major events in U.S. electricity and natural gas markets between 1875 and 1970. Significant technological advances and infrastructure development were accompanied by the creation of large companies to supply equipment, the Bonneville Power Administration and major utility companies, the initiation of state regulation, the formation of the Federal Power Commission, the National Electric Reliability Council, and the U.S. Environmental Protection Agency (EPA.) The era was characterized by ongoing significant year-over-year electric load growth and the expansion of U.S. energy systems.

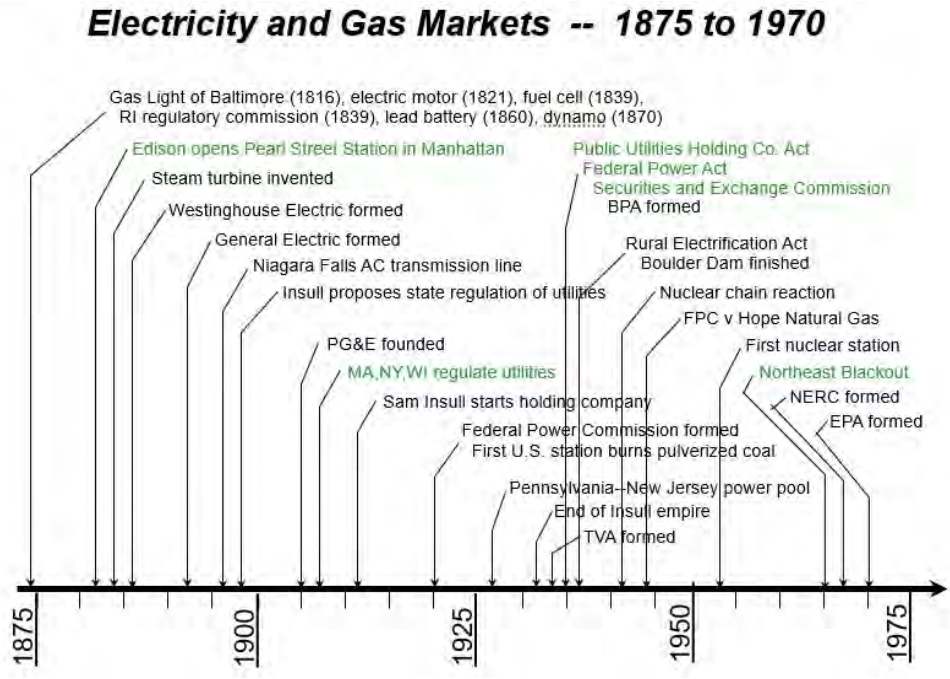

Figure 1. Key Events in U.S. Electricity and Natural Gas Markets – 1875 TO 1970

The Second Major U.S. Electric Energy Transition Began in the 1970s

The transition away from the utility-owned infrastructure model in the U.S. began in the late 1970's as governments and utilities responded to environmental and natural gas supply availability concerns by enabling power purchases at system "avoided costs," and by mandating minimum thermal efficiencies and prohibiting new natural gas-fueled plants. One result was that independent or merchant power producers could compete on price with utility-owned generators.

Figure 2 illustrates key U.S. events between 1970 and 1990, during the "Second Electric Energy Transition," which initiated many elements of the current market structure. Events included the formation of the U.S. Environmental Protection Agency (EPA) with accompanying clean air and clean water legislation and regulations, the founding of the Electric Power Research Institute, the OPEC oil embargo with impacts felt around the globe; PURPA, PIFUA and the NGPA legislation, and Federal Energy Regulatory Commission Orders affecting electricity, natural gas, oil and hydropower transactions, reliability standards, and the rates charged in interstate commerce.

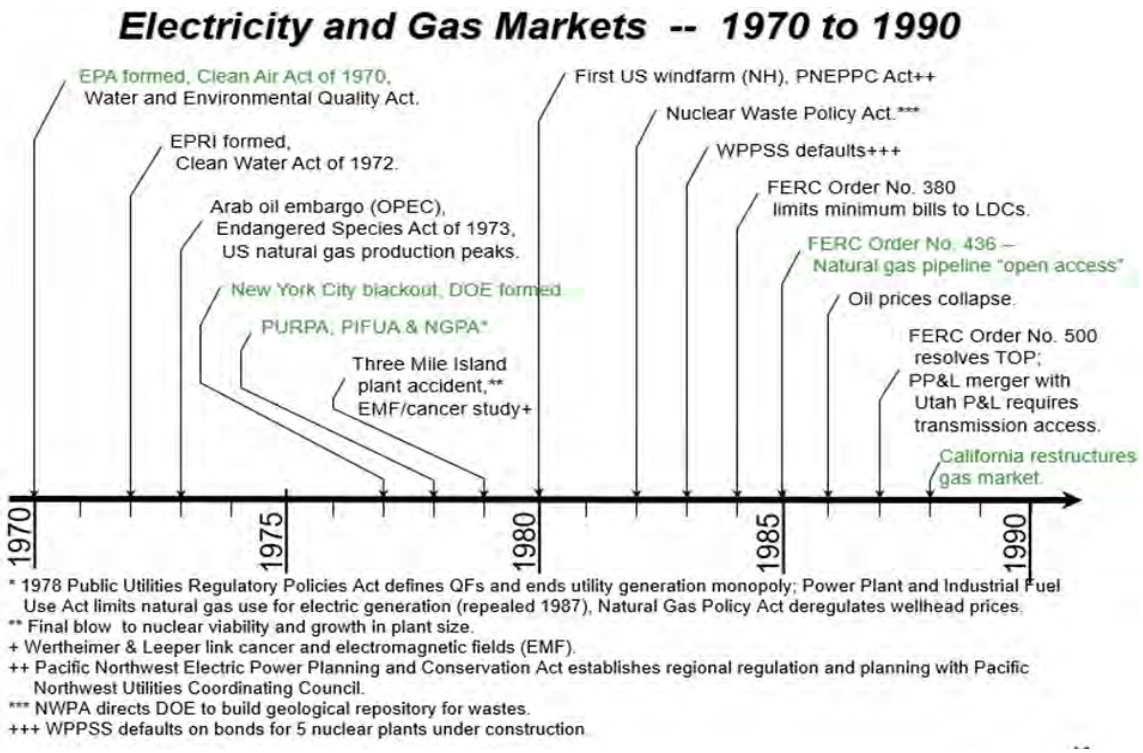

Figure 2. Key Events in U.S. Electricity and Natural Gas Markets Initiating the Second Electric Energy Transition, 1970 to 1990.

Legislation allowed more efficient energy resources, such as cogeneration, wind farms and biomass plants to be built and to create their own "learning curves." Learning curves for advanced technologies demonstrated cost reductions and performance improvements resulting from more deployment and "learning-by-doing." Independent System Operators (ISOs) and Regional Transmission Operators (RTOs) dispatched power plants on the basis of bids into hourly day-ahead and real-time wholesale electricity markets, paying market-clearing prices rather than costs-of-service.

During the 1990s grid operations became progressively more centralized by region. Natural gas combined cycle units became the preferred choice for capacity additions in many states. Open transmission access allowed wholesale markets to be designed and operated, and the electric utility industry was restructured.

Three major regional electricity grids now operate in the U.S. and Canada. The Western Interconnect extends from the Pacific Ocean to the Rocky Mountains; the Eastern Interconnect operates east of the Rocky Mountains, and the independent Texas Interconnected system is essentially only in Texas. Interstate wholesale power transactions are regulated by the Federal Energy Regulatory Commission (FERC) and retail transactions are regulated within most states by state Public Utility Commissions.

In 2024 the core architecture for regional power systems remains in place, as utilities, merchant generators, grid operators, Electric Service Providers (ESPs) and balancing authorities dominate the generation, dispatch and distribution of electricity. There are sixty-six U.S, one Mexican and

eight Canadian control areas that maintain the reliability of the major North American interconnected grids.

In the past, new technologies took decades to be developed, penetrate, and eventually dominate electricity capacity additions. These technological advances led oil, coal, natural gas and nuclear to become the primary fuels and also spawned immense supporting infrastructure and regulatory bodies that make transitions difficult. Nevertheless, the quest to reduce costs and decarbonize the U.S. economy has resulted in the significant expansion of low-cost, just-in-time natural gas production and pipeline transport methods to fuel gas-fired applications. Together with additions of renewable, intermittent solar and wind plants, the U.S. electricity industry has been able to achieve a reduction in annual CO_2 emissions of about 28% between 1995 and 2023. Today, the combustion of natural gas for power and heating buildings produces only about 40% of the greenhouse gas emissions (GHG) that burning coal would produce to provide an equivalent amount of combustion energy. Despite these improvements, natural gas cannot enable the US to achieve its "zero carbon" goals

The cumulative result of legislative and regulatory mandates has changed cost structures and created regional grids. Today's commodity power rates contain multiple and significant unbundled costs. Since the 1980s, electricity rates paid by end-use customers that are set by public utility commissions like the California Public Utilities Commission (CPUC) contain not only the costs of building, operating and maintaining power plants, transmission and distribution systems, but also include costs for ISO ancillary services, above-market costs of Qualifying Facilities and stranded assets, reliability must-run contracts, nuclear decommissioning and public benefits charges, among others. As a result, the relationship between the actual cost of generation and the price paid by the end-user has become increasingly decoupled. Figure 3 shows the results of this trend between 2006 and 2016, as the delivered cost of electricity rose continuously when compared to the cost of generating electricity.

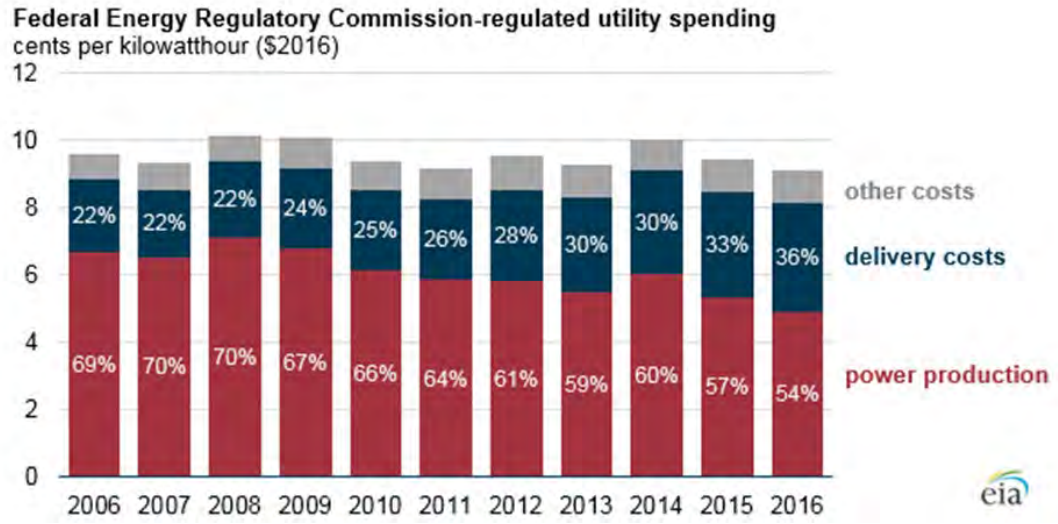

Source: US Energy Information Administration, FERC Financial Reports, September 2017

Figure 3. Electricity Prices Reflect Rising Delivery Costs and Declining Production Costs

The Third Electric Energy Transition

The Third Electric Energy Transition can be described as a move toward the general de-commodification of energy and, most specifically, electricity. A Megawatt-hour (MWh) is no longer just a unit of energy, but instead is energy generated and delivered with specific attributes such as price, price stability, scalability, reliability, environmental impacts, and resilience. Because participants in the energy market value these attributes differently, there is no longer one standard commodity value proposition.

Various attributes comprise the concept of energy assurance, even though each customer seeks its own balance of features. Attributes that were formerly understood as part of a standard offering of capacity and energy can now be differentiated and given separate valuations. Consequently, the Third Electric Energy Transition is spawning multiple types of solutions that enable organizations to contract for the bundle of energy attributes that best matches their specific priorities. Examples of this trend include energy efficiency, demand-side responses, distributed energy resources, microgrids, Community Choice Aggregators, resilient community grids, and self-generators.

In 2018 Sheldon Peterson, the former CEO of the National Rural Utilities Cooperative Finance Corporation, characterized the tasks facing the energy industry as Decentralization, Digitalization, Decarbonization, and Disintermediation (the 4-Ds).[2,3] Rapid electrification and volatile markets make accomplishing the 4-Ds complex and challenging. Traditional utilities and ESPs need to raise their rates high enough to cover increasing costs but keep rates low enough to retain enough customers to provide sufficient revenues to pay for the new obligations now part of the third energy transition. However, if too many customers depart as disintermediation occurs, then the risks of a potential Death Spiral are magnified, adding instability to our interrelated energy systems.

Although solar, wind and battery technologies have become essential contributors to increased electrification and decarbonization, they are not fully capable of addressing our 4-D challenges. The risk of greater reliance on inherently intermittent solar and wind grows proportionately with its prevalence in grid-delivered electricity. Worse, we cannot eliminate all the risks that impact wind and solar energy systems including powerful storms, wildfires, widespread episodes of extreme heat, coastal flooding, and rising sea levels. For example, past volcanic and weather events like the eruption of Mt. Tambora in 1815 would, if repeated, bring about a “year-without-sun,” causing global crop failures and rendering electric grids dependent on solar and wind largely inoperable. Other risks with very high consequences, such as war or sabotage, are largely ignored but could be mitigated by having a more diverse and robust set of energy supplies.

As a result, the widely used LCOE calculation (Levelized Cost of Energy) is no longer an accurate metric for comparing the true cost of generation technologies because it does not take into account intermittency and reliability. Hence, although wind and solar appear to have a cost advantage relative to other energy sources using standard LCOE calculations, when the cost of providing necessary “firming” power is included, the actual cost is much higher. Figure 5 below demonstrates that the estimated cost of “firming” the grid to overcome the intermittency of wind and solar now costs more than the wind or solar power itself in California.

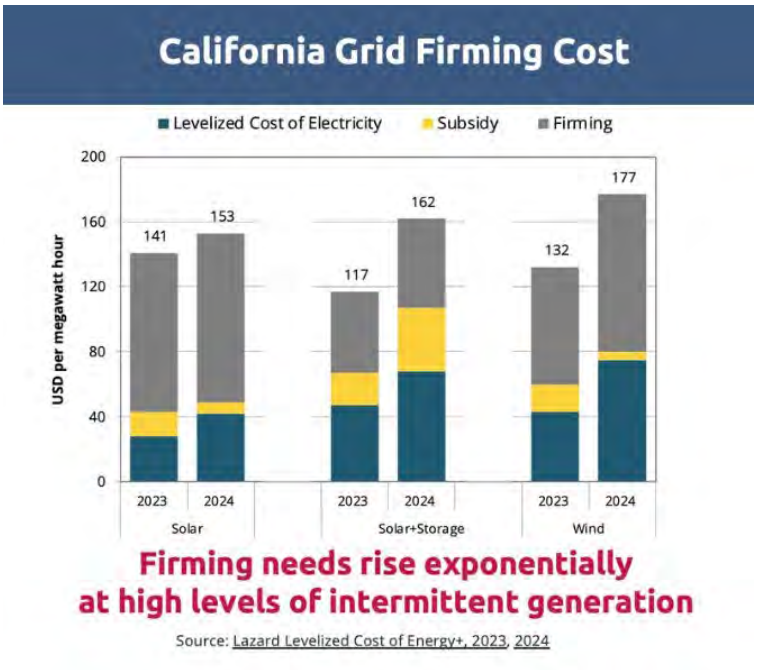

Figure 5 California Grid Firming Cost[4]

Multiple Factors Are Driving the Third Electric Energy Transition

The factors driving the Third Electric Energy Transition are fundamental, long-term, and structural.

Accelerating demand for clean energy sources

- The global demand for power has accelerated much faster than predicted, leading to shortages in many markets. For example in the United States "projections of electricity demand growth have doubled. The nationwide forecast of electricity demand growth by 2028 increased from a projection of 3.8% in 2022 to 7.8% in 2023".[5]
- National and regional climate policies, combined with low current natural gas prices, have substantially curtailed or eliminated the use of traditional baseload energy sources, such as coal and oil.
- Availability of energy has become a potentially significant constraint on growth.
- Manufacturing, in particular, needs thermal energy in addition to reliable, clean electric power.

Price Increases and Price Instability

- After decades of relative price stability, electric power consumers are confronted with the rapid escalation of power prices along with increased price volatility

Grid Instability

- As intermittent resources, such as wind and solar power generation, comprise a greater percentage of total grid capacity, the volatility of the energy supply increases.
- Prolonged power failures (sometimes with devastating impacts, as occurred in Texas in February 2021, during a winter storm), more frequent outages, brownouts, and power rationing have become increasingly common in both developed and emerging economies.
- Much of the electric grid is comprised of aging infrastructure and has shown its vulnerability to weather, fires and other disruptions.
- Power generation has become less predictable, because baseload coal and nuclear plants are being retired and non-geothermal renewables, including hydro power to a certain extent, are weather-dependent.

Regulatory and Legal Inertia

- Utilities are burdened by a complicated regime of regulations and restrictions that make it difficult to meet rapidly mounting demands for power.
- Existing powerlines are congested and building new transmission lines can require decades of contracting with multiple parties to permit, finance, and build.
- Intermittent power sources are inherently inefficient for large capacity power lines.

Energy Assurance and Other Key Attributes Are Required by Energy Intensive Organizations

To large energy-intensive organizations, “energy assurance” comprises multiple attributes in the right combination:

- **Availability**: sufficient energy must be available to accommodate expansion and growth. For example, some major textile plants in northeastern Spain have curtailed needed plant expansions, due to draught and regulatory controls that inhibit them from obtaining additional needed power.

- **Flexibility**: because using electric power to heat materials can be prohibitively expensive, the energy mix may require both heat and electric power,

- **Reliability and Resilience:** Reliability means a high level of uptime, and Resilience means resistance to and recovery from unforeseen events, such as major weather events or purposeful attacks. To energy intensive organizations, the consequences of power shortages and power instability have been nearly existential. Disrupted operations, damage to continuous process plants, and wasted materials have become a serious business risk. Predictably, vulnerable organizations no longer view energy as a commodity with assured availability. Instead, large power consumers consider their future power needs with respect to both reliability and resilience.

- **Stable affordability**: the energy supplied must be stable and cost-effective for the intended application. Today, geothermal power purchase agreements are being signed from

$70/MWh to $100/MWh for greenfield projects[6] and for $20 to $35/MWh for additional output from retrofits utilizing existing infrastructure.

- **Ancillary attributes:** Energy assurance alone is not sufficient. Other critical attributes sought by companies considering procuring their own energy supplies are:
  - Source: clean (ethical sourcing, reduced or no greenhouse gas emissions, limited water use & wastes),
  - Land: economical use of land and public acceptability,
  - Safety: low risks to employee and public welfare, health and safety,
  - Lifecycle costs and impacts: costs and impacts evaluated across the entire supply chain, including end-use and disposal over the project/product and its replacement's lifetimes.

Geothermal Energy Is A Key Element of the Third Energy Transition

As discussed in prior GRC papers,[7,8,9] geothermal energy could provide clean, carbon-free, around-the-clock, weather independent, energy secure, dispatchable, reliable, scalable and resilient power and heat in many more locations than it is used today, but only if interdisciplinary geothermal research, innovations and advances continue to achieve cost reductions and performance improvements like those occurring in recent months during 2023 and 2024.[10,11,12,13,14]

Figure 4 shows the value proposition and attributes provided by next-generation geothermal energy systems.

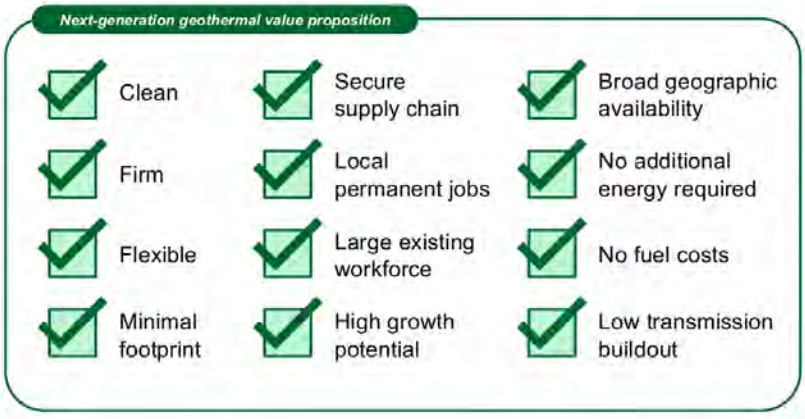

Figure 4 Features and Attributes of Next-generation geothermal projects[15]

Because the list of energy assurances required by consumers is comprehensive, it becomes obvious that geothermal energy is the ideal source to enable and accelerate the Third Energy Transition. No other renewable energy source provides clean energy in two forms (electrical and thermal) with high availability, reliability and resilience. Further, geothermal energy has far more global energy potential than coal, oil and gas combined, so it is inexhaustible in practical terms. In short, geothermal energy is uniquely suited to the requirements of the third energy transition.

Benefits of Co-location

These advantages can be made even more valuable by co-locating energy-intensive operations on top of or adjacent to geothermal resources. The clean, continuous, and reliable power generation from a "behind the meter" installation provides the energy assurance that energy-intensive organizations seek. They can:

- Avoid or mitigate utility price and rate increases,
- Eliminate grid vulnerabilities,
- Obtain both thermal energy and electric power,
- Meet clean energy and environmental stewardship goals,
- Reduce their energy footprint with land requirements 1/10 of solar and wind farms.

Having become aware of the significant benefits of geothermal energy, a number of industrial projects around the world are currently considering co-locating new facilities with geothermal energy operations. Such projects demonstrate the potential for geothermal to be a significant contributor to the third energy transition. Examples of such projects include:

- Data center companies that, due to the additional computing demands of artificial intelligence (A.I.) need to multiply the number of data centers by 4-fold, but can't get the added electric power, don't trust the grid, and want to control future prices,
- A carbon capture company that needs thermal energy to extract carbon, but knows heat is expensive and fossil energy is not low-emitting,
- Military bases that require absolute power assurance, hardened infrastructure, and resilience,
- A government-controlled power company that is directed to develop geothermal resources,
- Large textile companies that need to expand operations but cannot get additional power and are water constrained,
- Large chemical companies that need to expand operations but cannot get additional power, are water constrained and must meet GHG emission reduction goals.
- Steel manufacturing plants, which must have continuous power.
- Oil companies that need power for field operations and seek to convert depleted oil wells into geothermal power wells, thus displacing diesel generators.
- Companies mining bitcoins. It has been estimated that crypto currency operations consume 0.6% to 2.3% of all U.S. electricity demand in 2023. Of course, this electricity usage consumes resources and produces pollutants, while producing no realizable products.[16]

Advanced Geothermal Energy Systems Are Evolving to Match Customer Priorities

In order to realize its full energy assurance potential, geothermal power must be made more geographically available and scalable. While progress is being made across the entire spectrum of geothermal energy systems, Advanced Geothermal Systems (AGS) based on closed-loop architectures are particularly promising for third generation applications.

Closed-loop geothermal (CLG) energy systems make geothermal projects feasible in a much broader spectrum of resources than conventional hydrothermal systems and, in principle, more than Enhanced Geothermal Systems (EGS). This is because closed loops don't require the combination of large volumes of water and high subsurface permeability needed for conventional systems or the need for large-scale fracking, provided there is sufficient heat to extract. Closed-loop systems are much easier to permit because nothing is injected into the subsurface or extracted other than heat. A wide variety of CLG designs are now being developed and deployed that will provide the flexibility to use a variety of working fluids to enhance power output.

Two types of geothermal settings for "behind the meter" power projects

Organizations seeking energy assurance must evaluate many factors when deciding to co-locate a facility near a geothermal resource. However, the choice of geothermal resource will fundamentally determine the time, expense and control of the project. The key difference is whether the geothermal resource has already been at least partially developed or whether it is a "greenfield" project.

The fastest, least complicated way of providing additional geothermal energy is to work with existing projects. Such projects are in operation in many parts of the world with a combined capacity of about 16 GW. By applying closed-loop technology many of these projects can significantly expand production at an existing geothermal site. Choosing to co-locate with an existing geothermal operator has significant benefits:

- Most required permits have already been issued and additional permits should be relatively easy to acquire.
- The geothermal resource is proven, so project risk is small.
- Key infrastructure is already in place.
- Most projects have inactive wells and/or depleted permeability in fields that might be restored using closed-loop technology. Some projects also have idle electric generators that could be used.
- A contract can be executed to produce and deliver power from existing facilities or to finance and drill new wells and install additional generation.

Greenfield projects take longer to complete, but offer some advantages in terms of ownership, control, and flexibility.

- Industrial companies can do joint development of a given site to create a geothermal energy park, which is controlled by the participants.

- New projects should be able to take advantage of new forms of government subsidies and tax credits.

Increased Funding and Other Reforms Are Necessary to Continue the Third Energy Transition

The tasks required to implement the Third Energy Transition in the U.S and elsewhere are daunting and will require concerted, long-term investment by both the private and public sector.. According to the U.S. White House:

> "$3 trillion in private investments will be made over the next decade to address climate change, with 70% of these investments required to originate from utility and energy companies, clean energy developers, and financing institutions. While that may seem like a big number, it falls far short of the projections that indicate the need for annual investments to be nearly double that forecast, ranging from $4 trillion to $6.9 trillion just to meet the emissions reduction targets outlined in the Paris Agreement. This underscores the urgency and scale of finding clean ways to produce baseload power, and the need for substantial commitments from both the public and private sectors to drive meaningful change."[17]

For decades geothermal energy has been significantly underfunded by DOE and private investors compared to other energy systems. Even in 2022, the "Inflation Reduction Act and the Bipartisan Infrastructure Law concentrated clean energy investments in solar and wind, which are great near-term solutions for decarbonization, but neglected to invest sufficiently in continuous energy solutions like geothermal energy, which are necessary to reach full decarbonization in the long term." As also pointed out, "the increasing mix of intermittent renewable energy sources like solar and wind must be balanced by sources of clean firm power that are available around the clock in order to ensure grid reliability and reduce the need to overbuild solar, wind, and battery capacity. Geothermal power is a leading contender for addressing this issue."[18]

A January 2024 Federation of American Scientists report describes how increased government support could help commercialize clean energy, including geothermal power and heat technologies.

> "Next-generation geothermal technologies, such as enhanced geothermal systems (EGS), closed-loop [CLG] or advanced geothermal systems (AGS), and other novel designs, promise to allow access to a wider range of geothermal resources. Some designs can potentially also serve double duty as long-duration energy storage. Rather than tapping into existing hydrothermal reservoirs underground, these technologies drill into hot dry rock, engineer independent reservoirs using either hydraulic stimulation or extensive horizontal drilling, and then introduce new fluids to bring geothermal energy to the surface. These new technologies have benefited from advances in the oil and gas industry, resulting in lower drilling costs and higher success rates. Furthermore, some companies have been developing designs for retrofitting abandoned oil and gas wells to convert them into geothermal power plants. The commonalities between these two sectors present an opportunity not only to leverage the existing workforce, engineering expertise, and supply chain from the oil and gas industry to grow the geothermal industry but also to support a

> just transition such that current workers employed by the oil and gas industry have an opportunity to help build our clean energy future."[19]

> "The expansion of the [worldwide] geothermal industry presents considerable employment opportunities as well, with more than 196,000 individuals employed in 2021 according to the International Renewable Energy Agency's 2021 Annual Review. Many of these workers bring transferable skills and expertise from the oil and gas sector, facilitating a smooth transition."[20]

As proposed in May 2024, the 2025 federal budget promises to be instrumental in training and employing our vital future science and energy workforce.

A March 2024, New York Times article stated,

> "the growth of artificial intelligence requires huge data centers to train the evolving large-language models, making proximity to users less necessary…But as more of these sites start to pop up across the United States, there are new questions on whether they can meet the demand while still operating sustainably. The carbon footprint from the construction of the centers and the racks of expensive computer equipment is substantial in itself, and their power needs have grown considerably…Just a decade ago, data centers drew 10 megawatts of power, but 100 megawatts is common today."… "The Uptime Institute, an industry advisory group, has identified 10 supersize cloud computing campuses across North America with an average size of 621 megawatts…This growth in electricity demand comes as manufacturing in the United States is the highest in the past half-century, and the power grid is becoming increasingly strained."[21]

> "A.I. is only a small percentage of the global data center footprint. The Uptime Institute predicts A.I. will skyrocket to 10 percent of the sector's global power use by 2025, from 2 percent today"[22]

The May 5, 2024, Economist magazine cited the latest quarterly reports from Alphabet (Google's corporate parent), Amazon and Microsoft, stating that

> "the world's cloud-computing giants—collectively invested $40bn between January and March, most of it in data centres equipped to deal with growing artificial-intelligence (ai) workloads. Last month Meta, which does not have a cloud business but does run a data-hungry social-media empire, said its capital expenditure could reach $40bn this year as a result of AI-related projects. That is not far off the $50bn that Saudi Aramco, an oil colossus, is planning to splurge. Microsoft is likely to spend more."

Artificial Intelligence (A.I.) is poised to revolutionize the energy sector, mirroring the transformative effects of the Internet and mobile communications on global economic growth, according to a recent article by Wood Mackenzie.[23] A.I. promises to raise demand for energy, drive efficiencies, support low-carbon technologies, and address climate change while boosting the global economy. A.I.'s reliance on power-intensive data centers will necessitate massive investments in geothermal power generation to deliver power "behind the meter." As proof, tech companies are signing new power purchase agreements with early-stage geothermal companies.

And independent power producers are considering building data centers at existing generation facilities.[24]

In November 2023, Google announced that its data center project powered by geothermal energy is now operational:

> "To make the rapid progress needed to address climate change, we must accelerate a clean energy transition on a planetary scale. That's why we set an ambitious goal to operate our data centers and office campuses on 24/7 carbon-free energy (CFE) on every grid where we operate by 2030, with the ultimate aim of accelerating the decarbonization of the world's electricity systems.

Many industrial and commercial facilities around the world are seriously examining the feasibility of applying geothermal energy, particularly for plants operating in power systems where the costs of firm power have increased with higher penetrations of intermittent solar and wind generation. For example, Lazard's 2023 and 2024 Cost of Energy Studies[25] estimate how grid firming costs increase as the levels of intermittent generation go up in California. As illustrated previously in Figure 5, firming costs in California now exceed traditional LCOE values.

The Advantages of Geothermal Energy Today

Today, geothermal energy systems offer the most reliable, resilient, 24/7, continuous power and heat with the smallest footprint and lowest lifecycle costs of all renewable resources.

Geothermal projects add more jobs, have more secure domestic supply chains, and create more environmental benefits than solar or wind. Geothermal is largely carbon free and can also displace natural gas for heating. It can help balance the grid and provide baseload power and system diversity, as well as enhancing international energy security by reducing the risks of sabotage and deliberate disruptions in energy trade across borders.

Geothermal energy is weather independent and will still be operating when events like the explosion of Mt. Tambora in 1815 obscure the sun globally for months, and solar power systems cease to function.

What do we need to do?

Reductions in permitting time for projects, increased exploration and increased RD&D will make geothermal learning curves more robust and bring down costs. Geothermal technologies can provide energy assurance to individual companies, district heating projects and to regional electricity grids.

If we are serious about global decarbonization and electrification, we need to recognize that geothermal energy is now an essential energy resource.

Conclusions

Electricity continues to expand its share of the global energy market, as the need for energy in all forms surges beyond even optimistic estimates. At the same time, recent events have impacted

energy availability and electric grid reliability and stability, underscoring the essential importance of energy assurance. Consequently, energy intensive companies are prioritizing energy assurance and paying premium prices to obtain the mix of reliability, resilience, and stability they need. Among all clean energy sources, renewable geothermal energy offers a compelling value proposition that is driving intense interest in co-locating energy intensive companies near geothermal resources.

Thus, over the next several decades we must develop and deploy diverse clean technologies both upstream and behind-the-meter with essential reliability and resilience attributes. At the same time, we need to implement more workable markets, revise outdated government and regulatory policies, adapt the utility and energy supply business models, and encourage international cooperation.

To properly maintain and expand our complex electricity and energy systems, we need to evaluate the benefits of increased diversity and the role that continuous investments in RD&D must play to innovate, develop and build the future technologies we need to supply and deliver decarbonized heat and electricity in the U.S. and around the world.

REFERENCES

Blankenship, Doug, Gertler, Charles, Kamaludeen, Mohamed, O'Connor, Michael, Porse, Sean, "Pathways to Commercial Liftoff: Next-Generation Geothermal Power." U.S. Dept. of Energy, March 2024.

Crismundo, Kris," RE to power upcoming SteelAsia plants." Philippine News Agency. May 28, 2024. https://www.pna.gov.ph/articles/1225673

GreenFire Energy, July 2024 Newsletter, news@greenfireenergy.com

Kocis, Igor, "Deep Geothermal Can Solve the Need for Baseload Power." Power Magazine. March 20, 2024. https://www.powermag.com/deep-geothermal-can-solve-the-need-for-baseload-power/

Lazard, "Levelized Cost of Energy+ 2024. https://www.lazard.com/research-insights/levelized-cost-of-energyplus/ Graph by Isuru Seneviratne on LinkedIn Post : https://www.linkedin.com/posts/isurusen_lcoe-solar-wind-activity-7207789041553997824-Zp8x/?utm_source=share&utm_medium=member_ios

Muir, John, Van Horn, Andrew, Hill, Joe, "Geothermal Energy as a Premium Power Source – Resilient Continuous Power." Geothermal Rising Conference, Reno, NV. GRC Transactions, Vol. 46, 2022.

Norbeck, Jack and Latimer, Timothy, "Commercial-Scale Demonstration of a First-of-a-Kind Enhanced Geothermal System. Fervo Energy, September 2023 . https://eartharxiv.org/repository/view/5704/

Pan, David, "US Bitcoin Miners Use as Much Electricity as Everyone in Utah," Bloomberg. February 1, 2024. https://www.bloomberg.com/news/articles/2024-02-01/bitcoin-miners-in-us-consume-up-to-2-3-of-nation-s-electricity?embedded-checkout=true

Patel, Sonal, "Delving Deeper: New Optimism for Enhanced Geothermal Systems. POWER. April 2, 2024. https://www.powermag.com/delving-deeper-new-optimism-for-enhanced-geothermal-systems/

Quaise Energy, "Quaise Energy Raises $21 Million to Accelerate Terawatt-Scale Geothermal Energy." March 12, 2024. https://www.quaise.energy/news/quaise-energy-raises-21-million-to-accelerate-terawatt-scale-deep-geothermal-energy

Raza, Aftab, “The Future of Power: The 4 Ds that are Shaping the Energy Transition.” FynValue Inc. November 25, 2023. https://www.linkedin.com/pulse/future-power-4-ds-shaping-energy-transition-aftab-raza-tzt8c/

Ricks, Wilson, Voller, Katharine, Galban, Gerame, Norbeck, Jack and Jenkins, Jesse. "The role of flexible geothermal power in decarbonized electricity systems." Nature Energy, 2024. https://www.nature.com/articles/s41560-023-01437-y

Rystad Energy, “Global Energy Scenarios 2023.” “ https://pages.rystadenergy.com/energytransition-flagship-report

Sisson, Patrick, “A.I. Frenzy Complicates Efforts to Keep Power-Hungry Data Sites Green.” New York Times. Updated March 19, 2024. . https://www.nytimes.com/2024/02/29/business/artificial-intelligence-data-centers-green-power.html?unlocked_article_code=1.qU0.rFmF.R2i6ci3E3xni&smid=nytcore-ios-share&referringSource=articleShare

Smith, Scott, Jones, Ben, Wei, Jian, Amon, Carolyn, “A framework for the utility customer of the future.” Deloitte. February 18, 2019. https://www.deloitte.com/global/en/our-thinking/insights/industry/power-utilities-renewables/energy-platform-elevated-human-experience-utility-customer.html

Terrell, Michael, “A first-of-its-kind geothermal project is now operational.” Blog.google. https://blog.google/outreach-initiatives/sustainability/google-fervo-geothermal-energy-partnership/

Van Horn, Andrew, Amaya, Alvaro, Higgins, Brian, Muir, John, Scherer, Joe, Pilko, Robert, and Ross, Malcolm, "New Opportunities and Applications for Closed-Loop Geothermal Energy Systems." GRC Transactions, Vol. 44, 2020, pp 1123-1143, October 2020.

Van Horn, Andrew, Muller, Phillip, Pilko, Robert, Amaya, Alvaro, Muir, John and Scherer, Joseph. "The Benefits of Geothermal Power, Evolution of the U.S. Electricity Grid, and the Need for Geothermal Research." G Transactions, Vol. 45, 2021, pp 1878-1895.

Wu, Alice, ”Breaking Ground On Next Generation Geothermal Energy.” Federation of American Scientists (FAS), January 2024. p 1. https://fas.org/wp-content/uploads/2024/01/Wu_Breaking-Ground-on-Next-Gen-Geothermal_2024.pdf

ENDNOTES

---

[1] Rystad Energy, "Global Energy Scenarios 2023 . https://pages.rystadenergy.com/energytransition-flagship-report

[2] Smith, Scott, Jones, Ben, Wei, Jian, Amon, Carolyn, "A framework for the utility customer of the future." Deloitte. February 18, 2019. https://www.deloitte.com/global/en/our-thinking/insights/industry/power-utilities-renewables/energy-platform-elevated-human-experience-utility-customer.html

[3] Raza, Aftab, "The Future of Power: The 4 Ds that are Shaping the Energy Transition." FynValue Inc. November 25, 2023. https://www.linkedin.com/pulse/future-power-4-ds-shaping-energy-transition-aftab-raza-tzt8c/

[4] Lazard, "Levelized Cost of Energy+ 2024." Lazard. https://www.lazard.com/research-insights/levelized-cost-of-energyplus/ Graph by Isuru Seneviratne on LinkedIn Post https://www.linkedin.com/posts/isurusen_lcoe-solar-wind-activity-7207789041553997824-Zp8x/?utm_source=share&utm_medium=member_ios

[5] Blankenship, Doug, Gertler, Charles, Kamaludeen, Mohamed, O'Connor, Michael, Porse, Sean, "Pathways to Commercial Liftoff: Next-Generation Geothermal Power." U.S. Dept. of Energy, March 2024.

[6] Blankenship, Doug, Gertler, Charles, Kamaludeen, Mohamed, O'Connor, Michael, Porse, Sean, "Pathways to Commercial Liftoff: Next-Generation Geothermal Power." U.S. Dept. of Energy, March 2024. p 2 and p 13.

[7] Muir, John, Van Horn, Andrew, Hill, Joe, "Geothermal Energy as a Premium Power Source – Resilient Continuous Power." Geothermal Rising Conference, Reno, NV. GRC Transactions, Vol. 46, 2022.

[8] Van Horn, Andrew, Muller, Phillip, Pilko, Robert, Amaya, Alvaro, Muir, John and Scherer, Joseph. "The Benefits of Geothermal Power, Evolution of the U.S. Electricity Grid, and the Need for Geothermal Research." G Transactions, Vol. 45, 2021, pp 1878-1895.

[9] Van Horn, Andrew, Amaya, Alvaro, Higgins, Brian, Muir, John, Scherer, Joe, Pilko, Robert, and Ross, Malcolm, "New Opportunities and Applications for Closed-Loop Geothermal Energy Systems." GRC Transactions, Vol. 44, 2020, pp 1123-1143, October 2020.

[10] Patel, Sonal, "Delving Deeper: New Optimism for Enhanced Geothermal Systems. POWER. April 2, 2024. https://www.powermag.com/delving-deeper-new-optimism-for-enhanced-geothermal-systems/

[11] Ricks, Wilson, Voller, Katharine, Galban, Gerame, Norbeck, Jack, and Jenkins, Jesse. "The role of flexible geothermal power in decarbonized electricity systems." Nature Energy, 2024. https://www.nature.com/articles/s41560-023-01437-y

[12] Quaise Energy, "Quaise Energy Raises $21 Million to Accelerate Terawatt-Scale Geothermal Energy." March 12, 2024. https://www.quaise.energy/news/quaise-energy-raises-21-million-to-accelerate-terawatt-scale-deep-geothermal-energy

[13] Norbeck, Jack and Latimer, Timothy, "Commercial-Scale Demonstration of a First-of-a-Kind Enhanced Geothermal System. Fervo Energy, September 2023 . https://eartharxiv.org/repository/view/5704/

[14] Terrell, Michael, "A first-of-its-kind geothermal project is now operational." Blog.google. https://blog.google/outreach-initiatives/sustainability/google-fervo-geothermal-energy-partnership/

[15] Blankenship, Doug, Gertler, Charles, Kamaludeen, Mohamed, O'Connor, Michael, Porse, Sean, "Pathways to Commercial Liftoff: Next-Generation Geothermal Power." U.S. Dept. of Energy, March 2024.

[16] Pan, David, "US Bitcoin Miners Use as Much Electricity as Everyone in Utah," *Bloomberg*. February 1, 2024. https://www.bloomberg.com/news/articles/2024-02-01/bitcoin-miners-in-us-consume-up-to-2-3-of-nation-s-electricity?embedded-checkout=true

[17] Kocis, Igor, "Deep Geothermal Can Solve the Need for Baseload Power." *Power Magazine*. March 20, 2024. https://www.powermag.com/deep-geothermal-can-solve-the-need-for-baseload-power/

[18] Wu, Alice, "Breaking Ground On Next Generation Geothermal Energy." *Federation of American Scientists (FAS)*, https://fas.org/publication/breaking-ground-on-nextgeneration-geothermal-energy/. January 2024. p 1.

[19] Ibid, p 2.

[20] Kocis, Igor, "Deep Geothermal Can Solve the Need for Baseload Power." *Power Magazine*. March 20, 2024. https://www.powermag.com/deep-geothermal-can-solve-the-need-for-baseload-power/

[21] Sisson, Patrick, "A.I. Frenzy Complicates Efforts to Keep Power-Hungry Data Sites Green." *New York Times*. Updated March 19, 2024. . https://www.nytimes.com/2024/02/29/business/artificial-intelligence-data-centers-green-power.html?unlocked_article_code=1.qU0.rFmF.R2i6ci3E3xni&smid=nytcore-ios-share&referringSource=articleShare

[22] Ibid.

[23] Wood MacKenzie, "Artificial intelligence and the future of energy." *Wood MacKenzie*. June 27, 2024. https://www.woodmac.com/blogs/the-edge/artificial-intelligence-and-the-future-of-energy/

[24] GreenFire Energy, July 2024 Newsletter, news@greenfireenergy.com

[25] Lazard, "Levelized Cost of Energy+ 2024." *Lazard*. https://www.lazard.com/research-insights/levelized-cost-of-energyplus/

Maximizing the Kenyan Rift Geothermal Energy - The Otutu Rift Segment Case

Nyawir Erique Otienoh, Omenda Peter Ayodo, and Varet Jacques

KenGen PLC, P.O. Box 785-20117, Naivasha, Kenya, ENyawir@kengen.co.ke

Keywords

Enter keywords here <Keywords Style>

ABSTRACT

Otutu is part of the larger Kenya Central Rift and lies in between the Eburru and Elmenteita volcanic field, within the larger Kenya Rift Valley. The area covers a longer portion of the rift floor thus becomes a good representative of the active rift segment. Geological and geochemical surface exploration studies were undertaken in the area, an area outside the normal central volcanoes so as to understand the areas' geothermal relevance: volcanology, surface mineralogical and chemical characteristics of the volcanic lavas within the study area. This study gives us a better understanding of the behaviour of a rift segment. During fieldwork, several geological structures were mapped and several samples collected for further analysis. A wide variety of lava rocks were identified and these included alkali olivine basalts, trachytes and abundant. The petrochemical results from both ICP-MS and ICP-AES included the rock composition in terms of major oxides, trace and rare earth elements. These results were used to plot various diagrams that included the variation diagrams (for both major oxides, trace elements), Total Alkali-Silica diagram, the AFM diagram, CIPW Norm Classification and also normalized Rare Earth Elements plots. These results provided a complete view of the various kind of liquids emitted during the last million years along this active segment of the rift. It can, therefore, be concluded that the Otutu rift is an important heat release area. It possibly has a shallow underlying anomalous mantle along the rift axis, where successive magma rejuvenations have taken place. This is supported by the steam vents that are aligned along open fissures and faults synchronous and post-dating the volcanic events. These results are of interest for the future geothermal development of the area. However, further studies are recommended on the area in order to complete the surface study of this geothermal site.

1. Introduction

Otutu rift is part of a rift segment that is located on the floor of the KRV between the Eburru and Lake Elmenteita areas. It is approximately 140 km northwest of Nairobi, 11 km northwest of Lake

Naivasha. KRV is made of a succession of central volcanoes alternating with single rift segments. Otutu is one of the rifts spreading segments (characterized by fissure eruptions) located between the two central volcanoes of Eburru and Menengai (Figure 1).

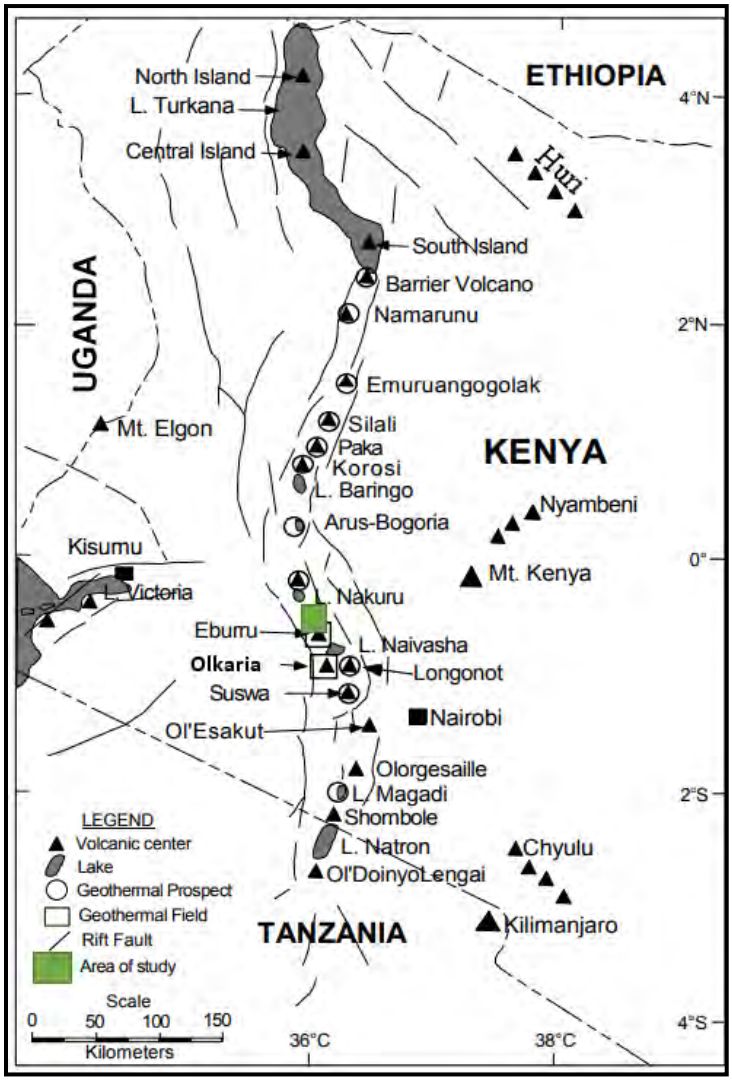

Figure 1: Map of the Kenya Rift showing the location of the Quaternary volcanoes (in black triangles) along the rift axis and the study area (in the green rectangle). Open circles are geothermal prospects in Kenya (Lagat, 2004).

The floor of the central KRV is characterized by two geologic settings: central volcanoes and flat-lying fissural volcanic fields. The central volcanoes have massifs of the order of 10 to 20 km wide with average reliefs of 100 to 500m above the rift floor. These central volcanoes are averagely-spaced 50 to 70 km from each other and alternate with flat-lying fissural volcanic fields occupying the low lands. The fissural fields are dominated by basaltic and intermediate lavas and interlayered by peralkaline silicic pyroclastic fall deposits that came from the surrounding central volcanoes and lacustrine sediments that originated from periods of high rift lake levels.

There are several grabens in the Kenya rift formed as a result of rifting. These fault troughs include the Elmenteita volcanic area, the area around Solai and Lake Nakuru. These areas are characterized

by widespread open fissures and normal faults showing long lasting crustal instability. These were formed during the Lower Pleistocene or Lower-Middle Pleistocene epoch, McCall (1957). McCall (1957) notes that the graben in Elmenteita experiences numerous volcanic activities as it is one of the least unstable troughs in the rift.

The noted line of instability, where thermal conditions are also noted, appears as the current axis of the rift spreading. This line extends southwards towards Eburru shoulders and further south passing through the western shores of Lake Naivasha towards Ol'Njorowa Gorge within the Hell's Gate National Park.

By looking at the bigger picture of the central segment of the KRV, it is observed that there is a succession of basaltic rift segments (B) that alternate with silicic central volcanoes (C). This can be seen by the following studied areas: Suswa is made of trachytic and phonolitic lavas (C), and thereafter we have the Akira plains with basaltic lavas (B); Olkaria and Longonot-Trachyte and rhyolites (C), then we have the Ndabibi-basalts (B), northwards occur Eburru trachytes and rhyolites (C), then Elmenteita Basaltic lavas (B); then Menengai – trachytes (C), (Clarke et al., 1990).

In terms of geothermal development, it is only in Eburru, Menengai, Olkaria and recently Paka and Korosi geothermal fields where deep drilling activities have taken place until now. Currently, appraisal and exploratory drilling is on-going at Paka and Korosi respectively. These two fields are far north of the earlier-mentioned three geothermal fields with more than 15 deep wells have been drilled so far between them. Geographically, the study area is bound between 0°27'S to 0°38'S and 36°11' to 36°21'.

The Kenya Electricity Generating Company, PLC (KenGen) together with Geothermal Development Company (GDC) have been exploring the KRV for its geothermal energy resources in the country so as to provide environmentally clean and low-cost energy for the country. KenGen is currently producing electricity from geothermal resources at Olkaria and Eburru while GDC has undertaken production drilling in Menengai and is currently carrying out exploratory drilling further north, in Paka volcano and Korosi areas.

Additionally, the Government of Kenya has licensed several other geothermal areas to private investors to explore and develop the resources for power generation and direct use. These includes Akiira and AGIL geothermal companies.

2. Results

2.1 Geology

Otutu rift was affected by rhythmic phases of spreading, during which dramatic volcano-tectonic events occurred, including both extensional tectonics and magmatic eruptions along the same active N-S trending faults and fissures of the rift axis. These volcanic activities in the rift axis are clearly linked with successive tectonic events characterizing the rift opening. During the fieldwork, it was noted that the whole volcanic activity in the study area is essentially characterized by lava flows, scoria cones and domes, without marked pyroclastic eruptions. The exception was noted in the areas influenced by the shallow water, thus producing hyaloclastites, which are generally easily altered and therefore difficult and unreliable to use for chemical analysis.

Quite a wide variety of differentiated products were observed in the study area, which is essentially a fissural area. It was also observed that shield structures tended to form, built on initial basaltic flows and intermediate terms (hawaiites, mugearites and trachyte flows). But these were cut by successive spreading events (normal faulting), allowing for a new magmatic cycle to occur (including basalts and highly differentiated products like rhyolites). It is worth noting that each of these eruption phases produced a variety of magma types that ranged from basaltic (basalts, basaltic trachy-andesites and trachy-andesites) lavas to trachytes and peralkaline rhyolites. The trachytes mainly occur on the slopes of the Eburru volcano both as shield building lavas and Late-phase flows, and this explains the close affinity with the Eburru Late-phase rhyolites with which they are associated in space. The basaltic lavas which occur at the foot of the Eburru volcano have been found not to co-genetic with the rhyolites and trachytes, which occur at the study area, along the same volcano-tectonic axis known as the Otutu rift. Whereas the evolution of the Eburru lavas was made possible by the thick overburden that allowed for the magma to differentiate at low pressures to form the trachytes and rhyolites, the Elmenteita lava evolved from small size magma chambers at mid-crustal depths. The results further demonstrate that even though the basaltic lavas occur in the same area, they were produced from different mantle sources. Below (from Plates 1 to 8) are some of the images taken of the study area and its surroundings.

Generally, normal faulting is in the same direction, N-S, and is well expressed in this study area with slight variations towards E-W. The exception is in areas that are covered by the most recent – sub-historic – Aa basaltic lava flow in Badlands. In the north-eastern part of the area, they tend to be visibly younger from east to west (that is, towards the rift axis) where they also affect more recent lava flows. The recent “Aa” basaltic flow (Plate 1) characterising the Badlands appears to extend mainly in a transverse, E-W direction. The SW limit of the flow is rectilinear and strikingly trending E-W. Due to its low viscosity, the basaltic flow flowed laterally towards the west, forming deep caves.

Plate 1: The researcher standing at the boundary of the Elmenteita volcanic basaltic flow, which is in the background, appearing as a highly vegetative field. In the far background are some of the structures that are aligned along the N-S Rift Axis.

Numerous cones are also observed, which correspond to former emission centres. Two variety of cones are clearly distinguished: hyaloclastite rings of large diameter, which pre-date the last sub-aerial basaltic lava flows, and subaerial scoria cones contemporaneous with this latest volcanic event, showing the emissive source of these Aa basalt flows. The largest and the most probably spectacular faulted hyaloclastite ring, is Losiriwe or “the Sleeping Warrior”. This spectacular structure is well seen from the Naivasha-Nakuru road crossing the active rift south of Lake

Elmenteita (Plate 2). It has a regular circular shape, with a basal diameter of 1.4 km and a maximum height of 120 m along part of the rim of this 900 m wide cone. This ratio of 1/10 between height and diameter is typical for such subaqueous hyaloclastite rings. As observed above, it is affected by normal faults on both sides and a small graben resulting from an open fissure along its axis, showing that this cone was at some stage in time the spreading axis of the rift. At present, the active axis of the rift is shifted 3 km east, at the level of the two other coalescent hyaloclastite cones elongated along the N-S trending rift axis with a sub-aerial eruptive phase having produced both subaerial scoria cone (Plate 3) and a lava lake of basaltic composition.

Plate 1: One of the distinct structures, Sleeping Warrior, a highly faulted dome that is located between the Elmenteita volcanic area and Lake Elmenteita.

Plate 3: View of the most recent scoria cone in the southern part of the Badlands.

Further south, these normal faults appear quite spectacular with important throws. Some of them clearly show that the tectonics affected the axis of an elongated shield volcano trending in the same meridian direction. Towards the active rift axis, normal faulting also affects very recent volcanic centres, such as a doubled rimmed scoria cone or an obsidian dome further south (Plate 4). On the western side of the rift axis, normal faulting is less visible, but open faults are still frequent, and attentive observations show that the tectonics was also quite violent there. Several hyaloclastite and scoria cones are cut by the N-S normal faults, which dip west, and some are left with only the western rim, with the central and eastern side having been down faulted and covered by more recent lava flows emitted along the rift axis as seen in Plate 5.

Plate 4: One of the Recent obsidian domes along the active rift axis cut by open and normal faults.

Plate 5: Cedar Hill, a recent rhyolitic dome made of anorthoclase porphyritic obsidian located to the SE of the Badlands area on the northern slope of Eburru volcano (photo by Varet, 2017).

2.2 Petrography

All the collected, over 120, rock samples were subjected to initial petrographic analysis in the field before taking samples to the laboratory for more analysis. Petrographic analysis was used to study the mineralogical evolution, confirm the rock type(s), the alteration minerals, and any other additional minerals not observed by the binocular microscope or the hand lens. Petrographic analysis assisted in;

i. Identification of the rock-forming minerals

ii. Characterization of the rock porosity

iii. Modal analysis (mineralogical composition)

iv. Analysis of the rock sample texture

Identifying the mineral phases and sequencing (phenocrysts were used as representatives of magmatic reservoir while groundmass used to depict the mode of eruption).

Rock types present in the study area range from alkali basalts to trachytes and peralkaline rhyolites. Both rhyolites and alkali basalts were found in areas around the Eburru volcano and also in the

volcanic field south of Lake Elmenteita. The collected samples were analyzed petrographically, and thereafter, 21 samples were picked based on their location, physical state and rock type for whole-rock analyses.

For petrographic microscope analysis, thin sections were prepared at KenGen's Geology lapidary laboratory in Olkaria, Kenya. The process included sawing of the rock samples, polishing, preparation and characterization in order to determine the samples' mineralogy. The thin sections were thereafter mounted on a petrographic microscope for analysis. For this project, thin sections were analysed in both KenGen' s Geology Laboratory in Kenya and the BRGM laboratory in France using Optika B-353POL and the LEICA DM 4500P Microscope, respectively.

2.3 Petrochemistry

Twenty-one (21) samples from the over 120 rock samples collected were subjected to whole-rock analysis (analysed for Major, Trace and Rare Earth Elements) using ICP-AES and ICP-MS in University of Occidental Britany (UBO), Brest, France. The samples were picked based on the surface outcrops and structures observed, in view of establishing a representative picture of the magmatic variations within Otutu rift, across and along the rift segment in particular. Therefore, aphyric or sub-aphyric samples were selected, as they directly allow to trace the evolution of the magmatic liquids. Of course, attention was also paid to the phenocrysts and their composition in the same magma types. It is noted that porphyritic samples were discarded during the critical selection of samples for petrochemical analysis as this study centred on the evolution of the liquid composition. This choice also explains some of the gaps observed in this sequence i.e. trachytes and rhyolites. Whole-rock analysis involved both major and trace/rare elements analysis. Major and trace elements are widely used to test petrogenetic models (Barberi et al. 1975; Reynolds et al., 1992; Bach et al., 1994; Perfit et al., 1994, 1996, 2001; Wendt et al., 1999; Sims et al., 2002).

2.3.1 Major Oxides

Lower Elmenteita basalts have SiO2 ranging from 48.26 to 55.46%. However, typical basalts would be in the range of 45 to 52%. This wide range of silica content can be attributed to fractional melting. The MgO and CaO values also range from 3.7 to 6.5% and 6.3 to 11.0%, respectively. These high MgO and CaO are typical major oxide trends of basalts. Upper Elmenteita Basalts have SiO2 ranging from 48.32 to 55.4%. They also have MgO and CaO values ranging from 3.8 to 6.0% and 6.5 to 10.4%, respectively. Generally, basalts are rich in MgO and Cao but low in silica.

The trachytes consist of Pliocene Gilgil Trachytes and Eburru shield-building trachytes. The early trachyte has 68.21% silica, 0.15% MgO, 0.56% CaO. This is relatively higher than what is noted in the shield building trachytes. The shield-building trachyte has SiO2 ranging from 63.28 to 67.37% with MgO and CaO being 0.01 to 0.17% and 0.61 to 1.38%, respectively.

The rocks occur on the Eburru volcano, and are dominantly on the northern slopes. The lavas have high SiO2 contents of 69.2-71.4%. The Fe2O3 (t) content are high as they range from 7.33 to 10.1%. The rocks have very low MgO contents of 0.01-0.14%. Their Na2O and K2O content ranges between 5.1-7.7% and 4.2-5.0%, respectively. The rhyolites at Eburru have been classified as pantellerites due to their low alumina content as compared to the alkalis (combination of K2O and Na2O). In this case, the alumina ranges between 7.11 and 8.8% while the alkali ranges from 9.40 to 11.16%.

a) Total Alkali-Silica classification

From Figure 2, the TAS Diagram shows a regular trend for all samples, slightly above the alkaline / sub-alkaline dividing line (dotted red on the diagram below), which is typical for all transitional series found elsewhere in the EARV, including Afar (Barberi et al., 1975). The rock sampled ranged from mafic through intermediate to silicic rocks (basalts, trachy-basalts, basaltic trachy-andesites, trachy-andesites, trachytes and rhyolites).

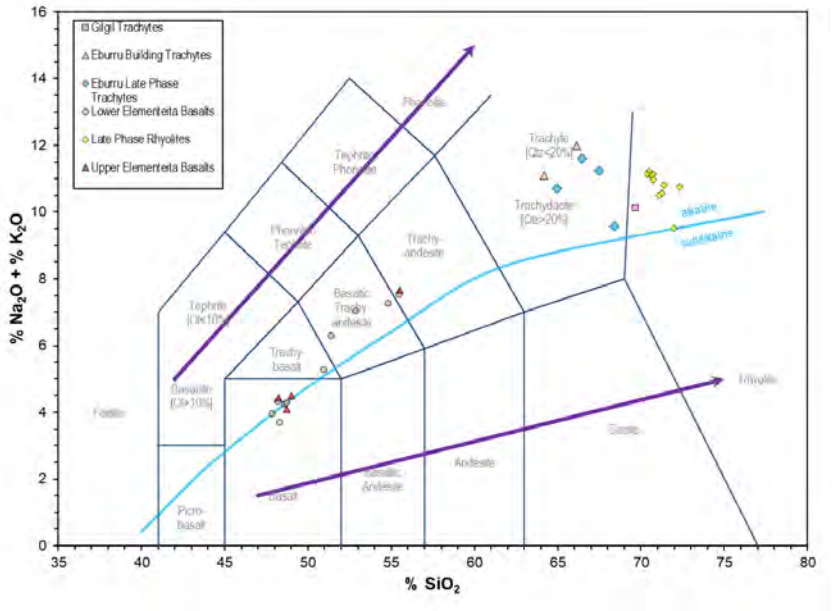

Figure 2: Total Alkali vs Silica Diagram for the study area.

Lower Elmenteita basalts vary in composition from basalt through trachy-basalt to basaltic trachy-andesite. Their alkali content varies from 3.69 to 7.51%, while their silica content varies from 48.31 to 55.46%. All the upper Elmenteita basalts samples except sample EN/EBLE 25A fall under the basalt category. Their normalized silica content varies from 48-49%, with the alkalis part ranging from 4.09-4.49%. Sample EN/EBLE 25A has a relatively high silica content (55.1%) and relatively high alkalis (7.66%).

Generally, the Upper Elmenteita basalts are low in both silica and alkali compared to the Lower Elmenteita basalts. They have a general composition of 45-52% SiO2 and 2 to 5% alkalis. This is noted in the upper Elmenteita suite but apparently the lower Elmenteita suite seems to be higher in their silica and alkali content. This varying composition noted in these basaltic suite (lower Elmenteita) could be as a result of fractional melting.

The one sample of Gilgil trachyte has high SiO2 (69.67%), which make it fall within the rhyolite field. However, the petrographic analysis clearly indicates that the lava is trachyte. The lava has an alkali content of 10.12%. Eburru shield trachytes all fell under the trachytes. They had alkali concentrations of 9.3-11.2%, with silica content ranging from 64.2 to 67.4%.

Generally, trachytes are feldspar-rich and thus have 60-65% silica content and an average of 7% alkali. Most of the samples had high silica and alkalic content and were plotted towards the tail end of the trachyte portion in the TAS diagram.

Rhyolite plot with an alkali content of 9.4 to 11.2% while the silica content was 70.4-71.4%. This is expected of rhyolites as they are the most silica-rich igneous rocks. They usually have higher SiO2 (69-77%) and alkali (>7%).

All the trachyte and rhyolite suites are all silica saturated with concentrations ranging between 64.18 and 71.4% by weight. The suites also have relatively high alkali contents that range between 9.3 to 11.2% and 9.4 to 11.2% by weight, respectively.

Therefore, all the samples plotting above or around the line that separates the alkaline and sub-alkaline rocks (Figure 2). This means that all the rocks sampled were alkaline/calc-alkaline rocks. Alkaline magmas are known to be derived from mantle-derived basaltic melts. These melts usually have had a residence in the crust and thereafter evolve through the assimilation and fractional crystallization (AFC) processes.

Sub-alkaline rocks can occur due to a variety of factors, including fractionation process affecting tholeiitic basaltic series, the influence of enriched mantle sources, crustal contamination, or the mixing of different magma types. In these instances, basaltic magmas derived from mantle melting can interact with continental crustal rocks or undergo assimilation and fractional crystallization processes, leading to the development of more evolved magmas with intermediate to felsic compositions. These evolved magmas may exhibit sub-alkaline or even calc-alkaline characteristics, similar to those found in convergent plate boundary settings.

b) AFM classification

AFM Diagrams, in their classification, distinguishes between the two usual types of parental magmas; alkali and tholeiitic (Figure 3).

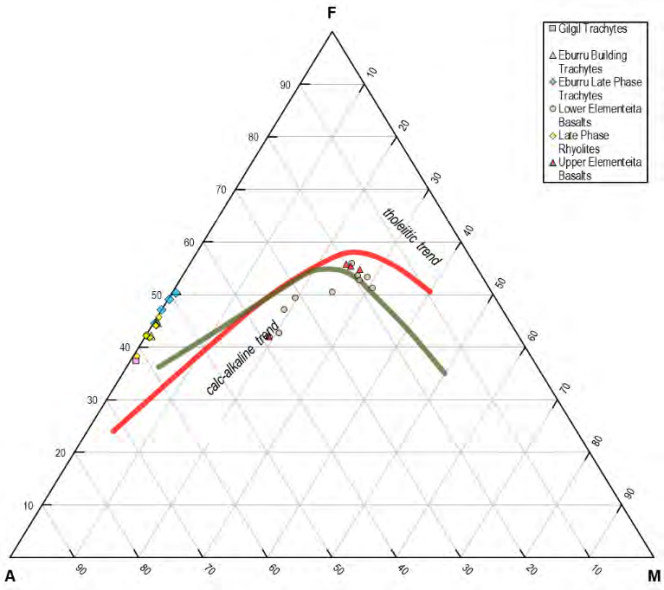

Figure 3: AFM Diagram for the Otutu study area.

It is noted that the lavas evolved through depletion of Fe and Mg and enrichment of alkalis. All the samples were plotted below the tholeiitic (sub-alkaline) series. It is noted that tholeiitic magmas

usually form at relatively shallow depths compared to alkalic magmas and differentiate into the SiO2 oversaturated rhyolites.

Figure 3 shows both trachytic and rhyolitic lavas plotting on the zero MgO axis due to their very low MgO contents while having high contents of alkali and Fe. The evolution of the Elmenteita and Eburru lavas can be described by the fractional crystallization process involving crystallization of ferromagnesian minerals (olivine, pyroxenes and plagioclases) as shown by decreasing Mg and Fe with an evolution from basalt through trachyte to rhyolite. The evolution is characterized by the enrichment of alkalis in the liquid phase.

c) Harker variation diagrams

Harker variation diagrams were plotted for the various rock suites in the study area. crystallization from basaltic liquids. Figure 4.

d) CIPW Norm Classification

The basaltic (lower and upper Elmenteita) samples contain no normative quartz but very high values of normative plagioclase and average normative orthoclase. This ranged between 52.4-62.1% and 5.2-22.3%, respectively. The normative diopside ranged from 10-19.5%, while the normative olivine values ranged from 4.5 to 12.2%. Normative ilmenite varied from 1.3 to 3.2%, and normative magnetite varied from 1.1-18%.

Normative nepheline values were generally low. Values ranging from 0.0 to 3.0% and 0.5 to 1.4% for normative nepheline and apatite, respectively, were also noted, with most samples containing no normative sodium silicate. Normative leucite was absent from all the basaltic samples, which is expected of all sub-alkaline bulk chemistry. The normative zircon ranged from 0.01 to 0.02%, while the normative chromite values were at 0.01%. All the other remaining normative minerals were absent or very low. These included acmite and calcite.

In the trachytic samples, normative quartz was noted. This ranged from 7.8% in sample 13 to 15.9-26.2% in the other samples. The samples also had relatively high values of normative plagioclase and normative orthoclase. This ranged between 22.3-42.3% and 27.7-32.6%, respectively. The normative diopside ranged from 1.8 to 4.6%, while the normative hypersthene values ranged from 5.8 to 10%. Normative acmite varied from 2.3 to 3.9%, while normative sodium silicate varied from 1.8 to 9.8%. Normative ilmenite was low and varied from 0.34-0.9%, while normative magnetite was very low (0.06%) and mostly absent. Normative apatite and zircon values were generally very low. Values ranging from 0.1 to 0.14 % and 0.0 to 0.1 % for normative apatite and zircon were noted, respectively. All the other remaining normative minerals were absent or very low. These included accessory minerals like nepheline, olivine, chromite and calcite.

In the rhyolitic samples, higher normative quartz was noted in comparison to the trachytic samples. This ranged between 30.0-33.1%. The samples also had relatively high values of normative plagioclase and normative orthoclase. This ranged between 14.5-24% and 26.0-28.2%, respectively. This lower plagioclase content in the rhyolites here (as compared to basalts and trachytes) is due to the low alumina deficit. The plagioclase effect usually plays a major role in the generation of peralkaline. The normative diopside was averagely low, ranging from 0.9 to 1.3%, though sample ES1 had 2.7% while the normative hypersthene values ranged from 7.1 to 9.7%. Normative acmite varied from 2.5 to 3.4%, while normative sodium silicate was averagely high,

varying from 5.8 to 11.1%. Normative ilmenite was averagely low and varied from 0.3-0.4%, while normative magnetite was very low (0.06%) and mostly absent. Normative apatite and zircon values were generally higher compared to basalts and trachytic suites. Values ranging from 0.02 to 0.08% and 0.18 to 0.24 % for normative apatite and zircon were noted, respectively. All the other remaining normative minerals were absent or very low. These included accessory minerals like nepheline, magnetite, olivine, chromite and calcite.

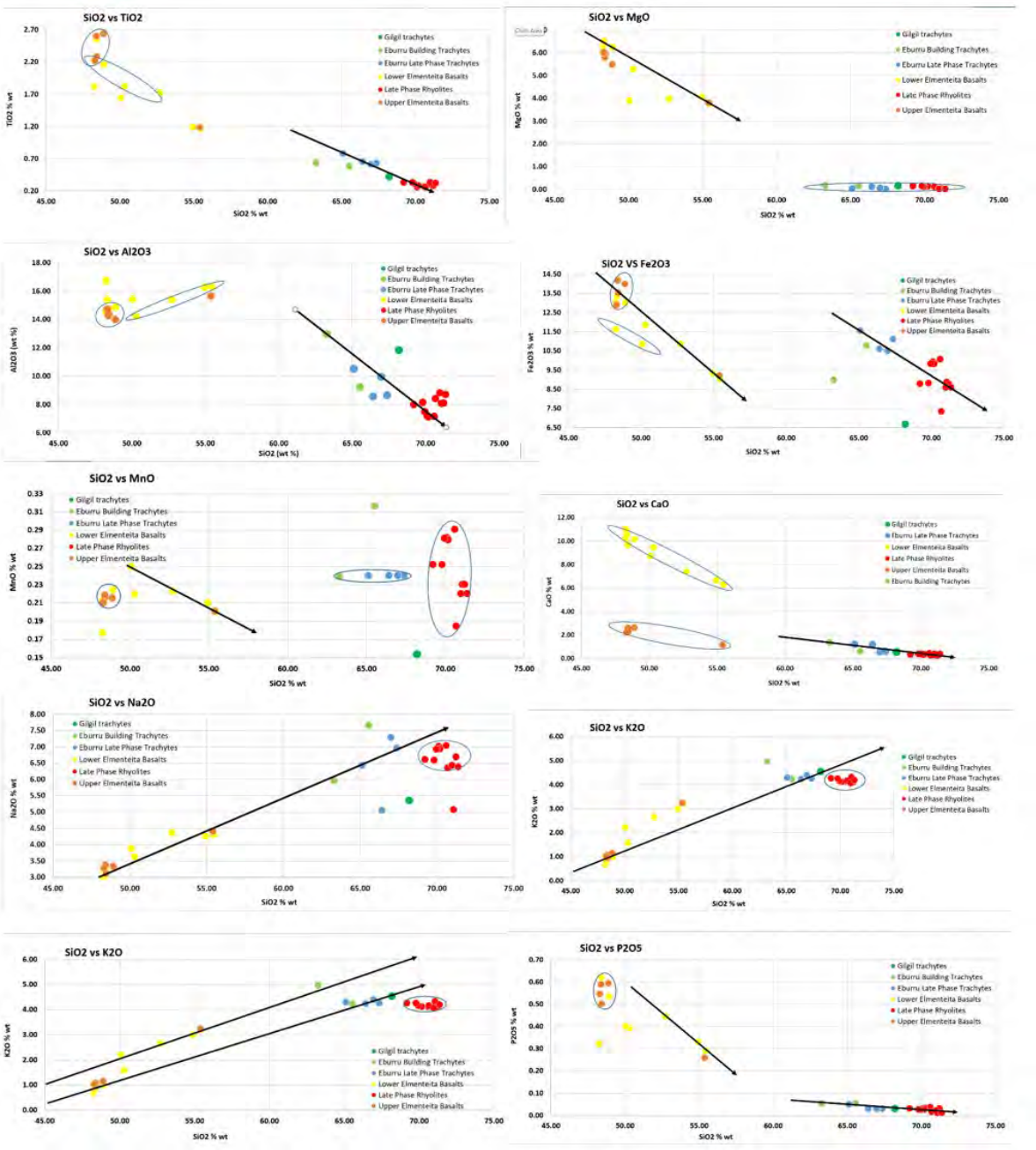

Figure 4: SiO2 vs Major Oxides variation diagram.

Generally, by CIPW classification, silicic rocks usually have normative quartz varying from the lower end trachytes through ignimbrites to the higher end rhyolites. The average quartz values are

1-4%, 17-21% and 22-30% for trachytes, ignimbrites and rhyolites, respectively. Silicic rocks also have averagely high values of plagioclase and orthoclase. For silicic rock as a whole, these ranges between 31-55% and 25-30%, respectively.

Most of the basalts show a good balance, with both olivine and hypersthene present, but not quartz (no tholeiite), whereas only 3 samples show the presence of nepheline, mostly as traces (ranging from 0.3-0.4%) with only one sample exceeding 1%, which confirm the transitional character of the basaltic magma source. Whereas olivine is always visible in thin sections under the microscope, orthopyroxene is not observed, which is classical in a basaltic environment (orthopyroxenes rather appear in plutonic environments). However, during the differentiation process, the magma progressively acquires a slight, then dominant, silica saturation in the end products.

Amphiboles are observed as phenocrysts in some intermediate lavas. They are not present in the normative analysis for the simple reason that the CIPW norm is based on “dry” mineral only – pyroxene in this case - and do not allow for amphibole (or mica) to occur. The amphiboles we observed frequently show signs of instability (mineral internally altered and rimmed with iron oxides) with the groundmass, indicating that these silica-deficient minerals formed at depth are not in equilibrium with the silica-saturated liquid containing them when emitted at the surface in more oxidizing and eventually “dryer” conditions, despite the fact that they have played a major role in the formation of silicic end products by fractionation of originally undersaturated magmas.

2.3.2 Trace Elements

The trace elements results obtained were plotted in variation diagrams while the multi elements (Rare Earth Elements) were normalized (chondrite normalized REE) and thereafter plotted for the study area to show the evolution chemistry.

a) Process Identification/Variation plots

Process identification plots (PIPs) were plotted to check on how the elements related to each other. PIPs are diagrams plotted of the ratio of two (2) incompatible elements against the abundance of the other. Incompatible elements are part of the trace elements. Figure 5 shows how these elements relate to each other.

b) Rare Earth Elements (REE)

Multi elements were normalized (chondrite normalized REE) and thereafter plotted for the study area to show the evolution chemistry, and this is illustrated in Figure 6.

One can observe a regular and parallel increase in REE elements with the evolution from basalt to rhyolites. From the diagram below, it is noted that there is a strong negative europium anomaly in trachyte and rhyolites due to the fractionation of feldspars. Barberi et al., (1975) described the negative Eu anomaly as resulting from the fractionation of alkali-feldspars since the element is incorporated in the lattice structure of the minerals.

Figure 5: SiO2 vs K2O variation diagram.

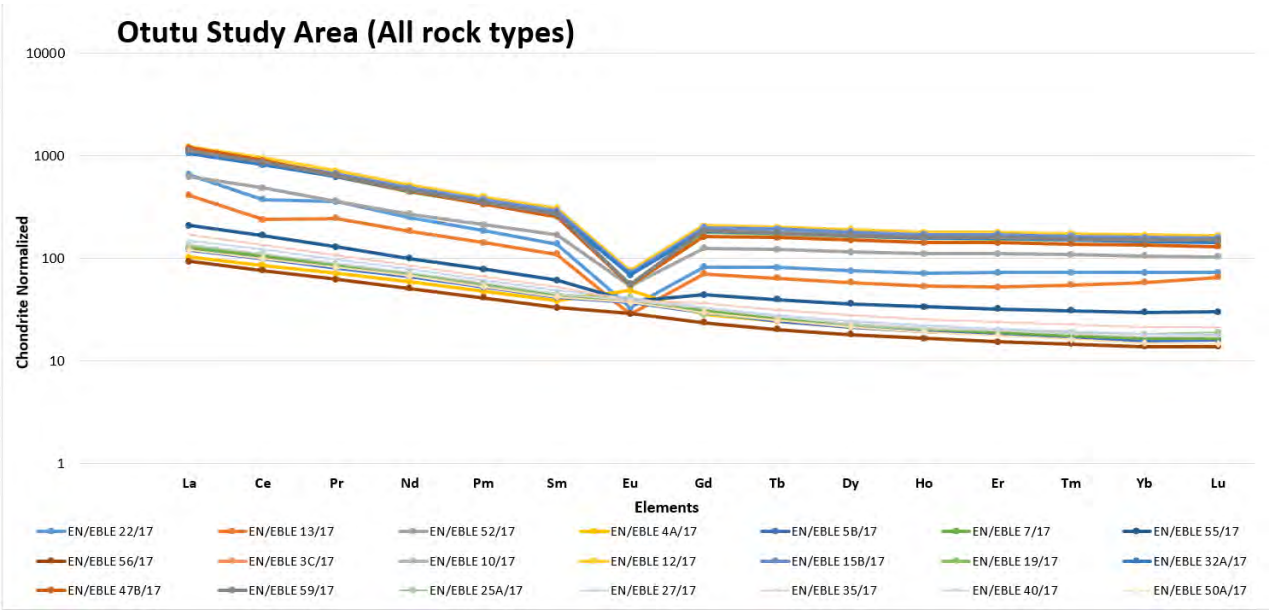

Figure 6: REE vs Chondrite normalized for all chemically analysed sampled rocks from the Otutu study area.

3. Conclusion

The Otutu rift study area is characterized by several volcano-structural features that include fissures, recent basaltic lava flows and shield structures. Important heat release along this rift axis is also noted all along the area. Steam vents are aligned along open fissures and faults synchronous and post-dating the volcanic events. Several hydrothermal zones are also noted resulting from fumarolic alteration. Though there are older or off-axis rock types that fall out of the fractionation line (the Gilgil Trachyte, the basalts sampled outside the rift axis and the Eburru rhyolites) but most rock types sampled within the rift axis of the study area still display a nice fractionation line. This clearly indicates the presence of a shallow steam-dominated reservoir underlying this rift axis. This reservoir is possibly heated by an underlying elongated magma chamber beneath it. The results also show that after the widespread trachyte emission that pre-dated the formation of the present rift, a variety of volcanic products were emitted. These happened during each of the successive steps of the rift segment development. The emission ranged from alkali-olivine basalts to pantellerites, with a few intermediate types. This means that, geothermally, the Otutu rift is not only fed by the fissural basalts originating from a deep-seated source but also from a shallow, elongated magma chamber that is along the rift axis.

Petrological investigations in this study allowed for the identification of the bimodal nature of the rocks in the area. The area has a large variety of both basic and acidic rocks. This variety of lava rocks ranged from alkali olivine basalts to mugearites, trachytes and pantelleritic obsidians, with a relative abundance of the later. Petrological analysis of the rocks and their interpretation shows that this evolution can simply be explained by the process of crystal fractionation occurring in the crust a few kilometres deep. It, therefore, appears that this linear volcano-tectonic context dominated by fissure eruptions along the rift axis allowed for this magma development. This could have occurred during the last few hundred thousand years. Successive magma chambers are interpreted as being elongated along the same axis with successive rejuvenations through basaltic magma injection from the relatively shallow underlying anomalous mantle.

Geochemical analysis carried on the selected fresh aphyric rock samples provided a complete view of the various kind of liquids emitted during the last million years along this active segment of the rift. The results showed that very dynamic magmatism had taken place that resulted in differentiation. This is evidenced by the different rock suites noted: basalts, trachytes and rhyolites. By use of trace elements, it is concluded that the magma sources for the various rock suites are at least three. This is due to the noted different elemental ratios noted in the plotted graphs. Incompatible elements ratios are less affected by FC than other element abundances. The ratios are usually similar in geochemical behavior, and rocks that are related by FC have a common/constant ratio. Therefore, the ratio of two incompatible elements in a magma will be more or less the same as that in the magma source.

The geological data collected in the field, the rock sample analysis, and the interpretation of the results in terms of geothermal implications have been included in a global geoscientific approach, thus allowing for a new conceptual model of the geothermal system in the rift segment to be proposed. As a result of the crystal fractionation and differentiation, this study alludes to presence of magma chambers below the study area. These results are thought to be of interest for the future development of the area, as well as – more generally – for the search for new geothermal resources along the East African Rift System away from the central volcanic units, i.e. along other active rifts segments, which represent much wider areas than the ones presently being targeted. Therefore, the possible heat source (s) in this type of environment should be investigated further and even confirmed by exploration drilling and exploited even if they differ in terms of size and shape with the central volcanoes.

4. Recommendations

The field work (rock-suites mapping), samples collection and analysis for major and trace element geochemistry provided only a limited insight into the petrogenesis of the Otutu rift. There is a need to undertake further studies in this area. The following studies are recommended: geochronological studies, a further detailed mineralogical study of a few key phases determining the major shifts in the fractionation process (e.g. how the amphibole pass from nepheline basalts to quartz trachytes and plagioclase pass from meta-aluminous to peralkaline liquids), close-knit geophysical surveys (preferably MT and magnetic surveys) to clearly map out the anomalies (thin, elongated heat sources), radiogenic isotope analysis, geochronological studies to evaluate not only the actual ages of the various rock series but also to quantify the periodicity of the magma injection and differentiation. This would go a long way in better understanding of this spreading axis in order to properly model the vertical dimensions of the rift segment and quantitatively define the whole geothermal conceptual model of this rift segment through the tectono-magmatic history.

Acknowledgement

The authors warmly thank Prof. Jean-Alix Barrat, the Geochemist Professor at the Geochemistry Laboratory, University of Occidental Britany (UBO), Brest, France, for his kind support in this project. He not only allowed access to the laboratory but also assisted in the analysis, sharing of relevant papers and advice for this study, as presented by Nyawir et al. (2018).

REFERENCES

Barberi F., Ferrara G., Santacroce R., Treuil M. et Varet J. (1975) - A transitional basalt-pantellerite sequence of fractional cristallization, the Boina Centre (Afar Rift, Ethiopia). Journal of Petrology, 16, p. 22-56.

Barberi F., and Varet J. (1975) - Recent volcanic units of Afar and their structural significance. In: Pilger A., and Rösler A. (edit.), Afar Depression of Ethiopia, Stuttgart (Schweizerbart), p. 174-178.

Clarke, M.C.G., Woodhall, D.G., Allen, D.J., Darling, W.G. (1990). Geological, Volcanological, and Hydrogeological Controls on the Occurrence of Geothermal Activity in the Area Surrounding Lake Naivasha, Kenya. Ministry of Energy, Kenya and British Geological Survey, Nairobi. pp138.

Lagat J. (2004). Geology, Hydrothermal Alteration and Fluid Inclusion Studies of Olkaria Domes Geothermal Field, Kenya. MSc Thesis, University of Iceland.

McCall G. J. H. (1957). Geology and Ground Water Conditions in the Nakuru Area. Ministry of Environment and Natural Resources Mines and Geological Department Geology and Ground Water Conditions in the Nakuru Area. Technical Report No. 3, pp22-27.

Nyawir, E., Barrat, J.A. & Varet, J. (2018). Geological, volcanological, petrological and geochemical approach to geothermal exploration of an axial rift segment of the central Kenya Rift Valley. Proceedings, 7th African Rift Geothermal Conference Kigali, Rwanda 31st October – 2nd November 2018. 14 p.

Perfit, M.R., Fornari, D.J., Ridlay, W.I., Kirk, P.D., Casey, J., Kastens, K.A., Reynolds, J.R., Edwards, M., Desonie, D., Shuster, R. And Paradis, S. (1996). Recent Volcanism in the Siqueiros Transform Fault: Picritic Basalts and Implications for Morb Magma Genesis. Earth Planet. Sci. Lett., V.141, pp91-108.

Perfit, M.R., Fornari, D.J., Smith, M.C., Bender, J.F., Langmuir, C.H. And Haymon, R.M. (1994) Small-Scale Spatial and Temporal Variations in Mid-Ocean Ridge Crest Magmatic Processes, Geology., V.22, pp. 375-379.

Perfit, M.R. (2001) Mid-Ocean Ridge Geochemistry and Petrology. Academic Press, University of Florida, P.11.

Reynolds, J.R., Langmuir, C.H., Bender, J.F., Kastens, K.A. And Ryan, W.B.F. (1992) Spatial and Temporal Variability in The Geochemistry of Basalts from The East Pacific Rise. Nature, V.359, Pp.493-499.

Sims, K.W.W., Goldstein, S.J., Blicher-Toft, J., Perfit, M.R., Kelemen, P., Fornari, D.J., Murrell, M.T., Hart, S.R., Depaolo, D.J., Layne, G., Ball, L., Jull, M.V. And Bender, J. (2002). Chemical And Isotopic Constraints On The Generation And Transportation Of Magma Beneath The East Pacific Rise. Geochim. Cosmochim. Acta, V.66(19), pp3481-3504.

Varet, J. (2017). Unpublished Report on Badlands (West from Gilgil): Structural Geology, Volcanology and Igneous Rocks Petrology. DeKUT/Géo2D for KenGen.

Wendt, J.I., Regelous, M., Niu, Y., Hekinian, R. And Collerson, K.D. (1999). Geochemistry Of The Lavas From The Garret Transform Fault: Insights From The Mantle Heterogeneity Beneath The Eastern Pacific. Earth Planet. Sci. Lett., V.173, pp.271-284.

Monetizing Low-Moderate Enthalpy Geothermal Reservoirs: Lessons Learned

R. Roundtree, B. Burke, J. Ostrum, L. Sedillos

Gradient Geothermal, Inc, Denver, CO

Keywords

Geothermal, Hydrothermal, Low-Enthalpy, Power Generation, ORC

ABSTRACT

Low and medium temperature hydrothermal reservoirs are differentiated from high-temperature geothermal reservoirs in several important ways: the predominant phase is liquid water, the reservoir temperature is usually less than 150 degrees Centigrade, the lithology is typically sedimentary rocks with primary pore space and permeability, and the pore space can be filled with other geofluids, including hydrocarbons. Most sedimentary systems are dominantly conduction-driven heat flow instead of convective.

In May 2022, a pilot geothermal energy plant at the Blackburn Field in northeast Nevada was installed to assess the integration of an Organic Rankine Cycle (ORC) engine with existing oil and gas facilities to generate electricity at an operating mature oil field.

The pilot project generated power as different process flow configurations were tested and the surface facilities integration of petroleum and geothermal resources were optimized to maximize power generation and minimize, or negate, operational interference with the oil and gas operator. The pilot project identified that thermal energy is lost in several processes between the reservoir and the ORC inlet at typical oil field flow rates creating forward opportunities for field optimization as project budgets allow. The project also validated the hypothesis of the geothermal operator that an intermediate flow loop is necessary to protect the heat exchanger in the ORC from the geofluids with residual petroleum compounds, high total dissolved solids content, and scaling tendencies.

1. Introduction

Physicists Richard Thomson, James Joule, and William Rankine theorized thermodynamic heat engines to transform thermal energy into mechanical work in the 1840’s and 1850’s (Smith, 1977).

Tabor and Bronicki (e.g., 1964) developed Organic Rankine Cycle (ORC) engines and opened the market for the use of ORC engines in heat waste power generation. ORC engines use a refrigerant with a boiling point below that of water to generate electricity for waste heat down to 65°C. Power generation at temperatures in the 65°-150°C range is of specific interest to well owners in sedimentary basins, particularly those in oil and gas where wells access similar reservoir temperatures (Johnson et al., 2020). Paired with geofluid flow rates that provide adequate thermal mass for power generation, the concept of geothermal power generation coproduced alongside oil and gas has been modeled and tested in several locations across the United States (e.g., ElectraTherm, 2012; Gosnold et al., 2017; Akhmadullin, 2017).

This paper discusses the results of the first phase of feasibility from a pilot project at the Blackburn oil and gas field in northeast Nevada. The location and history of the Blackburn field also prefaces the specific challenges and opportunities examined by the project in examining thermal energy loss throughout the geofluid gathering system and in optimizing the process flow of the fluids at the central facility to maximize power generation from both load and cumulative energy standpoints. The goals of the pilot project were to demonstrate the integration of geothermal power generation technology with an operating oil field. Specifically, the project identified the following goals:

- Document and monitor thermal energy loss across the geofluid gathering system
- Document and optimize the effect of oilfield central facility operations such as manifold flow gathering, separator, and pre-disposal water handling and storage on thermal energy loss
- Determine the optimal placement of geothermal power generation equipment within an oilfield
- Determine the feasibility of increasing power generation to 1 MW
- Plan for a specific scenario that increases power production and validates the 1 MW plan

2. Field Location & Selection

The Blackburn field is a conventional oil field located south of Carlin, Nevada, in Pine Valley, a narrow north-south oriented basin within the basin and range province of the western United States (Figure 1). This location was identified by Johnson et al. (2020) as having the ideal characteristics for piloting this type of operation.

The field was discovered in 1982 producing from a highly fractured dolomite at about 2440 meters depth (Scott and Chamberlain, 1988). The oil field is present because of the structural trapping of hydrocarbons. Over 2000 meters of Tertiary-aged volcanic deposits provide both an impermeable barrier to upward hydrocarbon migration and water flow creating in the Devonian-aged dolomite reservoir and artesian flow conditions with about 300 psi at surface. This pressure has been very consistent over the field's operations since 1982. The produced water has a total dissolved solids (TDS) content of about 2500 ppm. This low TDS value does not create mineralization or scaling issues for the oil and gas operator. The surface temperature at the well heads accessing the Devonian-aged Nevada Formation is about 116°C. Well log analysis and correction of bottom hole

temperature measuring during wireline logging of the wells in the 1980's and 1990's result in an estimated reservoir temperature of 138°C. The reservoir has zones with permeability as high as one Darcy.

The maturation of the field is a typical scenario for conventional oil and gas fields. The initial production was almost 100% oil with no gas in the early to mid-1980's. Total fluid production remained the same but the ratio of water to oil increased over time to its present number of just over 99% water to oil. In the early 2010's, atmospheric gas was pumped into parts of the field to create a gas cap in the reservoir and increase oil production by driving additional oil from its buoyancy-driven location at the very top of the reservoir to the perforations in some of the wells. This operation did not change the reservoir pressure of the field or the total fluids production volume but did increase the water to oil ratio temporarily.

3. Pilot Test Engineering

The pilot test generated electrical power from the approximately 4200 barrels per day (BPD) or 122.5 gallons per minute, of 116°C geofluid provided by the field operator. An ORC with a twin-screw induction generator and nameplate capacity 75 kW gross was used for power generation (Figure 2).

The geofluid production came from four wells: two wells in different fault blocks both penetrating the Nevada Formation and two wells penetrating the shallow Indian Wells formation. The two wells producing from the Nevada Formation provided the vast majority of the total production and the most thermal energy. These wells flowed naturally and were choked back by the oil and gas operator so that the central processing facilities at the field were not overwhelmed. The Indian Wells formation provided a few hundred barrels of oil and gas to the total fluid stream at temperatures around 90°C. The four individual flow lines joined at the central facility at manifold where the combined flow stream temperature was 107°C between the manifold and the inlet to the oil and water separators.

From the separators, oil is piped to holding tanks on one side of the central facility and water is piped to another tank in a different part of the pad. The separators flow water discontinuously to the water holding tank on a schedule known as a "dump schedule." One iteration of the pilot had the ORC and its heat conveyance sled directly downstream of the separators. The second iteration had the separators dump to a water tank and the ORCs were plumbed into the water tank for both inflow and outflow. The outcomes of those two plumbing configurations will be discussed in a later section.

The ORC as referred to in this paper is really two units: the ORC itself, which was configured with dry air-cooling fans, and a heat conveyance sled, which was the only direct point of contact between the produced geofluids and the geothermal power generation process. The direct point of contact was a plate-and-frame heat exchanger with gaskets selected for the separator dump pressures, geofluid chemistry, and the expected high temperature fluids. The heat exchanger was configured for a 5°C approach, meaning that the temperature conveyed to the ORC via the pipe loop was 5°C less than the input geofluid temperature. The intermediate pipe loop contained water in the warmer months and a mix of water and glycol for freeze production in the winter months.

4. Geothermal Pilot Outcomes & Learnings

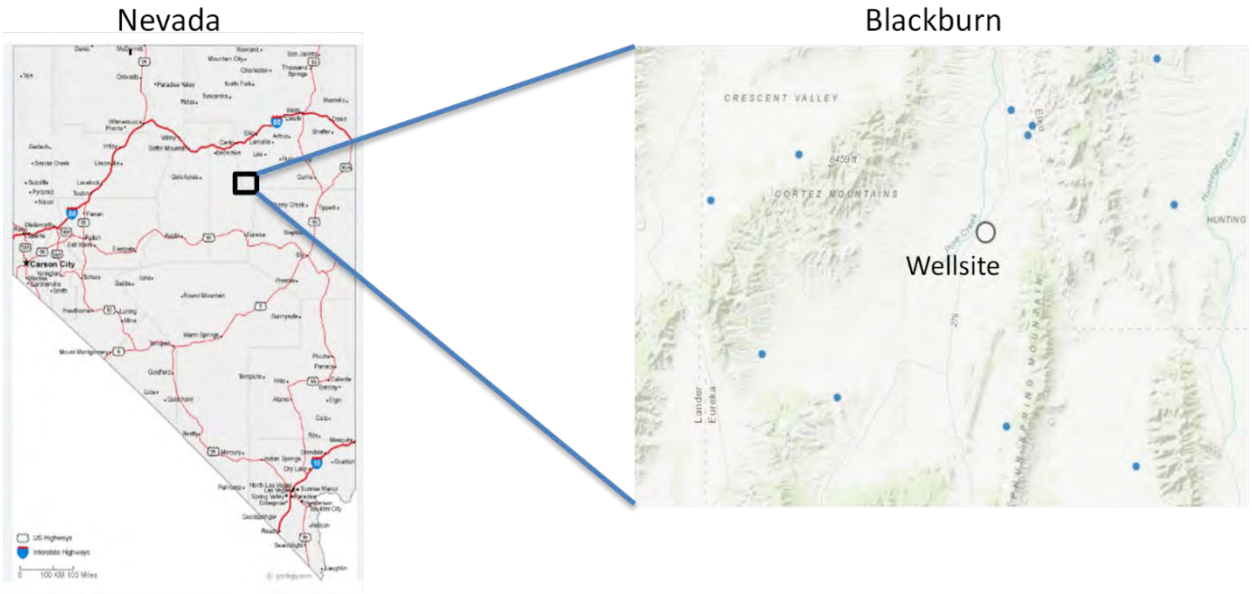

Figure 1 – Relative location of Blackburn field.

Figure 2 – Blackburn installed geothermal electricity generation equipment.

The geothermal pilot project commenced in May of 2022 and ran until March 2024 when the feasibility phase of the Wells of Opportunity project was completed. Simultaneous oil production and geothermal electricity generation was achieved throughout the project utilizing a fairly constant flow rate about 4200 BPD of produced water averaging between 93-104°C depending on where the take off point in the production stream was made. A custom and patent pending isolation heat exchanger (HXC) loop was engineered to protect the expensive ORC equipment from damage and contamination from the produced oil field waters. This HXC loop was run with a clean water and propylene glycol mixture to protect against freezing damage in colder times of the year. The entire system was remotely controlled and monitored through a 4G cellular network. In Figure 3 you can see the historical cumulative power production from a 75 kW nameplate capacity ORC from ElectraTherm. Of note is the slope of the line once continuous operations started in February 2023 versus the slope after October of that year. This lower power generation rate is due to re-piping the flow lines directly from the separator versus taking the output from the holding tank. The resulting average 11°C temperature drop is causing the lower power generation rate. The learning is that heat retention on surface is key to maximizing electricity output by placing the ORC equipment as close to the wellhead as possible if the necessary flow conditions can be attained by doing so.

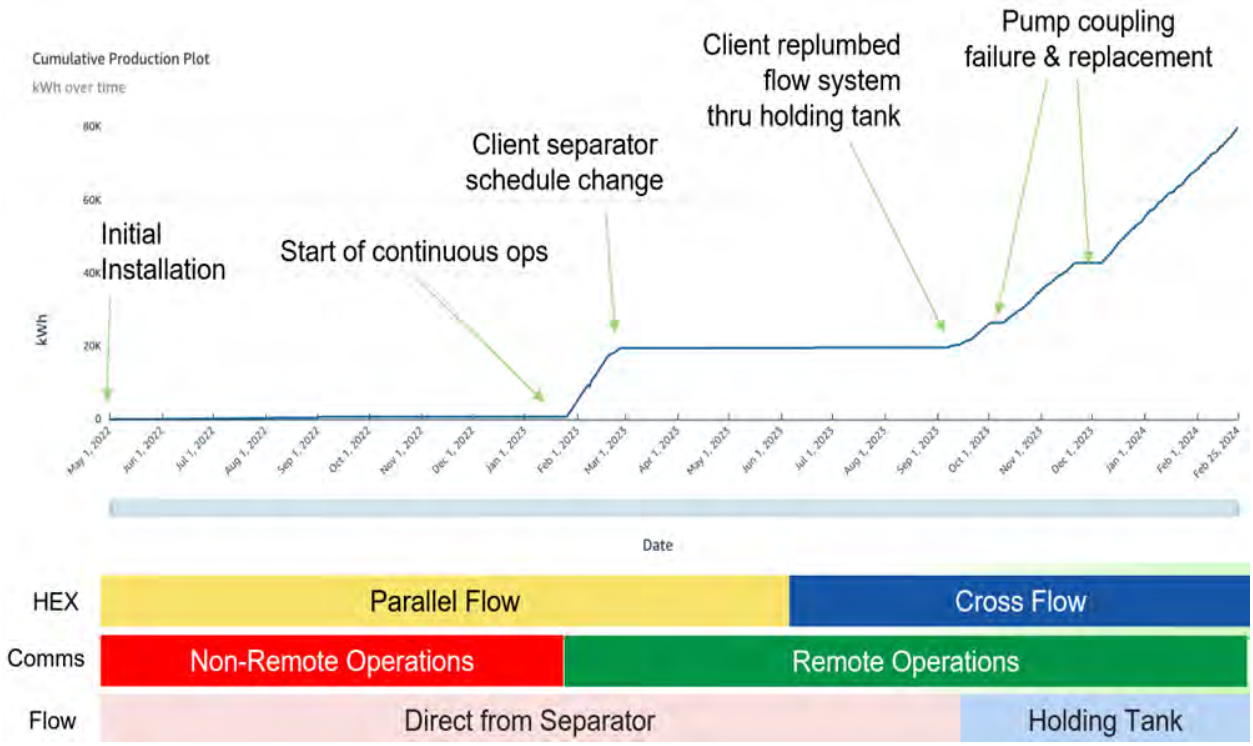

Figure 3 – Blackburn cumulative power production from feasibility phase.

Figure 4 demonstrates another important learning where the primary heat exchanger was modified from a parallel flow to a cross-flow orientation. As expected, the better heat transfer occurs when the HXC is plumbed in a cross-flow configuration. Contrary to many presentations, ORC's do in fact fluctuate in their power output when cooled using a dry air source. The geothermal heat source is almost constant from the organic heat flux within the earth and the gradual cooling of the reservoir at depth, but the mechanics of how the ORC works introduce sometimes substantial power output fluctuations. These changes cycle in both long term seasonal ambient temperature

changes from winter to summer seasons, but they also substantially fluctuate from hourly daytime and night-time ambient temperatures.

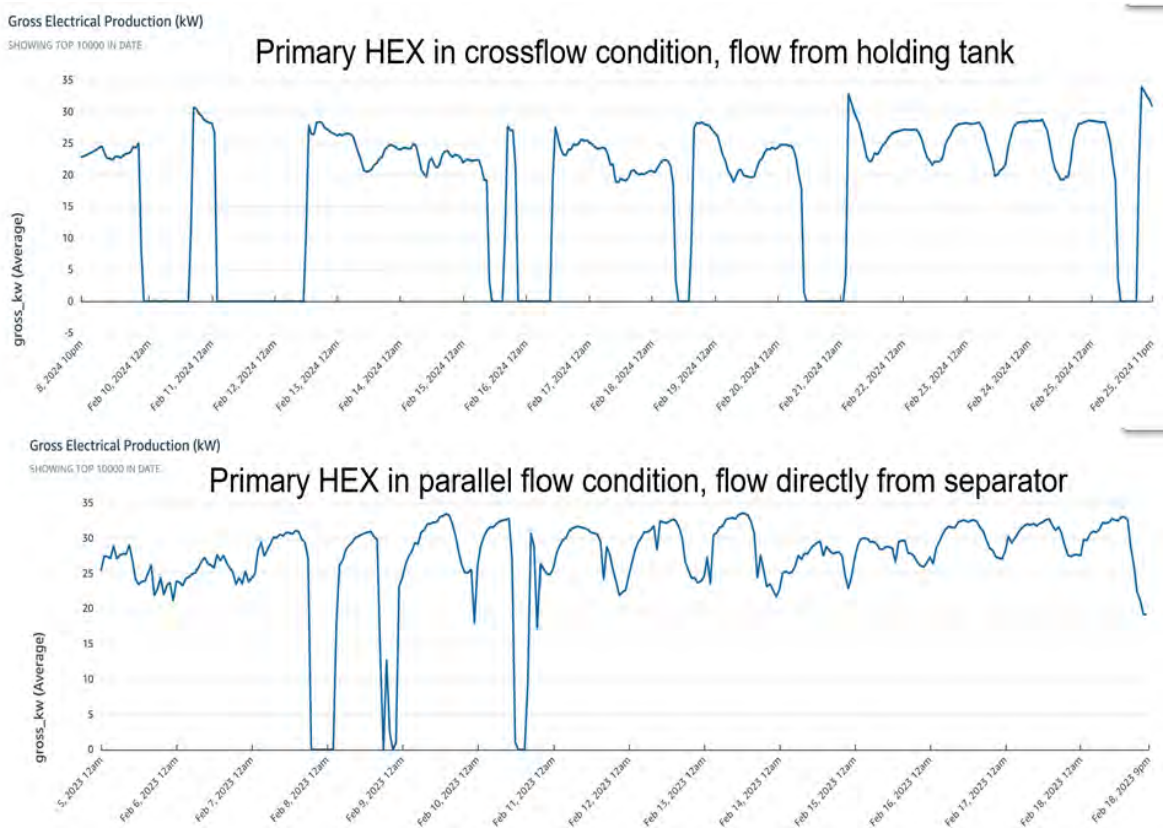

Figure 4 – Results of two simultaneous changes: HX plumbing from parallel to cross-flow, and change of heat source from separator to storage tank.

5. Effects of Ambient Temperature Variations on Modelled Output Power Generation

Using radiator cooling exploits the difference between the working fluid and ambient air temperatures to condense the working fluid to make it ready for the next power generation cycle. This is the most common cooling method utilized in ORC engines. This method has the convenience of allowing a modular and mobile solution for cooling and condensing the working fluid of the ORC. It has the disadvantage of high parasitic loads associated with the pumping and fan loads for the coolers. It also has the disadvantage of having strong seasonal and hourly variation in ambient temperatures. Figure 5, below, shows the seasonal variation in ambient temperature by month as well as the hourly temperature variation on a typical day. These variations cause ORC power output to also vary. Even with perfectly constant flow and hot water temperature, the ORC will have seasonal and hourly variation in power output for an air-cooled system. These variations need to be modeled on a case-by-case basis to accurately predict ORC system output throughout the day and over the course of months due to seasonal variation. In extreme cases the temperature swings can cause the ORC to shut down due to the fans no longer being able to cool and condense the working fluid. Output power can go to zero during the hottest portions of the day as shown in Figure 6. At higher latitudes the seasonal variation will be the dominant factor affecting ORC output variation. At lower latitudes, the hourly variation can often be the dominant factor affect

predicted ORC output variation. Each case needs to be modeled for reliable predictions of net power output from the ORC and the resulting project economics for the system.

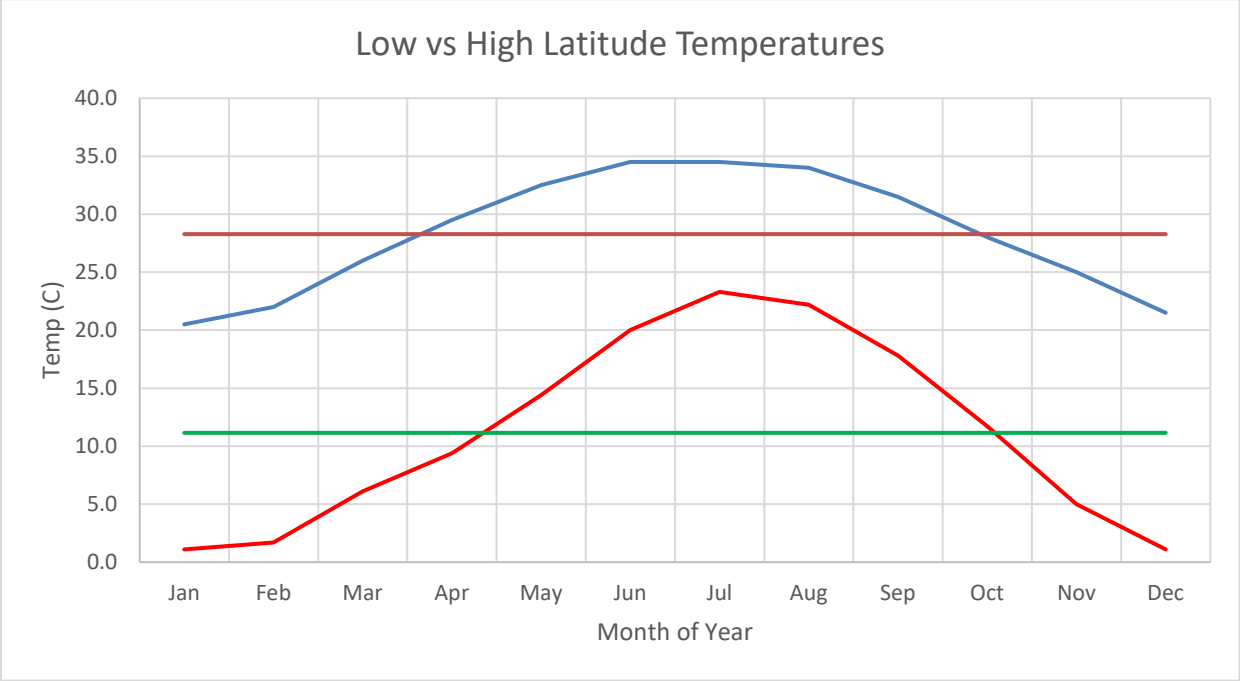

Figure 5 – Variation of seasonal and hourly temperatures at high and low latitudes.

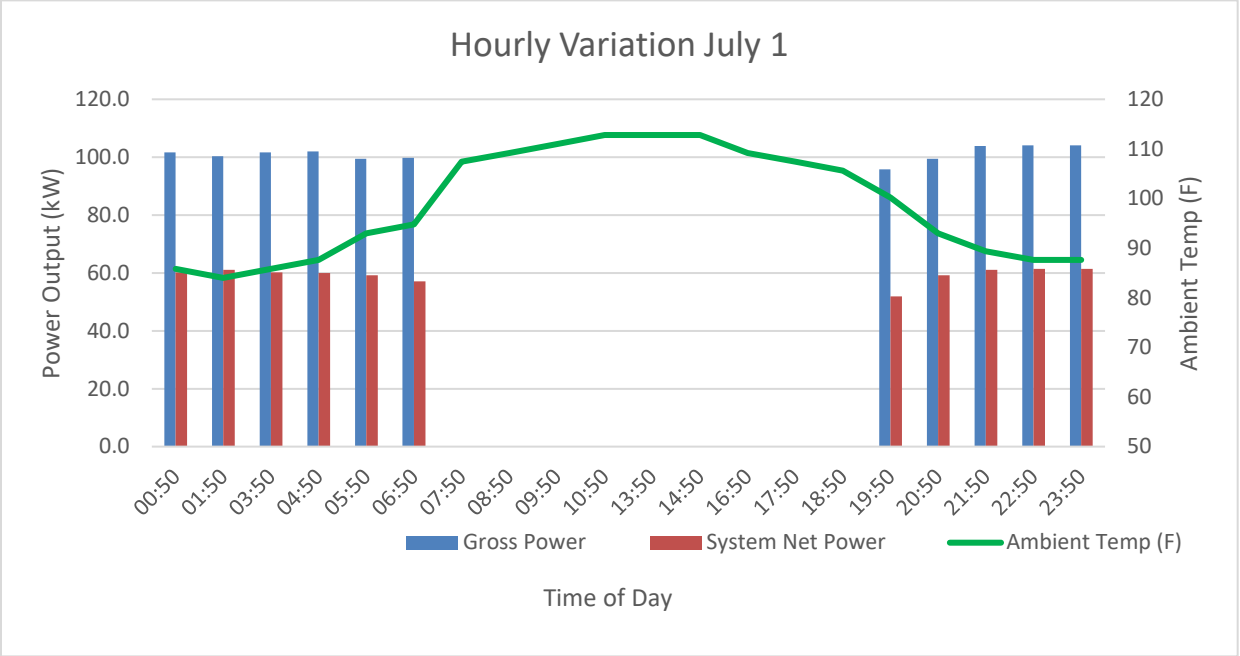

Figure 6 – Variation of seasonal and hourly temperatures at high and low latitudes.

6. Conclusions

Geothermal energy is one of the very best sources of non-carbon energy. The industry is in its infancy with many developments and improvements in store as it grows in the coming years. Virtually no forward-looking scenario of the growing energy demand is possible without a strong geothermal component as we look out 20, 30, or even 50 years into the future. The work force needs for the geothermal industry require skills and technologies from the oil and gas industry. It is reasonable to assume, much like in the case of cost reductions over time found in other renewable energy technologies, so too will geothermal energy development costs decline over time, especially in ORC design. With ORC's dependent upon ambient temperatures for air cooling of the working fluid, it is imperative to model both seasonal and hourly temperature variations to accurately forecast power output and project economics. The synergies gained by incorporating geothermal electricity generation capabilities to extract heat from existing oil and gas facilities is an obvious boost to lowering the hurdle rate for project economics. Generation near population centers also has the distinct advantage of being able to utilize the rejected ORC heat stream of slightly lower temperatures which are almost perfect for direct heating uses in communities or islanded industrial heating needs. As societal acceptance of these symbiotic approaches grows, and a much better full cycle use of the natural heat in the earth becomes commonplace, the future of geothermal in our future will be one of the most promising technologies and career paths over the next several decades.

Acknowledgement

This material is based upon work supported by the U.S. Department of Energy's Office of Energy Efficiency and Renewable Energy (EERE) under the Geothermal Technology Office and Wells Of Opportunity Incentive, Award Number DE-EE0009961.

This report was prepared as an account of work sponsored by an agency of the United States Government. Neither the United States Government nor any agency thereof, nor any of their employees, makes any warranty, express or implied, or assumes any legal liability or responsibility for the accuracy, completeness, or usefulness of any information, apparatus, product, or process disclosed, or represents that its use would not infringe privately owned rights. Reference herein to any specific commercial product, process, or service by trade name, trademark, manufacturer, or otherwise does not necessarily constitute or imply its endorsement, recommendation, or favoring by the United States Government or any agency thereof. The views and opinions of authors expressed herein do not necessarily state or reflect those of the United States Government or any agency thereof.

ElectraTherm, LLC, provided thermodynamic modeling and power modeling assistance. Grant Canyon Oil & Gas LLC provided sight access, field insight, and engineering support. The National Renewable Energy Laboratory (NREL) are our project partners and provided many insights to make this project successful.

REFERENCES

Akhmadullin, I., 2017. Utilization of Co-Produced Water from Oil Production: Energy Generation Case. SPE-184459-MS. SPE Health, Safety, Security, Environment, and Social Responsibility Conference – North America. New Orleans, LA., 18 April 2017.

Blankenship, D. et al (2024) Pathways to Commercial Liftoff: Next Generation Geothermal Power, U.S. Department of Energy report, March 2024. https://liftoff.energy.gov/wp-content/uploads/2024/03/LIFTOFF_DOE_NextGen_Geothermal_v14.pdf

Dupriest, F. and Noynaert, S. (2022) Drilling Practices and Workflows for Geothermal Operations. SPE-208798-MS.

Gosnold, W., Mann, M., Salehfar, H., 2017. The UND-CLR Binary Geothermal Power Plant. GRC Transactions 41.

ElectraTherm, 2012. Mississippi Oilfield Generates Low-Temperature, Emission Free Geothermal Energy at the Wellhead. https://www.smu.edu/~/media/Site/Dedman/Academics/Programs/Geothermal%20Lab/Documents/Oil%20and%20Gas%20Publications/2012_Denbury_White_Paper.ashx?la=en. Accessed on 07/01/2024.

Johnson, H., Kolker, A., Rhodes, G., and Taverna, N., 2020. Sedimentary Geothermal Resources in Nevada, Utah, Colorado, and Texas. Golden CO: National Renewable Energy Laboratory. NREL/TP-5500-76513. doi:10.2172/1660196.

Scott, C., Chamberlain, A., 1988. Blackburn Field, Nevada: A Case History, in Occurrence and Petrophysical Properties of Carbonate Reservoirs in the Rocky Mountain Region. Rocky Mountain Association of Geologists, Denver.

Smith, 1977. William Thomson and the Creation of Thermodynamics: 1840 – 1855, Archive for History of Exact Sciences 16, 231-288

Tabor, H., and Bronicki, L., 1964. Establishing Criteria for Fluids for Small Vapor Turbines, SAE Technical Paper 640823, https://doi.org/10.4271/640823.

Optimizing Flexible Geothermal Energy Generation: A Techno-Economic Analysis Using FGEM For EGS Huff-N-Puff

Lokesh Kumar Sekar[1], Mohammad Aljubran[2], Esuru Rita Okoroafor[1]

1 Texas A&M University, 2 Stanford University

Keywords

Flexible Geothermal Systems, Economic Modelling, huff-n-puff, EGS, Numerical Simulation, Sensitivity Analysis

ABSTRACT

Flexible energy resources are key for a reliable power supply in a decarbonized grid with a significant fraction of variable power source. Geothermal energy has always been an economic resource for baseload power and district heating. Recently, geothermal facilities have been expanding beyond baseload to supply flexible heat and electricity. Geothermal Energy can be harnessed through Enhanced Geothermal Systems (EGS). EGS involves creating an artificial reservoir by stimulating the natural permeability of hot rock formations beneath the Earth's surface. However, EGS may result in fast thermal depletion due to continuous fluid circulation. To slow down EGS thermal depletion due to continuous fluid circulation, we propose the Huff &Puff technique, which provides increased contact time between the injected working fluid and the hot geothermal rocks.

The primary objective of this work is to determine the technical and economic feasibility of harnessing geothermal energy from deep EGS using the huff-and-puff approach. To carry out these investigations, we use a 3-dimensional coupled thermo hydro mechanical numerical model to understand the system performance and the effect of different parameters on energy production. The outputs considered are wellhead temperature and production mass flow rates. Subsequently, we use a tool called FGEM, Flexible Geothermal Economics Modeling, to model the economics of EGS huff-n-puff systems.

The numerical simulation results show the feasibility of the huff-n-puff technique in EGS. The results from the economic modeling show that in the double well scenario, the Levelized Cost of Electricity (LCOE) for the huff-n-puff model is $0.40/KWh, slightly higher than the continuous model at $0.38/KWh. This is due to huff-n-puff's lower capacity factor from intermittent

production. However, huff-n-puff produces more cumulative water before thermal breakthrough, which occurs four times later than in the continuous model, supporting prolonged thermal storage feasibility. In contrast, the single well huff-n-puff model has a lower LCOE of $0.27/KWh, attributed to lower CAPEX and OPEX costs compared to the double well huff-n-puff model.

1. Introduction

Geothermal energy entails harnessing the heat from rocks beneath the Earth's surface to produce electricity (Barbier, 2002). In general, wells are drilled into the subsurface reservoir to extract hot fluids, with their application depending on the fluids' temperature and pressure: high-temperature fluids are primarily used for electricity generation, while low-temperature fluids are utilized for space heating and industrial processes (Barbier, 2002). Geothermal energy is unique among renewable energy sources because it is available continuously throughout the year, at any time of day, making it suitable for base load energy generation for both heat and power production (Agemar et al., 2014). Direct application of geothermal energy encompasses diverse uses like space heating and cooling, industrial processes, greenhouses, fish farming, and health spas. It relies on existing technology and basic engineering, utilizing both high- and low-temperature geothermal resources. The production cost for direct utilization varies but is often below US¢2/kWh (Fridleifsson, 2001). Despite statistics showing that geothermal energy contributes less to energy consumption than other low-carbon sources like solar, it offers several advantages that make it appealing for future energy development. These benefits include its consistency, significant untapped potential, widespread availability at depth, and a wide range of possible applications, especially where both power and heat are needed in varying proportions (Lund, 2000).

Despite these advantages, Michaelides (2016) reported that most of the world’s geothermal resources consist of low-temperature aquifers and hot dry rock resources, necessitating improved technologies for efficient power production from these sources. Additionally, a significant drawback is that these reservoirs can only be exploited for a limited time, until most of the contained fluid is extracted (Olasalo et al., 2016). These limitations have driven scientists to explore alternative solutions to mitigate the associated issues and ensure geothermal energy remains a viable and promising power source (Wong & Tan, 2015). The creation of artificial reservoirs has been proposed to decrease reliance on naturally occurring geothermal reservoirs. This alternative is known as "Enhanced Geothermal Systems" or EGS is an artificial reservoir constructed where the rock is hot, but there is insufficient fluid saturation and/or permeability in the rock (Okoroafor & Horne, 2024). Tester et al. (2006) led an interdisciplinary panel that defined EGS as "engineered reservoirs created to extract economical amounts of heat from geothermal resources with low permeability and/or porosity." For this assessment, this definition has been expanded to encompass all geothermal resources not currently in commercial production that require stimulation or enhancement (Breede et al., 2013).

One of the advantages of EGS over conventional geothermal reservoirs is that they can be harnessed in any location different from conventional hydrothermal geothermal locations. Despite being proposed as a viable solution, EGS still encounters significant challenges, such as requiring large contact time and contact area between the injected fluid and hot rock formations in continuous EGS operations (Okoroafor et al., 2022a). This drawback can result in slower heat transfer rates (Isaka et al., 2019). Advances in heat extraction strategies from geothermal rocks are crucial to meet increasing demand. Therefore, we consider the Huff & Puff technique as a possible

system for enhancing the contact time of injected working fluid with hot geothermal rocks and enabling higher cumulative heat extraction from the subsurface (Merzoug et al., 2023). In EGS, the Huff-n-Puff technique involves injecting a working fluid into wells, allowing it to soak for several days to enhance contact with hot rock formations. This process increases the fluid's temperature before resuming production, similar to its use in oil and gas recovery to optimize heat extraction (Isaka et al., 2019; Milad et al., 2021).

Assessing the feasibility of utilizing EGS with the huff-and-puff approach is essential for advancing and expanding this technique in future applications. Previous research on using the huff-and-puff technique in EGS is limited but promising. Recent studies on huff-and-puff EGS show advancements in thermal power extraction and optimization strategies, emphasizing factors like well spacing, fracture numbers, and operational parameters (Orzol et al., 2005; Tischner et al., 2010; Merzoug et al., 2023; Gudala et al., 2021 & Wu et al., 2023). Our study assessed the technical feasibility through numerical simulation, which replicated the subsurface EGS and implemented the Huff-n-Puff technique. In addition, the operational parameters are varied, and its impact is analyzed. This approach allowed for a comprehensive evaluation of the system's performance under varying conditions. The main parameter varied in this study is the number of wells drilled.

According to Lowry et al. (2014), the economic evaluation of EGS emphasizes that the Levelized Cost of Electricity (LCOE) is significantly influenced by pumping requirements. Therefore, determining economic feasibility is crucial for successful implementation alongside assessing technical feasibility. This dual evaluation ensures that EGS projects are both technically viable and economically sustainable. Thus, the primary objective of this work is to determine the feasibility of harnessing geothermal energy from EGS using the huff-and-puff approach both technically and economically.

Available software tools for evaluating geothermal power techno-economics include GETEM by Idaho National Lab, GEOPHIRES by NREL, and Hot Dry Rock economic by GTC Kappelmeyer GmbH. General-purpose tools such as PLEXOS, EnergyPLAN, GenX, and HOMER Energy are also utilized but are primarily designed for baseload geothermal projects and lack capabilities for modeling flexible geothermal operations (Aljubran & Horne, 2024). Hence, in our work for the economic feasibility analysis, we employed FGEM (Flexible Geothermal Economics Modeling), a specialized tool tailored for techno-economic assessments in flexible geothermal power generation. By applying FGEM, we conducted detailed economic modeling to optimize EGS Huff-n-Puff systems, ensuring that both technical and economic aspects were rigorously evaluated for feasibility.

2. Methodology

To determine the technical and economic feasibility of EGS huff-and-puff, we first used a 3-dimensional coupled thermo hydro mechanical (THM) numerical model to understand the system performance and the effect of different parameters on energy production. The outputs considered were wellhead temperature and production mass flow rates. The base case model had a top depth of 1200 meters and a reservoir temperature of 250°C with a single well used for both injection and production. We then compared the results of three different scenarios:

- **Single well Huff n Puff:** This strategy involves injecting fluid into the well and then allowing the well to rest before production.
- **Two well Huff n Puff:** Similar to the single well case, but here we have two wells, one for injection and one for production.
- **Two well continuous:** In this case, fluid constantly circulates between the two wells, continuously extracting heat.

For economics we used FGEM, Flexible Geothermal Economics Modeling, which is specifically designed for the techno-economic analysis of flexible geothermal power generation. We applied this tool to determine the economic viability of the huff-n-puff technique and further to optimize EGS huff-n-puff systems. The outputs from the FGEM tool include the Levelized Cost of Electricity (LCOE), Net Present Value (NPV), and payback period.

2.1 Numerical Model

The numerical model encompasses a reservoir with dimensions of 2000 feet in the x-direction, 300 feet in the y-direction, and 4000 feet in the z-direction. This model features a single horizontal well which is used as an injector and a producer. The base case scenario incorporates hydraulic fracturing by injecting slick water with a viscosity of 13.25 centipoise (cp) at surface temperature and 1.5 cp at reservoir temperature. This slick water carries a 100-mesh proppant and is injected at a rate of 80 barrels per minute (bpm). The fracturing schedule is divided into two phases: a fracturing phase and a production phase. In the base model, the fracturing phase lasts for 3.85 hours, followed by a shut-in period for the injection wells, amounting to a total of four days. Figure 1 illustrates the three-dimensional reservoir model, highlighting the fracture network and its distribution around the injection/production wells. The detailed model parameters and properties of the injected fluid are presented in Table 1. The reservoir model was assumed to be homogeneous with constant properties across the whole grid.

Table 1. Numerical model and injected fluid properties.

Parameter	Values
Model Parameters	
Model Size	2000*300 ft
Thickness	4000 ft
Reservoir Pressure	7250 psi
Reservoir Temperature	480 ^{o}F
Surface Temperature	60 ^{o}F
Well Depth	16400 ft
Heat transfer coefficient	9 BTU/(ft^2-hr)
Injected Fluid properties	
Fluid type	Water
Temperature	116 ^{o}F

The injection, soaking, and production schedule are detailed in Table 2. The injection and production scenarios are simulated under specific constraints. The rate constraint dictates that the maximum injection rate during the fracturing cycle is 80 barrels per minute (bpm), and during the injection cycle, it is 30 bpm. The wellhead pressure constraint stipulates that production must be maintained at a minimum pressure of 600 psi during both the fracturing and injection phases. This

wellhead pressure constraint effectively controls the bottomhole pressure and the wellhead production rate of the injected fluid. Following the establishment of the model as described, Huff 'n' Puff technique is implemented.

Table 2. Injection and Production Schedule

Phase	Process	Days
Fracturing cycle	Fracturing fluid injection	0.135
	Shut in	3.865
	Production	6
Huff n Puff Cycle 1	Injection Cycle – 1	10
	Soaking -1	5
	Production Cycle – 1	10
Huff n Puff Cycle 2	Injection Cycle – 1	10
	Soaking -1	5
	Production Cycle – 1	10

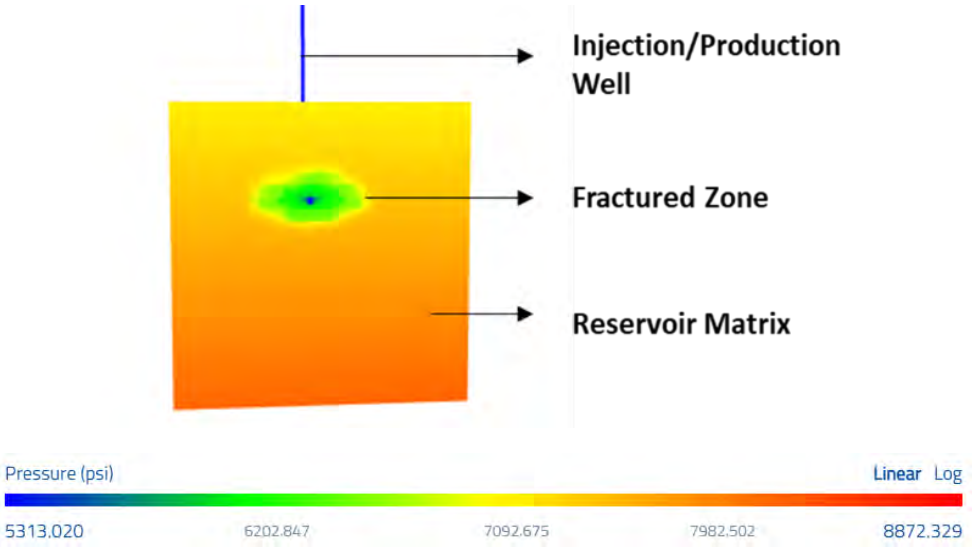

Figure 1: 3-Dimensional model showing the pressure after injection around the injection/production well

2.2 Numerical Model Validation

This study uses a coupled reservoir and fracture modelling simulator to replicate the subsurface enhanced geothermal system. To establish the suitability of the simulator for this study, we first validated the simulator results with already validated literature data. For the study validation, we used numerical simulation results from Okoroafor et al., 2022b. Fox et al., 2015 built a discretely fractured geothermal reservoir through a semi-analytical approach to study the effect of spatial aperture variations on EGS thermal performance. The model was developed by utilizing a hybrid method, including the finite element method for fracture to rock coupling and the boundary element method between the bulk rock. Okoroafor et al., 2022b modified and validated the work by Fox et al., 2021 for a square-shaped geothermal reservoir model to study the impact of fracture aperture anisotropy on EGS thermal performance using a commercial simulator (ECLIPSE E300).

In our validation study as a first step, we built the same reservoir model built by Okoroafor et al., 2022b and matched the bottomhole temperature from both models with a good degree of accuracy. The reservoir had a dimension of 50*50*45, grid cell counts of 112500, and a very thin fracture at a depth of 1295.5 m is considered. In the ECLIPSE model the fracture was initialized as a very thin layer with a thickness of 0.01 m. The temperature distribution in the fracture (X-Y) plane by Commercial simulator and Coupled fracturing Simulator is shown in Figure 2. Also, the graph showing the bottomhole temperature trend from commercial and coupled Hydraulic fracturing simulator is shown in Figure 3. The coupled Hydraulic fracturing simulator has the capability to integrate hydraulic fracturing and reservoir simulation into a single, unified model.

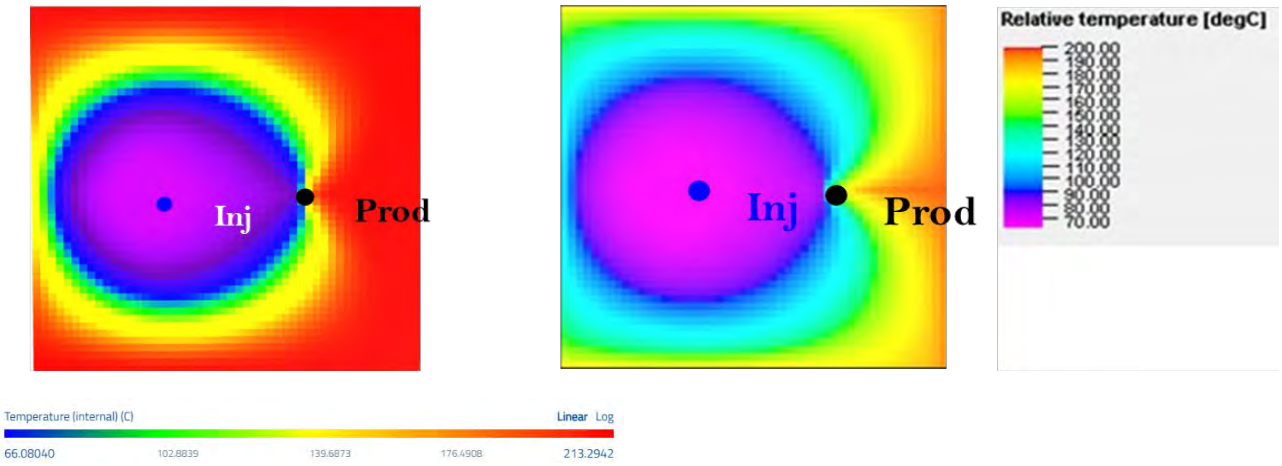

Figure 2: Temperature distribution in the fracture (X-Y) plane by Commercial simulator (right) and Coupled fracturing Simulator (left)

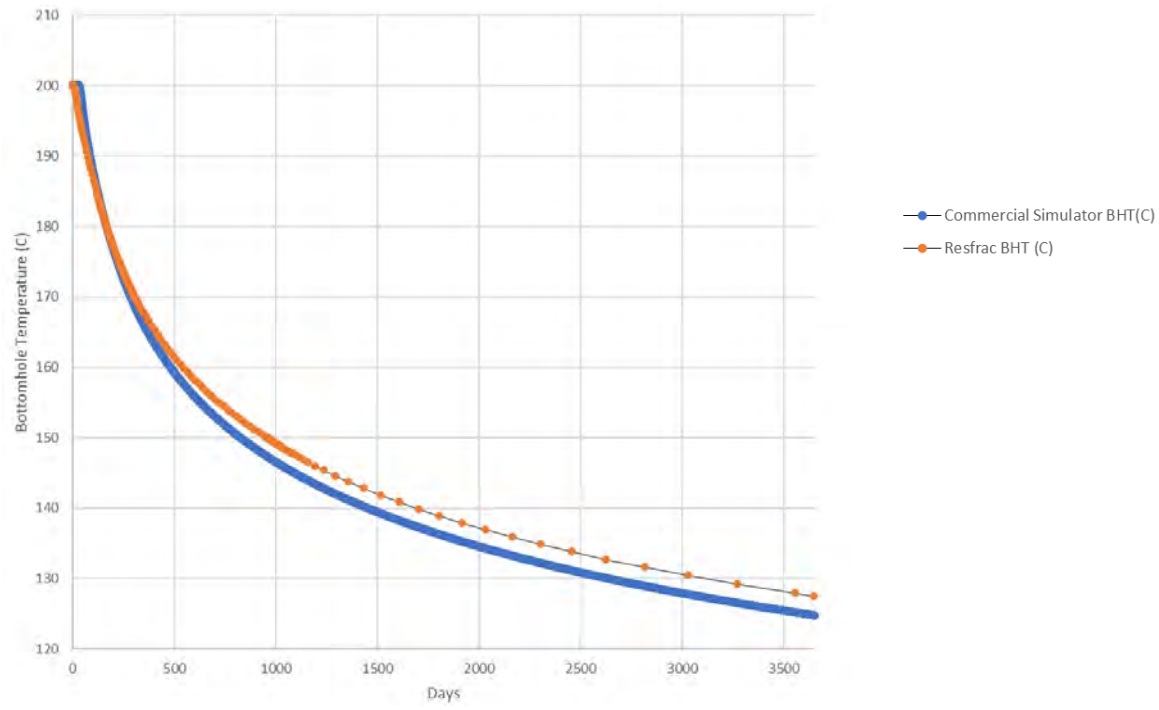

Figure 3: Graph showing the bottomhole temperature trend from commercial and coupled Hydraulic fracturing simulator

2.3 Sensitivity Analysis

After constructing and validating the numerical model, the optimal time of post-fracturing production is determined through a comprehensive sensitivity analysis. And in this study, for the injection, soaking and production schedule the values from Merzoug et al. (2023) and Sekar & Okoroafor (2024) were used. Studies have indicated that an optimal injection time of 10 days was most effective; five days were deemed too short to extract sufficient heat, while 15 days reduced injection and production rates due to storage volume saturation (Merzoug et al., 2023). Also, Sekar & Okoroafor (2024) determined the optimum soaking and production time to be 5 days and 10 days respectively. Subsequently, we compared the outcomes of single and double well huff-n-puff models to evaluate the technical feasibility of the huff-n-puff method in EGS.

2.4 Economic Feasibility Analysis through FGEM Flexible Geothermal Economic Modelling

After determining the technical and operational feasibility of the huff-n-puff technique, we used the open-source tool called FGEM (Aljubran & Horne, 2024). FGEM incorporates various parameters, including resource assessment, plant design, operational strategies, and market dynamics, to provide a comprehensive analysis of the economic viability of geothermal systems. FGEM requires three primary inputs: a configuration file in .json format, data files in .csv format, and a dispatch strategy implemented in Python code. These inputs collectively integrate detailed information on subsurface reservoir properties, power plant operations, and weather conditions. Table 3 presents the major input parameters used in the config. json configuration file for this case study. To accurately capture the dynamics of battery costs, weather patterns, wholesale energy prices users must provide the corresponding data files: battery.csv, weather.csv, wholesale.csv, and capacity.csv. These inputs regarding the reservoir, power plant and the weather are then validated and used to initiate the simulation run. Since our primary objective is to compare the continuous and Huff n Puff techniques for the double and single well type well configuration, we only changed the production temperature and mass flow rate while importing the data as a csv file (Aljubran & Horne, 2024).

2.4.1 Subsurface reservoir

FGEM seamlessly interfaces with numerical models like TOUGH2 and DARTS. It also allows for importing simulated reservoir outputs, such as wellhead temperature and mass flow rate stored in CSV files, to conduct comprehensive techno-economic evaluations (Aljubran & Horne, 2024). In our study, we will import our mass flow rates and wellhead temperature in the form of .csv files.

2.4.2 Weather

In this study for our economic modeling, we input one year of weather data and assume these patterns repeat annually over the project's lifetime.

2.4.3 Power Plant

The power plant component considers parameters like efficiency and reinjection water temperature, influenced by factors such as the power plant type (e.g., subcritical organic Rankine cycle (ORC) or single flash), entering geofluid temperature, and ambient conditions. Overall, this integrated approach with FGEM enables a thorough assessment of both the technical and economic

feasibility of implementing the huff-n-puff technique in EGS, leveraging detailed input parameters and sophisticated modeling capabilities.

Table 3. Major input parameters used in the config.json file for the double well case.

Metadata			
Initial Time	2024–01–01	State	Nevada
Economics			
Lifetime	25 $years$	Grid	130 $/kW
Discount	0.07	ITC	0.3
Inflation	0.02	TES	1434.53 $/m3
OPEX escalation	0.0	Battery	battery.csv
Downstream			
Plant type	Binary	Weather	weather.csv
PPC	12 MW	Wholesale	Wholesale.csv
CF	0.95	Capacity	Capacity.csv
Upstream			
Reservoir	Energy Decline	PRD count	1
Tr (0)	215 ◦ C	PRD-INJ ratio	1
Pr (0)	40 bars	Water loss	0%
Vr	5 km3	Pump efficiency	0.75
$Tsurf$	20 ◦ C	DSR	0.9
$Hwell$	1325 m	PI/II	20/20 kg/s/bar
$Dprd$	0.2159 m	$Dinj$	0.2159 m

Upon the end of the simulated project lifetime, records are stored, economics are computed, and various quantities are visualized. The visualized quantities include production temperature, mass flow rate and the net power generation (kWh) respectively. The outputs from the FGEM tool include the Levelized Cost of Electricity (LCOE), Net Present Value (NPV), and payback period.

3. Results and Discussions

We have conducted comprehensive simulations for single well huff-n-puff technique, focusing on their effectiveness in enhancing the temperature of the produced fluid through increased contact time of injected fluids. Initially, observations indicated that increased contact time could lead to higher temperatures in the produced fluid. By understanding the interplay between these parameters and their impact on the system's performance, we can ensure that the methods are not only technically sound but also ready for subsequent economic evaluation.

3.1 Determining the optimum post-fracturing production time

During the initial modeling phase, we observed that higher injection pressures result in greater vertical fracture propagation. On the other hand, reducing the injection pressure constraint led to model failure due to inadequate injection pressure, as illustrated in Figure 4. Prior to advancing the model development, we analyzed fracture propagation and discovered that a significant pressure decline post-fracturing mitigates the fracture propagation issue. Identifying the optimal production time post-fracturing is essential for managing fracture propagation and ensuring the required fluid injection volume. Sensitivity studies on the post-fracturing production period revealed that a production period of 6 days assists in pressure decline. This strategy stabilizes bottom hole pressure and effectively addresses fracture propagation challenges.

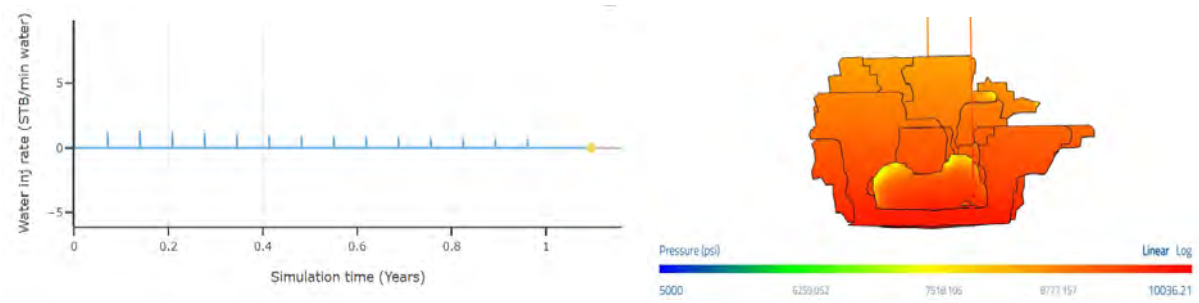

Figure 4: Figure showing the failed injection and higher fracture propagation issues

3.2 Determining the feasibility of single well Huff n Puff technique

Sekar and Okoroafor. (2024) compared the double well continuous and huff-n-puff long-term model and found that in the continuous model, the temperature declined from 475 to 375 ^{o}F and later it maintains the temperature around 375 ^{o}F for the next few years. But in the Huff n Puff case this decline is negligible. This is shown in Figure 5. These preliminary results prove the feasibility of huff-n-puff technique in EGS.

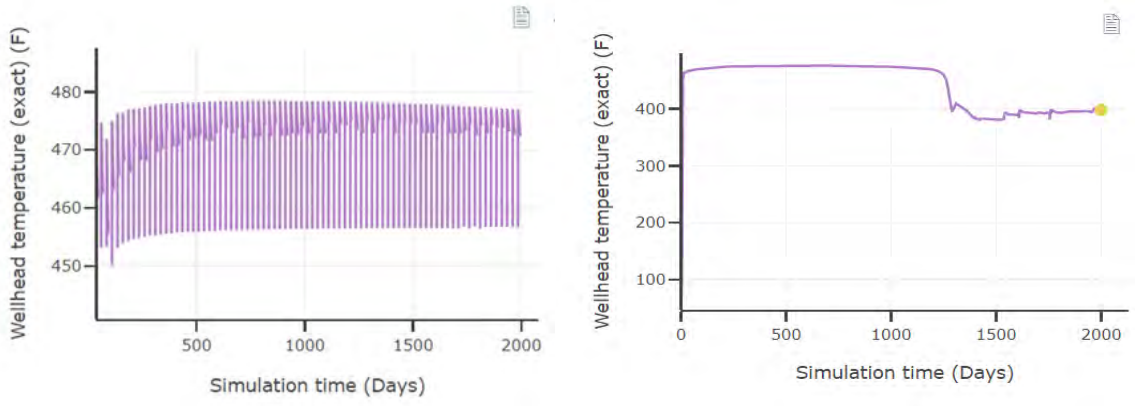

Figure 5: Comparison between the wellhead temperature of continuous (right) and Huff and Puff (left) Systems (Sekar & Okoroafor. 2024)

After simulating the single-well Huff n Puff models, we compared our results with the double-well huff-n-puff case by Sekar & Okoroafor (2024). The single well case shows a rapid decrease in the temperature and energy content (enthalpy) of the fluid coming out of the well (Figure 6). Also, our findings indicated that the average temperature values for the huff-n-puff technique in single wells is lower than that of double-well huff-n-puff. Even with a faster temperature decline, the CAPEX and OPEX values of single well case are anticipated to be less than that of the double well case. Thus, to demonstrate this fact and to identify the LCOE of the electricity generated, our next part of the study includes the economic analysis study using FGEM for all three cases, including the single and double well huff-n-puff models and double well continuous model.

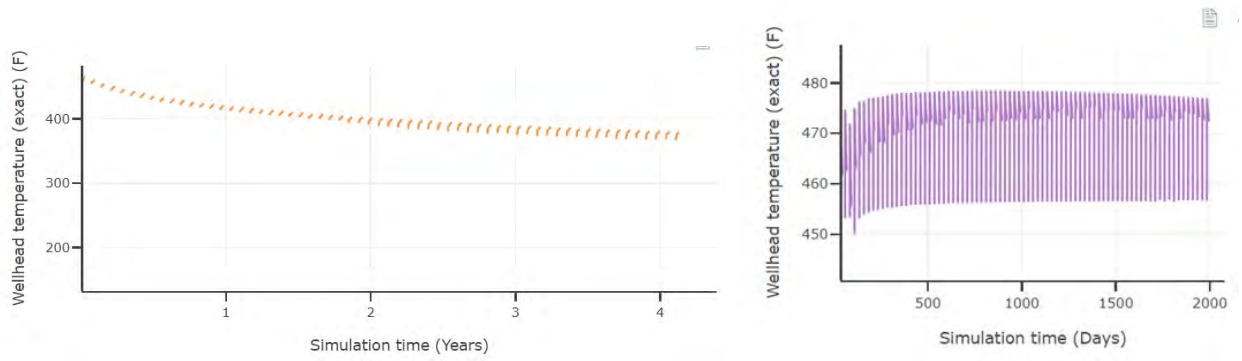

Figure 6: Comparison between the wellhead temperature of single well huff-n-puff (left) Systems and two well huff-n-puff (Sekar & Okoroafor. 2024) systems

3.3 Determining the economic feasibility of Huff n Puff technique

This study compares the double well continuous and huff-n-puff EGS models and the single well Huff-n-Puff model to determine the economic viability of the Huff-n-Puff technique and quantify its benefits over continuous extraction methods using a tool developed by Aljubran & Horne. (2024). We specifically demonstrate the application of FGEM (Flexible Geothermal Economics Modeling) to evaluate the techno-economic aspects of our simulated model, utilizing data from the Ormat Desert Peak II power plant located in Churchill County, Nevada. Post-economic modeling the wellhead temperature, thermal breakthrough time & LCOE for all three scenarios are tabulated in Table 4.

Table 4. Wellhead temperature, thermal breakthrough time & LCOE for different well count and injection scenarios.

Well Count & Injection Scenerio	Wellhead Temperature (°F) after 4 years	Thermal breakthrough time (days)	Levelized Cost of Electricity (dollars/KWh)
Double well continuous	375	1200	0.38
Double well huff-n-puff	475	4380	0.40
Single well huff-n-puff	390	1350	0.27

For the double well case, the Levelized Cost of Electricity (LCOE) for the Huff n Puff model (0.4 dollars/KWh) was higher than that of the continuous model (0.38 dollars/KWh). This slightly higher LCOE for the Huff n Puff technique is expected to be due to its intermittent production. Also, the single well huff and Puff showed an LCOE of 0.27 dollars/KWh. The low LCOE of single well huff-n-puff is anticipated to be due to the lower CAPEX cost for developing single well and the lower OPEX cost associated with it.

4. Conclusion

This study demonstrates the potential of the huff-n-puff technique to optimize energy extraction in EGS. The numerical simulation studies showed that the huff-n-puff approach showed superior heat extraction capabilities and maintained higher wellhead temperatures compared to continuous extraction, indicating its feasibility for sustainable geothermal energy production. Economic evaluations also highlighted the technique's viability, suggesting it could significantly improve the efficiency and longevity of EGS, thus contributing to a more reliable and flexible renewable energy

supply. The higher LCOE for the huff-n-puff technique is expected to be due to the lower capacity factor of huff-n-puff technique because of its intermittent production. Despite the slightly higher LCOE, the cumulative water produced before thermal breakthrough in the huff-n-puff technique was greater than in the continuous model. Additionally, the time for thermal breakthrough in the huff-n-puff model is four times longer than in the continuous model, ensuring the feasibility of prolonged thermal storage. The low LCOE of single well huff-n-puff is anticipated to be due to the lower CAPEX cost for developing single well and the lower OPEX cost associated with it. Economic modeling also proves the feasibility of huff-n-puff technique in EGS. Although this method may not supply continuous geothermal energy, it offers a viable option for heat storage and extended direct utilization. These insights represent a significant step towards the more efficient exploitation of geothermal resources, ultimately enhancing the overall energy recovery process in tight EGS reservoirs.

REFERENCES

Aljubran, M.J. and Horne, R.N., 2024. FGEM: Flexible Geothermal Economics Modeling tool. Applied Energy, 353, p.122125.

Agemar, T., Weber, J. and Schulz, R., 2014. Deep geothermal energy production in Germany. Energies, 7(7), pp.4397-4416.

Barbier, E., 2002. Geothermal energy technology and current status: an overview. Renewable and sustainable energy reviews, 6(1-2), pp.3-65.

Breede, K., Dzebisashvili, K., Liu, X. and Falcone, G., 2013. A systematic review of enhanced (or engineered) geothermal systems: past, present and future. Geothermal Energy, 1, pp.1-27.

Fox, D.B., Koch, D.L. and Tester, J.W., 2015. The effect of spatial aperture variations on the thermal performance of discretely fractured geothermal reservoirs. Geothermal Energy, 3, pp.1-29.

Fridleifsson, I.B., 2001. Geothermal energy for the benefit of the people. Renewable and sustainable energy reviews, 5(3), pp.299-312.

Gudala, M., Yan, B., Tariq, Z., & Sun, S. (2023). Doublet Huff and Puff (Dhp): A New Technology Towards Optimum Scco2 Sequestration with Stable Geothermal Recovery. Available at SSRN 4568399.

Isaka, B.A., Ranjith, P.G. and Rathnaweera, T.D., 2019. The use of super-critical carbon dioxide as the working fluid in enhanced geothermal systems (EGSs): A review study. Sustainable Energy Technologies and Assessments, 36, p.100547.

Lowry, T.S., Kalinina, E.A., Hadgu, T., Klise, K.A. and Malczynski, L.A., 2014. Economic valuation of directional wells for EGS heat extraction. In Thirty-Ninth Workshop on Geothermal Reservoir Engineering, Stanford University.

Lund, J.W., 2000. World status of geothermal energy use overview 1995-1999.

Merzoug, A., Zhang, J., & Okoroafor, E. R. Investigating the Feasibility of a Geothermal Huff-n-Puff: Implications for Enhanced Geothermal Systems.

Michaelides, E.E.S., 2016. Future directions and cycles for electricity production from geothermal resources. Energy Conversion and Management, 107, pp.3-9.

Milad, M., Junin, R., Sidek, A., Imqam, A., & Tarhuni, M. (2021). Huff-n-puff technology for enhanced oil recovery in shale/tight oil reservoirs: Progress, gaps, and perspectives. Energy & Fuels, 35(21), 17279-17333.

Okoroafor, E. R., Co, C., & Horne, R. N. (2022a). Numerical investigation of the impact of fracture aperture anisotropy on EGS thermal performance. Geothermics, 100, 102354. https://doi.org/10.1016/j.geothermics.2022.102354

Okoroafor, E. R., Williams, M. J., Gossuin, J., Keshinro, O., & Horne, R. N. (2022b). Fracture roughness considerations in comparing CO2 and water as enhanced geothermal system working fluids. Geothermics, 106, 102578. https://doi.org/10.1016/j.geothermics.2022.102578

Okoroafor, E. R., & Horne, R. N. (2024). Fracture aperture anisotropic effects on field scale enhanced geothermal system thermal performance. Geothermics, 118, 102897. https://doi.org/10.1016/j.geothermics.2023.102897

Olasolo, P., Juárez, M. C., Morales, M. P., & Liarte, I. A. (2016). Enhanced geothermal systems (EGS): A review. Renewable and Sustainable Energy Reviews, 56, 133-144.

Orzol, J., Jung, R., Jatho, R., Tischner, T., & Kehrer, P. (2005, April). The GeneSys-Project: Extraction of geothermal heat from tight sediments. In Proceedings World Geothermal Congress (pp. 24-29).

Sekar, L. K., & Okoroafor, E. R. (2024, June). Maximizing Geothermal Energy Recovery from Enhanced Geothermal Systems Through Huff-And-Puff: A Comprehensive Simulation Study. In ARMA US Rock Mechanics/Geomechanics Symposium (pp. ARMA-2024). ARMA.

Tester, J.W., Anderson, B.J., Batchelor, A.S., Blackwell, D.D., DiPippo, R., Drake, E.M., Garnish, J., Livesay, B., Moore, M.C., Nichols, K. and Petty, S., 2006. The future of geothermal energy. Massachusetts Institute of Technology, 358, pp.1-3.

Tischner, T., Evers, H., Hauswirth, H., Jatho, R., Kosinowski, M., & Sulzbacher, H. (2010, April). New concepts for extracting geothermal energy from one well: the GeneSys-Project. In Proceedings of the world geothermal congress, Bali (Vol. 2530).

Wong, K.V. and Tan, N., 2015. Feasibility of using more geothermal energy to generate electricity. Journal of energy resources technology, 137(4), p.041201.

Wu, Y., Salehi, S., & Karbalaeisaleh, F. (2023, June). Numerical Investigation of Geothermal Storage and Extraction Using Huff-N-Puff Wells. In ARMA US Rock Mechanics/Geomechanics Symposium (pp. ARMA-2023). ARMA.

Generating Value from Geothermal Non-Condensable Gas Emissions

P. Siratovich[1] A. Marsh[1], A. Blair[1], R. Lawson[1], M. Climo[1]

[1]Upflow Ltd

Keywords

Gas, Non-Condensable, Carbon Dioxide, Methane, Reinjection, Direct Use, Power Generation, Greenhouse Gases

ABSTRACT

The world is facing a climate crisis as a result of greenhouse gas (GHG)-driven warming. Many geothermal operators and researchers are actively implementing and finding new solutions to the challenge of abating GHG emissions from geothermal plants to ensure a sustainable future.

In geothermal power operations, non-condensable gases (NCG) are brought to the surface dissolved in / with the geothermal fluids. The most abundant geothermal gases are carbon dioxide (CO_2 - the most dominant NCG), hydrogen sulfide (H_2S) and methane (CH_4), with other gases considered trace gases. Their inability to condense (i.e., be turned into a liquid) by the cooling which occurs in geothermal power stations at the surface means NCGs are most often released to atmosphere during the power generation process. Decarbonization drivers for industry means reinjection of NCGs back into reservoirs is increasingly becoming standard practice at many locations globally, to close the emissions loop.

There is a need, and an opportunity, to find different uses and ways to abate the NCG emissions from geothermal plants that can be beneficial to operations, lower costs and potentially add value. In this paper, we examine several avenues of abatement through gas capture and re-use, into applications including horticulture, green fuels and chemicals production, and industrial uses, as an added benefit of geothermal energy production. Several pathways for utilization are illustrated that may have been overlooked.

1. Introduction

Geothermal power plants have high availability factors and, in most cases, produce significantly less GHG emissions than fossil-fuel driven plants, whilst having the constant output that other renewables do not have due to their reliance on daylight and weather conditions. However, geothermal plants can make contributions to decarbonization by addressing their GHG emissions profile.

Reinjection of GHG's back into reservoirs is increasingly becoming common practice. However, there are still challenges in this approach. For example, reservoirs may have limited ability to uptake reinjected gases without negative effects on production or scaling in the immediate vicinity. Additionally, flash-plant technology may have the challenge of oxygen introduced into the process

where direct contact condensers are used, which can increase the reactivity and corrosivity of the NCG stream.

Meanwhile, carbon dioxide, the most abundant NCG, is an essential processing gas in the modern world. Packaging, beverage production, agriculture, industrial processes, and several other industries rely on carbon dioxide gas as an essential input. There is an opportunity to capture and re-purpose NCGs for value-added uses, replacing fossil equivalents.

This paper summarizes the current challenges and opportunities for NCG abatement pathways. References are cited where data and experiences have been shared in the public domain, in many instances, the observations and recommendations stem from the authors' own experiences.

2. Non-Condensable Gas Emissions from Geothermal Power Plants

Produced geothermal fluids carry gases that are emitted in the process of extracting heat and power. These emissions challenge the notion that geothermal is an explicit 'green' source of energy. Geothermal power plants harness the heat stored in the Earth's crust to generate electricity from the fluids that permeate the subsurface. Geothermal fluid extracted from the underground reservoirs contains not only water, but also various dissolved gases, such as carbon dioxide (CO_2), hydrogen sulfide (H_2S), methane (CH_4), ammonia (NH_3) and nitrogen (N_2). During the geothermal production cycle, these gases must be processed using specialized gas trains as they do not stay condensed in the liquid phase at the operating conditions of the power plant. The NCGs are separated from geothermal steam in the condenser or binary heat exchanger and are usually vented to the atmosphere as byproducts, sometimes causing damage to site infrastructure and acting as environmental irritants.

Mclean and Richardson (2020) overview geothermal emissions from the New Zealand generation fleet, quantified in terms of CO_2e (CO_2 + methane equivalent), illustrating that overall, nearly 531 kilotonnes of CO_2e is emitted related to geothermal power generation. This highlights a significant emission profile for the nation's electricity production but also highlights an opportunity for finding innovative ways of repurposing these emissions since domestic CO_2 supply in New Zealand has become increasingly expensive (Olley, 2023).

2.1 Drivers to Reduce NCG & GHG Emissions

NCG emissions pose environmental and economic challenges for geothermal power generation as their emissions are closely regulated and, in New Zealand, bear the costs of emissions taxation, through the Emissions Trading Scheme (ETS). The New Zealand model taxes emissions similar to other jurisdictions where carbon taxation follows trading mechanisms and other cap-and-trade type initiatives (see Flues, 2020). Some financial benefits to consider in addressing GHG abatement for geothermal plants include:

- *Financial benefits of reducing carbon tax liability*: Reducing emissions from geothermal plants can save money by avoiding the costs of surrendering emission units under the emission trading schemes (where applicable), where costs are expected to increase over time.

- *Environmental benefits of reducing greenhouse gas emissions*: Reducing emissions from geothermal plants can help achieve climate change goals and demonstrate a commitment to sustainability and decarbonization.
- *Environmental benefits of reducing H_2S emissions*: Reducing H_2S emissions from geothermal plants can improve the local air quality and reduce the health and safety risks associated with exposure to toxic gas as well as ill-effects on plant infrastructure due to exposure to corrosive H_2S gas.

Even without financial incentives, operators may prefer to implement more sustainable solutions, such as reinjection or purification and sale of NCGs or derivatives, to boost their environmental performance and reputation. These actions show a commitment to corporate social responsibility, green energy, and earn the support of stakeholders. It also helps fight climate change and foster a low-carbon economy. However, operators of these plants are challenged to retrofit and repurpose the emissions in ways that will not affect plant operation and the sustainability and producibility of subsurface reservoirs.

3. Reinjection of NCGs into Reservoirs

Many locations around the world, including Iceland (Aradottir, *et al.*, 2020+1), New Zealand (Ruiz *et al.*, 2021) and Turkey (Layman, 2017; Yücetaş *et al.*, 2018), are now adopting the practice of sending GHG's back into reservoirs to close the emissions loop. The key advantage is the opportunity to dispose of GHGs, hydrogen sulfide and mercury emissions, which are often closely monitored and regulated.

Binary-cycle plants can usually capture NCGs and reinject them more easily than direct-contact condensing flash plants that use cooling circuits open to atmosphere that introduce air into the system. Geothermal flash plants can compress NCGs and inject them into brine handling systems, but there are challenges with methane, oxygen and nitrogen components that will not easily dissolve back into the brine and the increased corrosivity due to oxygen. Other challenges we believe need to be understood to achieve successful abatement through injection include:

- *Site Variability*: The uncertainty and variability of the NCG composition and flow rate at different sites and over time, which depend on the location, depth, and age of the reservoir, as well as the operational conditions of the power plant.
- *Chemistry & Geology*: The possible negative effects on the reservoir chemistry and geology, such as changing the pH, mineralogy, permeability, and fracture network of the rock formation, which could reduce the productivity and longevity of the reservoir.
- *Equipment*: The need for additional equipment, such as compressors, pipelines, and injection wells, increasing the capital and operational costs of the power plant.
- *Scaling & Corrosion*: The presence of oxygen from the condensing cycle introduces a major corrosion risk in brines, particularly those at high temperature and modified to reduce pH to control silica scale.
- *Energy consumption*: Energy intensity of gas abatement equipment and the parasitic loads on achieving economic success for geothermal power installations must be well understood and sensitivities tested.
- *Dissolved gases*: Keeping gases dissolved during transport to the well is critical for avoiding operational challenges, such as gas-locking of wellheads due to build-up of

pressure, as well as corrosion considerations from high gas concentrations in site infrastructure.
- *Containment failure*: There is a risk of releasing a gas cloud as a result of a containment failure in compressed gas lines or vessels.

Reinjection of NCGs into geothermal reservoirs requires careful evaluation of the technical, economic, and environmental feasibility of each case, as well as monitoring and modelling the reservoir behavior and performance (e.g. Figure 1). Considerations include:

- *Tracer test results*: Tracer tests can help indicate (e.g. Nyawir *et al.,* 2023; Kristjánsson *et al.*, 2016) what proportion of the injected fluid that returns to the production area. Operators can use this information to understand how much gas may find its way back to production areas (noting that mobility of gas-laden liquids may change compared with pre-injection results), which may increase both gas production from wells and possibly increase scaling risk.
- *Production and reinjection*: The production fluid is composed of a mixture of reservoir fluid unaffected by injection plus returns from reinjection. The reinjected fluid often has a higher gas concentration than that produced, due to evaporation.
- *Risks for the reservoir*: The main risks for the reservoir are scaling and plugging over widespread areas, and changes in gas concentrations that may affect the power output and injection capabilities (e.g., Byrne *et al.,* 2023; Kaya and Zarrouk, 2017). Concentration of gas may already be somewhat depleted if the plant has already been operating prior.
- *Concentration mechanism and model*: A concentration mechanism exists if all gases are forced into the reinjection stream and then return to the production area as demonstrated through modeling performed by Sevindik et al., 2023. The concentration changes expected due to returns can be estimated through models and validated during operation.
- *Best approach and learnings*: In our opinion, the best approach will be to slowly ramp up reinjection rates and monitor the system response over time as demonstrated by Abd Ghafar *et al.* (2022) at New Zealand's Ngatamariki field. The results at operations conducting gas injection are encouraging at locations like Ngatamariki, Ngāwha, Te Huka, and Hellisheidi (White, 2023, Abd Ghafar *et al.,* 2022, Ruiz *et al.,* 2021, Aradottir *et al.,* 2020), but are not directly applicable to all fields due to the different geologic setting and degrees of connectivity.

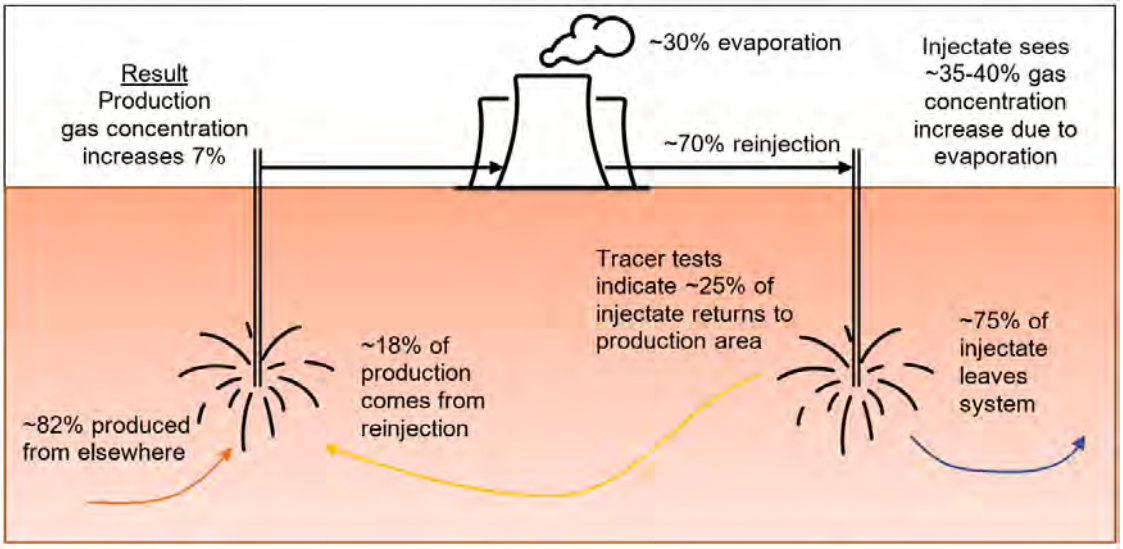

Figure 1: Conceptual model of Flash-Plant NCG reinjection. The pathway of NCGs reinjected into the reservoir will likely follow those seen in tracer testing but may also find new ways back to production areas particularly where gas or two-phase fluid zones exist.

4. Alternative Uses for CO_2 Emissions

Renewable energy sources such as geothermal, wind and hydro are anticipated to support the emergence of new low-carbon industries driven by electricity. Intermittency and market-driven electricity prices will favor technologies capable of flexible generation. Notably, there is potential in the concept of 'flexible geothermal' (Marsh *et al.*, 2023; Aljubran & Horne, 2023), particularly when aligned with the appropriate load or value-adding product. The flexible geothermal approach allows for large scale production and efficient storage when buffering electricity-heavy inputs during periods of low electricity prices, particularly where the storage duration is limited such as a daily oversupply cycle for electricity.

Likewise, a flexible approach to emissions management could realize economic and environmental benefits for operators. The examples below focus on CO_2, the most abundant NCG. While a known and vilified GHG, CO_2 is also an essential component of many industrial processes and is often produced as a byproduct of fossil fuels. By purifying and selling/using CO_2 from geothermal plants, new industries and supply vectors can be formed. This could create new revenue streams and support the development of low-carbon products and services, as well as displacing the need to produce CO_2 through traditional means.

4.1 Industrial Use of CO_2

There is the possibility of purifying and selling CO_2 from the geothermal NCG stream to a wholesaler or a direct user. This could reduce emissions, generate revenue, and provide a financial benefit from the avoided emissions taxation costs (where they exist). Liquid CO_2 is used in a variety of applications, including beverage carbonation, refrigeration, packaging, and fermentation. Gaseous CO_2 is used in a variety of applications, including packaging, fermentation, and animal stunning. An industrial user of gas would likely require specific levels of purification adapted from CO_2Meter (2019):

- Medical-grade CO_2 should be at least 99.5% pure and free of impurities, such as hydrocarbons, oxygen, and water.
- Food-grade CO_2 should be at least 99.9% pure and free of impurities, such as heavy metals, pesticides, and microbiological contaminants.
- Industrial-grade CO_2 should be at least 99% pure and free of impurities that could contaminate the product or process.

To meet the requirements of the food and beverage industry, the CO_2 would need to undergo purification and then be transported in liquid tanks or as bottled gas to customer/consumer markets (Brownsort *et al.*, 2019).

Direct collaboration with a new or established local industry is also possible. This approach offers several advantages, including enhanced certainty of supply volume and transport efficiencies (by piping directly) that can lead to competitive pricing. Moreover, partnering with an industrial entity nearby a geothermal site means access for the industry partner to renewable electricity, low-grade heat, fresh water, minerals, industrial-zoned land, and perhaps existing permits. There could be synergies with other local industries, such as in the New Zealand example at Kawerau or Wairakei/Tauhara where forestry offers a suitable feedstock for fuels production amongst other industrial outputs (McClintock *et al.*, 2020; Stephenson and Goodwin, 2019).

For horticulture, supplementation of CO_2 is a common practice in greenhouses. This is necessary because atmospheric CO_2 levels are typically low, and plants within closed greenhouse systems can rapidly deplete the available CO_2. By augmenting CO_2 levels, growers can enhance both the yield and quality of their crops (Nederhoff, 2021). Utilizing all the CO_2 from one power plant could support tens of hectares of glasshouse infrastructure by following the standard convention that 150 kg/Ha/hour of CO_2 is an optimal supply rate for closed greenhouse growing conditions (Nederhoff, 2022). For example, a 20-hectare glasshouse would require ~32,000 tons/annum of CO_2 to supplement growing, which would consume a significant portion of the ~37,578 tons/CO_2 per annum emitted at the Ngatamariki power station (Mclean & Richardson, 2020).

4.2 Geothermal CO_2 for Fuel & Chemical Production

Many efforts are being made globally to leverage CO_2 in the production of chemicals and fuels production (Grim *et al.*, 2022). This pathway offers several advantages: Firstly, it aids in mitigating overall greenhouse gas emissions by displacing more emissions-intensive production methods. Secondly, it promotes local production, reducing reliance on other countries and creates jobs for communities typically in need of employment opportunities. Some of the most common applications of CO_2 use in chemical and fuel production include:

- *Methanol*: A versatile chemical that can be used in a variety of applications, including as a fuel, a solvent, and as a raw material for other chemicals. Methanol can be produced from CO_2 by reacting it with hydrogen in the presence of a catalyst.
- *Urea*: A fertilizer that is used to improve crop yields. Urea can be produced from CO_2 by reacting it with ammonia.
- *Polycarbonates*: A type of plastic used in a variety of applications, including food packaging, electronics and construction. Polycarbonates can be produced from CO_2 by reacting it with epoxides.

- *Fuels*: CO_2 can be used to produce a range of fuels, including synthetic gasoline, diesel and jet fuel. These fuels can be produced by reacting CO_2 with hydrogen in the presence of a catalyst. Geothermal could potentially provide CO_2 through both NCG capture and direct-air capture (DAC) on-site, making for a circular fuel system (Figure 2).

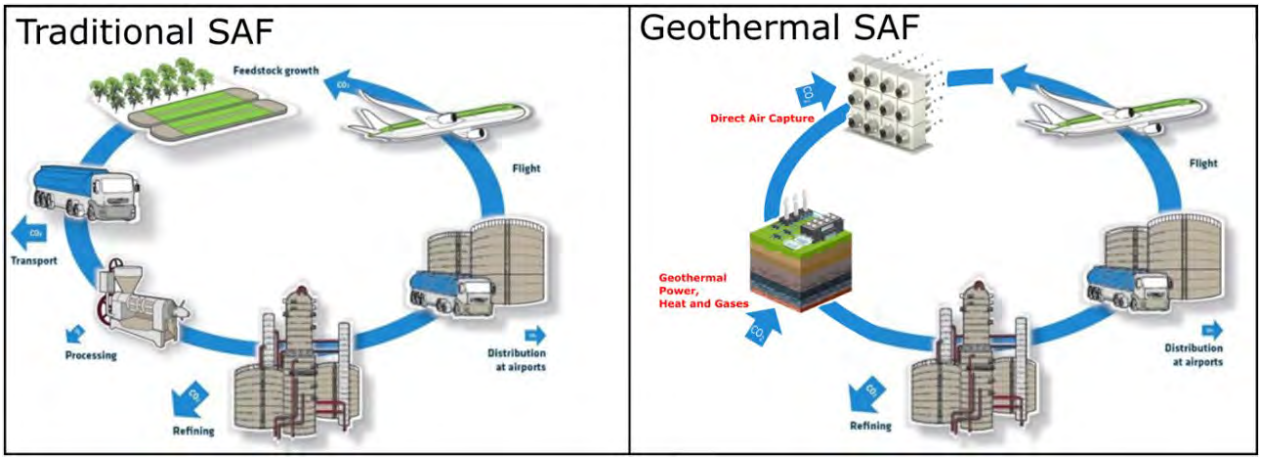

Figure 2: Traditional Sustainable Aviation Fuel (SAF) pathway versus a potential Geothermal SAF pathway. The need for external carbon feedstock is replaced by geothermal plant emissions and supplemented by direct-air capture (DAC) of CO_2 (Modified from Earth.org/sustainable-aviation-fuel-companies).

A compelling case study is that of Carbon Recycling International (Iceland) where an e-methanol pilot plant was developed using carbon emissions from a geothermal power plant in 2012. The George Olah Renewable Methanol plant is located within 1 km of the Svartsengi plant (IEA, 2019). In 2015, annual e-methanol production was 4,000 metric tons (1.1 million gallons) from this facility. The company is now focused on large scale international deployment of their technology into non-geothermal domains. This represents an example of how to meet the environmental goals of CO_2 reduction through repurposing of waste NCG streams.

5. Abatement Pathways

Whilst reinjection of CO_2 into geothermal reservoirs has recently increased, it is likely that a combination of abatement strategies will be needed to address the NCG emissions issue in its entirety. This paper has explored several avenues of abatement through both reinjection and via gas capture and re-use into non-geothermal commercial applications.

It is recommended that solutions be phased in a way to tackle the easiest to convert first, layering in more complex, and potentially more beneficial options as the technologies develop and mature. It is also likely that the economics will improve over time as fossil alternatives are gradually phased out. Table 1 shows a possible combination of pathways operators can consider in mitigating geothermal emissions.

Table 1: CO_2 abatement pathways for geothermal power-plants. Wholesale refers to selling CO_2 to a distributor; direct use refers to a model which the CO_2 is sold and utilized immediately adjacent to the existing geothermal production facility.

<table>
<tr><td colspan="3">No abatement
Some level of abatement will be possible at all plants, doing nothing should be avoided.</td></tr>
<tr><td>Reinject
Some reinjection will be possible, even beneficial, but stand-alone injection of all CO_2 will often be too risky.</td><td>Wholesale
Sale of all produced CO_2 may be possible but, depending on commercial terms, there are risks of varying returns and leaving significant value on the table long-term.</td><td>Direct Use
There may, eventually, be a direct use for all of the CO_2 in site adjacent new facilities (e.g. e-fuels), but this may take too long to build and secure.</td></tr>
<tr><td>Reinject + Wholesale
This option is best if there is some flexibility in the amount of CO_2 that can be injected to balance supply/demand changes in the wholesale market through a combined injection/sales strategy.</td><td>Wholesale + Direct Use
This option may be underpinned by strong demand for CO_2 where direct use and wholesalers compete for volume.</td><td>Reinject + Direct Use
Where there is strong and cheap CO_2 wholesale supply from that diminishes a need for geothermal CO_2, an industrial direct use would be needed to abate the balance not reinjected to the reservoir.</td></tr>
<tr><td colspan="3">Reinject + Wholesale + Direct Use
To achieve full abatement, it may be necessary to combine all three options in some proportion.</td></tr>
</table>

A significant effort would be required to decarbonize the global geothermal fleet in all locales and circumstances. The following list outlines recommended priorities for the geothermal industry to advance its knowledge base and, whilst not exclusive, gives a view as to what can be done to create a step-change in abatement of geothermal NCG emissions.

Advances in several fields of research are needed to provide solutions to geothermal emissions. These include:

- *Process Modeling* – Improved solubility and chemistry modeling, supported by laboratory testing of fluid mixtures. Widespread availability of gas process modeling tools to support projects and operations.
- *Carbon Measurement & Accounting* – Establish clear responsibilities within businesses. Design of new methods, and improvement to these methods, over time. Implement physical upgrades, such as better instrumentation.
- *Understanding Scaling / Corrosion* – Testing chemical reactions in the lab for each circumstance. Testing of plant side-streams, at pilot scale and full scale, and reporting these results. Corrosion product predictions and forecasting abilities for scaling. Improved data for corrosion rates in common geothermal steels for a wide range of dissolved gas chemistries.
- *Reinjection effects* – Results from different fields to build a picture of risk. Extensive tracer testing, repeated over time to understand return volumes times. Simulations to determine maximum injectable CO_2.

- *Overall Financial Evaluation* – Further developing financial models supports costs and benefits of emissions projects. Carbon credit price forecasting (with uncertainty) and investment triggers.
- *Plant Design and Estimation* – Short-listed plant design options and optioneering studies. Detailed estimates and equipment package development with pricing available. CAPEX and OPEX estimates for financial models.
- *State-of-the-art technology* – Forum for active developers and operators. Technology transfer from other industries. Further and wider strategy development.
- *Gas markets* – Conversation with existing gas suppliers. Negotiated commercial terms for sales. Evaluate sites and investments for CO_2 purification.
- *New Carbon Economies* – Strategize further how to engage and support new opportunities. Survey options and project the potential. Develop the commercial framework to capitalize, and triggers for investment. Monitor / ongoing support.
- *Regulatory Development* – Engage through geothermal associations to implement enabling policy statements and settings to support emissions abatement, particularly the re-use of gases.

6. Summary

The global geothermal industry can further contribute to reducing GHG emissions by reducing its own emissions profile. NCG emissions, containing GHGs such as CO_2 and CH_4, require dedicated thinking and consideration of how operators, in their particular circumstance, want to address these environmental degradants. As the world moves away from fossil-fueled industries, geothermal operators could add value through creative use of what has previously been regarded as waste byproduct. Solutions and potential uses for NCGs will be situation dependent. Whilst binary plants and flash plants with surface condensers have a marginally easier task to inject NCGs, they still face the issue of understanding how much NCG can be safely and sustainably injected back into the subsurface without harming the reservoir or wells. A combination of reinjection and gas off-take at the surface offers opportunities for gases to be utilized or repurposed as an industrial commodity and an enabler to extend the reach and positive impact of geothermal resources.

References

Abd Gafar et. al., Non Condensable Gas Reinjection Trial at Ngatamariki Geothermal Power Plant. New Zealand Geothermal Workshop, Auckland, New Zealand (2022).

Aljubran & Horne. Flexible Geothermal Power Dispatch Using Storage Tanks. World Geothermal Congress (2023).

Aradottir et al., Carbfix – Rock Solid Climate Action. Proceedings World Geothermal Congress 2020+1.

Byrne et al., The Effect of CO_2 Reinjection on Silica Scaling in Geothermal Reservoirs. New Zealand Geothermal Workshop. Auckland, New Zealand (2023).

Brownsort, P.A et al, Briefing on Carbon Dioxide Specifications for Transport. 1st Report of the Thematic Working Group on: CO_2 transport, storage and networks. 29th November, 2019. EU CCUS Projects Network (No ENER/C2/201765/SI1.793333)

CO2Meter. (2019). Why the Grade of CO2 Gas you are Using is Important. CO2Meter Inc. Blog, https://www.co2meter.com/blogs/news/co2-purity-grade-charts

Flues, F.A. Carbon pricing design: Effectiveness, efficiency and feasibility: An investment perspective. Paris: OECD Taxation Working Papers, No. 48, OECD Publishing. (2020).

Grim et al., Electrifying the production of sustainable aviation fuel: the risks, economics and environmental benefits of emerging pathways including CO_2. Energy Environ. Sci., 15, 4798, (2022).

International Energy Agency (IEA). Putting CO_2 to Use, Creating Value from Emissions. France, September 2019. https://www.iea.org/reports/putting-CO2-to-use. (2019).

Kaya, E. and Zarrouk, S. Reinjection of Greenhouse Gases into Geothermal Reservoirs. International Journal of Greenhouse Gas Control. 67, 111-129. (2017)

Kristjánsson et al., Comprehensive Tracer Testing in the Hellisheidi Geothermal Field in SW-Iceland. Proceedings of the 41st Workshop on Geothermal Reservoir Engineering. Stanford, California, February 22-24 (2016).

Layman, E. Geothermal Projects in Turkey: Extreme Greenhouse Gas Emission Rates Comparable to or Exceeding Those from Coal-Fired Plants. Proceedings 42nd Workshop on Geothermal Reservoir Engineering. Stanford, CA.(2017).

Marsh et al., Flexible Geothermal Application Within the New Zealand Electricity Market. New Zealand Geothermal Workshop, Auckland, New Zealand (2023).

McClintock et al., Lookahead from Kawerau, New Zealand: the Largest Geothermal Industrial Direct Use Complex in the World. World Geothermal Congress (2020).

Mclean and Richardson. Geothermal Greenhouse Gas Emissions In New Zealand In 2020: Lifecycle And Operational Emissions. New Zealand Geothermal Workshop, Auckland, New Zealand (2021).

Nederhoff, E. Innovative Technology for Transition to a Low-Carbon Greenhouse Industry. Tomatoes New Zealand, Vegetable NZ and EECA. (April, 2021).

Nederhoff, E. Energy Benchmarking in the Covered Crops Industry. Tomatoes New Zealand, Vegetable NZ and EECA. (March, 2022)

Nyawir et al., Evaluation of Tracer Test Results in Olkaria North-east Geothermal Field, Kenya and its Implications on Resource Management. World Geothermal Congress (2023).

Olley S. CO_2 Gas Prices Skyrocket by 600 Percent Amid Shutdown. Radio New Zealand, Business. https://www.rnz.co.nz/news/business/482383/co2-gas-prices-skyrocket-by-600-percent-amid-shutdown. (13 January 2023).

Ruiz N.C. et al. Passive NCG Reinjection at Te Huka Geothermal Binary Plant. New Zealand Geothermal Workshop, Auckland, New Zealand. (2021).

Stephenson and Goodwin. Geothermal on a Truck, The Nature's Flame Geothermal Direct Use Project. New Zealand Geothermal Workshop, Auckland, New Zealand (2019).

Sevindik et al., Modeling of Chloride and Carbon Dioxide Injection at Kizildere Geothermal Field. Stanford Geothermal Workshop (2023).

White, P. Clean wins at the environmental awards. https://ngawhageneration.co.nz/tell-me-about/news/clean-wins-at-the-environmental-awards. (24 July, 2023).

Yücetaş et al., Carbon Dioxide Injection Field Pilot in Umurlu Geothermal Field, Turkey. GRC Transactions Vol.42. (2018).

Greenhouse Gas Emissions Reduction: Global Geothermal Power Plant Catalog

Ian Richardson[1], Simon Webbison[2]

[1]Contact Energy, Te Aro Road, Wairakei, New Zealand

ian.richardson@contactenergy.co.nz

[2]Ormat Technologies, 6884 Sierra Center Parkway, Reno 89511, Nevada, USA

swebbison@ormat.com

Keywords

Carbon dioxide, hydrogen sulfide, greenhouse gas, reinjection, emissions reduction, ESG

ABSTRACT

Geothermal power generation typically (but not always) results in greenhouse gas emissions as a result of these gases being naturally present in geothermal fluids. Globally, there is an increasing focus on reducing naturally occurring emissions from geothermal electricity generation to contribute to wider decarbonization goals and efforts. Several countries have already implemented carbon emissions pricing, generally as a carbon-dioxide equivalent (CO_2e) value, or are in the process of considering doing so. Three major factors will increase the focus of operators in reducing emissions: (1) increased direct costs due to carbon pricing, (2) societal pressure from the general public, and (3) investment funds or funding institutions with ESG targets that influence the pricing and availability of funding for both new and existing projects.

This paper attempts to catalog details of global geothermal power plants that have meaningful greenhouse gas emissions reduction technologies in place, with details on the methods employed. The authors intend to republish this paper with an updated catalog regularly, and we encourage feedback from readers to ensure this catalog is updated accurately.

1. Introduction

Geothermal power generation is typically a low-emission, reliable and renewable source of electricity that is powered by earth's natural heat. Most geothermal power plants release a small amount (relative to fossil-fueled power plants) of greenhouse gases – primarily carbon dioxide (CO_2) and methane (CH_4). These gases are not created in the geothermal power generation

process. Still, they are contained naturally in the fluid from the geothermal reservoir and are then often released as a part of the power generation process. When pressure is reduced, the fluid from the reservoir boils, and due to Henry's law, these gases preferentially move into the steam phase, with minimal amounts retained within the separated geothermal water (also known as brine). The release of the gases from the power generation process is a result of the gases being non-condensable – such that when geothermal steam is condensed in a plant heat exchanger (typically a condenser in a flash plant and a vaporizer or pre-heater in a binary plant) the non-condensable gases remain as gases. In contrast, the steam is condensed into water. These non-condensable gases can interfere with the power generation process by restricting steam flow due to pressure build-up, so they must be removed from the process, and this typically results in them being released to the atmosphere (via a gas extraction system if the gases are at a pressure below atmospheric) and vented above a cooling tower or air cooled condenser to disperse the gases safely.

Several technologies are in use today to reduce gaseous emissions from geothermal power plants, and several drivers for emissions reduction from these power plants are described below.

2. Drivers for emissions reduction

Reducing geothermal emissions to the atmosphere can have multiple benefits, and as a result there are multiple drivers for reducing emissions, including some where emissions reduction is a secondary benefit to a different primary objective.

2.1 Odor nuisance and compliance

Odor nuisance and strict environmental limits on hydrogen sulfide emissions in some jurisdictions have resulted in several geothermal power plants undertaking non-condensable gas (NCG) reinjection where all of the geothermal gases exsolving from the production fluid are reinjected into the reservoir, including carbon dioxide and methane as an alternative to hydrogen sulfide scrubbing systems. The Puna geothermal plant in Hawaii, USA, has been reinjecting all of the non-condensable gases produced at the plant to meet environmental requirements (Richard, 1990) since the plant came online in 1993, whilst the Coso geothermal power plant in California operated with the NCG reinjected for a time to manage hydrogen sulfide emissions before changing to hydrogen sulfide abatement technology in lieu of NCG reinjection (Layman, 2017). The Hellisheidi geothermal plant in Iceland commenced injection of a concentrated hydrogen sulfide stream from its NCGs to meet air emissions requirements, which was known as SulFix, and has grown to also include the injection of carbon dioxide under the CarbFix program (Gunnarsson et al., 2015; Juliusson et al., 2015) with approximately 75% of hydrogen sulfide injected and 30% of carbon dioxide injected (Ragnarsson et al., 2023).

2.2 Greenhouse gas reduction

Given the typically low greenhouse gas emissions associated with geothermal power generation, employing additional technology to further reduce greenhouse emissions is not always seen as the best use of limited resources or is seen to apply risk or costs to the process. However, in jurisdictions with a direct cost of greenhouse gas emissions, such as New Zealand, the installation of greenhouse gas abatement technology has increased significantly over the past few years as emissions prices have increased. In the United States of America, whilst there is no direct cost of greenhouse gas emissions as seen in New Zealand (McLean, 2023; Carmichael and Zarrouk,

2023), there are increasing off-taker requirements observed in power purchase agreements in particular markets such as California which will likely drive continued pricing premiums for new zero carbon emissions geothermal electricity (Ormat, 2024) due to geothermal baseload reliability compared to other renewable zero carbon emission generation technologies such as wind or solar. Future production tax credits (PTCs) or similar appear to be requiring zero carbon emissions geothermal electricity to be eligible (Ormat, 2024).

Risks associated with reducing gas emissions that need to be managed to enable gas emission reductions to occur include, but are not limited to:

- Lower pH in the injected fluid stream whereby gas has been dissolved into, resulting in the increased likelihood of corrosion and, a reduction in the lifespan of the pipeline or well assets and an increased likelihood of reliability concerns. This is often managed through the application of a suitable chemical corrosion inhibitor or in some instances, an increase in the steel quality through the use of more corrosion-resistant alloys.
- The mixing of geothermal gases that include H_2S can result in an increase in the deposition and scaling of mineral deposits in reinjection systems, particularly in the mixing zone itself. Saturation of heavy metal sulfides such as antimony sulfides is common in geothermal reinjection systems where H_2S is dissolved in the reinjection fluid due to the increased sulfide concentration and decreased pH.
- Possibility of building up gas pockets within the injection line or wells, in particular for wells with high injectivity where the pressure of the injected fluid stream can reduce and cause flashing of what was a single-phase fluid stream. These gas pockets can cause challenges with flow dynamics, especially during plant upsets or plant start-ups. Condensation of the gases also poses a risk of low-pH conditions that can cause corrosion, and this is a risk, in particular in wellhead infrastructure for high permeability wells. The risk of gas pockets is often managed by having venting setups at appropriate locations through the pipework to support plant start-up processes.
- Reservoir feedback, particularly if gases are reinjected close to a production area and/or near a steam cap, there is a possibility that gas concentrations in the total production can increase, increasing the potential for calcite scaling in the production well and decreasing power plant efficiency due to the higher NCG content of the production fluid. The quantity of gas can overwhelm the power plant cycle by causing gas concentrations outside the design range of the plant.
- Safety considerations are essential for many emissions reduction systems where concentrated gas mixtures are conveyed at elevated pressure, with geothermal gas mixtures often containing significant concentrations of hydrogen sulfide, which is toxic even at low concentrations. Where gases are separated or purified, the potential of forming flammable gas mixtures also needs to be considered where the concentration of flammable species such as hydrogen and methane are high (Piggot et al., 2021; Olafsdottir et al., 2023)

2.3 Commercial use of carbon dioxide

Processing geothermal non-condensable gases to produce a commercial carbon dioxide product has been undertaken to provide both food and industrial-grade carbon dioxide (Simsek, 2003; Layman, 2017) and also carbon dioxide for greenhouse use (Ngethe and Jalilinasrabady, 2021). While this process may not reduce geothermal greenhouse gas emissions in a strict sense

depending on how the captured carbon dioxide is used. The use of geothermal-sourced carbon dioxide may offset the carbon dioxide produced by other means, such as the combustion or production of fossil fuels. Preparing commercial-grade gases from geothermal NCGs requires the removal of the unwanted components of the gas mixture – typically hydrogen sulfide, ammonia, mercury and hydrocarbons – although other unwanted species may also be present. Where the amounts of these unwanted species are low adsorbents may be used to remove them from the bulk gas flow. However, for higher concentrations more complex equipment may be required, such as a complex iron-sulfur recovery system for H_2S, while elevated levels of hydrocarbons may require the use of a catalytic oxidizer (Catox) or Regenerative Thermal Oxidizer (RTO). The removal of gases such as oxygen and nitrogen is likely to require liquefaction and reboiler systems in the purification of carbon dioxide to a high standard.

2.4 Reservoir support

The presence of dissolved gases in geothermal fluid results in a lower boiling point for depth than would otherwise be the case. This typically results in geothermal production wells being easier to flow than if the fluid did not contain dissolved gases (for wells producing 2-phase fluid – a mixture of water and steam) through a lighter column within the wellbore. In lower enthalpy systems, the gas content of the geothermal fluid can be critical in keeping production wells flowing without the need for pumps through the decreased fluid density and lower boiling point for depth that results from the presence of dissolved gases in the reservoir fluid.

2.5 Silica scale prevention (pH modification)

Carbon dioxide has the potential to be used in geothermal brine pH modification systems to reduce silica polymerization and scaling in geothermal reinjection systems. This is often seen in binary-type geothermal power plants where fluid outlet temperatures can be run at a relatively low level without the need for acid addition for pH modification – in this case, the condensate from the binary plant is typically acidic due to the presence of carbon dioxide and hydrogen sulfide, which when mixed with the brine reduced the pH sufficiently to inhibit silica polymerization long enough to return the reinjection fluid to the geothermal reservoir. While this is a benefit of NCG reinjection for both Binary and flash-type power plants, the authors are unaware of any power plants currently operating an NCG reinjection system for the sole purpose of inhibiting silica polymerization in the geothermal brine, however it is noted that this can be a factor in the technology selection process (Addison and Brown, 2012) and NCG reinjection was retained for a time at the Coso geothermal power plant for the purpose brine pH modification after an alternative H_2S abatement system was in service (Layman, 2017).

3. Technologies

There are three main technologies currently in use to reduce greenhouse gas emissions from geothermal power generation. (1) NCG Reinjection, where the gases are redirected into the geothermal reservoir – often dissolved in water but in some cases in a gaseous or supercritical state. (2) Pumped Binary technology – where the greenhouse gases remain dissolved in the geothermal liquid through the production, utilization and reinjection stages, and hence are not released to the atmosphere. (3) Gas purification involves preparing the geothermal gases (typically carbon dioxide) for commercial and industrial uses, such as in greenhouses or the food and beverage industry. Each of these technological approaches is discussed below.

3.1 NCG Reinjection

Non-condensable gas reinjection is a process that redirects the non-condensable gases that have been separated from the geothermal steam and condensate and directs the gas into the reinjection system, where the gas is returned to the geothermal reservoir. This technology can be used at both binary and flash-type geothermal power plants, although it is typically easier and simpler to employ at binary power plants due to more favorable operating conditions. These conditions include the exclusion of oxygen from the gas mixture to minimize corrosion, higher gas pressure that reduces or eliminates the need for gas compression, and often lower reinjection temperatures, which improves the solubility of the gases in the reinjection liquid. When used at binary plants, it is typical to route the NCGs from the vaporizer (or other heat exchanger where the gases would otherwise accumulate) to the reinjection fluid downstream of the preheaters – where the fluid is coldest. If the vaporizer pressure is high enough the NCGs can flow to the reinjection piping without the need for gas compression. For the purposes of this paper, NCG reinjection refers to deliberately routing the NCGs into the reinjection system (active reinjection) and does not refer to NCGs that dissolve in the condensate within the vaporizer (passive reinjection - Ruiz et al., 2021)

NCG reinjection can be applied to flash plants utilizing condensing steam turbines, however some extra design considerations are required. These include ensuring the presence of oxygen in the NCGs is minimized. This would typically require a surface condenser and well-designed and operated turbine gland steam system to minimize air ingress in the systems that operate under vacuum conditions. If a direct contact condenser is used, a system to remove oxygen and nitrogen from the NCG mixture will likely be required to minimize corrosion and breakout pressure issues, respectively. With both surface and direct contact condensing systems, a gas compression system will also be required to increase the NCG pressure to a suitable level for reinjection.

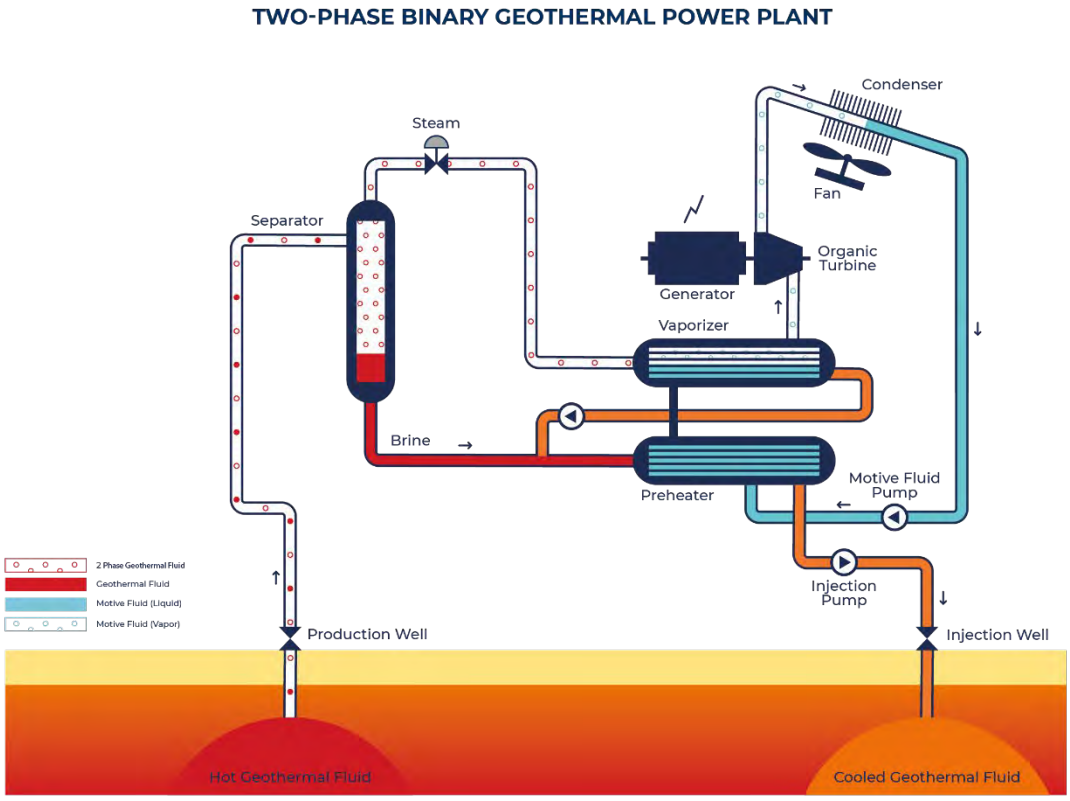

Figure 1: Two-phase Binary schematic

3.2 Pumped Binary

Pumped binary geothermal power plants are often the choice of plant design for low enthalpy and some medium enthalpy geothermal fields. The use of production pumps enables the development of non-artesian resources and can boost production in fields with low production pressures. Pumped binary systems can be temperature and depth limited, with these limitations dependent on pump and well designs as well as field conditions. While pumped binary geothermal power plants are typically zero emission (as described below), emissions may still occur if the geothermal fluid pressure is not maintained. This has been the case where the fluid has been exposed to atmosphere prior to reinjection (Bliem and Walrath), and when artesian systems have been converted to a pumped system while retaining the flash system (separator and steam systems) without implementing NCG reinjection.

Two major technological advancements have occurred throughout time to enable pumped Binary to be the leading technology employed for geothermal greenhouse gas reductions, with numerous power plants utilizing this combination of technology in low-medium enthalpy geothermal fields. The first is the development and evolution of binary power plant technology, with increases in efficiency and unit sizes. The other has been that well pump technology has evolved and become more reliable with the application of pumps increasing over time. Recently, in the United States

a number of original power plants on low-medium enthalpy geothermal fields have been repowered with new binary plants and making use of well pump technology, with more to come into the future with a repowered Beowawe facility coming online in 2024 (Ormat, 2023). Through the installation of pumps, the fluid does not flash in the wellbore or pipeline process, and therefore, any dissolved gases are kept in solution. This process is shown in the schematic in Figure 2. Pressures throughout the cycle are maintained at a suitably high level, and after energy extraction occurs through heat exchangers, the solubility of the gases increases as the temperature of the fluid is decreased, providing the ability to reduce pressures in the injection system without gas breakout occurring.

Lifecycle costs of the pumps tend to generally result in the installation of line-shaft pumps (LSPs) rather than electrical submersible pumps (ESPs). Cases where ESPs are utilized over LSPs are rare, except for where the well was deviated at a shallow depth and therefore LSPs cannot be utilized, or, where the depth required for the pump is extremely deep due to limited permeability in the wells formation or a deep water table. The primary reason for the lifecycle costs of LSPs being generally lower than ESPs is the operational lifespan between pump failures, with the main driver of this being that LSPs have electronic infrastructure on the surface rather than downhole.

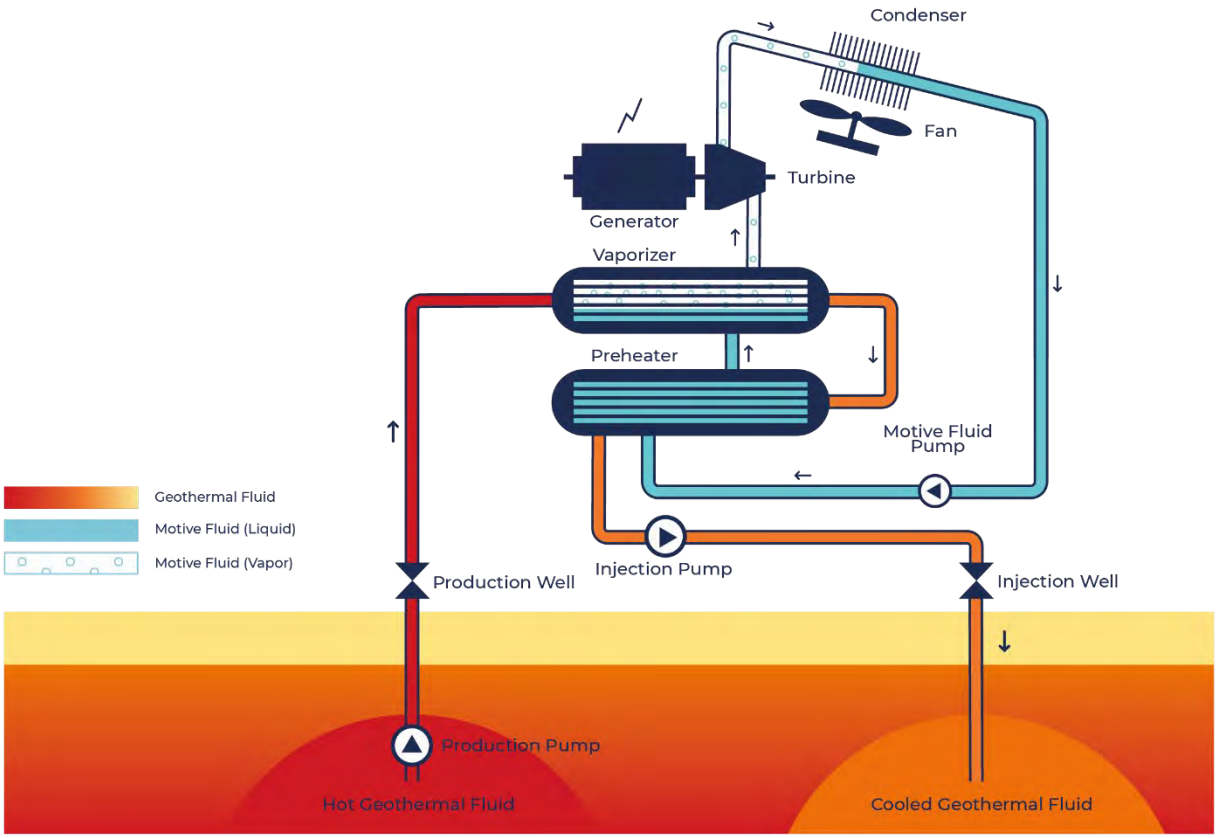

Figure 2: Pumped Binary schematic

3.3 Gas purification and reuse

Gas purification and reuse involves using one or more of the gases in the non-condensable gas mixture (typically carbon dioxide, although methane can also be captured for later use) for commercial or industrial use. The composition of a given NCG mixture and the intended downstream use will determine the various processing steps required to produce a gas that is commercially useful. Production of carbon dioxide suitable for industrial or food-grade use from geothermal sources may require significant processing, with removal materials found in geothermal such as hydrogen sulfide, ammonia, mercury, methane, non-methane hydrocarbons, nitrogen, hydrogen and argon (as well as oxygen if air ingress there is air ingress into the gas system) all having to be removed to a very high standard. It may often be the case that very high concentrations and volumes of carbon dioxide are required for a purification plant to be financially viable in addition to being located close to potential customers. For horticultural use, the required treatment may be reduced, especially where the presence of nitrogen and oxygen are of little consequence.

4. Examples

4.1 NCG Reinjection

4.1.1 Puna, Hawaii USA

The Puna geothermal power plant was commissioned in 1993 and is located on the Big Island in Hawai'i, USA. The stringent permitting conditions for the Puna power plant require that no hydrogen sulfide geothermal emissions are released from the power plant to alleviate concerns about impacts from nearby residents (Richard et al., 1989; Richard, 1990). This resulted in the design and installation of a 100% NCG reinjection system. The system involves collecting the NCGs from the vaporizers of the binary plants that receive the exhaust steam from the steam turbines. A gas compressor is used to increase the pressure of the gases such that they can be mixed with the geothermal brine and condensate that is also used in the power plant. This results in a 100% reinjection system, where all the geothermal brine, condensate and gases are returned to the reservoir. This system has been operating successfully since the plant was originally commissioned.

4.1.2 Carbfix, Hellisheidi, Iceland

The Carbfix project in Iceland is perhaps one of the best-known examples of NCG reinjection and greenhouse gas emissions reduction in the geothermal industry and is well reported in the literature. The Carbfix project aims to reduce greenhouse gas emissions by the reinjection of carbon dioxide into reactive rock formations where it can react and form stable minerals, thus avoiding emissions to the atmosphere. Commissioned at scale in 2014 at the Hellisheidi geothermal power plant (Aradottir et al., 2021), the Carbfix process has several key differences from most other geothermal NCG reinjection projects, including the use of either ground water (Carbfix 1) to dissolve the geothermal gases (although geothermal fluid can be used if there is a sufficient quantity available as was the case at Hellisheidi for Carbfix 2), and the use of a gas absorber - although this aspect is also used at Verkhne-Mutnovsky (Povarov and Nikolskyi, 2005) to promote dissolution of highly soluble gases (carbon dioxide and hydrogen sulfide) while

allowing for the venting of poorly soluble gases (such as methane and hydrogen). The use of non-geothermal water sources also allows for the geothermal gases to be reinjected outside of the geothermal reservoir, as long as the geology is suitable for the mineralization of the gases.

The Carbfix process, while more complex than some other NCG reinjection systems, enables more flexibility in the composition of NCG mixtures that can be used, and the type of geothermal plants that the process can be used with (potentially plants with direct contact condensers) as a result of the ability to largely remove poorly soluble gases from the gas stream.

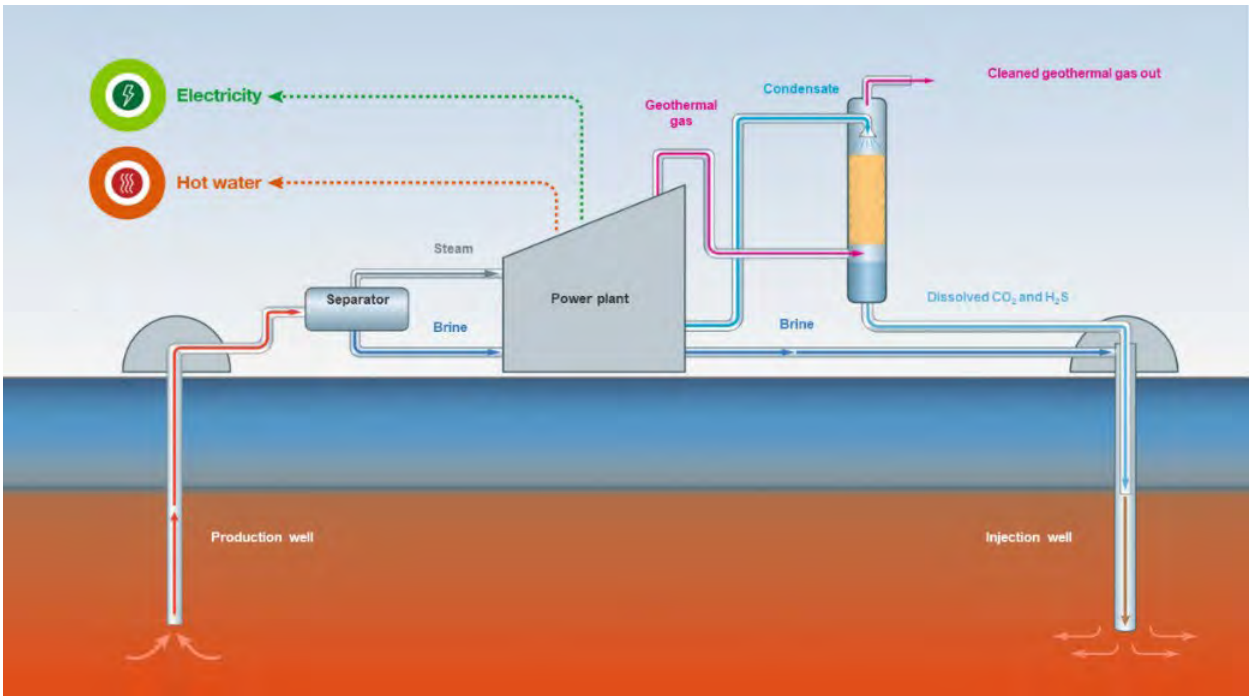

Figure 3: Basic Schematic of the Carbfix 2 process at Hellisheidi (from Aradottir et al., 2021)

4.1.3 Te Huka, Tauhara, New Zealand

The Te Huka geothermal power plant was commissioned in 2012 and is located in New Zealand and consists of two binary units utilizing geothermal brine and steam from the Tauhara geothermal field to produce a total of 25 MWe net. Under normal operating conditions the Te Huka plant released ~9,200t CO_2e per year as NCGs that did not naturally dissolve on the steam condensate under vaporizer conditions were vented to the atmosphere. In 2020, a project was commenced to reduce greenhouse gas emissions from geothermal generation by the plant's operator Contact Energy, which resulted in a redesign of the NCG venting system. Commissioning in 2022 this system resulted in a new NCG handling system to redirect the NCG flow from the atmosphere to the liquid reinjection system for the plant, where the NCGs are mixed with, dissolved into the reinjection liquid, and reinjected back into the geothermal reservoir. This enabled all of the gaseous emissions from the power plant to be reinjected as the plant conditions allowed for all of the gases to be dissolved in the surface equipment prior to reinjection, eliminating gas (and greenhouse gas) emissions from the power plant. The original design of the binary plant made these modifications relatively simple, with no gas treatment or compression required (Richardson et al., 2023).

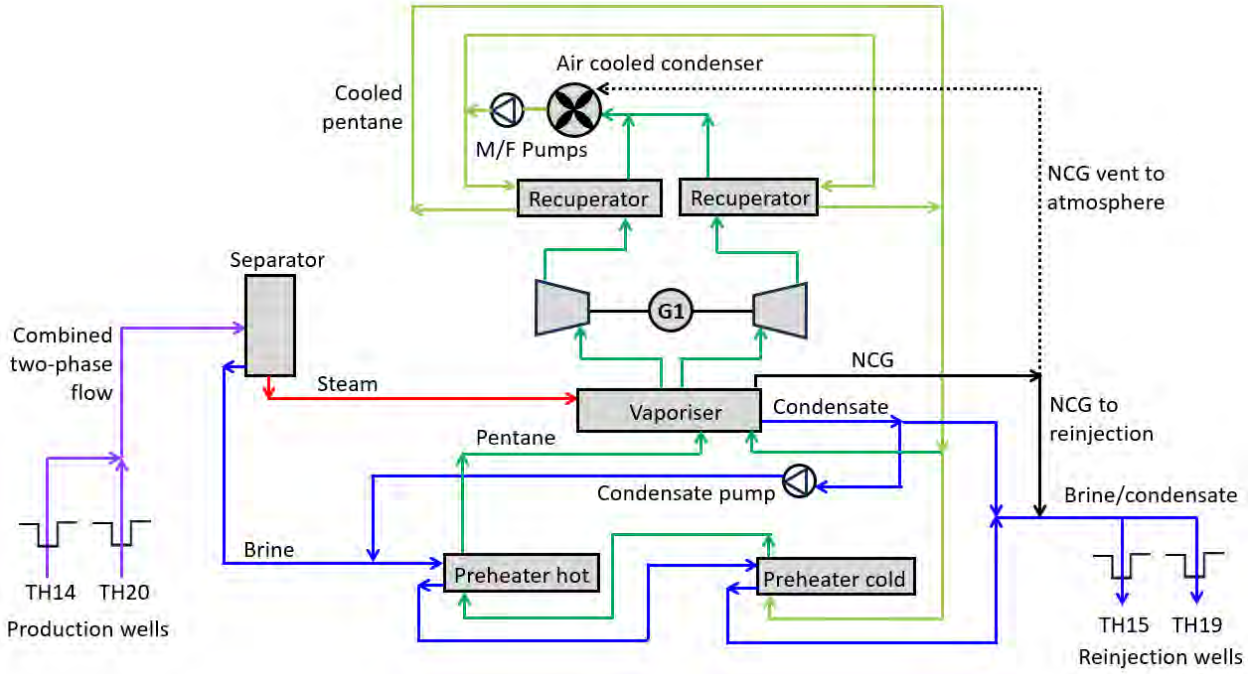

Figure 4: Te Huka flow schematic with NCG Reinjection (from Richardson et al., 2023)

4.2 Pumped Binary

4.2.1 McGinness Hills, Nevada USA

The McGinness Hills Geothermal Complex commenced generation in 2012, with three separate geothermal power plants in operation. The second plant came online in 2014, and the third in 2018. As of 2024 fields total capacity was 146 MW. All production wells make use of line-shaft pumps, which maintains pressure and prevents flashing. Therefore, the power plant has no separation equipment and throughout the whole process all gases are kept in solution.

4.2.2 Steamboat, Nevada USA

The Steamboat Geothermal Complex commenced its generation in 1986, with Steamboat 1 as a pilot project, and Steamboats 2 and 3 coming online in 1992. Significant development occurred over time on the field, with Ormat's subsequent consolidation of ownership. There are now 5 geothermal power plants operating as of the start of 2024 with a nameplate capacity of 79 MW, all featuring zero greenhouse gas emissions technology using binary power plants. The final major change in the field occurred in 2020 with the repower of the Steamboat Hills power plant with the binary Steamboat Hills Repower (Ormat, 2021).

Over time, numerous wells have been modified to pumped wells, with most of the Steamboat Hills section of the field having previously been all artesian wells historically, and these were almost all converted to pumped wells as part of the Steamboat Hills Repower (Akerley et al., 2021). Where good permeability was proven and economics allowed for it, new wells were drilled to enable the installation of line-shaft pumps. Where this was not the case and wells had a shallow kick-off

point or smaller casing, electric submersible pumps were installed. As of the start of 2024 only one artesian well remains on the field, well 24-5, and this feeds the Galena 2 plant then has infrastructure is designed to prevent any emissions from this well with a downhill pipe run to increase pressure by the time the fluid reaches the power plant and mixing with numerous pumped wells.

Figure 3: The original Steamboat Hills powerplant that was replaced with the new binary Steamboat Hills Repower in 2020.

4.3 Carbon Dioxide Reuse

Carbon dioxide reuse is a way to generate value from what would otherwise be a waste product from geothermal power generation. Perhaps the largest reuse of geothermal carbon dioxide can be found in Türkiye at the Kizildere facility operated by Zorlu Energy. The Kizildere 1 geothermal power plant was commissioned in 1984 and generated 18 MW of electricity. However, power generation in the field has increased substantially with the commissioning of Kizildere 2 and Kizildere 3. Kizildere delivers a part of its non-condensable gas flow to an adjacently located Linde gas processing plant, which uses the carbon dioxide contained in the NCG flow to produce high-purity carbon dioxide for commercial and industrial use. The high concentration and volume of carbon dioxide produced in the Kizildere geothermal plant (up to 99% of the non-condensable gas) results in a simpler, and more efficient processing system than would likely be required in many other geothermal fields to produce high-purity carbon dioxide.

Similar carbon dioxide recover plants were also in use at the Dora geothermal facilities in Türkiye. However, these were removed when the volume of gas from the power plants decreased to the point recovery was uneconomic, at which point gas reinjection was commenced (Asnük, 2024).

At the Svartsengi geothermal field in Iceland CO_2 from the NCG stream from the Svartsengi power plant is utilized to produce methanol (Ragnarsson 2023), at Carbon Recycling International's George Olah facility. While geothermally sourced carbon dioxide has been used for horticulture in Kenya, where the Oserian flower farm used carbon dioxide from the Olkaria geothermal system to support plant growth and increase output in its greenhouse operations (Ngethe and Jalilnasrabady, 2021).

5. Table of Power Plants with Greenhouse gas emissions abatement technology

This table is published with ownership and generation details as of 1 January 2024. This table excludes: temporary trials such as Umurlu, (Yucetas et al., 2018); plants that have ceased greenhouse gas abatement processes (e.g. Coso); plants smaller than 5 Mwe net in size; plants that are bottoming units or brine-only units; and, facilities that utilize geothermal CO_2 but do not generate electrical power (eg Haedarendi). This table is focused on greenhouse gas emissions abatement; for general emissions abatement from geothermal power plants Lenzi et al. (2021) provides a comprehensive overview.

Table 1: Details of facilities with Greenhouse gas emissions reduction practices in place as of 1 January 2024

Country	Field	Operator	MW	Emissions Reduction	Plant Type	Emissions Reduction Technology	Comments and References
USA	San Emidio	Ormat	39	Full	Binary	Pumped Binary	Includes San Emidio and North Valley plants
USA	Don A. Campbell	Ormat	30	Full	Binary	Pumped Binary	DAC1,2
USA	McGinness Hills	Ormat	146	Full	Binary	Pumped Binary	MGH1,2,3
USA	Steamboat	Ormat	79	Full	Binary	Pumped Binary and NCG Reinjection	Pumped Binary: Galena 1,3, Steamboat 2/3 and Steamboat Hills Repower Pumped binary and NCG Reinjection: Galena 2 has artesian well 24-5 as well as pumped wells
USA	Jersey Valley	Ormat	8	Full	Binary	Pumped Binary	
USA	Tuscarora	Ormat	17	Full	Binary	Pumped Binary	
USA	Tungsten	Ormat	41	Full	Binary	Pumped Binary	
USA	Raft River	Ormat	12	Full	Binary	Pumped Binary	
USA	Neal Hot Springs	Ormat	22	Full	Binary	Pumped Binary	
USA	Heber	Ormat	91	Full	Binary	Pumped Binary	Heber 1,2,South
USA	Ormesa	Ormat	36	Full	Binary	Pumped Binary	Field formerly known as East Mesa, consists of three separate plants: Ormesa 1,2,3
USA	Mammoth	Ormat	65	Full	Binary	Pumped Binary	G1,2,3, CD4
USA	Puna	Ormat	38	Full	Binary	NCG Reinjection	Conducted to prevent H_2S ambient discharge
USA	Stillwater	ENEL	12	Full	Binary	Pumped Binary	Acquired by Ormat in January 2024 - has some artesian wells but kept under pressure
USA	Salt Wells	ENEL	9	Full	Binary	Pumped Binary	Acquired by Ormat in January 2024
USA	Cove Fort	ENEL	18	Full	Binary	Pumped Binary	Acquired by Ormat in January 2024
USA	Blue Mountain	Cyrq	49.5	Full	Binary	Pumped Binary	
USA	Thermo	Cyrq	14.5	Full	Binary	Pumped Binary	
USA	Soda Lake	Cyrq	26.5	Full	Binary	Pumped Binary	
USA	Patua	Cyrq	48	Full	Binary	Pumped Binary	
USA	Lightning Dock	Cyrq	15.3	Full	Binary	Pumped Binary	Acquired by Zanskar in July 2024
USA	Star Peak	Open Mountain Energy	14	Full	Binary	Pumped Binary	

Country	Field	Operator	MW	Emissions Reduction	Plant Type	Emissions Reduction Technology	Comments and References
Russia	Mutnovsky	Geotherm JSC (PJSC RusHydro)	12	Full	Flash	NCG Reinjection	Povarov and Nikolskiy (2005)
New Zealand	Tauhara	Contact Energy	25	Full	Binary	NCG Reinjection	Te Huka plant NCG Reinjection commenced November 2022, Richardson et al. (2023)
New Zealand	Nga Tamariki	Mercury	82	Partial	Binary	NCG Reinjection	NCG Reinjection on one of four units, Ghafar et al. (2022)
New Zealand	Ngawha	Ngawha Generation (Top Energy)	57.5	Full	Binary	NCG Reinjection	NCG Reinjection commenced August 2022, Hanik (2024)
Iceland	Hellisheidi	ON Power (Reykjavik Energy)	303	Partial	Flash	NCG Reinjection	Carbfix, Gunnarsson et al. (2015)
Iceland	Nesjavellir	ON Power (Reykjavik Energy)	120	Partial	Flash	NCG Reinjection	Pilot plant, Carbfix (2024)
Iceland	Svartsengi	HS Orka	76	Partial	Flash	CO_2 Recovery	Methanol Production, Ragnarsson et al. (2023)
Türkiye	Babadere	MTN Energy	8	Full	Binary	Pumped Binary	
Türkiye	Kizildere	Zorlu	260	Partial	Flash	CO_2 Recovery	CO_2 utilized for commercial and industrial use, Simsek (2003), Layman (2017)
Türkiye	Salavatli	MEGE	18	Partial	Binary	Pumped Binary and NCG Reinjection	Asnük (2024)
Türkiye	Bukarkent	Limgaz	14	Full	Binary	Pumped Binary	Mertoglu and Basarir (2018)
Honduras	Platanares	Ormat	33	Full	Binary	Pumped Binary	
Germany	Dürrnhaar	Stadtwerke München	5.5	Full	Binary	Pumped Binary	
Germany	Kirchstockach	Stadtwerke München	5.5	Full	Binary	Pumped Binary	
Germany	Sauerlach	Stadtwerke München	5	Full	Binary	Pumped Binary	Bonafin (2021)
Germany	Traunreut	Equitix	5.5	Full	Binary	Pumped Binary	

6. Conclusions

While there are currently a significant number of geothermal power plants with greenhouse gas emissions reduction technology, this is dominated by pumped binary systems where the greenhouse gases remain in solution within the geothermal fluid throughout the power generation process. There are far fewer power plants where gases that have separated from the geothermal fluid are actively redirected into the reinjection process and examples of these plants are currently favored in binary plants due to the simplicity of adapting this process to typical binary plant designs. NCG reinjection in flash plants is more challenging both technically and economically. However as demonstrated in Iceland and Russia this technology is viable and likely to grow, particularly in jurisdictions where there is a significant benefit to greenhouse gas emissions reduction through a carbon price or other incentives. There are also plans for more commercial use of geothermally sourced carbon dioxide among geothermal plant operators as this is seen as an opportunity in some markets, and a potential requirement in others.

The use of carbon pricing, such as direct pricing in New Zealand, or indirectly through power purchase agreements like in California in the US, is driving more action towards zero greenhouse emission geothermal power plants. As other markets create either direct or indirect incentives, we expect significant increases to occur over time in the amount of geothermal power plants reducing their greenhouse gas emissions. The rapid pace of development of zero greenhouse emission geothermal power plants in New Zealand is an example where a market pricing incentive has resulted in outweighing risks associated with the activity, resulting in a significant deployment in a relatively short period time, generally as a function of a significant carbon price increase.

Acknowledgements

The authors wish to acknowledge the support of their respective organizations to publish this paper, Contact Energy Ltd and Ormat Technologies, Inc. Many thanks to those who have provided insight and review to ensure the information in this paper is as accurate as is possible, including: Alexander Richter, Anton Fiterman, Don Leger, Grimur Bjornsson, Ingvi Gunnarsson, Matteo Quaia, Sadiq Zarrouk, Þráinn Friðriksson and Yackov Yehoshua

REFERENCES

Addison, S.J. and Brown, K.L. (2012), “Ngatamariki Test Rig Results and Findings”, *Proceedings New Zealand Geothermal Workshop*

Akerley, J.; Eilan, B., Selwood, R., Darf, N. and Canning, B. (2021), “Drilling Challenges and Pumping Innovations for the Steamboat Hills Enhancement” *GRC Transactions, Vol. 45*

Askoy, N.; Gok, O., Mutlu, H. and Kilinc, G. (2021), “Drilling Challenges and Pumping Innovations for the Steamboat Hills Enhancement” *Proceedings World Geothermal Congress*

Asnük, B. (2024) *Personal Communication*

Aradottir, E., Sigfusson, B., Snaebjornsdottir, S., Marnarson, M., Ratouis, T., Helgason, K., Bragadottir, R., Clark, D., Marieni, C., Voigt, M., Gunnlaugsson, E., Elkers, E. and Gislason, S. (2021), “Carbfix – Rock Solid Climate Action”, *Proceedings World Geothermal Congress*

Bliem, C. and Walrath, L. (1983) “Raft River Binary-Cycle Geothermal Pilot Power Plant Final Report” Idaho National Engineering Laboratory, *United States Department of Energy*

Bonafin, J. (2021), “Update on European Geothermal Binary Units Delivered by Turboden”, *Proceedings World Geothermal Congress*

Carbfix (2024) https://www.carbfix.com/geothermalenergyccs

Carmichael, A. and Zarrouk, S. (2023) “A Review of Non-Condensable Gas (NCGs) Reinjection Within The Geothermal Industry and a Comparison With Other Carbon Capture and Storage (CCS) Technologies” *Proceedings New Zealand Geothermal Workshop*

Choudhary, A., Burnell, J., Hinkley, J., Elias, A. & Rayudu, R. (2021). “Reinjection as a solution to greenhouse gas emissions from high emitting geothermal power plants in New Zealand”, TENCON 2021 - 2021 IEEE Region 10 Conference

Ghafar, S., Allan, G., Ferguson, A., Siega, F., Rivera, M.and Murphy, B. (2022) “Non Condensable Gas Reinjection Trial at Ngatamariki Geothermal Power Plant”, *Proceedings New Zealand Geothermal Workshop*

Gunnarsson, I., Juliusson, B., Aradottir, E., Sigfusson, B. and Arnarson, M. (2015), “Pilot Scale Geothermal Gas Separation, Hellisheidi Power Plant, Iceland”, *Proceedings World Geothermal Congress*

Hanik, F. (2024) *Personal Communication*

Juliusson, B.M., Gunnarsson, I., Matthiasdottir, K.V., Markusson, S.H., Bjarnason, B., Sveinsson, O.G., Gislason, T. and Thorsteinsson, H.H. (2015) “Tackling the Challenge of H2S Emissions”, *Proceedings World Geothermal Congress*

Layman, E. (2017), “Geothermal Projects in Turkey: Extreme Greenhouse Gas Emission Rates Comparable to or Exceeding Those from Coal-Fired Plants”, *Proceedings 42nd Workshop on Geothermal Reservoir Engineering*, Stanford.

Lenzi, A., Paci, M., Tryggvadottir, L., Gunnarsson, T. and Ragnarsdottir, K. (2021) “Overview of Global Existence of Pollutant and GHG Abatement Facilities in GPPs”, *Proceedings World Geothermal Congress*

McLean, K., Montague, T., Alcaraz, S., Daysh, S., Doorman, P., Luketina, K., Tsui, K., White, B. and Zarrouk, S. (2023) “2020-2023 New Zealand Country Update”, *Proceedings World Geothermal Congress*

McLean, K. and Richardson, I. (2020), “Geothermal greenhouse gas emissions in New Zealand in 2020: lifecycle and operational emissions”, *Proceedings New Zealand Geothermal Workshop*

Mertoglu, O. and Basarir, N. (2018) “Geothermal District Heating and Power Generation Experience in Turkey”, *Proceedings European Geothermal Workshop*

Mountain, B., Sajkowski, L. and Rendel P.M. (2022), “CO_2 as an Effective Silica Scaling Inhibitor during Reinjection of Acid-Dosed Geothermal Brines: An Experimental Study”, *Goldschmidt Conference* <https://doi.org/10.46427/gold2022.12707>.

Ngethe, J. and Jalilinasrabady, S. (2021), “Optimisation of Geothermal Greenhouses Design for Kenyan Fresh-cut Flower”, *Proceedings Workshop on Geothermal Reservoir Engineering*, Stanford.

Olafsdottir, K., Gudmundsson, Y., Mamrosh, D., McIntush, K., Ryan, A., Piggott, B.,and Beitler, C. (2023) “Managing Flammable Species in CO_2 Capture Processes Utlilizing Water Scrubbing at Geothermal Power Plants” *GRC Transactions, Vol. 47*

Ormat (2020) https://investor.ormat.com/news-events/news/news-details/2020/Steamboat-Hills-Geothermal-Power-Plant-Enhancement-in-Nevada-Begins-Commercial-Operation/default.aspx

Ormat (2023) https://investor.ormat.com/news-events/news/news-details/2023/Ormat-Resumes-Operation-at-Its-Heber-1-Power-Plant-in-California-and-Completes-Expansion-of-the-Dixie-Valley-Power-Plant-in-Nevada/default.aspx

Ormat (2024) https://s1.q4cdn.com/231465352/files/doc_presentations/2024/Jun/20/Ormat-AD-Final-for-printing.pdf

Povarov, O. and Nikolskiy, A. (2005), “Experience of Creation and Operation of Geothermal Power Plants in Cold Climate Conditions”, *Proceedings World Geothermal Congress*

Piggott, B., McIntush, K., Mamrosh, D. and Beitler, C. (2021), “Non-Condensable Gas Composition Impacts on Carbon Capture and Water Injection”, *GRC Transactions, Vol. 45*

Ragnarsson, A., Steingrimsson, B. and Thorhallsson, S. (2023) “Geothermal Development in Iceland 2020-2022”, *Proceedings World Geothermal Congress*

Richard, M.A., Carey, D.L. and Russel, J.S. (1989) “Environmental Mediation and the Development of the Puna Geothermal Venture Project: Hawaii Tries a New Regulatory Process to Unlock a Decade of Confrontation”, *GRC Transactions, Vol. 13*

Richard, M.A. (1990), “The Puna Geothermal Venture Project Power for the Island of Hawaii”, *GRC Transactions, Vol. 14*

Richardson, I., Misa, T., Mclean, K., Castillo-Ruiz, N., Ferguson, A., Moodabe-Smith, V., Peral, D. and Wootton, D. (2023), “Non-Condensable Gas Reinjection at the Te Huka Geothermal Power Plant”, *GRC Transactions, Vol. 47*

Ruiz, N.C., McLean, K., Richardson, I., Misa, T., Ferguson, A., Altar, D., and Kaya, E. (2021). "Passive NCG Reinjection at Te Huka Geothermal Binary Power Plant" *Proceedings New Zealand Geothermal Workshop*

Yucetas, I., Ergicay, N. and Akin, S. (2018), “Carbon Dioxide Injection Field Pilot in Umurlu Geothermal Field, Turkey”, *GRC Transactions Vol 42*

Enhanced / Engineered Geothermal Systems

Experimental Investigation of the Flow Behavior of Ionic Liquids for use as Working Fluids in Enhanced Geothermal Systems

Christian Akhilome, Sushobhan Pradhan, and Prem Kumar Bikkina

Oklahoma State University

Keywords: *Enhanced geothermal systems, Ionic liquids, microfluidics, thermal short-circuiting*

Abstract

The heat recovery efficiency of an enhanced geothermal system (EGS) relies on the flow dynamics of the circulated working fluid in the natural and engineered fractures within the reservoir. The use of Ionic liquids (ILs) as geothermal working fluids is a promising alternative to conventional working fluids such as water due to their favorable properties including wide liquid range, high thermal stability, and shear thinning behavior. ILs are expected to offer enhanced flow hydraulics and address thermal short-circuiting, a potential issue in EGS operations. ILs dynamically adjust their rheological properties in response to localized temperature changes, enabling them to selectively traverse higher temperature flow paths with minimal resistance. Consequently, ILs can potentially eliminate flow shortcuts, thereby improving the overall heat recovery from the EGS.

This study investigates the flow behavior of ILs and their performance in EGS. Specifically, it examines correlations between flowrates and pressure drops of two ILs, viz., 1-butyl-3-methyl-imidazolium bromide ([bmim][Br]), and 1-hexylpyridinium bromide ([hPy][Br]), within idealized micro fractures. Experimental evaluations were conducted using a microfluidic set-up to simulate flow through micro channels in EGS, utilizing a variety of fluid samples, including De-ionized (DI) water, and 5%, 10%, and 25% solutions of [bmim][Br] and [hPy][Br]. Furthermore, the study also investigated the high-temperature flow behavior of [bmim][Br] at 18 ^{o}C, 50 ^{o}C, and 80 ^{o}C, comparing it to the performance of DI water under the same conditions. The reduction in the frictional pressure drops of the IL is compared to that of DI water, revealing significant hydrodynamic improvements with the IL. Particularly, as temperature increased, the IL showed better performance over DI water in terms of reduction in frictional pressure loss within the microchannels with an average reduction approximating four times larger than that of DI water. This research enhances our understanding of IL flow behavior in microchannels, which is crucial for optimizing heat recovery from EGS and advancing sustainable and cost-effective geothermal operations.

1. Introduction

The vast thermal energy resources found in the Earth's subsurface offer considerable potential for green and sustainable power generation. This thermal energy is mainly generated from heat conduction and convection from the Earth's core and exothermic decay of radioactive elements (Emujakporue, 2017). Bertani (2016) estimates that harnessing 1% of the Earth's crust heat could power the world for about three millennia, underscoring its enormity. Furthermore, the replenishment rate exceeds depletion, emphasizing the sustainability of geothermal energy. However, most high geothermal gradient areas are located within igneous rocks with very low permeabilities which makes harnessing this energy very challenging. Thus, the concept of enhanced geothermal systems (EGS) was developed to exploit these vast resources by creating flow paths that permit heat extraction from these reservoirs. EGS involves artificially stimulating hot dry rock (HDR) reservoirs to create a subsurface fracture network that allows circulation of a working fluid, traditionally water, between an injection well and a production well. Heat is exchanged from the HDR to the working fluid which is produced to the surface through the production well. Depending on the temperature of the produced fluids, they can be used for different purposes such as space heating for geothermal fluid temperatures as low as 80 ^{o}C and about 180 ^{o}C for economical electricity generation (Smith et al., 1975).

The efficiency of EGS is dependent on the temperature of the extracted fluid. Higher temperatures indicate better performance (Asai et al., 2019). The properties of the circulated working fluid are crucial for optimizing heat recovery from geothermal reservoirs. Various working fluids have been explored to improve the performance of EGS, with water and CO_2 being the most commonly used. Although water is relatively cheaper than other working fluids, its use in EGS is limited by issues related to mineral dissolution and precipitation. However, water does have higher thermal conductivity and specific heat capacity compared to CO_2 (André et al., 2006; Brown, 2000). Supercritical CO_2 ($ScCO_2$ – occurs when CO_2 is held above its critical temperature and pressure), prevents the silica precipitation and mineral dissolution challenges associated with water-based EGS projects. Furthermore, $ScCO_2$ yields a higher mass flow rate and net heat extraction for a given injection rate in EGS due to the existence of thermal siphoning between injection and production wells (T. Guo et al., 2019; Lei, 2022; Olasolo et al., 2016; Sun et al., 2018). In addition, unlike water, fluid losses in geothermal reservoirs may be beneficial when CO_2 is used as the working fluid due to the possibility of carbon sequestration, depending on suitable site conditions. A prevalent issue with both CO_2 and water geothermal working fluids is the possibility of flow channeling which can lead to early thermal breakthrough. Formation heterogeneities often lead to the creation of fractures with non-uniform properties when geothermal reservoirs are stimulated. This often leads to the creation of preferential flow paths in EGS due to the uneven hydraulic conductivities of the induced fractures (Gischig & Preisig, 2015; T. Li et al., 2016). Since preferential flow paths allow more flow compared to other fractures, the temperature of the surrounding rock decreases more rapidly. This cooling causes an increase in the fracture aperture due to thermal destressing, which in turn leads to even more channelized flow (Fu et al., 2016; B. Guo et al., 2016). This phenomenon, called thermal short-circuiting, can result in insufficient heat exchange and early thermal breakthroughs, leaving a large volume of reservoir rock untouched (S. Li et al., 2022). As a result, the temperature of the produced fluids reduces, thereby compromising the economic viability of the EGS project. Numerous field studies have documented evidence of thermal short-circuiting in EGS. For instance, Lu (2018) reviewed prominent EGS sites worldwide and noted that thermal short-circuiting contributed to the inability of projects like Rosemanowes

in the UK and Hijiori in Japan to achieve their target heat production over time, ultimately leading to the termination of operations at both sites. Different approaches have been suggested to mitigate thermal short-circuiting in literature including the use of temperature-sensitive proppants to modify fracture conductivity (Al Balushi et al., 2023; Hu et al., 2021), periodic shut-ins of injectors and producers (Fan et al., 2020), and the use of chemicals to plug highly conductive fractures (Zhang & Dahi Taleghani, 2023). However, there has been insufficient evidence to support the applicability of these remedies in practical terms.

Recently, ionic liquids (ILs) have been garnering significant attention in various fields, including thermal energy storage and EGS. ILs are salts composed entirely of ions and are generally liquids below 100 ^{o}C. ILs have emerged as promising alternatives to water and CO_2 due to their unique properties such as high thermal and chemical stability, low melting point, low vapor pressure, and shearing thinning which are favorable for EGS applications. Unlike water and $ScCO_2$, ILs significantly vary their rheological properties in response to temperature changes in the fractures which can potentially eliminate flow shortcuts. The underlying concept is that the viscosity of the ILs increases significantly when the temperature of the bounding rock matrix in channelized flow paths reduces. This increases the hydraulic resistance to flow in the preferential flow paths which leads to a redistribution of the working fluid into other regions in the EGS, thus, eliminating thermal shortcuts (Atashnezhad et al., 2023; Momoh et al., 2023). Despite this enormous potential, there is a relative scarcity of studies investigating the use of ILs as geothermal working fluids.

In this study, we investigated the performance of two ILs: 1-butyl-3-methyl-imidazolium bromide ([bmim][Br]) and 1-hexylpyridinium bromide ([hPy][Br]) as potential working fluids for EGS applications. We conducted a series of flowrate vs. pressure drop experiments using a microfluidic setup to mimic flow through a geothermal reservoir. Various fluid samples, including deionized (DI) water, and 5%, 10%, and 25% solutions of [bmim][Br] and [hPy][Br], were tested. Additionally, the study explored the high-temperature flow behaviors of [bmim][Br] at 18 °C, 50 °C, and 80 °C, comparing them to the performance of DI water under the same conditions. Our findings enhance the understanding of the flow behavior of ILs in microchannels, which is crucial for optimizing heat recovery from EGS and advancing sustainable and cost-effective geothermal operations. This research aims to contribute to the optimization of EGS by providing valuable insights into the flow dynamics of ILs as working fluids, potentially leading to more efficient and sustainable geothermal energy extraction methods.

2. Materials And Methods

2.1 Microchip

In this work, a 45 x 15 mm borosilicate glass microchip with three flow channels of varying widths was utilized. The microchip was designed and fabricated by Micronit Microtechnologies B.V., Netherlands. A Micronit Fluidic Connect Pro chip holder houses the microchip to ensure proper confinement and prevent fluid leaks during flow tests. Table 1 shows the dimensions of the microchannels in the chip while Figure 1 shows the chip holder and a detailed description of the microchip.

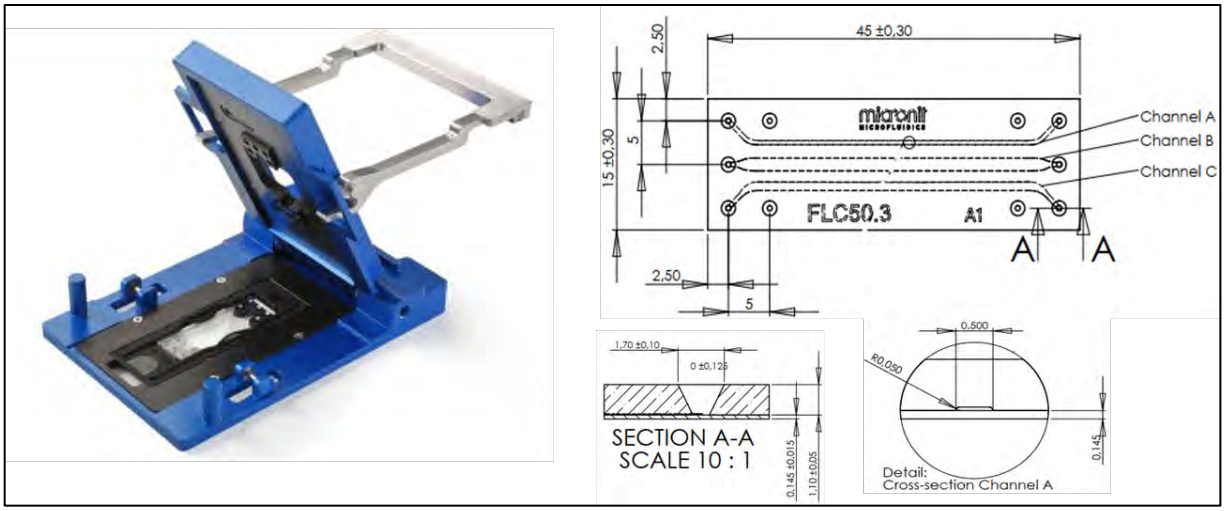

Figure 1: Pictorial description of the Fluidic Connect Pro chip holder (left) and the Microchip (right) (www.micronit.com)

Table 1: Dimensions of Microchannels.

Channel	Width (mm)	Length (mm)	Depth (mm)	Volume (µl)
A	0.5	42	0.05	1
B	1.5	40	0.05	2.8
C	1	42	0.05	1.9

2.2 Test Fluids

Two (ILs), 1-butyl-3-methyl-imidazolium bromide ([bmim][Br]) and 1-hexylpyridinium bromide ([hPy][Br]), were used to conduct the flow tests. The results obtained from the ILs were compared against those from deionized (DI) water). In addition, aqueous solutions of [bmim][Br] and [hPy][Br] were tested at three different concentrations of the ILs. The properties of the ILs, determined by Atashnezhad et al., (2023), are presented in Table 2 below.

Table 2: Properties of test fluids (Atashnezhad et al., 2023).

Fluids	Viscosity @ SR = 25-100 1/s & P = ~ 101.5 psi (cP)	Density (g/cc)	Thermal Stability (ºC)
[bmim][Br]	199-364	0.94	280
[hPy][Br]	697-715	1.105	380
DI Water	1	1.000	---

The viscosities of the aqueous test fluids were determined using a RheoSense microVISC viscometer. The viscometer uses an array of pressure sensors to measure the force required to pump fluids through a rectangular microfluidic channel which is indicative of the fluid's resistance to flow. Analytical solutions, such as the Hagen-Poiseuille equation, are then applied to estimate the shear stress and viscosity from the measured pressure drop. The densities of the aqueous samples were measured using a densitometer (Mettler Toledo DA-100M). The densitometer uses

the vibration frequency of a liquid-filled U-tube to determine the density of the liquid. Table 3 shows the viscosity and density of aqueous solutions of the ILs at 18 ^{o}C.

Table 3: Properties of test fluids continued.

	Viscosity @ 18 ^{o}C (cP)	**Density (g/cc)**
5% [bmim][Br]	1.402	1.0070
10% [bmim][Br]	1.528	1.0140
25% [bmim][Br]	2.007	1.0437
5% [hPy][Br]	1.258	1.0100
10% [hPy][Br]	1.340	1.0200
25% [hPy][Br]	1.791	1.0507

2.3 Experimental Facility

The microfluidic facility used to evaluate the reversibility of the ILs consists of several key components: i) constant pressure and constant rate syringe pumps for injecting and withdrawing the liquids into and from the chip; ii) a microchip and chip holders to simulate flow through fractures in EGS; iii) control valves; iv) differential pressure sensors to measure the pressure difference between the inlet and outlet of the microchip; v) a data acquisition device (DAQ) for real-time data gathering and performance analysis; vi) a workstation to monitor flow through the microchannels; vii) various fittings and PEEK tubings to facilitate fluid flow across the microchip. Figure 2 illustrates the process flow diagram of the experimental setup. For multichannel experiments, the Tee connectors at the inlet and outlet of the microchip are replaced by a union cross. The microchip features three idealized microfractures of varying widths but roughly the same length and depth.

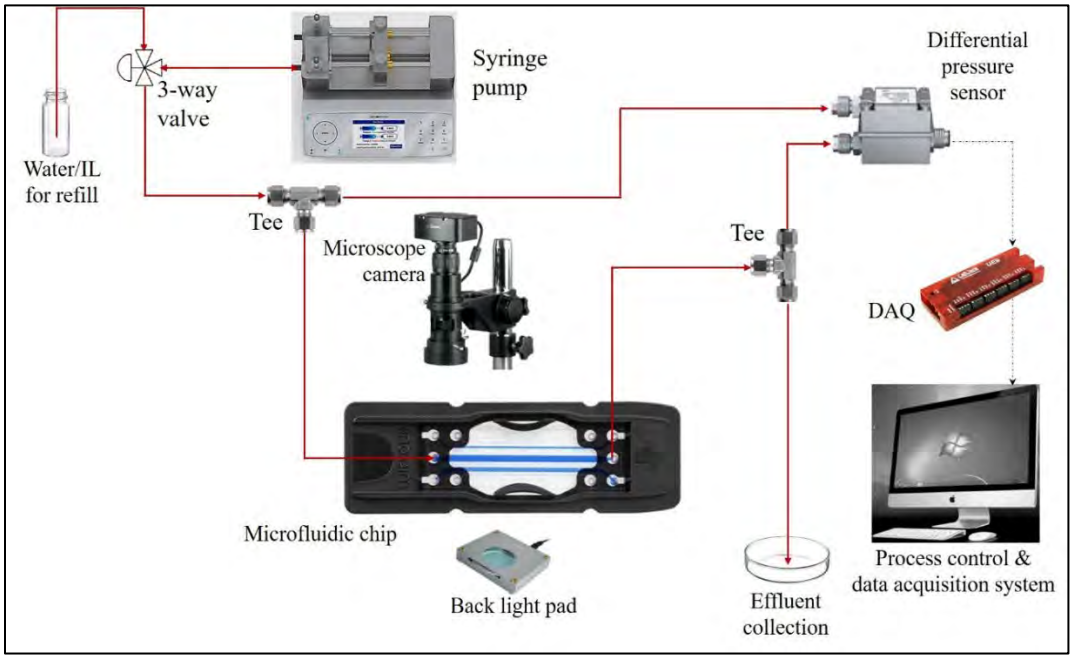

Figure 2: Process flow diagram for the experimental setup to conduct flow tests across the microchannel(s)

2.4 Pressure Drop across the Microfluidic Channels

A TDK minicell pressure sensor was used to measure the differential pressure across the microchannel(s). The pressure sensor records the voltage difference between the inlet and the outlet of a microchannel based on the piezoelectric effect. The measured voltage is transmitted through a LabJack UE9pro data acquisition device to a computer monitor. To convert the recorded voltage values to differential pressure (ΔP), the pressure sensor was calibrated to obtain a relation between voltage (V) and pressure drop (psi). The calibration was performed using a constant pressure injection pump (make: Teledyne ISCO; model: 260 D), yielding a linear relationship between the differential pressure and the voltage ($\Delta P = 35.711V - 17.162$, $R^2 = 0.9999$), as shown in Figure 3. This linear model was used to estimate ΔP from the voltage values recorded during the different flow experiments. By maintaining a constant flow rate through the microchannels, we recorded voltage values and applied the linear model to estimate ΔP which provided insights into the behavior of ILs in EGS.

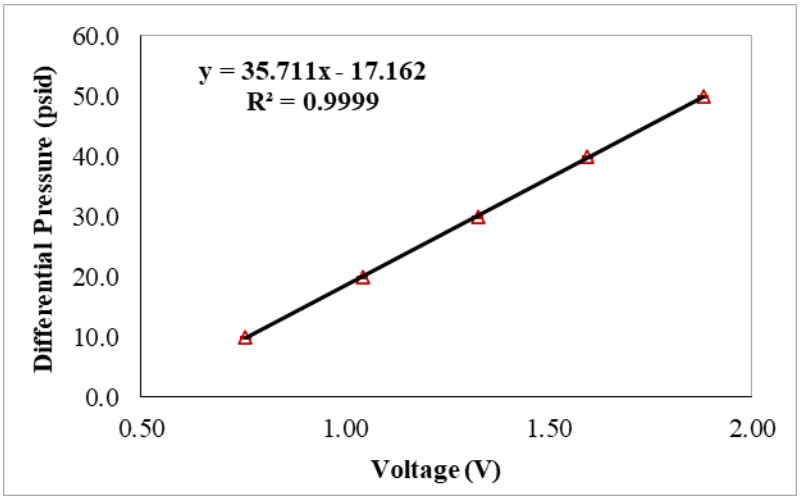

Figure 3: Calibration curve for the differential pressure sensor.

2.5 Procedures for Determining the Pressure Drop across the Microchannel(s)

2.5.1 Low Temperature Experiments

A Havard PHD Ultra syringe pump was used to conduct low-temperature experiments. Test fluids are withdrawn from the fluid reservoir into the syringe pump. They are then injected into the microchannel at a constant flow rate at room temperature (18 ^{o}C). The ΔPs across single microchannels are estimated using stabilized voltage readings i.e., when steady state flow exists in the microchannels. The flow rate is initially increased in steps until a predetermined rate is attained with the stabilized voltage values recorded at each flow rate. Next, the flow rate is reduced from the maximum to the minimum rate in the previous cycle while maintaining the same flow rate intervals. Finally, the flow rate is increased again from the lowest to the highest rate using the same step intervals in the first two cycles. This sequence is repeated for each test fluid, and the average of all three voltage values is used to estimate the pressure drop across the microchannel(s).

To minimize contamination of the test liquids, the microchannels and the pump's syringe are thoroughly cleaned with DI water and isopropyl alcohol (IPA) between experiments. This entire procedure is repeated for each test fluid and for both single- and two-channels.

2.5.2 High Temperature Experiments

For high-temperature experiments, a Chemyx Fusion 6000X syringe pump was used. Chemyx Fusion 6000X pump was used to pre-heat, regulate, and maintain the temperature of fluids in its syringe. The test fluids were preheated in a water bath to the desired temperature before withdrawing the liquids into the pump's syringe. The pump is then used to preheat the fluid again before injecting it into the microchannel. A thermal insulation tape was used to wrap the components of the setup, including the syringe, tubings, and fittings, to minimize heat losses. The procedures utilized to determine the pressure drop at the room temperature experiments were also adopted for the high-temperature experiments.

3. Results And Discussion

3.1 Aqueous Solutions

ILs may be diluted by water when utilized as geothermal working fluids, especially in hot wet rocks (HWR). It is therefore necessary to understand the flow behavior of aqueous solutions of the ILs utilized in this study. Flow behavior of 5%, 10%, and 25% solutions of [bmim][Br] and [hPy][Br] in the microchannels were examined in this work. The pressure drop vs. flowrate curves for these solutions are presented in the following sections.

3.1.1 Results for [bmim][Br]

The flow of fluid from one point to another in a system generally leads to a reduction in pressure due to three main factors: kinetic losses, potential losses, and frictional losses. The microfluidic setup consists of horizontally positioned and uniformly sized microchannels, thus eliminating potential and kinetic losses respectively. Frictional loss is a measure of a fluid's resistance to flow and is dependent on the fluid and system properties. Analytical solutions describing flow through microfluidic channels have shown that the pressure drop across microfluidic channels is dependent on the flowrate, fluid properties, and dimensions of the channel(s) (Estarki et al., 2023; Joseph et al., 2013). The viscosity of the fluid is the main fluid property that affects pressure drop, it describes the internal resistance of the fluid to flow. Thus, the more viscous the IL/aqueous solution, the higher its internal resistance and the consequent differential pressure across the channel/multichannel. Figure 4 shows the variation of pressure drop with flowrate for aqueous solutions of [bmim][Br] in single- and two-channels. It can be observed that the recorded ΔP increased with flowrate in all the cases considered. In addition, for a fixed flow rate, the pressure drop increased with increasing concentration of the [bmim][Br]. The increased pressure drop can be attributed to an increase in viscosity as the concentration of the IL increased from 5% to 25%. Readers are referred to Table 3 for the viscosities of the test fluids. Similarly, the differential pressure reduced with increase in the width of the channels because shear rate and flow resistance decreases as the width of the channels increases. This behavior was also noted in the two-channel experiments where the pressure drop derived from flowing through the single channel was always higher than the pressure drop recorded when a second channel was combined. The error bars on each data point in the plots represent the standard deviations of the mean ΔP value from three ΔP data points recorded in distinct experiments.

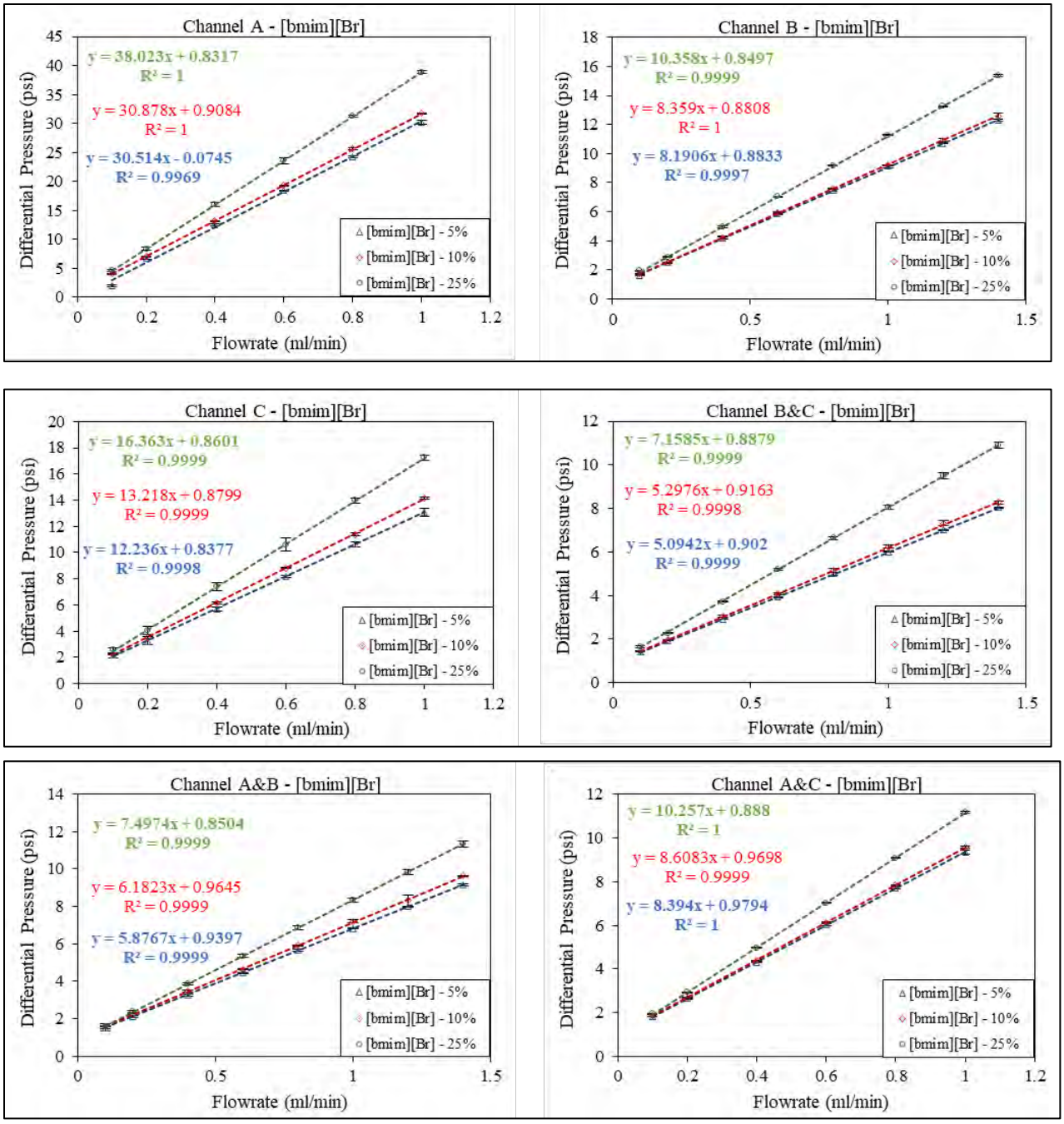

Figure 4: Variation of pressure drop (ΔP) with flow rate of [bmim][Br] in the microchannels

3.1.2 Results for [hPy][Br]

Similar trends were observed in the [hPy][Br] solutions as with the aqueous [bmim][Br] solutions. The pressure drop increased with both flowrate and concentration of the ILs, while it decreased with increasing channel width. It is important to note that the viscosity of 5% and 10% samples are closer compared to that of 10% and 25% concentrations which could explain the comparable ΔP-Q trends for 5% and 10% in all the cases.

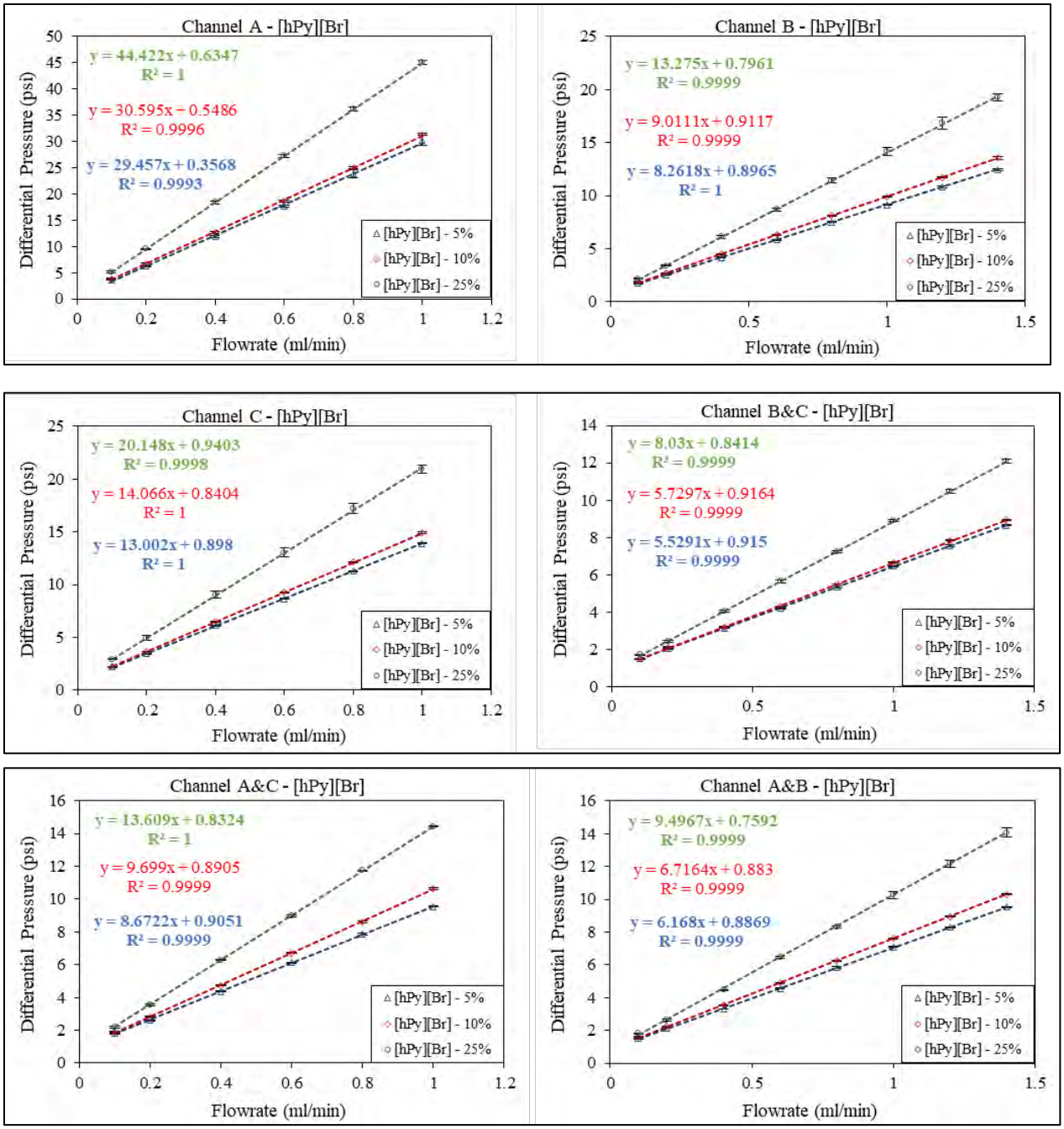

Figure 5: Variation of pressure drop (ΔP) with flow rate of [hPy][Br] in the microchannels

3.2 Results for [bmim][Br] and DI Water at High Temperature

Figures 6 and 7 show the effect of increasing the temperature of the DI water and [bmim][Br] on the pressure drop across a microchannel. As stated in previous sections, the pressure drop across each channel results from the frictional losses in the system which are mainly dependent on the viscosity of the flowing liquid and the internal conditions of the channel such as roughness, and channel dimensions. Temperature dependence of viscosity varies from fluid to fluid. The viscosity of [bmim][Br] reduces significantly when the temperature is increased. Thus, the measured pressure

drop across the channel at a constant rate reduces as the temperature of the IL increases. DI water, on the other hand, does not experience much viscosity reduction with increasing temperatures. For example, Korson et al., in 1969 estimated the viscosity of DI water at a temperature range of 0-100 ^{o}C. The viscosities of DI water at 18 ^{o}C, 50 ^{o}C, and 80 ^{o}C are approximately 1 cP, 0.55 cP, and 0.35 cP, respectively. As shown in Figure 6, the pressure drop across the channels did not change much when the temperature of DI water was increased from 18^{o}C to 50^{o}C and 80^{o}C.

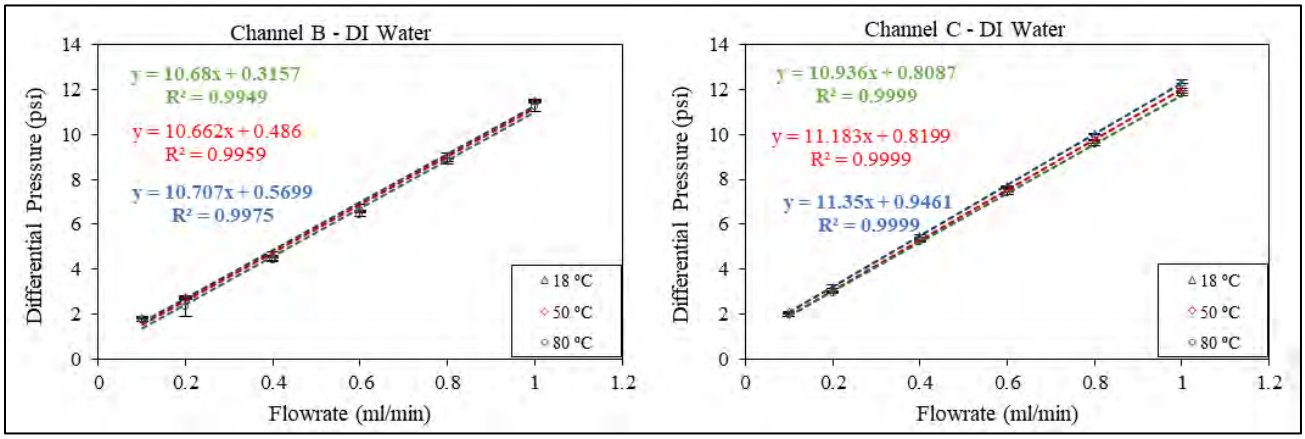

Figure 6: Variation of pressure drop (ΔP) with flow rate of DI water at 18 °C, 50 °C, and 80 °C in channel B and channel C

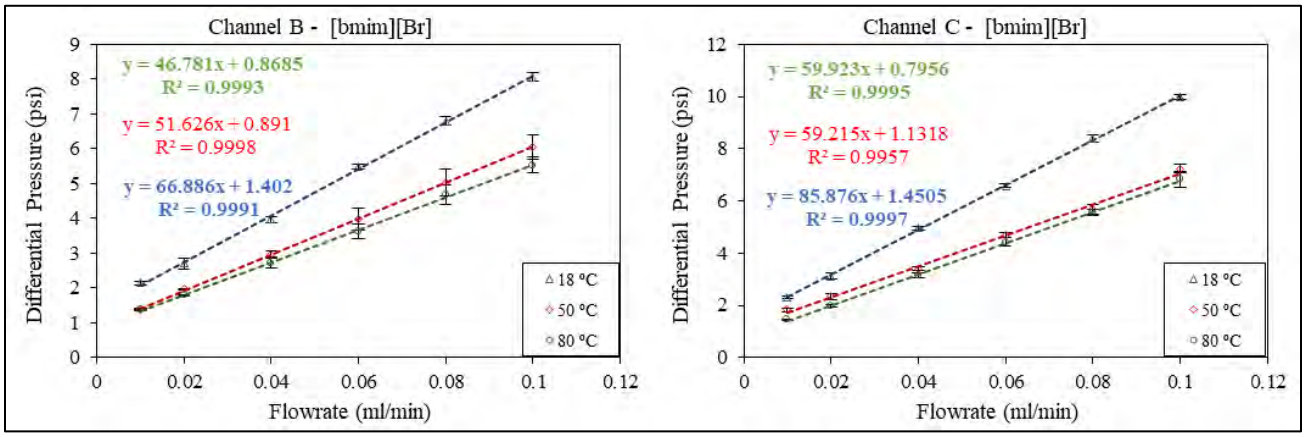

Figure 7: Variation of pressure drop (ΔP) with flow rate of [bmim][Br] at 18 °C, 50 °C, and 80 °C in channel B and channel C

Figure 6 and 7 demonstrates that [bmim][Br] exhibits enhanced hydrodynamic properties with increasing temperature compared to DI water at the microscale. This is further illustrated in Table 4 which shows the percentage reduction in pressure drop for both DI water and [bmim][Br], when a constant flow rate of 0.1 ml/min was maintained for both liquids.

Table 4: Recorded ΔP values and percent change of ΔP with temperature increase from 18°C to 80°C for DI water and [bmim][Br] in Channel B and Channel C.

Test fluid	Channel B						Channel C					
	DI Water			[bmim][Br]			DI Water			[bmim][Br]		
Temperature (°C)	18	50	80	18	50	80	18	50	80	20	50	80
ΔP (psi)	1.84	1.76	1.75	8.06	6.05	5.53	2.11	1.94	1.94	9.99	7.24	6.82
Percent reduction in ΔP	--	3.89	4.54	--	24.95	31.38	--	7.9	7.9	--	27.52	31.69

The frictional pressure loss reduction ratio, derived by comparing the percent reduction in ΔP of [bmim][Br] with that of DI water, is shown in Table 5.

Table 5: Frictional pressure loss reduction ratio of [bmim][Br] with respect to DI water.

Channel	Channel B		Channel C	
Temperature (°C)	50	80	50	80
Frictional pressure loss reduction ratio	6.4	6.9	3.5	4

Tables 4 and 5 show that the percent reduction in differential pressure with increasing temperature for DI water is much lower than the reduction experienced with [bmim][Br]. [bmim][Br] outperforms DI water in terms of the reduction in the frictional pressure loss in microchannels with increasing temperature. In channel B, [bmim][Br] exhibited a frictional pressure loss reduction seven times greater than that of DI water, while in channel C, it showed a four-fold reduction compared to DI water.

3.3 EGS Implications

As stated earlier, flow channeling can lead to thermal short-circuiting which can negatively impact the overall heat recovery efficiency of an EGS project. Unlike water, ILs have temperature-dependent viscosities, which can prevent thermal short-circuiting. As the viscosity of ILs increases in highly conductive, low-temperature flow paths, flow resistance increases, redirecting the ILs to lower conductivity, higher temperature paths. This redistribution into smaller, hotter fractures enhances the recovery efficiency of an EGS and can extend the project's lifespan. We can infer from the results that the use of [bmim][Br] (and similar ILs) as geothermal working fluids leads to greater frictional pressure loss which could cause more fluid flow in low-conductivity fractures. It is important to note that these experiments were conducted at a maximum temperature of 80°C due to the limitations of our experimental facility. In reality, higher temperatures exceeding 180°C have been recorded in EGS (Lu, 2018). Therefore, the frictional pressure loss ratio is expected to increase under actual EGS conditions, leading to improved flow hydraulics. However, drawing definitive conclusions from these findings requires further study to verify the flow behavior of ILs in fracture networks at the elevated temperatures typical of geothermal reservoirs.

4.0 Conclusions

The flow behaviors of [bmim][Br] and [hPy][Br] within idealized microfractures were evaluated using a microfluidic setup, and their potential as geothermal working fluids was discussed. The main findings from this study are:

- The ILs demonstrated pressure drops across single and multichannel proportional to the flowrate, viscosity of the ILs, and the dimensions of the single- and two-channels. [bmim][Br] showed a significant reduction in the frictional loss compared to DI water. The frictional pressure loss reduction of [bmim][Br] at 80^{o}C was about seven times that of DI water in channel B and four times greater than DI water in channel C.
- In EGS reservoir conditions, we expect a much higher viscosity increase ratio for the ionic liquids when temperature declines which can potentially eliminate short circuits.
- The use of ILs presents a dynamic solution to fracture tuning, enhancing the overall heat recovery and performance of EGS.

5.0 Acknowledgement

The research is based on work funded by the Department of Energy Office of Energy Efficiency and Renewable Energy (EERE) under the Geothermal Program Office Award Number DE-EE0009788.

We also thank our research collaborators Dr Al Dushaishi M., and Dr Atashnezhad A., for their work on the synthesis and characterization of the ILs.

References

Al Balushi, F., Zhang, Q., & Dahi Taleghani, A. (2023). Improving enhanced geothermal systems performance using adaptive fracture conductivity. *Applied Thermal Engineering*, *233*, 121206. https://doi.org/10.1016/j.applthermaleng.2023.121206.

André, L., Rabemanana, V., & Vuataz, F.-D. (2006). Influence of water-rock interactions on fracture permeability of the deep reservoir at Soultz-sous-Forêts, France. *Geothermics*, *35*(5), 507–531. https://doi.org/10.1016/j.geothermics.2006.09.006.

Asai, P., Panja, P., McLennan, J., & Deo, M. (2019). Effect of different flow schemes on heat recovery from Enhanced Geothermal Systems (EGS). *Energy*, *175*, 667–676. https://doi.org/10.1016/j.energy.2019.03.124.

Atashnezhad, A., Akhtarmanesh, S., Kjeldal, V. N., & Dushaishi, M. F. A. (2023). *Advancing Enhanced Geothermal Reservoirs with Ionic Liquids as Potential Geothermal Fluid*.

Bertani, R. (2016). Geothermal power generation in the world 2010–2014 update report. *Geothermics*, *60*, 31–43. https://doi.org/10.1016/j.geothermics.2015.11.003.

Brown, D. W. (2000). *A hot dry rock geothermal energy concept utilizing supercritical CO2 instead of water, PROCEEDINGS, Twenty-Fifth Workshop on Geothermal Reservoir Engineering Stanford University*. Stanford, California, January.

Emujakporue, G. O. (2017). Subsurface temperature distribution from heat flow conduction equation in part of chad sedimentary basin, Nigeria. *Egyptian Journal of Petroleum*, *26*(2), 519–524. https://doi.org/10.1016/j.ejpe.2016.07.003.

Estarki, H. E., Tareie, Z. S., & Latifi, H. (2023). Pressure drop measurement in microfluidics channel by the Fabry-Perot diaphragm-based flow sensor. *Flow Measurement and Instrumentation*, *91*, 102355.

Fan, H., Zhang, L., Wang, R., Song, H., Xie, H., Du, L., & Sun, P. (2020). Investigation on geothermal water reservoir development and utilization with variable temperature regulation: A case study of China. *Applied Energy*, *275*, 115370. https://doi.org/10.1016/j.apenergy.2020.115370.

Fu, P., Hao, Y., Walsh, S. D. C., & Carrigan, C. R. (2016). Thermal Drawdown-Induced Flow Channeling in Fractured Geothermal Reservoirs. *Rock Mechanics and Rock Engineering*, *49*(3), 1001–1024. https://doi.org/10.1007/s00603-015-0776-0.

Gischig, V. S., & Preisig, G. (2015). Hydro-fracturing versus Hydro-shearing: a critical assessment of two distinct reservoir stimulation mechanisms.

Guo, B., Fu, P., Hao, Y., Peters, C. A., & Carrigan, C. R. (2016). Thermal drawdown-induced flow channeling in a single fracture in EGS. *Geothermics*, *61*, 46–62. https://doi.org/10.1016/j.geothermics.2016.01.004.

Guo, T., Gong, F., Wang, X., Lin, Q., Qu, Z., & Zhang, W. (2019). Performance of enhanced geothermal system (EGS) in fractured geothermal reservoirs with CO2 as working fluid. *Applied Thermal Engineering*, *152*, 215–230. https://doi.org/10.1016/j.applthermaleng.2019.02.024.

Hu, X., Song, X., Wu, K., Shi, Y., & Li, G. (2021). Effect of proppant treatment on heat extraction performance in enhanced geothermal system. *Journal of Petroleum Science and Engineering*, *207*, 109094. https://doi.org/10.1016/j.petrol.2021.109094.

Joseph, J., Siva Kumar Gunda, N., & Mitra, S. K. (2013). On-chip porous media: Porosity and permeability measurements. *Chemical Engineering Science*, *99*, 274–283. https://doi.org/10.1016/j.ces.2013.05.065.

Korson, L., Drost-Hansen, W., & Millero, F. J. (1969). Viscosity of water at various temperatures. *The Journal of Physical Chemistry*, *73*(1), 34–39. https://doi.org/10.1021/j100721a006

Lei, H. (2022). Performance Comparison of H_2O and CO_2 as the Working Fluid in Coupled Wellbore/Reservoir Systems for Geothermal Heat Extraction. *Frontiers in Earth Science*, *10*, 819778.

Li, S., Wang, S., & Tang, H. (2022). Stimulation mechanism and design of enhanced geothermal systems: A comprehensive review. *Renewable and Sustainable Energy Reviews*, *155*, 111914.

Li, T., Shiozawa, S., & McClure, M. W. (2016). Thermal breakthrough calculations to optimize design of a multiple-stage Enhanced Geothermal System. *Geothermics*, *64*, 455–465. https://doi.org/10.1016/j.geothermics.2016.06.015.

Lu, S.-M. (2018). A global review of enhanced geothermal system (EGS). *Renewable and Sustainable Energy Reviews*, *81*, 2902–2921. https://doi.org/10.1016/j.rser.2017.06.097.

Momoh, I., Lee, H., Atashnezhad, A., & Al Dushaishi, M. (2023). *Fracture Conductivity Tuning in Granite under Triaxial Loading using Ionic Liquids: Implications for Enhanced Geothermal Systems*.

Olasolo, P., Juárez, M. C., Morales, M. P., D´Amico, S., & Liarte, I. A. (2016). Enhanced geothermal systems (EGS): A review. *Renewable and Sustainable Energy Reviews*, *56*, 133–144. https://doi.org/10.1016/j.rser.2015.11.031.

Smith, M. C., Aamodt, R. L., Potter, R. M., & Brown, D. W. (1975). *Man-made geothermal reservoirs*. Los Alamos Scientific Lab., N. Mex.(USA). https://www.osti.gov/servlets/purl/5132450.

Sun, F., Yao, Y., Li, G., & Li, X. (2018). Performance of geothermal energy extraction in a horizontal well by using CO2 as the working fluid. *Energy Conversion and Management*, *171*, 1529–1539. https://doi.org/10.1016/j.enconman.2018.06.092.

Zhang, Q., & Dahi Taleghani, A. (2023). Autonomous fracture flow tunning to enhance efficiency of fractured geothermal systems. *Energy*, *281*, 128163. https://doi.org/10.1016/j.energy.2023.128163.

EGS Reservoir Modeling for Developing Geothermal District Heating at Cornell University

Koenraad F. Beckers[1], Adam Hawkins[2], Burak Erdinc[2], Jefferson W. Tester[2]

[1]National Renewable Energy Laboratory, Golden CO, USA
[2]Cornell University, Ithaca NY, USA

Keywords

District Heating, Cornell University, Earth-Source Heat, EGS, Reservoir Modeling

ABSTRACT

Cornell University is pursuing development of an enhanced geothermal system (EGS) for providing heating to its main campus in Upstate New York. A ~3 km deep vertical observation well ("CUBO") was drilled in 2022 to characterize the subsurface using wellbore logging, borehole imaging, fluid sampling, mini-frac tests, coring, and drill cutting analysis. Down-hole temperatures measured at 3 km depth are about 80°C, sufficiently high for direct-use heating. The well drilled through generally low porosity and low permeability Paleozoic sedimentary formations and into metamorphic basement rock, encountered at about 2.8 km depth.

Leveraging subsurface data obtained through CUBO, we investigated technical feasibility and design requirements of a doublet well system with horizontal laterals connected to a fracture network created through hydraulic fracturing. The EGS reservoir is sized to provide a nominal heat output in the range 5 to 10 MW_{th} of continuous heating over a 15-year lifetime with limited thermal drawdown. We applied the Gringarten multiple parallel fractures model, the Cornell Discrete Fracture Simulator FOXFEM, and the commercial simulator ResFrac to estimate required heat transfer area and design a potential hydraulic stimulation treatment. Reservoir simulations indicate that, depending on fluid flow rate and injection temperature, 2 to 3 km^2 of effective fracture heat transfer area is required to supply the target heat output of 5 to 10 MW_{th} over 15 years.

1. Introduction

Cornell University aspires to become a carbon-neutral university by 2035 through its Climate Action Plan. A key pillar of this plan is decarbonizing the bulk of the heating load of the university's main campus in Ithaca, New York, with deep geothermal energy or "Earth Source Heat" (Tester et al., 2023). Over the past decade, various studies have been conducted to characterize the subsurface, investigate designs to integrate the geothermal system with the

existing campus energy infrastructure, and assess the overall technical and economic feasibility. In the summer of 2022, a 9,791 ft (2,984 m) deep exploratory well, named CUBO (Cornell University Borehole Observatory) was drilled to provide insights on the mechanical, thermal and hydrologic subsurface conditions using data collected through logging, coring, borehole imaging, mini-frac tests, assessing drill cuttings, and fluid sampling (Fulton et al., 2024). CUBO was drilled through about 9,400 ft (2,865 m) of Paleozoic sedimentary formations overlaying low-grade metamorphic basement rocks. Bottom-hole subsurface temperatures (after correcting for cooling due to drilling fluid circulation) are around 80°C, corresponding to a geothermal gradient of about 23°C/km. Analysis of mini hydraulic fracture testing combined with density logging suggests a strike-slip stress regime, i.e., the maximum and minimum principal stresses are horizontal and the intermediate principal stress is vertical.

Given the recent advances in EGS technology (e.g., by Fervo Energy and FORGE), this study explored developing a doublet system with long horizontal laterals at about 3 km vertical depth intersected by a large number of parallel vertical fractures created using multi-stage hydraulic stimulation (Figure 1). We leveraged three subsurface simulation models to explore potential reservoir designs capable of producing 5 to 10 MW_{th} of heat with limited thermal decline over a 15-year lifetime. Study objectives were (1) estimating the required number of fractures and required fracture area to sustain long-term heat production, (2) designing a potential hydraulic stimulation treatment program, and (3) comparing predicted reservoir performance across reservoir simulators.

2. Methodology

The three models applied to explore EGS reservoir performance are (1) the multiple parallel vertical fractures model by Gringarten et al. (1975) (Section 3), (2) the FOXFEM finite element simulator for heat transfer in fractures developed by Cornell (Fox, 2016; Hawkins, 2017; Section 4), and the commercial simulator ResFrac, allowing for simulating both hydraulic simulation and long-term fluid circulation (Section 5). The analytical Gringarten heat transfer model considers uniform flow through multiple parallel fractures. It does not calculate the pressure field, only the temperature field of the fluid. We applied the model as implemented in Python in GEOPHIRES (Beckers and McCabe, 2019; Ross and Beckers, 2023) and available on GitHub (NREL, 2024.). The model is easy to apply and provides a quick solution but assumes a simplified flow field with the fluid sweeping the entire area of the fracture with identical velocity.

The thermal-hydraulic FOXFEM simulator calculates the velocity field and corresponding pressure distribution of the fluid within the fracture, in addition to the fluid temperature field, thereby more accurately capturing the heat sweep with flow through a fracture. It can account for a variable aperture distribution but does not account for gravity (i.e., buoyancy effects due to difference in fluid density) and simulates only a single, discrete fracture. The tool is implemented in MATLAB and applies Green's functions in the Laplace domain to rapidly calculate the heat transfer between the fluid and the rock.

The thermal-hydraulic-mechanical simulator ResFrac is an advanced, commercial simulator that simulates both hydraulic stimulation to create fractures and long-term fluid circulation to estimate heat extraction. It is the most advanced simulator of the three applied, capable to simulate all relevant physics at play but has a steeper learning curve and simulations take a longer time (hours vs. seconds with the Gringarten model and minutes with the FOXFEM model).

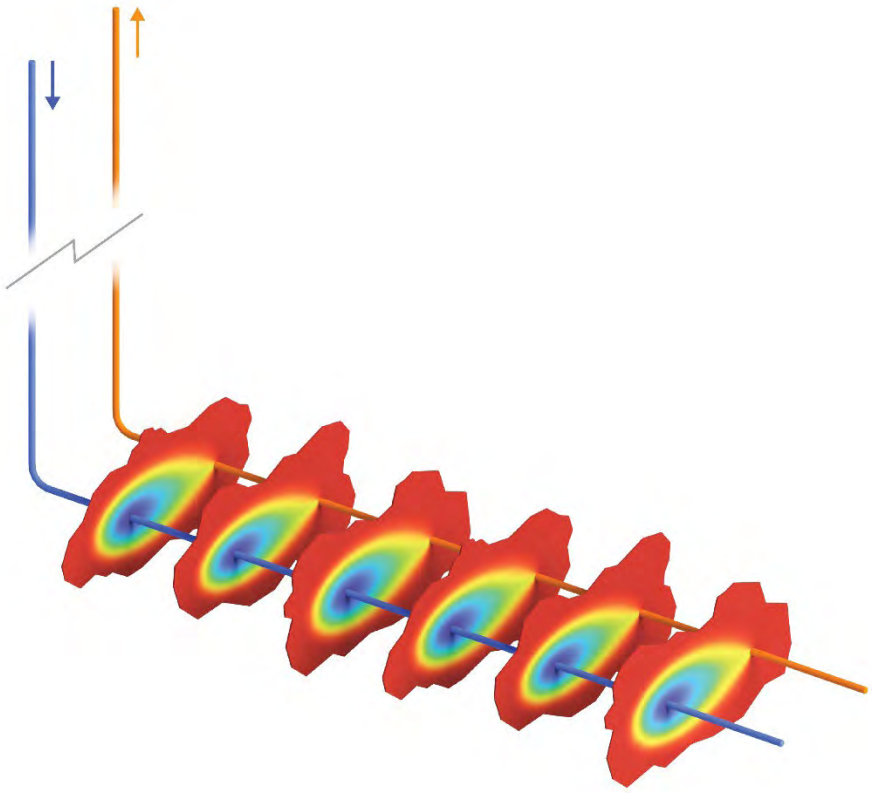

Figure 1: Simplified diagram of doublet EGS reservoir with multiple parallel vertical fractures connecting long horizontal laterals.

3. Thermal Simulations using Gringarten Multiple Parallel Fractures Model

We applied the analytical Gringarten et al. (1975) multiple parallel fractures model to investigate the required fracture heat transfer area to sustain heat production over a ~15-year lifetime. We considered four scenarios, exploring two different flow rates (30 and 50 kg/s) and two different injection temperatures (20° and 40°C). The design assumes two horizontal laterals spaced relatively close together at 150 m and with a fracture height of 150 m. The fracture spacing is set to 15 m. For comparison, Project Red in Nevada had a lateral well spacing of about 110 m (Norbeck and Latimer, 2023). For each scenario, we calculated the required number of fractures and corresponding lateral length to limit the temperature decline to 20°C after 20 years. The initial rock temperature is set to 80°C. All input parameters are listed in Table 1.

The required number of fractures (and corresponding lateral length and total heat transfer area) and initial and final thermal output for each scenario are presented in Table 1. All four scenarios have a similar production temperature profile (Figure 2a) but show a wide range in thermal output, with the initial thermal output ranging from 5 to over 12 MW_{th}, depending on the injection temperature and flow rate (Figure 2b). The lateral length required falls in the range of 1,200 to 2,300 m, and the number of fractures lies in the range of 85 to 157. For comparison, Project Red had a lateral length of about 1 km and about 100 perforation clusters in total (over 16 stages) (Norbeck and Latimer, 2023). The high thermal output scenario (Scenario 3) required the longest lateral length and highest number of fractures with a total fracture area of about 3.5 km^2. When flowing at only 30 kg/s instead of 50 kg/s (Scenario 1), a fracture heat transfer area of 2.1 km^2 is

sufficient to maintain a production temperature above 60°C. However, decreasing the flow rate also decreases the thermal output (initial thermal output drops from 12.5 to 7.5 MW_{th}).

Table 1: Input parameter and simulation results using Gringarten multiple parallel fractures model.

	Scenario 1	**Scenario 2**	**Scenario 3**	**Scenario 4**
Simulation Input Parameters				
Rock initial temperature	80°C			
Fluid injection temperature	20°C	40°C	20°C	40°C
Fluid flow rate	30 kg/s		50 kg/s	
Fluid density	1,000 kg/m3			
Fluid specific heat capacity	4,180 J/kg/K			
Rock thermal conductivity	2.8 W/m/K			
Rock density	2,800 kg/m^3			
Rock specific heat capacity	1,000 J/kg/K			
Fracture length = lateral spacing	150 m			
Fracture height	150 m			
Fracture spacing	15 m			
Number of fractures	94	85	157	142
Simulation Results				
Initial heat production	7.5 MW_{th}	5.0 MW_{th}	12.5 MW_{th}	8.4 MW_{th}
Heat production at 20 years	5.0 MW_{th}	2.5 MW_{th}	8.4 MW_{th}	4.2 MW_{th}
Production temp. at 20 years	59.8°C	59.8°C	60.0°C	60.0°C
Lateral length	1,380 m	1,245 m	2,325 m	2,100 m
Total heat transfer area	2.1 km^2	1.9 km^2	3.5 km^2	3.2 km^2

The required fracture geometry, and temperature and heat production results provided in Table 1 and Figure 2 are high-level estimates, given the simplifications in the Gringarten model. In Section 4, a more advanced simulator (FOXFEM) is applied, which calculates both the fluid velocity field and corresponding pressure distribution, in addition to the fluid temperature field.

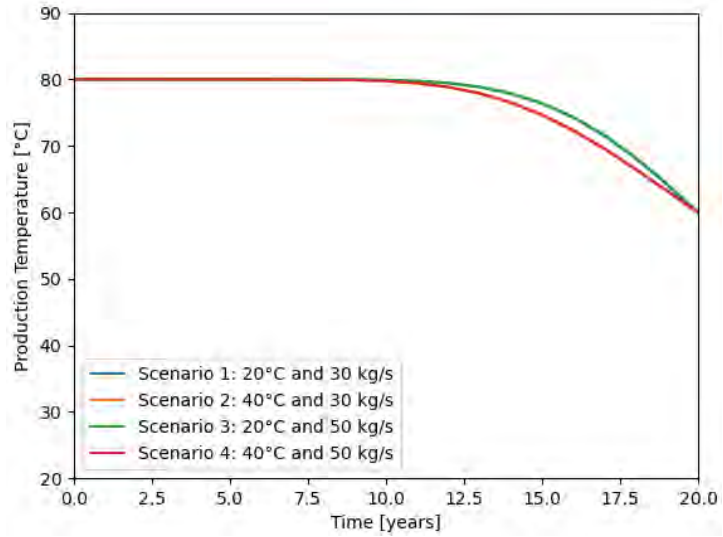

(a)

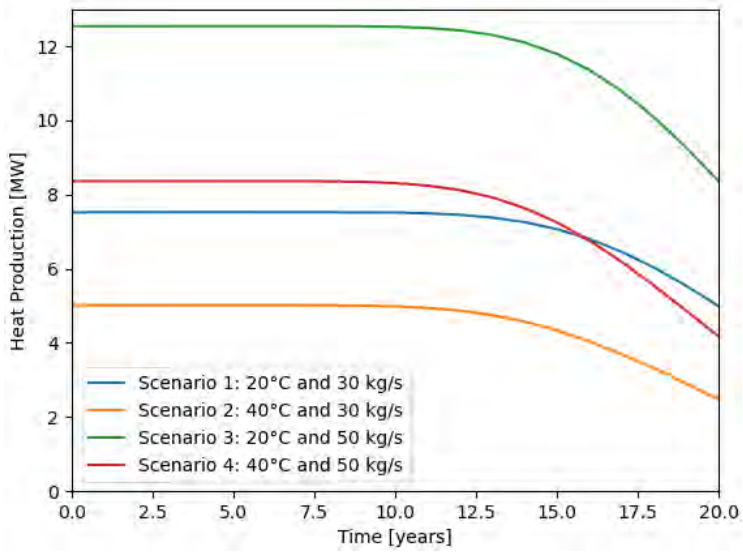

(b)

Figure 2: Production temperature (a) and corresponding heat production (b) for the four scenarios listed in Table 1. In all four scenarios, the number of fractures (and lateral length) was set to limit the production temperature decline to 20°C after 20 years of continuous operation. The heat production scales with the flow rate and difference between production and injection temperature, causing the wide range in heat production among the four scenarios. In (a), scenarios 1 and 3, and 2 and 4 overlap.

4. FOXFEM Thermal-Hydraulic Simulations

We applied the FOXFEM simulator, developed at Cornell, to estimate more accurately the heat extraction with fluid flow through a fracture located in a conduction-only medium. The tool only simulates a single fracture but simulates both the temperature and velocity field of the fluid, and can account for a variable aperture distribution.

We ran a simulation for a single fracture with FOXFEM to compare the heat sweep and effective heat transfer area with the Gringarten model, which for a single fracture simplifies to an error function. The fracture modeled is a circular fracture with a 160-m radius, with injection and production points spaced 150 m apart (Figure 3a). Rock and water properties are listed in Table 1, with water flow rate through the fracture set to 3 kg/s and injection temperature set to 20°C. The fluid temperature field after 20 years of operation is characteristic for a dipole flow field and indicates regions of the fracture with limited heat extraction from the rock (Figure 3b: yellow-colored regions). The production temperature for this case is shown in Figure 4 with the blue line, showing a temperature decline of about 30°C after 20 years. The same fracture area (0.081 km^2) with a uniform flow field as simulated with a modified Gringarten model for a single fracture shows a temperature drop of only 18°C after 20 years (red curve in Figure 4). The equivalent area with uniform flow to obtain the same temperature decline as with a dipole model is 0.054 m^2 (yellow line in Figure 4). This translates to roughly 66% heat sweep efficiency for a dipole model compared to the idealized uniform flow fracture model (assumed in Gringarten model). The heat sweep efficiency value can be different for different fracture geometries, flow rates, etc.

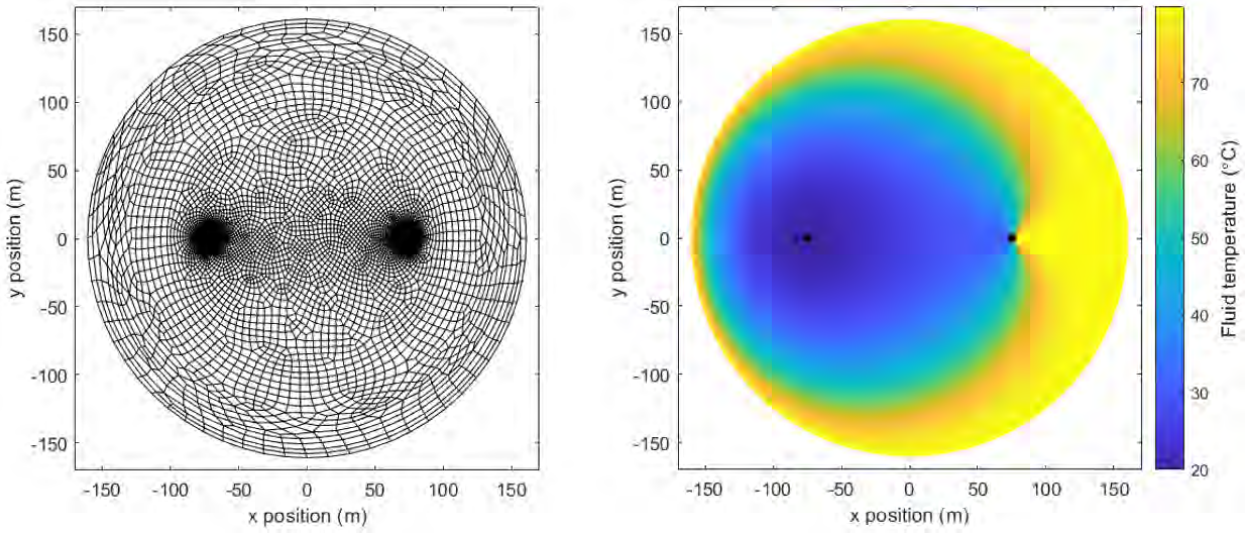

(a) (b)

Figure 3: Mesh (a) and fluid temperature field after 20 years of operation (b) for single fracture flow simulated with the FOXFEM simulator. Fracture has radius of 160 m with injection (left black dot) and production (right black dot) spaced 150 m apart.

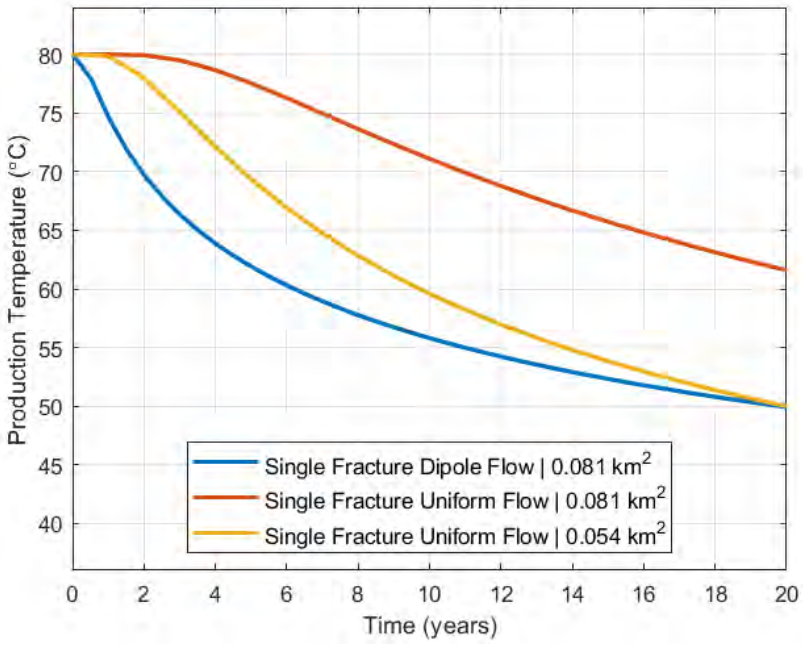

Figure 4: Production temperature profile for three scenarios: (1) single fracture dipole flow simulated with FOXFEM (as in Figure 3), (2) uniform flow in rectangular fracture for same fracture area, and (3) uniform flow in rectangular fracture with 34% reduction in fracture area.

The results shown in Figure 4 assume a uniform aperture field. Next, we explored the impact of the aperture distribution on the temperature field and production temperature. We considered three additional scenarios: a random aperture distribution between 0.5 and 2 mm (case 2), a high aperture flow path representing a "short-circuit" (case 3), and a low aperture blockage positioned in between the injection and production point (case 4). The aperture field and temperature field after 20 years for these three cases are shown in Figure 5. The production temperature profiles are presented in Figure 6. This analysis indicates the aperture field can have significant impact on the production temperature, particularly in the case of a channeled flow path, which concentrates the heat extraction along the flow path resulting in a low sweep efficiency. In real EGS reservoirs, proppants can be used to keep fractures open to facilitate obtaining high sweep efficiencies. Tracer testing can help with characterizing the effective heat transfer area. Techniques are currently being developed to mitigate high aperture flow paths, e.g., using temperature-dependent swelling particles.

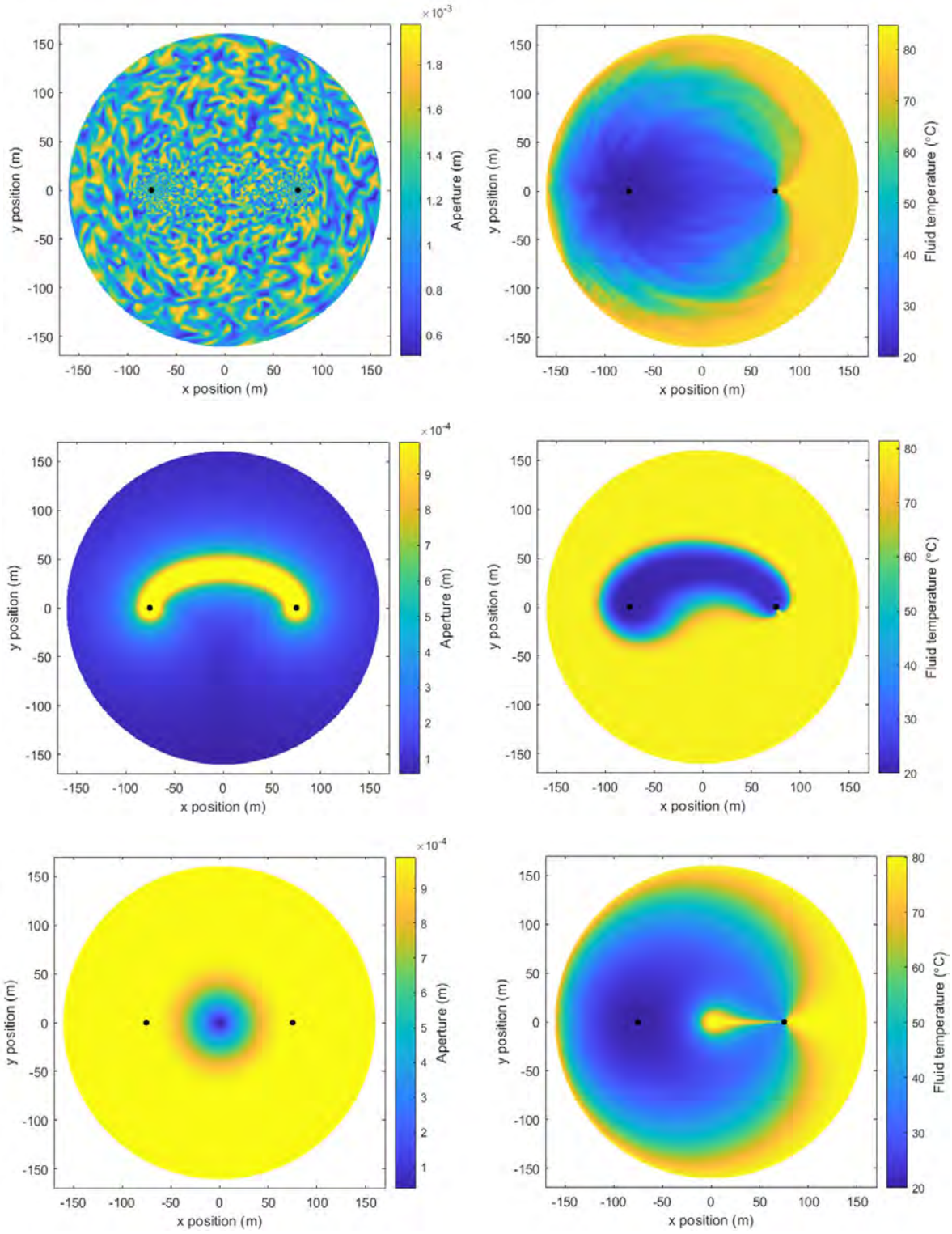

Figure 5: Fluid temperature field after 20 years (right column) for three additional aperture fields (left column): (case 2) random aperture (top), (case 3) high aperture flow path (middle), and (case 4) low aperture center blockage (bottom).

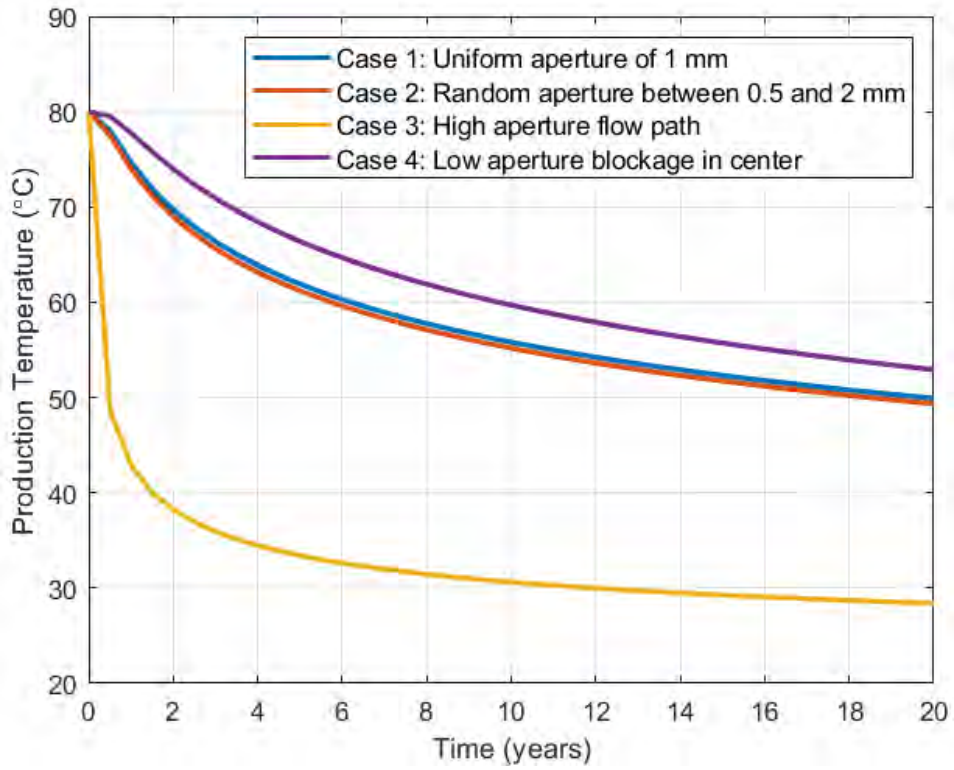

Figure 6: Production temperature profile for four aperture fields: (case 1) uniform aperture field (Figure 2), (case 2) random aperture field, (case 3) high aperture flow path, and (case 4) low aperture block in center. Corresponding aperture and temperature fields for cases 2, 3, and 4 are shown in Figure 5.

5. ResFrac Thermal-Hydraulic-Mechanical Simulations

5.1 LAS Data Processing

We utilized the commercial simulator ResFrac to explore hydraulic stimulation treatments and analyzed the corresponding thermal performance with long-term fluid circulation. We leveraged collected logging data from CUBO stored in a LAS file, provided as input to ResFrac. Figure 7 presents various logged properties with the entire profile shown on the left and the zoomed in profile for the bedrock shown on the right. The average values for the bedrock are provided as input to ResFrac, i.e., porosity of 3.9%, Young's modulus of 31 GPa, Poisson's Ratio of 0.32, and Biot coefficient of 0.58. A hydrostatic column is assumed for pore pressure with pressure gradient of 10.8 MPa/km.

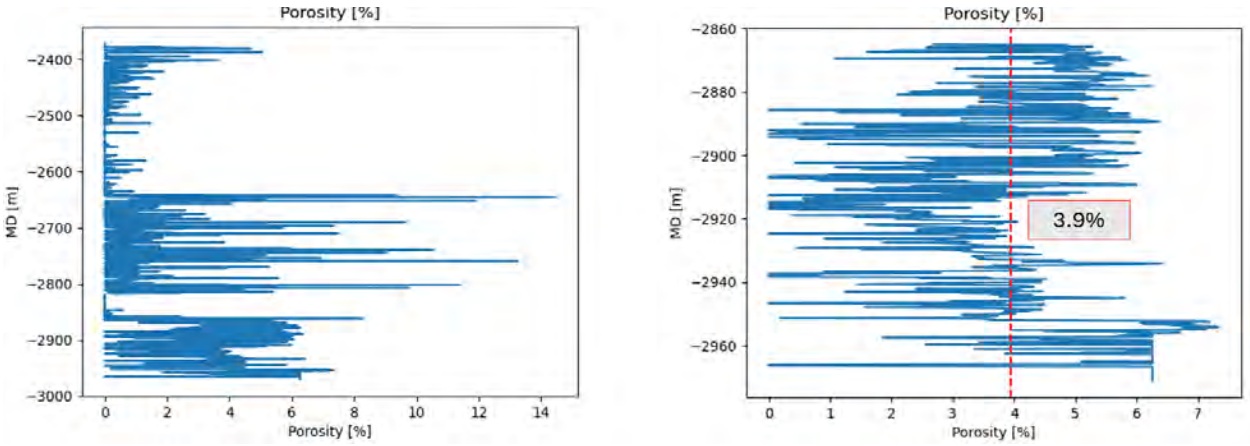
Porosity [%]
MD [m]
Porosity [%]
Porosity [%]
3.9%
MD [m]
Porosity [%]

(a)

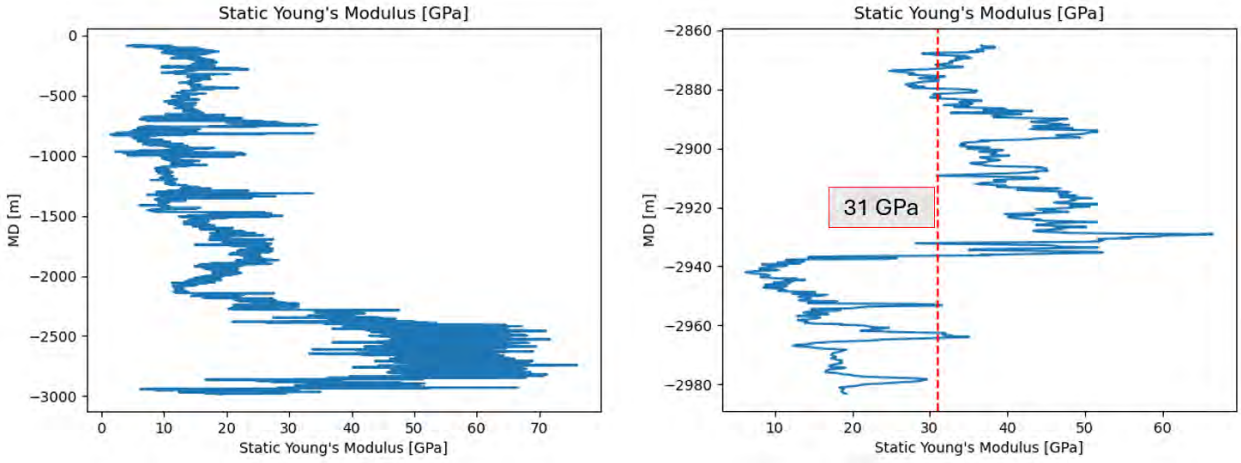
Static Young's Modulus [GPa]
MD [m]
Static Young's Modulus [GPa]
Static Young's Modulus [GPa]
31 GPa
MD [m]
Static Young's Modulus [GPa]

(b)

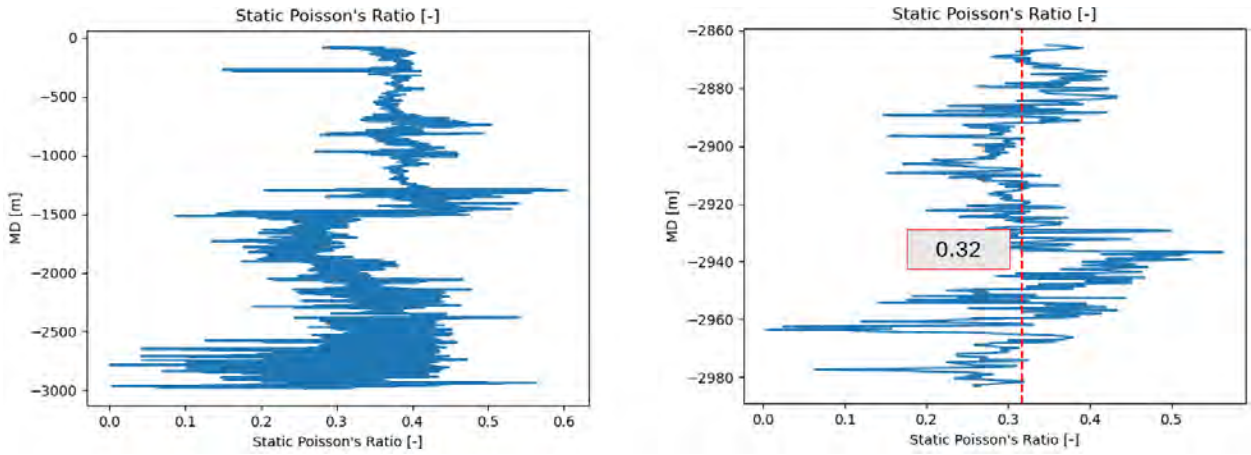
Static Poisson's Ratio [-]
MD [m]
Static Poisson's Ratio [-]
Static Poisson's Ratio [-]
0.32
MD [m]
Static Poisson's Ratio [-]

(c)

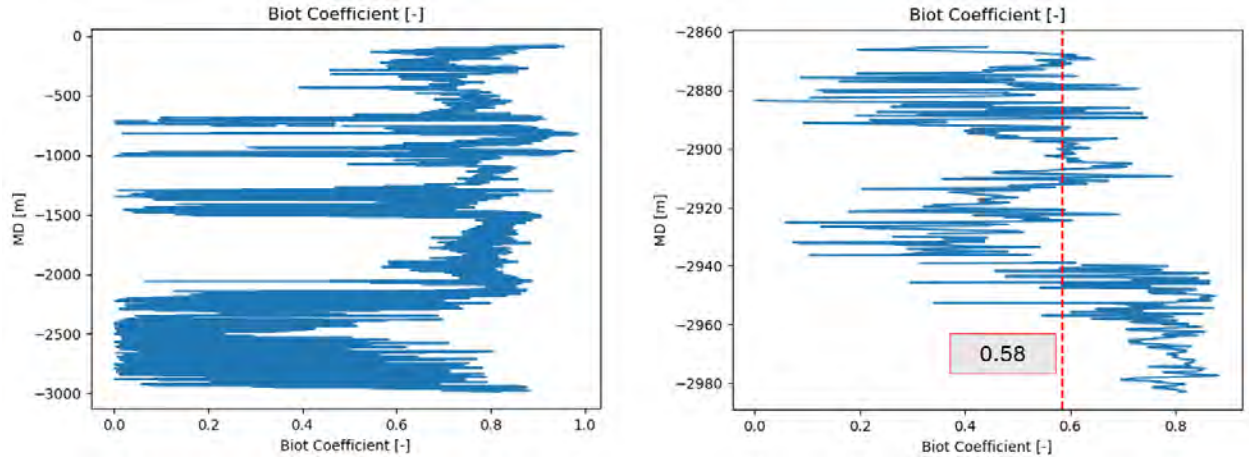

(d)

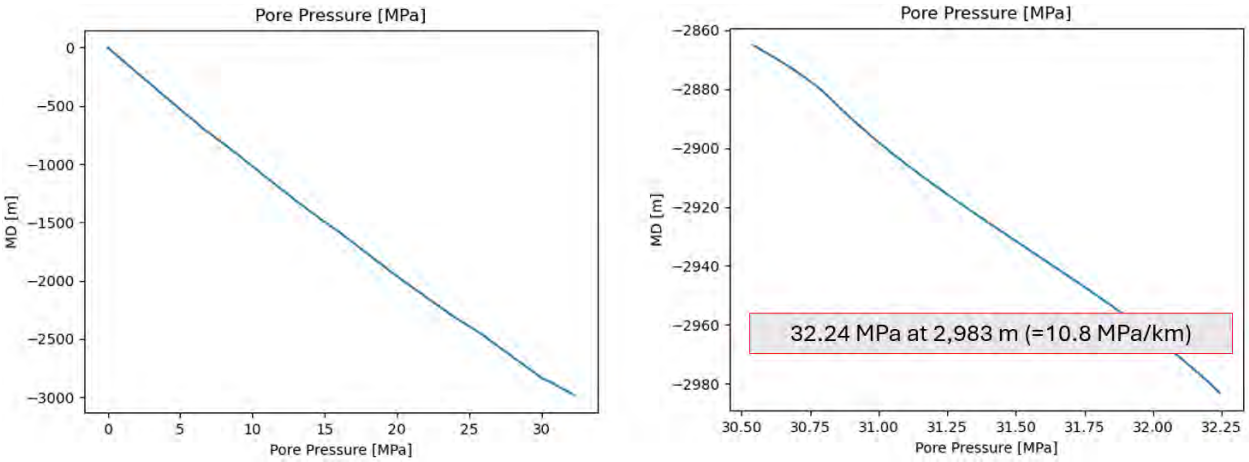

(e)

Figure 7: CUBO well LAS data for (a) porosity, (b) static Young's modulus, (c) static Poisson's ratio, (d) Biot coefficient, and (e) pore pressure. Plots on the left are for the entire well, and plots on the right are for the bottom part of the well in bedrock. Average values for bedrock are represented with red dashed lines and provided as input in ResFrac.

5.2 ResFrac Simulations

ResFrac simulations were conducted to design a potential hydraulic stimulation treatment and further explore the necessary number of fractures and fracture area to obtain long-term heat production with commercially acceptable thermal decline. Dozens of simulations were run considering different wellbore and stimulation designs. For this paper, we selected a promising case study with design parameters listed in Table 2 and simulation results presented in Figure 8. In this design, we considered 20 stages where each stage has five clusters, for a total of 100 fracture clusters. To save on computational time, only one stage was simulated using a no-flux condition as a domain boundary condition in between the stages. The injection and production lateral were spaced 150 m apart, the clusters were spaced 20 m apart, and we stimulated both laterals. The lateral length for each well is about 2 km. Stress field (with linear gradient) and uniform rock properties were specified using data from the wellbore logging (as stored in the LAS file; Section

5.1) and documented in Fulton et al. (2024). We limited the number of perforations per cluster to four and the perforation diameter to 0.01 m to enforce a sufficiently large pressure drop across the perforations, facilitating uniform fracture creation and uniform inflow across all fractures. The wellbore diameter was set to 0.18 m and the wellbore heat transfer coefficient to 50 $W/m^2/K$. We specified a matrix permeability multiplier of 10 when the pore pressure is 20 MPa above initial pore pressure in the matrix to account for effects such as small existing natural fractures opening at high pressures, causing increased leak-off. We used pure water instead of slickwater during stimulation and 100 mesh particles as proppants.

The production temperature for this design (Figure 8a) initially increases (due to diminishing wellbore heat losses) before dropping by about 5°C after 20 years. The production flow rate (Figure 8b) gradually increases to over 95% of the injection flow rate. Different designs such as a large wellbore field with alternating injection and production laterals may yield a smaller water loss rate. The injected proppant in all five fractures mostly settled in the bottom section of the fractures (Figure 8d), resulting in heat sweep of the hottest region of the fracture but also preventing fluid from accessing the entire fracture heat transfer area. Other treatments are currently being explored such as using proppants with smaller density or using slickwater instead of clean water during stimulation, which may result in a more uniform proppant distribution within the fractures. When simulating the same design with only 16 stages instead of 20 stages (i.e., 80 fractures instead of 100 fractures), the production temperature drops to 66°C after 20 years.

Table 2: Input parameters for preliminary base case design simulated with ResFrac.

Parameter	Value
Vertical depth of laterals	3 km
Lateral spacing	150 m
Fracture spacing	20 m
Rock density	2,800 kg/m^3
Rock specific heat capacity	1,000 J/kg/K
Rock thermal conductivity	2.8 W/m/K
Rock porosity	3.9%
Rock permeability	10^{-19} m^2
Rock initial temperature	81°C at 3 km depth
Minimum horizontal principal stress $S_{h,min}$	72 MPa at 3 km depth
Maximum horizontal principal stress $S_{h,max}$	108 MPa at 3 km depth
Vertical stress S_v	80 MPa at 3 km depth
Initial pore pressure	32 MPa at 3 km depth
Young's modulus	31 GPa
Biot coefficient	0.58
Poisson's ratio	0.32
Horizontal fracture toughness	2.2 MPa-m$^{1/2}$
Vertical fracture toughness	3.3 MPa-m$^{1/2}$
Rock thermal expansion coefficient	0.00001 1/°C
$E_{0,max}$	0.00027 m
90% closure stress	17 MPa
$E_{res,max}$	0.000001 m
Total number of fracture clusters	100
Stimulation treatment	Both injection and production well stimulated with 4 clusters per stage and 4 perforations per cluster. Injection sequence: 1. 10 min at 0.1 m^3/s (no proppant) 2. 80 min at 0.25 m^3/s with proppant (90 kg/m^3) 3. 80 min at 0.25 m^3/s with proppant (150 kg/m^3) 4. 10 min at 0.05 m^3/s (no proppant).
Long-term fluid flow rate	30 L/s
Long-term fluid injection temperature	30°C

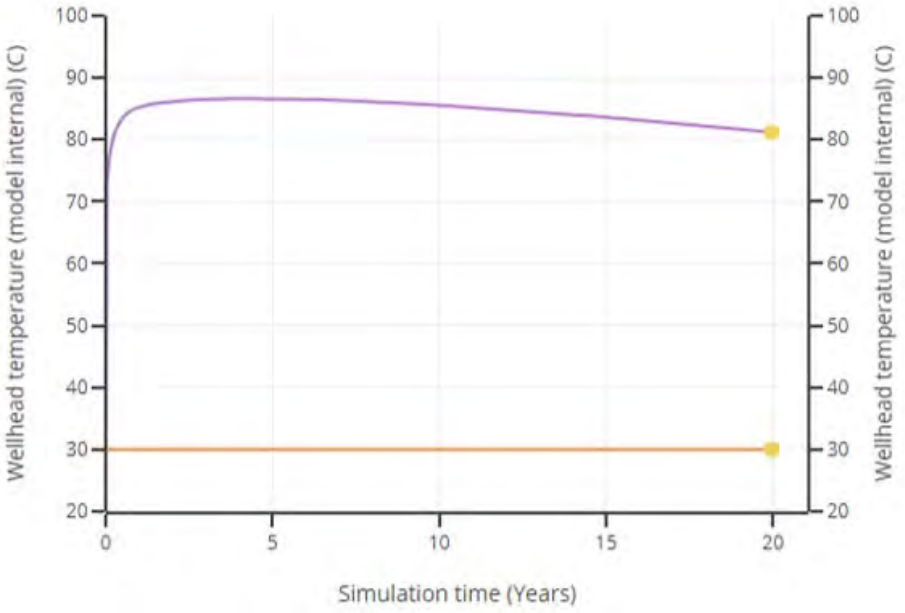
Wellhead temperature (model internal) (C)
100
90
80
70
60
50
40
30
20
0
5
10
15
20
Simulation time (Years)
Wellhead temperature (model internal) (C)

(a)

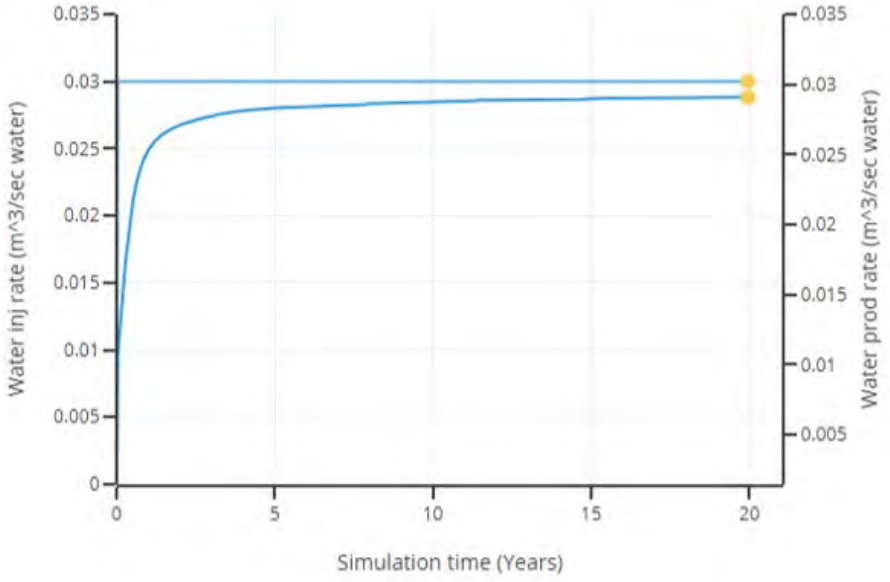
Water inj rate (m^3/sec water)
0.035
0.03
0.025
0.02
0.015
0.01
0.005
0
0
5
10
15
20
Simulation time (Years)
Water prod rate (m^3/sec water)

(b)

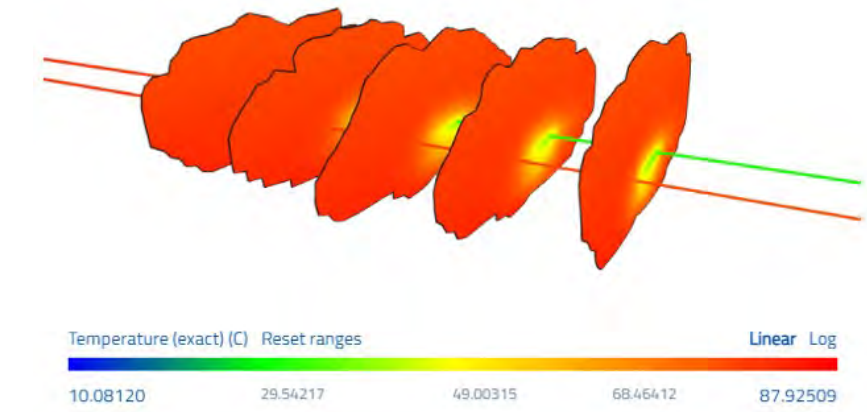

(c)

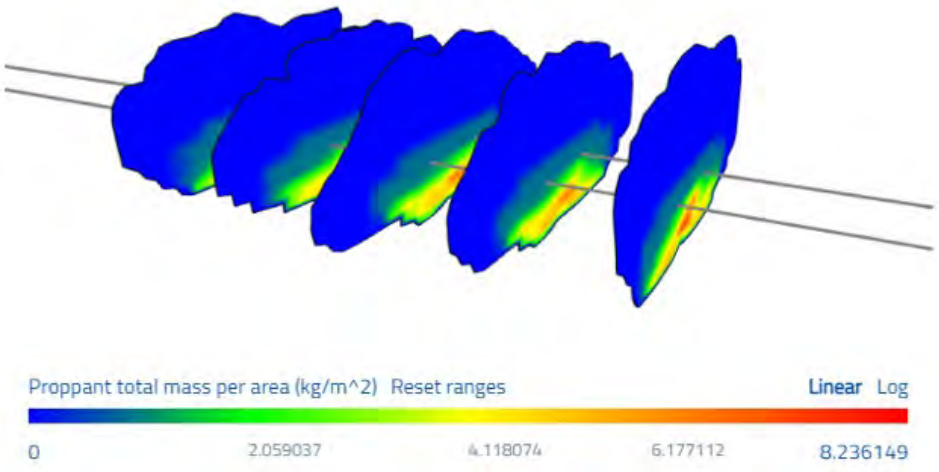

(d)

Figure 8: ResFrac Simulation Results. (a): Injection (orange) and production (purple) temperature profile; (b): injection and production flow rate (injection flow rate constant at 30 L/s); (c): fracture temperature distribution after 20 years; (d): proppant distribution after 20 years. Bottom figures have lateral extended by 10 times for better visibility of individual fractures.

6. Conclusions

In support of the Earth-Source Heat project at Cornell University, we conducted reservoir simulations to explore technical feasibility and design requirements of an EGS reservoir supplying 5 to 10 MW_{th} of heating to the university's district heating system. We applied three different simulators: (1) the thermal (T) Gringarten model, (2) the thermal-hydraulic (TH) FOXFEM simulator, and (3) the thermal-hydraulic-mechanical (THM) ResFrac simulator. We leveraged subsurface data obtained from the 3 km deep CUBO well drilled in 2022, including reservoir temperature, stress field, and thermo-physical properties.

Inspired by the recent EGS advancements, the EGS reservoir considered consists of an injection-production doublet at ~3 km vertical depth and ~2 km long horizontal laterals. The wells are spaced

about 100 to 150 m apart and connected with a network of ~100 vertical parallel fracture clusters. The initial rock temperature is 80°C, and water as heat transfer fluid is injected at 20° to 40°C and 30 to 50 L/s. Lower injection temperatures would require utilizing a heat pump for integrating with the existing district energy infrastructure.

The key study outcome, supported by all three simulators, is that, depending on injection temperature and flow rate, an *effective* heat transfer area on the order of 2 to 3 km^2 is required to provide 5 to 10 MW_{th} of heating continuously over 15 years with limited thermal decline. This total heat transfer area can be obtained with ~100 to ~150 fracture clusters where each fracture has an effective heat transfer area on the order of 20,000 m^2. ResFrac simulations indicate that stimulating both wells that are spaced 100 to 150 m apart with injecting proppants is a potential stimulation treatment to obtain a sufficiently large effective fracture heat transfer area. Previous work has shown that with today's drilling costs, integrating this doublet system with a heat pump into the existing district heating network has a cost-competitive levelized cost of heat on the order of $40/MWh (assuming 4.25% nominal discount rate).

Simulations with FOXFEM and ResFrac allowed quantification of the difference between fracture dimensions and effective fracture heat transfer area, as certain zones of the fracture may not be accessed by the circulating fluid. Reasons include flow not reaching the outer edges of the fracture, and preferential pathways within the fracture due to large aperture regions (e.g., proppants settling in the lower zone of the fracture.

Planned future modeling work includes conducting additional reservoir simulations to further explore sensitivity to subsurface conditions, including considering reservoir heterogeneity, different reservoir depths, and different wellbore designs. Further in-situ subsurface characterization is planned by deepening the CUBO well, installing permanent fiber, and running additional logs, stress field tests and flow tests. Finally, planning and design of a first doublet with horizontal laterals combined with multi-zone stimulation to provide heating to the campus is ongoing.

Acknowledgements

This work was authored in part by the National Renewable Energy Laboratory, operated by Alliance for Sustainable Energy, LLC, for the U.S. Department of Energy (DOE) under Contract No. DE-AC36-08GO28308. Funding provided by the U.S. Department of Energy Office of Energy Efficiency and Renewable Energy Geothermal Technologies Office. The views expressed herein do not necessarily represent the views of the DOE or the U.S. Government. The U.S. Government retains and the publisher, by accepting the article for publication, acknowledges that the U.S. Government retains a nonexclusive, paid-up, irrevocable, worldwide license to publish or reproduce the published form of this work, or allow others to do so, for U.S. Government purposes.

REFERENCES

Beckers, K.F., and McCabe, K. "GEOPHIRES v2.0: updated geothermal techno-economic simulation tool." *Geothermal Energy*, 7, (2019), 1-28.

Fox, D. "Thermal Hydraulic Modeling of Discretely Fractured Geothermal Reservoirs." Doctoral Dissertation, Cornell University, Ithaca, NY (2016).

Fulton, P., Clairmont, R., Fulcher, S., Pinilla, D., Purwamaska, I., Jamison, H., Fresonke, M., Puthur, R., Torres, J., Heaton, T., Beckers, K., Beyers, S., Bezner Kerr W., Bland, R., Erdinc, B., Olaf Gustafson, K., Carr, S., Sylvan, J., Fernandez, N., Jordan, T., and Tester, J. "Subsurface Insights from the Cornell University Borehole Observatory (CUBO): A 3km Deep Exploratory Well for Advancing Earth Source Heat Deep Direct-Use Geothermal for District Heating." *Proceedings, 49th Workshop on Geothermal Reservoir Engineering*, Stanford University, Stanford, CA (2024).

Gringarten, A.C., Witherspoon, P.A., and Ohnishi, Y. "Theory of heat extraction from fractured hot dry rock." *Journal of Geophysical Research* 80, no. 8, (1975), 1120-1124.

Hawkins, A.J. "Reactive tracers for characterizing fractured geothermal reservoirs." Doctoral Dissertation, Cornell University, Ithaca, NY (2017).

Macolm, R.I., and Beckers, K. "GEOPHIRES-X: An Object-Oriented Update to GEOPHIRES 2.0." *GRC Transactions* 47, (2023), 1573-1586.

Norbeck, J.H., and Latimer, T., "Commercial-scale demonstration of a first-of-a-kind enhanced geothermal system." Eartharxiv, (2023), https://doi.org/10.31223/X52X0B.

National Renewable Energy Laboratory (NREL), "GEOPHIRES-X", (2024), https://github.com/NREL/GEOPHIRES-X.

Tester, J., Gustafson, J.O., Fulton, P., Jordan, T., Beckers, K., and Beyers, S. "Geothermal direct use for decarbonization — progress towards demonstrating Earth Source Heat at Cornell." *Proceedings, 48th Workshop on Geothermal Reservoir Engineering*, Stanford University, Stanford, CA (2023).

Scaling and Thermal Penetration Depth in Enhanced Geothermal Energy Production

Sharat Chandrasekhar[(1)], P. V. (Suri) Suryanarayana[(2)], Udaya B. Sathuvalli[(1)], and Greg Asher[(2)]

[(1)] Blade Energy Partners

[(2)] Mazama Energy Inc

Keywords

Geothermal Wells, Multilaterals, Enhanced Geothermal Systems, Thermal Analysis

ABSTRACT

The thermal performance of an enhanced geothermal energy production system is analyzed. The system consists of a network of multilateral conduits which can be either drilled cylindrical holes or notionally rectangular ones generated by fractures. The steady state energy equation is coupled to that in the formation using a pseudo transient approach based on the Fourier Number. Expressions for the interface flux and penetration depth of the cold thermal front into the formation are developed for both drilled and fractured configurations. It is shown that the thermal performance of any multilateral or fracture-connected system can be characterized by a single parameter defined as the Number of Transfer Units (NTU), which is commonly used in heat exchanger analysis. The NTU in turn is proportional to the ratio of the Biot to Peclet numbers, and to the ratio of contact area to conduit area. Several examples are provided illustrating the approach. The results indicate that while the surface flux decays more rapidly in a planar (fractured) configuration, the significantly greater thermal contact area results in far superior thermal performance even after extended production times as large as 5 years.

1. Introduction

In recent years, a number of innovative concepts have been proposed to extract geothermal energy from hot dry resources. These include connecting multilaterals between injector and producer (Holmes, et al., 2021), thermal reach enhancement (Moncarz and Suryanarayana, 2022), closed loop geothermal (Beckers, et al., 2022), down-borehole exchange (all of which are increasingly referred to as Advanced Geothermal Systems, or AGS), and the classical Enhanced Geothermal Systems (EGS) that connect two (or more) wells through some form of fracturing or stimulation. The EGS approach has historically received the most attention and funding, since its beginnings in 1970s in Fenton Hill (Brown et al., 2012). The recent successes of Fervo (Norbeck, et al, 2023) and Utah FORGE (Allis and Moore, 2019) have brought EGS closer to reality. Both these demonstration projects were at temperatures around 200°C. More recently, the idea of using EGS in superhot rock (with resource temperatures greater than 375°C) has emerged as a viable and

scalable technique for the production of geothermal energy (US Department of Energy, 2024). Moncarz and Suryanarayana (2022) describe a novel AGS technique for exploiting superhot rock. The US DOE has recently increased its focus in this area by awarding a grant to Mazama Energy, to create EGS reservoirs in superhot rock.

All these methods involve the circulation of a working fluid through the fracture network in the resource to extract heat from the resource, which is then converted into electric power using an appropriate power cycle. The most commonly used working fluid is water.

Regardless of the concepts being proposed and tested, they all scale according to the parameters and properties governing heat transfer behavior in the resource. In this paper, we illustrate the heat transfer behavior of these systems using scaling parameters that govern the problem. It is shown that at pseudo-steady state, the non-dimensional temperature of the working fluid scales with the Biot number and a suitably defined Peclet number, as well as the ratio of the contact area to conduit area, thus encompassing all the parameters that govern heat transfer. The scaling curves provide a useful basis for comparing different heat extraction concepts, and for identifying improvements. It is shown that a single unified parameter known as the Number of Transfer Units, common in Heat Exchanger Analysis, can describe the thermal performance of practically any EGS or AGS.

One of the objectives of this study is to generalize the approach of the nearly 50-year-old study of Gringarten et al. (1975) who considered a network of very large (1 km^2) infinite planar fractures, and define a non-dimensional time parameter. While perhaps not practical at the time of their study, their results indicate the potential for substantial power generation with a properly constructed network of fractures in a hot dry resource.

Further, when extracting heat from hot, dry resources, depending upon the technique being used, the thermal penetration depth, and therefore, rate of thermal decline, vary. The thermal penetration depth is analogous to the drainage radius in oil and gas production. In this paper, we present a semi-analytical approach to determine the non-dimensional penetration depth, as a function of non-dimensional time (the Fourier number). Combining this with the scaling analysis above, we then investigate the expected thermal decline rate and the pseudo-steady state energy recovery for a number of examples. The notion of thermal recovery efficiency (analogous to the recovery factor in hydrocarbon reservoirs) is discussed in the context of these examples.

The authors believe that this work serves as a useful, generalized basis for quickly evaluating different thermal recovery concepts, and examining the impact of different modifications or improvements to heat recovery and recovery efficiency. This work complements the more sophisticated, but time-consuming, numerical simulations that are often used in literature to model heat recovery assurance. While it does not replace these numerical methods, it provides valuable insight into the thermal performance of different AGS and EGS systems.

2. Mathematical Model

Without loss of generality, an engineered “heat exchanger” created in a geothermal resource can be represented by two wellbores in the resource connected by one to several lateral conduits. The conduits can represent a single closed loop (as in a Closed Loop Geothermal System, or CLGS), a connected multilateral system, or a pair of wells connected by fractures. Figure 1 (left panel) shows a notional closed loop geothermal well with two vertical wellbores connected by a multilateral

system consisting of several widely spaced horizontal conduits of specified length and diameter, as indicated in the figure. An example of this concept is presented by Holmes et al. (2021).

The network can also consist of several fractures connecting the two vertical wells, as shown in the right panel of Figure 1. In this case, the fractures are assumed to be notionally rectangular with specified thickness (typically 3—5 mm), length, and height (breadth) of the planar fracture. Length and breadth are usually of the order of 100 m. Although the figure shows two vertical wells connected by planar fractures, the orientation of the wellbores and fractures can be arbitrary, as long as the fractures have constant width.

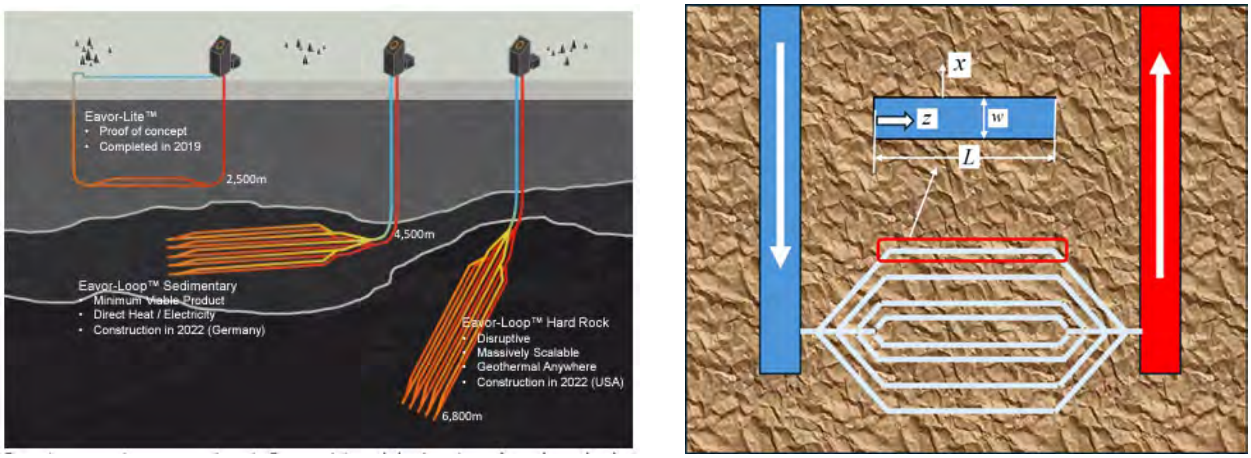

(a) Drilled Multilaterals **(b) Fractured Multilaterals**

Figure 1: Multilateral Configurations connecting two Vertical Wellbores.

The key geometrical parameters of the two types of connectivity are shown in Figure 2. Since the width b of the fractured multilaterals is generally several orders of magnitude larger than the thickness w, the hydraulic diameter can be approximated as $D_h \approx 2w$.

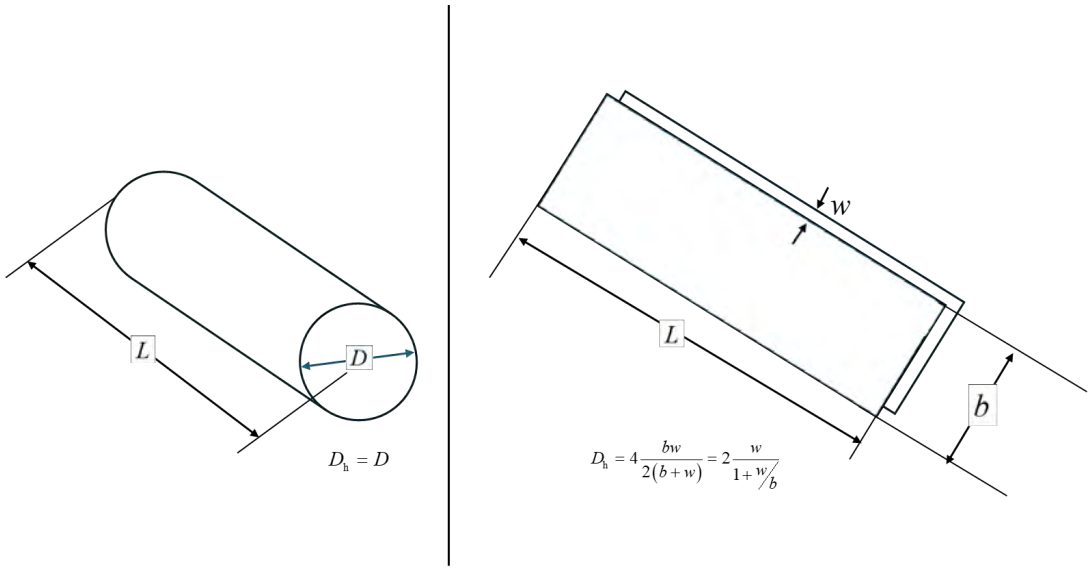

Figure 2: Geometry of a single Cylindrical (Drilled, Left) and Planar (Fractured, right) Conduit.

2.1 Governing Equations

Consider hydrodynamically fully developed flow in each horizontal conduit segment in Figure 1, under which the following assumptions are valid:

1. The resource is homogeneous, with constant thermophysical properties,
2. The flow is one-dimensional, with no thermophysical property variations or phase change in transverse directions (the implications of property variations or phase change on the scaling are discussed in the appendix),
3. The diameter of each conduit, or the width (aperture) of each fracture, is constant,
4. The sensible heat approach allows the enthalpy gradient to be represented by temperature and pressure gradients,
5. Transients are relegated to the formation and hence only to the conduit-formation interface flux, and
6. There is no thermal interference between individual conduits or fractures.

With the above assumptions, the quasi-steady (or pseudo-steady) non-conservative form of the transport equations of mass, momentum (Navier-Stokes), and energy in cylindrical coordinates reduce to

$$\frac{\mathrm{d}\dot{m}_\mathrm{c}}{\mathrm{d}z} = \frac{\mathrm{d}\dot{m}}{\mathrm{d}t}0 \Rightarrow V = \frac{\dot{m}}{\rho A_\mathrm{f}} \tag{1}$$

$$\frac{\mathrm{d}P}{\mathrm{d}z} = -\frac{1}{2} f \rho \frac{V^2}{D_\mathrm{h}} \tag{2}$$

and

$$\rho c_{\mathrm{p}} V \frac{\mathrm{d}T}{\mathrm{d}z} - \rho c_{\mathrm{p}} c_{\mathrm{JT}} V \frac{\mathrm{d}P}{\mathrm{d}z} = \frac{\dot{Q}(\bar{t})}{A_{\mathrm{f}}} \tag{3}$$

where the mass flow rate in each lateral conduit is the global mass flow rate divided by the number of conduits i.e., $\dot{m} = \dot{m}_{\mathrm{G}} \big/ N_{\mathrm{c}}$, and A_f is the conduit flow area. The heat flux $\dot{Q}(\bar{t})$ at the wellbore-formation evaluated at some snapshot $\bar{t}$ is obtained from the solution of the transient transverse formation heat diffusion problem. The friction factor can be evaluated in terms of the flow Reynolds number and the conduit relative roughness as

$$f = f\left(\mathrm{Re}, \frac{\varepsilon}{d}\right) = f\left(\frac{\rho V D_{\mathrm{h}}}{\mu}, \frac{\varepsilon}{d}\right) \tag{4}$$

from one of the many explicit forms of the Colebrook-White equation. The heat flux term $\dot{Q}(\bar{t})$ can also be expressed in terms of the instantaneous formation temperature gradient for drilled cylindrical multilaterals as

$$\dot{Q}(\bar{t}) = 2\pi h \frac{D}{2}\left(T_{\mathrm{W}} - T\right) = 2\pi R k_{\infty} \left.\frac{\partial T}{\partial r}\right|_{r=R} (z, \bar{t}) = 2\pi \bar{U}(\bar{t})\left(T_{\infty} - T\right) \tag{5}$$

and in the case of rectangular fractures, as

$$\dot{Q}(\bar{t}) = 2hb\left(T_{\mathrm{W}} - T\right) = 2bk_{\infty} \left.\frac{\partial T}{\partial x}\right|_{x=w} (z, \bar{t}) = 2\bar{U}(\bar{t})\left(T_{\infty} - T\right) \tag{6}$$

where the factor of 2 arises from the flux on each side of the rectangular conduit. In each case, the overall heat transfer conductance $\bar{U}$ relates the instantaneous heat flux at any axial location to the temperature difference between the undisturbed formation (T_∞) and the flowing stream (T).

The energy equation above is subject to the horizontal conduit inlet boundary condition

$$T(0) = T_{\mathrm{in}} \tag{7}$$

A set of dimensionless entities can be defined as

$$\xi = \frac{z}{L} \qquad\qquad \theta = \frac{T_{\infty} - T}{T_{\infty} - T_{\mathrm{in}}} \tag{8}$$

Accordingly, the energy equation can be expressed in non-dimensional form as

$$\frac{\mathrm{d}\theta}{\mathrm{d}\xi} = \Lambda - \Gamma\theta \tag{9}$$

where the frictional heating parameter (also known as the pressure gradient parameter) is

$$\Lambda = \frac{c_{\mathrm{JT}} L}{\left(T_{\infty} - T_{\mathrm{in}}\right)} \frac{\mathrm{d}P}{\mathrm{d}z}, \tag{10}$$

and

$$\Gamma = 2\pi^n \frac{\bar{U}L}{\dot{m}c_{\mathrm{p}}} = 2\pi^n \frac{\bar{U}}{k} \frac{kL}{\dot{m}c_{\mathrm{p}}} \tag{11}$$

The parameter Γ will be apparent to those familiar with heat exchanger analysis as the *Number of Transfer Units.* The index n is equal to 1 and 0 for cylindrical and planar geometries. The importance of this parameter is discussed in a later section.

With the above nondimensionalization, the boundary condition is

$$\theta(0) = 1 \tag{12}$$

In Appendix 1, it is shown how the *Number of Transfer Units* is also the governing parameter for the general case with variable thermophysical properties in an enthalpy-based formulation of the transport equation that is valid across trans-critical, supercritical and two-phase regimes.

2.2 Conduit Surface Flux

At any snapshot in time, the conduit surface flux represents the thermal interaction between the flowing stream, the conduit and the formation. Appendix 2 shows the mathematical details of the estimation of this flux, in terms of a dimensionless flux multiplier. For cylindrical geometry, the flux multiplier is given by

$$F(\tau) = \mathrm{L}^{-1}\left[\frac{1}{\sqrt{s}}\frac{K_1\left(\sqrt{s}\right)}{K_o\left(\sqrt{s}\right)}\right]\begin{cases} = \dfrac{1}{\sqrt{\pi\tau}}, & \tau \le 0.001, \\ \approx 10^{\sum_{k=0}^{5} p_k (\log_{10}\tau)^k}, & \tau > 0.001 \end{cases} \tag{13}$$

And for the planar geometry, the flux multiplier is

$$F(\bar{\tau}) = \left(\sqrt{\pi\tau}\right)^{-1} \tag{14}$$

These flux multipliers are pseudo-transient, in that they are functions of the nondimensional time

$$\tau = \left[\frac{4n}{D^2} + \frac{(1-n)}{w^2}\right]\alpha_\infty t \tag{15}$$

where n = 0 is for planar geometry, and n = 1 is for cylindrical geometry. but are evaluated at a snapshot in time.

The flux multiplier is useful when streamwise temperature variation at different time snapshots (elapsed time) is of interest. For each time snapshot, the flux multipliers can be evaluated, from which the conduit surface heat flux can be estimated. As a result, depending upon the case, a decay in outlet temperature can be seen as time progresses. This decay is an important result in determining the long-term performance of the system.

2.3 Thermal Penetration Depth

As the working fluid extracts thermal energy from the resource, the resource rock cools in the vicinity of the conduit. The thermal penetration depth is the normal distance from the conduit

centerline at which the resource temperature recovers to its undisturbed initial temperature. Thermal penetration depth affects heat extraction by the flowing fluid and decay in exit temperature with time. In Appendix 3, we describe how thermal penetration depth is calculated in this work, for both the cylindrical and planar geometries.

Figure 3 shows the normalized penetration depth as a function of the Fourier number, for the two geometries. It is seen that at large Fourier numbers (large times), the penetration depth in a planar configuration is larger. This suggests a more rapidly diminishing surface heat flux in a planar configuration, as compared with a cylindrical configuration. It also implies that a larger volume of the resource rock participates in the heat transfer, leading to higher cumulative thermal energy extraction. In both cases, the rate of increase of the penetration depth decreases logarithmically with time, suggesting that a pseudo-steady state approximation for the penetration depth is appropriate. Nevertheless, it should be noted that thermal penetration continues to evolve with time, and a true steady state is not achieved within the typical timeframes of interest (20-50 years).

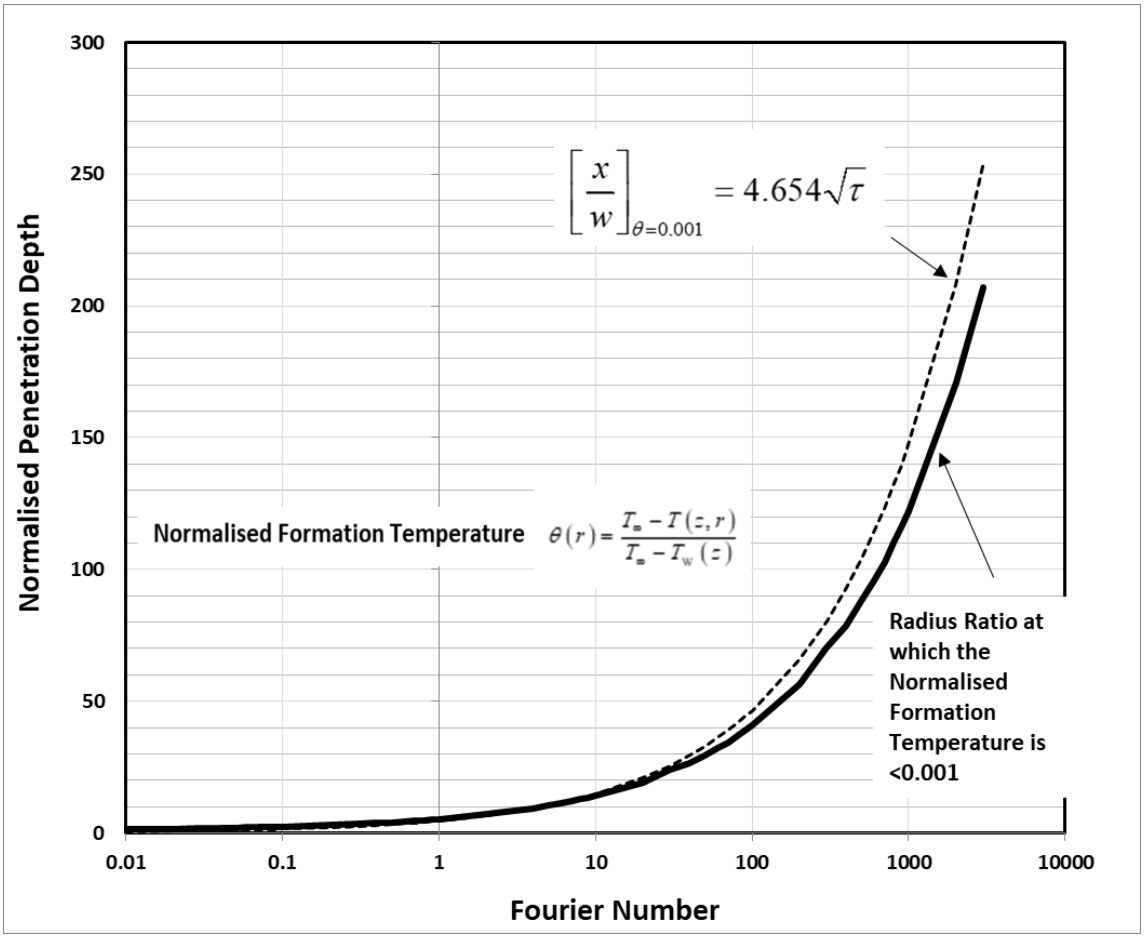

Figure 3: Thermal Penetration Depth as a function of the Fourier Number.

2.4 Temperature Field

Integration of Eq. (9) subject to the boundary condition in Eq. (12) leads to

$$\theta(\xi) = e^{-\Gamma\xi} - \frac{\Lambda}{\Gamma}\left(1 - e^{-\Gamma\xi}\right) \tag{16}$$

A plot of the dimensionless exit temperature θ (i.e., at $\xi = 1$) versus the Number of Transfer Units Γ is shown in Figure 4 for various values of the pressure gradient parameter Λ. Note that in order to facilitate an intuitive understanding of an increasing exit temperature with Γ, what is plotted in the figure is actually $1 - \theta_{\xi=1}$. It is seen that except for very large values of Λ (greater than 0.1) the exit temperature can be very accurately approximated as

$$\theta_{\xi=1} = e^{-\Gamma} \tag{17}$$

The negative Joule-Thomson effect is in evidence at Λ = 0.1, as a result of which the exit temperature is slightly higher than the undisturbed geothermal. This is similar to the phenomenon seen in prolific high pressure, high temperature hydrocarbon producer wells in which the arrival temperatures are often higher than the static bottom hole temperature. In the present context, this is purely academic, since the actual pressure gradients are substantially lower, rendering Λ values typically << 0.1.

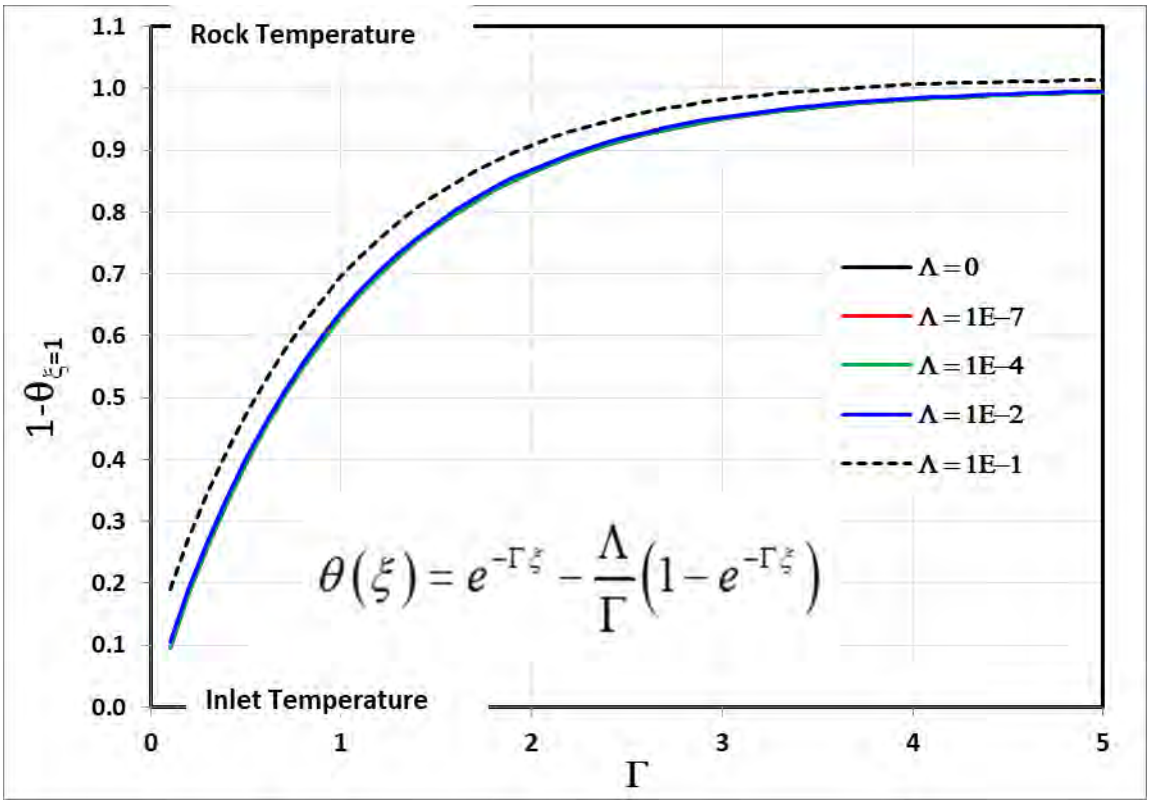

Figure 4: Dimensionless Exit Temperature as a function of the Number of Transfer Units (Γ) and the Pressure Gradient Parameter (Λ.)

2.5 Characterization of the Number of Transfer Units

An important result from this work is that the Number of Transfer Units (NTU) emerges as the key scaling parameter. It is therefore instructive to examine the Number of Transfer Units in the context of the operating parameters. We note that Eq. (11) can be written as

$$\Gamma = 2\pi^n \frac{k}{\rho V P c_p} \frac{\bar{U}}{k_\infty} \frac{k_\infty}{k} \frac{LP}{A_f} = 2\pi^n \frac{k}{\rho V P c_p} \frac{\bar{U}}{k_\infty} \frac{k_\infty}{k} \frac{A_c}{A_f} = 2\pi^n \frac{\mathrm{Bi}}{\overline{\mathrm{Pe}}} \frac{k_\infty}{k} \frac{A_c}{A_f} \tag{18}$$

where the Peclet and Biot numbers are

$$\overline{\mathrm{Pe}} = \frac{\rho V P c_p}{k} \tag{19}$$

and

$$\mathrm{Bi} = \frac{\bar{U}}{k_\infty} \tag{20}$$

and the product A_c of the conduit length and perimeter is the thermal contact area. It is more convenient to describe the Peclet number in terms of the key conduit dimension rather than the perimeter. Accordingly for the planar geometry, we have

$$\overline{\mathrm{Pe}} = 2\frac{\rho V w c_p}{k}\left(1+\frac{b}{w}\right) = \left[2\left(1+\frac{b}{w}\right)\right]\mathrm{Pe}_w \tag{21}$$

and for the cylindrical geometry,

$$\overline{\mathrm{Pe}} = \pi\frac{\rho V D c_p}{k} = \pi\mathrm{Pe}_D \tag{22}$$

Substitution into Eq. (18) results in

$$\Gamma = \gamma\frac{\mathrm{Bi}}{\mathrm{Pe}}\frac{k_\infty}{k}\frac{A_c}{A_f} \tag{23}$$

where

$$\gamma = \begin{cases} \dfrac{w}{w+b}, & \text{Planar Geometry} \\ 2, & \text{Cylindrical Geometry} \end{cases} \tag{24}$$

We see three important nondimensional groupings in the above equation: the ratio of the Biot number (*Bi*) to the Peclet number (*Pe*), the ratio of the formation conductivity to fluid conductivity, and the ratio of the thermal contact area (A_c) to the fluid flow area (A_f). The Number of Transfer Units (Γ) is *directly* proportional to the Biot number, the ratio of the areas, and the ratio of the conductivities. It is *inversely* proportional to the Peclet number (*Pe*). Since the higher the Γ, the more effective the thermal recovery (the higher the return temperatures), any strategy to improve

thermal recovery has to necessarily increase Γ. This can be achieved by increasing the area ratio (for example, increasing the contact area while reducing flow area), the conductivity ratio (for example, enhancing effective formation thermal conductivity), or *Bi*, or by reducing *Pe* (for example, by increasing the number of connecting conduits or fractures). In a previous work (Suryanarayana, et al, 2023), the authors have noted the importance of reducing *Pe* to increase the nondimensional exit temperature. This work expands upon this notion, and shows that NTU (Γ) is the fundamental governing nondimensional parameter for EGS and AGS.

2.6 Relationship to the nondimensional time parameter of Gringarten et al (1975)

It is interesting to note that the nondimensional time parameter t'_D defined by Gringarten et al (1975) is related to the NTU (Γ) of this work. In terms of the nomenclature of this study, their t'_D can be written as

$$t'_{\mathrm{D}} = \frac{\left(\rho c_{\mathrm{p}}\right)^2}{k_\infty \rho_\infty c_{\mathrm{p}_\infty}} \left(\frac{\dot{q}}{bz}\right)^2 t \tag{25}$$

setting $z = L$ at the conduit exit, and noting that $\dot{m} = \rho \dot{q}$ leads to

$$t'_{\mathrm{D}} = \left[\frac{k_\infty}{\rho_\infty c_{\mathrm{p}_\infty}} \frac{c_{\mathrm{p}}}{k_\infty} \frac{\dot{m}}{Lb^2} t\right] \frac{\dot{m} c_{\mathrm{p}}}{k_\infty L} = \left[\tau \frac{w^2}{b^2}\right] \left(\frac{\dot{m} c_{\mathrm{p}}}{k_\infty L}\right)^2 \tag{26}$$

Substitution of the definition

$$\frac{\bar{U}}{k_\infty} = \frac{b}{w} \frac{1}{\sqrt{\tau}} \tag{27}$$

into Eq.(26) results in

$$t'_{\mathrm{D}} = \left(\frac{\dot{m} c_{\mathrm{p}}}{\bar{U} L}\right)^2 = \Gamma^{-2} \tag{28}$$

leading to the key observation that the dimensionless time in the study of Gringarten et al. (1975) is effectively the inverse square of the NTU as defined in this study ($t'_D = 1/\Gamma^2$). Furthermore, if as Gringarten et al. (1975) did, internal thermal resistance is neglected at the conduit/formation interface (effectively Nu → ∞), then Eq. (27) is identical to Eq. (47) with the exception of the multiplier $\pi^{-1/2}$ of τ. The significance of this term however disappears at the large times considered in this study.

It is more intuitive to present the results in terms of NTU, as done in this work, as the different nondimensional groupings that control the thermal behavior are readily apparent, and make physical sense. Further, as we shall see, for a given system, NTU changes with time, which is important to observe when evaluating a given system.

Figure 4 is a useful representation of thermal recovery from EGS and AGS systems, and allows quick comparison of different systems. The basic approach is to calculate the NTU corresponding

to any given system, and read off the corresponding nondimensional temperature from Figure 4. In this manner, different concepts or modifications to concepts can be quickly evaluated.

3. Results and Discussion

We now examine a few EGS and AGS concepts using the above theory. In what follows, we present the results first in dimensional terms to provide physical context, and finally present them in nondimensional terms (Figure 4) to enable comparative assessment.

3.1 Cylindrical Drilled Multilaterals

Table 1 indicates a configuration with a 6000 m total lateral length. This mimics the connected multilateral system described in Holmes et al, (2021). A total of 5 laterals each with a diameter of 8.5 in are considered. With the assumed geothermal gradient of 0.08°C/m, the static rock temperature at the resource depth of 4500 m is 360°C. All thermophysical properties are evaluated at a reference temperature taken to be the average of the rock temperature and the specified inlet temperature of 100°C. The reference pressure is merely the hydrostatic pressure of pure water at the resource depth. For a specified mass flow rate of 20 kg/s, the estimation of all of the parameters leading to the pressure gradient parameter Λ and the Number of Transfer Units Γ are also shown. The pressure gradient parameter is several orders of magnitude lower than the Number of Transfer Units thereby justifying the use of the solid curve in Figure 4.

Table 1 Parameter Estimation with Drilled Multilaterals

Wellbore Parameters		Diameter (m)	0.2159		
# Laterals	5	Hydraulic Diam (m)	0.2159	Relative Roughness	9.41E-03
Length (m)	6,000	Flow Area (m^2)	3.66E-2	Aspect Ratio	27,790
Diameter (in.)	8.500	Perimeter (m)	0.6783	Prandtl Number	0.826
Resource Depth (m)	4500	Thermal Contact Area (m^2)	4,070		
		Reference Pressure (MPa)	44	Reynolds Number	1.87E+5
		Resource Temperature (°C)	360	Friction Factor	0.0375
Operational Parameters		Reference Temperature (°C)	230	Nusselt Number	356
Mass Flow Rate (kg/s)	20.0			Biot Number	0.231
Inlet Temperature (°C)	100	**Thermophysical Properties**		k-Ratio	2.967
Flow Duration (hrs)	10000	Density (kg/m^3)	861	Area ratio	1.11E+05
		Viscosity ($Pa.s^{-1}$)	1.26E-4	Geometry factor	2.000
Formation Properties		Specific Heat (J/kg-K)	4,409	τ	2.47E+03
Thermal Conductivity (W/m-K)	2.00	Thermal Conductivity (W/m-K)	0.674	F(τ)	0.23205
Thermal Diffusivity (m^2/sec)	8.00E-07	Joule-Thomson Coefft (m^2K/N)	-8.90E-8	U/k	0.686
Geothermal Gradient (°C/m)	0.08	Thermal Diffusivity (m2/s)	1.78E-7	Pe	1.54E+05
Roughness (in.)	0.08			Ac/Af.U/k	24,266
		Time Constant (s)	1.46E+4		
		Velocity (m/s)	0.127	Γ	**0.988** (NTU)
		Pressure Gradient (N/m^3)	-1.2	Λ	**2.47E-6**

The temperature variation along the conduit length is plotted in Figure 5 for different operating times. For each of these times, the Fourier number can be calculated from Eq. (48) from which the pseudo-transient conduit surface flux is approximated. There is decay with time, which appears to be stabilizing as physical time approaches 1 year, with the exit temperature dropping by about

25%. Figure 6 shows similar exit temperature curves, this time for a single lateral, as in classical closed-loop systems. Compared to Figure 5, the decay is more pronounced.

Figure 7 compares the decay of the exit temperature for a classical single-lateral closed-loop system with the five multilateral system discussed above. The figure starkly demonstrates the rapid decay of the single-lateral system, log scale of time notwithstanding, and underlines the need for long single laterals, or multiple laterals to obtain reasonable declines. This rapid decay of a single-lateral system was also remarked upon by Beckers, et al. (2022).

It is worth noting that the NTU reduces with time in both cases, and will approach a near-constant value at long times. More importantly, note that the NTU for the five-lateral system is an order magnitude higher than the single-lateral case, implying better thermal recovery.

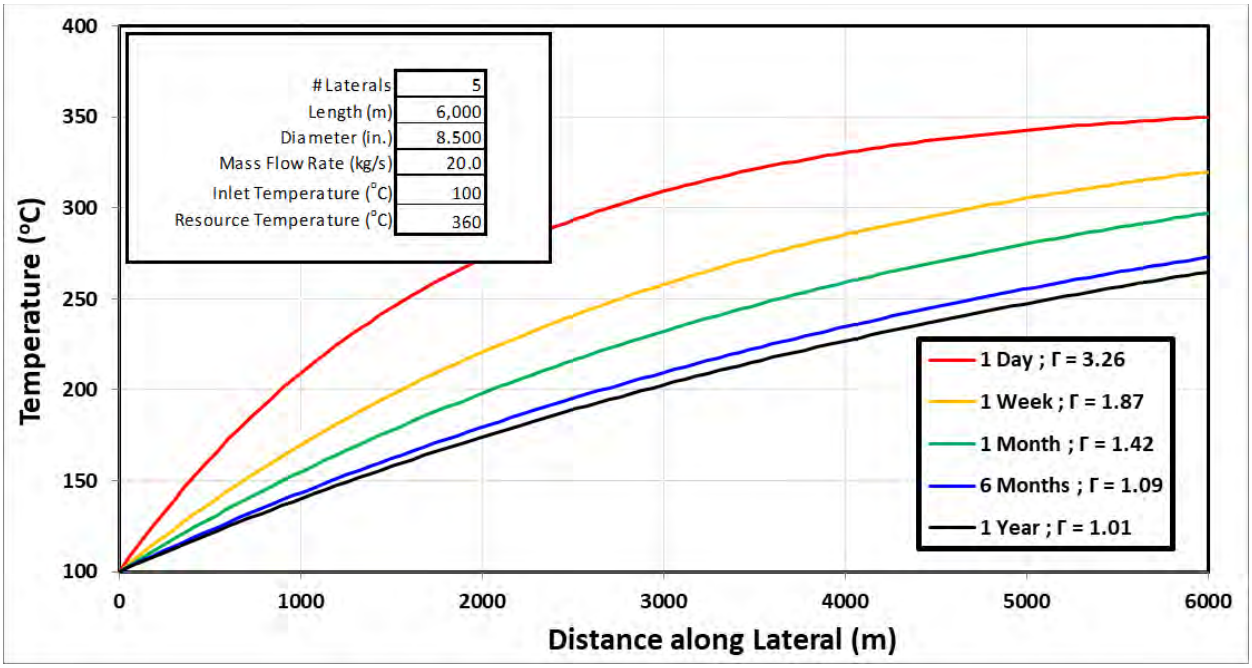

Figure 5: Streamwise Temperature Profiles at various operating times – 5 Drilled Multilaterals.

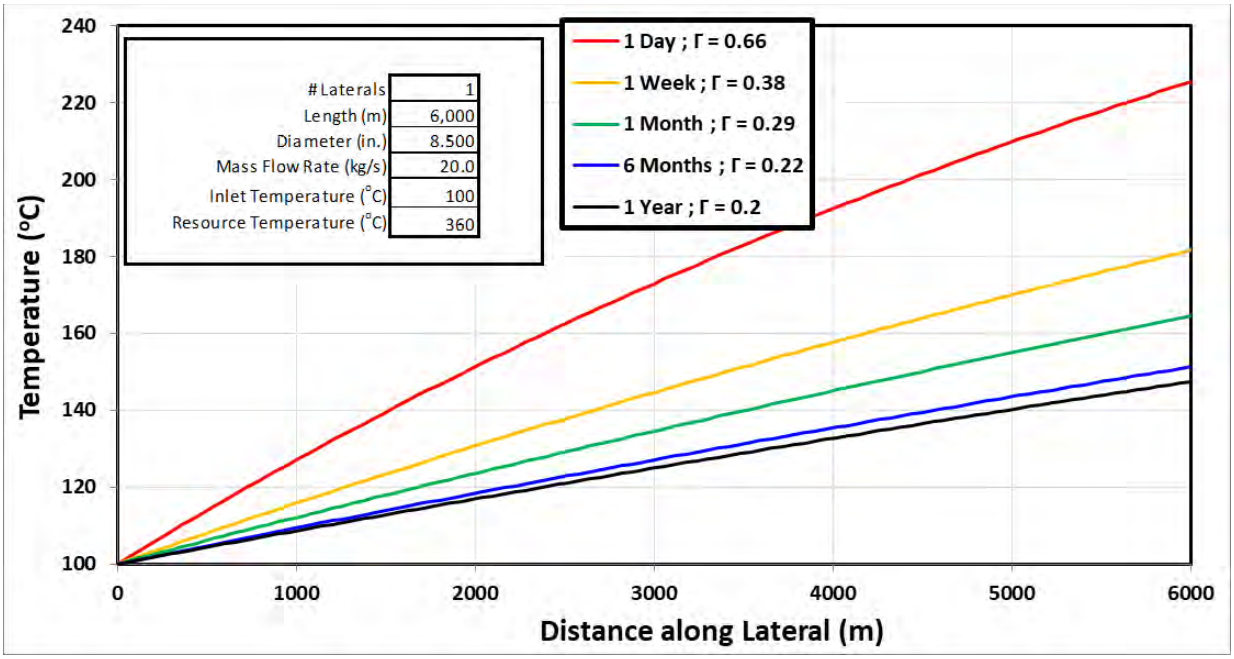

Figure 6: Streamwise Temperature Profiles at various operating times – 1 Drilled Multilateral.

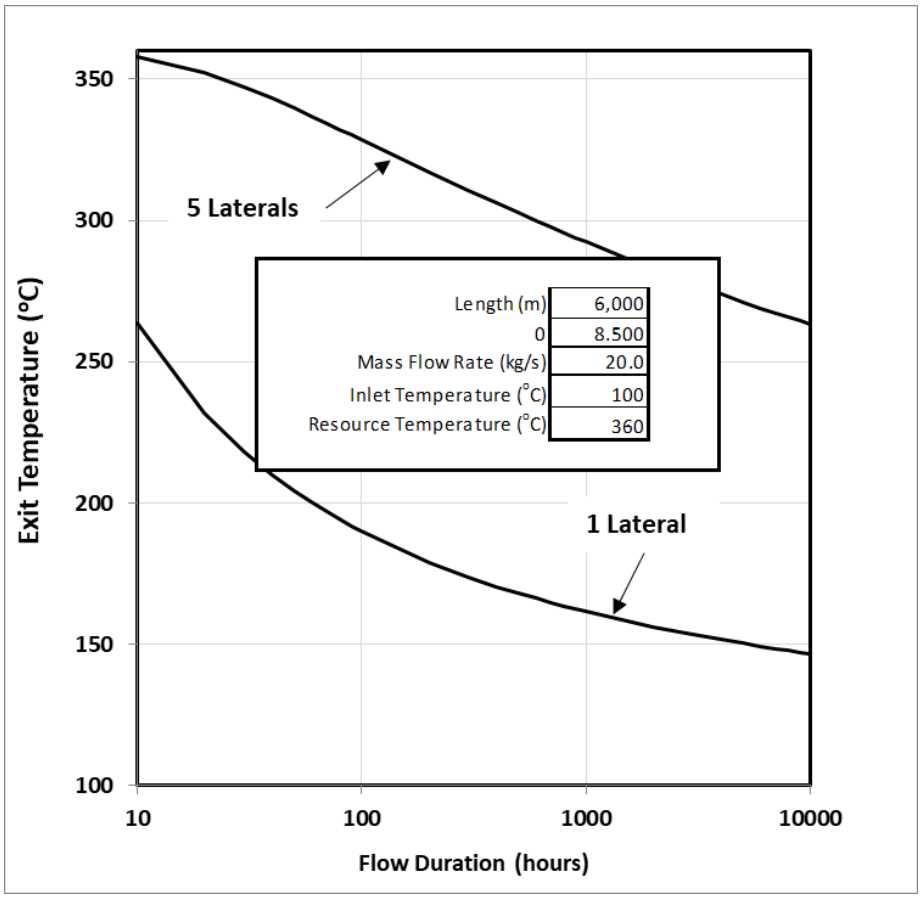

Figure 7: Decline of Exit Temperature with Time – 20 kg/s through 1 and 5 laterals.

3.2 Multiple Planar Fractures

In a planar configuration where several planar conduits caused by fracturing connect two vertical wellbores, the distance between wellbores is limited from practical considerations to 100 m. A total of 100 fractures, each of width 3 mm is assumed. The other parameters are exactly as in the case of cylindrical drilled multilaterals.

The temperature decay with time in the case of planar fractures is much lower than in the case of drilled multilaterals as evidenced in Figure 8. What is clear is that the greater contact area in the case of fractured multilaterals more than adequately compensates for the higher decay rate of the flux with time. Even after a 5-year producing period, the exit temperature at the given flowrate is still at the initial resource temperature. We also see that increasing the inter-wellbore distance is beneficial, with 70 m being a minimum in the case shown to avoid decline after 5 years. Also note the much higher values of NTU.

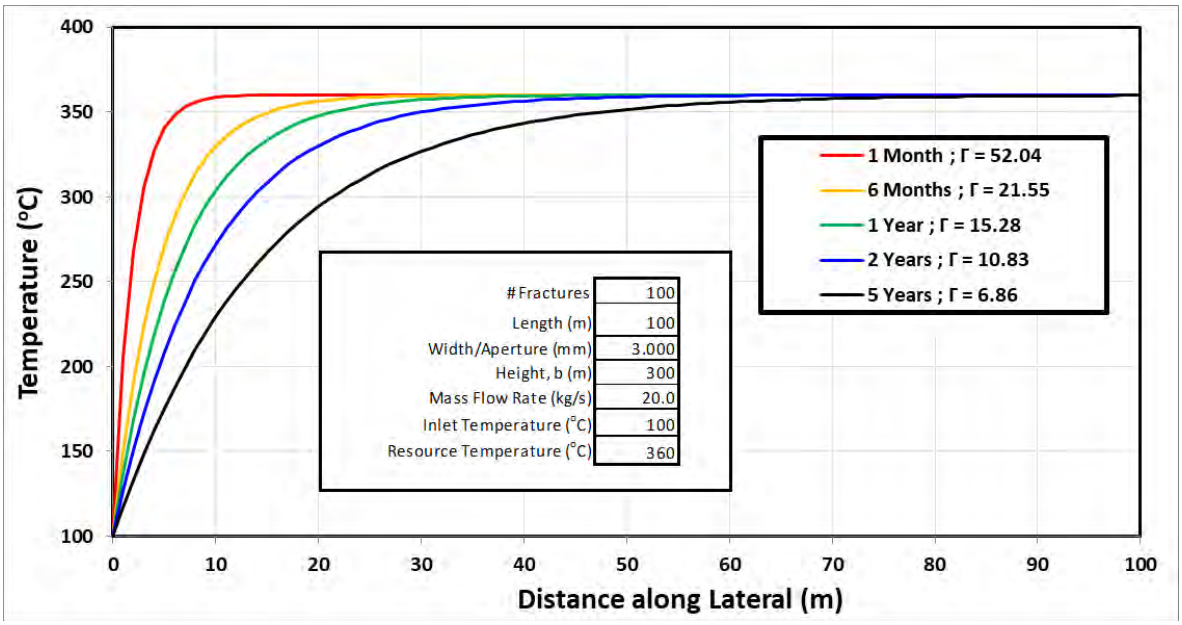

Figure 8: Streamwise Temperature Profiles at various operating times – 100 Planar Fractures at a Resource Temperature of 360 °C.

Figure 9 shows that with fewer planar fractures (in this case, five), thermal decay is more pronounced, implying that higher number of connected fractures is more beneficial to thermal recovery with lower rate of decline. This is in line with the conclusions of Gringarten, et al (1975).

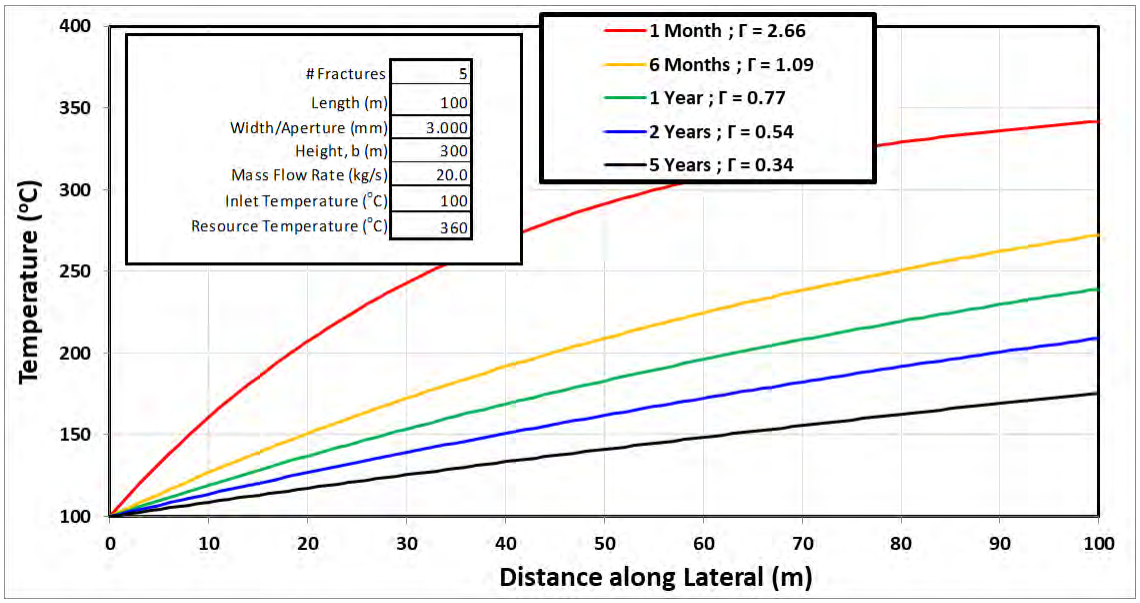

Figure 9: Streamwise Temperature Profiles at various operating times – 5 Planar Fractures at a Resource Temperature of 360 °C.

The effect of global mass flow rate - i.e., the total mass flow rate through all of the fractures is shown in Figure 10 at the end of an operating period of 5 years. This is for the 100 fractures case. Only for mass flow rates greater than 50 kg/s does the exit temperature drop substantially below undisturbed geothermal (resource temperature), indicating a respectable power generation capability. Further, the figure suggests that mass flow rates can be managed with time according to exit temperature or exit enthalpy constraints in practical systems.

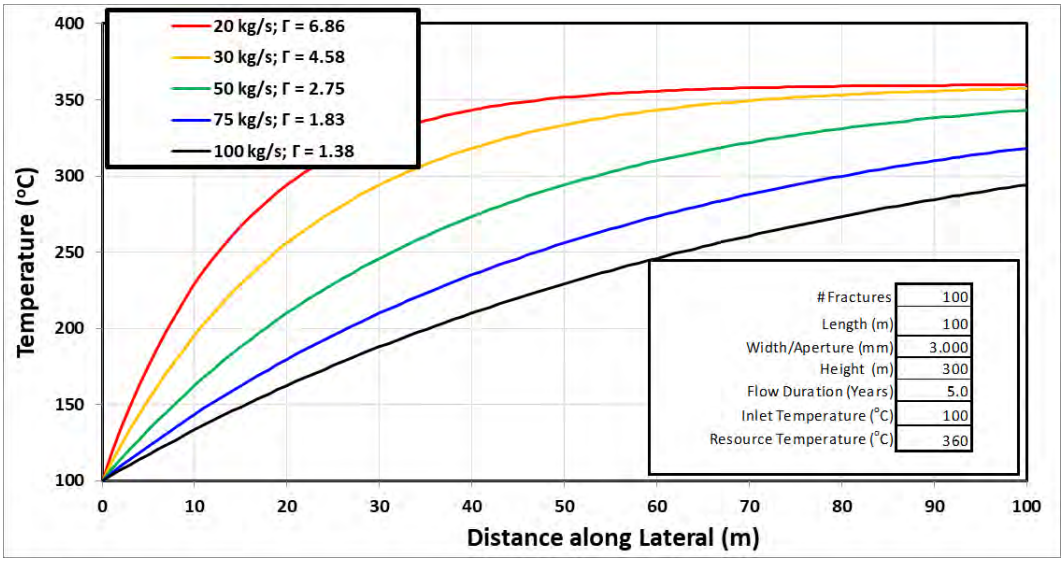

Figure 10: Streamwise Temperature Profiles at various Mass Flow Rates after 5 years – 100 Planar Fractures at a Resource Temperature of 360 °C.

Returning our attention to the scaling curve, the different operating scenarios evaluated in this work, corresponding to both cylindrical conduits and planar fractures, are indicated on the universal exit temperature vs NTU curve as shown in Figure 11. It should be noted that the mass flow rate has been kept constant in this illustration. In actual applications, the mass flow rate can be optimized for different extraction methods.

Any EGS or AGS concept not covered in this limited study can be similarly placed on this graph to assess its thermal performance. Likewise, the impact of modifications in flow rates, geometries, or thermal properties can be examined by calculating the NTU and using the graph to estimate the exit temperature.

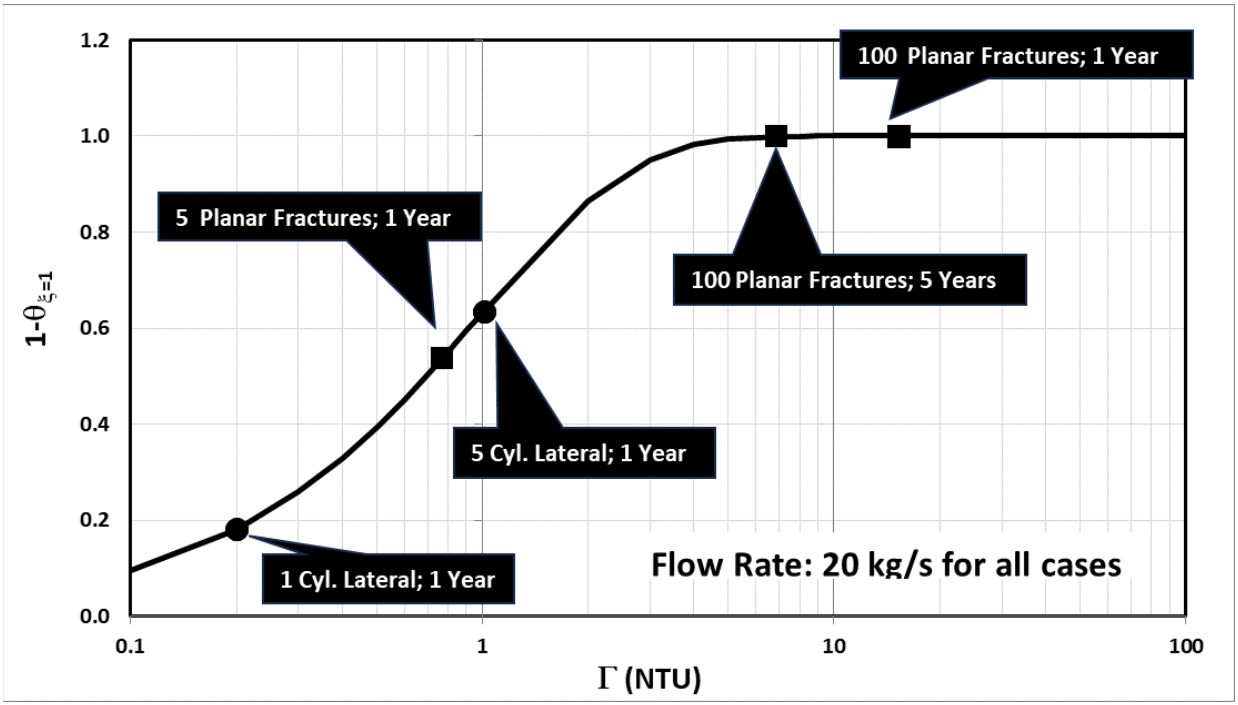

Figure 11: Various Operating Scenarios Superimposed on the Universal Exit Temperature vs Number of Transfer Units Curve.

3.3 Superhot Rock EGS – Illustrative Example

As noted in the introduction, there is increasing interest in the creation of EGS reservoirs within superhot rock (SHR, > 375°C) resources. In order to examine the thermal recovery from such systems, we look at an illustrative example. In this example, the following assumptions are made:

- Resource Temperature = 400 C
- Inlet temperature into the fracture network = 100 C
- Working Fluid is water
- Total Mass Rate = 50 kg/s
- Duration of Interest = 20 years
- Number of planar connecting fractures = 10 and 100
- Distance between Wells (Fracture Length) = 100 m
- Fracture height = 300 m
- Fracture width (aperture) = 3 mm
- Pressure gradient parameter is much less than 0.1

The streamwise thermal performance of this hypothetical system is shown in Figure 12 (10 fractures) and Figure 13 (100 fractures), in physical units, as a function of time. The transient surface flux term is calculated from the Fourier number corresponding to these times. With only

10 fractures (Figure 12), rapid decline is evident even after just a year. This is primarily because of the short distance between wellbores. The available contact area with ten fractures is not adequate to compensate for this. In order to arrest the decline, either the mass flow rate has to be reduced, or the distance (fracture length) has to be increased. However, with 100 fractures, for a significant length of time (2-5 years), we can see that the exit temperature is practically the same as the resource temperature (ignoring any production well heat loss). Clearly, the higher the number of connected fractures, the greater the thermal recovery. For completeness, we note that in order to create a large number of connected fractures, multi-stage fracturing of long deviated or horizontal wells may be required.

Even for the 100-fractures case, the exit temperature decays with time for long time, implying that the exit enthalpy will reduce with time. The reduction after 20 years (compared to the resource temperature) is not as drastic as in the drilled multilateral systems discussed earlier, and is about 20%. Still, it is not negligible, and should be considered in specific applications. Field development plans and operational strategies may need to manage either the number of wells or flow rates to maintain either a constant exit temperature or constant exit enthalpy over time, depending upon the design of the surface power facilities. Increasing the distance between the wellbores (fracture lengths) will also improve thermal performance. While detailed assessment of development strategies and operational management is beyond the scope of the current work, it serves to illustrate the need for more detailed analyses to support these activities.

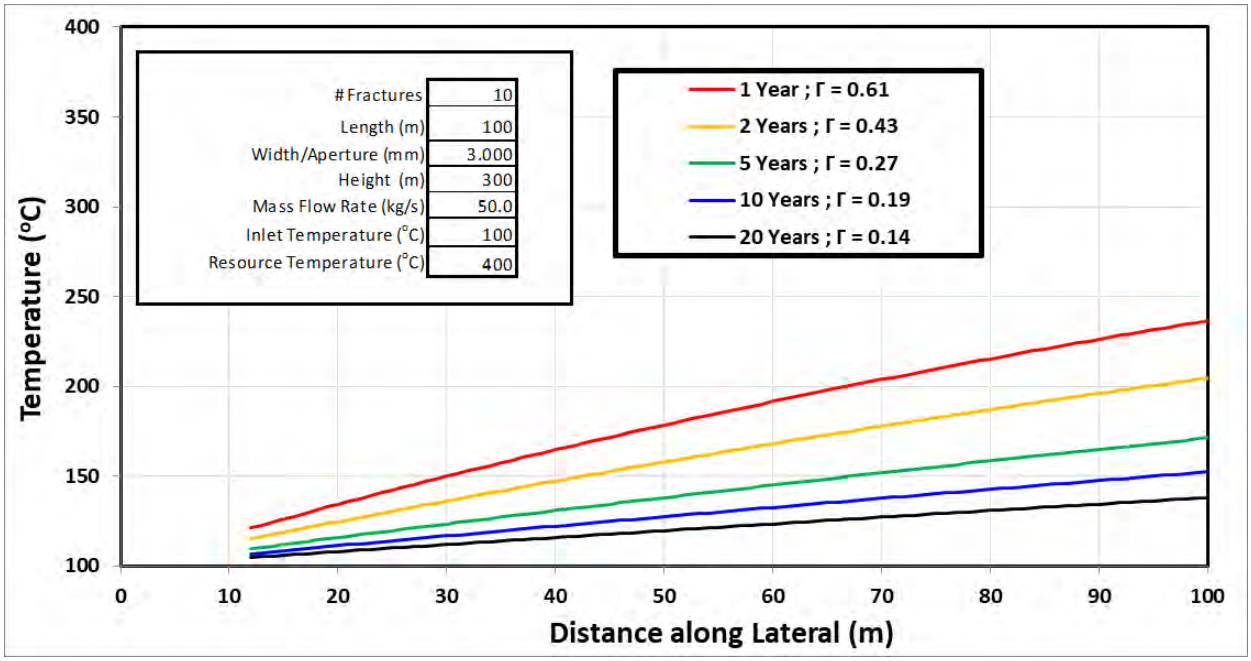

Figure 12: Streamwise Temperature Profiles at various operating times – 10 Planar Fractures at a Flow Rate of 50 kg/s and a Resource Temperature of 400°C.

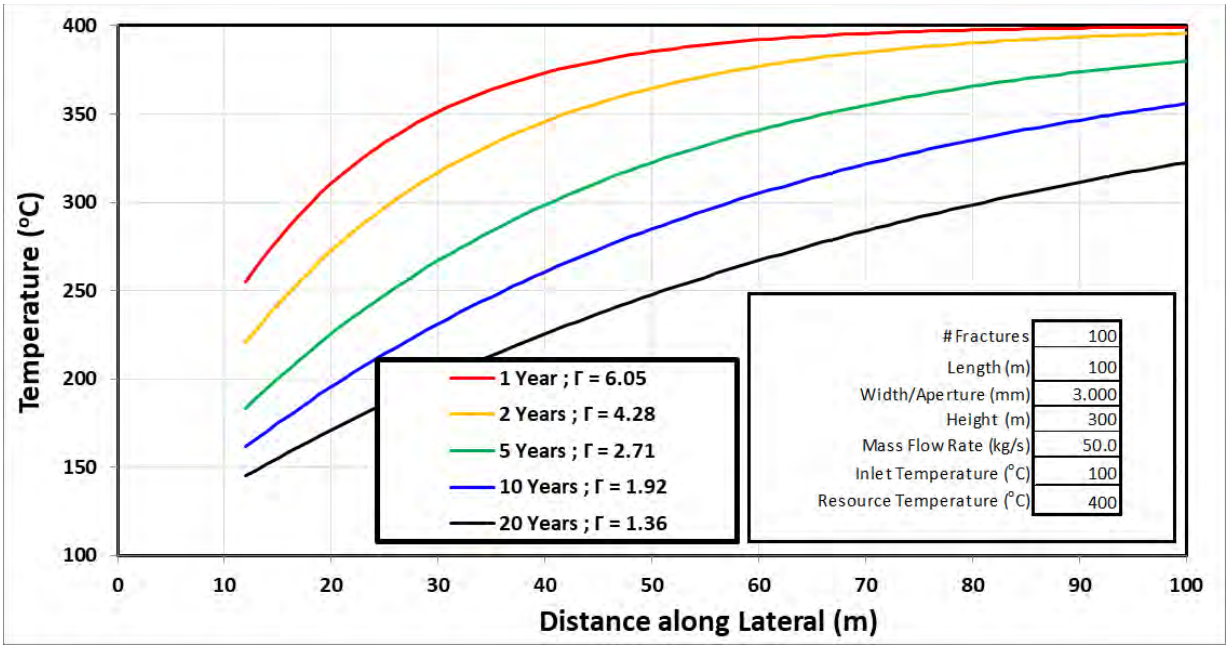

Figure 13: Streamwise Temperature Profiles at various various operating times – 100 Planar Fractures at a Flow Rate of 50 kg/s and a Resource Temperature of 400°C.

4. Conclusions

The thermal performance of enhanced (or engineered) geothermal energy production systems is analyzed in this study using a scaling approach. The system consists of a network of multilateral conduits which can be either drilled cylindrical holes or notionally rectangular planar fractures. The steady state energy equation is coupled to that in the formation using a pseudo transient approach based on the Fourier Number. Expressions for the interface flux and penetration depth of the cold thermal front into the formation are developed for both drilled and fractured configurations. It is shown that the thermal performance of any multilateral or fractured system can be characterized by a single parameter Γ, the Number of Transfer Units (NTU). NTU is a parameter that is commonly used in heat exchanger analysis. Therefore, it is not surprising that it emerges as the key scaling parameter here, as in essence, extraction of heat from hot, dry rock requires the creation of a heat exchanger in the resource.

The NTU is proportional to a) the ratio of the Biot to Peclet numbers; b) the ratio of the formation thermal conductivity to the fluid conductivity; and c) the ratio of the thermal contact area to flow area. In order to improve thermal recovery, NTU has to be maximized over the intended service life of a project. This can be achieved by designing and operating the extraction systems such that the above ratios are maximized.

Several examples of AGS and EGS concepts are provided to illustrate the main points of this work. Results indicate that while the surface flux decays more rapidly in a planar (fractured) configuration, the significantly greater thermal contact area results in far superior thermal performance even after extended production times as large as 5 years, particularly in superhot rock resources. Finally, it is shown that superior thermal performance and lower decline is possible with superhot rock EGS, especially when a large number of connected fractures can be created.

The scaling analysis and curves presented here are universal, and can be used to evaluate different concepts for heat extraction from hot dry rock resources. The authors hope that this work will be useful to quickly evaluate different heat extraction concepts, and to assess the impact of any modifications or improvements to the design or operation of such systems.

Acknowledgement

The authors thank the management of Mazama Energy for funding the work leading to this paper, and for allowing its publication. The authors are also grateful to Dr Ismail Ceyhan for his detailed review of the paper and his comments for improvement.

REFERENCES

R. Allis, and J. N. Moore, 2019, Geothermal Characteristics of the Roosevelt Hot Springs System and Adjacent FORGE EGS Site, Milford, Utah, Utah Geological Survey.

Beckers, K.F., Rangel-Jurado, N., Chandrasekar, H., Hawkins, A.J., Fulton, P.M., and Tester, J.W., 2022, "Techno-Economic Performance of Closed-Loop Geothermal Systems for Heat Production and Electricity Generation", *Geothermics*, v. 100, p. 102318.

Brown, D., Duchane, D., Heiken, G., and Hriscu, V., 2012, Mining the Earth's Heat: Hot Dry Rock Geothermal Energy, Springer

Carslaw, H. S., and Jaeger, J. C., Conduction of Heat in Solids, Oxford Clarendon Press, 1959.

Chandrasekhar S. Revisiting the Classical Problem of Transient Temperature Prediction in Complex Deepwater Wellbores with a New Semi-Analytical Approach", SPE/IADC Paper 199653. Galveston, TX , March 3--5, 2020.

Gringarten, A. C., Witherspoon, P. A., and Ohnishi, Y., 1975, "Theory of Heat Extraction from Fractured Hot Dry Rock", *Journal of Geophysical Research*, Vol 80, N0. 8, 1975.

Holmes, M., Toews, M, Jenkins, J., and Sepulveda, N., 2021, Multilateral Closed-Loop Geothermal Systems as a Zero Emission Load-Following Resource, GRC Transactions, Vol. 45.

Moncarz, P. D., and Suryanarayana, P. V., 2022, "Harvesting GeoHeat and the Impact of Enhancing Thermal Reach on Energy from Hot Dry Rock", United States Military Academy Special Colloquium on Computational Engineering Mathematics, West Point, October 21-22

Norbeck, J., Latimer, T., Gradl, C., Agarwal, S., Dadi, S., Eddy, E., Fercho, S., Lang, C., McConville, E., Titov, A., Voller, K., and Woitt, M., 2023, "A Review of Drilling and Stimulation of a Horizontal Geothermal Well System in North Central Nevada", 48th Stanford Geothermal Workshop, February 6-8, 2023.

M. N. Özisik, 1993, Heat Conduction, 2nd Edition, J. Wiley & Sons.

H. J. Ramey, Jr., 1962, "Wellbore Heat Transmission", SPE Paper 96, March 1962.

Suryanarayana, P. V., Chandrasekhar, S. V., and Asher, G., 2023, "A Review of Recent Concepts for Geothermal Energy Extraction with Focus on Thermal Reach", 3rd Philippine International Geothermal Conference, Manila, The Philippines.

US Department of Energy, "Pathways to Commercial Liftoff: Next-Generation Geothermal Power", Public Report, March 2024

APPENDIX 1

The quasi-steady state energy equation can also be cast in terms of the enthalpy derivative as

$$\rho V \frac{\mathrm{d}h}{\mathrm{d}z} = \frac{2\pi \bar{U}}{A_\mathrm{f}} \left(T_\infty - T \right) \tag{29}$$

subject to the boundary condition

$$h(0) = h\left(P_\mathrm{in}, T_\mathrm{in} \right) \tag{30}$$

where P_in and T_in are the inlet pressure and temperature. The momentum equation remains

$$\frac{\mathrm{d}P}{\mathrm{d}z} = -\frac{1}{2} f \rho \frac{V^2}{D_\mathrm{h}} \tag{31}$$

subject to its boundary condition

$$P(0) = P_\mathrm{in} \tag{32}$$

Temperature is extracted from enthalpy and pressure according to

$$T = T\left(P, h \right) \tag{33}$$

and the constitutive models for the overall heat transfer conductance and friction factor are as previously described in the body of the paper. If we define a reference conductance in terms of inlet properties as

$$\bar{U}_* = k_* \left[\frac{2}{\mathrm{Nu}_*} + \frac{1}{F(\tau)} \frac{k_*}{k_\infty} \right]^{-1} \tag{34}$$

and introduce the following set of dimensionless variables

$$\begin{aligned} \omega &= \frac{h - h(0)}{c_{\mathrm{p}_*} \left(T_\infty - T_\mathrm{in} \right)} \\ \xi &= \frac{z}{L} \\ \theta &= \frac{T_\infty - T\left(P, h \right)}{T_\infty - T_\mathrm{in}} \\ \phi &= \frac{\bar{U}}{\bar{U}_*} \end{aligned} \tag{35}$$

then the energy equation and its boundary condition are transformed to

$$\frac{\mathrm{d}\omega}{\mathrm{d}\xi} = \left[\frac{2\pi\bar{U}_{*}L}{\dot{m}c_{\mathrm{p}_{*}}}\right]\phi\theta = \Gamma_{*}\phi\theta$$
$$\omega(0) = 0 \tag{36}$$

The term Γ_{*} is the Number of Transfer Units defined in terms of inlet properties. As in the sensible heat formulation, the terms ω, θ, and ϕ are all of Order One. While Eq. (36) is not amenable to a closed form solution, it can be integrated numerically along the conduit in conjunction with a thermophysical property database[1] to yield profiles of enthalpy and hence temperature along the conduit. The velocity at any streamwise location is determined in accordance with mass conservation from

$$V = \frac{\dot{m}}{\rho A_{\mathrm{f}}} \tag{37}$$

For a flow that remains in the subcritical regime, which is typical of most operating scenarios, Figure 14 shows that despite the substantial thermophysical property variation along the conduit, the temperature profiles predicted by both the sensible-heat and enthalpy formulations are practically identical.

In a trans-critical flow scenario, with the operating pressure (and temperature) close to the critical pressure (and temperature), the differences in the predicted temperature profiles are more significant as shown in Figure 15.

[1] like NIST's REFPROP

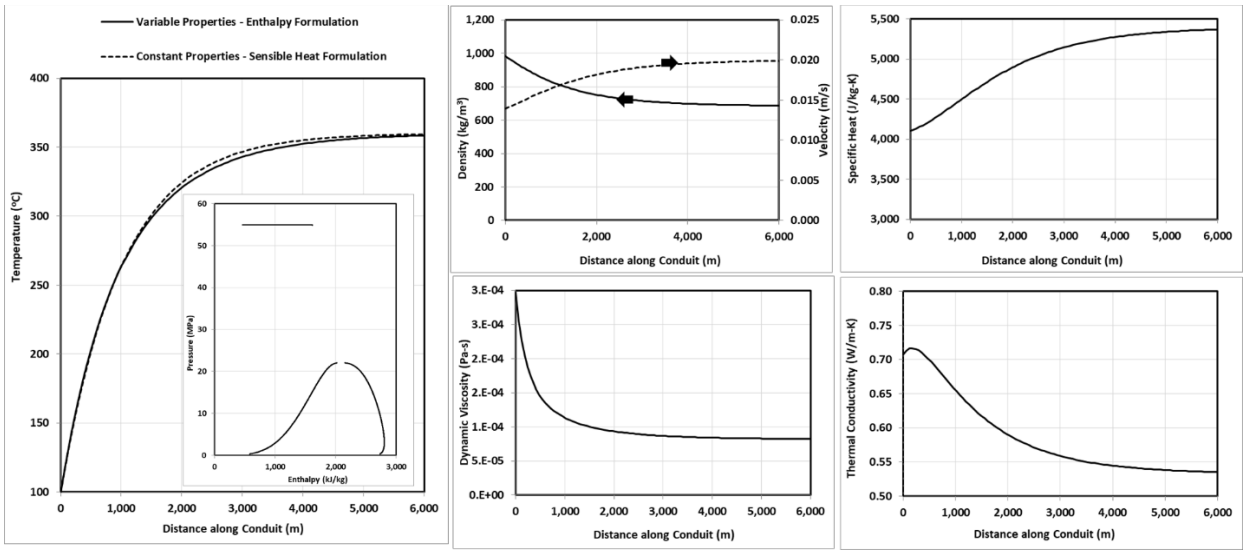

Figure 14: Temperature and Thermophysical Property Profiles for a Subcritical Flow Scenario (Resource Temperature 360°C and Inlet Pressure 55 MPa).

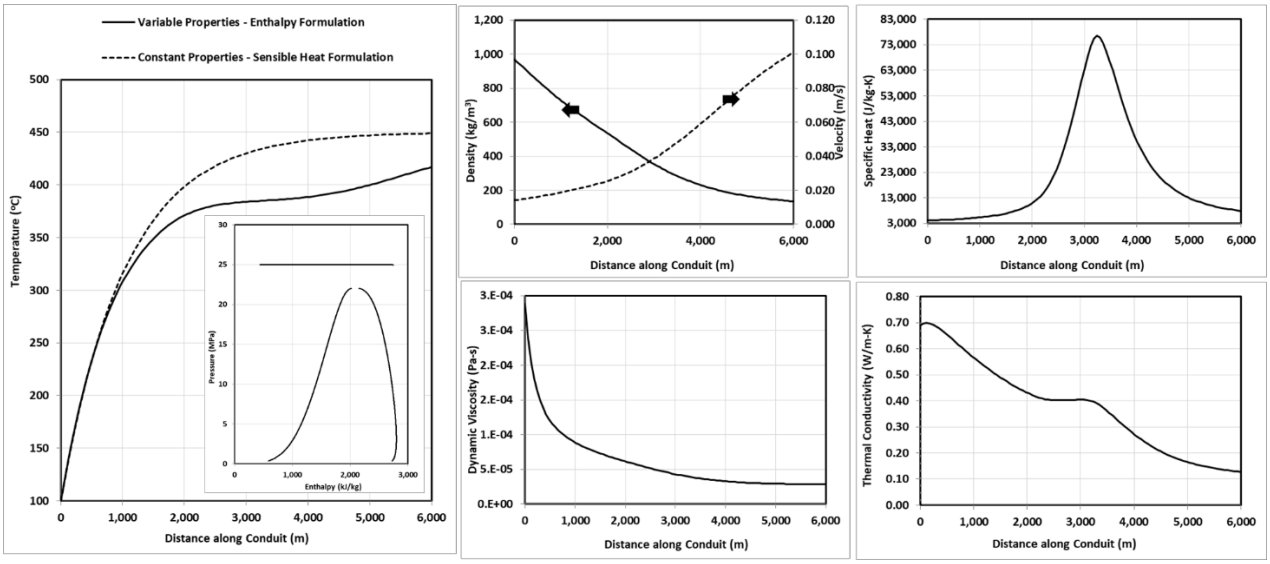

Figure 15: Temperature and Thermophysical Property Profiles for a Trans-Critical Flow Scenario (Resource Temperature 450°C and Inlet Pressure 25 MPa).

APPENDIX 2

Cylindrical Geometry (Drilled Multilaterals)

The flux at the interface of a cylindrical conduit and the formation is

$$\frac{\dot{Q}(t)}{2\pi} = Rk_{\infty}\left.\frac{\partial T}{\partial r}\right|_{r=R}(z,t) = k_{\infty}\left(T_{\infty}-T_{\text{in}}\right)\left.\frac{\partial \theta}{\partial \eta}\right|_{\eta=1}(\tau) = F(\tau)k_{\infty}\left(T_{\infty}-T_{\text{in}}\right) \tag{38}$$

where the dimensionless time is essentially a Fourier Number corresponding to the snapshot in time in question, and defined as

$$\tau = 4\frac{\alpha_\infty t}{D^2}, \tag{39}$$

where α_∞ is the formation thermal diffusivity. The pseudo-transient flux multiplier can be represented by the curve fit to solution of the one-dimensional radial diffusion problem of a cylinder embedded in a semi-infinite medium.

$$F(\tau) = \mathrm{L}^{-1}\left[\frac{1}{\sqrt{s}}\frac{K_1(\sqrt{s})}{K_o(\sqrt{s})}\right]\begin{cases} = \dfrac{1}{\sqrt{\pi\tau}}, & \tau \le 0.001, \\ \\ \approx 10^{\sum_{k=0}^{5} p_k (\log_{10}\tau)^k}, & \tau > 0.001 \end{cases} \tag{40}$$

In Eq. (40), $K_0(s)$ and $K_1(s)$ are the Modified Bessel Functions of the Second Kind, of Orders 0 and 1, respectively. For $\tau > 0.001$, the inverse Laplace Transform by contour integration – vide Carslaw and Jaeger (1959) – can be approximated by a polynomial as indicated in Eq. (40). The reader is referred to Chandrasekhar (2020) for details. Ramey (1962) approximated the cylindrical conduit as a line source in a semi-infinite medium and presented the approximation to the exponential integral solution as

$$F(\tau) = \ln\left(\frac{1}{2\sqrt{\tau}}\right) + 0.29 \tag{41}$$

The function $F(\tau)$ as given by both expressions is plotted in Figure 16, which also shows the coefficients in Eq. (40). It is seen that the simplified expression of Eq. (41) breaks down for very short times from the startup.

Following some algebra, we have

$$\frac{\bar{U}}{k} = \left[\frac{2}{\mathrm{Nu}} + \frac{1}{F(\tau)}\frac{k}{k_\infty}\right]^{-1} \tag{42}$$

where the Nusselt number is given by the Dittus-Boelter correlation according to

$$\mathrm{Nu} = \frac{hD}{k} = 0.023\,\mathrm{Re}^{0.8}\,\mathrm{Pr}^{0.3} \tag{43}$$

where the Reynolds and Prandtl numbers are

$$\mathrm{Re} = \frac{\rho V D}{\mu} \tag{44}$$

and

$$\mathrm{Pr} = \frac{\mu c_\mathrm{p}}{k} \tag{45}$$

Planar Geometry (Multiple Fractures)

For a planar geometry, the temperature profile in the transverse direction is given by Ozisik (1993). Differentiation with respect to the transverse coordinate yields

$$\left.\frac{\partial T}{\partial x}\right|_{x=w}(t)=\frac{\left(T_{\infty}-T_{\mathrm{w}}\right)}{\sqrt{\pi\alpha_{\infty}t}} \tag{46}$$

Substitution in Eq. (6), rearranging terms, and noting that in the limit $b/w \to \infty$ the hydraulic radius $R_{\mathrm{h}} \approx w$, yields

$$\frac{\bar{U}(t)}{k}=\left[\frac{1}{\mathrm{Nu}}\left(\frac{w}{b}\right)+\frac{w}{b}\frac{\sqrt{\pi\alpha_{\infty}t}}{w}\frac{k}{k_{\infty}}\right]^{-1} \approx \frac{b}{w}\left[\frac{1}{\mathrm{Nu}}+\sqrt{\pi\tau}\,\frac{k}{k_{\infty}}\right]^{-1} \tag{47}$$

where in this case the Fourier number is defined in terms of the fracture hydraulic diameter as

$$\tau=\frac{\alpha_{\infty}t}{R_{\mathrm{h}}^2}=\frac{\alpha_{\infty}t}{w^2} \tag{48}$$

and the pseudo-transient flux multiplier is

$$F\left(\bar{\tau}\right)=\left(\sqrt{\pi\tau}\right)^{-1} \tag{49}$$

suggesting that at very short times, the heat flux from a cylindrical body is similar to that from a plane. The Nusselt number in Eq. (47) is based on the conduit thickness, but the Reynolds number – also used to evaluate the friction factor – is based on the hydraulic diameter D_{h}.

The Fourier Number, which depending on the geometry (planar or cylindrical) can be defined in terms of the geometry index ($n=1$ for a cylindrical geometry and $n=0$ for a planar geometry), can be compactly expressed as

$$\tau=\left[\frac{4n}{D^2}+\frac{(1-n)}{w^2}\right]\alpha_{\infty}t \tag{50}$$

and a composite expression for the ratio $\bar{U}/k$ can be written as

$$\frac{\bar{U}}{k}=\left(\frac{w}{b}\right)^{1-n}\left[\frac{2^n}{\mathrm{Nu}}+\frac{1}{F(\tau)}\frac{k}{k_{\infty}}\right]^{-1} \tag{51}$$

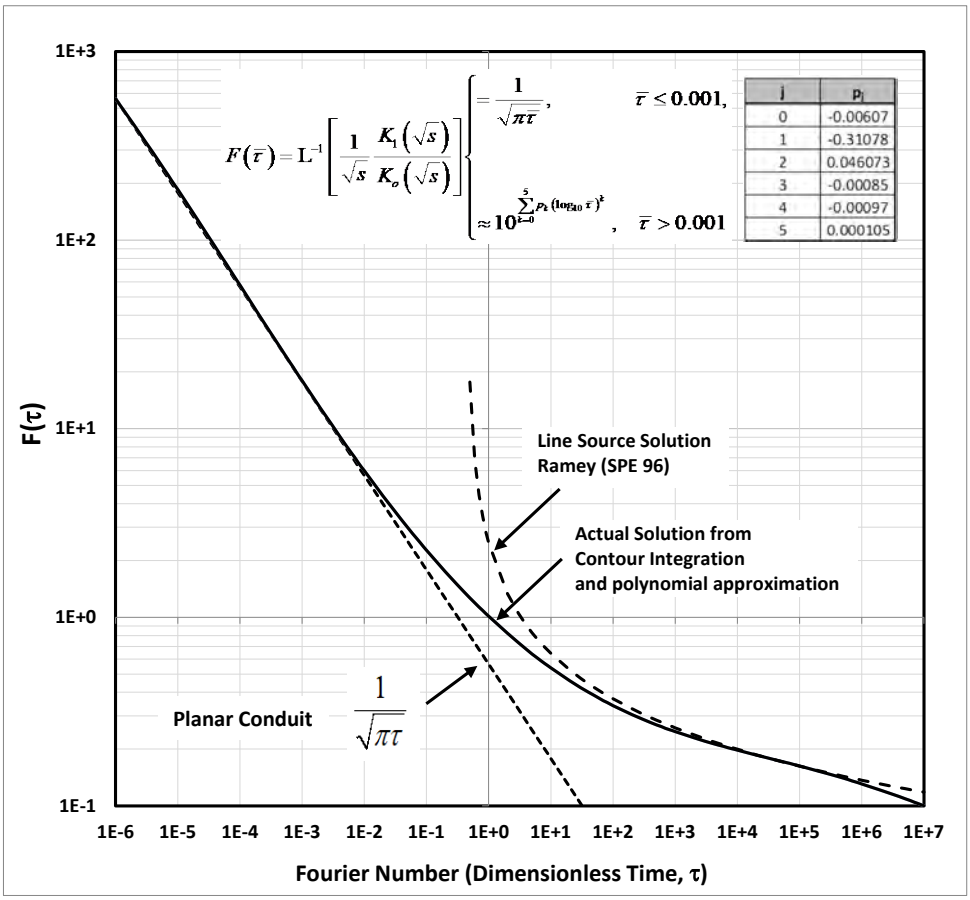

Figure 16: Decay of the Dimensionless Interface Flux from a cylinder embedded in a semi-infinite medium.

Appendix 3

Cylindrical Geometry (Drilled Multilaterals)

The normalized temperature in the formation at any streamwise location in a cylindrical conduit can be defined as

$$\theta(r) = \frac{T_\infty - T(z,r)}{T_\infty - T_{\mathrm{W}}(z)} \tag{52}$$

which is different from that in Eq. (8), as the normalizing temperature scale is the difference between the undisturbed geothermal and the instantaneous conduit surface temperature –as opposed to the conduit inlet temperature. If the radial position from the conduit is normalized with respect to the wellbore radius $R = D/2$ so that $\eta = r/R$, the radial temperature distribution is given by the inverse Laplace Transform

$$\theta(\eta) = \mathrm{L}^{-1}\left[\frac{\mathrm{K}_0\left(\sqrt{s}\eta\right)}{s\mathrm{K}_0\left(\sqrt{s}\right)}\right] \tag{53}$$

which can be evaluated following Carslaw and Jaeger (1959) using contour integration with a branch cut about the origin in the complex plane.

If the penetration depth is defined as the radial position at which the temperature decays to 0.001, this depth can be estimated by inverting Eq. (53). This is shown in Figure 3.

Planar Geometry (Multiple Fractures)

For planar geometries, the temperature variation with time and distance from the surface has been shown by Özisik (1993) to be

$$\theta = \mathrm{erf}\left(\frac{x}{2\sqrt{\alpha_\infty t}}\right) \tag{54}$$

which decays to 0.001 at

$$\left[\frac{x}{2\sqrt{\alpha_\infty t}}\right]_{\theta=0.001} = 2.327 \tag{55}$$

from which the distance normalized by the conduit width w can be determined as

$$\left[\frac{x}{w}\right]_{\theta=0.001} = 4.654\sqrt{\tau} \tag{56}$$

in terms of the same Fourier number definition as in (48).

Interpretation of Stimulated Permeability by Model Calibration with Data from Circulation Program at FORGE

Branko Damjanac[1], Zorica Radakovic-Guzina[1], Wei Fu[1], Aleta Finnila[2], Rob Podgorney[3]

[1] Itasca Consulting Group, Inc., Minneapolis, MN, USA

[2] WSP USA Inc., Redmond, WA, USA

[3] Idaho National Laboratory, Idaho Falls, ID, USA

Keywords

Geothermal, EGS, geomechanics, reservoir, stimulation, modeling

ABSTRACT

In April of 2022, three stimulation stages were carried out near the toe of well 16A(78)-32 at the Utah FORGE site. Based on the extent of the recorded microseismicity and modeling results, well 16B(78)-32 was drilled 100 m above well 16A(78)-32. In July of 2023, a circulation program was conducted between two wells. The aim was to implement low-rate injection to interrogate the reservoir between the injection and the production wells, 16A(78)-32 and 16B(78)-32, respectively, and to assess the effect of reservoir stimulation in April 2022. The circulation testing was designed to use low injection rates to prevent hydraulic fractures from being initialized or propagated. Back analysis of the circulation test was carried out using a coupled hydro-mechanical (HM) numerical model based on the distinct element method (DEM). The objective of the modeling was to interpret the state of the reservoir by matching the recorded injection pressures and rates at both wells. The model includes an explicit representation of the DFN. Some DFN fractures were generated to match the observed microseismic event locations, while most were generated stochastically. The model indicates that the stimulated reservoir permeability is a function of distance from the injection well. Although seismicity recorded during stimulation extended 100 m above the injection well, and the circulation test confirmed connectivity between the two wells, the back analysis indicated that the domain of increased permeability did not connect the two wells. Also, the circulation at rates of 5 bpm resulted in additional fracture propagation, which is evident from the injection pressure history and microseismicity recorded during circulation. The coupled thermo-hydro-mechanical (THM) model was subsequently used to simulate 80 days of water circulation between two wells by injection in three stages at the toe of well 16A (78)-32 to evaluate temperature decay with time.

1. Introduction

Utah Frontier Observatory for Research in Geothermal Energy (FORGE) is an Enhanced Geothermal System (EGS) project supported by the U.S. Department of Energy. The injection well 16A(78)-32 drilling was completed in December 2020. In April of 2022, three stages of reservoir

stimulation by fluid injection were conducted at the toe of well 16A(78)-32 (McLennan et al., 2023). In June of 2023, production well 16B(78)-32 was drilled within the extent of the microseismic cloud recorded during the stimulation, 100 m above 16A(78)-32. In July of 2023, after drilling the production well, circulation tests were conducted to assess the connectivity between wells 16A(78)-32 (injection) and 16B(78)-32 (production). The injection pressures recorded during the tests were analyzed by different teams using different methods, including analytical and numerical modeling approaches. In this article, we present the back-analysis of injection pressures recorded during Day 1 (on July 4, 2023) Circulation Test 1 (two tests were carried out on Day 1) using *XSite* (Itasca, 2020) with a hydro-mechanically (HM) coupled model based on the discrete element method (DEM) and lattice method. The objective of the back-analysis was to use the calibrated model (by matching the injection pressure history) to interpret the state of the reservoir near the toe of well 16A(78)-32 when the circulation tests commenced. The coupled thermo-hydro-mechanical (THM) model was subsequently used to predict the temperature decay of produced water in well 16B(78)-32 during 80 days of circulation between two wells.

2. Circulation Test Data

The circulation tests (including analysis of well connectivity) are discussed in detail by Xing et al. (2024). Only details of Day 1 of Circulation Test 1 relevant to the analysis described here are repeated. The geometry of the two wells and their completions at the time of Circulation Test 1 are illustrated in Figure 1. Three stages were stimulated near the toe of well 16A(78)-32. Stage 1 of stimulation was conducted in the openhole section of the well, while Stages 2 and 3 were carried out through perforated sections in the well casing.

Water was injected in all three stages along well 16A(78)-32 during the circulation tests. Recorded wellhead pressures for wells and injection rates in 16A(78)-3 are shown in Figure 2. The injection started at 0.5 bpm, increased to 2.5 bpm, and finally to a maximum rate of 5 bpm. The single pumping unit could not achieve 5 bpm at the wellhead pressure encountered, and a second (standby) unit was rigged up and brought online. Consequently, there were interruptions and oscillations in pumping rate and wellhead pressure.

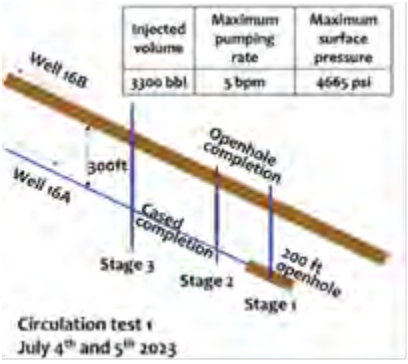

Figure 1 Illustration in vertical cross-section of the well toe geometries and completions during Circulation Test 1 (after Xing et al. 2024).

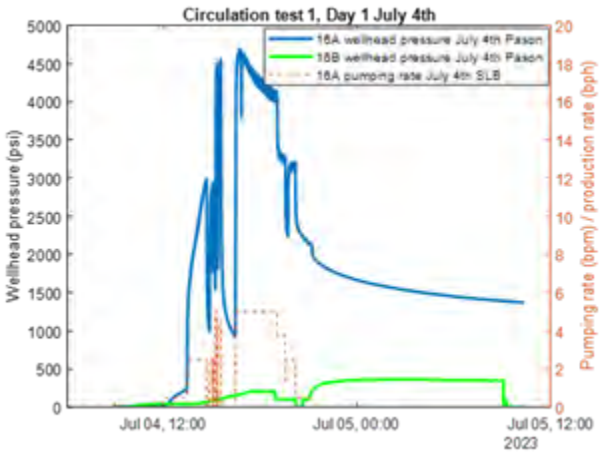

Figure 2 Wellhead pressure, injection, and production rates during Day 1 of Circulation Test 1 (after Xing et al. 2024).

Well 16B(78)-32 produced fluid and recorded a pressure response (Figure 2) during the first circulation test. About 40 minutes after injection initiation, the pressure increased (relative to the initial value) in well 16B(78)-32. The wellhead pressure in well 16B(78)-32 built up slowly with the flow line closed (i.e., the well was shut in at the surface, and the throttling valve to the pit from the production well was closed). When the wellhead pressure in 16B(78)-32 reached 200 psi, the throttling valve in the flow line was opened to maintain 200 psi as back pressure by flowing to the pit. Later, the back pressure was reduced to 100 psi during the pumping. After the injection stopped, the injection well and the production well were shut in. The pressure in well 16B(78)-32 built up to a maximum of 362 psi.

3. Discrete Fracture Network

Both the pre-existing natural fractures and new hydraulic fractures created during reservoir stimulation were explicitly represented in the model. Discrete stochastic fractures provided in the discrete fracture network (DFN) model have radii in the 10 to 150 m range and orientations matching the mean values of the four fracture sets identified from FMI logs (Finnila et al., 2021). The DFN was amended by adding fifteen fractures (Figure 3) inferred by interpreting the microseismic data recorded during the stimulation in 2022 (Finnila et al., 2023). Uncertainty in locations of the events recorded during stimulation of Stages 1 and 2 (and consequently in the geometry of the inferred fractures) is much greater than that for Stage 3 because, during Stages 1 and 2, fewer, more distant geophones were used to record microseismicity.

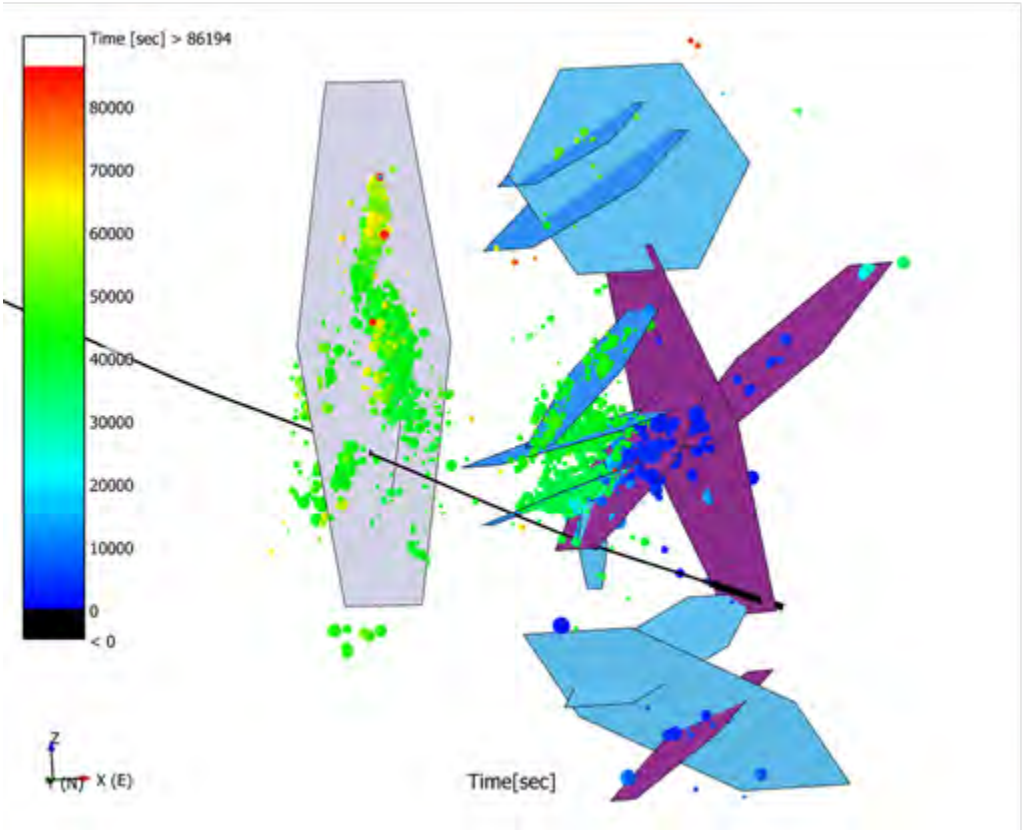

Figure 3 The geometry of the added fractures and the recorded microseismicity during reservoir stimulation in 2022. (The color scale indicates the timing of the microseismic events relative to the beginning of the injection.)

4. Numerical Models

The models were simulated using the numerical code *XSite*, which implements the synthetic rock mass (SRM) approach using the DEM and the lattice method (Damjanac et al., 2016). The model is fully coupled thermo-hydro-mechanically, and deformation and damage of the reservoir rock mass include the effects of deformation and damage of the intact rock (including hydraulic fracturing) and slip and opening of the pre-existing joints.

4.1 Short-Term Circulation

The thermal processes were not simulated in the short-term circulation models because of the relatively short duration of the tests. Modeling of the circulation test using *XSite*, with the capability to approximate hydro-mechanical coupling, is essential, particularly during injection at higher rates (e.g., 2.5 and 5 bpm) when the fluid pressures are expected to be sufficiently large to cause significant deformation of the fractures and change in their hydraulic apertures (i.e., permeability).

The material properties and initial stress conditions used by the models are listed in Table 1. It was assumed that all DFN, including the fractures created during stimulation, have a friction angle of 37°. After the excess pore pressures dissipated following the stimulation in 2022, it is assumed that the pore pressures returned to the initial hydrostatic state. The fractures closed if hydro-

shearing and placed proppant volume were negligible. Although the fractures have closed, it is assumed that there is a residual hydraulic aperture. The DFN residual aperture, a function of distance from the injection well, and the extent of the DFN that lost cohesive strength due to stimulation were calibration parameters used in this study.

The planned pumping schedule for Day 1 of Circulation Test 1 is shown in Figure 4. The rate oscillations that took place in the field were not reproduced in the model, in which fluid was injected at the (injection) points at the intersections between well 16A(78)-32 and the fractures. No perforation pressure drop was considered for any of the injection points. The fluid is injected in all three stages simultaneously, and the code resolves the rate distribution between the stages and injection points as a part of the model solution.

Table 1 Material properties and initial conditions for the circulation model with injection from well 16A(78)-32 (TVD 8490 ft, 2587.8 m).

Variable	**Value**
Young's modulus	55 GPa (8.0×10^6 psi)
Poisson's ratio	0.26
Fracture toughness	3 MPa×$m^{1/2}$ (2740 psi×$in^{1/2}$)
Fluid viscosity	Newtonian fluid, 2 cp
Pore pressure	0.0093 MPa/m (0.41 psi/ft), 24.0 MPa (3481 psi)
Minimum horizontal stress	0.0174 MPa/m (0.73 psi/ft), 42.68 MPa (6190 psi)
Maximum horizontal stress	0.0189 MPa/m (0.84 psi/ft), 48.80 MPa (7078 psi)
Vertical stress	0.0243 MPa/m (1.07 ft/ft), 62.80 MPa (9108 psi)

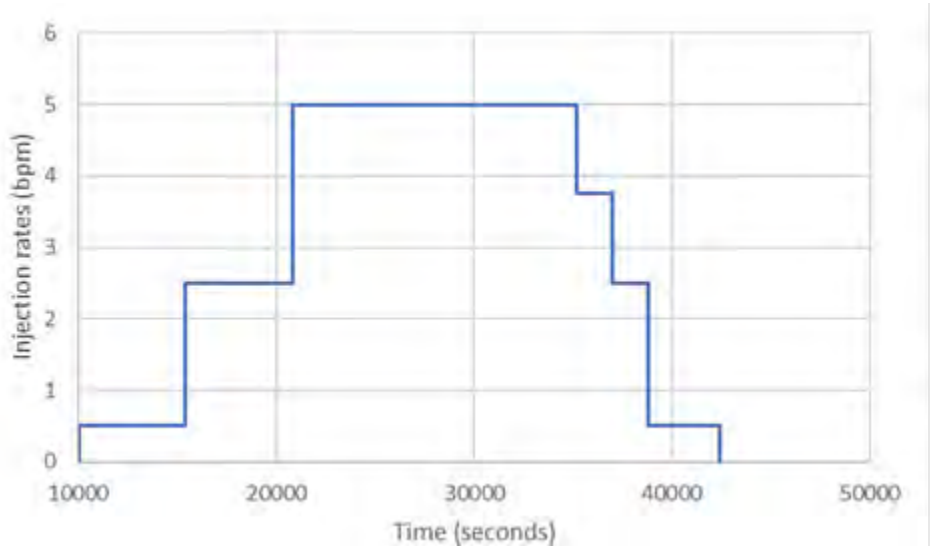

Figure 4 Simulated pumping schedule.

4.2 Long-Term Circulation

Water circulation between wells 16A(78)-32 and 16B(78)-32, when water is injected in three stages at the toe of 16A(78)-32, was simulated using a coupled THM model (Detournay et al., 2022). This model simulates heat advection with flowing fluid in fractures, convective heat transfer between fluid and rock, and heat conduction in the rock coupled with fluid flow in discrete fractures and a mechanical model of rock deformation. For computational efficiency, it is assumed that the flow model is continuously in a steady state and the mechanical model is continuously in equilibrium. Those assumptions are reasonable, considering that the characteristic time scales of the fracture flow and mechanical models are much smaller than the characteristic time scale of heat conduction (which is a relatively slow process). The model is advanced in time using heat transport processes, heat advection by flowing fluid, and heat conduction. The model is re-equilibrated mechanically at sufficiently small time intervals (i.e., sufficiently small thermally induced stress changes). Subsequently, the flow model is simulated to achieve a new steady state corresponding to changed apertures (i.e., permeability). The flow rates from the steady-state flow model are used in the advection model in the next thermal step.

The model simulates water circulation from well 16A(78)-32 to well 16B(78)-32. It is assumed that fluid percolation takes place only in stimulated pre-existing fractures and created hydraulic fracture (in Zone 3) as identified by interpreting the microseismic data shown in Figure 3. Water is injected at 5 bpm into all three stimulated zones at the toe of well 16A(78)-32.

5. Results

5.1 Model Calibration with Short-Term Circulation Data

The extent of the permeable DFN and contours of the hydraulic aperture calibrated to the field results are shown in Figure 5 (following preliminary results by Radakovic-Guzina et al. 2024). It includes the initially permeable (stimulated) DFN within the 50-m radius around 16A(78)-32. Outside that radius, the DFN is assumed to be impermeable with cohesion and tensile strength of

5 MPa. The permeability and hydraulic apertures within the permeable part of the DFN are considered to be variable depending on the distance from well 16A(78)-32. An initial hydraulic aperture of 0.4 mm is assumed within a radius of 25 m from well 16A(78)-32. The rest of the DFN within the permeable (stimulated) region (50 m radius) is assumed to have hydraulic apertures of 0.2 mm.

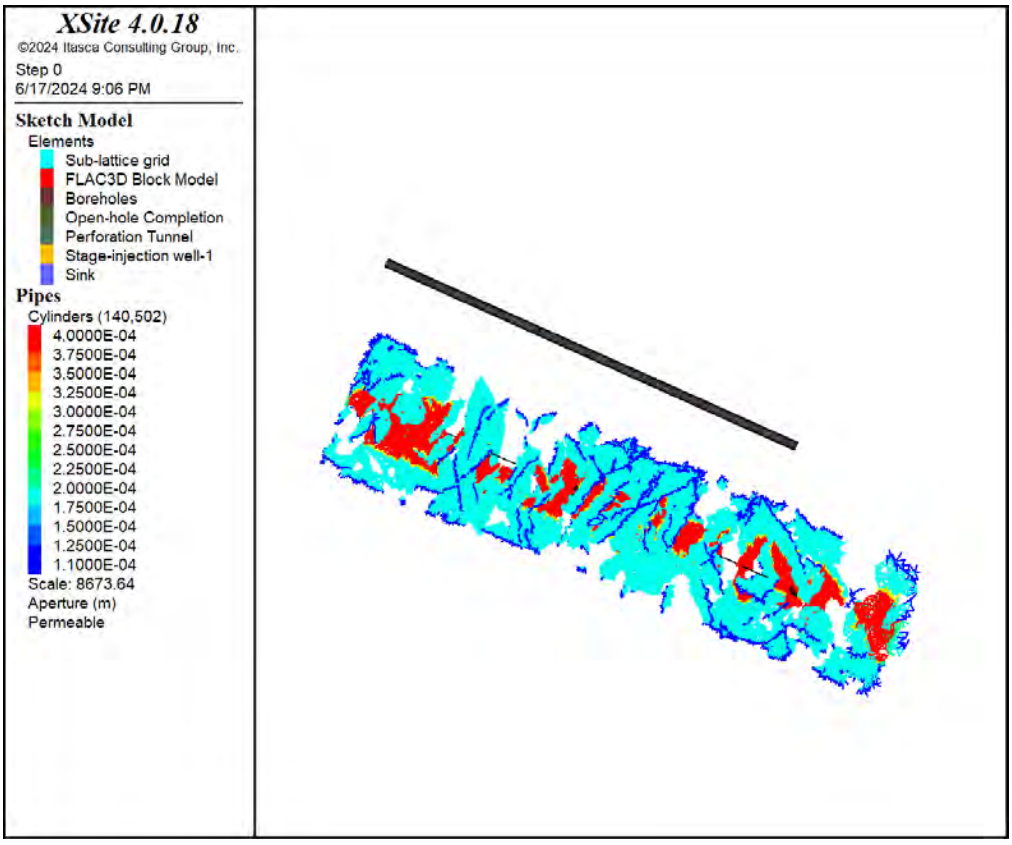

Figure 5 Initial hydraulic aperture (m) contours within the extent of initially permeable DFN (extending within a 50 m radius from well 16A(78)-32) are shown in a vertical cross-section along the sub-horizontal sections along two wells. The remaining DFN is impermeable and not shown in this plot. The wells are shown as inclined line segments (well 16A(78)-32 is shown as a thin line, and well 16B(78)-32 is shown as a cylindrical volume).

The contours of fracture fluid pressures and induced microcracks after 4.7 hours of injection, obtained by the calibrated model, are shown in Figure 6. The model indicates the response at 0.5 bpm injection rate governed by fluid pressure diffusion into a well-connected and stimulated DFN at pressures smaller than the minimum stress (i.e., through closed but permeable DFN, including fractures created during the 2022 stimulation). Hydro-mechanical coupling becomes important when injection rates increase to 2.5 and 5 bpm, resulting in additional stimulation of DFN and propagation of hydraulic fracture created in Stage 3 (indicated by new microcracks in Figure 6). The permeability of the reservoir at that stage of the circulation test is governed by the induced hydraulic aperture changes, not by the initial hydraulic apertures.

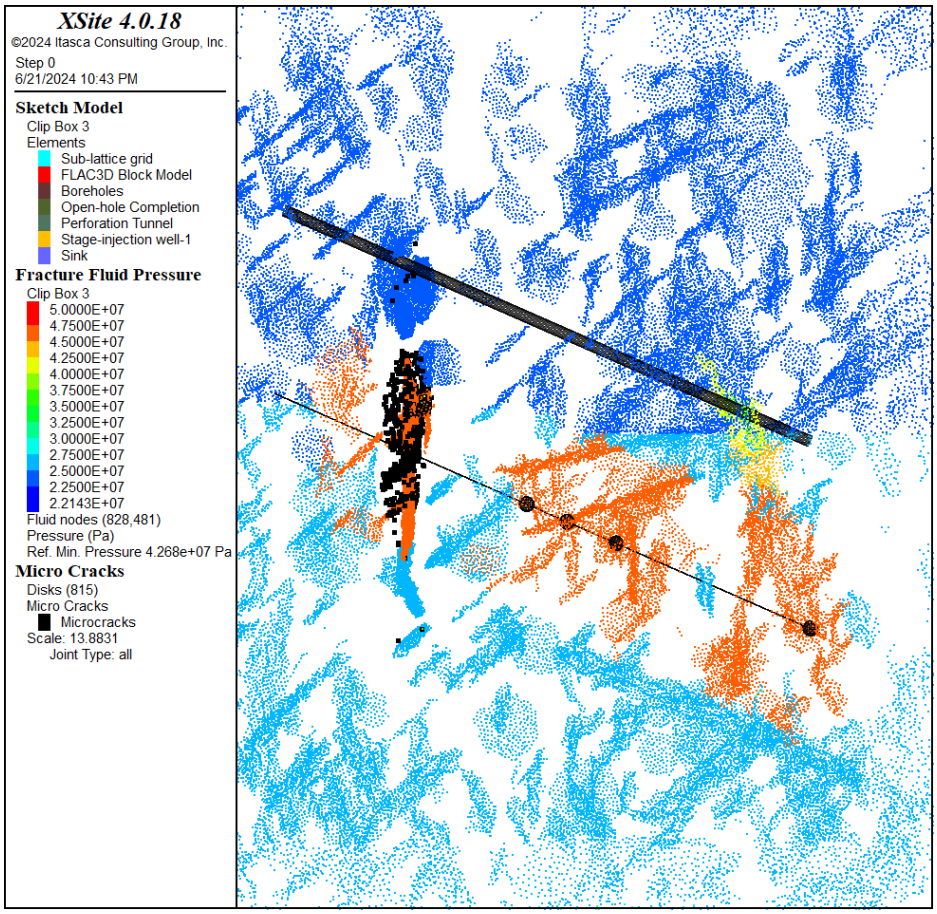

Figure 6 Fracture fluid pressure (Pa) contours and induced microcracks (black dots) after 4.7 hours of injection in a vertical section along the sub-horizontal section of well 16A(78)-32. The wells are shown as inclined line segments, and the injection points are spheres.

The downhole pressures obtained from the refined model compared with the pressures calculated using the recorded pressures (the downhole pressures calculated from the recorded surface pressures using the approach presented by Xing et al. 2023) are shown in Figure 7. This model matches the trends and magnitudes of the pressure history, indicating a reasonable approximation of the reservoir condition by the assumed permeability field (shown in Figure 5).

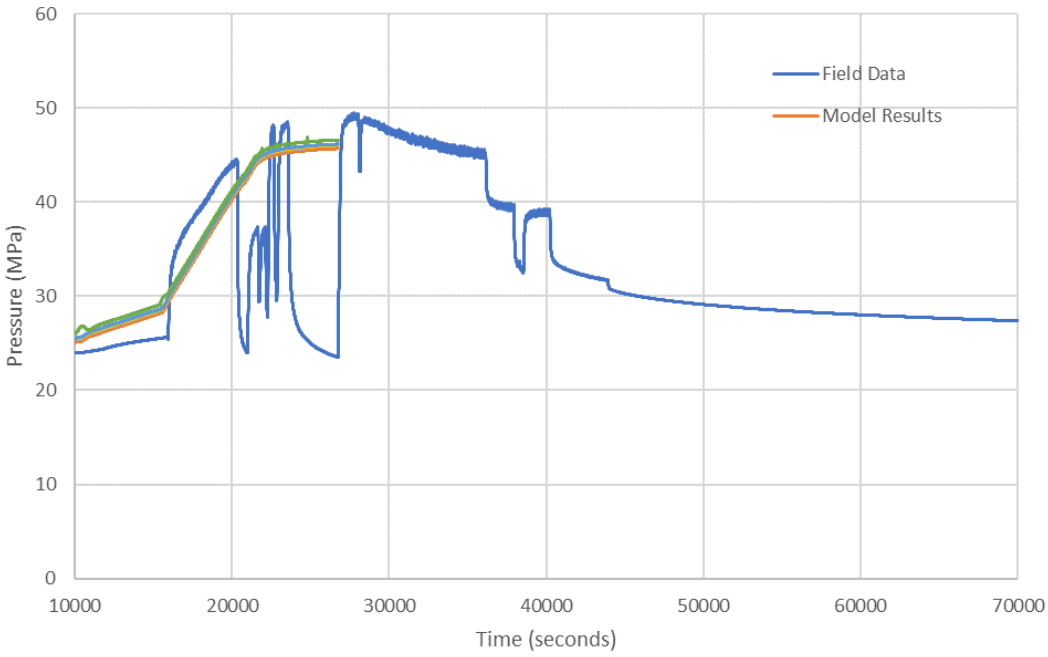

Figure 7 The downhole pressure histories as calculated from the field data and obtained from the calibrated model.

5.2 Long-Term Circulation

The fluid pressure contours after 80 days of fluid circulation by injection into three stages at the toe of well 116A(78)-32 are shown in Figure 8. The contours of fluid temperature after 80 days are shown in Figure 9. The history of produced water temperatures is shown in Figure 10. The entire injected water is recovered from the production well because a limited number of fractures completely disconnected from the rest of the DFN are included in the model. In that sense, this model is unconservative because it does not include any risk of losing some of the injected fluid. The temperature of the produced water is calculated by volume averaging temperatures of water produced from all fractures intersected by the production well. In 80 days, the temperature of the water produced drops 31°C (for a 100 m well spacing). The rock temperature contours, shown in the vertical cross-section along the wells in Figure 11, are consistent with the temperature histories of produced water. Only a “skin” of rock cools along the fracture length between wells 16A(78)-32 and 16B(78)-32. Skin cooling explains the relatively small effect of temperature changes on fracture apertures and injectivity observed in the model.

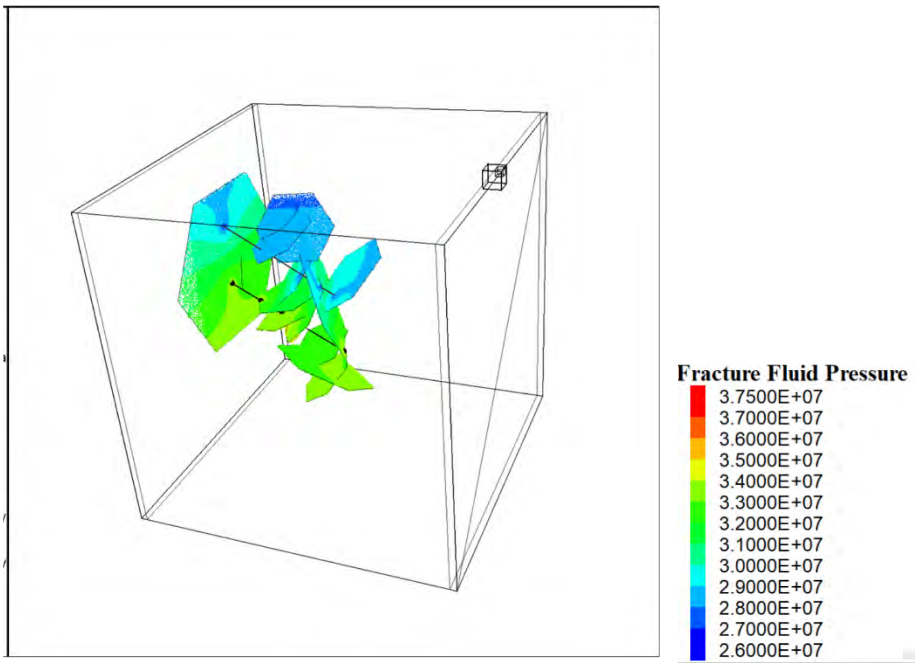

Figure 8 Fluid pressure (Pa) contours after 80 days of circulation.

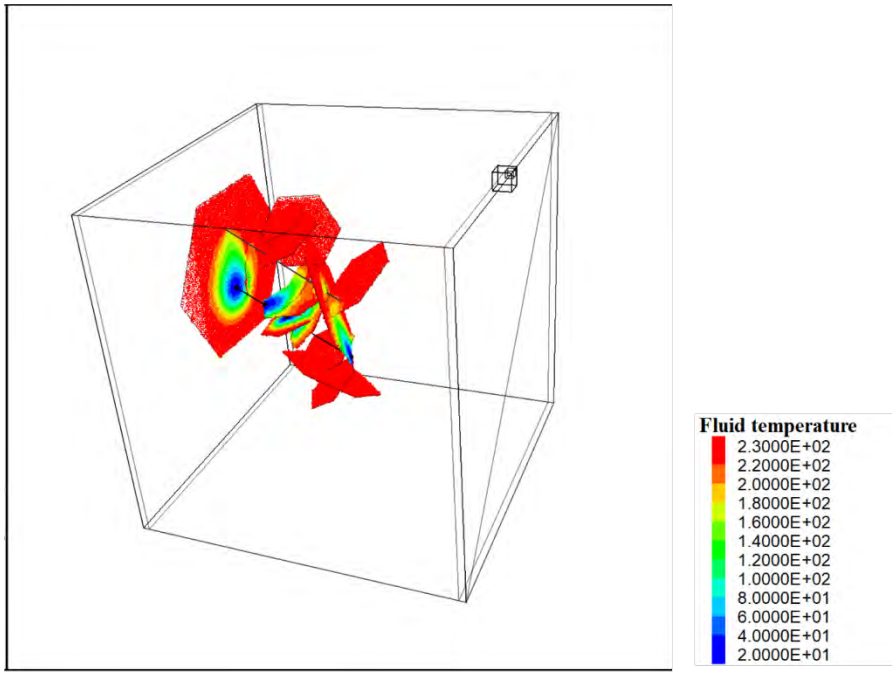

Figure 9 Fluid temperature (ºC) contours after 80 days of circulation.

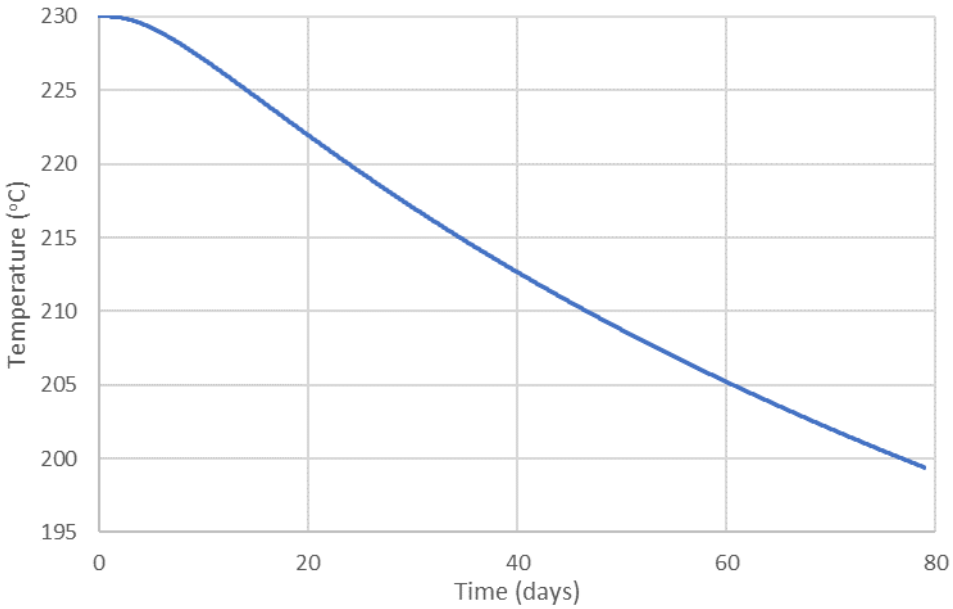

Figure 10 Temperature history of produced water.

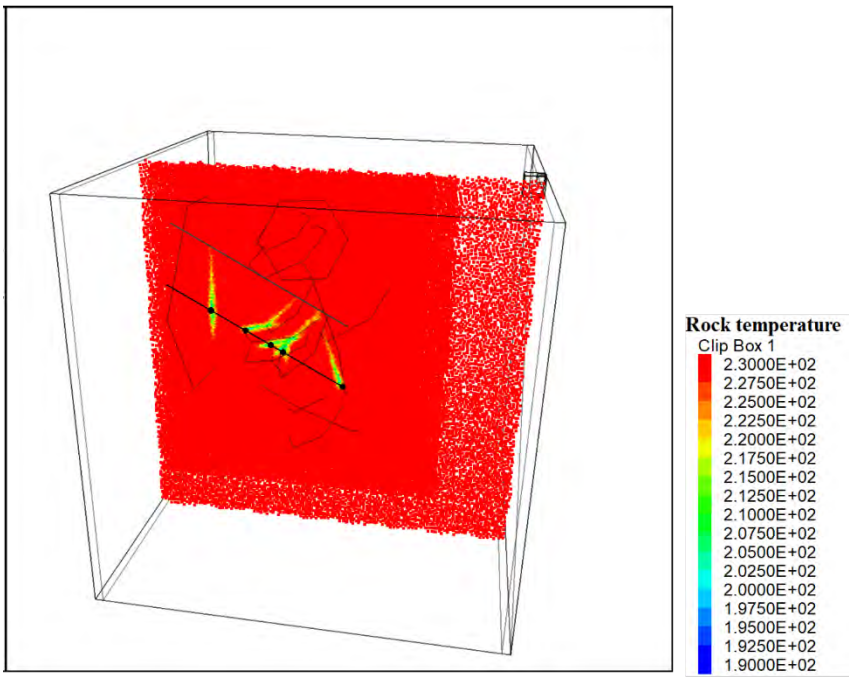

Figure 11 Rock temperature (°C) contours after 80 days of circulation.

6. Discussion

The injection pressure was recorded during Day 1 of Circulation Test 1. The results of the numerical model calibrated to those pressures indicate a stimulated volume around well 16A(78)-32 with some residual permeability for more than one year after stimulation. The extent of the domain with residual permeability is uncertain, but its radius around well 16A(78)-32 seems to be

tens of meters. The modeling results indicate that the stimulated reservoir volume (i.e., permeable and connected DFN) is smaller than the microseismic cloud.

During injection at 0.5 bpm, fluid percolates into the permeable and connected DFN without significant pressure and permeability increase. At rates of 2.5 bpm, the hydro-mechanical coupling becomes more dominant, causing hydraulic aperture changes greater than the initial apertures. Further increase of the rates to 5 bpm seems to result in fracture propagation.

A simulation of water percolation for 80 days at 5 bpm shows a relatively fast decrease in the temperature of the produced water. Thus, the flow rate through these three stages should be less than 5 bpm for long-term heat production.

7. Conclusion

A fully coupled hydro-mechanical model with explicit representation of the DFN and capability to simulate hydraulic fracturing was used to back-analyze Day 1 of Circulation Test 1 conducted at the FORGE project in July of 2023. The recorded injection pressure history was used to calibrate the numerical model. Day 1 of Circulation Test 1 was conducted from well 16A(78)-32 by fluid injection at relatively low rates, between 0.5 and 5 bpm, simultaneously in all three stages stimulated in April of 2022. The objective of the numerical modeling was to use a calibrated model to interpret better the effect of stimulation on reservoir (or DFN) permeability more than one year after the stimulation was conducted.

The modeling study results indicate a domain around well 16A(78)-32 with increased residual permeability more than one year after the stimulation. Such a domain is manifested by a relatively small pressure increase early and for a small injection rate (0.5 bpm). The stimulated domain with increased permeability seems smaller than the extent of the microseismic cloud. The model matched the pressure increase when the rate was increased to 2.5 bpm and hydraulic fracture propagation for the rate of 5 bpm if the DFN was assumed impermeable outside a cylinder with a 50-m radius around well 16A(78)-32.

A simulation of water percolation for 80 days indicates that the flow rate through these three stages should be less than 5 bpm for long-term heat production. Consequently, economical heat production would require a significantly larger number of stimulated stages.

Acknowledgment

The U.S. DOE-funded this work under grant DE-EE0007080, “Enhanced Geothermal System Concept Testing and Development at the Milford City, Utah FORGE Site.” We thank the many stakeholders supporting this project, including Smithfield, Utah School and Institutional Trust Lands Administration, Beaver County, and the Utah Governor’s Office of Energy Development.

This research used the resources of the High Performance Computing Center at Idaho National Laboratory, supported by the Office of Nuclear Energy of the U.S. Department of Energy and the Nuclear Science User Facilities under Contract No. DE-AC07-05ID14517.

REFERENCES

Damjanac, B., Detournay, C. and Cundall, P. A. “Application of particle and lattice codes to simulation of hydraulic fracturing.” *Computational Particle Mechanics*, 3(2), (2016), 249–261. https://doi.org/10.1007/s40571-015-0085-0

Detournay, C., Damjanac, B., Torres, M., Cundall, P., Ligocki, L., and Gil, I., Heat advection and forced convection in a lattice code – Implementation and geothermal applications, Rock Mechanics Bulletin, Volume 1, Issue 1, (2022), 100004, ISSN 2773-2304, https://doi.org/10.1016/j.rockmb.2022.100004.

Finnila, A., Doe, T., Podgorney, R., Damjanac, B., and Xing, P. “Revisions to the Discrete Fracture Network Model at Utah FORGE Site,” *GRC Transactions*, Vol. 45. (2021).

Finnila, A., Damjanac, B. and Podgorney, R. “Development of a Discrete Fracture Network Model for Utah FORGE using Microseismic Data Collected During Stimulation of Well 16A(78)-32.” In *Proceedings: 48th Workshop on Geothermal Reservoir Engineering*, Stanford University, Stanford, California, February 6-8, (2023), SGP-TR-224.

Itasca Consulting Group, Inc. *XSite* (Version 4.0.07), (2023), Minneapolis: Itasca.

McLennan, J., England, K., Rose, P., Moore, J. and Barker, B. “Stimulation of a High-Temperature Granitic Reservoir at the Utah FORGE Site.” In *SPE Hydraulic Fracturing Technology Conference and Exhibition*. (2023), January. OnePetro.

Pengju, X., Damjanac, B., Radakovic-Guzina, Z., Torres, M., Finnila, A., Podgorney, R., Moore, J., and McLennan, J. “Comparison of Modeling Results with Data Recorded During Field Stimulations at Utah FORGE Site.” In *Proceedings: 48th Workshop on Geothermal Reservoir Engineering*, Stanford University, Stanford, California, (2023), February 6-8, SGP-TR-224.

Pengju, X., England, K., Moore, J., Podgorney, R. and McLennan, J. “Analysis of Circulation Tests and Well Connections at Utah FORGE.” In *Proceedings: 49th Workshop on Geothermal Reservoir Engineering*, Stanford University, Stanford, California, (2024), February 12-14, SGP-TR-227.

Radakovic-Guzina, Z., Damjanac, B., Fu, W., Finnila, A., Podgorney, R., and McLennan, J. “Coupled Hydro-Mechanical Back-Analysis of Circulation Program at FORGE in July of 2023.” In *Proceedings: 49th Workshop on Geothermal Reservoir Engineering*, Stanford University, Stanford, California, (2024), February 12-14, SGP-TR-227.

Experimental Analysis of Fluid Hydraulics in Enhanced Geothermal Systems

Katrine J. M. Hareland, Vigleik N. Kjeldal, Eshan K. Maitra, Mohammed F. Al Dushaishi, and Geir Hareland

Oklahoma State University

Keywords

Enhanced Geothermal System, Geothermal Fluids, High-Temperature Flow Loop, Fracture Flow

ABSTRACT

The solidified and crystallized magma in the earth's crust forms igneous rocks such as quartzite and granite. Depending on the depth and geological age, the temperature of these formations is relatively high, and thus, they contain a considerable amount of thermal energy. These formations are not permeable nor contain pore fluid. However, they are brittle and can be stimulated by hydraulic fracturing to gain permeability. The stimulated igneous formations that contain a large amount of thermal energy are considered enhanced geothermal reservoirs. Extracting thermal energy from enhanced geothermal reservoirs requires the presence of a geothermal fluid. Water is the most common geothermal fluid with excellent specific heat capacity; however, the hydraulic properties of water can create undesirable fast paths through large fractures from an injection well to a production well. This phenomenon will reduce the enhanced geothermal reservoir's heat extraction efficiency and sustainability. A large-scale experimental setup of a high-temperature flow loop system was fabricated to simulate the geothermal fluid hydraulics in two different fracture apertures of granite rock slabs. The two fracture systems are equipped with heating jackets and insulated using high-temperature fiberglass insulation, and they can be controlled independently. The inlet and outlet pressures for the small fracture and the fluid temperature were monitored during the tests. Water as a geothermal fluid was tested to investigate the flow behavior in the small fracture. The initial results for water for single fracture tests flowing through the small fracture produced different pressure drop trends and heat transfer characteristics with varying flow rates. This paper presents the results for single fracture under varying temperatures. Preliminary results showed that heat absorption is a function of applied temperature, flow regime, and flow rate.

1. Introduction

Geothermal energy has been recognized as a valuable alternative to fossil fuels and nuclear power, as it is renewable and reliable. Deep geothermal energy, such as enhanced geothermal systems

(EGSs), has the potential to supply 60 gigawatts of electrical capacity (GeoVision, 2019). The process of geothermal heat extraction for EGS consists of deep injection and production wells drilled in a hot geothermal formation (Figure 1). The working fluid is circulated via the injector down into the hot formation, which flows through rock fractions and absorbs heat from the formation. The hot working fluid reaches the production wells and expands, generating electricity using turbines.

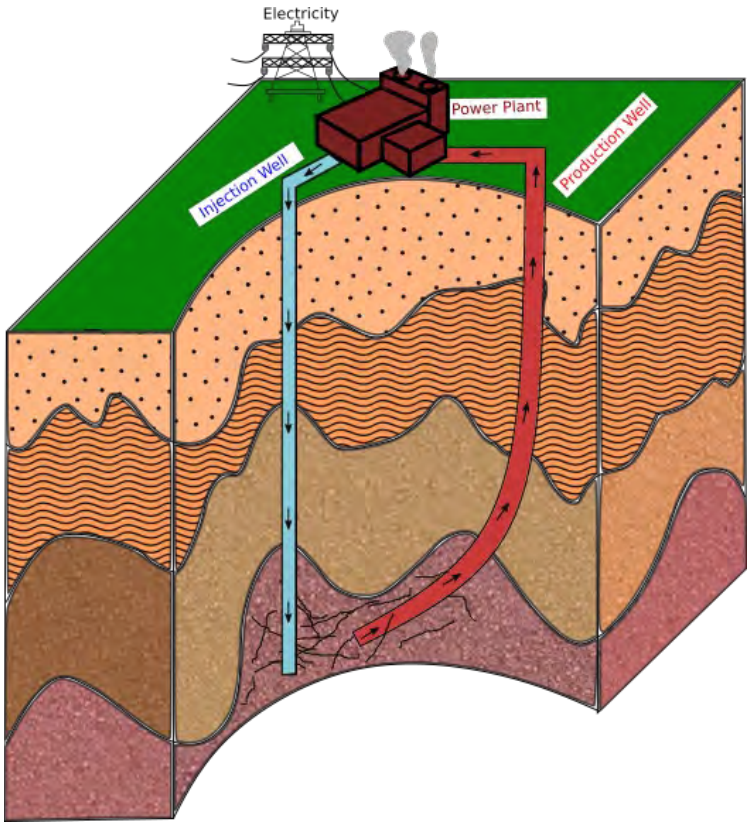

Figure 1: Enhanced geothermal system representation

Throughout the injection and production process, many factors can influence the heating potential of the working fluid. These factors include the working fluid, rock permeability, fracture size, and flow path. Working fluids play a crucial role in the operation of geothermal wells. They transfer heat from the hot rocks and fluids to the surface, which can be converted into electricity. Working fluids are selected based on their ability to transfer heat efficiently, compatibility with the geothermal reservoir, and environmental impact.

Water is commonly used as a working fluid; however, different fluids, such as supercritical CO_2 (Brown, 2000; Gao et al., 2023) and ionic liquids (Atashnezhad et al., 2023; Kazemi et al., 2020; Momoh et al., 2023) have been proposed as alternative fluids. Water as a geothermal working fluid is abundant and has excellent heat transfer properties, making it an efficient working fluid. It is also compatible with most equipment used in geothermal power plants. However, its usage may face constraints due to accessibility, quality, and ecological repercussions. The performance of geothermal systems is closely tied to the properties of the working fluid. Characteristics like heat capacity, thermal conductivity, viscosity, boiling point, corrosiveness, environmental impact, cost, and availability all play a role in determining the system's efficiency.

Some of the challenges EGS faces include the initial capital cost required for drilling and completing the wells. Geothermal reservoirs are characterized by low permeability, where reservoir stimulation is necessary. Another challenge with EGS is the rapid thermal decline of heat extraction, which is caused by fluid flowing through higher conductivity fractures, a phenomenon known as geothermal short-circuiting. The phenomenon of geothermal short-circuiting occurs when the injected fluid tends to flow through the path of higher conductivity, cooling the adjacent rock matrix and causing further fracture aperture increase and enhancing the flow concentration (Hu and Ghassemi, 2020). This phenomenon becomes an issue because the flow concentration only utilizes larger fractures, which decreases heat extraction efficiency as the smaller, hotter fractures are not utilized.

The effect of fracture aperture in a 1.5-inch granite core sample focused on chemical and mechanical attributes was investigated experimentally using a triaxial apparatus (Caulk et al., 2016). The experimental results indicated chemical dissolution was the primary mechanism for decreasing permeability over time. Similar triaxial apparatus experiments investigated heat transfer and fracture evolution (Huang et al., 2019; Zhang et al., 2022). The experimental investigation by Huang et al. (2019) indicated that fractures with large roughness decrease seepage, which is highly affected by confinement pressure. Zhang et al. (2022) experimental results showed that fracture apertures and permeability decreased using distilled water, while a decrease in aperture and permeability was noticed using simulated geothermal fluids. Using 3D printing technology, Xie et al. (2021) investigated the effect of fracture roughness in a 7.5-inch long cross-fracture flow, where it was found that a large rough fracture branch exhibits higher pressure drop loss, and with increasing injection pressure, the pressure drop loss tends to decrease. Hu and Ghassemi (2020) used a cubical 13-inch granite block consisting of an injector and several producers, where it was concluded that the effective fracture area controlling the heat extraction and the distance between the injection and production wells needed to be optimized.

Many experimental systems have been studied to investigate fluid flow and heat transfer characteristics in EGS. However, limited research has considered multi-fracture configurations. The multi-fracture EGS configurations still had limitations with varying fracture temperatures and singular inlet/outlet configurations (Cherubini et al., 2017; Hu and Ghassemi, 2020). Another limitation is the scalability of the proposed experiments, especially for heat extraction, as most of the performed experiments were on the core sample scale, i.e., less than 8 inches.

This work aims to design a large-scale dual fracture experimental flow loop to address fluid flow and heat transfer in EGS settings. The experimental design is a dual fracture system that can control each fracture temperature independently at constant and varying temperatures. This paper presents the experimental results for a single fracture with water as the working fluid.

2. Methodology

2.1 Experimental setup

The dual-channel experimental setup consists of granite rock slabs with specific dimensions to form the desired fracture anatomy for each channel. Each slab has a 10 ft long test section, as shown in the diagram of the experimental setup in Figure 2, and Figure 3 shows the setup configured in the laboratory.

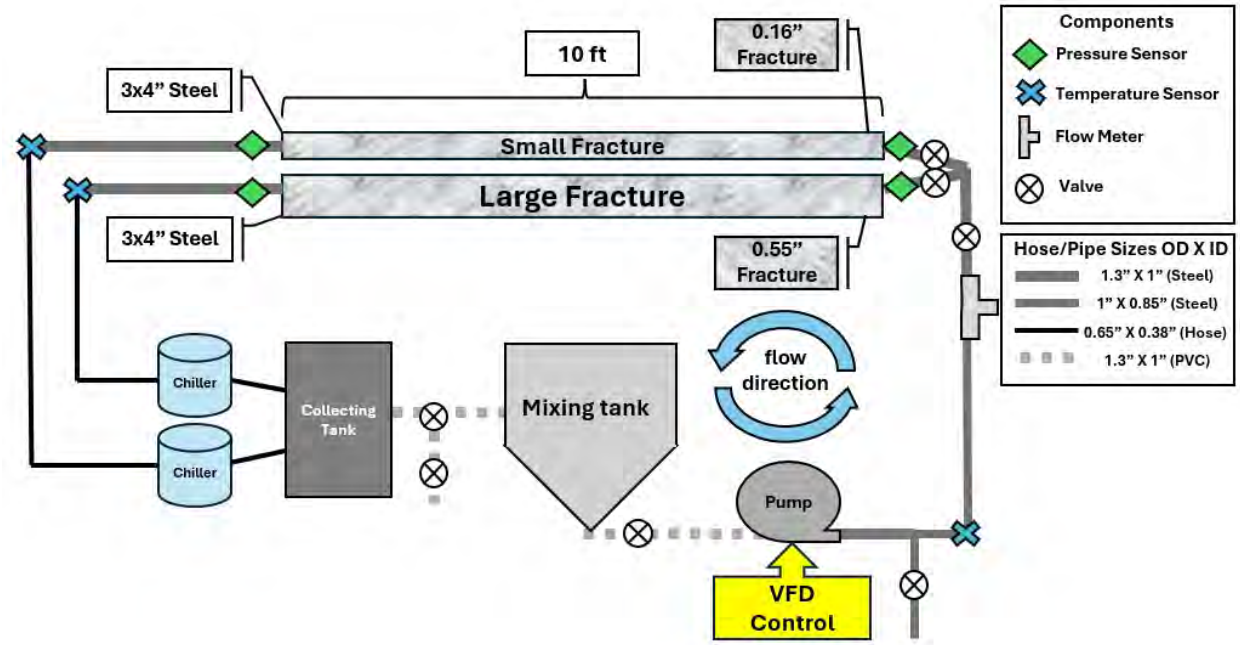

Figure 2: Experimental flow loop diagram

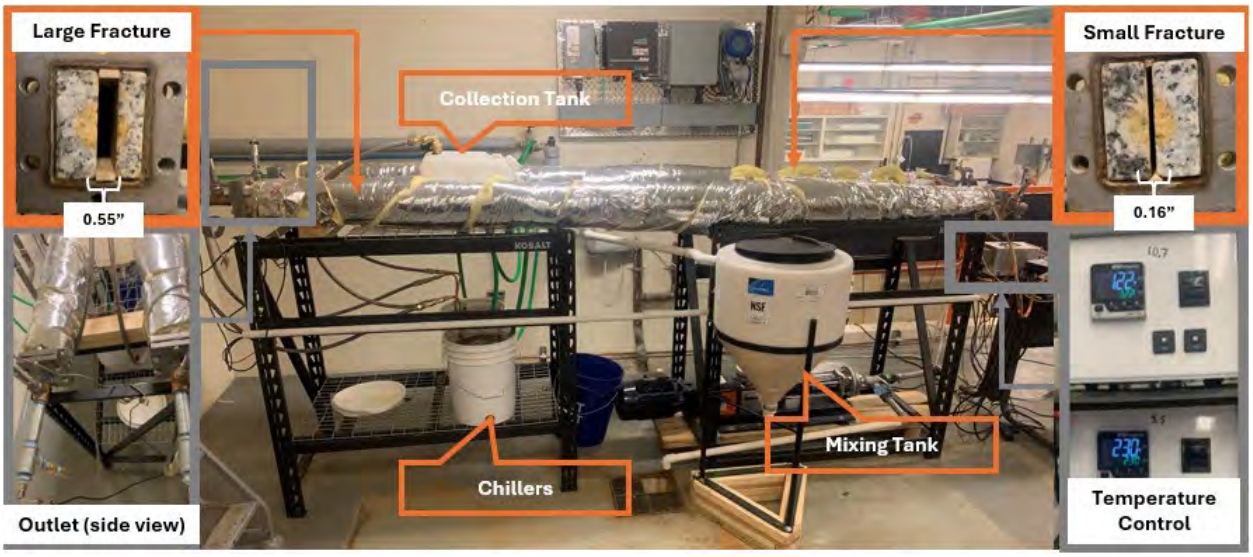

Figure 3: Geothermal flow loop design

A progressive cavity pump, controlled by a variable frequency device (VFD), injects the working fluid into a single pipe. Following the pump is a flow meter installed at the inlet, where the flow branches into the two fractures. Each branch consists of a valve at the inlet side, allowing the system to be used as a single fracture configuration and a dual fracture configuration. The 10 ft flow channels consist of a small fracture with an aperture of 0.16 in (4mm) and a large aperture fracture of 0.55 in (14 mm), as shown in Figure 3. Four pressure sensors are installed at the inlet and outlet of each fracture, and Resistance Temperature Detector (RTD) temperature sensors are installed at the inlet and outlet to collect the fracture's inlet and outlet temperatures. The small and

large fractures are heated and controlled independently with two heating cables on each fracture. Each flow channel is insulated with one high-temperature fiberglass layer and four aluminum-covered fiberglass layers. The data from the flow loop is collected from all the sensors using an analog data acquisition module. Once the working fluid has reached the end of each fracture, it flows into the chillers and is cooled by tap water. Following the chillers, the fluid is combined in the collecting tank, which then returns the fluid to the mixing tank, completing the flow loop and allowing for continuous circulation of the working fluid.

2.2 Testing procedure and data analysis

In this paper, the flow loop was configured to have the large fracture valve closed to analyze the behavior of the small fracture. Water was chosen as the working fluid for these experiments, and twenty different test scenarios were performed. The test scenarios consisted of five flow rates and four applied temperatures. The applied temperature was set for the small fracture by setting the thermostat for the temperature controller. The pump started with the VFD control using LabView, and pressure and temperature sensor data were collected for approximately 180 seconds, initiated by the user starting the data recording software.

The raw data was processed to generate pressure drop vs. flow rate analysis for each temperature to summarize the effect of each applied temperature scenario. The raw data was processed for the room temperature tests by removing the data during the start and end of the test and averaging the steady data to calculate the pressure drop across the fracture. For the tests where the temperature is applied, pressure drop behavior was analyzed at the maximum fluid outlet temperature period and 180 seconds from the start of the test to capture the fracture's heat loss behavior.

3. Results

The small fracture data was analyzed for twenty different data sets for each flow rate and applied fracture temperature. The raw datasets included inlet and outlet pressures, inlet and outlet temperature, and calculated pressure drop using the inlet and outlet pressures. The testing matrix consisted of four flow rates, including 1, 1.25, 1.5, 1.75, and 2 gallon/min (GPM), where the applied fracture temperature consisted of Room Temperature, 122 °F, 176 °F, and 230 °F.

The raw data for the room temperature tests for different flow rates is shown in Figure 4, where temperature indicates the measured outlet temperature of the fluid. The outlet temperature remained relatively constant at 75 °F for each room temperature test. The inlet and outlet pressures (P_i , P_o) and calculated pressure drop (ΔP) stay within the same 0.10-0.45 psi range. The system remains relatively constant over time, and the increase in flow rate causes an increase in pressure drop. Each test had a similar amount of fluctuation and no significant abnormalities.

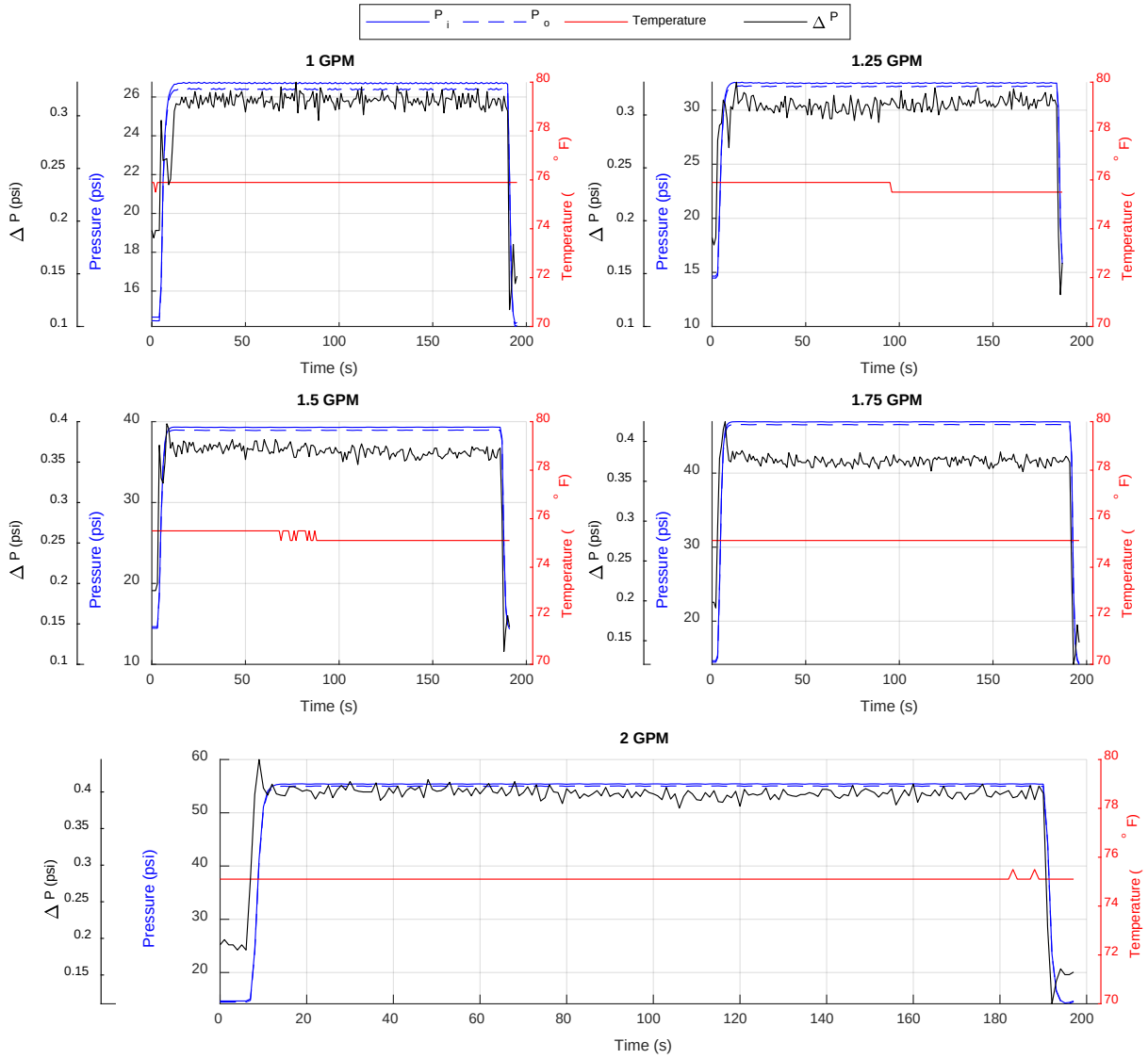

Figure 4: Experimental results showing the raw data for room temperature with different flow rates.

A single test was chosen to compare the raw data system behavior when the fracture is at a higher temperature and mid-range flow rate. Figure 5 shows the raw data for 1.25 GPM at an applied fracture temperature of 230 °F. The difference between the room temperature tests and the 230 °F applied temperature test is that the temperature readings for room temperature remain constant. In contrast, with the 230 °F applied fracture temperature readings, the outlet temperature decreases, and the inlet temperature increases with time. The pressure drop value exceeds the room temperature range at 0.1-0.6 psi. The pressure drop changes over time, increasing with increasing time. This behavior of increasing pressure drop with increasing temperature is due to increased water viscosity when the temperature decreases. As the granite begins to cool, the flow temperature decreases, which impacts the water's properties. Higher water viscosity creates higher resistance; therefore, more pressure drop is required to initiate flow movement. Overall, the raw data shows a difference between the system response when higher temperatures are applied.

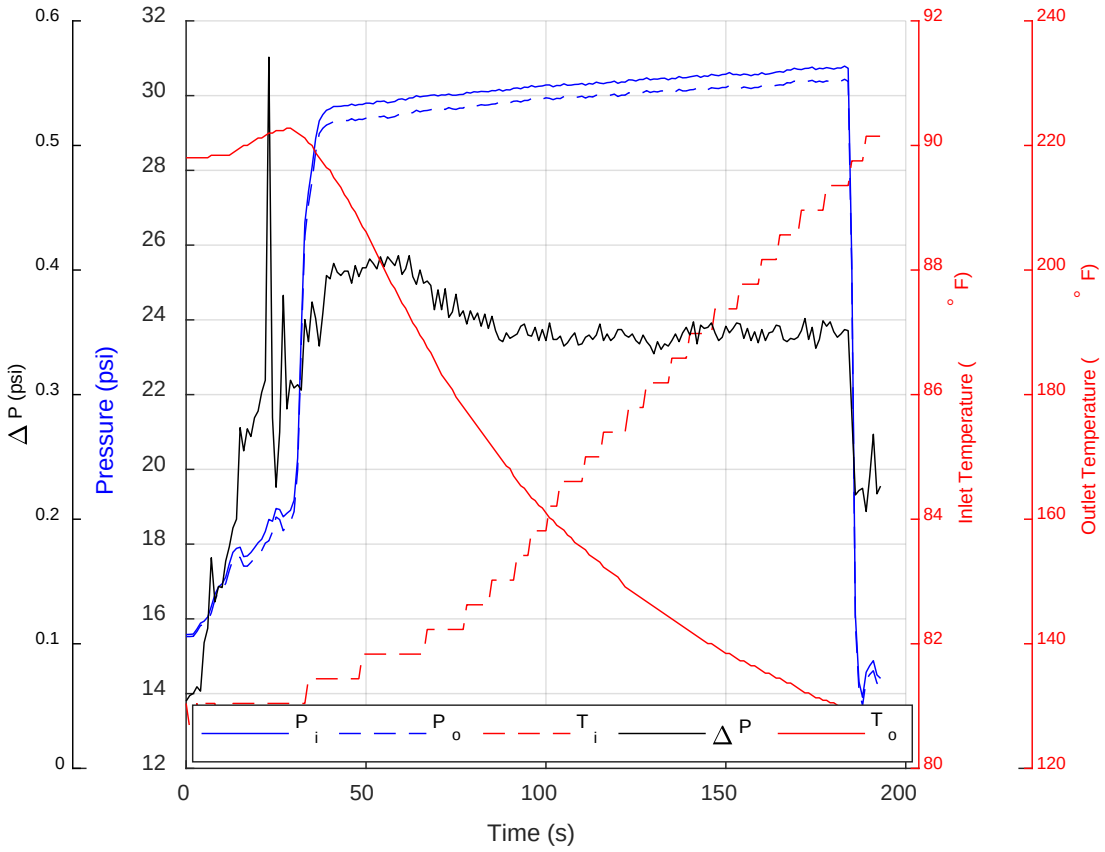

Figure 5: Raw flow loop data for 1.25 GPM at an applied temperature of 230 °F.

Figure 6 summarizes the effect of temperature on pressure drop when the maximum temperature is reached. Room temperature displayed an increasing pressure drop as the flow rate increased. For increasing temperature, the expected trend is to see a decrease in pressure drop compared to water due to a reduction in viscosity. However, not all the tests behaved consistently with increasing temperature. Tests at 122 °F and 176 °F primarily decreased in pressure drop with increased temperature compared to room temperature tests, but the 230 °F did not follow this trend. The 230 °F test followed this trend for only one flow rate at 1.75 GPM. The overall trend for comparing pressure drop versus flow rate is that pressure drop increases with increasing flow rate and decreases with increasing water temperature.

The pressure drop versus flow rate after 180 seconds of flow is shown in Figure 7. The pressure drop results after 180 seconds show a similar pattern for most applied temperatures compared to the pressure drop at the maximum temperature. The pressure drops tend to increase with increasing flow rate. When comparing room temperature to the other applied temperatures, there is a similar trend to the previous analysis, with 122 °F and 176 °F having decreasing pressure drops and 230 °F not following the same trend.

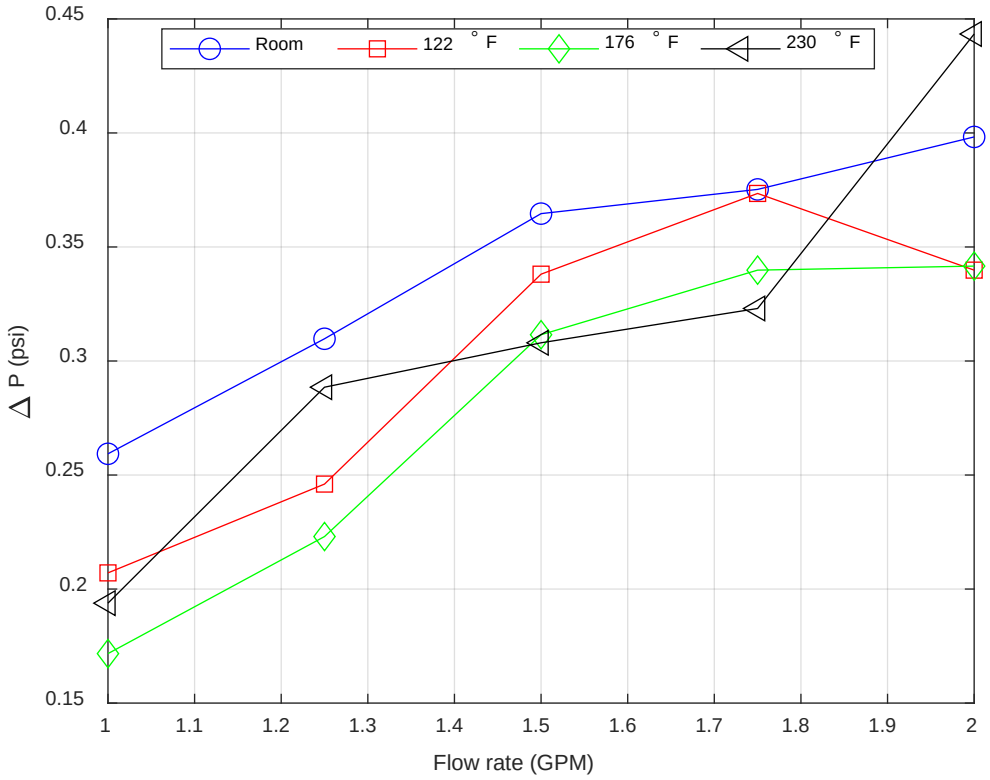

Figure 6: Pressure drops vs flow rate for varying temperatures at maximum fluid temperature.

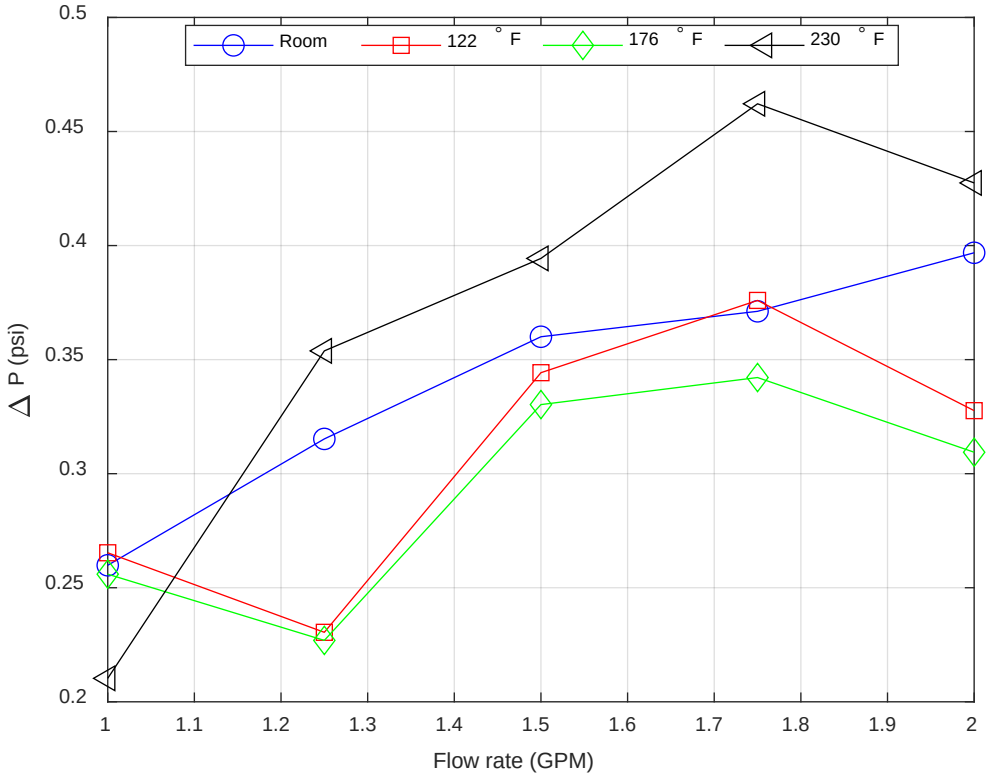

Figure 7: Pressure drops vs flow rate for varying temperatures after 180 seconds.

Overall, comparing the results at the maximum temperature and 180 seconds confirms the system's behavior is relatively consistent compared to room temperature tests, except for the 230 °F test. Due to 230 °F showing the most variation and inconsistency, additional analysis on flow regime behavior was performed to determine whether the temperature or flow regime is the more dominant factor in pressure drop analysis. Figure 8 shows the pressure drop vs Reynolds number for varying flow rates and applied fracture temperatures. This figure shows that most applied temperature tests have some turbulent behavior at differing flow rates. Room temperature remains primarily in the laminar and transitional flow regimes, while 230 °F is primarily in the turbulent flow regime region. This explains why the 230 °F tests did not follow a continuous pattern along with the other high temperature tests. This change in flow regime is also likely causing the 122 °F and 176 °F tests to vary after a specific flow rate is reached. Overall, this analysis with flow regime explains the variation in the pressure drop behavior and gives further insight into the behavior of the small fracture of the flow loop.

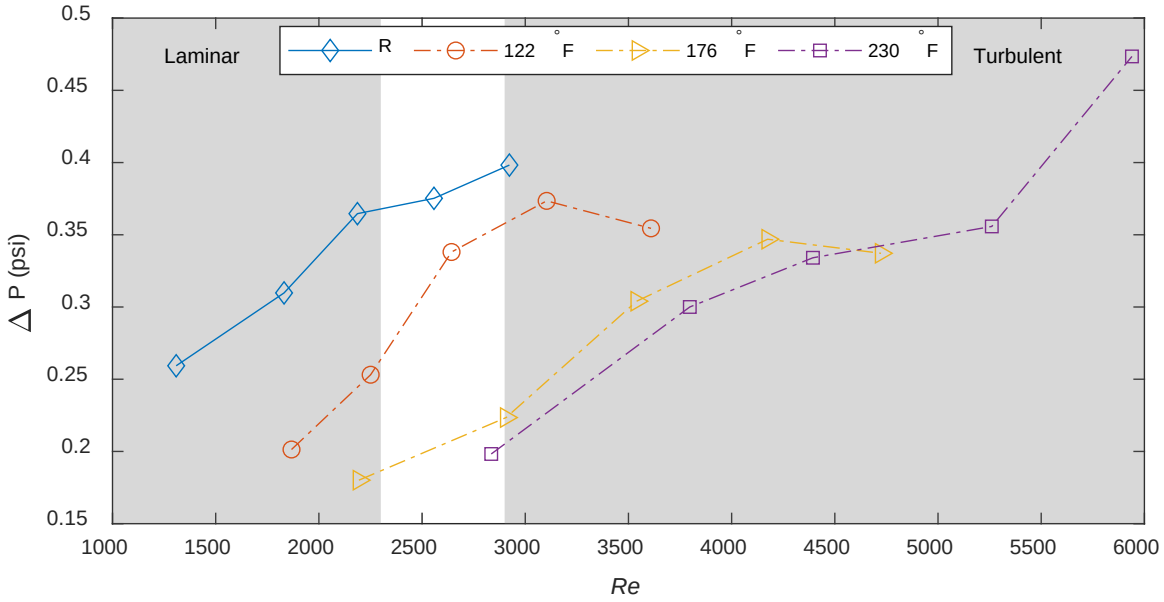

Figure 8: Pressure drop vs Reynolds number for varying flow rates and applied fracture temperatures

To analyze the decline in fluid temperature, i.e., heat extraction, the difference between the peak temperature and temperature at 180 seconds was calculated. This temperature difference was then divided by the time difference from peak temperature to the temperature at 180 seconds to obtain the rate of temperature change. This value was then plotted for each applied temperature as a function of flow rate, as shown in Figure 9, and the results are summarized in Table 1.

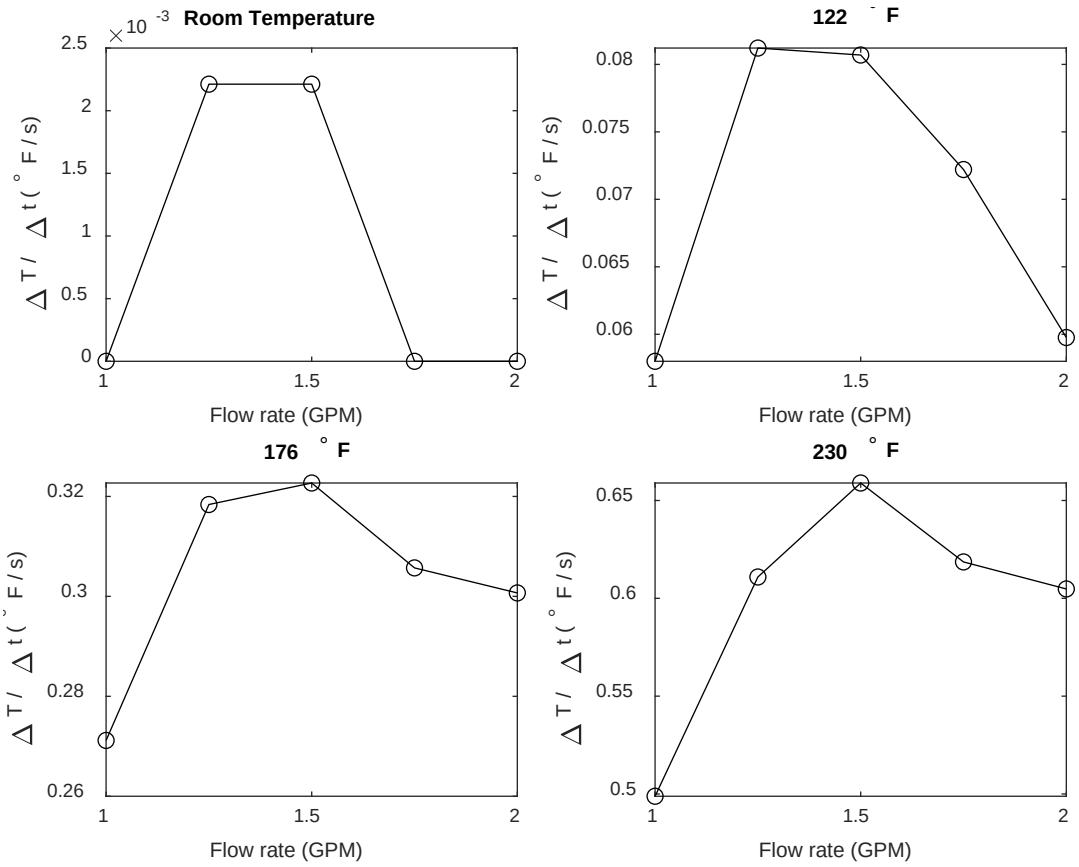

Figure 9: Rate of temperature change versus flow rate for varying applied temperatures.

Table 1: Summary of the rate of temperature change versus flow rate for varying temperatures.

Flowrate (GPM)	ΔT / Δt (°F / s)			
	Applied Temperature (° F)			
	Room	122	176	230
1	0.00	0.06	0.27	0.50
1.25	0.00	0.08	0.32	0.61
1.5	0.00	0.08	0.32	0.66
1.75	0.00	0.07	0.31	0.62
2	0.00	0.06	0.30	0.60

Figure 9 shows that the small fracture system reached a relatively consistent optimum heat extraction rate at a flow rate of 1.5 GPM. Additionally, Table 1 shows a consistent increase in temperature change over time as the applied temperature increased. Room temperature showed an expected result of little to no heat extraction, and 230 °F showed the highest heat rate at 0.66 °F/s. Overall, these results show a component of flow behavior that changes at 1.5 GPM, resulting in an optimal heat extraction rate.

4. Conclusion

The small fracture results for this project show relatively consistent behavior except for applied temperature tests at 230 °F. The tests were analyzed further with dimensionless number analysis to confirm that the flow regime affected the fracture's pressure drop, which caused some high temperature tests to have differing behavior. The results for the small fracture heat extraction rate over time for varying temperatures show promise for developing more efficient heat extraction strategies. These results show that the single fracture system reaches a consistent optimum value, creating the potential for further studies to investigate optimization techniques for enhancing geothermal heat extraction. Future work includes analysis of the large single fracture configuration data, dual constant temperature fracture analysis, varying large fracture temperature analysis, and running the same tests with different working fluids in the flow loop.

Acknowledgments

This material is based upon work supported by the U.S. Department of Energy's Office of Energy Efficiency and Renewable Energy (EERE) under the Geothermal Technologies Office Award Number DE-EE0009788.

REFERENCES

Atashnezhad, A., Akhtarmanesh, S., Kjeldal, V.N., and Al Dushaishi, M.F. 2023. "Advancing Enhanced Geothermal Reservoirs with Ionic Liquids as Potential Geothermal Fluid." Presented at the Presented at the Geothermal Rising Conference, Oct 1-4, Reno, NV, GRC Transactions, Vol. 47.

Brown, D.W. 2000. "A Hot Dry Rock Geothermal Energy Concept Utilizing Supercritical Co2 Instead Of Water." In Proceedings of the twenty-fifth workshop on geothermal reservoir engineering, Stanford University (pp. 233-238).

Caulk, R. A., Ghazanfari, E., Perdrial, J.N., and Perdrial, N. 2016. "Experimental Investigation of Fracture Aperture and Permeability Change within Enhanced Geothermal Systems." *Geothermics* 62 (July):12–21.

Cherubini, C., Pastore, N., Giasi, C.I., and Allegretti, N. M. 2017. "Laboratory Experimental Investigation of Heat Transport in Fractured Media." *Nonlinear Processes in Geophysics* 24 (1): 23–42. https://doi.org/10.5194/npg-24-23-2017.

Gao, X., Li, T., Meng, N., Gao, H., Li, X., Gao, R., Wang, Z., and Wang, J. 2023. "Supercritical Flow and Heat Transfer of SCO2 in Geothermal Reservoir under Non-Darcy's Law Combined with Power Generation from Hot Dry Rock." *Renewable Energy* 206 (April):428–40.

"GeoVision: Harnessing the Heat Beneath Our Feet." 2019.

Hu, L., and Ghassemi, A. 2020. "Heat Production from Lab-Scale Enhanced Geothermal Systems in Granite and Gabbro." *International Journal of Rock Mechanics and Mining Sciences* 126 (February):104205.

Huang, Y., Zhang, Y., Yu, Z., Ma, Y., and Zhang, C. 2019. “Experimental Investigation of Seepage and Heat Transfer in Rough Fractures for Enhanced Geothermal Systems.” *Renewable Energy* 135 (May):846–55..

Kazemi, S., Nor, M.I.M., and Teoh, W.H. 2020. “Thermodynamic and Economic Investigation of an Ionic Liquid as a New Proposed Geothermal Fluid in Different Organic Rankine Cycles for Energy Production.” *Energy* 193 (February):116722.

Momoh, I., Lee, H.P., Atashnezhad, A., and Al Dushaishi, M.F. 2023. “Fracture Conductivity Tuning in Granite under Triaxial Loading Using Ionic Liquids: Implications for Enhanced Geothermal Systems.” Presented at the Presented at the Geothermal Rising Conference, Oct 1-4, Reno, NV, GRC Transactions, Vol. 47.

Xie, J., Gao, M., Zhang, R., Liu, J., Liu, Y., Yang, B., Wang, M., and Wang, F. 2021. “Fluid Flow Characteristics of Cross-Fractures with Two Branch Fractures of Different Roughness Controlled by Fractal Dimension: An Experimental Study.” *Journal of Petroleum Science and Engineering* 196 (January):107996.

Zhang, P., Zhang, Y., Huang, Y., and Xia, Y. 2022. “Experimental Study of Fracture Evolution in Enhanced Geothermal Systems Based on Fractal Theory.” *Geothermics* 102 (June):102406.

Integrated Lifecycle Simulation for Utah FORGE: Part I – Fracture Geometry Calibration

Abdul Muqtadir Khan[1], John Mclennan[2], Olga Kresse[1], Kevin England[3], Pengju Xing[2], Brandon Hobbs[1], and Benoit Deville[1]

[1]SLB; University of Utah[2]; E-K Petro Consulting LLC[3]

Keywords

Enhanced Geothermal Systems, Complex Fracture Modeling, Fracturing Calibrations with Microseismic and Stain Data

ABSTRACT

The study explores the value extraction through the fracture geometry calibration component of end-to-end lifecycle simulations for the 16A(78)-32 and 16B(78)-32 injector-producer pair at the Utah Frontier Observatory for Research in Geothermal Energy (FORGE). Forward modeling was conducted with rigorous geomechanical, fracture propagation models calibrated with micro earthquake (MEQ), production logging, and strain data during fracturing and circulation.

The 3D geomechanical model was built from the structural geologic features and the thermal and mechanical properties profiles. In the first step of calibration, elastic properties were calculated from openhole logs and empirical core test data. A high-fidelity discrete fracture network (DFN) was used as an input in the 3D geo-model. The DFN was built based on data sets collected from five wells, microseismic monitoring during a 2022 stimulation campaign to constrain fracture orientations and intensity, and fracture characterization in well 16B(78)-32. The simulations were conducted in a 3D nonhomogenous mode with stress shadowing and fracture interactions. Next calibration was conducted using the MEQ data acquired in the stage 3 stimulation of well 16A(78)-32 in April 2022. The stress model, leakoff, DFN, stress anisotropy, fracture toughness were calibrated. Forward modeling was then conducted for phase2 stimulation in April 2024 with the calibrated properties. Connection efficiency of the doublet was also inferred from the modeling results. All the modeling results including fracture hits and connection efficiency were validated with the newly acquired MEQ, strain evolution, thermal strain datasets.

1. Introduction

Optimizing fracture propagation and network generation is critical for enhanced geothermal systems (EGS) development. The induced hydraulic fractures provide conductive systems through proppant packs. These enhanced flow-paths allow fluid to circulate throughout the fractured hot rock system and transfer heat through conduction. This heat is transported back to surface. An alternate success strategy for EGS could rely on large preexisting fractures such as in the Soultz project. But this precursor often does not exist in EGS candidates, pushing us to ensure successful fracture optimization. All the necessary, relevant aspects such as fracture propagation, stress interference, slurry flow, interaction with natural fractures, and materials selection (fracturing

fluid, proppant, circulation fluid) need to be considered. Also, changes in the thermoelastic, geomechanical, and geochemical dynamics during the lifecycle of EGS become pivot points for decision-making.

Integrated subsurface modeling facilitates strategy optimization for 15-30-year lifecycle of the project. The modeling needs to account for aspects related to fracturing, circulation, heat transfer mechanisms, and fluid-rock interactions. Coupled thermo-hydro-chemical-mechanical processes and stochastic techniques are critical. Kresse et al. (2024) have detailed a review study identifying research gaps and technological challenges in these domains.

Utah Frontier Observatory for Research in Geothermal Energy (FORGE) is a dedicated underground geothermal field laboratory for developing, testing, and accelerating breakthroughs in EGS technologies to advance geothermal resource development. Eight wells have been drilled at the Utah FORGE site. Five (58-32, 56-32, 68-32, 78-32 and 78B-32) are primarily for in-wellbore testing and monitoring purposes. A water well was drilled late in 2023 to provide water for a fracture stimulation program performed in April 2024 and an upcoming circulation test in early August 2024. There highly deviated 16A(78)-32 and 16B(78)-32 wells serve as doublets to evaluate the EGS concept. **Fig. 1** shows the location is on the flank of the structure separated from the conventional hydrothermal reservoir in the East Blundell power plant by the Opal Mount fault. The doublet subhorizontal wells are landed around 200°C with the deviated section covering from 6,000-ft to 8,000-ft in vertical depth. The reservoir comprises of low permeability granitic basement rock.

In the part-I of this paper related to the lifecycle simulations for the FORGE project, we cover the fracture simulations, measurements, and calibration component. All the logging and measurements from multiple wells, microearthquakes (MEQs), and strain data from fiber optics (FO) were used for the fracture modeling and calibrations.

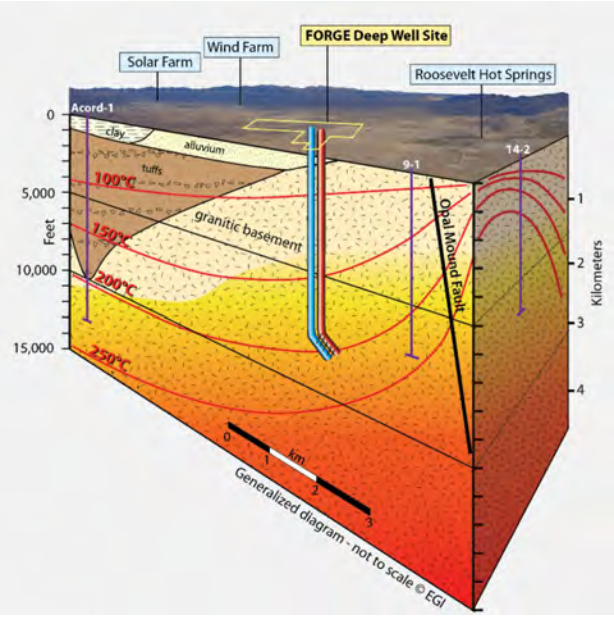

Figure 1: Cross section of the injector-producer doublet at the FORGE site with the subsurface isothermal contours (Moore et al. 2020).

2. Fracturing and Completion Summary at Utah FORGE

Injection well 16A(78)-32 was drilled and completed between October-2020 and January-2021. Following completion, injection tests were performed in the 200-ft openhole section below the 7” casing shoe to determine formation properties of the granite reservoir (Xing et al. 2021).

In April-2022, equipment was mobilized for fracturing treatments to determine fracture initiation and propagation behavior in the openhole section of the wellbore and through perforation intervals. Three fracturing stages were pumped (1 in openhole, 2 through perforations). The perforated stages were strategized to connect with the pre-existing fractures analyzed through image logs. Fracturing execution was conducted. The MEQ interpretation showed differences in fracture geometry and was used as the guide for drilling the production well to intersect the MEQ event clouds (McLennan et al. 2023).

In April-2023, the production well 16B(78)-32 was drilled with a 65° deviated section with the wellbore parallel, at the same azimuth, and 300 ft vertically directly above the 16A(78)-32 wellbore. A circulation test was performed by injecting water into 16A(78)-32 and monitoring the pressure and outflow from 16B(78)-32. Pressure increase was observed in 16B(78)-32 during two two-day injection periods, and outflow from 16B(78)-32 was still increasing during the second injection period when test was stopped. However, the outflow rate was very low compared to the injection rate into well 16A(78)-32. This was attributed to the recharge of the fracture network system between the two wells due to the large amount of fluid that flowed back from the fracturing treatments pumped in April 2022.

Three separate FO cable were run outside the 7” casing: two of the cables near the 7” casing shoe and one cable to a depth just after the end of the build section. The cable run to just below the end of the build section was for a pressure and temperature gauge that was ported into the 7” casing. After the special section of the wellhead was installed and the surface connections were completed and tested, the cementing treatment for the 7” casing was pumped and monitored by the fiber optic cables.

Following a wellbore cleanout run with the drillstring, a second circulation test was performed. The maximum injection rate was increase to 7.5-bpm from 5-bpm in the first circulation test. With the 7” casing cemented in place, the only place for the wells to communicate would be the 739-ft openhole section of 16B(78)-32. The second circulation test was also performed over a two-day period. On the first day, the injection rate into 16A(78)-32 was 5-bpm for most of the time and then increased to 7.5-bpm. Wellhead pressure and outflow rate were monitored on well 16B(78)-32, and results were similar. There was a very rapid pressure connection between the two wells, and the outflow rate was increasing throughout the injection; however, the outflow rate was still very low compared to the injection rate into 16A(78)-32. On the second day, a production logging tool (PLT) was run in 16A(78)-32 at rates of 2.5, 5.0 and 7.5-bpm to determine the distribution of fluid into the Stage 1 (openhole), Stage 2 (perforated) and Stage 3 (perforated) intervals. The results of both circulation tests are detailed by by Xing et al. (2024).

The second phase of multistage fracture stimulation at Utah FORGE was planned for commercial-scale treatment designs with a larger number of stages evaluating the effect of fluid viscosity, number of clusters per stage, cluster spacing, proppant type, etc. Since well 16B(78)-32 was equipped with FO, the design strategy was to pump all the stages in 16A(78)-32 and use the FO

strain data to fracture hit locations. In 16A(78)-32, the pump-down plug and guns multistage fracturing method was utilized. The 3-ft guns were loaded at 6 shots/ft with 60° phasing. The number of clusters varied from one to eight, and the cluster spacing ranged from 25 to 50 ft. The proppant pumped was 100-mesh and 40/70-mesh silica sand. In one of the stages, a 30/80-mesh ultralightweight proppant was added in addition to the silica sand proppant to evaluate the effect on proppant transport and post-closure placement within the proppant-pack. For well 16B(78)-32, the 4-ft perforation guns were loaded at 10/350° phasing and oriented to avoid perforating the FO cables. The perforation operations were performed via tubing-conveyed perforating (TCP). The proppant pumped in 16B(78)-32 was also 100-mesh and 40/70-mesh silica sand.

The first stage (3R) was a refrac of the three frac stages pumped in April 2022, with the addition of proppant. Stage 3R was pumped as designed with slickwater. Stage 4 was a single cluster pumped as designed with slickwater. Stage 5 was a single cluster pumped as designed with crosslinked CMHPG. Stage 6 was treated at high pressure, but the pump rate was not high enough to begin pumping proppant. The treatment was shut down and an additional perforation gun was run near the original perforation cluster. The stage schedule was restarted, but pressure was still at maximum allowable pumping pressure, with minimal improvement in injection rate. Stage 7 guns were pumped down and three clusters were perforated. Stage 7 behaved similarly to Stage 6 and no proppant was pumped. After shutdown, it was suspected that geological anomalies may have been the reason for the problems experienced in Stages 6 and 7. Stage 8 was perforated with eight clusters spaced 25-ft apart. The stage was pumped as designed with crosslinked CMHPG fluid and placed a total of 1,081,500 lb_m of proppant at a pump rate of 80-bpm. Stage 9 was also perforated with eight clusters and 25-ft spacing, and the fluid was slickwater. Treating pressure began to increase during the 40/70-mesh steps, and flush was started prematurely to avoid a screenout. A total of 730,000 lb_m of proppant was placed into the formation, which is 68% of the designed amount. Stage 10 was added to the schedule with the same design as Stage 6, which included the 30/80-mesh ultralightweight proppant added with the silica sand proppant. Stage 10 was pumped to completion as designed with slickwater.

After analysis of the FO data in well 16B(78)-32 during the 16A(78)-32 frac stages, it was determined to increase to five stages compared to the originally planned four stages, to accommodate the TCP gun string design conditions. The first four stages were all pumped to completion as designed. Unfortunately, Stage 5 was not able to be pumped because there were no frac plugs available to isolate Stage 4. Stage 5 was perforated and could be stimulated at a later time.

Fig. 2 below shows all the relevant steps to consider while modeling and calibrating fracture propagation and geometry. It illustrates Phase 1 and Phase 2 of fracturing and related activities, providing context to the steps taken in the modeling workflow.

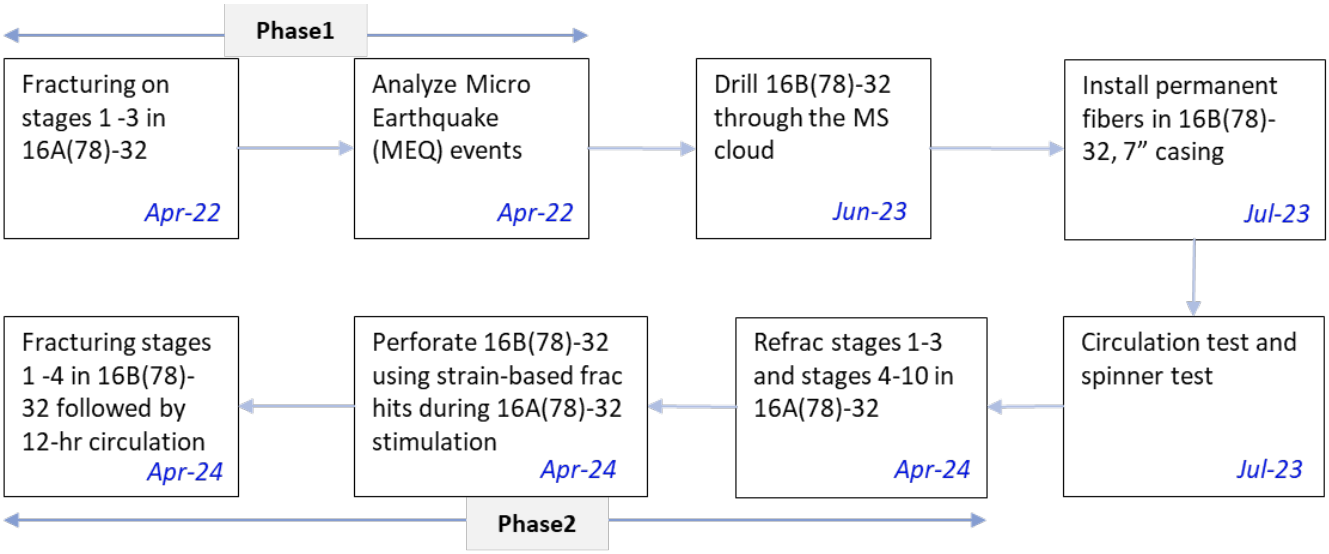

Figure 2: Event-wise workflow in phases 1 and 2 of fracturing at the FORGE site.

3. Geomodel Construction

The 3D model built for this study starts with the structural and geologic model based on faults and horizons. The model used here was built by Mulyani et al. (2024) and **Fig. 3** below shows the features and zonal 3D model based on the first steps in their work.

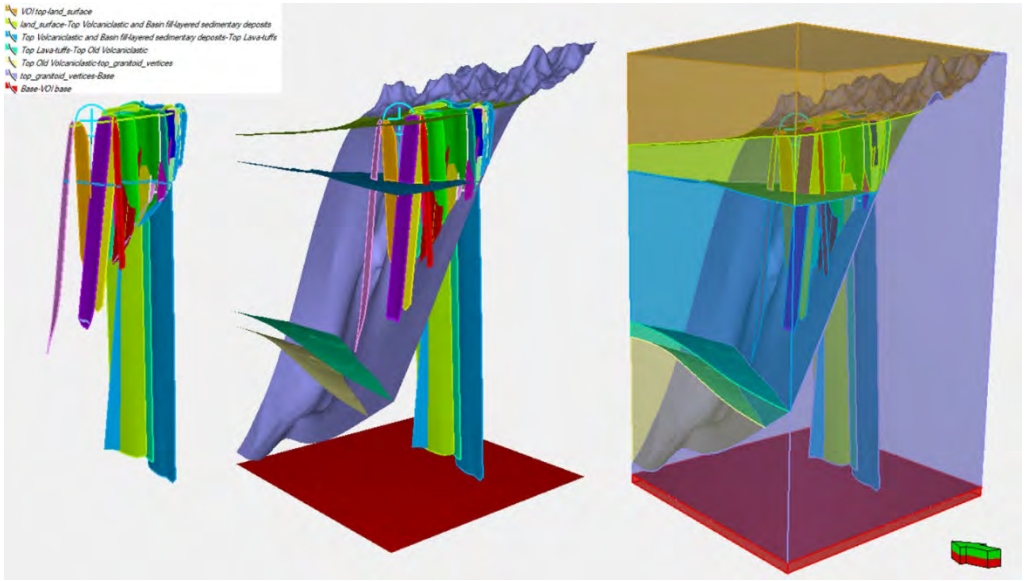

Figure 3: The geological structural model developed by Mulyani et al. (2024) showing (from L-R) faults, horizons, and zones constructed for 3D grid based on the horizon boundaries.

The structural tops (from top to bottom) used the volcaniclastic and basin fill layered sedimentary deposits, lava tuffs old volcaniclastic deposits, and granitoid vertices. The elastic properties model (in-situ stress, Young's Modulus, Poisson's ratio, etc.) demonstrated in **Fig. 4** was derived from

the continuous openhole logs measured in 16B(78)-32 across the lateral trajectory. The calculated elastic properties were propagated along the 3D structural model. Note that, compared with Figure 3 above, the 3D model is slightly truncated for fracture modeling. It captures the structural dip based on the isothermal contours, and the future parts will use the full structural model.

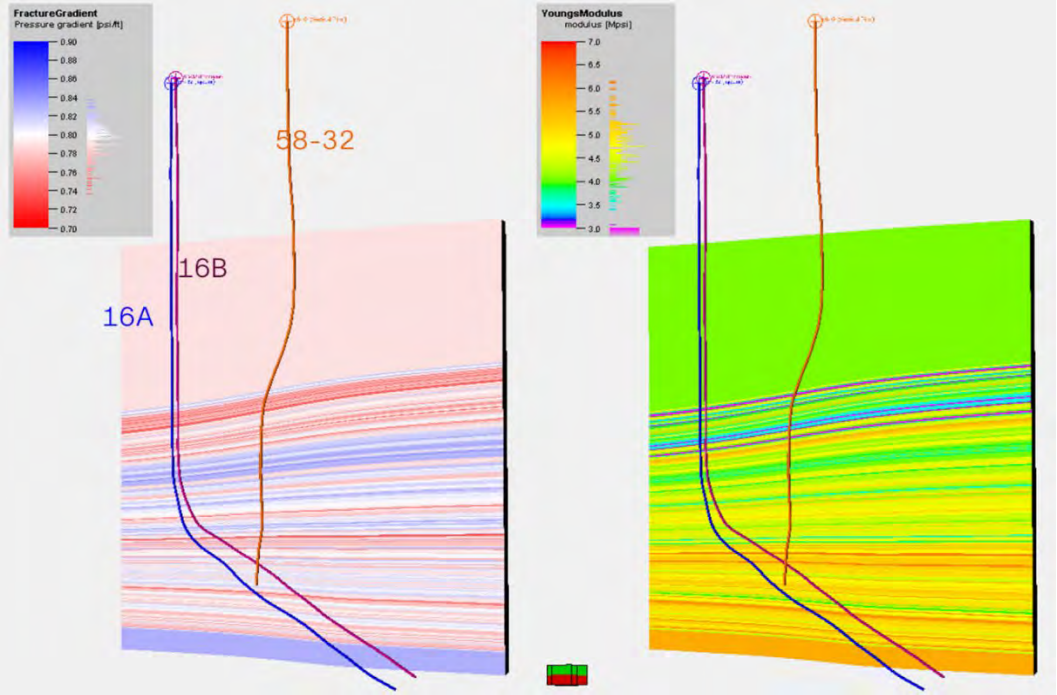

Figure 4: Elastic rock properties montage: (left) discretized fracture gradient and (right) Young's Modulus variation displayed in cross section across the vertical pilot well and the injector-producer doublet.

In addition to the layered zoneset, the properties used in the simulation model setup for the final calibrated model are detailed in **Table 1**. The tensile strength and fracture toughness inputs are from static triaxial testing conducted on the extracted cores (McLennan, 2018). The fracture azimuth (preferred fracture plane/S_{Hmax}) is taken from the 2000 fractures from FMI logs in well 58-32 (**Fig. 5**). The stresses in the base case model were slightly increased to match the MEQ data.

Table 1: Properties for the calibrated zone set model used for fracture simulations.

Fracture gradient	0.72 – 0.85	psi/ft
Young's Modulus	4 - 8	MMpsi
Poisson's Ratio	0.24 – 0.32	
Horizontal fracture toughness	1730	psi-in$^{1/2}$
Vertical fracture toughness	1520	psi-in$^{1/2}$
Tensile strength	1520	psi
Overburden gradient	1.13	psi/ft
S_{Hmax} gradient	0.79 – 0.92	psi/ft
Pore pressure gradient	0.46	psi/ft
S_{Hmax} azimuth	25	deg
Matrix permeability	0.00001	mD
Matrix porosity	0.2 - 2	%
Rock specific gravity	2.3	
Rock compressibility	1E-005	1/psi
Horizontal stress anisotropy	500 - 750	psi

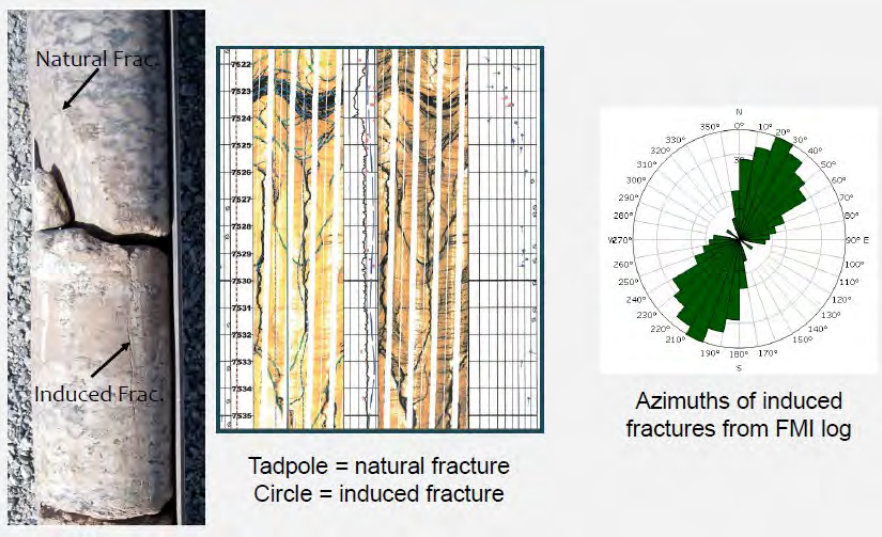

Figure 5: Core depiction, FMI log and rose diagram and poles predicted to upper hemisphere for induced fractures azimuth, in well 58-32. (Moore, 2019; McLennan et al. 2023)

The reference discrete fracture network (DFN) model for the FORGE, in this study is used to characterize both the natural fractures present in the reservoir and induced fractures created during hydraulic stimulation (Finnila and Jones, 2024). A deterministic set for fractures intersecting wells 58-32, 56-32, and 16A(78)-32 was included based on those features identified in the FMI log interpretation. It also includes fracture planes fitted to the seismic point cloud generated from the stimulation of well 16A(78)-32. In the most recent version, data from vertical well 78B-32 and deviated well 16B(78)-32 have been analyzed to refine fracture orientations and intensities.

Fracture sizes of this deterministic set were generated using the same truncated power-law distribution as the stochastic set, but only those larger than the minimum DFN size cutoff of 10-m radius were kept in the model. There are four fracture sets in total (refer to **Table 2** and **Fig. 6, left**). This 3D DFN was used to extract a total of 10,000 elements in a 2D DFN for fracture simulations (**Fig. 6, right**).

Table 2: Update fracture set parameterization (Finnila and Jones, 2024)

Set name	Description	Trend/Plunge [deg]	Strike/Dip [deg]	Fisher concentration	%
1	SSW-striking, vertical	114/2	204/88	22	30
2	South-striking, moderately dipping West	91/37	181/53	7	29
3	North-striking, moderately dipping East	230/52	320/38	4	21
4	East-striking, sub-vertical dipping South	354/16	84/74	9	20

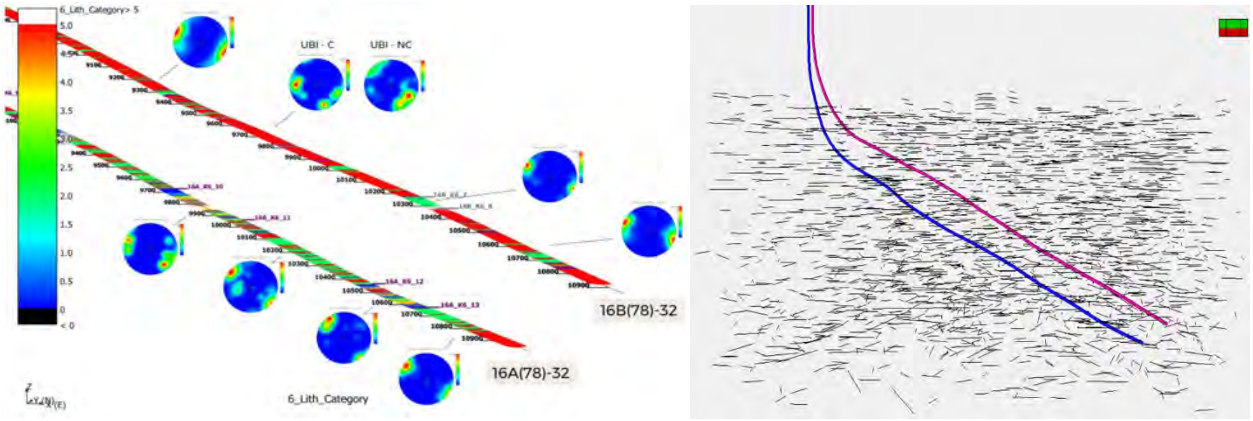

Figure 6: (left) Fracture pole orientations plotted in upper hemisphere stereonets for the deepest deviated sections of wells 16A(78)-32 and 16B(78)-32 (78)-32. Wells are colored by cluster label number using k=6 (Finnila and Jones, 2024); (right) Two-Dimensional DFN extracted from 3D DFN above for fracture simulations. Perspective looking north with the injector-producer doublet.

4. Fracture Model Exploration

The choice of an appropriate fracture model is crucial for obtaining comprehensive and reliable results on fracture shape. Historically, the development of hydraulic fracture models for oilfield applications started in the 1950s with simplified analytical and semi-analytical models. With the increase of the size of hydraulic fracturing treatments, the need for more advanced models applicable in layered reservoirs and needed for proper evaluation of the height of hydraulic fractures led to the development of Pseudo-3D (P3D) and eventually more complex planar 3D models. The review and description of these models could be found in Adachi et al, 2007.

While P3D models are CPU efficient, they are built on an assumption that reservoir elastic properties are homogeneous and averaged over all layers containing fracture height, which is applicable in many field cases. However, P3D models cannot handle complex reservoir stress profiles when the stresses vary non-monotonically as a function of depth or when unconfined height growth occurs. They cannot predict hourglass-shaped footprints when the middle layer in a multilayer system is stiffer than bordering layers. Planar 3D models were developed to handle these situations correctly while still considering the planar fracture geometry, predicting fracture growth in two-dimensional mesh, properly handling any stress profile for layered formations, and providing fully 3D width profile of the fracture (Adachi et al, 2007). Planar 3D models are successfully used in many field applications and considered as a “good enough” fracture propagation model for EGS applications. One of the disadvantages of these models is CPU performance, which has been considerably improved recently with the development of high-performance computing tools. However, planar 3D multi-cluster stimulations are still more expensive than P3D-based approaches and cannot handle interactions with pre-existing natural fractures. However, planar 3D multi-cluster stimulations are still more expensive than P3D-based approaches and cannot handle interactions with pre-existing natural fractures.

With the shale development, pressure analysis and matching, and by reviewing the MEQ events clouds in multiple wells and formations, it was concluded that fracture geometry is not always

planar, which could be attributed to interactions of hydraulic fractures with pre-existing discontinuities, stress shadow effect between closely located clusters, and to anisotropic 3D zone properties variation in some formations. These factors led to the development of complex fracture models (Kresse et al, 2012; Fu et al, 2012; McClure and Horne, 2013; Wu and Olson, 2015). The complex fracture models could be CPU intensive, so some simplifications are usually made to make them more CPU efficient while still capturing and properly handling the layer-related physics (Cohen et al, 2015). In many cases planar 3D models are used initially for fracture height evaluation, and then complex fracture models are applied with appropriate height restrictions.

When there is a need to pick the proper fracture model for EGS applications, several questions arise: What is the model expected to handle? What kind of formations, fluid Rheologies, proppant properties, and time scales are involved? Are there natural fractures or faults to be considered? The proper fracture model should be able to predict fracture propagation and height growth while accounting for the propagation regime and reservoir properties (impermeable, brittle, very hot rock), model fracture initiation, and model fluid and proppant transport while accounting for temperature and rheology changes. It should accommodate an advanced heat transfer model, including advection by fluids, heat transfer between the fracture and the rock, and heat conduction within the rock. It should also account for hydro-shearing and hydro-fracturing mechanisms in both stimulation and circulation phases, and account for thermoelastic and poroelastic stress changes and fracture reopening due to cooling during circulation.

We investigated both planar 3D and complex models (UFM) for EGS applications in this study to understand the implications of each and to determine the preferred one based on some observations.

5. Fracturing Simulations/Calibrations

This section will cover the calibration and forward modeling efforts with the available pumping data, acquired MEQ data, FO strain data, and PLT data (**Fig. 7** describes the workflow). The basecase was modeled to check the performance and compare with the MEQ point cloud, followed by the calibration workflow and forward modeling for all the stages on the lateral well 16A(78)-32. Note that in this part-I of the paper, the fluid flow modeling was not conducted.

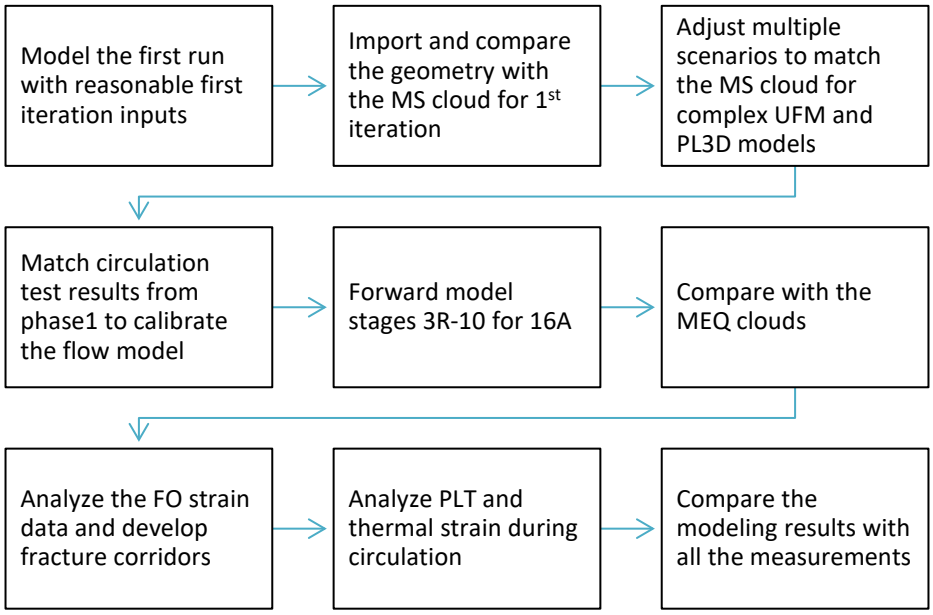

Figure 7: Modeling and calibration workflow using the MEQ, fiber and flow data.

5.1 Observations from the Microearthquake events

MEQ event cloud observations and interpretations and understanding are critical for calibration. **Fig. 8** shows the data from phase 1 of stimulation. Stage 1 showed the poorest event quantity (211 events) and quality (141-ft error) compared to Stage 2, which had 948 events and 41-ft error due to failure of some geophones. Stage 3 showed the best MEQ catalog with 1432 events with a mean error of 56-ft.

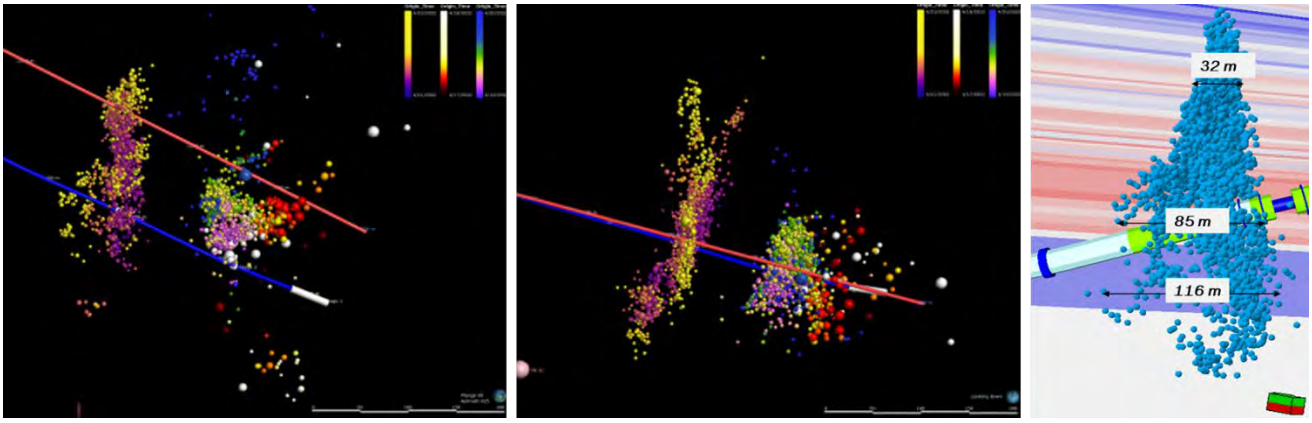

Figure 8: MEQ projection after 3-stage fracturing in phase 1. Perspectives looking north in vertical section (left) and plan view (middle). Events zoomed for stage 3 looking south showing the width of the network based on events up to 116-meters (right).

Finnila et al. (2023) provides some interesting observations in the process of extracting planes from the MEQ clouds. A total of 11 planes were fit to the full event cloud (4, 5, and 2 planes for Stages 1, 2, and 3, respectively), showing that Stages 1 and 2 grew in a relatively complex fashion

compared to stage 3. Even with Stage 3, there are two distinct planes, and focusing on the MEQ cloud, it also shows a width (S_{hmin} extent) of upto 116-meters, which indicates possible non-planarity. These two observations could be an impact of the DFN causing bending of the dominant fracture.

In phase 2, the event clouds show complex developments for the initial stages and stage 8 shows multiple networks. Stage 9 shows more planarity with some bending due to possible interaction. In the side view (**Fig. 9, middle; Fig. 9, right**), the complex event development is more evident. Moreover, the bottom barrier observed in phase 1 seems to be competent and most fracture height growth is observed towards the top which makes the producer lateral landing strategy viable (**Fig. 9, left**). The planarity of the fractures based on phase 2 data seems to be impacted by the treatment size and viscosity (crosslinked fluids).

MEQ events could either indicate the extending tensile fracture at the tip or a slip on a preexisting fault or plane of weakness. The latter would not contribute to fracture growth. Here, moment tensor inversion was conducted to impress the focal mechanism for tensional events. Additionally, a quality control exercise was performed to examine the magnitude and eliminate most of the shear slip events and noise.

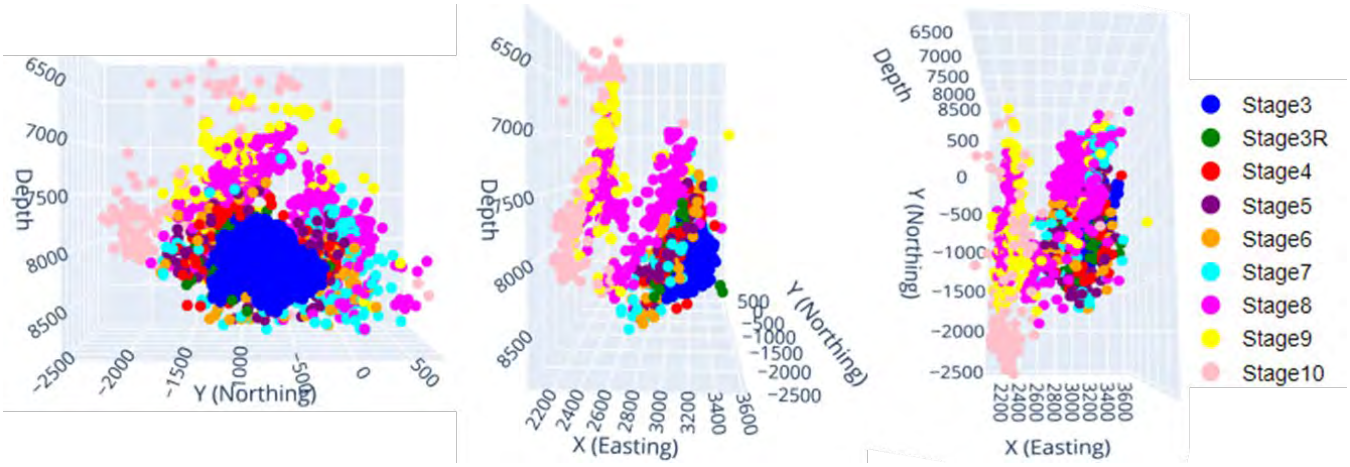

Figure 9: MEQ events projection during fracturing in phase 2. (left) gun-barrel view showing extension in the SHmax direction, i.e. fracture length; (middle) side view, network development in Shmin direction; (right) top view

5.2 Stimulation phase1 calibration workflow

Since Stage 3 gave the best MEQ event cloud with good accuracy, the chosen approach was to use Stage 3 to calibrate the basecase model. The modeling was conducted using complex UFM model as well as a planar 3D model. The leakoff model, stress model, and near-wellbore open perforations were changed for both models. Additionally, horizontal stress anisotropy and complexity index were calibrated for the UFM case. **Fig. 10** and **Table 3** show the comparison for both models. During the calibration exercise, it was observed that the length propagation was much higher for planar 3D model. We attempted to reduce the length propagation by increasing the total leakoff coefficient, but this significantly reduced the fracture height. It is important to note that if the

vertical (based on acoustic measurements) and lateral (structural consideration) variation in the 3D stress model is not considered, the upward height growth with the planar model can be misleadingly high. A constant stress gradient model across the vertical interval would lead to such modeling results. The UFM model matches the MEQ cloud better because of possible termination at a DFN element. Based on this observation and other compelling reasons provided by reservoir characterization through core testing, FMI logs, DFN modeling, etc. it was decided to utilize the UFM model for the forward modeling approach on the consequent stages.

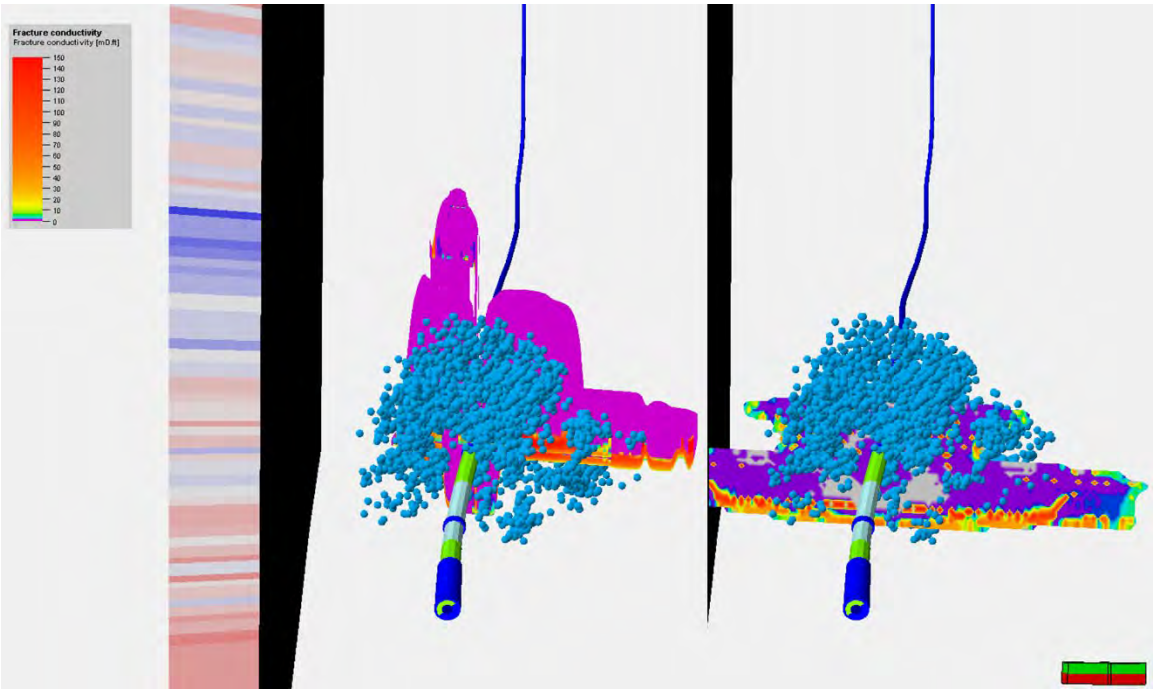

Figure 10: Fracture geometry after stress and leakoff model calibration with the complex UFM model (left) and the planar 3D model (right).

Table 3: Fracture geometry comparison for both propagation models.

	MEQ Point Cloud	UFM	Planar3d
Fracture half-length [ft]	522	596	1034
Max Fracture height [ft]	874	1159	519
Avg. Fracture conductivity [mD*ft]	NA	52.2	129.9

Another important aspect considered in this phase is to look at the expected downhole rheology of the fluid. The model uses rheology curves with exposure times at multiple temperature points. The viscosity is then interpolated by the solver as a function of temperature and exposure time at each grid block across the fracture. **Fig. 11** shows that most of the fracture geometry is exposed to a static rock temperature of 410°F, and the second largest fracture area is exposed to ~350°F. McLennan et al. (2023) presented a rheology curve for the CMHPG system, showing viscosity reduction below 40 cP and 10 cP after 2 and 3 hours of exposure, respectively. The same rheology profile was used in the model. Above 375°F, the viscosity input was 1 cP. It is noteworthy that the shear experienced by fluid is typically higher than tested in lab rheometers, so the expected fluid quality will be even lower. With these low viscosities, most of the proppant is expected to settle before fracture closure occurs. Hence, the conductivities in the upper part of the fractures could

cause multiple pinch points, affecting the connection efficiency between the doublets. This consideration was factored in phase 2 to account for accurate proppant transport, settling and also to conduct preliminary investigation on the impact of light weight proppant, pumped in Stage 10 of well 16A(78)-32.

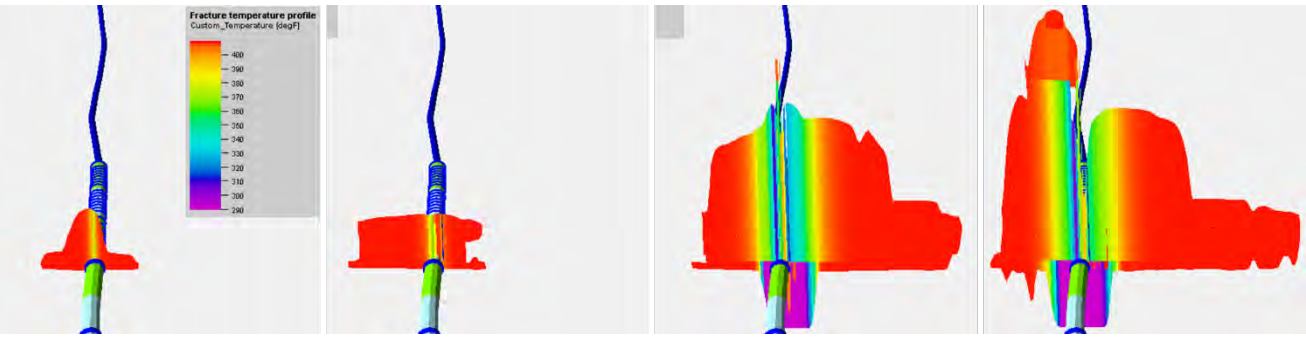

Figure 11: Temperature profile across fracture during pumping stage 3. Four snapshots at 1-hr intervals. The temperature scale here varies from 290°F to 410°F

5.3 Stimulation phase2 modeling

All the calibrated parameters from Phase 1 were used for the forward modeling presented in this section. Leakoff had to be reduced slightly for some of the stages to capture the larger fracture footprints. This could be due to the changes in system permeability as a consequence of DFN variations. Even though Stage 6 and Stage 7 were not successfully pumped, they were modeled because fluid was pumped in different attempts. **Fig. 12** shows a few perspectives of fracture network development. It is important to note that the middle and bottom figures have cutoffs implemented and do not represent the full hydraulic geometry. Stages 8, 9 and 10 show higher fracture conductivity development. The fracture propagation shows a limited impact of DFN in terms of complexity generation in the toe-side stages compared to heel-side. This is because the orientation of the fracture traces evolves from wellbore perpendicular to wellbore parallel as we move to the heel stage. The termination of a fracture when interacted with a DFN element depends on multiple criteria relevant to the fracture elements such as the approach angle, length, density, cohesive strength, etc. Hence, using the complex geomechanical propagation model is optimal whenever DFN is present in the formation. **Table 4** shows the comparison of the MEQ data with the modeling results. The relative results show a good agreement (also see figure 9), but the absolute results of the model are smaller. This is expected because the extent shown for MEQ is the furthest events captured and might just be due to critically stresses fracture slips or reactivation. The table also shows the Sh_{min} extent which is indicative of the fracture complexity versus planarity.

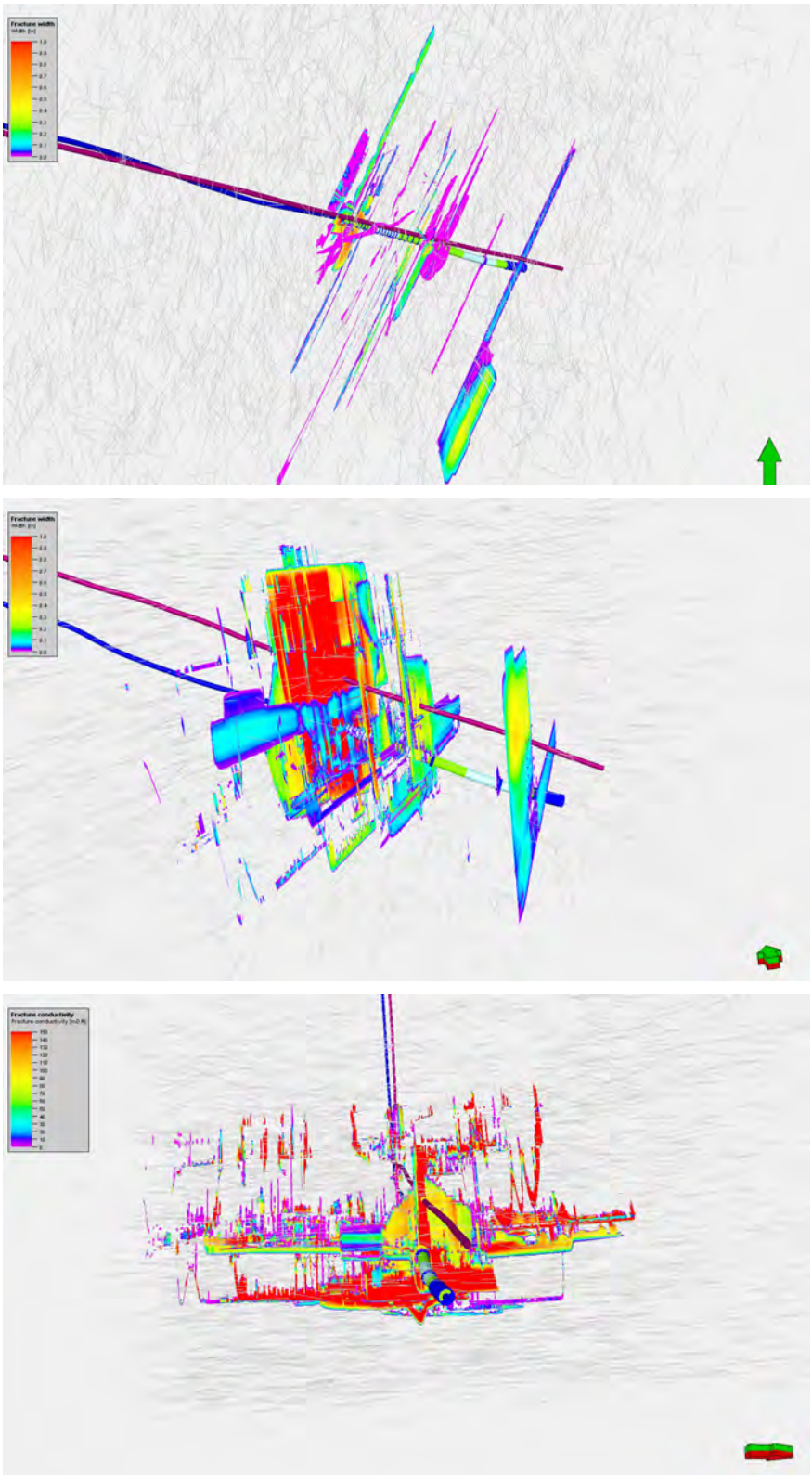

Figure 12: Fracture footprint for stages 1 – 10 with the DFN elements in grey. (top) fracture width profile in plan view; (middle) looking north with a fracture width cutoff of 0.1-in; (bottom) looking west, gun barrel, with conductivity cutoff of 1md.ft.

Table 4: Fracture geometry comparison (in principal stress directions) MEQ versus fracture modeling for phase2.

	MEQ		Fracture Model - UFM		MEQ
	S_{Hmax} Extent	Vertical Extent	S_{Hmax} Extent	Vertical Extent	S_{hmin} Extent
Stage 3R	1350	870	1193	1259	640
Stage 4	1500	1110	1561	984	680
Stage 5	1640	1280	1165	1347	670
Stage 6	1970	1360	1938	1266	650
Stage 7	2220	1650	2220	1084	910
Stage 8	2270	1900	1935	1441	1110
Stage 9	2230	2000	2493	1057	1430
Stage 10	3120	2530	1293	1680	1330

5.4 Production Logging Results Utilization

PLT results were insightful in modeling and understanding the large fracture geometries for stages 8 and 9. The fluid intensity was designed for 8 clusters but the cluster efficiency in these stages might have been ~50% with more fluid for the dominant clusters. The initial runs with the UFM model showed slightly higher cluster efficiency of 60-70% and the flux distribution data in **Fig. 13** helped calibrating that. The logging tool had limited access below stage 6. Low contribution from stage 7 stresses the importance of proppant. Stage 8 could not be decomposed to cluster level due to operational issues. Stage 9 highlights the heterogeneity and cluster non-uniformity considerations in EGS development.

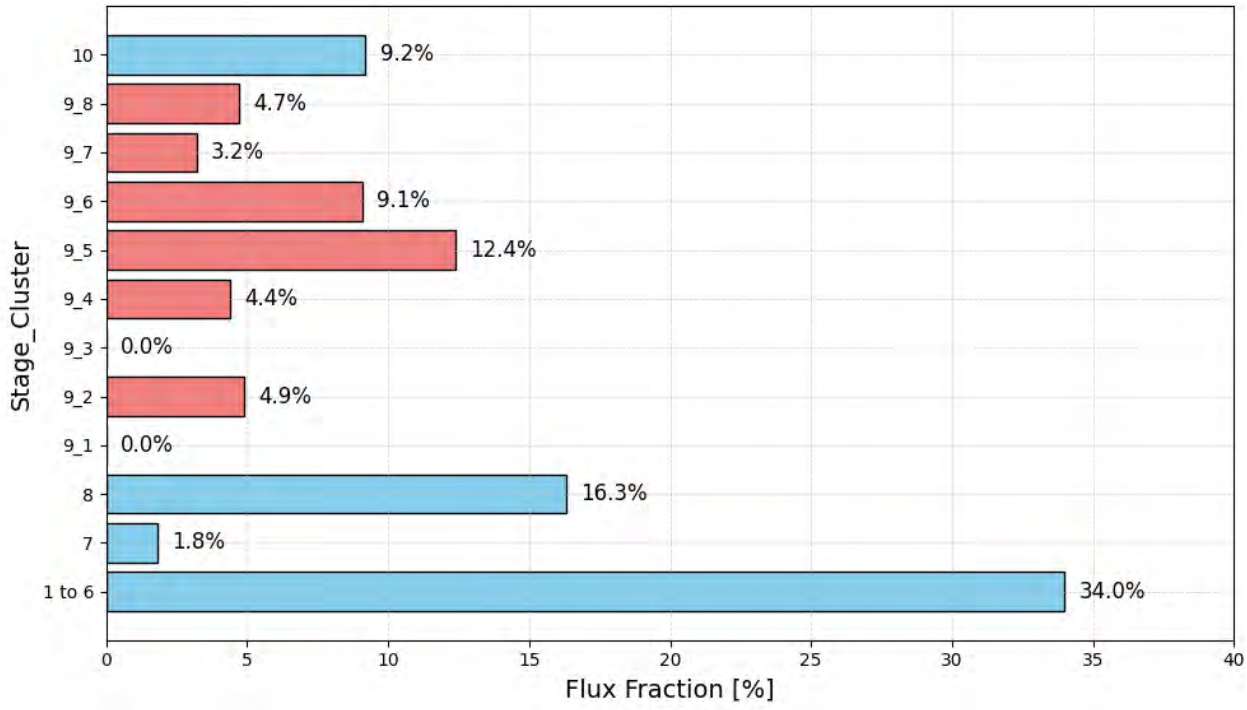

Figure 13: Production logging results after the 12-hr circulation test.

5.5 Fracture hits summary

The strain data was acquired during the 16B(78)-32 fracturing from the permanent FO installation in 16B(78)-32. A total of 49 hits were analyzed and fracture corridors were developed based on those (**Fig. 14, top**). Stages 8, 9 and 10 showed a lot of interaction with intersecting corridors. Analyzing the stage10 MEQ and strain data, it is evident that stage10 merged into a lot of existing fracture networks from previous stages. The large fracture geometry and multiple hits with much smaller fluid intensity can be explained through these interaction mechanisms. Also, stage 8 MEQ and strain data show a large network development. **Fig. 14, bottom** also shows a similar view from fracture modeling results. The corridors are very similar with obvious variations in stage 10 which are hard to predict.

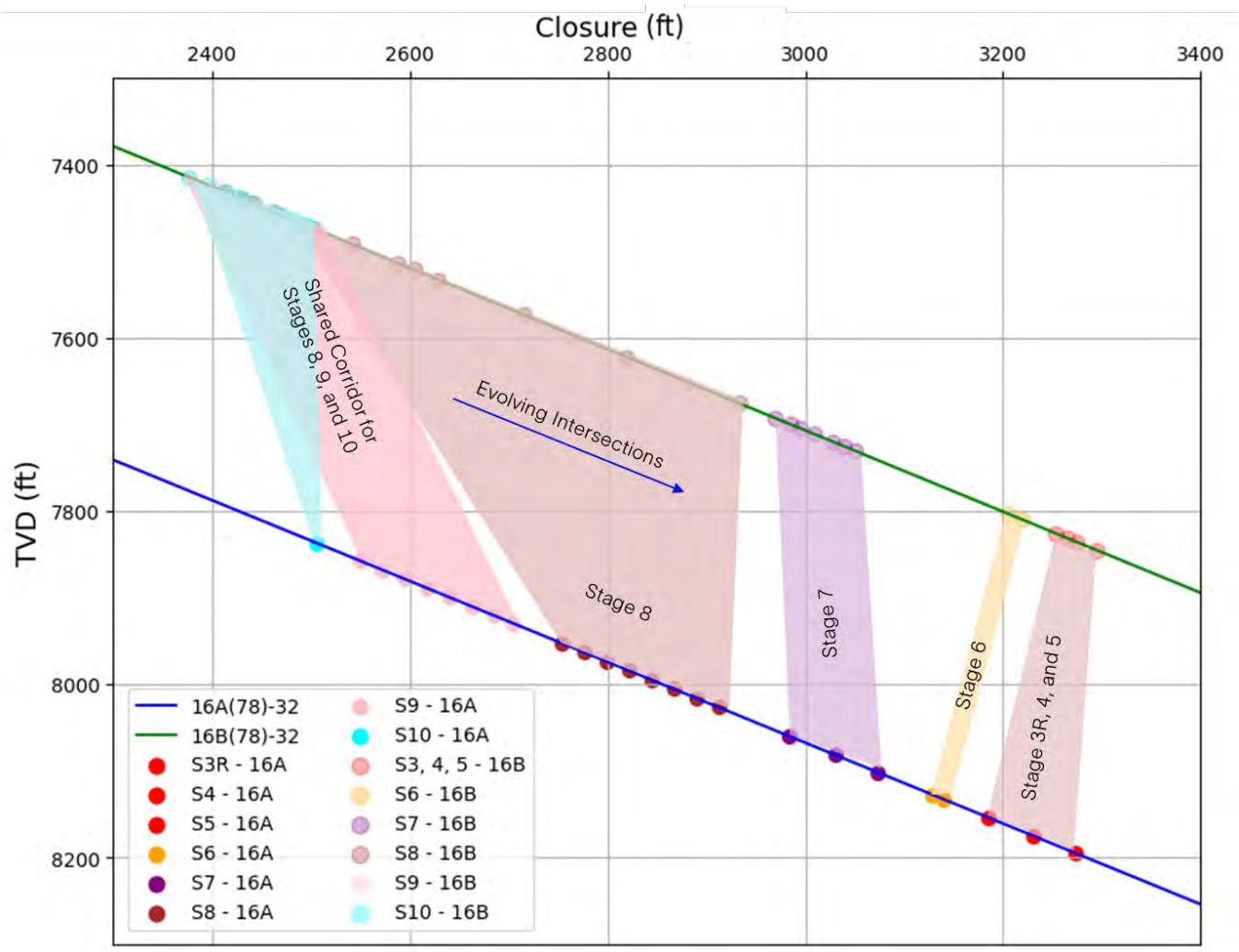

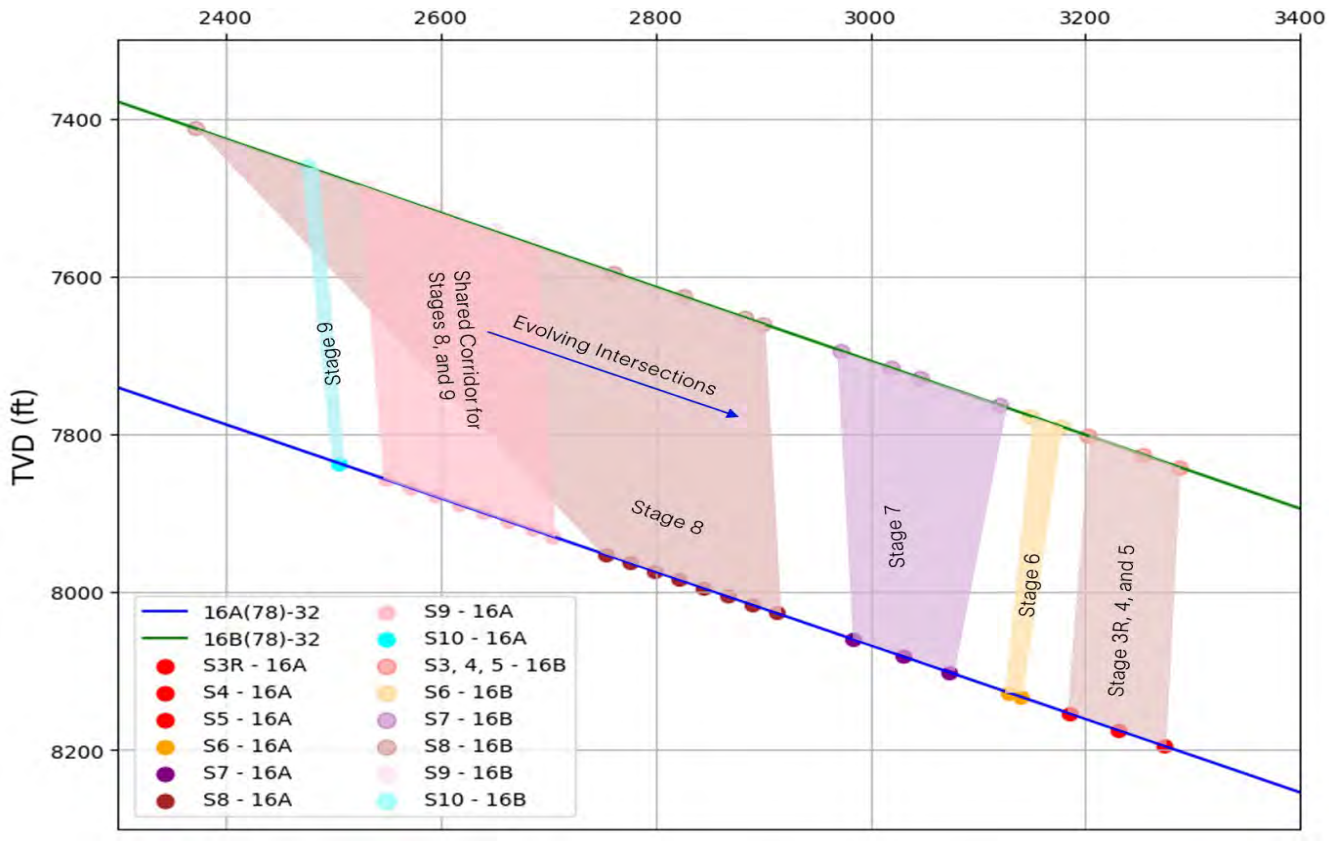

Figure 14: Fracture corridors constructed from 16A(78)-32 to 16B(78)-32 based on (top) fracture hits from Low Frequency DAS data; (bottom) fracture hits from the UFM complex fracture model.

Detailed analysis of fracture hits in the model revealed that most of the fracture hits show hydraulic width development but a 'near 0' end-of-treatment conductivity due to proppant settling and closure mechanics which could impact the connection efficiency. Hence the thermal strain analysis during the circulation test yields valuable insights into the interaction between injected cold fluid and hot fractured rock system, as well as the effectiveness of the fractures in facilitating fluid movement from the injector to the producer. Note that 4 fracturing stages were pumped with proppant in the 16B(78)-32 before the circulation. **Fig. 15** shows the thermal strain development in time. As the cold fluid enters the fractures, rapid temperature drop leads to rock contraction around the fracture, resulting in compressional strain. Hence, blue regions indicate the rock contraction and show that stages 9 and 10 were the first to receive and circulate the fluid. At the same time stages 7 and 8 show extensional behavior which could be a dynamic effect of the rock contraction in the nearby rock. For stages 9 and 10, as time progresses, the extensional (red) regions become more prominent, possibly due to the ongoing circulation of the cold fluid and the equilibration of thermal effects within the rock matrix. This transition might indicate areas where the fluid has moved further into the fracture network, causing redistribution of stress and inducing extensional strain. At this time stages 7 and 8 show compressional strains indicative of cold fluid arrivals here. Finally, cold fluid arrivals signals can also be seen in stages 3 through 6. This is intuitive based on the modeling and fracture corridors developed because even stage 8 shows strong interaction with the overlapping networks around stages 9 and 10. Moreover, the arrivals are faster and more conductive fractures are observed in areas where fracturing and proppant placement was done from injector and producer to overcome the 'near 0' conductivity at producer

purely from the injector stages. Also, the fracture driven strain curve peaks aligned with the waterfall show around 20 effective fractures which agrees with the fracture modeling results.

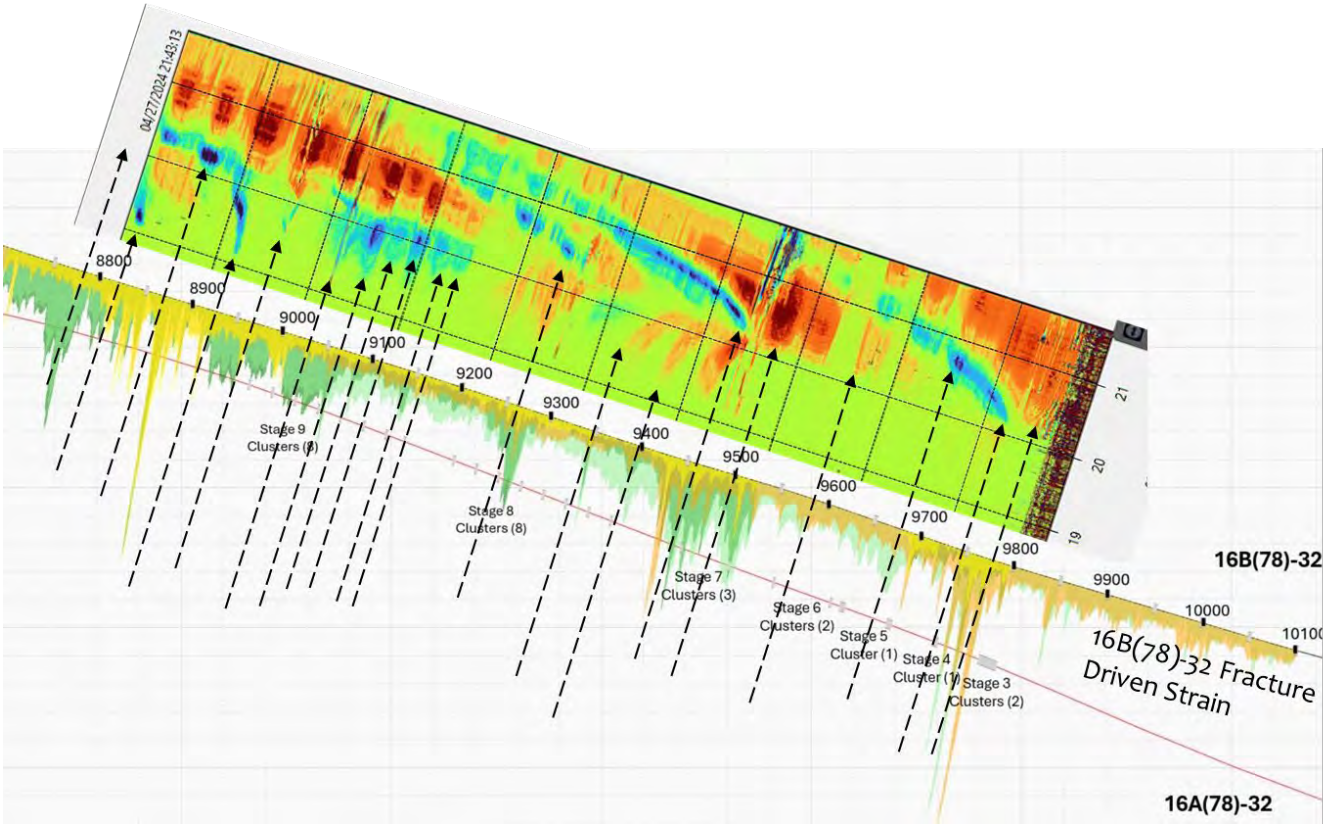

Figure 15: Thermal strain evolution (waterfall plot) during 12-hr circulation test (3 hour time scale shown on Y-axis) along with the fracture driven strain (continuous curve) along 16B(78)-32 (Courtesy Neubrex Energy Services).

Table 5 details the macro stagewise summary of the fracture hits achieved with well 16B(78)-32. The connection efficiency (>100%) observed from the strain-based frac hits dictates fracture network development more than planarity. The total effective fracture connection efficiency from the fracture driven strain during circulation agrees with the model, even though stage-wise distribution varies. Appendix-A provides details on the frac hit locations.

Table 5: Stagewise summary of frac hits from 16A(78)-32 to 16B(78)-32.

Stage#	Total Clusters	Cluster Spacing [ft]	Total frac hits			Connection Efficiency		
			DAS	Model	Circulation	DAS	Model	Circulation
3R	1	-	4	1	1	133.3%	100.0%	100.0%
4	1	-		1	1		100.0%	100.0%
5	1	-		1	1		100.0%	100.0%
6A, 6B	2	12.5	2	2	1	100.0%	100.0%	50.0%
7	4	50	7	4	2	175.0%	100.0%	50.0%
8	8	25	12	5	3	150.0%	62.5%	37.5%
9	8	25	12	5	7	150.0%	62.5%	87.5%
10	1	-	12	1	4	1200.0%	100.0%	400.0%
Total	26		49	20	20	188.5%	76.9%	76.9%

6. Discussion, Summary, and Way Forward

As much of the industry is beginning its journey of understanding how to put EGS concepts into practice, this paper presents a similar attempt. Using existing oil and gas simulators to try and plan and predict EGS work, up through future circulation events, brings various learning opportunities. As the authors discovered, these learned opportunities are larger than a single paper can encompass.

Part-I, encompasses the calibration of fracture systems and reservoir mechanical properties. Part-II will investigate strategies such as simultaneous injection to improve circulation efficiency and optimize the doublet connection efficiency. The optimization will also investigate DFN utilization to increase the circulating fluid's residency time, thereby increasing heat transfer. Hence, the 16B(78)-32 stimulation will be critical for part-II. Part-III will explore the end-to-end workflow investigating the circulation effect on the thermoelastic stress alterations of the rock and shear fractures generation. Part of this exploration will evaluate how the DFN properties manifest themselves and alter flow during long-term circulation.

Within this paper, much attention has been given to the model calibration, including the DFN. A lot of work has been dedicated to building the DFN using image logs and other tools to evaluate size, distribution, and orientation (Finnila and Jones, 2024). Even though some of the MEQ point clouds suggest planarity, a certain degree of complexity is possible based on the interpretations provided in this paper. While there may be an open debate about how to correctly predict fracture dimensions, what should be evident is that taking the DFN into account is critical in the long run for EGS. Even if the pumping schedule choice leads to less complexity, i.e., using crosslinked fluids, the DFN may still have an effect in reducing fracture growth in the preferred direction (as observed from phase 2 results). This effect will largely depend on the magnitude of stress anisotropy and principal stress reorientation during the EGS lifecycle in the circulation phase.

If we look at analogous shale plays such as Eagle Ford, which shows more planar features, or the Barnett, which shows complex MEQ cloud development, it becomes clear that a generic inference cannot be drawn. These observational findings can be extrapolated for EGS to infer that complex models will be more relevant than planar models for future EGS development. Moreover, if the system model neglects the DFN, then premature thermal breakthrough prediction with forward models could be missed, reducing the economic efficiency of the EGS installation.

Thermoelastic stress induction has not been considered in the fracture modeling here because, once the temperature transient equilibrates with the cooldown temperature, the thermal stress alterations would be minimal. However, in circulation phase, it is imperative to model this mechanism. McClure et al. (2024) have provided a robust forward modeling study using the thermoelastic effect during circulation and demonstrated stress changes upto 1,000s of psi, resulting in significant fracture apertures upto 1.5-in. Their results stress the importance to consider the systemic compliance changes (based on tensile strain) when DFN is also considered as a system

component. The next steps will be to calibrate the flow model from longer (30-day) circulation tests data and conduct forward modeling for 15-year and 30-year circulation tests results. As part of the ongoing study, propositions for the optimum fracturing strategy for EGS will also be made.

An important learning from the Phase 2 stimulation was the problems related to rock breakdown, injectivity, and proppant placement issues associated with Stages 6 and 7. This behavior is typical in high tectonic influence heterogenous clastic formations (Asif et al. 2024). This experience pronounces the importance of considering the vertical and lateral heterogeneity in the formation for EGS lifecycle modeling. Almutary et al. (2024) provide a data based approach to enhance placement quality. We will be investigating this using discrete indices calculated from the continuous logs and 3D geomodel, such as reservoir quality, completion quality, placement quality and geologic quality.

7. Conclusions

The paper provides a comprehensive workflow for calibrating and forward modeling for the FORGE EGS project. The subsurface structural and geologic model is used to build a 3D model along with a comprehensive DFN inclusion. The basecase inputs use the reservoir and rock characterization data conducted with triaxial core testing, openhole logs, and MEM calculation. Calibration utilizes the pumping pressures, MEQ event clouds, fiber optic, and PLT data. The modeling provides a comparison of complex and planar fracturing models and provides recommendation to use models that can incorporate DFNs, as their effect and potential impact can be critical for EGS lifecycle simulations. Significant proppant settling is observed due to the low viscosity, even with crosslinked fluids, as a temperature effect degrades the polymer. Fracture hit analysis and fracture corridor development from 16A(78)-32 to 16B(78)-32 was also presented, resulting in a 188%, 77% and 77% connection efficiency based on strain measurements during fracturing, modeling, and strain measurements during circulation, respectively. The fracture corridor development showed a marked similarly between the measured strain data and the model. These results can be explained by the hydraulic width development at the producer during fracturing but ‘near 0’ conductivity by the end of treatment leading to less effective connection quality.

REFERENCES

Adachi, J., Siebrits, E., Peirce, A., Desroches, J. “Computer Simulation of Hydraulic Fractures”. IJRMRE, 44 (2007), 739-757.

Almutary, T., Khan, A. M., Ugarte, E., and Hassan, N. “Placement Quality Index to Enhance Proppant Placement—Part I: The Machine-Learning Model” Paper presented at the SPE Conference at ADIPEC, Abu Dhabi, UAE, November. (2024).

Asif, A., Khan, A. M., Asiri, M. and El-Hassan, S. “Integrated Subsurface and Fracturing Treatment Analysis for Proppant Placement Enhancement in Tight Clastic Horizontal Well Fracturing” Paper presented at the SPE Gas and Oil Technology Showcase & Conference, Dubai, UAE, 7–9 May. (2024).

Cohen, C., Kresse, O., Weng, X. “A New Stacked Height Growth Model for Hydraulic Fracturing Simulations”. ARMA 15-75 (2015)

Finnila, A., Damjanac, B., and Podgorney, R. “Development of a Discrete Fracture Network Model for Utah FORGE using Microseismic Data Collected During Stimulation of Well 16A(78)-32” PROCEEDINGS, 48th Workshop on Geothermal Reservoir Engineering Stanford University, Stanford, California, February 6-8. (2023)

Finnila, A., and Jones, C. “Updated Reference Discrete Fracture Network Model at Utah FORGE” PROCEEDINGS, 49th Workshop on Geothermal Reservoir Engineering Stanford University, Stanford, California, February 12-14. (2024)

Fu, P., Johnson, S., Carrigan, C. “An Explicitly coupled Hydro-mechanical Model for Simulating Hydraulic Fracturing in Arbitrary Discrete Fracture Network”, IJNAM in Geomechanics (2012)

Kresse, O., Khan, A. M., Gutierrez-Sosa, L., Hobbs, B., Sosio, G., Emelyanov, D., and Mehay, S. “A Review of Enhanced Geothermal Systems Life Cycle Optimization: Laboratory Experimentation, Material Properties, and Numerical Modeling”. *GRC Transactions, Volume 48* (2024).

Kresse, O., Weng, X., Wu, R., and Gu, H. “Numerical Modeling of Hydraulic Fracture Interaction in Complex Naturally Fractured Formations”. *ARMA 12-292* (2012).

McClure, M., Horne, R. “Discrete Fracture Network Modeling of Hydraulic Stimulation: Coupling Flow and Geomechanics”, Springer, (2013).

McClure, M., Irvin, R., England, K., and McLennan, J. “Numerical Modeling of Hydraulic Stimulation and Long-Term Fluid Circulation at the Utah FORGE Project” PROCEEDINGS, 49th Workshop on Geothermal Reservoir Engineering Stanford University, Stanford, California, February 12-14. (2024)

McLennan, J. "Utah FORGE: Well 58-32 Core Analyses". United States. (2018). https://dx.doi.org/10.15121/1557418. https://gdr.openei.org/submissions/1162.

McLennan, J., England, K., Rose, P., Moore, J., and Barker, B. "Stimulation of a High-Temperature Granitic Reservoir at the Utah FORGE Site." Paper presented at the SPE Hydraulic Fracturing Technology Conference and Exhibition, The Woodlands, Texas, USA, January. (2023)

Moore, J. Characteristics of the Utah FORGE Site. Presentation at ARMA Conference Proceeding (2019).

Moore, J., McLennan, J., and Pankow, K. “The Utah Frontier Observatory for Research in Geothermal Energy (FORGE): A Laboratory for Characterizing, Creating and Sustaining

Enhanced Geothermal Systems" Presented at 45th Workshop on Geothermal Reservoir Engineering, Stanford University, Stanford, California, February 10-12, SGP-TR-216. (2020)

Mulyani, S., Khan A. M., Wisnubroto, B., Widiatmoko W., McLennan, J., Trikukuh J.S., and Puspa M.A. "Subsurface Stochastic Integrated Workflows with Downhole Measurements for Preferred Field Development Strategy: Utah Forge Case Study". The 10th Indonesia International Geothermal Convention and Exhibition (IIGCE) (2024).

Wu, K., Olson, J.E. "Numerical Investigation of Complex Hydraulic Fracture Development in Naturally Fractured Reservoirs". SPE-173326-MS, (2015).

Xing, P., Damjanac, B., Radakovic-Guzina, Z., Finnila, A., Podgorney, R., Moore, J., & McLennan, J. "Numerical Investigation of Stimulation from the Injection Well at Utah FORGE Site." In Using the Earth to Save the Earth - Geothermal Rising Conference, GRC, Vol. 45 (pp. 885-898) (2021)

Xing, P., England, K., Moore, J., Podgorney, R., & McLennan, J. "Analysis of Circulation Tests and Well Connections at Utah FORGE" PROCEEDINGS, 49th Workshop on Geothermal Reservoir Engineering Stanford University, Stanford, California, February 12-14. SGP-TR-227. (2024)

APPENDIX-A

This appendix provides a summary of the fracture hits observed during the Phase 2 stimulation of well 16A(78)-32. **Fig. A1** and **Table A1** detail the fracture hit locations.

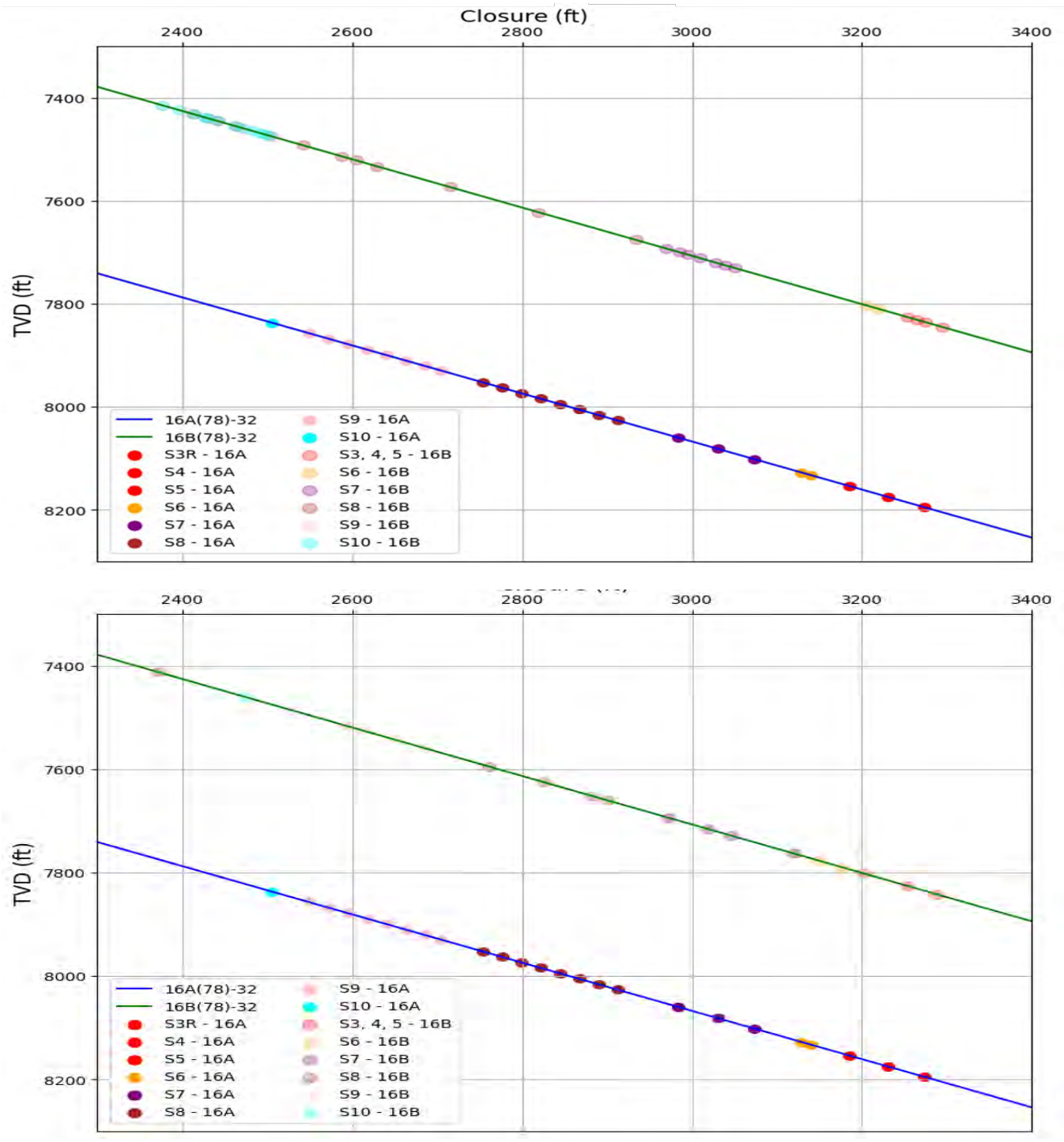

Figure A1: Summary of perforated clusters on 16A(78)-32 and fracture hits on 16B(78)-32- (top) fracture hits from Low Frequency DAS data; (bottom) fracture hits from the UFM complex fracture model.

Table A1: Stage wise fracture hit measured depth from the fracture model

Frac Hit#	Stager#	MD [ft]
1	3R	9784.14
2	4	9746
3	5	9690
4	6A, 6B	9631
5	6A, 6B	9662
6	7	9436
7	7	9488
8	7	9518
9	7	9599
10	8	8772
11	8	9202
12	8	9274
13	8	9337
14	8	9356
15	9	8948
16	9	9017
17	9	9037
18	9	9079
19	9	9121
20	10	8887

A Review of Enhanced Geothermal Systems Subsurface Life Cycle Optimization

Olga Kresse, Abdul Muqtadir Khan, Lesly Gutierrez-Sosa, Brandon Hobbs, Giovanni Sosio, Denis Emelyanov, and Sabine Mehay

SLB

Keywords

Enhanced geothermal systems, life cycle modeling

ABSTRACT

Enhanced geothermal systems (EGS) represent a promising avenue for sustainable energy production. However, the extreme temperatures pose an implementation and optimization challenge for EGS projects. Success depends on fracture propagation, proppant placement, and establishing circulation at sufficient rates to generate energy economically and efficiently. In this paper we review different aspects across different stages of the EGS life cycle and make some recommendations for data collection, rock characterization, and laboratory testing to understand material behavior, numerical modeling, etc.

1. Introduction

Naturally occurring geothermal systems require three elements for economic viability: heat, fluid, and permeability. In the absence of natural permeability, an EGS creates a man-made geothermal reservoir.

In EGS, hydraulic fractures open new or naturally-fractured pathways—creating permeability. Injected fluid circulates throughout the hot, fractured rock, absorbing the Earth's heat. Operators pump heated water to surface powerplants where it generates electricity.

Degradation of an EGS can occur when preferential flow channels open, short-circuiting the system. Long-term success depends on controlling flow distribution to achieve uniform heat sweeping.

The largest EGS projects within recent history are the Utah FORGE, Fervo's Projects Red and Cape. Smaller attempts such as the Newberry site, Ormat's wells in Desert Peak, Nevada, and Calpine's facility at The Geysers in California tried using "shear-fracturing" to connect nonproductive hydrothermal wells.

2. Prefracturing Phase

Forecasting the dynamic behavior of an EGS requires a thorough understanding of the initial states of (t)hermal, (h)ydraulic, (m)echanical, and (c)hemical (geochemistry) attributes (THMC). All the dynamic phenomena are governed by intrinsic properties of the host rocks and surroundings which must be modeled accurately and consistently. This process, known as "static modeling," is distinct from the numerical modeling of the system's behavior (section 3).

Characterizing and modeling such properties is challenging because of geological, structural, and mechanical complexity associated with EGS sites. The acquisition, interpretation and modeling techniques derived from other energy industries (oil and gas) may not be suitable for non-sedimentary rocks.

Different host-rock and natural-fracture properties will influence behavior during stimulation treatments or circulation regimes. These properties are often correlated, so it is crucial to adopt an integrated, multidisciplinary approach to characterize them—while preserving consistency across modeling stages.

2.1 Rock and Fracture Characterization

Understanding geothermal system geometry is the first step to build an integrated model. Suitable techniques to describe the system depends on geothermal type (IGA). Existing geological interpretation available from regional studies and public research institutions can be combined with surface sampling to infer flow paths from fluid, gas, and soil geochemistry, while accurate structural imaging is achieved through geophysical surveys (Wright et al., 1985).

Seismic surveying yields accurate results in sedimentary geothermal reservoirs, but gravity, magnetics, or magnetotellurics methods are better in volcanic contexts. Wellbore markers and borehole images enable refining the understanding of structure and stratigraphy. Integrated interpretation of these data enables building qualitative conceptual and structural models (Mulyani and Sarmiento, 2019), forming the basis of the site's static model.

Geophysical methods, surface sampling, and regional geological information can provide properties of different rock layers. Wellbore logs complement the information by providing insight on mineralogy. A combination of conceptual facies models and lithology logs are used to build 3D-lithofacies models (Mulyani and Sarmiento, 2019) to which numerical property models can be constrained.

While sedimentary reservoir modeling typically focuses on the rock matrix's hydraulic properties, e.g., porosity and permeability, EGS reservoirs contain negligible permeability, so the existence of natural-fracture networks, or the ability to create hydraulic fractures, becomes crucial for success.

The most accurate source of information to build realistic fracture models come from well logging and coring. Wellbore image logs are used to derive fracture geometry (density, inclination, and azimuth) and to infer some properties (mineralization and "openness") (Das et al., 2023). Resistivity images can be complemented with other logs, such as acoustic, flowmeter ("spinner logs"), temperature log anomalies, and observed drilling mud losses.

Rock thermal behavior is defined by its thermal conductivity and heat capacity. The thermal-response test (TRT) is commonly used for very low-temperature resources but, paradoxically, thermal properties can vary as a function of temperature.

Two groups of properties are required to model a rock's mechanical behavior: elastic moduli and rock strength properties. The thermoelasticity; i.e., additional stress and strain due to thermal energy, is defined by the thermal expansion coefficient.

2.2 Lab Experimentation

2.2.1 Fracturing Fluid, Proppant Testing

API_RP_39 (1998), *API_RP_19C* (2018), and *API_RP_19D* (2021) provide guidelines for fracturing fluid rheology, proppant specifications, and long-term conductivity, respectively. API procedures need enhancement for EGS:

1. Conditions: current temperatures up to 150°C, while EGS require up to 250°C.
2. Hysteresis: Temperature cycling during circulation requires fluid to go through heating-cooling cycles. A temperature ramp simulating these and comparing the upsweep/downsweep gives indications of thermal lag as a fluid quality indicator.
3. Chemical interactions: Due to the length of contact, material interactions (fluids, proppants, formation, etc.) should be characterized. Moreover, EGS fluid's properties (salinity, pH, TDS, etc.) may differ from oil and gas.
4. Proppant conductivity: Current tests measure 50-hour exposures for each stress point, and do not capture the proppant alterations on conductivity evolution.
5. Proppant dissolution: Temperature and geochemical alterations on proppant degradation is critical.
6. Corrosion and scaling: High temperatures require specialized chemistry, additives, and procedures.
7. Thermal breakthrough: Impact of thermal breakthrough on proppant channels and conductivity need study.

2.2.2 Triaxial Testing

Triaxial testing is crucial for understanding rock behavior and properties. Some laboratory experiments (Zhang et al., 2022) provide insight into fracturing mechanisms and processes but do not address issues with upscaling to extract critical parameters for field exploration. The influence of temperatures on fracture dynamics, as detailed by Hu et al. (2016), demonstrates generation of multiple fracture traces in the near-wellbore region, impacting fracturing pressure and flow resistance. Salazar et al. (2022) demonstrated equipment and testing with the integration of fiber optic sensors in triaxial testing devices. Below are some actionable areas:

1. True triaxial testing: Use apparatus capable of conducting testing with three independently controlled principal stresses and high temperatures (Frash and Gutierrez, 2012).
2. Testing conditions: Testing should achieve 250°C and 150 MPa.
3. Sample size and condition: Small sample sizes with smooth, enlarged, and lubricated end-platens to avoid high shear resistances (Liu et al., 2022).
4. Loading speed: Rapid loading and dynamic conditions are critical.

5. Other considerations: Due to complex interfacial properties, assuming a perfect bond between sample/loading platens might be invalid. Areas of focus are anisotropy, upscaling effects, data interpretation, and understanding fracture propagation and network development.

2.3 Fracturing Materials

2.3.1 Fracturing Fluid

Fracturing-fluid system requirements are typically: (a) sufficient viscosity to create fractures and suspend/transport the proppant; (b) be nondamaging to the proppant pack; (c) be nondamaging to the reservoir, i.e., limit plugging or precipitation within the rock matrix; (d) cost efficient; (e) low environmental impact. EGS needs are similar, but the host conditions (temperature, rock minerology) and requirements for circulation, e.g., thermal shocks through cooldown-warmback and continuous injection of nonnative fluid, bring further challenges.

Required viscosity is typically achieved by crosslinking high-molecular-weight polymers. At EGS temperatures, thermal degradation of polymers will be rapid - challenging for most fluid systems. Polymer residues on the fracture face that decrease circulation rates or heat transfer rate are further challenges.

A critical question in EGS applications is if the status quo of using water fracs (Project Red by Fervo—Norbeck et al., 2023) or existing crosslinked systems, i.e., FORGE, is appropriate. The authors' opinion is there should be continuous effort to keep looking for alternative systems.

Almulhim et al. (2020) and Almutary et al. (2021) successfully used CO_2-laden diutan-gum systems in Middle Eastern tight clastic and carbonate fields, respectively. Similar directions were explored at the laboratory scale comparing four systems: (a) water, (b) CO_2, (c) CO_2 with water, and (d) CO_2 with 1% polyallylamine (PAA) polymer, whose tests were conducted up to 200°C. The research found that CO_2 in hot dry rock (HDR) environment attains the highest conductivity during injection, followed by the CO_2 + 1% PAA system (Fig. 1, Jian et al., 2020).

Pumping water into HDR can cause supersaturated silica to precipitate and heal the fracture during cooldown or in the absence of flow. Therefore, the conductivity is less than 1 μm^3, for water, while CO_2-based systems are generally higher across various conditions.

To create complex networks in EGS, cryogenic options (liquid N_2) have been investigated. Due to thermal-stress effects, up to a 52% reduction in breakdown pressure (Yang et al., 2021) was achieved. Fracture patterns were characterized by cryogenic scanning electron microscopy and coiled tubing scanning.

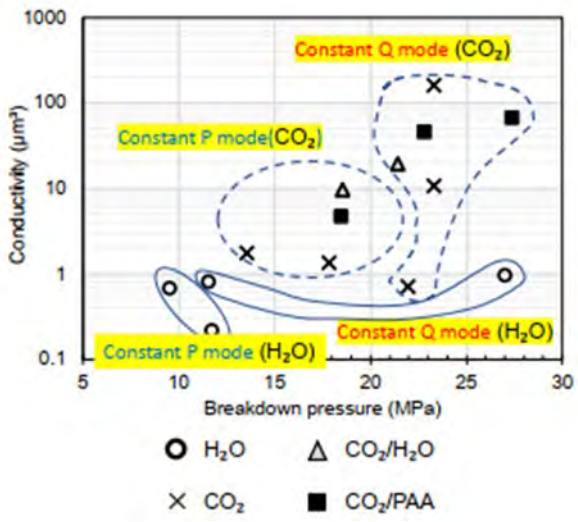

Figure 1: Conductivity at varying pressures for fluid systems at different injection modes (Jian et al., 2020).

EGS' needs invite multiple research areas for fracturing and circulation fluid chemistry. CO_2 and N_2, in energized and foamed conditions, should be investigated (Khan et al., 2023a). The introduction of free-polymer chains to nanoparticle superlattices can enhance thermal stability without disrupting internal organization, allowing for better control over particle interactions and the creation of ordered arrays in nanocomposites (Wang et al., 2021). Ruela et al. (2011) demonstrated an approach using a mixture of cationic or anionic polymers with specific zeta potential ranges, which exhibit salt tolerance and increased viscosity at temperatures above 150°C. Almubarak et al. (2018) developed a hybrid, dual-polymer hydraulic-fracturing fluid with enhanced thermal stability, stable to 205°C, by adjusting polymer loadings, using metallic crosslinkers, and incorporating buffers and oxygen scavengers.

2.3.2 Injection/Circulation Fluid

A good EGS circulation fluid should elevate heat transfer, reduce geochemical interactions, and be cost efficient. Fluids such as water, brine, and CO_2 all interact differently with rock. For example, groundwater injection leads to changes in mineralogy, impacting the reservoir's physical properties and circulation dynamics. To overcome this, pumping reactive fluids (weak acids) could enable continuous dissolution, thereby enhancing permeability and mass flow rates. Reactive transport modeling simulates fluid-rock interactions and predicts evolution of EGS projects by considering chemical reactions within the system (Adams et al., 2005).

As another example, supercritical CO_2 as the circulation fluid has potential because of its lower viscosity and density, leading to enhanced circulation efficiency and higher flow rates (Zhou et al., 2022). Toth and Bobok (2013) also investigated CO_2 as a circulation fluid in EGS. They found that heat transfer, for constant thermal mass, is lower for CO_2 than water (smaller thermal diffusion), but transport through fractured systems, because of lower pressure losses, and its ability for continuous carbonate dissolution, make it a viable option. Hence, comprehensive techno-economic analysis is critical during strategy planning to ensure a balance between energy output, cost effectiveness, and environmental considerations.

2.3.3 Proppant

The main function of proppant is to keep the tensile fracture open when pressure inside the fracture equalizes with reservoir pressure; thus older projects, such as the Newberry Volcano, which used hydroshearing as the main fracturing mechanism, did not use proppant. Norbeck et al. (2018) studied the Fenton Hill Field observations numerically, which indicated mixed-mode fracturing where generated tensile fractures closed shortly after treatment ended. This might explain its flow rate performance: Fenton Hill managed flow rates of ~7 L/s compared to ~64 L/s in Fervo's Project Red (~11% in comparison). Similar experience was seen at FORGE; this evolution shows promise in creating propped mixed-mode fractures to support conductivity of tensile fracture systems.

2.4 Proppant for EGS

At high temperatures proppant can become chemically unstable (dissolution and re-precipitation) depending on fracturing or circulation static and dynamic conditions. Understanding their long-term performance is important. In EGS context, a proppant should demonstrate higher chemical and thermal stability, mechanical strength, and acid resistance. Proppant solubility depends on the silica content of contacting fluids (reservoir or circulating). Waters with lower silica content demonstrate higher dissolution.

Brinton et al. (2011) studied bauxite, quartz, and their mixtures with granite at 200 to 230°C for up to 11 weeks in water, water-spiked silica, and the Raft River geothermal water (RRGW). Post-aging analysis showed higher dissolution of bauxite than quartz. This could be because RRGW is undersaturated in silica. Stoddard et al. (2010) found that conductivity is reduced by 48% at 90°C and 61% at 200°C.

Mattson et al. (2016) conducted a 2-month proppant strength study with a mixture of RRGW, granite, and bauxite/ceramic proppant, at unreacted and reacted conditions. The results confirm the significant crush-strength alteration over time (Fig. 2). However, Kryptosphere illustrated a higher degree of influence with proppant crushing ~9X higher post-chemical interactions at 13,000 psi.

Ko et al. (2023) investigated proppant pack performance for multiple proppants in the presence of water for 14 days up to 320°C. Noncoated proppant generated 3 to 4% additional fines at heated conditions. The rate of fines generation decreased with time, indicating proppant strength stabilization at a critical temperature where thermal damage plateaus.

Resin- and hydrophobic polymer-coated proppants showed 8 to 15% additional fines with removal of coating, cracks, and scale growth, leading to more crushing and lack of pack integrity (Fig. 3).

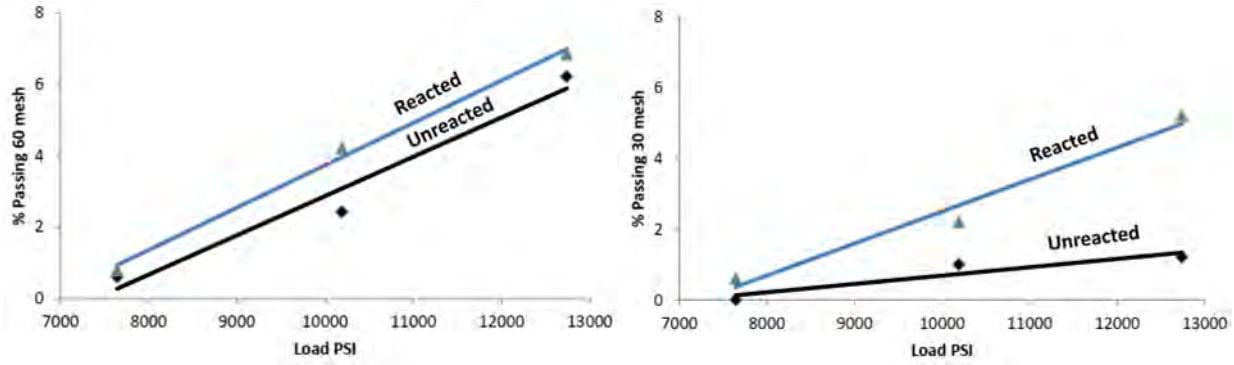

Figure 2: Crush-testing results for reacted and unreacted proppants at 250°C. (left) bauxite. (right) ceramic proppant (Mattson et al., 2016).

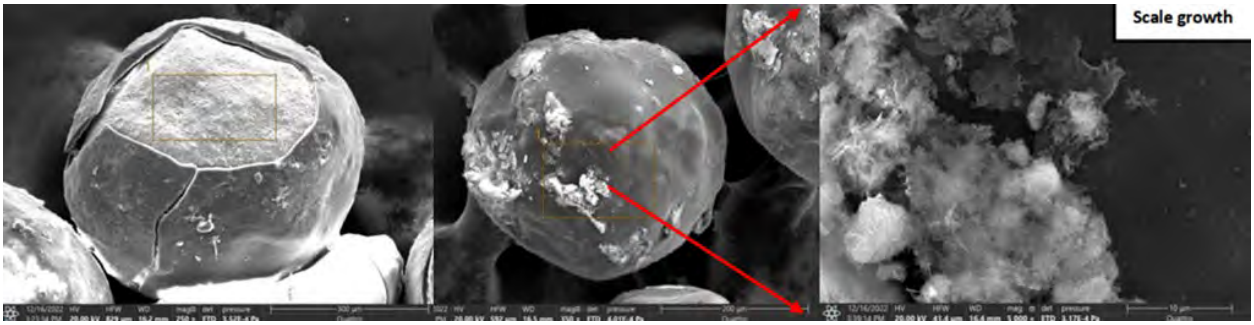

Figure 3: SEM scans of resin-coated proppant after 14 days at 320°C showing cracks and scale growth (Ko et al., 2023).

Lisabeth and Norbeck (2020) examined the impact of hydrothermal alteration on proppant brittleness and found that despite some surface changes, proppants retained mechanical integrity. Different proppant materials were reacted with brine and reservoir minerals (phyllite and diorite) up to 63 days at 250°C (Fig. 4). Results showed that quartz was most affected, resin-coated (RC) proppants are nonreactive, and high-feldspar proppants lead to dissolution and precipitation of clays but did not impact overall brittleness.

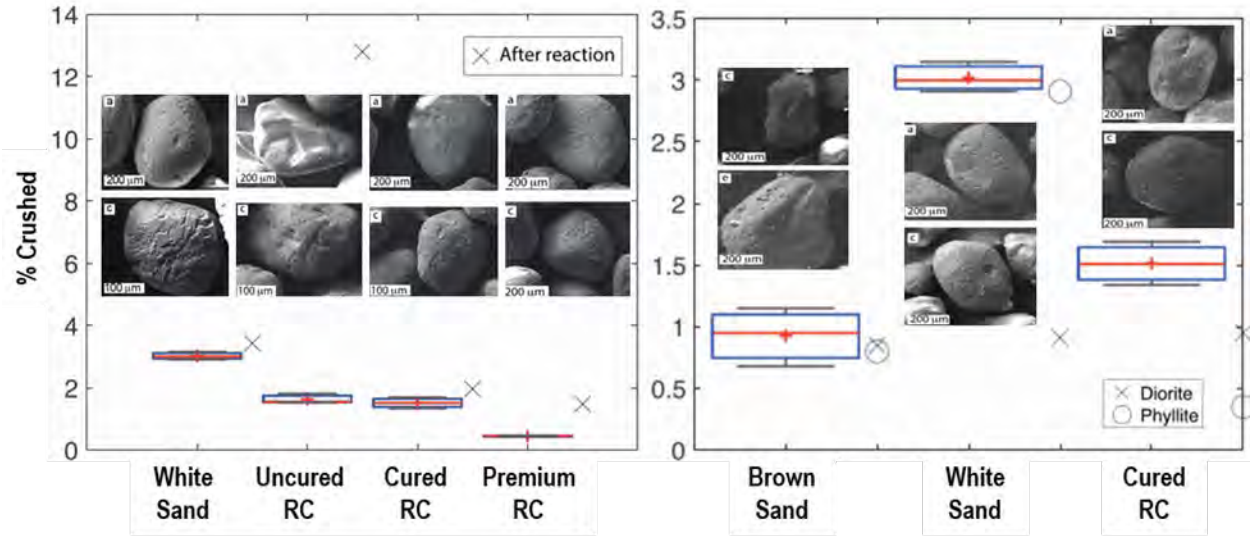

Figure 4: Summary of proppant testing showing % crush at 27.6 MPa and the inset images showing SEM scans (left) reaction for 7 days at 250ºC and 15.9 MPa. SEM scans show before (top) and after (bottom) reaction; (right) reaction for 63 days at 200ºC and 13.8 -Pa SEM scans show reaction with phyllite (top) and diorite (bottom (Lisabeth and Norbeck, 2020).

2.5 Innovative Materials, Techniques, and Avenues

Knox and Weaver (1989) evaluated multiple quartz proppants and quartz strengthened with alumina and zirconia. These showed better stability but still some dissolution. Nickel-plated sand showed good performance but was costly. Steam-resistant gravel (SRG) is highly resistant to dissolution and fines generation at 550°F.

Al Balushi et al. (2023) detailed proppants with negative thermal expansion coefficients, which demonstrate varying conductivity as a function of temperature, enabling uniform flow across fractures. This work posits that over 50 years, an additional 31.4% heat can be extracted. By optimizing flux through different parts of the network, this can effectively delay thermal breakthrough. This research presents a comprehensive workflow for proppant development (Fig. 5).

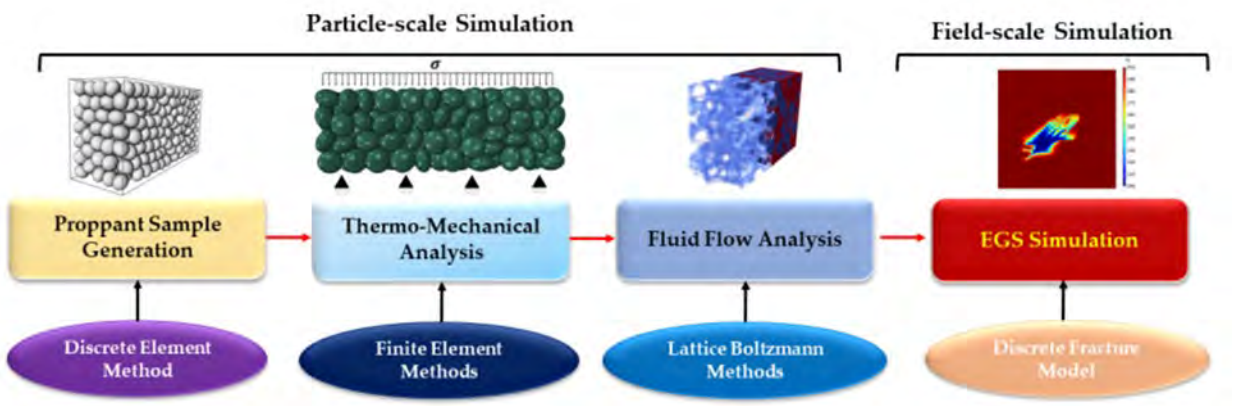

Figure 5: Comprehensive workflow combining interparticle modeling and field-scale analysis to study the novel proppant with negative thermal expansion (Al Balushi et al., 2023).

Kumar et al. (2019) have shown, numerically, that microproppants (~200 mesh) have potential in early EGS development to ensure uniform proppant placement in large networks.

Proppant flowback and redistribution is a major concern under various drawdown conditions. Similar damage is detrimental to EGS systems. High-aspect-ratio proppants, fibers, and 4D modeling can be effective (Khan et al., 2023c).

3. Numerical Modeling

To model and optimize EGS, one must consider various physical processes simultaneously, including fluid flow, heat transfer, geomechanics and geochemistry (Blöcher et al., 2010), necessitating multiple simulators. The key physical phenomena considered in multiphysics reservoir simulation are:

(1) Fluid dynamics: Fluid flow within porous media (Darcy's law, continuity equations), which consider hydrodynamical properties, pressure conditions, fluid properties, and heat transfer. Neglecting thermal effects could lead to inaccurate predictions, e.g., water-steam phase change, changes in hydrodynamical properties, cooling-induced fault reactivation, subsidence, etc. (Sullivan et al., 2001).

(2) Heat transfer within porous media: Temperature differences between injected and reservoir fluids, reservoir fluids and rock, and heat-source proximity. Three types of heat transfer mechanisms may occur: conduction, convection, and radiation (Zhao et al., 2015). However, radiation is often neglected because its contribution is insignificant in comparison.

(3) Geomechanics: Deformation of porous media caused by changes in pressure, temperature, and stress. Geomechanical deformation leads to changes in hydrodynamical properties of the rock and fractures (effective porosity and permeability), induced seismicity, and well stability (Li et al., 2020a).

(4) Geochemistry: Intense fluid-rock interaction can arise by injection of considerable volumes of working fluids (water, CO_2) during heat extraction (Gao et al., 2024). Fluid-rock interaction can lead to complex geochemical reactions (dissolution/precipitation of minerals, changes in rock

properties) and impact permeability and mechanical properties of the system as well as efficiency of heat extraction. Finally, corrosion risk on completion materials contacting fluid should also be addressed.

The main goal for fracturing in EGS is to permanently enhance permeability, thereby facilitating high fluid flow rates to produce economically.

Selecting a simulator that can model the creation of a hydraulic fracture network and is capable of evaluating fluid and heat transport between injector and production via the fracture network during the circulation phase is a challenge. Khan et al. (2024) presents an approach to life cycle modeling of EGS with complex fracture modeling.

3.1 During Fracturing

Hydraulic fracturing (HF) is the main part of EGS treatments and should be modeled simultaneously with wellbore and reservoir simulators.

Modeling of EGS HF simulation is intended to evaluate in-situ conditions and optimize EGS design to achieve sustainable heat production. Factors affecting EGS project success include creating a fracture surface area large enough to allow enough heat exchange to produce electrical energy at a commercial level and the ability to control the flow rate through fractures, lengthening thermal longevity and avoiding premature thermal breakdown (LBNL, 2021).

In oil and gas reservoirs, the target formation is stimulated to solely enhance the permeability of the formation. However, in EGS, the aim is to enhance the permeability and increase the contact area between hot rock and the circulating fluid. Having multiple fractures with smaller apertures is more advantageous than having a single fracture with larger aperture, as the fracture network provides larger contact areas for heat exchange.

Because heat extraction would decrease the temperature of the formation along the fracture, adjusting fracture conductivity to control flow rates would lead to more uniform heat extraction from the formation and therefore delay thermal breakthroughs. Thermal breakthroughs occur when preferential paths exist where the working fluid finds “shortcut” paths to quickly travel between the injector and producer wells. The fluid flow in EGS is dominated by flow in fractures rather than in rock matrix. For unpropped fractures, fracture conductivity is proportional to the cube of the fracture width, and wider fractures may provide higher conductivity (preferential flow path) to attract most of the circulating fluid, leaving massive amounts of untapped heat behind, and not allowing enough residence time for the passing fluid to heat up. This could shorten the lifetime of EGS. Controlling the flow rate through fractures to avoid premature thermal breakdown is crucial (LBNL, 2021).

More challenges for hydrofracturing for EGS include accounting for rock plasticity at high temperatures, creating large, simulated volumes with low water methods, and achieving minimum residency time for the circulating fluid to be heated. On the wellbore side it is necessary to ensure even governed flow distribution between the fractures (Kresse et al., 2023) and ensure high injection rates during an extended period.

Another uncertainty is the unpropped fracture conductivity at EGS conditions. High rates, limited-entry techniques, stress shadow effect, fracture complexity, and interaction with natural fractures contribute to larger offset/mismatch between fracture walls in field conditions than predicted by laboratory experiments.

HF simulators for EGS should include geomechanical components (stress orientation, rock strength), fracture mechanics (initiation and stimulation through hydrofracturing and hydroshearing, interaction with natural fractures, stress shadow effect), and fluid mechanics (fluid and proppant transport within the fractures, leakoff to reservoir rock) (Kresse and Weng, 2018; Kresse et al., 2024). Many oilfield-related simulators have been extended for EGS applications (Riahi et al., 2014; McClure and Kang, 2017; Kumar and Ghassemi, 2018; LBNL, 2021; Zheng et al., 2021; McClure et al., 2022; Kumar et al., 2023;). Among other studies we should mention Li and Lior (2015), Fu et al. (2016), Nadimi et al. (2018) and Cheng et al. (2019).

Proper HF models for EGS should include: fracture initiation criteria in impermeable, hard, brittle, very hot rock; fracture propagation during fluid circulation; stress changes caused by fracture opening due to temperature changes in the matrix; thermoelastic and poroelastic stress changes for fracture reopening during circulation; temperature-related material properties; multiphase flow; leakoff during heat extraction; 3D heterogeneous permeability; shear failure of rock matrix; permeable natural fractures; induced seismicity, etc.

HF models must involve advanced modeling of thermal effects in fractures accounting for temperature changes within the reservoir, including advection by fluid, heat transfer at the interface between fracture and rock, and heat conduction within the rock (Gringarten et al., 1975; Riahi et al., 2014; Fu et al., 2016; Hwang et al., 2022).

Two fracture simulation mechanisms may occur during hydraulic fracture treatment: hydrofracturing (creation of fractures in tension), and hydroshearing when overpressure induces slip along preexisting fractures, leading to irreversible permeability caused by rearrangement of asperities during shear dilation.

While permeability enhancement through shear slip has been considered by many as a standard for EGS, especially during circulation, HF can be used to achieve more conductive fractures at lower injected volume compared to hydroshearing. The review of historic EGS projects confirmed that both hydroshearing and hydrofracturing mechanisms occur and must be considered while modeling EGS.

3.2 Post-Fracturing Circulation Phase

Fractured systems in EGS could last up to 15+ years. This phase of long-term injection is less well-known and requires careful evaluation with proper predictions and analysis of multiple scenarios.

The main challenge for modeling circulation is to find the optimum conditions for sustainable heat production (LBNL, 2021; McClure et al., 2022; Kumar et al., 2023) considering that system properties could change during long-term cyclic heating and cooling or plastic creep.

3.2.1 Reservoir Simulation

Modeling EGS systems accurately while capturing the influence of each component; e.g., T, H, M, and C, and maintaining computational efficiency remains a challenge.

Fractured reservoirs can be modeled using equivalent continuum models (implicit approach), discrete fracture networks (DFNs) (explicit approach), or hybrid techniques (combination of explicit and implicit approaches) (Fig. 6).

The main limitations for the single-porosity model (a common equivalent continuum model) are that the rock and fractures are a volume-based average—an assumed single-permeability system. These simplifications cannot capture effects of THM coupling; e.g., heat transfer between rock and matrix or deformation of either.

The limitations of a dual-porosity model (two overlapping continua; Fig. 6c), (Barenblatt et al., 1960) are the idealized fracture network characteristics and simple fracture morphology.

Explicit representation of DFNs (Dershowitz et al., 2000) (Fig. 6d) are currently used in EGS simulations (Qarinurab et al., 2019). DFN models are more statistically data-demanding and computationally intensive than continuum models.

A hybrid model (Fig. 6e) combines the benefits of the continuum and discrete models (Cacas et al., 1990) but is still limited. Modern hybrid techniques; e.g., embedded discrete fracture model (EDFM), efficiently model matrix-fracture flow by embedding the DFN model into the 2D- and 3D-equivalent porous medium (Hajibeygi et al., 2011). EDFM, a generalized dual continuum (dual-permeability, dual-porosity), contains three connections (fracture-fracture, fracture-matrix, and matrix-matrix), to describe the fluid-heat exchange between fractures and matrix (Li et al., 2020a).

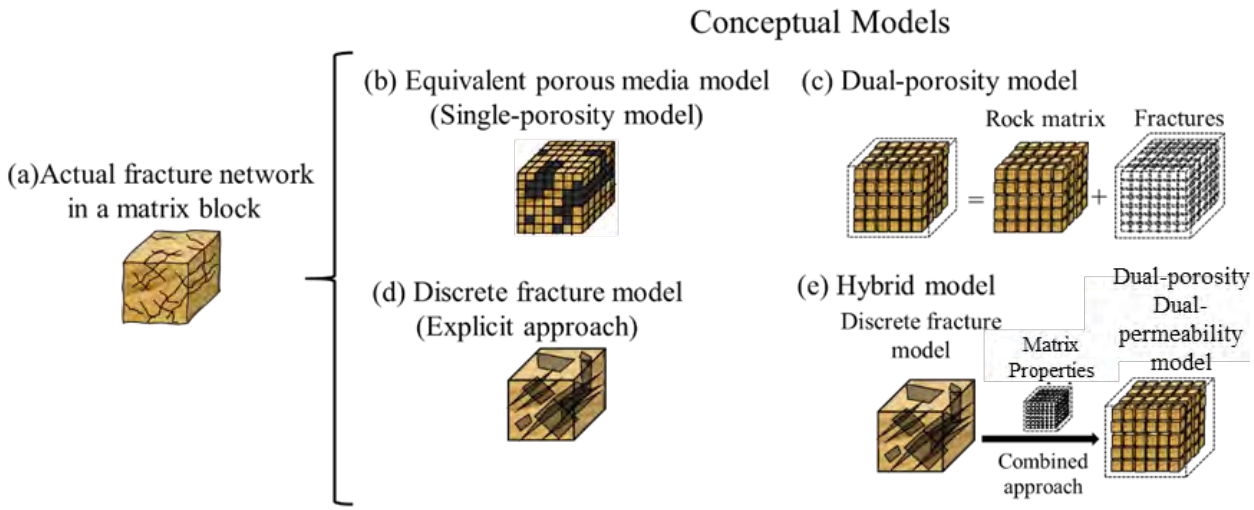

Figure 6: Model conceptualizations for fractured rock (a), equivalent porous medium (b), dual-porosity model (c), DFN model (d), and hybrid model (e).

The minimum modeling requirement for EGS can be achieved via thermohydrodynamically (TH) coupled models, which intend to represent the effects of the temperature gradients on hydraulic processes through changes in fluid density and viscosity with energy and mass conservation.

In Fig. 7, the coupling between the THM fields in a dual continuum (rock matrix and fracture) model is depicted as follows: items 3, 4, 5 and 19 illustrate stress and flow coupling; items 6, 7, 11 and 12 stress and temperature coupling; items 14, 18 and 19 for temperature and flow coupling. The most relevant coupling effects needed for EGS optimization are: (a) changes in stress due to temperature or pore pressure changes (items 11 and 19), (b) fracture aperture/permeability changes due to stress disturbance (items 3 and 4), (c) matrix porosity and permeability changes due to strain variations (item 5), (d) convective heat transfer in fractures (item 6), and (e) the heat conduction and convection modes of heat transfer (items 8, 9 and 18).

Geothermal numerical tools have been around for several decades, e.g., TETRAD and TOUGH2 (Pruess, 1990; Vinsome and Shook, 1991). Testing the accuracy and proficiency of geothermal simulators against historical data is still quite limited because of scarce or insufficient information. Furthermore, interpretating and processing data requires the human factor, which can invite biases.

The Geothermal Technologies Office (GTO) under the US Department of Energy (DOE) conducted a code comparison study program (White and Phillips, 2015). The program focused on examining existing codes, identifying dissimilarities, and modeling capabilities of several numerical simulators across six benchmark problems. This was redone in 2016 under the Code Comparison Study (GTO-CCS) to identify the capabilities and development areas of numerical simulation tools for EGS (U.S. Department of Energy, 2016), using seven benchmarks. In both analyses none of the simulators had all the necessary features to solve all problems (Ghassemi et al., 2015; U.S. Department of Energy, 2016).

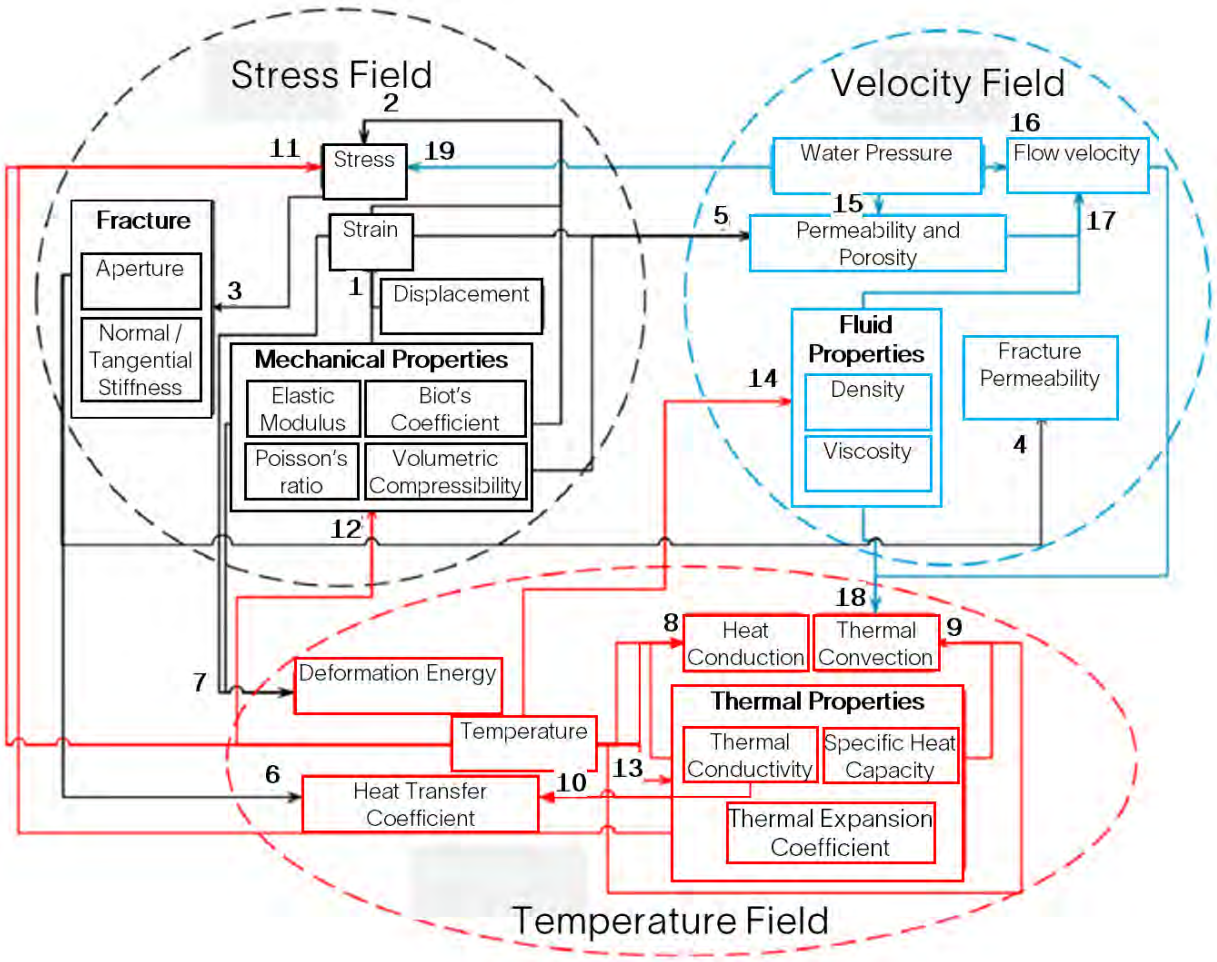

Figure 7: A scheme of a fully coupled THM model of a dual-continuum representation. Modified after Zhou et al. (2022).

In recent years, the HEATSTORE consortium (HEATSTORE, 2019) studied a variety of simulators to model operations at different sites, including high-temperature aquifer thermal energy storage (HT-ATES) sites. Among those numerical simulators were many respected software packages. The simulators comprise multiple numerical schemes. Mindel et al., (2021) concluded that although the simulators in the study were suitable to solve HT-ATES subsurface simulation problems some crucial discrepancies were discovered within the equations-of-state for thermal and enthalpy-injection modeling.

Another source of simulators comes from the oil and gas industry. (CMG Ltd., 2024; SLB, 2024a; SLB, 2024b; RFD, 2024) being the recognised simulators for thermal modeling.

Numerical simulations of multiphysics processes in EGS remain a valuable tool, enabling us to identify and evaluate risks to support management decisions. Furthermore, understanding underlying assumptions and model limitations can ensure better decisions.

3.2.2 Chemical Processes in Reservoir and Fractures

Chemical processes inside the reservoir and fractures include scale deposition, rock and proppant dissolution, change of fluid properties because of bulk or surface reactions, etc. Chemical compositions of circulating fluid can drastically change over short periods of time because of interactions with host rocks (<34 hours, Jones et al., 2023). These interactions can reduce porosity and permeability, leading to reduced injectivity and transmissivity. A reactive transport model that numerically simulates these processes is needed to predict chemical and physical evolution of the circulating fluids and associated reservoir damage, thereby mitigating scaling and corrosion.

Modeling of chemical processes is well established in geochemistry (e.g., Reed, 1982; Bethke, 2008; Bozau et al., 2015; Leal et al., 2017). However, with rapidly evolving fluid compositions, fluid-mineral equilibrium is unlikely during the life cycle of an EGS, and geochemical reactions should not be expected to be exclusively thermodynamically controlled. This also has implications for the use of aqueous geothermometers (Pang and Reed, 1998). Thermodynamic databases used in geochemical modeling are compiled from experimental and calculated data (Oelkers et al., 2009). Expanding and validating these databases over the pressure- temperature range and chemical (pH, salinity, and redox) conditions in geothermal systems are essential to enable accurate predictions of geochemical processes (Zhang et al., 2020).

Modeling chemical processes includes transport of components to and from the reaction site and the reaction itself. As shown in Fig. 8, the chemical process model needs fluid velocities to be used in the components transport model. As a result of the reactions, fluid properties may change, which should be accounted for in the fluid flow solution. Fracture geometry calculated in the geomechanics model defines boundary conditions for components transport and reaction models. At the same time, because of chemical processes, rock or proppant can be dissolved or their volume can be increased due to scale deposition; mechanical properties (Young's modulus) of the rock and proppant pack can also change and should be accounted for in the geomechanical solution. Temperature is an important input for chemical processes that comes from the heat transfer model. During the reaction, some heat may be released or absorbed, which should come back to the heat transfer model.

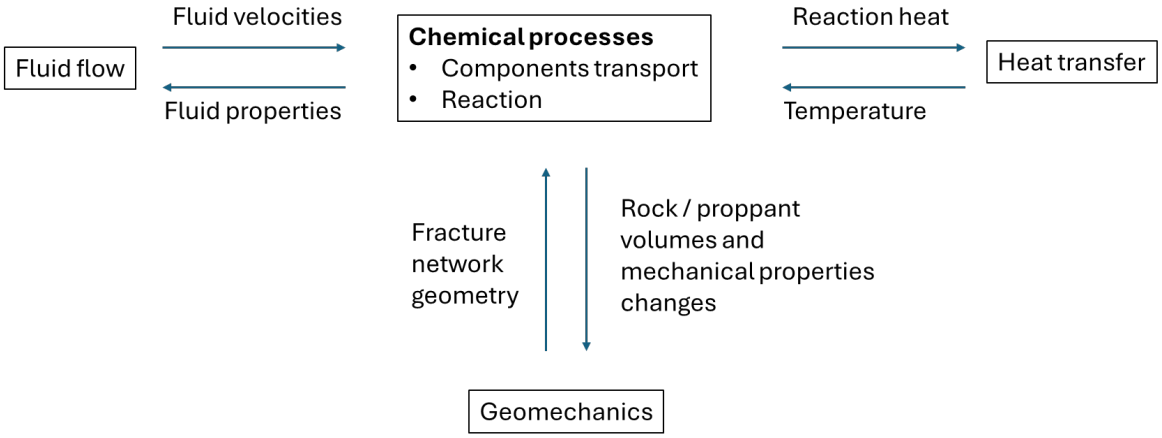

Figure 8: Chemical processes coupling.

Chemical processes coupled with fluid flow and heat transfer are part of the commercially available reservoir simulators or geochemical and reactive transport simulators.

Geomechanical coupling may be important when the rock and/or proppant volume decrease due to dissolution, which leads to reduction of in-situ stresses and subsequent opening or propagation of pressure-induced fractures. Such coupling is used in some acid fracturing models (Li et al., 2020b).

5. Conclusions

EGS projects resemble most shale installations from the past 15 years. Many components are similar; e.g., long-horizontal, multicluster wells using massive fracturing treatments. The US DOE (Smith, 2024) put it this way, “EGS technologies build on developments from the oil and gas industries—including directional drilling and fracking (or stimulation) technologies… Now, researchers supported by DOE and industry are working to adapt those technologies to geothermal conditions and applications.”

However, EGS’ needs in the modeling realm are different. For instance, EGS fractures will see continuous circulation throughout their life, requiring geomechanical modeling during the long-term circulation phase. Moreover, igneous and metamorphic rocks can behave radically different from shale and other sedimentary rocks.

Also, no longer can any of the models or decisions be siloed. EGS demands leveraging full THMC modeling to ensure a project can be delivered economically and efficiently.

In this paper we suggest key areas for EGS evaluation and differences from a conventional perspective. Currently, no single model or software considers all aspects, leaving room for improvement with each project.

REFERENCES

Adams, M., Moore, J., Bjornstad, S., et al. “Fluid-Mineral Equilibria and Injection in EGS — Effect of Injecting Groundwater.” *Environmental Science, Geology* (2005).

Al Balushi, F., Zhang, Q., and Taleghani, A. "Autonomous Fracture Conductivity Using Expandable Proppants in Enhanced Geothermal Systems." *SPE J.* 28 (2023): 2660–2674.

Almubarak, T., Li, L., Nasr-El-Din, H., et al. "Pushing the Thermal Stability Limits of Hydraulic Fracturing Fluids." *SPE Asia Pacific Oil and Gas Conference and Exhibition*, Brisbane, Australia, (2018).

Almulhim, A., Hamid, S., Khan, A. M., and Hoong, C. “A Novel Stimulation Design Approach Revives a Challenging Gas Field.” *SPE Asia Pacific Oil and Gas Conference and Exhibition*, Virtual, (2020).

Almutary, T., Purusharthy, N., Khan, A. M., and ElSebaee, M. “Study of Enhancing Stimulation and Maximizing Hydrocarbon Recovery from a Deep Heterogeneous Sub-Hydrostatic Carbonate Reservoir.” *23rd World Petroleum Congress*, Houston, TX, USA, (2021).

API RP 19C, Measurement of and Specifications for Proppants used in Hydraulic Fracturing and Gravel-packing Operations, second edition. (2018). Washington, DC: API.

API RP 19D, Recommended Practice for Measuring the Long-Term Conductivity of Proppants, second edition. (2021). Washington, DC: API.

API RP 39, Recommended Practices on Measuring the Viscous Properties of a Cross-Linked Water-Based Fracturing Fluid, third edition. (1998). Washington, DC: API.

Barenblatt, G., Zheltov, I., and Kochina, I. "Basic Concepts in the Theory of Seepage of Homogeneous Liquids in Fissured Rocks.” *JAMM* 24(5), (1960), 1286-1303.

Bethke, C.M. “Geochemical and Biogeochemical Reaction Modeling,” *Cambridge University Press*, (2008), 547 p.

Blöcher, M.G., Zimmermann, G., Moeck, I., et al. "3D Numerical Modeling of Hydrothermal Processes During the Lifetime of a Deep Geothermal Reservoir.” *Geofluids*, 10(3), (2010), 406-421.

Bozau, E., Häußler, S., and van Berk, W. “Hydrogeochemical Modeling of Corrosion Effects and Barite Scaling in Deep Geothermal Wells of the North German Basin using PHREEQC and PHAST.” *Geothermics*, 53, (2015), 540-547.

Brinton, D., McLin, K., and Moore, J. “The Chemical Stability of Bauxite and Quartz Sand Proppants Under Geothermal Conditions.” *36th Workshop on Geothermal Reservoir Engineering*, Stanford, CA, (2011).

Cacas, M.C., Ledoux, E., de Marsily, G., et al. "Modeling Fracture Flow with a Stochastic Discrete Fracture Network: Calibration and Validation: 1. The flow model.” *Water Resources Research*, 26(3), (1990), 479 - 489.

Cheng, Q., Wang, X., and Ghassemi, A.” Numerical Simulation of Reservoir Stimulation with Reference to the Newberry EGS.” *Geothermics*, 77, (2019), 327-343

CMG Ltd. *STARS*. Retrieved 05/06/2024, from https://www.cmgl.ca/solutions/software/stars/ (2024).

COMSOL Multiphysics. *COMSOL Multiphysics*. Retrieved 05/06/2024, from https://www.comsol.com/comsol-multiphysics/ (2020).

Das, S., Wray, A., Hamilton, D., et al. "A Fracture Characterization Case Study from an Enhanced Geothermal System," *4th EAGE Global Energy Transition Conference and Exhibition*, Paris, France (2023).

Dershowitz, B., LaPointe, P., Eiben, T., and Wei, L. "Integration of Discrete Feature Network Metho ds With Conventional Simulator Approaches." *SPE Reservoir Evaluation & Engineering.* 30(2), (2000) 165–170.

Frash, L.P. and Gutierrez, M. "Development of a New Temperature Controlled True-Triaxial Apparatus for Simulating Enhanced Geothermal Systems (EGS) at the Laboratory Scale." *37th Workshop on Geothermal Reservoir Engineering*, Stanford, CA, (2012).

Fu, P., Hao, Y., Walsh, S., and Carrigan, C. "Thermal Drawdown-Induced Flow Channeling in Fractured Geothermal Reservoirs," *RMRE*, 49, (2016), 1001–1024.

Gao, Z., LI, Y., Pang, Z., Huang, T., et al. "Geochemical Mechanisms of Water/CO2-rock Interactions in EGS and its Impacts on Reservoir Properties: A Review." *Geothermics*, 118, (2024).

Ghassemi, A., Kelkar, S., and McClure, M. "Influence of Fracture Shearing on Fluid Flow and Thermal Behavior of an EGS Reservoir - Geothermal Code Comparison Study." *40th Workshop on Geothermal Reservoir Engineering*. (2015) 1-14.

Gringarten, A.C., Witherspoon, P.A., and Ohnishi, Y. "Theory of Heat Extraction from Fractured Hot Dry Rock." *JGR*, 80, (1975), 1120-1124.

Hajibeygi, H., Karvounis, D., and Jenny, P. "A Hierarchical Fracture Model for the Iterative Multiscale Finite Volume Method." *JCP*, 230(24), (2011), 8729-8743.

HEATSTORE. (2019) Retrieved 05/06/2024 https://heatstore.eu/project.html

Hu, L., Ghassemi, A., Pritchett, J., and Garg, S. "Laboratory Scale Investigation of Enhanced Geothermal Reservoir Stimulation." *ARMA-2016*.

Hwang, J., Zheng, S., Sharma, M., et al. "Containment of Water-Injection-Induced Fractures: The Role of Heat Conduction and Thermal Stresses." *SPE Reservoir Evaluation & Engineering*, 25(2), (2022), 245-260.

IGA. "Best Practices Guide for Geothermal Exploration." Retrieved June 1, 2024, https://documents1.worldbank.org/curated/en/190071480069890732/pdf/110532-Geothermal-Exploration-Best-Practices-2nd-Edition-FINAL.pdf

Jian, G., Fernandez, C., A., Burghardt, J., et al. "Alternative, Less Water-Intensive, Fracturing Fluids for Enhanced Geothermal Systems." *ARMA-2020.*

Jones, C.G., England, K., Simmons, S., et al. "Stimulation, Tracers and Geochemistry at Utah FORGE," *48th Workshop on Geothermal Reservoir Engineering*, Stanford University, Stanford, CA, (2023).

Khan, A.M., BinZiad, A., Alshammari, F.O., and Glaznev, I. “Fiber Assisted Enhanced CO_2 Foam Fracturing and Proppant Placement.” *SPE Annual Technical Conference and Exhibition*, San Antonio, Texas, (2023a).

Khan, A.M., BinZiad, A., and Alsubaii, A. “Digital Degradable Chemistry Provides Solutions for Production Enhancement and Intervention in Challenging Wells.” *SPE International HFTC*, Muscat, Sultanate of Oman, (2023b).

Khan, A.M., BinZiad, A., Alsubaii, A., et al. “Proppant Flowback Control with High-Aspect Ratio Proppant and Advanced Modeling.” *SPE HFTC*, Muscat, Sultanate of Oman, (2023c).

Khan, A.M., Kresse, O., England, K., et al. “Integrated Lifecycle Simulation for Utah FORGE: Part I – Fracture Geometry Calibration.” GRC *Transactions*, Volume 48 (2024).

Knox J.A., and Weaver, J. “A Solution to Proppant Dissolution in Hydrothermal Environments.” *14th Workshop on Geothermal Reservoir Engineering*, Stanford, CA, (1989).

Ko, S., Ghassemi, A., and Uddenberg, M. “Selection and Testing of Proppants for EGS.” *48th Workshop on Geothermal Reservoir Engineering*, Stanford, CA, (2023).

Kresse, O., Sinkov, K., Hobbs, B. “Modeling Case Study: Optimizing Multicluster Stimulation Uniformity in Horizontal Wells.” *SPE HFTC*, The Woodlands, TX, (2023).

Kresse, O. and Weng, X. “Numerical Modeling of 3D Hydraulic Fractures Interaction in Complex Naturally Fractured Formations.” *RMRE*, (2018).

Kresse, O., Hobbs, B., and Pei, Y. “Challenges and Uniqueness of Dual-Fracture Model.” *ARMA-24-0453*, (2024).

Kumar, D. and Ghassemi, A. “Three-Dimensional Poroelastic Modeling of Multiple Hydraulic Fracture Propagation from Horizontal Wells.” *IJRMMS* 105 (2018), 192-209.

Kumar, D., Gonzalez, R.A., and Ghassemi, A. "The Role of Micro-Proppants in Conductive Fracture Network Development." *SPE HFTC*, The Woodlands, TX, (2019).

Kumar, D., Liu, B., and A. Ghassemi. “3D Modeling of the Utah Forge Reservoir Stimulation with Proppant Transport and Deposition.” *SPE Annual Technical Conference and Exhibition*, San Antonio, TX, (2023).

LBNL. “Performance Evaluation of Engineered Geothermal Systems Using Discrete Fracture Network Simulations.” United States. https://doi.org/10.2172/1775421, (2021).

Leal, A.M. M., Kulik, D.A., Smith, W.R., and Saar, M.O., “An Overview of Computational Methods for Chemical Equilibrium and Kinetic Calculations for Geochemical and Reactive Transport Modeling,” *Pure and Applied Chemistry*, 89, (2017), 145–166.

Li, M., and Lior, N. “Analysis of Hydraulic Fracturing and Reservoir Performance in Enhanced Geothermal Systems.” *JERT*, 137(4), (2015).

Li, S., Feng, X., and Pan, Z. “3D Numerical Analysis Using a Coupled Geomechanics and Fluid-Heat Flow Model for Heat Extraction from Enhanced Geothermal Reservoirs.” *Rock Mechanics for Natural Resources and Infrastructure Development*. (2020a)

Li, X., He, Y., Yang, Z., et al. “Fully Coupled Model for Calculating the Effective Acid Penetration Distance during Acid Fracturing.” *JNGSE*, 77 (2020b).

Lisabeth, H. and Norbeck, J. “Experimental Study of the Effect of Hydrothermal Alteration on Proppant Brittleness.” *GRC Transactions*, Vol. 44. (2020).

Liu, T., Jardine, R. J., Vinck, K., and Ackerley, S.K. "Optimization of Advanced Laboratory Monotonic and Cyclic Triaxial Testing on Fine Sands. ASTM International.” *Geotech. Test. J.*, 45(6) (2022), 1087–1107.

Mattson, E., Neupane, G., Plummer, M., et al. “Long-term Sustainability of Fracture Conductivity in Geothermal Systems using Proppants.” United States. https://www.osti.gov/servlets/purl/1348062 (2016)

McClure, Mark W., and Charles Kang. “A Three-Dimensional Reservoir, Wellbore, and Hydraulic Fracturing Simulator that is Compositional and Thermal, Tracks Proppant and Water Solute Transport, Includes non-Darcy and non-Newtonian Flow, and Handles Fracture Closure.” SPE-182593, Montgomery, TX. (2017)

McClure, M., C. Kang, and G. Fowler. “Optimization and Design of Next Generation Geothermal Systems Created by Multistage Hydraulic Fracturing,” *SPE HFTC* SPE-209186-MS, (2022)

Mindel, J., Alt-Epping, P., Armandine Les Landes, A., et al. "Benchmark Study of Simulators for Thermo-Hydraulic Modeling of Low Enthalpy Geothermal Processes.” *Geothermics,* 96. (2021).

Mulyani, S., Sarmiento, et al., “Calibrated Natural State Model in Sorik Marapi Geothermal Field, Indonesia”, IPTC-19221-MS, (2019).

Nadimi, S., Forbes, B., Finnila, A., et al. “Hydraulic Fracture/Shear Stimulation in and EGS Reservoir: Utah FORGE Program,” *ARMA 18-843*, (2018).

Norbeck, J.H. and Latimer, T. “Commercial-Scale Demonstration of a First-of-a-Kind Enhanced Geothermal System.” https://eartharxiv.org/repository/view/5704. (2023).

Norbeck, J., Latimer, T., Gradl, C., et al. “A Review of Drilling, Completion, and Stimulation of a Horizontal Geothermal Well System in North-Central Nevada” *48th Workshop on Geothermal Reservoir Engineering*, Stanford, CA (2023).

Norbeck, J., McClure, M. and Horne, R. “Field Observations at the Fenton Hill Enhanced Geothermal System Test Site Support Mixed-Mechanism Stimulation,” *Geothermics,* 74, (2018), 135-149.

Oelkers, E.H., Bénézeth, P., and Pokrovski, G.S. “Thermodynamic Databases for Water-Rock Interaction” *Reviews in Mineralogy and Geochemistry* 70, (2009), 1–46.

Pang, Z.-H. and Reed, M. “Theoretical Chemical Thermometry on Geothermal Waters: Problems and Methods,” *Geochimica et Cosmochimica Acta*, 62, (1998), 1083–1091.

PFLOTRAN. “A Massively Parallel Reactive Flow and Transport Model for Describing Subsurface Processes.” Retrieved 05/06/2024, from https://www.pflotran.org/.

Pruess, K. “TOUGH2–A General Purpose Numerical Simulator for Multiphase Fluid and Heat flow.” Berkeley, CA: Report: LBL-29400, (1990).

Qarinurab, M., Yasuharaa, H., Kinoshitaa, N., et al. "Numerical Investigation for Modeling Lahendong Geothermal Field, North Sulawesi, Indonesia.” *International Symposium on Rock*

Engineering for Innovative Future. *Japanese Society for Rock Mechanics*, Okinawa, Japan, (2019).

Reed, M.H, "Calculation of Multicomponent Chemical Equilibria and Reaction Processes in Systems Involving Minerals, Gases, and Aqueous Phase," *Geochimica et Cosmochemica Acta*, 46, (1982), 513-528.

Riahi, A., Damjanac, B., and Furtney, J. "Thermo-Hydro-Mechanical Numerical Modeling of Stimulation and Heat Production of EGS Reservoirs," *ARMA14-7741*, (2014).

RFD. *New Energy*. Retrieved 05/06/2024, from https://rfdyn.com/solutions/new-energy/.

Ruela, T., Martinez-Castro, N., Subramanian, K., et al. "Rheology Modifier Compositions and Methods of Use." United States Patent Appl. TVPP US201113026705. (2011).

Salazar, A., Selvadurai, P., Niu, Z., et al. "Insights into Triaxial Testing Using Coupled Acoustic Emission and Distributed Optical Fiber Strain Measurements." *ARMA-56*, (2022).

SLB. "ECLIPSE Geothermal." Retrieved 05/06/2024, from https: //www.slb.com/resource-library/technical-paper/geothermal/pham-eclipse-geothermal (2024a).

SLB. "Intersect." Retrieved 05/06/2024, from https://www.software.slb.com/products/intersect (2024b)

Smith, Morgan. "Enhanced Geothermal Systems (EGS): Frequently Asked Questions." *Congressional Research Service Report R48090*, (2024).

Stoddard, T., McLennan, J. and Moore, J. "Fracture Conductivity of a Bauxite-Propped Geothermal System." *Geothermal Resources Council*. 34, (2010).

Sullivan, M.J., Pruess, K., and Lippmann, M.J. "State of the Art of Geothermal Reservoir Simulation." *Geothermics*, 30, (2001), 395-429.

Toth, A. and Bobok, E. "Possibility to Use CO2 as EGS Fluid in Hungary." *38th Workshop on Geothermal Reservoir Engineering*, Stanford, CA, SGP-TR-198 (2013).

TOUGH3. *Software*. Retrieved 05/06/2024, from https://tough.lbl.gov/software/tough3/ (2020).

U.S. Department of Energy. "Benchmark Problems of the Geothermal Technologies Office Code." *PNNL-26016.* (2016).

Vinsome, P. and Shook, G. "Multi-Purpose Simulation." *JPSE*, 9(1), (1991), 29–38.

Wang Y., Liu P., Shi H., et al. "Enhancing the Stability of Polymer Nanostructures via Ultrathin Oxide Coatings for Nano-Optical Device Applications." *Nanotechnology*. 32(29), (2021).

White, M., and Phillips, B. "Code Comparison Study Fosters Confidence in the Numerical Simulation of Enhanced Geothermal Systems." *40th Workshop on Geothermal Reservoir*. Stanford, CA, (2015).

Wright, P.M., Ward, S.H., et al., "State-of-the-art geophysical exploration for geothermal resources". Geophysics, 50 (1985), 2666-2699.

Yang, R., Hong, C., Liu, W., et al. "Non-Contaminating Cryogenic Fluid Access to High-Temperature Resources: Liquid Nitrogen Fracturing in a Lab-Scale Enhanced Geothermal System," *Renewable Energy*, 165, Part 1, (2021), 125-138.

Zhao, Y., Feng, Z., Yang, D., and Liang, W. “THM (Thermo-hydro-mechanical) Coupled Mathematical Model of Fractured Media and Numerical Simulation of a 3D Enhanced Geothermal System at 573 K and Buried Depth 6000e7000 M.” *Energy*, 82, (2015), 193-205.

Zhang, G., Lu, P., Zhang, Y., et al. “SupPhreeqc: A Program for Generating Customized Phreeqc Thermodynamic Datasets from Supcrtbl and Extending Calculations to Elevated Pressures and Temperatures” *Computers & Geosciences* 143, (2020).

Zhang, T., Hu, Q., Chen, W., et al. “Analyses of True-Triaxial Hydraulic Fracturing of Granite Samples for an Enhanced Geothermal System.” *Lithosphere,* 5, (2022).

Zheng, S., Hwang, J., Manchanda, R., and Sharma, M. “An Integrated Model for Non-isothermal Multi-Phase Flow, Geomechanics and Fracture Propagation.” *JPSE*, 196, (2021).

Zhou, D., Tatomir, A., Sauter, M., and Tomac, I. “Optimization of Well Configuration for EGS Performance with Multi-Dimensional Two-Phase Flow Modeling.”*ARMA-56*, (2022).

Zhou, L., Zhu, Z., Xie, X., and Y., H. “Coupled Thermal Hydraulic Mechanical Model for an Enhanced Geothermal System and Numerical Analysis of its Heat Mining Performance.” *Renewable Energy*, 181, (2022), 1440-1458.

Understanding Impact of Complex Fracture Patterns in EGS In-Situ Stress Estimations Through Post-Peak Pressure Analysis from High-Temperature True-Triaxial Block Fracturing Experiments

Yunxing Lu[1], Fan Fei[2], Matteo Cusini[2], Andrew P. Bunger[1,3]

[1]Department of Civil and Environmental Engineering, University of Pittsburgh, USA

[2]Atmospheric, Earth, and Energy Division, Lawrence Livermore National Laboratory, USA

[3]Department of Chemical and Petroleum Engineering, University of Pittsburgh, USA

Keywords

In-situ stress estimation; Enhanced Geothermal Reservoir (EGS); FORGE; Thermo-hydro-mechanical coupling; Fracture complexity

ABSTRACT

Estimating in-situ stress in Enhanced Geothermal Systems (EGS) faces many complexities due to the limitations of simplified models used for traditional reservoir analysis and data interpretation. Due to the inherent high-temperature characteristics of EGS reservoirs, wellbore cooldown caused by injection and circulation can induce changes in the thermal stress field and create more complex fracture patterns. These conditions can also significantly influence the borehole pressure history recorded during fracturing tests, which will also cause problems for interpretation of hydraulic fracturing in-situ stress estimation methods. By implementing laboratory-scale block fracturing experiments under Utah FORGE conditions and analyzing post-peak wellbore pressure data, this study focuses on examining the validity of the classical interpretation methods, which are based on an assumption of simple planar fracture geometry. Incorporating the shut-in, reopen, and step-rate phases into the post-peak stage allows access to the closure pressure inferred by the laboratory G-function plot and reopening pressure by the reopen and step-rate tests. Our results indicate that the classical horizontal maximum stress estimation method does not provide stress estimates consistent with the actual applied stresses, particularly in cases with complicated fracture patterns that are likely caused by the substantial cooling of the wellbore prior to fracturing. Consequently, our work motivates future endeavors to develop a more robust approach for stress estimation in EGS reservoirs, accounting for near-wellbore fracture complexity caused by thermal stress induced by wellbore cooling.

1. Introduction

Accurately estimating in-situ stresses, especially minimum horizontal and maximum stresses, plays an important role in many engineering applications such as optimizing hydraulic fracturing designs, stabilizing the wellbore, and assessing fault reactivation (Bao & Burghardt, 2022; Kim et al., 2016; Xing et al., 2020). Classical theories and methods for estimating in-situ stresses mostly rely on two basic assumptions: the simplicity of fracture geometry and the simultaneous closing of the entire fracture surface (Cornet, 1981; Haimson & Cornet, 2003; Haimson & Fairhurst, 1967; Ito et al., 1999). However, these assumptions are based on ideal situations and may not reflect all cases encountered in practice. Following these basic assumptions, the estimation of in-situ stress can be determined by three components that can be captured or inferred from the hydraulic stimulation process: the breakdown stress (p_b), the fracture closure pressure (p_c), and the reopening pressure (p_r). The details of these definitions and their differences are well-explained by Guglielmi et al., 2023. However, more recent research (Guglielmi et al., 2023; Lu et al., 2024) has demonstrated that during the development of Enhanced Geothermal Systems (EGS), wellbore cooldown through injection and circulation can significantly alter the thermal stress field. Such changes are likely to generate more intricate and complex fracture patterns compared to those occurring in traditional reservoirs with low temperature. At the same time, this alteration substantially impacts the recorded borehole pressure history during fracturing tests, thereby rendering the interpretations of wellbore pressure less clear and perpetuating ongoing debates, particularly concerning the estimation of the maximum horizontal stress (σ_H). The original in-situ stress estimation equations were developed by Hubbert and Willis (1957). They initially proposed the expression for maximum horizontal stress (σ_H) as follows:

$$p_b = 3\sigma_h - \sigma_H + \sigma_t, \tag{1}$$

where the p_b is the breakdown pressure, σ_h is the minimum horizontal stress and σ_t is the tensile strength of the material. Subsequently, Haimson and Fairhurst (1967), Haimson et al. (2003), and Ito et al. (1999) introduced additional expressions for estimating the maximum horizontal stress, incorporating poroelastic effects and reopening pressures, respectively. Moreover, some researchers (Bredehoeft et al., 1976; Cornet, 1981; Gronseth & Kry, 1981) have pointed out that under certain circumstances, e.g., when fractures exhibit greater complexity than the sample geometry and when fractures do not completely close after each pressure cycle, the aforementioned theories and expressions for estimating the maximum horizontal stress may not be valid.

Considering these research gaps and challenges, we have undertaken a laboratory study and implemented analysis of post-peak pressure records from the triaxial loading hydraulic fracturing tests on 6-inch cubic granite blocks. Experiments were conducted under FORGE-relevant conditions. Laboratory-derived G-function, step-rate, and fracture reopening measurements can significantly enhance the identification of key components constituting the in-situ stresses. Additionally, this study provides an excellent opportunity to conduct numerous experiments, allowing us to quantitatively validate and examine the quality of current in-situ stress estimation methods under complex fracture pattern conditions. This approach not only augments our capacity to analyze and deduce in-situ stress in environments with complex fracture geometries, but also stimulates further research aimed at developing an accurate and more physically informed methodology for stress evaluation in Enhanced Geothermal Systems (EGS) reservoirs.

2. Experimental Setup and Methodology

The experimental setup involves testing 6-inch cubic granite blocks under two scenarios—room temperature and 200 degrees Celsius—using a hydraulic piston-actuated loading cell under true triaxial loading conditions with various combinations of in-situ stress. The St. Cloud Gray granodiorite is used here as the FORGE-analogue granite for laboratory testing purposes. This selection is primarily founded on acoustic anisotropy properties, assessed and calculated using the acoustic transmission system. This system can measure both S and P waves as they traverse the test sample. The velocity of these waves can serve as an indicator of the granite's anisotropy. To promote an even distribution of stress on the testing sample, aluminum loading plates with a minimum thickness of 3 inches are inserted between each side of the sample and the tilt saddle on the actuator. To further mitigate friction and prevent shear boundary conditions, Teflon sheets are placed between each face of the sample and the aluminum loading plate. For the second testing case, where the host block is heated to 200 degrees Celsius, thermal stress can be induced within the sample near the borehole by circulating room-temperature water through the borehole. As shown in Figure 1, this process results in a temperature drop of up to 140-150 degrees Celsius at the borehole wall when the circulation starts. The circulation time lasts around 15 minutes. During this time, a total of 2-4 liters of water is circulated through the borehole, and the borehole temperature continues to decrease, albeit at a slower rate, by approximately another 10 to 20°C. When the circulation is stopped, it waits for a period of time for the borehole temperature to recover to a relatively stable value. Then, the system's outlet is closed to initiate the hydraulic fracturing process. In the scenario without thermal stress, the hydraulic fracturing starts immediately after bleeding the air out of the system.

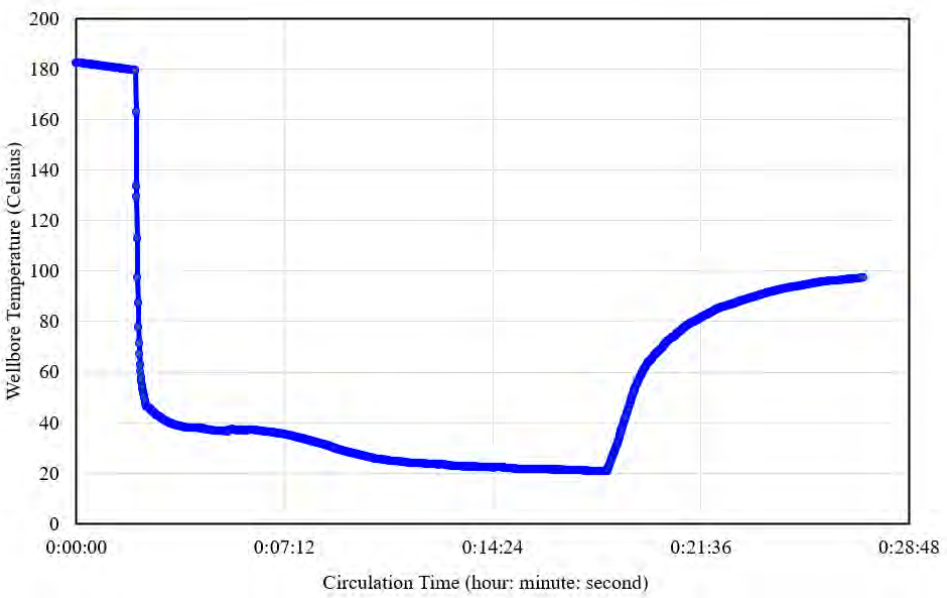

Figure 1: Wellbore temperature recording during water circulation.

During the hydraulic fracturing phase, the fluid is injected into the wellbore at a constant flow rate of 3 ml/min until the breakdown pressure is reached. After that, the injection is stopped and the wellbore pressure is monitored to observe post-peak pressure decline behaviors, which are referred to as the shut-in phase. The shut-in phase commences when the borehole pressure stabilizes at a constant value. After the shut-in phase, a reopening test is performed by injecting

the same fluid at the same flow rate into the borehole to observe pressure responses. Similarly, when the pressure reaches the peak in the reopening test, another shut-in phase is implemented. The procedure then moves to the step-rate pressure test, during which the borehole pressure increases in increments of 0.68 MPa (100 psi). Each subsequent step commences only after the current pressure level has stabilized at a constant flow rate. At each stage, the pressure level and corresponding flow rate are recorded and plotted for future analysis. Following the step-rate phase, another shut-in period occurs, after which the wellbore pressure decreases to ambient levels. With these steps completed, the entire test procedure is considered finished. These three phases constitute the whole process of the post-peak wellbore pressure analysis, as shown in Figure 2, and have provided the opportunity to infer the reopening pressure and minimum horizontal stress at different angles.

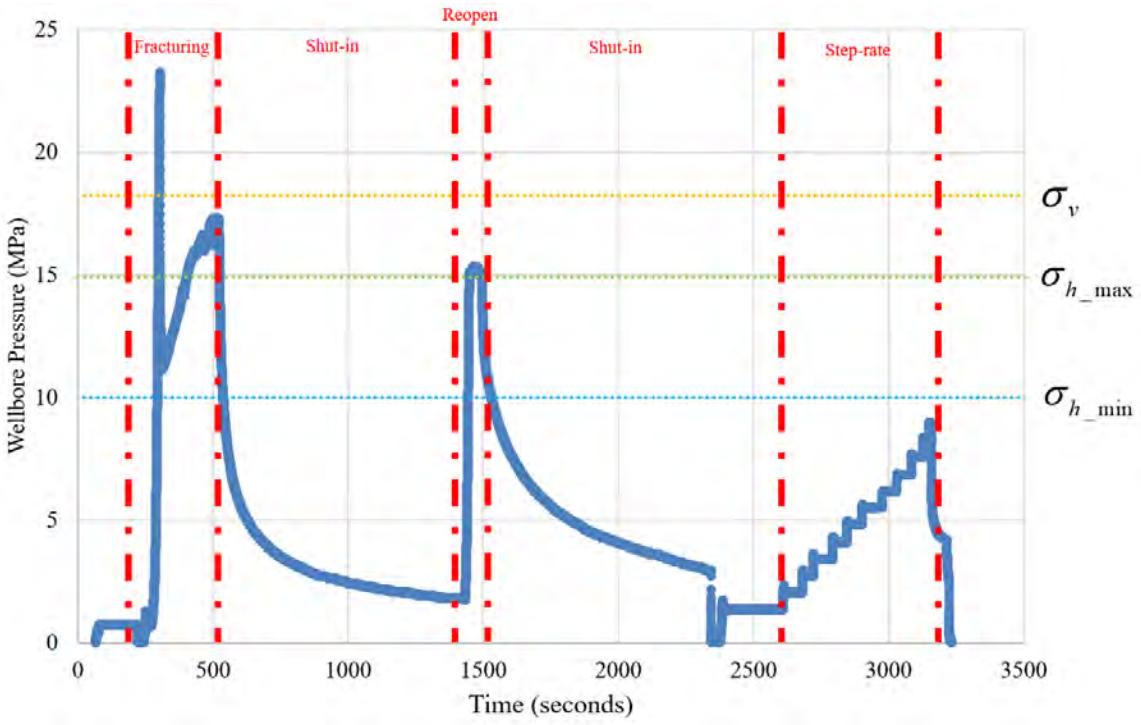

Figure 2: An example of full wellbore pressure record to show the lifecycle from fracturing to step rate testing.

3. Results

The testing scenarios covered in this section include three cases. In all these tests, the vertical and maximum horizontal stress are maintained at 17.5 MPa and 15 MPa, respectively. The borehole is parallel to the minimum horizontal stress direction. The magnitude of the minimum horizontal stress and the testing temperature are varied between tests. These tests are summarized below:

1) Horizontal well – Room temperature – Non-Thermal Stress with minimum horizontal stress values at 3 MPa (HR-NTS-3MPa)
2) Horizontal well – High temperature – Induced Thermal Stress with minimum horizontal stress values at 7 MPa (HH-ITS-7MPa)

3) Horizontal well – Room temperature – Non-Thermal Stress with minimum horizontal stress values at 7 MPa (HR-NTS-7MPa).

Figure 3 shows the results from testing case HR-NTS-3MPa, in which the hydraulic fracturing is carried out at room temperature without inducing any thermal stress. Figure 3 (a) shows the full pressure record during the four phases of the stimulation, i.e., hydraulic fracturing, shut-in, reopening, and the step rate. The breakdown pressure in this case is 42.5 MPa. By using the fracture compliance method (McClure et al., 2016), the G-function plot (Figure 3 b) from the first shut-in period indicates that the closure pressure is around 9 MPa, whereas the closure pressures picked up from the reopening tests (Figure 3 c) and the step rate (Figure 3 d) are around 14 MPa and 13 MPa, respectively. The fracture pattern observed within this testing is comprised of multiple-45-degree incline fractures, as shown in Figure 4.

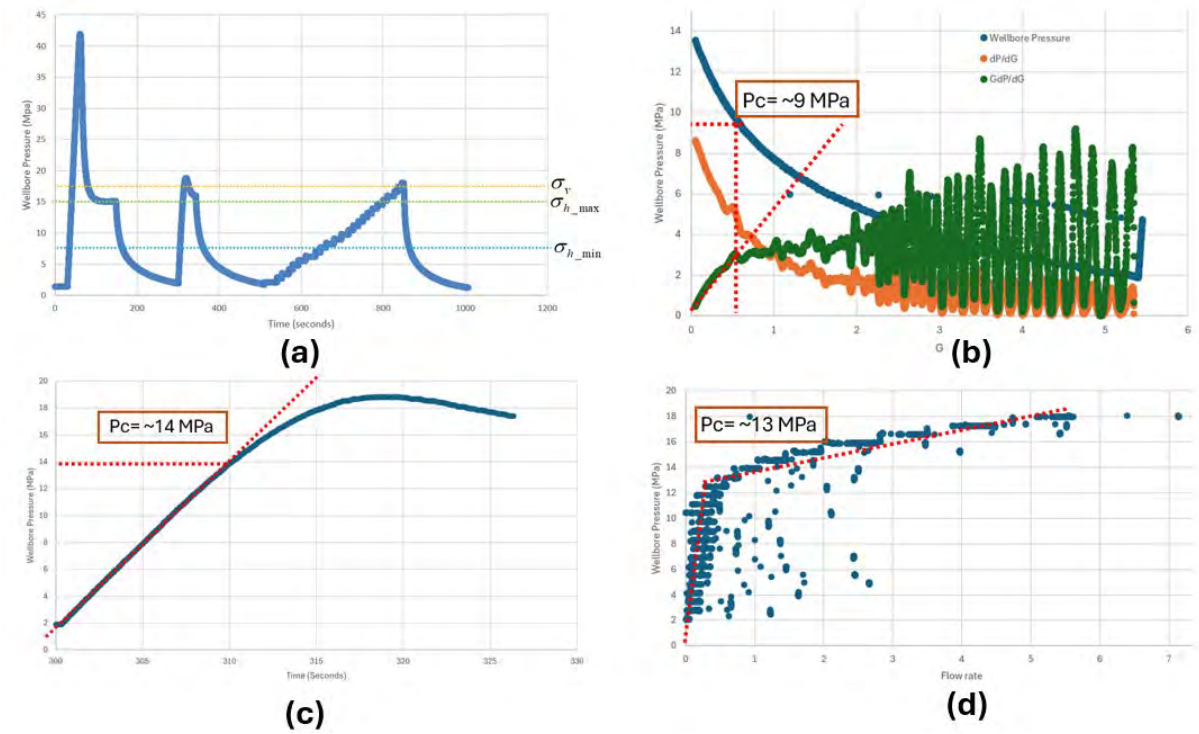

Figure 3: HR-NTS-3MPa test case: (a) Full wellbore pressure record; (b) G-function plot; (c) Reopening test pressure record; (d) Step rate plot.

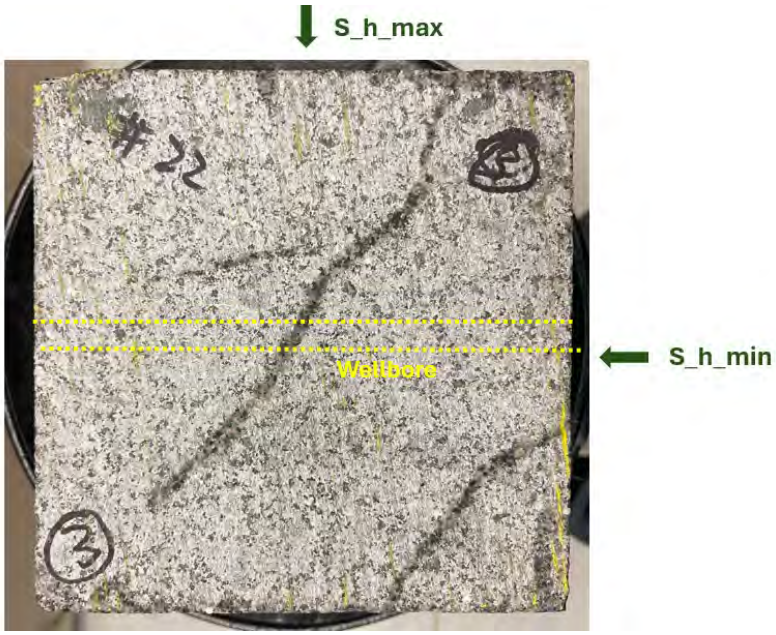

Figure 4: Fracture patterns observations from HR-NTS-3MPa.

In contrast to the non-thermal base case, the HH-ITS-7MPa testing case induces thermal stress by circulating cold tap water through the borehole in the center of the hot granite block (initially at 200 degrees Celsius) for 15 minutes before hydraulic fracturing starts. With the same applied stress combinations, the breakdown pressure shown in the Figure 5 is 15 MPa. Again, by the fracture compliance method (McClure et al. 2016), the fracture closure pressure picked from the G-function plot is 8 MPa, which almost aligns with the minimum stress applied in the experiment. In contrast, the closure pressures picked from the reopening and step rate tests are both 9 MPa, which is slightly above the applied minimum horizontal stress (7 MPa). The fracture patterns observed within this specimen consist of transversely oriented cracks, as shown in Figure 6.

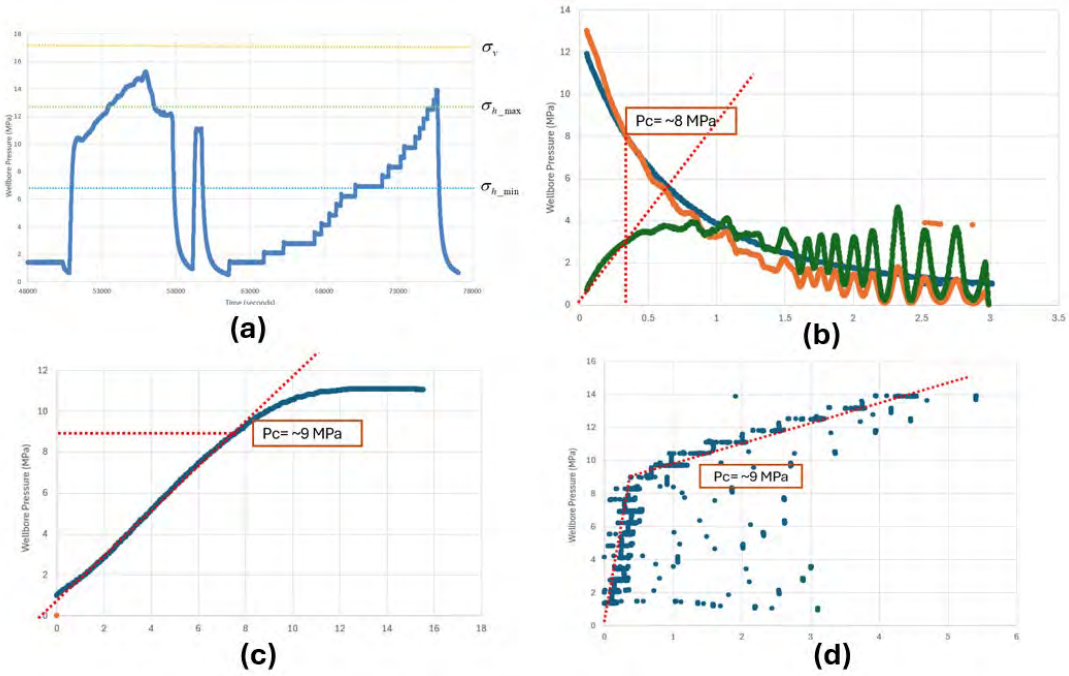

Figure 5: HH-ITS-7MPa test case: (a) Full wellbore pressure record; (b) G-function plot; (c) Reopening test pressure record; (d) Step rate plot.

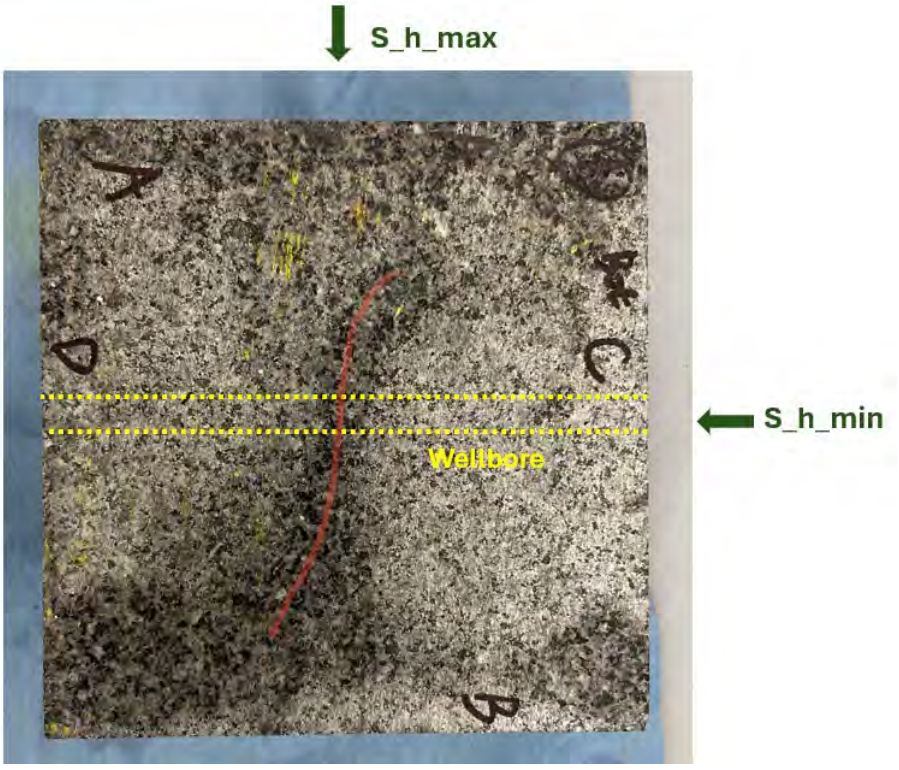

Figure 6: Fracture patterns observations from HH-ITS-7MPa (fracture location is indicated by red color).

The HR-NTS-7MPa testing case is different from the previous testing cases as no thermal stress is induced. As shown in Figure 7, the breakdown pressure is 21 MPa. The fracture closure pressures

derived from the G-function, reopening, and step rate tests are all around 6, 7 and 7 MPa. The fracture pattern observed, shown in Figure 8, consists of both longitudinal and transverse fractures.

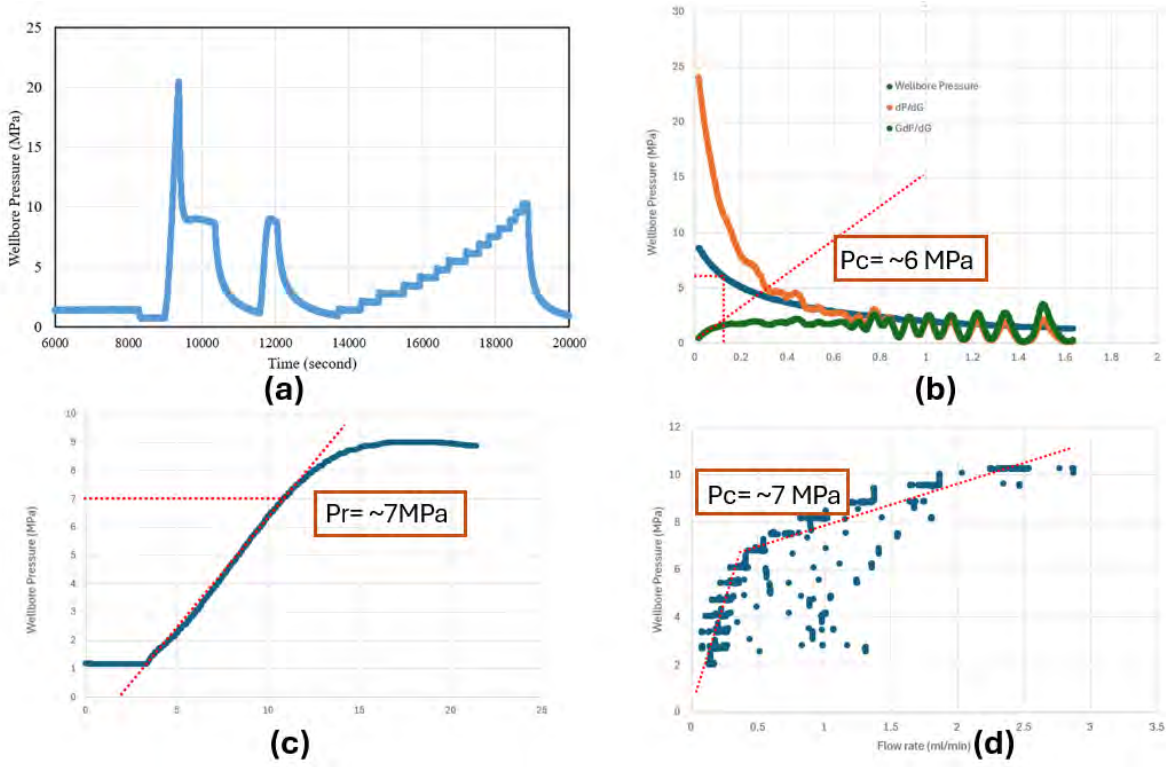

Figure 7: HR-NTS-7MPa test case: (a) Full wellbore pressure record; (b) G-function plot; (c) Reopening test pressure record; (d) Step rate plot.

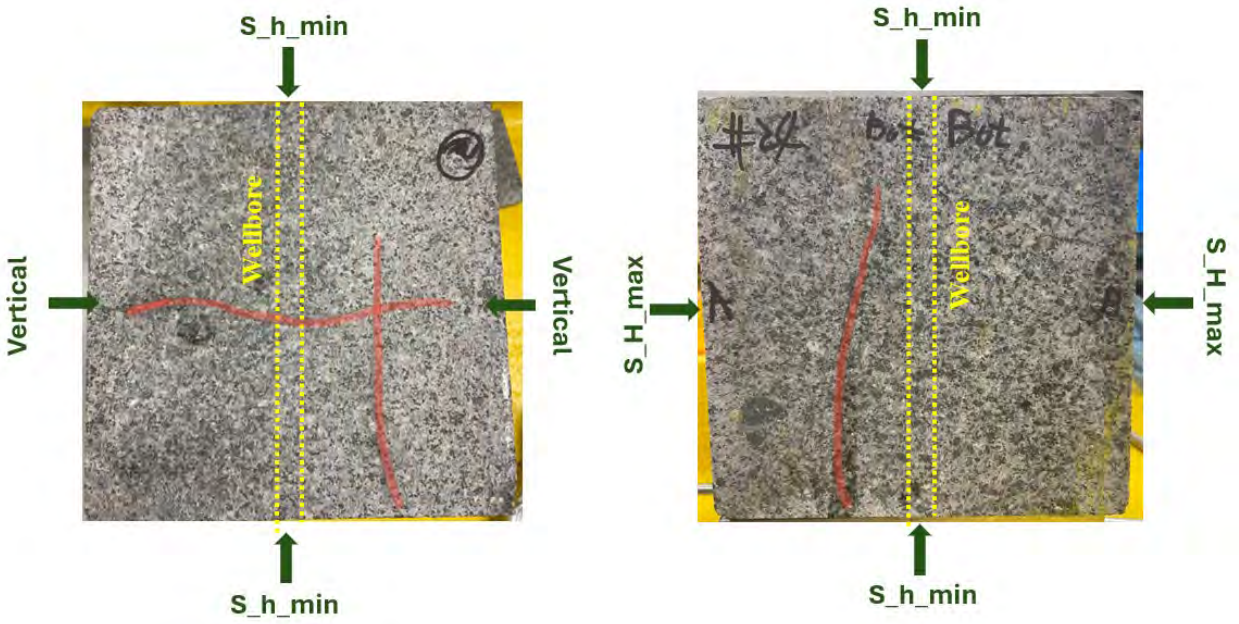

Figure 8: Fracture patterns observations from HR-NTS-7MPa.

4. Discussion

The results of the three testing cases covered in this paper are summarized in Table 1. First, by comparing the breakdown pressure between HR-NTS-7MPa and HH-ITS-7MPa, it is evident that the thermally induced stress from circulating room-temperature water into the hot testing sample can significantly lower the breakdown pressure. Secondly, by using Eq. (1) for each test, we determine the horizontal maximum stress by the actual applied minimum horizontal stress (σ_h) and p_b that is recorded from the experiment. These derived results are summarized in Table 1.

Examining these results, if the minimum horizontal stress is estimated by the closure pressure the G-function plot, and then reformulating Eq. (1), one obtains

$$\sigma_H = 3\sigma_h - p_b + \sigma_t. \quad \text{Eq. (2)}$$

Following the definition and explanations that Guglielmi et al., 2023 have provided about the relationships between the three terms, we can use the reopening pressure (p_r) to replace both the breakdown pressure (p_b) and tensile strength (σ_t), which leads to

$$\sigma_H = 3\sigma_h - p_r. \quad \text{Eq. (3)}$$

Table 1: Summary of the three testing case results

Testing Case	Closure Pressure G – function (MPa)	Reopen Pressure (MPa)	Step-rate Reopen Pressure (MPa)	Breakdown Pressure (MPa)	Actual Applied minimum horizontal Stress (MPa)	Actual Applied Horizontal Maximum Stress (MPa)	Calculated Horizontal Maximum Stress (MPa)
HR-NTS-3MPa	9	14	13	42.5	3	15	7.5
HH-ITS-7MPa	8	9	9	15	7	15	12
HR-NTS-7MPa	6	7	7	21	7	15	11

By using Eq. (3), we can estimate the maximum horizontal stress by using the closure pressure obtained from the G-function as an estimate of σ_h, and using the average value of the reopening pressure and step-rate reopening pressure as p_r. The calculated estimated maximum horizontal stress value is recorded in the last column of Table 1. For each case, the estimated horizontal maximum value deviates from the actual value by 20% to 50%. One possible reason for this difference is that the current maximum horizontal stress estimation model is built for an ideal fracture geometry. Let us consider the HH-ITS-7MPa case as an example where the generated fracture is almost ideally perpendicular to the direction of the minimum horizontal stress. The reopening pressure is around 9 MPa which is slightly above the minimum horizontal stress, and the estimated maximum horizontal stress would be approximately 12 MPa, slightly below the actual value. However, in the case of the HR-NTS-3MPa, because the generated fracture has a 45-degree inclination relative to the wellbore drilling direction —making it more complex than the ideal situation— using the reopening pressure under the 45-degree inclined fracture scenarios

could cause some deviation from the real value when using Eq. (3) to estimate the maximum horizontal stress. If one takes a step further, which could easily calculate the normal stress for this 45-degree incline fracture with the help of the well-known 2D stress transformation equation (Timoshenko & Gere, 2012), one could obtain the reopening pressure for this case as 11 MPa, which is not far from what has been recorded in the experimental measurements.

With this being said, the current theory underlying maximum horizontal stress estimation may not be suitable for application in complex EGS reservoir conditions, particularly when thermal stress is induced during the stimulation process. This thermal stress alters the original stress field, potentially generating a complex fracture pattern. This can be seen most clearly by comparing the testing cases of HR-NTS-7MPa and HH-ITS-7MPa, where the only difference is the latter case has introduced thermal stress. Due to the change in thermal conditions, the generated fracture geometry has altered from having both longitudinal and transverse fractures to having only transverse fractures. This example shows the potential for thermal stress to substantially impact fracture geometry. Furthermore, different combinations of in-situ stress could also generate very different fracture patterns under the EGS conditions. For example, when comparing the testing cases between HR-NTS-7MPa and HR-NTS-3MPa, where both cases are not induced with thermal stress and the only difference is the magnitude of the minimum horizontal stress, we can see that the fracture geometry is very different: the HR-NTS-7MPa has both longitudinal and transverse fractures, whereas the HR-NTS-3MPa has multiple-45-degree incline fractures.

5. Conclusions

Block tests have been performed on granite cubes subjected to true-triaxial confinement in which hydraulic fractures are created, allowed to close under shut-in conditions, and then reopened both rapidly and under step-rate conditions. This loading sequence enables analysis using classical in-situ stress estimation techniques. The testing cases are designed to examine the potential role of cooling of the wellbore prior to hydraulic fracturing along with evaluation of the impact of non-ideal fracture geometry on the fidelity of the stress estimations. By obtaining the relevant stress estimated the lab-scale G-function analysis, reopening pressure, and step-rate tests, we obtained estimated minimum horizontal stress and maximum stress. The results show that reopening occurs at a similar stress level for rapid repressurization and step-rate tests, and if evaluated in the classical way to obtain an estimate of the maximum horizontal stress, gives values that are around 20% - 50% above or below the actual applied values. Through a thorough analysis, we confirmed that the current maximum horizontal stress estimation method is valid when its assumptions are largely met, that is, the generated fractures are in a simple planar shape and in the desired direction. However, when the fractures become more complex, such as reoriented and multi-fractures crossed or even having longitudinal and transverse fractures simultaneously, the current horizontal maximum stress estimation method becomes less accurate. It must be realized that these complex fracture patterns are more prone to occurring under EGS conditions where thermal stress is induced from cooling via circulation. Overall, these findings have inspired us to conduct additional experiments under various EGS-related testing scenarios and to seek more accurate and physically interpretable expressions for estimating horizontal maximum stress under complex fracture patterns.

Acknowledgement

This work was performed at the University of Pittsburgh with funding provided by the DOE EERE Geothermal Technologies Office to Utah FORGE and the University of Utah under the project 'Enhanced Geothermal System Concept Testing and Development' at the Milford City, Utah Frontier Observatory for Research in Geothermal Energy (Utah FORGE) site. Support was received via Subcontract No. B651948. Parts of this work were performed under the auspices of the U.S. Department of Energy by Lawrence Livermore National Laboratory under Contract DE-AC52-07NA27344. Additional support for APB is provided by the RK Mellon Faculty Fellowship in Energy. We would like to express our gratitude to Charles Hager (PITT) for his outstanding technical contributions. We are also thankful for the support of our entire research group at the Hydraulic Fracturing Lab here at the University of Pittsburgh, particularly Olivia Hartz, Tess Harper, and Aubrey Green.

REFERENCES

Bao, T., & Burghardt, J. (2022). A Bayesian approach for in-situ stress prediction and uncertainty quantification for subsurface engineering. *Rock Mechanics and Rock Engineering, 55*(8), 4531-4548.

Bredehoeft, J., Wolff, R., Keys, W., & Shuter, E. (1976). Hydraulic fracturing to determine the regional in situ stress field, Piceance Basin, Colorado. *Geological Society of America Bulletin, 87*(2), 250-258.

Cornet, F. (1981). *Analysis of injection tests for in-situ stress determination.* Paper presented at the Workshop on Hydraulic Fracturing Stress Measurements, California, US.

Gronseth, J., & Kry, P. (1981). Instantaneous shut-in pressure and its relationship to the minimum in-situ stress. *Hydraul Fract Stress Meas, 139*, 147-166.

Guglielmi, Y., McClure, M., Burghardt, J., Morris, J. P., Doe, T., Fu, P., Knox, H., Vermeul, V., Kneafsey, T., & Ajo-Franklin, J. (2023). Using in-situ strain measurements to evaluate the accuracy of stress estimation procedures from fracture injection/shut-in tests. *International journal of rock mechanics and mining sciences, 170*, 105521.

Haimson, B., & Cornet, F. (2003). ISRM suggested methods for rock stress estimation—part 3: hydraulic fracturing (HF) and/or hydraulic testing of pre-existing fractures (HTPF). *International journal of rock mechanics and mining sciences, 40*(7-8), 1011-1020.

Haimson, B., & Fairhurst, C. (1967). Initiation and extension of hydraulic fractures in rocks. *Society of Petroleum Engineers Journal, 7*(03), 310-318.

Ito, T., Evans, K., Kawai, K., & Hayashi, K. (1999). Hydraulic fracture reopening pressure and the estimation of maximum horizontal stress. *International journal of rock mechanics and mining sciences, 36*(6), 811-826.

Kim, H., Min, K.-B., Bae, S., & Stephansson, O. (2016). *Integrated in-situ stress estimation by hydraulic fracturing and borehole observation at EXP-1 hole in Pohang of Korea.* Paper presented at the ISRM International Symposium on In-Situ Rock Stress, Tampere, Finland.

Lu, G., Kelley, M., Raziperchikolaee, S., & Bunger, A. (2024). Modeling the impact of thermal stresses induced by wellbore cooldown on the breakdown pressure and geometry of a hydraulic fracture. *Rock Mechanics and Rock Engineering*, 1-18. doi:https://doi.org/10.1007/s00603-024-03829-2

McClure, M. W., Jung, H., Cramer, D. D., & Sharma, M. M. (2016). The fracture-compliance method for picking closure pressure from diagnostic fracture-injection tests. *Spe Journal, 21*(04), 1321-1339.

Timoshenko, S. P., & Gere, J. M. (2012). *Theory of elastic stability*: Courier Corporation.

Xing, P., McLennan, J., & Moore, J. (2020). In-situ stress measurements at the utah frontier observatory for research in geothermal energy (forge) site. *Energies, 13*(21), 5842.

Learning Curve of Seismic Risk Mitigation for EGS Since Basel 2006 to Utah FORGE 2024 from the Perspective of a Project Developer

Peter M. Meier, Olivier Zingg, Andrés Alcolea Rodríguez, Falko Bethmann, Benjamin C. Dyer, Dimitrios Karvounis, Dieter Ollinger, Rémi Fiori, and Francisco Serbeto

Geo-Energie Suisse AG, Switzerland

Keywords

EGS, multistage stimulation, seismic risk mitigation

ABSTRACT

The experiences with the seismic risk in the EGS Basel project in 2006 were sobering and delayed the development of deep geothermal energy in Switzerland for almost 20 years. Since these dramatic experiences, there has been an increase in scientific progress as well as new setbacks, such as in the Pohang project. This failure has in turn provided many insights into mitigating seismic risks. Some of these lessons learned led to further developments that are now being tested, verified, and qualified in underground rock laboratories such as Bedretto (Switzerland) and in large-scale R&D field tests such at the Utah FORGE project (USA). These progresses include the field testing of multi-stage EGS stimulations, methodologies for risk studies, Advanced Traffic Light Systems, development of monitoring tools for high temperatures and their field verification and qualification. We will present an overview of the recent works and their implementation plans for the new EGS Haute-Sorne project in Switzerland.

1. Introduction

The lessons learnt from the Basel 2006 EGS project with a massive injection of 12’000 m^3 of water showed that control of seismic risk can be achieved by limiting the radius of each of the stimulated fracture surfaces to a few hundred meters (Meier et al., 2015). The fundamental consideration leading to this approach is based on observed data from many projects all over the world showing a clear correlation between the stimulated fracture plane areas and the seismic magnitudes. This correlation was also confirmed by detailed numerical modeling studies done for the risk study for the Haute-Sorne project.

A schematic representation of the massive hydraulic stimulation approach used in Basel compared to the planned multistage stimulation system in Haute-Sorne (Canton of Jura, Switzerland) is shown in Figure 1.

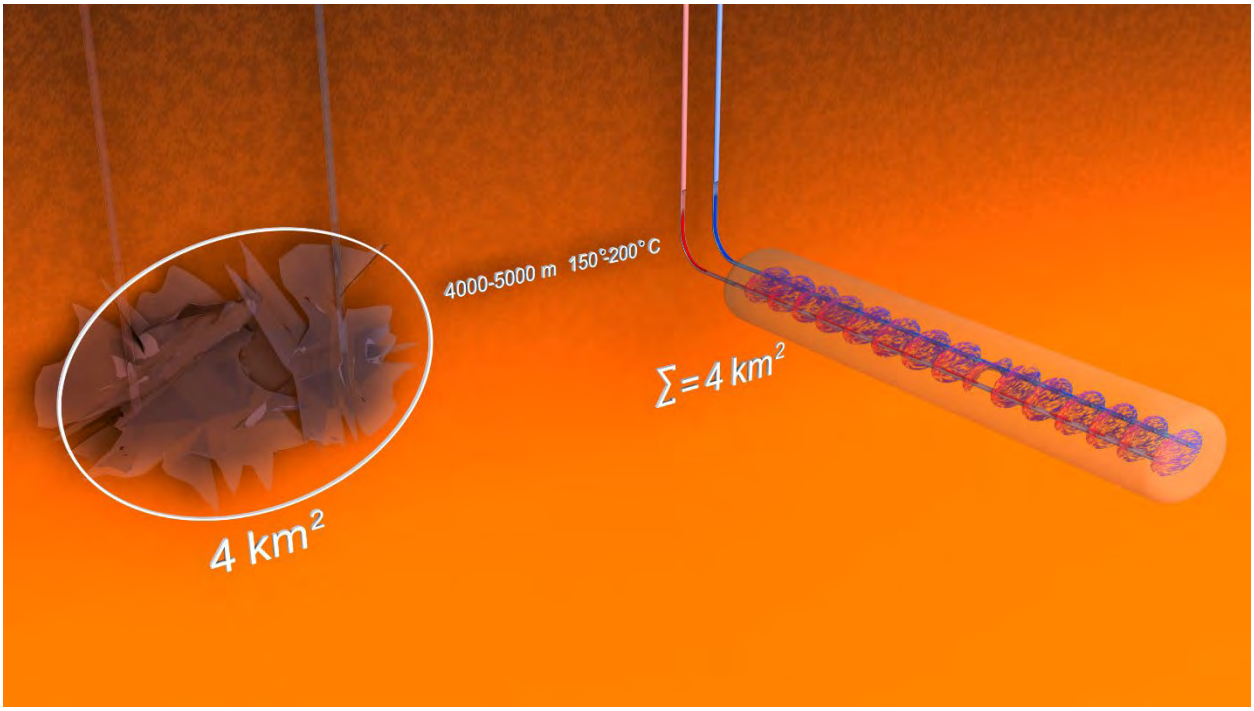

Figure 1: Schematic representation of the massive hydraulic stimulation concept like in Basel (left) in comparison to the multistage stimulation concept planned for future EGS projects in Switzerland (right).

2. Conclusions from the Pohang project

For nearly a year, several specialists from Geo-Energie Suisse analyzed and interpreted the data from the geothermal project and the earthquake of November 2017 in Pohang. These studies, requested by the permitting authorities of the Canton Jura shortly after the Geo-Energie Suisse had informed them, established that the very high-pressure water injections made in the vertical borehole probably played a decisive role in triggering the earthquake within a nearby fault.

The first vertical borehole did cross a major fault zone but not the second, which led to this fault being sandwiched between the two boreholes (this situation is represented schematically in Figure 2). For nearly two years, numerous water injections (stimulations) were carried out to try to circulate water between the two boreholes and thus produce energy on the surface. To achieve this, very high pressures, up to 900 bar at the surface, were applied in the vertical well. Such a pressure is more than 3 times the maximum injection pressure used in Basel.

The repeated injections at very high pressures into the vertical well led to an accumulation of pressure on a fault that was probably already in a naturally unstable state. Indeed, the study of the stress field and the numerical models carried out by Geo-Energie Suisse show that the local orientation of the natural tectonic stresses may have favored the activation of this fault (Meier et al. 2021; Bethmann et al., 2021; Alcolea et al. 2024).

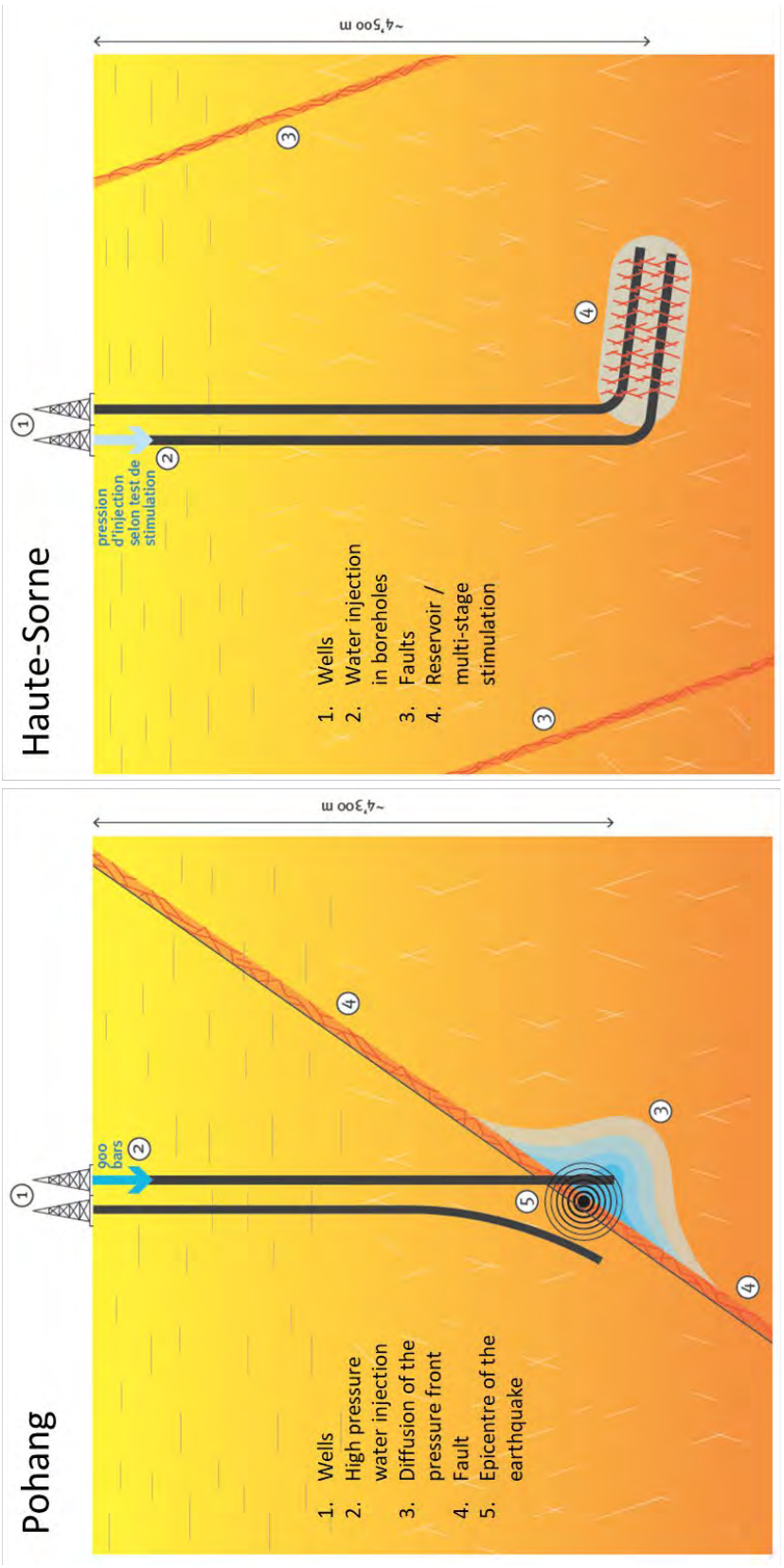

Figure 2: Comparison of the concepts of the Pohang and Haute-Sorne projects.

Timely parallel to the GES work but independently from each other the South Korean government had created official investigation commissions (ORAC/KERT) of the Pohang earthquake which published their report on March 20, 2019 (Geological Society of Korea (2019)). It is important to note that the main conclusions of both reports on the understanding of the trigger mechanisms of the Pohang earthquake are in very good agreement.

The realization of the Haute-Sorne project is subject to 136 conditions by the cantonal authorities. Of these, 21 address induced seismicity. The results of our investigations carried out on the Pohang project allow us to demonstrate that the application of authorization conditions similar to those of Haute-Sorne would have made it possible to stop and then abandon the Pohang project, as early as the first stimulation phase in January 2016 (Zingg and Meier, 2019).

Within the framework of the new Swiss energy law, which came into force on 1 January 2018, and in order to maximize the chances of success and further reduce the risks, Geo-Energie Suisse has reviewed its operational approach and decided to carry out its project in two phases (Figure 3). The first phase will be dedicated to exploration. The first well will be drilled to the depth of the reservoir. All measurements to characterize the deep crystalline rock mass such as fracturing state, permeability and stress field orientation will be carefully performed. Only a stimulation test carried out according to a predefined protocol in a particularly careful and monitored manner, with small injection volumes and low pressures, will be carried out.

Finally, the risk study will be updated on the basis of the parameters actually measured in the Haute-Sorne borehole and the lessons learned from the projects in the Bedretto underground rock laboratory and most importantly at the Utah FORGE site (Moore et al. 2023). Only then will it be possible to move on to the second phase, namely the drilling of the second well and stimulation of the reservoir.

3. Results from the R&D work in the Bedretto rock laboratory

The multi-stage hydraulic stimulation concept proposed by Geo-Energie Suisse, based on lessons learned from the Basel EGS project, was successfully demonstrated in 2020 and 2021 at the Bedretto underground rock laboratory in the granite of the Swiss Alps at a depth of 1100 m (Meier et. al. 2023). The three main success criteria were met: first, a significant increase in flow rates and thus an increase in the energy output of an EGS project; second, detailed monitoring and mitigation of induced seismicity; and third, validation and qualification of advanced multi-stage stimulation devices from the oil and gas industry for geothermal applications.

The increase in flow rates predicted in 2016 (Meier and Ollinger, 2016), using numerical modeling by factors between 3 and 6 for the multi-stage stimulation concept compared to single-stage stimulation was demonstrated in Bedretto in-situ at a reservoir scale of 1:3. Scaling the results from the field work to a deep EGS project such as Haute-Sorne in the Swiss canton of Jura yields a range of flow rates from 78 to 160 l/s. This value significantly exceeds the success criteria set at 65 l/s for the Haute-Sorne project. This is also a positive result given the inherent uncertainties. Applied to practice, this means that the electrical power of an EGS project can be increased from about 1.5 MW - if a single stimulation stage is carried out over the entire borehole reservoir section - to about 4.5 to 6 MW if a multi-stage stimulation approach is used.

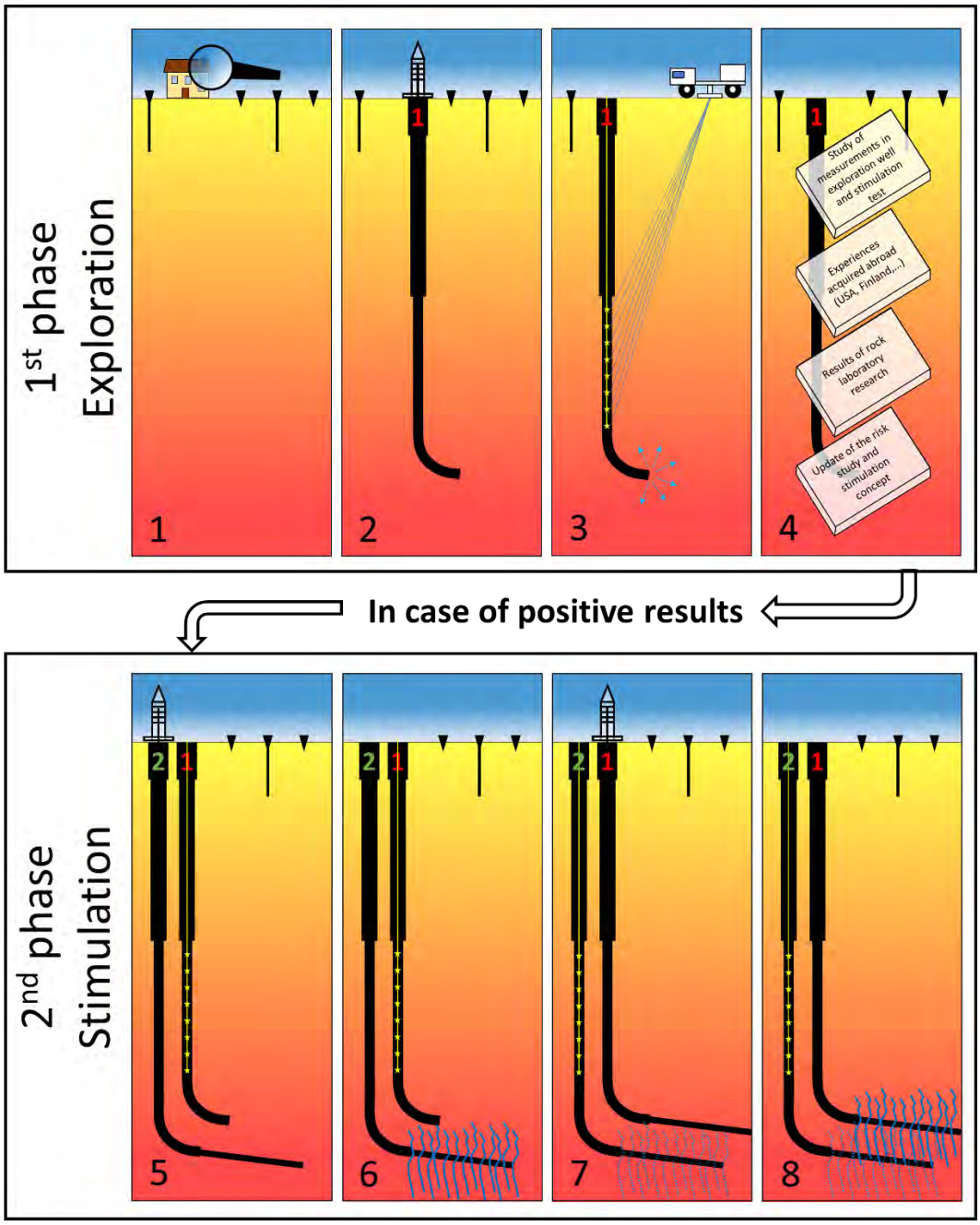

Figure 3: Steps for the implementation of the Haute-Sorne pilot project. Exploration phase: 1) Preservation of evidence and deployment of the seismic monitoring network (surface stations and boreholes) 2) Drilling of the first exploration borehole 3) Measurements in the reservoir and stimulation test with low pressures and small volumes 4) Study of the results of the measurements and stimulation test, integration of experience gained abroad and underground rock laboratory research, update of the risk study and the stimulation concept. Depending on the current state of planning, this is done in the absence of the drilling rig, but technical or logistical considerations may also decide otherwise. In case of positive results, transition to the Stimulation Phase: 5) Completion of the 2nd borehole; the first is equipped with a seismometer string to complete the seismic monitoring network 6) Stimulation of the reservoir under control of the seismic monitoring system 7) Completion of the 1st borehole, the second is equipped with the seismometer string and 8) if necessary, additional stimulation of the 1st borehole under control of the seismic monitoring system.

Real-time monitoring and mitigation of induced seismicity and associated risks - the second main criterion for proving success - was also successfully demonstrated. The maximum moment magnitude of -1.6 within the stimulated rock volume was lower than naturally occurring seismicity (up to a magnitude of 0.0) at greater distances of about 1000 m from the stimulated reservoir.

For years, there has been an intense debate among experts as to whether open-hole multi-packer systems or the classic cemented and perforated casing approach offer better hydraulic conditions for stimulation in fractured rocks. We have now been able to demonstrate, within the usual uncertainties of subsurface work, that in principle both methods are good for multi-zonal stimulation (Meier et al. 2022). This is good news for the geothermal industry. In planning borehole completions, drilling engineers can now focus on more reservoir-independent issues when deciding on one concept or the other, such as site-specific borehole conditions, borehole breakouts, borehole stability, temperature, equipment reliability, deployment risks, equipment availability and costs.

4. Results from seismic monitoring tools and advanced traffic light testing at the Utah FORGE site

Geo-Energie Suisse joined Utah FORGE (Moore et al., 2023) to provide high quality micro seismic locations and to qualify and verify high temperature down-hole monitoring tools, that can be utilized for longer term monitoring at the Haute-Sorne project. An important objective for monitoring the micro seismicity at Utah FORGE is to resolve the zonal isolation or overlap between the stimulation stages.

A special emphasis is put on the 3-component hodogram analysis from two- or multi-level three-component (3C) receiver strings, since in Haute-Sorne the stimulations in one of the two boreholes are planned to be monitored from the other deep well at a depth of more than 3500 m and temperatures in the range of 150 to 190 °C.

Geo-Energie Suisse also could improve the in-house seismic data processing and interpretation software by adding the capability to include seismic data from DAS (distributed acoustic sensing) cables that were installed behind casing or lowered inside of cased boreholes. In addition, Geo-Energie Suisse tested a prototype of fully fibre optic 3C receivers, that can support temperatures above 200 °C.

A plot with the preliminary evaluation of the micro seismicity during the main stimulation campaign in April 2024 is shown in Figure 4.

With respect to the performance of the monitoring system and individual tools the following general conclusions are:

- The high-temperature, digital, eight-level, three-component (3C) receiver strings worked up to about 3 weeks of continuous high temperature operation with satisfactory precision of the hodograms.
- The single or two-level retrievable, high-temperature 3C analog receivers worked for more than two months, after deployment related issues could be solved. The analysis of their hodogram precision is still on-going. If the hodogram precision is found to be acceptable, the analog receivers may be better suited for long term monitoring at Haute-Sorne than the digital tools.

- A combination of data from the DAS cable installed behind the casing with one or more 3C receiver strings has turned out to be very satisfactory.
- The first trials with a prototype of fully fibre optic 3C receivers are promising and considered to open new perspectives for long term seismic monitoring at high temperatures.

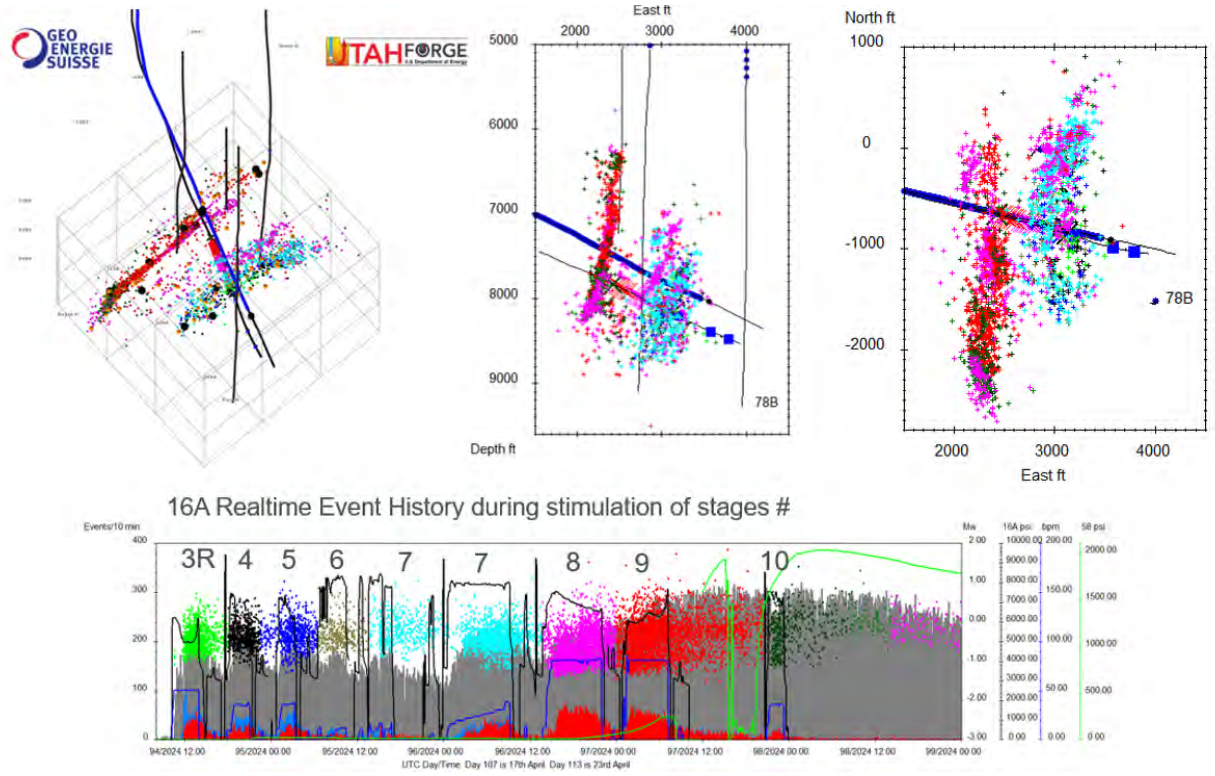

Figure 4: Distribution of micro seismicity during the stimulation of stages 3 to 10 in the deeper borehole 16A at Utah FORGE. Upper figures: 3D view (left), vertical view (middle), top view (right). Lower figure: Seismicity rate (grey: triggers, red: located events), injection rates (blue line) and injection pressure at 16A (black line) and pressure at observation well 58 (green line) during the main stimulation.

In addition to verifying and qualifying down-hole tools the abundant high quality data from several multi-stage stimulations provided a unique opportunity to test out the real time seismic risk forecasting procedure called Advanced Traffic Light System (ATLS). The ATLS provides a quasi-real time forecast of the probability that certain prefixed magnitude thresholds may be exceeded. As an example, the prediction for stimulation stage 3 is shown in Figure 5.

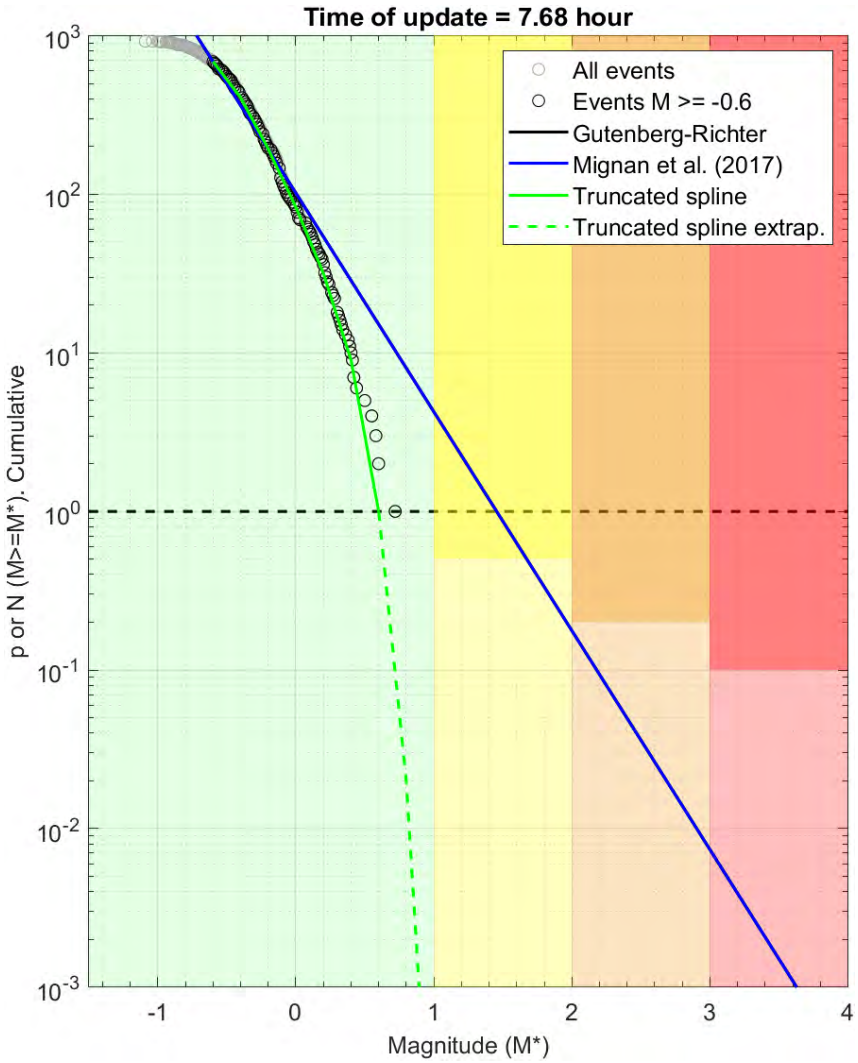

Figure 5: Advanced traffic light prediction at the end of the shut-in phase for stage 3. The predictions with the commonly utilized Gutenberg-Richter as well as the formulation after Mignan et al. (2017) overestimate the actual observed magnitudes. This behavior has been observed for most of the stimulated stages.

5. Transfer to the Haute-Sorne multi-stage stimulation project: stimulation test

Drilling of the first well has been started on May 21, 2024. The crystalline basement has been prognosed at depths between 1500 and 2500 m. After about one month of drilling through the typical sedimentary sequence of north-western Switzerland the crystalline basement has been reached at a depth of 1783 m. At the moment of writing no information is available on the rock mechanical properties of the targeted crystalline section.

The 13-3/8” casing covering the sedimentary formations will be set at a depth of 1820 m. The borehole information and the planned depth for the stimulation test are shown in Figure 6. At 4000 m depth the borehole with a diameter of 12-1/4” will be cased.

After a detailed analysis of the logging and cuttings data the most adequate depth for the test stimulation in the first quarter of 2025 will be determined. At that depth the casing will be

perforated such that several seismic monitoring 3C receivers of a digital tool string or the two-level analog 3C receivers evaluated at the Utah FORGE site can be placed with a cable that includes fiber optic lines for DAS below the perforations in order to avoid flow noise during injection.

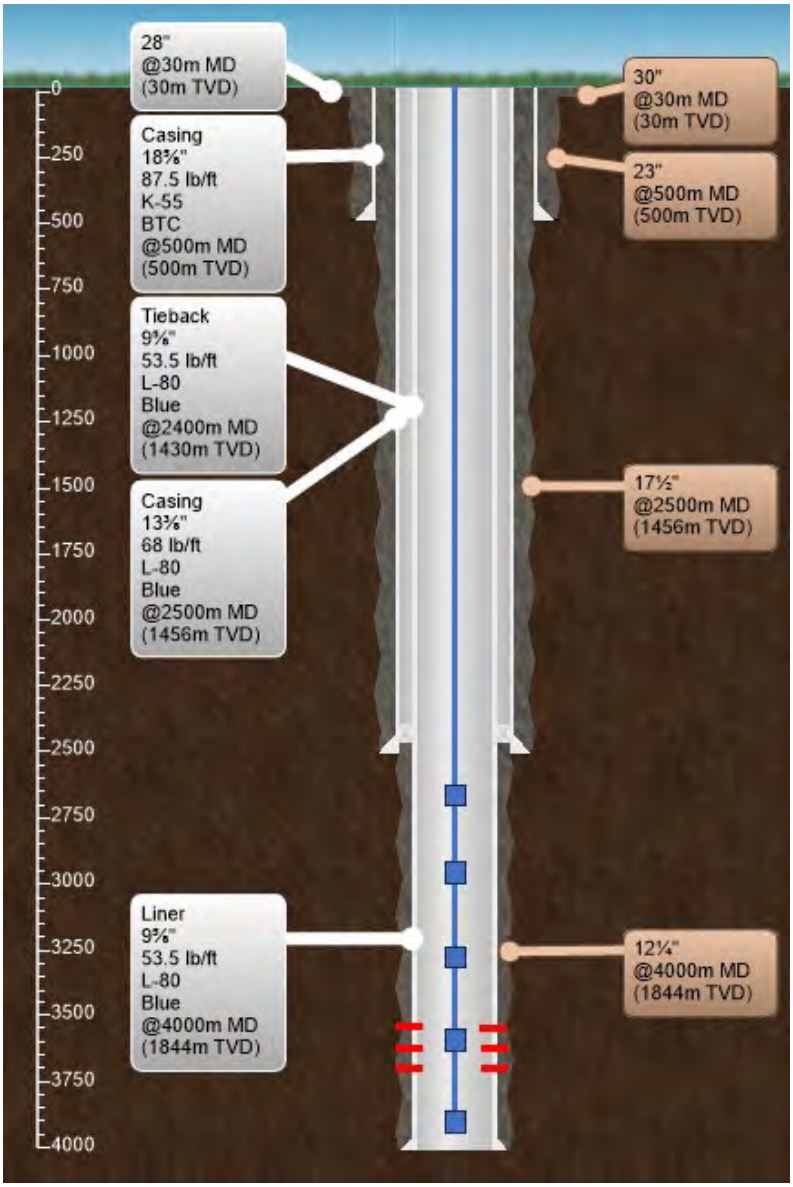

Figure 6: Borehole information with schematic drawing of the perforations and the seismic receiver string.

The stimulation test design will be based on data from Basel, Bedretto and Utah FORGE (Figure 7). The injected volume will be in the order of 500 m^3. We expect the moment magnitudes to attain values between the Basel and the Utah FORGE 2022 stimulations of stages 1 to 3 and the stimulated areas reaching an equivalent radius between 60 and 100 m.

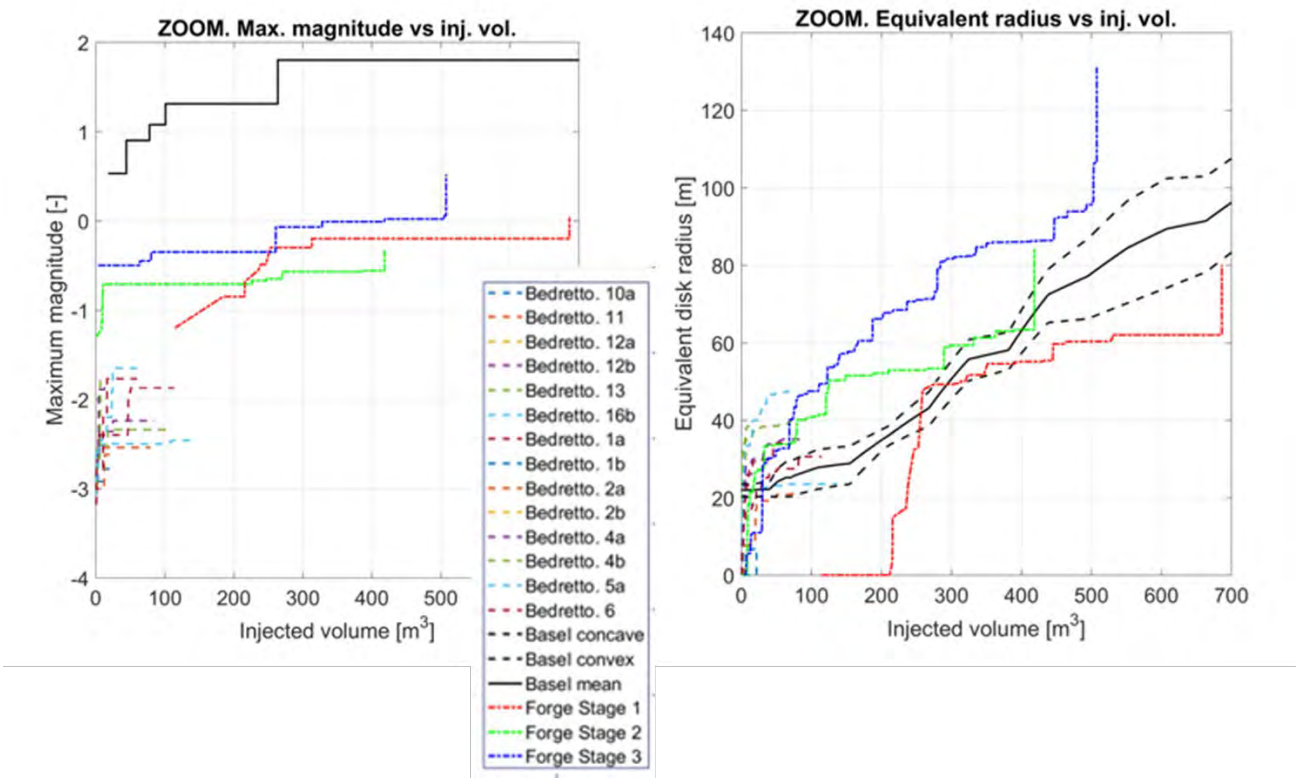

Figure 7: Design criteria for Haute-Sorne test stimulation: Maximum magnitudes (left) and radius of stimulated areas (right) as a function of injection volume at the Basel, Bedretto and Utah FORGE 2022 stimulations.

The current state of planning is summarized in the following sequential main steps:

1) Pressure static recovery (PSR): After installation of the geophone chain the well is shut-in at surface and pressures are monitored.

2) Constant head injection test including recovery for evaluating transmissivity before the test stimulation.

3) First test stimulation cycle:

a. Step-wise increase of injection rates with 10, 20, 45, 60 l/min. The duration of the first three steps is two hours each. The forth step is continued until the b-values can be estimated reliably from micro-seismicity. Adjust flow rate in function of the tolerable noise on the geophones.

b. Observation of pressures to identify processes of shearing, jacking or fracturing.

c. Stop injection if pressures at the wellhead are close to the equipment pressure limit of 50 MPa.

d. Stop injection if magnitudes Mw > 1.0.

e. Stop injection at an injected volume of 500 m3.

f. Prepare for backflow according to instructions of traffic light system (TLS).

g. Prepare for shut-in and/or backflow according to instructions of the advanced traffic light system (ATLS).

4) Shut-in: Pressure static recovery after shut-in at the wellhead for at least 24 hours or until a quasi-stable pressure trend will be attained for conducting a subsequent hydraulic test.

5) Constant head injection head test including recovery for evaluating transmissivity after the test stimulation.

6) After analyzing the data, a decision will be taken, if a second test stimulation cycle shall be performed.

6. Conclusions

The learning curve since the Basel 2006 EGS project has been long in time but important in know-how gain. The newest available technologies have been evaluated and thoroughly tested in field situations to mitigate seismic risks and maximize chances of success of a new EGS project in Switzerland. If the expected success can be realized, Switzerland will get its first power producing geothermal plant by 2029 in Haute-Sorne, Canton Jura. This example shows also the important role of R&D collaboration at experimental field sites between international partners for the development and realization of new technologies.

Acknowledgement

This work was financially supported by the Swiss Federal Office of Energy within the frameworks of the subsidy contract for the Haute-Sorne project (contract MF-021-GEO-ERK) and the ZoDrEx GEOTHERMICA project under contract SI/501720-01 as well as the Swiss State Secretariat for Education, Research and Innovation (SERI) under contract number 15-0316-1 for the DESTRESS Horizon 2020 EU-project. The opinions expressed and arguments employed herein do not necessarily reflect the official views of the Swiss Government.

REFERENCES

Alcolea Rodríguez, A., Meier, P.M., Vilarrasa, V., Olivella, S., and Carrera, J., “Hydromechanical modeling of the hydraulic stimulations in borehole PX2 (Pohang, South Korea)”, Geothermics, Volume 120 (2024).

Bethmann, F., Ollinger D., Tormann T., Heimlich C., Meier, P.M.: Seismicity Analysis with Spatial or Temporal Relation to the Pohang EGS Project, *Proceedings: World Geothermal Congress 2020*, Reykjavik, Iceland, April 26 – May 2 (2021).

Meier, P. M., Alcolea Rodríguez, A., and Bethmann, F.: Lessons learnt from Basel: New EGS projects in Switzerland using multistage stimulation and a probabilistic traffic light system for the reduction of seismic risk, *Proceedings: World Geothermal Congress 2015*, Melbourne, Australia, 19-25 April 2015 (2015).

Meier, P.M. and Ollinger, D., Monte Carlo flow rate simulations for the multi-stage EGS stimulation concept of the Haute-Sorne pilot project (Canton Jura, Switzerland), *Proceedings: European Geothermal Congress 2016*, Strasbourg, France (2016).

Meier, P.M., Bethmann, F., Zingg, O., Alcolea Rodríguez, A., Ollinger, D., Tormann, T., and Castilla, R. "Understanding the Pohang EGS Reservoir and the Need for Advanced Traffic Light Systems", *Proceedings: World Geothermal Congress 2020*, Reykjavik, Iceland, April 26 – May 2 (2021).

Meier, P.M., Serbeto, F., Christe, F., Alcolea, A., Castilla, R., Bethmann, F. and Dyer, B. "Results from benchmark testing of zonal isolation borehole completions for multi-stage EGS stimulation in the Bedretto underground rock laboratory in Switzerland." Proceedings: 56th U.S. Rock Mechanics/Geomechanics Symposium, Santa Fe, New Mexico, USA (2022).

Meier, P.M., Alcolea Rodríguez, A., Castilla, R., Karvounis, D., Bethmann, F., Dyer, B., Serbeto, F., Christe, F. and Ollinger, D. "Demonstration of an EGS multi-zonal stimulation system at the Bedretto underground rock laboratory." *Proceedings: World Geothermal Congress 2023* Beijing, China (2023).

Mignan, A., Broccardo, M., Wiemer, S. et al. Induced seismicity closed-form traffic light system for actuarial decision-making during deep fluid injections. Sci Rep 7, 13607 (2017)

Moore, J., McLennan, J., Pankow, K., Finnila, A., Dyer, B., Karvounis, D., Bethmann, F., Podgorney, R., Rutledge, J.; Meier, P., Xing, P., Jones, C., Barker, B., Simmons, S., and Damjanac, B. "Current Activities at the Utah Frontier Observatory for Research in Geothermal Energy (FORGE): A Laboratory for Characterizing, Creating and Sustaining Enhanced Geothermal Systems" 57th U.S. Rock Mechanics/Geomechanics Symposium, Atlanta, Georgia, USA (2023).

Zingg, O., and Meier, P.M. "Summary of the Investigations Conducted Following the November 2017 Earthquake in Pohang, South Korea, and Implications for the Haute-Sorne Multi-stage-stimulation EGS Project", Switzerland", GRC Transactions, Vol. 43 (2019).

Geopressured Geothermal Systems: An Efficient and Sustainable Heat Extraction Method

Mauricio A. Rivas, Victoria McGuire, Douglas Simpkins, and Lev Ring

Sage Geosystems

Keywords

Geopressured Geothermal Systems, backpressure, pressure-propped fractures, injection pump parasitic losses, system impedance, no proppant, modeling pressurized systems

ABSTRACT

Conventional geothermal systems rely on production from naturally occurring subsurface hot aquifers, while Hot Dry Rock (HDR) geothermal technology is a method of extracting geothermal energy from deep underground formations where there is hot but dry rock. A downhole heat exchanger is created by water being injected into the rock through one or several wells at high pressure, causing the rock to fracture and creating a network of permeable pathways. Water is then circulated through these artificial or natural fractures, absorbing heat from the hot rock and bringing this heat to the surface.

High impedance in the fracture network and near the wellbore area is a main contributor to high parasitic energy losses in HDR systems and makes commercial-scale implementation very difficult. The Fenton Hill Hot Dry Rock (HDR) tests, from the 1980s and early 1990s, showed that an increased backpressure can reduce markedly the impedance in the system. In so-called doublet (or two-well) Enhanced Geothermal Systems (EGS), horizontal sections of two wells are connected with fractures filled with proppant to prevent these fractures from closing and creating very high resistance to water circulation. This paper provides an alternative solution to the traditional EGS approach and discusses a recently introduced Geopressured Geothermal System (GGS) that keeps the surface and subsurface systems constantly pressurized above fracture opening pressure or, in other words, relying on pressure-propped fractures to keep impedance low.

Focusing on the hydro-mechanical (HM) performance of GGS, and reserving the full thermal-hydro-mechanical (THM) analysis for a later publication, the results show that the single-well pair GGS is superior to other systems in terms of HM performance. The methodology of this single-well pair GGS builds on that of mechanical storage in deep hydraulic fractures as field tested in South Texas in early 2023.

Numerical simulations were performed to demonstrate how properly engineered GGS resolves crucial surface challenges not previously addressed in heat extraction systems and how these geothermal systems experience a lower system impedance while maintaining commercial flow rates. Comparisons are made between GGS with the base case of a doublet EGS whose fractures are proppant-propped. The mathematical modeling of GGS is a natural extension of the recent modeling for mechanical storage that was additionally validated and calibrated against real-time field data.

1. Introduction

Extraction of heat from fractured hot dry rock (HDR) was first proposed in the Los Alamos National Laboratory in New Mexico in the early 1970s (Brown et al. 2012). An early theoretical approach to the heat extraction system studied there comprised two parallel vertical wells drilled to depths reaching dry hot rock with the second well intersecting the vertically oriented fracture produced by hydraulic fracturing the first well (Robinson et al., 1971). However, a more complex HDR system was created from the many years of field development and testing that ensued at Fenton Hill, New Mexico (physical site chosen by Los Alamos; see photo in Figure 1) and which continued until the mid-1990s. A great deal of valuable information was obtained from this pioneering HDR program.

Among the many lessons learned, the Fenton Hill field tests demonstrated that *impedance*, a measure of the resistance to circulation of a fluid through a subsurface system, is greatly reduced by holding an elevated backpressure on the production wellhead which assists in pressure propping the fracture(s) (DuTeau and Brown 1993; see Figure 1 for a recorded table). The potential for electric load-following methods was also verified, but the findings revealed that these backpressure operations: (1) demand a higher injection pumping capacity to maintain a pressurized subsurface system; and (2) expose the surface equipment to higher pressures (Brown and DuTeau 1995).

	LTFT	IFT	IFT2	IFT3
	7/28/92	9/29/92	12/10/92	12/27/92
Injection Pressure, MPa (psi)	27.29 (3958)	22.36 (3243)	27.32 (3963)	27.32 (3962)
Production Pressure, MPa (psi)	9.66 (1401)	9.65 (1399)	15.18 (2201)	12.40 (1798)
Production Flow Rate, l/s (gpm)	5.66 (89.7)	3.85 (61.1)	5.34 (84.6)	5.71 (90.5)
Production Temperature, °C (°F)	183 (361)	165 (329)	177 (351)	183 (361)
*Impedance, MPa/l/s (psi/gpm)	3.11 (28.5)	3.30 (30.2)	2.27 (20.8)	2.61 (23.9)

Figure 1: Photo of the HDR site at Fenton Hill, New Mexico (discover.lanl.gov) and field data demonstrating impedance reduction when applying backpressure via a choke (DuTeau and Brown 1993).

Geopressured Geothermal Systems (GGS), that pressurize the surface and subsurface systems as described in Section 2, are an alternative to previously proposed heat extraction systems as GGS address by design the challenges mentioned above. First, the use of a GGS surface injection kit

connected to a high-pressure binary plant allows the use of pressure energy usually wasted at surface to dramatically decrease power lost to the injection pump overcoming impedance; traditional systems simply vent pressures at surface from the production well. Next, fractures are *pressure propped*, defined here as fractures being inflated with fluid pressures above the minimum in-situ stress; the phrase 'fractures are *operated open'* is also often used. Pressure propped fractures: (a) considerably reduce system impedance, hence reduce friction losses; (b) allow larger lateral well spacing that enable larger fracture areas that are conducive for heat extraction (as opposed to having extensive fractures but short well-to-well distances in each fracture); and (c) enable a single-well pair solution for heat extraction when "huff-n-puff" (cyclical injection-production) operations are implemented instead. Lastly, GGS do not rely on proppants, which induce high friction losses and cannot be uniformly distributed, and thus the associated costs and time of proppant treatments are eliminated.

Because both temperatures and stresses generally increase with depth, a subsurface system reaching practical commercial geothermal temperatures will lead to higher surface pressures if fractures are pressure propped. Hence, the need for a GGS design that can operate with higher pressures both at surface and subsurface. It is noted that operating fracture fluid pressures above the minimum in-situ stress does pose risk to fractures growing. This may lead to fluid being lost as it can be trapped by the fracture at further distances away from the well. More importantly, if fracture growth is uncontrolled, fluid pressurization may trigger seismic activity, particularly if a fault is nearby. Therefore, fluid pressures in opened fractures are further restricted to be below fracture propagation pressures.

Mathematical models have been developed using coupled hydro-mechanical (HM) processes to compare Geopressured Geothermal Systems against a two-well EGS with fractures filled with proppant. A future work will compare the complete thermal-hydro-mechanical (THM) processes of GGS versus EGS. In particular, a future publication will show that the thermal drawdown behavior of a GGS is comparable or better than that of a proppant-laden EGS.

The framework of the engineered systems analyzed in this paper is introduced in Section 2, while Section 3 describes pumping power consumption and system impedance for traditional EGS versus GGS. Completed models are presented in Section 4 and include the deformation and multi-scale nature of fracture propagation; wellbore, perforation, and fracture frictional losses; pressure response due to fluid circulation that includes injection pumping and production; power lost to the injection pump; and system impedance. This section also presents the simulations for all systems and comparisons are made. The final section concludes that the single-well pair GGS, based on cyclic (or huff-n-puff) operations, outperforms any other system.

2. A Proppant-Laden EGS and Three Geopressured Geothermal Systems

The following systems are ordered according to the natural progression from a traditional two-well EGS to the single-well pair GGS design:

I. Two-well system with proppant-laden fractures and continuous circulation of fluid.
II. Two-well system with pressure-propped fractures and continuous circulation of fluid.
III. Three-well system with pressure-propped fractures and continuous circulation of fluid.
IV. Single-well pair system with pressure-propped fractures and huff-n-puff operations.

2.1 Traditional Two-well EGS versus a Two-well GGS.

A two-well Geopressured Geothermal System (GGS) is shown on the right of Figure 2, and this is compared directly with a traditional EGS shown on the left. Both systems have a subsurface design that includes an injection well whose lateral is hydraulically fractured, possibly by employing zonal isolation methods and limited entry completions, and a production well drilled to intersect the multiple fractures created. A first distinct characteristic of the two systems is that the traditional EGS has fractures filled with proppant whereas the GGS does not. In both systems, fluid is circulated down the injector well, through the fracture system and up the producer well.

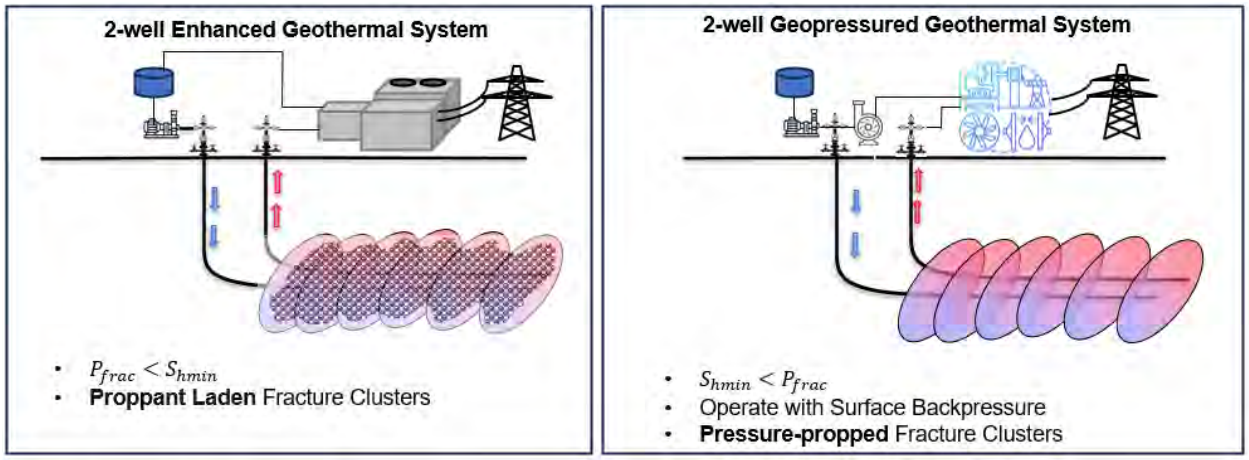

Figure 2: Comparison of a two-well EGS with a two-well GGS.

A second distinction is that the GGS is operated with an elevated backpressure maintained by a controllable choke that connects to the production wellhead. This backpressure is always maintained above fracture opening pressure and thus above the minimum in-situ stress allowing fluid to circulate with minimal impedance.

Although an elevated backpressure reduces the fracture impedance, the injection pump parasitic load increases and this leads to differences in surface design. In a GGS, a high-pressure binary plant (high pressure heat exchanger) maintains the high pressure from the production wellhead side to markedly reduce the pumping power needed by the GGS surface injection side. In this approach, the surface system utilizes pressure energy that is otherwise wasted (vented at surface) in traditional EGS, and allows the subsurface system to be maintained pressurized. A process flow diagram of the surface configuration of the two-well GGS is shown in Figure 3.

This coupling of surface and subsurface leads to a pressurized circulation loop that requires only make-up water to account for losses from evaporation and leak-off to the rock matrix. It should be noted that it is possible for a fracture wing not intersecting a producer well to potentially grow uncontrollably due to the high pressures; this situation is considered in Section 4.

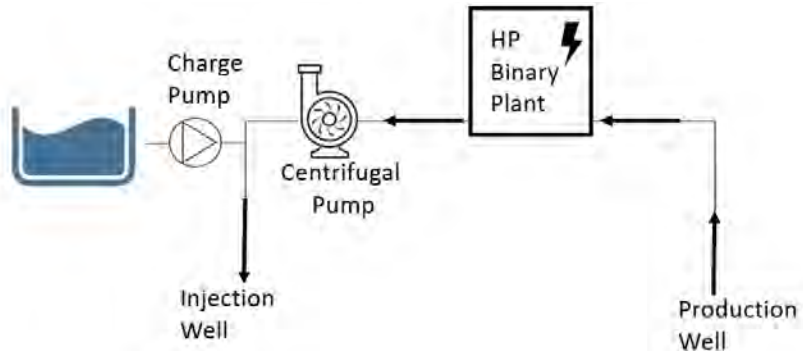

Figure 3: Process Flow Diagram for a two-well GGS; wells are connected at surface by a high-pressure binary plant and a GGS injection surface kit to pressurize the surface system.

2.2 A Pressure-propped Three-well System.

Drilling a second producer well to intersect the fractures of the previous two-well GGS, so that the lateral of the injector well is between both producer laterals, leads to the three-well GGS displayed in Figure 4 (Gedzius et al. 2011). The second producer intersecting the wings previously not containing a producer well reduces the risk of fractures growing out of control.

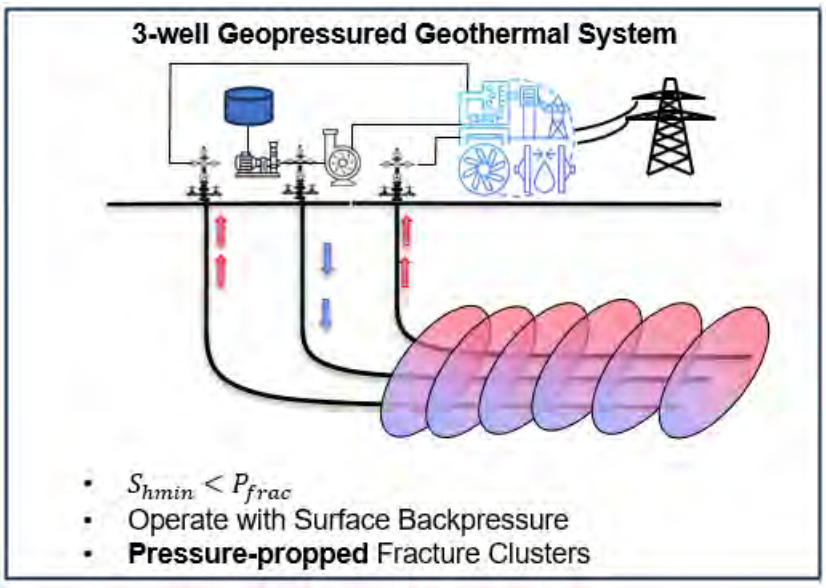

Figure 4: A three-well GGS as an extension of a two-well GGS.

In this design, fluid is circulated down the injector (middle) well, through the fracture cluster, and up through both producer wells. Fractures are opened by the elevated backpressure maintained by controllable chokes at the surface, one on each producer, with fracture fluid pressures maintained above the minimum in-situ stress. The high-pressure heat exchanger in the binary plant uses the high pressures flow from both production wells to significantly reduce the power required by the surface booster injection pump. As in the two-well GGS, this design does not require any proppants to be placed in the fractures.

2.3 A Single-well Pair Geopressured Geothermal System.

A single-well pair GGS operating at two different times is shown in Figure 5 as a 'huff-n-puff' system. In this design wells A and B are not connected in the subsurface and each well has its own set of fractures. This eliminates altogether the expensive task of connecting two or more horizontal wellbores with a fracture system created to establish subsurface circulation. The well stimulation operations are much simpler because each leg can be fracked individually and no intersections are required. The surface system is exactly the same as in other GGS where wells are connected at the surface by a high-pressure binary plant.

The system is initiated by injecting a pre-designed fluid volume and pressurizing fractures in both wells with fluid pressures above the minimum in-situ stress. Fractures in one well are given more fluid than fractures in the other well, and that extra percentage (around 20-30%) of the full fracture fluid volume will be the only volume that is moved back and forth between wells during the cyclic operations. The system is shut-in when the desired pressures and volumes (as calculated to meet power objectives) are reached. The system is now primed and cyclic operations may commence as described next.

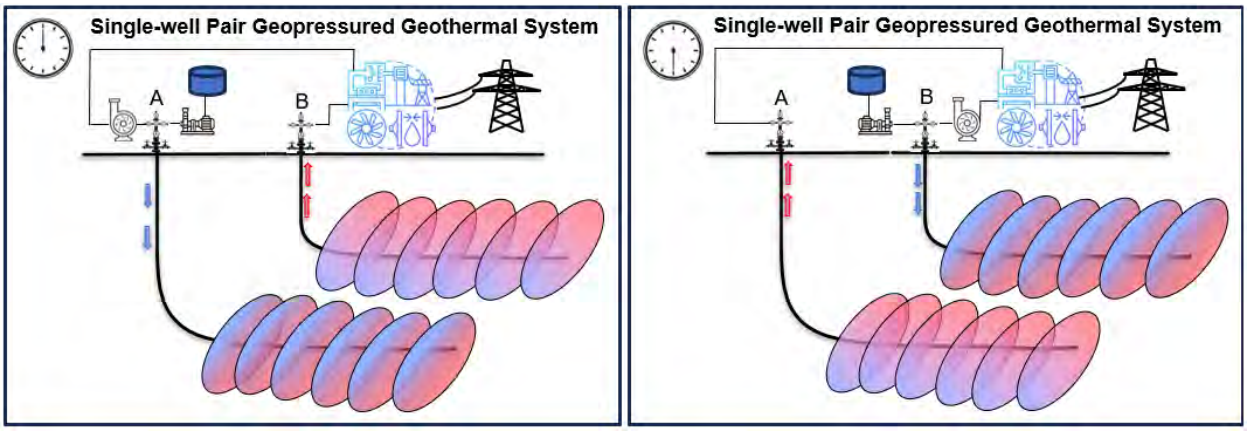

Figure 5: Framework of a single-well pair GGS. Wells are disconnected in the subsurface. Left shows producing from well B and injecting into well A, whereas the right shows producing from A and injecting into B. Surface equipment is not duplicated as flow paths at surface are simply redirected.

Using Figure 5 for illustration, a *cycle* starts at 12 o'clock when well B is opened and the produced fluid is produced to the high-pressure heat exchanger of the binary plant. Then the cooler fluid coming out of this heat exchanger is injected into well A while maintaining high pressure. As mentioned above, only a percentage of the total fluid volume is moved from well B fractures to well A fractures. The extra percentage of (cooler) fluid injected into well A fractures mixes with the volume of fluid injected during the initiation phase that is by now additionally heated. This percentage is calculated so that the system, in the example of Figure 5, runs until 6 o'clock, at which time well A fractures have the bigger fracture fluid volume. Now the wells are shut-in and then flow is reversed to begin the second half of the cycle, as in the right side of Figure 5. It is also possible to have a shut-in period before reversing the flow but this depends on power objectives. In this second half of the cycle, well A produces hot (due to mixing) pressurized fluid into the high-pressure binary plant and the same surface injection kit now injects the cooler fluid into well B. This A-to-B flow runs until 12 o'clock, the time when a full cycle is complete and well B fractures again have a larger volume than well A fractures. The wells are shut-in at 12

o'clock to then reverse the flow and start the second cycle. Running consecutive cycles creates the cyclic (or huff-n-puff) operations of this single-well pair GGS.

3. Minimizing the Power Lost to the Injection Pump and Impedance

The pressurized surface system in a general GGS arises from the need to decrease pump power consumption for the overall system to be practical. Since the power consumed by a pump is given by

$$Power_{pump} = \frac{(P_{pump} - P_{suction})\dot{m}_{inj}}{\rho_{inj}\eta_{pump}}, \quad (1)$$

where $(P_{pump} - P_{suction})$ is the pressure differential across the pump, $\dot{m}_{inj}$ is the mass flowrate at the injector well, ρ_{inj} the density of the fluid and η_{pump} is the efficiency of the injection pump, power is minimized by minimizing the pressure differential across the pump. An innovative solution to reduce the power consumed by the pump is to maintain the backpressure through the whole surface system. This leads to two types of surface systems where one operates with a low suction pressure (LSP) pump and the other with a high suction pressure (HSP) pump. In the simulations presented here, the efficiencies for the pumps are assumed to be 0.7 and 0.85, respectively, for the HSP and LSP pumps.

Figure 6 shows hydraulic schematics for two surface/subsurface systems where the subsurface system is either connected by fractures (left) or disconnected (right). The pump in either schematic may be LSP or HSP.

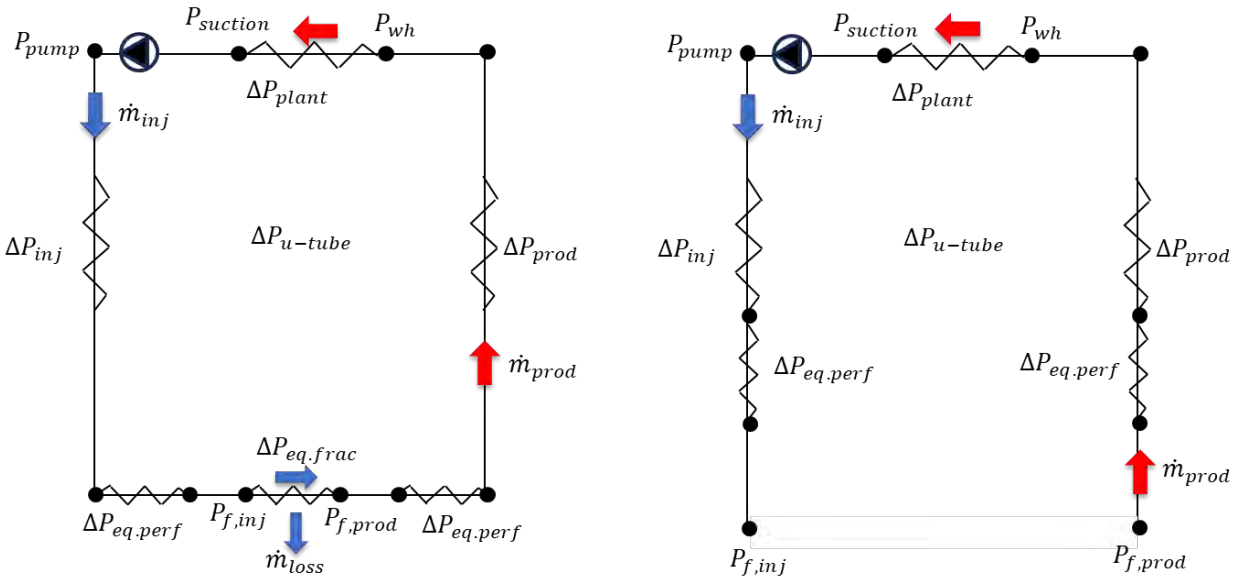

Figure 6: Hydraulic schematics of the surface/subsurface system comprising two vertical wells connected by fractures (left) and disconnected in the subsurface (right).

Using the hydraulic schematic on the left in Figure 6, the pressure balance for a system that circulates fluid is given by

$$P_{pump} - P_{suction} = \Delta P_{plant} + \Delta P_{wells} + \Delta P_{eq.perfs} + \Delta P_{eq.frac} + \Delta P_{u-tube} \quad (2)$$

where $P_{suction}$ is the suction pressure, ΔP_{wells} combines the injection and production well pressure losses denoted by ΔP_{inj} and ΔP_{prod}, respectively, $\Delta P_{eq.perfs}$ is pressure loss due to perforations, $\Delta P_{eq.frac}$ is fracture pressure loss, and ΔP_{u-tube} is the hydrostatic differential pressure between wells. The *system impedance* that the pump needs to overcome is

$$\text{Impedance} = \left(P_{pump} - P_{suction} - \Delta P_{u-tube}\right)/Q_{prod} \quad (3)$$

where Q_{prod} is the volumetric flowrate at the production side.

When wells are disconnected at subsurface (right side of Figure 6), both formulas are the same except that the fracture pressure difference $\Delta P_{eq.frac}$, between $P_{f,inj}$ and $P_{f,prod}$, refers to fracture fluid pressures in the same fracture (when circulating fluid between wells in the subsurface) or pressures in disconnected fractures (when cycling fluid between wellbores to surface, without subsurface connection). When more than one fracture or producer well is involved, then the schematics of Figure 6 extend, and so do the formulas, in a similar fashion as in parallel circuit analysis.

4. Modeling and Results for Pump Power Consumption and Impedance

Simulations for the GGS designs while in operation were made here with a hydro-mechanical (HM) solver. Fractures are assumed to be height constrained and below an effective stress and pressure sealing formation to prevent upward growth. The deformation and near-tip behavior of propagating fractures governed by competing processes is captured by the solver by modeling fractures as one-dimensional objects embedded in a two-dimensional reservoir. Fluid balances, leak-off, and fracture contact are also handled. The simulator includes wellbores connected to fractures with perforations and simulates the pressure response due to either circulating fluid through the entire subsurface system or cycling fluid between two disconnected well/fracs system. For the surface system, the simulator also calculates power lost to the injection pump and system impedance.

The wells for each of the modeled cases reach a true vertical depth of 7500 ft (2286 m), and laterals 3281 ft (1000 m) long connect with 100 fractures for all cases except the single-well pair GGS that only has 8 fractures on each of its 262 ft (80 m) long laterals; 7” casing for the entire lengths of the wells is assumed for each well; when wells are connected by fractures the spacing between laterals is set to be 656 ft (200 m). Pore pressure is taken to be hydrostatic and a gradient of 0.7 psi/ft is assumed for the minimum horizontal stress, with a normal fault regime. The reservoir rock at the given depth is assumed to have a permeability of 0.1 mD, a Young’s modulus of 20 GPa, and a Poisson’s ratio of 0.25.

The fluid in each of the systems is assumed to be water, and though temperature is not explicitly modeled, it is prescribed at 40 °C for injection wells and 150 °C for the reservoir/fractures and production wells. As fluid properties depend on pressure and temperature, thermophysical properties of the fluid are obtained by the equation of state using REFPROP (Lemmon et al. 2018).

All of the above also holds for the traditional two-well EGS, except that fractures are modeled differently. They are treated to be in the ideal case where each fracture is filled with uniformly distributed proppant so that a 0.5 porosity, a fracture conductivity of 25 md-ft, and a 1.5 mm aperture is assumed for each fracture.

4.1 Impedance and Pump Power Consumption in a Traditional Two-well EGS

A traditional two-well EGS, as in the left of Figure 2 but with 100 fractures, is modeled here under the assumptions given above. In the following, the simulator has filled the fracture/well system to initiate modeling of the system in full operation.

Figure 7 shows the simulated behavior of this two-well EGS operating for two days. A constant 50 l/s (793 gpm) injection flowrate is specified for the entire modeled time, while the backpressure is controlled to stepwise increase from a constant 100 psi (0.69 MPa) on the first day to a constant 200 psi (1.38 MPa) on the second day.

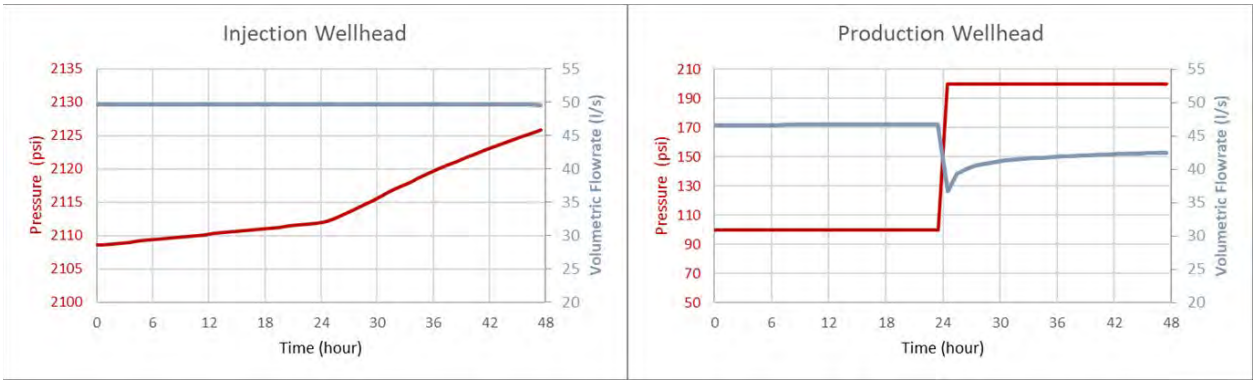

Figure 7: Simulated behavior of a traditional two-well EGS with 100 proppant-laden fractures operated with constant backpressures on each of the two days.

The simulation shows that on both days the production flowrate remains near constant, with approximately 47 l/s (745 gpm) on the first day and then drops and rebounds to the lower value of about 42 l/s (666 gpm) on the second day when the production backpressure is stepwise increased. The injection wellhead pressure builds up approximately linearly on both days, but at a much faster rate on the second day in response to the increased backpressure.

Figure 8 provides the friction pressure losses experienced during these two days of operation that circulates fluid down the injector well, through the 100 proppant-laden fractures and up the producer well; the part that makes up the U-tube effect is shown in the secondary vertical axis.

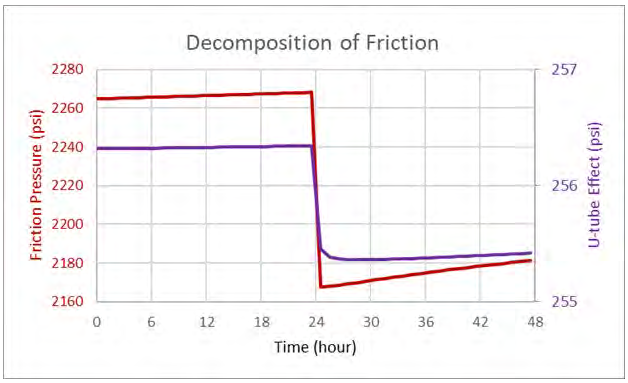

Figure 8: Friction pressure and U-tube effect of the two-well EGS with 100 proppant-laden fractures.

During the first day, the friction pressure remains around 2265 psi (15.62 MPa), and drops to 2167 psi (14.94 MPa) on the second day after the backpressure stepwise increases. This friction pressure

increases just slightly on the first day and moderately on the second day. It is observed that the U-tube effect follows a similar trend, but with magnitudes equal to 256 psi (1.77 MPa), on average, throughout the two-day operation.

Now the system impedance and pump consumption of power, are displayed in Figure 9. When the surface system is pressurized and an HSP pump used, then the system impedance on the first day is observed to be 0.35 MPa/(l/s) and increases and rebounds to 0.37 MPa/(l/s) on the second day as a consequence of the added resistance when the production backpressure is increased. When the surface system is not connected and an LSP pump is used, the impedance is 0.36 MPa/(l/s) on the first day and 0.40 MPa/(l/s) on the second day. This gives only a 3-8% drop in impedance when pressurizing the surface system.

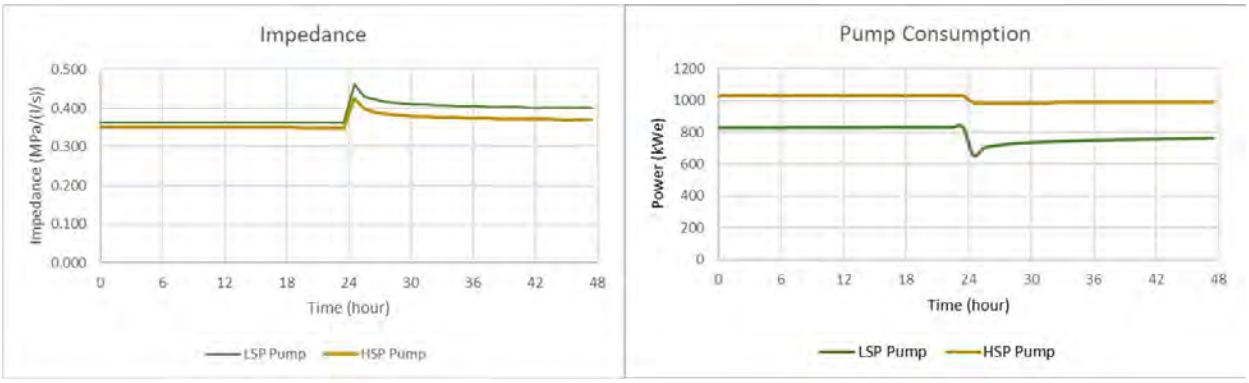

Figure 9: System impedance and pump power consumption for a traditional two-well EGS with 100 proppant-laden fractures.

When the EGS is operated with an LSP pump, the power consumed by the pump is 830 kWe, on average, during the first day of operation, and this drops but gradually increases to 762 kWe during the next 24 hours to overcome the stepwise increased backpressure. If, however, this two-well system is pressurized at surface and an HSP pump is used, then the pump consumption is about 1031 kWe during the first day and drops to 983 kWe and gradually increases to 990 kWe during the second day.

Modeling thus shows that maintaining the surface pressurized in a system where fractures are proppant propped leads to higher impedance and a power consumption increase of about 201 kWe during the first 24 hours and about 228 kWe during the next 24 hours. This translates to an energy increase of 4,824 kWh on the first day and 5,472 kWh on the second. Therefore, pressurizing the surface system when propping the fracture system with proppant is undesirable.

4.2 Reducing Impedance and Pump Power Consumption in a Two-well GGS

This subsection shows that hastily pressure propping fractures and pressurizing the surface system of a doublet system may be unwise and that careful attention is needed for a properly engineered GGS. Here, a two-well system is considered, as in the right of Figure 2 but with 100 fractures that are pressure-propped as opposed to proppant-propped. Since the fractures are operated open, i.e. with fluid pressures above the minimum in-situ stress, the deformation part of the simulator is enabled. In the following, the simulator has filled and pressurized the fracture/well system to initiate modeling of the system in full operation. Fractures fluid pressures are above the minimum in-situ stress but below the pressure that would lead to fracture propagation.

Figure 10 shows the simulated behavior of this two-well GGS operating for two days. A constant 50 l/s (793 gpm) injection flowrate is specified while maintaining a constant backpressure of 2132 psi (14.7 MPa) for the entire simulation.

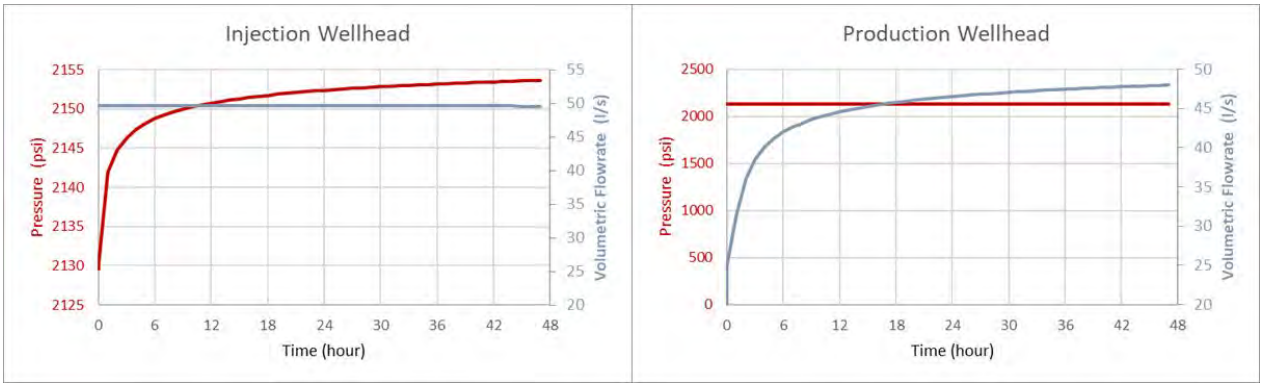

Figure 10: Simulated behavior of a two-well GGS with 100 fractures operated with a constant backpressure during the entirety of two days.

The simulation shows that the production flowrate increases from 25 l/s (396 gpm) to reach 48 l/s (761 gpm) at the 48th hour of operation as the increasing rate slows down. It is seen that the injection wellhead pressure builds up sharply during the initial 4 hours and continues to increase afterwards but at a much slower rate.

The friction pressure losses experienced by this pressurized system during these two days of operation is shown in Figure 11; the part that makes up the U-tube effect is again separated into the secondary vertical axis. The friction pressure is about 254 psi (1.75 MPa) for the 23 hours after having sharply increased in the first hour from the initial 156 psi (1.08 MPa). This friction pressure increases very slowly in the last 23 hours of operation. The U-tube effect is close to 233 psi (1.61 MPa) during the modeled time.

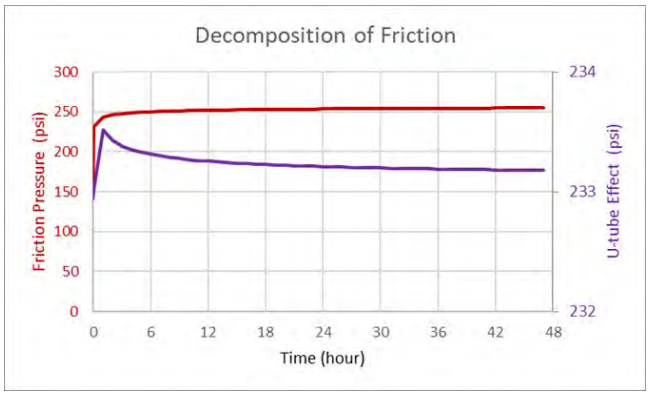

Figure 11: Friction pressure and U-tube effect of the two-well GGS with 100 fractures.

Figure 12 displays the system impedance and pump consumption of power. If the surface system is pressurized and uses an HSP pump, the system impedance is around 0.053 MPa/(l/s) for the majority of the two days, though it is gradually decreasing. If the surface is not pressurized and is equipped with an LSP pump, then the impedance is about 0.36 MPa/(l/s) throughout the modeled time. The impedance of the fully pressurized system is about an order of magnitude less than when the surface is not pressurized; this is also true when comparing with the proppant-laden EGS case.

Moreover, the maximum fracture aperture observed was 0.8 mm when fractures are pressured propped, almost half the aperture size of the proppant propped factures.

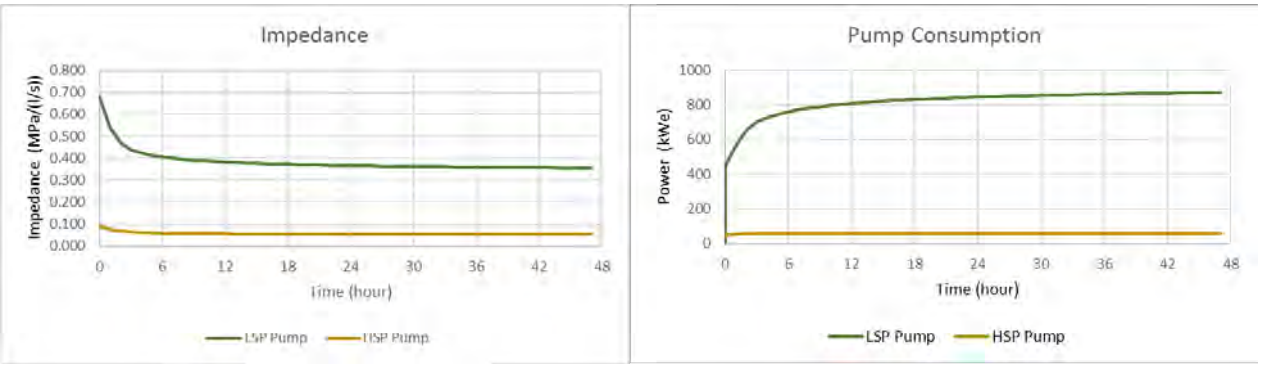

Figure 12: System impedance and pump power consumption for the two-well GGS.

Consider now the pump consumption behavior for this two-well system. Suppose first that this system is operated with an LSP pump. Figure 12 shows that the power consumed by the pump is 798 kWe, on average, during the two days of running the system. If, however, the surface system is pressurized and equipped with an HSP pump, then the pump consumption drops to 58 kWe during the modeled time. Thus, maintaining the surface system pressurized drastically reduced the power consumption of the pump. In fact, the drop in power consumed by the pumps implies an energy drop of 35,520 kWh during these two days.

The reduced impedance, the energy difference and the favorable system performance observed seems to undoubtedly warrant the use of a GGS surface injection kit for a two-well system. However, the simulations reveal a serious issue. Figure 13 shows a plan view of reservoir pressure focusing on one fracture in the system, and where the injector/producer well pair (two points) roughly are, respectively, at the centers of the red/blue region in the first frame, with this well distance fixed in all four frames. The simulation shows that the fracture keeps growing to the right, whereas the producer well serves as a pressure barrier and obstructs fracture growth to the left. Continued fracture growth is unwanted when continuously operating any heat extraction system as fluid is lost in the 'opposite direction'. More importantly, in scenarios of low fracture toughness, as in the simulation, the risk of uncontrolled fracture propagation is possible and may lead to seismic activity. As this may not always happen, operating a two-well system with fractures pressure propped and with a pressurized surface should be done with great caution if not avoided.

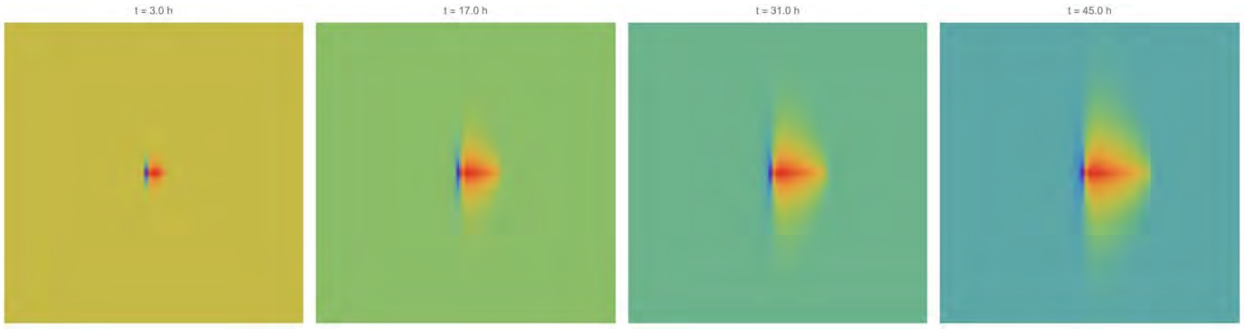

Figure 13: Plan view of reservoir pressure at hour 3, 17, 31 and 45 of the simulation displaying one fracture continuously growing to the right.

These modeled results align with the observations at Fenton Hill where the field tests of the (much more complex) subsurface system subjected to high injection and production pressures showed micro-seismic activity that implied further reservoir growth (Brown 1994). The recommendation from the Los Alamos National Laboratory to include a secondary production well, opposite the first relative to the injector well, is simulated next.

4.3 Reducing Impedance and Pump Power Consumption in a Three-well GGS

This subsection models operating a three-well GGS as in Figure 4 but with 100 fractures. As in the two-well GGS, fracture deformation is fully accounted for by the simulator. To initiate modeling of the system in full operation, the simulator fills the subsurface system and pressurizes the fractures with fluid pressures above the minimum in-situ stress but below the threshold that would lead to fracture propagation.

Figure 14 shows the simulated behavior of this three-well GGS operating for 48 hours. A constant injection flowrate of 50 l/s (793 gpm) is again specified for the entire modeled time, but the backpressure is controlled, in this case, to decrease stepwise from a constant 2132 psi (14.7 MPa) on the first day to a constant 2103 psi (14.5 MPa) on the second day.

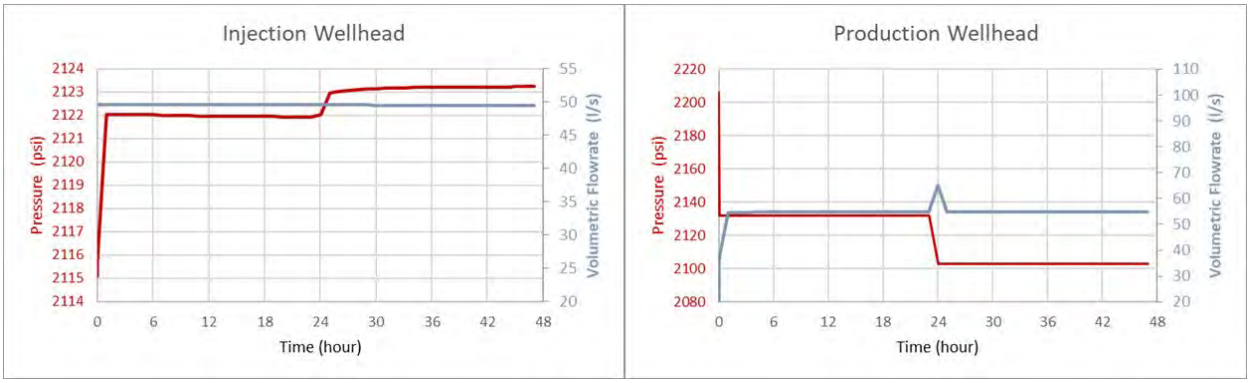

Figure 14: Simulated behavior of a three-well GGS with 100 fractures with fluid pressures above the minimum in-situ stress but below fracture propagation.

On both days the production flowrate remains a near constant of 55 l/s (872 gpm), with a small spike around the 24th hour when the backpressure is stepwise reduced. The injection pressure (approximately) stepwise increases from 2122 psi (14.63 MPa) on day one and to 2123 (14.64 MPa) on day two in response to the decreased backpressure in this system where fractures are operated open.

Figure 15 displays the friction pressure losses experienced during these two simulated days of injection and production; the part that makes up the U-tube effect is again on the secondary vertical axis. Compared with results for the EGS recorded in Figure 11, the friction pressure in this three-well GGS is lower by one order of magnitude. While operating this three-well system, the friction pressure loss is 223 psi (1.54 MPa) on the first day, and increases to 254 psi (1.75 MPa) on the second day after the backpressure stepwise decreases. The U-tube effect follows a similar stepwise increasing behavior, but is on average about 233.5 psi (1.61 MPa). Note that this U-tube effect, and that of the two-well GGS case, are close to the 256-psi average U-tube effect for the proppant-laden two-well EGS.

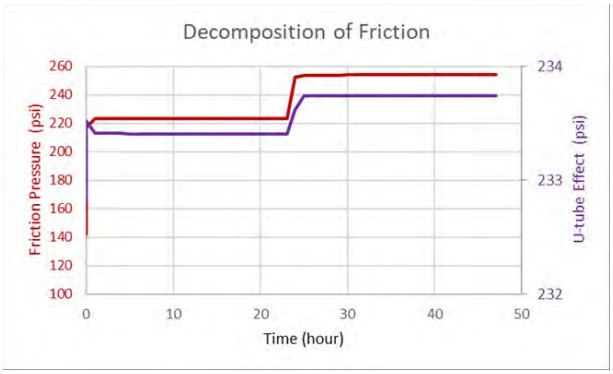

Figure 15: Friction pressure and U-tube effect of the three-well GGS with 100 fractures.

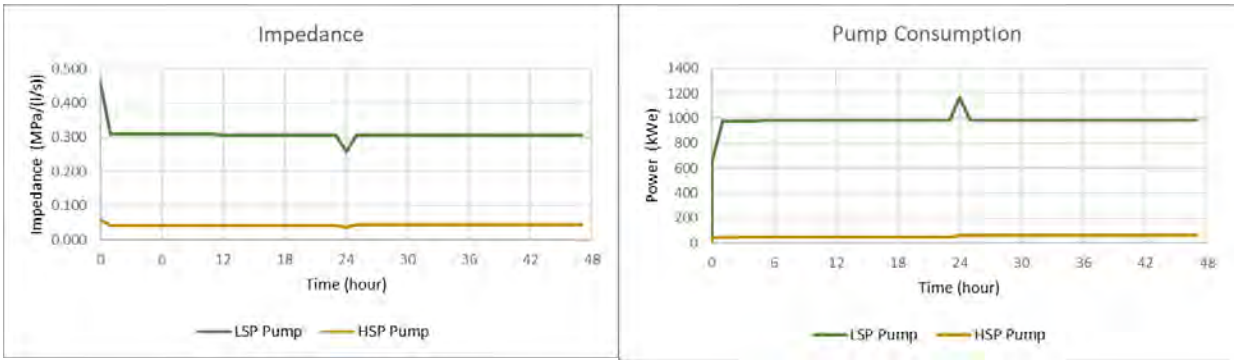

Figure 16: System Impedance and Pump Power Consumption for a three-well GGS with 100 fractures.

When the surface is pressurized and an HSP pump is used, Figure 16 shows that the system impedance is 0.041 MPa/(l/s) on the first day and increases to 0.044 MPa/(l/s) on the second day when the backpressure is stepwise decreased. When the surface is not connected and an LSP pump is used, the system impedance is 0.307 for the majority of the simulated time. As with friction pressure, the impedance of this pressurized system is an order of magnitude less than the unpressurized surface case; this observation is also true when comparing with the proppant-laden EGS case. The maximum fracture aperture observed when fractures were pressure propped was 0.95 mm, 37% less than the fracture aperture in the EGS case.

If the three-well subsurface system is operated with an LSP pump, the power consumed by the pump is 958 kWe during the two days simulated operation. However, if the surface system is pressurized and an HSP pump used, then the pump consumption stepwise increases from 43 to 58 kWe from day one to day two. This (small) jump results since the production backpressure is lower on the second day.

The simulations thus show that pressurizing the surface system leads to a power consumption drop of 907 kWe, on average, during the two-day operation. This translates to an energy drop of 43,536 kWh during this two-day simulation.

4.4 Reducing Impedance and Pump Power Consumption in a Single-well Pair GGS

This last design, the single-well pair GGS as in Figure 5 but with 8 fractures, is operated with cyclic, or huff-n-puff, operations, so the modeling results are displayed in a slightly different manner. As in the previous GGS designs modeled, fracture deformation is fully accounted for by the simulator as fractures are pressure-propped. To initiate modeling of the system in full operation, the simulator fills and pressurizes the fractures on both wells with fluid pressures above the minimum in-situ stress but below the pressure that would yield fracture propagation.

Figure 17 shows the simulated behavior of this single-well pair GGS operating for 52 hours. Consider first the flowrate profile of well A (in black). For the first 5.5 hours, fluid is being produced by well A at a rate of 50 l/s (793 gpm) and injected into well B; this is indicated in the plot by the negative volumetric flowrate value for well A. This production phase is followed by a one-hour shut-in phase of well A, and subsequently a 5.5-hour phase of injecting fluid (from well B) into well A at a rate of 50 l/s (a positive value in the plot). Another shut-in phase for one hour of well A follows, and then this production-injection process is repeated for well A. This creates the cyclic operation of well A, and well B is operated similarly but with the flow opposite that of well A. The accompanying plot shows that wellhead A pressure, for example, decreases when well A is producing, rebounds when shut-in, and increases when injecting into well A. Well B follows the same wellhead pressure behavior.

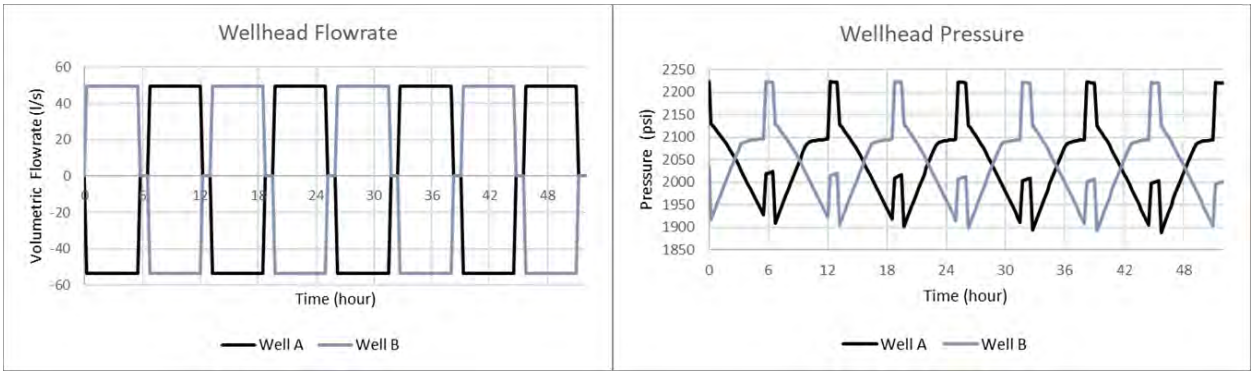

Figure 17: Simulated behavior of a single-well pair GGS with 8 fractures per well and huff-n-puff operations.

Figure 18 displays the friction pressure losses experienced during these 52 hours of huff-n-puff operations; the part that makes up the U-tube effect is shown in purple.

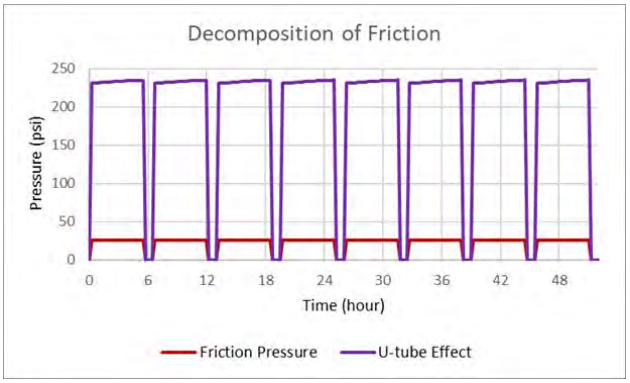

Figure 18: Friction pressure and U-tube effect of the single-well pair GGS with 8 fractures per well.

Unlike the other GGS designs, the friction pressure losses for the single-well pair GGS are one orders of magnitude lower than that experienced in the EGS with proppant-laden fractures; this single-well pair GGS has a friction pressure loss of 26 psi (0.18 MPa). The U-tube effect for the single-well pair GGS is 233 psi (1.61 MPa) when flowing, similar to the previous two GGS designs.

From Figure 19, the system impedance for the single-well pair design with the surface system pressurized (and thus with an HSP pump) has a value of 0.16 MPa/(l/s) when flowing. If the wells are not connected at surface and an LSP pump is used, then the system impedance is 1.16 MPa/(l/s), which is almost an order of magnitude higher than with the HSP pump. The maximum aperture observed for this case was 0.7 mm, which is less than half the aperture size in the EGS case.

If this two-well system is operated with an LSP pump, then the power consumed by the pump is 856 kWe, on average, during the simulated transfer of fluid. However, if the surface system is pressurized and an HSP pump is used, then the pump consumption is 80 kWe, on average, when flowing.

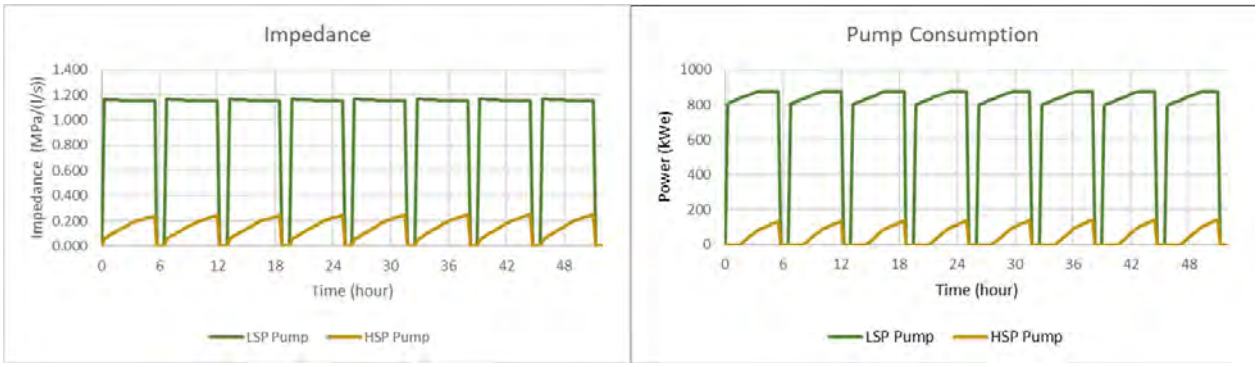

Figure 19: System Impedance and Pump Power Consumption for a single-well pair GGS.

Results from the simulation thus shows that maintaining the surface system pressurized leads to a power consumption drop of about 776 kWe during the 5.5 hours of flow. This translates to an energy drop of 4,265 kWh (on average) for each of these 5.5 hours of fluid transfer, or 34,144 kWh in the time when flowing.

5. Summary and Conclusion

These simulation results show that subsurface systems with pressure propped fractures have an impedance about one order of magnitude lower when the surface system is pressurized and when using a High Suction Pressure (HSP) pump versus not pressurizing the surface and only using a Low Suction Pressure (LSP) pump. This holds regardless if fluid is circulated through a connected subsurface or if huff-n-puff operations are used between two wells disconnected at the subsurface. The two-well and three-well designs where the surface and subsurface systems are pressurized have an impedance one order of magnitude lower than in the traditional two-well EGS with proppant propped fractures and an LSP pump. The pressurized single-well pair design with wells disconnected at the subsurface, but connected and pressurized at the surface, has half the impedance experienced in the EGS case.

If the surface system is pressurized and an HSP pump used when operating fractures open, then the power consumed by the injection pump is only 6-9% of the power consumed if an LSP pump is utilized (and if the surface system is not pressurized). In other words, maintaining the whole system pressurized, instead of wasting pressure on the production side, allows to drastically cut injection pump parasitic costs.

However, care should be taken when pressurizing the entire system. When applying this methodology to a two-well, multi-fracture system, the simulations show that continuous operation of the system (with practical performance at surface) leads to continued fracture growth, hence major fluid losses. Therefore, a GGS design should be operated with fracture fluid pressures above the minimum horizontal stress and below that which would induce fracture propagation. Both the three-well and single-well pressurized systems successfully use this pressure window. Longer lateral spacing is also demonstrated by the three-well design. The pressurized single-well pair design based on huff-n-puff operations is seen to be superior to the other systems in terms of the hydro-mechanical performance and it simplifies the stimulation operations and reduces the number of fractures by an order of magnitude.

Complementing the presented analysis of the GGS approach, a next publication will treat the full thermo-hydro-mechanical performance of GGS design.

Acknowledgement

Special thanks to our CTO Lance Cook at Sage Geosystems for the insightful subsurface design guidance.

REFERENCES

Brown, D. “How to Achieve a Four-fold Productivity Increase at Fenton Hill.” *GRC Transactions,* Vol. 18 (1994).

Brown, D., Duchane, D.V., Heiken, G. and Hriscu, V.T. “Mining the Earth’s Heat: Hot Dry Rock Geothermal Energy.” *Springer-Verlag,* Berlin Heidelberg (2012).

Dontsov, E.V., and Peirce, A.P. “A multiscale Implicit Level Set Algorithm (ILSA) to model hydraulic fracture propagation incorporating combined viscous, toughness, and leak-off asymptotics.” Comput. Methods Appl. Mech. Engrg. 313 (2017).

DuTeau, R. and Brown, D. "HDR Reservoir Flow Impedance and Potentials for Impedance Reduction." *Proceedings: 18th Workshop on Geothermal Reservoir Engineering,* Stanford University, Stanford, CA (1993).

Gedzius I, Teodoriu C. “Innovative Erschliesungskonzepte für Hot-Dry-Rock-Projekte im Norddeutschen Becken.” DGMK/€OGEW-Frühjahrstagung. Fachbereich Ausführung und Gewinnung (2011).

Glauser, W., McLenna, J. and Walton, I. “Do Perforated Completions have value for Engineered Geothermal Systems.” *ISRM International Conference for Effective and Sustainable Hydraulic Fracturing,* Brisbane, Australia (2013).

Lemmon, E.W., Bell, I.H., Huber, M.L., McLinden, M.O. “NIST Standard Reference Database 23: Reference Fluid Thermodynamic and Transport Properties-REFPROP.” Version 10.0, National Institute of Standards and Technology, Standard Reference Data Program, Gaithersburg (2018).

Murphy, H.D., Tester, J.W., Grigsby, C.O. and Potter, R.M. “Energy Extraction from Fractured Geothermal Reservoirs in Low-Permeability Crystalline Rock.” *Journal of Geophysical Research*, Vol. 86, No. B8, pp. 7145-7158 (1981).

Robinson, E.S., Potter, R.M., McInteer, B.B., Rowley, J.C., Armstrong, D.E., Mills, R.L. and Smith, M.C. “A preliminary study of the nuclear subterrane.” *Los Alamos Scientific Report*, Rept. LA-4547 (1971).

Simpkins, D., Rivas, M.A., Eros, M. and Ring, L. “Energy Storage in Deep Hydraulic Fractures: Mathematical Model and Field Validation.” *GRC Transactions*, Vol. 47 (2023).

High-temperature Polymers to Modify Fracture Permeability

John C. Stormont, Mahmoud Reda Taha, Nick Carroll, Pearl Tetteh, Daniel Murcia and Abigail Coffman

University of New Mexico

Keywords

Thermal short-circuiting, preferential flow, fracture permeability, fracture modification , nano-modified polymers, microcapsule transport

ABSTRACT

We are developing polymer-based materials that can be selectively injected into fractures to modify their permeability and consequently control the resulting flowrate through the fracture and the heat exchange with the formation. These polymer injectates offer an engineering solution for problems associated with preferential flow that can lead to thermal short-circuiting; namely, thermal breakthrough, decreasing energy extraction efficiency, and reduced service life. A nano-modified polymer has been developed and characterized that meets the target service requirements for geothermal applications; notably, they possess desirable properties (e.g., viscosity, bond strength) and do not degrade in temperatures up to 275 °C. Microcapsules are being developed to deliver the polymer catalyst and serve to control locations where the polymer will be deployed. We have fabricated monodisperse capsules with diameters ranging from 100 to 500 um and shell thickness ranging from a few hundred nanometers to many microns in radial thickness. We created microcapsules with two distinct monomeric blocks and demonstrated that capsules fabricated from these blocks have unique thermal degradation behavior at temperatures from ~ 250 °C to above 300 °C at ambient pressure. We are also investigating the movement of the microcapsules through rough fractures, with an emphasis on understanding the controls on microcapsule exclusion from small fractures that do not require permeability modification and microcapsule entry into larger fractures that are targeted for modification.

1. Introduction

Preferential flow can lead to thermal short-circuiting in enhanced geothermal systems (EGS), which is one of the most important challenges that must be overcome in order for EGS to be economically successful (Lowry et al., 2017). Thermal short-circuiting leads to thermal breakthrough, decreasing energy extraction efficiency, and reduced service life. We are developing polymer-based materials that can be injected into fractures at targeted locations away from the wellbore to modify their permeability and consequently control the resulting flowrate through the

fracture and the heat exchange with the formation. These polymer-based injectates offer an engineering solution for problems associated with preferential flow and thermal short-circuiting. The injectate could be used during initial stimulation and development of the EGS fracture network to tune the fracture network and optimize thermal productivity. Moreover, the injectate could be applied if there is an indication of thermal short-circuiting developing because of the thermal feedback loop. The injectate is designed to displace water from the fracture and harden to form a porous material which bonds to the rock surface (Stormont et al 2020). The injectate is designed to be durable at EGS temperature and pressure conditions. The degree of permeability modification will be adjustable so that the resulting permeability can be tailored for the specific needs of an EGS fracture network.

A schematic of the deployment of the polymer-based injectate is shown in Figure 1. The injectate is introduced into the fracture that is to be modified. The injectate is a mixture of four principal components: a polymer resin, a catalyst (i.e., hardener) to initiate polymerization, a pore-former (polyethylene glycol) and a high-temperature solvent that together will render the polymer porous. The catalyst, the pore former and the solvent can be delivered in microcapsules that incorporate a clocking mechanism based on temperature so they are released at a target location away from the wellbore. The porous nature of the material will allow control on the resulting permeability of the fracture, and prevents the treatment from completely sealing of the fracture. Microcapsules are sized to prevent entry into smaller fractures. Microcapsule rupture initiates as their temperature increases as the moving fluid is heated by the formation. Porous polymer begins to form and bond to the rock due to interaction of polymer resin, catalyst, and solvent. The permeability decrease can be progressively controlled by multiple applications of the injectate. Alternatively, the effect of the intervention can be reversed by adding select acids that will break the bond of the polymer to the rock, and thereby permitting the polymer to be displaced.

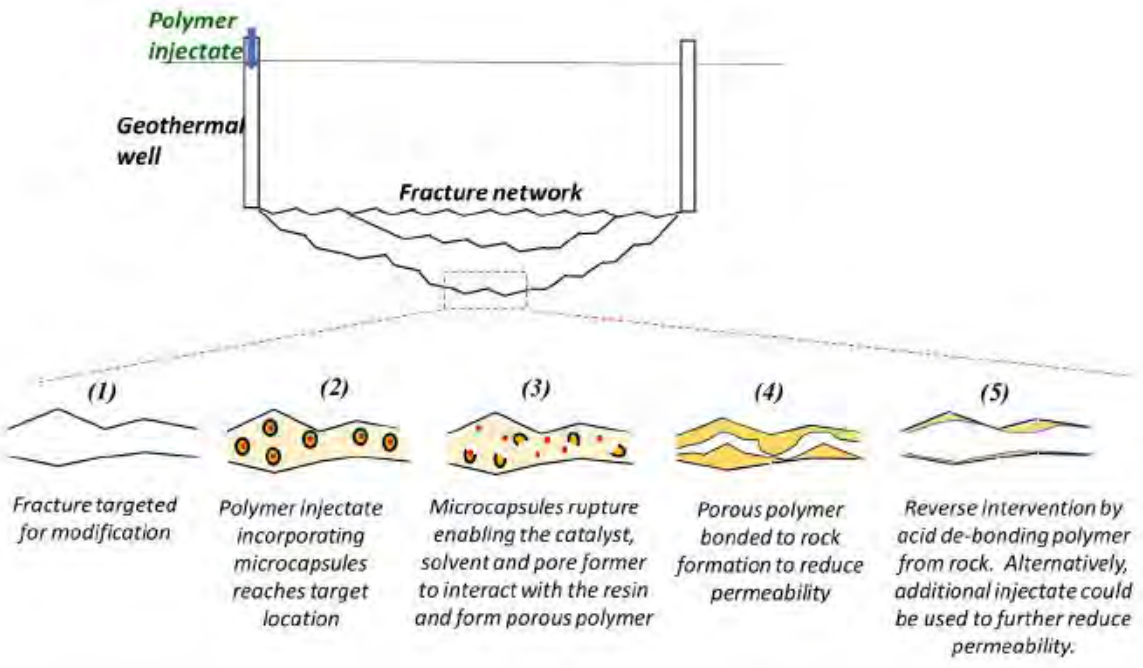

Figure 1: Deployment sequence of a porous polymer to modify fracture permeability.

In this paper, we summarize work directed at advancing this technology toward deployment. The project work is described in terms of polymer development, microcapsule fabrication, and microcapsule transport in rough fractures.

2. Polymer Development and Properties

A new nano-modified Resole-Phenol co-polymer resin was developed. The nanoparticles used were COOH-functionalized multi-walled carbon nanotubes (MWCNTs) or graphene nanoparticles (GNPs). The functionalization of the nanoparticles with the COOH carboxylic groups has been proven to improve the dispersion efficiency (Douba et al., 2017; Soliman et al., 2012). Five formulations of the nano-modified Resole-Phenol co-polymer resins were developed and characterized. The Resole resin was first deactivated using a Phenol deactivation agent then the Resole-Phenol co-polymer resin was reactivated using a curing agent. The degree of crosslinking was measured using differential scanning calorimetry (DSC) to quantify the degree of the Resole resin deactivation as shown in Figure 2. Formulation 5 of the Resole-Phenol co-polymer resin incorporating MWCNTs/Graphene nanoparticles showed the least degree of crosslinking of 15% and therefore was used in the subsequent step.

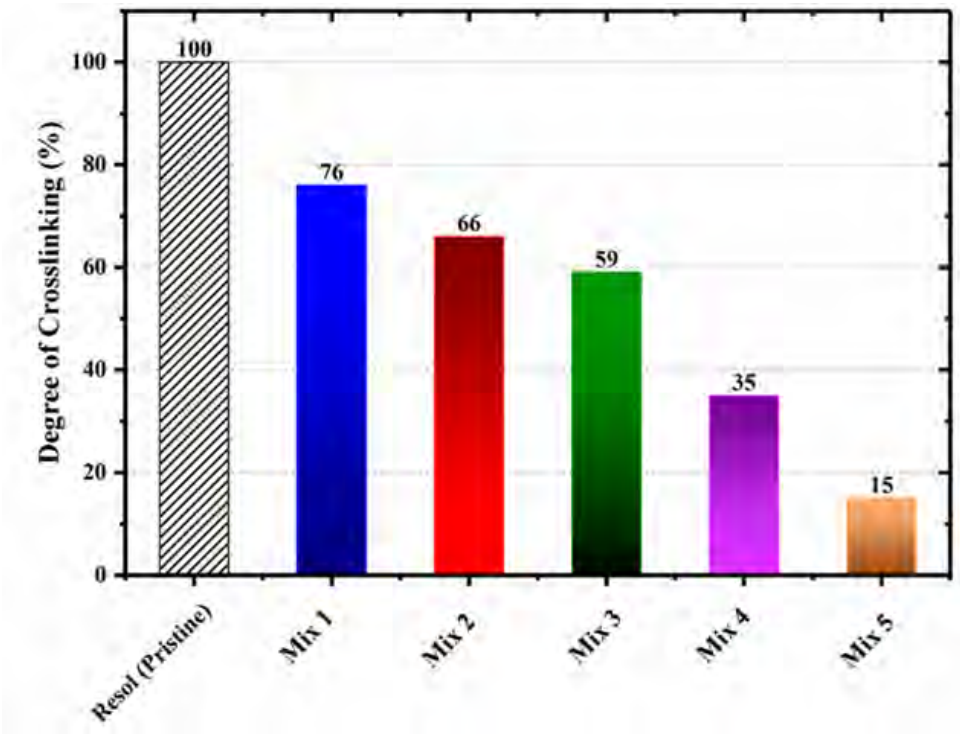

Figure 2: Degree of crosslinking of Pristine Resole resin and five Resole-Phenol formulations. The degree of cross-linking is used to describe the level of the new resin deactivation.

Rheological measurements using a high-temperature rheometer were performed for formulation 5 of the deactivated nano-modified Resole-Phenol co-polymer resin. High-temperature viscosity measurement was performed at 125℃ corresponding to the maximum weight loss observed from the thermal gravimetric analysis (TGA) of the deactivated resin. The new nano-modified Resole-

Phenol co-polymer resin showed a viscosity below 190 cP for 45 minutes which is a relatively low viscosity, very suitable for flow in wellbores and to penetrate microcracks.

Formulation 5 of the deactivated Resole-phenol resin was reactivated using a curing agent. Figure 3 shows the degree of cross-linking of 7 reactivated Resole-Phenol polymers using different curing agents and several mixing ratios. Experimental validation using DSC confirmed the chemical deactivation/reactivation processes, optimizing performance under varying conditions. Two formulations denoted Mix 5_3 and Mix 5_6 was shown to achieve the required level of deactivation necessary to be used as a polymer injectate.

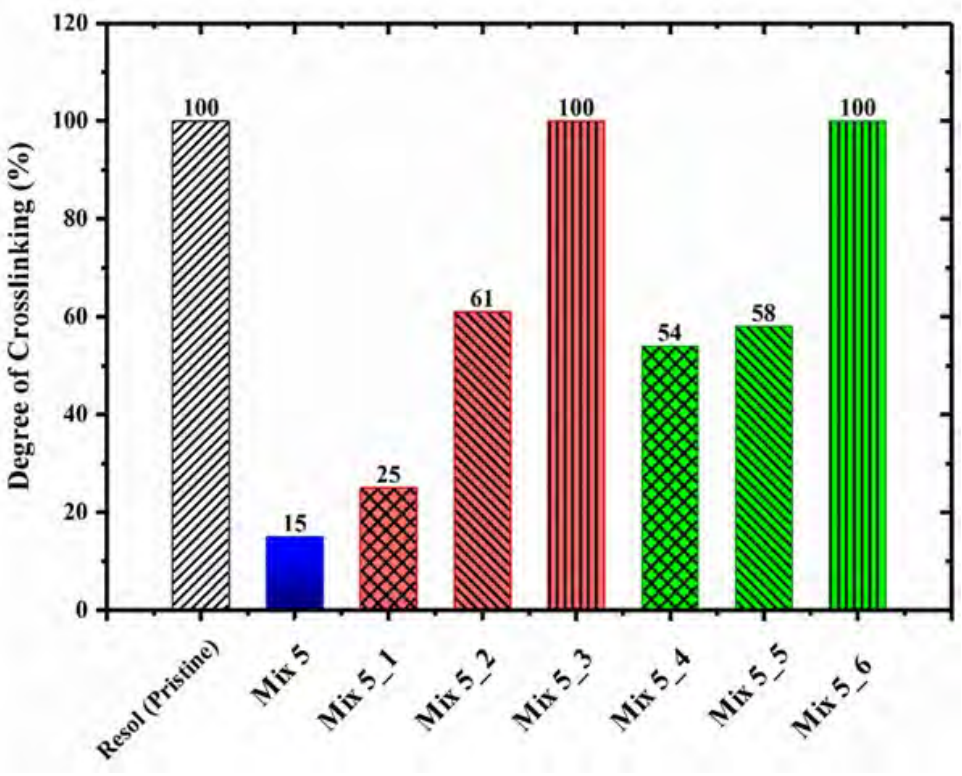

Figure 3: Reactivation of Formulation 5 using different curing agents and mixing ratios

TGA was used to characterize the thermal stability of the activated nano-modified Resole-Phenol co-polymer injectate. The new polymer injectate showed excellent post-curing thermal stability up to 475°C. Based on the analysis from Figure 4, Curing Agent 1 was chosen for further analysis since the activation temperature for Curing Agent 2 is very high. Moreover, using Curing Agent 2 results in the evaporation of the injectate at a temperature below 200°C before activation of the curing agent. Mix 5_6 was selected for further analysis based on the results above-mentioned. The DSC results showed no post-cured crosslinking, crystallization, or melting peaks for the nano-modified Resole-Phenol polymer injectate. The DSC results also showed an increased degree of crosslinking due to the incorporation of COOH-functionalized nanomaterials.

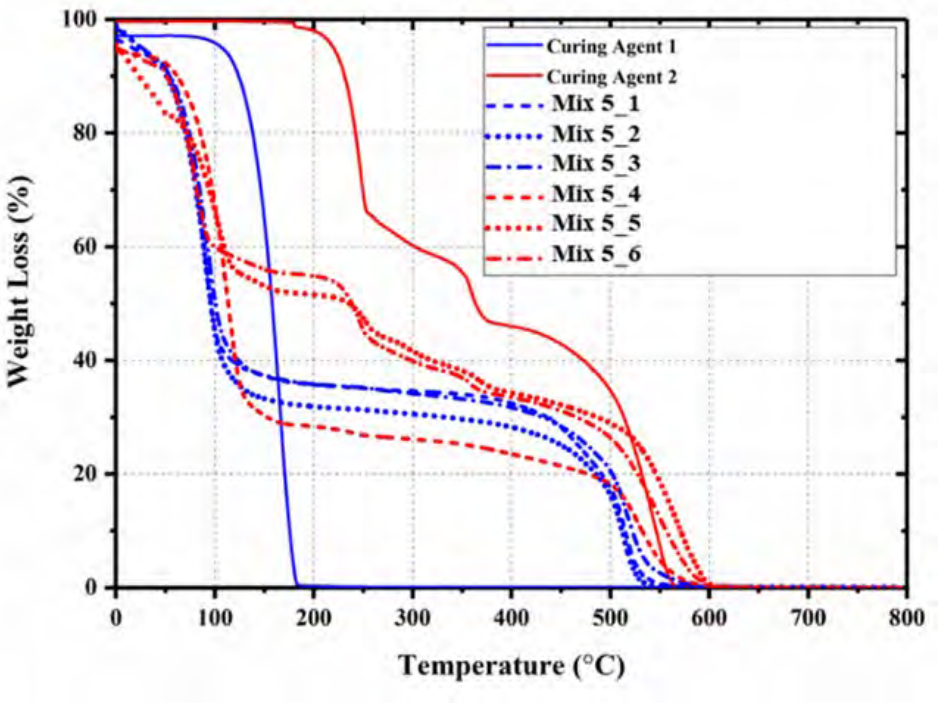

Figure 4: TGA analysis of the nano-modified Resole-Phenol polymer injectate

Characterization of the new nano-modified Resole-Phenol co-polymer injectate included identifying the gelation and setting times and comparing it with the pristine Resole. The new nano-modified polymer injectate showed a gelation time of about 30 minutes and a set time of about 45 minutes compared with 12 minutes of gelation time and 30 setting time for the pristine Resole. The 30-45 minutes of gelation and setting shall be sufficient to apply and use the new polymer injectate in the process to control the permeability of the geothermal wells. Furthermore, the radial and longitudinal shrinkage of the nano-modified Resole-Phenol co-polymer injectate was tested and showed no radial shrinkage and exhibited signs of longitudinal expansion, which could significantly enhance its sealing capabilities. We also performed some wettability measurements of the nano-modified Resole-Phenol co-polymer injectate and found its contact angle to range from 10-25^{o} in ambient temperature and to increase above 40^{o} at high temperatures. The above work showed the feasible development and use of nano-modified Resole-Phenol co-polymer injectate for geothermal wells.

3. Microcapsule fabrication

Thermally stable polymeric shell microcapsules (MCs) containing aqueous or organic cargo were fabricated using double emulsion templates. Droplet microfluidic devices as described previously (Arriaga et al., 2015; Nabavi et al., 2015) were used to fabricate double emulsion templates with liquid monomeric shell material (Figure 5) for chemically diverse acrylic microcapsules with well-defined and monodisperse diameters ranging from 100-500 microns and tunable shell thickness ranging from hundreds of nanometers to microns (see Figure 6), excellent thermal stability and tunable shell thermal decomposition temperatures and kinetics. Acrylic microcapsules are those formed by UV induced radical polymerization of acrylate-based monomers to produce thermosetting polymer shells. This strategy allows for the selection of diverse shell material

monomers to tune capsule (i) thermal stability at temperatures up to 250 °C and (ii) associated thermal decomposition induced release profiles.

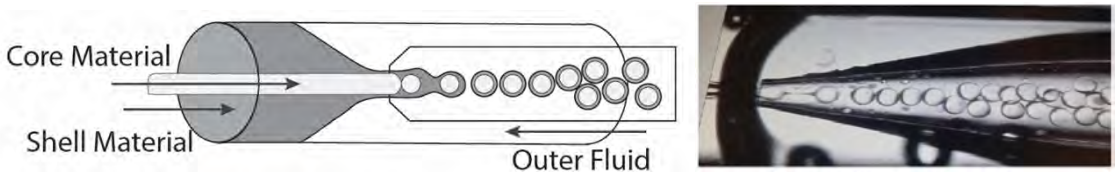

Figure 5: Schematic illustration (left) and microscopy image (right) of capillary microfluidic device used to fabricate double emulsion microcapsule templates.

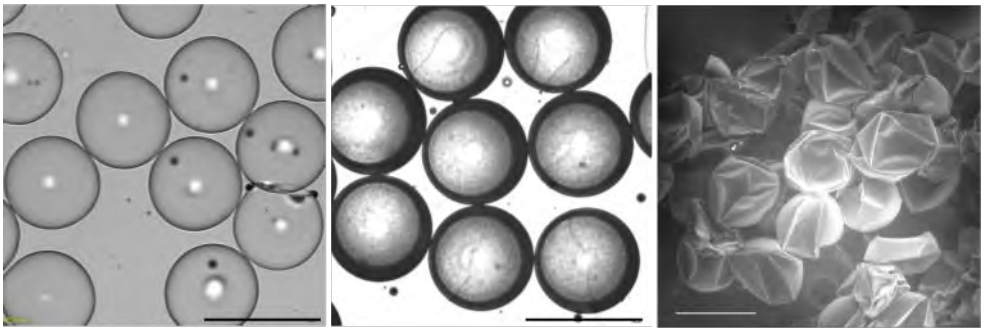

Figure 6: Optical (left, middle) and SEM (right) acrylic microcapsule images. Shell thicknesses can range from hundreds of nanometers (left, right) to microns (middle). Scale bars = 500 microns.

This tunable thermal decomposition behavior is highlighted in Figure 7 where TGA analysis of microcapsules with two different acrylic shells fabricated from acrylate or dimethacrylate monomer composites, respectively, shows resulting distinct thermal decomposition for the two monomers, ranging from around 250 to > 300 °C.

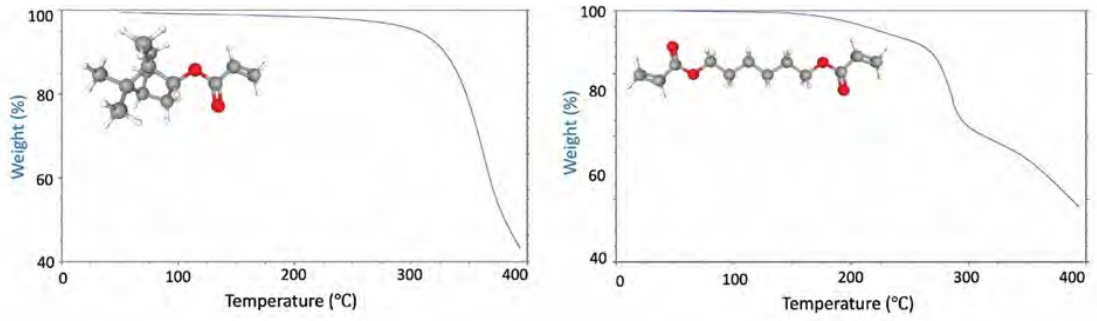

Figure 7: TGA signature curves for acrylate (left) and dimethacrylate (right) derived composite microcapsules.

With respect to thermally stable microcapsules that rupture at design time, we have demonstrated that dimethacrylate derived composite microcapsules rupture after 15 minutes at 320 °C under atmospheric pressure. The time path of rupturing for acrylic microcapsules was assessed by microscopy through imaging of capsules with an air core collected from a 320 °C heated sample (high temperature silicone oil as carrier fluid) at 5, 10, and 15 minutes. We replaced the aqueous core with air by evaporation because the capsules would undergo ‘steam explosions’ when exposed

to temperatures above 100 °C at atmospheric pressure. Results are shown in Figure 8 and reveal that thermal decomposition of the capsule shells results in the rupture of > 80% of the capsules at the 15-minute time mark.

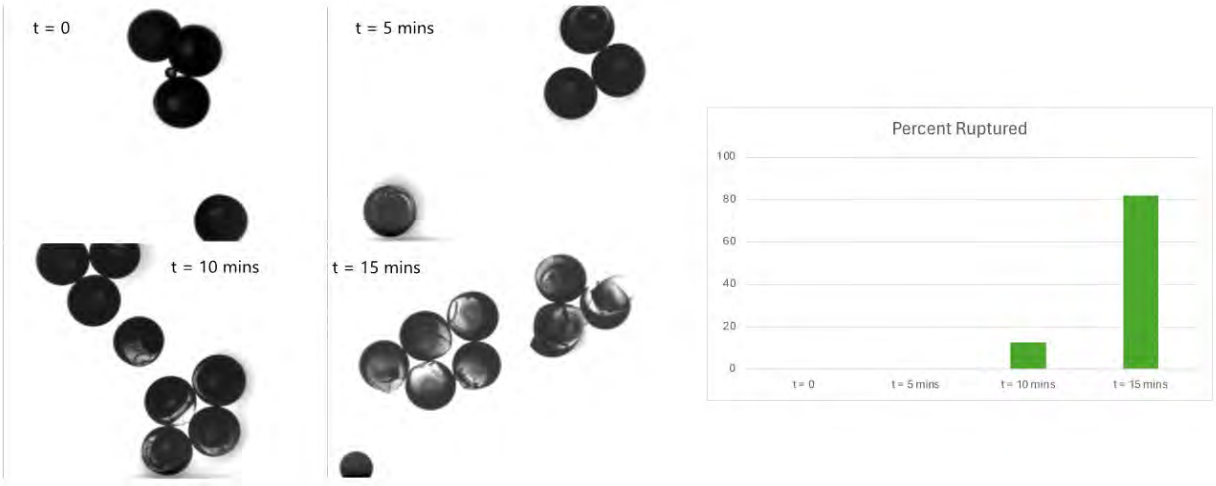

Figure 8: Time series microscopy images of acrylic microcapsules in silicone oil carrier fluid incubated at 320 °C indicate rupturing of >80% of the capsules at the 15-minute time mark.

4. Transport of microcapsules in rough fractures

An understanding of microcapsule movement into and through rough fractures is critical to the technology deployment: microcapsules should be excluded (blocked) from smaller fractures that are not meant to be modified with the polymer.

A flow visualization system has been developed to visualize microcapsule movement in rough fractures. This system has been used to measure microcapsule entry, transport and blocking within fractures to provide data to develop blocking functions for sheared and dilated fractures. The flow visualization system involves establishing steady flow through a transparent fracture replica, microcapsule introduction into the flow stream, video recording of the microcapsule movement, and application of particle tracking software.

Transparent fracture replicas were created from fractured granite specimens. Fracture topography data was obtained from profiling the fracture surface. The fracture replicas were integrated into a flow cell which allowed the fractures to be sheared and dilated to create a fracture network. Fluorescent 1 mm diameter microcapsules were passed through the fractures. By filming the experiments, we could determine the location and amount of blockage (retention) of the microcapsules in the fractures at different amounts of shear and dilation. In addition, a direct method to measure the aperture field of the fracture network was developed using a light transmission technique in which the light intensity through the fracture replica was measured with water and with a dye in order to interpret the fracture aperture field via the Beer Lambert Law. These results reveal that shear displacement creates complicated fracture networks that vary significantly with the amount of shear, consistent with the findings of others.

Particle trajectories within a fracture during flow are shown in Figure 9 for two conditions for the same fracture: normal displacement and shear displacement. When the fracture is normally

displaced, once the displacement allows microcapsules to enter, the flow of microcapsules is relatively uniform in the direction of the hydraulic gradient. In contrast, when this fracture is sheared, the flow of microcapsules is concentrated into channels and moves around locations of small aperture or where microcapsules become blocked.

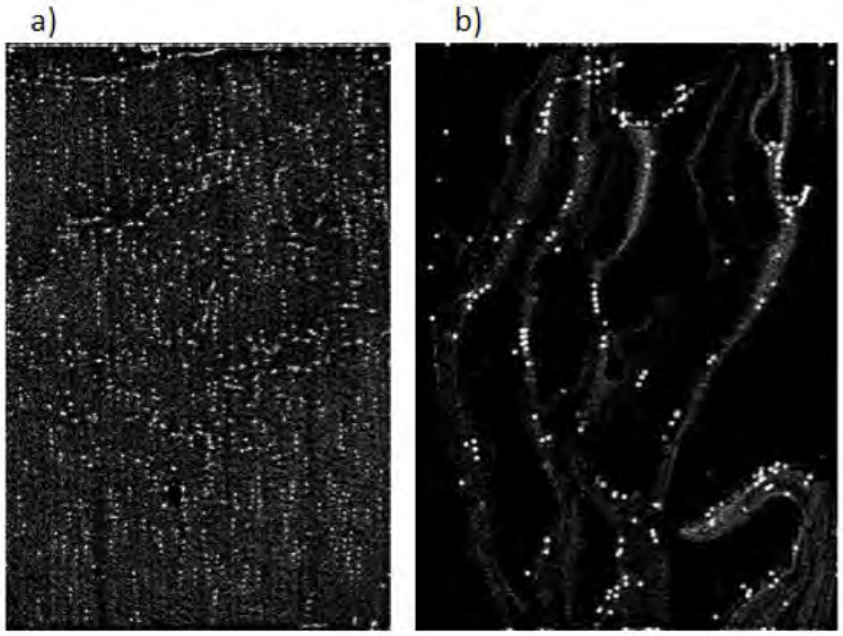

Figure 9: (a) Particle trajectories for normally displaced fracture revealing parallel flow paths over the entire fracture surface. (b) Particle trajectories for sheared fracture displaying tortuous flow concentrated in channels and excluded from large portions of the fracture. Flow direction is bottom to top of figure. White dots are microcapsules moving in well-connected flow paths.

We conducted tests on three different fractures with varying degrees of roughness: fracture C being the smoothest, fracture A of intermediate roughness, and fracture D being the roughest. We relate the blocking results to the hydraulic aperture of the fracture. The hydraulic aperture is the aperture of a smooth-walled parallel fracture that produces the same amount of flow as the rough-walled fracture, and can be related directly to the fracture permeability.

The ratio of hydraulic aperture to microcapsule diameter for complete blockage and no blockage is given in Figure 10. No blockage is the desired condition for fractures that we wish to modify: we can pass microcapsules into this region, and then they thermally degrade and the porous polymer will polymerize. Complete blockage including exclusion of microcapsules from the fracture is suitable for fractures we do not wish to modify, i.e., they are not preferential flow paths that lead to thermal short-circuiting. The results shown in the figure reveal that the hydraulic aperture for no blockage and complete blockage are different for different fractures. The rougher the fracture, the greater the hydraulic apertures are for these conditions. This suggests the blocking criterion may be a function of a roughness measure (such as the joint roughness coefficient or JRC) in addition to the hydraulic aperture.

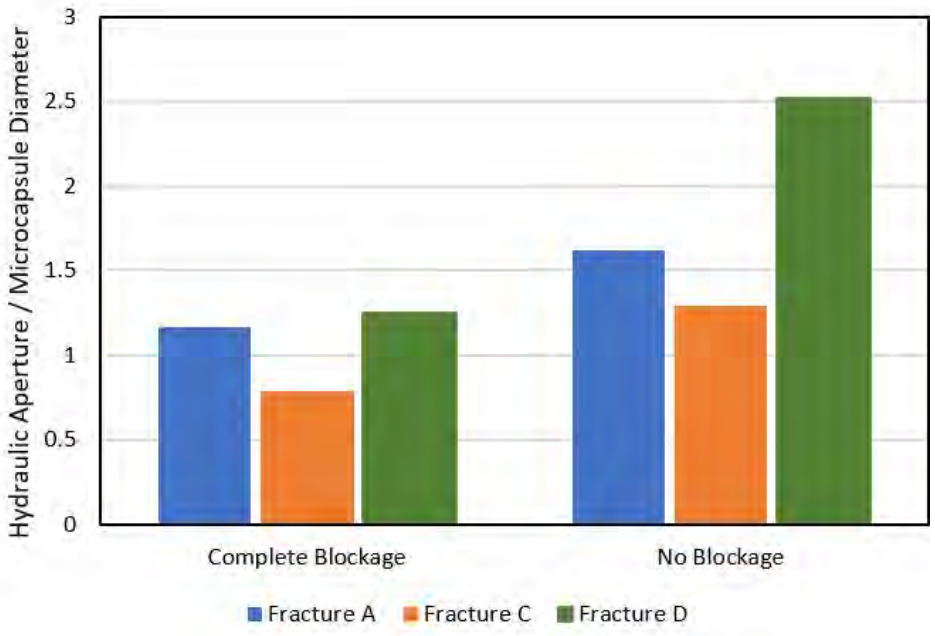

Figure 10: Hydraulic aperture to microcapsule diameter for complete and no blockage for three fractures of different roughness. Fracture C is the smoothest, followed by fracture A, and fracture D is the roughest.

5. Conclusions

Work to date has supported the concept of using a polymer injectate delivered by thermally degradable microcapsules to modify fracture permeability in geothermal wells. We have developed and tested a nano-modified Resole-Phenol co-polymer material, and have shown its properties are favorable for its use as an injectate in geothermal conditions. We have fabricated dimethacrylate derived composite microcapsules that rupture after 15 minutes at 320 °C, demonstrating cargo release as a function of time at geothermal-relevant temperatures. We have increased our understanding of microcapsule transport in rough fractures, demonstrating that the microcapsule to hydraulic aperture ratio for both complete exclusion from a fracture and free flow through a fracture with no blockage increases with the roughness of the fracture. Ongoing efforts are directed at verifying the permeability modification using the polymer in rough fractures, microcapsule survivability during injection, and tuning microcapsule release times for different temperatures.

Acknowledgement

This material is based upon work supported by the U.S. Department of Energy's Office of Energy Efficiency and Renewable Energy (EERE) under the Geothermal Technologies Office, Award Number DE-EE0009787. The views expressed herein do not necessarily represent the view of the U.S. Department of Energy or the United States Government. We acknowledge the contributions from former graduate students including Brittney Seaburn and Fatemeh Hamidi.

REFERENCES

Arriaga, L.R., Amstad, E., and Weitz, D.A.: Scalable single-step microfluidic production of single-core double emulsions with ultra-thin shells, Lab Chip, 15, (2015), 3335.

Douba, A., Genedy, M., Matteo, E., Kandil, U. F., Stormont, J., and Reda Taha, M. M., "The significance of nanoparticles on bond strength of polymer concrete to steel," International Journal of Adhesion and Adhesives, Vol. 74, pp. 77-85, 2017.

Lowry, T.S., Finger, J.T., Carrigan, C.R., Fors, A., Kennedy, M.B., Corbet, T.F., Doughty, C.A., Pye, S., and Sonnenthal, E.L., (2017), GeoVision Analysis Supporting Task Force Report: Reservoir Maintenance and Development, SAND2017-9977, Sandia National Laboratories.

Nabavi, S.A., Vladisavljević, G.T., Gu, S., and Ekanem, E.E.: Double emulsion production in glass capillary microfluidic device: parametric investigation of droplet generation behavior, Chem. Eng. Sci., 130, (2015), 183-196.

Soliman, E., Al-Haik, M., and Reda Taha, M. M., "On and off-axis tension behavior of fiber reinforced polymer composites incorporating multi-walled carbon nanotubes," Journal of Composite Materials, Vol. 46, No. 14, pp. 1661-1675, 2012.

Influence of Hydraulic Fracturing on Induced Seismicity Based on a Combined Flow and Geomechanical Model

Yuan Tian, Roland Horne

Dept. of Energy Science and Engineering, Stanford University

Keywords

Induced seismicity, hydraulic fracturing, fracture mechanics, fracture flow, EGS

ABSTRACT

This study used a combined flow and geomechanical model to investigate the important role that hydrological and mechanical properties of the stimulated hydraulic fracture played in the observed seismic sequences at the Pohang geothermal site, South Korea. According to the model, the elastic tensile stress transfer from opening of the hydraulic fracture contributed to the Mw 1.7 event that occurred around shut in. The model attributed the subsequent seismically dormant period to deactivation of the tensile stress caused by fracture closure, together with a delayed fluid pressure front. The Mw 5.5 event was explained in the model by a rapid increase in fluid pressure after arrival of the steep pressure front, which was influenced by pressure-dependent permeability in the hydraulic fracture.

1. Introduction

Induced seismicity during hydraulic stimulation in Enhanced Geothermal System (EGS) has been documented in several projects (Lee 2019, Deichmann 2009, Ellsworth 2019). The Mw 5.5 event in Pohang, Korea is the largest in EGS history resulting in huge economical loss and complete shutdown of the project. The Mw 5.5 earthquake occurred unexpectedly at the end of a seismic sequence in the final stimulation, which began with a relatively small seismic event (Mw 1.7) around shut in, which was followed by a seismically dormant period until the big Mw 5.5 event happened (Ellsworth 2019, Kim 2022). The failure of empirical relationships to constrain the maximum earthquake magnitude and the absence of small precursory seismic events to activate the mitigation strategy (the so-called traffic light system) indicates a gap in understanding of the underlying mechanisms. Therefore, there is a clear need to better understand the causal mechanisms to improve prediction and mitigation of induced seismicity.

Several mechanisms have been proposed for the observed seismic events at Pohang. A common effect shared by all the proposed mechanisms is fluid pressure (Ellsworth 2019) which suggests there was a connected hydraulic pathway between the injection well and the fault. The type of

hydraulic pathway influences the accompanying mechanisms in addition to the fluid pressure. One possibility is that the fault zone serves as the hydraulic pathway represented as a permeable porous medium for fluid to flow through. Ellsworth et al. (2019) proposed that pressure diffusion from the injection well to the fault was a key factor for the two largest seismic events in the two stimulations. Yeo et al. (2020) proposed that the combination of static shear transfer from seismic events in the previous stimulation, together with the fluid pressure, contributed to the Mw5.5 event. Chang et al. (2020) proposed that continuous poroelastic stressing accompanied with flow in the damaged zone, together with pressure diffusion, contributed to the Mw 5.5 event. For flow in permeable porous media, it is notable that both the pressure diffusion and the accompanying poroelastic stressing show a diffusive gradual evolution which could explain the occurrence of Mw 5.5 event but may not fully explain the seismically dormant period before it.

Another possibility is that the stimulated fracture served as the hydraulic pathway proposed by Kim et al. (2022). Mechanisms related to the hydraulic and mechanical properties of the stimulated fracture can provide alternative explanations for seismic events. Park et al. (2020) observed reversible and pressure-dependent permeability in the stimulated hydraulic fracture in PX-2, which contrasts to the less pressure-sensitive permeability in porous media. This pressure-dependent permeability results in a steeper pressure front compared to the smoother and more diffusive pattern in media with pressure-insensitive permeability such as a porous medium, which was analyzed in Hummel et al. (2009). The steep pressure front can result in a drastic increase in pressure after the arrival at the fault, which may shorten the time for fault slip to evolve into a large earthquake. Besides, the induced stress field associated with the deformation of the stimulated fracture can also perturb the in-situ stress of the fault and influence the pattern of seismic events. Kim et al. (2022) proposed that shear stress transfer from the hydroshearing fracture in PX-1 well could have contributed to the seismically silent period during PX-1 stimulation. It is possible that the tensile stress associated with the opening of the hydraulic fracture could also influence the induced seismicity in EGS although this has not yet been fully investigated for the case of Pohang. Evidence of the influence of tensile opening on perturbation of in-situ stress includes seismic anisotropy (Igonin et al., 2022) and the spatial-temporal distribution of seismic events (Kettlety et al., 2019). Therefore, further study is needed to better understand the role of tensile stress from fracture opening on seismic events in EGS.

We investigated the role that hydrological and mechanical properties of the stimulated hydraulic fracture may have played in the seismic sequences during the third stimulation in PX-2. The modelling results indicate that tensile stress transfer from the opening of the hydraulic fracture could have contributed to the relatively small seismic event (Mw 1.7) around the time of shut-in. The subsequent seismically dormant period can be explained by the deactivation of tensile stress because of fracture closure and the delayed arrival of the pressure front. The final large earthquake (Mw 5.5) could be attributed to a rapid increase in pressure once the pressure front arrived at the fault.

2. Problem formulation

This work investigated the influence of the hydraulic fracture in PX-2 well on the seismic sequence during the third stimulation where the large Mw 5.5 earthquake occurred with a two-month delay after the shut in. PX-2 is characterized as a hydraulic-jacking dominated well (Min et al. 2023) with the maximum wellhead pressure up to 90MPa, exceeding the minimal principal stress of

64MPa shown in Figure 1 (left). The third stimulation in PX-2 began in September 2017 with 2335 m^3 water injected. Figure 1 (right) shows the history of injection-volume and observed seismic events. An initial Mw 1.7 event happened around shut in, followed by a seismically dormant period with no detected seismic events. The Mw 5.5 earthquake then happened suddenly without observable increase in smaller precursory seismic events.

The conceptual figure of the model used to investigate the influence of hydraulic fracturing on induced seismicity is shown in Figure 2, which is based on the configuration of PX-2 injection well and the Mw 5.5 fault at Pohang. The stimulated fracture plane represents the hydraulic jacking dominated fracture in PX-2 which can intersect with a fault nearby. The blue point represents the injection well in PX-2 and the red point represents the fault which is 153m from the injection point. During the injection period, fluid pressure propagates towards the fault. The region around the injection point is under higher pressure and can induce opening when the fluid pressure exceeds the minimum principal stress. The induced tensile stress field associated with the opening can influence the stress field and perturb the in-situ stress of a fault nearby. Two contributions to the perturbation of the in-situ stress on fault are considered. One is fluid pressure which is active after the pressure front arrives. The other is tensile elastic stress transfer due to fracture opening as a long-range effect.

Figure 3 shows a flow chart of the modelling procedure. Based on the input injection strategy and hydrological parameters of the stimulated fracture, transient fluid pressure can be computed in the two-dimensional flow model. The pressure result is treated as an input into the fracture mechanics model to compute the tensile stress field away from the open hydraulic fracture. The total decrease of normal stress on fault is the sum of the tensile stress and the fluid pressure. The decrease is treated as input into the seismicity model, where slip evolution is computed as an indicator for seismic sequences.

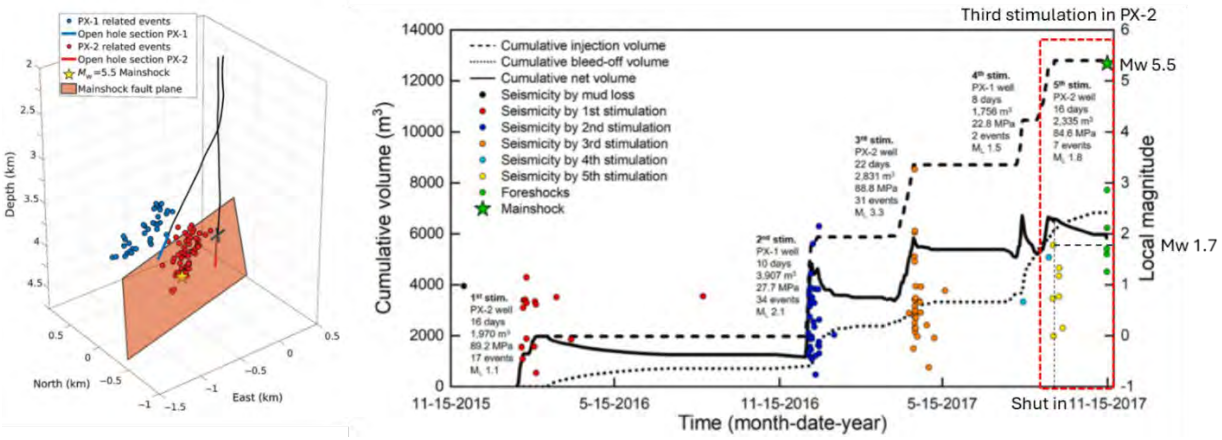

Figure 1: Configuration of PX-2 well and the Mw 5.5 fault (left) and history of injection volume and observed seismic events (right) in Kim et al. 2022

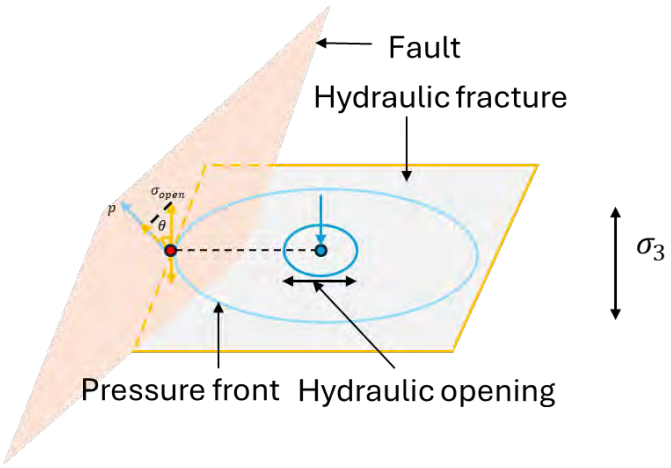

Figure 2: Induced seismicity on fault caused by the stimulated hydraulic fracture

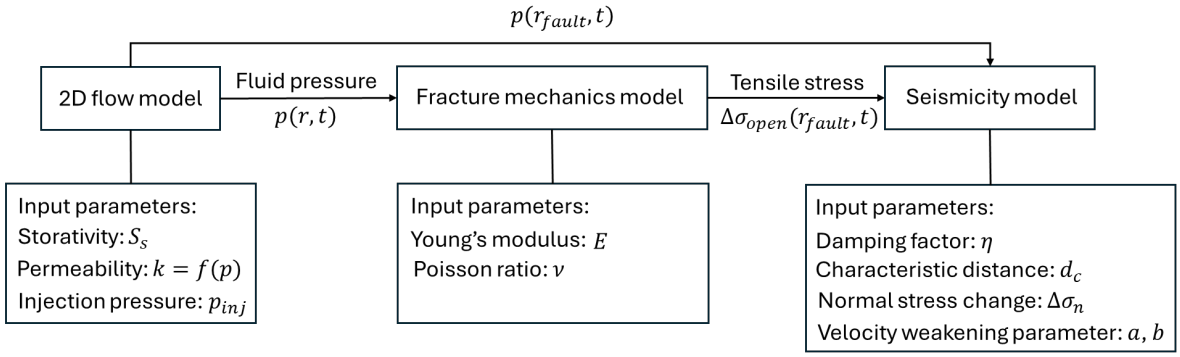

Figure 3: Flow chart of the modelling procedure: combine a flow model and a geomechanical model

2.1 Fluid flow: pressure diffusion in fracture

In Enhanced Geothermal Systems, fractures generally have larger permeability than the basement rock and are expected to become the dominant flow pathways. The permeability of fractures is dependent on the fracture aperture as described by the so-called cubic law in Witherspoon et al. (1980), which is influenced by effective stress on the fracture plane. This results in pressure-dependent permeability in fractures. Park et al. (2020) observed that the permeability of the stimulated fracture in PX-2 well showed nonlinear and reversible changes with wellhead pressure as shown in Figure 3 (left). When the wellhead pressure exceeds the minimal principal stress (around 60MPa), the aperture increases more rapidly. Hummel et al. (2009) analyzed the difference in pressure distribution under pressure-dependent permeability and constant permeability, showing that the pressure-dependent aperture combined with the cubic law results in a steeper pressure front compared to the smoother and more diffusive pressure distribution in the case of constant permeability. Therefore, it is necessary to account for the pressure-dependent permeability in fracture flow to obtain a more accurate pressure distribution. In this work, pressure-dependent permeability was considered based on the observed relationship between permeability and wellhead pressure in well PX-2.

2.1.1 Governing equations

The pressure diffusion equation is:

$$\rho S \frac{\partial p}{\partial t} = \nabla \left(\frac{\rho k}{\mu} \nabla p \right) + q_m \tag{1}$$

where $\rho(kgm^{-3})$ is fluid density, $S(Pa^{-1})$ is the specific storage coefficient, $k(m^2)$ is permeability, $\mu(Pa \cdot s)$ is fluid viscosity and $q_m(kgm^{-3}s^{-1})$ is a mass source. The permeability and the aperture-pressure relationship is expressed as:

$$k = \frac{b^2}{12} \tag{2}$$

$$b = b_0 e^{d_0 p} \tag{3}$$

$$k = f(p) = \frac{{b_0}^2 e^{2d_0 p}}{12} \tag{4}$$

2.1.2 Model settings

Figure 4 shows the geometry of the flow model used to simulate the two-dimensional radial flow on the stimulated fracture plane. The model geometry is a square in Figure 1(left) with fluid injected into the element in the center. Only the overpressure caused by injection is modelled and formation pressure is ignored. Initial pressure is 0MPa. It should be noted that the boundary condition at the injection point represents the wellbore. The wellbore condition used in the work is a simplification of the actual injection history. In the model, constant pressure control was used, and the injection pressure was fixed at 90MPa during injection, which was the maximum wellhead pressure during stimulation in PX-2. In future modeling, the real injection history will be implemented and a detailed calibration on the flow model parameters will be done by matching the wellhead pressure history given the injection rate history.

The aperture-pressure relationship can be matched with the observation data in Park et al. (2020) shown in Figure 3 (left) by an exponential function described in Rutqvist et al. (2003) shown in Figure 3 (right). The pressure-dependent permeability relationship is used in the flow model. Figure 3 (right) shows that permeability of the PX-2 fracture varies over three orders of magnitude from 10^{-12} to 10^{-8} m^2 from 0 to 90 MPa.

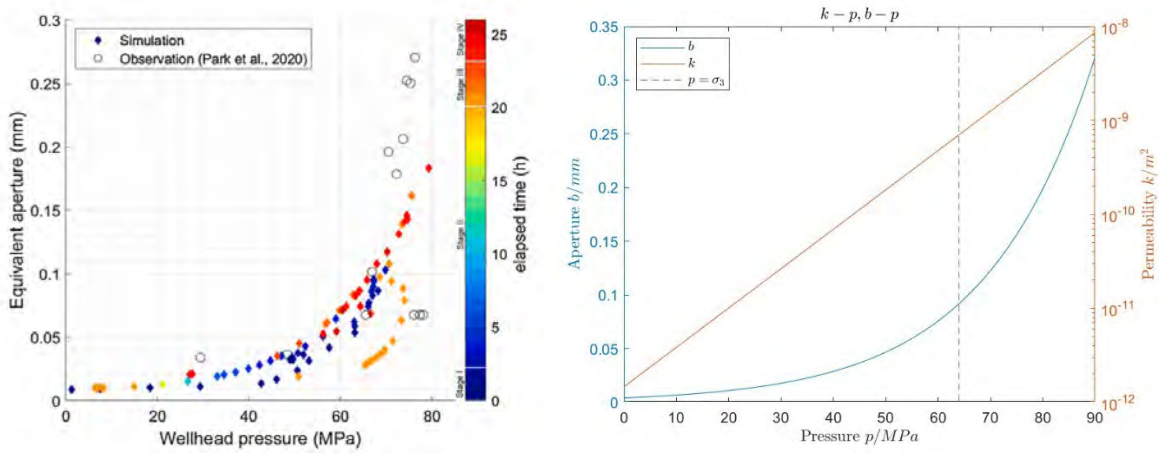

Fig 3: Observation on aperture-wellhead pressure relationship in PX-2 well (left) in Park et al. 2020, permeability-pressure and aperture-pressure relationship used in the simulation (right)

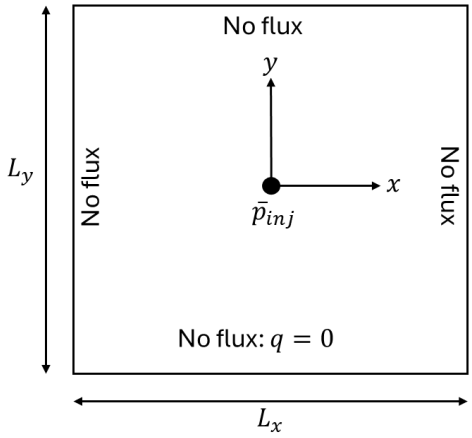

Fig 4: Flow model: geometry and boundary condition

Table 1: Parameter settings in the fluid flow model

Parameter	Value
Storage coefficient S	0.1
Initial aperture b	0.0042 mm
Curvature of aperture- pressure relationship d_0	0.0482 MPa^{-1}
Fluid viscosity	0.001 $Pa \cdot s$
Fracture length L_x, L_y	720 m
Injection pressure $\bar{p}_{inj}$	90 MPa
Duration of injection time t_{inj}	31200 s
Total time t_{end}	62400 s

2.1.3 Model limitations and future work

A key limitation of the current work is how well the spatial-temporal fluid pressure distribution produced by the fluid flow model represents the actual conditions at Pohang. As the first step in the modelling procedure shown in Figure 2, the accuracy of the fluid pressure results directly influences two factors contributing to the seismicity on fault: fluid pressure and tensile stress. Fluid pressure is influenced by hydrological properties (storativity coefficient, permeability), fracture length (model size) and injection strategy (boundary condition on the injection point). In this study, a simplified input injection strategy with an injection period and a subsequent shut in period was used. In comparison, the real scenarios at Pohang involved multiple cycles of injection and shut-in known as the cyclic injection, evidenced by the periods of stable injection volume shown in the injection volume-time data in Kim et al. (2022). Besides, model parameters including the hydrological properties and the fracture length need to be constrained by the output pressure at the injection point to match the wellhead pressure history observed in Pohang.

2.2 Fracture mechanics: Tensile stress caused by fracture opening

Based on the fluid pressure, the region where pressure is larger than the minimal principal stress σ_3 is identified as hydraulic opening segments The fracture opening, denoted as $[u]_n$, is assumed to develop under net pressure as p_{net} which is the difference between the fluid pressure and the minimal principal stress. The elastic opening is associated with a tensile stress field extending beyond the opening segments, which perturbs the stress field in the surrounding rock and influences the in-situ stress on a fault nearby.

2.2.1 Governing equations

Within the open hydraulic fracture $r < R_{open}(t)$ where r denotes the distance away from the injection point, the fracture opening can be related to the net pressure acting as the normal traction by the force equilibrium of rock with embedded displacing fractures. Because shear stress is assumed to be zero in the open fracture, the force equilibrium in three directions can be simplified to only in the normal direction shown in Eq. (5). The interaction coefficient matrix **C** relates the normal discontinuity (opening) and the normal traction on the fractures. The matrix is influenced by the fracture geometry and the mechanical properties of the rock as Young's modulus and Poisson's ratio. In this work, **C** was computed using the open-source Displacement Discontinuity Method code (DDFS) developed by Wong et al. (2021).

$$\boldsymbol{C}[\boldsymbol{u}]_n = \boldsymbol{p}_{net} \tag{5}$$

$$\boldsymbol{p}_{net}(t) = \boldsymbol{p} - \sigma_3 \tag{6}$$

For the region beyond the open hydraulic fracture $r > R_{open}(t)$, the stress field is influenced by the elastic tensile stress associated with the hydraulic opening fracture.

$$\sigma_{open}(r,t) = -\frac{E}{(1-\nu^2)4\pi}\int_0^{R_{open}(t)} \frac{\partial [u]_n(s,t)}{\partial s}\frac{sds}{r-s} \tag{7}$$

Based on the radius of the hydraulic fracture R_{open} and the net pressure inside $p_{net}(r)$ in the two-dimensional radial flow model, the tensile stress caused by the hydraulic opening beyond the hydraulic fracture $\Delta\sigma_{open}(r,t)$ can be obtained from the fracture mechanics model. The tensile stress $\Delta\sigma_{open}$ is perpendicular to the stimulated fracture and parallel to the minimal principal stress σ_3. r refers to the distance from the injection point.

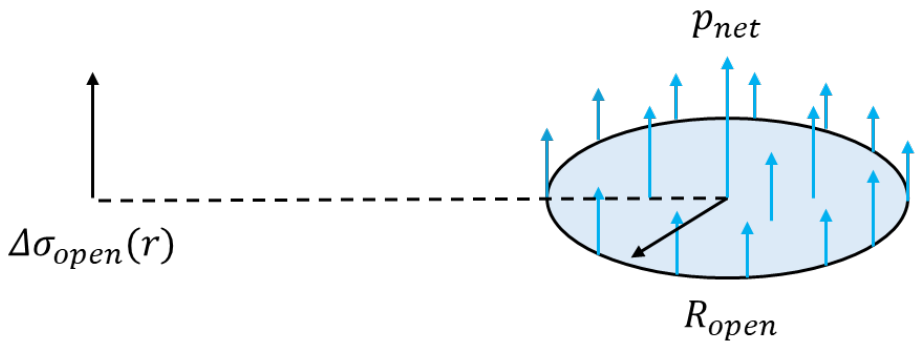

Fig 5: Tensile stress on associated with the opening of the hydraulic fracture

2.2.2 Model settings

A two-dimensional fracture plane embedded in the infinite elastic rock is modelled to simulate the opening in the open segments and the tensile stress beyond the opening fracture. Inside the radius of the open hydraulic fracture, the fracture opens up in the normal direction of the plane under the net pressure distribution. Tensile stress associated with the opening is computed based on the distance from the injection point.

Table 2: Parameter settings in the fracture mechanics model

Parameter	Value
Fracture radius R_{open}	Based on p
Net pressure distribution p_{net}	Based on p
Young's modulus	0.0482 MPa^{-1}
Poisson ratio	0.001 $Pa \cdot s$

2.3 Induced seismicity

From observations, induced seismicity often occurs as a series of seismic sequences. When in-situ stress of a fault is perturbed, the slip velocity and shear stress on the fault evolve in stages including nucleation, rupture propagation, rupture arrest and fault restrengthening. The rate-and-state friction model (Dieterich et al., 1992) is one of the commonly used constitutive models for friction coefficient, which can effectively capture the fault frictional behavior in induced seismicity (McClure et al., 2011).

2.3.1 Governing equations

$$\tau - \eta v = f(v,\theta)\sigma_n \tag{8}$$

$$\sigma_n = \sigma_n^0 - \Delta\sigma_n = \sigma_n^0 - \sigma_{open} - p \tag{9}$$

$$f(v,\theta) = f_0 + alog\frac{v}{v_0} + blog\frac{\theta}{\theta_0} \tag{10}$$

$$\frac{d\theta}{dt} = 1 - \frac{\theta v}{d_c} \tag{11}$$

The evolution of shear stress (τ) and slip velocity (v) in a seismic cycle under quasi-dynamic equilibrium can be described by Eq. (8). η is the damping factor accounting for the energy dissipation in slip. $f(v,\theta)\sigma_n$ is the shear resistance based on the normal stress σ_n. In the rate-and-state friction model, the friction coefficient depends on the slip velocity v and state variable θ described in Eq. (10). The state variable considers the influence of slip history described in Eq. (11). In this work, induced seismicity was assumed to be driven by a decrease of normal stress ($\Delta\sigma_n$) which includes contribution from the tensile stress from opening (σ_{open}) and fluid pressure (p).

2.3.2 Model settings

In this work, the fault was simplified to a single point at the intersection with the stimulated fracture, shown as a single red point in Figure 2. The evolution of slip velocity at the point driven by perturbation on normal stress of fault $\Delta\sigma_n$ was modelled to indicate the observable seismic magnitude. Eq. (8) to -Eq. (11) are solved using a third-order Runge-Kutta method (McClure 2011, Noda 2009, Ozawa 2023).

Table 3: Parameter settings in the seismicity model

Parameter	Value
Reference friction coefficient f_0	0.6
Reference slip velocity v_0	$10^{-6}\,m/s$
Direct effect parameter a	0.01
State evolution parameter b	0.013
State evolution distance d_c	$0.0015m$
Radiation damping coefficient η	50MPa·s/m
Stiffness	2.5MPa/m
Initial shear stress τ_0	60MPa
Initial normal stress σ_{n0}	99.5MPa
Initial state variable θ_0	0.6

3. Results and discussion

3.1 Transient pressure with pressure-dependent permeability

Figure 6 shows the pressure distribution in one dimension with the pressure-dependent permeability at the time of shut in and at the end of the simulated time. Figure 8 and Figure 9 show

the pressure and permeability distribution in two dimensions. A steep pressure front is observed in Figure 6 where the pressure changes rapidly within a small distance. Inside the pressure front, pressure is relatively high and close to the injection pressure. However, pressure drops to almost zero beyond the front. For comparison, the pressure distribution under constant permeability is shown in Figure 7 with high and low permeability levels. In the constant permeability case, pressure shows a smoother diffusive pattern. In addition, the pressure decrease around the injection point is more distinct compared to the pressure-dependent permeability case.

Based on the pressure distribution in the pressure-dependent permeability case, the length of the opening fracture which initiates around the injection point grows during injection. However, the length of the opening hydraulic fracture is smaller and almost zero under both constant high and low permeability cases shown in Figure 7 because of the large pressure drop around the injection point. After shut in, the pressure front under pressure-dependent permeability keeps going forward which is still steeper than constant permeability but smoother than during injection. For places far away from the injection point, it is possible that the fluid pressure front arrives after shut in and causes a large pressure increase.

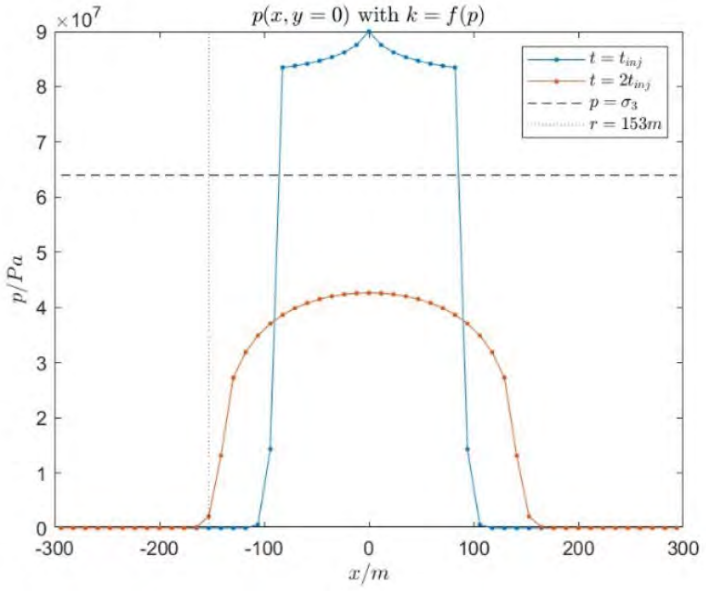

Fig 6: Fluid pressure on $y = 0$ at $t = t_{inj}$ and $t_{end} = 2t_{inj}$: pressure-dependent permeability

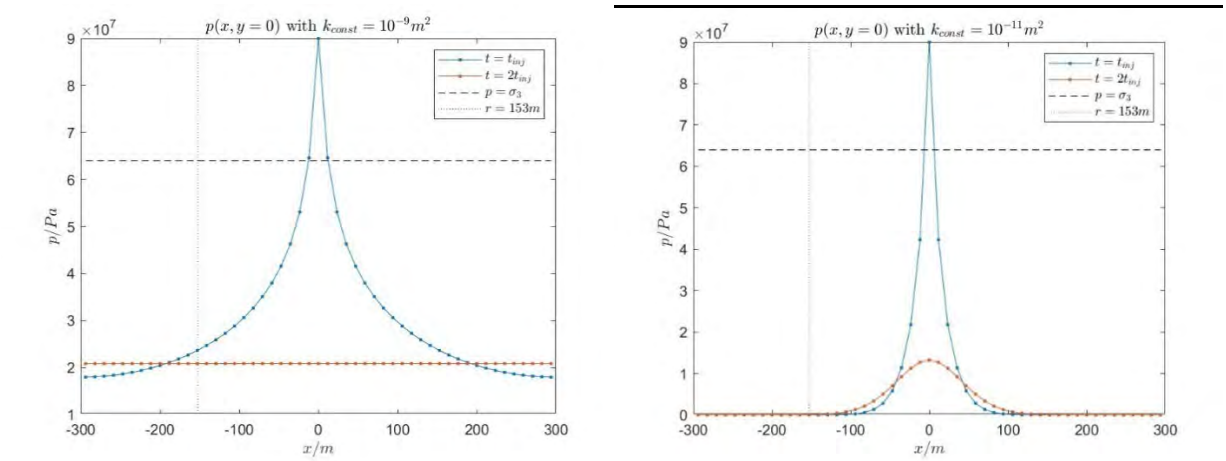

Fig 7: Fluid pressure on $y = 0$ at $t = t_{inj}$ and $t_{end} = 2t_{inj}$: constant permeability

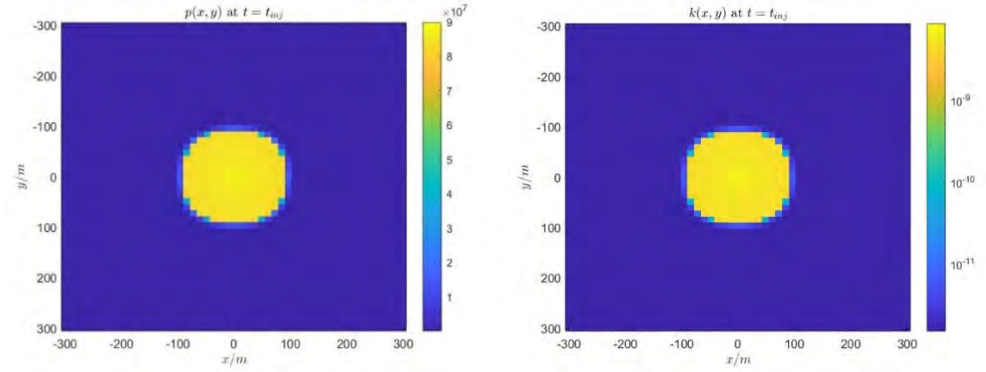

Figure 8: Fluid pressure and permeability on the fracture plane at $t = t_{inj}$: pressure dependent permeability

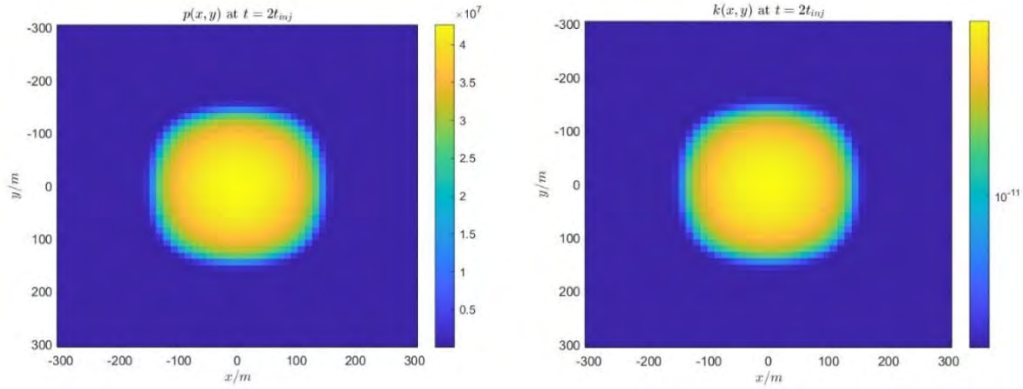

Figure 9: Fluid pressure and permeability on the fracture plane at $t_{end} = 2t_{inj}$: pressure dependent permeability

3.2 Tensile stress accompanied with opening in hydraulic fracture

Figure 10 shows the net pressure distribution within the open hydraulic fracture and the tensile stress beyond the fracture associated with the fracture opening. The tensile stress decreases with

distance away from the injection point in 1/r order. It has been noted that earthquake events can be triggered on critically stressed faults when the perturbation in normal stress on the fault reaches 0.01MPa (Ellsworth et al., 2019). In Pohang, the net pressure at the wellhead can reach up to 20 MPa. Based on the injection strategy used in this work, Figure 10 (right) shows that σ_{open} can exceed 0.01MPa when $r/R_{open} < 2$. This suggests that tensile stress can contribute significantly to the total change in normal stress change if the fault is located inside a region with a specific distance from the injection point. The distance from the PX-2 well and the activated Mw5.5 fault ranges around 200m. The fault was represented as a single point located at $r = 153m$ in the work.

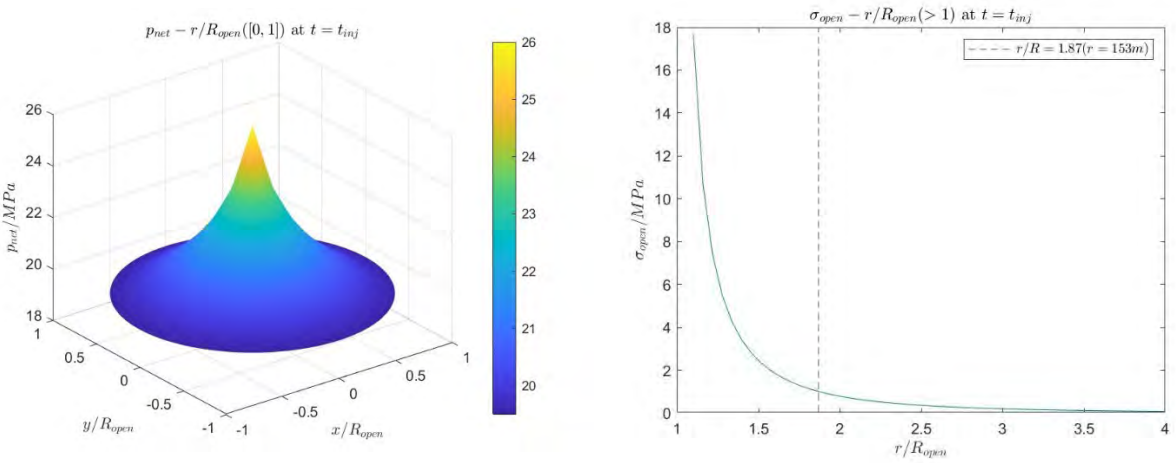

Figure 10: Tensile stress σ_{open} with distance away from the injection point r (left), net pressure p_{net} inside the hydraulic open fracture (right)

Figure 11 shows the evolution of the tensile stress and fluid pressure at the fault where $r = 153m$. Two key contributions to the total normal stress change on a fault include the tensile stress σ_{open} and the fluid pressure p. The simulated period can be divided into four stages based on the activation of the two sources.

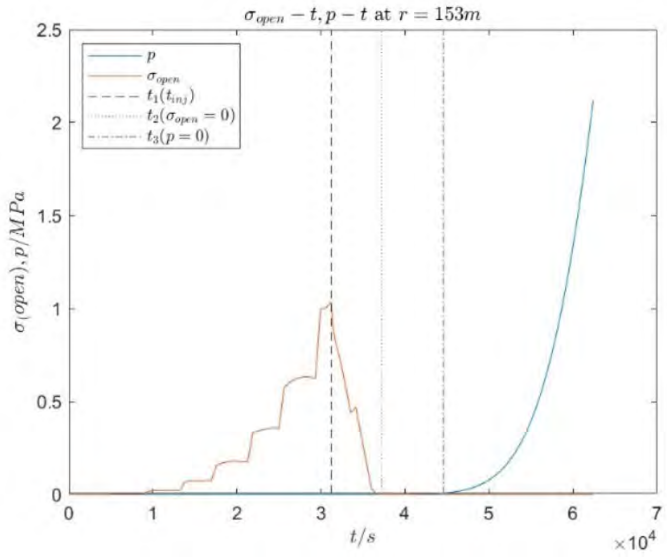

Figure 11: Tensile stress σ_{open} and fluid pressure p with time on the fault ($r = 153m$)

During the first stage from $t = 0 \sim t = t_1(t_{inj})$, only the tensile stress σ_{open} is prominent. The magnitude of σ_{open} increases with time because of the lengthening of opening fracture and reaches a peak around 1MPa at t_1 before injection stops at shut-in. Fluid pressure has not reached to the fault and the contribution from p is inactive. The second stage occurs from $t_1(t_{inj})$ to $t_2(\sigma_{open} = 0)$ during which σ_{open} decreases to zero in a short time after shut-in. After shut-in, the pressure around the injection point drops significantly and falls below σ_3. This pressure drop leads to the closure of the open hydraulic fracture and leads to inactivation of the tensile stress. The third stage ranges from $t_2\big(\sigma_{open} = 0\big)$ to $t_3(p = 0)$ during which both σ_{open} and p are inactive. The fourth stage occurs from $t_3(p = 0)$ to t_{end}. During that stage, the pressure front reaches the fault, causing a rapid rise in fluid pressure p over a short period. The maximum p is 2MPa reached by the end of the simulated time.

Based on the injection strategy, geological parameters in hydrology and mechanics, and fault location assumed in this work, the contributions of fluid pressure p and tensile stress σ_{open} on fault were active at different times throughout the stimulation. The tensile stress σ_{open} becomes active sooner than pressure p because of the long-range character of elastic stress transfer which outpaces the transport of the pressure front.

At the start, only tensile stress σ_{open} is active until around the time of shut-in, reaching its maximum value at the shut-in. Shortly after the shut-in, σ_{open} decreases to zero as the hydraulic opening closes. There is an interval between $t_2\big(\sigma_{open} = 0\big)$ and $t_3(p = 0)$ where both σ_{open} and p are inactive. Eventually, the pressure front arrives after some delay after shut-in causing a rapid increase in p. The maximum pressure is reached at the end of simulated time with a magnitude twice that of the maximum tensile stress.

3.3 Evolution of slip velocity on the fault

The tensile stress accompanying the hydraulic opening σ_{open} , together with the fluid pressure p contributes to the total decrease of normal stress on fault $\Delta\sigma_n$ as shown in Figure 12. Considering that the $M_w 5.5$ fault of Pohang seems to have been in a critical state (Ellsworth et al., 2019), the in-situ stress at the point representing the fault in this work was also assumed to be in a critical state. At this point, the initial shear stress τ_0 is balanced with the product of the static friction coefficient f_0 and the initial normal stress as σ_{n0}. When the normal stress decreases, it triggers the onset of a seismic cycle, with the evolution of slip velocity shown in Figure 13.

In Figure 13, slip velocity starts to increase as the injection starts, driven by the rising $\Delta\sigma_n$ contributed by the tensile stress from opening σ_{open}. A local peak in slip velocity is reached at the time of shut-in, coinciding with the maximum $\Delta\sigma_n$, which may indicate the occurrence of a small seismic event. Although the increase in slip velocity happens after the pressure surge upon arrival of the pressure front, the slip velocity spikes with four orders of magnitude increase from 10^{-6} m/s to 10^{-2} m/s over a short time, which could suggest the occurrence of a large earthquake at the end of the simulated time, considerably later than the shut-in.

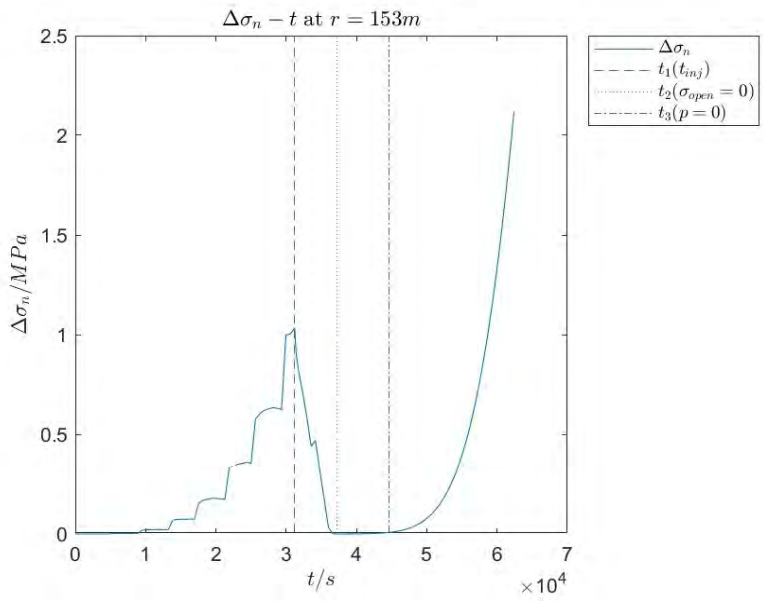

Figure 12: Total decrease in normal stress with time on $r = 153m$

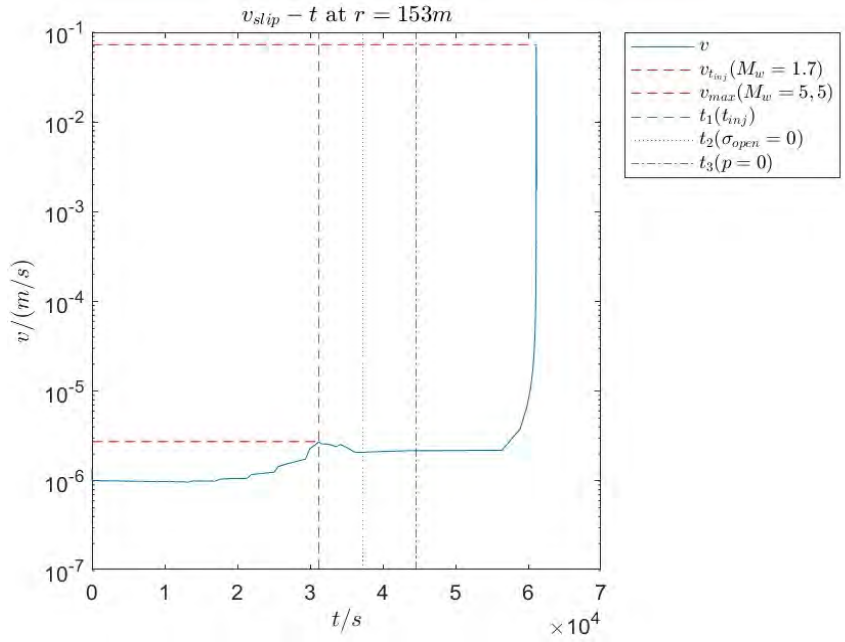

Figure 13: Slip velocity with time under the total decrease in normal stress on $r = 153m$

3.4 Discussion on the proposed alternative mechanism for seismic events in Pohang compared with the existing mechanisms

This work investigated the influence of stimulated hydraulic fractures in well PX-2 on the seismic events observed in the third stimulation of well PX-2. During the stimulation, a small seismic event Mw 1.7 was observed around the shut-in time, followed by a seismically dormant period before a large seismic event Mw 5.5 that occurred two months after the shut-in.

The combined effects of the mechanical and flow properties of the hydraulic fracture could be an alternative mechanism explaining the observed seismic events. Tensile stress transfer from the opening of the hydraulic fracture initiates the slip contributing to the Mw 1.7 event around shut-in, which is shown as a local velocity peak in Figure 13. Tensile stress becomes inactive shortly after shut in due to the fracture closure resulting from the pressure drop. The fluid pressure pattern, which is influenced by the pressure-dependent permeability of the stimulated hydraulic fracture, accounts for both the seismically dormant period and the occurrence of the Mw 5.5 earthquake later. The spatial distribution of pressure shows a steep pressure front under the pressure-dependent permeability condition compared with the smoother, more diffusive pressure pattern under the constant permeability condition. Before the pressure front arrives, the fluid pressure remains inactive which contributes to the seismically dormant period shown as relatively low slip velocity. The rapid increase in fluid pressure after the arrival of the front contributes to the delayed large Mw5.5 earthquake shown as a spike in slip velocity.

Several mechanisms have been proposed to account for the observed seismic events in Pohang during alternative stimulation between the two wells and cyclic stimulation in a single well. The proposed alternative mechanism shares some similarities with these existing mechanisms but also differs in both the mechanism and the specific time range of the seismic events it focuses on. A common mechanism shared by all the mechanisms is the fluid pressure, which assumes a connected hydraulic pathway between the injection point and the fault. Different types of the assumed hydraulic pathway result in different accompanying mechanisms besides fluid pressure.

On one hand, the hydraulic pathway can be provided by the fault zone, with fluid flowing from the injection point to fault through a permeable porous medium with either homogeneous or heterogeneous permeability. Studies by Yeo et al. (2020) and Ellsworth et al. (2019) considered a fault zone with heterogeneous permeability, characterized by a high-permeability damaged zone around the injection point and a low-permeability fault core. The damaged zone facilitates pressure propagation from the injection point, while the fault core slows down the diffusion around the fault. Ellsworth et al. (2019) shows that fluid pressure on the fault which is hundreds of meters away from the injection point can reach the level capable of triggering the earthquakes and the pressure can persist months after the injection period. This pressure behavior contributed to the Mw 3.4 event and the delayed Mw 5.5 event later associated with the PX-2 well. Yeo et al. (2020) proposed that static shear transfer from the Mw 3.4 event in the previous stimulation, combined with fluid pressure, contributed to the delayed Mw 5.5 event. Chang et al. (2020) assumed a constant permeability fault zone and proposed that the continuous poroelastic stressing under alternate stimulation between two wells, together with pressure diffusion along the fault, contributed to the Mw 5.5 event.

Another possibility is that the stimulated fracture serves as the hydraulic pathway connecting the injection point and the fault (Min et al., 2022). Mechanisms related to the hydraulic and mechanical properties of the stimulated fracture can provide alternative explanations for seismic events. A decrease in permeability after shut in as a result of the pressure-dependent permeability could slow down pressure diffusion and contribute to the delayed Mw 5.5 event after shut-in of PX-2. Additionally, shear stress transfer caused by hydroshearing fractures in well PX-1 decreases shear stress on part of the fault contributing to the seismic dormancy during PX-1 injection.

This work assumed that the stimulated hydraulic fracture in PX-2 connects the injection point and the fault. Based on this assumption, the results suggest that the tensile stress transfer from the

hydraulic opening and the fluid pressure under the pressure-dependent permeability could serve as an alternative mechanism accounting for the seismicity sequences observed during the third stimulation of PX-2.

4. Conclusions

This study proposes an alternative mechanism explaining the observed seismic sequences during the third stimulation of well PX-2 at Pohang, focusing on the role of stimulated hydraulic fracture. Distinct observations of seismicity include a relatively small seismic event (Mw 1.7) around shut-in, followed by a seismically dormant period until the larger seismic event (Mw 5.5) happened long after shut-in. In the model, the Mw 1.7 event was attributed to the tensile stress transfer from the opening in hydraulic fracture before injection stops. The subsequent seismically dormant period was explained by deactivation of the tensile stress due to fracture closure after shut-in, together with the delayed arrival of fluid pressure front. The Mw 5.5 event is explained by a rapid increase in pressure after the arrival of the steep pressure front caused by the pressure-dependent permeability in the stimulated fracture.

REFERENCES

Chang KW, Yoon H, Kim YH, Lee MY. (2020). " Operational and geological controls of coupled poroelastic stressing and pore-pressure accumulation along faults: induced earthquake in Pohang, South Korea." *Nature Communications.*

Deichmann N, Giardini D. (2009). "Earthquakes induced by the stimulation of an enhanced geothermal system below Basel (Switzerland)." *Seismological Research Letters*.

Dieterich JH. (1992). "Earthquake nucleation on faults with rate-and-state dependent friction." *Tectonophysics*.

Ellsworth WL, Giardini D, Townend J, Ge S, Shimamoto T. (2019). "Triggering of the Pohang Korea, earthquake (Mw 5.5) by enhanced geothermal system stimulation." *Seismological Research Letters*.

Hummel N, Muller T. (2009). "Microseismic signatures of non-linear pore-fluid pressure diffusion." South Korea." *Geophysical Journal International.*

Igonin N, Verdon JP, Eaton DW. (2022). "Seismic anisotropy reveals stress changes around a fault as it is activated by hydraulic fracturing." *Seismological Research Letters.*

Kettlety T, Verdon JP, Werner MJ, Kendall JM. (2020). "Stress transfer from opening hydraulic fractures controls the distribution of induced seismicity." *Journal of Geophysical Research.*

Kim H, Park YS, Yim J, Xie LM, Min K, Rutqvist J. (2022) "Induced and triggered seismicity by immediate stress transfer and delayed fluid migration in a fractured geothermal reservoir at Pohang, South Korea." *International Journal of Rock Mechanics and Mining Sciences.*

Lee K, Ellsworth WL, Giardini D et al. (2019). "Managing injection-induced seismic risks The Pohang quake shows the need for new methods to assess and manage evolving risk." *Science*.

McClure MW, Horne RN. (2011). "Investigation of injection-induced seismicity using a coupled fluid flow and rate/state friction model." *Geophysics*.

Min KB, Park S, Kim KI, Yoo H, Kwon S, Yim J, Rutqvist J. (2023). "Findings and lessons learnt from hydraulic stimulations for Pohang Enhanced Geothermal Systems project." *In: 48th Workshop on Geothermal Reservoir Engineering. Stanford, California, USA.*

Noda H, Dunham E, Rice J. (2009). "Earthquake ruptures with thermal weakening and the operation of major faults at low overall stress levels." *Journal of Geophysical Research: Solid Earth.*

Ozawa S, Ida A, Hoshino T, Ando R. (2023). "Large-scale earthquake sequence simulations of 3D geometrically complex faults using the boundary element method accelerated by lattice H-matrices." *Geophysical Journal International.*

Park S, Kim KI, Xie L, Yoo H, Min KB, Kim M, Yoon B, Kim KY, Zimmermann G, Guinot F, Meier P. (2020). "Observations and analyses of the first two hydraulic stimulations in the Pohang geothermal development site, South Korea." South Korea." *Geothermics.*

Rutqvist J, Tsang CF. (2003). "Analysis of thermal-hydrologic-mechanical behavior near an emplacement drift at Yucca Mountain." *Journal of Contaminant Hydrology.*

Witherspoon PA, Wang JSY, Iwai K, Gale JE. (1980). "Validity of cubic law for fluid flow in a deformable rock fracture." *Water Resources Research.*

Wong L, Cui X. (2021). " DDFS3D: A set of open-source codes leveraging hybrid 3D displacement discontinuity method and fictitious stress method to simulate fractures." *Engineering Analysis with Boundary Elements.*

Yeo IW, Brown MRM, Ge S, Lee KK. (2020). "Causal mechanism of injection-induced earthquakes through the Mw 5.5 Pohang earthquake case study." *Naure Communications.*

Analysis of the Stimulated Volume and Seismicity Migration in Utah FORGE Stimulations

Zhi Ye[1,2] and Ahmad Ghassemi[1]

1. **Reservoir Geomechanics and Seismicity Research Group, University of Oklahoma**

2. **Now at Department of Geology and Geological Engineering, South Dakota Mines**

Keywords

FORGE EGS, Natural fracture, Fracture Shearing Growth, SRV, Induced Seismicity

ABSTRACT

In April 2022 and July 2023, a series of hydraulic stimulation and fluid circulation experiments were executed at the Utah FORGE injection well 16A(78)-32, accompanied by high-resolution seismic monitoring. These experiments have shown a consistent pattern of upward migration in seismic cloud development, indicating the ascendant propagation of both hydraulic fractures (HF) and natural fractures (NF) upon fluid injection. Building on our prior numerical simulations, the results have demonstrated that the upward growth of hydraulic fractures may interact with natural fractures leading to a more complex stimulated reservoir volume (SRV) consisting of a HF/NF network (Kumar, Liu, & Ghassemi, 2023). In this study, we performed a theoretical analysis to further analyze fracture propagation behavior in response to fluid injection in Utah FORGE. Leveraging rock properties derived from FORGE core samples, in-situ stress assessments from borehole image logs (Ye et al., 2022; Ye & Ghassemi, 2024), and stochastic fracture set orientations within the Utah FORGE context (Finnila & Jones, 2024), our investigation aimed to analytically evaluate the growth of the SRV and fracture evolution. Our findings indicate that fracture set 2 (South-striking, moderately dipping West) and fracture set 4 (East-striking, sub-vertical dipping South) are likely to be among the first to slip and propagate during fluid injection. Additionally, our analysis reinforces the dominance of upward fracture migration as the primary propagation mechanism within the FORGE stimulations. We also discuss the results with reference to the hydroshearing conceptual model and its implications for SRV size and geometry.

1. Introduction

Enhanced geothermal systems (EGS) are proposed as a solution to unlock the vast potential of geothermal energy from hot-dry rocks at depth, which are typically deficient in water and permeability. Despite nearly a dozen EGS field demonstrations conducted worldwide since the 1970s, fundamental technical barriers persist, limiting the large-scale commercial production of

geothermal energy. The Utah FORGE project, sponsored by the U.S. Department of Energy (DOE), aims to develop and test new technologies for characterizing, creating, and sustaining continuous fluid flow and energy transfer within an EGS reservoir (Moore et al., 2020). At Utah FORGE, a pair of highly deviated wells were drilled for injection (well 16A(78)-32) and production (well 16B(78)-32). Hydraulic stimulations were conducted, and may continue to be conducted, to create an EGS system in granitoid rocks with bottom-hole temperatures near 230 °C.

The EGS reservoir rocks at Utah FORGE are characterized by an abundance of natural fractures of varying scales and sizes, identified as four major sets through borehole image logs and core samples (Finnila & Jones, 2024). During pressurized fluid injection for stimulation, these natural fractures play a critical role in influencing reservoir permeability and induced seismicity. In April 2022 and 2024, a series of hydraulic stimulation experiments were conducted at the injection well 16A(78)-32, accompanied by high-resolution seismic monitoring. These experiments consistently demonstrated an upward migration pattern in seismic cloud development, indicating the ascendant propagation of both hydraulic and natural fractures upon fluid injection. Moreover, the complex geometry of the seismic clouds further suggests a stimulated reservoir volume likely involving interactions between hydraulic and natural fractures. Building on our prior numerical simulations, the results indicate that the upward growth of hydraulic fractures may interact with natural fractures, leading to a more complex SRV comprising a hydraulic fracture/natural fracture (HF/NF) network (Kumar, Liu, & Ghassemi, 2023).

The shear stimulation or hydroshearing approach is a conceptual model considered in the FORGE project. A critical research objective in FORGE stimulation is to investigate the role of natural fractures in EGS stimulation and the associated seismicity activities. Therefore, analyzing the shearing behaviors of natural fractures at the FORGE stimulation site is of significant interest. Following our previous modeling studies (Kumar, Liu, & Ghassemi, 2023; Lee & Ghassemi, 2023), we conducted a theoretical analysis to further understand fracture propagation and seismicity migration in response to fluid injection at Utah FORGE, aiming to provide insights into the operation and characterization of hydraulic stimulation at this site. Initially, we performed laboratory experiments to characterize the relevant geomechanical properties of granitoid rocks from the Utah FORGE reservoirs. The experimental results, along with in-situ stress data and fracture characteristics (e.g., orientation) identified from borehole image logs, were then used to conduct a theoretical analysis of the response of FORGE natural fracture sets to fluid injection. The analysis employed the approach proposed by Pine & Batchelor (1984), which was modified by Nygren & Ghassemi (2005). Using static analysis, the spatial migration of the stimulated volume was assessed by comparing the gradients of the driving shear forces and the resisting shear strength. This analysis also demonstrated the criticality of different fracture sets at the toe of the FORGE injection well as a function of their properties.

2. Experimental Characterization of FORGE Reservoir Rocks

To determine the related mechanical properties for the theoretical analysis of fracture shearing migration, a series of laboratory experiments were conducted on the granite samples from the FORGE reservoir. The Young's modulus and Poisson' ratio determined from a triaxial compressive test are 62 GPa (9.0×10^6 psi) and 0.27, respectively. The uniaxial compressive strength (UCS) is 121 MPa (1.7×10^5 psi).

In addition, multistage triaxial shear tests were conducted on a saw-cut smooth fracture (Figure 1(a)) and a tensile-induced rough fracture (Figure 1(b)) to estimate the friction properties of FORGE natural fractures. During a triaxial shear test, a given confining pressure, σ_3, is first applied, and then differential stress (σ_1- σ_3) is raised until the fracture slips. However, results under different confining pressures are required to construct the shear strength envelope. Thus, a multistage test strategy was applied: progressively, for each consecutive stage, a different confining pressure was applied, and the axial load was increased via strain control until fracture slip occurred. Then, the axial load was lowered to the applied confining pressure level and a new stage was started at a higher confining pressure.

(a) (b)

Figure 1: (a) Saw-cut fracture created on a FORGE granite sample at ~2074 m (6802.92 ft.); (b) Rough fracture created on a FORGE granite sample at ~2073 m (6802.73 ft.). The procedure regarding creating saw-cut or rough fracture on cylindrical granite samples can be referred from Ye & Ghassemi (2018).

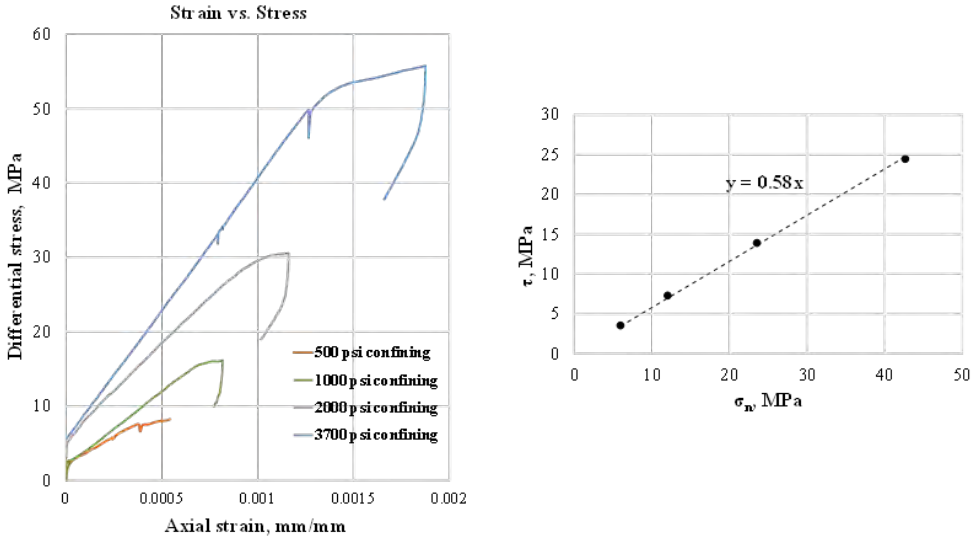

(a) (b)

Figure 2: (a) Saw-cut fracture created on a FORGE granite sample at ~2074 m (6802.92 ft.); (b) Rough fracture created on a FORGE granite sample at ~2073 m (6802.73 ft.). The procedure regarding creating saw-cut or rough fracture on cylindrical granite samples can be referred from Ye & Ghassemi (2018).

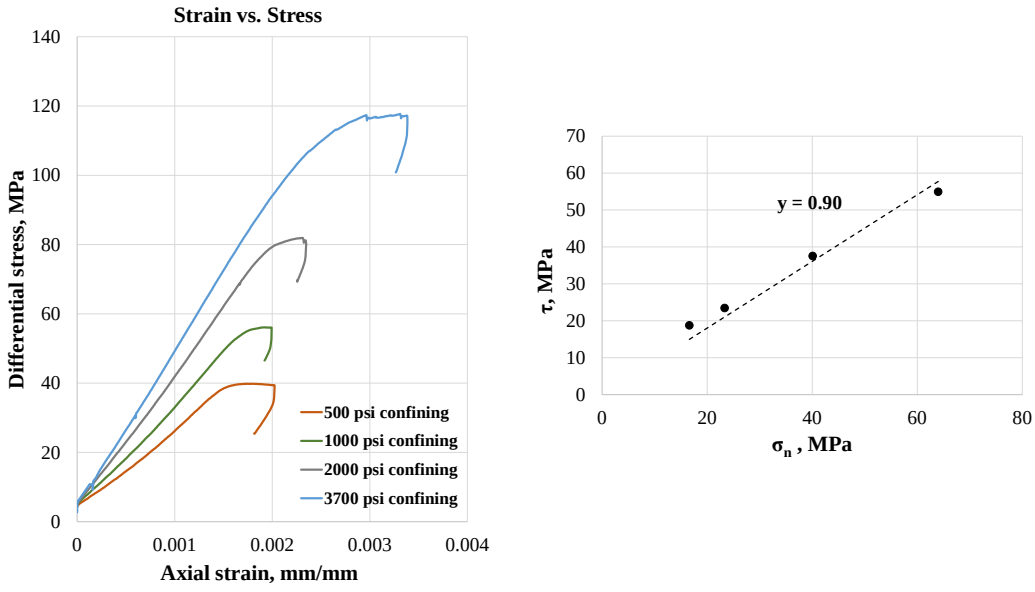

Figure 3: (a) stress-strain curve of triaxial shear test on FORGE granite sample at ~2073 m (6802.73 ft.) with a tensile-induced fracture; (b) shear strength envelope of the tensile-induced fracture test with a friction angle of 42º.

According to the results from several stages with different confining pressures, the shear strength envelope and frictional properties can be determined based on the tests conducted on a single rock fracture (Ye & Ghassemi, 2016). The results of multistage shear tests for the two fractures (one saw-cut smooth fracture and one rough fracture) are shown in Figure 2 and Figure 3, respectively. As expected, the tensile-induced fracture with rough fracture surfaces has a larger shear strength and friction coefficient than that of the saw-cut fracture. The friction angle of the tensile-induced fracture is ~42°, while the saw-cut fracture has a friction angle of ~30°. Considering natural fractures are generally with various surface topography/roughness, a reasonable range of the friction angles of FORGE natural fractures can be estimated as from 30º-50º.

3. Theoretical Analysis of Fracture Shearing in FORGE Stimulation

3.1 Natural Fractures and In-situ Stresses at FORGE

Four major sets of natural fractures have been identified from the data of borehole image logs and core samples in FORGE stimulation site (Finnila & Jones, 2024). The intensity and orientations of the natural fracture sets are listed in Table 1.

Table 1: General intensity and orientation of the natural fractures in the FORGE stimulation zone

		F1: SSW-striking, vertical	F2: South-striking moderately dipping West	F3: North-striking, moderately dipping East	F4: East-striking, sub-vertical dipping South
	[%]	30	29	21	20
Mean Set Orientation	Strike [deg]	204	181	320	84
	Dip [deg]	88	53	38	74
	Fisher Concentration	22	7	4	9

The in-situ stresses at the FORGE reservoir are detailed in Table 2. The vertical stress (σ_v) determined from the density logs is 25.56 MPa/km (1.13 psi/ft, Moore et al., 2020), and the pore pressure (P_p) is considered as 9.79 MPa/km (0.433 psi/ft, hydrostatic pressure gradient). The minimum principal stress (σ_h) is estimated to be an average value of 16.85 MPa/km (0.75 psi/ft) by reexamining the injection tests carried out in the stimulation well 16A(78)-32 in January 2021. The maximum principal stress (σ_H) is constrained to an average value of 21.15 MPa/km (0.94 psi/ft) based on drilling-induced fractures and breakouts observed from the borehole image logs (Ye et al., 2022; Ye & Ghassemi, 2024). The in-situ values of the friction angle (ϕ')) for the fracture sets are not known. Therefore, laboratory test results conducted on FORGE reservoir rocks (including both smooth and rough fractures), described in Sec. 2, will be used as a proxy, suggesting that the friction angle (ϕ')) ranges from 30° to 50°. Other relevant mechanical properties, also derived from the laboratory tests, are listed in Table 2.

Table 2: In-situ stress and geomechanical properties at the FORGE stimulation zone

Parameter	Value	Source
Vertical stress (σ_v)	25.56 (MPa/km)	Integration of density logs, Moore et al., 2020
Minimum horizontal principal stress (σ_h)	16.85 (MPa/km)	Reexamining DFIT tests of 16A(78)-32
Maximum horizontal principal stress (σ_H)	21.15 (MPa/km)	Constrained by image logs (Ye & Ghassemi, 2024)
Pore pressure (P_p)	9.79 (MPa/km)	Hydrostatic pressure, Moore et al., 2020
Friction angle	30° - 50°	Lab tests on FORGE cores (see Sec. 2)
Unconfined compressive strength	121 MPa	
Young's modulus	62 GPa	
Poisson's ratio	0.27	

3.2 Failure Criterion for Natural Fractures

In this theoretical analysis, a linear failure criterion (Mohr-Coulomb criterion) is used to assess the response of natural fractures to injection pressure. This criterion assumes that fracture slip is independent of the intermediate principal stress and occurs in the plane defined by the maximum principal stress (σ_1) – minimum principal stress (σ_3). Considering that Utah FORGE is likely situated in a normal faulting zone (Ye et al., 2022; Ye & Ghassemi, 2024), the σ_v - σ_h plane is assumed to be the failure plane (see Figure 4).

The linear failure criterion for the planes of weakness (e.g., natural fractures) is obtained by considering the normal and shear stresses acting on them:

$$\sigma_n = P_o - S_o \cos(2\theta) \quad (1)$$

$$\tau = S_o \sin(2\theta) \quad (2)$$

where $P_o = \frac{\sigma_1+\sigma_3}{2}$ and $S_o = \frac{\sigma_1-\sigma_3}{2}$ are the mean and deviatoric stress components, respectively. The angle θ represents the fracture angle with respect to the maximum principal stress, while β represents the fracture angle with respect to the minimum principal stress, where θ = 90° - β. In a normal faulting regime, β is equal to the dip angle.

Eqns. (1) and (2) are then substituted into a Mohr-Coulomb failure criterion for the fractures:

$$\tau_f = C + \sigma_n' \tan\phi' = C + \left(\sigma_n - P_p\right) \tan\phi' \quad (3)$$

where τ_f is the shear stress, σ_n' is the effective normal stress, σ_n is the normal stress, P_p is the pore pressure, and ϕ' is the friction angle of natural fractures. C is the cohesion, which is generally assumed to be very small and is considered to be zero for fractures.

Substitution of Eqs. (1) and (2) into Eq. (3) yields:

$$\sigma_1 - \sigma_3 = \frac{2(S_o+\sigma_3 \tan\phi')}{(1-\tan\phi' \cos\beta)\sin 2\beta} \quad (4)$$

According to the experimental results in Sec. 2, in this work we consider a broader range of friction angle values from 30º to 50º as a sensitivity analysis. Differentiating Eq. (4) with respect to β and setting it equal to zero yields (Jaeger et al., 2009):

$$\tan 2\beta_{crit} = -\cot\phi' \text{ or } \phi' = 2\beta_{crit} - \frac{\pi}{2} \quad (5)$$

Eq. (5) represents the least stable fracture orientation for a given friction angle. Applying the 30º-50º friction angle values to Eq. (5) shows that β_{crit} equals 60º-70º, aligning with the dip angles of fracture set 2 (south-striking, moderately dipping west) and fracture set 4 (east-striking, sub-vertical dipping south). This implies that shear slips are most likely to first occur on fracture set 4 during injection.

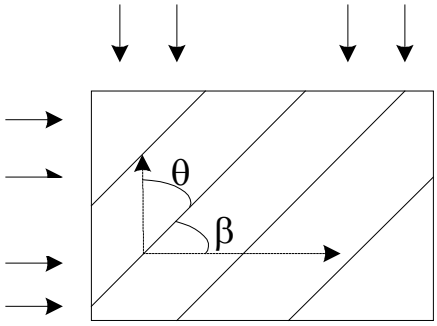

Figure 4: Conceptual model of fractures in the target stimulation zone, illustrating the definition of angles used in the analysis. At the FORGE site, which is characterized by normal faulting, σ_1 corresponds to σ_v, and σ_3 corresponds to σ_h. The angle θ represents the fracture angle with respect to the maximum principal stress, while β represents the fracture angle with respect to the minimum principal stress, where θ = 90° - β. In a normal faulting regime, β is equal to the dip angle.

3.3 Limiting Stress Conditions

The limiting value of the critical stress ratio, R, for a range of possible friction angles is determined in this section. This ratio is found by manipulation of Eq. (4) (Goodman, 1980; Pine & Batchelor, 1984):

$$R = \frac{\sigma_1'}{\sigma_3'} = \frac{1 + \tan\phi'(\sin 2\theta + \tan\phi' \cos 2\theta)^{-1}}{1 - \tan\phi'(\sin 2\theta + \tan\phi' \cos 2\theta)^{-1}} \quad (7)$$

It represents the stress condition required for limiting equilibrium of fractures in terms of their angle from the major principal stress and their friction angle. Plots of R with respect to θ for different friction angles ($\boldsymbol{\phi'}$) are shown in Figure 5, which demonstrates that as the friction angle increases the limiting value of R also increases. In a normal faulting regime, the vertical stress is the maximum principal stress, and the minimum horizontal stress is the minimum principal stress. The in-situ stress ratio value before fluid injection ($R_i = \sigma_v'/\sigma_h'$) for the estimates of the stress state at FORGE is 2.23 (see the blue horizontal line in Figure 5). As can be seen in Figure 5, the minimum of each curve represents the least stable fracture orientation. These least stable fracture orientations are 20º, 22.5º, 25º, 27.5º, and 30º for ϕ' = 50º, 45º, 40º, 35º, and 30º, respectively. Most of these least stable fracture orientations fall within a range close to fracture sets 2 and 4, particularly fracture set 4 (see Figure 5). This suggests that the natural fractures within fracture sets 2 and 4 are primarily near a critical state and might slip first following fluid injection. Additionally, the R values for each set of fractures are larger than the in-situ stress ratio (R_i), indicating that an increase in fluid pressure within the fractures is required to trigger fracture slip due to the fractures not being in critical state. In the following section, the critical pore pressure required to initiate fracture slip will be discussed within a theoretical framework based on the Mohr-Coulomb failure criterion.

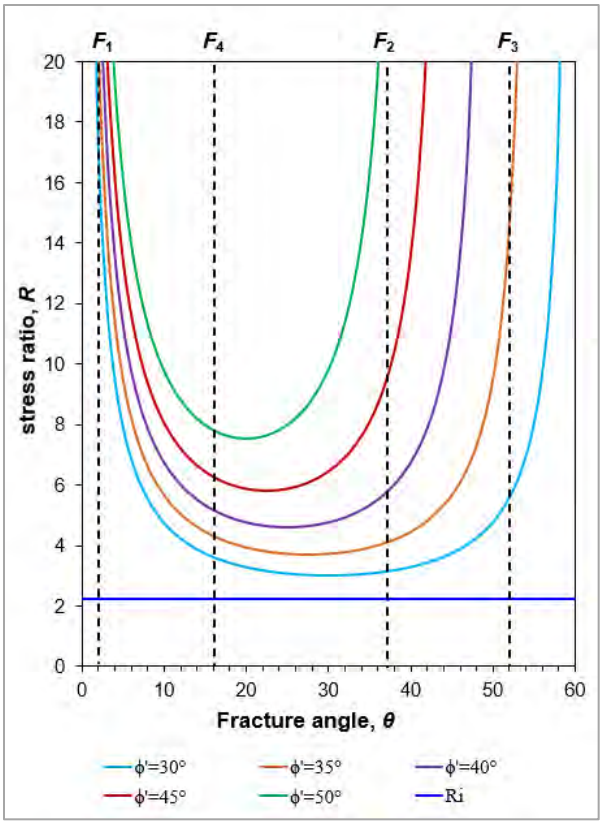

Figure 5: *R* Values for the range of friction angles chosen (ϕ'=30° - 50°). R_i represents the in-situ stress ratio at the FORGE site, which is the ratio of σ'_v/σ'_h. The four black-dashed lines from left to right indicate the four fracture sets at the FORGE site with dips of 88° (fracture set 1), 74° (fracture set 4), 53° (fracture set 2), and 38° (fracture set 3), respectively.

3.4 Critical Injection Pressure Required for Fracture Reactivation

Since the natural fractures at the toe of the stimulation well are not in a critical state (as illustrated in Figure 5), pressurized fluid injection is necessary to reactivate the fractures during hydraulic stimulation. It is important to determine the amount of fluid pressure needed to critically stress these fractures and induce slip. Upon stimulation of a reservoir, a unit increase in fluid pressure within a fracture will decrease the effective stress by the same amount, according to Terzaghi's definition of effective stress. For pre-existing or natural fractures, the critical injection pressure (P_c^{joint}) required to induce shearing must satisfy the following equation according to the Mohr-Coulomb criterion:

$$\tau_f = C + \left(\sigma_n - P_c^{joint}\right) tan\,\phi' \tag{8}$$

Substitution of Eqs. (1) and (2) into Eq. (8) yields:

$$P_c^{joint} = \frac{\sigma_1 + \sigma_3}{2} - \frac{\sigma_1 - \sigma_3}{2}\left(\frac{sin\,2\theta + cos\,2\theta\,tan\,\phi'}{tan\,\phi'}\right) + \frac{C}{tan\,\phi'} \tag{9}$$

The critical pore pressures required for the reactivation of the natural fractures in the FORGE reservoir (at a depth of 2.6 km) with different friction angles are shown in Figure 6. In Figure 6, all the curves of critical pore pressure decrease until a critical fracture orientation is reached, after

which they increase. It is evident that fractures oriented from θ = 15º to 35º (corresponding to dip angles β = 55º to 75º) are among the first to slip. This suggests that fracture sets 2 and 4 are likely to slip first during hydraulic stimulation. Additionally, for natural fractures with shallow dipping orientations (dip angles β < 20˚), the required pore pressure increases significantly.

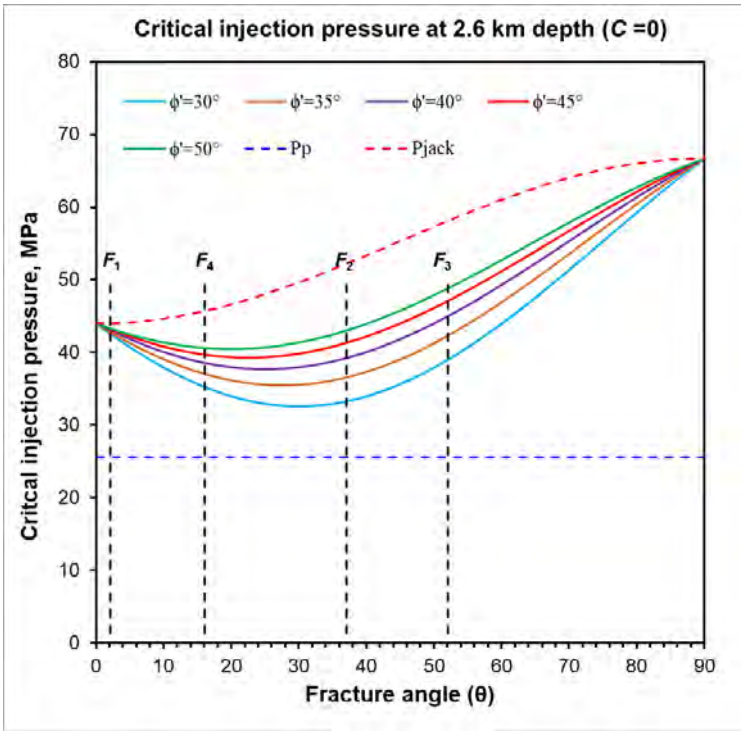

Figure 6: Critical injection pressures required for inducing shear slip and jacking on various fracture orientations and friction angles at a depth 2,609 m (the toe of stimulation well). In the plot, the four black-dashed lines indicate the four primary fracture sets at the FORGE site with dips of 88° (fracture set 1), 74° (fracture set 4), 53° (fracture set 2), and 38° (fracture set 3), respectively.

3.5 Critical Injection Pressure Required for Inducing Hydraulic Jacking

Pressurized fluid injection can also induce hydraulic jacking, which reopens natural fractures. Theoretically, for hydraulic jacking, the effective normal stress acting on the fracture becomes zero. Therefore, the critical fluid pressure required for hydraulic jacking (P_{jack}^{joint}) is given by the following equation:

$$P_{jack}^{joint} - \sigma_n - T = 0 \tag{10}$$

Substitution of Eqs. (1) and (2) into Eq. (10) yields:

$$P_{jack}^{joint} = \frac{\sigma_1 + \sigma_3}{2} - \frac{\sigma_1 - \sigma_3}{2} cos\, 2\theta + T \tag{11}$$

where T is the tensile strength of natural fractures, which can be assumed to be negligible.

From Eq. (11), it can be observed that the critical pressure for hydraulic jacking is not influenced by the friction angle of fractures. Additionally, when θ = 0º or 90º, and assuming that both cohesion

and tensile strength of natural fractures are negligible, P_{jack}^{joint} is equal to P_c^{joint} according to Eqs. (9) and (11), as illustrated in Figure 6.

In Figure 6, it is noticed that slip is generally initiated before jacking during injection. The critical pore pressure (P_c^{joint}) and the net fluid pressure ($P_p^+ = P_c^{joint} - P_p$) for the fracture sets 1, 2, 3 and 4 are reported in Table 3. The net fluid pressure is referred to the surface pressure required for fracture reactivation. The values in Table 3 are calculated at an injection depth of 2,609 m (the toe of stimulation well) where the pore pressure (P_p) is 25.54 MPa. In Table 3, we can see that fracture sets 2 and 4 require a relatively lower fluid pressure to be activated by shear stimulation. This is consistent with the predictions suggested by the above analysis of limiting stress conditions.

Table 3: Critical Pore Pressure ($\boldsymbol{P_c^{joint}}$) and net pore pressure ($\boldsymbol{P_p^+}$) in MPa required to reactivate the four sets of natural fractures for different friction angles □'□ at FORGE

	β = 88° (fracture set 1)		**β = 53° (fracture set 2)**		**β = 38° (fracture set 3)**		**β = 74° (fracture set 4)**	
ϕ'	P_c^{joint}	P_p^+	P_c^{joint}	P_p^+	P_c^{joint}	P_p^+	P_c^{joint}	P_p^+
30°	42.62	17.08	33.28	7.74	38.98	13.44	35.27	9.73
35°	42.86	17.32	36.60	11.06	42.33	16.79	37.10	11.56
40°	43.05	17.51	39.18	13.64	44.94	19.4	38.52	12.98
45°	43.20	17.66	41.28	15.74	47.05	21.51	39.67	14.13
50°	43.33	17.79	43.03	17.49	48.83	23.29	40.64	15.10

3.6 Fracture Growth and Shearing Migration

When non-horizontal fractures/faults slip, shear growth can occur upward or downward. One of the critical challenges in the development of an EGS system is to predict and control the growth of the stimulated fractures and ensure the appropriate connections of the injection well, the stimulated zone, and the production well. Hence, it is necessary to analyze the possible migration of fracture shearing under the reservoir conditions. The shearing migration of natural fractures during fluid injection can be predicted by considering the difference in the pressure increase per unit depth required for inducing shear slip above and below the injection point. If the pore pressure increment difference is positive, downward shear growth is expected since slip propagates downward where less pressure is required. On the other hand, if the pore pressure increment difference is negative, upward shear growth is likely the primary shearing mode. The analysis of shearing migration is a function of the variation of fracture properties and in-situ stress with depth. Indeed, a change in shear growth can occur at a critical depth if the stress gradient is non-linear. Therefore, the downward or upward shear growth can be expressed as (Pine & Batchelor, 1984):

$$G = \frac{dP_p^+}{dz} = \frac{1}{2}\left(\frac{d\sigma_1'}{dz} + \frac{d\sigma_3'}{dz}\right) - \frac{\sin 2\theta + \tan\phi' \cos 2\theta}{2\tan\phi'}\left(\frac{d\sigma_1'}{dz} - \frac{d\sigma_3'}{dz}\right) \quad (12)$$

where z is depth. Solving Eq. (12) for the critical fluid-pressure gradient (G), upward growth is predicted for positive values of G, while negative values of G suggest downward growth. The derivatives on the right-hand side of Eq. (12) are the gradient of the effective maximum principal stress ($\frac{d\sigma_1'}{dz}$) and the gradient of the minimum principal stress ($\frac{d\sigma_3'}{dz}$).

Plotting the critical pressure gradient (G) in Figure 7. It is noticed that the values of G for the four fracture sets are positive under the friction angles from 30º to 50º, indicating the upward shearing migration/growth.

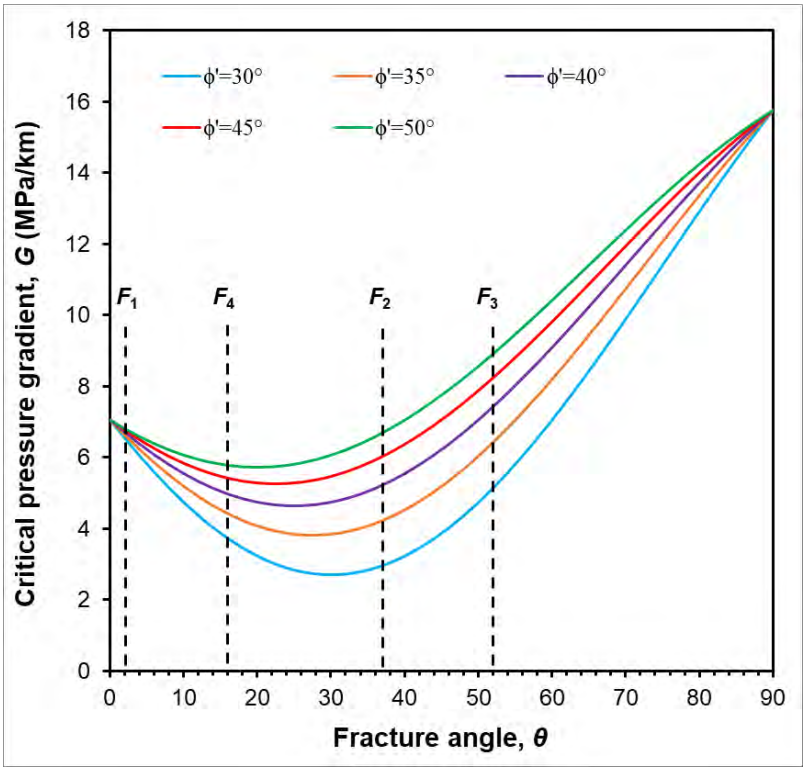

Figure 7: Critical fluid-pressure gradient for the four natural fractures various friction angles in FORGE site. In the plot, $G > 0$ indicates upward growth of fracture shearing. the four black-dashed lines indicate the four primary fracture sets at the FORGE site with dips of 88° (fracture set 1), 74° (fracture set 4), 53° (fracture set 2), and 38° (fracture set 3), respectively.

4. Discussion

Since April 2022, several hydraulic stimulations have been conducted at the toe of injection well 16A(78)-32, and a series of fluid circulation tests have been performed between injection well 16A(78)-32 and production well 16B(78)-32. These injection tests are accompanied by high-resolution seismic monitoring, providing an opportunity to analyze the Stimulated Reservoir Volume (SRV) and seismicity growth. Using seismicity data from the three-stage stimulation in April 2022 and four flow circulation tests in July 2023, we have plotted the seismic clusters observed during these tests, as shown in Figure 8. This analysis helps in understanding the spatial distribution and growth of seismic events, offering insights into fracture behavior and reservoir response to hydraulic stimulations and fluid circulation. The upward growth of the seismicity cloud induced by fluid injection suggests that fractures tend to propagate and/or shear upwards. Additionally, the complex geometry of these seismic clouds indicates the likely involvement of hydraulic fracture-natural fracture (HF-NF) interaction during hydraulic stimulation and fluid circulation. These observations from induced seismicity align well with the results of our theoretical analysis, suggesting that the presented analytical model can reliably predict the growth

of the SRV and seismicity, as well as estimate the net fluid pressure required to induce fracture slip.

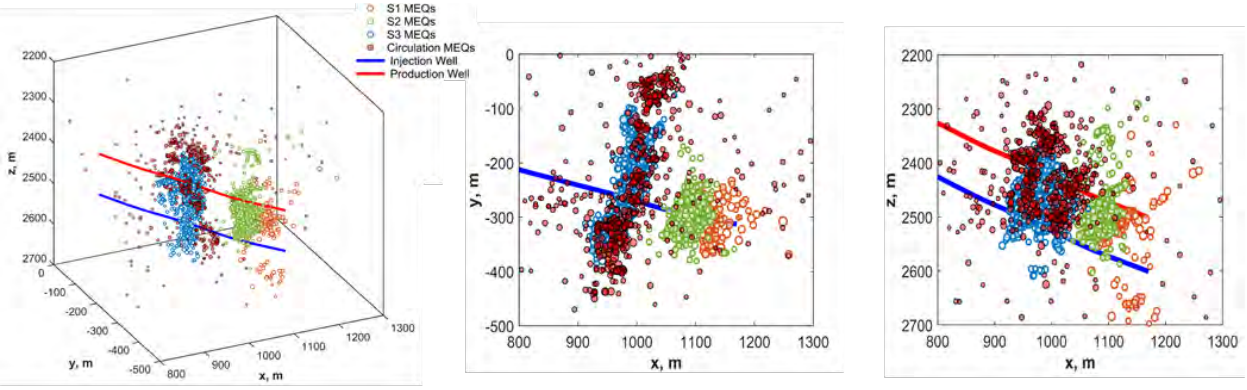

Figure 8: Seismic clusters observed during the three-stage stimulation in April 2022 and the four flow circulation tests in July 2023 conducted in the Utah FORGE reservoir. The inclined blue and red lines represent the deviated portions of the injection well and the production well within the FORGE reservoir, respectively. The blue, green, and red hollow circles represent the seismic events induced during the three-stage stimulations, while the red solid circles represent the seismic events induced during the fluid circulation tests.

It should be noted that the upward or downward shearing of pre-existing fractures depends on the gradients of the effective principal stresses, the friction angle, and the dip angle of the individual fracture. Therefore, spatial or temporal changes in the stress regime, due to continuous fluid injection and the associated cooling during the stimulation phase and later the production phase, might alter the slip tendency and shearing migration during hydraulic injection.

5. Conclusions

In this study, a series of laboratory experiments were conducted on FORGE reservoir rocks to characterize their mechanical properties, including the friction coefficient, Young's modulus, Poisson's ratio, and unconfined compressive strength (UCS). The experimental results, along with in-situ stress data and natural fracture data, were used to perform a theoretical analysis based on the linear Mohr-Coulomb failure criterion to evaluate the shearing behaviors of natural fractures in the FORGE reservoir. The critical stress analysis demonstrates that none of the four major fracture sets at FORGE reservoir are currently in a critical state, with fracture sets 2 and 4 being relatively less stable than fracture sets 1 and 3. Consequently, fracture sets 2 and 4 are likely to slip first during fluid injection. According to this theoretical analysis, the critical injection pressures required to induce fracture slip and jacking were estimated. Additionally, the analysis of the critical fluid-pressure gradient (G) suggests that upward shearing is likely the primary mode of shearing migration at FORGE. The predicted upward shearing migration is consistent with the growth of microseismic clouds observed during the stimulation and fluid circulation tests conducted in the FORGE reservoir, supporting the reliability of this model. The results of this analysis are expected to provide valuable insights into the design and operation of hydraulic stimulation and the mitigation of induced seismic risks at the Utah FORGE site.

REFERENCES

Finnila, A., & Jones, C. (2024). Updated Reference Discrete Fracture Network Model at Utah FORGE. In *Proceedings, 49th Workshop on Geothermal Reservoir Engineering, Stanford University, Stanford, CA*.

Goodman, R. E.: *Introduction to rock mechanics*, (1980), New York: Wiley.

Jaeger, J. C., Cook, N. G., & Zimmerman, R.: *Fundamentals of rock mechanics*, (2009), John Wiley & Sons.

Kumar, D., Liu, B., & Ghassemi, A. (2023). 3D Modeling of the Utah Forge Reservoir Stimulation with Proppant Transport and Deposition. In *SPE Annual Technical Conference and Exhibition?* (p. D022S011R002). SPE.

Lee, S. H., & Ghassemi, A. (2023). Modeling and Analysis of Stimulation and Fluid Flow in the Utah FORGE Reservoir. In *Proceedings: 48th Workshop on Geothermal Reservoir Engineering, Stanford University, Stanford, California*.

Moore, J., McLennan, J., Pankow, K., Simmons, S., Podgorney, R., Wannamaker, P., ... & Xing, P. (2020). The Utah Frontier Observatory for Research in Geothermal Energy (FORGE): a laboratory for characterizing, creating, and sustaining enhanced Geothermal systems. In *Proceedings of the 45th Workshop on Geothermal Reservoir Engineering*. Stanford University.

Nygren, A., & Ghassemi, A.: Influence of Cold Water Injection On Critically Stressed Fractures in Coso Geothermal Field, CA, *Proceedings*, 40th U.S. Symposium on Rock Mechanics (USRMS), Anchorage, Alaska, USA (2005).

Pine, R. J., & Batchelor, A. S.: Downward migration of shearing in jointed rock during hydraulic injections, *International Journal of Rock Mechanics and Mining Sciences & Geomechanics Abstracts*, **21**(5), (1983), 249-263.

Ye, Z., & Ghassemi, A. (2024). The Updated Wellbore Stress Models for Utah FORGE. In *Proceedings, 49th Workshop on Geothermal Reservoir Engineering, Stanford University, Stanford, CA*.

Ye, Z., & Ghassemi, A.: Deformation Properties of Saw-Cut Fractures in Barnett, Mancos and Pierre Shales, *Proceedings*, 50th US Rock Mechanics/Geomechanics Symposium, Houston, TX, USA (2016).

Ye, Z., Fang, Y., Ghassemi, A., & McLennan, J. (2022). A Preliminary Wellbore In-situ Stress Model for Utah FORGE. In *ARMA US Rock Mechanics/Geomechanics Symposium* (pp. ARMA-2022). ARMA.

Operation Strategy to Avoid Thermal Short-circuit in EGSs with Horizontal Wells

Qitao Zhang and Arash Dahi Taleghani

Department of Energy and Mineral Engineering, Pennsylvania State University, State College, 16801, USA

Keywords

Enhanced geothermal systems, Thermal short-circuit, Downhole flow control, Heat extraction efficiency, and Distributed temperature sensing.

ABSTRACT

Enhanced geothermal systems face a significant obstacle: thermal short-circuiting, where fluid flows through only a few fractures, limiting efficiency. This issue is particularly problematic for horizontal wells with multiple fractures. To address this challenge, we introduce a revolutionary temperature-sensitive flow management system. Equipped with real-time sensors and dynamic flow control devices, this innovative system optimizes injection and production across the lateral, effectively preventing thermal shortcuts. Utilizing this flow management system, operation strategies can be designed to determine when and where to adjust the injection and production rates within a twin-horizontal well Enhanced Geothermal System (EGS). Our numerical simulations demonstrate the system's impressive long-term impact. Over a 50-year period, it maintains a produced fluid temperature 40 K higher than uncontrolled systems, and thus the heat extraction efficiency can be increased significantly by simply applying the presented operation strategy. Our innovative approach has the potential to transform horizontal wells into high-performance EGS, unlocking a future of sustainable and efficient energy production.

1. Introduction

The Enhanced geothermal system (EGS) is a type of geothermal technology that utilizes hydraulic stimulation to improve fluid flow within deep, impermeable hot dry rock (HDR) formations. This method creates fractures in the rock, increasing the permeability and allowing for greater circulation of hot fluids. Consequently, EGS systems have the potential to extract significantly more heat compared to traditional geothermal systems, such as closed-loop systems. (Liu and Dahi Taleghani, 2023a; Liu and Dahi Taleghani, 2023b). However, thermal short-circuiting is a significant issue that can severely limit the efficiency and productivity of EGS reservoirs (Liu et al., 2020). It occurs when the injected fluid preferentially flows through a limited number of

fractures or high-permeability pathways within the reservoir, resulting in an inefficient heat exchange with the surrounding rock formation. The primary mechanism behind thermal short-circuiting is the development of localized cooling zones around these high-flow pathways. As the injected fluid, typically cooler than the reservoir rock, flows through these pathways, it absorbs heat from the adjacent rock, gradually decreasing the rock temperature in the vicinity of the flow paths. Over time, this localized cooling effect creates a thermal short-circuit, where a significant portion of the injected fluid flows through these cooled zones without effectively extracting heat from the bulk of the reservoir. Thermal short-circuiting can be exacerbated by several factors. Reservoirs with highly heterogeneous fracture networks or permeability fields are more susceptible, as the injected fluid tends to follow the path of least resistance, concentrating flow in a few high-permeability channels (Al Balushi et al., 2023a). Improper well spacing or configuration can also increase the likelihood, for instance, if the injection and production wells in a doublet system are too close together, allowing the injected fluid to preferentially flow through a direct pathway between them (Li et al., 2016). Additionally, the stress state and orientation of fractures within the reservoir can influence flow patterns and potentially promote thermal short-circuiting if the fractures are favorably aligned with the well trajectories (McLean and Espinoza, 2023).

Thermal short-circuiting has severe consequences for EGS operations. As the injected fluid bypasses a significant portion of the reservoir through the short-circuiting pathways, the amount of heat extracted from the rock formation is significantly reduced, leading to lower reservoir productivity and energy output. The rapid flow through these pathways can also cause premature thermal breakthroughs at the production well, where the injected fluid returns to the surface without sufficient heat extraction. Moreover, over time, the continuous injection of cooler fluid through the short-circuiting pathways can lead to progressive cooling of the reservoir, further reducing its thermal potential and lifespan. Recently, horizontal drilling or basically horizontal wells in the form of new drilling or repurposing existing wells (Santos et al., 2022) has been considered as a potential option to boost the efficiency of EGS, however, well configuration and multistage stimulations in parallel horizontal wells may increase the risk of thermal short-circuiting, significantly. Mitigating thermal short-circuiting is crucial for enhancing the efficiency and longevity of EGS reservoirs. Strategies such as optimizing well placement, stimulating additional fractures, and implementing advanced flow control techniques may help address this challenge and improve the overall performance of EGS systems with some limitations.

Before we present the potential application of flow control systems, we review some of the field observations regarding this problem. The inherent heterogeneity and anisotropy (unequal properties in different directions) of geothermal formations often cause the working fluid to concentrate in just a few fractures. Studies like those at Rosemanowes, UK (Parker, 1999) and Soultz, France (Tester et al., 2006) revealed how a single fracture can dominate fluid flow, carrying over half the injected fluid despite the presence of multiple potential pathways. This uneven distribution highlights the critical role of fracture conductivity in EGS projects. By controlling the conductivity of individual fractures, we can potentially mitigate the formation of dominant flow paths (plane-channeling) between injection and production wells. Unfortunately, current technologies lack the finesse to achieve truly uniform heat extraction from all fractures. This research aims to bridge that gap by exploring innovative methods, like Inflow and Injection Control Devices (ICDs) and real-time temperature monitoring, to manipulate flow within the reservoir and optimize heat extraction efficiency.

Even though operators hope to avoid thermal short-circuiting between horizontal wells in EGS, delaying or preventing early thermal breakthroughs. However, achieving uniform thermal flow between wells is challenging for two reasons. Firstly, the geometry of induced fractures is difficult to control underground. Secondly, the natural variations within rock formations make it nearly impossible to adjust the fluid flow for even heat extraction precisely. One solution we proposed before is tunable fracture conductivity, which can adjust the fracture conductivity according to the local temperature and thus temporarily seal preferential fracture flow pathways. (Al Balushi et al., 2023b; Zhang and Dahi Taleghani, 2023; Zhang and Dahi Taleghani 2024). However, these methods highly depend on the special agents, and their durability and actually performance in the field practice have not been tested. By contrast, in this research, we are presenting some techniques that have been widely used in the oil and gas industry. Our approach in this paper focuses on modifying the heat harvesting process, not the reservoir. We propose controlling flow injection and production based on real-time temperature measurements from the production well. In the oil and gas industry, inflow and injection control devices (ICDs) successfully manage flow across wellbore lengths. These versatile tools can be installed even in open-hole completions. ICDs restrict flow in highly permeable zones, promoting flow in less productive areas. This helps prevent bypassing valuable resources and improves fluid recovery. Similarly, ICDs can be adapted for geothermal systems, working independently of the fracture network or geological formations. Since they reside within the wellbore, they offer the advantage of being independent of geology or completion methods. Additionally, distributed temperature sensors (DTS) using fiber optics can reliably provide temperature data along the wellbore at various depths. It's important to note that this research is not endorsing specific products, but rather exploring potential advancements through adopting such technologies in the geothermal field.

This research investigates a novel subsurface flow management system designed to combat thermal short-circuiting, a longstanding challenge in enhanced geothermal systems (EGS). By strategically directing fluid flow between wells, this system has the potential to significantly improve heat extraction. The study unfolds in several parts: first, we introduce the system and its method for eliminating thermal short-circuits. Second, a numerical model specifically designed for EGS with horizontal wells is built, with the key capability of integrating the flow management system. Third, the system is incorporated into the EGS model to numerically explore its operational benefits. This research, by tackling thermal short-circuiting with this innovative approach, paves the way for substantial improvements in heat extraction, ultimately fostering a more efficient and sustainable future for geothermal energy.

2. Methodology

2.1 Mathematica model

Assuming the reservoir matrix has been fully saturated, then fluid flow in the reservoir matrix can be described by Darcy's law. The corresponding kinematic equation for the fluid flow is as follows:

$$\boldsymbol{u} = -\frac{k_m}{\mu_f}\left(\nabla p - \rho_f \boldsymbol{g}\nabla z\right) \tag{1}$$

where **u** is the vector of Darcy's seepage velocity in the reservoir matrix. k_m represents the permeability of the reservoir matrix. μ_f and ρ_f are the viscosity and density of working fluid, respectively. p is the reservoir pore pressure. ∇ represents the Hamiltonian operator which

calculates the gradient of a scalar. **g** represents the gravitational acceleration in the vertical direction and $\rho_f \mathbf{g}\nabla z$ represents the whole gravity terms.

The continuity equation for the fluid flow in the reservoir matrix can be expressed as follows:

$$\frac{\partial(\phi_m \rho_f)}{\partial t} + \nabla \cdot (\rho_f \boldsymbol{u}) = 0 \tag{2}$$

where ϕ_m denotes the porosity of the reservoir matrix.

For the fluid flow in discrete fractures, the kinematic equation can be expressed as follows:

$$\boldsymbol{u}_f = -\frac{k_f}{\mu_f}(\nabla_T p_f + \rho_f \boldsymbol{g} \nabla_T z) \tag{3}$$

where $\mathbf{u}_f$ is the vector of fluid velocity in discrete fractures. $\nabla_T p_f$ is the pressure gradient tangent to the fracture surface. k_f represents the permeability of fracture.

Heat transfer in EGS consists of heat conduction and heat convection. During production, convection plays a dominant role in heat extraction from EGS. Assuming the local equilibrium is achieved in the porous media, which means the temperature for the fluid at the rock surface equals the temperature of the rock, then the temperature distribution in the reservoir matrix can be calculated as follows:

$$(\rho c)_{\text{eff}} \frac{\partial T}{\partial t} + \rho_f c_f \boldsymbol{u} \cdot \nabla T - \nabla \cdot (\lambda_{\text{eff}} \nabla T) = 0 \tag{4}$$

where T is temperature. c_f is the heat capacity of the working fluid. λ_{eff} is the effective heat conductivity. Assuming the heat conduction in solid and fluid phases happens in parallel, then the effective heat conductivity is the weighted arithmetic of the heat conductivity of the solid phase and fluid phase.

Heat transfer in discrete fractures can be expressed as follows:

$$d_f (\rho c)_{\text{eff}} \frac{\partial T}{\partial t} + d_f \rho_f c_f \boldsymbol{u} \cdot \nabla_T T - \nabla_T \cdot (d_f \lambda_{\text{eff}} \nabla_T T) = 0 \tag{5}$$

Based on the mathematical models presented above, the operation of EGS can be simulated. In the next section, we are going to introduce the novel real-time downhole flow control system. We will simulate the EGS operated with such a system based on the mathematical models presented in this section.

2.2 Real-time Downhole Flow Control System

To prevent thermal short-circuiting between horizontal wells in EGS and boost heat extraction efficiency, we propose a real-time flow management system for intelligent fluid distribution. The presented flow management system for EGSs consists of two parts.

The first component of the flow management system comprises temperature sensors strategically placed within the production well. These sensors continuously transmit real-time data on downhole temperatures. This system utilizes distributed temperature sensors (DTS) installed within the production well, similar to those used in the oil & gas industry for downhole monitoring. DTS technology offers real-time (less than 60 seconds) and high-resolution (less than 1 meter) temperature data, allowing operators to identify hot and cool zones along the wellbore. This information is crucial for the second part of the flow management system, which is yet to be

revealed but will likely leverage this data to adjust fluid flow and prevent thermal short-circuiting. While previous geothermal projects primarily used DTS in vertical wells for monitoring purposes (Patterson et al., 2017), its application in horizontal EGS wells holds significant promise for detecting thermal short-circuiting in real-time. This combined approach has the potential to significantly improve heat extraction and pave the way for a more efficient and sustainable future of geothermal energy.

Secondly, the system utilizes Inflow and Injection Control Devices (ICDs) installed in the injection well and production well. Similar to their application in oil & gas for problems like water breakthroughs, ICDs can be adapted for geothermal use with minimal modifications. By analyzing the temperature data from the production well, operators can identify fractures or stages producing cooler water. This information allows them to precisely control fluid flow through these specific fracture flow pathways, ultimately limiting cold water production in the corresponding production well. This targeted approach prevents thermal short-circuiting and optimizes heat extraction efficiency.

Inefficient heat extraction plagues geothermal systems due to thermal short-circuiting, where water preferentially flows through some specific, highly conductive fractures. This bypasses untapped heat pockets and leads to early thermal breakthroughs. Our proposed flow management system tackles this challenge. Distributed temperature sensors (DTS) act as our downhole sentinels, pinpointing the problematic fracture by detecting its abnormally low temperature. In response, downhole inflow control devices (ICDs) strategically intervene, restricting flow through this "shortcut". This intervention fosters a more uniform temperature distribution across the reservoir, enabling balanced heat extraction from each zone. By eliminating the thermal shortcut and promoting even flow, our system significantly boosts heat extraction efficiency, maximizing the geothermal system's potential.

3. Numerical Implementation

Based on the aforementioned methodologies, the numerical model for the simulation of EGS operation with the real-time downhole flow control system is presented in this section. Figure 1 shows the 3-D geometry model and this model consists of (a) underburden and overburden layers for potential energy support; (2) a targeted layer for the heat extraction purpose as highlighted in red box ~ formation height is 150 m; (3) an injection horizontal well and a production horizontal well for fluid circulation ~ these two well are drilled parallelly and the well spacing is 400 m; (4) 11 induced fracture connecting the injection and production well ~ fracture spacing is equal, i.e., 100 m and fractures fully penetrate the geothermal formation. It is assumed that all fractures are fully propped and thus the thermal distressing effect has few impacts on fracture width. We also assume that the injection and production wells are completely cased and injected fluid circulates through the perforations. Detailed dimensions of the model can be found in Figure 1.

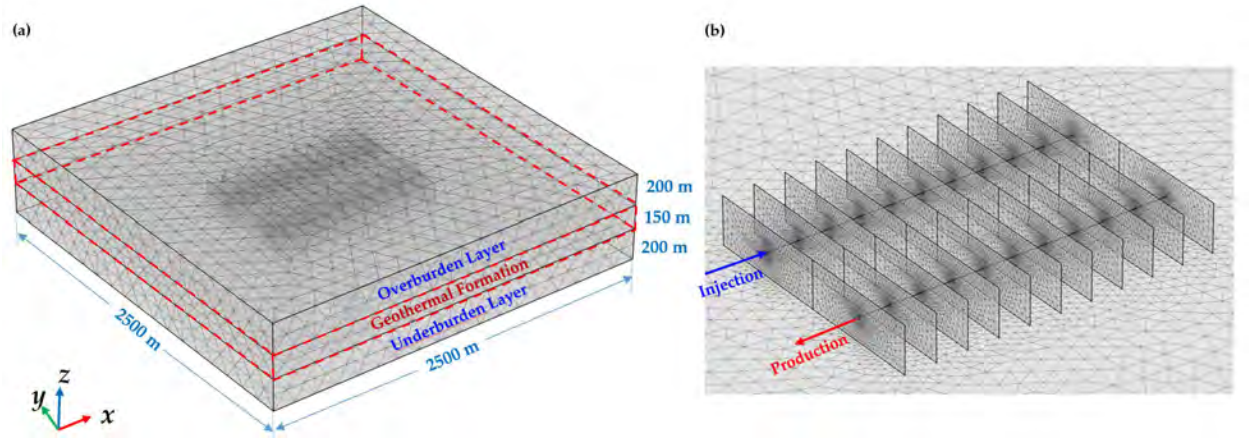

Figure 1: The 3-D geometry model and mesh generation.

The detailed parameters for the numerical simulation are listed in Table 1.

Table 1: Parameters for the simulation model

Parameter	Value	Unit
Size of the reservoir	2500×2500×550	m^3
Height of geothermal formation	150	m
Permeability of reservoir matrix	1	10^{-3} μm^2
Initial porosity of reservoir matrix	10	%
Initial porosity of fracture	20	%
Initial reservoir pressure	3.0×10^7	Pa
Initial reservoir temperature	473.15	K
Production rate	50	kg/s
Injection rate	50	kg/s
Injection temperature	313.15	K
Total calculation time	50	Year

Here, we assume that the hydraulic conductivities of each fracture are different, and distinct hydraulic conductivities in different fractures leave a great chance to form thermal shortcuts. The designed comparison of hydraulic conductivities among 11 fractures is shown in Figure 2. Fractures #2, #6, and #10 have higher hydraulic conductivity which can naturally accommodate more fluid flow through them.

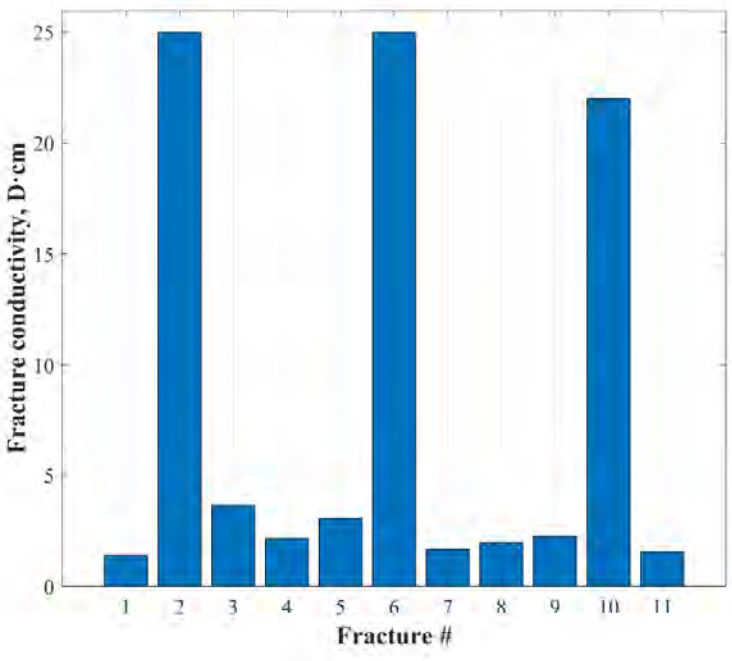

Figure 2: Distribution of fracture hydraulic conductivities in different fractures.

In this section, several simulation scenarios are designed for comparison, which are described as follows

- Case #1: No flow control in injection well or production well.
- Case #2: Flow control is implemented in both injection and production wells. The flow rate in each stage is calculated based on the produced fluid temperature at that stage as:

$$q_{\text{in}}^{a} = \frac{T_{\text{out}}^{a} - T_{\text{in}}}{\sum_{i=1}^{n}\left(T_{\text{out}}^{i} - T_{\text{in}}\right)} q_{\text{in,total}}, \; q_{\text{out}}^{a} = -q_{\text{in}}^{a}, \tag{6}$$

where $T_{\text{out}}{}^{a}$ is the produced fluid temperature from fracture #*a*. T_{in} is the injection temperature which is 313.15 K in this study. $q_{\text{in, total}}$ is the total injection rate. $q_{\text{in}}{}^{a}$ is the injection rate through fracture #*a*. $q_{\text{out}}{}^{a}$ is the production rate from fracture #*a*. *n* is the total fracture number, i.e., 11.

Based on the established numerical model and simulation scenarios, numerical simulations are conducted to investigate real-time flow rate adjustment using produced fluid temperature data.

4. Results and Discussions

Simulations reveal a stark contrast between scenarios with and without the proposed flow management system. Figure 3a depicts the temperature distribution within the fracture system after 50 years in a case without flow management (Case #1). The figure exposes the detrimental effects of thermal short-circuiting, particularly in stages #2, #6, and #10. where significantly cooler temperatures indicate bypassed heat. Conversely, Figure 3b showcases the temperature profile after 50 years in a case with the flow management system implemented (Case #2). The injection

and production rates are adjusted based on Eq. (5) after each time step during the numerical simulation. The figure convincingly demonstrates the system's effectiveness. Instead of concentrated hot zones, a more uniform and balanced temperature distribution is evident across all stages, signifying efficient heat extraction throughout the entire fracture system. This visualization underscores the significant improvement in overall heat extraction efficiency achieved by the proposed flow management system.

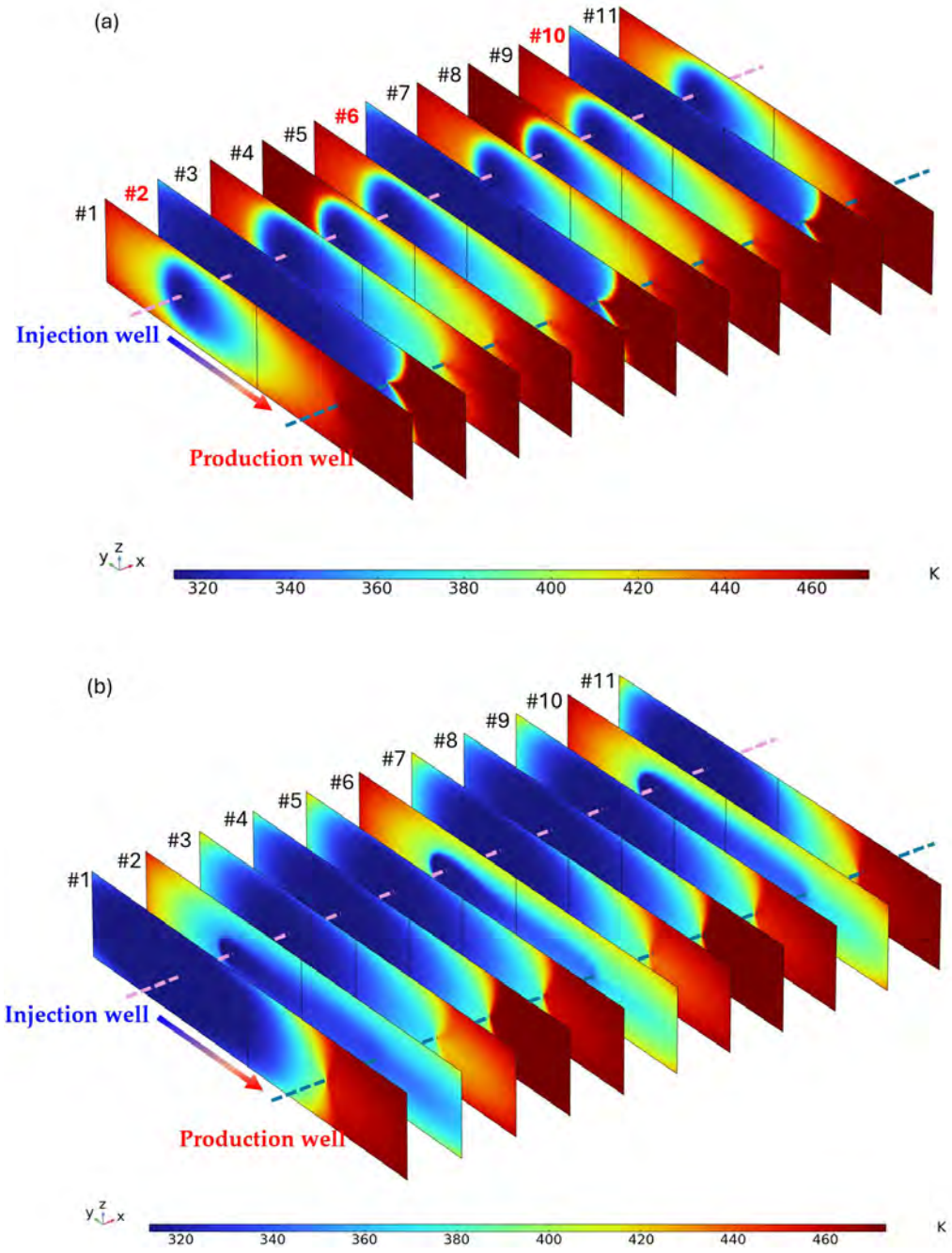

Figure 3: Distribution of fluid temperature distribution in the fracture system: (a) without flow control; (b) with proposed flow control.

Figure 4 shows the produced fluid temperature from different fractures over 50 years of operation. It could be seen that due to high hydraulic conductivities, fractures #2, #6, and #10 have larger decline rates regarding the temperature drop, which indicates a potential thermal short-circuit. However, given the installment of the real-time downhole flow control system, there are inflection points that appear on these 3 curves at around 3rd year of operation, which significantly delay the temperature drop in these fractures and thus prevent the thermal short-circuiting to get worse (The timing of inflection points is the time of early thermal breakthrough in these fractures). These inflection points are generated due to the adjustment of the injection rate and the production rate, which also suggests that the application of the flow management system can significantly enhance production efficiency.

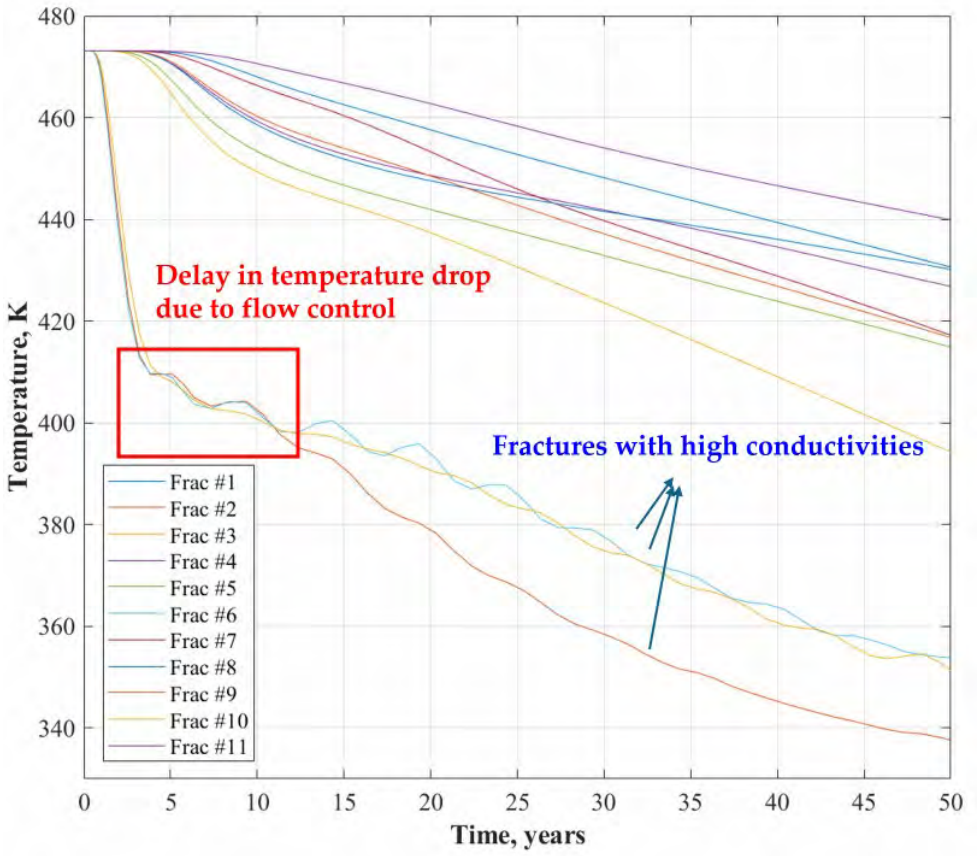

Figure 4: Comparison of temperature of produced fluid from different fractures over 50 years of operation.

Figure 5 shows a comparison of real-time injection and production rates in different fractures over 50 years of operation. At the beginning of the EGS operation, since there are 11 fractures that share 50 kg/s fluid circulation, each fracture has an initial circulation rate of 4.545 kg/s. After that, the ICDs adjust the flow rate in different fractures continuously. It could be seen that, since fractures #2, #6, and #10 have much larger hydraulic conductivities and lower local temperatures (see Figure 4), the installed valves in the injection well and production well are lowering the circulation rates through these fracture for the entire 50 years. After 50 years of operation, the circulation rate in fracture #2 declined from 4.545 kg/s to 1.248 kg/s, which is a 72.5% decline. By contrast, for those fractures that maintain high produced fluid temperature, the installed valves in the injection well and production well increase the circulation rates through these fractures for the entire 50 years.

For instance, after 50 years of operation, the flow rate in fracture #11 has increased by 44.3%, from 4.545 kg/s to 6.559 kg/s. This real-time management of flow rate across the system ensures that the geothermal system is operating in a highly efficient way.

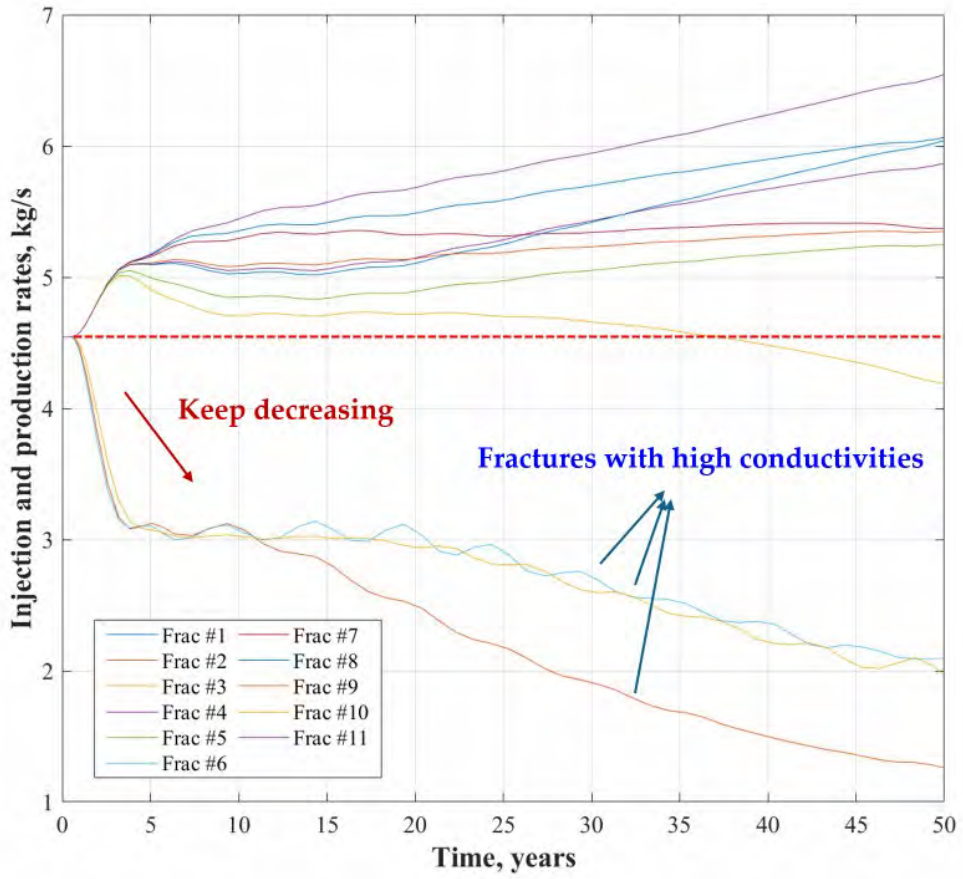

Figure 5: Comparison of real-time injection and production rates in different fractures over 50 years of operation.

Figure 6 shows a quantitative comparison of the overall temperature of produced fluid between cases 1 and 2. It can be seen from the figure that, when the ICDs are not installed, we are not able to control the fluid flow into the production well. The temperature of the produced fluid would keep decreasing from the beginning to the end. Over the 50 years of production, the temperature of the produced fluid in case 1 decreases by 30.18 K, from 473.15 K to 378.67 K. However, when the autonomous subsurface valves are installed in the geothermal system, the temperature of the produced fluid would be much higher than that in Case 1, decreasing from 473.15 K to 414.77 K. In other words, the application of a flow management system can effectively increase the temperature of the produced fluid. By utilizing the proposed flow management system, operators can expect a higher production temperature even after long-time production, and thus the effective operation time for the EGS can be effectively prolonged.

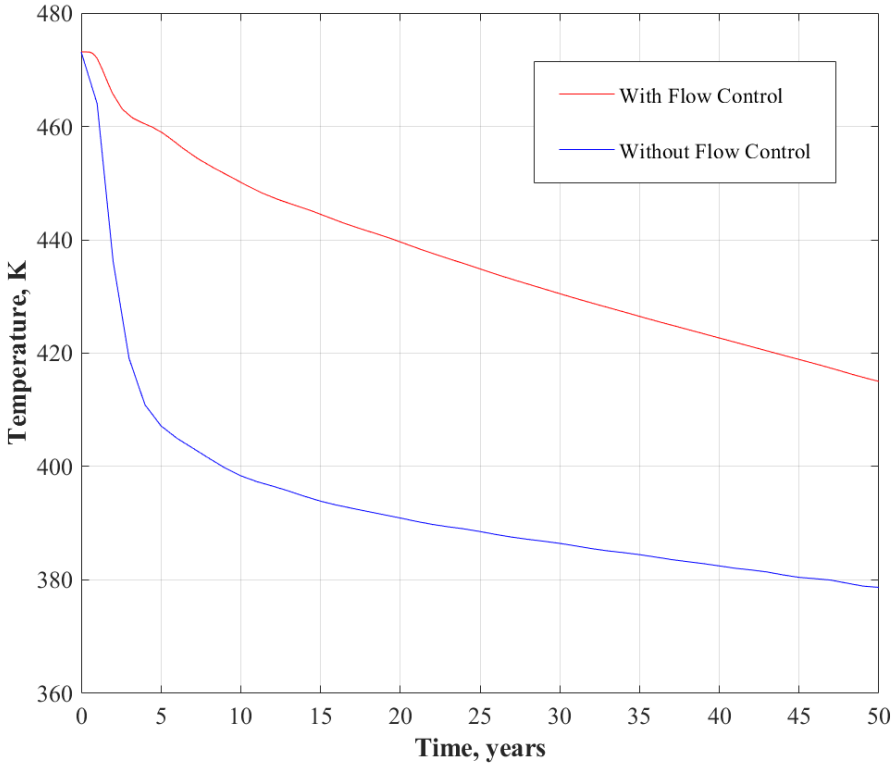

Figure 6: Comparison of overall produced fluid temperature over 50 years of operation.

5. Conclusion

This paper introduces a novel downhole flow management system for enhanced geothermal systems (EGS) utilizing horizontal wells to significantly improve heat extraction. These temperature-sensitive devices reside within the wellbore, dynamically adjusting injection rates in different sections based on the real-time temperature of the produced fluid. This targeted approach tackles the pervasive issue of thermal short-circuiting, where preferential flow paths exploit specific fractures, bypassing vast areas of untapped geothermal energy. We investigated the system's effectiveness in mitigating this challenge. By leveraging real-time downhole data, the system autonomously manages thermal shortcuts along the wellbore, restricting cold water injection into corresponding zones. Our numerical simulations demonstrate a substantial improvement in heat extraction: with constant pressure in the EGS, the produced fluid temperature can be about 40 K higher compared to a system without Inflow Control Devices (ICDs). The benefits of this system are even more pronounced in EGS with significant variations in fracture conductivity. This research provides valuable insights into the efficient management of fluid circulation within horizontal well EGS, paving the way for substantially increased heat extraction and a more sustainable future for geothermal energy.

Acknowledgment

This material is based upon work supported by the U.S. Department of Energy's Office of Energy Efficiency and Renewable Energy (EERE) under the Geothermal Technologies Office, Award Number DE-EE0009787.

REFERENCES

Al Balushi, F., Zhang, Q., and Dahi Taleghani, A. Autonomous Fracture Conductivity Using Expandable Proppants in Enhanced Geothermal Systems. *SPE Journal*, (2023a), 28(05), 2660-2674.

Al Balushi, F., Zhang, Q., and Dahi Taleghani, A. Improving enhanced geothermal systems performance using adaptive fracture conductivity. *Applied Thermal Engineering*, (2023b), 233, 121206.

Li, T., Shiozawa, S., and McClure, M. W. Thermal breakthrough calculations to optimize design of a multiple-stage Enhanced Geothermal System. *Geothermics*, (2016), 64, 455-465.

Liu, H., Wang, H., Lei, H., Zhang, L., Bai, M., and Zhou, L. Numerical modeling of thermal breakthrough induced by geothermal production in fractured granite. *Journal of Rock Mechanics and Geotechnical Engineering*, (2020), 12(4), 900-916.

Liu, S., and Dahi Taleghani, A. Analysis of an enhanced closed-loop geothermal system. *Geoenergy Science and Engineering*, (2023a), 231, 212296.

Liu, S., and Dahi Taleghani, A. Factors affecting the efficiency of closed-loop geothermal wells. *Applied Thermal Engineering*, (2023b), 222, 119947.

McLean, and M. L., Espinoza, D. N. Thermal destressing: Implications for short-circuiting in enhanced geothermal systems. *Renewable Energy*, (2023), 202, 736-755.

Parker, R. The Rosemanowes HDR project 1983–1991. Geothermics, (1999), 28 (1999) 603–15.

Patterson, J.R., Cardiff, M., Coleman, T., Wang, H., Feigl, K.L., Akerley, J., and Spielman, P., Geothermal reservoir characterization using distributed temperature sensing at Brady Geothermal Field, Nevada. *The Leading Edge*, (2017), 36(12), 1024a1-1024a7.

Santos, L., Dahi Taleghani, A., and Elsworth, D. Repurposing abandoned wells for geothermal energy: Current status and future prospects. *Renewable Energy*, (2022), 194, 1288-1302.

Tester, J.W., Anderson, B.J., Batchelor, A.S., Blackwell, D.D., DiPippo, R., et al. The future of geothermal energy. Massachusetts Institute of Technology, (2006), 358 (2006)1-3.

Zhang, Q., and Dahi Taleghani, A. Autonomous fracture flow tunning to enhance efficiency of fractured geothermal systems. *Energy*, (2023), 281, 128163.

Zhang, Q., and Dahi Taleghani, A. Intelligent fluid flow management for enhanced geothermal system in fractured horizontal wells. *Applied Thermal Engineering*, (2024), 239, 122191.

Geochemistry

Predicting Hydrothermal Reservoir Depth from Chemical Geothermometers Using a Three-Dimensional Temperature Model in the Great Basin, USA

Jacob DeAngelo[1], Erick R. Burns[1], and Stanley P. Mordensky[2]

[1]U.S. Geological Survey, Moffett Field CA 94035, USA

[2]U.S. Geological Survey, Spokane WA 99201, USA

Keywords

Chemical geothermometers, Great Basin, temperature, geothermal, strain rate, crustal thickness, permeability, hydrothermal, heat flow

ABSTRACT

Recent work in the Great Basin region of the western United States has made it possible to predict the depth of hydrothermal reservoirs (i.e., the depth at which heat is accumulated prior to ascent via hydrothermal upflow) identified through geochemistry and to contextualize the spatial patterns of these reservoir depths. Chemical geothermometers use the chemical and mineral constituents of hydrothermal fluids to predict the temperature at which fluids equilibrated with the host rocks at depth. Assuming that most of the Great Basin is dominated by conductive conditions until a vertically connected hydrothermal flow path is created (e.g., by faulting), geothermometers reflect the chemical and thermal conditions at the depth interval that the fluid has conductively equilibrated over a long period before a vertical conduit allows convective upflow. By pairing geothermometer temperature estimates with our recent three-dimensional temperature model of conductive heat flow in the Great Basin, we estimate the corresponding reservoir depths and construct a map of circulation depths.

The predicted depths from geothermometers have spatial patterns across the Great Basin that relate to patterns seen in other geologic and geophysical data. Deeper springs generally occur disproportionately in areas with higher strain rates and in basins. We posit that current elevated strain rates reflect patterns of historic deformation where ongoing tectonic activity maintains permeable pathways to deeper reservoirs, some of which are estimated to exceed 6 km depth. Basins, as expected, contain a disproportionate number of these deep systems, because the underlying aquifers are closer to the surface in basins, thus requiring less water pressure to reach the surface than in mountain ranges. Most springs estimated to have their source in a deep reservoir occur at places known to host a hydrothermal system; these refined depth estimates of the source

reservoir can help to better constrain the source depth for many known hydrothermal systems across the Great Basin.

1. Introduction

We extract depth estimates from chemical geothermometer estimates (hereafter, geothermometers) in the Great Basin using a recent three-dimensional conductive heat flow temperature model (Burns et al., 2024; DeAngelo and Burns, 2024). Geothermometers use the chemical and mineral constituents of hydrothermal fluids to predict the temperature at which these fluids equilibrated with the host rocks. Equilibration occurs whenever water spends sufficient time residing or flowing through a depth interval (e.g., permeable geologic layer), so the geothermometer represents the most recent equilibrium before rapid ascent of the water through a hydrothermal conduit (Kennedy et al., 2020); the term "rapid" only implies that travel time is fast relative to chemical reaction rates, so that the mineral content of the water still represents temperature and compositional conditions at the depth interval of the most recent equilibration. The reservoir depth estimates therefore represent an estimated depth of equilibration (i.e., the depth at which lateral flow is accumulated and starts its rapid ascent). The Burns et al. (2024) temperature model is a one-dimensional conductive heat flow model that uses a recent conductive heat flow map of the Great Basin (DeAngelo et al., 2023a) along with equations from Williams and DeAngelo (2011) that assume steady-state conditions, negligible convective heat flow, uniform constant radiogenic heat production with depth, and varying sedimentary unit thickness to estimate temperature between 0 and 7 km depth. The heat flow model (DeAngelo et al., 2023a) took steps to remove the influence of wells reflecting hydrothermal upflow and groundwater recharge, thus depicting only broad regional heat flow variations. This results in a temperature model that does not represent convective heat flow from hydrothermal systems or local effects from groundwater recharge; it depicts conductive conditions only with thermal gradients that are nearly linear within sedimentary units or underlying rock.

2. Methods

2.1 Geothermometer Data

Geothermometer temperatures for wells and springs in the Great Basin were obtained from the Nevada Bureau of Mines and Geology (Mlawsky and Ayling, 2020, Fig. 1). For each well or spring location, all available geothermometer temperatures were used to extract corresponding depths from the 2024 U.S. Geological Survey (USGS) three-dimensional temperature model of the Great Basin (Burns et al., 2024). Three geothermometers were present in the data, one cation and two silica geothermometers: the cation geothermometer Na-K-Ca (Fournier and Truesdell, 1973); and silica geothermometers: quartz and chalcedony (Fournier, 1977), though many of the wells and spring samples had only some or none of the geothermometers present. The geothermometers used the following equations:

Na-K-Ca: $$T = \frac{1647}{\log\left(\frac{Na}{K}\right) + \beta\left[\log\left(\frac{\sqrt{Ca}}{Na}\right)+2.06\right] + 2.47} - 273.15$$ Fournier and Truesdell (1973) (1)

Quartz (SiO_2): $$T = \frac{1309}{5.19 - \log\left(SiO_2\right)} - 273.15$$ Fournier (1977) (2)

Chalcedony (SiO_2): $$T = \frac{1032}{4.69 - \log\left(SiO_2\right)} - 273.15$$ Fournier (1977) (3)

Where T, Na, K, Ca, SiO_2, are temperature in °C, sodium concentration in mg/L, potassium concentration in mg/L, calcium concentration in mg/L, and silica concentration in mg/L, respectively. For the Na-K-Ca geothermometer, $\beta = 1/3$ if $\left[\log\left(\frac{\sqrt{Ca}}{Na}\right) + 2.06\right] < 0$, otherwise $\beta = 4/3$ unless the resulting temperature exceeds 100°C, in which case $\beta = 1/3$.

Different geothermometers produce valid results within different temperature ranges. Equations for silica geothermometers (e.g., quartz, chalcedony) presented in Fournier (1977) are described as relating silica content to temperature in the range of 0-250°C but further states: "*The quartz geothermometer probably works best in the temperature range 150-225°C"*. The Na-K-Ca geothermometer (Fournier and Truesdell, 1973) was developed using data ranging in temperature from 4-340°C, though Li (2000) recommends its use above 200°C. The maximum temperatures reported for the Na-K-Ca, quartz, and chalcedony geothermometers were 284°C, 243°C, and 234°C, respectively.

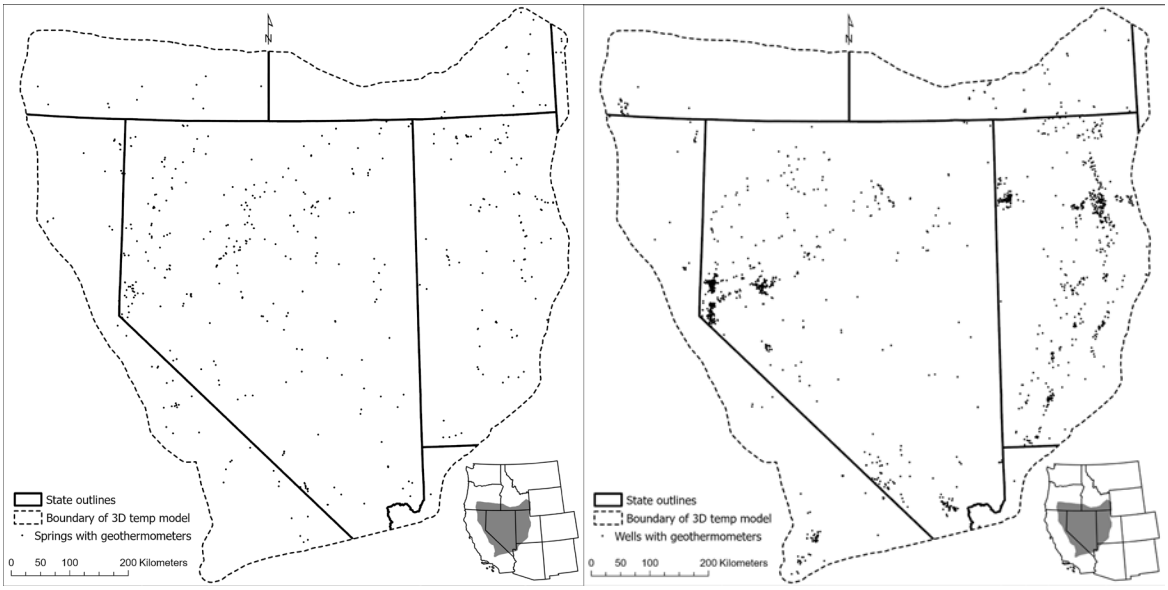

Figure 1: Distribution of springs (left) and wells (right) containing geothermometer temperatures with charge balance not exceeding ± 5% (Mlawsky and Ayling, 2020) shown above the boundary of the temperature model (Burns et al., 2024) and state outlines (U.S. Geological Survey, 2023b).

2.2 Estimation of Depth

Depth was estimated using the nearest thermal profile of Burns et al. (2024) by linearly interpolating depth proportionally between the two temperatures bracketing each geothermometer temperature. The Burns et al. (2024) model assumes conductive conditions only; it does not depict convective effects from known hydrothermal systems or groundwater flow. Associated depth estimates, therefore, assume a conductive gradient. The Burns et al. (2024) model estimates temperature up to 7 km depth; any geothermometers with a corresponding depth greater than 7 km were labeled as having a 7 km depth and can be assumed to be greater than 7 km depth.

2.3 Conceptual Model

For a spring at the surface to release water from a deep reservoir, there must be permeable pathways leading to that deep reservoir. These pathways must be maintained with new fractures

generated from faulting more quickly than they seal shut from mineral precipitation as fluids migrate through changing temperature, pressure, and compositional conditions. However, if a fracture pathway intersects shallower reservoirs, the water at the surface will be dominated by water from the shallower reservoirs with geothermometers reflecting the lower temperatures , even if hydraulic properties are the same. This is because flow path resistance is proportional to flowpath length (Darcy, 1856), with shorter flowpaths being the easier path. A spring discharging water from a deep reservoir must therefore have very few connections to shallower reservoirs along its path. There is likely some mixing along the way, but to have geochemical conditions reflecting a high temperature, most of the flow must have originated from a single deep horizon that equilibrated with the surrounding conductive temperature conditions at depth.

2.4 Histogram Maps

To visualize regional depth estimates, we plotted histograms (examples in Fig. 2) for 50 by 50 km cells in our study area depicting the count of nearby (within a radius reaching from the cell center to the corner) depth estimates for the different geothermometer types. Samples with a charge balance exceeding ± 5% are not considered valid for reliable geothermometer estimates and were therefore excluded (Nordstrom et al., 1989; Appelo and Postma, 2005). To account for geographic clustering of data, all well or spring observations in geographically clustered areas aside from the minimum, median, and maximum values within a 1 by 1 km cell were excluded.

The different styles of plots in Fig. 2 depict: A) the *raw* count with each plot showing a maximum of 20 records per bin; B) a *scaled* depiction where the maximum number of depicted records is equal to the size of the largest bin; and C) a *presence /absence* plot where a full color bar is given if any observations fall into the bin. These are included to offer visualizations that allow one to see where deeper reservoirs are predicted, even when there are relatively few observations. The individual histograms seen in Fig. 2 comprise the 50 by 50 km blocks in the histogram plots in subsequent figures. Colors in the histogram correspond to depth to make it easier for an observer to see where deeper depths were predicted.

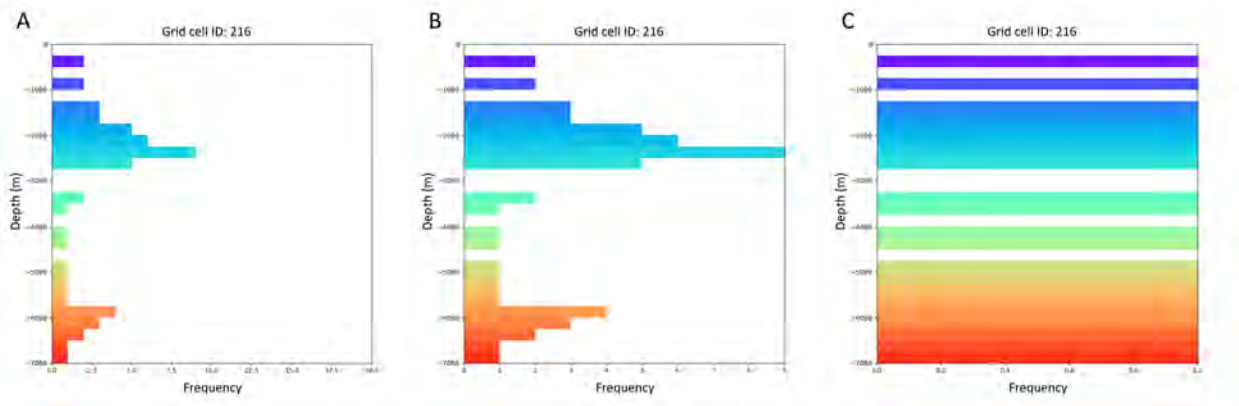

Figure 2: Example histograms for a single 50 km grid cell depicting the frequency of depth estimates based on geothermometers. These three histograms depict the same data and show, A) the raw counts, B) scaled to maximum to emphasize the local pattern, and C) presence/absence to emphasize depth intervals that may be permeable.

2.5 Comparison to Other Regional Maps

We compare geothermometer depth estimates to regional models for strain rate (Zeng, 2022), heat flow (DeAngelo et al., 2023a), and derivatives of elevation data that separate the local basin and range elevation signal from regional trends in elevation (DeAngelo et al. 2023b). We select the strain rate model (i.e., the second invariant of strain derived from geodetic observations) from Zeng et al. (2022) to examine how deeper geothermometer estimates correspond to rates of overall deformation under the hypothesis that elevated strain rates may be an indication of increased tectonism that could provide a continued connection to deeper reservoirs. We select the conductive heat flow from DeAngelo et al. (2023a) to see whether deeper geothermometer estimates fall disproportionately in areas of higher or lower heat flow. We select elevation trend from DeAngelo et al. (2023b) as a proxy for crustal thickness to test whether thermal springs with estimated deep sources occur disproportionately in areas with thinner crust. We also look at detrended elevation from DeAngelo et al. (2023b), which depicts elevation relative to the basin-range interface (generally with positive values in ranges and negative values in basins) to see whether deeper springs fall disproportionately in basins.

To understand whether deeper reservoir estimates preferentially fall in areas with disproportionately higher or lower values of the features mentioned above, we inspect the rank order of said features at locations of relatively deep springs. By isolating the rank order for features at only the deeper springs (deeper than 3 km using quartz estimates), we compare the distribution of rank values for deeper springs to the values from the entire study area. Proportionally higher ranks indicate preferentially higher values in features; likewise, proportionally lower ranks preferentially indicate lower feature values.

3. Results

Fig. 3 shows the combined counts of estimated depth from all declustered wells and springs at each 50 by 50 km cell (as illustrated in Fig. 2) across the study area to provide a visualization of where geothermometer estimates correspond to relatively deep source depths. The columns in Fig. 3 show the three different styles of histograms (raw, scaled, presence/absence); the rows show the three geothermometer types (Na-K-Ca, quartz, chalcedony). Most frequently, reservoir depths are in the range 0-2 km, as shown by blue histogram bars across most of the Great Basin in all visualizations in Fig. 3, but reservoir depths over 6 km are present over parts of the study area, shown by the warmer (i.e., redder) colors. Areas with deeper estimates suggest deep reservoirs and tend to be near northwest Nevada or along the Wasatch Front (i.e., areas known to host hydrothermal activity [Faulds et al., 2021]), with the greatest proportion in the northwest quadrant of Nevada and relatively few in the central Great Basin in the areas surrounding the Nevada-Utah border.

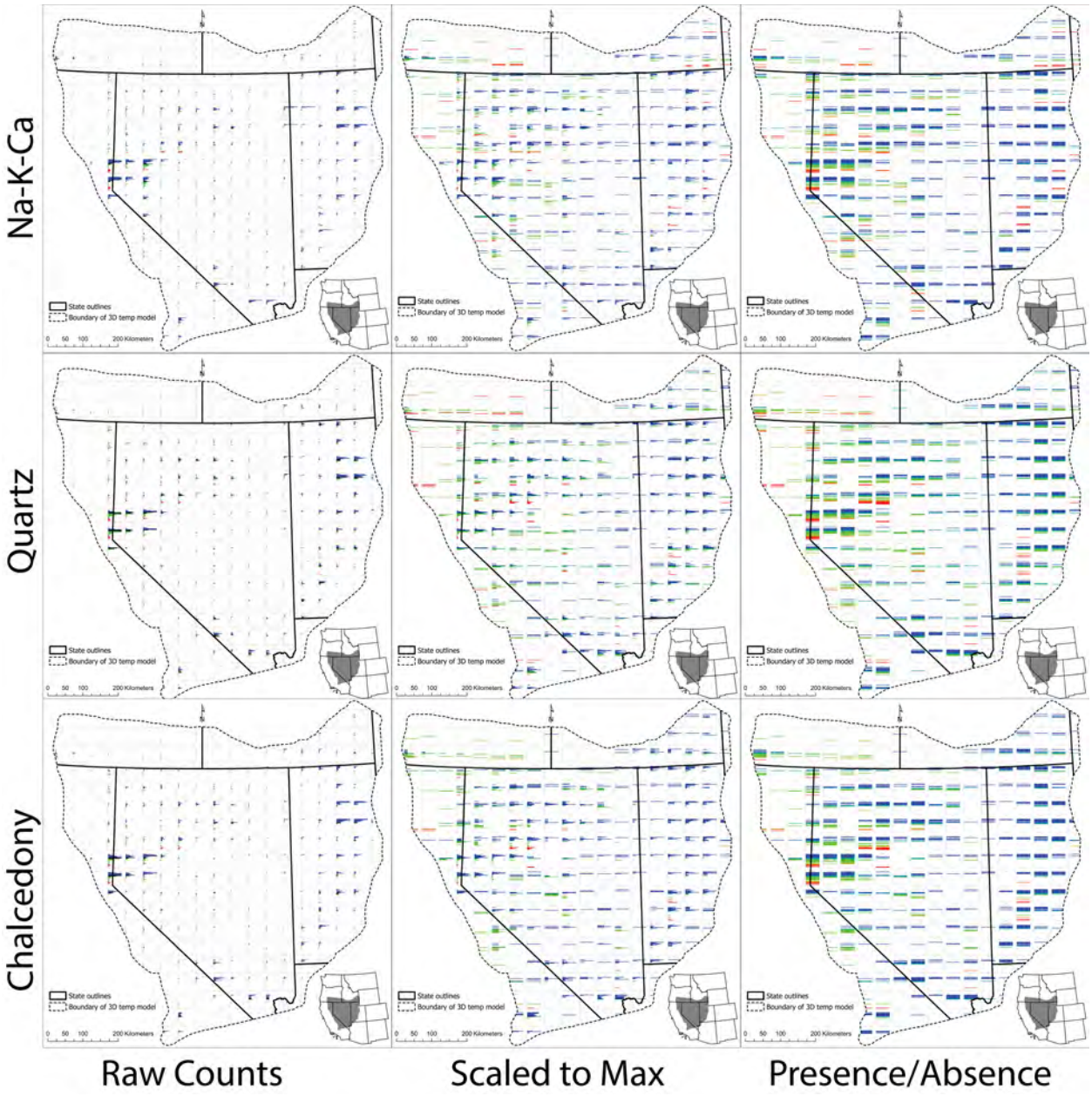

Figure 3: Histogram plots for the Na-K-Ca, quartz, and chalcedony geothermometers (rows from top to bottom), with raw, scaled, and presence/absence plotting styles (columns from left to right). All plots contain histograms showing the frequency of nearby depth values predicted from a combined data set of all declustered wells and springs with charge balance not exceeding ± 5%.

4. Discussion

Maps in Figs. 4A-C compare only springs (i.e., not wells) to known hydrothermal systems (Fig. 4A; Faulds et al., 2021), geodetic strain rate (Fig. 4B; Zeng, 2022), and detrended elevation (Fig. 4C; DeAngelo et al., 2023b). Most of the deeper springs (deeper than 3 km using quartz estimates with charge balance not exceeding ± 5%) are associated with known hydrothermal systems (Fig.

4A). These hydrothermal systems do not have reported values for estimated reservoir depths; however, extrapolating depths informed by the geothermometer estimates from the Burns et al., (2024) temperature model allows for a better understanding of the possible reservoir depths of known geothermal systems.

Fluids from deeper reservoirs (e.g., 6 km; Fig. 3) require permeable pathways to reach the shallow subsurface. The results presented in Figs. 4B and D suggest that active ongoing tectonic deformation in these areas correlates with maintaining these permeable pathways (Kennedy et al., 2020). The current strain rates reflect current deformation, but likely also reflect past deformation. Areas with deeper predicted reservoirs generally have been experiencing higher deformation rates relative to the larger study area, which may have been creating and maintaining sufficiently high permeability to outpace mineral precipitation in the pathways from deep reservoirs. Fig. 4D shows that deeper springs tend to be correlated with higher strain rates, as the blue line is higher than the 1:1 'Entire Great Basin' line throughout, with approximately 40% of deep springs being in areas in the top 80% of strain values. These deeper reservoirs must have some component of lateral flow, and perhaps they exist in horizontally permeable strata throughout the Great Basin (either primary or secondary permeability). Although the evidence shows springs with estimated depths deeper than 5 km depth in many areas across the Great Basin, we do not see this in all areas. We postulate strain rates are insufficiently high in most areas to regularly establish and maintain vertical conduits with geologic units at 6 km depth, and therefore, there may exist hidden reservoirs at this depth in other areas (i.e., the absence of evidence does not imply the evidence of absence), and future studies could strive to develop methods to identify deep reservoirs that are currently untapped by hydrothermal circulation.

DeAngelo et al. (2023b) describe how patterns in regional elevation trends are likely a good proxy for variations in crustal thickness in the Great Basin, and that heat flow and crustal thickness appear to be inversely related in much of the Great Basin, because thinner crust results in less insulation between the atmosphere and the hot interior of the Earth. We sought to discover whether thinner crust (~1 km thickness differences observed across the Great Basin [DeAngelo et al., 2023b]) might also be allowing more surface expressions like deeper thermal springs to manifest from reservoirs that exist at the same sea level in areas with thicker crust, simply because there is a shorter path to the surface. Fig. 4D shows no evidence of this; deeper springs do not appear to be correlated with thinner crust, as the orange line for crustal thickness mostly has little divergence from the 1:1 'Entire Great Basin' line. We next looked at detrended elevation to see whether these deeper springs fell disproportionately in areas above or below the range front. These deeper springs overwhelmingly tended to fall in areas with low detrended elevation values (i.e. basins, see Figs. 4C, D); this is to be expected, because springs emerge at the surface in basins far more frequently than in ranges because the underlying aquifers are closer to the surface in basins, thus requiring less water pressure to reach the surface than in mountain ranges. Fig. 4D also shows a curve for raw elevation (U.S. Geological Survey, 2023a), which falls between the crustal thickness and detrended elevation curves. This is likely because the elevation data contain a mixture of signals for both detrended elevation and regional elevation (reflection of crustal thickness), and springs correlate strongly with the signal from detrended elevation, causing a correlation magnitude with raw elevation to fall between that of crustal thickness and detrended elevation. Additionally, heat flow exhibited only a modest amount of correlation with deep springs (Fig. 4D).

The discussion herein has ignored possible confounding effects of volcanism. Strain conditions that create vertical paths for water upflow could also conceivably create conduits for magma upwelling. Studies have shown that modern volcanism correlates with hydrothermal favorability (Smith and Shaw, 1975; Williams and DeAngelo, 2008). Therefore, in some cases, upwelling magma might conceivably bias depth estimates made from geothermometers. As the northwest corner of the study area occupies the transition between the Great Basin and the Northwest Volcanic Province (Sherrod and Keith, 2018, Glen et al., 2004), we postulate that some of the deeper estimates are likely affected by rising magma; the same could be occurring in volcanic areas of eastern California. Hence, the associations we identify between estimated geothermometer depths and strain rate are broad trends rather than a complete explanation.

This paper is intended as a proof of concept to begin discussions about using geothermometers as a tool to estimate reservoir depths in the Great Basin. Future work could focus on better understanding the reliability of the various geothermometers based on whether minimum chemical concentrations should be present, whether pH should be within certain limits, whether other geothermometers should be generated to provide additional support, and other related considerations. Herein, the focus has been on the temperature estimates made from hydrothermal waters, but future efforts might also consider the chemistry of these fluids to answer questions like:

- Does the chemistry and/or mineralogy tell us anything about the reservoir itself?
- Can we compare this chemistry across regions to postulate whether these deep reservoirs extend for great distances?
- Does the water chemistry show evidence of magmatic degassing?

Understanding these questions could help to uncover whether deep reservoirs may exist laterally at a great scale throughout the Great Basin.

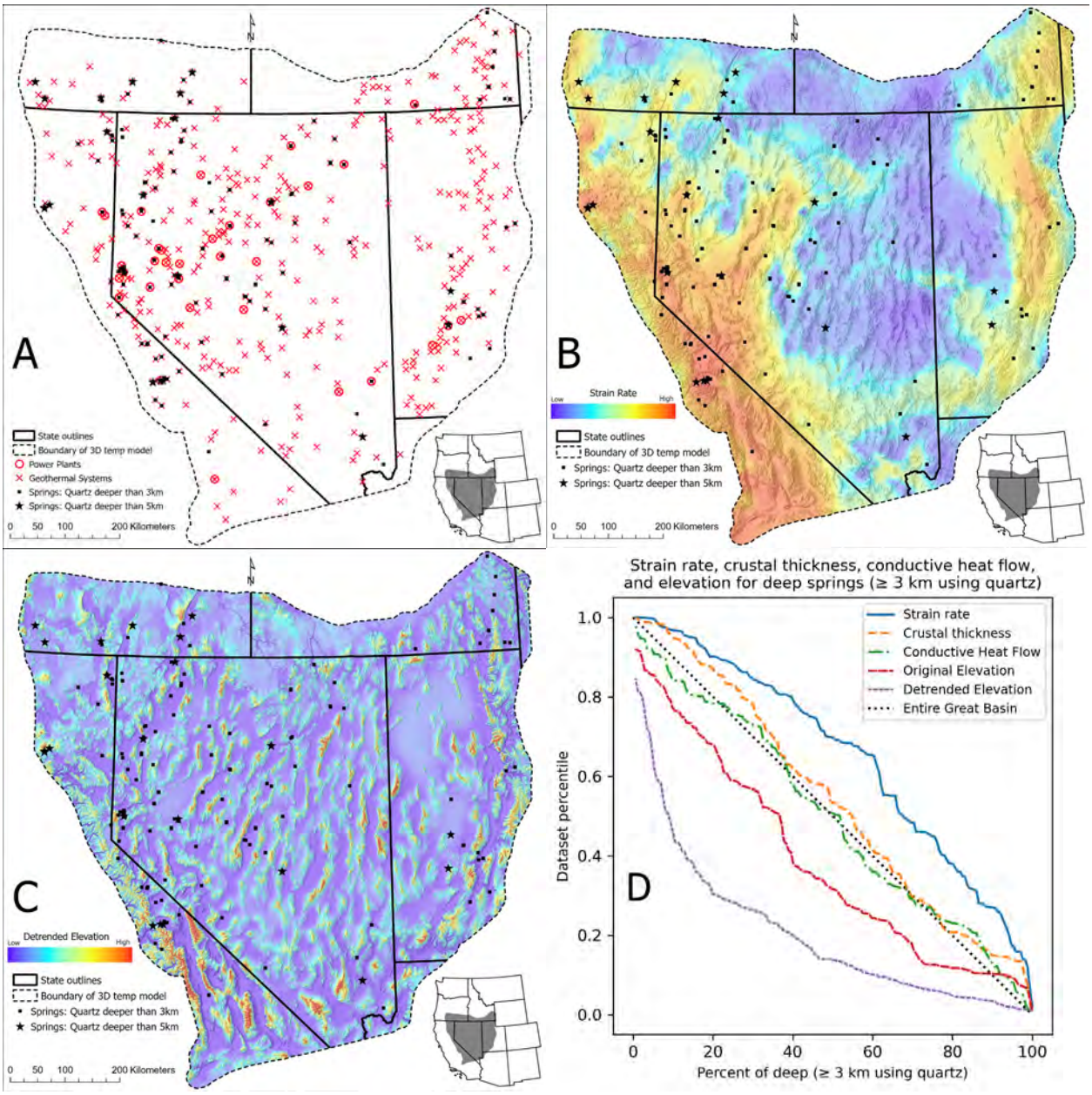

Figure 4: A) Springs with relatively deep (≥ 3 or ≥ 5 km) quartz geothermometer reservoir estimates overlain upon locations of known geothermal systems and power plants (Faulds et al., 2021). B) Strain rate (Zeng, 2022) with deep quartz springs plotted, C) Detrended elevation (DeAngelo et al., 2023b) with deep quartz springs plotted, D) Predictive skill for all features examined: the 1:1 "Entire Great Basin' line depicts values across the entire study area and the curves for features that depart from the 1:1 line show that deeper springs (≥ 3 km using quartz) have disproportionately high strain rate and low detrended elevation (i.e. basins). Hillshade for B) and C) is derived from USGS National Atlas (National Atlas of the United States, 2012).

5. Data Release

A USGS data release (DeAngelo and Burns, 2024) that supports this paper contains the well and spring data with estimated depths from all available geothermometers, including those with a

charge balance exceeding ± 5%; the data release also contains the georeferenced histogram plots shown in Fig. 3.

Acknowledgement

This study was funded by the U.S. Geological Survey Energy Resources Program and the U.S. Department of Energy - Geothermal Technologies Office under award DE-EE0009254 to the University of Nevada, Reno for the INnovative Geothermal Exploration through Novel Investigations Of Undiscovered Systems (INGENIOUS). Any use of trade, firm, or product names is for descriptive purposes only and does not imply endorsement by the U.S. Government.

REFERENCES

Appelo, C.A.J., Postma, D., 2005, *Geochemistry, Groundwater and Pollution*, 2nd edition. A.A. Balkema, Rotterdam.

Burns, E.R., DeAngelo, J., and Williams, C.F., 2024, *Updated three-dimensional temperature maps for the Great Basin*, USA, Proceedings 49th Stanford Geothermal Workshop, Stanford, California, February 12-14, 2024, SGP-TR-227.

Darcy, H., *Les Fontaines Publiques de la Ville de Dijon*, Dalmont, Paris, 1856.

DeAngelo, J., Burns, E.R., 2024, *Depth predictions of chemical geothermometers estimated using a three-dimensional temperature model in the Great Basin*, USA: U.S. Geological Survey Data Release, https://doi.org/ 10.5066/P14B8XOH.

DeAngelo, J., Burns, E.R., Gentry, E., Batir, J.F., Lindsey, C.R., Mordensky, S.P., 2023a, *New Maps of Conductive Heat Flow in the Great Basin, USA*: Separating Conductive and Convective Influences, Proceedings 48th Stanford Geothermal Workshop, Stanford, California, 6-8 February 2023.

DeAngelo, J., Burns, E.R., Mordensky, S.P., Lindsey, C.R., 2023b, *Detrending Great Basin Elevation to Identify Structural Patterns for Identifying Geothermal Favorability*. Geothermal Rising Conference Transactions. Reno, Nevada, 47, October 1-5, 2023.

Faulds, J. E., Coolbaugh, M. F., Hinz, N. 2021, *Inventory of structural settings for active geothermal systems and late Miocene (~8 Ma) to Quaternary epithermal mineral deposits in the Basin and Range province of Nevada*. Reno, NV: The Great Basin Center for Renewable Energy.

Fournier, R.O., 1977, *Chemical geothermometers and mixing models for geothermal systems.* Geothermics 5, 41–50.

Fournier, R.O., Truesdell, A.H., 1973. *An empirical Na-K-Ca geothermometer for natural waters*. Geochim. Cosmochim. Acta 37, 1255–1275.

Glen, J.M., McKee, E.H., Ludington, S., Ponce, D.A., Hildenbrand, T.G., Hopkins, M.J., 2004, *Geophysical terranes of the Great Basin and parts of surrounding provinces*: U.S. Geological Survey Open-File Report 2004-1008, 10.3133/ofr20041008.

Kennedy, B.M., Farquhar, A., Hilderman, R., Villeneuve, M.C., Heap, M.J., Mordensky, S.P., Kilgour, J., Jolly, A., Christenson, B., Reuschlé, T., 2020, *Pressure Controlled Permeability in a Conduit Filled with Fractured Hydrothermal Breccia Reconstructed from Ballistics from Whakaari (White Island), New Zealand*. Geosciences, 10(4), 138; https://doi.org/10.3390/geosciences10040138.

Li, J., Sagoe, G., Li, Y., 2020, *Applicability and limitations of potassium-related classical geothermometers for crystalline basement reservoirs*. Geothermics 84, 101728.

Mlawsky, E., Ayling, B.F., 2020, *GBCGE Subsurface Database Explorer and APIs, data set*, retrieved from: https://dx.doi.org/10.15121/1987556.

National Atlas of the United States, 2012, *100-Meter Resolution Elevation of the Conterminous United States. National Atlas of the United States*. Available at: http://purl.stanford.edu/zz186ss2071.

Nordstrom, D.K., Ball, J.W., Donahoe, R.J., Whittemore, D., 1989, *Groundwater chemistry and water-rock interactions at Stripa*. Geochim. Cosmochim. Acta 53, 1727–1740.

Sherrod, D.R., and Keith, M.K., 2018, *GIS database and discussion for the distribution, composition, and age of Cenozoic volcanic rocks of the Pacific Northwest Volcanic Aquifer System study area*: U.S. Geological Survey Open-File Report 2018–1030, 16 p., https://doi.org/10.3133/ofr20181030.

Smith, R.L., Shaw, H.R., 1975, Igneous-related geothermal systems, in White, D.F. and D.L. Williams, eds., *Assessment of geothermal resources of the United States – 1975*, United States Geological Survey Circular 726, 155p.

Sonney, R., Vuataz, F. D., *Validation of chemical and isotopic geothermometers from low temperature deep fluids of Northern Switzerland*, Proceedings World Geothermal Congress, vol. 14, no. 1423, pp. 1–12, 2010.

U.S. Geological Survey, 2023a, *3D Elevation Program 30-Meter Resolution Digital Elevation Model*, accessed August 01, 2022 at URL https://www.usgs.gov/the-national-map-datadelivery.

U.S. Geological Survey, 2023b, *USGS National Boundary Dataset (NBD) Downloadable Data Collection*: U.S. Geological Survey.

Williams, C.F., DeAngelo, J., 2008, *Mapping geothermal potential in the western United States*. Geothermal Resources Council Transactions, 32, p.181.

Williams, C. F., and DeAngelo, J., 2011, *Evaluation of Approaches and Associated Uncertainties in the Estimation of Temperatures in the Upper Crust of the Western United States*: GRC Transactions, Vol. 35.

Zeng, Y., 2022, *GPS Velocity Field of the Western United States for the 2023 National Seismic Hazard Model Update*. Seismological Research Letters, 93(6), 3121-3134. doi:10.1785/0220220180.

Stable Isotope Characterization of the High-Temperature Steam Reservoir of the Northwest Geysers: Review of Data Acquired During Step Out Drilling Program and Integration into 3D Geological Model

Steve DeOreo and Melinda Wright

Calpine Corporation

Keywords

Stable isotopes, 18-Oxygen, The Geysers

ABSTRACT

The high-temperature reservoir (HTR) in the northwest Geysers inherently produces steam of varying quality, for example, higher volatile chlorides than the normal-temperature reservoir (NTR) in the central and southeast Geysers. HTR rocks from the northwest central Prati area (formerly Central California Power Agency) have distinct delta18-Oxygen (δ18-O) isotopic signatures compared to rocks of the NTR, but HTR rocks from the nearby Aidlin and High Valley areas have isotopic signatures like the rocks of the NTR. Reservoir metagraywackes of the NTR have silicate δ18-O values as low as +3 ‰, while anomalously high values in metagraywackes in productive portions of the central northwest Prati HTR typically range from +8 to +10 ‰. This δ18-O anomaly in the Prati portion of the NW Geysers reservoir is particularly striking given that is bounded to the SW (Aidlin) and the NE (High Valley) by blocks which produce steam of comparable pressure and temperature from similar depths, suggesting that the deep Prati reservoir is not hydrologically isolated even if it is isotopically distinct.

Many previous studies have concluded that the primary cause of isotopically “light” rock compositions in the main Geysers field was pervasive flushing of the permeable reservoir rock by meteoric waters with an average value of -8‰, while permeable reservoir rock in the Prati HTR has not been pervasively flushed and is therefore producing steam from boiled connate and / or magmatic waters with δ18-O values near 0‰. Some studies have suggested mechanisms by which water flushing of the Geysers reservoir could have reached far northwest into the HTR sections of Aidlin and High Valley without impacting the HTR in the Prati area. One key line of evidence for such models is the overall lower noncondensable gas (NCG) content of steam produced from Aidlin and High Valley versus Prati HTR sections. Although stable isotope systematics have always been considered as supporting evidence in such studies, detailed software-based mapping of rock 18-O data has not previously been done at The Geysers.

Whole-rock and steam condensate samples have been collected continuously during drilling and flow testing of new geothermal wells between 2018 and 2024, and these samples have added to the existing legacy data set of >1,000 silicate 18-O analyses. Sampling from a new step-out drilling program in the northwest Geysers has also significantly increased data density in both the NTR and HTR sections in this area. The entire Geysers δ18-O whole rock isotope catalogue (now ~1,400 δ18-O analyses) has been turned into an interpolated 3D model using the radial basis function in Leapfrog Energy software. Integration of this new isotopic model with fault mapping, micro-earthquake (MEQ) hypocenter alignments, and lithology data has allowed for new insights into the possible fault controls for meteoric water flushing in the Northwest Geysers and its impact on HTR steam quality. This isotope map has also been used to assist in the planning and targeting of new geothermal wells at The Geysers.

1. Introduction

1.1 Overview of Oxygen Isotopes Systematics

Regional scale δ18-O compositional mapping of silicate minerals was first recognized as a prospecting tool in mining geology where large, economic ore bodies are created by deep circulation of heated meteoric waters which cause hydrothermal alteration of magma bodies and surrounding country rock (e.g. Criss et al., 1991 and references therein). Criss et al. noted that steep δ18-O gradients and "bullseye" map patterns generally pointed towards the centers of such deposits. Since large hydrothermal ore bodies are essentially the rock record of extinct geothermal systems, many workers realized that the Oxygen and Deuterium (O / D) stable-isotope systematics of ore bodies could be applied to understanding active geothermal systems, including The Geysers in northern California. Craig (1963) noted that most geothermal systems worldwide are composed of boiling meteoric water. As a result, typical water / rock interactions in hydrothermal systems consist of isotopically light meteoric water causing initially isotopically heavy δ18-O values of unaltered rock to be depleted to values closer to zero ‰, though exact isotope values of both waters and rocks will vary by region. In the Geysers / Clear Lake region, unexchanged metagraywackes of the Franciscan Formation outside of the geothermal field have values as high as δ18-O +17‰ (Hulen and Moore, 1995), and meteoric waters have δ18-O values of -7 to -8‰ (White et al 1973). Inside the Geysers geothermal reservoir, steam-condensate samples have δ18-O values of +3.2 to -6.8‰ (Lowenstern and Janik, 2003; Geysers unpublished data), and δ18-O values in silicate-mineral samples from reservoir-depth metagraywacke and granitoid intrusions ("the felsite") range from +2 to +10‰ (Geysers unpublished data).

As this wide range of δ18-O silicate and δ18-O / D water values suggests, The Geysers reservoir is not contained in a single homogeneous body of uniformly exchanged rock, but rather contains notable vertical and lateral δ18-O isotopic gradients which have been extensively studied and published on over the last 40+ years with implications for not only conceptual understanding of reservoir emplacement and evolution but also practical understanding of exploration, development and extraction. For example, the SE to NW increase in rock δ18-O values was used to interpret the magnitude and direction of meteoric water flushing (Truesdell et al., 1987; Walters and Beall, 2002); abrupt lateral shifts from low to high rock δ18-O values were used to infer fault bounded reservoir compartments in the northwest Geysers (Walters et al., 1996); δ18-O rock isotopic gradients were correlated with primary and secondary mineralogy profiles of well bores that approach and penetrate the felsite pluton that intruded the central and southeast Geysers (Moore and Gunderson, 1995); anomalously high 18-O water and rock isotopes in the northwest Geysers

were used to identify and characterize a distinct HTR component in the CCPA / Prati area (Haizlip, 1985; Truesdell, 1991; Walters et al., 1992); fluid inclusion studies of 18-O / D isotopes were employed to help characterize the fluid in multiple generations of vein paragenesis (Moore and Gunderson, 1995; Jones et al., 2016); and correlations have been made between low isotopic exchange in the reservoir with poor steam quality, i.e. high NCG and high chloride content (Gunderson, 1989, Beall et al., 2007).

1.2 Novel Application

This paper is written in the context of all the above research, but it is focused on the utility of the Geysers rock δ18-O isotopic database itself as an applied science tool that leverages all the research cited above. The sheer sample size, areal extent and data density of the dataset makes it an ideal candidate for interpolation into a geo-referenced 3D mesh body. This was done using the radial basis function in Leapfrog Energy software, though any similar 3D interpolation tool on various industry-standard software platforms could have been employed to achieve similar results. The resulting data visualization does not supplant any of the conceptual models referenced above, but rather helps validate them and leverage them into an exploration and well- targeting tool by integration with other data sets in 3D model space. Calpine is now using subsurface variation in rock δ18-O values to develop targets for new wells, which is a novel application of stable isotope data at The Geysers.

1.3 High-Temperature Reservoir (HTR)

The Geysers vapor-dominated system primarily produces steam from the normal-temperature reservoir (NTR) at temperatures up to 240° C. Starting in the 1980s, deeper drilling in the northwest Geysers encountered steam temperatures of up to 346° C (Walters et al., 1988; Unocal unpublished reports), which contained varying NCG concentrations and high volatile chlorides. Today, Calpine's Resource team delineates the top of the high-temperature reservoir (HTR) when reservoir temperature reaches 260° C and temperature gradients switch from convective to conductive. Recent drilling in the northwest Geysers validates the ongoing use of these criteria (Calpine unpublished data). Although the NTR and the HTR have distinct temperatures and geochemical characteristics, they are nonetheless connected, with no hydrologic or structural boundary between them (Walters et al. 1996). In some areas of the field (e.g. Aidlin), HTR steam was utilized commercially, while in other parts of the field, some HTR steam was initially considered not economically viable, e.g. former CCPA areas 2 and 3 (Walters et al. 1996). Steam with the highest NCG content was consistently found in HTR rocks that were less isotopically exchanged (Walters and Beall 2002). The northwest Geysers Enhanced Geothermal System (EGS) demonstration project deepened existing wells in the former CCPA leases farther into the HTR and encountered reservoir temperatures of 400° C (Garcia et al., 2016). Whole-rock δ18-O values from reservoir metagraywacke samples taken from the productive EGS reservoir ranged from +10 to +12‰, which are comparable to cap rock values in the rest of The Geysers (Lutz et al., 2012). The Geysers EGS project showed that injection of tertiary-treated recycled water could reduce the NCG content of the steam by up to 90% (Garcia et al., 2016), which significantly improves its economic viability, but the fundamental underlying observation that the deep northwest central (Prati / CCPA) Geysers HTR has experienced no natural meteoric-water flushing remains true, irrespective of these injection derived benefits to the reservoir. Further discussion of injection impacts at The Geysers are beyond the scope of this paper but are summarized in Beall et al. (2007).

2. Methods

The data set used to create the 3D model described in this study contains ~1,400 unique samples (with more pending at the lab) and is a fully validated and quality-controlled compendium of all the rock isotope data from the Geysers and surrounding delineation wells, including much (if not all) of the rock isotope data used in the references cited in the introduction. Figure 2 is a summary histogram of all δ18-O rock isotope data with a bin size of 0.5‰.

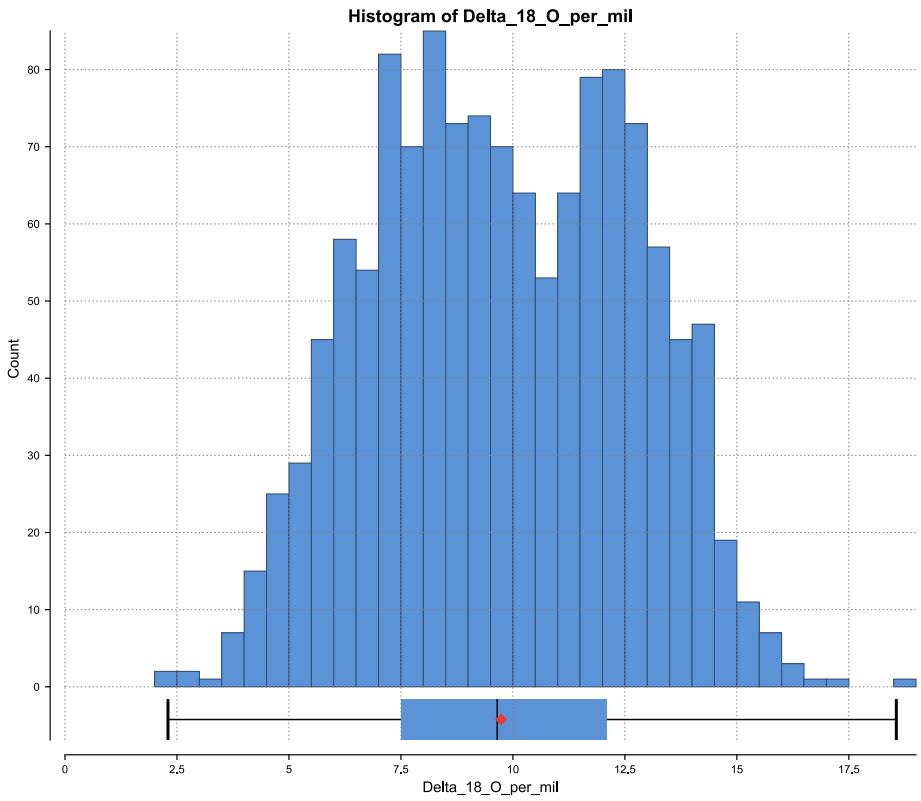

Figure 1: Histogram summarizing the entire δ18-O rock isotope database used to create the 3D rock isotope model described in this section. The catalogue was screened for anomalous values, and all georeferencing for each well's data set was cross checked against original well files and sampling notes.

Since 2019, ~300 new analyses have been completed, primarily on samples collected from new wells that Calpine has drilled at The Geysers. In 2021, 36 additional legacy samples were obtained from The EGI Geothermal Sample Laboratory in order to fill in some spatial gaps in the central and southeast Geysers. Rock isotope sampling has become part of Calpine's mud-logging and sampling standard operating procedure, including for recent drilling. Sample collection starts at ~2,000 feet (ft) measured depth in each newly drilled well and continues at ~500-ft intervals to total depth, hole conditions and rock type allowing. Only intervals logged as ≥80% graywacke or 100% felsite are considered for analysis. Samples are collected even in the shallow caprock to improve data density in the 3D model and to capture any isotopic variations that might occur in

the transition from caprock to the top of the steam reservoir. Steam-condensate samples are also collected for 18-O / D sampling at various stages during drilling and flow testing, but discussion of steam condensate isotopes is beyond the scope of this paper.

Samples were prepared following the same procedures that have been applied by various Geysers resource groups (multiple operating companies) since the mid 1990's, so that new data can be compared directly to historical data. Sample preparation procedures are described in Gunderson and Moore (1994) and bromine pentafluoride digestion of samples to extract oxygen from silicates is described in Clayton and Mayeda (1963). Analytical results in this paper are reported in delta notation relative to standard mean ocean water (SMOW). The Calpine Geysers Resource group and other previous resource groups have primarily employed the stable isotope lab at Southern Methodist University for the majority of the rock and water sample analyses continuously from the mid 1990's to the present.

3. Results

The primary utilities of the 3D rock isotope model are: 1) improved data visualization, 2) integration into existing conceptual models, and 3) application to well targeting. This section will give examples of each of these categories.

3.1 Data Visualization

Before discussing improved data visualization capabilities provided by this rock isotope 3D modeling effort, it should be said that using software interpolation to convert point clouds in the format (X,Y,Z + data) into body models is not a novel technique, nor is using various subsurface modeling software platforms to create map views and cross-sections of such data. Therefore, the intent here is to show that these well-established techniques have added value to a large and valuable Geysers legacy data set that was not previously utilized to its maximum potential. Previous renderings of the rock isotope data for The Geysers reservoir had been limited to plan view contour maps of average values from a wide range of reservoir depths shown at a single representative datum (e.g., Walters et al., 1996), or hand drafted cross sections which were time consuming to create and thus limited to one or two major section lines traversing the steam field per project (e.g. Garcia et al., 2015). Figure 2 is a series of map view depth slices of the rock isotope model focused on the northwest Geysers study area. This sequence of depth slices elucidates several features of the northwest Geysers reservoir that have long been understood (as discussed in section *3.2* below) but that have never been depicted in the context of detailed rock isotope maps at multiple elevations. Similarly, the cross section A-A' (Figure 3) shows the result of integrating the rock isotope model with fault data, well course locations plus "Top Steam" and "Top High Temperature Reservoir" interpreted surfaces (imported from the Geyser's SKUA GoCAD model and described in Hartline et al., (2016; 2019)). Beyond the obvious utility of generating cross sections at any view angle and refreshing on demand as new drilling data are added, this particular section view has provided several new insights. It has provided evidence that certain faults mapped at the surface penetrate to reservoir depths (see section *3.2* below) and also led to a significant re-targeting of one of the planned steam production wells in the area (see section *3.3* below).

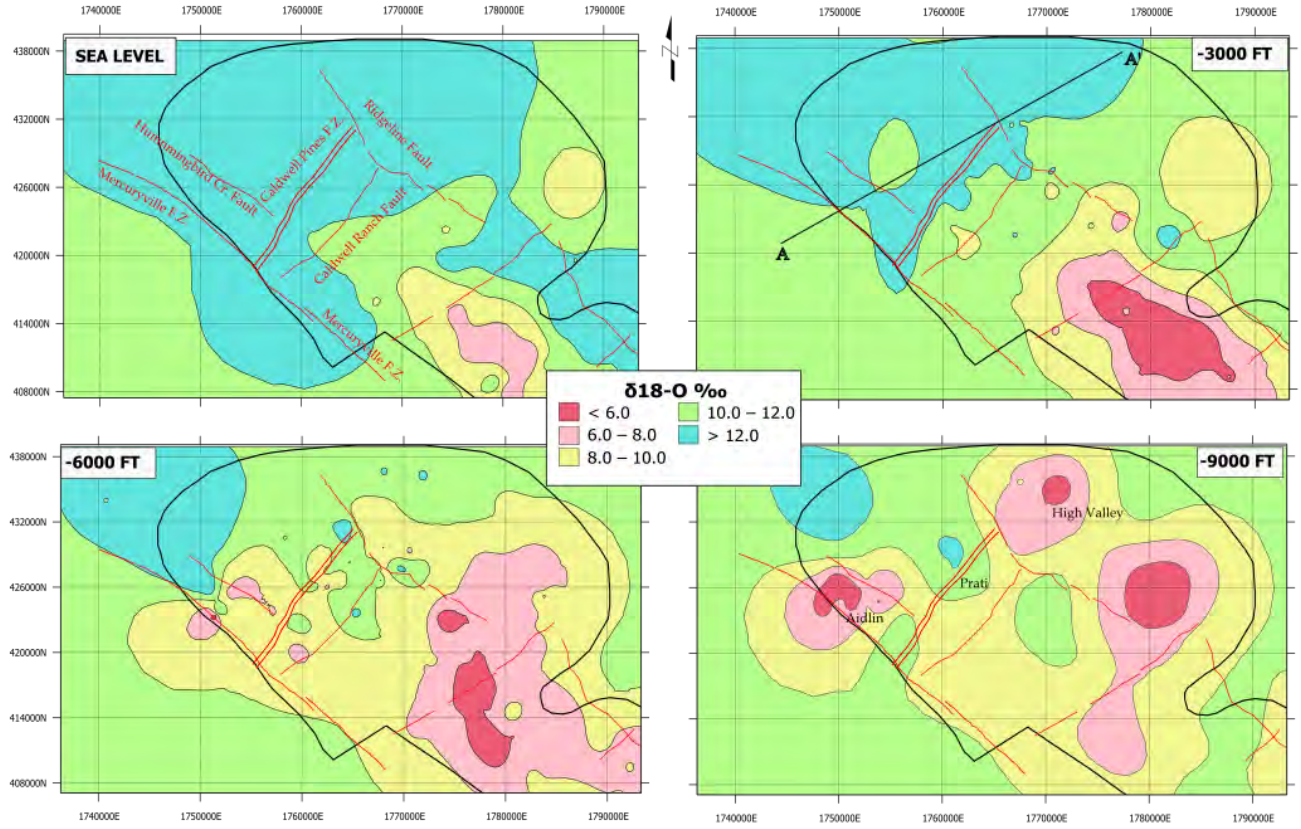

Figure 2: Figure 2. Map-view depth slices of 18-O rock isotope model in the northwest Geysers study area. The deep "lobes" of highly exchanged rock in the Aidlin and High Valley areas visible only in the slice at -9000 ft with respect to mean sea level (MSL) can only be accessed by drilling 10,000- to 12,000-ft' wells. The Prati / Caldwell Pines area (former CCPA leases) hosts normal temperature and high temperature steam reservoirs at depths from -3000 ft to -9000 ft MSL in rocks that are much less exchanged than any other reservoir rocks at The Geysers. Isotope values are contoured per the color key inset in center of figure. The Geysers reservoir limit is the solid black line, and surface fault traces are red lines. Labeling in the sea level map applies to all four views. The cross-section line for the subsequent figure is shown in the -3000 ft. map.

3.2 Comparison with Existing Conceptual Models

Previous published work referenced in Section *1.2* above has established the validity of using δ18O rock isotope data from silicates to assess the degree of water / rock interaction in the Geysers reservoir and has thus established isotopic exchange in reservoir rocks at The Geysers as a proxy for meteoric water flushing. This line of evidence has been used in the development of many conceptual models of The Geysers, some of which are summarized in Section *1.1* above and are too numerous to review here, so this discussion will instead focus on one example.

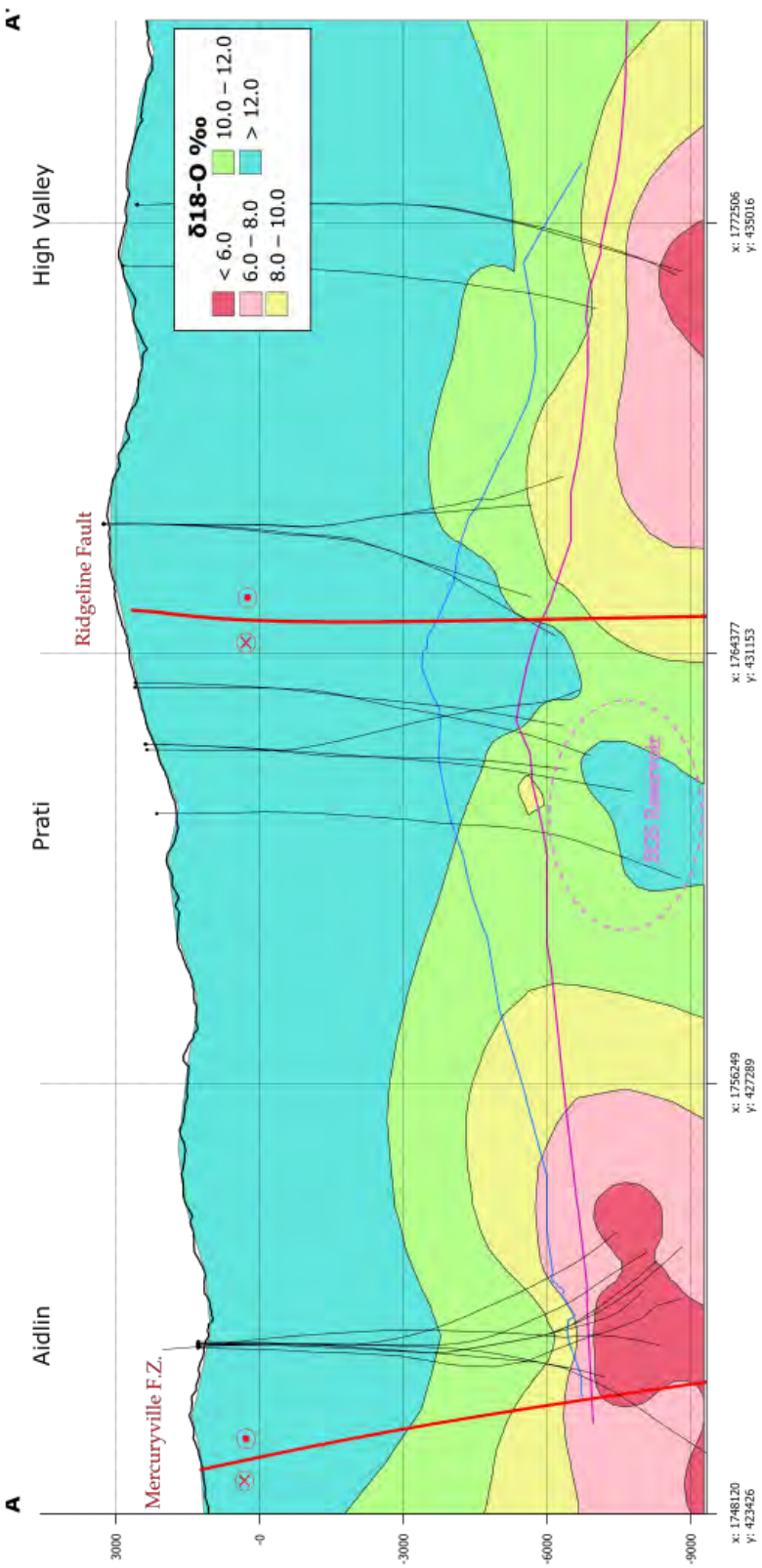

Figure 3: Cross section A-A' (southwest to northeast, see Figure 2 for location map). In this view, the 18-O stable isotope model is integrated with: a) The Geysers well course map (black lines – well names withheld), b) software projections of mapped surface faults into the subsurface (thick red lines) and interpreted surfaces "Top Steam" and "Top High Temperature Reservoir) imported from The Geysers SKUA GoCAD 3D model. This view emphasizes that the HTR of the northwest Geysers is broken into three distinct blocks: Aidlin, Prati (CCPA) and High Valley, where the two highly exchanged "lobes" of reservoir rock described in the -9000' MSL panel of Figure 2 clearly flank the less isotopically exchanged Prati block with abrupt lateral transitions on both sides. On the northeast side, this transition is spatially correlated with the Ridgeline Fault at depth. Although the Prati block of the HTR hosts many productive steam wells, NCG concentrations can exceed 60,000 ppmw, which has been correlated to the higher rock 18-O values, i.e. less meteoric water flushing.

3.2.1 Timing and Spatial Distribution of Meteoric Water Flushing

Beall et al. (2007) explained the pre-development initial condition distribution of NCG concentrations, which were lower in the southeast Geysers and higher in the northwest Geysers using a meteoric water flushing model. Their hypothesis detailed where meteoric water first entered the Geysers reservoir, and subsequent direction of flow. Figure 4A below illustrates this hypothesis. Because the southeast Geysers had the lowest initial NCG, the shallowest steam reservoir and nearby hot springs, this was the suggested entry point for the major water flushing event that occurred during a postulated tectonic breach of the reservoir and concurrent boil down from two phase into vapor dominated reservoir (see Moore and Gunderson 1995). The blue lines and arrows in Figure 4A depict the inferred SE to NW travel direction of the infiltrating water, which was determined by following the "troughs" in the NCG contours. Although Beall et al. did note that silicate δ18-O values indicative of pervasive water-rock exchange in the path of the hypothesized meteoric water flushing front were permissive of this interpretation, the isotope data were not presented in detail, nor were they plotted in map view. Figure 4B below is modified from Beall et al. 2007 figure and replaces the NCG contours with the δ18-O isotope contours at -9000 ft MSL derived from the new 3D model. Notably, the inferred meteoric water sinks from the 2007 map correspond to the deep areas of pervasive isotopic exchange in the Aidlin and High Valley reservoirs. Meanwhile, the gassier CCPA (Prati) contour block in 4A correlates to the 10‰ closed contour "island" seen in 4B.

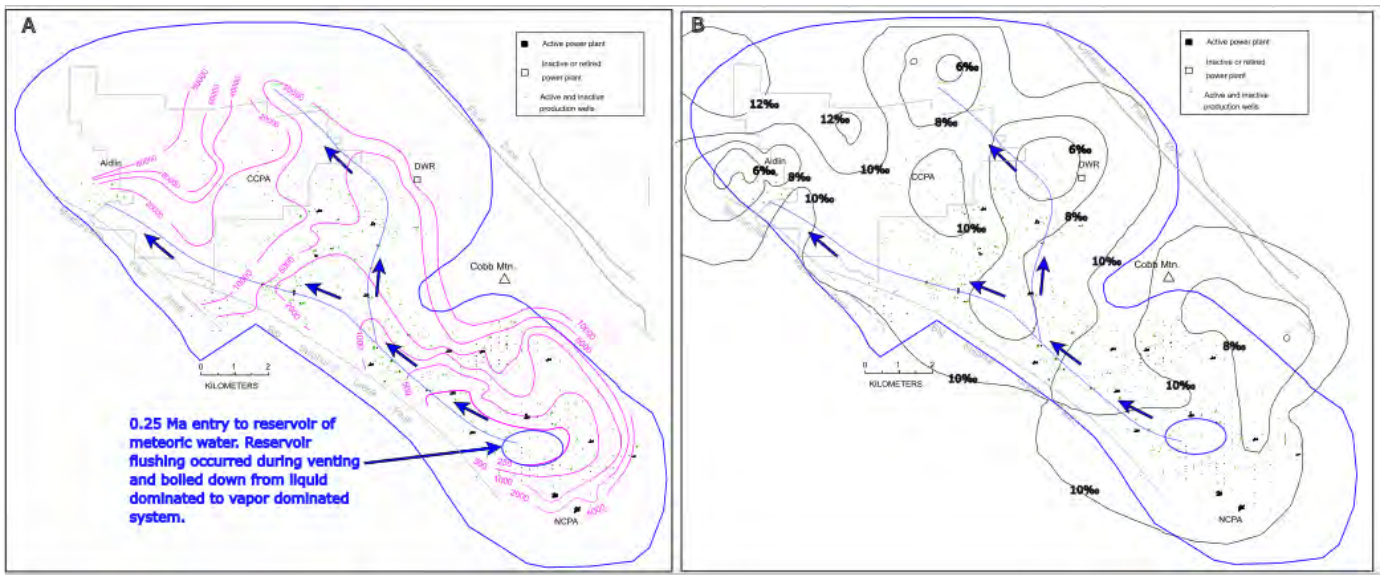

Figure 4: (modified after Beall et al., 2007) A. Conceptual model showing inferred entry of meteoric water into SE Geysers (blue oval) and interpreted path of water invasion and flushing of the steam reservoir from SE to NW, illustrated by blue lines and arrows. NCG concentrations are contoured in pink lines with values labeled in units of parts per million by weight (ppmw). B. Same as (A), but NCG contours replaced with silicate δ18-O values at -9000 ft MSL contoured in black lines with values labeled in ‰. The δ18-O contours show that the deep reservoir sections of Aidlin and High Valley have lower NCG and more isotopic exchange, while the Prati (CCPA) area has higher reservoir NCG and less isotopic exchange.

3.3 Example of Well Targeting Application

As part of Calpine's current step-out drilling program, thirteen new geothermal wells will be drilled utilizing four existing well pads. The northeast-most of these well pads is represented in the cross-section above (Figure 3). This pad is located on the northeast side of the Ridgeline fault, and has four existing wellbores, two drilled to the southwest and two drilled to the northeast. In the process of developing the 3D isotope model and integrating all the observations described above, it was noted that the two wells drilled to the northeast are reaching out towards the High Valley block of the reservoir, though their bottom hole locations are shallow with respect to the zone of maximum isotopic exchange depicted in core of this feature at ~9,000 ft MSL. In light of that observation, the original well targets planned from this pad were reconsidered as described below.

The following description references Figure 5 below for the northeast-most step-out well pad in Figure 3. The first well to be drilled on that pad was planned with a Geysers "standard" well trajectory with a kickoff point at ~3,000 ft MD and a directionally drilled section building to an inclination angle of 22° from vertical (pink line in figure). Although other factors were considered in the planning of this trajectory, it was determined that designing a different well that intersected with (and penetrated into) the modeled 10‰ isosurface at depth would improve the well prognosis by increasing the chance intersecting High Valley "type" steam, which is known to have lower NCG. The revised trajectory is shown by the black line in Figure 5. The final planned bottom hole location of this well is 1,500' deeper in true vertical depth (TVD) than the original planned trajectory.

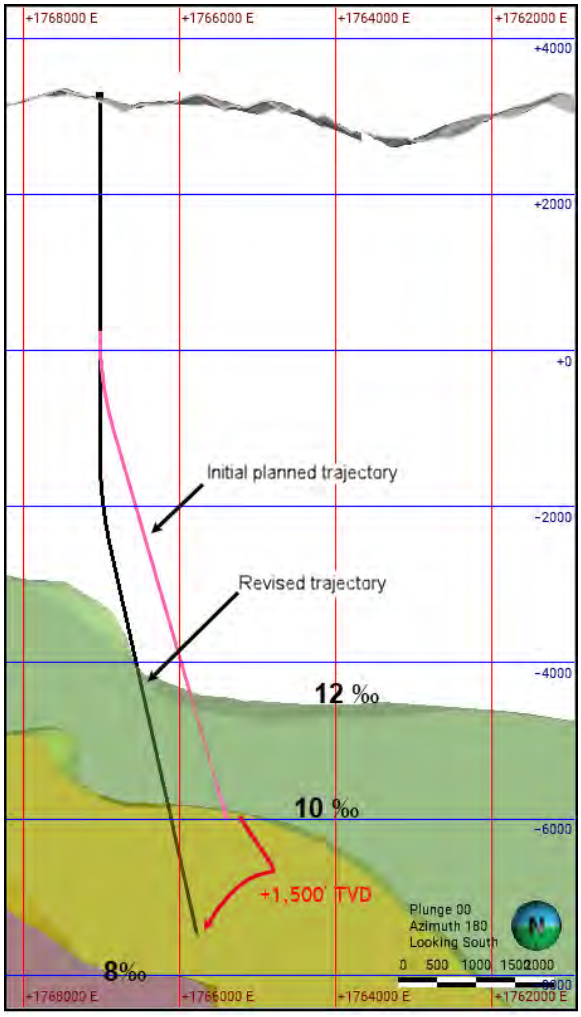

Figure 5: Cross sectional view of two planned well trajectories for Calpine's step out drilling program. The pink trajectory was planned using a "Geysers standard" well plan with a kick off point (KOP) of ~3,000 ft measured depth and a directional drilling program building to an angle of ~22° off vertical. Using the 3D rock isotope model as a guide, the well trajectory was redesigned (black line) to reach deeper into the more isotopically exchanged body of reservoir rock by using a deeper KOP and by limiting the build angle to ~18°.

Conclusions

The new δ18-Oxygen rock isotope 3D model of the Geysers reservoir was created by using software interpolation on a dataset of ~1,400 samples, which was composed of 1,000 + legacy data points and 300+ new analyses done since 2019 as part of Calpine's ongoing drilling program. The creation and use of this dataset has been done in the context of the extensive research that has already been completed on 18-Oxygen and Deuterium isotope systematics of geothermal systems in general, and of The Geysers specifically. Within that body of work are several dominant conceptual models based on integration of stable isotope data with structural data, steam condensate geochemistry, MEQ data, and operating company production and injection data. The

purpose of the present study is not to supplant any of those models, but rather to cross reference, validate, and possibly improve those models by leveraging the maximum value out of a previously underutilized dataset. This study has demonstrated that software integration has allowed Geysers rock isotope data to be incorporated into 3D model space and rapidly viewed in the context of other spatial data in ways commonly seen with potential fields in geophysical data. From that software platform, the isotope maps were also used to validate and expand upon the hypothesis of Beall et al.(2007) that meteoric water flushing started at an infiltration point in the southeast Geysers and moved deeper and to the northwest, eventually impacting the Aidlin and High Valley high temperature reservoir blocks. Finally, the isotope model has already been demonstrated to have value as a well planning tool, where an upcoming steam well trajectory in Calpine's step out drilling program was significantly changed in order to improve its chances of encountering a part of the deep high temperature reservoir where higher oxygen isotope exchange has previously been correlated with lower NCG concentrations in produced steam.

Acknowledgements

The authors wish to acknowledge Mark Waters and Joe Beall, both of whom have passed away. Their influence lives on at The Geysers. We also thank Ian Richards and John Robbins from the SMU stable isotope lab. Their consistent, quality work has been the backbone of decades worth of Geysers stable isotope research. The EGI Geothermal sample laboratory provided the authors with access to archived drill cuttings samples for isotope analysis with generous facilitation from Clay Jones and David Langton.

Disclaimer:

The views expressed in this paper are those of the author(s) and do not necessarily reflect the views of Calpine Corporation or its affiliates. Any opinions, findings, conclusions, or recommendations expressed in this paper are solely those of the author(s) and do not represent the opinions or policies of Calpine Corporation or its affiliates.

All intellectual property rights related to the content of this paper, including but not limited to data, text, graphics, images, and other materials, are owned by Calpine Corporation. No part of this paper may be used, reproduced, distributed, relied upon, or transmitted in any form or by any means without the prior written permission of Calpine Corporation.

REFERENCES

Beall, J.B., Wright, M.C., Hulen, J.B. "Pre- and Post-Development Influences on Fieldwide Geysers NCG Concentrations." *Geothermal Resources Council Transactions*, 31, (2007), 427-434.

Clayton, R.N. and Mayeda, T.K., "The Use of Bromine Pentatlouride in the Extraction of Oxygen from Oxides and Silicates for Isotopic Analysis." *Geochimica et Cosmochimica Acta*, 27, (1963), 43-52.

Craig, H. “The Isotopic Geochemistry of Water, and Carbon in Geothermal Areas.” In *E. Tongiorgi (Ed.), Nuclear Geology on Geothermal Areas.* Consiglio Nacionale delle Ricerche, Laboratorio di Geologia Nucleare, (1963), 17-53.

Criss, R., Fleck, R., and Taylor, P. "Tertiary Meteoric Hydrothermal Systems and their Relation to Ore Deposition, Northwestern United States and Southern British Columbia." *Journal of Geophysical Research,* 96 No. B8, (1991), 13,335-13,356.

Garcia, J., Hartline, C., Walters, M., Wright, B., Rutqvist, J., Dobson, P.F., and Jeanne, P. “The Northwest Geysers EGS Demonstration Project, California Part 1: Characterization and ReservoirR to Injection.” *Geothermics*, 63, (2016), 97-119.

Gunderson, R. “Distribution of Oxygen Isotopes and Noncondensable Gas in Steam at The Geysers.” *Geothermal Resources Council Transactions*, 19, (1989), 439-445.

Gunderson, R.P. and Moore, J. N., “Oxygen Isotope Geochemistry of The Geysers Reservoir Rocks, California.” *Proceedings: 19th Workshop on Geothermal Reservoir Engineering*, Stanford University, Stanford, CA, (1994), 237-244.

Haizlip, J. “Stable Isotopic Composition of Steam from Wells in the Northwest Geysers, The Geysers, Sonoma County, California.” *Geothermal Resources Council Transactions*, 9, Part 1, (1985), 311-316.

Hartline, C.S., Walters, M.A., Wright, M.C. “Three-Dimensional Structural Model Building Constrained By Induced Seismicity Alignments at The Geysers Geothermal Field, Northern California.” *Geothermal Resources Council Transactions*, 43, (2019), 937-960.

Hartline, C.S., Waters, M.A., Wright, M.C., Forson, C., Sadowski, A. “Three-Dimensional Structural Model Building and Induced Seismicity Analysis at the Geysers Geothermal Field, Northern California” *Proceedings: 41st Workshop on Geothermal Reservoir Engineering*, Stanford University, Stanford, CA, (2016), 241-246.

Hulen, J.B., and Moore, J.N., “Secondary Mineralogy and Oxygen-Isotope Geochemistry of Two Peripheral Steam-Exploration Boreholes at The Geysers Geothermal Field, California.” *Geothermal Resources Council Transactions*, 19, (1995), 451-456.

Jones, C.G., Moore, J.N., Bowman, J.R., and Walters, M. “High-temperature Hydrothermal Metamorphism at the Geysers Geothermal Field, California: an Investigation of Mineral Chemistry and Vein Paragenesis from an Active Contact Metamorphic Environment.” In, *Proceedings: 41st Workshop on Geothermal Reservoir Engineering,* Stanford University, Stanford, CA, (2016), 1-18.

Lowenstern, J.B., and Janik, C.J., “The Origins of Reservoir Liquids and Vapors from The Geysers Geothermal Field, California (USA).” *US Society of Economic Geologists Special Publication*, 10, (2003), 181-195.

Lutz, S.J., Walters, M., Pistone, S., and Moore, J.N.. “New Insights into the High-temperature Reservoir, Northwest Geysers.” *Geothermal Resources Council Transactions*, 36, (2012), 907-916.

Moore, J.N., and Gunderson, R.P. “Fluid Inclusion and Isotopic Systematics of an Evolving Magmatic-hydrothermal System.” *Geochimica et Cosmochimica Acta*, 59 (19), (1995), 3887-3907.

Truesdell, A.H., Haizlip, J.R., Box Jr, W.T., and D'Amore, F., "Fieldwide Chemical and Isotopic Gradients in Steam from The Geysers." In *Proceedings: 12th Workshop on Geothermal Reservoir Engineering*, Stanford University, Stanford, CA, (1987), 241-246.

Truesdell, A.H. "The Origin of High-temperature Zones in Vapor-dominated Geothermal Systems." In *Proceedings: 16th Workshop on Geothermal Reservoir Engineering*, Stanford University, Stanford, CA, (1991), 15-20.

Walters, M., and Beall, J., "Influence of Meteoric Water Flushing on Noncondensable gas and Whole-rock Isotope Distributions in the Northwest Geysers." *Geothermal Resources Council Transactions*, 26, (2002), pp. 379-384.

Walters, M.A., Moore, J.N., Nash, G.D., and Renner, J.L. "Oxygen Isotope Systematics and Reservoir Evolution of the Northwest Geysers, CA." *Geothermal Resources Council Transactions*, 20, (1996), 413-421.

Walters, M.A., Haizlip, J.R., Sternfeld, J.N., Drenick, A.F., and Combs, J. "A Vapor-dominated High-temperature Reservoir at The Geysers California." In C. Stone (Ed.), *Monograph on The Geysers Geothermal Field*, Geothermal Resources Council, (1992), 77-87.

Walters, M.A., Sternfeld, J.N., Haizlip, J.R., Drenick, A.F., and Combs, J. "A Vapor-dominated Reservoir Exceeding 600°F at The Geysers, Sonoma County, California." In *Proceedings: 13th Workshop on Geothermal Reservoir Engineering*, Stanford University, Stanford, CA, (1988), 73–81.

White, D.E., Barnes, I., and O'Neil, J.R. "Thermal and Mineral Waters of Nonmeteoric Origin, California Coast Ranges." *Geological Society of America Bulletin*, 84(2), (1973), 547-560.

Development of a New Screening Method for Low Silica Adhesion Resin Materials Based on the Ab Initio Quantum Chemical Approach

Tianlong Jiang [1], Yukari Okada [1], Azusa Wada [1], Daisuke Fukuda [2], Shigeto Yamada [1]

[1] Fuji Electric Co., Ltd., [2] JMC Geothermal Engineering Co., Ltd.

Keywords

Silica scale, Low adhesion, Resin materials, Ab initio calculation, Quantum chemistry

ABSTRACT

Silica scaling results in flow rate reduction or improper performance in power generation. To preserve the power generation capacity, it is necessary to take measures to prevent silica adhesion. One of the issues is to improve the surface properties of the components by surface coating or applying alternative materials to metal.

In this work, *ab initio* calculation based on the quantum chemistry was applied to clarify the mechanism of silica adhesion and to predict the silica adhesion properties of the resin materials. The calculations have been performed for seven kinds of resin materials which contains polytetrafluoroethylene (PTFE), polyvinyl chloride (PVC), polybutylene terephthalate (PBT), polyethylene terephthalate (PET), sheet molding compound (SMC), polymethyl methacrylate (PMMA) and polycaprolactam (Nylon 6). According to the calculation results, it is found that the seven kinds of resin materials could be divided into two groups. The low silica adhesion group which contains PTFE, PVC, PMMA and Nylon 6, and the high silica adhesion group which contains PBT, PET and SMC.

Field tests for verification were performed with the same resin materials at one geothermal power plant in the northeast part of Japan. According to the field test results, the low silica adhesion group and the high silica adhesion group were in excellent agreement with the calculation results.

Therefore *ab initio* quantum chemical calculation is considered to be a powerful research methodology for predicting the adhesion properties between silica and the candidate resins. Furthermore, an efficient and effective screening method for low silica adhesion resin materials has been developed in this work.

1. Introduction

In order to realize the big goal of carbon neutral target in 2050, various renewable energies are attracting attention at this moment. In particular, geothermal power generation is a renewable energy that can generate power sustainably with almost zero CO_2 emissions, and is said to be a "baseload power source" that can generate power stably without being influenced by natural conditions such as weather, in contrast to other renewable energies, for example solar power and wind power (Imamura et al., 2016) .

In geothermal power plants, geothermal fluid is exploited for power generation. However, reduction of power generation due to silica scale is a serious issue which affects many geothermal projects. Once silica scale adheres to the inner surface of the pipes, valves or other parts on the brine line, such silica scaling results in flow rate reduction or improper performance. As the solutions to this issue, some new approaches have been proposed.

For example, one of the approaches is to predict the amount of generated silica scale for scheduling the maintenance works in order to preserve the power generation capacity (Jiang et al., 2023). Another one is to improve the surface properties of the components by surface coating, such as diamond like carbon (DLC) coat (Nakashima et al., 2022 and 2023).

DLC has been verified to be effective in reduction of silica adhesion and has been used as the surface coating for the blade of the turbines. On another hand, since the uniformity of the DLC surface coating has been reported to be very important, DLC is considered to be not suitable for some large parts on the brine line such as the inner surface of the pipes. Therefore, it is considered to be necessary to separate the materials for the surface coating based on the target and situation.

In this case, resin materials are expected to be a good choice. There are various kinds of resin materials in the world with wide range of properties (Ebbing and Gammon, 2016). The studies on the performance design and synthesis of the resin materials have been widely discussed. It is considered that some new alternative materials which are easy-to-install on geothermal field with high durability and low silica adhesion property could be found.

However, it is said to be such a tough problem because the experiments which take a lot of time and effort are required to verify the silica adhesion properties for the large number of resin materials. Hence, a new screening method for predicting the low silica adhesion resin materials would be necessary. As a solution to the issue, the *ab initio* calculations based on the quantum chemical approach has been applied in this work.

2. Methodologies for theoretical analysis

2.1 The frontier molecular orbital theory

The major process of silica adhesion is considered to be chemical phenomena. From the point of view of chemistry, the chemical properties of the materials are determined by the molecular orbital and the electronic state of the molecules. It is well known that a good approximation for reactivity could be found by analyzing the Highest Occupied Molecular Orbital (HOMO) and the Lowest Unoccupied Molecular Orbital (LUMO), based on the famous frontier molecular orbital theory which won the Nobel Prize in Chemistry (Fukui et al., 1952). The theory has been widely utilized

in many fields for resin material researches, for example to find suitable materials for the polymeric binders in lithium-ion batteries (Kanamura, 2003).

In the case of silica adhesion, the passage of the electrons from silica to the molecules of geothermal power plant equipment result in the adsorption reaction. It is considered that the resin molecules with low LUMO energies are predisposed to adsorb silica and the ones with high LUMO energies are not predisposed to adsorb silica. Therefore the LUMO energies of resins could be an important indicator for predicting the reactivity between silica and the candidate resin materials.

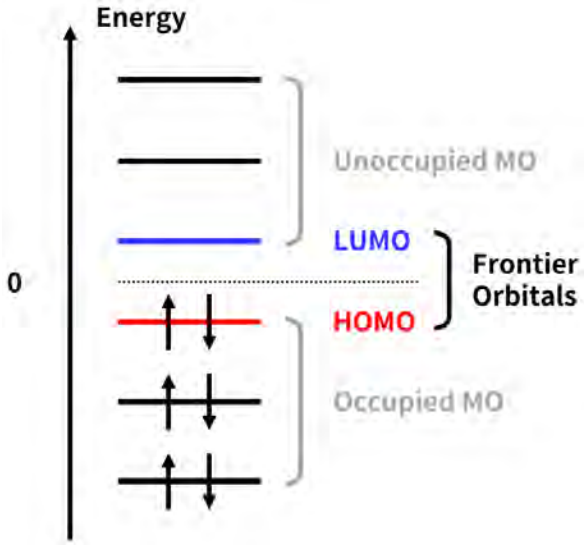

Figure 1: The overview of frontier molecular orbital theory.

2.2 Overview of the ab initio calculations

The theoretical analysis has been carried out following the procedure shown in Figure 2.

The initial structures for the resin molecules were built using the GaussView 6.0 program (Dennington et al., 2016).

Optimization calculations were composed of two processes, the optimization with the density function theory (DFT) method and the optimization with the molecular orbital (MO) method, in order to obtain reasonable structures with low calculation cost.

Molecular orbital calculations for the optimized structures were performed with the MO method, and the LUMO energies were estimated to evaluate the silica adhesion properties of the resins.

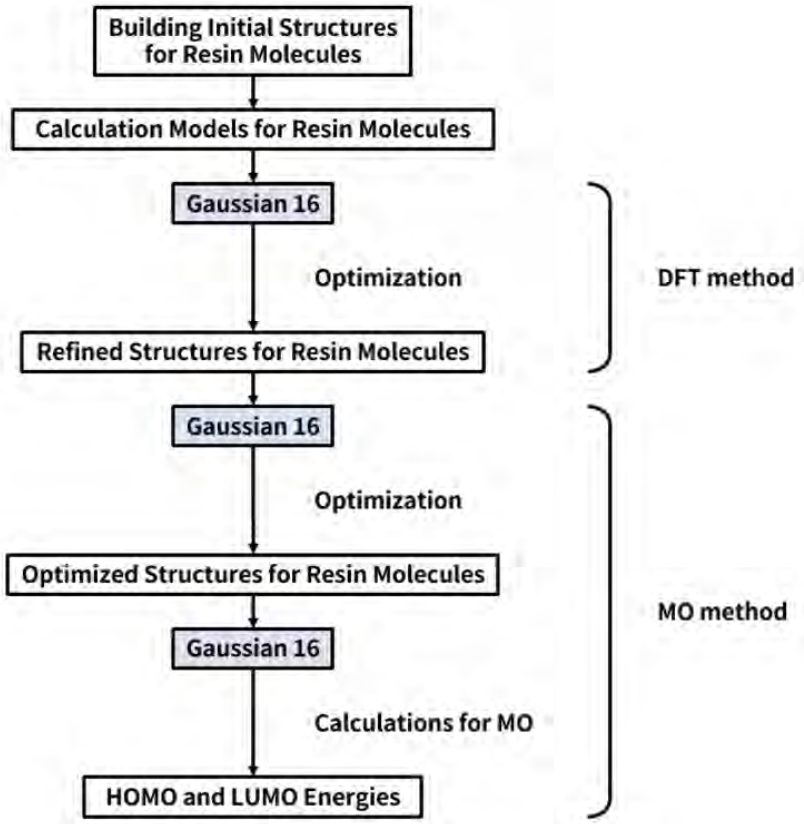

Figure 2: Flowchart of the theoretical analysis for estimating the LUMO energies to evaluate the silica adhesion properties of the resin molecules.

2.3 Optimization for the resin molecules

As described in section 2.2, the optimization calculations were composed of two processes.

The first-step optimizations were performed by the DFT method at B3LYP/6-31G level using the Gaussian 16 package (Frisch et al., 2016). Parallel computing was applied with 96 threads.

The second-step optimizations were performed by the Møller–Plesset (MP) perturbation theory, which is one of the commonly used MO method, at MP2/cc-pVDZ level using the Gaussian 16 package. It improves on the Hartree–Fock method by adding electron correlation effects by means of Rayleigh–Schrödinger perturbation theory (RS-PT) to second order (MP2) in this work.

2.4 Molecular orbital calculations for the resin molecules

Molecular orbital calculations were performed by the Møller–Plesset (MP) perturbation theory at MP2/cc-pVDZ level with the Merz-Singh-Kollman analysis using the Gaussian 16 package. The LUMO energy analysis were carried out based on the calculation results.

3. Methodologies for field test

3.1 Experimental apparatus

The field test was carried out by branching geothermal water from the reduction pit to the test section at one geothermal power plant in the northeast part of Japan.

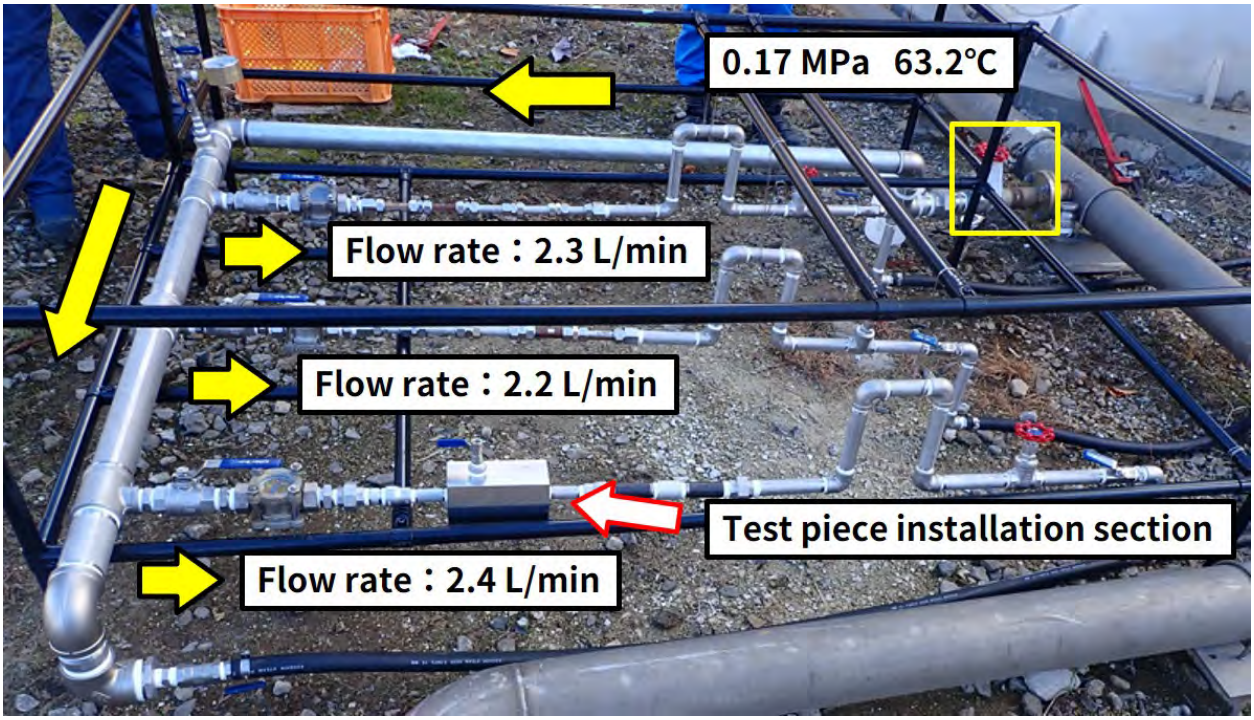

Figure 3: Experimental apparatus of the field test.

The schematic diagram of the flow test with the resin test pieces is shown in Figure 4. The main part of this apparatus was consisted of one routing line from the geothermal water pit, three test lines, and one resin test piece installation section. A ball valve and a pressure gauge for passing geothermal fluid through the routing line were installed, and three test lines were installed in the latter part as well. Field tests could be performed independently on each test line in parallel by providing ball valves at the upper and lower of them. In addition, the condition of geothermal fluid and the presence or absence of foreign matter contamination were confirmed by providing a sight glass at the upper part of each test line.

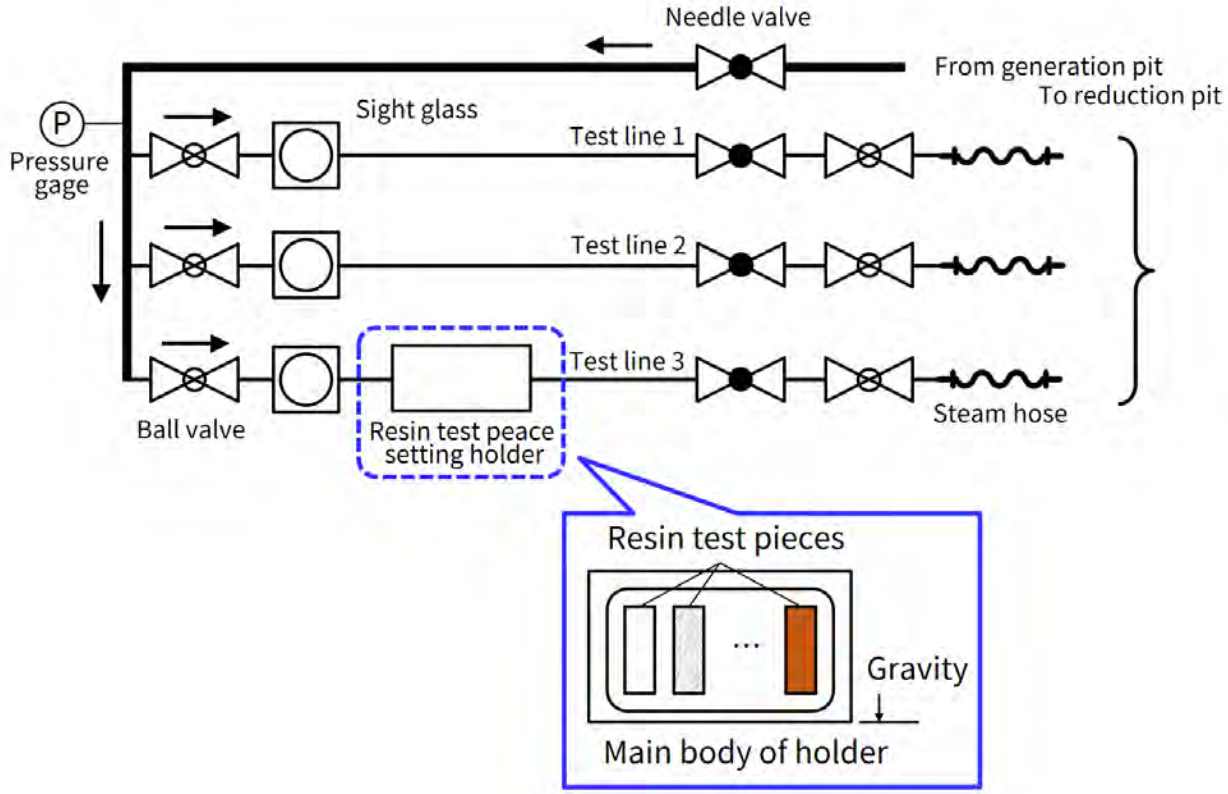

Figure 4: The schematic diagram of the local water flow test of the resin test piece.

Resin test pieces were mounted in the test piece installation holder of the test line 3. The resin test pieces were secured by screws to the inner side of the test piece installation holder in a vertical direction as shown in Figure 5, to prevent weight-impact deposition of the suspension in the geothermal fluid on the test pieces.

In addition, seven types of resin test pieces were installed, and the information of the resins is summarized in Table 1. All dimensions were in 40 mm × 10 mm × 3 mm, in order to make the impact of the shape of the test pieces on the fluidic flow uniform. At the latter stage of the test line, a needle valve for adjusting each flow rate was provided, and a steam hose was installed at the last stage, so that the geothermal fluid was returned to the pit.

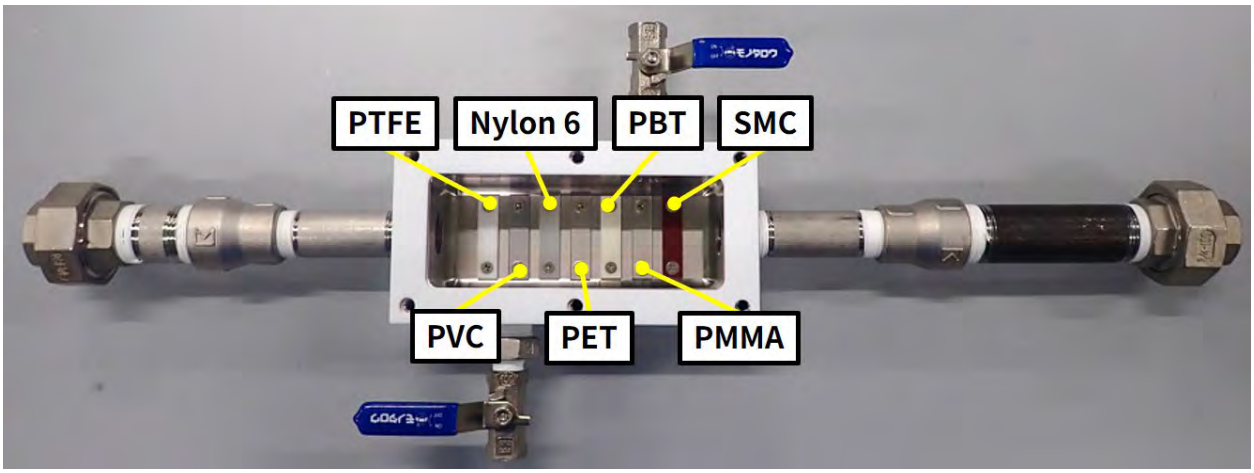

Figure 5: The inner side of the test piece installation holder.

Table 1: Summary of the information of the resins.

No.	Resin material	Glass ransition temperature [K]	Max allowable working temperature [K]	Melting point [K]	Density [g/cm^3]	Coefficient of water absorption [wt%] (24h)
1	PTFE	338	533	600	2.13 ～ 2.20	0.01
2	PVC	353	333	358	1.35 ～ 1.45	0.04 ～ 0.40
3	Nylon 6	323	413	498	1.13	1.10 ～ 1.90
4	PET	343	353	533	1.38	0.10 ～ 0.20
5	PBT	333	413	503	1.31 ～ 1.38	0.06 ～ 0.09
6	PMMA	343	363	378	1.18	0.20 ～ 0.40
7	SMC	353	423	—	1.65 ～ 2.60	0.05 ～ 0.50

3.2 Experimental method

Geothermal water of 63°C, 0.17 MPa and default flow rate 2.4 L/min was passed through the test line 3 on which the resin test pieces were installed for about 50 days. The flow rate measurement method was calculated by taking the water flow rate from the wastewater section (steam hose) of each test line into the graduated cylinder and using the water intake rate and time. Within this test period, flow rate adjustment was not performed, so that the natural flow rate attenuation due to silica adhesion was allowed. Resin test pieces to which silica adhered were subjected to ultrasonic cleaning and drying in a laboratory, and then subjected to elemental analysis by a SEM-EDX.

The sample preparation and SEM-EDX were performed following the procedure below.

(1) The samples are immersed in pure water for ultrasonic cleaning

(2) Dry in an auto dry desiccator for at least 24 hours.

(3) Compositional analyses are performed on five randomly selected sites in SEM-EDX.

(4) Calculate the ratio of adhered substance/substrate at each point and compare it with the average value.

(5) When the ratio of adhered substance/substrate was large, it was judged that many scales with strong adhesion force remained.

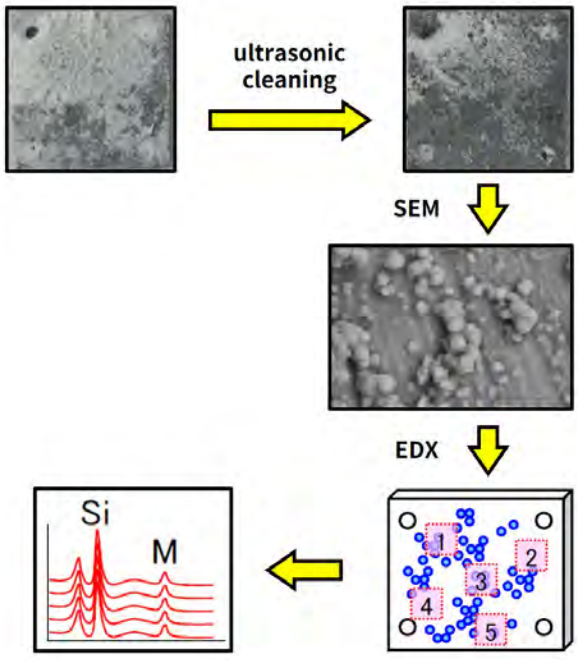

Figure 6: The procedure of sample preparation and SEM-EDX.

4. Results and discussions

The optimization calculation as mentioned in section 2.3 have been performed for seven kinds of resin materials which contains polytetrafluoroethylene (PTFE), polyvinyl chloride (PVC), polybutylene terephthalate (PBT), polyethylene terephthalate (PET), sheet molding compound (SMC), polymethyl methacrylate (PMMA) and polycaprolactam (Nylon 6). The structure refinement were carried out and the structure of the resin molecules were obtained theoretically as shown in Figure 7, Figure 8 , Figure 9, Figure 10, Figure 11, Figure 12 and Figure 13.

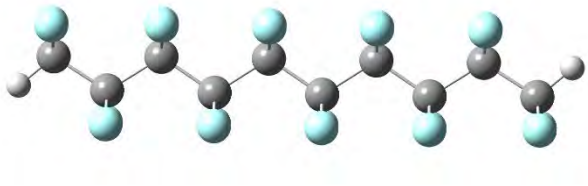

Figure 7: The Structure of PTFE molecule.

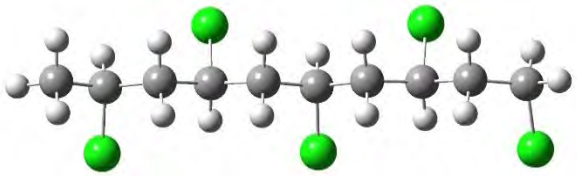

Figure 8: The Structure of PVC molecule.

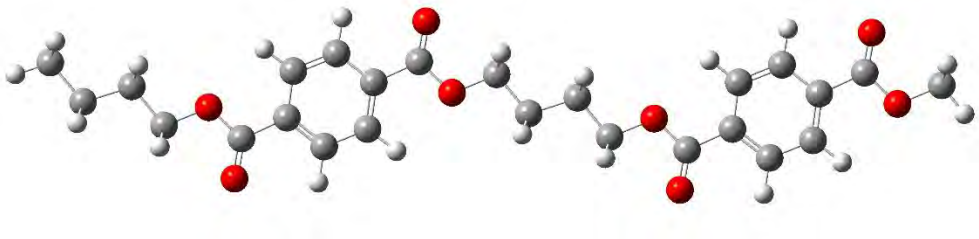

Figure 9: The Structure of PBT molecule.

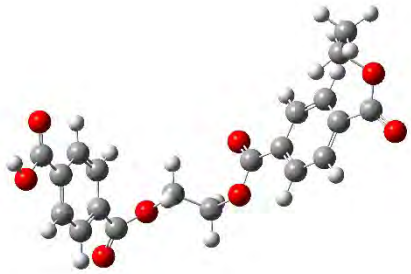

Figure 10: The Structure of PET molecule.

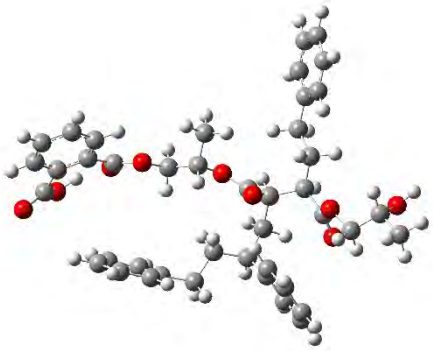

Figure 11: The Structure of SMC molecule.

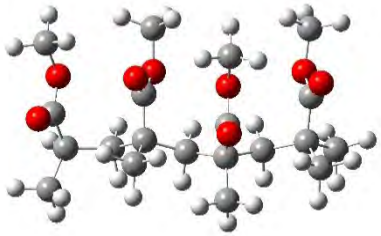

Figure 12: The Structure of PMMA molecule.

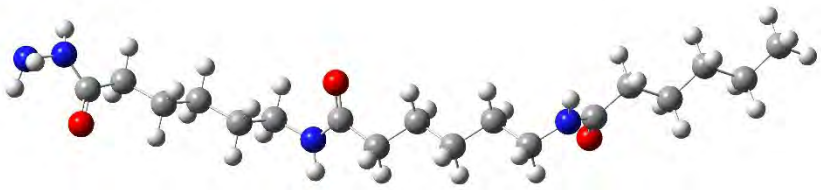

Figure 13: The Structure of Nylon 6 molecule.

The molecular orbital calculations for the seven kinds of resins were performed and the LUMO energies, which are considered to be the important indicator for predicting the reactivity between candidate resin materials and silica have been estimated. The calculation results are summarized as shown in Figure 14.

The LUMO and HOMO energies of some resins such as PTFE, have been reported by other experiment groups in past studies (Choi et al., 2015). The LUMO and HOMO energies of PTFE is reported to be about 3 eV and -15 eV. On the other hand, in this work the LUMO and HOMO energies of PTFE were estimated to be 3.49 eV and -13.90 eV. Thus, the calculation result is considered to be reasonable.

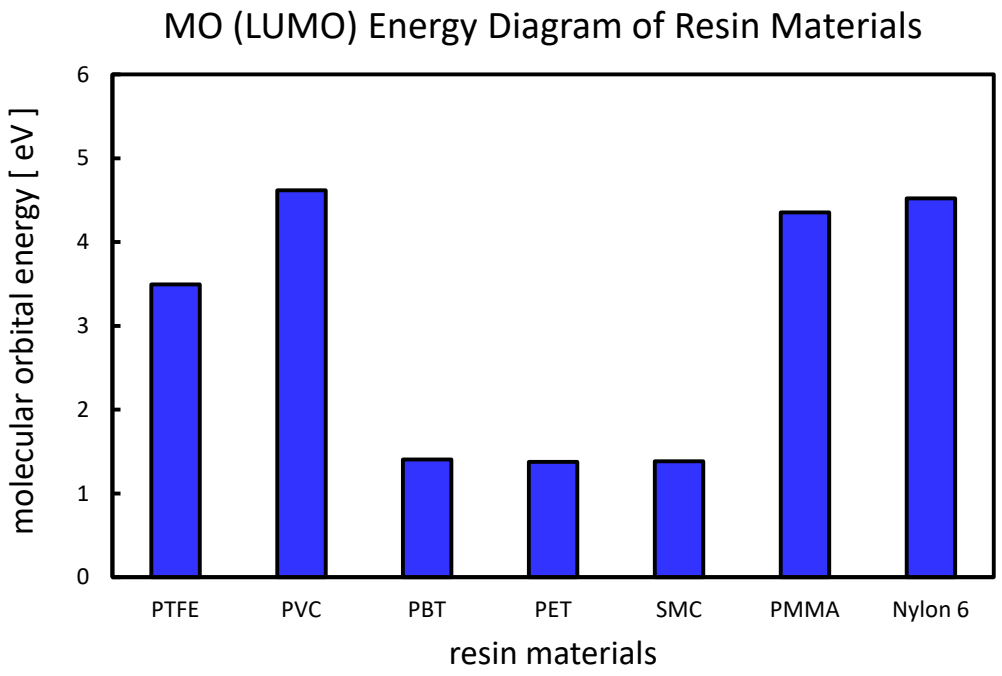

Figure 14: The calculation results of LUMO energies for the resin.

As mentioned in section 2.1, it is considered that the resin molecules with lower LUMO energies are predisposed to adsorb silica and the resin molecules with higher LUMO energies are not predisposed to adsorb silica. From the calculation results, it is found that the seven kinds of resins could be divided to one low silica adhesion group (PTFE, PVC, PMMA and Nylon 6) and one high silica adhesion group (PBT, SMC and PET).

The field test for verification were carried out as mentioned in section 3.1 and 3.2. The state of the test pieces before ultrasonic cleaning and after ultrasonic cleaning is shown in Figure 15. The appearance of silica adhesion seems to be the same as the calculation results. The analysis by SEM-EDX were also performed as shown in Figure 16.

The appearance of silica adhesion seems to be the same as the calculation results.

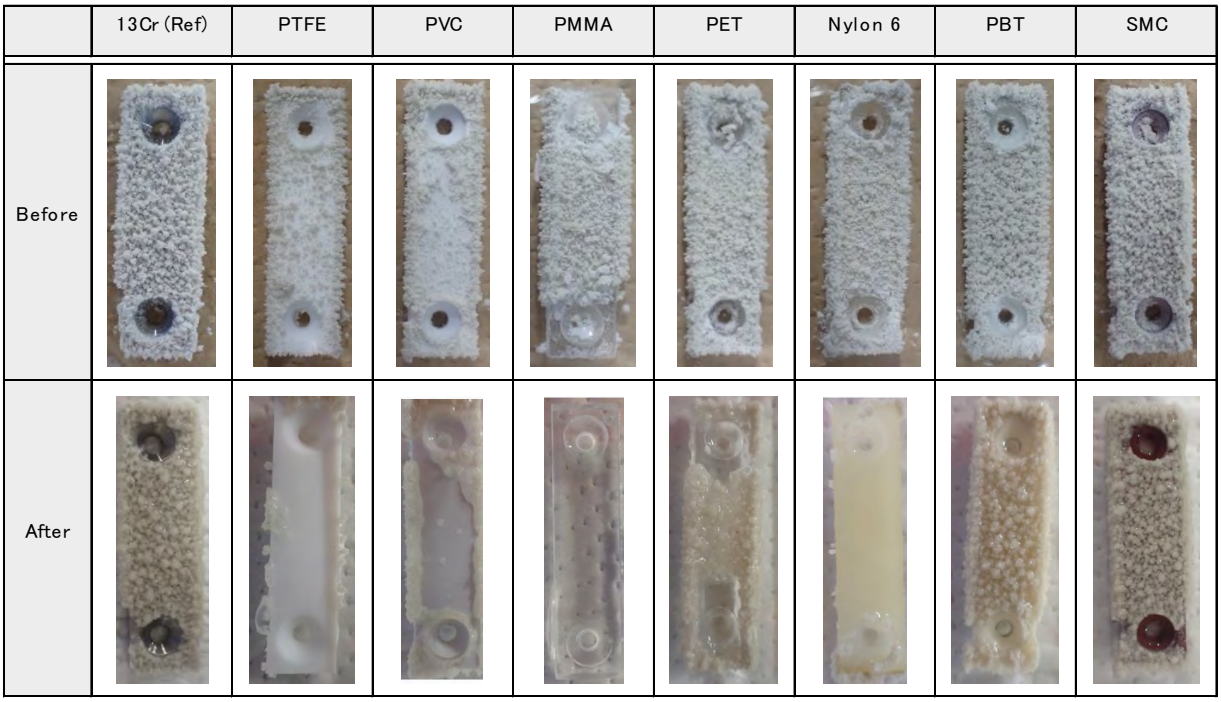

Figure 15: The state of the test pieces before ultrasonic cleaning and after ultrasonic cleaning.

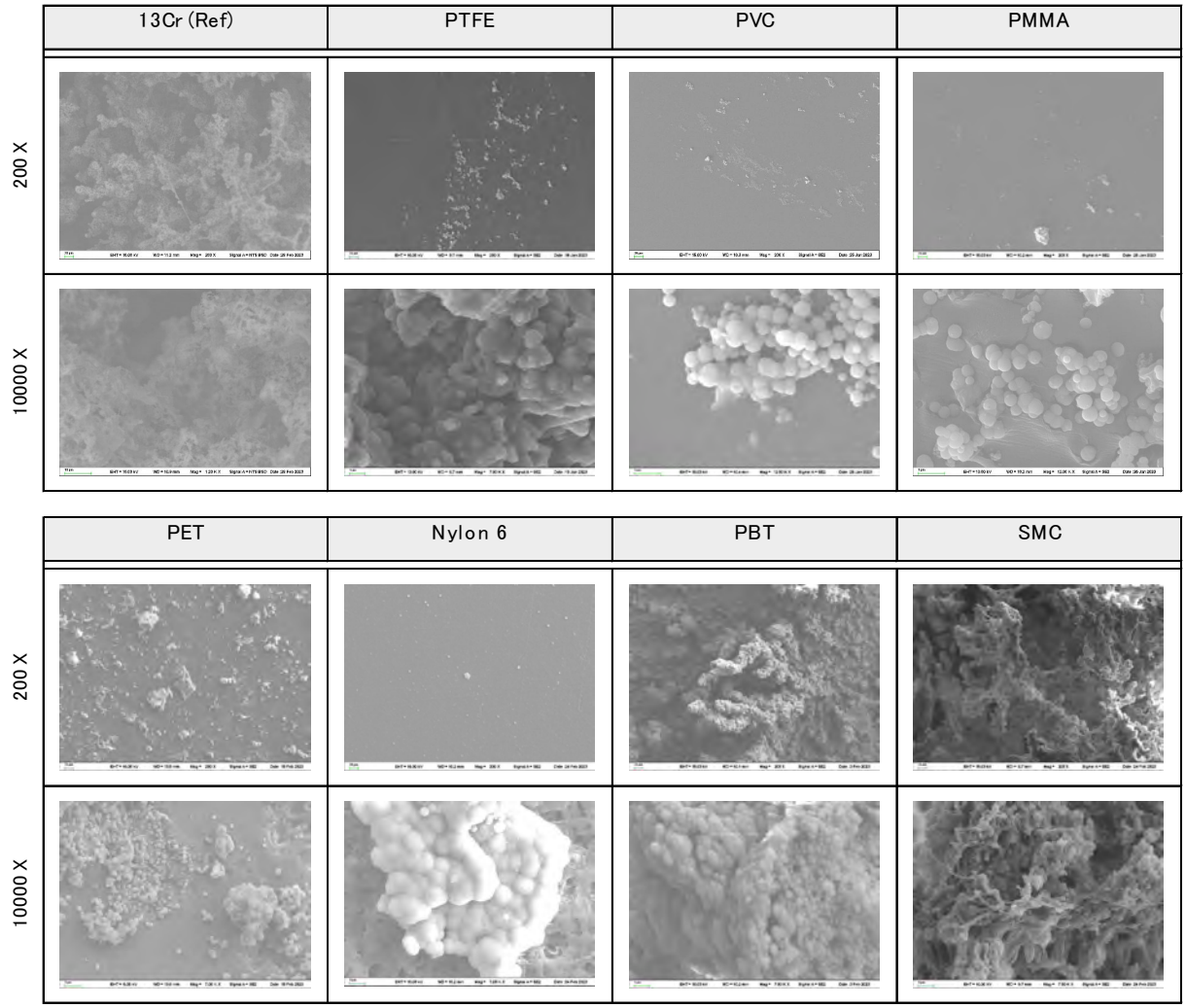

Figure 16: The observation results of SEM-EDX.

Furthermore, the ratio of adhered substance/substrate estimated from the SEM-EDX results were summarized with the calculation results as shown in Figure 17. It is found that the calculation results of the silica adhesion properties agrees with the field test results very well. The low silica adhesion group and the low silica adhesion group were revealed as predicted.

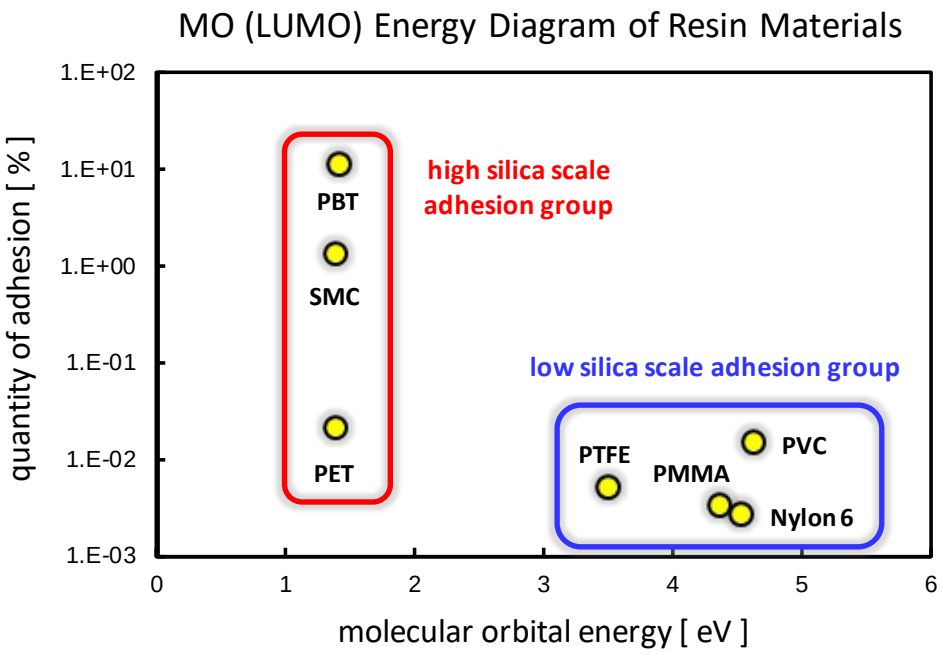

Figure 17: Summary of the calculation results and the field test results.

5. Conclusions

In the present work, to clarify the mechanism of silica adhesion and to predict the silica adhesion properties of the resin materials, *ab initio* calculation based on the quantum chemistry has been introduced. The calculations as well as the field tests have been performed for seven kinds of resin materials which contains PTFE, PVC, PBT, PET, SMC, PMMA and Nylon 6.

As a result of comparing the silica adhesion properties of the resins predicted by the calculations with the field test results, it is found that the field test results were in excellent agreement with the calculation results. The seven kinds of resins could be divided to one low silica adhesion group and one high silica adhesion group, which reveals that the silica adhesion properties of the resins could be predicted non-empirically with theoretical approach.

According to our results, *ab initio* quantum chemical calculation is considered to be a powerful research methodology for predicting the reactivity between candidate resin materials and silica. Furthermore, an efficient and effective screening method for low silica adhesion resin materials has been developed in this work. By utilizing this screening method, considering the strength and heat resistance of resin materials, it would be possible to quickly find the resin materials suitable for geothermal power plants. It is expected that the low silica adhesion resin materials for production lines and injection lines, or lining injection well as coating materials, could greatly contribute to the preservation of the power generation capacity.

REFERENCES

Imamura E., Iuchi M. and Bando S. "Comprehensive Assessment of Life Cycle CO_2 Emissions from Power Generation Technologies in Japan". *Central Research Institute of Electric Power Industry Report.* 2016, Y06.

Jiang T., Wada A., Ui S., Fukuda D. and Yamada S. "Theoretical Analysis of Predicting the Amount of Generated Silica Scale in Water with Temperature and pH Dependence". *GRC Transactions*. 2023, **47**, 2963-2710.

Nakashima Y., Umehara N., Kousaka H., Tokoroyama T., Murashima M. and Murakami K. "Influence of Defects in Graphene-Like Network of Diamond-Like Carbon on Silica Scale Adhesion". *Tribol. Lett.* 2022, **71**, 17.

Nakashima Y., Umehara N., Kousaka H., Tokoroyama T., Murashima M. and Mori D. "Carbon-based coatings for suppression of silica adhesion in geothermal power generation". *Tribol. int.* 2023, **177**, 107956.

Ebbing D. and Gammon S. D. "General Chemistry". *Cengage Learning*. 2016.

Fukui K., Yonezawa T. and Shingu H. "A Molecular Orbital Theory of Reactivity in Aromatic Hydrocarbons". *J. Chem. Phys*. 1952, **20**, 722–725.

Kanamura K. "Lithium Secondary Battery Technology". *CMC Press*. 2003.

Dennington R., Keith T. A. and Millam J. M. GaussView, Version 6.0. Semichem Inc., Shawnee Mission, KS, 2016.

Frisch M. J., Trucks G. W., Schlegel H. B., Scuseria G. E., Robb M. A., Cheeseman J. R., Scalmani G., Barone V., Petersson G. A., Nakatsuji H., Li X., Caricato M., Marenich A. V., Bloino J., Janesko B. G., Gomperts R., Mennucci B., Hratchian H. P., Ortiz J. V., Izmaylov A. F., Sonnenberg J. L., Williams-Young D., Ding F., Lipparini F., Egidi F., Goings J., Peng B., Petrone A., Henderson T., Ranasinghe D., Zakrzewski V. G., Gao J., Rega N., Zheng G., Liang W., Hada M., Ehara M., Toyota K., Fukuda R., Hasegawa J., Ishida M., Nakajima T., Honda Y., Kitao O., Nakai H., Vreven T., Throssell K., Montgomery J. A. Jr., Peralta J. E., Ogliaro F., Bearpark M. J., Heyd J. J., Brothers E. N., Kudin K. N., Staroverov V. N., Keith T. A., Kobayashi R., Normand J., Raghavachari K., Rendell A. P., Burant J. C., Iyengar S. S., Tomasi J., Cossi M., Millam J. M., Klene M., Adamo C., Cammi R., Ochterski J. W., Martin R. L., Morokuma K., Farkas O., Foresman J. B. and Fox D. J. Gaussian 16, Revision C.01. Gaussian, Inc., Wallingford CT, 2016.

Development of Reactive Transport Models for Very High Temperature Heat Aquifer Storage (VESTA) at a Pilot Site in Germany

Ram Kumar[1,2], Ghanashyam Neupane[1,2], Wencheng Jin[1], Trevor Atkinson[1,2], Travis McLing[1,2], Robert Smith[2,3], Yingqi Zhang[4], Patrick Dobson[4], Eva Schill[4,5], Thomas Kohl[5], Florian Bauer[5], Fabian Nitschke[5], Judith Bremer[5]

[1]Idaho National Laboratory, Idaho Falls, Idaho, U.S.A., 83415
[2]Center for Advanced Energy Studies, Idaho Falls, Idaho, U.S.A., 83401
[3]Earth and Spatial Sciences, University of Idaho, Moscow, Idaho, U.S.A, 83844
[4]Lawrence Berkeley National Laboratory, Berkeley, California, U.S.A., 94720
[5]Karlsruhe Institute of Technology, Eggenstein-Leopoldshafen, Germany, 76344

Keywords

HT-RTES, Site Characterization, Geochemistry, Reactive Transport Processes, Thermal Short-circuiting, Scaling, Permeability Evolution

ABSTRACT

Thermal energy storage at large scale has significant potential for large scale clean energy deployment. However, it is necessary to understand and address the challenges (Dobson et al., 2023) associated with high temperature reservoir thermal energy storage (HT-RTES). Lessons learned from the previous demonstrations identify insufficient site characterization, thermal short-circuiting, lack of available heat, scaling, corrosion, and biofouling as key factors affecting the performance of HT-RTES. The objective of this paper is to develop reactive transport modeling strategies to understand the geochemical processes associated with HT-RTES in high-saline reservoirs by evaluating the significance of changes in temperature, pressure, mineralogy, and porosity of the formation during the HT-RTES operation. The results from the model will also evaluate the retrograde solubility of minerals, changes in permeability, and changes in redox conditions during the HT-RTES operation.

For this study, an isolated injection-production well doublet is used for injecting hot and cold fluids during the seasonal cycle. During summer, brine at 75 °C is surface heated to 140 °C and injected into the reservoir with 15% porosity. Produced brine from the heat-exchanger at 60 °C is injected back into the cold well during winter. Reactive transport simulations are carried out using TOUGHREACT-EOS7(Dobson et al., 2004; Sonnenthal et al., 2021) for 5 years of cyclic RTES operation. Representative geochemical data were obtained from the depleted Leopoldshafen oil field of Leopoldshafen around the DeepStor site (Banks et al., 2021).

After a five-year operational period, the model estimates a 1.5% increase in the porosity in the vicinity of the hot wells. Near the cold wells, there is a negligible decrease in porosity, roughly

0.1%, within the same duration. These observations imply that dissolution of minerals is more prominent near the hot well because of the increase in temperature and the injection of slightly acidic brine, while mineral precipitation tends to occur near the cold well where the temperature falls. Iron minerals such as goethite show dissolution near the hot wells and precipitation in the relatively colder brine slightly away from the hot well. Also, changes in permeability have been evaluated using a cubic law of porosity-permeability correlation. There is no significant interference of hot and cold plumes, which indicates that thermal short-circuiting has not occurred under the simulated operating conditions. Future work will include a modeling scenario under strong oxidizing conditions such as presence of dissolved oxygen in the injection brine, which can better quantify the possibility of corrosion and scaling due to air intrusion.

1. Introduction

As the shift from fossil fuels to Variable Renewable Energy (VRE) technologies gains momentum for electricity generation and heating, the need for energy storage becomes more critical. While numerous energy storage systems are being developed to manage short-term needs, the significant seasonal fluctuations in VRE output and energy demand pose a greater challenge. Seasonal energy storage technologies, capable of transferring energy from periods of surplus such as summer to times of deficit like winter, are emerging as a vital solution. High-temperature reservoir thermal energy storage (HT-RTES) is being considered as a viable option for long-duration energy storage. This method allows the storage of surplus thermal energy in permeable geological formations like aquifers or depleted hydrocarbon fields over several months. While RTES demonstrates significant promise for geothermal energy applications at moderate temperatures (Fleuchaus et al., 2020), concerns about its long-term viability arise due to potential issues such as corrosion, scaling, and well clogging due to changes in geochemistry during the operation (Dobson et al., 2023) when shifting to higher temperatures.

This study aims to establish a method for assessing the impact of hydrogeochemical processes on RTES through the application of reactive transport modeling. The specific goals are 1) construct a numerical model for analyzing the reactive-transport processes relevant to RTES systems, 2) examine the geochemical factors which can impact system performance or diminished efficiency during cyclical operations, 3) determine the rates at which mineral precipitation and dissolution occur, and 4) assess alterations in porosity and permeability.

In terms of formation water chemistry, the DeepStor site at the Karlsruhe Institute of Technology (Germany) is used in this simulation. Notable research papers evaluating the potential of the DeepStor site for geothermal use include those by Banks et al. (2021), Frey et al. (2022), Bremer et al. (2022), Nitschke et al. (2023), Stober et al. (2023), Schill et al., (2024), and Stricker et al. (2024). Banks et al. (2021) conducted a preliminary geochemical evaluation, identifying potential risks such as mineral scaling and structural damage in the reservoir due to reactive transport processes, with a particular emphasis on reduced porosity around the thermal wells. The study utilized a model based on equilibrium thermodynamics to simulate the dissolution and precipitation of minerals. However, equilibrium thermodynamics may not yield precise predictions for the rates of mineral dissolution and precipitation. To enhance the accuracy of modeling results, it is important to incorporate reaction kinetics. Nitschke et al. (2023) conducted an analysis of brine-rock interactions and scaling potential, employing the MulT_predict geothermometer to analyze the chemical system's temperature control. The study identified key scaling minerals such as iron hydroxides, calcite, celestite, and barite, noting distinct scaling mechanisms during both

the testing phase with open pond storage and the operational phase with a two-well system for cyclic storage and production. However, the study did not integrate transport processes, which could impact the geochemical processes related to brine-rock interaction during cyclic RTES operations.

This study aims to bridge current knowledge gaps by evaluating the DeepStor site for RTES through a reactive-transport modeling approach.

2. Methodology

2.1 Geologic and Hydraulic Setting at DeepStor site

The DeepStor site is situated at KIT Campus North, nestled within the central portion of the Upper Rhine Graben (URG), a key segment of the European Cenozoic Rift System. This region is known for Germany's most significant temperature anomaly, reaching approximately 170°C at 3,000 meters depth (Baillieux et al., 2013). Over 2,000 meters of sediment have accumulated at the DeepStor location, predominantly under shallow marine conditions, leading to substantial marl deposits interspersed with layers of sand. The targeted strata for DeepStor, the calcareous fine-grained sandstones of the Niederrödern and Froidefontaine Formations, are found at depths of approximately 800 and 1,300 meters, respectively (Bremer et al., 2022). These sandstone layers reach thicknesses of up to 10 meters and exhibit subsurface temperatures between 70-90°C. The hydrologic and thermal characteristics of the sandstones in the Meletta beds from the Froidefontaine Formations have been described by Banks et al. (2021) and Stricker et al. (2024). These properties have been employed while setting up simulations in the current study. To generalize the approach, the site-specific and rather limited thickness of the sandstone layer of the Niederrödern and Froidefontaine Formations has been increased to a thickness of 220 m. In the first approach, the vertical temperature gradient has been neglected. Also, precipitation of minerals during the surface heating and cooling processes are not considered in this study.

Table 1: Hydrologic and thermal properties of the units used in modeling, adapted from Banks et al. (2021) and Stricker et al. (2024).

Unit	Porosity	Permeability (m^2)	Thermal Conductivity ($Wm^{-1}K^{-1}$)	Grain Heat Capacity (J/kg/°C)	Grain Density (kg/m^3)
Sandstone	0.15	6.6×10^{-14}	2.50	850	2680
Caprock	0.01	2.1×10^{-18}	1.50	964	2630

2.2. Numerical modeling approach

Reactive transport modeling was performed using TOUGHREACT V4 (Sonnenthal et al., 2021). The Equation of State module (EOS7) used for the modeling considers aqueous phases not as mixtures of water and salt but as mixtures of water and brine. The salinity of the aqueous phase is described by means of the brine mass fraction, and density and viscosity are interpolated from the values for the water and brine endmembers. The brine is modeled as NaCl solution. The model does not account for changes in enthalpy due to salinity. Fluid flow within this system are governed

by Darcy's law, as described by Pruess et al. (1999), while heat transfer is facilitated by both conduction and convection, incorporating both sensible and latent heat changes.
In the liquid phase, aqueous species are transported and interact with the solid and gas phases. The chemical transport equations use total dissolved concentrations, including primary species and their secondary aqueous counterparts (Sonnenthal et al., 2021). The kinetics of mineral dissolution and precipitation are based on the Transition State Theory, following the work of Steefel and Lasaga (1994) and Xu and Pruess (2001), expressed as follows:

$$r_n = \pm A_n k_n \left(1 - \Omega_n^{\theta}\right)^{\eta} \quad \text{n = 1…N}_q \tag{1}$$

where k_n is the rate constant (moles/mineral surface area/time), A_n is the specific reactive surface area/kg of H_2O, Ω_n is the ratio of the activity product (Q) divided by the equilibrium constant (K). A positive value of r_n indicates mineral dissolution and a negative value indicates mineral precipitation.
Permeability changes are calculated from porosity change using ratios of permeabilities calculated from the Carman-Kozeny relation (Bear, 1972) as follows:

$$k = k_i \frac{(1-\phi_i)^2}{(1-\phi)^2} \left(\frac{\phi}{\phi_i}\right)^3 \tag{2}$$

ϕ_i and k_i denotes initial porosity and initial permeability respectively.

2.3. Griding and RTES parameters

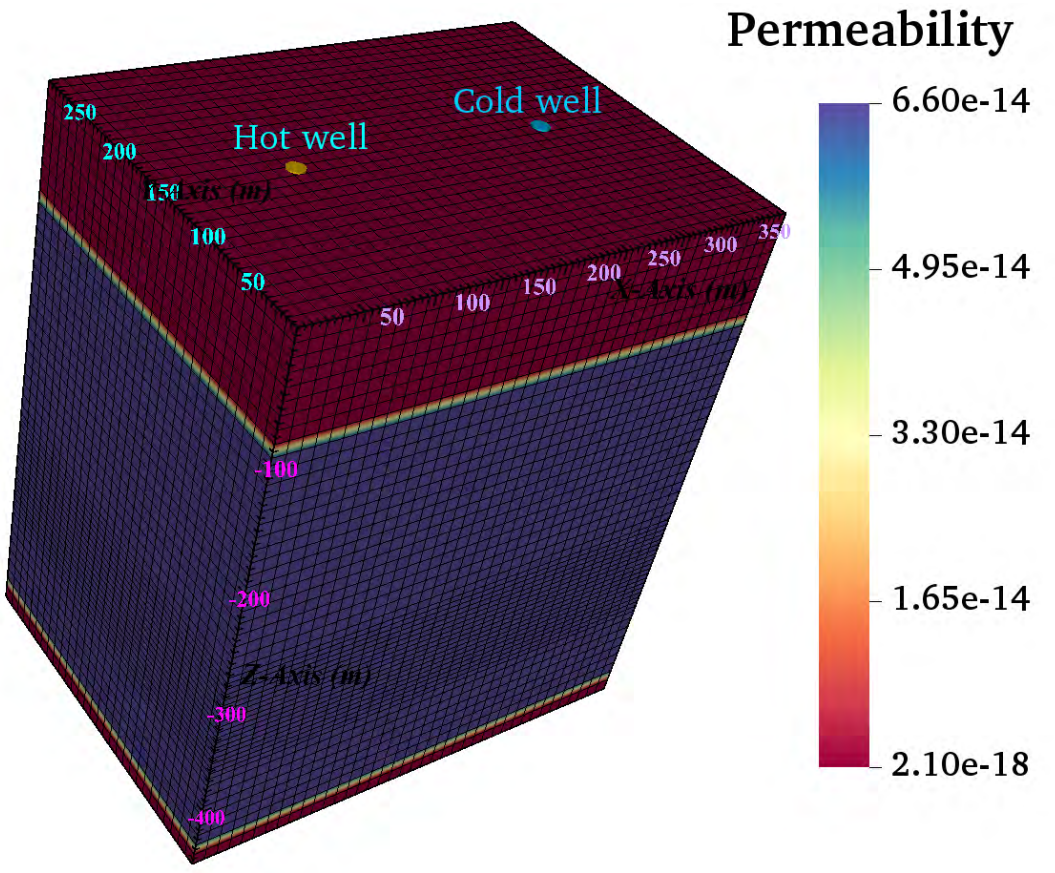

Figure 1: 3-D gridding of the mesh with initial permeability.

A finely discretized three-dimensional grid has been developed, tailored to the characteristics of the storage rock formations. The initial permeability for both the Niederrödern and Froidefontaine Formations has been uniformly set across the grid, with increased resolution near the injection zones as shown in Figure 1. The constructed mesh omits the overlaying strata up to a depth of 1000 meters, focusing exclusively on the Niederrödern and Froidefontaine Formations to optimize computational efficiency. The grid incorporates site-specific vertical pressure gradients to establish initial pressure conditions, maintaining a constant temperature profile. At the base level of the grid (Z=0 meters) represents the pressure conditions found at 1 kilometer depth at the actual site location. To avoid the thermal short-circuiting during injection and extraction processes, hot and cold wells are positioned 200 meters apart (Figure 1), each with a 50-meter screen segment, operating at a flow rate of 5 kg/s. In first run a steady state simulation is performed to obtain hydrostatic pressure conditions, and the results form this run is used as boundary condition in second run to simulate undisturbed natural state conditions with throughflow of mass and heat. In third run, the operational cycle begins with the injection of hot brine at 140°C into the hot well for six months during the summer, while the cold well simultaneously produces at the same rate. For the following six months, brine at 60°C is injected into the cold well, with the hot well producing at an equivalent rate. The study simulates this cyclic procedure over a period of five years.

2.3. Mineralogy and brine chemistry

For the reactive transport simulations, the mineral compositions and proportions are informed by Banks et al. (2021) and comprise primary minerals such as quartz, calcite, dolomite, albite, muscovite, microcline, annite, clinochlore, and kaolinite. Additionally, secondary minerals such as goethite, hematite, and ferrihydrite have been incorporated into the model. The mineral kinetic rate parameters are adapted from Palandri and Kharaka (2004).

The brine chemistry or fluid composition (Table 2) at Meletta Beds of Froidefontaine Formation in the Leopoldshafen field is reported by on Banks et al. (2021). Al^{3+} is calculated by assuming equilibrium with albite. The brine is further speciated for near steady state concentrations with minerals at 75°C using the thermodynamic database from Blanc et al. (2007). The steady-state brine chemistry is also speciated at 60°C and 140°C to align the temperatures of injection fluids in cold and hot wells respectively.

First scope calculations have been conducted accounting for a DeepStor type system consisting of a doublet with a warm and a cold leg. The calculations adopt the DeepStor strategy assuming the wells to be separated not to exchange thermal energies in the underground. These conceptual models intend to demonstrate the possible influence of hydrochemistry on thermal storage systems.

Table 2: Brine speciation calculated to mimic near steady-state brine composition with minerals at 75°C and 140°C. Al^{3+} is estimated by equilibrating the solution with albite using Blanc et al. (2012).

Primary Species	Speciated concentration at 75°C (molal)	Speciated concentration at 140°C (molal)
pH	7.24	6.53
Ca^{2+}	9.250×10^{-02}	9.249×10^{-02}
Fe^{2+}	1.207×10^{-05}	1.207×10^{-05}
Mg^{2+}	3.348×10^{-02}	3.349×10^{-02}
Na^{+}	1.647×10^{-00}	1.647×10^{-00}
K^{+}	1.557×10^{-02}	1.557×10^{-02}
Cl^{-}	1.907×10^{-00}	1.908×10^{-00}
HCO_3^{-}	2.310×10^{-04}	2.311×10^{-04}
SO_4^{2-}	5.166×10^{-03}	5.166×10^{-03}
Al^{3+}	1.734×10^{-8}	1.738×10^{-8}
$SiO_2(aq)$	5.822×10^{-04}	5.823×10^{-04}
$O_2(aq)$	3.153×10^{-63}	3.154×10^{-63}

3. Results and discussion

3.1. Evolution of temperature during seasonal operation

Figure 2 illustrates the temperature variations in the hot and cold wells after 5 years of seasonal operations. The spatial distribution of thermal energy across the XZ-plane at Y=145 m is depicted, highlighting the thermal dynamics around the wells. The cold well is injected with brine at 60°C, resulting in a cooler region surrounding them. Conversely, the hot well receives heated brine at 140°C, which then propagates outward, eventually encountering and mixing with the native colder brine, creating a cooler thermal front further from the well.

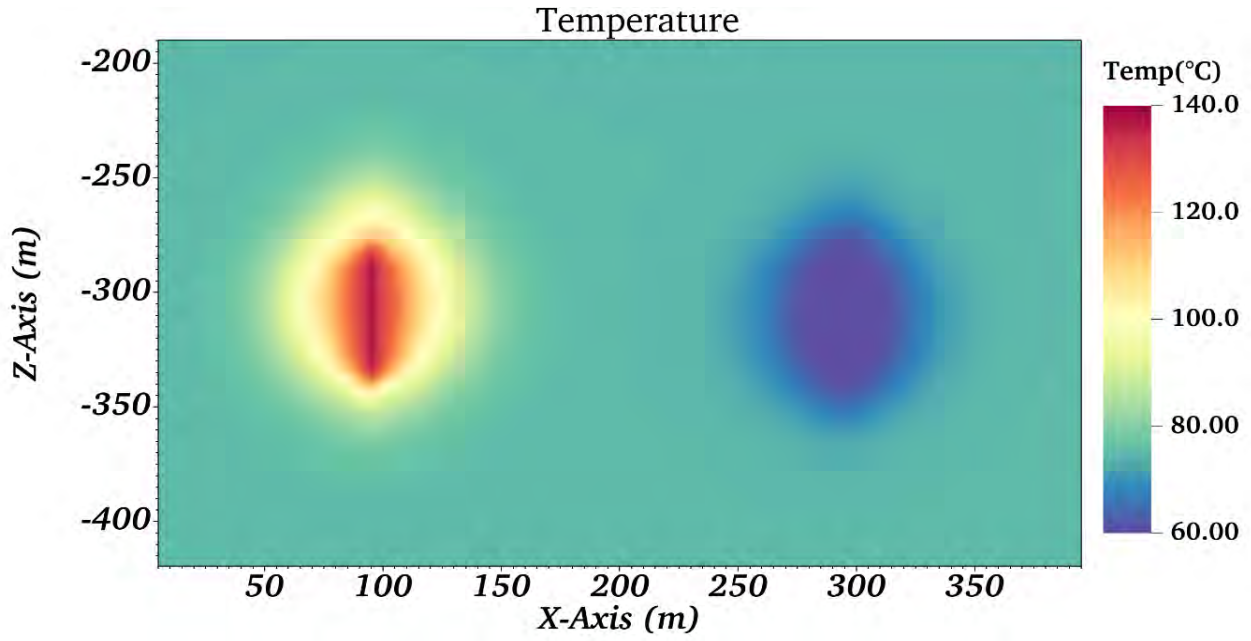

Figure 2: Variation of temperature at a hot and a cold well after 5 years of seasonal injection and production cycles.

3.2. pH and concentrations of iron species

Variations in pH and the concentrations of iron species (Fe^{2+} and Fe^{3+}) serve as significant indicators of the extent to which brine chemistry can influence mineral dissolution and precipitation, as well as the redox potential for iron oxidation, which are critical factors in the formation of scale and the occurrence of corrosion. In Figure 3, the pH levels around the hot and cold wells are depicted, indicating an increase in pH to about 7.5 near the cold well and a decrease to approximately 6.4 around the hot well. These pH shifts can be ascribed to the water-rock interactions and the temperature-dependent changes in the activity coefficient of H^+ associated with change in dissociation constant of water.

Figures 4 and 5 show the concentrations of ferrous (Fe^{2+}) and ferric (Fe^{3+}) ions respectively, with a notable increase in iron species concentrations around the hot wells relative to the cold wells. Plotting individual ferrous and ferric ion concentrations instead of total concentrations provides insight into the oxidizing or reducing conditions that may result in the precipitation of iron-containing minerals. This situation could pose a risk of corrosion to the well bore and tubing. The marked contrast between the concentrations of Fe^{2+} and Fe^{3+} suggests that the current model does not incorporate the effects of oxygen intrusion or potent oxidizing conditions. In oxidizing environments, there would likely be a greater conversion of Fe^{2+} to Fe^{3+}, which in turn could amplify the risk of precipitation of Fe (III) minerals such as goethite. At this point, the study doesn't consider intrusion of oxygen at the surface.

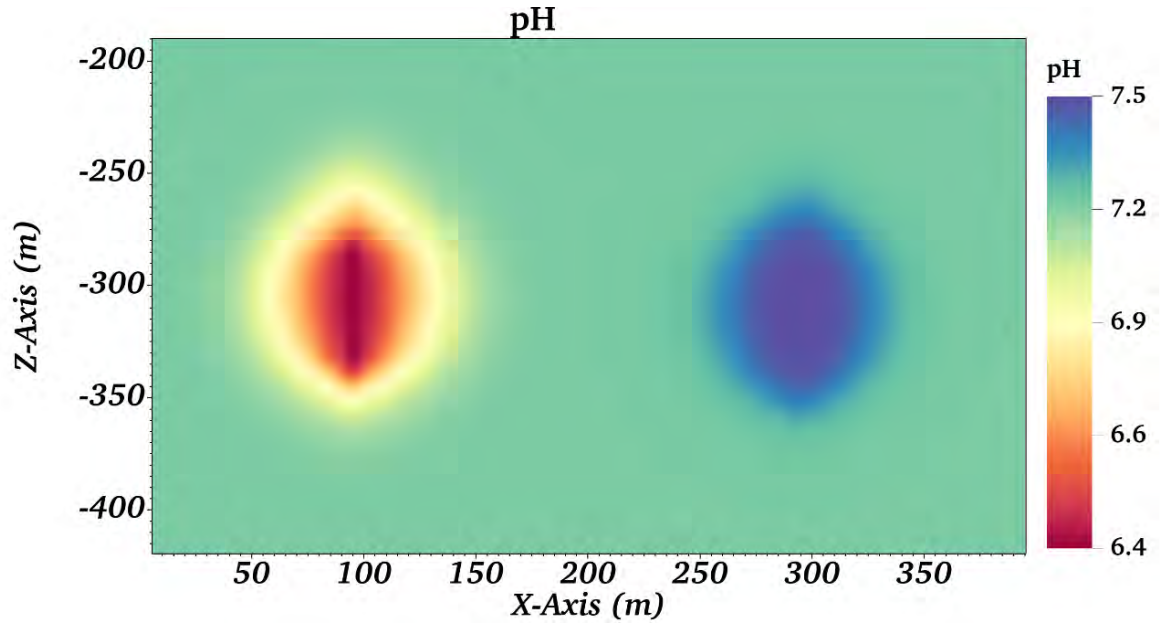

Figure 3: pH distribution in the XZ-plane (Y=145 m) after 5 years of seasonal injection and production cycles.

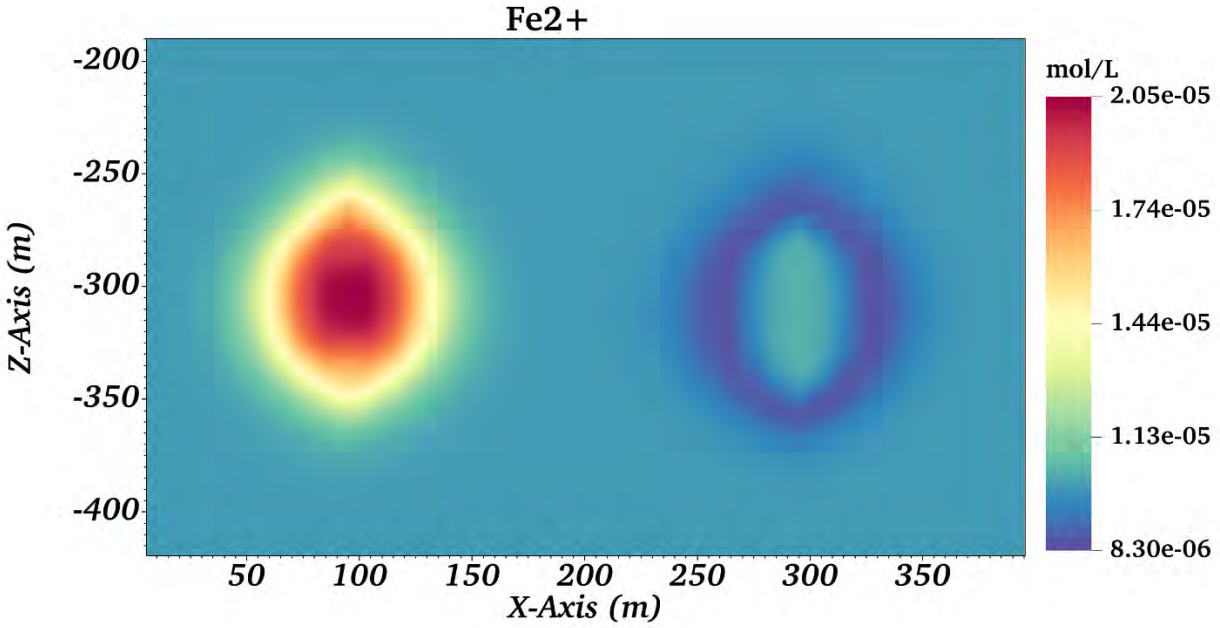

Figure 4: Concentration (mol/L) of Fe^{2+} in the XZ-plane (Y=145 m) after 5 years of seasonal injection and production cycles.

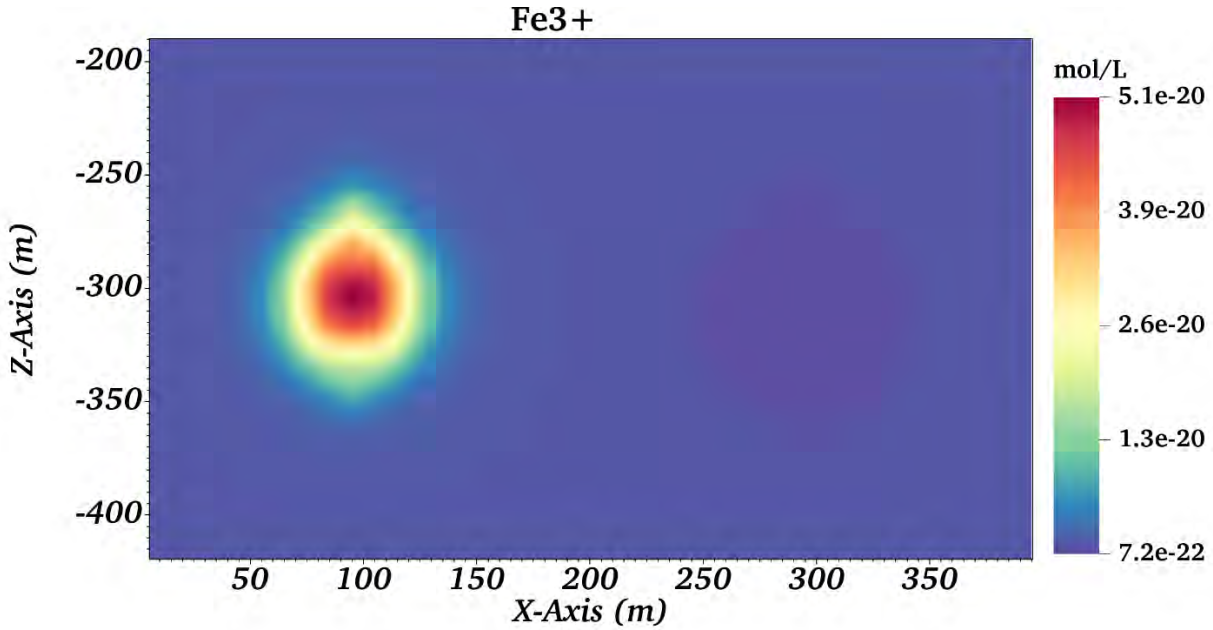

Figure 5: Concentration (mol/L) of Fe^{3+} in the XZ-plane (Y=145 m) after 5 years of seasonal injection and production cycles.

3.3. Changes in mineralogy

3.3.1. Changes in calcite and dolomite

Changes in calcite and dolomite in terms of volume fraction of total minerals are plotted in Figure 6 and 7, respectively. The model forecasts the dissolution of calcite near the hot well, likely due to the mildly acidic characteristics of the injected brine when subjected to elevated temperatures. However, the formation of dolomite is predicted in the areas adjacent to the hot well. Near the cold well, the situation reverses with calcite forming and dolomite dissolving. It is important to note that the mineralogical alterations of calcite and dolomite near the cold well are approximately an order of magnitude less compared to those near the hot well.

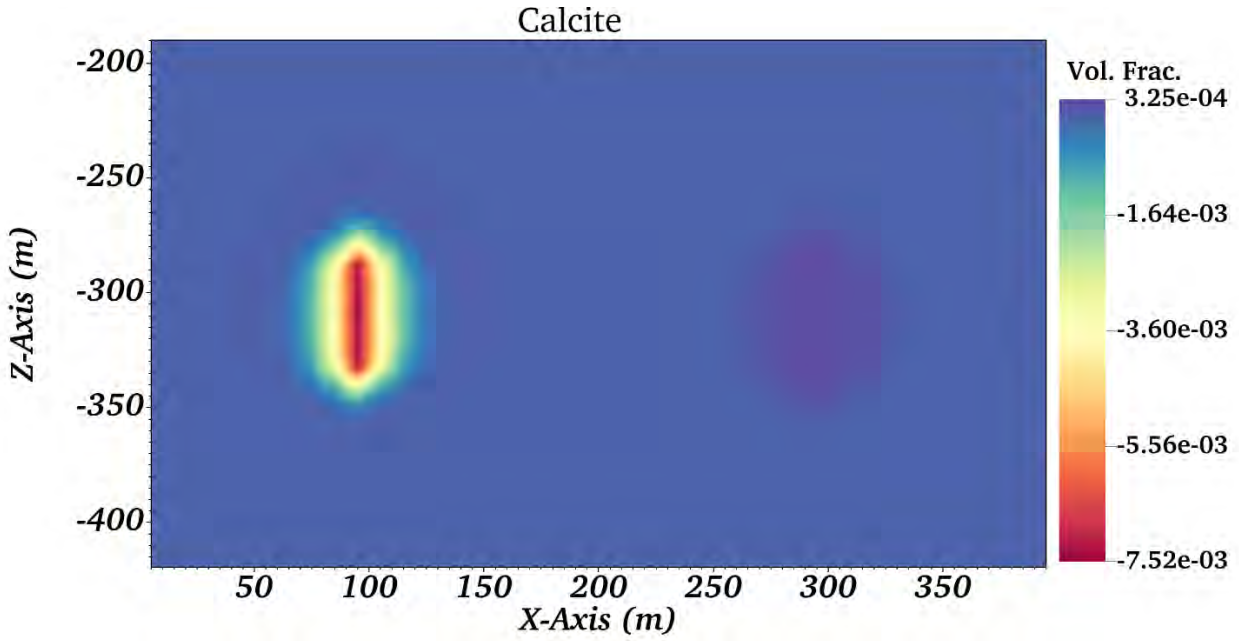

Figure 6: Calcite changes (volume fraction) in the XZ-plane (Y=145 m) after 5 years. A negative value on color bar indicates dissolution whereas a positive value indicates precipitation.

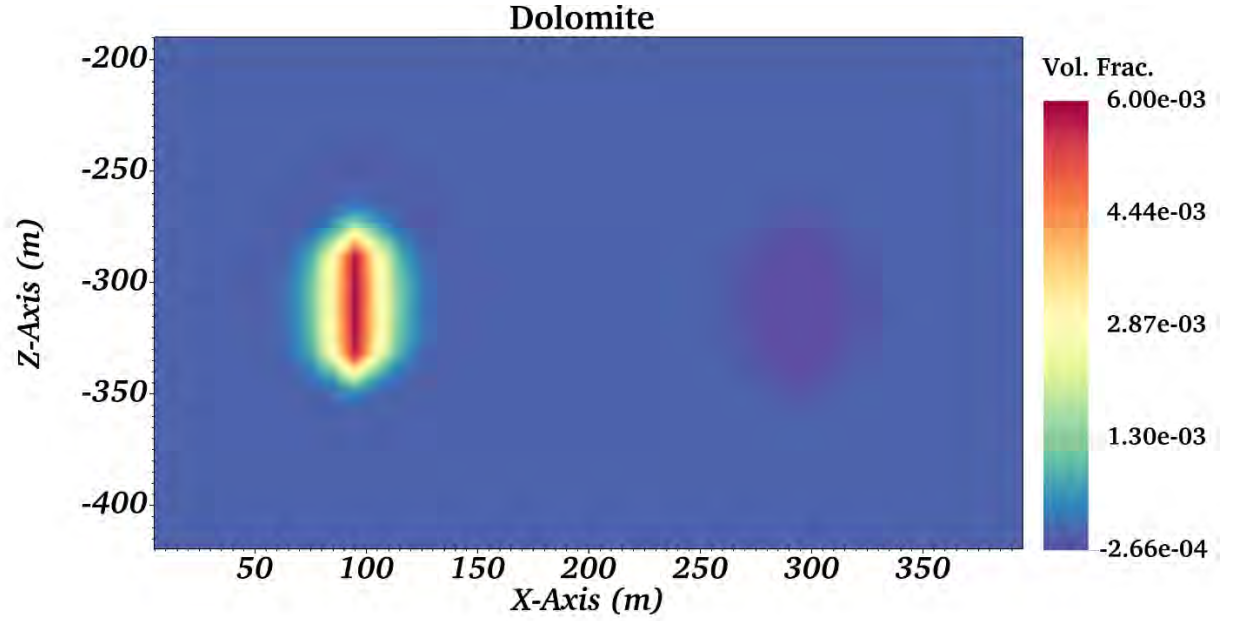

Figure 7: Dolomite changes (volume fraction) in the XZ-plane (Y=145 m) after 5 years of seasonal injection and production cycles.

3.3.2. Changes in quartz and microcline

Figures 8 and 9 illustrate that quartz and microcline undergo dissolution in proximity to the hot well, while precipitation of these minerals near the cold wells is observed to be substantially lower, with the rate of precipitation being about 20 and 50 times smaller in magnitude relative to the dissolution rates.

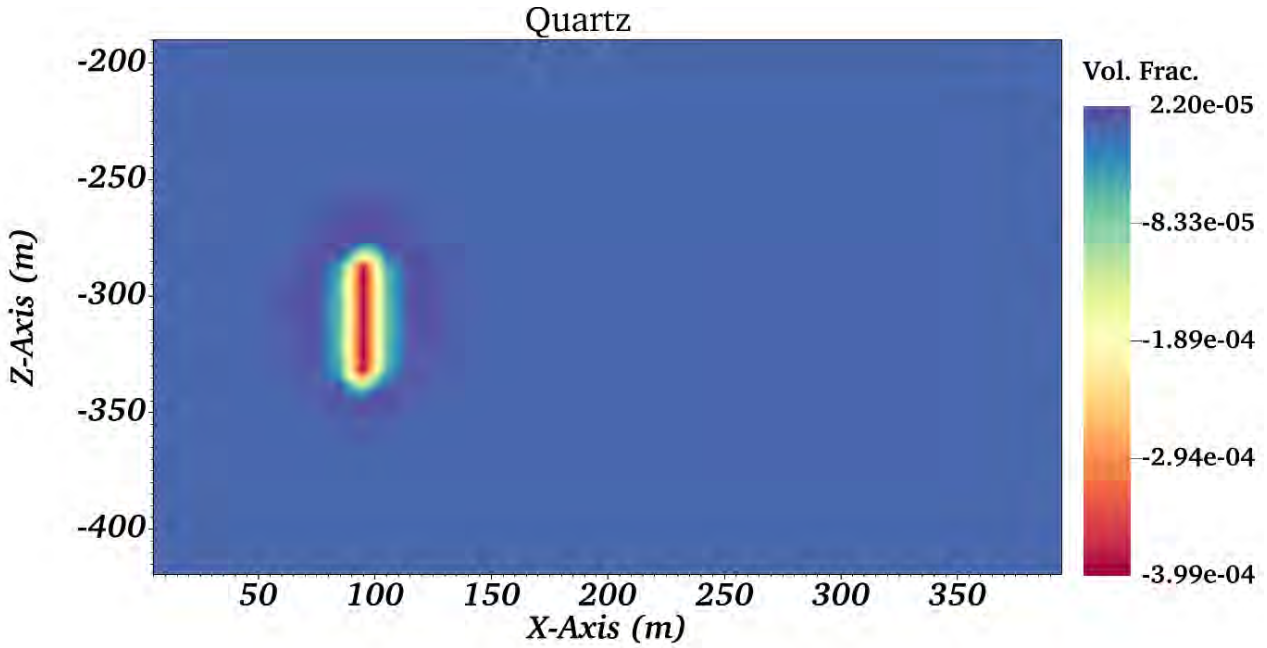

Figure 8: Changes in quartz (volume fraction) in the XZ-plane (Y=145 m) after 5 years of seasonal injection and production cycles.

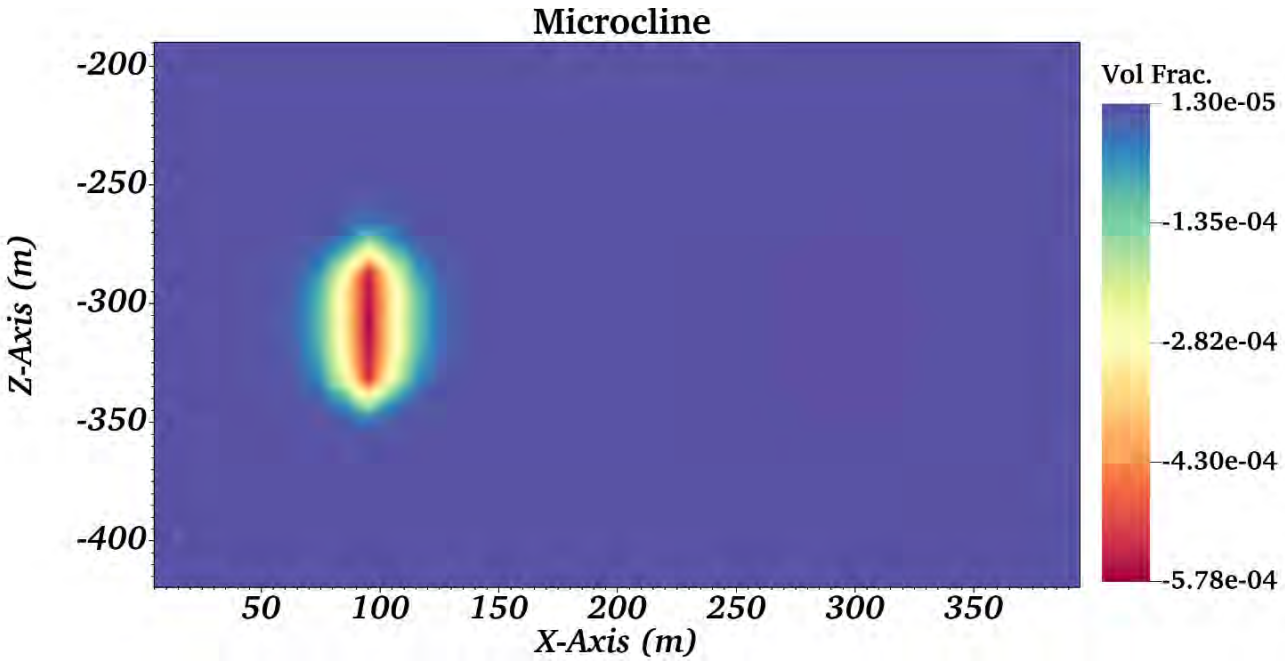

Figure 9: Changes in microcline (volume fraction) in the XZ-plane (Y=145 m) after 5 years of seasonal injection and production cycles.

3.3.3. Changes in goethite and hematite

In Figure 10, it is observed that goethite dissolves near the wellbore where the temperature is around 140°C. However, at a distance from the wellbore where the temperature drops, goethite precipitation occurs, matching the scale of dissolution seen in the warmer region. The precipitation of hematite (Figure 11) near the hot well is observed to be roughly 15 times less in magnitude

compared to the changes in goethite. Neither of the iron minerals, hematite and goethite, exhibit significant changes in the vicinity of the cold wells.

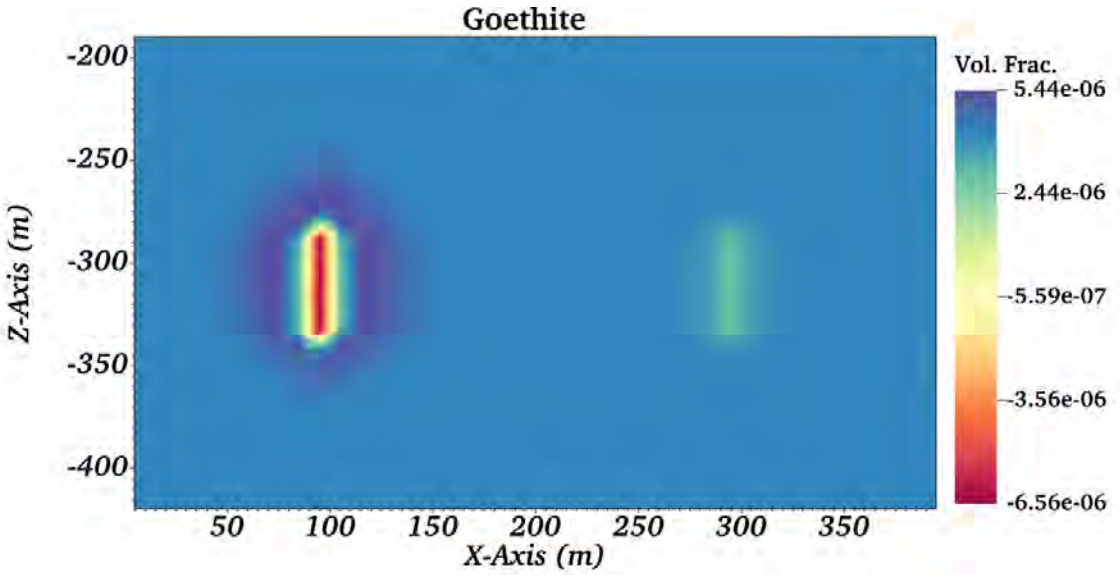

Figure 10: Changes in goethite (volume fraction) in the XZ-plane (Y=145 m) after 5 years of seasonal injection and production cycles.

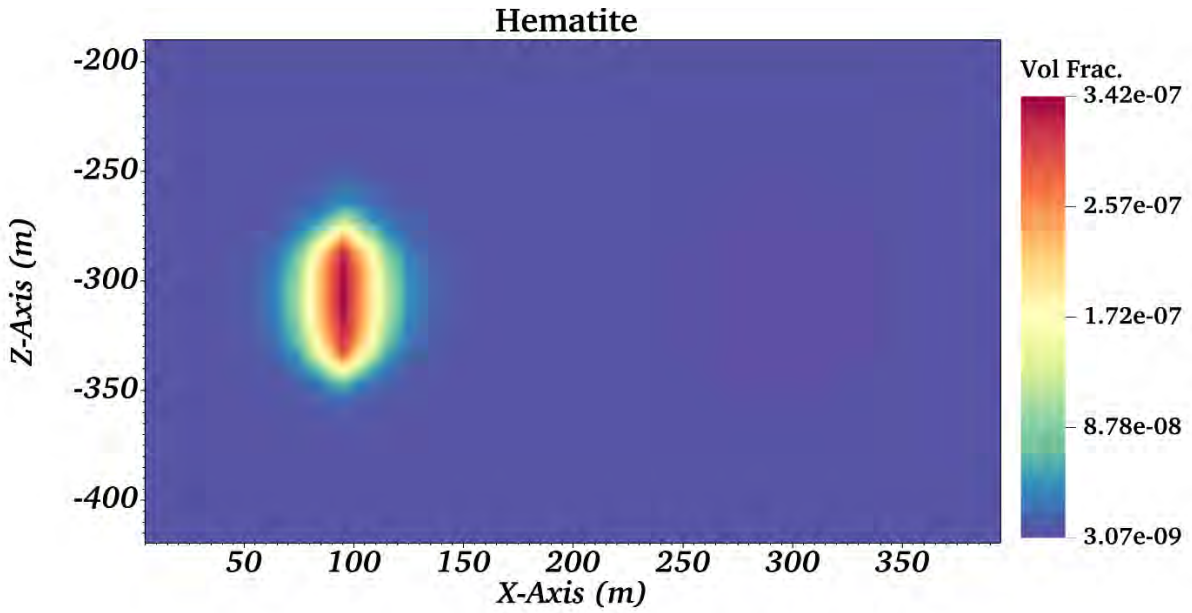

Figure 11: Changes in hematite (volume fraction) in the XZ-plane (Y=145 m) after 5 years of seasonal injection and production cycles.

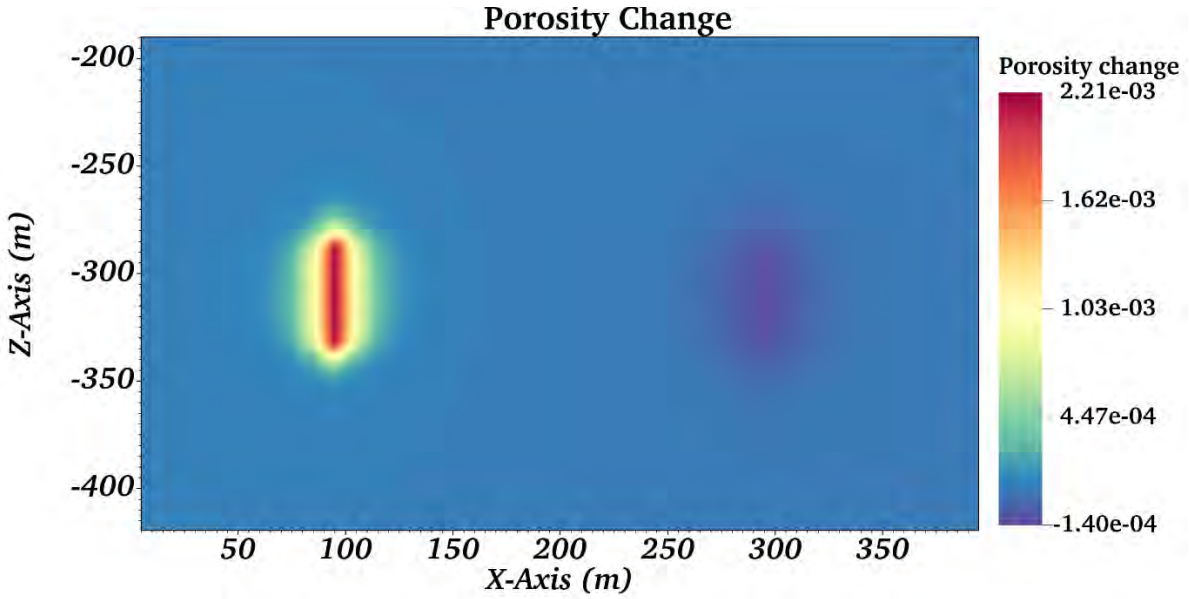

Figure 12: Changes in porosity in the XZ-plane (Y=145 m) after 5 years of seasonal injection and production cycles.

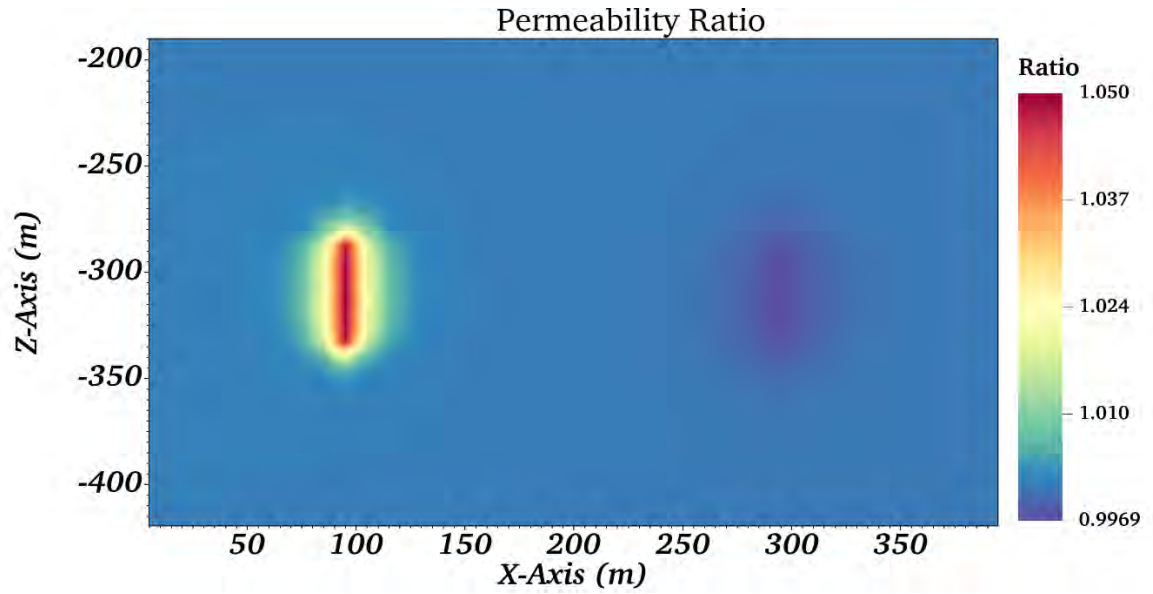

Figure 13: Permeability ratio in the XZ-plane (Y=145 m) after 5 years of seasonal injection and production cycles.

3.4. Changes in porosity and permeability

Figure 12 illustrates the overall variations in porosity attributed to the dissolution and precipitation of minerals. The modeling indicates an increase in porosity of around 1.5% in the area surrounding the hot well, while a decrease of approximately 0.1% in porosity is predicted near the cold well. The enhanced porosity observed near the hot well can be linked to the dissolution of calcite, quartz, and microcline, with calcite undergoing the most significant amount of dissolution among these minerals. The amount of dolomite that precipitates near the hot well is not as substantial as the combined dissolution of these minerals, which leads to a net increase in porosity. This augmented

porosity adjacent to the hot well may improve the efficacy of the injection process for long-term storage, and the minimal decrease in porosity near the cold well is considered to have little impact. Figure 13 depicts the permeability ratio, which is calculated as the current permeability divided by the initial permeability. This ratio is derived from changes in porosity, using a cubic law for the calculation.

4. Conclusions and future work

The conceptual model integrates operational conditions, hydrogeologic attributes, and mineralogical data to simulate outcomes such as heat distribution, the likelihood of thermal short-circuiting, and variations in pH, brine composition, mineralogy, porosity, and permeability. The conclusions drawn from this study reveal that, over a five-year period, the operation of the RTES system within the established operational and reservoir parameters carries no significant risk. Results from the reactive transport modeling can guide the optimization of operational practices to enhance the effectiveness of thermal energy storage and reduce the incidence of operational failures owing to corrosion and scaling, which stem from retrograde solubility and the precipitation of iron minerals. Additionally, the findings from this study can be utilized to develop preventative measures to circumvent these issues, thereby promoting the sustainability of long-term reservoir thermal energy storage.

Future directions for this research will account for a refined geometrical setting and will include modeling scenarios with strong oxidizing conditions, like the presence of dissolved oxygen, to better quantify the potential for corrosion and scaling resulting from air intrusion. Also, it will be necessary to refine the grid resolution around the well to millimeter-scale accuracy to more precisely quantify the precipitation of iron hydroxides on the well screen. Also, a detailed wellbore simulation can be integrated with the reservoir simulation to better quantify the mineralogical changes at well screens.

Acknowledgement

We express our gratitude to the United States Department of Energy (DOE) and the German Federal Ministry of Education and Research (BMBF) for their financial contribution to our research as part of the VESTA project. We also acknowledge the support from Neptune Energy GmbH and their consortium partners. The research is funded by the U.S. Department of Energy's Office of Energy Efficiency and Renewable Energy, Geothermal Technologies Office, with Lawrence Berkeley National Laboratory being funded under Award Number DE-AC02-05CH11231 and Idaho National Laboratory under Award Number DE-AC07-05ID14517.

REFERENCES

Baillieux, P., Schill, E., Edel, J.-B., and Mauri, G. "Localization of temperature anomalies in the Upper Rhine Graben: insights from geophysics and neotectonic activity". *International Geology Review*, v. 55, no. 14, (2013), p. 1744-1762.

Banks, J., Poulette, S., Grimmer, J., Bauer, F., and Schill, E. "Geochemical Changes Associated with High-Temperature Heat Storage at Intermediate Depth: Thermodynamic Equilibrium

Models for the DeepStor Site in the Upper Rhine Graben, Germany". *Energies*, v. 14, no. 19, (2021), p. 6089.

Bear, J., 1972, "Dynamics of Fluid in Porous Media", New York, Dover Publications, Inc.

Blanc, P., Lassin, A., Piantone, P., Azaroual, M., Jacquemet, N., Fabbri, A., and Gaucher, E. C. "Thermoddem: A geochemical database focused on low temperature water/rock interactions and waste materials". *Applied Geochemistry*, v. 27, no. 10, (2012), p. 2107-2116.

Blanc, P., Lassin, A., Piantone, P., and Burnol, A. "Thermoddem a database devoted to waste minerals". *Bureau de Recherches Géologiques et Minieres (Orléans, France)*, (2007), p.

Bremer, J., Nitschke, F., Bauer, F., Schill, E., Kohl, T. Kaymacki, E., Koelbel, T., El-Alfy, A., Ollinger, D., Meier, P., Pei, L., Blöcher, G., Klein, S., Hahn, F., Atkinson, T.A., McLing, T., Jin, W., Zhang, Y., Dobson, P., Rutqvist, J., Hörbrand, T., and Jahrfeld, T. "VESTA – Very-high-temperature heat aquifer storage". European Geothermal Congress 2022, Berlin, Germany, (2022), 5 p.

Dobson, P. F., Atkinson, T. A., Jin, W., Acharya, M., Akindipe, D., Li, B., McLing, T., and Kumar, R., Hybrid Uses of High-Temperature Reservoir Thermal Energy Storage: Lessons Learned from Previous Projects, SPE Energy Transition Symposium, 2023, p. D011S001R001.

Dobson, P. F., Salah, S., Spycher, N., and Sonnenthal, E. L. "Simulation of water–rock interaction in the Yellowstone geothermal system using TOUGHREACT". *Geothermics*, v. 33, no. 4, (2004), p. 493-502.

Fleuchaus, P., Schüppler, S., Godschalk, B., Bakema, G., and Blum, P. "Performance analysis of Aquifer Thermal Energy Storage (ATES)". *Renewable Energy*, v. 146, (2020), p. 1536-1548.

Frey, M., Bär, K., Stober, I., Reinecker, J., van der Vaart, J., and Sass, I. "Assessment of deep geothermal research and development in the Upper Rhine Graben". *Geothermal Energy*, v. 10, no. 1, (2022), p. 18.

Nitschke, F., Ystroem, L., Bauer, F., and Kohl, T. Published, "Geochemical constraints on the operations of high temperature aquifer energy storage (HT-ATES) in abandoned oil reservoirs", *in* Proceedings *Proceedings, 48th Workshop on Geothermal Reservoir Engineering, Stanford University, Stanford, California (2023).*

Palandri, J. L., and Kharaka, Y. K. "A compilation of rate parameters of water-mineral interaction kinetics for application to geochemical modeling". U.S. Geological Survey Open File Report 2004-1068, 2004.

Pruess, K., Oldenburg, C. M., and Moridis, G. "TOUGH2 user's guide version 2". Lawrence Berkeley National Lab.(LBNL), Berkeley, CA (United States), 1999.

Schill, E., Knauthe, R., Garipi, X., and Bauer, F. DeepStor - Heat cycling in the deep and medium-deep subsurface. Proceedings, 49th Workshop on Geothermal Reservoir Engineering, Stanford University, Stanford, CA, (2024).

Sonnenthal, E., Spycher, N., Xu, T., and Zheng, L. "TOUGHREACT V4.1-OMP reference manual: a parallel simulation program for non-isothermal multiphase geochemical reactive transport". University of California, Berkeley., (2021).

Steefel, C. I., and Lasaga, A. C. "A coupled model for transport of multiple chemical species and kinetic precipitation/dissolution reactions with application to reactive flow in single phase hydrothermal systems". *American Journal of Science*, v. 294, (1994), p. 529-592.

Stober, I., Jägle, M., and Kohl, T. "Optimizing scenarios of a deep geothermal aquifer storage in the southern Upper Rhine Graben". *Geothermal Energy*, v. 11, no. 1, (2023), p. 34.

Stricker, K., Egert, R., Schill, E., and Kohl, T. "Risk of surface movements and reservoir deformation for high-temperature aquifer thermal energy storage (HT-ATES)". *Geothermal Energy*, v. 12, no. 1, (2024), p. 4.

Xu, T., and Pruess, K. "On fluid flow and mineral alteration in fractured caprock of magmatic hydrothermal systems". *Journal of Geophysical Research: Solid Earth*, v. 106, no. B2, (2001), p. 2121-2138.

Inhibition of Iron Sulfide to Prevent Brine Pump Capacity Decline

Fritz Earwin Monterozo

Nalco Water, An Ecolab Company

Keywords

Brine pump, mineral scaling, and iron sulfide

ABSTRACT

In geothermal systems, iron sulfide can be considered as one of the most challenging scales because of the impacts of the deposits formed. This type of scale is usually intermixed with amorphous silica and metal silicates, which in turn, forms tenacious and hard deposits that can be observed in both surface and subsurface facilities. In one case in the Philippines, deposition of iron sulfide along the brine reinjection system negatively impacts the capacity of the brine pump. Aside from scaling along the pipelines, iron sulfide deposition was also observed inside the pump casing which causes the rapid decline of pump capacity. Without operable pumps, the plant is forced to shutdown and do manual cleaning to regain normal operations. A new inhibition program was studied based on existing cases of Nalco Water and check if the same principle can show positive impact on this type of application. The goal of the inhibition program is to preserve the capacity of the brine pump by minimizing scaling. This will maintain existing or reduce (or to some extent, eliminate) brine dumping rate. The trial was conducted from Oct. 19, 2023, and ended on Feb. 19, 2024. Nalco Water silica inhibitor blend was used targeting metal silicates/sulfides/oxides and amorphous silica. The Nalco program has started under an existing dumping condition. It can be observed that before the new inhibition program, the brine dumping rate increases steeply over time. The Nalco program was able to slow down the steep increase of the dumping rate. This was further demonstrated after the silencer cleaning where it can be observed that the brine dumping rate was consistently controlled for 1 month. Aside from brine dumping data, monomeric silica levels were also monitored during the trial. Comparing to the baseline, monomeric silica retention increased during the trial which is a good indicator of lesser scaling potential. Silica may not be visible in the XRF or XRD analyses because the sample was limited to the brine pump internals only. It is possible that the conditions inside the brine pump are not conducive to silica scaling, and thus scaling involving silica might be observed upstream or downstream of the brine pump. Aside from quantitative measurements, qualitative observations were also made during the trial. It is worth noting that during an outage where the brine pump was put out of service, no manual

barring was done to restart the pump. This was a good indication of the benefits of the chemical program in comparison to the previous experiences of the site.

1. Introduction

Mineral scaling in different geothermal systems is known to be a considerable limiting factor in achieving operational efficiency. It can occur at any location in a geothermal power station where temperature, pressure, pH or velocity changes, thereby affecting component concentrations that lead to scaling (Jamero et. al., 2018). Aside from amorphous silica and its derivatives, metal sulfide scaling in geothermal surface facilities can drastically reduce the output of the power plant. The formed hard and tenacious scales can reduce pipeline internal diameter which has severe adverse consequences on both operational and economic considerations (Andritsos & Karabelas, 1995).

Iron sulfide is one of the most common metal sulfide scales found in geothermal systems. It can be considered as the most abundant component in sulfide-rich scales. Observed iron sulfide scales in geothermal can exist in various forms. Geothermal wells in Paris Basin have large concentration of dissolved sulfide which forms mackinawite, pyrite and pyrrhotite (Criaud & Fouillac, 1989). A two-phase pipeline in the Philippines showed formation of pyrite and pyrrhotite co-depositing with magnetite and hematite (Jamero et. al., 2018). Another crystalline phase identified and observed in a geothermal facility in the US is troilite (Gallup et al., 1990). Among the crystalline phases observed, pyrite can be considered as the most stable phase. At relatively high temperatures conditions of 200 ℃ and above, pyrite and pyrrhotite are the dominating structures while other metastable sulfide phases can exist at lower temperatures and atmospheric conditions (Taylor, 1980).

Like mineral scaling in general, iron sulfide scaling is affected by both thermodynamic and kinetic considerations. Factors like flow velocity, pH and concentration of scale-inducing species (supersaturation) have strong influence on the scaling potential.

1.1 Factors Affecting Iron Sulfide Formation

According to the study of Andritsos & Karabelas (1995), aside from saturation conditions, pH, flow velocity and temperature have varying effects on the deposition behavior of iron sulfide. In terms of pH, the observed deposition behavior (assuming constant species concentration, temperature, salinity and velocity), resembles a “bell” shape curve with peak at pH 6.2.

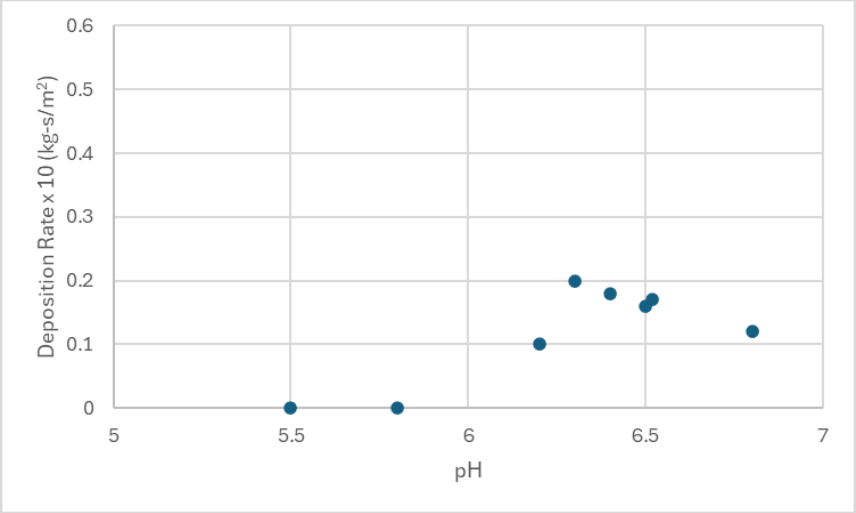

Figure 1. Effect of pH on deposition rate of iron sulfide. Reference: Andritsos & Karabelas, 1995)

Flow velocity has a considerable impact on deposition rate at fixed pH value. It can be generally observed that increasing velocity also increases the deposition tendency of iron sulfide. However, there is no direct impact on the morphology of the developed scales, having larger or smaller crystal structure (Andritsos and Karabelas, 1991). For temperature, a retrograde solubility curve of iron sulfide deposition was observed. An increase in temperature significantly increased the deposit formation rate. Unlike other sulfides where temperature has an impact on the pH range of deposition, this was not observed specifically for iron sulfides.

1.2 Geothermal Brine Pump Deposition

A geothermal site in the Philippines experiences brine pump capacity decline due to mineral scaling. Without enough capacity, diversion of the brine to the reinjection system can be challenging. To maintain the level inside the separator vessel, dumping of brine to collection ponds is being done. In worst case, production wells are being shut or throttled to manage limited reinjection capacity.

The nature of the deposition was studied by getting actual samples from pump casing and impeller. Figure 2 shows the actual scale samples obtained and analyzed.

Pump Casing

Impeller

Figure 2. Actual scale samples obtained and analyzed from the brine pump.

The samples were submitted to an analytical laboratory in Singapore for X-ray Fluorescence (XRF) and X-ray Diffraction (XRD) analyses. Below is the summary of the analyses:

Downstream Deposit Analysis

Elemental Analysis by X-ray Fluorescence — **Test Method: CP17000**

The sample preparation was: Dried at 105 °C

Iron (Fe)	50 wt %
Sulfur (S)	47 wt %
Arsenic (As)	1 wt %
Copper (Cu)	1 wt %

Total From XRF: 99 wt %

The following elements were not detected or were below the reporting limit (< 0.5%):

Al Sb Ba Bi B Br Cd Ca Ce Cs Cl Cr Co Dy Er Eu F Gd Ga Ge Au Hf Ho In I Ir La Pb Li Lu Mg Mn Hg Mo Nd Ni Nb Os Pd P Pt K Pr Re Rh Rb Ru Sc Sm Se Si Ag Na Sr Ta Te Tb Sn Tm Ti W Tl Th U V Yb Y Zn Zr

Analysis by X-ray Diffraction

The XRD was performed on: Dried at 105 °C

Iron Sulfide (Pyrite) - FeS2

Some amorphous material present.

Figure 3. XRF and XRD analyses of the scale samples obtained from the brine pump.

The primary identity of the scale is iron sulfide (pyrite), which explains the general dark gray color of the scale. This type of scale was also observed in other geothermal facilities like Leyte, typically from mixing an acidic well which carries the iron ions and a neutral well which causes the increase in prevailing pH (Jamero et al., 2018). Analysis of the brine that passes through the brine pump shows pH around 6.4. Based on Andritsos & Karabelas (1995) and as confirmed with our site experiences, pH is considered as the main driving factor of iron sulfide scaling. The pH of the brine is within the pH range of 6 to 6.8 at which this scale is expected to precipitate. Concentration of scale-forming ions is also an important factor to consider, especially for systems that we are expecting an influx of iron.

2. Methodology

From a similar site experience on addressing iron sulfide scaling, the same program principle was proposed. The program focuses on addressing the metal-based scales and preventing potential metal silicate formation both in the brine pump internals and downstream pipeline. This may help maintain the overall capacity of the pump.

In this case, a combination of metal silicate/sulfide/oxide inhibitor blend was used alongside with a silica inhibitor. These chemistries were blended on-site into a single product and dosed upstream of the brine pump. The details of the chemical program are summarized below:

Chemical	Function	Target Dosage (based on brine chemistry)
GEO981	Minimizes monomeric silica deposition by crystal structure modification and colloidal silica dispersion.	5 ppm
GEO962 and GEO939	Inhibition of metal silicates/sulfides/oxides to prevent further co-deposition with amorphous silica forming much harder scales.	10 ppm

The proposed program was applied for a period of 4 months. Brine dumping rate was the main key performance indicator involved. Ideally, the program should maintain the initial dumping rate to say the inhibition performance is favorable.

3. Results

For the trial, the key indicators that were agreed upon were reduction in the increase of dumping rate, which ultimately will have an impact on the actual time in-between cleaning of the brine pump. To gain additional data during the trial, monomeric silica was also measured. Scaling coupons were also installed both upstream and downstream of the brine pump.

The trial started on Oct. 19, 2023, with a target 4-month run which was to end on Feb. 19, 2024. During the testing, several outages were encountered which affected the trial. One was from Nov. 9 to Nov. 17 due to dosing pump issues, and the other one was from Dec. 5 to Dec. 17 for silencer dump cleaning.

Figure 4 shows the brine dumping trend from September 15, 2023 to January 22, 2024, along with level-control valve (LCV) positions during this period.

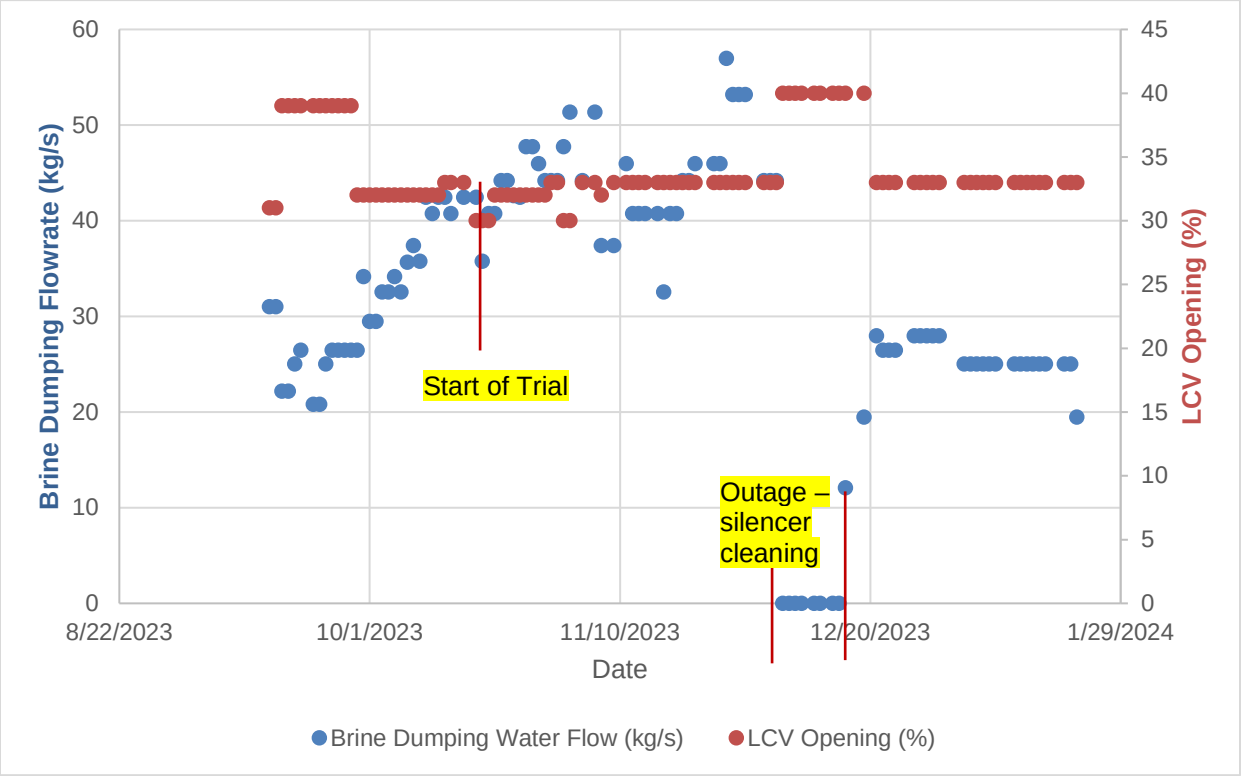

Figure 4. Brine dumping rate before and during the trial.

The test program started under an existing dumping condition. It can be observed that before the new inhibition program, the brine dumping rate was increasing steeply over time. The proposed program was able to slow down the steep increase of the dumping rate. This was further demonstrated after the silencer cleaning, where it was observed that the brine dumping rate was consistently controlled for 1 month.

Aside from brine dumping data, monomeric silica levels were also monitored during the trial.

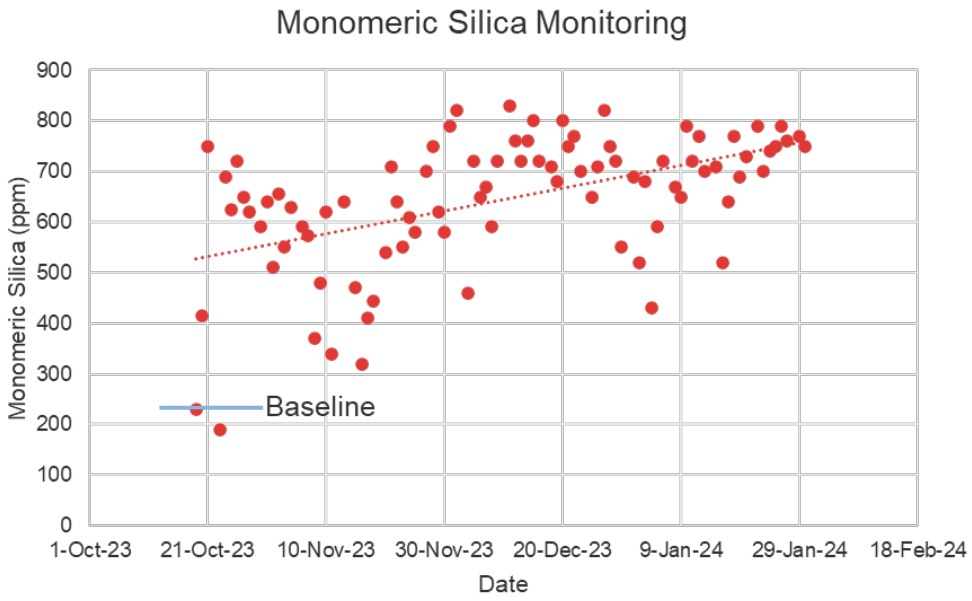

Figure 5. Monomeric silica levels along the brine pump line

Comparing to the baseline, monomeric silica retention increased during the trial which is a good indicator of decreasing scaling potential. Silica may not be visible in the XRF or XRD analyses because the sample was limited to the brine pump internals only. It is possible that the conditions inside the brine pump were not conducive to silica scaling, and thus scaling involving silica might have been occurring upstream or downstream of the brine pump.

Scale coupons were also used to monitor the progress of the trial, but the data can be considered as inconclusive since there was an outage during one of the observation periods. Here is the summary of the measurements:

Treatment	Days Inserted	Initial Weight (g)	Final Weight (g)	% Increase	Remarks
Baseline 1 (BP-B)	15	25.2	27.9	10.7	Inserted without BP-B cleaning
Baseline 2 (BP-A)	31	27.3	28.5	4.4	Started clean
Treatment Program	33	27.2	28.8	5.9	Inserted without BP-A cleaning; with 9 days outage

Aside from quantitative measurements, qualitative observations were also made during the trial. It is worth noting that during an outage where the brine pump was put out of service, no manual barring was done to restart the pump. This was a good indication of the benefits of the chemical program in comparison to the previous experiences by the site.

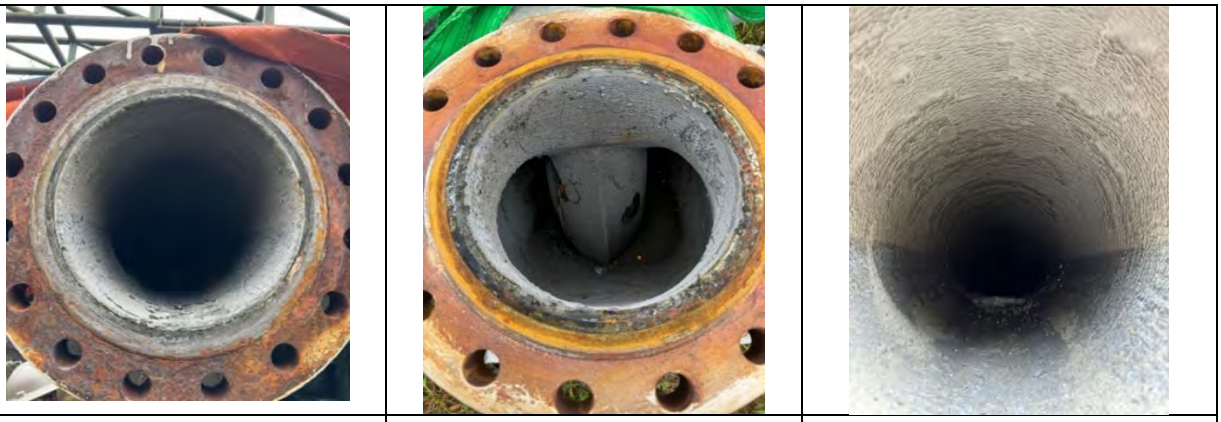

Upstream	Brine Pump Internal	Downstream

Figure 6. Brine pump inspection after the 4-month trial run.

According to the studies done by Andritsos and Karabelas (1995), the brine condition is favorable for the formation of iron sulfide. It can be considered that saturation conditions as well as pH are the main driving factors for the deposition. In comparison to the dosing behavior along the lines and inside the brine pump, it was observed that iron sulfides where mainly deposited inside the brine pump, and a combination of iron sulfides and amorphous silica scaling was present on the upstream and downstream pipelines. The hypothesis is that iron sulfide deposition is more pronounced inside the brine pump due to turbulence. The turbulent nature of the flow enhances particle interaction and increases agglomeration (Afkhami et al., 2019).

4. Conclusions and Recommendations

The condition inside the brine pump as well as the brine characteristics are contributing factors to the deposition of iron sulfide. General dispersion and inhibition were considered for the selection of a suitable treatment program. Quantitative and qualitative results show that the new program used for scale inhibition in the brine pump line is promising. The positive impacts of the program were observed firsthand. These are related to maintaining the dumping rate prior to the start of the program and obvious differences like elimination of manual barring to restart the pumps.

Ideal scenarios for the conduct of the program are the following:

1. The dosing program should ideally start with a clean system – to be able to fully demonstrate the inhibition capabilities. Pre-existing scales usually serve as seed for other scales so this can have an impact on the parameters being measured.

2. Brine dumping should be eliminated prior to the start of the dosing program. This will help to clearly demonstrate the benefits of having a preventive approach.

3. A brine sampling point should be available downstream of the brine pump. This will capture the true monomeric silica retention and clarify the relation to scaling downstream of the system.

4. Scale coupons should be installed on a clean system prior to the start of the program.

In relation to item 2, there was an observation of soft white deposits at the dump area of the silencer. Based on initial XRF results, these are purely amorphous silica. Compared to previous deposition behavior, these white deposits are easier to clean and do not form hard deposits. However, the deposition rate is faster compared to the conditions before. This can be attributed to the further concentration of silica downstream of the silencer which forces the inhibitor-colloidal silica bonds to be unstable. The result is precipitation of amorphous silica instead of complexing with metal ions. This leads to a strong recommendation that the inhibitor program should be dosed in systems where we will not expect re-concentration (exposure to atmosphere/flashing) and drastic temperature reduction that will increase the silica saturation index beyond an allowable range.

Acknowledgement

The author would like to thank Nalco Water for the support and opportunity.

REFERENCES

Afkhami, M. et al., 2019: Effect of Reynolds number on particle interaction and agglomeration in turbulent channel flow. *Powder Technology*, Vol. 343, 908 – 920.

Andritsos, N. & Karabelas, A. J., 1995: An experimental study of sulfide scale formation in pipes. *World Geothermal Congress Proceedings 1995*, Firenze, Italy, 2469 – 2474.

Andritsos, N. & Karabelas, A.J., 1991: Sulfide scale formation and control: the case of lead sulfide. *Geothermics*, Vol 20, 343 – 353.

Criaud, A. & Fouillac, C., 1989: Sulfide scaling in low enthalpy geothermal environments: a survey. *Geothermics*, Vol 18. 73 – 81

Gallup, D. et al., 1990: Heavy metal scaling in production well at the Salton Sea geothermal field. *Geothermal Resources Council Transactions*, Vol. 15, 1583 – 1590.

Jamero, J., Zarrouk, S. J. & Mroczek, E., 2018: Mineral scaling in two-phase geothermal pipelines: two case studies. *Geothermics*, Vol. 72, 1 – 14.

Development of Carbon-based Coating to Suppress Silica Scale Accumulation on the Inner Surface of Pipes

Yuya Nakashima[1)], Shinya Ui[1)], Shigeto Yamada[1)], Risako Imai[2)], Hiroyuki Kousaka[3)]

[1)]Fuji Electric Co., Ltd., [2)]Graduate school of Natural Science and Engineering, Gifu Univ.,[3)] Center of applied research of plasma, Faculty of Engineering, Gifu Univ.

Keywords

Low-adhesion coating, Silica scale, Diamond like Carbon

ABSTRACT

Silica scale accumulation on the inner surface of pipes such as heat exchanger causes power reduction or frequent maintenance to remove it. This problem is caused by blocking fluid flow due to scale accumulation. This work aimed to reduce silica accumulation by using Diamond-Like Carbon (DLC) coating. DLC is a carbon-based amorphous thin film that consists of a diamond structure and graphite structure and a low-adhesion performance against silica scale was confirmed in previous our studies. However, DLC is generally coated to outer surface due to limitation of deposition method. In this study, new coating method specialized for an inner surface has been developed, and its chemical structure was evaluated by X-ray Analysis Fine Structure (XAFS) and Elastic Recoil Detection Analysis (ERDA). As a result of chemical structure, a half-length of pipe in 500 mm received the DLC coating, while the other side was coated with a polymer-like carbon (PLC). Furthermore, geothermal brine was flowed in the coated pipes to validate the effect on silica scale accumulation. The accumulated silica morphology and accumulated amount was observed by Scanning Electron Microscope and Energy Dispersive X-ray microanalyzer. On the non-coated surface, silica scale completely covered the inner surface of pipes. The DLC-coated surface also accumulated silica. However, the silica peeled off by itself during observation, and eventually the amount of silica on the DLC surface reduced to 3% of the accumulation for the non-coated surface.

1. Introduction

Geothermal power plants produce renewable energy and they emit only 1 – 3 % CO_2 compared to emissions from fossil-fired thermal power plants [1],[2]. Additionally, geothermal power plants provide stable electricity supply in contrast to the other renewable power sources such as solar and wind power which fluctuate depending on time and weather [2]. However, geothermal brine contains a certain amount of dissolved silica, which precipitates and accumulates on the inner surfaces of pipes in heat exchangers.

Figure 1 shows examples of scale accumulation on the inner surface of the pipes in the shell and tube type heat exchanger. The silica accumulation eventually reduces the power generation because the accumulated silica blocks the geothermal-brine flow paths. Chemical and physical combined methods for removal of accumulated silica (such as fluorine acid washing and water jets) are routinely adopted to mitigate this issue [3]. However, power plants are typically shut down for these operations. Therefore, a method to suppress silica adhesion without power plant shutdowns is required. In a previous study, Nakashima et al. reported that diamond-like carbon (DLC) coatings could reduce silica adhesion to 2% of levels without coatings (compared with 13% Chromium steel) based on silica adhesion testing which imitates silica accumulation experimentally [4]. Therefore, the use of DLC coatings could be effective in suppressing the silica adhesion without power plant shutdowns. DLC is a carbon-based amorphous thin film with diamond- and graphite-like structures with sp^3 and sp^2 hybridization state, respectively [5]. DLC can be categorized as hydrogen-free and hydrogen-containing DLC; these are designated as amorphous carbon (a-C) or tetrahedral amorphous carbon (ta-C) (depending on the sp^3 fraction) and a-C:H, respectively. The ta-C coatings are excellent hard materials which provide anti-wear properties. The a-C:H coatings are generally deposited by chemical vapor deposition (CVD), resulting in lower hardness. However, it is a suitable coating method for complex shapes. DLC coating is generally applied to outer surfaces due to limitations of coating methods. The physical vapor deposition (PVD) method is a kind of sputter process, therefore, surfaces hidden from the coating source (such as inner surface of the pipes) have difficulty getting deposition. Figure 2 shows the schematic illustration of inner surface deposition. The CVD method also needs to generate plasma for deposition, however inner surface is narrow and plasma is hard to get into that space. Therefore, there were few research about DLC coatings on inner surface of pipes and evaluation of it against silica accumulation. In this study, a new coating method was developed specifically for the inner surfaces of pipes. The PVD and CVD methods require putting the surfaces to which we want to apply the coatings inside a vacuum chamber. The new coating method treats the pipes as the vacuum chamber, and we could generate the plasma needed for CVD deposition inside the pipes, and DLC could be deposited on the inner surface of the pipes. Then, chemical structure of DLC on the pipes was evaluated, and it was exposed to geothermal brine to validate the suppression of silica accumulation.

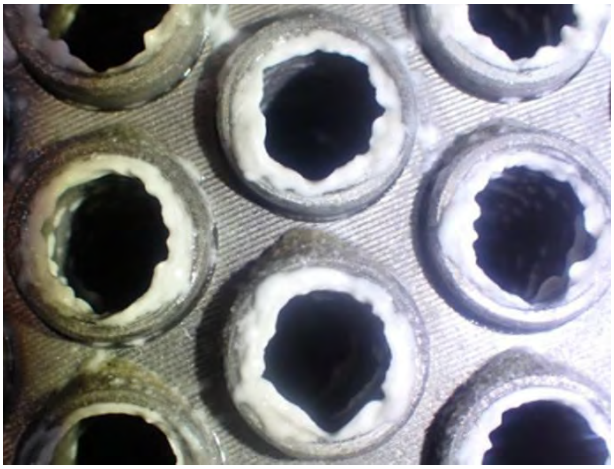

Figure 1: Example of scale accumulation on the surface of inner pipes

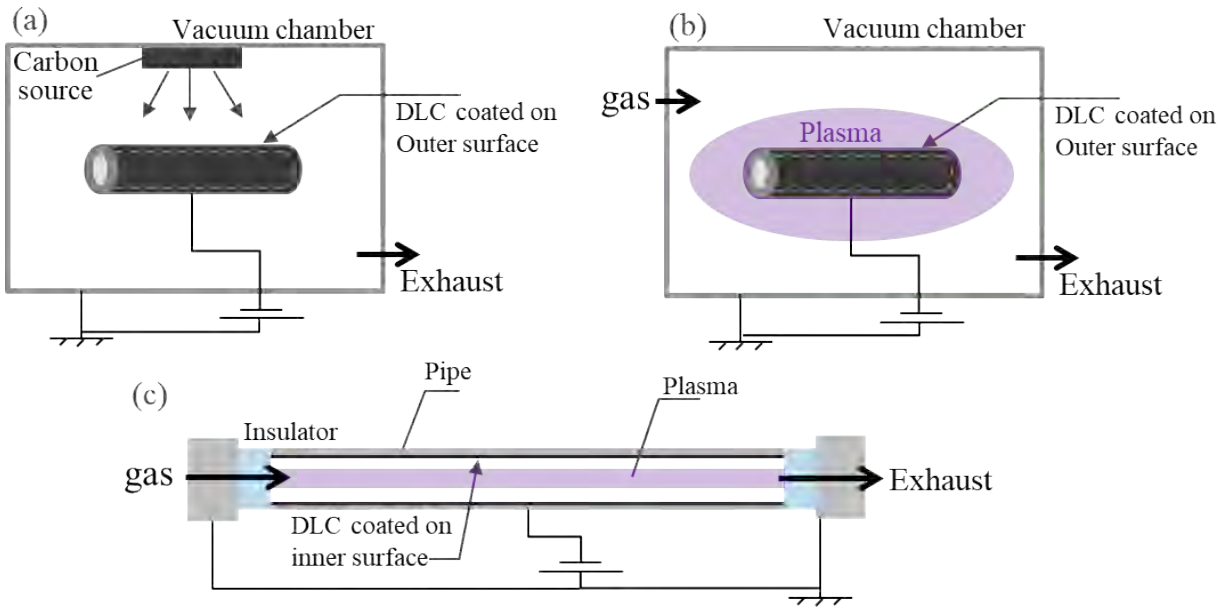

Figure 2: Schematic illustration of DLC deposition method

(a)PVD, (b)CVD, (c) Inner surface coating developed in this study

2. Experimental procedure

2.1 Test materials and DLC coating procedure

In this study, stainless steel (AISI 304, SUS304 in JIS) pipes, which is generally used in the corrosive environment, was adapted for coating substrate. The outer diameter, thickness, and length of pipes were 19.05, 1.65, 500 mm, respectively. This pipes diameter and thickness is same as that in a heat exchanger adapted in the binary geothermal power plant. Additionally, in order to evaluate the chemical structure and composition of DLC coating, 10 × 10 × t1 plate substrate consist of stainless steel (AISI420, SUS420J1 in JIS). This plate substrate was buff finished to Ra 0.01μm for chemical structure evaluation. Figure 3 shows schematic illustration of the DLC coating equipment. There are 3 jigs to connect steel pipes or quartz pipes, and it has spaces to contain the plate substrate (10 × 10 × t1). Therefore, both tip and midpoint of pipes were able to be evaluated. Since DLC coating requires to apply a bias voltage to pipes, quartz pipes were adopted for the electrical insulation. Bottom jig was connected to gas supply and top jig was connected to vacuum pump. In order to generate plasma in DLC coating process, pressure adjustment was implemented by flow rate of gases and vacuum pump adjustment. The 3 jigs (top, midpoint and bottom) were used for the chemical structure evaluation of top, midpoint and bottom positions. However, the midpoint jig was removed in the DLC coating process for the scaling test at site to apply the DLC coating to 500 mm pipes which was suitable in the scaling test. The deposition conditions for the chemical structure evaluation and the scaling test were same.

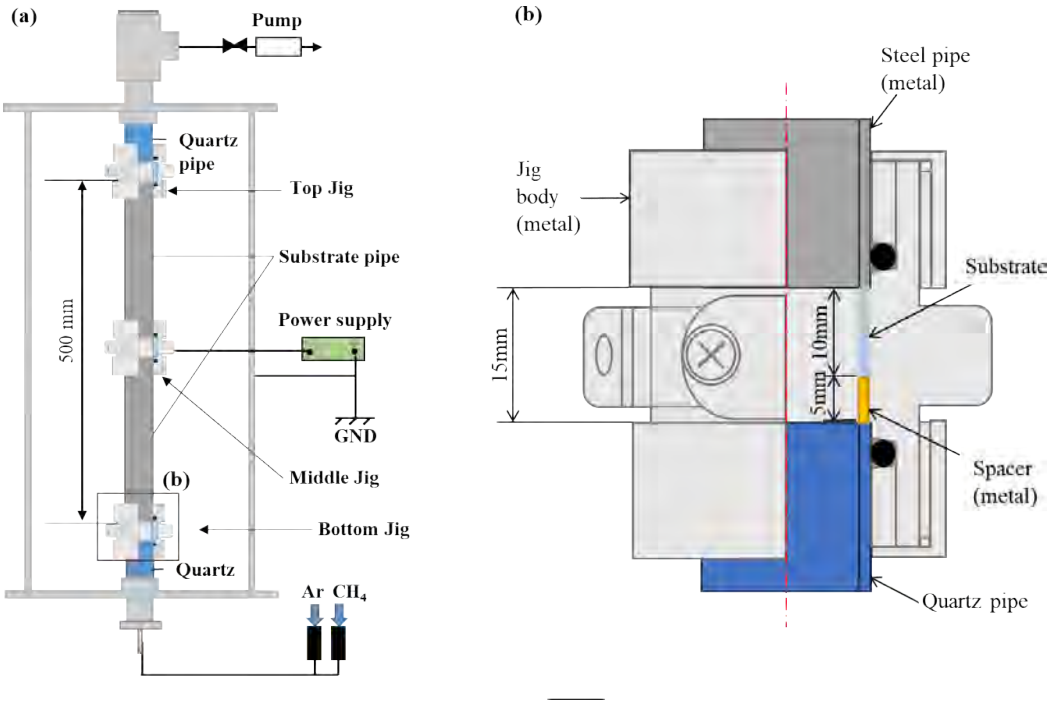

Figure 3: Schematic illustration of coating equipment (a) overview of coating equipment, (b) details of bottom jig[6]

Table 1 shows the deposition condition of DLC coatings. Bias voltage was applied as pulse direct current with a duty ratio of 0.75% to avoid the temperature increase during coating process. Ar gas was adopted as to generate plasma, and CH4 was adopted as carbon source of DLC coating. The back pressure of exhaust gas was set as 33 Pa, it was adjusted to generate plasma. Before the DLC coating process, plasma cleaning was applied to remove contamination or oxidation layer on the inner surface of pipe by exposing that surface under Ar gas plasma.

Table 1 Deposition conditions of DLC coating

Average Voltage		-840	V
Duty rate		0.075	%
Deposition time		80	min
Pressure		33	Pa
Gas flow	Ar	75	sccm
	CH_4	18.5	sccm

2.2 Analysis methods used to measure DLC coating properties

In order to measure the sp^2 bond fraction on the outermost surface, X-ray analysis of the fine structure (XAFS, Aichi synchrotron BL7U) was conducted. Highly oriented pyrolytic graphite (HOPG) was employed as a reference with 100% sp^2 binding, and the sp^2 bond fraction ($sp^2/(sp^2+sp^3)$) of the DLC coating was calculated by comparing the spectrum regions by utilizing the π^* orbitals in sp^2 bonds at 285.4 eV in the HOPG and DLC coatings[7]. XAFS can be employed to measure the sp^2 fraction at different depths depending on the type of electron yield. It was previously mentioned that the auger electron yield (AEY) comes from 0–2 nm depth and that the total electron yield (TEY) comes from 0–50 nm depth51). Therefore, the sp^2 bond fraction calculated from the AEY was defined as that of the outermost surface structure of the DLC coating, and the fraction obtained from the TEY was defined as that of the bulk structure.
In order to measure the depth profile of the hydrogen amount, high-resolution elastic recoil detection analysis (HR-ERDA, HRBS500) was performed with 480 keV N+ ion input, and recoiled H+ ions were detected. The hydrogen amount was calculated from the reference DLC coating, for which the hydrogen amount was already known.

2.3 Scaling test at site

In order to confirm the suppression of silica accumulation at DLC coating on the inner surface of pipes, non-coated and DLC coated pipes was exposed under actual geothermal brine at the actual geothermal plant. The geothermal brine was branched from the hot brine line at the geothermal binary plant and led to the test section. Figure 4 shows test section. Non-coated and coated pipe was connected in series, and geothermal brine was flowed through the pipes with 0.65t/hr for 75 days.

After the test, both non-coated and DLC coated pipes were cut and the silica accumulation morphology was evaluated using Scanning electron microscopy (SEM) to confirm the difference of silica accumulation between non-coated and DLC coated pipes.

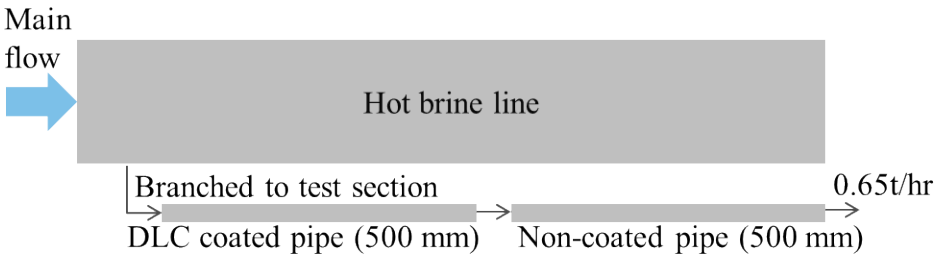

Figure 4: Test section of scaling test

In addition, scale suppression effect was confirmed by comparing the accumulated amount of scale on the coated and non-coated pipes. The accumulated amount of scale was defined as following.

$$A = \frac{Si}{M}$$

where A, Si, M are accumulated silica amount, detected Si atom amount [wt%], and detected atoms derived from coating or substrate amount, respectively. Therefore, summation of the amount of Fe, Cr, C is used for M. The accumulated amount of scale on the coating was calculated from A of the coating divided by that of non-coated one.

3. Results

3.1 DLC coating on the inner surface of pipes

Figure 5 shows coating equipment for pipes in process and appearance of plate substrate after deposition set inside of jig at (a) 0 mm (bottom), (b) 250 mm (midpoint) (c) 500 mm (top). Plasma light was evident at both ends of the pipe, and it is thought that plasma was generated and coating deposition occurred over the entire length of pipe. Points (a), (b), (c) had colored areas where coating deposited. DLC coating has generally black color derived from carbon. Therefore, these colors of substrate were caused by interference color depending on the thickness of coating. Figure 6 shows appearance of DLC coating on 500 mm pipe. Each position of the inner surface of pipe got black colored, indicating that entire surface of pipe got deposited with coating. However, the color of the coating was different from plate substrate, as shown in Figure 5. The inner surface of pipes shown in Figure 6 had no color gradation. In contrast, the plate substrate as shown in Figure 5 had color gradation on the substrate, and it was not of a black color. Therefore, the color change in the plate substrate was caused by thickness difference, since the jig shape was different from the pipe, and the plasma state was also different from that of the pipe. In contrast to the black color at the inner surface of pipe at (a), (b), (c), the substrates at these positions showed brownish black, greenish black, and black, respectively. It is thought that the chemical structures were different at each position. Therefore, in order to differentiate the chemical structure of coatings deposited on the inner surface of pipe, XAFS and ERDA analysis was performed on the plate substrates.

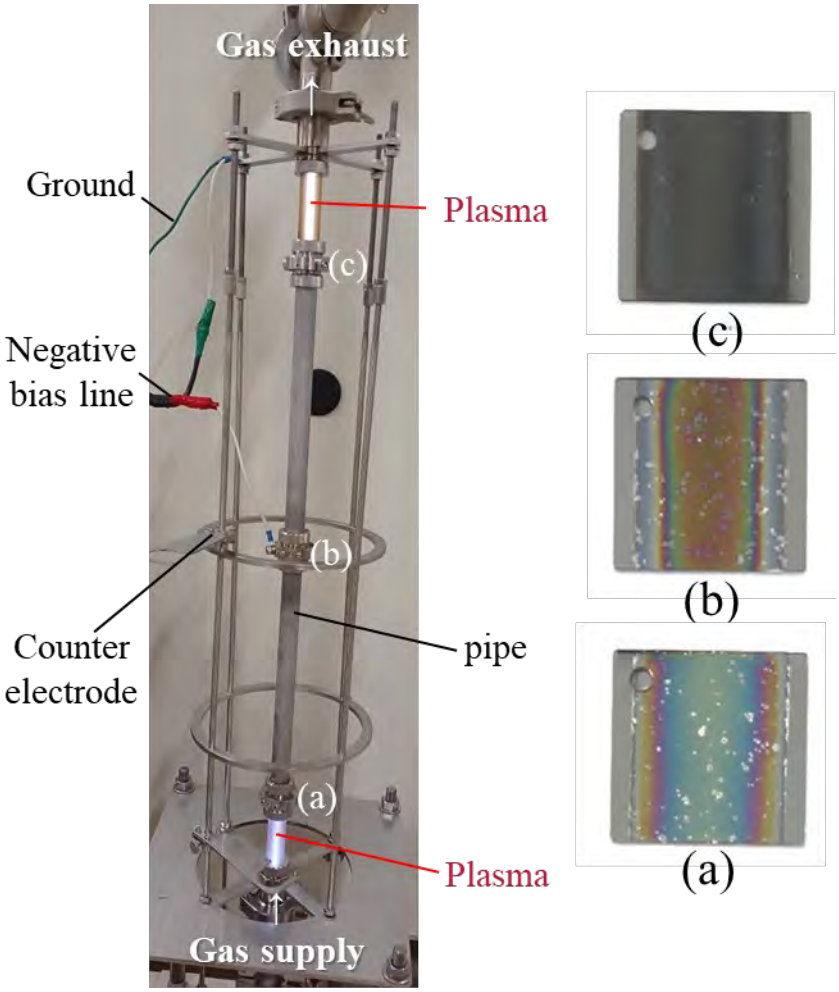

Figure 5: Coating equipment in deposition process, appearance of plate substrate after deposition set inside of jig at (a) 0 mm (bottom), (b) 250 mm (midpoint) (c) 500 mm (top)

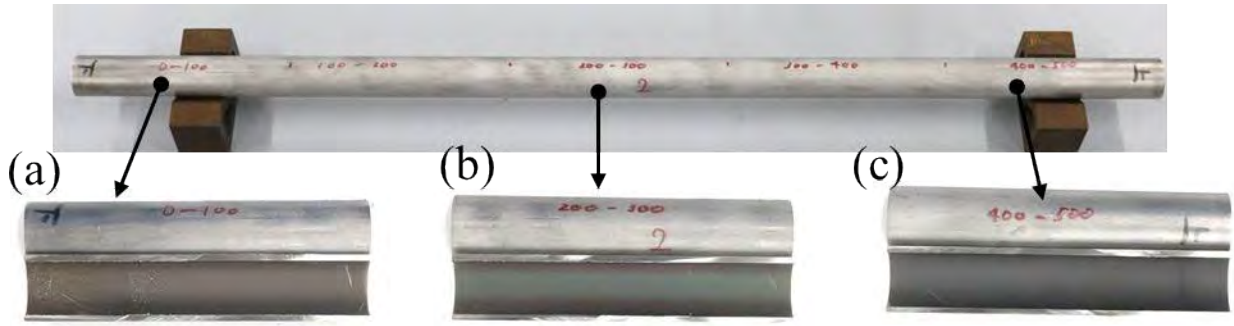

Figure 6: Appearance of DLC coating on 500 mm pipe from gas supply at (a)0 – 100 mm, (b) 200-300, (c) 400 – 500 mm

Figure 7 shows spectrum of XAFS with the analysis of outermost surface in 0 – 2 nm. The XAFS spectrum describes peaks derived from π, σ bonding of carbon atoms which represent the sp^2 and sp^3 hybridization state of DLC coatings. Our previous study [4] indicated that a low sp^2 fraction (described as peak area of $sp^2/(sp^2+sp^3)$ in the XAFS spectrum) could reduce silica adsorption energy and eventually suppress the amount of accumulated silica. Therefore, the sp^2 fraction was analyzed at 0, 250, 500 mm from the gas supply position. DLC is an amorphous coating, which indicates that the XAFS spectrum should have broad peaks. Therefore, the XAFS spectrum at the (b) 250 mm and (c) 500 mm positions indicated the presence of DLC coatings. However, the

XAFS spectrum at the (a) 0 mm position had multiple peaks in the σ bonding region. These multiple peaks are characteristic of graphite [7], and it indicated that little of the coating at (a) was in an amorphous state. Therefore, the area of 0 -100 mm from the tip of pipe was coated with polymer-like carbon (PLC) rather than the DLC coating. However, at least the area of 300 – 500 mm was coated with DLC coating.

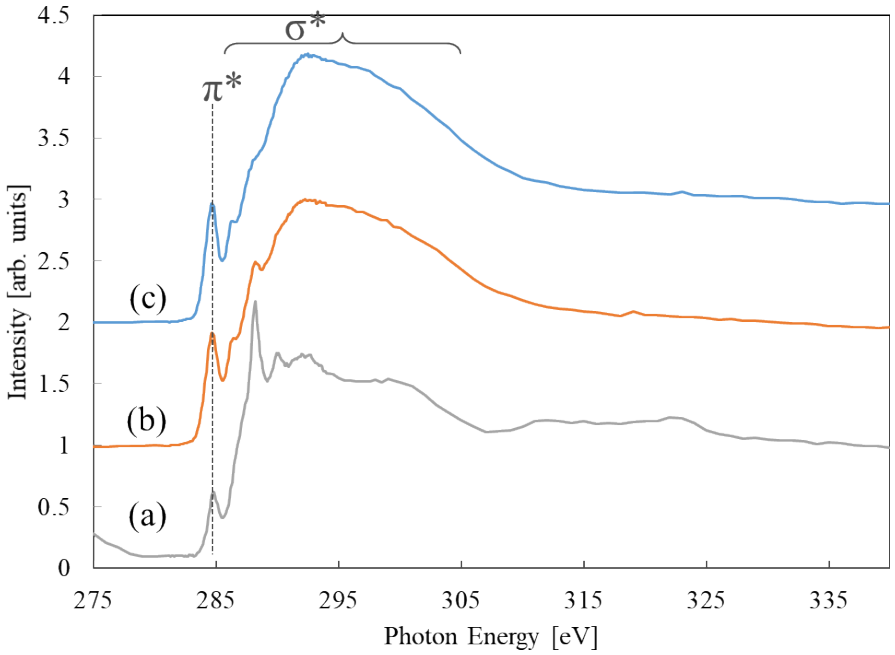

Figure 7: XAFS spectrum of plate substrate set in the position of (a) 0 mm, (b) 250 mm, (c) 500 mm

Figure 8 shows hydrogen content distribution from surface of coating by ERDA analysis. Our previous studies indicated that higher hydrogen content could suppress silica accumulation [8]. Each position (a) – (c) had hydrogen distribution at depth and a different trend in the outermost surface around 0 – 5 nm. At the outermost surface, hydrogen content is higher in order of (a) 0 mm, (c) 500 mm, (b) 250 mm. Therefore, (c) 500 mm had a lower-adherence DLC coating than the other positions since that position had highest hydrogen content in DLC. In this coating method, the chemical structures of the coatings were quite different depending on the position along the pipe length. (a) was polymer-like carbon (PLC) coating as indicated by XAFS analysis. Therefore, (a):PLC had higher hydrogen content than (b),(c):DLC [5]. Conventional coating method has enough space to contain the coating gas, however, inner pipe coating method had less space to contain the coating gases (CH_4) than conventional one, as illustrated in Figure 3. Therefore, coating gas was consumed along with the length of pipe, and much amount of hydrogen derived from CH_4 were in (c) than (b) position. Therefore, I inferred that hydrogen content results in order of (a), (c), (b).

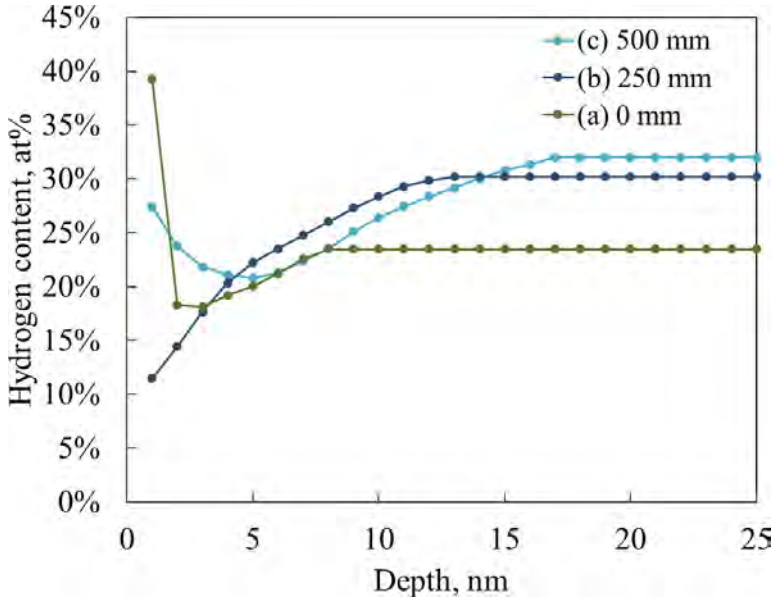

Figure 8: Hydrogen content distribution from surface of coating at (a) 0mm, (b)250mm, (c)500 mm

3.2 Scale accumulation on the inner surface of pipes

In order to confirm that the suppression effect of accumulated scale at the DLC coating depends on its chemical structure, accumulated scale morphology was observed by SEM-EDX for non-coated and several positions of coated pipes corresponding to chemical structure analyses of the previous section. Figure 9 shows accumulated scale morphology on the inner surface of SUS304 pipe. Scale covered the entire surface. Its morphology was made of cohesive spheres, which is characteristic of amorphous silica[9]. Table 2 shows chemical composition of accumulated scale on the inner surface of SUS304 pipe. Si and O atoms were mainly detected, and Al, Ca, Ca, Na atoms were also detected. Few Fe atoms which derived from substrate were detected. Therefore, it is thought that the accumulated scale was mainly made from amorphous silica.

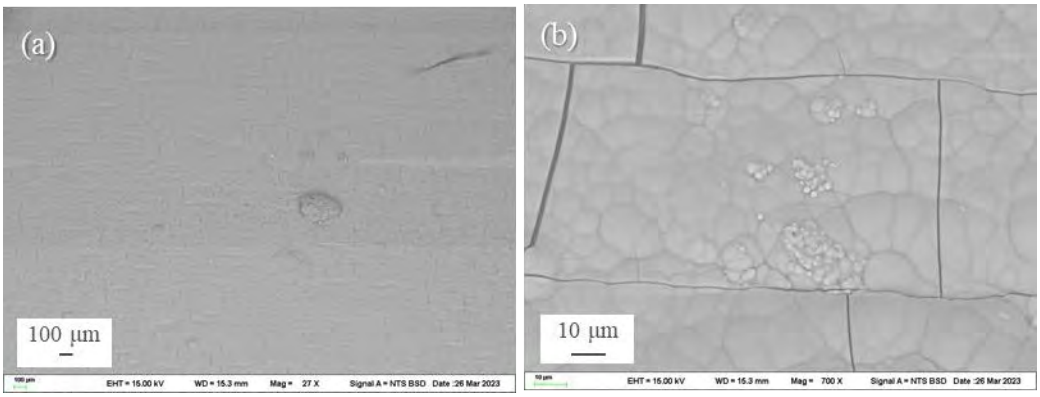

Figure 9: SEM image on the inner surface of SUS304 pipe.

Table 2: Chemical composition of accumulated scale on the inner surface of SUS304 pipe

Chemical composition [wt%]							
C	O	Na	Al	Si	K	Ca	Fe
1.72	53.45	1.26	6.24	31.41	1.40	3.91	0.61

Figure 10 shows SEM images of accumulated scale morphology on the inner surface of coated pipe. Each position of pipe accumulated scale with cohesive sphere morphology; therefore it is thought that the scale accumulation consisted mainly of amorphous silica. At the (b) position, which had DLC coating with a hydrogen content 11 at% at the outermost surface, the surface got covered entirely with accumulated scale. In contrast, at the (a) position, which had a polymer-like carbon coating with hydrogen content of 39 at% at the outermost surface, the scale partly peeled off. At the (c) position, which had DLC coating with hydrogen content of 27 at% at the outermost surface, the accumulated scale peeled off almost the entire surface. Figure 11 shows the accumulated scale amount at the surface of coated pipe. The reference amount for 100% accumulated scale is that of uncoated SUS304 pipe. However, DLC coating was partly peeled off. Therefore, the effectiveness of scale suppression was in the following order: (c), (a), (b). Moreover, DLC coating with higher hydrogen content at (c) could attain a level of 0.5 % of scale accumulation compared with SUS304. In our previous study [4],[8], DLC coating with high hydrogen content could reduce the accumulated silica amount. Therefore, the (c) position, at which the DLC coating had the highest hydrogen content could reduce more scale accumulation than the other positions.

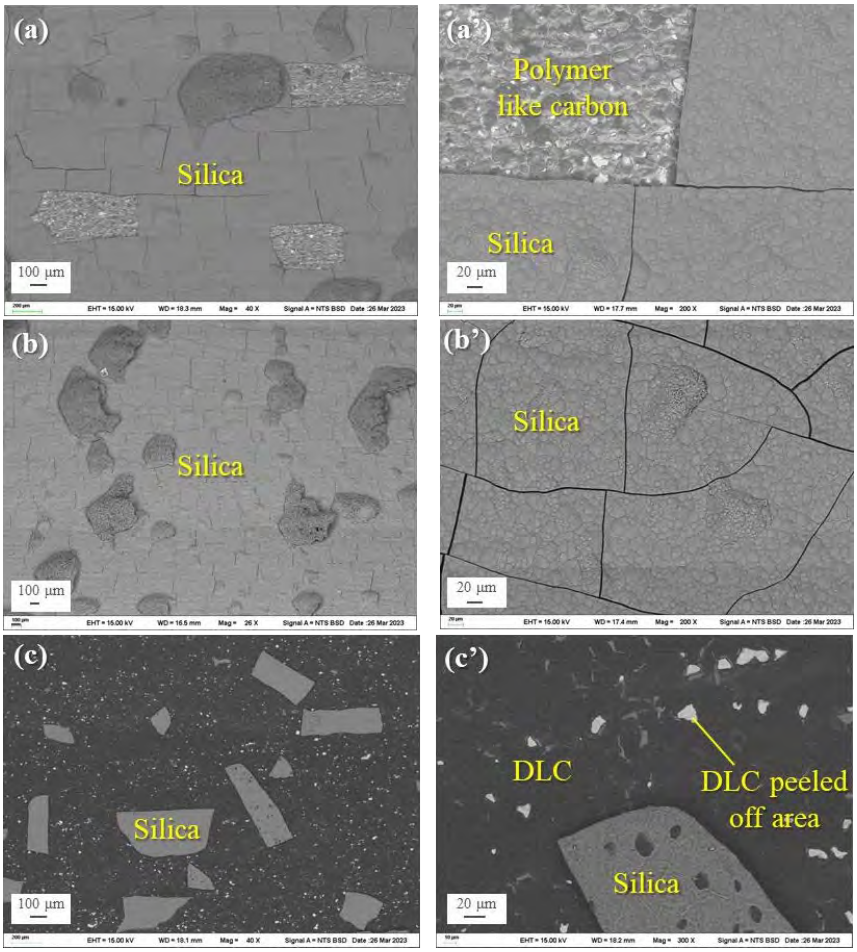

Figure 10: SEM image on the inner surface of coated pipe
(a)(a')0 - 100 mm, (b)(b') 200 – 300 mm, (c)(c') 400 – 500 mm

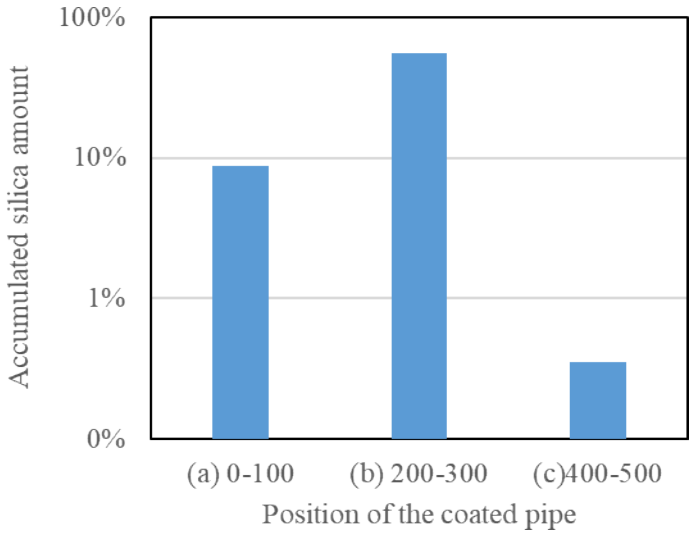

Figure 11: Accumulated scale amount at the surface.

4. Discussion

4.1 Suppression mechanism of silica scale accumulation by DLC coating

In order to discuss the suppression mechanism of scale accumulation by DLC coating, accumulated scale morphology was additionally observed. Figure 12 shows accumulated scale and DLC-coated surface comparison on the inner surface of DLC-coated pipe at the position of 400 – 500mm, which had highest suppression effect against the scale. SEM image of (a) and (b) is the corresponding surface with peeled-off scale and DLC coating, as described in the illustration. The white dotted line in the (a) and (b) images indicates the corresponding area. At the DLC-coated surface, there were many rough surface with polygonal shapes. It is thought that these polygonal shapes derived from grains of austenite in the SUS304. There was no silica inside of the grains; however on the groove located at the border of grains, accumulated silica remained. Figure 13 shows the surface of scale corresponding to the grooves shown on the DLC-coated surface. There is flat surface in the peeled scale at locations corresponding to the grooves, indicating that scale in the grooves got fractured, and the scale eventually peeled off. Therefore, it is thought that adhesion force between the DLC and scale was weak. However, when grooves derived from the substrate surface worked as anchor for the scale, then silica scale adhered at that area. Figure 14 shows the visual appearance of inner surface of the DLC-coated pipe at (c) 400-500mm after scale test. At this part of coated pipe before the SEM observation, there was silica scale entirely on the surface; however, it was peeled off after the SEM observation. It is indicated that the accumulated silica adhered to the coated surface through the groove area as Figure 13, and scale was already peeled off on almost the entire surface. Therefore, it is inferred that a small impact by vacuum during SEM observation caused scale removal.

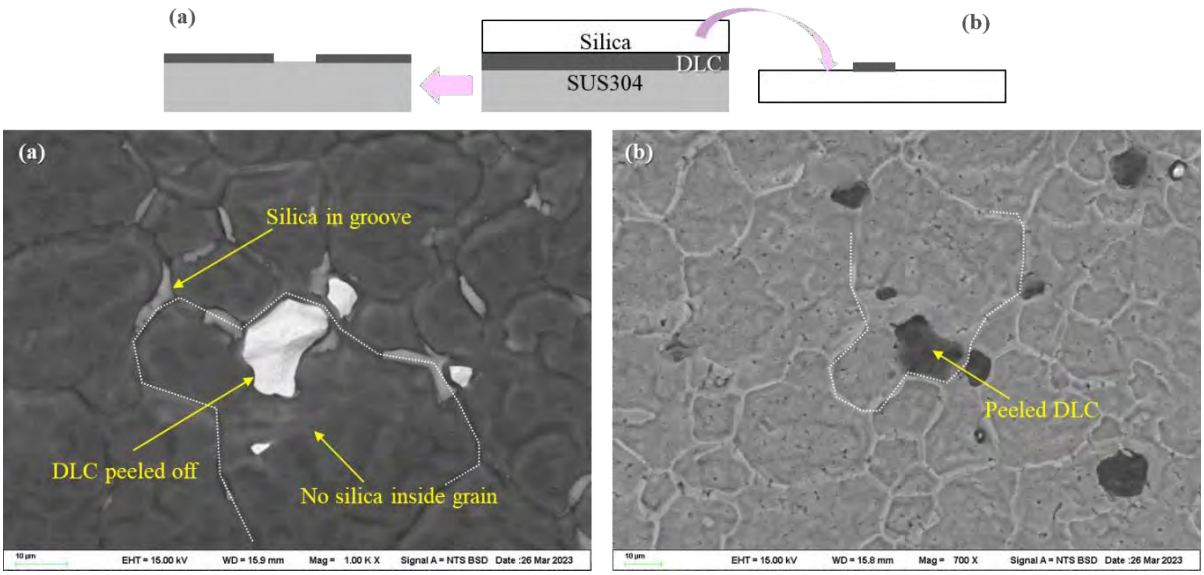

Figure 12: silica and calcium based scale accumulation above iron sulfide on the 13%Cr steel.

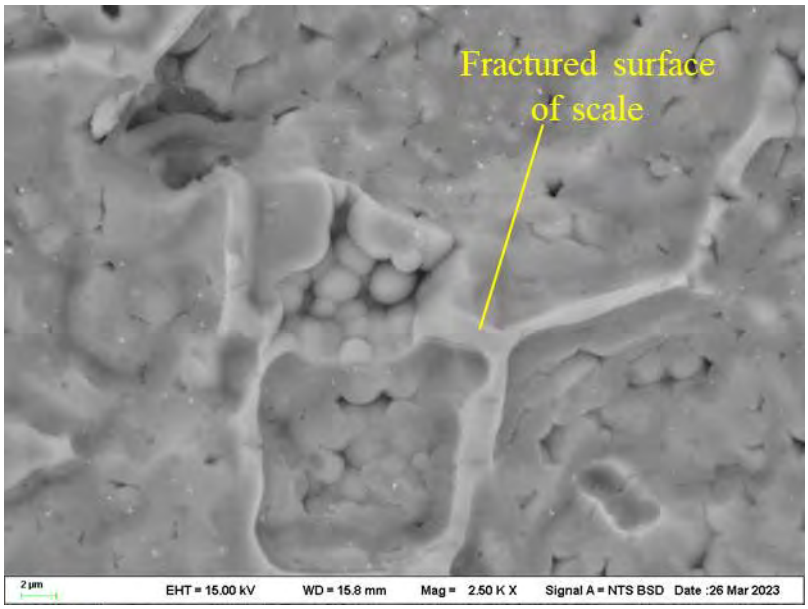

Figure 13: Scale accumulation model on the (a) 13%Cr steel, (b) DLC coating, and accumulated morphology of scale model on the (a') 13%Cr steel, (b') DLC coating

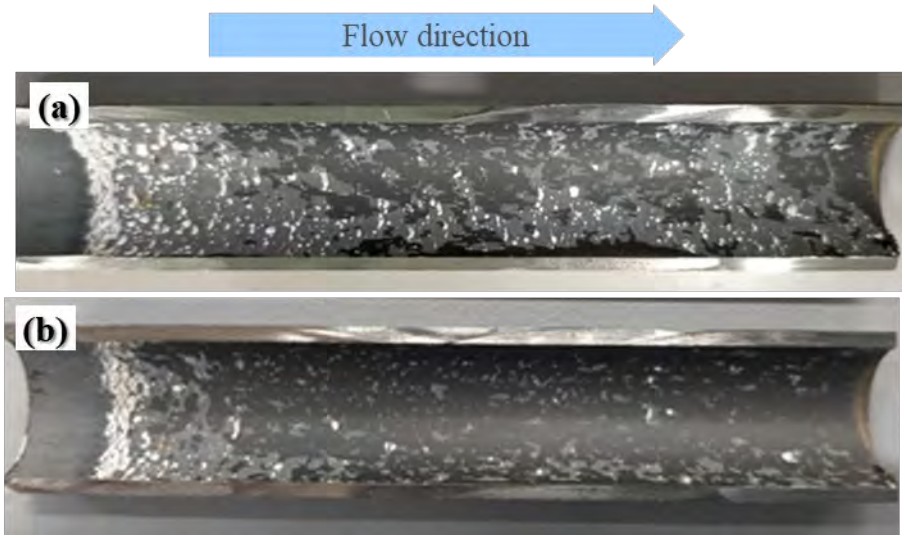

Figure 14: Visual appearance of inner surface of the DLC-coated pipe at position (c) 400-500mm after scale test, (a) before, (b) after SEM observation.

5. Conclusion

In order to suppress silica accumulation on the inner surface of pipes used for heat exchangers, a new deposition method of DLC coating for the pipes was developed, and the scale suppression effect was evaluated through field testing at a geothermal power plant. The new deposition method could deposit DLC coating on the inner surface of pipes by using the pipes themselves as vacuum chambers. Moreover, some positions along the pipe had high hydrogen content in the DLC coating, which was expected to suppress scale accumulation, and was able to suppress accumulated scale amount dramatically compared with stainless steel pipe. Therefore, it is believed that DLC coating is potentially applicable as a new method to reduce silica scale on geothermal turbine blades. The evaluation results are as follows.

- Pipe with an inner diameter of 16 mm and a length of 500 mm was used for the inner surface coating substrate, and coating was deposited along the entire length of the pipe. Polymer-like carbon coating was deposited at 0 mm from the tip of the pipe, and DLC coating was deposited at 250 and 500 mm, as distinguished by XAFS analysis.
- DLC coating at the 250-mm and 500-mm positions had hydrogen contents of 11% and 27%, respectively. The higher hydrogen content at 500 mm was expected to have higher suppression effect for scale accumulation.
- Based on the amount of amorphous silica scale that accumulated during the field test, the DLC coating at 500 mm could reduce the amount of accumulated silica to 0.5 % of the amount observed with non-coated pipe made from SUS304.

Acknowledgement

The authors are grateful to involved in the Takigami binary power plant for their long-term proper maintenance and management of the scale accumulation test equipment and for their fruitful discussions.

REFERENCES

[1] Imamura E, Iuchi M, Bando S. "Comprehensive Assessment of Life Cycle CO_2 Emissions from Power Generation Technologies in Japan." *Central Research Institute of Electric Power Industry Report*, (2016), Y06.

[2] Yonekura H. "Overview of Policies on Geothermal Development in Japan", https://www.irena.org/-/media/Files/IRENA/Agency/Events/2013/Jan/11_4/11_Yonekura.pdf?la=en&hash=B3A8454BF076F83053364120562261A32FAF8979 (accessed 1 July 2023).

[3] Yamamura T, Ishizaki T, Takasu K. "Descaling System for Geothermal Fluid Pipes Using Special Pigs". *Journal of the Japan Geothermal Energy Association*. 28, 4, (1991), 297-307.

[4] Nakashima Y, Umehara N, Kousaka H, Tokoroyama T, Murashima M, Mori D. "Carbon-based coatings for suppression of silica adhesion in geothermal power generation", *Tribology International*, (2023), 177

[5] Ferrari AC, Robertson J. "Interpretation of Raman spectra of disordered and amorphous carbon". *Physical Review B,* 61, 20, (2000), 14095.

[6] Imai, R., Kousaka H., Nakashima, Y, Nakajima, Y., “Development of in-pipe DLC deposition technology to suppress scaling on the inner surface of pipes for geothermal power generation”, *Prod. 23rd machine design and tribology conference*, JSME (MDT 2024), 2A2-2. [in Japanese]

[7] Saikubo A, Yamada N, Kanda K, Matsui S, Suzuki T, Niihara K, et al. "Comprehensive classification of DLC films formed by various methods using NEXAFS measurement". *Diam Relat Mater*. 17, 7–10,(2008)1743–1745.

[8] Nakashima, Y., Umehara, N., Kousaka, H., Tokoroyama, T., Murashima, M., Murakami, K. "Influence of defects in graphene-like network of diamond-like carbon on silica scale adhesion". *Tribology Letters*, 71, 1, (2023). 17.

[9] Iler RK. THE CHEMISTRY OF SILICA. *Wiley interscience*. 1979

A Simple Predictive Tool for Geothermal Amorphous Aluminosilicate Scales: Correlation with Field Examples

Claire J Newton, Sadiq J. Zarrouk, Bridget Y Lynne, Eylem Kaya

Department of Engineering Sciences, University of Auckland, Private Bag 92019, Auckland, New Zealand

Keywords

Aluminosilicate, scale, silica, aluminium hydroxide, boehmite, kinetic, experiment, colloid, model, tool, predictive, precipitation, reaction, hydroxyaluminosilicate, reservoir, reinjection, mitigation, prevention.

ABSTRACT

Amorphous aluminosilicate scales are a common occurrence within infrastructure at many geothermal fields around the world, often resulting in the unexpected fouling of surface infrastructure and injectivity decline in geothermal reinjection wells. Amorphous aluminosilicate scales often form under conditions at which pure amorphous silica scales would not be expected. Such conditions include temperatures significantly higher than that predicted for amorphous silica polymerisation and extreme low pH, such as the formation of blockages in sulfuric acid injection quills. Additionally, the formation of aluminosilicate scale does not share the kinetic limitations displayed by its pure amorphous silica counterpart, having been observed to nucleate quasi-instantaneously both in the laboratory and in the field. Given these unique characteristics, a novel formation mechanism triggered by the precipitation of aluminium (oxy)hydroxide was tested in laboratory experiments, leading to a simple predictive tool for the occurrence of aluminosilicate scales. These results and tool are then compared to examples of and formation conditions of aluminosilicate scales within geothermal power stations at 3 separate geothermal fields. These examples include a rapidly formed aluminosilicate material deposited en masse during a binary plant excursion, leading to the first reported observation of the aluminium (oxy)hydroxide mineral, boehmite, in a geothermal scale,

1. Introduction

The purpose of this paper is to highlight the formation mechanism of many amorphous aluminosilicate scales encountered within the geothermal industry, and a means to predict their occurrence. This report is primarily aimed at assisting geothermal infrastructure operators identify risk areas and likely causes of apparently anomalous aluminosilicate scaling where pure

amorphous scaling is not anticipated. The formation mechanism discussed here (Newton, 2020) is also relevant to natural hydrothermal settings under conditions of significant physico-chemical disequilibrium, such as during boiling events within hydrothermal veins and mixing zones where downflowing near-surface derived acidic sulphate fluids interact with up flowing neutral pH geothermal waters. However, the focus of this report is scaling affecting the industrial utilization of geothermal resources including direct use for heating, and particularly power generation scenarios. It should be noted, however, that many of these physico-chemical scenarios are also often analogous to those occurring within natural hydrothermal systems.

Aqueous Al is typically undersaturated with respect to boehmite in the deep production zones of geothermal reservoirs, with aqueous Al concentration instead being controlled by the solubility of stable aluminosilicate mineral phases such as felspars and clay minerals. Unlike crystalline aluminosilicate minerals, amorphous aluminosilicate materials produced under rapid changes in fluid chemistry and temperature during which boehmite becomes supersaturated are instead quasi-stable. Although these quasi-stable aluminosilicate solid phases are not well preserved in the geologic record within extinct hydrothermal systems, these amorphous aluminosilicate materials are of primary significance within the comparatively short time spans relevant to human use of a geothermal resource.

The experimentally tested observation that the supersaturation of Al with respect to boehmite in presence of aqueous silica triggers the quasi-instantaneous formation of amorphous aluminosilicate material (Newton, 2020) has resulted in the development of a relatively simple excel-based tool to predict the onset of amorphous aluminosilicate scaling. This tool calculates boehmite saturation concentration and based on input values of fluid temperature and pH, and then compares this to the measured Al concentration as Al^{3+} (due to Al concentration typically being stated in terms of this species in laboratory analytical reports). Similar to the calculation of a silica saturation index (SSI) (Fournier, 1986), this tool yields a boehmite saturation index (BSI), which can be used to predict the onset of amorphous aluminosilicate scale deposition. Analogous with SSI, BSI is simply the concentration of aqueous Al divided by the solubility of Al with respect to boehmite. This tool also calculates SSI, however it uses a somewhat more sophisticated method after Fleming and Crerar (1982), rather than that of Fournier (1986) or Gunnarsson and Arnórsson (2000), in that it also takes pH into account for the amorphous silica solubility calculation.

At a pH of ~6 and above the Si/Al ratio of amorphous aluminosilicate scales are 3 and above, and more commonly between 5 and 10 (Gallup, 1997; Newton, 2020). The Si/Al mole ratio of the scale appears to be largely influenced by aging of the scale and its deposition rate (Newton et al.,2018, Newton, 2020), with the initially deposited amorphous aluminosilicate scale gradually taking up silica brine as it ages (Newton et al., 2018; Newton, 2020). Amorphous aluminosilicate scales also take up cations, such as Na^{+}, K^{+}, and Ca^{2+}. This as a result a of tetrahedrally coordinated Al^{3+} being substituted for Si^{4+} in the tetrahedral silica lattice, which imparts a charge imbalance. This imbalance is neutralised via the incorporation of positively charged metal cations (Gallup, 1997; Newton, 2020).

Aluminosilicate scales formed below a pH of ~6 have a Si/Al mole ratio below 3, commonly close to 1.0, and do not incorporate cations, such as Na^{+}, K^{+}, and Ca^{2+} into their short-range structure. This is likely due, depending on Si/Al mole ratio of the material, to Al being either entirely octahedrally coordinated, or partially octahedrally coordinated, with any tetrahedrally coordinated Al being so in a different manner to aluminosilicate scales produced under near neutral conditions

(Exley and Birchall, 1993: Doucet et al., 2001a; Strekopytov and Exley, 2006; Tokoro et al., 2014; Leiviska et al., 2014; Beardmore et al., 2016).

Such geothermal scales have not been discussed elsewhere in the geothermal literature to the knowledge of the author. However, these materials appear to be readily formed where acidic fluids mix with near neutral pH geothermal brine. Examples include zones where diluted sulfuric acid mixes with hot geothermal brine within brine acid dosing static mixers, and where acidic steam condensate mixes with neutral pH brine within binary plant heat exchangers and interconnect pipes. These scales are often combined with antimony, and occasionally arsenic sulphides. Although such materials appear to have received little recognition within the geothermal literature, they are likely the higher temperature analogue to some well-studied low Si/Al mole ratio aluminosilicate materials produced at lower temperatures. These include allophane like materials deposited by some acidic low temperature freshwater springs (Childs et al., 1990; Newton, 2020), and artificially produced hydroxyaluminosilicate (HAS) materials, also produced at near ambient conditions (Exley and Birchall, 1993: Doucet et al., 2001a; Strekopytov and Exley, 2006; Tokoro et al., 2014; Leiviska et al., 2014; Beardmore et al., 2016).

2. **Methodology**

2.1 Scale Sampling and Analysis

Scales sampled from geothermal fields A and B were analysed for bulk (qualitative) elemental composition in the field via a handheld Olympus Vanta X-ray fluorescence (XRF) analyser. Scales from geothermal field C were analysed at the University of Waikato for bulk (quantitative) composition via Bruker WDXRF S8 Tiger XRF analyser, and mineral phase composition and structure with a Panalytical Empyrean X-ray diffractometer (XRD). Handheld XRF analyser results are reported as elemental ratios as the analyser was not calibrated for rock samples. Nonetheless, results for samples which have been analysed via both handheld and quantitative XRF were found to be very close for the elements of interest (Si, Al, Na, K, Ca). Scales from all three geothermal fields were examined via Scanning Electron Microscopy (SEM) using Energy-Dispersive X-ray Spectroscopy (EDS) at the University of Auckland.

2.2 Silica Solubility (SSI) Calculation

A full description of the method after Fleming and Crerar (1982) used to calculate SSI by the scaling model used in this study is beyond the scope of this report, however an overview of the calculation is provided below.

$$S = K_C{}' \left[1 + \frac{10^{pH}\, K_B\, K_w}{\gamma_{H_3(OH)_4^-}}\right] \quad (1)$$

Where S, K_c', K_B, K_w, and γ are the total equilibrium solubility of silica in water (molal), silica solubility product constant (at neutral pH), silicic acid dissociation constant, water dissociation constant, and the activity coefficient of the silicic acid ion. In the scale prediction tool discussed

in this report, the total equilibrium solubility of silica is calculated from input values of temperature and pH only, with the constants given above calculated within the tool from empirically derived data.

This the solubility values derived from this tool are in very close agreement with more commonly used simpler solubility calculations, such as that of Fournier (1986) (equation 2) below a pH of approximately 8.5, above which the singly ionized silicic acid anion increasingly contributes to the total solubility of amorphous silica in water.

$$t = -42.196 + 0.28831(C) - 3.6685 \times 10^{-4}(C^2) + 3.1665 \times 10^{-7}(C^3) + 77.034(logC) \quad (2)$$

Where t and C are temperature in ºC and silica concentration in mg/kg, respectively.

2.3 Aluminium (oxy)hydroxide Solubility (BSI) Calculation

Boehmite solubility is calculated using the solubility product constants (K_{spB}) (infinite dilution) obtained for boehmite by Bénezeth et al. (2001) (Table 1). Although the K_{spB} utilized are for a solution state of infinite dilution, in practice the calculated solubility values obtained from them provide an excellent match, both experimentally and from field observations for the low Al concentration dilute chloride fluids encountered within geothermal systems used for power generation. This approximation has the advantage of greatly simplifying the use of this scale prediction tool.

For completeness it should also be noted that there is a phase transition of the solid crystalline aluminium (oxy)hydroxide phases against which the solubility of Al in water is referenced l within the temperature range of this scaling tool. The phase transition of gibbsite (Al-hydroxide) to boehmite (Al-oxyhydroxide) occurs above approximately 80ºC (Wefers and Misra, 1987; Palmer and Wesolowski, 1992). This phase boundary, however, has no meaningful consequence for rapidly polymerised Al-(oxy)hydroxide structures which then proceed to rapidly react with silica under typical geothermal conditions. This is due to amorphous Al-(oxy)hydroxide being more soluble than crystalline Al (oxy)hydroxide. However, in near-neutral solutions, the solubility curve of gibbsite/boehmite very closely approaches the precipitation onset condition (Okada et al., 2002). Therefore, this simplified model of boehmite solubility is used here to estimate Al-(oxy)hydroxide precipitation-onset conditions, which has proven to be effective in practice, both in laboratory experiments and in the field.

The calculation of boehmite solubility and hence BSI is achieved by solving the solubility equilibria (equations 3 to 7) below using the solubility product constants for the relevant species and temperature in Table 1. For temperatures which fall between values referenced in Table 1, K_{spB} is estimated via linear interpolation.

$$AlOOH_{(s)} + 3H^+ \overset{K_{sB0}}{\longleftrightarrow} Al^{3+} + 2H_2O \quad (3)$$

$$AlOOH_{(s)} + 2H^+ \overset{K_{sB1}}{\longleftrightarrow} Al(OH)^{2+} + H_2O \quad (4)$$

$$AlOOH_{(s)} + H^+ \overset{K_{sB2}}{\longleftrightarrow} Al(OH)_2^+ \quad (5)$$

$$AlOOH_{(s)} + H_2O \overset{K_{sB3}}{\longleftrightarrow} Al(OH)_3^0 \quad (6)$$

$$AlOOH_{(s)} + 2H_2O \overset{K_{sB4}}{\longleftrightarrow} Al(OH)_4^- \quad (7)$$

Table 1. Solubility product constants (K_{spB}) for boehmite at infinite dilution (Bénézeth et al., 2001) used by the aluminosilicate scale prediction tool used in this report.

	Al^{3+}	$Al(OH)^{2+}$	$Al(OH)_2^+$	$Al(OH)_3$	$Al(OH)_4^-$
T °C	log K_{sB0}	log K_{sB1}	log K_{sB2}	log K_{sB3}	log K_{sB3}
0	9.43	3.58	-2.80	-7.83	-16.41
25	7.64	2.69	-3.09	-7.72	-15.14
50	6.03	1.83	-3.17	-7.60	-14.32
75	4.65	1.09	-2.24	-7.90	-13.62
100	3.46	0.46	-3.30	-7.49	-13.02
125	2.42	-0.09	-3.36	-7.38	-12.50
150	1.49	-0.59	-3.40	-7.27	-12.06
175	0.68	-1.03	-3.41	-7.16	-11.69
200	-0.06	-1.42	-3.48	-7.06	-11.40
225	-0.07	-1.77	-3.52	-6.95	-11.18
250	-1.31	-2.09	-3.55	-6.84	-11.05
275	-1.85	-2.38	-3.58	-6.73	-11.01
300	-2.35	-2.64	-3.60	-6.62	-11.07

Due to the simplifying assumptions discussed above, only temperature (to determine the appropriate K_{spB}) and pH (to obtain $x[H^+]$ for each equilibrium reaction calculation) are required as inputs for this scale prediction tool. The results of each equilibrium equation are then summed to obtain total Al (molar) and then converted to ppm (as Al^{3+}) for easy comparison with brine laboratory chemistry analyses. Measured Al^{3+} from laboratory analyses is then divided by calculated equilibrium Al concentration with respect boehmite to yield a BSI value.

3. Results and Discussion

3.1 Geothermal Field A: Amorphous aluminosilicate scaling induced by brine-acid dosing

The power station at geothermal field A consists of a two-stage turbine with a direct contact condenser. The deep reservoir temperature and pH of this geothermal field is ~290°C and 6.8 (pH calculated via the geochemical calculation program WATCH), respectively. Reservoir silica and

aqueous aluminium concentrations are ~680ppm (as SiO_2) and 1.5ppm (in terms of Al^{3+}), respectively. HP steam and brine are separated at ~190°C, with LP steam and brine being subsequently separated at ~130°C. HP brine is dosed with diluted sulfuric acid to mitigate silica scaling within a static mixer (Figure 1 and 2), located in the HP brine line between the HP and LP steam separators. The 98% v/v concentration sulfuric acid is prediluted using a side stream of HP brine via a tantalum quill housed in a removeable spool (Figure 2) in the 3" side stream pipeline.

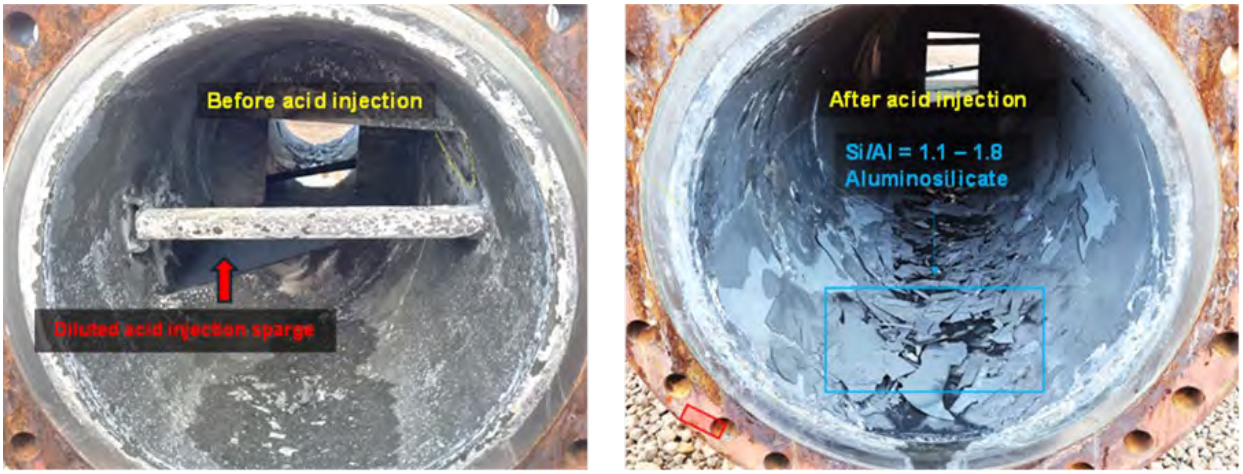

Figure 1: Acid static mixer from geothermal field A. There is minimal scaling prior to acid injection, which consists of a <1mm think extremely hard glassy material. Scaling post acid addition is voluminous downstream of the dilute acid injection sparge bar. The Si/Al mole ratio of this scale ranges between 1.0 and 2.0 for the aluminosilicate component of the scale. The dark colour of the scale is imparted by sulfides which begin being deposited approximately 2 metres downstream of the dosing sparge. Calculated SSI and BSI prior to acid addition are 0.84 and 0.33, respectively. SSI and BSI post acid addition are 0.92 and 300.48, respectively.

Aluminosilicate scale was found to be deposited immediately downstream of the acid dosing point within the static mixer at geothermal field A, accompanied by sulfides. (Figure 1). This scale was very aluminium-rich, with a Si/Al mole ratio ranging between 1.0 and 2.0; Aluminosilicate scale was also found to be deposited immediately adjacent to acid injection points both within the main acid static mixer (Figure 2) and within the brine dilution line opposite the neat acid injection quill (Figure 3). Surprisingly, aluminosilicate scale was also found inside and partially blocking the neat acid injection quill (Figure 4). The aluminosilicate scale deposited within the main static mixer is compositionally zoned, which appears to be correlated with degree of acid mixing with the main brine flow. Areas closest to where the center of the diluted acid plume from the sparge nozzles impinges on the static mixer wall and fins possess the lowest Si/Al mole ratios, ranging between 1.0 and 2.0. Further from the center of the acid plume, Si/Al increases in the deposited material up nearly 6 (Figure 2). Even further from the inferred acid plume the scaling drops to near zero, with the mixer wall appearing the same as that upstream of the acid mixer sparge.

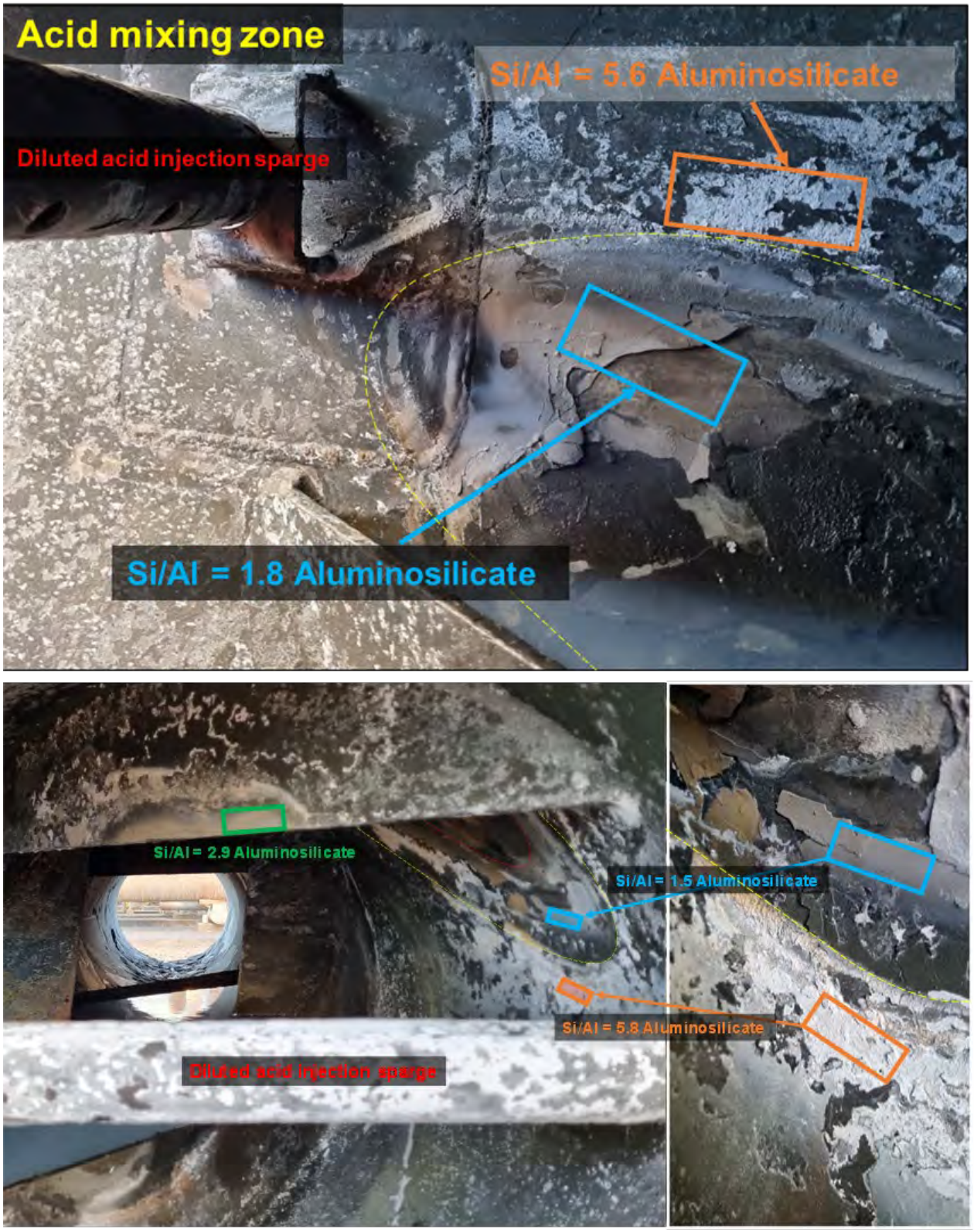

Figure 2. Compositionally zoned aluminosilicate scales deposited in the acid-brine mixing zone within the acid static mixer of geothermal field A. The Si/Al mole ratio reported for each zone is the average of several analyses.

Calculated SSI before acid dosing of the HP brine is calculated to be 0.84, and post acid dosing it is 0.92 (Figure 4). This indicates that there should be no risk of silica scaling, post acid dosing in the HP line, both due to the low pH and SSI remaining below 1.0. Conversely BSI increases precipitously from 0.33 pre acid dosing to 300.48 post acid dosing (Figure 5). As predicted by the BSI tool, this coincides with the immediate appearance of aluminosilicate scale. This occur within both the main brine-acid static mixer, and surprisingly in the likely turbulent mixing zone surrounding the neat sulfuric acid injection quill, and within the tantalum acid injection quill (Figure 4).

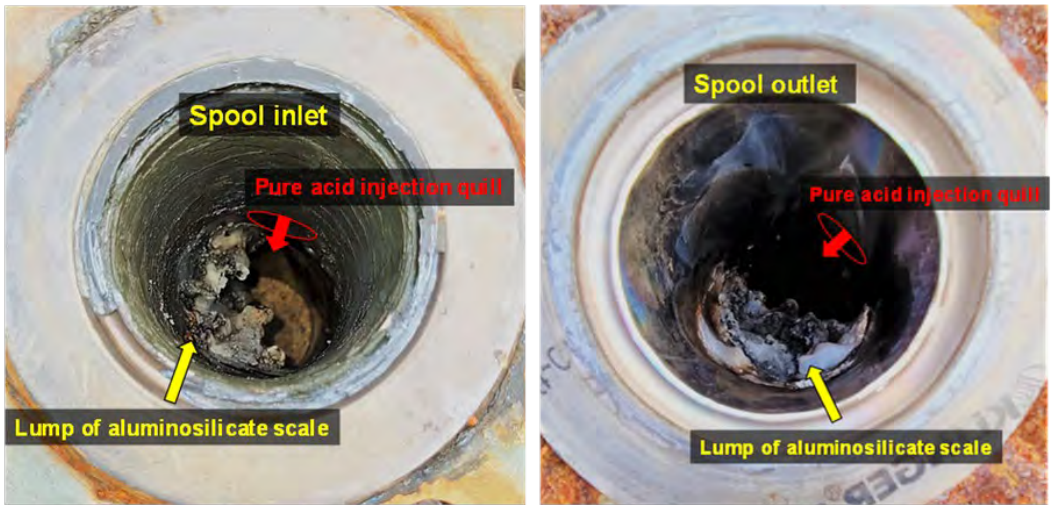

Figure 3. Amorphous aluminosilicate scale buildup surrounding a sulfuric acid (98% v/v) injection quill within the dosing spool at geothermal field A. The scale occurs as a large, isolated build up localised on the 3" pipe wall opposite the tantalum dosing quill. No scale is visible downstream of the of the dosing quill, which is likely due to the extreme acidic conditions in the ~1% v/v sulfuric acid-brine mixture.

Figure 4. Tantalum acid injection quill partly obstructed by aluminosilicate scale (Si/Al = 5.7).

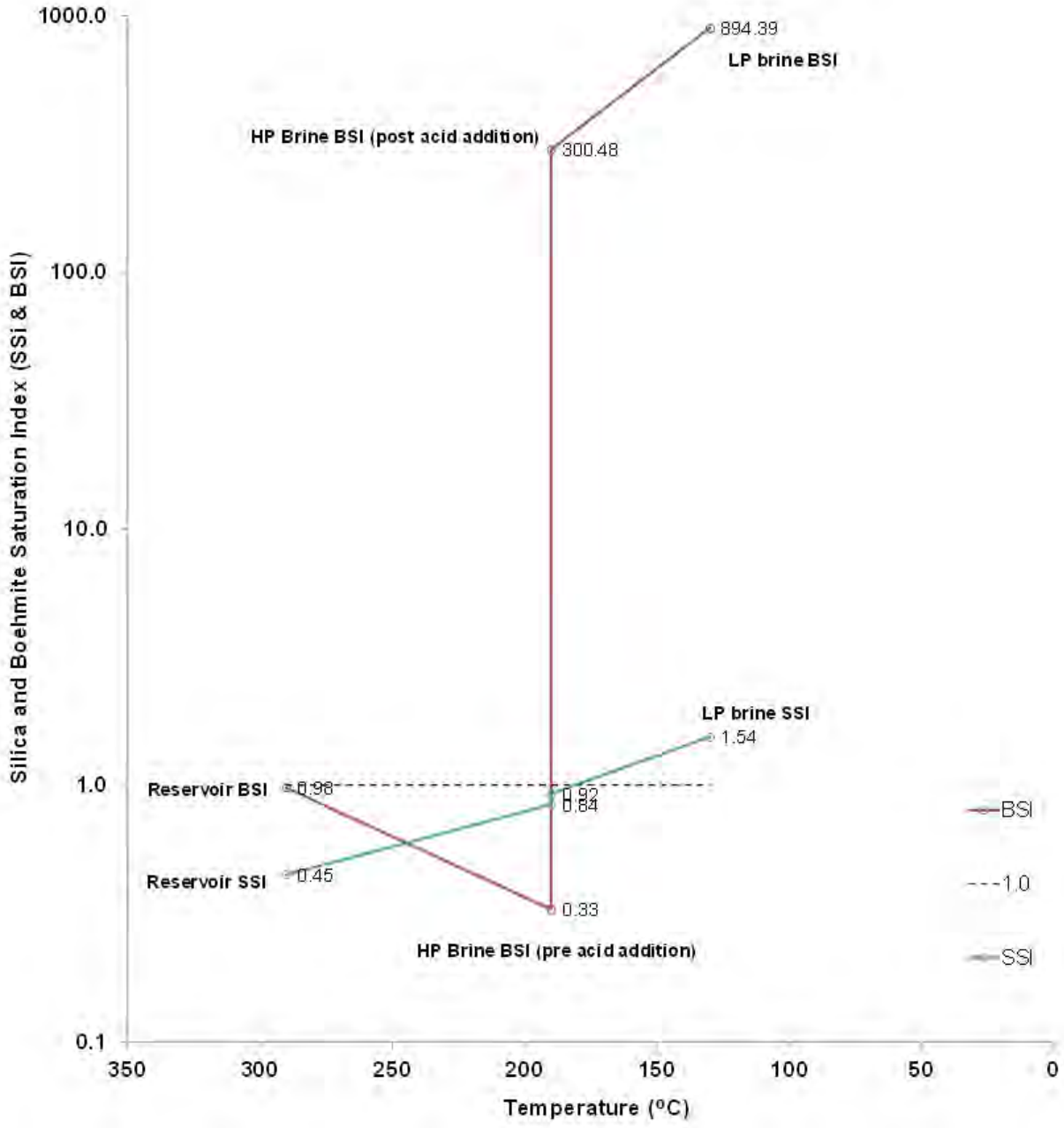

Figure 5. Calculated SSI and BSI path for the produced brine at geothermal field A from the reservoir feed zone, through the HP steam-brine separator, acid dosing plant, and finally the LP steam-separator.

3.2 Geothermal Field B: Amorphous aluminosilicate scaling coinciding with cooling and brine-acidic steam condensate mixing

The power station at geothermal field B consists of a binary Ormat Energy Converter (OEC) unit which makes use of both brine (220°C and pH 6.65) and steam condensate (200°C and pH 5.0) in separate heat exchangers, the outlet fluids are then mixed prior to reinjection, yielding a fluid with a temperature of 135°C, pH of 5.5, aqueous silica (as SiO_2) concentration of 780ppm and Al (as Al^{3+}) of 0.75 ppm. At the brine-condensate mixing point, a voluminous black and relatively soft scale is formed. This scale is an approximately 50:50 mixture (by mass) of stibnite and aluminosilicate scale (Figure 6).

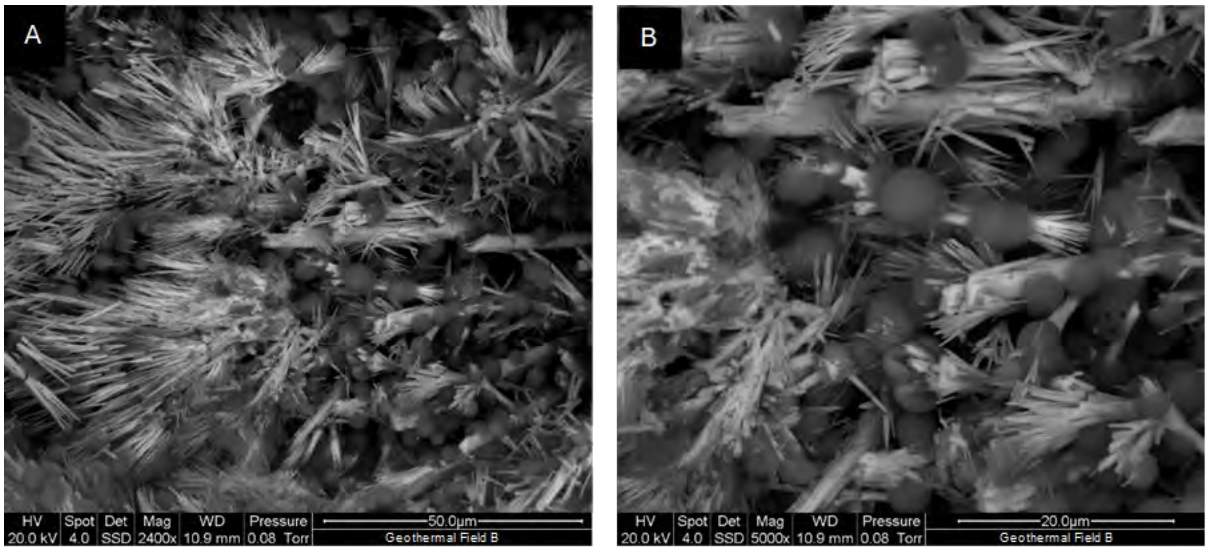

Figure 6. SEM images of the scale formed at the OEC outlet brine-condensate mixing point at power station of geothermal field B. This scale is composed of a mixture of stibnite (long radiating fibers) and aluminosilicate scale (spheres suspended within the scale). A: SEM image of the combined stibnite/aluminosilicate scale at 2400x magnification. The brightest grey-white hued radiating needles are stibnite, with the darker spheroids comprising aluminosilicate material. The brightness of the stibnite is due to the SEM instrument being operated in backscatter mode, with the larger/heavier antimony nuclei causing a greater proportion of emitted electrons to be scattered back toward the electron detector than that of the lighter elements comprising the aluminosilicate spheroids. B: A: SEM image of the combined stibnite/aluminosilicate scale at 5000x magnification. The greater magnification in this image provides a better view of the aluminosilicate spheroids within the loose stibnite matrix of the scale. The aluminosilicate spheroids were found to have a Si/Al mole ratio of 1.0 in all 3 EDS measurements.

Although the SSI at OEC brine outlet is 1.65 (Figure 7), pure amorphous silica is unlikely due to the rapid transit of the heat exchanger and consequent insufficient time for pure amorphous silica polymerisation to occur (Rothbaum et al., 1979). This assumption was confirmed by no pure amorphous silica scale being observed in the OEC brine outlet line, with only some thin, hard aluminosilicate scale being found. SSI is reduced at the brine-condensate mixing point due to brine dilution with the steam condensate. The chance for pure silica scaling is further reduced due to the low pH caused by mixing of the near-neutral pH brine with the acidic condensate retarding silica polymerisation (Brown, 2011). Conversely, BSI rises from approximately 1 at the brine heat

exchanger inlet to over 140 at the brine-condensate mixing point, indicating the strong possibility of aluminosilicate scale to form here. Dilution by the acidic steam condensate has a relatively minor effect on BSI due to the exponential relationship between boehmite solubility and both pH and temperature (Figure 8). As predicted by this tool, this significant increase in BSI at the steam condensate-brine mixing point is again associated with the deposition of aluminosilicate scale where pure amorphous silica would not be expected to occur.

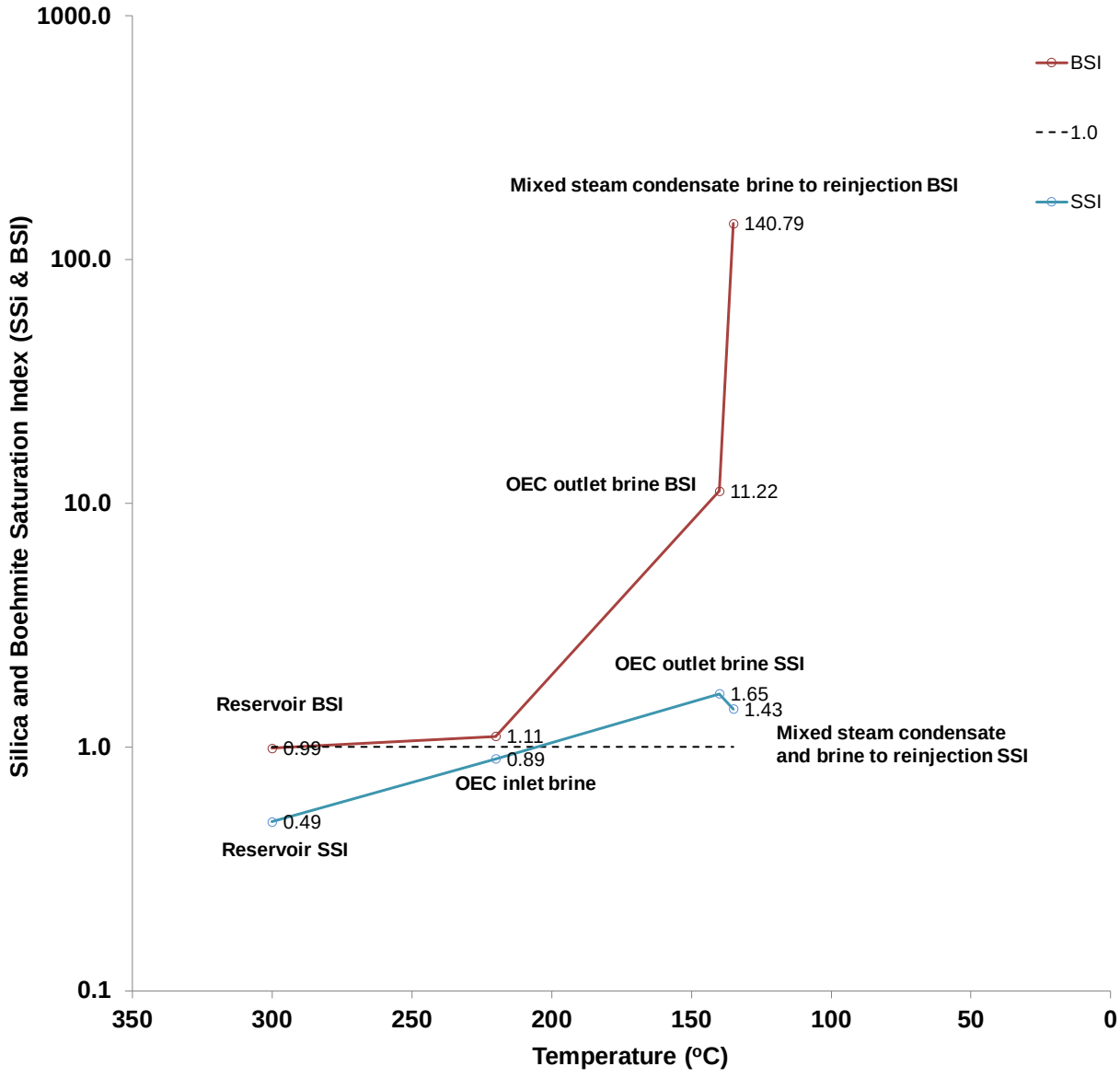

Figure 7. Calculated SSI and BSI path for the produced brine at geothermal field B from the reservoir feed zone, through the OEC brine heat exchanger to the steam condensate-brine mixing point/reinjection.

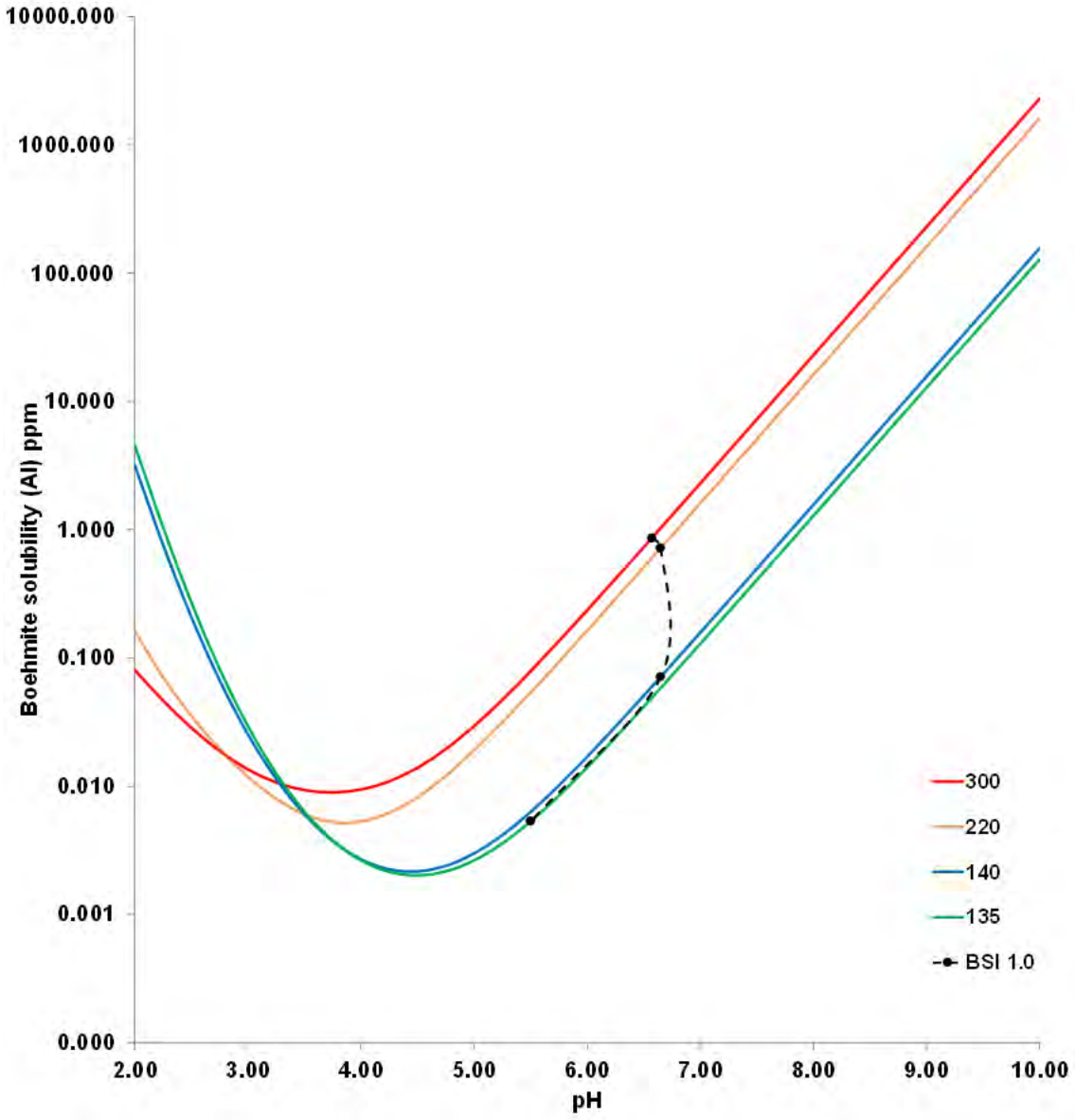

Figure 8. Dashed black line: Boehmite solubility path (BSI 1.0) as a function of temperature and pH at geothermal field B from the reservoir feed zone, through the OEC brine heat exchanger to the steam condensate-brine mixing point/reinjection. Solid colour lines: Boehmite solubility curves as a function of pH at each temperature through the OEC unit at geothermal field B.

The potential for the nucleation of the aluminosilicate scale being induced by the precipitation of stibnite does not appear likely due to the clear separation between the phases that can be seen in Figure 6. Conversely, the aluminosilicate spheroids deposited at the steam condensate-brine mixing point may be supporting the growth of the stibnite needles. This possibility is indicated by the scale becoming progressively aluminosilicate rich toward the fluid-facing scale surface, with

the stibnite needles being longer and more developed with depth closer to the basal, pipe wall adjacent, layers of the scale.

3.3 Geothermal field C: Amorphous aluminosilicate scale from steam condensate + brine mixing and from neutral pH brine during a process excursion

The power station at geothermal field C consists of an OEC unit which makes use of both brine (195^{o}C and pH 6.55) steam (195^{o}C), and a mixture of brine and steam condensate through separate heat exchangers. The inlet temperature and pH of the mixed fluid used by the 3rd heat exchanger is 180^{o}C and pH 5.5, respectively, with an outlet temperature of 140^{o}C. Aqueous silica (as SiO2) concentration is 820ppm at the inlet of the brine heat exchanger (stage 1), and 660 at the inlet of the mixed steam condensate-brine heat exchanger (stage 2). Al (as Al3+) concentration is approximately 1.0ppm at the at the inlet of the brine heat exchanger (stage 1), and 0.85 at the inlet of the mixed steam condensate-brine heat exchanger (stage 2).

Within the stage 2 heat exchanger a light brown aluminosilicate scale with a Si/Al mole ratio of between 1.2 and 3.0 is formed within the tubes and on the tube bundle face of the heat exchanger (Figure 9). The SSI within this heat exchanger ranges between 0.8 at the vessel inlet and 1.14 at the vessel outlet (Figure 10). Meanwhile, BSI ranges between 0.99 prior to mixing of the stage 1 outlet brine with steam condensate, to 36.92 post mixing/the stage 2 heat exchanger inlet, and finally 134.92 at the stage 2 vessel outlet (Figure 10). Although pure amorphous silica is slightly over saturated by the time the steam condensate-brine mixture exits the stage 2 heat exchanger, pure amorphous silica scaling is unlikely. This is due to both the rapid transit of the fluid though the heat exchanger and consequent insufficient time for pure amorphous silica polymerisation to occur (Rothbaum et al., 1979), and the relatively low pH of the fluid which retards polymerisation of aqueous silica (Brown, 2011). Conversely, BSI rapidly increases from just under 1.0 just prior to the steam condensate-brine mixing point to over 130 at the stage 2 heat exchanger exit. This sudden supersaturation of Al with respect to boehmite again coincides with the sudden appearance of aluminosilicate scales. It should be noted that some very thin, hard and glassy aluminosilicate scales do also form upstream of the stage 2 heat exchanger, however the accumulation rates are very slow, unlike for the stage 2 heat exchanger, which requires regular mechanical cleaning.

Interestingly, the aluminosilicate scale with the stage 2 heat exchanger appears to rapidly undergo a change in composition following deposition, with Si/Al ratio dropping from 3.0 at the fluid facing surface of the scale (Figure 9) to approximately 1.4 less than a micrometre below the surface of the scale. This change in composition is accompanied by a change in apparent structure of the scale, with the aluminosilicate material appearing to convert to something which looks very much like a clay mineral in SEM images (Figure 9). None the less it is X-ray amorphous (Figure 11), and therefore does not possess any crystalline structure, and is therefore not a mineral, clay or otherwise. This material does however display the characteristic lowered peak intensity and intensity maximum shifted to ~25^{o} 2θ CuKα of other amorphous aluminosilicate scales, compared to the greater peak intensity and intensity maximum located at ~22^{o} 2θ CuKα of pure amorphous silica (Newton, 2020).

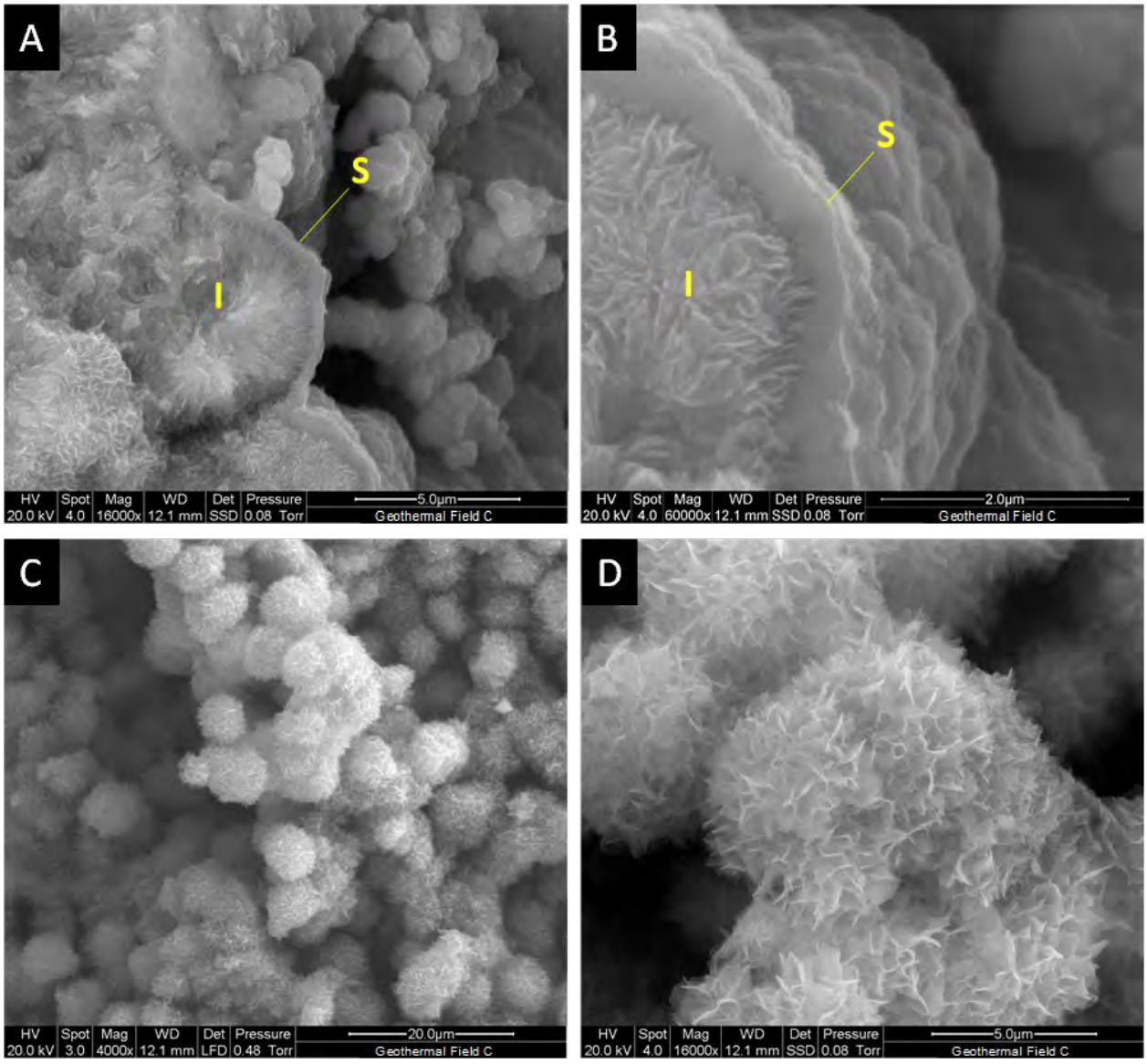

Figure 9. SEM images of aluminosilicate scale deposited within the geothermal field C stage 2 heat exchanger. A: Cross-sectional view of the top fluid-facing surface of the scale. "S" indicates the surface 'rind' of the scale, which has a Si/Al mole ratio of 3.0 and does not appear to incorporate Na, Ka, or Ca into its short-range structure. "I" indicates the interior of the scale spheroidal structure, which has a Si/Al mole ratio of 1.4 and similarly does not appear to incorporate Na, Ka, or Ca into its structure. B: Magnified view of the surface and interior of the top-fluid facing scale surface shown in image A. C: Cross-sectional view of the deeper interior of the stage 2 heat exchanger a scale. This material has a Si/Al ratio of between 1.2 and 1.4, with the Si/Al ratio of most EDS analyses clustering closer to 1.4. D: Magnified view of the spheroidal structures visible in image C.

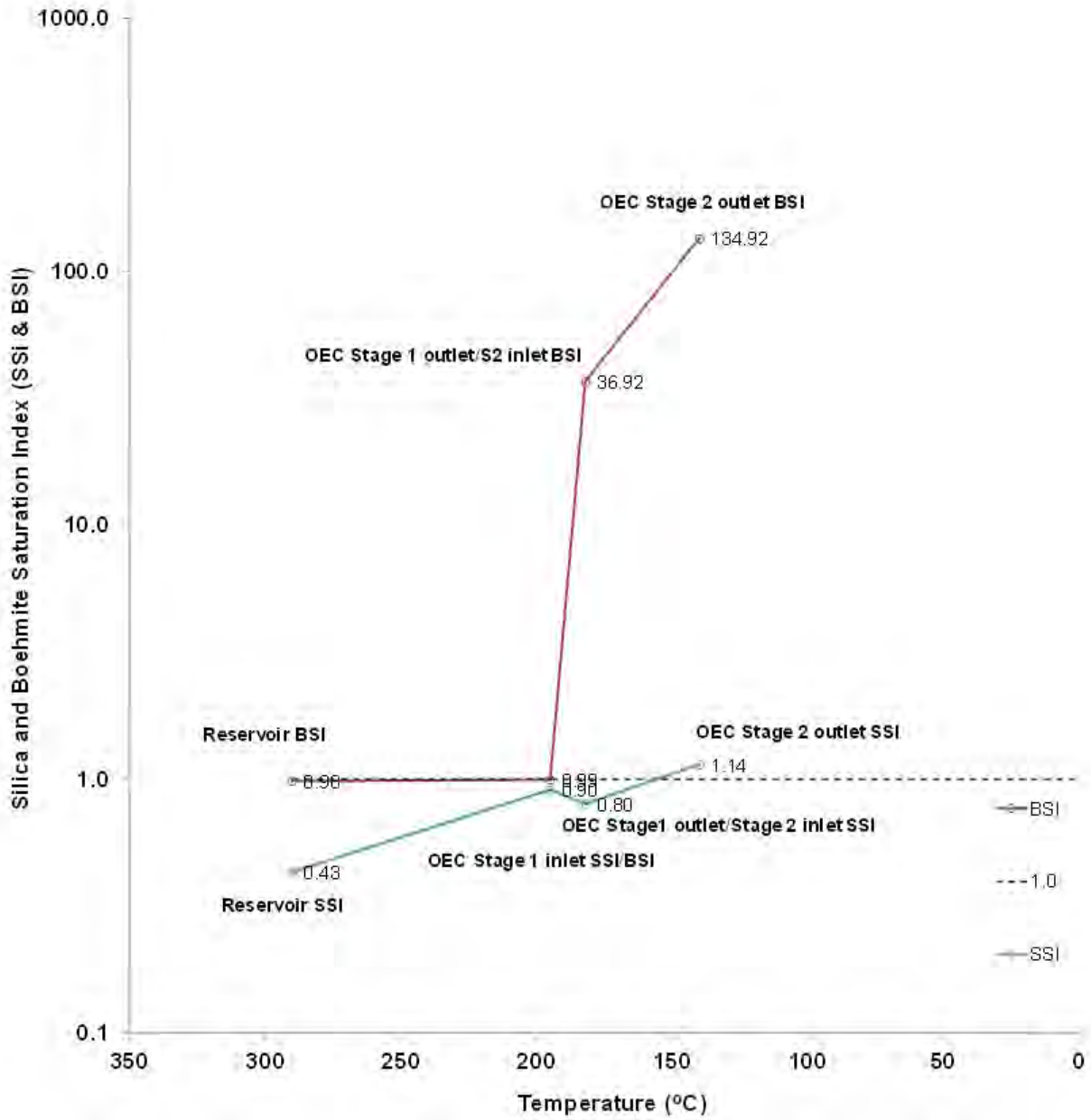

Figure 10. Calculated SSI and BSI path for the geothermal fluid at geothermal field B from the reservoir feed zone and through both OEC brine/steam condensate + brine mixture heat exchangers.

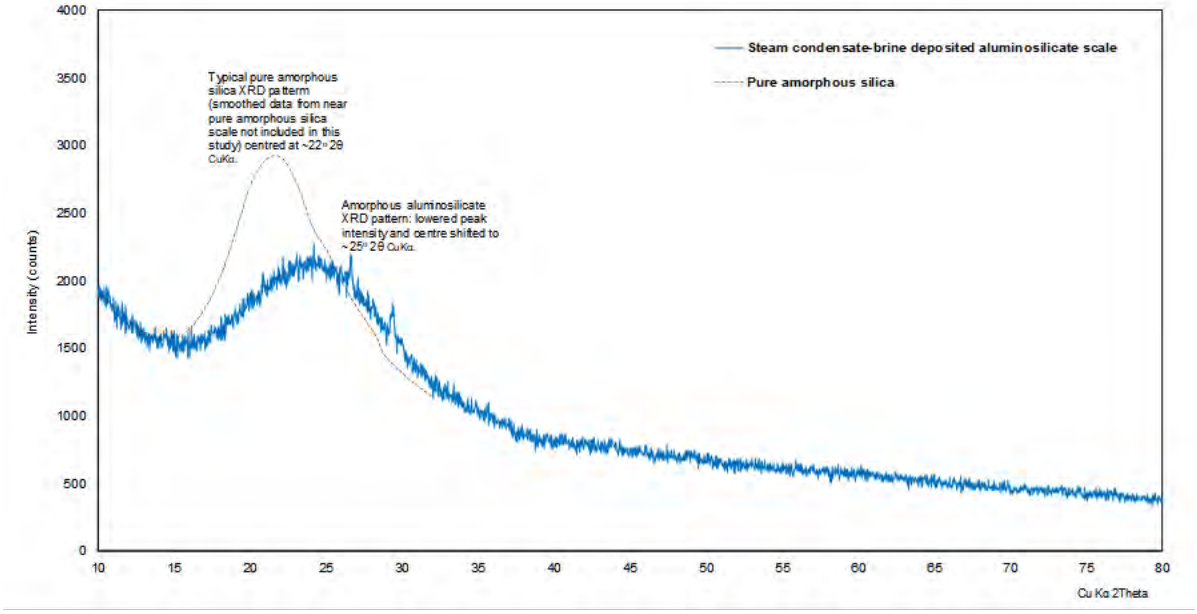

Figure 11. Geothermal field C stage 2 heat exchanger aluminosilicate scale XRD pattern.

A process excursion within the stage 1 heat exchanger also led to the rapid formation of an aluminosilicate scale. In contrast to the examples given above, this scale was formed at neutral pH and was likely caused by a local drop in brine temperature. This process excursion consisted of the rapid blockage of the first pass tubes of the stage 1 brine heat exchanger with debris from upstream in the brine line during a plant start up (Figure 12).

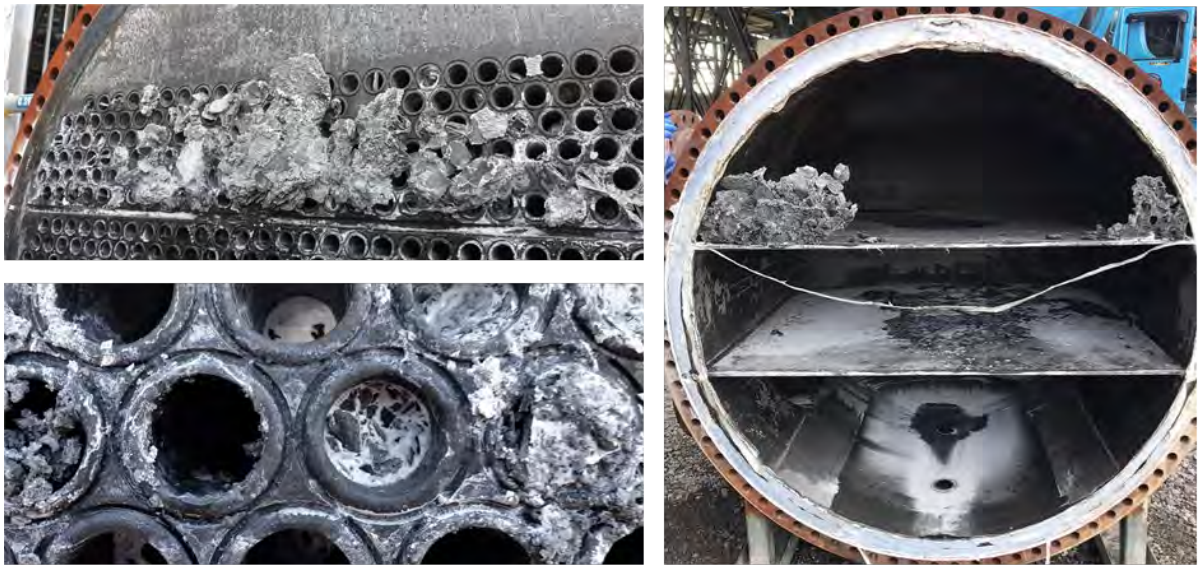

Figure 12. Scale material blocking the tubes and tube face of the stage 1 brine heat exchanger at geothermal field C.

These dark coloured debris were subsequently ‘cemented’ with a white aluminosilicate material (Figure 12), which was actively being produced until the unit was shut down for cleaning approximately 8 weeks following the inception of the incident. The deposition of the white aluminosilicate cement resulted in the gradual increase in pressure differential (dP) of approximate 3 bar across the heat exchanger over time as it built up. The mechanism inferred to be the cause of the precipitation of the white aluminosilicate cement is localised reduction in brine temperature caused by boiling induced by the pressure drop. As the blockage occurred at the inlet of the heat exchanger, the brine was still very close to saturation temperature following steam separation, so that only a small pressure drop is necessary to induce boiling.

Figure 13. White aluminosilicate powder located downstream of the tube blockages. Top image: Middle divider plate. Bottom left image: Endcap drain. Bottom right image: Middle divider plate edge close-up view.

The material which formed the white ‘cement’ was also found as a white powder mantling horizontal surfaces within the heat exchanger. (Figure 13) immediately downstream of the first-pass tubes. This powder has a Si/Al mole ratio of 4.3 (Table 2) and does incorporate cations such as Na+ and K+ to balance the negative charge induced by Al substituting for Si in the short-range structure of the scale (Table 2). Structurally, this material appears to be like other aluminosilicate scales, with the characteristic lowered XRD pattern peak intensity and intensity maximum shifted to ~25º 2θ CuKα (Figure 14), compared to the greater peak intensity and intensity maximum located at ~22º 2θ CuKα of pure amorphous silica Newton (2020). A significant difference

between this material and the other largely amorphous aluminosilicate scales is the presence of the aluminium oxyhydroxide phase, boehmite (Fig. 14).

Table 2. Compositional comparison between stage 1 heat exchanger white powder and rapidly precipitated synthetic aluminosilicate produced in lab experiments (80F02, Newton, 2020). Ratios calculated on a mole basis.

Material	Si/Al	(Na+K+2Ca)/Al	$(K/Na_{(scale)})/(K/Na_{(brine)})$
White aluminosilicate powder	4.3	0.75	7.45
Synthetic aluminosilicate	3.6	0.78	7.29

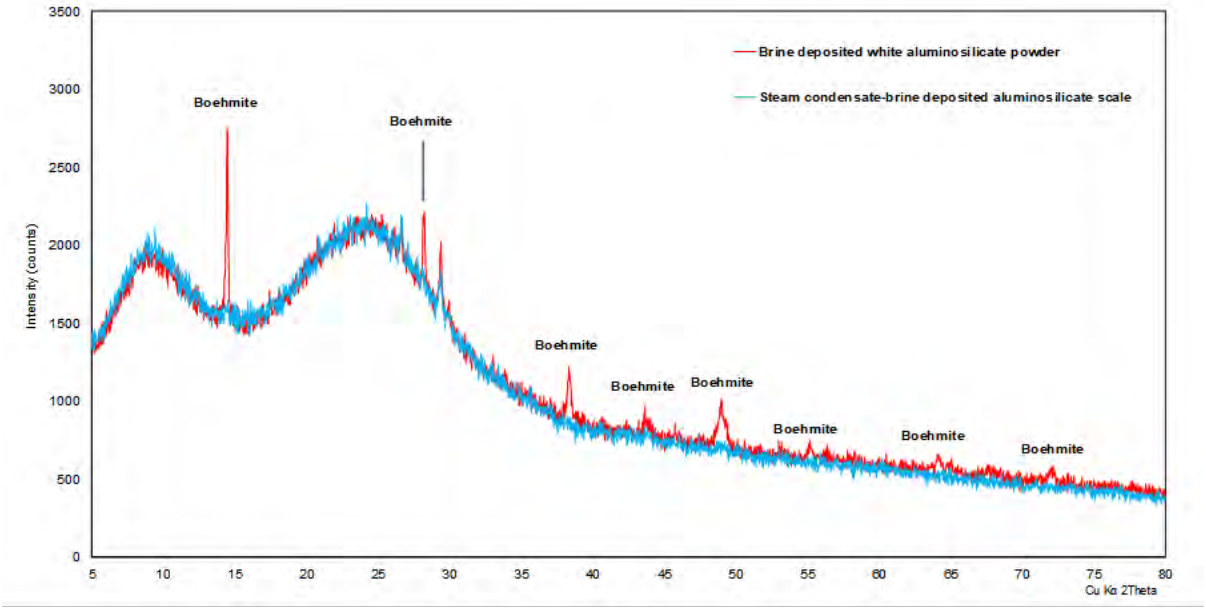

Figure 14. Comparison of geothermal field C stage one heat exchanger white powder XRD pattern (red trace) with that of the stage 2 heat exchanger aluminosilicate scale (blue trace). Boehmite diffraction peaks in the red trace are labelled as 'Boehmite" in black.

As the white aluminosilicate powder was being rapidly formed right up until the heat exchanger was shut down and opened up for cleaning, this material is likely very 'young'. Potentially only formed between several seconds and several hours before the unit was shut down.

The stage one heat exchanger white aluminosilicate powder was likely being rapidly formed right up until the heat exchanger was shut down and opened up for cleaning. This is indicated by its loose fine texture and improbable extended residence on the smooth surface of the heat exchanger divider plate amidst the high velocity and turbulence of the brine's direction change between the 1st and 2nd heat exchanger passes. This in turn suggests this material is likely very 'young', potentially only formed between several seconds and several hours before the unit was shut down, and still retains some of the structure from its initial formation. Consequently, it still contains boehmite, which has not been fully consumed by silica (boehmite is not stable in aqueous silica-

rich environments). A similar phenomenon was observed by Yokoyama et al. (1999) in aluminium-containing silica scales from Hachobaru geothermal power station in Kyushu, Japan. Within this material, the recently deposited scale was found to contain a significant portion of octahedrally coordinated Al, which was rapidly converted to tetrahedral coordination deeper within the same deposit.

Additionally, the composition and probable short-range structure of the white aluminosilicate powder closely resemble those of rapidly precipitated synthetic geothermal aluminosilicate produced under temperature, pH, and compositionally controlled laboratory experiments (Newton, 2020) (Table 2). The compositional similarities also extend to the $K/Na_{scale}/K/Na_{brine}$ ratio of the materials. This cation enrichment value has been found to typically be in the range of 4 to 6 in nearly all scales formed at neutral pH analysed by the author (Newton, 2020). In experiments where synthetic aluminosilicate scales were formed, the rapid precipitation of synthetic aluminosilicate was triggered by the supersaturation of aqueous Al with respect to boehmite, independent of silica concentration in the test brines (Newton, 2020).

The brine entering the stage 1 heat exchanger is very close to boehmite saturation, with a BSI of 0.99. A small reduction in localised temperature by, for example 5ºC, induced by flashing is enough to increase the BSI to 1.2, and therefore the production of boehmite and hence aluminosilicate scale would be predicted by the BSI/aluminosilicate tool. Given the notable boehmite content in the stage 1 heat exchanger aluminosilicate powder, its rapid precipitation, and the silica-undersaturated formation conditions (SSI ~0.87), it is highly plausible that the chemical mechanism identified in the synthetic aluminosilicate experiment led to the formation of stage 1 heat exchanger aluminosilicate powder.

4. Conclusion

Four instances of amorphous aluminosilicate scaling formed under a variety of physico-chemical conditions at three different geothermal fields were compared against a tool developed to predict their formation. This tool is based on laboratory experiments Newton (2020) which indicated that the supersaturation of aluminium with respect to boehmite in the presence of dissolved silica results in the quasi-instantaneous formation of amorphous aluminosilicate material. In each of the four instances of amorphous aluminosilicate scaling studied, the BSI calculated by the aluminosilicate scaling ‘prediction’ tool indicated that aluminosilicate scaling was likely, while SSI calculations indicated that siliceous scales were not likely. This tool therefore shows promise for future use in anticipating otherwise unexpected silica scales in geothermal fluid handling equipment. Anticipation of potential aluminosilicate scaling allows for planning for mitigation ahead of time where required to prevent unplanned and expensive shutdowns. Examples of aluminosilicate scaling which may result in unexpected plant maintenance are fouling of brine acid injection systems and binary station heat exchangers. Therefore, the ability to anticipate geothermal aluminosilicate scaling is valuable, both during the plant design stage, and for troubleshooting problems once equipment is in operation.

Acknowledgements

This work was possible through the support of New Zealand Ministry of Business, Innovation and Employment (MBIE) through the Reversing Carbon Emissions in Geothermal Energy Industry – Template for Emissions – Intensive Industries project funds (UOAX2211).

REFERENCES

Beardmore, J., Lopez, X., Mujika, J.I. and Exley, C., 2016. What is the mechanism of formation of hydroxyaluminosilicates? Scientific reports, 6, p.30913.

Brown, K., 2011, May. Thermodynamics and kinetics of silica scaling. In *International Workshop on Mineral Scaling* (p. 8). Manila, Philippines.

Bénézeth, P., Palmer, D.A. and Wesolowski, D.J., 2001. Aqueous high-temperature solubility studies. II. The solubility of boehmite at 0.03 m ionic strength as a function of temperature and pH as determined by in situ measurements. *Geochimica et Cosmochimica Acta*, *65*(13), pp.2097-2111.

Doucet, F.J., Rotov, M.E. and Exley, C., 2001a. Direct and indirect identification of the formation of hydroxyaluminosilicates in acidic solutions. Journal of inorganic biochemistry, 87(1-2), pp.71-79.

Exley, C. and Birchall, J.D., 1993. A mechanism of hydroxyaluminosilicate formation. Polyhedron, 12(9), pp.1007-1017.

Fleming, B.A. and Crerar, D.A., 1982. Silicic acid ionization and calculation of silica solubility at elevated temperature and pH application to geothermal fluid processing and reinjection. *Geothermics*, *11*(1), pp.15-29.

Fournier, R.O. (1986) Reviews in Economic Geology Volume 2. Geology and Geochemistry of Epithermal Systems. Society of Economic Geologists. Editors Berger and Bethke. pp 45 – 61

Gallup, D.L., 1997. Aluminum silicate scale formation and inhibition: scale characterization and laboratory experiments. Geothermics, 26(4), pp.483-499.

Gunnarsson, I. and Arnórsson, S., 2000. Amorphous silica solubility and the thermodynamic properties of H4SiO 4 in the range of 0 to 350 C at Psat. Geochimica et Cosmochimica Acta, 64(13), pp.2295-2307.

Leiviskä, T., Rämö, J., Lanzani, G., Huhtakangas, S., Laasonen, K. and Pehkonen, S.O., 2014. Quasi-quantitative determination of elemental relationships and surface properties in aqueous aluminium-silicon systems. Journal of Water Process Engineering, 1, pp.54-63.

Newton, C.J, Zarrouk, S., Lawless, J., Rowe, M., Guidos, J., Brown, K.: Aluminium-Rich Silica Scaling: San Jacinto-Tizate Geothermal Energy Project, Nicaragua. Proc. 40th New Zealand Geothermal Workshop 2018, Taupo, New Zealand. (2018).

Newton, C.J: Interaction of Aluminium with Silica in Geo-fluids: Investigation of a Proposed Compositional Control Mechanism of Natural Waters and Aluminosilicate Precipitation

Reactions in Aqueous Systems. (2020). Master's Thesis, University of Auckland, New Zealand. (2020).

Okada, K., Nagashima, T., Kameshima, Y., Yasumori, A. and Tsukada, T., 2002. Relationship between formation conditions, properties, and crystallite size of boehmite. Journal of colloid and interface science, 253(2), pp.308-314.

Palmer, D.A., Bénezeth, P. and Wesolowski, D.J., 2001. Aqueous high-temperature solubility studies. I. The solubility of boehmite as functions of ionic strength (to 5 molal, NaCl), temperature (100–290 C), and pH as determined by in situ measurements. Geochimica et Cosmochimica Acta, 65(13), pp.2081-2095.

Palmer, D.A. and Wesolowski, D.J., 1992. Aluminum speciation and equilibria in aqueous solution: II. The solubility of gibbsite in acidic sodium chloride solutions from 30 to 70 C. Geochimica et Cosmochimica Acta, 56(3), pp.1093-1111.

Rothbaum, H.P., Anderton, B.H., Harrison, R.F., Rohde, A.G. and Slatter, A., 1979. Effect of silica polymerisation and pH on geothermal scaling. Geothermics, 8(1), pp.1-20.

Strekopytov, S., Jarry, E. and Exley, C., 2006. Further insight into the mechanism of formation of hydroxyaluminosilicates. Polyhedron, 25(17), pp.3399-3404.

Tokoro, C., Suzuki, S., Haraguchi, D. and Izawa, S., 2014. Silicate removal in aluminum hydroxide co-precipitation process. Materials, 7(2), pp.1084-1096.

Wefers, K. and Misra, C., 1987. Oxides and hydroxides of aluminum (Vol. 19, pp. 1-92). Pittsburgh, PA: Alcoa Laboratories.

Yokoyama, T., Sato, Y., Nakai, M., Sunahara, K. and Itoi, R., 1999. Siliceous deposits formed from geothermal water in Kyushu, Japan: II. Distribution and state of aluminum along the growth direction of the deposits. Geochemical journal, 33(1), pp.13-18.

How Important Is the Hydrothermal Alteration in the Upper Rhine Graben for Geothermal Lithium Assessment?

Jeanne Vidal[1], Catherine Lerouge[2], Philippe Lach[2], Claire Aupart[2], N'Zé Emmanuel Traoré[1], Bernard Sanjuan[2]

[1] Lithium de France, 16 rue des Couturières, 67240 Bischwiller, France

[2] Bureau des Recherches Géologiques et Minières, Orléans, France

Keywords

Geothermal lithium, Li-bearing minerals, X-Ray diffraction, laser ablation, Upper Rhine Graben (URG), GLITER project

ABSTRACT

The Upper Rhine Graben (URG) benefits from an extensive geothermal history with several industrial projects on stream since the beginning of the 21st century. Several deep wells have demonstrated that hydrothermal brines circulate inside a complex network of natural fractures developed in the Triassic sandstones and the altered granitic basement with temperatures up to about 210°C and Li concentrations up to 210 mg/L. More recently, scientific studies have revealed that geothermal lithium could be extracted from this brine. The opportunity for lithium extraction combined with a low CO_2 emission heat gave a second life to the geothermal exploration in the URG. A better knowledge of lithium sources will be based on mineralogical and geochemical characterization of the potential reservoir rocks. Representative samples were collected, i.e., several facies from the base to the top of the Triassic and Permian sandstones and granites of Hercynian basement from quarries in Vosges mountains as well as from deep wells. Micro-analytical techniques were correlated to petrological and geochemical data to discuss the Li resource circulations at the regional scale. Further investigations in other samples of the URG will be compared to attempt to upscale the Li rich rocks assessment at the regional scale and elucidate the Li enrichment in the brines.

1. Introduction

In the 1970s, the discovery of lithium concentrations until 400 ppm in the Salton Sea geothermal field in California attracted curiosity of researchers among the world (Werner, 1970). In the Upper Rhine Graben (URG), a first geochemical analysis of geothermal fluid from the Cronenbourg geothermal exploration borehole near Strasbourg, reveals high lithium levels of 210 ppm (Pauwels et al., 1993). The URG presents unique geological conditions, characterized by elevated geothermal gradient and brines upflow along major faults associated to regional thermal anomalies

that make it an ideal region for geothermal exploitation (Baillieux et al., 2013; Pribnow and Schellschmidt, 2000). Over the year, several reservoirs have been investigated for geothermal projects. Projects with the highest flowrate targeted fracture and fault zones in the granitic basement, while projects targeting the sandstones reservoir remain with lower flowrate (Vidal and Genter, 2018). Today, five high-temperature geothermal plants operate in Alsace (France), in Palatinate and in Baden-Württemberg (Germany), producing heat and power, with lithium concentrations in the deep geothermal brines ranging from 166 to 203 ppm (Bosia et al., 2021; Sanjuan et al., 2016) (Figure 1). Similar Li concentrations were analyzed in the brines from deep geothermal wells recently drilled in the granite basement at Vendenheim (Sanjuan et al., 2021) and Illkirch, in Alsace (Bosia et al., 2021). This ongoing research and development highlights the potential of geothermal lithium as a sustainable energy resource. In this framework, the GLITER project (Integrative multiscale investigation of heat and lithium source and pathways in Deep Geothermal System in a rift context: Focus on the Upper Rhine Graben), cofunded by the French National Research Agency, investigates, among other things the Li sources and Li fluid concentration processes in the URG. A petrological and geochemical characterisation is conducted on the selected samples of sandstones, and granite of the URG from deep wells, quarries and outcrops in order to determine the major Li-carrier minerals and correlate them to fluids concentration at the regional scale.

A geothermal well, named VDH, from the Strasbourg area is presented in this study. Cuttings from several facies of Triassic and Permian sandstones as well as Carboniferous granitic basement intersected below 3.5 km depth were sampled. These formations reached temperature above 200°C in VDH well and were affected by several hydrothermal events. The well intersected permeable fracture and fault zones that channelize deep circulations in both sandstones and granite. The circulating geothermal brine in VDH well has a high Li content between 162 and 200 ppm and a Total Dissolved Solids around 100 g/L. The Li range observed is explained by different sampling methods under different conditions, with production tests carried out on the early and late development stages of the well and having timelines ranging from few days to several weeks of circulations.

The preliminary results of the mineralogical and geochemical studies conducted on these samples are compared to existing literature, but also other analyses acquired in the framework of the GLITER ANR project; core samples at the sediments-basement interface from the EPS1 well at Soultz-sous-Forêts as well as sandstones samples from Adamswiller and Rothbach quarries in the western border of the URG (Figure 1). By synthesising these data, the goal of the project is to elucidate where the brines are enriched in depth and how they make it possible to mobilize the lithium available in the rock formations.

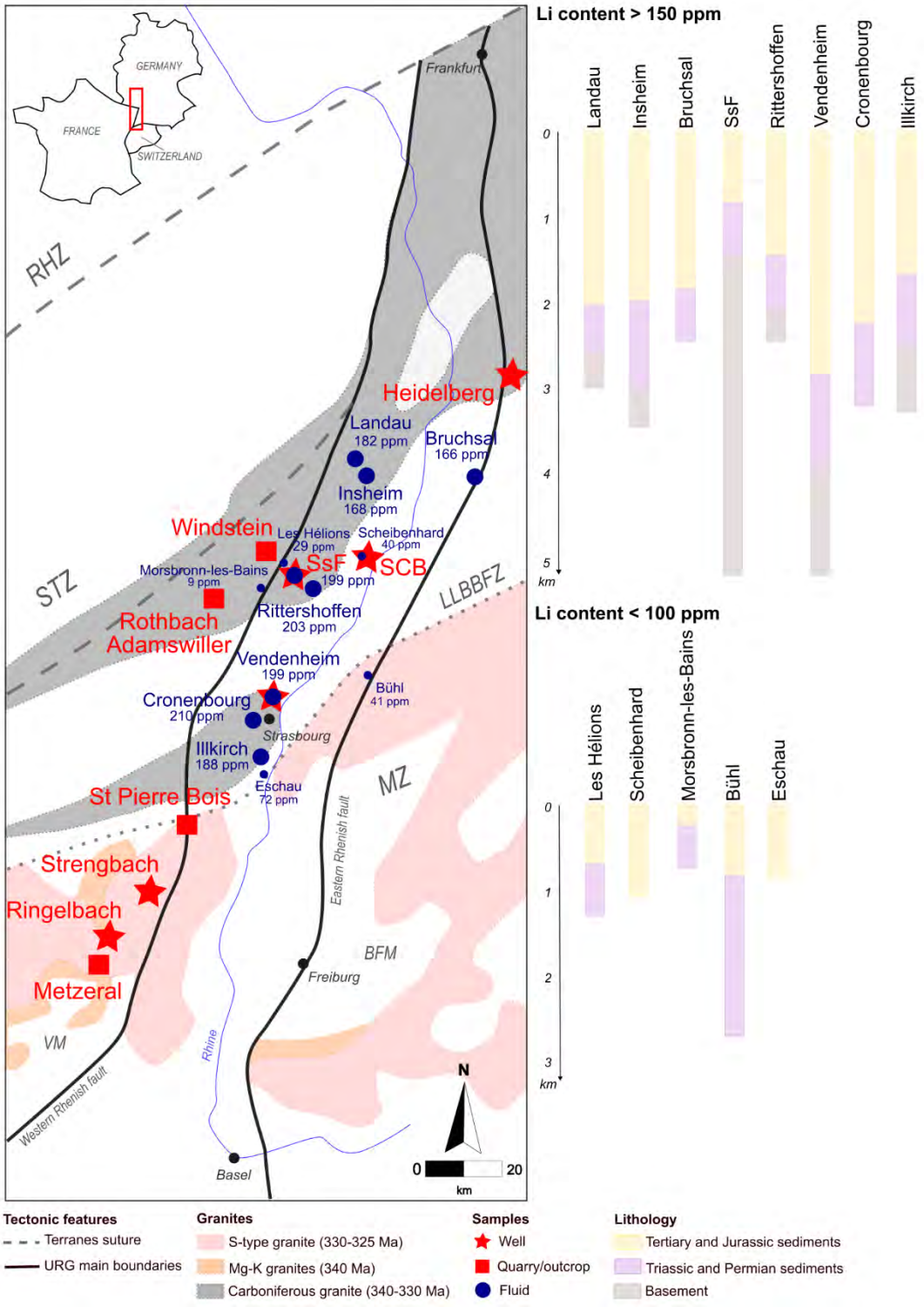

Figure 1: Map of Li distribution in fluids of the URG superimposed to the granite and granitoids emplacement. Li contents in fluids are from (Bosia et al., 2021; Pauwels et al., 1993; Sanjuan et al., 2016). Granites emplacement are extrapolated from the geological map and interpretative signature of the basement from Edel and Schulmann (2009). RHZ = Rhenohercynian zone, STZ = Saxothuringian zone, MZ Moldanubian zone, LLBBFZ = Lalaye-Lubine fault zone, VM = Vosges Mountains, BFM = Black Forest Mountains

2. Sampling and methodology

Cuttings were sampled in representative formations intersected by the VDH well at Vendenheim: Voltzia sandstones in the Upper Buntsandstein, Vosgian sandstones in the Middle Buntsandstein, Permian sandstones, the hydrothermalized granitic basement. The goal was to conduct analysis on fresh and fractured and altered levels to compare the impact of alteration on Li resource. In EPS-1 well at Soultz-sous-Forêts, Permian sandstones as well as the first few hundred meters of biotite-amphibole granite described in Dezayes and Lerouge (2019) were sampled. Voltzia sandstones were sampled from Adamswiller quarry while Vosgian sandstones are from Rothbach quarry. Other rock samples identified on Figure 1 will be presented in further studies to correlate the results of this paper.

For VDH well, mineral phases were identified by binocular (Figure 2) and quantified using X-ray diffraction on bulk rock and Rietveld refinement (Figure 3). XRD were performed on powder mounts using a D8 Advance Brucker AXS diffractometer (CuKα, from 2° to 70°2θ with a step-scan 0.02° increments per second, counting time 1s per increment, 30 mA, 40 kV) at IC2MP laboratory at the University of Poitiers. Then, bulk rock geochemistry was analyzed by Multi Collector Inductively Coupled Plasma Mass Spectrometer from major and trace elements in cuttings samples of representative formations.

In all samples from wells and quarries, analyses of major elements (^{23}Na, ^{24}Mg, ^{27}Al, ^{29}Si, ^{39}K, ^{48}Ti, ^{56}Fe) and lithium (^{7}Li) in minerals were performed using a UVl laser-ablation microsampler CETAC® Excite (193 nm) coupled to an Agilent triple quadrupole plasma mass spectrometer at the French Geological Survey laboratory in Orléans (France), according to the laser configuration of Monnié et al. (2018). Ablation spots 35 μm in diameter were performed at 8 Hz frequency with energy of ~6 J/cm^2 for quartz and ~4 J/cm^2 for other silicates. Analysis time for each spot was 60 s, including 20 s of background measurement with the laser off and 40 s of analysis time with the laser on. Quantification was performed with Glitter® software. All data were calibrated against the external standard NIST SRM 612 (Pearce et al., 1997), and the internal standard of the Si value in the mineral.

3. Results

3.1 VDH deep well from Strasbourg area

The Voltzia sandstones are micaceous sandstones presenting a very low matrix porosity and permeable levels associated to fractures. Fracture filling of the all Permo-Triassic sequence intersected is mainly barite (Figure 2). Li measurements on illite and muscovite range between 30 and 50 ppm (Table 1).

The Vosgian sandstones are quartz-rich sandstones with heterogeneous porosity mainly due to variation of grain size and occurrences of fractures. Li average content of illite is higher (127±57 ppm) than in the Voltzia sandstones (Table 1). Li contents of scarce biotite (143 ppm) and chlorite (317 ppm) are also higher than that measured in the Voltzia sandstones (13 and 96 ppm respectively. However, the bulk rock geochemistry reveals similar Li content of 20-25 ppm in the Triassic sequence (Figure 3).

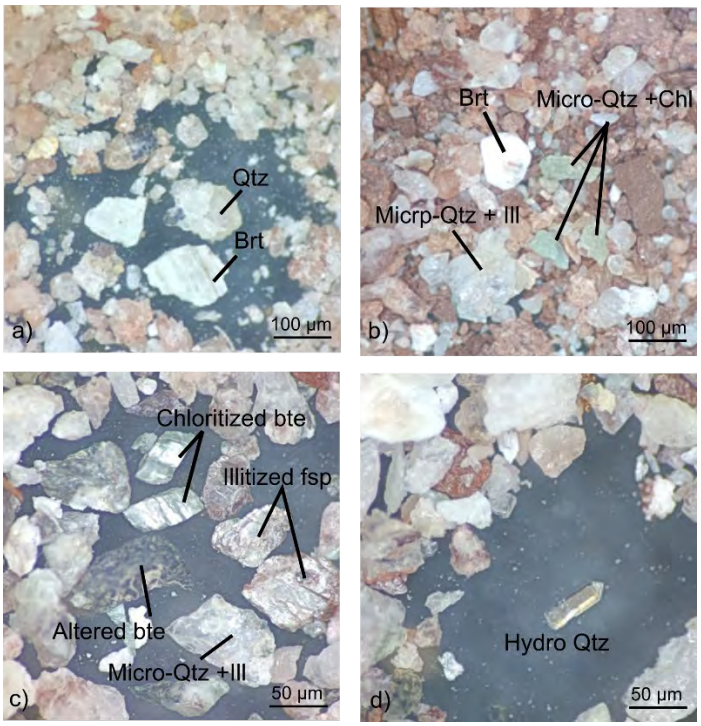

Figure 2: Mineralogical observations of cuttings samples in (a) Vosgian sandstones (b) Permian sandstones (c) altered granitic basement (d) fault zone in granitic basement. Qtz = quartz, Hydro Qtz = hydrothermal quartz, Bte = biotite, Brt = barite, Chl = chlorite, Fsp = felspar, Ill = illite

The Permian sandstones contain a low clay ratio similar to Voltzia sandstones. However, the Li content of the bulk rock ranges between 65 and 75 ppm, the highest values measured in the well. The Li content in minerals was not yet measured in the sample. It would be relevant as a major permeable fracture zone was intersected in this formation.

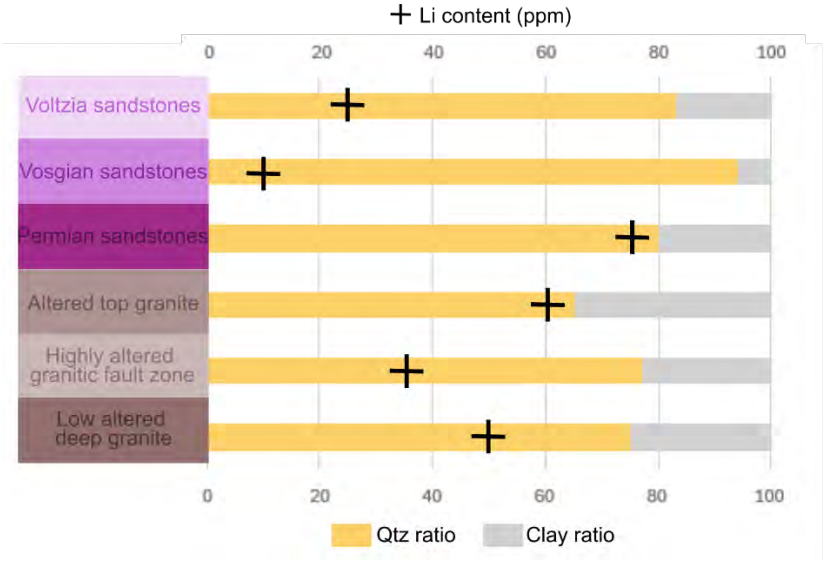

Figure 3: Clays and quartz ratio (in %) estimated from XRD as well as distribution of Li content (in ppm) measured in bulk rock. Clays include muscovite, illitic minerals (illite and illite-smectite mixed layers), biotite and chlorite.

Table 1: Li contents (in ppm) measured in minerals by laser ablation. Bte = biotite, Chl = chlorite, Ill = illite and illite-smectite mixed layers), Qtz = magmatic quartz, Amp = amphibole, ave = average, sd = standard deviation

Lithology	Sample	Bte		Chl		Ill		Qtz		Amp	
		ave	*sd*	ave	*sd*	ave	*sd*	ave	*sd*	ave	*sd*
Voltzia sandstones	VDH well	13	*6*	96	*28*	39	*8*	-	-	-	-
	Adamswiller quarry	~320		-	-	321	*541*	-	-	-	-
Vosgian sandstones	VDH well	143	*3*	317	*86*	127	*57*	14	*8*	-	-
	Rothbach quarry	-	-	-	-	109	*143*	-	-	-	-
Permian sandstones	EPS1 well	-	-	-	-	219	*339*	-	-	-	-
Altered top granite	VDH well	105	*32*	439	*67*	108	*48*	47	*83*	67	*39*
	EPS1 well	501	*124*	504	*103*	55	*5*	10	*2*	10	*3*

In the Hercynian basement, petrographic observations provide evidence of biotite, amphibole, quartz, feldspars, chlorite, illite, carbonates in cuttings of granite, suggesting that it consists of a biotite-amphibole granite affected by an intense weathering marked by the abundance of clay minerals including illite, chlorite, and the presence of hydrothermal microquartz and carbonates (Figure 2).

The Li contents of bulk rock vary considering the grade of alteration. The whole Li content is around 50-60 ppm in zones where chlorite and residual biotite prevail, and around 30-35 ppm in zones where illite, carbonates and hydrothermal quartz are dominant (Figure 3). The Li contents of minerals vary a lot: 105±32 ppm in altered biotite, 67±39 ppm in amphibole, 439±67 ppm in chlorite or chloritized biotite, 108±48 ppm in illitic minerals (Table 1). Quartz analyzed with laser ablation in granite is mainly magmatic one (47±83 ppm) as hydrothermal quartz in fault zone is more difficult to target.

3.2 Additional work on EPS1 deep well from Soultz-sous-Forêts

Core samples in Permian sandstones intersected by EPS1 well indicate very heterogeneous Li content of detrital micas ranging between 3 and 1444 ppm.

Some samples from the first few hundred meters of biotite-amphibole granite present preserved magmatic biotite showing high Li content (501±124 ppm) compared to amphibole (10±3 ppm). Chlorite associated to the diffuse propylitic alteration observed in the less altered samples shows similar high Li content (504±103 ppm) to that of biotite. In the most intense altered samples, illite in fractures (55 ±5 ppm) and in the granite wallrock (<40 ppm) has significantly lower Li contents than ferromagnesian minerals. It is noteworthy that hydrothermal quartz fills in fractures exhibits high Li content (353±152 ppm) compared to magmatic quartz (10±2 ppm).

3.3 Sandstone quarries

Voltzia sandstones from Adamswiller quarry exhibit a large range of Li concentrations in illitic minerals (1-2247 ppm, median = 86 ppm) and contain scarce biotite flakes (around 320 ppm). Vosgian sandstones from Rothbach quarry present a large range of Li concentrations in illitic minerals too (1-717 ppm, median = 62 ppm).

4. Discussion

In sandstones, illitic minerals with minor detrital chlorite, muscovite, and biotite are the primary Li-carrier minerals. Micro-analytical measurements on cuttings samples are likely less reliable than those on rock materials. Analyses of clays and mica in sandstones show a wide range of Li contents, suggesting significant heterogeneity in the sources. One mica flake can present a very high Li content, while a neighboring one may have a very low content. The overall Li content of Middle Buntsandstein sandstones, ranging from 20-25 ppm, is consistent with literature values: 20-40 ppm from a deep well in Bruchsal (Kölbel et al., 2023) and 13-17 ppm from a quarry in the Black Forest (Orywall et al., 2017). The highest Li content in Permian sandstones up to 70 ppm, or even 80 ppm in Bruchsal (Kölbel et al., 2023), might be due to a proximal source of dismantled granitic bedrock in the Permian basin, whereas the Middle Buntsandstein's extensive fluviatile context transported weathering products over several thousand kilometers.

The granite intersected in the VDH well from the Strasbourg area consists of biotite-amphibole granite. The first few hundred meters show intense alteration, with at least two stages identified: 1) diffuse propylitic alteration marked by biotite chloritization, and 2) fracture wallrock alteration associated with hydrothermal circulations, marked by prevalent matrix illitization, carbonate fills in fractures, and hydrothermal quartz fills in permeable levels. The Hercynian basement intersected by the VDH well is similar in terms of magmatic rock and alterations to that intersected at Soultz, aged from Carboniferous (330-340 Ma) (Genter, 1989).

In the VDH well, the granitic basement shows heterogeneous Li distribution mainly due to the type and intensity of alteration. The highest whole-rock Li contents correspond to zones where propylitic alteration (biotite chloritization) prevails and residual primary magmatic biotite remains. Lower values are found in fractured zones affected by matrix illitization and carbonate and quartz fills in fractures. These results are consistent with bulk rock data from Soultz; 25 ppm for illitized facies vs 37 ppm for facies dominated by propylitic alteration (Genter, 1989). High Li contents in biotite and chlorite and low ones in illite, measured in VDH and EPS1 wells, are similar to findings by Dugamin et al. (2024). The high Li contents measured in hydrothermal quartz in the EPS1 well and some quartz spots in the Strasbourg well confirm data from Dugamin et al. (2024) (623-1043 ppm). These high Li contents were also identified in a major fault outcropping in the St Pierre Bois quarry on the western shoulder of the URG (Dezayes et al., 2021).

These preliminary results, correlated with existing literature, suggest that ferromagnesian primary minerals of the Carboniferous granitic basement could be a possible source of lithium. The dissolution of Li-bearing ferromagnesian minerals during brine circulations in fracture and fault zones could lead to brine Li-enrichment (Figure 4). Simple seawater evaporation during the Triassic cannot explain the Li content observed in present-day fluid (Dugamin et al., 2024). Li resources migrate in the Permo-Triassic and Carboniferous reservoir rocks through fracture and fault networks where water-rock interactions are intense.

The decrease in Li contents from the propylitic alteration to an intense hydrothermal alteration (illite-carbonates-quartz) and the Li content in hydrothermal quartz suggest lithium mobilization from the granite into the hydrothermal fluids. This underscores the need for further analysis of other granite types in the URG, such as Mg-K granite or biotite-muscovite S-type granite (Tabaud et al., 2015). The latter are peraluminous granites known as sources of Li, and understanding

differentiation processes during granitic intrusion and granitoid emplacement could help elucidate Li distribution at a regional scale (Figure 1).

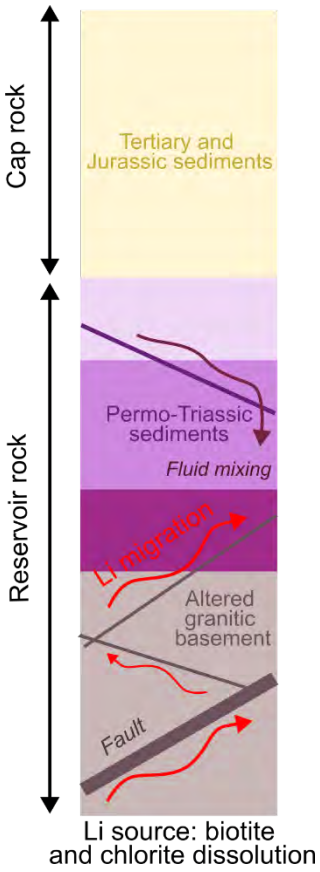

Figure 4: Conceptual model of the geothermal lithium play in the URG

5. Concluding remarks and perspectives

These preliminary results highlight the high-level content in ferromagnesians minerals from the Carboniferous granite making them potential sources of lithium during brine's enrichment. When the brine suffers disequilibrium and precipitate it can lead to Li-rich newly formed quartz. As the Permo-Triassic rocks result from granite's dismantling, the sedimentation context and grade of alteration of the minerals will impact the Li distribution in the reservoir rocks. The Li content of the reservoir rocks associated to an illite-facies is lower than a biotite-chlorite-facies.

The lithium behavior in alteration processes is only partially understood due to the lack of data on the lithium distribution in fresh minerals and their alteration products. Further analysis will be conducted in different sites and rock formations of the URG to strengthen the understanding of lithium enrichment in brines.

Acknowledgement

A part of the data presented was acquired in the framework of the GLITER project (ANR-22-CE50-0027) cofunded by the Agence Nationale de la Recherche.

REFERENCES

Baillieux, P., Schill, E., Edel, J.-B., Mauri, G., 2013. Localization of temperature anomalies in the Upper Rhine Graben: insights from geophysics and neotectonic activity. International Geology Review 55, 1744–1762. https://doi.org/10.1080/00206814.2013.794914

Bosia, C., Mouchot, J., Ravier, G., Seibt, A., Jähnichen, S., Degering, D., Scheiber, J., Dalmais, E., Baujard, C., Genter, A., 2021. Evolution of Brine Geochemical Composition during Operation of EGS Geothermal Plants (Alsace, France), Proceedings of 46th Workshop on Geothermal Reservoir Engineering. Stanford University, California, USA.

Dezayes, C., Lerouge, C., 2019. Reconstructing Paleofluid Circulation at the Hercynian Basement/Mesozoic Sedimentary Cover Interface in the Upper Rhine Graben. Geofluids 2019, 4849860. https://doi.org/10.1155/2019/4849860

Dezayes, C., Lerouge, C., Innocent, C., Lach, P., 2021. Structural control on fluid circulation in a graben system: Constraints from the Saint Pierre Bois quarry (Vosges, France). Journal of Structural Geology 146, 104323.

Dugamin, E.J.M., Boiron, M.-C., Cathelineau, M., Richard, A., Peiffert, C., Lebreton, A., Banks, D.A., Despinois, F., 2024. Brine-granite interaction and lithium leaching in a continental rift (Soultz-sous-Forêts, Rhine Graben, France). Lithos 478–479, 107604. https://doi.org/10.1016/j.lithos.2024.107604

Edel, J.-B., Schulmann, K., 2009. Geophysical constraints and model of the “Saxothuringian and Rhenohercynian subductions – magmatic arc system” in NE France and SW Germany. Bulletin de la Societe Geologique de France 180, 545–558. https://doi.org/10.2113/gssgfbull.180.6.545

Genter, A., 1989. Géothermie roches chaudes sèches: le granite de Soultz-sous-Forêts (Bas-Rhin, France). Fracturation naturelle, altérations hydrothermales et interaction eau-roche (PhD thesis). Université d’Orléans, France.

Kölbel, L., Kölbel, T., Herrmann, L., Kaymakci, E., Ghergut, I., Poirel, A., Schneider, J., 2023. Lithium extraction from geothermal brines in the Upper Rhine Graben: A case study of potential and current state of the art. Hydrometallurgy 221, 106131. https://doi.org/10.1016/j.hydromet.2023.106131

Monnier, L., Lach, P., Salvi, S., Melleton, J., Bailly, L., Béziat, D., Monnier, Y., Gouy, S., 2018. Quartz trace-element composition by LA-ICP-MS as proxy for granite differentiation, hydrothermal episodes, and related mineralization: The Beauvoir Granite (Echassières district), France. Lithos 320-321, 355–377. https://doi.org/10.1016/j.lithos.2018.09.024.Orywall, P., Drüppel, K., Kuhn, D., Kohl, T., Zimmermann, M., Eiche, E., 2017. Flow-through experiments on the interaction of sandstone with Ba-rich fluids at geothermal conditions. Geothermal Energy 5, 20. https://doi.org/10.1186/s40517-017-0079-7

Pauwels, H., Fouillac, C., Fouillac, A.-M., 1993. Chemistry and isotopes of deep geothermal saline fluids in the Upper Rhine Graben: Origin of compounds and water-rock interactions. Geochimica et Cosmochimica Acta 57, 2737–2749. https://doi.org/10.1016/0016-7037(93)90387-C

Pearce, N.J., Perkins, W.T., Westgate, J.A., Gorton, M.P., Jackson, S.E., Neal, C.R., Chenery, S.P., 1997. A compilation of new and published major and trace element data for NIST SRM 610 and NIST SRM 612 glass reference materials. Geostandards and Geoanalytical Research 21, 115–144.

Pribnow, D., Schellschmidt, R., 2000. Thermal tracking of upper crustal fluid flow in the Rhine Graben. Geophysical Research Letters 27, 1957–1960. https://doi.org/10.1029/2000GL008494

Sanjuan, B., Millot, R., Innocent, Ch., Dezayes, Ch., Scheiber, J., Brach, M., 2016. Major geochemical characteristics of geothermal brines from the Upper Rhine Graben granitic basement with constraints on temperature and circulation. Chemical Geology 428, 27–47. https://doi.org/10.1016/j.chemgeo.2016.02.021

Sanjuan, B., Négrel, G., Le Lous, M., Poulmarch, E., Gal, F., Damy, P.-C., 2021. Main geochemical characteristics of the deep geothermal brine at Vendenheim (Alsace, France) with constraints on temperature and fluid circulation, in: Proceedings World Geothermal Congress 2020+1. Reykjavik, Iceland

Tabaud, A.-S., Janoušek, V., Skrzypek, E., Schulmann, K., Rossi, P., Whitechurch, H., Guerrot, C., Paquette, J.-L., 2015. Chronology, petrogenesis and heat sources for successive Carboniferous magmatic events in the Southern–Central Variscan Vosges Mts (NE France). Journal of the Geological Society 172, 87–102. https://doi.org/10.1144/jgs2013-123

Vidal, J., Genter, A., 2018. Overview of naturally permeable fractured reservoirs in the central and southern Upper Rhine Graben: Insights from geothermal wells. Geothermics 74, 57–73. https://doi.org/10.1016/j.geothermics.2018.02.003

Werner, H.H., 1970. Contribution to the mineral extraction from supersaturated geothermal brines Salton Sea Area, California. Geothermics, Proceedings of the United Nations symposium on the development and utilization of geothermal resources 2, 1651–1655. https://doi.org/10.1016/0375-6505(70)90492-X

Geology

Structural Setting and Geothermal Potential of Northeastern Reese River Valley, North-Central Nevada: Highly Prospective Detailed Study Site for the INGENIOUS Project

James E. Faulds[1], Tait E. Earney[2], Jonathan M.G. Glen[2], John H. Queen[3], Jared Peacock[2], Nicole Hart-Wagoner[1], Kurt Kraal[1], Cary Lindsey[1], Quentin Burgess[1], and Mary Hannah Giddens[1]

[1]Great Basin Center for Geothermal Energy, Nevada Bureau of Mines and Geology University of Nevada, Reno, NV 89557

[2]U.S. Geological Survey, Moffett Field, CA 94035

[3]Hi-Q Geophysical, Inc., Ponca City, OK, 74601

Keywords

Geothermal exploration, structural controls, Great Basin, Nevada, favorable structural settings, geophysical data

ABSTRACT

The northeastern part of the Reese River basin situated ~15 km southeast of Battle Mountain, Nevada, scored highly in the Nevada geothermal play fairway analysis (PFA) for hosting potential hidden geothermal systems. This site (also referred to as Argenta Rise) was therefore chosen for detailed study in the INGENIOUS project (INnovative Geothermal Exploration through Novel Investigations Of Undiscovered Systems). The high PFA scores resulted primarily from favorable structural settings (e.g., fault intersections and pull aparts) with relatively high slip rates on Quaternary faults. The INGENIOUS project is utilizing additional parameters and more rigorous analytical techniques to further advance exploration at this site. This includes integration of geological (e.g., Quaternary fault mapping) and new geophysical datasets (e.g., gravity, magnetics, MT data, and five reprocessed seismic reflection profiles) to build a structural model and to identify specific favorable sites for potential geothermal upwellings. Two-meter temperature surveys were also conducted in the area (139 measurements).

This part of north-central Nevada is characterized by systems of intersecting northerly and ENE-striking faults within the broader Humboldt structural zone, a poorly understood belt of ENE-striking faults and relatively high heat flow extending across northern Nevada. Kinematic analysis of exposed fault surfaces shows that ENE-striking faults have accommodated sinistral-normal slip,

and normal slip characterizes N- to NNE-striking faults. Northeastern Reese River Valley lies within a broad left step between major ENE-striking fault zones on the northern flanks of the Argenta Rim and Shoshone Range and thus corresponds to a broad pull-apart in the ENE-striking sinistral-normal fault system. Notably, the nearby Beowawe geothermal system in Whirlwind Valley (with abundant sinter, hot springs, and a geothermal power plant) occupies a fault intersection in a relatively small left step in a major ENE-striking sinistral-normal fault and may serve as an analogue for a potential hidden system in northeastern Reese River Valley. Existing geological maps, high-resolution lidar, and seismic reflection data demonstrate that northeastern Reese River Valley is structurally complex with multiple intersections between the ENE- and N- to NNE-striking fault systems. Some of these fault intersections correspond to low resistivity anomalies, magnetic lows, and/or very subtle 2-m temperature anomalies, which may indicate hidden geothermal upwellings. Three-dimensional modeling and temperature-gradient drilling are planned to further evaluate these sites for geothermal activity.

1. Introduction

The primary goal of the INGENIOUS project is to accelerate discoveries of new, commercially viable hidden geothermal systems in the Great Basin region of the Basin and Range province in the western USA, while substantially reducing the exploration and development risks for all geothermal resources (Ayling et al., 2022, Faulds and Richards, 2023). The Great Basin region is a world-class geothermal province with >1200 MWe of installed nameplate capacity from ~28 geothermal systems (e.g., Muntean et al., 2021; Figure 1). However, studies indicate far greater potential for conventional hydrothermal systems in the region (Williams et al., 2009; U.S. Department of Energy, 2019), but most of these resources are hidden or blind (Coolbaugh et al., 2007a).

Most geothermal systems in the Great Basin region, especially those ≥120°C, reside along normal faults in complex interaction zones, such as fault terminations, fault intersections, step-overs or relay ramps, accommodation zones, displacement transfer zones at the ends of strike-slip faults, and releasing bends or pull-aparts in strike-slip faults (Curewitz and Karson, 1997; Faulds and Hinz, 2015; Faulds et al., 2021a; Figure 1). These fault interaction zones contain higher fault and fracture densities, more permeable fault breccia in lieu of impermeable clay gouge, and typically correspond to critically stressed areas (Faulds and Hinz, 2015; Siler et al., 2018; Siler, 2023a, b). These characteristics lead to enhanced permeability and promote long-term fluid flow (Micklethwaite and Cox, 2004).

Because most systems in this region are controlled by Quaternary normal faults (Bell and Ramelli, 2007), they generally reside near the margins of actively subsiding basins, which can lead to development of blind or hidden systems. Fault-hosted upwelling fluids commonly flow into permeable sediments in the basin without emerging directly along the surface trace of the reservoir-hosting fault(s). Geothermal outflow may therefore surface kilometers away from the deeper source or remain *hidden* (or blind) with no surface manifestations (Richards and Blackwell, 2002).

Thus, techniques are needed to identify and characterize structural settings associated with increased permeability and relatively high potential to host a hidden system. The discovery of the McGinness Hills hidden system in central Nevada, which is currently the largest producing system in Nevada (~150 MWe; Figure 1; Nordquist and Delwiche, 2013), suggests that many such systems

are yet to be discovered in the region and that some of these hidden systems may be capable of becoming large producers.

The technical challenge is to develop methodologies to locate such systems with minimal risk. The geothermal play fairway concept is one approach to reduce this risk, and it has been applied to evaluate undeveloped and potential hidden systems in various settings in the conterminous western U.S. (Faulds et al., 2015a; 2015b; 2018; 2019; Forson et al., 2016; Shervais et al., 2016; Siler et al., 2017; Craig, 2018; Craig et al., 2021). In Nevada, play fairway analysis was applied to a 96,000-km^2 study area (Figure 1) and resulted in the discovery of new hidden systems in Gabbs Valley and Granite Springs Valley (Faulds et al., 2021b, c; Craig et al., 2021).

However, geothermal play fairway analysis is a relatively 'youthful' methodology, and previous play fairway projects encountered challenges such as how to objectively estimate relative weights for input datasets, incomplete datasets, lack of key datasets, and limited numbers of training sites (Faulds et al., 2020). More broadly, the geothermal community has recently made major achievements on multiple fronts, including play fairway analysis (e.g., Faulds et al., 2015a, 2018, 2021b, c; Shervais et al., 2016; Siler et al., 2017; Wannamaker et al., 2017), 3D and conceptual modeling (e.g., Siler et al., 2019; Craig et al., 2021), resource capacity estimation, feature engineering (Hart-Wagoner et al., 2023), machine learning (e.g., Smith et al., 2023), the application of advanced geostatistics, and value-of-information (VOI) analysis to identify prospective geothermal resources and reduce exploration risk. However, these techniques have yet to be integrated together into a holistic, practical, best-practices workflow for a broad region.

The INGENIOUS project aims to fully integrate these techniques for the entire Great Basin region to develop a comprehensive exploration workflow toolkit that includes predictive geothermal play fairway maps at both regional- and local-scales, updated regional geological and geophysical data compilations, detailed 3D maps and conceptual models of four individual prospects, software tools to facilitate practical use of our refined exploration workflows, and ultimately a Developers' Playbook for the entire region (e.g., Ayling et al., 2022). The study area encompasses 494,269 km^2, including most of Nevada, western Utah, southern Idaho, southeastern Oregon, and easternmost California (Figure 1). Building on geothermal play fairway efforts in central Nevada (Faulds et al., 2015a, b, 2021b, c), NE California/NW Nevada (Siler et al., 2017), and western Utah (Wannamaker et al., 2017), we have expanded these study areas to the broader Great Basin region and have generated preliminary geothermal potential maps of this region (Figure 1; Hart-Wagoner et al., 2023, 2024).

Concurrently, we moved several promising blind prospects forward with detailed geological and geophysical analyses to be followed by thermal-gradient hole drilling (Faulds and Richards, 2023). The detailed study sites for the INGENIOUS project extend from northwestern Nevada into southwestern Utah (Figure 1). Our first detailed study site in Granite Springs Valley in western Nevada was initially identified in the Nevada play fairway analysis project in which detailed studies and temperature-gradient drilling documented an apparent hidden geothermal system (Faulds et al., 2019, 2021b). The INGENIOUS project extended this analysis by developing a 3D conceptual model and potentially locating the primary zone of upwelling (Kraal et al., 2023). Lessons learned from the regional and local-scale analyses in the Nevada play fairway project guided our strategy in locating and defining the next two detailed sites in northeastern Reese River Valley and the Buffalo Valley/Jersey Summit area, both in north-central Nevada. Selection of the fourth detailed study site at Lund North in southwestern Utah built on all prior experiences in this

and previous related projects. The three new detailed study sites (northeastern Reese River Valley, Buffalo Valley/Jersey Summit, and Lund North) cover areas not previously addressed with detailed studies in the Nevada play fairway analysis or in other projects.

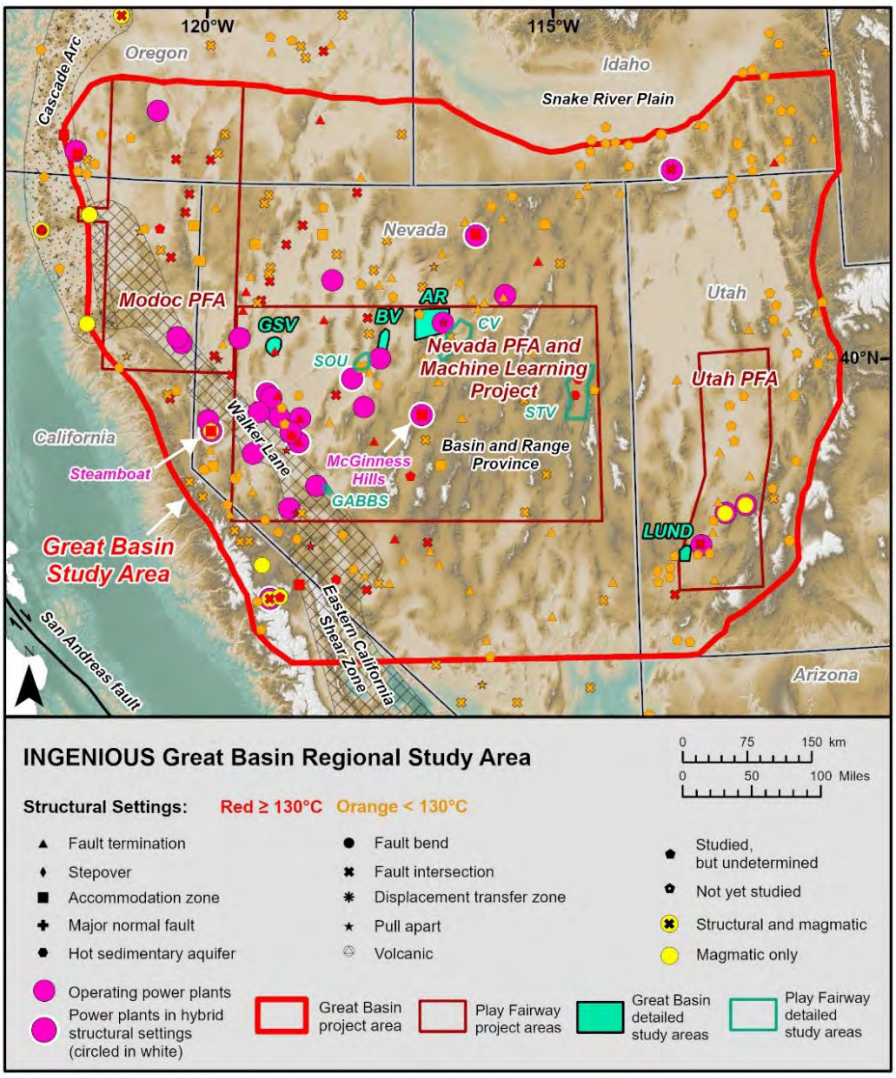

Figure 1: Great Basin study area for INGENIOUS project, with locations of known geothermal systems, identified structural settings, previous play fairway analysis (PFA) projects (Modoc, Nevada, and Utah), and detailed study areas for both the INGENIOUS project (Granite Springs Valley-GSV; Argenta Rise-AR [northern Reese River Valley], Buffalo Valley/Jersey Summit-BV, and Lund, Utah-LUND) and Nevada PFA (Crescent Valley-CV; SE Gabbs Valley-GABBS; Sou Hills-SOU; and Steptoe Valley-STV). Base map is from the ArcGIS online map server (Esri, 2024)

This paper provides a progress report on detailed geological and geophysical investigations of the study site in northeastern Reese River Valley known as Argenta Rise. First, we provide an overview of the area and then describe the detailed geological and geophysical analyses, followed by a brief discussion of the implications for potential hidden systems and planned temperature-gradient drilling in the area. We focus on the structural framework of the area, particularly the possible influence of the geometry and kinematics of complex intersecting fault zones on potential geothermal activity in prospective sites for hidden geothermal systems.

2. Northeastern Reese River Valley (Argenta Rise)

2.1 Regional Setting

The study area lies within the northeastern part of the Reese River Valley ~15 km southeast of Battle Mountain in north-central Nevada (Figure 2). It largely occupies a broad basin bounded to the southeast by the northern Shoshone Range, to the east by the Argenta Rim, and to the west by the Battle Mountain Range. This area was chosen for detailed analysis in the INGENIOUS project, because it scored highly in the Nevada geothermal play fairway analysis for hosting potential hidden geothermal systems. The high play fairway scores resulted primarily from the presence of favorable structural settings (e.g., fault intersections and pull aparts) with relatively high slip rates on Quaternary faults. We informally refer to this area as Argenta Rise due to its proximity to Argenta Rim directly to the east and slightly elevated topography relative to lower parts of Reese River Valley in the Battle Mountain area.

Northeastern Reese River Valley lies within a broad region of northern Nevada extending from near Reno to the Idaho border characterized by high heat flow and east-northeast-striking fault zones that disrupt the typical more northerly trending structural grain of the Great Basin region. This zone of faulting and high heat flow has been referred to as the Humboldt structural zone (Rowan and Wetlaufer, 1981). Several major geothermal fields in northern Nevada, including Bradys, Desert Peak, Beowawe, and Tuscarora reside within the Humboldt structural zone. From west to east, major east-northeast- to north-northeast-striking faults in the Humboldt structural zone include the Olinghouse fault (Sturmer and Faulds, 2018), faults along the northern margin of the Carson Sink, Midas trough, Argenta Rim and Northern Shoshone Range faults in the Argenta Rise study area (Figure 2), and Malpais fault near Beowawe (Struhsacker, 1980; Benoit and Stock, 1993; Watt et al., 2007). These east-northeast-striking normal faults intersect and are kinematically linked to the more common north- to north-northeast-striking normal faults in the Great Basin region and are generally presumed to accommodate sinistral normal slip. However, few detailed studies have documented the kinematics along these faults (Sturmer and Faulds, 2018). The Humboldt structural zone is oriented nearly orthogonal to the Walker Lane in the western Great Basin, which corresponds to a zone of dextral shear accommodating ~25% of the motion between the North American and Pacific plates (e.g., Hammond and Thatcher, 2004; Faulds and Henry, 2008).

The western margin of the northern Nevada rift cuts across northeastern Reese River Valley. The northern Nevada rift is a long, narrow, north-northwest-trending alignment of middle Miocene volcanic and hypabyssal rocks and epithermal gold-silver and mercury deposits formed during west-southwest to east-northeast extension (Zoback, 1989; Zoback et al., 1994; Wallace and John, 1998). It formed ~16 Ma to 14 Ma (Zoback et al., 1994). Mafic, mantle-derived magmas were emplaced along a deep-seated, north-northwest-trending fracture system that cut Paleozoic, middle Tertiary, and early Miocene formations.

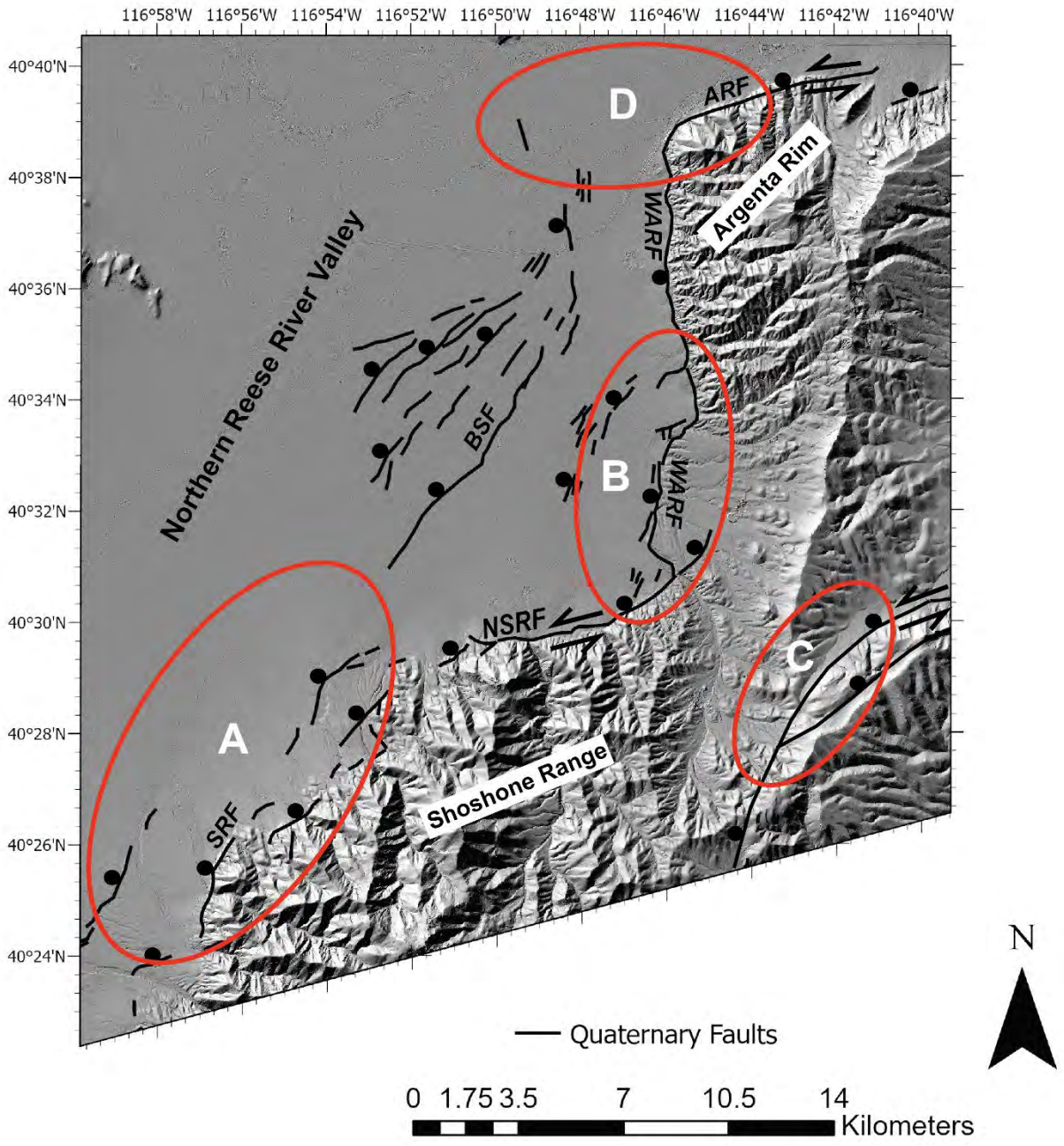

Figure 2: DEM hill-shade (U.S. Geological Survey, 2024) of the study area in northeastern Reese River Valley, also known as Argenta Rise. Quaternary faults are shown as black lines, with balls on downthrown sides and arrows indicating sinistral component of motion on ENE-striking faults. Individual favorable structural settings within the broader study area are outlined by red ellipses and labeled with letters. A, displacement transfer zone and fault intersection; B, fault intersection, pull apart, and step-overs; C, small pull apart and fault intersection; D, fault intersection. Major faults: ARF, Argenta Rim fault; BSF, Bateman Spring fault; NSRF, Northern Shoshone Range fault; SRF, Shoshone Range fault; WARF, West Argenta Rim fault.

2.2 Stratigraphic and Structural Framework

The bedrock stratigraphy of the Argenta Rise study area is characterized by Paleozoic rocks that are overlain by Tertiary volcanic rocks and Miocene to Quaternary basin-fill sediments (John and Wrucke, 2003; Gilluly and Gates, 1965; Ramelli et al., 2001). Formations of both the upper and lower plate of the Roberts Mountains thrust are present at Argenta Rise. The upper plate formations include the Ordovician Valmy Formation, the Silurian Elder Sandstone, and the Devonian Slaven Chert. The lower plate formations include the Shwin Formation and the Roberts Mountains Limestone. The western flank of the northern Shoshone Range is dominated by the upper plate of the Roberts Mountains thrust, with less extensive units of the lower plate present as windows in the thrust sheets (Gilluly and Gates, 1965; John and Wrucke, 2003).

A package of Cenozoic sedimentary and volcanic units unconformably overlie the Paleozoic sedimentary units of the Roberts Mountain allochthon. The volcanic units are extensive and range in age and composition. The oldest Cenozoic unit within the study area is the Caetano Tuff, a 33.8 Ma rhyolitic ash-flow tuff (John et al., 2008; Colgan et al., 2014). The tuff is widespread to the south and southeast of the study area, but the unit is only locally exposed within the study area. Overlying the Caetano Tuff and the Paleozoic section is a package of middle Miocene volcanic rocks that range in composition from basalt to dacite. These rocks are associated with the northern Nevada rift and are extensive in the eastern part of the study area, capping the Argenta Rim. Intruding the Paleozoic basement rock in the western part of Argenta Rim is a swarm of north-northwest-striking basaltic dikes that are potential feeder dikes to associated basalt flows. The Quaternary geology of the northern part of the Reese River basin has been mapped extensively (House et al., 2000; Ramelli et al., 2001, 2017). The ages of the Quaternary units range from Pleistocene to Holocene, with depositional environments including alluvial fan, alluvial flat, fluvial, and eolian deposits.

The structural framework of the study area is dominated by gently to moderately tilted Cenozoic fault blocks and associated half graben basins typical of the Basin and Range province. The northeastern part of the Reese River basin lies adjacent to the northern flank of the Shoshone Range and western margin of the Argenta Rim (Figure 2). The northern Shoshone Range is a north-northeast-trending, east-tilted fault block, and Argenta Rim is a southeast-tilted fault block (John and Wrucke, 2003). The study area is situated in a broad left step between the east-northeast-striking, north-dipping Argenta Rim fault on the north flank of Argenta Rim, and the east-northeast-striking, north-dipping fault that bounds the north end of the Shoshone Range (here referred to as the Northern Shoshone Range fault; Figure 2). These east-northeast striking faults are linked by a north-northwest-striking, west-dipping, fault zone that bounds the western flank of the Argenta Rim and is here referred to as the West Argenta Rim fault. Major fault intersections reside at the northern and southern ends of the West Argenta Rim fault with the Argenta Rim and Northern Shoshone Range faults, respectively. This area forms a broad pull apart between east-northeast-striking sinistral-normal faults. This favorable setting for geothermal activity was noted in the Nevada play fairway project (Faulds et al., 2015a). Notably, the nearby Beowawe geothermal system (with abundant sinter, hot springs, and a geothermal power plant) occupies a fault intersection in an apparent left step (or small pull apart) in the Malpais fault, a major east-northeast-striking sinistral-normal fault (Zoback 1979; Struhsacker 1980; Watt et al., 2007; Figure 7), and may serve as an analogue for a potential hidden system in the Argenta Rise area.

Quaternary fault scarps permeate the northeastern part of the Reese River basin (Figure 2) and commonly cut Holocene alluvial fan deposits. Paleoseismic studies along the northern Shoshone Range noted scarps with progressively greater offset across progressively older surfaces, indicating multiple deformational events. At least two paleoseismic events took place along this fault zone in the past 10,000 years (Wesnousky et al., 2005). The most recent event occurred ~3,317 years B.P. and resulted in 0.4 m of offset. From this, a slip rate of 0.1 mm/yr was calculated. In Whirlwind Valley directly to the east, which contains the Beowawe geothermal system and operating power plant, Quaternary scarps also cut Holocene fan deposits. The paleoseismic events along these faults have a recurrence interval of ~10,000 years (Wesnousky et al., 2005). The most recent event occurred ~7,450 years B.P. and resulted in 0.7 m of vertical offset, which yields a slip rate of 0.09 mm/yr.

3. Methods and Results

The INGENIOUS project has integrated geological and geophysical datasets to build a structural model and to identify specific favorable sites for potential geothermal upwelling. We have also conducted a 2-meter temperature survey.

3.1 Geological Studies

Geologic studies have included compilation of preexisting geological mapping, analysis of high-resolution lidar, and kinematic analysis of fault surfaces. We concluded that existing geologic mapping in the area was adequate for geothermal investigations and development of detailed models, if supplemented by analysis of lidar to locate and analyze (e.g., recency and slip rates) Quaternary faults. Kinematic analysis of exposed fault surfaces (Figure 3) showed that east-northeast-striking faults have accommodated sinistral-normal slip, and normal slip characterizes north- to north-northeast-striking faults. This is an important finding, as east-northeast-striking faults are common in north-central Nevada and intimately linked to arrays of northerly striking faults, but slip along these faults has rarely been characterized. Knowledge of the fault kinematics can help in defining the location and type of favorable structural settings and ultimately in modeling slip and dilation tendency and potential geothermal upwellings in 3D.

Analysis of lidar and field reconnaissance showed that major Quaternary faults in the study area, have several fault interaction zones that are conducive to geothermal activity. This includes major intersections between the West Argenta Rim fault and both the Northern Shoshone Range and Argenta Rim faults and a major step-over (relay ramp) near the southern end of the West Argenta Rim fault (Figure 2; areas B and D). In addition, the Northern Shoshone Range fault has several small steps and also intersects a major north-northeast-striking west-dipping fault on the west flank of the Shoshone Range (Figure 2, area A), which continues south of the study area for tens of kilometers and is here referred to as the Shoshone Range fault.

A 2-meter temperature survey with 139 measurements was completed across the area but did not identify any definitive thermal anomalies (Figure 4). Two very subtle anomalies were found but are either isolated to a single station or below the typical detection limit. Therefore, the shallow temperature survey at Argenta Rise was inconclusive. However, the two very small anomalies may suggest a hidden geothermal resource, which is possibly masked by a shallow cool aquifer or is relatively deep compared to other systems in the region that have yielded definitive shallow thermal anomalies (e.g., Coolbaugh et al., 2007b).

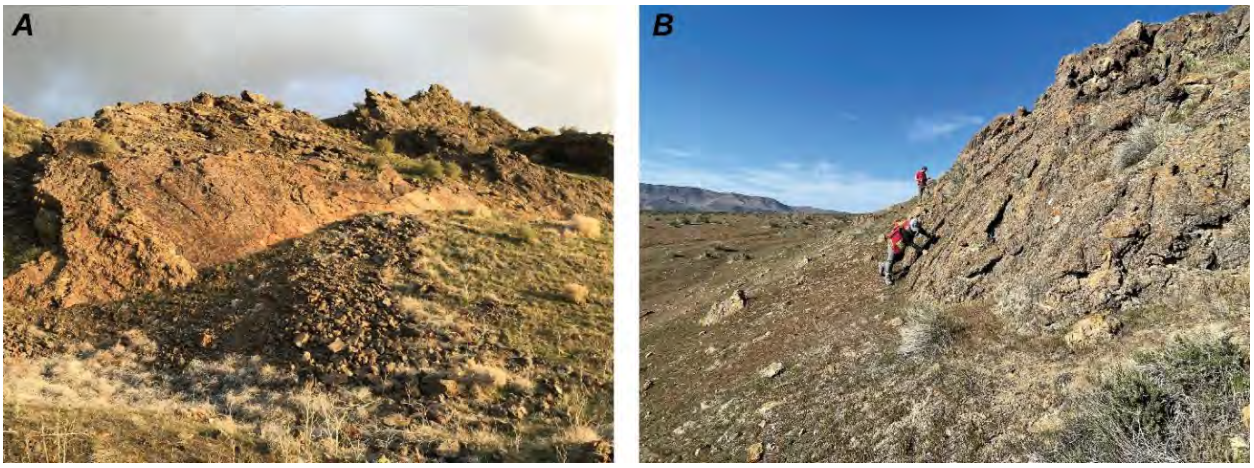

Figure 3: A. Well-exposed fault surface along the Argenta Rim fault, a major ENE-striking, N-dipping fault on north side of Argenta Rim. Fault surface is ~10-15 m in height. Kinematic indicators (e.g., fault striae, corrugations, and Riedel shears) indicate sinistral-normal displacement. B. N-striking, W-dipping fault on west flank of Argenta Rim (West Argenta Rim fault), with dip-slip normal displacement. Photos taken by James Faulds.

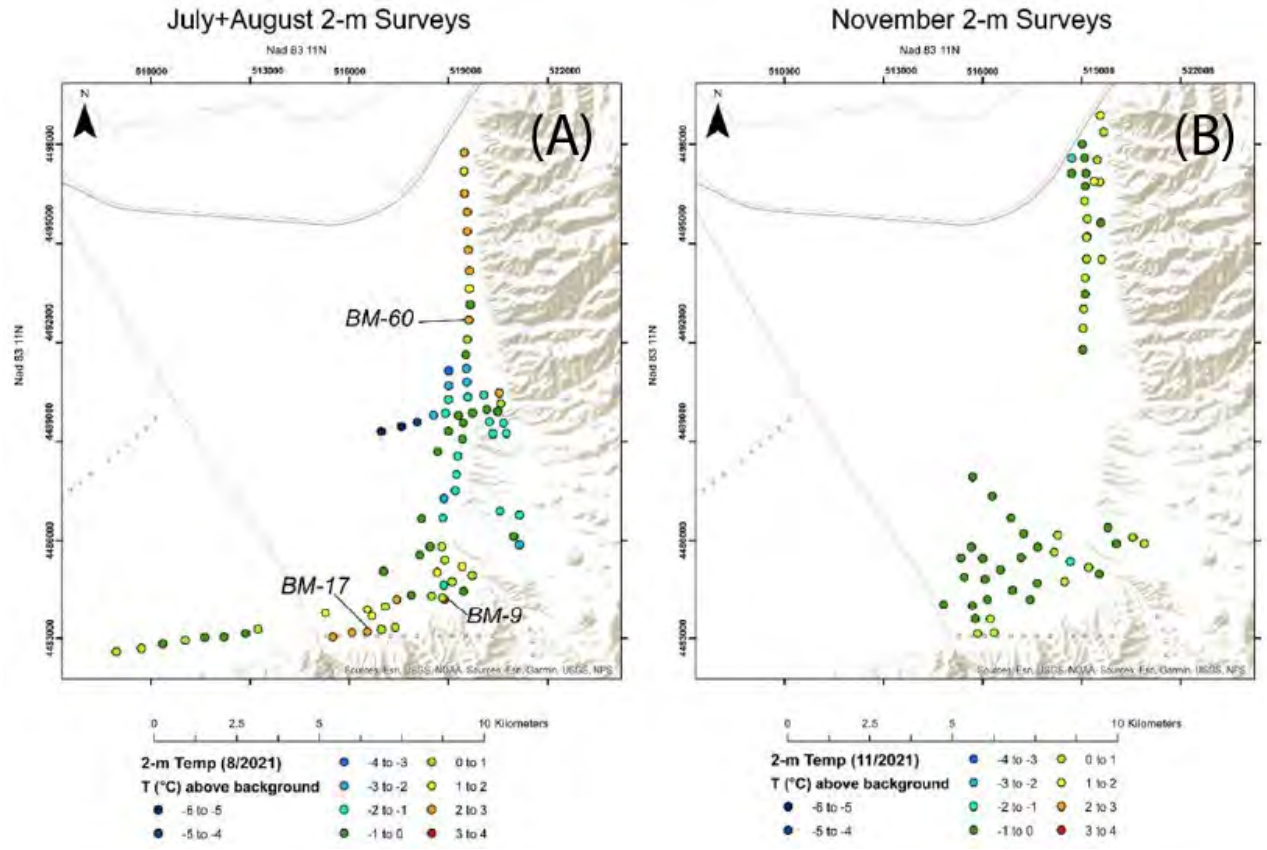

Figure 4: Shallow (2-meter) temperature surveys of the Argenta Rise study area. (A) Survey from July and August 2021. (B) Survey from November 2021. DEM hillshade is from U.S Geological Survey (2024).

3.2 Geophysical Investigations

New geophysical surveys for the Argenta Rise area in the INGENIOUS project have included gravity, magnetic, and MT data acquisitions, which were carried out by the U.S. Geological Survey (Earney et al., 2022, 2023, 2024). Data acquisitions included 1,207 gravity stations, ~70 line-km of magnetic profiles, 43 MT stations, and numerous rock property samples and outcrop measurements (254 hand samples collected for density, 76 outcrop magnetic susceptibility measurements, and 17 paleomagnetic cores taken from two sites) to help constrain potential field model rock properties (Figure 5). New gravity and magnetic grids were generated, and geophysically inferred structural mapping was derived from the gravity and magnetic datasets (Figures 6 and 7). A depth-to-basement inversion model was also developed from the new gravity compilation. Finally, a new 3D resistivity model was developed for the area based on the 43 MT stations. The MT slice at 500 m below sea level or ~2 km depth shows low resistivity anomalies occupying favorable structural settings (e.g., fault intersections and pull aparts) along the northern range-front fault of the Shoshone Range (Figure 8). Details of these datasets and resulting interpretations are reported in an accompanying paper in this volume (Earney et al., 2024).

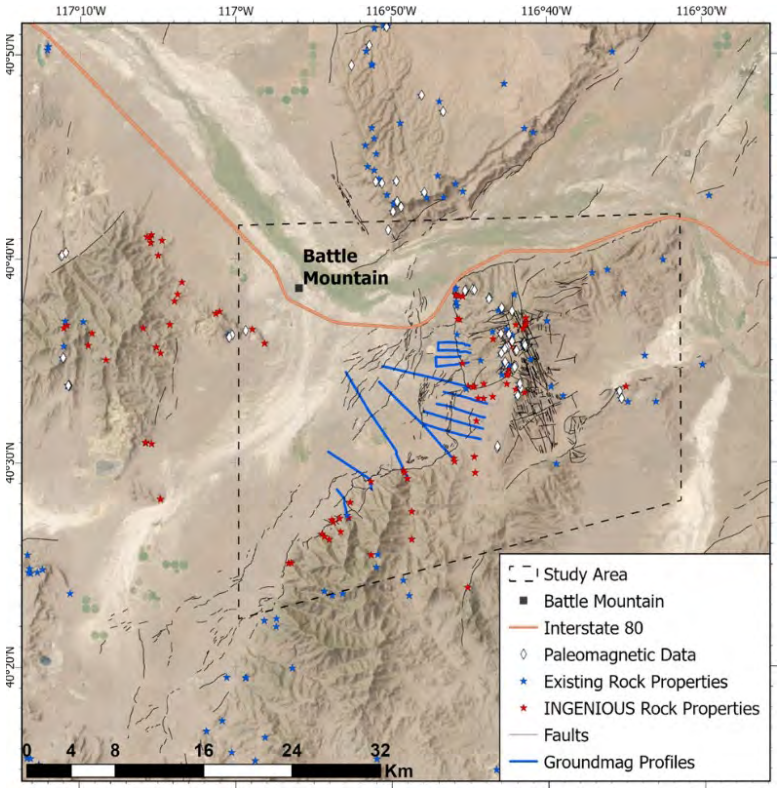

Figure 5: Ground magnetic, rock property, and paleomagnetic field data collection at Argenta Rise. Base map is from the ArcGIS online map server (Esri, 2024).

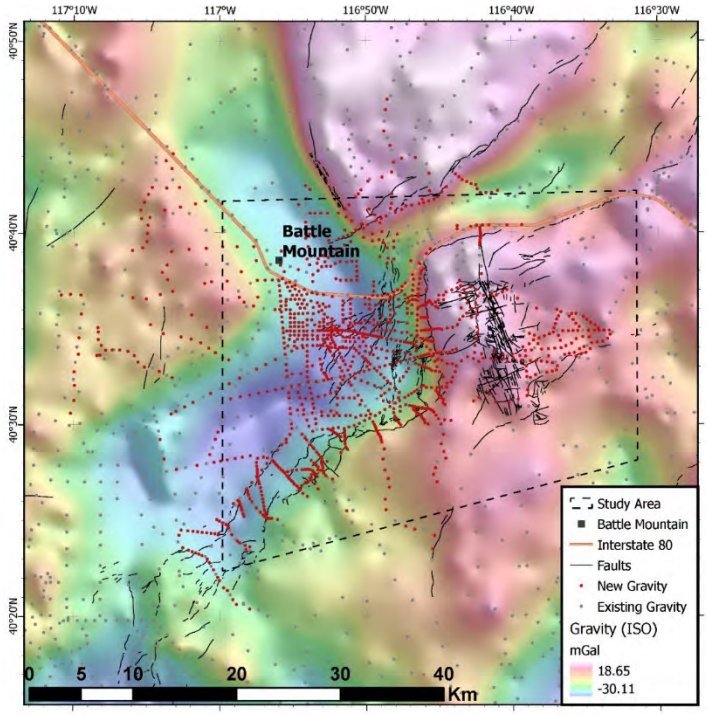

Figure 6: Isostatic gravity grid of the Argenta Rise area based on new and re-reduced existing data. Gravity station coverage includes existing (gray) and new field data (red). Quaternary faults compiled in this project are shown in black.

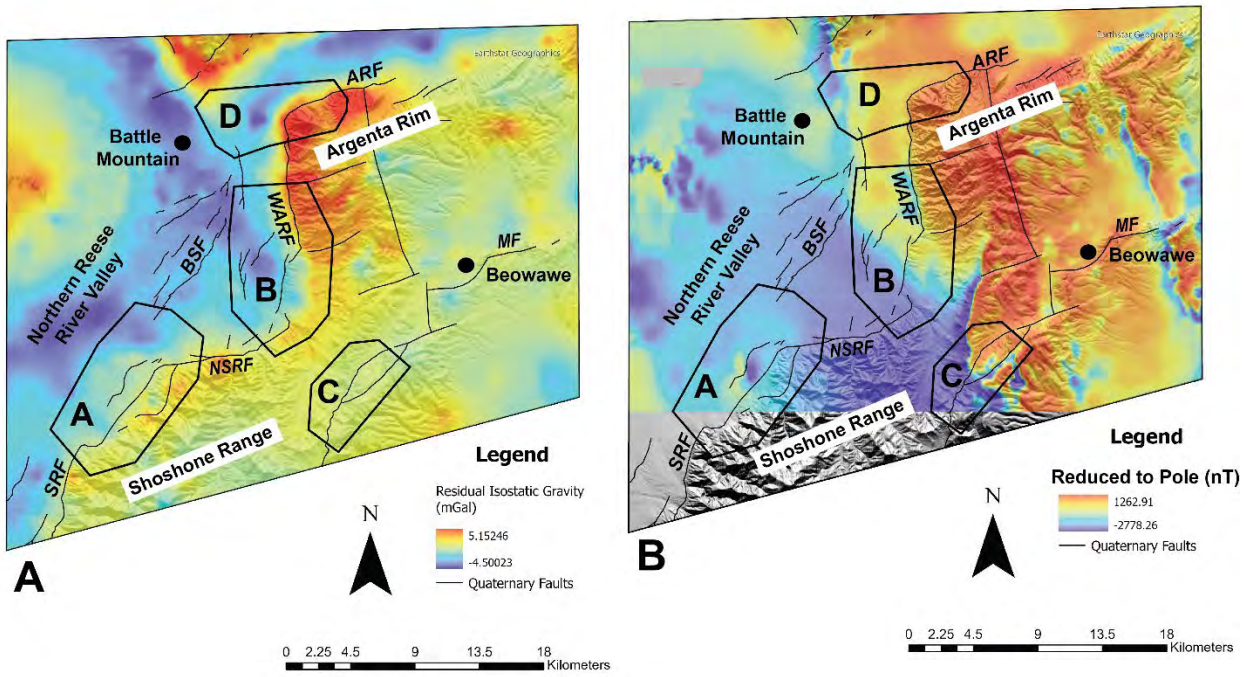

Figure 7: A. Preliminary isostatic residual gravity map for the Argenta Rise area. B. Preliminary magnetic anomaly map (reduced to pole). Black polygons outline the local-scale, individual favorable structural settings identified in this area based on both the geological and geophysical data (see text for discussion), with letters corresponding to those shown on Figures 2 and 8. MF, Malpais fault; see Figure 2 for explanation of other fault labels. DEM hillshade is from U.S Geological Survey (2024).

The rights to interpret six preexisting 2D seismic reflection profiles in the Argenta Rise area were purchased from Seismic Exchange, Inc. Based on the original quality of these profiles, we determined that it would be cost-effective to reprocess the profiles. Pre-stack depth migration (PSDM) results produced through the reprocessing showed substantial improvement for all profiles. A number of coherent reflection events can be tracked, and faulting is also indicated by offsets in some of these reflection events. This improvement in the processed results is related to careful unraveling of the source and geophone coordinates, the application of advanced tomographic refraction statics analysis, and the application of state-of-the-art pre-stack migration velocity analysis.

The reprocessed seismic reflection profiles and revised depth-to-basement horizon estimates for these profiles, based on their gravity inversion models, were interpreted for faults and stratigraphic horizons. Multiple faults were readily interpretable and correlate with major gravity gradients and faults mapped at the surface. Several faults were also noted that are concealed and have not ruptured the surface. This includes a major east-dipping fault on the west side of the northern Reese River basin, which corresponds to a major gravity gradient in that area. In addition, the proprietary seismic reflection data generally indicate that the northern Reese River basin is gently tilted toward the east (data not shown).

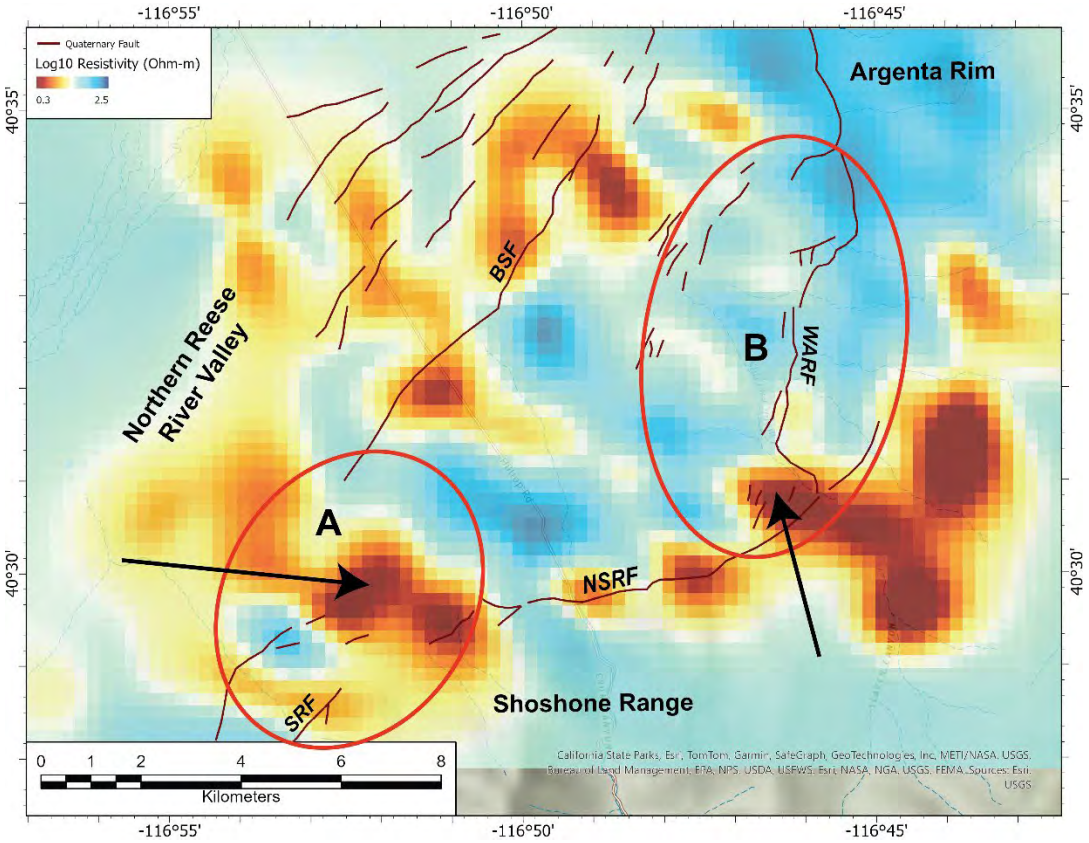

Figure 8: MT grid for the Argenta Rise site at 500 m below sea level or ~2 km depth. Low resistivity anomalies can indicate the presence of clay caps and/or geothermal reservoirs. Red ellipses highlight two favorable structural settings that are marked by low resistivity anomalies (red arrows), with letters corresponding to those shown in Figures 2 and 7. See Figure 2 for explanation of fault labels.

4. Discussion

The geological and geophysical datasets indicate a complex system of intersecting east-northeast-striking sinistral normal and north- to north-northeast-striking normal faults within the northeastern part of the Reese River basin (Argenta Rise area). This pattern of faulting is evident in surface geological data, including relatively abundant Quaternary fault scarps, and also in gravity, magnetic, and MT data. Reprocessed seismic reflection data also show these faults, with major faults imaged on the reflection profiles generally corresponding to gravity and/or magnetic gradients as well as, in many cases, to surface fault scarps.

The Argenta Rise study area occupies a large left step in a system of east-northeast-striking sinistral normal faults and thus represents a broad pull apart. However, this area covers many tens of square kilometers, and thus is impractical due to its size for an economical geothermal drilling program. It is therefore critical to vector into the most prospective parts of this area to reduce the risks in drilling. Three favorable structural settings for geothermal activity have been identified in the northeastern part of the Reese River basin. A fourth setting was defined directly to the east (Figures 2 and 7). Most of these settings lie within the broader favorable structural area noted in the Nevada play fairway project. Identifying additional prospective areas at a finer scale reflects the natural progression from regional- to local-scale exploration, as demonstrated in other detailed studies in the region (McConville et al., 2017; Faulds et al., 2019; Craig et al., 2021).

The newly identified favorable structural settings include three hybrid settings and a fault bend (Figures 2, 7, and 8). Structural setting A is a hybrid of several favorable settings, including a left step in the east-northeast-striking Northern Shoshone Range fault, a possible left step in a northeast-striking intrabasinal fault (Bateman Spring fault), an intersection between the Bateman Spring and Northern Shoshone Range faults, and a displacement transfer zone at the apparent western terminus of the Northern Shoshone Range fault. The displacement transfer zone contains a discrete elliptically shaped, north-trending magnetic low (Figure 7B) and a low resistivity anomaly (Figure 8). Structural setting B (Figures 2, 7, and 8) is also a hybrid of several favorable settings, including a left step in the north-striking West Argenta Rim normal fault and fault intersections between the West Argenta Rim fault and both an obscure intrabasinal east-north-northeast-striking fault and the east-northeast-striking Northern Shoshone Range fault. This setting is part of the broad pull apart between east-northeast-striking sinistral-normal faults. It is marked by large gravity gradients that correspond to mapped Quaternary faults (Figure 7A) and a low resistivity anomaly in its southern reaches (Figure 8). Additionally, there are two anomalous magnetic lows along the western range front of Argenta Rim (Figure 7B). Structural setting C (Figures 2 and 7) lies just to the southeast of our primary study area in the northeastern Reese River basin and is a fault bend in an east-northeast-striking to a north-northeast-striking fault zone. The orientation of this fault bend relative to a regional west-northwest-trending extension direction makes it optimally oriented for dilation and enhanced permeability. The fault bend is also associated with minor magnetic lows along the mapped fault trace. Structural setting D is a hybrid of two favorable settings, including a possible left step in the east-northeast-striking sinistral-normal Argenta Rim fault and a fault intersection between the Argenta Rim fault and northerly striking West Argenta Rim normal fault. This setting encompasses large gravity and magnetic gradients marking concealed faults. Proposed temperature-gradient drilling, planned for late 2024, will focus on structural settings A and B (Figures 2, 7, and 8).

Acknowledgment

This project is funded by U.S. Department of Energy - Geothermal Technologies Office under award DE-EE0009254 to the University of Nevada, Reno. Results presented in this paper reflect the many contributions of the entire INGENIOUS team. Any use of trade, firm, or product names is for descriptive purposes only and does not imply endorsement by the U.S. Government. Reviews by Jacob Anderson and an anonymous individual improved this paper.

REFERENCES

Ayling, B. and others, 2022, INGENIOUS Phase 1 (budget period 1) progress report: Department of Energy DE-EE0009254 Report, 116 p.

Bell, J.W. and Ramelli, A.R., 2007, Active faults and neotectonics at geothermal sites in the western Basin and Range: Preliminary results: Geothermal Resources Council, v. 31, p. 375-378.

Benoit, D., and Stock, D., 1993, A case history at the Beowawe, Nevada geothermal reservoir: Geothermal Resources Council Transactions, v. 17, p. 473-480.

Colgan, J.P., Henry, C.D., and John, D.A., 2014, Evidence for large-magnitude, post-Eocene extension in the northern Shoshone Range, Nevada, and its implications for the structural setting of Carlin-type gold deposits in the lower plate of the Roberts Mountains allochthon: Economic Geology, v. 109, p. 1843-1862.

Coolbaugh, M.F., Raines, G.L., and Zehner, R.E., 2007a, Assessment of exploration bias in data-driven predictive models and the estimation of undiscovered resources: Natural Resources Research, v. 16, no. 2, p. 199-207.

Coolbaugh, M., Sladek, C., Faulds, J., Zehner, R., and Oppliger, G., 2007b, Use of rapid temperature measurements at a 2-meter depth to augment deeper temperature gradient drilling: Proceedings, 32nd Workshop on Geothermal Reservoir Engineering, Stanford University, Stanford, California, SGP-TR-183, p. 109-116.

Craig, J.W., 2018, Discovery and analysis of a blind geothermal system in southeastern Gabbs Valley, western Nevada [M.S. Thesis]: University of Nevada, Reno, 111 p.

Craig, J.W., Faulds, J.E., Hinz, N.H., Earney, T.E., Schermerhorn, W.D., Siler, D.L., Glen, J.M., Peacock, J., Coolbaugh, M.F., and Deoreo, S.B., 2021, Discovery and analysis of a blind geothermal system in southeastern Gabbs Valley, western Nevada, USA: Geothermics, v. 97, p. 102–177.

Curewitz, D. and Karson, J.A., 1997, Structural settings of hydrothermal outflow: fracture permeability maintained by fault propagation and interaction: Journal of Volcanology and Geothermal Research, v. 79, p. 149-168.

Earney, T.E., Glen, J.M.G., Ayling, B., Faulds, J., Siler, D., Dean, B., Zielinski, L.A., Schermerhorn, W.D., Williams, N., Wagoner, N., Morales-Rivera, A., 2022, Characterizing structure and geology with potential field geophysics to asses geothermal resource potential near Battle Mountain, NV: Geothermal Rising Conference, v. 46.

Earney, T.E., Glen, J.M.G., Peacock, J., Faulds, J.E., Schermerhorn, W.D., Rea-Downing, G., Anderson, J.E., 2023, Preliminary geophysical maps and models of a potential blind geothermal system near Battle Mountain, Nevada: Geothermal Rising Conference, v. 47.

Earney, T.E., Glen, J., Peacock, J., Faulds, J., Schermerhorn, W., Rea-Downing, G., Anderson, J., Lindsey, C., and Richards, M., 2024, Geophysical Modeling of a Possible Blind Geothermal System Near Battle Mountain, NV: Geothermal Resources Council Transactions, v. 48, 21 p.

Esri, ArcGIS Map Service, 2024, accessed from: https://services.arcgisonline.com/ArcGIS/rest/services/Reference/World_Reference_Overlay/MapServer, (accessed, 8/2024).

Faulds, J.E., and Henry, C.D., 2008, Tectonic influences on the spatial and temporal evolution of the Walker Lane: An incipient transform fault along the evolving Pacific – North American plate boundary, *in* Spencer, J.E., and Titley, S.R., eds., Circum-Pacific Tectonics, Geologic Evolution, and Ore Deposits: Tucson, Arizona Geological Society, Digest 22, p. 437-470.

Faulds, J.E., and Hinz, N.H., 2015, Favorable tectonic and structural settings of geothermal settings in the Great Basin Region, western USA: Proxies for discovering blind geothermal systems: Proceedings, World Geothermal Congress 2015, Melbourne, Australia, 6 p.

Faulds, J.E., Hinz, N.H., Coolbaugh, M.F., Shevenell, L.A., Siler, D.L., dePolo, C.M., Hammond, W.C., Kreemer, C., Oppliger, G., Wannamaker, P., Queen, J.H., and Visser, C., 2015a, Integrated geologic and geophysical approach for establishing geothermal play fairways and discovering blind geothermal systems in the Great Basin region, western USA: Final Technical Report, Department of Energy (DE-EE0006731), 106 p. https://gdr.openei.org/files/756/Faulds-DE-EE0006731-Report-v2.pdf.

Faulds, J.E., Hinz, N.H., Coolbaugh, M.F., Shevenell, L.A., Siler, D.L., dePolo, C.M., Hammond, W.C., Kreemer, C., Oppliger, G., Wannamaker, P.E., Queen, J.H., and Visser, C.F., 2015b, Integrated geologic and geophysical approach for establishing geothermal play fairways and discovering blind geothermal systems in the Great Basin region, western USA: A progress report: Geothermal Resources Council Transactions, v. 39, p. 691-700.

Faulds, J.E., Craig, J.W., Coolbaugh, M.F., Hinz, N.H., Glen, J.M., DeOreo, S., 2018, Searching for blind geothermal systems utilizing play fairway analysis, western Nevada: Geothermal Resources Council Bulletin, v. 47, p. 34-42.

Faulds, J.E., Hinz, N.H., Coolbaugh, M.F., Ramelli, A., Glen, J.M, Ayling, B.A., Wannamaker, P.E., DeOreo, S.B., Siler, D.L., and Craig, J.W., 2019, Vectoring into potential blind geothermal systems in the Granite Springs Valley area, western Nevada: Application of the play fairway analysis at multiple scales: Proceedings 44th Workshop on Geothermal Reservoir Engineering, Stanford University, Stanford, California, SGPTR-214, p. 74-84.

Faulds, J.E., Brown, S. Coolbaugh, M., DeAngelo, J., Queen, J.H., Treitel, S., Fehler, M., Mlawsky, E., Glen, J.M., Lindsey, C., Burns, E., Smith, C.M., Gu, C., and Ayling, B.F., 2020, preliminary report on applications of machine learning techniques to the Nevada geothermal play fairway analysis: proceedings, 45th Workshop on Geothermal Reservoir Engineering, Stanford University, SGP-TR-216, 6 p.

Faulds, J.E., Coolbaugh, M.F., and Hinz, N.H., 2021a, Inventory of structural settings for active geothermal systems and late Miocene (~8 ma) to Quaternary epithermal mineral deposits in

the Basin and Range province of Nevada: Nevada Bureau of Mines and Geology Report 58, 28 p.

Faulds, J.E., Hinz, N.H., Coolbaugh, M., Ayling, B., Glen, J., Craig, J.W., McConville, E., Siler, D., Queen, J., Witter, J. and Hardwick, C., 2021b, Discovering blind geothermal systems in the Great Basin region: An integrated geologic and geophysical approach for establishing geothermal play fairways: All phases: Department of Energy, Geothermal Technologies Office, Final Technical Report on Award DE-EE0006731, 74 p.

Faulds, J.E., Hinz, N.H., Coolbaugh, M.F., Craig, J.W., Glen, J.M., Ayling, B.F., Sadowski, A.J., Siler, D.L, and DeOreo, S., 2021c, The Nevada geothermal play fairway project: Exploring for blind geothermal systems through integrated geological, geochemical, and geophysical analyses: Proceedings World Geothermal Congress 2021, Reykjavik, Iceland, 12 p.

Faulds, J. and Richards, M., 2023, INGENIOUS Transitions from regional to local scale to find hidden geothermal systems: Geothermal Resources Council Transactions, v. 47, 17 p.

Forson, C., Czajkowski, J. L., Norman, D. K., Swyer, M. W., Cladouhos, T.T. and Davatzes N., 2016, Summary of phase 1 and plans for phase 2 of the Washington state geothermal play-fairway analysis: Geothermal Resources Council Transactions, v. 40, p. 541-550.

Gilluly, J., Gates, O., Plouff, D., and Ketner, K. B., 1965, Tectonic and igneous geology of the northern Shoshone Range, Nevada: U.S. Geological Survey Professional Paper 465, https://doi.org/10.3133/pp465.

Hammond, W.C., and Thatcher, W., 2004, Contemporary tectonic deformation of the Basin and Range province, western United States: 10 years of observation with the Global Positioning System: Journal of Geophysical Research, v. 109, B08403, doi:10.1029/2003JB002746

Hart-Wagoner, N.R., Coolbaugh, M., Faulds, J.E., and Mlawsky, E., 2023, Feature engineering of fault attributes for play fairway analysis, Great Basin region, USA: Geothermal Resources Council Transactions, v. 47, 23 p.

Hart-Wagoner, N., Coolbaugh, M., Faulds, J.E., Mlawsky, E., Lindsey, C., & Trainor-Guitton, W. (2024). Preliminary Regional Play Fairway Workflow for the Great Basin Region, USA. In: Proceedings of the 49th Workshop on Geothermal Reservoir Engineering, Stanford University, Stanford, California, February 12-14, 2024. SGP-TR-227.

House, P.K., Ramelli, A.R., Wrucke, C.T., and John, D.A., 2000, Geologic map of the Argenta quadrangle, Lander County, Nevada: Nevada Bureau of Mines and Geology Open-File Report 2000-07.

John, D. A., and Wrucke, C. T., 2003, Geologic map of the Mule Canyon quadrangle, Lander County, Nevada: Nevada Bureau of Mines and Geology Map 144.

John, D.A., Henry, C.D., and Colgan, J.P., 2008, Magmatic and tectonic evolution of the Caetano caldera, north-central Nevada: A tilted, mid-Tertiary eruptive center and source of the Caetano Tuff: Geosphere, v. 4, p. 75–106.

Kraal, K.O, Ayling, B.F., Hart-Wagoner, N., and Faulds, J.E., 2023, Resource conceptual model and power capacity estimates for the northern Granite Springs Valley blind geothermal prospect, Pershing County, Nevada: Geothermal Rising Conference Proceedings, 1 p.

McConville, E.G., Faulds, J.E., Hinz, N.H, Ramelli, A.R., Coolbaugh M.F., Shevenell L., Siler, D.L., Bourdeau-Hernikl, J., 2017, A play fairway approach to geothermal exploration in Crescent Valley, Nevada: Geothermal Resources Transactions, v. 41, p. 1213-1221.

Micklethwaite, S., and Cox, S.F., 2004, Fault-segment rupture, aftershock-zone fluid flow, and mineralization: Geology, v. 32, p. 813–816, doi:10.1130/G20559.1.

Muntean, J.L., Davis, D.A., and Ayling, B., 2021, The Nevada mineral industry, 2020, Nevada Bureau of Mines and Geology Special Publication, MI-2020, 105 p.

Nordquist, J., and Delwiche, B., 2013, The McGinness Hills geothermal project: Geothermal Resources Council Transactions, v. 37, p. 58–64.

Ramelli, A.R., House, P.K., Wrucke, C.T., John, D.A., 2001, Geologic map of the Stony Point quadrangle, Lander County, Nevada: Nevada Bureau of Mines and Geology Map 131.

Ramelli, A.R., Wrucke, C.T., House, P.K., 2017, Geologic map of the Bateman Spring quadrangle, Lander County, Nevada: Nevada Bureau of Mines and Geology Map 185.

Richards, M., and Blackwell, D., 2002, A difficult search: Why Basin and Range systems are hard to find: Geothermal Resources Council Bulletin, v. 31, p. 143-146.

Rowan, L.C., and Wetlaufer, P.H., 1981, Relation between regional lineament systems and structural zones in Nevada: American Association of Petroleum Geologists Bulletin, v. 65, p. 1414-1452.

Shervais, J.S., Glen, J.M., Nielson, D., Garg, S., Dobson, P., Gasperikova, E., Sonnenthal, E., Visser, C., Liberty, L.M., DeAngelo, J., Siler, D., Varriale, J., and Evans, J.P., 2016, Geothermal play fairway analysis of the Snake River Plain: Phase 1, Proceedings, 41st Workshop on Geothermal Reservoir Engineering, Stanford University, SGP-TR-209, 7 p.

Siler, D.L., Zhang, Y., Spycher, N.F., Dobson, P.F., McClain, J.S., and Gasperikova, E., 2017, Play-fairway analysis for geothermal resources and exploration risk in the Modoc Plateau region: Geothermics, v. 69, p. 15–33.

Siler, D.L., Hinz, N.H., and Faulds, J.E., 2018, Stress concentrations at structural discontinuities in active fault zones in the western United States: Implications for permeability and fluid flow in geothermal fields: Geological Society of America Bulletin, v. 130, no. 7-8, p. 1273-1288; https://doi.org/10.1130/B31729.1.

Siler, D.L., Faulds, J.E., Hinz, N.H., Dering, G.M., Edwards, J.H., and Mayhew, B., 2019, Three-dimensional geologic mapping to assess geothermal potential: Examples from Nevada and Oregon: Geothermal Energy, v.7, no. 2, 32 p., https://doi.org/10.1186/s40517-018-0117-0.

Siler, D., 2023a, Structural discontinuities and their control on hydrothermal systems in the Great Basin, USA: Geothermal Resources Council Transactions, v. 47, 12 p.

Siler, D.L., 2023b, Structural discontinuities and their control on hydrothermal systems in the Great Basin, USA: Geoenergy, v.1, no. 1, https://doi.org/10.1144/geoenergy2023-009.

Smith, C.M., Faulds, J.E., Brown, S., Coolbaugh, M., DeAngelo, J., Glen, J.M., Burns, E., Siler, D.L., Treitel, S., Mlawsky, E., Fehler, M., Gu, C., and Ayling, B.F., 2023, Exploratory analysis of machine learning techniques in the Nevada geothermal play fairway analysis: Geothermics, v. 111, https://doi.org/10.1016/j.geothermics.2023.102693.

Struhsacker, E.M., 1980, The geology of the Beowawe geothermal system, Eureka and Lander counties, Nevada: University of Utah Research Institute, Earth Science Laboratory report, no. 37, p. 78.

Sturmer, D.M., and Faulds, J.E., 2018, Kinematic evolution of the Olinghouse fault and the role of a major sinistral fault in the Walker Lane dextral shear zone, Nevada, USA: Journal of Structural Geology, v. 115, p. 47-63.

U.S. Department of Energy (DOE), 2019, GeoVision: Harnessing the heat beneath our feet: U.S. Department of Energy, DOE/EE-1306, www.energy.gov/eere/geothermal/geovision.

U.S. Geological Survey, 2024, 3D Elevation Program 10-meter resolution digital elevation model, accessed from URL https://www.usgs.gov/the-national-map-data-delivery, (accessed, 8/2024).

Wallace, A.R., and John, D.A., 1998, New studies of Tertiary volcanic rocks and mineral deposits, northern Nevada rift (Chapter 22): U.S. Geological Survey Open-File Report 338, p. 264-278.

Wannamaker. P.E., Moore, J.N., Pankow, K.L., Simmons, S.F., Nash, G.D., Maris, V., Trow, A., and Hardwick, C.L., 2017, Phase II of play fairway analysis for the eastern Great Basin extensional regime, Utah: status of indications: Geothermal Resources Council Transactions, v. 41, p. 2368-2382.

Watt, J. T., Glen, J. M., John, D. A., and Ponce, D. A., 2007, Three-dimensional geologic model of the northern Nevada rift and the Beowawe geothermal system, north-central Nevada: Geosphere, v. 3, p. 667-682.

Wesnousky, S.G., Barron, A.D., Briggs, R.W., Caskey, S.J., Kumar, S., and Owen, L., 2005, Paleoseismic transect across the northern Great Basin: Journal of Geophysical Research, v. 110, p. 1–25, doi: 10.1029/2004JB003283.

Williams, C.F., Reed, M.J., DeAngelo, J., and Galanis, S.P. Jr., 2009, Quantifying the undiscovered geothermal resources of the United States: Geothermal Resources Council Transactions, v. 33, p. 995-1002.

Zoback, M.L., 1979, A geologic and geophysical investigation of the Beowawe geothermal area, north-central Nevada: Stanford University Publications in the Geological Sciences, v. 16, p. 79.

Zoback, M. L., 1989, State of stress and modern deformation of the northern Basin and Range province: Journal of Geophysical Research: Solid Earth, v. 94, p. 7105-7128.

Zoback, M. L., McKee, E. H., Blakely, R. J., and Thompson, G. A., 1994, The northern Nevada rift: Regional tectono-magmatic relations and middle Miocene stress direction: Geological Society of America Bulletin, v. 106, p. 371-382.

Geothermal Resource and Opportunities Assessment of Colorado

Emilie Gentry, Joe Batir

Teverra

Keywords

Colorado geothermal, resource assessment

ABSTRACT

Colorado has a long history of mining and hydrocarbon production as well as recent developments of wind and solar energy. Additionally, hot springs and thermal wells exist across the state, suggesting potential for geothermal resources. Previously, limited studies aimed to characterize these individual geothermal sites, with plans for local development. The statewide geothermal resource has been generally known and mapped in the state in past years, but there is significantly more data now available, which means resource understanding can be improved through a new resource assessment. Additionally, no recent public studies have examined the best pathway for economic development of these resources in Colorado that could substantially assist the energy needs of the state.

As part of a larger geothermal resource study for the state of Colorado, an initiative by the Colorado Energy and Carbon Management Commission (ECMC), Teverra completed a thermal resource evaluation with new data and produced new geothermal resource maps. In addition to evaluating the geothermal resource in Colorado, the study also examined utilization opportunities given the determined resource potential.

The geothermal resource across the state was examined for electricity production, direct use, and geothermal heat pump applications. There are several prominent sedimentary basins with significant development that may be an opportunity for well repurposing, which is also examined. There is resource with temperatures 100-175 °C throughout the state at depths that are currently drilled. In these areas, power generation could be a possibility, and technologies to utilize lower temperature resources are likely to have the greatest economic impact and benefit for the majority of the state.

This study demonstrates a new approach to understanding the geothermal resource for the state, and compares this work to what work had been previously completed on geothermal potential in Colorado.

1. Introduction

Colorado has a rich history of geothermal resource utilization dating back to pre-Columbian times, primarily through the exploitation of thermal springs (CNAIS, 2020). However, the oil crisis of the early 1970s sparked a renewed interest in exploring and harnessing geothermal energy in the state. This period saw a surge in geothermal exploration efforts, culminating in numerous localized basin and thermal spring studies and a few comprehensive statewide assessments (Dick, 1976; Dick and Pearl, 1978; Galloway, 1980; Gwinn, 1981; Ringose, 1980, Zacharakis, 1981).

The Colorado Geological Survey (CGS) played a pivotal role in documenting and evaluating Colorado's geothermal potential. Prior to 2000, CGS published over 40 reports detailing various aspects of geothermal resources. These reports encompassed assessments of thermal springs, wells, geothermal gradients, and heat flow across the state. The most recent comprehensive study, led by Paul Morgan in 2016, provided detailed insights into Colorado's geothermal potential.

In recent years, Colorado has set goals to reduce statewide greenhouse gas emissions, underscoring the need for innovative energy solutions. Geothermal technology has emerged as a promising option, leveraging the Earth's heat for electricity generation, heating, cooling, and other energy applications. This has spurred significant interest and investment from both public and private sectors at state and federal levels.

Recognizing the potential of geothermal energy, recent legislative measures have given the Colorado Energy Conservation Management Commission (ECMC) the role of overseeing geothermal development among other technologies aligned with its expertise in oil and gas. To aid in this transition, legislation also mandated ECMC to complete a study to assess Colorado's geothermal resources comprehensively, identifying optimal technologies and opportunities for integrating existing infrastructure into the state's evolving energy landscape.

This paper examines the findings of this study, offering insights into the suitability of various geothermal technologies within Colorado's geological framework. It highlights emerging opportunities and strategies aimed at advancing geothermal energy as a cornerstone of the state's sustainable energy future. This new study represents a significant advancement in our understanding of Colorado's geothermal resources. Leveraging enhanced data collection and technological capabilities, the maps and assessments in this report offer a comprehensive update on the state's geothermal potential. Improved geological modeling and additional data have enabled a finer resolution analysis of geothermal gradients, heat flow, and resource potentials across different geological formations and regions of Colorado.

By comparing and contrasting past assessments with current data sets, this report identifies changes and trends in resource availability, offering valuable insights for future development and policy formulation. This iterative approach ensures that stakeholders and decision-makers have access to the most up-to-date information when evaluating the feasibility and economic viability of geothermal projects throughout the state.

2. Updated Thermal Resource Characterization

To complete a thermal resource characterization for the state of Colorado, well and thermal springs data was used to explore geothermal resource potential, model the geothermal gradient, and

calculate new thermal properties. The results of this work include a new understanding of the greater thermal regime and geothermal resource potential.

Subsurface temperature data were collected from well information. Bottomhole temperature (BHT) data for oil and gas wells in all the producing sedimentary basins in the state of Colorado were provided by CGS (Figure 1). This included only public well data. BHT data require a correction to estimate true formation temperature, as the raw data are impacted by circulating drilling fluids and are commonly cooler than the true formation temperature. Well data are limited to areas where wells exist, which is in sedimentary basins where the wells were drilled for oil and gas development. Maps created from the thermal calculations should be viewed with the knowledge that there are areas that are interpolated where well data do not exist.

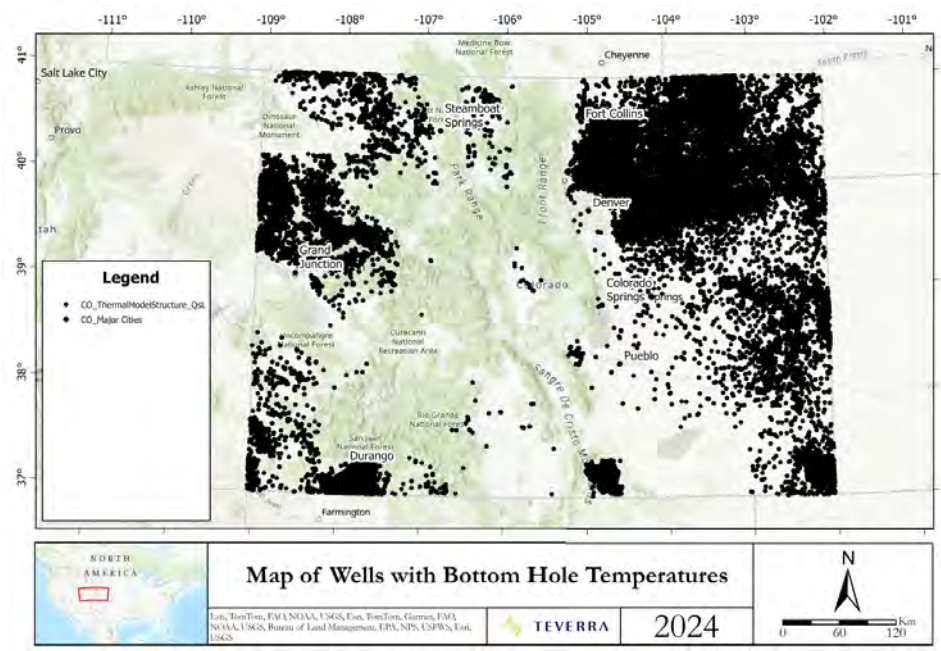

Figure 1: Map of oil and gas wells that contain BHT data provided by the Colorado Geological Survey.

To complete the thermal resource characterization, geothermal gradient, thermal conductivity models, heat flow and temperature at depth were calculated.

The geothermal gradients for all CGS-provided data points were computed and are depicted in Figure 2 in °C/km. The well data trends on the map indicate gradients ranging from 25°C-32°C/km (1.37°F-1.76°F/100 ft). This range exceeds the average continental geothermal gradient for the US, which is 25°C/km (1.37°F/100 ft), highlighting areas with a stronger thermal signature. These findings align well with previous CGS research, confirming higher gradients in specific regions. The updated geothermal gradient resource map offers enhanced data resolution across various areas. Resulting geothermal gradient values were utilized for heat flow and temperature at depth calculations.

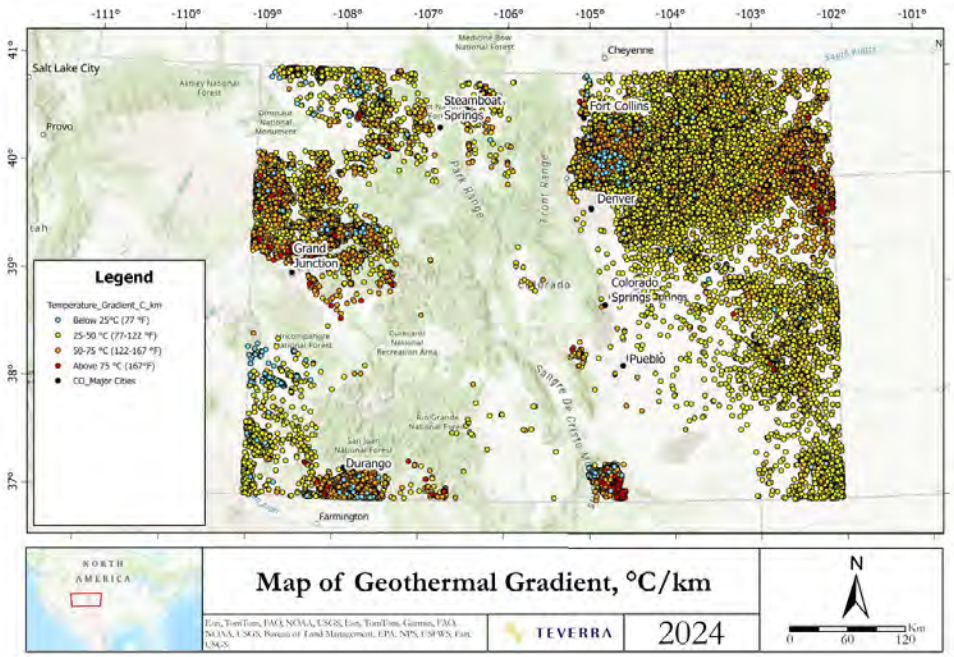

Figure 2: Map of geothermal gradient calculated for wells in Colorado.

In this study, the Bullard method (Bullard, 1940) was used to calculate heat flow, which requires a comprehensive stratigraphic column for the thermal conductivity model. The Bullard method utilizes thermal resistance (the reciprocal of thermal conductivity) to compute cumulative thermal resistance from the surface to the depth of temperature measurement. By plotting temperature against thermal resistance, the slope of the resultant line corresponds to the heat flow.

For our thermal conductivity model, formation lists and thicknesses were derived from supplied stratigraphic columns by CGS and the Correlation of Stratigraphic Units of North America (COSUNA) (AAPG, 1994). The COSUNA segments divide the state into approximately 13 sections based on distinct stratigraphy, each providing estimated thicknesses for their respective layers. These COSUNA segments were cross-referenced with CGS stratigraphic columns to ensure completeness and accuracy in thermal conductivity assignments. Estimated thermal conductivities were assigned based on lithology and formation using data from Gallardo and Blackwell (Gallardo, 1999) and Reiter et al. (1983, 1979, 2010). In cases where specific values were unavailable, generic values for the respective rock types were utilized.

All new heat flow values in this comprehensive study were derived from the Bottom Hole Temperature (BHT) data supplied by CGS. Additionally, equilibrium heat flow data collected statewide by CGS were incorporated into the analysis (Figure 3). The resulting heat flow map of Colorado (Figure 4) integrates the newly computed BHT-derived heat flow values along with approximately 140 measured equilibrium heat flow points provided by CGS. The 140 equilibrium heat flow points complement the BHT derived heat flow wells in that they have a greater spatial coverage in the regions lacking BHT coverage.

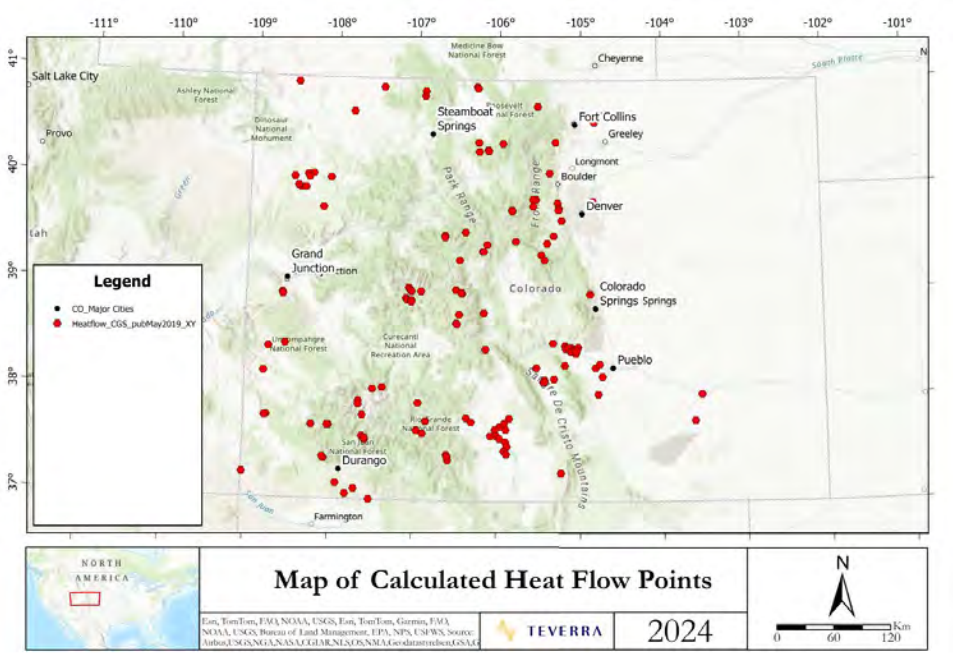

Figure 3: Map of heat flow point provided by CGS.

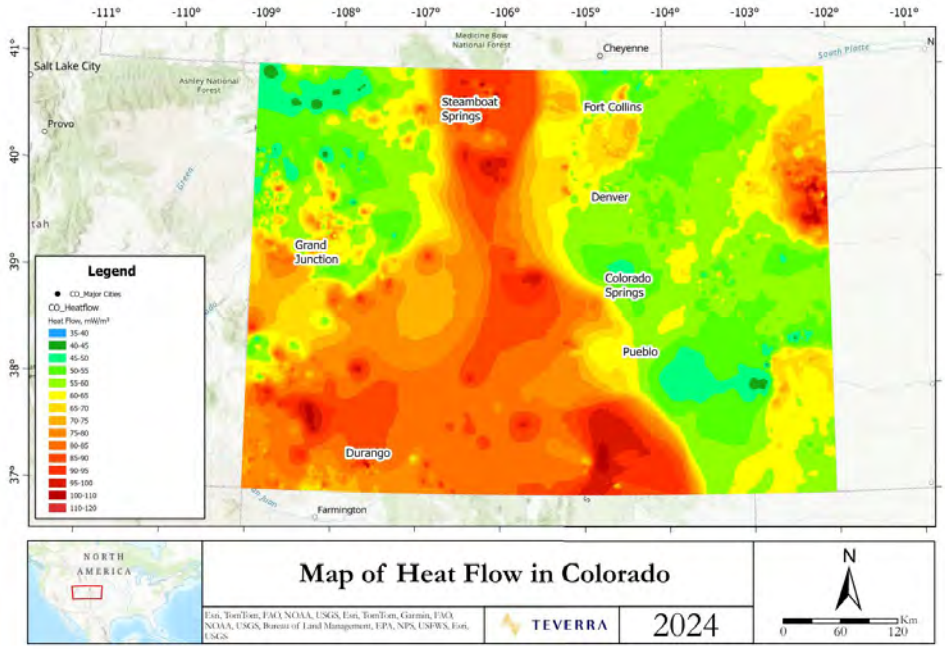

Figure 4: Map of estimated heat flow for the state of Colorado.

Across the state, heat flow varies, with some areas registering values at or below 50 mW/m² and others exceeding 80 mW/m². The global continental average heat flow stands at approximately 67 mW/m² (Lucazeau, 2019), highlighting certain areas in Colorado with above-average heat flow characteristics. Notably, southwestern Colorado, the Piceance Basin, and the central region exhibit the highest heat flows, ranging between 60 and 120 mW/m², albeit with considerable variability.

The statewide heat flow pattern shows a prominent central area of high heat flow, consistent with previous public maps (Blackwell et al., 2011). The inclusion of additional well data in this study enhances resolution and understanding, particularly in sedimentary basins across Colorado. Lower heat flow is observed in the High Plains region, with a poorly constrained low in the northwest corner of the state. Despite limited data, indications suggest a prevalence of high heat flow in the central region. The interpolation of high heat flow values is supported by the presence of numerous hot springs in this area, although the scarcity of data points challenges the accuracy of this interpolation. The abundance of hot springs in the central region suggests significant geothermal energy potential, although further assessment is needed to quantify these opportunities effectively.

Using the calculated heat flow, temperature versus depth was modeled and maps made of temperature at defined depths. These maps are provided to identify geothermal anomalies. Here, we utilized the Batir and Richards (2020) methodology to calculate the subsurface thermal regime. Note that this model assumes a crustal component with exponential decay of radiogenic heat production. This assumption, while used extensively for temperature—depth modeling in continental settings, may be an oversimplification of temperature distribution and heat flow throughout the crust, especially for areas with more recent tectonic activity and areas with variable crustal Petrology.

The most frequently drilled well depth in Colorado is less than 2.5 km (8,202 ft) (Figure 5). In this analysis, we present interpolated temperatures at the depth of 2.5 km (8,202 ft), incorporating temperature data points with maximum depths up to 2.5 km (8202 ft). Across the majority of the state at this depth, temperatures are generally below 100°C (212°F).

Areas extending from the San Juan Basin to the Raton Basin, and northward to the Piceance Basin, exhibit slightly higher temperatures ranging from approximately 100°C to 124°C (212°F to 255°F), with localized spots exceeding 150°C (302°F). Specifically, the Raton Basin shows temperatures between 100°C and 125°C (212°F to 255°F) at 2.5 km (8,202 ft) depth. Within the Denver Basin, the Wattenberg field demonstrates elevated temperatures ranging from 100°C to 110°C (212°F to 230°F) at depth. As previously noted, there is a localized area of elevated temperatures along the eastern border of the state. At a depth of 2.5 km (8202 ft), temperatures in this region are mapped up to 150°C (302°F).

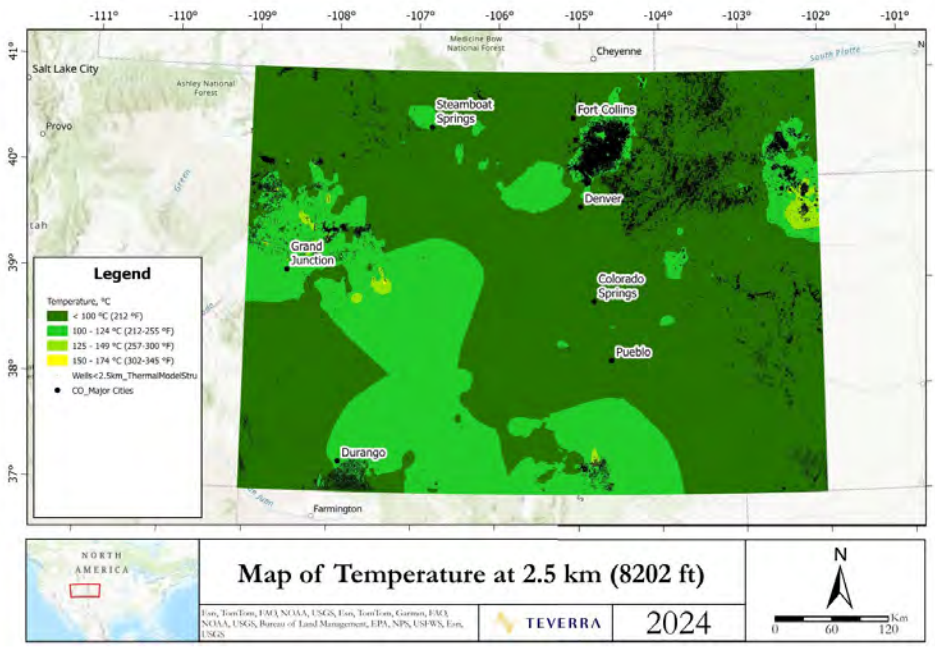

Figure 5: Map of calculated temperature at 2.5 km (8200 ft), used to represent the potential temperature at a common drilling depth for Colorado. The black dots are wells with temperature data that have a total depth of 2.5 km and shallower.

The temperature at 5 km (16,404 ft) represents the practical drilling limit for geothermal exploration in Colorado (Figure 6). While there are a few wells deeper than 5 km (16,404 ft) and plans for additional deep drilling, such wells are uncommon at present. Therefore, 5 km (16,404 ft) is currently considered the maximum feasible depth for geothermal exploration in the state.

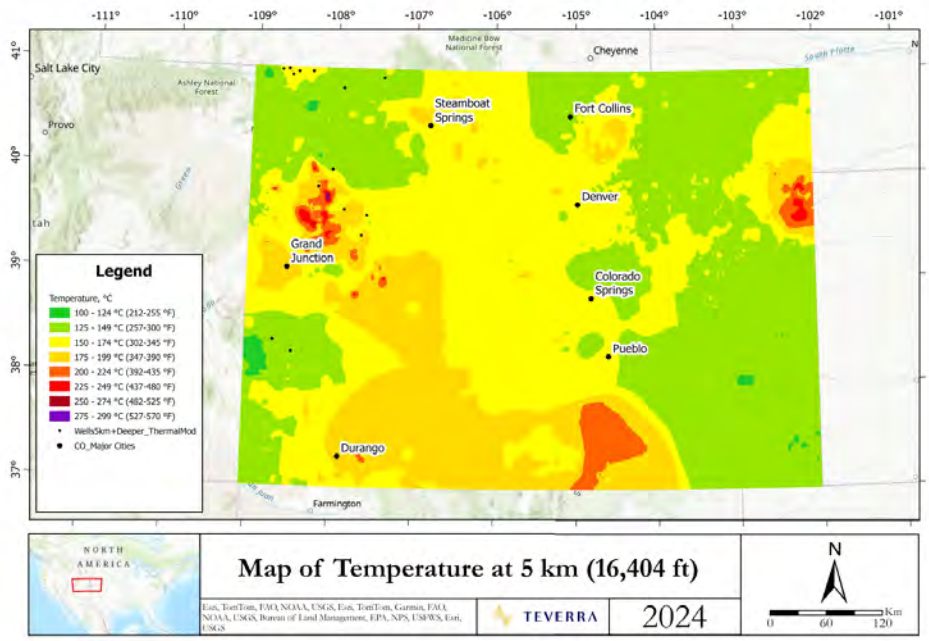

Figure 6: Map of calculated temperatures at 5 km (16,404 ft) depth, the estimated current technical limit for drilling.

Across most of the state, temperatures at 5 km (16,404 ft) are notably higher. The Piceance Basin, for instance, exhibits a thermal low in its northern area but generally maintains a high thermal regime with temperatures ranging from 180°C to 200°C (356°F to 392°F), and localized anomalies reaching 250°C to 300°C (482°F to 572°F). Due to abundant well data in this region, these elevated thermal readings are considered more reliable. In southwestern Colorado, temperatures typically range from 150°C to 200°C (302°F to 392°F), with the Paradox Basin along the western border displaying lower temperatures in the 100°C to 150°C (212°F to 302°F) range at depth. The central part of the state generally records temperatures at 5 km (16,404 ft) ranging from 150°C to 175°C (302°F to 347°F), except for the Raton Basin where temperatures slightly exceed 212°C (414°F). Eastern Colorado predominantly registers temperatures between 125°C and 150°C (257°F and 302°F) at this depth. The Wattenberg Field, situated in this area, reaches temperatures of 175°C to 182°C (347°F to 360°F). An extrapolated thermal high along the eastern border suggests temperatures up to 230°C (446°F), but this is based on shallow data and introduces greater uncertainty with depth.

Overall, drilling to 5 km (16,404 ft) offers greater potential for geothermal power production and higher temperature applications compared to depths of 2.5 km (8,202 ft). However, such deep drilling operations incur higher costs, aligning with current standard drilling depths for the region.

Lastly, temperature data at 7 km (22,966 ft) is presented to emphasize the potential for future deep drilling endeavors (Figure 7). Thermal trends observed at this depth parallel those at 5 km, albeit with markedly higher temperatures. The coolest temperatures, ranging from 150°C to 200°C (302°F to 392°F), are found in the Sand Wash Basin, Paradox Basin, and much of eastern Colorado.

Significantly elevated thermal regimes at 7 km (22,966 ft) are concentrated in the Piceance Basin, San Juan Basin, Raton Basin, the Wattenberg Field in the Denver Basin, eastern Denver Basin, and central Colorado, where temperatures range from 200°C to 300°C (392°F to 572°F). This depth holds substantial potential for electricity generation, but the advancement of deep drilling technologies is crucial for these resources to become economically viable for production. It is also important to note, few wells exist at these depths for ground truthing of the temperature-depth model. There is high potential, but also potential for high uncertainty.

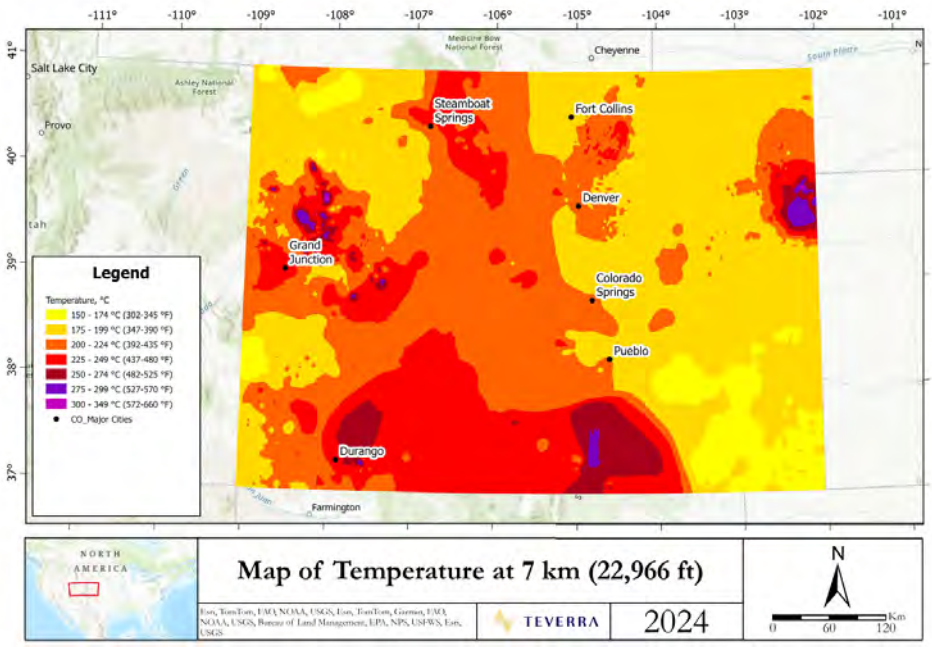

Figure 7: Map of temperatures at 7 km (22,966 ft) depth, presented as potential future deep drilling potential.

Overall, the temperature necessary for the desired utilization, whether direct use applications or geothermal power generation, can be reached. This becomes more of a parameter of how deep to drill to reach the desired resource. These maps are created from well data and are an interpolation from the well specific data. Therefore, these maps should not be considered adequate for site-specific exploration. Rather, these maps indicate where existing data can be used to suggest potential for thermal anomalies that may warrant exploration. Additionally, uncertainty analysis of the associated data points show where there are not enough data to make a discrete analysis, indicating where maps should be used with caution.

3. Discussion on Previous and Present Work Completed

For comparison of previous work to the new updated resource assessment in this study, regional state-wide maps and assessments will be discussed. While there are several focused studies completed on Colorado's sedimentary basins and localized thermal springs, these are much more detailed than what was assessed in this resource study.

An Interpretive Geothermal Gradient map (Figure 5) for the state was published in 2010 (Berkman and Watterson, 2010). In 2008, an Interpretive Geothermal Heat Flow map (Figure 6) was developed using the Southern Methodist University, University of North Dakota, and University

of Michigan databases and an additional 40 data points CGS calculated from borehole temperature-depth logs (Berkman and Carroll, 2008). In 2016, Paul Morgan presented at AAPG an updated Colorado Geothermal Map (Figure 7), which maps geothermal gradient by geologic formation and is refined through hand contouring (Morgan, 2016). Heat flow data points are mapped with the geothermal gradient. Mapping was focused where data was sufficiently spatially dense to avoid interpolation. Additionally, the isotherms of 50°C and 75°C were hand contoured where BHTs came close to the isotherm shown.

In this study, Teverra created a thermal conductivity model that was defined by geologic formations and formation thicknesses of thirteen areas throughout the state. The thermal conductivity values assigned were specific to the geologic formation assigned in that area and where no measurement was available, a general thermal conductivity value was used. The thermal conductivity model specific to lithology and local lithology thickness was then used to calculate the heat flow and temperature-at-depth. In other words, the heat flow and temperature at depth results were calculated for the appropriate geologic formation at depth. Furthermore, this method incorporated depth to basement as an estimation of sedimentary thickness and scaled all calculations to agree with total sediment package thickness.

The Interpretive Geothermal Gradient map of Colorado (Figure 8) has more interpolation and interpretation than the geothermal gradient map developed in this study (Berkman and Watterson, 2010). While this study mapped geothermal gradient as well data points, Berkman and Watterson (2010) extrapolated the data to cover the entire state in an interpretive map. Despite the mapping style differences, the overall data and mapped trends agree between the two maps. High and low geothermal gradients are agreeable between the 2010 and 2024 assessment maps.

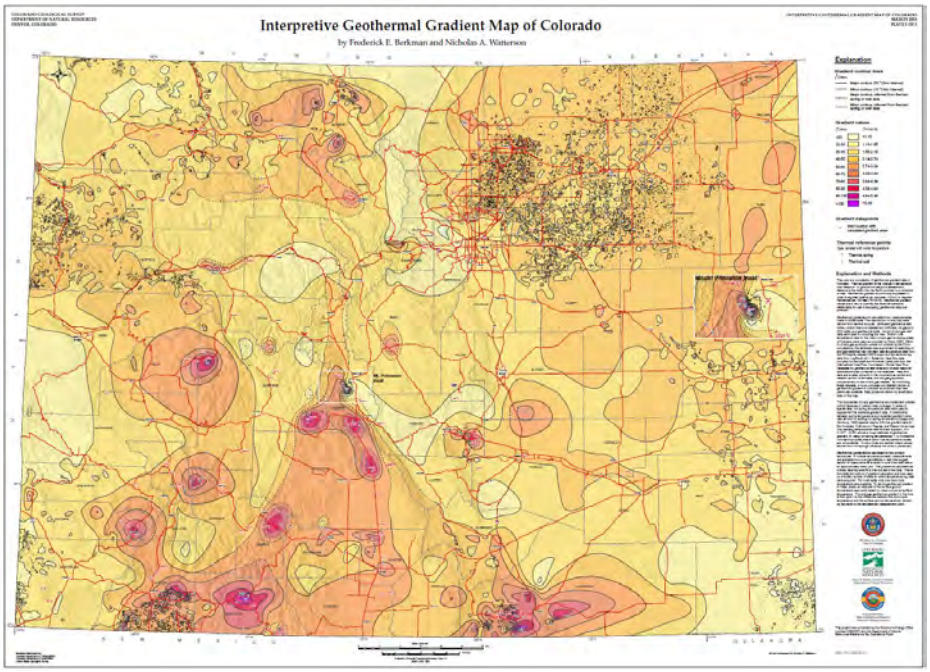

Figure 8: Interpretive Geothermal Gradient map published by CGS (Berkman and Watterson, 2010).

The Interpretive Geothermal Heat Flow map (Figure 9) published in 2008 shows heat flow trends that are mimicked by the heat flow assessment completed in this study. These two maps are in

agreement that there are three main heat flow provinces. The Great Plains province which has normal heat flow in majority eastern Colorado with an exceptional high for the Raton Basin. The Southern Rocky Mountains have an elevated heat flow in several localized areas, and the San Luis Valley where Mt. Princeton exists is the highest mapped heat flow. Slight differences occur in the heat flow values. The 2008 assessment contains some higher heat flow values and more detail on Mt. Princeton that was not available in the 2024 study. The location of the high heat flow areas align, but the exact values may slightly differ. The 2008 assessment has values over 200 mW/m^2 whereas the 2024 assessment specifically set a high value limit at 120 mW/m^2. The cause for this difference is likely due to differences in data and gridding procedures versus hand gridding.

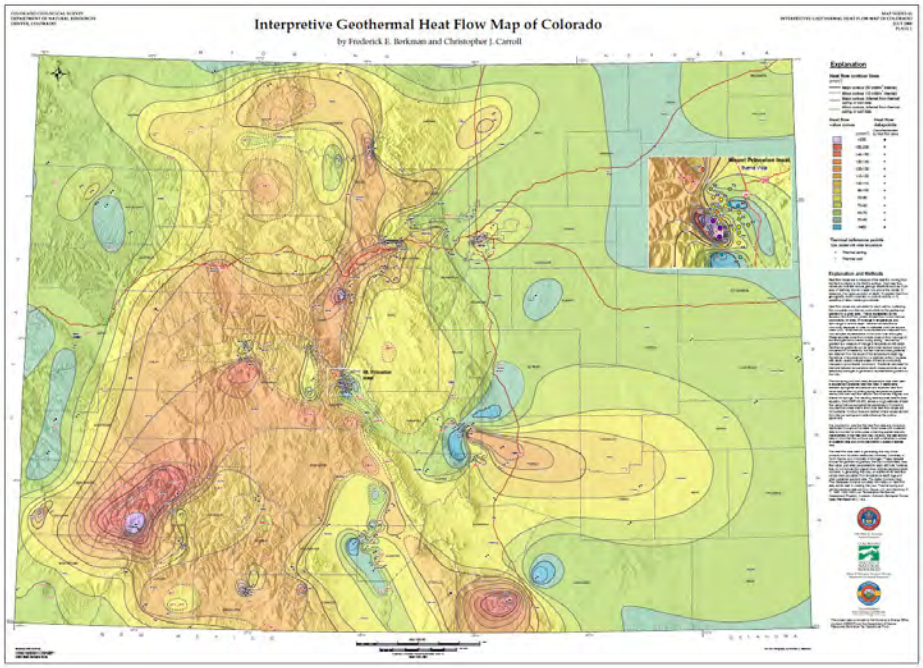

Figure 9: Interpretive Geothermal Heat Flow map published by CGS (Berkman and Carroll, 2008).

A visual comparison of the Colorado Geothermal Map (Figure 10) and the geothermal model in this study and resulting maps may show minor differences (Morgan, 2016). These differences are derived from the level of detail mapped and the slight differences in calculation methodology. The Colorado Geothermal Map provides more detail for each sedimentary basin as a formation evaluation only where adequate data points exist. The maps in this report are a large-scale exploration assessment and include interpolation at depth where the spatial database is limited. In these areas of interpolation, evaluation must be considered with the data density assessments. Visual differences between these maps do not necessarily suggest disagreement, but instead likely represent additional characterization of specific geologic formations in certain areas.

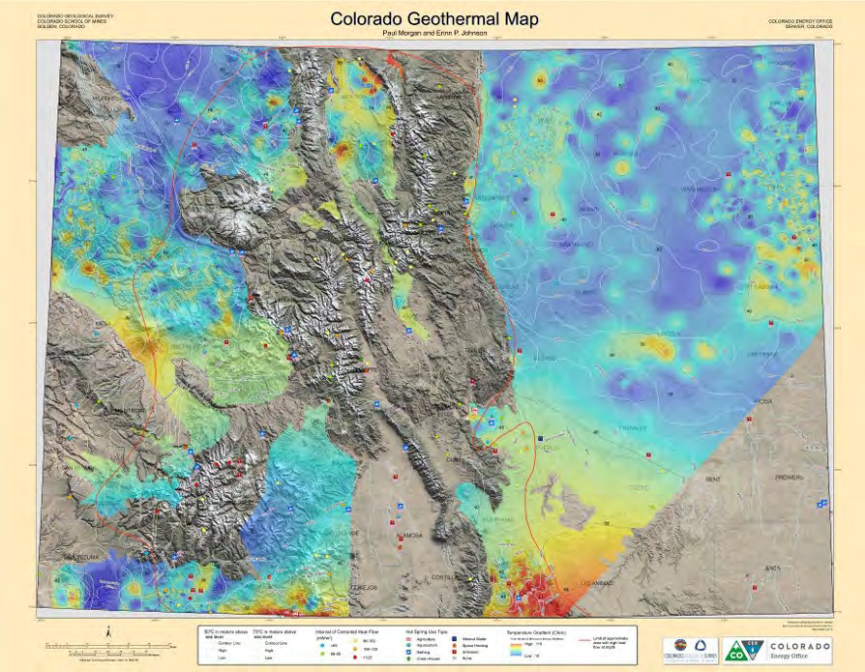

Figure 10: Colorado Geothermal map published by Paul Morgan, 2016.

4. Emerging Geothermal Utilization

Various types of geothermal utilization were examined based on available thermal resources to establish a hierarchy of opportunities, as depicted in Figure 11. High-temperature utilization technologies are constrained by minimum temperature thresholds, whereas low-temperature technologies can operate in the same areas if they are optimal for end-users. Therefore, locations utilizing high-temperature applications like Enhanced Geothermal Systems (EGS) for power production are suitable also support low-temperature uses such as direct heating.

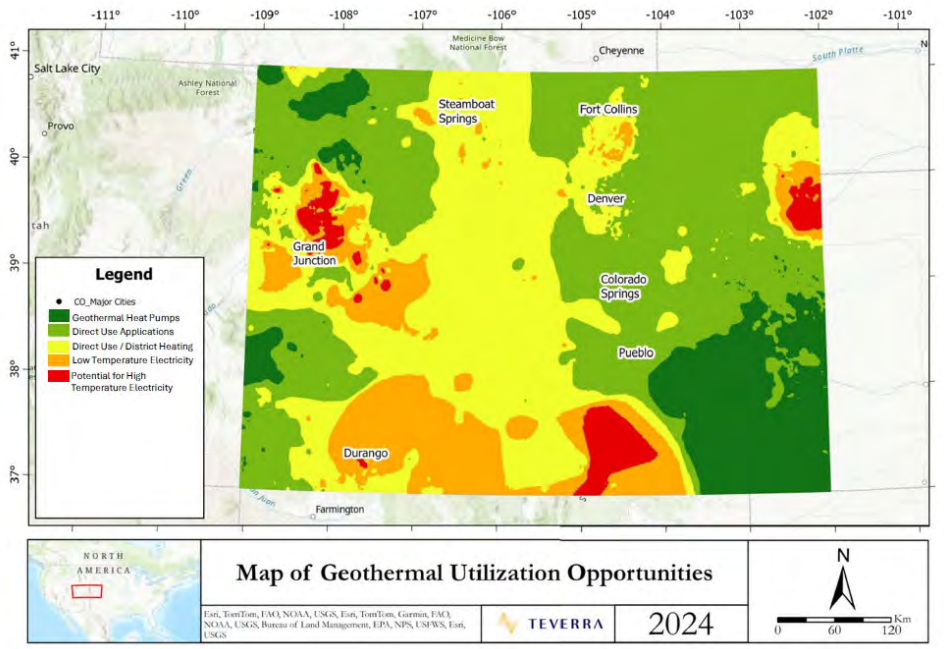

Figure 11: Map that indicates the geothermal utilization opportunities in Colorado. The uses here are cumulative.

In Figure 11, areas shaded dark green are most conducive to geothermal heat pumps due to their very low-temperature thermal resources. Light green and yellow areas are well-suited for direct use applications and thermal energy networks. Orange areas indicate potential for low-temperature electricity generation alongside direct use applications. Regions marked in red show potential for high-temperature power generation, depending on drilling depth, and also support low-temperature power generation, direct use, and thermal energy networks.

Energy storage solutions are particularly applicable in sedimentary basins where geological reservoirs are widespread and accessible. This framework helps prioritize geothermal utilization strategies tailored to the varying thermal characteristics and resource potentials across Colorado.

5. Conclusions

This statewide geothermal resource assessment was completed to comprehensively understand Colorado's geothermal potential, comparing current findings with historical knowledge. The assessment utilized oil and gas well data, equilibrium temperature logs and geothermal exploration data, and thermal spring geothermometry to analyze the thermal regime, revealing localized areas with high-temperature geothermal reservoir potential, though these are not widespread across the state. Instead, much of Colorado's geothermal resource at viable depths falls within the low-temperature range (< 180°C or < 356°F), with isolated pockets of higher temperatures exceeding 180°C (356°F).

Comparing this study to previous work completed by CGS reveals that the updated assessment and corresponding maps are largely consistent with previous research, yet benefit from enhanced data inputs that increase confidence and provide greater detail in certain regions. Although minor discrepancies may arise from differences in data sources or methodologies used for mapping and

assessment, the overall trends remain unchanged. The additional data significantly enriches our understanding and characterization of Colorado's geology and geothermal resources, offering deeper insights into potential energy opportunities across the state.

Given the geothermal resource of Colorado, there are many options for utilization. The geothermal industry typically targets temperatures above 180°C for power production, highlighting potential areas for high-temperature geothermal exploration in Colorado. However, present opportunities lie predominantly in utilizing low-temperature geothermal energy, supported by technologies such as direct use applications, thermal energy networks, and binary power production units. Direct use technologies, particularly suitable near population centers, offer prospects for heating buildings, homes, manufacturing facilities, and greenhouses. Furthermore, the repurposing of existing wells, especially those in the oil and gas sector, presents over 2,000 potential sites for generating geothermal electricity using binary systems.

Overall, the comprehensive study provides deeper insights into Colorado's geology and geothermal resources, offering a foundation for future exploration and utilization strategies in the state.

Acknowledgement

This project was funded by the Colorado Energy and Carbon Management Commission. A special acknowledgement to the project leaders Michael Rigby, John Morgan, and Marie Hoerner.

All data used in this project came from the Colorado Geological Society. Paul Morgan and Nathan Rogers were integral to organizing and providing data for this study.

REFERENCES

AAPG. “CSDE, COSUNA, and Geothermal Survey Data.” *Am. Assoc. of Petroleum Geologists*, (1994).

Batir JF, Richards MC. “Analysis of Geothermal Resources in Three Texas Counties.” Dallas, TX, Southern Methodist University, (2020), p. 60, DE-EE0008971.

Berkman, Frederick E., and Nicholas A. Watterson. “MS-51 Interpretive Geothermal Gradient Map of Colorado.” *Geothermal Map Series.* Denver, CO, Colorado Geological Survey, Department of Natural Resources, (2010), https://coloradogeologicalsurvey.org/publications/interpretive-geothermal-gradient-map-colorado.

Berkman, Frederick E., and Christopher J. Carroll. “MS-45 Interpretive Geothermal Heat Flow Map of Colorado.” *Geothermal Heat Flow Map Series*, Denver, CO, Colorado Geological Survey, Department of Natural Resources, (2008), https://coloradogeologicalsurvey.org/publications/interpretive-geothermal-heat-flow-map-colorado.

Blackwell D, Richards M, Frone Z, Batir J, Ruzo A, Dingwall R, et al. “Temperature-At-Depth Maps For the Conterminous US and Geothermal Resource Estimates.” *GRC Trans*, (2011), 35:1545–50, https://www.osti.gov/biblio/1137036

Bullard E. “Heat flow in South Africa.” *Proc R Soc Lond A*, (1940), 222:428–50.

CNAIS. Center for Native American and Indigenous Studies (CNAIS). “Colorado Places: Their Native American Names.” (2020) [cited 2024 July 30]. Available from: https://www.colorado.edu/cnais/resources/colorado-places-theirnative-american-names

Dick JD. “Geothermal Reservoir Temperatures in Chaffee County, Colorado” [MS Thesis], Northeast Louisiana Univ., (1976).

Dick JD, Pearl RH. “Exploration for nonelectric geothermal resources in Colorado.” *Am Assoc Pet Geol Bull*, (1978), 62(5):882–3.

Gallardo J, Blackwell D. “Thermal structure of the Anadarko Basin.” *AAPG Bull*, (1999), https://archives.datapages.com/data/bulletns/1999/02feb/0333/0333.htm

Galloway MJ. “Hydrogeologic and Geothermal Investigation of Pagosa Springs, Colorado.”. Denver, CO: *Colorado Geological Survey*, (1980), p. 96. (Special Publication). Report No.: SP-10.

Gwinn C. “Miscellaneous Maps and Logging Information for Holes C-TH-1 Through C-TH-12, San Luis and Canon City, Colorado”. *Southern Methodist University*, (1981), p. 5. (Unpublished report).

Lucazeau F. “Analysis and mapping of an updated terrestrial heat flow data set.” *Geochem Geophys Geosystems*, (2019), 20(8):4001–24, https://onlinelibrary.wiley.com/doi/abs/10.1029/2019GC008389

Morgan, P., “Producing Practical and Useful State Geothermal Maps.” In *AAPG Annual Convention and Exhibition*, (2016).

Reiter M, Clarkson G. “Relationships between heat flow, paleotemperatures, coalification and petroleum maturation in the San Juan Basin, northwest New Mexico and southwest Colorado.” *Geothermics*,(1983), 12(4):323–39, https://www.sciencedirect.com/science/article/pii/0375650583900056

Reiter M, J. Mansure A, Shearer C. “Geothermal characteristics of the Colorado Plateau.” *Tectonophysics*, (1979), 61(1):183–95, https://www.sciencedirect.com/science/article/pii/004019517990297X

Reiter M, Chamberlin RM, Love DW. “New data reflect on the thermal antiquity of the Socorro magma body locale, Rio Grande Rift, New Mexico.” *Lithosphere*, (2010), 2(6):447–53, https://doi.org/10.1130/L115.1

Ringose CD. “OF-80-12 Temperature-Depth Profiles in the San Luis Valley and Canon City Areas, Colorado.” *Colorado Geological Survey*, (1980), p. 18. (Open File Report). Report No.: OF-80-12.

Zacharakis TG. “SP-16 Geothermal Resource Assessment of Waunita Hot Springs, Colorado.” *Colorado Geological Survey*, (1981), p. 69. (Special Publication). Report No.: DOE/ET/28365-14.

Characterizing Sedimentary Geothermal Reservoirs: Case Study from the Great Salt Lake Basin

Kellen Gunderson[1] and Christian Hardwick[2]

[1]Projeo Corporation

[2]Utah Geological Survey

Keywords

Sedimentary basins, reservoir characterization, Great Basin, exploration

ABSTRACT

Sedimentary geothermal resources are an emerging resource play in many basins in the United States. While many different exploration plays have been recognized as having sedimentary geothermal potential, detailed studies that refine drilling targets and characterize geothermal reservoirs are lacking. Because sedimentary basins have been the focus of decades of successful and unsuccessful petroleum exploration, many of these basins contain a wealth of legacy data that can be used for geothermal exploration. Here, we present a case study from the Great Salt Lake (GSL) basin where legacy data is integrated with outcrop analysis to characterize a deep sedimentary geothermal reservoir. Seismic structural cross sections, petrophysical data from legacy oil and gas wells, and outcrop analog studies are integrated to define potential drilling targets and inform techno-economic modeling and development concepts.

Oil and gas companies exploring the GSL basin in the 1970's and 1980's conducted extensive seismic surveys and exploration drilling. Structural mapping from regional gravity and seismic reflection data defines major extensional faults and three major sub-basins where sedimentary geothermal reservoirs are buried by 2–3 km (6,561–9,842 ft) of Miocene-recent sediment. These are the Gunnison Bay Basin, the Gilbert Bay Basin, and the Willard Bay Basin.

Exploration well data is used to build a stratigraphic framework and characterize potential geothermal reservoirs. The most prospective reservoirs are fractured Paleozoic carbonates, which reach temperatures greater than 150 °C (302 °F) at 3 km (9,842 ft) depth in the Gunnison Bay basin. Stratigraphic units of interest are the Ordovician Fish Haven Dolomite, Silurian Laketown Dolomite, and the Cambrian Nounan and St. Charles Dolomites. These formations which are massively bedded, commonly vuggy, and pervasively fractured. Fractures measured in Paleozoic carbonates in the Promontory Mountains show two consistent subvertical fracture sets oriented E-W and NNE-SSW.

Analysis of petrophysical logs indicate porous and permeable reservoirs in carbonate units below the 150 °C (302 °F) isotherm. Conservative estimates of log-derived porosity for these carbonates

varies between 5-15%, which is higher than many analogous fractured commercial petroleum reservoirs and comparable to other sedimentary geothermal developments.

The reservoir characterization is used to generate techno-economic models of conceptual sedimentary geothermal development and highlight fairways where sedimentary resources could be developed. While much of the GSL basin will be difficult to develop due to sensitive environmental issues or the challenges of drilling and developing under the lake, the northern extent of the Willard Bay Basin is onshore, above the GSL high stand and represents a favorable greenfield sedimentary geothermal exploration target area with no deep well penetrations. The approach detailed here is also beneficial as it can be applied to other sedimentary reservoirs and plays in basins containing legacy oil and gas exploration data.

1. Introduction

Geothermal exploration and development are currently expanding in the United States. New geothermal play concepts are being tested that were not previously considered economic (Norbeck and Latimer, 2023; Marcia, 2024). These exploration plays include sedimentary and enhanced geothermal systems (EGS), which typically have different geologic characteristics from conventional hydrothermal exploration plays. By most classifications, the vast majority of the operating geothermal power plants in the United States are conventional hydrothermal systems, except for sedimentary developments in the Salton Sea (Ramirez et al., 2023) and a single EGS production well near Blue Mountain, NV that began production in late 2023 (Fercho, 2023). A sedimentary geothermal play is currently under development by DEEP Earth Energy in the Williston Basin, in the province of Saskatchewan in Canada (Marcia, 2024). At that development the target reservoir is the Cambrian Deadwood formation that is between 120–125 °C (248–257 °F) at ~3.5 km (11,483 ft) depth and will be developed with horizontal wells that have 2 km (6,561 ft) long lateral sections.

These new EGS and sedimentary geothermal projects have opened many new basins to geothermal exploration. Of particular interest are basins where oil and gas exploration (both successful and not) has occurred, because those basins contain legacy data that can be re-used for geothermal exploration in a cost-effective way. In this study we present a workflow for how legacy petroleum exploration data can be used to detail play fairways, identify drilling targets, and characterize potential geothermal reservoirs. We use the Great Salt Lake (GSL) basin as a case study for this workflow.

The GSL basin has been identified as an area with the potential of hosting geothermal resources capable of power generation (Allis, et al., 2011; 2013; Blackett et al., 2018). The basin lies within a region of elevated heat flow in the Basin and Range province (Figure 1), which is the region containing most of the commercial power geothermal plants in the United States. In the GSL basin, the presence of elevated temperatures from oil and gas wells, in conjunction with deep, extensional Neogene sedimentary basins, has led several researchers to point out the potential for stratigraphic geothermal reservoirs there (Allis, et al., 2011; 2013; Edwards and Chapman, 2013; Blackett et al., 2018). While these previous studies have highlighted the high-level geothermal potential of the basin, none of them have detailed the various geothermal exploration concepts or characterized the potential geothermal reservoirs. Here, we re-examine and synthesize the available geothermal, geophysical, and geologic data in the GSL basin to create and describe potential exploration plays

and drilling targets in the basin, characterize the reservoir, and create a feasible economic model for development.

2. Geologic Setting

The geologic setting of the GSL basin has the potential to host conventional hydrothermal or sedimentary geothermal systems. The oldest rocks in the basin are Precambrian basement that unconformably underlie passive margin Paleozoic carbonates (Hintze, 1988). During the Sevier Orogeny, these rocks were folded and thrusted. The overthrusted structures can be observed in ranges like the Promontory Range (Crittenden, 1988) and in deep seismic sections (Velasco et al., 2010). Basin and Range extension began during the Neogene time and continues to the present day. This extension formed several deep sedimentary basins that are contained within the larger GSL basin. These basins are filled with alluvial and lacustrine sediments, with interbedded volcanics (Bortz, 1987).

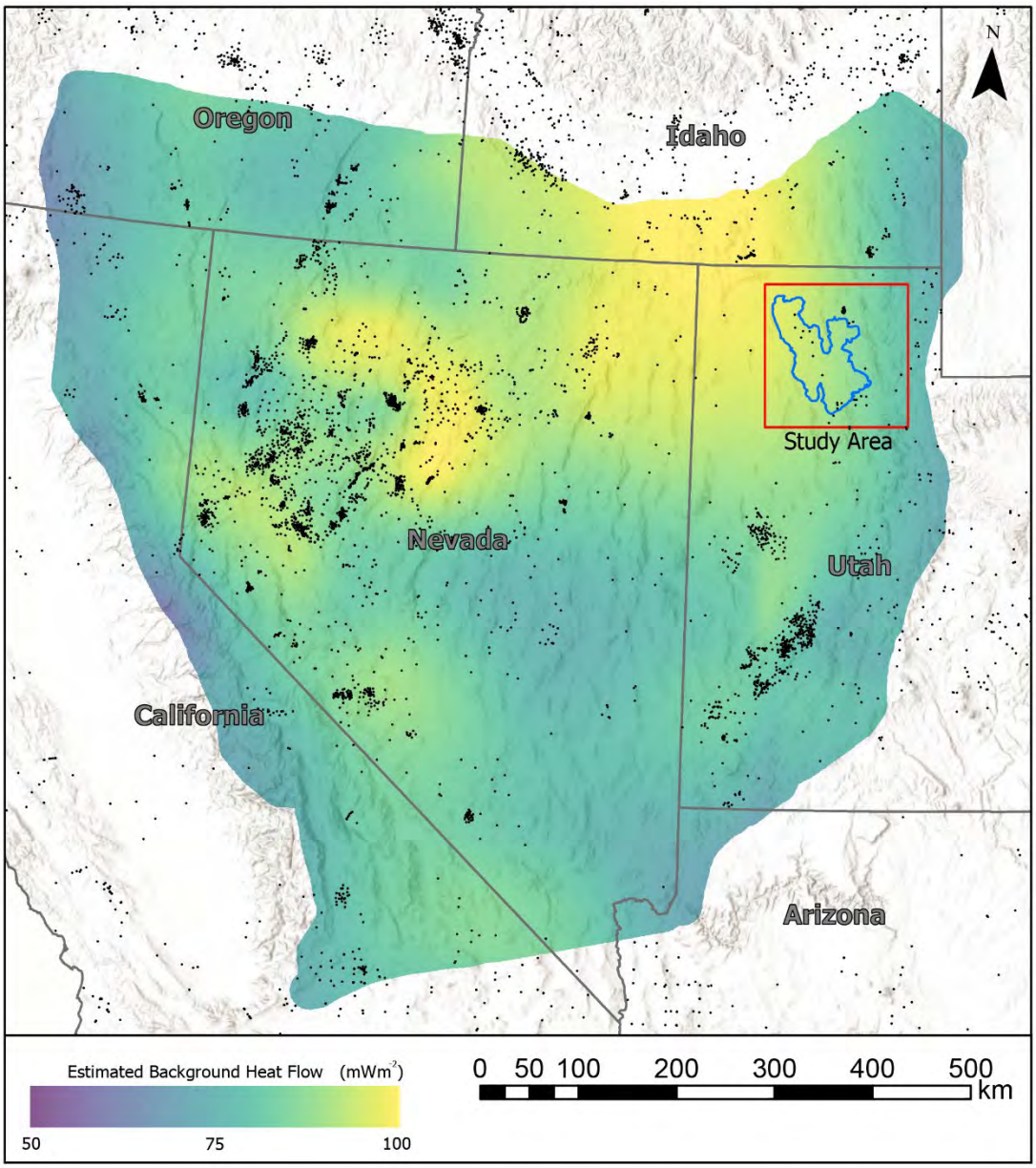

Figure 1: Great Basin estimated background heat flow map (mW/m^2) from DeAngelo et al. (2022) showing thermal data points (black dots) with the Great Salt Lake and study area outlined. The GSL Basin lies within an area of higher heat flow within Northern Utah.

3. Gravity

An isostatic gravity map for the GSL basin study area (Figure 2) was created from a public gravity dataset layer originally part of a larger Great Basin geothermal study (Glen et al, 2022). Gravity lows are generally interpreted to represent basins with sedimentary fill, due to the lower density of basin sediments compared with basement rocks (Hinze, et al., 2013; Paterson and Reeves, 1985). In the GSL area, several sub-basins can be delineated by the gravity data, which are named the

Gunnison Bay Basin (northeast), Gilbert Bay Basin (south), and Willard Bay Basin (northwest). These basins appear to be asymmetric, with interpreted N-S trending basin-bounding faults that correlate with many of the mapped quaternary faults across the basin (Bowman and Arabasz, 2017).

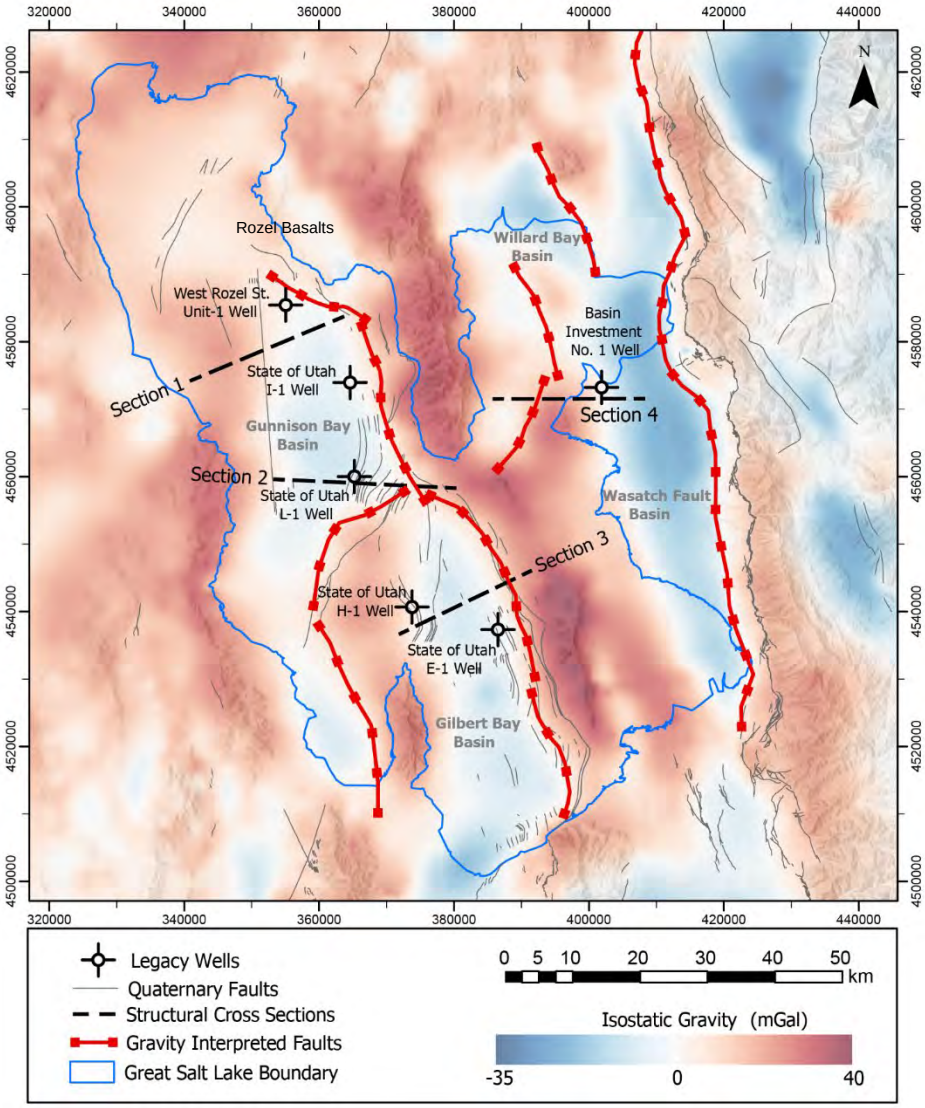

Figure 2: Isostatic gravity structure map encompassing the larger GSL basin showing the location of major sub-basins, structural elements, structural cross sections, and relevant deep oil and gas wells (source of gravity data from Glen et al., 2022). The Great Salt Lake shoreline is outlined by the solid blue line. The thick dashed black lines show the locations of legacy seismic lines and cross sections in this study. The thin grey lines represent quaternary faults from the Utah Geological Survey quaternary fault database (Bowman and Arabasz, 2017). Gravity lows are interpreted to represent major sub-basins. The red lines represent interpretations of major basin bounding faults from gravity data. There are three major sub-basins investigated in this study, the Gunnison Bay, Gilbert Bay, and Willard Bay basins. The depths and general structure of these sub-basins are also constrained by legacy deep oil and gas wells and seismic reflection data. These basins are useful analogs for other nearby sub-basins, like the Wasatch Fault Basin, that are less data constrained.

The gravity high in the northern part of the Gunnison Basin and extending onshore towards the Promontory mountains is due to the presence of the Rozel Basalts. These basalts were encountered in several oil and gas wells and are the reservoir rock for the only producing oil fields in the basin (Bortz, 1987).

4. Temperature

Several legacy deep oil and gas wells in the study area have temperature surveys that were used to understand variations in regional conductive geothermal gradients. These wells extend from 1,500 m (4,921 ft) to over 3,200 m (10,498 ft). The maximum temperature encountered is over 210 °C (410 °F) at the bottom of State of Utah I-1 well (Figure 3), which is in the center of the Gunnison Bay Basin (Figure 2). The State of Utah L-1 well, at the southern end of the Gunnison Basin reaches 150 °C (302 °F), which is commonly used as a threshold for economic power production in the Great Basin. The State of Utah E-1 well in the Gilbert Bay Basin reaches temperatures over 120 °C (248 °F) but is likely not in the hottest part of the basin. The well is located close to a basin-bounding fault (Figure 4) and is missing the Paleozoic carbonate section, which appears to be faulted out due to ~5 km (16,404 ft) of heave on the fault (Figures 4 & 5). There were no temperature surveys in the public database from the Willard Bay Basin.

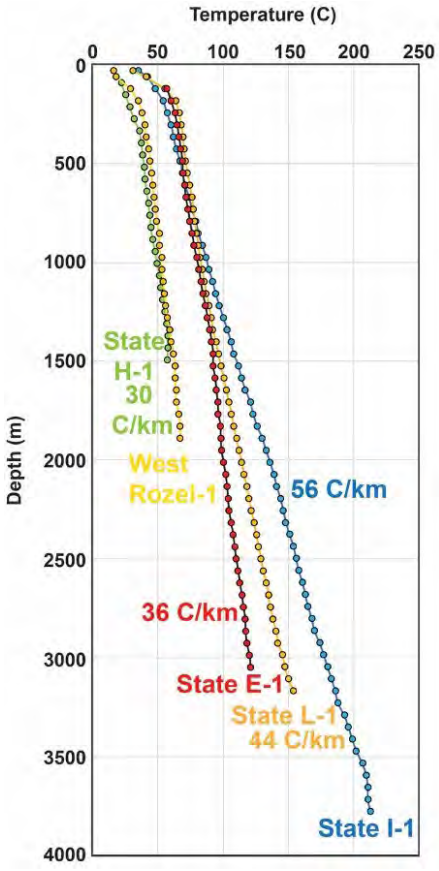

Figure 3: Temperature profiles from deep oil and gas wells in the Gunnison Bay and Gilbert Bay basins shown in Figure 2 (UDOGM, 2023). The wells in the Gunnison Bay basin have higher geothermal gradients and are the only wells that reach over 150 °C (302 °F) within the well's total depth. These profiles demonstrate a conductive geothermal gradient, and none of the examined wells encountered fault-hosted convection, even though the State of Utah E-1 well drilled through a large basin-bounding normal fault (Figure 4).

4. Seismic Reflection Profiles

Newly interpreted line drawings from published seismic sections across the major extensional basins in the Great Salt Lake area are shown in Figure 4. These seismic lines detail the major structural and stratigraphic features relevant to geothermal exploration. The deep petroleum exploration wells provide stratigraphic control on these structural interpretations. The seismic interpretations show dominantly asymmetric basins with west-dipping listric basin-bounding normal faults. Younger strata thicken significantly towards the fault in the hanging-wall, indicating these are growth strata deposited synchronously with fault activity and span a period of Miocene to recent time. The seismic line through the Willard Bay basin (Section 4) shows a buried horst block bounded by oppositely dipping extensional faults on both sides. The basin fill here is generally less thick due to small throw on the faults. This is consistent with the gravity map in Figure 2, which shows a gravity high across this seismic line. Figure 2 also shows a gravity low north of the Section 4 seismic profile, where the basin structure is likely more similar to the structure observed in the Gunnison Bay seismic profiles (Sections 1 & 2).

Synthetic and antithetic faults are common in hanging-wall anticlines; however, these faults primarily are contained within the growth strata units, and commonly do not reach the deeper Paleozoic carbonates or basin-bounding fault (Figure 4- Sections 2 & 3). Because of this, these faults are unlikely to host deep fluid heat convection. This could be significant since upflow along deep faults is thought to feed the sedimentary systems at the Brawley, Ormesa, and Salton Sea sedimentary geothermal fields, even though those fields produce from primary porosity and permeability in place (Ramirez et al., 2023).

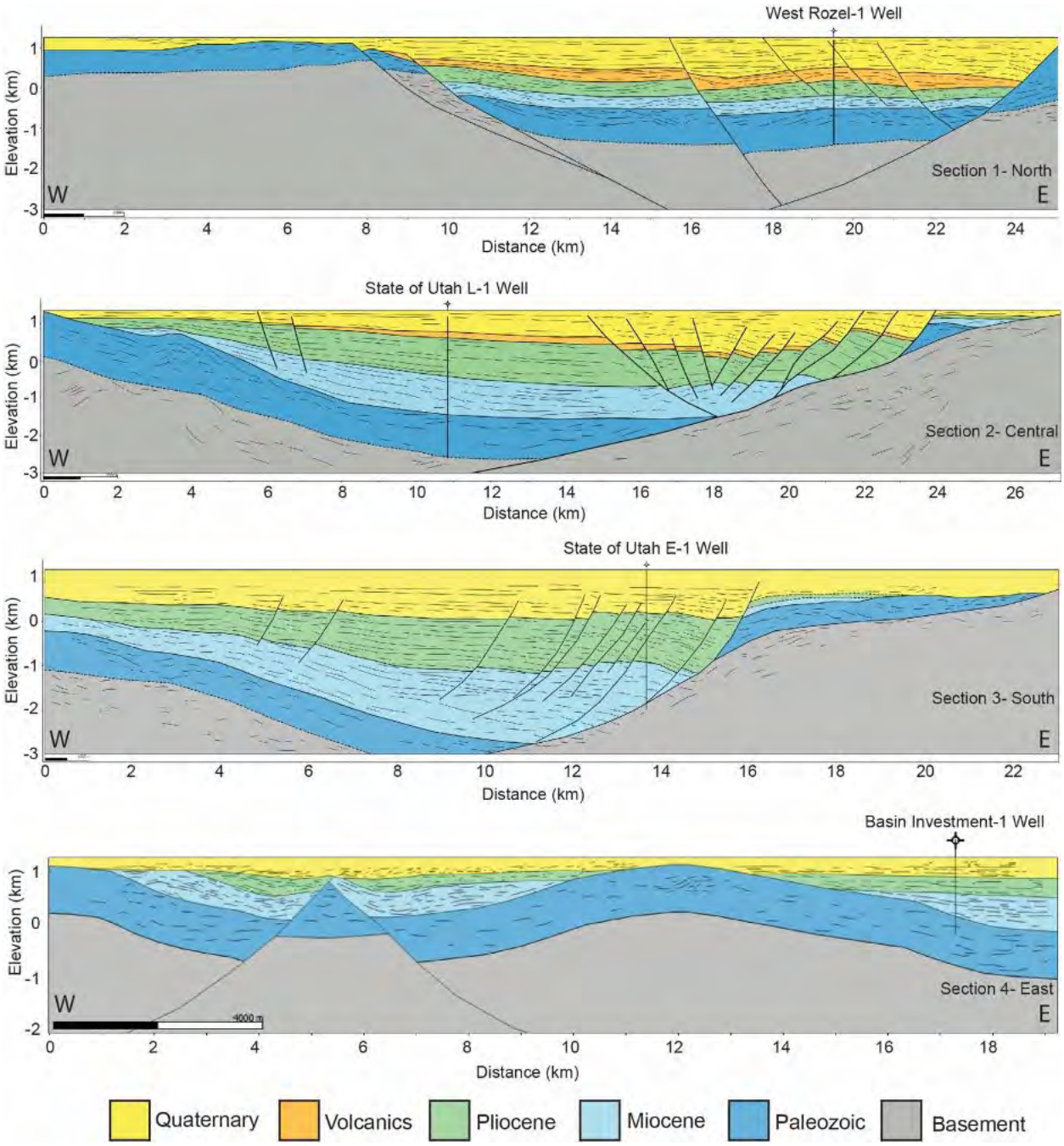

Figure 4: Line drawing interpretations of seismic reflection sections across the GSL basin. Locations of sections are shown in Figure 2. Nearby offset wells projected onto each section were used to define stratigraphic horizons. (A) Section across the northern Gunnison Bay basin, interpreted from Bortz (1987). (B) Section across the southern Gunnison Bay basin, interpreted from Velasco (2009). (C) Section across the Gilbert Bay basin, interpreted from Petropoulos (1994). (D) Section across the Willard Bay basin, interpreted from McNeil and Smith (1991).

5. Geothermal Reservoirs

5.1 Basin Stratigraphic Framework

Mud log reports from drilling were used to interpret major lithostratigraphic units in deep wells and correlate them across the basin (Figure 5). The uppermost unit is interpreted to be quaternary in age and consists almost entirely of fine-grained siltstones and shales. In the northern part of the basin, there are basalts underlying these fine-grained clastic rocks. These fractured basalts are part of the Rozel volcanic field and are the reservoir rocks for the legacy Rozel oil field (Bortz, 1987; Figure 2). Below the mudstones is a major lithostratigraphic unit that is ~500–700 m (1,640–2,296 ft) thick and is interpreted to be Pliocene in age. This unit consists mostly of shale with some thin sandstone beds. In the State of Utah E-1 well in the southern part of the study area, the top of this unit has a several hundred-meter-thick sandstone package. Underlying the Pliocene clastic rocks is a unit of interbedded shales and carbonates interpreted to be Miocene in age. Individual carbonate beds tend to be a few to tens of meters (10–100 ft) thick according to mud log reports. The basal stratigraphic unit consists of massively bedded limestones and dolomites. Mapping in the nearby Promontory Mountains (Crittenden, 1988) indicates these carbonates range from Cambrian-Pennsylvanian age.

These lithostratigraphic units also correlate to major stratigraphic packages observed in the regional seismic lines (Figure 4). The Miocene-Quaternary units exhibit growth geometries consistent with active extensional faulting during that period.

By integrating temperature data with this stratigraphic framework, potential geothermal reservoirs can be evaluated. The Miocene-Quaternary basin-fill sand and carbonate layers are likely too thin to be commercial reservoirs except for the 500 m (1,640 ft) thick sandstone unit encountered in the Gilbert Bay Basin. However, this sand is shallow and likely only ~60 °C (140 °F), far below the threshold needed for geothermal power production. The most prospective lithostratigraphic units in terms of temperature and lithology are the Paleozoic carbonates, which are especially prospective in the Gunnison Bay Basin, where these units are thick and reach temperatures over 200 °C (392 °F).

It is assumed that sedimentary geothermal reservoirs that are thick and not interbedded with shales are more desirable, because they will likely be more efficient at sweeping heat from a larger area when production wells are operating. The detailed geologic mapping by Crittenden (1988) in the Promontory Mountains identifies the Upper Cambrian Nounan and St. Charles Dolomites, the Ordovician Fish Haven Dolomite, and the Silurian Laketown Dolomite as carbonate units that are thick and massively bedded with few or no shaly interbeds. The Fish Haven and Laketown formations are described as commonly vuggy and all these units are described as having extensive fracture development, which can enhance reservoir quality in carbonate reservoirs.

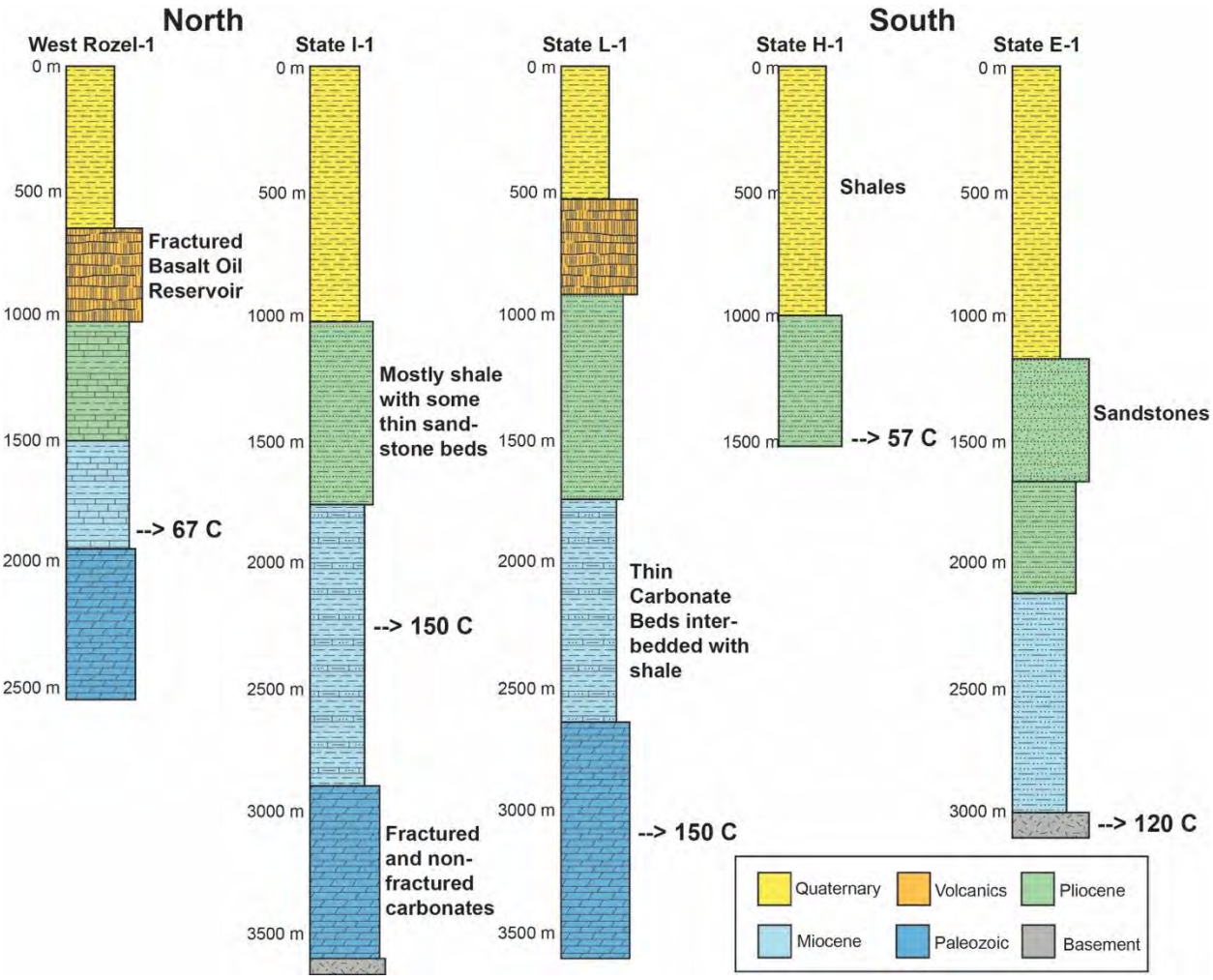

Figure 5: Stratigraphic cross section of deep oil and gas wells shown in Figure 2 showing the major lithostratigraphic framework of the GSL basin. Some temperature benchmarks from the temperature logs in Figure 3 are also shown.

5.2 Fracture Characterization

Naturally occurring fractures often play a critical role in contributing to porosity and permeability in carbonate reservoirs. Outcrop analysis of fractures in potential reservoir units was conducted to understand possible fracture density in the geothermal reservoir. The Paleozoic carbonate units that are encountered in the deep GSL basin wells are exposed in the Promontory Range, which is a major N-S trending horst block that separates the Gunnison and Willard Bay basins (Figure 2). Outcrops along the northern edge of the Promontory Range were visited and characterized for their potential as subsurface geothermal reservoirs (Figure 6).

Outcrops consisted of blue-gray, medium thickly bedded, heavily fractured limestones and dolostones interbedded with thin siltstones, mudstones, and cherts (Figure 6A). Fractures observed were closely spaced, with two primary fracture orientations measured: a generally E-W subvertical fracture set and a NNE-SSW trending subvertical fracture set (Figure 6B). These orientations were

consistent across the range and on oppositely dipping limbs of a small anticline, suggesting fracture development occurred after overthrusting of the Paleozoic units and could be regionally continuous. While some fractures were calcite filled, many were open with apertures ranging from <1–10mm (0.04–0.4 inches).

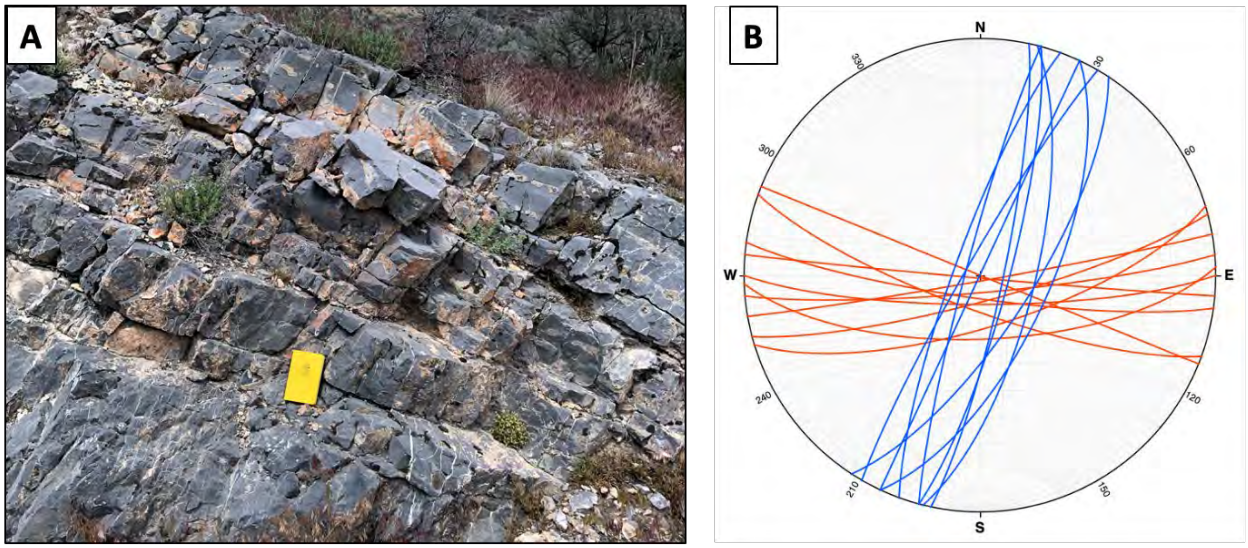

Figure 6: (A) Outcrop image of a fractured carbonate reservoir analog exposed along the northern edge of the Promontory Range. The image showed parallel, closely spaced fractures; some of which are calcite filled, while others are open. (B) Lower-hemisphere stereonet of measured fracture planes, consisting of an E-W trending subvertical set (red) and an NNE-SSW trending subvertical set (blue).

5.3 Well Log Interpretation and Reservoir Properties

Reservoir properties of Paleozoic carbonate units were investigated using well logs for the deep wells in the basin (UDOGM, 2023). Data availability for each well varies, but most of the wells in the GSL basin have mud logs and gamma-ray logs, and some have additional density, neutron porosity, resistivity, and/or sonic logs in raster log format. Figure 7 shows the typical log responses for a ~1,000 m (3,280 ft) of the State of Utah I-1 well (Indian Cove) well beginning near the top of the Paleozoic Carbonates. This well had the highest bottom-hole temperature of the wells in this study, with a temperature > 200 °C (392 °F).

Based on the well data, the Paleozoic Carbonates can be split into five stratigraphic units:

(1) 2,895–3,109 m (9,500–10,200 ft)- Characterized by medium and variable gamma ray, highly variable neutron porosity, medium and variable resistivity, and a caliper log with large spikes suggesting borehole cave-ins. Mud log reports interbedded dolomite/limestone and shales/anhydrites. Based on the mud log and well log signatures, it appears that the alternating carbonate/shale successions are thin to medium bedded, with the only thick carbonate unit being a massive 30 m (100 ft) dolomite interpreted at ~2,933 m (9,625 ft). The porous and conductive zones also correlate with caliper spikes and shale units on the mud log, suggesting the interbedded carbonates here are likely tight with low porosity.
(2) 3,109–3,127 m (10,200–10,260 ft)- Characterized by high gamma ray, high porosity, and low resistivity. Mud log reports a ~18 m (60 ft) section of shale.

(3) 3,127–3,352 m (10,260–11,000 ft)- Characterized by generally low gamma ray with short spikes, low porosity, and low resistivity. Mud log reports interbedded dolomite/limestones and shales, but with generally fewer and thinner shale units. Spikes in gamma, porosity, and resistivity are correlative and likely indicate the presence of shale units.
(4) 3,352–3,566 m (11,000–11,700 ft)- Characterized by low gamma ray with more infrequent but larger spikes, low and less variable neutron porosity, and low variable resistivity. Mud log reports primarily dolomite and limestones with few shales. Carbonates could be muddy, contributing to spikes in the log data.
(5) 3,566–3,672 m (11,7001–2,050 ft)- Characterized by low gamma ray, elevated neutron porosity, and low resistivity. Mud log reports dolomite with few to no interbedded shales. The top of the unit has a porosity spike that correlates with resistivity and caliper log lows. This suggests a major porous and permeable zone possibly capable of hosting a geothermal reservoir. Below this is another smaller porosity high that correlates with a conductive zone but is not accompanied by a significant change in the caliper log.

Unit 5 is interpreted to be the primary drilling target for geothermal reservoir exploration and the depths and temperatures associated with that unit are included in the economic models for this study. The measured temperature at the top of this unit is 210 °C (410 °F) and this prospective reservoir correlates with a small section of an isothermal temperature gradient in the temperature log (Figure 3).

The observed reservoir properties compare favorably with analogous systems for both petroleum and geothermal production. Log-derived porosity values for the carbonate reservoir in State of Utah I-1 well are shown in Figure 8 and compared with a potential analog reservoir from Railroad Valley, Nevada (Anna et al., 2007). The analog reservoir is an actively producing oil and gas reservoir and consists of Paleozoic carbonates. The Nevada reservoir has low matrix porosity and natural fractures are thought to be significant contributors to fluid flow.

Another analogous reservoir is the Cambro-Ordovician Deadwood Formation in the Williston Basin of Canada and North Dakota (USA) where DEEP Earth Energy is actively developing a sedimentary basin geothermal power project. The Deadwood Formation there has porosity ranging from 10-16% with 260 md permeability (Marcia, 2024) at 3,500 m (11,483 ft) depth. The DEEP Earth team has drilled several wells, performed long-term flow tests and plan to drill production wells with 2 km (6,561 ft) lateral sections that can sustain flow rates >1,000 gal/min with these reservoir properties (Marcia, 2024).

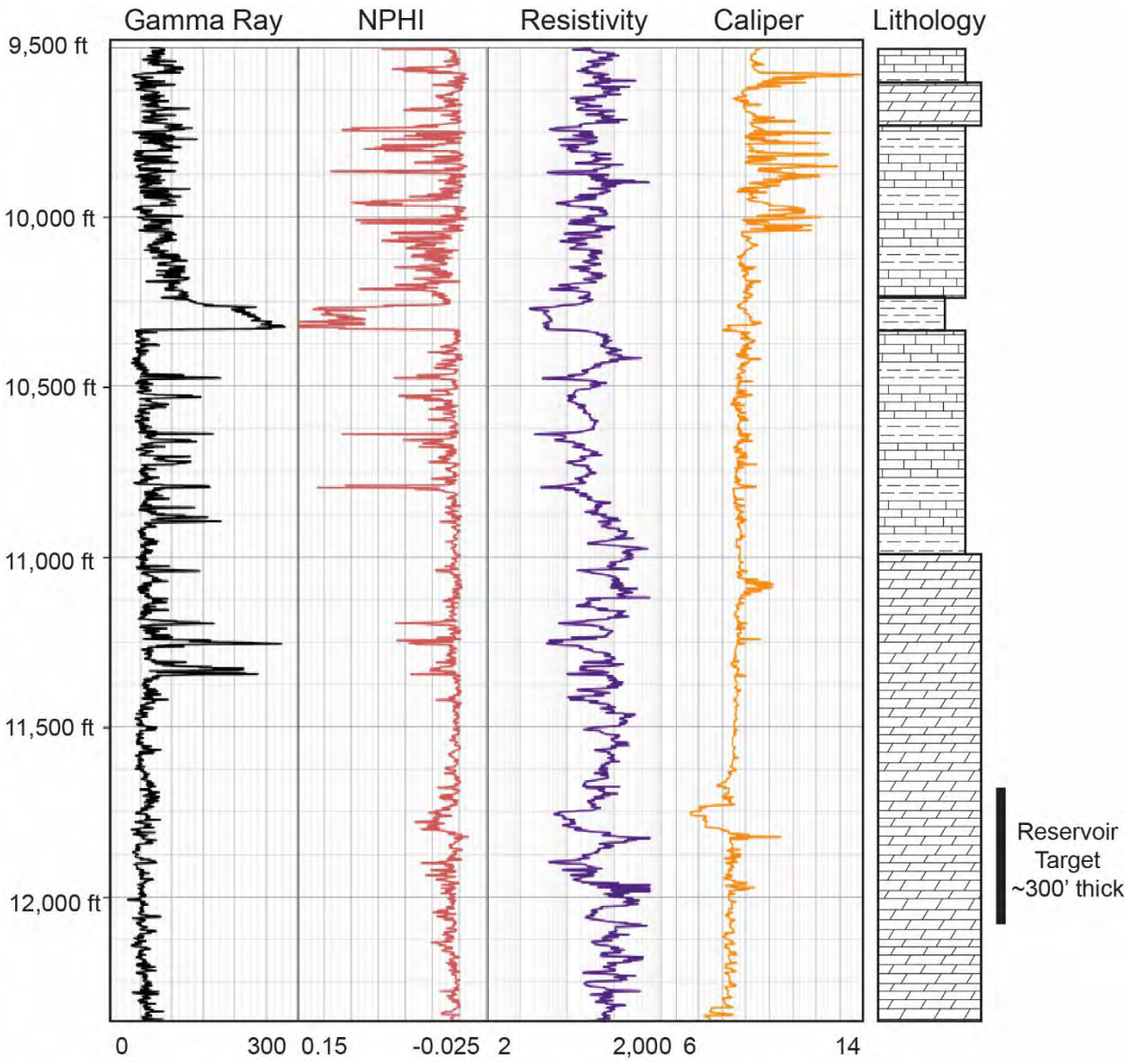

Figure 7: Example of standard well log responses and mud-log lithology from a selected interval in the State of Utah I-1 well. This 853 m (2,800 ft) section of well can be separated into 5 major lithologic units that have distinctive log responses.

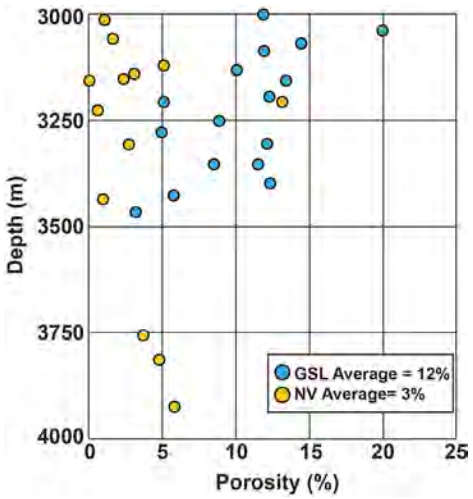

Figure 8: Log-derived porosity depth plot for Paleozoic carbonates in the State of Utah I-1 well (blue) and Railroad Valley, Nevada producing oil carbonate reservoirs (orange) (Anna et al., 2007) which serve a potential analog. Porosity values from Nevada are obtained from core, which might explain some of the measurement difference.

6. Discussion

6.1 Techno-economic Modeling

The geologic characterization described here can be used to model the economics of different development scenarios. NREL's Geophires techno-economic modeling tool (Beckers et al., 2019) was used to model the power production and levelized cost of electricity (LCOE) of a conceptual sedimentary geothermal development. For the scenario shown in Figure 9, a development consisting of 10 production wells and 8 injections wells at a depth of 3.5 km (11,483 ft) was modeled. For wells flowing with a pump at 1250 gal/min, the development would produce 56 megawatt electric (MWe) of net power with an LCOE of $63/MWh. While the modeled reservoir can handle an increased flow rate, the system becomes increasingly inefficient, relying on a large parasitic load to power downhole pumps. This is an example of one development scenario, but it demonstrates that reasonable reservoir inputs provide modeled outputs for power generation per well and LCOE that are economic in most modern offtake markets.

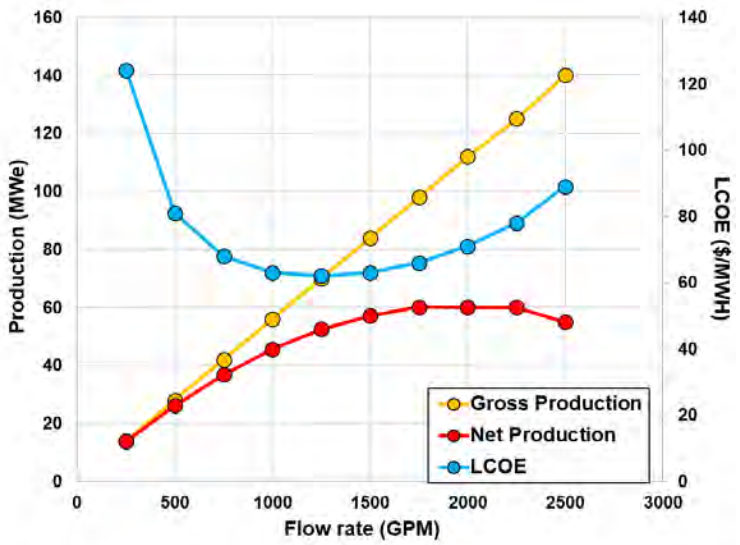

Figure 9: Output from a techno-economic model using the Geophires geothermal economic modeling tool (Beckers and McCabe., 2019) showing gross power (orange) net power (red) and levelized cost of electricity (LCOE; blue). This development concept is for a development consisting of 10 production wells and 8 injection wells at 3.5 km (11,483 ft) depth with a production temperature of 210 °C (410 °F).

6.2 Environmental Considerations & Development Concepts

The Great Salt Lake is a critical environmental resource to the state of Utah. Recently, the decreasing lake levels have brought increased attention to the role the lake plays in the local ecosystem and economy. Due to the environmental sensitivity of the lake, it is unlikely that geothermal development can be pursued in any part of the lake below the historical lake level high stand. While it might be intriguing to attempt to develop the sedimentary geothermal reservoirs under the lake from deviated wells drilled from onshore (i.e. drilling into the East Side of Gunnison Bay Basin from Western side of Promontory Mountains- Figure 2), the basin bounding faults have several miles of heave as observed in the seismic reflection lines (Figure 4). Reaching the carbonate drilling targets would likely require extended-reach drilling, which is a costly drilling technique that would likely make a geothermal development uneconomic.

Another approach would be to explore for and develop sedimentary geothermal reservoirs in areas of the basin that are above the Great Salt Lake shoreline high stand and are less environmentally sensitive. One such example is the northern end of the Willard Bay Basin, where a gravity low suggests a deep sub-basin (Figure 2). Unfortunately, there are no deep wells drilled in this sub-basin, but the insights gained from the offset wells in other parts of the basin, as detailed in this study, can be applied to exploration efforts in this area.

Our suggestion for successful exploration in an area like the onshore portion of the Willard Bay Basin would involve the following: collection of 2D seismic reflection profiles, magnetic, electromagnetic, and gravity data to constrain basin geometry; detailed studies on cuttings and core from nearby wells in adjacent basins that can be used as analogues; shallow and intermediate-depth temperature data; modeling heat flow and reservoir properties using data constrained from offset wells in the basin; and outcrop studies of potential reservoir hosting lithologies in the adjacent ranges to further help constrain fractures, and reservoir properties. These data would be

used to site a deep vertical exploration well that would be designed in a way so that it could be re-entered and side-tracked for a lateral leg in a proven reservoir.

One of the innovations of DEEP Earth Energy's Williston Basin sedimentary geothermal project is their well field layout, termed a "rib-cage" wellfield, which is a novel development concept for geothermal drilling and development. The concept drills a series of alternating production wells and injection wells, at regular intervals (e.g. 0.5 km or 1,640 ft), with the lateral legs parallel to each other. From each well pad, a twin well would be drilled in the opposite direction to minimize surface disturbance, permitting, and infrastructure. For the Northern Willard Bay development example in this study, a rib-cage geometry would work well, with the lateral legs oriented perpendicular to one of the two primary fracture sets in Figure 6 to maximize intersections with fracture systems that could connect between injection and production wells.

7. Conclusions

Sedimentary geothermal reservoirs are emerging geothermal resource plays in the United States and merit detailed geologic characterization to choose the right development location and concept. In many basins where oil and gas exploration has occurred, there is a wealth of legacy data that is in the public domain or can be obtained cheaply. We used an example from the Great Salt Lake Basin, Utah to show how this legacy data can be used to characterize a potential geothermal reservoir, determine drill targets, and model the economics of potential developments in a greenfield setting.

Acknowledgements

We would like to thank management at the Utah Geological Survey and Projeo for supporting the publication of this manuscript. This paper was improved by helpful reviews from Adrian Wiggins and Kelly Blake.

REFERENCES

Allis, R., Moore, J., Blackett, B., Gwynn, M., Kirby, S., and Sprinkel, D. "The potential for basin-centered geothermal resources in the Great Basin." *Geothermal Resources Council Transactions*, (2011). v. 35, 683-688.

Allis, R., Moore, J. N., Anderson, T., Deo, M., Kirby, S., Roehner, R., and Spencer, T. "Characterizing the power potential of hot stratigraphic reservoirs in the Western US." *Proceedings Thirty-Eight workshop on Geothermal Reservoir Engineering* (2013). SGP-TR-198

Anna, L. O., Roberts, L. N., and Potter, C. J. "Geologic assessment of undiscovered oil and gas in the Paleozoic-Tertiary composite total petroleum system of the Eastern Great Basin, Nevada and Utah." *Nevada and Utah: US Geological Survey Digital Data Series DDS-69-L*, (2007). v.*2*, 50.

Beckers, K. F., and McCabe, K. "GEOPHIRES v2. 0: updated geothermal techno-economic simulation tool." *Geothermal Energy*, (2019). v. *7*, p. 1-28.

Blackett, R., Gwynn, M., Hardwick, C., and Allis, R. “Stratigraphic geothermal potential in deep sedimentary basins, Northeastern Great Basin, Utah.” *Utah Geological Association Publication*. (2018). v:47:04

Bortz, L. C. “Heavy-Oil Deposit, Great Salt Lake, Utah: Section V. Exploration Histories.” *AAPG Studies in Geology: Vol. 25: Exploration for Heavy Crude Oil and Natural Bitumen*, (1987). p. 555-563.

Bowman, S. D., and Arabasz, W. J. “Utah earthquakes (1850–2016) and Quaternary faults.” *Utah Geological Survey Map*, (2017). v. *277*(1).

Crittenden Jr, M. D. “Bedrock geologic map of the Promontory Mountains, Box Elder County, Utah.” *US Geological Survey*. (1988). No. 88-646.

DeAngelo, J., Burns, E.R., Gentry, E., Batir, J.F., Lindsey, C.R.,and Mordensky, S.P., “Heat flow maps and supporting data for the Great Basin, USA.” *U.S. Geological Survey data release*, (2022) https://doi.org/10.5066/P9BZPVUC.

Edwards, M., and Chapman, D. “Geothermal resource assessment of the Basin and Range province in western Utah”. *Masters Thesi, Department of Geology and Geophysicss at University of Utah.* (2013).

Fercho, S., Norbeck, J., McConville, E., Hinz, N., Wallis, I., Titov, A., and Latimer, T., “Geology, state of stress, and heat in place for a horizontal well geothermal development project at Blue Mountain, Nevada.” *Proceedings, 48th Workshop on Geothermal Reservoir Engineering, Stanford University, Stanford, CA.* (2023)

Glen, J.M.G, Earney, T.E., Zielinski, L.A., Schermerhorn, W.D., Dean, B.J., and Hardwick, C., 2022, Regional geophysical maps of the Great Basin, USA: U.S. Geological Survey data release, https://doi.org/10.5066/P9Z6SA1Z.

Hinze, W. J., Von Frese, R. R., Von Frese, R., and Saad, A. H. “Gravity and magnetic exploration: Principles, practices, and applications.” *Cambridge University Press*. (2013).

Hintze, L. F. “Geologic history of Utah.” *Brigham Young Univ. Geology Studies, Spec. Publ,* (1988). v. *7*, 202p.

Norbeck, J. H., and Latimer, T. “Commercial-scale demonstration of a first-of-a-kind enhanced geothermal system.” *EarthArXiv* (2023). https://doi.org/10.31223/X52X0B

Marcia, K. “DEEP Earth Energy: Sedimentary Geothermal Power Development in Southern Saskatchewan.” *Geothermal, Lithium Hydrogen: New Energy from Subsurface Fluids*, AAPG-GRC joint meeting. (2024).

McNeil, B. R., and Smith, R. B. “Upper crustal structure of the northern Wasatch Front, Utah, from seismic reflection and gravity data.” *Master's thesis, Dept. of Geology and Geophysics, University of Utah* (1991).

Paterson, N. R., and Reeves, C. V. “Applications of gravity and magnetic surveys; the state-of-the-art in 1985.” *Geophysics*, (1985) v.*50*(12), 2558-2594.

Petropoulos, G. S. “Structure and relationships between Tertiary normal faults and Mesozoic thrust faults beneath the Great Salt Lake, Utah.” *Masters Thesis, Department of Geosciences, University of Arizona.* (1994).

Ramirez, G., Zuza, R., Johnson, A., Murphy, J., and Akerley, J., “Integrated Conceptual Model of Sedimentary Basin-Hosted Geothermal Fields in Imperial Valley, CA.” *GRC Transactions*. (2023) Vol 47.

UDOGM. “Utah Deparment of Natural Resources Division of Oil, Gas, & Mining, Online Data Explorer”, https://dataexplorer.ogm.utah.gov/ (2023) Accessed January 2023

Velasco, M. S. “Eastern Basin and Range crustal extension: A view from seismology and geodesy.” Doctoral dissertation, Department of Geosciences, University of Arizona. (2009).

Velasco, M. S., Bennett, R. A., Johnson, R. A., and Hreinsdóttir, S. “Subsurface fault geometries and crustal extension in the eastern Basin and Range Province, western US.” *Tectonophysics,* (2010). v. *488*(1-4), 131-142.

Exploring Geothermal Potential of Great Basin Sub-Regions

Nicole R. Hart-Wagoner[1], Cary Lindsey[1], Whitney Trainor-Guitton[2], Mark Coolbaugh[1], and James E. Faulds[1]

[1]Great Basin Center for Geothermal Energy, Nevada Bureau of Mines and Geology, University of Nevada, Reno

[2]National Renewable Energy Laboratory (NREL)

Keywords

INGENIOUS, Great Basin, sub-region, geothermal, exploration, statistics, PCA, k-means

ABSTRACT

The INnovative Geothermal Exploration through Novel Investigations Of Undiscovered Systems (INGENIOUS) project aims to discover new, economically viable hidden geothermal systems in the Great Basin region by building on previous work in play fairway analysis and machine learning. A key objective of this project is to develop an exploration workflow to reduce geothermal exploration risks for hidden geothermal systems. A single preliminary play fairway workflow was developed from the assessment of the regional INGENIOUS geological, geophysical, and geochemical datasets. This workflow provided new preliminary predictive geothermal fairway maps for the INGENIOUS study area, which encompasses most of Nevada, western Utah, southern Idaho, southeastern Oregon, and easternmost California. However, a recent study (incorporating machine learning techniques) of a portion of Nevada identified four geologic domains and determined that the relative importance of individual datasets or features as indicators of geothermal potential may differ across these domains. The INGENIOUS study area includes a much larger and more geologically diverse region; therefore, additional geologic domains or sub-regions are expected. To assess the sub-regions in the INGENIOUS study area, principal component analysis and k-means clustering were applied. Preliminary results indicate that the INGENIOUS regional data cluster into groups that relate to different geologic domains in the Great Basin region. These include domains such as the Walker Lane, extensional western Great Basin region, broad lower strain region in the eastern Great Basin of western Utah and eastern Nevada, Quaternary volcanic fields, and the area adjacent to the Snake River Plain. These clusters are assessed to determine the key geologic drivers of the identified clusters. Understanding this variability can provide key insights for the exploration and characterization of hidden geothermal systems in the Great Basin region and could indicate the need to develop multiple geothermal conceptual models and play fairway workflows for the INGENIOUS study area.

1. Introduction

The Great Basin region in the western United States (Figure 1) is a world-class geothermal province. In Nevada alone, the installed geothermal capacity is reported to be 786 MWe (Muntean

et al., 2021), and researchers have proposed that geothermal potential could be much higher (e.g., Williams et al., 2009). Many of the historical discoveries of conventional hydrothermal systems in the Great Basin region have surface thermal features. However, future geothermal potential is thought to lie mostly in hidden or blind geothermal systems that lack surface thermal features such as hot springs (e.g., Coolbaugh et al., 2007; Faulds et al., 2019). In recent years, there has been an extensive effort to identify and develop more hidden geothermal systems (e.g., Faulds and Hinz, 2015; Faulds et al., 2021 a,b,c; Craig et al., 2021). The INnovative Geothermal Exploration through Novel Investigations Of Undiscovered Systems (INGENIOUS) project aims to discover new, economically viable hidden geothermal systems in the Great Basin region by integrating new and established techniques to develop a play fairway workflow that can reduce exploration risk. The study area for the project includes most of Nevada, western Utah, southern Idaho, southeastern Oregon, and easternmost California (Figure 1). A single preliminary play fairway workflow was developed from the assessment of the regional INGENIOUS geological, geophysical, and geochemical datasets, which provided new preliminary predictive geothermal fairway maps for the INGENIOUS study area (Hart-Wagoner et al., 2024). While the preliminary play fairway workflow is a crucial first step in producing updated predictive geothermal fairway maps, additional refinements are being evaluated to enhance that workflow.

One refinement being evaluated is the use of sub-regions in the regional play fairway workflow. This approach stems from the findings of Smith et al. (2023), who applied PCAk to the Nevada PFA study area in northern Nevada. They identified four geologic domains including the Walker Lane, western Great Basin, central Nevada seismic belt, and the carbonate aquifer. PCAk was applied to the Nevada PFA study area to determine the relative importance of individual features, as indicators of geothermal potential may differ across the region in the different geologic domains. The INGENIOUS study area includes a much larger and more geologically diverse region; therefore, additional geologic domains or sub-regions are expected. The existence of these geologically distinct sub-regions could indicate the need to develop multiple conceptual models and play fairway workflows for the INGENIOUS study area. Principal component analysis and k-means clustering were applied to the identified known geothermal systems within the INGENIOUS study area. Subsequently, the clusters were analyzed to determine how they might relate to geologically distinct sub-regions of the Great Basin region. We then weigh the key contributing features for known geothermal system clusters, providing insight into 1) the viability of the single preliminary play fairway workflow (Hart-Wagoner et al., 2024) and 2) the need for different geothermal conceptual models and exploration workflows for sub-regions of the INGENIOUS study area in the Great Basin region.

2. Data and Methods

2.1 Data

In Phase I of the INGENIOUS project, a regional-scale geoscience compilation of 14 datasets was completed for the 494,269 km² study area. These included: 1) location of Quaternary faults, 2) slip rates on Quaternary faults, 3) age or recency of faulting, 4) slip-dilation tendency (TSTD) on Quaternary faults, 5) active and paleo-geothermal features, 6) Quaternary volcanic distribution, 7)

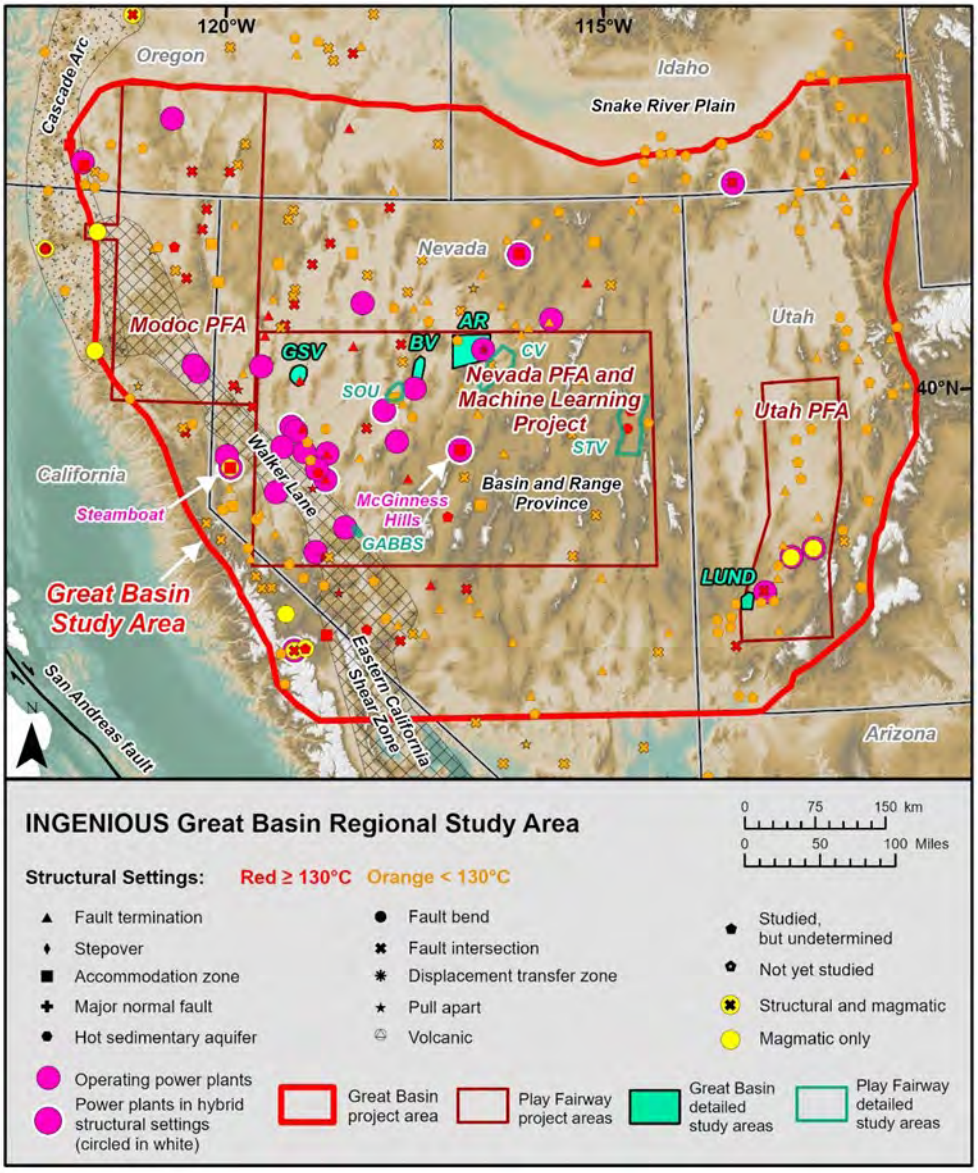

Figure 1: Regional setting of Great Basin study area for the INGENIOUS project, with locations of known geothermal systems, identified structural settings, previous PF projects (Modoc, Nevada, and Utah), and current detailed study areas (Granite Springs Valley-GSV; Argenta Rise-AR, Buffalo Valley-BV, and Lund). From Faulds and Richards (2023).

gravity data and models, 8) magnetic data and models, 9) magnetotelluric (MT) data and models, 10) geodetic strain rate, 11) earthquake distribution, 12) regional heat flow/temperatures, 13) temperature-geochemical data from wells and springs, and 14) two-meter temperature data. These datasets are a mixture of categorical and continuous numerical data. Many of the continuous numerical datasets were utilized in this study in their original form. However, categorical data needed to be transformed to continuous numerical datasets through feature engineering. An example was combining the fault and fault attribute data to generate Quaternary fault models for recency and slip rate (Hart-Wagoner et al., 2023). In this case, Euclidean distance and Euclidean allocation were utilized to transform these datasets into continuous grids. Then, weights-of-evidence (WofE) analysis was used to identify statistical relationships between known geothermal

systems and the data to build new Quaternary fault attribute models that were continuous gridded surfaces (Hart-Wagoner et al., 2023).

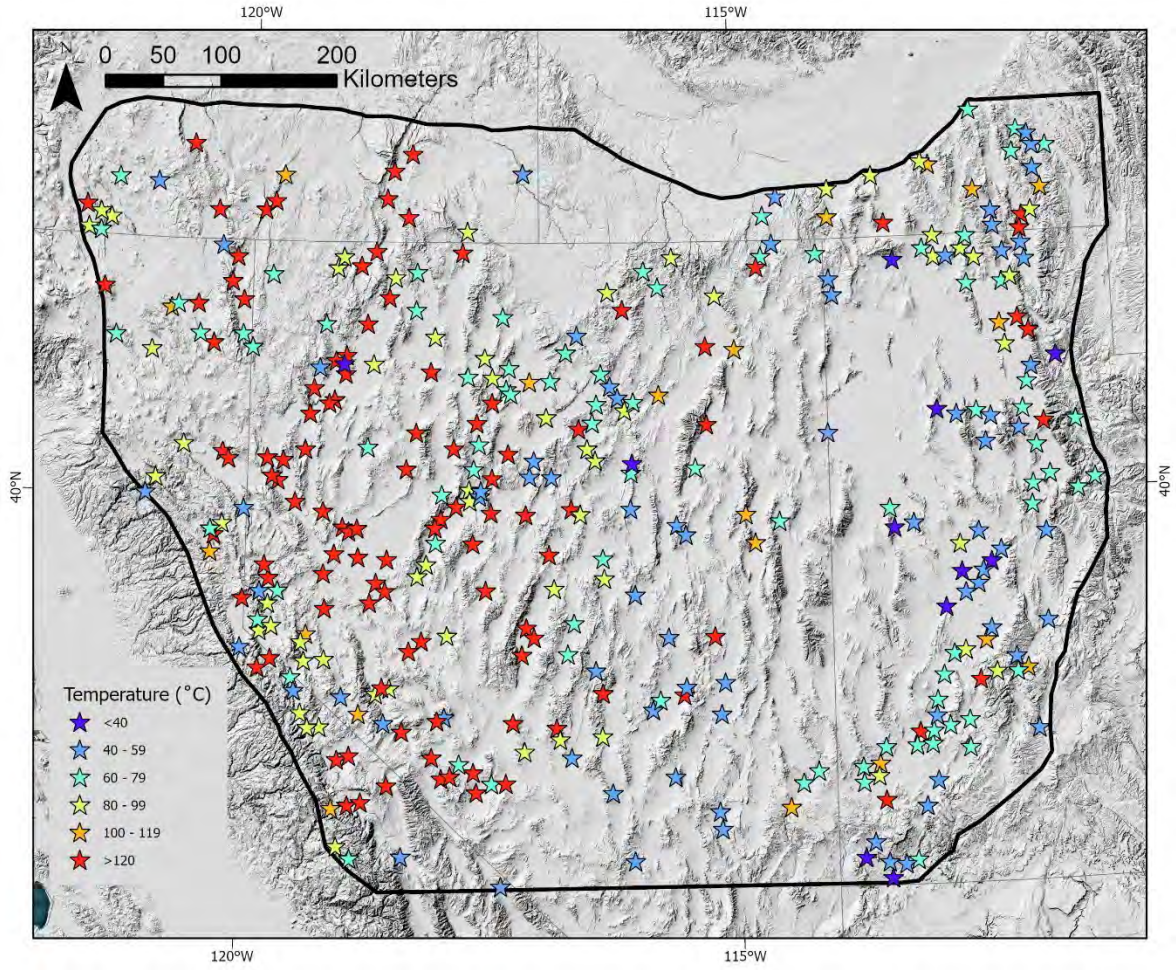

Figure 2: Compiled known geothermal systems in the INGENIOUS study area >37˚C. Data from the INGENIOUS datasets were extrapolated at each of these sites.

The data utilized in this study included features for earthquake rate density (Ayling et al., 2022), electrical conductance depth slices estimated from modeling of MT data (Peacock and Bedrosian, 2022), conductive heat flow (DeAngelo et al., 2022), depth to basement and potential field geophysical data (Glen et al., 2022), geodetic data (Ayling et al., 2022), Quaternary faults and fault attributes (Hart-Wagoner et al., 2023), and Quaternary volcanic vent composition. From these datasets, a total of 22 features were assessed in this analysis. The earthquake features included one independent (i.e., main shock) and one dependent earthquakes (i.e., aftershocks, foreshocks, and swarms) rate density model using N = 100 and an α value of 0.15 (N is the nearest number of earthquakes that were considered in generating the earthquake rate density map and α is a "declustering parameter" that distinguishes between independent and dependent earthquake events). The MT features included depth slices for: near-surface (2-12 km), middle crust (12-20 km), lower crust (20-50 km), upper mantle (50-90 km) and mantle (90-200 km). The potential field geophysical derived features included isostatic residual gravity anomalies, horizontal gravity gradient, magnetic intensity, horizontal magnetic gradient, and depth to basement. The geodetic

features included the second invariant, the dilatation rate, and the shear rate. The Quaternary fault features included recency, slip rate, and TSTD models. Lastly, the Quaternary volcanic features included distance to felsic, intermediate, and mafic volcanic vents.

A total of 354 known geothermal systems with known or estimated temperatures >37˚C in the INGENIOUS study area were identified as training sites for this analysis (Figure 2). These systems are either producing geothermal systems (i.e., contain operating geothermal power plants), identified geothermal systems that have not yet been developed, or geothermal systems that have been identified from measured well temperatures or temperatures estimated using geothermometry. A data value from each of the features listed above was extracted at each of the 354 known geothermal systems. These data were then utilized for PCAk modeling.

2.2 Unsupervised PCAk Modeling

Principal component analysis (PCA) (e.g., Pearson, 1901; Hotelling, 1933; Jolliffe, 2002) and k-means clustering (e.g., MacQueen, 1967; Lloyd, 1982; Jain, 2010) are unsupervised machine learning techniques that have been utilized for exploratory data analysis to support dimensionality reduction and to group and visualize multidimensional data. These methods have previously been used in tandem (PCAk) and shown utility in developing geothermal potential maps and guiding geothermal exploration studies at a finer regional scale (e.g., Smith et al., 2023). A similar approach is applied here to a different set of features to evaluate variability in the identified known geothermal systems of the much larger INGENIOUS study area.

PCA is a dimensionality reduction method that rotates and transforms the data to identify the principal components that account for the most variance in the input data. Since we are considering many potential features to characterize INGENIOUS known geothermal systems, PCA can be utilized to balance the consideration of these features, while maximizing the amount of explained variance considered in the analysis in fewer dimensions. The principal components are ordered by the proportion of the variance that they account for in the dataset, with lower principal component numbers accounting for more variance. A plot of the explained variance ratio can therefore be utilized to determine the number of principal components that should be considered in the analysis. These principal components also have loading values that indicate the contribution of each original feature to the principal components (e.g., Smith et al., 2023). These values can be used to identify which features are most influential in explaining the variance captured by each principal component.

K-means clustering is a method to group and visualize data for a user-defined number of clusters (k). The number of clusters can be defined by testing various number of clusters and calculating the within-cluster sum of squares for each tested k value. As the number of clusters increases, the within-cluster sum of squares generally decreases. The optimal number of clusters is usually determined where the within-cluster sum of squares difference becomes marginal. Once the optimal number of clusters is determined, K-means can build on the identified principal components by identifying data clusters and optimal centroid locations from the identified principal components. These clusters can then be mapped to illustrate the spatial extent of known geothermal system clusters. The loading values from the PCA analysis can be utilized to assess the importance of the features in each cluster (e.g., Smith et al., 2023). The ranking of features in each cluster can be used to evaluate the variability of known geothermal systems between different clusters.

3. Results

3.1 PCA Results

The PCA results indicate that none of the identified principal components explains more than 23.6% of the total variance of the dataset (Figure 3A). Four principal components are required in order to explain ~50% of the variance, while 10 components are required to explain 80% of the variance, and 14 components are required to explain ~90% of the variance (Figure 3B). To reduce dimensionality while still maximizing the amount of variance utilized in k-means, 14 principal components were retained and utilized in k-means clustering.

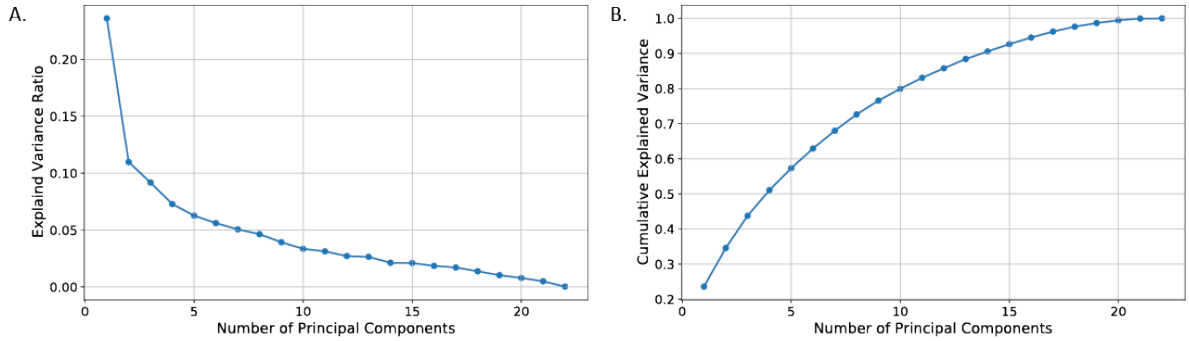

Figure 3: PCA scree plots. A. Explained variance ratio for each individual principal component. B. Cumulative explained variance ratio for combined principal components.

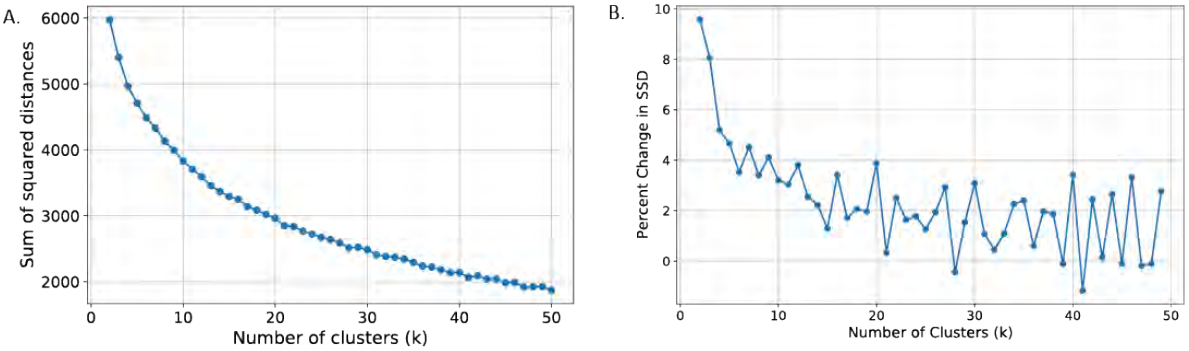

Figure 4: K-means scree plots. A. Within-cluster sum of squares for different k values. B. Percent change in the within-cluster sum of squares between different k values.

3.2 K-means Results

K-means clustering was completed using the PCA-transformed data (14 principal components). To identify the optimal number of clusters, k values from two to 50 were tested. The within-cluster sum of squares (Figure 4A) and the percent change of within-cluster sum of squares (Figure 4B) were utilized to identify six clusters for these data. If more than six clusters were utilized, there was only a marginal decrease in the within-cluster sum of squares.

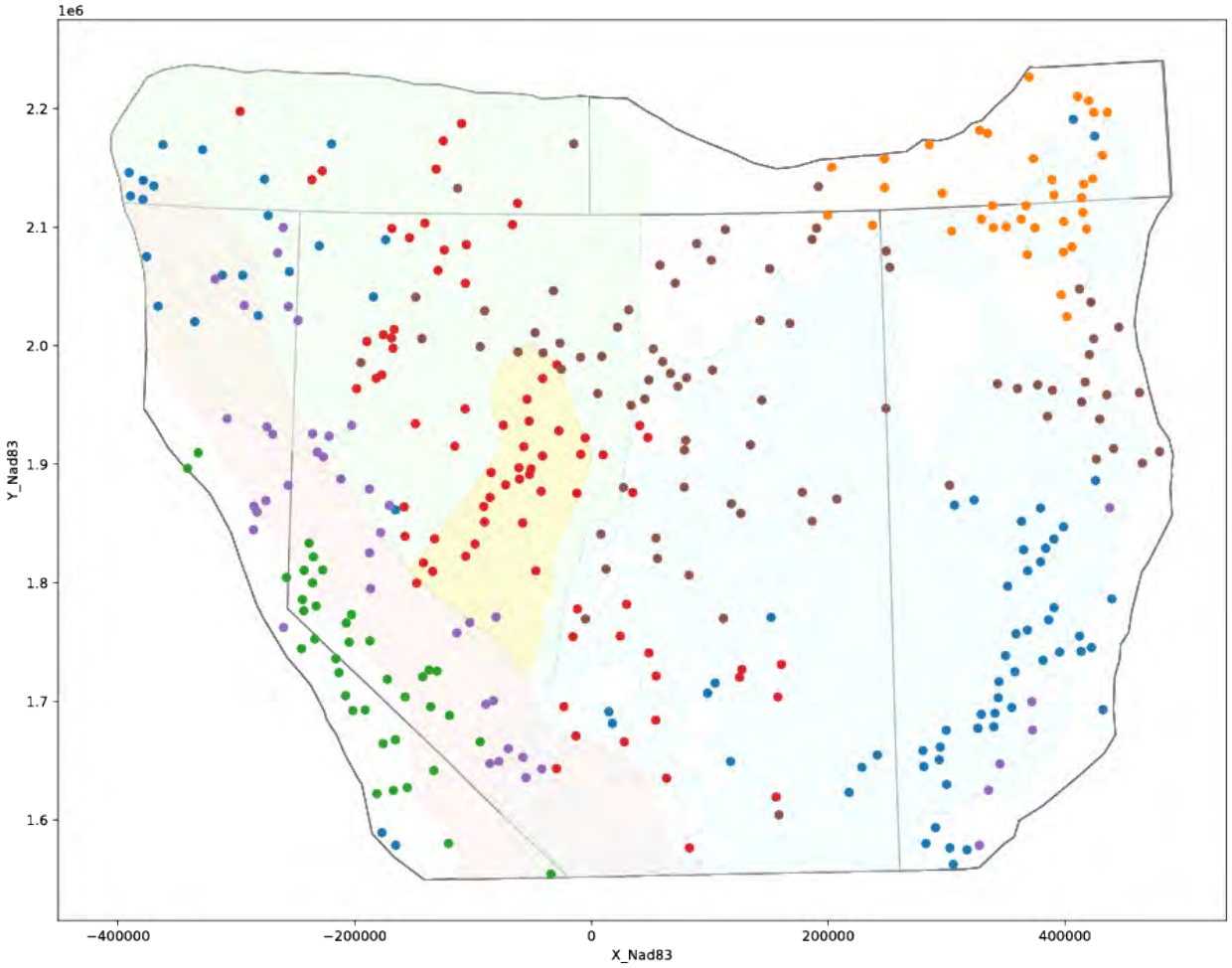

Figure 5: PCAk cluster map for the resulting six clusters. Different clusters of known geothermal systems are represented by different colored points. Polygons are based on the geologic domains utilized by Smith et al. (2023) and illustrate potential geologic sub-regions: green polygon – western Great Basin, red polygon – Walker Lane, yellow polygon – central Nevada seismic belt, blue polygon – carbonate aquifer.

The six clusters were then mapped to illustrate the geographic extent of the clusters (Figure 5). The sum of loading values from PCA were utilized to assess feature importance within each cluster (Figure 6). The features in each cluster were ordered based on the sum of loading scores to illustrate the relative contribution of features to the cluster (Figures 7-9). A high positive loading value indicates a strong contribution to the cluster and a positive relationship between the high feature values and high PC scores. A high negative loading value also indicates a strong contribution to the cluster and a negative relationship between high feature values and high PC scores.

The green cluster has 38 known geothermal systems, which are generally clustered in the southwest margin of the study area along the southwestern edge of the Walker Lane (Figure 5). Within the green cluster, the sum of loading values for this cluster has the strongest positive and negative relationships (Figure 6). The strongest contributing features with positive relationships are geodetic data, earthquake rate density, and Quaternary faults, and the strongest contributing features with negative relationships are isostatic gravity and distance to Quaternary volcanic vents (Figure 7A). These results indicate that the known geothermal systems in this cluster have an

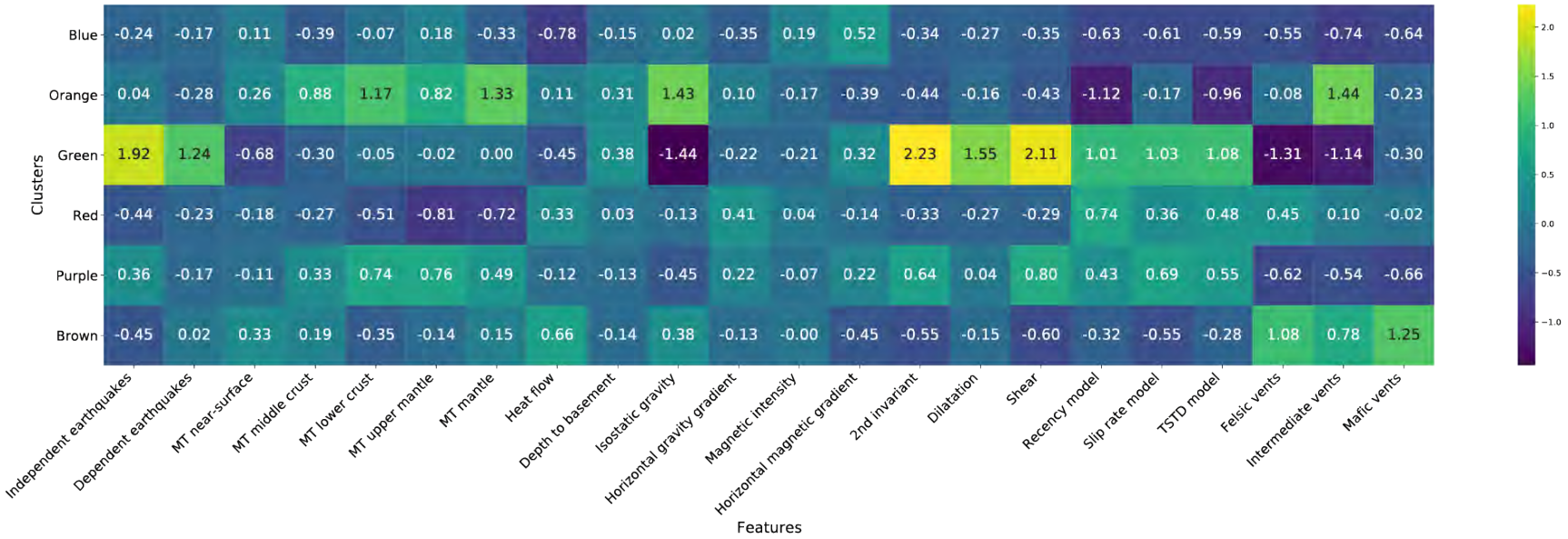

Figure 6: PCAk feature matrix for feature influence in each cluster. The value in the box is the sum of the loading values which is either negative or positive. Warmer colors indicate a positive relationship, and cooler colors indicate a negative relationship.

association with high second invariant and shear rates, high earthquake rate density, low isostatic gravity values, long distances to Quaternary volcanic vents, and high TSTD and slip rate.

The purple cluster has 43 known geothermal systems and is generally clustered along the southwest margin of the study area but more interior than the green cluster along the northeastern edge of the Walker Lane (Figure 5). Compared to some of the other clusters, the sum of loading values for this cluster are all relatively low (Figure 6). The strongest contributing features with positive relationships are geodetic data, MT, and Quaternary faults, and the strongest contributing factors with negative relationships are distance to volcanic vents (Figure 7B). These results indicate that the known geothermal systems in this cluster have an association with high shear rates, high conductance in the upper mantle and lower crust, high slip rates, and short distances to Quaternary volcanic vents.

The red cluster has 79 known geothermal systems and is generally more dispersed in the western part of the Great Basin study area (Figure 5). Compared to some of the other clusters, the sum of loading values for this cluster are all relatively low (Figure 6). The strongest contributing features with negative relationships are MT and earthquake rate density, and the strongest contributing features with positive relationships are Quaternary faults and distance to felsic volcanic vents (Figure 8A). These results indicate that the known geothermal systems in this cluster have an association with low conductance in the lower crust, upper mantle, and mantle, low earthquake rate density, long distances to Quaternary volcanic vents, and high TSTD.

The brown cluster has 80 known geothermal systems and is a bit more dispersed in the eastern part of the Great Basin study area (Figure 5). Compared to the other clusters, the sum of loading values for this cluster are higher with strong positive relationships (Figure 6). The strongest contributing features with positive relationships are distance to volcanic vents and heat flow, and the strongest contributing features with negative relationships are geodetic data and slip rate of Quaternary faults (Figure 8B). These results indicate that the known geothermal systems in this cluster have an association with long distances to Quaternary volcanic vents, high conductive heat flow, low second invariant and shear rates, and low slip rates.

The orange cluster has 37 known geothermal systems and is generally clustered in the northeast corner of the study area, adjacent to the Snake River Plain (Figure 5). Relative to some clusters, the sum of loading values for this cluster are higher with strong positive relationships (Figure 6). The strongest contributing features with positive relationships are distance to intermediate volcanic vents, isostatic gravity, MT, and a negative relationship with Quaternary fault recency and TSTD (Figure 9A). These results indicate that the known geothermal systems in this cluster have an association with long distances to Quaternary intermediate volcanic vents, high isostatic gravity values, high conductance in the mantle and lower crust, low TSTD, and older recency.

The blue cluster has 77 known geothermal systems and is generally clustered in the northwest corner of the study area near the Modoc Plateau and along the southern edge of the Wasatch Front (Figure 5). Compared to some of the other clusters, the sum of loading values for this cluster are all relatively low and exhibit stronger negative relationships (Figure 6). The strongest contributing features with negative relationships are heat flow, distance to volcanic vents, and Quaternary fault attributes (Figure 9B). These results indicate that the known geothermal systems in this cluster have an association with low conductive heat flow values, short distances to Quaternary volcanic vents, older recency, low slip rate, and low TSTD.

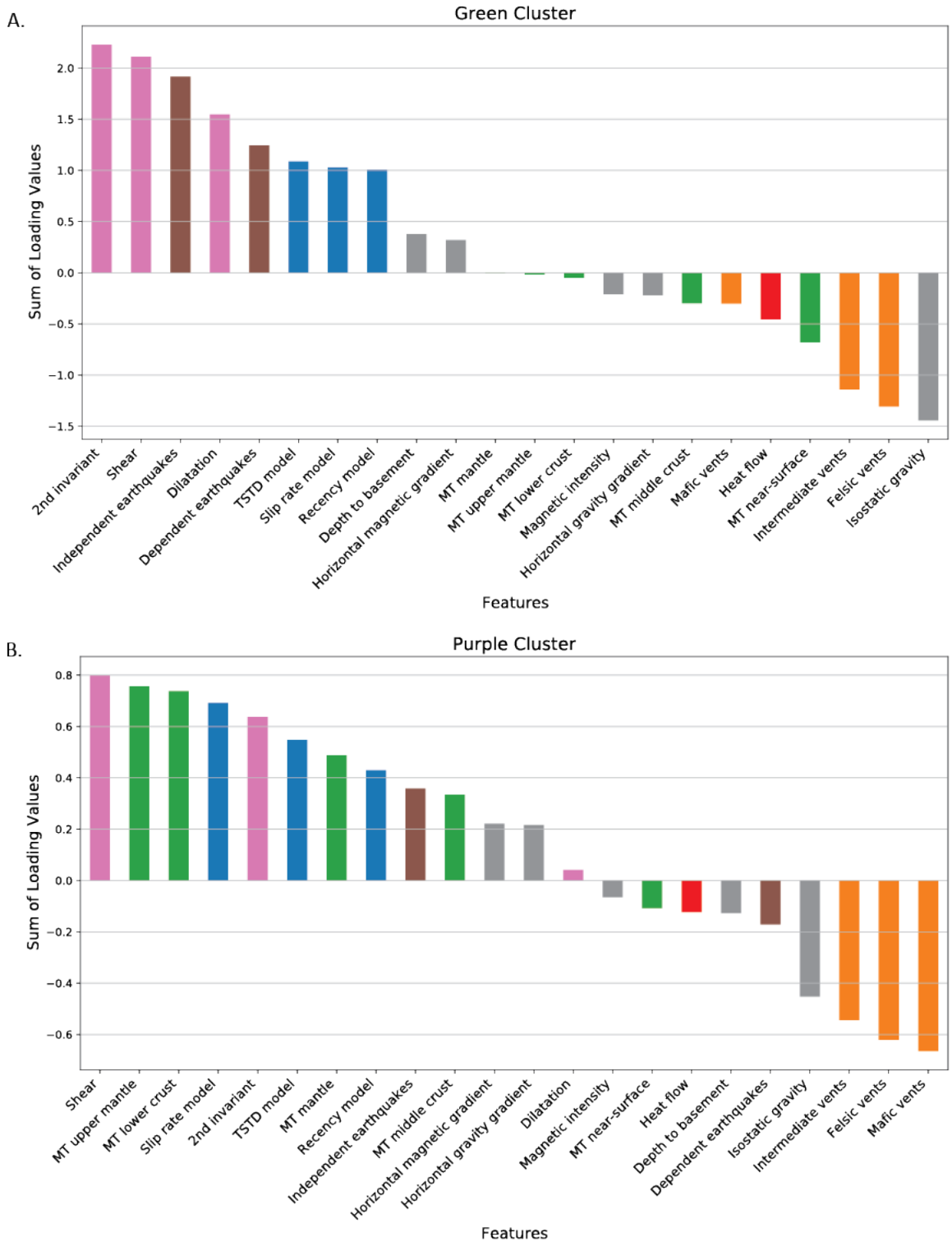

Figure 7: Relative sum of loading values ranking from high to low for the green (southwest Walker Lane) cluster (A) and Purple (northeast Walker Lane) cluster (B). Bars are colored for like data types; pink: geodetic, red: heat flow, orange: Quaternary volcanic vents, green: MT, blue: Quaternary fault attributes, brown: earthquake rate density, gray: potential field.

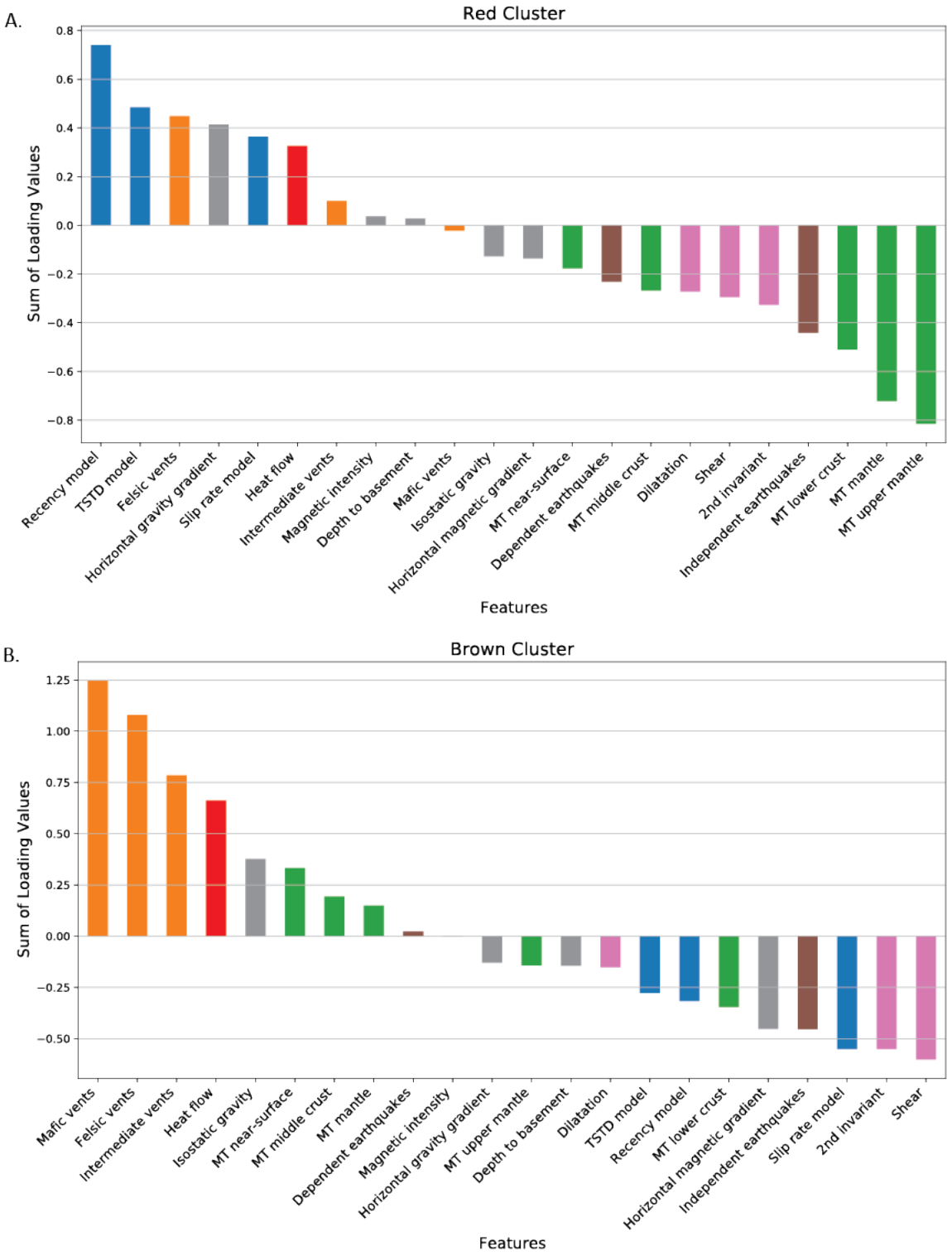

Figure 8: Relative sum of loading values ranking from high to low for the red (western Great Basin) cluster (A) and the brown (eastern Great Basin) cluster (B). Bars are colored for like data types; pink: geodetic, red: heat flow, orange: Quaternary volcanic vents, green: MT, blue: Quaternary fault attributes, brown: earthquake rate density, gray: potential field.

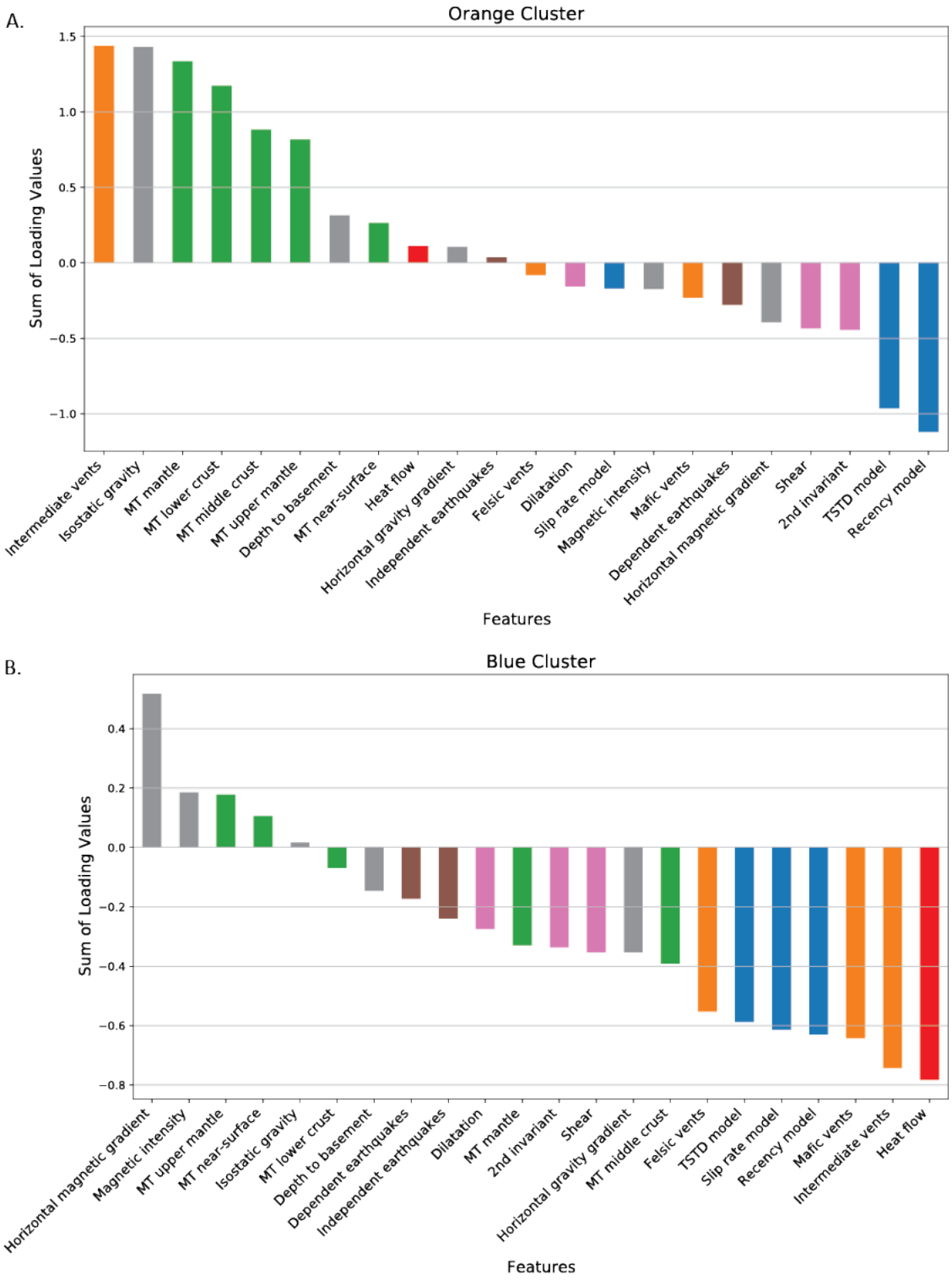

Figure 9: Relative sum of loading values ranking from high to low for the orange (adjacent to the Snake River Plain) cluster (A) and the blue (Quaternary volcanic field) cluster (B). Bars are colored for like data types; pink: geodetic, red: heat flow, orange: Quaternary volcanic vents, green: MT, blue: Quaternary fault attributes, brown: earthquake rate density, gray: potential field.

4. Discussion

4.1 PCA and K-means

These preliminary results indicate that while dimensionality reduction can be utilized, there are still many principal components required to explain the variance in the datasets. This was consistent in all the tests using different numbers of input features. The number of retained principal components utilized for k-means was also tested. If the number of principal components varied, the resulting clusters did not change significantly. The resulting clusters were still grouped in geographic areas that can be related to different geologic domains, independent of using geographic location data or assigning known geothermal systems to different geologic domains. As the number of principal components varied, the most variation in cluster designation occurred along the Wasatch Front. The geographic distribution of clusters in the western Great Basin remained largely consistent across the various tested numbers of principal components.

4.2 Clusters

Due to the western Great Basin clusters remaining largely consistent, this indicates high confidence in the differentiation of the clusters in the western Great Basin region. This includes the distinction of the green cluster on the southwestern side of the Walker Lane and the purple cluster on the northeastern side of the Walker Lane. The differentiation of these clusters seems to be mostly driven by geodetic data with higher strain rates in the green cluster and still high, but slightly lower strain rates in the purple cluster. Another difference noted in these clusters is that the green cluster is associated with slightly higher slip rates and slightly longer distances to some Quaternary faults than the purple cluster. This could be another line of evidence to support that geothermal systems in the green cluster may be associated with slightly longer distances to Quaternary faults potentially due to the high slip rates that commonly correspond to strike-slip faults or to very long and linear normal faults that are not as favorable for geothermal activity except in transtensional pull-apart basins or displacement transfer zones (Faulds et al., 2010, 2021b,c). These long linear normal faults may lack structural complexity and discontinuities, which could limit geothermal favorability, or these faults with high slip rates may generate more clay gouge that limits the permeability of the fault and lowers geothermal favorability (Faulds et al., 2010, 2021a,b,c; Hart-Wagoner et al., 2023). Either way, the variability between these clusters could be utilized to better characterize the geothermal systems along the Walker Lane.

These results also help to distinguish between the more dispersed clusters in the western and eastern Great Basin. The main distinguishing factor for these two clusters seems to be Quaternary fault attribute data. The brown cluster of the eastern Great Basin appears to have lower slip rates and older Quaternary faulting. This cluster also has longer distances to Quaternary faults and paleo-geothermal deposits, which could indicate that there is some difference in how the geothermal systems in the brown and red clusters interact with the near sub-surface to surface. It has previously been suggested that geothermal systems in the eastern Great Basin could be concealed within the carbonate aquifer domain (e.g., Smith et al., 2023). The longer distances to Quaternary faults and paleo-geothermal deposits identified in this study may support that hypothesis, as concealment could cause geothermal fluids to travel greater distances through the subsurface before reaching the surface. From the analysis of the features utilized in this study, it is not clear what feature could be causing potential concealment of geothermal systems in the

eastern Great Basin. Additional features, such as lithological data (Smith et al., 2023) may provide more insight into the factors that could be causing concealment in this sub-region.

The orange cluster that is adjacent to the Snake River Plain has strong positive contributing features of MT depth slices (middle crust to mantle) and isostatic gravity. This indicates that in this sub-region, there may be a conductive and dense body in the sub-surface. More work is needed to identify how this is impacting geothermal systems in this sub-region. This cluster also has strong negative contributing factors indicating that these systems have a relationship with low TSTD and older recency. This may indicate that these older Quaternary faults may not be oriented optimally to slip or dilate. This may suggest that Quaternary faulting is not as significant of a positive factor for geothermal systems in this sub-region.

The blue cluster is the only cluster that includes two geographic areas of the study area. While this cluster has weaker contributing factors than most of the other clusters, the key contributing feature for this cluster is distance to Quaternary volcanic vents, and this cluster aligns with the major Quaternary volcanic fields of the Great Basin. While Quaternary volcanic fields and this cluster do not compose a large portion of the Great Basin, they are still an important distinction because they offer insight into how the relationships between features and geothermal systems in these volcanic regions vary from other sub-regions of the Great Basin. Generally, these results show inverse relationships with many of the features that are key contributing features in much of the rest of the Great Basin, such as geodetic data, earthquake rate density, and Quaternary fault attributes. The distinctions that this cluster provides are key to more accurately model geothermal favorability in the volcanic fields of the INGENIOUS study area.

4.3 Distribution of Known Geothermal Systems between Clusters

The number of known geothermal systems in each cluster ranges from 37-80, with the highest number of geothermal systems occurring in the brown (n=80), red (n=79), and blue (n=77) clusters and nearly half as many geothermal systems in the orange, green, and purple clusters. This indicates that there are more identified geothermal systems in the eastern Great Basin, western Great Basin, and Quaternary volcanic field domains. However, this count considers both lower and higher temperature geothermal systems. If only the higher temperature systems are considered, the distribution of geothermal systems from highest to lowest is: red (n=42), purple (n=23), brown (n=15), green (n=13), blue (n=13), and orange (n=3). This could imply that the potential for higher temperature geothermal systems is greater in the western Great Basin and along the Walker Lane. Alternately, this could also suggest that current geothermal exploration has not found the key to identifying higher temperature geothermal systems in the other sub-regions.

The estimated temperatures of the higher temperature systems in each cluster were also assessed (Figure 10). This shows that the blue cluster (Quaternary volcanic fields) contains the highest temperature systems but also has the largest range in temperature. The mean temperature for this cluster is 175 ˚C. While the orange cluster (adjacent to the Snake River Plain) only has a few higher-temperature known geothermal systems, these have the smallest temperature range and a mean temperature of 172˚C. This could suggest that while there are few identified systems in this sub-region, there may be high potential for additional higher temperature systems, if we can isolate the best exploration approach for identifying hidden systems in this sub-region. Similarly, the brown cluster (eastern Great Basin) has a mean temperature of 170˚C, indicating there may be high potential to identify additional higher temperature systems in the eastern Great Basin as well.

The mean temperatures for geothermal systems in the green, red, and purple clusters (Walker Lane and the western Great Basin) were 160˚C, 158˚C, and 153˚C, respectively.

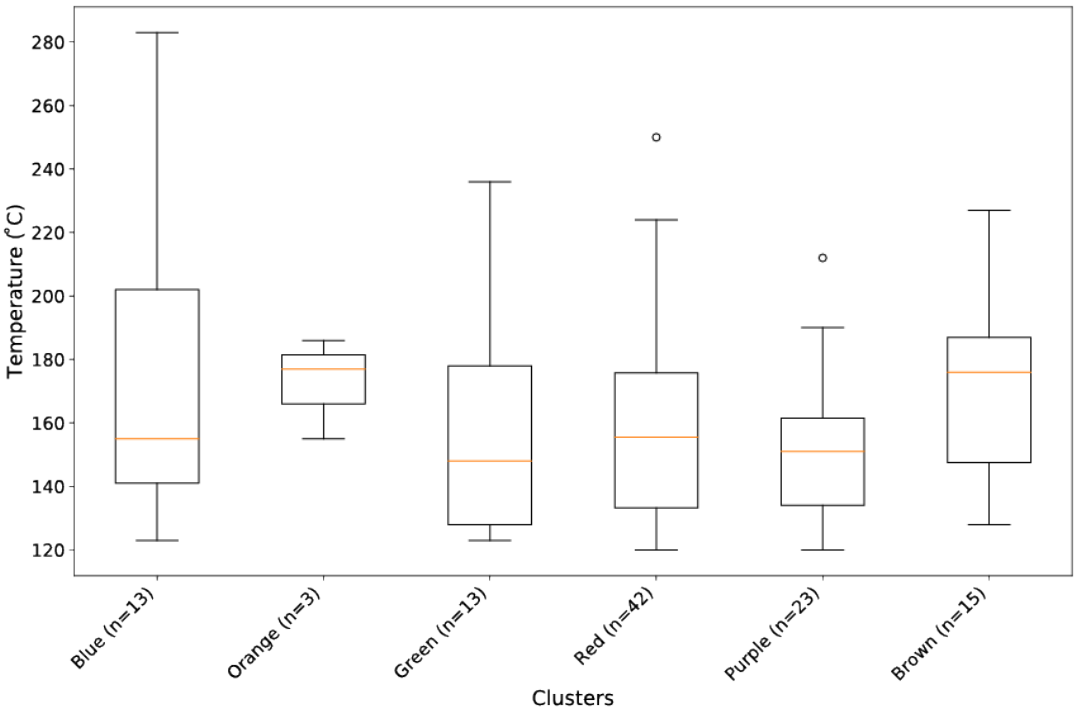

Figure 10: Box and whisker plot of the estimated temperatures for the known geothermal systems in each cluster.

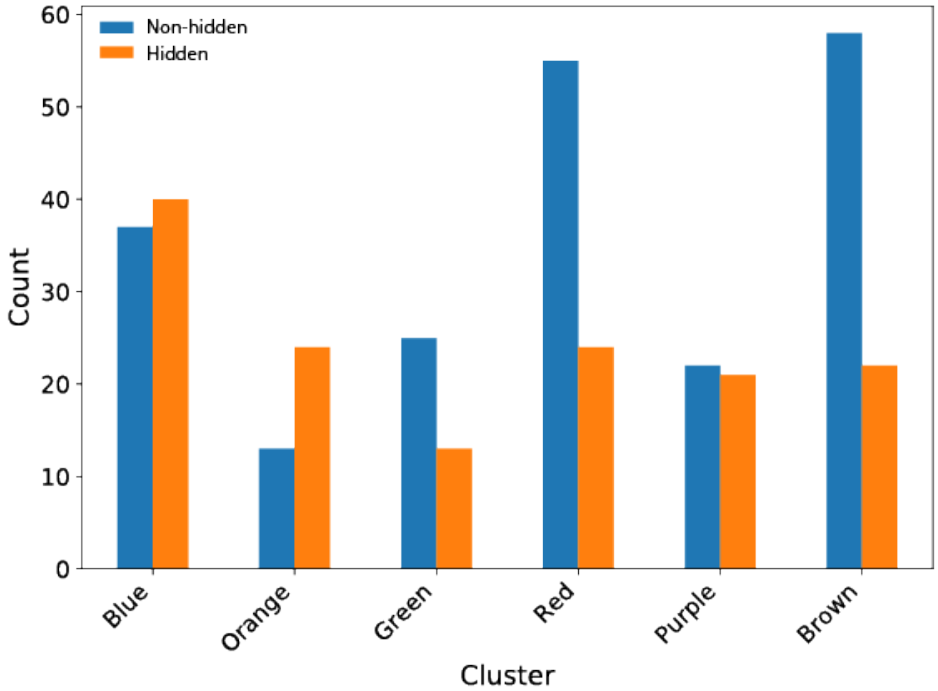

Figure 11: Number of hidden and non-hidden geothermal systems in each cluster.

It has been estimated that nearly three quarters of the geothermal resources in the Great Basin region lack surface expressions (e.g., Faulds et al., 2015). To understand the distribution of hidden and non-hidden geothermal systems in the clusters, the known geothermal systems were classified as hidden (no active surface thermal features) or non-hidden (has active surface thermal features such as a hot spring). Figure 11 shows the distribution of hidden and non-hidden geothermal systems in each cluster. The brown (eastern Great Basin), red (western Great Basin), and green (southwestern Walker Lane) clusters have significantly more non-hidden geothermal systems. This could suggest that these sub-regions have a higher potential for geothermal fluids to interact with the surface and form surface thermal features. In contrast, the orange (adjacent to the Snake River Plain) cluster has a higher proportion of hidden geothermal systems, which could suggest a higher likelihood for geothermal systems in this sub-region to be hidden. The blue (Quaternary volcanic fields) and purple (northeastern Walker Lane) have similar proportions of hidden and non-hidden systems.

There are not many known geothermal systems that are categorized as magmatic systems in the Great Basin region. Some of the magmatic systems that have been identified reside in the blue cluster, which is associated with Quaternary volcanic fields. However, there are also several that are in the green cluster, which is associated with the southwestern side of the Walker Lane. This suggests that while it might be limited, there may be a magmatic component in this Walker Lane sub-region.

Lastly, we identified the clusters where the current Great Basin geothermal power plants reside. The clusters with the highest concentration of actively producing geothermal power plants are the red cluster (western Great Basin) and the purple cluster (northeastern Walker Lane), each containing 27% of the power plants. The blue cluster (Quaternary volcanic fields) contains 19% and the brown (eastern Great Basin) cluster has 15% of the power plants. The green (southwestern Walker Lane) cluster and the orange cluster (adjacent to the Snake River Plain) have the lowest concentration, with 8% and 4% of the active power plants, respectively.

4.4 Implications for Modeling Geothermal Favorability

A cut-off of 120˚C is commonly used for assessing higher temperature geothermal systems (e.g., Hart-Wagoner et al., 2023), but here we utilized a lower temperature threshold to increase the number of systems utilized in the analysis. Even though some of these systems are lower temperature, having additional training sites in some of the areas with few identified higher temperature systems may help better characterize the geologic variability of geothermal systems in these regions. However, an analysis of just the higher temperature systems may provide more insight on the potential of the most productive geothermal systems in the study area.

Many of the higher temperature known geothermal systems are located in the western Great Basin. These higher temperature systems are commonly utilized in statistical techniques to develop relationships between geothermal favorability and these known geothermal systems. If these relationships are utilized to model geothermal favorability across the entire Great Basin, it is likely that the high contribution features, identified through this study, in the western Great Basin region are disproportionately favored in these models. Therefore, if these models are applied to areas such as the eastern Great Basin, geothermal favorability may not be modeled appropriately for that sub-region. This study is aligned with results from the Nevada PFA study area (e.g., Smith et al., 2021; Trainor-Guitton and Rosado, 2023) and suggests that the identified features may need to be

weighted differently for sub-regions to more accurately model geothermal favorability across the sub-regions of the INGENIOUS Great Basin region study area. More work is needed to assess the high contributing features in each of these clusters or sub-regions and how they relate fundamentally to the conceptual model for Great Basin geothermal systems. Additionally, these results need to be assessed for how they can be integrated into the INGENIOUS regional play fairway workflow to model geothermal favorability across the Great Basin sub-regions.

5. Preliminary Conclusions

This preliminary PCA analysis has shown that while dimensionality reduction can be applied, there are still many principal components required to explain the variance of the dataset. Additionally, the k-means clustering analysis utilized six clusters, and independent of assigning geologic domains to the known geothermal systems, the known geothermal systems cluster geographically and align with various geologic sub-regions of the Great Basin region. These include sub-regions such as the Walker Lane, extensional western Great Basin region, broad lower strain region in the eastern Great Basin, the area adjacent to the Snake River Plain, and Quaternary volcanic fields. The identified clusters were also assessed to discern the key contributing features and their positive and negative relationships to better assess geothermal variability between the clusters and sub-regions. The identified clusters also provide insight into the temperature distributions, proportion of hidden and non-hidden geothermal systems, and geothermal potential in each sub-region. Finally, the results of this study suggest that features may need to be weighted differently for individual sub-regions to more accurately model geothermal favorability across the sub-regions of the Great Basin.

Acknowledgements

This project is funded by U.S. Department of Energy - Geothermal Technologies Office under award DE-EE0009254 to the University of Nevada, Reno. Thank you to the entire INGENIOUS team (Great Basin Center for Geothermal Energy, Nevada Bureau of Mines and Geology, University of Nevada Reno, Aprovechar Lab L3C, Cyrq Energy, Inc., Geothermal Resource Group, Hi-Q Geophysical, Inc., Idaho Geological Survey, Innovate Geothermal Ltd, Lawrence Berkeley National Laboratory, National Renewable Energy Laboratory, Petrolern Ltd., U.S. Geological Survey, and the Utah Geological Survey) for their contributions to the INGENIOUS project, which supported this work. Any use of trade, firm, or product names is for descriptive purposes only and does not imply endorsement by the U.S. Government.

REFERENCES

Ayling, B. and others, 2022, INGENIOUS Phase 1 (budget period 1) progress report: Department of Energy DE-EE0009254 Report, 116 p.

Coolbaugh, M.F., Raines, G.L., and Zehner, R.E., 2007, Assessment of exploration bias in data-driven predictive models and the estimation of undiscovered resources: Natural Resources Research, v. 16, p. 199-207.

Craig, J.W., Faulds, J.E., Hinz, N.H., Earney, T.E., Schermerhorn, W.D., Siler, D.L., Glen, J.M., Peacock, J., Coolbaugh, M.F., and Deoreo, S.B., 2021, Discovery and analysis of a blind

geothermal system in southeastern Gabbs Valley, western Nevada, USA: Geothermics, v. 97, p. 102–177.

DeAngelo, J., Burns, E.R., Gentry, E., Batir, J.F., Lindsey, C.R., Mordensky, S.P., 2022, Heat flow maps and supporting data for the Great Basin, USA: U.S. Geological Survey data release, https://doi.org/10.5066/P9BZPVUC

Faulds, J., Coolbaugh, M.F., Bouchot, V., Moek, I., and Oguz, K., 2010, Characterizing structural controls of geothermal reservoirs in the Great Basin, USA, and Western Turkey: developing successful exploration strategies in extended terranes: In World Geothermal Congress, 11 p.

Faulds, J.E., and Hinz, N.H., 2015, Favorable tectonic and structural settings of geothermal settings in the Great Basin Region, western USA: Proxies for discovering blind geothermal systems: Proceedings, World Geothermal Congress 2015, Melbourne, Australia, 6 p.

Faulds, J., Hinz, N.H., Coolbaugh, M.F., Shevenell, L.A., Siler, D.L., dePolo, C.M., Hammond, W.C., Kreemer, C., Oppliger, G., Wannamaker, P.E., Queen, J.H., Visser, C.F., 2015, Integrated Geologic and Geophysical Approach for Establishing Geothermal Play Fairways and Discovering Blind Geothermal Systems in the Great Basin Region, Western USA: A Progress Report: Geothermal Resources Council Transactions, v. 39, 10 p.

Faulds, J., Hinz, N.H., Coolbaugh, M.F., Ramelli, A., Glen, J.M, Ayling, B.A., Wannamaker, P.E., Deoreo, S.B., Siler, D.L., and Craig, J.W. 2019, Vectoring into potential blind geothermal systems in the Granite Springs Valley Area, western Nevada: Application of the play fairway analysis at multiple scales: Proceedings, 44th Workshop on Geothermal Reservoir Engineering, Stanford University, Stanford, CA.

Faulds, J.E., Coolbaugh, M.F., and Hinz, N.H., 2021a, Inventory of structural settings for active geothermal systems and late Miocene (~8 ma) to Quaternary epithermal mineral deposits in the Basin and Range province of Nevada: Nevada Bureau of Mines and Geology Report 58, 28 p.

Faulds, J.E., Hinz, N.H., Coolbaugh, M., Ayling, B., Glen, J., Craig, J.W., McConville, E., Siler, D., Queen, J., Witter, J. and Hardwick, C., 2021b, Discovering blind geothermal systems in the Great Basin region: An integrated geologic and geophysical approach for establishing geothermal play fairways: All phases: Department of Energy, Geothermal Technologies Office, Final Technical Report on Award DE-EE0006731, 74 p, https://doi.org/10.2172/1724080.

Faulds, J.E., Hinz, N.H., Coolbaugh, M.F., Craig, J.W., Glen, J.M., Ayling, B.F., Sadowski, A.J., Siler, D.L, and DeOreo, S., 2021c, The Nevada geothermal play fairway project: Exploring for blind geothermal systems through integrated geological, geochemical, and geophysical analyses: Proceedings World Geothermal Congress 2021, Reykjavik, Iceland, 12 p.

Faulds, J. and Richards, M., 2023, INGENIOUS Transitions from regional to local scale to find hidden geothermal systems: Geothermal Resources Council Transactions, v. 47, 17 p.

Glen, J.M.G, Earney, T.E., Zielinski, L.A., Schermerhorn, W.D., Dean, B.J., and Hardwick, C., 2022, Regional geophysical maps of the Great Basin, USA: U.S. Geological Survey data release, https://doi.org/10.5066/P9Z6SA1Z.

Hart-Wagoner, N.R., Coolbaugh, M., Faulds, J.E., and Mlawsky, E., 2023, Feature engineering of fault attributes for play fairway analysis, Great Basin region, USA: Geothermal Resources Council Transactions, v. 47, 22 p.

Hart-Wagoner, N.R., Coolbaugh, M., Faulds, J.E., Mlawsky, E., Lindsey, C., Trainor-Guitton, W., 2024, Preliminary Regional Play Fairway Workflow for the Great Basin region, USA: Proceedings, 49th Workshop on Geothermal Reservoir Engineering, Stanford University, Stanford, CA.

Hotelling, H., 1933, Analysis of a complex of statistical variables into principal components: Journal of educational psychology, v. 24(6), p. 417.

Jain, A. K., 2010, Data clustering: 50 years beyond K-means: Pattern recognition letters, v. 31(8), p. 651-666.

Jolliffe, I. T., 2002, Principal component analysis for special types of data: Springer New York, p. 338-372Peacock, J.R. and Bedrosian, P., 2022, Electrical Conductance Maps of the Great Basin, USA: U.S. Geological Survey data release, https://doi.org/10.5066/P9TWT2LU.

Lloyd, S., 1982, Least squares quantization in PCM: IEEE transactions on information theory, v. 28(2), p. 129-137.

MacQueen, J., 1967, Some methods for classification and analysis of multivariate observations: In Proceedings of the fifth Berkeley symposium on mathematical statistics and probability, v. 1, No. 14, p. 281-297.

Muntean, J.L., Davis, D.A., and Ayling, B., 2021, The Nevada mineral industry 2020, Nevada Bureau of Mines and Geology Special Publication, MI-2020, 105.

Peacock, J.R. and Bedrosian, P., 2022, Electrical Conductance Maps of the Great Basin, USA: U.S. Geological Survey data release, https://doi.org/10.5066/P9TWT2LU.

Pearson, K., 1901, LIII. On lines and planes of closest fit to systems of points in space: The London, Edinburgh, and Dublin philosophical magazine and journal of science, v. 2(11), p. 559-572.

Smith, C.M., Faulds, J.E., Brown, S., Coolbaugh, M., DeAngelo, J., Glen, J.M., Burns, E., Siler, D.L., Treitel, S., Mlawsky, E., Fehler, M., Gu, C., and Ayling, B.F., 2023, Exploratory analysis of machine learning techniques in the Nevada geothermal play fairway analysis: Geothermics, v. 111, https://doi.org/10.1016/j.geothermics.2023.102693.

Trainor-Guitton, W., & Rosado, S., 2023, A VOI Web Application for Distinct Geothermal Domains: Statistical Evaluation of Different Data Types within the Great Basin: Geothermal Resources Council Transactions, v. 47, 16 p.

Williams, C.F., Reed, M. J., DeAngelo, J., and Galanis Jr, S. P., 2009, Quantifying the undiscovered geothermal resources of the United States: Geothermal Resources Council Transactions, v. 33.

Geological Mapping Standards for Developing Geothermal Resource Conceptual Models; Survey Design, Applications, Pitfalls and Remedies

Nicholas H. Hinz[1], Alex Milton[1], William Cumming[2], and James E. Faulds[3]

[1]Geologica Geothermal Group, Inc.

[2]Cumming Geoscience

[3]Nevada Bureau of Mines and Geology, University of Nevada, Reno

Keywords

Geologic Mapping, Conceptual Modeling, Best Practices, Risk, Well Targeting, Resource Assessment

ABSTRACT

Geological mapping is a vital component of geothermal exploration programs because faults penetrating formations with rock properties favorable to forming open space fracture permeability are an important conceptual element of almost all geothermal reservoirs developed for power generation. Depending on exposures and site access, geologic maps typically have several relevant components including stratigraphy, faults, structural data, active and inactive geothermal surface manifestations, type, and extent of alteration and, for volcano-associated systems, eruption vents and age. Each of these components contributes to the interpretation of geophysics and geochemistry and the integration of these with thermodynamics in a geothermal resource conceptual model.

Geological mapping projects begin with reviews of earlier maps, but most geological maps are produced for purposes other than the assessment of a specific geothermal prospect, such as characterizing regional tectonics, assessing hazards, or exploring for minerals. Although the fundamentals of geological mapping are the same for these applications, their differing scales and objectives can limit their relevance to geothermal exploration. For example, a regional study might provide important overall context regarding a major strike-slip fault that extends through a geothermal prospect, but it might omit the local step-over in the fault that accounts for the geothermal upflow. Where structures are obscured by recent volcanic ash eruptions or alluvial deposits within a prospect, regional structures are typically interpolated, implying greater local uncertainty. When a team is integrating a wide range of data sets into geothermal resource conceptual models used to assess well target risk and resource capacity, geoscientists who are not geologists must understand how to appropriately weight the evidence from a range of geological maps. To address these needs, we have reviewed best-practice standards for the specialists who produce geological maps for the geothermal industry, and we have proposed a checklist that we recommend prospect assessment teams and managers use to weight evidence from geologic maps.

1. Introduction

Geological maps provide the overall context for the interpretation of geochemistry, geophysics, hydrology and well data for geothermal resource characterization and reservoir management. They also provide surface evidence for interpreting the structures and formation properties that constrain the permeable pathways hosting hot geothermal upflows and buoyant outflows and, commonly just as importantly, cold meteoric downflows and crossflows.

Geological mapping provides 2D constraints that, when integrated with other geoscience data, can be projected into a 3D subsurface model of the lithology and structural elements of geothermal resource conceptual models. These maps integrate the line and point observations obtained from geological fieldwork with remote sensing image analysis, well data, geophysics and, increasingly, Light Detection and Ranging (LiDAR) data. The fundamentals of geologic mapping for geothermal purposes are the same as those for exploration of other natural resources, for hazard assessment and for geoscience research but there are major differences in emphasis that are commonly not appreciated within the industry. After airborne and satellite remote sensing imaging became widely available through the mid-1900s and especially after computer analysis of lineaments, structures, and general geomorphology became ubiquitous in the late-1900s, they have become essential for planning field mapping and interpolating between surface measurement points. In recent years, the technology used in field mapping has advanced significantly with the advent of high-resolution LiDAR imaging, integrated into electronic displays with GPS and cameras supporting the insertion of photographs of mapped features directly into a geolocated field map database. However, the fundamental concepts of field geology have not changed (e.g., Compton, 1985, 2017; Freeman 1999; Walker and Cohen, 2009; Spencer, 2017).

High quality geologic mapping provides the principal constraint on several important elements of geothermal resource conceptual models used in geothermal exploration and development. For example, faults are associated with the fracture permeability of upflows in both deep circulation systems (Faulds and Hinz, 2015) and most magmatically heated systems (Hinz et al., 2016). Reservoir boundaries are also commonly associated with mapped faults and lithologic contacts. Geologic mapping supports the interpretation of permeability patterns associated with structural settings, stress orientations, Quaternary fault activity and stratigraphy. The extent, type and activity of exposed alteration is correlated with the existence and size of geothermal reservoirs (Stelling et al., 2016). Geologic mapping also helps identify potential holes in the smectite cap that protects geothermal reservoirs from cold meteoric downflows commonly associated with recent volcanic domes and vents and exposed fractured crystalline rocks. In addition to its support for building the conceptual model, geological mapping sometimes identifies new areas for geochemistry sampling and usually supports the design of geophysical surveys. Ideally, geological mapping should be treated as an iterative collaboration among geoscientists; for example, local field geology might follow up a gap in a smectite cap detected by MT or an offset in shallow formations wells consistent with faulting not shown in existing maps. The crucial step for effectively using geologic mapping is its consistent integration with geochemistry, geophysics and supporting data in the geothermal resource conceptual model.

Although making a lineament map from remote sensing images is an essential step in the process of producing effective geologic maps, the mistaken assumption that lineament maps alone can reliably constrain subsurface structural geology is a common pitfall in the geothermal industry. Because of the higher cost and much more demanding level of expertise and physical fitness

required to effectively conduct field mapping, geologic maps used for geothermal exploration and development have been mainly based on lineaments derived from remote sensing data, with little or no ground verification. Given the larger number of features typically included in lineament maps relative to ground-verified geologic maps, the lineament maps are often given more emphasis in well targeting decisions, resulting in a confirmation bias in favor of using such maps, even if the predictive value of the lineament maps is much poorer than ground-truthed geologic maps. Although LiDAR lineament analyses are an important aid to field mapping, the use of lineament maps rather than geological maps consistent with best practice mapping standards tends to increase risk in resource evaluation and well targeting (Stark et al., 2022).

This paper summarizes the best practices of geologic mapping programs for geothermal applications. In Section 2 we propose a brief checklist that geologists, other geoscientists, and decision-makers can apply when assessing what weight to give to geologic map elements in an integrated conceptual model and what priority to give to acquiring new geology data. In Section 3, we supply a quality assurance checklist that geologists can use to assess the adequacy of existing maps and determine suitable objectives for new or infill geologic mapping. Section 4 recommends steps for planning geologic mapping fieldwork and recording field observations, including desktop analysis of LiDAR and integration of supporting data prior to completing fieldwork. Section 5 reviews established best practice standards for completing a geologic map, supporting cross-sections and an accompanying geologic report. To illustrate these points, we review three published case studies that include older and revised geological maps and highlight pitfalls and successes related to the maps, along with comparisons to other geoscience data and conceptual models of the resources. These case studies include Sorik Marapi (Indonesia), Kibiro (Uganda) and Blue Mountain (United States). Other geothermal areas are discussed in brief with citations to highlight key applications, pitfalls, and remedies.

2. Assessing Confidence in Geologic Map Elements and the Need for New Mapping

Some types of geologic mapping are almost always available for any geothermal prospect, but these geologic maps are usually not been developed with a focus on characterizing a specific geothermal prospect. These maps can have a broad range in scales, quality, and detail. Therefore, the first step in geologic mapping is an assessment of the suitability of the existing geologic map data for the geothermal application. This initial assessment is typically completed by a geologist but the same information is relevant to non-specialists assessing whether to acquire more geology data or considering what weight to give to particular map features when integrating the evidence from the map with other geoscience data in conceptual models used to target wells and assess resource geometry.

To facilitate the review of existing mapping by geologists, other geoscientists and resource managers, a simplified checklist is provided in Table 1 below. To illustrate the application of this checklist, two side by side geologic maps of the same geothermal area have been provided in Figure 1 to show examples of each checklist item.

Table 1: Checklist for evaluating the quality of existing geologic mapping and gaps that may pose a risk to guiding an exploration program. Examples of this checklist are provided in Figure 1.

A check in this list indicates high risk	Missing a check in this list indicates high risk
☐ Does the map mainly show lineaments without detailed ground checking of "faults" important to the interpretation?	☐ Are types of faults indicated (normal, srike-slip, etc.)?
☐ Are "faults" straight lines in every direction creating the appearance of shattered glass?	☐ Are dip and sense motion shown?
☐ Are many of the faults intersecting, but not offset each other?	☐ Are formation dips shown and are they consistent with fault dips in the section?
☐ Are faults given names that are not previously documented and lack reliable measurements at several exposures or data types showing dip, throw and motion?	☐ Are faults dotted or narrowed to indicate extrapolation across alluvium?

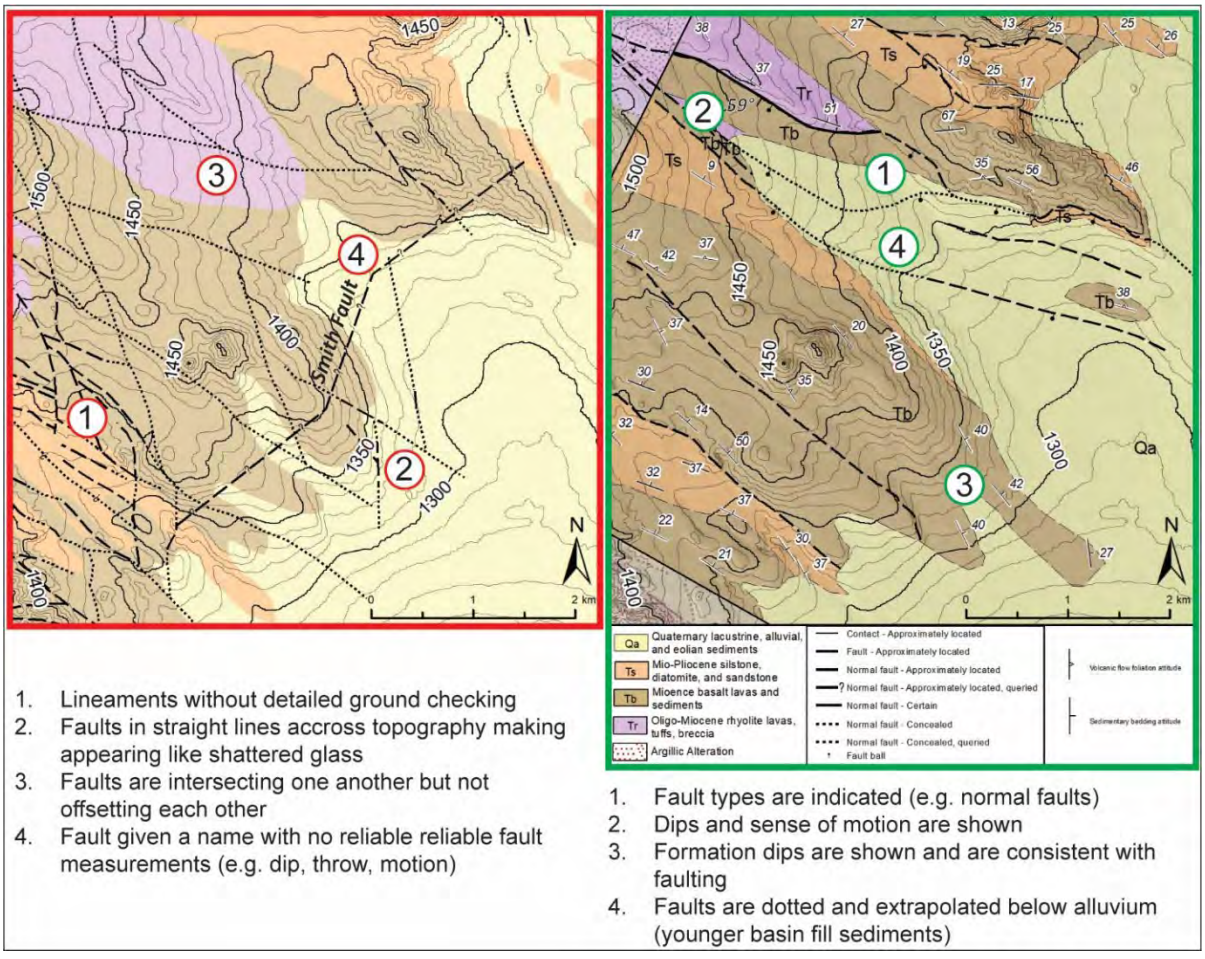

1. Lineaments without detailed ground checking
2. Faults in straight lines accross topography making appearing like shattered glass
3. Faults are intersecting one another but not offsetting each other
4. Fault given a name with no reliable reliable fault measurements (e.g. dip, throw, motion)

1. Fault types are indicated (e.g. normal faults)
2. Dips and sense of motion are shown
3. Formation dips are shown and are consistent with faulting
4. Faults are dotted and extrapolated below alluvium (younger basin fill sediments)

Figure 1: Two geologic maps of the same area with checklist elements from Table 1 listed by number to locate examples on each map. The map on the left outlined in red is an example of a high-risk geologic map (checking all four boxes on left column of Table 1). The map on the right outlined in green is an example of the high-quality mapping required for successful geothermal exploration and development (checking all four of the boxes on the right column in Table 1).

If the checklist in Table 1 indicates relatively high risk in using the existing geological maps, then the next step may be to review whether circumstances are favorable for significantly improving the map quality. In some cases, improving the map might be problematic, say because alluvium obscures structure. In these cases, alternative data sets like MT and/or temperature gradient wells might more suitably constrain resource decisions. Some circumstances warrant a more detailed data gaps analysis that considers the impacts of gaps relative to each other and the project goals. If additional mapping is warranted for a given project, best practices for implementing a geologic mapping program are provided in the following sections.

3. Determining Map Area and Mapping Objectives

The first step in geologic mapping is to determine the area that needs to be covered. Start by reviewing the quality of existing geologic maps (Section 2) and well data (if available) to design and plan details of the geologic mapping program. Planning the area for mapping should consider access restrictions and geology questions related to both resource assessment and to the design of supporting surveys.

In geothermal exploration there is typically a specific lead that attracts initial interest, such as hot springs, fumaroles, alteration, hot wells, silica sinter or a pattern of resistivity (Stelling et al., 2016; Sewell et al., 2024). The area of the likely range of geothermal conceptual models associated with the lead is the focus of exploration. A geologic map should be focused on key conceptual model elements that can be controlled by geology (e.g., permeability, hot upflow, hot/warm outflow, cold influx, acid influence, and cap rock). The proposed map area should cover the likely stratigraphy and structure associated with the geothermal resource. The map area does not need to be rectangular or even linear on any edge. Typically, the lateral extent is several times larger than the lateral extent of the anticipated resource area as indicated by potentially analogous reservoirs, including both upflows and outflows. All likely geometries should be covered, and sufficient area should be reviewed to capture the broader structural and stratigraphic frameworks.

The map area can be extended in greater distance parallel to the structural trend and a lesser distance perpendicular to it. This will ensure that a greater understanding of the local and broader regional structural framework is captured in the geologic mapping. Since even high-quality geological mapping is relatively low cost, it is usually better to capture a larger area surrounding the lead than would be considered for geophysical surveys. Different elements of the map might cover different areas. A larger area might be the focus of field checks for key stratigraphic and structural controls of the geothermal resource that may not be located at the surface in the immediate vicinity of the initial geothermal lead. To help focus the geologic map area, mapping objectives and ensure that they are accounted for when designing the map area and implementing the field work, a general checklist for review of geologic mapping objectives is provided in Table 2.

4. Implementing a Geologic Mapping Survey

This section focuses on implementation of the objectives identified in the previous section.

3.1 LiDAR and Aerial or Satellite Photo Analysis

A beginning step for many geothermal mapping projects is to complete a desktop analysis of LiDAR data to assess Quaternary fault traces. These data help geological mapping efforts and give insights into local and regional structural complexities that could control permeable pathways for hot fluids (Faulds et al., 2015), reservoir boundaries (Hinz et al., 2021). When planning LiDAR acquisition or analysis, it includes an area 25-50% larger than the expected geologic map area to help integrate local and regional fault patterns. Although LiDAR data significantly improves the efficiency and reliability of the geologic mapping process, they are not essential to complete a geologic map suitable for geothermal exploration and development in most settings.

Table 2: Geologic map review check list. A check mark in the table below indicates that the related data is more likely to be reliable and in turn have valuable utility to geothermal resource conceptual modeling.

Geologic Map Objectives		
Is it present? ("√" if yes)	***Map element***	***Description***
	Stratigraphy	Unit extent shown in map and age sequence in legend, with accompanying text describing of each unit, even if only one or two units in an entire map area.
	Structural data	Include bedding attitudes, and fault dips if surface outcrops are available.
	Fault symbology	Faults and contacts drawn to indicate confidence based on exposed/not exposed, uncertainty of location or existence. Examples may include **Solid** = certain; **Dashed** = approximate; **Dotted** = concealed; Queried = fault or contact uncertain (symbolized with **dashed lines** and "**?**"). Faults should also be clearly distinguished from lineaments with different symbology.
	Fault kinematics	If kinematic evidence is available, kinematic labels should be included (e.g., up/down, strike-slip arrows)
	Fault trace geometry	Map traces of faults should include kinematic labels. Examples include: -Strike-slip faults typically very straight along strike -Normal or reverse faults typically sinuous along strike -Low angle normal or thrust faults are very sinuous along strike
	Realistic fault network pattern	Most geothermal prospects include only a few well-defined active major faults with kinematically consistent subsidiary faults and older faults that may be less consistent. Realistic fault patterns rarely look like randomly broken glass.
	Geothermal features	If present, location, and alteration details should be included with geothermal surface manifestations.
	Cross section	Geologic maps should include at least one cross section each.
	Regional correlation	The geology of the map area fits the regional geology.
	Well data	If well data is available, well lithology observations fit with available geologic map data in a supporting cross-section.

Figure 2 illustrates a typical LiDAR and structural analysis workflow. This typically includes evaluating geomorphic features associated with faults visible in low sun-angle hillshades and/or from slope shades in LiDAR images (Figure 2a). These geomorphic features can include fault scarps which are ramps in the ground surface that connect offset depositional or erosional surfaces (e.g., Bennett et al., 2018). A high-resolution elevation profile like Figure 2b can detect subtle fault motion related to scarps and a series of profiles can help sort out the continuity of faults, often iterating with field observations. Other features include scissoring of fault scarps, closed depressions, contractional ridges along strike-slip faults (e.g., Hunter et al., 2011; Gold et al., 2014) or pop-up wedges or ground folds associated with reverse or thrust faults (e.g., Koehler and Woods, 2013). Although LiDAR resolution of the ground surface below dense tropical forest is typically lower than would be expected for the arid desert environment shown in Figure 2, the value of LiDAR is comparable because it significantly offsets the greater difficulty of field mapping in tropical forest. Therefore, structure relevant to geothermal exploration can be mapped with LiDAR globally across all fault types and through most vegetation cover.

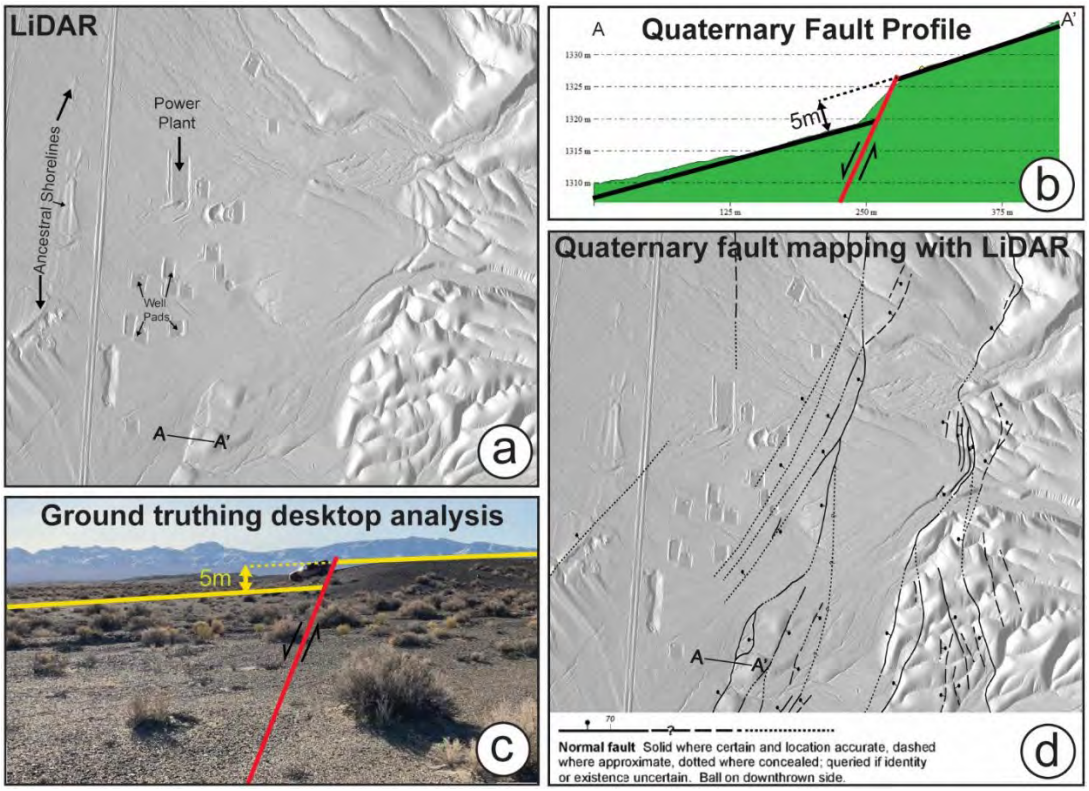

Figure 2: Example dataset and workflow for Quaternary fault focused LiDAR analysis. a: raw hill shade exported from LiDAR data of the Star Peak geothermal area (Fercho et al., 2020) with examples of non-fault lineaments, anthropogenic features, and cross section A-A' across a Quaternary active fault scarp in the younger basin fill sediments. b: elevation profile of A-A' showing the planer and near parallel surfaces of the basin fill sediments offset by a ~5 m normal fault. c: an example of in field ground truthing of the features identified in LiDAR with a pickup truck parked on the steep slope of a fault scarp. d: The resulting map after the desktop analysis and ground truthing of the LiDAR (Fercho et al., 2020).

Geomorphic features visible in LiDAR data that can be confused with fault scarps include fluvial scarps, the break-in-slope features associated with differential erosion between separate stratigraphic horizons, and paleo-shorelines of lakes (Figure 2). Other natural features that are

commonly identified as LiDAR lineaments but typically do not directly correspond to faults include river or stream channels, edges of lava flows, edges of mud flows and tops of ridges (Figure 2). Non-geologic features that may be confused with fault scarps include anthropogonic ground disturbances like roads and vegetation alignments that have not been eliminated in the processing of the raw LiDAR data to generate the Bare Earth DEM. The ambiguity of the interpretation of such features can be reduced by interpreting the LiDAR images together with aerial or satellite photo imagery and supporting geophysical data but, in most cases, additional field mapping will be required to fully characterize faults initially identified using LiDAR (Milton et al., 2023).

At the exploration stage of a project, it has seldom been feasible to conduct a drone-based thermal infrared + visible (RGB) photo survey over a sufficient area to be decisive but this option should be considered if practical at a suitable cost.

The desktop analysis of LiDAR and satellite photo imaging supports the preparation of an overall field strategy and a list of specific field objectives and priorities. These include confirming Quaternary fault traces, collecting field data on suspected fault traces, assessing any questionable features in the LiDAR that may be faults (Figure 2) and checking any evidence of potential alteration detected in the satellite photo images (or any drone-based surveys).

3.2 Geologic Field Mapping

Field notes should be recorded whenever observations can be found that are key to part of the overall mapping objectives of any given study. The spacing of locations in which field observations are recorded is based on geological complexity and availability of features that can be investigated. The geologic map should be updated with acquisition of each significant field point and at the end of each day the geologic map should be reviewed to make sure all updates have been incorporated. The next day's list of field objectives should also be revised to address new or remaining questions.

All field observations should include GPS (or similar) location data (including coordinate system used), a general description of the site location and photographs, with scale, if relevant to the type of feature described. A digital tablet/smartphone using appropriate software can significantly automate this task and promote the integration of LiDAR and other supporting data. Further details of the notes necessary for each site depend on the available geologic features, the geologic reason for selecting the site for recording observations and/or obtaining quantitative measurements. Each observation point may include focus on one or more of the following categories with requisite information required for each category based on field data available.

Stratigraphic Framework: Clearly delineate the stratigraphic framework, including bedrock and unconsolidated surficial deposits, contact relations and relative ages, distribution, thickness, overall composition, and compositional variation in 3D space. Where possible, attitudes in the bedrock units should be collected. When field analysis of outcrops and hand samples is not sufficient to clearly delineate lithologic units, collecting samples and completing thin section analysis can help define lithology. Key stratigraphic observations and map elements include:

- Unit descriptions include color, texture, mineralogy, and variability of these qualities. Provide interpretation of lithology and formation as applicable.
- Contacts

    - Record which unit is exposed on either side of the contact and if the contact is depositional, intrusive, faulted, or a combination thereof
    - Record the dip of the contact
    - Observe and record the degree and type of alteration if present
- Attitudes of stratigraphic units (e.g., bedding, foliation)

Structural Framework: Determine the structural framework, including geometry, kinematics, magnitude of offset, recency, and slip rates as data is available. Emphasis should be placed on determination of Quaternary active faults, including ones that may be immediately adjacent to geothermal prospects and acting as one of the primary faults in a major fault step-over, pull-apart, or other key structural setting. Key structural observations and map elements include:

- Faults
    - Attitudes of faults
    - Damage zone characterization (if applicable)
        - Width
        - Fabric and composition (breccia, clay gouge)
        - Alteration mineralogy, type, and intensity
    - Kinematic data from fault surfaces with photos to document features
        - Trend and plunge or rake of striae in fault plane
        - Riedel shears or steps along a fault surface (e.g., van der Pluijm and Marshak, 2004; Fodor, 2007)
        - Offset planar or linear features along the fault
    - Quaternary fault scarp characterization such as trend or strike, vertical offset of surfaces (apparent offset), slope, single or multi-event, observations relative to determining if normal, reverse, oblique, or strike-slip. Photos as applicable.
- Folding
    - General description
    - Measure and record geometry as data is available
- Metamorphic fabrics
    - Describe type(s) of fabric (e.g., planar, linear)
    - Record orientations of strike and dip or trend and plunge as necessary depending on the fabrics present.

Alteration: Determine if alteration is present at the surface. If so, map the extent, type, intensity (e.g., Gifkins et al., 2005). If areas of alteration are present, determine relative age(s) such as recent/active or relict. Relict could be 10s or 100s of thousands of years old or millions of years old. If a suitable analog provides a potential guide to alteration association and age, note which analog is used and why. Alteration assemblages can be difficult to identify in hand sample. Collecting rock samples in the field for lab analysis (e.g., x-ray diffraction and/or thin section analysis) can help define the alteration associated with modern and relict geothermal systems. Ideally, a shallow soil temperature probe should be inserted to refusal into soft clay alteration to assess its current state and, if the temperature is significantly higher than ambient, the feature should be identified as a thermal manifestation and labeled hot altered ground. Key alteration observations and map elements include:

- Alteration descriptions (e.g., Thompson et al., 1996)
    - Describe the alteration relative to the protolith (e.g., primary, or secondary)

- Describe color, texture, minerology, and alteration intensity

Surface Manifestations: Map active and inactive geothermal surface manifestations. These may include thermal springs, steaming ground, fumaroles, gas seeps, hot altered ground, or spring deposits such as travertine or sinter. Key geothermal surface manifestation observations that should be noted by field geologists and included as map elements include:

- Geothermal surface manifestation description, temperature, any odor of sulfur, photos, and notes on whether the location is associated with stratigraphic and/or structural elements.
- Hot spring observations should include temperature, pH and chloride content using test strips. More complete geochemistry sampling might be warranted if access is limited.
- Mineral spring deposits (e.g., sinter, travertine) characterization, description, photos

Table 2 is a summary of these key geologic map elements and serves as a checklist of key observations and structural elements for a geologist when planning and implementing geologic mapping focused on a geothermal resource. The absence of one or more of these key observations is not necessarily a reflection of the quality of the geological map. In fact, the common practice of setting quotas on the numbers of fault observations that field geologists must find tends to greatly degrade the quality of the resulting maps since most lineaments are not correlated with faults and so expertly confirming that the fault does not exist is an important goal of the field geologist. Therefore, it is important to detail in the geologic map and report those key structural elements that are observable in the field and those lineaments and previously interpreted faults that could not be confirmed in the field.

Additional details of potential observations and approaches to collecting observations on each type of geologic feature can be found in many geologic mapping reference books (e.g., Compton, 1985, 2017; Freeman 1999; Walker and Cohen, 2009; Spencer, 2017).

4. Final Geologic Map Production and Reporting

After fieldwork is complete, a final map needs to be generated with colors, symbols, and labels of polygon, line, and point data clearly presented. Faults need to be attributed as concealed where they extended under young surficial deposits or bedrock units and where the fault does not extend to the surface. Faults also need to have kinematic indicators on the map (where this is known) such as which side is up or down or if strike-slip if left-lateral or right-lateral. A unit list, unit descriptions, and unit/age correlation diagram or chart should accompany the map. To illustrate the interpreted geologic framework in the subsurface, one or more geologic cross sections should accompany each part of the map area that is of exploration interest and differs significantly from other sections. Typically, cross sections are generated perpendicular to the overall structural strike across a given map area to communicate framework geology most effectively. Information from nearby wells and geophysical cross-sections should be considered in the making the geology cross-section and, in many cases, it will be advantageous to align a geological cross-section with such data. Finally, a checklist of map components and cartographic details can be helpful as part of the final internal review of a map product. Examples are available through multiple state and federal geologic surveys globally (e.g., Nevada Bureau of Mines and Geology: NBMG).

A geologic report should accompany all mapping projects and should include summaries of the field mapping accomplished, including integration of multiple datasets as available, and comments on map data accuracy and remaining data gaps based on limitations of field access or exposures.

The core of the report should provide a summary of the stratigraphic and structural framework, alteration, and distribution of surface geothermal features, as relevant. Annotated field photos, inset map figures, and plots of structural data typically strengthen the report and summary interpretations relevant to supporting geothermal exploration and development projects. The final map and accompanying report, along with assessments of remaining data gaps can then be used as an effective tool at identifying structural target areas (e.g., Fauld and Hinz, 2015; Faulds et al., 2021; and Hinz et al., 2023) along with integrating with geophysics, geochemistry, and well data, as available, for conceptual modelling purposes.

5. Case Studies

Three representative case studies compare old mapping that illustrates pitfalls and new mapping completed according to geologic mapping best practices. These examples illustrate several key components of geologic maps in a range of geological settings, including volcanic and non-volcanic geothermal prospects in dense forests and deserts. Sorik Marapi, located in Indonesia, is an operating field in a volcanic arc setting with a field area mostly covered by dense tropical forest and locally covered by agricultural fields. Kibiro, located in Uganda, is an undeveloped deep-circulation system with moderate vegetation coverage in the western branch of the East African Rift System. Blue Mountain, located in the United States, is deep circulation system associated with an operating field in an arid desert region.

Although these three case studies are representative of geological mapping efforts in a variety of settings, geological mapping best practices have been applied successfully in many other areas. This includes geothermal fields in the Great Basin region of the western USA, fields in the eastern and western branches of the East African Rift System (EARS), and in subduction arc settings. Many publications describe geological maps that are consistent with the standards outlined in this paper and, together with subsequent papers on resource development, illustrate how important such maps can be to the conceptual models of the related geothermal fields, including:

- in the US Basin & Range region, at Desert Peak (Faulds et al., 2010, 2012), Bradys (Faulds et al., 2010, 2017), Desert Queen (Dellerman, 2021; Faulds et al., 2010, 2022), Patua (Faulds et al., 2011), Emerson Pass (Anderson, 2013; Anderson et al., 2013), Black Warrior area (Sadowski, 2016; Sadowski and Faulds, 2016), San Emidio/North Valleys (Rhodes, 2011; Rhodes et al., 2011), Lee-Allen (Hinz et al., 2010), Salt Wells (Hinz et al., 2011), Wabuska (Hinz et al., 2013), southeastern Gabbs Valley (Craig, 2018; Craig et al., 2021); Reese River Narrows (Hinz et al, 2013); Crescent Valley (McConville, 2018); Tuscarora (Dering, 2013; Dering and Faulds, 2013); Steptoe Valley (Hinz et al., 2020b); and Neal Hot Springs (Edwards, 2013).
- in the East African Rift, at Suswa, Kenya (Haizlip et al., 2020); Menengai, Kenya (Riedl et al, 2019); Songwe, Tanzania (Hinz et al., 2018); Panyimur, Uganda (Hinz et al., 2018); Buranga, Uganda (Natukunda et al., 2024); Faile, Djibouti (Guellah et al., 2023), Bweengwa, Zambia (Hinz et al., 2020c).
- in arc settings, at Akutan, USA (Stelling et al., 2015), Sokoria, Indonesia (Hinz et al., 2020a). Many other geology maps of geothermal prospects may meet the standards advocated here but either are not published or are published only after so much subsurface data is available that the initial surface mapping standards are not emphasized (e.g., Muara Laboh, Indonesia, Stimac et al., 2019; Salak, Indonesia, Stimac et al., 2010; Rantau Dedap, Indonesia, Ramadhan, et al., 2021).

In addition, where geophysical imaging and/or well data has been available, 3D geological models have increasingly enhanced conceptual models of geothermal systems in many areas worldwide (Siler et al., 2021, 2023).

Sorik Marapi, Sumatra, Indonesia

The Sorik Marapi geothermal project is located on the northeast flank of the Sorik Marapi volcano, and along a major active strand of the Sumatra fault system, on Sumatra, Indonesia (Figure 3). Drilling began in 2016 with the first 45MW installed by 2019. As of 2023, the field has been operating for four years with a current installed capacity of 180 MW. Multiple geologic maps have been published for this field and four of these are reviewed relative to geologic best practices and to how effectively they inform the conceptual model of Hinz et al. (2021).

The geologic aspects of the 2024 conceptual model for the Sorik Marapi reservoir (Figures 4 and 5) remain mostly unchanged from that published in Hinz et al. (2021). In this model, the vapor core of Sorik Marapi is isolated to a chimney underlying the volcano's summit area and the geothermal reservoir is a hydrologically separate, neutral >320°C upflow about 1 km west of the main strand of the active SFS, with associated elongate <260°C outflows to the north and south. The inferred upflow area is based on well temperature data, fluid geochemistry, locally elevated non-condensable gases, and permeability patterns. Overall, the upflow appears to be elongated NE-SW, possibly associated with a concealed NE-striking fault zone. A NE-striking fault that connects the major western and eastern strands of the dextral NNW-striking Sumatra fault system in this area could function as a pull-apart, a common structural setting of operating geothermal systems in Sumatra.

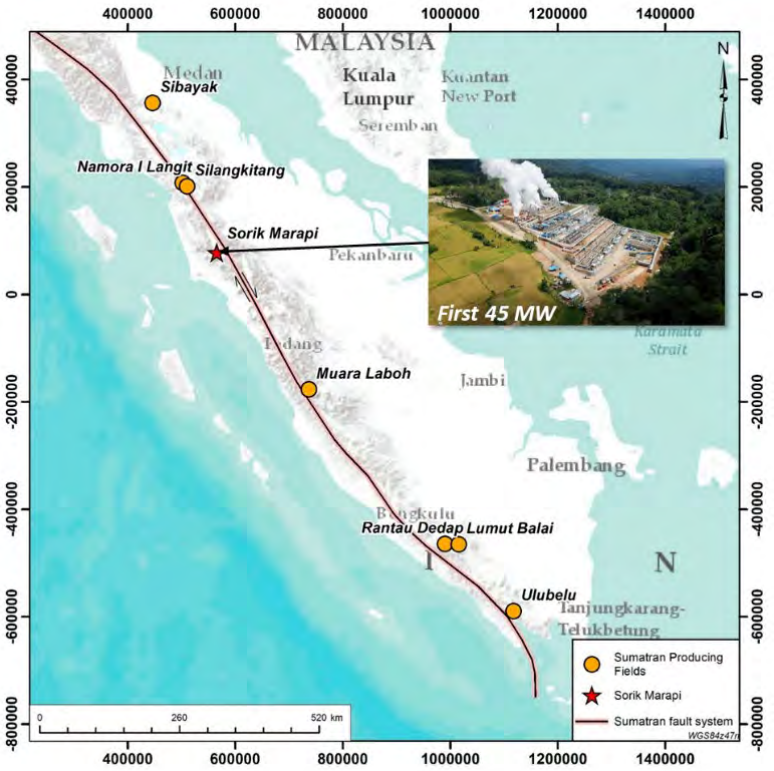

Figure 3: Location map of Sorik Marapi geothermal project (from Hinz et al, 2021).

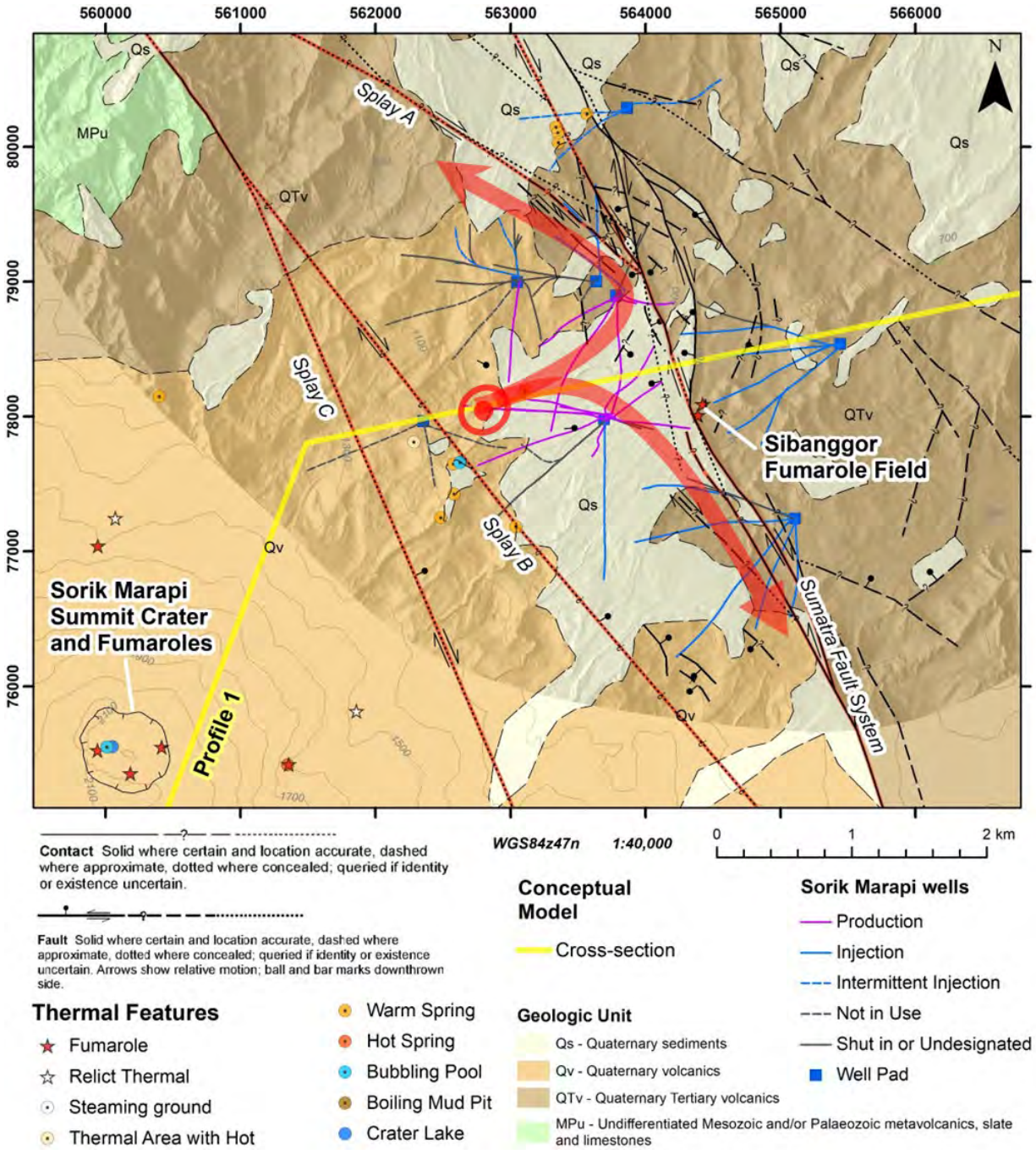

Figure 4: Geologic map of the Sorik Marapi field, modified from Hinz et al. (2021). Wells drilled within the currently developed Sorik Marapi Geothermal Reservoir. Red lines highlighting some faults correspond to major strands of the Sumatra fault system and are discussed in the text. Key conceptual model elements are also shown; upflow (arrowed circle) and outflow pathways (red arrows).

The reservoir is largely hosted in pre-Cenozoic metamorphic rocks and late Cenozoic intrusive rocks. Image data indicate that fractures are predominantly oriented with an approximate NNE-strike and moderate to steep dips both east and west; however, permeable fractures have been encountered with a large range of strikes and dips (Hinz et al., 2021). Of note, most of the major faults identified in the reservoir from drilling data do not reach the surface or are covered by young

volcanics and can only be identified by subsurface data. The northern and eastern margins of the reservoir are bound by major strike-slip faults and the western margin has also been hypothesized to be bound by a major strike-slip fault (Kim et al., 2020, 2024; Hinz et al. 2021; Turk et al., 2024).

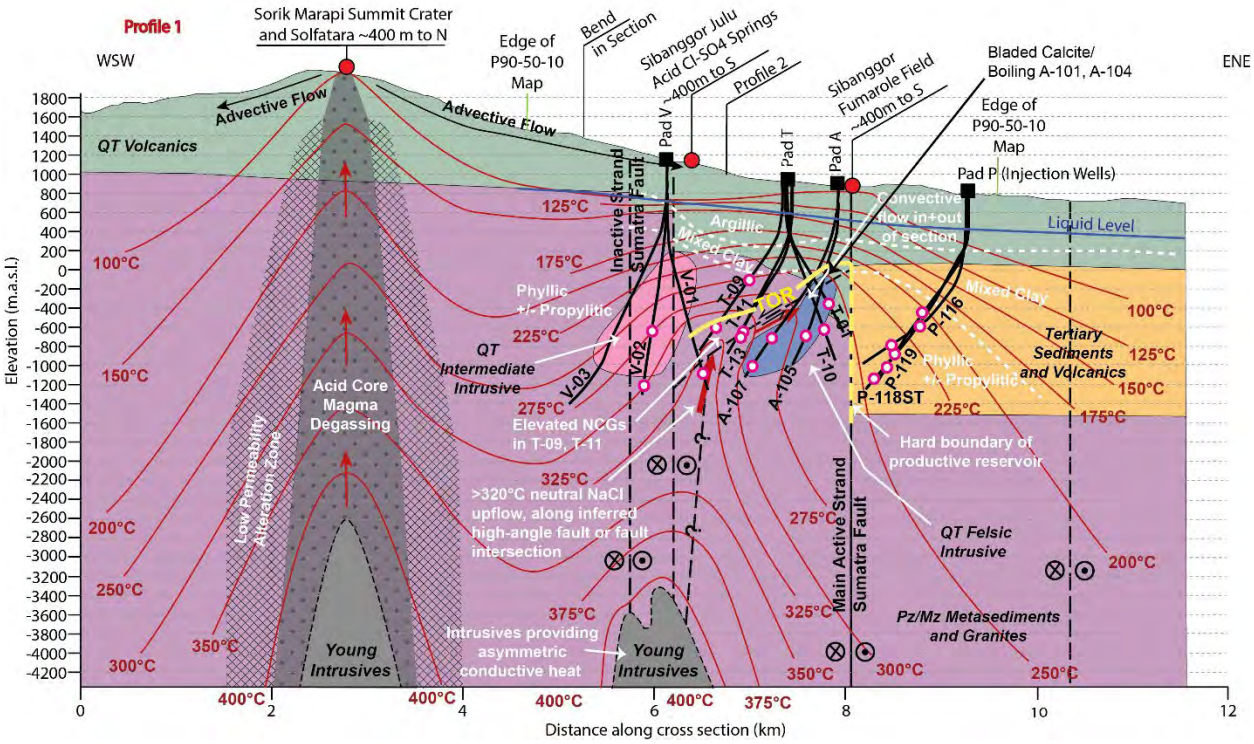

Figure 5: Geologic cross section of the Sorik Marapi field, modified from Hinz et al. (2021) and borrowed from Turk et al. (2024). Cross-section crosses through Figure 4 and full extent is shown on the map in Hinz et al. (2021).

Multiple geologic mapping efforts have been completed at different scales by government and private companies. Of these, four maps have been published, two pre-drilling (Rock et al., 1983; Rezkey and Hermawan, 2015), and two during exploration and development drilling (Sarmiento et al., 2017; Hinz et al, 2021). The surface manifestations (fumaroles and hot springs) were first mapped in detail by SKM (2011), and all subsequent maps have confirmed this distribution. There is acid-sulfate and argillic alteration exposed at and near the locations of the active surface manifestations. None of the maps have identified any major areas of relict high rank alteration that could indicate cap erosion and areas that could host cool down-flow. Although the map investigations of surface manifestations and alteration are similar, there are key differences in the stratigraphic and structural framework between these maps. Thus, the stratigraphic and structural framework elements of these maps are reviewed relative to geologic mapping best practices and to the current conceptual model to highlight predictive value and data gaps.

Rock et al. (1983): This map provided broad regional coverage with major strands of the Sumatra fault system, and major stratigraphic units from Cenozoic volcanics and sediments to older pre-Cenozoic metamorphic and granitic rocks (Figure 6: upper left). Some of the value for early exploration of this field is that it shows discontinuous coverage of Quaternary and Tertiary volcanics across the region, supporting that at least in part of the reservoir is likely hosted in pre-Cenozoic metamorphic and/or plutonic rocks. There are no kinematic indicators associated with

the fault traces and no structural data plotted on this map. One could assume that the NNW-striking faults probably have dextral strike-slip or oblique strike-slip motion based on the geologic setting. However, even if some of these data were included, the resolution at 1:250,000 scale is typically insufficient for identifying key kinematic structural models to guide exploration.

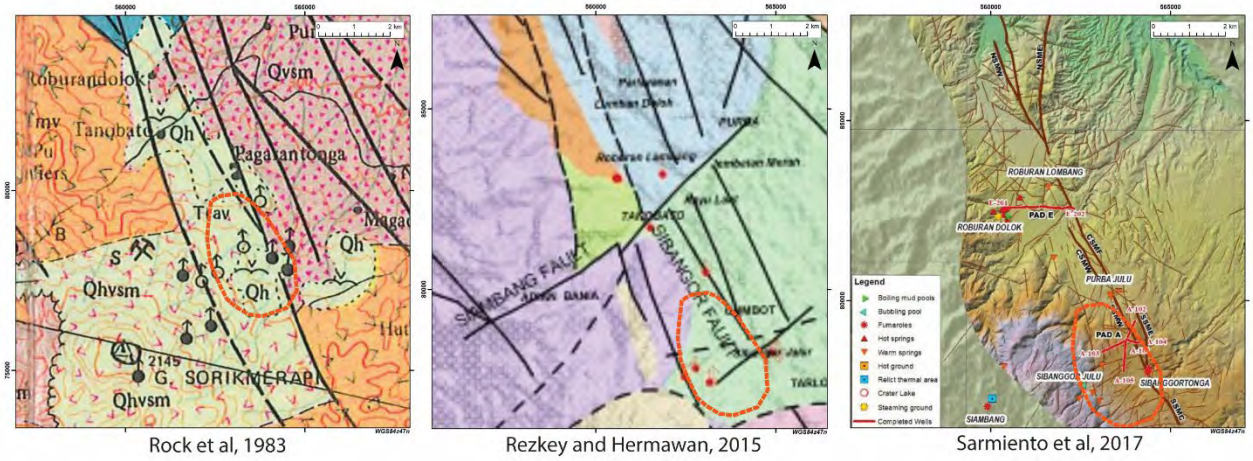

Figure 6: Three maps of the Sorik Marapi geothermal prospect at the same scale (1:60,000) showing the variability in geologic map detail and the same reservoir area (dashed red polygon) modified from Hinz et al, 2021).

Rezkey and Hermawan (2015): This map shows slight differences to lithologic contacts relative to Rock et al., (1983) and a different fault pattern. A key implication for conceptual modeling is that the Cenozoic volcanic rocks are likely relatively thin, and the reservoir is likely hosted in pre-Cenozoic strata. However, like the previous map, there are no kinematic indicators associated with the fault traces and no structural data plotted on this map indicates the likely geometry of the pre-Cenozoic rocks. No cross section was available to illustrate subsurface expectations based on the map data.

Sarmiento et al. (2017): This map is the first publication of this field to include lineament analysis of LiDAR data which could support a detailed geomorphic evaluation of this part of the Sumatra fault zone (Figure 6). The main strands of the Sumatra fault are symbolized with a bold red line while all other lineaments are thin red lines; however, the publication does not report how the individual primary or secondary lineaments were selected (e.g., general topographic feature, fault scarp, fault surface, and/or offset stratigraphy). Missing descriptive elements for the lineaments include kinematic indicators (e.g., strike-slip, normal slip), designation of recency, and concealed versus exposed fault segments. There is also no update of the stratigraphy based on surface mapping. The reported stratigraphic framework was updated in the subsurface based on well data, indicating that the cap and reservoir were entirely comprised of volcanic stratigraphy. Having the reservoir hosted in volcanic stratigraphy is a departure from earlier models such as SKM (2011) that hypothesized that the reservoir was likely hosted largely, or in part, in metamorphic and/or crystalline rock based on the initial mapping of the area by Rock et al. (1983).

Hinz et al., (2021): The geological map in Figure 4 and the cross-section in Figure 5 were based on the stratigraphy from Rock et al. (1983), reanalysis of LiDAR data in 2018 and 2019, field mapping in 2019 and 2021, and new detailed well lithologic logs compiled in 2019 and 2020. Below is a summary of the stratigraphy and structure.

- The stratigraphic framework for the developed geothermal area based on surface exposures and drilling data includes the following: Quaternary volcanics and sediments (Qv and Qs, respectively), Quaternary-Tertiary volcanics (QTv). Metasedimentary rocks (MPu).
- The structural framework is dominated by strands of the Sumatra fault zone. The main active trace, labeled Sumatra Fault System on Figure 4, is associated with fault scarps along much of the length, with some segments covered by recent sediments (Qs). In cross-section, this main strand is associated with a major offset in stratigraphy with a thick section of Tertiary sediments (Ts) to the east of the fault and Cenozoic volcanics (Qs and QTv) overlying metamorphic and intrusive rocks to the west (Figure 5). There is also evidence for dextral offset of stream and river channels along this primary segment (Hinz et al., 2021).
- In addition to the main active trace of the Sumatra fault there are three other segments based on drilling data and geophysics, each with variable surface exposures. These fault segments are labeled Splay A, B, and C on Figure 4. Splay A is associated with a discontinuous series of fault scarps along the trace and an abrupt change in the base of the low resistivity smectite clay alteration detected by MT, shallow over the reservoir and much deeper to the northeast of the Splay A. Splay B is exposed where volcanics are juxtaposed against metamorphic rocks northwest of the reservoir, which is locally supported by drilling data. Slay B likely extends to the northwest based on possible fault scarps north of the map in Figure 4 (Hinz et al., 2021). In cross section there is an abrupt thickening of the Cenozoic volcanics across Splay B from west to east (Figure 5). Splay C is a branch of Splay B and is supported by drilling data and map data to the south of Figure 4 (Hinz et al., 2021).

A key lesson from geologic mapping in this field is that the major strike slip faults bounding the reservoir have typically acted as permeability barriers, whereas the relatively minor faults within the reservoir that are directly contributing to permeability and are not well-exposed on the surface. This is a key pattern in other fields in Sumatra and around the world (e.g., Geysers, California) where major strike-slip faults act as boundaries to reservoirs. Permeability is often associated with the damage zone on one side of the fault, but permeability across the main fault strand is very low, likely due to gouge in the fault core. At Sorik Marapi, the permeability of the reservoir outflow is likely controlled by geomechanics associated with an extensional step-over between two major strands of the Sumatra Fault System, whereas the structural control on the upflow is still not confirmed. The current theory is that upflow is hosted along a ~NNE- to NE-striking high angle fault segment in the west central part of the well field (Hinz et al., 2021).

Kibiro, Uganda

Figure 7: Kibiro location indicated by red star.

The Kibiro geothermal prospect is in Uganda along the east side of Lake Albert (Figure 7). Geothermal investigations at Kibiro were initiated by Ugandan government in 1993 with multiple studies continued intermittently through 2016. As reported in Hinz et a., (2018), new detailed geologic mapping was completed at Kibiro in 2018.

Previous mapping is shown in Figure 8A, where the Northern Toro Bunyoro (NTB) fault is shown as perfectly straight. The new mapping shows that the Kibiro geothermal area is located along a complex system of fault step-overs with a combined length over 1.5 km and width of up to 150 m (EAGER, 2018a; Figure 8B). Each step is also associated with one or more fault intersections in the footwall and/or hanging-wall side.

Fault dip measurements on the upper splay of the NTB fault and the Kachuru fault are 65° NW and 46° to 50° NW, respectively. The 65° dip measurement of the upper splay of the NTB fault matches with the drill-hole data-derived 65° dip estimate on the main strand of the NTB fault north of Kibiro (Alexander et al., 2016a) and the 2D MT inversion model (Figure 9B). Quaternary scarps are associated with both strands of the NTB fault and the first 2-3 km of the Kachuru fault as it extends south from the NTB fault. Based on the distribution of fault scarps it is probable that Quaternary slip on the north end of the Kachuru fault is synchronous with slip along the NTB fault zone.

Surficial geothermal features include four clusters of hot springs, inactive oil seeps, bedrock alteration, and an area of steaming ground (Figure 8B). The hottest cluster of springs ranges from 77 to 87°C and emanates from the NE end of the upper NTB fault adjacent to where it merges with the outer main NTB fault. Three other clusters of hot springs are present outboard of the main NTB fault and are aligned along a possible concealed NE-SW striking step-faults. An area of steaming ground (labeled fumarole) with 45°C temperature was discovered at the SW end of the step-over in an area of intense argillic bedrock alteration, native sulfur, and bitumen (Hinz et al., 2018). The fumarole extends the distance of surface thermal features about 750 m SW of the previously identified hot springs. Results of the previous soil CO_2 and soil temperature studies (Alexander et al., 2016) are consistent with the distribution of active thermal manifestations at either end of the double-ended step-over along the NTB fault.

To revise the conceptual model, the updated structural mapping and the TEM conductance were overlaid as in Figure 9A to support the subsurface structural and MT resistivity cross-section in Figure 9B. The previous UNEP structural model (Alexander et al., 2016) involved a single fault intersection between the NTB fault and the Kachuru fault, suggesting that the upflow was likely focused along a narrow, steeply plunging fault intersection. However, the width of the step-over region along the NTB fault and the extent of the anomalous soil temperatures closely correlated with the NE-SW extent of the high TEM conductance (low average resistivity in orange to red areas) interpreted as smectite alteration in the basin-fill sediments. The consistency between the thermodynamic implications of geology, surficial thermal data, and TEM conductance provides increased confidence in a larger extent of the conceptual model along strike.

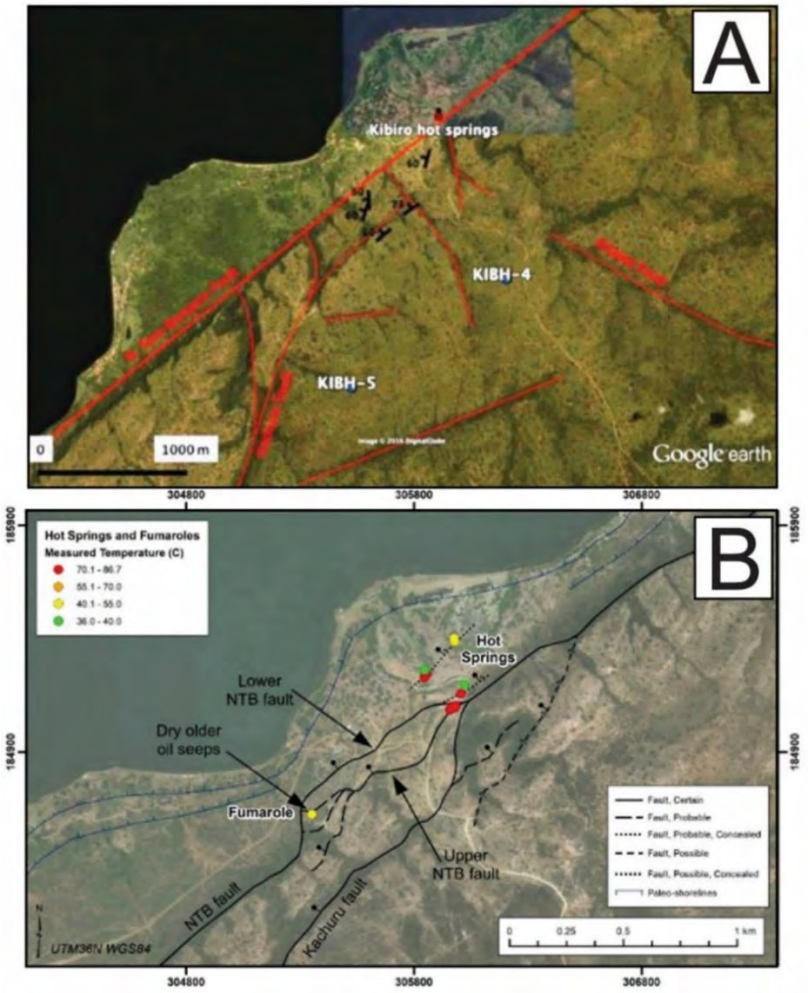

Figure 8: Figure modified from Hinz et al., (2018): (A) Previous geologic map of Kibiro on left (Alexander et al., 2016). (B) New structural geologic map of Kibiro (EAGER, 2018a).

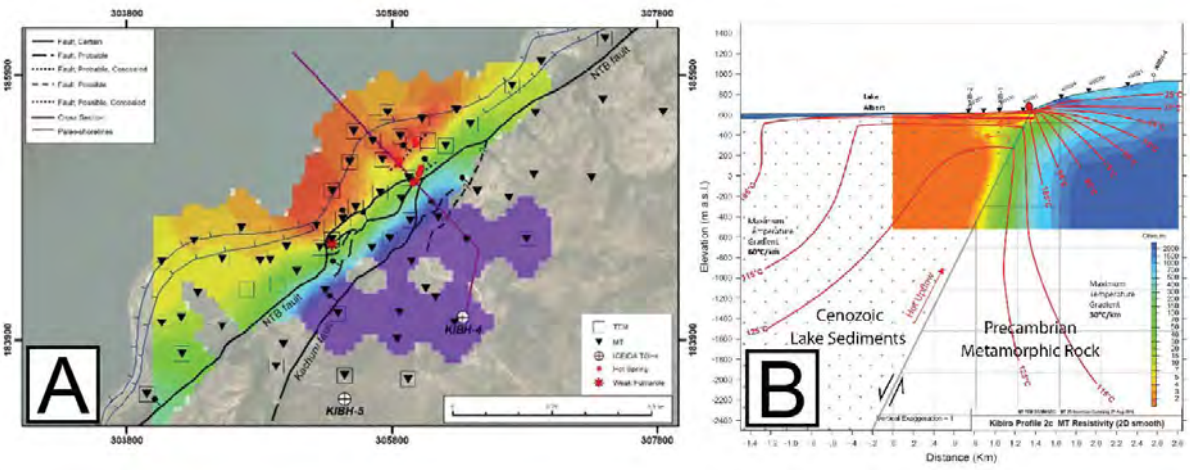

Figure 9: Figures modified from Hinz et al, 2018: (A) Map of TEM conductance to 200 m depth from Alexander et al. (2016) plotted on the new generated structural map (Hinz et al., 2018). (B) MT 2D cross-section with conceptual model isotherms associated with upflow in a fault with 65° dip and outflow into shallow gravels.

The additional data collected in 2018 support the previous model (Alexander et al., 2016) with these additions: 1) higher confidence in achieving commercial production from within the NTB fault zone, and 2) equal or greater confidence in achieving commercial production from within stratigraphic-hosted outflow given higher confidence in fault-hosted up-flow, which suggests a broader area of combined fault and formation-hosted reservoir compared with the previous model. The main uncertainty with respect to targeting the potential outflow is the unknown permeability of the coarser basin-fill deposits and this remains unchanged by this study (a secondary risk issue is its likely lower temperature). The main risk with respect to targeting the upflow in the fault zone is the variable permeability within such fault zones.

An updated median conceptual model cross-section is presented in Figure 9B with isotherms illustrating a 125°C upflow in the NTB fault dipping 65°. Given the higher confidence that the step-over along the NTB fault provides the conduit for deep circulation, the updated conceptual model is constructed to >2000 m a.s.l. to illustrate the control that convection along this structure has on the isotherms.

Blue Mountain, Nevada, United States

Figure 10. Location of the Blue Mountain geothermal area, Nevada, USA.

The Blue Mountain geothermal area in Nevada and has been operating since 2009, with 25 MWe net power capacity as of 2021 (Figure 10). The upflow is >225°C and most production is from a 175-200°C hot outflow. Twenty-six wells have been drilled and of these, seven have been successful as producers. A comparison of recent mapping by Fercho et al. (2023) to previous generations of maps and associated models illustrates what improvements in geological mapping might have contributed to well targeting success.

Six geologic maps (Figure 11) were published for the Blue Mountain geothermal area from 1999 to 2016. All of these maps show a variety of structural complexity at the nose of the mountain range that juts into the basin. Four of these (Fairbank and Ross, 1999; Melosh et al., 2008; Casteel et al., 2010, Swyer et al., 2016) were compiled from a combination of surface observations, geophysics, and well data. However, all four maps lack fault recency and kinematic data needed to develop a kinematic-structural model that could be used to predict subsurface permeability patterns. The map by Wyld (2002) provides kinematic data, but focuses on the Mesozoic basement rocks exposed in the mountain range and does not provide detail on faults that extend into the basin where the reservoir is located. The map by Faulds and Melosh (2008) provide a map with kinematic data, characterization of fault recency, photos and descriptions of Quaternary active fault segments, and they used these data to identify three possible structural setting models for how the geothermal reservoir could be hosted where the mountain range points into the basin. The mapping by Faulds and Melosh (2008) was regional in scale, and they recommended that more detail would be needed to refine the structural model options used to predict subsurface permeability and characterize uncertainty in targeting.

Fercho et al., (2023) picked up from where the mapping by Faulds and Melosh (2008) left off with the new mapping defining that the structural setting is a displacement transfer zone whereby NE-striking, NW-dipping normal faults splay off the north side of a WNW-striking dextral-normal fault (Figure 12). The mapping of the WNW-striking fault is based on multiple fault surface

exposures where dip and kinematic data were measured. Furthermore, the mapping N- and NNE-striking fault segments were based on bedrock exposures of fault surface and fault scarps in Quaternary alluvium. In the updated conceptual model, upflow is along a major normal fault close to where it splays north form the dextral-normal fault. Outflow is between normal faults to the NE. This updated structural model is consistent with one of the previous models identified by Faulds and Melosh (2008).

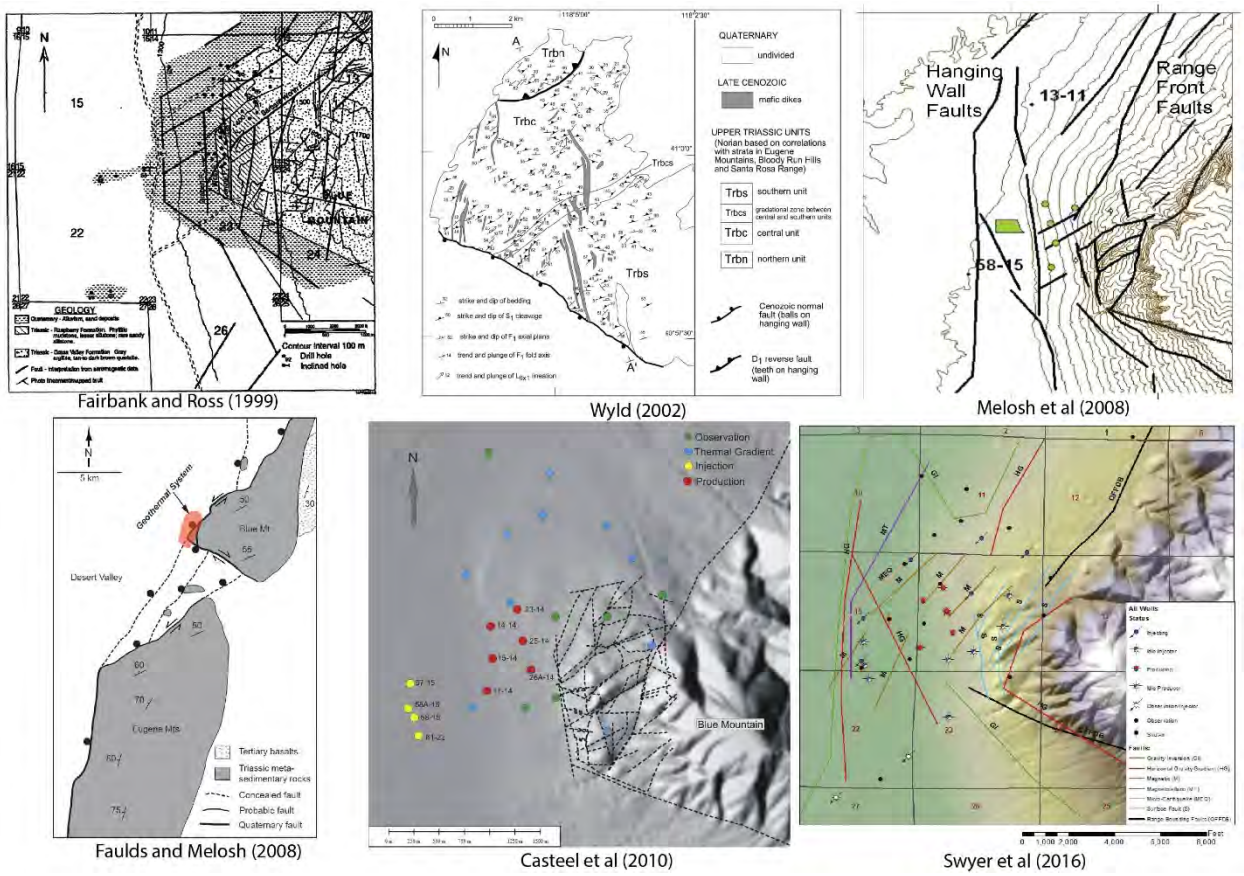

Figure 11: Historic geologic maps from the Blue Mountain geothermal area.

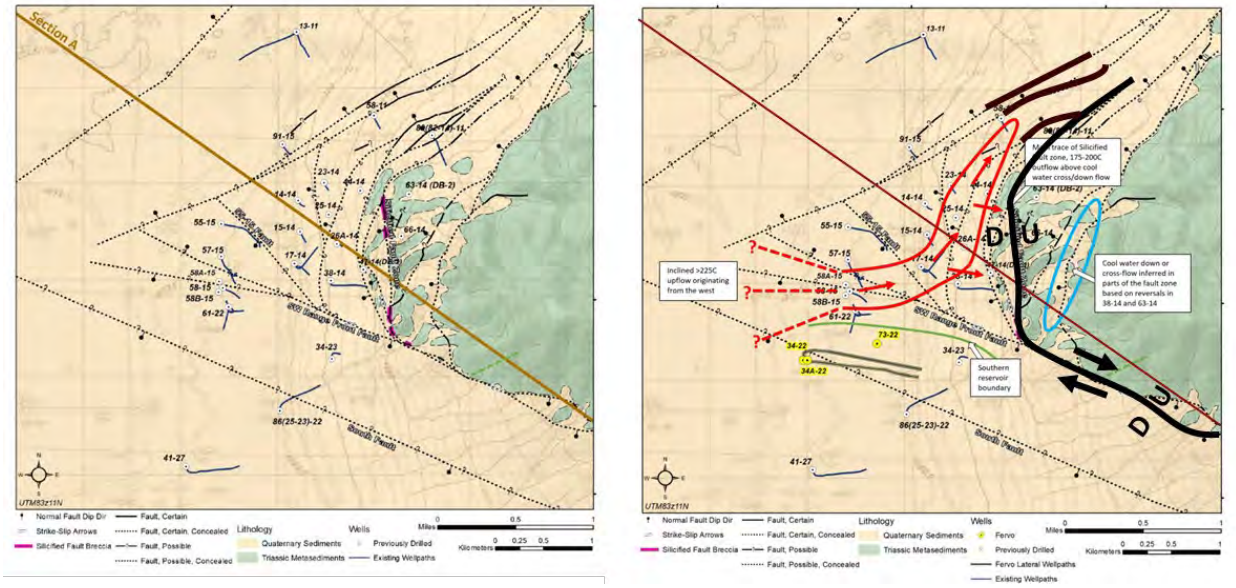

Figure 12:Updated geologic map (left) and conceptual model (right) from the Blue Mountain geothermal area (Fercho et al., 2023).

6. Conclusions

Geologic mapping is an important dataset used to support the development of geothermal resource conceptual models for both high and low temperature geothermal systems in all geological settings worldwide. When initially exploring a prospective resource, previous geologic mapping is typically available. Evaluating the quality and utility of existing geologic mapping is critical to planning exploration and developing resource conceptual models. The consistent use of a checklist like Table 1 can help identify the need for new geologic maps and can help assess the weight given to elements of a geologic map when constructing a conceptual model or targeting a well. When an update is required, geologic mapping based on best practices outlined in this paper can provide geologic maps suitable for integration with conceptual models. Checklists like those presented in Table 2 can help improve the acquisition and interpretation of geologic surface maps so that they will be more predictive of the subsurface.

Geologic mapping is an iterative process that should be periodically revisited as exploration and development progresses and other data sets are acquired. For example, at the Rantau Dedap geothermal field in Sumatra, MT resistivity detected several gaps in the low resistivity smectite cap, one near the proposed upflow target area. Surface geological mapping detected relict higher temperature clay alteration at the surface that well data subsequently showed was related to advanced argillic surrounding an intrusion that is correlated with the current upflow (Ramadhan et al., 2021). The same case history illustrates how a shallow landslide block can obscure the deep structure that is most closely correlated with reservoir permeability. Although geological mapping is initially conducted to predict subsurface conditions in geothermal fields, as development proceeds, surface mapping can be refined to diagnose geothermal resource development issues.

Issues not addressed in this discussion include quantifying the uncertainty of projections of structure into the subsurface based on surface geologic maps. This is becoming particularly important in 3D visualizations that are commonly misinterpreted as having much less uncertainty

than is implied by the supporting data. Further comparisons of surface maps of structure to well data, production zones and wellbore image logs (e.g., Wallis et al., 2012, 2023) would help characterize how predictive surface mapping can be, extending results like that of Guevarra-Segura et al. (2015).

REFERENCES

Alexander, K.B., Cumming, W., and Marini, L., 2016, Geothermal resource assessment report: Kibiro Geothermal Prospect, Uganda: Final Report-September 2016: Confidential report to UNEP and GRD/MEMD.

Anderson, R.B., 2013, Structural controls of the Emerson Pass geothermal system, Washoe County, Nevada: [M.S. thesis] University of Nevada, Reno, 101 p.

Anderson, R.B., Faulds, J.E., and Dering, G.M., 2013, Preliminary geologic map of the central Lake Range, southern Fox Range, and northern Terraced Hills, Emerson Pass geothermal area, Washoe County, Nevada: Nevada Bureau of Mines and Geology Open-File Report 13-10, 1:24,000 scale, 9 p. text.

Bennett, S.E.K., DuRoss, C.B., Gold, R.D., Briggs, R.W., Personius, S.F., Reitman, N.G., Devore, J.R., Hiscock, A.I., Mahan, S.A., Gray, H.J., Gunnarson, S., Stephenson, W.J., Pettinger, E., and Odum, J.K., 2018, Paleoseismic results from the Alpine Site, Wasatch fault zone, timing and displacement data for six Holocene earthquakes at the Salt Lake City-Provo Segment Boundary: Bulletin of the Seismological Society of America, v. 108, p. 3202–3224.

Casteel, J., Trazona, R., Melosh, G., Niggemann, K., and Fairbank, B., 2009, A preliminary conceptual model for the Blue Mountain geothermal system, Humboldt County, Nevada: Geothermal Resources Council Transactions, v. 33, p. 917–920.

Compton, R.R., 1985, Geology in the Field: New York, Wiley.

Compton, R.R., 2017, Geology in the Field: Scotts Valley, CA, CreateSpace Independent Publishing Platform.

Craig, J.W., 2018, Discovery and analysis of a blind geothermal system in southeastern Gabbs Valley, western Nevada: [M.S. thesis] University of Nevada, Reno, 111 p.

Dellerman, N.P., 2021, Application of geothermal play fairway analysis to the Desert Queen geothermal prospect, northern Hot Springs Mountains, Churchill County, Nevada: [M.S. thesis] University of Nevada, Reno, 133 p.

Dering, G.M., 2013, Structural controls of the Tuscarora geothermal field, Elko County, Nevada: [M.S. thesis] University of Nevada, Reno, 82 p.

Dering, G.M., and Faulds, J.E., 2013, Preliminary geologic map of the Tuscarora geothermal area, Elko County, Nevada: Nevada Bureau of Mines and Geology Open-File Report 13-5, scale 1:24,000.

EAGER, 2018, Review of Kibiro prospect structural geology with implications on the conceptual model and drilling program: Confidential Report to GRD, April.

Edwards, J.H., 2013, Structural controls of the Neal Hot Springs geothermal system, eastern Oregon: [M.S. thesis] University of Nevada, Reno, 84 p.

Fairbank, B., and Ross, H., 1999, Geology and temperature gradient surveys, the Blue Mountain geothermal discovery, Humboldt County, Nevada: Geothermal Resources Council Transactions, v. 23, p. 513–517.

Faulds, J.E., and Melosh, G., 2008, A preliminary structural model for the Blue Mountain geothermal field, Humboldt County, Nevada: Geothermal Resources Council Transactions, v. 32, p. 273–278.

Faulds, J.E., Coolbaugh, M.F., and Hinz, N.H., 2021, Inventory of structural settings for active geothermal systems and late Miocene (~8 Ma) to Quaternary epithermal mineral deposits in the Basin and Range province of Nevada: Nevada Bureau of Mines and Geology Report 58, 27 p.

Faulds, J.E., Coolbaugh, M.F., Benoit, D., Oppliger, G., Perkins, M., Moeck, I., and Drakos, P., 2010, Structural controls of geothermal activity in the northern Hot Springs Mountains, western Nevada: The tale of three geothermal systems (Brady's, Desert Perk, and Desert Queen): Geothermal Resources Council Transactions, v. 34, p. 675–683.

Faulds, J.E., Koehler, R.D., Dellerman, N.P., and Green, H.L., 2022, Geologic map of the Parran quadrangle, Churchill County, Nevada: Nevada Bureau of Mines and Geology Open-File Report 2022-02, scale 1:24,000, 6 p.

Faulds, J.E., Ramelli, A.R., and Perkins, M.E., 2011, Preliminary geologic map of the Hazen Quadrangle, Lyon and Churchill Counties, Nevada: Nevada Bureau of Mines and Geology Open-File Report 11-8, scale 1:24,000.

Faulds, J.E., Ramelli, A.R., Coolbaugh, M.F., Hinz, N.H., Garside, L.J., and Queen, J.H., 2017, Geologic map of the Bradys geothermal area, Churchill County, Nevada: Nevada Bureau of Mines and Geology Open-File Report 17-4, 2 sheets, 1:12,000 scale, 6 p. text.

Faulds, J.E., Ramelli, A.R., Garside, L.J., Coolbaugh, M.F., and Green, H.L., 2012, Preliminary geologic map of the Desert Peak Quadrangle, Churchill County, Nevada: Nevada Bureau of Mines and Geology Open-File Report 12-5, scale 1:24,000.

Faulds, N.H., and Hinz, N.H., 2015, Favorable tectonic and structural settings of geothermal settings in the Great Basin Region, western USA: Proxies for discovering blind geothermal systems: World Geothermal Congress, Melbourne, Australia.

Fercho, S., Hinz, N., Casteel, J., and Turk, J., 2020, Analysis of natural and drilling induced fractures from newly acquired borehole image logs at the Star Peak geothermal field, NV: Implications for localized stress field rotation within a normal fault step-over: *GRC Transactions*, v. 44, p. 557–571.

Fercho, S., Norbeck, J., McConville, E., Hinz, N., Wallis, I., Titov, A., and Latimer, T., 2023, Geology, state of stress, and heat in place for a horizontal well geothermal development project at Blue Mountain, Nevada, in Proceedings, 48th Workshop on Geothermal Reservoir Engineering, Stanford University, Stanford, CA, February 2023.

Fodor, L.I., 2007, Segmentation linkage and the state of stress in transtensional transfer zones: Field examples from the Pannonian Basin, in Cunningham, W.D., and Mann, P., eds., Tectonics of Strike-slip Restraining and Releasing Bends: London, Geological Society of London, p. 417–431.

Freeman, T., 1999, Procedures in field geology: Wiley-Blackwell.

Gifkins, C., Herrmann, W., and Large, R., 2005, Altered volcanic rocks: Centre for Ore Deposit Research, University of Tasmania.

Gold, R.D., Briggs, R.W., Personius, S.F., Crone, A.J., Mahan, S.A., and Angster, S.J., 2014, Latest Quaternary paleoseismology and evidence of distributed dextral shear along the Mohawk Valley fault zone, northern Walker Lane, California: *Journal of Geophysical Research: Solid Earth*, v. 119, p. 5014–5032, https://doi.org/10.1002/2014JB010987.

Guellah, D.A., Mohamed, C., Mohamed, J., Davis, L., Haizlip, J., and Hinz, N., 2023, Preliminary results of the geothermal exploration project of EDD in Fialé, Asal Rift, Djibouti: *GRC Transactions*, v. 47, p. 290–304.

Guevarra-Segura, I., Ejera, V., and Stark, M., 2015, Are faults effective targets in the deep reservoir? A case study from Bulalo Reservoir, Laguna, Philippines: World Geothermal Congress.

Haizlip, J.R., Cumming, W., Hinz, N., Melosh, G., Alexander, K., Harvey, M., Magnusson, R., and Reynisdóttir, S.B., 2020, Conceptual model of Suswa geothermal prospect, Kenya: World Geothermal Congress, 16 p.

Hinz, N., Cumming, B., and Sussman, D., 2018, Exploration of fault-related deep-circulation geothermal resources in the western branch of the East African Rift System: Examples from Uganda and Tanzania, in Proceedings of the 7th African Rift Geothermal Conference.

Hinz, N.H., and Faulds, J.E., 2011, Preliminary geologic map of the Reese River geothermal area, Lander County, Nevada: Nevada Bureau of Mines and Geology Open-File Report 11-3, scale 1:24,000.

Hinz, N.H., Cumming, C., Matson, G., Haizlip, J., Sussman, D., Fercho, S., Fishbin, A., Sanjaya, D., Sagala, B., and Tang, Y., 2020a, Conceptual Model Update of the Sokoria Geothermal Field, Flores, Indonesia: World Geothermal Congress, 12 p.

Hinz, N.H., Faulds, J.E., and Bell, J.W., 2011, Preliminary geologic map of the Bunejug Mountains Quadrangle, Churchill County, Nevada: Nevada Bureau of Mines and Geology Open-File Report 11-9, scale 1:24,000.

Hinz, N.H., Faulds, J.E., and Oppliger, G.L., 2010, Preliminary geologic map of the Lee-Allen geothermal area, Churchill County, Nevada: Nevada Bureau of Mines and Geology Open-File Report 10-06, scale 1:24,000.

Hinz, N.H., Faulds, J.E., Coolbaugh, M.F., Hardwick, C., Gwynn, M., Queen, J., and Ayling, B., 2020b, Play fairway analysis of Steptoe Valley, Nevada: Integrating geology, geochemistry, geophysics, and heat flow modeling in the search for blind resources: *Geothermal Resources Council Transactions*, v. 44, p. 593–612.

Hinz, N.H., Matson, G., Sussman, D., Haizlip, J., Turk, J., Fercho, S., and Letvin, A., 2021, Conceptual model update of the Sorik Marapi Geothermal Prospect, Sumatra, Indonesia: *Geothermal Resources Council Transactions*, v. 45, p. 2225–2242.

Hinz, N.H., Ramelli, A.R., and Faulds, J.E., 2013, Preliminary geologic map of the Wabuska Quadrangle, Lyon County, Nevada: Nevada Bureau of Mines and Geology Open-File Report 13-08, scale 1:24,000.

Hinz, N.H., Vivian-Neal, P., Haizlip, J., Matson, G., Cumming, W., Harrison, P., and Campbell, S., 2020c, Zambia: Conceptual Model and Drilling Update of the Deep Circulation Bweengwa River Geothermal Prospect: World Geothermal Congress, 16 p.

Hunter, L.E., Howle, J.F., Rose, R.S., and Bawden, G.W., 2011, LiDAR-assisted identification of an active fault near Truckee, California: *Bulletin of the Seismological Society of America*, v. 101, no. 3, p. 1162–1181.

Kim, K., Finsterle, S., Garg, S., Haizlip, J., Hinz, N., Fercho, S., and Tang, Y., 2020, Natural-state reservoir model of Sorik Marapi geothermal field: World Geothermal Congress.

Kim, K., Haizlip, J., Hinz, N., Turk, J., Garg, S.S., Brown, Z., Pardede, F., Triananda, W., and Yuono, R.T., 2021, Updates of numeric reservoir model for Sorik Marapi geothermal field: *GRC Transactions*, v. 48, p. 13.

Koehler, R.D., and Woods, R.-E.F., 2013, Paleoseismic and LiDAR investigations along the Cathedral Rapids and Dot "T" Johnson faults, interior Alaska: State of Alaska Department of Natural Resources Division of Geological and Geophysical Surveys Report of Investigations, 2013-4, p. 26.

McConville, E.G., 2018, Detailed analysis of geothermal potential in Crescent Valley, north-central Nevada [M.S. thesis]: University of Nevada, Reno, 122 p.

Melosh, G., Casteel, J., Niggemann, K., and Fairbank, B., 2008, Step-Out Drilling Results at Blue Mountain, Nevada: *Geothermal Resources Council Transactions*, v. 32, p. 49–51.

Milton, A., Hinz, N., Fishbin, A., Alali, A., Lundquist, M., Chandra, V.R., and Alhani, A., 2023, Exploration for blind, deep circulation, geothermal resources along Gulf of Aqaba coastal region of NEOM, Saudi Arabia: *Geothermal Resources Council Transactions*, v. 47, p. 1484–1498.

Natukunda, J.F., Bahati, G., Hinz, N., and Sewell, S., 2024, Geothermal energy exploration at Buranga prospect, Uganda - Status update, in Proceedings, 10th African Rift Geothermal Conference, Dar es Salaam, Tanzania, 13–15 November, 16 p.

Ramadhan, I., Sewell, S., Stimac, S., Ganefianto, N., and Azis, H., 2021, Conceptual interpretation of MT resistivity at the Rantau Dedap field, Sumatra, Indonesia: *GRC Transactions*.

Rezky, Y., and Hermawan, D., 2015, Geothermal System of Sorik Marapi-Roburan-Sampuraga, North Sumatera, Indonesia, in Proceedings, World Geothermal Congress.

Rhodes, G., 2011, Structural control on the Empire-San Emidio Desert geothermal system, northwestern Nevada [M.S. thesis]: University of Nevada, Reno, 72 p.

Rhodes, G.T., Faulds, J.E., and Ramelli, A.R., 2011, Geologic map of the northern Lake Range, San Emidio geothermal area, Washoe County, Nevada: Nevada Bureau of Mines and Geology Open-File Report 10-3, scale 1:24,000.

Riedl, S., Melnick, D., Mibei, G.K., Njue, L., and Strecker, M., 2019, Continental rifting at magmatic centres: structural implications from the Late Quaternary Menengai Caldera, central Kenya Rift: *Journal of Geological Society*, p. 17, https://doi.org/10.1144/jgs2019-021.

Rock, N. M. S., Aldiss, D. T., Aspden, J. A., Clarke, M. C. G., Djunuddin, A., Kartawa, W., Miswar, S. J., Thompson, R., and Whandoyo, R., 1983, The geology of the Lubuksikaping Quadrangle (0716), Sumatra, scale 1:250,000: *Geological Survey of Indonesia*.

Sadowski, A., 2016, Structural controls on the Black Warrior blind geothermal system, Washoe-Churchill Counties, Truckee Range, Nevada [M.S. thesis]: University of Nevada, Reno, 144 p.

Sadowski, A.J., and Faulds, J.E., 2016, Preliminary geologic map of the Black Warrior geothermal area, Truckee Range, Washoe and Churchill Counties, Nevada: Nevada Bureau of Mines and Geology Open-File Report 16-7, scale 1:24,000, 6 p.

Sarmiento, Z. F., Bjornsson, G., Licup, A. C., Esberto, M. B., Indra, T., Baltasar, A. S. J., and Chandra, V. R., 2017, Update on the exploration and development drilling at the Sorik Marapi Geothermal Field, North Sumatra, Indonesia: In *Proceedings of the 5th Indonesian International Geothermal Convention and Exhibition (IIGCE)*.

Siler, D.L., Faulds, J.E., Hinz, N.H., and Queen, J.H., 2021, Three-dimensional geologic map of the Brady geothermal area, Nevada: U.S. Geological Survey Scientific Investigations Map 3469, 2 sheets, pamphlet 20 p., https://doi.org/10.3133/sim3469.

Siler, D.L., Witter, J.B., Craig, J.W., Earney, T.E., Schermerhorn, W.D., Fournier, D., Faulds, J.E., Glen, J.M., and Peacock, J.R., 2023, Three-dimensional geologic map of the southeastern Gabbs Valley area, Nevada: U.S. Geological Survey Scientific Investigations Map 3498, 29 p., 1 sheet and 1 video, https://doi.org/10.3133/sim3498.

Spencer, E. W., 2017, *Geologic Maps: A Practical Guide to Preparation and Interpretation* (3rd ed.): Waveland Press.

Stark, M. A., Estrella, C. M., Ejera, V. G., and Baxter, C., 2022, Quantitative evaluation of drilling targets: *Geothermal Resources Council Transactions*, v. 46, p. 2174–2187. Geothermal Rising, https://www.geothermal-library.org/index.php?mode=pubs&action=view&record=1034736.

Stelling, P., Hinz, N.H., Kolker, A., and Ohren, M., 2015, Exploration of the Hot Springs Bay Valley (HSBV) Geothermal Resource Area, Akutan, Alaska: *Geothermics*, v. 57, p. 127–144.

Stimac, J., Sihotang, A.M., Mussofan, W., Baroek, M., Jones, C., Moore, J.N., Schmitt, A.K., 2019, Geologic controls on the Muara Laboh geothermal system, Sumatra, Indonesia: Geothermics, v. 82, p. 97-120.

Stimac, J., Baroek, M., Suminar, A., Sagala, B., 2010, Integration of surface and well data to determine structural controls on permeability at Salak (Awibengkok), Indonesia: Proceedings World Geothermal Congress 2010 Bali, Indonesia, 25-29 April 2010, 7 p.

Swyer, M. W., Uddenberg, M., Nordin, Y., Cladouhos, T. T., Hinz, N., and Magnuson, J., 2022, Structural controls on the Newberry Geothermal Field: *Geothermal Rising Conference*, Reno, NV.

Wallis, I.C., McNamara, D., Rowland, J.V., and Massiot, C., 2012, The nature of fracture permeability in the basement greywacke at Kawerau geothermal field, New Zealand: Proceedings of the 37th Workshop on Geothermal Reservoir Engineering, Stanford University, Stanford, California, January 30–February 1, 2012, SGP-TR-194.

Wallis, I., Milton, A., Brown, Z., Davis, L., Casteel, J., and Peters, B., 2023, Faults, fractures, formation, and stress at Fish Lake: Controls on wellbore-scale permeability in a deep

circulation geothermal system: Geothermal Resources Council Transactions, v. 47, p. 1852–1871, Davis, California, Geothermal Rising.

Evaluation of the Geothermal Potential of the Southern San Luis Basin, Taos County, New Mexico

Shari Kelley

New Mexico Bureau of Geology and Mineral Resources, New Mexico Institute of Mining and Technology, shari.kelley@nmt.edu

Keywords
temperature logs; discharge temperatures; San Luis Basin, Taos County, Rio Grande rift

ABSTRACT
Temperature-depth measurements from shallow water wells and deep monitoring wells are used to investigate the affects of fluid flow in faults and fluid flow in aquifers on the thermal structure of the southern San Luis Basin (SLB) in north-central New Mexico. Two areas with the highest geothermal gradients are located in the Miranda graben on southern margin and in the No Agua-Cerro de los Taoses area on the western margin of the basin. The ENE-striking, north-down, left-lateral Embudo fault system is an accommodation structure connecting two Rio-Grande-rift half-graben basins, the west-dipping Española Basin to the south and the east-dipping SLB to the north. The Embudo fault cuts the older, north-striking, 8-km-wide Picuris-Pecos fault zone, a Laramide structure that generally is an east-down, strike-slip fault. Toward the east, the Embudo fault transitions to the north-striking, west-dipping, 2-km-wide, Sangre de Cristo fault zone by progressively changing to a dip-slip fault. The intense fracturing of basement rocks caused by the complex interactions among these faults provides pathways to connect deep aquifers with shallow aquifers. Within the Picuris-Pecos fault zone, a series of horsts and grabens, referred to collectively as the Miranda graben, controls the location of Ponce de Leon warm springs. Three water wells (128 to 273 m deep) were logged in Miranda Canyon. Geothermal gradients (32–58°C/km) in all three wells are modified by flowing water. The highest elevation well records downflow and the two lower elevation wells record upflow. Discharge temperatures at the low-elevation end of this system are as high as 35°C.

A second area with elevated geothermal gradients and discharge temperatures extends from the No Agua rhyolite dome along the western margin of the basin eastward to Cerro de los Taoses near the center of the basin. Three thermal profiles collected near No Agua record lateral fluid flow in a thin zone (1–5 m) in a basalt interval. The well at No Agua displays upflow of 33°C water from the screened interval (276–330 m) within a sandstone just above granite basement. In contrast, the three wells at Cerro de los Taoses, which were measured in air, have linear gradients of 50 to 70°C/km in wells 120 to 170 m deep. The temperature data, in combination with published water chemistry data, indicates that the recharge area for this system lies to the west in the Tusas

Mountains. The meteoric water has circulated deeply, picking up heat and chemical constituents and is discharging along buried faults.

Temperature profiles collected from 24 shallow wells scattered throughout the basin are disturbed by fluid flow through vesicular and flow-breccia intervals in the basalt flows of the Taos Plateau volcanic field, masking the deeper thermal structure of the basin. Three deep monitoring wells (410–900 m deep) penetrate below the basalt into the underlying rift-fill sediments. These wells have geothermal gradients of 26.4–28.3 °C/km.

1. Introduction

This investigation focuses on evaluating the geothermal potential of the southern San Luis Basin (SLB) in Taos County, NM (Fig. 1). This basin is part of the Rio Grande rift, a north-striking zone of extension that started forming at 30 to 25 Ma. The heat flow in this particular section of the rift is 71 to 130 mW/m^2 (Edwards et al., 1978). Previous resource evaluations were primarily based on collecting and modeling aqueous and gas geochemistry data from the three known hot springs in the area: Manby (sometimes called Stagecoach spring, 32.8–38°C); Black Rock spring(sometimes called Hondo; 36.9–41°C), and Ponce de Leon spring (34.0–34.6°C). Early water and gas chemistry collection studies include Summers (1976), Swanberg (1980, 1984), and Norman and Bernhardt (1982). Trainer and Lyford (1979) used mixing models of existing data to conclude that the thermal waters are much diluted, hot spring discharge is low, and based on the low temperatures recorded in the chalcedony geothermometers (<100°C) , that the fluids have traveled far from the source of heat.

A systematic analysis of all thermal data available in the southern SLB from a geothermal perspective has yet to be completed. In this study, temperature-depth measurements from shallow water wells and deep monitoring wells are used to investigate the affects of fluid flow in faults and in aquifers within basalt flows and in rift-fill sediments on the thermal structure of the southern SLB. Both local and regional-scale, topographically driven, deep circulation and heating of fluid in an elevated heat flow thermal regime variably controls the elevated gradients observed in the SLB.

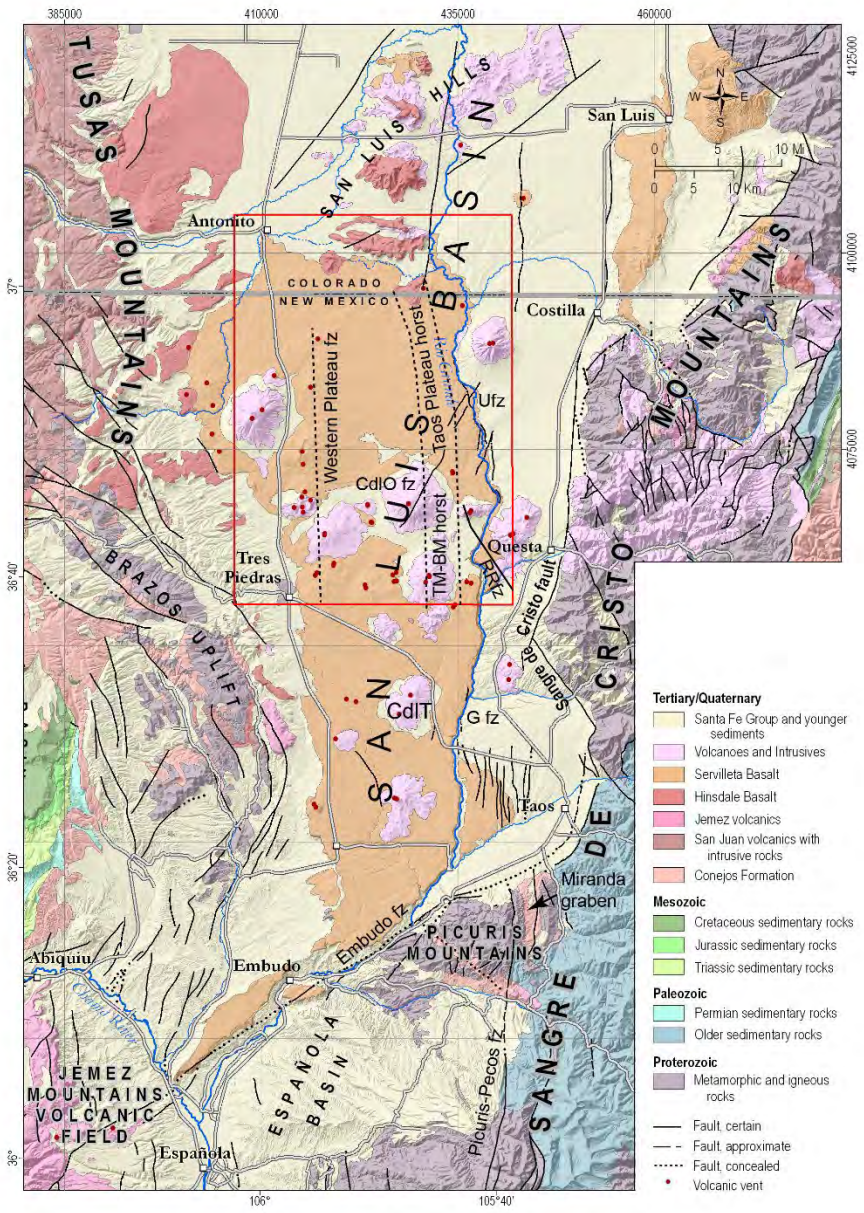

Figure 1. Simplified geologic map of the southern San Luis Basin and the surrounding mountains modified from Johnson and Bauer (2012) The red box shows the extent of the Johnson and Bauer (2012) hydrogeologic study. fz=fault zone; Ufz=Ute Mountain fault zone, CdlO fz=Cerro de la Olla fault zone; G fz=Gorge fault zone; CdlT=Cerro de los Taoses.

2. Geologic Setting

The southern SLB is in the northern part of the Rio Grande rift, a zone of extension that bisects the state of New Mexico. The Sangre de Cristo Mountains are located to the east of the basin and the basement-cored Tusas Mountains lie to the west (Fig. 1). The Picuris Mountains, bounded on the northwest by a left-lateral strike slip fault, the Embudo fault, form the southern boundary of the basin; this fault has a minor north-side-down normal component. The Picuris Mountains are separated from the Sangre de Cristo Mountains by the north-striking Picuris-Pecos fault zone that was active during Proterozoic, Laramide, and Rio Grande rift episodes of deformation (Miller et al., 1963, Bauer and Kelson, 2004; Cather et al., 2011). Gravity and aeromagnetic surveys reveal that the SLB is deepest along a narrow zone next to the west-dipping, western bounding faults of Sangre de Cristo Mountains (Cordell, 1978; Keller et al., 1984). This narrow feature, the Taos graben, is bordered on the west by the buried east-dipping Gorge fault (Grauch and Keller, 2004). Manby and Black Rock hot springs emerge from one of the few strands of the Gorge fault that reaches the surface. An intrarift horst on the west side of the Taos graben is marked at the surface by exposures of Oligocene volcanic rocks on Timber Mountain and Brushy Mountain (Lipman and Mehnert, 1979; Thompson et al., 1991; Grauch et al., 2017)). Johnson and Bauer (2012) extend this feature to the north into Colorado as the buried Taos Plateau horst (Fig. 1). The Jemez lineament, a zone of NE-striking low-velocity mantle that is associated with < 10 Ma volcanism, including the 6 to 1 Ma Taos Plateau volcanic field (Lipman and Mehnert, 1979; Appelt, 1998), crosses the area of interest. Basalt flows of the Taos Plateau field cover the central and western parts of the basin.

Several tectonic events, including Proterozoic continental assembly, Pennsylvanian Ancestral Rocky Mountain, Late Mesozoic to Early Cenozoic Laramide, and Middle to Late Cenozoic Rio Grande Rift deformation, have shaped the structural and depositional elements of the basin. Volcanic and volcaniclastic rocks derived from the Late Eocene to Miocene San Juan volcanic field to the northwest and the Oligocene to Miocene Latir volcanic field on the eastern margin of the basin near Questa are preserved throughout the region. As extension in northern New Mexico began at 30–25 Ma, the developing rift basin filled with debris shed from the surrounding highlands. As extension continued, prominent, rounded andesitic to dacitic to rhyolitic domes erupted between 5 and 3 Ma at the same time that Servilleta basaltic shield volcanoes were active 5.2 to 3.6 Ma, thus creating the Taos Plateau volcanic field. Extension has continued; both the Sangre de Cristo fault and the Embudo fault zones have been active during Quaternary time (Menges, 1990).

3. Aquifers

The principal aquifers in the southern SLB in proximity to the town of Taos are sedimentary units in the Late Oligocene to Miocene Santa Fe Group. This unit includes (from oldest to youngest): alluvial/fluvial basin-fill deposits (Chama-El Rito Member of the Tesuque Formation), well-sorted eolian sands (Ojo Caliente Sandstone Member of the Tesuque Formation), and a younger set of alluvial and fluvial basin-fill deposits assigned to the Chamita Formation. The basalt lava flows of the Taos Plateau volcanic field assigned to the Servilleta Formation (Drakos et al., 2004; Johnson and Bauer, 2012; Johnson et al., 2016). The middle Pleistocene Lama Formation is intercalated with and overlies the basalt flows. The Lama Formation is comprised of distal-alluvial-fan sand and gravel derived from the Sangre de Cristo Mountains. This unit was deposited before the development of the Rio Grande gorge. All basin-fill units and the basalts generally thin towards

the south and east, eventually pinching out against the mountain fronts (Johnson et al., 2016). Fractures in the fault damage zones in the basement rocks are generally open (Johnson et al., 2016). In contrast, fault damage zones in the Santa Fe Group are generally filled with clay (Johnson et al., 2016); thus, aquifers within the Santa Fe Group tend to be compartmentalized. The basalts are also important aquifers. Columnar jointing is common and basal flow breccias and vesicular flow tops facilitate groundwater flow.

The Servilleta Formation is the principal aquifer in the western portion of the SLB in northern New Mexico (Johnson and Bauer, 2012). The basalt flows are thick, continuous and are interbedded with clay and silt. Permeability in the basalt is high due to the presence of columnar joints, vesicular flow tops, basal breccias, and lava tubes. The Santa Fe Group underlies the basalt flows of the Servilleta Formation. In the western part of the basin, the Oligocene Hinsdale basalt that was derived from volcanic centers in Colorado is an important deep aquifer that delivers groundwater from the Tusas Mountains to the SLB (Johnson and Bauer, 2012).

4. Important Structures

4.1 Southern basin

Johnson et al. (2016), building on the earlier work of Bauer et al. (2004), document that the complex interaction between the older, north-striking, 8-km-wide Picuris-Pecos fault zone and the younger, ENE-striking, north-down, left-lateral Embudo fault system. This interaction intensely fractured the basement rocks on the southern margin of the SLB, thus providing pathways to connect deep aquifers with shallow aquifers. Overall, the Picuris-Pecos fault zone is an E-down, strike-slip fault, but in detail in the Miranda graben near Talpa, the zone actually consists of a series of horsts and grabens. The Miranda graben developed during Laramide offset along the Pecos-Picuris fault. The graben was filled by the 28.35±0.11 Ma Picuris Formation derived from the San Juan Mountains; these sediments were subsequently cut by the fault (Johnson et al., 2016). The Picuris-Pecos system continues northward and is buried beneath the rift-fill deposits of the SLB. The buried fault appears to have been reactivated as the Los Cordovas system that offsets alluvial fans as young as Quaternary (early to middle Pleistocene). Latest motion on the Embudo fault system is constrained to be late Pleistocene to Holocene. Toward the east, the Embudo fault transitions to the N-striking, W-dipping, 2-km-wide, Sangre de Cristo fault zone by progressively changing to a dip-slip fault.

4.2 Western basin

Johnson and Bauer (2012) identified four surface faults that cut the volcanic rocks of the Taos Plateau volcanic field and two possible buried structures that control groundwater flow in the SLB west of the Rio Grande (Fig. 1). The four surface faults are the northwest-striking, east-down Red River fault zone, the northeast-striking, east-down Ute Mountain and Cerro de la Olla faults, and complex Gorge fault zone largely identified using aeromagnetic data (Machette et al., 2007). The Red River fault zone cuts Pleistocene gravels (Kelson et al., 2008). Older Oligocene volcanic rocks are exposed on the Timber Mountain-Brushy Mountain horst. Johnson and Bauer (2012) extend this horst, named the Taos Plateau horst, northward into Colorado based on the presence of elevated discharge temperatures, water chemistry, and aeromagnetic data. The presence of the Western Plateau faults is based on the alignment of volcanic vents and on a decrease in hydraulic gradient across the proposed structure.

5. Temperature Measurement Methods

Johnson and Bauer (2012) and Johnson et al. (2016) identified several open wells with no pumps (either monitoring wells or undeveloped wells) for data logger installation. These types of wells are perfect for equilibrium temperature log analysis. Eighteen thermal logs measured in open wells were collected as part of this study. In addition, we compiled thermal profile data from published thermal gradient/heat flow studies (Swanberg, 1984; Edwards et al., 1978; Reiter et al., 1975, Reiter and Sandoval, 2004). Published thermal profiles from deep monitoring and production wells have not been previously analyzed in the context of rock types encountered in the wells. We gathered data from driller's logs and available geophysical logs and compared these data to variations in geothermal gradient in each well to determine the influence of rock type on geothermal gradient and to evaluate conductive versus convective affects.

The New Mexico Bureau of Geology and Mineral Resources temperature-logging equipment uses a thermistor attached to a wireline cable to measure resistance as a function of depth. Resistance is translated to temperature using a laboratory calibration. Resistance is recorded at 1-m depth intervals using a digital multimeter and a computer. Profiles in the southern basin were measured with a sensor designed to measure resistance in water; consequently, the air readings for these logs are not in thermal equilibrium. In contrast, many of the open holes west of the Rio Grande are dry, so a different, fast-response thermistor was used to measure temperature in the vadose zone. The logging rate varied from one to 4 m/minute.

The distribution of temperature measurements discussed in this paper is illustrated in Figure 2. Many of the shallow wells are disturbed by shallow fluid flow, masking the geothermal potential of the deeper system (e.g., Fig. 3G). Consequently, this investigation will primarily focus on the deeper monitoring and water wells highlighted by yellow dots on Figure 2, although a few warm, shallow wells are included in the analysis.

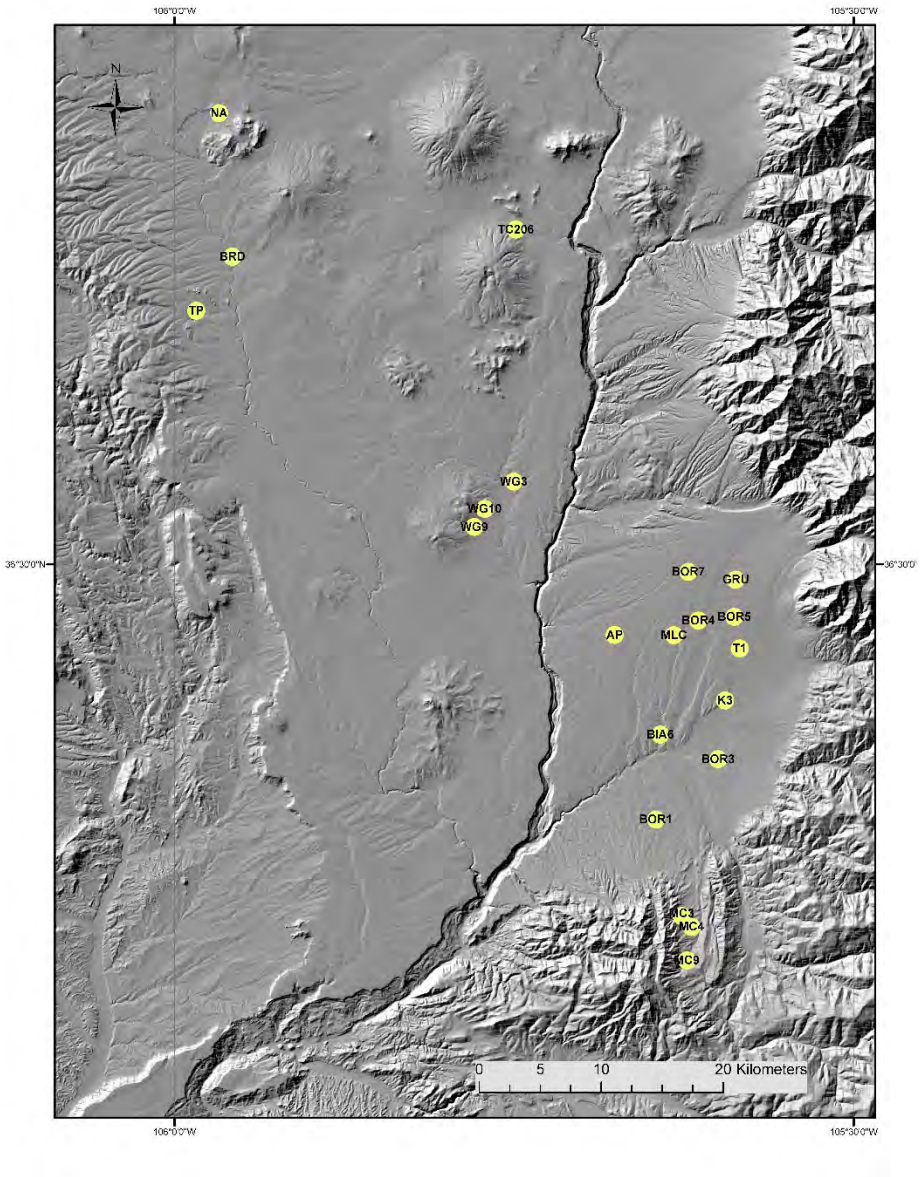

Figure 2. Location of the water and monitoring well included in this analysis.

6. Temperature Log Results

The discussion of the results is organized by location within the southern SLB. Fluid movement in aquifers influences thermal profiles from deep monitoring wells and intermediate-depth water wells east of the Rio Grande. Measured temperatures in the Miranda graben are potentially affected by fluids moving through highly fractured rocks in the Embudo and Picuris-Pecos fault zones and contain information about both recharge and discharge. Anomalously high geothermal gradients characterize the data from the west side of the basin between Cerro de los Taoses and Tres Piedras.

6.1 East of the Rio Grande (Eastern Basin)

Eight deep (305 to 944 m) monitoring and production wells and two shallow water were logged in an area that is within a few kilometers north, west, and southwest of the town of Taos. Reiter and Sandoval (2004) published temperature logs from five monitoring and production wells drilled by the Bureau of Reclamation in cooperation with the town of Taos, and one well was re-logged as part of this study. BOR1 is a deep monitoring well (610 m) drilled south of the basalt pinch out. A shallow well (140 m) is part of the piezometer nest. BOR1 was completed on 11/22/99 and Reiter and Sandoval (2004) logged the well August 2002. As part of this study, we logged both the co-located shallow and deep monitoring wells on 7/17/12. The temperatures in both the shallow and the deep piezometers measured in 2012 at depths less than 140 m are nearly identical; however, the temperature in the deep BOR1 borehole has changed significantly between 2002 and 2012 (Fig. 3A). At depths shallower than 500 m, the well has cooled about 1.6°C, and the well has warmed about 0.7 °C below 500 m between 2001 and 2012. Wells do equilibrate through time as the surrounding rocks recover from thermal changes caused by drilling. The usual trend is warming through time, but cooling has been observed. Furthermore, purging of monitoring wells during water sampling may modify the temperature distribution in a well. The most recent thermal profile is disturbed by cool water flowing through gravel and sand intervals at 403–433 m (flowing around the well casing) and 439–488 m (coincides with the upper-screened interval). Linear gradients in the shallow part of the deep BOR1 and in shallow well are 24–26 °C/km; analysis of the Reiter and Sandoval (2004) log over this same depth range yields a similar result. Gradients in the deeper part of BOR1 are 30–33°C/km.

Well BOR3 (Fig. 3B) penetrates the Servilleta and Chamita formations, and the Chama-El Rito Member of the Tesuque Formation. The gradient shows a small inflection at the contact between the Servilleta Formation and the Chamita Formation that is likely related to thermal conductivity contrast between rock types; the gradient is slightly higher in the basalt. The gradient is linear (20.1°C/km) through the upper part of the Chamita Formation, and then the gradient becomes nearly isothermal below 420 m. Cold water enters the well at the top of the screen and appears to move down the well (Reiter, 2004).

Deep monitoring well BOR4 (Fig. 3C) penetrates Servilleta Formation, Chamita Formation, and the Chama-El Rito Member of the Tesuque Formation. The gradients in BOR4 are moderately disturbed by upflow, with water coming into the borehole near the top of the screen in the Chamita Formation. The geothermal gradient below the disturbed interval is 28.7°C/km.

Chamita Formation, and the Ojo Caliente and Chama-El Rito members of the Tesuque Formation are encountered in BOR5 (Fig. 3D); the well bottoms in one of the older basalts. Two zones of cold water, one a ~205 m and one at ~460 m locally modify the gradient. The upper cold zone is in the Chamita Formation and the cool water is flowing around the casing. The lower cold zone is in the Chama-El Rito Member. Water enters the borehole within the screened interval. The gradient in the relatively undisturbed middle section of the well is 35°C/km.

BOR7 (Fig. 3E), the deepest well logged (900 m), goes through thick Lama Formation, Servilleta Formation, Chamita Formation and both members of the Tesuque Formation. The top of the log is greatly affected by cold water flowing through Servilleta Formation basalt. Below the basalt, the geothermal gradient is linear (28°C/km) and the slight changes in gradient line up with changes in rock type. The maximum measured temperature in this deep drillhole is 38°C.

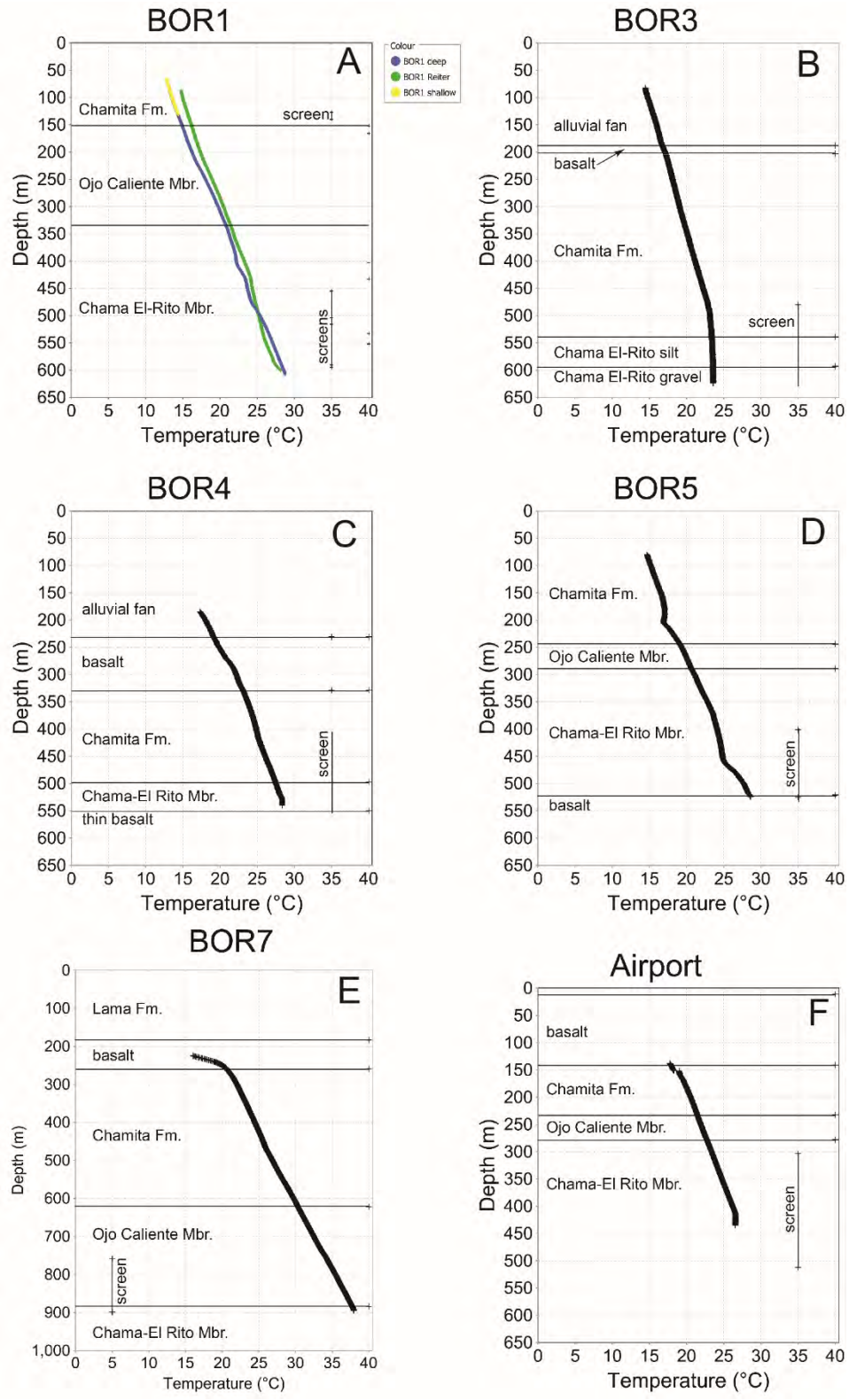

Figure 3A-F: Thermal profiles in deep boreholes near Taos from Reiter and Sandoval (2004). The rocks units in each well were added as part of this investigation. The Ojo Caliente and the Chama-El Rito are members of the Tesuque Formation.

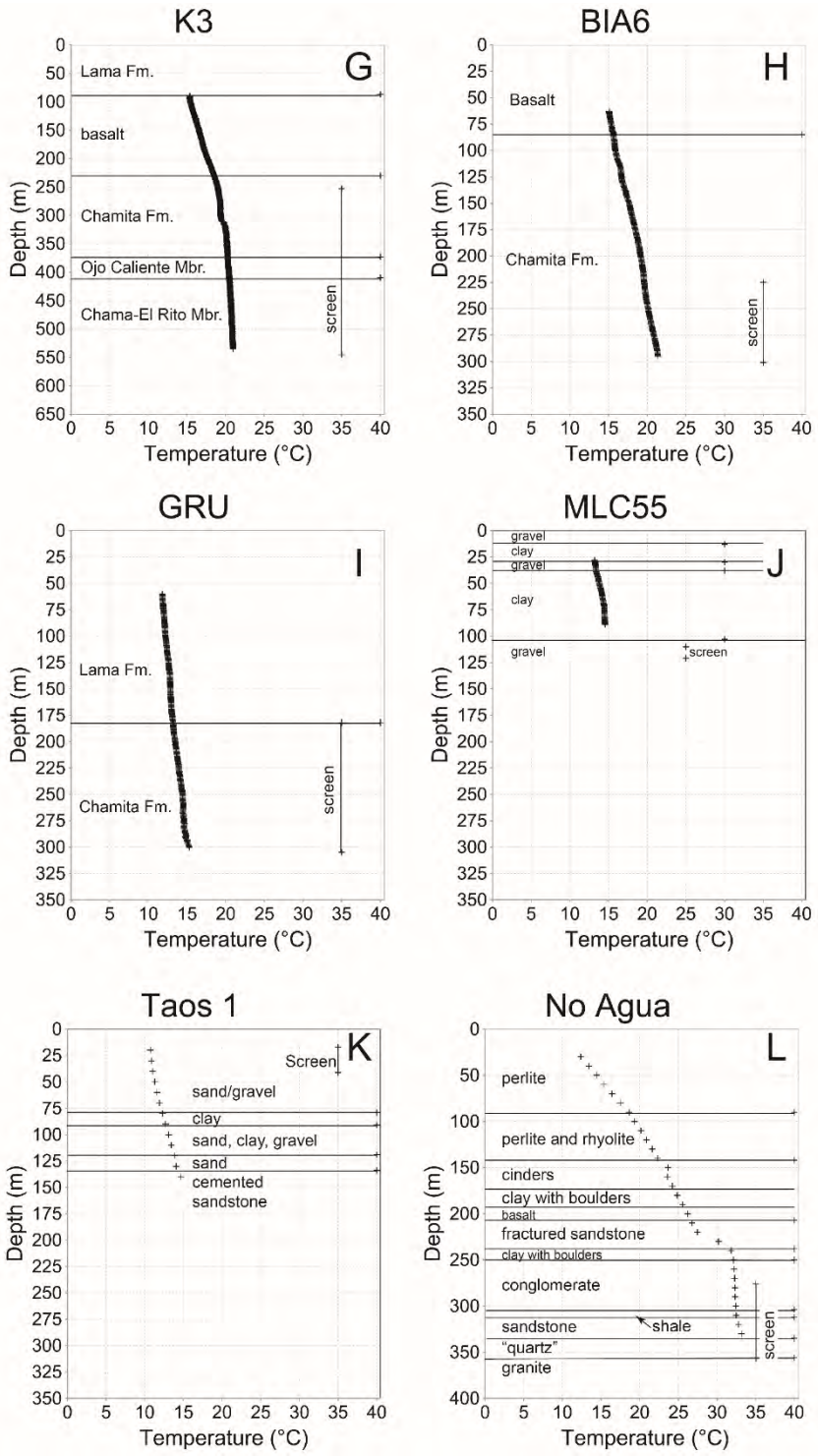

Figure 3G-L: Temperature-depth logs from Reiter (2004; G, H, I), this study (J); Edwards et al. (1978; K) and Reiter et al. (1975; L). The rocks units in each well were added as part of this investigation.

The deep well at the Taos Airport (Fig. 3F), which is located closer to the center of the Taos Plateau, has a conductive gradient of 28°C/km through the Chamita Formation and both members of the Tesuque Formation. Minor cooling near the top of the log may be related to cool water flowing through the overlying Servilleta Formation.

K3 (Fig. 3G) encounters Lama, Servilleta, and Chamita formations and the Ojo Caliente and Chama-El Rito members of the Tesuque Formation. The geothermal gradient through the Servilleta Formation is 23°C/km. Cool water enters the drill hole through the screen at 230 m, indicating a downward hydraulic gradient (Reiter and Sandoval, 2004).

BIA6 (Fig. 3H), which is located near the Rio Pueblo de Taos (Fig. 2), is in Servilleta Formation basalt above 85 m and the well is completed in Chamita Formation. Water coming into the well near the top of the screen is flowing up the borehole. The gradient above the disturbed interval is 25°C/km.

The Lama and Chamita formations were encountered in GRU (Fig. 3I); the Servilleta Formation is not present. This well generally has a low geothermal gradient (19°C/km), likely due to its proximity to the Sangre de Cristo mountain front. Two minor influxes of cool water are within the screened interval, one near the Lama/Chamita contact, and the second in the Chamita Formation near the bottom of the well.

One shallow well, MLC-55 (Fig. 3J), was logged as part of this study. The drillers log indicates that the well encountered alternating layers of gravel and clay. Cool water enters the well through the screen and flows up, indicating an upward hydraulic gradient. The geothermal gradient between 40 to 70 m is 31°C/km. A second shallow well, Taos 1 (Fig. 3K), was measured by Edwards et al. (1978) and is drilled into sand, gravel, and clay of the Santa Fe Group. Small variations in gradient correlate to rock type changes, indicating conductive heat flow in this well. Measured gradients are 37 to 42°C/km.

6.2 Miranda graben

Three wells that are 128 to 273 m deep were logged in Miranda Canyon (Fig. 4C). Geothermal gradients in all three wells are modified by flowing water. The calculated gradients for two of the wells are estimated from short linear segments that may not coincide with changes in rock type. The shape of the thermal profile in Miranda Canyon 3 is typical of slow upflow in the wellbore. The gradients measured in the middle part of the Miranda Canyon 4 hole coincide with fine-grained (57.8°C/km) and coarse-grained interval (51.2°C/km) interpreted from the driller's logs. Water from a cool aquifer enters the Miranda Canyon 4 well at the screened interval. Miranda Canyon 9 penetrates alternating beds of sand and gravel and one clay layer. Cold water appears to flow around the top of the wellbore. A background gradient of 32.4°C/km was calculated for depths greater than 103 m.

6.3 Western margin

Previous measurements of heat flow by Reiter et al. (1975) identified two wells with elevated geothermal gradients on the western margin of the Taos Plateau. The well at Tres Piedras (Fig. 4 B, TP) is about 170 m deep; no driller's logs are available. The average linear geothermal gradient is 51°C/km through the middle of the well, and warm water enters the well at ~140 m. The second well with published heat flow data is the water well that supplies the No Agua perlite mine (Figs.

3L, NA on Fig.4B). The upper part of the well, which is in perlite and rhyolite, is conductive. The drillers log mentions lost circulation in the sandstone interval. Warm water flows around the well near the top of a basalt flow at a depth of 150 m. Sandstone, conglomerate, and clay that likely belongs to the Santa Fe Group underlies the basalt. Warm water enters the well through the screen near the bottom of the hole and flows up the well bore. The well bottoms in Proterozoic rocks**.** Interval gradient in the No Agua well are 64.3 to 100.9°C/km.

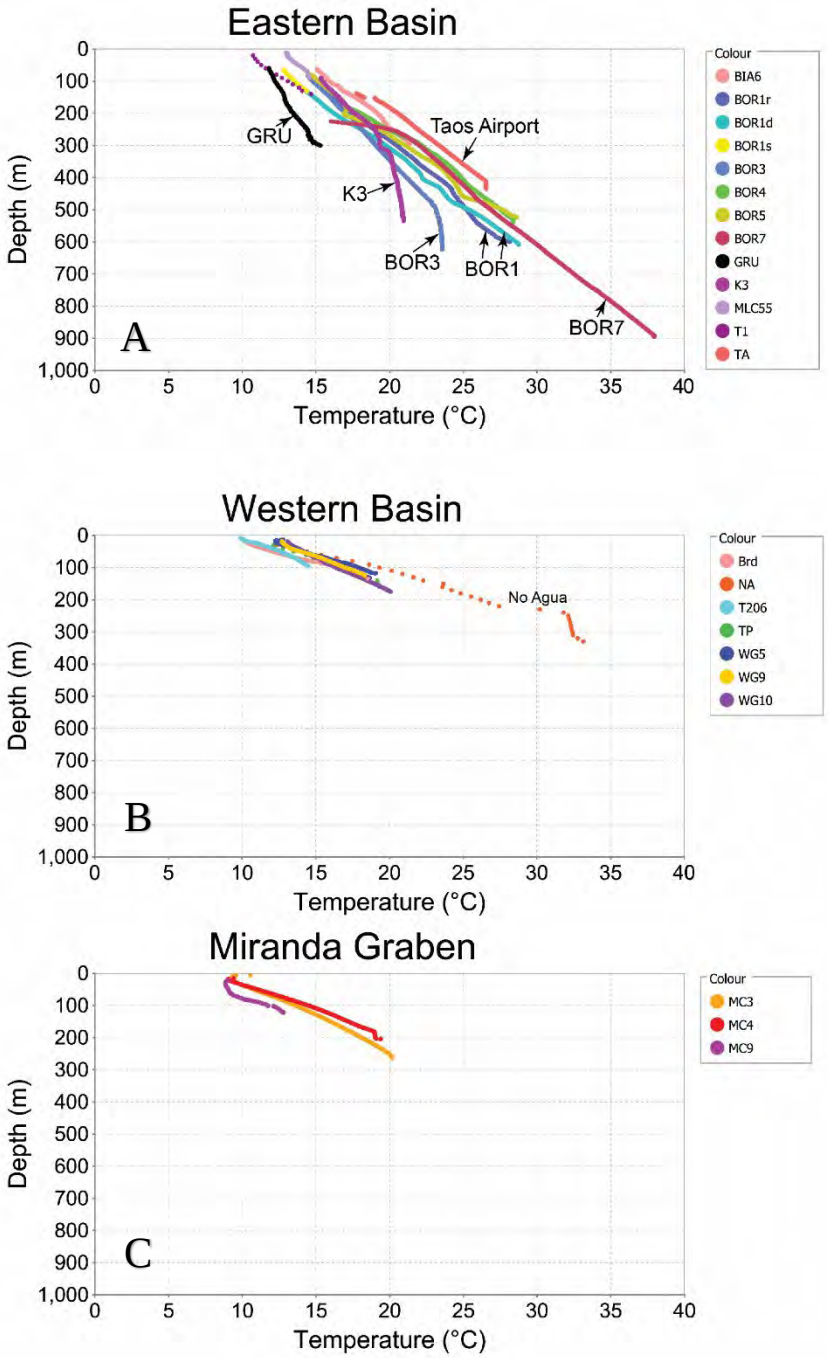

Figure 4: Comparison of temperature logs from the southern San Luis Basin.

Five wells west of the Rio Grande were logged as part of this study. T206 (Fig. 4B) is located in the middle of the basin north of Highway 64. Well T206 has conductive gradients ranging from 51 (shallow) to 36 (deep) °C/km; no driller's log is available for this well. Three wells were logged near Highway 64 west of the Rio Grande in the Cerros de los Taoses. WG5 (Fig 4B) is a dry hole that penetrates Lama Formation, Servilleta Formation basalt flows and intercalated clay or sand and gravel beds, and bottoms in the Chamita Formation. The thermal profile is noisy because the casing has been removed and vadose zone moisture appears to be moving along flow breaks and within the basalt flows. A rainstorm at the surface during the time of logging might also have contributed to the noise. The linear gradient through a thick clay layer at the bottom of the well is 55.7 °C/km. WG9 (Fig. 4B) is a dry hole that penetrates 153 m of "andesite" and interbedded sandstone. Linear gradients range from 56 (shallow) to 44 (deep)°C/km. WG10 (Fig. 4B) is a dry well with no driller log, but the hole is likely in the Servilleta Formation. The linear gradient near the bottom of the hole is 50 °C/km. The final well logged in this region was the Bradley (Fig. 4B, Brd) well, a dry hole about 106 m deep that bottoms in Proterozoic granite on the west side of the basin adjacent to the Tusas Mountains. This warm well has gradients that vary from 74 (shallow) to 112 (deep) °C/km.

7. Discussion

7.1 Margins of the basin

Two areas of geothermal interest along the southern and western margins of the SLB that appear to be structurally controlled are characterized by elevated geothermal gradients compared to the gradients in the eastern part of the basin (east of the Rio Grande; Fig. 4). One area is associated with the well-known Ponce de Leon warm spring located at the north end of the Miranda graben (Fig. 1). This hydrologic system is controlled by flow pathways along strands of the N-striking Picuris-Pecos fault zone interacting with the northeast-striking Embudo fault zone. The new temperature logs from the Miranda graben provide information about the recharge area and the flow paths that lead to discharge of the spring. Johnson et al. (2016) describe the hydrogeologic framework of the southern margin of the SLB using a combination of major and trace element geochemistry and isotopic analysis. These authors document elevated groundwater discharge temperatures associated with the Ponce de Leon thermal spring along the south edge of the SLB. The temperatures are 21.9 to 34.9 °C in a zone about two km north of the spring. Elevated temperatures in the outflow plume extend 7.5 km northeast into a shallow aquifer along extrapolated projections of the buried Picuris-Pecos fault zone. The chemistry of the groundwater at the Ponce de Leon spring (Na-Cl-SO_4) is unique compared to groundwater in the headwaters in the Miranda graben (Ca-Mn-Mg-HCO_3). Johnson et al. (2016) suggest that the chemistry of the Ponce de Leon system is related to deep circulation of groundwater through Pennsylvanian carbonates and evaporites and volcaniclastic Picuris Formation within and beneath the graben.

The second prospect is located along the western margin of the Taos Plateau north of the village of Tres Piedras. The presence of elevated geothermal gradients in this area has long been known (Reiter et al., 1975), but new data collected during this investigation expand the zone of high geothermal gradients eastward into the Cerros de los Taoses. Johnson and Bauer (2012) identified elevated discharge temperatures in several wells on and just west of the No Agua rhyolite dome that range from 25 to 31 °C. These authors propose a model of deep underflow from the Tusas Mountains into the western SLB through the Hindsdale basalt and fractured Proterozoic basement

based on the chemistry of the Ca-Mg-rich HO_3 groundwater that characterize this area. Oxygen and deuterium data from this region support the concept of deep circulation within the Tusas Mountains. Deuterium depletion suggests that the groundwater originated at high elevation and a positive ^{18}O shift (0.5 to 1.0%, fig. 32, Johnson and Bauer, 2012) indicates water-rock interactions at high temperatures. Groundwater residence times are 8000–5500 radiocarbon-years before present.

7.2 East of the Rio Grande

In contrast to the basin margins, the thermal architecture of the SLB east of the Rio Grande near the town of Taos reflects the interaction between the regional geothermal gradient and groundwater flow in aquifers. Cool water flowing through basalt flows and though discrete beds in Santa Fe Group sedimentary units is documented in several wells. The aquifers at depth are confined. Differences in hydraulic gradient cause upflow and downflow within wellbores, which is observed in the thermal profiles of several wells in this region. Johnson et al. (2016) also note differences in hydraulic gradient in piezometer nests in this area. The gradients is slightly down near Rio Grande del Rancho, but near Rio Pueblo de Taos, the gradient is up (Johnson et al., 2016). The background geothermal gradient is 28°C/km east of the river.

7.3 Other prospective areas

7.3.1 Red River fault zone

Johnson and Bauer (2016) measured relatively warm discharge temperatures of 16.5–18.1°C from wells near the northwest-striking Red River fault zone (Fig. 1) and its projection northward into the buried Taos Plateau horst. Three warm springs (16.5–17.5°C) discharge from the fault zone. The groundwater near projections of the Red River fault zone and its intersection with the Cerro de la Olla-Ute Mountain faults zone is Na-rich with relatively high concentrations of Cl and SO_4. A relatively elevated Cl/Br ratio of 190 was measured in this area.

7.3.2 Sunshine Valley

Temperature logs for the three wells were measured by Rawling and Kelley (2020); all three were isothermal due to groundwater flow in the basalt in that area, with warmer temperatures measured near the village of Costilla just south of the Colorado border. Warm discharge temperatures of 16.4 to 23.8 °C were measured in two wells near Costilla. An important finding from that study was that, based on chloride mass balance calculations, more than half of the recharge occurs as groundwater underflow into the aquifer directly from the Sangre de Cristo mountain block. The steep topography and geologic features of the Questa caldera probably influence the large amount of recharge by underflow in this part of the SLB.

7. Conclusion

In general, groundwater flow in aquifers in the Servilleta Formation basalt flows and in permeable layers within the Santa Fe Group mask the true geothermal potential of the southern SLB. Despite this challenge, local, structurally controlled, deep-circulation systems in the Miranda graben and north of Tres Piedras have been identified using a combination tof temperature logs, spring and

well discharge temperatures, and groundwater geochemistry. Other areas that warrant further investigation are located along the Red River fault zone and near the village of Costilla.

Acknowledgement

Jeff Pepin helped with the fieldwork. Paul Bauer provided important information about the rock units in the BOR wells.

REFERENCES

Appelt, R.M., "$^{40}Ar/^{39}Ar$ geochronology and volcanic evolution of the Taos Plateau volcanic field, northern New Mexico and southern Colorado." *Unpublished M.S. thesis, New Mexico Tech, Socorro,* (1998),58 pp.

Bauer, P.W., and Kelson, K.I., "Fault geometry and Cenozoic kinematic history of the southeastern San Luis Basin near Taos, New Mexico." *New Mexico Bureau of Geology and Mineral Resources Bulletin, 160*, (2004), 70–95.

Cather, S.M., Read, A.S., Dunbar, N.W., Kues, B.S., Krainer, K., Lucas, S.G., and Kelley, S.A., "Provenance evidence for major post-Early Pennsylvanian dextral slip on the Picuris–Pecos fault, northern New Mexico." *Geosphere*, 7, (2011) 1175–1193.

Cordell, L., "Regional geophysical setting of the Rio Grande rift." *Geological Society of America, Bulletin*, 89, (1978), 1073–1090.

Drakos, P., Lazarus, J., Riesterer, J., White, B., Banet, C., Hodgins, M., and Sandoval, J., 2004a, "Subsurface stratigraphy in the southern San Luis Basin, New Mexico." *New Mexico Geological Society Guidebook*, 55, (2004) 374–382.

Edwards, C. L., Reiter, M., Shearer, C., and Young, W., "Terrestrial heat flow and crustal radioactivity in northeastern New Mexico and southeastern Colorado." *Geological Society of America Bulletin*, 89, (1978), 1341-1350.

Grauch, V.J.S., and Keller, G.R., "Gravity and aeromagnetic expression of tectonic and volcanic elements of the southern San Luis Basin, New Mexico and Colorado." *New Mexico Geological Society Guidebook*, 55, (2004), 230–243.

Grauch, V.J.S., Bauer, P.W., Drenth, B.J., and Kelson, K.I., "A shifting rift—Geophysical insights into the evolution of Rio Grande rift margins and the Embudo transfer zone near Taos, New Mexico." *Geosphere*, 13, (2017) 870–910, doi: 10 .1130 /GES01425.1.

Johnson, P.S., and Bauer, P.W, "Hydrogeologic investigation of the northern Taos Plateau, Taos County, New Mexico." *New Mexico Bureau of Geology and Mineral Resources Open-File Report 544*, (2012), 78 p. plus plates and appendices.

Johnson, P.S., Bauer, P.W., and Felix, B., :Hydrogeologic investigation of the southern Taos Valley, Taos County, New Mexico." *New Mexico Bureau of Geology and Mineral Resources Open-File Report 581*, (2016), 96 p. plus 2 plates and appendices.

Keller, G.R., Cordell, L., Davis, G.H., Peeples, W.J., and White, G., A geophysical study of the San Luis Basin." *New Mexico Geological Society Guidebook*, 35, (1984) 51–57.

Kelson, K. I., Bauer, P. W., and Thompson, R. A., "Preliminary geologic map of the Guadalupe Mountain 7.5-minute quadrangle, Taos County, New Mexico." *New Mexico Bureau of Geology & Mineral Resources, Open-File Geologic Map OF-GM 168*, (2008), scale 1:24,000.

Lipman, P. W. and Mehnert, H. H., "The Taos Plateau volcanic field, northern Rio Grande rift, New Mexico." in Riecker, R. C., ed., *Rio Grande rift – Tectonics and magmatism*: American Geophysical Union, Washington D.C., (1979), 289–311.

Machette, M. N., Coates, M-M., and Johnson, M. L., "2007 Rocky Mountain Section Friends of the Pleistocene Field Trip—Quaternary geology of the San Luis Basin of Colorado and New Mexico, September 7–9, 2007." *U.S. Geological Survey Open-File Report 2007–1193*, (2007), 197 p.; available at pubs.usgs.gov/of/2007/1193.

Menges, C.M., "Late Quaternary fault scarps, mountain-front landforms, and Pliocene-Quaternary segmentation on the range-bounding fault zone, Sangre de Cristo Mountains, New Mexico." *Neotectonics in earthquake evaluation: Geological Society of America Reviews in Engineering Geology*, 8, (1990), 131-156.

Miller, J.P., Montgomery, A., and Sutherland, P. K., "Geology of part of the Sangre de Cristo Mountains, New Mexico." *New Mexico Bureau of Mines and Mineral Resources, Memoir 11*, (1963), 106 pp.

Norman, D. I. and Bernhardt, C. A., "Assessment of geothermal reservoirs by analysis of gases in thermal waters." *New Mexico Energy Research and Development Institute Report EMD 2-68-2305*, (1982), 130 p.

Rawling, G., and Kelley, S., "Sunshine Valley hydrogeology study." *New Mexico Bureau of Geology and Mineral Resources Open-file Report 607*, (2020), 68 pp.

Reiter, M., and Sandoval, J. "Subsurface temperature logs in the vicinity of Taos, New Mexico." *New Mexico Bureau of Geology Guidebook, 55*, (2004), 415-419.

Reiter, M., Edwards, C. L., Hartman, H., and Weidman, C., "Terrestrial heat flow along the Rio Grande rift, New Mexico and southern Colorado." *Geological Society of America Bulletin*, 86, (1975), 811-818.

Swanberg, C. A., "Chemistry, origin, and geothermal potential of thermal and non-thermal waters in New Mexico." *unpublished report submitted under US Geological Survey Grant 14-08-0001-6-255*, (1980), 99 p.

Swanberg, C.A., "Geothermal resources of the Rio Grande rift." *New Mexico Energy and Development Report NMERDI 2-69-2208*, (1984), 165-183.

Summers, W. K, "Catalog of thermal waters in New Mexico." *New Mexico Bureau of Mines and Mineral Resources Hydrologic Report*, 4 (1980),80 p.

Thompson, R. A., Johnson, C. M., and Mehnert, H. H., "Oligocene basaltic volcanism of the north Rio Grande rift: San Luis Hills, Colorado." *Journal of Geophysical Research*, 96, (1991), 13,577–13,592.

Trainer, F. W. and Lyford, F. P., "Geothermal hydrology in the Rio Grande rift, north-central New Mexico." *New Mexico Geological Society Guidebook*, 30, (1979), 299–306.

Remote Sensing Case Studies for Detection and Interpretation of Geothermal Surface Materials for Geothermal Exploration in the Basin and Range, Nevada, USA

Kurt O. Kraal and Paul C. Schwering

Sandia National Laboratories

Keywords

BRIDGE, SWIR, Hyperspectral, Remote Sensing, Exploration, Sinter, Great Basin

ABSTRACT

"Blind" geothermal systems, lacking active geothermal surface manifestations such as hot springs or fumaroles, are difficult to discover. However, there are often surface or near-surface materials indicative of subsurface geothermal activity above a blind system. These are typically products from springs/fumaroles related to the system that are no longer active or exposure of hydrothermal alteration minerals due to faulting and/or erosion. Examples of shallow or surface materials indicative of possible geothermal activity include silica polymorphs (e.g., opal/chalcedony, found in silica sinter, silicification or veining), carbonates (e.g., tufa, travertine, calcite veining), advanced argillic alteration (e.g., kaolinite, alunite), intermediate argillic alteration (smectite, illite) and borates. We utilize publicly available airborne hyperspectral data in the visible and short-wave infrared (SWIR) wavelength range over western Nevada to create thematic maps of geothermal indicator minerals over known geothermal systems and prospects for use in exploration. We map several benchmark areas with known geothermal surface materials: Salt Wells, and Lee Allen. We then apply these techniques to produce mineral maps of prospective resource areas in Gabbs Valley, Hawthorne, and Bell Flat, Nevada. We synthesize these maps with existing data to explore how they may inform exploration activities and potential conceptual models.

1. Introduction

The goal of this paper is to demonstrate the use of publicly available hyperspectral data in the Great Basin region of the western USA for geothermal exploration by identifying geothermal surface materials and paleo-geothermal deposits. This work, funded by the U.S. Department of Energy's Geothermal Technologies Office, is part of the Basin & Range Investigations for Developing Geothermal Energy (BRIDGE) Project to advance the exploration practices of discovering and characterizing hidden (or "blind") geothermal resources in the region (Schwering

et al., 2022). First, we will describe a conceptual framework for the shallow environment of geothermal systems and the formation of various hydrothermal minerals. We will then review previous examples of using remote sensing techniques to map geothermal surface materials. We will then look at two benchmark locations where previous mapping has identified sinter and silicified sediments (i.e., Lee Allen Hot Springs and Salt Wells Geothermal Field, Nevada) and evaluate techniques and data quality for geothermal exploration activities. We will then apply those techniques and data sources for geothermal exploration in several greenfield locations with high geothermal resource potential.

1.1 Conceptual Framework

Geothermal systems produce distinctive mineral products and landforms on the surface or in the near subsurface through the discharge of various fluid types (Sillitoe, 2015; e.g., Figure 1). These landforms and mineral products can be the product of surface hot springs and/or fumaroles or be formed in the subsurface and exposed by faulting and/or erosion. Even when there are no active hot springs or fumaroles, such as at a blind geothermal system, there may be relict paleo-geothermal deposits that were active in the past. These surface features and shallow hydrothermal alteration zones can be identified by distinct minerals or mineral mixtures. Several of these materials can be detected with remote sensing techniques, including silica (opal/chalcedony), carbonates (calcite, aragonite), and phyllosilicates (smectite, kaolinite, illite; e.g., Figures 2 & 3).

Silica polymorphs (e.g., opal and chalcedony) can be found in several shallow and surficial geothermal environments with neutral-pH chloride thermal waters. The classic example is silica sinter discharged at the surface in hot springs, and the presence of sinter is considered a good indicator for a high temperature geothermal reservoir (greater than ~175 °C per Fournier, 1983). Hot springs can only occur where the water table intersects the surface, which may occur proximal or distal to the inferred upwelling location, or not at all. Hot fluids (~100 °C) supersaturated in silica precipitate opal-A (amorphous silica) in cones, aprons, terraces, pools or marshes producing several distinct sinter facies (e.g., Cady & Farmer, 1996). As it ages over ~50,000 years, the opal-A will transition through several intermediary steps to microcrystalline quartz (chalcedony) (Sillitoe, 2015). Historically active sinter terraces are present at Steamboat Springs (White et al., 1964) and Beowawe geothermal fields in Nevada (Rimstidt & Cole, 1983). Common features observed at high temperature geothermal fields in the Great Basin are silicified sediments, such as at Salt Wells and Desert Peak, often found alongside sinter and is sometimes exposed at the surface through erosion (Garside & Schilling, 1979; Coolbaugh et al., 2004, Yap et al., 2018; Ayling et al., 2022). In a lacustrine environment, as were many basins in the Great Basin during the Pleistocene epoch (Russel, 1885, Adams & Wesnousky, 1999; Benson et al., 2011), silica can be precipitated as amorphous silica sediments, hydrothermal chert or silicified lacustrine sediments (Sillitoe, 2015). Additional near-surface formation environments for silica polymorphs are as water table silicification (opal) beneath steam-heated zones, and in veins (see below).

Carbonates can be found as surficial deposits of travertine, tufa, or calcite veins. Travertine and tufa are distinguished by their textures and inferred formation environment. Travertine is formed when CO_2 rich fluids degas in springs, causing supersaturation with and precipitation of

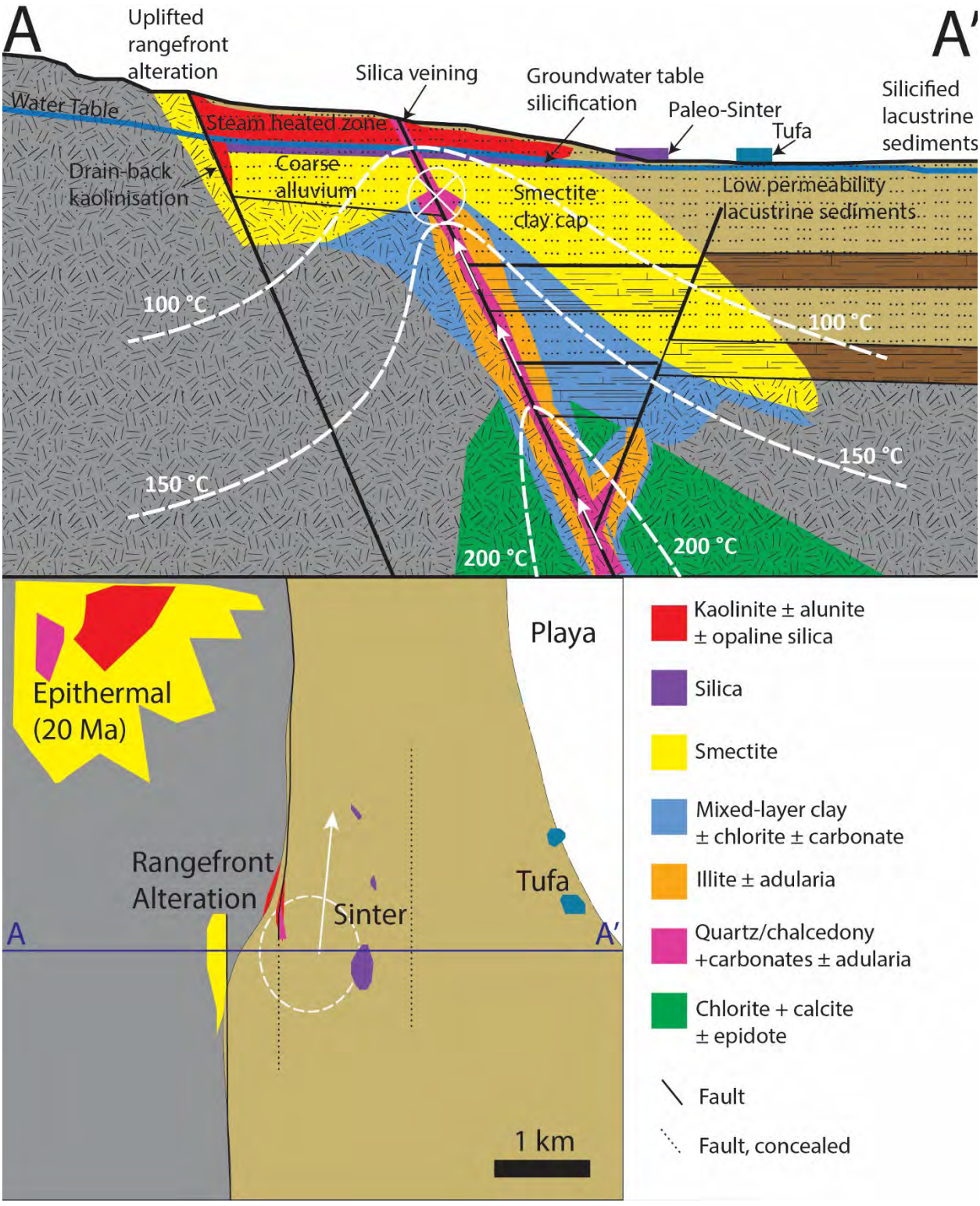

Figure 1: Conceptual model for hydrothermal alteration mineral zonation and paleo-geothermal deposits for deep-circulation-type geothermal systems in the Great Basin region. Adapted from and/or inspired by observations of the authors, Cole and Ravinsky, (1984), Reyes, (1990); Hedenquist et al., (2000), Richards and Blackwell, (2002), Simmons et al., (2005), Cumming (2009), Hinz et al., (2014), Sillitoe (2015), Delwiche et al., (2018), Siler et al., (2019), Jolie et al., (2021), Hedenquist & Arribas (2022), Kraal, (2023).

$CaCO_3$. Travertines form terraced-mounds, fissure-ridges or eroded sheets (Hancock et al., 1999). Tufa is formed in lakes where calcium enriched subaqueous spring fluids mix with CO_2 saturated lake waters (Bensen, 1994; Coolbaugh et al., 2009), and is characterized by a crumbly texture and deposits shaped like cones, towers, and pinnacles (Hancock et al., 1999). It is uncertain if travertine and tufa are directly related to high-temperature geothermal reservoirs or epithermal mineral systems, since many springs forming travertine are cold, and distal to the geothermal reservoir or mineral deposit (Sillitoe, 2015). However, in the Great Basin region, it has been found that many large tufa deposits are associated with thermal springs, some with high geothermometry (e.g., 150-170 °C at Needle Rocks and Pyramid Rock, NV per Coolbaugh et al., 2009), and therefore they are a resource exploration target.

The shallowest hydrothermal alteration zone typically encountered in geothermal systems is the steam-heated zone (Figure 1). The steam-heated zone is formed in the vadose zone above the water table where H_2S bearing steam condensates, producing oxidized low (2-3) pH fluids that form a the so-called "advanced argillic" alteration assemblage (opaline silica, alunite, anhydrite, kaolinite, diaspore; Sillitoe 2015, Hedenquist & Arribas, 2022). Commonly also present is native sulfur, and hematite that originally formed as pyrite but quickly oxidized (Sillitoe, 2015). Beneath the steam-heated zone, laterally extensive silicification (opal->chalcedony) can form where acidic fluids dissolve silica and deposit it at the groundwater table (Sillitoe 1993; Hedenquist et al., 2000; Sillitoe, 2015). Kaolinite (± smectite ± siderite ± pyrite) can also be formed by weakly acidic fluids (pH 4-5) where CO_2-rich condensates in the shallow hydrothermal environment below the groundwater table, commonly referred to as intermediate argillic alteration (Hedenquist & Arribas, 2022). Acidic fluids formed in the shallow environment can sometimes downwell along permeable pathways and produce drain-back kaolinization (Sillitoe, 2015). Active steam-heated zones in the Great Basin region are found at Steamboat Hills, Nevada, San Emidio, Nevada, and Cove Fort/Sulfurdale, Utah.

Studies of hydrothermal alteration minerals in active geothermal field around the world have found characteristic temperature-dependent mineral zonation with depth (Browne, 1978; Henley and Ellis, 1983; Cole and Ravinsky, 1984; Reyes, 1990; Figure 1). The specifics of this zonation are a product of the fluid chemistry, temperature, water/rock ratio, time, wall rock characteristics, and geologic structure (e.g., Reed, 1997). To generalize for near-neutral pH fluids: at shallowest depths/temperatures (<150 °C) smectite clay is predominant, along with carbonates, opal, and zeolites. This smectite zone is typically termed the "clay cap" and is a target for exploration geophysics as smectite has a low electrical/electromagnetic resistivity (Usher et al., 2000; Cumming, 2009; Folsom et al., 2020; Sewell et al., 2023). At intermediate temperatures (~150-200 °C), mixed-layered clays (illite/smectite or chlorite/smectite), are predominant. More proximal to fluid flow pathways, illite and adularia are common hydrothermal phases. In the center of the hydrothermal upflow, typically quartz or chalcedony, carbonates ± adularia is precipitated. At higher depths/temperatures (>180 °C), but with lower water/rock ratio, chlorite + calcite is formed, ± epidote where temperature is >250 °C. When exploring for active geothermal fields, deeper (hotter) alteration mineral assemblages observed at the surface, such as chlorite + calcite ± epidote are not a good indicator of active geothermal activity, because significant uplift and/or erosion must occur to expose them. Similarly, large (>0.5 km^2) zones of clay alteration within the range are most likely related to older paleo-geothermal fields (such as those that produce epithermal mineral deposits) that are no longer active. However, Quaternary-Pliocene aged epithermal deposits are often found proximal to high (>150 °C) geothermal systems in the region

(Coolbaugh et al., 2005). Smaller (1-500 m^2) zones containing smectite, kaolinite, or silicification exposed in the footwall of Quaternary faults may be a good target for geothermal exploration because their exposure can be relatively recent and they indicate the presence of these minerals just beneath the surface (as observed at Tungsten Mountain, Delwiche et al., 2018; Kraal, 2023).

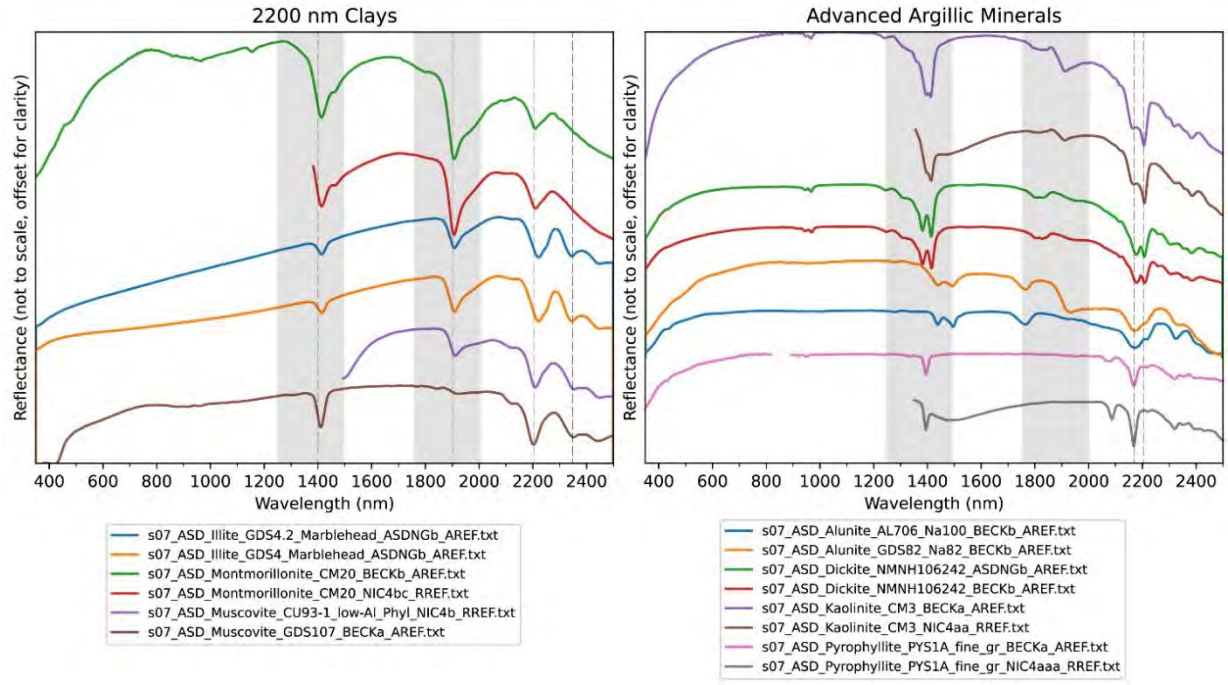

Figure 2: Example library mineral spectra from Kokaly et al., (2017), showing "2200 nm clays", or minerals with distinct 2200 nm absorption features associated with argillic/illitic/phyllic alteration (montmorillonite, illite, muscovite), and minerals associated with advanced argillic alteration (kaolinite, dickite, alunite, pyrophyllite). Grey areas are obscured by atmospheric effects.

Therefore, the most reliable paleo-geothermal deposits or hydrothermal alteration mineral targets for exploration using remote sensing are as follows: Silica (found in sinter, silicified sediments, groundwater table silicification, and silica veining); Carbonate (found in tufa, or in veins), kaolinite (found in steam-heated zones and shallow geothermal environments), and smectite (found in the clay cap). Outcrops of these in basins, or along a range front, are prioritized. The location of these minerals relative to Quaternary faults, complex structural settings, shallow low-resistivity anomalies, and shallow temperature anomalies can provide the foundation for multi-disciplinary greenfield geothermal exploration for blind systems.

1.2 Previous applications of SWIR remote sensing to geothermal exploration

Infrared reflectance spectroscopy in the Short-Wave Infrared Range (SWIR) is commonly used for identification and mapping of many hydrothermal alteration minerals, in particular phyllosilicates and other O-H bearing silicates, carbonates, and phosphates, because these minerals have diagnostic "absorption features" in the SWIR (1000-2500 nm) and are associated with distinct hydrothermal alteration mineral assemblages (Thompson et al., 1999). The shape and location of absorption features in a measured mineral's spectra are compared with standard mineral reference libraries for mineral or mineral mixture identification (e.g., Kokaly et al., 2017; Figures 2 & 3). Use of SWIR spectroscopy for remote sensing, field, and laboratory applications is common in the

mineral exploration industry to map zonation of hydrothermal alteration minerals (e.g., Thompson et al., 1999; Agar & Coulter, 2007). It has also been applied for geothermal exploration activities (e.g., Kratt et al., 2010a; van de Meer et al., 2014; Calvin et al., 2015; Calvin and Pace, 2016; Hart-Wagoner et al., 2022; Kraal, 2023). As additional high-quality, publicly available hyperspectral data is acquired in the coming years (e.g., through the USGS Earth MRI program, and new satellites), there is potential for the discovery of new blind geothermal systems in the western USA.

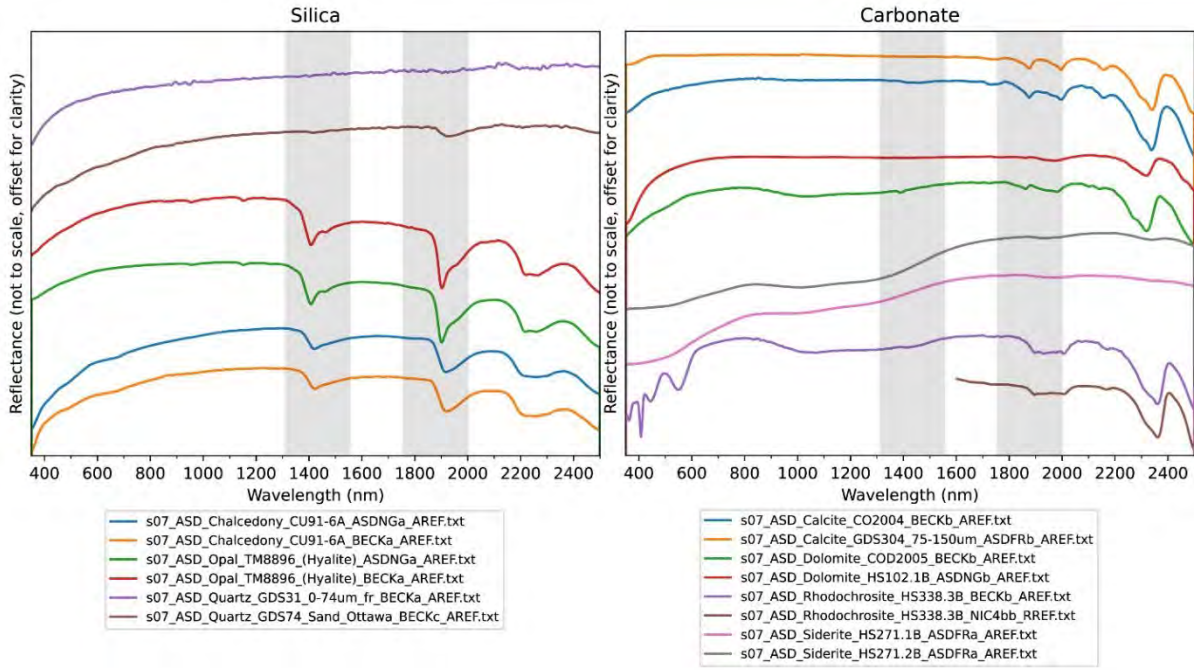

Figure 3: Example library mineral spectra from Kokaly et al., (2017) showing silica phases (quartz, chalcedony, opal) and carbonate phases (calcite, dolomite, rhodochrosite, siderite). Note that quartz does not have absorption features in this wavelength range.

2. Methods

2.1 Data Source

Remote sensing data for this study was collected by the Airborne Visible/Infrared Imaging Spectrometer classic (AVIRIS-c) instrument operated by the Jet Propulsion Laboratory (JPL). The AVIRIS-c instrument collects data over 225 spectral channels from 400 to 2500 nm with a pixel size of 14 m. The data was converted from radiance to reflectance and available to download from the AVIRIS Classic Data Portal website. Bands between 1312-1492 and 1800-2066 nm are not analyzed due to atmospheric interference. Additional residual atmospheric contamination artefacts obscure the region between 2350-2500 nm, as observed by Kokaly et al., (2021). Portions of the following AVIRIS lines were interpreted: f180828t01p00r07, f180605t01p00r07, f180604t01p00r12, f180828t01p00r06.

2.2 Data Processing Techniques

Remote sensing data was processed and interpreted using ENVI software. Several statistical and expert driven approaches are performed to classify spectra in the image and identify endmember

spectra to use in supervised classification. The general procedure is to utilize false color images emphasizing specific absorption features (such as at 2200 nm for clay and opal/chalcedony, or 2165 for kaolinite) to identify areas with minerals of interest. Endmember pixels identified using either statistical or expert driven techniques are collected using ENVI's Region of Interest (ROI) tool. Class statistics of each ROI are used to determine if they represented scene endmembers well. Comparison with the USGS spectral reference library (Kokaly et al., 2017) are used to classify scene endmembers by mineral or mineral mixture, (or other material, such as vegetation).

The ROIs then served as inputs for the Matched Filtering (MF) supervised classification algorithms. In addition to using ROIs for Matched Filtering, we also utilize library mineral spectra from the USGS library (Kokaly et al., 2017). This is performed where specific minerals of interest (such as opal or chalcedony) were not easily identifiable in the scene. MF is an algorithm for finding user-defined endmembers within a scene by performing partial unmixing. This technique is useful because it does not require knowledge of every endmember within a particular scene. Threshold based ROIs are then used to create a thematic map. Threshold minimum of 0.5 was found to work best for many endmember classes based on analysis of class statistics, and spatial coherence in map view. The matched filtering algorithm was applied in most scenes to the wavelengths between 2140 and 2300 nm, where data quality was the highest and the most diagnostic spectral features are located for the minerals of interest in this study (opal, chalcedony, smectite, kaolinite). Due to the atmospheric residual artefacts in the 2350-2500 nm wavelength region, it is difficult to distinguish smectite from illite or muscovite, which can usually be distinguished by an absorption feature at 2350, and therefore these minerals are grouped in our analysis. Carbonate minerals were also difficult to identify/distinguish when the mineral abundances are low due to these data artefacts.

The results produced in this study are thematic maps showing the location of minerals of interest utilizing the MF algorithm. We grouped the results into 2-4 endmembers per map: "2200 nm clays", representing smectite, illite, and/or muscovite; kaolinite (possibly kaolinite + smectite); carbonate (calcite); and silica (opal and/or chalcedony). There is a balance between using conservative thresholding to produce more accurate thematic maps (i.e., every pixel in map the map contains the intended spectra), with the risk of missing some pixels, and utilizing wider thresholds that may produce "false positives". Here, we utilize the more conservative approach, which we find to be the most useful for exploration applications. A conservative thresholding approach combined with manual classification of missed pixels based on visual inspection of spectra could improve the spatial coherence of mapped zones, however this approach was not undertaken in this study because our goal is to utilize these techniques for exploration and identify previously unknown paleo-geothermal deposits rather than to make the most accurate map.

We compared the newly interpreted hyperspectral data in this study to pre-existing hydrothermal alteration maps of the Basin and Range province compiled from interpretation of multi-spectral Advanced Spaceborne Thermal Emission and Reflection Radiometer (ASTER) Data (Mars, 2013). Mars utilized Interactive Data Language logical operator algorithms to map hydrothermally altered rocks, grouping them into (1) hydrothermal silica-rich rock, (2) propylitic rocks, (3) argillic rocks, and (4) phyllic rocks, and available to download as ArcGIS shape files. Argillic and phyllic rocks are mapped by Mars with 30-m spatial resolution and identified based on the 2165 nm and 2200 nm absorption features. The hydrothermal silica-rich rock is mapped with 90-m resolution, based

on the O-H absorption feature between 2260-2400 nm, and the thermal infrared band associated with the 9090 nm quartz absorption feature.

3.0 Results

3.1 Benchmark Sites

To validate that the publicly available remote sensing data has sufficient spectral and spatial resolution, as well as sufficient data quality to detect paleo-geothermal deposits, we investigated two areas with known paleo-geothermal deposits. Salt Wells and Lee Allen Springs have been previously mapped by Coolbaugh et al., (2004, 2006), and/or Hinz et al., (2011, 2014), both located in the vicinity of Fallon, NV.

3.1.1 Lee Allen

Lee Allen is the location of the Lee "Hot Spring", formed from a blown-out well from the 1930s, and the Allen Springs (adjacent to Allen Ridge). Hinz (2010) mapped silica-cemented sands of Pleistocene age, and Tufa of Miocene age adjacent to the Lee and Allen springs (Figure 4, Left). Currently, geyserite is forming in the Lee "Hot Spring". Quartz geothermometry indicate equilibration at ~165 °C (Mariner, 1974).

Four scene endmembers are mapped in the thematic map: silicified zones (opal, or chalcedony), kaolinite, 2200 nm clay (likely smectite or illite), and carbonate (likely calcite) (Figures 4 & 5). The silicified zones are distinguished in the scene by a sharp dip in reflectance at ~2190 nm, and a relatively broad/rounded absorption or flat zone between 2200-2300 nm (Figure 5). The largest silicified sediments zone mapped by Hinz et al., (2010) was easily identifiable in the AVIRIS dataset (mapped in Figure 4A, to the northwest of "Allen Springs" label). The smallest, northern area of silicification mapped by Hinz et al, (2010) was not discernable using this dataset (Figure 4C). Individual pixels in the southern silicified area (northwest of "Lee" label, Figure 4B) had characteristic spectra associated with opal/chalcedony but were difficult to map using the matched-filtering technique without also classifying too many non-silica pixels in the map area.

Kaolinite and 2200 nm clay signatures are observed near the small northern silicified zone, possibly related to hydrothermal alteration (Figure 4C). The large kaolinite zone in the north of the map (Figure 4G) is associated with a rhyolite dome and the Tuff of Campbell Creek units, and sediments derived from these units (Hinz et al., 2010), and may be the product of weathering. Carbonate spectra were also observed throughout the map area and are co-located with mapped tufa deposits and mounds (Figure 4D), and beach deposits of late Miocene age (Figure 4E, Hinz et al., 2010). The multispectral map from Mars (2013) did not identify the silica sinter in the area immediately around the Lee and Allen springs (Figure 6).

Figure 6 shows hyperspectral and multispectral thematic maps in the wider Lee Allen area. In the northern portion of the map, silica is identified but appears to be associated with Tertiary Rhyolitic breccias, sands, and gravels of middle Miocene age mapped by Hinz et al., (2010), and unlikely to be related hydrothermal activity. Several small outcrops of Tertiary volcanics - Tcc (Tuff of Campbell Creek) and unknown Tuff (Ttu) are associated with 2200 nm clay and kaolinite in both maps (Figure 6, Hinz et al., 2010). In the west, small kaolinite and silica zones are co-located with faulting of Miocene basalt lavas and interbedded diatomite (Figure 6, Hinz et al., 2010).

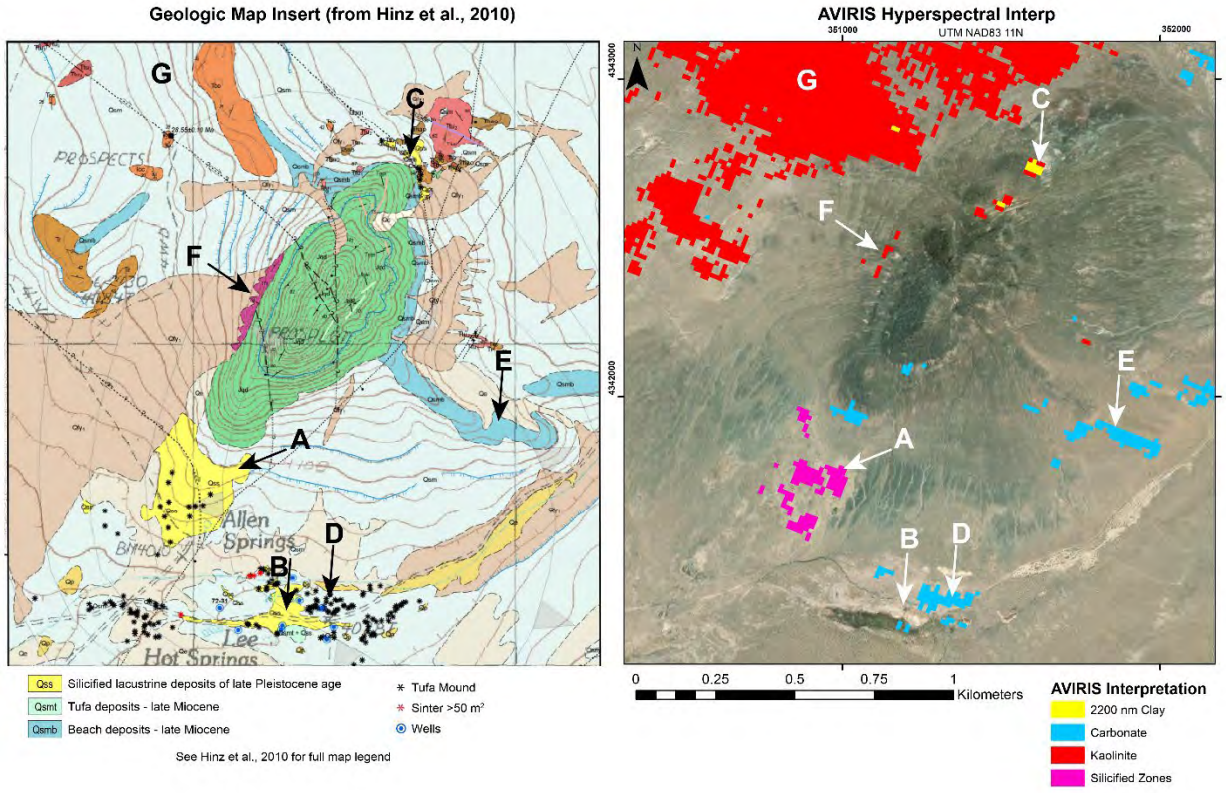

Figure 4: Arrows indicate locations discussed in the text. Left: Map from Hinz et al., 2010 showing geology, faults, and paleo-geothermal deposits at the Lee and Allen springs area. Right: Thematic map showing the interpretation of the AVIRIS Hyperspectral data, showing silicified zones, carbonate rich zones, kaolinite rich zones, and 2200 nm clay zones.

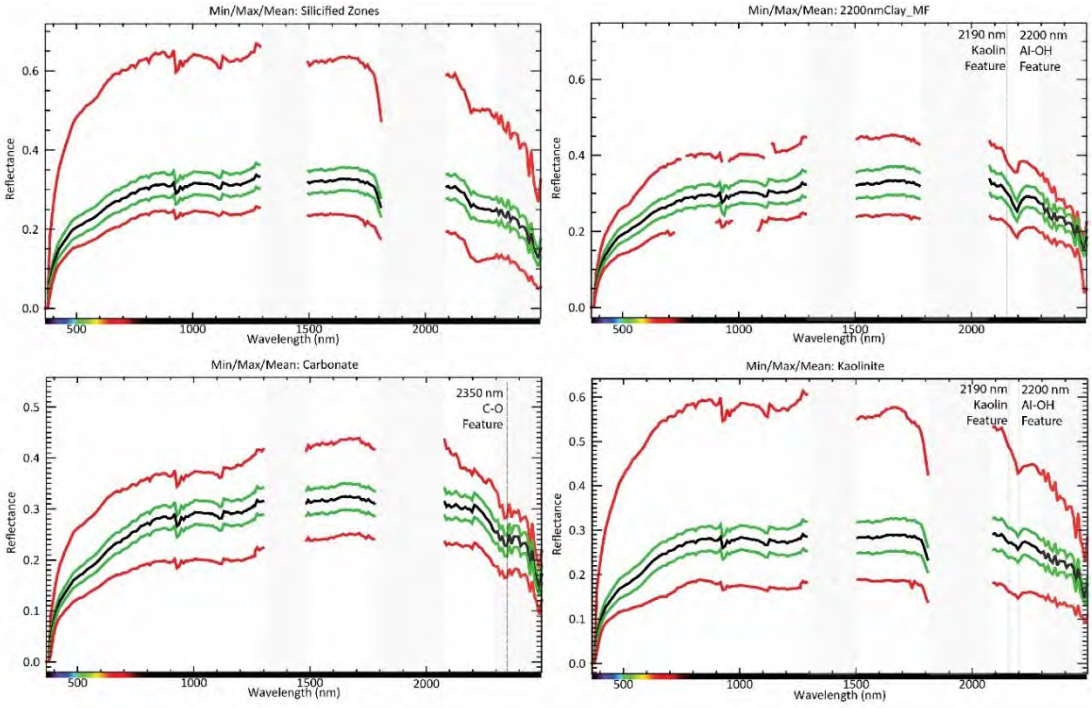

Figure 5: Class statistics for thematic mineral maps of Lee Allen (Figure 4, Figure 6).

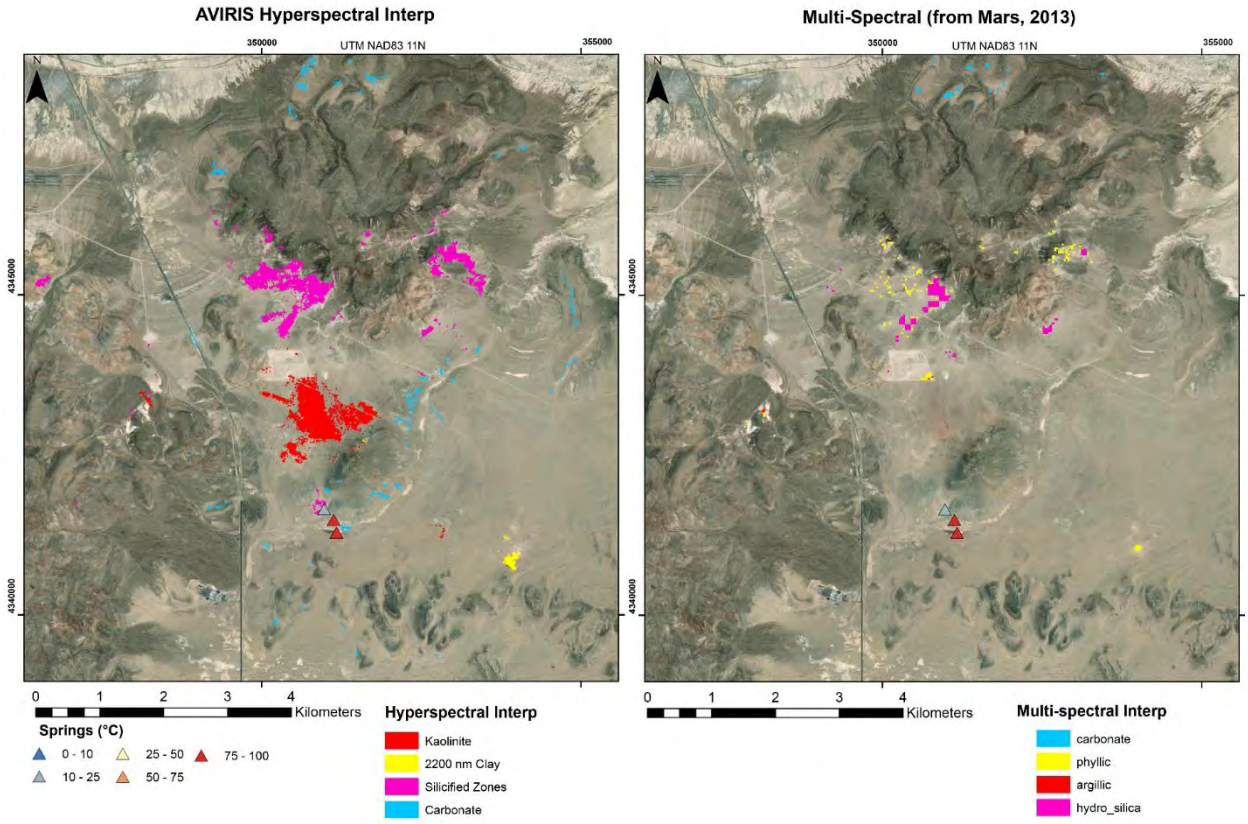

Figure 6: Thematic maps from AVIRIS hyperspectral mineral interpretation, and Mars, (2013) multi-spectral interpretation of the wider Lee Allen area.

3.1.2 Salt Wells, Nevada

The Salt Wells geothermal field producing 9.6 net MWe as of 2022 (Jowitt et al., 2023), and currently operated by Ormat Technologies, Inc. Thermal features currently active at Salt Wells are a few areas of warm ground, however hot springs were active into the early 20th century (Coolbaugh et al., 2004 citing Garside and Schilling, 1979). There are 3 types of sinter present at Salt Wells: massive opaline material, siliceous oolites, and silicified roots, mud and algal matter (Coolbaugh et al., 2004). Often the silicified sands are overlain by 5 cm – 2m thick lenses of sinter, and sometimes tufa (Coolbaugh et al., 2004). In addition, Hinz et al. (2014) mapped several argillic-altered bedrock outcrops near the silica deposits.

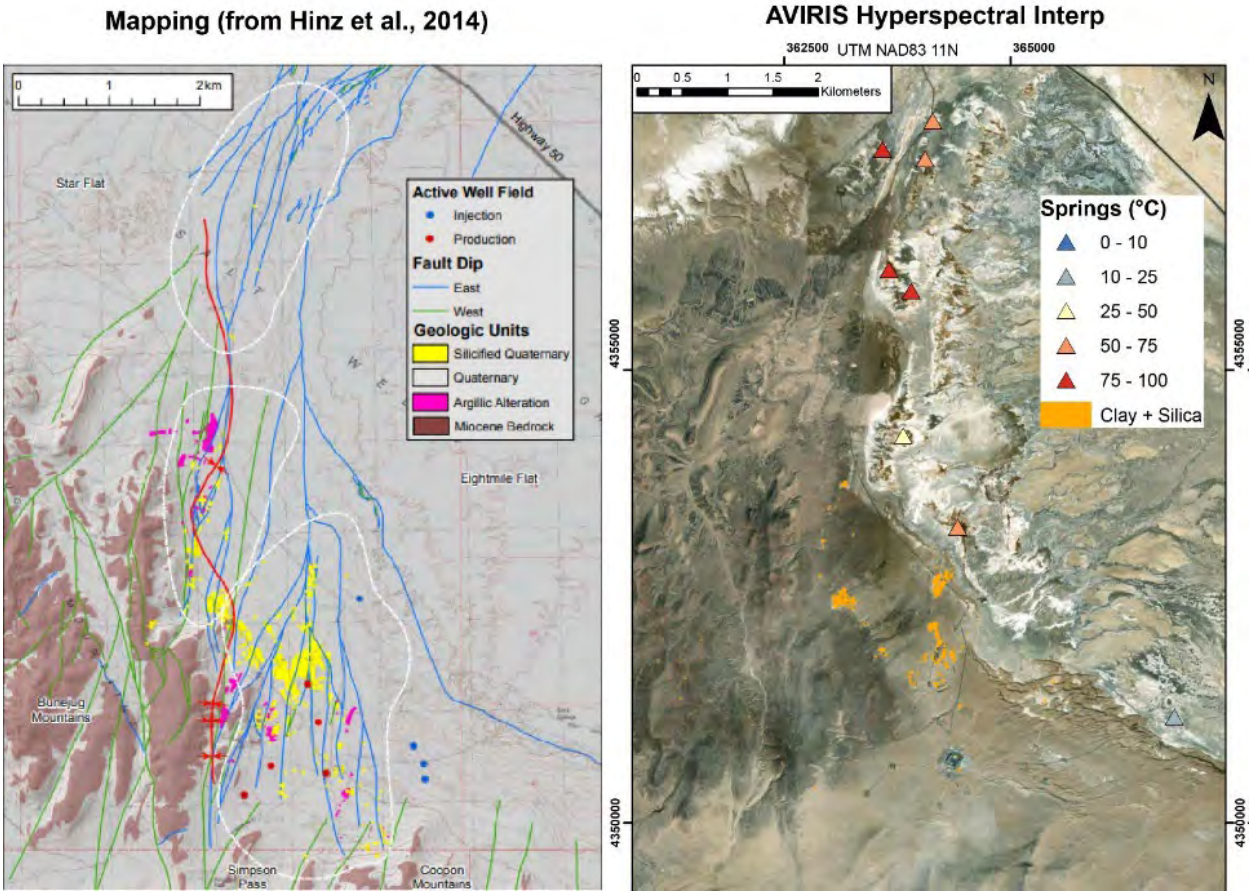

Figure 7: Paleogeothermal deposits of Salt Wells, Nevada. Both maps are the same scale/location. Left: Map from Hinz et al., 2014, showing the location of mapped paleogeothermal deposits, faults, and the active well field at Salt Wells. Right: Results of AVIRIS hyperspectral interpretation showing zones of clay + silica (orange) that roughly corresponds to mapped silicified quaternary sediments. Also shown is the location of hot springs.

Silicified zones mapped by Coolbaugh et al., (2004; 2006), and Hinz et al., (2014) were co-located with a distinct 2200 nm clay signature in the AVIRIS data (Figure 7), rather than a pure opal/chalcedony spectrum, likely a product of mixed 2200 nm clay + kaolinite + silica composition (Figure 8). This spectral signature was distinct enough to be mapped using matched filtering technique, and the macro-level geometry of these deposits are consistent with previous mapping. These clay/silica areas were not mapped in the Mars (2013) multi-spectral compilation. The

argillic-altered bedrock mapped by Hinz et al., (2014) was not discernable in the hyperspectral data, perhaps because the exposures were too small for the spatial resolution of the data.

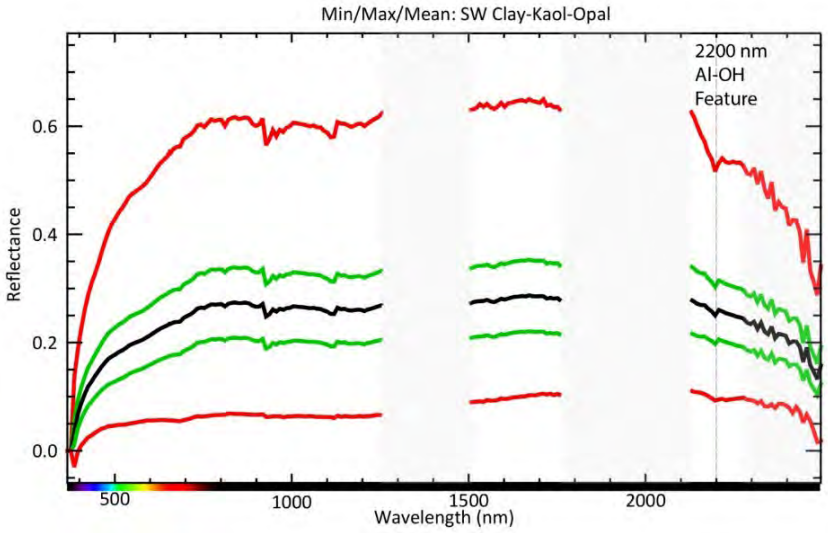

Figure 8: Class statistics for Clay + Silica zone, consistent with mapped silicified sediments from Salt Wells. Note that the 2200 nm Al-OH absorption feature is the most prominent.

3.2 Exploration Case Studies

3.2.1 Gabbs Valley

Gabbs Valley is the location of several known geothermal systems and prospects, including the Don. A Campbell geothermal power plant operated by Ormat Technologies Inc. with 26.1 MWe net production in 2022 (Jowitt et al., 2023). Known thermal anomalies are also present, including Petrified Springs, North Gabbs, Rawhide Hot Spring, near the town of Gabbs, and near the warm "Gene Sawyer" well. Additional prospects without temperature data identified during the BRIDGE project include Kaiser and Dead Cow Splay (Downs et al., 2023; Figure 9, Figure 10).

Figure 9 shows the results of the AVIRIS hyperspectral interpretation from this study (Left), and the multi-spectral interpretation by Mars (2013; Right) in northern/central Gabbs Valley. The largest kaolinite and 2200 nm clay zones occur in the northern Montecristo Mountains, adjacent to the Kaiser Fluorspar mining area (labeled "F"). Several opal/silica signatures are observed near the Starfire Opal Mine (labeled "O"). Near the 2-m temperature anomaly at North Gabbs (NG), there is some kaolinite and 2200 nm clay detected, co-located with the northern termination of the Montecristo western range-bounding fault and fault step-overs within (Figure 9A), however it is uncertain if this argillic zone is associated with the larger (likely older) alteration around the Kaiser Mine area. On the other side of the range, there are small patches of clay alteration along the range-front adjacent to the Kaiser geothermal prospect (co-located with the northern termination of the faults bounding the east side of the Montecristo mountains; Figure 9B). Near the Rawhide Hot Springs (RHS), there is small patches of kaolinite and 2200 nm clay alteration ~1.5 km east along Fissure Ridge, within a Miocene or Oligocene tuff unit (Figure 9C; Ekren & Byers, 1986) that is relatively anomalous, given that the other tuffs of this unit are not altered adjacent to this location. Lastly, there is possible silicification along strike two fault segments that stepover mapped by Ekren and Byers (1986) near Cobble Cuesta (CC; Figure 9D).

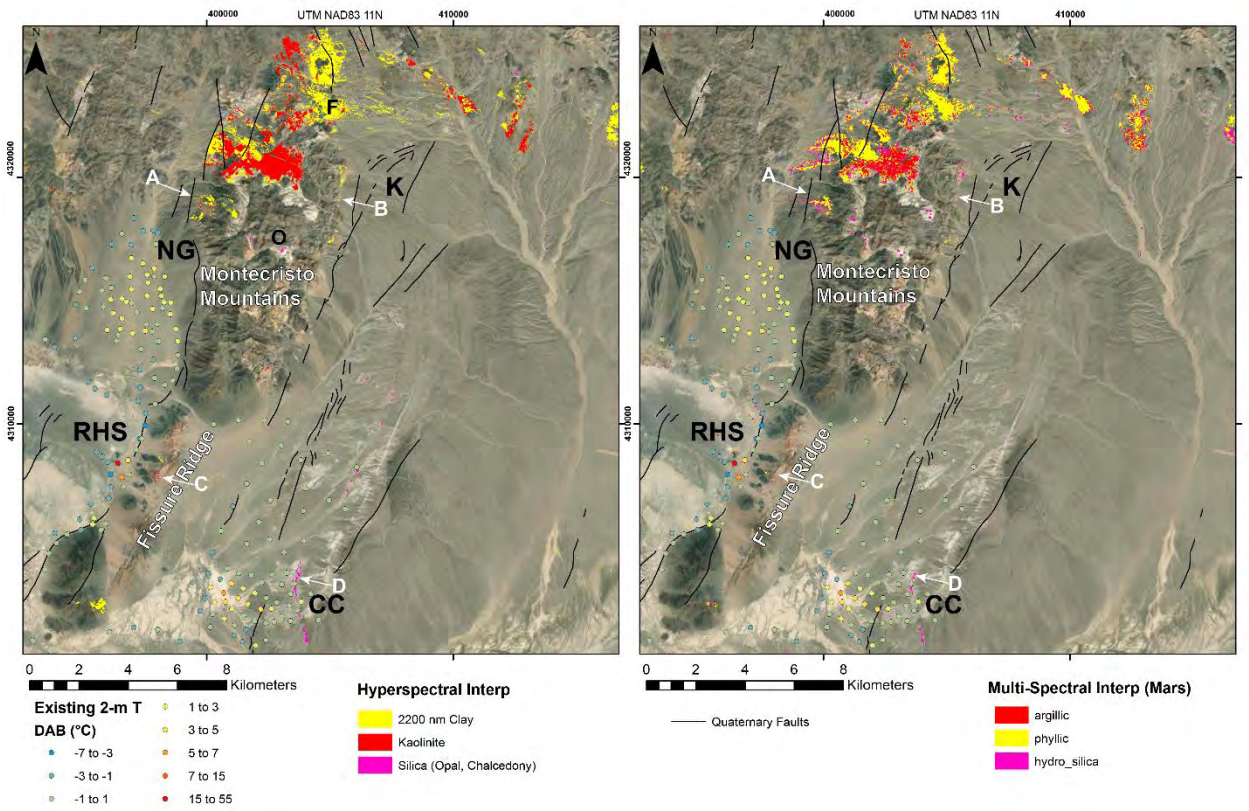

Figure 9: North Central Gabbs Valley, centered on Fissure Ridge. Several geothermal prospects are in this map, including North Gabbs (NG), Rawhide Hot Springs (RHS), Cobble Cuesta (CC) and Kaiser (K). White arrows refer to areas discussed in the text.

Figure 10 shows the hyperspectral interpretation thematic mineral map for southern Gabbs Valley, the location of the Don A. Campbell geothermal plant, and the Petrified Springs and Dead Cow Splay geothermal prospects. Large kaolinite and 2200 nm clay rich zones occur associated with known mineral resources, such as to the southwest (Au, Ag, Blue Sphinx Property, Gold Pen Mine, Lone Star Group, Randall property etc.), and the to the southwest (Hg, Au, Paradise Peak Mine, Finger Rock Mercury prospect). Several smaller kaolinite or 2200 nm clay rich zones occur along or near Quaternary faults such as at location 10A, 10B, 10C, 10D and 10F, some of which are associated with Au or Hg mineral resources (Figure 10). Location 10E has several small 2200 nm clay patches and is associated with a “Fire Clay” silica mine, adjacent to Dead Cow Splay. There does not seem to be any surface hydrothermal alteration associated with Don A. Campbell or Petrified Springs.

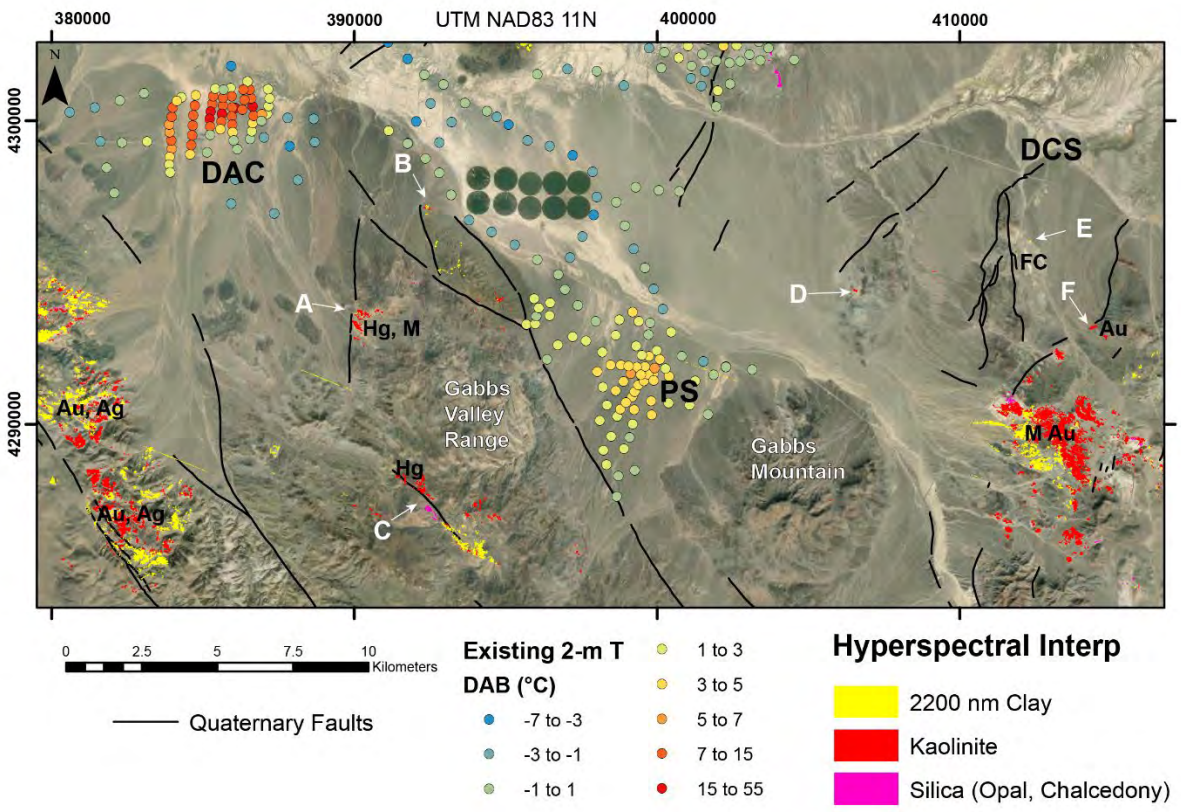

Figure 10: Southern Gabbs Valley hyperspectral interpretation thematic map, along with two-meter temperature data. DAC refers to Don A Campbell geothermal plant, PS refers to petrified springs geothermal prospect, and DCS refers to Dead Cow Splay geothermal prospect. Also shown are the location of known mineral occurrences from the Mineral Resources Data System (Mason and Arndt, 1996).

3.2.2 East Hawthorne

East Hawthorne is a geothermal prospect within the Hawthorne Army Depot identified from shallow temperature surveys (Kratt et al., 2010b; Figure 11) and temperature gradient drilling. Resent geophysical analysis by the BRIDGE team found a shallow dipping conductor co-located with the 2-m temperature anomaly (Sewell et al., 2023). Preliminary analysis of geophysical data suggest that this anomaly is associated with a displacement transfer zone where a northwest striking strike-slip fault connects with one or more northeast striking normal faults. Several clay anomalies are observed in Mesozoic highly silicified meta-volcanic units mapped by Hinz et al., (2010). A small outcrop of kaolinite mapped in both hyperspectral and multi-spectral data ~2 km east of 2-m T anomaly (Figure 11B). Another kaolinite-altered outcrop mapped in the hyperspectral data is ~4 km south of the 2-m T anomaly, ~ 1 km east of the inferred intersection of the strike-slip and normal fault inferred from geophysics (Figure 11C). There is a large 2200 nm clay anomaly near the 2-m T anomaly, possibly related to low-resistivity zone seen in geophysics datasets (Figure 11A). Additional widespread 2200 nm clay to the south within the range, likely unrelated to recent geothermal activity, and co-located with known gold mines and prospects. The remote sensing did not detect carbonate near a known tufa deposit, perhaps because it is too small (Figure 11D), and it is uncertain if this tufa is related to the thermal anomaly zone outlined by the temperature surveys.

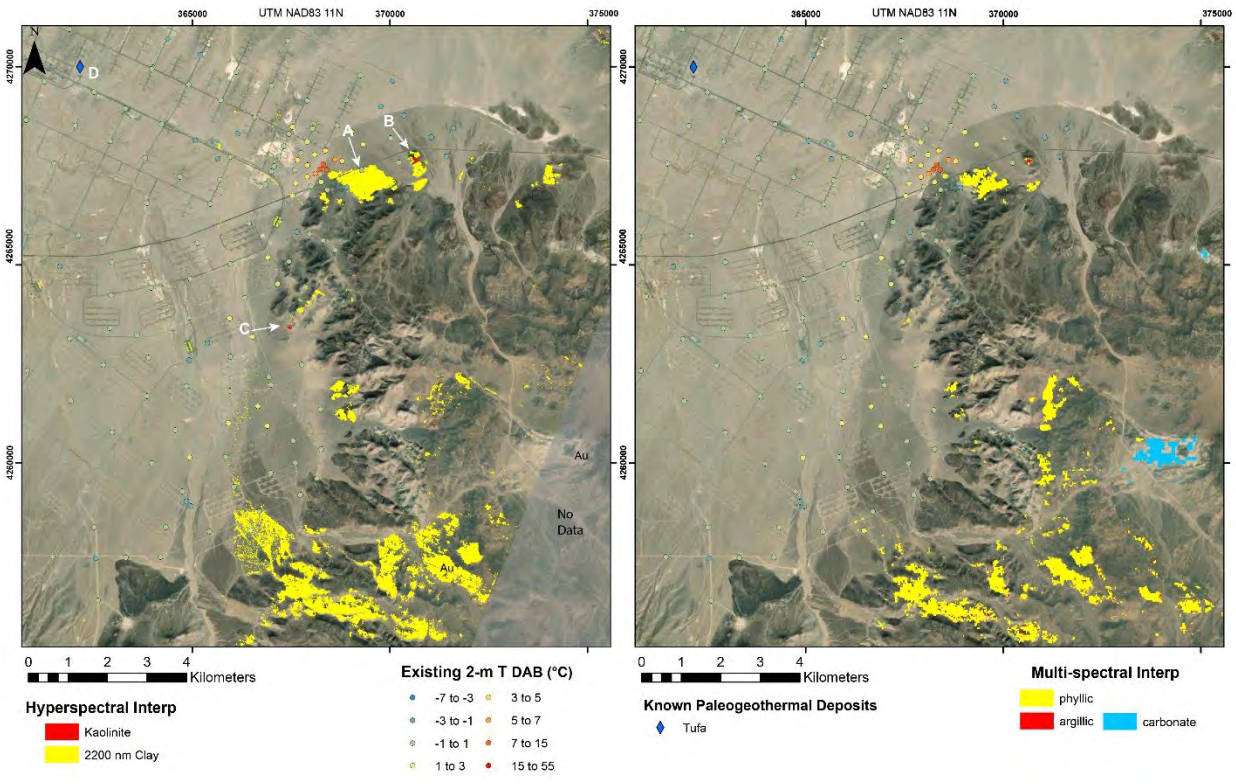

Figure 11: Thematic mineral maps of the East Hawthorne geothermal prospect.

3.2.3 Bell Flat

Bell Flat is a basin just north of Gabbs Valley in NV with no known thermal anomalies. However, active faulting (including historical ruptures, Caskey et al., 1996) and multiple favorable structural settings (step-overs, fault terminations, and fault intersections) contribute to its high favorability for hosting undiscovered blind geothermal resources. Several locations along the Fairview Fault Zone on the western margin of the basin have 2200 nm clay and kaolinite anomalies as indicated by the remote sensing hyperspectral data (Figure 12). Zone 12A is the location of kaolinite and 2200 nm clay alteration, associated with a minor step-over in the range bounding fault. Zone 12B contains kaolinite and clay anomalies within a larger normal fault step-over. Therefore, these locations would be good targets for shallow temperature surveying based on the presence of favorable structural features and possible argillic alteration.

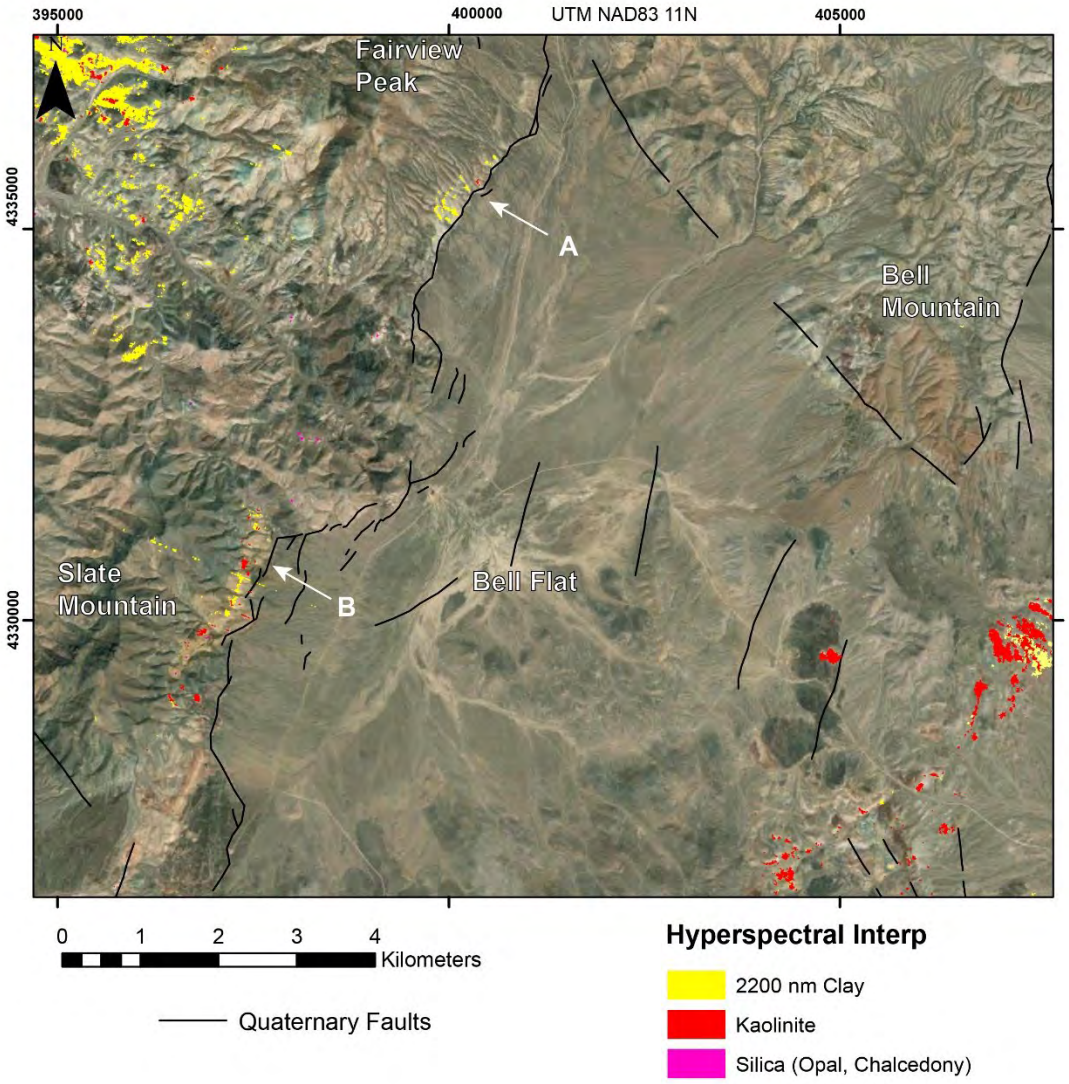

Figure 12: Thematic remote sensing mineral map of Bell Flat, Nevada.

4. Conclusion

Remote sensing using publicly available hyperspectral data can be successfully and efficiently used for geothermal exploration by mapping minerals and mineral mixtures commonly found on the surface or in shallow portions of active geothermal systems. Generally there is agreement between the hyperspectral and multispectral interpretations reviewed here. Higher spatial and spectral resolution allowed for (a) more detail in the maps produced from the hyperspectral data and (b) identification of additional hydrothermally altered outcrops. When a conceptual model framework is applied, these mineral maps can help inform further exploration activities and decisions about resource potential. Caution must be used to discern potentially recent hydrothermal alteration minerals, commonly found in basins or along active fault traces, versus relict Cenozoic or older hydrothermal alteration minerals associated with past hydrothermal activity or the results of weathering. Future work includes field verification of mapped hydrothermally altered zones and laboratory analysis of field samples to validate the SWIR interpretations.

Acknowledgement

This material was based upon work supported by the U.S. Department of Energy, Office of Energy Efficiency and Renewable Energy (EERE), Office of Technology Development, Geothermal Technologies Office under the FY2020 Hydrothermal and Low Temperature Multi-Topic Funding Opportunity Announcement DE-FOA-0002219. Sandia National Laboratories is a multimission laboratory managed and operated by National Technology & Engineering Solutions of Sandia, LLC, a wholly owned subsidiary of Honeywell International Inc., for the U.S. Department of Energy's National Nuclear Security Administration under contract DENA0003525. This paper describes objective technical results and analysis. Any subjective views or opinions that might be expressed in the paper do not necessarily represent the views of the U.S. Department of Energy or the United States Government. The United States Government retains, and the publisher, by accepting the article for publication, acknowledges that the United States Government retains a non-exclusive, paid-up, irrevocable, world-wide license to publish or reproduce the published form of this manuscript, or allow others to do so, for United States Government purposes.

REFERENCES

Adams, K. D., & Wesnousky, S. G. (1999). The Lake Lahontan highstand: Age, surficial characteristics, soil development, and regional shoreline correlation. *Geomorphology*, *30*(4), 357-392.

Agar, B., & Coulter, D. (2007, September). Remote sensing for mineral exploration–A decade perspective 1997-2007. In *Proceedings of Exploration* (Vol. 7, pp. 109-136).

Ayling, B., Faulds, J., Morales Rivera, A., Koehler, R., Kreemer, C., Mlawsky, E., Coolbaugh, M., Micander, R., dePolo, C., Kraal, K. and Wagoner, N., (2022). INGENIOUS-Great Basin Regional Dataset Compilation (No. 1391). USDOE Geothermal Data Repository (United States); GBCGE, NBMG, UNR.

Benson, L., (1999). Carbonate deposition, Pyramid Lake Subbasin, Nevada: 1. Sequence of formation and elevational distribution of carbonate deposits (tufas). Paleogeography, Paleoclimatology, and Paleoecology, 109, 55-87.

Benson, L. V., Lund, S. P., Smoot, J. P., Rhode, D. E., Spencer, R. J., Verosub, K. L., ... & Negrini, R. M. (2011). The rise and fall of Lake Bonneville between 45 and 10.5 ka. *Quaternary International*, *235*(1-2), 57-69.

Cady, S.L., & Farmer, J.D., (1996). Fossilization Processes in Siliceous Thermal Springs: Trends in Preservation along Thermal Gradients. In: Bock, G.R., Goode, G.A. (Eds.), pp. 150–173.

Calvin, W. M., Littlefield, E. F., & Kratt, C. (2015). Remote sensing of geothermal-related minerals for resource exploration in Nevada. *Geothermics*, *53*, 517-526.

Calvin, W. M., & Pace, E. L. (2016). Mapping alteration in geothermal drill core using a field portable spectroradiometer. *Geothermics*, *61*, 12-23.

Caskey, S. J., Wesnousky, S. G., Zhang, P., & Slemmons, D. B. (1996). Surface faulting of the 1954 Fairview Peak (MS 7.2) and Dixie Valley (MS 6.8) earthquakes, central Nevada. *Bulletin of the Seismological Society of America*, *86*(3), 761-787.

Cole, D.R., & Ravinsky, L.I. (1984). HYDROTHERMAL ALTERATION ZONING IN THE BEOWAVE GEOTHERMAL SYSTEM, EUREKA AND LANDER COUNTIES, NEVADA'. Economic Geology, v. 79, pp. 759-767.

Coolbaugh, M.F., Sladek, C., and Kratt, C., (2004). Digital mapping of structurally controlled geothermal features with GPS units and pocket computers: Geothermal Resources Council Transactions, v. 28, p. 321-325.

Coolbaugh, M.F., Sladek, C., Kratt C., Shevenell, L., & Faulds, J.E., (2006). Surface indicators of geothermal activity at Salt Wells, Nevada, USA, including warm ground, borate deposits, and siliceous alteration: Geothermal Resources Council Transactions, v. 30, p. 399-405.

Delwiche, B., Peters, B., Sophy, M., Smith, C., & O'Brien, J. (2018). Successful deployment of a multi-crossing directional drilling method at Ormat's new Tungsten Mountain Geothermal Field in Churchill County, Nevada. PROCEEDINGS, 43rd Workshop on Geothermal Reservoir Engineering, Stanford University, Stanford, California, SGP-TR-213.

Downs, C., Schwering, P., Sewell, S., Winn, C., Hinz, N., Zimmerman, J., Blake, K., Sabin, A., Lopeman, J., Milton, A., Siler, D., & Cumming, W. (2023). Development of the Prospect Portfolio and Initial Surface Exploration Studies in the Basin & Range Investigations for Developing Geothermal Energy (BRIDGE) Project. GRC Transactions, 47.

Ekren, E. B., & Byers Jr, F. M. (1986). Geologic map of the Mount Annie NE, Mount Annie, Ramsey Spring, and Mount Annie SE quadrangles, Mineral and Nye counties, Nevada (No. 1579).

Folsom, M., Libbey, R., Feucht, D., Warren, I., & Garanzini, S. (2020). Geophysical observations and integrated conceptual models of the San Emidio Geothermal Field, Nevada. Proceedings, 45th Workshop on Geothermal Reservoir Engineering, Stanford University, Stanford, California. SGP-TR-216.

Fournier, R.O (1985). The behavior of silica in hydrothermal solutions. In: Berger, B.R., & Bethke, P.M (eds) Geology and geochemistry of epithermal systems. Reviews in Economic Geology, 2, 45-61.

Garside, L J, & Schilling, J H. (1979). Thermal waters of Nevada. United States: N. Web.

Hancock, P. L., Chalmers, R. M. L., Altunel, E. R. H. A. N., & Cakir, Z. (1999). Travitonics: using travertines in active fault studies. *Journal of Structural Geology, 21*(8-9), 903-916.

Hedenquist, J.F. Arribas, A.R., Gonzalez-Urien, E. (2000). "Exploration for Epithermal Gold Deposits", Gold in 2000, Steffen G. Hagemann, Philip E. Brown. Society of Economic Geologists.

Hedenquist, J. W., & Arribas, A. (2022). Exploration implications of multiple formation environments of advanced argillic minerals. Economic Geology, 117(3), 609-643.

Hart-Wagoner, N., Calvin, W., & Ayling, B.F. (2022). Remote Sensing Applications for Geothermal Exploration in the Black Rock Desert, Nevada. GRC Transactions, 46, 1075-1092.

Hinz, N. H., Faulds, J. E., & Oppliger, G. L. (2008). Structural controls of Lee-Allen Hot Springs, southern Churchill County, western Nevada: A small pull-apart in the dextral shear zone of the Walker Lane. Geothermal Resources Council Transactions, 32, 285-290.

Hinz, N. H., Faulds, J. E., Moeck, I., Bell, J. W., & Oldow, J. S. (2010). Structural controls of three blind geothermal resources at the Hawthorne Ammunition Depot, west-central Nevada. *Geothermal Resources Council Transactions*, *34*, 785-790.

Hinz, N. H., Faulds, J. E., & Oppliger, G. L. (2011). Preliminary geologic map of the Lee-Allen geothermal area. Churchill County, Nevada: Nevada Bureau of Mines and Geology Open-File Report, 10-6.

Hinz, N. H., Faulds, J. E., & Coolbaugh, M. F. (2014). Association of fault terminations with fluid flow in the Salt Wells geothermal field, Nevada, USA. Geothermal Resources Council Transactions, 38, 3-10.

Jowitt, S.M., Micander, R., Richards, M., & Reynolds, D. (2023). The Nevada mineral industry 2022: Nevada Bureau of Mines and Geology Special Publications MI-2022, 82 p.

Kraal, K.O. (2023). *Application of Hydrothermal Alteration Mineral Analysis to Geothermal Reservoir Characterization for Three Geothermal Fields in the Western United States* (Doctoral dissertation, University of Nevada, Reno).

Kratt, C., Calvin, W. M., & Coolbaugh, M. F. (2010a). Mineral mapping in the Pyramid Lake basin: Hydrothermal alteration, chemical precipitates and geothermal energy potential. *Remote Sensing of Environment*, *114*(10), 2297-2304.

Kratt, C., Sladek, C., & Coolbaugh, M. (2010b). Boom and bust with the latest 2 m temperature surveys: Dead Horse Wells, Hawthorne Army Depot, Terraced Hills, and other areas in Nevada. *GRC Transactions*, *34*, 567-574.

Kokaly, R. F., Swayze, G. A., Livo, K. E., Hoefen, T. M., Hubbard, B. E., Meyer, J. M., ... & Gnesda, W. R. (2021, July). Imaging spectroscopy applied to mineral mapping over large areas: Impact of residual atmospheric artefacts in reflectance spectra on mineral identification and mapping. In *2021 IEEE International Geoscience and Remote Sensing Symposium IGARSS* (pp. 1855-1858). IEEE.

Mariner, R.H., Rapp, J.B., Willey, L.M & Presser, T.S. (1974). The Chemical Composition and Estimated Minimum Thermal Reservoir Temperatures of the Principal Hot Springs of Northern and Central Nevada, US Geological Survey, no. 74-1066.

Mars, J. L. (2013). Hydrothermal alteration maps of the central and southern basin and range province of the United States compiled from advanced spaceborne thermal emission and reflection radiometer (ASTER) data (No. 2013-1139). US Geological Survey.

Mason, G.T., & Arndt, R.E. (1996). Mineral Resources Data System (MRDS): USGS Data Series 20, https://doi.org/10.3133/ds20.

Reed, M.H. (1997). Hydrothermal alteration and its relationship to ore fluid composition. *Geochemistry of hydrothermal ore deposits*, 303-366.

Reyes, A. G. (1990). Petrology of Philippine geothermal systems and the application of alteration mineralogy to their assessment. *Journal of Volcanology and geothermal research*, *43*(1-4), 279-309.

Richards, M., & Blackwell, D. (2002). A difficult search: Why Basin and Range systems are hard to find. Geothermal Resources Council Bulletin, 31(4), 143-146.

Rimstidt, J. D., & Cole, D. R. (1983). Geothermal mineralization; I, The mechanism of formation of the Beowawe, Nevada, siliceous sinter deposit. *American Journal of Science*, *283*(8), 861-875.

Russel, I.C., (1885). Geological history of Lake Lahontan, a Quaternary lake of northwestern Nevada. U.S. Geological Survey Monograph 11, 288 pp.

Schwering, P., Lowry, T., Hinz, N., Matson, G., Sabin, A., Blake, K., Zimmerman, J., Sewell, S., & Cumming, W. (2022). The BRIDGE Project – Hidden Systems Reconnaissance in Western Nevada. GRC Transactions, 46.

Sewell, S., Cumming, W., Schwering, P., Hinz, N., Downs, C., Zimmerman, J., Bedrosian, P., Robinson, B., Murray, D., & Schlutz, A. (2023). Using Helicopter Time-Domain Electromagnetic (HTEM) Resistivity Surveys with Supporting Geoscience Data to Target Temperature Gradient Wells and Discover Hidden Geothermal Systems in the U.S. Basin and Range. GRC Transactions, 47.

Siler, D. L., Faulds, J. E., Hinz, N. H., Dering, G. M., Edwards, J. H., & Mayhew, B. (2019). Three-dimensional geologic mapping to assess geothermal potential: examples from Nevada and Oregon. *Geothermal Energy*, *7*, 1-32.

Sillitoe, R.H. (1993). Epithermal models: genetic types, geometrical controls and shallow features. In: Kirkham, R.V., Sinclair, W.D., Thorpe, R.I., & Duke, J.M. (eds) Mineral deposit modeling. Geol Assoc Can Spec Pap 40, 403-417.

Sillitoe, R. H. (2015). Epithermal paleosurfaces. Mineralium Deposita, 50(7), 767-793.

Simmons, S.F., White, N.C., John, D.A., (2005). "Geological Characteristics of Epithermal Precious and Base Metal Deposits", One Hundredth Anniversary Volume, Jeffrey W. Hedenquist, John F. H. Thompson, Richard J. Goldfarb, Jeremy P. Richards. Society of Economic Geologists.

Thompson, A.J.B., Hauff, P.L. & Robitaille, A.J. (1999). Alteration mapping in exploration: application of shortwave infrared (SWIR) spectroscopy: Society of Economic Geologists Newsletter 39, p. 1, 16–27.

White, D. E., Thompson, G. A., & Sandberg, C. H. (1964). *Rocks, structure, and geologic history of Steamboat Springs thermal area, Washoe County, Nevada* (No. 458-B).

Yap, L., Ayling, B.F., Hinz, N. (2018). Mapping sinter and travertine outcrops in the state of Nevada. GRC Transactions vol. 42.

Final Results of the Hawai‘i Play Fairway Project

Nicole Lautze[1], Donald Thomas[1], Garrett Ito[1], Neil Frazer[1], Stephen Martel[1], Nicholas Hinz[2]

[1]University of Hawai‘i, Hawai‘i Groundwater and Geothermal Resources Center
[2]Geologica Geothermal Group, LLC

Keywords
Hawai‘i, geothermal, Play Fairway

ABSTRACT

The Hawai‘i Play Fairway project produced the State of Hawai‘i’s first statewide geothermal resource assessment since the 1980s and Hawai‘i’s first quantitative geothermal resource probability model. Funded $2.3 million by the U.S. Department of Energy, the project operated over three phases from 2014 to 2021. During the first two phases, the project developed a statewide geothermal resource probability map and a Play Fairway methodology and identified 10 locations for geothermal prospecting. During the third phase, the project tested the methodology, drilled a temperature observation well on Lāna‘i Island to a depth of ~1km, and developed final statewide probability maps. At 1-km depth, the temperature within Lāna‘i Well 10 exceeds those of two wells in Kīlauea’s East Rift Zone and a third well in the Saddle region of Hawai‘i Island that exhibited an elevated temperature gradient from 1-2km depth. The Phase 3 work reconsidered some of our earlier evaluations in the production of final statewide probability of heat maps. In our final assessment, we now take fluid probability of Fluid and exclude probability of Permeability due to a dearth of data at anticipated resource depths. This differs from our Phase 1 presentation of a combined resource probability achieved by multiplying the three together.

1. Introduction

Despite a 100% renewable policy objective and a significant continuing reliance on fossils fuels, surprisingly little is known about Hawai‘i’s geothermal resource potential. Geothermal exploration in the 1970’s and 80’s was concentrated within Kīlauea’s East Rift Zone (KERZ) on Hawai‘i Island, where several exploratory wells were drilled. Outside of Kīlauea’s summit and ERZ, Hawai‘i’s geothermal resources are blind, and prior to the Hawai‘i Play Fairway project, little work had gone into the exploration of blind resources over the rest of the state.

Areas of high heat in Hawai‘i reflect recent intrusions, including unerupted magma, so prospecting for heat naturally targets the main pathways of magma movement through Hawaiian shield volcanoes: calderas, rift zones, and volcanic vents. In most locations in the state, rock in the upper 1-2 km of the volcanoes has high permeability, which results in a relatively deep water table. We, therefore, expect geothermal resources statewide to be 2 km or more below the ground surface.

The Hawai‘i Play Fairway project took place over 3 phases. The results of the first two project phases are summarized across four publications in the journal Geothermics (Lautze et al., 2017a, 2017b, 2020; Ito et al., 2017). The main task in Phase 3 was to execute a drilling project on Lāna‘i Island, the detailed results of which are expected to be published soon (Lautze et al., in review, Geothermics). In Phase 3, we incorporated the Lāna‘i drilling data in our probability model and also updated our rationale on the probabilities of fluid and permeability at resource depths, such that the Probability of Fluid across the state is equal to 1 (due to the expectation that resources will be below sea level), and the Probability of Permeability is excluded from analysis at this time as we lack data to constrain it. Therefore, given current state of knowledge, we advocate for using our final probability of heat, and our confidence in this probability, to guide the next phase of exploration. We regard further development of geothermal energy in Hawai‘i as essential to enable the state to achieve its 100% renewable policy objective and look forward to enabling Hawai‘i’s transition from fossil fuels through geothermal discovery and development.

2. Final Probability and Confidence Calculations

Our published maps for each island in the State of Hawai‘i from project Phase 1 show a) calculated probabilities of three attributes: Heat (Pr_H), Fluid (Pr_F), and Permeability (Pr_P); b) the combined probability of a Resource (Pr_R), calculated as the product of the individual three probabilities:

$$PrR(x)=PrH(x)PrF(x)PrP(x) \quad (1)$$

and c) our computed Confidence in Pr_R (Ito et al.; 2017). In this discussion, an “x” denotes a location on the map. We refer to equation (1) as the “Veto Equation” because the probabilities Pr_H, Pr_F, and Pr_P are independent and range between 0 and 1 and if any one of them is low, so too will be the resource probability $Pr_R(x)$. The approximation in this product of probabilities is the same as that of the naive Bayesian classifier in which conditional probabilities are estimated by marginal probabilities (e.g., Domingos and Pazzani, 1997). As seen in Figure 1 and as is generally true statewide (Ito et al., 2017; Lautze et al., 2017b), the calculated Phase 1 resource probabilities (Pr_R) are low. In fact, our calculated Pr_R was less than 10% across most of the state, only above 30% off of Hawai‘i Island, and only 45% at the state’s only proven site, Puna Geothermal Venture (PGV).

We now consider that our Phase 1 results were too conservative. Upon further interpretation, we consider that everywhere in Hawai‘i, Pr_F will be approximately equal to 1 at resource depths below sea level (so across all of the state except its highest volcanic peaks). Further, due to the paucity of deep drilling data in Hawai‘i outside the one known geothermal resource region along KERZ, we have little data to constrain Pr_P at expected resource. We therefore suggest that the statewide maps of Pr_H and Confidence in Pr_H guide future exploration activities, however we are also aimed at better constraining subsurface permeability, for example through core drilling.

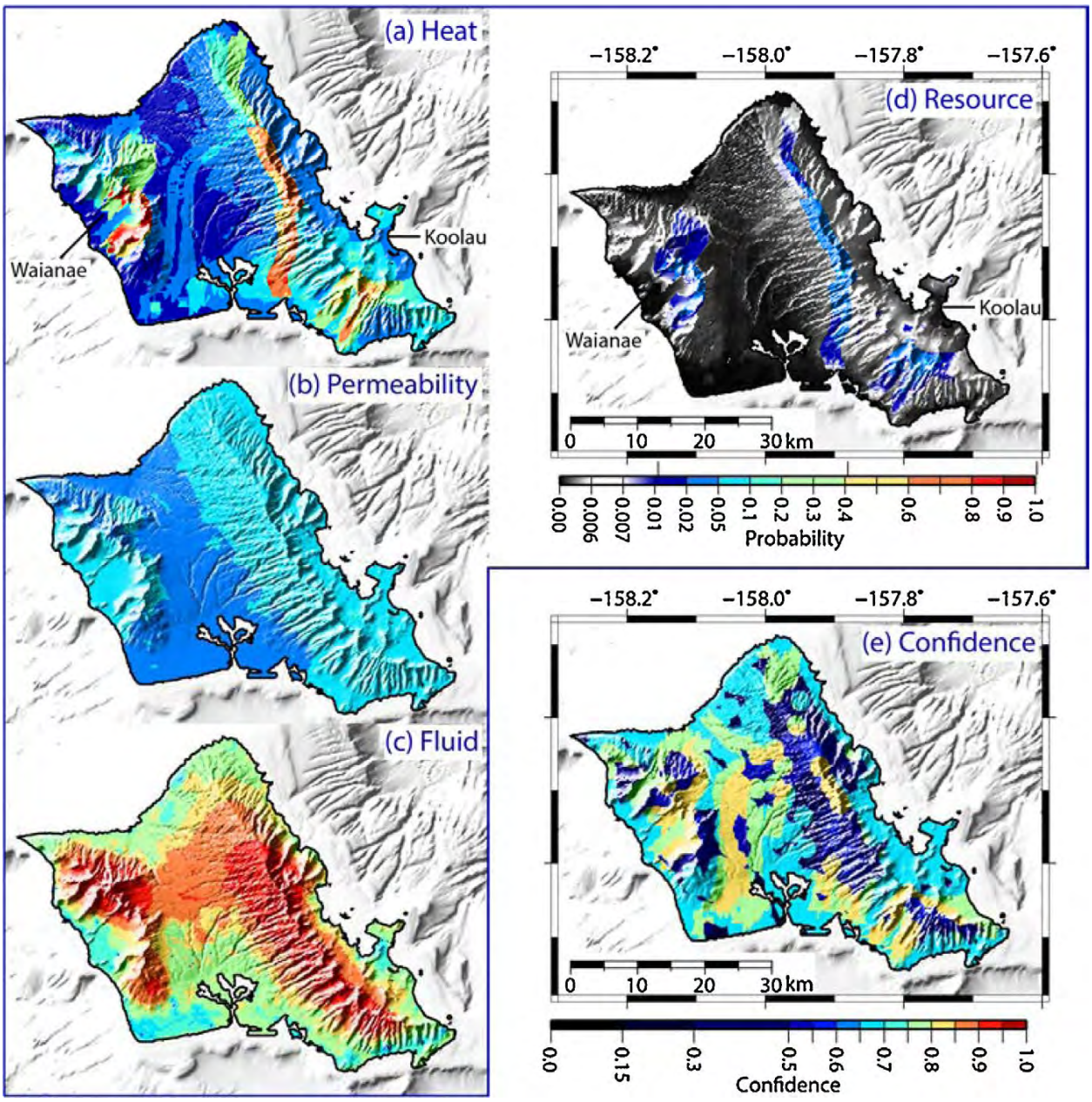

Figure 1. Phase 1 Probability and Confidence results for the Island of Oʻahu. This is Fig. 6 in Ito et al. (2017).

2.1 Phase 3 probability of heat (PR_H) calculation: updated heat loss with time function based on Lānaʻi drilling results

Figures 2 and 3 show the probability of heat in the subsurface across the State of Hawaiʻi, calculated following the method outlined by Ito et al. (2017), but excluding all evidence used during Phase 1 from groundwater data due lack of confidence in groundwater flow directions. Figure 3 shows the same probability results as Figure 2 but with water well temperatures overlaid for qualitative analyses. These final probability values incorporate all of the Phase 2 geophysical data, as well as an updated function for "heat decay with time since last eruption" based on the

new Lāna‘i Well 10 (Phase 3 drilling) temperature measurements (Lautze et al., in review, Geothermics).

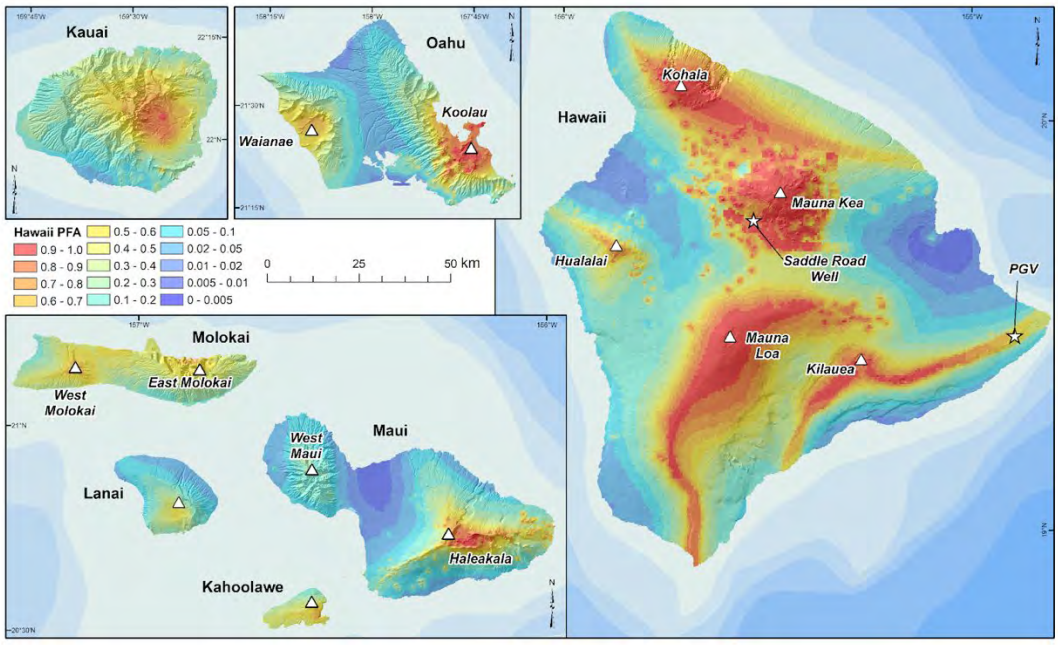

Figure 2. Probability of subsurface Heat across the State of Hawai‘i.

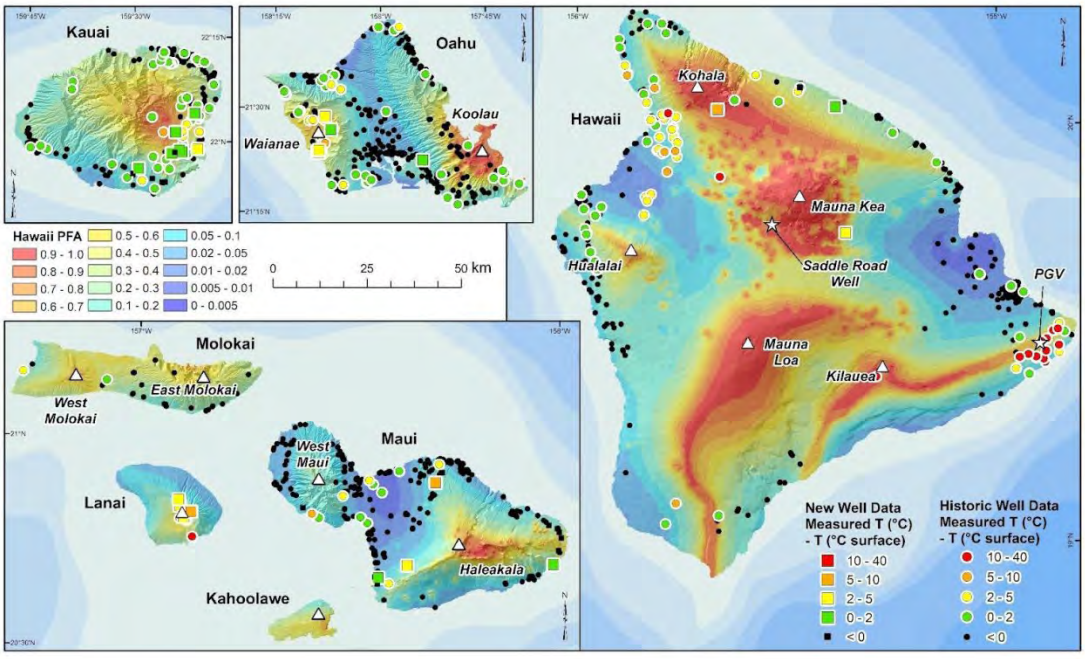

Figure 3. Probability of subsurface Heat across the State of Hawai‘i, overlaid with the location and temperature of groundwater wells. “New Well Data” (squares) were collected in Phase 2 of this Play Fairway project. Wells without any known temperature anomalies are shown as small black circles.

3. Discussion of PR_H Results

Figure 2 indicates a probability of heat above 50% at each shield volcano in the state except West Maui, with the largest and highest probabilities near the summit regions of the active Kīlauea and Mauna Loa volcanoes. Each shield volcano on Hawai‘i Island has a probability of heat >90% except Hualālai at ~70%. Haleakalā has a Pr_H of 70-80% at the summit, decreasing to 60% or below along its rift zones; Lāna‘i, West and East Moloka‘i, and Wai‘anae have a Pr_H ~60 -70 %, and Kaua‘i and Ko‘olau have a slightly higher Pr_H at ~80%. These probabilities in general accord with the size and lifespan of the volcanoes, and are further supported by groundwater data. Figure 3 shows a presence of notably warm groundwaters in the vicinity of PGV along KERZ, along Mauna Loa's South rift, on and South of Kohala volcano (waters to the south have a mixed source from Kohala and Mauna Kea; Tachera 2018), on Lāna‘i, in Wai‘anae caldera, and on Kaua‘i. Broadly, and not surprisingly, the statewide Pr_H shown in Figure 2 closely aligns with our current state-of-knowledge regarding Hawai‘i's volcanic geology.

4. CONCLUSIONS

This paper presents final Hawai‘i statewide maps of the probability of a geothermal resource (Pr_R). In contrast to our prior maps of Pr_R, which were based on the products of the computed probabilities of substantial Heat, Fluid, and Permeability, PrR(x)=PrH(x)PrF(x)PrP(x), our updated maps presume PrR(x)=PrH(x). The probability of fluid is now approximated as being equal to one because extensive evidence indicates that fluid is pervasive in the Hawaiian crust below sea level, which coincides with the expected subsurface depths of Hawai‘i's geothermal resources where production would be viable. Calculations of the probability of permeability Pr_P are presented to motivate future measurements of this property, but large uncertainties in these calculations render them useless for the calculation of Pr_R. We also present an updated map of confidence in our Probability of Heat based on the number and quality of data at a given location which shows highest confidence near eruptive centers and where geophysical data have been collected.

Overall, the Hawai‘i Play Fairway project represents a major advancement in the exploration of geothermal resources in Hawai‘i. We have now compiled all relevant data into maps of Pr_H, which provide a roadmap for future exploration activities. With $20M to $200M invested in geothermal exploration over the next 5-10 years, Hawai‘i would be able to better define the nature and extent of its geothermal resource and have an informed conversation on where and how further development could begin.

Acknowledgements

We thank the U.S. Department of Energy's Geothermal Technologies Office for funding and management of this project, under award number DE-EE0006729, and a generous donation from Pūlama Lāna‘i in their support of this project. We are deeply grateful to the too-numerous-to-mention students, field assistants, drilling and core-archiving crews, water well-owners and landowners who enabled this project's success.

REFERENCES

Domingos, P., Pazzani, M., 1997. On the optimality of the simple Bayesian classifier under zero-one loss. Machine Learning, 29, 103–130.

Ito, G., Frazer, N., Lautze, N.C., Thomas, D.M., Hinz, N., Waller, D., Whittier, R., Wallin, E., 2017. Play Fairway Analysis of Geothermal Resources across the State of Hawai‘i: 2. Resource Probability Mapping. Geothermics, 70, 393–405. https://doi.org/10.1016/j.geothermics.2016.11.004

Lautze, N.C., Ito, G., Thomas, D.M., Frazer, N., Martel, S., Hinz, N., Tachera, D., Hill, G., Pierce, H., Wannamaker, P., Martin, T., 2020. Play Fairway Analysis of geothermal resources across the State of Hawai‘i: 4. Updates with new groundwater chemistry, subsurface stress analysis, and focused geophysical surveys, Geothermics 86. https://doi.org/10.1016/j.geothermics.2019.101798.

Lautze, N.C., Thomas, D.M., Haskins, E., in review. Play Fairway Analysis of Geothermal Resources across the State of Hawai‘i: 5. Slim hole drilling on Lāna‘i Island. Geothermics.

Lautze, N.C., Thomas, D.M., Hinz, N., Ito, G., Frazer, N., Waller, D., 2017. Play Fairway Analysis of Geothermal Resources across the State of Hawai‘i: 1. Geological, geophysical, and geochemical datasets. Geothermics 70, 376–392. https://doi.org/10.1016/j.geothermics.2017.02.001.

Lautze, N.C., Thomas, D.M., Waller, D., Hinz, N., Frazer, N., Ito, G., 2017. Play Fairway Analysis of Geothermal Resources across the State of Hawai‘i: 3. Use of Development Viability as one criteria to prioritize future exploration activities. Geothermics 70, 406–413. https://doi.org/10.1016/j.geothermics.2017.07.005.

Characterisation of Core from a New Zealand Geothermal Field and its Potential Reaction to Receiving CO_2-rich Injection Fluids.

Bridget Y. Lynne[1,2], Eylem Kaya[1] and Alex Morriss[1]

[1]University of Auckland, 70 Symonds St, Auckland, New Zealand

[2]Geothermal Scientific Investigations Ltd, 11 Kyle Rd, Greenhithe 0632, Auckland, New Zealand

Keywords

CO_2-entrapment, injectate, tonalite, fluid-rock interaction

ABSTRACT

The University of Auckland's "Reversing Carbon Emissions in the Geothermal Industry" five-year project, aims to mitigate Green House Gas (GHG) emissions by employing innovative techniques in carbon capture and storage. A key focus of the project involves developing processes that will enable trapping of gases, especially CO_2, in solid form at optimal distances from the injection point, thereby promoting negative-emissions energy generation. A high-temperature-pressure reactor is currently under construction to carry out laboratory experiments involving saturating cored samples with CO_2-rich fluid. Prior to these experiments, it is critical to fully characterise the physical properties of the cored samples. Our experiments are designed to identify the favourable fluid-rock interactions and trapping mechanisms that govern CO_2 entrapment. Following our experiments, we will model fluid-rock interactions and the storage capabilities of the rock. We present the mineralogical, textural, and elemental characterisation of cored samples immediately adjacent to an injection depth, prior to it being used for reinjection, from one New Zealand geothermal field. Methods for rock characterisation include; (1) scanning electron microscopy to assess microscopic void dimensions, distribution, and connectivity and to examine reactive surfaces, (2) petrography to determine mineral relationships, mineral percentages and textural components, (3) X-ray fluorescence and energy dispersive spectroscopy to identify elemental compositions, (4) computerised tomography to establish rock density, and connected flow pathways. We are working with our industry partners to undertake field trials following completion of our experiments. New Zealand is taking significant steps in addressing climate change and minimising its environmental footprint. This MBIE-funded project is a notable advancement towards achieving this goal.

1. Introduction: Reversing carbon emissions (RCE) project overview

Geothermal fluids carry a variety of gases, primarily CO_2 along with traces of H_2S, NH_3, CH_4, and H_2. Currently these gases are captured directly without dilution (without mixing with the air) in

steam condensers. However, geothermal wastewater presents an opportunity to dissolve and permanently capture the GHG before reinjection, a focus of numerous international trials. For example, projects in Iceland (Gislason et al. 2018), the USA (Richard, 1990), Japan (Yanagisawa, 2010; Kaieda et al. 2009), Türkiye (Yücetaş et al. 2018), and the Philippines (Joselito et al. 2005) have explored this concept. Some of these trials utilise mineral entrapment of gases in specific deep geological formations, such as basalt (Gislason et al. 2018). The potential for CO_2 sequestration in basalts has also been investigated extensively by McGrail et al. (2006), Matter et al. (2007), and Snæbjornsdottir et al. (2014), in the United States and Iceland, on land and offshore. Keeping CO_2 underground in mineral form is important for long-term storage because mineralisation provides a stable and predictable means of storing CO_2, significantly reducing the volume of stored CO_2, and mitigating risks regarding potential CO_2 leakage, migration, and associated operational and environmental impacts.

New Zealand has committed to a 50% reduction in net greenhouse gas emissions by 2030, as announced during the UN's COP26 climate summit. To facilitate this transition, the Renewable Energy Strategy has been established, aimed at expanding the energy supply and achieving net-zero carbon emissions status by 2050. This research initiative seeks to contribute to these goals by developing processes that will enable trapping gases, especially CO_2, in solid form while boosting fluid production from geothermal resources. This will require characterising the unique geochemical, geological, petrophysical, and fluid dynamic properties to investigate potential mechanisms for trapping GHGs, to allow negative-emission energy generation.

Throughout this five-year project, we will assess the suitability of various host rocks in the Taupō Volcanic Zone (TVZ) for GHG entrapment. The programme involves an innovative stepwise approach:

- Step one consists of analysing and characterising rocks from injection depths. These analyses will include X-Ray Diffraction (XRD), Scanning Electron Microscopy (SEM), Energy Dispersive Spectroscopy (EDS), Computerised Tomography (CT), petrographic microscopy, rock strength compressibility tests, and density and porosity measurements.
- Step two involves constructing a pressure-temperature chamber. Experiments will be conducted on characterised TVZ geothermal host rocks placed inside the chamber, exposing them to varying amounts of CO_2-rich fluid. Changes within host rocks before and after exposure to the experimental conditions of the pressure chamber will be documented. The novel aspect of this programme involves injecting chemical agents into the pressure chamber to increase the quantity of available cations, which will promote permanent entrapment of GHG.
- In step three, we will determine the optimal chemical agents required for injection that will favour permanent GHG entrapment, and identify the most suitable TVZ formations to be targeted for our field trials.
- Step four will involve modelling the predictive behaviour of chemical reactions based on our laboratory results and field trials.

We are collaborating with our industry partners on laboratory and field-scale tests. The utilisation of large-scale field data will validate and enhance our research on the influence of GHG-rock-geothermal wastewater interactions, assess the short- and long-term impacts of GHG reinjection, and identify potential risks to the environment and geothermal development operations.

Concurrently, we will quantify the benefits of reservoir pressure support resulting from the injected GHG, ultimately leading to higher generation efficiency.

2. Ngā Tamariki Geothermal Field, New Zealand and NM9 injection well

Ngā Tamariki Geothermal Field is located within the Taupo Volcanic Zone (TVZ), North Island of New Zealand (Fig. 1). This geothermal field is a high enthalpy geothermal system comprised of three different aquifers; a shallow meteoric groundwater zone, chloride-bicarbonate waters at depth, and a chloride geothermal reservoir of 290 °C below 1000 m depth (Bignall, 2009). There are very few natural surface thermal manifestations at Ngā Tamariki. Only minor hot springs and steam-heated features are present (Mongillo and Clelland, 1984). Situated at the northern extent of the field is Pavlova Spring which discharges dilute alkali chloride-bicarbonate water (Campbell et al. 2002). Brotheridge (1995) has documented hydrothermal eruptions in the area.

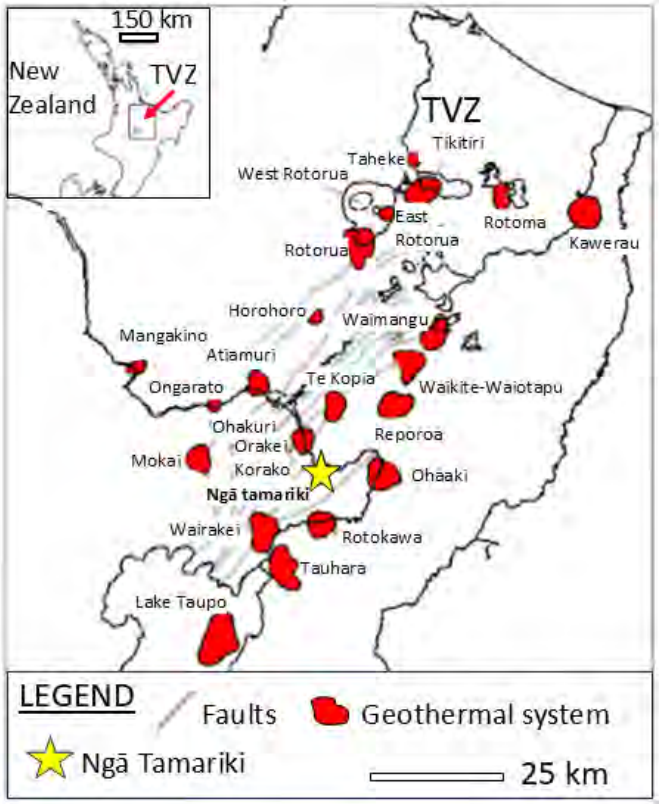

Figure 1: Location of Ngā Tamariki geothermal field and other geothermal fields within the Taupo Volcanic Zone (Kissling and Weir, 2005).

We selected the Ngā Tamariki Geothermal Field as a primary focus for this paper due to its implementation of CO_2 reinjection practices aimed at minimising carbon emissions. As part of this initiative, non-condensable gases (NCGs) from one of its units are injected back into the reservoir through a designated reinjection well (NM9). This ongoing CO_2 reinjection trial at Ngā Tamariki has been operational at one of its four units since October 2021, injecting 25% of the total station's emissions per year, amounting to over 8,000 tons of CO_2 equivalent annually.

The general geology of the field is fairly typical of a TVZ geothermal system (Fig. 2A). Hydrothermal alteration at depth predominantly results from fluid-rock interaction with high

temperature, neutral-pH fluids, leading to the formation of minerals such as illite, chlorite, epidote and pyrite (Chambefort et al., 2014).

However, Ngā Tamariki exhibits unique geological features. Drillholes NM4, NM8 and NM9, located in the north of the field (Fig. 2A), have intersected an intrusive complex consisting of diorite and tonalite between 2300 m and 3500 m depth. This intrusive complex has an associated magmatic-hydrothermal alteration halo representative of a high-intermediate-sulfidation state, epithermal mineralization (Chambefort et al., 2014). This relict high temperature advanced argillic to potassic hydrothermal alteration halo consists of biotite and magnetite with rare K-feldspar, quartz, pyrophyllite/muscovite, and rare andalusite and topaz (Arehart et al., 2002; Christenson et al., 2002; Lewis et al., 2013; Chambefort et al., 2014; Fig. 2B).

Injection wells NM8 and NM9 were drilled in 2012. Clearwater et al., (2015) documented two key observations; (i) initially these wells increased in injectivity for differing lengths of time which was attributed to thermal contraction of the rock expanding fractures, and (ii) both wells experienced a decline in injectivity which was attributed to silica scaling in the formation. Clearwater et al., (2015) also report fluctuations in injectivity that do not appear to be explained by temperature variation of the injectate. Their investigation highlighted the need for further analyses on compositional changes of the injectate, including variability in the gas content of the reinjection fluid.

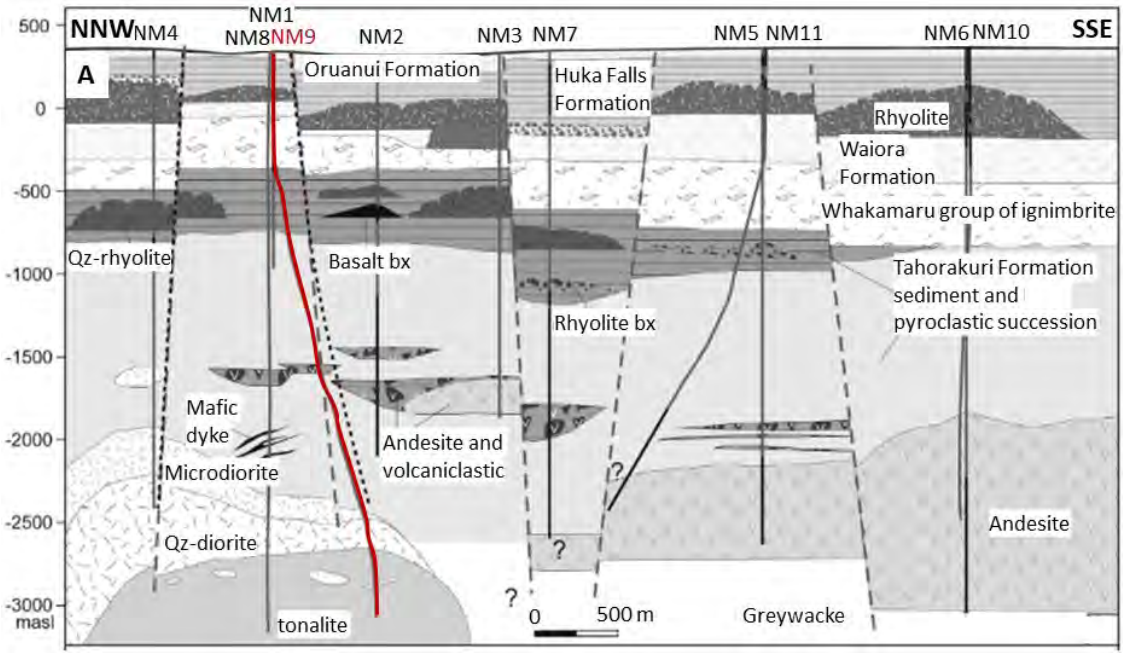

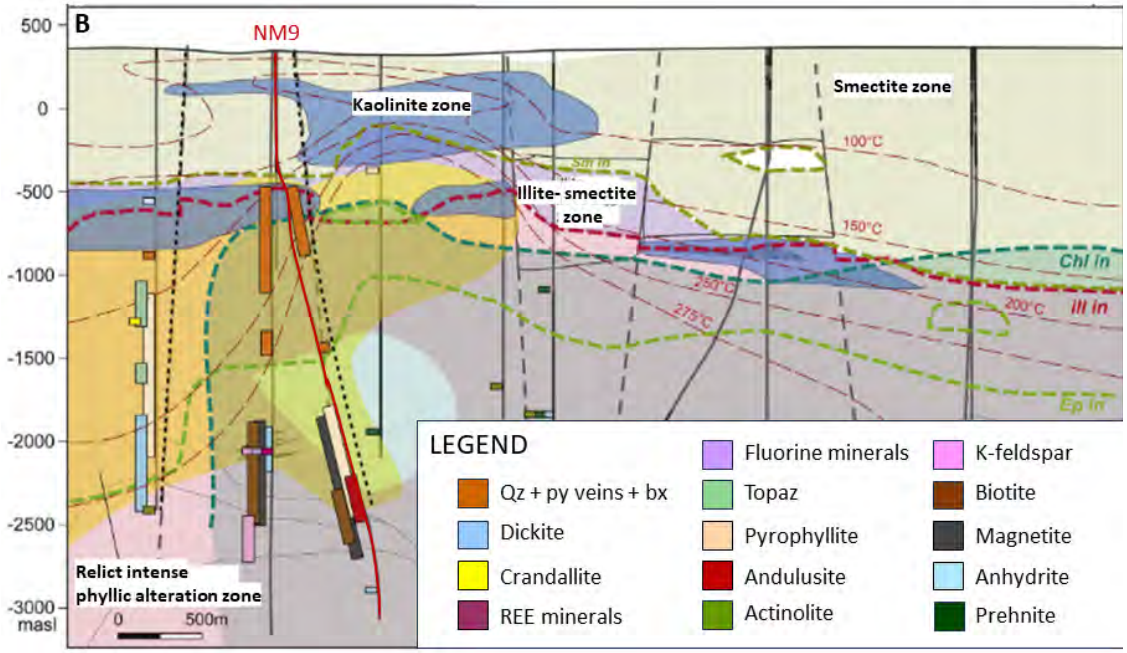

Figure 2: Cross-sections through Ngā Tamariki Geothermal Field with the location of injection well NM9 highlighted in red (Chambefort et al., 2016). (A) Geological cross-section with rock types shown. (B) Cross-section showing isotherms and mineralogy (Chambefort et al., 2016).

Step one of our 5-year RCE project is reported herein. Step one involves characterising the textural, elemental and mineralogical characteristics of the tonalite from NM9, located immediately below the current injection depth. The samples analysed in step one, have not been exposed to reinjection fluid as they were recovered prior to well NM9 being used for reinjection. Step two involves fluid-rock experiments in a specifically-designed test chamber. The purpose-built chamber is designed to sample and analyse the tonalite core at various time intervals, after exposure to different CO_2-rich fluid concentrations. Core characterisation pre- and post-experiments will be conducted using identical analytical techniques so a direct comparison of fluid-rock interaction can be assessed, with the aim of documenting how the tonalite intrusive complex is reacting to CO_2-rich injectate fluid. Step three involves modelling the predicted behaviour of the rocks using real fluid-rock input data. Step four includes modelling the predictive behaviour of chemical reactions based on our laboratory results and field trials.

3. NM9 core samples

For our RCE project, Mercury Energy donated a 0.45 m core of tonalite from injection well NM9, from 3201.1 to 3201.55 m depth (Fig. 3A), located immediately below the current injection depth. This core is referred to as the RCE core.

In 2013, prior to the RCE project, Mercury Energy provided four pieces of tonalite core from injection well NM9, for characterisation of void distribution, connectivity and dimensions, specifically using Scanning Electron Microscopy (SEM) and Energy Dispersive Spectroscopy (EDS). The four samples were from depths between 3204 m and 3206.9 m (Fig. 3B-3E). The results presented by Lynne (2013) provide valuable information on the void characteristics of the

NM9 tonalite core between 3204 m and 3206.9 m depth. As fluid is contained in and travels through voids in rocks such as pore spaces, fractures and mineral defects, the results from Lynne (2013) on void connectivity, dimensions, distribution and quantity is relevant to the RCE project and have been included in this study. Inclusion of these samples extends the tonalite characterisation from NM9 injection well from 0.45 m to 6.8 m.

All the core samples analysed in this study were collected before well NM9 was used as an injection well. Therefore, they have not yet reacted with injectate fluid.

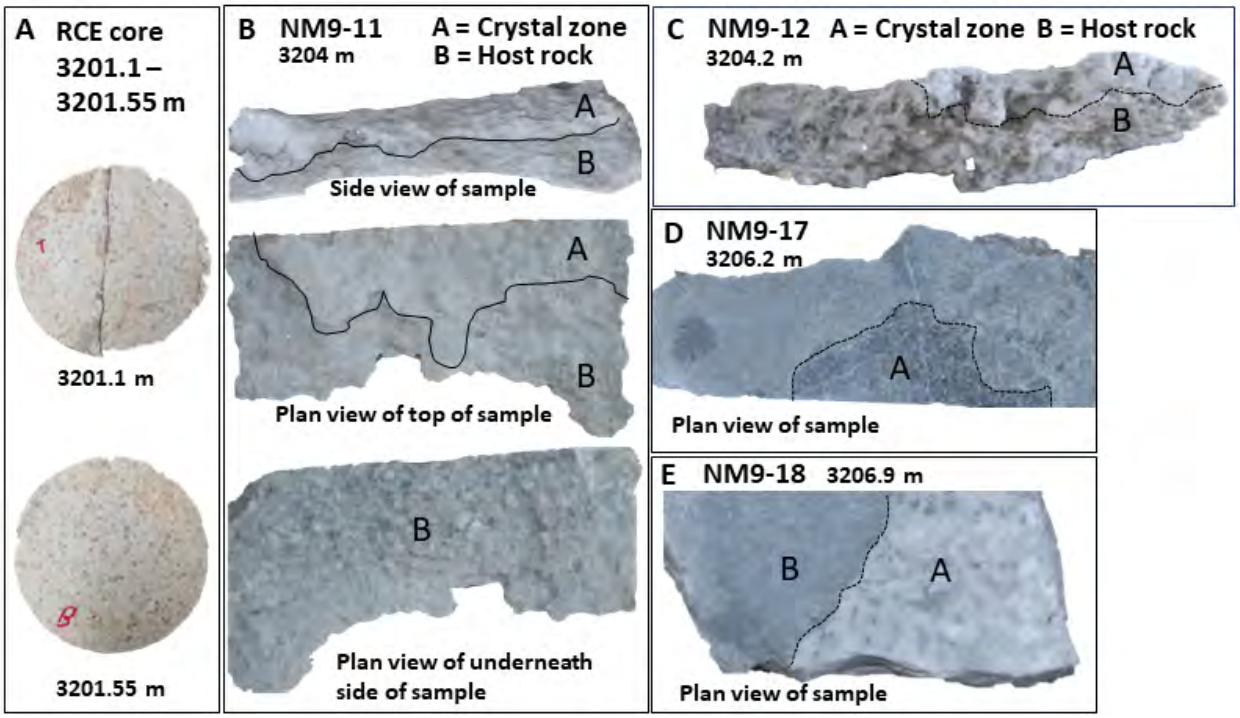

Figure 3: Samples of tonalite core from the Ngā Tamariki geothermal field. (A) Mildly-altered white tonalite from 3201.1 to 3201.55 m depth. (B-C) Highly-altered tonalite core from 3204 m depth with crystal zones (A) and host rock areas (B). (D) Grey tonalite core from 3206.2 m depth with dark grey alteration halo and white infilled fractures. (E) Boundary between grey and white tonalite core from 3206.9 m depth. Least altered core. (B-E) Samples from Lynne, (2013).

4. Methods

A multi-analytical-technique approach was chosen for Step One of the RCE project and is aimed at characterising the core prior to Step Two. Analytical methods have been chosen that will enable void characterisation, reveal potential reactive surface areas, determine the textural, elemental and mineralogical composition and establish the rock strength, before interacting with CO_2-rich fluids in our experimental chamber.

The 0.45 m long tonalite RCE core from NM-9 was examined using petrography, micro-CT scanning, X-Ray Fluorescence (XRF), and Scanning Electron Microscopy (SEM). Void, reactive surfaces and elemental composition of the tonalite core from 3204 m to 3206.9 m depth have been characterised using SEM and EDS (Lynne, 2013). Planned for later this year, but not available at

the time of writing this paper is X-Ray Diffraction (XRD) and compressibility testing on the samples. Prior to placing the samples in the experimental chamber, a full set of analyses will be completed on all samples.

4.1 Petrography

Petrographic thin sections of the upper and lower sections of the RCE core were made at the University of Christchurch. They were analysed on a Nikon Eclipse LV100 PDL petrographic microscope and photographed on a Nikon DS-Ri1 camera.

4.2 Elemental composition (XRF and EDS)

Bulk composition of the RCE core was determined via X-Ray Fluorescence (XRF). Samples were taken from both the upper (3201.1 m depth) and lower sections of the tonalite core (3201.55 m). Samples were crushed in a rock crusher before being sieved through a 710 µm sieve. Once sieved, the samples were cleaned in distilled water in a Bandelin Sonorex Digitec ultrasonic bath. The samples were then dried for 24 hours at 60°C prior to being placed in a rock mill for 2 minutes each, to produce a powder. All samples were heated to 200°C for 48 hours to find the ignition loss. The major oxide concentration (%) was evaluated by the glass bead method which was prepared by the 1:3 dilution method. This means that 3g of a sample was combined with 9g of flux. The flux that was used contained 67% $Li_2B_4O_7$ and 33% $LiBO_2$. For trace element analysis, samples were prepared by the pressed pellet technique in which 7.5g of sample was mixed with 2.5g of binder. XRF analysis was conducted using an S8 TIGER (Series 2) wavelength dispersive X-ray fluorescence spectrometer (WDXRF).

Energy Dispersive Spectroscopy (EDS) was used to analyse mineral-specific compositions in samples NM9-11, NM9-12, NM9-17 and NM9-18. EDS analyses were performed to obtain semi-quantitative compositional data on the mineral phases. EDS operating conditions were 20 keV accelerating voltage, with a spot size of 5 µm, and a working distance of 5 mm. No EDS scans were collected on the RCE core as the EDS was out of action.

4.3 Density measurements

Micro-Computerised Tomography was used to determine the bulk density of the sample and to examine void networks and fracture infill. Two 40 mm wide slabs were cut from the top of the tonalite core at 3201.1 m depth. No sample could be prepared from 3201.55 m depth due to a problematic fracture. Samples were cut using the Metkon Geocut Geological Cutter. Once slabbed, the samples were cored using a 10 mm diameter core drill bit to gain 6.5mm diameter sub cores. One sample was taken from each 40 mm slab. For analysis, the samples were placed in a plastic straw and mounted in a Bruker Skyscan 1272 micro-CT scanner. The acquisition parameters were: 85 kV, 110 µA beam current, 3750 mS exposure time, 2x Al filters, 2 µm pixel resolution, camera pixels 2452 x 1640. Scan parameters were: 0.25° rotation step, 2x frame averaging, 3 random movement and 360° rotation. The imaging time was 5.5 hours per sample. The images were reconstructed using InstaRecon CBR Server Premium 15K in conjunction with Nrecon 2.2.2 and subsequently visualised in 3D using CTVox V 3.3. Analysis was completed using CTAn V1.18.4.0.

4.4 Scanning Electron Microscopy (SEM) and Energy Dispersive Spectroscopy (EDS)

SEM was used to document the microscopic void size, abundance, distribution and connectivity. For the RCE core SEM imaging, analysis was conducted on fresh surface specimens produced from the sub-core drilling process as outlined in the micro-CT methods. A TESCAN CLARA instrument, working at a voltage of 10 keV, was used to conduct the SEM analysis. These images were used to assess the pore spaces within the samples and the degree to which they are interconnected. EDS would normally be conducted alongside SEM; however, the University of Auckland Science Department's EDS machine was out of order at the time of SEM analysis.

For samples NM9-11, NM9-12, NM9-17 and NM9-18, each sample was mounted on an aluminium stub and powder coated with platinum (10 nm coating thickness) for ~7 minutes at 10 mA using a high resolution Polaron SC7640 sputter coater. Samples were examined using a Phillips (FEI) XL30S field emission gun SEM. SEM operating conditions were 10 keV accelerating voltage, spot size of 3 μm, and a working distance of at least 5 mm. Energy Dispersive Spectroscopy (EDS) was performed on selected areas within the samples to obtain semi-qualitative compositional data. EDS operating conditions were 20 keV accelerating voltage, with a spot size of 5 μm and a minimum working distance of 5 mm. SEM and EDS equipment was located at RCSMS, University of Auckland.

5. Results

5.1 Characterisation of tonalite core from 3201.1 to 3201.55 m depth (RCE core)

5.1.1 Mineralogy and textures

At 3201.1 m depth, petrographic images reveal primary plagioclase feldspars are partially altered to calcite, anhydrite, muscovite, K-feldspar and epidote. Opaque minerals are also present. Primary quartz phenocrysts are fractured and infilled with clay. Some remnant primary minerals have completely altered to anhydrite and/or calcite (Fig. 4A-B). At 3201.55 m depth petrographic observations indicate primary plagioclase with secondary minerals of calcite, biotite, muscovite, adularia, epidote, pyrophyllite, K-feldspar and chlorite. Chlorite occurs as veins and alteration rims around primary plagioclase phenocrysts. The matrix consists of microcrystalline quartz with disseminated opaques and minor pyrophyllite alteration (Fig. 4C-D).

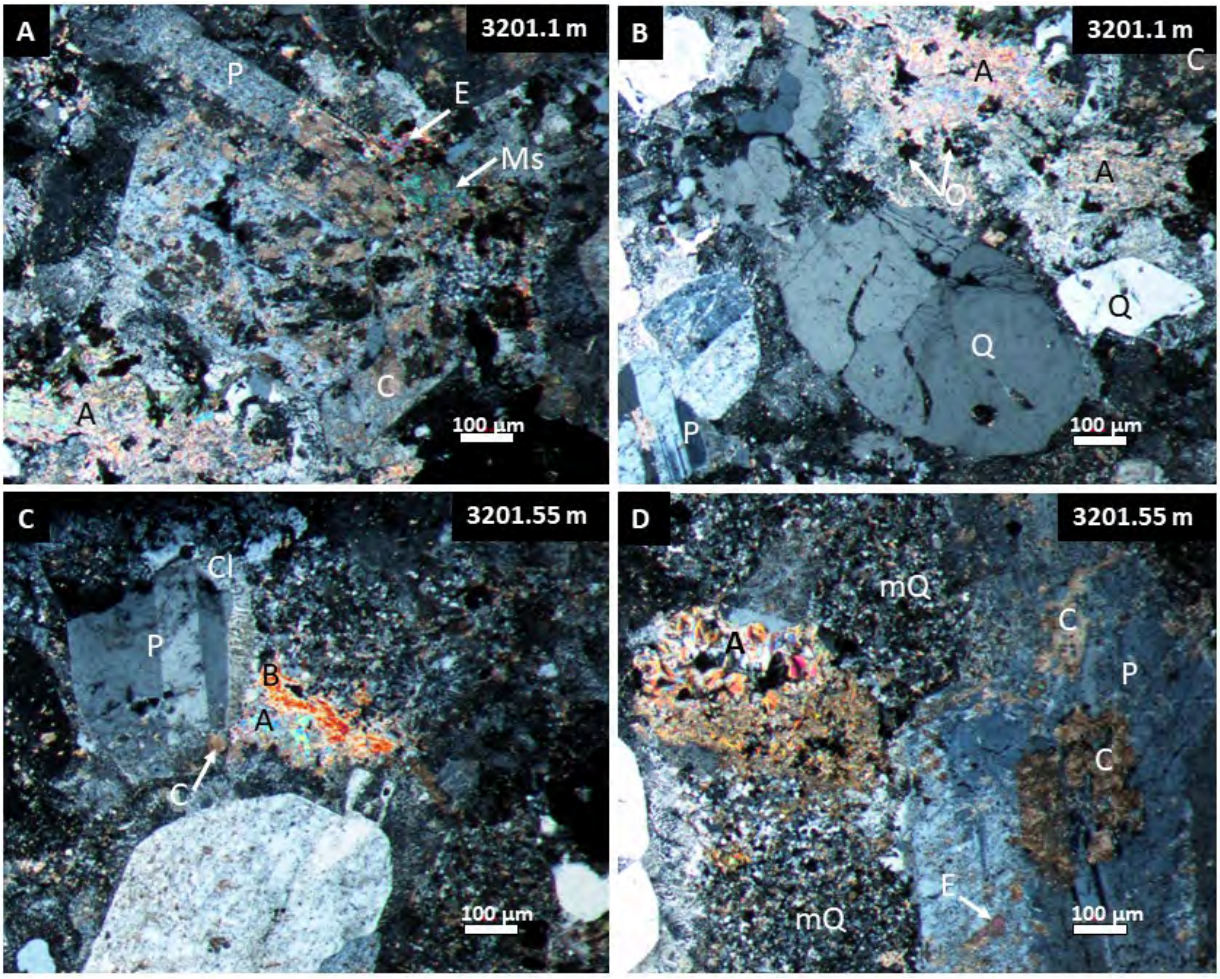

Figure 4: Petrographic thin section images of RCE core. (A-B) 3201.1 m depth. (A) Patchy alteration of primary plagioclase feldspar phenocryst to secondary calcite, anhydrite, muscovite, and epidote. (B) Large, fractured, quartz phenocryst with fractures infilled with clay. Remnant primary phenocrysts completely altered to anhydrite with disseminated opaques and calcite. (C-D) 3201.55 m depth. (C) Hydrothermal alteration of primary plagioclase to biotite and muscovite. Calcite and chlorite veins within microcrystalline quartz matrix are present. (D) Remnant phenocryst displays intense pyrophyllite alteration. Patchy calcite alteration, as well as minor epidote, is visible. Matrix consists of microcrystalline quartz with minor pyrophyllite alteration (Q = quartz, A = anhydrite, B = biotite, C = calcite, Cl = chlorite, E = epidote, mQ = microcrystalline quartz, O = opaques, Ms = muscovite, P = plagioclase feldspar).

5.1.2 Elemental composition (XRF)

Eleven major oxides (Table 1) and 28 trace elements were analysed using XRF. SiO_2 and Al_2O_3 dominate the major oxides with lesser amounts of Na_2O, K_2O and CaO.

Table 1: XRF results for the RCE core showing concentrations of major oxides, prior to experiments.

Major Oxides (%)		
Formula	**Tonalite (3201.1m)**	**Tonalite (3201.55m)**
Na_2O	3.83	3.88
MgO	0.40	0.53
Al_2O_3	13.46	13.84
SiO_2	72.92	71.72
P_2O_5	0.037	0.053
MnO	0.010	0.013
SO_4	1.78	2.32
K_2O	3.29	2.39
CaO	2.19	2.79
TiO_2	0.27	0.26
Fe_2O_3	1.41	1.92
LOI (Loss of Ignition)	0.040	0.040
Sum	99.62	99.76

5.1.3 Mapping RCE core density

Micro-Computerised Tomography (CT) performed on the sample revealed this sample is a fairly uniform low-density sample but with isolated patched of higher density mineralisation. With the rare exception, fractures remain unfilled (Fig. 5).

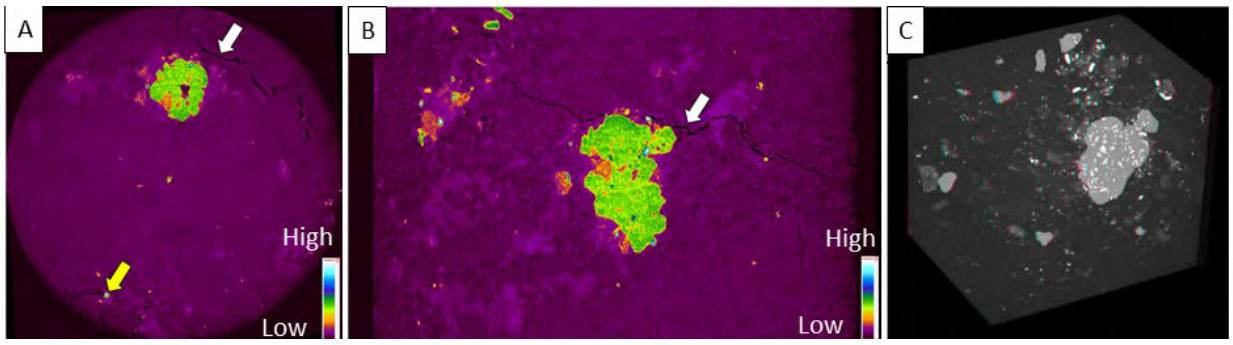

Figure 5: Micro-CT scans of the RCE sample. (A) Transaxial view. (B) Lateral view. (A-B) High-density phenocryst with some alteration within a relatively homogeneous low-density matrix. Fractures are dominantly unfilled (white arrows) but there is rare mineralisation in fractures (yellow arrows). (C) 3D model demonstrates density variations related to spatially patchy mineralisation within the core.

5.1.4 Morphology (SEM) and elemental composition (EDS)

SEM images of the RCE cored sample demonstrate a lack of void connectivity at depths of 3201.1 to 3201.55 m (Fig. 6). At 3201.1 m depth isolated voids range in size up to 15 µm x 5 µm (Fig. 6A-C), while at 3201.55 m depth, isolated voids are smaller with maximum dimensions of 6 µm x 3 µm (Fig. 6D-F). Rare fractures are observed at 3201.55 m depth that are 4 µm wide and continuous over >100 µm (Fig. 6D-E).

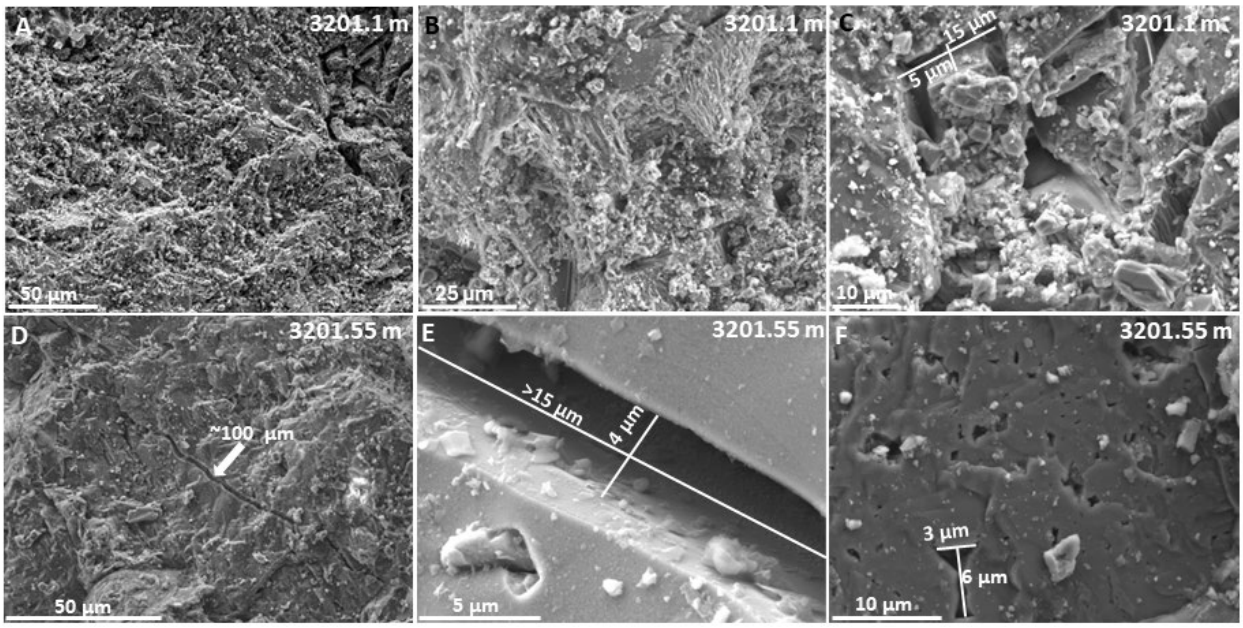

Figure 6: SEM images of the RCE core. (A-C) Depth 3201.1 m. (D-F) Depth 3201.55 m. (A) Overview of sample. (B) Minimal to no voids present. (C) Isolated voids up to 15 µm x 5 µm. (D) Rare fracture >100 µm in length. (E) Fracture >15 µm x 4 µm with minor clay platelets on inner fractured surface. (F) Isolated voids 3 µm x 6 µm.

5.2 Mineralogical and morphological characterisation of NM9 core from 3204 m, 3206.2 and 3206.9 m depth

5.2.1 NM9-11 Depth 3204 m

Sample NM9-11 consists of a crystal-rich fracture zone that overlies the host rock (Fig. 3B). SEM and EDS examination of the crystal-rich zone (Area A on Fig. 7A) revealed intergrowths of high temperature hydrothermal alteration minerals of epidote (>250 °C) and illite (>220 °C) on large quartz and Ca-rich silicate crystals (Fig. 7A-D). The underlying host rock (Area B on Fig. 3) does not reveal high temperature hydrothermal minerals, suggesting the flow of high temperature fluids was confined to the fracture zone, at this depth. Abundant connected voids around crystals in Area A vary in size up to 500 µm x 300 µm (Fig. 7C). Voids within Area B host rock are common, vary in size and many are isolated (Fig. 7E-F). Abundant reactive surfaces are present within this sample that would facilitate ongoing fluid-rock reactions.

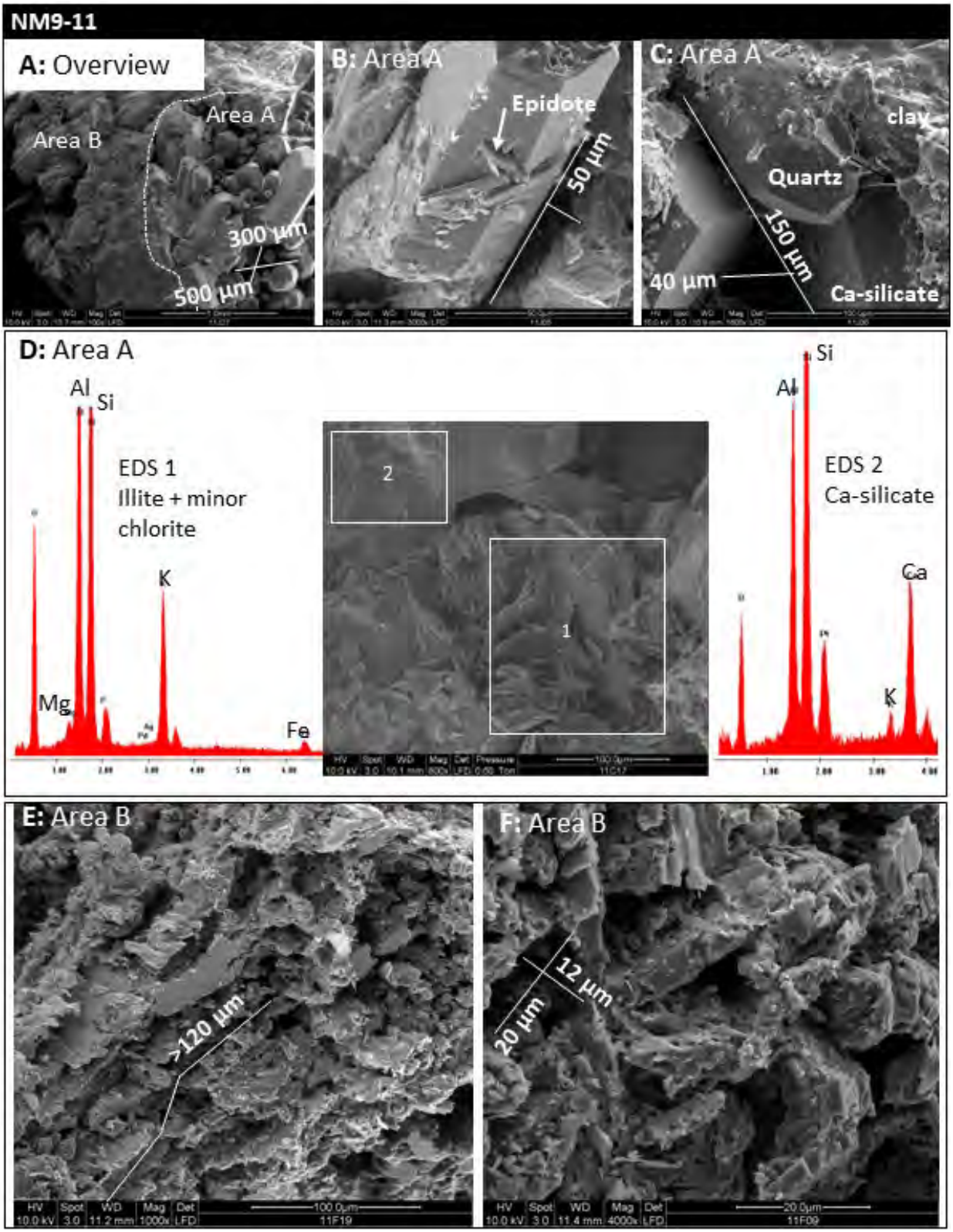

Figure 7: SEM images sample NM9-11. (A) Overview of sample shows a crystal-rich fracture zone (Area A) and the underlying host rock (Area B). (B-D) Quartz, Ca-silicate, epidote and illite in Area A. (E-F) Variation in void size and connectivity within Area B.

5.2.2 NM9-12 depth 3204 m but below NM9-11

Sample NM9-12 (Fig. 3C) revealed hydrothermal alteration minerals of quartz, epidote (>250 °C) and calcite growing into open space within a fracture (Fig. 8A-C, 8E-F). Illite (>220 °C) is also observed in the host rock (Fig. 8D, 8F). Connected voids in the fracture zone are >200 µm in length. Isolated voids of ~50 µm in length occur in the host rock. Abundant reactive surfaces occur within the fracture zone but are limited in the host rock.

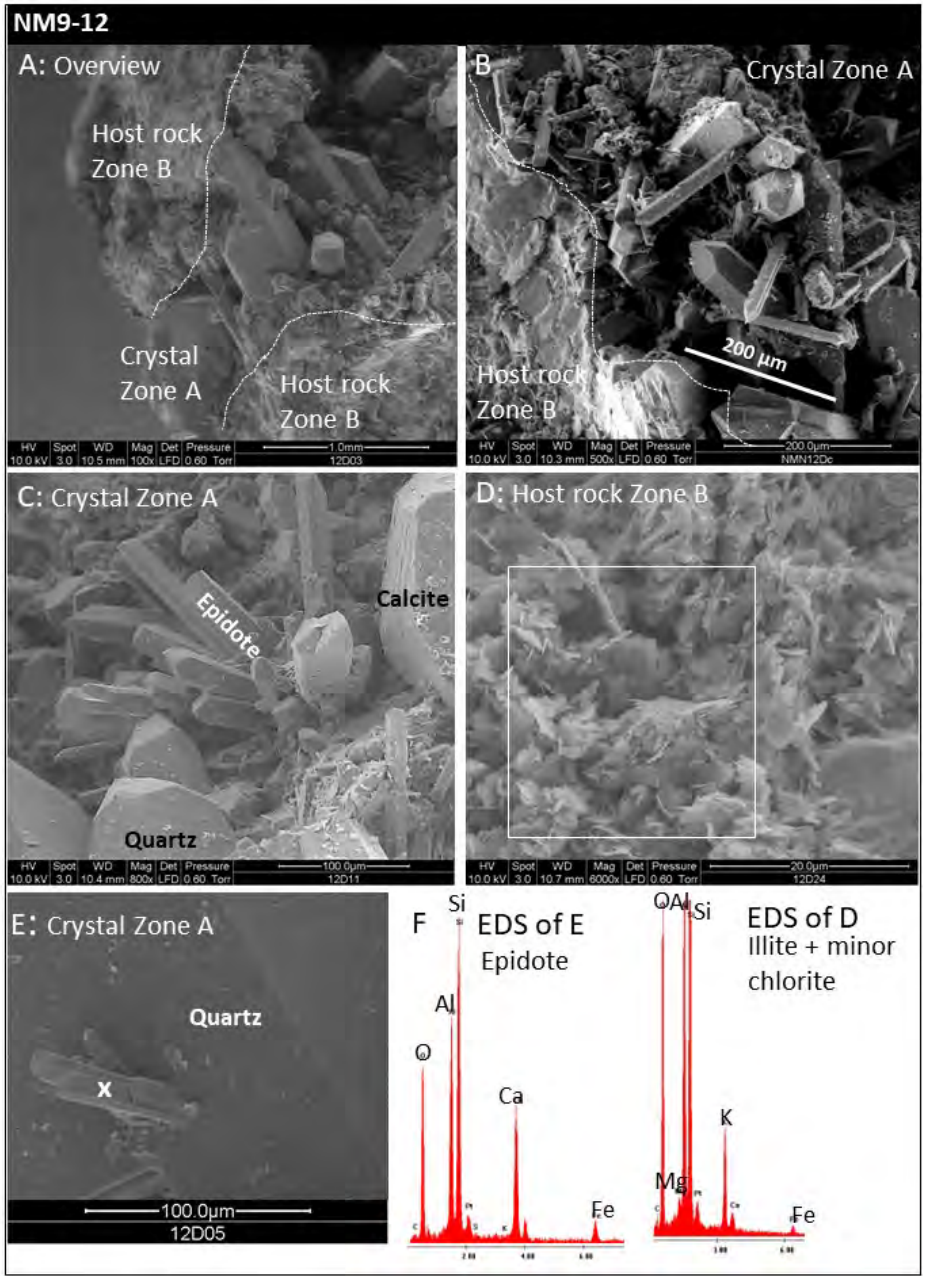

Figure 8: SEM images sample NM9-12. (A) Overview of sample. (B-C and E-F) Crystal-rich fracture zone partially infilled with hydrothermal alteration minerals of epidote, calcite and quartz. (D) Alteration to illite within host rock. White box is site of EDS shown in F. (E) Epidote and quartz in crystal rich fracture zone A. X marks site of EDS shown in (F). (F) EDS scans of x in (E) and white box in (D).

5.2.3 NM9-17

Sample NM9-17 (Fig. 3D) revealed the presence of hydrothermal alteration minerals of anhydrite, illite and chlorite (Fig. 9). Voids are limited to between individual clay platelets and fractures within anhydrite crystals.

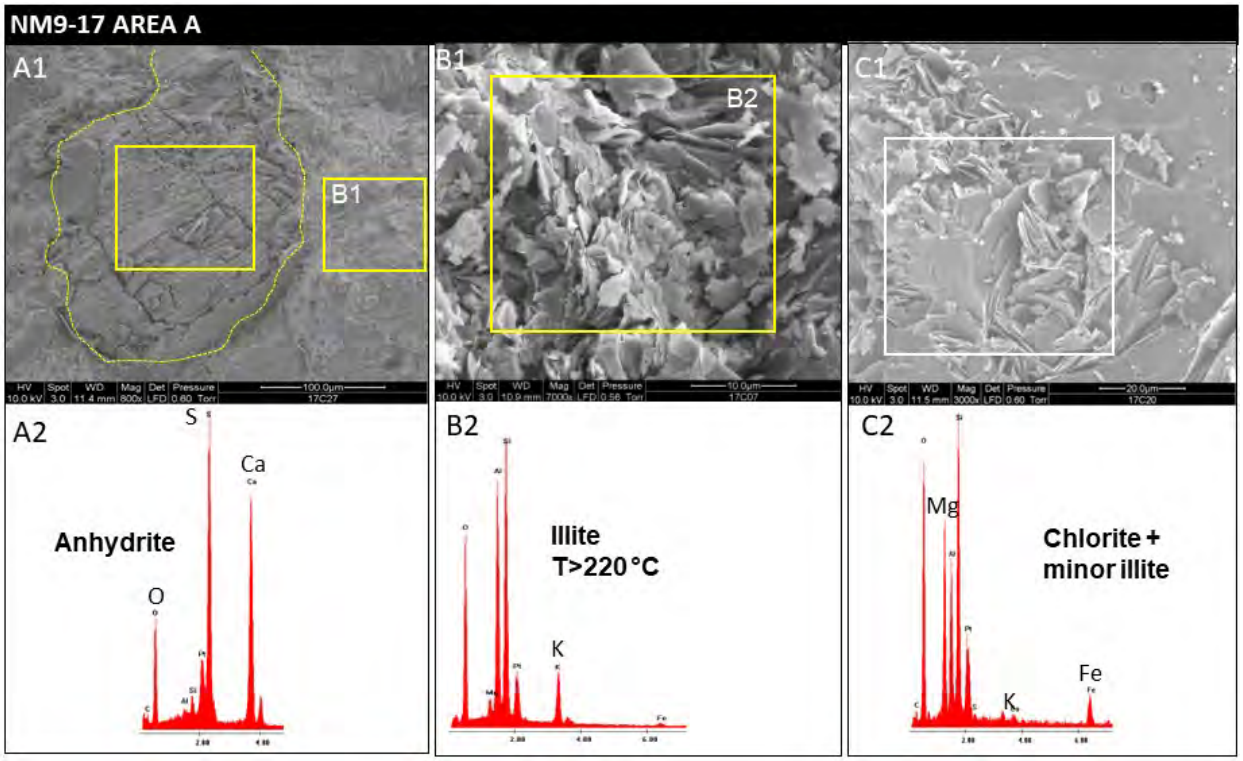

Figure 9: SEM and EDS images of sample NM9-17. (A1-A2, B1-B2) Large, fractured, anhydrite crystals surrounded by illite. Boxed areas indicate sites of EDS scans. (C1-C2) Chlorite and minor illite shown by EDS scan of boxed area.

5.2.4 NM9-18

Core sample NM9-18 (Fig. 3E) shows a boundary between grey (NM9-18B) and white (NM9-18A) tonalite. Both NM9-18A and NM9-18B revealed varying quantities of illite and chlorite. Chlorite dominates the grey tonalite, while illite dominates the white tonalite. Hydrothermal alteration minerals of anhydrite were observed in the grey tonalite but not in the white tonalite. Voids are dominantly limited to open spaces between clay platelets in both samples and are minimal (Fig. 10).

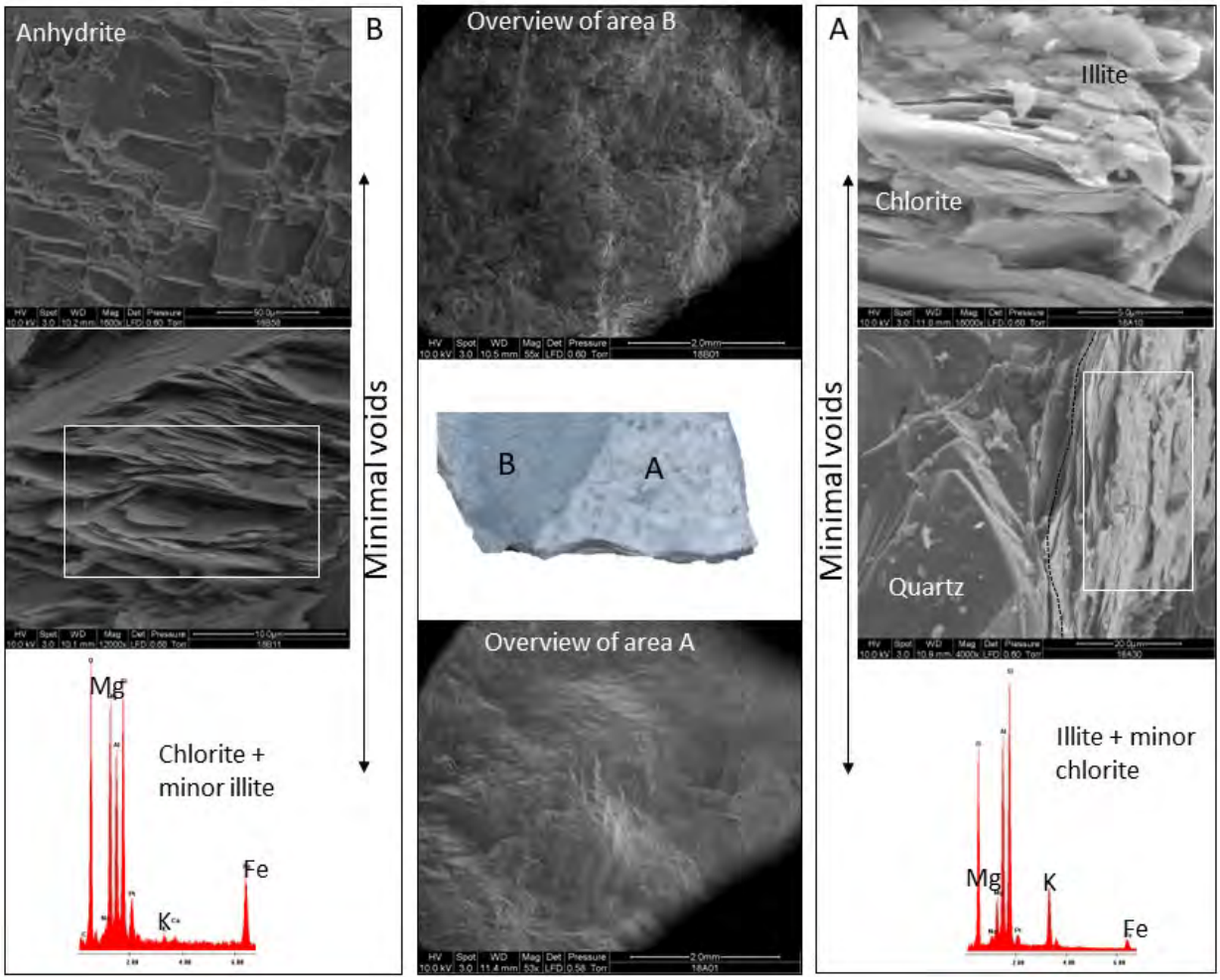

Figure 10: SEM images of sample NM9-18. Overview of sample (centre). (Left) Grey tonalite (area B) with hydrothermal alteration minerals of chlorite, minor illite and anhydrite. (Right) White tonalite (area A) shows areas of illite and chlorite, and large quartz crystals.

5.3 Elemental composition characterisation of core from 3204 m, 3206.2 and 3206.9 m depth

Crystals and clays within each of the four samples were examined by EDS to determine their elemental composition (Fig. 11). As CO_2-rich injectate will readily react with Ca-bearing minerals, it is important to document the occurrence of Ca, trapped in Ca-bearing minerals, their specific elemental composition and their depths. Our results indicate that the concentration of Ca in Ca-bearing minerals and clays varies within the tonalite host rock, within the fracture versus non-fracture zones and with depth.

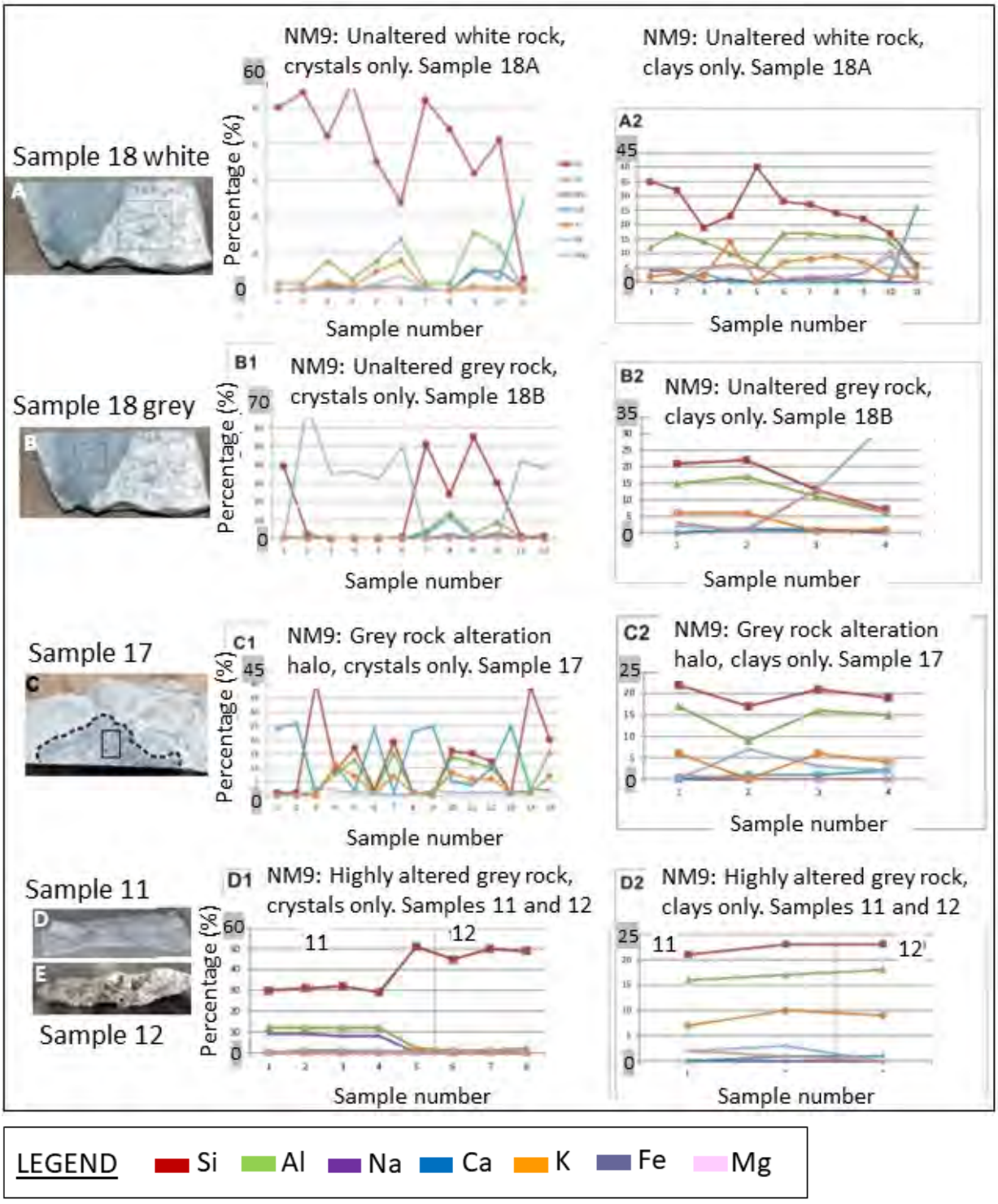

Figure 11: Summary of EDS results for the four tonalite samples between 3204 m and 3206.9 m depth.

6. Discussion

The presence of tonalite, an igneous, intrusive rock, within a TVZ hosted geothermal system such as Ngā Tamariki, is quite unique. Tonalite is of felsic composition, rich in feldspars and silica. The

feldspars are usually oligocase (Na-rich) or andesine (Na-Ca-rich) with <10% alkali feldspars (K-feldspar) and >20% quartz. However, the tonalite in Ngā Tamariki NM9 injection well is associated with magmatic-hydrothermal alteration representative of high-intermediate-sulfidation state epithermal mineralisation (Chambefort et al., 2017). Over the 6.8 m of core analysed we document the presence of quartz, alkali feldspar, and plagioclase feldspar primary minerals and hydrothermal alteration minerals of chlorite, illite, calcite, anhydrite, epidote, quartz, and adularia.

CO_2 mineral entrapment can be enhanced or inhibited by the availability of cations, reactive surfaces, host rock mineralogy, rock textures, voids, fractures, crystal size and crystal shape. Our multi-analytical approach has characterised host rock from injection well NM9 at Ngā Tamariki geothermal field. We documented;

- The presence of Ca-bearing minerals such as anhydrite, calcite and epidote, thus favouring chemical reactions and potentially facilitating CO_2 entrapment when in contact with CO_2-rich injectate fluid,
- Our EDS results document elemental composition variability over 6.8 m of core.
- Voids decrease with depth over the 6.8 m length of core,
- Connected voids are dominantly limited to isolated fractures in the RCE core and the crystal-rich fracture zones of samples NM9-11 and NM9-12,
- The dominance of crystals within the fracture zones of NM9-11 and NM9-12 provide abundant reactive surfaces for continued reactions to occur, when exposed to CO_2-rich fluid experiments,
- The open fractures provide space for future mineral growth and CO_2-mineral entrapment processes,
- Large isolated voids, such as those in the host rock of NM9-11, would increase the fluid storage capacity of the rock but fluid-rock interaction and/or CO_2-entrapment could only occur if fluid was able to reach the voids,

The pre-experimental characterisation of the tonalite core from NM9 injection well (step one) highlights the complex interplay of multiple parameters that will control permanent CO_2 entrapment. It also demonstrates the heterogeneity of the tonalite core over 6.8 m. These results emphasize why it is important to fully characterise the rocks in order to understand and predict how rocks of the same type, but at different depths, may react upon contact with CO_2-rich injectate. Rock variability within the same formation as shown in this study, will influence the rocks suitability for CO_2 uptake. By understanding the variable characteristics of formations in injection wells, the most ideal injection depth for CO_2 uptake can be better targeted.

Step two of the study involves the experimental laboratory work on the NM9 tonalite core characterised in this study. Step two will provide real-time data showcasing mineral reactions under known; (i) fluid-rock conditions, (ii) mineralogy, elemental composition and textures, (iii) density, void and fracture characteristics.

Following on from the post-experiment characterisation of the tonalite core, will be field geochemical and geophysical monitoring, and reactive transport and numerical modelling, using real rock data. These are all essential tools necessary to assess and predict the behaviour of CO_2 within the reservoir rocks. In collaboration with our industry partners, we are actively working on creating numerical models which can serve as a tool for investigating fluid-rock interaction parameters within reservoir-scale investigations. This comprehensive approach aims to unlock

insights into potential precipitation mechanisms, specifically those linked to NCG reinjection. This also allows us to identify primary and secondary minerals that have been identified in the various host rocks common in the diverse reservoir rocks prevalent within the TVZ geothermal systems.

Acknowledgements

This work was supported by the NZ Ministry of Business, Innovation and Employment for funding the work through MBIE Research Programme: UOAX2211 “Reversing Carbon Emissions in the Geothermal Energy Industry: Template for Emission-Intensive Industries”. We would also like to thank Mercury Energy for access to the core samples. The work by Lynne (2013) was supported by the Foundation of Research Science and Technology, project number 3608884. We also thank Mercury Energy (formerly Mighty River Power) for supplying the cored rock samples for the 2013 study.

REFERENCES

Arehart, G.B., Christenson, B.W., Wood, C.P., Foland, K.A., Browne, P.R.L., “Timing of volcanic, plutonic, and geothermal activity at Ngatamariki, New Zealand.” *Journal of Volcanology and Geothermal Research, 116*, (2002), 201-214.

Bignall, G., 2009. “Ngatamariki geothermal field geoscience overview.” *GNS Science Consultancy Report 2009/94*, (2009), 41 pp.

Brotheridge, J.M.A. “Surface manifestations – past and present – of the Ngatamariki Geothermal Field, Taupo Volcanic Zone, New Zealand.: *M.Sc. Thesis University of Auckland, New Zealand*, (1995), 154 pp.

Campbell, K.A., Rodgers, K., Brotheridge, J.M.A., Browne, P.R.L. “An unusual modern silica-carbonate sinter from Pavlova Spring, Ngatamariki, New Zealand.” *Sedimentology, 49(4),* (2002), 835-854.

Chambefort, I., Lewis, B., Wilson, C.J.N., Rae, A.J., Bignall, G., Coutts, C., Ireland, T.R. “Stratigraphy and structure of the Ngatamariki geothermal system: New U-Pb geochronology and its implications for Taupo Volcanic Zone evolution.” *Journal of Volcanology and Geothermal Research, 274*, (2014), 51-70.

Chambefort, I., Buscarlet, E., Wallis, I.C., Sewell, S., Wilmarth, M. “Ngatamariki Geothermal Field, New Zealand. Geology, geophysics, chemistry and conceptual model.” *Geothermics 59*, (2016), 266-280.

Chambefort, I., Lewis, B., Simpson, M.P., Bignall, G., Rae, A.J., Ganefianto, N. “Ngatamariki Geothermal system: Magmatic to Epithermal Transition in the Taupo Volcanic Zone, New Zealand.” *Economic Geology, 112*, (2017), 319-346.

Christenson, B.W., Mroczek, E.K., Kennedy, B.M., van Soest, M.C., Stewart, M.K., Lyon, G. “Ohaaki reservoir chemistry: Characteristics of an arc-type hydrothermal system in the Taupo Volcanic Zone, New Zealand.” *Journal of Volcanology and Geothermal Research 115*, (2002), 53-82.

Clearwater, J., Azwar, L., Barnes, M., Wallis, I., Holt, R. “Changes in Injection Well Capacity During Testing and Plant Start-Up at Ngatamariki.” *Proceedings World Geothermal Congress, Melbourne, Aus.* (2015).

Gíslason, S. R., Sigurdardóttir, H., Aradóttir, E. S., Oelkers, E. H. “A brief history of CarbFix: challenges and victories of the project's pilot phase.” *Energy Procedia 146,* (2018), 103–114.

Joselito P. Villena; Edwin H. Alcober; Romeo G. Jabonillo; Danilo H. Cruz; Jose Rufino S. Peñaranda; Dennis R. Sanchez; Guillen., H. V. “Evaluation of the Results of the Tongonan-1 CO_2 Gas Injection Project, Leyte, Philippines.” *In Proceedings World Geothermal Congress, 2005; Antalya, Turkey, 24-29 April 2005, (2005).*

Kaieda, H., Kubota, K., Wakahama, H., Ueda, A. “Field experiments for studying on CO_2 sequestration in solid minerals at the Ogachi HDR Geotheraml site Japan.” *34th Workshop on Geothermal Reservoir Engineering, SGP-TR-187,* (2009).

Kissling, W. M., Weir, G.J. “The spatial distribution of the geothermal fields in the Taupo Volcanic Zone, New Zealand.” *Journal of Volcanology and Geothermal Research 145, 136-150,* (2005).

Lewis, B., Chambefort, I., Rae, A., Bignall, G., Coutts, C. “Magmatic-hydrothermal alteration at Ngatamariki: implications for the deep roots of TVZ geothermal systems.” *Proceedings, 35th New Zealand Geothermal Workshop, Rotorua, New Zealand,* (2013).

Lynne, B.Y. “Scanning Electron Microscopy Pilot Study of core from NM9 well, Ngatamariki, New Zealand.” Institute of Earth Science and Engineering, University of Auckland (2013), 38 pp.

McGrail, B.P., Schaef, H.T., Ho, A.M., Chien, Y.J., Dooley, J.J., Davidson, C.L. “Potential for carbon dioxide sequestration in flood basalts”. *Journal of Geophysical Research, 111,* (2006), B12201, 1–13.

Matter, J.M., Takahashi, T., Goldberg, D. “Experimental evaluation of in situ CO_2-water-rock reactions during CO_2 injection in basaltic rocks: implication for geological CO_2 sequestration.” *Geochemistry, Geophysics and Geosystems, 8,* (2007), 1-19.

Mongillo, M.A., Clelland, L. “Concise listing of information on the thermal areas and thermal springs of New Zealand.” *Department of Scientific and Industrial Research, Geothermal Report 9, Wellington*. (1984), 228 pp.

Richard, M A. “The Puna Geothermal Venture Project Power for the Island of Hawaii.” *Geothermal Resource Council Transactions. Vol. 14,* (1990).

Snæbjornsdottir, S.O, Wiese, F., Fridriksson, T., Armansson, H., Einarsson, G.M., Gislason, S.R. “CO_2 storage potential of basaltic rocks in Iceland and the oceanic ridges.” *Energy Procedia, 63,* (2014), 4585–6000.

Yanagisawa, N. “Ca and CO_2 Transport and Scaling in the Hijiori HDR System, Japan.” *Proceedings World Geothermal Congress, Indonesia,* (2010).

Yücetaş I., Ergicay, N., Akin, S. “Carbon Dioxide Injection Field Pilot in Umurlu Geothermal Field, Turkey.” *Geothermal Resource council Annual Meeting,* (2018).

Geothermal Play Fairway Analysis (GPFA) - Part II: Texas/Gulf Coast Mechanisms of Heat Generation

Kevin McCarthy[1]*, Will Pettitt[1], Rich Priem[2]

[1] Baker Hughes [2] Priemere GeoTechnology

Keywords

Geothermal, Play Fairway Analysis (PFA), Exploration

ABSTRACT

Geothermal Play Fairway Analysis (GPFA) is an exploration process adopted to geothermal, that integrates data of critical risk elements inherent to that specific geothermal play type. The key function of GPFA is to reduce risk and increase focus for improving exploration success rates. GPFA begins at the regional/basin scale, and progressively focuses in on the play scale. It then examines the critical risk element data to highlight which play areas have the highest likelihood of success (prospects).

The outputs from the GPFA process are Common Risk Segment (CRS) & Composite Common Risk Segment (CCRS) Maps. CRS maps define areas that contain the same general Probability of Success (PoS) for each individual risk element based on the input data. Operator analyzed/ determined cutoff values or classes are then applied to each map with color assignments indicating high (red), medium (yellow) and low (green) risk areas for each element under consideration. Each individual CRS map is then composited into a single CCRS map.

Publicly available data on hundreds of thousands of boreholes in Texas and the Gulf Coast demonstrate excellent potential for geothermal electricity generation from either current or abandoned oil and gas wells. Near-surface geothermal resources, at depths of 3 km (9,842 ft) or less, are generally less than 150°C (302°F) in Texas. Economically feasible electricity generation is possible with available subsurface temperature conditions within reasonable depths—generally greater than 120°C (248°F) within 4 km (13,123 ft) – given the prolific oil and gas well drilling. Extensive data exists to depths as much as 8 km (26,246 ft), indicating temperatures in excess of 300°C (572°F).

When initiating an investigation into a new geothermal exploration area, a "high-level first pass" should be conducted for the heat resource before initiating the full GPFA process or detailed feasibility assessment. This is an important first step prior to conducting a detailed study so that you can determine if there is a heat resource to be exploited prior to investing significant time and effort on an extensive study. The initial step is to investigate for any temperature data to determine

geothermal gradients within the exploration area. This will usually be in the form of borehole temperature/completion logs from previously drilled oil and gas wells and any available publications. It is critically important in the GPFA process not to only identify areas of adequate geothermal (heat) resource but to also understand the mechanisms driving the existence of these geothermal gradients. Understanding the subsurface geology and mechanics of heat generation will allow the investigator to identify the most critical risk parameters particular to that prospect.

1. Introduction - Geothermal Systems

Geothermal fields are found throughout the world in a range of geological settings and are increasingly being developed as a significant long-term energy resource. Geothermal systems have distinct characteristics which are reflected in the chemistry of the geothermal fluids and their potential applications. However, they all have in common a heat source which drives water present in the upper sections of the Earth's crust into convection. Many geothermal resources can be used for space heating applications (e.g., urban district heating schemes, greenhouse heating, etc...) while higher temperature systems (>150°C) are used to generate electricity through the production of steam. Before moving into the application of GPFA, it is important to understand the defining characteristics of a “geothermal system”.

If you are involved with the geothermal world, you have likely heard the terms "hydrothermal" and "Geothermal Heat Pump", which are correlated with conventional geothermal systems. Additionally, terms like "Enhanced Geothermal Systems (EGS)" and "Advanced Geothermal Systems" which are linked to unconventional geothermal systems. While these are one way to "define" a geothermal system, we are not discussing that here. In this context, we are looking at the general characteristics that are associated with geothermal systems; liquid vs. vapor dominated, low or high temperature, sedimentary or volcanic, etc.

Geothermal systems are commonly classified by a series of descriptive terms:

Reservoir equilibrium state: This is the fundamental division between geothermal systems and is based on the circulation of the reservoir fluid and the mechanism of heat transfer. Systems in dynamic equilibrium are continually recharged by water entering the reservoir. The water is heated and then discharged out of the reservoir, either to the surface or to underground permeable horizons. Heat is transferred through the system by convection and circulation of the fluid. Systems in static equilibrium have minor to no recharge in the reservoir and heat is transferred only by conduction.

Fluid type: The reservoir fluid can be composed mainly of liquid water (liquid-dominated) or steam (vapor-dominated). In the majority of reservoirs, both steam and liquid water exist in varying proportions as two-phase. Liquid-dominated systems are most common, some which contain a steam cap which can expand or develop on exploitation as happened at Wairakei, New Zealand. Systems which discharge only steam are rare - the best known are Larderello, Italy and The Geysers, USA. Note that liquid-dominated systems are sometimes called water-dominated; this is not a good term since all hydrothermal fields are composed of water in either the liquid or vapor phase. Vapor-dominated systems are also referred to as steam fields.

Reservoir temperature: The temperature (or enthalpy) of geothermal reservoirs is an important parameter in terms of fluid chemistry and potential resource usage. Systems are commonly

described as low-temperature (<150°C) or high-temperature (>150°C). Low-temperature systems are used for "direct-use" applications (e.g., heating), while high-temperature systems can be used for electricity generation as well as direct-use applications.

Host rock: The rocks which contain the geothermal reservoir (the "host rocks") react with the geothermal fluid. As fluid-rock interactions determine the final composition of the geothermal waters and gases, a knowledge of the host rocks is important for application of geothermometers and understanding potential scaling problems if the field is developed. Volcanic, clastic-sedimentary, and carbonate-sedimentary rocks (and the metamorphic equivalents of these lithologies) all yield geothermal fluids with contrasting and distinct chemistries. If the subsurface geology is poorly understood, it may be possible to predict the lithologies from the water chemistry.

Heat source: The heat source for the system is a function of the geological or tectonic setting. If the heat flow is provided by a magma, then such systems are termed volcanogenic and are invariably high-temperature systems. Heat is not always supplied by magma, and a geothermal system can be generated in areas of tectonic activity. For example, heat may be supplied by the tectonic uplift of hot basement rocks, or water can be heated by unusually deep circulation created by movement of a permeable horizon or faulting. These are termed non-volcanogenic systems and include examples of both high and low-temperature reservoirs.

2. Geothermal Play Fairway Analysis (GPFA)

GPFA, an exploration process developed by the oil and gas industry and now adopted to Geothermal, integrates data of critical risk elements inherent to that specific geothermal play type (Nielson et al., 2015). The key function of GPFA is to reduce risk and increase focus for improving exploration success rates.

GPFA was first applied to petroleum systems and is now being developed for understanding geothermal systems. The elements required for a conventional petroleum play or “petroleum system” are a source rock, reservoir rock, migration pathway, and seal (Figure 1). To be considered a prospect (high PoS), the play must also contain structural or stratigraphic traps, and have a source rock sufficiently heated to generate hydrocarbons at a time – the critical moment – when all the other required elements (e.g., reservoirs, pathways, seals, traps) were in place.

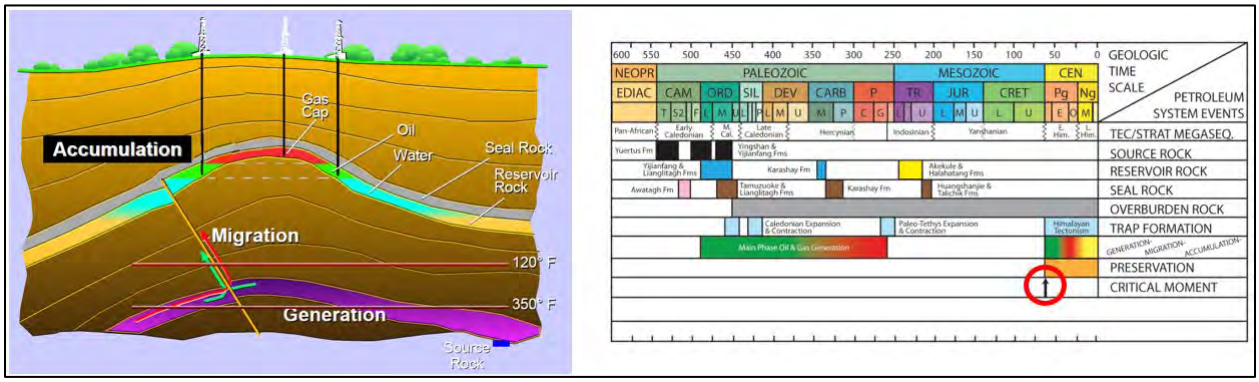

Figure 1: Elements required for a conventional petroleum play or “petroleum system”; source rock, reservoir rock, migration pathway, and seal.

The elements required for an unconventional petroleum play or "petroleum system" are inherently different from a conventional system as the source rock is also the reservoir (Figure 2). The low permeability organic rich shale reaches required thermal maturity to produce hydrocarbons which are then produced through hydraulic fracturing (artificial permeability network).

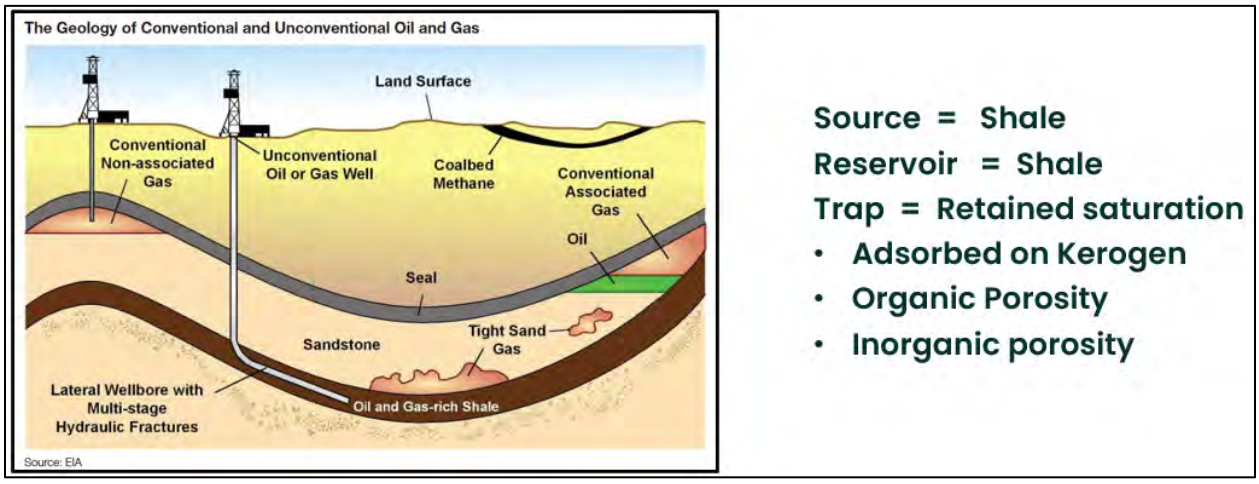

Figure 2: Elements required for an unconventional petroleum play or "petroleum system" are inherently different from a conventional system as the source rock is also the reservoir.

GPFA begins at the regional/basin scale, and progressively focuses in on the play scale (Figure 3). It then examines the critical risk element data to highlight which play areas have the highest likelihood of success (prospects).

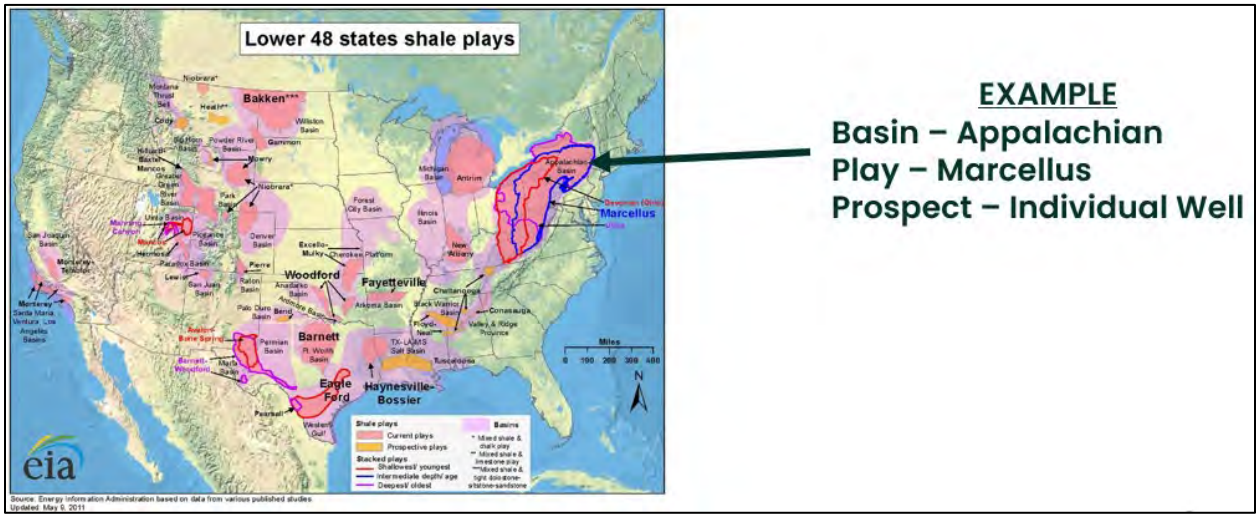

Figure 3: GPFA begins at the regional/basin scale, and progressively focuses in on the play scale (Jordan, Teresa et al., 2016).

3. Common Risk Segment (CRS) & Composite Common Risk Segment (CCRS) Maps

The outputs from the GPFA process are Common Risk Segment (CRS) & Composite Common Risk Segment (CCRS) Maps (Figure 4). CRS maps define areas that contain the same general Probability of Success (PoS) for each individual risk element based on the input data (Faulds,

James E., et al., 2021). Operator analyzed/ determined cutoff values or classes are then applied to each map with color assignments indicating high (red), medium (yellow) and low (green) risk areas for each element under consideration. Each individual CRS map is then composited into a single CCRS map. In conventional petroleum exploration, the risk elements are the reservoir, source, charge, and trap.

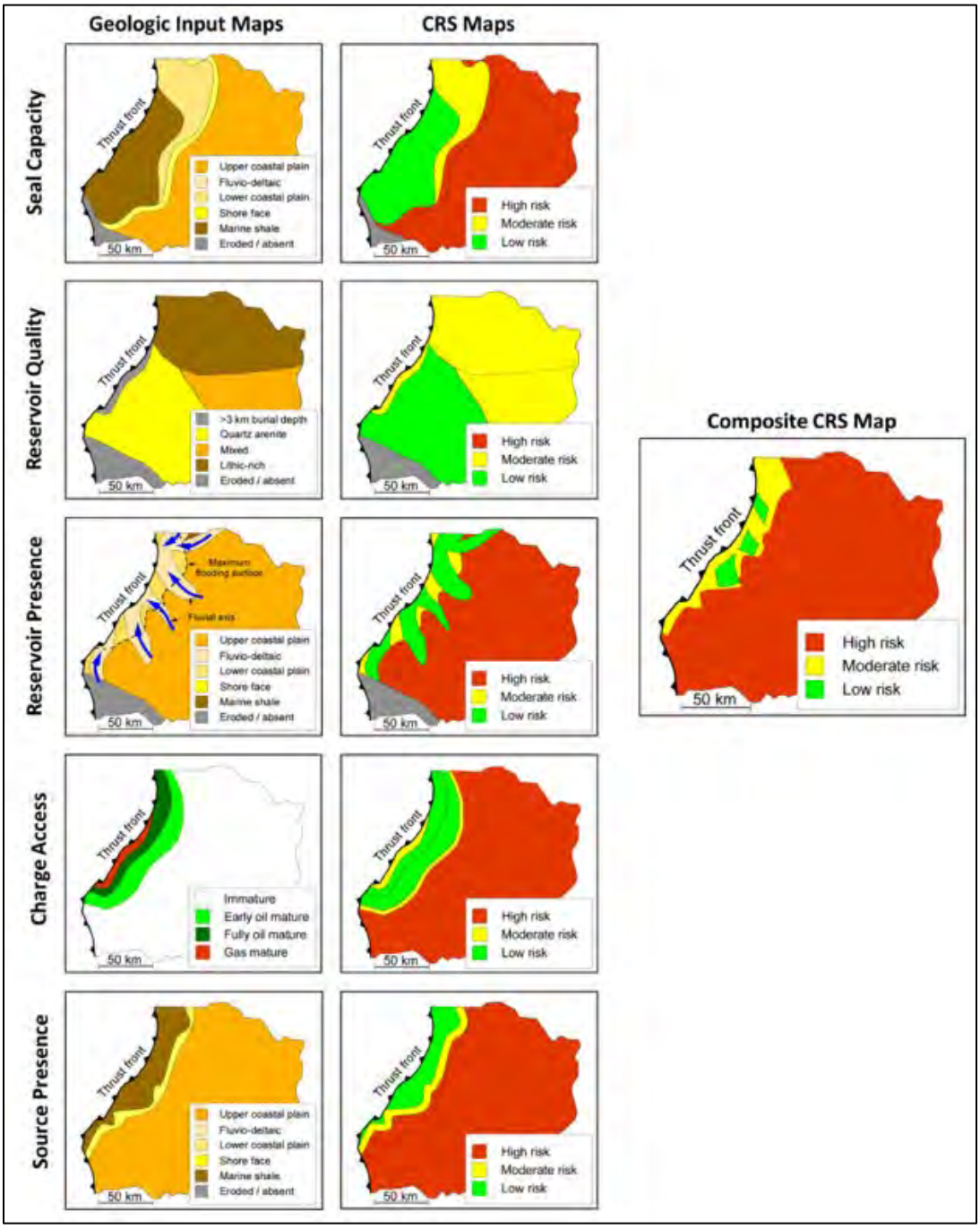

Figure 4: Common Risk Segment (CRS) & Composite Common Risk Segment (CCRS) Maps. CRS maps define areas that contain the same general Probability of Success (PoS) for each individual risk element. Source: Bump, 2021. Common risk segment mapping: Streamlining exploration for carbon storage sites, with application to coastal Texas and Louisiana

For an unconventional petroleum system, here are some examples of the critical risk elements and their associated risk cutoff values (Figure 5). Note the asterisk for EGS next to the % clay critical risk parameter. In an unconventional petroleum system that requires fracturing, if the % clay gets too high, the rock is too ductile, and the fractures will not remain open. The same would apply to EGS, which requires the generation of a fracture network.

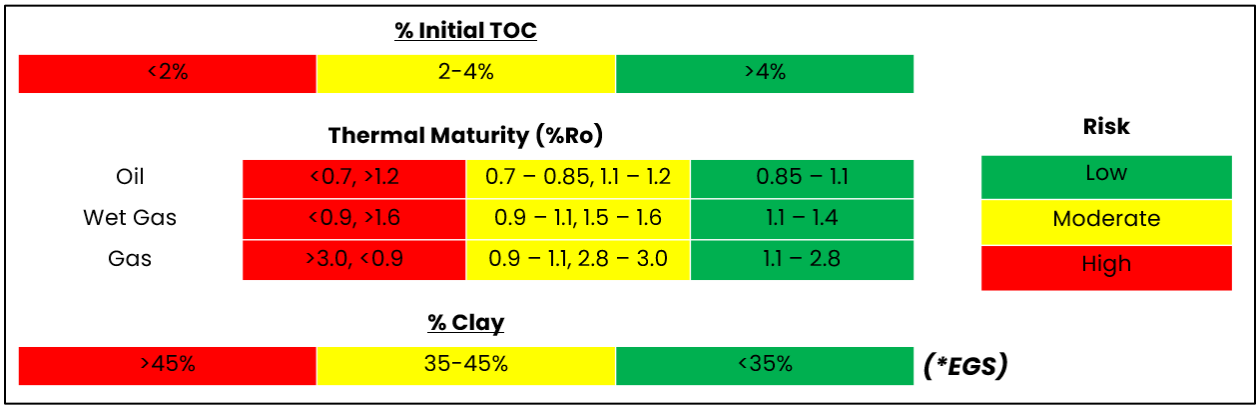

Figure 5: Critical risk elements and their associated risk cutoff values.

The CRS/CCRS workflow using heat flow (mW/m^2) as an example (Figure 6):

1. Gather risk element data
2. QC data
3. Import data into GIS system
4. Conduct interpolation to create continuous surface
5. Apply cutoff value colors (green, yellow, red)
6. Single layer risk CRS created
7. Integrate/stack individual CRS layers to create CCRS

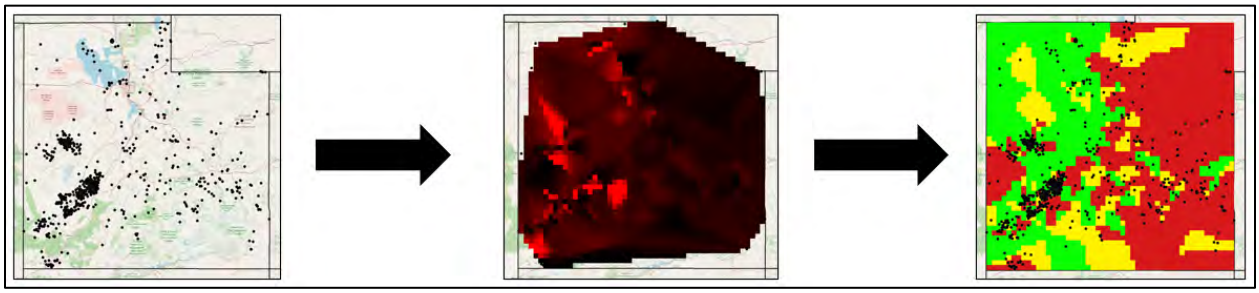

Figure 6: CRS/CCRS workflow using heat flow data (mW/m^2) as an example. Heat flow data points (mW/m^2) imported into GIS, followed by an IDW/TIN interpolation continuous surface and final risk value colors applied to form a single CRS layer.

4. Geothermal CRS Elements

In a geothermal play or system, the main exploration risk elements for this study are (a) heat resource, (b) permeability, (c) recharge and (d) seal.

a: Heat: While trivial that a high-level heat source is the principal requirement for an effective and economic geothermal system, accessibility depth for drilling and evaluation purposes, as well as interval complexity are important factors.

b: Permeability: Geothermal reservoirs are reliant on natural fracture permeability, associated with fracturing related to tectonic and magmatic processes, or through stimulated fractures if feasible.

c: Temperature recharge capacity of the migration of fluids within the geothermal system is critical to maintaining a long-lived resource with economic heatflow dynamics.

d: A seal keeps fluid from escaping or mixing with colder shallower aquifers. It also acts as a thermal insulator to the geothermal reservoir.

In the following GPFA example conducted in the Tularosa Basin (Bennett, Carlon R. et al., 2015), we see the individual CRS elements combined into a final CCRS map (Figure 7):

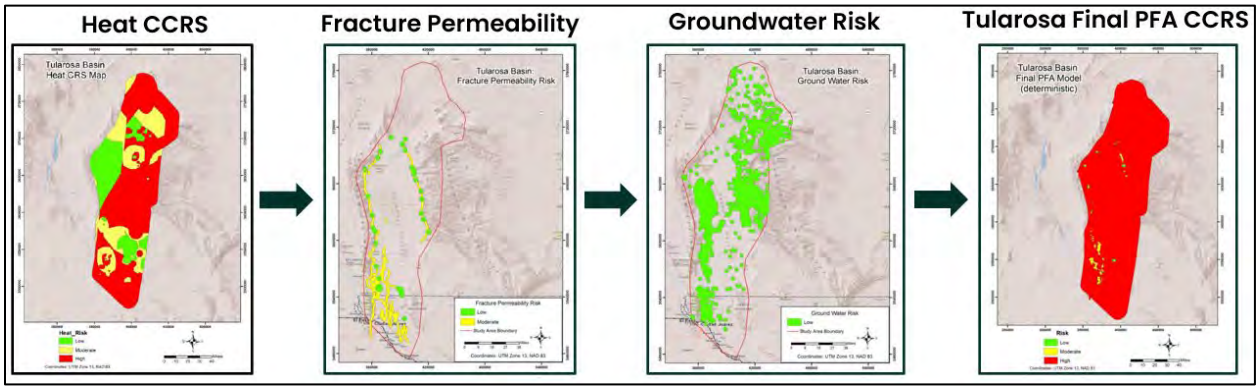

Figure 7: GPFA example from the Tularosa Basin. Source: Department of Energy, Office of Energy Efficiency and Renewable Energy (EERE), Geothermal Technologies Office DE-EE0006730; Innovative Play Fairway Modelling Applied to the Tularosa Basin.

Through the application of GPFA and screening for critical risk elements inherent to a functional geothermal system (heat, groundwater, and fracture permeability), this study was able to reduce an exploration area of approximately 6500 km2 into 8 specific high graded potential plays/target sites (Figure 8). These prospects represent areas where all the critical risk elements coincide with a low-risk determination.

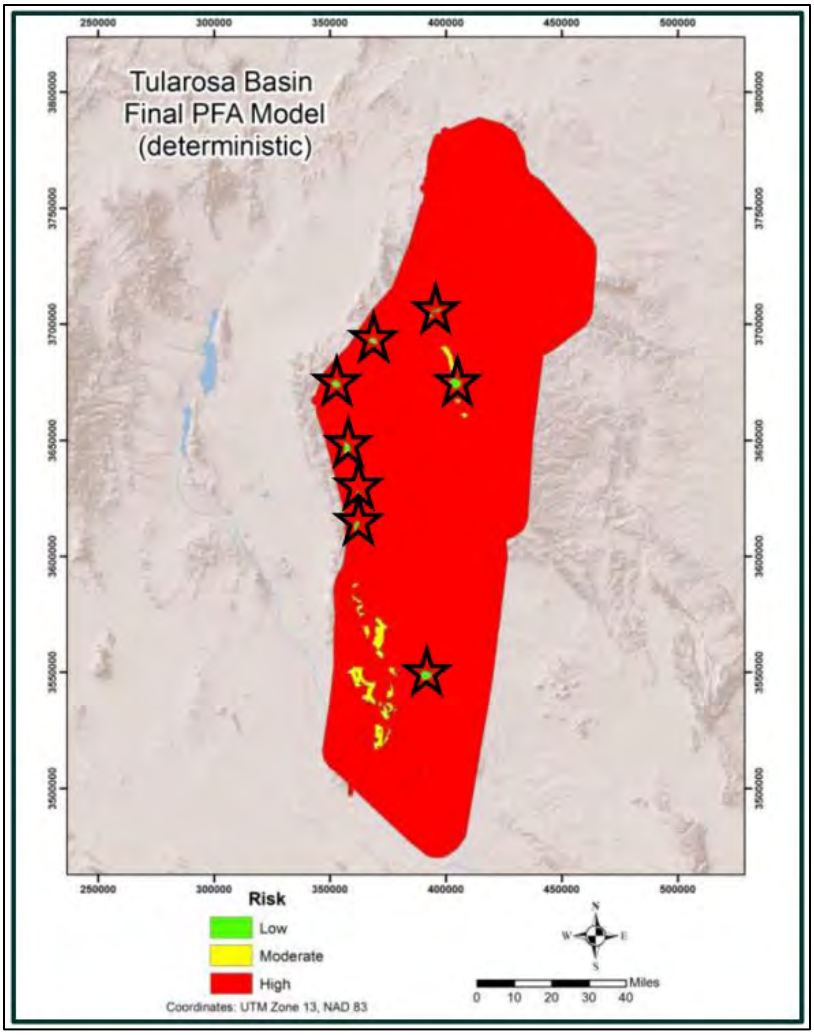

Figure 8: GPFA CCRS final map from the Tularosa Basin. Source: Department of Energy, Office of Energy Efficiency and Renewable Energy (EERE), Geothermal Technologies Office DE-EE0006730; Innovative Play Fairway Modelling Applied to the Tularosa Basin.

Here we present some example heat geothermal risk elements and their associated risk cutoff values:

1. Temp. Gradient °C/km
   - 0 °C/km – 35 °C/km = High Risk (Red)
   - 35 °C/km – 50 °C/km = Moderate Risk (Yellow)
   - > 50 °C/km = Low Risk (Green)
2. Quartz Geothermometer °C
   - 0 °C/km – 60 °C/km = High Risk (Red)
   - 60 °C/km – 80 °C/km = Moderate Risk (Yellow)
   - >80 °C/km = Low Risk (Green)
3. Heat Flow mW/m^2
   - 55 – 70 mW/m^2 = High Risk (Red)
   - 70 – 85 mW/m^2 = Moderate Risk (Yellow)
   - >85 mW/m^2 = Low Risk (Green)

The most important risk element for geothermal is heat; you can think of this as the equivalent to the source rock in petroleum systems. Without a source rock, there simply isn't a petroleum system to be investigated. Similarly, if you don't have the necessary heat resource, there is no functional geothermal system.

5. Hi-Fi Advancements

After understanding the basics of GPFA, we recommend advancing to more sophisticated and automated analysis with a high-fidelity solution. Again, leveraging the knowledge base of the petroleum industry, the results below (Figure 9) were produced using the Power Risk Optimizer from the Priemere Power Tools for ArcGIS (Help@Priemere.com). With the same data & parameters as above, the same eight Prospects (Hot/Go Spots) were identified.

However, the final hi-fi results can be classified at any desired level of detail, and there is greater resolution to consider with the six colors utilized. And as a further diagnostic aid, the polygon labels indicate the critical risk factor (CRF) as the element with the greatest impact within each area. These automated features facilitate rapid iteration on various models and parameters to achieve a more thorough and accurate understanding of the GPFA system.

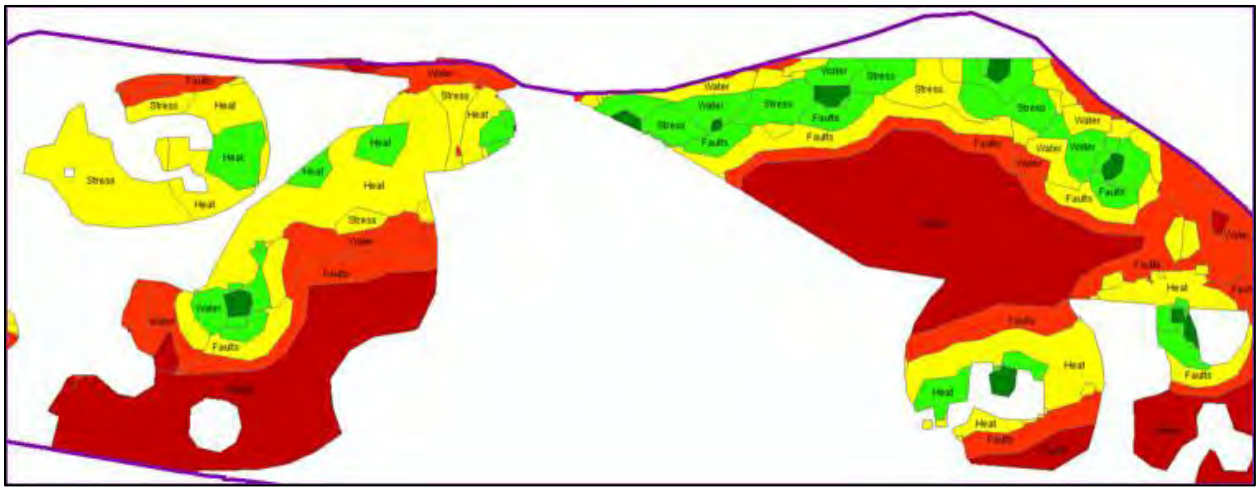

Figure 9: Hi-Fi GPFA example for the Tularosa Basin from the Priemere Power Risk Optimizer.

6. Initial GPFA Screening

When initiating an investigation into a new geothermal exploration area, a "high-level first pass" should be conducted for the heat resource before initiating the full Geothermal Play Fairway Analysis (GPFA) process or detailed feasibility assessment. This is an important first step prior to conducting a detailed study so that you can determine if there is a heat resource to be exploited prior to investing significant time and effort on an extensive study.

The initial step is to investigate for any geothermal gradient data that may be available within the exploration area. This will usually be in the form of borehole temperature logs from previously drilled oil and gas wells. In the United States, you can generally find this data across most geothermal exploration areas. An example resource for this is the Southern Methodist University (SMU) National Geothermal Data System.

This detailed database has provided the means to create some key geothermal maps in the United States, such as the Geothermal Map of North America (Figure 10), Heat Flow Map of the Continental U.S. (Figure 11) and the NREL Favorability of Deep Enhanced Geothermal Systems (Figure 12):

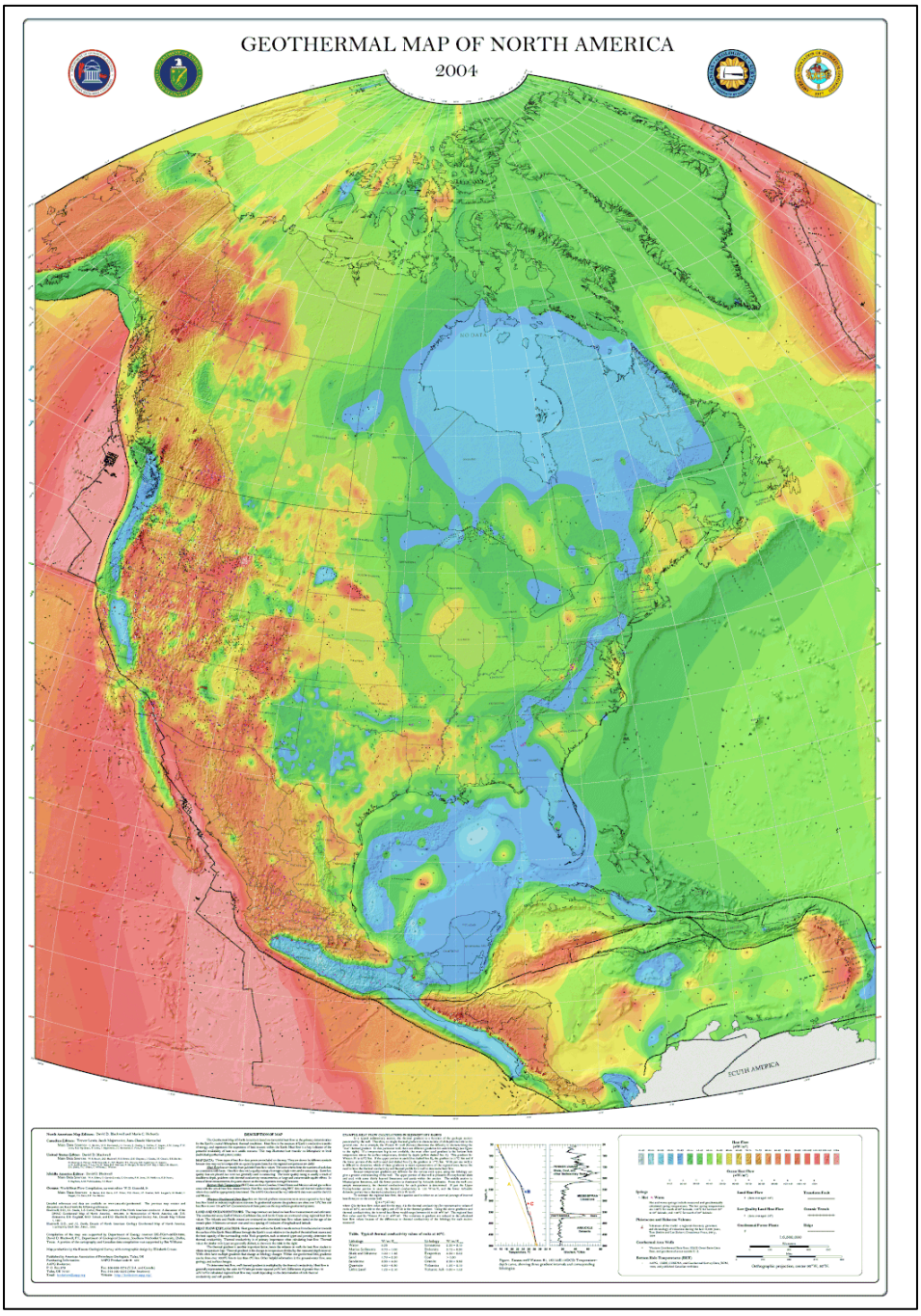

Figure 10: Geothermal Map of North America. Source: Blackwell, D.D., and M. Richards, Geothermal Map of North America, AAPG Map, scale 1:6,500,000, Product Code 423, 2004.

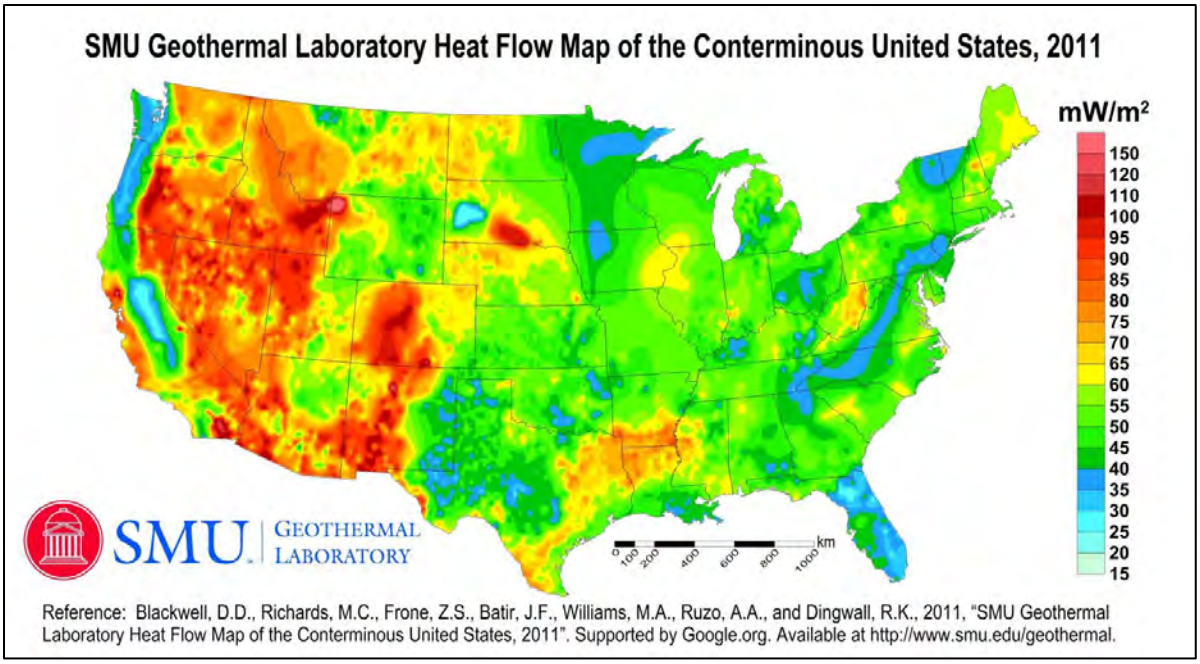

Figure 11: Heat Flow Map of the Continental U.S. Source: Blackwell, David, M. Richards, Z. Frone, J. Batir, A. Ruzo, R. Dingwall, and M. Williams 2011, Temperature at depth maps for the conterminous US and geothermal resource estimates, GRC Transactions, 35 (GRC1029452).

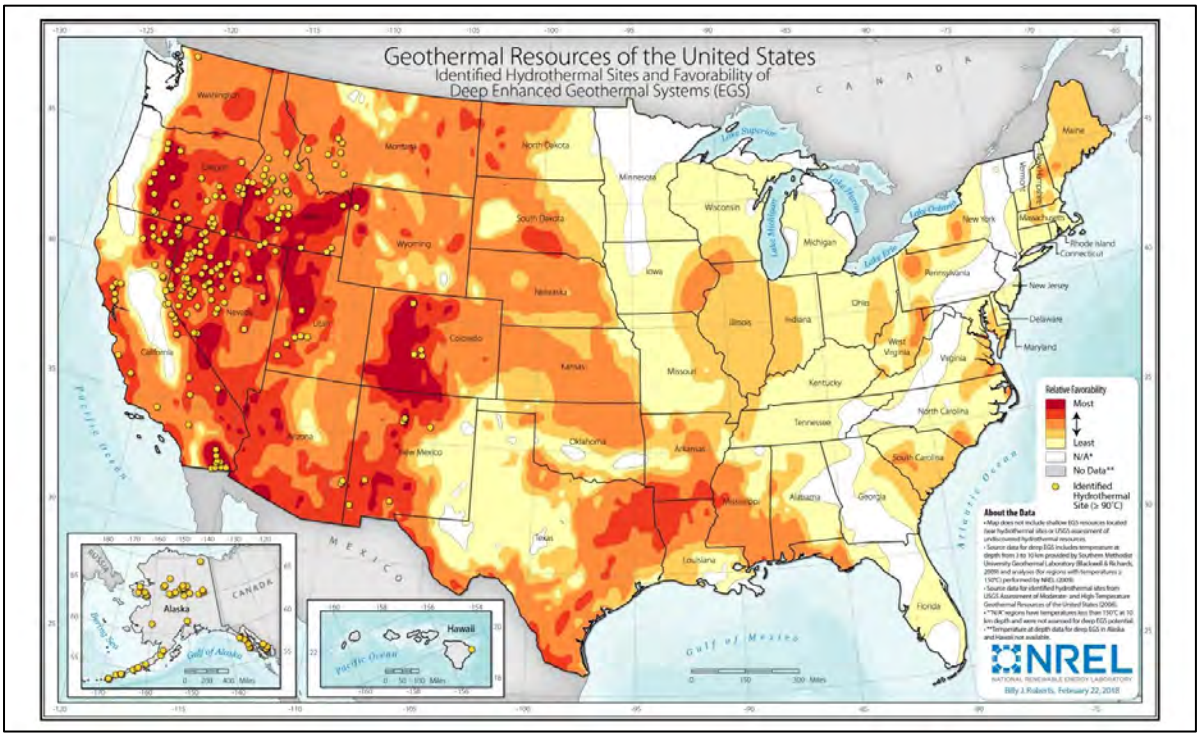

Figure 12: NREL Favorability of Deep Enhanced Geothermal Systems. Source: [NREL Geothermal Resources of the United States—Identified Hydrothermal Sites and Favorability of Deep Enhanced Geothermal Systems]

The main reason we want to look at geothermal gradients from these borehole temperature logs first is to determine if the exploration area is even suitable to geothermal development and economically feasible (Shervais, John W., et al., 2021). The previously described risk cutoffs generally applied to geothermal gradients are as follows:

Temp. Gradient °C/km

- 0 °C/km – 35 °C/km = High Risk (Red)
- 35 °C/km – 50 °C/km = Moderate Risk (Yellow)
- > 50 °C/km = Low Risk (Green)

Geothermal gradients > ~ 50 °C/km are amenable to large scale electricity/power generation and provide a temperature resource capable of supporting the full spectrum of geothermal applications. Between ~ 35 °C/km to 50 °C/km, geothermal low enthalpy/direct use applications are viable and will likely require an Organic Rankine Cycle (ORC), which includes additional costs. At gradients below ~ 35 °C/km, geothermal development is generally not viable. This is primarily due to two reasons; a) an appreciable heat resource is not present and b) you have to drill too deep to reach the required temperatures and therefore it becomes economically unfeasible since the largest cost associated with geothermal projects is drilling. For example, if you have to drill to 8-10 km just to reach 150 °C (which is the base temperature generally required for closed-loop systems and even higher temperatures for EGS), the drilling cost is too significant, making it difficult to attain an ROI within a reasonable timeframe. Notice in the NREL favorability map above, they didn't even consider areas where 150 °C were not reached by 10 km exactly for this reason.

For example, in a recent study a client was looking to investigate geothermal resource development in Louisiana (LA) for closed-loop applications. Prior to initiating a full GPFA study, a first high-level pass for the heat resource was conducted. The parish areas they were initially evaluating are shown in Figure 13.

Figure 13: Louisiana Parish Map. The exploration areas of interest are circled in red.

For the first pass, these parishes were evaluated from a temperature/geothermal gradient perspective (Figure 14 and 15):

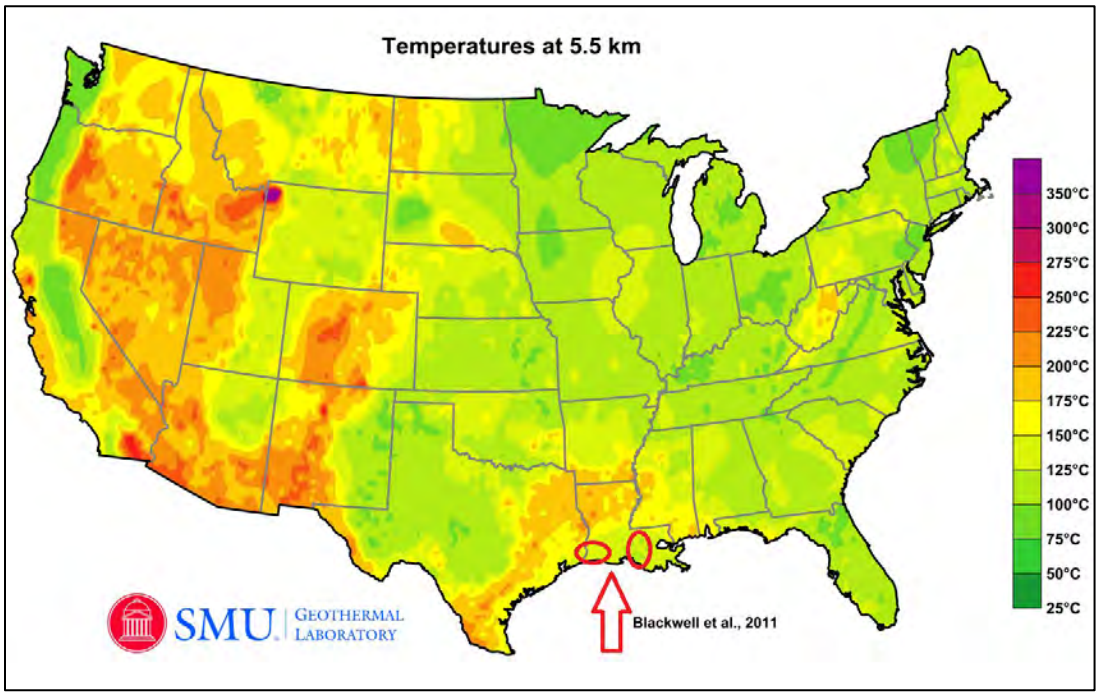

Figure 14: Temperatures at 5.5 km depth with identified counties in red. Source: Blackwell, D., Richards, M., Frone, Z., Ruzo, A., Dingwall, R., & Williams, M. (2011). Temperature-At-Depth Maps For the Conterminous US and Geothermal Resource Estimates. *GRC Transactions,* 35(GRC1029452).

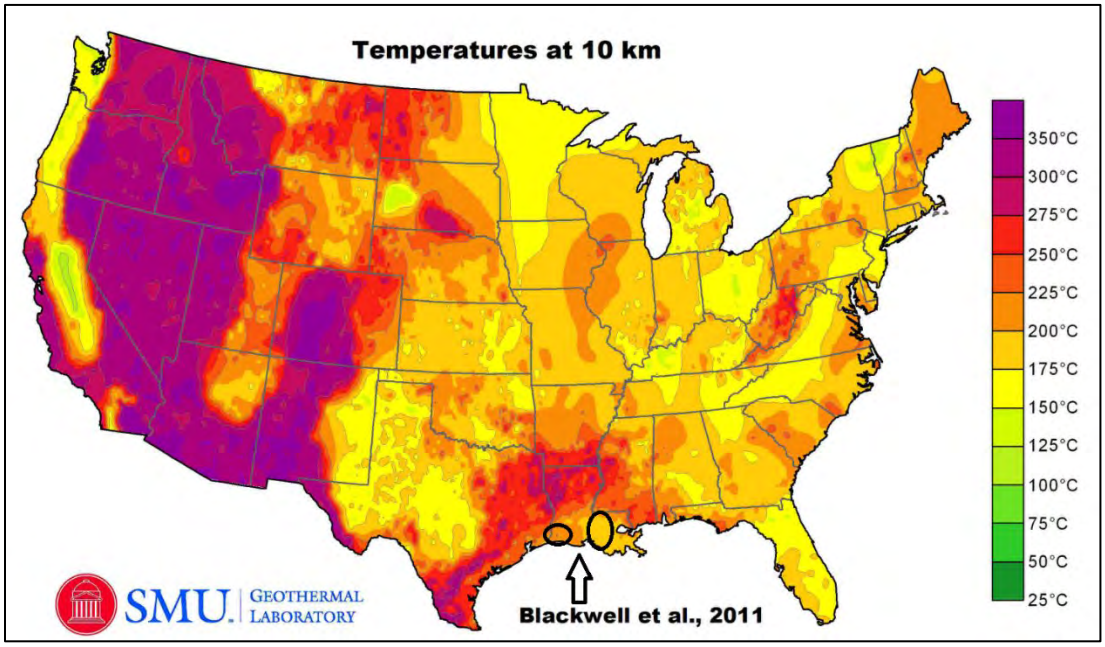

Figure 15: Temperatures at 10 km depth with identified counties in red. Source: Blackwell, D., Richards, M., Frone, Z., Ruzo, A., Dingwall, R., & Williams, M. (2011). Temperature-At-Depth Maps For the Conterminous US and Geothermal Resource Estimates. *GRC Transactions,* 35(GRC1029452).

As can be seen, the client would have to drill to ~10 km to even reach temperatures above 150 °C, base temperatures generally required for optimal closed-loop geothermal systems. This would require significant drilling costs that would make a geothermal project in the area economically unfeasible. This first-pass heat resource assessment provided the client key information that saved them significant time and money.

In this case, the client had interests across the state of LA, and as can be seen in the pictures above, the geothermal gradients in the northern part of the state are amenable to geothermal development.

The geothermal regimes between Northern & Southern LA are completely different from each other due to the Sabine and Monroe Uplifts in the north. These resulted in igneous intrusions that have higher radiogenic heat production (RHP) that provide higher heat flow and also have higher thermal conductivities, creating higher present day geothermal gradients in northern LA. These are absent to the south, where geothermal gradients are significantly lower. Additionally, there are large salt domes present in northern LA and not present in southern LA. Salt domes act as "thermal wicks" and are very efficient at wicking heat from its deeper base up to the top of the salt dome, resulting in locally higher temps at shallower depths.

7. GPFA Screening Applied to The Texas/Gulf Coast Region

Texas produces more oil and natural gas than any other state and to date remains the largest producer of these natural resources, with approximately 4 million barrels per day (MMbbl/d) of oil and more than 20 billion cubic feet per day (Bcf/d) of gas. There is no other state or region worldwide which has been as extensively explored or drilled for oil and natural gas as Texas. Currently, there are ~187,401 active oil wells and 98,709 active gas wells producing oil and natural gas in the state, according to the Railroad Commission of Texas. Additionally, over 7000 of these wells have been abandoned and require significant financial expenses to properly plug and decommission. The assessment supports the imperative need for these wells to be analyzed and assessed for their significant geothermal energy resource potential as an extension of the well life and return on investment of deployed capital, as well as benefiting corporate and societal carbon neutrality goals.

As previously stated, the most critical GPFA element is the heat resource, which is intimately tied to the existing geothermal gradient. In Texas and the Gulf Coast Region, areas with the highest geothermal gradients are found in Southwest Texas (Eagle Ford) and East Texas/Northwest Louisiana (Haynesville), as depicted in the regional geothermal gradient (°C/km) CRS map (Figure 16). The cutoffs applied in this CRS map are as follows: 0-35 °C/km (red) = no geothermal potential, 35-50 °C/km (yellow) = potential for low enthalpy/direct use applications, 50-100 °C/km (green) = electricity/power generation potential.

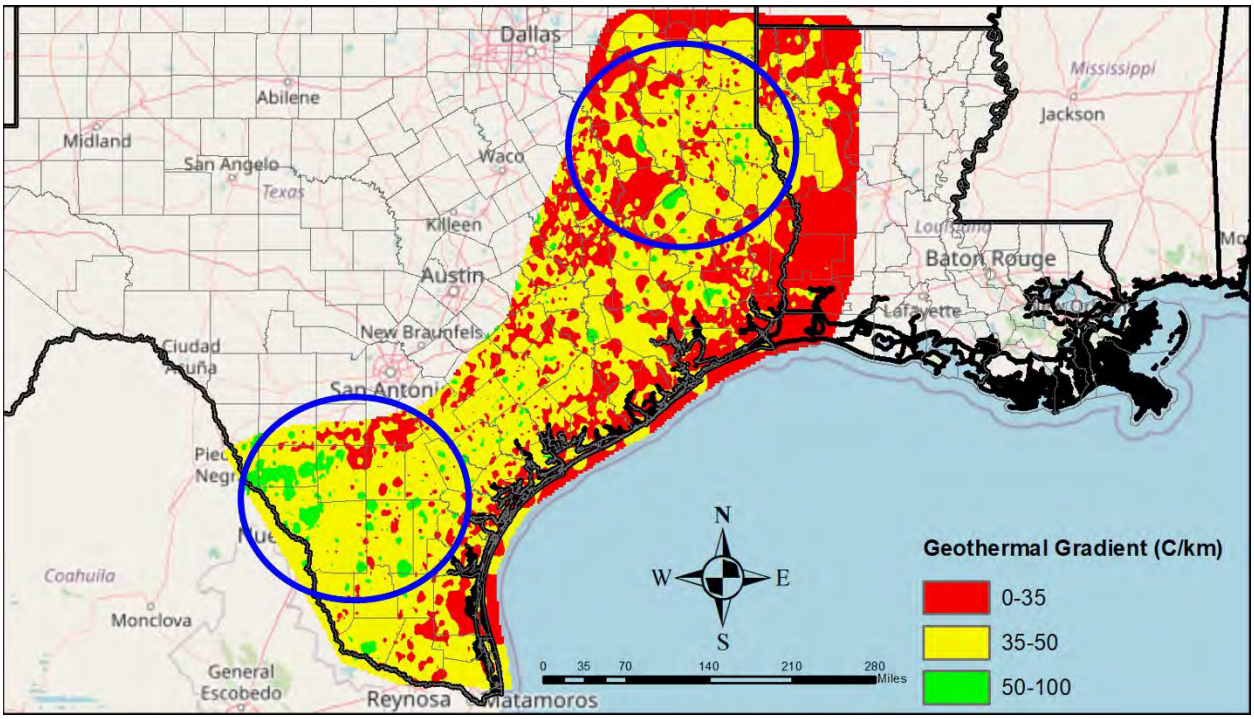

Figure 16: Regional TX/LA Geothermal Gradient CRS Mapping.

The mechanisms behind these two elevated geothermal gradient regions are different. In the Northeast, as can be viewed below (Figure 17), the Haynesville region heat flow values are in excess of 60 – 85 mW/m^2, which is anomalously high compared to the surrounding region. This higher heat flow is attributed to greater radiogenic heat production (RHP) in the igneous basement rocks and the presence of salt domes/diapirs, which have a thermal conductivity 2 to 4 times greater than any other sedimentary rocks (Gray and Nunn, 2010).

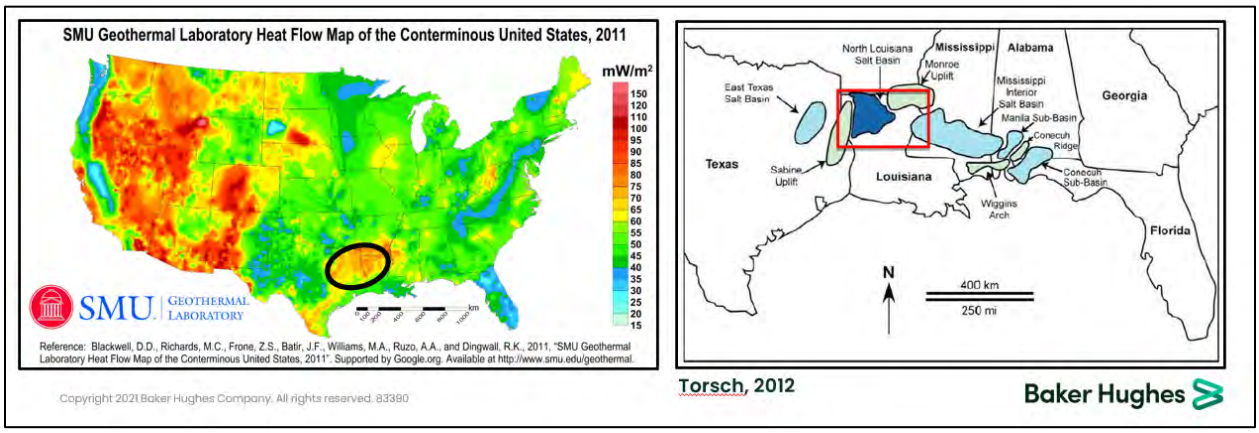

Figure 17: Haynesville Geothermal Potential.

The salt diapirs are of particular interest in geothermal development and exist across the Haynesville region, as shown in the map cross section A-A´ (Figure 18).

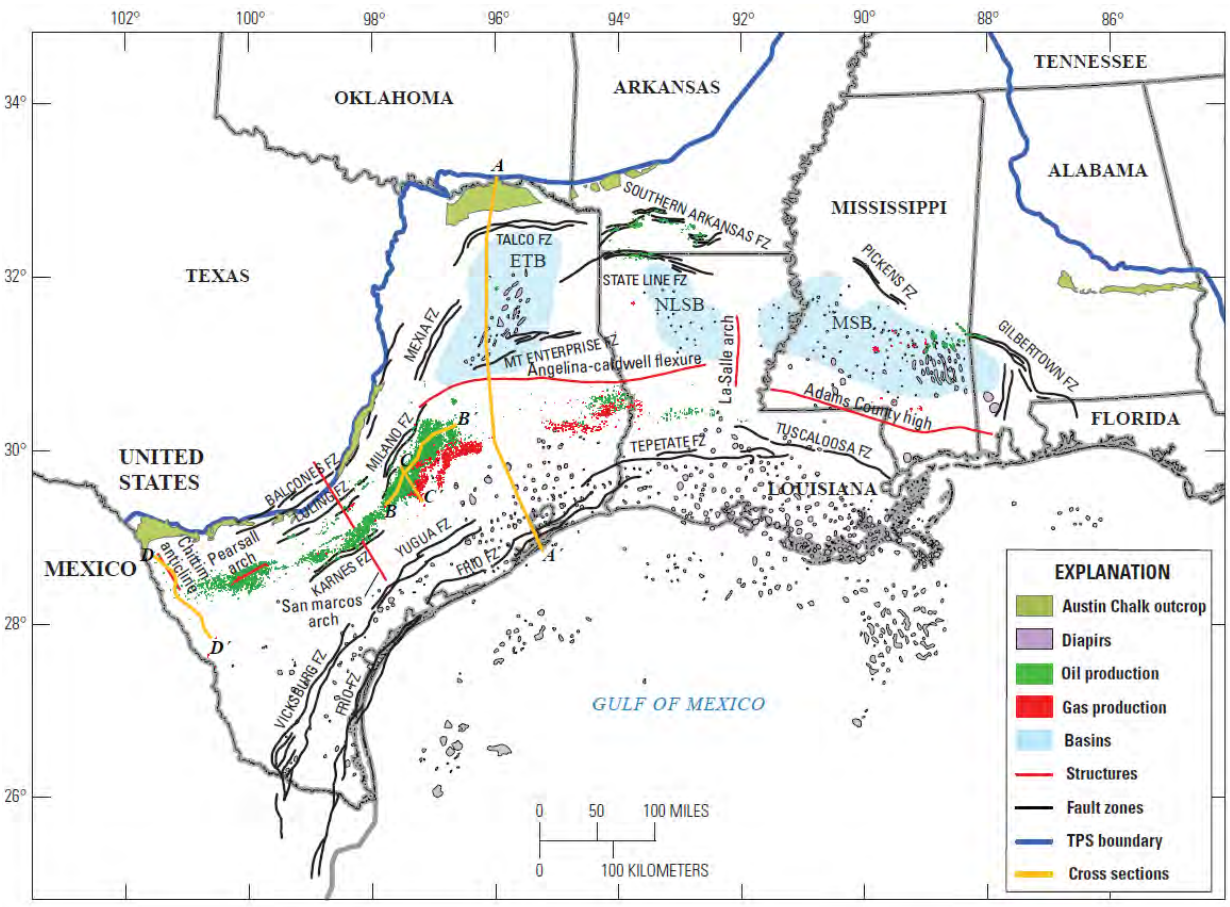

Figure 18: Map cross section A-A´ showing the location of salt diapirs (Pearson, 2012).

When viewing the cross section A-A´, it can be seen these salt diapirs are large vertical columnar structures that can extend to depths nearing 10 km and upwards to the near surface (Figure 19). These high thermal conductivity diapirs can act as “thermal wicks”, where they capture or “wick” much higher temperatures near their base to the top of the diapir. There will be some heat loss along the upward flow of the diapir but due to their high thermal conductivity/heat transfer capability, much higher temperatures can be “wicked” up to the top of the diapir, creating a localized elevated geothermal gradient that can be significantly higher than the surrounding area. In viewing individual well data, areas near these diapirs can often have geothermal gradients between 60-90 °C/km, whereas ambient background for the region is ~ 35 – 40 °C/km. While drilling into a diapir would need to be avoided due to their ductile/plastic nature, higher geothermal gradients could be exploited around them for geothermal energy. The elevated geothermal gradients would reduce drilling costs to attain required functional temperatures and provide greater energy production, although more research must be applied in understanding the extent of this localized diapir effect.

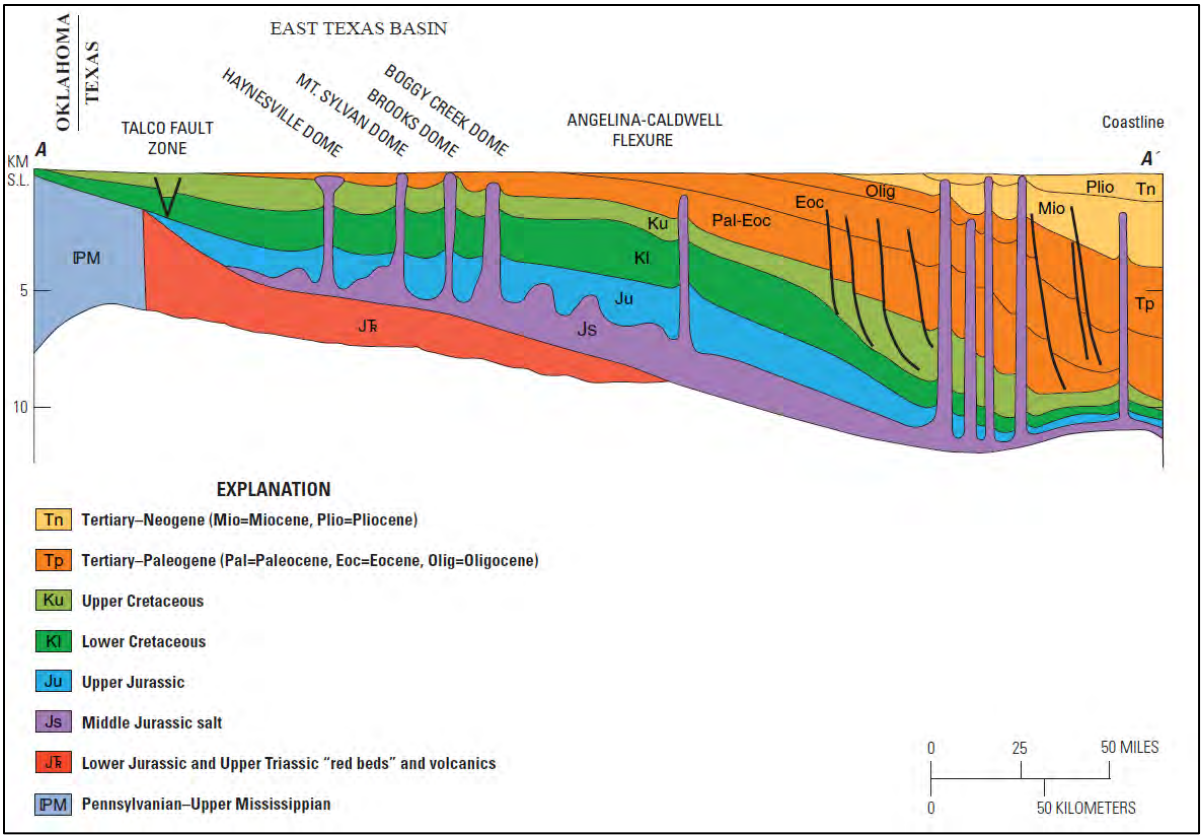

Figure 19: Cross section A-A´ with salt diapir structures from OK to the TX Gulf Coast (Pearson, 2012).

As demonstrated in the NREL Geothermal Favorability Map, the vast majority of Haynesville oil and gas wells depicted below (Figure 20) lie within a high geothermal favorability area, with bottom hole temperatures that are amenable to closed-loop applications and excellent candidates for repurposing.

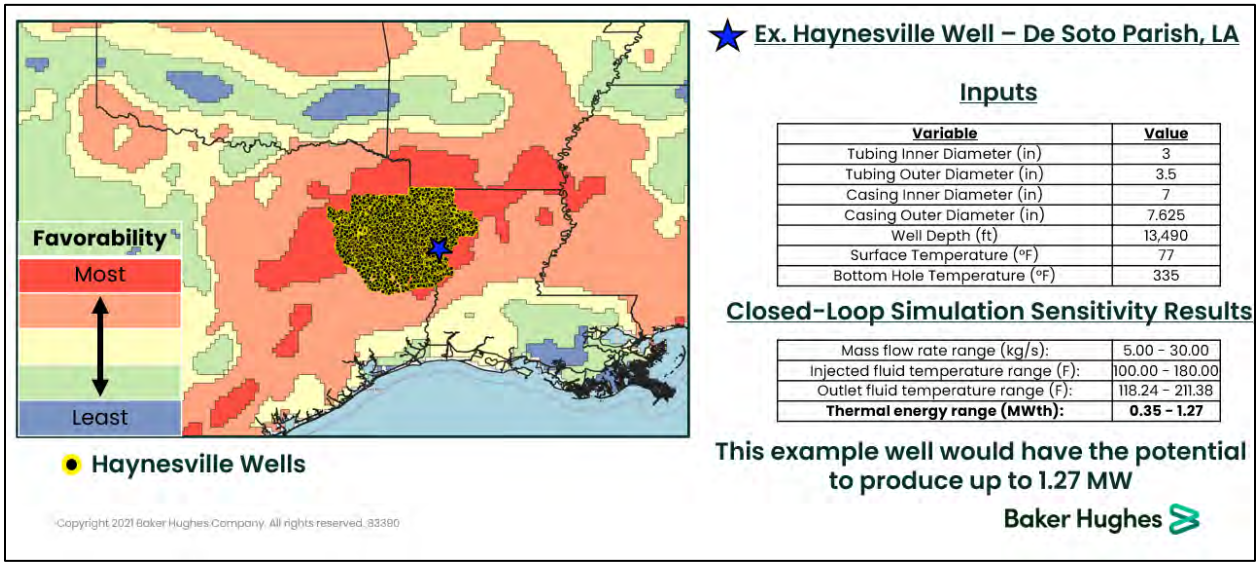

Figure 20: Haynesville Geothermal Potential – Closed-Loop Applications

The example well shows potential to produce up to 1.27 MWth and with thousands of wells like it within the Haynesville region, the potential for large scale power generation is significant.

The mechanism for the higher geothermal gradients in Southwest Texas (Eagle Ford) is likely tied to geopressured zones that are known to exist along the Texas Gulf Coast/Gulf of Mexico region. When reaching overpressure levels (>.70 psi/ft) due to rapid deposition and compaction, hot fluids can be driven upward along fault planes, resulting in elevated geothermal gradients. This was shown in the following two figures (Figure 21 & 22), where a study clearly demonstrated the correlation between depth to overpressure and geothermal gradients. Where the depth to top of overpressure was shallower, the depth to 300 °F was also less, resulting in elevated geothermal gradients.

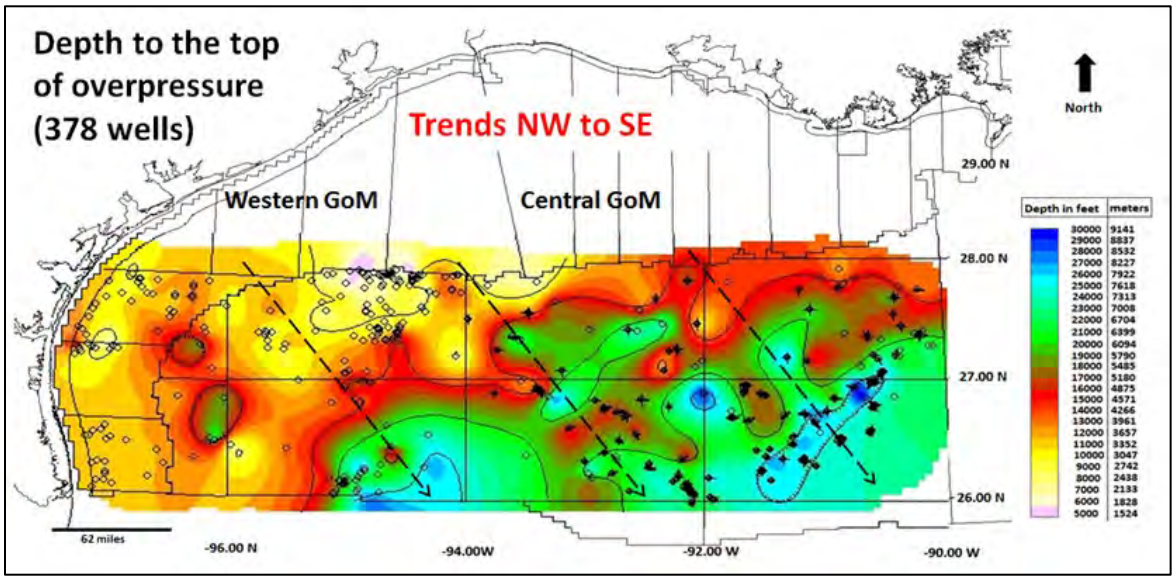

Figure 21: Depth to the top of overpressure computed from 378 GoM wells (Cornelius, 2020).

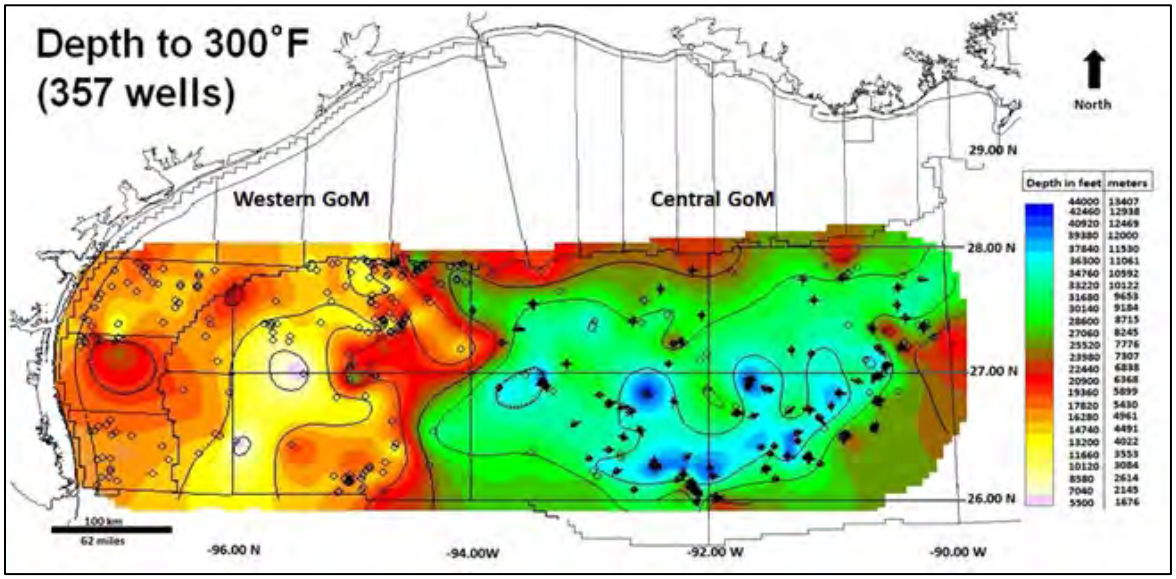

Figure 22: Depth to 300° F computed from 357 GoM wells (Cornelius, 2020).

Additionally, applying the NREL Geothermal Favorability Map to the Southwest Texas Eagle Ford Region (Figure 18) and some example well data from the Enverus DrillingInfo Database, it can be seen that many existing wells are in high geothermal favorability areas that are also amenable to repurposing from oil and gas into geothermal wells.

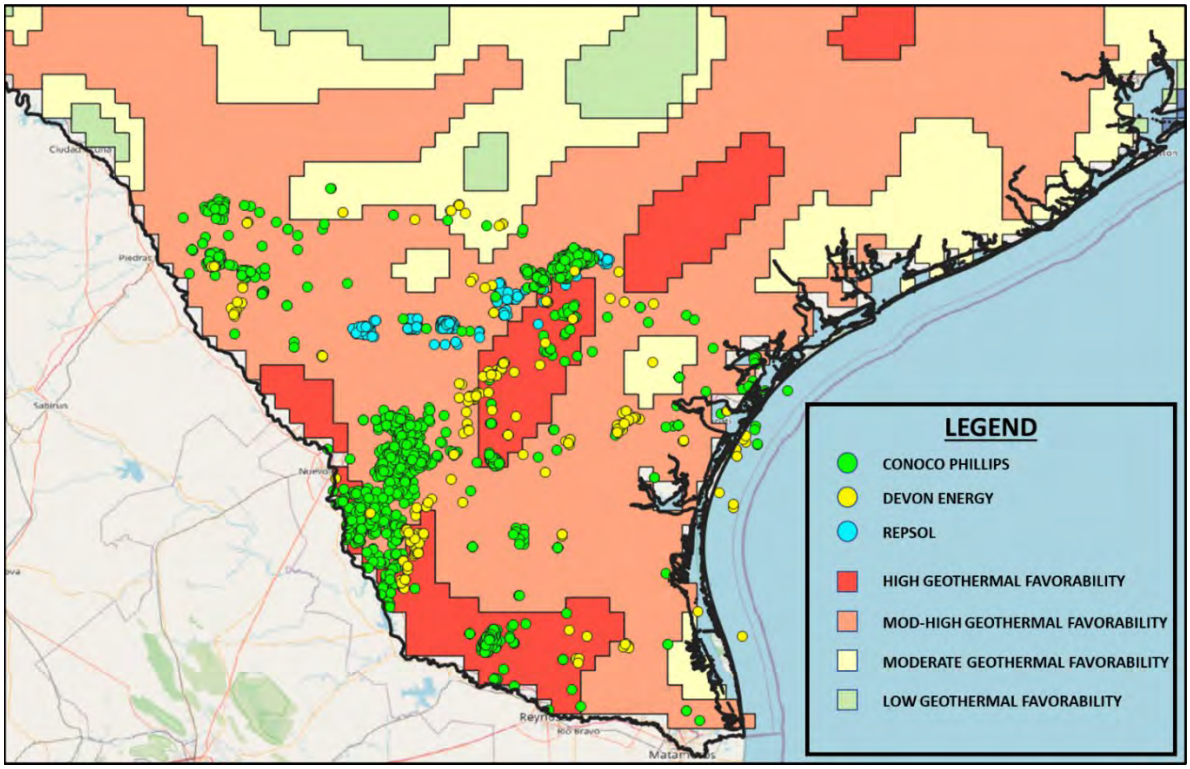

Figure 23: Southwest Texas (Eagle Ford) Geothermal Potential – Repurposing and Closed-Loop Applications

This clearly demonstrates an exploitable geothermal heat resource CRS element, which would then be combined with CRS maps for permeability, recharge, and seal to create a composite CCRS map identifying locations within these regions with functional geothermal systems that have potential for large scale power generation.

8. Conclusions

Geothermal resources have been recognized for some time as a possible significant source of energy but to date have seen marginal increases in their development and application. Much of this is attributed to the substantial upfront costs associated with geothermal projects coupled with a lack of reservoir characterization. While the resource potential is recognized, investors have been hesitant to proceed with these high risk, long return on investment (ROI) scenarios.

GPFA will provide significant value in geothermal exploration by:

- Reducing Exploration Risk
- Increasing % Probability of Success (PoS)
- Increasing the Return on Investment (ROI)

Though many cost reducing technologies are being developed in the geothermal industry right now, continued refinement and development of GPFA workflows and their associated risk reduction will continue to increase investor confidence and support the full-scale growth of geothermal in the coming energy transition.

REFERENCES

Bennett, Carlon R., et al. The Convergence of Heat, Groundwater & Fracture Permeability. Innovative Play Fairway Modelling Applied to the Tularosa Basin Phase 1 Project Report. No. Phase 1 Final Report. Ruby Mountain Inc., Salt Lake City, UT (United States), 2015.

Bump, Alexander P., Susan D. Hovorka, and Timothy A. Meckel. "Common risk segment mapping: Streamlining exploration for carbon storage sites, with application to coastal Texas and Louisiana." International Journal of Greenhouse Gas Control 111 (2021): 103457.

Cornelius, Sharon & Emmet, Peter. (2020). Relationship between Geothermal and Geopressure Gradients in the Western Gulf of Mexico (expanded abstract for GeoGulf 20, annual meeting of the Gulf Coast Association of Geological Societies to be held in October, 2020 in Lafayette, Louisiana).

Faulds, James E., et al. Discovering Blind Geothermal Systems in the Great Basin Region: An Integrated Geologic and Geophysical Approach for Establishing Geothermal Play Fairways: All Phases. No. DOE-UNR-06731-01. Univ. of Nevada, Reno, NV (United States); ATLAS Geosciences, Inc., Reno, NV (United States); US Geological Survey, Menlo Park, CA (United States); Hi-Q Geophysical, Inc., Ponca City, OK (United States); Innovate Geothermal Ltd, Vancouver (Canada); Utah Geological Survey, Salt Lake City, UT (United States), 2021.

Gray, T. A., and J. A. Nunn, 2010, Geothermal Resource Assessment of the Gueydan Salt Dome and the Adjacent Southeast Gueydan Field, Vermillion Parish, Louisiana: Gulf Coast Association of Geological Societies Transactions, v. 60, p. 307-323.

Jordan, Teresa E., et al. Low Temperature geothermal play fairway analysis for the Appalachian basin: phase 1 revised report November 18, 2016. No. DE-EE0006726. Cornell Univ., Ithaca, NY (United States), 2016.

Nielson, Dennis L., et al. "Geothermal play fairway analysis of the Snake River Plain, Idaho." Proceedings of the 40th workshop on geothermal reservoir engineering. Stanford. 2015.

Pearson, K. (2012). Geologic models and evaluation of undiscovered conventional and continuous oil and gas resources: Upper Cretaceous Austin Chalk, U.S. Gulf Coast. U.S. Department of the Interior, U.S. Geological Survey.

Priem, Richard M. Priemere Power Tools for ArcGIS. 2004-2023.

Shervais, John W., et al. Play Fairway Analysis of the Snake River Plain, Idaho. No. DOE-USU-0006733. Utah State Univ., Logan, UT (United States), 2021.

Fracture Permeability in Basement Greywacke for Supercritical Geothermal Drilling Planning

Sarah D. Milicich[1], Cécile Massiot[1], Isabelle Chambefort[1], Drestanta Yudha Satya[2]

[1]GNS Science, New Zealand

[2]Mercury NZ Ltd., New Zealand

Keywords

Basement greywacke, fractures, resistivity borehole image, outcrop, supercritical

ABSTRACT

Supercritical geothermal resources have potential to decarbonise industry and power sustainable economic growth opportunities. It is inferred that fractured, low matrix-permeability metasedimentary basement rocks (greywacke) that underly much of the Taupō Volcanic Zone (TVZ), New Zealand, could host supercritical geothermal resources. These rocks have complex fracturing patterns resulting from a long history of deposition, burial, faulting, and hydrothermal activity. Supercritical fluid circulation will likely be through fractures, so it is important to understand fracture distribution and fracture permeability in greywacke. A resistivity image from a >2 km-deep well in the Kawerau Geothermal Field provide the deepest fracture dataset collected in TVZ greywacke. The borehole observations are complemented by structural information from outcrops that are not hydrothermally altered.

Observations at two outcrops of low-grade metasediments and schist show that metamorphic veins are pervasive, of varied orientation, sometimes 10s meters long, and areal density can vary a lot over 10s meters. Parameters such as faulting seem to have a larger influence on vein density than rock type or metamorphic grade.

In the borehole image, potentially permeable fractures have orientation consistent with current tectonics. Resistive (mineralised) fractures have moderate dip magnitude and no preferred strike orientation, consistent with them being mostly of metamorphic origin. Conductive fractures are interpreted as having a combination of metamorphic and tectonic origins, with some likely to have been of metamorphic origin reactivated under current tectonics. Overall, there are more fractures in sandstone than mudstone, but this is less pronounced for conductive (potentially permeable) fractures than for resistive fractures (mineralised) or resistive fractures with conductive halo (potentially permeable). Differences between lithologies are less pronounced when considering volumetric fracture densities. Lithological controls on fracturing differ amongst the three

permeable zones. The two minor permeable zones are in intervals of sandstone, mudstone and interbedding mixes. The third, major permeable zone is in dominantly sandstone and an interbedded mixture of sandstone and mudstone. Potentially permeable fractures of high thickness (>20 mm) are more common within the two minor feed zones than outside feed zones. Fracture density is higher in the major feed zone than outside feed zones.

When considering both outcrop and borehole image fracture data, overall, faults and fractures consistent with current tectonics seem to matter more than lithology for permeability. The veins of varied orientations observed in outcrops seem to remain in the geothermal reservoir (i.e., the resistive fractures), and the permeable fractures in the geothermal system may be either new ones or metamorphic discontinuities (veins, layering boundaries) reactivated under current tectonic stresses.

1. Introduction

Future deep supercritical geothermal exploration and utilisation in New Zealand will likely be in metasedimentary basement rocks (greywacke) that underly much of the Taupō Volcanic Zone (TVZ; Te Ahi Tupua), New Zealand. Greywacke has a complex history of sedimentation, metamorphism, rifting, and hydrothermal activity, with fractures formed at various stages. Intact greywacke has low matrix porosity and permeability (Melia et al., 2022; Mielke et al., 2016) so fluids dominantly circulate through fractures. Given that greywacke is a strong rock (Melia et al., 2022), it is likely that pre-existing discontinuities that are critically stressed, i.e., well oriented for slip with regard to current in-situ stress, are being reactivated during rifting, with additional fractures potentially created. In geothermal reservoirs, hydrothermal alteration may infill and/or dissolve fracture infill. It is therefore important for current and future geothermal development in New Zealand to understand the potential effects of greywacke rock type on fracture permeability in the TVZ.

Currently, two geothermal fields production reservoirs are hosted in greywacke: Kawerau in the TVZ and Ngāwhā in Northland, where permeability is controlled by fractures and faults due to very low matrix porosity. In this paper, we assess fracture characteristics and permeability as a function of greywacke rock types interpreted from a borehole resistivity image at the Kawerau Geothermal Field. Borehole image interpretations are put in the context of outcrop observations of non-hydrothermally altered greywacke near Whakatāne and low-grade schist in the South Island at Rarangi (Figure 1).

Borehole images provide a narrow (<0.5 m width) but long (hundreds of meters) observations of layers and fractures directly in geothermal reservoirs, that can be linked to other downhole measurements to assess the fractures origin, characteristics and permeability potential. Hydrothermally altered greywacke outcrop analogues are scarce in New Zealand, hence the use of outcrops near the Kawerau Geothermal Field that have not experienced the effects of a geothermal system.

In this study, we have quantitatively assessed fractures in a 907 m-long resistivity borehole image from a >2 km-deep well in the Kawerau Geothermal Field and qualitatively assessed fractures for several greywacke outcrops.

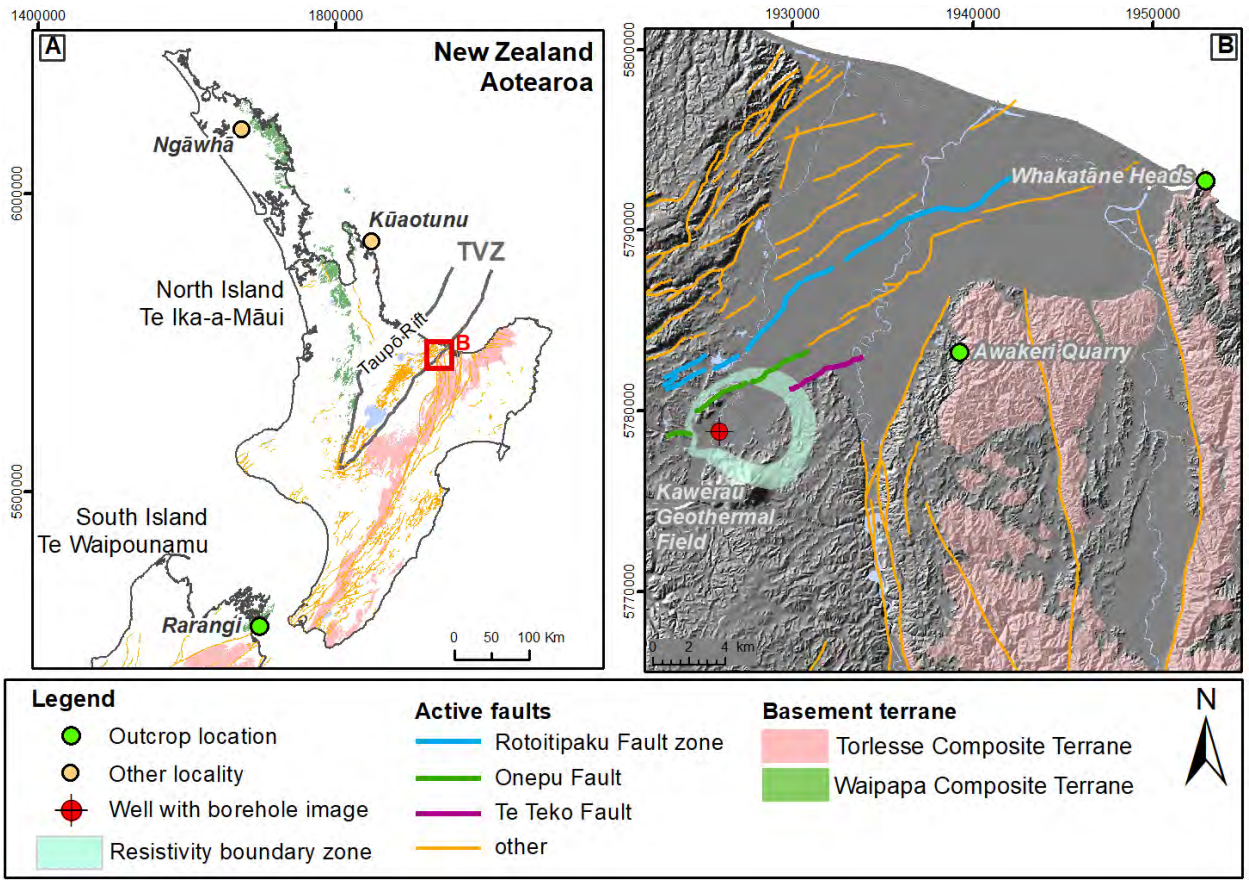

Figure 1: A) Locations with greywacke basement referred to in this study and surface outcrop of greywacke (Heron, 2023). The Taupō Volcanic Zone (TVZ; Te Ahi Tupua) hosts the Taupō Rift, an intra-arc rift with steeply dipping normal faults striking NE-SW to ENE-WSW (Villamor et al., 2017). B) Resistivity boundary zone of the Kawerau Geothermal Field at about 500 m depth with the geothermal well with borehole image in this study (bracketed by the 20 and 50 Ωm resistivity contours; after Allis, 1997), active faults (Langridge et al., 2016), surface greywacke (Heron, 2023), and location of the Awakeri Quarry and Whakatāne Heads outcrops. The subsurface greywacke at Kawerau is Waipapa Composite Terrane.

1.1 Greywacke basement rocks

The basement rocks in and around the TVZ area are greywacke, formed during the Jurassic and Cretaceous periods (about 200-100 million years ago). The sandstone and mudstone that dominate the greywacke were formed in oceans by the accumulation of coarse- to fine-grained material. Due to burial, heat and pressure, these were variably metamorphosed into metasedimentary conglomerate, sandstone and mudstone, and in some places low-grade schist (Leonard et al., 2010; Mortimer et al., 2023). Subsequent exhumation caused further fracturing and deformation. Fractures are commonly filled with minerals such as clay, quartz, and calcite. The greywackes underlying the TVZ geothermal fields comprise the Torlesse and Waipapa composite terranes (Figure 1), with the Waipapa rocks having intermediate SiO_2 (andesitic) compositions and Torlesse consisting of higher SiO_2 quartzo-feldspathic compositions (Wood et al., 2001; Mortimer et al., 2023).

The character of the greywacke varies regionally, making exploration of deep geothermal resources challenging. Basement rocks have been reached by drilling in multiple TVZ geothermal

fields. Exploration for permeability in greywacke has shown rock at Kawerau and Ngāwhā to be good hosts for geothermal reservoirs (Figure 1), with only limited success at other geothermal fields that intersect greywacke.

1.2 Kawerau Geothermal Field and Outcrop Locations

The Kawerau Geothermal Field (Figure 1) is the northeastern most of the active high–temperature geothermal fields in the TVZ (Bibby et al., 1995; Kissling and Weir, 2005; Rowland and Simmons, 2012). Kawerau wells are drilled into greywacke of the Waipapa Composite Terrane (Milicich et al., 2016; Milicich et al., 2021b) comprising primarily metasedimentary sandstone and mudstone. These rocks have very low matrix porosity but host both geothermal production and injection wells, with fluid flow localised in fault and fracture networks.

The only surface faults known in the area are the Te Teko, Onepu and Rotoitipaku faults (Figure 1), but 3D geological modelling of the subsurface indicates additional major faults (Milicich et al., 2014; Langridge et al., 2016). These are roughly striking NE-SW and steeply dipping, consistent with the Taupō Rift. In addition, faults with lesser throw than the main NE-SW faults strike NW-SE. These faults in the subsurface have a steep dip magnitude (>75°), to the NW and NE. In contrast, the metamorphic layering is likely to be much more variable, and potentially lower dip magnitude.

Wallis et al. (2012) investigated lithological controls the thickness and frequency of fractures in greywacke in wells KA50 and PK08 based on interpretation of acoustic borehole images and reported larger fracture thickness and higher frequency occurring in sandstone intervals.

Fracture patterns were observed at three locations. Whakatāne Heads and Awakeri quarry near the Kawerau Geothermal Field, and Rarangi in the northern part of the South Island (Figure 1). Whakatāne Heads and Awakeri quarry include metasedimentary sandstone, mudstone, and conglomerate, with Whakatāne Heads being located in a mélange zone, i.e., bodies of deformed rocks characterised by the inclusion of tectonically mixed fragments or blocks (Leonard et al., 2010). Rarangi is metasedimentary sandstone and mudstone with a low-grade schist overprint (Begg and Johnston, 2000).

2. Data and Method

2.1 Outcrop observations

Outcrop observations were made at three outcrops (Figure 1). Whakatāne Heads shows veins in deformed layers of sandstone and mudstone as part of the mélange (Whakatāne mélange; Leonard et al., 2010). At the nearby Awakeri quarry, lithologies comprise conglomerate, sandstone and finely layered mudstone. Although the Awakeri quarry is part of the Whakatāne mélange, rocks are less deformed than at Whakatāne Heads. One possible fault occurs in the study area but is not mapped in the New Zealand active fault database (Langridge et al., 2016) and does not show displacement. At Rarangi, the schist outcrop is dominated by sandstone with steeply-dipping foliation and includes a small fault. Observations were visual at all outcrops. For quantitative results, additional detailed vein mapping was conducted using orthophotographs acquired by drone photogrammetry at Awakeri quarry (~750 m long outcrop exposure), and hand-held cameras at Rarangi (~40 m long exposure).

2.2 Borehole image

The resistivity image obtained in 2013 using a formation micro imager (FMI) and was processed and interpreted following the methodology of McNamara et al. (2019). All orientations are with reference to geographic north, and borehole deviation (<10°) has been taken into account. Fracture thickness is corrected for both fracture and borehole orientations, i.e., it is the orthogonal distance between fracture walls. Texture and layering features were carefully differentiated from natural fractures and stress-induced features (Davatzes and Hickman, 2010; Halwa et al., 2013; Milicich et al., 2021a).

Fracture classification for the resistivity image includes natural (conductive and resistive fractures, micro-faults, halo fractures, partial fractures, and enhanced fractures; Figure 2 and Table 1) and induced (drilling induced tensile fractures and petal centreline fractures) features. Halo fractures are conductive fractures with a high resistivity halo around them (Figure 2). Enhanced fractures are ambiguous stress-enhanced fractures, many present as partial fractures and commonly with straight line sections that are not sinusoidal (Barton et al., 2010). Since enhanced fractures likely do not extend far from the borehole wall and unlikely to contribute to fluid flow, they are not considered in this fracture analysis. Conductive fractures are interpreted as most likely to be permeable (Massiot et al., 2017a; McNamara et al., 2019). McNamara et al. (2019) showed that halo fractures in ignimbrites in the Wairakei Geothermal Field, TVZ tended to be more permeable. Resistive fractures are not considered to be permeable as they are commonly mineralised (Massiot et al., 2017a).

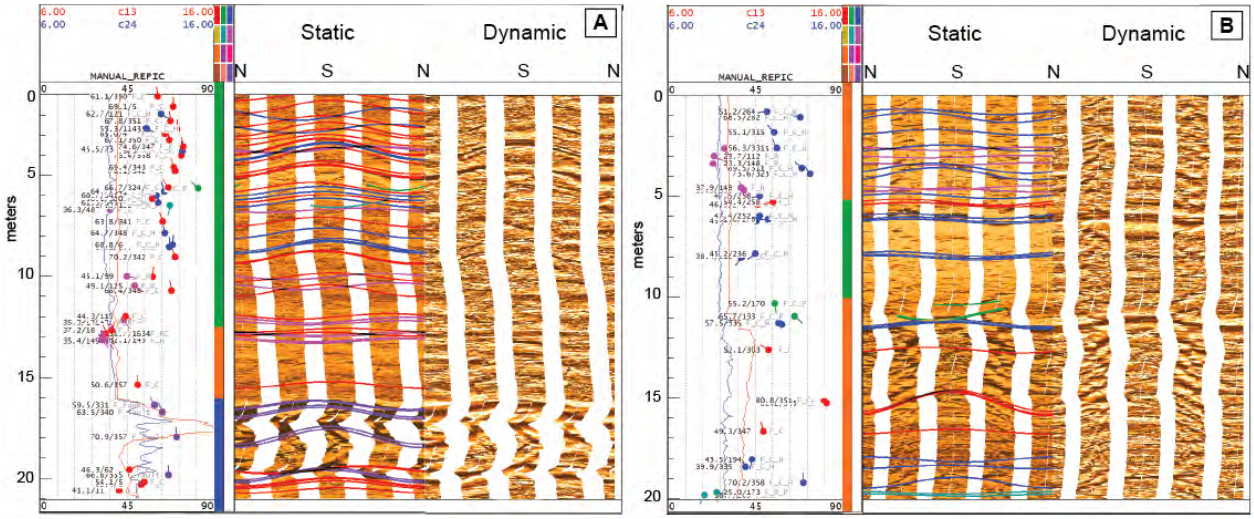

Figure 2: Borehole image examples of fractures in permeable zones. A) A feed zone with a damage zone associated with a series of micro-faults. B) A feed zone with multiple conductive fractures with halos. See Table 1 for colours. Borehole images are presented unwrapped along the north orientation, so that planar features intersecting the cylindrical borehole appear as sinusoids. From left to right: tadpole and mechanical calipers (C13 and C24), statically normalised, and dynamically normalised images (Hansen and Buczak, 2010).

Table 1: Natural fracture classification

Fracture	Definition	Trace type and acronym	Permeability potential	Number	Symbol Figure 2
Conductive	Planar conductive (dark), discordant features that can be traced around the borehole.	Full (F_C)	moderate	472	
		Partial (F_C_P)	low	202	
Conductive halo	Planar conductive (dark) discordant feature with clear indication of resistive (bright) halo.	Full (F_C_H)	high	191	
		Partial (F_C_H_P)	moderate	46	
Resistive	Planar resistive (bright) discordant feature.	Full (F_R)	none (infilled)	300	
		Partial (F_R_P)	none (infilled)	74	
Micro-fault	Planar discordant features that show obvious displacement or truncation of other image features.	Full (F_fault)	high if part of a wider fractured zone	8	

Mudstone intervals generally appear dark in statically-normalised images, whereas sandstone-dominated intervals appear bright because they are richer in quartz (Figure 3). There are many intervals with clear layering. Even though metamorphosed, there are still primary sedimentary bedding features present e.g., cross bedding. There are also bedding parallel fractures, which are commonly difficult to differentiate from bedding, although some may be included in the low dip magnitude fracture features.

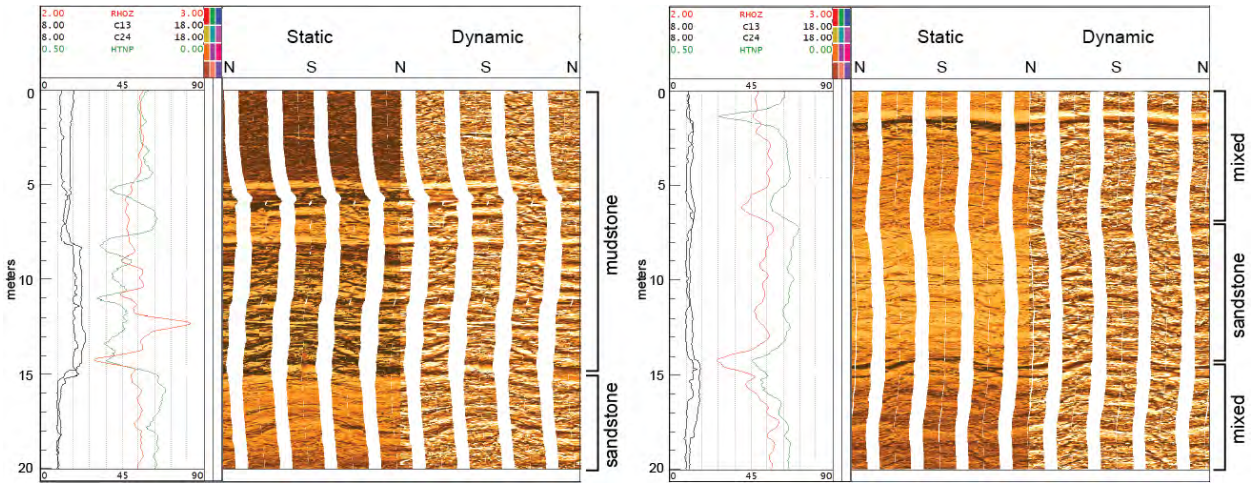

Figure 3: Representative examples of lithofacies (Table 2) in resistivity image. Left) Mudstone and sandstone. Right) Sandstone and mixed. Curves shown are mechanical calipers (C13 and C24), thermal neutron porosity (HTNP) and density (RHOZ). Images are statically normalised, and dynamically normalised (Hansen and Buczak, 2010).

Three permeable (feed) zones were interpreted from pressure, temperature and spinner logs (PTS) obtained from completion tests (Mercury pers comm, 2020). Due to commercial sensitivity, the depths and PTS data are not published here. To examine the effect of rock type on fractures, the relative abundance of sandstone and mudstone was determined. Seven lithofacies were initially determined in Schlumberger (2013) following the scheme described in Wallis et al. (2012). The classification was done with a binning technique using resistivity cutoffs applied to a scaled

resistivity image. The binning also considered neutron-density and resistivity downhole measurements. The initial seven lithofacies were simplified to three to produce a statistically meaningful lithofacies fracture analysis (Table 2).

Table 2: Greywacke lithofacies.

Lithofacies	Description	% mudstone
Sandstone	Sandstone and sandstone with very minor mudstone	0-25
Mixed	Interbedded intervals of sandstone and mudstone	25-75
Mudstone	Mudstone and mudstone with very minor sandstone	75-100

To provide reliable fracture statistics, we have only considered intervals of image where >25% azimuthal coverage was deemed reliable, i.e., where the fracture density is reliable (Massiot et al., 2017b). The 774 m of borehole image included in this analysis are made of two intervals large enough for reliable fracture statistics (125 m and 649 m, respectively). For statistical analysis, partial fractures have been grouped with continuous fractures.

3. Results

3.1 Outcrop observations: Whakatāne Heads, Awakeri quarry, Rarangi

Veins at the three outcrops show similarity of patterns with high variability over small distances (Figure 4). At Whakatāne Heads, some veins are thicker and more focused in sandstone than mudstone (Figure 4A). At all three outcrops, veins occur along, across or terminate at interfaces between layers of sandstone and mudstone (Figure 4B-D). Veins associated with faults are localised (Figure 4B-C) and commonly show splays (Figure 4B). Splaying, anastomosing, and merging of veins is common even in the absence of faulting (Figure 4E). Long (>2 m) and thin (1-3 mm) veins are common in all lithologies, and at Awakeri quarry, form connected vein groups of >10 m-long that cross interfaces between large conglomerate clasts. At all three outcrops, orientations of veins are varied and at varied angle to bedding.

Quantitative analysis of areal vein density at Awakeri quarry and Rarangi reveals that similar densities are found away from faults in different lithologies, and whether the host rock is of low-metamorphic grade or foliated schist. By contrast, density is locally increased within 1 m of a fault at Rarangi, with numerous short (<0.5 m) and thick (1-3 cm) veins; and near possible fault strands at Awakeri, presenting as a network of thin (1 mm) cross-cutting veins. A section of Rarangi outcrop presents thick (1-8 cm) veins of >1 m-long (measurement limited by the outcrop exposure) although it does not appear to be associated with a visible fault. Quantitative analysis of fractures in outcrop will be continued in future work.

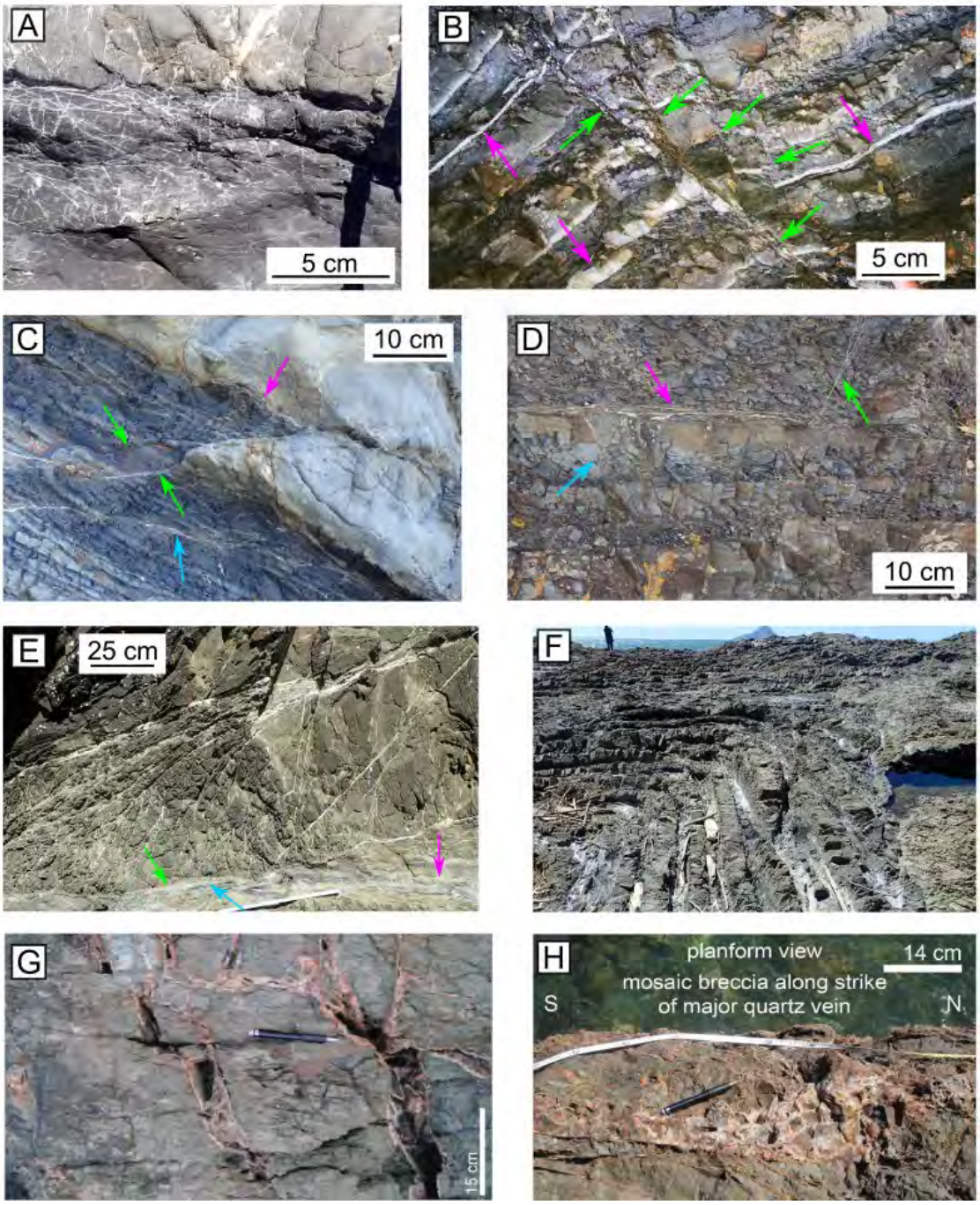

Figure 4: Veining at Whakatane Heads (this study) and Kūaotunu epithermal deposit (reproduced from Lawrence, 2015). A) Thick veins in grey sandstone and dispersed thin veins in darker mudstone. B) Fault splay (green arrows) displacing layers of sandstone and mudstone. Some veins are along layers (pink arrows). C) Fault oblique to layering displacing sandstone and mudstone layers, with veins along (pink arrow) and crossing (blue arrow) beds, and along the fault (green arrows). D) Veins along (pink arrow), crossing (blue arrow) and arresting (green arrow) on layers. E) Vein splaying in sandstone. Some veins have the same thickness and orientation modifications in the mudstone layer (blue arrow) while other become more diffuse or terminate at the mudstone interface (green arrow). Some veins are along the interface between mudstone and sandstone (pink arrow). F) Fold with veins along and across layers. G) Fractures parallel to and crossing weak cleavage parallel to pen (Lawrence, 2015). H) Localised brecciation along quartz vein (Lawrence, 2015).

3.2 Borehole image: lithology

Over the interpreted interval of the borehole image, there is more mixed lithology than pure mudstone and sandstone (Table 3). We deem the total length of sandstone intervals (178 m) to be sufficient for statistical purposes. Individual intervals of single lithologies range from 1 to 43 m-long (median of 6 m). Feed zones 1 and 2 comprise dominantly mudstone and mixed lithologies. Major feed zone 3 is dominantly in a mixed lithology with little mudstone.

Table 3: Relative percentage of lithofacies in feed zones (FZ) and the interpreted interval.

Interval	Mudstone	Mixed	Sandstone
FZ1 (minor; 33 m)	38%	41%	21%
FZ2 (minor; 82 m)	48%	35%	17%
FZ3 (major; 48 m)	11%	56%	33%
Interpreted interval (774 m)	34%	43%	23%

3.3 Borehole image: fractures

3.3.1 Orientation and thickness

Fracture orientation depends on the fracture type (Figure 5). Resistive fractures have dip magnitudes dominantly between 30° and 60° (median of 45°), and when averaged for the entire borehole image, no preferential strike orientation. In contrast, conductive fractures have a dominant strike of NE-SW to E-W dipping to NW to N, with dip magnitudes >45° (median 58°). Micro-faults have the same orientation as the dominant orientation of conductive fractures. Conductive fractures with a resistive halo have the same dominant orientation as conductive fractures, but also have more variable orientations. Orientation of halo fractures thus appears similar to both conductive and resistive fractures. These orientation patterns do not change in or outside of permeable zones.

Fracture thickness ranges from 1 to 159 mm with a median of 5 mm. Conductive, halo and resistive fractures have the same median thickness (5 mm) while the 8 micro-faults are thicker (median of 37 mm). The thickest fractures (>20 mm) consist of 18 conductive (maximum of 159 mm, likely a densely fractured zone rather than a single fracture), 16 resistive (maximum of 49 mm), 5 micro-faults (maximum of 61 mm) and 2 halo (maximum of 32 mm).

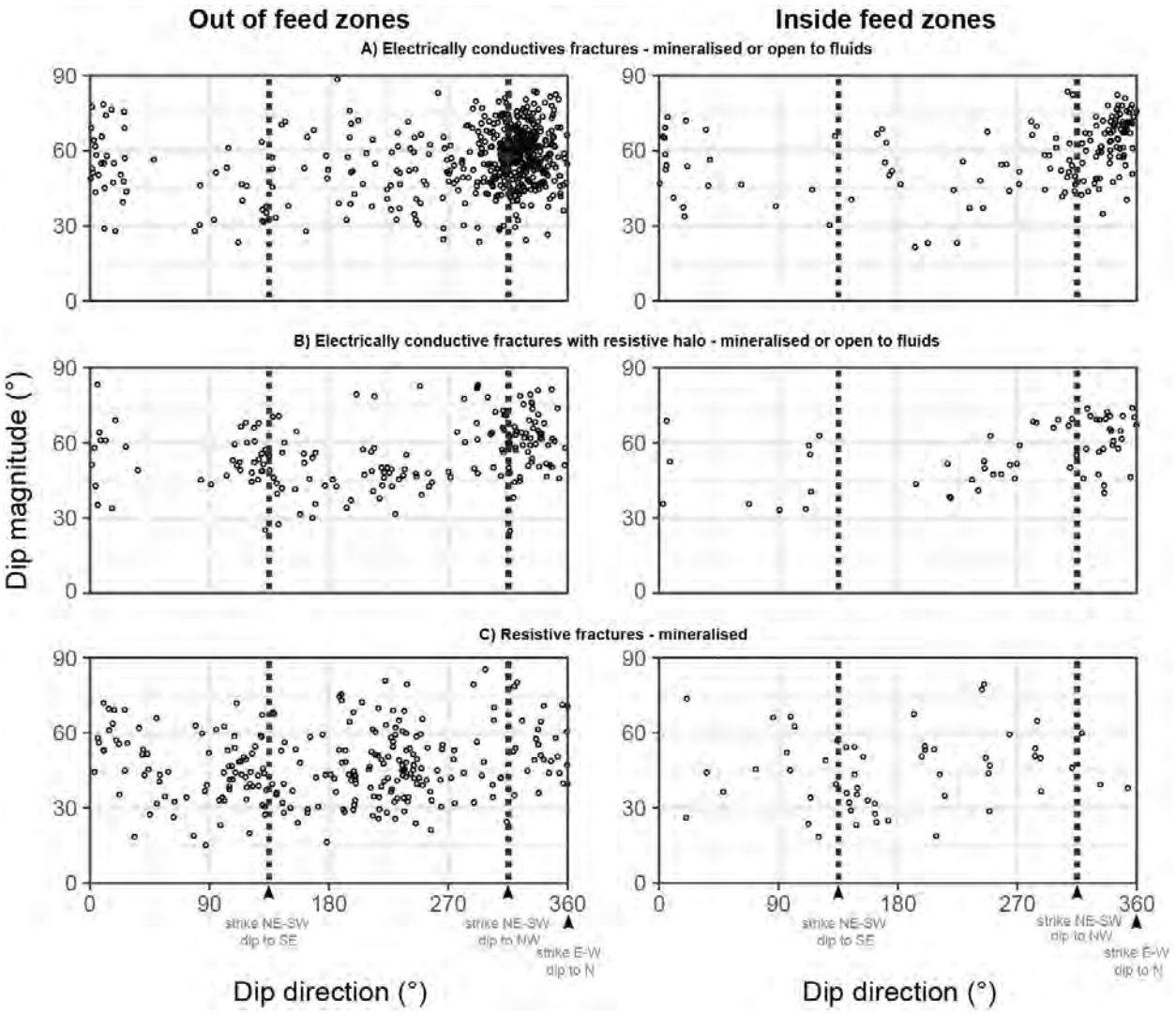

Figure 5: Dip magnitude versus dip direction for each fracture type. Left: fractures outside feed zones. Right: Fractures in feed zones.

3.3.2 Fracture density

The fractures are distributed throughout the imaged interval. Some intervals have fracture clusters with a higher density of halo, conductive and resistive fractures.

The density of natural fractures along the borehole (P10) considering all fracture types and lithologies is 1.50 m^{-1} (Figure 6A). Fracture density is twice as high for conductive (0.81 m^{-1}) than resistive (0.39 m^{-1}) and nearly three times that of halo (0.30 m^{-1}) fractures. Density is low for micro-faults (0.01 m^{-1}). The statistical difference of lithological for micro-faults is not reliable because of the small data set, with five micro-faults in mixed lithologies, three in mudstone and none in sandstone.

Fracture density is higher in sandstone (1.95 m^{-1}) than in mixed lithologies (1.52 m^{-1}) and mudstone (1.16 m^{-1}). This higher P10 for sandstone than mudstone is most clearly the case for halo fractures, but only moderately so for conductive and resistive fractures. The lithological difference

for conductive fractures is restricted to partial conductive fractures (0.32 m^{-1} in sandstone; 0.16 m^{-1} in mudstone), while continuous conductive fractures have the same density in all three lithologies (0.5-0.6 m^{-1}).

In the transformation from linear (P10 – Figure 6A) to volumetric (P33 – Figure 6B) densities, fractures of high dip magnitude and/or thickness have a relatively higher weight than other fractures. On average, fractures (open to fluid flow or mineralised) form about 2% of the rock volume. When considering all natural fracture types, P33 is slightly lower in mudstone (1.8%) than in mixed and sandstone (both 2.3%). Overall, the relative proportions of P33 by fracture types are similar to those from P10, with some slight variations. Micro-faults have higher dip magnitude and thickness than other dip types, yielding relatively higher P33.

Resistive fractures have moderate dip magnitude and have few thick fractures, yielding relatively lower P33. Some conductive fractures have high thickness, yielding relatively higher P33. Difference of P33 between lithologies are very small for conductive and resistive fractures and reduced for halo fractures compared to P10.

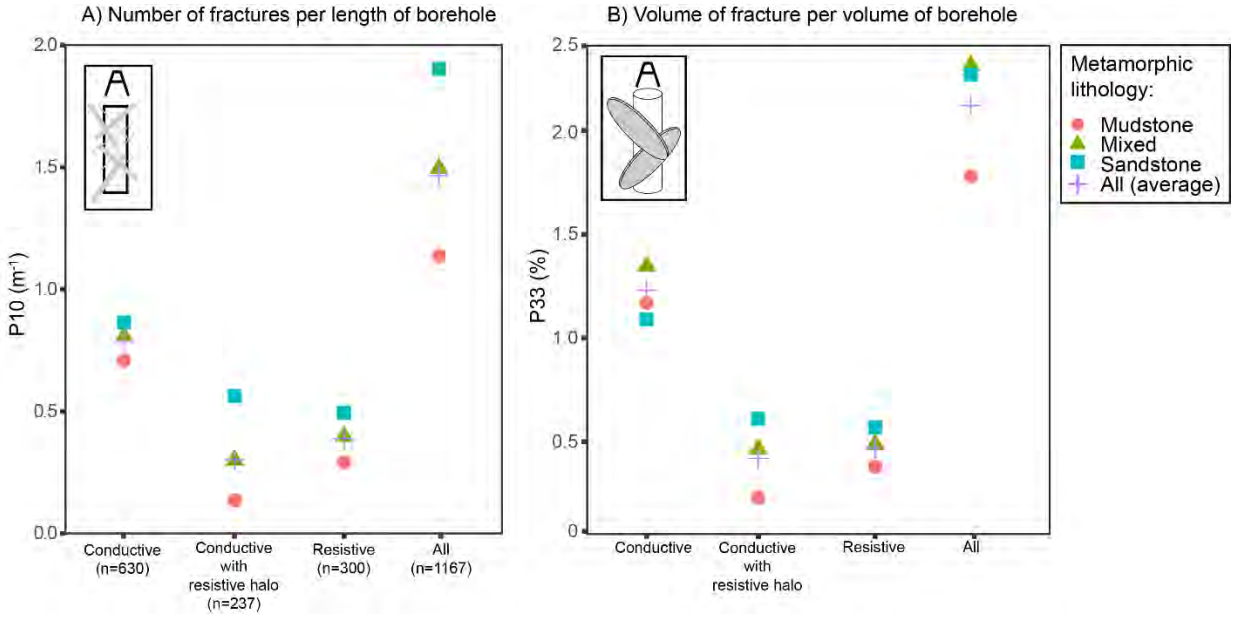

Figure 6: Natural fracture density as a function of fracture type and metamorphic lithology. A): P10, number of fractures per meter of borehole. B) P33, volume of fractures per volume of borehole.

3.3.3 Permeable zones

The orientation of potentially permeable fractures (i.e., conductive, conductive fractures with halo and micro-faults) within feed zones (FZ) is generally consistent with the Taupō Rift (steeply dipping with NE-SW strike) (Figure 7). There are some variations, in particular with FZ2 having a more ENE-WSW striking fractures. There are subordinate orientations in each feed zone (NNW-SSE and N-S strike). Resistive fractures have more varied strike, along with lower dip magnitudes. Fractures of all strike are found outside of permeable zones.

Permeability is not clearly associated with either high fracture density, high thickness, or type. Fracture density (P10) is higher in major feed zone 3 (2.2 m^{-1}) than outside feed zones (1.5 m^{-1}). This different density is not observed in the two other feed zones (1.6 m^{-1} and 1.3 m^{-1}). Density of

halo fractures is higher in major FZ3 (0.8 m^{-1}) than outside feed zones (0.2 m^{-1}), but lower in the two minor feed zones (0.1 m^{-1}). There are four micro-faults in FZ2 but none in the two other feed zones. Other fracture types have similar densities within and outside feed zones.

Potentially permeable fractures of elevated apparent thickness (i.e., >20 mm) are more common within the two minor feed zones than outside feed zones, but this is not observed for the major feed zone. There is only one resistive fracture of elevated thickness in feed zones (FZ2).

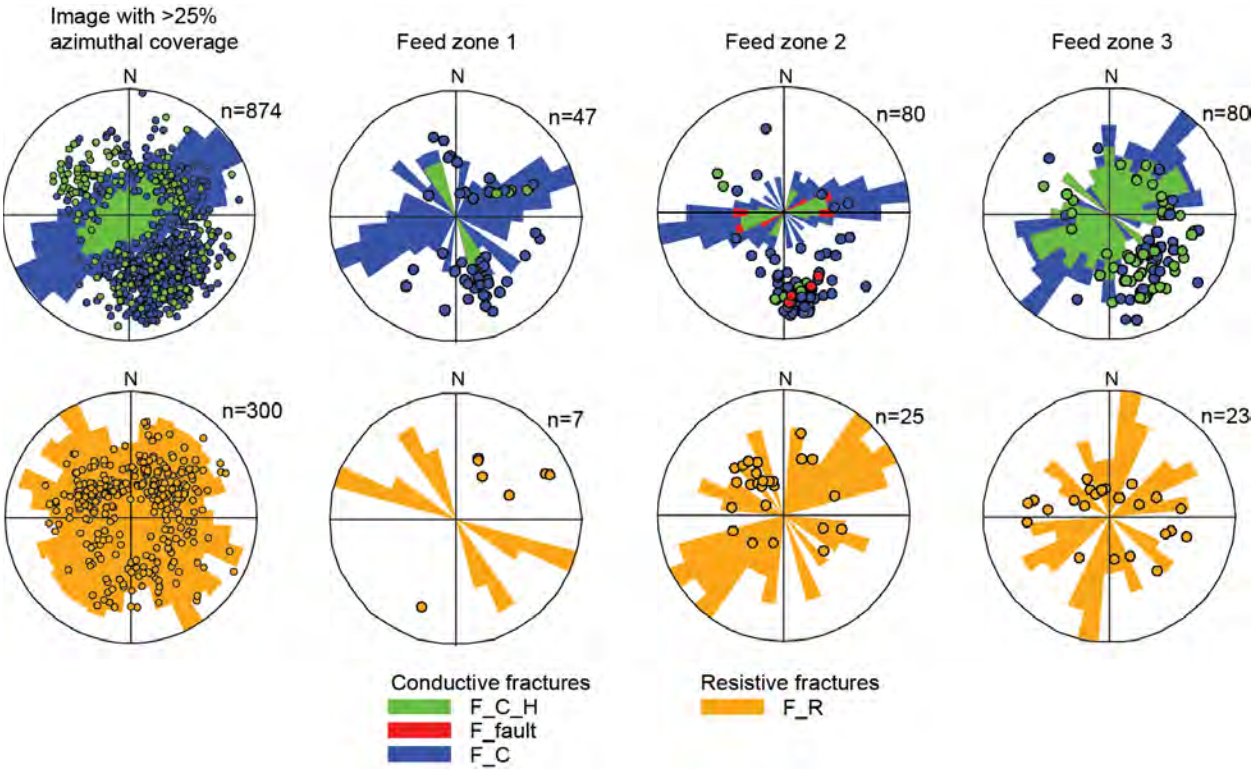

Figure 7: Fracture orientations in the imaged interval with >25% azimuthal coverage and the three feed zones. Partial and full fractures are grouped in this figure. In Schmidt projection stereonets, lower hemisphere. n = total feature count. Due to commercial sensitivity, the depths are not specified here.

4. Discussion

The high-resolution resistivity image provides an excellent detailed view of the borehole wall for lithological analysis and fracture characterisation. However, from a reservoir management point of view, it is difficult to determine which fracture is more likely to be permeable, or those resulting from either metamorphic veining or recent and current tectonic activity. Resistivity images acquired in ignimbrites at the Wairakei Geothermal Field also revealed numerous details on fracturing, layering and bedding (McNamara et al., 2019), but the metamorphic veining in greywacke adds a layer of complexity in image interpretation.

The different fracture orientation and density of different fracture types suggests different origins. Resistive fractures have moderate dip magnitude and no preferential strike throughout the entire imaged interval. In addition, resistive fractures have higher linear fracture density (P10) in sandstone than in mudstone. This suggests that resistive fractures are metamorphic veins rather

than reactivated fractures or fractures generated by current tectonics. Based on outcrop observations, some of those resistive fractures may have formed along layering in an orientation that is not well-oriented for reactivation prior to current Taupō Rift tectonics. The higher density of partial conductive fractures in sandstone compared to mudstone, and the more varied fracture orientation of these partial fractures suggest a possible metamorphic origin, similar to the varied orientations measured in outcrop.

Continuous conductive fractures have orientations consistent with steep normal faults striking parallel to the Taupō Rift faults, with linear fracture density similar in all lithologies. We infer that these fractures are tectonic-related fractures and veins. They have been formed by either reactivating metamorphic veins that are critically stressed (as defined by Barton et al., 1995), or newly formed, under the current stress regime. The localised nature of feed zones is consistent with outcrop observations of increased veining density in the near-vicinity of faults, that occur at multiple scales (Figure 4B-C-H, Seebeck et al., 2014; Ellis et al., 2023).

The higher density of halo fractures in sandstone and mudstone, combined with orientations intermediate between conductive and resistive fractures suggests that halo fractures are a mix of metamorphic veins and tectonic fractures. Contrary to the Wairakei Geothermal Field (McNamara et al., 2019), they are not as useful prediction of permeability.

In the studied well, there is a higher linear fracture density (P10) in sandstone than in mudstone; and the major FZ3 that has a high fracture density intersected more mixed and sandstone lithologies than other feed zones. However, we suggest that these observations cannot be used as a general rule that sandstone intervals are more fractured than mudstone, nor that sandstone are more permeable than mudstone. Firstly, the difference in fracture density relates only to some fracture types, including the resistive fractures that are not permeable. The density and orientation of continuous conductive fractures (some of which are permeable) is not obviously affected by metamorphic lithologies. Secondly, volumetric fracture densities (P33) show smaller differences between lithologies than linear densities (P10). This echoes outcrop observations where thinner but more numerous veins in mudstone may provide similar vein volume as the thicker but fewer veins in sandstones. Thirdly, fracturing and associated permeability also strongly depends on proximity to faults, in-situ stress (Barton et al., 1995; Townend and Zoback, 2000) and connectivity to fracture networks (Kissling and Massiot, 2023) that have not been considered in this preliminary work.

Linear fracture density (P10) in this well is high enough (1.1 m^{-1} considering conductive fractures and conductive fractures with halo) to yield a fully connected fracture network at reservoir scale (>0.3 m^{-1}), based on fracture network modelling by Kissling and Massiot (2023). The fracture density at borehole scale, and the combination of varied vein orientation and long veins (and vein groups) in outcrop suggest that, in a reservoir, some of the veins would be well-oriented for being reactivated in any stress field and could provide connectivity and/or storage for fluids. Increased veining in close vicinity of faults in outcrops suggests a very focused enhanced permeability, as suggested by other studies of greywacke in New Zealand (Seebeck et al., 2014; de Ronde et al., 2001; Ellis et al., 2023). Similarly, at Kūaotunu epithermal deposit, Lawrence (2015) made observations of veining and breccias mainly associated with faults, locally affected by the rock fabric and with high spatial variability (Figure 4G-H).

The implication from borehole and outcrop studies is that there will likely be permeable fractures in supercritical wells drilled into greywacke. In supercritical conditions, fluids need connected fracture networks, but not necessarily fractures of elevated aperture, as fluids have low viscosity (Wagner & Pruβ, 1995). As suggested by laboratory and numerical modelling of granite samples, small cloud-fracture networks may be sufficient to provide sufficient permeability (Watanabe et al., 2019; Liu et al., 2022), though granite are much more isotropic than greywacke rocks. Further studies on the effect of stress, metamorphic fabric and hydrothermal alteration are needed to confirm this, in addition to supercritical exploratory drilling.

5. Conclusion

In this resistivity borehole image acquired in greywacke at the Kawerau Geothermal Field, we interpret resistive fractures as being of dominantly metamorphic origin. Conductive fractures and micro-faults are interpreted as mostly representing fractures initiated or reactivated under the current extensional stress field. Conductive fractures with resistive halos are interpreted to result from a mixture of tectonic and metamorphic origins.

In this well, borehole resistivity image interpretation shows that there are more fractures in sandstone than mixed lithologies and again than in mudstone, but this affects some dip types more than other, and is not so pronounced when considering volumetric densities. This higher density in sandstone than in mudstone is also subtle when only considering potentially permeable fractures rather than resistive fractures (closed veins). Halo fractures are not as good indicator of permeability than they were in ignimbrites at the Wairakei Geothermal Field.

When considering fracture density and fracture patterns at both borehole and outcrop scale, there is likely to be a well-connected fracture network at reservoir scale whether drilling into either sandstone or mudstone dominated greywacke.

In future work, we will interpret data from this well in the context of nearby faults and will compare results from other wells. Future integration with quantitative outcrop observations will also strengthen findings on controls on fracture and associated permeability in TVZ greywacke.

Acknowledgement

This study is part of GNS Science's Geothermal the Next Generation research programme, led by Isabelle Chambefort, funding of which was provided as an Endeavour fund by the Government of New Zealand (Contract number CO5X1904). We thank Mercury NZ Ltd. for the provision and permission to publish well data. Thanks to J-swap for access to the Awakeri Quarry.

REFERENCES

Allis, R.G. "The natural state and response to development of Kawerau geothermal field, New Zealand". *Proceedings Geothermal Resources Council*, Davis, California, United States (1997).

Barton, C.A., Zoback, M.D., and Moos, D. "Fluid flow along potentially active faults in crystalline rock." *Geology*, 23.8, (1995), 683-686.

Barton, C.A., and Moos, D. “Geomechanical Wellbore Imaging: key to managing the asset life cycle”. In M. Poppelreiter, C. Garcia-Carballido, and M. Kraaijveld (Eds.), Dipmeter and borehole image log technology. *AAPG Memoir*, 92, (2010), 81–112.

Begg, J.G. and Johnston, M.R. “Geology of the Wellington area: scale 1:250,000”. Lower Hutt: Institute of Geological & Nuclear Sciences. Institute of Geological & Nuclear Sciences 1:250,000 geological map 10. 64 p. (2000).

Bibby, H.M., Caldwell, T.G., Davey, F.J., and Webb, T.H. “Geophysical evidence on the structure of the Taupo Volcanic Zone and its hydrothermal circulation”. *Journal of Volcanology and Geothermal Research*, 68, (1995), 29–58.

Davatzes, N.C. and Hickman, S.H. “Stress, fracture, and fluid-flow analysis using acoustic and electrical image logs in hot fractured granites of the Coso geothermal field, California, USA”. In Poppelreiter, M., Garcia-Carballido, C. and Kraaijveld, M. eds. Dipmeter and borehole image log technology. *AAPG Memoir*, 92, (2010), 259-293.

de Ronde, C.E.J., Sibson, R.H., Bray, C.J., and Faure, K. “Fluid chemistry of veining associated with an ancient microearthquake swarm, Benmore Dam, New Zealand”. *Bulletin of the Geological Society of America*, 113(8), (2001), 1010–1024.

Ellis, S.M., Hill, M., and Little, T.A. “Structure and topology of a brittle-ductile fault swarm at Crawford Knob, Franz Josef, New Zealand”. *New Zealand Journal of Geology and Geophysics*, 1–22, (2023).

Halwa, L., Wallis, I.C., and Lozada, G.T. “Geological analysis of the volcanic subsurface using borehole resistivity images in the Ngatamariki Geothermal Field, New Zealand”. *Proceedings New Zealand Geothermal Workshop*, Rotorua, New Zealan d (2013).

Hansen, B. and Buczak, J. “Making interpretable images from image logs”. In Poppelreiter, M., Garcia-Carballido, C. and Kraaijveld, M. eds. Dipmeter and borehole image log technology. *AAPG Memoir*, 92, (2010), 51-66.

Heron, D.W. (custodian). “Geological map of New Zealand 1:250,000 [digital data]”. 4th ed. Lower Hutt (NZ): GNS Science. (GNS Science geological map; 1). (2023), doi: 10.21420/5XTJ-5718.

Kissling, W.M. and Massiot, C. “Modelling of flow through naturally fractured geothermal reservoirs, Taupō Volcanic Zone, New Zealand”. *Geothermal Energy*, 11(1), (2023), 20.

Kissling, W.M. and Weir, G.J. “The spatial distribution of the geothermal fields in the Taupo Volcanic Zone, New Zealand”. *Journal of Volcanology and Geothermal Research*, 145, (2005), 136–150.

Langridge, R.M., Ries, W.F., Litchfield, N.J., Villamor, P., Van Dissen, R.J., Barrell, D.J.A., Rattenbury, M.S., Heron, D.W., Haubrock, S., Townsend, D.B., and Lee, J.M. “The New Zealand active faults database”. *New Zealand Journal of Geology and Geophysics*, 59(1), (2016), 86-96.

Lawrence, M.J. “Characterisation of fracture properties in greywacke reservoir rock utilising the Kuaotunu epithermal deposit as a fossil analogue”. MSc Thesis, (2015), University of Auckland. http://hdl.handle.net/2292/25190.

Leonard, G.S., Begg, J.G., Wilson, C.J.N. (comps). “Geology of the Rotorua area: scale 1:250,000”. Lower Hutt: GNS Science. Institute of Geological & Nuclear Sciences 1:250,000 geological map 5. 102 p. (2010).

Liu, B., Suzuki, A., Watanabe, N., Ishibashi, T., Sakaguchi, K., and Ito, T. “Fracturing of granite rock with supercritical water for superhot geothermal resources”. *Renewable Energy*, 184, (2022), 56–67.

Massiot, C., McLean, K., McNamara, D.D., Sepulveda, F., and Milicich, S.D. “Discussion between a reservoir engineer and a geologist: permeability identification from completion test data and borehole image logs integration”. *Proceedings New Zealand Geothermal Workshop*, (2017a), Rotorua, New Zealand.

Massiot, C., Townend, J., Nicol, A., and McNamara, D.D. “Statistical methods of fracture characterization using acoustic borehole televiewer log interpretation”. *Journal of Geophysical Research: Solid Earth*, 122, (2017b).

Melia, A., Faulkner, D.R., and McNamara, D.D. “Physical property characterization of the Waipapa Greywacke: an important geothermal reservoir basement rock in New Zealand”. *Geothermal Energy*, 10, (2022).

McNamara, D.D., Milicich, S.D., Massiot, C., Villamor, P., McLean, K., Sepulveda, D., and Ries, W.F. “Tectonic controls on Taupo Volcanic Zone geothermal expression: insights from Te Mihi, Wairakei Geothermal Field”. *Tectonics*, 38, (2019), 3011-3033.

Mercury Pers. Comm. Feed zone depths from interpretation of well completion data, (2020).

Mielke, P., Weinert, S., Bignall, G. and Sass, I. “Thermo-physical rock properties of greywacke basement rock and intrusive lavas from the Taupo Volcanic Zone, New Zealand.” *Journal of Volcanology and Geothermal Research*, 324, (2016), 179-189.

Milicich, S.D., Bardsley, C., Bignall, G., and Wilson, C.J.N. “3-D interpretative modelling applied to the geology of the Kawerau geothermal system, Taupo Volcanic Zone, New Zealand”. *Geothermics*, 51, (2014), 344-350.

Milicich, S.D., Clark, J.P., Wong, C., and Askari, M. “A review of the Kawerau geothermal field, New Zealand”. *Geothermics*, 59, (2016), 252-265.

Milicich, S., Massiot, C., McNamara, D.D., and Sepulveda, F. “Volcanic texture identification and influence on permeability using borehole resistivity image logs in the Taupo Volcanic Zone, New Zealand”. *Proceedings Stanford Geothermal Workshop*, (2021a). Stanford, United States.

Milicich, S.D., Mortimer, N., Villamor, P., Wilson, C.J., Chambefort, I., Sagar, M.W., and Ireland, T.R. “The Mesozoic terrane boundary beneath the Taupo Volcanic Zone, New Zealand, and potential controls on geothermal system characteristics”. *New Zealand Journal of Geology and Geophysics*, 64(4), (2021b), 518-529.

Mortimer, N., Charlier, B.L., Rooyakkers, S.M., Turnbull, R.E., Wilson, C.J., Negrini, M., Bannister, S., Milicich, S.D., Chambefort, I., Miller, C.A., and Kilgour, G. “Crustal basement

terranes under the Taupō Volcanic Zone, New Zealand: Context for hydrothermal and magmatic processes". *Journal of Volcanology and Geothermal Research*, (2023), p.107855.

Rowland, J.V. and Simmons, S.F. "Hydrologic, magmatic, and tectonic controls on hydrothermal flow, Taupo Volcanic Zone, New Zealand: implications for the formation of epithermal vein deposits". *Economic Geology*, 107, (2012), 427–457.

Schlumberger. "FMI image interpretation report, prepared for Mighty River Power". Image analyst F.A. Kalukal (2013).

Seebeck, H.C., Nicol, A., Walsh, J.J., Childs, C., Beetham, R.D., and Pettinga, J. "Fluid flow in fault zones from an active rift". *Journal of Structural Geology*, 62, (2014), 52–64.

Townend, J., and Zoback, M.D. "How faulting keeps the crust strong." *Geology*, 28.5, (2000), 399-402.

Villamor, P., Litchfield, N.J., Gómez-Ortiz, D., Martin-González. F., Alloway, B.V., Berryman, K.R., Clark, K.J., Ries, W.F., Howell, A., and Ansell, I.A. "Rapid evolution of subduction-related continental intraarc rifts: The Taupo Rift, New Zealand." *Tectonics*, 36.10, (2017), 2250-2272.

Wagner, W. and Pruβ, A. "The IAPWS Formulation 1995 for the Thermodynamic Properties of Ordinary Water Substance for General and Scientific use". *Journal of Physical Chemistry*. Reference Data, Vol 31/2, (2002).

Wallis, I.C., McNamara, D., Rowland, J.V., and Massiot, C. "The nature of fracture permeability in the basement greywacke at Kawerau Geothermal Field, New Zealand". *Proceedings Thirty-Seventh Workshop on Geothermal Reservoir Engineering*, (2012), Stanford, California, United States.

Watanabe, N., Sakaguchi, K., Goto, R., Miura, T., Yamane, K., Ishibashi, T., Chen, Y., Komai, T., and Tsuchiya, N. "Cloud-fracture networks as a means of accessing superhot geothermal energy". *Scientific Reports*, 9(1), (2019), 1–11.

Wood, C.P., Brathwaite, R.L., and Rosenberg, M.D. "Basement structure, lithology and permeability at Kawerau and Ohaaki geothermal fields, New Zealand". *Geothermics*, 30(4), (2001), 461-481.

Mount Augustine: Exploring For A New Geothermal Resource In South-central Alaska

Guy Oliver[1], Moamen Gasser[2], Marcus Oesterberg[1], Anthony Pennino[3] and Paul Craig[3]

[1] Ignis Energy Inc., [2] Texas A&M University, [3] GeoAlaska Inc.

Keywords

Railbelt region, Renewable Energy Portfolio Standard, Mount Augustine, Stratovolcano, Upper Jurassic Naknek Formation, Resource Assessment, Monte Carlo Analysis, Power Density Potential, Volumetric Heat Recovery

ABSTRACT

South-central Alaska holds significant geothermal potential due to its location along the Pacific Ring of Fire, a region globally known for its volcanic activity and geothermal resources. The Cook Inlet Region lies above the Pacific Plate subduction zone and contains active volcanoes, including Mt. Augustine.

Alaska has some of the highest residential and commercial electricity prices in the nation, while its per capita energy consumption is the second highest, in part because of the State's small population, cold climate, and energy-intensive industries. South-central Alaska houses approximately 550,000 people (75% of the entire Alaskan population). Power sales in 2020 exceeded 4,408 GWh, of which 82% came from fossil-fuel produced electricity (natural gas and coal) and 18% from renewables (primarily hydroelectric). In December 2021, the Governor of Alaska requested a study on the potential impacts of achieving an 80% renewable energy portfolio for South-central Alaska.

Mt. Augustine is an andesitic stratovolcano typical of subduction zones and located in the Kamishak Bay in the southern part of the Cook Inlet, approximately 60 miles west of Anchor Point and 175 miles SW of Anchorage. Numerous previous researchers have concluded that it contains a shallow magma chamber making it attractive for geothermal exploitation. In September 2022, GeoAlaska was awarded a permit to explore for geothermal resources across 3 onshore tracts of land, totaling 3,048 acres on the southern part of Augustine Island, primarily where the Upper Jurassic Naknek Formation outcrops.

In the summer of 2023, Acoustic Magnetotelluric (AMT) data from 28 sites and gravity data from a further 215 locations were acquired, processed, and interpreted. Additionally, 20 rock samples

were collected from cliff sections along the southern margin of the island, primarily from within the outcropping Naknek Formation.

The jointly inverted geophysical data reveal an area in the southern part of the island of low resistivity and high density strata lying above a zone of higher resistivity. We interpret this as the sub-crop of the Naknek Formation acting as a seal, trapping a potential hydrothermal system below, within the fractured basement. The Naknek Formation is likely to underly much of the southern part of the island and is such an effective seal, it has all but limited any above sea-level surface geothermal features that one would expect for a typical andesitic geothermal resource. As such, we describe this Mt Augustine resource as being an atypical blind geothermal system, suggesting a largely horizontal circulation pattern. An analogue for this system could be Cerro Pabellón GPP in northern Chile, which has a current installed capacity of approximately 83 MWe.

As a result of this collected data, additional exploration activity will be undertaken during 2024/25 including the drilling of an exploration well.

1. Introduction and Context

GeoAlaska LLC was founded in 2020 with a desire to identify and exploit geothermal opportunities in Alaska, and to provide baseload carbon-free electricity for the benefit of the Alaskan people. In March 2023 Ignis Energy Inc, a sister company to Geolog International B.V., partnered with GeoAlaska in order to provide technical and project management support. Since 2021, GeoAlaska has created a geothermal exploration position that includes 2 prospective locations on State owned land and close to the Alaskan South Central Rail Belt Region, including 10,830 acres on the southern flank of Augustine Island (geothermal prospecting permits ADL 394080 and ADL 394374) and 6,376 acres on the southern/central flank of Mt. Spurr (geothermal resource leases 394178, 394179 and 394180). This paper focuses on exploring the geothermal potential at Augustine Island.

South-central Alaska holds significant potential due to its proximity to the Pacific Ring of Fire, a region globally known for its volcanic activity and geothermal resources (U.S. Energy Information Association, 2022). The Cook Inlet basin is a NW-SE trending forearc basin lying above the Aleutian subduction zone of southern Alaska (Haeussler, *et al*., 2000) which contains active volcanoes, including Mt. Augustine.

Alaska's electricity market has been growing rapidly, with a strong recent emphasis on renewable energy. In late May 2024, House Bill 50 was passed by House Alaskan lawmakers which included more favorable conditions to encourage geothermal prospecting in the State. There are no geothermal power plants operating in the State with an installed capacity greater than 0.5 MW.[1]

Alaska's per capita energy consumption is the second highest in the nation (U.S. Energy Information Association, 2024) in part because of the State's small population, cold climate and energy-intensive industries. Alaska also has some of the highest residential and commercial

[1] The Chena power plant located at Chena Hot Springs near Fairbanks has been in operation since 2006 and has an installed capacity of 0.4MW (Erkan *et al.*, 2008).

electricity prices in the nation (U.S. Energy Information Association, 2024). Finally, 70% of the Alaskan population lies within South-central Alaska's 'Railbelt region' (Asmus *et al.*, 2023).

The 'Railbelt region' refers to the interconnected electric grid that stretches approximately 700 miles from the city of Fairbanks in the north through Anchorage to the Kenai Peninsula in the south. About 75% of Alaska's population (approximately 550,000 residents) are served by the Railbelt region. As the largest electrical grid in the State, it is vital for statewide economic and community development. Based on 2020 usage, power sales were calculated to top 4,408 GWh, of which 82% came from fossil-fuel-produced electricity (primarily natural gas and coal) and 18% from renewables (primarily hydroelectric, Dahlstrom *et al.*, 2023). In 2022, the State passed and signed legislation through the Renewable Energy Portfolio Standard (RPS) that will allow Alaska to join 30 other States and 2 Territories in creating a renewable portfolio standard, that can be applied to the Railbelt region. A key element of the Governor's RPS is a firm commitment to transitioning to 30% sustainable power by 2030 and 80% by 2040 (Dahlstrom *et al.*, 2023).

There are concerns in the Cook Inlet region over the reliability of long-term natural gas supplies, with natural gas-fired power plants currently providing the bulk of electrical production in the region. Imported LNG may become necessary in the near future, would almost certainly lead to a higher price of electricity to the consumer (ENSTAR, 2024). In a recent 2023 survey conducted by the Alaska Center for Energy and Power (ACEP) 82% of 275 respondents 'somewhat' or 'strongly' favored geothermal technology as a future carbon neutral solution for the Railbelt region (Asmus, *et al*., 2023).

Geothermal power produced at Augustine Island could replace the current coal-fired power plants operating in the interior of Alaska and within the Railbelt region. These coal fired power plants produce a total of 816,000 MWh over a typical 12 month period, emitting a total of 1.7m tonnes of CO2e per year (Goodfellow and Birnbaum, 2023).

2. Geological Setting of Augustine Island

Augustine Island (otherwise referred to as Augustine Volcano or Mt. Augustine) is located in the southwestern Cook Inlet, south-central Alaska, approximately 175 miles southwest of Anchorage and 60 miles west of Anchor Point on the Kenai Peninsula (Figure 1).

Augustine Volcano, an andesitic stratovolcano began erupting before the late Wisconsin glaciation, some 75,000 years ago (Waitt and Begét, 2009) although Waythomas and Waitt, 1998 place the timing of the initial volcanic intrusion at approximately 40,000 years ago, on a small island of upper Jurassic Naknek Formation to upper Cretaceous sedimentary rock, in the Cook Inlet, Alaska (Waitt and Begét, 2009). Augustine Volcano most recently erupted in 2006 and prior to that, during the late 20th Century (Kamata et al., 1991, Power et al., 2006, Swanson and Kienle, 1988 and Waitt and Begét, 2009).

Several have postulated that Augustine volcano contains a relatively shallow magma chamber (Koulakov *et al.*, 2023, Eichelberger *et al.*, 2023, Power, 2023 (*pers comm)*) and we concur. Koulakov *et al.*, 2023 used arrival time data from local seismicity recorded by a number of seismic stations on the island to identify a shallow rigid core composed of igneous rocks but strongly fractured and saturated with fluids and melts. Above this the authors note a zone associated with degassing of deep fluids. We explore this further. Eichelberger *et al.*, 2023 and Power, 2023 (*pers*

comm) have postulated that the Augustine Volcano magma chamber is estimated to be at a depth of only 4 km with an expected temperature of 840°C and a de-gassing zone of approximately 300°C at around 1 km below sea level.

2.1 The southern flank of Augustine Island

Outcropping on the southern flank of Augustine Volcano are a approximately 500ft thick series of approximately 1 mile^2 gently dipping sedimentary rocks attributed to the Upper Jurassic Naknek Formation (Figure 2, Detterman and Reed, 1964, Detterman and Jones, 1974, Buffler, 1976, amongst others).

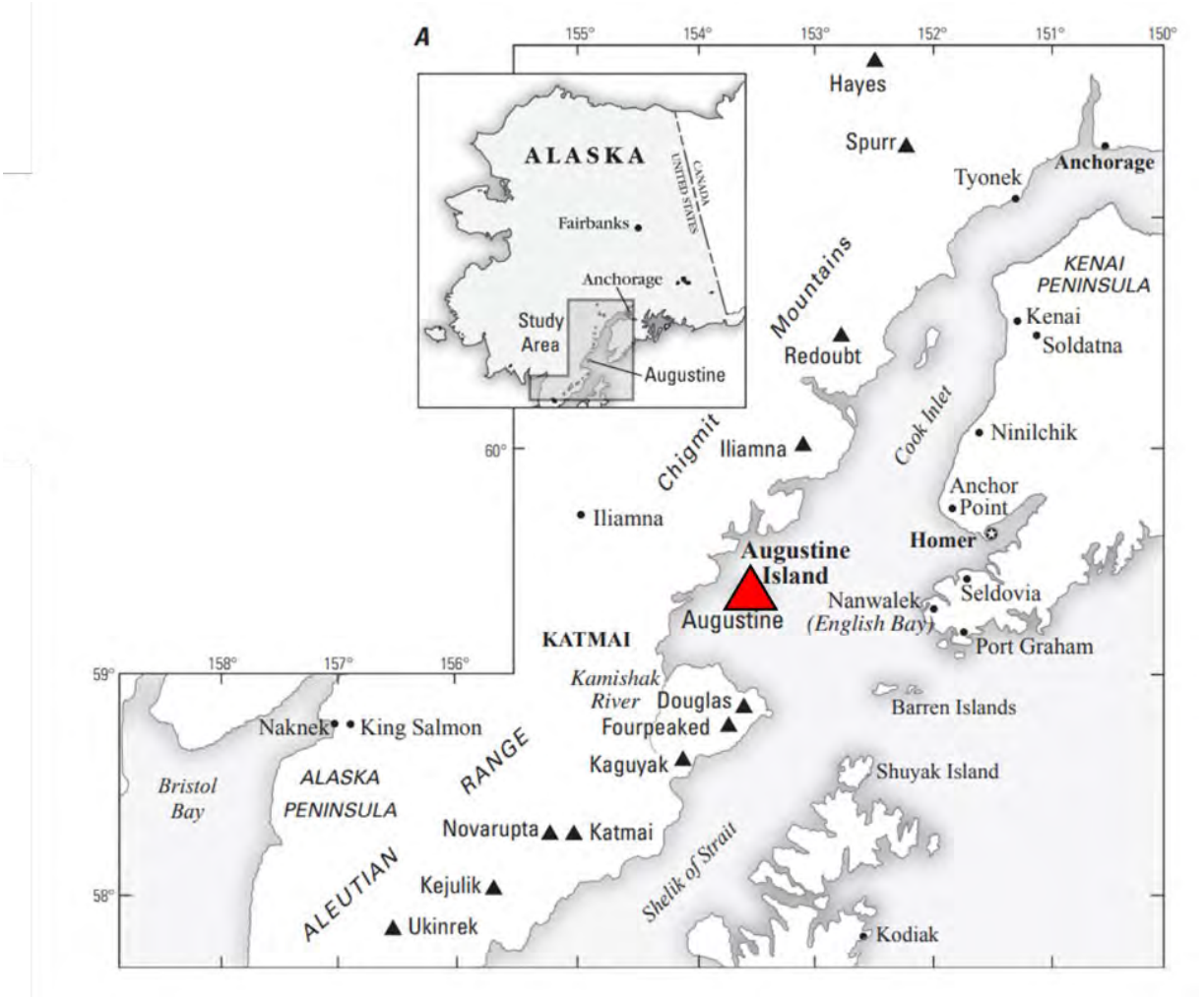

Figure 1: Cook Inlet area, Alaska; volcanoes shown as triangles, towns/cities as dots. Augustine Volcano shown as red triangle (modified from Waitt and Begét, 2009).

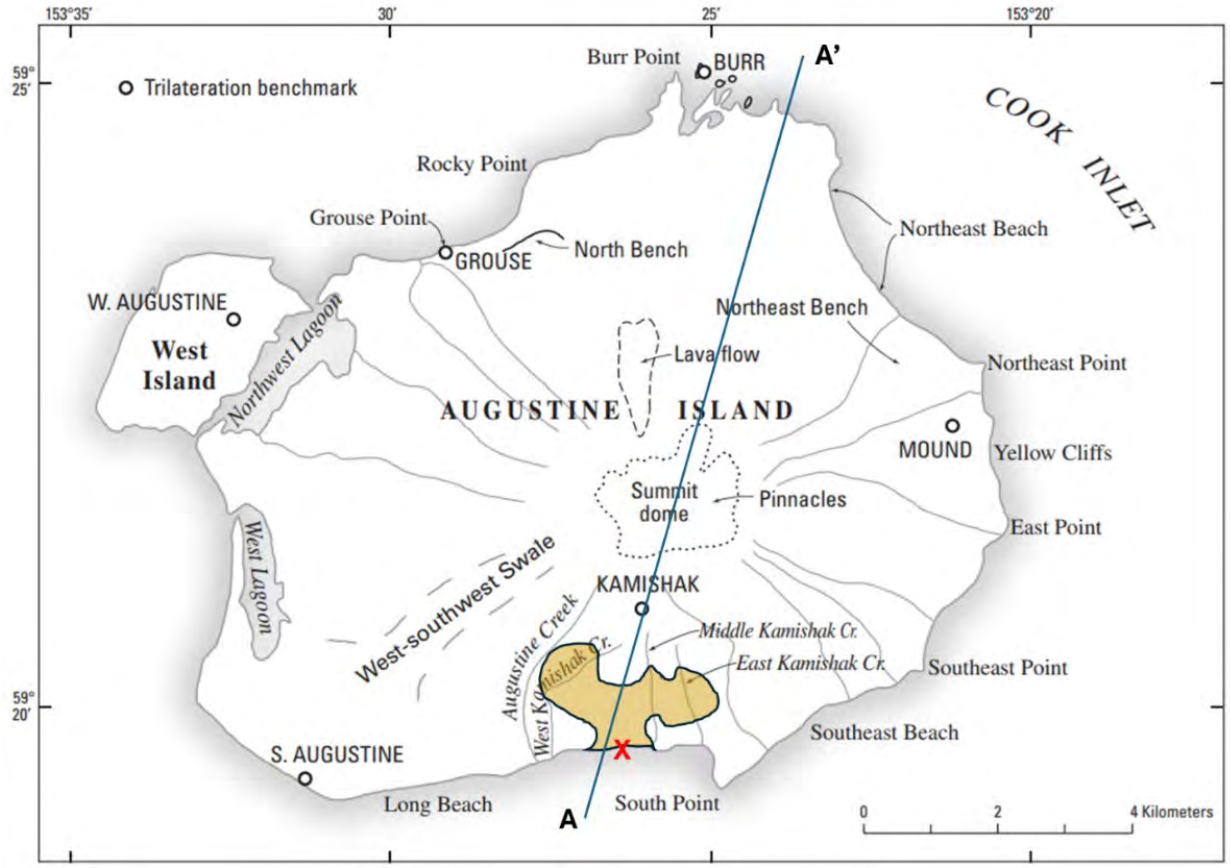

Figure 2: Approximate outcrop of Upper Jurassic Naknek Formation (brown shading) on the southern flank of Augustine Island (modified from Waitt and Begét, 2009). The red 'X' marks the location of the outcrop sampling (see below).

On Augustine Island, the Naknek Formation comprises a lower member of thin-bedded dark-gray siltstone to very fine sandstone and an upper member of thickly bedded medium to fine grained sandstone in places showing evidence of trough cross-bedding, lignite clasts and petrified wood (Waitt and Begét, 2009). The Naknek Formation on Augustine Island suggests deposition in a shallow restricted nearshore bay environment (Waitt and Begét, 2009). Interestingly, approximately 80 miles further north at Chisik Island, the Naknek Formation consists of deep-water channel deposits in sub-marine canyons (Herriott, T., *et al.*, 2016). Other workers (*e.g.* Koulakov *et al.*, 2023b and Syracuse *et al.*, 2011) have reported that the uplifted Jurassic section is commonly zeolitized.

2.1.1 Outcrop sampling

During the Fall of 2023, GeoAlaska sub-sampled various sedimentary strata exposed in the beach and cliff section at the eastern extent of Long Beach (see Figure 2 for location). In total, 15 samples were collected of which 13 are of a sedimentary origin and 11 likely representative of different facies within the Naknek Formation (Figure 3 and Table 1). These sedimentary samples ranged from well cemented siltstone containing calcite cemented fractures to well cemented medium to coarse grained oxidized sandstones. Abundant bivalves were identified in some of the samples. XRD and XRF data from these outcrop samples indicate a clay mineralogy indicative of

chlorite and smectite (up to 29% in sample 20) with minor illite, throughout. In addition, in samples 13, 19 and 21 zeolites were identified ranging from 7.6 weight% (sample 21, Clinoptilolite) to 17.9 weight% (sample 13, Laumontite). Sample 19 was found to contain 10.7 weight% Heulandite.

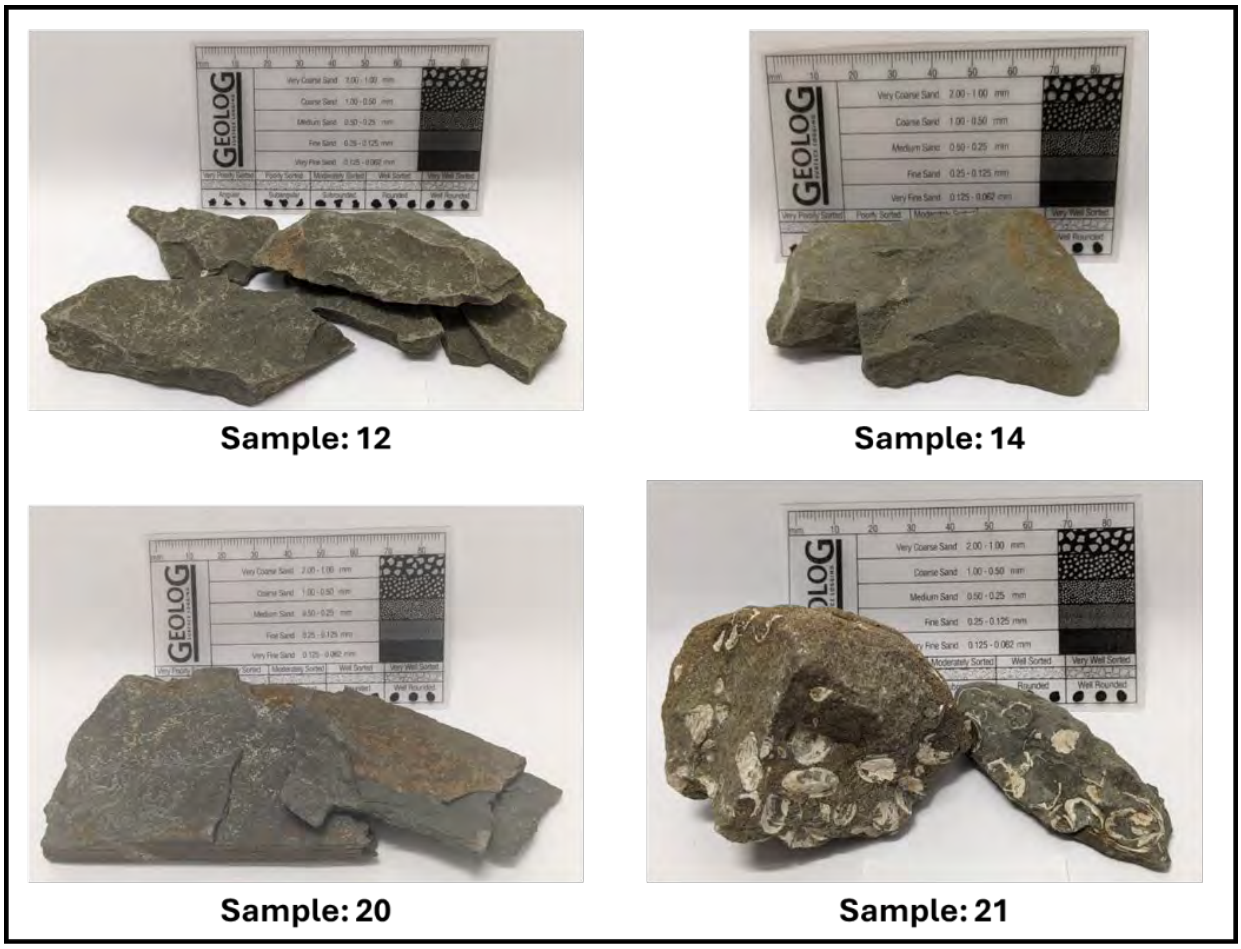

Figure 3: Outcrop samples from Long Beach, south Augustine Island. See Figure 2 for location of sampling.

2.1.2 Cross section

In their 2009 publication, Waitt and Begét include a NNE/SSW cross section of Augustine Island (see Figure 1 for cross section line) the southern portion of which is displayed in Figure 4 below. Note their assumptions of the Jurassic sub-crop, which this paper will explore further based on new MT, gravity and seismic data. It is the location, extent and composition of this Jurassic sub-crop that is a key component of the geothermal resource potential of the southern flank of Augustine Island.

3. Available Database

Table 2 summarizes the available data utilized for the exploration campaign to-date. In addition to the outcrop samples collected during the Fall of 2023, an initial Acoustic Magnetotelluric

(AMT) and Gravity survey was commissioned by GeoAlaska during the summer season of 2023 covering the entire ADL 394080 permit area. The MT survey consisted of 28 MT stations (Figure 5A) while the Gravity survey consisted of 215 stations (Figure 5B).

Table 1: Outcrop samples from Long Beach, south Augustine Island, sedimentological description. Highlighted rows refer to samples displayed in Figure 3.

Sample	Lithology	Colour	Density (g/cm^3)	Notes	Interpretation
1	Porfyric lava	Medium Grey (N5)	2.33	Hard, visible femic minerals (and some Obsidian), plagioclases and feldspars in a greyish groundmass.	Probable volcanic deposits
4	Porfyric lava	Grayish Red (10R 4/2)	2.52	Hard, millimeter sized feldspars and reddish femic crystals in a reddish groundmass.	
2	Claystone	Moderate Yellowish Brown (10YR 5/4)	1.94	Loose clay.	Probable recent Pleistocene to Late Holocene deposits
3	Claystone	Moderate Brown (5YR 4/4)	1.86	Soft claystone with some volcanic and sedimentary grains	
10	Sandstone	Dark Grey (N3)	2.42	Medium hard layered sandstone with cleavage. Presence of black fossils.	Probable Upper Jurassic sandstone and shale Naknek Formation
11	Sandstone	Olive Grey (5Y 4/1)	2.37	Hard coarse sandstone, reddish oxidation on some sides of the rock sample.	
12	Sandstone	Dark Grey (N3)	2.30	Hard fine grained sandstone. Presence of thin veins.	
13	Sandstone	Olive Grey (5Y 4/1)	2.33	Poorly well cemented coarse grained sandstone. Presence of fine-grained layers. Presence of dark micas.	
14	Sandstone	Olive Black (5Y 2/1)	2.15	Moderately hard. Presence of localized oxidation.	
15	Sandstone	Olive Black (5Y 2/1)	2.30	Hard fine grained layered sandstone. Presence of veins.	
17	Calcite veins in sandstone	Dark Grey (N3)	2.42	Pseudo-acicular/prysmatic veins witihn a fine grained sandstone. Calcite veins are coated by iron oxides.	
18	Siltstone	Dark Grey (N3)	2.52	Very hard cemented siltstone. presence of veins (calcite?).	
19	Sandstone	Olive Grey (5Y 4/1)	2.24	Moderately hard coarse grained sandstone. Slightly layered.	
20	Siltstone/Sandstone	Dark Grey (N3)	2.25	Moderately hard laminated coarse grained siltstone/fine grained sandstone . Slightly cemented.	
21	a) CG Sandstone; b) FG Sandstone	a) Light Olive Grey (5Y 5/2); b) Dark	2.42	a) Moderately hard, cemented, abundant fossils (bivalves) ; b) Hard, presence of fossils (bivalves) and veins.	

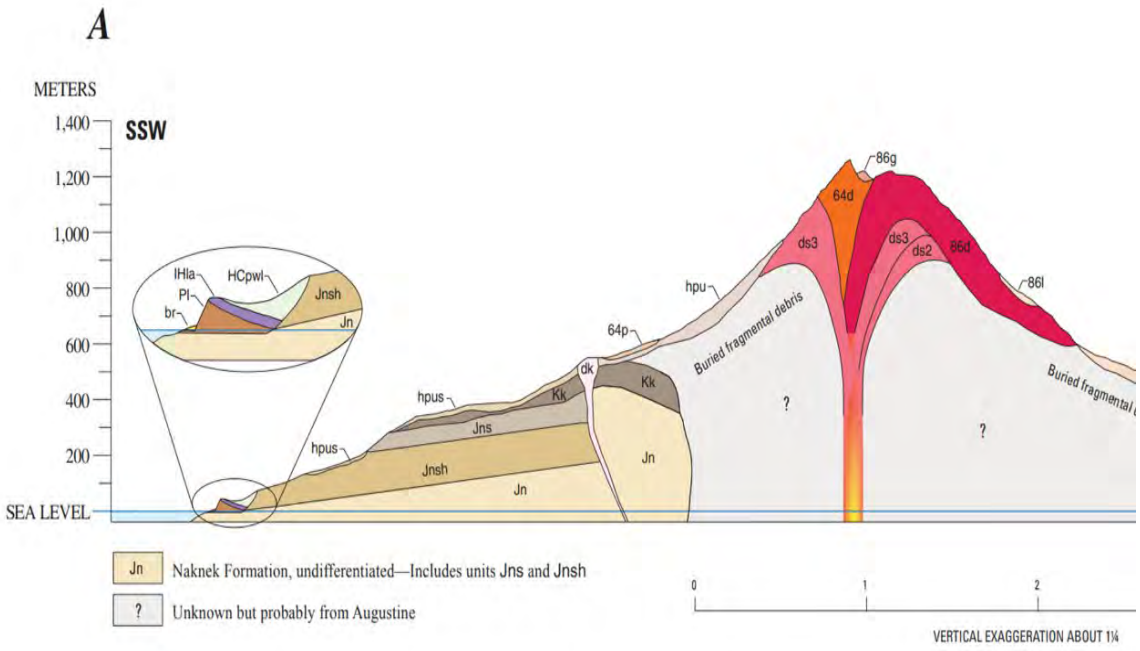

Figure 4: Cross section of the southern flank of Augustine Island (after Waitt and Begét, 2009).

Table 2: Summary of the available data utilized to-date for the exploration campaign on Mt. Augustine.

Data Type	Raw Data	Output Data	Interpreted Data	Notes	Reference
Geologic Structure	Yes	Yes	Yes	-	(Waitt and Begét, 2009) (Syracuse et al., 2011) (Koulakov et al., 2023b) Field studies, 2023
Temperature Logs for Shallow Wells	No	No	No	-	-
MT Data	Yes	Yes	Yes	AMT not MT.	Field studies, 2023
Resistivity Survey	Yes	Yes	Yes	With AMT Data above.	Field studies, 2023
Seismic Survey	Yes	Yes	Yes	The data is given in DAT file by (Koulakov et al., 2023b). The raw provided by USGS	(Syracuse et al., 2011) (Koulakov et al., 2023b)
Water Chemistry	Yes	Yes	Yes	Summit fumarole gas measurements from 2008 (5) & 2010 (3)	(Evans et al., 2015)
Gravity Data	Yes	Yes	Yes	In conjunction with AMT survey	Field studies 2023
Eruptions	Yes	Yes	Yes		(Kamata et al., 1991; Power et al., 2006; Swanson and Kienle, 1988)

In addition, GeoAlaska used catalog data provided by the Alaska Volcano Observatory (AVO) which includes arrival times of seismic *P* and *S* waves recorded by permanent seismic networks operating on the volcano. In this study we used data from January 2001 to December 2017, which included 6624 events recorded by 15 permanent stations deployed on the flanks of the volcano.

4. Geophysical Data Interpretation and Modelling

4.1 AMT and Gravity Data

From the AMT and Gravity data, a combined 3D inversion model was built using Geotools and RLM-3D code. The resulting 3D resistivity and density volumes were uploaded into Leapfrog Energy software where depth and vertical slices were extracted to visualize any low-resistivity and high-density anomalies. The visualizations were complemented by uploading the geological map of Mt. Augustine including the location of any potential geothermal elements.

The generated model revealed a sector with a convergence of low resistivity and high-density volumes on the southern flank of Augustine Volcano that could represent a working hydrothermal system, underlying a geothermal clay cap.

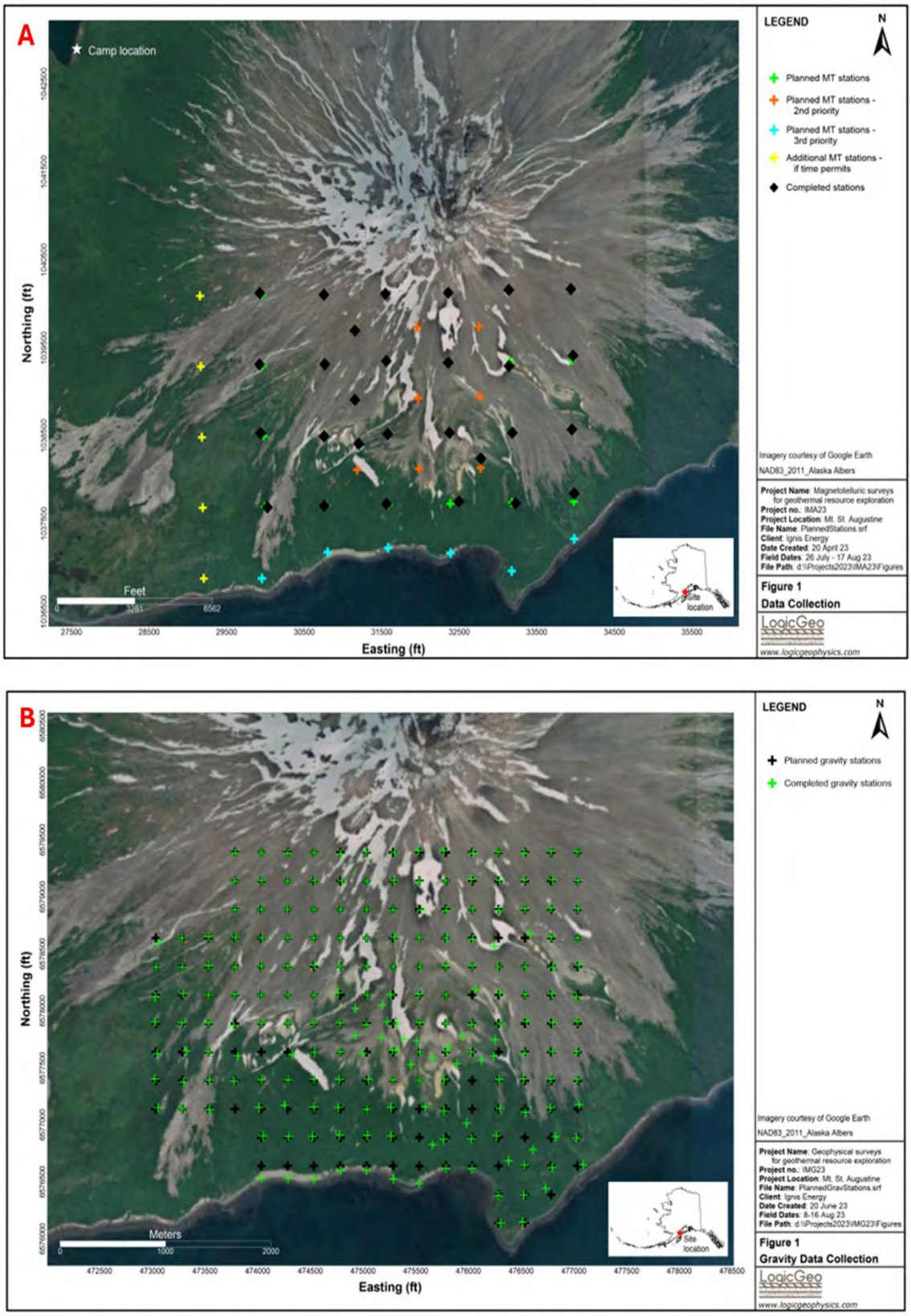

Figure 5: Maps showing the location and number of collected data from AMT (A) and Gravity (B)

4.2 Seismic Data

LOTOS code has been used for the seismic inversion and to construct the 3D visualization of Mt Augustine seismic data (Koulakov, 2009). The *P* and *S* wave velocities have been analyzed to get an insight on the potential geothermal reservoir tomography. The limitation and details of the code are beyond the scope of this article so the reader is referred to Koulakov, (2009); Koulakov et al., (2023b); Koulakov, (2020) for more information. The 3D inversion was sliced into 4 vertical cross-sections Figure 6) and 5 horizontal cross-sections. The data filtration was based on the approach of Koulakov, *et al.* 2023 which resulted in a total of 3,127 events with 10,680 P-wave picks and 11,080 S-wave picks. Although our approach is similar to Koulakov *et al.* (2023), their main focus was the volcanic pluming system, while our main focus is identifying a potential geothermal resource. Figure 7 shows the absolute P (V_P) and S (V_S) waves velocities for vertical and horizontal cross-sections. Also, the anomalies in P (dV_P) and S (dV_S) wave velocities are presented in Figure 8. The relatively similar count for P-wave picks and S-wave picks made it easier to obtain the ratio of dV_P/dV_S (shown in Figure 8). It is noted that in each of the cross-sections displayed in Figures 7 and 8, the lack of seismic events away from the central region is due to a limited number of seismic stations over the flanks of the volcano.

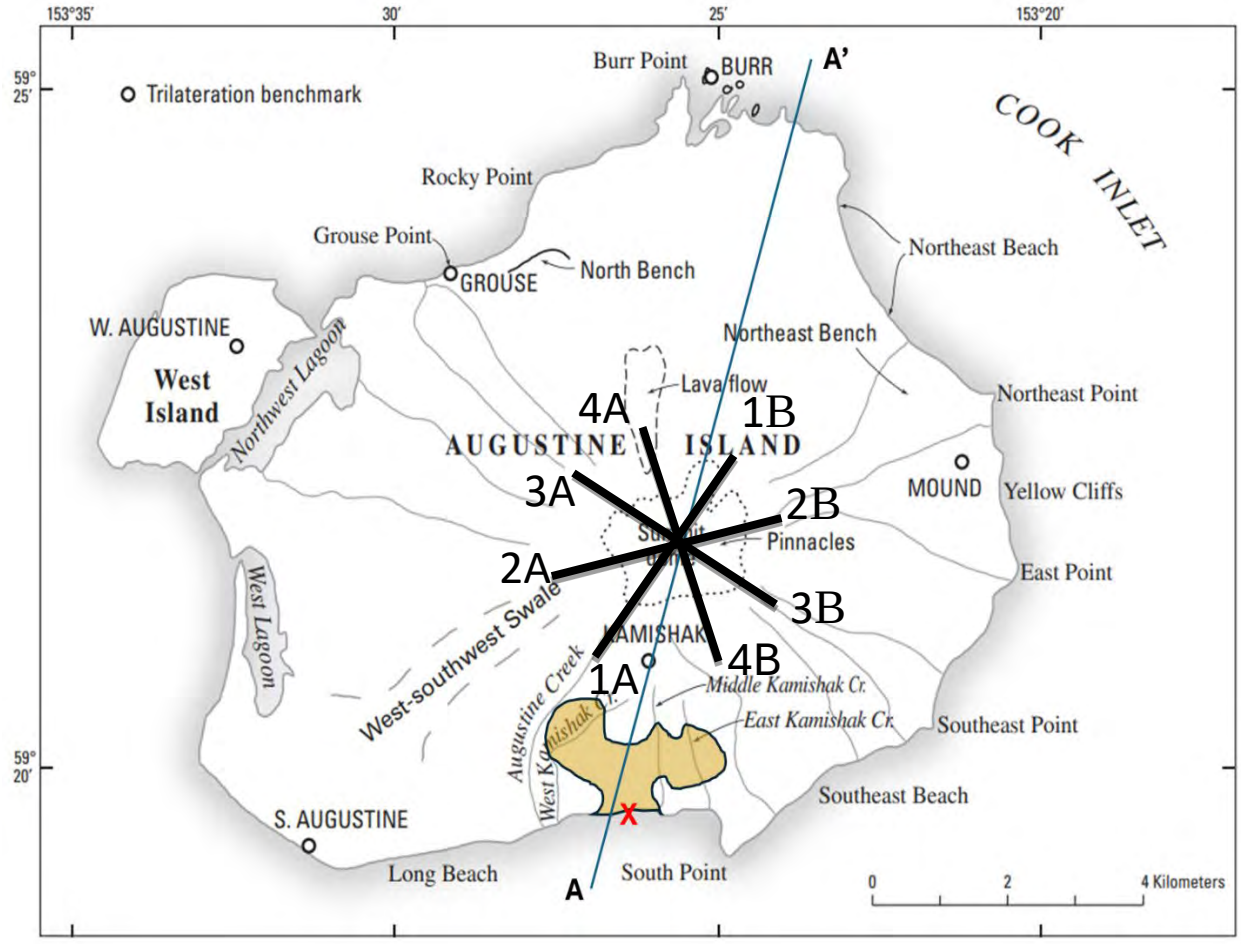

Figure 6: Locations of the 4 vertical seismic sections across Mt Augustine. Sections 1A-1B and 4A-4B are most relevant to this paper and will be discussed further.

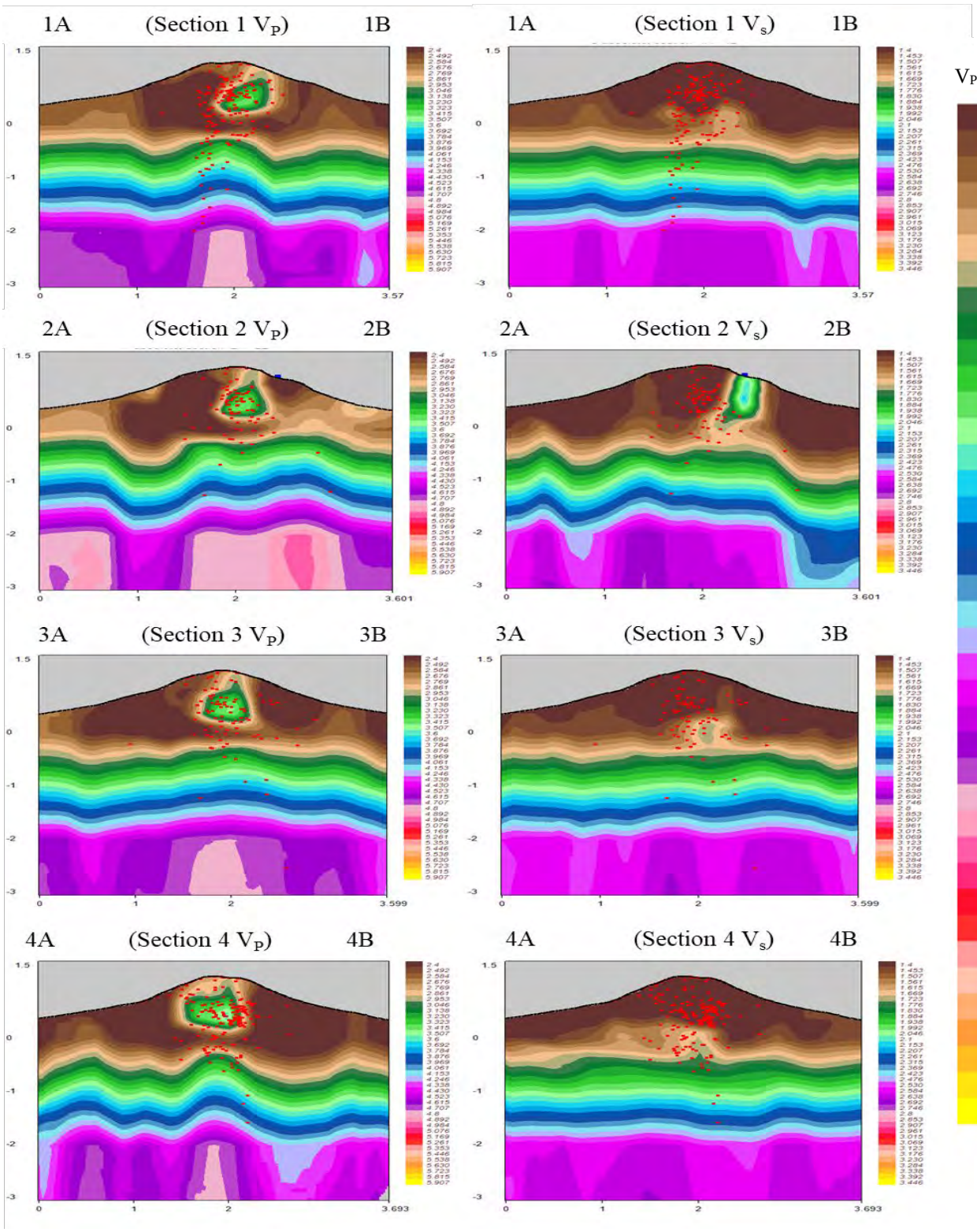

Figure 7: V_P (left column) and V_S (right column) measured in Km/sec for the 4 vertical sections (1 to 4) shown in Figure 6. The red dots represent measured seismic events, Y-axis is the elevation/depth above/under sea-level in Km and X-axis is horizontal displacement in Km along the 4 vertical seismic sections (shown in Figure 6) starting from 0 at point A and ending at point B in all subfigures.

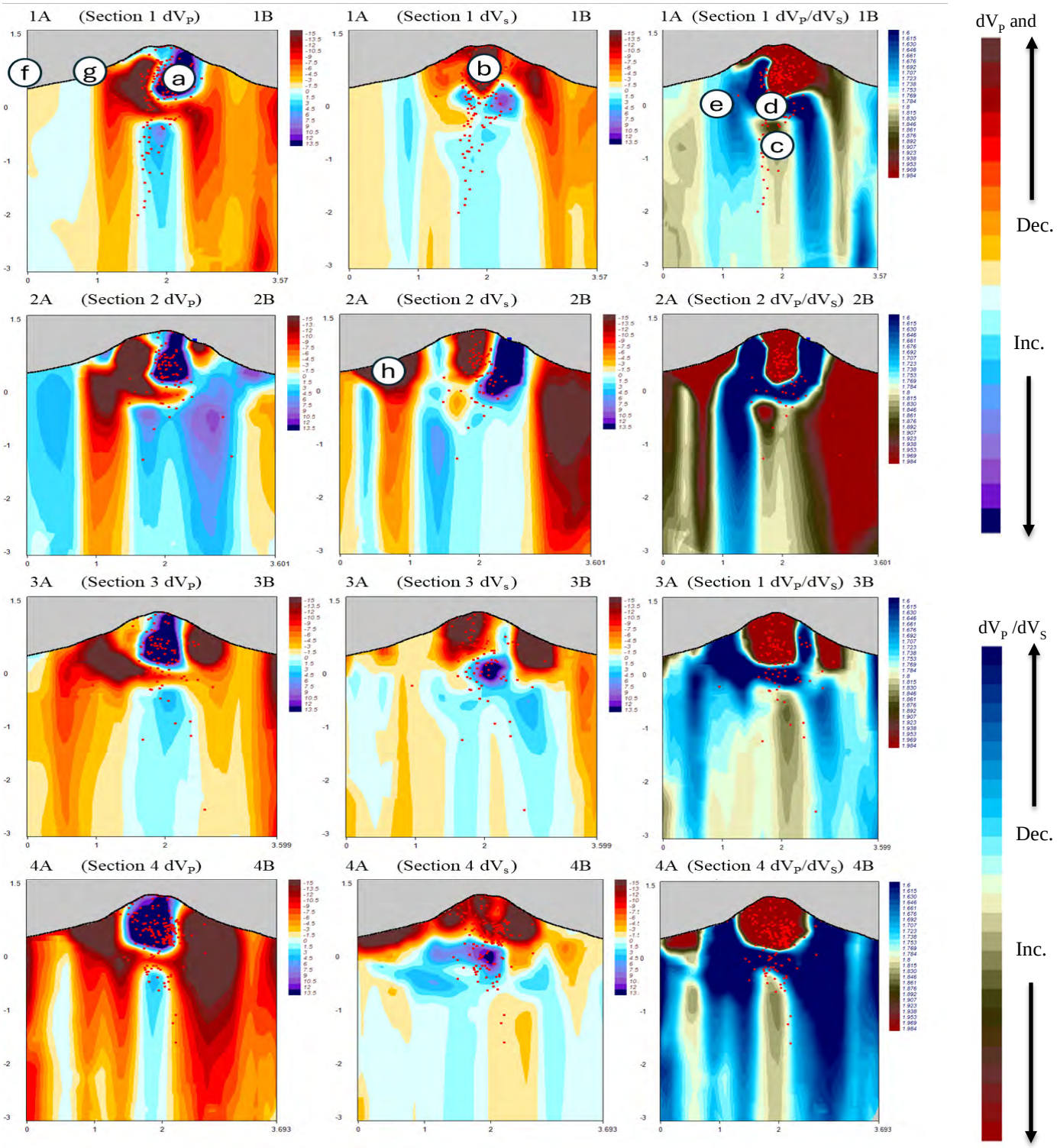

Figure 8: Shows dV_P (%) in the left column, dV_S (%) in the middle column and dV_P/dV_S (dimensionless) in the right column for the 4 vertical sections (1 to 4) shown in Figure 6. The red dots, Y-axis and X-axis are the same as described in Figure 7. See text for explanation of annotations a through h.

5. Subsurface Modelling

5.1 Geological Model (incorporating the AMT and Gravity data)

Figure 9 below is adapted from Waitt and Begét, 2009 and illustrates the geological model of the potential geothermal resource below the southern flank of Augustine Volcano. Outcrop data suggests that the Upper Jurassic sedimentary pile (light brown color on Figure 9, and acronyms Jnsh and Jns) has been faulted due to compression, probably as a result of the initial volcanic intrusion. These faults are likely to have been clay smeared reducing their effectiveness to form conduits to vertical fluid flow. It is more likely that any downward meteoric fluid flow occurs through or at the contact between the more porous volcanic sediments that onlap the Jurassic sub-crop.

XRD data from outcrop samples reveals that the Jurassic sediments can contain up to 29% smectite. In the sub-surface where there is interaction between super-heated brines and the sedimentary rock (yellow surfaces in Figure 9) this percentage volume is likely to be more and thus the Jurassic sub-crop is predicted to form an excellent seal or clay cap to any underlying hydrothermal system contained within the fractured basement (pink polygons in Figure 9). In fact, we believe the Jurassic sub-crop is such a good seal, it is preventing any upward movement of hydrothermal fluids, resulting in a more horizontal circulation pattern for the trapped hydrothermal fluids (Figure 9). A working hypothesis is that hydrothermal fluids could be reaching the surface on the sub-sea lower flanks of Augustine Island, although as of yet, there is no direct evidence to corroborate this.

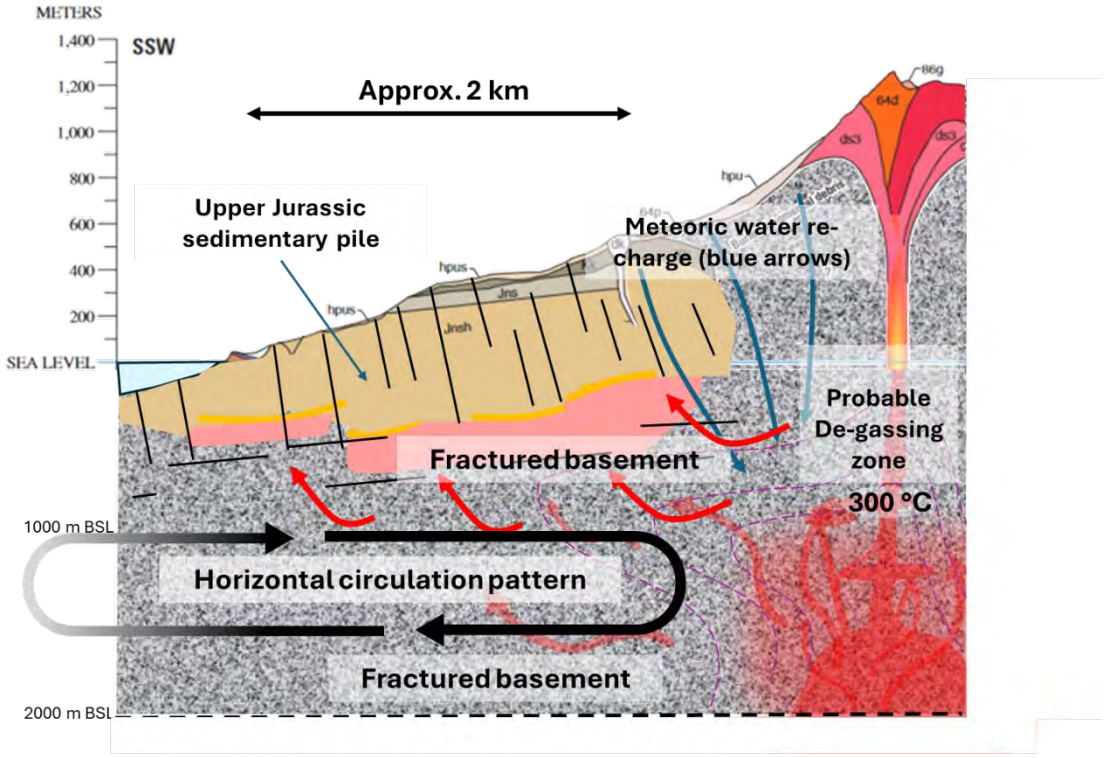

Figure 9: Geological model of potential geothermal resource under the southern flank of Augustine Volcano. See text for further information (modified from Waitt and Begét, 2009, see reference for acronym explanation).

The combined resistivity and density data from the 3D AMT/gravity datasets corroborates the above findings. The convergence of low resistivity and high density volumes on the southern flank of the island represents the Upper Jurassic sediment seal or geothermal clay cap sitting above a higher zone of resistivity which is likely to represent the hydrothermal system. (Figure 10).

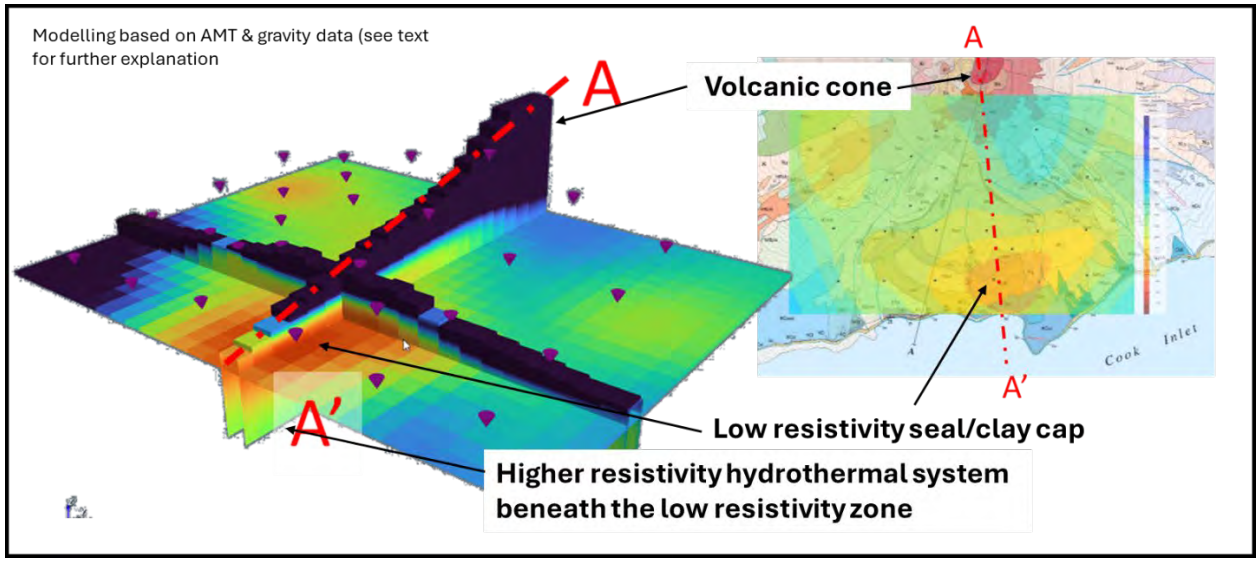

Figure 10: 3D modelling of AMT and Gravity data revealing a volume of low resistivity and high-density within the southern part of Augustine Island

5.2 Seismic model

In all vertical sections a strong anomaly of very high dV_P was observed within the edifice of the volcano which is interpreted as the igneous rock structure within the edifice (see Figure 8, point a). Conversely a very low dV_S was observed within the edifice which can be interpreted as fractures filled with fluids and melts (see Figure 8, point b). Also, the data reveals a high dV_P, low to moderate dV_S columnar anomaly associated with high dV_P/dV_S observed at a greater depth below the edifice which is interpreted as a slender magma conduit (see Figure 8, point c). In addition, a sudden change in dV_P/dV_S from high to low values is observed between the edifice and the magma conduit. This behavior is associated with high, dense seismicity and could be the result of a zone of degassing region (see Figure 8, point d).

The Southern flank of Mt Augustine represents a high potential for geothermal resource development. In section 1A-1B we observe the presence of a columnar anomaly of relatively high dV_P, high dV_s and relatively low dV_P/dV_S (see Figure 8, point e). This anomaly could be interpreted as a brittle zone where degassed fluids form fractures and quickly propagate upwards (Koulakov et al., 2023a). Also, in section 1A-1B both dV_P and dV_S increase as we go further away from the shoreline (see Figure 8, point f to g). This increase could be due to the decrease in the saturation of water further away from the shoreline. Aside from the magma conduit and edifice, the Upper Jurassic silts and sands were observed to have a higher V_P and V_S. This observation coincides with the theory of having a thermally altered clay layer that works as a seal between the fractured saturated basement below and the silts and sands, above. Similar anomalies were observed for section 4A-4B and the interpretation of these anomalies is the same.

In section 2A-2B, a relatively high dV_P associated with low dV_S which results in high dV_P/dV_S anomaly is observed under the southern flank of the volcano (see Figure 8, point h). Our interpretation is that dV_P is less in this region because of the Upper Jurassic sedimentary lithology (Takei, 2002; Waitt and Begét, 2009) when compared to the igneous structure of the edifice. On the other hand, another reason for dV_P to increase is the presence of water. This assumption is verified by the low dV_S and high dV_P/dV_S in the area (Adam and Otheim, 2013).

Combining the geological, resistivity, gravity and seismic data, the basis of a working hydrothermal system is identified under the southern flank of Augustine Volcano (Figure 11). The geological, resistivity and gravity data support the identification of an effective seal/clay cap, while the seismic data identifies a fluid filled zone of fractured basement directly beneath this. The areal extent of the seal/clay cap has been calculated as 3000 m^2 while the underlying hydrothermal resource volume has been calculated as 1,200,000 m^3 (based upon currently available data).

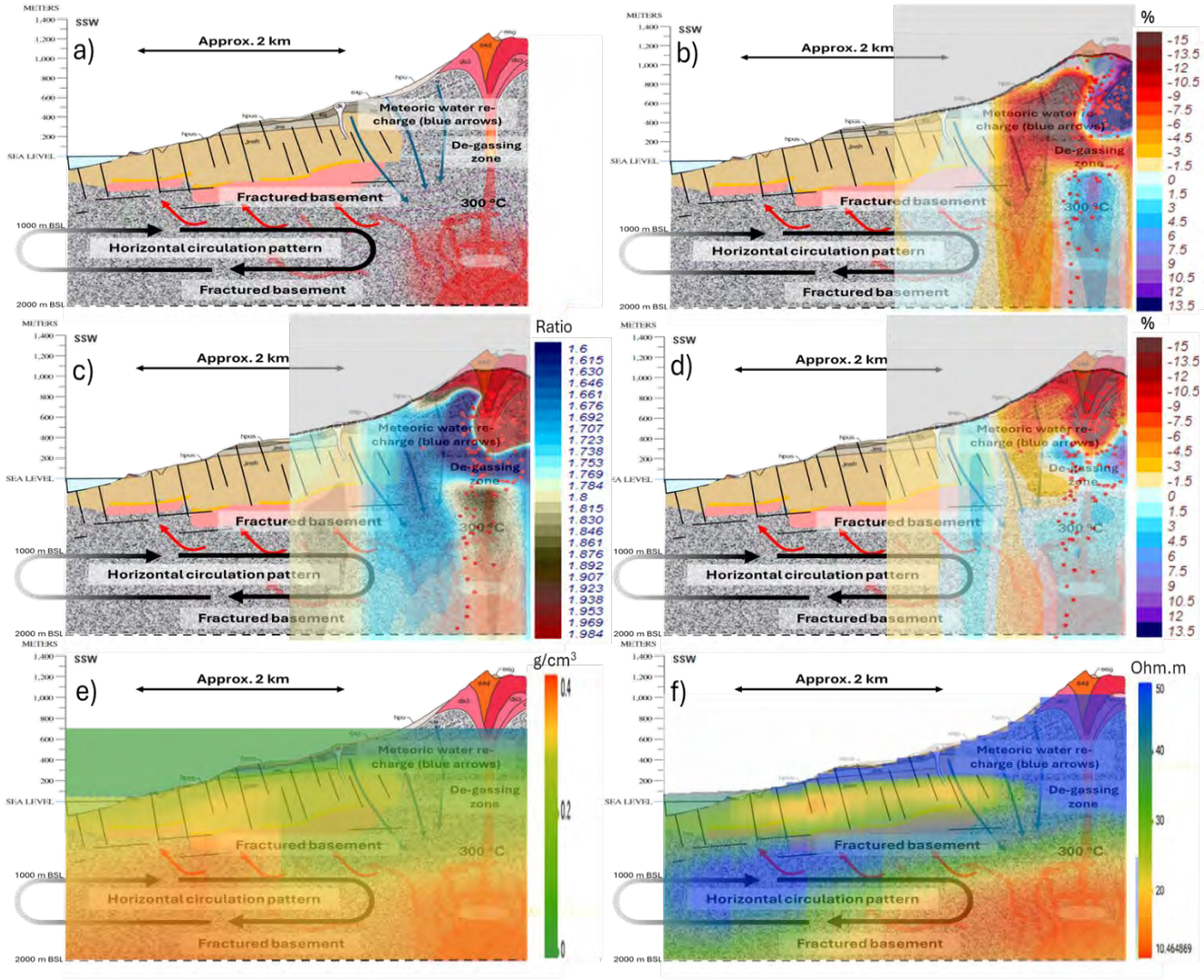

Figure 11: Full sub-surface model combining the (a) geologic model with (b) dVP, (c) dVP/ dVS, (d) dVS, (e) gravity and (f) AMT data.

5.3 Discussion

Due to the presence of the Jurassic seal/clay cap, we describe this geothermal resource as 'atypical'. A typical geothermal resource on a volcanic flank normally requires hydrothermal alteration of volcanic sediment/basement in order to create an effective seal. In addition, and due to the absence of identified surface manifestations, the potential geothermal resource identified at Augustine Volcano could be described as 'blind'. Blind geothermal systems are hydrothermal systems that lack surface thermal features (*e.g.* hot springs, mud volcanoes, *etc*). However, they share many features in common with conventional identified hydrothermal systems. Dobson, 2016 identifies a number of geologic factors that could prevent the rise of hot, buoyant fluids from reaching the surface including,

- Blind systems may have thicker, better developed seals
- Faults associated with blind systems may not reach the surface or may be fault-sealed
- Blind systems may contain depressed water tables that result in no surface thermal manifestations
- Blind systems may be obscured by an overlying cold-water aquifer
- Blind systems may be smaller than identified hydrothermal systems in the same geologic setting
- Blind systems may be deeper than their identified geothermal counterparts

There are good examples of blind geothermal systems located in volcanic zones that have been developed for geothermal power production including Puna Geothermal Venture, Hawaii and Cerro Pabellón Geothermal Field, Chile. Cerro Pabellón is located in a subduction zone volcanic center and is located on the eastern flank of the Apacheta volcano, and thus has a similar geological setting to Mt. Augustine. A thick altered clay seal consisting of smectite-illite mix has formed over the geothermal reservoir, blocking any vertical migration of fluids, thus resulting in a dominant horizontal circulation pattern (Maza *et al.*, 2021, Baccarin *et al.* 2021). Despite the lack of surface manifestations, Cerro Pabellón geothermal system has a current installed power capacity of 83 Mwe.

Based on the data collected from Augustine Volcano to date, we believe that the potential identified geothermal resource shows many similarities with Cerro Pabellón which could represent a good analogue for future development.

6. Volumetrics and Uncertainties

Based on the results from the seismic, AMT, gravity, and geological data, a potential hydrothermal resource was identified in the southern part of the island and within the original permit area. In order to volumetrically evaluate this potential hydrothermal resource, two reservoir estimation methods (the volumetric method and the power density method) were evaluated.

The volumetric method is widely used to quantify geothermal resource capacity. Equation 1 is used to estimate the megawatts of electric power that can be generated from a geothermal resource (Muffler, 1979). Equation 2 is used to determine the thermal energy (q) measured in joules (J) (Garg and Combs, 2015; Muffler and Cataldi, 1978).

$$MWe = \frac{qXR_fX\eta_{\text{conv}}}{FXL} \quad (1)$$

$$q = q_r + q_f = Ah(T_i - T_f)[(1-\varphi)\rho_R c_R + \varphi(X_L \rho_L c_L + X_V \rho_V c_V) \quad (2)$$

X_L and X_V can be calculated using Equation 3 (O'Sullivan and O'Sullivan, 2016). While the rock is considered fully saturated where $X_L + X_V = 1$ and their entropies are obtained using the steam tables for two-phase saturated fluid. All the variables and their units are summarized in Table 3.

$$X_V = \frac{S_{L@Ti} - S_{L@Tr}}{S_{V@Tr} - S_{L@Tr}} \quad (3)$$

Table 3: Variables and corresponding units for parameters used in Equations 1 through 3.

Symbol	Name	Unit
MWe	Power Potential	Mwe
Q	Thermal energy	MJ
R_f	Recovery factor	%
L	Power plant lifespan	Seconds
η_{conv}	Conversion factor	%
F	Load factor	%
A	Area	m^2
H	Thickness	m
T_i	Initial reservoir temperature	°C
T_r	Reference Temperature	°C
T_f	Final abandonment temperature	°C
$\rho_i c_i$	Volumetric heat capacity	$J/m^3°C$
X_L	Liquid fraction	%
X_V	Vapor fraction	%
S_L	Entropy of liquid phase	J/K
S_V	Entropy of vapor phase	J/K

The power density method is another way to estimate potential power generation per area (Mwe/Km^2). The simple calculation and the few assumptions for power density make it a favorable choice especially in an early exploration phase. Wilmarth and Stimac, (2015) have developed Figure 12 for 53 geothermal fields based on tectonic settings in correlation with reservoir temperature.

Based on the current dataset, potential power generation was calculated using both power density and volumetric methods and averaged for further calculations. Since there are a lot of uncertainties associated with any green field prospect like Mt Augustine, Monte Carlo simulation (MCS) with 10,000 iterations was utilized to reduce the level of uncertainty. Figure 13 shows the histogram distribution for the potential MWe for Mt Augustine. The P_{50} has been calculated as 70 MWe with a P_{90}-P_{10} range of 49 MWe to 93 MWe. These numbers will change as GeoAlaska collects additional quantitative data.

Once the power production potential is calculated it can then be used to estimate the number of wells required to effectively produce the resource. The MWe/number of wells is assumed to be 3.5 MWe/well for slim wells (Alarcón, 2023) and 8.5 MWe/well for conventional wells, both of which agree with the Cerro Pabellón Field full field development plan (Lobos Lillo et al., 2023). Tables 4 and 5 summarize all the key data and assumptions used in the power production potential calculation. Once the optimum number of wells is calculated, the technical assessment is concluded, and the economic assessment can commence.

Based on the current dataset and the results of the volumetric modelling, the optimal number of wells required to develop the prospect is 11 conventional wells or 27 slim wells.

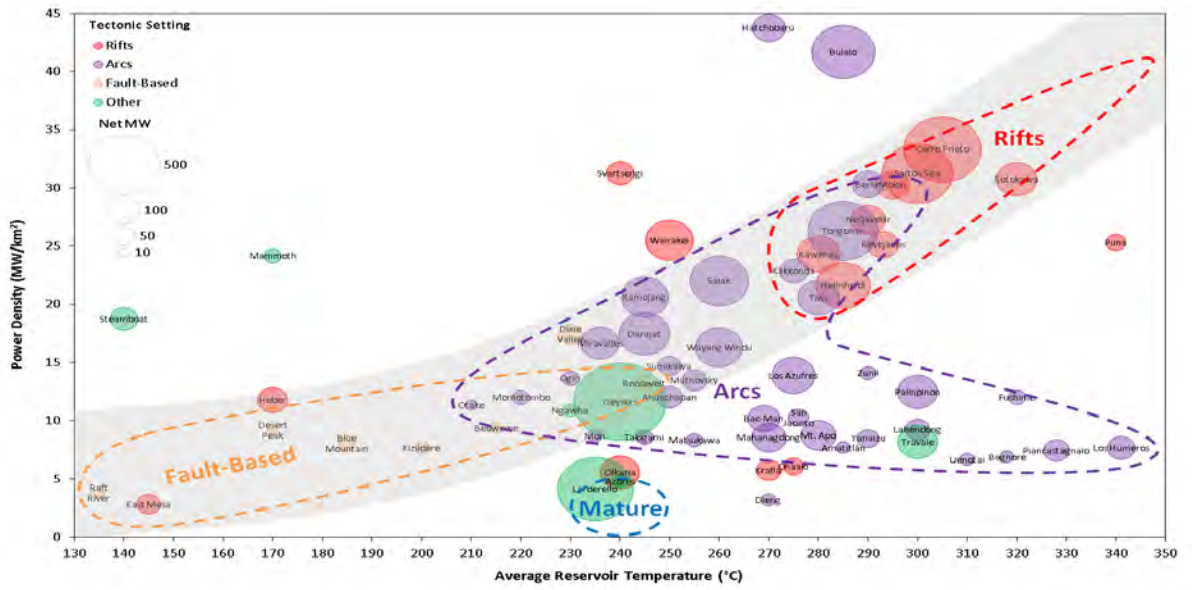

Figure 12: Clusters of geothermal wells and the correlation of their power density with measured reservoir temperature, (Wilmarth and Stimac, 2015).

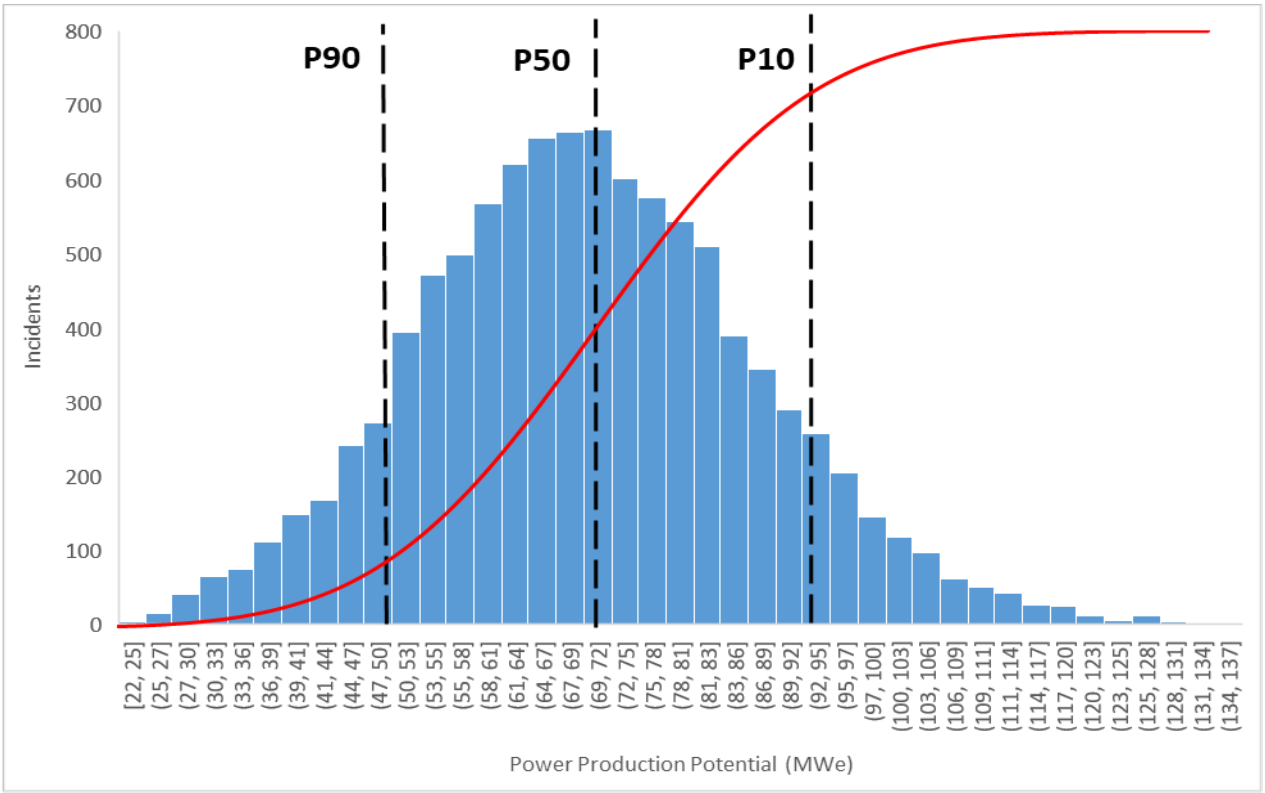

Figure 13: MCS histogram distribution for power production potential in MWe. 70 MWe is the P50 and a P90-P10 range of 49 MWe to 93 MWe. CDF is the cumulative distribution function of power production potential to be equal a certain value or less.

Table 4: Summary of the variable data utilized for MCS modelling.

Parameter	Most Likely	Minimum	Maximum	Unit	Reference
Rock porosity (φ)	10	5	15	%	(Ciriaco et al., 2020)
Recovery Factor (Rf)	15	5	20	%	(Garg and Combs, 2015)
Conversion efficiency (η_{conv})	75	70	80	%	(Garg and Combs, 2015)
Abandonment temperature (T_f)	100	100	151.831	°C	(Aravena et al., 2016)
Area	3.5	3	4	Km^2	2023 AMT Data
Thickness	400	200	600	m	2023 AMT Data
Production decline rate	0.15	0	0.5	%	(Alarcón, 2023)
Cost Increase rate	2	0	10	%	(Alarcón, 2023)
Power Density range	15	10	25	MWe/Km2	(Wilmarth and Stimac, 2015)

Table 5: Summary of the fixed data utilized for MCS modelling.

Parameter	Value	Unit	Reference
Reference Temperature	15	°C	(Sanyal et al., 2004) (Williams 2004) (Basel et al. 2010)
Initial Reservoir Temperature	280	°C	(Eichelberger et al. 2023)
Volumetric heat capacity of the rock ($\rho_R c_R$)	2700	$KJ/m^3°C$	(Aravena et al., 2016)
Lifespan (L)	30	Years	(Ciriaco et al., 2020)
Capacity factor (F)	95	%	(Aravena et al., 2016)

The economic assessment assumes the delivery of electrical power to the shoreline of Mt. Augustine and does not consider transfer of power to the mainland. It is divided into three main parts, CAPEX, OPEX and Revenue. Firstly, CAPEX can be divided into development costs and construction costs. The development cost includes surface exploration, project management, testing and reservoir management, infrastructure (well pads, etc.), drilling of production wells, drilling of injection wells, design and engineering, land, permitting, environmental management and contingency reserve. The construction cost includes powerplant engineering, procurement and construction (EPC), insurance, management and others (Martínez Ruiz et al., 2022; Osorio Luna, 2018). Powerplant EPC can be calculated using Equation 4 (Martínez Ruiz et al., 2022; Sanyal, 2005).

$$EPC = KW * CC = KW * CPP * e^{-0.0025(MW-5)} \quad (4)$$

Where, CC is the capital cost in USD/kW, CPP is the cost per kW of the powerplant, and W is the gross power output of the power plant in MW. The cost per kW of the powerplant (CPP) varies depending on the type of powerplant and any changes in the technologies involved. CPP ranges between 1,700 USD/kW to 2000 USD/kW (Alarcón, 2023).

OPEX calculations also include such costs as insurance, easements, concession leases, selling and administrative expenses, environmental mitigation, utilities, auxiliary power, OandM externalization and royalties. The net potential generation capacity is calculated by subtracting the parasitic loads shown in Table 6 from total potential capacity. Based on Table 6 calculations, the net potential generation capacity is 89% of the total potential capacity.

Based on the current dataset and assumptions the economic modelling predicts a total CAPEX investment to range from \$181 to \$287 million USD as P_{10} and P_{90}, respectively. P_{50} for total CAPEX is \$234 million USD which represents a 3.4 million USD/MWe CAPEX investment per power generation. Figures 15 shows the range of P10 to P90 for CAPEX investment per MWe.

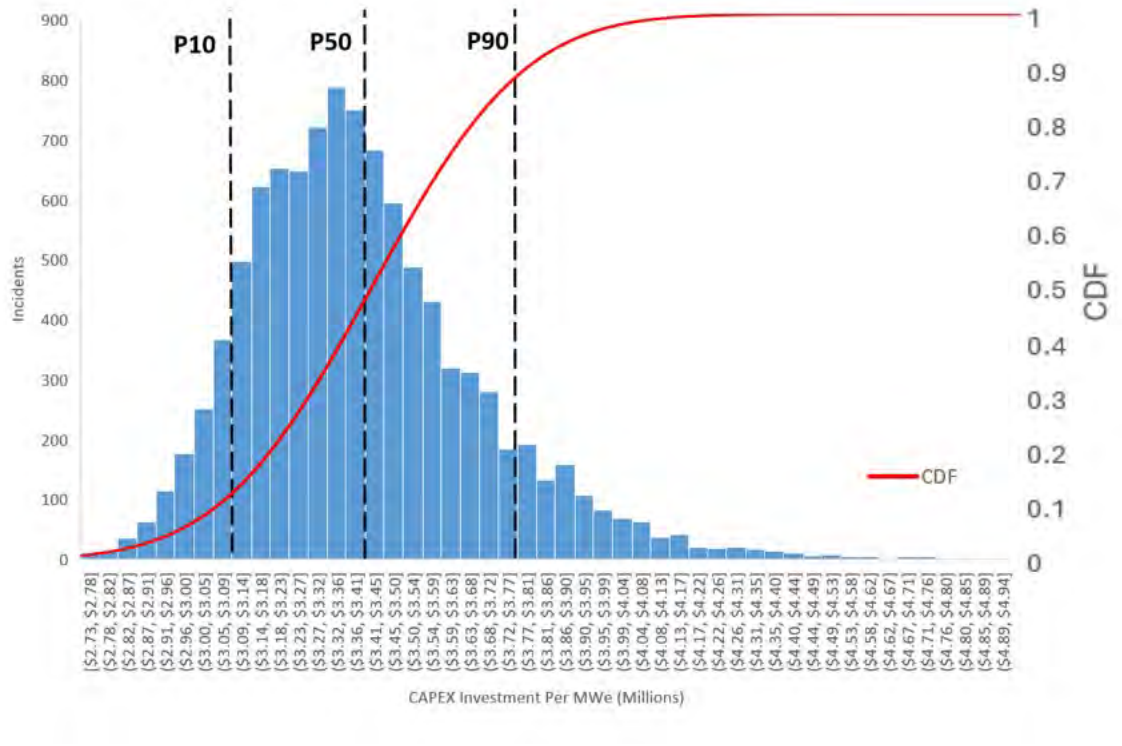

Figure 15: MCS histogram distribution for CAPEX investment per MWe. \$3.4 million /MWe is the P50 while P90-P10 range from \$3.1 to \$3.8 million/MWe. CDF is the cumulative distribution function of CAPEX investment per MWe to be equal a certain value or less.

7. Full Field Development Plan

Any development efforts are accompanied by an underlying business plan that relies on carefully derived assumptions and is updated as new information is revealed. Economic evaluation criteria include the internal rate of return (IRR) and net present value (NPV). Current assumptions in determining the viability of this project neglect beneficial tax breaks, carbon offset credits, and debt leverage from project finance. The location also warrants high capital expenditure and operating cost to mitigate against geohazards, as well as costs associated with the remote location. Finally, the financial calculations assume a zero-terminal value for the power plant after 35 years even though other geothermal plants around the world operate long after their design life spans., Figure 16 plots undiscounted cumulative net cash flow for the full project life cycle versus time.

Lastly, an overview of the full evaluation process for Mt Augustine is presented in Figure 18 and Table 7.

Based on the results obtained from the full field evaluations, the payout time for Mt Augustine is between the year 2034 to 2035, assuming a start date of January 1st 2022. The IRR for the project has an 80% probability to be between the range of 16.44% and 20.42% with P50 equal to 18.48%. Figure 17 show the histogram distribution for IRR as it calculates today.

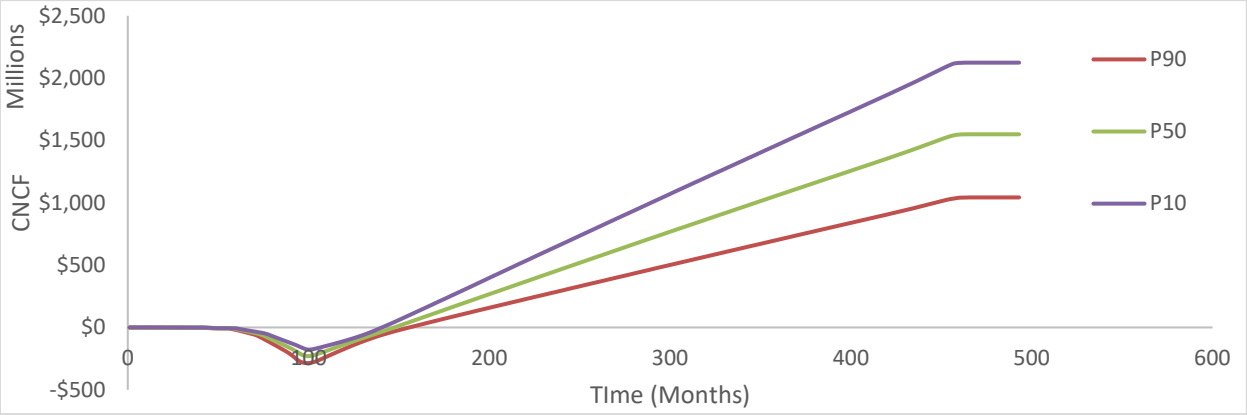

Figure 16: Undiscounted CNCF before tax versus time for different scenarios.

Table 6: Summary of the parasitic loads (Alarcón, 2023).

Type of Load	Percentage of the total capacity
Average powerplant consumption	6%
Average reinjection pumps	2.75%
Average contingency systems	2.25%
Total	11.00%

Table 7: Summary of the undiscounted economic results before tax, credits, depreciation, and project finance considerations.

Output	10%	50%	90%
Total Installed CAPEX	$ 181,496,071	$ 233,861,921	$ 287,315,152
Net Power Production Potential (MWe)	49	70	93
Number of Wells	8	11	14
Number of Slim Wells	18	27	36
CAPEX Investment Per MW	$ 3,091,623	$ 3,402,422	$ 3,771,093
IRR (35 Years)	16.44%	18.48%	20.42%
NPV (35 Years)	$ 71,403,695	$ 126,446,230	$ 185,064,641
Payout (Months)	140	147	155

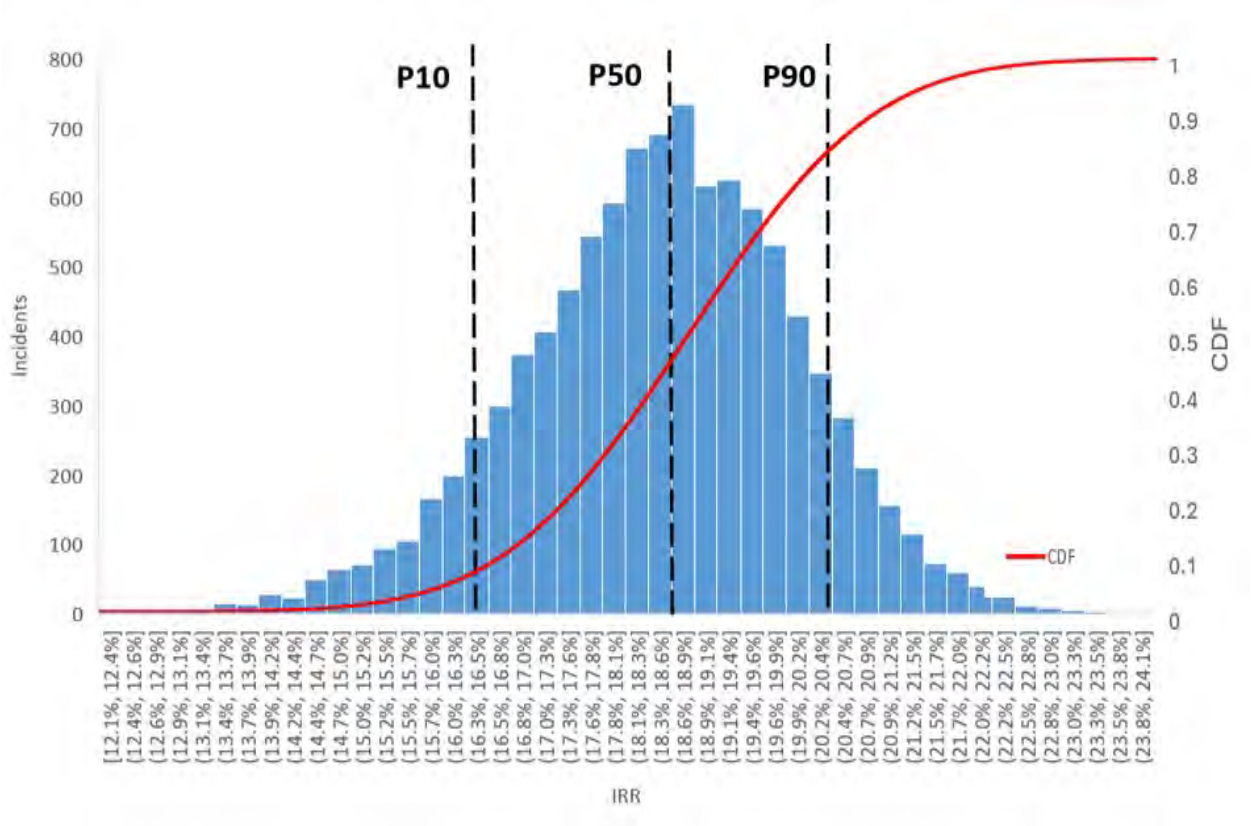

Figure 17: MCS modelling histogram distribution for IRR after 35 years. 18.48% is the P50 while P90-P10 range from 16.44 to 20.42%. CDF is the cumulative distribution function of IRR to be equal a certain value or less.

8. Next Steps

Figure 19 displays GeoAlaska's plans for exploration, appraisal. and development of the Augustine Volcano's potential geothermal resource. Our aim is to contribute to a 24/7 reliable baseload energy supply for Alaskans residing within the Railbelt Region of South-central Alaska.

GeoAlaska has commissioned additional MT data collection, processing and 3D modelling to further resolving the depth to base of the Jurassic seal, and the volume of the potential hydrothermal system identified from the 2023 dataset. GeoAlaska has expanded the survey area with the recent lease expansion; additional data will be collected across the entire south of Augustine Island to delineate the spatial extent of this and other potential prospects. During 2025, GeoAlaska intends to drill its first exploration well, the location of which will be determined by the results of the MT data analysis. The intention of the exploration well will be to penetrate beyond the base of the Jurassic seal and into the reservoir to gain information on the reservoir, fluid type, fluid flow, and temperature. This data should enable GeoAlaska to improve plans for development drilling.

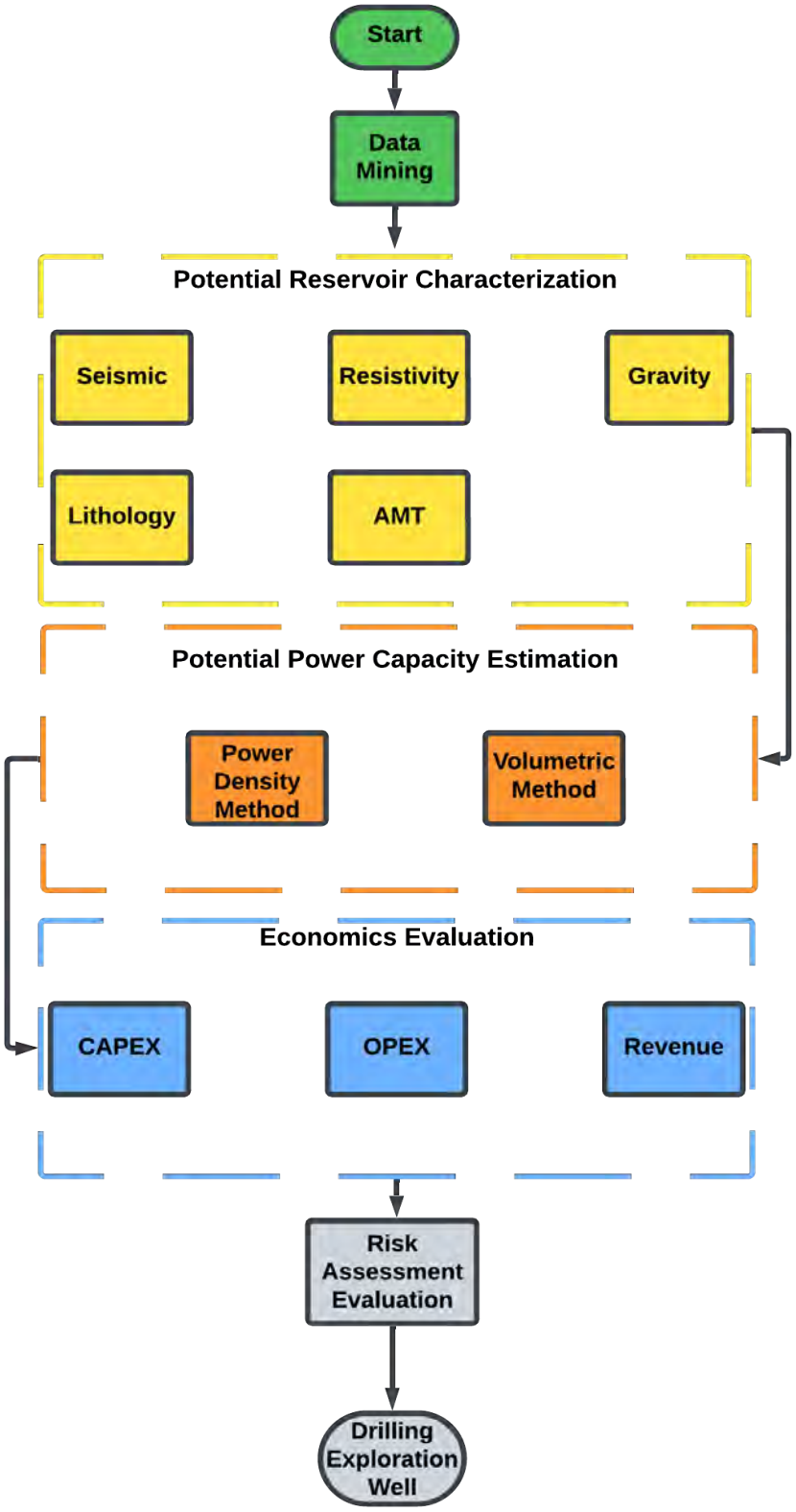

Figure 18: Mt Augustine full evaluation process.

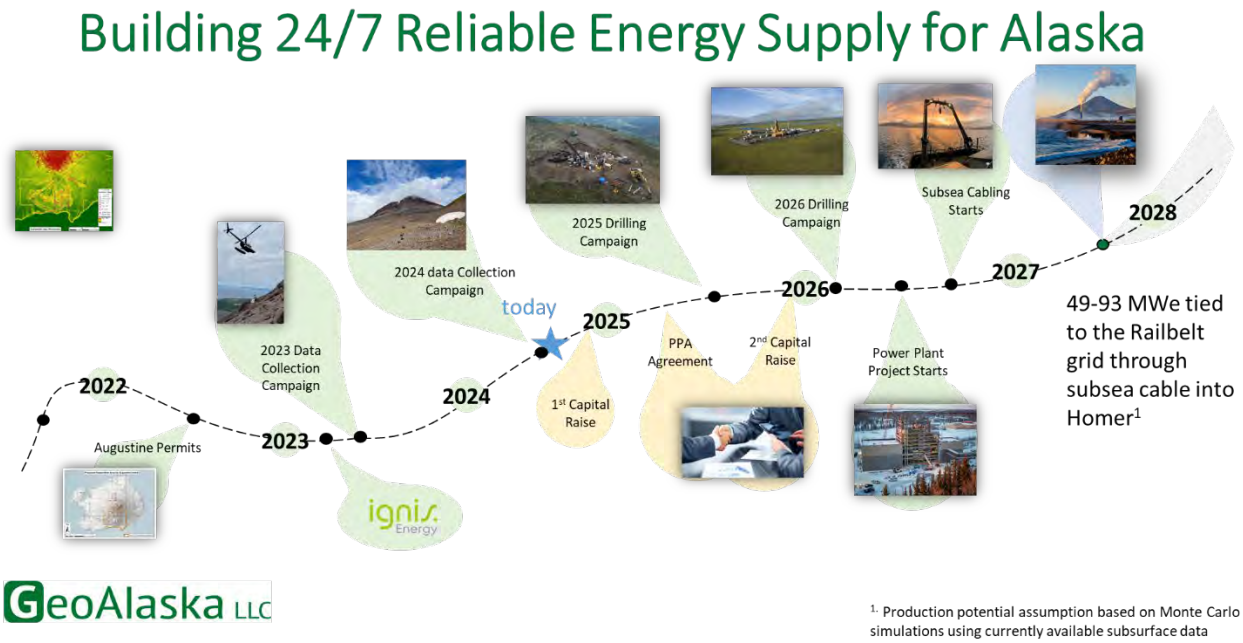

Figure 19: Expected exploration, appraisal and development timeline for Augustine Volcano geothermal project.

9. Conclusions

1. Augustine Volcano (Mt. Augustine) is an active stratovolcano located in the southwestern Cook Inlet, South-central Alaska, approximately 60 miles west of Anchor Point, Kenai Peninsula, and adjacent to the Railbelt Region of Alaska which houses approximately 550,000 residents whose current power generation is dominated by natural gas and coal.
2. The Governor of Alaska recently requested a study on the potential impacts of achieving an 80% renewable energy portfolio for South-central Alaska including any potential geothermal resource.
3. Since 2021, GeoAlaska and its partner Ignis Energy have permitted 10,830 acres and extended the original lease holding on the southern flank of Mt Augustine, with a view to explore its full geothermal potential.
4. Outcropping on the southern flank of the island are a series of silt-grade to coarse-grained Upper Jurassic Naknek Fm. sediments. Outcrop studies confirmed that these sediments can contain up to 29% smectite.
5. During the summer of 2023, AMT and Gravity data were collected over a portion of the southern flank of the island, corresponding to the first tract of geothermal prospecting permits.
6. Inversion and 3D modelling of these data suggest the presence of a low resistivity and high density seal or clay cap, corresponding to the Upper Jurassic sub-crop overlying a zone of higher resistivity which is likely to represent the underlying hydrothermal system. Based on these data, the area of the clay cap is measured at 3 km^2, while the thickness of the underlying reservoir is thought to be around 400 m.

7. GeoAlaska utilized catalog seismic data provided by the Alaska Volcano Observatory. These data corroborate the identification of a sedimentary clay cap overlying a fluid-filled zone of fractured basement.
8. Based on the assumed reservoir temperature of 280° C and all other assumptions, the potential power production was estimated using two methods, the volumetric method and the power density method. A Monte Carlo simulation predicts a P50 of 70MWe and a range (P90-P10) of 49MWe to 93MWe.
9. According to the above-mentioned economic analysis the development of Mt Augustine will require around 3.4 million USD per MWe. The IRR ranges between 16.44% to 20.42% with a payout time of 12 years from project start.
10. GeoAlaska continues to collect additional sub-surface data as a means of further de-risking the geothermal prospect(s) and to identify a suitable location to drill its first exploration well during 2025.

Acknowledgements

GeoAlaska and its partner Ignis Energy would like to acknowledge and thank the following, all of whom have assisted and contributed significantly to this project to-date:

Alaska Oil and Gas Conservation Commission (AOGCC)

Alaska Volcano Observatory (AVO)

Logic Geophysics and Analytics

Pollux Aviation Ltd.

JRG Energy Consultants Ltd.

Geolog International B.V.

Geotech labs, Milan (a Division of Geolog International B.V.)

Texas AandM University

Professor Nathan Meehan (Harold Vance Department of Petroleum Engineering, Texas AandM University) and Danny Rehg (VP Operations, Ignis Energy Inc.) both of whom provided valuable and constructive comments on the content of this manuscript.

REFERENCES

Adam, L., Otheim, T., 2013. Elastic laboratory measurements and modeling of saturated basalts. *JGR Solid Earth 118*, 840–851. https://doi.org/10.1002/jgrb.50090

Alarcón, A.I.M., 2023. Technical, economic, social, and environmental assessment of geothermal resources in Chile.

Asmus, P., Rogers, B., Cicilio, P., Colt, S., Burtness-Adams, F. and Hansen, J., 2023. Railbelt Decarbonization Pathways Study Public Comment Summary. *Alaska Center For Energy and Power Technical Report* UAF/ACEP/TP-01-001, June 2023.

Buffler, R., 1976. Geologic map of south Augustine Island, lower Cook Inlet, Alaska. *Alaska Department of Natural Resources, Division of Geology and Geophysical Surveys*, Open-File Report AOF-96, 3 pages and map.

Ciriaco, A.E., Zarrouk, S.J., Zakeri, G., 2020. Geothermal resource and reserve assessment methodology: Overview, analysis and future directions. *Renewable and Sustainable Energy Reviews 119*, 109515. https://doi.org/10.1016/j.rser.2019.109515

Garg, S.K., Combs, J., 2015. A reformulation of USGS volumetric "heat in place" resource estimation method. *Geothermics 55, 150–158.*

Dahlstrom, N., Thayer, C. and Koplin, C, 2023. *Alaska Energy Security Task Force Report, Volume 1*.

Detterman, R. and Jones, D., 1974. Mesozoic fossils from Augustine Island, Cook Inlet, Alaska. *American Association of Petroleum Geologists Bulletin, v. 58*, pages 868-870.

Detterman, R. and Reed, B., 1964. Preliminary map of the geology of the Iliamna quadrangle, Alaska. U.S. *Geological Survey Miscellaneous Investigations Map I-407, scale 1:250,000*.

Dobson, P., 2016. A review of exploration methods for discovering hidden geothermal systems. *Geothermal Rising Conference Transactions, Vol. 40*, 2016, pages 695-706.

Eichelberger, J., Foster, M. and Holdmann, G., 2023. Augustine Volcano, Cook Inlet, Alaska has Magma Storage at Shallow Depth and Merits Geothermal Exploration. *Geothermal Rising Conference Transactions, Vol. 47*, 2023

ENSTAR, 2024. Cook Inlet Update Report, February 7th, 2024.

Erkan, K., Holdmann, G., Benoit, W. and Blackwell, D, 2008. Understanding the Chena Hot Springs, Alaska, geothermal system using temperature and pressure data from exploration boreholes. *Geothermics, Volume 77*, Issue 6, December 2008, pages 565-585.

Evans, W.C., Bergfeld, D., Neal, C.A., McGimsey, R.G., Werner, C.A., Waythomas, C.F., Lewicki, J.L., Lopez, T., Mangan, M.T., Miller, T.P. and Diefenbach, A., 2015. Aleutian Arc Geothermal Fluids: Chemical Analyses of Waters and Gases Sampled in Association with the Alaska Volcano Observatory. *US Geol. Surv. Data Release*.

Goodfellow, P. and Birnbaum, M., 2023. Alaska Greenhouse Gas Emissions Inventory 1990-2020. *Alaska Department of Environmental Conservation Division of Air Quality*, May 25, 2023 report.

Hinga, B.D.R., 2015. Ring of Fire: An Encyclopedia of the Pacific Rim's Earthquakes, Tsunamis, and Volcanoes. *Bloomsbury Publishing USA*.

Haeussler, P., Bruhn, R. and Pratt, T., 2000. Potential seismic hazards And tectonics of the upper Cook Inlet basin, Alaska, based in analysis of Pliocene and younger deformation, IN. *Geological Society of America Bulletin, Vol. 112, Issue 9*, pages 1414 – 1429.

Herriott, T., Wartes, M. and Decker, P., 2016. Record of a late Jurassic deep-water canyon at Chisik Island, south-central Alaska: Further delineation of Naknek Formation depositional

systems in Lower Cook Inlet. In, Herriott T. (ed), Petroleum-related geologic studies in lower Cook Inlet during 2015, Iniskin-Tuxedni region, south-central Alaska: *Alaska Division of Geological and Geophysical Surveys Preliminary Interpretative Report 2016-1*, 78 pages.

Kamata, H., Johnston, D.A., Waitt, R.B., 1991. Stratigraphy, chronology, and character of the 1976 pyroclastic eruption of Augustine volcano. *Alaska. Bulletin of Volcanology 53*, 407–419. https://doi.org/10.1007/BF00258182

Koulakov, I., 2009. LOTOS Code for Local Earthquake Tomographic Inversion: Benchmarks for Testing Tomographic Algorithms. *Bulletin of the Seismological Society of America 99*, 194–214. https://doi.org/10.1785/0120080013

Koulakov, I., D'Auria, L., Prudencio, J., Cabrera-Pérez, I., Barrancos, J., Padilla, G.D., Abramenkov, S., Pérez, N.M., Ibáñez, J.M., 2023a. Local Earthquake Seismic Tomography Reveals the Link Between Crustal Structure and Volcanism in Tenerife (Canary Islands). *JGR Solid Earth 128*, e2022JB025798. https://doi.org/10.1029/2022JB025798

Koulakov, I., Qaysi, S.I., Izbekov, P., Browne, B.L., 2023b. Structure of shallow magma sources beneath Augustine Volcano (Alaska) inferred from local earthquake tomography. *Journal of Volcanology and Geothermal Research 444*, 107965.

Koulakov, I.Yu., 2020. BASIC TOMO: an educational tool for investigating the role of controlling parameters and observation geometry in tomography problems. *Russian Journal of geophysical technologies 40–54*. https://doi.org/10.18303/2619-1563-2020-1-40

Lobos Lillo, D., Delgado, F., Pritchard, M.E., Cardona, C., Franco, L., Pedreros, G., Amigo, A., 2023. Documenting surface deformation at the first geothermal power plant in South America (Cerro Pabellón, Chile) by satellite InSAR time-series. *Journal of Volcanology and Geothermal Research 441*, 107869. https://doi.org/10.1016/j.jvolgeores.2023.107869

Martínez Ruiz, Y., Duque, D.F.M., Ramírez Malule, H., 2022. Geothermal Power Projects Valuation Model, in: García Alcaraz, J.L., Realyvásquez Vargas, A. (Eds.), *Algorithms and Computational Techniques Applied to Industry*. Springer International Publishing, Cham, pp. 29–46. https://doi.org/10.1007/978-3-031-00856-6_2

Maza, S., Collo, G., Morata, D., Taussi, M., Vidal, J., Mattioli, M., and Renzulli, A., 2021. Active and fossil hydrothermal zones of the Apacheta volcano: Insights for the Cerro Pabellón hidden geothermal system (Northern Chile). *Geothermics, 102206*.

Muffler, L.J.P., 1979. Assessment of geothermal resources of the United States, 1978 (No. USGS-CIRC-790). *Geological Survey, Reston, VA (USA). Geologic Div.* https://doi.org/10.2172/6870401

Muffler, P., Cataldi, R., 1978. Methods for regional assessment of geothermal resources. *Geothermics 7*, 53–89. https://doi.org/10.1016/0375-6505(78)90002-0

Osorio Luna, G.E., 2018. Análisis de sinergias en la minería de la región de Antofagasta (Master's). Pontificia Universidad Catolica de Chile (Chile), Chile.

O'Sullivan, M.J., O'Sullivan, J.P., 2016. 7 - Reservoir modeling and simulation for geothermal resource characterization and evaluation, in: DiPippo, R. (Ed.). *Geothermal Power Generation. Woodhead Publishing*, pp. 165–199. https://doi.org/10.1016/B978-0-08-100337-4.00007-3

Power, J.A., Nye, C.J., Coombs, M.L., Wessels, R.L., Cervelli, P.F., Dehn, J., Wallace, K.L., Freymueller, J.T., Doukas, M.P., 2006. The reawakening of Alaska's Augustine volcano. *EoS Transactions 87*, 373–377. https://doi.org/10.1029/2006EO370002

Sanyal, S.K., Klein, C.W., Lovekin, J.W. and Henneberger, R.C., 2004. National assessment of US geothermal resources-a perspective. *Geothermal Resources Council Transactions, 28*, pp.355-362.

Sanyal, S.K., 2005. Cost of Geothermal Power and Factors that Affect It.

Swanson, S.E., Kienle, J., 1988. The 1986 Eruption of Mount St. Augustine: Field Test of a Hazard Evaluation. *J. Geophys. Res. 93*, 4500–4520. https://doi.org/10.1029/JB093iB05p04500

Syracuse, E.M., Thurber, C.H., Power, J.A., 2011. The Augustine magmatic system as revealed by seismic tomography and relocated earthquake hypocenters from 1994 through 2009. *J. Geophys. Res. 116*, B09306. https://doi.org/10.1029/2010JB008129

Takei, Y., 2002. Effect of pore geometry on V P / V S : From equilibrium geometry to crack. *Journal of Geophysical Research 107*. https://doi.org/10.1029/2001JB000522

U.S. Energy Information Administration, 2022. Geothermal explained. Where geothermal energy is found. Update February 15th, 2022.

U.S. Energy Information Administration, 2024. State Profile and Energy Estimates Overview. Update April 18th, 2024.

U.S. Energy Information Administration, 2024. Electric Power Monthly, Table 5.6.A, average price of electricity to ultimate customers by end-use sector. Update March 2024.

Waitt, R.B., Begét, J.E., 2009. Volcanic processes and geology of Augustine Volcano, Alaska. *U.S. Geological Survey Professional Paper, 1762*, 78 p., 2 plates, scale 1:25,000.

Waythomas, C. and Waitt, R., 1998. Preliminary volcano-hazards assessment for Augustine Volcano, Alaska. *U.S. Geological Survey Open-File Report 98-106*, 39 pages.

Wilmarth, M., Stimac, J., 2015. Power Density in Geothermal Fields. *Proceedings World Geothermal Congress 2015*. Melbourne, Australia 19-25 April

Characterizing Subsurface Structures and Determining In-Situ Stress Orientations: A Case Study from the Tuchang Geothermal Prospect Area, Northeastern Taiwan

Tito Satria Putra Perdana[1], Bing-Chen Chen[2], Ming-Wei Liao[2], Li-Wei Kuo[3], Andy Min-Hao Wang[1], Wei-Cheng Huang[2], Roger Henneberger[1]

[1] SLB; [2] CPC Corporation Taiwan; [3] National Central University, Taiwan

Keywords

Borehole High-Resolution Resistivity Imaging Tool, Borehole Image, Subsurface Structure, Fracture Analysis, Fracture Classification, Fracture Orientation, Conductive Fracture, Conductive Fault, In-Situ Stress Orientation, Metamorphic Rocks, Lushan Formation, Tuchang, Yilan, Taiwan

ABSTRACT

Targeting structurally controlled permeability in geothermal fields remains a challenge due to the difficulties in characterizing subsurface structures in terms of their hydraulic behavior within the reservoir. Measurement sensitivity in combination with approximately 80% circumferential coverage (in an 8-1/2-inch wellbore) makes the Borehole High-Resolution Resistivity Imaging Tool useful for identifying subsurface structures and providing direct data on in-situ stress orientations in the formation intersected in the logged interval. Accurate, high-resolution wellbore images paired with skilled image interpretation enables fractures and faults to be characterized as open (hydraulically conductive) or closed (non-conductive, typically due to mineral deposition). Knowledge of the depths and orientations of permeable structures is beneficial at the local scale (within the logged wells) and at the reservoir scale. The improved understanding of permeability distribution is used to optimize operations and improve decisions about future well targets in conventional hydrothermal projects.

In 2020, two exploration wells were logged on behalf of CPC Corporation Taiwan utilizing the Borehole High-Resolution Resistivity Imaging Tool, the Advanced Neutron-Gamma Logging Tool, the High-Resolution Resistivity Array Tool, and the Pressure-Temperature (PT) Logging Tool. The exploration wells are located in the Tuchang Geothermal Prospect Area, Yilan County, Northeastern Taiwan. These logs were run mainly in the 8-1/2-inch diameter production interval of the wells, and the results have been analyzed and interpreted. This has enabled improved classification of fractures and faults, including basic properties (direction), and determination of whether the fractures and faults are open or healed.

Conductive fractures and faults are observed in much of the logged interval in each exploration well; together, they show a dominant strike orientation of NE-SW, with dips measured in the range of 5°-90°. Drilling-induced fractures and borehole breakouts are also observed, with a dominant strike orientation of NNE-SSW to NE-SW for drilling induced fractures and NW-SE for borehole breakouts. The interpretation of the logging results is consistent with the predominant structural / tectonic trend in the area as most mapped faults are oriented NE-SW. conductive fractures and faults are important contributors to permeability in both exploration wells. Large conductive fractures and faults with NE-SW, NW-SE, and N-S strike orientations have been correlated to permeability indicators such as the presence of thermal plumes and sudden increases in temperature.

1. Introduction

Fluid flow in geothermal reservoirs in active tectonic regions like Iceland, Indonesia, Taiwan, the Philippines, and New Zealand is controlled mainly by permeable structures (fractures and faults) in the subsurface. Therefore, examining the location and characterization of permeable structures is an important step towards estimating the productivity of a reservoir (Brehme et al., 2016).

Targeting structurally controlled permeability remains a challenge in geothermal fields, because of the difficulties in characterizing subsurface structures and their behavior within the reservoir. The sensitivity of measurement in combination with approximately 80% circumferential coverage (in an 8-1/2-inch wellbore) makes the Borehole High-Resolution Resistivity Imaging Tool useful for identifying subsurface structures and providing direct data on in-situ stress orientations in the formation in the logged interval. Accurate, high-resolution resistivity borehole images (hereinafter referred to as 'borehole images') paired with skilled image interpretation enables fractures and faults to be characterized as conductive (possibly “open”, hydraulically conductive) or resistive (“closed”, non-conductive, typically due to mineral deposition).

In 2020, CPC Corporation Taiwan (“CPC”) drilled two deep exploration wells (X-1 and X-2) in the Tuchang Geothermal Prospect Area, Yilan County, Northeastern Taiwan (Figures 1, 2, and 3). The wells were drilled from the same well pad because it is difficult to find flat surfaces for drilling. Well X-1 (completed on 31 May 2020) was deviated SSE, with a maximum deviation of about 47° from vertical; well X-2 (completed on 15 September 2020) was deviated WSW with a maximum deviation of approximately 38° from vertical (Figure 3). Wells X-1 and X-2 encountered bottom-hole temperatures of 151°C and 134.5°C, respectively; the highest temperature measured in well X-2, however, was 150°C (at a depth of 550 meters measured depth [mMD]). Well X-1 shows a gradient of approximately 6°C/100 m at 2,000 mMD, and well X-2 encountered a slightly higher gradient of 7°C/100 m at 1,500 mMD. The temperature profiles of wells X-1 and X-2 suggest, to varying degrees, a “thermal plume” in the approximate interval of 450 to -100 m a.s.l. No losses of circulation were reported during drilling. The temperature profiles of wells X-1 and X-2 are presented in Sub-Section 4.3.

Production wells X-1 and X-2 were logged on behalf of CPC using Borehole High-Resolution Resistivity Imaging Tool, the Advanced Neutron-Gamma Logging Tool, the High-Resolution Resistivity Array Tool deployed by SLB, and Pressure-Temperature (PT) logging tool deployed by Industrial Technology Research Institute (ITRI). The Borehole High-Resolution Resistivity Imaging Tool was run mainly in the 8-1/2-inch-diameter intervals, which pass through Tertiary-age metamorphic rocks.

For the intervals where borehole image data were collected, we conducted the following analyses: borehole image processing, borehole image interpretation, and integrated fracture interpretation. This integrated analysis utilized borehole images, temperature and pressure logs, caliper logs, standard open-hole logs (including gamma ray [GR], resistivity, neutron-porosity, and density), lithological log plots from cuttings analysis, and lost circulation intervals (from drilling reports). The primary objective of this study was to deliver a comprehensive analysis of subsurface structures, encompassing fracture and fault classification, as well as the determination of the orientation and density of subsurface fractures and faults.

2. Geologic Setting

2.1 Regional Geologic Setting

The Tuchang geothermal prospect area is located approximately 30 km southwest of the city of Yilan in Yilan County, northeastern Taiwan (Figure 1). It lies in a mountainous area (known as the Central Mountain Range) with the valleys of the TuoWen and TienKuJen rivers running through it (Figures 1, 2, and 3). It is also near the Yilan plain, a major plain in northeastern Taiwan. The prospect area is approximately 1.5 km northeast of the JenTse prospect area and about 15 km southwest of the operating geothermal field at Chingshui which has a total installed capacity of 4.95 MW as of June 2024 (Figure 1).

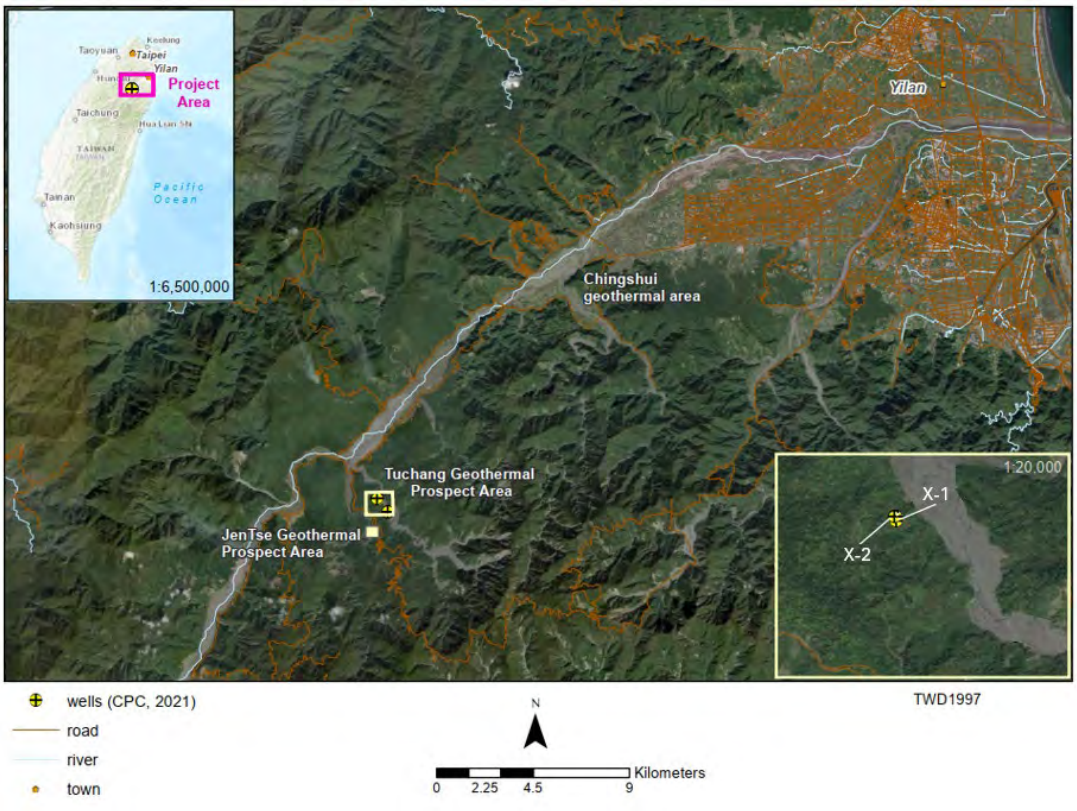

Figure 1: Location map of the Tuchang Geothermal Prospect Area, Yilan County, Northeastern Taiwan

Taiwan is a site of active orogenesis caused by the northwestward movement of the Philippine Sea Plate and its collision with the Eurasian Plate (Shyu et al., 2005; Teng, 1996) (Figure 1). The

Philippine Sea Plate subducts beneath the Eurasian Plate, leading to the formation of the Ryuku Arc in Northern Taiwan. The Okinawa Trough, extending from southwestern Kyushu Island in Japan to the Yilan Plain, is a back-arc basin in the Ryuku Arc-Trench system (Figure 2). To the south of the Yilan Plain, the northern Central Mountain Range (where the Tuchang prospect is located) has undergone a transition from a tectonic compressional regime to an extensional regime (Teng, 1996) (Figure 2). The earlier tectonic collision formed the high mountains and metamorphic rocks. The later eastward extension of the Okinawa Trough has caused the regional extension and the development of the Yilan Plain (Lai et al., 2009). The latest extension that may have occurred within the past million years in the southwestern portion of the Okinawa Trough is characterized by normal faults with vertical to sub-vertical offsets that have existed since the Late Pleistocene (Shih et al., 2018; Shyu et al., 2005).

Abundant hot springs indicate the existence of geothermal potential in the Yilan Plain and the northern Central Mountain Range (Liu et al., 2015). Borehole data and geochemical studies suggest that the temperature of the geothermal systems in the northern Central Mountain Range is on the order of 200-230°C at depths of 2,000 to 3,000 m (Liu et al., 2015; Tong et al., 2008).

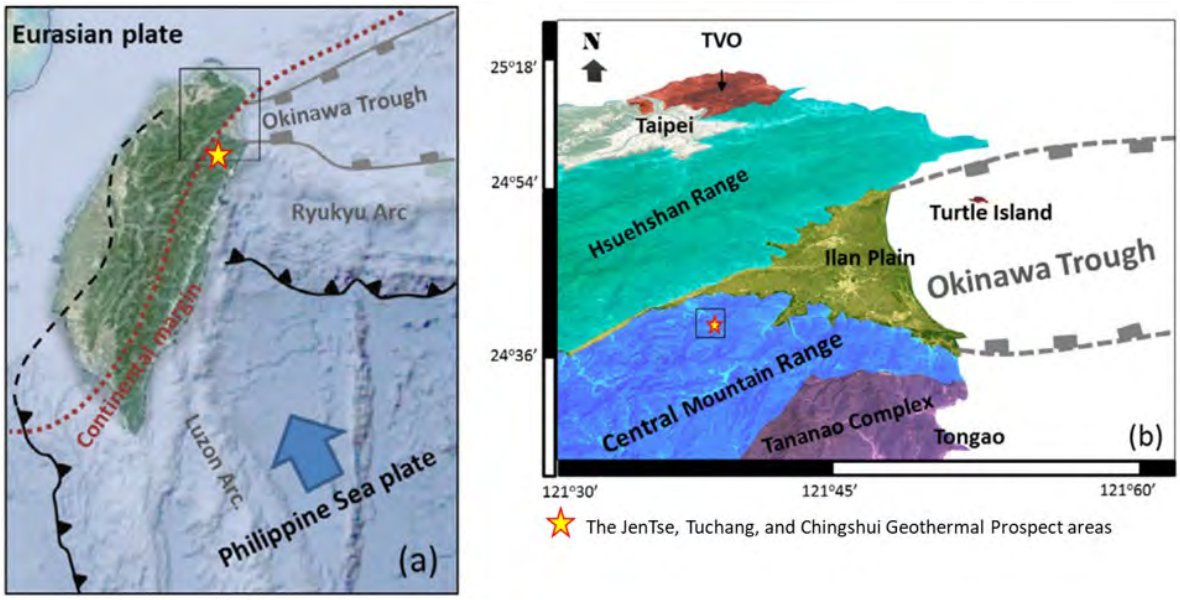

Figure 2: Regional geologic setting of the Yilan Plain and Northern Central Mountain Range (modified from Lu et al., 2017)

The primary heat source of the geothermal systems of the northern Central Mountain Range is believed to be the high-temperature metamorphic rocks in the rapidly uplifted mountain belts (Lin, 2000). In this model, the heat source of the geothermal system is the residual heat of rock formations in the Central Mountain Range which have been rapidly uplifted in the past 5 million years. Lu et al. (2017) indicated that the hydrogen and isotopic compositional data of natural hot springs and thermal water has a meteoric origin with a recharge area located at an altitude above 1,000 m, and circulates to deep levels through a fracture network controlled by regional fault systems. The meteoric water infiltrated into, and was heated by, deep rocks with a high geothermal gradient and then rose to the shallower reservoir or to the surface as hot springs.

Some geophysical and geochemical studies, however, suggest that there may be a deeper magma-related heat source in this area (Lu et al., 2017; Tong et al., 2008). Based on geologic and geophysical data, there is a possibility that the high heat flow and geothermal gradient may result from the existence of a magma chamber within the shallow crust or from shallow intrusive dikes underneath the Tuchang prospect area. There is an E-W trending high magnetic anomaly onshore (in the Yilan Plain) and a low-velocity zone underneath the offshore crust that indicate possible magmatic intrusion related to the back-arc opening of the Okinawa Trough (Lu et al., 2017 citing Tong et al., 2008; Yu and Tsai, 1979).

Geologically, the Tuchang and JenTse geothermal prospect areas are in a tectonically active region that has undergone a transition from compression to crustal extension. In principle, a graben structure in this setting would be an area of crustal thinning that is favorable for magmatic intrusion into the crust, providing a heat source for the formation of geothermal systems. A series of normal faults and opening fractures demonstrate an extensional structural setting (e.g., the NE-SW trending Dashi Fault). These faults may provide conduits for magma to rise easily and erupt at the surface as a volcano (e.g., Kueishantao to the NE of Yilan Plain), and to intrude beneath the Tuchang prospect area and the Yilan Plain. Lu et al. (2017) inferred that the fluid for hydrothermal alteration in the area was probably related to the magmatic source; this is also supported by oxygen and carbon isotopes.

The "Slate Belt" of the northern Central Mountain Range is one of the regions of high geothermal potential in Taiwan. It is mainly comprised of tight host rocks (slate formations) which have low primary porosity; these host rocks are also impermeable if they are not faulted and/or fractured (Liu et al., 2015; Song and Lu, 2019). Fault-related and/or fracture-related permeable structures are believed to be the main migration paths for geothermal fluid in the northern Central Mountain Range (Chang et al., 2014; Lu et al., 2017, 2020; Tong et al., 2008; Chiang et al., 2015). However, studies suggest that not all the faults (and their associated fractures) in this region are effective geothermal fluid conduits (Chang et al., 2014; Chiang et al., 2015; Lu et al., 2018, 2020; Tong et al., 2008). It has also been demonstrated that Tertiary-age metamorphic rocks of the Central Mountain Range have lost their original porosity; thus, fault and/or fracture permeability is essential for production of thermal fluids (Chen, 1985). Several explored geothermal reservoirs in the Central Mountain Range area are hosted by Tertiary-age metamorphic rocks, with production from faults and/or fractures in slate and metasandstone; the latter is generally more productive, having higher fracture permeability than slate (Chen, 1985).

2.2 Lithology and Structural Setting of the Tuchang Prospect Area

2.2.1 Lithology

The slightly fractured sub-metamorphic slate of the Miocene Lushan Formation is the predominant rock widely exposed in the Tuchang geothermal prospect area. The Miocene Lushan Formation is part of the "Slate Belt" discussed above. The Lushan Formation can be divided into three members based on lithological differences: the Kulu Member (which exhibits good development of slaty cleavage, with a few beds of fine-grained metasandstones; it does not crop out in the prospect area); the Chingshuihu Member (mainly composed of slate or phyllite with thin beds of metasandstones; it crops out in the western and northwestern portions of the prospect area); and the JenTse member (composed mainly of very-fine-grained metasandstone intercalated with slate,

with some fine-grained to medium-grained metasandstones [up to 35 m thick] on the bottom; it is highly fractured, and crops out in the central and eastern portions of the prospect area) (Figure 3).

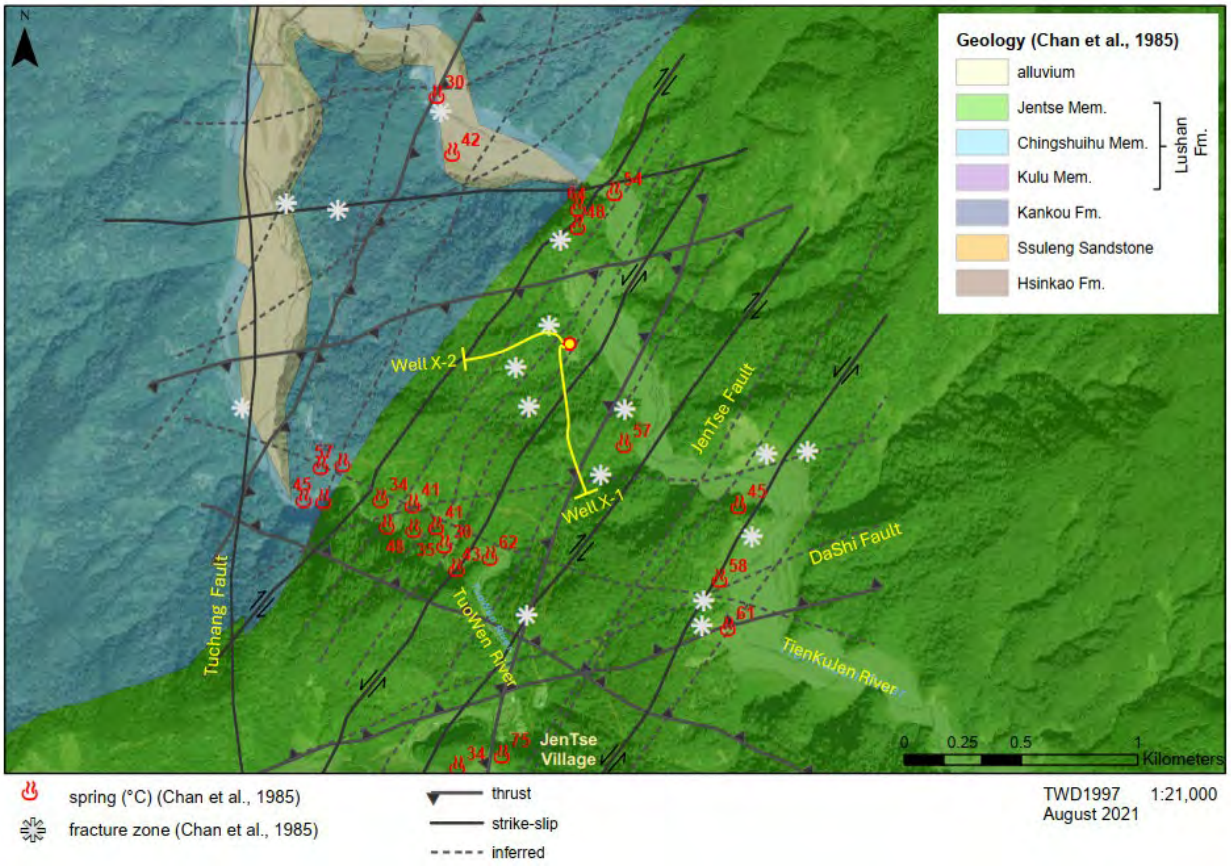

Figure 3: Geologic map of the Tuchang Geothermal Prospect Area

2.2.2 Structural Setting

The Tuchang geothermal prospect area is transected by prominent faults trending NE-SW, with some faults trending NW-SE, N-S, and ENE-WSW also present in the area (Figure 3). The widths of the fault zones range from less than one meter to tens of meters on outcrops; their offsets, however, are minor. The extensions of the faults / fault zones are difficult to determine due to poor continuity of the outcrops.

Some low- to high-temperature springs and fracture zones in the Tuchang geothermal prospect area are associated with certain faults and/or areas of fault intersections (Figure 3). Some major right lateral strike-slip faults, thrust faults, and normal faults have been identified from surface geologic mapping (Figure 3).

Outcrop data indicate that fractures are well developed in the Tuchang prospect area, mainly along faults or fault zones (Figure 3). Mapping by previous investigators (e.g., Hsiao and Chiang, 1979) indicates that fractures are well developed mainly in the JenTse Member of the Lushan Formation. Two dominant fracture sets in the area were reported: (1) NE-SW striking fractures dipping 70° to 80° to the southeast; and NW-SE striking fractures dipping 60° to 90° to the southwest.

The rugged terrain in the Tuchang area may be related to the development of fracture systems (Hsiao and Chiang, 1979). Rivers and valleys in the area trend almost parallel to the faults and/or fractures (N-S, NW-SE, and NE-SW) (Figure 3).

2.2.3 Geothermal Manifestations

The important geothermal manifestations in the Tuchang prospect area consist of several low- to high-temperature springs with minor associated hydrothermal alteration. They appear mainly along the banks of the TuoWen and TienKuJen Rivers and rock cliffs (Figure 3). Temperatures of the springs range from 30°C to more than 75°C with pH from 7.0 to 8.0. The springs issue mainly from the JenTse Member of the Lushan Formation, and are associated with faults, areas of fault intersections, and fracture zones (Figure 3).

3. Borehole Image Processing and Interpretation

3.1 Data

Wells X-1 and X-2 were logged using Borehole High-Resolution Resistivity Imaging Tool, the Advanced Neutron-Gamma Logging Tool, the High-Resolution Resistivity Array Tool, and PT logging tool. In well X-1, these logs were run in the intervals of 10 to 300 mMD (17-inch section of the well), 300 to 747 mMD (12-1/4-inch section), and 753 to 1,980 mMD (8-1/2-inch section). In well X-2, they were run in the interval of 250 to 1,480 mMD (8-1/2-inch section).

3.2 Borehole Image Processing

The primary purpose of computer processing of resistivity data is to convert the raw data into the best visual representation of the borehole. Proper conditioning of the data is achieved using certain correction algorithms, prominent examples of which are:

3.2.1 Image Correction / Equalization

Processing of the borehole image data was carried out on the SLB's Techlog* wellbore software platform using the Well Bore Imaging (WBI) workflow. A basic quality control test of the inclinometry data from raw images was used to determine if the borehole image is correctly oriented. This test computed the offsets needed to correct accelerometer and magnetometer variables and determined if correction was required. The main Speed correction module in Techlog was used, using frame time and Z-axis acceleration to compute tool acceleration and tool velocity at every depth. Tool sticking is detected to avoid incorrect computation of the variables when the tool is temporarily stuck. The speed-corrected image is then normalized using the Histogram Equalization module.

3.2.2 Image Orientation

The image is oriented with respect to the north of the borehole.

* Mark of SLB

3.2.3 Image Depth Shift / Depth Match

When logging tools are run in sequence, differences occur in depth from tool to tool and from run to run due to differential cable stretch. Stretch can be pronounced when the logging string sticks or temporarily hangs up in the hole. All logging measurements must be adjusted to a common depth reference before data processing can continue. All depths should be referenced to a base log selected from a logging tool where strong or forceful tool positioning is not used (e.g., GR log from the Advanced Neutron-Gamma Logging Tool). Free-moving tools travel through the borehole more smoothly than tools that are pushed with great force against the borehole wall. For this reason, logs run with strongly centralized tools (e.g., Borehole High-Resolution Resistivity Imaging Tool) are not selected as the base log.

3.2.4 Image Normalization

The image is normalized by assigning a color spectrum of user-defined bins to the resistivity data to obtain image pixels that are representative of a particular bin size. When all pixels are viewed together the normalized image is produced. Two types of normalization – static and dynamic – are performed.

In static normalization a preferred spectrum of colors, in this case 128, is distributed over the data interval. This technique provides a good overall representation of the data, highlighting major resistivity variations. Higher resolution normalization is achieved through the process of dynamic normalization, where a preferred spectrum of colors (up to 128) is distributed over a 1-meter window length. A sliding window method is applied to the whole data interval. The normalized images produce an optimized image of the resistivity data and are usually presented side-by-side on interpretation plots.

3.2 Borehole Image Interpretation

The processing of borehole images was followed by interactive dip picking and feature classification using normalized images. The dip picking enabled computation of the dip angle of lithological boundary, fracture, fault, and/or any other planar features. Drilling-induced fractures and borehole breakouts were also easily recognizable in most situations. Interactive dip picking was performed manually using a sine wave, with its amplitude and azimuth fitted to planar features on the image.

3.3 Integrated Fracture Interpretation and Analysis using Borehole Images and Standard Open-Hole Logs

Integrated fracture interpretation and analysis using borehole image and standard open-hole logs (e.g., GR, resistivity, neutron-porosity, density, pressure, and temperature) are conducted to better classify the natural fractures, to get the fracture properties (direction and density / intensity), to better determine whether the fractures are (possibly) open or closed, and to assess the permeability of the subsurface fault or fracture. With the sensitivity of the measurement of borehole imaging (in combination with their circumferential coverage), the natural fractures, possible faults, beddings / foliations, drilling-induced fractures, and borehole breakouts are reliably characterized.

4. Results of Borehole Image Processing and Interpretation

4.1 Borehole Image Log Quality and Borehole Conditions

Borehole log inclinometry data from wells X-1 and X-2 (collected using the General-Purpose Inclinometry Tool, or GPIT) show good coherency with the wells' deviation and azimuth data, indicating that the tools were correctly oriented in the boreholes and that the calculated dips are correct.

The borehole conditions of both wells are generally good, with only a few large and minor washouts, and the image quality is generally good to excellent.

The Borehole images are in general on-depth with standard open-hole logs.

4.2 Borehole Image Manual Dip Classification

Structural features were picked manually using sine waves, with their amplitudes and azimuths fitted to planar features on the borehole image. The lowest point of the sinusoid troughs defines the dip azimuths, and the amplitude of the sinusoids define the dip magnitudes.

All dip interpretations have been made using a combination of static and dynamic normalized images, along with gamma-ray, resistivity, and neutron-porosity logs, and results of cutting analysis.

In resistivity images, the fractures that have conductive traces (represented by dark colors) are termed conductive fractures. The fractures are further classified into three types based on their appearance and continuity across the borehole diameter:

- Conductive Fractures: the predominant fracture type, they appear as low- to high-angle planar features with good continuity across the borehole and strong contrast with the surrounding rock (Figure 4[a]).
- Bedding Fractures: rare compared to the conductive fractures, mostly recognized in or near the fault zones. These fractures appear as medium- to high-angle planar features with good continuity across the borehole and strong contrast with the surrounding rock. Due to their similarity to bedding planes, these features are classified as Bedding Fractures (Figure 4[b]).
- Fissures: these fractures appear as low- to moderate-angle planar features with relatively poor continuity across the borehole and weak contrast with the surrounding rock (Figure 4[a]).

The study focused especially on conductive fractures which, due to conductive drilling mud, are conventionally assumed to be open and hydraulically conductive, although care must be taken with such an assumption because conductive fractures can also be clay-filled or pyrite-filled.

Fractures with resistive traces (represented by white / light colors) are termed resistive fractures. Resistive fractures are generally considered to be closed or healed (filled with resistive minerals such as calcite and quartz) (Figure 4[c]).

Conductive faults or possible faults have also been identified (Figure 4[d]), with diagnostic features including (but not restricted to): indications of large conductive events developed across

the wellbore (Figures 4[d] and 5[c]), enlarged hole at faults, abrupt termination of fractures and/or bedding surfaces on the fault plane (Figure 5[c]), sharp facies changes, dip magnitude and / or azimuth changes of beddings (Figure 5[c]), and the presence of fractures around the fault (Figure 4[d]).

Drilling-induced tensile fractures and borehole breakouts were identified where they occur on opposite sides of the borehole wall (Figures 5[a] and 5[b]). Although these features do not have a dip direction or dip magnitude, their strikes can be defined and used to indicate the maximum and minimum horizontal stress directions.

The intervals logged in wells X-1 and X-2 are comprised of metamorphic rock formations. The lithologies are mainly slate and metasandstone of the JenTse Member of the Lushan Formation. Bedding of these lithologic units can be observed on the borehole image (Figures 4[b] and 5[d]).

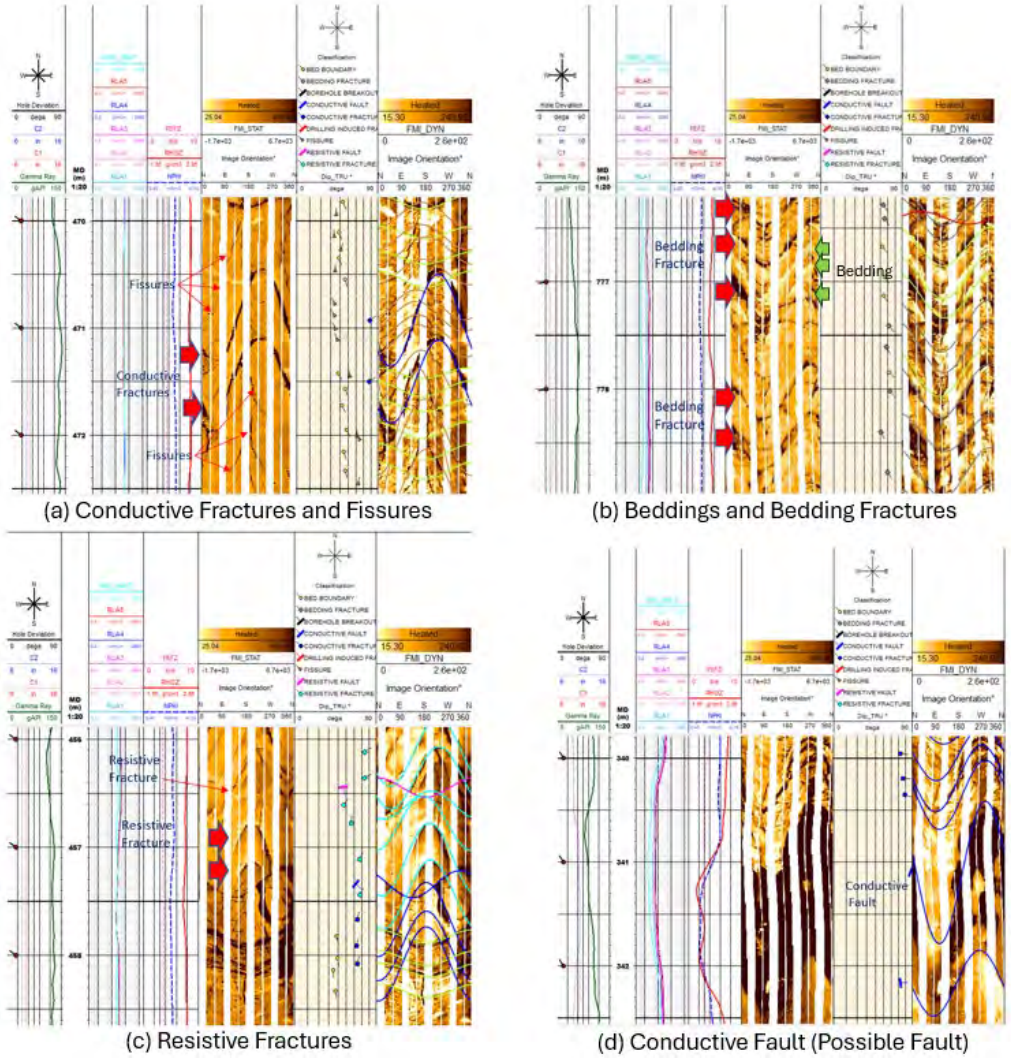

Figure 4: Borehole image examples of conductive fractures and fissures (a), beddings and bedding fractures (b), resistive fractures (c), and conductive fault / possible fault (d) from wells X-1 and X-2

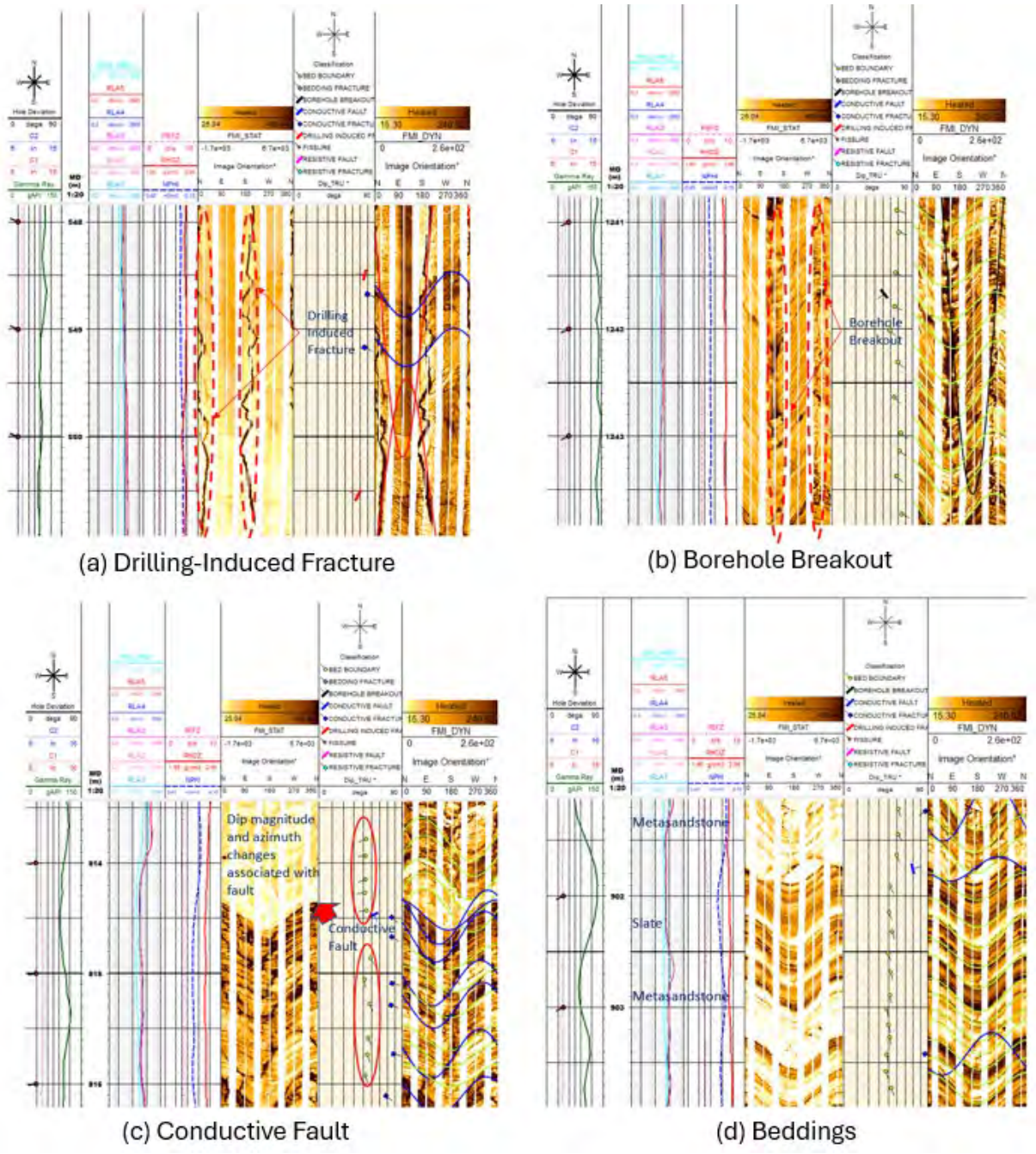

Figure 5: Borehole image examples of drilling-induced fracture, borehole breakout (b), conductive fault (c), and bedding (d) from wells X-1 and X-2.

4.3 Borehole Structural Interpretation

4.3.1 Borehole Image Structural Interpretation of Well X-2

Structural interpretation includes identifying and determining the orientation of fractures and faults and determining the present-day tectonic stress field orientation from drilling-induced features and borehole breakouts. Detailed structural analysis was performed for the interval of 250 to 1,480 mMD (within the 8-1/2-inch section of the well).

Bedding is observed on the borehole image; it is developed mainly in the slate and appears as a repetitive layering (which can be conductive and/or resistive) (Figure 5[d]). Bedding dip statistics in the interval show a dominant azimuth orientation of southeasterly, though some northwesterly dips are also present. Bedding dip magnitudes are from approximately 5° to vertical. High-angle bedding is usually associated with faults / fault zones. These bedding orientations reflect the major structural / tectonic trend in the area.

Fractures are well developed over almost the entire interval logged. The fractures identified from borehole images are almost exclusively conductive (considered to be open). Some resistive (considered to be closed) fractures were also recognized. Fracture types and morphology in well X-2 are described below:

- Conductive Fractures: the predominant fracture type. Conductive-fracture dip statistics over the interval show dominant strike orientations of NE-SW, NW-SE, and N-S with NE, SE, E, and W azimuths (Figures 6 and 7). Dip magnitudes for this fracture type are highly variable, from approximately 5° to vertical. These conductive fracture orientations reflect the major structural / tectonic trend in the area as discussed in Section 2.
- Bedding Fractures: bedding-fracture dip statistics in the interval indicate dominant strike orientations of NE-SW with SE azimuth. The dip magnitudes of the bedding fractures vary from approximately 10° to nearly vertical. These bedding fracture orientations reflect the major structural / tectonic trend in the area, as discussed in Section 2.
- Fissures: in well X-2, fissures were recognized in a few intervals near the fault zones. Fissure dip statistics in the interval indicate dominant strike orientations of ENE-WSW, NNE-SSW, and WNW-ESE with W, NNW, and N azimuths. The dip magnitudes of the fissures are from 30° to 40°.
- Resistive Fractures: resistive-fracture dip statistics over the interval demonstrate dominant strike orientations of NW-SE with NE azimuths. Dip magnitudes for this fracture type are highly variable, from approximately 10° to vertical.

Conductive faults (or possible faults) were recognized on the borehole images. Their dip statistics show dominant strike orientations of NE-SW with SE and NW azimuths (Figures 6 and7). Dip magnitudes for conductive faults vary from approximately 15° to vertical. These orientations reflect the major structural / tectonic trend in the area as discussed in Section 2. Well X-2 was drilled near some mapped NE-SW trending faults; in the subsurface this well might encounter some of these faults / fault zones.

The temperature data of well X-2 suggest a thermal plume at 50-600 mMD, and large conductive fractures and faults are well developed within this interval (Figure 7). Conductive-fault and conductive-fracture dip statistics over the interval of 250 to 600 mMD demonstrate dominant strike orientations of NE-SW, N-S, and NW-SE, with SE, E, NE. and W azimuths (Figure 7). Dip magnitudes for conductive fault and conductive fracture over the interval of 250 to 600 mMD are highly variable, from approximately 15° to vertical.

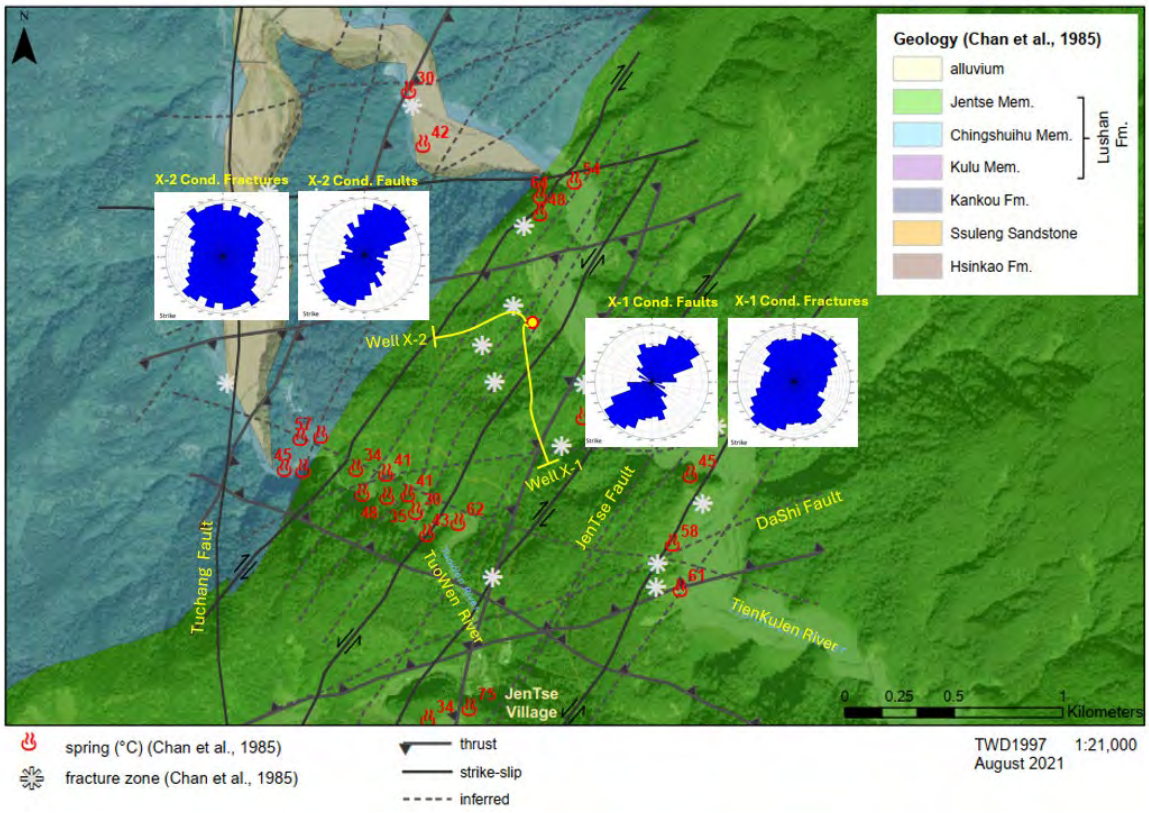

Figure 6: Geologic map of the Tuchang Geothermal Prospect Area showing surface geologic structures and strike orientations of conductive fractures and faults from wells X-1 and X-2.

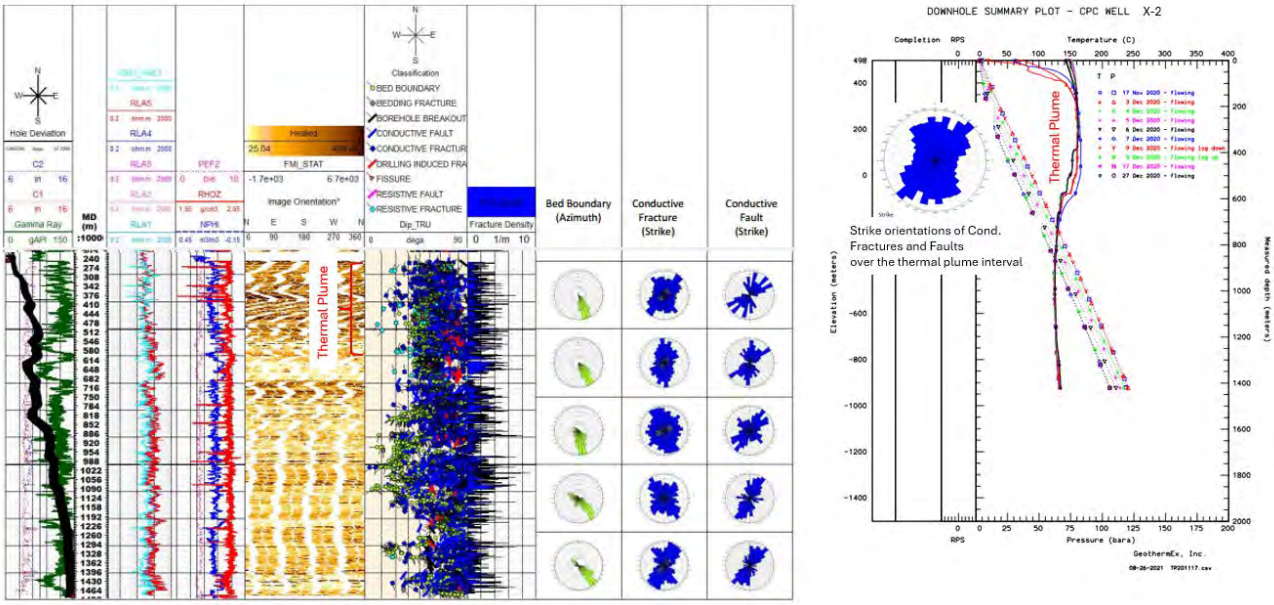

Figure 7: Integrated fracture interpretation and analysis of well X-2. The temperature data suggests a thermal plume in an interval of 50-600 mMD, and large conductive fractures and faults are well developed within this interval. Conductive-fault and conductive-fracture dip statistics over the interval of 250 to 600 mMD demonstrate dominant strike orientations of NE-SW, N-S, and NW-SE.

4.3.2 Borehole Structural Interpretation of Well X-1

Detailed structural analysis of well X-1 was performed for the intervals of 10 to 300 mMD (17-inch section of the well), 300 to 747 mMD (12-1/4-inch section), and 753 to 1,980 mMD (8-1/2-inch section).

Like X-2, the interval logged in well X-1 is comprised of metamorphic rock formations, mainly slate and metasandstone of the JenTse Member of the Lushan Formation. Bedding is observed on the borehole image, with dip statistics showing dominant azimuth orientations of southeasterly and northwesterly. Main dip magnitudes are from approximately 30° to 50° and 65° to 85°. High-angle foliation surfaces are usually associated with fault(s) / fault zone(s). These foliation surface orientations reflect the major structural / tectonic trend in the area. A major change in bedding dip azimuth is observed at a depth of approximately 1,450 mMD; this change is associated with a major fault / fault zone.

Fractures are developed over almost the entire interval logged in well X-1. The fractures identified from borehole images are almost exclusively conductive (considered to be open). Resistive fractures were also recognized in the studied interval.

- Like well X-2, conductive fractures are the dominant fracture type in well X-1. Conductive-fracture dip statistics over the interval demonstrate dominant strike orientations of NE-SW and NW-SE, with NW, NE, and SE azimuths (Figure 6). Dip magnitudes for this fracture type are highly variable, from approximately 5° to vertical. These conductive fracture orientations reflect the major structural / tectonic trend in the area as discussed in Section 2.
- Bedding fractures are rare compared to the conductive fractures. Bedding-fracture dip statistics in the interval indicate dominant strike orientations of NE-SW with SE and NW azimuths. The dip magnitudes of the bedding fractures vary from approximately 20° to vertical. These bedding fracture orientations reflect the major structural / tectonic trend in the area as discussed in Section 2.
- In well X-1, fissures were recognized in some intervals near the fault zones. Fissure dip statistics in the interval indicate dominant strike orientations of NW-SE with NE and SW azimuths. The dip magnitudes of the fissures vary from approximately 10° to vertical.
- Resistive fractures were also recognized on the borehole image, with dip statistics indicating dominant strike orientations of E-W and NW-SE, with N, NE, and SE azimuths. The dip magnitudes vary from approximately 15° to vertical.

Conductive faults (or possible faults) were recognized on the borehole images. Conductive-fault dip statistics over the interval demonstrate dominant strike orientations of NE-SW with SE and NW azimuths (Figure 6). Dip magnitudes for conductive fault vary from approximately 5° to vertical. These orientations reflect the major structural / tectonic trend in the area as discussed in Section 2.

Temperatures measured in well X-1 suggests a thermal plume in an interval of 60 to 650 mMD. Some large conductive fractures and faults are developed in this interval. Conductive-fault and conductive-fracture dip statistics over the interval of 60 to 650 mMD demonstrate dominant strike orientations of NE-SW and NW-SE, with NW, SE, NE, and N azimuths. Dip magnitudes for conductive faults and conductive fractures over the interval of 250 to 600 mMD are highly

variable, from approximately 10° to vertical. However, a 9-5/8-inch casing has been set in this interval, thus, the well currently produces from a deeper reservoir whose top is at a depth of approximately 1,450 mMD. A major fault / fault zone is observed at about 1,450 mMD; it is associated with a major dip azimuth change of the bedding and good development of conductive fractures. Well X-1 also demonstrates a "positive" deflection of temperature (to higher readings) in this fault / fault zone, which might be associated with permeable fractures and/or fracture network. Conductive fractures around 1,450 mMD depth show dominant strike orientations of NW-SE and NE-SW, with dip magnitudes from about 10° to near vertical. Conductive faults around this depth show dominant strike orientation of NE-SW with dips mainly steeper than 80°.

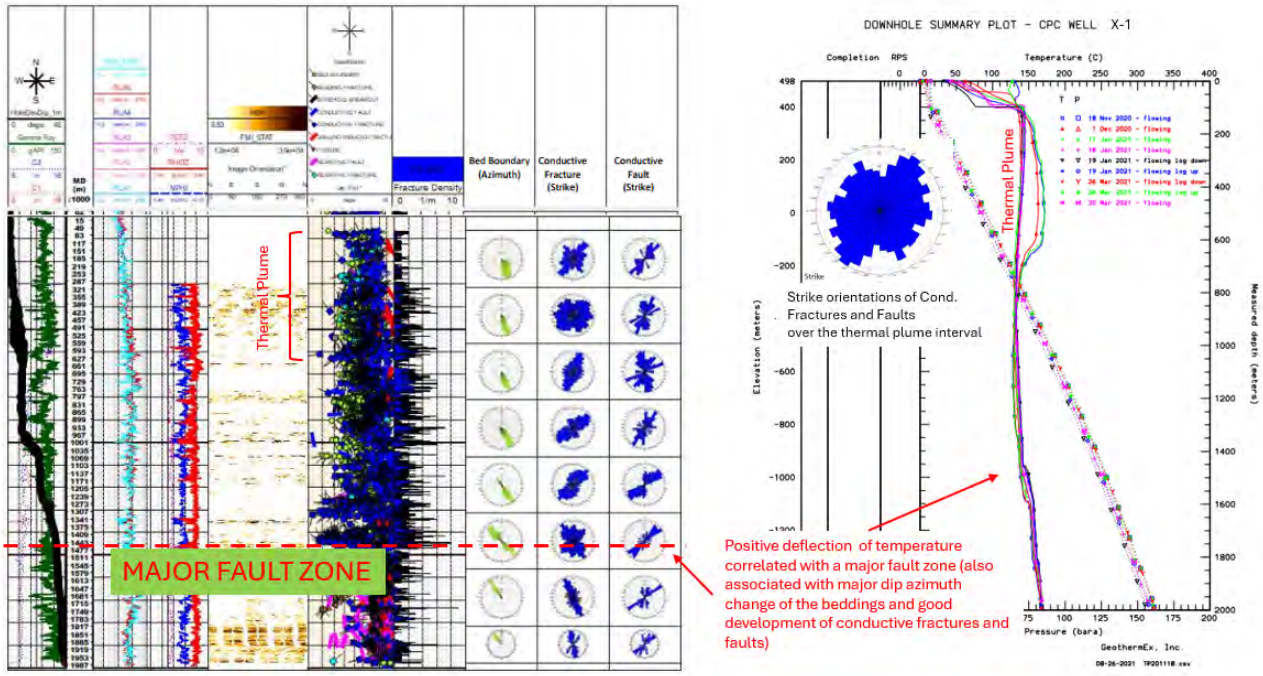

Figure 8: Integrated fracture interpretation and analysis of well X-1. The temperature data suggests a thermal plume in an interval of 60-650 mMD, and large conductive fractures and faults are well developed within this interval. Conductive-fault and conductive-fracture dip statistics over the interval of 60 to 650 mMD demonstrate dominant strike orientations of NE-SW and NW-SE. A "positive" deflection of temperature (observed at a depth of 1,450 mMD) is correlated with a major fault zone (that is associated with a major dip azimuth change of the beddings and good development of conductive fractures and faults. Conductive fractures and faults around 1,450 mMD depth show dominant strike orientations of NW-SE and NE-SW).

4.3.3 Analysis of *In-Situ Stress Orientations*

The Earth's crust rarely stays in a lithostatic stress condition (with stresses equal in all directions; that is, $\sigma1 = \sigma2 = \sigma3$). The equilibrium of the stress state is generally disturbed by movements of tectonic plates, leading to the formation of a regional stress system, which may itself be partially or completely overprinted by localized stresses associated with faults, folding, diapirism, volcanism and so forth. The orientation of such local stresses may change abruptly over short distances in any area.

Wells drilled in areas subjected to unbalanced stresses often exhibit two types of borehole failures (shear failure and tensile failure) when the rocks they penetrate are replaced by drilling fluid. The

rocks can bear both compressive and shear stresses, but the fluid filling the borehole can bear only compressive stress. Consequently, concentration of stresses takes place around the borehole in the form of hoop stress or tangential stress. When the mud weight is too low (i.e., radial stress = mud weight minus pore pressure), the maximum hoop stress becomes much higher than the radial stress. Consequently, a shear failure of rocks exposed to the borehole takes place; this appears as borehole elongation on the orthogonal calipers and as long dark regions on the borehole images that are 180 degrees apart.

Conversely, when the mud weight is too high, the radial stress increases and the hoop stress decreases; consequently, the rock around the borehole comes under tension and fails in tension. The fractures thus created are called drilling-induced fractures, which appear as fractures seen in the borehole images oriented at 180 degrees from each other.

Generally, in vertical to near-vertical wells, the axis of borehole elongation is aligned with the trend of minimum horizontal stress, and the strike of drilling-induced fractures is aligned with the trend of maximum horizontal stress. However, this may not be the case for deviated wells, particularly those that are not aligned with either of the two horizontal stresses. In such wells, the orientations of borehole breakouts and drilling-induced fractures may not represent the true orientation of the two horizontal stresses, because all three principal stresses (vertical and two horizontal) act obliquely to the borehole.

In the intervals logged in well X-1, both drilling-induced fractures and borehole breakouts are developed. Drilling-induced fractures demonstrate a strike orientation of NNE-SSW/NE-SW, and borehole breakouts show a strike orientation of NW-SE.

Both drilling-induced fractures and borehole breakouts are also developed in the interval logged in Well X-2. Some drilling-induced fractures demonstrate a strike orientation of NNE-SSW/NE-SW (Figure 5[a]). Some borehole breakouts show a strike orientation of NW-SE (Figure 5[b]).

Wells X-1 and X-2 have maximum deviations of approximately 47° and 38° from vertical, respectively; thus, the strikes of drilling induced fractures and borehole breakouts may not align with the trends of maximum and minimum horizontal stress, respectively, though in general they agree with the major structural / tectonic trend. The maximum horizontal stress direction (S_{Hmax}) observed in the image logs aligns with the dominant structural strike trend (NNE-SSW/NE-SW) observed in the prospect area.

5. Conclusions

Surface exploration indicates that the Tuchang geothermal prospect area is transected mainly by faults trending NE-SW, with some faults trending NW-SE, N-S, and ENE-WSW also present. Outcrop data indicate that fractures are well developed in the prospect area, mainly along faults or fault zones. There are two dominant fracture sets in the area: NE-SW and NW-SE.

Subsurface data (i.e., borehole images) indicate that fractures are well developed over almost the entire intervals logged in exploration wells X-1 and X-2. Conductive fracture is the predominant fracture type. Conductive-fracture dip statistics over the intervals logged in wells X-1 and X-2 demonstrate dominant strike orientations of NE-SW, NW-SE, and N-S with NW, NE, SE, E, and

W azimuths. Dip magnitudes for this fracture type are highly variable, from approximately 5° to vertical. These orientations reflect the major structural / tectonic trend in the area.

Conductive faults (or possible open faults) were also recognized on the borehole images, with dip statistics that show dominant strike orientations of NE-SW with SE and NW azimuths. Dip magnitudes for conductive faults are highly variable, from approximately 5° to vertical. These orientations reflect the major structural / tectonic trend in the area. Wells X-1 and X-2 were drilled near some NE-SW trending mapped faults; in the subsurface the wells might encounter some of these faults / fault zones.

In general, the *in-situ* horizontal stress orientations agree with the major structural / tectonic trend. The maximum horizontal stress direction (S_{Hmax}) observed in the image logs aligns with the dominant structural strike trend (NNE-SSW/NE-SW) observed in the field.

Conductive fractures and faults (or possible faults) are important contributors to permeability in both wells. Large conductive fractures and faults have been correlated with permeability indicators, e.g.:

- Thermal plume intervals observed in Tuchang's exploration wells X-1 (at 60 to 650 mMD) and X-2 (50-600 mMD / 250-600 mMD [the Borehole High-Resolution Resistivity Imaging Tool was not logged from 50-250 mMD]) are associated with good development of large conductive fractures and faults which trend mainly NE-SW, NW-SE, and N-S.
- A "positive" deflection of temperature (to higher readings) in well X-1 (observed at a depth of 1,450 mMD) is correlated with a major fault zone, which is associated with a major dip azimuth change of the bedding and good development of conductive fractures and faults. Conductive fractures and faults around 1,450 mMD depth show dominant strike orientations of NW-SE and NE-SW.

REFERENCES

Brehme, M., Blöcher, G., Cacace, M., Deon, F., Moeck, I., Wiegand, B., Kamah, Y., Regenspurg, S., Zimmermann, G., Sauter, M., and Huenges, E. "Characterizing permeability structures in geothermal reservoirs – A case study in Lahendong". *Proceedings: 1st Workshop on Geothermal Reservoir Engineering* 2016, Stanford, California, USA (2016).

Chang, P., Lo, W., Song, S., Ho, K., Wu, C., Chen, C., Lu, H. "Evaluating the Chingshui Geothermal Reservoir in Northeast Taiwan with a 3D Integrated Geophysical Visualization Model. *Geothermics,* 50, (2014), 91–100.

Chen, C. "Chemical Characteristics of Thermal Waters in the Central Range of Taiwan, R.O.C." *Chemical Geology*, 49, (1985), 303-317.

Chiang, C., Hsu, H., Chen, C. "An Investigation of the 3D Electrical Resistivity Structure in the Chingshui Geothermal Area, NE Taiwan." *Terr. Atmos. Ocean. Sci*., 26 (3), (2015), 269-281.

Hsiao, C., Chiang, S. "Geology and Geothermal System of the Chingshui – Tuchang Geothermal Area, Ilan, Taiwan." *Petroleum Geology of Taiwan*, 16, (1979), 205-213.

Lai, K., Chen, Y., Wu, Y., Avouac, J., Kuo, Y., Wang, Y., Lin, K. "The 2005 Ilan Earthquake Doublet and Seismic Crisis in Northeastern Taiwan: Evidence for Dyke Intrusion Associated with On-land Propagation of the Okinawa Trough." *Geophys. J. Int.*, 179 (2), (2009), 678-686.

Lin, C.H. "Thermal Modeling of Continental Subduction and Exhumation Constrained by Heat Flow and Seismicity in Taiwan." *Tectonophysics*, 324 (3), (2000), 189-201.

Liu, C., Song, S., Kuo, C. "Silica Geothermometry Applications in the Taiwan Orogenic Belt." *Terr. Atmos. Ocean. Sci.*, 26 (4), (2015), 387-396.

Lu, Y., Song, S., Wang, P., Wu, C., Mii, H., MacDonald, J., Shen, C., John, C. "Magmatic-like Fluid Source of the Chingshui Geothermal Field, NE Taiwan Evidenced by Carbonate Clumped-Isotope Paleothermometry." *Journal of Asian Earth Science*, 149, (2017), 124-133.

Lu, Y., Song, S., Taguchi, S., Wang, P., Yeh, E., Lin, Y., John, C. "Evolution of Hot Fluids in the Chingshui Geothermal Field Inferred from Crystal Morphology and Geochemical Vein Data." *Geothermics*, 74 (June), (2018), 305-318.

Lu, Y., Song, S., Lin, P., Taguchi, S., Wang, C., Lai, Y., Lee, H. "Thermal Fluid Changes after Operating a Geothermal System: A Case Study of the Chingshui Geothermal Field, Taiwan." *Geothermics*, 87, (2020), 101878 .

Teng, L.S. "Extensional Collapse of the Northern Taiwan Mountain Belt." *Geology*, 24 (10), (1996), 949-952.

Tong, L., Ouyang, S., Guo, T., Lee, C., Hu, K., Lee, C., Wang, C. "Insight into the Geothermal Structure in Chingshui, Ilan, Taiwan." *Terr. Atmos. Ocean. Sci.*, 19 (4), (2008), 413-424.

Shih, R., Wang, C., Chen, W., Wang, Y., Kuo, H., Yen, T., Huang, C., Chang, Y., Chung, C., Hunag, M., Chang, Y. "Seismic Reflection Profiling of the First Deep Geothermal Field in Taiwan." *Geothermics*, 74, (2018), 255-272.

Shyu, J., Sieh, K., Chen, Y., Liu, C. "Neotectonic Architecture of Taiwan and Its Implications for Future Large Earthquake." *Journal Geophysics Res. Solid Earth*, 110, (2005), B08402.

Song, S., Lu, Y. "Geothermal Explorations on the Slate Formation of Taiwan." *Renewable Geothermal Energy Explorations*. IntechOpen, (2019).

Yu, S., Tsai, Y. "Geomagnetic anomalies of the Ilan plain, Taiwan." *Petrol. Geol. Taiwan*, 16, (1979), 19-27.

Discrete Reservoir Characteristics Within Lahendong Geothermal System

Imam M. Prasetyo, Teguh Prabowo, R.M. Tofan Sastranegara

PT. Pertamina Geothermal Energy Tbk.

Keywords

Lahendong, geothermal system, reservoir characteristic, reservoir compartment

ABSTRACT

Lahendong geothermal field is located in North Sulawesi Province about 30 km south from Manado City. The exploration of geothermal resources in Lahendong and surrounding area has been initiated since early 1980's by PT. Pertamina and identified two prospects which are Lahendong and Tompaso on north and south part of the field respectively. Lahendong geothermal field is the pioneer of geothermal power generation in North Sulawesi region and currently is operating 4 x 20 MW.

39 (thirty-nine) wells have been drilled in Lahendong Geothermal field to support the power generation. Integrated geoscientific and reservoir data from the wells reveal interesting fact that the reservoir in Lahendong is compartmentalized with discrete reservoir characteristics. There are at least 2 (two) main upflows which are upflow from beneath Linow volcanic crater lake and upflow from beneath Kasuratan volcano. The later hydrology is also divided into 2 (two) blocks which are North Kasuratan and South Kasuratan. They also having distinct characters.

Identification of discrete reservoir within Lahendong geothermal system is manifested in the conceptual model and later provided the foundation for numerical model. This knowledge is also important for determining production and injection strategy for sustainable exploitation of geothermal fluid.

1. Introduction

Lahendong geothermal prospect is located within two administrative areas which are Minahasa County and City of Tomohon, North Sulawesi Province (Figure 1.1). Exploration of geothermal resources in Lahendong has been initiated since 1982-1983 by conducting geoscientific surveys (geology, geochemistry and geophysics). There are 2 prospects identified in Lahendong Geothermal Concession which are Lahendong and Tompaso on North and South part of the field respectivley. Both prospects have their own geothermal system although they are located within greater Tondano Caldera volcanic complex.

Currently Lahendong geothermal field is operating 4 x 20 MW geothermal power plants (GPP) and delivering 80 MW to North Sulawesi electricity grid system by PT. Pertamina Geothermal

Energy Tbk (PGE). Understanding of geothermal system and reservoir characteristic of Lahendong field is crucial as the basis for managing sustainable reservoir for years of contract lifetime.

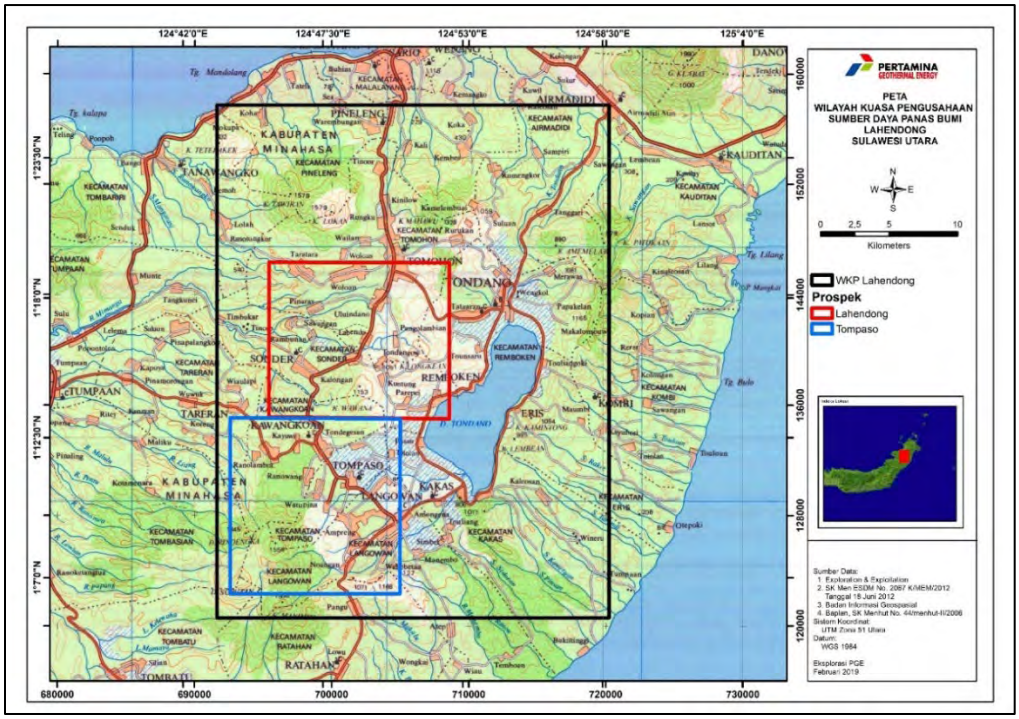

Figure 1. Map of Minahasa geothermal concession map consisting of Lahendong and Tompaso on north (red box) and south (blue box) respectively.

2. Lahendong Geothermal System

Lahendong Prospect lies in Pangolombian Caldera which is located within Tondano Caldera. The caldera is about 4 km wide, and it erupted about 0.45 mya according to the latest dating of its deposits. It is located on the west side of Tondano Lake and inside of the Pangalombian Caldera. Several younger quaternary volcanic edifices may act as potential heat sources of Lahendong geothermal system, such as Mount Kasuratan, Mount Tampusu, Linau Crater Lake and Mount Lengkoan. They are volcanoes related to the Pangalombian Caldera.

The lithology in Lahendong consists of predominantly Quaternary volcanic rocks. Although there are some Tertiary Volcanics and carbonate rocks intersected by deep exploration wells in Lahendong, those rocks are not found on the surface. The rock composition in Lahendong is mainly andesitic to rhyolitic. Pyroxene andesite is common as the product of andesitic lavas from volcanoes such as Kasuratan and Tampusu. while pumice, pumiceous tuff, obsidian is some of the products from rhyolitic volcanoes.

The structural geology of the field is mainly affected by the subduction of Halmahera Plate beneath the Sulawesi plate on the east. Although the local stress regime may be modified due to the resultant of regional stress regime. The main structural trends in Lahendong consist of NE-SW and NW-SE with minor N-S directions.

The components of geothermal system of Lahendong field consist of: 1. Potential heat sources from diorite intrusions beneath Mt. Kasuratan and Linow lake; 2. The hydrothermal activity in shallow part resulting impermeable argillic clay cap mainly developed inside Pangalombian Caldera and extent toward north and south; 3. The reservoir rocks consist of primary permeability from Tuff, Lapilli Tuff and volcanic breccia whereas NE-SW and N-S faults provide secondary permeability from fractures; 4. The origin of fluid is coming from meteoric water sources mainly from Mt. Lengkowan area in the south-west.

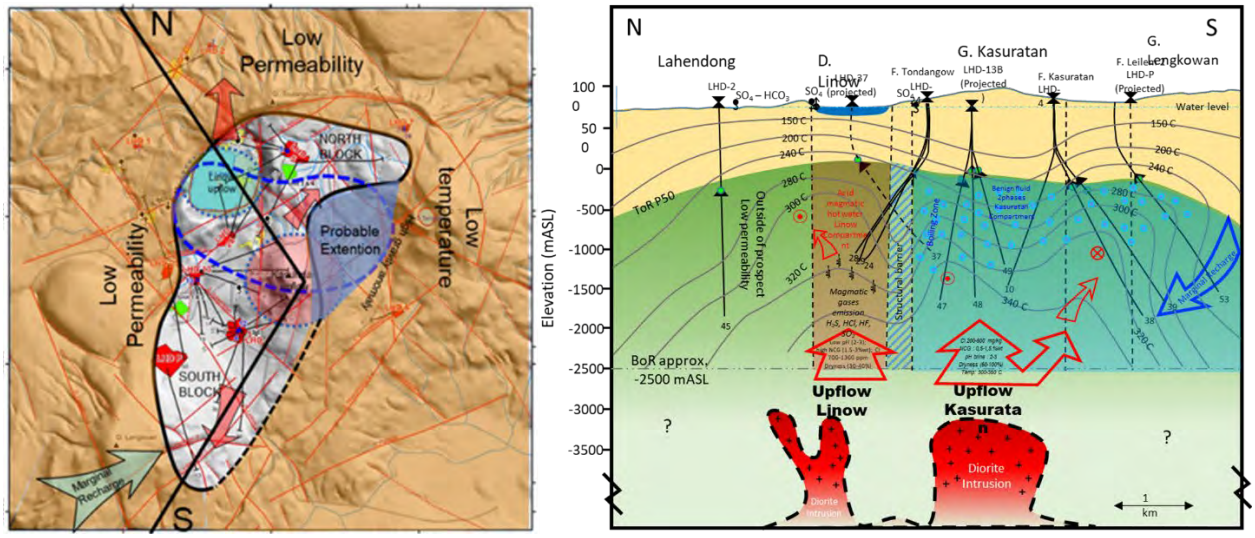

Figure 2. Hydrology and conceptual model of Lahendong geothermal system.

There are two upflows in Lahendong which are rising from beneath Mt. Kasuratan and Linow crater lake. Both have been confirmed by wells and geochemical characteristics. The fluid up flows from Kasuratan and moves laterally toward north and south. Hydrothermal fluid also rises beneath Linow crater lake and outflows to the north. The later system is young and influenced by magmatic components.

3. Reservoir Characteristics

Lahendong Geothermal field is naturally a water-dominated geothermal system which has relatively shallow water table. It has very high temperature characteristics with a range of 250 to 360^{0}C. The highest temperature anomaly distribution lies in the middle and south, especially around the Mt. Kasuratan area with measured temperature range of 320 to 360^{0}C. The reservoir pressure of the Lahendong is in the range of 100 to 160 bar with the reservoir water level at an elevation of about 750-800 masl. The feedzone depths around -300 s.d -1100 mdpl with range of permeability medium to high. The dryness has also wide range numbers between 11 – 100 % with current production decline of 4%/year. This wide range of numbers in reservoir parameters is mainly due to compartmentalized reservoir.

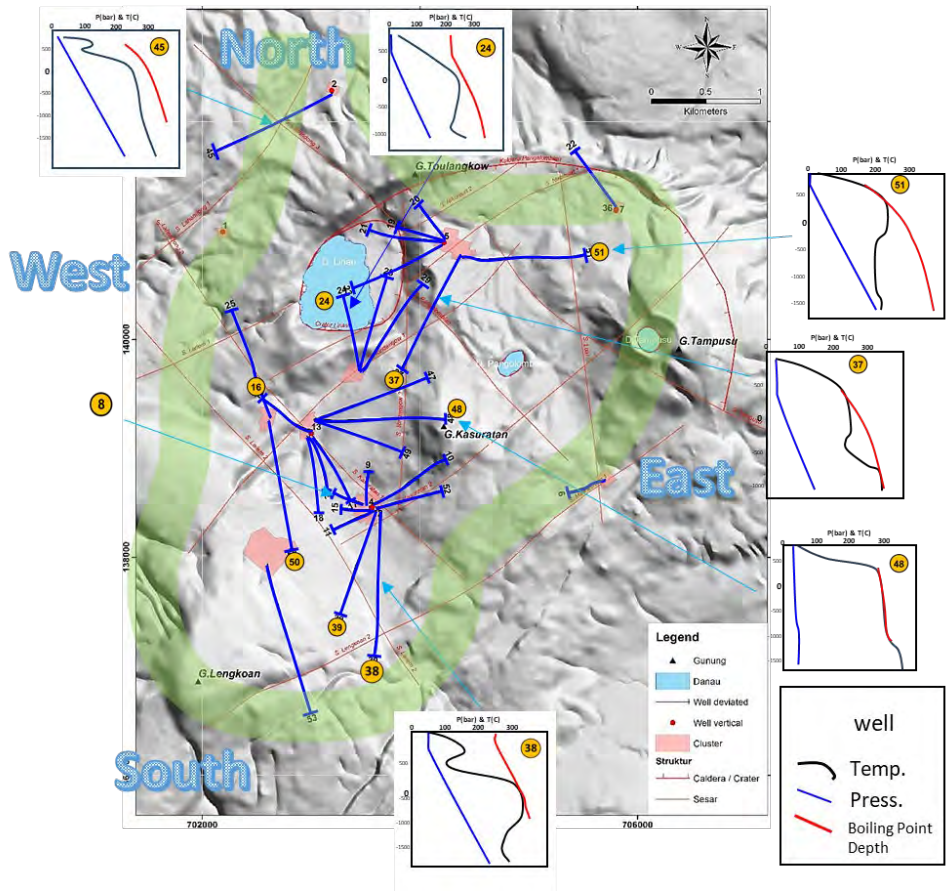

Figure 3. Distribution of temperature across Lahendong reservoirs.

3.1 Reservoir Compartmentation

Mainly there are 2 reservoir compartments inside the Pangalombian Caldera which hosts Lahendong geothermal system, they are:

Linow Compartment

Linow reservoir is located in Linow eruption crater at the North West edge of Pangalombian Caldera. The reservoir compartment is restricted by the collapse rim of Linow Lake. The main feature of this compartment is the influence of acid magmatic fluid. The characteristics of this reservoir compartment are as follow:

- Hot water dominated system with initial dryness of 40-60%
- Reservoir temperature ranges of 280-300 C and enthalpy of 1500-1800 kj/kg
- High permeability but located in limited area around LHD-23 and 28
- The chemistry of fluid shows low pH (2-3), High NCG (1.5-3%wt), and chloride concentration of 700-1300 ppm.

Kasuratan Compartment

Kasuratan reservoir is located around Mt. Kasuratan as the main upflow zone. It is divided into 2 blocks which have distinct characterics. The blocks are as follow:

- *North Block:* covers the area of Pangalombian and east of Linow lake. The characteristics of this reservoir block are: Hot water dominated reservoir (dryness 11-15%), Temperature range of 230-250 C and enthalpy of 900-1000 kJ/kg; high permeability (ii=80-2000 lpm/ksc); the chemistry of fluid shows benign (pH 7-8), NCG (0.2-0.5%wt), and chloride concentration of 300-400 ppm.
- *South Block:* covers area of Mt. Kasuratan, South and South West flank of Mt. Kasuratan, and E – SE flank of Mt. Lengkowan. This block is characterized by its 2-phase vapor dominated reservoir (60-100% dryness); high temperature and enthalpy (300-360 C and 1900-2600 kJ/kg respectively); low to medium permeability (ii 0.025 – 336 lpm/ksc); The chemistry shows benign fluid (pH 6-7) with NCG (0.2-1.3 wt%) and Chloride concentration of 300-500 ppm.

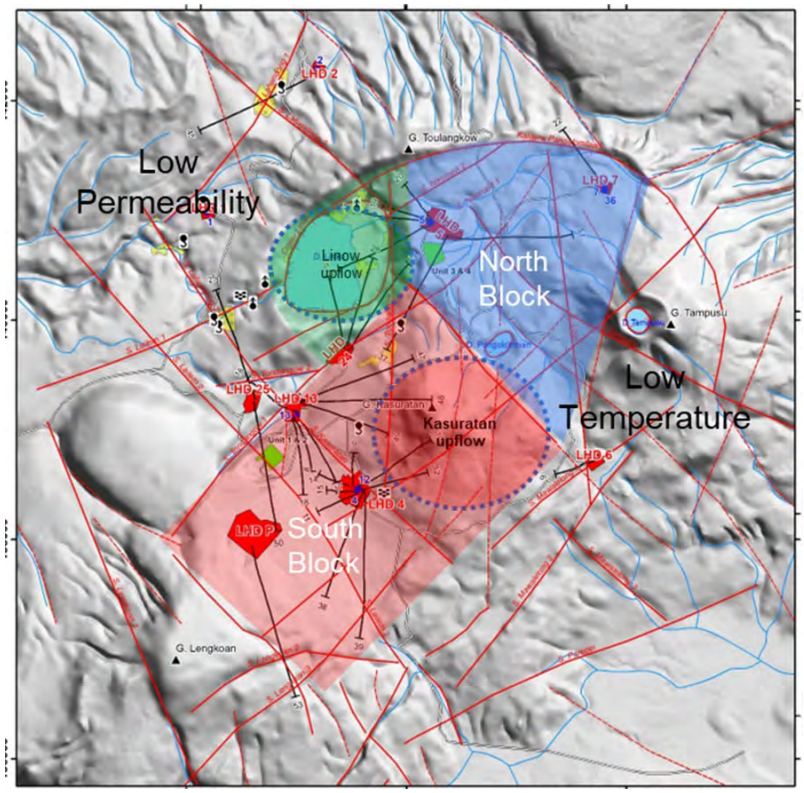

Figure 4. Reservoir compartments of Lahendong geothermal system.

4. Discussion

Lahendong geothermal field features a unique system that combines both two-phase high enthalpy and lower enthalpy reservoirs within Mt. Kasuratan reservoir compartment. Additionally, an acid magmatic upflow rises beneath Linow Lake, isolated from other compartments. The boundaries between these compartments and reservoir blocks are governed by geological structures. The Linow Lake compartment is bounded by the crater rim of Linow Lake, while the North and South blocks of Mt. Kasuratan are divided by the Kasuratan Fault. These geological structures play a crucial role in distinguishing the reservoir characteristics.

The overall heat anomaly in the Lahendong prospect is notably high. The temperature in the south block of Mt. Kasuratan reaches a maximum of 360°C, the highest recorded temperature among PGE fields. This high temperature correlates with low to medium permeability. However, due to

the high enthalpy of the two-phase system, well output remains substantial. Conversely, the north block of Mt. Kasuratan has a lower temperature but higher permeability, resulting in lower enthalpy and dryness. This also necessitates significant brine management or injection.

5. Conclusion & Recommendation.

Understanding reservoir characteristics in a geothermal field is crucial for its development. When a field has discrete characteristics, effective reservoir management is necessary to sustain production and identify opportunities for expansion.

In the Lahendong field, the south block of Mt. Kasuratan serves as the main production zone, while the north block is used for injection. Some wells in the north block can flow at low pressure, presenting an opportunity to install low-pressure turbines and binary plants in the future. Linow Lake wells continue to be used for production, with appropriate treatment of acid magmatic fluid.

Acknowledgement

We would like to express our appretiation to the management of PGE for the opportunity to publish this paper.

REFERENCES

Koestono, H., Siahaan E.E., Marihot Silaban, M., Franzson, H.: Geothermal model of the Lahendong Geothermal Field, Indonesia, Proc. World Geothermal Congress 2010 Bali, Indonesia, 2010.

Prasetyo, I.M., Sardiyanto, Larasati, D., Abdurachman, F.H., Adi, T., Hastuti, P. Lahendong Field Conceptual Model Update, Internal Report, PT. Pertamina Geothermal Energy, 2021.

Siahaan, E.E., Soemarinda, S., Fauzi, A., Silitonga, T., Azimudin, T., Raharjo, I.B. (2005) Tectonism and volcanism study in the Minahasa compartment of the north arm of Sulawesi related to Lahendong geothermal field, Indonesia. Proc. World Geoth. Congress. (2005).

Sullivan, J.O., Abdurachman, F.H., Bignall, G., Bromley, C., Dekkers, K., Ghassan, M., Gravatt, M., Hastuti, P., Indra, A., Nugraha, R., Pasaribu, F., Popineau, J., Prasetyo, I.M., Rai, V., Renaud, T., Yuniar, D., O'Sullivan, M. Multidisciplinary collaboration to create a new numierical model of Lahendong geothermal field. Proc. 48th Workshop on Geothermal Engineering, Stanford, California, Feb. 6-8, 2023.Verma, A., and Pruess, K. "Enhancement of Steam Phase Relative Permeability Due to Phase Transformation Effects in Porous Media." Proceedings: 11th Workshop on Geothermal Reservoir Engineering, Stanford University, Stanford, CA (1986).

Utami, P., Widarto, D.S., Atmojo, J.P., Kamah, Y., Browne, P.R.L., Warmada, I.W., Bignall, G., and Chambefort, I., 2015. Hydrothermal Alteration and the Evolution of the Lahendong Geothermal System, North Sulawesi, Proc. World Geothermal Congress 2015 Melbourne, 19-25 April 2015, p.

Conceptual Model of the Puna Geothermal System

Drew Spake, Zach Reynolds, Derek Caro, Nick Prina, John Murphy, Adam Johnson, Paul Spielman, Robin Zuza, Simon Webbison

Ormat Technologies, Inc.

Keywords

Geology, Drilling, Conceptual Model, Image Log Analysis

ABSTRACT

The Puna Geothermal Venture (PGV) is a 38-MW combined cycle power plant producing from a two phase, liquid-dominated, 280-320°C (±535-610°F) resource located at a prominent left-step in Kilauea's East Rift Zone on the Island of Hawai'i. Drilling results and interpretation of available geoscientific datasets reveal a deep reservoir with fracture-dominated permeability controlled primarily by rift-parallel fractures with some contribution from rift-cutting features.

The 2018 Kilauea eruption forced plant shutdown and resulted in a recovery campaign which brought the plant back online in 2020. Following plant restart a new drilling campaign was completed, adding two new wells to the production field and one new well to the injection field and bringing PGV generation to over 32 MW for the first time since the eruption. An acoustic borehole image log was successfully acquired for the first time at PGV during this drilling campaign, providing new insights into subsurface conditions and permeability controls. In this paper we integrate available geologic, geophysical, and geochemical to provide a conceptual framework for the PGV system.

1. Introduction

Exploration for naturally occurring geothermal systems as a source of independent power production has been ongoing in the state of Hawai'i since at least the early 1960s. Numerous state and federally funded projects have studied Hawai'i's geothermal potential through a variety of geological, geophysical, and geochemical surveys, as well as exploration drilling to test hypotheses resulting from surface exploration (e.g., Furumoto et al., 1977; Thomas, 1986; Lautze et al., 2017; Warren et al., 2023). The Island of Hawai'i was the focus of early exploration efforts due to its active volcanism and the presence of surface manifestations of geothermal systems, such as hot springs, which other islands lack. Kilauea volcano and its associated rift zones are the most favorable regions for Hawaiian geothermal exploration due to the colocation of necessary elements for the formation of hydrothermal systems: elevated shallow heat flow (from young volcanism), a

fluid-saturated subsurface (implied by the high annual rainfall and location on an oceanic island), and permeable fluid pathways to support natural convective processes (suggested by active tectonic dilation along the rift zones).

Geothermal exploration on the Island of Hawai'i began in 1961 with the drilling of four exploration wells by Hawaii Thermal Power Company in Kilauea's Lower East Rift Zone (LERZ) near a prominent left step in the rift zone's fissures. The wells (TH-1, -2, -3, & -4) encountered elevated groundwater temperatures ranging from 109° to 203°F (43° to 95°C) at depths from 216 to 686 ft but were plugged and abandoned, lacking temperatures high enough for energy production (DPED, 1982). Following an extensive geophysical survey of the LERZ from 1973-1975, the Hawai'i Geothermal Project utilized federal, state, and county grant funds to drill the HGP-A resource discovery well near Pu'u Honua'ula, the initial eruptive fissure for the 1955 LERZ eruption. HGP-A was completed in April 1976 to 6450 ft (1966 m) measured depth (MD) with a bottom hole temperature of 676°F (358°C) (Takahashi et al., 1985). The well produced 110 kph at 166 psig with ~43% steam fraction to a 3MW turbine generator from 1981-1989, marking the onset of geothermal energy production in Hawai'i. Additional exploration drilling along the LERZ during the 1980-1990s by competitor companies and the State of Hawai'i/University of Hawai'i demonstrated the existence of high temperatures along the LERZ, but high permeabilities were never encountered and production was not sustained from any of the Lanipuna, Ashida, or Scientific Observation Hole (SOH) locations (Figure 1).

Figure 1: Regional map of Kilauea's Lower East Rift Zone. The PGV lease area is shown in hatched blue, with faults shown in black (Moore and Trusdell, 1991) and fissures from the 2018 eruption in red (Zoeller et al., 2020). Geothermal exploration wells are shown in white, and warm springs in orange.

PGV was the first and only commercially productive geothermal power plant in Hawaii and provided 31% of the island's electrical demand in 2017. PGV began commercial operation of a >600°F (315°C) naturally occurring geothermal system with an Ormat-supplied 30 MW combined cycle power plant with 100% reinjection of produced fluids in 1993. The project was acquired by Ormat in June 2004, and over the years generation has increased by upgrading the facility, through resource development, and with the addition of two bottoming OECs (Ormat Energy Converter) which produced more energy from the brine. As of 2012, the facility was comprised of a combined cycle (steam turbine with binary condenser) air cooled plant and two brine binary units with a nameplate capacity of 38 MW. The plant operated continuously from startup in 1993 until plant shutdown in May 2018 due to a volcanic eruption along the LERZ. Recovery efforts to the facility began in early 2019 following cessation of the eruption in late September 2018. The plant was brought back online in November 2020 after an extensive campaign to restore both the power plant and wellfield, which included workovers, re-drills, and initially the drilling of 3 new wells.

Following plant restart, a drilling campaign from 2022-2023 successfully three new wells, with the additional production brine helping to increase PGV's generation to >32 MW for the first time since the eruption. As part of the planned completion testing for the campaign an acoustic borehole image log was acquired in the northernmost well, the first successful image log at PGV.

As of this writing (June 2024), there have been 20 full-sized "KS" (Kapoho State) wells drilled at PGV with a total of 39 discrete legs considering original holes (OH), twins (e.g., KS-1A), multi-leg completions (ML), redrills (RD), and sidetracks (ST). Production wells are primarily clustered on the southern side of the wellfield, with injection wells primarily on the northern side of the field (Figure 2).

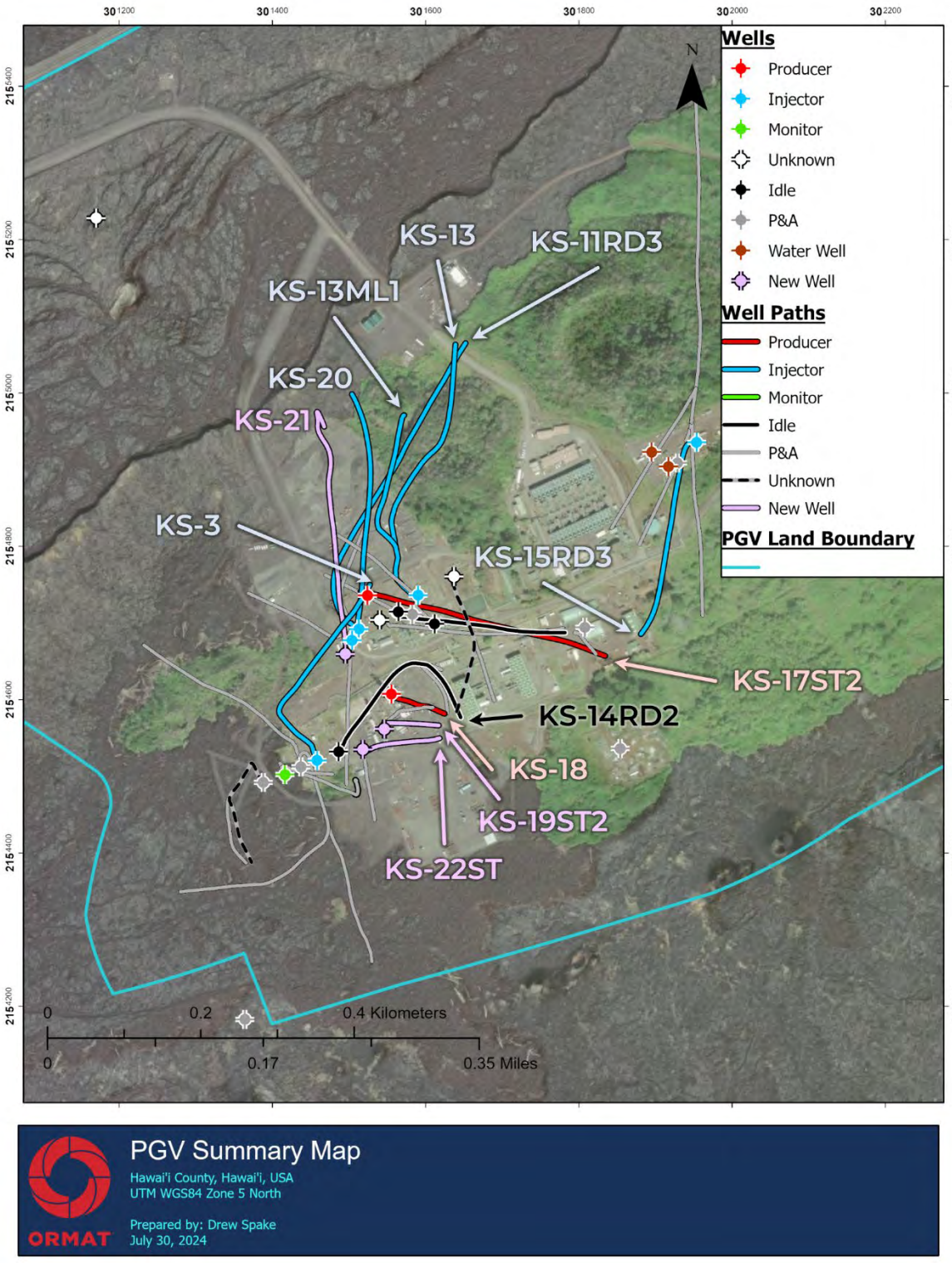

Figure 2: PGV wellfield map. Directional well paths are shown with colors corresponding to the well's status, with new wells completed during the 2022-2023 drilling campaign indicated separately. The bottom hole location of new wells and active production/injection wells are labeled (other wells left unlabeled for clarity).

2. Geology

2.1 Regional Geology and Tectonic Setting

The hydrothermal system at PGV is located in a volcanic rift zone associated with the Kilauea volcano on the Island of Hawai'i. The Hawaiian-Emperor island chain is a string of 8 major and 129 minor islands and seamounts formed by a mantle plume hot spot over the past ±70 MA (Wilson, 1963). The Island of Hawai'i is the youngest, southernmost member of the archipelago and encompasses five major shield volcanoes (from oldest to youngest: Kohala, Mauna Kea, Hualālai, Mauna Loa, & Kilauea). An older, sixth volcano, Māhukona, lies beneath sea level off the northwestern tip of the island, while Kama'ehuakanaloa (formerly Lō'ihi), represents active growth of the newest volcano in the chain southeast of Kilauea (Sherrod et al., 2021).

Magma supply to Hawaiian volcanoes originates with upwelling of mantle melt at an intraplate "hot spot" (Wilson, 1963; Morgan, 1971). On the Island of Hawai'i, Kilauea and Moana Loa share magma supply from the hot spot but likely have separate, though proximal, storage chambers (Poland et al., 2014). The general model for Kilauea's magma plumbing system is that magma generated in the mantle at 30-60 km depth ascends and is stored at neutral buoyancy in reservoirs that are 2-4 km beneath the summit and almost wholly molten rift zones at 3-10 km beneath the surface (Eaton and Murata, 1960; Ryan, 1988) (Figure 3).

Hawaiian volcanoes are built through successive stages of volcanism, quiescence, and erosion. An idealized model of Hawaiian volcano evolution involves four eruptive stages: (1) a pre-shield submarine alkalic stage, (2) a tholeiitic shield-building stage, depositing ≥95% of the volume of the volcano, (3) a post-shield alkalic stage which deposits a thin cap of alkalic basalt and differentiated lavas, and (4) an alkalic rejuvenation stage characterized by isolated vent eruptions following several million years of dormancy and erosion (Clague and Dalrymple, 1987). Deposits found on the Island of Hawai'i represent stages 1-3, with the active Mauna Loa and Kilauea depositing primarily tholeiitic basalts through shield-stage volcanism (Sherrod et al., 2021).

Kilauea's oldest deposits are ±275 ka alkalic, pre-shield submarine basalts which were sampled from the southern slope of the volcano by remotely operated submersibles, presumably representing submarine lava flows (Lipman et al., 2002). The SOH-1 exploration core hole drilled on the eastern flank of the volcano records a transition from subaerial to submarine deposits at ±551 m below sea level in a sequence comprised entirely of tholeiitic lava flows and dikes (Trusdell et al., 1999; Sherrod et al., 2021). Surface mapping shows that Kilauea's subaerial stratigraphy is composed of three major units (oldest-youngest): (1) the Hilina Basalt, (2) the Pahala Ash, and (3) the Puna Basalt (Sherrod et al., 2021). The Hilina Basalt is exposed only in fault scarps located along the southern flank of the volcano, while the Puna Basalt covers nearly the entire surface of Kilauea (Langenheim and Clague, 1987; Sherrod et al., 2021).

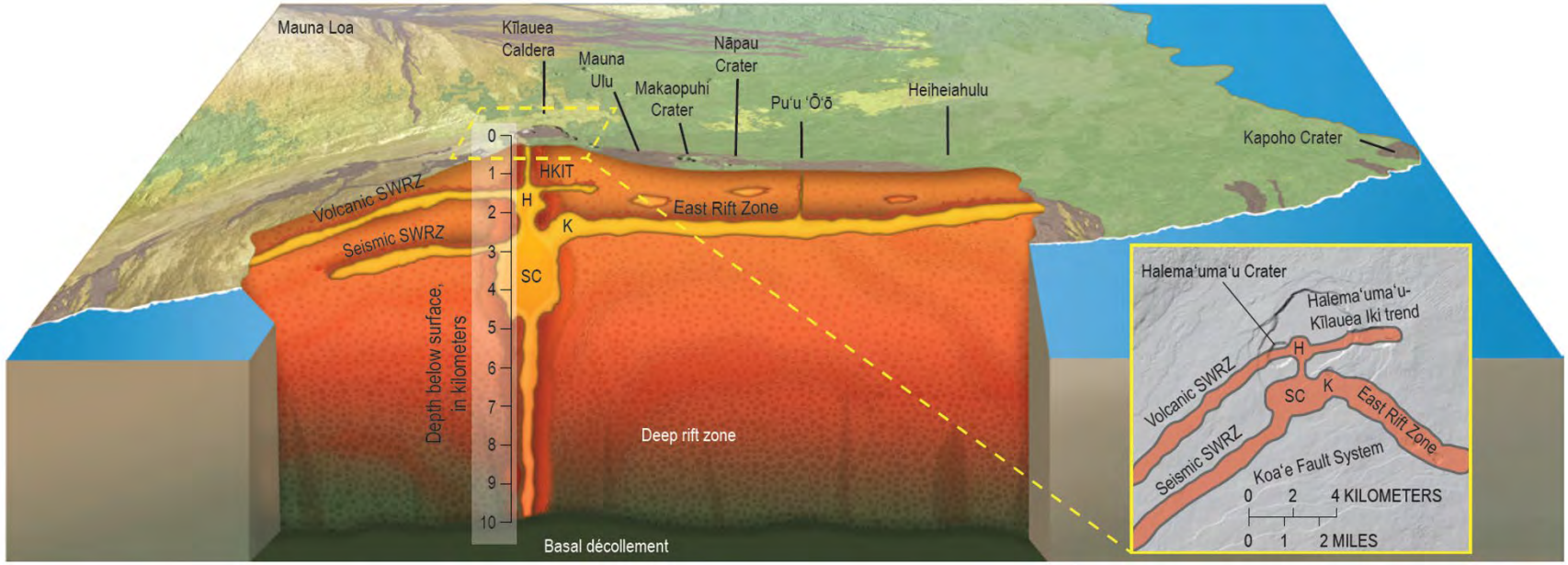

Figure 3: Illustration of Kilauea's magma plumbing system. Schematic cross section depicts the magma pathways and storage areas (exaggerated in size). K, Keanakāko'i reservoir; SC, south caldera reservoir; SWRZ, Southwest Rift Zone. Schematic viewing direction is from south to north. Plan view gives the relations of magma pathways to surface features and topography in the vicinity of Kilauea Caldera. (Figure and text reproduced from Poland et al., 2014).

Kilauea is cut by two rift zones which emanate from the summit caldera: the East Rift Zone (ERZ) and Southwest Rift Zone (SWRZ) (Figure 4). The two rift zones are bridged by the Koa'e Fault and Hilina Fault zones, deeply rooted normal fault systems accommodating southeastward displacement along the rift zones (Lipman et al., 1985, Duffield, 1975). Beginning in the 1950s, the ERZ became the most active part of Kilauea's magmatic system (Poland et al., 2014). Magma movement along the rift is facilitated by seaward extension of Kilauea's mobile southern flank, which acts to dilate the rift zone (Patrick et al., 2020). Motion of the south flank is likely accommodated by slip along a basal decollement 6-11 km deep at the interface between pre-Mauna Loa oceanic crust and the overlying volcanic edifice (Lipman et al., 1985).

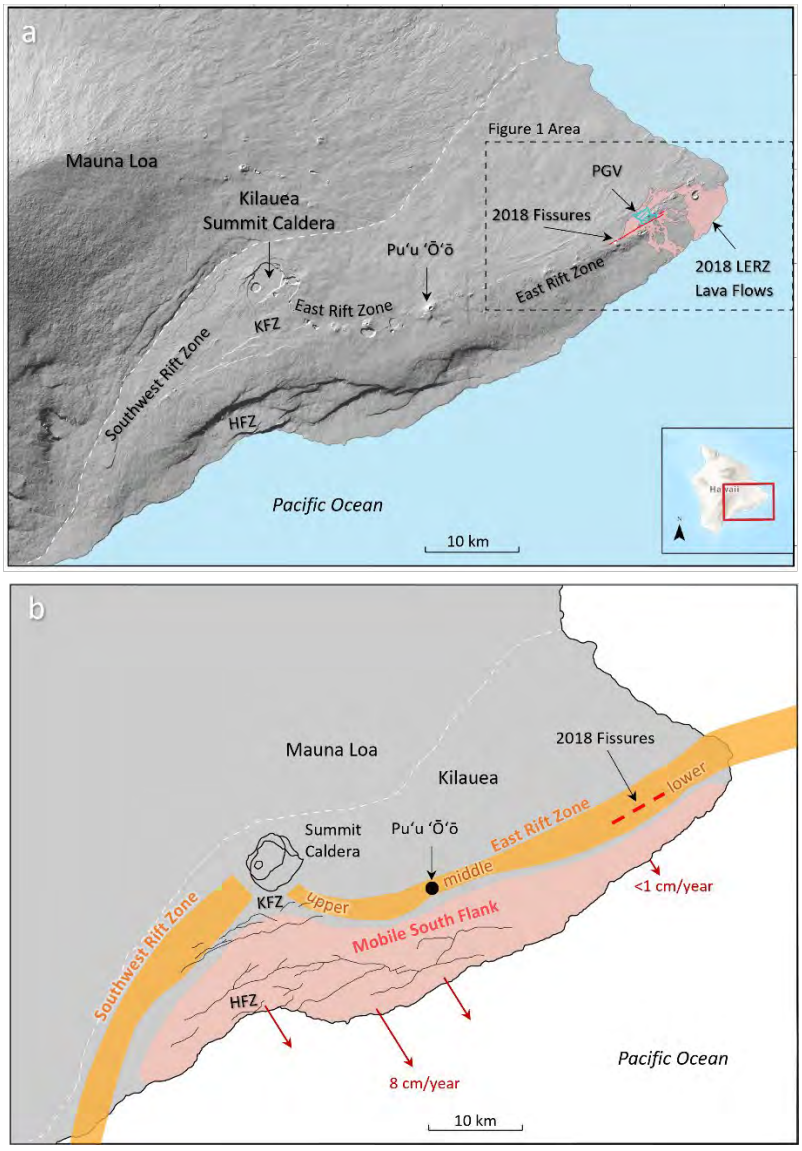

Figure 4: (a) Map of Kilauea volcano. The approximate boundary between Mauna Loa and Kilauea lavas is denoted by the dashed white line and the area of Figure 1 is shown by the black dashed box with PGV's location indicated in hatched blue. (b) Schematic structural map of Kilauea volcano showing the summit region and two rift zones. The mobile south flank exhibits steady southeast motion and is tightly coupled with the rift magmatic system. KFZ: Koa'e Fault Zone. HFZ: Hilina Fault Zone. (Figure modified from Patrick et al., 2020).

The East Rift Zone extends southeast from the summit caldera for approximately 7 km, then trends ±063° (N63°E) toward and beyond the end of the land surface. The rift is loosely subdivided into upper, middle, and lower sections and is one of the main conduits for lateral migration of magma from the holding chamber beneath Kilauea's summit caldera, with eruptions in the lower portion of the rift having occurred as recently as 1790, 1840, 1955, 1960, 1961, and 2018 (Moore and Trusdell, 1991).

The subaerial portion of the LERZ strikes 063°, is 3-4 km wide and about 23 km long, extending for an additional 70 km offshore as the submarine Puna Ridge. The LERZ is a constructional ridge characterized by low spatter deposits and cones up to ~200 ft (60 m) high (Moore and Trusdell, 1991). Its elevation gently decreases from southwest to northeast and ranges from a high of 1,713 ft (522 m) above sea level at Heiheiahulu to sea level at Cape Kumukahi (Swanson et al., 1976). The overall vent and fracture lineaments align strongly along the 063° trend and typically exhibit a pattern of en echelon step-overs.

Underlying the surface expression of the ERZ is a much broader (±12- 20 km wide) intrusive dike complex inferred by gravity (Broyles et al., 1979) and magnetic data (Kinoshita et al., 1963). This complex is thought to consist of an aggregate of closely spaced, parallel to subparallel, vertical to steeply dipping dikes intruded into a sequence of Mauna Loa and Kilauea lava flows. Individual dikes are likely <1 m to 5 m in width, though may be vertically and laterally extensive (Swanson et al., 1976; Wilson and Head, 1988).

2.2 Local Geology and Structure

All the rocks in the vicinity of PGV are Holocene tholeiitic basalts with varying abundances of olivine and pyroxene phenocrysts reflecting the relative amount of fractionation of magmas in subsidiary magma chambers along the rift zone (Moore and Trusdell, 1991; Langenheim and Clague, 1987). Pahoehoe and a'a lava flows as well as spatter deposits and small cinder cones dominate the landscape, representing eruptive events from about the year 1601 up to the most recent eruption in 2018, which overran part of the PGV wellfield and covered older deposits. Two small cinder cones and associated spatter deposits known as Pu'u Honua'ula from an eruption ±373 years before present form prominent hills on the PGV property. The power plant is constructed on a small topographic high formed by flows from the 1955 eruption which emanated from fissures at the base of the two cones. This small plateau prevented the plant from being consumed by the 2018 lava flows.

Eruptive vents on the southern side of the LERZ are commonly en echelon and right-stepping in the region west of Puulena Crater (~800 m southwest of the PGV lease). The linear alignment of vents abruptly terminates here, shifting left (northwest) by ~1 km, where they resume the 063° trend but are organized in left-stepping en echelon arrangement. The left step is well documented by seismic and magnetic datasets, however no transverse faults striking perpendicular to the main rift trend have been identified. The differential motion of the southern flank may result in failure of structural blocks bound by NW-striking faults, causing the stepover (Moore, 1992).

2.3 Downhole Geology and Structure

Subsurface geology is informed by the relatively high-density drilling over the small areal extent at the PGV project area, with additional context and regional constraints provided by publications on the early exploration wells, particularly HGP-A and the SOH holes.

Wells drilled at PGV document 3 major correlatable units, in order from shallowest to deepest: l) subaerial basalt flows 2) a transitional, near-shore assemblage dominated by hyaloclastites, and 3) submarine pillow basalts. Diabase dikes are found throughout the stratigraphic sequence but increase in frequency and width with depth. These lithologic assemblages are not internally homogeneous, and geologists working at Puna have divided the basalt stratigraphy into the following primary divisions based on physical characteristics: scoria (cinders), lavas (vesicular, aphanitic), hyaloclastite, diabase dikes (porphyritic), highly altered (observable parent texture i.e., vesicular or aphanitic) and clay (indistinguishable parent texture commonly associated with hyaloclastite and/or tephra). The hydrothermal reservoir is hosted within fractured submarine basalt flows and diabase dikes starting about 4200 ft (1280 m) below ground level (bgl) (approximately -3600ft/-1100 rSL (relative to sea level)).

The depositional environment directly affects the physical appearance of all three basalt types. Subaerial basalts, mostly a'a and pahoehoe, occur as solid flows separated by rubblized interflow breccias or sometimes totally fragmented and rubblized flows. Submarine basalt flows occur as dense conglomerates of pillows and pillow fragments infilled by ocean floor clays and silica. Dikes are typically coarser grained tabular bodies that intruded pre-existing flow basalts. Hyaloclastites are deposits of grit to sand sized granular glass fragments formed when hot, fluid basalt flows into the ocean creating phreatic explosions. The hyaloclastite material may be deposited off or near shore as black sand beaches or on shore as littoral cones and tuff rings depending on the prevailing winds and intensity of the lava-water reaction. Primary olivine tholeiites as well as differentiated basalts can be found as subaerial, submarine, hyaloclastite, or intrusive dike deposits.

Permeable fractures are commonly, but not ubiquitously, associated with the intersection of diabase dikes. Dike rock is recognized by its relatively coarse grained, hypidiomorpic, subhedral texture, its fresh, unaltered appearance, and general scarcity of secondary mineralization. In many wells the permeable fractures were encountered in the footwall side of a diabase dike after drilling through several tens of feet of diabase.

Dikes and permeable fractures are primarily interpreted to be aligned with the local strike of the LERZ (063°) and subvertical or steeply northwest dipping. Permeable fractures at PGV are generally named for the first well to have intersected the feature, e.g., the KS-5 Fracture hosts current production from the KS-19ST2 and KS-22ST wells. Key production fractures include the KS-5, KS-8, and KS-14 Fractures, and injection is hosted in the 1955 Fissure (distinguished by discrete North and South fracture zones), KS-3, and KS-20 Fractures.

In addition to the SW-NE striking features, the conceptual and numerical models include permeable pathways oriented perpendicular to the rift (NW-SE) (Murphy et al., 2024), which is supported by observed tracer return pathways and consistent with PGV's location at the major left-step in the LERZ (Figure 5). A key purpose for image log acquisition during the 2022-2023 drilling campaign was to establish if such fractures are identifiable in the subsurface.

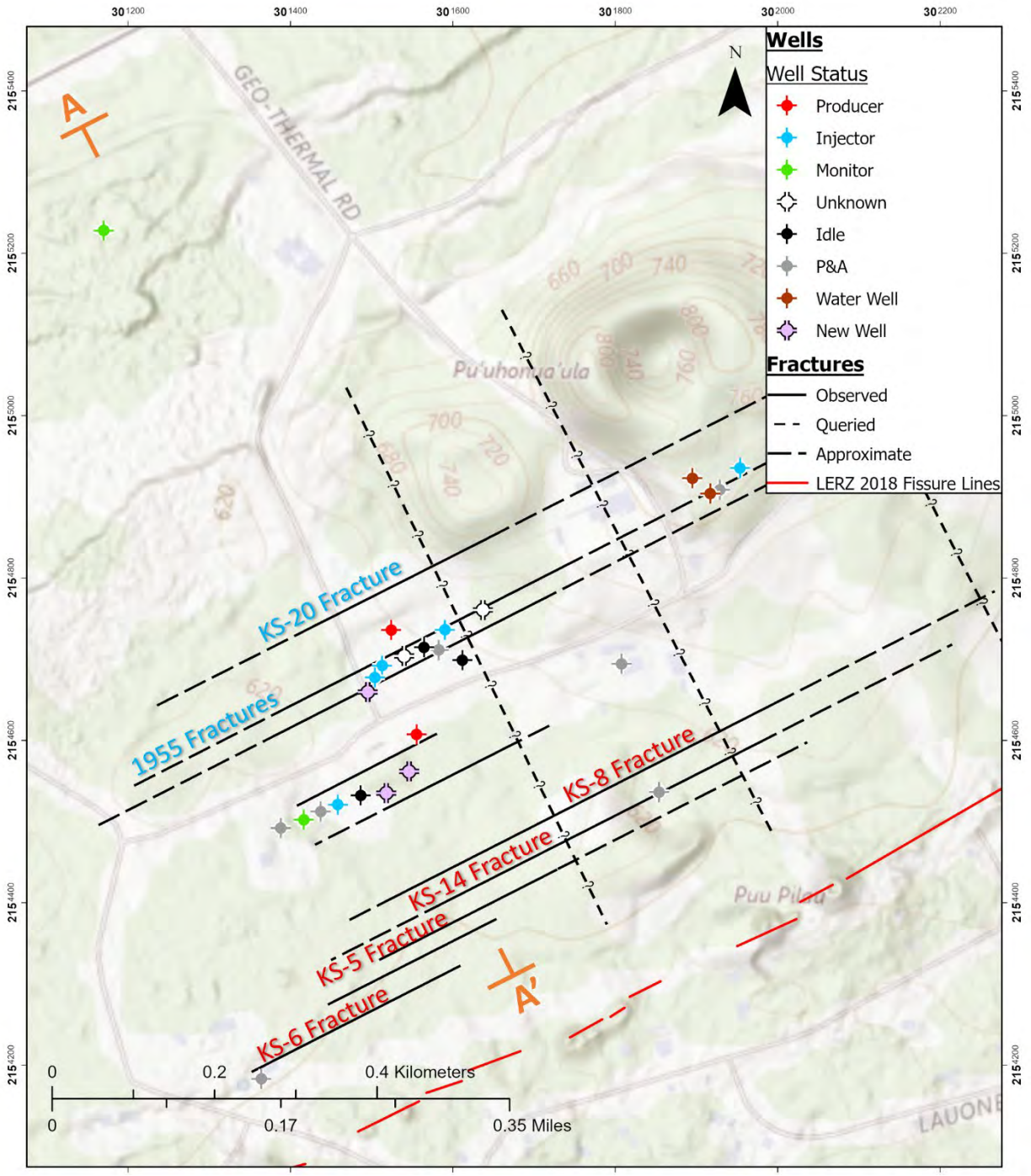

Figure 5: Map of the PGV wellfield showing known and hypothesized subsurface fracture pathways. Key production and injection structures are labeled in red and blue, respectively. Figure 10 cross section extents indicated by A-A' line (orange symbology).

2.4 Image Log Results

Borehole image logs are an invaluable dataset which allow quantification of fracture attitudes and in some cases the orientation of the stress field, data points which allow ground truthing of key elements of a conceptual model, and for this reason acquisition of an acoustic image log was an important component of the logging and testing plan for the northernmost well drilled in the 2022-2023 campaign. The borehole geometry and stability conditions were considered continuously throughout drilling and the decision-making process of calling TD, and these components were essential to making an informed, risk-based plan and decision for log acquisition. For example, below 6900 ft MD the borehole "inverts", changing azimuth by ~180° as designed to re-cross the target fracture zone, and this geometry was an important component of selecting the image log interval. With no significant fill on bottom observed during drilling or reaming (which could indicate borehole sloughing or collapse), the borehole was considered to be in stable condition and approval was granted to run a PTS survey followed by image log acquisition. However, to maintain borehole stability throughout logging operations it was decided that the wellbore would remain filled with drilling mud rather than switching over to water, as is common for acquisition of acoustic image logs.

The image log was successfully acquired from the casing shoe (3634 ft) to 6900 ft MD. The image quality is poor overall due to suspended solids in the fluid column from the drilling mud causing attenuation of the acoustic signal, but interpretation of important features is still possible. Analysis of the image log identified 248 discrete features over the 3266 ft log interval. Most structures identified are rift-parallel and sub-vertical, dipping both NNW and SSE (supporting key elements of the conceptual model), with a minor population of NW-trending, SW-dipping features identified.

Southeast-striking (rift-cutting) fractures captured in the image log have strikes ranging from ±105°-160°, with the mode of the population oriented approximately 112°/75° (strike/dip) (Figure 6). Mapped surface representations of these features, represented as queried fractures in Figure 5, strike 154°; this attitude is based on combined analysis of regional to local gravity and magnetic surveys, LiDAR lineaments, and tracer studies, and is consistent with the range of fracture attitudes implied by image log interpretation. Whether there are throughgoing, high permeability fractures present in the field, as the mapped traces imply, or if NW-SE trending fractures are found as a distributed population throughout the subsurface, as they manifest in the image log interval, is a remaining uncertainty in the conceptual model with important implications for reservoir management and well targeting.

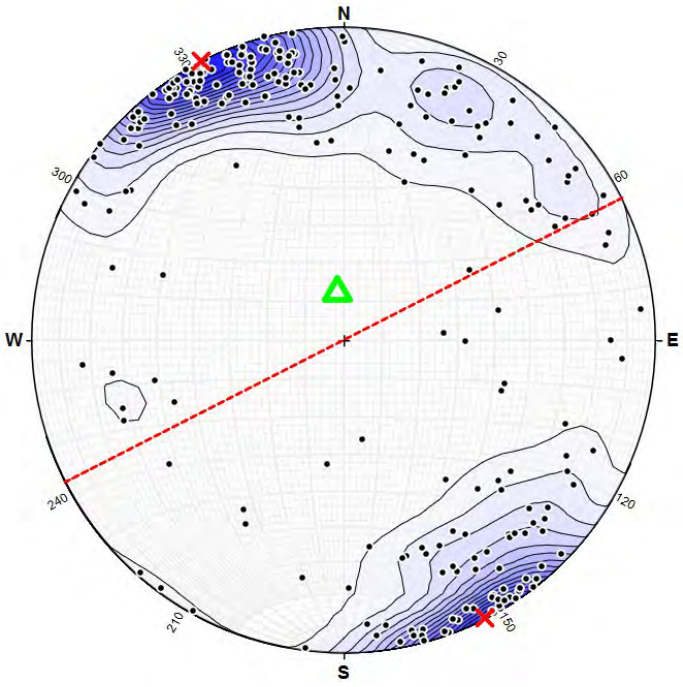

Figure 6: Lower hemisphere stereonet with poles to planes plotted and contoured for all fractures identified in the image log (n=248). The trend of the LERZ (063°/243°) is indicated by the dashed red great circle, and poles to that vertically dipping plane are indicated by red X's. The average (median) attitude of the borehole through the imaged interval is plotted as a bold green triangle.

Drilling induces damage to the borehole wall may be preserved as borehole breakouts (BO), petal-centerline fractures (PCF), or drilling induced tensile fractures (DITF), structures which can be used to infer the orientation of the modern stress state in the subsurface (e.g., Davatzes and Hickman, 2010; Moos and Zoback, 1990, Zoback et al., 1985). Three pairs of DITFs were identified in the image log. DITFs at ±3650 ft and 4450 ft are oriented NE-SW, indicating that S_{Hmax} is roughly aligned with the trend of the LERZ (Figure 7) and fractures subparallel to the rift should be well-oriented for dilation and fluid flow (e.g., Heffer, 2002). However, the final pair of DITFs identified at ±6270 ft are oriented NW-SE (116°/299°), an approximately 60° shift from the shallower pairs, which would place rift-parallel fractures under compression and preferentially favor fluid flow along NW-SE trending structures. This rotation may be local, with the attitude of S_{Hmax} reverting to a NE-SW orientation beyond the logged interval. Alternatively, this stress field rotation may imply that deep permeable zones in the northern wellfield are more likely to be channelized along rift-perpendicular fractures, which may facilitate rapid breakthrough of injectate back to the production field and thus unfavorable cooling of the reservoir. Additional testing, particularly a long-term reservoir tracer test, is required to better understand the fluid pathways from the injection to production fields.

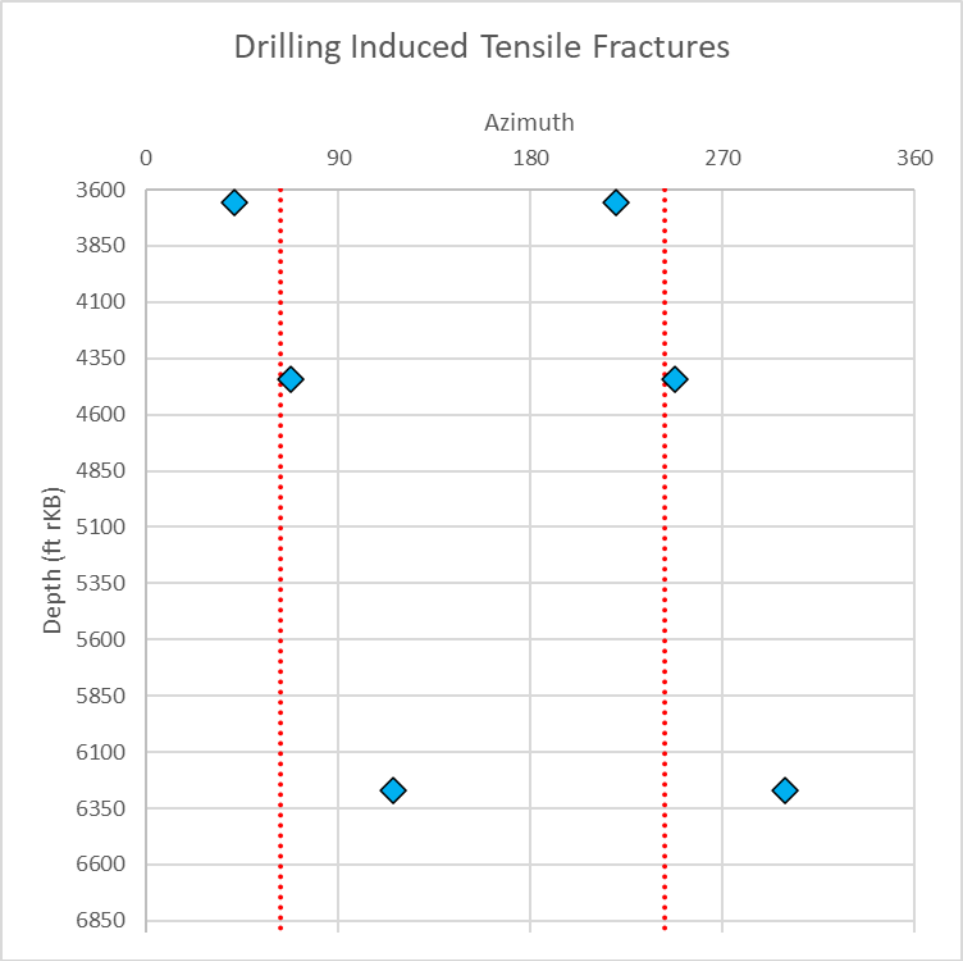

Figure 7: Drilling induced tensile fractures (blue diamonds) identified in image log plotted against borehole depth. The trend of the LERZ is plotted as red dotted lines.

2.5 Alteration Systematics

Hydrothermal alteration of basaltic to diabasic host rocks occurs as replacement mineralization and fracture or vesicle filling secondary mineral deposits. Replacement minerals include clays, chlorite, and disseminated pyrite, with replacement mineralization first appearing at ±1500 ft MD (±455 m) and becoming more pervasive below ±4000 ft MD (±1220 m).

High clay content logged in drill cuttings is a function of both temperature-dependent alteration processes and host rock lithology, with abundant clay found in glassy hyaloclastites of the transitional zone/near shore depositional environment. Widespread clay begins at ±2600 ft (792 m) bgl (-1110 ft/ -580 m rSL) and is logged to variable depths that are interpreted to represent the size and shape of the clay caprock overlying the convective hydrothermal system. Thick expanses of clay are interbedded with unaltered basalt flows and hyaloclastite deposits, indicating the incomplete alteration of the host rock and imperfect nature of the caprock. This incomplete alteration combined with structural discontinuities from tectonic fracturing allow minor leakage of fluids and steam from the underlying hydrothermal system in the natural state. This phenomenon is well-documented in geothermal systems around the world where surface manifestations

overlying the reservoir document leakage of steam and fluids through the caprock (e.g., Rowland and Simmons, 2002).

Four distinctive fracture filled mineral assemblages are recognized. The stratigraphically highest, lowest temperature assembly consists of amorphous silica (opaline silica and chalcedony) + anhydrite + pyrite ± clay/chlorite ± zeolite(s) ± calcite. A moderate to high temperature assemblage is composed of anhydrite + pyrite + quartz + chlorite ± garnet ± chalcopyrite. The highest temperature, deepest stratigraphic assemblage consists of quartz + epidote + chlorite ± actinolite ± anhydrite.

A quantitative relationship between reservoir temperatures and these mineral assemblages has not been well established due to the propensity of higher temperature fluids from deep in the reservoir to flow upwards within the wellbore and mask the flow from the upper, cooler entries. From mineralogical and fluid temperature correlations from other known geothermal fields, the low temperature mineral assembly probably represents reservoir temperatures of 300-400°F, the moderate temperature assembly represents temperatures of 400-550°F, and the high temperature group ≥550°F.

Mineralogical precursors to entry into high-temperature production zones are not well-developed in the Puna field. In shallower portions of the high-temperature system, such as that encountered in KS-7, a hydro-fractured texture consisting of brecciated basalt, re-cemented with silica and anhydrite, may be present along with bladed pyrrhotite. Below 3500 ft depth, minor occurrences of euhedral epidote have been noted within 100 feet of entry into producing fractures. However, it is stressed that mineralogical precursors may be rare or absent immediately prior to entry into a producing fracture.

3. Geophysics

Geophysical data acquired near PGV reveal that measurable variations within the rocks of the LERZ are subtle, primarily due to the island's lithologic homogeneity. Gravity data indicate a lack of significant density contrast between rock units, resulting in a relatively attenuated gravitational signature. Several generations of resistivity surveys have been completed with varying degrees of success, including 4 CSAMT lines in 1993 and a regional magnetotelluric (MT) survey focused on imaging magma reservoirs and conduits within Kilauea and the East and Southwest rift zones. While the CSAMT data is of limited use due to the high levels of anthropogenic noise near the power plant, Hoversten et al. (2022) demonstrates that MT resolves the rift zones as extensive low resistivity anomalies and provides insight into successful MT acquisition in the challenging field conditions found near Kilauea.

An airborne magnetic survey collected in 1978 with flight line spacings of 0.8 and 1.6 km demonstrated that magnetics is a useful tool for imaging the regional structure of the LERZ (Flanigan & Long, 1987). Ormat collected an airborne magnetic survey over PGV which enhances the resolution of key features, revealing strong magnetic highs that correlate with mapped eruptive vents and faults along the LERZ (Reynolds et al., 2024). The survey shows that sharp magnetic highs aligned with the trend of the LERZ, interpreted as shallow dikes with high magnetic susceptibility, make a left-step near PGV, consistent with the rift geometry implied by vents and fissures. Lineaments linking the two main rift segments in this area trend approximately perpendicular to the rift, supporting the existence of NW-SE (±333°/153°) trending fractures in

the vicinity of the geothermal system. It should be noted that the survey is not interpreted as imaging alteration and destruction of magnetic minerals associated with the upper portions of the hydrothermal system due to the depth to the resource (>3000 ft). Rather, breaks in magnetic highs associated with the rift trend are interpreted as possible structures which may extend into the subsurface and influence permeability pathways (Figure 8).

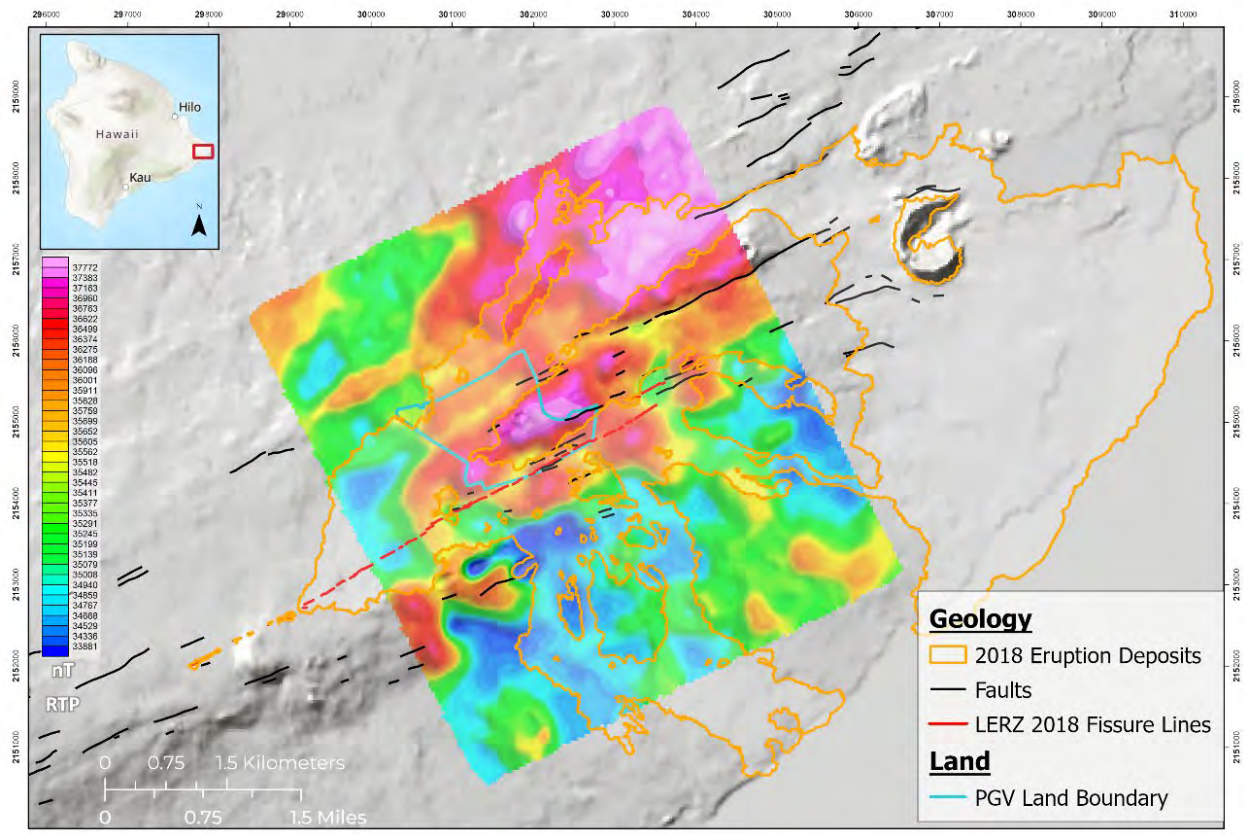

Figure 8: RTP (reduced to pole) magnetic data overlain on a 30 m DEM of the LERZ and PGV. Basalt deposits from the 2018 eruption are shown outlined in orange; mag anomalies do not follow the deposits, indicating that deeper structures are resolved by the method.

4. Geochemistry

Production fluids from PGV are a combination of two-phase flow from intra-wellbore boiling, as well as two-phase brine and steam in the reservoir based on enthalpy measurements and quarterly tracer flow tests (TFTs). Reservoir brines at PGV are moderate TDS (up to ±23,000 ppm), Na-Cl fluids with reservoir pH generally estimated between 5-6. The fluids are variably mixed, thermally altered meteoric-modified seawater brine with up to 70% modified seawater (Figure 9). Gas composition is dominated by H_2S and CO_2 with total discharge of less than 0.5 wt.%.

The basal groundwater aquifer above the PGV hydrothermal resource is predominantly a mixture of meteoric and altered seawater, with temperatures ranging between 30-65°C. The basal aquifer within the LERZ experiences a high degree of natural spatial and temporal chemical heterogeneity. This is likely a result of near well structures, such as highly permeable lava flows being intersected with impermeable dikes, which may isolate shallow aquifers and limit fluid flow. In addition to

structural controls, changes in the rates of recharge into these aquifers varies the degree of input from seawater versus meteoric water sources (Novak, 1995; Thomas, 1987 and Sorey and Colvard, 1994). Further, some minor degree of natural steam leakage into the system is inferred based on slightly depressed pH values and elevated sulfate concentrations in some monitoring wells such as MW-1.

There are no surface manifestations related to the PGV system. There are, however, a series of warm springs and seeps that occur to the SSE along the coast and isolated steam vents within the rift associated with the 1955 and 2018 fissure eruptions. Based on lower expected resource temperatures inferred from geothermometery and differences in the degree of seawater dilution, the springs are hypothesized to be related to a separate hydrothermal system (Janik et al., 1994).

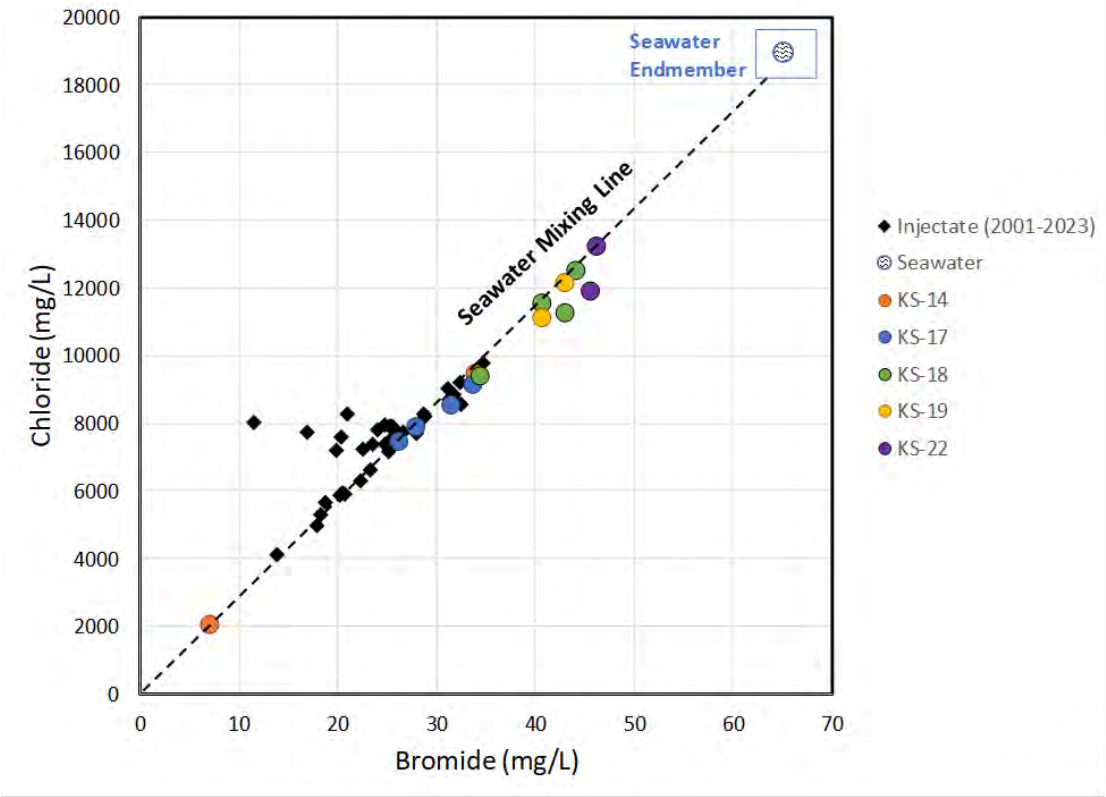

Figure 9: Chloride/Bromide cross plot showing the relationship between PGV brines and seawater. Production brines and injectate plot on the seawater mixing line.

5. Conceptual Model

The Puna reservoir is a high temperature, two-phase, liquid-dominated system with a varying steam fraction confined within Kilauea's Lower East Rift Zone. Heat for the system is supplied by active magma migration and the very high heat flow through the rift. Intrusion of magma into the rift zone displaces the southern flank of the volcano, promoting dilation along the rift. A prominent left step in the rift in the vicinity of PGV generates and maintains a zone of locally enhanced permeability in basalt flows and dikes with low natural porosity and permeability. The high permeability production and injection structures are subvertical, rift-parallel fractures that often associate with diabase dike margins, with fractures perpendicular to the rift formed as a function

of the stepover facilitating injection returns to production. The system is overlain by a caprock formed by hydrothermal alteration of pahoehoe & a'a flows, hyaloclastite, and pillow basalts which alters mafic minerals and volcanic glass to smectite-rich clay. The glassy groundmass characterizing hyaloclastite makes them particularly susceptible to clay alteration and the caprock is largely coincident with the extents of these transitional marine deposits. Departures of the clay caprock from the modeled extents of the transitional zone are interpreted based on the distribution of the natural state temperatures of the system, with the caprock closely following the 200°C isotherm due to the instability of smectite clays above that temperature (e.g., Reyes, 1990). Clay alteration is not homogenous and the caprock is likely breached in places by tectonic dilation over the lifecycle of a long-lived geothermal system, but naturally occurring leakage into overlying strata is thought to be relatively minor and transient in nature as the leaking structure self-seals due to hydrothermal alteration. Surface manifestations are suppressed by the deep resource depths, the clay caprock, and the vigorous groundwater system overlying the reservoir, all working in conjunction to keep the system hidden at surface. The water table within the resource area occurs at an elevation of approximately sea level (0 mRSL), corresponding to a depth of 188m (620 ft).

The distribution of interpreted static-state temperatures in PGV suggest that upflow originates along steeply northwest-dipping fractures. Note that the isotherms displayed in Figure 10 represent the post-eruption conditions, not the natural state of the system, and reflect significant cooling of the northern reservoir by a long history of injection.

Steep NW-SE thermal gradients through the field are a function of high permeability and convection along sub-vertical fractures within the rift zone versus unfractured zones adjacent to the rift to the north and south. The occurrence of permeable rift-perpendicular fractures as integrated into the conceptual and numerical models based on surface geology and tracer returns, a hypothesis which has been further substantiated by a recent airborne magnetic survey, which clearly images the left-step in the LERZ, and analysis of an acoustic borehole image log, which demonstrates the existence of NW-SE trending fractures throughout the logged interval. However, a key uncertainty remaining in the conceptual model is whether (a) there are large, high permeability NW-SE pathways (as the queried faults in Figure 5 would imply), or (b) NW-SE trending fractures represent a distributed fracture set that is present throughout the field but not localized into a handful of high permeability pathways.

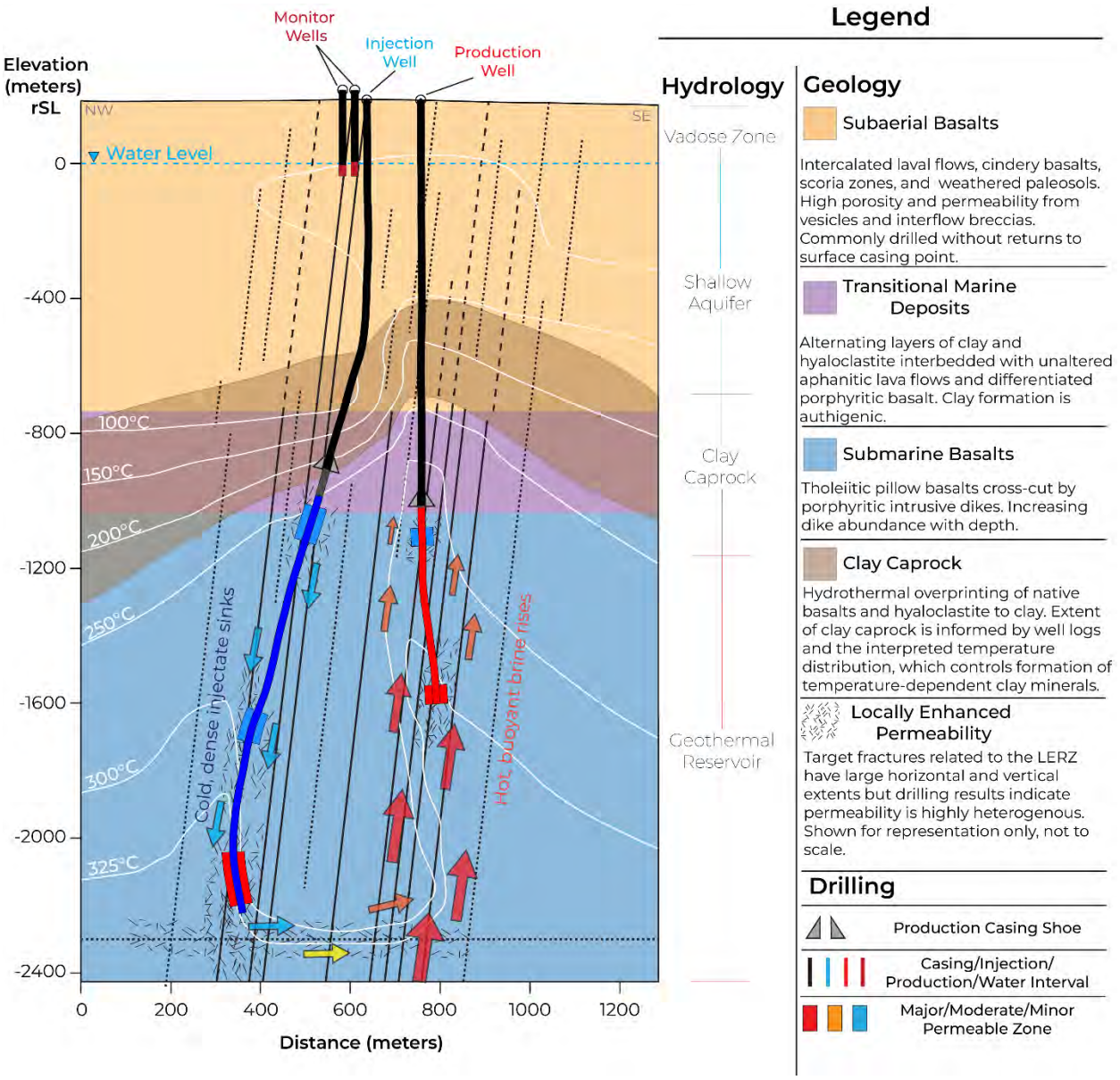

Figure 10: Schematic diagram of the PGV hydrothermal system conceptual model, including interpreted post-eruption natural state isotherms which depict significant cooling of the reservoir at injection depths. Vertical exaggeration 0.75x.

6. Conclusion

The Puna Geothermal Venture represents a high-temperature, naturally occurring geothermal system found in the active Lower East Rift Zone of Kilauea. The geothermal system's location is due in part to the occurrence of a prominent left-step in the rift zone which creates locally enhanced permeability. Fracture-dominated permeability and upflow of thermal fluids at PGV are controlled primarily by rift-parallel fractures. Rift-perpendicular permeability pathways were previously hypothesized based on surface mapping, geophysical datasets, and reservoir tracer studies, and have been confirmed for the first time at PGV by analysis of an acoustic borehole image log. Additional reservoir testing is required to understand the impact of rift-perpendicular fractures and

the connection between production and injection following the successful completion of a recent drilling campaign.

7. Acknowledgements

We would like to thank the PGV operators, Ormat's Wellfield and Resource staff who contributed to post-eruption recovery effort and who continue to operate and maintain PGV as a flagship geothermal power plant, as well as Peter Drakos for his more than 15 years of geoscience contribution to the field.

REFERENCES

Broyles, M. L., Suyenaga, W., & Furumoto, A. S., "Structure of the lower east rift zone of Kilauea volcano, Hawaii, from seismic and gravity data," Journal of Volcanology and Geothermal Research, 5(3-4), (1979), 317-336.

Clague, D. A., & Dalrymple, G. B., "The Hawaiian-emperor volcanic chain," US Geol. Surv. Prof. Pap., 1350, (1987), 5-54.

Davatzes, N. C., & Hickman, S. H., "The feedback between stress, faulting, and fluid flow: Lessons from the Coso Geothermal Field, CA, USA," in Proceedings World Geothermal Congress, Vol. 2010, (April 2010).

Department of Planning and Economic Development (DPED), State of Hawaii, "Geothermal Power Development in Hawaii. Volume I. Review and Analysis," Department of Energy Report, DOE/ET/27133, (1982).

Duffield, W.A., "Structure and origin of the Koae fault system, Kilauea Volcano, Hawaii." USGS Professional Paper 856. (1975).

Eaton, J. P., & Murata, K. J., "How Volcanoes Grow: Geology, geochemistry, and geophysics disclose the constitution and eruption mechanism of Hawaiian volcanoes," Science, 132(3432), (1960), 925-938.

Flanigan, V.J., & Long, C.L., "Aeromagnetic and Near-Surface Electrical Expressions of the Kilauea and Moana Loa Volcanic Rift Systems," Volcanism in Hawaii, 1, pg. 935-946, (1987).

Furumoto, A. S., MacDonald, G. A., Druecker, M., & Fan, P. F., "Preliminary studies for geothermal exploration in Hawaii, 1973-1975," (1977).

Heffer, K., "Geomechanical influences in water injection projects: An overview," Oil & Gas Science and Technology, 57(5), (2002), 415-422.

Hoversten, G.M., Gasperikova, E., Mackie, R., Myer, D., Kauahikaua, J., Newman, G.A., Cuevas, N., "Magnetotelluric Investigations of the Kilauea Volcano, Hawaii," Journal of Geophysical Research: Solid Earth, 127.8, (2022).

Janik, C.J., Nathenson, M., & Scholl, M.A. "Chemistry of spring and well waters on Kilauea Volcano, Hawaii, and vicinity." USGS Open File Report 94-586, (1994).

Kinoshita, W.T., Krivoy, H.L., Mabye, D.R., MacDonakd, R.R., "Gravity survey of the island of Hawi'i, Geologic Survey Research 1963," U.S. Geol. Surv. Prof. Pap., 475, (1963), 114-116.

Langenheim, V. A., & Clague, D. A., "The Hawaiian-Emperor Volcanic Chain. Part II. Stratigraphic framework of volcanic rocks of the Hawaiian Islands," USGS Prof. Pap, 1350, (1987), 55-84.

Lautze, N., Thomas, D., Hinz, N., Apuzen-Ito, G., Frazer, N., & Waller, D., "Play fairway analysis of geothermal resources across the State of Hawaii: 1. Geological, geophysical, and geochemical datasets," Geothermics, 70, (2017), 376-392.

Lipman, P. W., Lockwood, J. P., Okamura, R. T., Swanson, D. A., & Yamashita, K. M., "Ground deformation associated with the 1975 magnitude-7.2 earthquake and resulting changes in activity of Kilauea volcano, Hawaii," (1985), No. 1276.

Lipman, P. W., Sisson, T. W., Ui, T., Naka, J., & Smith, J. R., "Ancestral submarine growth of Kilauea volcano and instability of its south flank," in Hawaiian volcanoes: deep underwater perspectives, 128, (2002), 161-191.

Moore, R. B., "Volcanic geology and eruption frequency, lower east rift zone of Kilauea volcano, Hawaii," Bulletin of Volcanology, 54, (1992), 475-483.

Moore, R. B., & Trusdell, F. A., "Geologic map of the lower east rift zone of Kilauea Volcano, Hawaii," (1991), No. 2225.

Morgan, W. J., "Convection plumes in the lower mantle," Nature, 230(5288), (1971), 42-43.

Moos, D., & Zoback, M. D., "Utilization of observations of well bore failure to constrain the orientation and magnitude of crustal stresses: application to continental, Deep Sea Drilling Project, and Ocean Drilling Program boreholes," Journal of Geophysical Research: Solid Earth, 95(B6), (1990), 9305-9325.

Murphy, J., Prina, N., Spielman, P., & Spake, D., "Permeability and Numerical Modeling of the Puna Geothermal Venture," GRC Transactions, Vol. 48, (2024).

Patrick, M. R., Houghton, B. F., Anderson, K. R., Poland, M. P., Montgomery-Brown, E., Johanson, I., ... & Elias, T., "The cascading origin of the 2018 Kīlauea eruption and implications for future forecasting," Nature Communications, 11(1), (2020), 5646.

Poland, M. P., Miklius, A., & Montgomery-Brown, E. K., "Magma supply, storage, and transport at shield-stage Hawaiian volcanoes," (2014), No. 1801-5, 179-234.

Novak, S.P. "A conceptual model of shallow groundwater flow within the Lower East Rift Zone of Kilauea Volcano, Hawaii." Masters Thesis, University of Hawai'i at Manoa. Honolulu, Hawaii, 170, (1995).

Rowland, J.V., & Simmons, S.F., "Hydrologic, magmatic, and tectonic controls on hydrothermal flow, Taupo Volcanic Zone, New Zealand: Implications for the formation of epithermal vein deposits." Economic Geology 107, no.3, 427-457, (2012)

Reyes, A. G., "Petrology of Philippine geothermal systems and the application of alteration mineralogy to their assessment," Journal of Volcanology and Geothermal Research, 43(1-4), (1990), 279-309.

Reynolds, Z., Spake, D., Caro, D., Prina, N., Feucht, D., Blake, K., Libbey, R., & Delwiche, B., “Detailed Airborne Magnetic Survey of the Puna Geothermal Venture and the Lower East Rift Zone, Island of Hawai’i,” GRC Transactions, Vol. 48 (2024).

Ryan, M. P., "The mechanics and three-dimensional internal structure of active magmatic systems: Kilauea Volcano, Hawaii," Journal of Geophysical Research: Solid Earth, 93(B5), (1988), 4213-4248.

Sherrod, D. R., Sinton, J. M., Watkins, S. E., & Brunt, K. M., "Geologic map of the State of Hawaii," (2021), No. 3143.

Sorey,M.L., & Colvard, E.M., “Potential Effects of the Hawaii Geothermal Project on Ground-Water Resources on the Island of Hawaii.” Water Resources Investigation Report 94-4028, USGS, (1994).

Swanson, D. A., Duffield, W.A., & Fiske, R.S., "Displacement of the south flank of Kilauea volcano: The result of forceful intrusion of magma into the rift zones," US Geol. Surv. Prof. Pap., 963, (1976), 39.

Takahashi, P., Seki, A., & Chen, B., "A Pacific-wide geothermal research laboratory: the Puna Geothermal Research Facility," Uniiversity of Hawaii, 2540 Dole Street, Honolulu, Hawaii 96822, (1985), No. SGP-TR-84; CONF-850107-33.

Thomas, D. M., "Geothermal resources assessment in Hawaii," Geothermics, 15(4), (1986), 435-514.

Thomas, D.M., , “Geochemical model of the Kilauea east rift zone.” Volcanism in Hawaii, ch. 56. (1987) U.S. Geological Survey Open File Report 93-82.

Trusdell, F.A., Novak, E., Evans, S.R., & Okano, K., "Core lithology from the State of Hawaii Scientific Observation Hole 1, Kilauea Volcano, Hawaii," U.S. Geological Survey Open-File Report 99–389, (1999), 67 p., http://hdl.handle.net/10125/21548.

Warren, I., Friedel, M. J., Wallin, E., Lautze, N., Hou, Z. J., Vasco, D. W., ... & Rhodes, G., "Innovative Subsurface Learning and Hawaiian Exploration using Advanced Tomography (ISLAND HEAT) Phase 1 Final Report," National Renewable Energy Laboratory (NREL), Golden, CO (United States), (2023), No. NREL/TP-5700-87316.

Wilson, J. T., "A possible origin of the Hawaiian Islands," Canadian Journal of Physics, 41(6), (1963), 863-870.

Zoback, M. D., Moos, D., Mastin, L., & Anderson, R. N., "Well bore breakouts and in situ stress," Journal of Geophysical Research: Solid Earth, 90(B7), (1985), 5523-5530.

Zoeller, M. H., Perroy, R. L., Wessels, R., Fisher, G. B., Robinson, J. E., Bard, J. A., Peters, J., Mosbrucker, A., & Parcheta, C. E., "Geospatial database of the 2018 lower East Rift Zone eruption of Kilauea Volcano, Hawaii [Data set]," U.S. Geological Survey, https://doi.org/10.5066/P9S7UQKQ.

Identifying Sedimentary Geothermal Play Types in the Cretaceous Strata of South Texas Through High-Resolution Temperature-Depth Mapping Based on Corrected Bottom-Hole Temperature Measurements

J. Eric Stautberg and Steven A. Sonnenberg

Department of Geology and Geological Engineering, Colorado School of Mines

Keywords

Sedimentary basins, Texas Gulf Coast, bottom-hole temperature correction, temperature mapping, isotherm, time since circulation

ABSTRACT

Accurate formation temperature is a pivotal part of geothermal resource assessments in sedimentary basins. Bottom-hole temperature (BHT) measurements from well logs are an abundant data set in these basins but are also notoriously unreliable because of several reasons such as the vintage of the measurement, type of tool used, ambient surface temperature at the time of logging, thermal properties of the drilling mud, time since circulation (TSC), rate of penetration (ROP) while drilling, human error, and the thermal conductivity of the formation and formation fluids (oil, natural gas, or brine) where the temperature is measured. Consequently, BHT correction methods vary depending on the basin and available data. In south Texas, where oil and gas wells dominate the landscape, the Waples et al. (2004) correction method is commonly used because it incorporates TSC data and ambient surface temperature to correct for the cooling effects of drilling mud on the formation while the well was being drilled.

A 12,500 square mile area in south Texas was designated for BHT correction and temperature-depth mapping because it contains most of the key sedimentary geothermal elements of the Texas Gulf Coast. These elements include: 1) the location of geopressured reservoirs in Paleogene formations, 2) the location of the Aptian and Albian shelf margins, 3) the type of transitional crust beneath the sedimentary section, 4) the location of salt diapirs, and 5) the shallowest depth to 250º F in Texas. To help identify geothermal play types in the Cretaceous strata of south Texas, BHT measurements from 826 wells north of the Aptian and Albian shelf margins were corrected for temperature-depth mapping. Of these 826 wells, 267 had TSC data and were subsequently corrected using the Waples et al. (2004) BHT correction methodology. This method resulted in an average temperature increase of 19.66%, which aligned with temperature measurements from

cement bond logs, drill stem tests (DSTs), and regional BHT correction studies completed by other researchers.

Corrected BHT measurements for 267 wells were then used to calculate a temperature log from the surface to 25,000 ft for each well. Using IHS Markit's Petra cross section and mapping software, temperatures were correlated from well to well across the research area at 25º F increments from 200º F to 500º F. This methodology resulted in two important products for geothermal play type identification: 1) a high-resolution series of temperature-depth maps for play fairway identification and 2) a set of temperature logs that can be incorporated into petrophysical analysis for temperature-based reservoir characterization calculations.

1. Introduction

The Texas Gulf Coast region of the greater Gulf of Mexico Basin contains the necessary geothermal elements for low-temperature geothermal development for both utility scale electrical power generation and direct use applications. Deposition of thick Mesozoic and Cenozoic sedimentary rocks, coupled with passive margin tectono-stratigraphic relationships provides the necessary geologic framework to support geothermal exploration here. Previous researchers from the Bureau of Economic Geology at the University of Texas in Austin (BEG), the Department of Energy (DOE), Southern Methodist University (SMU), the National Renewable Energy Lab (NREL), the U.S. Geological Survey (USGS), and many others have laid the groundwork for the development of clean, renewable, stable, dispatchable, baseload electricity in this basin and others across the United States.

Despite decades of subsurface research completed by these researchers and others, however, no commercial scale geothermal development has yet occurred on the Texas Gulf Coast. Consequently, the focus of this project is to provide a detailed subsurface characterization of an approximately 12,500 square mile area in south Texas to: 1) encourage geothermal exploration along the Texas Gulf Coast and in other sedimentary basins, 2) provide an exploration-based workflow for identifying and characterizing geothermal reservoirs, and 3) pinpoint specific geothermal play fairways in this region through high-resolution temperature-depth mapping.

To achieve these goals, understanding the distribution of subsurface temperatures across the basin is extremely important but often very challenging because of the inaccuracy in bottom-hole temperature measurements from wireline logs. These temperature measurements are the most common datasets used in sedimentary basins for subsurface temperature mapping because of their abundance but are also notoriously unreliable for many reasons including: 1) the vintage of the measurement, 2) type of tool used, 3) ambient surface temperature at the time of logging, 4) the thermal properties of the drilling mud, 5) time since circulation (TSC), 6) rate of penetration (ROP) while drilling, 7) human error, and 8) the thermal conductivity of the formation and formation fluids (oil, natural gas, or brine) where the temperature is measured. For these reasons, multiple different types of correction methodologies have been developed in sedimentary basins across the world. Subsequent correction methods and mapping techniques are discussed here, with the goal of building a high-resolution and comprehensive set of temperature-depth maps across a region of south Texas that can be used as a case study for further temperature-depth mapping across the Texas Gulf Coast.

2. Methods

2.1 Geothermal Elements of the Texas Gulf Coast

Understanding the basinwide geologic controls on the spatial and temporal distribution of potential geothermal play types along the Texas Gulf Coast is the first step in exploring for these resources. Fortunately, oil and gas exploration and development over the past century has provided an excellent subsurface dataset for geothermal explorers to use to characterize the potential resources here. Combining the results from previous researchers in this region yields five major structural and stratigraphic features that appear to have the most significant controls on the location of potential geothermal targets. These features are: 1) the location geopressured reservoirs in Paleogene formations (Bebout et al., 1978; Loucks et al., 1978; Bebout et al., 1979; Bebout et al., 1982), 2) the location of the Aptian and Albian shelf margins (Ewing, 1991), 3) the composition of the crust that underlies the sedimentary formations (Ewing and Galloway, 2019), 4) the location of salt diapirs (Condon and Dyman, 2006), and 5) the depth to 250º Fahrenheit (F) (Figure 1). Combining all these elements together shows that the south Texas region contains all of these overlapping geologic elements and was consequently chosen to be the focus of this study.

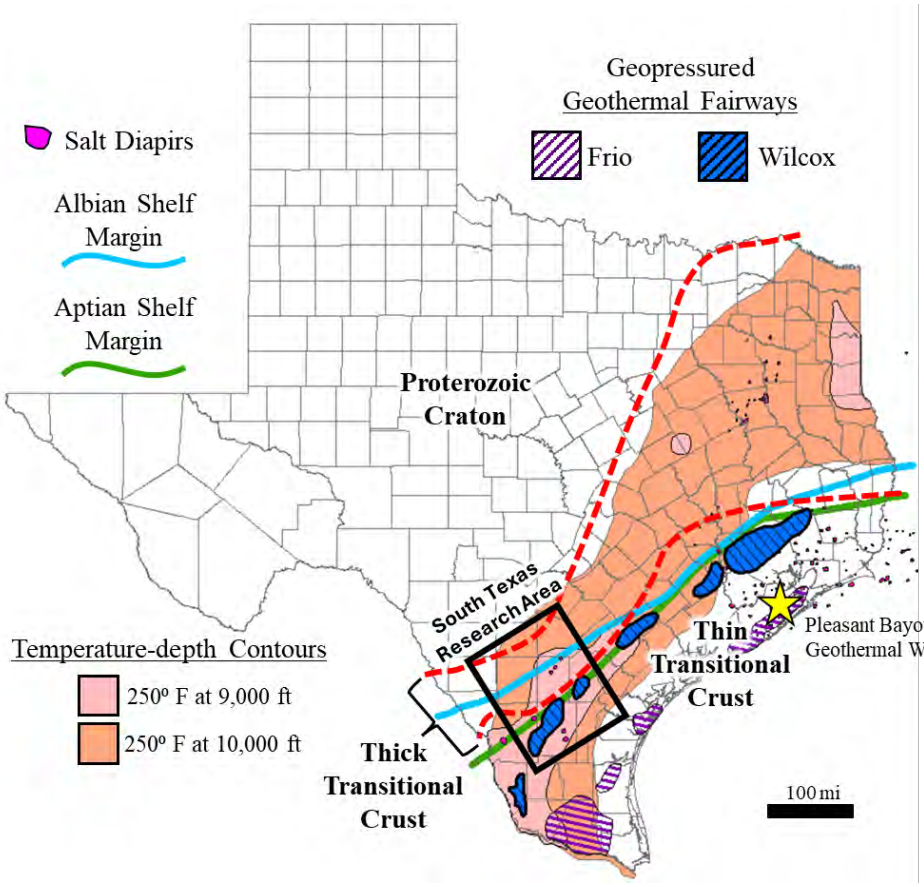

Figure 1: Location of the basinwide geologic elements of the Texas Gulf Coast that influence the location and types of potential geothermal reservoirs. Map elements from Bebout et al., 1982; Blackwell et al., 2010; Condon and Dyman, 2006; Ewing, 1991; and Ewing and Galloway, 2019. Modified from Stautberg and Sonnenberg, 2024.

An approximately 12,500 square mile area covering 10 counties was selected to identify and characterize all the major geothermal play types in this region that then could be applied to the rest of the Texas Gulf Coast (Figure 2A). The research area is cross-cut by both the Aptian and Albian shelf margins, the main Wilcox fault zone, the boundary between thick transitional crust to the north and thin transitional crust to the south, it contains six salt diapirs, and there are two geopressured-geothermal zones in the Wilcox Formation previously identified by Bebout et al. (1982). Additionally, the approximate depth to 250° F is represented by the color-filled contours as previously mapped by Blackwell et al. (2010). This temperature is important because it is often considered the lowest temperature that can be used for electrical power generation, although there are other controlling factors that ultimately affect the minimum temperature required for the power generation process.

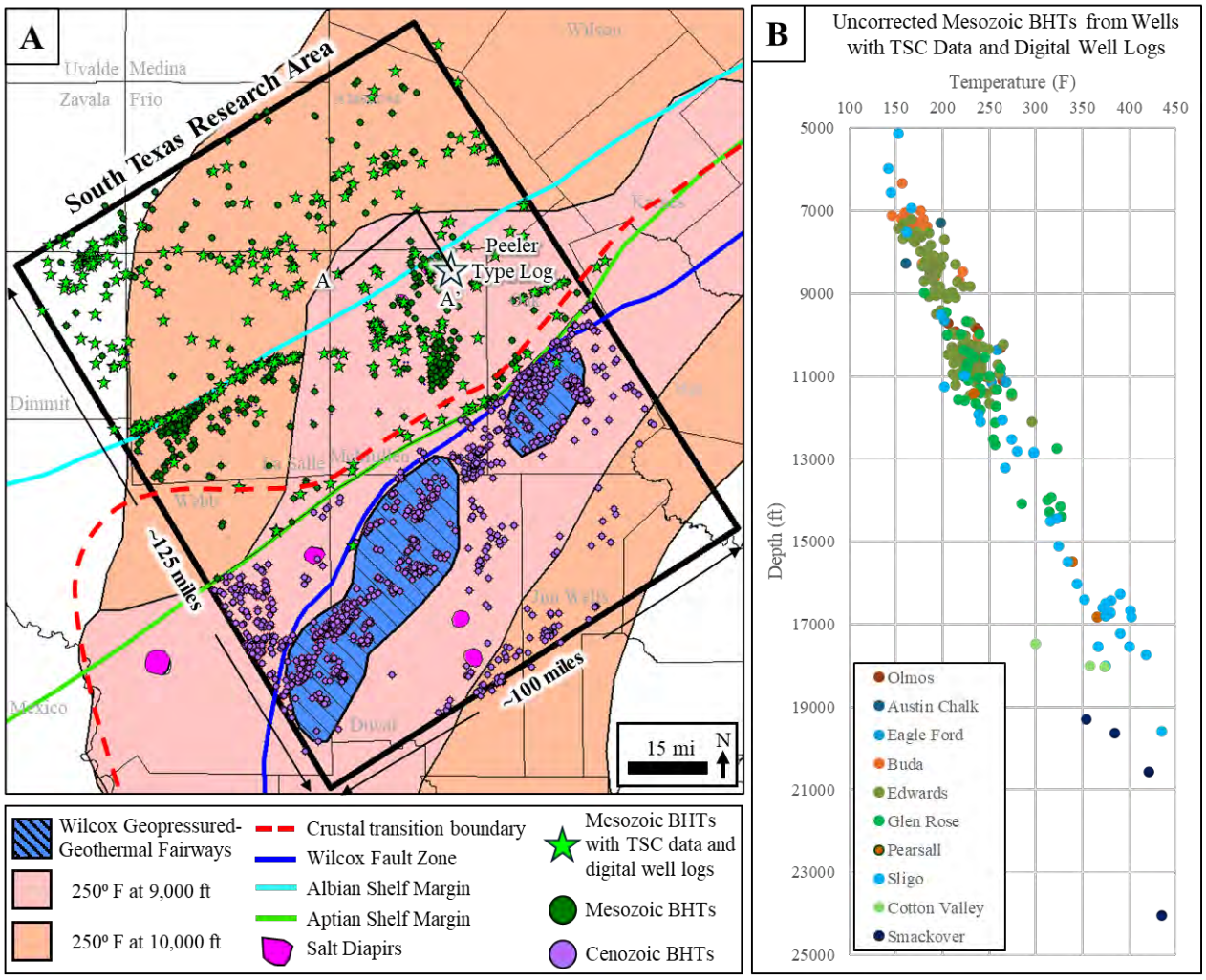

Figure 2: A) Location of the south Texas research area showing the location of geologic elements that control the location and type of geothermal play types along with the location of wells with BHT measurements in Mesozoic and Cenozoic formations. B) Temperature versus depth plot for 267 wells with BHT measurements in Mesozoic formations and that also contain digital well logs. Map elements from Bebout et al., 1982; Blackwell et al., 2010; Condon and Dyman, 2006; Ewing, 1991; and Ewing and Galloway, 2019.

2.2 Bottom-hole Temperature Data

A dataset of 1,864 wells with one or multiple BHT measurements was compiled from the National Geothermal Data Systems website for BHT correction and subsurface temperature mapping (Figure 2A). This dataset was then divided based on the age of the formations that the BHT measurement was taken in (Mesozoic versus Cenozoic) and the crustal type underlying those subsequent formations. In the northern half of the research area, the Mesozoic sedimentary rocks are underlain by thick transitional crust, whereas the southern half of the research area is underlain by thin transitional crust and contains thick Cenozoic formations. Consequently, the BHT dataset is divided based on boundary between these two crustal types from Ewing and Galloway (2019). These two geologic elements influence the basal heat flow from the underlying basement, heat flow within different sedimentary packages, thickness and age of the sedimentary packages, and thermal conductivity of the different formations. However, for this study only the BHT correction methods and temperature-depth mapping for the Mesozoic formations will be discussed.

The Mesozoic dataset contains 826 wells with BHT measurements and was subsequently divided again based on the availability of both digital well log and TSC data. Of these wells, 267 were selected for temperature mapping because they contain both TSC times and digital well logs that cover most of the Cretaceous and Jurassic formations (Figure 2B). The location of these wells is shown in Figure 2 along with the relationship between uncorrected BHT measurements and depth for the Cretaceous and Jurassic formations. Bottom-hole temperature measurements for these 267 wells are from the Olmos, Eagle Ford, Buda, Edwards, Glen Rose, Pearsall, Sligo, Cotton Valley, and Smackover formations (Figures 2 and 3).

2.3 Bottom-hole Temperature Correction

One of the cruxes of subsurface temperature mapping in sedimentary basins is accurately correcting the BHT measurements for external variables that affect the quality and accuracy of the temperature measurement. In sedimentary basins, most subsurface temperature data comes from measurements from wireline logging tools when the well was logged. Subsurface temperature measurements can also come from drill stem tests (DSTs), cased-hole temperature logs, and cement bond logs, however, these types of data are less common and will be discussed in the following section. Temperature measurements from these three other sources are considered to be best representative of true formation temperature because they are typically collected long after the well was drilled, so the temperature of the wellbore is back to its original temperature.

Temperature correction is required for BHT measurements obtained from wireline logs for the many reasons discussed previously. In the Gulf of Mexico Basin, a BHT correction methodology from Waples et al. (2004) is commonly used because it incorporates depth, TSC, and ambient surface temperature when the well was logged to correct for some of the variables that affect the temperature at the bottom of the wellbore. This correction methodology was adopted and applied to the dataset used in this study. Other correction methodologies (Blackwell and Richards, 2004; Corrigan, 1997; Crowell et al., 2010; Forster et al., 1995; and Kehle et al., 1970) rely mainly on depth of the temperature measurement for correction and were developed in other basins, so their correction method is not directly applicable to the south Texas region of the greater Gulf of Mexico Basin.

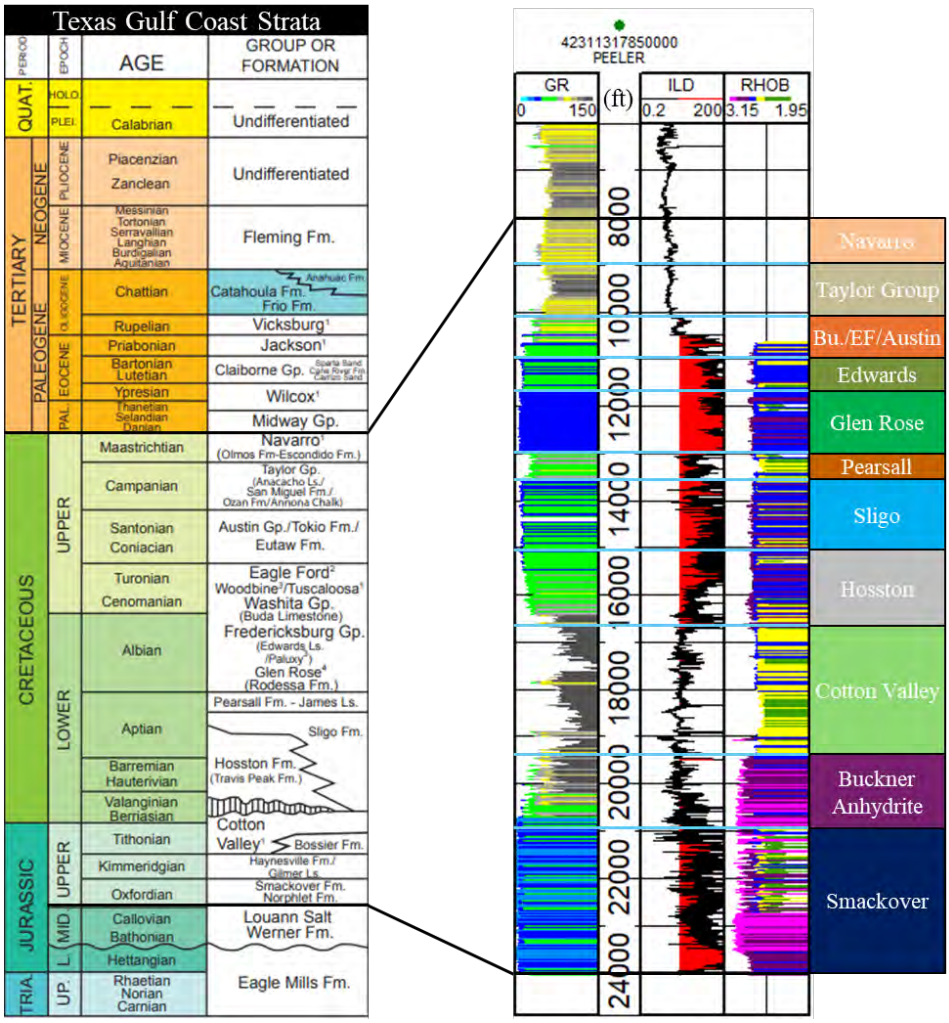

Figure 3: Stratigraphic column for south Texas tied to the Peeler#1 well in northeastern McMullen County. Gamma-ray (GR), resistivity (ILD), and bulk density (RHOB) were used to correlate Cretaceous and Jurassic formation tops across the 267 wells that contain digital well logs and BHT measurements. Stratigraphic column is modified from Swanson et al., 2013.

Equation 1 shows the formula derived by Waples et al. (2004) where the true formation temperature (T_{true}) is a product of the ambient surface temperature in Celsius at the time of logging ($T_{surface}$), the formation factor (f) which incorporates the TSC data, the measured BHT in Celsius ($T_{measured}$), and the depth in meters (Z). Temperatures and depths were converted from Celsius and meters to Fahrenheit and feet after the BHT correction was completed.

$$T_{true} = T_{surface} + f * (T_{measured} - T_{surface}) - 0.001391 * (Z - 4{,}498) \quad (1)$$

Depths, BHT measurements, and TSC times were obtained from well headers of raster logs for 267 wells with both temperature measurements and digital log data in the Cretaceous and Jurassic formations. Ambient surface temperature for the month, county, and year in which the well was logged came from the National Oceanic and Atmospheric Administration (NOAA) database (Figure 4A). Ambient surface temperature at the time of logging ranged from 49° F to 89° F, and the average was 70° F. All these variables were recorded in an Excel spreadsheet so they could be input into Equation 1 for accurate BHT correction.

3. Results

3.1 Corrected Bottom-hole Temperature Measurements

Using the Waples et al. (2004) correction methodology discussed above yields on average a 19.66% increase in temperature for the 267 wells in the Mesozoic BHT dataset (Figure 4B). Temperature correction ranges from an increase of 26.24% to a decrease of 4.65%. The resulting corrected BHTs for this entire dataset are shown in Figure 4C and are compared to the uncorrected values (shown in black). To calibrate the accuracy of the Waples et al. (2004) correction method, temperature measurements from 10 cement bond logs and 22 cased-hole temperature logs are shown in Figure 4C. Most of these equilibrium temperature measurements fall within the cloud of corrected temperature measurements, which suggests that this methodology of BHT correction is valid. A linear best fit line (green) that more closely follows the slope of the equilibrium temperature data points (red and orange dashed lines respectively) was applied to the corrected BHT data by adjusting the y-intercept to intersect the average ambient surface temperature (70° F) and 0 ft measured depth (MD). Consequently, the origin of this graph represents the average surface temperature when these wells were logged.

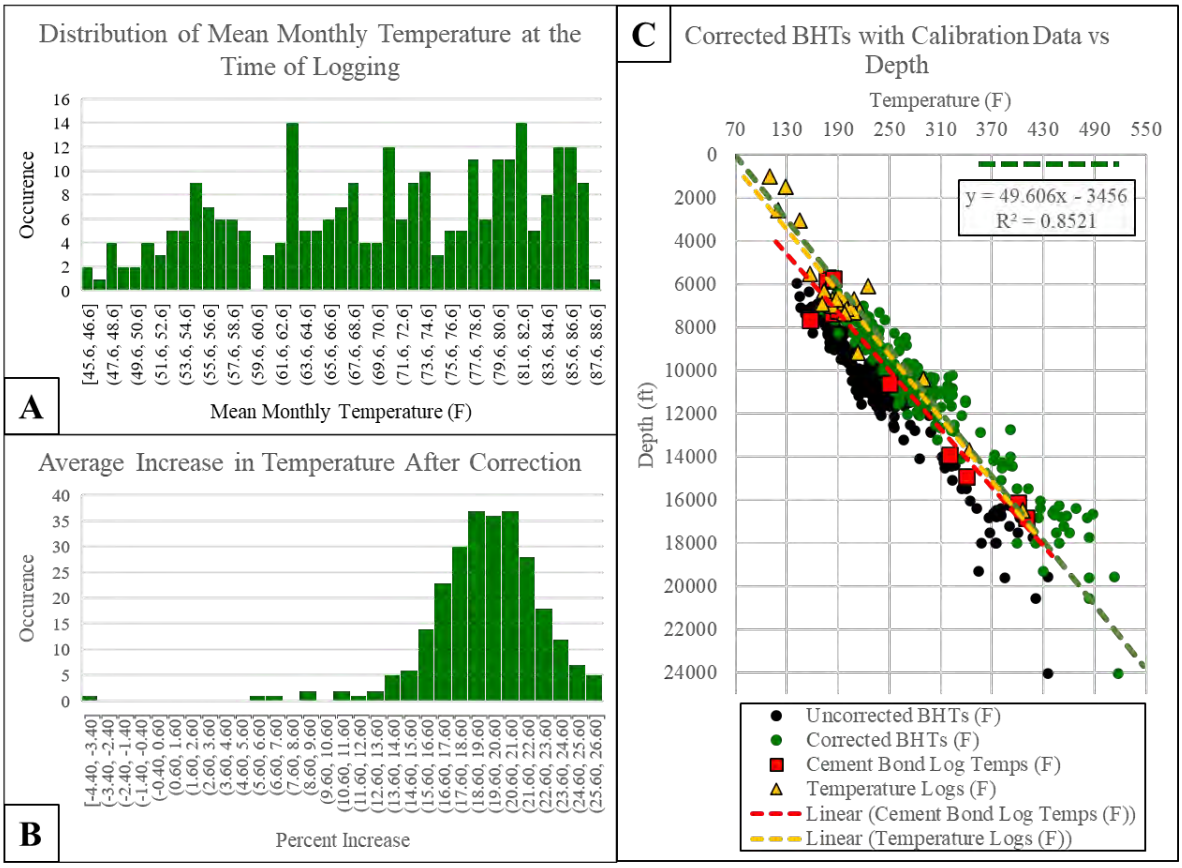

Figure 4: A) Distribution of the mean monthly temperature for the 267 wells with TSC data based on the county and year in which the well was logged. Wells with multiple logging runs at different dates have multiple different ambient temperatures based on the dates of each logging run. B) Average percent increase in temperature using the Waples et al. (2004) method shown in Equation 1. C) Uncorrected versus corrected BHT measurements with calibration data in the form of temperatures from cement bond logs (red squares) and cased-hole temperature logs (orange triangles).

Some of the temperature measurements between 16,000 ft and 18,000 ft in the Sligo Formation are elevated compared to the cement bond logs and cased-hole temperature logs at equivalent depths. This suggests that the Waples et al. (2004) correction methodology might be overestimating true formation temperature at deeper depths. More calibration datapoints are needed below 16,000 ft to verify this but only a few other wells penetrate these depths in the study area. Despite this observation, this method of BHT correction seems valid for the south Texas region of the greater Gulf of Mexico Basin.

3.2 Corrected Bottom-hole Temperature Logs

For geothermal exploration in sedimentary basins, building a comprehensive set of subsurface temperature-depth maps is the main goal of correcting BHT measurements. One of the additional challenges with using BHT measurements for temperature mapping is that they usually span a wide range of depths and are not measured in the same formation. In the Mesozoic dataset, temperature measurements are found in eight Cretaceous and two Jurassic formations and represent discrete points in each well (Figure 2B). Consequently, geothermal gradients from the corrected BHT measurements need to be calculated to estimate the true formation temperature in formations above and below where these datapoints were collected. Using both the ambient surface temperature at the time of logging and the corrected BHT measurement, temperature can be estimated between the base of the well and the surface using the geothermal gradient calculated for each well. In doing so, a series of temperature-depth logs can be created for mapping temperature between wells and within each formation of interest.

Corrected BHT measurements, the depth at which the measurement was acquired, and the ambient surface temperature at the time of logging for the Mesozoic BHT dataset was loaded into IHS Markit's Petra software to calculate a temperature-depth log for each well. Equation 2 shows the relationship between these variables and how Petra creates temperature-depth logs for these wells.

$$T_{depth} = ((T_{true} - T_{surface})/Z_1)*Z_2+T_{surface} \quad (2)$$

In this equation T_{depth} is the temperature calculated at any depth between the surface and 25,000 ft, T_{true} is the corrected BHT, $T_{surface}$ is the ambient surface temperature at the time of logging, Z_1 is the depth of the BHT measurement, and Z_2 is a depth log in 0.5 ft increments from surface to 25,000 ft. With this equation, the corrected BHT and the depth of that measurement is converted into a geothermal gradient for each well and the ambient surface temperature at the time of logging becomes the shallowest temperature for each calculated temperature log. Geothermal gradients for the Mesozoic BHT dataset range from 2.15-3.27° F/100 ft with an average gradient of 2.66.

These variables are then used to calculate a temperature at any given depth throughout the wellbore at a 0.5 ft increments. Subsequent temperatures are stored in the depth log (Z_2 from Equation 2) and Petra creates a LAS file for each well that this equation is run on. This produces a corrected temperature log for each well with a corrected BHT measurement at a 0.5 ft increment from surface to 25,000 ft (Figure 5). These corrected temperature logs can then be displayed in a cross-section, where isotherms can be physically correlated from well to well like a formation top. Additionally, since the corrected temperature logs are at 0.5 ft increments, they can be incorporated into petrophysical calculations or models to be compared to other petrophysical variables (porosity, permeability, water saturation, mineralogy, etc.).

Figure 5 is a well log cross section that contains corrected temperature logs (CTDL) for each well. The color pattern on the temperature logs is at 25° F increments and the black lines are the Cretaceous and Jurassic formation tops. Using this methodology, the relationship between temperature and depth can easily be mapped in the subsurface and at any temperature increment that is desired. This results in a temperature-structure map that shows the depth to the desired temperature measurement.

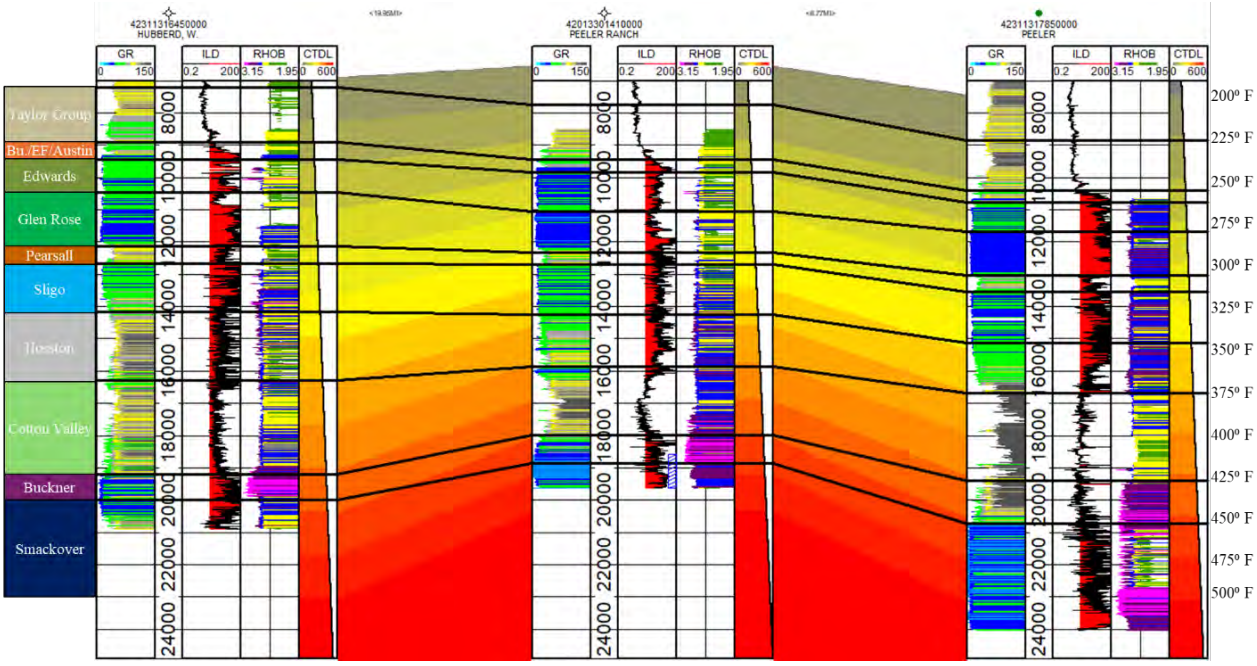

Figure 5: Cross-section A-A' (shown on Figure 2A) showing the relationship between structure and temperature. Calculated temperature-depth logs (CTDL) are displayed in track four of each well and the color fill between each well shows the temperature in Fahrenheit (F). Formation tops for Cretaceous and Jurassic formations are displayed in black.

3.3 Temperature-depth Mapping

Using the cross-section display above, isotherms can easily be correlated from well to well resulting in a series of temperature and depth values for each isotherm in every well. Consequently, either a computer based contouring method or hand contouring method can be used to map the relationship between temperature and depth. Figure 6 shows the depth to 250° F across the research area, contoured with a combination computer contouring and hand contouring method.

This map shows a similar trend to the Blackwell et al. (2010) contours from Figure 2A, where the depth to 250° F is shallower to the south and deeper to the north (Figure 5). However, the depth to 250° F using the methodology discussed above shows that the depth to the 250° F isotherm is slightly shallower than the Blackwell et al. (2010) map to the south and slightly deeper to the north. This is likely a result of differing BHT correction methodologies and a different dataset. Between the Aptian and Albian shelf margins the depth to 250° F ranges from 7,000-9,000 ft, whereas north of the Albian shelf margin the depth is consistently greater than 9,000 ft. This is similar to the depth trends observed in temperature-depth maps from Blackwell et al. (2010) and Gardner and Birdwell (2023), however, their maps are on a much more regional scale that spans the entire Texas Gulf Coast.

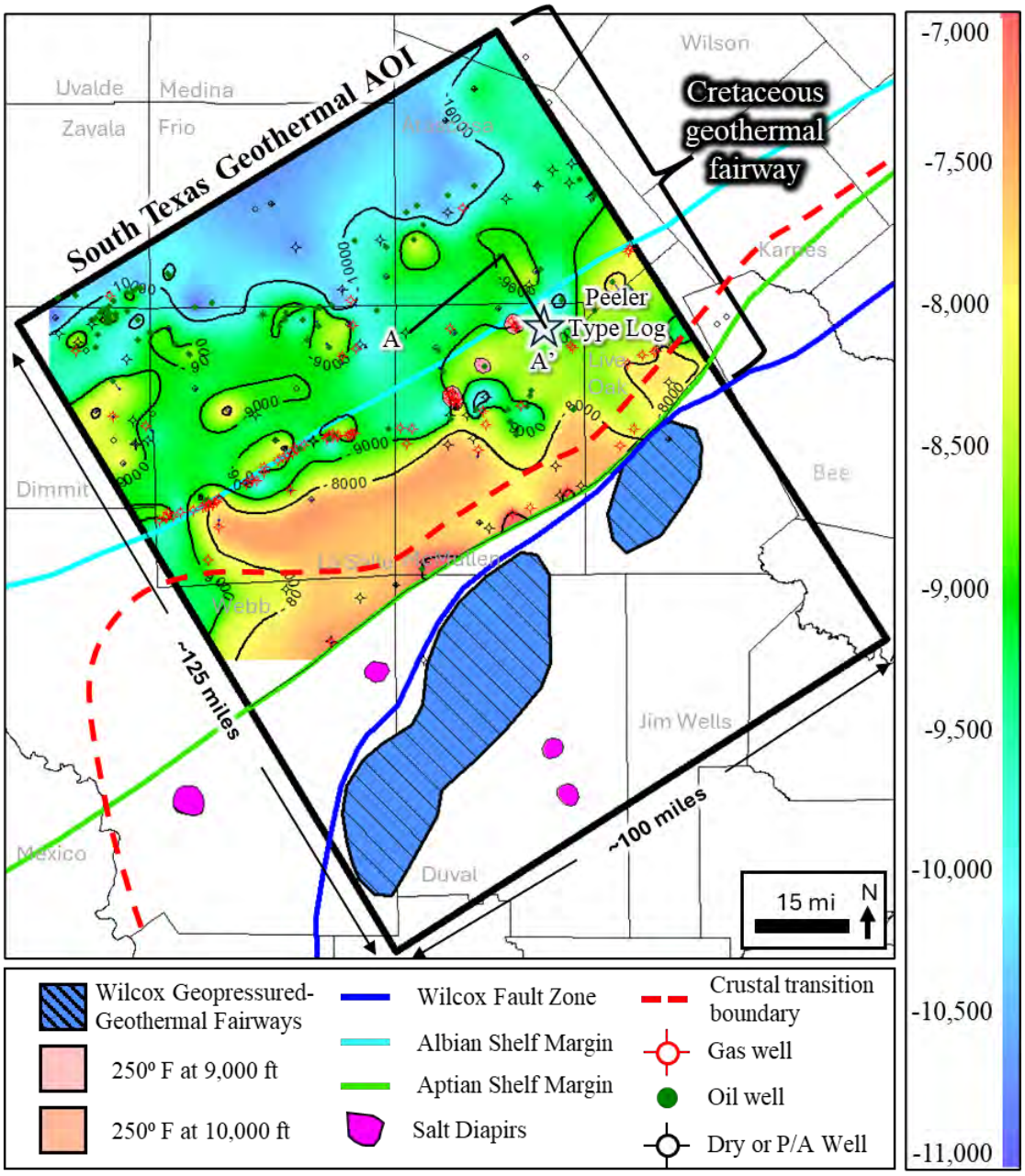

Figure 6: Temperature-depth map for the 250º F isotherm based on 267 wells with BHT measurements in Cretaceous and Jurassic formations that overly thick transitional crust. This temperature surface dips to the north and ranges in depth from about 7,000 ft to almost 11,000 ft.

4. Conclusions and Future Work

Temperature mapping is a fundamental part of geothermal exploration in sedimentary basins but often is one of the most challenging reservoir properties to calculate and map. Many external factors at the time of logging ultimately affect the accuracy of the BHT measurement and careful consideration of these factors is required when compiling a BHT dataset for correction and mapping. The Waples et al. (2004) correction methodology used here, combined with calibration

temperatures from cement bond logs and cased-hole temperature logs, appears to be a valid method for correcting BHTs in the Mesozoic strata of south Texas.

Temperature mapping based on temperature-depth logs calculated from corrected BHT measurements is one approach to high resolution temperature mapping in the subsurface. Using this method, geothermal explorers can easily hand contour temperature-depth maps and correlate temperature between wells in any formation of interest. However, comparing this method of temperature mapping to other methods, such as basin modeling, would help to compare the accuracy of each temperature mapping method. The next step in temperature-depth mapping in this research area is to repeat the methodology discussed here but on the wells with BHT measurements in Cenozoic formations (Figure 2A). This will show if there are any differences between the BHT measurements in Mesozoic formations compared to Cenozoic formations, and if the underlying type of crust is the cause these differences. Temperature mapping and BHT correction in sedimentary basins is a challenging aspect of geothermal exploration, but using the concepts and methodologies discussed above will help to ensure the accuracy and legitimacy of subsequent maps and resource estimates produced from corrected BHT measurements.

Acknowledgement

Funding for this project was provided by the Mudrocks and Tight Oil Characterization Consortium (MUDTOC) in the Department of Geology and Geological Engineering at Colorado School of Mines. Digital and raster log data was graciously provided by TGS.

REFERENCES

Bebout, D.G., Loucks, R.G., and Gregory, A.R. "Evaluation of An Energy Resource – Geopressured Geothermal Zone." *Texas Gulf Coast Society of Petroleum Engineers 53rd Annual Fall Technical Conference and Exhibition*, (1978), 8 p.

Bebout, D.G, Weise, B.R., Gregory, A.R., and Edwards, M.B. "Wilcox Sandstone Reservoirs in the Deep Subsurface Along the Texas Gulf Coast, Their Potential for Production of Geopressured Geothermal Energy." *Bureau of Economic Geology Final Report*, (1979), 198p.

Bebout, D.G., Weise, B.R., Gregory, A.R., and Edwards, M.B. "Wilcox sandstone reservoirs in the deep subsurface along the Texas Gulf Coast: their potential for production of geopressured geothermal energy." *Bureau of Economic Geology Report of Investigations*, (1982), No. 117, 140 p.

Blackwell, D.D., and Richards, M. "Calibration of the AAPG Geothermal Survey of North America BHT Database." *American Association of Petroleum Geologist Annual Meeting*, Dallas, TX, (2004).

Blackwell, D.D., Richards, M., and Stepp, P. "Texas Geothermal Assessment for the I35 Corridor East." *Texas State Energy Conservation Office Final Report*, (2010), 87 p.

Condon, S.M., and Dyman, T.S. "2003 Geologic Assessment of Undiscovered Conventional Oil and Gas Resources in the Upper Cretaceous Navarro and Taylor Groups, Western Gulf

Province, Texas." *U.S. Geological Survey Digital Data Series DDS-69-H*, (2006), Chapter 2, 42p.

Corrigan, J. "Correcting Bottom Hole Temperature Data." *AEPT Research Memo RM 97-0007*, (1997).

Crowell, A.M., Ochsner, A.T., and Gosnold, W. "Correcting Bottom-Hole Temperatures in the Denver Basin: Colorado and Nebraska." *GRC Transactions*, Vol. 36, (2012).

Ewing, T.E. "Structural framework." *in* Salvador, A. ed., *The Gulf of Mexico Basin*, Boulder, Geological Society of America, The Geology of North America, (1991), v. J, p. 3-52.

Ewing, W.E., and Galloway, T.E. "Evolution of the Northern Gulf of Mexico Sedimentary Basin." *in* Miall, A.D. ed., *The Sedimentary Basins of the United States and Canada (Second Edition)*, Elsevier, (2019), p. 627-694.

Förster, A., Merriam, D.F., and Davis, J.C. "Statistical Analysis of Some Bottom-hole Temperature (BHT) Correction Factors for the Cherokee Basin, Southeastern Kansas. " *Tulsa Geologic Society Transactions*, (1996), p. 3-9.

Gardner, R., and Birdwell, J.E. "Hidden System Identification: Basin Modeling as a Tool for Examining Sedimentary Geothermal Resource Potential." *GRC Transactions*, (2023), Vol. 47.

Kehle, R.O., Schoeppel, R. J., and Deford, R. K. "The AAPG Geothermal Survey of North America." *Geothermics*, Special Issue 2, U.N Symposium on the Development and Utilization of Geothermal Resources, Pisa, Italy, Vol. 2, Part 1, (1970).

Loucks, R.G. "Sandstone Distribution and Potential for Geopressured Geothermal Energy Production in the Vicksburg Formation Along the Texas Gulf Coast." *Bureau of Economic Geology Geological Circular 79-4*, (1978), 34 p.

Stautberg, J.E., and Sonnenberg, S.A. "Geologic Controls on the Spatial and Temporal Distribution of Sedimentary Geothermal Play Types on the Texas Gulf Coast." *GeoGulf Transactions*, v. 73, (2024), p. 131-141.

Swanson, S.M., Karlsen, A.W., and Valentine B.J. "Geologic Assessment of Undiscovered Oil and Gas Resources—Oligocene Frio and Anahuac Formations, United States Gulf of Mexico Coastal Plain and State Waters." *U.S. Geological Survey Open-File Report 2013–1257*, (2013), 66 p.

Waples, D.W., Pacheo, J., and Vera, A. "A Method for Correcting Log-derived Temperatures in Deep Wells, Calibrated in the Gulf of Mexico." *Petroleum Geoscience*, Vol 10, (2004), pp.239-245.

Alteration Assemblages and Paragenesis at the Sorik Marapi Geothermal Prospect, Sumatra, Indonesia

Jesse Turk[1], Jim Stimac[2], Nicholas Hinz[1], Jill, Haizlip[1], David Sussman[1], Tio Ferdinand[3], Alfiady [3]

[1]Geologica Geothermal Group, Inc., 75 Caliente Street, Reno, NV 89502
[2]Stimac Geothermal Consulting, 342 Whiteoaks Dr NE, Albuquerque, NM 87122
[3]PT Sorik Marapi Geothermal Power, Recapital Building 5th Floor, Jl Adityawarman Kav 55, Jakarta Selatan 12160

Keywords

Alteration mineralogy, vein paragenesis, volcano-hosted geothermal system, Sumatran fault, conceptual model, wairakite

ABSTRACT

The Sorik Marapi Geothermal Field is a volcano-hosted geothermal system located in North Sumatra, Indonesia. The project has been developed in four phases by PT Sorik Marapi Geothermal Power (SMGP) for a total of 180 MWe installed capacity of power generation. Wells drilled to depths of 1500 to 2715 m have proven a commercial geothermal resource at 245 – 320°C with neutral pH in an approximately 3 km (N-S) x 2 km (E-W), irregularly shaped area along the Sumatran Fault System (SFS). Like other geothermal resources, the base of the argillic cap provides a good marker for the top of the reservoir in some areas of the reservoir (mainly under Pad A and some Pad T wells). However, across much of the reservoir, the reservoir top does not align with the smectite cap and is instead commonly capped by phyllic or overlapping phyllic and propylitic alteration. In all areas across the field the appearance of wairakite, rather than epidote which is typical of volcanic-associated geothermal systems, is most diagnostic of the top of the reservoir. Vein paragenesis determined from thin section petrography illustrates that where wairakite is observed, it is consistently the most recent vein filling mineral observed throughout the reservoir. In this paper, we examine the spatial patterns between permeability, alteration mineralogy and paragenesis, and present conceptual model and alteration elements in map, 1-D, and 2-D cross-section views to illustrate these relations. This work was done as part of Geologica supporting SMGP develop the Sorik Marapi geothermal field (Sorik Marapi).

1. INTRODUCTION

Sorik Marapi is located on the northeast flank of Sorik Marapi volcano and along a major strand of the Sumatran Fault System (SFS) in North Sumatra (Figure 1). Unlike some other geothermal systems in the world adjacent to active volcanoes that have been impacted by magmatic acid vapor cores or supergene acid influx, there is no evidence that the Sorik Marapi geothermal reservoir has

experienced either, rather the reservoir is geochemically similar to many other entirely neutral systems developed worldwide. Sorik Marapi Geothermal Field can therefore be considered an example of paired (but separate) acid vapor core and neutral systems. The first thorough geothermal assessment of Sorik Marapi was completed by Sinclair Knight Merz (SKM) in 2011 (SKM, 2011), which concluded that up to four possible resource areas were present along distinct parts of the SFS northeast of Sorik Marapi volcano. Starting in 2016 and continuing into 2024, Sorik Marapi Geothermal Power (SMGP) has drilled >40 wells in Sibanggor, the southernmost of the four prospect areas identified (Figure 2) that have proven a ~245° to 325°C geothermal resource extending over an area of approximately 3 x 2 km. Between 2019 and 2023 SMGP constructed and is currently operating multiple power plants with a installed capacity of 180 MWe.

In this paper, we examine the spatial patterns between geometry of the productive reservoir, permeability patterns within the reservoir, alteration mineralogy and paragenesis, and present conceptual model and alteration elements in map, 1-D, and 2-D cross-section views to illustrate these relations. Below is a list of the key datasets used for this evaluation.

- Mud Logs: During development drilling, cuttings were collected approximately every 3 meters and analyzed under a binocular microscope. The first 25 wells were relogged by binocular scope to refine lithologic units (Hinz et al., 2021).
- MeB: Methylene Blue (MeB) estimates of the smectite clay content were completed at 9 m intervals in all production and injection wells.
- Thin Sections: Cuttings from intervals of interest were selected for thin section preparation and analysis (~10 samples per well). The thin sections were prepared by Wagner Petrographic and analyzed by Jim Stimac. Samples were stained for K-feldspar and calcite to simplify estimating abundance of these minerals (Stimac, 2023).
- Well Testing: Upon the completion of drilling, temperature and pressure (±spinner) logs were run by wireline as part of completion tests.

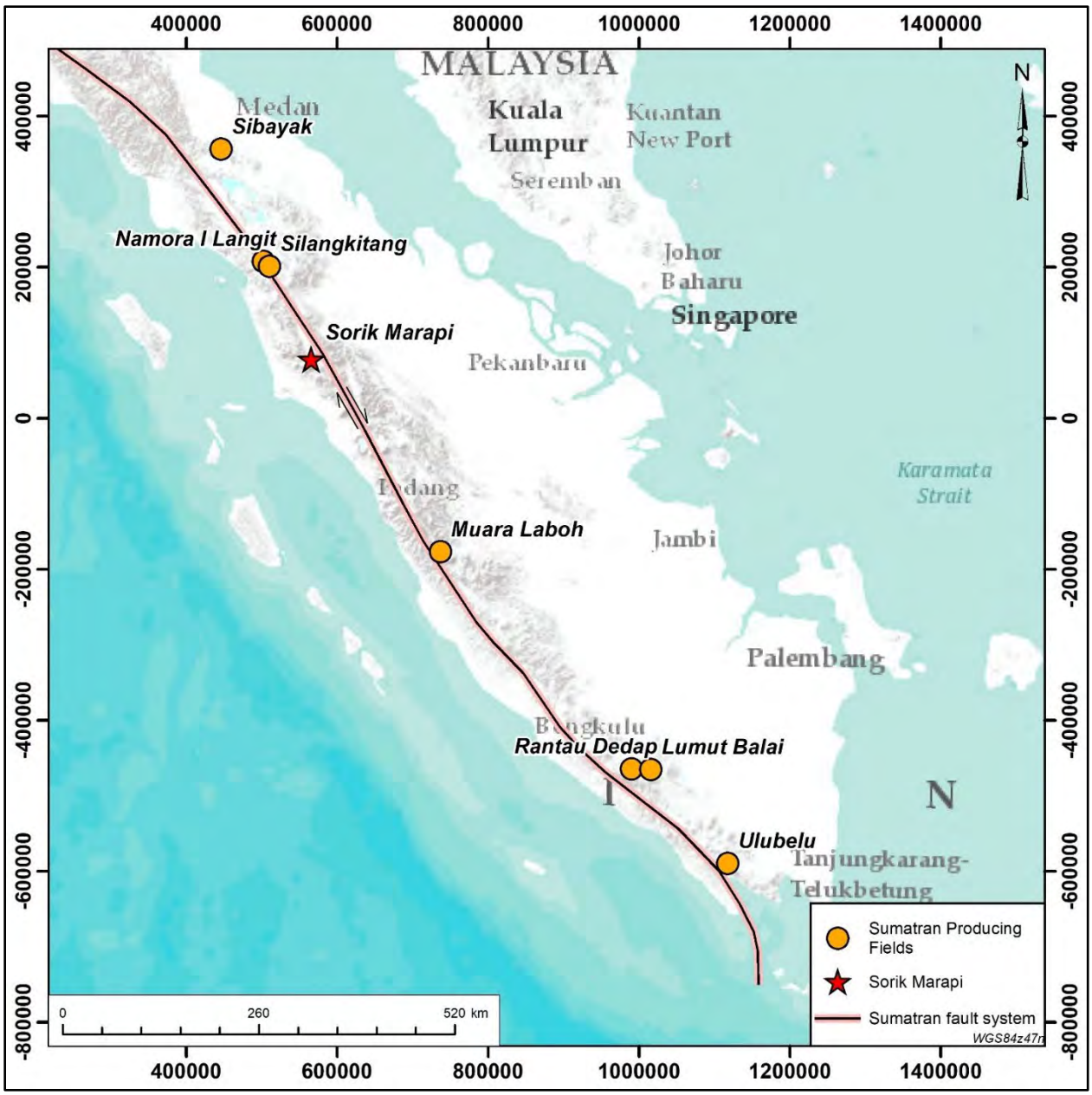

Figure 1. Overview map of Sumatra showing location of the Sorik Marapi and other operating geothermal fields.

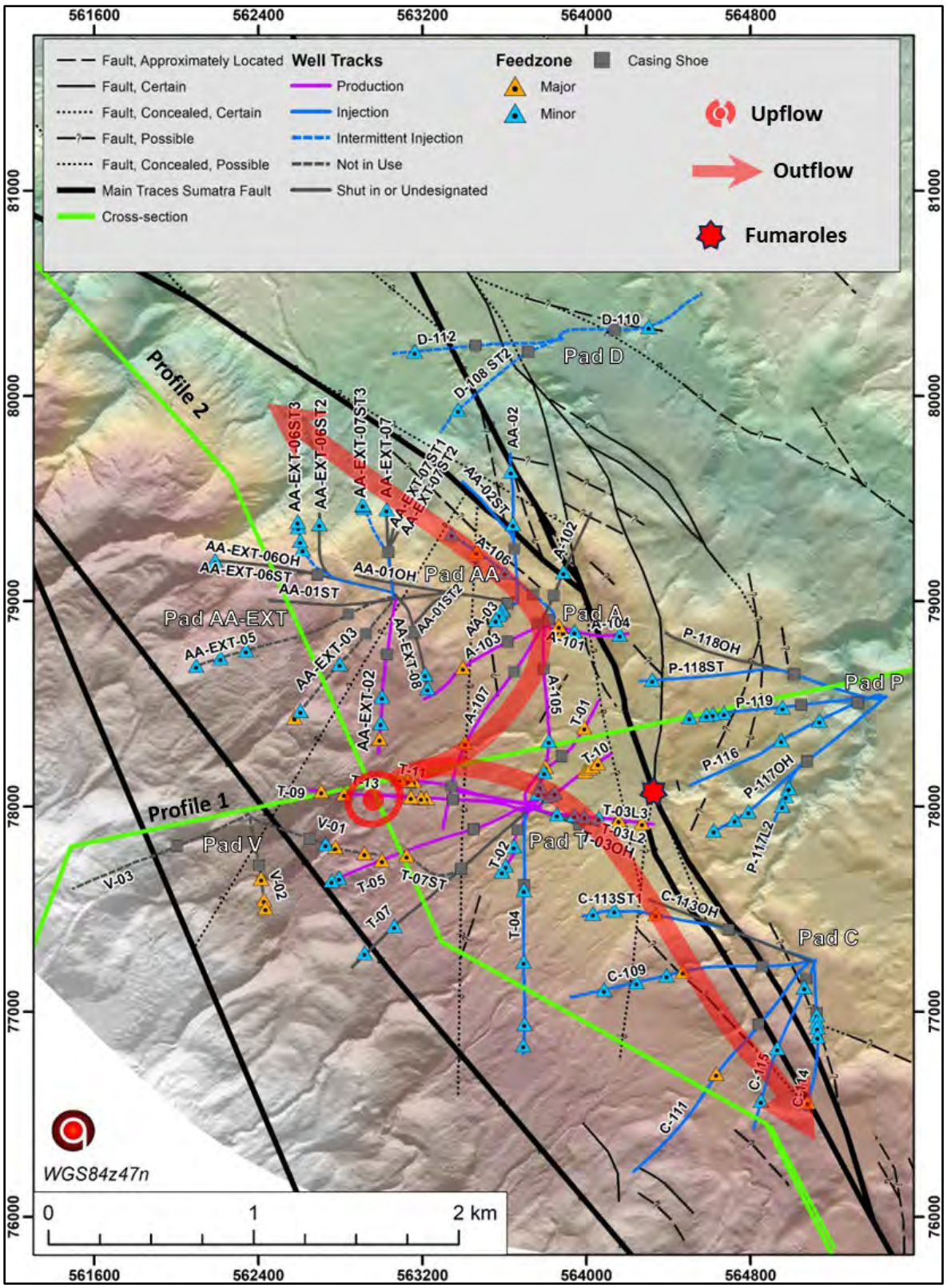

Figure 2. Wells drilled within the currently developed Sorik Marapi Geothermal Reservoir. Heavy black lines are NW-SE trending faults of the SFS. Key conceptual model elements include upflow (arrowed circle) and outflow pathways (red arrows). The green lines correspond to the cross-sections in Figures 4 and 5.

Through the development of the resource, the conceptual model has been continuously updated to incorporate geologic and well testing data from new wells. The most recent published conceptual model was in Hinz et al. (2021). This paper presents a summary of the current conceptual model used to guide ongoing development through 2024 and discusses the patterns among the initial appearance of wairakite, hydrothermal vein paragenesis, and the commercial reservoir as determined from temperature profiles and feedzones in the wells.

2. CONCEPTUAL MODEL SUMMARY

The conceptual model for the Sorik Marapi reservoir remains largely unchanged from that published in Hinz et al. (2021). In this previous conceptual model, a neutral >320°C upflow zone separate from the acid core occurs about 750 m west of Pad T (Figure 2). The inferred upflow area is based on well temperature data, fluid geochemistry, locally elevated noncondensable gases (NCG), and permeability patterns. Overall, the convective upflow appears to be elongated NE-SW and inclined upward towards the E from the area between Pads T and V towards Pad A at a moderate angle beneath a west-dipping cap rather than a subvertical upflow (Figure 4). This apparent elongate orientation of the upflow is likely associated with a NE-striking fault zone. One option for such a fault zone is a NE-striking fault that connects the major western and eastern strands of the Sumatra fault zone in this area. There is an initial eastward rollover and lateral outflow from the upflow zone which fans out eastward across Pad T and A wells, which intersect 260 to 280°C fluids. This eastward flow is under an inclined cap dominated by phyllic (sericite/illite-quartz-pyrite) to mixed-layer clay (illite-smectite, chlorite-smectite) to argillic (smectite) alteration assemblages, rising from below -1,100 masl west of Pad T to >100 masl beneath Pad A. As the outflow approaches the main strand of the SFS, it branches to the southeast and north-northwest. The southeast branch of outflow carries 250 to 260°C fluids southeast through the T-04, C-113ST, and C-109 area at -600 to -1,100 masl under a phyllic to phyllic-propylitic alteration assemblage cap (Figure 5). The north-northwest branch of outflow is inferred to carry <260°C fluid NW of A-106 within fractured metasediments and between major strands of the SFS between -600 and 0 masl below a mixed clay to argillic cap (Figure 2 and Figure 5). The zones of highest permeability in the reservoir are associated with the upflow and the outflow where it forks north and south along the SFS in the shallow Pad A wells and eastern Pad T wells.

The top of the reservoir (TOR) has been determined by the top of isothermal intervals in stable static temperature logs and feedzones identified through analysis of PT(S) surveys taken after completion testing. Throughout the productive reservoir, the depth to the TOR varies from ~250 masl to -1,200 masl. In this previous model, the base of the argillic cap provides a marker for the top of the reservoir near the eastern parts of the Pads A and T wells. However, across much of the reservoir outside this area, the reservoir top does not immediately coincide with the base of the argillic cap and is instead commonly capped by transitional/mixed clay, phyllic or phyllic-propylitic alteration area (Figures 4 and 5). This, along with paragenetic analysis suggests that reservoir permeability and temperature may have extended further than today.

The 2024 conceptual model includes two updates. One is that there are likely two major splays of SFS along the western part of the well field (Figure 2 and Figure 4). The interpretation for these splays is the variation in elevation of the contact between Tertiary volcanics and the underlying metamorphic rocks. The other conceptual model update is that there is an ~1-km diameter

hypabyssal intrusion under Pad V that is similar in size to the intrusion under Pad A but is intermediate in composition rather than felsic (Figure 4). The inferred upflow area under T-09 is inferred to be between these intrusions. The intrusions pre-date the modern reservoir and feedzones are distributed both within and outside the intrusions.

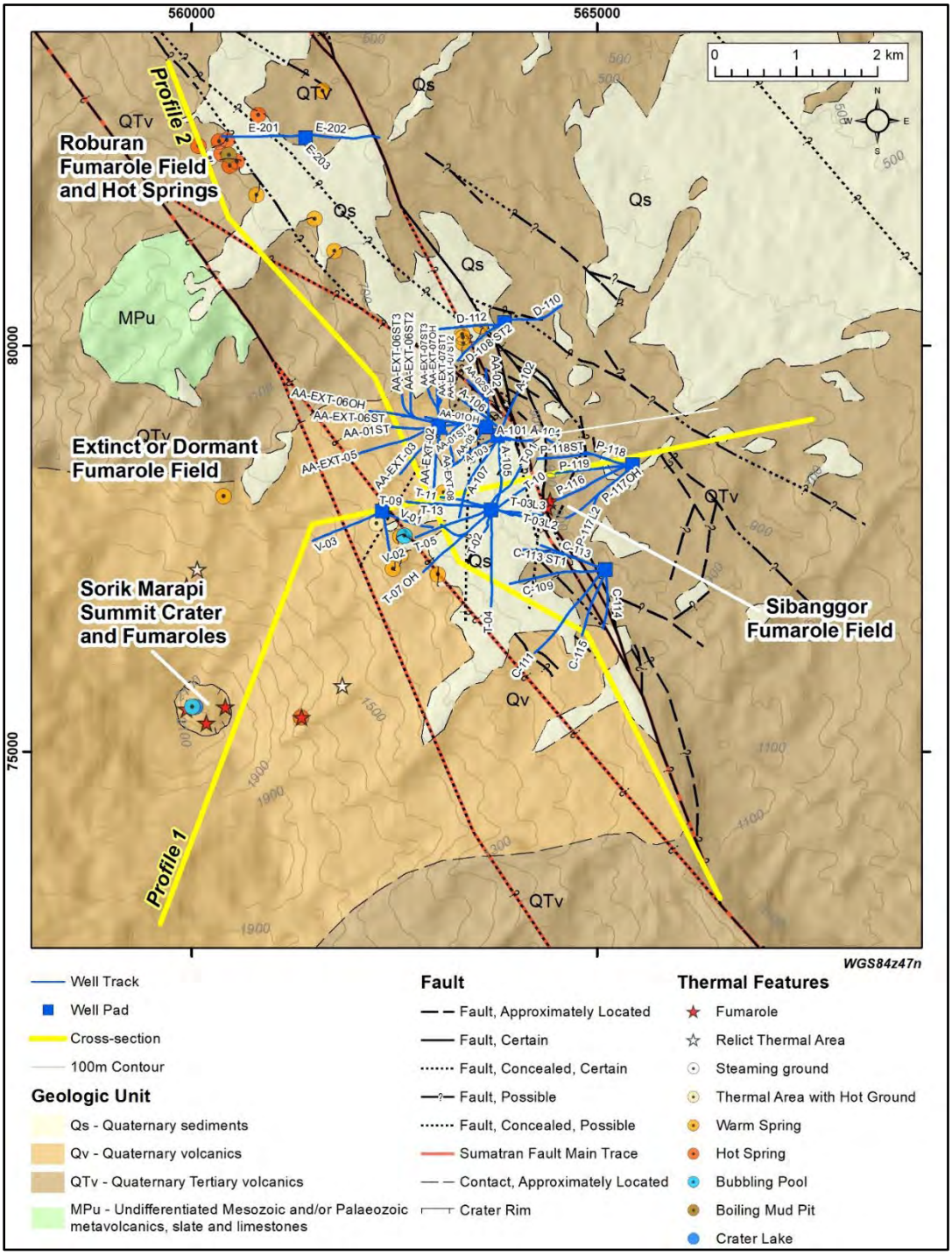

Figure 3. Map of Sorik Marapi with well tracks and conceptual model cross-section lines. The summit crater and associated magmatic fumaroles and the active solfataric (acid core) system are located about 3 km southwest of the wellfield. Modified from Hinz et al. (2021).

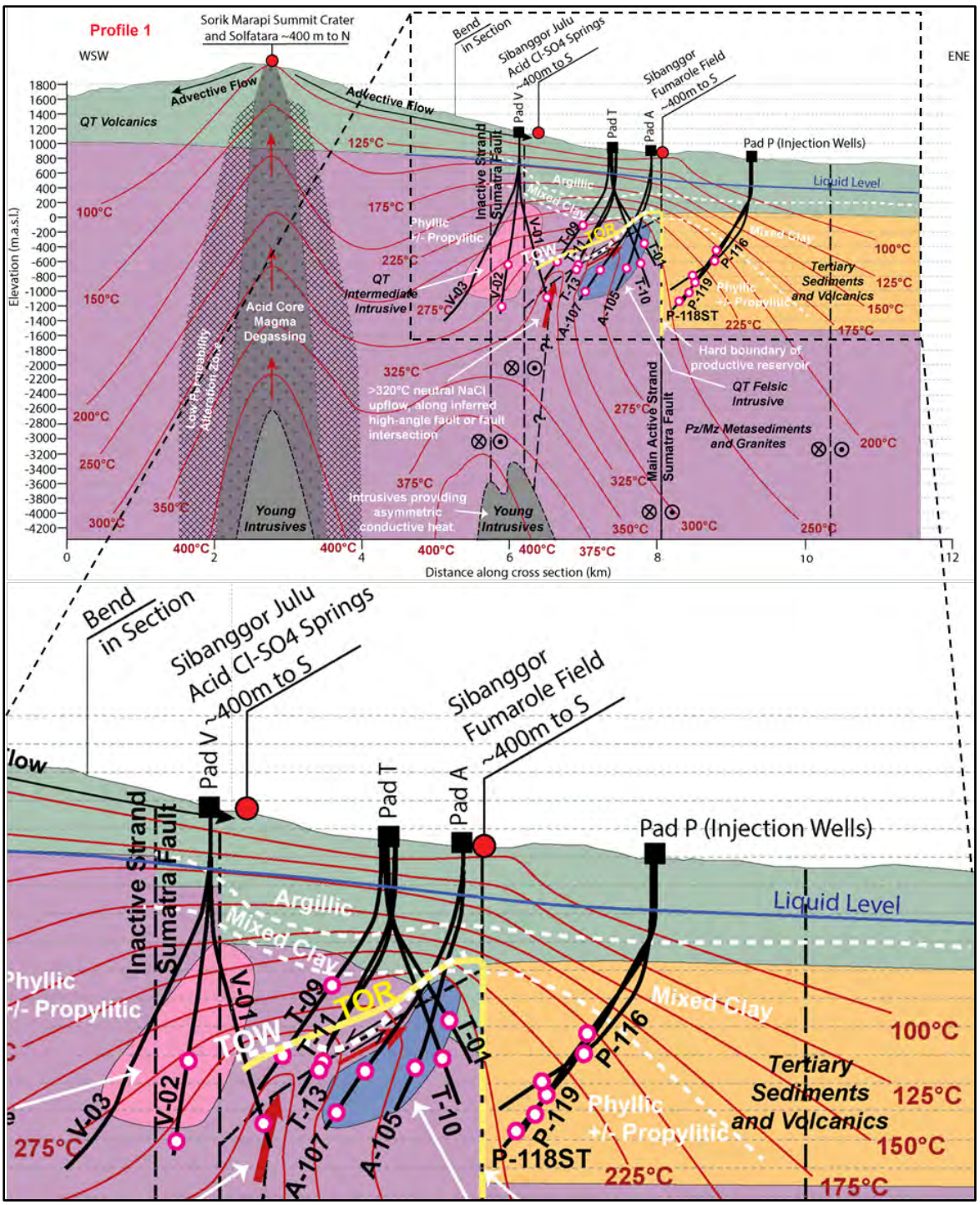

Figure 4. Top - Conceptual model cross-section along Profile 1 (location shown in Figures 2 and 3). The key features of the model include simplified geologic units, temperature isotherms, the top of the reservoir (TOR) shown as a yellow line, the top of wairakite (TOW) shown as a heavy dashed white line, major structures (dashed black lines), and hydrothermal alteration zones (white dashed lines and text). Well courses are solid black lines, and major feedzones are shown as open red circles. Bottom – a zoomed in view of the conceptual model cross-section showing the relations between the TOW, TOR, and feedzones. Modified from Hinz et al. (2021). The acid core system beneath Sorik Marapi volcano is based on surface observations and modeled after Reyes et al. (1993).

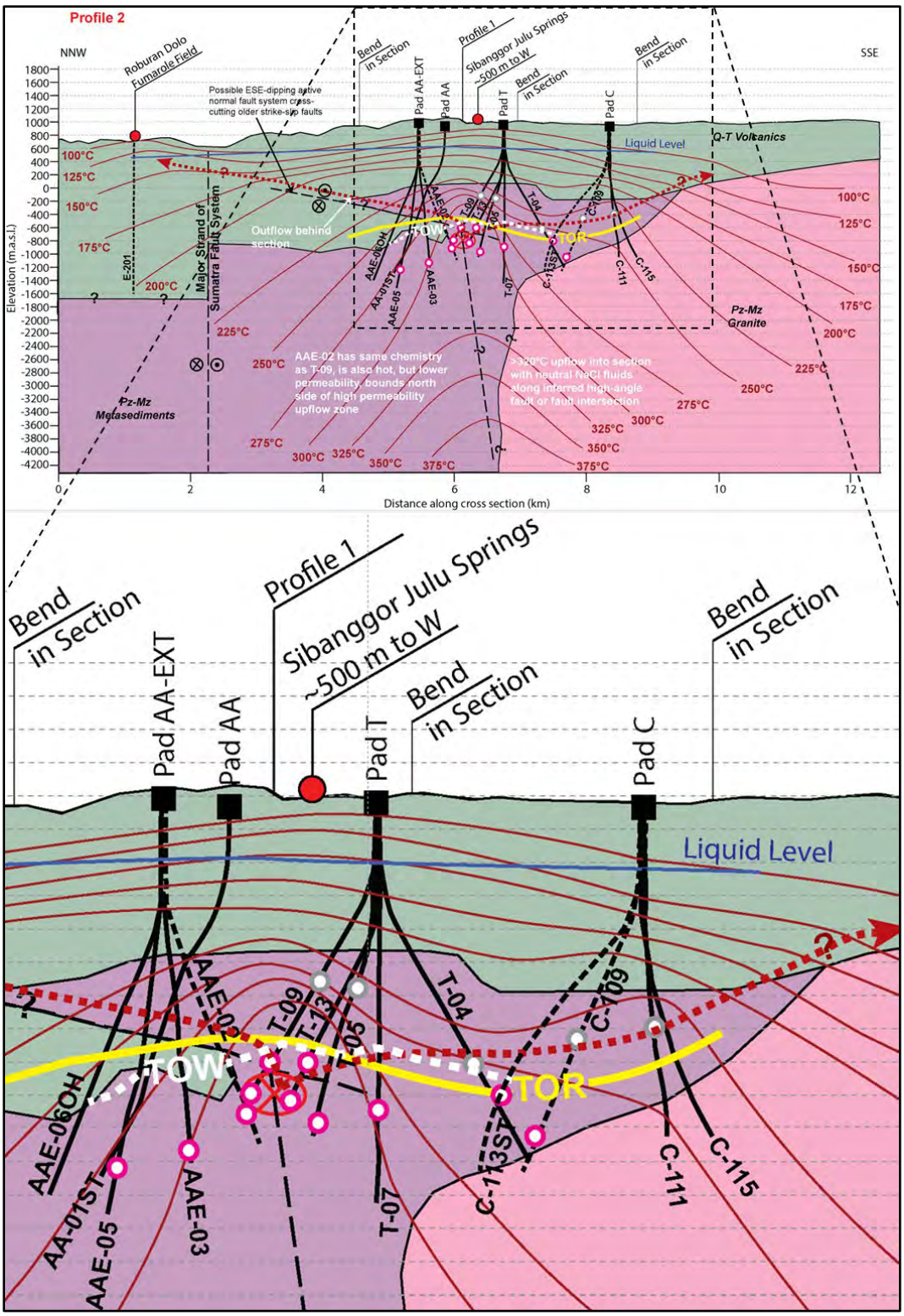

Figure 5. Top - Conceptual model cross-section along Profile 2 (location shown in Figures 2 and 3). The key features of the model are shown in the same manner as in Figure 4. Outflow to N and S are shown as dashed red lines and portray flow behind section. Bottom – a zoomed view of the conceptual model cross-section showing the relations between the top of wairakite, top of the reservoir, and feedzones. Modified from Hinz et al. (2021).

3. HYDROTHERMAL ALTERATION

Hydrothermal alteration in geothermal systems is well understood and can be separated into distinct mineral assemblages based on the chemistry of circulating fluid (e.g., Browne, 1978; Reyes, 1991). Evaluation of mineral paragenetic sequence in veins provides an additional level of understanding of system evolution and status (Stimac, 2023). In particular, comparison of the formation sequence of key calc-silicate minerals and the abundance of open space in veins to measured temperatures and well permeability provides insight into the evolution of the system to its current state.

Analysis of well temperature and alteration mineralogy data has identified that the alteration of the cap overlying the reservoir varies from argillic (smectite) to mixed-layer clay (smectite-illite and smectite-chlorite) to phyllic-propylitic (Hinz et al., 2021). Phyllic-propylitic alteration consists of overlapping dominant quartz-sericite-pyrite and subordinate quartz-chlorite-epidote-pyrite. Where both epidote and illite/sericite are present in a sample, we determine the dominant assemblage by which key mineral is more abundant.

The metasedimentary rocks such as phyllite and schist are atypical reservoir rocks in volcanic systems but are important in the Sorik Marapi system. Their presence favors formation of illite/sericite-quartz-titanite-pyrite-calcite, rather than epidote and other calc-silicates. Conversely the assemblage epidote-adularia-chlorite-quartz-pyrite is more prevalent in plutonic rocks that form another important reservoir lithology in the Sorik Marapi system. In these rocks epidote is distributed as matrix alteration or in filled veins where it is encapsulated in later quartz, calcite, or prehnite. This contributes to the poor correspondence between epidote and the current reservoir top of this system. More broadly this suggests the existence of precursor hydrothermal systems that formed in the same area as the modern system or earlier stages of fluid-rock interaction in this geothermal system.

The cap geometry over major feedzones in production wells on Pads A, AA, AA-EXT, T, and C shows that the reservoir top deepens to the southwest from Pad A and is deepest in the T-05 and T-09 area. In general, decreases in MeB values provide the most consistent marker for the top of the reservoir in the Pad A area, coupled with the appearance of chlorite replacement of phenocrysts; this is typical of the argillic to transitional/mixed-layer clay transition. Note the argillic alteration is correlative to the volcanics and is not observed in the underlying metamorphic rocks. As the cap further deepens to the SW in the west-directed Pad T wells (i.e., T-05 and T-09), it transects below the volcanic rock and enters the metamorphic rock and is characterized by phyllic-propylitic alteration, and the underlying reservoir is most consistently marked by the appearance of wairakite.

3.1 Implication of Wairakite in Analogue Systems

In typical high-temperature (> 240°C) neutral-chloride volcano-hosted geothermal systems, the first vein minerals to form upon fracture initiation and upflow of heated meteoric water circulation are epidote ± adularia ± quartz (Stimac, 2023). As temperatures decline, prehnite ± quartz commonly form. Wairakite ± calcite ± anhydrite commonly form later as temperature declines or pH declines due to admixture with steam condensate (Moore et al., 2004; Figure 7). Calcite ±

anhydrite may also form from descending peripheral steam-heated waters as system temperatures and pressures wane. Secondary mineral growth tends to result in permeability loss unless fractures are being reopened or new ones are being formed. Progressive infilling of veins records the life of the system, although rejuvenation and repeated paragenetic cycles are possible.

Moore et al. (2004) summarized characteristics of wairakite at Tiwi, Bulalo (Philippines) and Karahabodas (Indonesia) geothermal fields. Constraints from fluid inclusions in coprecipitated phases gave temperatures of about 235 to about 300°C. Similarly, at Copahue (Argentina), quartz coexisting with wairakite had fluid inclusions temperatures of 240 to 280°C (Mas et al., 1995). These authors interpreted that the coexistence of vapor- and liquid-rich inclusions in the same quartz crystal as suggesting that boiling was taking place when wairakite was precipitated.

Moore et al. (2004) highlighted that wairakite typically forms late, commonly after epidote and prehnite, but before calcite and anhydrite. However, at Bulalo episodes of epidote and wairakite alternated. At Karahabodas, wairakite postdates early epidote, then prehnite and later anhydrite + calcite. In these examples Moore et al. (2004) noted that wairakite typically forms from lower pH or lower aCa^{+2} fluid than epidote (i.e., lower aCa^{+2}/aH^{+}). They emphasized that, based on phase relations, a decrease in temperature favors prehnite over epidote but a decrease in pH favors wairakite relative to epidote.

Although epidote is typically used to define high-temperature geothermal reservoir volumes, in some cases wairakite may be the most reliable indicator of the reservoir top and extent. Wairakite is common in high-temperature geothermal systems (>220°C) dominated by propylitic alteration (Browne and Ellis, 1970; Moore et al., 2004). They observed wairakite forming after epidote ± prehnite and either before or after late anhydrite ± calcite. They interpret this sequence of deposition to indicate evolution from system initiation and upflow (epidote), to minor cooling (prehnite), to mixing with descending steam condensates (wairakite), and descent of sulfate and bicarbonate-rich steam heated waters (anhydrite ± calcite). This general sequence, or variations on it, is extremely common, especially in the upper portions of geothermal reservoirs (Moore et al., 2004; Stimac, 2023). Wairakite is stable at relatively low concentrations of dissolved CO_2. At higher concentrations of CO_2, it is replaced by calcite (Browne and Ellis, 1970; Thompson and Thompson, 1996; Moore et al., 2004).

3.2 Wairakite at Sorik Marapi

At Sorik Marapi wairakite is commonly the most abundant calc-silicate mineral (Figure 6 and Figure 8). It is found partially filling late-stage veins that appear to have formed at or near current system conditions. It is particularly useful in determining the top of the reservoir since epidote is commonly distributed above and/or laterally away from the reservoir or is sparse to absent. Wairakite locally encapsulates needles of earlier formed epidote, actinolite, or prehnite, and it is found in close association with quartz, calcite, and anhydrite.

Geochemical data from wells indicate that the Sorik Marapi reservoir fluid is a dilute (TDS ~1500-1900 mg/kg) neutral Na-Cl brine (Hinz et al., 2021) with low non-condensable gas (up to 0.1 wt% total NCG) primarily composed of CO_2, with minor proportions of H_2S and trace amounts of NH_3, N_2, CH_4, and H_2. Steam is formed from depressurization of these reservoir fluids and condensed would likely be an acid sulfate fluid. However, steam zones at the current Sorik Marapi reservoir

appear to be production induced and limited to shallow parts of the reservoir. Wairakite is found deeper in the reservoir at high temperature as well as at the top of the reservoir. Alternating episodes of boiling and cooling, rupture, and down flux of condensed steam may be the processes which yielded the formation of wairakite at Sorik Marapi and the association of wairakite with quartz and bladed calcite or anhydrite. Such ruptures may be related to the close spatial relationship of the reservoir to active splays of the SFS.

Figure 6. Wairakite found at 1635 m-MDRF in well T-09. The depth at which this wairakite was observed coincides with an increased loss rate of drilling fluids, indicating that an open-fracture was intercepted.

The shallowest depth at which wairakite is found is 877 m-MD (26 masl) in well A-104, where the downhole temperature is almost 260°C. Meanwhile, wairakite is noted in well AA-EXT-05 from 1,699 m-MD (-650 masl) to 2,653 m-MD (-1,466 masl) which is the deepest depth it is observed. Generally, wairakite in Sorik Marapi is observed in the productive reservoir west of the

main strand of the SFS where Pads A, AA, AA-EXT, and T are located (Figures 2, 3, and 12) and is largely absent in Pad C, D, and P wells.

The abundance of both wairakite and phyllic alteration at Sorik Marapi is consistent with an increasing aK+ and/or aH+ relative to aCa++ compared typical neutral-Cl waters producing propylitic alteration. However, diaspore or kaolinite/dickite, characteristic of advanced argillic alteration, are rarely observed at Sorik Marapi and produced fluids are benign. Wairakite is also observed as the latest vein filling mineral in phyllic altered zones in well A2 at about 710 m-MDRF at Muara Laboh (Baroek et al., 2018).

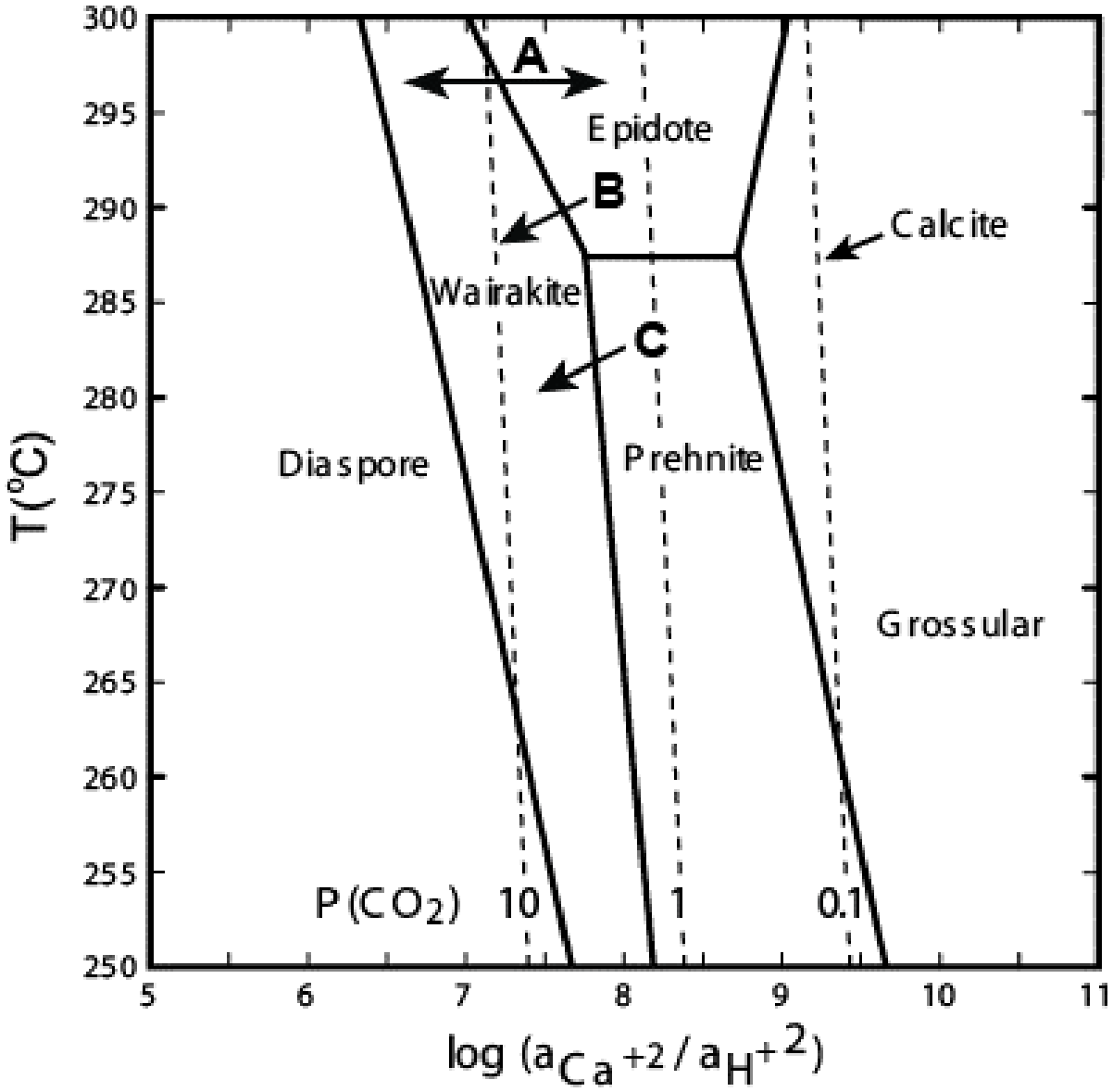

Figure 7. Phase relations between epidote, prehnite and wairakite for a fluid composition precipitating illite (from Moore et al., 2004). Arrows illustrate paths between epidote, prehnite, and wairakite: A) is a path for changing aCa++/aH+ at the same temperature, B) and C) are for concurrent cooling and decreasing aCa++/aH+ for epidote and prehnite to wairakite, respectively.

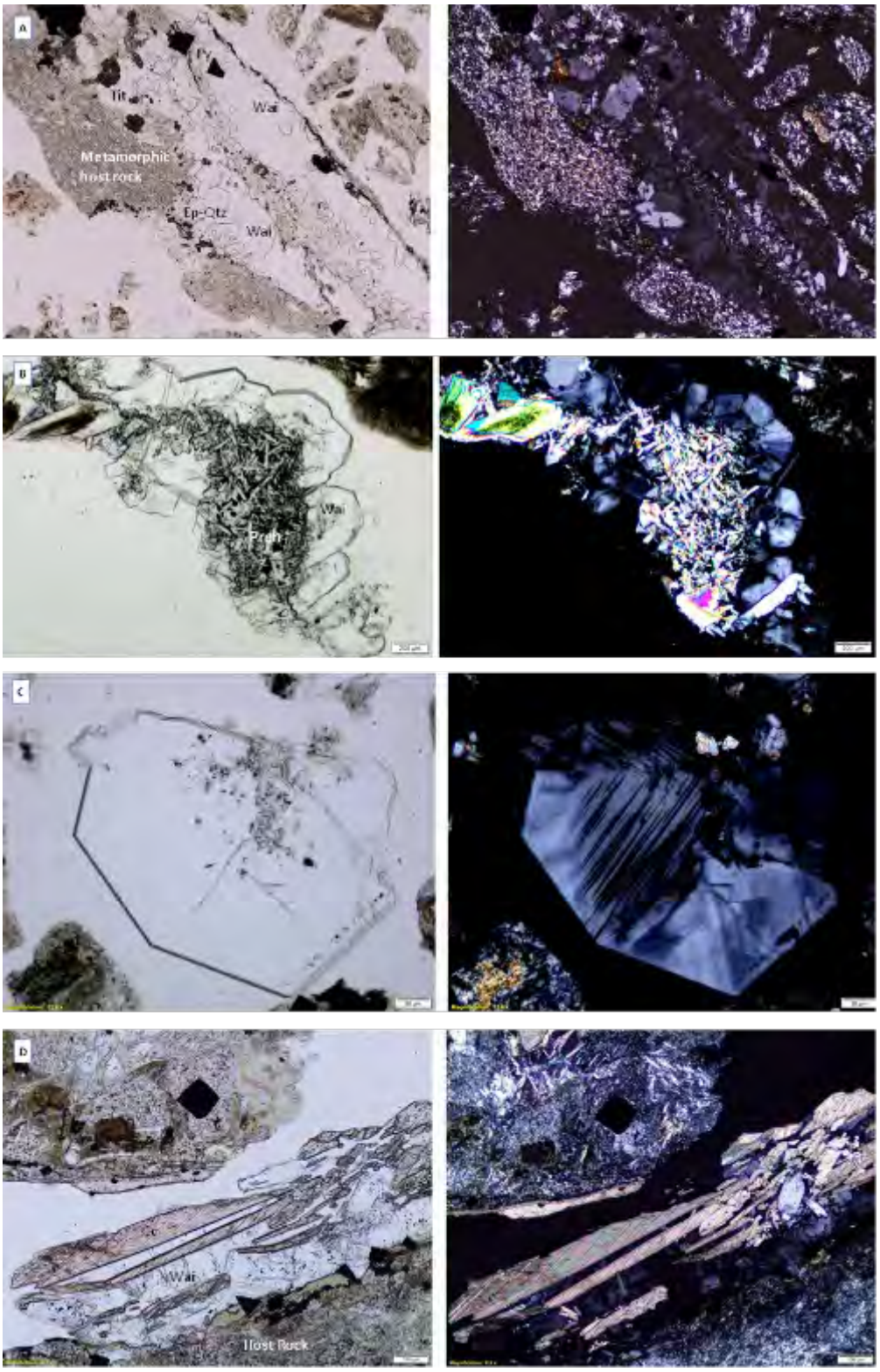

Figure 8. Wairakite at Sorik Marapi. A) Wairakite (Wai) infilling open veins with early quartz (Qtz). B) Wai encapsulating earlier prehnite (Prh). C) Euhedral Wai indicating growth in an open vein, possibly encapsulating minor calcite and epidote. D) Intergrown bladed calcite (Cc) and Wai suggesting boiling conditions.

3.2 Open Space Textures

Numerous petrographic studies of cuttings and core indicate that higher permeability is more likely when open space textures such as euhedral or subhedral intergrowths of common vein minerals are observed (e.g., Stimac, 2023). Conversely, filled vein samples may signal that system permeability has declined in that area. Commonly the onset of significant open space in veins corresponds with the top of the deep reservoir. Within the permeable Sorik Marapi reservoir veins with open space are commonly very abundant in the vicinity of major entries. This is evidenced by both open space textures such as euhedral crystals and a high abundance of vein fragments in cuttings samples (reaching 20-30%).

There is also evidence for hydrothermal and tectonic breccias with overgrowths of new vein minerals indicating that open space was created multiple times in some areas. For example, in well A-107 breccias consisting of both host rock and vein mineral fragments are overgrown by wairakite and wairakite-adularia (Figure 9). Wairakite, quartz (Figure 10), prehnite, and adularia are the most common minerals in these occurrences.

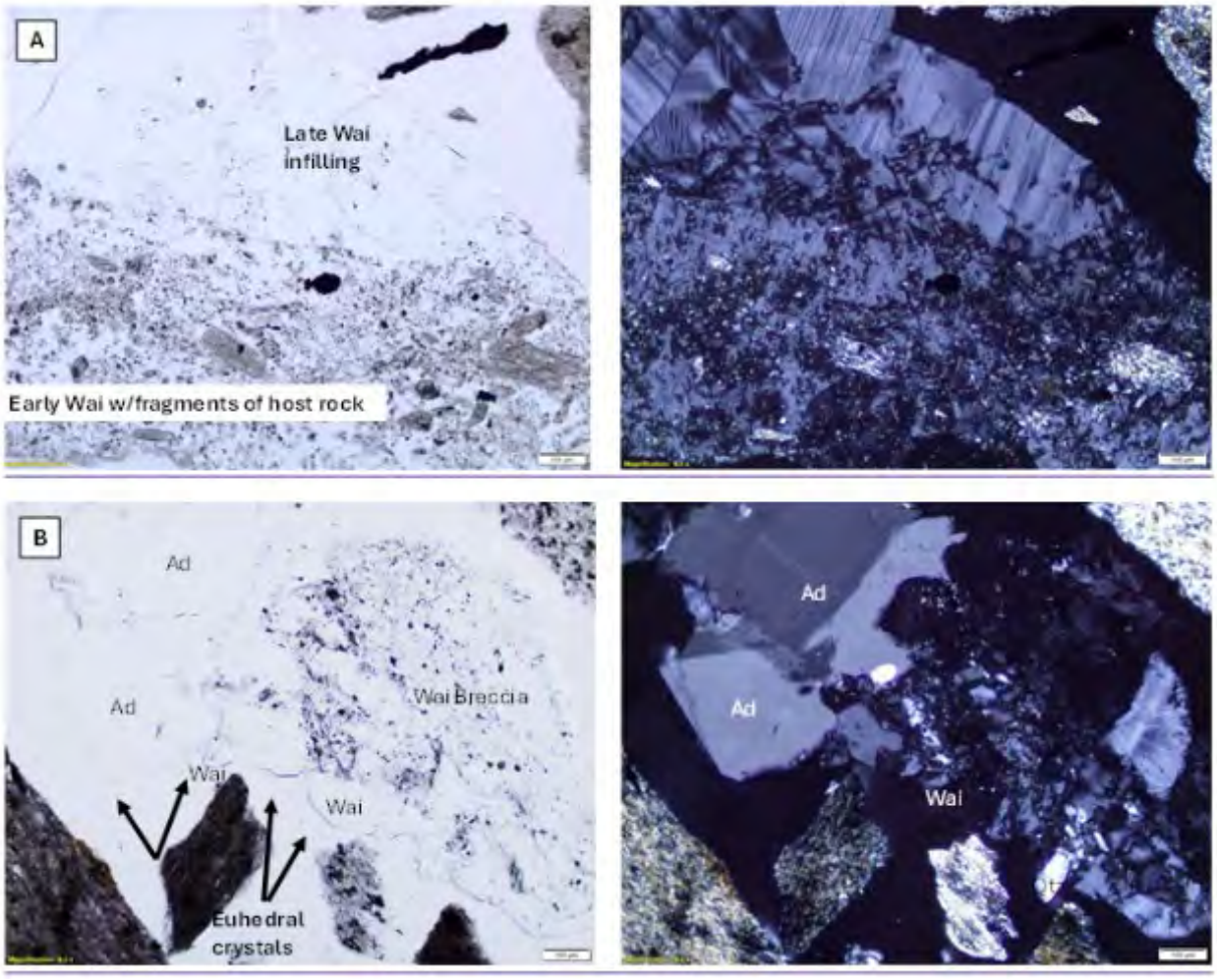

Figure 9. A) A-107 1393 m-MDRF – Multiple episodes of wairakite with clastic debris of host rock; B) A-107 1393 m-MDRF - Multiple episodes of wairakite with evidence of open space adularia-wairakite.

Figure 10. Open space mineral indicator, drusy quartz, from 1109 m-MDRF in well T-03. Drusy quartz grew with secondary silica as its platform.

4. WAIRAKITE DISTRIBUTION AND RESERVOIR PERMEABILITY

Across the productive Sorik Marapi reservoir, there is a correlation between the initial appearance of wairakite in wells and the top of the reservoir (Figures 4 and 5). The top of the reservoir has been determined by the top of isothermal intervals in stable static temperature logs and feedzones identified through analysis of PT(S) surveys taken after completion testing. Most feedzones in productive wells are in metamorphic rocks or intrusions, although a few feedzones have been observed in volcanics (e.g., A-101 and A-104). There are no clear permeability patterns at the margins of intrusions as have been observed at some other geothermal fields (e.g., The Geysers, USA). It is therefore likely that all the feedzones are associated with faults or major fractures. Wells A-101, C-113ST, T-01 and T-09 provide examples throughout the upflow and outflow zones of the relation between the appearance of wairakite, feedzones, and the top of the reservoir (Figure 11). Well T-09 is located near the >320°C upflow zone, well T-01 is in an easterly outflow, well A-101 resides in the shallowest part of the reservoir where a thin natural steam cap is inferred to exist prior to development, and C-113ST is in outflow to the south. The depths of the appearance of wairakite, feedzones, and isothermal intervals in these wells are presented in Table 1. While

wairakite can be distinguished under the binocular microscope when logging chips, it can be difficult to distinguish from other similarly colored minerals. The maximum vein abundance noted in thin sections from these wells varies widely from 6% in C-113ST to 100% in A-101. However, in the production section of each respective well vein abundance generally increases near the first observance of wairakite (Figure 11).

Table 1. Correlation between wairakite, feedzones, and isothermal intervals in select Sorik Marapi wells.

Well	Depth of Wairakite (m-MDRF; masl)	Feedzone Depth (m-MDRF)	Start of Isothermal Zone in Temperature Profile (m-MDRF)
A-101	870; 50	830	~870
C-113ST	1640; -700	1710	~1710
T-01	1010; -100	1440	~1010
T-09	1635; -750	1200 to 1840	~1170

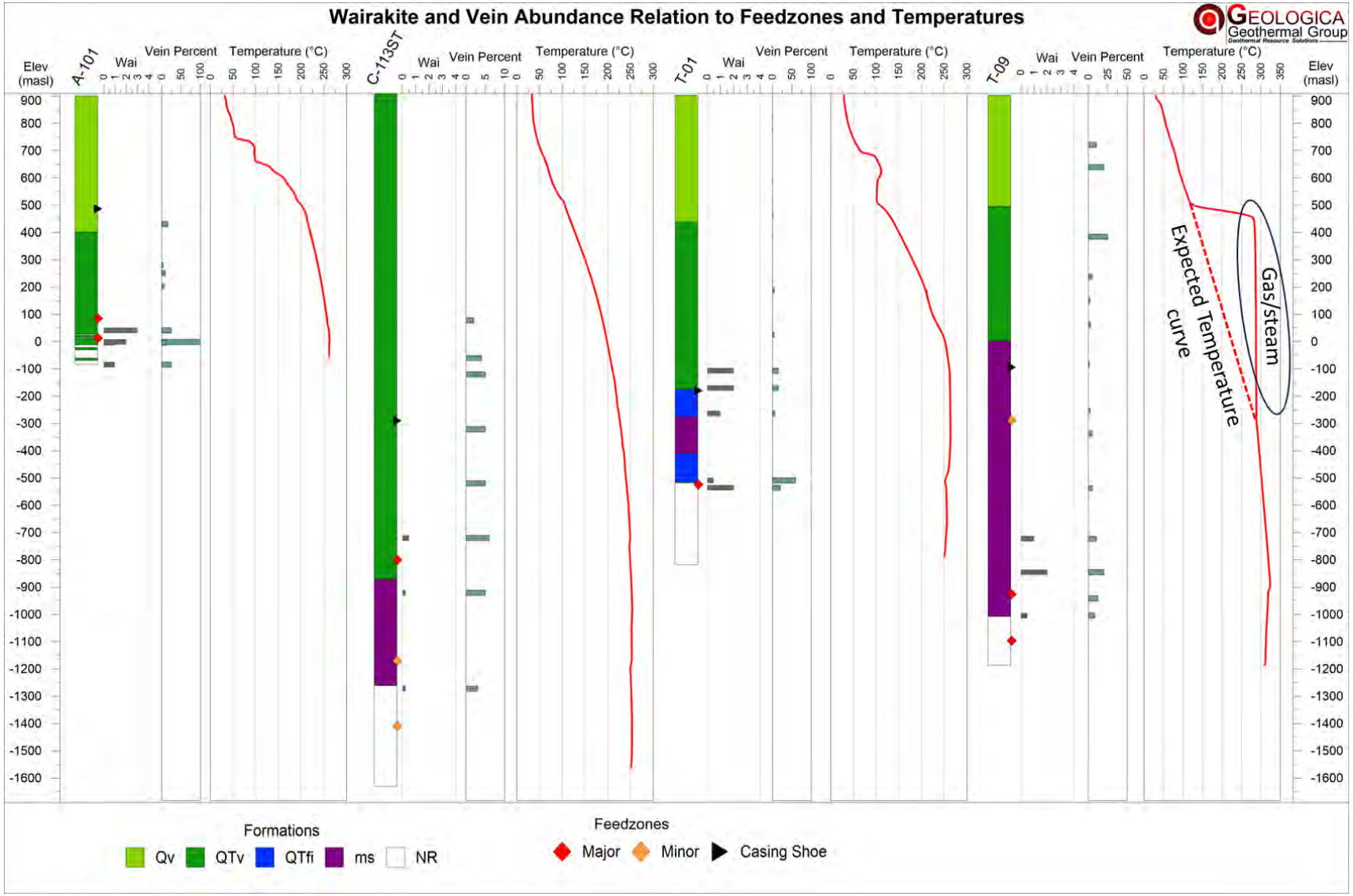

Figure 11. Select SMGP wells showing correlation of wairakite and vein abundance to reservoir permeability. Formations: Qv – Quaternary volcanics; QTv – Quaternary to Tertiary volcanics; ms - Paleozoic-Mesozoic metasediments; NR - no returns.

There is generally good spatial distribution of wairakite abundance (Figures 12 and 13) relative to permeability in the reservoir as defined by injectivity indices of feedzones. As shown in Figures 12 and 13, the highest qualitative abundance (see figures for key) of wairakite noted in thin sections is seen in wells near the upflow zone (near wells T-05 and T-09) and in Pad A wells where the top of the reservoir is shallowest (Figure 4). However, there are likely some high wairakite abundance areas within the reservoir that are aliased due to thin section sample selection (e.g., no thin section samples from A-105, V-02, and V-03), total lost circulation in productive wells (e.g., T-03L3 and T-10 have major feedzones below TLC intervals), and distribution of well tracks in 3D space. There is another area of higher wairakite abundance near well AA-EXT-05 that does not have a high injectivity index. This may represent an area that had higher permeability in the past but has not had fractures re-opened by fault activity in recent geologic time. Northeast of the main strand of the SFS, there are only two instances of wairakite in thin sections. This aligns well with the conceptual model which posits the main strand of the SFS is predominately a permeability barrier and a reservoir boundary. To the south of the productive reservoir, wairakite is only observed in the northernmost Pad C well, C-113ST.

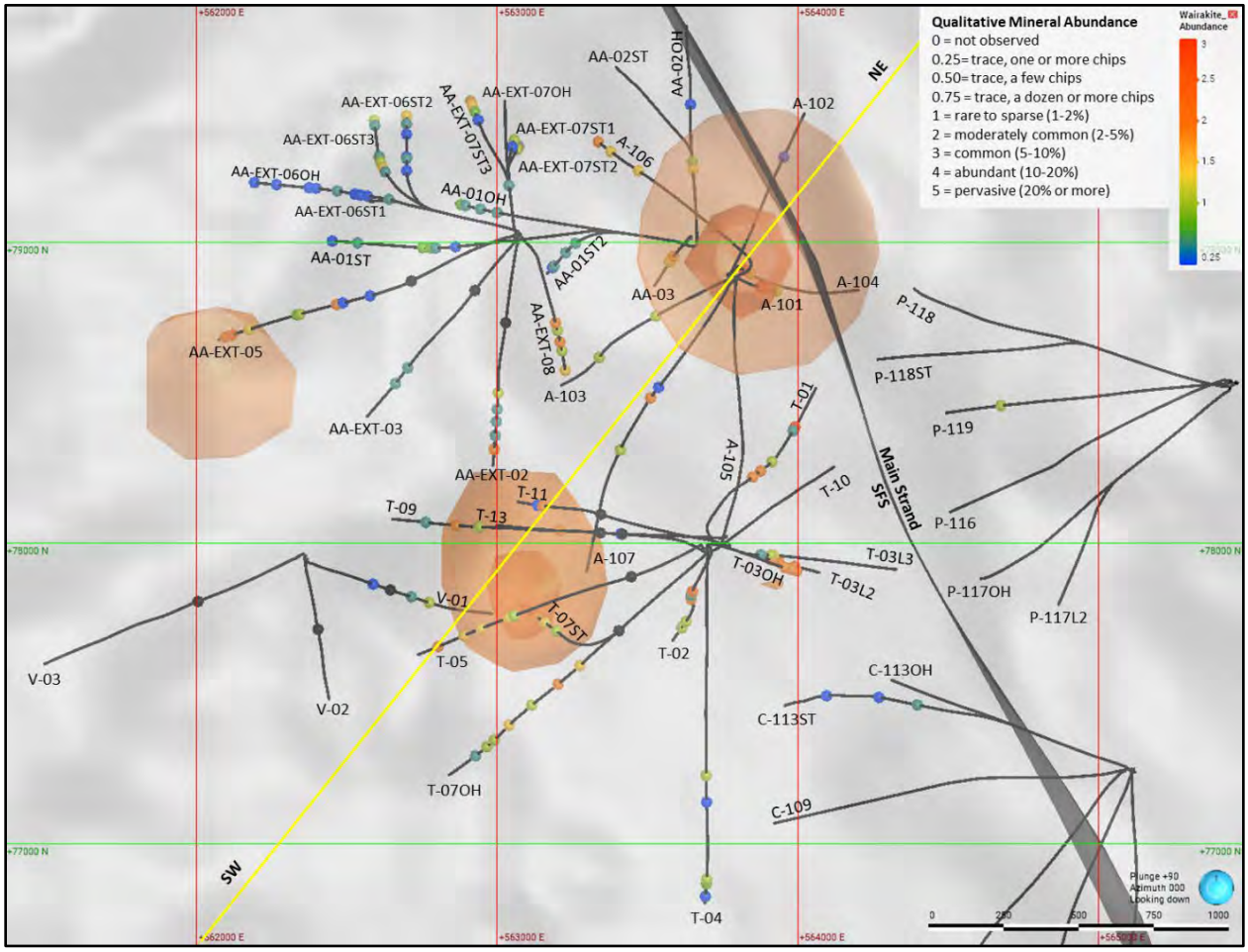

Figure 12. Plan view of drilled well tracks and wairakite qualitative abundance from thin sections (color-scaled spheres) with higher abundance areas emphasized (2.0 and 2.5 isosurfaces); black spheres are production casing shoes. Cross-section profile (SW-NE) used in Figure 13 is shown for reference.

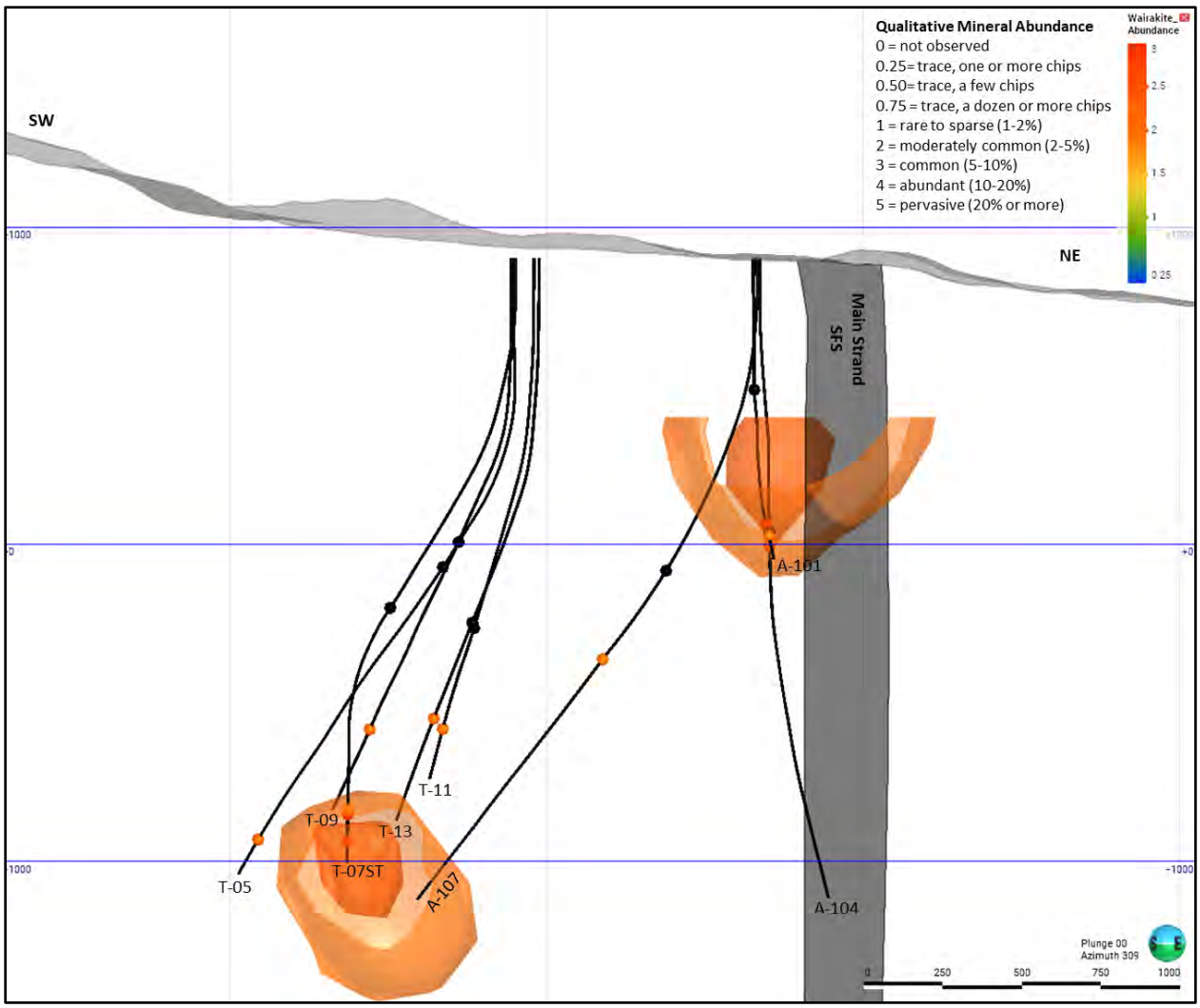

Figure 13. Section view showing wairakite qualitative abundance 2.0 and 2.5 spheres along well tracks and isosurfaces; black spheres are production casing shoes. These higher abundance zones are near deep upflow (e.g. near T-05, T-09) and the shallowest part of reservoir below Pad A (e.g. A-101, A-104).

5 CONCLUSIONS

There is a close correlation between the productive reservoir at Sorik Marapi and the presence of wairakite. Conversely, in wells outside of the productive reservoir, wairakite is generally not present. The top of the reservoir of the Sorik Marapi geothermal resource transects two major formations and includes metamorphic rocks in the deeper parts and volcanic rocks in the shallower parts. In the part of the cap that is made up of volcanic rocks, the alteration of the cap is argillic to mixed clay. In the part of the cap that is made up of metamorphic rock, the alteration in the cap is phyllic or phyllic-propylitic. In all areas across the field, independent of reservoir rock lithology or depth, the appearance of wairakite is most diagnostic of the top of the reservoir. This observation is based on vein paragenesis determined from thin section petrography illustrates where wairakite is observed, it is consistently the most recent vein filling mineral. This association with the top of

the reservoir and the recency of wairakite in vein paragenesis indicate it is the alteration mineral that is most closely linked with current reservoir conditions.

In general, wairakite is favored over epidote at lower pH and temperature. Over the past couple of decades, a pattern of later stage wairakite has continued to be recognized in several fields (e.g., Maura Laboh, Sumatra, Indonesia, Baroek et al., 2018; Rantau Dedap, Sumatra, Indonesia, Mussofan et al., 2021; outflow of Bacman, Philippines; Dimabayao and Rowe, 2020). Moore et al. (2004) made a case that late wairakite is typically related to mixing of steam condensate with reservoir fluid. At Sorik Marapi, the acidic or cooler conditions conducive to the formation of wairakite could be produced by alternating episodes of boiling and cooling, rupture, and down flux of condensed steam or steam mixed with peripheral waters. This work could benefit from selection of additional intervals of cuttings for thin section preparation and evaluation to farther refine the distribution of wairakite, and additional reservoir fluid sampling for geochemistry analysis to help determine the main mechanism responsible for forming wairakite at Sorik Marapi.

REFERENCES

Baroek, M., Stimac, J., Sihotang, A.M., Putra, A.P., Martikno, R. “Formation and fracture characterization of the Muara Laboh Geothermal System, Sumatera, Indonesia”. *Proceedings Geothermal Resource Council 42* (2018).

Browne, P.R.L. “Hydrothermal alteration in active geothermal fields”. *Annual Rev. Earth Planet. Sci.* 6, (1978), 229-248.

Browne, P.R.L. and Ellis, A.J. “The Ohaki-Broadlands hydrothermal area, New Zealand mineralogy and related chemistry”. *Am. J. Science* 269, (1970), p. 97-131.

Hinz, N., and 12 others. “Conceptual Model Update of the Sorik Marapi Geothermal Prospect, Sumatra, Indonesia”. *Proceedings Geothermal Resource Council 45* (2021).

Mas, G., Mas, L, Bengochea, L. “Zeolite zoning in drill holes of the Copahue geothermal field, Neuquen, Argentina”. *Proceedings World Geothermal Congress* (1995).

Moore, J., Bruton, C., Powell, T. “Wairakite: A Potential Indicator of Fluid Mixing”. *Proceedings Geothermal Resource Council* 28, (2004), 495-498.

Reyes, A.G. “Petrology of Philippine geothermal systems and the application of alteration mineralogy to their assessment”. *Journal of Volcanology and Geothermal Research,* 43, (1990), 279-309.

Reyes, A.G., Giggenbach, W.F., Saleras, J.R.M., Salonga, N.D., Vergara, M.C., 1993, Petrology and geochemistry of Alto Peak, a vapor-cored hydrothermal system, Leyte Province, Philippines: Geothermics, v. 22, p. 479-519.

Stimac, J. “Petrography as a Cost-Effective Approach to Understanding Geothermal System Evolution”. *Proceedings Geothermal Resource Council 47* (2023).

Thompson, A.J.B., Thompson, J.F.H. (Editors) “Atlas of Alteration – A Field and Petrographic Guide to Hydrothermal Alteration Minerals. *Geol. Soc. Canada MDRU,* (1996).

SKM, “Sorik Marapi Preliminary Resource Assessment Report”. Proprietary report, (2011), 369 p.

A Comprehensive Exploration and Modeling Approach for Heat and Geothermal Lithium Extraction in the Upper Rhine Graben

Jeanne Vidal[1], Ricardo Perez[1], Bastien Poux[2], Taha Sy[1], Mathieu Darnet[3], David Soubeyrand[1]

[1] Lithium de France, 16 rue des Couturières, 67240 Bischwiller, France

[2] Aetna Geothermal Ltd, Vancouver, Canada

[3] Bureau des Recherches Géologiques et Minières, Orléans, France

Keywords

Geothermal lithium, 3D seismic, CSEM, Leapfrog, OpenFlow, Upper Rhine Graben

ABSTRACT

Since August 2022, an exploration campaign has been conducted in Northern Alsace, France, to enhance the understanding of the area and build 3D models integrating geological, geophysical, and geochemical data. These 3D models aim to mitigate the risks associated with future lithium extraction by modeling the effects of extraction on the subsurface. This comprehensive integrative approach will help lithium resource assessments and targeting future projects.

1. Introduction

Launched in 2020, Lithium de France's project aims to produce hot, lithium-rich fluid naturally circulating within a fracture network in the Upper Rhine Graben (URG). The primary target in their exploration license, named Les Sources, is the natural circulations within the fractured and faulted reservoir at the sediments-basement interface. Understanding and predicting these brine circulations inside the fault network are crucial for the success of geothermal projects.

Several geophysical acquisitions were implemented in Les Sources to build a 3D representation of the hydrothermal system. By integrating these geophysical surveys, this approach will aid selecting targets for future projects. Aware of the unresolved issues in subsurface exploration and the concerns of local populations, these 3D models are used to mitigate risks, prepare drilling operations, predict reservoir behavior during exploitation, and assess the lithium resource.

The preliminary forecasts for sustainable exploitation will help to facilitate the development of future projects. These models are designed to evolve with future drilling operations, well-data acquisition, and hydraulic tests.

2. Geophysical exploration

2.1 3D seismic campaigns

Two seismic surveys were conducted in 2022 and 2023 in Les Sources (Figure 1). Special attention was given to imaging deep-seated basement features, such as the top of the basement and the intricate network of faults and fractures within. In an onshore context with irregular surveys due to dense urban environments and high level of anthropogenic noise, several approaches were implemented to enhance the clarity of the deep-seated basement features and improve the interpretation workflow:

- A dense, irregular source configuration, with mid-size vibrators operating in high productivity mode using the simultaneous random sweep (SRS) configuration.
- An extra set of vibration points, using a single fleet of sparser, low-frequency sweeps emitted by three vibrators (Strobbia et al., 2024).

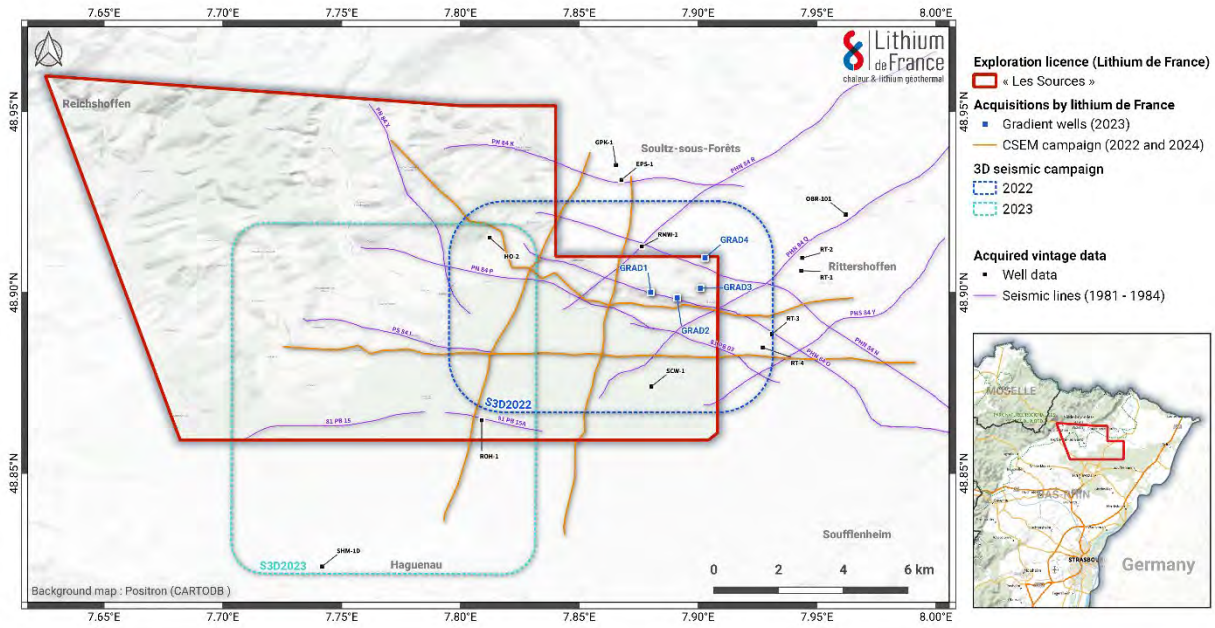

Figure 1: Exploration campaign; 3D seismic surveys, CSEM lines, and reprocessed 2D seismic lines conducted since 2022 in the Les Sources license area.

These two approaches enhance vertical resolution and signal penetration, benefiting the interpretation of geological structures (Figure 2a). Two main families of faults affecting the sediments-basement interface were observed:

- A major set striking in the Rhenish direction (N-S +/-20°) with large offsets, intersecting the entire sedimentary cover and rooting in the basement. These normal faults were well identified with 2D seismic lines, but their location and geometry were enhanced from the 3D survey.

- A minor set striking from the Rhenish to Hercynian (SE-NW to ESE-NWN) direction with moderate offsets, affecting the base of the sedimentary cover and rooting in the basement.

These faults were known at the well scale but poorly imaged on legacy 2D lines (Sausse et al., 2010).

Faults observed at the sediment-basement interface root several hundred meters into the basement. Improved fault connections through the 3D seismic survey reveal potential pathways for deep circulations and thus potential targets.

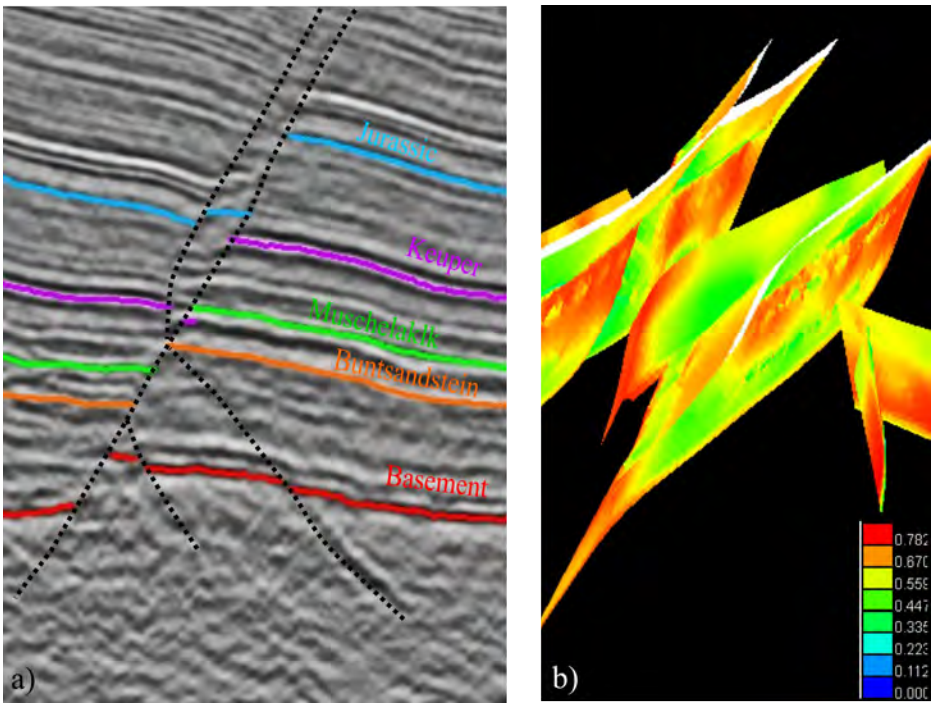

Figure 2: a) Interpreted crossline from the 3D seismic survey b) Slip tendency mapped along fault planes.

2.2 2D Controlled-source Electromagnetic surveying

Electromagnetic (EM) methods have proven effective for characterizing geothermal reservoir geometry in volcanic areas, hydrocarbon reservoir geometry in offshore sedimentary regions, and onshore mineral exploration (Constable, 2010; Coppo et al., 2016; Darnet et al., 2020; Hokstad and Kruber, 2023). Lithium de France, in collaboration with the French Geological Survey, developed this methodology to de-risk targets with high geothermal and lithium potential in deep fractured reservoirs, despite the high levels of anthropogenic noise (Darnet et al., 2023). Four Controlled-source Electromagnetic (CSEM) lines were acquired between 2022 and 2024 within the footprint of a 3D seismic acquisition (Figure 1).

The CSEM survey involved electric-field sensors distributed at nominal 500m intervals along 2D profiles. Along each profile, several grounded electric dipole transmitters, ranging from 1km to 3km in length, were deployed. To combat the anticipated high levels of EM noise, short boreholes (3 m deep) were drilled and equipped with metallic rods as injection electrodes. Additionally, multiple square wave signals with a wide range of fundamental frequencies (from 16 seconds to 512 Hz) were transmitted to maximize the signal-to-noise ratio at the receivers, regardless of the noise spectrum typology.

CSEM data were processed in the frequency domain using a robust processing approach (Smai and Wawrcyniak, 2020) and inverted using a 3D finite-difference scheme (CustEM, see Rochlitz et al., 2019). Frequencies with the best signal-to-noise ratios and the highest sensitivity to the target depth were selected, specifically 16s, 8s, 2s, 2Hz, 8Hz, 32Hz, and 128Hz.

The resulting resistivity model after inversion identified low resistivity anomalies following traces of faulted structures. These anomalies could be related to increased porosity within the fault zone and/or the presence of hotter and/or more saline hydrothermal fluids (Figure 3). These anomalies match with thermal anomalies known from past hydrocarbon exploration wells and provide new insights into permeable features of the reservoir that could not be detected based on seismic data alone.

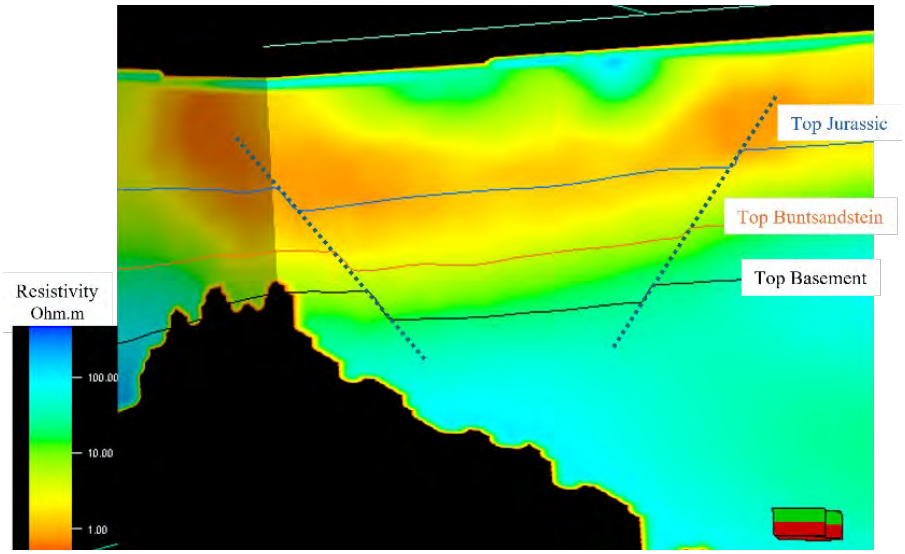

Figure 3: Random cross-sections from the 3D resistivity model derived from the inversion of CSEM data acquired in Les Sources license. Black dotted lines represent the faults identified on seismic data.

3. Geological 3D model

3.1 Building a static model

A 3D geological model was built using Leapfrog software (Seequent) to create a spatial representation of the project's geology based on results from the seismic survey interpretations. The stratigraphic contacts from the wells were used to calibrate the time-to-depth conversion of the seismic data and served as a control tool rather than an input for the geological model.

Five interpreted horizons were imported into Leapfrog as high-resolution point files, serving as the base for each of the five main lithological units and to model the faults present in the project area. Lithological surfaces were generated from these point files, with a threshold of 0.2 meters applied to remove points in zones of limited elevation change. This process allowed for the creation of simplified surfaces, reducing the processing time that would have been required if high-resolution point files were used. The newly created lithological surfaces were then utilized to create the fault surfaces by digitizing and connecting the visible fault offsets on each of the five surfaces (Figure 4a). This procedure was applied to both the main regional faults and other faults with limited vertical and lateral extents. It is important to note that the visible fault dip on each of the

lithological surfaces does not correspond to the actual fault dip; this is a normal artifact resulting from the seismic interpretation of fault zones rather than fault surfaces. This workflow is used to generate a fault surface passing through the center of the fault damage zone.

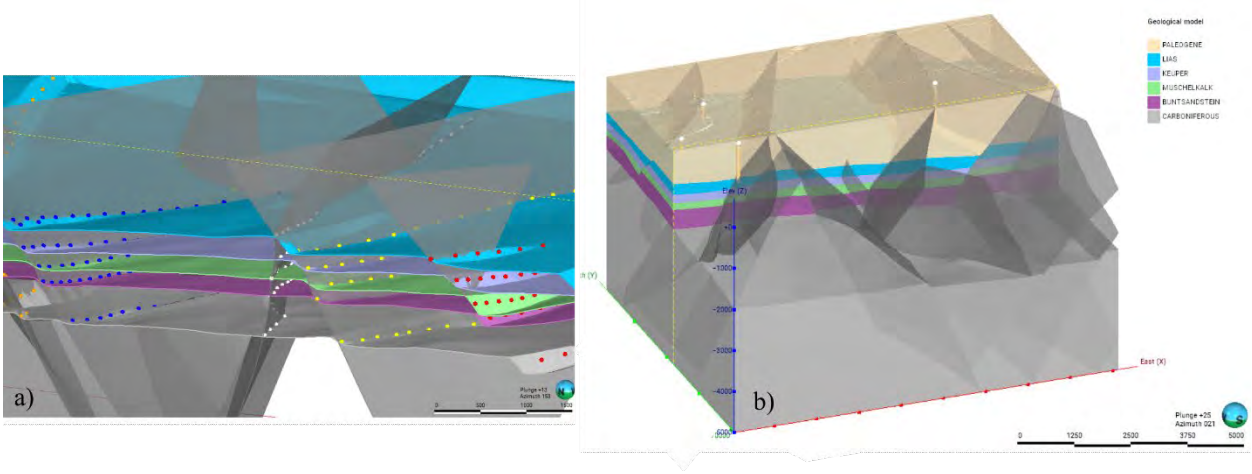

Figure 4: 3D geological model built with Leapfrog software (Seequent): a) fault construction b) lithological surfaces and fault planes used for geological modeling.

The triangulated points from the lithological surfaces were extracted and used in the Leapfrog geological modeling tool to build smooth surfaces between the main faults and generate the final geological model (Figure 4b). Using triangulated points rather than the lithological surfaces eliminates the fault offset artifact, as it creates separate contact surfaces in each block separated by the main faults. This 3D geological model is utilized for well planning and updating temperature modeling in the area.

3.2 Shallow temperature wells

In Les Sources license, the temperature model was poorly constrained by deep well measurements. In the northern area of the license, four shallow temperature wells were drilled down the first 200 m depth for geothermal gradient measurements (Figure 1). They are coherent to the highest geothermal gradient from hydrocarbon and geothermal wells existing in Northern Alsace. Based on the temperature profile of the deepest wells that reached the basement, the temperature of the deep reservoir was extrapolated, i.e. at 2 km depth in the license (Figure 5a).

With these additional data, the temperature model was updated using the Radial Basis Function (RBF) algorithm in Leapfrog (Figure 5b). This algorithm has the advantage of considering all available data in the model without limiting its interpolation between points based on a user-defined search radius, while giving more importance to the closest datapoints. The resulting model presents good coherence with known temperature anomalies from the literature and helps predict the upwelling of Li-rich hot fluids.

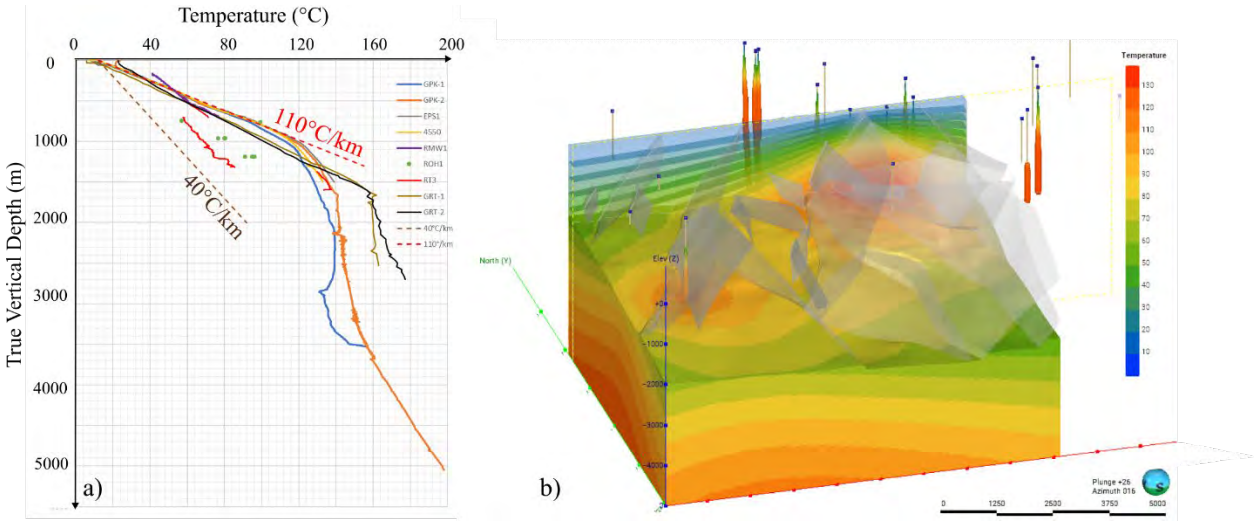

Figure 5: a) Temperature data from shallow temperature wells, legacy hydrocarbon, and geothermal wells in the area; dashed lines are geothermal gradient b) 3D temperature model from Leapfrog software (Seequent).

3.3 Mineralogical and geochemical observations

A comprehensive conceptual model was developed incorporating a large legacy database from hydrocarbon and geothermal observations. Mineralogical observations were conducted on deep existing wells that intersected the reservoir to identify alteration phases that could seal the fractures and faults but also delineate the thickness of damage zones and fault cores (Figure 6a & b) (Sy et al., 2023). A special focus was paid on clay minerals as they are known to affect the natural permeability of the reservoir but also as they are identified as Li-bearing source (Dugamin et al., 2024; Humphreys et al., 2023; Genter et al., 2024; Vidal et al., 2024). X-ray diffraction on clay fractions as well as Short Wave Infrared spectroscopy were conducted for a semi-quantitative approach in deep geothermal wells that reached Triassic and Permian sandstones and granitic basement. Inductively coupled plasma mass spectrometry (ICP-MS) measurements on deep cuttings samples provide Li distribution in the reservoir. Illite-rich facies are associated to low Li content (20-30 ppm) whereas zones dominated by ferromagnesians minerals reach 70 ppm. In parallel, geochemical data in fluids seems to be more homogeneous, between 166 and 210 ppm Li measured in deep wells from the Upper Rhine Graben (Figure 6c).

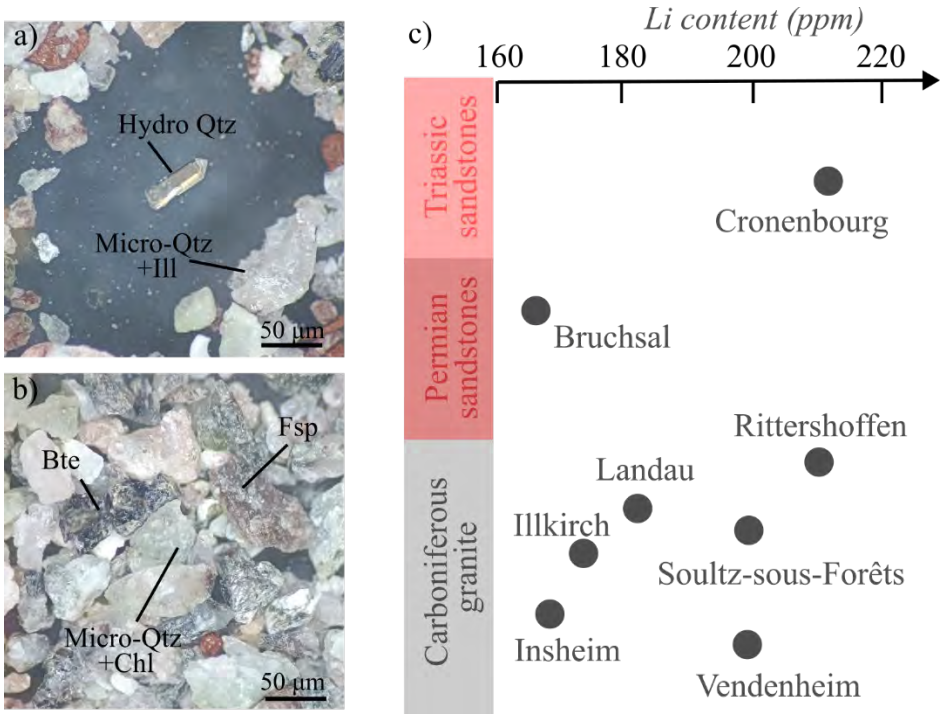

Figure 6: Mineralogical observation in granitic basement at (a) permeable level and (b) illitized zones. (c) Lithium content in ppm of deep geothermal fluids in the URG from Bosia et al. (2021), Pauwels et al. (1993) and Sanjuan et al. (2016). Qtz = quartz, Bte = biotite, Fsp = felspar, Chl = chlorite, Ill = illite.

4. Using modeling as prediction tool

4.1 Slip tendency

Following the Good Practice Guide for Induced Seismicity Mitigation co-published by the French Geological Survey in 2023, a slip-tendency study was conducted using 3DStress software (Southwest Research Institute). Utilizing a stress model based on Valley and Evans (2007), the slip tendency for fault structures in the 3D geological model was mapped (Figure 2b). Slip tendency of faults varies according to the dip and azimuth variations of fault planes, with higher values occurring in the strike of the horizontal stress. Information from the slip tendency map can be used with other geomechanical parameters to plan for the mitigation of seismicity.

It is important to note that slip tendency alone is not a criterion for seismicity, as many other geomechanical parameters can influence seismicity, such as fault friction and cohesion. Additional thermo-hydro-mechanical (THM) modeling is being conducted to further characterize potential induced seismicity (Wynants-Morel et al., 2024).

4.2 Thermo-Hydraulic modeling

A 3D TH model was developed using the OpenFlow suite (Beicip-Franlab) to evaluate exploitation scenarios. The natural state was calibrated based on historical data, including pseudo-hydrostatic profile, temperature gradients or petrophysical models, the traditional dual-porosity *Warren & Roots* approach, and previously presented acquisitions. The fracture model incorporated the two fault families discussed on section 2.1 3D seismic campaigns, featuring a damage zone of variable

thickness, as well as the hydrothermal alterations zones, discussed on the section 3.3 Mineralogical and geochemical observations (Figure 7).

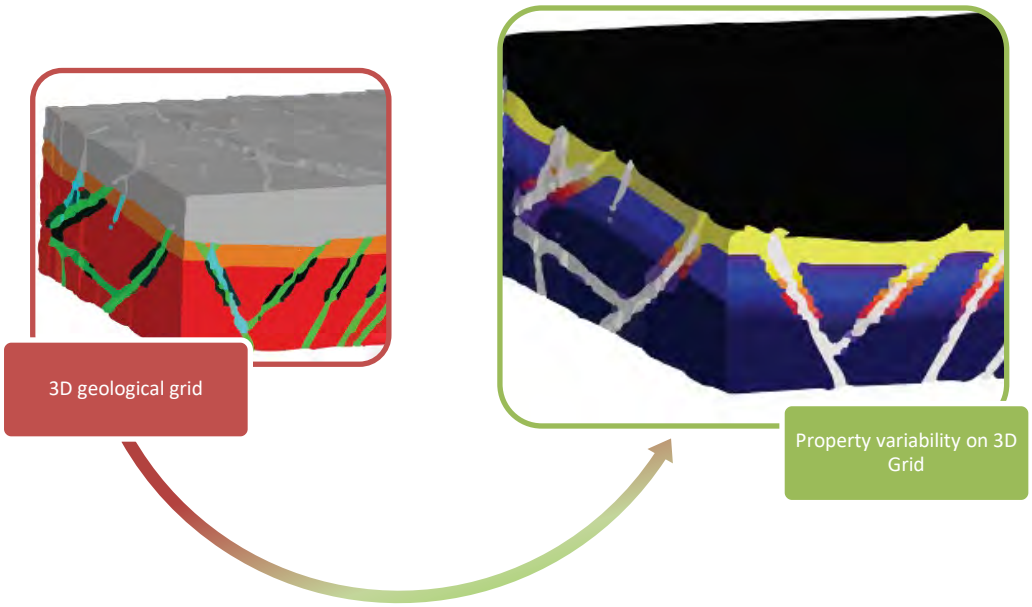

Figure 7: Schematic 3D Les Sources TH model.

Lithium was modelled as an inert tracer and its concentration and mass variability was investigated through time. Several scenarios were run to evaluate the impact of well locations, targeted structures, or the contribution of the damage zones, among others.

4.3 Lithium resource assessment

The sites proposed for the resource assessment were GRC, PUN, KON and KIL (Figure 8a):

- The GRC site had 2 J-wells spaced by 1km (GRC1-prod and GRC2-inj) and targeted a main fault affecting the porous and permeable sandstones with a variable production flowrate in order to consider the impact of flowrate on recovery.
- The PUN site had 2 vertical wells spaced 2.7km apart (GTPunA-prod and GTPunB-inj), targeting a minor fault zone in the sandstones layer for GTPunA and the damage zone of a major fault zone in the altered granitic basement for GTPunB.
- The KON site had two vertical wells GTKonA and GTKonB with 1km in between (GTKonA-prod and GTKonB-inj) targeting a major fault zone at the sandstones-granite interface for GTKonA and a damage zone of a major fault zone affecting the granite fo GTKonB.
- The KIL site had 2 vertical wells GTKilA and GTKilB, distanced apart by 2.7km (GTKilA-prod and GTKilB-inj) and targeting a minor fault zone affecting the sandstones for GTKilA and a major one affecting the sandstones fot GTKilB. Both faults targeted did not present associated damage zone.

All the scenarios were run with a mean flowrate of 3600 m3/d (42 L/s) except for one case of GRC. A conservative concentration of 180 mg/L was also used for the initialization of the lithium distribution on the 3D model (Figure 8).

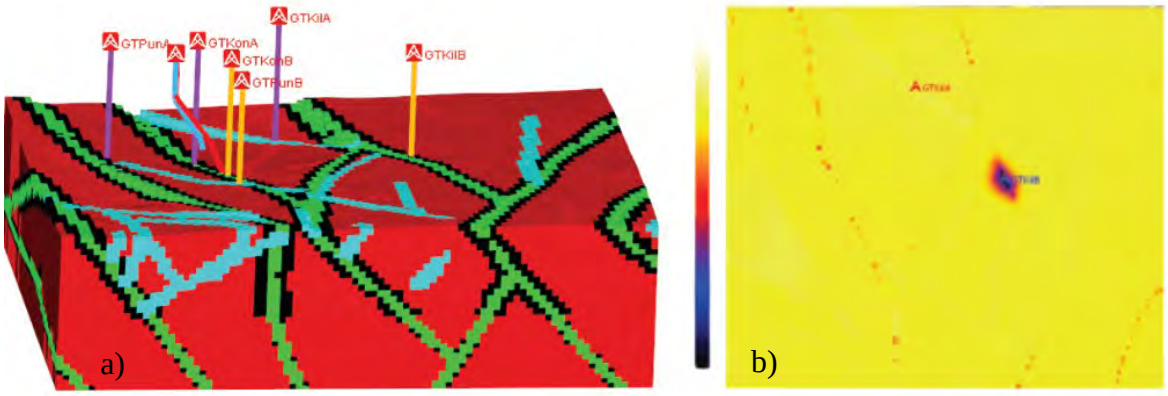

Figure 8: (a) Sites configuration for the lithium assessment. (b) Lithium depletion on the KIL site.

Between PUN, KON and KIL sites; the exploitation for KON showed the only receding trend for Li2CO3 or Lithium Carbonate Equivalent (LCE) over time with an annual mean decrease of 0.56% (Lithium concentration went from ~180 mg/L to ~155 mg/L over 25 years), see Figure 9. KIL and PUN sites had little changes on LCE with 0.03% mean annual decrease for both. The total LCE production was ~6000, ~6200 and ~6300ton for KON, KIL and PUN sites.

For the resource assessment on the GRC site, as mentioned, was decided to test a 3600 and a 3000 m3/D flowrate (42 and 35 L/s respectively). The reason behind this was to evaluate lithium recovery at different flowrates. The changes on lithium content were too small, having an annual mean decrease of 0.02% for the higher flowrate, and an annual mean increase of 0.01% for the latter. The total LCE produced for GRC1 was ~6200 and ~5200 ton over 25 years respectively.

When GTKilA and GTKonA are compared, differences between both fault families discussed on section 2.1 3D seismic campaigns are observed. The KON site intersecting a major fault produced about 3% less lithium than KIL site intersecting a minor one. Comparing GTKilA and GTPunA, reveals the production of GTPunA is more advantageous with 1% more of LCE produced over 25 years, than the GTKilA because the latter does not intersect the damage zone of the fault whereas GTPunA targets a large porous and permeable damage zone. This suggests that as long as the well is connected to the natural fractured reservoir, neither the fault family nor the damage zone thickness would have a significant impact on the lithium exploitation.

The availability of the lithium resource on the reservoir is quite important. At the exploitation of the KIL site (Figure 8b), no lithium depletion is taking place around the production well (GTKilA). The concentration is decreasing with the injection of depleted water on the reservoir, around the injection point (GTKilB).

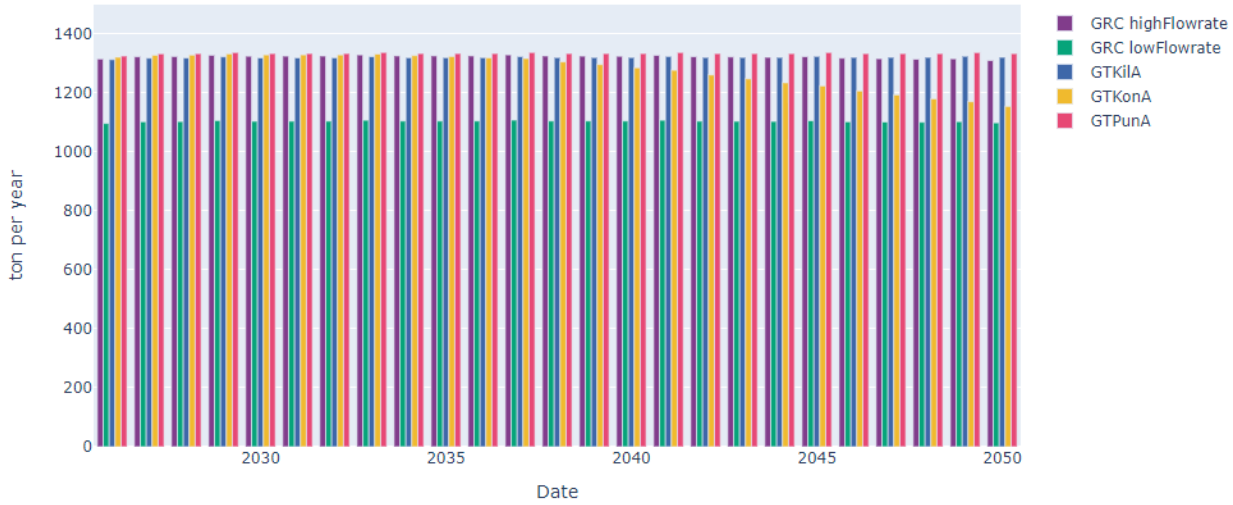

Figure 9: LCE production for the hypothetical exploitation of GRC, KIL, KON and PUN sites.

5. Concluding remarks and perspectives

The integrative approach for exploration campaign allows to identify the hydrothermal system architecture with cap rocks, reservoir rocks and source rocks as well as importance of fracture and faults contribution for circulations of hot Li-rich brine. It also underlines the importance of fault network with all striking, not only the major Renish one but also the deeper Hercynian one that enhance deep circulations for brine. Within our models, lithium concentration in the fluid is homogeneous on the reservoir, regardless of the lithology or the fault occurrences or the rock alteration degree. However, the distribution of the resource is uneven and heterogeneous because this is a function of the petrophysical parameters of the model. When the model is run in the exploitation, the lithium depletion is related directly to the injection of depleted water, pushing Li-rich brine on the fractured network towards the production well. This needs to be studied further, but it could mean that several different scenarios like the screening observed on the Enhanced Recovery Techniques for the O&G industry is necessary for lithium extraction.

REFERENCES

Bosia, C., Mouchot, J., Ravier, G., Seibt, A., Jähnichen, S., Degering, D., Scheiber, J., Dalmais, E., Baujard, C., Genter, A., 2021. Evolution of Brine Geochemical Composition during Operation of EGS Geothermal Plants (Alsace, France), Proceedings of 46th Workshop on Geothermal Reservoir Engineering. Stanford University, California, USA.

Constable, S., 2010. Ten years of marine CSEM for hydrocarbon exploration. GEOPHYSICS 75, 75A67-75A81. https://doi.org/10.1190/1.3483451

Coppo, N., Darnet, M., Harcouet-Menou, V., Wawrzyniak, P., Manzella, A., Bretaudeau, F., Romano, G., Lagrou, D., Girard, J.-F., 2016. Characterization of Deep Geothermal Energy Resources in Low enthalpy sedimentary basins in Belgium using Electro-Magnetic Methods – CSEM and MT results, in: European Geothermal Congress 2016. Strasbourg, France.

Darnet, M., Wawrzyniak, P., Coppo, N., Nielsson, S., Schill, E., Fridleifsson, G.Ó., 2020. Monitoring geothermal reservoir developments with the Controlled-Source Electro-Magnetic

method — A calibration study on the Reykjanes geothermal field. Journal of Volcanology and Geothermal Research 391, 106437. https://doi.org/10.1016/j.jvolgeores.2018.08.015

Darnet, M., Soubeyrand, D., Roche, P., Vidal, J., Bretaudeau, F., Beauois, F., François, B., 2023. Characterizing Geothermal and Lithium Resources in the Upper Rhine Graben (France) with Active Electromagnetic Methods. The Fourth EAGE Global Energy Transition Conference and Exhibition, European Association of Geoscientists & Engineers, Issy-les-Moulineaux, France, pp. 1–4. https://doi.org/10.3997/2214-4609.202321019

Dugamin, E.J.M., Boiron, M.-C., Cathelineau, M., Richard, A., Peiffert, C., Lebreton, A., Banks, D.A., Despinois, F., 2024. Brine-granite interaction and lithium leaching in a continental rift (Soultz-sous-Forêts, Rhine Graben, France). Lithos 478–479, 107604. https://doi.org/10.1016/j.lithos.2024.107604

Genter A., Baujard C., Dalmais E., Glaas C., Maurer V., Ravier G., 2024. EGS development in Europe based operational geothermal projects, Chapter 2, EGS: the future energy-road ahead, Editors D. Chandrasekharam and A. Baba, Taylor and Francis, CRC Press, UK.Constable, S., 2010. Ten years of marine CSEM for hydrocarbon exploration. GEOPHYSICS 75, 75A67-75A81. https://doi.org/10.1190/1.3483451

Coppo, N., Darnet, M., Harcouet-Menou, V., Wawrzyniak, P., Manzella, A., Bretaudeau, F., Romano, G., Lagrou, D., Girard, J.-F., 2016. Characterization of Deep Geothermal Energy Resources in Low enthalpy sedimentary basins in Belgium using Electro-Magnetic Methods – CSEM and MT results, in: European Geothermal Congress 2016. Strasbourg, France.

Darnet, M., Wawrzyniak, P., Coppo, N., Nielsson, S., Schill, E., Fridleifsson, G.Ó., 2020. Monitoring geothermal reservoir developments with the Controlled-Source Electro-Magnetic method — A calibration study on the Reykjanes geothermal field. Journal of Volcanology and Geothermal Research 391, 106437. https://doi.org/10.1016/j.jvolgeores.2018.08.015

Hokstad, K., Kruber, C., 2023. Multigeophysical Inversion for Geothermal Exploration, in: GRC Transactions. Presented at the Geothermal Rising Conference.

Humphreys, J., Brounce, M., McKibben, M.A., Dobson, P., Planavsky, N., Hoover, H.R., Wenzel, B., 2023. Distribution, isotopic composition, and origin of Li in the Salton Sea Geothermal Field. Proceedings of 48th Workshop on Geothermal Reservoir Engineering Stanford University, California, USA

Pauwels, H., Fouillac, C., Fouillac, A.-M., 1993. Chemistry and isotopes of deep geothermal saline fluids in the Upper Rhine Graben: Origin of compounds and water-rock interactions. Geochimica et Cosmochimica Acta 57, 2737–2749. https://doi.org/10.1016/0016-7037(93)90387-C

Rochlitz, R., Skibbe, N., & Günther, T., 2019. custEM: Customizable finite-element simulation of complex controlled-source electromagnetic data. Geophysics, 84(2), F17-F33.

Sanjuan, B., Millot, R., Innocent, Ch., Dezayes, Ch., Scheiber, J., Brach, M., 2016. Major geochemical characteristics of geothermal brines from the Upper Rhine Graben granitic basement with constraints on temperature and circulation. Chemical Geology 428, 27–47. https://doi.org/10.1016/j.chemgeo.2016.02.021

Sausse, J., Dezayes, C., Dorbath, L., Genter, A., Place, J., 2010. 3D model of fracture zones at Soultz-sous-Forets based on geological data, image logs, induced microseismicity and vertical seismic profiles. Comptes Rendus Geoscience 342, 531–545. https://doi.org/10.1016/j.crte.2010.01.011

Smaï, F., & Wawrzyniak, P., 2020. Razorback, an open source Python library for robust processing of magnetotelluric data. Frontiers in Earth Science, 8, 296.

Strobbia, C., Chapart, A., Sweeney, D., Roche, P., Soubeyrand, D., Vidal, J., Foss, S., Bakke, R., Bianchi, T., 2024. Onshore Broadband Seismic Exploration for Geothermal Targets Using a Multiscale Shooting Grid. Presented at the 85th EAGE Annual Conference & Exhibition (including the Workshop Programme), European Association of Geoscientists & Engineers, https://doi.org/10.3997/2214-4609.2024101276

Sy, T., Vidal, J., Wynants-Morel, N., Roche, P.-H., Perez, R., Soubeyrand, D., 2023. Developing conceptual model for geothermal reservoir exploration in Northern Alsace (France), in: Proceedings of European Geothermal Workshops. Utrecht, The Netherlands.

Valley, B.C., Evans, K.F., 2007. Stress state at Soultz-sous-Forêts to 5 km depth from wellbore failure and hydraulic observations, Proceedings of 32nd Workshop on Geothermal Reservoir Engineering. Stanford University, California, USA.

Vidal, J., Lerouge, C., Sanjuan, B., Lach, Ph., Aupart, C., Traoré N.E., 2024. How important is the hydrothermal alteration in the Upper Rhine Graben for geothermal lithium assessment? Proceedings of 48th GRC Transactions, Hawaï, USA.

Wynants-Morel, N., Vidal, J., Soubeyrand, D., 2024. Including Permeability Anisotropy in Fault Zones Models Helps Coping with Both Geothermal Reservoir Storage Estimation and Induced Seismicity, Proceedings of 49th Workshop on Geothermal Reservoir Engineering. Stanford University, California, USA.

Towards a Conceptual Model of Deep Circulations in Cerro Pabellón Geothermal System (Andean Cordillera, Northern Chile)

Vidal J.[1*], Patrier P.[2], Beaufort D.[2], Maza S.[1], Galarce F.[1], Daniele L.[1], Rivera G.[3], Volpi G.[3] and Morata D.[1]

[1] Department of Geology and Andean Geothermal Center of Excellence (CEGA). Facultad de Ciencias Físicas y Matemáticas, University of Chile, Plaza Ercilla 803, Santiago, Chile

***now at : Lithium de France, 16 rue des Couturières, 67240 Bischwiller, France**

[2] University of Poitiers, CNRS UMR7285, IC2MP, HydrASA, Bat B8, Rue Albert Turpain, TSA51106, F-86073 Poitiers Cedex 9, France

[3] ENEL Green Power Chile, Av. Santa Rosa 76, Santiago, Chile

Keywords

geothermal energy, high-enthalpy system, clay minerals, hydrothermal circulations, Cerro Pabellón, Chile, Andean Cordillera

ABSTRACT

Located at 4500m a.s.l in Andean cordillera (Northern Chile), Cerro Pabellón (CP) geothermal powerplant is the first commercial power plant in South America that exploits the Na-K-Cl fluid circulating in the fractured volcanic formations. This study focuses on hydrothermal alteration of the geothermal reservoir based on four production wells drilled on both sides of a graben structure and presenting unlike hydraulic properties. Cuttings were sampled and analyzed using X-ray diffraction (XRD) to observe the mineral distribution and variations of crystal-chemistry of clays (fraction <5 μm). Then, scanning electron microscopy coupled with energy dispersive spectroscopy (SEM-EDX) were used to perform chemical microanalysis of hydrothermal minerals. These results suggest a high heterogeneity of the reservoir in term of alteration: a pervasive alteration dominated by trioctahedral clays (saponite to chlorite sequence through corrensite and C-Crr mixed layers) was observed in all samples whereas a multi-event fracture-controlled alteration was only observed locally. A first event was observed at shallow depth in the active part of the reservoir composed of adularia + Ba-rich feldspar + feathery quartz + chalcedony + calcium arsenates + illite suggesting boiling processes. Another event dominated by dioctahedral clays (illite-smectite mixed layers with more than 90% of illite and illite) occurs in all permeable fracture zones intersected by wells. This multi-event alteration seems strongly controlled by the eastern graben fault and the wide fracture network connected to this structure.

1. Introduction

The geothermal system of Cerro Pabellón (CP) is located ~100 km northeast of Calama city (Antofagasta region, Northern Chile), near the Chile-Bolivia border, inside the Pabelloncito graben. Located at 4500 m a.s.l, this extensional structure affected by highly dipping and NW-striking faults hosts deep Na-K-Cl fluid circulations (>250°C). Since 2017, Geotérmica del Norte (GDN), a joint venture between Enel Green Power Chile and ENAP (Chilean National Oil Company), has exploited 13 wells for a power capacity of 83 MWe (Cappetti et al., 2021). These deep wells are unique witnesses of the reservoir, that remains hardly accessible in Andean geothermal system and could help to understand factors controlling deep hydrothermal circulations (Vásquez et al., 2014; Vidal et al., 2021). A total of 142 samples were examined in four deep wells: CP5A- (300-1000 m) and CP6A (400-1400 m), both located in the central part of the graben in the most active zone of the reservoir, CP2A (850-1550 m), located inside the graben but outside the core of the reservoir in term of productivity and CP4A (1500-2700 m), located in outside the graben. This study focuses on hydrothermal alteration of the reservoir and more specifically on clay minerals because they are very sensitive to temperature, rock and fluid chemistry, timing, fluid/rock (F/R) ratio, between other variables (Flexser, 1991; Inoue and Kitagawa, 1994; Patrier et al., 1996; Vásquez et al., 2016; Vidal et al., 2018). Thus, they are considered as good markers of past and present hydrothermal circulations. Spatial distribution and crystal-chemistry of clay minerals were investigated thanks to petrographic observations, X-Ray diffraction (XRD) conducted on the clay fraction (< 5 μm). Chemical microanalyses were performed with Scanning Electron Microscope coupled to Energy Dispersive Spectroscopy (SEM-EDX). Nature and the amount of hydrothermal parageneses associated to deep rocks would help to understand geodynamics of the deep system. Such a contribution may be of interest for other Andean geothermal systems with more limited geological information and may help in the further development of geothermal projects in the Chilean Andes and neighboring countries.

2. Area of study

The CP geothermal system belongs to the graben structure called the Pabelloncito graben (Figure 1). This depression of 20 km long and 3 km wide is framed between two main normal faults, N53°W to N60°W direction, and a secondary fault system in between with the same orientation affects the geological units (Rivera et al., 2021; Urzúa et al., 2002). The eastern border fault is divided in three strands North of the Pabellón dome. Exploration and deep wells drilled at CP confirmed deep circulations of geothermal fluid channelized into permeable fault and fracture zones (FZs) and sealed by a 300-m thick clay cap (Baccarin et al., 2021; Maza et al., 2018; Rivera et al., 2021; Vidal et al., 2022).

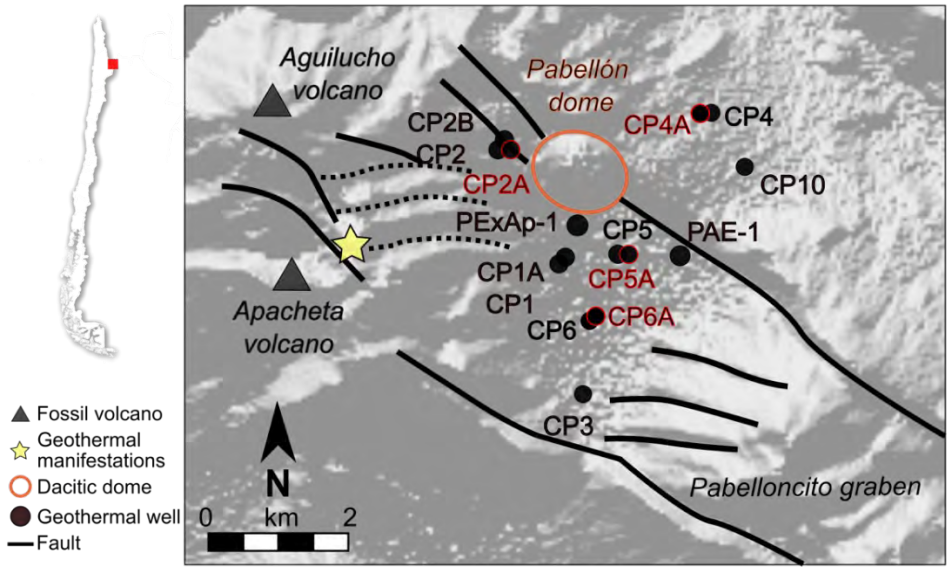

Figure 1: Map of Cerro Pabellón (CP) geothermal system with main normal faults of Pabelloncito graben and morphological lineaments in dashed lines. The studied production wells are represented in red.

The 3D thermal model of the CP reservoir shows a dome shape of the isotherms (Baccarin et al. 2021). The apex of the thermal dome marks the center of the upflow zone of the geothermal fluid in the eastern edge of Pabelloncito graben. This study is based on four wells intersecting andesitic lavas as well as lithic and dacitic tuffs.

- CP2A well is located in the northern margin of the thermal dome, with a temperature decreasing gradually. The well was drilled vertically above the median strand of the eastern fault. The temperature acquired ten months after drilling operations reached 245°C at 1800 m depth (Figure 2a). The main inflow of the well is observed at 1530 m depth, considered as the intersection of the northern strand of the fault, with an injectivity index of 10 m^3/h/bar (Rivera et al., 2018). However, partial mud losses were observed at 925 m depth in the andesitic lavas at the top of the convection. Production test of the well revealed a total fluid flow rate of 190 t/h with a wellhead pression of 8 bar and a title of vapor of 7% (Rivera et al., 2018).
- CP4A well is located outside the graben structure. The well was drilled down to 2700m MD and even if it is located in the peripheral limit of system, a good hydraulic connection to the main reservoir was discovered (Baccarin et al., 2021). The temperature acquired several months after drilling to reach 235°C at the bottom of the well (Figure 2b). A negative T anomaly from 2525 to 2650 depth matches a main permeable FZ which probably controls the hydraulic behavior of the well. The well presents a high injectivity with an absorption of 310 m^3/h without wellhead pressure (Rivera et al., 2018).
- CP5A well is located in the apex of the thermal dome. The well was drilled vertically until 1936 m depth above the eastern border fault of the graben. The temperature was acquired, one year after drilling operations, until 600 m where it reaches 220°C (Figure 2c). A permeable FZ was identified at 447 m depth, in andesitic lavas, with total mud losses during drilling and a negative temperature (T) anomaly in the T profile. However, the injectivity index of this FZ is low (Rivera et al., 2018). Partial mud losses were also observed at 525 m depth even thought the structural model of Baccarin et al (2021) does

not identify permeable FZ at this depth. A permeable FZ at 700 m depth is identified as the main structure responsible of the major injectivity (circa 7 m^3/h/bar) (Rivera et al., 2018). Total mud losses occurred at 1000 m depth making collection of cuttings impossible below this depth. The graben border fault was intersected at this depth according to the structural model of Rivera et al. (2021). Production test of the well revealed a total fluid flow rate of 305 t/h with a title of vapor of 18% (Rivera et al., 2018).

- CP6A well is also located in the *hot core* of the thermal dome. The well was drilled down to 2300m MD. The deep temperature reached 230°C few months after drilling operations (Figure 2d). A double T anomaly, positive one from 1210 to 1290m MD matches a first permeable FZ at 1240m MD and a negative one from 1290 to 1360m MD matches a second permeable FZ at 1320m MD from the structural 3D model. The structural model indicates at least 3 others deep FZs intersected by the well. The deepest one is interpreted as a local fault intersected at 2200m MD. CP6A well presents the highest injectivity index of the geothermal system with 20 m^3/h/bar (Rivera et al., 2018).

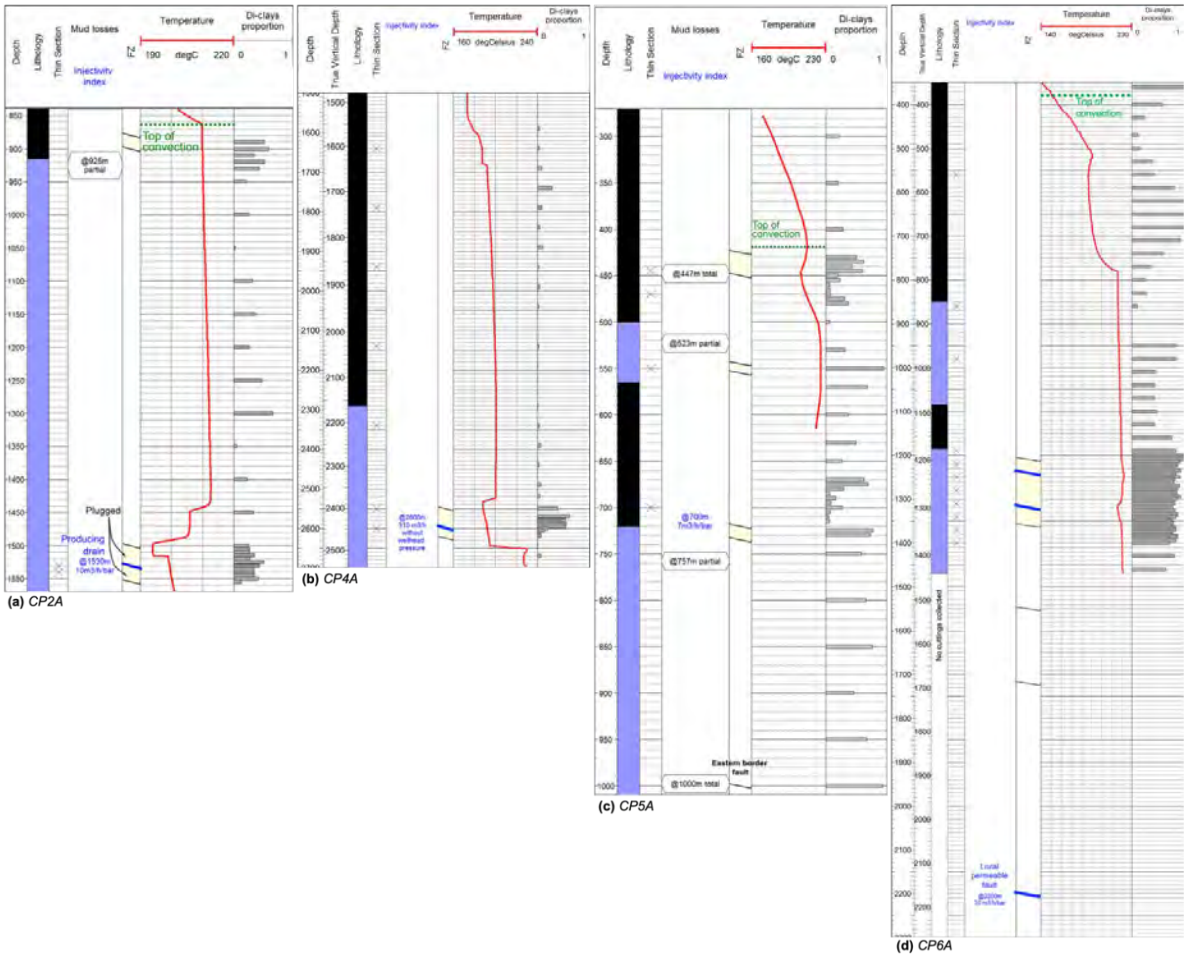

Figure 2: Lithology, mud losses, measured injectivity index, permeable fracture and fault zones (FZ), temperature profile and proportion of dioctahedral clays in a) CP2A well, b) CP4A well, c) CP5A well and d) CP6A well. The thickness and depth of the FZs are deduced from clay signature and thus, are constrained by the sampling.

In this study, special attention was paid to clay signature in order to evaluate factors controlling fluid flow and how tectonic control of the northern border fault influences the reservoir productivity.

3. Methodology

Petrographic investigations were carried out in thin sections of cuttings fixed in epoxy. As cutting samples present an average size between 0.5 and 2mm, spatial resolution is low and textural relations between minerals are hardly observed.

Identification of clays was conducted by XRD on the less than 5 µm fraction of 28 cutting samples in CP2A, 35 in CP4A 39 in CP5A and 72 in CP6A. Cutting samples were immersed in distilled water in absence of preliminary grinding, and then disaggregated by ultrasonic treatment to properly dispersed the clay particles in suspension. Oriented powders were prepared from sedimentation of the <5 µm grain size clay separate of the suspension on glass slides. Clay minerals were identified by X-Ray Diffraction (XRD) of air-dried and ethylene– glycol (EG)-saturated oriented powders carried out on a Bruker D8 Advance diffractometer (CuKα radiation, 40 kV, 40 mA). The analytical conditions were as follows: angular domain: 2.5–30° 2θ; step increment: 0.025 2θ; and counting time per step: 3s. Processing of the diffractometers was conducted using Match! Software (Crystal Impact). The clay minerals were identified according to Brindley and Brown (1980). All deconvolution processed are described in Vidal et al (2022). The proportion of dioctahedral clays was estimated from the peak areas according to the ratio: *(I-S area + Ill area Ill) / (I-S area + Ill area + Chl area + C-Crr area + Crr area).*

Chemical microanalyses of primary and secondary minerals were acquired on thin sections of CP5A and CP2A wells using a SEM JEOL JSM-IT500 SEM equipped with a BRUKER linxeye EDX associated with SPIRIT software at the IC2MP laboratory at the University of Poitiers. The analytical conditions were as follows: 15 kV; 1 nA; counting time: 50 s; and working distance: 11 mm. The analyzed elements were Si, Al, Fe, Mg, Mn, Ti, Ca, Na and K. The system was calibrated with a variety of synthetic oxide and natural silicate standards. The reproducibility of the standard analyses is approximately 1%, except for Na, which had a reproducibility of 1.5%.

Fluid-clay minerals equilibrium was simulated with PHREEQC software (USGS) based on the chemistry of geothermal fluid, gases and minerals. The software was used to calculate clay mineral saturation indices relative to chemical composition of geothermal fluid described by Giudetti and Tempesti (2021) and a recalculated pH of 5.7. Because water analyses lacking Al and Fe, concentrations of these both elements were estimated in order to force the water to be at equilibrium with Al-bearing mineral as suggested by Pang and Reed (1998).

4. Results

4.1 Alteration petrography

All samples collected in the four wells show evidence of hydrothermal alteration involving at least two alteration type: a pervasive one and a fracture-controlled one.

A pervasive alteration is observed in all samples with a moderate to intense stage. This alteration pattern is particularly well expressed away from permeable FZs. Pervasive alteration is characterized by the replacement of most of the original rock-forming mafic minerals (pyroxenes,

volcanic glass, biotite) and, at a lesser degree, of igneous feldspars by a great variety of trioctahedral clay species ranging from smectite to chlorite through corrensite and chlorite-corrensite mixed layers (Figure 3a & 2b). The fact that chloritic minerals may replace smectite in the altered pyroxenes or in the groundmass, suggests that the trioctahedral clay minerals may have occurred sequentially during the progress of the pervasive alteration (Figure 3i). Trioctahedral minerals are observed mostly in association with titanite, needle-shaped hematite and epidote (Figure 3b). In CP5A well, they are observed associated to numerous inclusions of arsenic minerals, calcite and quartz (Figure 3i). In CP4A and CP6A wells, Fe,K-rich minerals green clay minerals from the celadonite-glauconite group are observed in a lesser degree (Figure 3c).

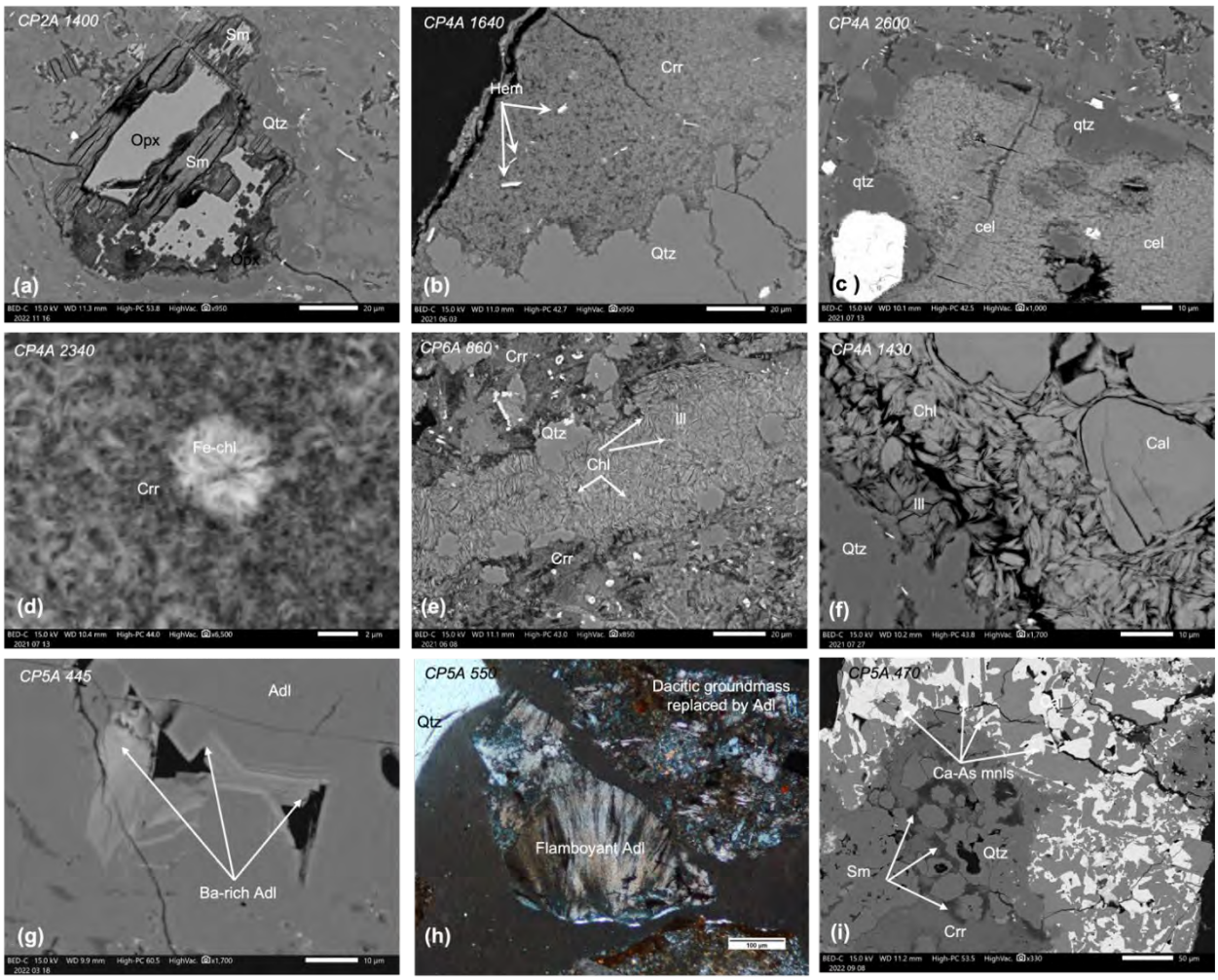

Figure 3: Mineral associations representative of pervasive alteration (a – c) and fracture-controlled alteration dominated by illitization processes (d – f) and boiling processes (g – i). Observations conducted by SEM in thin sections of cuttings fixed in expoxy in CP2A, CP4A, CP5A and CP6A wells. Adl = adularia, Cal = calcite, Chl = chlorite, Crr = corrensite + C-Crr mixed layers, Hem = hematite, Ill = illite, Opx = orthopyroxens, Qtz = quartz, Sm = smectite.

Close to permeable FZs, there has been highly destructive alteration characterized by destruction of the original texture of volcanic rocks, igneous minerals (excepting quartz in dacitic rocks) and minerals from pervasive alteration, as well as development of a vein network and cementation of open spaces (cracks and dissolution voids) (Figure 3d to 2i). This fracture-controlled alteration is characterized by illitic minerals that seem to precipitate together with chlorite +/- carbonates,

mainly calcite but also sometimes dolomite (Figure 3e & 2f). Co-precipitation of illite and chlorite suggests the occurrence of at least one other generation of chlorite than the one observed previously in association with epidote and titanite (Figure 3d). In shallow FZs of CP5A, an earlier fracture-controlled event is observed with a massive precipitation of adularia as microcrystalline aggregates in groundmass, and direct deposition from solutions into open spaces where it forms rhombic crystals (Figure 3g & 2h). Chemical zoning observed in rhombic crystals of adularia at the wall of open spaces is indicative of periodic increase in Ba for K substitution in the crystal lattice during their crystal growth (Figure 3g). Quartz and calcite are frequently associated with adularia. Specific texture of hydrothermal minerals in veins, such as flamboyant and feathery quartz, crustiform-collomorph bands including quartz or chalcedony and adularia and blade shape calcite are typical of precipitation from boiling fluids (Figure 3h).

4.2 Occurrences of clay minerals

From the XRD mineral identification, trioctahedral clays (i.e. smectite, corrensite, mixed chlorite-corrensite layers and chlorite) are present throughout in wells but appear strongly obliterate by dioctahedral clays in main permeable FZs (Figure 4). At the most one can note a rough trend to decreasing content of the highly expandable minerals (smectite, corrensite) in the total amount of trioctahedral clays with increasing depth. The proportion of dioctahedral clays in the bulk clay material is particularly high (higher than 50%) in the permeable FZ as well as in lithic tuffs. Dioctahedral clays consist uniquely in K-bearing minerals (i.e. I-S and discrete illite) (Figure 4). The I-S R1 (with smectite between 60% and 80%) are particularly abundant above the top of the fluid convective zone where temperature is lower than 200°C (Figure 4b). I-S R3 (with ill>90%) and illite are closely associated in depths where a very weak thermal gradient is observed traducing convective heat transfer. Locally, the percentage of illite in the I-S R3 increases slowly in the vicinity of both FZs with a maximum of illitic component at the depth of main permeable drains of FZs (Figure 4).

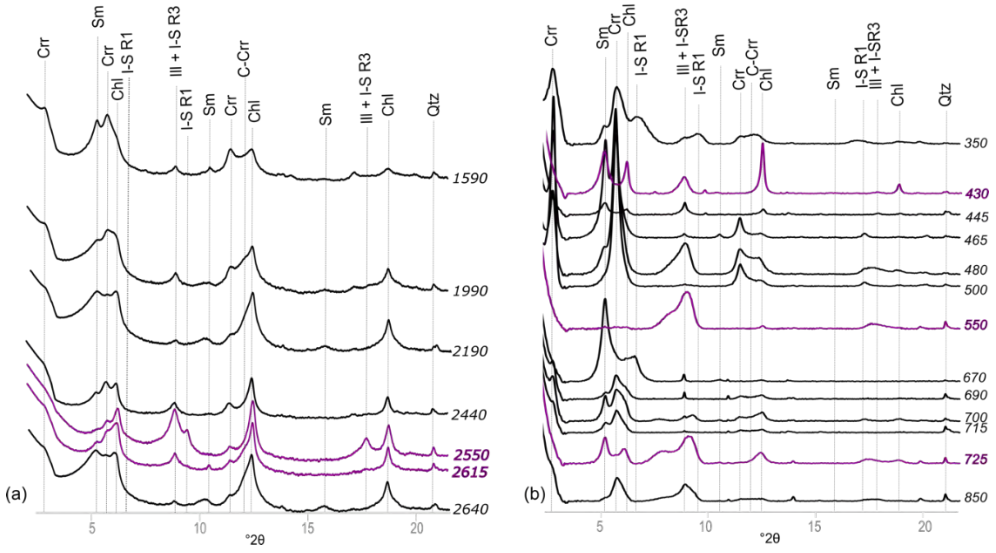

Figure 4: X-Ray diffractograms of EG-saturated oriented powder (<5 µm clay fraction) a) 1590, 1990, 2190, 2440, 2550, 2615 and 2640 in CP4A well b) samples 350, 430, 445, 465, 480, 500, 550, 600, 670, 690, 700, 715, 725 and 850 in CP5A well. Samples from permeable FZs are indicated in purple. Chl: chlorite, C-Crr: chlorite-corrensite mixed layers, Crr: corrensite, Ill: illite, I-S: illite-smectite mixed layers, Sm: smectite, Qtz: quartz.

4.3 Chemical compositions of clay minerals

Chemical analyses of trioctahedral clays reveal a wide compositional field that spread over clay species from saponite to chlorite through corrensite and C-Crr (Figure 5). From a crystallochemical point of view, all smectite are saponite presenting XFe ratios (Fe/(Fe+Mg)) between 0.2 to 0.5 probably relative to the chemistry of the mineral that they are replacing. Corrensite-to-chlorite transition is marked by a strong increase of the iron content at the expense of the magnesium content in the octahedral sheets; XFe increases from 0.1 to 0.47 from corrensite to chlorite. Two types of chlorite are distinguished based on XFe ratio. The Fe-Mg chlorite with 0.2<XFe<0.5 are observed in association with corrensite and C-Crr in replacement of all ferromagnesian magmatic minerals. These chloritic minerals are related to the pervasive alteration. The Fe-chlorite with 0.55<XFe<0.80 precipitate mainly with illitic minerals in veins. Sometimes, they are observed in replacement of Fe-Mg chlorite and corrensite from the pervasive alteration. This second generation of Fe-chlorite is related to the argillic alteration developed in FZ. When they co-precipitate with illitic minerals, the interlayer charge is slightly higher due to contamination. Some measurements of chlorite are in between both. Chemical analyses of dioctahedral clays (I-S R1, I-S R3 and ill) do not present major variations with depth and in both wells (Table S6). The interlayer charge is essentially satisfied by potassium and is between 0.70 and 0.90 for I-S and higher than 0.90 for pure illite. Detailed microanalyses of clay minerals are given in Vidal et al. (2022).

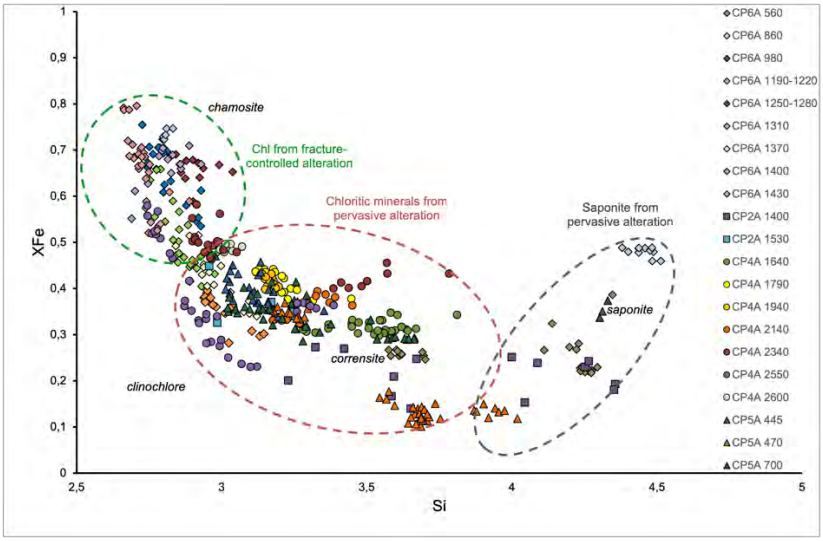

Figure 5: Plot of structural formulae of trioctahedral clays in a diagram of XFe versus Si for CP5A and CP2A wells (XFe = Fe/(Fe + Mg). All the samples are represented with a relative structure containing 14 oxygen atoms and assuming that the total iron content was composed of Fe2+. Theoretical compositions of chamosite, clinochlore, corrensite and saponite are provided for reference as black crosses.

4.4 Equilibrium of clay minerals

The state of fluid mineral equilibrium can be used to explain dissolution-precipitation of clay minerals. Figure 6 shows saturation index for clay minerals for a Na-K-Cl geothermal fluid (> 230 °C) with low gas content. Results from PHREEQC modeling are quite consistent with petrographic observations; negative saturation index for saponite and Fe-Mg chlorite suggesting an obliteration of clays from pervasive alteration by illite and Fe-chlorite from fracture-controlled alteration as

suggested by positive saturation index. The precipitation of Fe-chlorites directly from circulating geothermal fluid suggests reducing conditions of crystallization.

Regarding gases, CO_2 is the dominant species that is consistent with precipitation of carbonates' precipitation whereas H_2 and CH_4 are strongly depleted. However, the fluid sampling occurs in surface and fluid probably suffers degassing that led to an increase of solutes compared to the deep reservoir and these preliminary results of saturation index of clay minerals need to be improve with further fluid samples and geochemical studies.

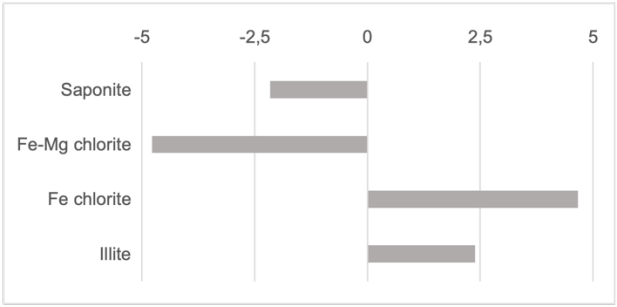

Figure 6: Modeling of saturation index for clay minerals with PHREEQC software

5. Discussion

The study of hydrothermal alteration in CP2A, CP4A, CP5A and CP6A wells demonstrated a great spatial and temporal heterogeneity of alteration within in the deep reservoir. At least two different styles of alteration were identified:

(1) A weak to moderate pervasive alteration style which is characterized by little change of the original textures and by the replacement of most of the original rock-forming minerals by trioctahedral clays (saponite, corrensite, chlorite-corrensite mixed layers (C-Crr) and Fe-Mg chlorite), calco-silicates (epidote, titanite, zeolites) and less frequently clays from celadonite-glauconite group. It is a propylitic alteration very common during cooling of magmatic intrusive bodies resulting from interactions between igneous minerals with stagnant fluids of diverse in pores or microcracks (Lowell and Guilbert, 1970; Thomasson and Kristmannsdottir, 1972). In the context of the andesitic volcanism, it is mainly dominated by trioctahedral clays and is representative of hydrothermal alteration in inactive flow regimes (Beaufort et al., 1990).

(2) A fracture-controlled alteration style which is characterized by a strong destruction of the original textures and in which both the original rock forming minerals and the minerals of the pervasive alteration have been dissolved and replaced. Two fracture controlled events were observed:

- A first mineral paragenesis characterized by *adularia + Ba-rich feldspar + silica polymorphs (quartz, chalcedony) + calcium arsenates + calcite + illite* was observed in shallow permeable FZs of CP5A well, that are possibly at a liquid/steam interface at about 4100m a.s.l., i.e 400 m depth (Baccarin et al., 2021). These hydrothermal parageneses are common in low-sulphidation epithermal deposits reported in the literature (Dong et al., 1995; Dong and Morrison, 1995; Patrier et al., 2013; Rowland and Simmons, 2012; Simmons and Browne, 2000). Adularia, blade shape calcite, quartz, chalcedony and their flamboyant, feathery and crustiform-collomorph textures suggest boiling processes that were already mentioned in PAE-

1 well (Urzúa et al., 2002). At the end of boiling processes, when pressure increases and pH decreases, illite with a very high interlayer charge (close to mica) can locally and temporarily precipitate until another boiling event occurs. The fact that these minerals assemblages are observed in CP5A well could be linked to the intersection of the graben border fault that allows unimpeded fluid upflow.

- A second mineral paragenesis characterized by *illite + illite-smectite mixed layers (I-S) + Fe-chlorite + carbonates (mainly calcite)* was observed in all permeable FZs in all wells of the CP geothermal system. Morphology of clays observed in permeable FZs suggest abrupt changes in the flow regime such as mixing of geothermal fluids that lead to explosive nucleation of small clay crystallites and promote occurrences of heterogeneous mineral assemblages, such as I-S (Beaufort et al., 1996; Mas et al., 2006).

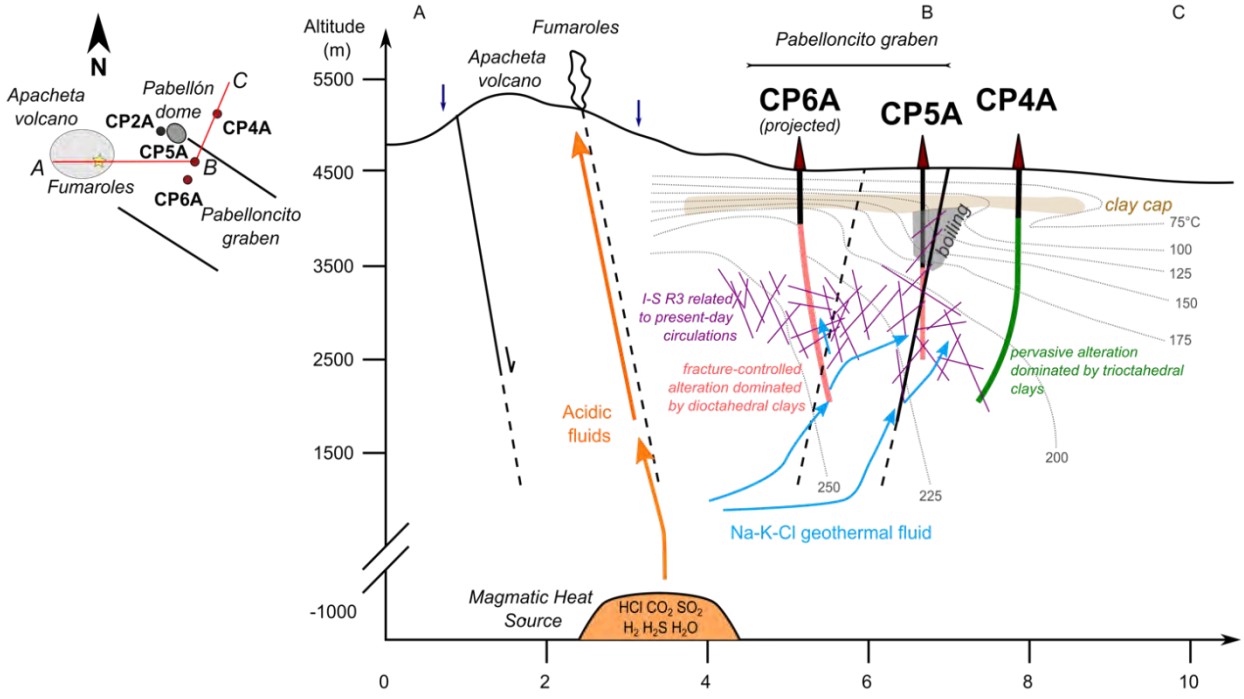

Figure 7: Conceptual model of the hydrothermal alteration occurring through the eastern border fault of the graben acting as a conduit and the wide permeable fracture network associated to it. Isotherms, structures and fluid circulations are schematically represented from Giudetti and Tempesti (2021), Maza et al. (2018), Urzúa et al. (2002) and updated with results of clay signature in CP2A, CP4A, CP5A and CP6A wells. The large-scale faults are from the structural model of Rivera et al. (2021) and the wide permeable fracture network developed in its vicinity follows the trace of the low resistive anomaly in the 3D magnetotelluric model from Baccarin et al. (2021). The depth of the magmatic heat source is from Gorini et al. (2018). I-S R3 refers to illite-smectite mixed layers with less than 10% of smectite.

These three alteration events can be spatially and temporally superimposed. The propylitic alteration probably started before but continues even if locally in the permeable levels, a multi-event fracture-controlled alteration occurred erratically. As an active system, dynamics of the fluid leads to a heterogeneous alteration; the dioctahedral sequence is mainly expressed in CP6A well, in the *hot core* inside the graben whereas the trioctahedral sequence is mainly expressed in CP4A, outside the graben (Figure 7). However, illitic minerals and more particularly I/S R3 ml (ill>90%) are observed as clay signature for FZs in all wells inside and outside the graben suggesting a unique source for the fluid circulating in the reservoir. Thus, the eastern border fault of the graben does

not act as an impermeable barrier and an interconnected fracture network is developed in the vicinity of the fault channelizing the geothermal fluid. The proximity of both wells to each other (circa 2 km between bottoms of the wells) and the injectivity index of CP4A confirms a good connection to the deep geothermal reservoir. However, the sudden decrease of the isotherms and the dominance of propylitic alteration in CP4A suggest limited fluid circulations outside the graben restricted to few FZs compared to the center of the graben. Intense paleo-circulations can lead to a sealing of the fracture network as suggested by the clay pattern in CP2A well where a significant amount of dioctahedral clays could seal the median strand of the eastern fault probably intersected by the well. In CP5A well, the eastern border fault acts as a preferential pathway for unimpeded fluid flow with evidence of boiling process at shallow depths (Figure 7). This eastern border fault is a complex structure in terms of fluid flow and circulations occur spatially and temporarily heterogeneously.

6. Conclusion

As the CP reservoir is an active system, it demonstrates high heterogeneity in terms of alteration mineralogy. Typical clay signatures observed along deep wells suggest a complex multi-event history of fluid circulations controlled by the eastern border fault of the Pabelloncito graben. The latter controls the narrow thermal plume promoting focused vertical fluid flow at the South of the Pabellón dome whereas the hydrothermal activity collapsed in response to intense illitization which plugged the fault zone at the North of the Pabellón dome. However, the eastern graben fault does not behave as barrier. The same clay signature is observed inside and outside the graben suggesting a wide permeable fracture network channelizing fluids in both side of the border fault. As exploitation of the geothermal system leans on well-connected fracture network providing sufficient permeability, the study of hydrothermal alteration and more specifically clay minerals is important for future geothermal development of CP system as well as other Andean geothermal systems. Moreover, recent results indicate that clays are the primary lithium-bearing minerals, and understanding their properties is crucial for advancing prospects of geothermal lithium co-extraction.

Acknowledgement

Our thanks to Geotérmica del Norte (GDN) for authorizing the use of wells data of Cerro Pabellón Power Plant project. The study has benefited the scientific and financial support of the Andean Geothermal Center of Excellence (CEGA), Anid-Fondap projects #15090013, 15200001 & ACE210005. It was published in the framework of the ANID-Fondecyt postdoctoral grant n° 3210150 attributed to J. Vidal.

REFERENCES

Baccarin, F., Volpi, G., Rivera, G., Giorgi, N., Arias, A., Giudetti, G., Cei, M., Cecioni, M., Rojas, L., Ramirez, C., 2021. Cerro Pabellón Geothermal Field (Chile): Geoscientific Feature and 3D Geothermal Model, in: Proceeding of the World Geothermal Congress 2020+1. Reykjavik, Iceland.

Beaufort, D., Papapanagiotou, P., Patrier Mas, P., Fouillac, A.M., Traineau, H., 1996. I/S and C/S mixed layers, some indicators of recent physical-chemical changes in active geothermal systems: The case study of Chipilapa (El Salvador), in: Proceedings of Seventeenth Workshop on Geothermal Reservoir Engineering. Stanford University, California, USA.

Beaufort, D., Westercamp, D., Legendre, O., Meunier, A., 1990. The fossil hydrothermal system of Saint Martin, Lesser Antilles: geology and lateral distribution of alterations. J. Volcanol. Geotherm. Res. 40, 219–243. https://doi.org/10.1016/0377-0273(90)90122-V

Brindley, G.W., Brown, G., 1980. X-ray Diffraction procedures for clay mineral identification, in: Crystal Structures of Clay Minerals and Their X-Ray Identification. Mineralogical Society, London, Great Britain, pp. 305–360.

Cappetti, G., Giorgi, N., Arias, A., Volpi, G., Rivera, G., Cei, M., Fedeli, M., Di Marzio, G., Pasti, M., Massei, S., Baccarin, F., 2021. The Cerro Pabellón Geothermal Project (Chile): from Surface Exploration to Energy Production, in: Proceeding of the World Geothermal Congress 2020+1. Reykjavik, Iceland.

Dong, G., Morrison, G., Jaireth, S., 1995. Quartz textures in epithermal veins, Queensland - classification, origin, and implication. Econ. Geol. 90, 1841–1856. https://doi.org/10.2113/gsecongeo.90.6.1841

Dong, G., Morrison, G.W., 1995. Adularia in epithermal veins, Queensland: morphology, structural state and origin. Miner. Deposita 30, 11–19. https://doi.org/10.1007/BF00208872

Flexser, S., 1991. Hydrothermal alteration and past and present thermal regimes in the western moat of Long Valley caldera. J. Volcanol. Geotherm. Res. 48, 303–318. https://doi.org/10.1016/0377-0273(91)90048-5

Giudetti, G., Tempesti, L., 2021. First Geochemical Data from Cerro Pabellón Geothermal Project (Apacheta Region, Chile), in: Proceeding of the World Geothermal Congress 2020+1. Reykjavik, Iceland.

Gorini, A., Ridolfi, F., Piscaglia, F., Taussi, M., Renzulli, A., 2018. Application and reliability of calcic amphibole thermobarometry as inferred from calc-alkaline products of active geothermal areas in the Andes. J. Volcanol. Geotherm. Res. 358, 58–76. https://doi.org/10.1016/j.jvolgeores.2018.03.018

Inoue, A., Kitagawa, R., 1994. Morphological characteristics of illitic clay minerals from a hydrothermal system. Am. Mineral. 79, 700–711.

Lowell, J.D., Guilbert, J.M., 1970. Lateral and vertical alteration-mineralization zoning in porphyry ore deposits. Econ. Geol. 65, 373–408. https://doi.org/10.2113/gsecongeo.65.4.373

Mas, A., Guisseau, D., Patrier Mas, P., Beaufort, D., Genter, A., Sanjuan, B., Girard, J.P., 2006. Clay minerals related to the hydrothermal activity of the Bouillante geothermal field (Guadeloupe). J. Volcanol. Geotherm. Res. 158, 380–400. https://doi.org/10.1016/j.jvolgeores.2006.07.010

Maza, S.N., Collo, G., Morata, D., Lizana, C., Camus, E., Taussi, M., Renzulli, A., Mattioli, M., Godoy, B., Alvear, B., Pizarro, M., Ramírez, C., Rivera, G., 2018. Clay mineral associations in the clay cap from the Cerro Pabellón blind geothermal system, Andean Cordillera, Northern Chile. Clay Miner. 53, 117–141. https://doi.org/10.1180/clm.2018.9

Pang, Z.-H., Reed, M., 1998. Theoretical Chemical Thermometry on Geothermal Waters: Problems and Methods. Geochim. Cosmochim. Acta 62, 1083–1091. https://doi.org/10.1016/S0016-7037(98)00037-4

Patrier, P., Bruzac, S., Pays, R., Beaufort, D., Bouchot, V., Verati, C., Gadalia, A., 2013. Occurrence of K-feldspar-bearing hydrothermal breccias in the Bouillante geothermal field (Basse Terre – Guadeloupe). Bull. Société Géologique Fr. 184, 119–128. https://doi.org/10.2113/gssgfbull.184.1-2.119

Patrier, P., Papapanagiotou, P., Beaufort, D., Traineau, H., Bril, H., Rojas, J., 1996. Role of permeability versus temperature in the distribution of the fine (< 0.2 μm) clay fraction in the Chipilapa geothermal system (El Salvador, Central America). J. Volcanol. Geotherm. Res. 72, 101–120. https://doi.org/10.1016/0377-0273(95)00078-X

Rivera, G., Cecioni, M., Volpi, G., 2018. Modelo Integrado 3D del Sistema Geotérmico "Cerro Pabellón" al Término de la Etapa de Construcción. Internal Report. (Internal Confidential Report). Geotérmica del Norte S.A.

Rivera, G., Morata, D., Ramirez, C., Volpi, G., 2021. Volcanic and Tectonic Evolution of Azufre – Inacaliri Volcanic Chain and Cerro Pabellón Geothermal Field (Northern Chile), in: Proceeding of the World Geothermal Congress 2020+1. Reykjavik, Iceland.

Rowland, J., Simmons, F., 2012. Hydrologic, Magmatic, and Tectonic Controls on Hydrothermal Flow, Taupo Volcanic Zone, New Zealand: Implications for the Formation of Epithermal Vein Deposits. Econ. Geol. 107. https://doi.org/10.2113/econgeo.107.3.427

Simmons, S.F., Browne, P.R.L., 2000. Hydrothermal Minerals and Precious Metals in the Broadlands-Ohaaki Geothermal System: Implications for Understanding Low-Sulfidation Epithermal Environments. Econ. Geol. 95, 971–999. https://doi.org/10.2113/gsecongeo.95.5.971

Thomasson, J., Kristmannsdottir, H., 1972. High temperature alteration minerals and thermal brines, Reykjanes, Iceland. Contrib. Mineral. Petrol. 36, 123–134. https://doi.org/10.1007/bf00371183

Urzúa, L., Powell, T., Cumming, W.B., Dobson, P., 2002. Apacheta, a new geothermal prospect in Northern Chile, in: Geothermal Resources Council Transactions. Geothermal Resources Council, Davis, California, pp. 65–69.

Vásquez, M., Bauluz, B., Nieto, F., Morata, D., 2016. Illitization sequence controlled by temperature in volcanic geothermal systems: The Tinguiririca geothermal field, Andean Cordillera, Central Chile. Appl. Clay Sci., Clay mineral indices in palaeo-geothermal and hydrothermal studies 134, 221–234. https://doi.org/10.1016/j.clay.2016.04.011

Vásquez, M., Nieto, F., Morata, D., Droguett, B., Carrillo-Rosua, F.J., Morales, S., 2014. Evolution of clay mineral assemblages in the Tinguiririca geothermal field, Andean Cordillera of central Chile: an XRD and HRTEM-AEM study. J. Volcanol. Geotherm. Res. 282, 43–59. https://doi.org/10.1016/j.jvolgeores.2014.05.022

Vidal, J., Patrier Mas, P., Betancourt, C., Maza, S., Morata, D., 2021. First results of the vein alteration in the deep well PGC1 of Irruputuncu geothermal system, Andean Cordillera, Northern Chile., in: World Geothermal Congress 2020+1. Reykjavik, Island.

Vidal, J., Patrier, P., Beaufort, D., Maza, S., Rivera, G., Volpi, G., Morata, D., 2022. Clay Minerals in the Deep Reservoir of the Cerro Pabellón Geothermal System (Northern Chile). Minerals 12. https://doi.org/10.3390/min12101244

Vidal, J., Patrier, P., Genter, A., Beaufort, D., Dezayes, C., Glaas, C., Lerouge, C., Sanjuan, B., 2018. Clay minerals related to the circulation of geothermal fluids in boreholes at Rittershoffen (Alsace, France). J. Volcanol. Geotherm. Res. 349, 192–204. https://doi.org/10.1016/j.jvolgeores.2017.10.019

Evolution of Shallow Temperature Surveys

Maxwell Wilmarth[1] and Drew Siler[2]

[1]Baseload Power U.S., [2]Geologica Geothermal Group

email: maxwell.wilmarth@baseloadpower.us

Keywords

Shallow temperature survey, 2m probe, Puchuldiza

ABSTRACT

Exploration drilling for geothermal resources is expensive and the risk of not discovering an economic resource with exploration drilling is high. Lower cost, shallower direct measurements of the subsurface have therefore been conducted as part of early-stage geothermal exploration since at least the late 1970s. These surveys prioritize low cost and rapid data gathering over a wide field area. Since the mid-2000s the technique has been further developed and data corrections have become more sophisticated. This paper compares three shallow temperature (2 m probe) systems used by public and private groups. Additionally, findings are described from a shallow temperature survey conducted in 2010 at Puchuldiza, Chile. The results indicate that shallow temperature surveys are an effective method for discovering and characterizing geothermal resources.

1. Introduction

Exploration drilling for geothermal resources is expensive with high risk of not discovering an economic resource with exploration drilling. A variety of geological, geochemical, and geophysical surveys are typically conducted to lower the risk of failure. One of these techniques is shallow temperature surveys, which have been conducted in the Basin and Range province of the United States since at least the 1970s. The goal of a shallow temperature survey is to locate a thermal anomaly quickly and at low cost so that further exploration surveys can focus on an area of interest.

2. Shallow vs deep drilling

Deep drilling (>1000 m) costing on the order of $1MM to $10MM is required to discover a geothermal resource (**Figure 1**). Consequently, explorationists trade lower cost for shallower and less representative information about temperature distribution. Slim wells to ~1000 m at a cost of ~$1MM are sometimes cost-effective, and handfuls of temperature gradient holes drilled from ~50 m to 150 m for $10k to $50k each are commonly used as well (e.g., Basin and Range, Salton Sea). Pushing this cost/depth relationship to its limit leads to shallow temperature surveys at depths of

~0.5 m to 2 m for a cost of <$500 per hole. A nominal depth of 2 m has become the standard in the industry for these types of surveys. A large number of these holes can be drilled for the same cost as a single temperature gradient (TG) hole and provide a much higher spatial density than a TG program. However, these shallow holes carry a higher risk of being impacted by surface effects and meteoric water than deeper TG holes.

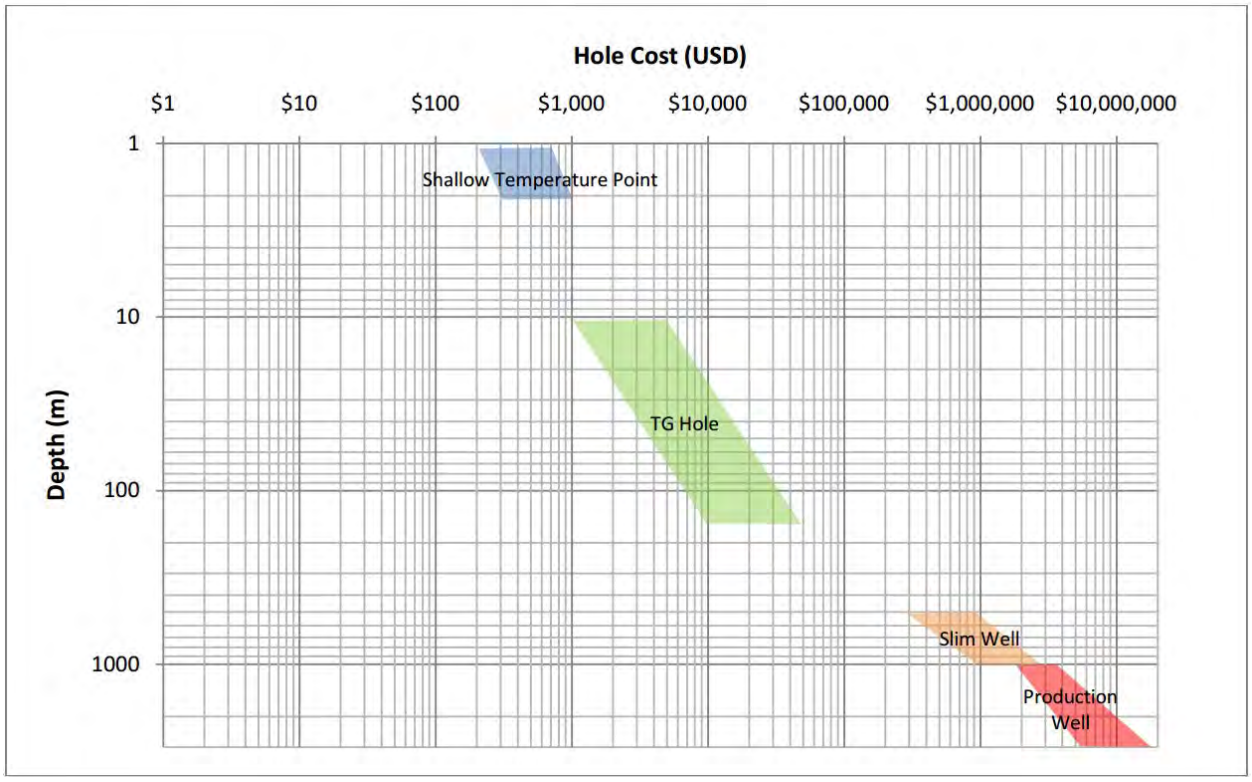

Figure 1. Hole cost vs depth relationship

The goal of a shallow temperature survey is to identify anomalously high shallow temperatures that may be associated with a geothermal reservoir at depth. Shallow temperatures on the order of 1 m depth are affected by many non-geothermal surface processes which can cause variations in temperature equal to or greater than the magnitude of the thermal anomaly above the background temperature. Wet or damp soil and shallow cold aquifers can mask a geothermal reservoir and so the method has only been used in arid regions like the Basin and Range. The diurnal temperature cycle is dampened sufficiently at depths as shallow as 0.5 m. The seasonal cycle is significant to a depth of 10 m or more, but changes slowly enough that it can be ignored during a short survey or compensated for with seasonal monitoring.

Since the temperature signal measured at 2 m from a geothermal reservoir can be <5°C above background, various corrections to the 2 m temperature data are usually required, including corrections for elevation, albedo, and slope aspect. These are discussed further below.

TG hole programs investigate even deeper. A shallow temperature survey does not replace a TG hole program. Rather it provides a low-cost data set on temperature distribution for the development of a conceptual model early in the exploration phase of a geothermal prospect. Together with other low-impact exploration techniques like fluid geochemistry, structural

mapping, and geophysical surveys such as MT and gravity, it can help target a TG hole program while environmental studies and drilling permits are obtained.

3. History of the technique

Shallow temperature surveys for geothermal exploration are first represented in the literature starting in the late 1970s and early 1980s. They were first used at depths of 1-2 m to investigate many known geothermal systems in the Basin and Range. The equipment used in these surveys is unknown but assumed to be a truck-mounted drill rig. A summary of the history of these studies is provided in Kraal et al (2024)

In the mid-2000s, the survey technique was revived by the Great Basin Center for Geothermal Energy (GBCGE) at the University of Nevada, Reno (UNR) to map a large number of greenfield geothermal projects and especially blind systems. GBCGE discovered at least seven previously unknown thermal anomalies in Nevada: Southern Gabbs Valley, Teels Marsh, Rhodes Marsh, Columbus Marsh, East Hawthorne, Emerson Pass, and Petrified Springs (Kraal et al, 2024). The GCBGE system utilized a side-by-side Utility Task Vehicle (UTV) with a hand-held electric hammer which pounds closed-bottom steel pipe (the probes) into the ground (**Figure 2**). This method of inserting the probes works well in soft sediment but is difficult or impossible in rocky soil. GBCGE has also used a 2-stroke gasoline rock drill with mixed success. This system is still in use at the time of this writing by GBCGE and graduate students at UNR.

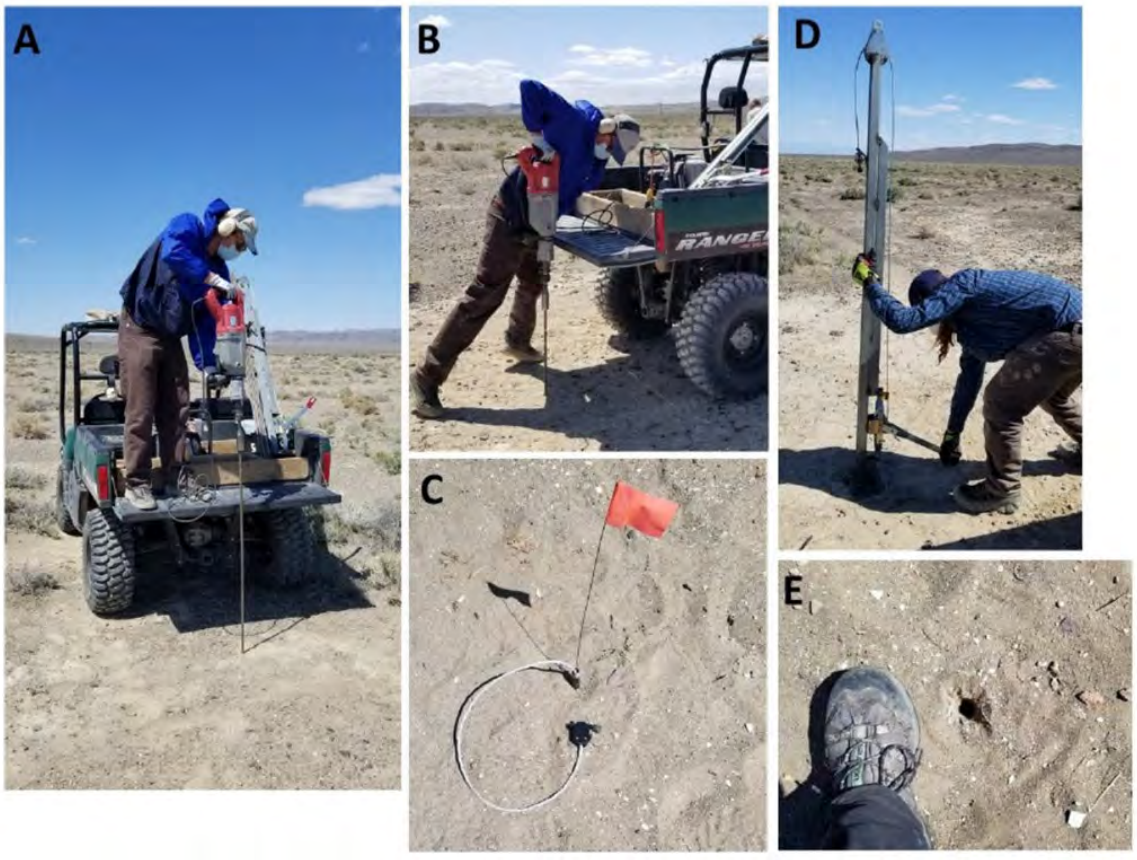

Figure 2. The GBCGE 2 m probe rig as described in Kraal et al (2024).

In 2009, a purpose-built rig mounted on a side-by-side and utilizing a custom mast-mounted electric rotohammer and ¾" concrete drill bits was built by Geoglobal Energy (GGE) for use in the Altiplano of Chile, where arid conditions similar to the Great Basin predominate (**Figure 3**). Details of this system and the data collected at the Puchuldiza project in Chile are discussed below. The fate of this rig is unknown but it is assumed to still be warehouse in northern Chile.

In 2010, an upgraded version of the GGE rig was used by Nevada Geothermal Power at Blue Mountain, Nevada. This rig was parted out and sold sometime in 2011-2012.

Figure 3. The GGE rig in use at Puchildiza, Chile.

In the early 2020s, at least one company in Nevada utilized a direct-push type drilling rig commonly used in the environmental and geotechnical industries. This type of system can work well, but is limited to fine-grained sediment and roads traversable by trucks.

In early 2024, a new 2 m probe purpose-built rig designed and built for Baseload Power U.S. (BPUS) by Double R Drilling of Reno, Nevada for use in the Basin and Range. The innovations of this rig include a tiltable mast-mounted rotohammer and custom-made 2 m fully-fluted concrete bits (**Figure 4**). This system is discussed in detail below.

Figure 4. The 2 m prove rig designed and built for BPUS by Double R drilling.

4. Methodology

The methodology of inserting the temperature probes is similar for all three systems discussed in this paper: 1) a side-by-side UTV is used to carry personnel and equipment to the field, 2) 2 m long probes are inserted into the ground, 3) after thermal equilibration temperature measurements are made down the hollow probe with a resistive temperature device (RTD) on a wire, and 4) the probe is removed from the ground and re-used.

The GBCGE system has generally used a handheld electric hammer to pound hollow steel rods (probes) into sediment. This works well in fine-grained sediments and rocky soils with clast size up to ~2-4 cm. The disadvantages of this system are that the electric hammer is hand-held which fatigues the crew, it is difficult or impossible to penetrate rocky soil, and the probes must be laboriously jacked out of the ground by hand to remove them.

By contrast, the GGE system employed a hinged mast and track system with a winch to mount a rotohammer. The mast allowed for remote operation with a tether and was significantly less laborious to operate. The rotohammer could be used to either pound probes in the ground, similar to the GBCGE system, or to drill holes using ¾” concrete bits available off-the-shelf. The holes could be blown clean with an on-board air compressor and a long, thin, tube attachment. The bits were 2 m long but the flights only continued ~1 m. This required repeated hole cleaning after 1 m depth which significantly increased the total drilling time.

The newest system created by BPUS and Double R used a pivoting mast built from unistrut with a track that allows the rotohammer to move up and down. The mast can be tilted back onto the rig while driving and redeployed to the vertical position at the next location. The winch in the mast can also be used to pull rods after the measurements are complete. Two people can operate the rig (**Figure 4**) comfortably. Upon reaching the desired depth, the hole can be blown clean with air and a hollow steel rod is dropped into the hole. A tap on the rod with a sledge hammer ensures good contact with the formation. An RTD (**Figure 5a**), is threaded on a wire down the rod (**Figure 5b**).

A small amount of water can be poured into the pipe to ensure good conductive thermal contact with the RTD.

Although the RTD only needs seconds to minutes to thermally equilibrate, the steel rod requires up to an hour or more to equilibrate with the formation. We prefer to leave the rods in overnight before making a measurement. To make a measurement the RTD is plugged into an electronic meter and the temperature is read off the display (**Figure 5c**).

Figure 5. RTD and meter (a); Threading the RTD down the probe (b); and reading the temperature (c).

5. Corrections

Various corrections must be made to the raw temperature data in order to correctly map the shallow temperature distribution. These corrections have been detailed in Sladek et al (2009) and Kraal et al (2024). In the Puchuldiza and BPUS surveys, the most useful corrections were found to be 1) seasonal drift, 2) elevation, and 3) albedo, in that order. Other attempted corrections included slope aspect and total solar insolation, but were not found to be significant. Examples of the Puchuldiza survey seasonal trend (**Figure 6**), and negative correlations with shallow temperature for elevation (**Figure 7**) and albedo (**Figure 8**) are shown below.

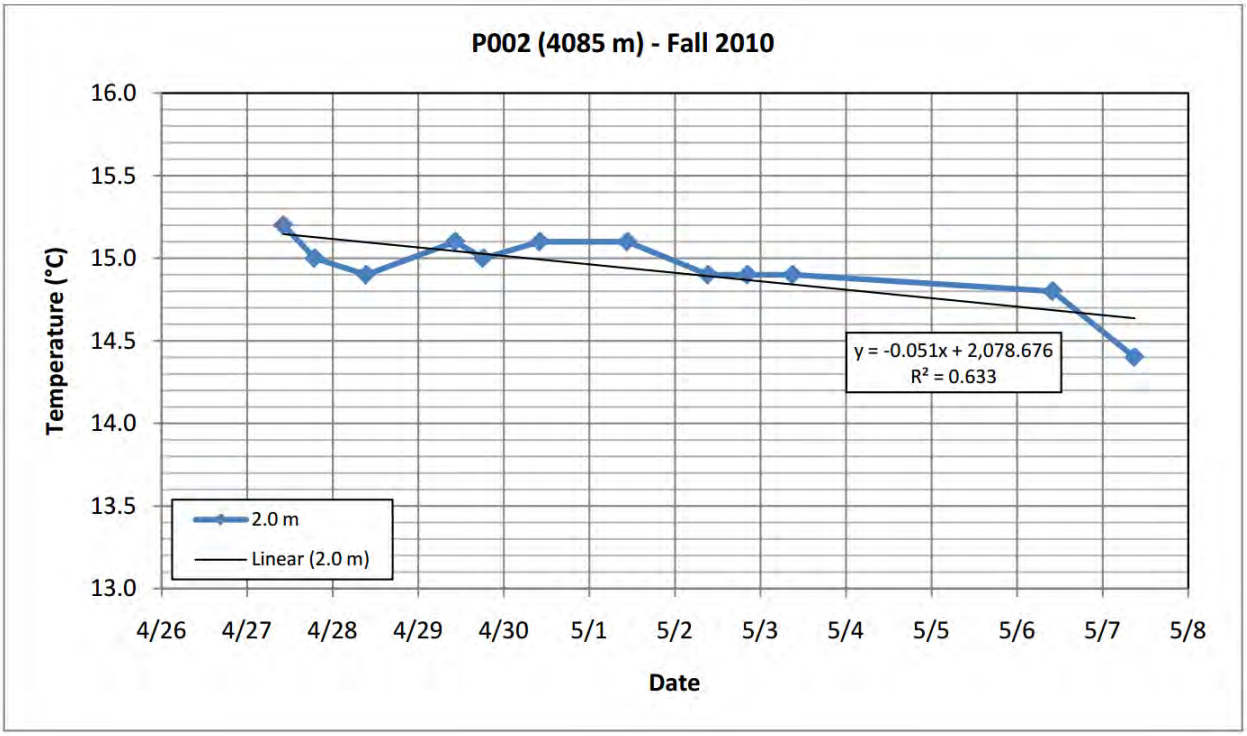

Figure 6. April/May monitoring of Puchuldiza base station P002. There was a small cooling trend at 2.0 m.

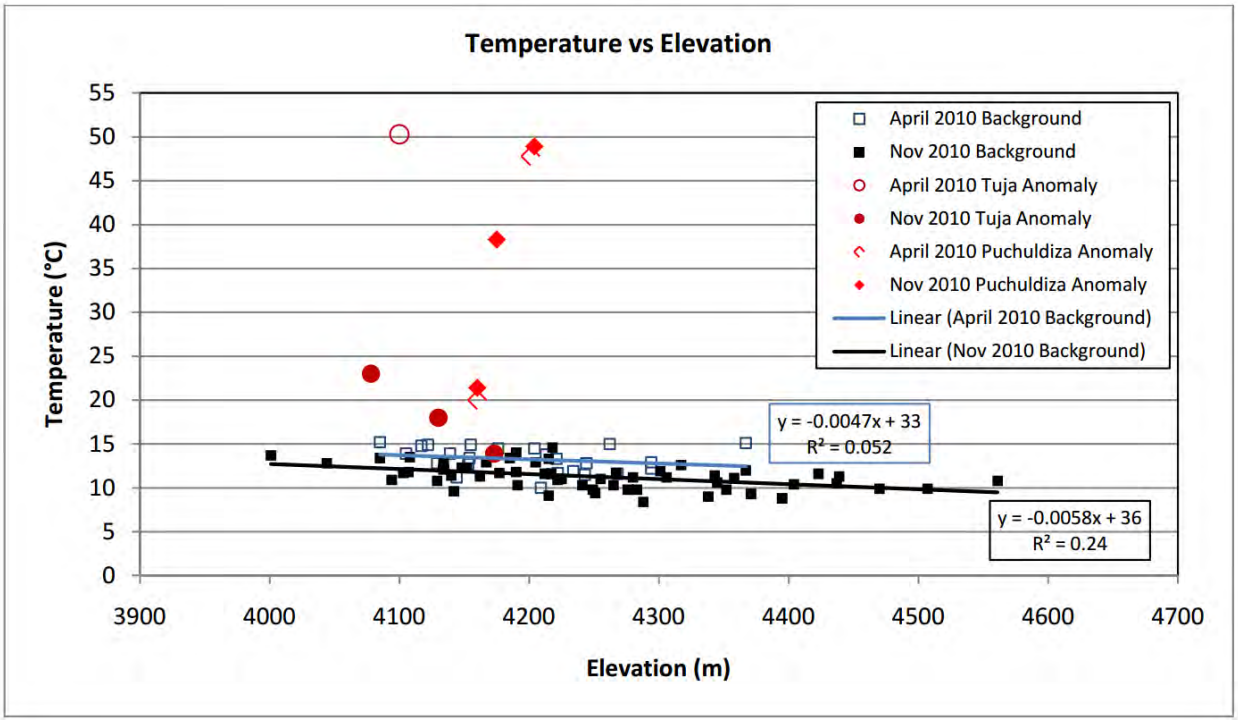

Figure 7. Puchuldiza uncorrected temperature vs elevation. There is a small negative correlation.

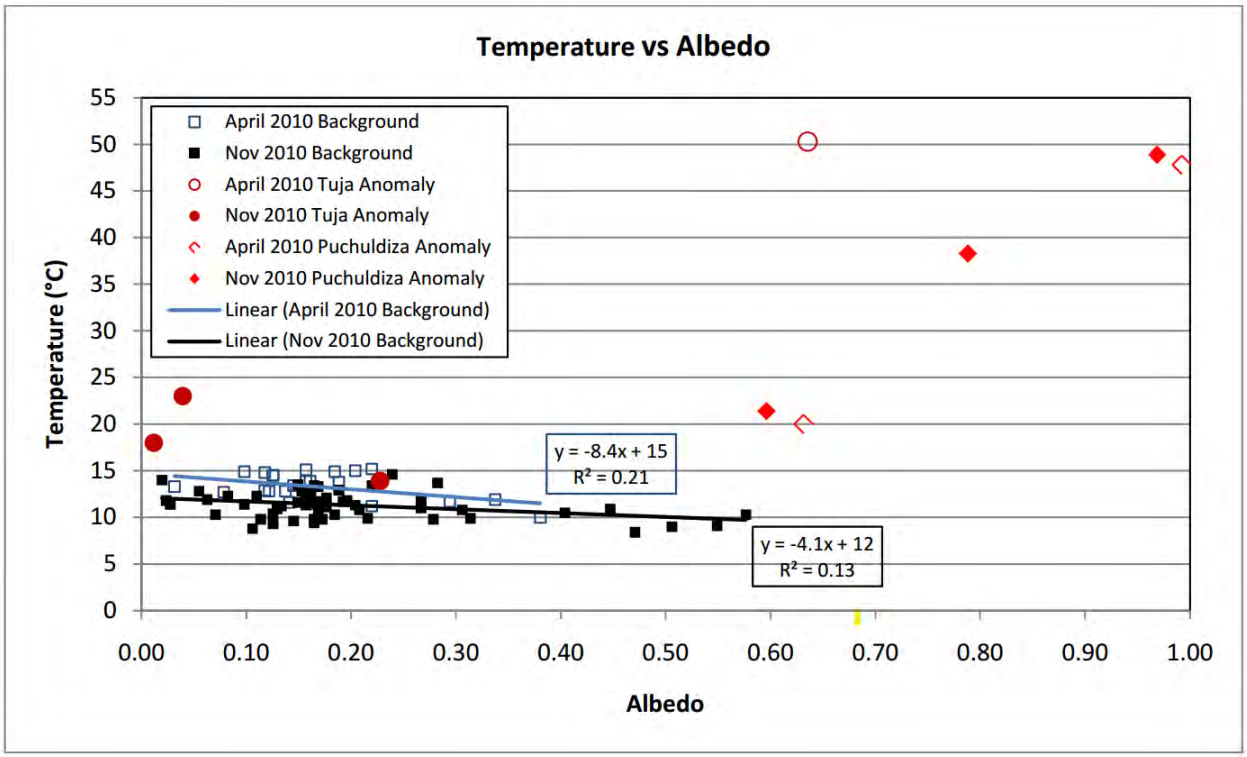

Figure 8. Puchuldiza uncorrected temperature vs albedo. There is a small negative correlation.

6. BPUS Standard Operating Procedures

The following Standard Operating Procedures have been developed by BPUS in concert with Geologica Geothermal Group. These SOPS build on the procedures used in the Puchuldiza surveys and borrow from the procedures of Kraal et al (2024).

6.1. Survey Operation

The essential aspects of 2 m surveying are 1) installing a 2-meter-long hollow rod (probe) into the ground, 2) waiting an appropriate period of time (typically at least two hours) for the probe to equilibrate with the ground temperatures, 4) recording the temperatures at 2 m depth, and 4) pulling the probe for later re-use.

6.2. Survey Design

The survey design consists of 1) at least two ‘base stations’ (label Base-1, Base-2, etc.) and 2) several dozen or more measurement locations (labelled 1, 2, etc.). It is critical that the field crew has a GPS-capable device (e.g. tablet or handheld GPS) that the survey design has been loaded onto prior to mobilization. This will ensure that data are collected in the correct locations.

6.3. Install Base Stations

On the first day of the survey, the first task is to install base stations. These probes are to remain in place for the entire duration of the survey. Locate each ‘Base’ location and install a probe.

Record the name of site (e.g., ‘Base-1’) and the time and date the probe was installed on the attached data sheet.

6.4. Installing Probes

To maximize time efficiency, it is recommended to install many (>10) probes, then return to measure the temperatures at each one and remove each one. The locations in the survey design are numbered (1, 2, 3…etc.), probes should be inserted in the same order as the numerical order of survey design. Locate and travel to location 1, install a probe. Record the name of site (e.g., ‘1’), the GPS coordinates, (Latitude and Longitude), and the time and date the probe was installed on the attached data sheet. Cap the probe with PVC cap (to keep out dust), and add flagging (so it can be easily found later, not accidental run over). Travel to 2 and repeat.

A typical survey might look like:

Day 1: Install two base stations
Install probes 1-15
Measure temperatures at both base stations
Measure temperatures and remove probes 1-15
Take a photo of data collection sheet and email it to office (if not using digital data input)

Day 2: Measure temperature at both base stations
Install probes 16-30
Measure temperatures and remove probes 16-30
Take a photo of data collection sheet and email it to office

Day 3: Measure temperature at both base stations
Install probes 31-50
Measure temperatures and remove probes 31-50
Measure temperature at both base stations, remove both base station probes
Take a photo of data collection sheet and email it to office

6.5. Making Temperature Measurements

Once many (>10) probes are installed, enough time (at least two hours) is likely to have elapsed, so the temperature of the probe is now in equilibrium with the temperature of the ground. Return to the first probe installed (e.g. 1). Insert the RTD, ensure that the RTD goes all the way to the bottom of the probe. Wait for the temperature readings to ‘settle’ on a single temperature. Typically, this takes less than 5 min. The RTD should be left at bottom for a minimum of 2 minutes. Record the time the measurement was taken, and the temperatures at 2m on the attached data sheet. Travel to the next probe, repeat.

6.6. Transmitting the Data

At the end of each day’s data collection take a photograph of the day’s data sheet and the base station data sheet and email it to the office. Depending on the day-to-day results, some adjustments to the survey design may be made. If adjustments are made, a new KMZ file will be emailed to

the field crew. On the final day of the survey measure temperatures at the base stations, pull the base station probes and send a photograph of the final day's data sheet and the base station data sheet to the office.

7. Quick Reference Guide for Standard Operating Procedure (SOP) at each survey location

The following Table (**Figure 9**) details the order of events that should occur at each survey location, including base stations.

ALWAYS WEAR PROPER PPE (Minimum: SAFETY GLASSES & WORK GLOVES)
2m probe survey: Probe installation
1) Locate and drive to the planned survey location. a. It is acceptable to deviate by up to 50 feet from the planned location to avoid areas that have obstacles (e.g. fence, debris, culvert, steep drainage channel, animal burrows etc.) b. Do not install a probe if there is standing or running water on the surface, relocate to the nearest dry area. Avoid drainage channels, even dry channels may have ground water just below the surface. 2) Install the probe to 2 meters (6 ft, 3 and 1/3 inches). a. In the event of a failed installation (less than 2 meters), re-locate by several feet and try again. 3) Record the survey point name (e.g., 1) and GPS location (latitude and longitude) in decimal degrees format with 6 digits in the decimal (e.g. 38.828714, -117.579906) even if it is identical to the plan, on the attached data sheet. 4) Save the location in a GPS or tablet as a point. 5) Record the time that the probe was inserted on the attached data sheet. 6) Record any site-specific information (e.g., had to move because of fence) on the attached data sheet. 7) Cap the probe with PVC cap. 8) Mark the probe with flagging or cone so it can be re-located easily and to prevent others from driving over it. 9) Travel to the next location.
2m probe survey: Temperature measurement
1) Relocate to the probe location. 2) Confirm that >2 hrs have passed since the probe was inserted. 3) Remove the PVC cap and insert the RTD. 4) Make sure the RTD goes all the way to the bottom of the probe (2m). 5) Wait at least 2 minutes for the RTD to equilibrate. 6) Record the time of the temperature measurement on the attached data sheet. 7) Record temperatures at 2m on the attached data sheet. 8) Photograph location, include station number (written on small white board or notepad) and meter with screen showing 2m temperature reading. 9) Pull the probe and move to the next station.

Figure 9. SOP Quick Reference Guide.

Conclusion

Shallow temperature surveys have been conducted as part of early stage geothermal exploration since at least the late 1970s. These surveys prioritize low cost and rapid data gathering over a wide field area. Since the mid 2000s the technique has been further developed and data corrections have become more sophisticated. So too has the custom equipment used in these surveys become more sophisticated. The 2 m probe survey methodology developed by the GBCGE, and private companies such as GGE and BPUS can be applied to a large area of the Basin and Range to explore for new geothermal systems, especially blind systems.

Acknowledgement

This work relied heavily on assistance from many people. The Puchuldiza survey was greatly assisted by the work of GGE team members Pedro Muñoz, Jim Stimac, Silke Lohmar, Domingo Maldonado, Sergio Iriarte and Andrea Gonzalez. Data analysis and report preparation benefitted from special contributions by Anna Colvin and Esther Mandeno, and from review by Glenn Melosh, Jim Stimac and David Sussman. The BPUS survey was heavily dependent on Chris Reede from Double R Drilling who designed and built the rig from BPUS specifications, and led the testing and data collection. Geologica staff contributed to the BPUS system design and testing including Peter Drakos, Matthew Folsom, and Leland Davis.

REFERENCES

Coolbaugh, M.F., Sladek, C., and Kratt, C., 2010, Compensation for seasonal and surface affects of shallow (two-meter) temperature measurements, GRC Transactions, v. 34, p. 851-856.

Kraal, K., Lindsey, C., Zimmerman, J., Sladek, C., and Burgess, Q. 2024, Development of shallow (2-m) temperature survey standard operating procedures and interpretation workbook. PROCEEDINGS, 49th Workshop on Geothermal Reservoir Engineering, Stanford University, Stanford, California, February 12-14, 2024. SGP-TR-227.

Sladek, C., Coolbaugh, M.F., and Kratt, C., 2009, Improvements in shallow (two-meter) temperature measurements and data interpretation, GRC Transactions, v. 33, p. 535-542.

Implication of Geothermal Conduits with the Relationship Between Fracture Intensity and Fault Distribution in the Central Mountain Area of Taiwan

Ming-Yu Wu[1], Chyi Wang[2], Wei Lo[1], and Sheng-Rong Song[2]

[1]Institute of Mineral Resources Engineering, National Taipei University of Technology

[2]Department of Geosciences, National Taiwan University

Keywords

Fracture intensity, Structural features, Geological map, Geothermal conduits

ABSTRACT

In recent years, Taiwan has become actively to develop renewable energy sources and investigate geothermal resources. One area of interest is the Lushan region, known for its numerous hot spring outcrops. Preliminary surveys suggest that it holds potential for geothermal development. Successful geothermal energy development relies on the existence of an enough heat source and appropriate pathways for the heat to rise to shallow depths, and a detailed geological map is a must for effective and cost-efficient exploration.

This study bases on the previous geological map covering the western fringe at the middle part of the Central Mountain Range and zooming in the Lushan area with more detailed mapping. While the ongoing Quaternary orogeny in Taiwan has created a unique geological environment and the rapid uplift has brought in abundant heat sources, the compressed slate and meta-sandstone formations have resulted in complex subsurface structures, and the rugged mountain ranges and deep valleys also prevent a thorough geological field work. Finding additional and creative methods to build more precise geological map in such a challenging area for interpreting underground rock types and structures has become a pressing need.

Our approach is to gather data from field survey works, digital elevation model (DEM), and previous literatures for exploring various geological structure patterns, then fracture network analysis is executed to categorize those data for the fracture strength map. Five factors, including outcrop fracture density, rock porosity, outcrop fracture intensity, outcrop fracture connectivity, and surface lineament intensity, are determined for the analytical process. The normalized score from each factor is calculated and assigned into grid map for the final fracture strength index. The existence and trend of projected fault zones and other structural features are confirmed by comparison with the fracture strength index map in the Lushan area.

Our integrated results strongly indicate the important value of digital processing, which is not only capable of consistently describing outcrop information, but also effectively complements field

surveys in a remote area. Through the fracture strength index map, this study also implies the potential areas of the geothermal reservoir and hot fluid conduits, providing valuable information for geothermal exploration.

1. Introduction

In Taiwan, electricity generation primarily relies on thermal power, but the high dependence on imported coal leads to high generation costs and air pollution. In recent years, with increasing environmental awareness, clean energy sources have gained more attention, especially geothermal energy. As a base-load power source, geothermal energy poses no risks associated with nuclear power, making it one of the choices for energy development in Taiwan. (Song et al., 2015)

Taiwan's active Quaternary orogeny has created a unique geological environment with rapid crustal uplift providing extensive heat sources, making geothermal resource development favorable (Chen, 1975; Huang et al., 1997; ITRI, 1984; Lee et al., 1994; Song and Lu, 2018; Teng et al., 2013). However, the deeply buried and compressed metamorphic environment also results in complex underground structures. To effectively develop geothermal resources, more methods are needed to create more precise geological maps, interpret subsurface formations and structures, and subsequently construct a better geothermal model.

In geothermal development, when heat sources are sufficient, hydrothermal channels become a key investigation factor. When rocks fracture under stress, they form interconnected spaces that can serve as channels for hydrothermal fluids during power generation. Therefore, fault structures are a primary focus of the investigation. Fault activity generates fault damage zones around it, where new secondary fractures are formed in the rocks within the damage zone. These new fractures connect with existing ones, creating natural fracture networks (Faulds, 2014). Rock formation with higher fracture intensity is prone to have more porosity and/or permeability. Understanding areas with high fracture intensity can help determine the potential distribution of geothermal reservoir and hydrothermal conduits.

This study investigates the fractures in the Lushan area, applying topological network methods to calculate the fracture intensity and connectivity (Sanderson and Nixon, 2015; Hansberry et al., 2021). This is combined with surface lineament data interpreted from shaded relief maps, rock porosity, and joint density data. Each factor is normalized and scored to create a fracture strength index map, which aims to confirm the structure patterns in the geological map, and further identify the higher fracturing areas as potential geothermal development targets in the Lushan area.

This study concludes that our approach successfully employed a digital sampling method for efficient field sample handling, enhanced geological maps by incorporating supplementary DEM data for hard-to-reach remote areas, effectively utilized fracture strength analysis to verify structural patterns on the geological map, and most importantly, suggested the correlation between fracture intensity and the rock properties of porosity and permeability in metamorphic slate area.

2. Geological Background

Taiwan is situated at the boundary between the Eurasian Plate and the Philippine Sea Plate (Figure 1). The collision and compression of these two plates have produced complex geological structures

and a significant amount of thermal energy. During the Quaternary orogeny, rapid crustal uplift occurred, and the residual heat from this process has become the main source for geothermal development in Taiwan. (Lee et al., 2006; Wang et al., 2021)

Previous geothermal resource development and surveys in Taiwan have identified several hot spring outcrops in the Lushan area, located on the western flank of the Central Mountain Range in Nantou. The surface hot water temperatures in this area range from 54°C to 98°C, with substantial water flow rates, indicating a potential for geothermal development (Chang and Chiao, 1979). Identifying optimal locations for hydrothermal channels can facilitate further geothermal exploration.

The Lushan area comprises Tertiary meta-sedimentary rocks, specifically low-grade metamorphosed thick mudstone formations known as the Lushan Formation from the Miocene epoch (Hsiao et al., 1980). Based on lithological and stratigraphic variations, the Lushan Formation is subdivided into three members (Figure 1): the Chunyuan Member, the Yuanfeng Member, and the Kunyang Member, from bottom to top. The Chunyuan Member, the lowest layer, consists of slate interbedded with thin layers of fine-grained meta-sandstone. The Yuanfeng Member, the middle layer, consists of interbedded meta-sandstone and slate. The Kunyang Member, the uppermost layer, consists of slate interbedded with meta-sandstone (Lo and Yang, 2002).

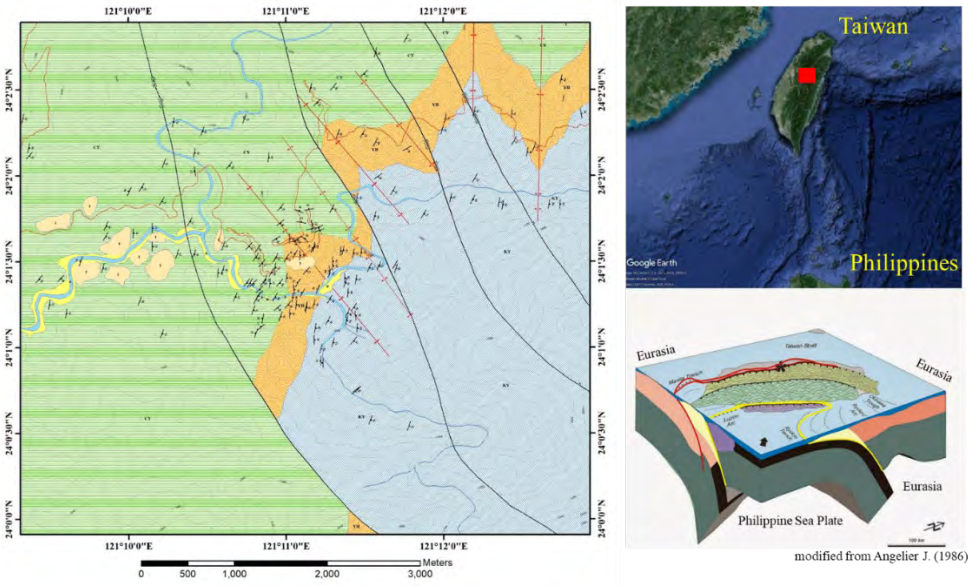

Figure 1: Geological map of the Lushan area, Taiwan. The green represents the Chunyang member, the orange represents the Yuanfeng member, and the blue represents the Kunyang member.

Although these metamorphic rocks have relatively low porosity, they are prone to fracturing due to the external forces during metamorphism. These fractures create void spaces that could serve as conduits for fluid flow, enhancing the reservoir properties. The well-developed cleavage in the slates from the Lushan area, coupled with the presence of four fault zones, should have generated extensive fracture zones, providing favorable conditions in geothermal exploration due to high porosity and permeability properties.

3. Data and Methods

3.1 Data elements

After a fault occurs, it generates a fault damage zone, which is usually accompanied by secondary faults and fractures (e.g., Bruhn et al., 1994; Billi et al., 2003; Odling et al., 2004; Berg and Skar, 2005; Faulkner et al., 2010; Choi et al., 2016), resulting in higher degree of fracturing in these areas compared to the wall rock. This study aims to identify areas influenced by fault damage zones through its characteristic features. We collect the following three types of data to investigate the degree of fracturing in the Lushan area:

(1) Outcrop scale fractures

Outcrops in the field directly reflect whether they have been affected by fault activity. If affected, more fractures or secondary fault structures can be observed on the outcrops. Therefore, it is necessary to conduct field surveys on the freshly exposed outcrops, measure the orientation data of fractures, and take photographs. In addition to the data obtained from field surveys, this study also references the results of the joint density survey of the Lushan area by Hsiao et al., 1980. In his survey, the number of joints present on outcrops was recorded every 100 meters, and the joint density was classified into six levels (Figure 2), showing the distribution of joint density at the outcrop locations.

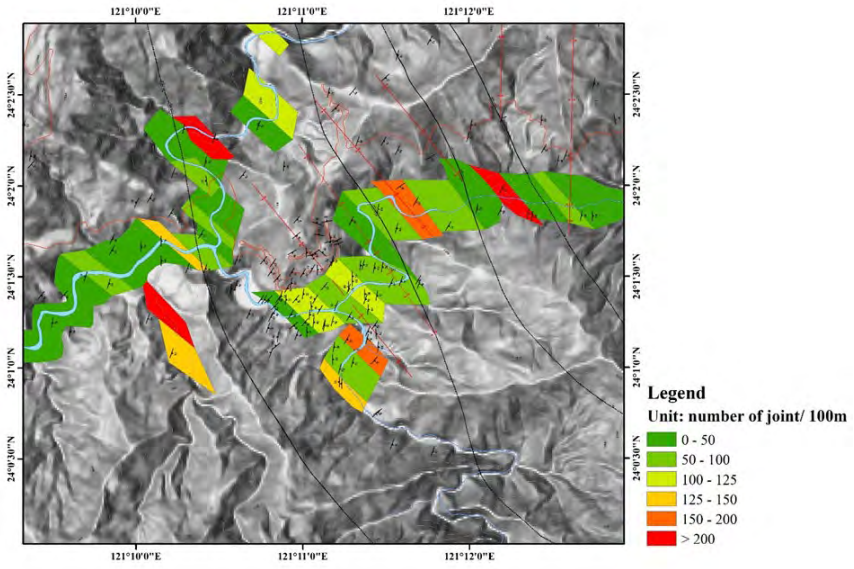

Figure 2. Fracture Density Distribution Map (revised from Hsiao et al., 1980)

(2) Remote sensing scale lineaments

During the field survey of outcrops, it was found that due to the steep terrain and high elevation of over 1,100 meters in the Lushan area, along with rapid river erosion, surveying outcrops in the river valleys is rather difficult. To obtain more comprehensive fracture data, this study uses a DEM to generate a shaded relief map, which effectively displays linear features on the surface, representing fracture patterns at that resolution (Henderson et al., 1996). This method compensates

the lack of surface information due to the difficulty of surveying certain areas in the Lushan region, and introduces substitutes through converted remote sensing data.

(3) Rock porosity

The quantity and morphology of fractures generated in different lithologies would look differently. For examples, lithologies with higher internal porosity tend to have lower compressive strength (Baud et al., 2014), making them more prone to fracturing under stress. The lithology of our study area mainly consists of slate and meta-sandstone. Based on the amount of meta-sandstone present in the three lithological units, the relative porosity content can be estimated. Thus, the meta-sandstone content in the three lithological units, from highest to lowest, is Yuenfeng Member, Kunyang Member, and Chunyang Member, corresponding to their relative porosity levels.

3.2 Processes and methods

Each dataset undergoes various processing steps before being classified into five factors for spatial grid analysis, culminating a fracture strength map (Table-1). Outcrop-scale fracture data are processed into two factors: fracture intensity and fracture connectivity. Remote sensing scale lineaments are processed into the surface lineament intensity factor. Plus the survey results on joint density in the Lushan area (Hsiao et al., 1980) represent the fracture density factor, while the relative porosity factor is demonstrated by the lithology. Five relevant factors are proposed by fracture intensity, fracture connectivity, surface lineament intensity, fracture density, and rock porosity. These are used for spatial grid analysis and produce a fracture strength map in the Lushan area.

Table-1: work flow

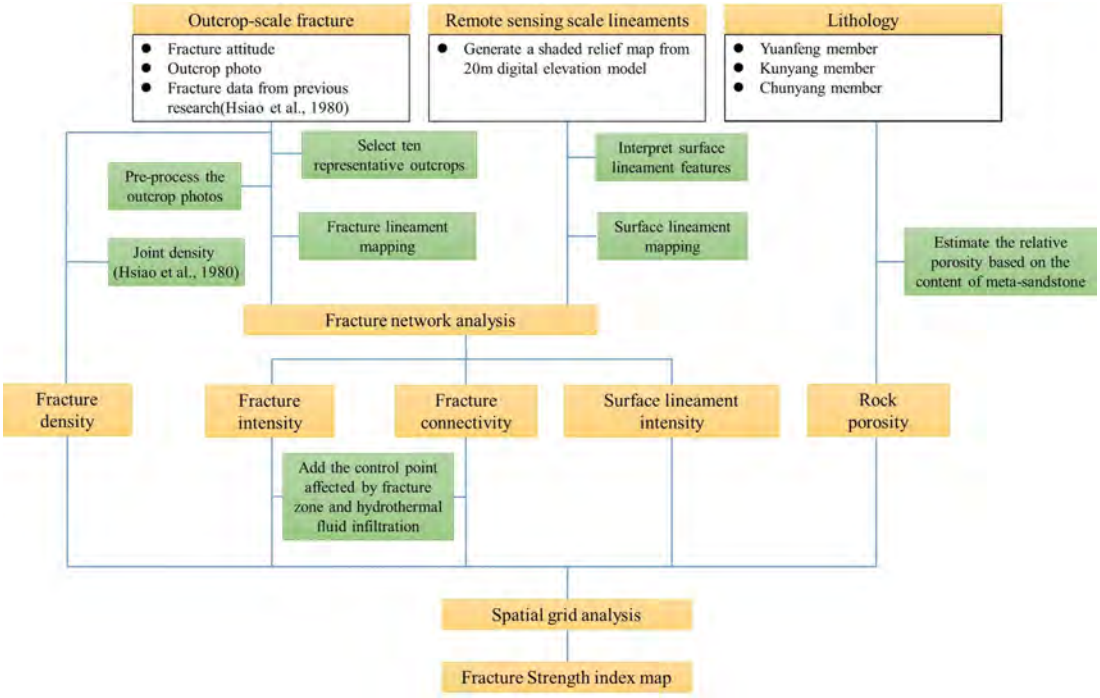

The processing methods for outcrop-scale fracture data and remote sensing scale lineaments are explained as follows:

3.2.1 Outcrop scale fracture lineament mapping

Before converting the surveyed outcrop data into parameters for fracture intensity and fracture connectivity, it is necessary to map the fracture lineaments on the outcrops. To improve analysis efficiency, reduce subjective bias, and shorten the time required for mapping fractures, this study adopts three steps to complete the fracture lineament mapping:

(1) Selection of Representative Outcrops

Based on the distribution of survey locations, the weathering condition, and fracture types, ten representative outcrops are selected from the field for efficiency purpose.

(2) Preprocessing and fracture recognition

To reduce subjective bias and maintain consistent fracture recognition rules, photographs of the representative outcrops were taken (Figure 3a). Adobe Photoshop was used to preprocess these photographs, removing areas that were not part of the outcrops and those with excessive vegetation. Next, the filter tool was used to convert the images into sketch effects, transforming the outcrop photographs into sketch lineament maps (Figure 3b), thereby completing the fracture lineament recognition.

(3) Lineament mapping

To shorten the time required for mapping lineaments, ArcGIS geographic information system software was used. With the ArcScan tool in ArcMap, the black parts of the sketch lineament maps were vectorized into line features, thus completing the fracture lineament mapping (Figure 3c).

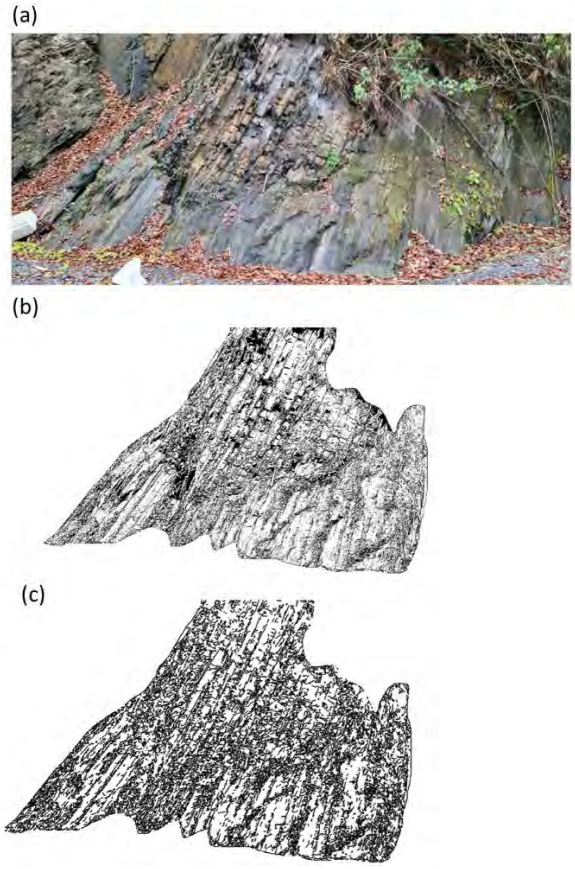

Figure 3. (a) Original outcrop photo before conversion to sketch effect; (b) Outcrop photo after conversion to sketch effect; (c) Conversion of sketch diagram to line features to complete fracture lineament mapping.

3.2.2 Outcrop fracture intensity and fracture connectivity

The fracture lineaments from the outcrops are converted into linear features to analyze fracture intensity and fracture connectivity. The parameters for fracture intensity and connectivity are analyzed based on the geometric and topological characteristics of the fracture network (Sanderson and Nixon, 2015). This analysis method involves calculating the types and quantities of nodes and branches based on the endpoints and intersection points of the fracture lineaments (Figure 4). Then, using formulas from Table-2, the two-dimensional fracture intensity (P_{21}) and average number of connections per branch (C_B) are determined, yielding the fracture intensity and connectivity values for each outcrop (Sanderson and Nixon, 2015; Sanderson and Nixon, 2018; Hansberry et al., 2021).

The P_{21} for fracture intensity is defined by the PXY system (Sanderson and Nixon, 2015). This system provides a specific definition for describing the degree of rock fracturing (Figure 5): P represents the parameter, X is the dimension of the sample, and Y is the dimension of the sampled feature. Thus, P_{21} represents the total fracture length per unit area. C_B, used for calculating fracture connectivity, is a dimensionless network connectivity indicator that measures the connectivity of the fracture network, with values ranging from 0 to 2. A value of 0 indicates no connectivity, 2 indicates full connectivity, and a C_B value of 1.5 suggests sufficient connectivity for fluid flow (Sanderson and Nixon, 2018). To quickly calculate these parameters, the study utilized the

Network Geometry and Topology toolbox developed by Nyberg et al. (2018). This tool provides an automated method for constructing the node topology of fracture networks, reducing the time and potential errors in manually identifying and calculating nodes and branches.

After calculating the fracture intensity and connectivity parameters for representative outcrops, these values are interpolated across the entire area using the Inverse Distance Weighted (IDW) method, with the representative outcrop locations as control points. This interpolation yields the fracture intensity and connectivity distribution in the Lushan area. During field surveys, those control points were observed that some outcrops had fault-induced fracture zones. When mapping fractures, the boundaries of these fracture zones are often marked, and due to extensive fracturing within the zones, the number of fractures may be lower. Some outcrops also have mineral deposits from thermal fluids (e.g., gypsum, sulfur, and calcite) covering the surface, which can affect the mapping of fractures and potentially introduce errors in the calculations of fracture intensity and connectivity. Although efforts are made to avoid selecting these affected areas when choosing representative outcrops, they still hold significance. Fault-induced fracture zones typically indicate the extent of fault damage, and the presence of thermal deposits is evidence of fluid outflow. Therefore, the fracture intensity and connectivity in these areas might be higher. To account for these factors in the analysis, the study includes outcrops with fracture zones and thermal deposits in the analysis, using the highest levels of fracture intensity and connectivity parameters as control points to minimize errors.

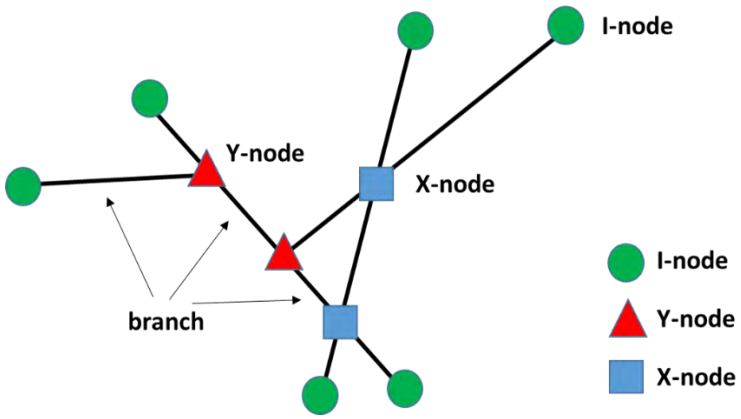

Figure 4. Example of nodes and branches presented by fracture lineaments (modified from Sanderson and Nixon, 2015)

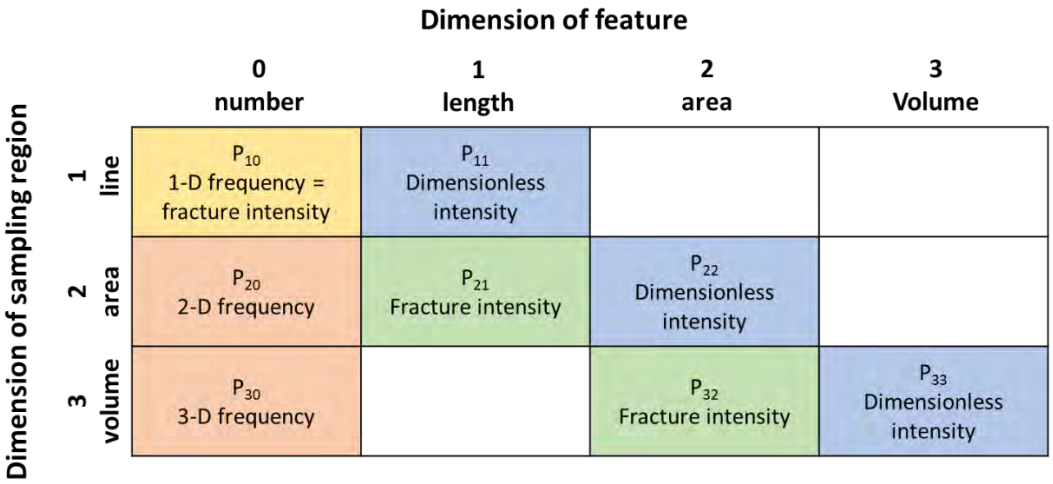

Figure 5. Dimensional significance of the PXY system according to the sampling area and recorded feature dimensions (modified from Hansberry et al., 2021)

Table-2. The topological parameters used in this study

parameter	Notation	Equation or description
Nodes	I,X,Y	Isolated, abutting, crossing
Number of Nodes	N_I, N_Y, N_X	
Number of Lines	N_L	N_L =(NI+NY)/2
Number of Branches	N_B	N_B =(NI+3NY+4NX)/2
Connections per branch	C_B	C_B =(3NY+4NX)/NB
Characteristic (ave.) length	L_C	Average length of lines
Intensity	P_{21}	P_{21} =$N_L L_C$/area

3.2.2 Surface Lineament Intensity

Surface lineament intensity is derived from the surface lineament features identified in the shaded relief map and is calculated using the P_{21} formula. The difference between fracture intensity and surface lineament intensity lies in the scale of analysis: fracture intensity is based on fracture lineaments interpreted from outcrops, while surface lineament intensity is derived DEM.

In this study, the shaded relief map was generated using a 20-meter resolution DEM. To calculate surface lineament intensity at different locations in the study area, the area was divided into 100-meter by 100-meter grids. The P_{21} parameter was calculated for each grid, illustrating the distribution trend of surface lineament intensity.

3.3 Integration of Correlation Factors

After calculating the values for the five relevant factors, it is necessary to integrate all factors to present the geothermal fluid channel scores for various locations in the Lushan area. Considering that the numeric scales of each factor differ, normalization must be performed before they can be

compared and combined. This study uses normalization based on the value ranges of each factor, employing the natural breaks method to categorize the data into five levels. Scores from 5 to 1 are assigned from high to low. Subsequently, the scores for each relevant factor at the same location are summed to determine the geothermal fluid channel score for that location.

4. Results

4.1 Field fracture intensity and fracture connectivity

The locations of the 10 selected representative outcrops and 27 control points are shown in Figure 6. The P_{21} and C_B values for fractures were calculated using the Network Geometry and Topology Toolbox, with the results presented in the table within Figure 6. The fracture intensity values in this area range from 0.021 to 0.069, with the highest at sample #2 and the lowest at sample #7; the branch connectivity values range from 1.049 to 1.702, with the highest at sample #8 and the lowest at sample #10.

Since these outcrop locations were selected as representative, the P_{21} and C_B values were interpolated to other locations using the Inverse Distance Weighted (IDW) method. The data were then categorized into 5 classes using the Natural Breaks (Jenks) method (Figure 7). Based on these classes, the highest classification levels were used to incorporate outcrops with fault-induced fracture zones and those with thermal mineral deposits into the analysis, resulting in the fracture intensity and connectivity factor distribution maps for the Lushan area (Figure 8). The high-intensity regions for fracture strength are mainly located in the southwest and northeast areas. The southwest area is situated along the first fault, suggesting that high fracture strength is due to the fault-induced fracture zone. Since there is no outcrop survey data in the northwest and southeast regions, the interpolated results in these areas remain unchanged, reflecting the same intensity levels, which is a less accurate aspect. The high-intensity regions for fracture connectivity are primarily found in the northeastern area and, to a lesser extent, around the first and second faults. However, when directly observed from the numerical values (Figure 7), there is generally no significant variation across the area.

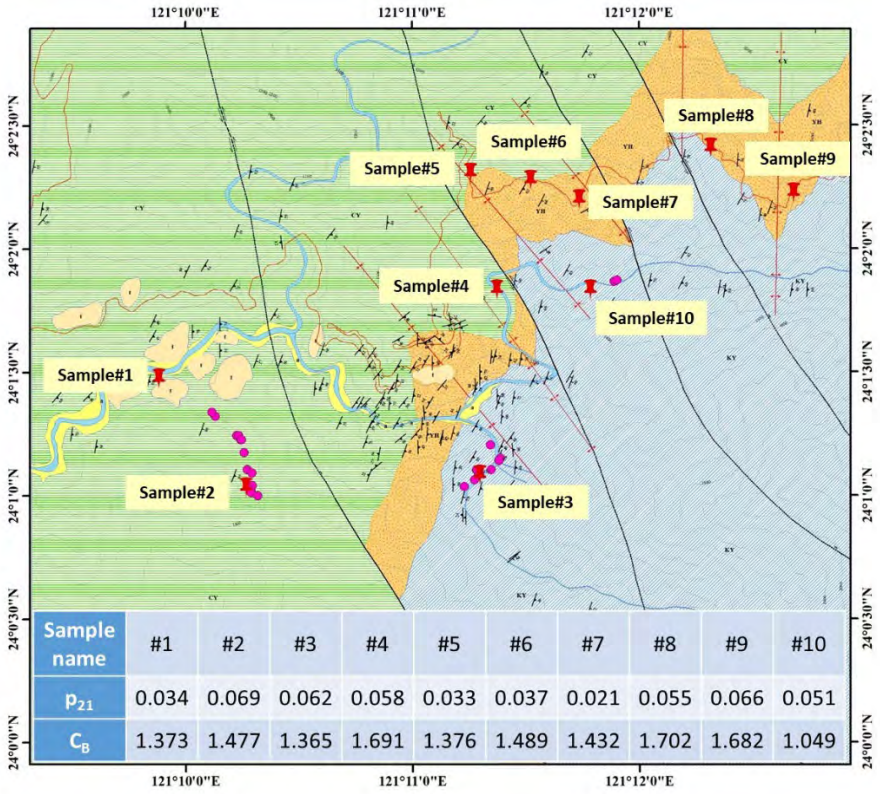

Sample name	#1	#2	#3	#4	#5	#6	#7	#8	#9	#10
P_{21}	0.034	0.069	0.062	0.058	0.033	0.037	0.021	0.055	0.066	0.051
C_B	1.373	1.477	1.365	1.691	1.376	1.489	1.432	1.702	1.682	1.049

Figure 6. Locations of the representative outcrops (10 samples), control points (27 pink circles), and the calculated P_{21} and C_B parameters for each location.

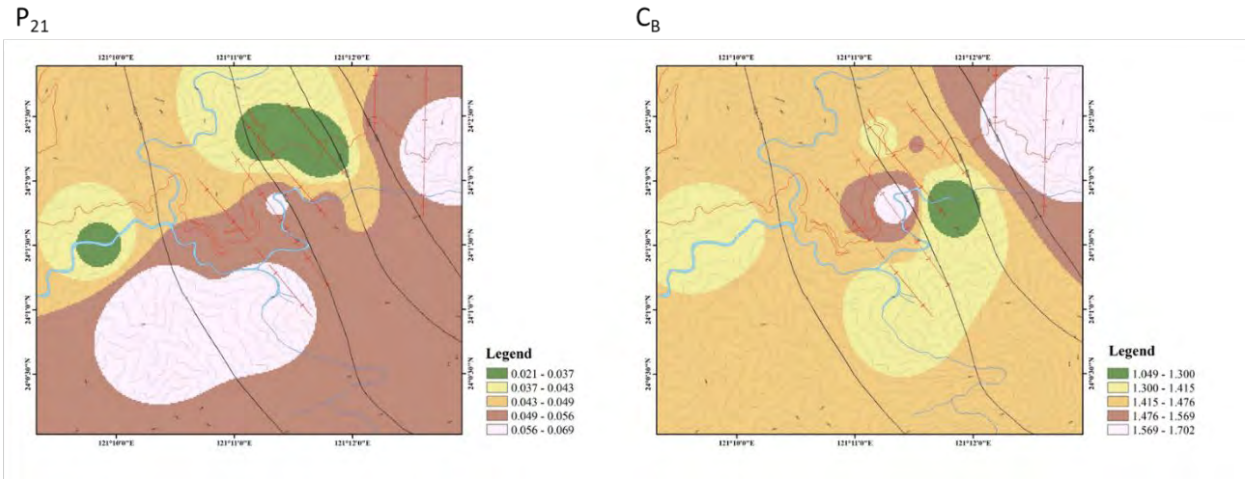

Figure 7. Distribution maps of fracture intensity factor (P_{21}) and fracture connectivity factor (C_B)

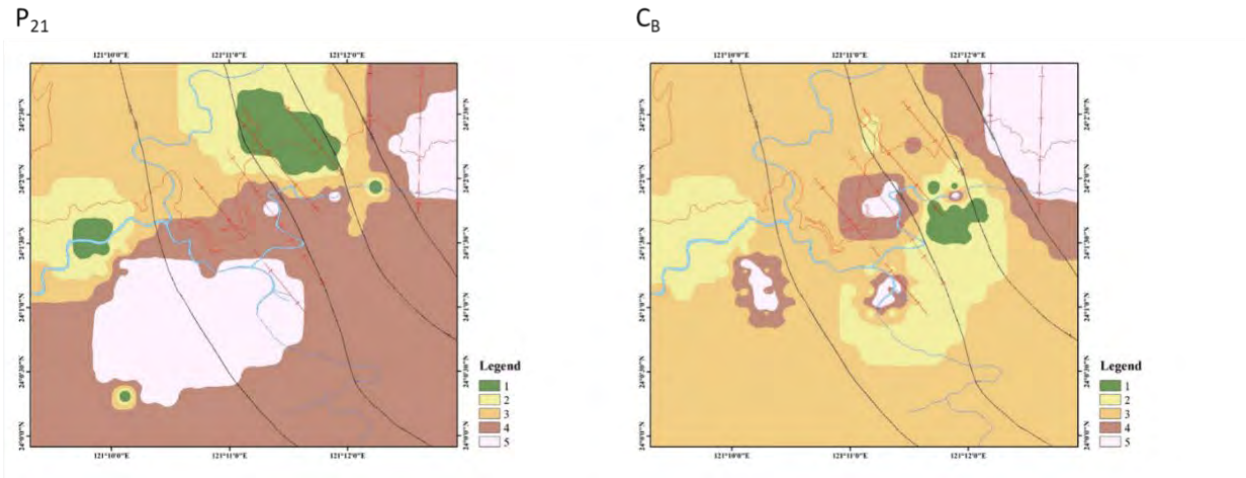

Figure 8. Distribution maps of fracture intensity factor(P_{21}) and fracture connectivity (C_B) factor grades.

4.2 Surface Lineament Analysis

Using a 20-meter resolution DEM, a hill-shade map was generated, and surface lineament features were mapped, as shown in Figure 9a. A total of 769 surface lineaments were mapped. These lineaments primarily display two dominant orientations (Figure 9b): N10°W-S10°E and N45°W-S45°E, with secondary orientations including N20°E-S20°W, N60°E-S60°W, and N85°E-S85°W. Given that the four left-lateral faults on the geological map extend in the N20°W direction, the related fractures generated due to these faults' displacements are shown in Figure 9c, where R-shear, R'-shear, and P-shear directions are N35°W, N85°E, and N10°W, respectively (Woodcock and Schubert, 1994). These directions are reflected in the surface lineaments, indicating that the lineaments are influenced by faulting and that the intensity of lineaments varies in specific areas.

The study area was divided into 100-meter by 100-meter grids to calculate the P_{21} values for each grid. The P_{21} values were then classified into 5 grades using the natural breaks method, resulting in the surface lineament intensity distribution map for the Lushan area (Figure 10). Except for the northeastern region, high-intensity lineament areas are mainly concentrated around fault zones. Comparison of these results with the fracture intensity factor grade distribution map (Figure 8) reveals similar results, except for some differences at the northern end of the third fault. However, due to the comprehensive nature of the surface lineament mapping, intensity trends are also observed in the northwest and southeast parts of the study area.

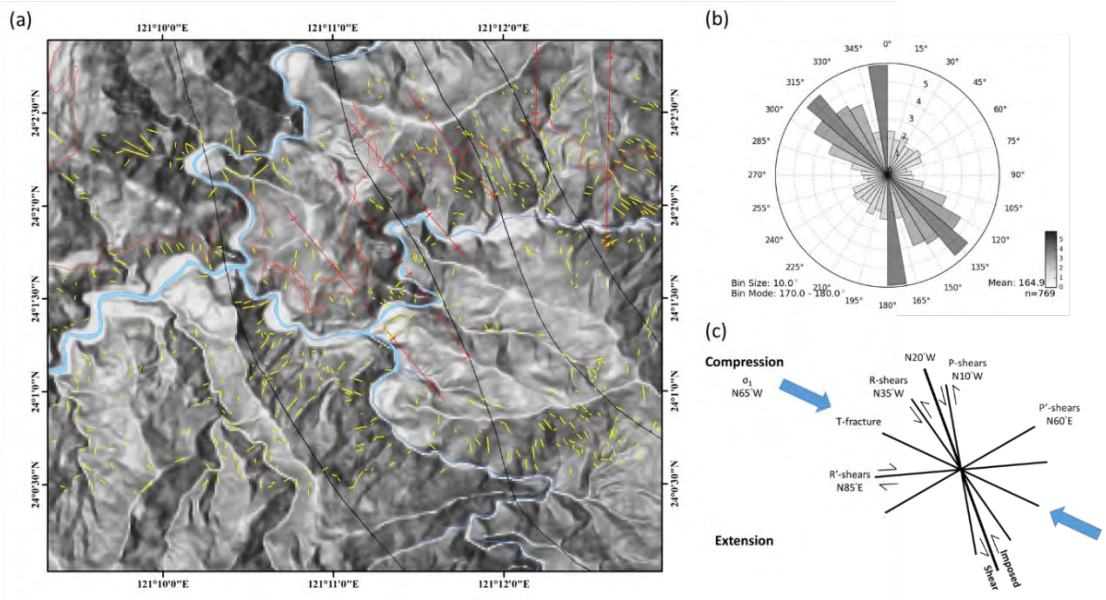

Figure 9. Surface lineament analysis. (a) Yellow lines represent the mapped surface lineament features. (b) Rose diagram of the directions derived from the surface lineament features. (c) Directions of fractures related to left-lateral faults in the Lushan area.

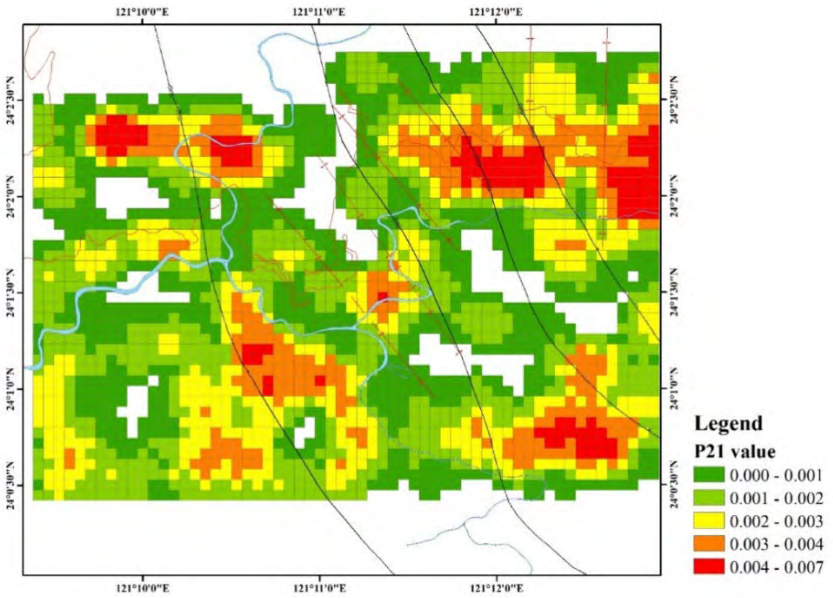

Figure 10. Distribution map of surface lineament intensity.

4.3 Fracture strength index map

Integration of surface lineament-related factors requires normalization before aggregation. To present the fracture strength distribution in the Lushan area, the study area was divided into grids

of 300 meters by 300 meters. Each grid's fracture index score was collected, and then Inverse Distance Weighted (IDW) interpolation was applied to display the fracture strength in five intensity levels (Figure 11).

According to our fracture strength index map, the highest scores are found in the northeastern region, followed by the central part of the study area, and lowest scores are around the western and northern parts. Such a result from this map is consistent with the locations of many geothermal manifestations.

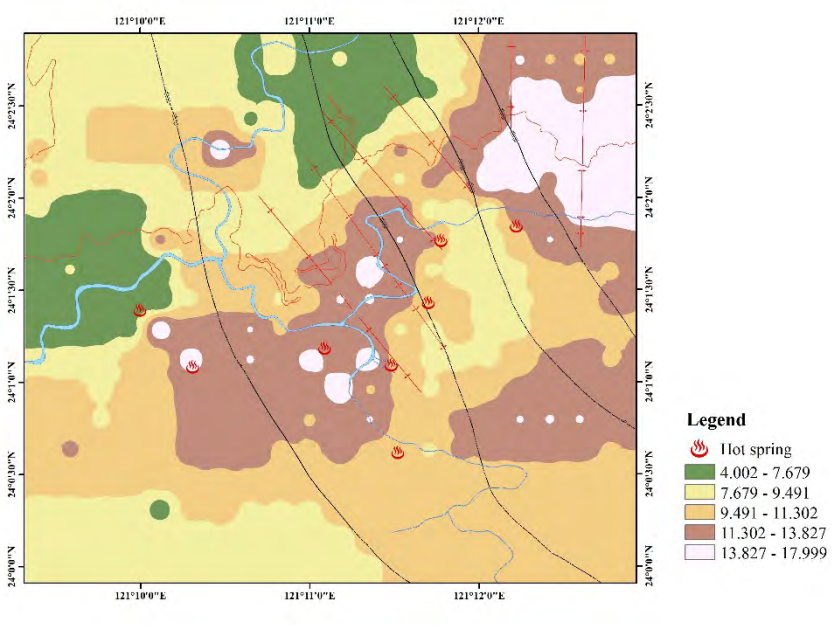

Figure 11. Fracture strength index map

5. Discussion

5.1 Advantages of using photo processing to record field fracture lineament data

Fracture analysis typically involves recognition and drawing fracture lineaments, which is often a time-consuming and labor-intensive task. Prolonged observation and analysis can lead to visual fatigue and decreased attention, making interpreters prone to missing details or making errors. Additionally, subjective factors such as the interpreter's expertise, experience, and personal biases can contribute to variability in fracture lineament interpretation (Bond, 2015). These subjective factors leading to inconsistent or inaccurate results should be eliminated or minimized through certain standard procedures and auxiliary techniques.

To mitigate such error-prone issues, this study employs a software tool in Photoshop for preprocessing into well recognizable fracture lineaments. The procedure starts with removing non-target areas in an outcrop photo, and then utilizes filters to convert the picture into simple black-

and-white line drawings. A digitized vector data can be imported to the ArcGIS platform for other processes.

However, such a conversion process using Photoshop may be failed to produce quality results and even worse than manual recognition. This could result from the complexity of the photo content, such as significant vegetation covers or severe weathering on the outcrop surface, where weathering crusts and other materials may be mistakenly interpreted as lines. These falsely recognized lines can impact the final fracture lineament drawing. Therefore, choosing high quality outcrop photos with a clean and fresh rock surface for the software processing is also a vital step.

5.2 Allocation of weight ratios for factors

In this study, the final fracture strength scores were calculated by summing the normalized scores of each five factors using equal weighting, implying that all factors are considered equally important. However, analysis results suggest that some data are more reliable, while some factors are deemed more relevant. By adjusting the weights according to the data accuracy, data precision, or the relevance of correlation, the result may be improved and closer to the reality.

For example, in this study, the orientation of surface lineaments is consistent with the fracture directions generated by fault movements, and it aligns with the fracture strength results at the outcrop scale. This consistency enhances the credibility of the surface lineament data, suggesting that its weight ratio should be increased. Conversely, the results for fracture connectivity show less variation, reducing the significance of this data and justifying a decrease in its weight ratio. For a better result, the weight ratios for each factor in Fracture Intensity, Fracture Connectivity, Surface Lineament Intensity, Rock Porosity, and Cleavage Density may be adjusted to 20%, 10%, 40%, 10%, and 20%, respectively.

5.3 The relationship between fracture patterns and fault distribution

The geological map drawn in this study (Figure 1) is based on the additional field investigations and references to previously published geological maps at this area (Chang and Chiao, 1979; Hsiao rt al., 1980; ITRI, 1984; Lo and Yang, 2002). While the general trends of the geological structures in those previous studies are similar, there were some specific faults and folds that have been interpreted differently, also regarding the location of fault structures and their impact on the Lushan area. To reconcile these geological maps and provide a clearer picture of the distribution and effects of fault structures in this region, this study investigates the characteristics of fractures formed by fault movement.

The fractures measured from the field survey were categorized into six area, labeled A to F, based on their proximity from West to East (Figure 12b). By organizing the fractures in each area, a total of six fracture sets were identified. The abundance of fractures in each area was categorized into three levels: high (red), medium (blue), and low (green), and presented in the table grid (Figure 12a).

Among these six fracture sets, all but the third set correspond to fractures generated by the left-movement faults (Figure 12c). In area B, C, and D, secondary faults or fault-induced fracture zones are commonly observed. These areas are primarily dominated by the fifth and sixth fracture sets, corresponding to the R-shear and T-fracture generated by faults (Figure 12c). Moving from area E towards area F, the number of R-shear fractures are fewer in area E than that in area F. Conversely, the number of T-fractures in area F drops to a medium level, with the dominant fracture set becoming the first set, R'-shear.

The variation in the number of R-shear and T-fractures suggests that area B, C, D, and E are within major deformation zones interacting with the three main faults from the central of our study area in the Lushan region, with similar changes in fracture sets and quantities. The right-most fault affects area F locating westerly in a separated deformation area, which is probably influenced by other factors at the northeast direction outside of our study area.

From above observations of trends and quantities in each fracture set, we may conclude that one major deformation area is at the center of our study area, including area B, C, and D, two faults, and along the Yuanfeng Member that containing relatively more meta-sandstone component; the other deformation area is located at northeastern corner of our study area, including area E and passing by one fault.

(a)

Area \ fracture set	Set 1 R'-shear	Set 2 P'-shear	Set 3 cleavage or other fracture	Set 4 P-shear	Set 5 R-shear	Set 6 T-fracture or other fracture
A	E-W/ 80-90˚S E-W/ 65-90˚N	N60˚E/ 75-90˚S	N35˚E/ 75-90˚N N35˚E/ 80-90˚S	N-S/ 50-75˚W	N45˚W/ 85˚S	N60˚W/ 60-90˚S
B			N30˚E/ 0-30˚N	N15˚E/ 0-30˚N	N30˚W/ 40-70˚S N30˚W/ 30-40˚N	N70˚W/ 70-90˚S N70˚W/ 80-90˚N
C			N30˚E/ 35-40˚N	N15˚W/ 70˚S	N45˚W/ 70-90˚S	N60˚W/ 65-80˚S
D		N60˚E/ 85˚S		N15˚E/ 30˚N	N45˚W/ 70-90˚S	N60˚W/ 75-90˚S
E	E-W/ 75-85˚S	N60˚E/ 10-20˚S	N40˚E/ 60-85˚N	N15˚E- N15˚W/ 70-90˚W	N40˚W/ 75-90˚S	N60˚W/ 70-90˚S
F	E-W/ 80-90˚S E-W/ 65-90˚N	N70˚E/ 80-90˚S N70˚E/ 75-90˚N	N35˚E/ 75-90˚N N35˚E/ 80-90˚S	N-S/ 50-75˚W	N30˚W/ 55-60˚S	N55˚W/ 60-90˚S

the main set intermediate set least prevalent set

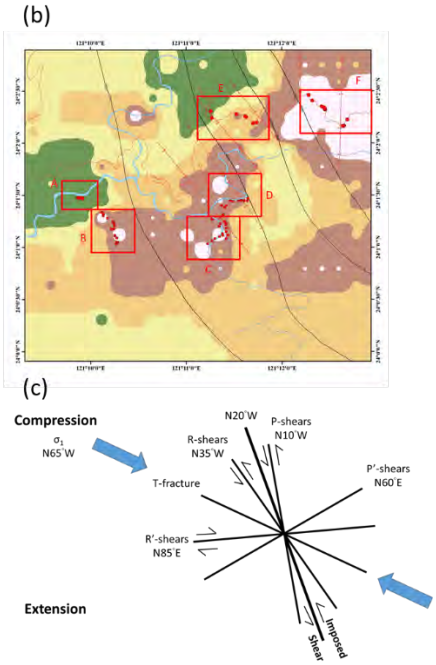

Figure 12. (a) The fracture set for each area. (b) same as Figure 11. (c) same as Figure 9c.

5.4 The implication between fracture intensity pattern and geothermal reservoirs and fluid pathways

Good targets of traditional geothermal reservoirs typically exist in rocks having higher porosity, permeability, and fracture networks such as basalts and sandstones. Geothermal development in

Taiwan faces unique challenges, as the primary geothermal targets are in metamorphic rocks with low porosity where the heat sources are associated with rapid crustal uplift and plate collision activities in the Central Mountain Range. Thus, relying solely on rock porosity is not effective for projecting potential reservoir and fluid pathway locations, and other critical factors must be considered.

Fracture patterns are an important consideration. Extensive fractures can act as conduits for fluid flow and/or as reservoirs confined by more compact rocks. Metamorphosed sandstones, which are structurally uniform and compressed, often have larger fracture spaces and relatively straightforward fracture networks; metamorphic sandstone and slate interlayers, often create a complex fracture network in slate than meta-sandstones are typically more suitable as reservoirs than slates. However, research in the Lushan area reveals that the P21 and CB values for meta-sandstones in the Yuanfeng Member (sample #5, #6, and #7 in Figure 6) are lower, while the data for the Chunyuan Member and Kunyang Member are higher (sample #2, #3, #4, and #10 in Figure 6).

This study hypothesizes that this may be due to the slates, after being affected by faults, forming stronger and more continuous fracture zones due to the interaction between fault-generated fractures and the dense cleavage developed in the slates. Based on the above assumption, we may speculate that the slate region within the Lushan area may offer a more favorable environment for potential geothermal reservoirs and hydrothermal conduits. However, additional research is necessary to substantiate this hypothesis.

5.5 Future attempts

The main factors analyzed in this study are based primarily on surface survey data. While this data can show the distribution of surface rupture severity and serve as a reference for subsurface fragmentation, it is hard to reflect actual subsurface conditions. If any subsurface data (e.g., MT data, optical imaging logging data from boreholes, etc.) were incorporated into the analysis, it would allow for a more comprehensive understanding of the three-dimensional fragmentation distribution in the Lushan area. Therefore, the future plan is to include subsurface data in the correlation factors and analyze them together to create a three-dimensional map of fragmentation intensity distribution for the Lushan area or any other potential targets.

Conclusion

- This study utilizes common image processing software to preprocess outcrop photos, simplifying the complexity of outcrop fracture recognition. By applying consistent criteria, this approach also enhances the accuracy of future fracture analysis.
- Representative outcrops are used as control points in this study, and interpolation methods are employed to extend the data across the entire area, together with the use of lineament features from DEM, addressing the issue of having few or difficult-to-reach outcrops.

- Combining the geological and fracture strength maps, slaty area tends to produce stronger fracture intensity than meta-sandstone area, affected by the trends of faulting and cleavage pattern.
- The fracture strength index map from this study may be relevant to the hydrothermal channel or geothermal reservoir in the Lushan area, offering important reference data for geothermal exploration in the region.

Acknowledgement

This study, including data obtained from field surveys and the mapping process, is supported by the project “Three-dimensional geological model construction of the Lushan area, Nantou” (Project #B11228), funded by the Central Geological Survey, Ministry of Economic Affairs.

REFERENCES

Angelier, J. ,1986. "Preface to the special issue of Geodynamics of the Eurasian-Philippine Sea plate boundary." *Tectonophysics*, 125, IX-X.

Bruhn, R.L., Parry, W.T., Yonkee, W.A., and Thompson, T., 1994. "Fracturing and hydrothermal alteration in normal fault zones." Pure Appl. *Geophys.* 142, 609–644.

Billi, A., Salvini, F., and Storti, F., 2003. "The damage zone–fault core transition in carbonate rocks: implications for fault growth, structure and permeability." *J. Struct. Geol.* 25, 1779–1794.

Berg, S.S., and Skar, T., 2005. "Controls on damage zone asymmetry of a normal fault zone: outcrop analyses of a segment of the Moab fault, SE Utah." *J. Struct. Geol*. 27, 1803–1822.

Baud, P., Wong T.F., Zhu, W., 2014. "Effects of porosity and crack density on the compressive strength of rocks." *International Journal of Rock Mechanics & Mining Sciences*, 67, 202-211.

Bond, C. E., 2015. "Uncertainty in structural interpretation: Lessons to be learnt." *Journal of Structural Geology*, 74, 185-200.

Chang, P.-T., and Chiao, C.-H., 1979. "Geology of Lushan Geothermal Area." *Mining &Metallurgy*, 23(2), 65-72.

Chen, C.H., 1975. "Thermal waters in Taiwan, a preliminary study. In: Proceedings of the Grenoble Symposium, August 1975." Pub. #119. *International Association of Hydrological Sciences*, pp. 79–88.

Choi, J.H., Edwards, P., Ko, K., and Kim, Y.S., 2016. "Definition and classification of fault damage zones: A review and a new methodological approach." *Earth-Science Reviews*, 152, 70-87.

Faulds, J., Coolbaugh, M., Bouchot, V., Moea, I., and Oguz, K., 2010. "Characterizing Structural Controls of Geothermal Reservoirs in the Great Basin, USA, and Western Turkey: Developing

Successful Exploration Strategies in Extended Terranes." World Geothermal Congress 2010, Apr 2010, Bali, Indonesia. 11p. hal-00495884

Faulkner, D.R., Jackson, C.A. L., Lunn, R.J., Schlische, R.W., Shipton, Z.K., Wibberley, C.A. J., and Withjack, M.O., 2010. "A review of recent developments concerning the structure, mechanics and fluid flow properties of fault zones." J. Struct. Geol. 32, 1557–1575.

Hansberry, R.L., King, R.C., Holford, S.P., Hand, M., and Debenham, N., 2021. "How wide is a fault damage zone? Using network topology to examine how fault-damage zones overprint regional fracture networks." Journal of Structural Geology. 146, 104327.

Henderson, D.B., Ferrill, D.A., and Clarke, K.C., 1996. "Mapping geological faults using image processing techniques applied to hill-shaded digital elevation models." Proceeding of Southwest Symposium on Image Analysis and Interpretation, San Antonio, TX, USA, 1996, 240-245, doi: 10.1109/IAI.1996.493760.

Hochstein, M. P., 1990. "Classification and assessment of geothermal resources." In: Dickson, M. H., and Fanelli, M. (Eds.), Small Geothermal Resources: A Guide to Development and Utilization, pp. 31-57.

Hsiao, P.-T., Tseng, C.-S., and Wey, S.-K., 1980. "Geology and Geothermal Potential of the Lushan Area, Nantou." Petroleum Geology of Taiwan, No17, 107-123.

Huang, C.Y., Wu, W.Y., Chang, C.P., Tsao, S., Yuan, P.B., Lin, C.W., and Xia, K.Y., 1997. "Tectonic evolution of accretionary prism in the arc–continent collision terrane of Taiwan." Tectonophysics 281, 31–51.

ITRI, 1984. "Report on Exploration and Assessment Of Geothermal Resources In Taiwan — Lushan Geothermal Area." EMRO Report, 207.

Lee, C.-R., Chiang, T.-I., and Chen, J.-H., 1994. "Compilation of Geothermal Exploration Data of Taiwan." Research Report of Energy Research Development Foundation, Energy Commission, Ministry of Economic Affairs, 06-3-83-0252-2. (in Chinese).

Lee, Y.-C., Chen, C.-C., Liu, T.-K., Ho, H.-C., Lu, H.-Y., and Lo, W., 2006. "Mountain building mechanisms in the Southern Central Range of the Taiwan Orogenic Belt – From accretionary wedge deformation to arc-continental collision." Earth Planet. Sci. Lett. 252, 413–422.

Lo, W., and Yang, C.-N., 2002. "Wushe – Geological map of Taiwan, scale 1:50,000." Central Geological Survey, MOEA.

Nyberg, B., Nixon, C.W., and Sanderson, D.J., 2018. "NetworkGT: A GIS Tool for Geometric and Topological Analysis of Two-Dimensional Fracture Networks." Geosphere, 14(4).

Odling, N.E., Harris, S.D., and Knipe, R.J., 2004. "Permeability scaling properties of fault damage zones in siliclastic rocks." J. Struct. Geol. 26, 1727–1747.

Sanderson, D.J., Nixon, C.W., 2015. "The use of topology in fracture network characterization." Journal of Structural Geology. 72, 55–66.

Sanderson, D.J., Nixon, C. W., 2018. "Topology, connectivity and percolation in fracture networks. " Journal of Structural Geology. 115, 167–177.

Song, S.-.R., and Team Members of Geothermal Focus Center, NEP-II, MOST, 2015. "Exploration of deep geothermal resources and evaluation of sites for enhanced geothermal system in the Ilan area." *Annual Report of Geothermal Focus Center*, NEPII, MOST.

Song, S.-.R., and Lu, Y..-C., 2018. "Geothermal explorations on the slate formation of Taiwan: In: Ismail." Basel I. (Ed.), *Renewable Geothermal Energy Explorations*, IntechOpen, doi: 10.5772/intechopen.81157.

Teng, L.S., Song, S.R., Yeh, E.C., Lin, A.T., Liu, C.M., and Tsai, Y.L., 2013. "Tectonic appraisal of geothermal potential of Taiwan." Western Pac. *Earth Sci.* 13, 1–38.

Wang, C., Lo, W., Song, S-R, and Wu, M-Y, 2021. "Geothermal energy development roadmap of Taiwan by play fairway analysis." *Geothermics*, 97, 2021, 102242, https://doi.org/10.1016/j.geothermics.2021.102242.

Geophysics

Exploration of Deep Hot Sedimentary Aquifer Geothermal Systems in The Midyan Basin of Saudi Arabia by ENOWA-NEOM

[1] Ahmed Alhani, [1]Ammar Alali, [1]Chelsea Cervantes, [1]Vicky Ray Chandra, [2]Lukman Sutrisno, and [2]Jon Jonsson

[1]Strataphy

[2]ENOWA

Keywords

Geothermal, Hot Sedimentary Aquifer, Midyan Basin, Saudi Arabia

ABSTRACT

This study was conducted to investigate the potential for a hot sedimentary aquifer geothermal system within the NEOM area in the northwest of Saudi Arabia using regional geophysics and 2D seismic lines covering the main known basins along the Red Sea coast. The thickness of each basin was investigated to determine the maximum depth to basement within each basin. The Red Sea sedimentary basin deposition started as part of the Red Sea rift sequence and is mainly influenced by tectonic activity within each subregion of the early rift. The Red Sea rift began ~32 Ma and has created the basin that includes the modern-day Red Sea and the Gulf of Suez. The rift presents itself as a series of half grabens that extend from Bab Al-Mandab Strait in the south to the Mediterranean in the north. This tectonic arrangement was superimposed in the northern Red Sea by the strike-slip tectonics of the Gulf of Aqaba in which began movement ~12 Ma as part of the left-lateral Dead Sea Fault system.

This is the first attempt at geothermal exploration in these sedimentary basins, where currently no known systems exist. The basis for designing this exploration work is on the premise of conduction heat flow, with no impact of convection or magmatic processes that would diverge away from the background heat gradient. Using the known heat gradient in the area from oil and gas wells, the intent is to drill into a reservoir at a depth that delivers the necessary temperature for use as geothermal power, heating, and refrigeration. Using a greenfield exploration approach, the workflow has included the analysis of regional geology, heritage well data, published technical papers, geologic map data, 2D imagery, airborne magnetic and gravity data, along with the acquisition and interpretation of 180 km of 2D seismic. Of the mapping completed thus far, several targets were identified in the Midyan area where the investigation suggests deep basins which could host Hot Sedimentary Aquifer geothermal systems. The targets in the area lie in syn-rift sedimentary reservoir-seal pairs that are deeper than 3 km at present and are either within marine

turbidite sands, or early-rift continental sands capped by marine shales. The 2D seismic interpretation along with the assessment of other existing data will form the basis of discussion as to how the identified prospects were chosen.

1. Introduction

NEOM is the planned independent economic zone in the northwest of Saudi Arabia. It is born out of the ambition of Saudi Arabia's Vision 2030 to see the country develop into a pioneering and thriving model of excellence in various important areas of development. ENOWA is a 100% subsidiary of NEOM that is tasked with delivering NEOM's energy related vision to life. This vision is to become the world's most advanced renewable energy hub and the first at-scale fully renewable electrical system. NEOM aspires to have a high degree of electrification, which results in increased electricity requirements compared to traditional economies. To provide affordable renewable electricity, ENOWA aims to develop geothermal resources.

One of the main geothermal plays in development in the NEOM region is the hot sedimentary aquifer (HSA) geothermal system within the Midyan Basin. This is the first attempt at geothermal exploration in these sedimentary basins, where currently no known systems have been proven to exist, nor has geothermal infrastructure been established. This paper will discuss the exploration of the Midyan Basin's potential to host a hot sedimentary aquifer geothermal system from the standpoint of both existing and acquired geophysical data, and the identification of potential geothermal prospects that have resulted from the assessment.

2. Available Data

2.1 Published Regional Work

While there are not yet any published works about the NEOM development specifically, regional studies of the larger Red Sea and Midyan Basin areas have assisted in creating the framework and context of the depositional and structural history of the basin. Published geophysical studies of the area have also provided a baseline for the planning and expectations of further surface exploration.

2.1.1 Regional tectonic history

Bosworth (2015) provides a detailed description of the geological evolution of the Red Sea, along with Hughes & Johnson (2005), which in turn provides a detailed account of the lithostratigraphy of the Red Sea Region. These regional studies guide our understanding of the tectonic history of the Midyan Basin region and provide detailed information on the different lithological units that exist within the larger basin. The lithostratigraphy of the region is described in further detail in Section 3.3.

2.1.2 Regional magnetics and gravity

Regional gravity and magnetic data are available from SGS Saudi Arabia. This dataset was interpreted and used in choosing the locations of the 2D seismic lines for the seismic field study as described in sub-section 2.4. It is also used to de-risk the seismic interpretation by linking the newly acquired 2D seismic lines to the non-seismic surveys.

2.1.3 Published seismic profiles

In 2014, Tubbs et al., through one of the Saudi Aramco geologic field programs, acquired onshore 3-D, transition zone 2-D and offshore 2-D seismic data in the Midyan Basin to provide further insight into the geological history of the region. This study provides a detailed assessment of the structural interpretation of the Midyan Basin, along with a lithostratigraphic and seismic stratigraphic interpretation of the Midyan area.

2.2 Outcrop Geology

The surface geology of the NEOM area is based on a regional geological map of the NEOM area. Supporting surface geological interpretation includes satellite imagery maps and structural maps that have assisted in mapping structural faulting and observable lineaments.

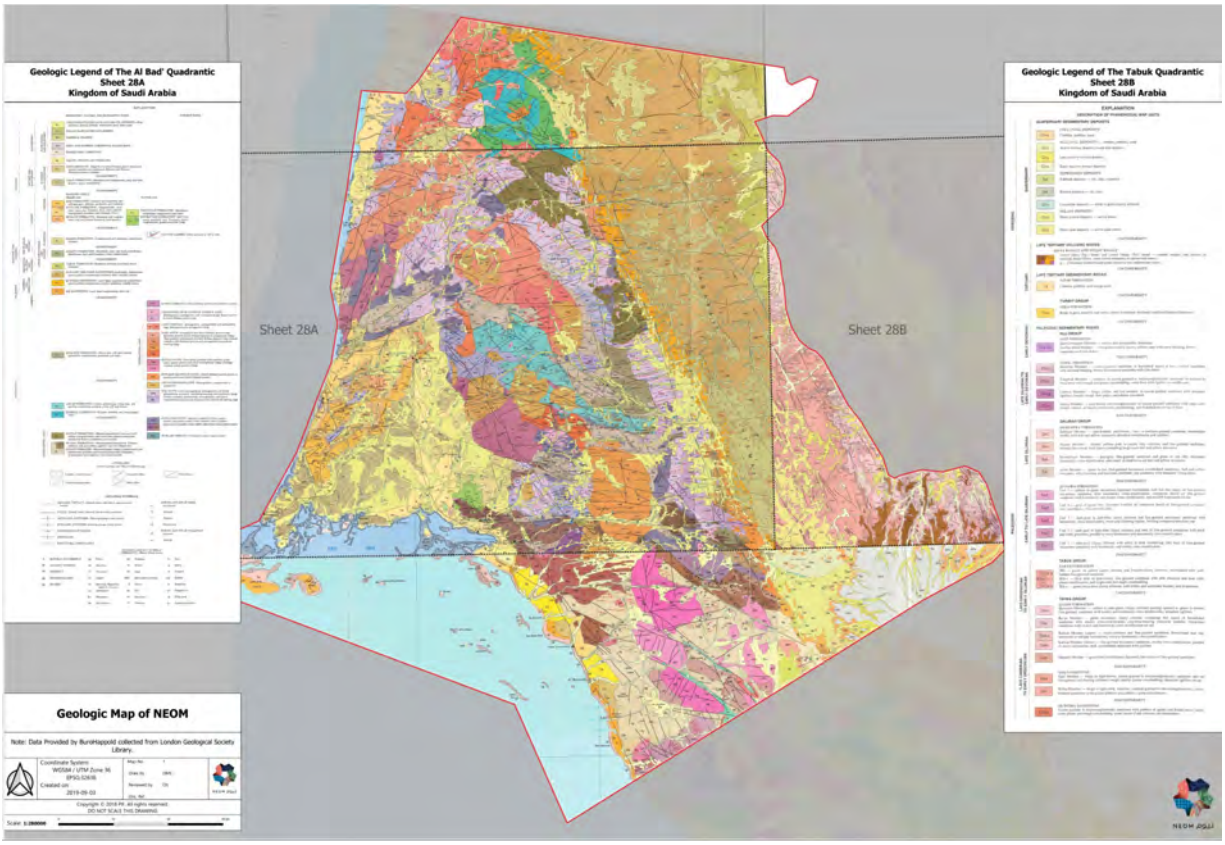

Figure 1. A regional surface geological map of the NEOM area. A more detailed regional context is provided in figures 5 and 6.

With these maps as a basis for field exploration, evidence of late Quaternary faulting was investigated during a field visit in August of 2022. From what was observed, it is thought that scarps found in the field were possibly associated with recent faulting and salt movement.

2.3 Legacy Well Data

Temperature surveys from 5 shallow (< 3000 m total depth) oil and gas wells drilled in the Midyan Basin were obtained. Measured temperatures in these wells reveal conductive geothermal gradients between 30-35 °C/km.

Limited information from shallow water wells that have been drilled in the area were also obtained, with majority of the wells drilled in the area of Tabuk, which is a town directly northeast of the border of the NEOM area. The wells that were drilled in Tabuk reach up to 600-1250 m in depth, and temperatures around 40 °C.

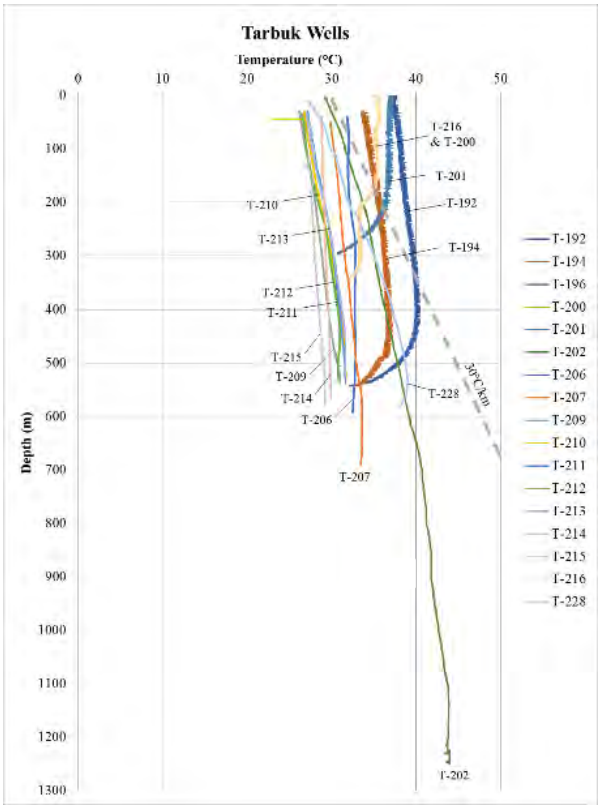

Figure 2. Temperature of water wells drilled NW of the town of Tabuk, directly NE of the NEOM area.

In addition, 1201 shallow geotechnical boreholes have been drilled along the western coast of Saudi Arabia and along the eastern shore of the Gulf of Aqaba. These wells do not surpass a depth of 60 m and present information of the shallowest formations in the area.

2.4 Newly Acquired 2D Reflection Seismic Data

As part of the study to identify areas of potential geothermal resources, 15 (fifteen) 2D onshore seismic lines were acquired in 2023 in the NEOM area to gather detailed subsurface information,

characterize the reservoir, identify structural features and reduce exploration risks. The seismic survey reached a total length of 180 km. The results of this seismic field survey helped identify the Midyan Basin as one of the main areas of interest for hot sediment aquifer exploration. The processing sequence follows a full production Pre-Stack Time Migration (PSTM) sequence to improve the overall structural imaging and resolution.

Figure 3. The locations of the seismic profiles in the Midyan area of the seismic survey of March 2023.

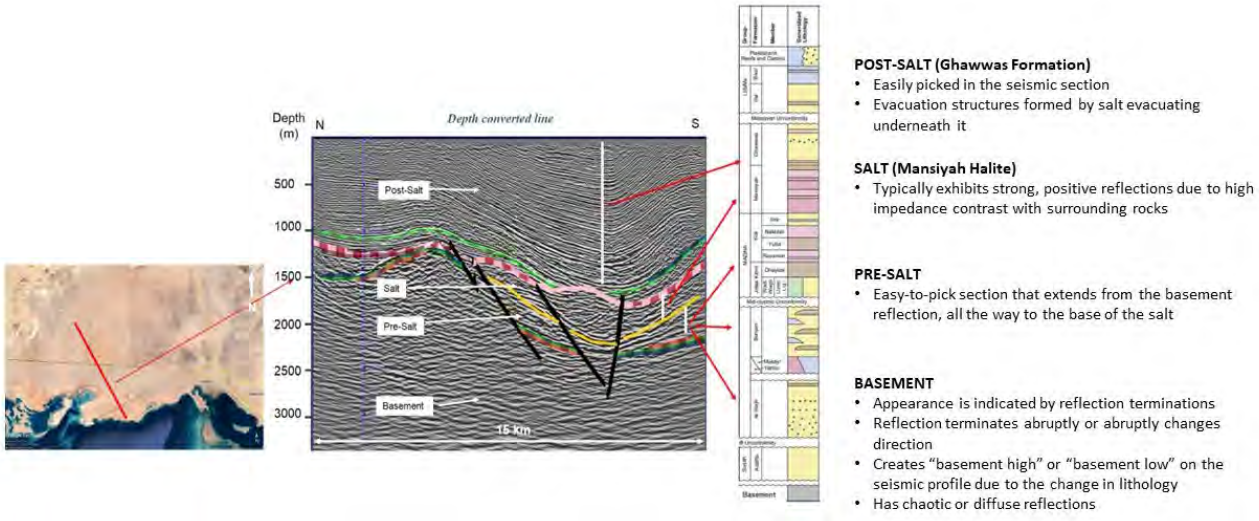

Figure 4. An example of a seismic line and interpretation from the 2023 seismic survey conducted in the NEOM area.

3. Regional Geology and Structural Style

3.1 Regional Geology

The regional area of interest is in the northwestern part of Saudi Arabia, directly northeast of the Red Sea Basin, which is a divergent plate margin. The Red Sea basin was formed by a continental rift that started 30-32 million years ago by initiation of the Afar Plume (Figure 6-a and -b) (Bosworth, 2015), and eventually developed into an oceanic rift that now hosts the Red Sea, and forms part of the boundary between the African and Arabian plates. The Red Sea basin started as an asymmetric rift that propagated from the south to the north in a series of deep half grabens all along the Red Sea. At the beginning of the rift, the Gulf of Suez was considered part of the Red Sea and shared the same history and structural trends. All along the Red Sea basin, there are several zones of half grabens that dip towards the Arabian plate, and others that dip towards the African plate with accommodation zones in between associated with oblique cross-basinal arches. These have been studied in detail in the Gulf of Suez and have also been demonstrated along the main Red Sea.

Pre-Miocene formations are considered to predate the development of the rift. Cretaceous formations are the oldest in the section, and are thickest within Gulf of Suez, and thin towards the south until they disappear offshore and in outcrop (on the Saudi Arabian side) within the northern areas of the Red Sea (Adaffa and Usfan Formations; Hughes, 2005). Some Cretaceous outcrops are preserved with down dropped basin grabens in outcrops within the NEOM area (e.g., Adaffa Sandstone Formation). There are some other Cretaceous outcrops preserved within grabens along the Saudi coast that extend to the south, nearly reaching the Yemen border.

The early stage of the rift resulted from rift-normal extension that is postulated to have opened the whole 2,200 km long Red Sea simultaneously (Figure 6-c) (Bosworth, 2015). At this stage, the Early Oligocene rift deposits were the continental sands of Al Wajh formation, which are present everywhere in the Red Sea as continental red beds and lacustrine deposits that reach up to 2200 m in thickness. This was followed by a marine incursion that deposited the deep marine turbidites of the Burqan formation where the rift was most active tectonically; in these areas the Burqan is the thickest formation.

A change in depositional environment is marked by outcrops revealing the intra-Burqan mid-clysmic unconformity (~17.5-18Mya) that ended the deposition of the Maqna group (Figure 8) (Tubbs et al, 2014). The Maqna group shows clear signs of low tectonic activity and of basin wide restriction where several regional anhydrite formations, interbedded with clastic and carbonate formations, were deposited. The basin restriction developed into a basin wide salinity crisis linked to the Mediterranean Messinian restriction, and the Red Sea that deposited the massive Mansiyah halite (Gargani, 2008).

Around 14-12 million years ago, the Gulf of Aden rift developed into an oceanic ridge with seafloor spreading and the Arabian and the Eurasian plates collided, rotating the Arabian plate around a north-African Euler pole counterclockwise and causing the Red Sea to switch to a rift-oblique extension (Figure 6-d) (Bosworth, 2015). The new shift in extensional direction caused reactivation of some faults, and strike-slip deformation as the faults moved to accommodate the differential extension.

The opening of the Gulf of Aqaba in the Late Miocene (5-12 million years ago) occurred after the Red Sea Rift had already stopped its initial rifting (~14 million years ago). Its opening helped accommodate the plate rotation, and the extension along the Gulf of Suez was abandoned, making it a dead rift. This also created late strike-slip deformation across the basin especially in the northern Red Sea and within the Midyan peninsula, creating pull-apart basins and further deepening the basin as a whole.

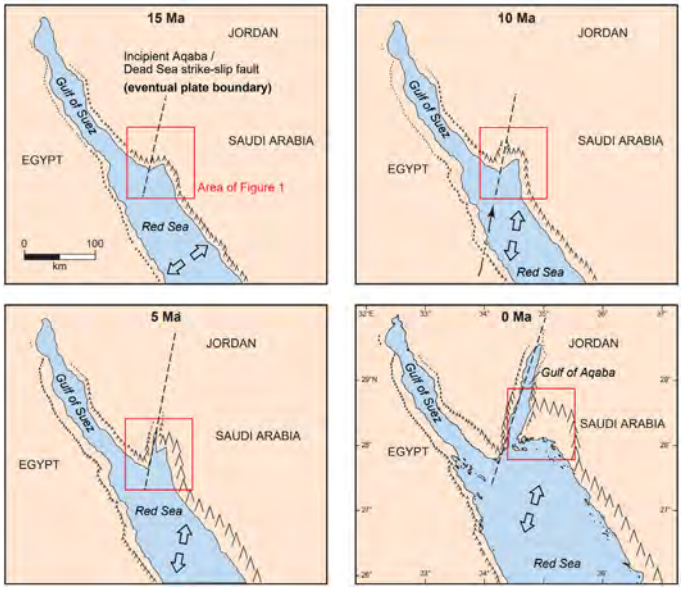

Figure 5. A schematic of the opening of the Gulf of Aqaba as illustrated by Tubs et al. (2014)

The Red Sea changed into a drift regime with the extension localized to the center of the Red Sea while the plate moved along the Aqaba strike-slip system to reach a total left-lateral displacement of 107 km (Quennell, 1959). The southern end of the Red Sea opened an extra 26 km due to the plate rotation. The combined displacement caused several pull-apart basins along transtensional bends to develop. The Gulf of Aqaba Sea is one large pull apart basin separating the Sinai Peninsula from the NEOM region.

Around 5 million years ago, seafloor spreading initiated in the southern Red Sea, and a ridge formed that transferred most of the deformation to the center of the sea (Figure 6-f). Continental rifting ceased in the south and only localized deformation continued offshore in the north.

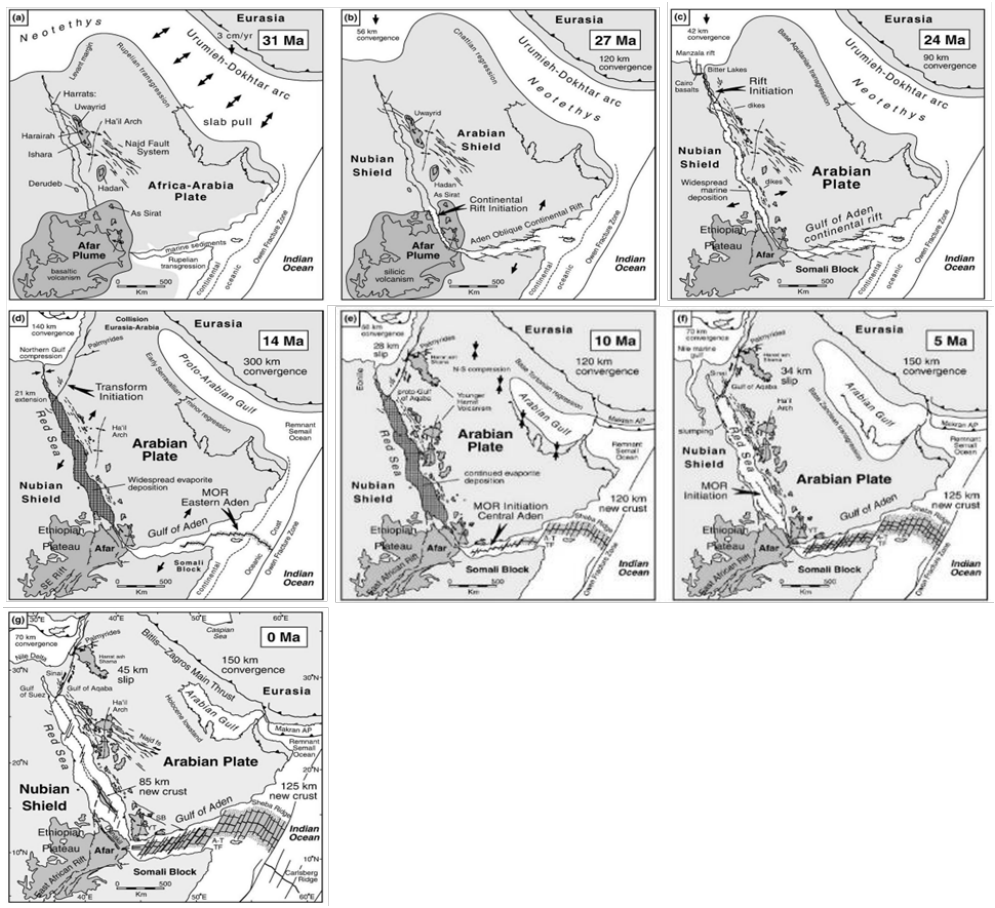

Figure 6. The evolution of the Red Sea rift from the initiation of the Afar plume, through the rift climax, strike slip initiation and rotation axis change, and to modern day system. (Bosworth, 2015)

3.2 Regional Structural Setting

The Red Sea developed as an asymmetric rift associated with oblique extension starting in the Oligocene through Late Miocene. A schematic of an asymmetric rift system can be seen in Figure 7-a. Under transtensional strain, a geometry of half grabens bounded by synthetic faults formed across the width of the basin (Figure 7-b). The dip polarity of the half grabens flips in several regions of the Red Sea and Gulf of Suez at several transfer zones from east- to west-dipping and west- to east-dipping. These transfer or accommodation zones link the displacement across regions of the sea and represent cross-basinal arches where dip directions rotate. The regional structural framework can help guide exploration by adding context to rift geometry at subregional scale.

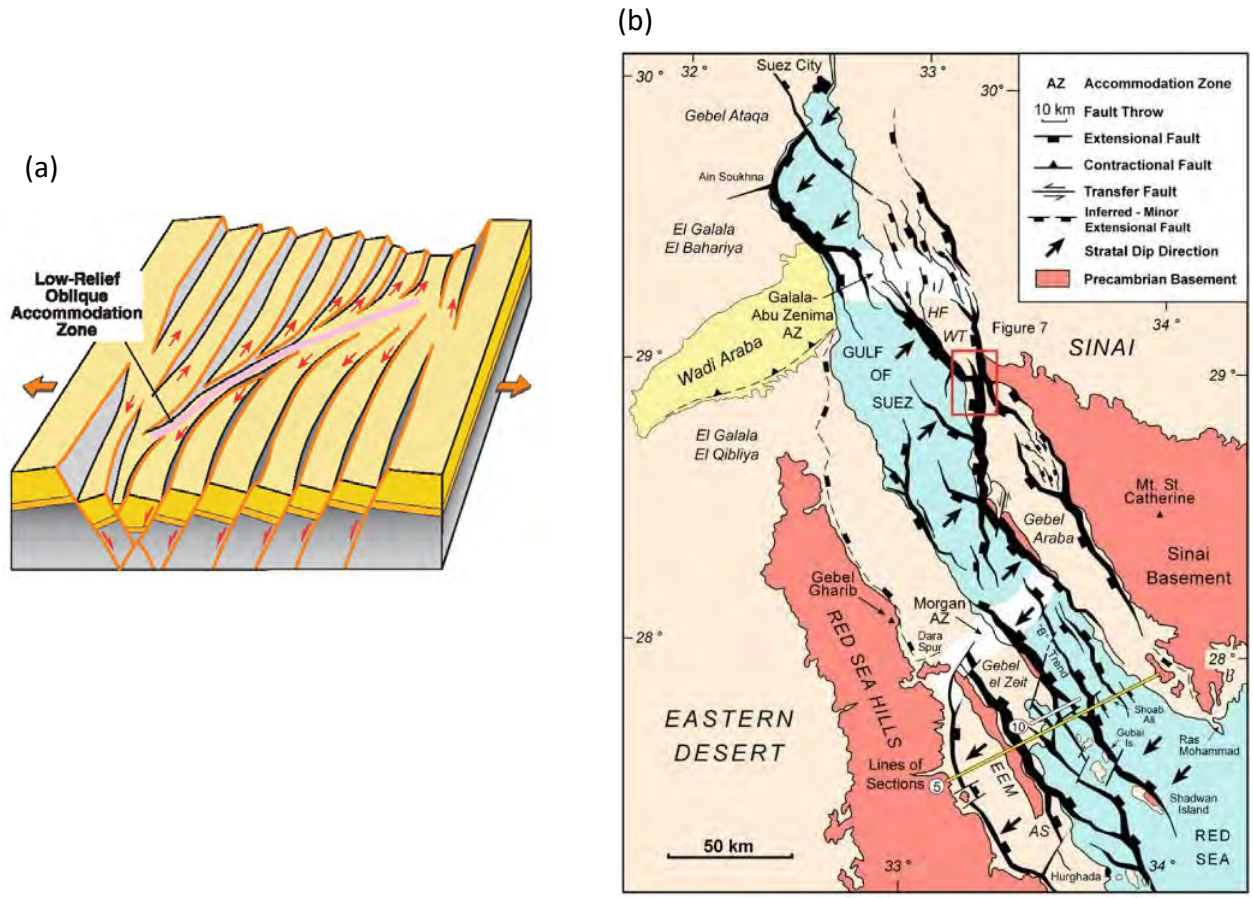

Figure 7. (a) Schematic of the transfer zone in asymmetric fault systems from a sandbox experiment. (McClay, 2002) (b) Faults in the Gulf of Suez with different transfer zones labelled. (Bosworth, 2005)

3.3 Stratigraphic Framework

The Red basin stratigraphic section is dominantly related to the tectonic history of the Red Sea rift. Overall, the pre-rift section is thin, and the rift sequence is often directly overlying crystalline basement. Therefore, a clear character to defining the stratigraphic section is in relation to the rift stage. This is especially useful because the kinematics of the rift itself are the largest influence on the depositional environment, as well as the basin shape and accommodation space. Hence, the section can be divided into a pre-rift, syn-rift, late rift, and post-rift. These must also be contextualized within the overall understanding of the space creation within the different zones of the Red Sea, the fact that the faults along the rift margin are no longer active, and the plate motion is accommodated by space creation offshore. There are several hypotheses related to the onset of the ocean crust formation, as well as hyper-extension of the offshore continental crust. The method in this report by which we define the rift formation relates to the rift fault kinematics onshore. The understanding of the onshore basin is calibrated by published literature on the onshore drilling results, and outcrop studies.

There are 6 formations that are a major part of the Red Sea Basins. From youngest to oldest, these formations include:

1. Ghawwas Formation (~12 to ~6 Ma)
   The Ghawwas formation is a post-salt formation dominated by sandstones with minor intercalated carbonates deposited within salt mini-basins controlled by accommodation space within the halite body.

2. Mansiyah salt formation (15.3 to ~12 Ma)
   The Mansiyah formation is a massive halite deposition formed during a basin wide salinity crisis that can be linked to the Mediterranean Messinian restriction. This formation acts as a regional marker in the area.

3. Maqna Group (17.5 to 15.3 Ma)
   The Maqna Group is a pre-salt formational group comprising interbedded fine to medium-grained clastics and carbonates that was formed during a period of low tectonic activity and basin-wide restriction.

4. Burqan Formation (20.5 to 18 Ma)
   The Burqan is a pre-salt deep marine turbidite that was deposited by a marine incursion.

5. Al Wajh Formation (33 to 21 Ma)
   The Al Wajh is a pre-salt high porosity sandstone formation that was deposited during the earliest stage of the rift.

6. Neoproterozoic Basement
   There is an unconformity present due to the transitional zone between the sedimentary units and the Neoproterozoic granitic basement. It is of note that the basement can also potentially host permeable faulting, below the sediments, however the nature of these faults has not yet been studied in depth.

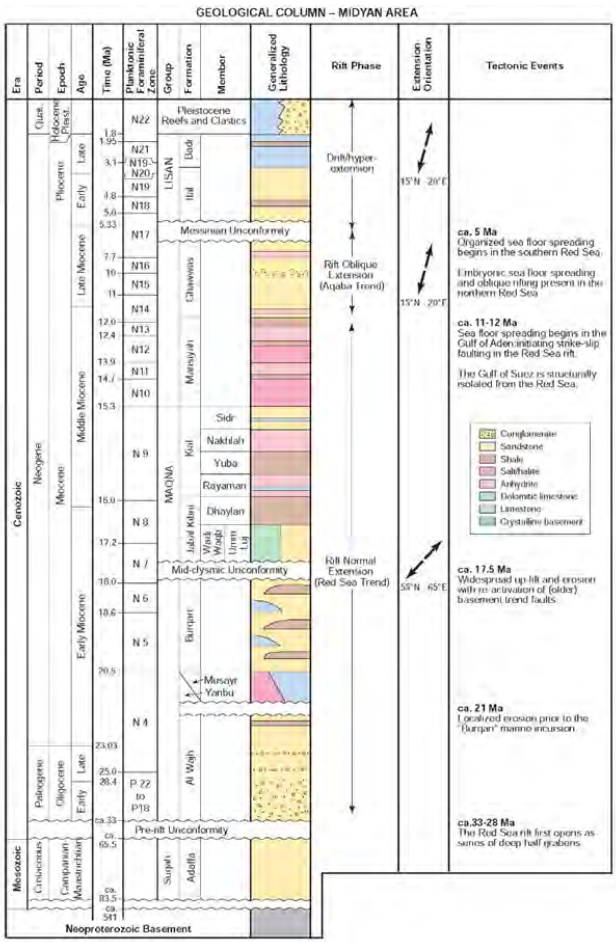

Figure 8. Generalized lithostratigraphy of the Midyan Basin.

4. Geothermal Workflow and Results

From the data presently available, the Midyan Basin has been assessed using a greenfield exploration approach, while under the assumptions associated with a hot sedimentary aquifer (HSA) play. In an HSA geothermal play, the reservoir is heated by conduction with no impact of convection or magmatic processes that would diverge the reservoir temperature away from the background heat gradient. The temperature that would need to be reached for geothermal commercial purposes would thus be a function of depth and background gradient. The permeability of the subsurface is below the convective threshold, but the conductive heat input to deep aquifers with local elevated permeability producing conditions suitable for a productive HSA that can be targeted by exploration. In an HSA play, there is a balance required in locating sufficient temperatures and permeability; temperature will increase with depth in a conductive temperature regime, however an increasing overburden with depth will also decrease the permeability of aquifer-hosting rocks. In the Midyan Basin, from oil and gas well temperature data, the geothermal gradient has been shown to be between 32-35 °C/km. To reach >100 °C it would be necessary to drill at least 3 km into the subsurface.

The exploration approach followed a typical greenfield exploration methodology. A desktop study was performed to assess the known information of the Midyan Basin from the standpoint of scientific literature and public data. This supported field visits directed at observing outcrops and verifying previously reported faulting.

The basin geometry was interpreted using potential field methods with the first interpretation based on the regional magnetics and gravity data from SGS Saudi Arabia, with supporting input from Tubbs et al. (2014). From the regional magnetic map below, there can be observed two magnetic lows, one in the south of the Midyan Basin close to the coast, and another low present in the back-basin, close to Al-Bada.

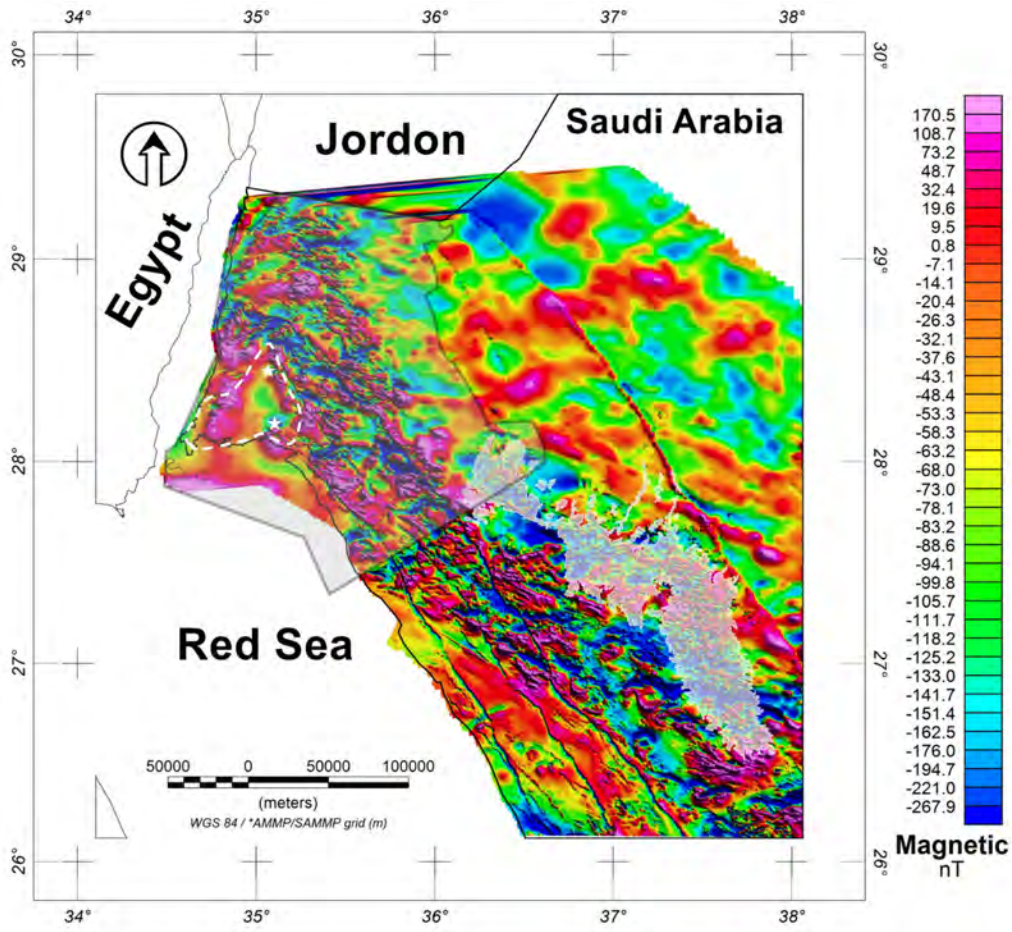

Figure 9. Regional magnetic map of Saudi Arabia. The NEOM area is outlined by the translucent polygon, while the Midyan Basin is outlined by the white dashed-line.

The observed magnetic lows were found to correspond to an interpreted low in the seismic lines presented by Tubbs et al. (2014). Comparing the seismic section in Figure 9 from Tubbs et al. (2014) to the magnetic anomaly map in Figure 10 , the location of the northernmost magnetic low in the Midyan Basin (shown as the northernmost white star in Figure 9) coincides with the deeper

basement depicted in the seismic section northward towards A'. Similarly, the basement also seems to be dipping southwest towards the coast as shown in the seismic section in Figure 10. This also corresponds with a magnetic low in the south, as seen in Figure 9.

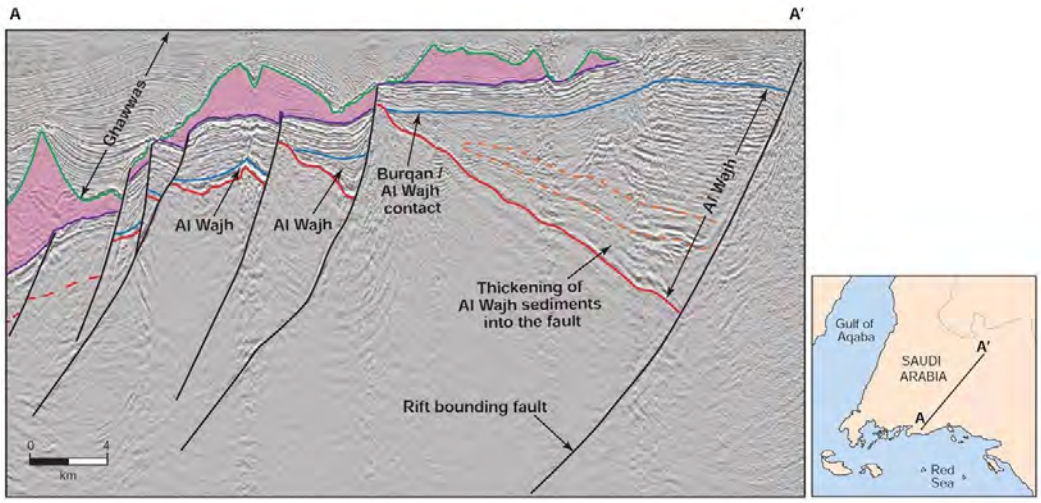

Figure 10. Interpreted pre-stack depth-migrated 3-D seismic section from Tubbs et al. (2014). Black lines = faults; green = top Mansiyah Formation; purple = top Maqna Group; cyan = top Al Wajh Formation, red = top basement. Highlighted in pink is the Mansiyah Formation. In this interpretation, the basement is deepening towards the northeast, towards A'.

The implied basin geometry derived from published regional magnetics and gravity along with the published seismic profiles from Tubbs et al. (2014) helped guide the location of seismic lines for a present day 2D seismic study which was performed to confirm the findings and further interpretation from already existing scientific literature. The resulting seismic profiles were used to map and confirm the depths to the granitic basement, map basin bounding faults and to define the sedimentary packages of the basin. Overall, the ideal geothermal targets in the Midyan Basin were determined to be found where the depth of the basement was the deepest, in that both a temperature of >100 °C and where permeable formations could be accessed. Numerous lithological units in the basin would make ideal reservoir targets, namely the Ghawwas, Maqna, Burqan and Al Wajh Formations. It will be required for any of these formations to be >3 km deep in order meet the target subsurface temperature of ≥100 °C.

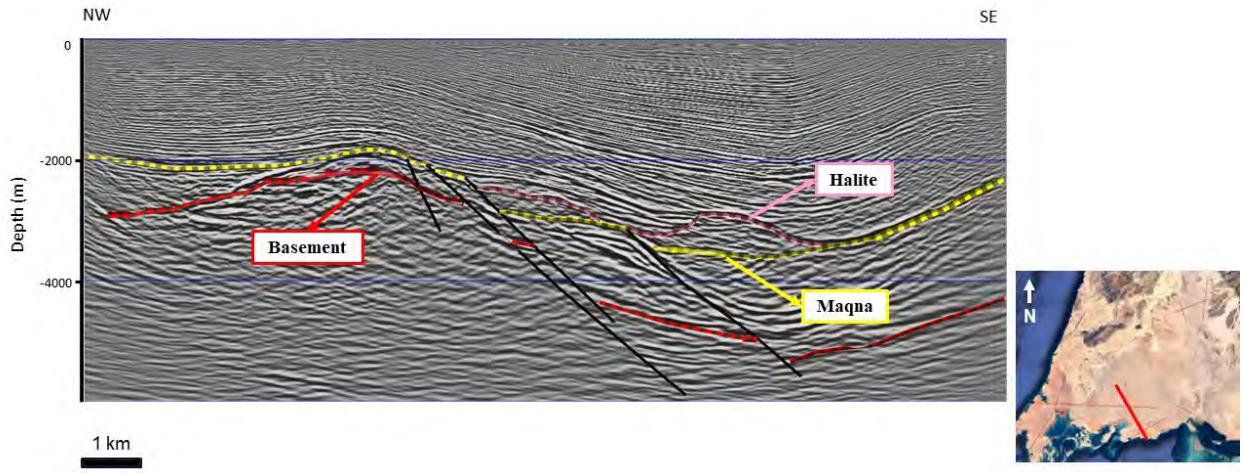

Figure 11 Newly acquired seismic showing the depth to basement exceeding 4 km on depth converted seismic sections. This makes the area attractive for geothermal development.

Based on the legacy data interpretation, the new seismic lines were acquired. Once processed, the 2D seismic sections revealed basin boundaries and depths. Detailed interpretations of the 2D data were performed and integrated with existing geologic information. Interpretation of the formation picks were divided into Basement, Pre-Salt (Maqna, Burqan and Al Wajh Formations), Salt (Mansiyah Halite), and Post-Salt segments (Ghawwas Formation). On the newly interpreted seismic lines, four (4) potential geothermal well locations were proposed in the Midyan Basin; three of the locations are closer to the coast in the northwest of Saudi Arabia, while the other is located more inland, farther north in the basin. It is in these locations where magnetic lows are encountered and where the basement is interpreted to be the deepest in the basin, thus increasing the likelihood of attaining both commercially viable temperature and permeability for geothermal utilization. These locations were either the center of the pull-apart basin from strike-slip displacement or the deepest points in the graben next to the basin bounding fault.

5. Conclusion

This study has demonstrated the potential of the Midyan Basin in the northwest of Saudi Arabia to host hot sedimentary aquifer (HSA) geothermal systems. Through a comprehensive exploration approach that included the analysis of regional geology, legacy well data, and newly acquired 2D seismic lines, several promising geothermal targets have been identified. These targets are located within deep syn-rift sedimentary reservoir-seal pairs that are deeper than 3 km and are predominantly found in marine turbidite sands or early-rift continental sands capped by marine shales.

The exploration work revealed that the Red Sea basin's tectonic history, characterized by stages of rifting and fault propagation, has significantly influenced the current structural configuration and sediment deposition. The depth to basement, a critical factor for geothermal exploration, was mapped using regional geophysics and seismic data. The deepest parts of the basin, where temperatures exceed 100 °C, were identified as the most viable for geothermal exploitation. These

areas correspond to magnetic lows observed in regional magnetic maps and seismic profiles, indicating significant sediment thickness and optimal conditions for geothermal reservoirs.

The Midyan Basin's geological setting, with its complex interplay of rift and strike-slip tectonics, provides a unique opportunity for geothermal development. The identification of key lithological units such as the Ghawwas, Maqna, Burqan, and Al Wajh formations as potential reservoirs further underscores the basin's suitability for geothermal projects. The successful exploration and eventual development of these geothermal resources can contribute significantly to NEOM's vision of becoming a leading renewable energy hub, providing sustainable power, heating, and cooling solutions.

In summary, the exploration efforts in the Midyan Basin have laid a strong foundation for future geothermal development. The current study highlights the potential of the Midyan Basin to support large-scale geothermal energy projects, aligning with Saudi Arabia's Vision 2030 and the ambitious goals of the NEOM project. Future work should focus on detailed reservoir characterization, drilling exploratory wells, and conducting feasibility studies to further de-risk the identified geothermal prospects and pave the way for commercial geothermal exploitation in the region.

Acknowledgement

We would like to thank ENOWA-NEOM for their sponsorship of this work and approval to publish this paper.

REFERENCES

Bosworth, William. "Geological evolution of the Red Sea: historical background, review, and synthesis." The Red Sea: *The formation, morphology, oceanography and environment of a young ocean basin* (2015): 45-78.

Gargani, Julien, Isabelle Moretti, and Jean Letouzey. "Evaporite accumulation during the Messinian Salinity Crisis: the Suez rift case." *Geophysical Research Letters* 35.2 (2008).

Hughes, Geraint Wyn ap Gwilym, and Robert S. Johnson. "Lithostratigraphy of the Red Sea region." *GeoArabia* 10.3 (2005): 49-126.

McClay, K. R., et al. "4-D evolution of rift systems: Insights from scaled physical models." *AAPG bulletin* 86.6 (2002): 935-960.

Quennell, Albert M. "Tectonics of the Dead Sea rift." *Proceedings of the 20th international geological congress, Mexico*. 1959.

Tubbs, Robert E., et al. "Midyan Peninsula, northern Red Sea, Saudi Arabia: seismic imaging and regional interpretation." *GeoArabia* 19.3 (2014): 165-184.

Verma, A., and Pruess, K. "Enhancement of Steam Phase Relative Permeability Due to Phase Transformation Effects in Porous Media." *Proceedings: 11th Workshop on Geothermal Reservoir Engineering*, Stanford University, Stanford, CA (1986).

Preliminary Ground and Airborne-based Geophysical Mapping and Modelling of an Active Hydrothermal System at Mammoth Lakes, California

Jacob Anderson[1], Jonathan M.G. Glen[1], Claire Bouligand[2], Grant Rea-Downing[1], Tait Earney[1]

[1]U.S. Geological Survey, Moffett Field, CA

[2]Univ. Grenoble Alpes, Univ. Savoie Mont Blanc, CNRS, IRD, Univ. Gustave Eiffel, ISTerre, 38000 Grenoble, France

Keywords

Aeromagnetics, Gravity, Geophysics, Potential Fields, Geothermal Resources, California, Faulting, Magmatism, Mammoth Lakes, Thermal Infrared, Gas, Long Valley Caldera, Sierra Nevada

ABSTRACT

Mammoth Lakes, California hosts a productive hydrothermal system within the seismically active south moat of Long Valley Caldera. Surficial evidence of the shallow hydrothermal system includes discrete zones of tree-kill dispersed between Shady Rest Park and the Casa Diablo Geothermal Power Plant (40 MW), as well as east of the power plant. The tree-kill areas are associated with elevated diffuse CO_2 emissions, heated ground, hydrothermal alteration, diffuse soil H_2S emissions, and gas vents. Previous mapping delineates prominent north and northwest trending structures within the south moat along the southwestern edge of the resurgent dome that may accommodate gas and fluid flow at the Shady Rest Park and Basalt Canyon tree kill areas (SRTKA and BCTKA, respectively). Both tree-kill areas are also located along contacts between resurgent rhyolite, mafic lavas, and surficial deposits which may provide additional pathways for gas and fluid migration in the shallow subsurface.

Characterizing structure and lithology using geophysical anomalies can help identify primary structural controls on the hydrothermal system and the extent of subsurface alteration at these sites. We conducted ground and airborne-based potential field geophysical surveys to map gravity and magnetic anomalies. These anomalies were then used to model subsurface geology, structure, and hydrothermal alteration. Here we present our preliminary geophysical mapping and modelling results at both tree-kill locations. Gravity and magnetic data suggest complex structural intersections are coincident with heated ground and gas emissions at the SRTKA and BCTKA. Hydrothermal systems are often observed or interpreted to exploit fault intersections which can serve as highly permeable pathways for hydrothermal fluid and gas discharge, enabling economic

geothermal energy production. Geophysical mapping and modelling are an effective means of investigating such structural complexity at Mammoth Lakes due to the presence of unidentified and concealed structures.

1. Introduction

The Long Valley Caldera (Figure 1) hosts an active hydrothermal system sustained by ongoing volcanic heat flux below the western moat of the caldera near Deer Mountain (Peacock et al., 2016; Sorey et al., 1991) and shallow permeable horizons arising from lithologic variations (Suemnicht et al., 2007) near Casa Diablo (Figures 1 and 2). Moderate hydrothermal fluid temperatures in and around Casa Diablo (150-170 °C; Bergfeld et al., 2006) enable geothermal productivity (40-Megawatt electric capacity; Suemnicht et al., 2007) adjacent to the town of Mammoth Lakes. Surface alteration, heated ground, gas vents, and areas of tree kill within the vicinity of Casa Diablo hot springs motivated a detailed geophysical study of this region to understand what structural controls contribute to the present state of subsurface hydrothermal activity and surface expression. Furthermore, the accessibility at Shady Rest Park has enabled continued experimentation with a variety of airborne-based tools to assess active surface processes (Zielinski et al., 2022). Small uncrewed aerial systems (sUAS) provide increased data coverage capabilities and cost effectiveness for small to moderately sized areas of interest. The roughly 5- by 3-km region of interest for geophysical mapping, extending from the Basalt Canyon tree-kill area (BCTKA) to the Shady Rest tree-kill area (SRTKA), is uniquely suited for sUAS (Figure 3). The current work focuses on presenting results from multi-year geophysical surveys that indicate the existence of magnetic lows coincident with known zones of tree-kill, soil and rock alteration, and gas emissions. Importantly, the shape of these zones of low magnetization has been refined better than previous regional magnetic surveys were capable of (Ponce, 2019). Gravity and magnetic anomaly mapping using data obtained from 2021 – 2024 provides a higher resolution look at anomalies within and surrounding areas of tree-kill.

Forward modelling of gravity anomalies provides a way to distinguish concealed structures that can be resolved by modelling variations in density that arise from faults and contacts. These inferred structures are non-unique in that the observed data can reflect faults, contacts, intra-unit density variations, or other structures that places rocks adjacent to each other with density differences great enough to yield a gradient. Forward modelling of magnetic data also results in non-unique solutions but provides information about differences in magnetic properties (induced and remanent magnetization) at the surface and at depth. Joint modelling of both gravity and magnetic data can strengthen model confidence because a good fit must match both observed gravity and magnetic data.

From 2021 to 2024, we collected gravity data in the vicinity of the SRTKA and BCTKA, as well as regionally within the south moat, to constrain gradients across potential concealed structures and construct preliminary potential-field models. We also collected aeromagnetic data across both tree-kill areas (Figure 3) to aid in mapping alteration zones, concealed structures, and young volcanic deposits. This joint method of forward modelling may be advantageous to identify and characterize concealed structures that lie beneath the south moat and may control the geothermal system.

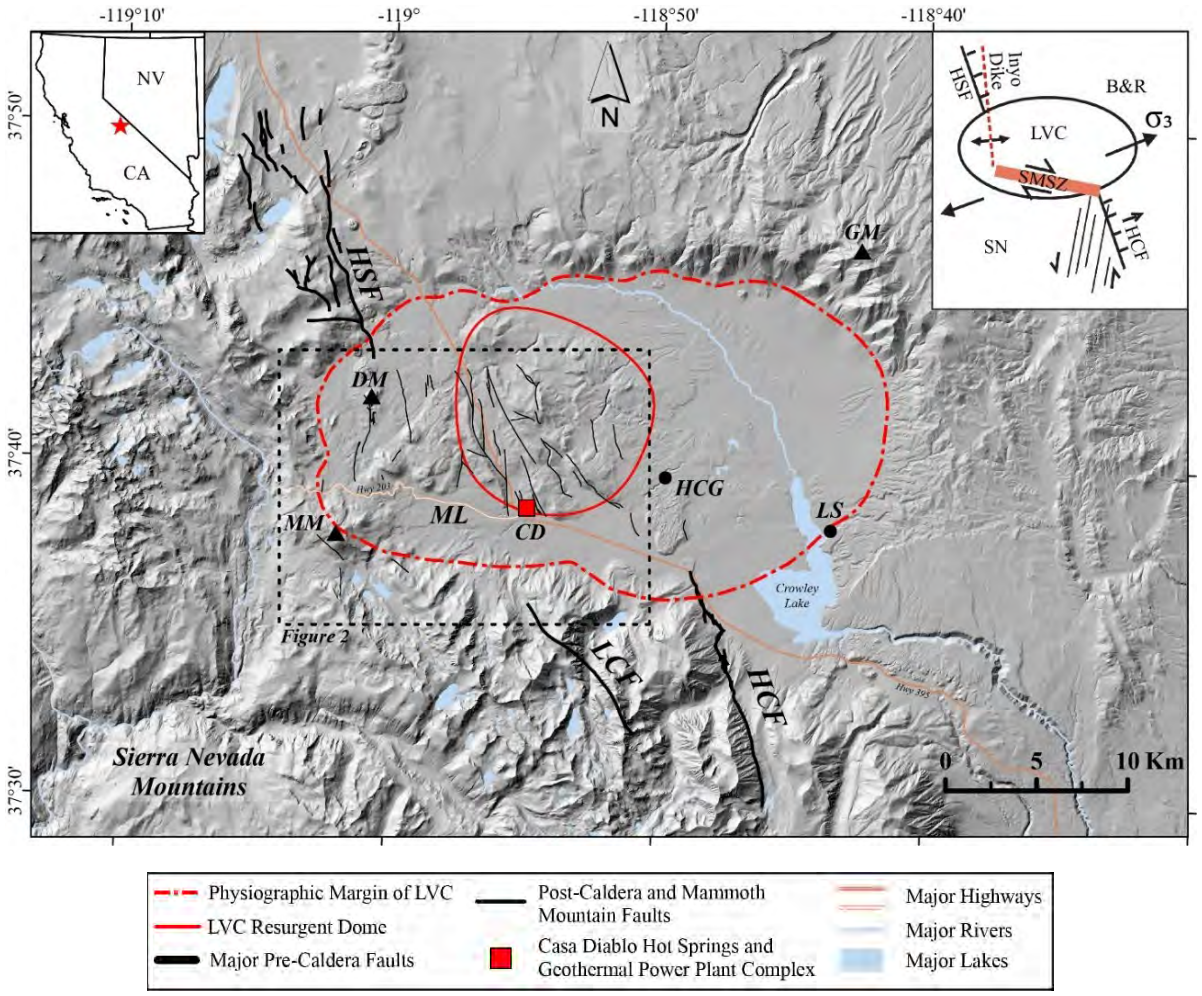

Figure 1: Digital Elevation Model (DEM) hillshade (USGS, 2024) of the Long Valley Caldera region. Sierran range front faults (HCF, HSF) from U.S. Geological Survey (2020). Laurel-Convict Fault (LCF) from Strand (1967). Post-Caldera and Mammoth Mountain faults from Hildreth & Fierstein (2016). LVC, Long Valley Caldera; HCF, Hilton Creek Fault; HSF, Hartley Springs Fault Zone; HCG, Hot Creek Gorge; LS, Layton Springs; MM, Mammoth Mountain; ML, town of Mammoth Lakes; DM, Deer Mountain; GM, Glass Mountain. Top right inset (modified from Hill & Montgomery-Brown (2015), Figure 1): Conceptual structural outline of Long Valley Caldera region; SMSZ, south moat seismic zone; σ3, local orientation of least stress; SN, Sierra Nevada; B&R, Basin and Range Province; Inyo Dike, Mono-Inyo volcanic chain. Top left inset: geographic location of LVC in red star.

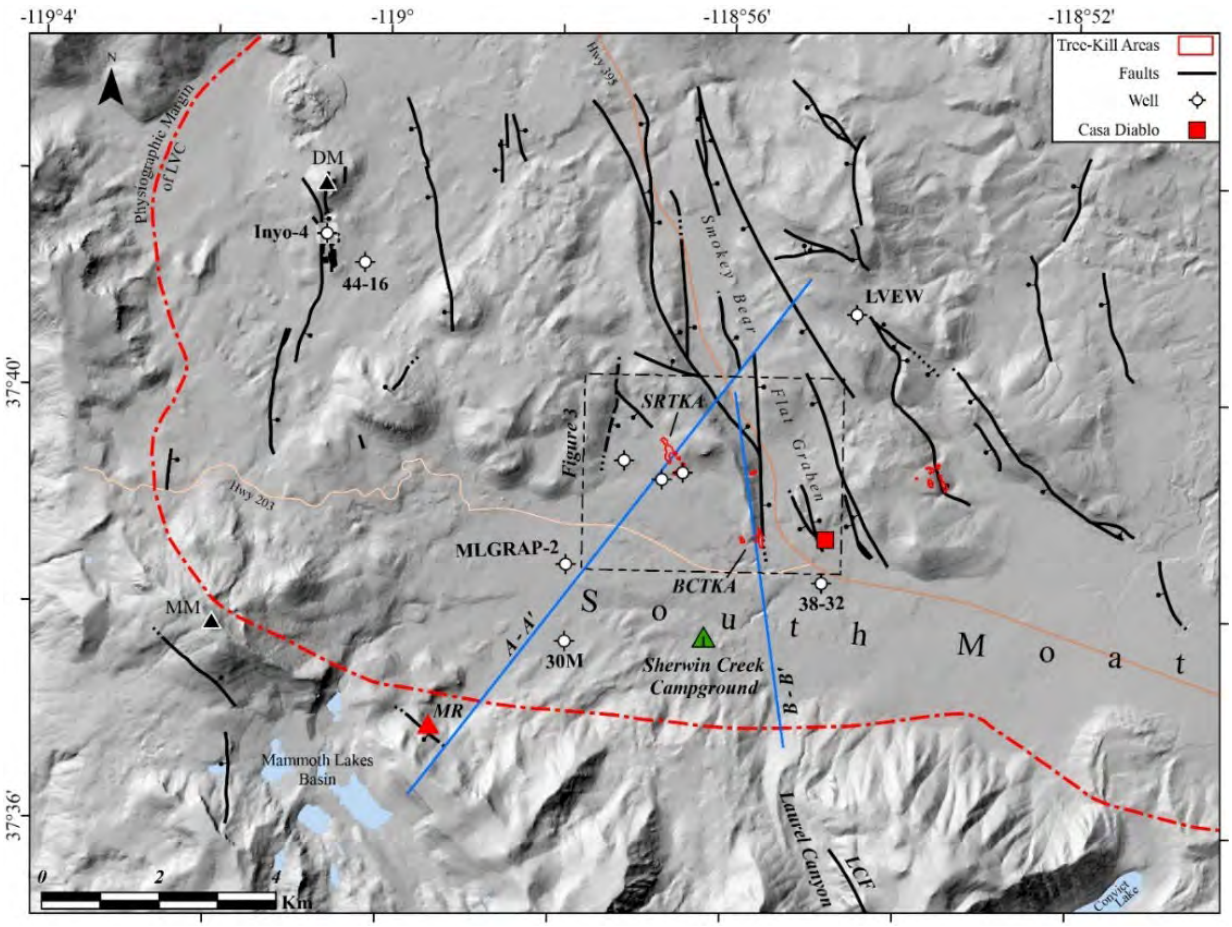

Figure 2: Digital Elevation Model (DEM) hillshade (USGS, 2024) of the south moat of Long Valley Caldera and town of Mammoth Lakes. SRTKA, Shady Rest tree-kill area; BCTKA, Basalt Canyon tree-kill area; LCF, Laurel-Convict Fault; MR, Mammoth Rock; LVEW, Long Valley exploration well. Faults and physiographic margin outline from Hildreth & Fierstein (2016). LCF fault from Strand (1967). White circles are locations of wells discussed in this work and used in modelling. Wells within dashed box are identified in Figure 3.

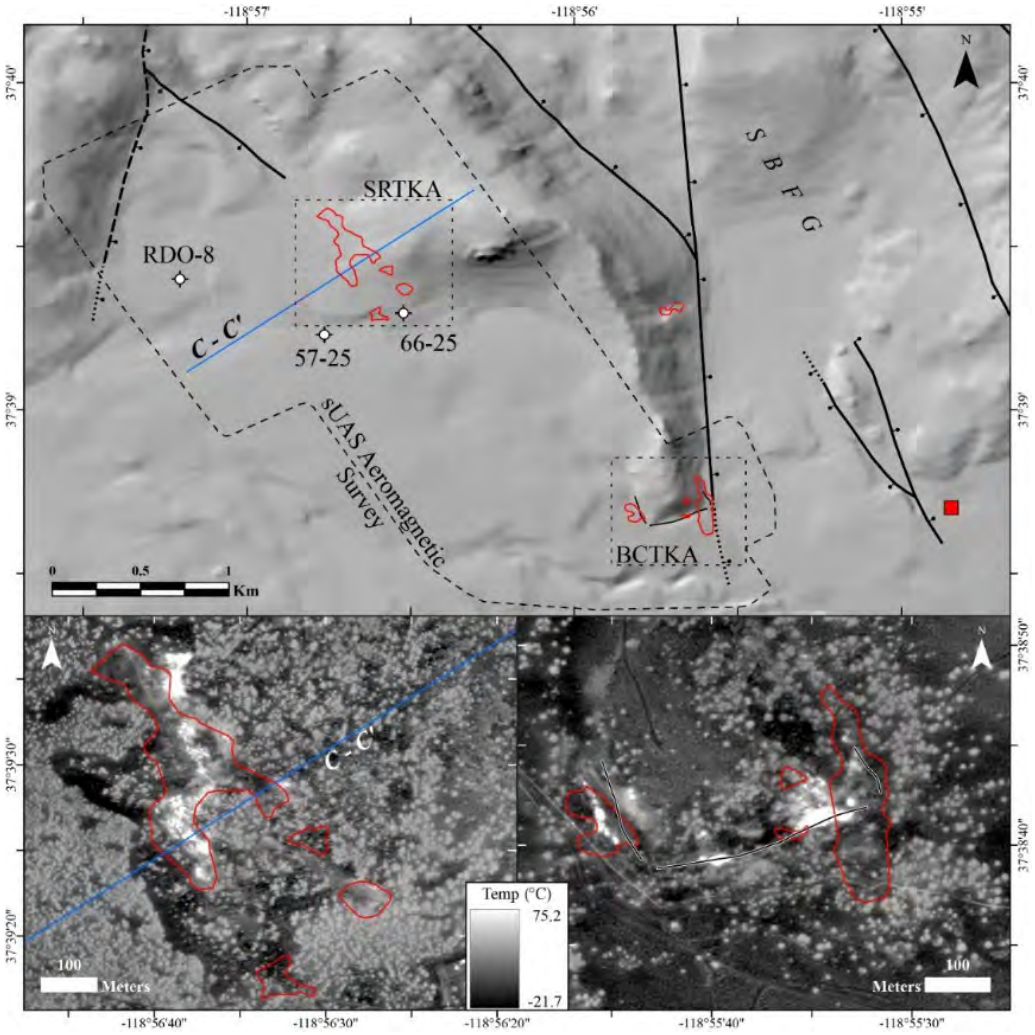

Figure 3: Digital Elevation Model (DEM) hillshade (USGS, 2024) with tree-kill areas from Shady Rest Park to Casa Diablo and sUAS survey shown. Lower two Figures are thermal infrared orthomosaics from Vaughan et al. (2018) zoomed to SRTKA (lower left) and BCTKA (lower right). SBFG, Smokey Bear Flat Graben. Thick black lines are faults from Hildreth and Fierstein (2016). Thin black lines at BCTKA are faults mapped by Bergfeld et al. (2006). White circles are locations of wells discussed in this work and used in modelling.

2. Geologic Setting

Long Valley Caldera (Figure 4) developed ~767 ka when a caldera-forming eruption released more than 650 km^3 of Bishop Tuff from a 5-km deep magmatic reservoir (Hildreth and Fierstein, 2016; Wallace et al., 1999). During eruption, a landslide of precaldera basement rock on the south wall broke loose and slid into the southern region of the caldera, reaching all the way to present-day Casa Diablo (Suemnicht et al., 2007). The subsequent 100 ka following caldera collapse sustained a series of intracaldera eruptions which emplaced rhyolitic flows, domes, and tuffs (Hildreth et al., 2017; Hildreth and Fierstein, 2016), herein referred to informally as early rhyolite (Bailey et al., 1976). This resurgent volcanism was followed by 400-500 meters of uplift from approximately 670 – 540 ka (Hildreth et al., 2017).

The hydrothermal system at Long Valley has experienced two major periods of activity. Th/U age samples collected from altered breccia zones, silicified veins, and calcite veins in the central and eastern caldera suggest a period of high hydrothermal flux between 300 – 200 ka (Sorey et al., 1991). Additional sampling at Casa Diablo, Hot Creek, and Layton Springs (Figure 1) reveals the latest period of hydrothermal activity initiated around 40 ka (Sorey et al., 1991). These ages indicate a primary period of hydrothermal activity centered in the central and eastern caldera, whereas the present system extends across the south moat as far west as Mammoth Mountain (Figures 1 and 2). The present-day hydrothermal system is sustained by a magmatic reservoir on the western margin of Long Valley, likely beneath the west moat and/or below Mammoth Mountain (Peacock et al., 2016; Sorey et al., 1991). Geothermal well logging indicates hydrothermal fluids upwell near Deer Mountain along deep basement faults and flow laterally southeast/east between the early rhyolite and Bishop Tuff toward Casa Diablo and then along the south moat before discharging at Hot Creek Gorge and other hot springs as far as the Owens River (Peacock et al., 2016; Sorey et al., 1991). The buried, syneruptive landslide block near Casa Diablo serves as a hydrologic barrier between cooler recharge waters within the Bishop Tuff and hotter hydrothermal waters within intracaldera fill (Suemnicht et al., 2007).

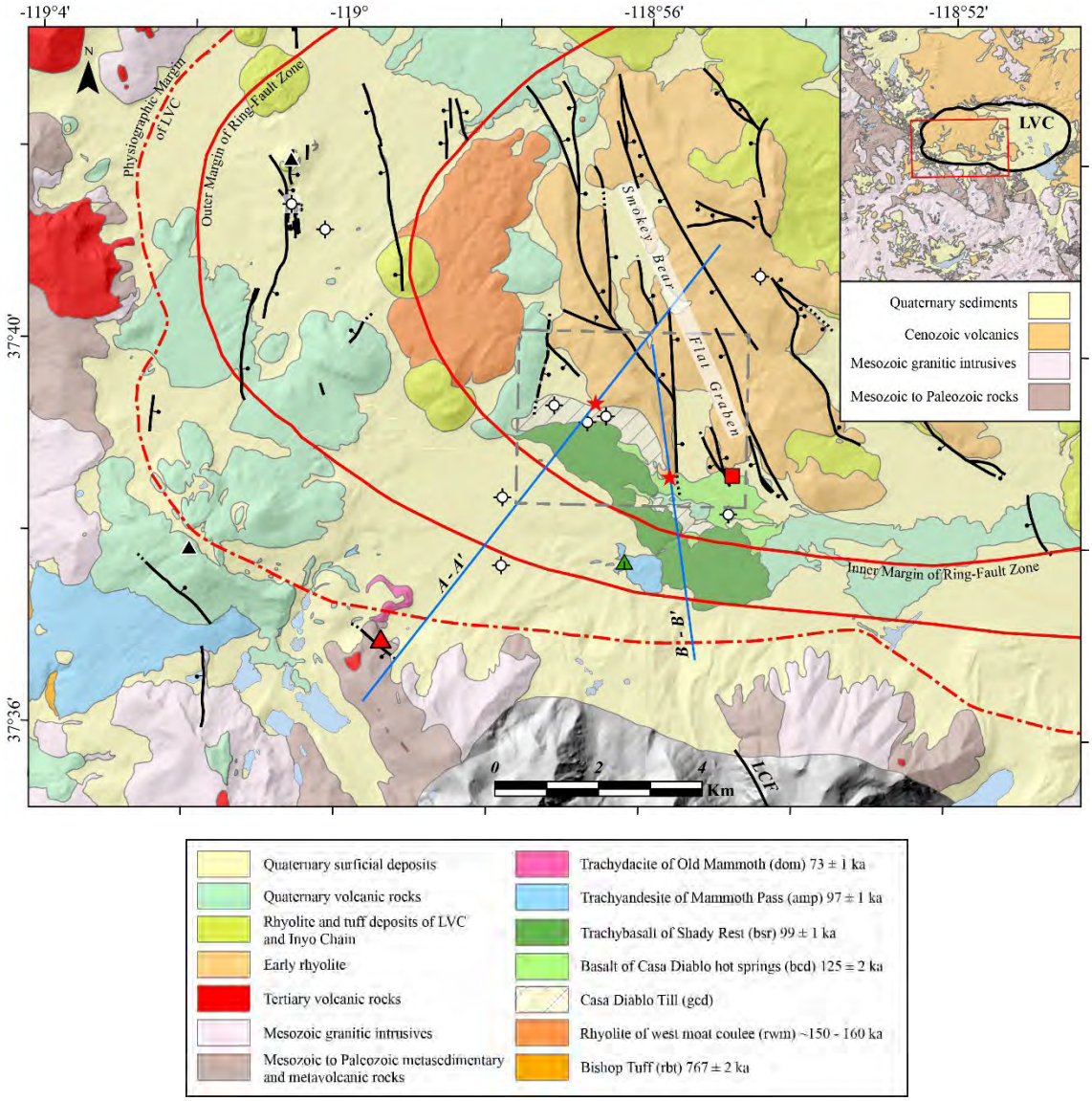

Figure 4: Digital Elevation Model (DEM) hillshade (USGS, 2024) overlain by geology of western Long Valley Caldera (LVC) adapted from Hildreth and Fierstein (2016). Top right inset shows DEM hillshade overlain by generalized geology adapted from Strand (1967) and red rectangle showing Figure extent. Ages of individual units from Hildreth and Fierstein (2016). Stars indicate locations of SRTKA and BCTKA. White circles are wells identified in Figures 2 and 3. See Figures 1 – 3 for regional feature identification.

3. Previous Geophysical Investigations

Long Valley has a long history of geophysical investigation, much of it centered on determining the extent and status of the Long Valley magma chamber. Geophysical and geological evidence indicate the chamber is moribund (Hildreth, 2017). However, seismic and geodetic data suggest active uplift beneath the early rhyolite is induced by “second boiling” fluid migration caused by progressive crystallization of the magma chamber. Recent tomographic models by Biondi et al.

(2023) of Long Valley Caldera (LVC) also support this second-boiling model to explain seismicity and uplift. The fluid migration is accompanied by earthquakes within the south moat seismic zone (SMSZ) (Hildreth, 2017; Shelly, 2016). Earthquake relocation indicates active seismicity at 3 – 9 km depths (Prejean et al., 2002) within the SMSZ. Although regionally active seismicity predominates in the extracaldera (Hildreth, 2017), the abundance of seismicity within the SMSZ and general absence within the rest of the caldera, as well as no evidence of elevated heat flow beneath the center of resurgent uplift indicate there are no active magmatic intrusions within the structural caldera. Surface expression of SMSZ faults and the ring fault system is lacking (Hildreth and Fierstein, 2016). However, active fumaroles, gas vents (Bergfeld, 2006), heated ground (Vaughan et al., 2018; Figure 3), and tree-kill (Figures 4 and 5) coincident with inferred zones of seismicity (Prejean et al., 2002) within the vicinity of Casa Diablo hot springs may indicate permeability is enhanced by SMSZ structures identified by Prejean et al. (2002).

A relatively thin zone of caldera fill in the south moat inferred from Kane et al. (1976), in addition to a WNW-ESE trending gravity gradient, and a complex magnetic low extending as a lobate tongue from the southern margin of the caldera to Casa Diablo may result from hydrothermal alteration and mineralization (Kane et al., 1976). Hydrothermal alteration may dissolve and remove magnetic material and mineralization can decrease porosity and locally increase observed gravity anomalies. However, the gravity gradient generally reflects the shape of the caldera, suggesting a conservative interpretation is warranted on inferences about caldera structure and lithology in the south moat. The tight gradient contouring the caldera boundary does broaden in the south moat but the coincidence of hydrothermal mineralization and Mammoth Mountain volcanic deposits in the south moat complicates a structural and lithologic interpretation of the gradient given the resolution of the survey presented by Kane et al. (1976). Similarly, the magnetic gradients from both the low- and high-level aeromagnetic surveys within the south moat align with ~NW SMSZ seismic inferences (Prejean et al., 2002) and fault interpretations (Hill and Montgomery-Brown, 2015; Riley et al., 2012) but Kane et al. (1976) posits the continuation of the magnetic low from Casa Diablo into the metamorphic basement rocks exposed along the south wall of Long Valley suggests the low may be explained in part by these rocks extending beneath the western caldera. The gravity and magnetic anomalies within the south moat suggest a variety of factors (hydrothermal activity, pre-caldera structure, active tectonics) are imposing these geophysical fabrics.

4. Data and Methods

Magnetic data were collected with a sUAS from 2021-2024 to supplement regional magnetic data collected at 400-m spacing and 150-m flight height (Ponce, 2019; Figure 6). The sUAS survey covers both the SRTKA and BCTKA (Figure 3). Aeromagnetic data were acquired using a Sensys MagDrone R3 fluxgate magnetometer flown at a height of 60 meters above ground with 60-meter line spacing at a speed of 10 m/s. sUAS calibration and compensation were conducted after Kaub et al. (2021) to remove flight heading effects. Aeromagnetic surveys were diurnally corrected using a Geometrics G-856 proton precession magnetometer with a base station located within the survey area. Flight lines were flown at a NE trend because of the strong NW orientation of mapped structure, contacts, and tree-kill at SRTKA (Figure 5). Tie lines were flown orthogonal (SE) to flight lines and used to level the surveys collected across all years (Figure 7). Flight lines and tie lines were used to grid the magnetic data at a grid cell size of 15 meters. Individual lines were minimally edited to reduce the presence of flight lines artifacts that place gradients along flight

lines. “Observed” magnetic anomalies in this work refer to values interpolated from the sUAS and regional aeromagnetic grids, used in the modelling.

More than 850 new gravity stations were collected within the Mammoth Lakes region between 2021-2024 using Scintrex CG-5 and CG-6 gravimeters. Gravity readings were processed by removing gravitational contributions from latitude according to the reference ellipsoid, earth-tide effects dependent on latitude and time, instrumental drift, the free-air effect arising from elevation above sea level, terrain effects within 167 km (complete Bouguer), and isostatic effects from topographic compensation at depth. Isostatic residual anomalies represent lateral variations of density in the middle and upper crust (Blakely, 1995) that provide insight into crustal structure. These data were subsequently merged with existing regional data from Langenheim et al. (2024), which were reprocessed for this study.

Tree-kill areas were outlined in 2016 by visual inspection of aerial imagery from 2014 and prior years (personal comm., Mads O’Brien 8/23/24). Geophysical mapping and modelling products and interpretations use gridded gravity data. “Observed” gravity anomalies in this work refer to interpolated values from a gravity grid. Profiles A – A’ and B – B’ fit data from 400-m cell size grids (Figures 9, 10), and profile C – C’ fit data from 100-m cell size grids (Figure 11) because of the dense station coverage in and around SRTKA.

Gravity and magnetic gradients yield insight into the location of possible structural boundaries (Blakely and Simpson, 1986). To aid our geophysical interpretations, we used pseudogravity (PSG) and reduced-to-pole (RTP) transformations to center anomalies over source bodies. The RTP transformation converts an observed anomaly to one where the magnetization and ambient field are vertically oriented whereas the PSG transformation involves replacing the distribution of magnetization with an equivalent density distribution to convert a magnetic anomaly into a representative gravity anomaly. Fundamentally, this transformation converts the observed magnetic field into a magnetic potential (Blakely, 1995). Using the resultant PSG anomalies, we calculated the horizontal gradient magnitude (HGM) points that indicate where the gradient is steepest. This derivative method is effective at producing lineations that lie along steep dipping structures, where rocks of differing density or magnetization are juxtaposed. Plotting the HGM maxima (maxspots) on top of the RTP anomaly grid simplifies geophysical interpretation. We connected these maxspots, representing ridges in a HGM grid, into continuous lines using an automated routine developed by Athens (2018). A HGM analysis was also carried out on gravity anomalies to identify structures arising from density contrasts.

We also collected rock samples of geologic units across the south moat to conduct density and magnetic property measurements to constrain the model parameters. Grain, saturated-bulk, and dry-bulk densities were calculated for collected samples by weighing samples in dry air, under saturated and submerged conditions, and saturated in air. Magnetic susceptibility measurements of hand samples were conducted using a ZH instruments SM30 meter with a resolution of $1x10^{-7}$ SI units. In addition, field-based outcrop susceptibility measurements were taken because these reflect unit properties more accurately compared to hand sample susceptibility measurements. Lastly, the well-documented geologic and tectonic history of this region (Hildreth and Fierstein, 2016; Bailey, 1976) and previous geophysical modelling work (Carle et al., 1988) provided constraints for assigning physical properties and delineating subsurface interpretations for the 2D geophysical models constructed in this work.

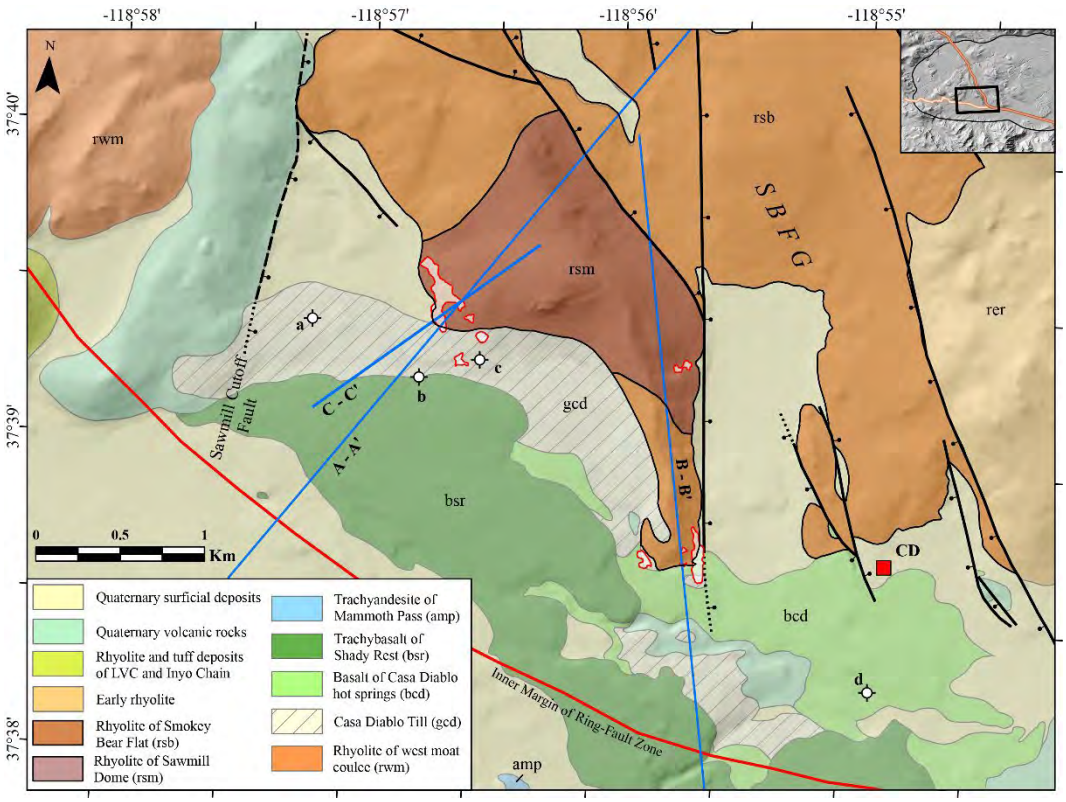

Figure 5: Digital Elevation Model (DEM) hillshade (USGS, 2024) overlain by geology in the south moat, adapted from Hildreth et al. (2017) and Hildreth and Fierstein (2016). Outline of early rhyolite subunits rsm and rsb were adapted from Figure 2 in Hildreth et al. (2017). Wells within this Figure: a, RDO-8; b, 57-25; c, 66-25; d, 38-32. CD, Casa Diablo Geothermal Plant and hot springs; SBFG, Smokey Bear Flat Graben. Top right inset shows DEM hillshade with thick black rectangle showing Figure extent, LVC physiographic margin in thin black outline, and major highways in orange.

5. Geophysical Mapping

Identifying structures at regional and local scales was conducted prior to the construction of 2D forward models. Geophysical mapping helps identify potential concealed structures that may be relevant to understanding the geothermal system. A particular interest was to investigate the concealed ring-fault zone of LVC (Figures 4 and 5) given its seismic activity and alignment with observed magnetic and gravity anomalies extending into zones of local interest (i.e., SRTKA & BCTKA; Figure 6). Regional scale magnetic and gravity mapping do not provide irrefutable geophysical evidence of ring faults, but anomalous bodies and major gradients in the south moat did inform 2D forward modelling.

5.1 Potential Fields

5.1.1 Regional Aeromagnetic Anomalies

Regional magnetic anomalies (Ponce, 2019) of interest are outlined in Figure 6. Boundaries were informed from (1) HGM maxspots on the PSG aeromagnetic grid and (2) significant anomalous bodies from the RTP grid. Bodies 1 (B1) and 8 (B8) are defined by HGM maxspots and correlate with exposures of Mesozoic plutons in the south wall of LVC (Figure 4). Body 4 (B4) is informed

by both HGM maxspots and RTP contours to emphasize the extensive magnetic low present at SRTKA and BCTKA. Body 5 (B5) is a north-trending magnetic high coincident with the mapped extent of unit rwm (Figure 4). The east side of B5 is well defined with HGM maxspots, and the western margin is informed by RTP contours. Bodies 6 and 7 (B6, B7) are well defined from HGM maxspots and correlate with mapped exposures of Mesozoic plutons (B7) and the Mammoth Mountain edifice (B6).

In addition to outlining bodies of interest, HGM maxspots delineated lineations that agreed well with mapped and inferred structure. Figure 6 shows line 1 (L1) parallel to the inferred inner margin of the ring-fault zone, traceable from well 38-32 (Figure 2) to the southwestern extent of B4. Lines 2 and 3 (L2, L3) align well with Smokey Bear Flat Graben (SBFG) faults north of SRTKA. Line 4 (L4) is well defined by HGM maxspots and may represent the concealed contact between Mesozoic plutonic rocks and Mammoth Mountain volcanic deposits.

Body 2 (B2) is a lobate magnetic high on the north side of Mammoth Rock (Figures 2, 6). The southeastern boundary of B2 is well defined by HGM maxspots, but the remainder of the outline is informed from RTP contours. Body 3 (B3) is a linear, east-west trending magnetic high defined by RTP contours. The magnetic high extends beyond Sherwin Creek Campground and appears to diminish where it intersects with the inferred inner margin of the ring fault zone. A minor saddle separates B2 and B3 northeast from Mammoth Rock. The coincidence of B2 and B3 with volcanic flows from Mammoth Mountain (Figure 4) and the inferred ring-fault zone motivate a further look at possible explanations of these features because profile A – A’ crosses over these anomalous bodies.

B2 correlates well with the mapped exposure of the informal trachydacite of Old Mammoth (Figure 4; unit dom, Hildreth and Fierstein, 2016). Between the western edge of B3 and Sherwin Creek Campground, the informal trachyandesite of Mammoth Pass (Figure 4; unit amp, Hildreth and Fierstein, 2016) is concealed by surficial deposits. Well 30M (Figure 2) encounters unit amp at ~40 meters depth and passes through ~120 meters of Mammoth Mountain volcanics down to a total depth of 195 meters (Hildreth and Fierstein, 2016, their Figure 6). Surface mapping and well logs support the hypothesis that B3 results from a buried source of high magnetization between outcropping unit dom and Sherwin Creek Campground.

Unit dom is only exposed at the foot of Mammoth Rock (Figures 2 and 4) and not encountered further east according to surface mapping and well logs (Hildreth and Fierstein, 2016). Unit amp is more widely exposed, outcropping west of Mammoth Mountain and as far east as Sherwin Creek Campground. Unit amp erupted prior to the construction of the Mammoth Mountain edifice (97 +/- 1 ka, Hildreth and Fierstein, 2016) and is older than unit dom by ~24 ka (Figure 4, legend). If B3 results from a buried flow, it is likely unit amp and/or older volcanic flows encountered in well 30M. Nevertheless, other reasonable alternatives should be considered. (1) This anomaly may arise from a buried ring dike. However, no such feature has been identified in the literature. (2) Faults on the north and south sides of B3 may account for the observed signal. The magnetic low on the south side of B3 attributable to metasedimentary units suggest a lithologic source instead. Nevertheless, the gradient on the north side of B3 may represent a ring fault structure.

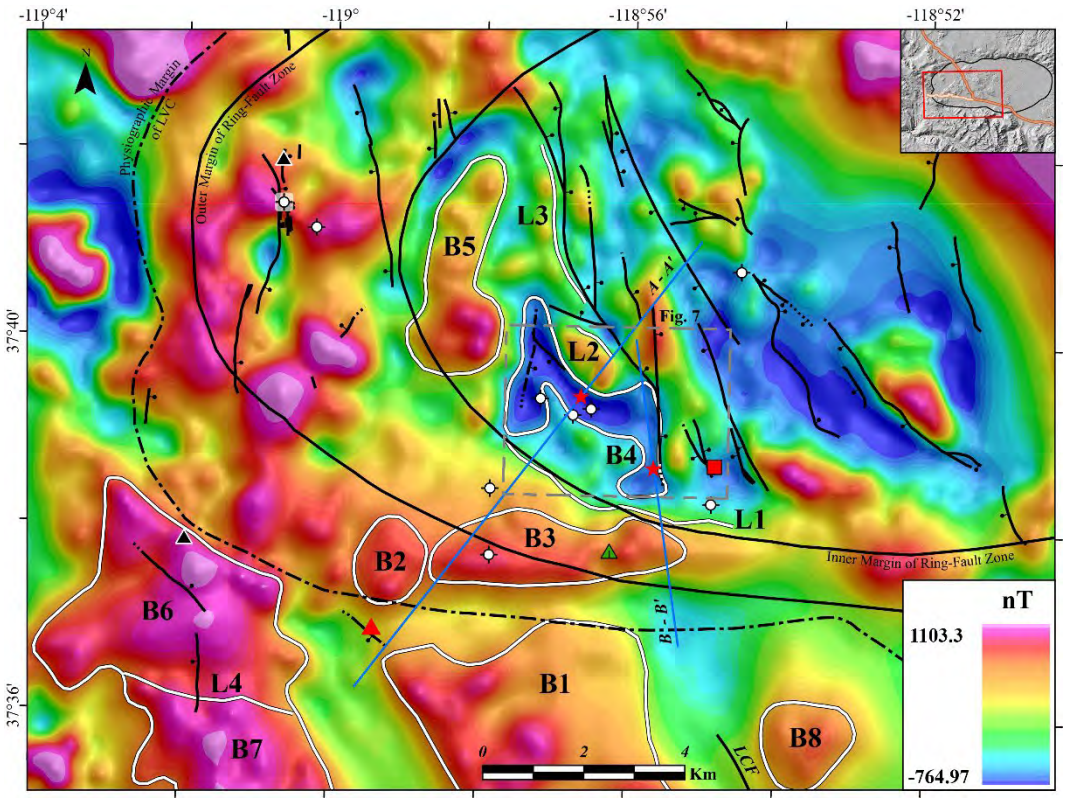

Figure 6: Regional aeromagnetic (reduced to pole) data from Ponce (2019). Faults are from Hildreth and Fierstein (2016). LCF, Laurel-Convict Fault from Strand (1967). White outlines delineate magnetic features discussed in text. Red stars mark tree-kill areas. Red box is Casa Diablo Geothermal Plant and hot springs. Black triangles are geographic features identified in Figure 1. Red triangle is Mammoth Rock (Figure 2). Green triangle is Sherwin Creek Campground. White circles are wells identified in Figures 2 and 3. A – A' and B – B' are model cross section lines shown in Figures 13 – 14. Top right inset shows DEM hillshade with red rectangle showing Figure extent, LVC physiographic margin in thin black outline, and major highways in orange.

Although more analysis is needed to definitively determine the source of the B3 anomaly, the presence of volcanic flows logged in wells from Hildreth and Fierstein (2016) presented irrefutable evidence that was used for 2D forward modelling in this work. Additionally, the inferred outer ring-fault margin from Hildreth (2017) was used to inform the placement of this major structure in the subsurface.

5.1.2 sUAS Magnetics

The magnetic anomalies observed with the sUAS (Figure 7) reveal greater resolution of regional features shown in Figure 6. Magnetic lows of note are northwest of SRTKA, within SRTKA, and at BCTKA. The dominant orientation of magnetic gradients (dotted black lines) is NW and shows good agreement with gravity HGM lineations (Figures 7 and 11). The NW-SE trending lineation northeast of SRTKA suggests a continuation of the fault that intersects the Sawmill Cutoff Fault. Additionally, cross-cutting lineations are indicated at the termini of SRTKA. An ENE striking magnetic low terminates at the northeastern extent of SRTKA, orthogonal to the main magnetic fabric. This feature is likely a contact between the informal rhyolite of Smokey Bear Flat and rhyolite of Sawmill Dome (Hildreth et al., 2017; Figures 7 and 5). At the southern extent of

SRTKA, an ENE striking magnetic lineation near well 57-25 (Figures 7 and 3) may indicate a potential cross-cutting structure.

A geophysically inferred structural intersection is also present at BCTKA. Magnetic lineations trend N-S along the west and eastern sides of BCTKA, paralleling the contact between the informal basalt of Casa Diablo hot springs (bcd) of Hildreth and Fierstein (2016), Casa Diablo Till (gcd), and early rhyolite (subunit rsb) (Figures 7 and 5). Also, an E-W magnetic lineation cuts directly through BCTKA coincident with faults mapped by Bergfeld et al. (2006) (Figure 3). Although the gravity lineations (white dotted lines) show good agreement with the N-S trending magnetic lineations, an E-W lineation is not present in the gravity HGM analysis. Magnetic data are more sensitive to shallow geologic heterogeneity and may be reflecting (1) shallow alteration present at BCTKA, (2) inherent differences between magnetic properties of unit rsb and unit bcd, and (3) terrain effects present across BCTKA.

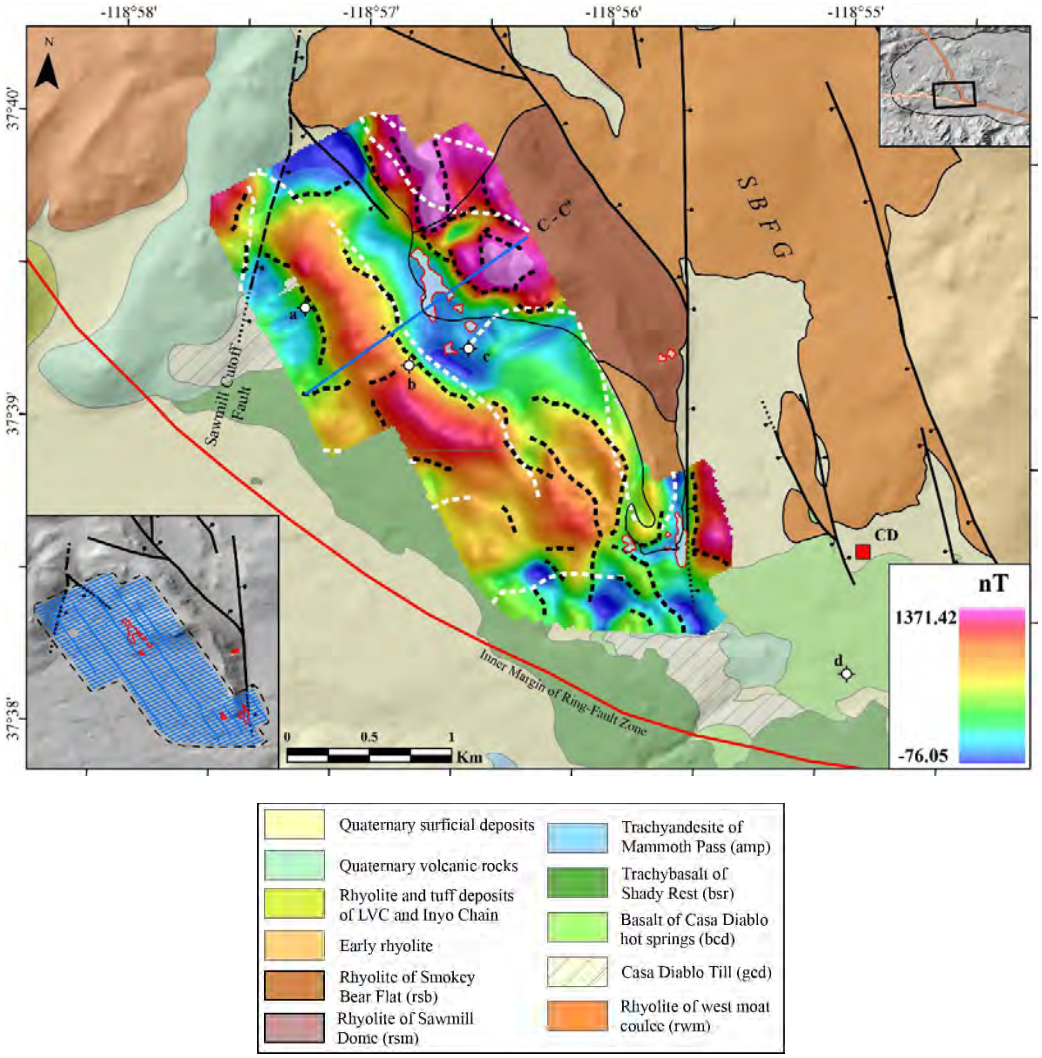

Figure 7: Reduced to pole magnetic anomaly map from sUAS acquisition. Black dotted lines are HGM lineations calculated from the pseudogravity magnetic grid. White dotted lines are HGM gravity lineations from Figure 11. Early rhyolite subunits rsm and rsb are included as thin black lines, see Figure 5 for geologic map. Red square is Casa Diablo Geothermal Plant and hot springs. Red outlines are tree-kill areas (see Figure 3). Wells symbols are identified in Figures 2 and 3. Bottom left inset shows sUAS

survey extent in dashed line, blue lines showing flight lines (NE oriented), and tie lines used to level the survey data (SE oriented). Wells within this Figure: a, RDO-8; b, 57-25; c, 66-25; d, 38-32. CD, Casa Diablo Geothermal Plant and hot springs; SBFG, Smokey Bear Flat Graben. Top right inset shows DEM hillshade with thick black rectangle showing Figure extent, LVC physiographic margin in thin black outline, and major highways in orange.

To assist the interpretation of observed magnetic anomalies, we computed magnetic topographic anomalies (Figure 8) across the survey extent using the method of Bouligand et al. (2016) with the assumption of a constant magnetization direction (equal to the direction of the ambient magnetic field) and intensity (1 A/m) in the subsurface. Correlated features in topographic and observed anomalies indicate topography contributes to the observed signal. However, the absence of a correlation suggests that the observed magnetic anomalies reflect magnetization variations at depth. A magnetic high over the early rhyolite (both subunits rsb and rsm), north and east of SRTKA, appears in both the observed anomaly and topographic anomaly, suggesting that this magnetic high can be explained by topography (Figures 7 and 8). The same applies for the early rhyolite outcropping near BCTKA.

The major NW trending magnetic high west of SRTKA (Figure 7) has a topographic contribution southeast from well 57-25 (Figure 8). This suggests that the magnetic high between BCTKA and well 57-25 has a topographic contribution to explain the observed signal. This region also is where mafic flows (units bsr and bcd) have been mapped on the surface by Hildreth and Fierstein (2016). However, northwest from well 57-25 (Figure 3), we see that the topographic effect is low compared to the observed signal. This suggests that this portion of the magnetic high results from a highly magnetized body concealed beneath surficial deposits.

The crossing structure at the northeastern end of SRTKA is coincident with a topographic anomaly, suggesting the magnetic low observed is in part due to topography. However, pre-existing structures (the contact between rsm and rsb) may predispose this zone to increased erosion due to a juxtaposition of physical properties, driving weathering, erosion, and topographic development. The correspondence between the subunit contact and magnetic anomaly should not be discarded as simply an artifact of topography. The crossing structure at the southern end of SRTKA does not show a significant topographic effect, indicating that the anomaly associated with this structure can be explained by subsurface magnetization variations that may result from a lithologic or structural contact between unit bsr and unit bcd.

The magnetic low at and around SRTKA is not associated with a magnetic low in the topographic anomalies, indicating that this area is characterized by lower magnetization. However, the magnetic low at BCTKA is partly observed in the topographic anomalies. This precludes the conclusion that this area is associated with a significant lower magnetization. Surficial alteration, heated ground, and gas vents are observed here, but less well developed and long-lived subsurface alteration at BCTKA (as compared to SRTKA) may account for this discrepancy.

The northwest trending HGM lineations on the west and eastern sides of SRTKA suggest some structure may be present on either side. The fault mapped north of SRTKA (intersecting the Sawmill Cutoff Fault just outside of the survey area) may extend into SRTKA if these lineations represent the continuation of this fault. These NW lineations intersect NE lineations at the northern and southern extents of SRTKA. These intersections may host enhanced permeability and control subsurface alteration. Notably, the northern end of SRTKA hosts a significant thermal anomaly (Figure 3) as outlined in Vaughan et al. (2018).

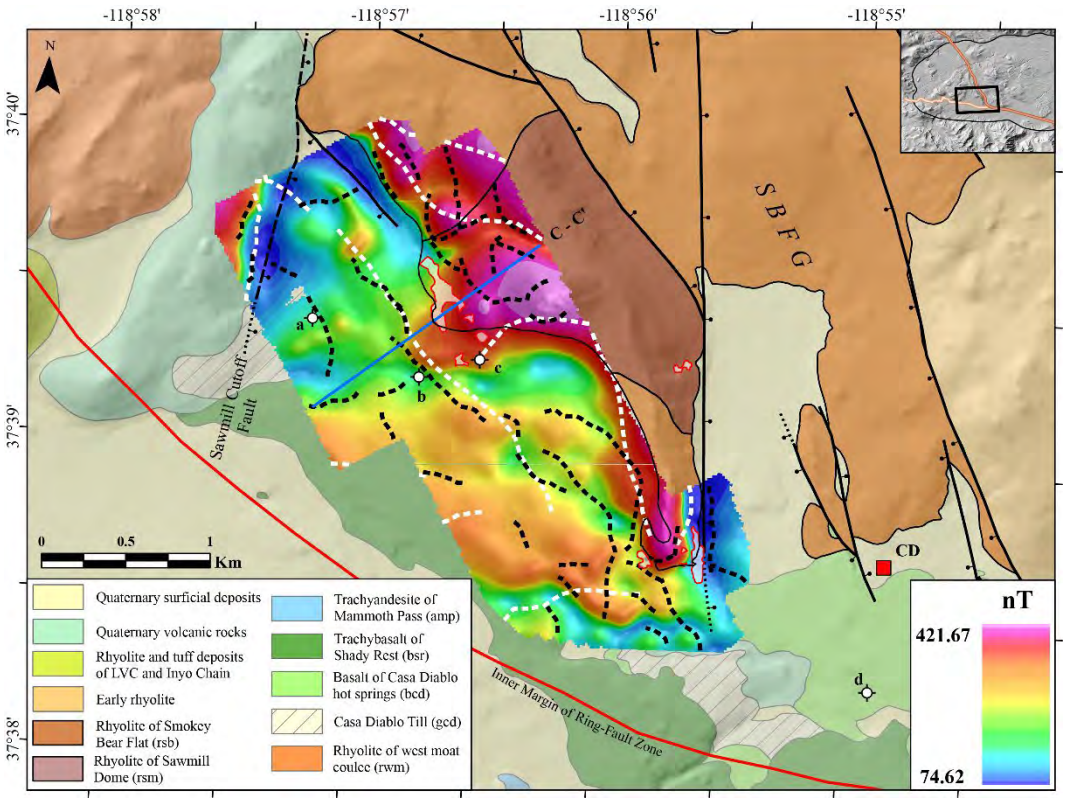

Figure 8: Magnetic anomalies resulting from topography. A constant magnetization of 1 A/m was assumed across the entire extent of the survey. Black dotted lines are HGM lineations calculated from the pseudogravity magnetic grid. White dotted lines are HGM gravity lineations from Figure 11. Early rhyolite subunits rsm and rsb are included as thin black lines. Red square is Casa Diablo geothermal plant and hot springs. Red outlines are tree-kill areas (see Figure 3). Wells within this Figure: a, RDO-8; b, 57-25; c, 66-25; d, 38-32. CD, Casa Diablo Geothermal Plant and hot springs; SBFG, Smokey Bear Flat Graben. Top right inset shows DEM hillshade with thick black rectangle showing Figure extent, LVC physiographic margin in thin black outline, and major highways in orange.

5.1.3 Regional Gravity

Gradients in gravity anomalies in the south moat (Figures 9 and 10) align with large-scale structures that have been inferred from seismicity (Prejean et al., 2002) and geologic studies (Hildreth, 2017; Hildreth and Fierstein, 2016). A major NW trend in the gravity gradient along the southern margin of LVC is subparallel to the inferred ring-fault zone (Figure 9). A closer look reveals a NW-trending gravity high extending from BCTKA to SRTKA (Figure 10). A minor saddle in the gravity high suggests a NE oriented structure may be present between BCTKA and the southern extent of SRTKA (Figure 10). A local gravity low, located where profile A – A' intersects the inferred inner margin of the ring-fault zone (Figure 10) suggests low density fill may be thicker. The agreement between regional gravity highs and lows with regional aeromagnetic anomalies near SRTKA and BCTKA (Figures 6, 9, 10) suggest that structure and/or alteration affect both density and magnetic properties of rocks in the subsurface.

Gradients near the BCTKA are predominately E-W and N-S trending (Figures 10 and 11). An oblate, E-W oriented gravity high south of BCTKA extends to Casa Diablo geothermal plant but appears to be cut off by the SBFG (Figure 11). Regional magnetic anomalies also indicate a strong E-W fabric in the gradients near BCTKA (Figure 6).

A N-S oriented gravity high along the eastern side of the SBFG is unexpected because one would expect a gravity low from thicker, low-density fill on the down-dropped (east) side of the fault. This likely reflects the low density of early rhyolite compared to mafic flows or a zone of mineralization because the regional aeromagnetic anomalies indicate a coincident magnetic high (Figure 6). The mineralized body would need to be highly magnetic to account for this observed anomaly, which suggests a mafic flow is more likely.

The regional gravity anomalies agree well with gradients from the regional aeromagnetic anomalies. Orthogonal fabrics at SRTKA (NW/NE) and BCTKA (N/E) suggest tree-kill areas are generally coincident with structural intersections, but a closer look at the gravity gradients in comparison with the sUAS survey will clarify the spatial correspondence with tree-kill areas using a HGM analysis.

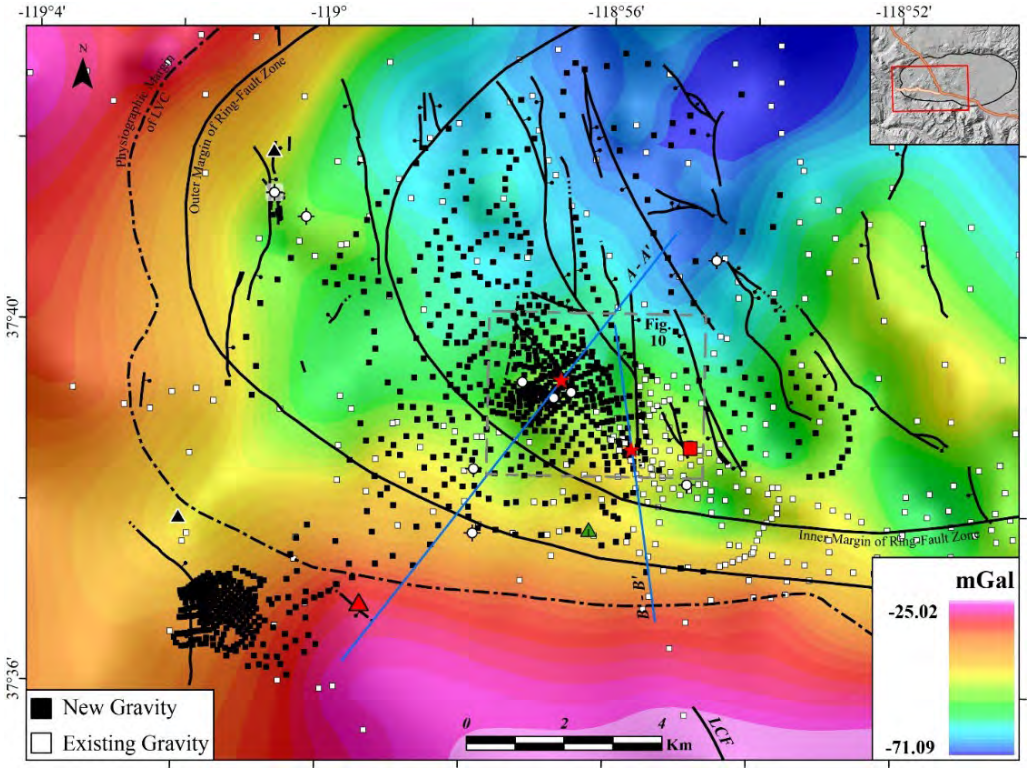

Figure 9: Isostatic gravity anomaly grid, 400-m cell size. Existing gravity coverage from Langenheim et al. (2024). Faults are from Hildreth and Fierstein (2016). Red stars are tree-kill areas, red square is Casa Diablo Geothermal Plant and hot springs. Other feature labels can be found in Figure 2. Top right inset shows DEM hillshade with red rectangle showing Figure extent, LVC physiographic margin in thin black outline, and major highways in orange.

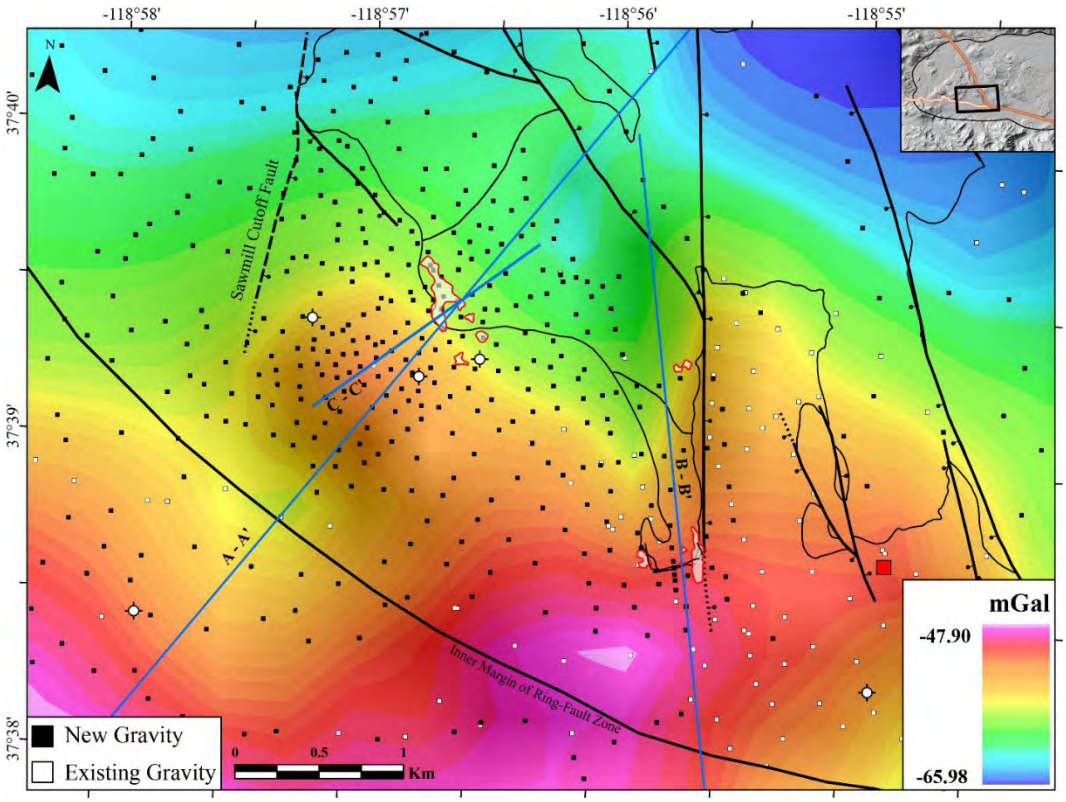

Figure 10: Isostatic gravity anomaly grid, 100-m cell size. Existing gravity coverage from Langenheim et al. (2024). Faults are from Hildreth and Fierstein (2016). Red outlines are tree-kill areas. Red square is Casa Diablo Geothermal Plant and hot springs. Top right inset shows DEM hillshade with thick black rectangle showing Figure extent, LVC physiographic margin in thin black outline, and major highways in orange.

5.1.4 Detailed Gravity

Gridding the gravity at 100-m cell size reveals finer details across the study area, but also agrees well with regional gradient orientations discussed in sections 5.1.1 and 5.1.3 with some differences. The NW fabric observed at SRTKA in regional aeromagnetic anomalies, sUAS magnetic anomalies, and regional gravity is present in the detailed gravity HGM lines (Figure 11, white dotted lines). However, the cross-cutting NE gradient inferred from a minor saddle in the regional gravity anomaly grid, postulated to be present somewhere between BCTKA and the southern extent of SRTKA, does not appear in the detailed gravity HGM analysis. However, a minor saddle is present at the southern extent of SRTKA.

The NE oriented HGM line near the southern extent of SRTKA is resulting from the juxtaposition of early rhyolite next to glacial deposits (Figure 5, unit gcd). This contact is interpreted as a glacial feature by Hildreth et al. (2017). No other NE trending HGM lineations are present near SRTKA, suggesting that any crossing structures here are shallow.

In addition, the gravity HGM lines do not coincide with the magnetic HGM lines paralleling the eastern side of SRTKA that suggest the continuation of a mapped fault. The lack of gravity HGM lines may indicate that this structure is shallow or that fault throw decreases to the southeast. The gravity HGM lines on the west side of SRTKA do agree well with the sUAS magnetic HGM lines,

supporting the hypothesis that some buried body of anomalous density and magnetization is present, juxtaposed against the western margin of SRTKA by a concealed structure (contact or fault).

Gravity lineations at BCTKA agree well with sUAS magnetic lineations along a NS trend on the western and eastern sides of BCTKA (Figure 11). In contrast, the EW gravity HGM line near BCTKA is offset toward the southwest. This lineation may represent the contact of mafic flows at their thickest here in the south moat. Although a definitive intersection is not found here at BCTKA between magnetic and gravity HGM lineations, the agreement with NS lineations supports the presence of structures that may regulate subsurface processes related to hydrothermal alteration, gas and fluid migration, and thermal diffusion. The discrepancy between gravity and magnetic HGM lineations suggest any structure or contact present here is shallow.

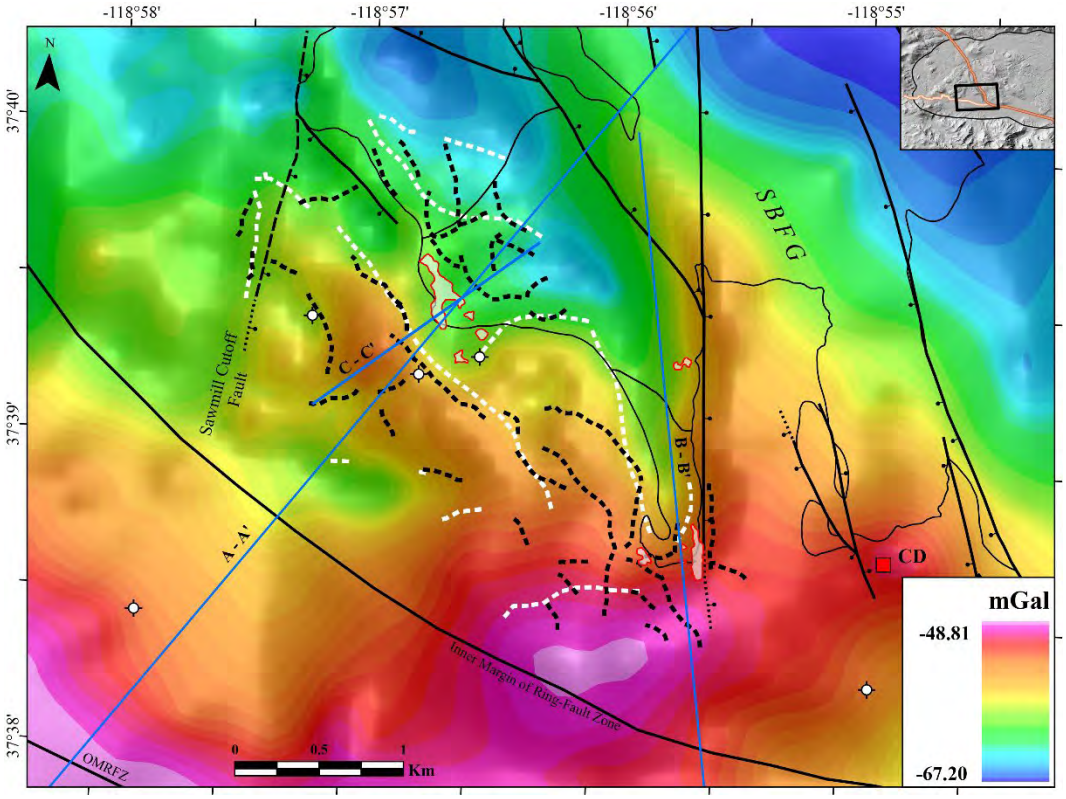

Figure 11: Isostatic gravity anomaly grid, cell size 100 m. Black dotted lines are HGM lineations on the magnetic grid. White dotted lines are HGM lineations on the isostatic gravity grid. Red outlines are tree-kill areas. Faults are from Hildreth and Fierstein (2016). OMRFZ, inferred outer margin of the ring-fault zone; SBFG, Smokey Bear Flat Graben, CD, Casa Diablo Geothermal Plant and hot springs.

6. Geophysical Modelling

6.1 Model Rock Properties

Rock density properties were determined by measuring collected samples for density and magnetic susceptibility, and supplemented from the literature (Ponce, 2021; Hildreth et al., 2014; Stevens and Greene, 1999; Palmer, 1996; Carle, 1988; Mankinen, 1986; Berkman, 1978; Williams, 1977;

Sheridan, 1970; Currie et al., 1953) when no samples were available to directly measure. Model properties for units included in the 2D profiles are in Figure 12.

6.1.1 Density

Saturated bulk densities (SBD) are used for all units on the assumption that the water table is relatively shallow compared to the depth of the model. Mafic flows, alteration zones, early rhyolite, sinter deposits, granitic rocks, and metasedimentary rock density values were determined from hand samples collected in the field and measured in a rock property laboratory. Metasedimentary densities are calculated from collected hand samples and data available from Ponce (2021). The lithology of the Morrison Block from Stevens & Greene (1999) was used to select rock types and calculate density from data from Ponce (2021). Welded and unwelded Bishop Tuff density values were computed by using grain density values from Carle (1988) and porosity estimates from Sheridan (1970). Pore space is assumed to be completely saturated with water. Welded Bishop Tuff SBD is determined to be 2,250 kg/m^3 with 5-10% porosity (Sheridan, 1970) for a grain density of 2,350 kg/m^3 (Carle, 1988). Unwelded Bishop Tuff is determined to be 1,630 kg/m^3 with 20-60% porosity (Sheridan, 1970) for a grain density of 2,050 kg/m^3 (Carle, 1988). The “high density and magnetic body” density value was adjusted to fit the gravity anomaly.

6.1.2 Magnetic Properties

Early rhyolite paleomagnetic directions are incorporated from Mankinen et al. (1986), using a Fisher mean to average between both subunits present in the study area (rhyolite of Sawmill Dome, Mankinens site 1; rhyolite of Smokey Bear Flat, Mankinens site 2). Magnetization values for early rhyolite are taken from Williams et al. (1977). Paleomagnetic directions from mafic flows were averaged (Fisher mean) using data from Hildreth et al. (2014) (their supplemental file 2). Magnetizations for the mafic flows are taken from Mankinen (1986) (his table 1, late basalts and trachyandesites). The paleomagnetic directions for the Bishop Tuff are taken from Palmer et al. (1996) and magnetization values are from Williams et al. (1977). Magnetization values for granitic rocks are taken from Currie et al. (1953). Magnetization values for metasedimentary rocks are taken from Berkman (1978). Paleomagnetic directions for both granitic and metasedimentary rocks are assumed to be a geocentric axial dipole (GAD) field at a latitude of 37.65 degrees given the typically poor ability for these rock types to retain a remnant magnetization. Susceptibility values from measured samples were used or informed by literature when not available. The paleomagnetic direction of the ”high density and magnetic body” was assumed to be the same as early rhyolite given its stratigraphic position. Its magnetization and susceptibility were adjusted to fit the observed magnetic anomaly.

	Unit	Density (kg/m^3)	Susc. (SI)	Mag. (A/m)	Inc. (°)	Dec. (°)
	Unconsolidated surficial deposits and till (0 - 200m)	2050	*	*	*	*
	Unconsolvidated surficial deposits and till (200 - 600m)	2150	*	*	*	*
	Mafic flows	2450 - 2500	0.01285	4 - 5	45.5	2.8
	High density and magnetic body	2600	0.0145	2.7	59.7	7.6
	Early rhyolite (high magnetization)	1960 - 2350	0.00413	2.5 - 5.6	59.7	7.6
	Early rhyolite (average magnetization)	1960 - 2280	0.00413	2.3	59.7	7.6
	Early rhyolite (below average magnetization)	2180 - 2350	0.00413	2	59.7	7.6
	Early rhyolite (low magnetization)	1960 - 2350	0.00134	0.5 - 1	59.7	7.6
	Sinter deposits	1940	*	*	*	*
	Landslide breccia	2250	*	*	*	*
	Bishop Tuff (unwelded, high magnetization)	1630	0.00258	3 - 4	53	348
	Bishop Tuff (unwelded, average magnetization)	1630	0.00258	2.2	53	348
	Bishop Tuff (unwelded, low magnetization)	1630	0.00258	1	53	348
	Bishop Tuff (welded)	2250	0.00258	2.2	53	348
	Granitic rocks	2670 - 2700	0.016	0.365	57	0
	Metasedimentary rocks	2640 - 2700	0	0.005	57	0

Figure 12: Model rock properties. See text for sources of rock property data.

6.2 Profile Description

6.2.1 Profile A – A'

Profile A – A' crosses the south moat and directly through SRTKA. Joint forward modelling (Figure 13) suggests that the ring fault zone is not geophysically discernable with the available resolution of interpolated regional aeromagnetic data and regional isostatic gravity data. An early rhyolite (ER) body of low magnetization (0.5 – 1 A/m) relative to average values adjacent to SRTKA is necessary to fit observed gravity and magnetic values. However, an ER block of below average magnetization (2 A/m) within the low magnetization zone is needed to fit the magnetic high observed southwest adjacent to SRTKA. Welded Bishop Tuff is modelled as substantially thicker than unwelded Bishop Tuff to fit the observed gravity values. Low frequency magnetic anomalies between the basement exposures and SRTKA are fit by adjusting the thickness of buried mafic flows. This fit agrees with the conclusion that the E-W trending magnetic high along the southern caldera (feature B3 in Figure 6) wall can be explained from buried mafic flows. Thickening mafic flows toward the southern caldera wall are also consistent with the south moat being a local topographic low in relation to the uplifted early rhyolite (the resurgent dome, see Figure 1). Volcanic effusions from Mammoth Mountain periphery flow downhill along the south moat and pile up.

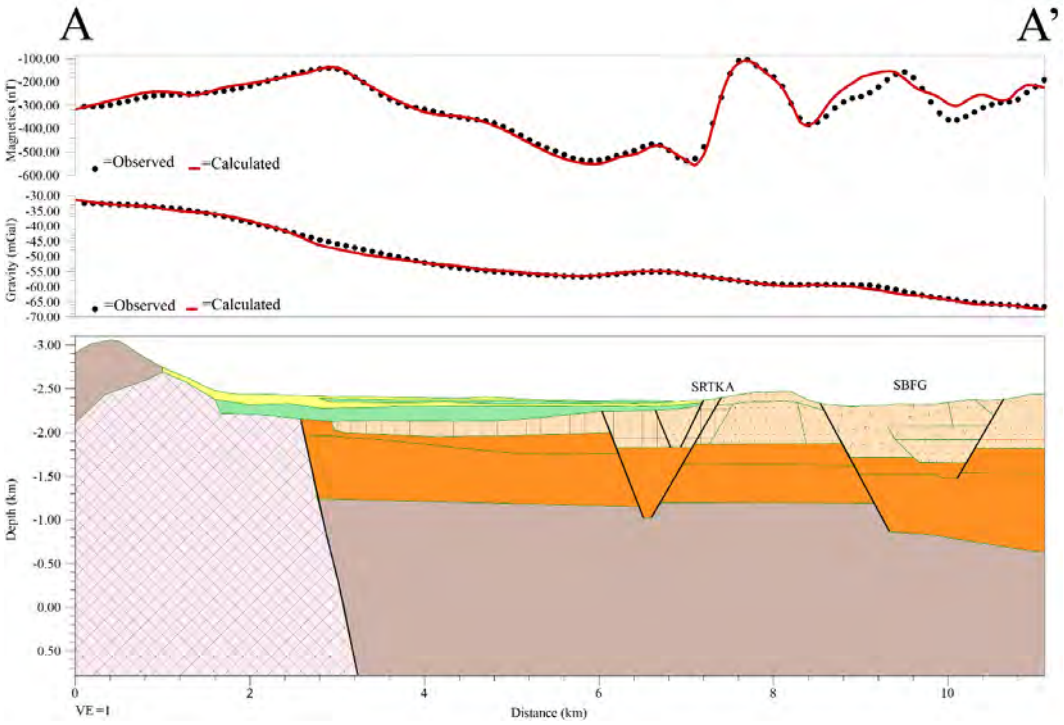

Figure 13: A – A' Preliminary forward model with Shady Rest tree-kill area (SRTKA) and Smokey Bear Flat Graben (SBFG) labeled. Magnetic anomalies modelled are from the total magnetic field (TMF) data from Ponce (2019). Gravity anomalies modelled are from 400-m gridded data (Figures 9 and 10). Thick black lines are major structures inferred by geophysics (ring fault at southern end, SRTKA structures discussed in geophysical mapping sections) or mapped (SBFG mapped by Hildreth and Fierstein (2016)). See Figures 2 and 4 for profile line locations.

6.2.2 Profile B – B'

Profile B – B' (Figure 14) extends from lower Laurel Canyon (Figure 2) across BCTKA and outcrops of early rhyolite. Similar to profile A – A' and conclusions in Carle (1988), welded Bishop Tuff is thicker than unwelded Bishop Tuff to fit the observed gravity anomalies (Figure 14). A large landslide block is modelled beneath early rhyolite but overlaying Bishop Tuff. This block agrees with findings by Suemnicht et al. (2007) that a syneruptive landslide block is extensive at depth in the Casa Diablo area.

The dominant magnetic high in the southern portion of the profile (at ~1-2 km profile distance) is fit by modelling early rhyolite of average magnetization overlain by undulatory mafic flows extending to BCTKA. Low magnetization of early rhyolite adjacent to BCTKA provides a good fit to the observed magnetic low. The low magnetization of early rhyolite upslope from BCTKA agrees well with observed alteration by this work's authors north from BCTKA and alteration mapped by Bailey (1976). A low magnetization block of early rhyolite beneath BCTKA agrees with the mapping that found BCTKA is better defined by magnetic anomalies than gravity anomalies (section 5.1.4). As in Profile A – A', observed magnetic and gravity data can be fit without incorporating multiple ring fault structures. This suggests that either (1) the resolution of the gravity and magnetic data used for these models do not permit delineation of this structure and/or (2) density and magnetic properties at depth are not sufficiently different to produce strong signals.

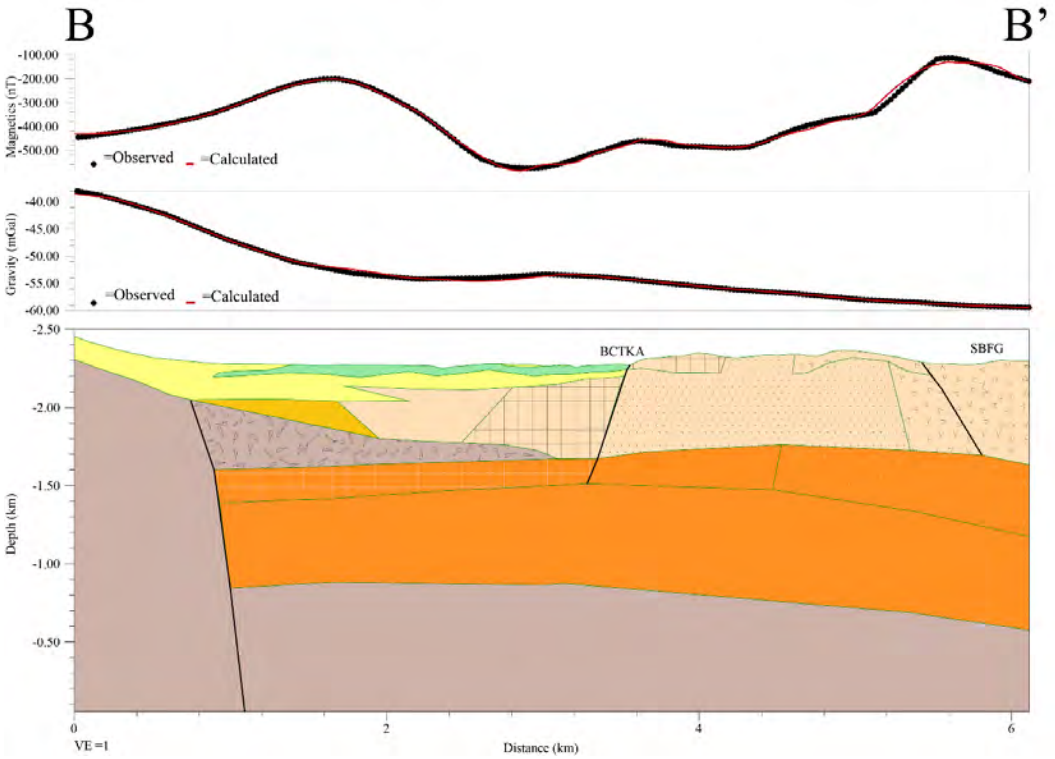

Figure 14: B – B' Preliminary forward model with Basalt Canyon tree-kill area (BCTKA) and Smokey Bear Flat Graben (SBFG) labeled. Magnetic anomalies modelled are from the total magnetic field (TMF) data from Ponce (2019). Gravity anomalies modelled are from 400-m gridded data (Figures 9 and 10). Thick black lines are major structures inferred by geophysics (ring fault at southern end) or mapped (fault mapped by Bergfeld et al. (2006), and SBFG mapped by Hildreth and Fierstein (2016)). See Figures 2 and 4 for profile line locations.

6.2.3 Profile C – C'

A short profile was modelled across SRTKA using sUAS magnetics data gridded as described in previous sections and gravity gridded values shown in Figure 11. As modelled in profiles A – A' and B – B', a thicker sequence of welded Bishop Tuff is needed to fit the observed gravity (Figure 15). Additionally, a zone of low magnetization early rhyolite is included beneath SRTKA to fit the magnetic low across the southern portion of the profile. Intra-unit gradational magnetization was incorporated within early rhyolite to fit the observed magnetic values at the NE end of the profile. Given the alteration needed at depth to fit the magnetic low, this model cannot conclusively determine whether a fault is merited as indicated by the geophysical mapping (Figure 7). An approximately 150-meter thick, 600-meter-wide zone of high density and magnetization is required to fit the observed gravity and magnetic values (the "high density and magnetic body"). This may represent a zone of hydrothermal mineralization, lithologic variation within early rhyolite or adjacent moat rhyolite units, or a buried mafic flow. Conducting an electrical resistivity tomography (ERT) or seismic reflection survey across this buried feature and SRTKA may elucidate subsurface electrical property variations and seismic velocity changes that could inform a robust interpretation concerning the source of the magnetic and gravity anomalies.

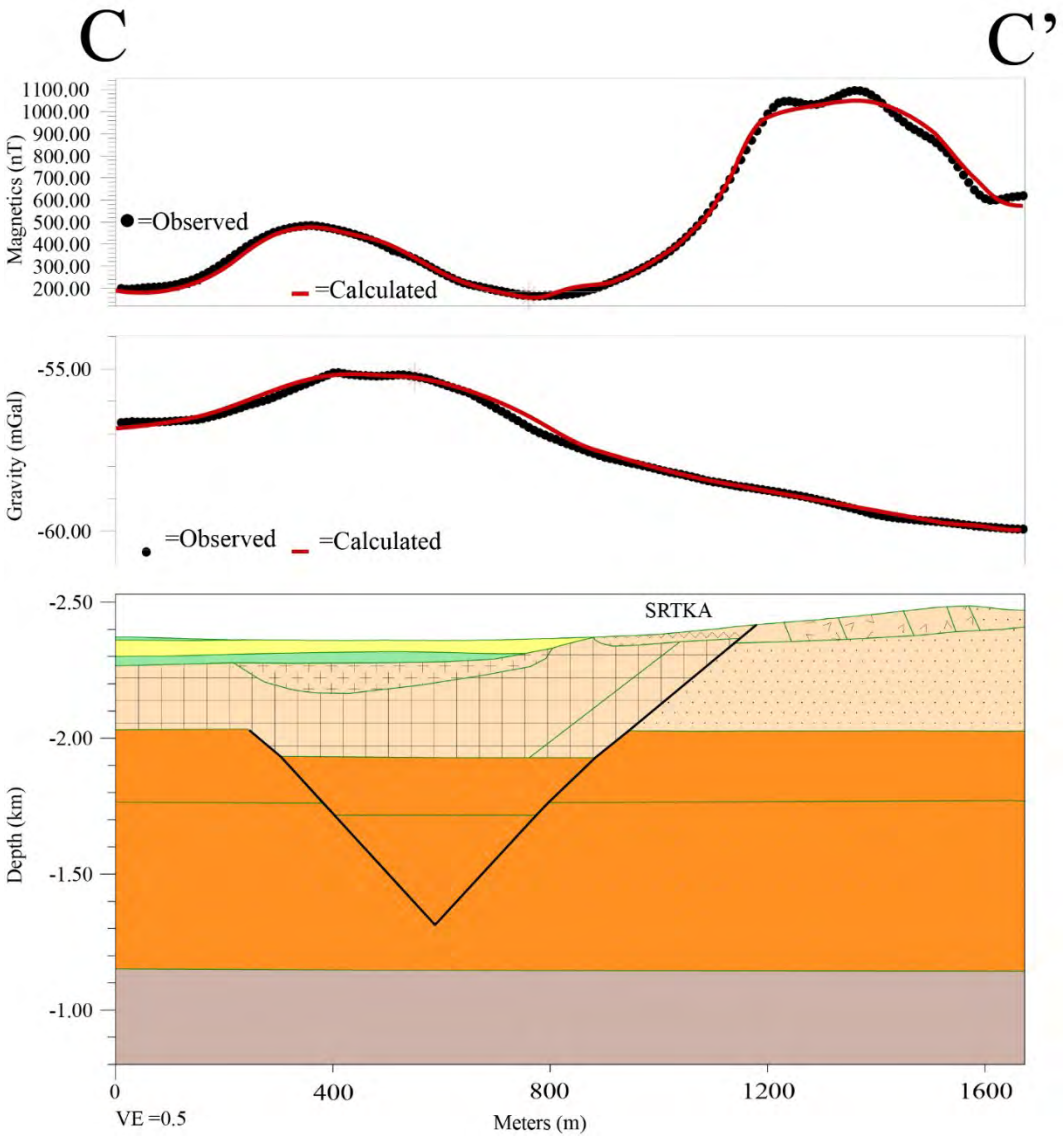

Figure 15: C – C' Preliminary forward model. Shady Rest tree-kill area (SRTKA) location is labeled. Magnetic anomalies modelled are from the total magnetic field (TMF) data from Ponce (2019). Gravity anomalies modelled are from 100-m gridded data (Figure 11). Thick black lines are major structures inferred by geophysics. See Figures 3 and 5 for profile line locations.

7. Conclusion

Geophysical data collected from 2021 – 2024 at Mammoth Lakes provide insight into the present state of surface and subsurface alteration and structure. Interpretation of potential field data provides new perspectives on the controls on localization of hydrothermal surface expression and subsurface alteration. Gravity and magnetic HGM mapping reflect previously known WNW structures along the SMSZ and suggest structural complexity may play a role in hydrothermal surface manifestations at SRTKA and partly at BCTKA. Although the preliminary 2D joint models proposed here cannot uniquely map these complex structures, they do reveal a subsurface architecture that requires significant density and magnetic juxtaposition to account for observed

anomalies. Continued work to characterize the subsurface rock property variability will enhance understanding and characterization of a structural model of the south moat.

Acknowledgements

Many thanks to Wes Hildreth and Judy Fierstein for providing valuable insight into the geologic history of Long Valley and pointing me toward useful resources. Thanks to Peter Kelly, Bill Evans, Deborah Bergfeld, Jennifer Lewicki, and Sara Peek for their cooperation and valuable insight into gas flux at Shady Rest and Basalt Canyon. Thanks to Greg Vaughan for assistance with thermal infrared interpretation and support in devising better TIR workflows. Additional thanks to Stuart Wilkinson, David Shelly, Alicia Hotovec-Ellis, Stephanie Prejean, Jared Peacock, Grace Walker, Benjamin Morbeck, and Leyla Namazie. Thanks to Victoria Langenheim, Wes Hildreth, Karen Christopherson, Steve Sewell, and Paul Schwering for their helpful and thorough reviews of this manuscript. ISTerre is part of Labex OSUG@2020 (ANR10 LABX56). Any use of trade, firm, or product names is for descriptive purposes and does not imply endorsement by the U.S. Government.

REFERENCES

Athens, N. “Maxspots Curvature”, software available at: https://github.com/nathens/maxspots_curvature, (2018)

Bailey, R.A., Dalrymple, G.B. and Lanphere, M.A. “Volcanism, structure, and geochronology of long valley caldera, mono county, california.” Journal of Geophysical Research, (1976), 81(5), pp.725-744.

Bergfeld, D. and Evans, W.C. ”Monitoring CO2 emissions in tree kill areas near the resurgent dome at Long Valley Caldera, California.” US Geological Survey, (2011), (No. 2011-5038).

Bergfeld, D., Evans, W.C., Howle, J.F. and Farrar, C.D. “Carbon dioxide emissions from vegetation-kill zones around the resurgent dome of Long Valley caldera, eastern California, USA.” Journal of volcanology and Geothermal Research, (2006), 152(1-2), pp.140-156.

Berkman, F.E. “Magnetic model study of the Long Valley caldera, California, A.” 1970-1979-Mines Theses & Dissertations, (1978).

Blakely, R.J. “Potential theory in gravity and magnetic applications.” Cambridge University press, (1995).

Bouligand, C., Coutant, O., Glen, J.M.G. “Sub-surface structure of La Soufrière of Guadeloupe lava dome deduced from a ground-based magnetic survey.” J. Volcanol. Geotherm. Res. 321, (2016), 171–181. https://doi.org/https://doi.org/10.1016/j.jvolgeores.2016.04.037

Carle, S.F. “Three-dimensional gravity modeling of the geologic structure of Long Valley caldera.” Journal of Geophysical Research: Solid Earth, (1988), 93(B11), pp.13237-13250.

Currie, R.G., Grommé, C.S. and Verhoogen, J., 1963. Remanent magnetization of some Upper Cretaceous granitic plutons in the Sierra Nevada, California. Journal of Geophysical Research, 68(8), pp.2263-2279.

Hildreth, W., Fierstein, J., Champion, D. and Calvert, A. “Mammoth Mountain and its mafic periphery—A late Quaternary volcanic field in eastern California.” Geosphere, (2014), 10(6), pp.1315-1365.

Hildreth, W. and Fierstein, J. “Eruptive history of Mammoth Mountain and its mafic periphery, California.” US Geological Survey, (2016), (No. 1812).

Hildreth, W. “Fluid-driven uplift at Long Valley Caldera, California: geologic perspectives.” Journal of Volcanology and Geothermal Research, (2017), 341, pp.269-286.

Hildreth, W. “Concealed Ring-Fault Zone of Long Valley Caldera” US Geological Survey, (2017), (No. 2017-5022-L).

Hildreth, W., Fierstein, J. and Calvert, A. “Early postcaldera rhyolite and structural resurgence at Long Valley Caldera, California.” Journal of Volcanology and Geothermal Research, (2017), 335, pp.1-34.

Hill, D.P. and Montgomery-Brown, E. “Long Valley Caldera and the UCERF depiction of Sierra Nevada range-front faults.” Bulletin of the Seismological Society of America, (2015), 105(6), pp.3189-3195.

Kane, M.F., Mabey, D.R. and Brace, R.L. “A gravity and magnetic investigation of the Long Valley caldera, Mono County, California.” Journal of Geophysical Research, (1976), 81(5), pp.754-762.

Kaub, L., Keller, G., Bouligand, C. and Glen, J.M. “Magnetic surveys with Unmanned Aerial Systems: Software for assessing and comparing the accuracy of different sensor systems, suspension designs and compensation methods.” Geochemistry, Geophysics, Geosystems, (2021), 22(7), p.e2021GC009745.

Langenheim, V.E., Dean, B.D., Earney, T.E., Anderson, J.E, Sisson, T.W., Moore, J.M., Roberts, M.A., Ritzinger, B., Zielinski, L.A., Schmidt, K.M., Chuchel OU, B.A., Walker, G.C., Morbeck, B.L., Comstock, K.H. “Gravity, density, and magnetic property measurements of the Sierra Nevada, California and Nevada” U.S. Geological Survey data release, (2024), https://doi.org/10.5066/P13KZVHQ

Mankinen, E.A., Grommé, C.S., Dalrymple, G.B., Lanphere, M.A. and Bailey, R.A. “Paleomagnetism and K-Ar ages of volcanic rocks from Long Valley Caldera, California.” Journal of Geophysical Research: Solid Earth, (1986), 91(B1), pp.633-652.

Palmer, H.C., MacDonald, W.D., Gromme, C.S. and Ellwood, B.B. “Magnetic properties and emplacement of the Bishop tuff, California.” Bulletin of volcanology, (1996), 58, pp.101-116.

Peacock, J.R., Mangan, M.T., McPhee, D. and Wannamaker, P.E. “Three-dimensional electrical resistivity model of the hydrothermal system in Long Valley Caldera, California, from magnetotellurics.” Geophysical Research Letters, (2016), 43(15), pp.7953-7962.

Ponce, D.A. “High-Resolution Aeromagnetic Survey of Mono Basin and Long Valley, California” U.S. Geological Survey data release, (2019), https://doi.org/10.5066/P9671UZU.

Ponce, D.A. “Density and Magnetic Properties of Selected Rock Samples from the Western U.S. and Alaska” U.S. Geological Survey data release, (2021), https://doi.org/10.5066/P9FONTGS

Prejean, S., Ellsworth, W., Zoback, M. and Waldhauser, F. “Fault structure and kinematics of the Long Valley Caldera region, California, revealed by high-accuracy earthquake hypocenters and focal mechanism stress inversions.” Journal of Geophysical Research: Solid Earth, (2002), 107(B12), pp.ESE-9.

Riley, P., Tikoff, B. and Hildreth, W. “Transtensional deformation and structural control of contiguous but independent magmatic systems: Mono-Inyo Craters, Mammoth Mountain, and Long Valley Caldera, California.” Geosphere, (2012), 8(4), pp.740-751.

Shelly, D.R., Ellsworth, W.L. and Hill, D.P. “Fluid-faulting evolution in high definition: Connecting fault structure and frequency-magnitude variations during the 2014 Long Valley Caldera, California, earthquake swarm.” Journal of Geophysical Research: Solid Earth, (2016), 121(3), pp.1776-1795.

Sheridan, M.F. “Fuarmolic mounds and ridges of the Bishop Tuff, California.” Geological Society of America Bulletin, (1970), 81(3), pp.851-868.

Sorey, M.L., Suemnicht, G.A., Sturchio, N.C. and Nordquist, G.A. “New evidence on the hydrothermal system in Long Valley caldera, California, from wells, fluid sampling, electrical geophysics, and age determinations of hot-spring deposits.” Journal of Volcanology and Geothermal Research, (1991), 48(3-4), pp.229-263.

Strand, R. “Mariposa Sheet” State of California, the Resources Agency, Department of Conservation, Division of Mines and Geology, (1967)

Stevens, C.H. and Greene, D.C. “Stratigraphy, depositional history, and tectonic evolution of Paleozoic continental-margin rocks in roof pendants of the eastern Sierra Nevada, California.” Geological Society of America Bulletin, (1999), 111(6), pp.919-933.

Suemnicht, G.A., Sorey, M.L., Moore, J.N. and Sullivan, R. “The shallow hydrothermal system of Long Valley caldera, California.” Geothermal Resources Council Transactions, (2007), 30, pp.465-469.

U.S. Geological Survey: 3D Elevation Program 10-Meter Resolution Digital Elevation Model, accessed from URL https://www.usgs.gov/the-national-map-data-delivery, (accessed, 2/2024).

U.S. Geological Survey. “Quaternary Fault and Fold Database for the Nation.” U.S. Geological Survey data release, (2020), https://doi.org/10.5066/P9BCVRCK

Vaughan, R.G., Bergfeld, D., Evans, W.C., Wilkinson, S., Miwa, C. and Diabat, M. “A Baseline Thermal Infrared Survey of Ground Heating Around the Casa Diablo Geothermal Plant, Mammoth Lakes, CA.” Geothermal Resources Council Transactions, (2018).

Wallace, P.J., Anderson Jr, A.T. and Davis, A.M. “Gradients in H2O, CO2, and exsolved gas in a large-volume silicic magma system: Interpreting the record preserved in melt inclusions from the Bishop Tuff.” Journal of Geophysical Research: Solid Earth, (1999), 104(B9), pp.20097-20122.

Williams, D.L., Berkman, F. and Mankinen, E.A. “Implications of a magnetic model of the Long Valley Caldera, California.” Journal of Geophysical Research, (1977), 82(20), pp.3030-3038.

Zielinski, L.A., Glen, J.M., Earney, T.E., Rea-Downing, G.H., Vaughan, R.G., Kelly, P.J., Keller, G.H., Dean, B.J. and Schermerhorn, W. “UAS-based tools for mapping and monitoring

hydrothermal systems: An example from Mammoth Lakes, California.” Geothermal Resources Council Transactions, 46, (2022), pp.1618-1637.

Base of Clay Cap Temperature Characterization in Sumatra Island, Study Case in PGE Fields

Muhammad Tajul Arifin[1], Aditya Abdurrahman Juanda[1], Mulyanto[1]

[1]PT Pertamina Geothermal Energy Tbk

Keywords

Cap, Conductor, Sumatra, Resistivity, Temperature

ABSTRACT

The formation of clay cap and its expected temperature are closely related to the geological setting of each geothermal field. In Sumatra Island, the overall geological setting is highly influenced by the interplay between a field's distance to the Great Sumatran Fault Zone and its pre-existing geological conditions. This interplay shapes both geological structures and hydrothermal fluid flow patterns, complicating the correlation of the base of clay cap with temperature.

To characterize the base of clay cap temperature in Sumatra Island, a comprehensive assessment was conducted of magnetotelluric (MT) data and borehole data such as the methylene blue (MeB) measurement of smectite clay in cuttings and temperature logs from five explored and developed geothermal fields of Pertamina Geothermal Energy (PGE). First, the consistency of the 3D resistivity model from MT surveys was evaluated by comparing it with the 1D model. Subsequently, the 1D model was refined using MeB data from wells to identify the base of the clay cap. We then examined the correlation between the base of the clay cap and temperature by analyzing nearby wells selected close to MT station locations.

The findings reveal a strong correlation between the base of the clay cap and the associated temperature. The details of this correlation vary depending on the geological setting of the geothermal system and especially the geothermal system evolution. This characterization offers a preliminary method for estimating the temperature of geothermal systems known or assumed to exist below the base of clay cap in Sumatra and, potentially, globally, tailored to specific geological settings and geothermal system evolution.

1. Introduction

The idealized model for a convective geothermal system has a cap that seals the hot fluids within the reservoir flowing upward to the surface. The sealing properties of the cap is derived from its main mineral composition, commonly consisting of hydrated smectite clay or mixed-layer clay. Due to the high cation exchange capacity and resulting high interface conduction that characterizes hydrated smectite clay, the geothermal reservoir cap typically has a low resistivity value of below

10 ohm-m (Ussher, 2000; Cumming, 2016). As temperature increases, the smectite clay of the argillic zone transitions to mixed-layer smectite-illite clay or to smectite-chlorite clay. A transition from smectite clay to a phyllic cap comprised of abundant illite is a special case also correlated with a moderate increase in resistivity. The transition to the more brittle illite or chlorite clay associated with the propylitic alteration characteristic of a high temperature reservoir would be correlated with an increase to much higher resistivity (Johnstone, et al., 1992; Cumming, 2016). The correlation of alteration and temperature data from wells with MT resistivity will better characterize the values of resistivity and temperature that correlate with these transitions in different geothermal settings.

Many of the earliest studies of the relationship between low resistivity and smectite clay and its importance in the exploration for geothermal resources have originated from Indonesia (e.g. Whittome and Salveson, 1990; Cumming and Matson, 2021). More recently, the importance of the base of clay cap and base of conductor in geothermal interpretation has been studied thoroughly at several geothermal fields in Sumatra such as Muara Laboh, Rantau Dedap, and Sorik Marapi (Dyaksa, et al., 2016; Ramadhan, et al., 2021; and Matson et al., 2021). The base of conductor found in these fields has resistivity ranging as low as 3 ohm-m up to 20 ohm-m. The higher "intermediate" resistivity cap corresponds to a mixed-layer clay cap. Both Rantau Dedap and Sorik Marapi have the base of conductor lying above and below the water table, depending on whether the underlying geothermal reservoir is boiling or not boiling, respectively. However, these publications tend to focus on the application of resistivity and smectite data to the assessment of reservoir geometry and well targets. The properties of the base of the low resistivity smectite cap have not been systematically studied and published for Indonesian geothermal fields, for example, in the manner that Ardid et al. (2019) compiled for the top and base of the smectite cap at Wairakei. Therefore, to support interpretations of geothermal fields, we have compiled and analyzed data on the properties of the base of the clay cap from five geothermal fields in Indonesia.

This study investigated and compiled data from the base of the smectite clay cap for five geothermal fields in Sumatra Island, namely: Kerinci, Bukit Daun, Hululais, Lumut Balai and Ulubelu. These field are located in the southern volcano-tectonic domain of the Sumatran Arc (Sutrisno, et al., 2020) (Figure 1). All of these fields are located close to the NW-SE dextral strike-slip segmented Sumatra Fault Zone, except for Lumut Balai where the shortest distance between the field to the closest Kumering segment of the Sumatra Fault Zone is 35 km. Ulubelu is located around 12 km from the splay of the Semangko Segment to the southwest, while Kerinci, Hululais and Bukit Daun are only 2 to 4 km from the nearest segment (Figure 1). All these fields are high enthalpy, volcano-hosted geothermal fields with benign hydrothermal fluids. They have a large range in likely capacity from 10s to 100s of MWe. At the surface, the five geothermal fields are covered by Quaternary volcanics, mainly derived from local volcanic eruption vents such as Bukit Gedang Hululais, Bukit Daun, Gunung Kunyit, Bukit Rindingan, Bukit Lumut and Bukit Balai (Gafoer et al., 1993; Gafoer et al., 1992; Amin et al., 1993; Kusnama, et al., 1992). Although fracture permeability is important to these fields, especially the upflows, matrix permeability of the Oligo-Miocene volcanics of the Hulusimpang Formation are responsible for much of reservoir permeability within the Kerinci, Bukit Daun, Ulubelu and Hululais reservoirs (Ikhwan, et al., 2023).

This study has utilized borehole logs and surface data. The borehole data includes temperature logs and MeB, x-ray diffraction (XRD) and petrography from cuttings. These are integrated with

the 3D and 1D resistivity models from magnetotelluric (MT) inversions to interpret the base of clay cap and infer its resistivity and temperature. Therefore, this study will improve the understanding of the temperature and resistivity distribution at the base of the clay cap in geothermal fields in Sumatra.

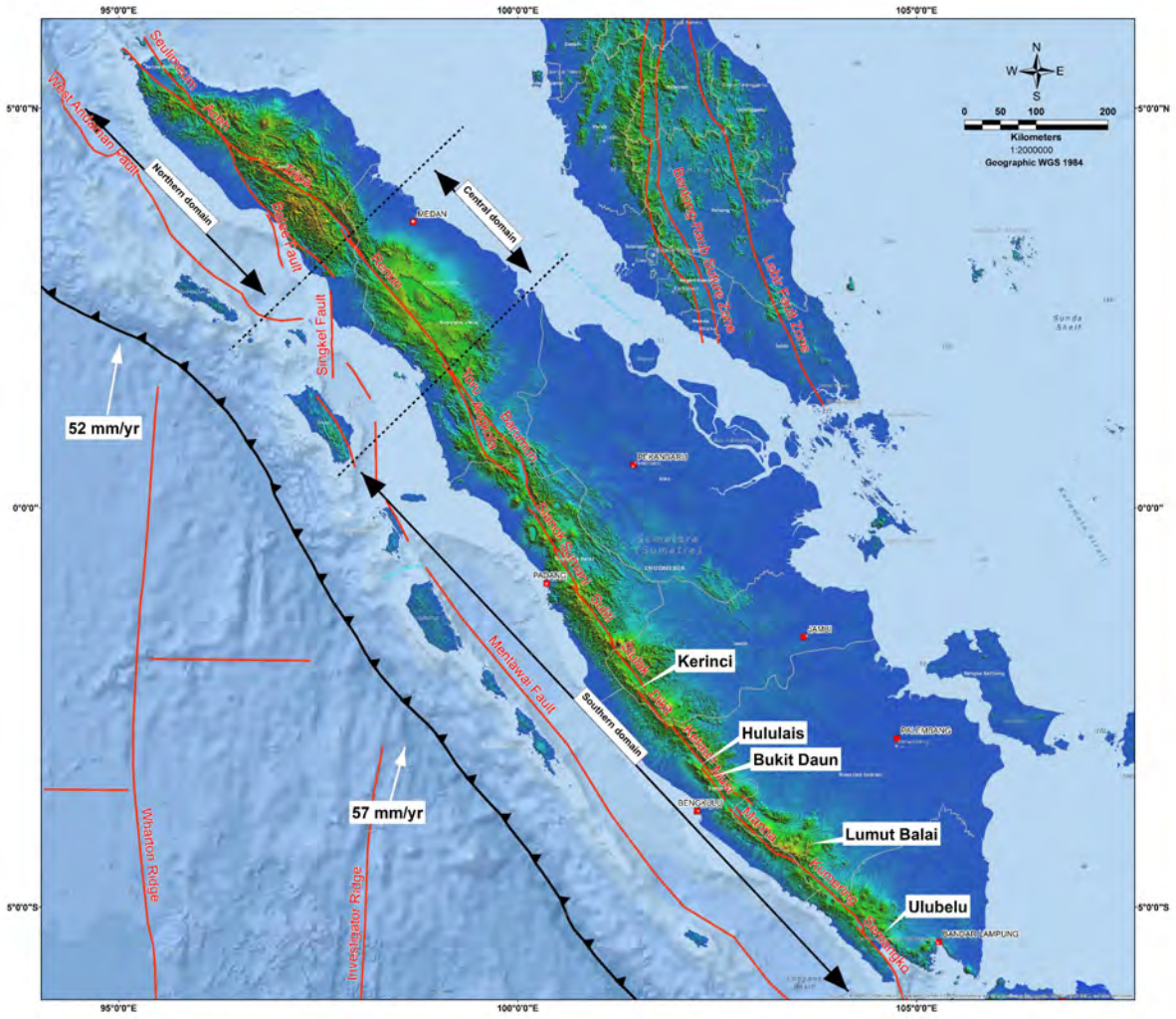

Figure 1. Location of reviewed geothermal fields overlain with DEMNAS, regional tectonic setting, Sumatran Faults, and related features (Sieh & Natawidjaja, 2001; Pour, et al., 2016), subdivision of geothermal system in Sumatra (Sutrisno, et.al., 2020)

2. BASE OF CLAY CAP IDENTIFICATION APPROACH

Before determining the base of clay cap, the consistency of the 3D MT resistivity model was qualitatively compared with 1D MT resistivity models. Resistivity values were obtained for the wells from the intersection of the wellbores with the model blocks from the 3D MT inversion, which are later used to obtain the resistivity distribution of the base of clay cap.

The base of the smectite clay cap in each well is identified by analyzing the general trend of methylene blue (MeB) index value, supported by X-Ray Diffraction (XRD) analyses. The MeB

test is commonly used during geothermal drilling to roughly quantify the smectite content in the rock (Gunderson, et al., 2000). The MeB index values are based on the procedure of Utomo, et al. (2022), using the equation as follows:

$$Methylene\ blue\ index\ (\%) = \frac{Volume\ of\ MeB\ (ml)}{Weight\ of\ the\ cuttings\ (gram)}\ x\ 3$$

The XRD results are derived from the interpretation of samples treated in three ways, air dried, glycolated and heated to 550°C. These helps differentiate the occurrence of different clay minerals. For example, a smectite response is expected from the glycolated samples but smectite should be absent from the samples heated to 550°C.

The clay transitions at the base of the clay cap determined from clay measurements is correlated with the temperature logs to derive the temperature distribution at the different clay transitions. The temperature log representative of the natural state temperature of the wells is identified based on the sequence heat-up temperature log measurements where several heat-up temperature profiles are close to each other, implying close to static temperature.

Therefore, this study integrated 3D/1D MT resistivity models, borehole geology data and temperature logs measured in five geothermal fields, Kerinci, Bukit Daun, Lumut Balai, Hululais and Ulubelu. Out of the 124 wells in these 5 geothermal fields, 92 have both temperature logs and MeB data. However, 7 wells lack temperature log measurements and are excluded from the assessment. For wells that only have temperature logs, the base of clay cap is identified using resistivity values from surrounding wells within the same well pad and supplemented by XRD measurements of cuttings or cores, if available.

3. RESULT AND DISCUSSION

3.1 Magnetotelluric (MT) Resistivity Results

MT resistivity data from all five fields involved in this study have been supplied by PT Pertamina Geothermal Energy. In general, the quality of field measurement data and the processing of MT data from each field has yielded acceptable results. The 3D MT resistivity model serves as a reference for determining the bottom of clay cap, which is the focus of this study. To check whether the smoothing applied to the 3D MT inversion might adversely affect the correlations with well data, the 3D results were compared to a simplified 1D inversion at each MT measurement (Figure 2). In the context of geothermal exploration, when we observe an area with low resistivity at a shallow depth, it is likely indicative of a high content of smectite clay (Cumming, 2016). This smectite clay alteration may cap a geothermal reservoir upflow or outflow or it may correspond to smectite clay unrelated to a geothermal field, an issue resolved by an integrated conceptual model interpretation. Where a low resistivity zone does cap a geothermal reservoir, this study characterizes the range of temperature and resistivity that may be correlated with the transition from the base of the smectite cap to the reservoir in different geothermal settings.

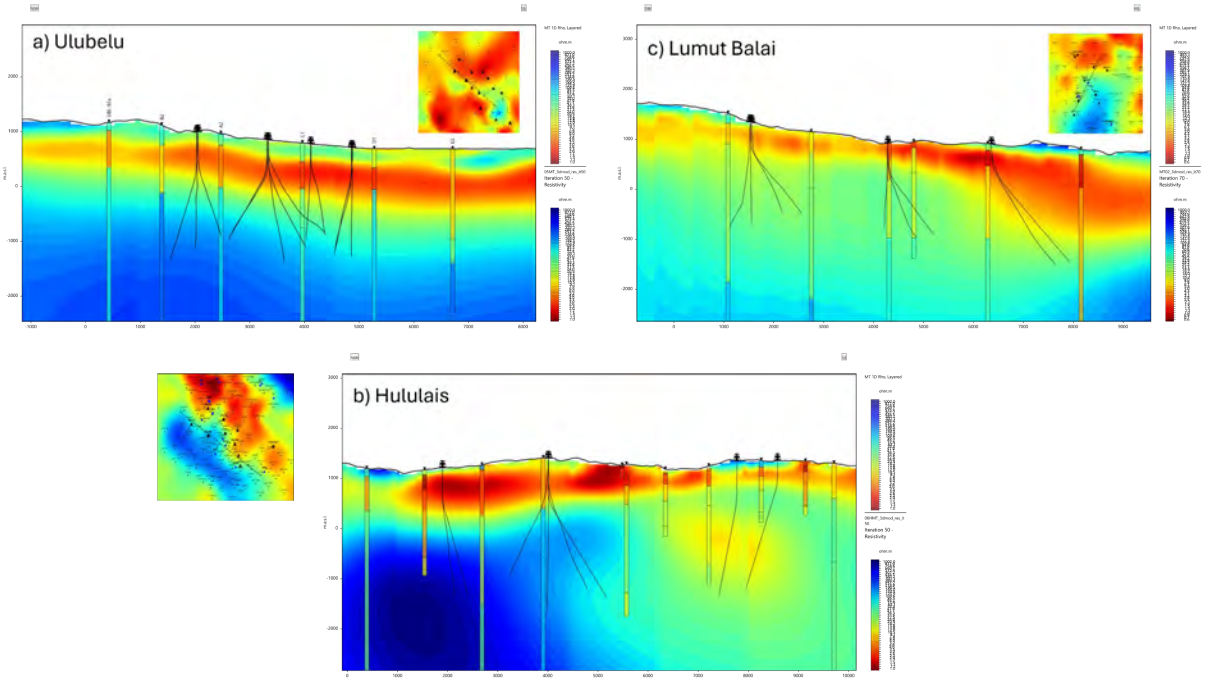

Figure 2. The 3D MT compared to 1D MT of Ulubelu, Lumut Balai and Hululais. In general, the 3D MT result is acceptable on resolving the low resistivity/conductor distribution.

3.2 Base of Clay cap Characterization

This study divided the base of clay cap into two categories, the base of smectite clay and the base of mixed/transitional clay. This grouping was based on borehole geology data, specifically the occurrence of temperature-sensitive clay minerals and the type of transition (Cumming, 2016; Matson, et al., 2021). The base of smectite clay cap was defined as the transition at the base of the argillic zone of mainly smectite clay (expected to be low resistivity) and at the top of a zone of transitional/mixed-layer clays (expected to be low to moderate resistivity). The base of mixed/transitional clay cap corresponds to transition at the base of the transitional/mixed-layer clay (expected to be low to moderate resistivity) and at the top of propylitic/phyllic alteration (expected to be much more resistive).

The base of smectite clay has been identified using the transition from values of the MeB index generally greater than 10 to values consistently below 10. At values greater than 10, the clay in the rock mainly consists of smecite clay, as confirmed by XRD. This situation also exists in the Muara Laboh and Rantau Dedap geothermal fields where an MeB index lower than 10 corresponds to a significant decrease in the content of smectite-clay (Dyaksa, et al., 2016). The base of mixed/transitional clay is identified by the transition of the relatively erratic values of the MeB index near values of 10 to more constant values below 3 to 6 of the MeB index. The base of mixed/transitional clay correlates with a transition derived from XRD where mixed-layer clay declines, and first epidote also transitions to the more crystalline form of continuous epidote as a marker of propylitic alteration (Figure 3).

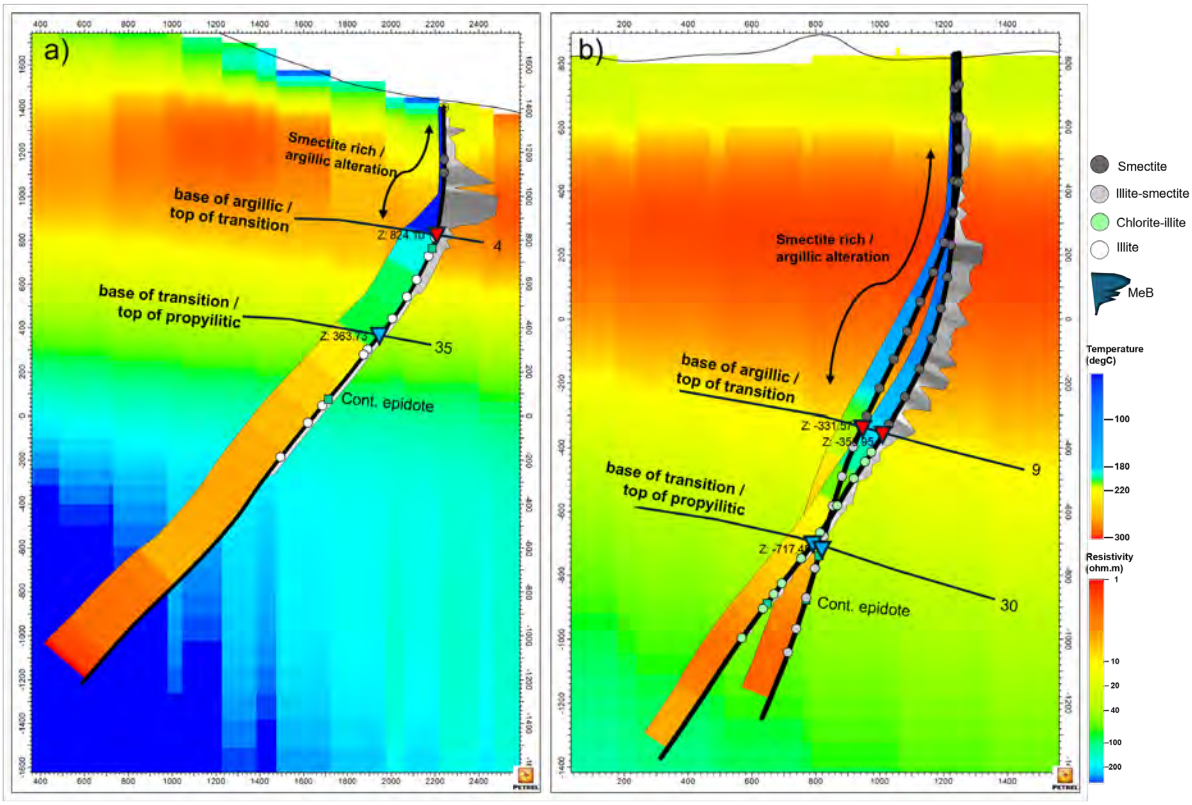

Figure 3. Base of argillic/top of transition and base of transition/top of propylitic are interpreted based on the MeB index value trend and the occurrence of clay mineral from XRD (a & b). When a well does not have MeB, besides the 3D resistivity MT the nearby well data is used to determine the base of clay cap (b).

The analyses and data compiled from the five geothermal fields investigated in this study reveal a consistent pattern of cap transitions and temperature in Figure 4a. The base of smectite clay category that corresponds to the base of the argillic/top of the transition, has a median temperature distribution of 152°C. Additionally, temperatures below 180°C account for 75% of the data, while those below 220°C comprise 93% of the P10 dataset (Figure 3). For the base of mixed/transitional clay category, equivalent to the base of transition/top of propylitic alteration zone, the temperature distribution is skewed to higher temperature in Figure 3, where the median temperature of the base of mixed/transitional clay is 207°C and 93% of the P90 dataset is below 250°C.

The correction of temperature with the petrological transitions at the base of clay cap in this study are consistent with those in the other fields in Sumatra. For instance, the base of conductor at Rantau Dedap bounds the isotherm below 180°C (Ramadhan, et al 2021). In a broader context for neutral/benign pH high enthalpy geothermal systems worldwide such as in the Philippines, this observed pattern is close to the range of smectite alteration zone of below 180°C and the transition alteration zone range from 180°C to 220°C (Reyes, 1990). Similarly, in New Zealand, the base of the conductor that overlies the reservoir unit in Wairakei-Tauhara has a median temperature of 198°C (Ardid et al., 2021), which is close to the median of the temperature at the base of mixed/transitional clay in this study at 207°C.

Shifting focus to resistivity, the value of resistivity at the base of argillic (or top of transition) zone for 80% and 90% of the data is less than 10 ohm-m and less than 15 ohm-m respectively, in Figure 4b. It is characterized by a strong skewness to lower resistivity and a median of 6 ohm-m. Meanwhile, the base of transition (or top of the propylitic) zone is more widely distributed to more intermediate and higher resistivity values, with a median value of 15 ohm-m and 90% of the data is under 42 ohm-m.

The median resistivity of 6 ohm-m at the base of argillic (top of transition) zone obtained from this study correlates with those in Sorik Marapi, Muara Laboh, and Rantau Dedap. At Sorik Marapi the intense smectite alteration of the argillic cap has a resistivity of 3 to 5 ohm-m but in some areas where reduced smectite content within the cap occurs, resistivity is 7 to15 ohm-m (Matson, et al., 2021). At both Muara Laboh and Rantau Dedap, the base of a 5 ohm-m zone corresponds to decreasing smectite content (MeB < 10) (Dyaksa, et al., 2016). This pattern also fits with the generalized geothermal system where both smectite and mixed layer caps are commonly found with resistivity values less than 10 omh-m (Johnstone, et al., 1982 and Cumming, 2016).

The base of the argillic (top of transition) zone in this study is located at a median elevation of about 150 mASL, while the base of the transition (top of propylitic) zone is at a median elevation of -84 mASL, implied a median separation of the zone of about 230 m. These numbers are given only to give a sense of the elevation distribution for the base of clay cap since the depth is significantly influenced by local topography in each field.

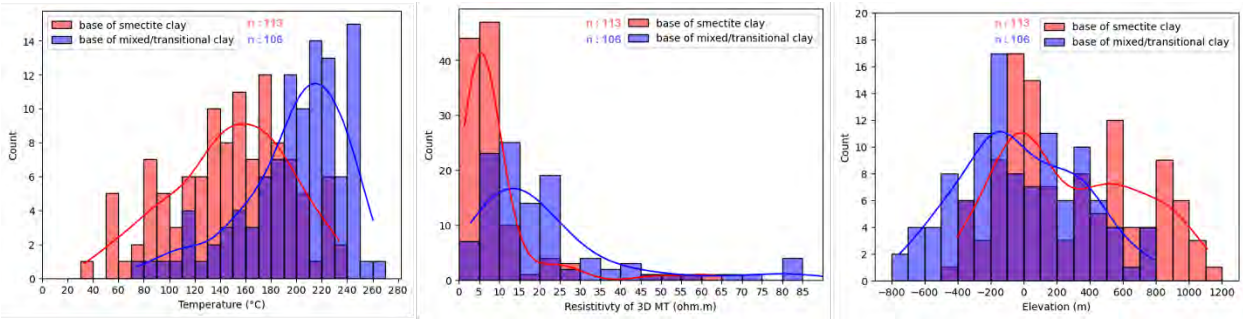

Figure 4. The histogram of temperature (left), resistivity (middle) and elevation (right) at the base of argillic (red) and base of transition (blue). The temperature distribution at the base of transition is skewed to the right to higher temperature, median 207°C. The resistivity at the base of argillic is heavily skewed to the left below 10 ohm-m, while at the base of transition is more widely distributed to intermediate resistivity value (median = 15 ohm-m). The elevation distribution at the base of argillic is more fluctuated compared to the base of transition elevation.

3.3 The Outliers

There are 6 wells in Lumut Bali that have higher than typical resistivity values for both the base of argillic (top of transition) zone (20-40 ohm-m) and base of the transition zone (60-80 ohm-m). In addition, 2 wells in Hululais have anomalous resistivity values at the base of transition (average 80 ohm-m).

In Hululais, the base of transition in those two wells sits on andesite breccia and andesite with medium to intense alteration intensity (20-50 alteration index) which consists of abundant calcite, common chlorite, illite, quartz, and illite-smectite, reflecting a mixed-layer clay or transition alteration zone (Figure 5a). These two wells have a maximum temperature of 215°C since they are

located on the northwestern margin of the field at the periphery of the northern trending outflow about 3 km north of the >300°C Hululais upflow (Figure 2b). The north-south hydrology of the outflow zone at Hululais follows the direction of north-south maximum horizontal stress, accommodating the open north-south structures (Nurseto, et al., 2020). Other wells that intersected the upflow and outflow have relatively higher alteration intensity, and higher injection index indicating higher permeability (Arifin, et al., 2020). Thus, the higher resistivity values in these two wells are interpreted as being associated with lower permeability and less intense alteration.

In the generally higher temperature southern and central parts of the Lumut Balai field, the conductor is thin, the base of conductor is shallower, and the conductor in this part of the field is generally more resistive than the conductive zone in the northern and northeastern parts of the field (Figure 2c). The MeB, XRD and petrographic analyses of the borehole cuttings from the southern and central wells show that the first epidote and continuous epidote found in cuttings are also associated with the occurrence of smectite and mixed-layer clay. The smectite clay is in equilibrium with the measured temperature, implying that the epidote is relict at those depths (Figure 5b). Garnet and veins of quartz-chlorite-epidote, indicating temperatures over 300°C, also occur with mixed-layer and transitional clay consistent with temperatures below 200°C. The maximum measured temperature in the Lumut Balai wells is 265°C. The retrograde alteration occurred at these depths, which the more resistive high temperature alteration is now relict and has been overprinted by more recent argillic clay. The cause for retrograde alteration in these wells is still debatable and needs further investigation.

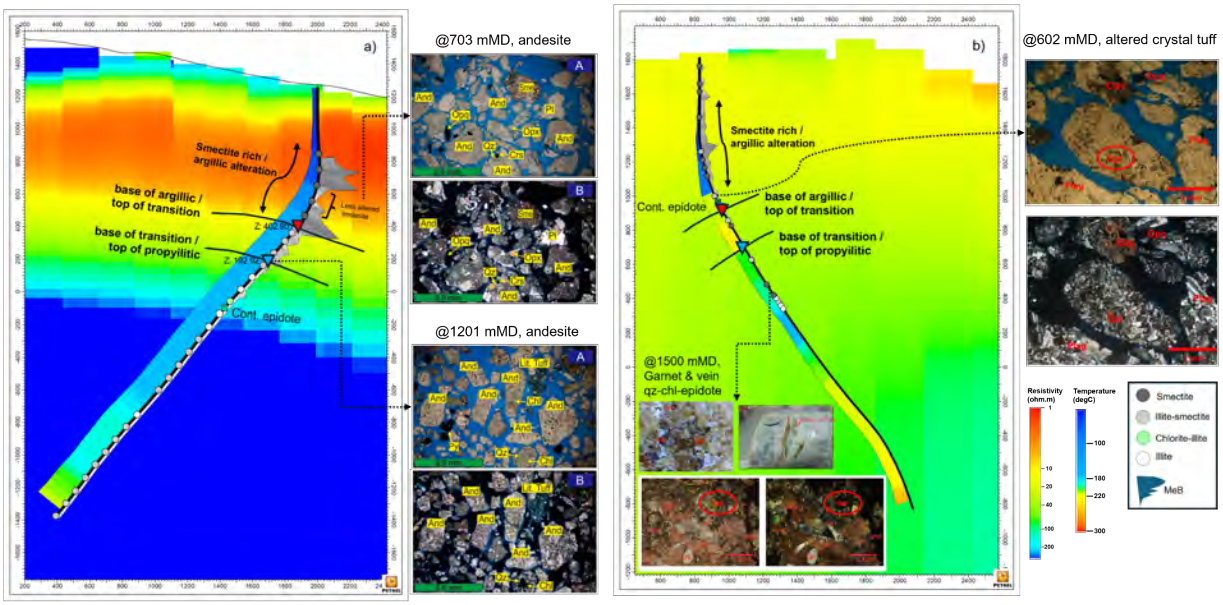

Figure 5. The outlier wells in Hululais field (a) and in Lumut Balai (b). Showing the high resistivity anomalies found in both wells and the geological findings in the cuttings.

4. CONCLUSIONS

Detailed correlations between MT resistivity and borehole cuttings, alteration and natural state temperature from 113 boreholes in five geothermal fields in Sumatra have characterized the range

of resistivity and temperature expected at the clay transitions at the base of the impermeable cap and top of the permeable reservoirs.

Although 3D inversion of MT data tends to smooth the resistivity model, the uncertainty of resistivity values can be evaluated by checking the consistency of the 3D resistivity model with respect to 1D Mt resistivity models.

Although a strong correlation is demonstrated between borehole temperature and the base of the clay cap determined from smectite and XRD measurements, the details vary based on the evolution of geothermal systems. Based on this study, the resistivity value of the base of argillic cap in Sumatra is typically below 10 ohm-m, whereas the base of transition zone or top of reservoir ranges from 10 to 25 ohm-m. The temperature range for the base of argillic zone varies from 120 to 200°C, whereas the temperature range for the base of the transition zone varies from 180 to 240°C.

Although the analyses used in the study have been limited to geothermal fields operated by PT PGE, Tbk. in Sumatra Island, similar results published for other geothermal fields indicate that the results have broader applicability for interpreting resistivity patterns and characterizing geothermal system temperatures.

In general, the temperature, resistivity and elevation at the base of clay cap presented in this study could be used as an analogue for other geothermal fields in Sumatra and elsewhere for at least two purposes. Firstly, within an area known to host a high temperature geothermal field, the results of this study can be used to interpret resistivity or estimate a likely range of temperature with respect to the base of argillic clay (top of transition) zone and the base of transition (top of propylitic) zone. Secondly, because the observations of the base of the clay cap are all in the cased and cemented section of the wells, the estimate of temperature and formation properties could support drilling engineering decisions regarding the borehole casing plan and cementing process. The specific correlations of resistivity, temperature and alteration transitions will vary depending on the conceptual model of a particular geothermal field, which requires the integration of the MT resistivity model with the geology, geochemistry and other geoscience data and, importantly, with the well data as it becomes available.

Acknowledgement

Special thanks to PT Pertamina Geothermal Energy Tbk and Jayanti Anggraini for giving the opportunity to present the paper, Dhanie Marstiga Yuniar, Ahmad Fahmi Fanani and Fadiel Evan Marastio for the fruitful discussion regarding reservoir pressure & temperature logs.

REFERENCES

Amin, T.C., Sidarto, S. S., and Gunawan, W., “Geological Map of the Kotaagung Quadrangle, Sumatra”, Geological Research and Development Centre, Bandung (1993).

Ardid, A., Archer., R., Bertrand, E., Sepulveda, F., Tarits, P., & Dempsey, D., “Heat transfer through the Wairakei-Tauhara geothermal system quantified by multi =-channel data modelling”, Geophysical Research Letters, 48, e2020GL092056 (2021).

Arifin, M., T., Nurseto, S., T., Nusantara., V., D., M., Pratama., G., R., Marastio, F., E.,” Feedzone Evaluation in Hululais Geothermal Field, Bengkulu, Indonesia”, Proceedings: 42nd New Zealand Geothermal Workshop (2020).

Badan Informasi Geospasial, “DEMNAS BIG. Seamless Digital Elevation Model (DEM) dan Batimetri Nasional”, Retrieved from https://tanahair.indonesia.go.id/demnas/#/#Info (2023)

Cumming, W., “Resource Conceptual Models of Volcano-Hosted Geothermal Reservoirs for Exploration Well Targeting and Resource Capacity Assessment: Construction, Pitfalls and Challenges”, GRC Transactions, Vol. 40 (2016).

Cumming, W. and Matson, G., “ Conceptual Challenges in Applying Geophysics to Geothermal Exploration in Indonesia.” Invited Abstract In: Geophysics in Geothermal Energy – Today and Tomorrow. Society of Exploration Geophysics Workshop. 12-13 October 2021, Jakarta.

Dyaksa, D. A., Ramadhan, I., Ganefianto, N., “Magnetotelluric Reliability for Exploration Drilling Stage: Study Cases in Muara Laboh and Rantau Dedap Geothermal Project, Sumatra, Indonesia”, Proceedings: 41st Workshop on Geothermal Reservoir Engineering, Stanford University, Stanford, California, SGP-TR-209 (2016)

Gafoer S., Amin, T.C., and Pardede, R., “Geological Map of the Baturaja Quadrangle, Sumatra", Geological Research and Development Centre, Bandung (1993).

Gafoer S., Amin, T.C., and Pardede, R., “Geological Map of the Bengkulu Quadrangle, Sumatra”, Geological Research and Development Centre, Bandung (1992).

Gunderson, R., Cumming, W., Astra., D., Harvey, C., “Analysis of Smectite Clays in Geothermal Drill Cuttings by The Methylene Blue Method: For Well Site Geothermometry and Resistivity Sounding Correlation”, Proceedings: World Geothermal Congress, Kyushu – Tohoku, Japan (2000).

Ikhwan, M., Prasetyo, I. M., Suryanto, S., Sastranegara, R. M. T., “The Role of The Hulusimpang Formation in Well-Scale Permeability of the Central Southern Sumatra Geothermal Fields”, Proceedings: World Geothermal Congress 2023, Beijing, China (2023)

Johnstone, J. M., Pellerin, L., Hohmann, G.W.,” Evaluation of Electromagnetic Methods for Geothermal Reservoir Detection, Geothermal Resources Council Transactions, Vol. 16 (1992).

Kusnama, Pardede, R.S., Andi Mangga and Sidarto, “Geological Map of the Sungaipenuh and Ketaun Quadrangle, Sumatra”, Geological Research and Development Centre, Bandung (1992).

Matson, G., Cumming, W., Hinz, N., “Interpretation of Magnetotelluric Resistivity Models of Sorik Marapi Geothermal Prospect, Sumatra, Indonesia”, GRC Transactions, Vol. 45 (2021)

Nurseto, S., T., Arifin, M. T., Pratama, G., R., Nusantara, V., D., M., Thamrin, M. H.,” Geology Fault Network of Hululais Geothermal System, Bengkulu, Indonesia”, Proceedings: 42nd New Zealand Geothermal Workshop (2020).

Pour, A. B., Hashim, M., Makoundi, C., Zaw, K., “Structural Mapping of the Bentong-Raub Suture Zone Using PALSAR Remote Sensing Data, Peninsular Malaysia: Implications for Sediment-hosted/Orogenic Gold Mineral Systems Exploration”, Resource Geology, Volume 66, Issue 4, p. 368-385 (2016).

Ramadhan, I., Sewell, S., Stimac, J., Ganefianto, N., Azis, H., Baroek, M. C., “Conceptual Interpretation of MT resistivity at the Rantau Dedap Field, Sumatra, Indonesia”, GRC Transactions, Vol. 45 (2021).

Reyes, A., G., “Petrology of Phillippine Geothermal Systems and the Application of Alteration Mineralogy to Their Assessment”, Journal of Volcanology and Geothermal Research, 43. 279-309, Elsevier Science Publishers B.V., Amsterdam (1990).

Sieh, K., and Natawidjaja, D., “Neotectonics of the Sumatran fault, Indonesia”, Journal of Geophysical Research, Vol 105, No. B12, Pages 28,295-28,326 (2000).

Sutrisno, L., Bonte, D., Daud, Y., Smit, J., Beekman, F., Purwanto, W., Van Wees, J. D., “Regional Characterization of the Sumatran Geothermal Systems, Indonesia”, Proceedings: World Geothermal Congress 2020+1, Reykjavik, Iceland (2021).

Ussher, G., Harvey, C., Johnstone, R., and Anderson, E., “Understanding the resistivities observed in geothermal systems” In: Proceedings: World Geothermal Congress, Tokyo, Japan. (2000).

Utomo, D. A., Saputro, I. J., Abiyudo, R., Husein, M., 2022, Determining Clay Mineral on Methylene Blue (MeB) Analysis on Drilling Cutting Based on XRD Analysis, Case Study: Blawan-Ijen Field, Indonesia, Proceedings: The 8th Indonesia International Geothermal Convention & Exhibition (IIGCE) 2022, Jakarta.

Whittome, A. and Salveson, J., “Exploration and Evaluation of the Darajat Geothermal Field, West Java, Indonesia” Geothermal Resources Council Transactions (1990).

Meso-scale Geophysical Characterization of the Geothermal System in Montserrat, W.I.

Racine Basant[1], Graham Ryan[1] and Oshaine Blake[2]

[1] The University of the West Indies, Seismic Research Centre, [2] The University of the West Indies, Department of Chemical Engineering

Keywords

Triaxial testing, seismic velocities, core samples, Caribbean

ABSTRACT

Geothermal energy development in Montserrat, West Indies, can help to improve energy security and reduce the island's heavy reliance on fossil fuels. A more detailed understanding of the spatial variation in physical properties across the lithologies which host the reservoir can greatly increase the ability to harness this renewable resource. Previous work was largely based on macro-scale characterization of the geothermal reservoir using geophysical techniques including seismic tomography. To enhance our understanding of the large-scale geophysical models we measured P- and S-wave velocities on three cores retrieved from the Montserrat's third geothermal well using a servo-controlled triaxial apparatus. Our results showed that P-wave velocity decreased by 9 % when temperature was increased to 150 Degrees Celsius. Our data also assessed the relationship between seismic properties and parameters such as porosity, lithology and alteration. These important relationships improve our ability to interpret geophysical data and target productive geothermal wells.

1. Introduction

Conceptual modelling contributes to reducing the risks associated with drilling geothermal wells in geologically complex volcanic regions. Exploration surveys consisting of geological, geochemical and geophysical studies contribute to building a conceptual model about the region of interest (Cumming 2009; Cumming 2016; Seyedrahimi-Niaraq et al. 2017). Amongst the aforementioned studies, geophysical surveys provide the best visual representation of the subsurface region at the exploration phase. For example, seismic tomography surveys of higher resolutions have been used to understand deeper areas in volcanic regions. As useful as these geophysical models are, geophysical inversions are non-unique and ill-conditioned.

Laboratory data provide the best opportunity to validate and improve on geophysical modelling. Several studies have utilized geophysical measurements on outcrop and borehole rocks to

develop a better understanding of the factors that influence variations in geophysical parameters (Heap et al. 2014; Siratovich et al. 2014; Siratovich et al. 2016; Heap et al. 2016; Mordensky et al. 2018; Kushnir et al. 2018; Goupil, Heap, and Baud 2022). Cores, a direct representation of the subsurface environment, offer the most realistic interpretation of the deep-seated geothermal environment.

Cores obtained in Montserrat, provide an avenue for investigating the meso-scale geophysical properties within the geothermal system. The island of Montserrat, located in the northern section of the Lesser Antilles arc (Figure 1a), comprises of four volcanic bodies: Silver Hills, Centre Hills, Soufrière Hills and South Soufrière Hills (Figure 1b). The north to south alignment of the four volcanic bodies reflect the geological history and migrating volcanism on the island (Harford et al. 2002; Hatter et al. 2018). Soufrière Hills is the only active volcano on the island. In 1995 began a series of phreatic explosions from the Soufrière Hills volcano which destroyed many of the existing thermal features on the island (Young et al. 1997; Wadge et al. 2014). The Hot water pond remains the only thermal manifestation on the island (Figure 1c). Andesitic composition is prevalent on all volcanic centres and topographic features on the island except for South Soufrière Hills. Basaltic to andesitic composition is characteristic at this centre (Harford et al. 2002; Hatter et al. 2018; Kiddle et al. 2010; Rea 1974).

The Montserrat geothermal field was mapped in the southern part of the island in the St. George's Hill – Garibaldi Hill – Richmond Hill (Figure 1c). Rea (1974) suggested that Garibaldi Hill and St. George's Hill were parasitic centres related to Centre Hills. Evidence of pumice fall deposits on the hills however led Harford et al. (2002) to propose that these areas were tectonically uplifted volcaniclastic deposits either from Centre Hills or Soufrière Hills. The tectonic setting of St. George's Hills is left lateral-transtensional where NW, WNW and NE structures abound and intersect to create rhombic fault patterns.

Using a joint interpretation approach, Ryan et al. (2013) found that a low velocity body, mapped in the south-west of the island from a seismic tomography survey (Shalev et al. 2010), was spatially aligned below a low resistivity region, mapped from a magnetotellurics survey (Ryan et al. 2009). The authors interpreted this as a fracture controlled geothermal system sitting below the conductive clay cap region in St. George's Hill. By integrating Ryan et al's study with geological and geochemical interpretations of the Montserrat geothermal system, two wells, MON-1 and MON-2, were drilled in this region to total depths of 2298 m and 2870 m respectively. In 2016, a third well, MON-3, was drilled to the north-east of the prior wells, also in the St. George's Hill region (Figure 1c). To further characterize the region, Ryan and Shalev (2014) utilized the high resolution seismic tomography data to model the temperature distribution within the geothermal system. Ryan and Shalev (2014) investigation of the one-dimensional velocity profile (Shalev et al. 2010) and the temperature profiles from MON-1 and MON-2 led the authors to hypothesize that the anomalous seismic velocities could be influenced by hydrothermal alteration. Temperature profiles of the wells are shown in Basant et al. (2022) and Ryan et al. (2014). The authors observed a decrease in anomalous velocities to 1750 mbsl followed by an increase in anomalous velocities. The authors suggested that at depths above 1750 mbsl the formation of phyllosilicate clays and in particular illite, acts to plasticize the rocks and reduce seismic velocities up to temperature of 200 ºC. Furthermore, the authors stated that below 1750 mbsl propylitic alteration, which involves the alteration of silicates such as epidote, quartz, and adularia, could be the cause for the velocity to increase.

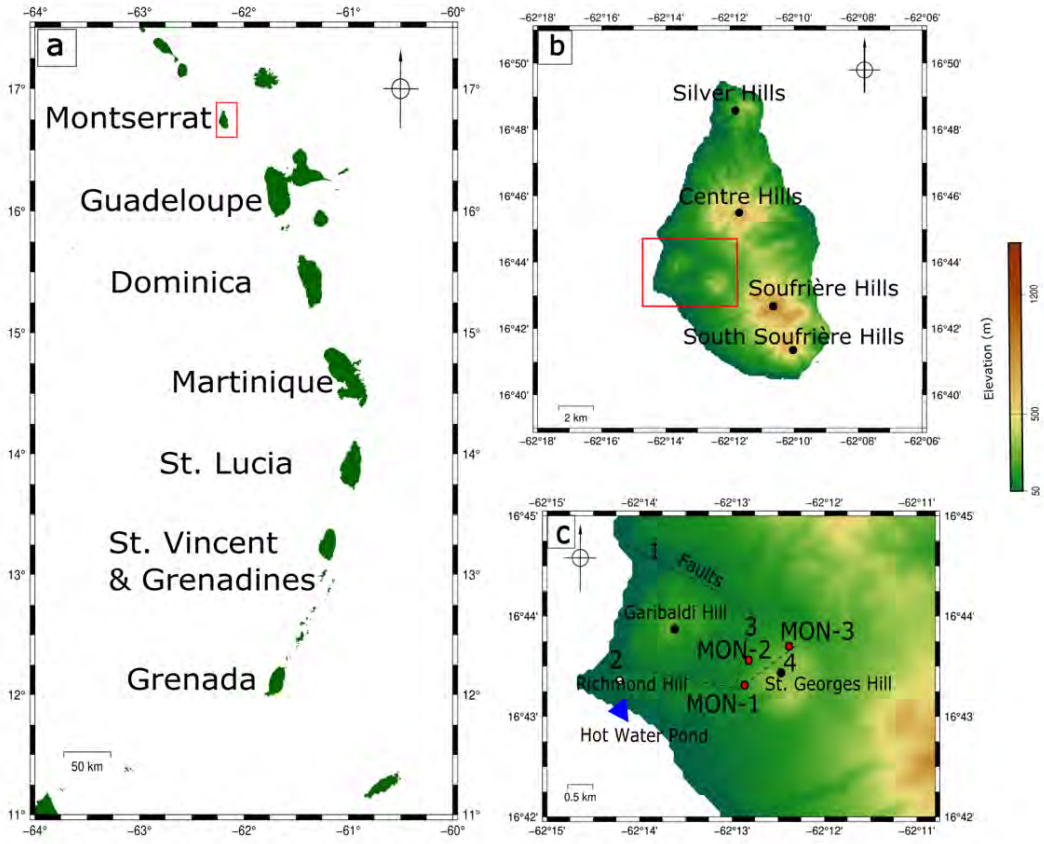

Figure 1:) Map of the Lesser Antilles arc b) Volcanic centres in Montserrat. Red square is the location of the Montserrat geothermal field c) Montserrat geothermal field showing the Hot water pond (blue triangle), faults (black dotted lines) and three wells, MON-1, MON-2 and MON-3 (red circles). Core samples were extracted from the MON-3 well (Basant et al., 2022)

In this study, laboratory geophysical studies on samples obtained from three cores are conducted to investigate and validate the seismic velocity variation in the Montserrat geothermal system, Montserrat, Lesser Antilles. With no prior work done on the core samples, we aim to understand the relations of P- and S- waves velocities with parameters such as porosity, lithology and degree of alteration. This advancement may help to guide future seismic exploration on the island.

2. Method

29 samples (~20 mm diameter) were plugged (both vertical and horizontal directions to the axis of the cores) from three 4 inch diameter cores (Core 1, Core 2 and Core 3). Core 1 and Core 2 are andesite lavas while Core 3 consists of various volcaniclastic sediments (siltstones, sandstones and mudstones) and limestones. XRD analysis on the cores showed that Core 1's alteration assemblage as smectite ± chlorite-smectite ± laumontite ± vermiculite ± calcite ± quartz. Core 2's alteration assemblage as chlorite-smectite ± prehnite ± calcite ± quartz ± laumontite ± anhydrite. Core 3's assemblages were classified as calcite ± quartz ± laumontite ± illite-smectite ± chlorite ± wairakite ± pyrite ± anhydrite ± chlorite-smectite ± rectorite.

The ends of the 20 mm samples were squared to a tolerance of ± 0.02 mm using a precision end

face grinder, were washed and then dried for a minimum of 24 hours at 50 °C. The samples were thermally equilibrated to ambient conditions before any measurements were taken. The dry bulk density was calculated using the measured weight and calculated volume of each sample. Porosity was measured using the PoroPerm equipment (porosimeter from Vinci Technologies, Inc). The PoroPerm measures grain and bulk volume. The Boyle-Mariotte's Law is used to determine grain and pore volume from the expansion of a known mass of nitrogen into a matrix cup of the PoroPerm apparatus. Porosity is calculated from the ratio of the pore volume (difference in bulk volume and grain volume) to the bulk volume.

Measurements of ultrasonic P- and S-waves were performed at the Geomechanics Laboratory, University of West Indies. A high-pressure-temperature servo-controlled triaxial deformation apparatus was used to measure the ultrasonic P- and S-wave velocities following the pulse transmission technique (Birch 1960, 1961). The apparatus consists of a hydrostatic pressure vessel with oil as the confining medium, a pulse generator and receiver, digital oscilloscope, and P- and S-wave piezoelectric transducers (fundamental frequency of 1.5 MHz) at the top and bottom to the core samples. More details on the apparatus are discussed in Iyare, Blake, and Ramsook (2021) and Blake et al. (2021). The apparatus can produce confining and pore pressures of up to 200 MPa and temperatures up to 200 ℃.

P- and S-wave travel times were measured on saturated samples. The samples were saturated by placing in a bath of deionized water under vacuum. The samples were next inserted into the triaxial apparatus where de-ionized water was pumped at a pressure of 10 MPa into both ends of the samples using the upstream and downstream pore pressure connections. Reservoir pore pressures, determined as the product of the density of water, sample depth and the gravitational constant (9.81 m/s), were next set. During this process, the confining pressure was always 5 - 10 MPa more than the pore pressure. Effective pressures were determined as the difference between the confining and pore pressures. The saturated samples were measured in a pressurization and depressurization cycle with effective pressures varying from 10 - 110 MPa. After measuring P- and S-wave travel times on saturated rocks, the temperature of the triaxial apparatus was set to 150 ℃ and the system was allowed to stabilize for 30 minutes. P- and S-wave travel times were measured on the samples at the set temperature.

The P- and S- wave velocities, $V_{p,s}$, were calculated by dividing the sample's length by the P- and S- wave travel times as shown in equation 1.

$$Vp,s = \frac{L}{trock} \tag{1}$$

where L is the length of the rock's plug and t_{rock} is the total one way travel time of the P- or S-wave though the core sample and the system i.e. $t_{rock} = t_{observed} - t_{system}$.

3. Results

We utilize the P- and S- wave velocities at the reservoir pressure for this analysis. The influence of temperature is first reported. An increase in temperature to 150 ℃ caused reductions in P-waves between 2 - 9 %. S-waves were not obtained at 150 ℃ as the waveforms were significantly

attenuated.

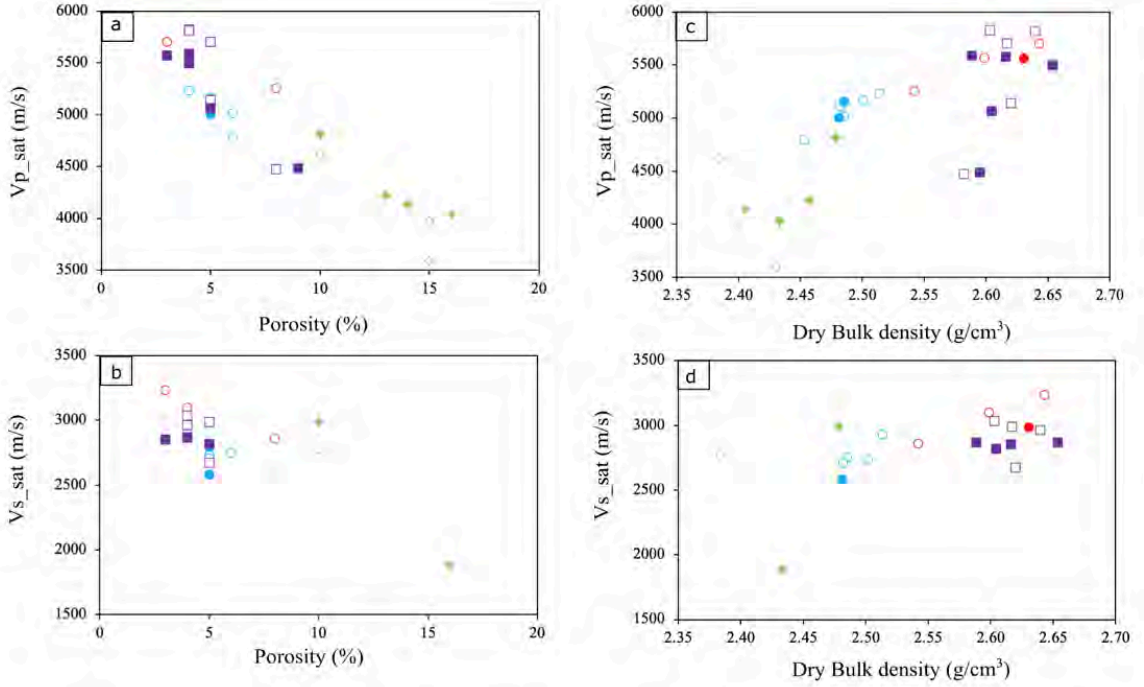

Figure 2: Variations in P- and S- wave velocities with porosity and bulk density under saturated conditions for core samples in Montserrat. Blue circles are Core 1 samples. Red circles are Core 2 samples. Green diamonds are Core 3 volcaniclastic sediment samples and purple squares are Core 3 limestones. The unfilled symbols represent vertical samples. The filled symbols represent horizontal samples.

The variations in lithology, porosity and dry bulk density with the saturated P- and S-wave velocities are shown in Figure 2. The volcaniclastic sediments of the highest porosities (10 – 16 %) and lowest densities (2.38 – 2.48 g/cm^3) measured the lowest P- and S-waves. Meanwhile, andesite lavas and limestones of relatively lower porosities (2 – 10 %) and higher dry bulk densities (2.43 – 2.65 g/cm^3) related to higher P- and S- waves. Differences in P- and S-waves were also observed between horizontal and vertical oriented samples (Figure 2). For the andesite lavas, variations in both P- and S- waves were no more than 100 m/s when comparing measurements on both horizontal and vertical samples. For the limestones, P- and S- waves on horizontal samples were lower (up to 639 and 172 m/s respectively) than the vertical samples. For the volcaniclastic sediments, the P-waves for the horizontal samples were higher (up to 443 m/s) compared the vertical samples. S-waves were highly attenuated at saturated conditions for this lithotype.

Taking into account only vertical samples, variations in seismic velocities are still observed in each lithology. For example, for the lavas, Core 2 samples have higher P- and S-waves (up to 1000 m/s) compared to Core 1 (Figure 2). Figure 2 shows that Core 2 samples were of higher bulk densities compared to Core 1. While porosity is relatively similar, both cores showed varying mineral assemblages. In particular, Core 1 contained smectite clays while Core 2 contained

chlorite-smectite. We expect the bulk and shear moduli for chlorite-smectite to be between the end member clays (i.e. higher than smectite), thus resulting in higher P- and S- wave velocities. For both the limestones and volcaniclastic sediments, the P-waves (for vertical samples only) varied up to 1500 m/s (Figure 2) within each lithology. Variations in porosity, alteration assemblages and textures observed amongst the samples may be reasons for this observation.

4. Discussion

We utilize our laboratory data to further investigate and validate the seismic velocity variation in the Montserrat geothermal system. Firstly, seismic velocities from the seismic tomography model at 1500 mbsl, 1700 mbsl and 2000 mbsl were 3.36 km/s, 3.63 km/s and 4.11 km/s respectively. The average velocities of Core 1, Core 2 and Core 3 were however greater than 4.8 km/s. The higher laboratory P-waves than the modelled P-waves may be due to the effects of temperature and scaling. A 9 % correction for temperature (150 ℃), based on our findings (maximum value), reduces the laboratory velocities. Jaya et al. (2010) and Janssen et al. (2021) observed similar reductions at this measured temperature. The authors however reported further reductions in P-waves between 10 – 40 % when temperature was increased from room temperature to 250 ℃ on rocks obtained from geothermal systems in the Krafla and Hengil geothermal fields, Iceland and Kızıldere geothermal system in Turkey respectively. With higher temperatures measured in the Montserrat geothermal system (Ryan et al., 2014), we expect a further reduction in the seismic velocities. To understand the effects of scaling, assuming a P- wave velocity of 5000 m/s, the corresponding wavelength is 500 m at 10 Hz (average seismic frequencies of the seismic tomography study), but only 3 mm at the ultrasonic frequency of 1.5 MHz (used in this study). The larger rock volumes sampled would include fractures, that may be up several meters long, again accounting for the differences in the field and laboratory velocities.

Despite the influence of scaling, the ultrasonic P-waves highlight important variations at the centimeter scale that can be used to help investigate and validate Ryan et al.'s (2014) previous hypothesis. Ryan et al. (2014) suggested that the anomalous seismic velocities in the Montserrat geothermal system could be influenced primarily by hydrothermal alteration. Ryan et al. (2014) investigated the influence of temperature, porosity and hydrothermal alteration based on logical reasoning supported by laboratory studies on volcanic rocks on geothermal systems (Kristinsdóttir et al. 2010; Boitnott 2003; Kiddle et al. 2010; Jaya et al. 2010). The potential influence of these factors is re-investigated using our new data with considerations for scaling.

Temperature logs obtained in the geothermal wells (MON-1, MON-2 and MON-3) showed increasing temperature in the Montserrat geothermal reservoir with bottomhole temperatures between 200 ℃ and 300 ℃ (Ryan et al. 2014). As mentioned earlier, increasing temperature is expected to cause further reductions in P-waves. Jaya et al. (2010) suggested reductions in P-waves were influenced by change of state in the fluid. At temperatures above 175 ℃ the formation of steam bubbles was interpreted to reduce the bulk moduli of the rock and thus, decrease the P-wave velocities. The influence of steam as a potential factor for lowering seismic velocities in the Montserrat geothermal system seems highly unlikely as reservoir geochemistry analysis conducted on the MON-1 and MON-2's producing fluid indicated that Montserrat's reservoir is likely to be a single-phase liquid system (EGS 2014).

Porosity is roughly the same from Core 1 (1478 mbsl) to Core 2 (1700 mbsl) which also do not support the lowest velocity perturbation observed at 1750 mbsl in the seismic tomography model. The effect of scaling, which considers potentially larger fractures, could however be a cause for

the anomalous velocities. The presence of a fault at ~1750 mbsl in the Montserrat geothermal system is again implausible as feeder zones were observed at ~1200 mbsl in the MON-1 and MON-2 wells (EGS 2014). While structural porosity may not a potential factor for the anomalous velocities modelled in the Montserrat geothermal system, stratigraphically related porosity could be a plausible explanation. Our dataset revealed that the volcaniclastic sediments are ~20 % slower than other lithotypes. Volcaniclastic sediments however appear both above and below 1750 mbsl in the Montserrat geothermal system (Basant et al. 2022) which again do not support the velocity perturbation depth profile.

Regarding the effects of hydrothermal alteration, our results showed the lowest velocities for the samples with the highest smectite content amongst the andesite lavas. The petrological findings from Core 1 depict that smectite is higher where the low velocity anomaly is observed (Basant et al. 2022). However, the smectite content is only consistent up to 1200 mbsl unlike the velocity anomaly. This is also supported by the lack of smectite in Core 2 and petrological findings reported in Basant et al. (2022). Ryan and Shalev (2014) proposed the particular influence of illite for anomalous velocities. Our analyses did not detect illite with the MON-3 samples which cannot validate this proposition. The XRD on the samples showed chlorite-smectite clay percentages increases to a maximum at 1700 mbsl and then decreases system (Basant et al. 2022). This variation supports the anomalous variation in seismic velocities. It is however important to note it is challenging to solely segregate the effects of chlorite smectite from other factors.

Overall, the petrological evidence shows that the spatial pattern in chlorite-smectite could be cause for the variations in the anomalous seismic velocities, however further work is needed to fully validate this statement. Also, Ryan et al. (2014) proposed the influence of propylitic alteration assemblages in particular episode below 1750 mbsl. None of our sample however contained epidote, an alteration mineral characteristic of propylitic alteration. Future work is thus proposed for investigating the effects of higher temperatures (> 200 ℃), particularly in the S-waves, increasing core samples that considers varying assemblages. Also, we propose a deeper investigating into the anisotropy of volcaniclastic and sedimentary rocks

5. Conclusion

We investigated the meso-scale properties in the geothermal system in Montserrat, West Indies using 20 mm core samples. Using the high precision triaxial apparatus at the University of the West Indies, we showed that P-wave velocity decreased by 9 % when temperature was increased to 150 Degrees Celsius. Our data show that variations in lithologies, porosity and hydrothermal alteration can cause changes in both P- and S- wave velocities. Using our meso-scale characterization, we hope to improve our ability to interpret geophysical data and target productive geothermal wells.

Acknowledgement

We thank the government of Montserrat for permission to use the geophysical data. We are also very grateful for FCDO for providing some funding. Moreover, we thank the University of the West Indies Campus Research and Publication for funding some of the materials used in the lab and for the X-ray diffraction analyses

REFERENCES

Basant, R.A., Bridget L.Y, Ramsook R., Ryan G.A, Blake O.O, and Utley, J. 'Utilizing cores for characterising the temperature and permeability regimes in a litho-stratigraphic model of the Montserrat geothermal system, Montserrat (Lesser Antilles arc, West Indies)', *Geothermics*, 100, (2022), 102341.

Birch, F. 'The velocity of compressional waves in rocks to 10 kilobars: 1', *Journal of Geophysical Research (1896-1977)*, 65, (1960), 1083-102.

Birch, F. 'The Velocity of Compressional Waves in Rocks to 10 Kilobars, Part 2', *Journal of Geophysical Research*, 66, (1961), 2199-224.

Blake, O., Ramsook, R. D. Faulkner, and Iyare, U. 'Relationship Between the Static and Dynamic Bulk Moduli of Argillites', *Pure and Applied Geophysics*, 178, (2021), 1-16.

Boitnott, G. N. 2003. "Core Analysis for the Development and Constraint of Physical Models of Geothermal Reservoirs."

Cumming, W. 'Geophysics and resource conceptual models in geothermal exploration and development.' in Ronald DiPippo (ed.), *Geothermal Power Generation* (Woodhead Publishing) (2016)

Cumming, William. 'Geothermal resource conceptual models using surface exploration data', *Proceedings:* 34th Workshop on Geothermal Reservoir Engineering Stanford University, Stanford, California, (2009)

Goupil, M., Heap M., and Baud. P. 'Permeability anisotropy in sandstones from the Soultz-sous-Forêts geothermal reservoir (France): implications for large-scale fluid flow modelling', *Geothermal Energy*, 10, (2022), 32.

Harford, C., Pringle, M., Sparks, R. and Young, S. 'The volcanic evolution of Montserrat using 40Ar/39Ar geochronology', *Geological Society, London, Memoirs*, 21, (2002), 93.

Hatter, S., Palmer, M., Gernon, T., Taylor, R., Cole, P., Barfod, D., and Coussens, M. 'The Evolution of the Silver Hills Volcanic Center, and Revised 40Ar/39Ar Geochronology of Montserrat, Lesser Antilles, With Implications for Island Arc Volcanism', *Geochemistry, Geophysics, Geosystems*, 19, (2019) 427-52.

Heap, M. J., Kennedy, B., Farquharson, J., Ashworth, J., Mayer, Letham-Brake, M., Reuschlé, T., Gilg H., Scheu, B., Lavallée, Y., Siratovich, P., Cole, J., Jolly, A., Baud, P., and Dingwell, D. 'A multidisciplinary approach to quantify the permeability of the Whakaari/White Island volcanic hydrothermal system (Taupo Volcanic Zone, New Zealand)', *Journal of Volcanology and Geothermal Research*, 332, (2016).

Heap, M. J., Lavallée, Y., Petrakova,L., Baud, P., Reuschlé, T., Varley, N., and Dingwell, D. 'Microstructural controls on the physical and mechanical properties of edifice-forming andesites at Volcán de Colima, Mexico', *Journal of Geophysical Research: Solid Earth*, 119, 2014, 2925-63.

Iyare, U., Oshaine, B., and Ramsook, R., 'Estimating the Uniaxial Compressive Strength of Argillites Using Brazilian Tensile Strength, Ultrasonic Wave Velocities, and Elastic Properties', *Rock Mechanics and Rock Engineering*, 54 (2021).

Janssen, M., Barnhoorn, A., Draganov, D., Wolf, K., and Durucan. S. 'Seismic Velocity Characterisation of Geothermal Reservoir Rocks for CO2 Storage Performance Assessment', *Applied Sciences*, 11, (2021) 3641.

Jaya, M., Shapiro, S., Kristinsdóttir, L., Bruhn, D., Milsch, H., and Spangenberg. E. 'Temperature dependence of seismic properties in geothermal rocks at reservoir conditions', *Geothermics*, 39, (2010), 115-23.

Kiddle, E., Edwards, B., Loughlin, S., Petterson, M., Sparks, R., and Voight. B. 'Crustal structure beneath Montserrat, Lesser Antilles, constrained by xenoliths, seismic velocity structure and petrology', *Geophysical Research Letters*, 37, (2010).

Kristinsdóttir, L., Flovenz, O., Árnason, K., Bruhn, D., Milsch, H., Spangenberg, E., and Kulenkampff, J. 'Electrical conductivity and P-wave velocity in rock samples from high-temperature Icelandic geothermal fields', *Geothermics*, 39, (2010), 94-105.

Kushnir, A., Heap, M.J., Baud, P., Gilg, A., Reuschlé, T., Lerouge, C., Dezayes, C., and Duringer. P., 'Characterizing the physical properties of rocks from the Paleozoic to Permo-Triassic transition in the Upper Rhine Graben', *Geothermal Energy*, 6, (2018), 16.

Mordensky, S. P., Villeneuve, M., Kennedy, B., Heap, M.J., Gravley, D, Farquharson, J., and Reuschlé, T. 'Physical and mechanical property relationships of a shallow intrusion and volcanic host rock, Pinnacle Ridge, Mt. Ruapehu, New Zealand', *Journal of Volcanology and Geothermal Research*, 359, (2018), 1-20.

Rea, J.W. "The volcanic geology and petrology of Montserrat, West Indies', *Journal of the Geological Society*, 130, (1974), 341.

Ryan, G., and Shalev, E. 'Seismic Velocity/Temperature Correlations and a Possible New Geothermometer: Insights from Exploration of a High-Temperature Geothermal System on Montserrat, West Indies', *Energies*, 7, (2014) 6689-720.

Ryan, G., Onacha, S., Shalev, E., and Malin, R., 'Imaging the Montserrat geothermal prospect using Magnetotellurics (MT) and Time Domain Electromagnetic induction(TDEM) measurements.' (2009)

Ryan, G., Peacock, J., Shalev, E., and Rugis. J., 'Montserrat geothermal system: A 3D conceptual model', *Geophysical Research Letters*, 40, (2013) 2038-43.

Seyedrahimi-Niaraq, M., Faramarz D., Younes N., and Soheil P. 'Development of an updated geothermal reservoir conceptual model for NW Sabalan geothermal field, Iran', *Geothermal Energy*, 5, (2017), 14.

Shalev, E., Kenedi, C., Malin, R., Voight, V., Miller, V., Hidayat, D., Sparks, R., Minshull, T., Paulatto, M., Brown, L., and Mattioli. G. 'Three-dimensional seismic velocity tomography of Montserrat from the SEA-CALIPSO offshore/onshore experiment', *Geophysical Research Letters*, 37, (2010).

Siratovich, P. A., Heap, M., Villeneuve, M., Cole, J., Kennedy, B., Davidson, J., and Reuschlé, T. 'Mechanical behaviour of the Rotokawa Andesites (New Zealand): Insight into permeability evolution and stress-induced behaviour in an actively utilised geothermal reservoir', *Geothermics*, 64, (2016), 163-79.

Siratovich, P., Heap, M., Villenueve M., James, C., and Reuschlé. T. 'Physical property

relationships of the Rotokawa Andesite, a significant geothermal reservoir rock in the Taupo Volcanic Zone, New Zealand', *Geothermal Energy*: 1-31, (2014).

Wadge, G., Voight, B., Sparks, R., Cole, P., Loughlin, S., and Robertson, R. 'An overview of the eruption of Soufrière Hills Volcano, Montserrat from 2000 to 2010, in Wadge, G., et al., eds., The Eruption of Soufrière Hills Volcano, Montserrat from 2000 to 2010', *Geological Society of London Memoir*, 39, (2014), 1-39.

Young, S., White, R., Wadge, G., Voight, B., Toothill, J., Stevens, N., Stewart, R., Stasiuk, M., Sparks, R., Skerrit, G., Shepherd, J., Scott, W., Robertson, R., Power, J., Norton, G., Murphy, M., Miller, A., Miller, C., Lynch, L., and Ambeh, W. 'The Ongoing Eruption in Montserrat', *Science*, 276, (1997), 371-72.

Buffalo Valley and Surrounding Temperature Data: Heat Flow Calculation and Implications for Geothermal Exploration

Joseph Batir, Jerjes Porlles, Emilie Gentry

Teverra LLC

Keywords

Buffalo Valley, Temperature, Heat Flow, Geothermal, Exploration

ABSTRACT

Temperature measurements for thermal mapping are a primary indicator of potential thermal resources and location for a hydrothermal geothermal system. As such, various temperature measurements are often collected as part of geothermal exploration. In association with the INGENIOUS project, new heat flow values were calculated for the Buffalo Valley wells 72-23 and 31-26 and were interpreted for local context and exploration best practices. Heat flow values were calculated using the existing temperature logs and newly measured thermal conductivity values from the two wells. These new heat flow values are being utilized for geothermal concept model refinement and new well spotting. Additionally, existing temperature measurements of variable depth were examined in comparison to the deeper 72-23 and 31-26 wells, as well as virgin rock temperature calculations versus the existing temperature logs. Two primary observations were made that will be included in the INGENIOUS exploration workbook. First, virgin rock temperature is nominally higher than the temperature logs collected shortly after drilling. Bottom hole temperature in 72-23 increased by only 6% and 2% after 9 and 32 hours since drilling fluid circulation, respectively. This suggests that the calculation of virgin rock temperature may be unnecessary in some exploration circumstances and wait time between drilling and logging can be reduced without accuracy compromise for this specific location. Second, shallow nearby temperature measurements in the upper 175 m all have linear gradients, which would suggest regional heat flow; however, these gradients vary significantly from what is interpreted as background, increasing to what would be interpreted as near a geothermal system. This observation highlights the variation in quality and use of different temperature measurements and the necessary accompanying data when being used for exploration purposes.

1. Introduction

The INnovative Geothermal Exploration through Novel Investigations of Undiscovered Systems (INGENIOUS project) is a research project funded by the U.S. Department of Energy (DOE) Geothermal Technologies Office (GTO) to accelerate the discovery of new and commercially

viable hidden geothermal systems. Hidden geothermal systems do not exhibit surface manifestations like hot springs or steam vents, making them more challenging to locate and explore. The INGENIOUS project aims to develop and apply innovative techniques to identify and characterize these hidden geothermal systems, thereby expanding the tools to increase geothermal resource discovery and de-risk development of this clean energy resource. One key tool that will be produced is a geothermal exploration playbook, providing data types, collection methodologies, and other key parameters to de-risk exploration. Development of the exploration playbook is being supported by confirmation drilling that has taken place associated with INGENIOUS identified hidden geothermal systems. While this work is being performed within the Great Basin of the Western United States, the intention is that the exploration playbook will be useful and applicable for exploration in adjacent and analogous areas to the Great Basin.

One location being studied in detail as part of the INGENIOUS project in Buffalo Valley (Figure 1). The precursor and initial INGENIOUS play fairway analysis (PFA) maps identify this region as a potential geothermal target. Similarly, Buffalo Valley was previously identified as a potential geothermal resource area, partially due to the existing hot springs (Sass et al., 1976; Burgess and Faulds, 2024). This previous identification led to exploration activities, including a gravity survey, drilling of multiple shallow thermal gradient holes (~125 m) and drilling of 2 deep slim holes. Temperature logs were collected in the two slim holes. To date, no development has taken place in Buffalo Valley. Burgess and Faulds (2024) performed a more extensive assessment of the larger Buffalo Valley region to test and improve the INGENIOUS PFA methodology, including a 2-m temperature probe survey in Southern Buffalo Valley.

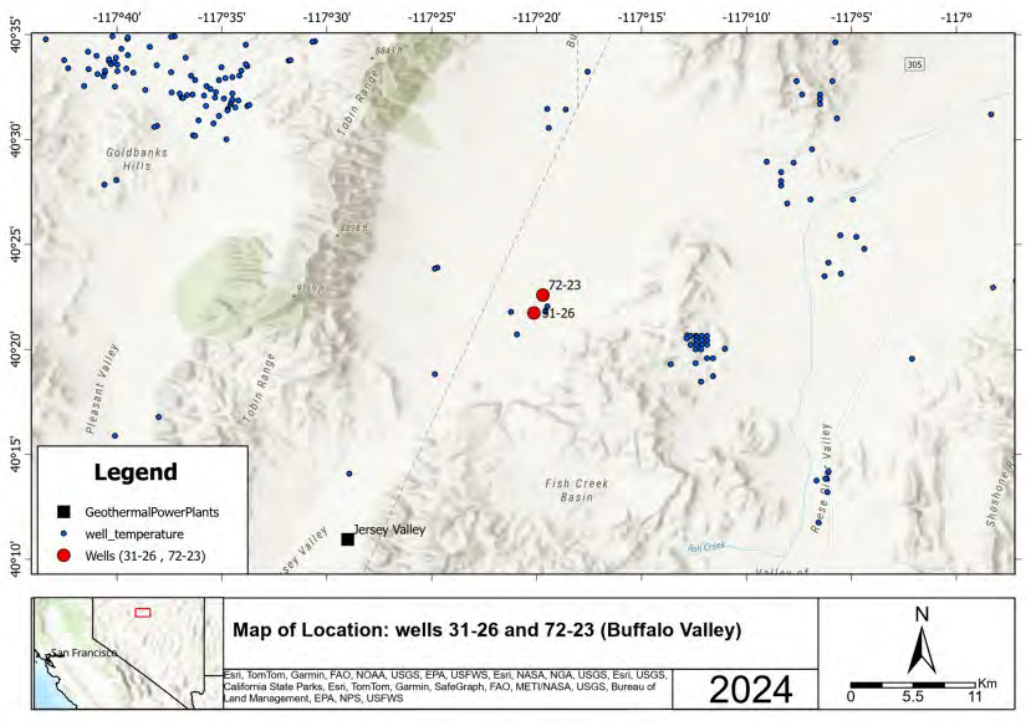

Figure 1. Map location wells BV 31-26 and BV 72-23.

To provide additional support for this PFA confirmation work, Teverra calculated and evaluated heat flow for the Buffalo Valley slim holes, using the temperature logs from the two wells, BV 31-

26 and BV 72-23, using traditional equilibrium temperature heat flow calculation methodologies (Beardsmore and Cull, 2001). As an additional test, the Virgin Rock Temperature (VRT) was calculated using the Horner plot method and compared to the supplied temperature logs. A sensitivity analysis was performed to determine heat flow uncertainty. Finally, temperature measurements from previous studies (Sass et al., 1976) were compared with the deep temperature logs for exploration insight and guidance development for the exploration workbook.

2. Methodology

Data available for this work included shallow (~125 m deep) temperature logs, 2 deeper (500 – 1000 m deep) slim holes, wells BV 31-26 and BV 72-23 with equilibrium temperature logs, and core samples for thermal conductivity measurements from the respective deeper slim holes. Given these data, equilibrium heat flow values were calculated for the deep slim holes and were used to establish regional thermal regime context. Equilibrium heat flow calculation was completed using the 1D heat conduction equation (Beardsmore and Cull, 2001). Detailed calculation methodology for the respective heat flow components is provided within each data section. Heat flow uncertainty was calculated based on the variability of geothermal gradient, thermal conductivity, and the variability of heat flow within the respective lithologies. Furthermore, applicability of deep versus shallow temperature data were examined, comparing the shallow temperature logs with the slim hole temperature logs.

2.1 Heat Flow Calculation

Heat flow is the rate at which heat is transferred from the Earth's interior to the surface (equation 1). Regional heat flow calculations are often simplified to 1D, utilizing multiple assumptions about the input data and the local subsurface conditions. Assumptions include: 1) conductive geothermal gradient, 2) constant heat flow within the near surface, 3) no thermal disturbance within the temperature data, 4) homogeneous thermal conductivity within individual lithologies. Utilizing these assumptions, heat flow can be calculated for individual lithologic sections, and variability between lithology sections show measurement uncertainty.

$$Q = dT/dz * k \quad (1)$$

Where:

Q = Heat Flow, mW/m^2

dT/dz = Geothermal Gradient, °C/km

k = Thermal Conductivity, W/m*k

2.2 Temperature Data

The primary temperature data used to calculate geothermal gradient for heat flow include temperature logs from the two exploration slim holes in Buffalo Valley, wells BV 31-26 and BV 72-23. These wells have multiple temperature – pressure surveys and lithology logs for stratigraphic correlation (Figure 2). The multiple temperature logs were collected at various times since drilling, which does show a re-equilibrating of the wellbore after drilling. The multiple temperature measurements enable thermal numerical modeling of the wellbore to estimate virgin rock temperature (VRT) following the Horner method (Ali et al., 2006; Beardsmore & Cull, 2001),

which is discussed later. Additionally, these temperature logs were examined for regionally representative geothermal gradient sections to use directly for heat flow calculations.

A geothermal gradient is considered regionally representative if it is deep enough to: 1) not be disturbed by climatic signals, 2) sufficiently separated from any known anomalous subsurface features such as hot springs 3) has no clear indicators of inter-borehole fluid flow and 4) contains a conductive gradient section, preferably 50 m in length (Richards et al., 2012). A regionally representative gradient is desired for heat flow calculations so that the heat flow represents the regional thermal regime and can then be compared to other regional data to comparatively rank potential thermal resource. A conductive geothermal gradient is identified within a temperature log as a temperature that is increasing linearly with depth. Both wells have large sections with conductive geothermal gradients, sufficient for heat flow calculation.

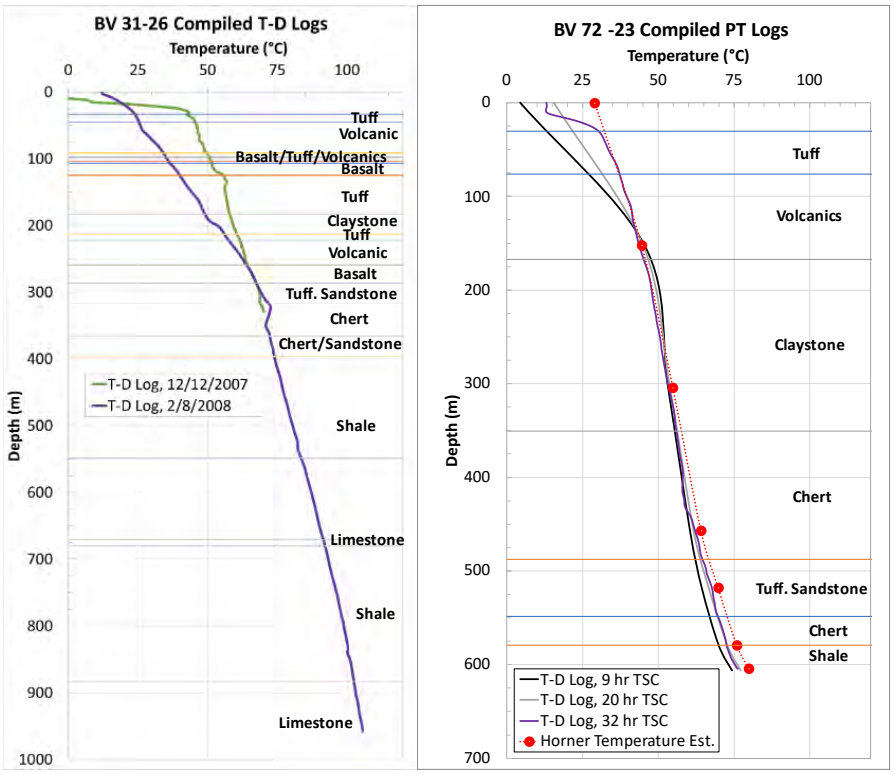

Figure 2. Temperature logs and associated lithologies for BV 31-26 (Left) and BV 72-23 (right).

Geothermal gradient is the change in temperature with depth within the Earth's subsurface. As stated previously, a conductive geothermal gradient is visualized in a temperature log as a linear increase in temperature with depth. Geothermal gradient, as the derivative of the temperature versus depth, will be a constant value with depth. Geothermal gradient is dependent on the thermal regime, specifically the heat flow and the thermal conductivity of the specific lithology. For both wells, the geothermal gradient starts high, above 100 °C/km and gradually decreases. In well BV 72-32, there is a section from ~100 – 350 m with relatively consistent thermal gradient, although more variation. In well BV 31-26, the thermal gradient between 300 and 1000 m is more consistent, showing variations correlated to lithology, with an average of 55 °C/km (Figure 3).

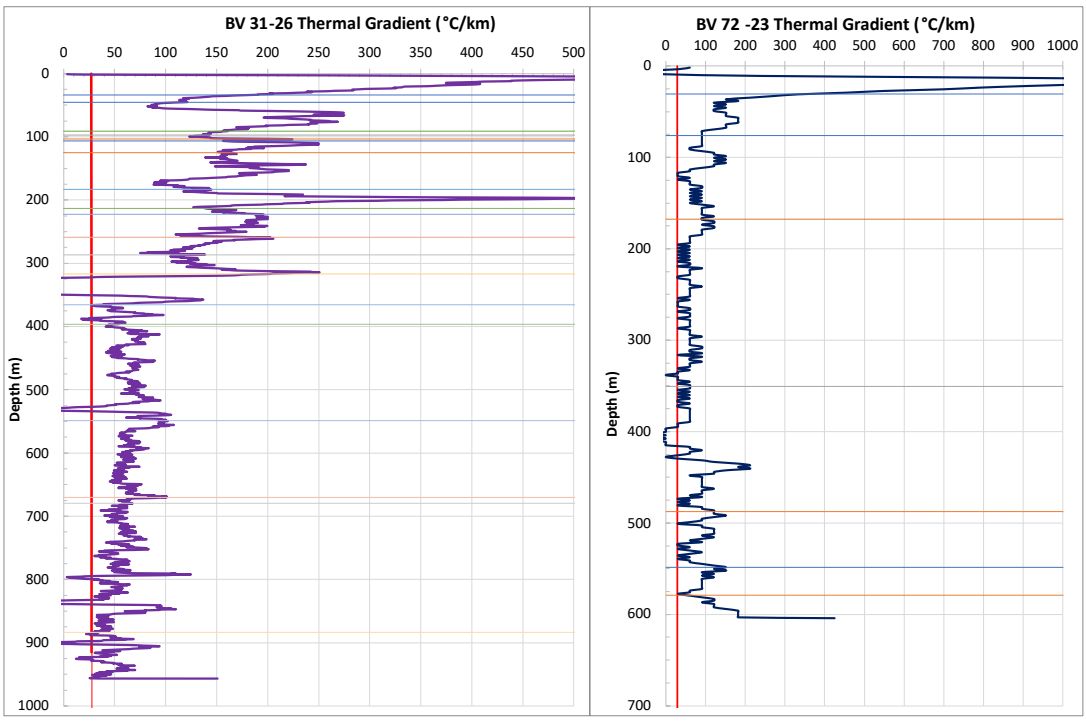

Figure 3. Thermal gradient BV 31-26 (left) and BV 72-23 (right). The red line represents a gradient of 27 °C/km.

2.3 Thermal Conductivity

Thermal conductivity is the rate at which heat is transferred through a material. For heat flow calculations, the material heat is traveling through are the respective lithologies encountered within the wellbore and documented on the lithology log. Thermal conductivity of rocks (and other materials) can be measured using multiple different methods and if often sample availability dependent. For rocks, thermal conductivity varies based on petrologic factors such as mineral composition, porosity, pore fluid, temperature, and pressure, which can vary significantly within a given rock type such as sandstone (Beardsmore and Cull, 2001). As such, measured thermal conductivity from rock samples within wellbores with temperature logs is the preferred method to increase accuracy of heat flow measurements. When rock samples aren't available, thermal conductivity is estimated based on previously measured values, introducing significant opportunity for uncertainty and heat flow calculation error.

For wells BV 31-26 and BV 72-23, both lithology logs and rock samples were available and were utilized for thermal conductivity measurement and heat flow calculation. Rock samples were collected from the major rock types and thermal conductivity was measured using the divided bar measurement device. Measurements were performed at the SMU Geothermal Laboratory, with samples being run a minimum of two times for repeatability and measurement uncertainty analysis (Richards, 2024). Where no rock samples were able to be acquired, generic rock type thermal conductivity estimates were used (Beardsmore and Cull, 2001). Lithology logs for wells BV 72-23 and BV 31-26 are presented in Table 1 and Table 2, respectively, and measured thermal conductivity for relevant rock types, Table 3. Note rock samples from specific lithologies were encountered in both wells. Uncertainty assessment was performed for lithologic groups from both wells to increase statistical significance and total number of thermal conductivity measurements

per lithology. Figure 4 shows the thermal conductivity values as a function of lithology and depth of the wells BV 72-23 and BV 31-26 that were utilized for heat flow calculations. As seen in Figure 4, thermal conductivity from the rock samples was propagated throughout the depth of the associated rock formation. Note that rock samples were not able to be collected from all lithologies.

Table 1: Lithology BV 72-23

From MD (m)	To MD (m)	Total Thickness (m)	Lithology	Short Description/Formation
30.5	76.2	45.7	Tuff	Fish Creek Mtn tuff
76.2	167.6	91.4	Volcanics	Ash/Volcanic breccia
167.6	350.5	182.9	Clay/Claystone	
350.5	487.7	137.2	Chert	Havallah/Pumpernickel
487.7	548.6	61.0	Tuffaceous Sandstone	China formation?
548.6	579.1	30.5	Chert	Havallah/Pumpernickel
579.1	605.9	26.8	Shale	Havallah/Pumpernickel

Table 2: Lithology BV 31-26

From MD (m)	To MD (m)	Total Thickness (m)	Lithology	Short Description/Formation
33.5	45.7	12.2	Tuff	Fish Creek Mtn tuff
45.7	91.4	45.7	Volcanics	Volcanic breccia
91.4	97.5	6.1	Basalt	Qt cinder cone?
97.5	103.6	6.1	Volcanics	Volcanic ash
103.6	106.7	3.0	Tuff	Fish Creek Mtn tuff
106.7	125.0	18.3	Basalt	Qt cinder cone?
125.0	182.9	57.9	Tuff	Fish Creek Mtn tuff
182.9	213.4	30.5	Claystone	
213.4	222.5	9.1	Tuff	Fish Creek Mtn tuff
222.5	259.1	36.6	Volcanics	Volcanic breccia
259.1	286.5	27.4	Basalt	Qt cinder cone?
286.5	317.0	30.5	Tuffaceous Sandstone	China Mountain?
317.0	365.8	48.8	Chert	Havallah/Pumpernickle
365.8	396.2	30.5	Chert/Sandstone	Havallah/Pumpernickle
396.2	548.6	152.4	Siliceous Shale	Havallah/Pumpernickle
548.6	670.6	121.9	Siliceous Shale	Havallah/Pumpernickle
670.6	679.7	9.1	Limestone	Havallah/Pumpernickle
679.7	883.9	204.2	Siliceous Shale	Havallah/Pumpernickle
883.9	944.9	61.0	Limestone	Havallah/Pumpernickle

944.9	951.0	6.1	Limestone	Havallah/Pumpernickle
951.0	964.7	13.7	Limestone	Havallah/Pumpernickle
579.1	605.9	26.8	Shale	Havallah/Pumpernickel

Table 3: Rock thermal conductivity (Richards, 2024; Beardsmore & Cull, 2001)

Well	Type of rock	Depth (m)	K ($Wm^{-1}K^{-1}$)	Std. Dev.
BV 72-23	Fish Creek Rhyolite Tuff	64	1.40	± 0.35
BV 72-23	Claystone	198	1.37	± 0.40
BV 72-23	Chert Havallah	503	2.19	± 0.35
BV 31-26	Fish Creek Rhyolite Tuff	427	2.38	± 0.25
BV 31-26	Basalt Cinders	137	1.16	± 0.30
BV 31-26	Chert Siliciclastic	259	1.23	± 0.25
BV 31-26	Limestone Pumpernickel	341	5.35	± 0.35

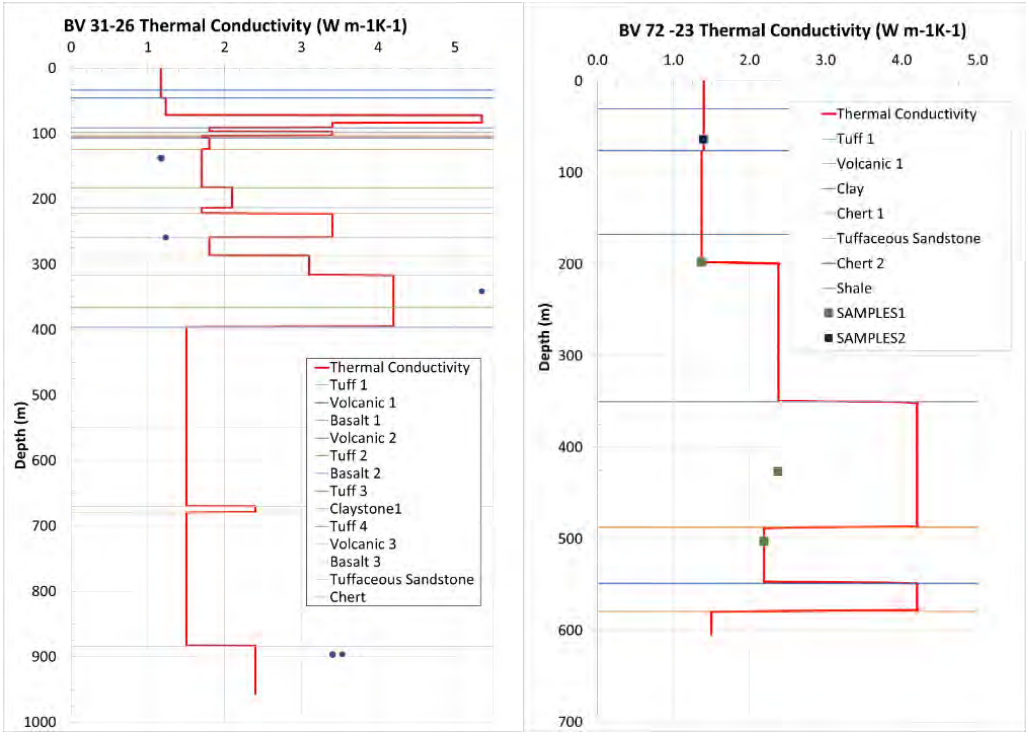

Figure 4. Thermal Conductivity wells BV 31-26 (left) and BV 72-23 (right).

2.4 Horner Plot Analysis

The Horner plot method is a graphical technique used to determine the virgin rock temperature (VRT) in a borehole. VRT is the temperature of the undisturbed rock mass at the depth of the borehole in which temperature was measured. The method is based on the principle that the temperature of a borehole will approach the VRT as the borehole equilibrates with the surrounding rock mass (Ali et al., 2006; Beardsmore & Cull, 2001). Since originally discovered, several equations have been tested to calculate VRT (Lachenbruch and Brewer, 1959; Cao et al., 1988).

The Horner plot method involves plotting the bottom-hole temperature (BHT) of the borehole against the time elapsed since drilling or other activities that may have disturbed the temperature of the rock mass. The BHT is measured at several time intervals over days or weeks. The resulting plot will typically show an initial rapid increase in temperature followed by a gradual approach to a constant value. The VRT is estimated by extrapolating to “infinite” time since drilling.

The Horner plot method is a simple and effective way to estimate the VRT in a borehole. However, it is important to note that the method is only valid in boreholes with conductive thermal regimes (i.e., no significant fluid flow within the wellbore), and can only accurately be calculated with a minimal of 3 temperature versus time data points, preferably with more that show the logarithmic thermal warming (Deming, 1989).

Well 72-23 provided values of temperature logs at different times, which was sufficient to evaluate the virgin rock temperature (VRT). Table 4 shows the values of depth and temperature. Two methodologies of Horner style corrections were tested using the time-series of temperature logs within B 72-23, Cao et al. (1988) and Lachenbruch and Brewer (1959).

Table 4: Temperature logs at different times Lithology BV 72-23

9 hr 10/21/08		20 hr 10/21/08		32 hr 10/22/08	
DEPTH (m)	TEMP (oC)	DEPTH (m)	TEMP (oC)	DEPTH (m)	TEMP (oC)
0.0	4.4	0.0	15.6	0.0	23.9
152.4	45.6	152.4	45.0	152.4	44.8
304.9	53.3	304.9	53.9	304.9	54.6
457.3	60.6	457.3	61.7	457.3	63.6
518.3	64.4	518.3	66.7	518.3	68.7
579.3	70.0	579.3	72.8	579.3	74.5
606.4	74.4	606.4	77.2	604.6	78.4

3. Results

Utilizing the available data, heat flow was calculated for the wells BV 31-26 and B 72-23, including an estimation on measurement error. In addition to heat flow and measurement error, VRT calculations were made and analysis performed to examine shallow temperature data, deep temperature data, and VRT versus temperature logs.

3.1 Heat Flow

Geothermal gradient was calculated from the temperature logs provided for BV 31-26 and BV 72-23 and thermal conductivity was measurement for rock samples collected for the two wells. For both wells, the heat flow anomalously high in the upper section from approximately 0 to 400 m. In BV 31-26, there is a consistent heat flow of 89 ±36 mW/m² from 400 m to 900 m. In BV 72-23, there is a consistent section of heat flow of 125 ±41 mW/m² from 130 m to 350 m (Figure 5). Both wells show these sections of relatively consistent geothermal gradient and respective heat flow, although there is a high standard deviation associated with these sections. The high standard deviation is particularly high. Here, we attribute this high uncertainty value to the large spikes in geothermal gradient within the wellbore. These small spikes are likely minor zones of flow or

minor lithology changes that cause a drastic increase in gradient. These large fluctuation zones were not examined in detail since this region and this work was meant to build regional setting. Note that both wells increase in heat flow at the base of the wellbores. In BV 31-26, this could be an artifact of being at the base of the wellbore and logging procedure of sitting on the bottom of the well. For BV 72-23, there is a clear increase in calculated heat flow, which is variable. This could be an indication of recorded fluid flow, indicating that the base of BV 72-23 may not be in a conductive thermal regime.

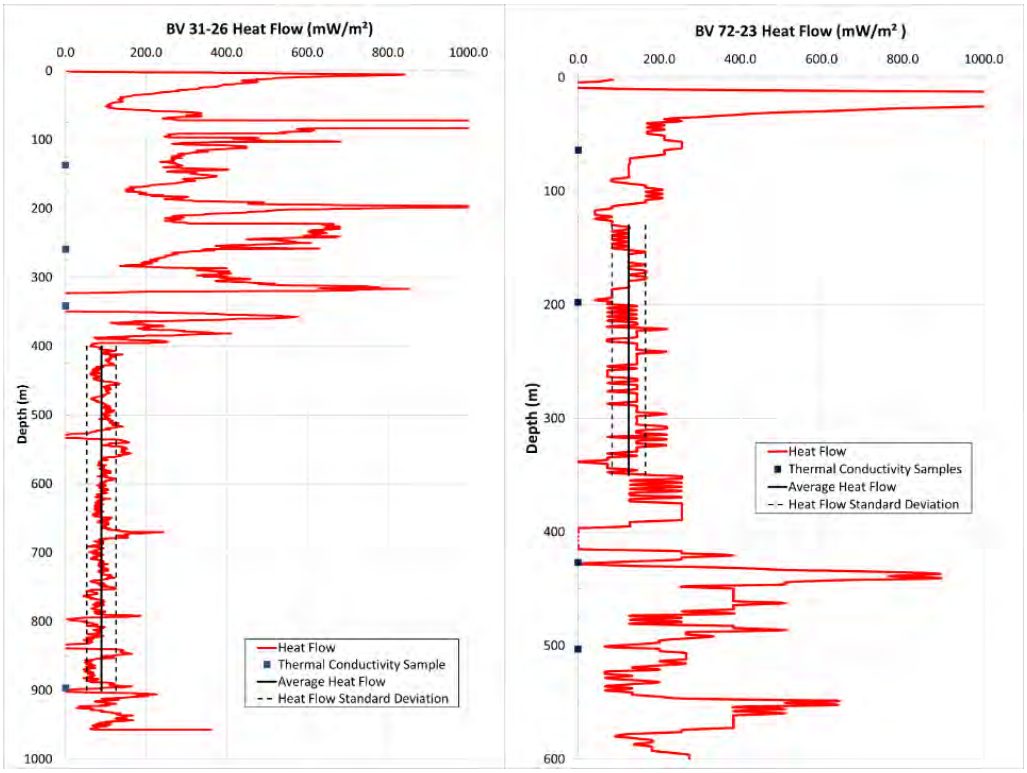

Figure 5. Calculated heat flow values for wells BV 31-26 (left) and BV 72-23 (right).

3.2 Virgin Rock Temperature Calculations

Figure 6 shows the virgin rock temperature results with the Hermanrud, Cao, and Lerche method. However, that method is also one of the least precise. The Horner method (Lachenbruch & Brewer, 1959) is considered more precise based on an observed similarity in the behavior of *in situ* temperature and pressure when disturbed by drilling. Figure 7 shows temperature plotted against Ln(1+(tc/dt)) to calculate the VRT. A straight line of best fit through all points from the same depth yields the VRT for that depth at the temperature axis intercept.

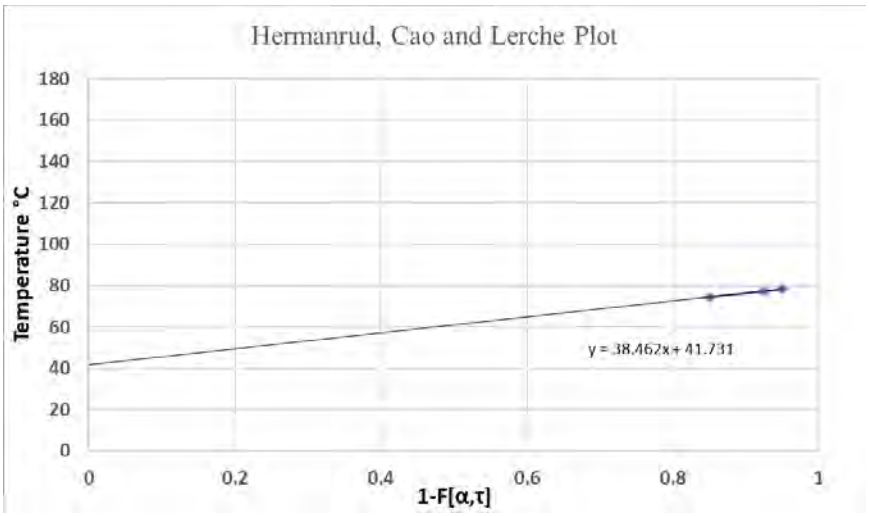

Figure 6. Hermanrud, Cao, and Lerche method BV 72-23.

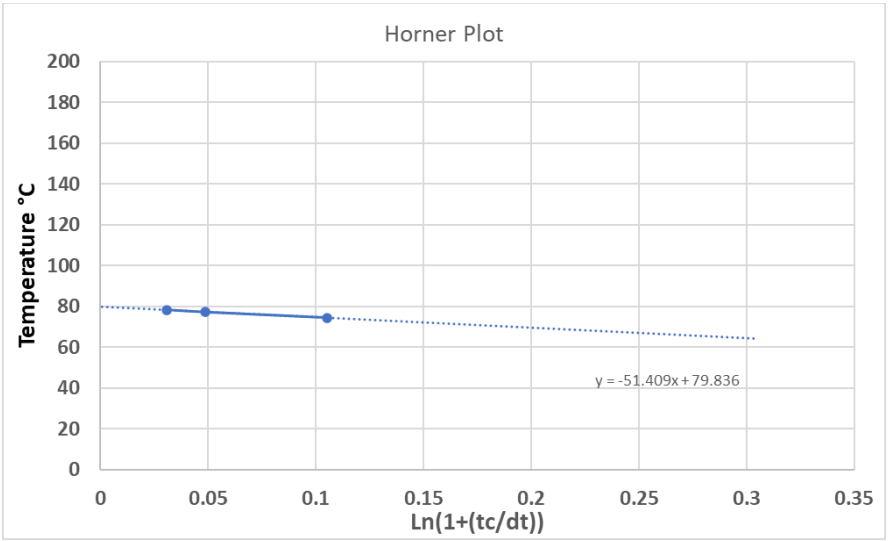

Figure 7. Horner Plot BV 72-23.

The temperature measurements of variable depth were compared to the deeper 72-23, as well as VRT calculations versus the existing temperature logs. Analysis shows a nominal increase in VRT compared to temperature logs collected shortly after drilling. VRT in BV 72-23 was greater than the measured bottom hole temperature by only 6% and 2% after 9 and 32 hours since drilling fluid circulation, respectively (Figure 2). In this specific location and exploration circumstance, wait time between drilling and logging could be reduced without accuracy compromise. This implies that the calculation of VRT may be unnecessary in some exploration scenarios.

4. Comparison of Deep and Shallow Temperature Measurements

Similar to VRT, existing shallow temperature data were compared to the two deeper wells in Buffalo Valley. These shallow nearby temperature measurements were in the upper 175 m and all have linear gradients, suggesting they are in a conductive thermal regime, and may represent regional heat flow. When compared with deep wells, though, the shallow gradients are

significantly higher than the interpreted background geothermal gradient (Figure 9). This is a similar result produced here where BV 31-26 shows a high heat flow anomaly in the shallow subsurface from 0 - 300 m depth. The key challenge identified here is how exploration activities can identify a regional thermal anomaly or a local geothermal system related thermal anomaly.

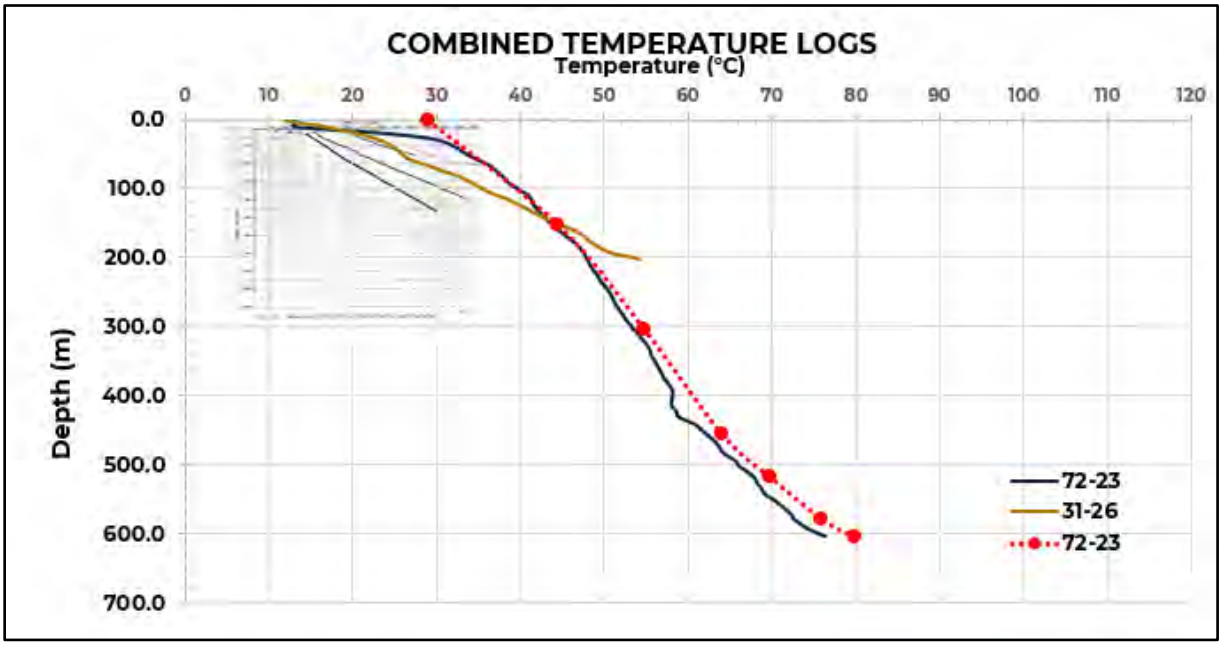

Figure 8. Combined temperature logs compared with Horner values (Well BV72-23).

CONCLUSIONS

This study calculated heat flow for two wells (BV 31-26 and BV 72-23) as part of the INGENIOUS project. Temperature logs and lithology were analyzed to determine geothermal gradient, measure thermal conductivity, and calculate heat flow values. As part of this work, comparison was made between the deep temperature logs discussed here with other existing, shallow temperature data within the Buffalo Valley region. This comparison was made to develop additional insights and recommendations for exploration procedures moving forward.

The temperature measurements of variable depth were compared to the deeper BV 72-23, as well as virgin rock temperature calculations versus the existing temperature logs. Two observations were made to be included in the INGENIOUS exploration workbook. First, virgin rock temperature is nominally higher than temperature logs collected shortly after drilling, increasing by only 6% and 2% after 9 and 32 hours since drilling fluid circulation, respectively. This infers that the calculation of virgin rock temperature may be unnecessary in some exploration circumstances and wait time between drilling and logging may be reduced without accuracy compromise. This should be further examined. Second, shallow nearby temperature measurements in the upper 175 m all have linear gradients, suggesting regional heat flow, but these gradients vary significantly from what is interpreted as background, which could erroneously highlight this area as an exploration target. Further analysis will be performed of this observation to determine how best to incorporate this comparison knowledge.

ACKNOWLEDGEMENTS

The INGENIOUS project is funded by the U.S. Department of Energy Geothermal Technologies Office under award DE-EE0009254 to the University of Nevada, Reno. Teverra performed this work as a subcontract on the INGENIOUS grant. Any use of trade, firm, or product names in this paper is for descriptive purposes only and does not imply endorsement by the U.S. Government. The authors thank Quentin Burgess, Maria Richards, Dr. Cary Lindsey and others on the INGENIOUS team for discussion that contributed to this work. Maria Richards performed the thermal conductivity measurements that were input for these heat flow calculations.

REFERENCES

Ali, S., Musto-Onuoha, K., & Orazulike, D. (2006). “Bottom-hole temperature correction – the Chad Basin, N.E., Nigeria case study.” *Global Journal of Geological Sciences*, 3(2). https://doi.org/10.4314/gjgs.v3i2.18720

Beardsmore, G., & Cull, J. (2001). “Crustal Heat Flow: A Guide to Measurement and Modeling.” Cambridge University Press.

Burgess, Q., & Faulds, J. (2024). “Characterization and Analysis of a Potential Hidden Geothermal Resource in the Jersey Summit Area, North-Central, Nevada.” *Proceedings, 49th Workshop on Geothermal Reservoir Engineering*, Stanford University, Stanford, CA. SGP-TR-227.

Cao, S., Lerche, I., & Hermanrud, C. (1988). “Formation temperature estimation by inversion of borehole measurements.” *Geophysics*, 53(7), 979–988. https://doi.org/10.1190/1.1442534

Deming, D. (1989). “Application of bottom-hole temperature corrections in geothermal studies.” *Geothermics*, 18(5), 775–786. https://doi.org/https://doi.org/10.1016/0375-6505(89)90106-5

Lachenbruch, A., & Brewer, M. (1959). “Dissipation of the temperature effect of drilling a well in Arctic Alaska.” https://doi.org/10.3133/b1083C

Sass, J. H., Olmsted, F. H., Sorey, M. L., Lachenbruch, A. H., Munroe, R. J., & Galanis, S. P. (1976). “GEOTHERMAL DATA FROM TEST WELLS DRILLED I N GRASS VALLEY AND BUFFALO VALLEY, NEVADA* +.”

Richards, M., (2024). “THERMAL CONDUCTIVITY SAMPLES (Run as crushed samples) GBCGE-INGENIOUS Project January 2024.” Southern Methodist University. SMU Geothermal Lab.

Microseismic Monitoring During a Next Generation Enhanced Geothermal System at Cape Modern, Utah

Sireesh Dadi[1], Jack Norbeck[1], Aleksei Titov[1], Ben Dyer[2], Ahmad Mohammadi[3], Yu Geng[4], Kanu Obinna[1], Nori Nakata[5] and Gabe Matson[1]

[1]Fervo Energy, [2]Geo-Energie Suisse, [3]Texas A&M University, [4]Nanometrics Inc, [5]Lawrence Berkely National Laboratory

Keywords

Microseismic, induced seismicity, fiber optic sensing, offset pressure monitoring

ABSTRACT

The Cape Modern project, a next-generation Enhanced Geothermal System (EGS) field, is being developed in Southwest Utah. The initial phase of the project involved the stimulation of three horizontal wells using a plug-and-perf hydraulic stimulation technique. To ensure comprehensive monitoring of induced seismic activity associated with EGS operations, an extensive microseismic network was deployed, comprising shallow borehole sensors, a surface nodal array, deep borehole fiber optic sensors, and 3-component (3C) passive sensors. A key observation from this setup was that the high-precision double-difference-based locations derived from the sparse regional shallow borehole array provided spatial resolution comparable to that of the deep borehole sensors, achieving accuracy down to a few hundred feet in real-time during injection operations. The high-resolution microseismic data from the deep borehole fiber optic-based Distributed Acoustic Sensing (DAS) revealed extensive linear features reactivated during the stimulation process. Interestingly, the orientation of these linear features was misaligned with the maximum horizontal stress (SHmax) orientation, suggesting the reactivation of preexisting natural fractures, faults, or lithological boundaries within the host rock and intrusive bodies. During the operations, a total of five seismic events with magnitudes greater than 2.0 were recorded, necessitating the activation of the Traffic Light System (TLS). Injection had to be paused three times out of the five, while the other two events occurred when there was no active injection. The largest event was measured at a local magnitude of 2.3, according to the USGS ComCat catalog. Importantly, ground motion levels near the nearest town remained low, well below the threshold likely to cause any noticeable effects or damage. Following each amber-level alert, seismicity levels returned to normal, indicating the effectiveness of the TLS in managing induced seismicity. This highlights the importance of real-time monitoring and responsive management in mitigating seismic risks during geothermal operations, ensuring minimal impact on surrounding communities.

1. Introduction

A recent commercial liftoff report by the Department of Energy (DOE) estimated a substantial opportunity for next-generation geothermal energy, projecting a potential capacity of 2-5 GW by 2030 and up to 125 GW by 2050 (Blankenship. D., 2024). Realizing this potential will necessitate breakthrough innovations in drilling, stimulation techniques, resource identification and characterization, and risk mitigation. This paper focuses on seismic monitoring while optimizing Enhanced Geothermal Systems (EGS) in horizontal wells stimulated using plug-and-perf techniques—a method extensively tested and proven in the Unconventional Oil and Gas industry

A crucial aspect of the monitoring program involves mitigating induced seismicity. The primary mechanisms identified to cause induced seismicity include direct pressure increases in faults, poroelastic stressing, and thermoelastic stress changes (Buijze et al., 2019). Direct pressure increases occur when fluid injection or production alters the pore fluid pressure within a fault. This pressure change reduces the effective normal stress on the fault, potentially bringing it closer to failure. The elevated pressure can diffuse away from the injection site over time, potentially inducing seismic events at the edge of the faults and even after the injection has stopped. This mechanism is particularly important in fractured rock masses, where fluid flow is dominated by fractures, leading to pressure diffusion and seismicity over larger areas (Deichmann et al., 2014). Poroelastic stressing refers to the stress changes within and around a pressurized rock volume due to changes in pore pressure (Segall & Fitzgerald, 1998, Mossop & Segall, 1997). This mechanism results in volumetric strain of the rock mass, which can either compress or expand the rock, depending on the location relative to the pressure source. This stress change can lead to fault reactivation, especially in areas where the initial stress state is near critical failure. Thermoelastic stress changes occur due to temperature differences between injected fluids and the surrounding rock, leading to thermal contraction or expansion of the rock mass. This thermal strain induces additional stress changes, which can contribute to fault instability. For example, the cooling of the rock around a reinjection well can reduce the total stress, making faults within and near the cooled volume more prone to seismic slip (Rutqvist et al., 2015).

The potential for induced seismicity is highly site-specific and depends on factors such as lithology, depth, and proximity to critically stressed faults. Norbeck and Latimer (2023) successfully demonstrated the feasibility of a commercial-scale, first-of-its-kind Enhanced Geothermal System (EGS) utilizing a horizontal doublet well design. The project, carried out by Fervo Energy in northern Nevada, involved drilling and stimulating horizontal wells within a high-temperature geothermal reservoir. The EGS development phases included drilling, stimulation, and a 37-day flow test, which confirmed the hydraulic connectivity between the wells. The seismic activity throughout the entire operation remained below magnitude two, indicating that the innovative approach to geothermal energy extraction can be achieved with minimal seismic risk (Norbeck & Latimer, 2023). Seismicity during the initial drilling, stimulation, and flow test phases was thoroughly examined by Dadi et al. (2024), where all recorded seismic events were found to be below magnitude 2. The seismicity continued to be monitored beyond the flow test phase, encompassing the production phase that began in October 2023 and extended through to July 2024. Throughout this period, all seismic events remained under magnitude 2, with the largest recorded event near the Fervo Doublet registering a local magnitude of 1.87 (Figure 1a). Significantly higher number of seismic events with magnitudes greater than 2, 3, and 4 are observed in the Nevada Basin and Range, which are attributed to natural processes and other anthropogenic activities such as mining, distinct from the EGS operations at the Fervo site (Figure 1b). This comparison

highlights the relatively low seismic impact of the Fervo Doublet operations in contrast to the broader regional seismicity.

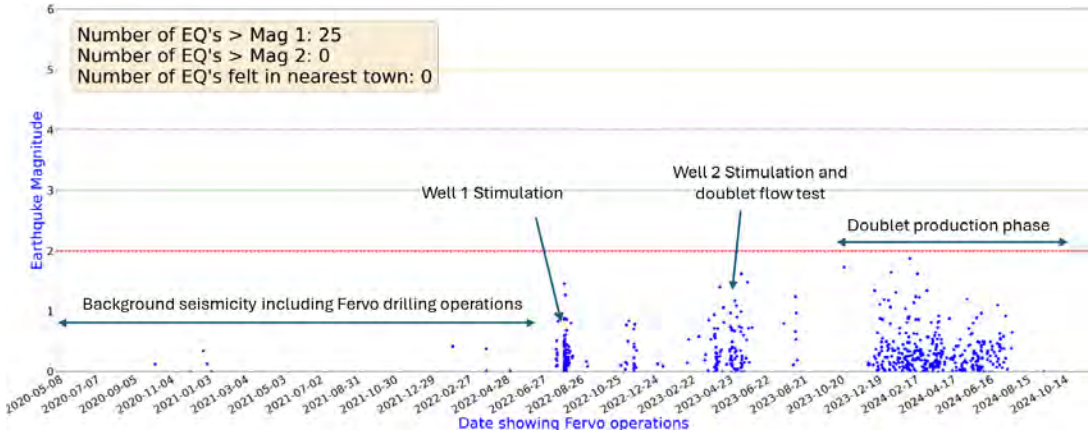

(a)

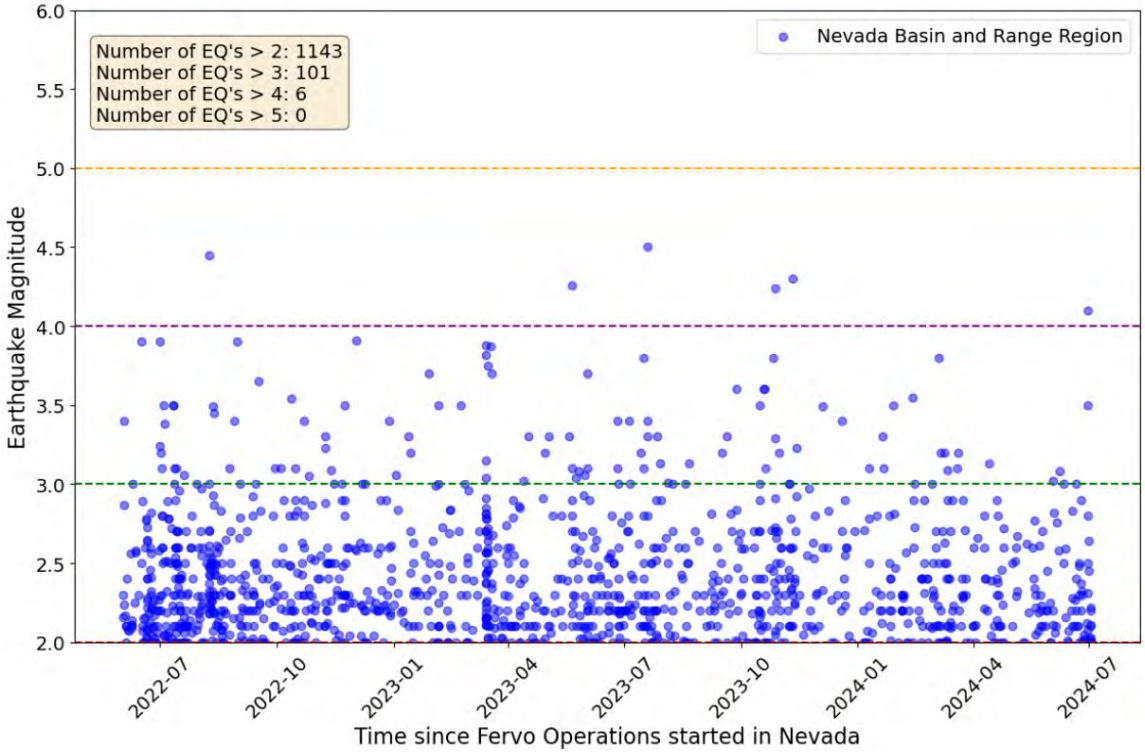

(b)

Figure 1: (a) Seismicity recorded near the Fervo Doublet in northern Nevada from July 2022 to July 2024. The plot shows the number of earthquakes (EQs) with magnitudes greater than 2.0, 3.0, 4.0, and 5.0. Despite ongoing geothermal operations, including drilling, stimulation, and production phases, all recorded events remained below magnitude 2.0, indicating minimal induced seismicity associated with the Enhanced Geothermal System (EGS) activities. (b) Seismicity in the Nevada Basin and Range region over the same period, highlighting a higher frequency of seismic events with magnitudes exceeding 2.0, 3.0, and 4.0, which are primarily attributed to natural seismic processes and other anthropogenic activities like mining.

Microseismic monitoring also plays a crucial role in optimizing Enhanced Geothermal System (EGS) operations, particularly in refining completion designs that involve key parameters such as stage length, the number of clusters, perforation designs, fluid injection volumes per stage, and fluid types. To determine the most effective completion parameters, design of experiments methodologies is often employed alongside a tailored monitoring program. The EGS system design and deployment framework we seek to pioneer encompasses four critical phases: (1) resource identification and optimal planning and drilling of wells, (2) stimulation of wells to establish hydraulic connectivity, (3) injection and crossflow tests to validate system productivity, and (4) the production phase. Effective monitoring across all phases is essential to defining and optimizing the EGS system.

Advanced monitoring tools are increasingly being used to enhance EGS efficiency. These include pressure diagnostics such as Instantaneous Shut-In Pressure (ISIP), offset pressure monitoring, and sealed wellbore monitoring; fiber optic sensing for temperature and low-frequency strain measurements (Titov et al., 2024); and microseismic monitoring using multi-well Distributed Acoustic Sensing (DAS) (Dadi et al., 2024) and 3-component (3C) geophones. For instance, pressure measurements provide critical insights into the fracture gradient of the reservoir, the Volume to First Response (VFR) required to generate hydraulic fractures that propagate to offset wells, and fracture propagation velocity. Microseismic monitoring, on the other hand, is instrumental in characterizing the stimulated rock volume, fracture morphology, and out-of-zone injection, which could elevate the risk of induced seismicity.

In this paper, we present findings from microseismic monitoring of three horizontal wells, utilizing data from shallow borehole arrays, deep borehole fiber optics, and 3C geophones. The performance of the shallow borehole array, installed at 23 locations by the University of Utah and Fervo, is compared with results obtained from multi-well DAS-based microseismic data. Additionally, we discuss how real-time monitoring, in conjunction with a predefined Traffic Light System (TLS) and effective communication with the operations team, successfully mitigated induced seismicity during the stimulation of the three horizontal wells. The stimulated wells underwent successful flow testing in July and August 2024; however, the detailed flow results and seismicity data from this period are beyond the scope of the present paper. These findings will be comprehensively reported in a subsequent publication.

2. Geologic setting

Cape Modern is located adjacent to the Utah FORGE site in Milford Valley, Utah. The reservoir comprises granitic basement rocks, including granite, granodiorite, diorite, and Precambrian gneiss. Figure 2 displays a fault map of the area near Cape Station, highlighting three main fault structures: the Opal Mound Fault, the Mag Lee Fault, and the Mineral Mountains West Fault System. The Mineral Mountains West Fault System has a surface expression visible on LiDAR and terminates south of the area of interest (Fercho et al., 2024).

The drilling campaign at Cape Modern included a deep vertical monitoring well (Delano 1-OB) and four deep horizontal wells (Frisco 1-I, 2-P, 3-I, 4-T), as shown in Figure 3. The Frisco 1-I and 3-I wells serve as horizontal injectors, while the Frisco 2-P and 4-T wells function as producers. The injector wells are deeper than the producer wells. The vertical monitoring well is drilled deeper than both the injectors and producers and is equipped with a permanent fiber optic cable behind

the casing and a pressure gauge outside the casing at the reservoir depth. This vertical well extends further down to record microseismic data significantly deeper than the horizontal wells.

The project utilized three-dimensional geologic and temperature models derived from existing data from the nearby Blundell and FORGE wellfields, which were iteratively updated with new drilling results. The orientations of the horizontal wells were guided by the maximum horizontal stress (SHmax) indicators from adjacent wells, indicating a consistent SHmax of 10°-15° (NNE) across the field (Figure 4). SHmax refers to the direction of the maximum horizontal compressive stress in the Earth's crust. Understanding SHmax is crucial because it influences the orientation and propagation of induced fractures during hydraulic stimulation. By aligning wells approximately perpendicular to SHmax, we maximize the effectiveness of the fracturing process, as fractures tend to open and propagate perpendicular to the minimum principal stress direction. This approach enhances the connectivity of the fracture network, which is essential for efficient geothermal energy extraction. In our case, the wells were oriented at angles of 75°–80° relative to SHmax, which is close to perpendicular. This slight deviation from the ideal 90° was due to operational constraints and geological considerations, but it still effectively enhances fracture development. The stratigraphy at Cape ranges from Miocene basin-fill deposits to granitic basement rocks. A comprehensive 3D geologic model was developed and refined using well logs, gravity profiles, and cuttings analyses, providing critical insights for well targeting and improving model accuracy with each drilled well (Figure 3).

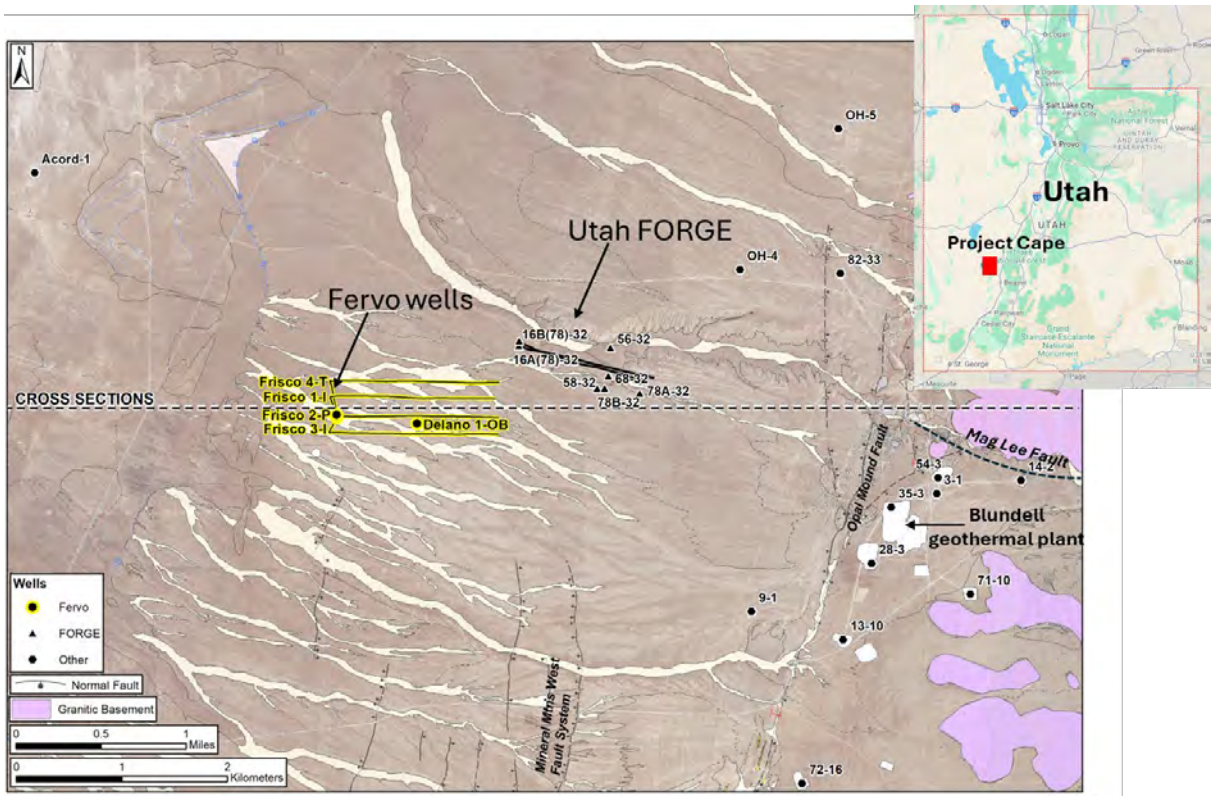

Figure 2: Map view of the Frisco wells, Delano 1-OB vertical observation well, Utah FORGE wells and the Blundell geothermal plant wells. The wells of interest in this paper are the Frisco 1-I, Frisco 2-P and the Frisco 3-I wells. In the figure, the Frisco and Delano wells are highlighted in yellow. The Utah FORGE wells are represented by solid triangles, while the Blundell wells are depicted as solid circles

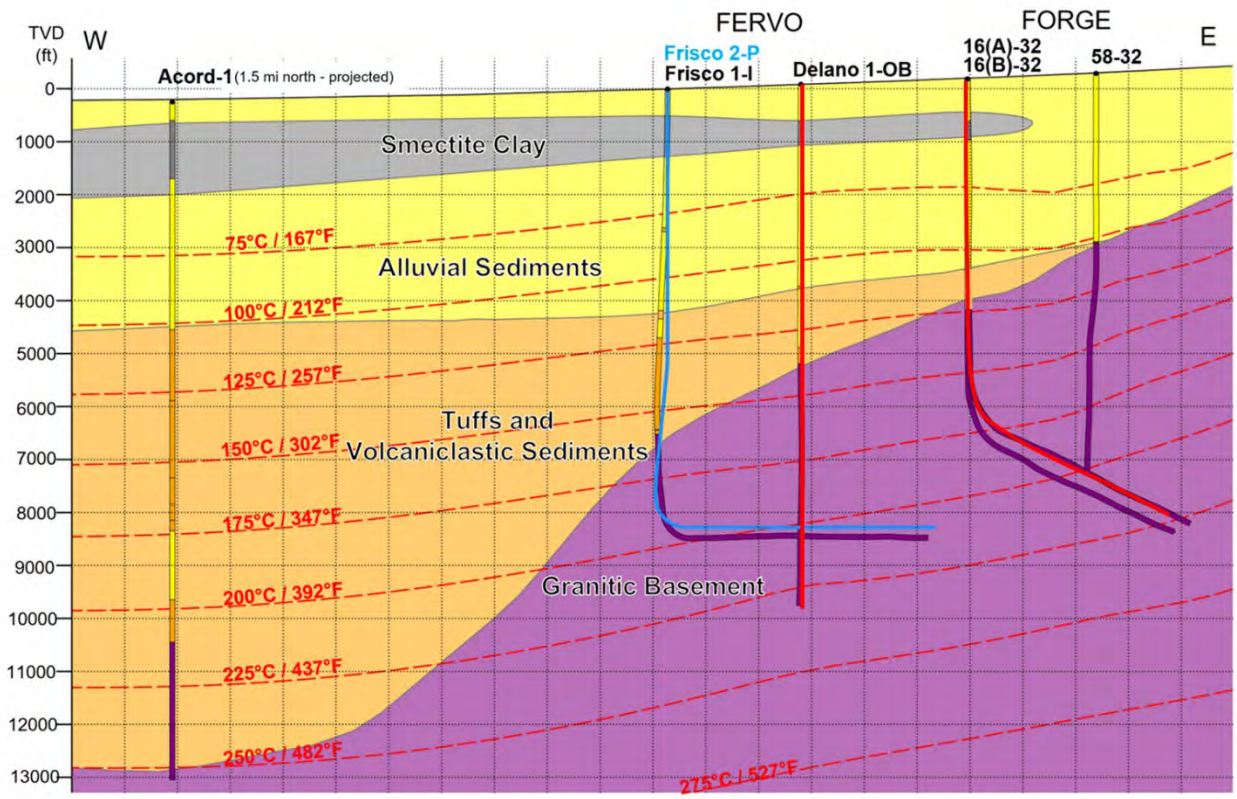

Figure 3: Cross section view of the Frisco wells, Delano 1-OB well and the FORGE wells. The red lines show the fiber optic cables permanently installed behind casing on the Delano 1-OB and the 16B well. Data from both the fiber optic cables along with a 3C sensor in 56-32 are used for microseismic monitoring.

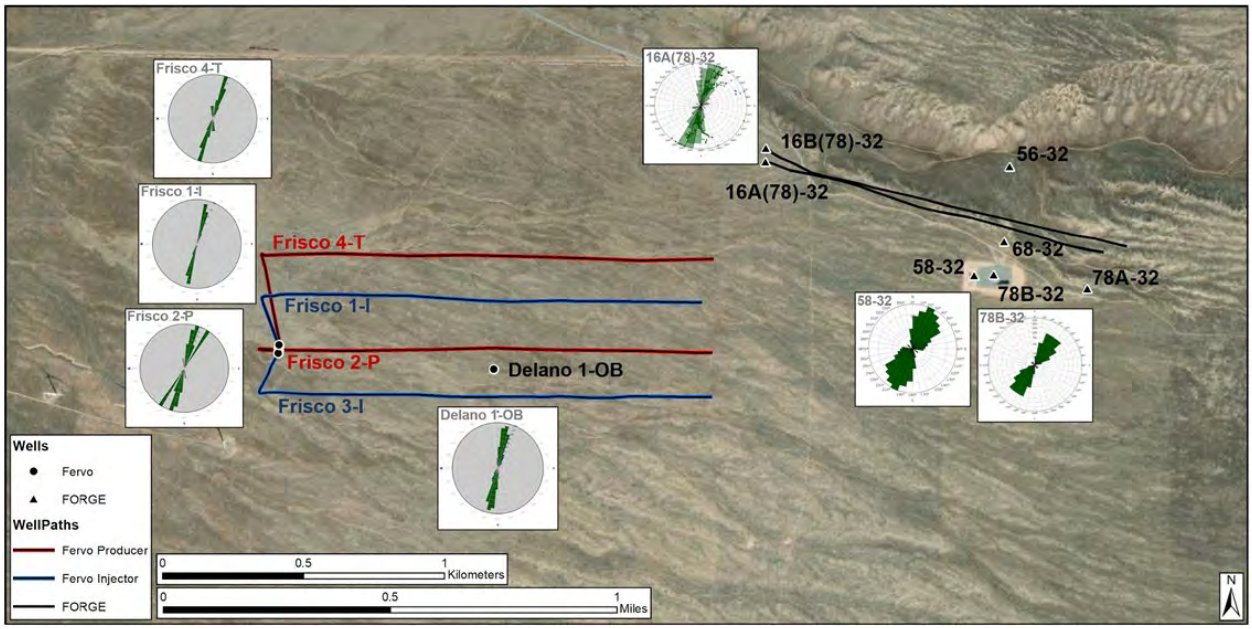

Figure 4: Orientation of the drilling induced fractures in Fervo and Utah FORGE wells showing NNE-SSW orientation representative of the SHmax.

3. Monitoring Acquisition summary

3.1 Shallow borehole array:

A local seismic monitoring network was installed at Cape Station as part of the Utah FORGE project in December 2016 and has been operational since. The network comprises a total of seventeen stations installed by the University of Utah Seismograph Stations (UUSS) and six additional stations installed by Fervo Energy and Berkeley National Lab. The seventeen UUSS stations monitor the Utah FORGE project, while the six additional stations infill the UUSS network and serve as backups in case the UUSS FORGE network fails during critical operations conducted by Fervo.

The seismic monitoring network includes a variety of sensors: fourteen broadband sensors, seven strong motion sensors, and two short-period sensors. These sensors are distributed as shown in Figure 5, spaced approximately 2 km, 8 km, and 12 km from Cape Station. Additionally, there are strong motion accelerometers at the Blundell geothermal plant and Milford High School to measure ground motion both for background levels and during stimulation activities. This comprehensive seismic monitoring network ensures robust data collection and enhances the ability to monitor and mitigate induced seismicity in the area.

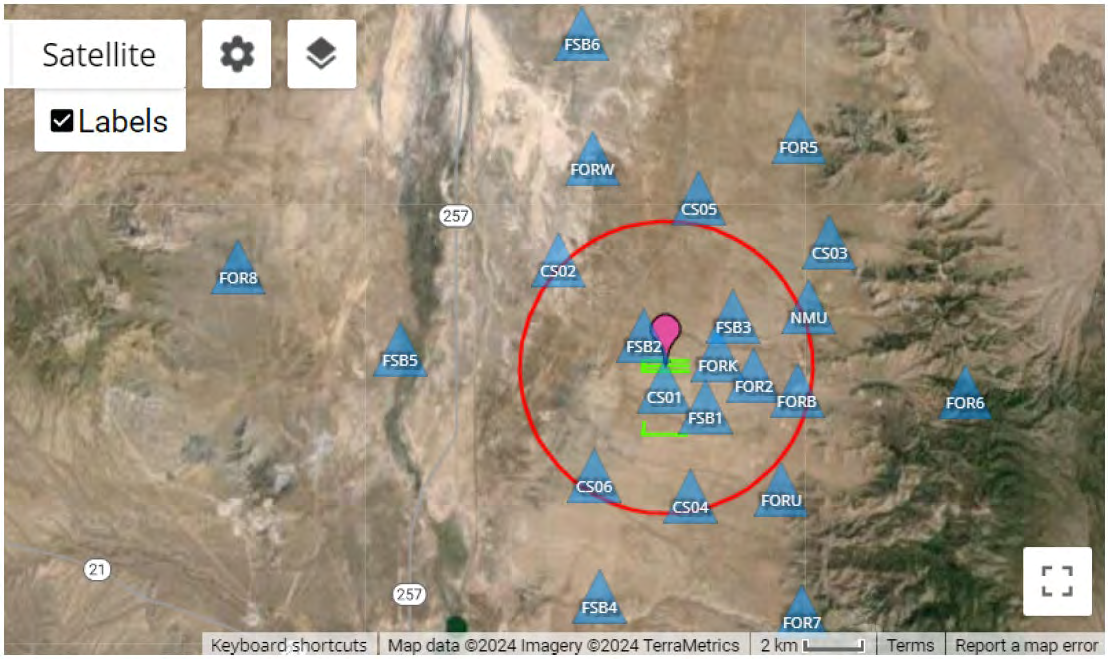

Figure 5: Location of the Shallow Borehole array around the Cape Modern area. The green lines are the drilled Fervo horizontal wells. The red circle shows the 5 km buffer area where the Traffic Light System is active.

3.2 Deep Borehole Fiber Optic DAS and 3C geophones

Two permanent fiber optic cables, installed behind the casing in the Delano 1-OB and 16B wells (shown in red in Figure 3), are used to detect microseismic events. Additionally, a passive 3C

sensor is located in the 56-32 FORGE well (not shown here). During the stimulation of Frisco 1-I, a temporary wireline fiber was deployed in the horizontal Frisco 2-P well. Similarly, a temporary disposable fiber was deployed in the Frisco 3-I well. However, the deployment in Frisco 3-I achieved only partial success because the bare disposable fiber was not rated for the high temperatures encountered in the well.

4. Operations summary

Out of the four wells drilled at the Frisco site, three—Frisco 1-I, Frisco 2-P, and Frisco 3-I—were stimulated. Each well was stimulated with 27 stages, except for Frisco 2-P, which was stimulated with 28 stages using a plug-and-perf technique. The stimulation was conducted in two phases. The first phase, carried out in February/March 2024, involved the stimulation of all 27 stages of Frisco 1-I, all 27 stages of Frisco 3-I, and 2 stages of Frisco 2-P. Due to operational issues beyond the scope of this paper, the remaining 26 stages of Frisco 2-P were stimulated in June 2024. Notably, stages 10 and 11 of Frisco 3-I and stages 2 and 3 of Frisco 2-P were stimulated using a zipper frac style.

In addition to the stimulations at the Frisco well pad, the Utah FORGE project conducted additional stimulation activities in March/April 2024. The shallow borehole array used for monitoring the regional area was able to detect the microseismic events corresponding to the Utah FORGE stimulations, providing a comprehensive view of the seismic activity in the region.

5. Observations

5.1 Seismic monitoring

5.1.1 UUSS/USGS monitoring:

The Shallow Borehole Network includes stations from both the University of Utah Seismograph Stations (UUSS) and those installed by Fervo/LBNL. UUSS oversees seismic monitoring at the FORGE site and given that Fervo's operations are within a 3 km buffer radius of FORGE, they also monitor seismic activity related to Fervo's operations. All raw waveforms from both UUSS stations and the Fervo/LBNL stations (designated with the 6K* station code) are accessible for download from the IRIS Data Management Center (DMC). UUSS event locations are archived and searchable through the USGS ComCat. Fervo conducts its own real-time seismic monitoring, utilizing both UUSS stations and six additional stations that enhance the UUSS network.
Figure 6 provides a comparison of seismic activity with magnitudes greater than 2 near the Cape Station against seismicity across the Lower 48 states since the beginning of 2024, while Figure 7 presents a similar comparison focused on the state of Utah. All events in this figure were located by UUSS. There have been ten events with magnitudes greater than 2 recorded at the Cape Station in the USGS catalog, with the largest event registering a local magnitude of 2.3. For context, between the start of 2024 and August 26th, when this paper was submitted, there have been 4,952 earthquakes with magnitudes greater than 2 across the Lower 48 states.
Out of all the events shown, UUSS/USGS generated one ShakeMap, as illustrated in Figure 8. The peak ground acceleration (PGA) value for this event in Milford, Utah, was approximately 0.05% g, which is below the commonly accepted lower limit felt threshold of 0.1% g (Richter, 1958).

Fervo proactively engaged with the communities in Milford and Beaver during and after the stimulation activities, and no felt reports were received from these towns.

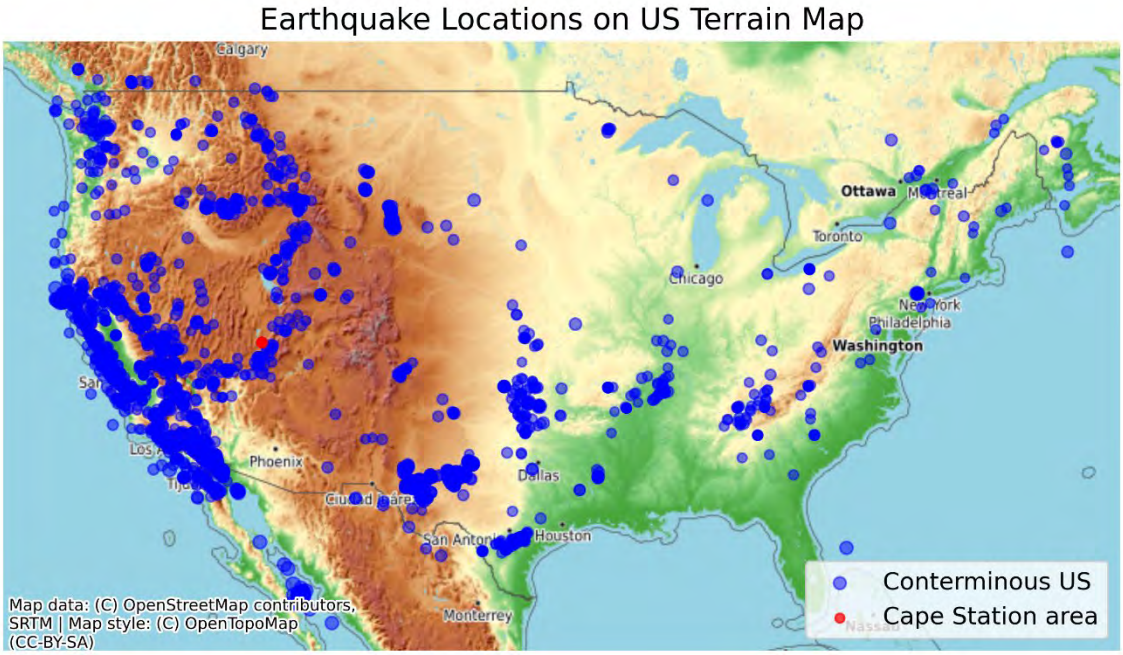

(a)

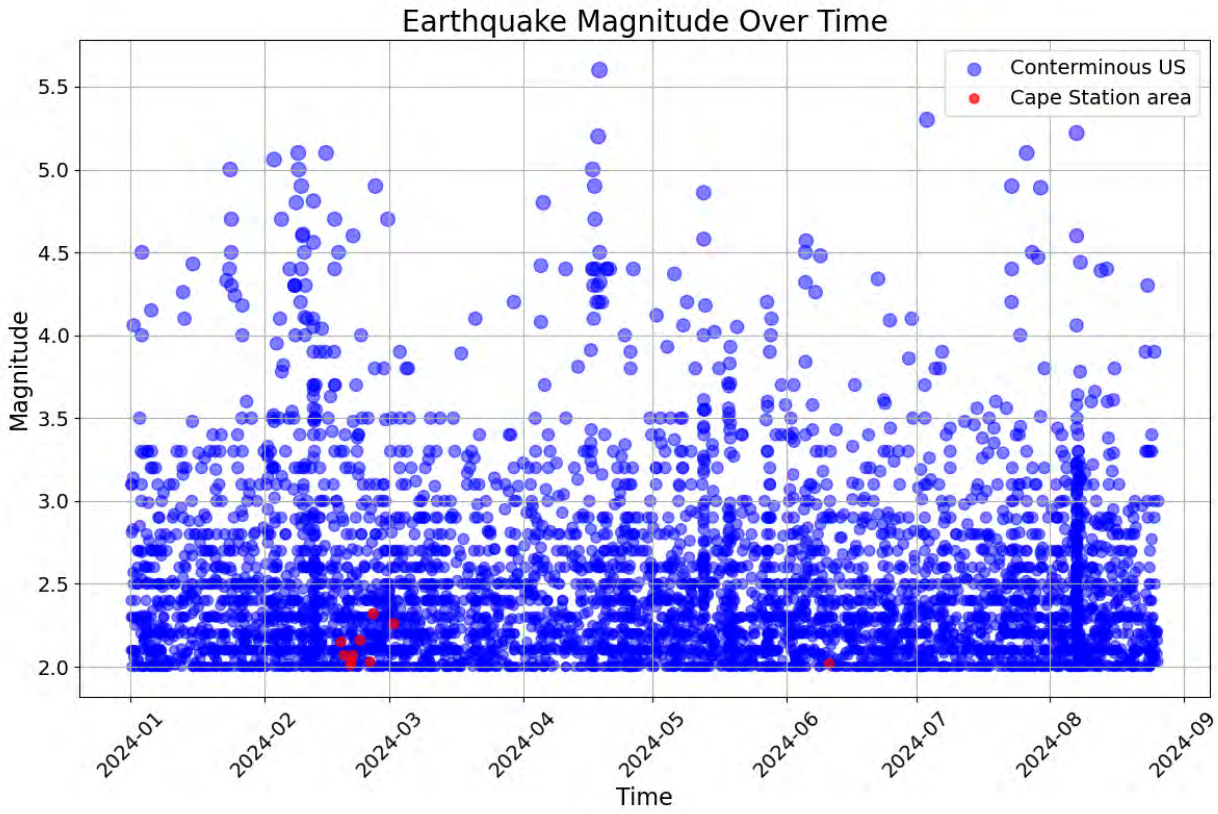

(b)

Figure 6: (a) Map showing the locations of all earthquakes with magnitudes greater than 2 across the Conterminous United States, as retrieved from the USGS ComCat database. (b) Magnitude versus time plot for these earthquakes, with red dots representing earthquakes near the Cape Station and blue dots indicating earthquakes in other parts of the US. The duration of the extracted catalog is from the beginning of 2024 to August 26th 2024.

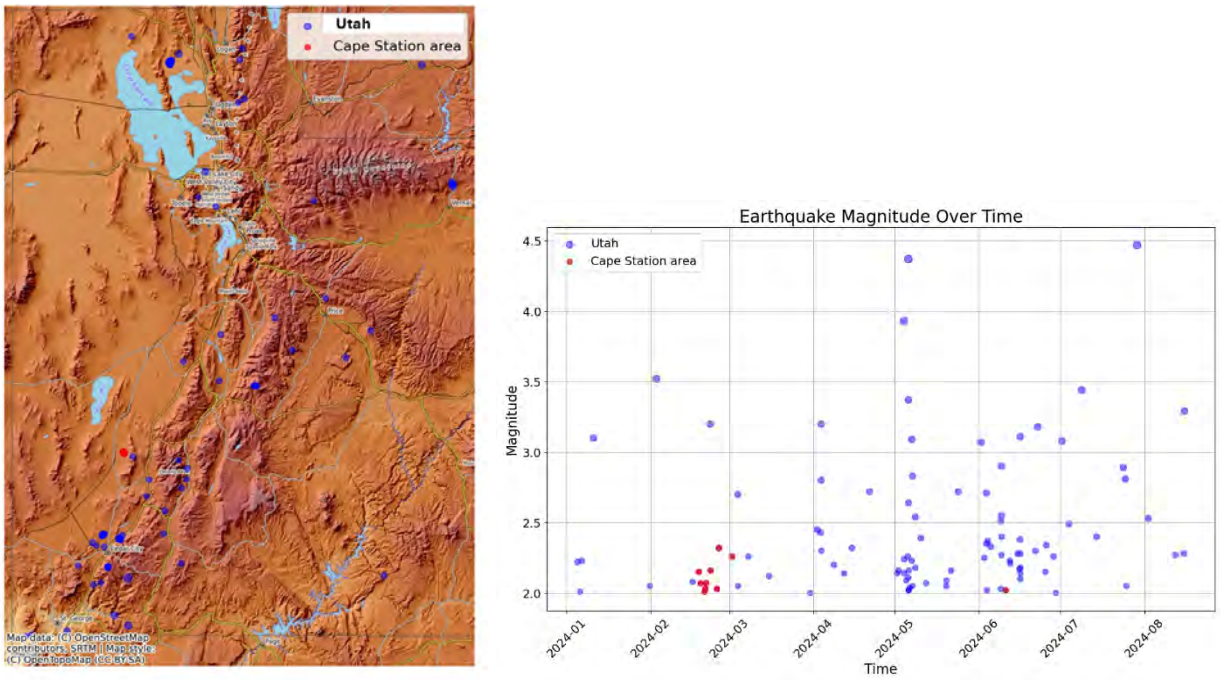

(a) (b)

Figure 7: (a) Map showing the locations of all earthquakes with magnitudes greater than 2 across the state of Utah, as retrieved from the USGS ComCat database. (b) Magnitude versus time plot for these earthquakes, with red dots representing earthquakes near the Cape Station and blue dots indicating earthquakes in Utah. The duration of the extracted catalog is from the beginning of 2024 to August 26th, 2024.

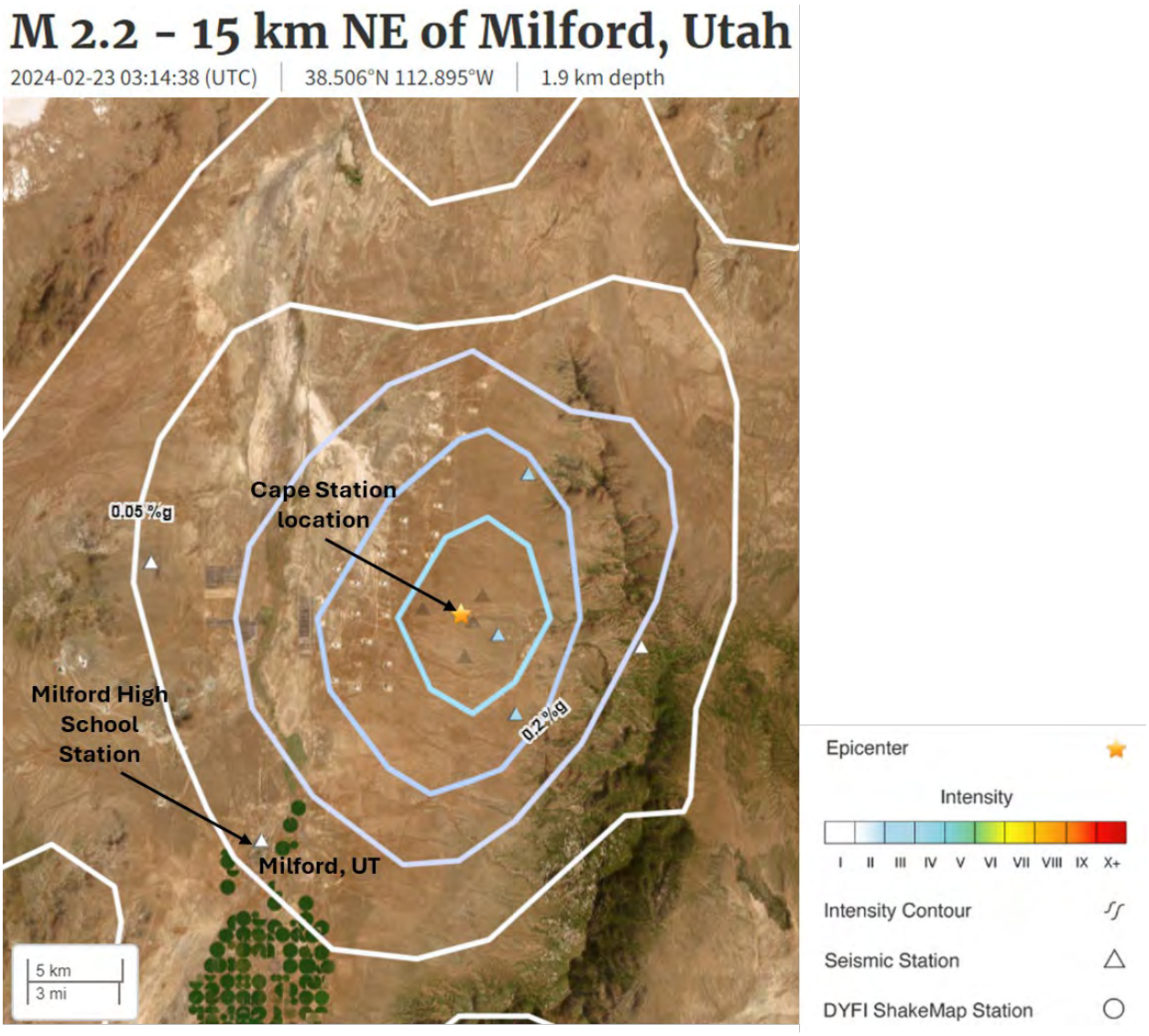

Figure 8: Map showing the location and intensity contours of a magnitude 2.2 earthquake that occurred 15 km northeast of Milford, Utah, on February 23, 2024, at 03:14:38 UTC. The earthquake's epicenter is marked by a star, with surrounding intensity contours illustrating varying levels of ground shaking. The Cape Station and Milford High School seismic stations are indicated on the map, with intensity values recorded at different distances from the epicenter (USGS event ID uu80046841).

5.1.2 Fervo seismic monitoring

Fervo's real-time seismic monitoring is conducted with the assistance of a vendor, resulting in differences in the number of detected events and their estimated magnitudes compared to UUSS monitoring. Fervo's detection thresholds are intentionally set lower to capture smaller magnitude events during drilling activities. For the purposes of this paper, it is important to note that Fervo's magnitude estimates are calculated using slightly different parameters, leading to variations in reported magnitudes. It is well understood that magnitudes of smaller earthquakes can vary depending on the method used for estimation. Through personal communication with UUSS

personnel and a comparison of the methodologies used in the UUSS and Fervo catalogs, several key differences were identified:

1. **Magnitude Estimation Method:** UUSS estimates duration-based magnitudes (Md) for smaller events, typically those below magnitude 1, and uses local magnitudes (Ml) for events greater than magnitude 1. In contrast, Fervo consistently reports local magnitudes for all events.

2. **Calculation Differences:** UUSS calculates local magnitudes following the methodology detailed in Pechmann et al. (2007, BSSA, 97, 557-574), whereas Fervo uses the equation from Hutton and Boore (1987, BSSA, 77, 2074-2094).

3. **Instrument Response Differences:** Differences in the damping constant and static magnification (gain) in the Wood-Anderson frequency response also contribute to variations in magnitude estimates between the two catalogs.

These points highlight some of the reasons for the observed differences, though this is not an exhaustive list. Since the beginning of 2024, the Fervo catalog has recorded seven earthquakes with magnitudes greater than two near the Cape Station area. Of these, five coincided with Fervo's stimulation and injection activities, while two occurred during FORGE injection operations. The two largest events in the Fervo catalog were recorded with local magnitudes of 2.67 and 2.51. Table. 1 shows the PGV and PGA values for the five greater than 2 magnitude earthquakes during Fervo operations. Based on the PGA/PGV thresholds established in the literature, none of the events with magnitudes ranging from 2.09 to 2.65 recorded at the UU.MHS2 station would be felt at the nearest town, Milford, UT. The peak ground accelerations (PGA) are well below the 0.3% g threshold, and the peak ground velocities (PGV) are significantly lower than the 0.1 cm/s felt threshold. Consequently, these events are unlikely to have been perceptible to people in the vicinity (Richter, 1958; Siskind et al., 1980; Worden et al., 2012).

Table 1: Ground motion parameters for seismic events with magnitude greater than two during Fervo operations recorded near the Cape Station. Each table presents peak ground acceleration (PGA) and peak ground velocity (PGV) values across three channels (ENE, ENN, and ENZ) from UUSS station UU.MHS2. The MHS2 station is located at Milford High School in the nearest town to Cape Station.

M_L = 2.65

Channel	Intensity	PGA (cm/s²)	PGV (cm/s)
UU.MHS2.01.ENE	I	0.1596	0.0054
UU.MHS2.01.ENN	I	0.1353	0.0044
UU.MHS2.01.ENZ	I	0.1806	0.0041

M_L = 2.17

Channel	Intensity	PGA (cm/s²)	PGV (cm/s)
UU.MHS2.01.ENE	I	0.2012	0.0034
UU.MHS2.01.ENN	I	0.1195	0.0019
UU.MHS2.01.ENZ	I	0.1290	0.0022

M_L = 2.51

Channel	Intensity	PGA (cm/s²)	PGV (cm/s)
UU.MHS2.01.ENE	I	0.3859	0.0058
UU.MHS2.01.ENN	I	0.2183	0.0034
UU.MHS2.01.ENZ	I	0.1858	0.0047

M_L = 2.12

Channel	Intensity	PGA (cm/s²)	PGV (cm/s)
UU.MHS2.01.ENE	I	0.1403	0.0036
UU.MHS2.01.ENN	I	0.0920	0.0019
UU.MHS2.01.ENZ	I	0.1382	0.0026

M_L = 2.09

Channel	Intensity	PGA (cm/s²)	PGV (cm/s)
UU.MHS2.01.ENE	I	0.1262	0.0019
UU.MHS2.01.ENN	I	0.1262	0.0021
UU.MHS2.01.ENZ	I	0.2791	0.0024

Fervo employs a predefined Traffic Light System (TLS) to manage induced seismicity, with a green threshold set at magnitude 2 and a red threshold at magnitude 3. This detailed TLS protocol is designed to ensure prompt and effective response to seismic events and a detailed description of

the TLS is included here. Among the five events with magnitudes greater than 2, three occurred during active injection, triggering the TLS and resulting in immediate operational adjustments to mitigate seismic risks. The remaining two events occurred after injection activities had ceased, leading to a suspension of operations in accordance with the TLS guidelines until the required pause period was satisfied. This approach underscores Fervo's commitment to proactive and adaptive management of induced seismicity.

5.2 Seismicity rate analysis with pressure and injection volumes

Prior to the stimulation at the Frisco Pad, the seismicity in the area primarily concentrated near the Blundell Geothermal plant bounded by the Opal Mound fault to the east and the Mag Lee fault to the north. From 2020, there seem to be periods of high- and low-density seismicity which could be due to the occurrence of natural seismicity in the area or some of the stations are occasionally dysfunctional. Based on the seismicity identified on the surface/borehole stations there is no elevated seismicity during the three stage stimulation at 16A(78)-32 in April 2022.

The stimulation of the Frisco 1-I produced significant microseismic activity above the background seismicity level clearly demonstrating the microseismic is due to the stimulation operations (Figure 9). During the stimulation when there is pause in operations as shown by the constant cumulative injection rate (black curve in Figure 10a) there is steep decline in seismicity in a few hours. The pressure gauge at the reservoir level measured reservoir pressure during the stimulation. There is spike in the pressure when the stimulation in Frisco 1-I is nearest to the Delano 1-OB well and the pressure decreases as the stimulation progressed to the heel stages (as shown in the green curve in Figure 10a). A similar but larger spike is observed during the stimulation of the Frisco 3-I stimulation. The larger spike is due to the proximity of the Delano 1-OB observation well to Frisco 3-I well compared to the Frisco 1-I well. The total injected volume and the cumulative seismic moment is correlated very well during the Frisco 1-I and 3-I stimulation. The seismicity rate dropped significantly as soon the stimulation was complete as seen by the flat cumulative seismic moment after the stimulation.

A similar increase in seismicity level was noticed during the Frisco 2-P stimulation during June 2024. During the interval between the two stimulation phases, seismicity levels returned to background levels, except during the FORGE stimulation and an injection test in the Frisco 1-I well. The pressure gauge in the Delano 1-OB well generally shows similar behavior as the Frisco 1-I and 3-I stimulation as there is a spike in pressure when the stimulation is closer to the observation well (Figure 11a). However, the pressure started increasing from the beginning of the stimulation of Frisco 2-P. This suggests a high connectivity of the hydraulic network during the Frisco 2-P stimulation. The cumulative seismic moment during the Frisco 2-P stimulation is also well correlated to the injection volumes (Figure 11b). There is a continued increase in cumulative seismic moment after the Frisco 2-P stimulation due to continued pumping operations as soon as the stimulation is complete. The injection rates are not available at the time of submission of this article to include in the cumulative injection curve (pink curve in Figure 11b).

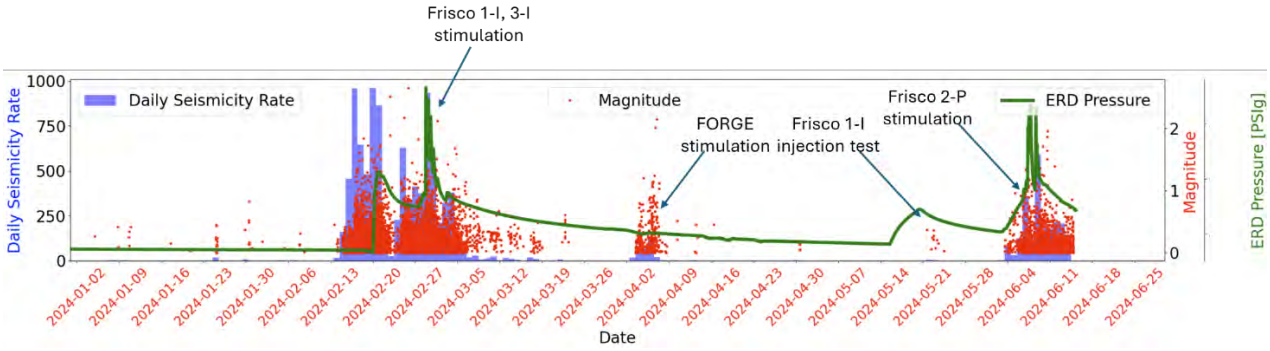

Figure 9: The figure illustrates the seismicity rate as a blue histogram, spanning from the beginning of January until June 15th, 2024. It highlights the time periods during which the Frisco stimulations occurred. The green curve represents the downholegauge pressure at the reservoir level outside the casing on the Delano 1-OB well. For confidentiality reasons, the actual pressure values have been masked. This visualization aims to correlate seismic activity with reservoir pressure changes and stimulation events over the specified timeframe.

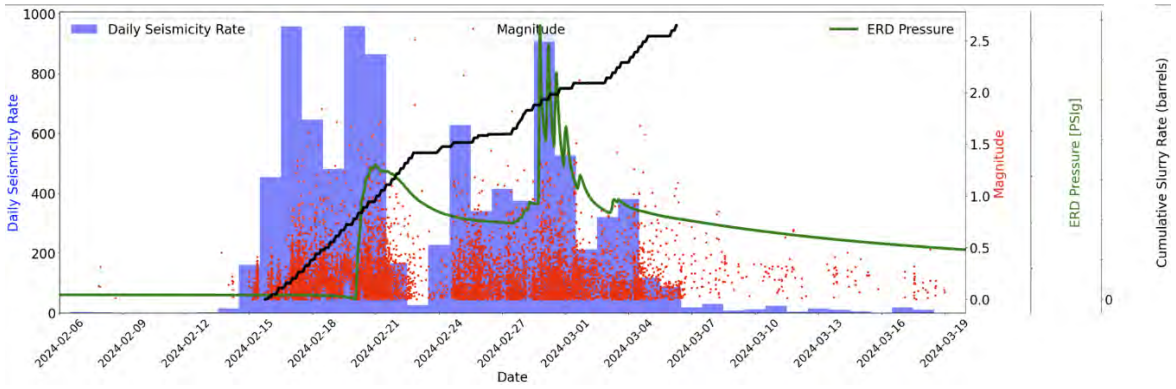

(a)

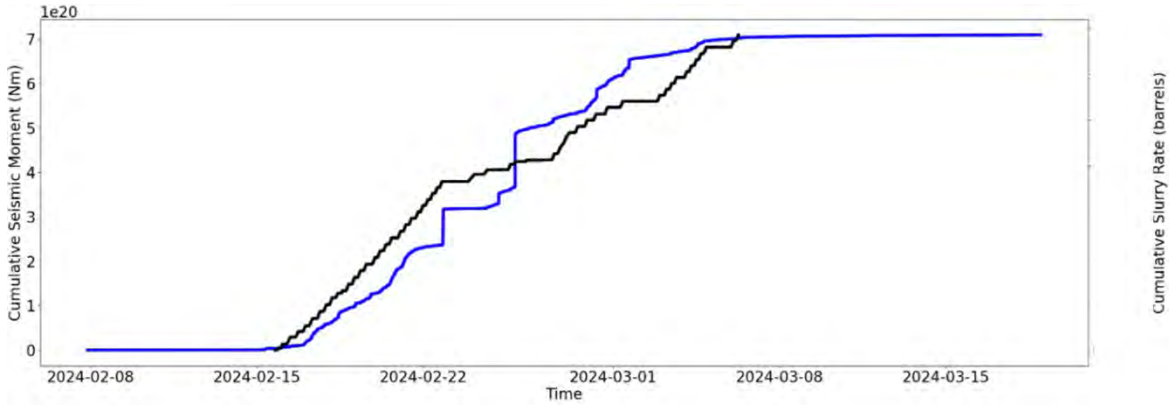

(b)

Figure 10: (a) Figure displays the seismicity rate and downhole pressure data, along with the magnitudes of the seismic events during the stimulation of Frisco 1-I and Frisco 3-I wells. The black curve represents the cumulative injection rate. This detailed view allows for a closer examination of the relationship between seismicity, reservoir pressure, and injection activities during the stimulation periods. (b) This plot shows the cumulative injection rate against the cumulative seismic moment released from all seismic events during the stimulation of Frisco 1-I and Frisco 3-I wells.

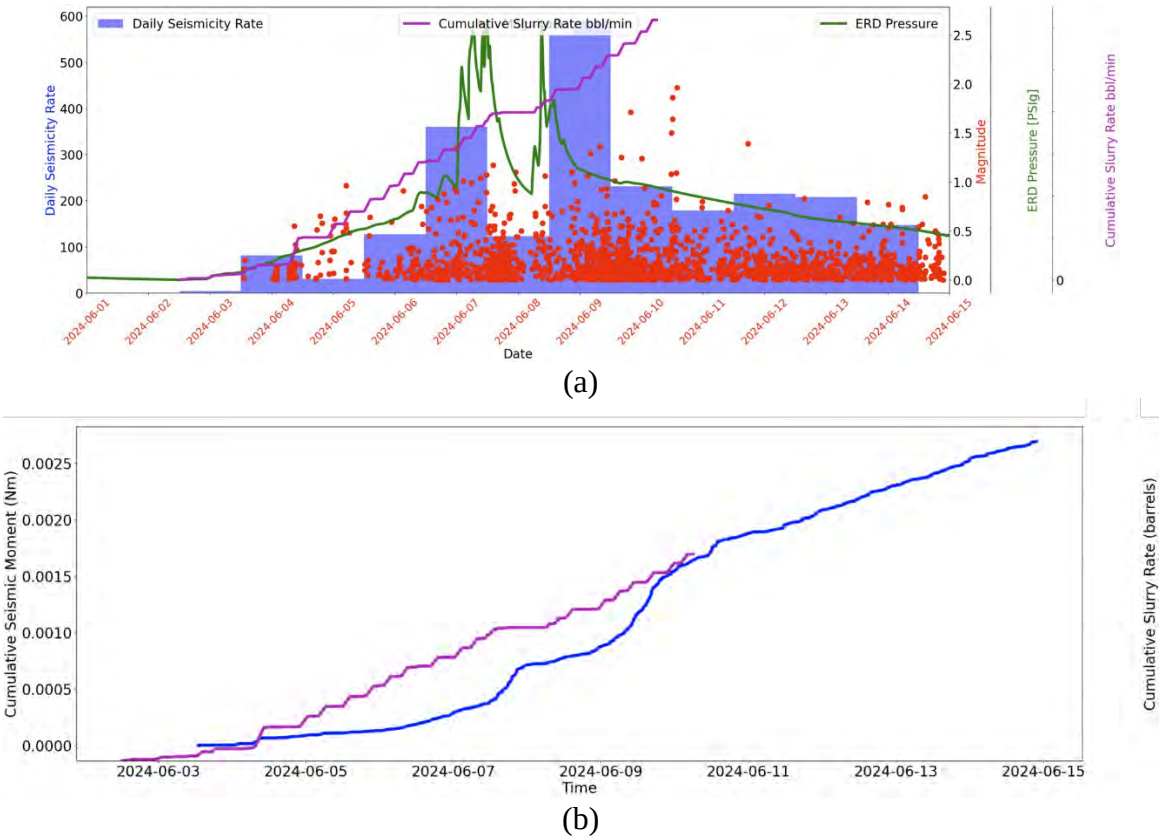

Figure 11: (a) Figure displays the seismicity rate and downhole pressure data, along with the magnitudes of the seismic events during the stimulation of Frisco 2-P. The black curve represents the cumulative injection rate. This detailed view allows for a closer examination of the relationship between seismicity, reservoir pressure, and injection activities during the stimulation periods. (b) This plot shows the cumulative injection rate against the cumulative seismic moment released from all seismic events during the stimulation of Frisco 2-P.

The seismic analysis of the Frisco 1-I and 3-I stimulation phases shows a higher number of events with magnitudes greater than one and two compared to the Frisco 2-P stimulation and post-stimulation phases, with 125 and 26 events exceeding magnitude 1, respectively (Table 2). The magnitude-frequency distributions reveal a b-value of 1.509 for Frisco 1-I and 3-I, indicating a relatively higher frequency of smaller events, while the b-value for Frisco 2-P and post-stimulation is slightly higher at 1.787, suggesting a steeper decay in event frequency (Figure 12). The **b-value** is a parameter from the Gutenberg-Richter law, which describes the relationship between earthquake frequency and magnitude in a given region. A higher b-value indicates that smaller magnitude events are relatively more frequent than larger ones, while a lower b-value suggests a flatter distribution with a higher proportion of larger events. Both b-values during the two stimulation phases are higher than the typical tectonic b-value of 1, indicating that induced seismicity from the stimulation phases results in a greater proportion of smaller earthquakes. These findings imply that the stimulation activities are associated with seismicity characterized by a higher occurrence of smaller events compared to natural tectonic processes.

Table 2: Seismic activity summary for the Frisco 1-I and 3-I stimulation phases compared to the Frisco 2-P stimulation and post-stimulation phases.

	Frisco 1-I and 3-I stim	Frisco 2-P stim and Post Stim
No of Events with Mag > 1	125	26
No of Events with Mag > 2	5	None
No of Events with Mag > 3	None	None
No of Events felt in nearest towns	None	None
Total No of Events	29967	19579
Mc	-0.162	-0.3
b-value	1.509	1.7
Mmax	2.67	1.88

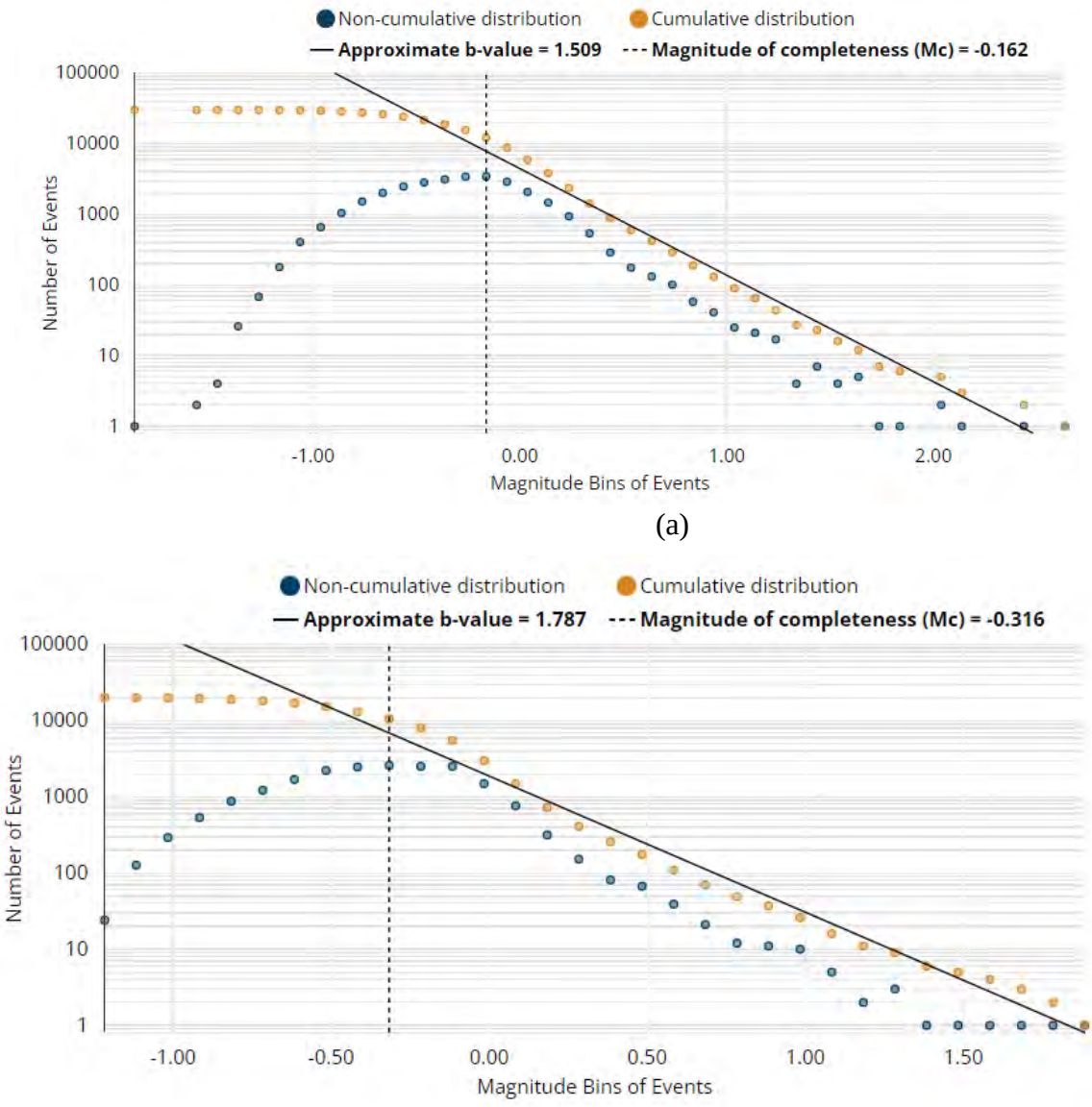

Figure 12: (a) Magnitude-frequency distribution for seismic events during the Frisco 1-I and 3-I stimulation phases, showing both non-cumulative (blue dots) and cumulative (orange dots) distributions. (b) Magnitude-frequency distribution for seismic events during the Frisco 2-P stimulation and post-stimulation phases, also showing both non-cumulative and cumulative distributions.

5.3 Microseismic catalogs

A 3D velocity model was constructed using all available Sonic logs from Utah FORGE wells and Fervo wells, including Delano 1-OB, Frisco 1-I, along with the top of the basement from 3D seismic and gravity data (Figure 13). A constant basement velocity of 5649.1 m/sec was estimated based on the hypocentral distance versus travel time (pick time minus event origin time) plot shown in Figure 14.

Figure 15 compares the microseismic activity during the stimulation of all three Frisco wells using data from the shallow borehole array and deep borehole DAS and 3C geophone data. Both datasets reveal linear features oriented either N-S or 10°-15° NNW-SSE, which is not aligned with the SHmax orientation shown in Figure 4. The likely reason for this is that the linear features represent existing natural fractures and faults, which are reactivated because they are optimally oriented for failure under the SHmax orientation, as determined from the image logs. While the number of detected events is significantly larger with the deep borehole array-based locations, the general geometry and extent of the features are similar in both datasets.

To better understand the hydraulic behavior of one of the fault features (Figure 15b), the microseismic cloud associated with that specific fault was isolated, and a microseismic diffusion analysis was conducted. The hydraulic diffusivity was estimated by modeling the migration of the triggering front of microseismic events (MEQ) using a diffusion model. The relationship $r=\sqrt{4\pi D\Delta t}$, where r is the distance from the wellbore, D is the hydraulic diffusivity, and Δt is the time since fluid injection, was applied to the data. Different values of D were fitted to the observed microseismic event data to capture the best-fit diffusivity, with the resulting curves compared against the actual event distribution to estimate the hydraulic properties of the fault zone. The data points and the model curves were plotted to visualize how varying diffusivity values influence the spread of seismicity over time. The estimated hydraulic diffusivity for the fault feature in this study of 0.1 - 0.15 m^2/s (Figure 16) is significantly higher than values reported from other experiments, such as the EGS Collab, where a diffusivity of D=0.008 m^2/s was fitted across different stimulation episodes (Yu et al., 2024). In contrast, the hydraulic diffusivity estimated during the third stage of the FORGE stimulation in April 2022 ranges between D = 0.15 - 0.2 m^2/s, suggesting a much more permeable fault zone at the FORGE site (Yu et al., 2024). This indicates that the hydraulic properties at the FORGE site and at Cape Station are more conducive to fluid flow, likely leading to a more rapid propagation of the seismic triggering front compared to the EGS Collab site.

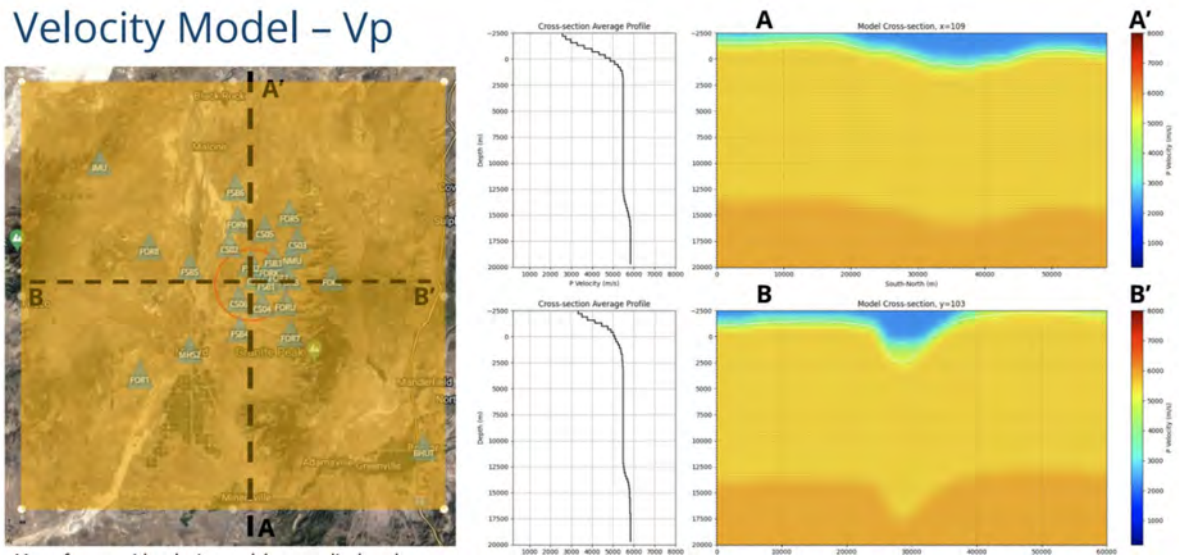

Figure 13: (a) Map of array with velocity model extent displayed as orange box. Cross-sections shown to the right are highlighted as black dashed line. (b) Vp cross-sections: Right image shows velocity variation across the section, left plot displays cross-section average profile.

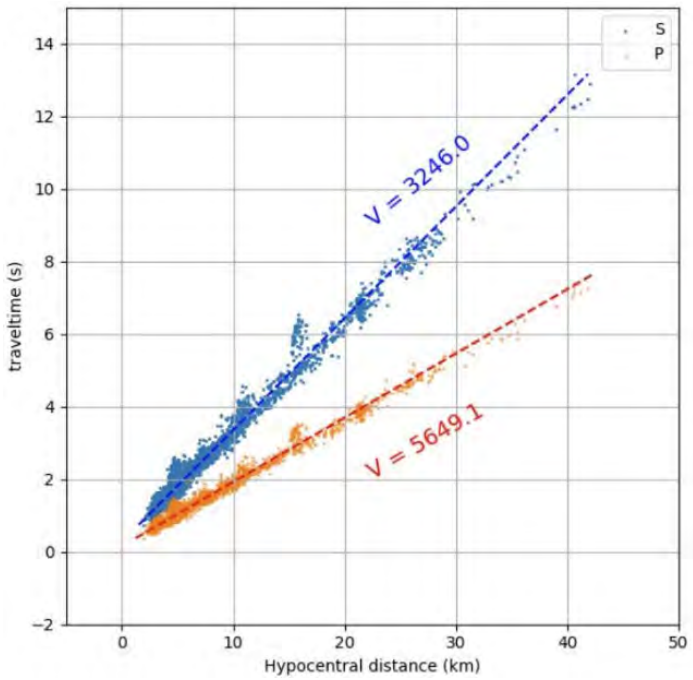

Figure 14: Plot for traveltime (pick time minus event origin time) vs hypocentral distance per phase per event per station, dashed lines are the fitted lines with estimated Vp and Vs velocity values.

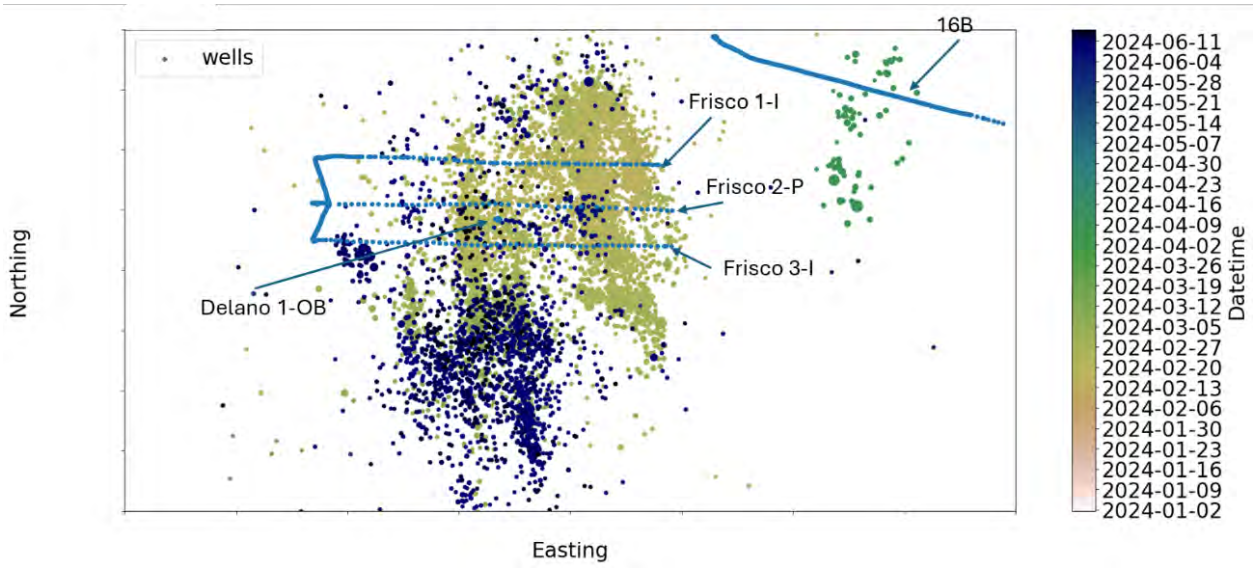

(a)

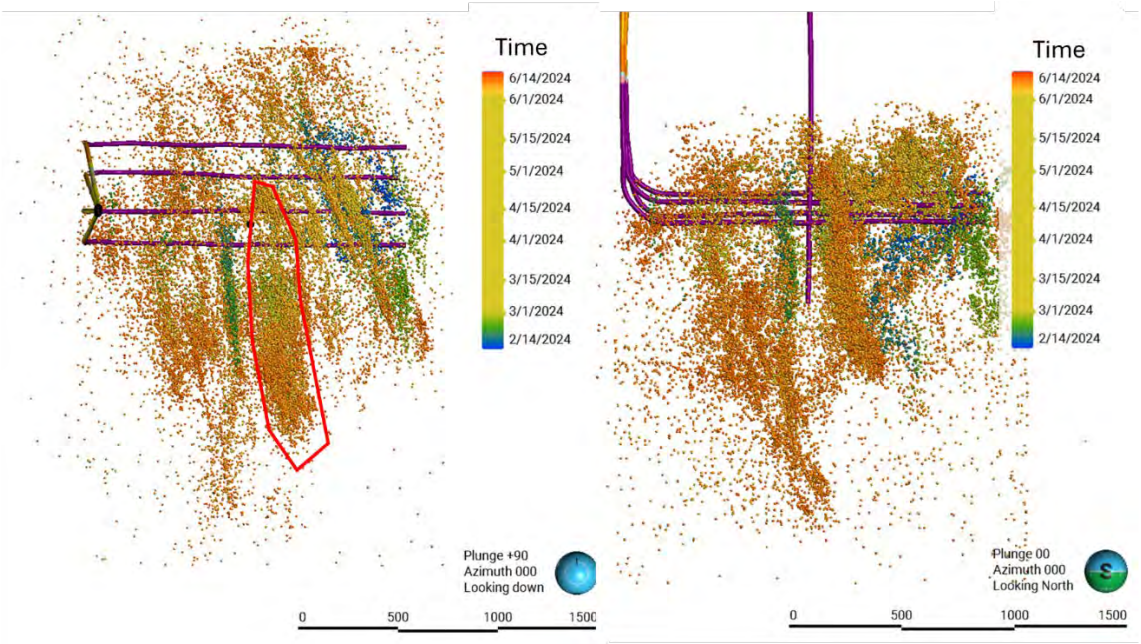

(b)

Figure 15: (a) Microseismic catalog during the Frisco 1-I, 2-P and 3-I stimulation based on the Shallow Borehole array data. (b) Microseismic catalog during the Frisco 1-I, 2-P and 3-I stimulation based on the deep borehole fiber optic DAS and 3C sensors in the 56-32 well. The figure on the left is the map view and the figure to the right is the cross-section depth view of the microseismic. The red polygon in Figure YY indicates the reactivated fault feature where the hydraulic diffusivity is estimated during Frisco 1-I ad 3-I stimulation.

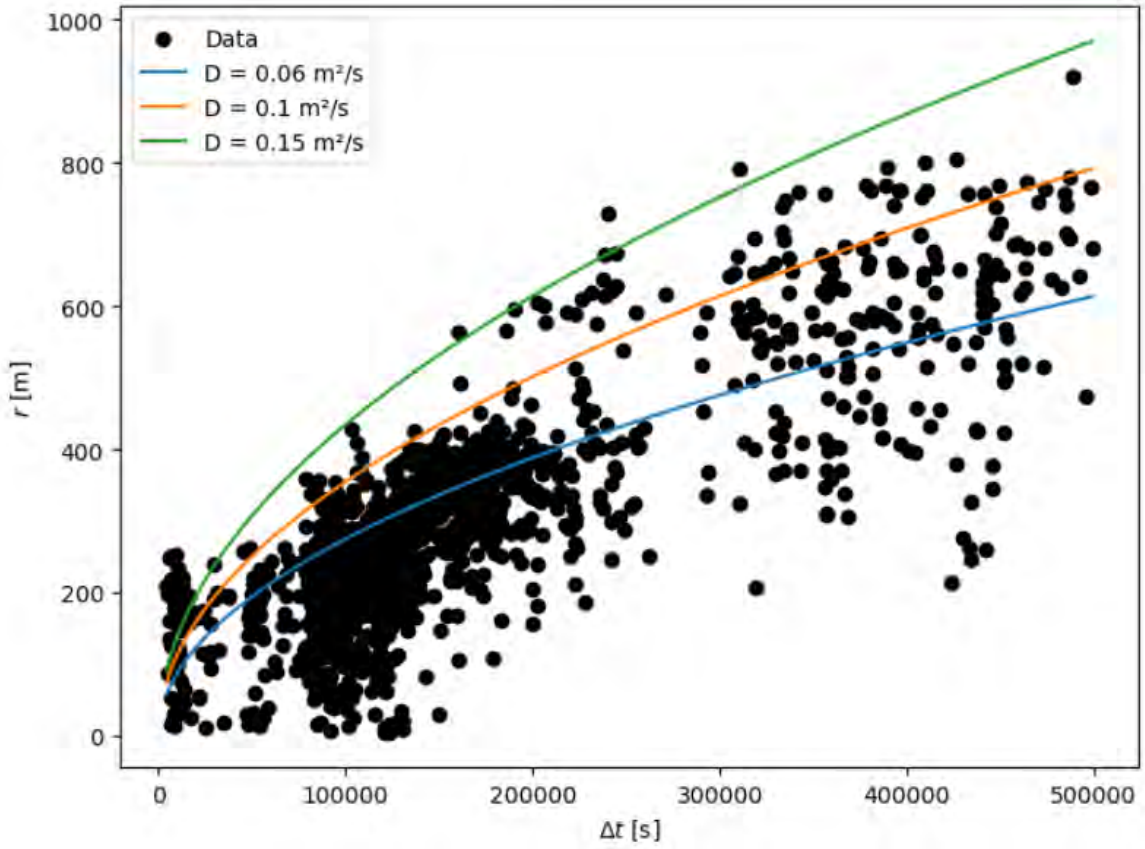

Figure 16: Plot showing the relationship between the distance r in meters of microseismic events from the wellbore and the time elapsed since the initiation of fluid injection (Δt) near the fault of interest. The red polygon in Figure 10 indicates the reactivated fault feature where the hydraulic diffusivity is estimated. The black dots represent the observed microseismic event data. The colored curves represent the modeled distances for different values of hydraulic diffusivity D within the fault: D=0.06 m^2/s (blue), D=0.1 m^2/s (orange), and D=0.15 m^2/s (green). The plot illustrates how different diffusivity values influence the spread of seismicity over time, aiding in the estimation of hydraulic properties of the fault zone.

5.4 Focal mechanism analysis

In addition to the shallow borehole network and deep borehole measurements, a surface nodal array has been deployed around the Frisco Pad area, actively recording data since February 2024. Further details on the nodal array's geometry and acquisition setup can be found in Nori et al., 2024.

This paper includes the focal mechanisms of seismic events from the Frisco 1-I and 3-I stimulation phases in February and March 2024. To predict P and S wave arrival times and phase polarity, we utilized the EQNet model (https://github.com/AI4EPS/EQNet), an advanced version of PhasNet (Zhu and Beroza., 2019). In our analysis, we selected only those picks where the P phase score was 0.8 or higher to ensure the reliability of our focal mechanism estimations. To improve the accuracy of S-wave amplitude estimation, we rotated the three-component signals—originally in the vertical, north, and east directions—into vertical, radial, and transverse components based on

the event-station azimuth. We then estimated the P-wave amplitude on the vertical (Z) component and the S-wave amplitude on the transverse (T) component. Following these processing steps, we generated a refined database of 1,719 events.

For the focal mechanism inversion, we employed the SKHASH Python package (Skoumal., 2024), a modernized version of the widely used HASH package originally developed in Fortran over two decades ago. SKHASH leverages recent advancements to better constrain focal mechanisms for small-magnitude or poorly recorded earthquakes. In our workflow, we varied the 3D earthquake locations and velocity models to identify acceptable solutions. As input for the focal mechanism solutions, we used P-wave first-motion polarity and enhanced the constraints by incorporating S/P wave amplitude ratios. Additionally, we included horizontal and vertical location uncertainties in the inversion process to minimize errors related to event location.

Using the aforementioned technique, focal mechanism solutions were successfully derived for 1,719 events, with 1,564 of these classified as A and B quality, indicating solutions with low uncertainty (Figure 17a). To classify the faulting regimes and determine the maximum horizontal stress (Shmax) for each event, the methodology described by Zoback (1992) was applied. This approach enabled the events to be categorized into distinct faulting regimes, including strike-slip (SS), normal faulting (NF), and thrust faulting (TF) (Figures 17b, 18 and 19). Additionally, hybrid regimes were identified, such as transtension (NS), which combines features of NF and SS, and transpression (TS), which combines features of TF and SS, consistent with the classifications proposed by Zoback (1992). The dominant faulting mechanism for the study area is strike-slip with more reverse faulting patterns in the East and North sections, which can be normal faults that reactivate as reverse faults.

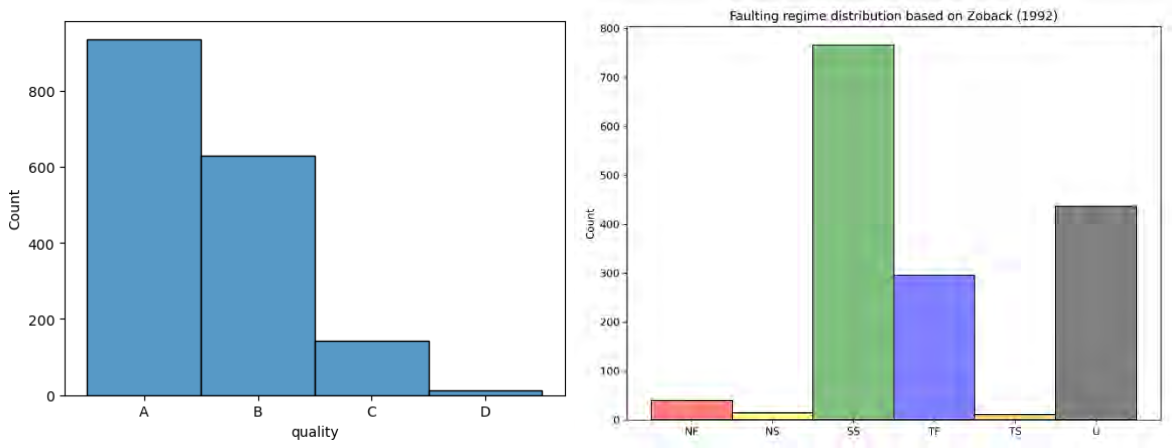

(a) (b)

Figure 17: (a) Distribution of the SKHASH focal mechanism solutions by quality, with classifications ranging from A to D, indicating varying levels of uncertainty. (b) Faulting regime distribution based on the criteria outlined by Zoback (1992), categorizing events into normal faulting (NF), strike-slip (SS), thrust faulting (TF), transtension (NS), transpression (TS), and undefined (U) regimes.

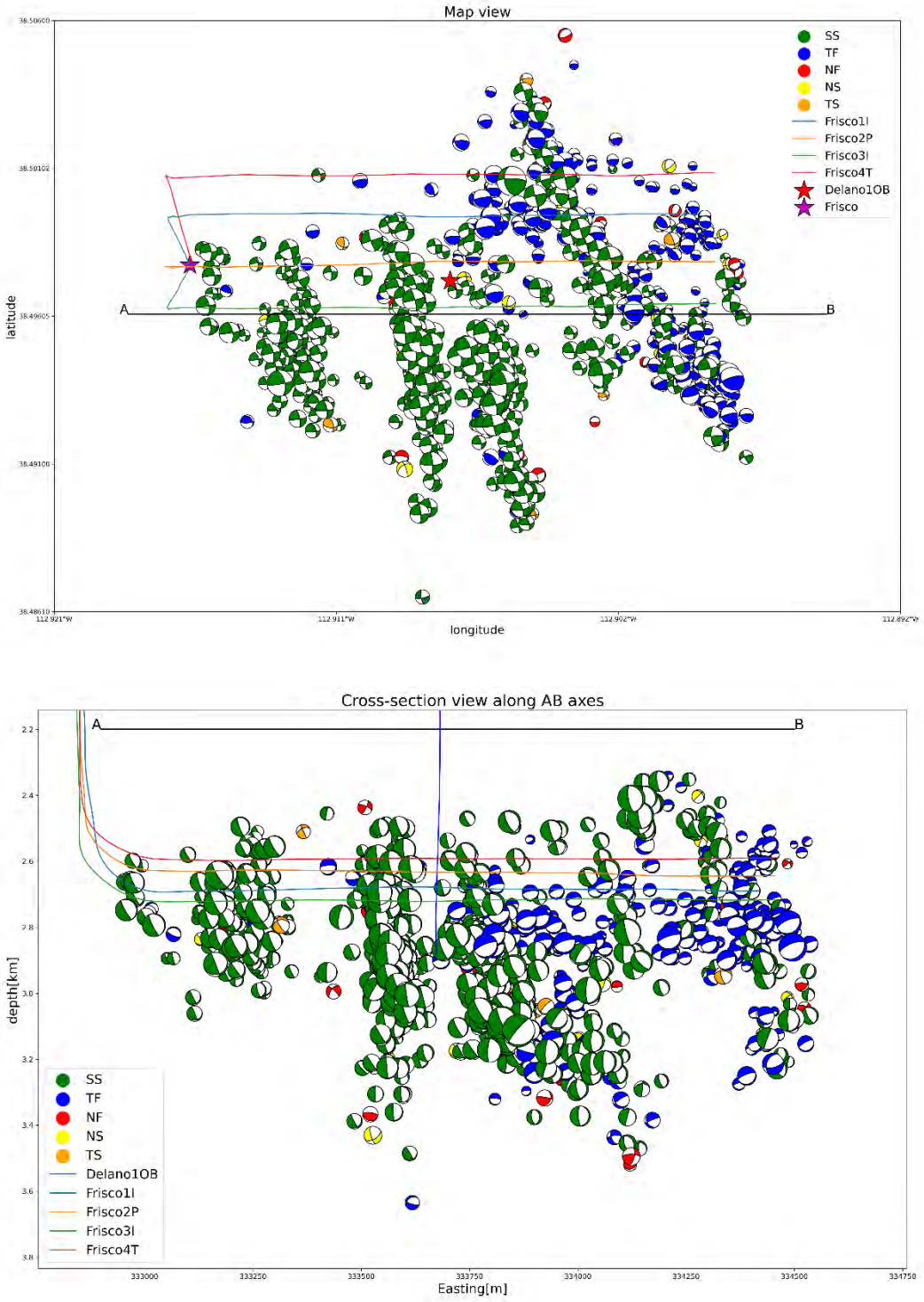

Figure 18: Top view (above) and cross-section view along the AB axes (below) of the study area, showing the distribution of focal mechanisms for the seismic events categorized by faulting regimes, including strike-slip (SS), thrust faulting (TF), normal faulting (NF), transtension (NS), and transpression (TS). The map also highlights the location of various wells, including Frisco 1-I, Frisco 2-P, Frisco 3-I, and Frisco 4-T, as well as the Delano 1-OB well.

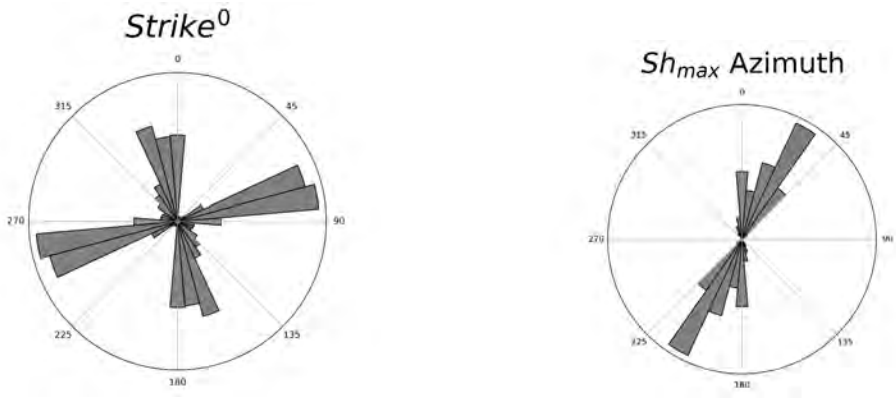

(a) (b)

Figure 19: (a) Rose diagrams showing the distribution of nodal plane strike angles (top) and (b) the orientation of maximum horizontal stress (Shmax) azimuths (bottom) for the seismic events analyzed. These diagrams provide insights into the dominant faulting directions and the stress field orientation within the study area.

6. Conclusion

The Cape Modern project represents a significant advancement in the development of Enhanced Geothermal Systems (EGS), particularly in the application of comprehensive microseismic monitoring and real-time management strategies. The project involved the stimulation of three horizontal wells using a plug-and-perf completion design, a technique adapted from the unconventional oil and gas industry, which proved effective in creating hydraulic connectivity within the reservoir. The microseismic data revealed a trend of increasing seismicity correlating with the volume of fluid injected during stimulation. The real-time monitoring system provided reliable updates that were instrumental in making timely operational adjustments. When seismic events with magnitudes of 2.0 or greater were detected, these real-time data allowed for immediate activation of the Traffic Light System (TLS), leading to pauses in injection and other mitigation strategies to control seismicity. Additionally, the downhole pressure gauge installed in the monitoring well played a crucial role in managing induced seismicity. A clear relationship between downhole pressure and seismicity was observed, suggesting that pressure monitoring can be effectively used to anticipate and control seismic events. This proactive approach ensured that even as seismicity increased with fluid injection, the safety of operations was maintained, with the largest event recorded at a local magnitude of 2.3, resulting in ground motion levels lower than “felt” threshold near the nearest town. Active community engagement was a key component of the project’s success. Fervo Energy actively engaged with the local community before, during, and after the injection activities, providing clear communication about the induced seismicity protocols in place. This included holding informational sessions and sharing a seismicity education blog that detailed Fervo’s approach to managing induced seismicity. This proactive engagement helped build trust and understanding within the community, ensuring that residents were informed and reassured about the safety measures implemented throughout the project. The successful integration of real-time seismic monitoring, pressure monitoring, adaptive operational strategies, and active community engagement underscores the importance of a holistic approach to managing geothermal operations.

Acknowledgements

The author would like to thank Fervo Energy for allowing us to publish the data and results. This work is partially supported through the LBNL MEQ project by the U.S. Department of Energy, Office of Energy Efficiency and Renewable Energy (EERE), Geothermal Technologies Office, under Award Number DE-AC02–05CH11231 with Lawrence Berkeley National Laboratory. This work is partially supported by the U.S. DOE under grant DE-EE0007080 “Enhanced Geothermal System Concept Testing and Development at the Milford City, Utah FORGE Site”. One of the authors, Ahmad Mohammadi from Texas A&M University, received support through the NSF Geothermal Internship Program.

REFERENCES

Blankenship, D., Gertler, C., Kamaludeen, M., O’Connor, M., & Porse, S. (2024). *Pathways to Commercial Liftoff: Next-Generation Geothermal Power*. U.S. Department of Energy. https://liftoff.energy.gov/next-generation-geothermal-power/

Buijze, L., van Bijsterveldt, L., Cremer, H., Paap, B., Veldkamp, H., Wassing, B.B., Van Wees, J.D., van Yperen, G.C., ter Heege, J.H. and Jaarsma, B., (2019). Review of induced seismicity in geothermal systems worldwide and implications for geothermal systems in the Netherlands. *Netherlands Journal of Geosciences*, *98*, p.e13.

Dadi, S., Norbeck, J., Titov, A., Payeur, T., Machovoe, S., Joern, K., & Chinaemerem, K. (2024). Microseismic Monitoring of a Horizontal EGS System: Case Study and State of the Art. *Proceedings of the 49th Workshop on Geothermal Reservoir Engineering*, Stanford University, Stanford, California, February 12-14, 2024

Deichmann, N., Kraft, T., & Evans, K. F. (2014). Identification of faults activated during the stimulation of the Basel geothermal project from cluster analysis and focal mechanisms of the larger magnitude events. *Geothermics*, *52*, 84-97.

Fercho, S., Matson, G., McConville, E., Rhodes, G., Jordan, R., and Norbeck, J. *"*Geology, Temperature, Geophysics, Stress Orientations, and Natural Fracturing in the Milford Valley, UT Informed by the Drilling Results of the First Horizontal Wells at the Cape Modern Geothermal Project.*"* *Proceedings: 49th Workshop on Geothermal Reservoir Engineering*, Stanford University, Stanford, CA (2024).

Hutton, L. K., & Boore, D. M. (1987). The ML scale in southern California. *Bulletin of the Seismological Society of America*, *77*(6), 2074-2094.

Mossop, A., & Segall, P. (1997). Subsidence at The Geysers geothermal field, N. California from a comparison of GPS and leveling surveys. *Geophysical Research Letters*, *24*(14), 1839-1842.

Nakata, N., S.-M. W., C. Hopp, Y, Jung, L. Luo, H. Lisabeth, E. Sonnenthal, T. Smith, M. Robertson, D. W. Vasco and S. Dadi (2024) Microseismicity observation and characterization at Cape Modern, Utah, *Geothermal Rising Conference, Oct 27-30, 2024, Hawaii, USA*

Norbeck, J. H., & Latimer, T. (2023). Commercial-scale demonstration of a first-of-a-kind enhanced geothermal system. https://eartharxiv.org/repository/object/5704/download/11142/

Pechmann, J. C., Nava, S. J., Terra, F. M., & Bernier, J. C. (2007). Local magnitude determinations for Intermountain Seismic Belt earthquakes from broadband digital data. *Bulletin of the Seismological Society of America*, *97*(2), 557-574.

Richter, C. F., (1958) Elementary Seismology, *W. H. Freeman,* San Francisco.

Rutqvist, J., Dobson, P. F., Garcia, J., Hartline, C., Jeanne, P., Oldenburg, C. M., ... & Walters, M. (2015). The northwest Geysers EGS demonstration project, California: Pre-stimulation modeling and interpretation of the stimulation. *Mathematical Geosciences*, *47*, 3-29.

Segall, P., & Fitzgerald, S. D. (1998). A note on induced stress changes in hydrocarbon and geothermal reservoirs. *Tectonophysics*, *289*(1-3), 117-128.

Siskind, D. E. (1980). Structure response and damage produced by ground vibration from surface mine blasting (Vol. 8507). *US Department of the Interior, Bureau of Mines*.

Skoumal, J., Jeanne, H., and Peter, S., "SKHASH: A Python Package for Computing Earthquake Focal Mechanisms." *Seismological Research Letters 95, no. 4 (2024): 2519-2526.*

Titov, A., Dadi, S., Galban, G., Norbeck, J., Almasoodi, M., Pelton, K., Bowie, C., Haffener, J. and Haustveit, K., (2024). Optimization of Enhanced Geothermal System Operations Using Distributed Fiber Optic Sensing and Offset Pressure Monitoring. In *SPE Hydraulic Fracturing Technology Conference and Exhibition* (p. D021S003R001). SPE.

Worden, C. B., Gerstenberger, M. C., Rhoades, D. A., & Wald, D. J. (2012). Probabilistic relationships between ground-motion parameters and modified Mercalli intensity in California. *Bulletin of the Seismological Society of America*, *102*(1), 204-221.

Yu, P., Mali, A., Velaga, T., Bi, A., Yu, J., Marone, C., ... & Elsworth, D. (2024). Crustal permeability generated through microearthquakes is constrained by seismic moment. *Nature communications*, *15*(1), 2057.

Zoback, M. L., "First-and second-order patterns of stress in the lithosphere: The World Stress Map Project." *Journal of Geophysical Research: Solid Earth 97, no. B8 (1992): 11703-11728.*

Zhu, W., and Beroza, G. "PhaseNet: a deep-neural-network-based seismic arrival-time picking method." *Geophysical Journal International 216, no. 1 (2019): 261-273.*

Geophysical Modeling of a Possible Blind Geothermal System Near Battle Mountain, NV

[1]Tait Earney, [1]Jonathan Glen, [1]Jared Peacock, [2]James Faulds, [1]William Schermerhorn, [1]Grant Rea-Downing, [1]Jacob Anderson, [2]Cary Lindsey, [2]Maria Richards

[1]U.S. Geological Survey, Moffett Field, CA 94035

[2]University of Nevada, Reno, Great Basin Center for Geothermal Energy, Nevada Bureau of Mines and Geology, Reno, NV 89557

Keywords

Geothermal, hydrothermal systems, geophysics, gravity, magnetic, magnetotelluric, 2D modeling, 3D modeling, Argenta Rise, Basin and Range, Nevada

ABSTRACT

The northeastern portion of the Reese River basin in north-central Nevada is the focus of detailed geophysical and geological studies as part of the INGENIOUS project, which aims to identify new, commercially viable hidden geothermal systems in the Great Basin region of the western U.S. This location, herein referred to as Argenta Rise, occupies a broad (~15km wide) left-step between major range-front fault systems along the northwestern edge of the Shoshone Range and Argenta Rim, with numerous ENE-striking intra-basin faults presumably accommodating sinistral-normal oblique slip across the step-over. Four discrete regions have been identified within the study area that have favorable structural settings for hosting a blind hydrothermal system. However, with no definitive or extensive surface manifestations of an active hydrothermal system (e.g., geysers, steam vents, sinter, etc.), detailed geophysical studies are necessary to resolve subsurface geology and structure, and identify zones of enhanced structural complexity that may promote hydrothermal fluid flow. Hence, we collected high-resolution gravity, MT, and rock property data (density, magnetic susceptibility), and analyzed the recently acquired GeoDAWN aeromagnetic data to characterize potential geothermal resources in this region. Using the new geophysical datasets, we jointly modeled gravity and magnetic data along a series of intersecting 2D profiles that integrated information from recent, local-scale fault mapping. Rock property measurements performed on outcrops and hand samples throughout the study area constrained the models. The MT data were used to construct a 3D resistivity model that highlights the location of inferred alteration and fluids in the subsurface. Combined MT and potential field results reveal which structures may be most important for controlling hydrothermal fluid migration, as well as which geologic units may host hydrothermal fluids. Our gravity derived depth to basement surface

coincides well with the base of shallow conductive anomalies, suggesting hydrothermal fluids may be confined to basin fill sediments and volcanics. This work supports our development of 3D geophysical and geologic models that are focused along the western flank of the northern Shoshone Range and aids the process of selecting sites for temperature gradient drilling.

1. Introduction

The northeastern Reese River basin was initially identified for having high geothermal resource potential in the Nevada Play Fairway Analysis (PFA; DeAngelo, 2019; Faulds et al., 2019). Subsequently, this area was chosen for detailed geological and geophysical investigations as part of the Innovative Geothermal Exploration through Novel Investigations Of Undiscovered Systems (INGENIOUS) project (Ayling et al., 2022; Earney et al., 2022; Williams et al., 2022; Earney et al., 2023). Argenta Rise is located approximately 15 km southeast of Battle Mountain, NV, along the western flank of the northern Shoshone Range within the north-central Basin and Range Province (Figure 1). The Beowawe Geysers, an active geothermal area with numerous geysers and sinter deposits is ~15 km further east of Argenta Rise at the southern end of Whirlwind Valley. The Beowawe flash powerplant was established in 1985, and produced 16.7 MW from a roughly 200°C resource (Benoit and Stock, 1993). Although the geothermal resource at this location has degraded over time (Benoit and Stock, 1993), presumably due to recharge of cold meteoric water, the powerplant generated 13.7 MW of electricity in 2018 (Ayling, 2020). Argenta Rise lacks definitive surface manifestations of active thermal features, such as those observed at the Beowawe Geysers; however, it occupies a favorable structural setting thought to be conducive to hydrothermal up-flow (Faulds et al., 2011; Faulds and Hinz, 2015; Faulds et al., 2024). Faulds et al. (2024) identified two discrete regions with potentially elevated shallow temperatures proximal to the range-front fault zone on the western side of the northern Shoshone Range (Figure 1, inset map). To further refine areas favorable for geothermal activity at Argenta Rise, we conducted high-resolution gravity, magnetotelluric (MT), and physical property surveys, and analyzed Geoscience Data Acquisition for Western Nevada (GeoDAWN; Glen and Earney, 2023, 2024) aeromagnetic data to map and model subsurface geology and structure. Model parameters are constrained by physical property measurements (density, magnetic susceptibility) collected from hand samples and outcrops of the relevant geologic units throughout the northern Reese River basin and adjacent ranges. Our results support ongoing efforts to develop three-dimensional (3D) geologic and structural models, and identify specific sites for temperature gradient drilling.

2. Geologic Framework

Argenta Rise occupies a nearly 15 km wide left-step between major ENE-trending range-front fault systems along the northwestern edge of the Shoshone Range and at Argenta Rim (Figure 1). Numerous ENE-striking intra-basin faults presumably accommodate sinistral-normal oblique slip across the step-over. Beyond the favorable structural setting, there are two large-scale crustal features that make this region particularly favorable for geothermal resource investigations: 1) the Northern Nevada Rift (NNR); and 2) regionally high background conductive heat flow (Figure 1, index map). The NNR is a series of several narrow, arcuate, NNW-trending features that extend for at least 500 km from southern Nevada to the Nevada-Oregon border (McKee and Noble, 1986; Blakely and Jachens, 1991). The eastern segment of the NNR (Stewart et al., 1975; Zoback, 1979; Glen and Ponce, 2002) passes just east of the study area. Studies have proposed that the NNR was caused by a highly magnetic, mafic dike swarm that intruded the upper crust through deep-seated

crustal fractures that were reactivated in the middle Miocene during the passing of the Yellowstone hotspot along the Oregon-Idaho border (Zoback and Thompson, 1978; Glen and Ponce, 2002). The stresses induced by magma emplacement, and the contrast in physical properties between NNR-related intrusions and the surrounding country rock likely make the boundaries of the NNR structurally weak, and prone to faulting and fracturing. In regions with high strain rates, such as the Basin and Range (Zeng, 2022), these structures can frequently be reactivated, maintaining permeable pathways for deep circulating hydrothermal fluids. Thus, characterizing faults and fractures associated with the NNR will play an important role in understanding and identifying potential geothermal resources at Argenta Rise. This area also has anomalously high background conductive heat flow, largely as a result of regional extension within the Basin and Range. The study area sits on the eastern edge of the Battle Mountain High, a lobe of high heat flow in north-central Nevada with average surface heat flow estimates of 100+ mW/m^2 (Sass et al., 1971). Based on new maps of conductive heat flow within the Basin and Range (DeAngelo et al., 2022), estimated surface heat flow values at Argenta Rise are ~97.6 mW/m^2, and across the entire Basin and Range heat flow values are on average ~78.6 mW/m^2. These data suggest, at least regionally, that there is a higher potential of encountering geothermal resources at economically feasible depths in the north-central Basin and Range.

At Argenta Rise, the stratigraphy pertinent to our modeling efforts consists of highly deformed and thrusted Paleozoic siliciclastic and carbonate rocks that are overlain by minor deposits of Mesozoic sediments and intruded by Mesozoic and Tertiary granitoids (Crafford, 2007). Overlying these units are locally voluminous packages of Cenozoic volcanics and basin fill sediments (Crafford, 2007). The Paleozoic units, exposed along the northern Shoshone Range, at Battle Mountain, and in small outcrops at the southern end of the Sheep Creek Range, are presumed to be the primary basement lithologies throughout the northern Reese River basin. Although discrete intrusive bodies (i.e., dikes) related to the NNR are mapped at the surface in the northern Shoshone Range (Ramelli et al., 2001; John and Wrucke, 2003; Ramelli et al., 2017), the bulk of these rocks occur at depth along a NNW-trend through the northern Shoshone Range and Sheep Creek Range on the east side of the study area (Watt et al., 2007). For the purposes of two-dimensional (2D) and 3D modeling in this project, we generalize the Nevada state geological map (Crafford, 2007) within the region surrounding the study area by grouping together units that would be expected to have similar physical properties (density, magnetic susceptibility, magnetic remanence; Figure 1).

The two predominant fault orientations observed at Argenta Rise trend NNW and ENE, recording the transition from NNR-related ENE-WSW directed extension in the middle Miocene to the NW-SE directed extension characteristic of the modern-day Basin and Range, respectively (Zoback et al., 1994). Complex interactions between these opposing fault sets create numerous structurally favorable zones for promoting hydrothermal fluid flow within the study area (Faulds et al., 2011; Williams et al., 2022; Faulds et al., 2024). The geophysical data presented herein delineate concealed intra-basinal faults, and resolve subsurface fault interactions, providing a more complete view of subsurface fault complexity.

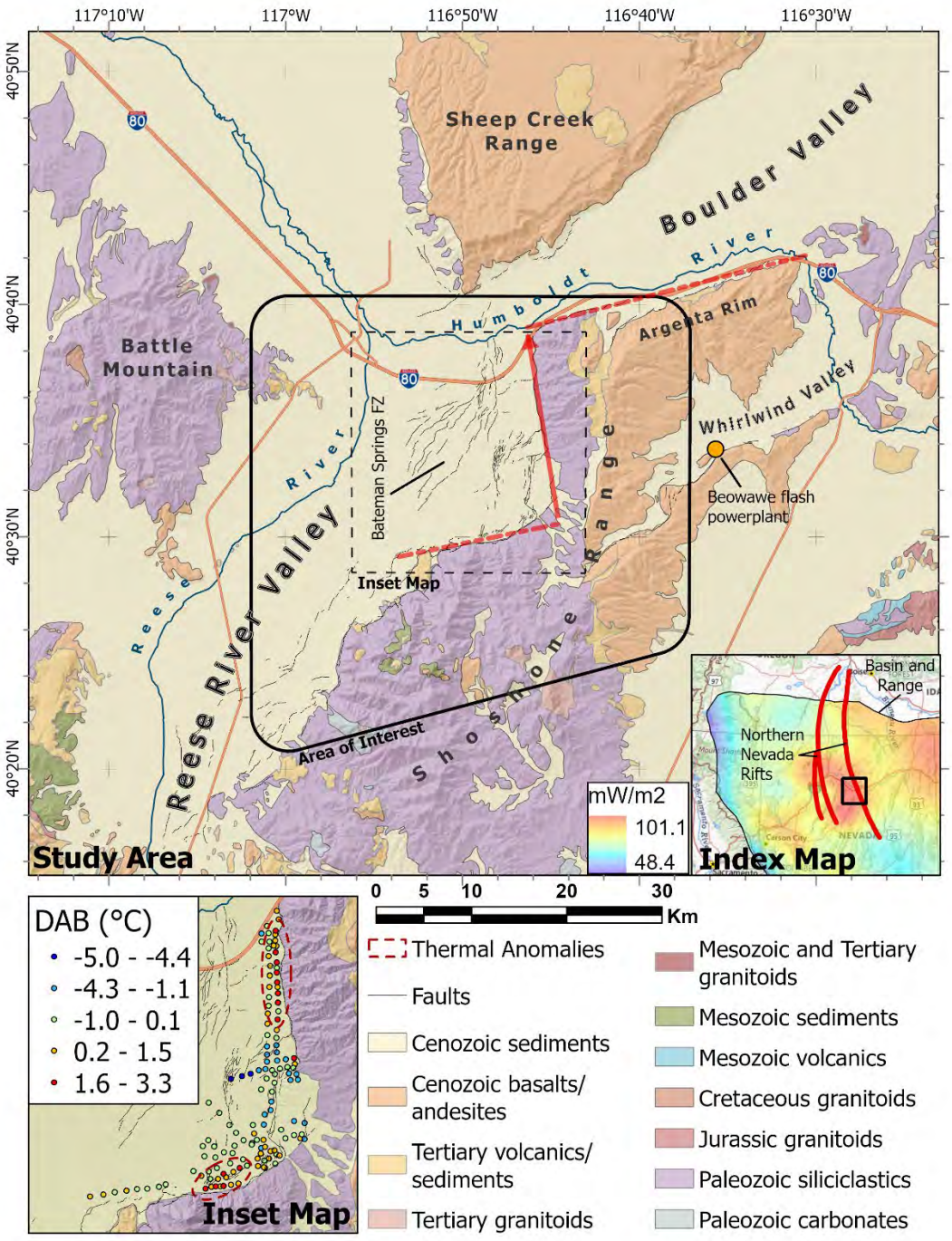

Figure 1: Study Area – Digital elevation model (DEM) hillshade (U.S Geological Survey, 2021a) overlain by simplified geologic map (adapted from Crafford, 2007). Faults are a compilation of existing (USGS, 2021a), and newly identified faults mapped by the University of Nevada, Reno (UNR) using lidar (U.S. Geological Survey, 2021b). The dashed red lines and red arrow indicate the left-step between range-front fault zones along the northwestern edge of the Shoshone Range (southern dashed red line) and Argenta Rim (northern dashed red line). Inset Map – 2-meter temperature survey conducted by UNR in July and November 2021 measured in degrees above background (DAB; Faulds et al., 2024). Index Map – Regional location map showing the location of the study area, the boundary of the Basin and Range, traces of the NNR (Glen and Ponce, 2002), and background conductive heat flow (DeAngelo et al., 2023).

3. Geophysical Data

Geophysical methods are valuable tools for investigating geothermal systems because they facilitate mapping of subsurface structures which may inhibit or host fluid flow and can be used to help resolve basin depths and geometries. Natural variations in gravity, magnetic, and electrical fields arise due to lateral and vertical contrasts in physical properties (e.g., density, magnetic susceptibility/remanence, and conductivity, respectively), which can reflect facies changes, presence of hydrothermal fluids, alteration products of hydrothermal fluids, offset across faults, and/or geological contacts. At Argenta Rise, the geology is quite varied, consisting of mafic igneous rocks, siliciclastic and carbonate rocks, granitoid intrusives, and tuffaceous and sedimentary rocks. The strong contrast in physical properties between these geologic units leads to distinct gravity, magnetic, and conductivity anomalies. We present new gravity, magnetic, and magnetotelluric data collected across the northern Reese River basin. We use various derivative, filtering, and modeling methods to characterize concealed geology and structures.

3.1 Gravity

A total of 1,207 new gravity measurements were collected in 2021 and 2022, encompassing ~2,000 km^2 of the northern Reese River basin and adjacent ranges. These data augmented an existing network of 3,899 gravity measurements from the surrounding region (Ponce, 1997; Hildenbrand et al., 2002 [PACES]; PACES database was made available from University of Texas, El Paso on 5/29/2018 [Ben Drenth, U.S. Geological Survey, written comm., March 2021]), improving regional coverage in areas of sparse control and providing detailed coverage (200 to 300 m station spacing) across range front and intra-basin structures. Isostatic anomaly values were calculated using standard gravity reduction methods (Blakely, 1995), assuming an average crustal density of 2,670 kg/m^3, a density contrast of 400 kg/m^3 at the crust-mantle boundary, and a sea level crustal thickness of 25 km. The isostatic anomalies were gridded using a minimum curvature routine with a cell size of 400 m. A residual isostatic anomaly map was subsequently generated (Figure 2) to facilitate structural mapping and interpretation of subtle anomalies produced by shallow crustal features that might otherwise be difficult to recognize in the presence of regional fields.

3.2 Magnetics

Magnetic data reveal subtle fluctuations in the magnetic field that reflect variations in the magnetization of rocks in the subsurface, and are particularly useful in regions where bedrock may be concealed by young basin fill sediments. In the northern Reese River basin, the strong contrast in magnetic properties (magnetic susceptibility and remanent magnetization) between the predominant lithologies (young sedimentary deposits [low magnetic properties], Cenozoic volcanics [high magnetic properties], and Paleozoic basement rocks [low magnetic properties]) results in distinct magnetic anomalies. These anomalies delineate structures such as faults and contacts that may provide natural permeable pathways for hydrothermal fluids.

The recently acquired GeoDAWN survey included a high-resolution aeromagnetic survey over northern and western Nevada and eastern California (Glen and Earney, 2024), and spans our study area at Argenta Rise. The survey was flown with a nominal flight height of 150 m above terrain over areas with low topographic relief and 200 m above terrain over mountain ranges. Flight lines were flown along an azimuth of 90 degrees and spaced 400 m apart, while tie lines were flown along an azimuth of 180 degrees and spaced 4,000 m apart. Magnetic data were recorded at 10 Hz.

The total field (TF) magnetic anomaly was gridded using a cell size of 100 m. We applied a number of derivative and filtering methods to this grid to simplify anomalies and aid interpretations of structural features. The reduced-to-pole (RTP) transformation (Blakely, 1995) was applied to the TF magnetic anomaly map to effectively center magnetic anomalies over their sources (Figure 3A). Additionally, several residual grids were created to highlight very subtle, shallow anomalies associated with young intra-basinal Quaternary faults (Figure 3B). To produce the residual grids, we upward continued the TF map a distance of 50 m and subtracted the result from the original TF map, then recalculated the RTP anomaly.

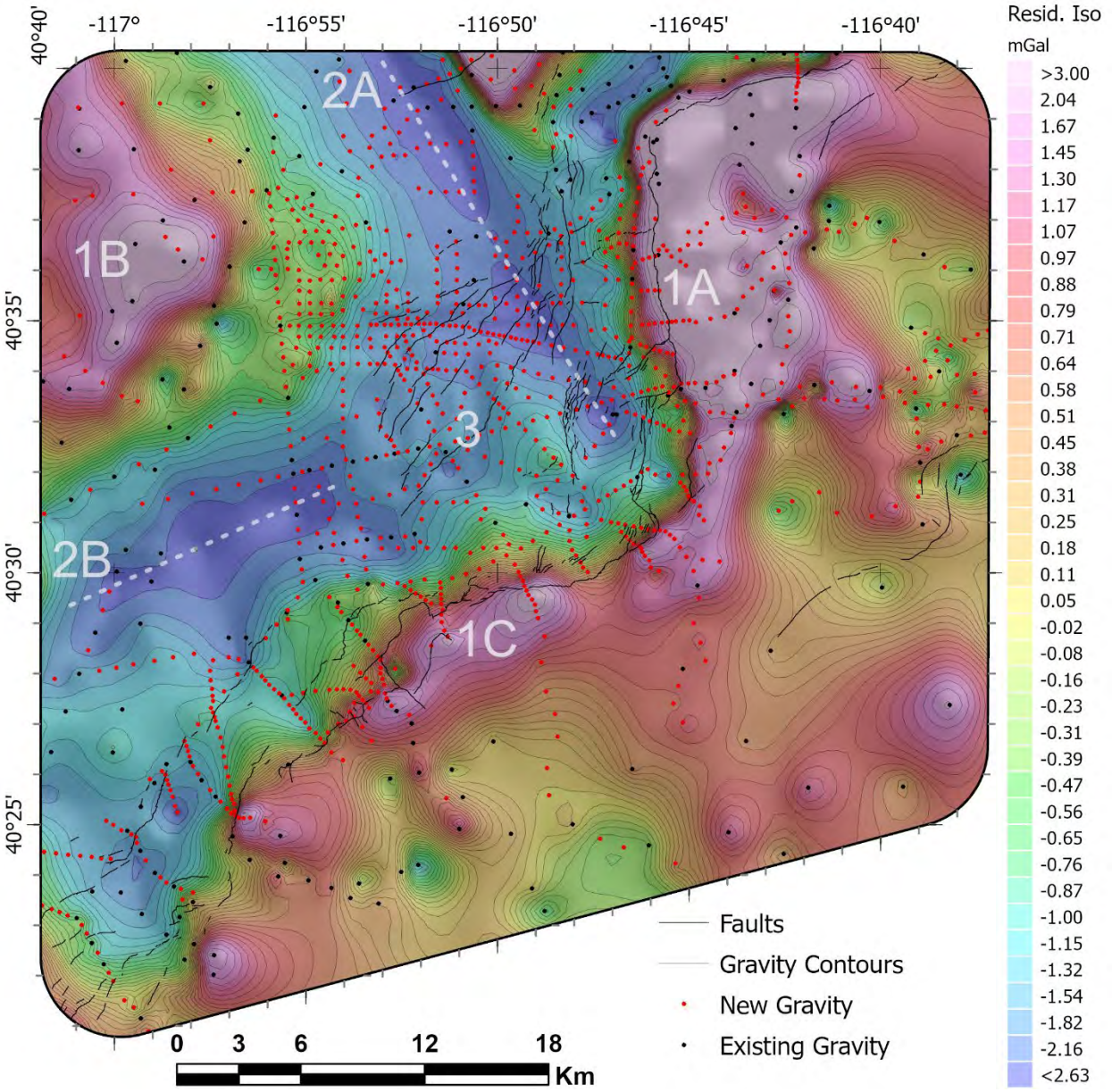

Figure 2: Residual isostatic anomaly map overlain by faults (dark black lines), gravity contours (light black lines; contour interval corresponds to bins in the 'Resid Iso' color bar), new gravity stations (red dots), and existing gravity stations. Labeled features are described in the Discussion section of this manuscript.

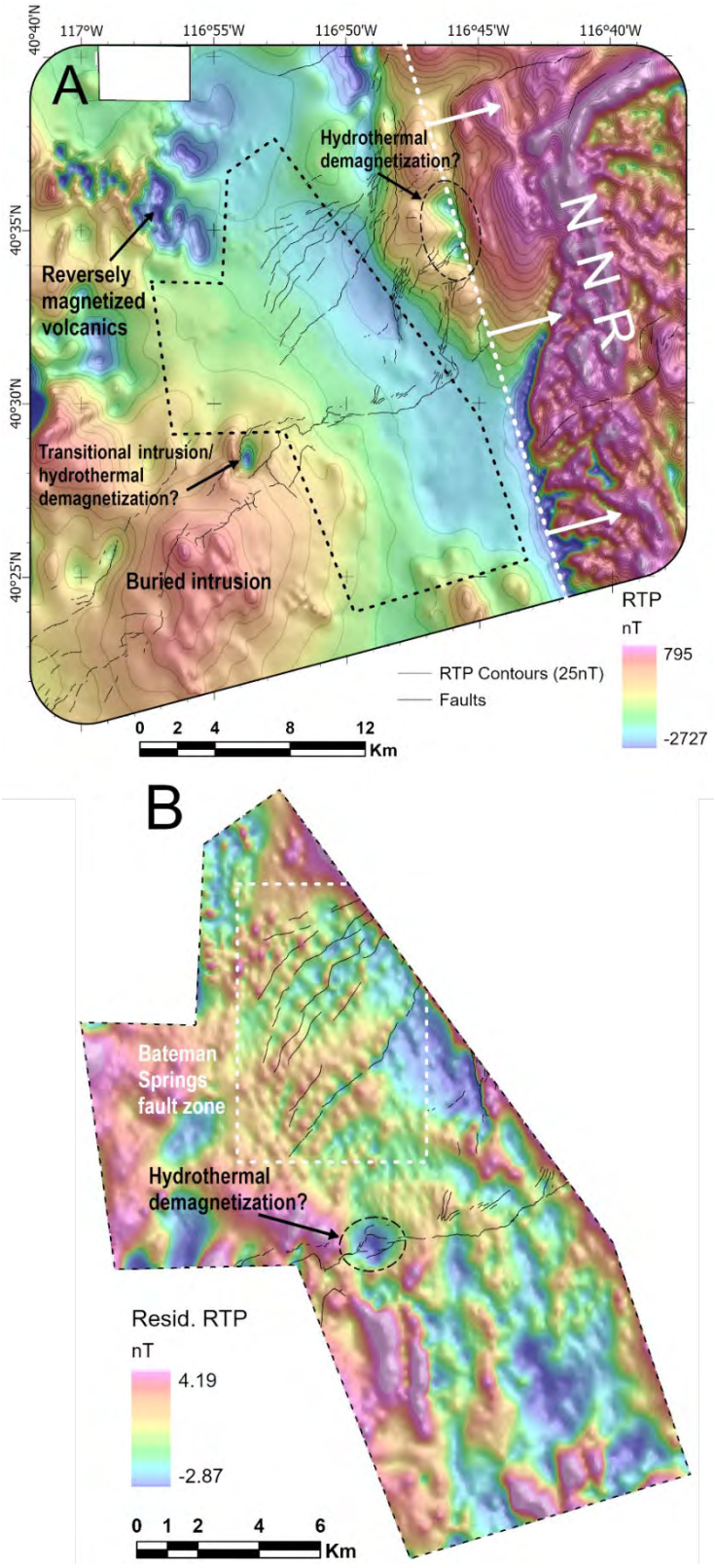

Figure 3: RTP magnetic anomaly (A), and residual RTP magnetic anomaly (B) overlain by faults (black lines). Dashed black line on panel A indicates the extent of the grid in panel B. Features pertinent to this study are labeled and described in the Discussion section of this manuscript.

3.3 Magnetotellurics

Magnetotellurics (MT) is a passive electromagnetic geophysical method that can be used to infer subsurface electrical conductivity structure by measuring the Earth's electrical response to natural time-varying magnetic fields. The MT method is particularly well suited for geothermal studies as it can facilitate imaging of subsurface clay caps, zones of hydrothermal alteration, heat sources, hydrothermal fluids, and thermally enhanced zones (Newman et al., 2008; Munoz, 2014).

In May 2022, MT data were collected at 43 locations spanning an area of ~200 km^2 across the core of the study area. Magnetic fields were measured with Zonge International Inc. ANT4 induction coils (Tucson, AZ). Electric fields were measured with Borin Stelth 1 Ag-AgCl electrodes (Culver City, CA) placed in saturated bentonite clay bags for better contact resistance. Both the magnetic and electric fields were recorded with ZEN data loggers developed by Zonge International Inc. (Tucson, AZ). The instruments were left recording for about 24 hours, providing reliable resolution of the subsurface conductivity structure for the upper two to three kilometers of the Earth's crust. MT data were used to generate a 3D electrical conductivity model of the subsurface using ModEM (Kelbert et al., 2014). From the 3D model, we extracted 2D plan maps at pre-determined depths (relative to sea level) to highlight conductive anomalies at various depths of investigation that might indicate the locations of hydrothermal fluids or their alteration products (Figure 4). Additionally, we extracted 2D cross sections from the 3D model along our 2D geophysical profiles to facilitate the interpretation of which structures may host hydrothermal fluid flow in the shallow subsurface.

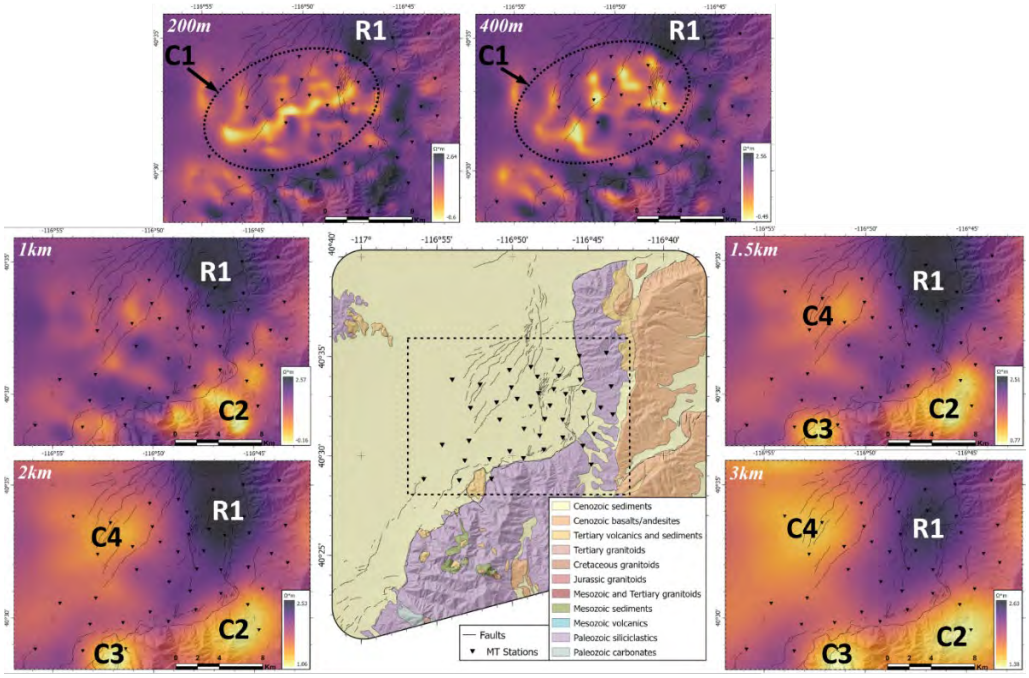

Figure 4: Depth slices through 3D conductivity model. (Center) DEM (U.S. Geological Survey, 2021) hillshade overlain by the generalized geologic map, faults (black lines) and MT stations (inverted black triangles). The dashed black rectangle indicates the extent of the depth slices. These images highlight the conductivity structure at depths of 200 m (upper left), 400 m (upper right), 1 km (mid left), 1.5 km (mid right), 2 km (lower left), and 3 km (lower right) beneath Argenta Rise. Conductive and resistive anomalies (i.e., C1-4, R1, respectively) are described in the Discussion section of this manuscript.

4. Structural Mapping

We performed a horizontal gradient analysis of the gravity and magnetic grids to detect abrupt lateral changes in density and magnetization, and thereby elucidate subsurface structural patterns. Subsurface structures typically manifest as steep gradients in potential field data, and can be mapped by analyzing horizontal gradient maxima (HGM; Grauch and Cordell, 1987; Cordell and McCafferty, 1989; Blakely and Simpson, 1986), which tend to lie over sub-vertical structures. For the TF magnetic data, we first calculated the pseudogravity (Blakely, 1995). The pseudogravity transformation effectively centers TF magnetic anomalies over their respective source bodies, and simplifies their interpretation. We then calculate horizontal gradient maps of the gravity and pseudogravity grids, and following Phillips et al. (2007), calculate HGM using a routine that identifies laterally continuous ridges in horizontal gradient maps. Discrete maxima were then connected into continuous lines (or lineations) based on user specified distance and azimuth tolerance relationships to adjacent maxima (Athens, 2018; Figure 5).

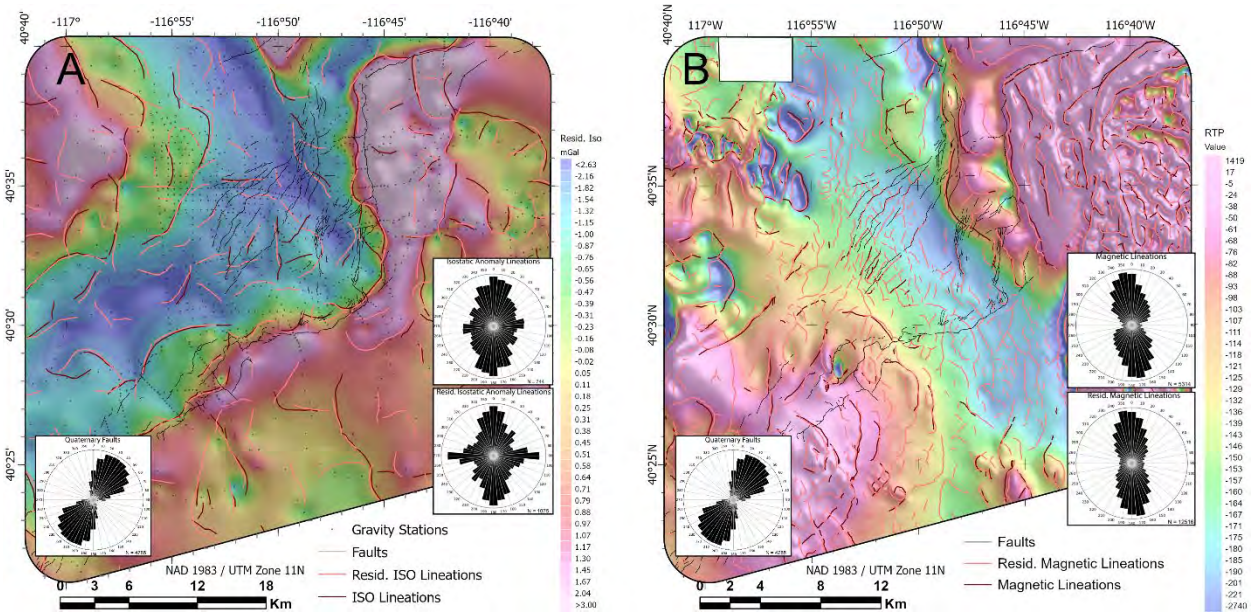

Figure 5: A) Residual isostatic anomaly overlain by gravity stations (black dots), faults (black lines), and lineations derived from the isostatic and residual isostatic anomalies (dark red and light red lines, respectively. Rose diagrams show trends of Quaternary faults (lower left), lineations derived from the isostatic anomaly (upper right) and lineations derived from the residual isostatic anomaly (lower right). B) RTP magnetic anomaly overlain by faults (black lines) and lineations derived from the magnetic and residual magnetic anomalies (dark red and light red lines, respectively). Rose diagrams show trends of Quaternary faults (lower left), lineations derived from the pseudogravity anomaly (upper right), and lineations derived from the residual pseudogravity anomaly (lower right).

5. Geophysical Modeling

To characterize subsurface stratigraphy and structure we constructed 2D and 3D potential field models utilizing both forward and inverse methods. Physical property measurements (density, magnetic susceptibility, magnetic remanence) from hand samples and outcrops of relevant geologic units throughout the region informed model parameters. All models are consistent with the mapped surface geology represented in the generalized geological map.

5.1 Depth to Basement

We perform a 3D inversion of gravity anomalies, using methods described by Jachens and Moring (1990), to estimate the geometry of the pre-Cenozoic basement surface beneath the northern Reese River basin (Figure 6). This method is an iterative procedure that combines gravity data, surface geology, and an estimate of the density of Cenozoic deposits to approximate the thickness of young basin fill. We separated the isostatic anomaly into two components: 1) a basement gravity field (representing crystalline, pre-Cenozoic, and intrusive rocks); and 2) a basin fill gravity field (representing overlying Cenozoic basin fill deposits). We simplify the surface geology of the Nevada state geologic map (Crafford, 2007), and reclassify all units into two categories: basement (generally any crystalline, pre-Cenozoic, or intrusive rocks) and Cenozoic deposits. For the purposes of this project, we reclassify all Cenozoic volcanics as Cenozoic sediments being that there are no volcanic units that are both thick enough (greater than several hundred meters) and dense enough to appreciably affect the regional gravity field in the study area. During the inversion the basement density is allowed to vary laterally while a vertical density gradient function (Jachens et al., 1996) is enforced in the basin fill deposits (see 'Quaternary Sediments', Table 1). To constrain the inversion solutions, we incorporate publicly available well data from three sources: oil and gas (Nevada Bureau of Mines and Geology, 2023b), geothermal (Nevada Bureau of Mines and Geology, 2023a), and water wells (Nevada Division of Water Resources, 2023).

This style of depth to basement estimate contains a substantial amount of uncertainty and is often only accurate to within 20% of the total basin depth in areas without well constraints (Jachens et al., 1996). Ambiguity in the gravity method, local density-depth variations in overlying basin fill deposits, and the assumption that basin fill density varies in the vertical direction only will often lead to an underestimation of true basin depth. Furthermore, basement lithologies, while modeled as a single unit in the inversion, are highly variable and heterogeneous throughout the study area, representing a wide range of densities. Nonetheless, our inversion results provide a qualitative characterization of relative variations in the basement surface. We use that characterization to guide regional interpretations of basin geometry and inform the development of our 2D and 3D geophysical models.

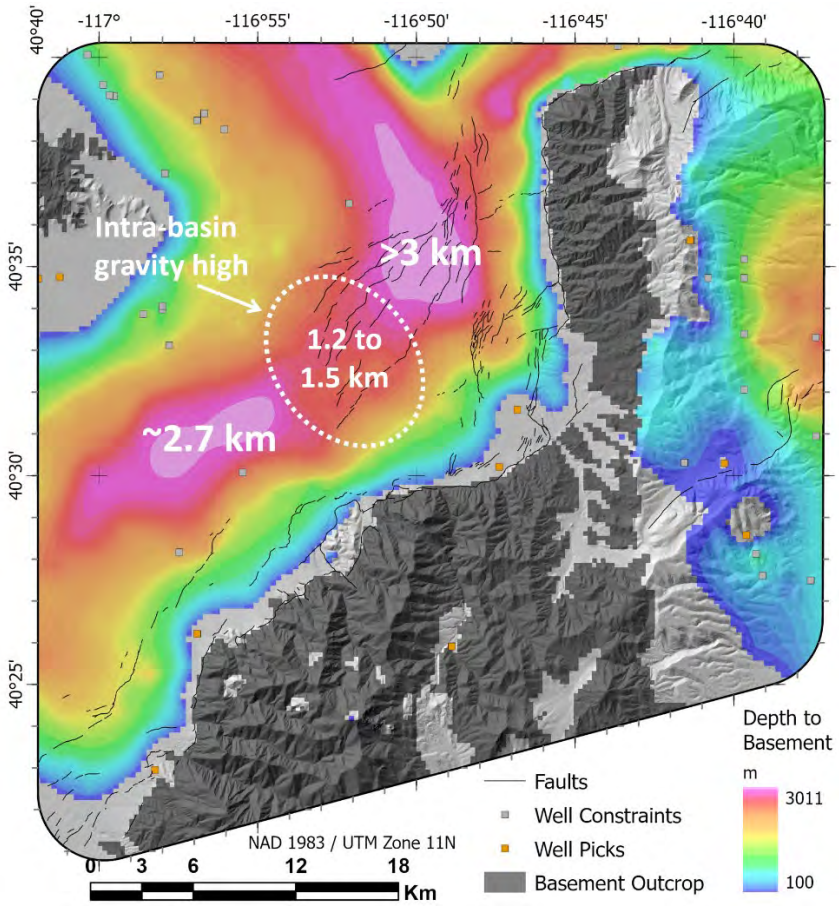

Figure 6: DEM (U.S. Geological Survey, 2021) hillshade overlain by depth to pre-Cenozoic basement map, faults (black lines), minimum constraint wells (i.e., wells not intercepting the basement; grey squares), basement intercepting wells (orange squares), and locations of basement outcrop (dark grey areas). Light grey areas are locations where basement is interpreted to be <100 m below the surface.

5.2 2D Modeling

A series of 12, 2D joint gravity and magnetic potential field models were created along profiles spanning the northern Reese River basin (Figure 7). Six of these profiles (WV1, WV2, WV3, WV4, WV5 and NNRA) were adapted from Watt et al., (2007) and updated to be consistent with the modeling goals of this study. Although geophysical models are typically placed orthogonal to the primary structural trend that is being characterized, we also consider the underlying gravity data density and attempt to focus on regions with dense data coverage that still captures key features and structures that may be important for controlling hydrothermal activity. Profile data are extracted from the gravity (isostatic anomaly) and magnetic (total field anomaly) grids with a sampling interval of 100 m along the profiles. Model bodies are assigned densities and magnetic susceptibility and remanence values based on physical property measurements when available (Table 1). Model body geometries are made to be consistent with the generalized surface geology. A total of 31 geologic units are modeled, representing 23 generalized 2D model layers with differing densities based on depth, and different remanent magnetizations. The model bodies are adjusted iteratively using a process of forward and inverse methods to reproduce the observed potential field anomalies within the limits imposed by the physical property data and surface geology (Figure 8).

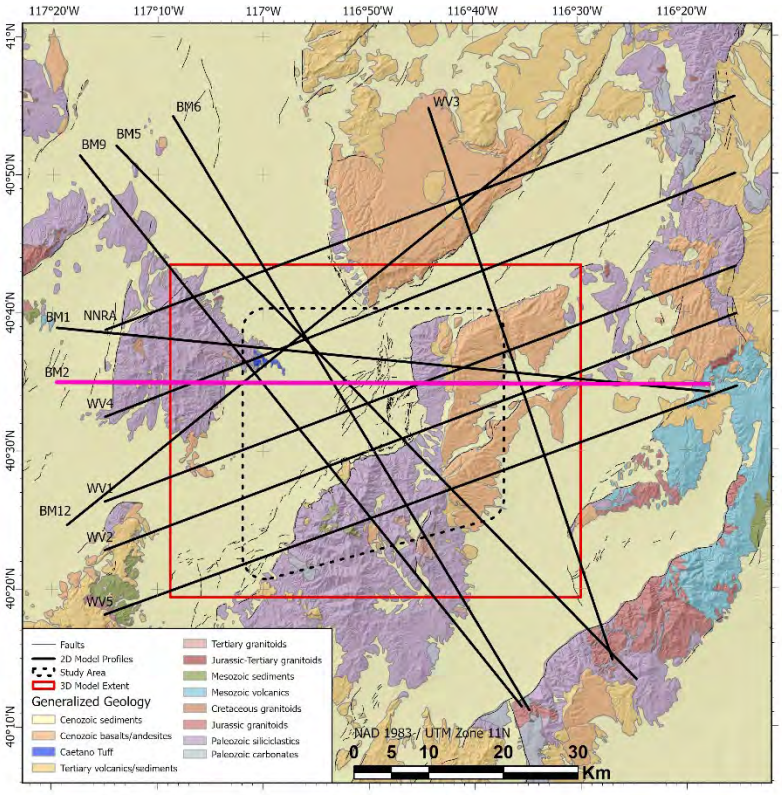

Figure 7: DEM (U.S. Geological Survey, 2021) hillshade overlain by generalized geologic map, faults (thin black lines), 2D model profile locations (thick black lines), the Argenta Rise study area (dashed black polygon), and the 3D model extent (red polygon; Figure 9). The 2D model profile indicated by the thick pink line (BM2) is presented herein (Figure 8).

Table 1: Physical property values used in 2D and 3D modeling. Physical properties include density (measured in kilograms/meter^3), magnetic susceptibility (Susc.; unitless, values reported in 10^{-3} SI), magnetic remanence (Rem.; measured in Ampere/meter), inclination (Inc.; measured in degrees), and declination (Dec.; measured in degrees). Values determined by measurements performed on hand samples and outcrops for this project.

Unit	Description	Density kg/m^3	Susc. ($x10^{-3}$) SI	Rem. A/m	Inc. degrees	Dec. degrees
QTs	Quaternary sediments: 0 – 200 m	2,020	*	*	*	*
	Quaternary sediments: 200 – 600 m	2,120	*	*	*	*
	Quaternary sediments: 600 – 1200 m	2,320	*	*	*	*
	Quaternary sediments: >1200 m	2,420	*	*	*	*
QTba	Quaternary - Tertiary basalts/andesites	2,550	0.025	1	64	12.5
Caetano	Tertiary Caetano Tuff	2,120	0.005	1.9	-66.5	156.3
Tvs	Tertiary volcanics/sediments	2,400	0.013	*	*	*
Ti	Tertiary granitoids	2,670 – 2,720	0.007 – 0.013	*	*	*
Ki	Cretaceous granitoids	2,670 – 2,720	0.008 – 0.013	*	*	*
Ji	Jurassic granitoids	2,670 – 2,750	0.006 – 0.013	*	*	*
TKJi	Mesozoic and Tertiary granitoids	2,670 – 2,750	0.035	*	*	*
Ms	Mesozoic sediments	2,600	*	*	*	*
Mv	Mesozoic volcanics	2,600	0.010	*	*	*
Pzu	Paleozoic siliciclastics	2,660	0.001	*	*	*
Pzc	Paleozoic carbonates	2,700	*	*	*	*
NNR2	NNR (lightly intruded basement)	2,670 – 2,770	0.005 – 0.025	0.5	64	12.5
NNR1	NNR (heavily intruded basement)	2,700 – 2,800	0.031 – 0.038	1	64	12.5

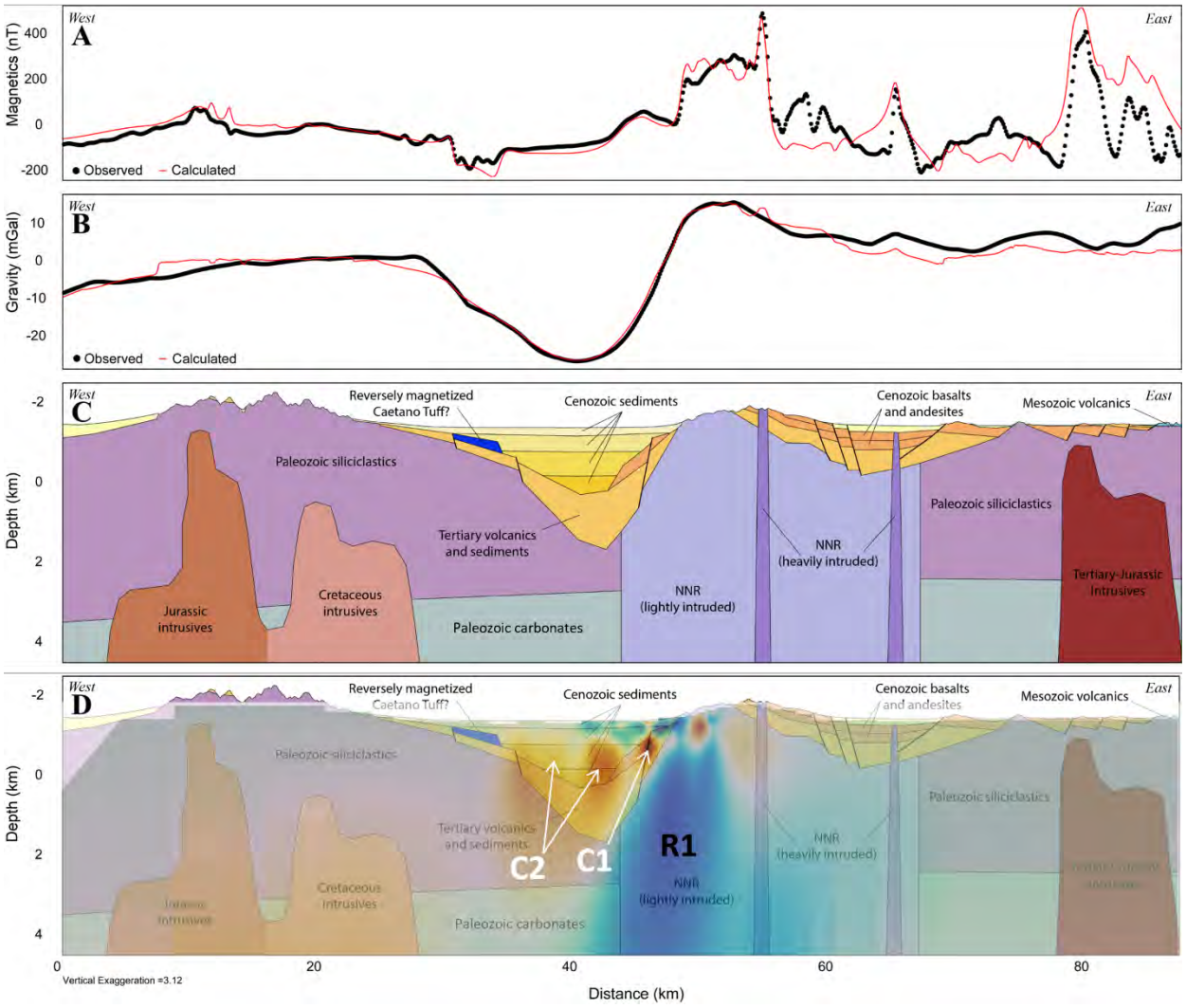

Figure 8: Joint gravity and magnetic potential field model along profile BM2 (profile location indicated by pink line on Figure 7). Magnetic data (panel A) are extracted from the total field anomaly and gravity data (panel B) are extracted from the isostatic anomaly. Observed anomalies are indicated by the black dots, and the calculated model responses are indicated by the red lines. Model bodies (panel C) are assigned densities and magnetic susceptibility and remanence values based on physical property measurements performed on outcrops and hand samples collected in Reese River basin and surrounding ranges. Resistivity anomalies (panel D) overlain on model bodies highlight near surface conductors that could represent hydrothermal fluids and/or zones of alteration along faults and contacts. Conductive and resistive anomalies (i.e., C1, C2, and R1) are described in the Discussion section of this manuscript.

5.3 3D Modeling

A 3D joint gravity and magnetic potential field model is developed using the Oasis Montaj® GM-SYS 3D Modeling software extension (Seequent, 2023). The 23 generalized 2D model layers are further simplified to 10 layers for the 3D model and provide initial constraints. Surfaces in the 3D model are adjusted through structural inversions to minimize misfit between the observed and calculated anomalies (Figure 9). There are several ambiguities in the model area related to the depth and geometry of sources. One of the layers, representing young, reversely magnetized

volcanics, did not reproduce either the geometry, or magnitude of the magnetic low at the southeast corner of Battle Mountain (see 'Reversely magnetized volcanics' on Figure 9). We attribute this to the fact that this anomaly is relatively small, isolated, and not adequately represented in the 2D models. Therefore, we removed this layer from the 3D model, and instead created a voxel model over this anomaly and inverted on magnetic susceptibility, deriving a closed body isosurface, which when imported back into the 3D model, reproduces the magnetic low quite well. Another ambiguity pertains to the geometry and depth of the granitoids. Surficial outcrops of these units are relatively small, and we do not have an extensive inventory of physical property information on them. The density contrast between the granitoids and surrounding basement lithologies is presumed to be minor. However, some of the granitoids appear to have distinct magnetic anomalies associated with them. To model the granitoids in 3D, we performed a series of magnetic structural inversions on the granitoid layer, creating a tiered geometry in which the granitoids are more voluminous at depth, and more laterally restricted closer to the surface.

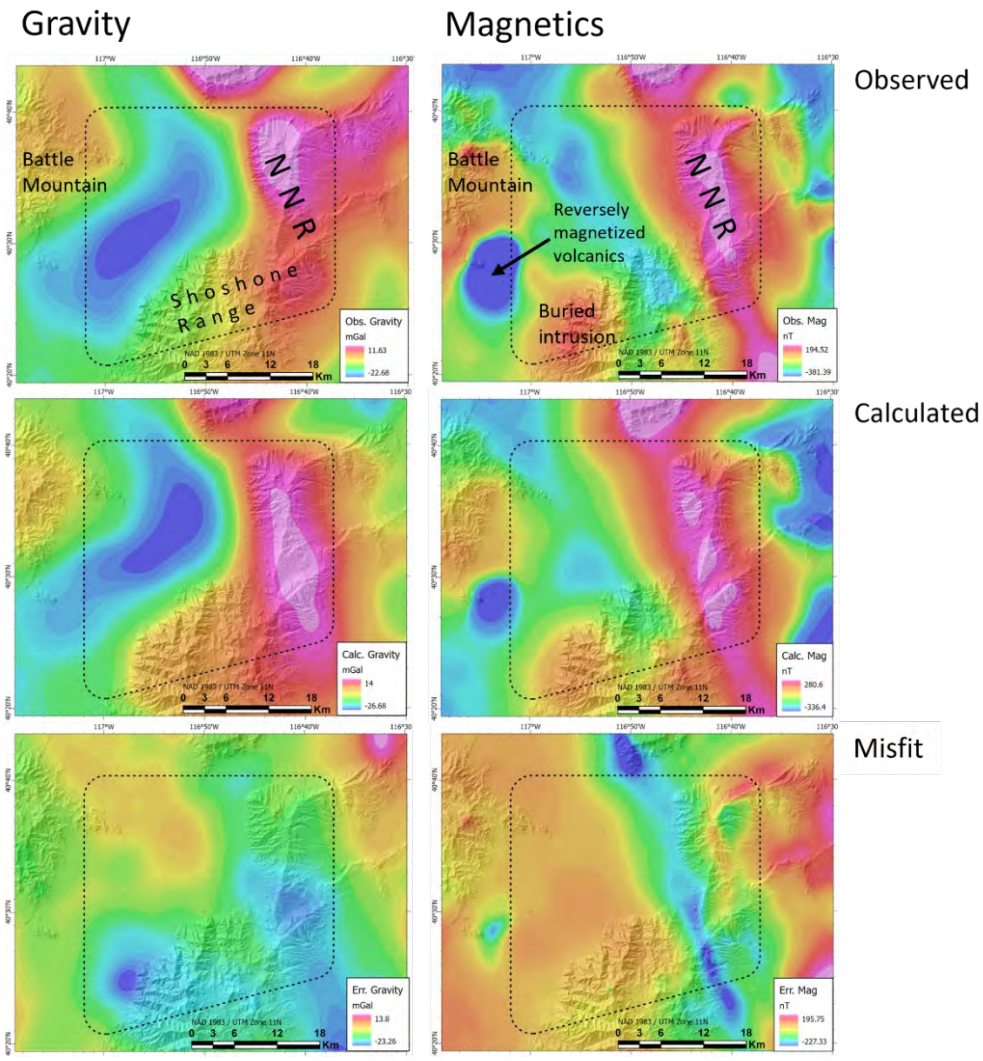

Figure 9: DEM (U.S Geological Survey, 2021) hillshade overlain by results of 3D joint gravity and magnetic potential field model showing observed gravity and magnetic anomalies (top), calculated model responses (middle), misfit between the observed and calculated anomalies (bottom). The Argenta Rise study area is indicated by the black dashed polygon. Model extent is indicated on Figure 7.

6. Discussion

The geophysical data and models presented here-in, reveal basin-bounding and concealed intra-basinal structures that may influence the development of a hydrothermal system at Argenta Rise. Anomalies observed in the gravity, magnetic and magnetotelluric datasets are used to constrain basin geometry and basin depth, delineate concealed contacts, faults, and fault extensions, and identify regions with subsurface fluid flow and/or hydrothermal alteration. Interpretations of these features are incorporated in the 2D and 3D models to provide a robust characterization of subsurface geology at Argenta Rise.

The gravity maps and depth-to-basement results constrain basin geometry and basin depth in the northern Reese River valley. The highs (areas 1A, 1B, and 1C on Figure 2) correspond to outcrops and near surface bodies of Paleozoic siliciclastic and carbonate rocks and middle Miocene NNR-related mafic intrusives, which tend to be relatively dense compared to other lithologies in the region. The two most prominent gravity lows (areas 2A and 2B on Figure 2) delineate two structurally controlled sub-basins beneath the northern Reese River basin; one trending NNW (area 2A) and the other trending ENE (area 2B). The NNW-trending sub-basin is asymmetric, with the trough of the gravity low displaced towards the east relative to the central axis of the basin between Battle Mountain and the northern Shoshone Range. The eastern edge of the gravity low has a distinct NNW-trend, which is notably different than the much more northerly trend of the current range-front fault zone bounding the western edge of the northern Shoshone Range. We interpret this gradient to represent the concealed, southeastward extension of the NNW-trending range-front fault zone bounding the west side of the southern Sheep Creek Range. Gravity values in this sub-basin gradually increase to the west, suggesting vertical deformation is primarily accommodated by the eastern range-front fault zones. The ENE-trending sub-basin is relatively more symmetric and truncated along its eastern extent by an approximately 10 km wide series of subtle intra-basin gravity highs (area 3 on Figure 2) that also delineate the west side of the southern portion of the NNW-trending sub-basin. The intra-basin gravity highs form a ridge-like feature across the Reese River basin and may be indicative of structural relief in the basement surface.

Our gravity derived depth-to-basement results (Figure 6) indicate maximum basin depths of >3 km in the southern portion of the NNW-trending sub-basin and ~2.7 km in the ENE-trending sub-basin. An intra-basin gravity high (area 3 on Figure 2; Figure 6) is situated between these two regions. Basin depths above the intra-basin gravity high are 1.2 to 1.5 km. If this feature is structurally controlled, it suggests that there could be 1.2 to 1.8 km of cumulative vertical displacement across the structures inferred along its periphery. The intra-basin gravity high could be a barrier to lateral flow of subsurface fluids between the NNW- and ENE-trending sub-basins or, alternatively the structural complexity may locally enhance permeability, promoting the vertical transport of fluids between the deep and shallow subsurface (Earney et al., 2018; Craig et al., 2021).

One of the most prominent features apparent in the GeoDAWN aeromagnetic data (Glen and Earney, 2023, 2024) is a NNW-trending region of magnetic highs in the eastern portion of the study area (labeled ‘NNR’ on Figure 3A). Numerous aforementioned studies (Stewart et al., 1975; Zoback and Thompson, 1978; Zoback, 1979; McKee and Noble, 1986; Blakely and Jachens, 1991; Glen and Ponce, 2002) have concluded that this feature is caused by a highly magnetic, mafic dike swarm that was emplaced in the middle Miocene. Large-scale crustal features, such as the NNR, typically have highly faulted and fractured boundaries which can serve as conduits for deep

circulating hydrothermal fluids. Numerous other features are interpreted from the aeromagnetic data, including shallowly buried, reversely magnetized volcanics (Figure 3A), buried intrusive bodies (Figure 3A), zones of possible demagnetization due to hydrothermal alteration (Figure 3A and 3B), and very subtle anomalies associated with young Quaternary faults along the Bateman Springs fault zone (Figure 3B). The residual magnetic lineations overall show a very strong northerly trend (Figure 5B). However, over the basin where magnetic gradients are much lower, there are numerous lineations with a distinct NNW-trend, a trend that is not well represented in Quaternary fault patterns within the study area. This trend is very similar to the trend of the NNR. Therefore, we interpret these features to represent relatively older structures that may relate to emplacement of the NNR. Many of the NNE-trending intra-basin faults associated with the Bateman Springs fault zone have subtle, but mappable anomalies associated with them (Figure 3B). Furthermore, the horizontal gradient analysis reveals that many of these faults extend further than they are currently mapped, in addition to identifying new structures that are currently unmapped. The recognition of these features and, more importantly, where these features intersect with northerly- and NNE-trending Quaternary faults may help identify additional areas with enhanced structural complexity that could support the development of a hydrothermal system.

Overall, the MT results (Figure 4) correlate well with the gravity derived depth-to-basement results (Figure 6) with nearly all of the conductors lying within the basin or slightly above the basement-basin fill contact (bottom panel on Figure 8 shows one example of this). As an exception, however, we note that strong conductors appear within basement lithologies at depth in the southern portion of the survey area (C2 and C3 on Figure 4). As there are currently no mapped hot springs in these areas, we interpret these anomalies as possible recharge zones, where meteoric fluids are entering the subsurface through a network of deep-seated fractures in the basement. Shallow and deep conductors (C1 and C4 on Figure 4, respectively) within the basin appear to line up nicely with the region of dispersed NE-striking faults associated with the Bateman Springs fault zone, and may represent the presence of saline groundwater or, alternatively, could be due to hydrothermal upwelling. A resistive body (R1 on Figure 4) is consistently present at all depths in the northeastern portion of the survey area, becoming more pronounced and expanding south and westward at deeper depths. This resistive body is interpreted to reflect the geometry of the basement surface at this location.

The 2D geophysical modeling we performed constrained the locations and relative amounts of offset along major faults and highlights which faults may be more conducive to hosting hydrothermal fluid flow. One of the primary advantages of 2D geophysical models is the ability to leverage high resolution geophysical data where available to make detailed structural interpretations that can be difficult to characterize in 3D. The 2D geophysical model presented here (Figure 8), has several correlations with the MT data that may indicate the presence of shallow hydrothermal activity. The strongest conductive anomaly (C1 on Figure 8) along the profile is co-located with a major, northerly-trending fault on the east side of the basin. The anomaly appears confined to a perched volcanic unit that overlies a package of mixed sedimentary and volcanic basin fill (Cenozoic basalts/andesites and Tertiary volcanics/sediments). However, the conductive anomaly does not appear to extend much deeper than the perched volcanic unit, suggesting that if this anomaly is due to the presence of hydrothermal fluids and/or alteration, the primary zone of upwelling may be occurring off-axis of this profile. Alternatively, this anomaly may reflect the presence of a shallow groundwater aquifer that is confined to the volcanics and localized around the fault due to an enhancement of permeability. The slightly less conductive, but more extensive

anomaly just to the west (C2 on Figure 8), correlates spatially with the Bateman Springs fault zone, and may indicate hydrothermal activity, or the presence of sediment-hosted meteoric groundwater. The large resistive body (R1 on Figure 8) is interpreted as NNR-intruded basement.

The 2D geophysical models provide discrete, detailed structural information about the subsurface. However, subsurface geology is inherently complex and difficult to characterize via 2D methods alone. The 3D geophysical model, presented here (Figure 9), provides a more robust means of testing the validity of our 2D models and, by extension, our conceptual model of the subsurface. Overall, the calculated gravity and magnetic responses of our 3D model layers agree quite well with the observed data as indicated by the relatively low error estimates. Inconsistencies within the 3D model are largely due to poor data distribution (primarily the sparse gravity data coverage in the south and southeastern portion of the Shoshone Range), and the complex, heterogeneous nature of the geology being modeled. Some of the misfit could be minimized by incorporating additional 2D model constraints. Nevertheless, the data from the 2D and 3D geophysical models provide insight regarding stratigraphic, structural and physical property relationships of subsurface geology at Argenta Rise.

7. Conclusions

We characterize the subsurface geology, constrain basin geometry, and map basin-bounding and concealed intra-basin structures at Argenta Rise using high-resolution geophysical data (i.e., newly collected gravity, MT, and physical property data and aeromagnetic data) to model geophysical anomalies and assist with identifying structural settings that are favorable to hydrothermal fluid flow. The gravity and depth-to-basement maps reveal two sub-basins beneath Argenta Rise with a potential structurally controlled, intra-basin high separating these two basins. Maximum basin depths are near 3 km. The horizontal gradient analysis of the aeromagnetic data suggests the presence of previously unmapped intra-basin structures (e.g., new faults and extensions of mapped faults), as well as extensions to mapped faults, and highlights subsurface structural complexity. When combined with the 2D geophysical models, the MT data indicate regions of potential hydrothermal activity, in some cases with strong conductive bodies co-located with faults and contacts. The 3D geophysical model shows that our conceptual model of basin geometry and structure (represented in the 2D geophysical models) is relatively accurate throughout the study area as indicated by the low error estimates. These data will support our planned development of a 3D geological model and aid the process of selecting sites for temperature gradient drilling.

Acknowledgements

This project is funded by U.S. Department of Energy – Geothermal Technologies Office under award DE-EE0009254 to the University of Nevada, Reno, and with support from the U.S. Geological Survey Energy Resources Program under the Geothermal Resource Investigation Project. Any use of trade, firm, or product names is for descriptive purposes only and does not imply endorsement by the U.S. Government. We thank Karen Christopherson, Randall Mackie, Stanley Mordensky, and Jacob DeAngelo for their thoughtful reviews of this manuscript.

REFERENCES

Athens, N. “Maxspots curvature.” software available at: https://github.com/nathens/maxspots_curvature, (2018).

Ayling, B. “35 years of geothermal power generation in Nevada, USA: A review of field development, generation, and production histories.” *Proceedings: 45th Workshop on Geothermal Reservoir Engineering*, Stanford University, Stanford, CA (2020), p. 12

Ayling, B., Faulds, J.E., Clark, A., Morales-Rivera, A., Sladek, C., Berti, C., Kreemer, C., Siler, D., Mlawsky, E., Gentry, E., Kleber, E., Burns, E., Warren, I., Batir, J., DeAngelo, J., Peacock, J., Witter, J., Queen, J., Glen, J.M.G., Kraal, K., Mann, M., Wagoner, N., Williams, N., Dobson, P., Micander, R., Koehler, R., Kirby, S., Brown, S., Earney, T.E., Cladouhos, T., Rickard, B., Trainor-Guitton, W., Lifton, Z. “INnovative Geothermal Exploration through Novel Investigations Of Undiscovered Systems (INGENIOUS) Project Introduction and Activity Update.” *Proceedings: GRC Transactions*, 46, (2022).

Benoit, D., and Stock, D. “A case history at the Beowawe, Nevada geothermal reservoir.” *Proceedings: GRC Transactions*, 17, (1993).

Blakely, R.J., and Simpson, R.W. “Approximating edges of source bodies from gravity or magnetic data.” *Geophysics*, 51, (1986), doi: 10.1190/1.1442197.

Blakely, R.J., and Jachens, R.C. “Regional study of mineral resources in Nevada: Insights from three-dimensional analysis of gravity and magnetic anomalies.” *Geological Society of America Bulletin*, 103, (1991).

Blakely, R. J. “Potential Theory in Gravity and Magnetic Applications.” *New York, Cambridge University Press*, (1995).

Cordell, L., and McCafferty, A.E. “A terracing operator for physical property mapping with potential field data.” *Geophysics*, 54, (1989), doi:10.1190/1.1442689.

Crafford, A.E.J. “Geologic map of Nevada.” *U.S. Geological Survey Data Series*, 249, (2007).

Craig, J.W., Faulds, J.E., Hinz, N.H., Earney, T.E., Schermerhorn, W.D., Siler, D.L., Glen, J.M., Peacock, J., Coolbaugh, M.F., DeOreo, S.B. “Discovery and analysis of a blind geothermal system in southeastern Gabbs Valley, western Nevada, USA.” *Geothermics*, 97, (2021).

DeAngelo, J. “Nevada geothermal favorability mapping, weights of evidence smoothed functions and refined methodology.” *San Francisco State University*, masters thesis, (2019).

DeAngelo, J., Burns, E.R., Gentry, E., Batir, J.F., Lindsey, C.R., Mordensky, S.P. “Heat flow maps and supporting data for the Great Basin, USA.” *U.S. Geological Survey Data Release*, (2022), doi: 10.5066/P9BZPVUC.

Earney, T.E., Schermerhorn, W.D., Glen, J.M.G., Peacock, J., Craig, J., Faulds, J., Hinz, N., Siler, D. “Geophysical investigations of a blind geothermal system in southern Gabbs Valley, Nevada.” *Proceedings: GRC Transactions*, 42, (2018).

Earney, T.E., Glen, J.M.G., Ayling, B., Faulds, J., Siler, D., Dean, B., Zielinski, L.A., Schermerhorn, W.D., Williams, N., Wagoner, N., Morales-Rivera, A. “Characterizing structure and geology with potential field geophysics to assess geothermal resource potential near Battle Mountain, NV.” *Proceedings: GRC Transactions*, 46, (2022).

Earney, T.E., Glen, J.M.G., Peacock, J., Faulds, J.E., Schermerhorn, W.D., Rea-Downing, G., Anderson, J.E. “Preliminary geophysical maps and models of a potential blind geothermal system near Battle Mountain, Nevada.” *Proceedings: GRC Transactions*, 47, (2023).

Faulds, J.E., Coolbaugh, M.F., Hinz, N.H., Cashman, P.H., and Kratt, C., Dering, G., Edwards, J., Mayhew, B., and McLachlan, H. “Assessment of favorable structural settings of geothermal systems in the Great Basin, western USA.” *Proceedings: GRC Transactions*, 35, (2011).

Faulds, J.E., and Hinz, N. “Favorable tectonic and structural settings of geothermal systems in the Great Basin region, western USA: Proxies for discovering blind geothermal systems.” *Proceedings, World Geothermal Congress*, (2015).

Faulds, J.E., Hinz, N., Coolbaugh, M., Ayling, B., Glen, J.M.G., Craig, J., McConville, E., Siler, D., Queen, J., Witter, J., and Hardwick, C. “Discovering blind geothermal systems in the Great Basin region: An integrated geologic and geophysical approach for establishing geothermal play fairways. Final technical report for Phases 1-3 (DE-EE0006731).” *Department of Energy*, (2019).

Faulds, J., Earney, T.E., Lindsey, C., Glen, J.M.G., Queen, J.H., Burgess, Q., Giddens, M.H. “Structural Setting and Geothermal Potential of Northeastern Reese River Valley, North-Central Nevada: Highly Prospective Detailed Study Site in the INGENIOUS Project.” *Proceedings: GRC Transactions*, 48, (2024) *Same conference*.

Glen, J. M., and Ponce, D. A. “Large-Scale Fractures Related to the Inception of the Yellowstone Hotspot.” *Geology*, 30, (2002), doi: 10.1130/0091-7613(2002)030<0647:LSFRTI>2.0.CO;2.

Glen, J.M., and Earney, T.E. “New high resolution airborne geophysical surveys in Nevada and California for geothermal and mineral resource studies.” *Proceedings: GRC Transactions*, 48, (2023).

Glen, J.M.G., and Earney, T.E. “GeoDAWN: Airborne magnetic and radiometric surveys of the northwestern Great Basin, Nevada and California.” *U.S. Geological Survey Data Release*, (2024), https://doi.org/10.5066/P93LGLVQ.

Grauch, V.J.S., and Cordell, L. “Limitations of determining density or magnetic boundaries from the horizontal gradient of gravity or pseudogravity data.” *Geophysics*, (1987), doi: 10.1190/1.1442236.

Hildenbrand, T., Briesacher, A., Flanagan, G., Hinze, W., Hittleman, A., Keller, G., Kucks, R., Plouff, D., Roest, W., Seeley, J., Smith, D., and Webring, M. “Rationale and Operational Plan to Upgrade the U.S. Gravity Database.” *U.S. Geological Survey Open File Report*, 02-463, (2002), doi: 10.3133/ofr02463.

Jachens, R.C., and Moring, B.C. “Maps of the Thickness of Cenozoic Deposits and the Isostatic Residual Gravity Over Basement for Nevada.” *U.S. Geological Survey Open File Report*, 90-404, (1990), doi: 10.3133/ofr90404.

Jachens, R.C., Moring, B.C., and Schruben P.G. “Thickness of Cenozoic Deposits and the Isostatic Residual Gravity Over Basement” *Chapter 2 in Singer, An Analysis of Nevada's Metal-Bearing Mineral Resources, Nevada Bureau of Mines and Geology Open-File Report*, 96-02-02, (1996).

John, D.A., and Wrucke, C.T. “Geologic map of the Mule Canyon Quadrangle, Lander County, Nevada.” *Nevada Bureau of Mines and Geology*, Map 144, (2003).

Kelbert, A., Meqbel, N., Egbert, G.D., Tandon, K. “ModEM: A modular system for inversion of electromagnetic geophysical data.” *Computers and Geosciences*, 66, (2014).

McKee, E.H., and Noble, D.C. “Tectonic and magmatic development of the Great Basin of western United States during late Cenozoic time.” *Modern Geology*, 10, (1986).

Munoz, G. “Exploring for Geothermal Resources with Electromagnetic Methods.” Surveys in *Geophysics*, 35, (2014).

Nevada Bureau of Mines and Geology. “Geothermal Well Information.” Accessed from URL https://nbmg.unr.edu/geothermal/WellInfo.html, (accessed, 3/2023a).

Nevada Bureau of Mines and Geology. “Oil and Gas Well Search.” Accessed from URL https://nbmg.unr.edu/Oil&Gas/WellSearch.html, (accessed, 3/2023b).

Nevada Division of Water Resources. “Well Driller Reports.” Accessed from URL https://data-ndwr.hub.arcgis.com/datasets/NDWR::well-driller-reports/about, (accessed, 3/2023).

Newman, G.A., Gasperikova, E., Hoversten, G.M., Wannamaker, P.E. “Three-dimensional Magnetotelluric Characterization of the Coso Geothermal Field.” *Geothermics*, 37, (2008).

Phillips, J.D., Hansen, R.O., and Blakely, R.J. “The use of curvature in potential-field interpretation.” *Exploration Geophysics*, 38, (2007).

Ponce, D.A. “Gravity Data of Nevada.” *U.S. Geological Survey Data Series*, 42, (1997), doi: 10.3133/ds42.

Ramelli, A.R., House, P.K., Wrucke, C.T., John, D.A. “Geologic map of the Stony Point Quadrangle, Lander County, Nevada.” *Nevada Bureau of Mines and Geology*, Map 131, (2001).

Ramelli, A.R., Wrucke, C.T., House, P.K. “Geologic map of the Bateman Spring Quadrangle, Lander County, Nevada.” *Nevada Bureau of Mines and Geology*, Map 185, (2017).

Sass, J.H., A.H. Lachenbruch, R.J. Munroe, G.W. Green and T.H. Moses, Jr. “Heat flow in the western United States.” *Journal Geophysics Research*, 76, (1971).

Seequent, Oasis Montaj, 2023.2, (2023).

Stewart, J.H., Walker, G.W., and Kleinhampl, F.J. “Oregon-Nevada lineament.” *Geology*, 3, (1975).

U.S. Geological Survey: 3D Elevation Program 10-Meter Resolution Digital Elevation Model, accessed from URL https://www.usgs.gov/the-national-map-data-delivery, (accessed, 8/2021a).

U.S. Geological Survey: 3D Elevation Program 1-Meter Resolution Digital Elevation Model, accessed from URL https://www.usgs.gov/the-national-map-data-delivery, (accessed, 8/2021b).

U.S. Geological Survey: Quaternary Fault and Fold Database for the United States, accessed from: https://www.usgs.gov/natural-hazards/earthquake-hazards/faults, (accessed, 7/2021).

Watt, J.T., Glen, J.M.G., John, D.A., Ponce, D.A. “Three-dimensional geologic model of the northern Nevada rift and the Beowawe geothermal system, north-central Nevada.” *Geosphere*, 3, (2007), doi: 10.1130/GES00100.1.

Williams, N., Faulds, J.E., Ayling, B., Glen, J.M.G., Earney, T.E., Siler, D., Kraal, K., Wagoner, N., Morales-Rivera, A. “Analysis of a Blind Geothermal System in the Northern Reese River Basin.” *Proceedings: GRC Transactions*, 46, (2022).

Zeng, Y. “GPS Velocity Field of the Western United States for the 2023 National Seismic Hazard Model Update.” *Seismological Research Letters*, 93, (2022), doi:10.1785/0220220180.

Zoback, M.L., and Thompson, G.A. “Basin and range rifting in northern Nevada: Clues from a mid-Miocene rift and its subsequent offsets.” *Geology*, 6, (1978), doi: 10.1130/00917613(1978)6<111:BARRIN>2.0.CO;2.

Zoback, M.L. “A geologic and geophysical investigation of the Beowawe geothermal area, north-central Nevada.” *Stanford University Publications in the Geological Sciences*, 16, (1979).

Zoback, M.L., McKee, E.H., Blakely, R.J., Thompson, G.A. “The northern Nevada rift: Regional tectono-magmatic relations and middle Miocene stress direction.” *Geological Society of America Bulletin*, 106, (1994).

Reducing Costs and Mitigating Risk for Geothermal Energy with Permeable Fracture Imaging

Jeffrey Eppink, James Geiser, Peter Geiser, Peter Malin, Austin Mathews, Anastasia Stroujkova

Enegis, LLC

Keywords

Permeable Fracture Imaging, Reservoir Characterization, Permeability, Fractures, Seismic Imaging, Geothermal Reservoir

ABSTRACT

To mitigate risk and maximize the chances for sustained fluid flow in geothermal reservoirs, knowledge of permeability field architecture is vital. We achieve this by mapping permeable fractures with a non-microearthquake seismic listening method: Permeable Fracture Imaging, PFI. Enegis has demonstrated the viability of PFI technology on a lease operated by AltaRock Energy at the Newberry Volcano in Oregon and funded by the Advanced Research Projects Agency–Energy and Quaise Energy.

The PFI signal is created by minute elastic vibrations of fluid-filled voids and fractures activated by the propagation of episodic stress waves through the crust. The PFI directly addresses the knowledge gap of the heterogeneous permeability field—not by modeling—but by directly mapping the permeable fractures. The result is a five-dimensional (space, time, energy) map of fracture permeability.

In October 2023, we conducted a ~1,000 geophone survey over a ~27 km^2 area on the west flank of Newberry caldera. Passive recording was conducted over 4 ½ days. The survey imaged a 1.6 x 1.6 km target zone centered on a lease well. Our deepest imaging volume was at 2200 m depth.

Based on independent near-well observations, the PFI survey recorded active permeable fractures along the well and mapped them far beyond the well. Sub-regional NNW-SSE fault and fracture zone trends are clearly observed. Further, the PFI results correlate with independent lithology, density, and resistivity data. They also are consistent with a lower-resolution map of the magnetotelluric-delineated clay cap and observed Bouguer gravity anomalies.

The PFI method is empirical and repeatable, supplying actual data, not simulations, which contrasts with traditional reservoir modeling. The technique also can provide accurate reservoir

monitoring. Except for the velocity model, the PFI technique requires no modeling assumptions. Relative to microearthquake techniques, which require three component geophones at similar grid size to PFI surveys, PFI is less costly. It also is not subject to the need to have the sensors in-place during MEQ swarms. Compared to the linear geometry of single fiber optic DAS cable, the 2D PFI geophone grid provides significantly better target locations.

We have performed technoeconomic analyses for PFI surveys using cost data from DOE models. These studies show that the PFI technique could reduce reservoir development life-cycle costs and monitoring by 40% compared to the status quo for seismic methods. The PFI technique materially helps minimize the "drilling blind" problem that has plagued geothermal development, leaving it behind in the race for investment compared to wind and solar. The PFI technique results in a direct mapping of permeability field architecture as opposed to computer simulations, which can be driven by assumptions. The PFI technique also has potential for application in geologic carbon storage, wastewater injection and delineation of blind mineral deposits.

1. Introduction

Enegis, LLC, (Enegis) applied for and was awarded an ARPA-E Small Business Innovative Research (SBIR) grant under the Supporting Entrepreneurial Energy Discoveries (SEED) program in September 2022. The award is entitled Ambient Seismic Imaging (ASI) Technology for Low Cost and Effective Geothermal Resource Exploration, Development, and Management. A geothermal lease on Newbery Volcano in Oregon is the site of the project. Of note, Enegis re-branded ASI as Permeable Fracture Imaging (PFI) as a means of focusing technology's impact on the critical technical geothermal reservoir parameters of active permeability and fluid flow.

Permeable Fracture Imaging technology uses seismic emission tomography methods and passively listens to vibrations due to stress-change-induced fluid-rock interactions. These interactions are episodically created by the earth's flux of stresses that form the Transient Stress Field (TSF) whose variation is at a time scale measured in seconds (P. Geiser and P. Malin, personal communication, 2024). The data comprising the TSF are part of the seismic "noise" or endogenous radiation spectrum, which in recent years has also been called "seismic emissions". This noise is the subject of considerable interest, e.g., Chebotereva (2000). Research has revealed that the noise is the product of natural non-random sources of seismic energy that affect the brittle crust and manifest in the seismic record e.g., oceanic waves, e.g. (Aster, R., C., et al, 2023), atmospheric loadings, e.g. (Rodrigues 2007), Earth tides, volcanic tremors, etc.

Wavelet analysis by J. Geiser (2024, personal communication) of the natural rock permeability-associated vibrations shows that they are episodically periodic with episodes common over periods of many minutes. The heterogeneous permeability field of the Earth's brittle crust has long been a challenge for the extraction of fluid resources. Our seismic method solves this problem—not by modeling—but by directly mapping the permeability field architecture quantitatively and temporally. The PFI signal is due to minute elastic vibrations of fluid-filled fractures and voids activated by the near-continuous movement of episodic stress waves through the crust. We note that the PFIs we develop are active surfaces that can be associated with fractures. Our product is a five-dimensional (space, time, energy) permeability field map, taken from Geiser et al. (2023), which the broader group of us recently published. (Figure 1).

This article describes the geological setting, previous germane, technical work conducted on the West flank of Newberry Volcano, our data acquisition process, the field survey, data processing, interpretation, and results. Of note, given the funding limitations of the ARPA-E grant, we could only design the field survey to confidently image to depths of ~2100 m, which is shallower than the target objective of the NWG 55-29 well.

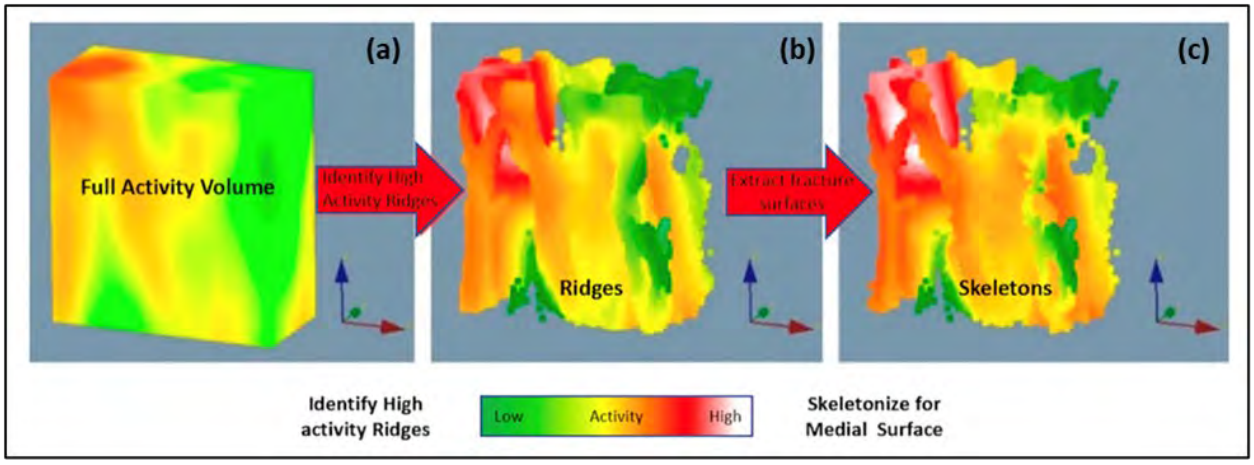

Figure 1. Processing of survey data for semblance full activity volumes (FAVs). (a) FAV, (b) Isolation of ridges, (c) Peak picking on the FAV to find local areas of connected high activity voxels. In 3D form "clouds" of high-activity permeability field (HaPF) emissions, which are skeletonized to form 1-voxel-thick medial HaPF surfaces (from Geiser et al., 2023).

2. Geological and Geophysical Background

Located within central Oregon, Newberry Volcano (Figure 2b, Newberry shown as point "A") is situated near the conjunction of three distinct geologic zones, including the Cascade Volcanic Arc to the west, the Basin and Range province to the south and southeast, and the Columbia Plateau in the northeast and east. Newberry Volcano is a large shield construct located approximately 60 km east of the axis of the Cascade Range, and approximately 35 km from the city of Bend, Oregon.

As a broad shield volcano, Newberry has shown evidence of volcanic activity for the last 600,000 years. The volcano is bimodal in nature skirted with predominantly felsic, caldera-centered eruptions, and mostly mafic eruptions on the flanks, generally composed of ash/lahar deposits, as well as basalts, andesites, and cinder cones, while the caldera contains obsidian flows, rhyolitic tephra, cinder cones, maars, and vents, with heavy faulting penetrating the units in the caldera. A geologic map of the Newberry volcano is depicted in Figure 2a.

Newberry's youngest lava flow is called the Big Obsidian Flow, which is approximately 1,300 years old (Robinson et al., 2015). Due to Newberry's recent volcanic activity, the United States Geological Survey (USGS) has classified it as the 13th most threatening volcano in the United States (Ewert et al., 2018).

2.1 Structural Trends

The stress state of the Newberry region has been examined in previous work using focal mechanisms from earthquakes. Regionally, the least compressive stress (σ3) is generally oriented ENE/WSW (264° ± 29°), the principal compressive stress (σ1) is near vertical, and the intermediate stress (σ2) is oriented approximately north to south (or NNW/SSE) (Crider, 2001). Other stress indicators, such as dikes, cinder cones, and the orientation of faults (such as the Sisters fault zone near Bend, Oregon) suggest similar stress orientations (Newberry Geothermal Energy, 2016).

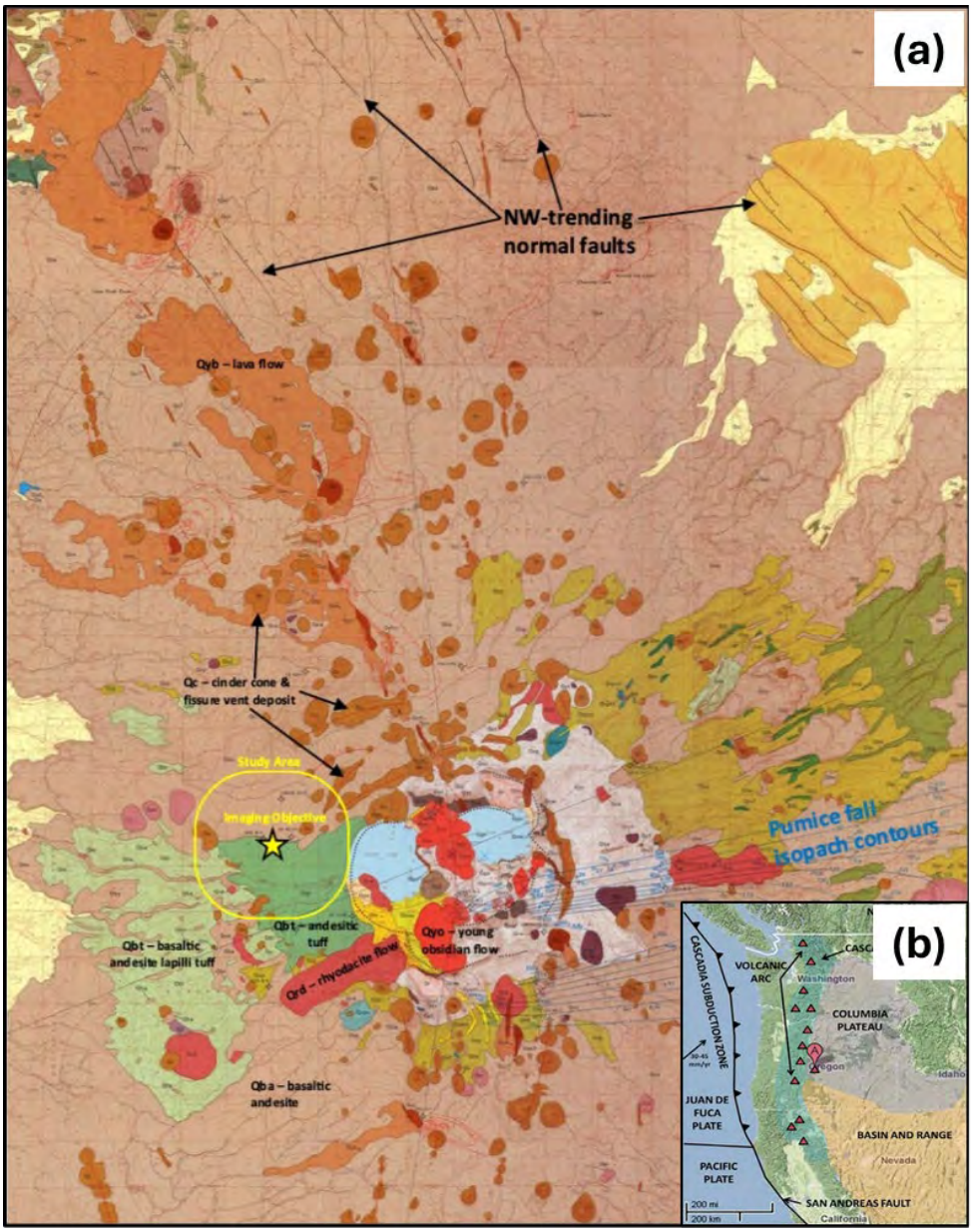

Figure 2. (a) Geologic Map of Newberry Volcano (MacLeod et al., 1995). (b) Geologic Provinces of the Pacific Northwest (Newberry Geothermal Energy, 2016).

The faults in the region are characterized by two dominant orientations (Figure 3a), including a set of tectonically related northwest-striking faults (shown in yellow), and a separate set of faults and fractures that developed as a result of volcano formation (shown in red and orange). Scarps around Newberry volcano are generally oriented N-S and the fissures tend to be oriented NNW (Cladouhos et al., 2011). The recent lava flows of Newberry volcano also strike in the NNW/SSE direction in what is known as the Northwestern Rift Zone (Figure 3b). This NNW structural trend is also reflected in several surficial lineaments within LiDAR imagery.

Well NWG 55-29, the imaging objective of the study, underwent a stimulation in 2014 and gathered microearthquake (MEQ) data to characterize the fault-slip kinematics of the reservoir (Figure 3c). The distribution of P (compression) and T (extension) axes form a thrusting fault-plane solution with slight obliquity that strikes NNW and accommodates ENE-WSW shortening. The fault set exhibits structural trends that generally match the regional stress orientation.

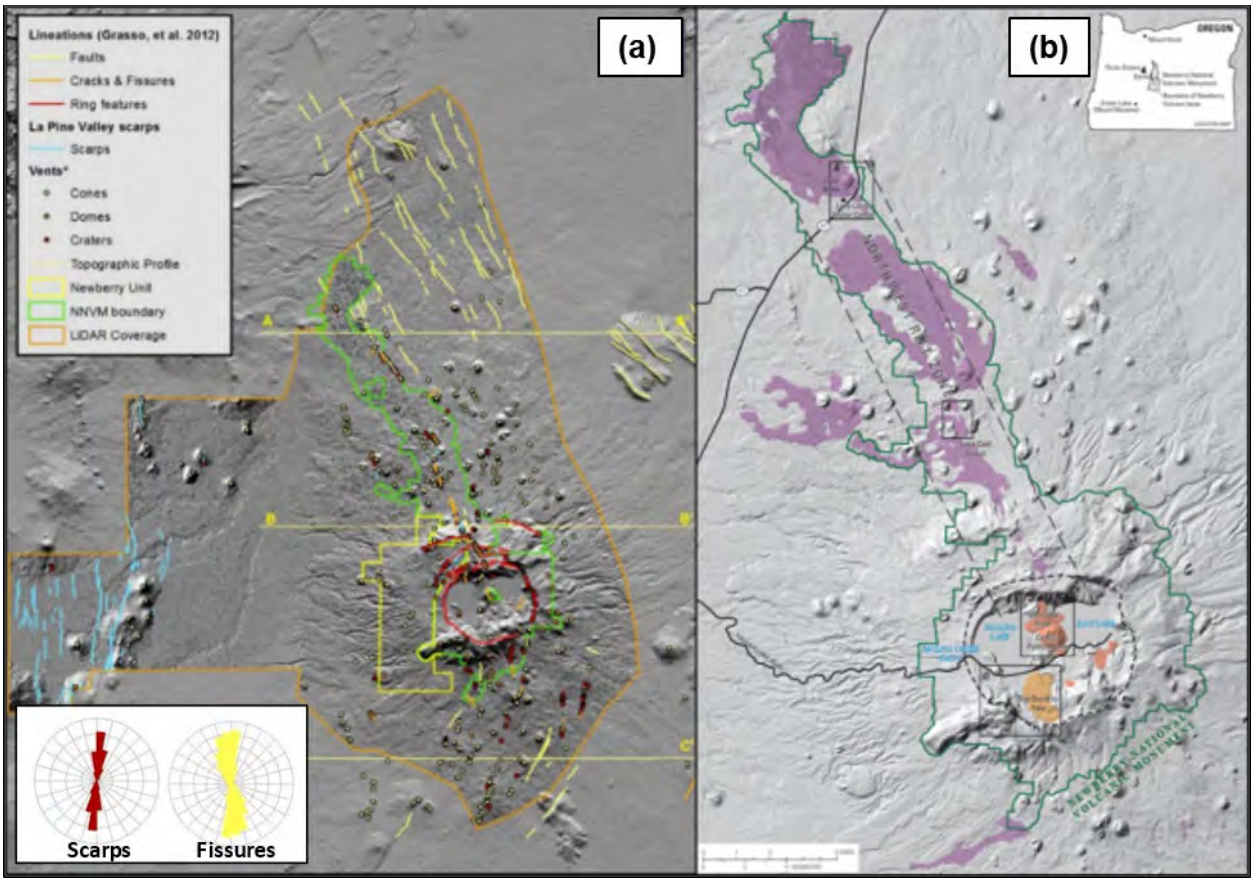

Figure 3. (a) Newberry Fault Zones (from Newberry Geothermal Energy, 2016; Cladouhos et al., 2015). (b) Northwestern Rift Zone (from Robinson et al., 2015).

2.2 Volcano-scale Geophysics

Several geophysical investigations have been conducted on the west flank of Newberry Volcano in attempts to elucidate the nature of the subsurface geology. Gravity surveys, collected in 2007 and 2010, are presented in the complete Bouguer Anomaly map in Figure 4a (Waibel et al., 2012).

The edge of the volcano's structure is inferred from gravity data trends NNW/SSE, consistent with the regional stress orientation. The high-density rocks (shown in purple) and high geothermal gradients present in the western flank of the volcano suggest that the pluton is young enough to still maintain its high heat. Taverna et al. (2024) found gravity anomalies were present beneath the caldera and on the western and northwestern flank, and these coincide with areas of high favorability for enhanced geothermal systems (EGS) development.

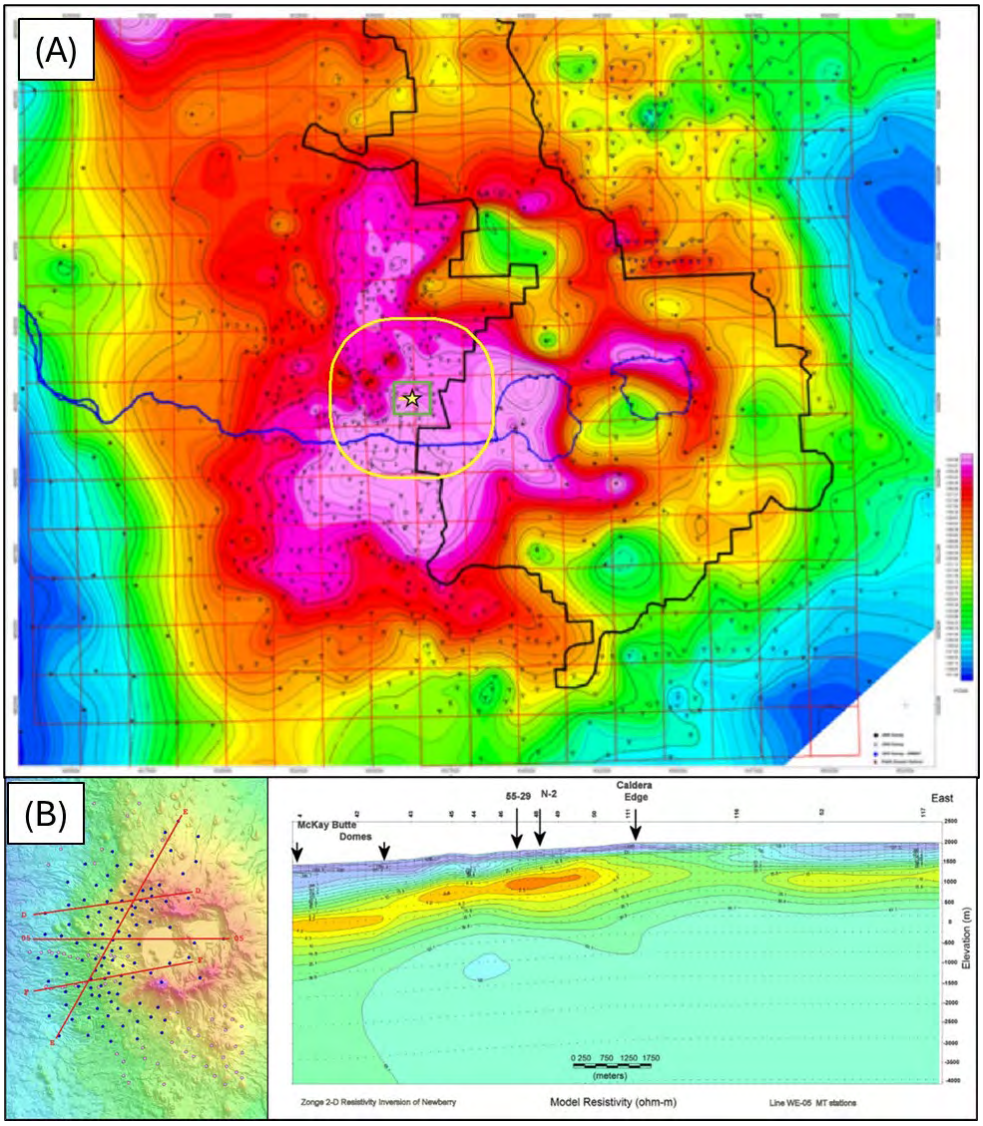

Figure 4. (A) Complete Bouguer Anomaly with density reduction value of 2.5 g/cc (Waibel et al., 2012) (B) 2D MT slice, Line 05 (Waibel et al., 2012).

The electrical resistivity of the reservoir beneath Newberry volcano was studied using magnetotelluric (MT) surveys (Figure 4b), which are affected by the presence of fluids, rock composition, temperature variations, porosity, and permeability. At Newberry, there is a shallow, electrically conductive layer on the west flank of the volcano that is underlain by an electrically resistive mass. Generally, the base of the shallow conductive layer is indicative of an interface

between lower temperature clay/zeolite alteration and high temperature greenschist facies alteration (Waibel et al., 2012). NWG 55-29, the target objective of this study, is located at the western edge of this zone.

3. Data Planning and Acquisition

3.1 PFI Net Design

We designed the survey using a nominal 175 m spacing based on imaging objectives and economic constraints for the number of geophones that we could use for the project. We then raytraced our nominal layout based on certain criteria, including:

- land access
- the physical and ecological geography of the field area
- randomization
- efficient positioning of the geophones

The final survey layout depicted in Figure 5 covers 25 km^2 and comprises about 1000 stations. Each station was to be occupied by a geophone, recorder, and battery as a single unit called a Nodal Recording Unit (NRU).

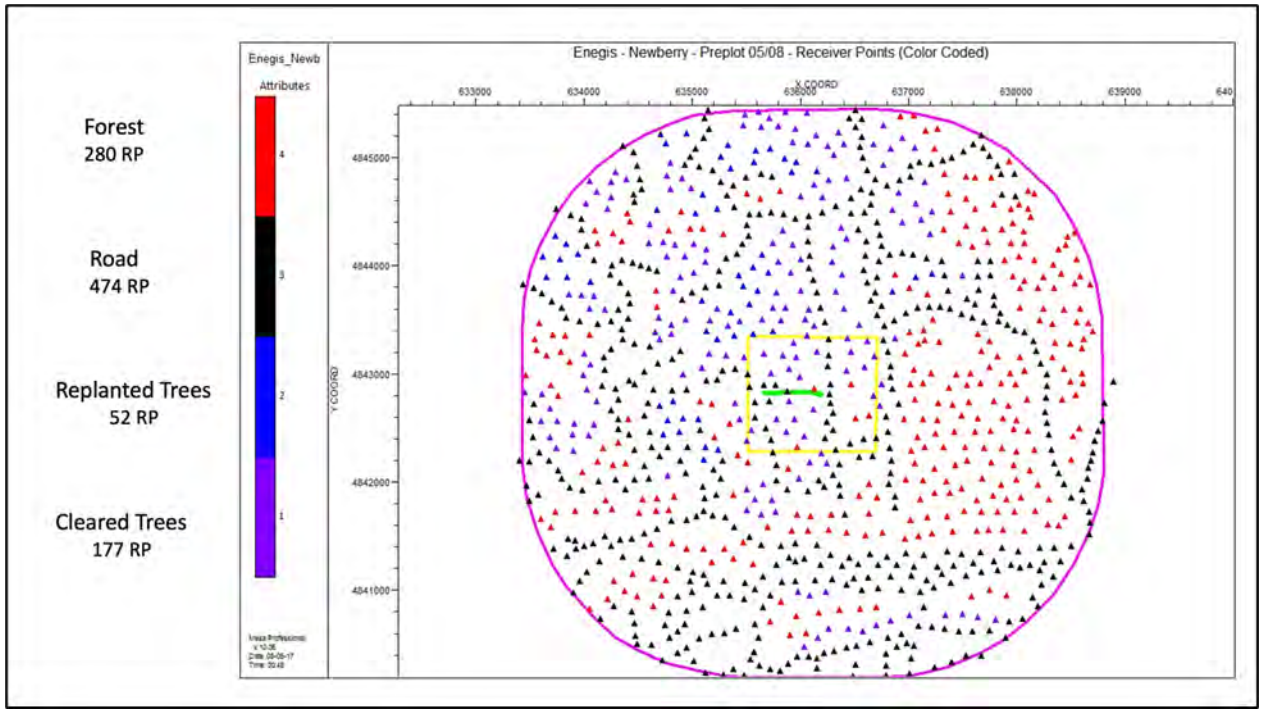

Figure 5. Nodal Recording Unit layout

3.2 Permitting and Field Survey

Material difficulties were encountered in obtaining land access permits from the U.S. Forest Service (FS) due to bureaucratic delays beyond Enegis' control. Upon our field permit issuance

28 September 2023, Enegis mustered multiple field crews and implemented the survey from 7 to 19 October, allowing for 5.5 days to emplace nearly 1000 geophones, recorded for 4.5 days and 3 days of pick-up. Each NRU was emplaced in a shallow (~10 cm) hole that was dug with a slide hammer ((b) in Figure 6), geopositioned with a Juniper Geode unit (c). The computed field positioning of the NRUs is shown in (d). Four days following our survey, the survey area was covered in about 15 cm of snow (e).

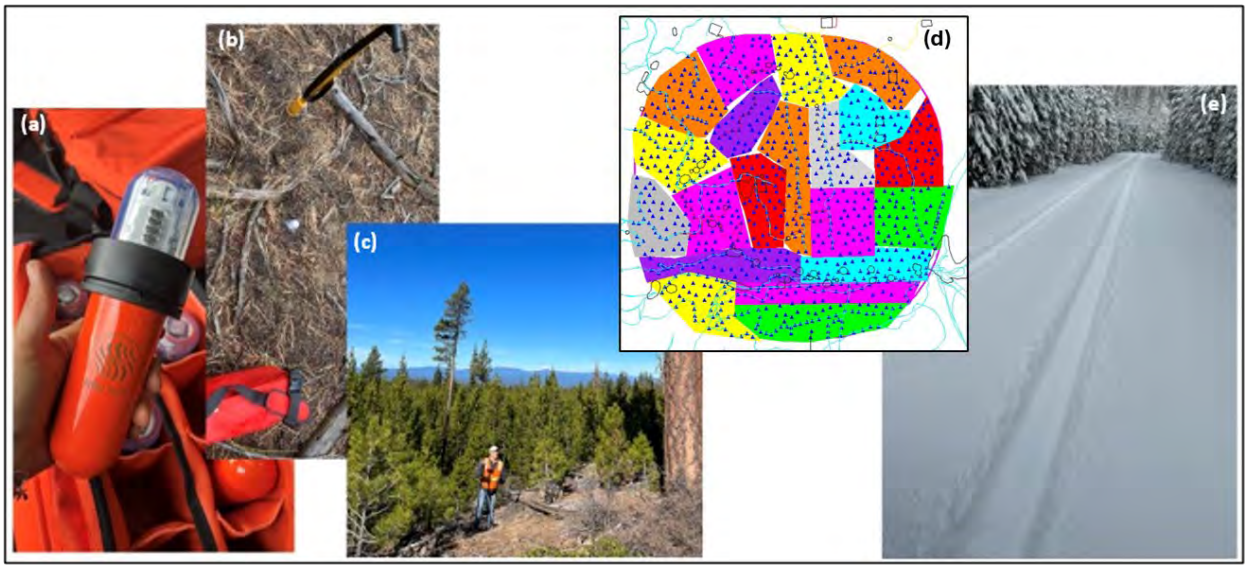

Figure 6. Newberry Volcano field program. (a) a typical NRU, (b) an emplaced NRU, (c) geopositioning of the node, (d) the emplaced field nodal array and (e) field conditions 4 days following the survey

The full array comprised 982 geophone nodes, for which we had a 99.5% success rate for recording, resulting in 977 NRUs with recorded data. Figure 7 depicts the semblance fold at 2100 m aperture in our imaging cube, which is the number of receivers that a given depth point has available to it for imaging. The fold coverage in red is over 600, which provided an excellent basis for developing PFIs.

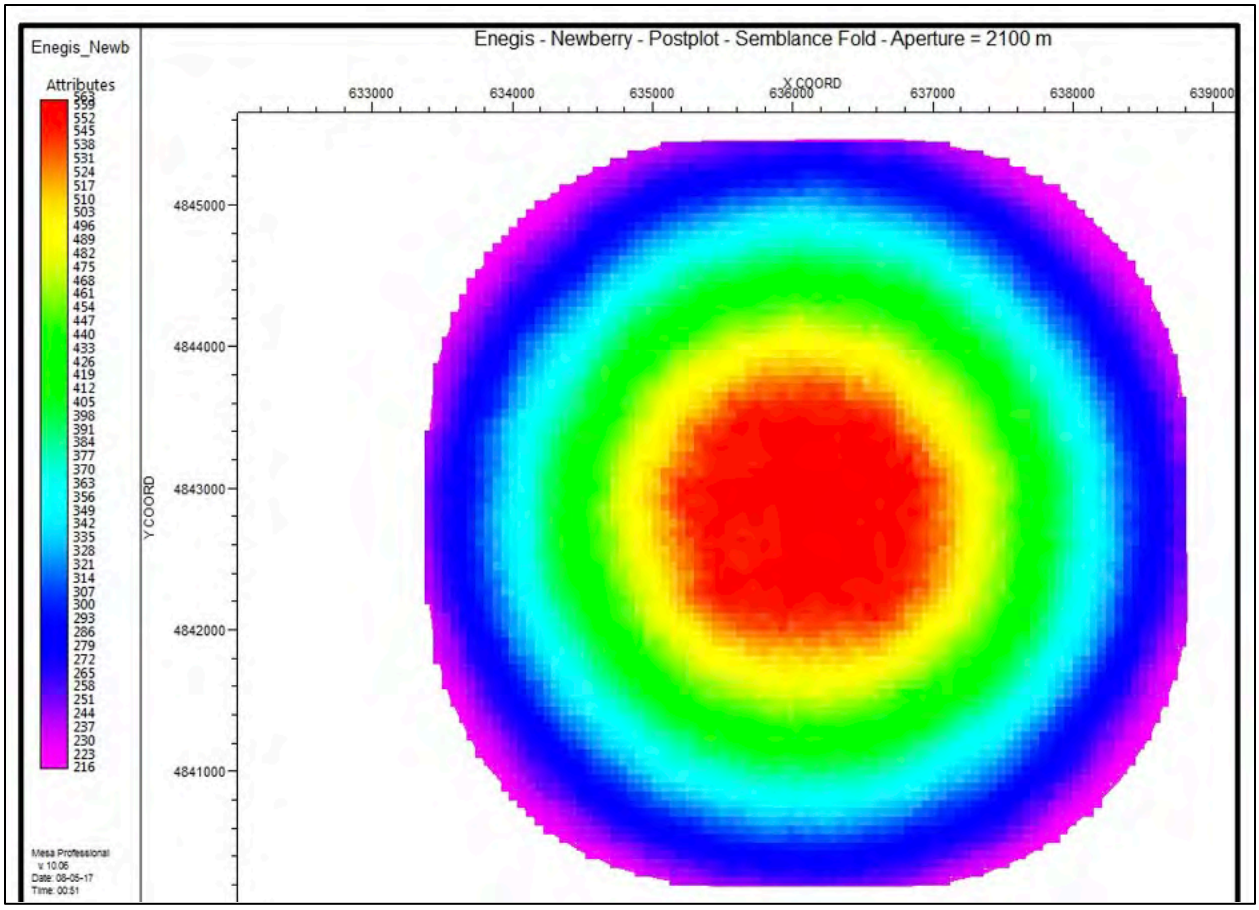

Figure 7. Survey fold coverage.

3.3 Noise Analysis

Seismic noise can significantly degrade the quality of seismic measurements and affect the performance of ambient noise imaging. Cultural noise from moving vehicles and operating machinery (pumps, generators etc.) poses problems during the day. Other noise sources include rain, wind, running water in the creek, local and remote earthquakes and microseisms.

We analyzed seismic amplitudes from all array nodes during the time of the experiment to determine the noisy locations and time intervals. Figure 8a shows the full grid root mean square (RMS) amplitudes averaged over each minute during the full array spread. Notice the diurnal pattern with higher amplitudes during the day and lower amplitudes at night. Figure 8b-e shows the amplitudes for each node averaged over 6-hour intervals highlighted in a. Strong cultural noise is observed on Saturday afternoon (b) with the highest amplitudes following the road and various tourist attractions in the southern part of the array. Figure 8c and e show the array amplitudes between midnight and 6AM on 15 and 17 October. The noise level during these time intervals is significantly lower than during the Saturday afternoon. Figure 8d shows the array amplitudes between 6 AM and noon on 16 October. High noise level observed during this time interval is spread over the entire array, although the amplitudes vary between the nodes. 15 October appears to be the quietest day overall.

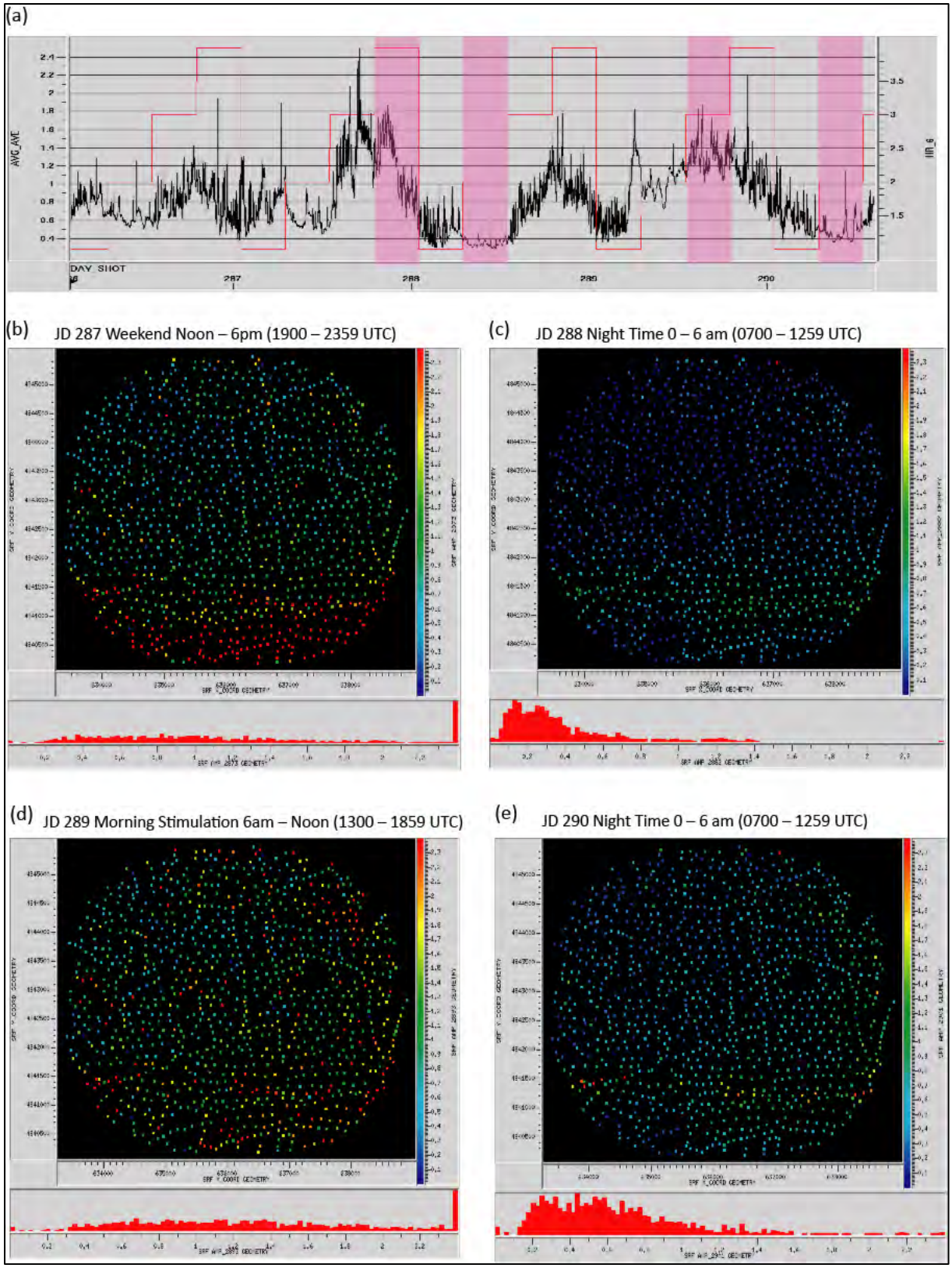

Figure 8. (a) Full grid RMS amplitudes. (b) Array amplitudes on 14 October 2023. (c) Quiet time interval on Sunday, 15 October 2023. (d) Monday, 16 October (e) Quiet time on Tuesday, 17 October.

4. Data Processing

The PFI method used to identify regions with high fracture density is based on conventional reflection seismic signal processing algorithms modified to deal with one-way travel times between the fracture sources and the receivers. The processing of the seismic data is performed in the following major steps: (1) Noise suppression: (2) estimation of elevation and residual statics; (3) building the earth velocity model; and (4) one-way travel time depth migration for a continuous signal source. The processing steps are outlined below.

4.1 Signal Denoising, Enhancement, and Quality Control

Data from 977 nodes were recorded during the array deployment. We used the data acquired during the full array spread between 13 and 17 October 2023 to analyze and reduce the noise. Success in using fracture seismic recordings for mapping fractures requires extensive trace editing, signal enhancement and noise suppression (Sicking et al., 2016). To identify high- and low-noise time intervals we calculated RMS amplitudes averaged over each minute for each receiver during the array full spread period and then summed them over time.

The first step in the preprocessing, involving removal of the bad traces, train noise and unexplained high amplitudes, resulted in some reduction in the noise amplitude. Significant improvements have been achieved after applying a median filter and dropping individual receivers in noisy locations.

The next step in noise reduction is cepstral filtering, which is used to remove stationary noise persistent for long periods of time. This type of noise is common in populated areas and appears as noise background added to the consistent, slowly changing, harmonic character of fracture seismic signals. The noise is significantly reduced after the filter application. Using the full grid array average, we identified the low-noise 5-hour time intervals used in the final processing steps. These quiet intervals occurred during the nighttime on 15 and 17 October 2023. The intensity volumes were then estimated during these low-noise time intervals.

4.2 Estimation of Elevation and Residual Statics

Elevation and residual statics are used to account for the differences in the elevation and near-surface velocity variations between the array geophones. The elevation statics are applied by taking the difference between the surveyed elevation of each geophone and the chosen constant elevation datum, then computing the travel time for the elevation difference using the near surface velocity. The computed travel time shifts are applied to the traces before the one-way depth migration.

4.3 Building the Earth Velocity Model

Our velocity model is set within the geologic context of Newberry Volcano. Existing velocity data comes from several seismic experiments utilizing both active and passive sources, including a 1983 seismic refraction profile (Cotton and Catchings, 1989), a 1984 active source seismic experiment (Dawson and Stauber, 1986), and a 2008 active source seismic experiment (Beachly et al., 2012). A comparison of several existing velocity models is presented in Figure 9b. In this study we used a model modified from Beachly et al. (2012) by warping on topography.

Due to significant topographic features in the study area, estimation of 3D seismic travel times is required to perform the imaging. Using 3D raytracing is computationally intensive compared to

using a simple layered velocity model. A 3D velocity model was developed using a flat image datum at the elevation of 2000 m. To build the velocity model, small time shifts were added to re-datum the receiver data from the surface to a smoothed elevation-based surface. The final step involves filling the shallow velocity layer to the datum elevation. Figure 10 shows the slice through the final 3D velocity model.

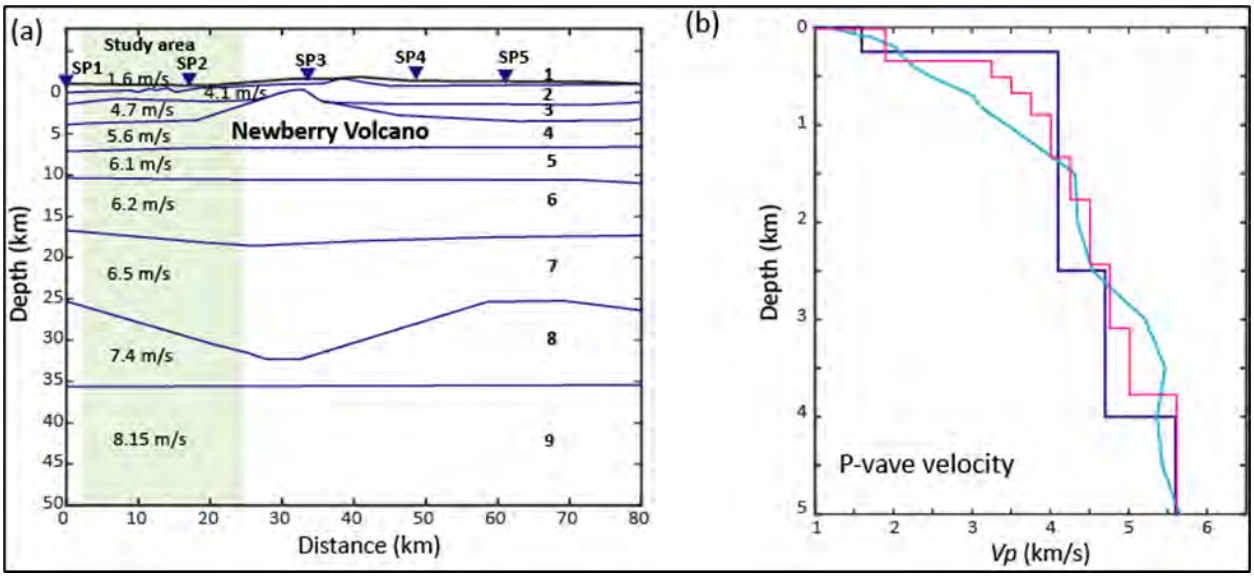

Figure 9. (a) Seismically derived crustal velocity model (from Catchings & Mooney, 1988). Numbers 1-9 refers to layers 1-9 described in the text. (b) Seismic velocity structure for the Newberry area: blue – from Catchings & Mooney, 1988; magenta – from Beachly et al., 2012; cyan – from Templeton et al., 2014.

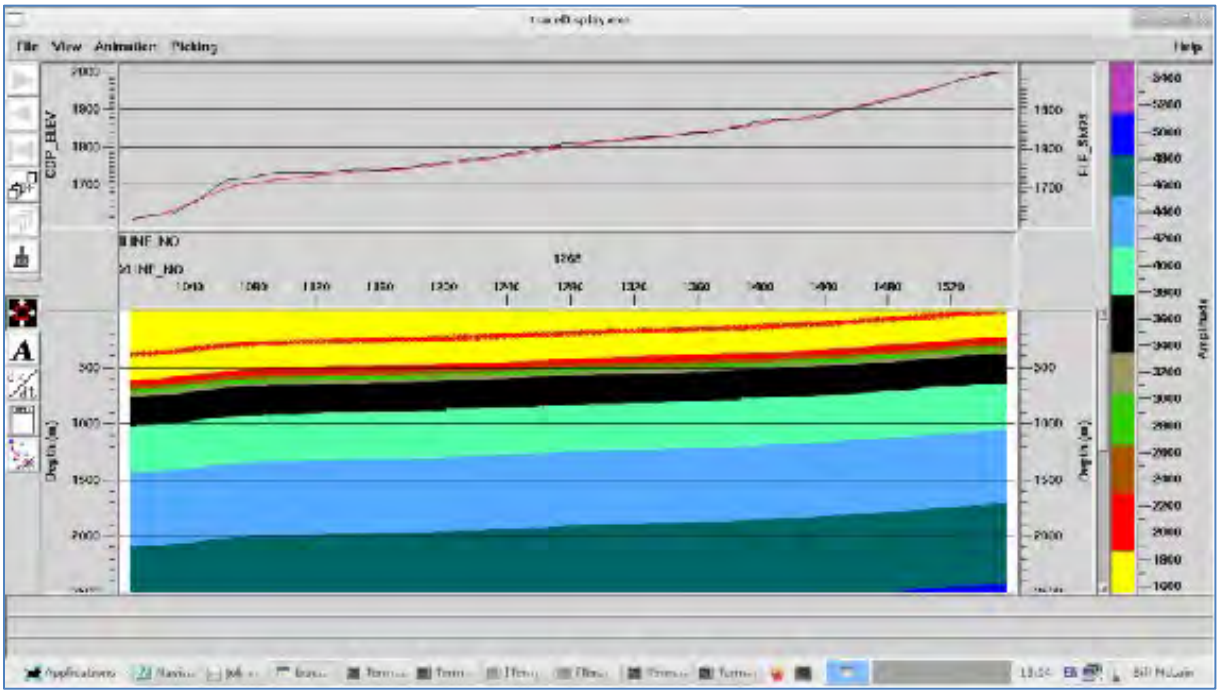

Figure 10. 3D velocity model based on Beachly et al (2012) with the velocity of 1575 m/s in near-surface layer

4.4 One-way Travel Time Depth Migration for a Subsurface Signal Source

The PFI volumes are produced using Kirchhoff depth migration with one-way travel times computed from each voxel within the volume to every receiver on the surface. Kirchhoff migration is a two-step process that first applies a time shift to each trace equal to the travel time from the voxel to the surface geophone and then images across all the time shifted traces.

Figure 11 schematically shows the processing steps used to compute the 3D seismic intensity volumes. An intensity volume is computed for each 200-millisecond time window of the trace data with a move up of 100 milliseconds between the intensity volumes. This produces a new fracture seismic intensity depth volume at 100 millisecond steps.

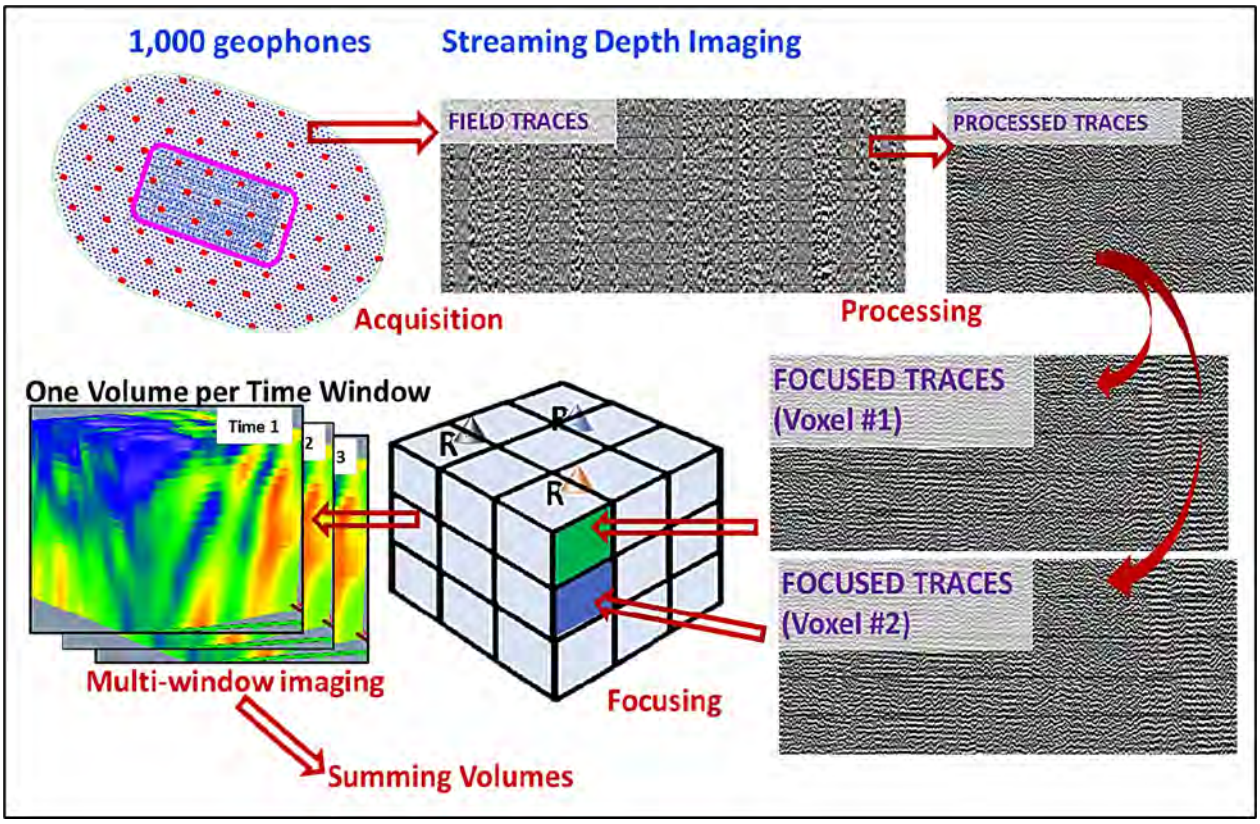

Figure 11. Workflow for one-way travel time depth migration. After trace processing and velocity model building and calibration, the traces are depth-migrated for each time window and each depth voxel for the time interval that will be summed; (from Sicking & Malin, 2019).

The survey was focused on a 1.5 x 1.5 km area at depths of 450 to ~2200 m and processed to achieve voxel sizes of 40 x 40 x 40 m and interpolated down to 10 x 10 x 10 m. The resolution of the survey is estimated to be 37 to 50 m. The final fracture seismic intensity volume is computed by summing all the volumes that are not deleted to create FAVs.

Figure 12a-b shows the horizontal slices thorough the semblance volumes stacked over the 5-hour periods with the lowest noise for 15 and 17 October. The 3D images of the intensity volumes with semblance values greater than 605 are shown in Figure 12c.

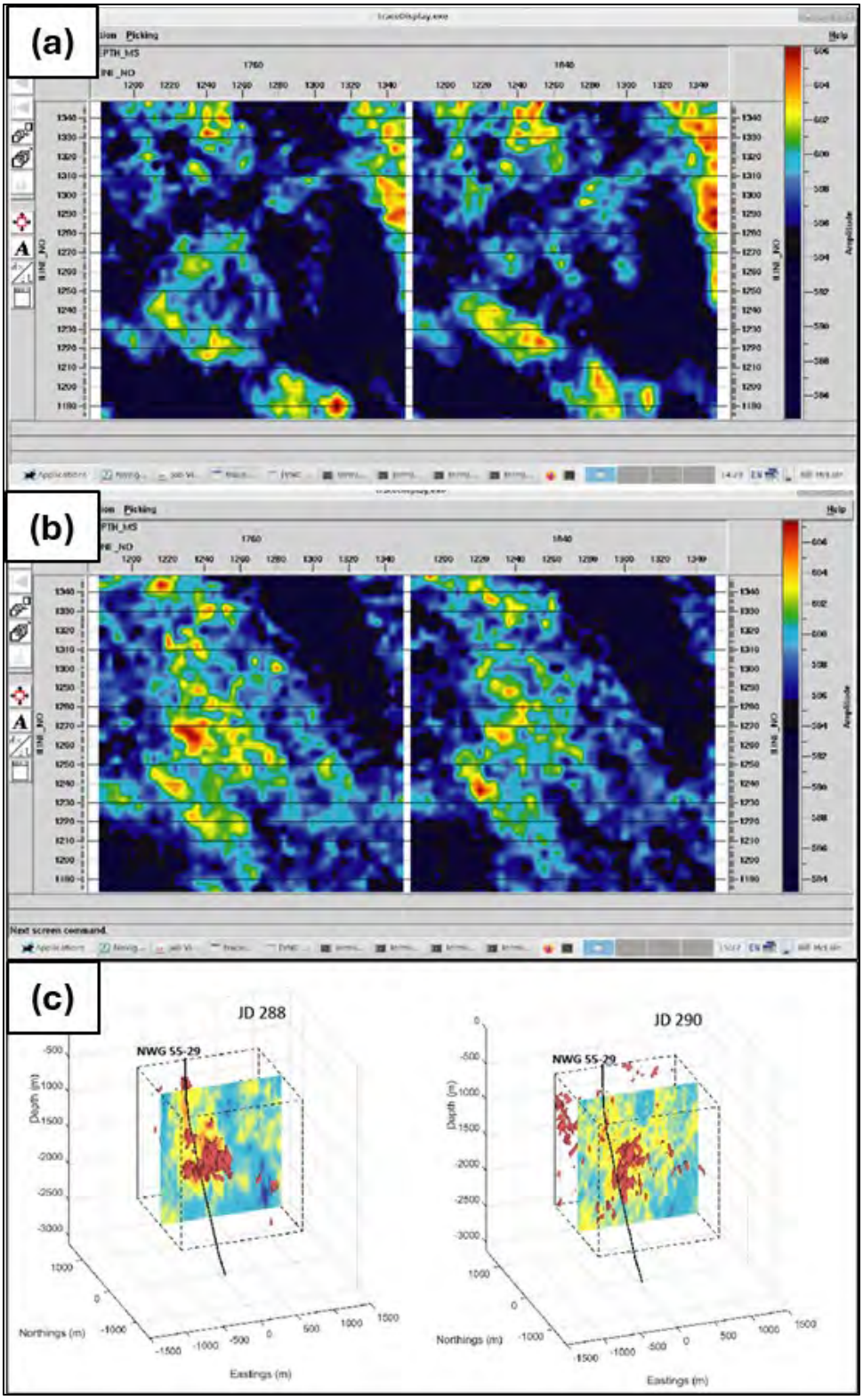

Figure 12. Five-hour stacks for the depth slices Z = 1760 m (left panels) and Z = 1840 (right panels) for the time intervals: (a) 15 October, 07:40 – 12:39 UTC and (b) 17 October, 07:40 – 12:39 UTC. (c) Five-hour semblance FAV volumes for the time intervals: 15 October, 07:40 – 12:39 UTC (left) and 17 October, 07:40 – 12:39 UTC (right).

5. Data Interpretation

5.1 The Aperture Imaging Volume Schematic

A schematic of the relative imaging quality of Newberry PFI survey is shown in Figure 13. The relative quality values shown by the color scheme are based on the number of signals included in the 2.1 km aperture centered on each subsurface point - the stack fold. This aperture was found to provide the optimal improvement of PFI signal to noise: larger apertures included low signal traces, and smaller apertures reduced the stack fold. The depth imaging capabilities of the PFI method also depend on three other factors: (1) the maximum offset from the edges of the target zone, (2) the accuracy of the seismic velocity versus depth, and (3) local control of near-surface travel time differences between individual stations.

Compared to the East and West edges of the Newberry survey, the relative signal-to-noise improvement in the NWG 55-29 well target box was a factor of ~9 greater. As the available aperture diminishes near the survey boundaries, both the stacking fold and depth imaging quality diminishes. The progressive graying – loss of signal quality and resolution – can be seen at the bottom and edges of the PFI imaging ellipsoid.

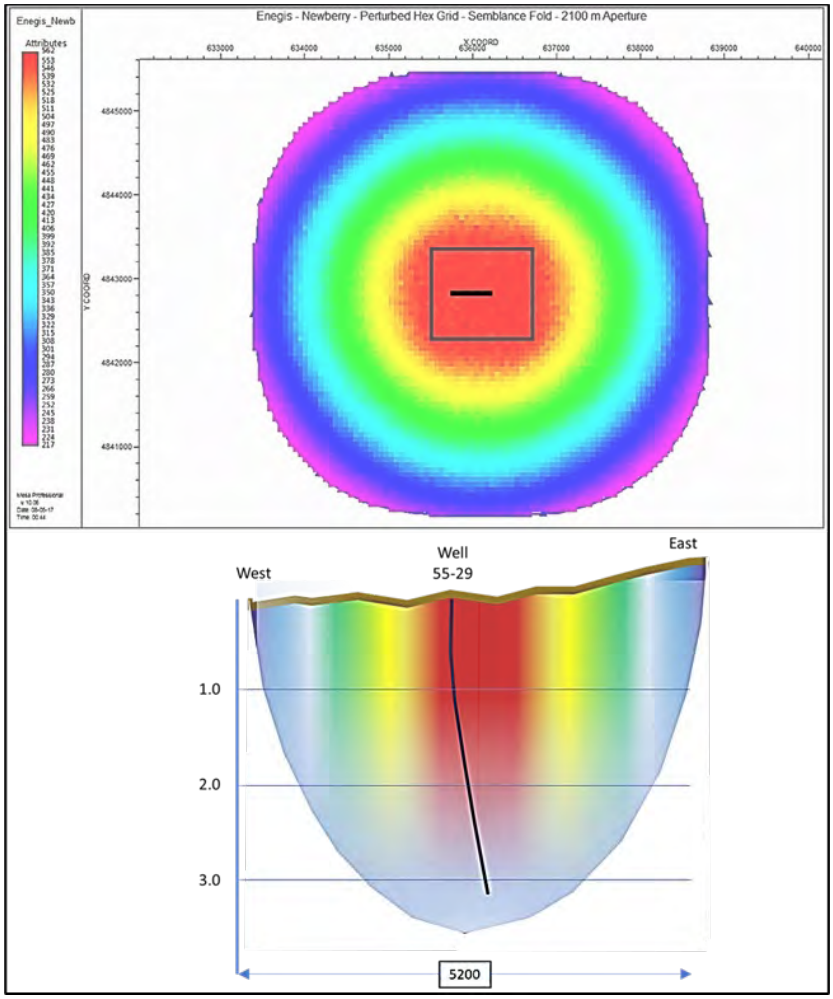

Figure 13. A map and cross section of the relative PFI image quality resulting from the stacking folds and aperture offsets of the Newberry survey. (Surface area designation is in meters. Depth is in kilometers.)

5.2 Density and Stratigraphy Log Correlation

The density and lithology logs shown below (Figure 14) are part of the well logs previously done in the NWG 55-29 borehole (Cladouhos et al., 2015). It is present here and used later as a significant marker in our first pass interpretation of the Newberry PFI data.

Comparison of the two logs suggest that crystalized flow and welded and lithified extrusive rocks have the highest and least scattered densities. Similar relations have been found in many equivalent volcanic systems.

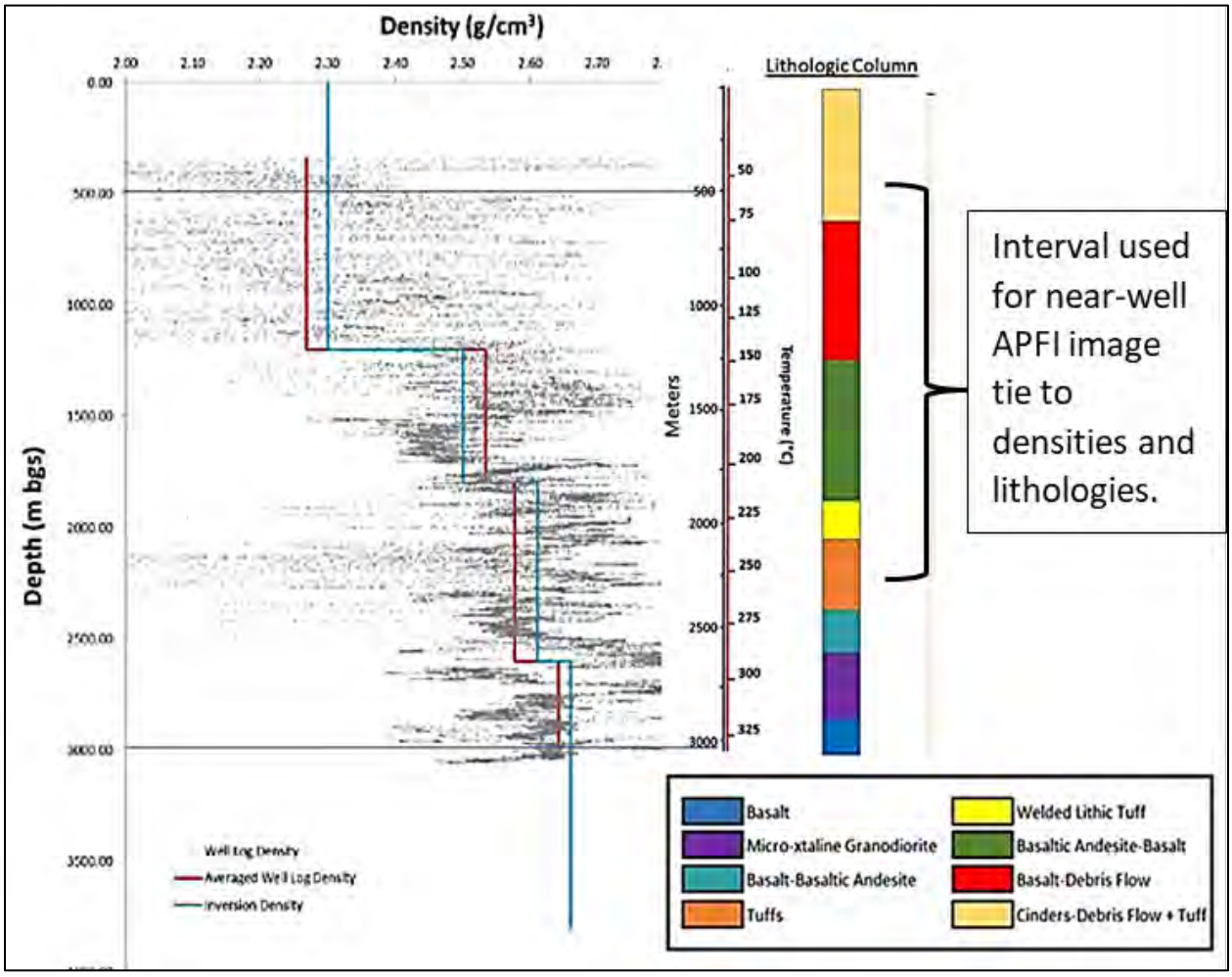

Figure 14. Density and lithology log observed in well NWG 55-29 (Cladouhos et al., 2015)

Well lithified and uniformly dense rocks have well defined fractures and are mechanically more coupled, allowing for connected fluid flow channels and efficient, low energy loss wave propagation. Therefore, naturally flowing geothermal systems are consistently associated with fractured basalt, igneous, and metamorphic rocks.

5.3 Near-well PFI

Geophysical methods such as PFI that map broad areas are difficult to interpret if they cannot be tied to some form of collocated physical property and lithology observations. Thus, in this section we show that significant PFI features are present in the near well environment of borehole NWG 55-29 – the target zone of the Newberry PFI survey. We subsequently interpret these features in the near well environment of NWG 55-29 in terms of the rock density and lithology observed in this well, and their association with ambient seismic signals from fluids in permeability structures – the Active Permeability Field. The observed correlations and their PFI interpretation are then used to extend the near well results to other portions of the target zone.

The vertical sections in Figure 15 below were taken at decreasing offset from well NWG 55-29. The sections span the density and lithology log interval shown above. They reveal the link between the Newberry PFI observations and the density/lithology of NWG 55-29 logs. This correlation is used to extend the near well result to other areas in the target zone.

Reading from the left to the right, the vertical sections in the upper and lower rows in this Figure are as viewed from the south. The section offset is listed and indicated on the map in the central row. As indicated in Figure 15 and the density/lithology log, the vertical section covers the basalt-debris flow, unwelded tuff, and cinder/volcanic ash as well as the basaltic andesite-basalt and welded tuff.

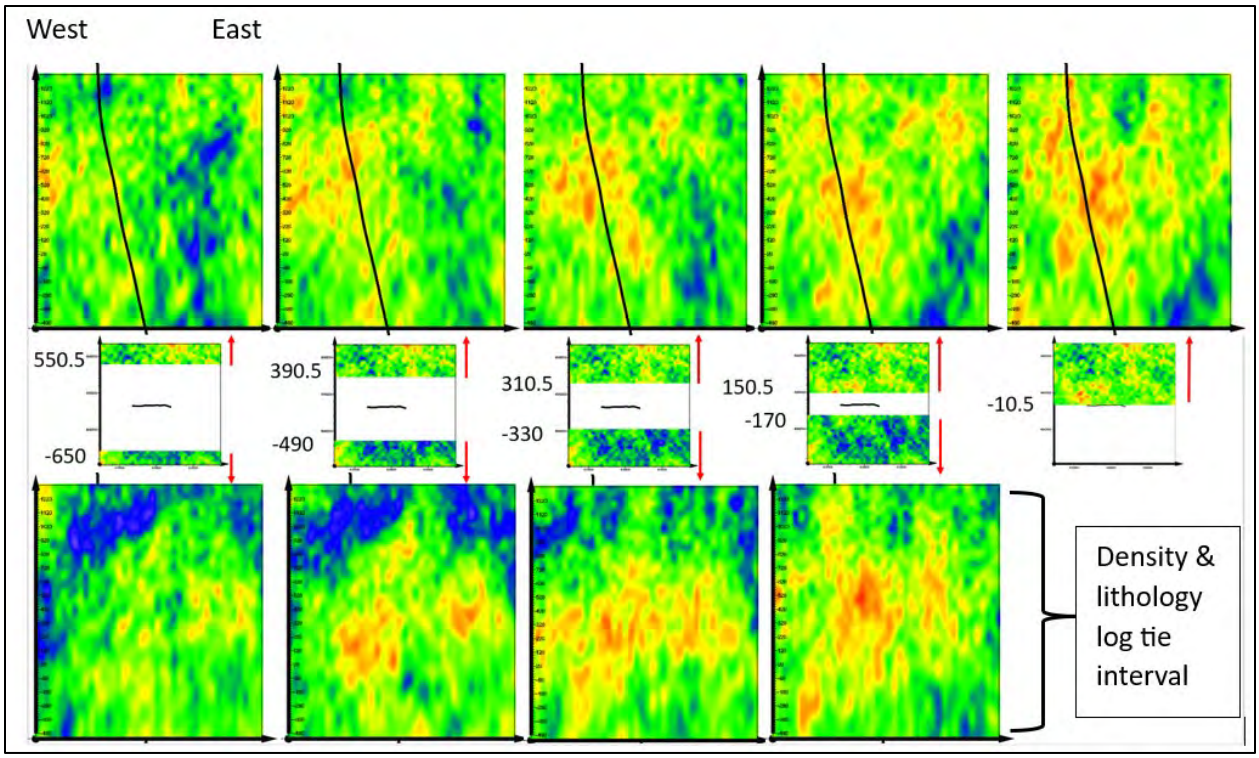

Figure 15. West to East vertical PFI X-sections. The orange color intensity depicted correlates with lithology.

These specific relations are not the focus of this section as they will be made directly explicit in the following sections. Here the important result is observation of responses from permeable fractures near the ground truth of the NWG 55-29 well logs. As seen on the right-hand side of the vertical sections, there is a significant signal response contributing to PFI directly associated with NWG 55-29.

The active volume cube, comparing map slices and PFI volumes with vertical slices above is shown in Figure 16. The numbered features in Figure 16 are also shown annotated in the vertical offset sections within Figure 17.

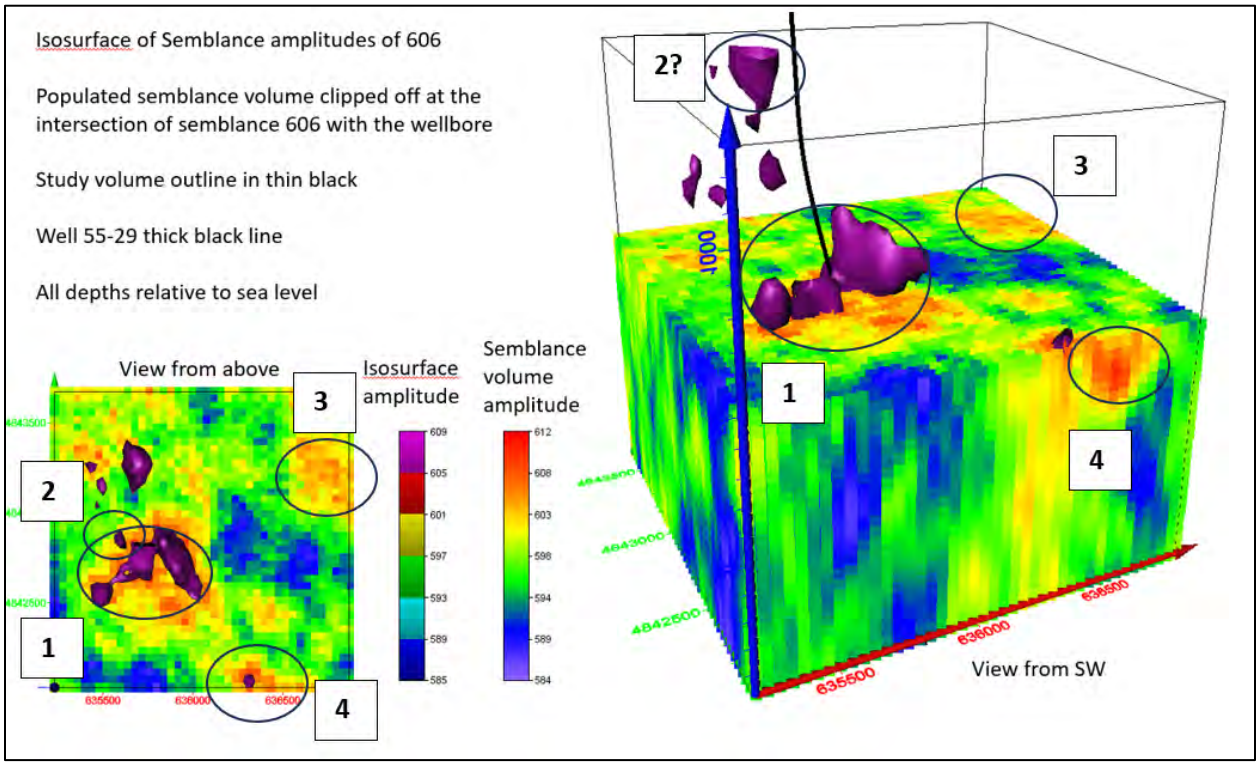

Figure 16. Active volume cube. The vertical slice and block figures above (Figure 15) reveal four notable PFI permeability isosurfaces (Geiser, et al, 2023). The map slice at 1400 m below ground surface (bgs) and block diagram shows higher semblance, near well, NNW trending and connected, conjugate, SW trending PFI structures. There are also higher semblance features to the NNW of NWG 55-29 and to the NE of this well. Numbered features indicate of high relative permeability.

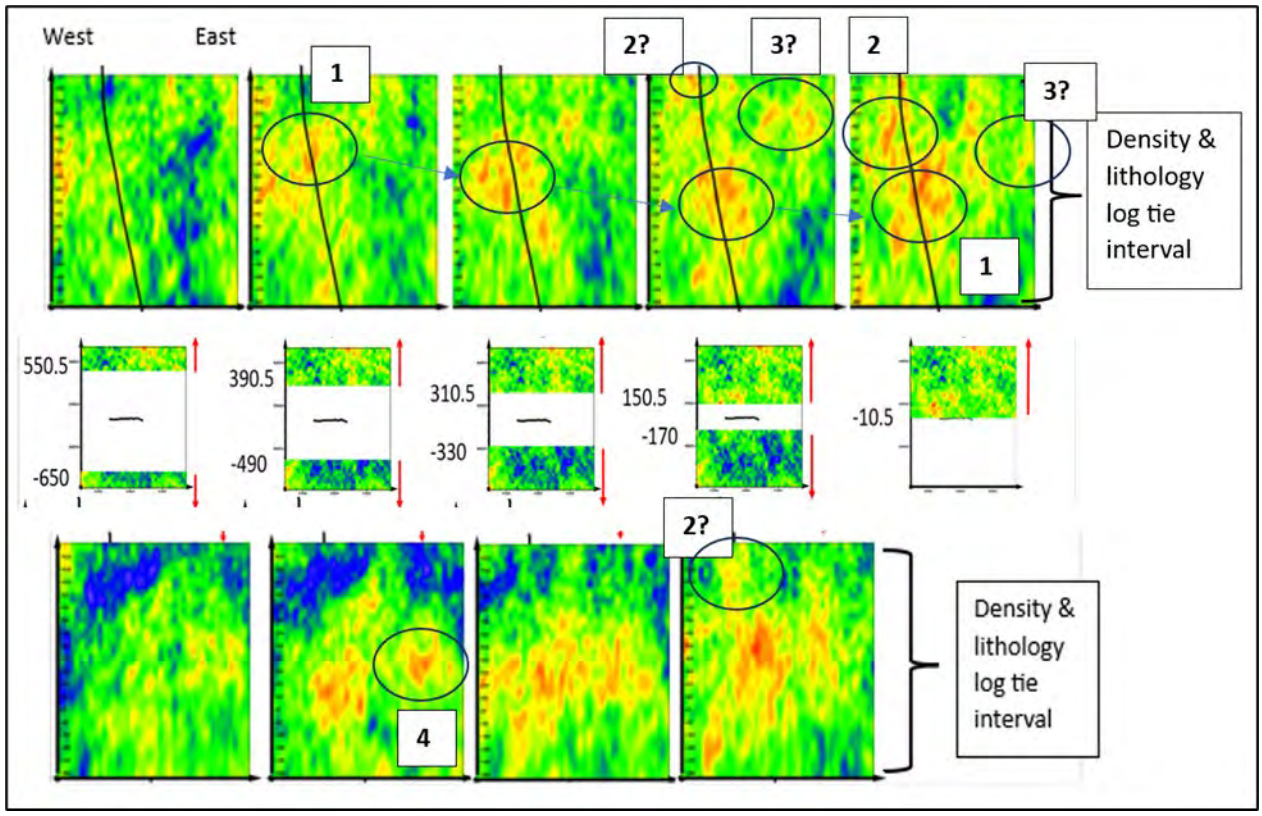

Figure 17. As the progressive vertical slices approach the NWG 55-29 from the north, a high semblance PFI feature, labeled 1, progresses to deeper depths and connects with the well. A second feature, indicated by 2, appears to follow along NWG 55-29 downward, but begins a few hundred meters above the one that approaches from the north. Features 3 and 4 appear respectively north and south of the well.

5.4 Near-well tie to well logs and lithology/stratigraphy

As noted by several studies (e.g., Geiser et al., 2023; Geiser et al., 2012; Engelder et al., 2022), the variation of rock mechanical properties and fracture density result in differences in energy emission that are reflected by the semblance value. We use these relations to interpret our PFI images.

The geological cross section model of the Newberry volcanics suggests a layered, but laterally heterogeneous, lithology column. As shown in the near well vertical section below (Figure 18), which is coordinated with the density and lithology logs, the layering shown by the high semblance amplitudes is consistent with the geology. Feature 1 appears to be associated with the higher, more uniform density basalt-andesite-basalt and welded tuff layers. Accordingly, this feature may in fact be mapping fluid filled permeability structures. Tracing this high semblance zone back to the north, where it appears to be at shallower depths may reflect a general rise in the andesite-basalt layer.

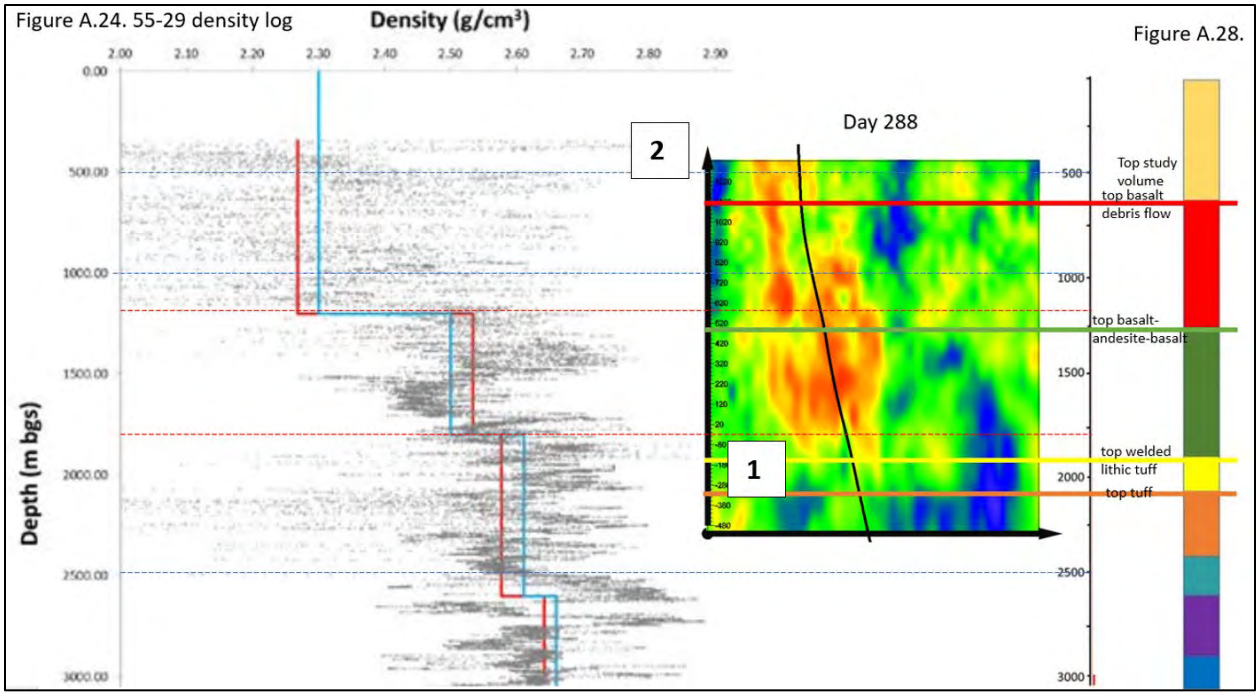

Figure 18. Correlation of density and lithology of Newberry well NWG 55-29 to a vertical PFI slice along the well

The most noticeable and consistent PFI features are labeled as in the figures above. The main association appears to be with the more uniform density basalt-andesite-basalt and welded tuff layers. As discussed in the next section, the more linear feature labeled 2 may result from fluid filled fracture along normal faults in the overlying debris flows and unwelded tuff.

5.5 Tie to Regional Geology

The set of successive map slices shown below (Figure 19) are spaced 80 meters apart, at 800, 880, and 960 m depth. They show that the NNW - SSE trending clouds of maximum semblance have a clear linear boundary on their eastern side. This boundary becomes sharply defined with increasing depth. This suggests that this boundary is one of the many NNW-SSE normal faults seen in regional geology. A second more diffuse but also generally NNW-SSE area occurs to the northeast of the sharply defined trend near well NWG 55-29.

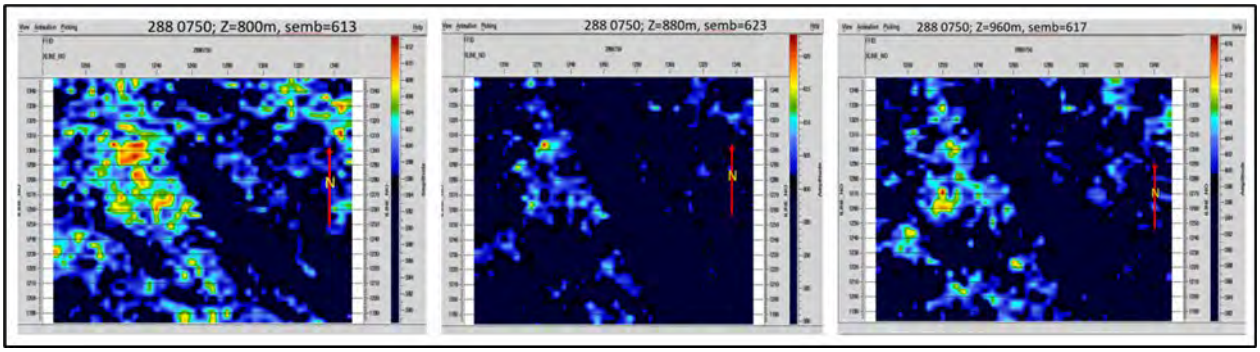

Figure 19. Shallower, 800-960 m bgs PFI images

Two other features are present in these images: a SE-ward deepening of the highest semblance features and secondary SW-NE trending edges in the semblance clouds. All three features are seen in the map and vertical section views below in Figure 20. In map view (left hand Figure 20), the NNW-SSE and SW-NE trends are interpreted as part of the regional faulting structure. In block diagram view, the NNW-SSE PFI features are interpreted as the normal faults that extend up into the debris flows and unwelded tuffs.

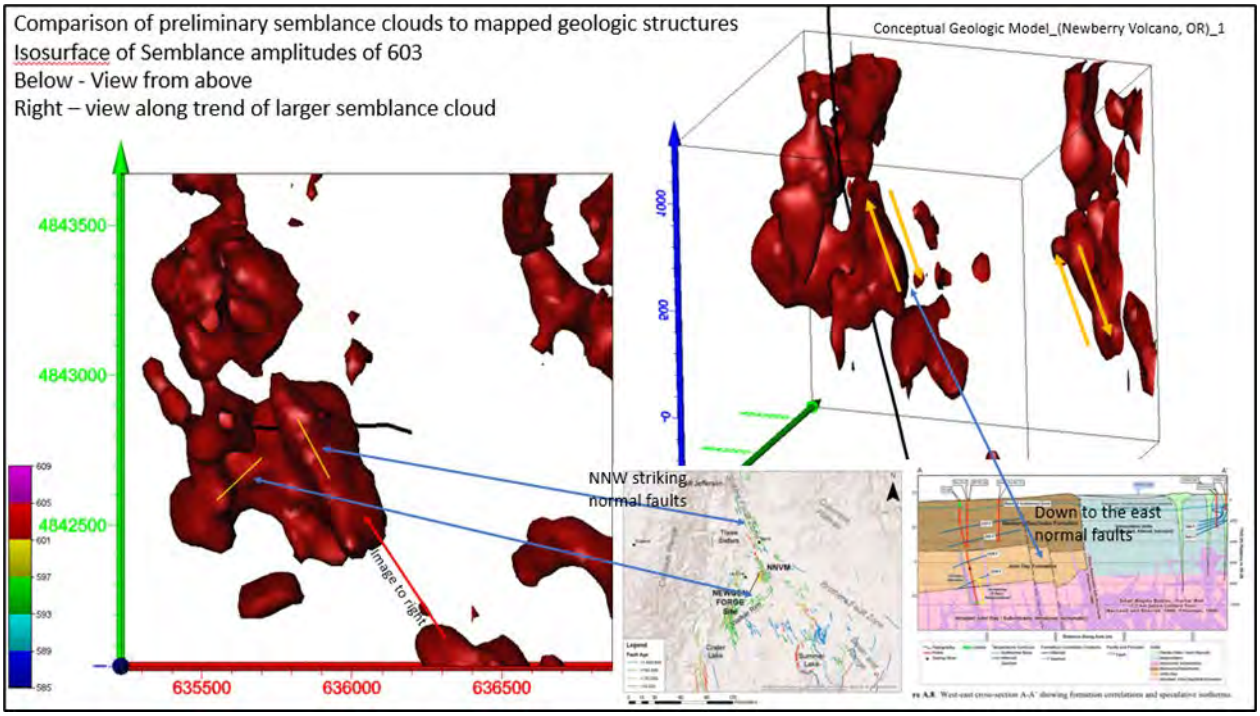

Figure 20. Map projection and block view of 3 significant PFI features suggestive of normal faulting in the near-well volume of 55-29

Figure 21 shows active permeable fractures. In the image at 1200 m (a), this is near the top of the andesite/basalt layer. At a depth of 2000 m, which is below the casing shoe in the well within a slotted liner, the depth slices are reflective of the andesite-basalt layer (b).

The region immediately north of the Newberry Volcano is (or was) under a Regional Stress field with the Maximum Horizontal stress (SHmax) oriented NNW resulting in NE – SW extension. This results in normal faults that strike NNW – SSE, essentially parallel to the dominant orientation of maximum semblance trends shown in the map slices. This structural trend is also reflected in the strike of the recent lava flows of Newberry, stress orientations from earthquake focal mechanisms, surficial lineaments in LiDAR imagery, and the orientation of MEQs because of the 2014 stimulation of NWG 55-29.

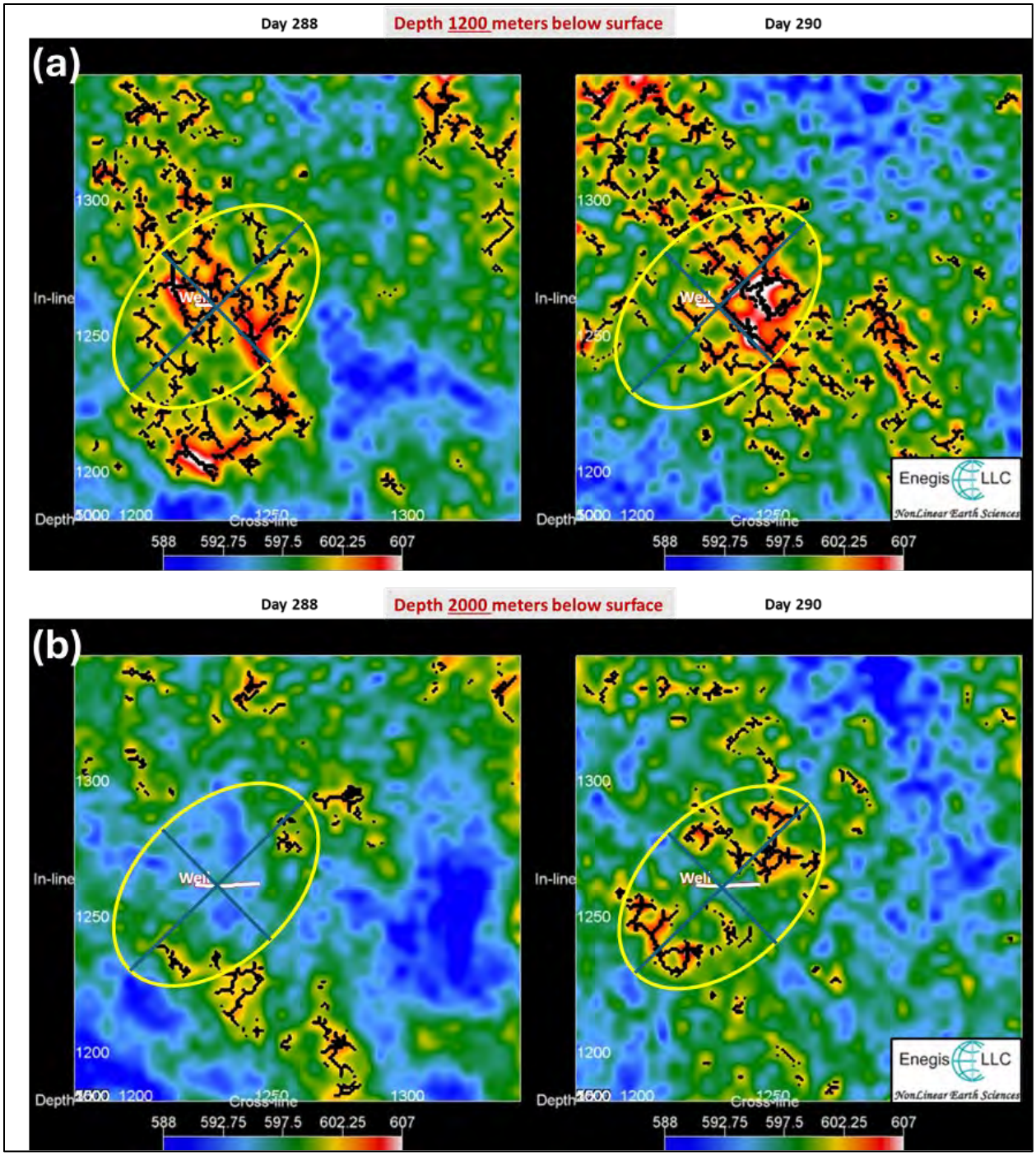

Figure 21. Depth slices of skeletonized FAVs with maximum fracture density delineated in black lines

6. Conclusions

6.1 Summary of Results

As the result of the field program, the Newberry project has provided robust results in a technically challenging environment. The ARPA-E project has provided a viable demonstration of the PFI technique in geothermal application, notably:

- The PFI technique results in markedly improved imagery showing the extent of active fluid filled fracture systems that extend beyond the NWG 55-29 wellbore on the order of a few hundred meters. The results correlate with the density and lithology logs from NWG 55-29
- Comparison of the PFI results with MT data leads to the conclusion that PFI resolution is about two orders of magnitudes greater and differentiates the fracture system between the heterogeneous debris flow and the more homogeneous andesite/basalt layer (Figure 22). The lower resistivity of the MT data is interpreted as the result of hydrothermal alteration (hydrated clays). This zone is seen to lie above the active PFI zone, which we interpret as having lower permeability and hence reduced active fluid flow pathways.

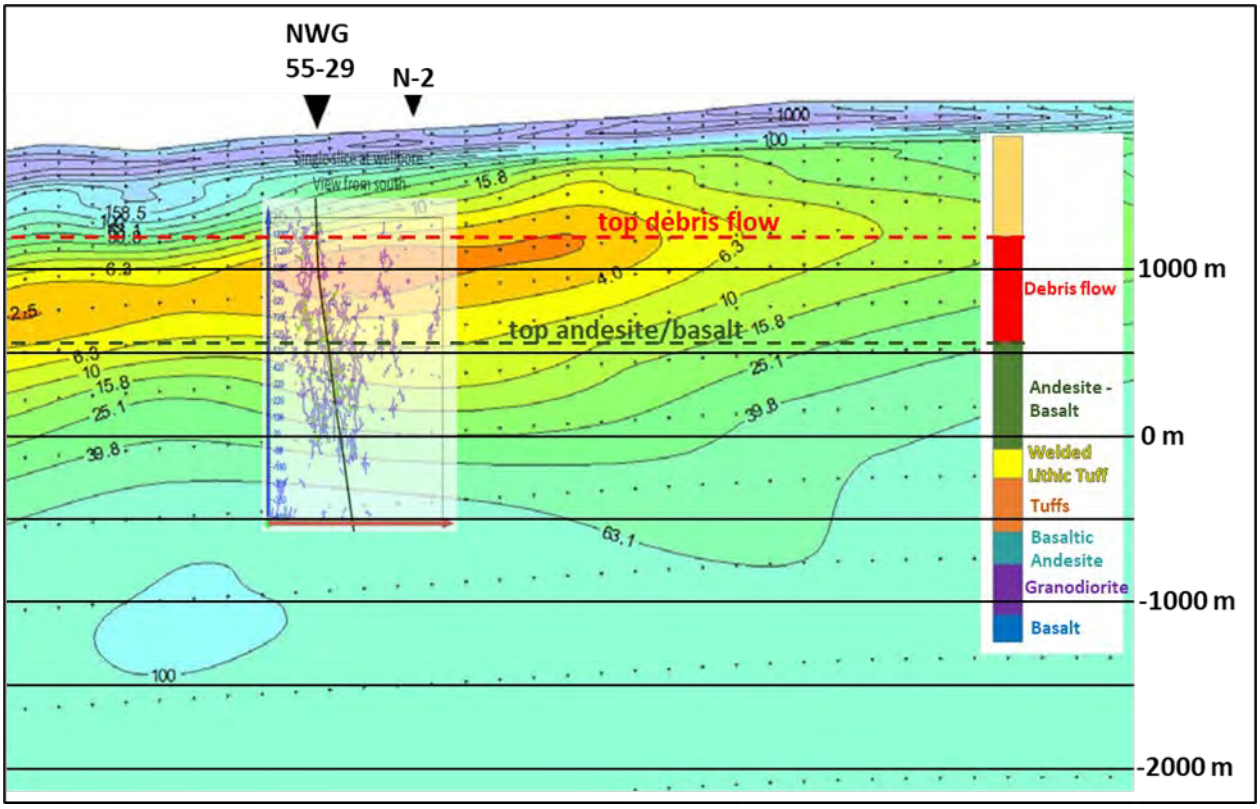

Figure 22. PFI and MT datasets correlated with lithology.

Our ARPA-E project has achieved its purpose—that of demonstrating the viability of PFI technology in a geothermal application. Resource limitations of budget constrained our ability to image deeper than ~2100 m. To extend PFI down to the ~2600 m objective of well NWG 55-29,

we recommend that the survey radius be increased by about 20% resulting in an approximate 38 square km area compared to the 25 square km achieved with this project.

6.2 What practicably differentiates PFI technology?

The PFI technique results in a direct mapping of permeability field architecture as opposed to computer simulations that can be driven by assumptions. In terms of the geothermal marketplace, in contrast with traditional reservoir characterizations, the PFI method is empirical, supplying actual data, not driven by assumptions. It does not depend on modeling (except for a velocity model, a standard in seismology), and contrasts with traditional reservoir modeling, which takes far more steps and assumptions (Figure 23). Further, the PFI technique is not dependent on MEQs since it utilizes ambient seismic emissions.

We believe that, based on technoeconomic modeling, that geothermal project development life-cycles costs could be >50% less compared to the status quo. Additionally, we believe PFI technology can provide reliable reservoir monitoring that enhances public trust concerning issues such as induced seismicity.

There are also additional energy sectors where the PFI technology can have application:

- Geologic carbon storage (GCS) requires an understanding of the target reservoir's properties to minimize risks during sequestration efforts. Also, the injection and disposal of wastewater requires subsurface characterization and monitoring. There are growing concerns about induced seismicity due to fluid injections, with seismic events up to M 3.5 caused by fluid injection occurring in the U.S. (Verdon & Bommer, 2021). PFI can be used to record the micro and macro-seismic events and measure their magnitudes, monitor fluid injections over time, and even take advantage of any seismic emissions from the induced seismicity to image the reservoir
- PFI technology could be useful for delineating ore bodies, where the boundaries provide seismic velocity contrasts and could be the sites of fluid flow that the PFI technology could image
- PFI can be used in compressed air energy storage (CAES) projects to image the potential air storage reservoirs and monitor the reservoirs during operations

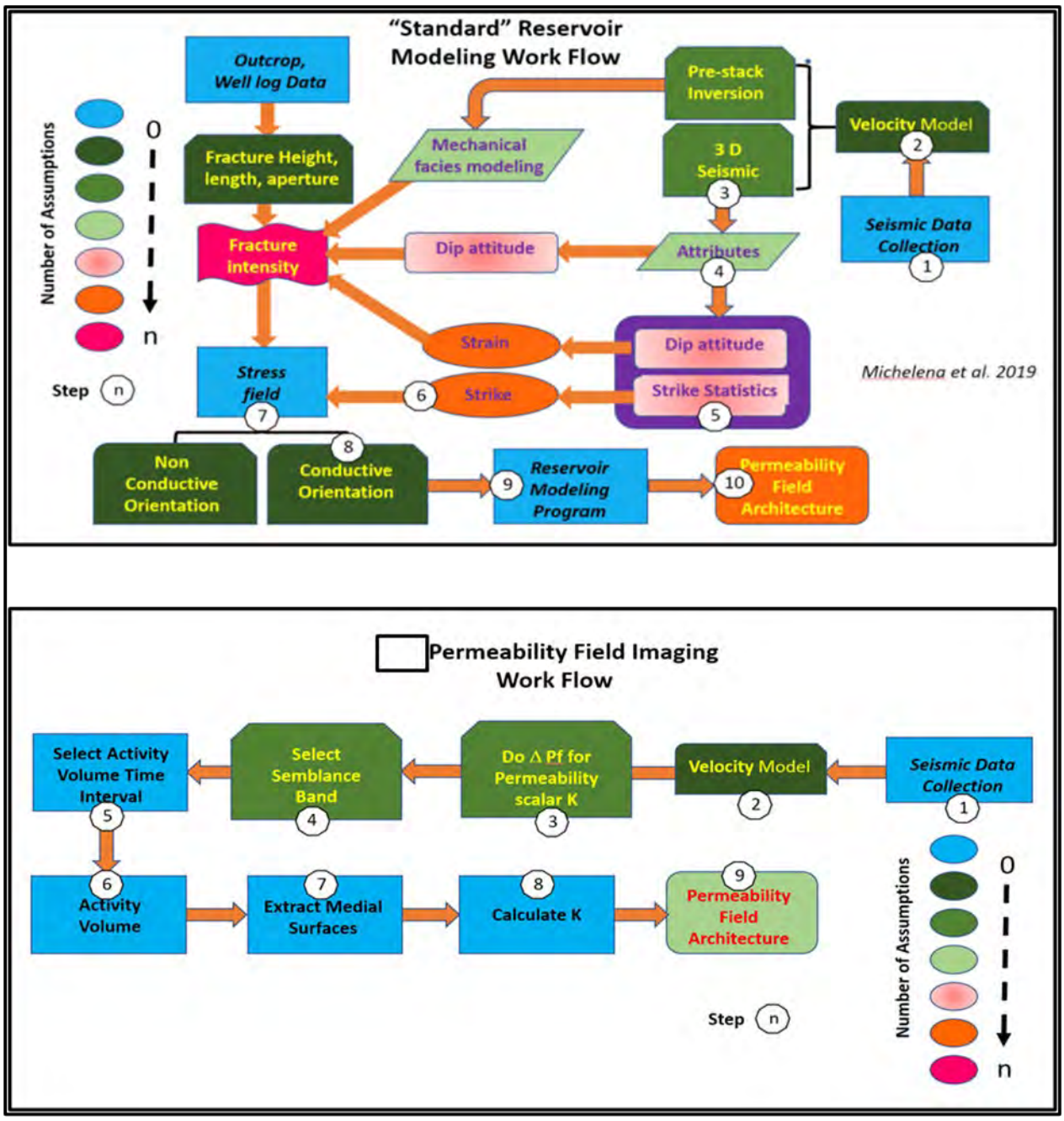

Figure 23. Standard reservoir modeling vs. PFI imaging

Acknowledgement

The information, data, or work presented herein was funded in part by the Advanced Research Projects Agency-Energy (ARPA-E), U.S. Department of Energy, under Award Number DE-AR0001660. The views and opinions of authors expressed herein do not necessarily state or reflect those of the United States Government or any agency thereof.

REFERENCES

Aster, R., Ringler, A., Anthony, R., and Lee, T. “Increasing ocean wave energy observed in Earth’s seismic wavefield since the late 20th century.” *Nature Communications*, vol. 14, 2023, https://doi.org/10.1038/s41467-023-42673-w

Beachly, M., Hooft, E., Toomey, D., and Waite, G. "Upper crustal structure of Newberry Volcano from P-wave tomography and finite difference waveform modeling." *Journal of Geophysical Research*, vol. 117, no. B10, 2012.

Catchings, R., and Mooney, W. "Crustal structure of east central Oregon: Relation between Newberry Volcano and regional crustal structure." *Journal of Geophysical Research*, vol. 93, no. B9, 1988, pp. 10081-10094.

Chebotareva, I., Nikolaev, A., and Sato, H. “Seismic emission activity of Earth’s crust in Northern Kanto, Japan.” *Physics of the Earth and Planetary Interiors*, vol. 120, 2000, pp. 167–182

Cladouhos, T., Petty, S., Callahan, O., Osborn, W., Hickman, S., and Davatzes, N. "THE ROLE OF STRESS MODELING IN STIMULATION PLANNING AT THE NEWBERRY VOLCANO EGS DEMONSTRATION PROJECT." *Thirty-Sixth Workshop on Geothermal Reservoir Engineering*, 2011.

Cladouhos, T., Petty, S., Swyer, M., Uddenberg, M., and Nordin, Y. "2014 Results from Newberry Volcano EGS Demonstration." AltaRock Energy Inc., 2015.

Cotton, J., and Catchings, R. "Data report from the 1983 US Geological Survey East-central Oregon Seismic Refraction Experiment." U.S. Geological Survey, 1989.

Crider, J. "Oblique slip and the geometry of normal-fault linkage: mechanics and case study from the Basin and Range in Oregon." *Journal of Structural Geology*, vol. 23, 2001, pp. 1997-2009.

Dawson, P., and Stauber, D. "Data report for a three-dimensional high-resolution P-velocity structural investigation of Newberry Volcano, Oregon, using seismic tomography." U.S. Geological Survey, 1986.

Engelder, T., Vermilye, J., Lacazette, A., Geiser, P., Sicking, C., and Hooker, J. "Seismic emissions reveal the mechanical stratigraphy of the Middle Paleozoic section under the Appalachian Plateau, Pennsylvania." *Geological Society of America Special Paper*, vol. 557, 2022, pp. 239-266.

Ewert, J., Diefenbach, A., and Ramsey, D. "2018 Update to the U.S. Geological Survey National Volcanic Threat Assessment." U.S. Geological Survey, 2018.

Geiser, P., Lacazette, A., and Vermilye, J. "Beyond 'dots in a box': An empirical view of reservoir permeability with tomographic fracture imaging." *First Break*, vol. 30, no. 7, 2012, pp. 63-69.

Geiser, P., Malin, P., Boyer, S., and Geiser, J. "Permeabilty Field Imaging: Mapping the geocritical crust’s permeability field." *AAPG Bulletin*, vol. 107, no. 9, 2023, pp. 1581-1608.

Heath, B., Hooft, E., Toomey, D., and Bezada, M. "Imaging the magmatic system of Newberry Volcano using joint active source and teleseismic tomography." *Geochemistry, Geophysics, Geosystems*, vol. 16, 2015.

MacLeod, N., Sherrod, D., Chitwood, L., and Jensen, R. "Geologic Map of Newberry Volcano, Deschutes, Klamath, and Lake Counties, Oregon." U.S. Geological Survey, 1995.

Michelena, R., Gilman, J., and Zahm, C. “Seismic, geologic, geomechanics, and dynamic constraints in flow models of unconventional fractured reservoirs: Example from a south Texas field.” *THE LEADING EDGE*, 2019, p. 116 -122, https://doi.org/10.1190/tle38020116.1.

Newberry Geothermal Energy. "Establishment of the Frontier Observatory for Research in Geothermal Energy (FORGE) at Newberry Volcano, Oregon, Appendix A Conceptual Geologic Model." 2016.

Pinzon-Rincon, L., Lavoué, F., Mordret, A., Boué, P., Brenguier, F., Dales, P., Ben-Zion, Y., Vernon, F., Bean, C., and Hollis, D. "Humming Trains in Seismology: An Opportune Source for Probing the Shallow Crust." *SRL*, vol. 92, no. 2A, 2021, pp. 623-635.

Robinson, J., Donnelly-Nolan, J., and Jensen, R. "Newberry Volcano’s Youngest Lava Flows." U.S. Geological Survey, 2015.

Rodrigues, E. “Estimation of crustal vertical movements due to atmospheric loading effects by GPS observations.” *Revista Brasileira de Geofisica* vol. 25, no. 1, 2007, pp.45-50.

Sicking, C., and Malin, P. "Fracture Seismic: Mapping Subsurface Connectivity." *Geosciences*, vol. 9, no. 12, 2019, pp. 508.

Sicking, C., Vermilye, J., and Fish-Yaner, A. "Pre-drill Reservoir Evaluation Using Passive Seismic Imaging." *Unconventional Resources Technology Conference*, 2016.

Taverna, N., Pauling, H., Trainor-Guitton, W., Kolker, A., Mibei, G., Dobson, P., Sonnenthal, E., Tu, X., and Schultz, A. "De-risking superhot EGS development through 3D play fairway analysis: Methodology development and application at Newberry Volcano, Oregon, USA." *Geothermics*, vol. 118, 2024.

Templeton, D., Matzel, E., Johannesson, G., Myers, S., and Goebel, M. "Final Report: Mapping Fracture Network Creation with Microseismicity During EGS Demonstrations." Lawrence Livermore National Lab, 2014.

Verdon, J., and Bommer, J. "Green, yellow, red, or out of the blue? An assessment of Traffic Light Schemes to mitigate the impact of hydraulic fracturing-induced seismicity." *Journal of Seismology*, vol. 25, 2021, pp. 301-326.

Waibel, A., Frone, Z., and Jaffe, T. "Geothermal exploration at Newberry Volcano, Central Oregon." 2012.

Sibayak Geothermal Field: New Insights from Updated MT Model

Inusa P Fauzi, Aditya A Juanda, Sotarduga S Nainggolan, and Mulyanto

PT. Pertamina Geothermal Energy

Keywords

Magnetotelluric, Inversion Model, Sibayak, Bottom of Clay Cap, Enhanced Conductivity, Pyrite, Saline Fluids

ABSTRACT

Re-evaluating the Sibayak geothermal reservoir in North Sumatra, Indonesia, this study utilizes recent magnetotelluric (MT) data in 2023 to refine the existing 2D model into a 3D model. Compared to the 1996 model, a significant feature, an enhanced conductive body (0.1-1 Ω.m) was identified extending from outside the Singkut Caldera towards Mt. Pratektekan. Though past studies did not identify this conductive body, this discovery was confirmed by 1D and 2D MT inversions and intersects existing wells. The delineation of the base of the clay cap with the underlying enhanced conductive body presents a challenge due to the absence of a distinct boundary between the two in our 3D resistivity model. Meanwhile, 1D models could separate the bottom of clay cap and enhanced conductive body. While the exact cause remains under investigation, there are two possible causes of an enhanced conductive body which are saline fluids and sulfide minerals. This study emphasizes the value of updated geophysical data in understanding geothermal reservoirs and paves the way for further exploration and development in the Sibayak field.

1. Introduction

The Sibayak geothermal field, situated in North Sumatra, has been a contributing factor to Indonesia's geothermal energy production since 1996. Initially generating 2 MW, the field's capacity expanded to 12 MW in 2008 with the addition of two 5 MW units. However, an inactive steam sales contract with an Independent Power Producer (IPP) since 2012 prompted Pertamina Geothermal Energy (PGE) to re-evaluate Sibayak's potential to contribute to its ambitious 1 GW geothermal target.

Pertamina had conducted several geophysical data acquisitions. Initially, DC resistivity (Schlumberger) surveys were conducted to explore geothermal prospects with depth of investigation around 1000 meters, continued by an MT survey in 1992 and time domain electromagnetic (TDEM) for static shift correction in 1997 (Mulyadi, 2000). A gravity survey was also conducted by PT. Gondwana in 1989 – 1990 using a Lacoste Romberg gravity-meter (Daud, et al., 2001). In addition to the geophysical surveys, PGE undertook an update of the Sibayak reservoir model. The original model, developed in 2001, incorporated data from 10 wells drilled in the field (Atmojo, et al., 2001). Recognizing the potential impact of production history on reservoir characteristics, PGE created a new model in 2024 utilizing the available data since 2008 from the same 10 wells and incorporating post-production conditions. (Firanda, et al., 2024).

A team of geoscientists and reservoir engineers from PGE re-evaluated the Sibayak geothermal field's potential. This re-evaluation employed updated magnetotelluric (MT) data acquisition and resistivity inversion techniques to analyze the depth of the clay cap. Well cutting data from 10 wells provided information on clay content, which will be useful in evaluating the clay cap. The updated resistivity model revealed a previously unidentified, enhanced conductive anomaly (less than 5 ohm.m) extending from the surface to a depth of approximately 4,000 meters below sea level with a lateral extent of about 4,000 meters. This anomaly exhibits an oval shape and trends southwest-to-northeast beneath Mount Sibayak. Notably, this anomaly was absent in previous resistivity models, However, PGE's recent MT data acquisition and resistivity model was thoroughly evaluated, resulting in minor data masking for all decades above 160s (0.01 Hz) which PGE considered as satisfactory. It is also challenging to delineate the bottom of clay cap on our 3D resistivity model due to this high conductive body positions near the clay cap, resulting in a more smoothed and lower resolution view of the bottom of the clay cap (Cumming & Mackie, 2010). The nature of the high conductive anomaly remains an open question. This paper will study delineating the base of the clay cap including potential causes for enhanced conductivity based on well data.

1.1 Field Overview

Sibayak field is a volcanic geothermal system inside Singkut caldera which formed at ~44 ka (Forni, et al., 2024) with two small conduit strato-volcano (Hochstein & Sudarman, 2015). Figure **1** shows two schematic conceptual models describing a volcanic hosted system and isotherms with alteration zone background derived from temperature log of the wells. The conceptual model was also used to update the numerical simulation of Sibayak Field (Firanda, et al., 2024) which consists of geothermal upflow beneath Mt. Sibayak outflowing towards southeast and northeast. Sibayak complex manifestations were found in the crater of Sibayak Mountain and flank of Sibayak inside the Singkut caldera (Fahmi, et al., 2021). Figure 2 is the geological map of Sibayak with structure orientation NW-SE. Although Sibayak is a volcanic hosted system, tertiary sediments play major roles for the permeability in Sibayak reservoir.

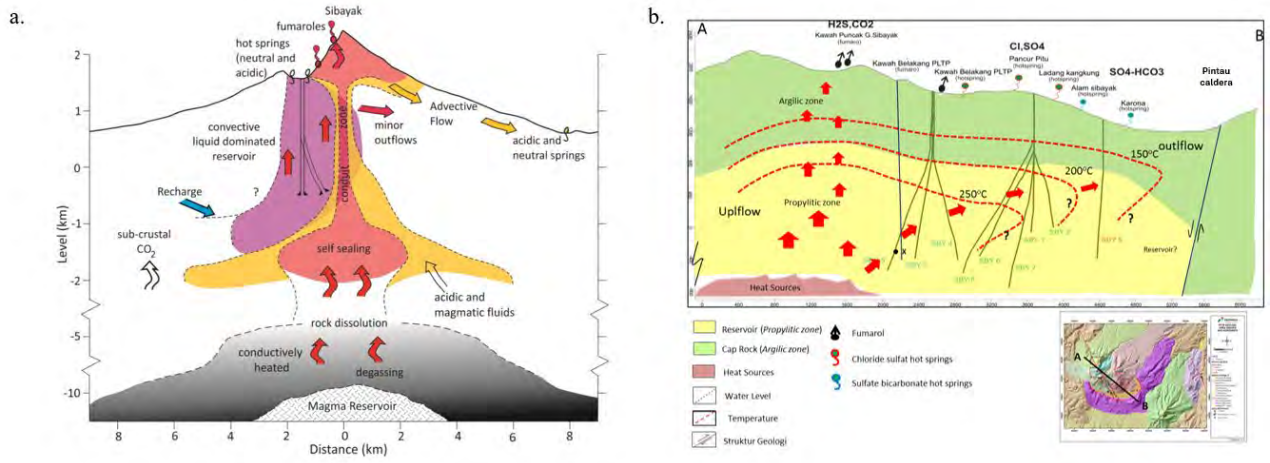

Figure 1. a. Sketch of Sibayak volcanic hosted conceptual model (Hochstein & Sudarman, 2015) and b. Isotherm conceptual model with hydrological setting of Sibayak along the alteration zone background developed from well temperature log (PT. Pertamina Geothermal Energy Tbk, 2022)

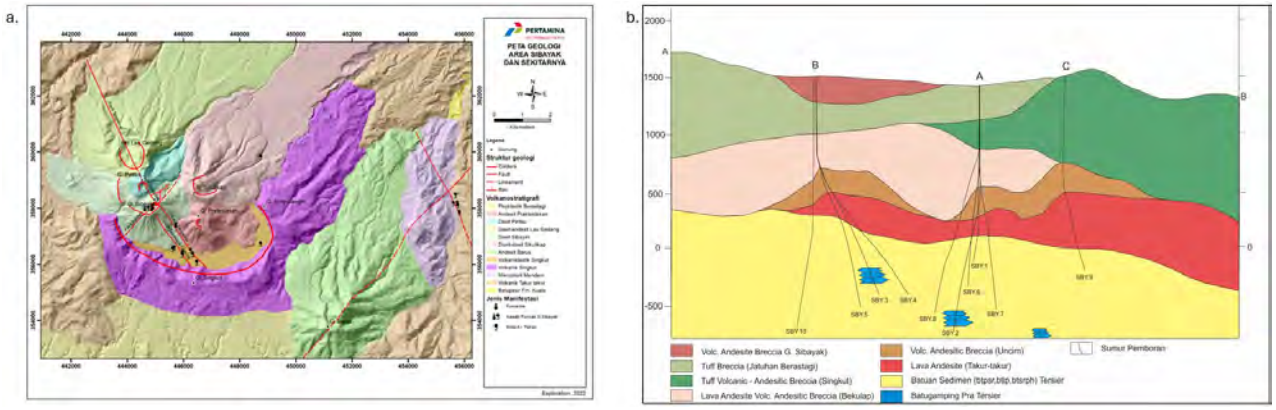

Figure 2. a. Updated geological map with stratigraphy of Sibayak field (PT. Pertamina Geothermal Energy Tbk, 2022) and b. Geological cross section interpreted from well cuttings data (PT. Pertamina Geothermal Energy Tbk, 2016)

2. Sibayak MT Surveys

Sibayak's MT data, acquired in 1991 by PT Alico and in 1997 by PT Qodharwan Wirasta Konsultan, with total 51 MT stations, were utilized for 2D inversion techniques to verify the reservoir structure and its extent (Daud, et al., 2002). To achieve a more comprehensive understanding of the Sibayak geothermal field using modern software and technology, a 3D inversion approach was carried out. This re-modeling process aimed to enhance the three-dimensional visualization of the Sibayak Field, improving the accuracy of the geothermal resource assessment. However, limitations were encountered due to the incomplete recovery of historical MT data. To address this challenge and refine the remodeling efforts, a new MT data acquisition campaign was conducted. PGE's in-house geophysics department acquired 54 MT stations using proprietary tools and standardized acquisition procedures.

A three-receiver magnetotelluric (MT) system, including two operational units and one backup, facilitated simultaneous data acquisition at two stations per day in Sibayak. Each station utilized

three MTC-80H coils with a frequency range of 1 kHz to 10,000 seconds and 4 electrode pots. Time series data processing was run in-house using SSMT software resulting in 4 excellent datasets, 48 good datasets and 2 fair datasets.

Figure 3 shows MT stations designed for characterizing the Sibayak reservoir. The station distribution was expected to be grid spaced or spread evenly with a target of 500 to 1000 m spacing in the inner core and 1500 m to 2000 m for the outer core with area of surveys around 100 m^2. Overall, the data acquisition met the target although in some areas such as in the northeast of Sibayak Mountain and south of Singkut Caldera MT data could not be acquired due to dense forest with minimum access and densely populated areas with high voltage power line.

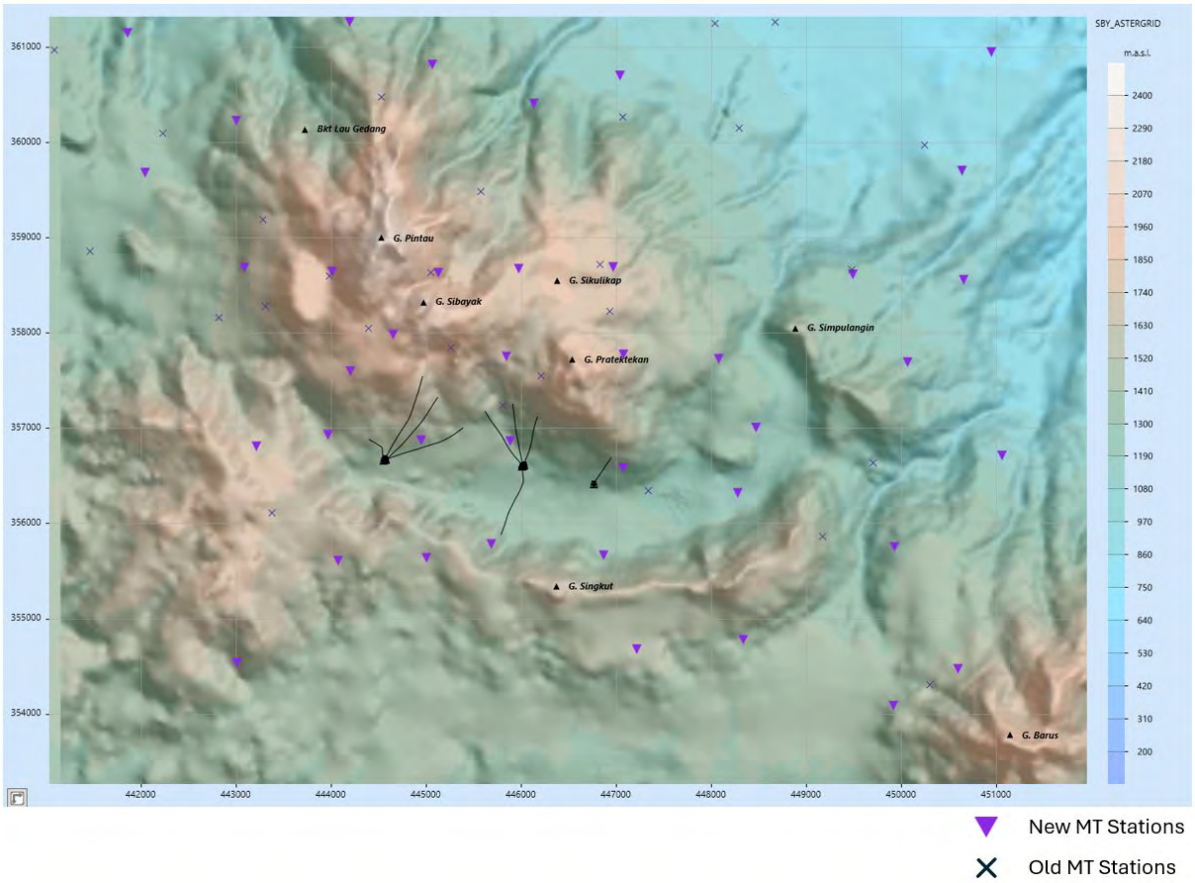

Figure 3. Distribution of MT stations from data acquisition in 2023 (purple triangle) and 1991 & 1997 (cross).

3. Sibayak MT Inversions

Prior to this study, previous MT datasets from the Sibayak geothermal field had undergone several analyses. The first study showed that 1D inversions could be used to delineate the clay cap, reservoir and subsurface structure (Mulyadi, 2000). Understanding the limitation of 1D inversion, 2D inversions were carried out to improve the interpretation of reservoir and basement from 1D inversions due to strong indication of 2D or 3D effects (Daud, et al., 2002). Advancements in technology have facilitated the routine application of 3D inversion techniques in recent years. Using a well-prepared MT dataset with recent technology, PGE conducted 3D inversion to create a better understanding of Sibayak reservoir.

Prior to 3D inversion, the data were rotated to 0 degrees (North) and edited to mask out noisy data, which was was only necessary for frequencies below 0.006 Hz due to anomalous behavior in the YX component at lower frequencies (Figure 4**)**. Both MT impedances and the vertical magnetic transfer function (tipper) were inverted. Additionally, we carried out in-house 1D and 2D inversions using Geotools software. The resulting 3D resistivity model revealed a previously unidentified, enhanced conductive anomaly extending from the outer Singkut Caldera towards Sibayak Mountain. The validity of this anomaly was investigated through further analyses such as comparing it to the previous model, conducting 1D and 2D inversions and lastly conducting a 3D sensitivity analysis.

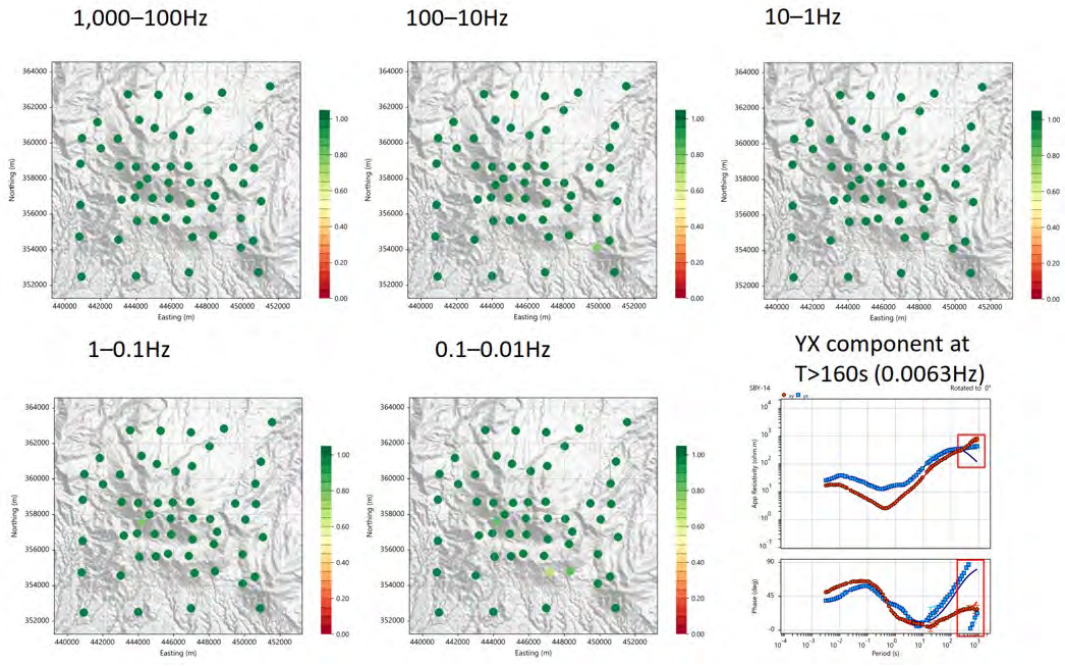

Figure 4. Data masking of MT datasets in every frequency start from 1000 – 0.01 Hz. Color bar green-red describing the percentage of data masked, value 1 or green means no data masking performed.

3.1 Comparisons of MT Inversion Models

To verify the existence of the newly identified high conductive anomaly, several attempts were made to reconcile it with previous findings. As the original MT datasets used to generate the old 2D resistivity model were unavailable, the datasets of the old MT stations were plotted on the new 3D model, and the published image of the old 2D model was visually compared (Figure 5). Stations SBK-205, SBK-216, SBK-211, and SIB-128 are located within the footprint of the anomaly on the new 3D model. However, the old 2D model did not image a conductive body at these locations. This could be due to several reasons. First, the highly conductive anomaly might exhibit a 3D effect that could not be adequately captured by the older 2D inversion algorithms. Second, due to the deep 3D nature, input data for the 2D model were restricted from 0.003 down to 30 seconds period (Daud, et al., 2002).

An additional effort to reconcile the anomaly with previous findings involved comparing published old MT curves to new MT curves nearby. Around 200 meters from SBK-211 is SBY-20 station

with the same MT curve response (Figure 6). The most notable difference observed was a significantly higher initial resistivity (around 750 ohm.m) in the new SBK-211 curve compared to the old SBY-20 curve (around 40 ohm.m). This discrepancy could be attributed to the application of static shift correction using TDEM data in the processing of the old MT data, which was not employed for the new dataset. Both curves exhibited a deflection in the Rho-YX component at a period of 1 second, while the Rho-XY component deflection occurred before 1 second in both datasets.

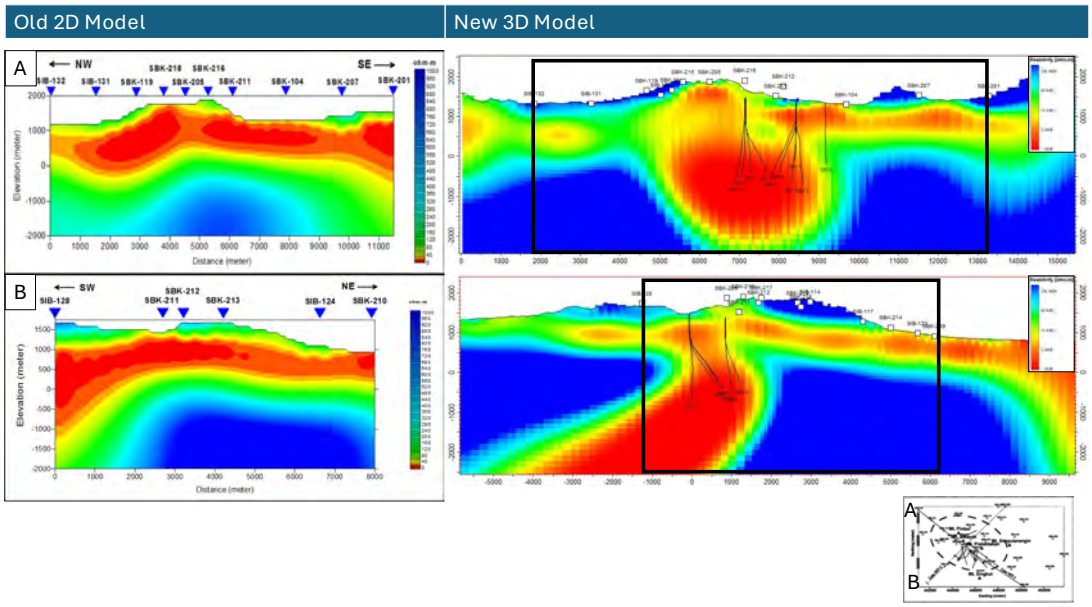

Figure 5. Cross-section comparation between old 2D model (left) and new 3D model (right). The boundary of the old 2D model is visualized in a black box.

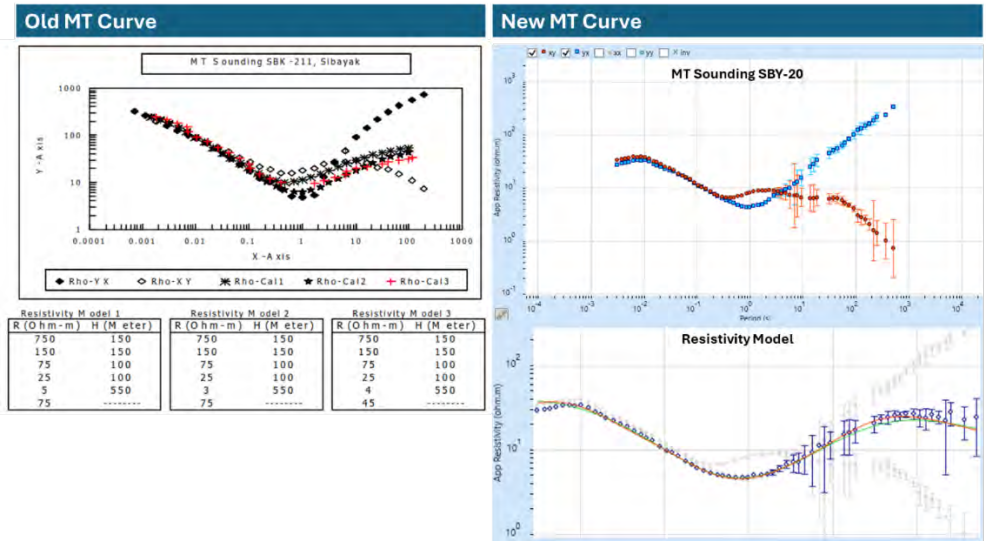

Figure 6. Comparison of nearby station between SBK-211 (old MT dataset) and SBY-20 (new MT dataset) including each 1D inversion.

3.2 New MT Inversions of 1D, 2D and 3D Models

While 1D and 2D MT inversions using Geotools software offered a complementary approach, they presented limitations compared to 3D inversion. Unlike 3D models, which invert for distortion matrices, 1D and 2D inversions relied on static shift corrections obtained from TDEM surveys. This dependence on the type of static shift correction can potentially introduce distortions in the geometry of the geothermal clay cap as interpreted from the 1D and 2D models. However, the information derived from 1D and 2D models, when combined with alteration mineral data from wells, could still contribute to a comprehensive interpretation of the geothermal system.

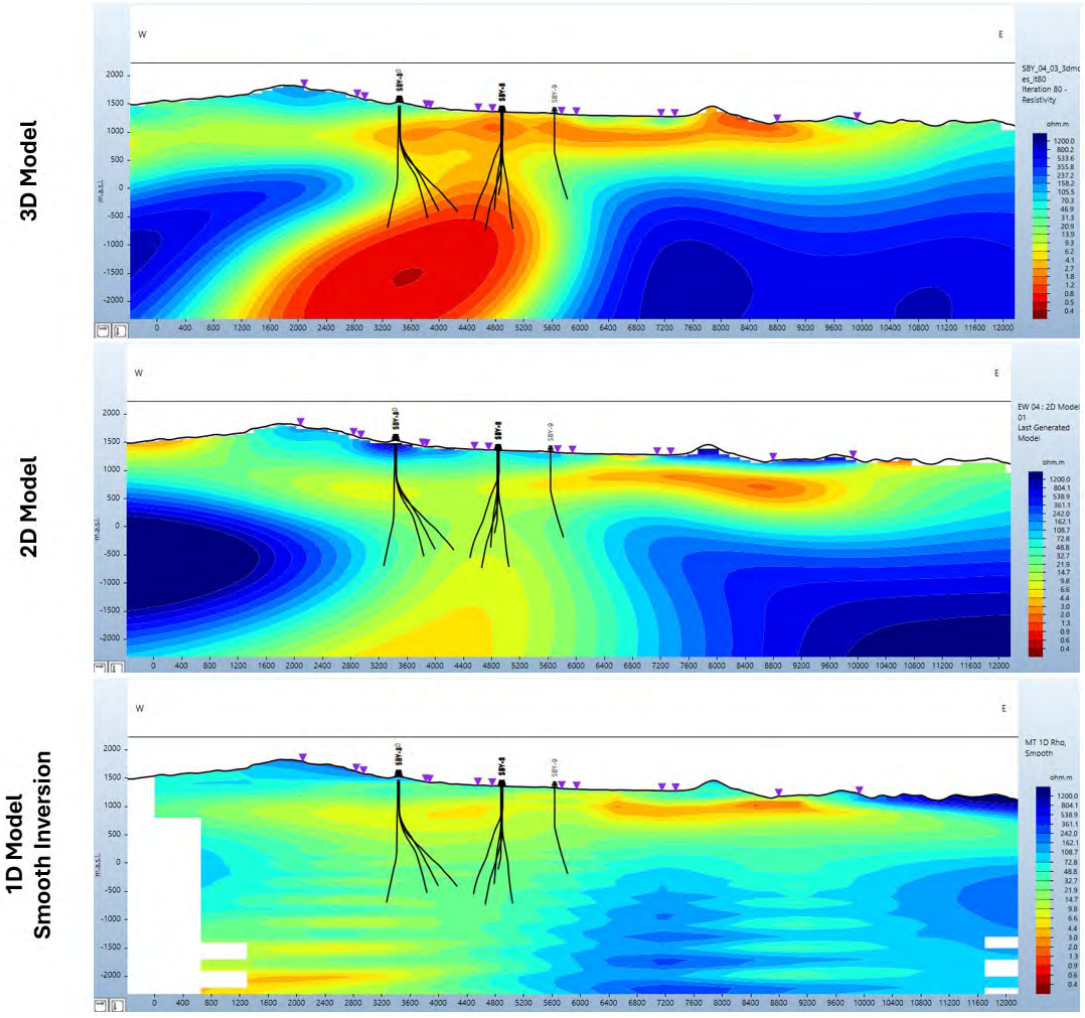

Figure 7. Three West-East Cross-Sections, crossing wells trajectory from 3D, 2D and 1D model sequentially.

To generate 1D models, a smooth inversion (Occam) method was performed as it was good enough to delineate the resistivity of the geothermal clay cap (Cumming & Mackie, 2010). These 1D models were generated for all data within a frequency range of 1000 Hz to 0.001 Hz, incorporating a 5% apparent resistivity noise floor. Subsequently, the 1D Occam models were horizontally interpolated to create a cross-sectional image (Figure 7**).** The resulting 1D model provides a smooth representation of the resistivity down to a depth of approximately 1000 meters, with

increased scatter at greater depths. This scattering might be attributed to the influence of 2D and 3D effect.

A 2D inversion was conducted utilizing TE and TM mode curves within the frequency range of 1000 to 0.01 Hz, as determined by data masking. Typically, 2D inversions serve as a preliminary step to refine inversion parameters before progressing to 3D modeling.

The 3D inversion was initiated with a uniform 50 ohm-m initial model and a 5% error floor, converging after 80 iterations to a root mean square (RMS) value of 1.08. By incorporating data from 0.006 to 251 Hz, reliable depth resolution was achieved to a depth exceeding 5000 meters. This depth coverage adequately captured the high conductive anomaly extending from outside the Singkut Caldera towards Sibayak Mountain. Notably, nine of the ten wells are located within the outer core of this conductive anomaly. However, a cautious interpretation is warranted due to the age of the well reports, which precludes further detailed analyses such as X-ray diffraction (XRD).

3.3 Sensitivity Test

To assess whether the deep conductive anomaly was an artifact of the inversion process or parameters, a sensitivity analysis was conducted (CGG Geoscience, Multiphysics, 2023). A modified 3D resistivity model (Figure 8.a) was created by replacing the enhanced conductive anomaly with a less conductive body (50 ohm.m). The impact of this modification on the forward response was evaluated by comparing the TE-TM mode curves of the original and modified models at stations within the southwestern study area (Figure 8.b). The apparent resistivity and phase curves from the original model (points) displayed significant deviations from those of the modified model (solid lines). This substantial difference in the forward responses demonstrates that the MT data possess sensitivity to the enhanced conductive body, suggesting its presence is required to accurately fit the observed data.

4. The Bottom of the Clay Cap from 1D and 3D MT

Delineating the bottom of the clay cap using 3D resistivity models is often straightforward and typical for geothermal field evaluations. However, in the Sibayak field, the presence of an enhanced conductive body positioned near the clay cap in the 3D model presented a significant challenge. This proximity resulted in a blurred interface between the conductive clay cap and the anomaly, hindering clear separation. To address this limitation, 1D MT inversions were employed to provide a higher-resolution characterization of the clay cap (Figure 7). Figure 7 illustrates a clear separation between the bottom of the clay cap (interpreted at 10 ohm.m) and the enhanced conductive body in the 1D model, in contrast to the ambiguity observed in the 3D model.

The absence of static shift correction in the 1D model presented a significant challenge. While the integration of well data, including alteration zones, enhanced the interpretation of the geothermal system, the direct correlation between the 1D and 3D model-derived clay cap depths and well data proved to be inconsistent (Figure 9). The lack of Methylene Blue tests (MBT) in the legacy well reports, an uncommon practice at the time, hindered a more precise correlation between the clay cap and the argillic alteration zone.

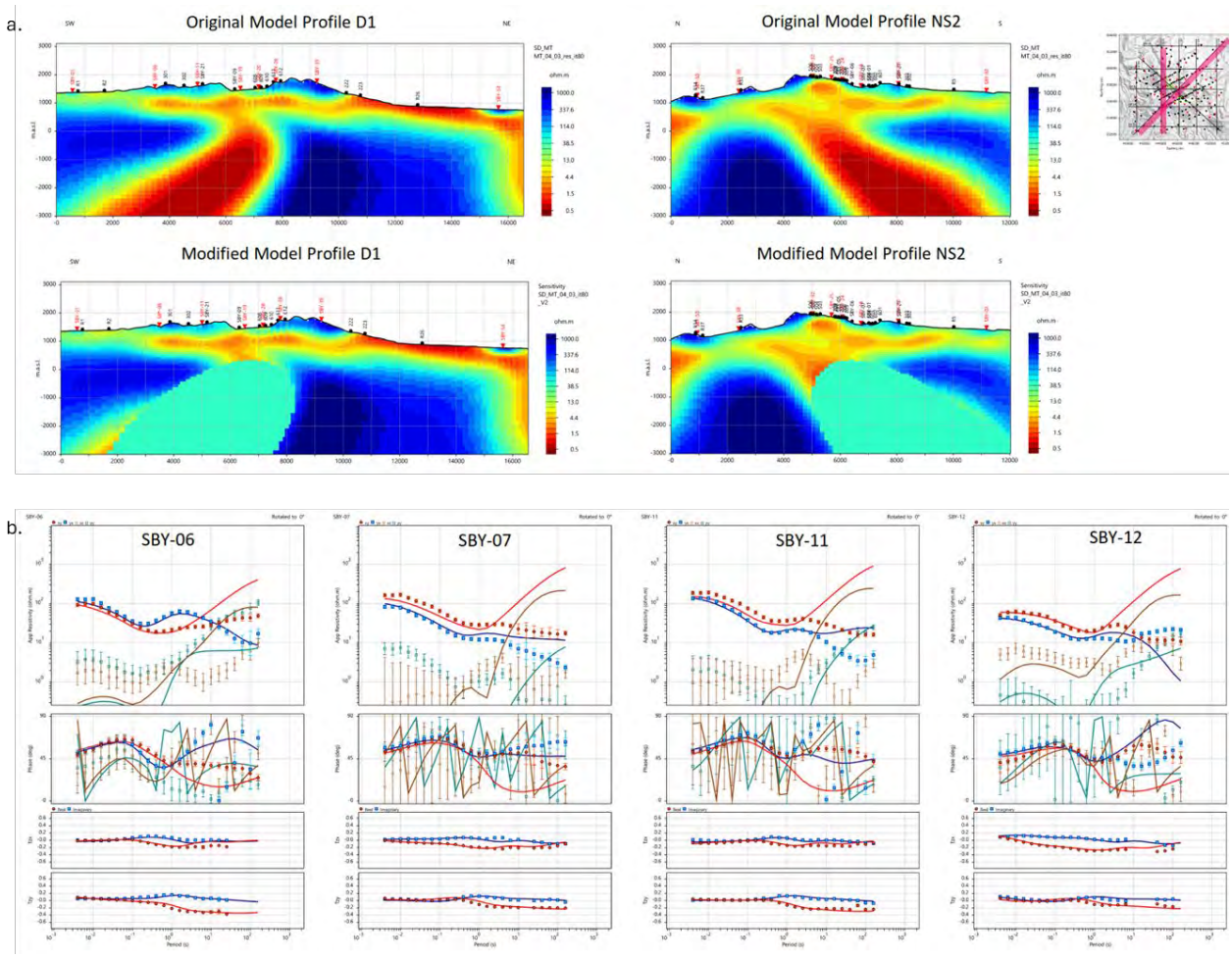

Figure 8. a. Cross-sections of two profiles comparing between modified 3D model from high conductivity into 50 ohm.m body. b. MT-curves sampled from MT stations above the high conductive body with MT curve from forward modelling of the modified body (solid lines) and original data (dots).

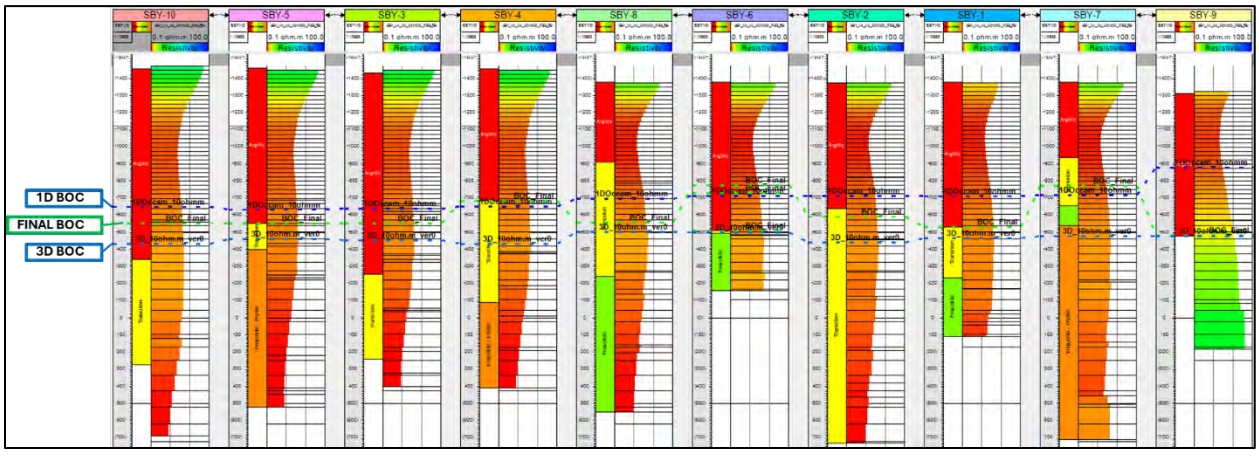

Figure 9. 1D and 3D interpreted bottom of clay cap with alteration data from Sibayak wells.

To address these limitations, a combined approach was adopted. The bottom of the argillic alteration zone was used as a primary constraint, and the general trend of the bottom of clay cap from the 1D model was incorporated into the 3D model using minimum curvature interpolation. This strategy aimed to mitigate the negative impacts of the low resolution associated with blurred resistivity value of the high conductive body and the clay cap on the 3D model Figure 10.

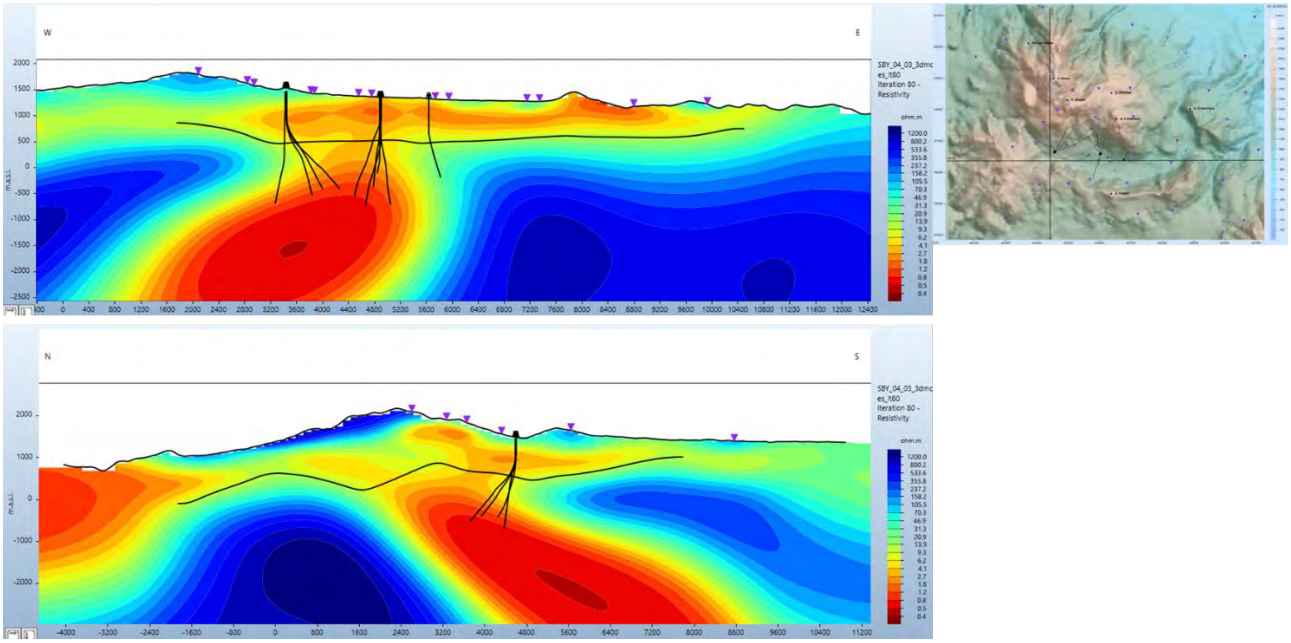

Figure 10. Cross-sections of 3D model with the interpolated bottom of clay cap from 3D interpretation BOC bound with well data and 1D BOC trends.

5. Possible Causes for Enhanced Conductivity

Potential causes for enhanced conductivity include graphite, ore minerals, saline fluids, and partial melting (Schilling, et al., 1997). However, given the likely presence of an impermeable barrier confining fluids, saline fluids are considered the most plausible explanations (Jones, 1992). A modeled electrical conductivity of sandstones saturated with NaCl solution (3.5wt% – 4wt%) as a function of porosity show electrical resistivity ranging from 1 to 5 ohm.m with 25% porosities (Jenkins, et al., 2023).

The other possible cause is that laboratory studies have established a correlation between high electrical conductivity and the presence of ore minerals, particularly sulfides. However, while this association is commonly observed, it is not universally applicable. Numerous case studies demonstrate that high conductivity can occur both with and without the presence of detectable sulfides (Lin, et al., 2023).

5.1 Saline fluid

Deeper geothermal brines sampled from Sibayak wells contain average sodium (Na^+) and chloride (Cl^-) concentrations of 500 and 1300 ppm, respectively, equivalent to a salinity of 0.18 wt%. These salinity levels are typical for geothermal brines. Yet, Figure 2.b presents a simplified geological model of Sibayak based on well cuttings data. Upper tertiary sandstones were found on those wells

ranging from 800 to 0 masl. Although sandstones should have high permeability, permeability derived from well productivity in Sibayak were found to have small to intermediate permeability (< 30 milliDarcy) (PT. Pertamina Geothermal Energy Tbk, 2016) based on permeability category (Wheaton, 2016). This discrepancy is likely attributed to silica or calcite scaling within the sandstone formations. Such scaling may create impermeable barriers, potentially trapping saline fluids and consequently enhancing electrical conductivity as observed in the resistivity model.

5.2 Sulfide

Pyrite is a sulfide mineral commonly appearing and reported during geothermal drilling. By utilizing this data, we can map the distribution of Pyrite within the Sibayak model. Figure 11a illustrates the distribution of Sibayak wells, incorporating alteration models, Pyrite content (ranging from 10 to 30 wt% as indicated by pink to red shading), and resistivity logs derived from 3D MT inversions. A horizon of Pyrite with 10wt% was mapped from the wells to know the distribution of Pyrite.

Figure 11b is a West to East cross-section presenting Sibayak wells with Pyrite content and a filtered <10 ohm.m 3D resistivity model as a background. An interpreted horizon of Pyrite > 10wt% was delineated with a dotted line and coinciding with the top of a conductive dome-shaped body. This correlation suggests a potential link between the enhanced conductivity and the presence of a sulfide body, warranting further investigation.

6. Discussions

In this study, 2D inversion was used to verify the presence of the highly conductive body identified in the 3D model, particularly its position relative to the production wells. The 2D inversion confirmed the existence of the conductive body, although its depth was estimated to be greater than that observed in the 3D model (Figure 7). This discrepancy underscores the importance of accurate static shift correction in both 1D and 2D inversions. Although static shift correction was not applied, the interpolated BOC is a success as shown in Figure 10 & Figure 11b.

To know more about the relationship between porosity, salinity, resistivity and temperature we could refer to a study by Ussher, et al., 2000. It is clear that the resistivity of Sibayak well brine sample data from Figure 12a could be ranging from 10 – 3 ohm.m, while an effective model in Figure 12b with temperature ranging from 250 – 300 ^{o}C, Sibayak sandstone should have porosity more than 20%. Unfortunately, porosity data for Sibayak sandstones are currently unavailable.

The other possibilities are using a model generated by Clennell, et al., 2010 with 100% brine saturated sandstone with Pyrite bearing sandstones. By incorporating Pyrite contents ranging from 10 to 30%, as observed in Sibayak, resistivity values below 10 ohm.m can be simulated (Figure 13). This modeling approach can be further refined by incorporating detailed mineral composition data from the Sibayak wells.

If the high conductivity is attributed to trapped saline fluids, future development efforts should prioritize targeting the conductive body. This approach is supported by the observation that production wells are located within the conductive zone, while non-production wells (e.g., SBY-9) are situated outside this area.

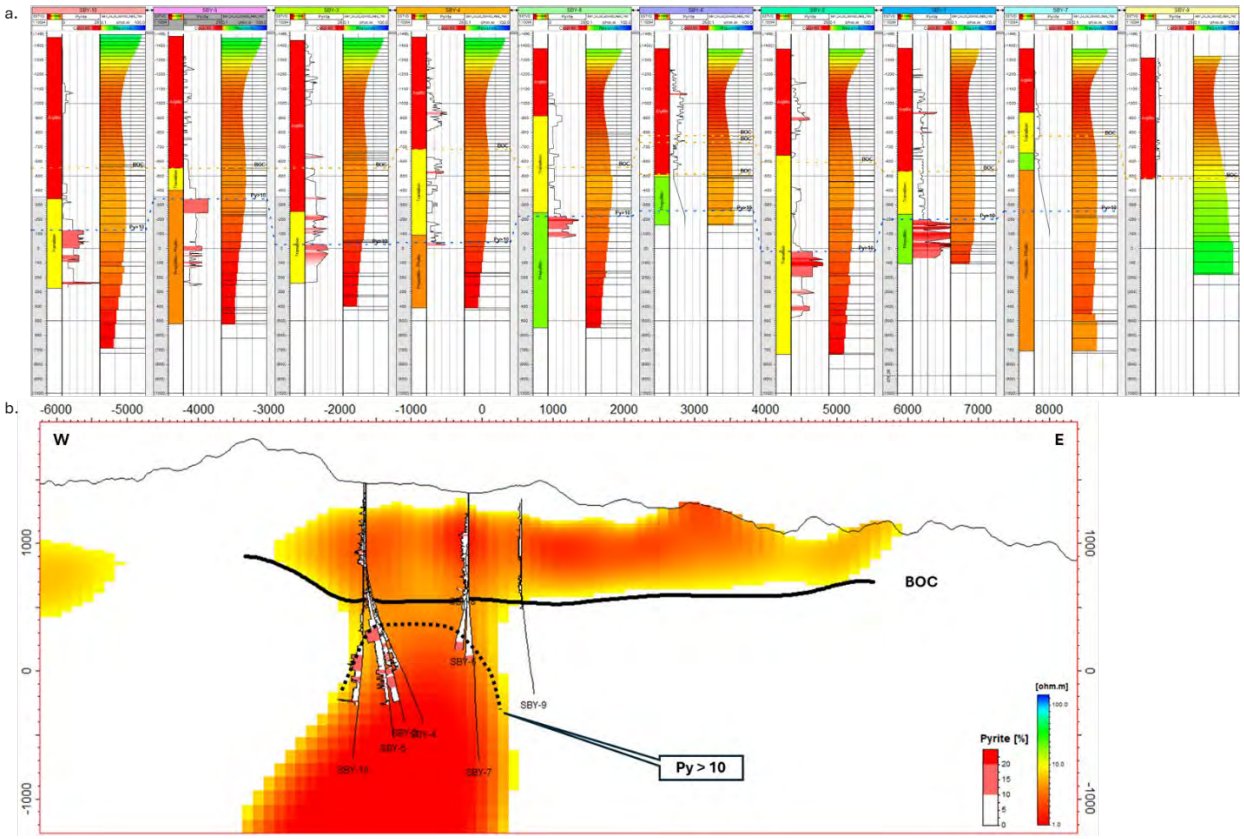

Figure 11. a. Distribution of Pyrite content in percentage (%) : pink to red is more than 10% contents, b. W-E cross-section with a filtered less than 5 ohm.m resistivity model background and Sibayak wells with each Pyrite content, a dotted line is an interpreted line of Pyrite with more than 10% content.

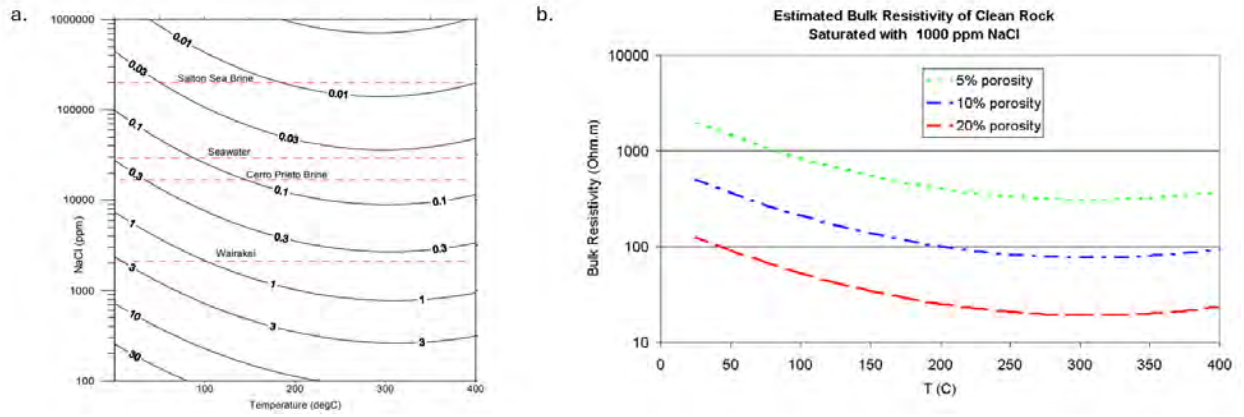

Figure 12. Relationship of salinity, porosity, temperature and resistivity (Ussher, et al., 2000) a. Variation of resistivity in ohm.m of Nacl solutions from measurements (Ucok, et al., 1980) modified by (Ussher, et al., 2000). b. a modelled Archie's Law bulk resistivities for "clean" rocks containing saturated 1000 ppm NaCl.

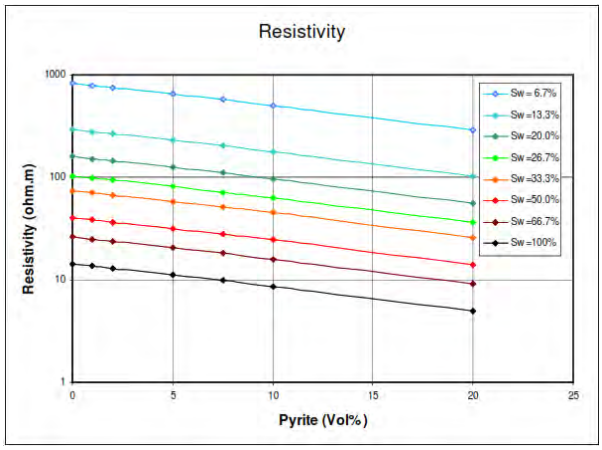

Figure 13. Resistivity of brine-saturated Pyrite bearing sandstones model with variable gas saturation, using Hanai-Bruggeman method (Clennell, et al., 2010).

Conversely, if sulfide mineralization is the primary cause of the enhanced conductivity, a comprehensive exploration program focused on identifying and evaluating rare mineral potential is warranted. Regardless of the underlying mechanism, drilling a new well into the core of the conductive body is essential to advance understanding of the system and assess its economic viability.

7. Conclusions

The integration of 1D and 3D inversion results with well data has significantly improved the delineation of the bottom of the clay cap (BOC), particularly in differentiating the clay cap from the underlying, highly conductive zone. Even though the causes of a deep enhanced conductivity in Sibayak are unclear, an enhanced conductive body is visible in all 1D, 2D and 3D MT inversions.

To explain the origin of enhanced conductivity, a combination of approaches is recommended. Drilling a new well targeting the conductive zone, coupled with resistivity logging, would provide direct evidence of the causative factors. Alternatively, rock physics modeling using methods like Hanai-Bruggeman or Archie's law could be employed to estimate formation factors for the Sibayak Tertiary sandstone. However, the lack of detailed rock property data limits the accuracy of such models.

Acknowledgement

This study was supported by PT. Pertamina Geothermal Energy Tbk, Geoscience Exploration & Development Region 1 Division, Geoscience Department. Thank you for the support and permission to publish this paper.

REFERENCES

Atmojo, J. et al., 2001. *Numerical Modelling Study of Sibayak Geothermal Reservoir, North Sumatra, Indonesia.* Stanford, California, Twenty-Sixth Workshop on Geothermal Reservoir Engineering.

CGG Geoscience, Multiphysics, 2023. *Pertamina Geothermal Energy Internal Report of 3D MT Inversion Modeling - Sibayak,* s.l.: CGG Geoscience, Multiphysics.

Clennell, M. B. et al., 2010. *The influence of pyrite on rock electrical properties : a case study from NW Australian gas reservoirs.* s.l., SPWLA 51st Annaul Logging Symposium.

Cumming, W. & Mackie, R., 2010. *Resistivity Imaging of Geothermal Resources Using 1D, 2D and 3D MT Inversion and TDEM Static Shift Correction Illustrated by a Glass Mountain Case History.* Bali, Indonesia, World Geothermal Congress.

Daud, Y., Sudarman, S. & Ushijima, K., 2001. *Sibayak Geothermal Field (Indonesia): Structure Assessed From Gravity and Hydrogeological Considerations.* s.l., s.n.

Daud, Y., Sudarman, S. & Ushijima, K., 2002. *Imaging Reservoir Structure of the Sibayak Geothermal Field (Indonesia) Based on Magnetotelluric Observations.* s.l., s.n.

Fahmi, F. L. et al., 2021. *Geochemistry Monitoring of Surface Thermal Manifestation in Sibayak, North Sumatra, Indonesia.* Reykjavik, Iceland, World Geothermal Congress.

Firanda, E. et al., 2024. *Updating Numerical Simulation Model of Sibayak Field, Indonesia.* Standford, California, Forty-Ninth Workshop on Geothermal Reservoir Engineering.

Forni, F. et al., 2024. Remobilization and eruption of an upper crustal cumulate mush at the Singkut Caldera (North Sumatra, Indonesia). *Journal of Volcanology and Geothermal Research,* Volume 445.

Hochstein, M. P. & Sudarman, S., 2015. *Indonesian Volcanic Geothermal Systems.* Melbourne, Australia, World Geothermal Congress.

Jenkins, A. P., Rust, A. C., Blundy, J. & Biggs, J., 2023. Magnetotelluric investigations at Andean volcanoes: Partial melt or saline magmatic fluids?. *Journal of Volcanology and Geothermal Research.*

Jones, A. G., 1992. Electrical conductivity of the continental lower crust. In: D. M. Fountain, R. J. Arculus & R. W. Kay, eds. *Continental Lower Crust.* s.l.:Elsevier, pp. 81-143.

Lin, W., Yang, B., Han, B. & Hu, X., 2023. A Review of Subsurface Electrical Conductivity Anomalies in Magnetotelluric Imaging. *Sensors,* 23(1803).

Mulyadi, 2000. *Magnetic Telluric Method Applied For Geothermal Exploration in Sibayak, North Sumatra.* Kyushu - Tohoku, s.n.

PT. Pertamina Geothermal Energy Tbk, 2016. *Internal Report : Geological, Geochemistry, Geophysical and Reservoir Evaluation of Sibayak Geothermal Field, North Sumatra,* Jakarta, Indonesia: Resource Management Division of Planning and Development Directorate.

PT. Pertamina Geothermal Energy Tbk, 2022. *Internal Report : Geological Mapping Report of Sibayak Area,* Jakarta, Indonesia: Geoscience Region I Exploration Division of Exploration and Development Directorate.

Schilling, F. R., Partzsch, G. M., Brasse, H. & Schwarz, G., 1997. Partial melting below the magmatic arc in the Central Andes deduced from geoelectromagnetic field experiments and laboratory data. *Physics of the Earth and Planetary Interiors,* Volume 103, pp. 17-31.

Ucok, H., Ershaghi, I. & Olhoeft, G., 1980. Electrical resistivity of geothermal brines. *Journal of Petroleum Technology.*

Ussher, G., Harvey, C., Johnstone, R. & Anderson, E., 2000. Understanding the resistivities observed in geothermal systems. *World Geothermal Congress.*

Wheaton, R., 2016. *Fundamentals of Applied Reservoir Engineering.* s.l.:Gulf Professional Publishing.

A Direct Comparison of Resistivity Models from Helicopter Transient Electromagnetic and Magnetotelluric Datasets Collected over a Blind Geothermal System in East Hawthorne, Nevada, USA.

Matthew Folsom[1], Steven Sewell[2], William Cumming[3], Jade Zimmerman[4], Andy Sabin[4], Christine Downs[5], Nick Hinz[1], Carmen Winn[1], Benjamin Seiderman[6] and Paul Schwering[5]

[1]Geologica Geothermal Group, [2]Australis Geoscience Ltd., [3]Cumming Geoscience, [4]Navy Geothermal Program Office, [5]Sandia National Laboratories, [6]KLM Geoscience.

Keywords

Blind geothermal system, magnetotellurics, helicopter transient electromagnetics, gravity, shallow low resistivity zones, geothermal outflow.

ABSTRACT

Blind geothermal systems are believed to be common in the Basin and Range province and represent an underutilized source of renewable green energy. Their discovery has historically been by chance but more methodological strategies for exploration of these resources are being developed. One characteristic of blind systems is that they are often overlain by near-surface zones of low-resistivity caused by alteration of the overlying sediments to swelling clays. These zones can be imaged by resistivity-based geophysical techniques to facilitate their discovery and characterization.

Here we present a side-by-side comparison of resistivity models produced from helicopter transient electromagnetic (HTEM) and ground-based broadband magnetotelluric (MT) surveys over a previously discovered blind geothermal system with measured shallow temperatures of ~100°C in East Hawthorne, NV. The HTEM and MT data were collected as part of the BRIDGE project, an initiative for improving methodologies for discovering blind geothermal systems. HTEM data were collected and modelled along profiles, and the results suggest the method can resolve the resistivity structure 300 – 500 m deep. A 61-station MT survey was collected on an irregular grid with ~800 m station spacing and modelled in 3D on a rotated mesh aligned with HTEM flight directions. Resistivity models are compared with results from potential fields datasets, shallow temperature surveys, and available temperature gradient data in the area of interest.

We find that the superior resolution of the HTEM can reveal near-surface details often missed by MT. However, MT is sensitive to several km deep, can resolve 3D structures, and is thus better suited for single-prospect characterization. We conclude that HTEM is a more practical subregional prospecting tool than is MT, because it is highly scalable and can rapidly discover shallow zones of low resistivity that may indicate the presence of a blind geothermal system. Other factors such as land access and ground disturbance considerations may also be decisive in choosing the best method for a particular prospect. Resistivity methods in general cannot fully characterize the structural setting of a geothermal system, and so we used potential fields and other datasets to guide the creation of a diagrammatic structural model at East Hawthorne.

1. Introduction

Blind geothermal systems are those that have no active surface manifestations such as hot springs, fumaroles or steaming ground. A subset of these, referred to as hidden systems, may have exposures of young or relict sinter, travertine, silicified sediments or acid-sulfate alteration. Going as far back to the mid-1800s in the western U.S., such systems have been discovered by chance by drilling water wells (e.g., Humboldt House) and later by petroleum exploration wells and mineral exploration holes in the 1900s.

Blind and hidden geothermal systems represent an underutilized source of renewable green energy in the Basin and Range province. Some have estimated that about 70% of the convective geothermal resources in the Basin and Range province (Coolbaugh et al., 2006a) are blind resources and that only about half of these blind resources have been discovered thus far in the Basin and Range. Over the past decade, exploration strategies for these systems have evolved towards a unified methodology. Examples of recent contributions have been made using targeting key structural settings (Faulds and Hinz, 2015; Hinz et al. 2015), Play Fairway analysis (Faulds et al. 2015, 2016; Siler et al. 2017 and others) by using machine learning (Faulds et al. 2020; Ayling et al., 2022) and by large-scale prospecting using airborne EM methods (Schwering et al., 2022, Sewell et al., 2023, Folsom et al., 2024). In this study, we examine how helicopter transient electromagnetics (herein referred to as HTEM) compare with ground based Magnetotellurics (MT). The objectives of this paper are twofold: (1) Perform a real-world side-by-side comparison of the two methods in the context of a classic blind geothermal system, and (2) to advance the understanding the blind geothermal system at East Hawthorne, NV.

Central to this effort is the basic observation that geothermal systems in the Basin and Range, blind or not, are frequently overlain by shallow zones of low resistivity (generally < 10 – 15 ohm.m). These zones can extend above the local water table, they occur largely within unconsolidated alluvium, and they tend to correlate with shallow thermal anomalies. The mechanism responsible for this pattern is the generation of low-resistivity hydrated smectite clays, which is enhanced above boiling or near-boiling shallow fluids that are exsolving gas. In systems that are well understood, these zones do not always occur directly over power-capable reservoirs. Instead, they are found where hot fluids rise near the surface, such as along outflow paths or near current or relict springs. The offset between these features and a typical geothermal reservoir can be several kilometers long. It is important to note that there are other geologic causes for shallow zones of low resistivity besides those of geothermal origin.

The dominant method for resistivity exploration used by the geothermal industry has been MT, a ground-based, passive technique that has a depth of investigation of many kilometers. The method

has practical advantages for the explorer. The acquisition systems are reliable, easy to transport and install without specialized tools, and cause minimal ground disturbance. Contractor costs are very reasonable. Challenges include long permitting timelines, requirements imposed by regulatory agencies, and the need to model the data with specialized codes. Modeling MT data in 3D, which is generally recommended for larger datasets, is computationally intensive and can be expensive, although costs are declining. When best practices for data processing and modelling are not followed, the results can contain artefacts that are misleading. Finally, MT surveys collected with wide station spacing (> 1 km) can easily miss the alteration associated with a geothermal system, which can sometimes encompass small areas (< 2 km^2). For this reason, MT can be a poor tool for reconnaissance of larger areas.

An alternative to using MT is to deploy an HTEM method instead. Transient electromagnetic systems are active-source, sending a large current in discrete pulses though a coil to generate a vertical, time-varying magnetic field that induces electrical currents in the subsurface. Secondary fields created by these currents are measured in a receiving coil. The depth of investigation for the system deployed in this study is generally 300 m – 500 m deep in the basins of Nevada (Sewell et al., 2023). Advantages to the explorer include excellent resolution, zero ground disturbance, a simple and fast permitting workflow, and the ability to rapidly cover large areas. Disadvantages include a limited depth of investigation, and high mobilization costs that make smaller surveys less practical.

Regardless of the method, resistivity alone is not sufficient to characterize the structural and stratigraphic setting of a geothermal system, which controls the distribution of permeability and ultimately guides well targeting efforts. Other methods must be deployed to accomplish this goal, such as geologic mapping, LiDAR analysis and potential fields geophysics (gravity and magnetic methods).

The BRIDGE project (Schwering et al., 2022) is part of a DOE-funded program to improve exploration efficiency in the discovery and characterization of blind geothermal systems in the Basin and Range province. The primary tool of this project was the deployment of a regional-scale HTEM survey, (Figure 1) which has been followed by a multidisciplinary exploration methodology.

An example of the results is shown for one HTEM line that bisects Gabbs Valley, NV, and crosses both the developed Don A. Campbell geothermal field, which is a blind system, and the Rawhide geothermal prospect, which has a hot spring. The resistivity model, shown in the lower panel of Figure 1, shows that shallow low-resistivity zones drape over both systems. In this figure and others like it in this report, a depth of investigation cut-off is denoted by a transition from solid to transparent colors. This is determined by the inversion algorithm, and values below this transition may be poorly constrained. The transparent portions extend to a constant depth of 600 m.

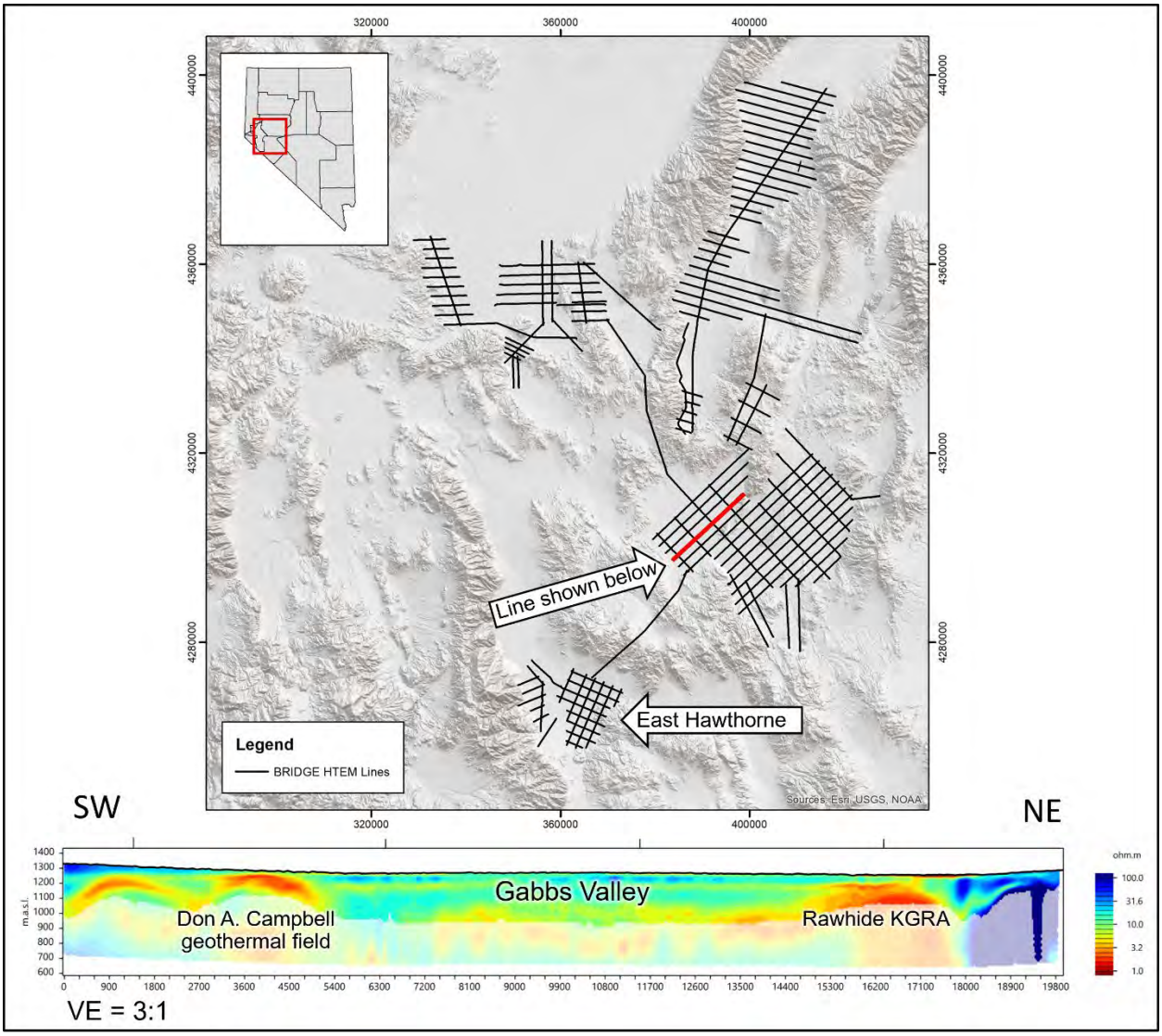

Figure 1: BRIDGE HTEM flight lines, and one sample resistivity profile from a transect crossing Gabbs Valley, NV. The approximate locations of the Dan A. Campbell geothermal field and the Rawhide known geothermal resource area (KGRA) are shown for reference. Note the 3x vertical exaggeration (VE) of the THEM resistivity profile.

1.1 Background

The blind geothermal prospect at East Hawthorne lies on the northwestern edge of the Garfield Hills, within the Walker Lake Basin near the town of Hawthorne, and inside the Hawthorne Ammunition Depot. A shallow temperature anomaly was defined in detail by a 2m temperature probe survey commissioned by the U.S. Navy in 2008 and 2009 (Kratt et al., 2010) that followed a thermal anomaly identified by water wells and temperature gradient drilling by the University of Nevada, Reno (Trexler, 1981). Additional surface studies were also conducted in 2009 in parallel

with the 2m temperature probe survey and that included geologic mapping, geochemistry studies, geophysical surveys, and 3D modeling (Hinz et al., 2010, Bell and Hinz, 2010; Kratt et al., 2010; Moeck et al., 2010; Lazaro et al., 2010; Penfield et al., 2010; Schoffner et al., 2010; 2011). Following these surface studies, a temperature gradient drilling program was completed in 2010 (Meade et al., 2011). A maximum temperature of 83.4°C was encountered at 55 m deep above a cooler deeper aquifer, indicating that hot lateral cross-flow was occurring at this location. Also in 2010, a slim well, HAD-1, was drilled to 914 m depth at East Hawthorne (Figure 2). This well encountered drilling losses 167 m depth at the contact between alluvium and quartz diorite. It is uncertain if the contact is depositional or a fault contact, however it is co-located with the highest temperatures in the well of 98.9°C above a temperature reversal (Figure 2; Meade et al., 2011; Blake et al., 2017). To date, there has been no geochemical analysis of fluids from East Hawthorne, limiting estimates of potential resource temperatures without having geothermometry calculations available.

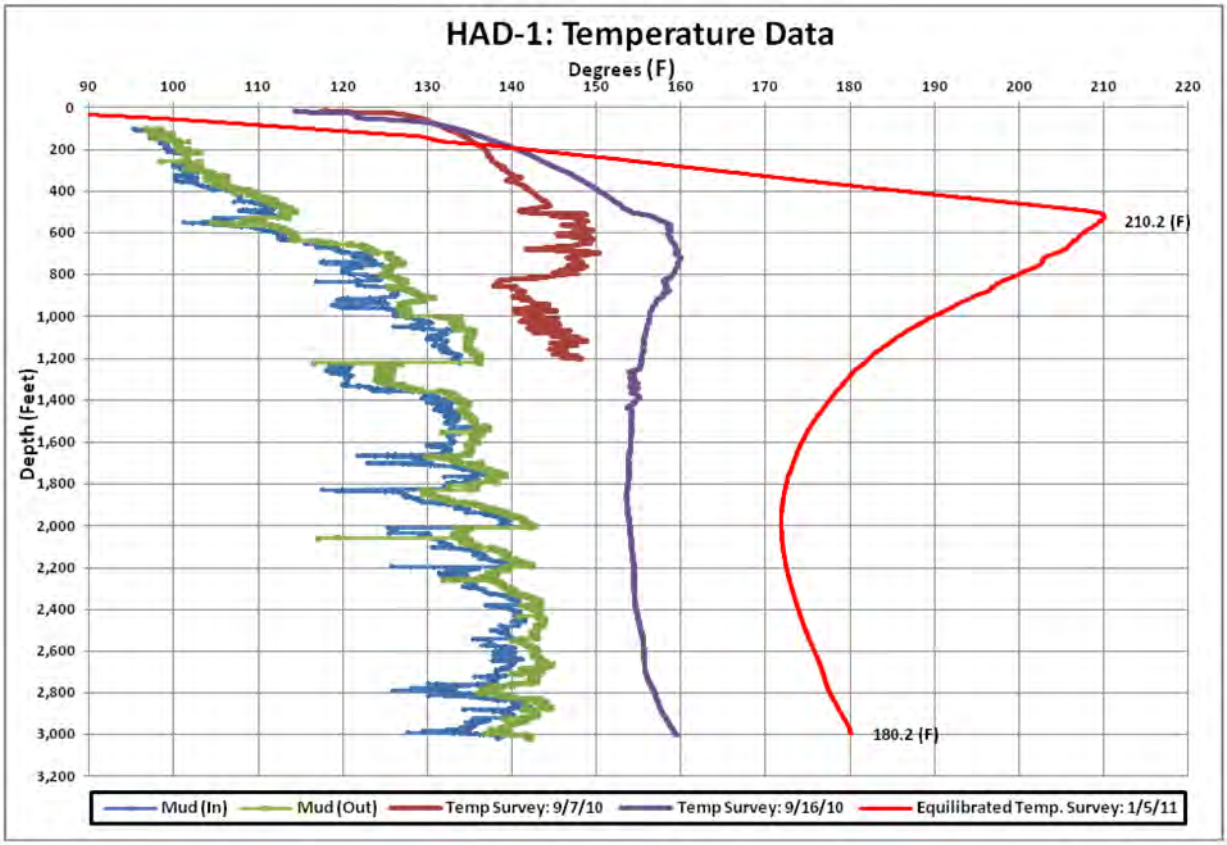

Figure 2: Drilling mud temperatures and temperature survey data for HAD-1 (figure from Meade et al., 2011).

XRD clay analysis of cuttings from HAD-1 confirmed smectite clay alteration in the alluvial section, which terminates at the contact with Mesozoic quartz diorite (Blake et al., 2017). Below this, the alteration regime switches to mixed-layer clays of illite-smectite, and illite-chlorite. The smectite clay zones that overlay the near-boiling outflow were shown to align with low-resistivity zones imaged by the HTEM (Sewell et al., 2023). Hence, the shallow low-resistivity zones here were confirmed to be of geothermal origin. The mixed layer clay alteration in the Mesozoic rocks

may be related to relict higher temperature alteration as noted in adjacent surface outcrops (Hinz et al., 2010).

The BRIDGE project followed up this observation with a 61-station MT survey, conducted in two phases. Data were then modelled in 3D, enabling a deeper image to be generated, and allowing direct comparison with the HTEM results.

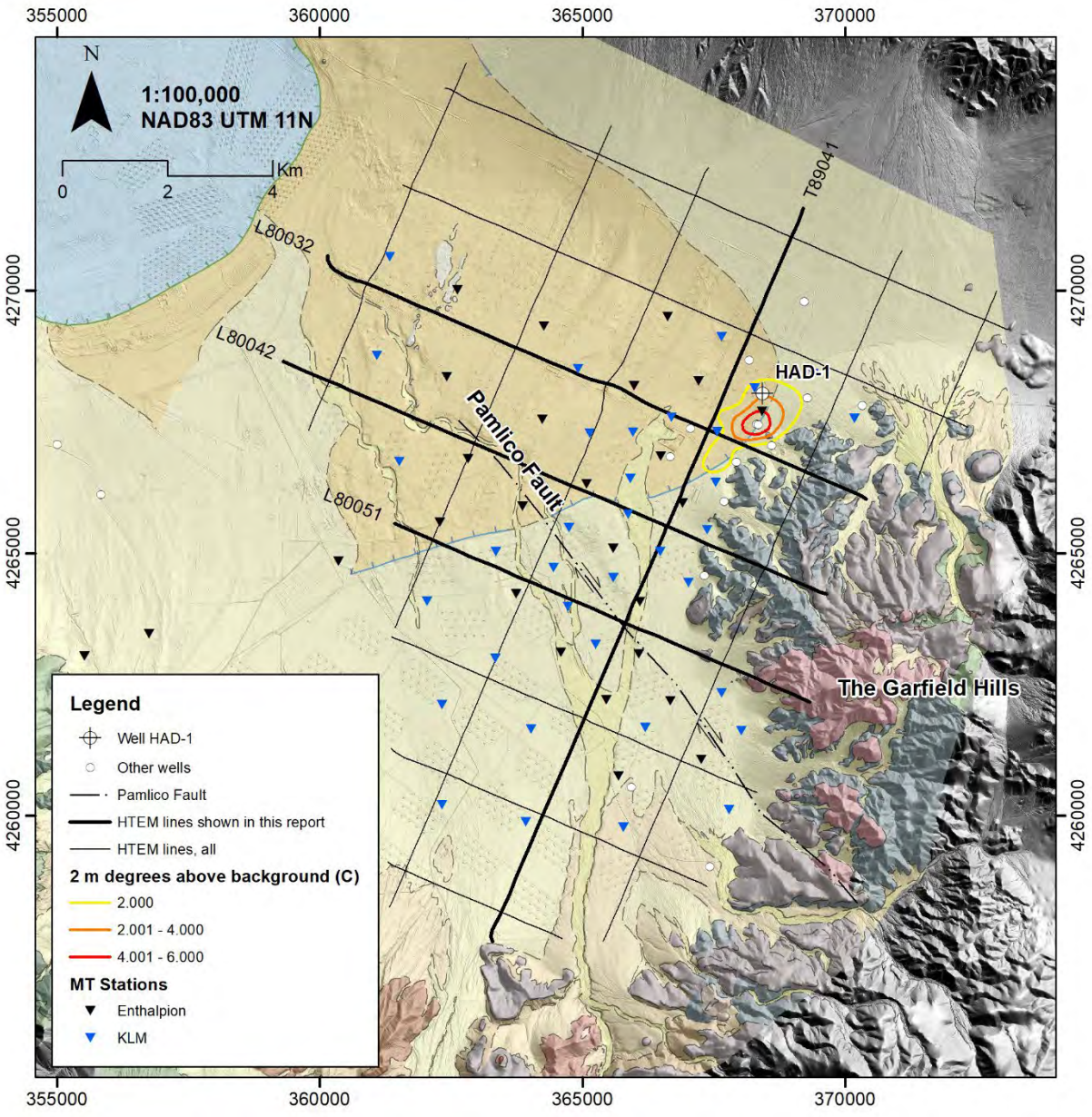

Figure 3: Map of East Hawthorne, including wells and HAD-1 locations (white circles), MT stations (triangles), HTEM flight lines (black lines), contoured 2-meter temperature results (yellow, orange and red lines), and select geologic features from Hinz et al., 2010.

1.2 Geologic Setting

The Walker Lake Basin lies on the western margin of the Walker Lane, which is a sub-unit of the Basin and Range Province dominated by NW-striking dextral strike slip faults. These strike slip features are often kinematically linked with normal faults. The basin is inferred to be a complex half-graben (Hinz et al., 2010), bound on its western side by the Wassuk Range-front fault. The Garfield Hills are composed of thin Tertiary volcanics overlying mostly of Mesozoic metamorphic rocks with some granitic plutons, including one intersected by HAD-1 (Blake et al., 2017). The NW corner of the Garfield hills are cut by NW-striking dextral faults and NE-striking sinistral oblique faults. The Pamlico Fault (Figure 1) is a NW-striking strike-slip fault that is both mapped at the surface (Hinz et al., 2010; Hinz 2024, personal communication) and is observed to correlate with a strong gradient in the gravity data. This gradient implies that the Pamlico Fault also drops low density alluvial fill against higher density basement rocks. Strong gravity gradients also suggest a concealed NE-striking, NW-dipping normal fault zone across NW margin of the Garfield Hills. No evidence of this fault zone is apparent at the surface, but its shallower extent may have been encountered by HAD-1.

2. Data

2.1 HTEM

HTEM data were collected along 1,877 line-km in the western Basin and Range (Figure 1). 2 km line spacing was considered adequate for prospecting purposes and enabled a large area to be surveyed for reasonable cost. One downside to the large line spacing is that the results cannot be contoured in plan-view without aliasing features. Lines were chosen to be perpendicular to structures. In the East Hawthorne area only, tie-lines were spaced equally at 2 km.

HTEM data were contracted through Xcalibur Multiphysics using their HELITEM™ system. This system deployed a 962 m^2 loop with four turns of wire. A 7.5 Hz, 146 A current with 50% duty cycle was transmitted to the coil. Returns were measured in 25 time-gates at a central-loop, multicoil (X, Y, Z) receiver. An independent magnetometer was also deployed just aft of the receiver coil. Flight speed averaged 110 km/h with an average sensor height of 35 m.

2.2 MT

MT data were collected in two phases. 26 sites were collected in 2022 by Enthalpion Energy using customized 32-bit receivers, custom magnetic field sensors and PbCl non-polarizable electrodes. Each station recorded vertical magnetic data. Stations were left to record for two nights each and recorded simultaneously with two sets of remote reference coils at distant locations. A ‘far’ remote was operated in northwestern Oregon, and a ‘local’ remote was installed approximately 70 km east of the survey center. All data were processed using dual-remote references, which is an approach designed to reduce the impact of geomagnetically induced currents in grounded power transmission lines. The contractor noted, however, that there was little evidence of bias in the results due to these sources. Final transfer functions include MT responses from 440 Hz – 0.00055 Hz.

In a second phase, KLM Geoscience was commissioned to add 35 MT locations to the original grid, reducing the station spacing to ~800 m. KLM deployed Phoenix RXU-8A receivers, MTC-155 broadband magnetic sensors and Cu-CuSO4 porous pot electrodes. Vertical magnetic data was

not collected. Each station collected data overnight and each were recorded simultaneously to a single remote reference station located 20 km to the east of the survey grid. Final transfer functions include MT responses from 10,000 Hz – 0.001 Hz.

Figure 4 shows sample transfer functions from both deployments. Apparent resistivity and phase are shown as edited prior to the modeling routing, with masked points in grey. Solid red and blue lines represent the rho+ synthetic model, which is used as proxy for data quality, although it makes certain 1D assumptions. (Parker and Booker, 1996).

Phase tensors (Caldwell et al., 2004) from all stations are shown over a range of periods in Figure 5. Because they are computed from edited data, many are missing at longer periods and within the dead band. Ellipses are colored by the geometric mean of the phase. Phase tensors are derived from components of the impedance phase, are rotationally invariant and are free from the effects of galvanic distortion. Parameters extracted from the phase tensors provide useful insights on the dimensionality of the structure. The long axis of the ellipse denotes the preferred direction of current flow, which are skewed some by 3D effects if they are present. Data quality is good to excellent for the majority of stations, with few outliers.

2.3 Gravity and Magnetics

Gravity data were compiled from the open-source dataset described by Ponce (1997) and from two separate deployments collected by the U.S. Navy in 2001 and 2009 (Schoffner, 2011). For this project, data were re-merged from the original files, terrain corrections were re-calculated digitally using LiDAR data, and the results were reduced to complete Bouguer anomaly (CBA) using standard methods (Hinze et al., 2007). After editing some spurious points, a total of 998 gravity stations covers the southern portion of the Walker Lake Basin. The CBA, along with its horizontal gradient magnitude (HGM) and first vertical derivative (1VD) are shown in panels A-C of Figure 6.

Aeromagnetic data was clipped out of the GeoDAWN dataset collected by the USGS (Glen and Earney, 2024). In this region, line spacing is 400 m and the mean terrain clearance was 237 m above ground. Flight lines were oriented east-west. The reduced-to-pole magnetic residual (RTP) is shown in panel D of Figure 6.

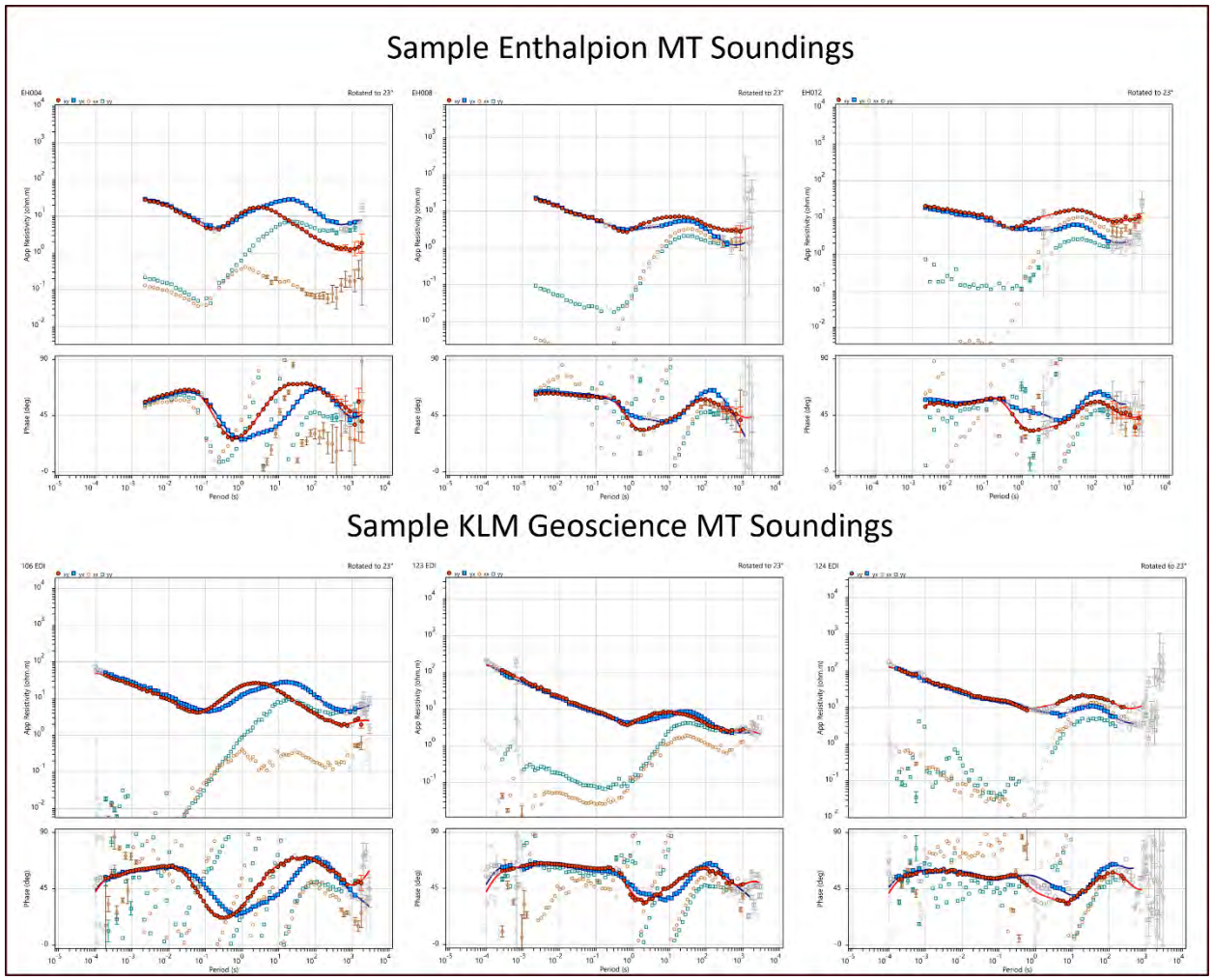

Figure 4. Sample MT sounding plots from the Enthalpion and KLM surveys. The upper portion of each sub plot shows the apparent resistivity, and the lower portion shows the impedance phase. All tensor components are shown. Solid red and blue lines are the Rho+ synthetic model, which is used a proxy for data quality.

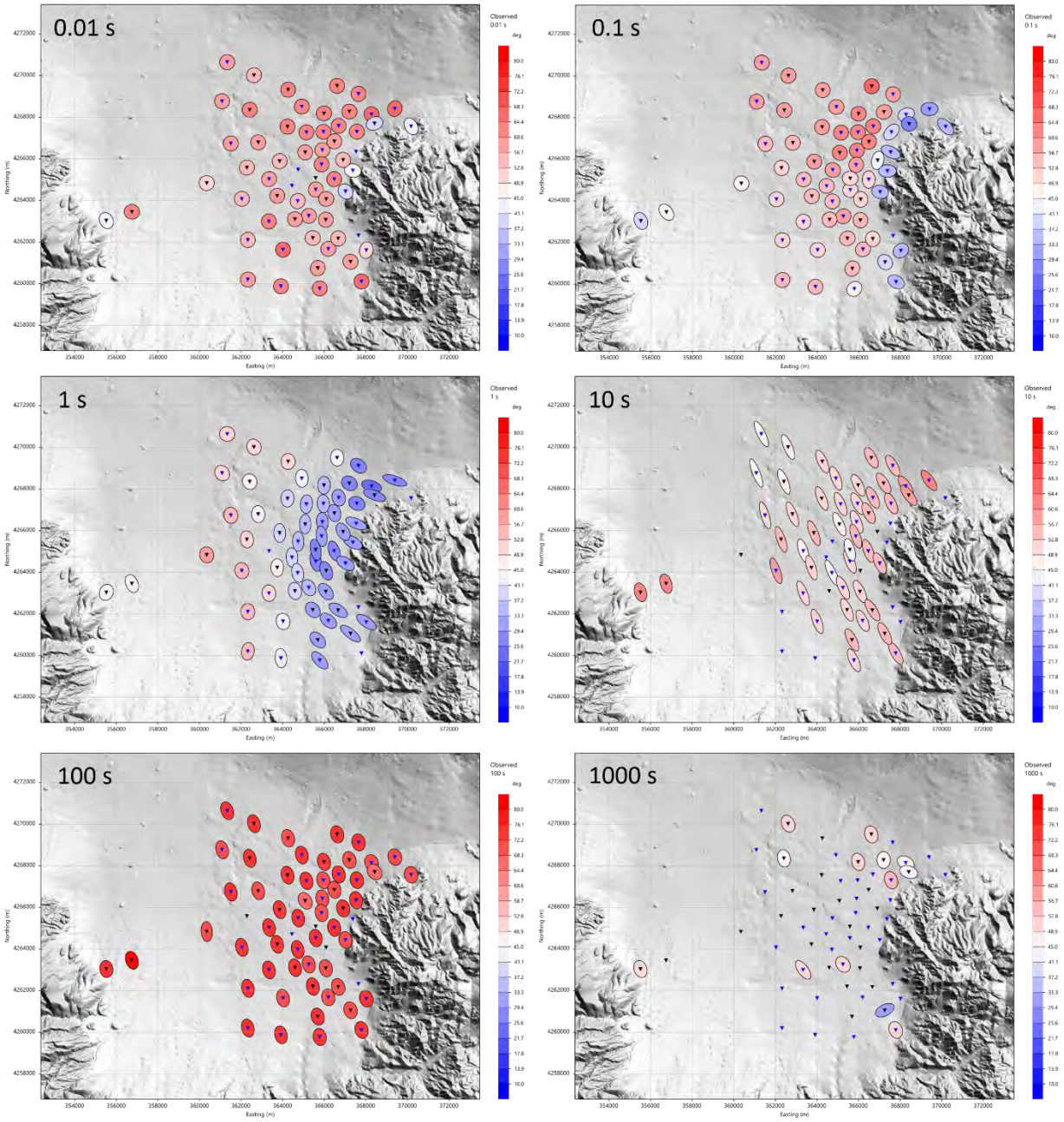

Figure 5: Phase tensors at select periods, noted in the upper left corner of each panel in units of seconds. Ellipses are colored by the geometric mean of the phase. Phases above 45° (red) indicate a decrease in resistivity with depth, and phases below 45° (blue) indicate an increase in resistivity with depth. This is true only where the data are 1D in nature.

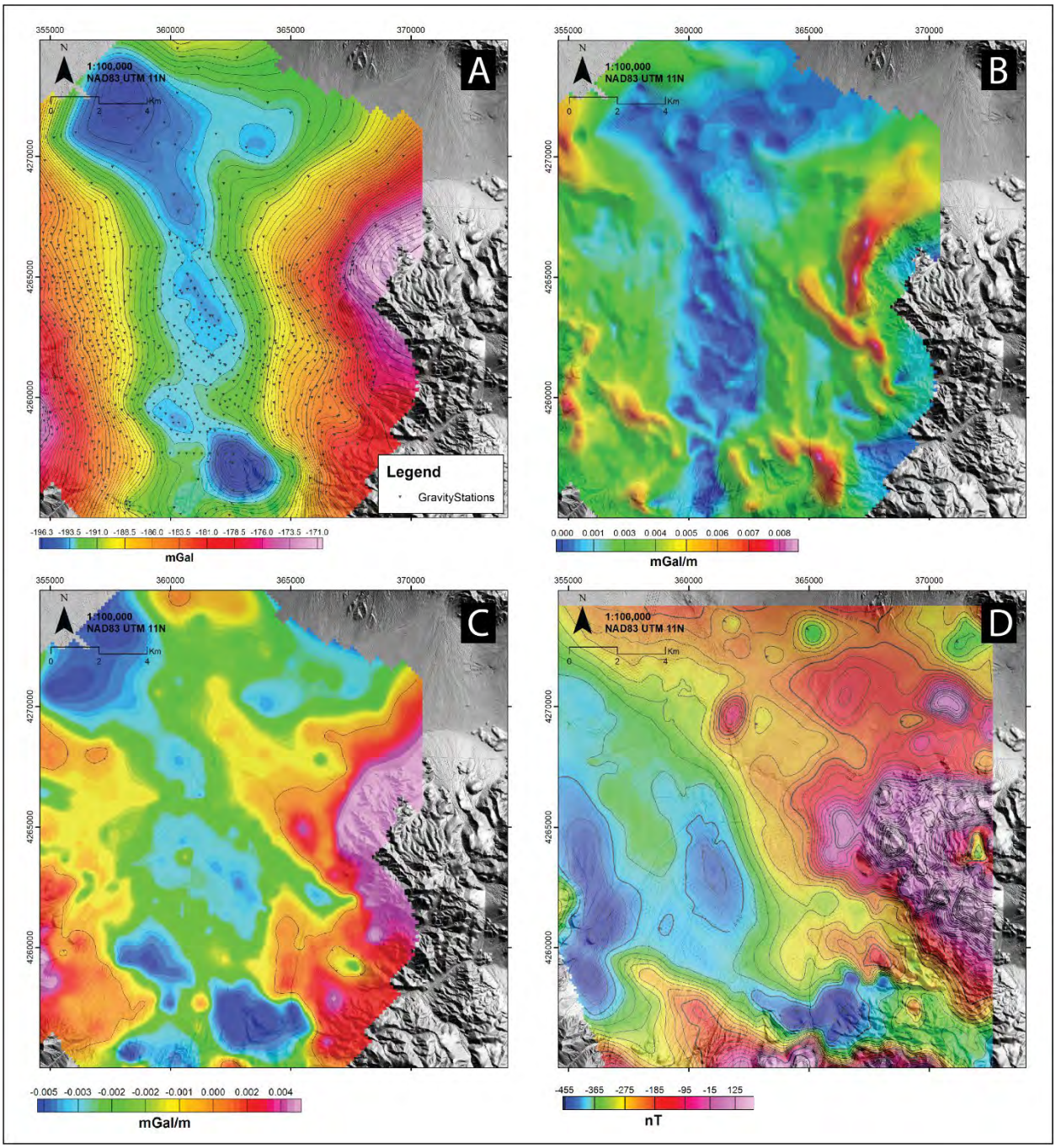

Figure 6. Gravity and magnetic data from East Hawthorne. Panel A: Complete Bouguer anomaly (CBA) reduced at 2.45 g/cc and gridded at 150 m, with gravity station locations shown as small black triangles. Panel B: Horizontal Gradient Magnitude of the CBA. Panel C: First vertical derivative of the CBA. Panel D: Reduced-to-pole magnetic anomaly from the GeoDAWN dataset (Glen and Earney, 2024).

3. Methods and Results

3.1 HTEM

Laterally constrained, 1D deterministic inversions of the HTEM data were carried out by the USGS using the Aarhus Workbench Airborne TEM module. The depth of investigation was determined, which is an estimate of the depth at which the modelled results can resolve the resistivity structure given local signal and noise levels. This is shown in the HTEM figures in this report as a transition from opaque to transparent. Note that this depth is variable and dependent on the overlying resistivity values. In areas with near surface conductors, the depth of investigation is decreased.

In many areas at East Hawthorne, noise from anthropogenic sources such as railways, ammunition bunkers, power lines and buried utilities caused problems with the results. These issues are generally easy to identify and present themselves as localized early-time transients in the receiving coil. Care was taken to edit these points prior to modeling, which results in blank strips in some of the models. Induced-polarization (IP) effects are also present in the data, which can occur in strong central-loop TEM systems. This effect causes rapid decay of transient voltages followed by a polarity reversal (El-Kaliouby, 2001).

3.2 MT

The model mesh used to perform the 3D inverse modeling was rotated to align with the HTEM flight lines (Figure 7). The mesh accounts for topography and was constructed using a finer inner core and coarser outer core to reduce the total number of cells. Padding cells extend for 50 km in the X, Y and Z directions. The total number of model cells is about 1.2 million. Data were rotated 23° CW from north to align with the mesh, and then edited of spurious points prior to modeling.

The data were then modelled using the RLM-3D inversion code (V.3.3.3.12526) as described in Soyer et al., (2020). This code follows a minimum structure Tikhonov approach (Tikhonov and Arsenin 1977), deploying regularized least-square methodology, where an objective function is iteratively minimized using the method of non-linear conjugate gradients.

A summary of the model mesh, inversion parameters and data fit results are shown in Figure 7. A total of eight models were run to explore the inversion space. The final model started from a homogeneous 20 ohm.m subsurface resistivity and ran for 50 iterations using a higher (smoother) vertical regularization setting (tauV). The model was then re-started using a smaller tauV setting and ran for 30 more iterations, achieving a final RMS fit of ~1.2 while using a 3% error floor on all tensor components.

Constant elevation map slices through the final 3D MT model are shown in Figure 8.

3.3 A Direct Comparison of Results

Figure 9 and Figure 10 show direct comparison of the HTEM results to the 3D MT model, extracted along four lines. Select wells are projected to the cross sections, including HAD-1. 1D layered models of the MT data, made from the invariant mode are shown over the cross-sections for reference.

Both the 3D MT model and the HTEM models can clearly resolve shallow low-resistivity features associated with the blind geothermal system at East Hawthorne. In cross-section, the HTEM

models have superior resolution, and image complexities not seen in the MT. In several cases, the MT sees a single low resistivity body, but the HTEM results suggest it is made from two discrete layers. Often, the HTEM places a flat-lying conductors ~100 m deep within the alluvium. These are only sometimes resolved within the MT model. Interpretation of such features remains incomplete, but they may indicate soil horizons, the water table, or geothermal outflow features. In several instances, the HTEM results match the shallow 1D models from the MT data better than they do the 3D MT model. This effect was made worse on 3D inversions run with smoother regularization settings, and so it seems likely to be related to the nature of minimum structure modeling techniques. Despite these doubts about shallow results in the 3D resistivity model, the MT model appears to be well constrained to several km in depth.

In plan-view, the 3D MT model provides valuable observations on the extent of the shallow low resistivity zones and can be compared directly with other mapped data such as results from gravity. This would be possible using HTEM also, had closer line spacing been deployed.

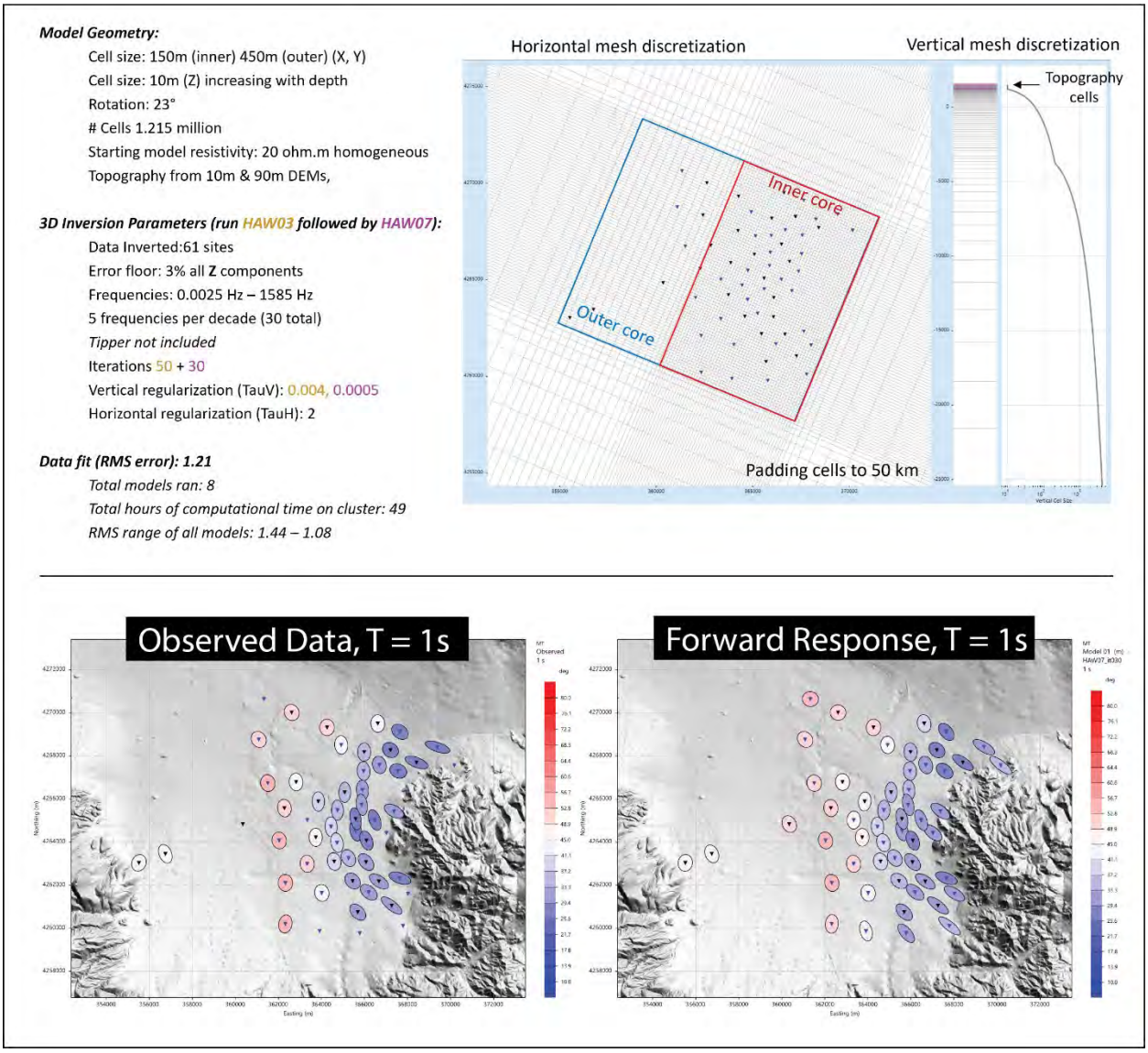

Figure 7. Summary of mesh geometry, inversion parameters and resulting data fit. Lower panels show phase tensors at a period of 1 second, from the observed data (left) compared to the forward response (right).

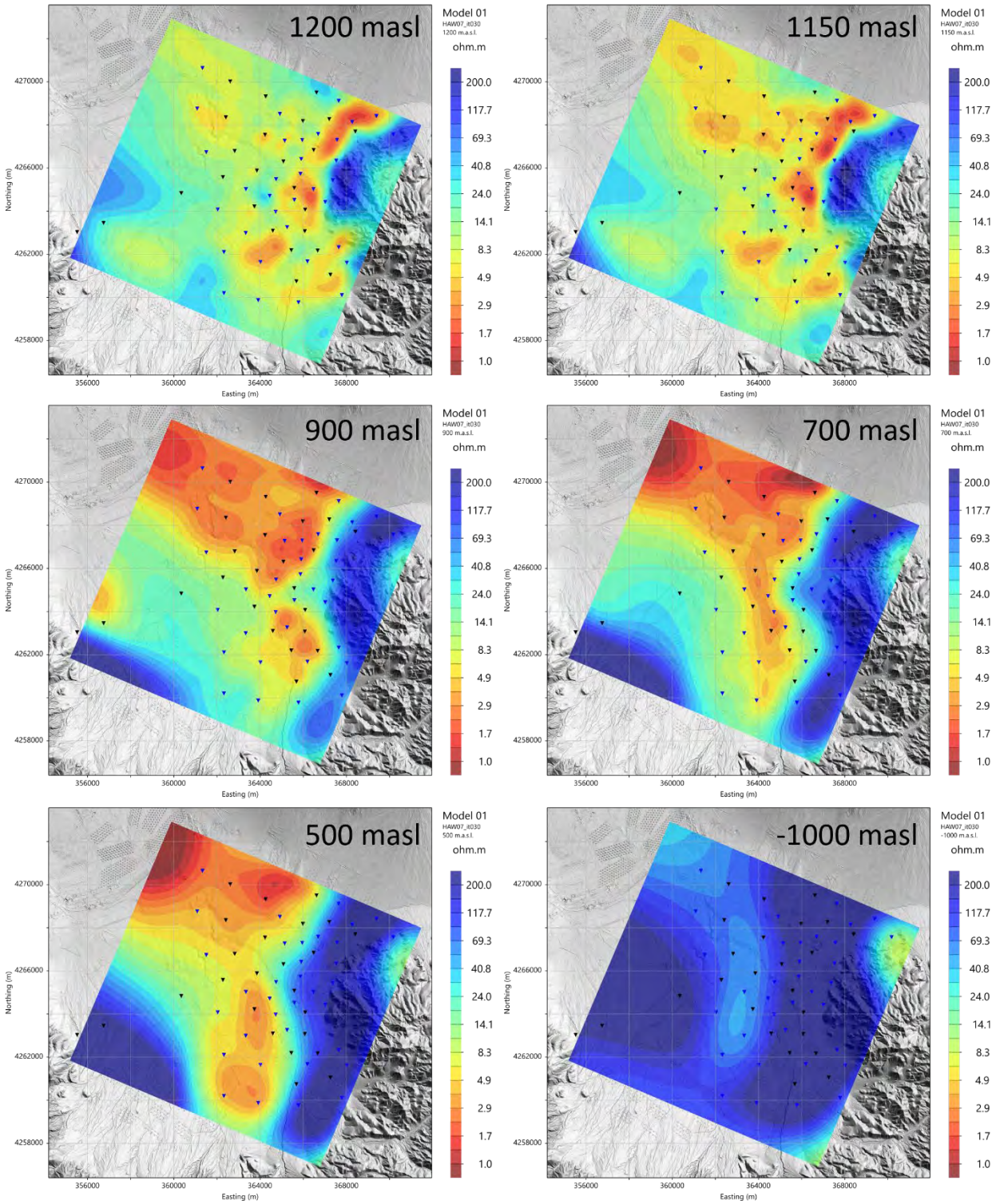

Figure 8: Constant elevation slices, noted in meters above sea level (masl), at select intervals through the final 3D MT model.

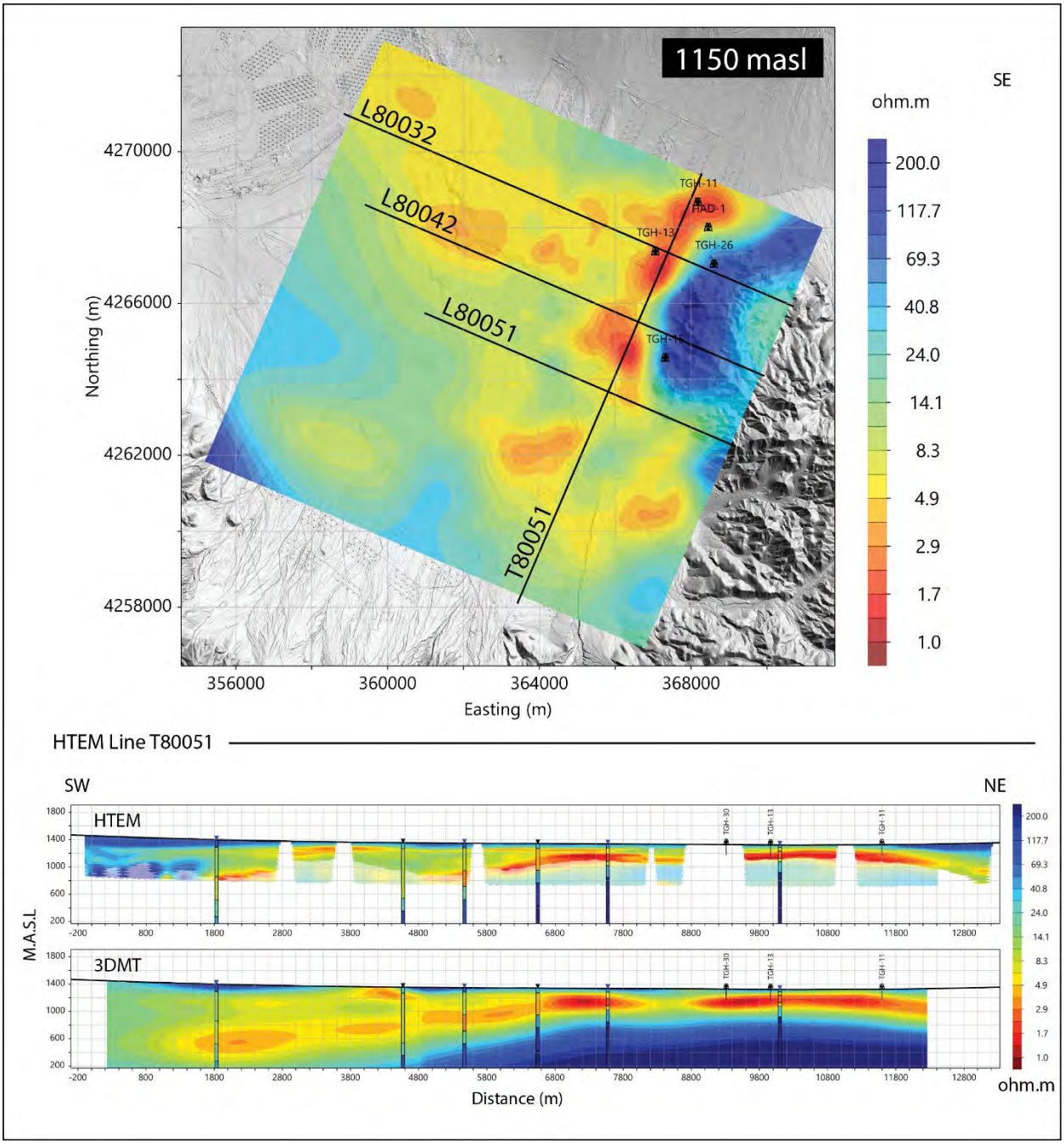

Figure 9: A direct comparison of HTEM and 3D MT results. Upper panel shows the 3DMT model sliced at 1150 masl, with select profiles chosen for comparison. Wells projected onto to the cross sections are shown with black symbols. Lower panel compares the two results on HTEM line T80051. Layered results from 1D MT models of the invariant mode are shown as colored bars.

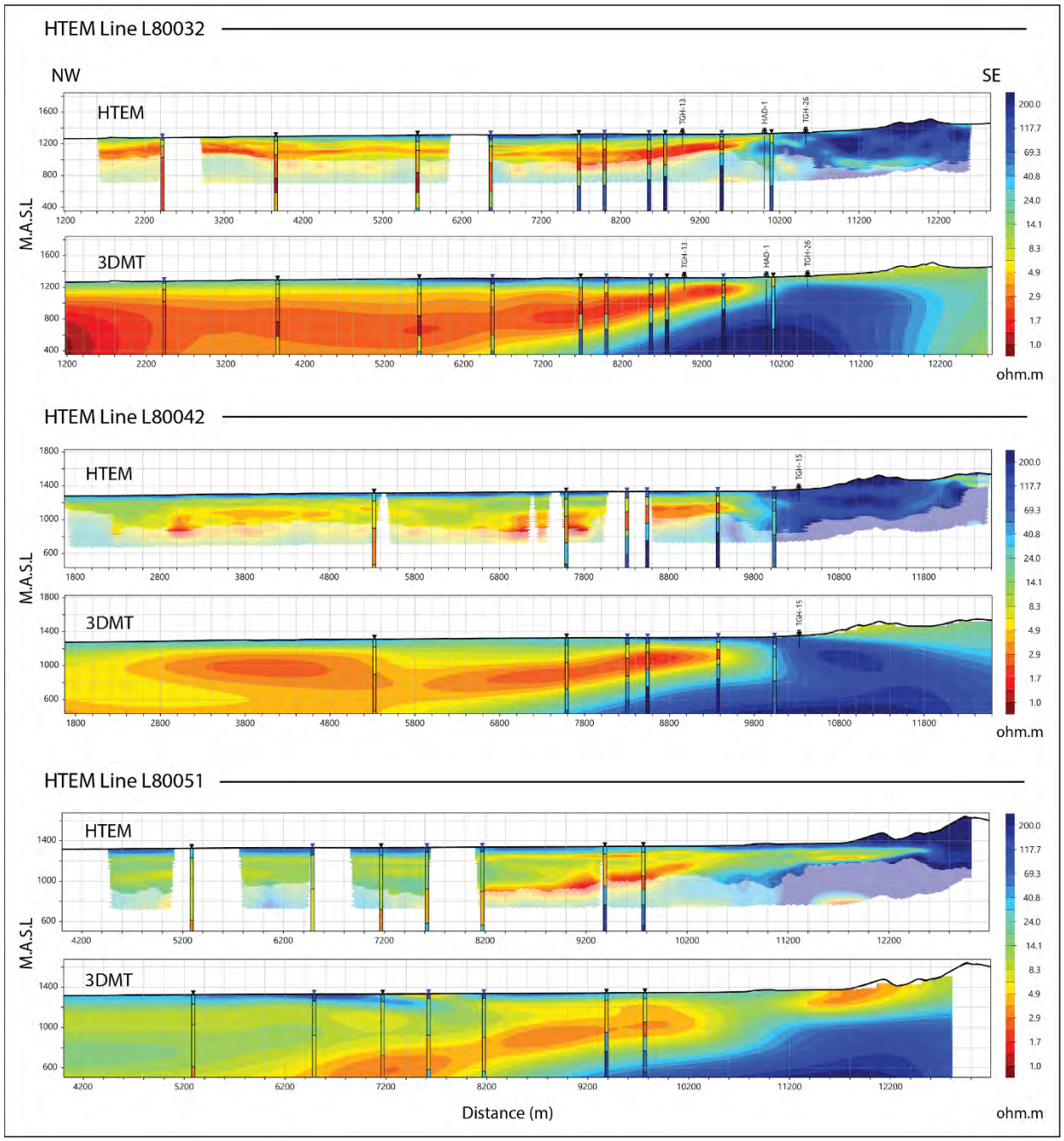

Figure 10: A direct comparison of HTEM and 3D MT results on lines L80032, L80042 and L80051. Layered results from 1D MT models of the invariant mode are shown as colored bars.

4. Interpretation and Discussion

Combining the results from the HTEM, MT and potential fields datasets provides an opportunity to construct a preliminary structural model at East Hawthorne and guide some conceptual model elements of the geothermal system there. The horizontal gradient magnitude of the gravity CBA indicates two strong, nearly perpendicular high gradient zones, which we interpret as major, basin-offsetting faults (Figure 11, panel A). These faults are also suggested by mapped contacts on the ground in the case of the Pamlico Fault, and an inferred fault contact at the base of alluvium in HAD-1, supporting the NE-striking normal fault. These observations follow from the so-called horizontal gradient method, where such contacts are picked along gravity gradient maxima (Cordell, 1979; Cordell and Grauch, 1985). Similar conclusions can be derived from the magnetic data (Figure 11, panel B). Finally, this pattern of two intersecting fault zones is echoed in the MT model, where at shallow depths the low-resistivity zones are confined to the down-dip portions of the normal fault, and north of the Pamlico Fault (Figure 11, panel C). At an elevation of 900 masl in the MT model, a sharp corner intrudes into the low resistivity zone, also suggesting an intersection here. Other faults in Figure 11 are mostly diagrammatic and meant to convey a zone of complexity that likely occurs where these two fault zones intersect.

In the Basin and Range Province, certain structural settings have been shown to correlate with active geothermal systems and epithermal mineral deposits (Faulds et al., 2021; Faulds and Hinz, 2015). These settings include fault step-overs and relay-ramps, among others. The system at East Hawthorne is categorized by these studies as a fault intersection, however, work from this paper suggests that it is a displacement transfer zone instead. In this setting, a strike-slip faulting is kinematically linked to near-perpendicular normal faulting. Producing fields that share this type of geometry include Don A. Campbell, Wabuska, and Blue Mountain. Notable prospects that are believed to host similar setting include South Gabbs (Craig et al., 2021) and Rhodes Marsh (Faulds et al., 2021).

Interpretation of the results suggests two possible end members for the location of an up-flow and geothermal reservoir. The first is that the system lies near the 2-meter temperature anomaly, down-dip along the NE-striking normal fault. HAD-1 encountered near-boiling lateral outflow, and it appears to have been targeted too far up-dip to encounter the resource.

An alternative model is that the system lies closer to the junction of the Pamlico and NE-striking normal faults. Where these two faults meet, a shallow zone of low resistivity is also located, and it overlies an intermediately resistive corner (20 – 40 ohm.m) that intrudes into a conductive background. This geometry is characteristic of other analogue geothermal up-flow zones. This model implies that the observations at HAD-1 and the 2-meter survey are caused by a ~ 4 km long geothermal outflow plume, traveling along-strike with the NE normal fault, although potentially channelized by stratigraphic layers. Such an outflow is not unprecedented in Basin and Range systems. For example, a ~5 km boiling outflow plume is well documented at the San Emidio Field (Folsom et al., 2020, Rhodes et al., 2010, Matlick, 1995) and an 8 km long 140 to 90°C shallow (<150 m deep) outflow is documented at Salt Wells, which is part of a 12 km long shallow thermal anomaly (Edmiston and Benoit, 1984; Coolbaugh et al., 2004, 2006b; Hinz et al., 2014).

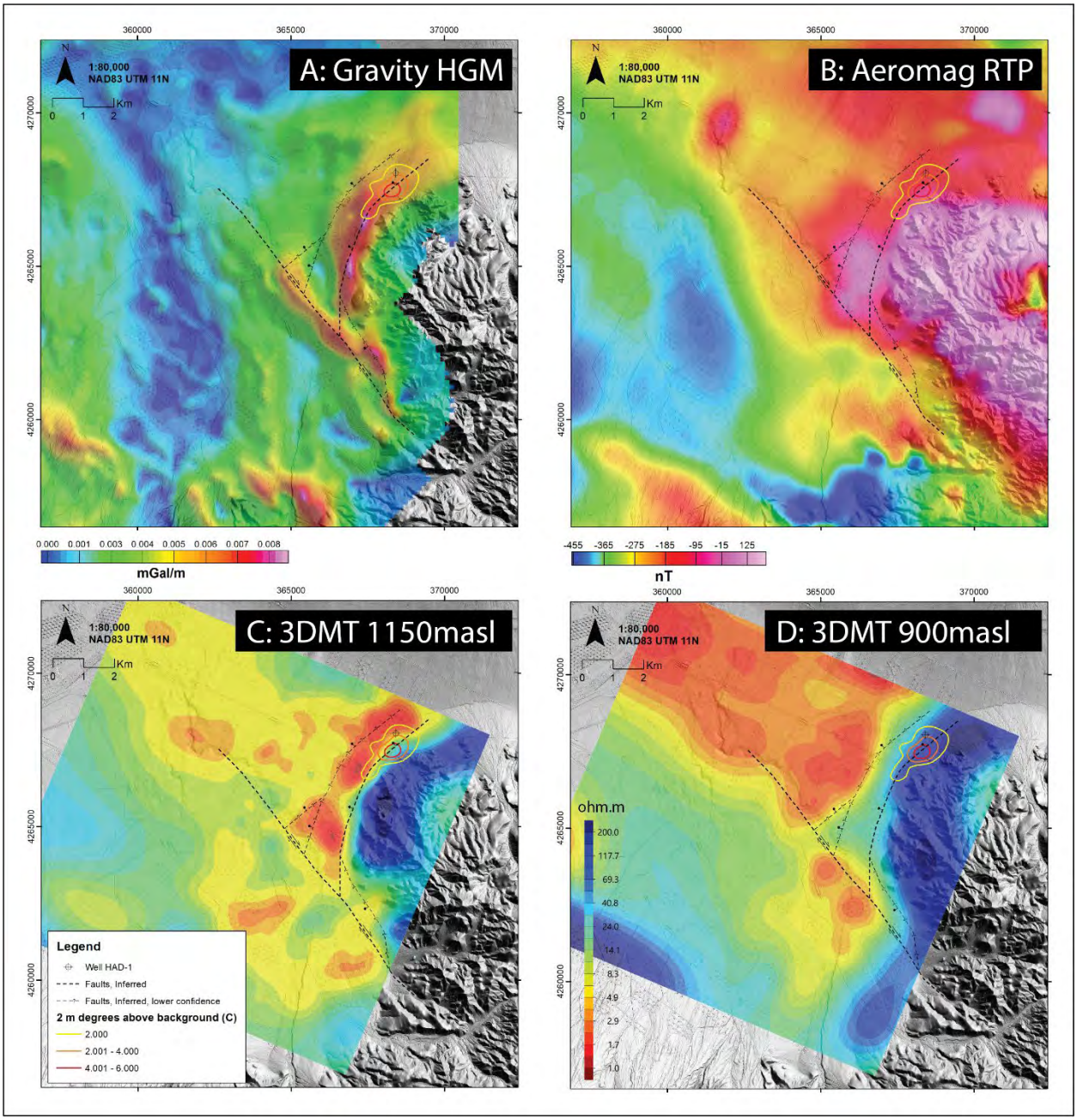

Figure 11: Preliminary structural model informed by geophysics. In each panel, inferred faults and the 2-meter temperature anomaly are shown against different geophysics results. Panel A: Gravity horizontal gradient magnitude (HGM). Panel B: Reduced-to-pole aeromagnetic anomaly (Aeromag RTP). Panel C: Elevation slice at 1150 masl from the 3DMT model. Panel D: Elevation slice at 900 masl from the 3D model.

5. Conclusions

The blind geothermal system studied at East Hawthorne is characterized by low resistivity zones (< 5 ohm.m) that extend across a large area (~8 km^2 at 150 m depth). At the location of well HAD-1, these zones correlate with smectite clay alteration. A preliminary analysis of MT, gravity and magnetic data, supplemented by observations from mapped faults and well data, suggests that the system is hosted within a displacement transfer zone, consistent with generalized models for this area (Hinz et al., 2010). This structural setting is favorable for hosting geothermal upflow as illustrated by both producing fields and prospects elsewhere in the Basin and Range (Faulds and Hinz, 2015). Although several geothermal conceptual models are consistent with the data at East Hawthorne, we prefer a model where an up-flow is hosted near the intersection of the Pamlico strike-slip fault and a NE-striking, NW-dipping normal fault, and below the shallow low-resistivity zone here. This implies a ~4 km long outflow path that connects with the 2m temperature anomaly.

Shallow, low resistivity features relevant to the geothermal system at East Hawthorne are successfully imaged by models created from both HTEM and MT data. Direct comparison of the results demonstrates that, while they each have advantages and limitations, they are ultimately complementary methods for the explorer. The 3D MT model, owing to its survey geometry, is better at characterizing the extent of the shallow low-resistivity zones. In cross-section, the HTEM results have superior resolution, and can resolve the upper portions of typical Basin and Range geothermal systems. Given that HTEM causes no ground disturbance, is straightforward to permit, can access remote locations and rapidly cover large areas, we conclude that it is a better method for geothermal prospecting than MT. However, MT is more practical and cost-effective for assessing a single prospect, it can see much deeper than HTEM and inherently contains 3D information. Despite difficulties with permitting and the complexities of modeling MT in 3D, we conclude that it remains a better choice for developing conceptual models, assessing well targets and estimating resource capacity.

Acknowledgements

This material was based upon work supported by the U.S. Department of Energy, Office of Energy Efficiency and Renewable Energy (EERE), Office of Technology Development, Geothermal Technologies Office under the FY2020 Hydrothermal and Low Temperature Multi-Topic Funding Opportunity Announcement DE-FOA-0002219. Sandia National Laboratories is a multimission laboratory managed and operated by National Technology & Engineering Solutions of Sandia, LLC, a wholly owned subsidiary of Honeywell International Inc., for the U.S. Department of Energy's National Nuclear Security Administration under contract DENA0003525. This paper describes objective technical results and analysis. Any subjective views or opinions that might be expressed in the paper do not necessarily represent the views of the U.S. Department of Energy or the United States Government. The United States Government retains, and the publisher, by accepting the article for publication, acknowledges that the United States Government retains a non-exclusive, paid-up, irrevocable, world-wide license to publish or reproduce the published form of this manuscript, or allow others to do so, for United States Government purposes. Access to lands and airspace was authorized in coordination with representatives of the U.S. Navy, Army,

and Bureau of Land Management – the authors very much appreciate this support and cooperation. The authors are also grateful to the Xcalibur Multiphysics and Heli Carrier team for coordinating and conducting the HTEM survey safely and effectively. Our thanks to Paul Bedrosian at the USGS for his great care in modeling the HTEM data. We’d like to thank the diligent and professional work performed by Enthalpion and KLM Geoscience while collecting the MT data.

REFERENCES

Ayling, B., Faulds, J., Morales Rivera, A., Koehler, R., Kreemer, C., Mlawsky, E., Coolbaugh, M., Micander, R., dePolo, C., Kraal, K., Wagoner, N., Siler, D., DeAngelo, J., Glen, J., Peacock, J., Batir, J., Gentry, E., Berti, C., Lifton, Z., Clark, A., Kirby, S., Hardwick, C., & Kleber, E. (2022). INGENIOUS – Great Basin Regional Dataset Compilation. U.S. D.O.E. Geothermal Data Repository. https://doi.org/10.15121/1881483

Bell, J. W., & Hinz, N. (2010). Young Walker Basin faults provide new insights into structural relations controlling geothermal potential at the Hawthorne army weapons depot, central Nevada Transactions Geothermal Resource Council, 34, 751-754.

Caldwell, T. G., Bibby, H. M., & Brown, C. (2004). The magnetotelluric phase tensor. Geophysical Journal International, 158(2), 457-469.

Coolbaugh, M.F., Sladek, C., & Kratt, C. (2004). Digital mapping of structurally controlled geothermal features with GPS units and pocket computers: Geothermal Resources Council Transactions, v. 28, p. 321-325.

Coolbaugh, M. F., Raines, G. L., Zehner, R. E., Shevenell, L., & Williams, C. F. (2006a). Prediction and discovery of new geothermal resources in the Great Basin: Multiple evidence of a large undiscovered resource base. In GRC 2006 Annual Meeting: Geothermal Resources-Securing Our Energy Future, Vol. 30, pp. 867-873.

Coolbaugh, M.F., Sladek, C., Kratt, C., Shevenell, L., and Faulds, J.E. (2006b). Surface indicators of geothermal activity at Salt Wells, Nevada, USA, including warm ground, borate deposits, and siliceous alteration: Geothermal Resources Council Transactions, v. 30, p. 399-405.

Cordell, L. (1979). Sedimentary facies and gravity anomaly across master faults of the Rio Grande rift in New Mexico. Geology, 7(4), 201-205.

Cordell, L., & Grauch, V. J. S. (1985). Mapping basement magnetization zones from aeromagnetic data in the San Juan Basin, New Mexico. In The utility of regional gravity and magnetic anomaly maps (pp. 181-197). Society of Exploration Geophysicists.

Craig, J. W., Faulds, J. E., Hinz, N. H., Earney, T. E., Schermerhorn, W. D., Siler, D. L., ... & Deoreo, S. B. (2021). Discovery and analysis of a blind geothermal system in southeastern Gabbs Valley, western Nevada, USA. Geothermics, 97, 102177.

El-Kaliouby, H. (2001). Extracting IP parameters from TEM data. In Handbook of Geophysical Exploration: Seismic Exploration (Vol. 30, pp. 307-326). Pergamon.

Edmiston, R.C. & Benoit, W.R. (1984). Characteristics of basin and range geothermal systems with fluid temperatures of 150°C to 200°C: Geothermal Resources Council Transactions, v. 8, p. 417-424.

Faulds, J. E., Coolbaugh, M. F., & Hinz, N. H. (2021). Inventory of Structural Setting for Active Geothermal Systems and Late Miocene (~ 8 MA) to Quaternary Epithermal Mineral Deposits in the Basin and Range Province of Nevada. Nevada Bureau of Mines and Geology.

Faulds, J. E., Brown, S., Coolbaugh, M., DeAngelo, J., Queen, J. H., Treitel, S., ... & Ayling, B. F. (2020). Preliminary report on applications of machine learning techniques to the Nevada

geothermal play fairway analysis. In 45th workshop on geothermal reservoir engineering (pp. 229-34).

Faulds, J.E., Hinz, N.H., Coolbaugh, M.F., Siler, D.L., Shevenell, L.A., Queen, J.H., dePolo, C.M., Hammond, W.C., & Kreemer, C. (2016). Discovering geothermal systems in the Great Basin region: an integrated geologic, geochemical, and geophysical approach for establishing geothermal play fairways: Proceedings, 41st Workshop on Geothermal Reservoir Engineering, Stanford University, Stanford, CA, Feb. 22-24, 15 p.

Faulds, J., Hinz, N., Coolbaugh, M., Shevenell, L., Siler, D., dePolo, C.M., Hammond, W.C., Kreemer, V., Opplinger, G., Wannamaker, P., Queen, J.H., & Visser, C. (2015). Integrated geologic and geophysical approach for establishing geothermal play fairways and discovering blind geothermal systems in the Great Basin region, western USA: A progress report. GRC Transactions, 39(DOE-UNR-06731-05).

Faulds, J., & Hinz, N. (2015). Favorable tectonic and structural settings of geothermal systems in the Great Basin region, western USA: Proxies for discovering blind geothermal systems. In Proceedings World Geothermal Congress, Melbourne, Australia, 19-25 April 2015

Folsom, M., Winn, C., Milton, A., Zimmerman, J., Blake, K., Sabin, A., Downs, C., Sewell, S., Krall, K., Nale, S., Huang, W. & Schwering, P. (2024). An Early-Stage Exploration Update on the Grover Point Blind Geothermal System in Dixie Valley, Nevada: Highlights of Geophysics Results and Conceptual Modeling. In Proceedings of the 49th Workshop on Geothermal Reservoir Engineering, Stanford University, Stanford, CA, USA.

Folsom, M., Libbey, R., Feucht, D., Warren, I., & Garanzini, S. (2020). Geophysical observations and integrated conceptual models of the San Emidio geothermal field, Nevada. In Proceedings of the 45th Workshop on Geothermal Reservoir Engineering, Stanford University, Stanford, CA, USA.

Glen, J.M.G. & Earney, T.E. (2024). GeoDAWN: Airborne magnetic and radiometric surveys of the northwestern Great Basin, Nevada and California: U.S. Geological Survey data release, https://doi.org/10.5066/P93LGLVQ.

Hinz, N. H., Faulds, J. E., Moeck, I., Bell, J. W., & Oldow, J. S. (2010). Structural controls of three blind geothermal resources at the Hawthorne Ammunition Depot, west-central Nevada. Geothermal Resources Council Transactions, 34, 785-790.

Hinz, N.H., Coolbaugh, M.F, Faulds, J.E., Siler, D.L., & Dering, G.M. (2015). Building the next generation of regional geothermal potential maps: Examples from the Great Basin region, western USA: Proceedings, World Geothermal Congress 2015, Melbourne, Australia, 12 p.

Hinze, W. J., Aiken, C., Brozena, J., Coakley, B., Dater, D., Flanagan, G., ... & Winester, D. (2005). New standards for reducing gravity data: The North American gravity database. Geophysics, 70(4), J25-J32.

Kratt, C., Sladek, C., & Coolbaugh, M. (2010). Boom and bust with the latest 2m temperature surveys: dead horse wells, Hawthorne Army Depot, terraced hills, and other areas in Nevada. Transactions, Geothermal Resources Council 34, 567–573.

Lazaro, M., Page, C., Tiedeman, A., Sabin, A., Bjornstad, S., Alm, S., Meade, D., Shoffner, J., Mitchell, K., Crowder, B., GBCGE, & Halsey, G. (2010). United States Department of the Navy geothermal exploration leading to shallow and intermediate/deep drilling at Hawthorne

Ammunition Depot, Hawthorne, NV. Transactions, Geothermal Resources Council 34, 595–598.

Matlick, S. (1995). San Emidio Geothermal System, Empire, NV. GRC Field Trip – October 1995. Mesquite Group, Inc.

Meade, D., Lazaro, M., Bjornstad, S., Alm, S., Tiedeman, A., Sabin, A., & Page, C. (2011). Results of the US Navy Geothermal Program Office 2010 drilling project at Hawthorne Army Depot, Nevada. Transactions, Geothermal Resources Council 35, 193–195.

Moeck, I., Hinz, N., Faulds, J., Bell, J., Kell-Hills, A., & Louie, J. (2010). 3D geological mapping as a new method in geothermal exploration: A case study from central Nevada: Geothermal Resources Council Transactions, v. 34, p. 807–812.

Parker, R. L. & Booker, J. R. (1996). Optimal one-dimensional inversion and bounding of magnetotellurics apparent resistivity and phase measurements. Physics of the Earth and Planetary Interiors, 269-282.

Penfield, R., Zehner, R., Coolbaugh, M., Shevenell, L., Hastings, J., Johnson, G., Snyder, W., Morgos, D., Kurz, K., Sabin, A., Lazaro, M., Bjornstad, S., & Halsey, G. (2010). Geothermal site assessment using the National Geothermal Data System (NGDS), with examples from the Hawthorne ammunition depot area. Transactions, Geothermal Resources Council 34, 709–714.

Rhodes, G. T., Faulds, J. E., & Teplow, W. (2010). Structural Controls of the San Emidio Geothermal Field, Northwestern Nevada. GRC Transactions, Vol. 34.

Schwering, P., Lowry, T., Hinz, N., Matson, G., Sabin, A., Blake, K., Zimmerman, J., Sewell, S., & Cumming, W. (2022). The BRIDGE Project - Hidden Systems Reconnaissance in Western Nevada. GRC Transactions, Vol 46, 2022.

Shoffner, J., Li, Y., Hinz, N., Sabin, A., Lazaro, M., & Alm, S. (2010). Understanding fault characteristics and sediment depth for geothermal exploration using 3D gravity inversion in Walker Valley, California: Geothermal Resources Council Transactions, v. 34, p. 633-636.

Shoffner, J. D. (2011). Understanding the utility of gravity and gravity gradiometry for geothermal exploration in the southern Walker Lake basin, Nevada. 2011-Mines Theses & Dissertations.

Sewell, S., Cumming, W. Schwering, P., Hinz, N., Downs, C., Zimmerman, J., Bedrosian, P., Robinson, B., Murray, D., & Schlutz, A. (2023). Using helicopter time-domain electromagnetic (HELITEM) resistivity surveys with supporting geoscience data to target temperature gradient wells and discover hidden geothermal systems in the US Basin and Range. Geotherm. Res. Council Bull., 47

Siler, D.L., Zhang, Y., Spycher, N.F., Dobson, P.F., McClain, J.S., Gasperikova, E., Zierenberg, R.A., Schiffman, P., Ferguson, C., Fowler, A. & Cantwell, C. (2017). Play-fairway analysis for geothermal resources and exploration risk in the Modoc Plateau region. Geothermics, 69, pp.15-33.

Tikhonov, A.N. & Arsenin, V.Y. (1977). Solutions of ill-posed problems, V. H. Winston and Sons.

Trexler, D.T., et al. (1981). Low-to-Moderate Temperature Geothermal Resource Assessment For Nevada, Area Specific Studies, Nevada Bureau of Mines and Geology, UNR, Reno, NV, DOE/NV/10039-3, prepared for U.S. Department of Energy.

The Influence of Pre-existing Structures on Geothermal Springs: Inferences from Potential Field Mapping in Surprise Valley, CA and Other Sites in the Northwestern Great Basin

Jonathan M.G. GLEN, Tait Earney

U.S. Geological Survey, Moffett Field, CA 94035

Keywords

Surprise Valley, Basin and Range, aeromagnetics, gravity, geophysics, geothermal resources, Nevada, California, Great Basin, dike swarm, faulting, magmatism

ABSTRACT

Surprise Valley, located in the northwestern Great Basin, is an asymmetric extensional basin that marks a major tectonic transition between the relatively un-extended volcanic Modoc Plateau to the west, and the Basin and Range to the east that has undergone 10-15% extension. In addition, it sits just north of the Walker Lane which accommodates up to 20% of dextral slip associated with Pacific-North American plate interactions.

Thermal springs issue from eight areas within Surprise Valley. Most of these occur within the basin and are not situated on the main basin forming range-front faults. As a result, efforts to resolve the structural setting of the valley's hydrothermal system have relied on geophysics to characterize basin structure and geology.

Extensive efforts to map the basin with ground and airborne magnetics have revealed a >35 km-long linear, intra-basin magnetic high, interpreted as a buried dike swarm. Geothermal springs on the eastern side of the valley, including Seifert hot springs, Leonards hot springs, and Surprise Valley hot springs (SVHS), are all situated along the magnetic high and occur at local breaks and bends in the anomaly, suggesting that fracture permeability is enhanced along the feature and particularly at these discontinuities.

Recent studies, including drilling over the anomaly near SVHS that likely intersected dike material, as well as subsequent mapping and sampling of dikes outcropping along the anomaly on the playa surface south of SVHS, confirm (as previously inferred) that mafic intrusives are the

principal source of the anomaly. Similar interpretations made in two other valleys (in southern Oregon and northwestern Nevada), where inferred intra-basin dikes appear to be spatially correlated with hot springs or prospective geothermal resource areas, suggest that the impact of pre-existing basement structure on hydrothermal activity may pertain more generally to other hydrothermal settings throughout the Great Basin. If so, efforts to map basement may enhance understanding structural controls on some geothermal systems.

Furthermore, similarities across these disparate sites suggest that magmatism may play a much larger role in accommodating extension and influencing basin evolution across the western Great Basin than previously recognized.

1. Introduction

1.1 Geologic Setting

Surprise Valley is located in northeastern California and situated between the relatively un-dissected Modoc Plateau to the west, and the Great Basin to the east, forming the westernmost deep extensional graben of the Great Basin that is characterized by basin and range physiography (Figure 1). The valley also marks a major tectonic transition from north to south, as it sits immediately north of the Walker Lane, which accommodates up to 20% of dextral slip associated with Pacific-North American plate interactions, and just south of the low-strain High Lava Plains region (Hammond and Thatcher, 2005, 2007).

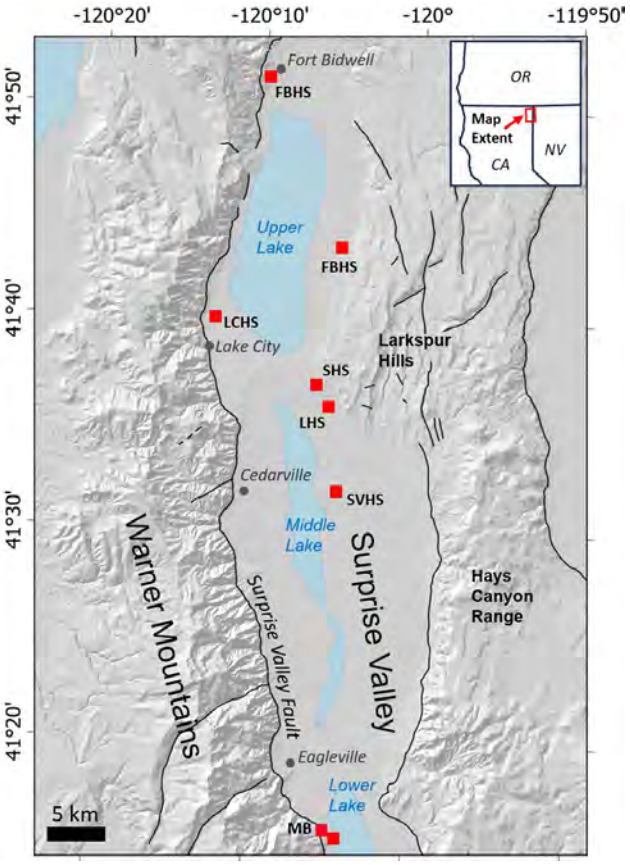

Figure 1. Index map of study area showing the location of faults (black lines, after Egger and Miller, 2011) and hot springs (red squares). SVHS – Surprise Valley hot springs, FBHS – Fort Bidwell hot springs, LCHS – Lake City hot springs, SHS – Seifert hot springs, LHS – Leonards hot springs, MB – Menlo Baths.

The valley is bounded to the west by the Warner Mountains that form the footwall of the east-dipping Surprise Valley normal fault (SVF). The SVF is the dominant basin-forming structure that has experienced at least 8 km of dip-slip offset (Egger and Miller, 2011; Personius et al., 2009). Several parallel secondary structures have been identified within the basin outboard of the SVF (Glen et al., 2008) that may have developed to accommodate more recent extension in response to continued tilting of the Warner Mountains Range and shallowing of the SVF. The valley is flanked on the east by the Larkspur Hills and Hays Canyon Range, which have been exhumed along a west-dipping normal fault, and dissected by numerous Quaternary faults that indicate the area is still actively extending (Hedel, 1984). However, most of the extension has been accommodated along the SVF resulting in an asymmetric basin that is deepest to the west and comprised of west-dipping stratigraphy.

Geochronologic studies (Carmichael et al., 2006) reveal that basalt volcanism occurred in the region during three episodes at 3–4.5 Ma, ~6 Ma, and 7–8 Ma. Faulting initiated ~14-12 Ma (Egger and Miller, 2011), though the faults in the Larkspur Hills were mainly active over approximately the same time period as basalt volcanism and are no longer active (Ritzinger, 2014). Extension in Surprise Valley likely occurred in two episodes, initiating in the mid-to-late Miocene as horst and graben style faulting that resulted in roughly a third of the total basin extension (Egger and Miller, 2011; Colgan et al., 2008). The second phase of fault activity began after ~3 Ma. Slip on the Surprise Valley fault is interpreted to have begun during the early phase of extension ~14 Ma.

This was reactivated during Pliocene extension and has continued to the present. Together, this has resulted in an estimated 8 km of dip-slip offset on the SVF that has contributed to an accumulated extension of roughly 15% across the basin (Egger and Miller, 2011).

1.2 Geothermal resources

Surprise Valley hosts numerous thermal springs throughout its extent, though exploration of the valley's geothermal resources first began following a remarkable mud volcanic eruption near Lake City in 1951 (White, 1955). Exploratory drilling occurred in the 1970's and again in the early 2000's, mostly focused near Lake City on the west side of the valley where near-boiling geothermal fluids and hydrothermal siliceous deposits occur at the surface. Drillholes at Lake City reveal temperatures as high as 165 ºC at depths between 686 and 1,036 m, and the presence of alteration minerals at >1,415 m that are indicative of formation temperatures over 260 ºC (Benoit et al., 2005). Results from a drillhole (WME-E1) taken on the east side of the valley near the Surprise Valley hot springs (Holt et al., 2023) yield reservoir temperature estimates from geothermometry ranging from 90˚C to 143˚C, and a maximum borehole temperature of 110˚C. These estimated reservoir temperatures suggest there is potential to support electrical generation in addition to applications for municipal and residential heating, agriculture and other commercial needs, though to date, resources in the valley have yet to be developed beyond limited direct-use purposes.

Many of the thermal springs occur within the basin and do not appear to be directly related to the main range-front fault (Figure 1). As a result, more recent studies of the valley's geothermal systems have focused on geophysical methods (gravity, magnetic, seismic, paleomagnetic) aimed at characterizing subsurface geology and structure that may control hydrothermal fluid flow (Egger et al., 2010, 2014; Glen et al., 2008, 2013). These structures include a NW-trending accommodation zone that intersects hot springs on both sides of the valley, and a prominent NNW-trending linear intra-basin magnetic high interpreted as a buried dike or dike swarm that appears to control several hot springs on the east side of the valley (Glen et al., 2013; Athens et al., 2016).

Based on the presence of young silicic volcanic rocks on the eastern margin of the valley, Duffield and Fournier (1974) suggested that the geothermal system may be related to residual heat associated with Tertiary magma chambers, but more recent published age data indicate that the youngest volcanic rocks are 3.8 Ma (Carmichael et al., 2006). Although a magmatic source cannot be ruled out, it seems more likely that present-day geothermal fluids originate from deep crustal circulation of meteoric water, similar to other Basin and Range extensional systems that exhibit higher-than-average crustal heat flow (e.g., Kennedy and van Soest, 2006).

2. Geophysics

Past regional geophysical investigations in Surprise Valley have involved gravity, magnetotelluric, seismic, and paleomagnetic studies across the basin (Glen et al. 2008, 2013; Egger et al., 2010, 2014; Athens et al., 2011, 2016; Lerch et al., 2008, 2010; Ritzinger, 2014) aimed at constraining basin geometry, structure and geology, to better understand basin tectonics and evolution, and to study the area's geothermal resources.

It is widely considered that geothermal springs in extensional geothermal systems commonly occur in complex structural settings, such as at fault terminations or intersections (Curewitz and Karson,

1997; Faulds et al., 2010), thus much of the research on the valley's geothermal resources has relied on geophysical methods to resolve subsurface geology and structure that is concealed beneath young basin fill.

Progress in understanding the controls on hydrothermal fluid flow, in the eastern part of the valley, has come from efforts to map the magnetic field. Earliest efforts conducting hiked profiles with portable magnetometers revealed a prominent magnetic high within the basin that was traceable between multiple profiles across several kilometers. Subsequent efforts using ATV-borne magnetometer systems (Athens et al., 2011), that permitted rapid data collection on the playa surface, revealed the magnetic anomaly formed a long narrow prominent magnetic high spanning over 35 km (Figure 2). These data also showed that the major hot springs in the eastern part of the valley (Seifert, Leonards, and Surprise Valley) were coincident with the magnetic anomaly, suggesting that the magnetic source, interpreted as a shallow buried mafic dike (Glen et al., 2013), had some influence on hydrothermal fluid flow. Support for the dike interpretation came from recent mapping in the Hays Canyon Range, located 7 km east of the anomaly, of numerous mafic dikes having similar trends to the overall basin magnetic anomaly trend (Sawyer, 2022). Joint gravity and magnetic modeling across the anomaly, combined with a coordinated seismic survey (Athens et al., 2016) indicated the anomaly in the upper basin is most likely due to a shallow (150 m) buried, fault-controlled dike or dike swarm.

Significant gaps in coverage of the magnetic high, however, remained in the most critical areas around hot springs where access on the ground was limited by vegetation, surface water, dangerous thermal conditions, and private lands. Mapping these areas was necessary to better understand the relationship between the source of the magnetic high and the springs. This was achieved by employing the use of drone-based magnetometer systems that were able to overcome limited ground access. The first such surveys were conducted in 2012 with the use of a relatively large NASA fixed-wing platform (Glen et al., 2013). The combined ground and airborne magnetic mapping provided key details around the springs on the east side of the valley that revealed they lie along the edge of the magnetic high, at structural transitions where the high undergoes steps, bends, or breaks (Glen et al., 2013).

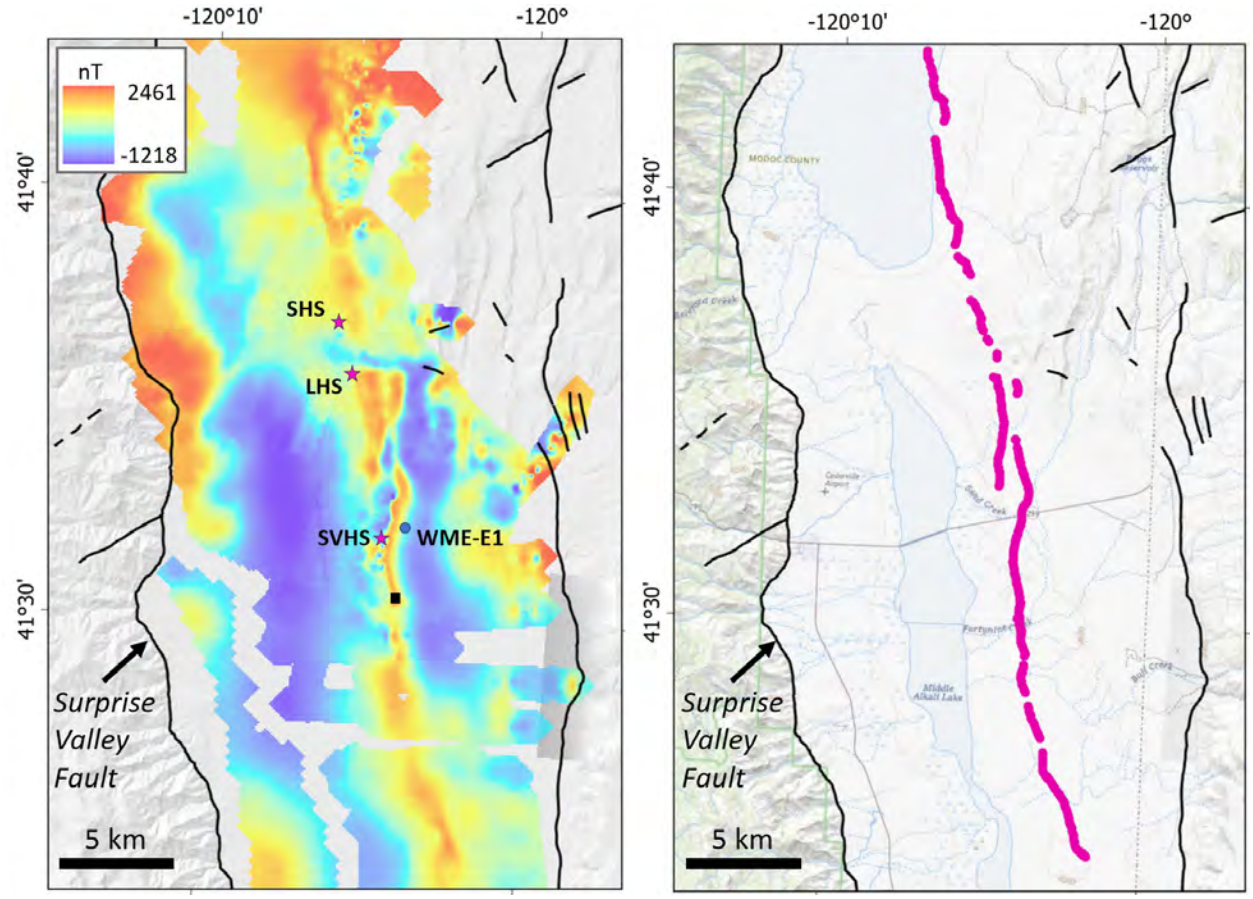

Figure 2. (Left) Magnetic anomaly map that reveals a prominent narrow basin magnetic anomaly resulting from a strongly magnetic mafic dike swarm. Also shown are faults (black lines), hot springs (pink stars), drillhole WME-E1 (blue circle), and the location of figure 3 (black square). (Right) Figure showing the crest of the magnetic anomaly derived from horizontal gradient minima. Base map is from the ArcGIS online map server (Esri, 2024).

Additional support for the dike interpretation for the basin magnetic high comes from an exploratory well (WME-E1; Holt et al., 2023), situated on the magnetic anomaly near the Surprise Valley hot springs. After completing the well, a borehole televiewer was employed to map fractures, cracks and breakouts, and determine stress orientations. The tool, which got stuck at the bottomhole depth at 1,097 m was eventually freed. When the tool was extracted from the hole, it was discovered that a 5-cm long rock chip was stuck between the tool and the centralizers used to align the tool in the borehole. Thin section and chemical analyses of the rock chip identify it as serpentinized peridotite (M.Clynne, U.S. Geological Survey, written comm. August 2019), that we interpret was most likely sourced from an inclusion within the dike, because no outcrops of peridotite exist in the region.

Confirmation of the dike interpretation was ultimately made when a string of low-relief outcrops of dikes, having the same trend as the anomaly, were discovered immediately south of the SVHS and situated on the anomaly (Figure 3). Our most recent efforts have entailed sampling, photogrammetry, detailed ground-based magnetic and gravity surveys, and airborne magnetic surveys of the basin dikes and those outcropping in the Hays Canyon Range. Paleomagnetic, geochemical and geochronologic analyses of these samples are planned. Although the poor

exposure precludes direct observation of faulting, preliminary structural mapping and modeling of potential field data across the playa dike outcrops support a model of faulting coincident with the dike swarm that may reflect dike-capture by a pre-existing fault, as was inferred >15 km north along the anomaly in the upper basin (Athens et al., 2016). Further field measurements and observations are planned in order to refine modeling of the dikes.

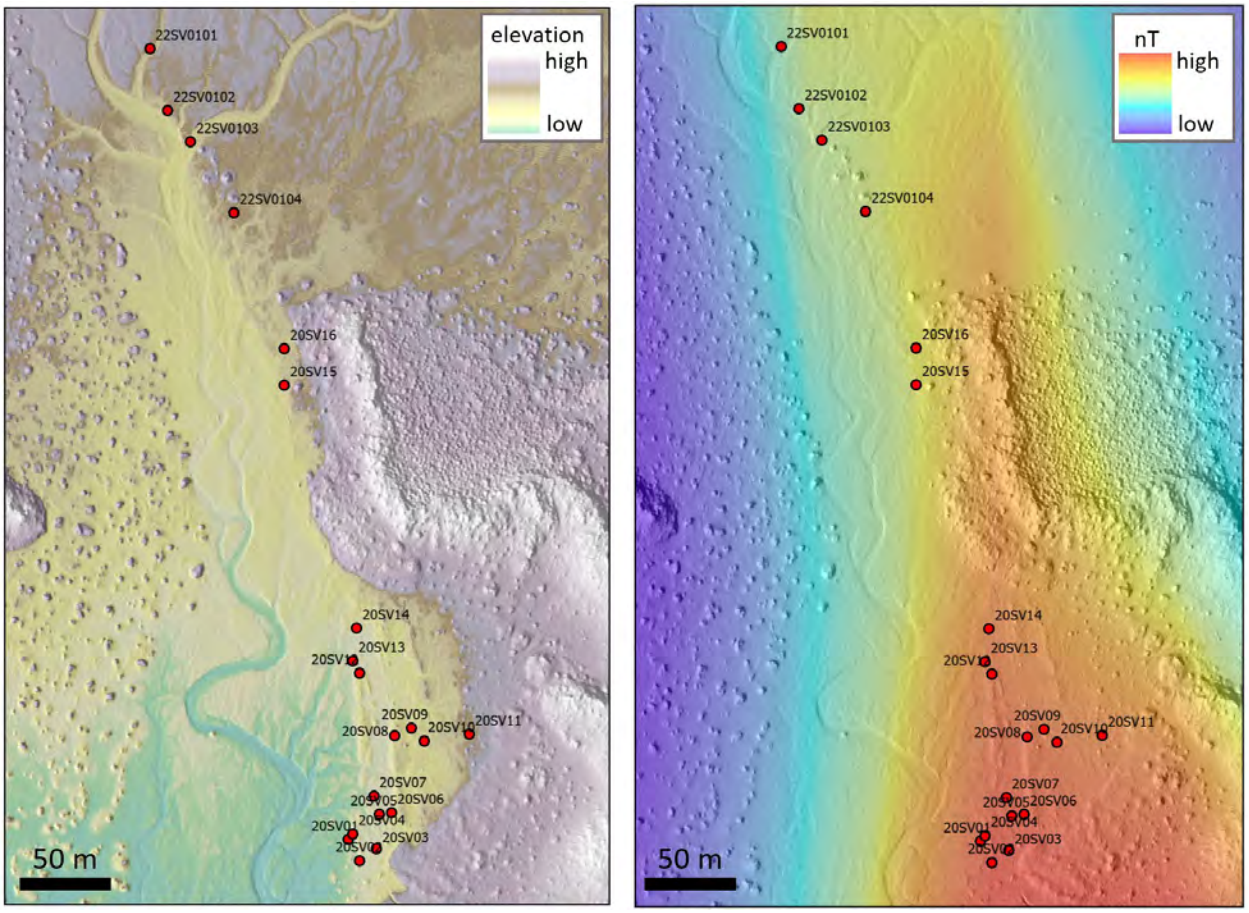

Figure 3. Paleomagnetic sampling sites of dikes outcropping along the basin magnetic high (red dots) plotted on (Left) color shaded relief and (Right) magnetic anomaly grid. The location of these figures is shown on Figure 2.

3. Discussion

Recent field and geophysical mapping of dikes within the basin and across the Hays Canyon Range reveals a potentially important component of extension accommodated through magma-injection. Furthermore, magma-assisted extension may be substantially underestimated, because it is likely many smaller dikes have gone undetected. It has been proposed that the cumulative amount of extension on numerous small faults can be significant (e.g., Marrett and Almendinger, 1992; Scholz et al., 1993; Athens et al., 2016). A similar case can be made for dikes, namely that substantial extension may be accommodated by as yet undetected dikes, provided their distribution is subject to similar scaling laws as for faults. Regardless, the influence of presently mapped and geophysically inferred dikes across Surprise Valley likely has important implications for basin evolution in Surprise Valley beyond their impact on the estimated total basin extension.

Lerch et al. (2010) speculated that initial rapid slip along the SVF would have raised the brittle-ductile transition (Figure 4). This in turn, may have promoted asthenospheric melting that fed diking across the eastern basin. The fact that the mapped dikes reside east of the depocenter of the basin is consistent with the expected displacement of the asthenosphere that would occur at the deepest reaches of the SVF where the fault extends under the eastern basin (Figure 4). Furthermore, diking would presumably have alleviated extensional stresses and suppressed faulting across the eastern part of the valley, which may explain the pronounced basin asymmetry. Feedback between magma addition to the east, that would inhibit brittle faulting across the eastern bounding range-front faults, and continued faulting along the SVF, that would drive continued melting, would promote basin asymmetry.

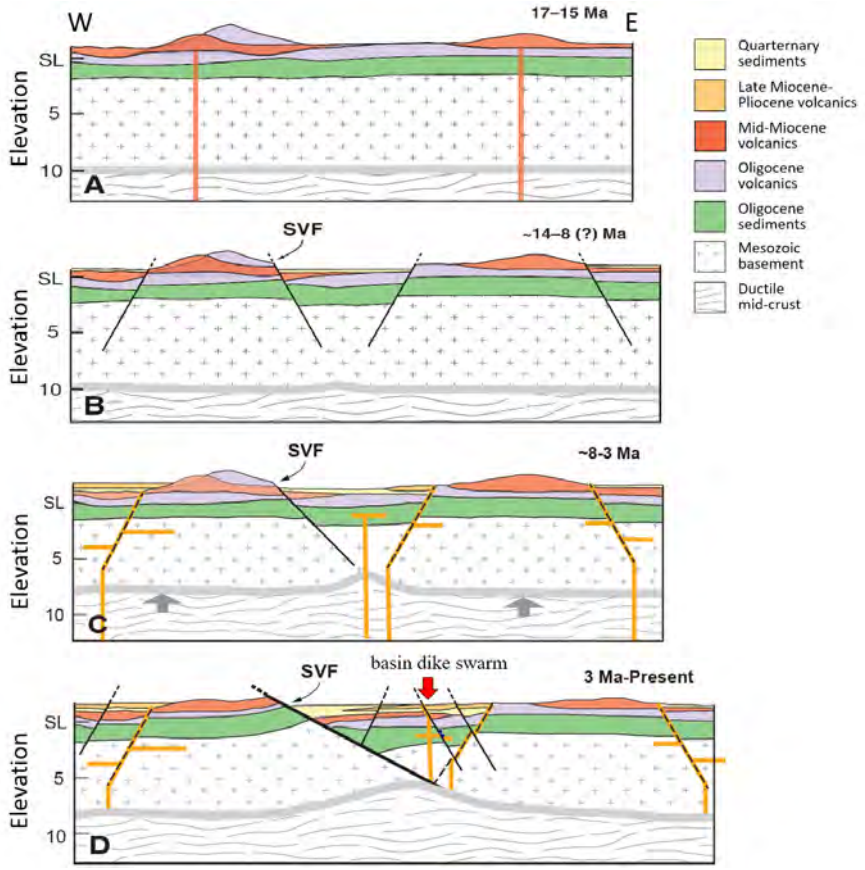

Figure 4. Cartoon showing the extensional history of Surprise Valley showing time periods from 17-15 Ma (A), ~14-8 Ma (B), ~8-3 Ma (C), 3 Ma to Present (D). Faults are shown as black lines (solid – active; dashed – inactive), intrusives (dikes and sills) are shown as orange lines. The brittle-ductile transition is shown as a thick grey line. Figure modified from figure 7 of Egger and Miller (2011).

The Surprise Valley Fault is a major basin and range style normal fault that has accommodated up to 8km of dip-slip motion since the middle Miocene. Paleoseismic studies across the fault reveal Holocene rupture (Personius et al., 2009) that indicate the fault is still active. This is consistent with geodetic measurements (Hammond and Thatcher, 2005) that document strong present-day velocity gradients suggesting active extension across Surprise Valley. Although the geodetic data indicate dominantly EW-oriented extension, a component of right-lateral strike-slip is predicted (Hammond and Thatcher, 2007) across the valley.

The high-resolution magnetic maps provided by the drone surveys reveal details of the basin magnetic high that may support a claim for longer-lived strike-slip deformation. Overlapping strands of the anomaly south of the SVHS resemble a left stepping pair of en echelon segments that may indicate extension was oblique to the trend of the regional anomaly (Glen et al., 2013). Such en echelon segments can form when dikes undergo shear stress during emplacement. If this was the cause for this feature along the intra-basin magnetic high, the relative offset of the anomaly segments would indicate right-lateral shear present at the time of dike emplacement.

If strike-slip deformation is occurring across Surprise Valley, it is unlikely to be accommodated on the SVF, given the lack of evidence from trenching, and the highly corrugated trace of the fault that precludes oblique slip on the fault (Egger and Miller, 2011). Likewise, mapping in the Larkspur Hills shows no evidence of strike-slip motion (Ritzinger, 2014). Egger et al. (2010) suggest that strike-slip motion may be partitioned on buried intrabasin faults. Strike-slip motion may alternatively be distributed more diffusely across a wide network of normal faults or through block rotation (Wesnousky et al., 2012). If strike slip is occurring, we suggest that the dike swarm is a probable candidate for accommodating some or most of it. Indeed, the dike swarm's north-northwest orientation, steep dip, and relatively straight trace (compared to the corrugated nature of the SVF and faults in the Larkspur Hills) are favorable for accommodating NW-oriented slip, both during emplacement when traction along the plane of the dikes is low, and subsequently via faulting that might exploit weaknesses along the dike margins (e.g., by reactivating fractures induced in the country rock during dike emplacement). Indeed, modeling results from Athens et al. (2016) indicate there is strong evidence for dike-fault interactions (involving both syn- and post- dike-emplacement faulting). Preliminary modeling in the Middle Basin south of the SVHS indicates a very similar relationship revealing intra-basin faulting coincident with the margin of the dike swarm. Dike-induced damage to country rock, and subsequent post-emplacement faulting along the dike, may both contribute to enhanced permeability that could explain the close correlation between hot springs in Surprise Valley and the intra-basin dike swarm.

The tie between the valley's geothermal system, dike swarm, and faulting suggests that basin tectonics and hydrothermal activity are influenced by pre-existing basement structure. This relationship may pertain more generally to other hydrothermal settings throughout the Great Basin. If so, a focus on mapping basement geology and structure may enhance understanding of structural controls on a class of geothermal systems. Indeed, two other examples in Summer Lake, Oregon (Figure 5; Earney and Glen, 2024), and Granite Springs Valley, Nevada (Figure 6; Glen et al., 2022) show striking similarities to Surprise Valley. Both sites are also characterized as north-south elongated asymmetric basins that developed dominantly by slip along a principal west-bounding range front fault that resulted in the deepest parts of the basins being displaced to the west, while to the east they display evidence for significant diking. The surprising similarity of these valleys suggest that they may be characterized by similar tectonic conditions. Indeed, the basins are all regionally aligned (with each other and with the trend of inferred dikes) and situated between areas characterized by shear across the Walker Lane and more classical basin-and-range extension (Figures 7&8). Although speculative, this may indicate that oblique extension has played a key role in influencing basin evolution in these settings.

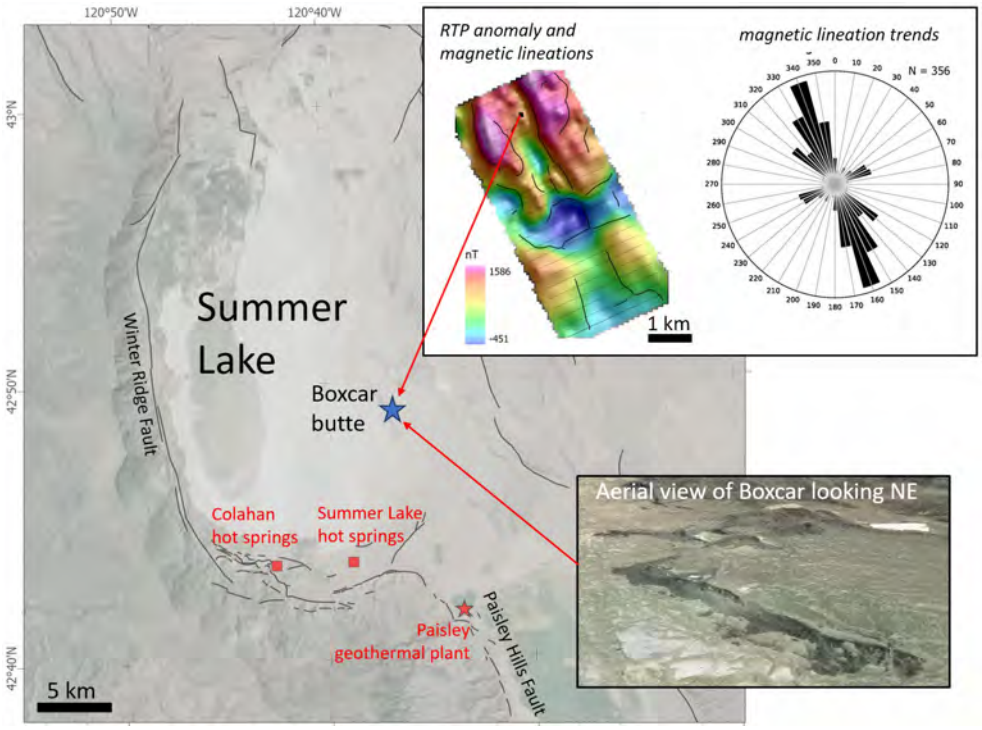

Figure 5: Digital elevation model (DEM) hillshade of Summer Lake (U.S. Geological Survey, 2024) overlain by aerial imagery (Esri, 2024), showing the Boxcar butte feature interpreted as a mafic dike (blue star), Quaternary faults (black lines; U.S. Geological Survey, 2024), hot springs (red squares), and the Paisley Geothermal plant (red star). Insets show: a shaded reduced-to-pole (RTP) magnetic anomaly map of the region around the Boxcar (Earney and Glen, 2024), rose diagram of magnetic lineations (Earney and Glen, 2024), and oblique aerial view of the Boxcar (Google Earth Pro, 2024).

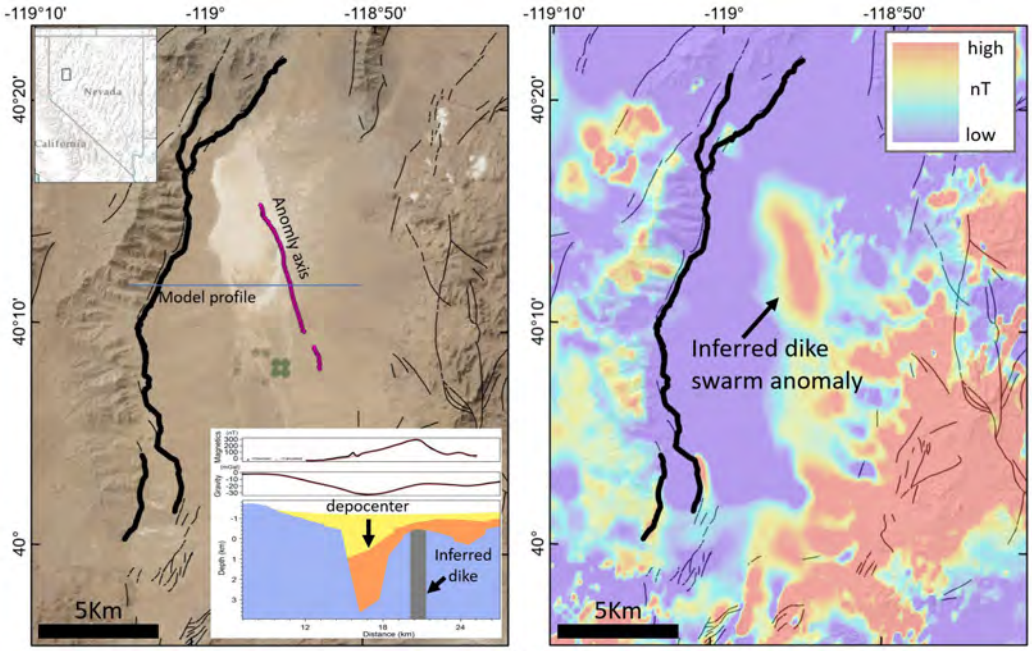

Figure 6. (Left) Digital elevation model (DEM) hillshade (U.S. Geological Survey, 2024) of Granite Springs Valley, NV overlain by aerial imagery (Esri, 2024), showing the axis of an intra-basin magnetic high (pink lineations), faults (black lines; U.S. Geological Survey, 2024), and location of potential field profile. Thick black line represents the main west-bounding range-front fault. Inset shows potential-field model that indicates inferred dikes east of the main depocenter (after Glen et al., 2022; depicting basement rocks in blue, volcanics in orange, and basin fill in yellow). (Right) magnetic anomaly map (Glen and Earney, 2024) of Granite Springs Valley, NV, showing faults (black lines).

Figure 7. Topographic map showing the locations of Surprise Valley, CA-NV, Summer Lake, OR, and Granite Springs Valley, NV. Base maps come from the ArcGIS online map server (Esri, 2024).

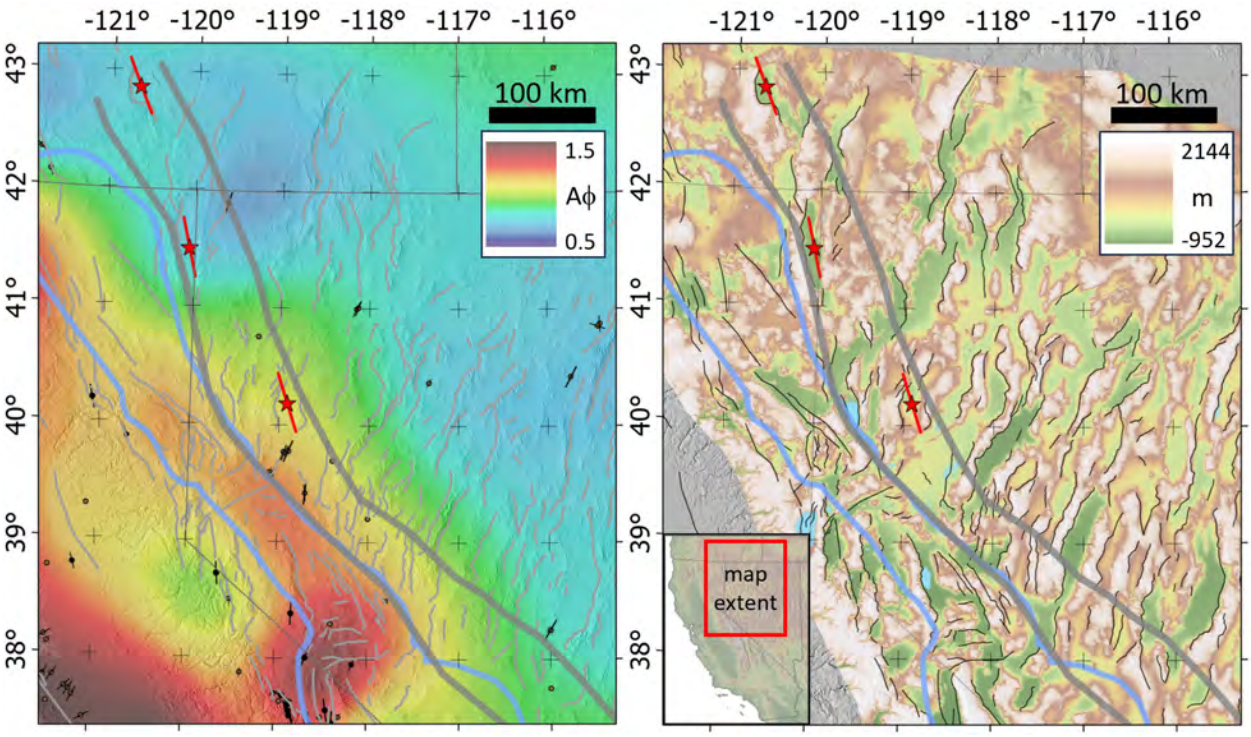

Figure 8. Map showing the locations (from north to south) of Summer Lake, OR, Surprise Valley, CA-NV, and Granite Springs Valley, NV (red stars) and the trends of their associated magnetic anomalies (red lines) displayed on (Left) a base map of relative stress magnitudes [based on Aϕ stress values ranging between normal faulting (0.5) and strike-slip faulting (1.5); Lund Snee and Zoback (2020)]; and (Right) a base map of detrended topography (DeAngelo et al., 2023). Also shown are faults (grey on left and black on right), extent of Walker Lane (light blue polygon, after Faulds and Henry, 2008), and a zone, inferred here, marking the transition between the Walker Lane and Great Basin that is mostly characterized by north-south oriented basins (delineated by thick grey lines).

Acknowledgments

We are grateful to Roy Mink for showing us outcrops of the playa dikes. We thank William Schermerhorn, Jacob Anderson, Karen Christopherson, and Randall Mackie for constructive reviews of this manuscript. Any use of trade, firm, or product names is for descriptive purposes only and does not imply endorsement by the U.S. Government. This work was funded with support from the U.S. Geological Survey Energy Resources Program.

REFERENCES

Athens, N.D., Glen, J.M.G., Klemperer, S.L., Egger, A.E., and Fontiveros, V.C. “Hidden intrabasin extension: Evidence for dike-fault interaction from magnetic, gravity, and seismic reflection data in Surprise Valley, northeastern California.” *Geosphere*, 12, 1, (2016), 15–25, doi: 10 .1130/GES01173.1.

Athens, N.D., Glen, J.M.G., Morin, R.L., and Klemperer, S.L. “ATV magnetometer systems for efficient ground magnetic surveying.” *The Leading Edge*, 30, (2011), 394-398, doi: 10 .1190 /1 .3575284.

Benoit, D., Moore, J., Goranson, C., and Blackwell, D. D. “Core Hole Drilling and Testing at the Lake City, California geothermal field.” *Geothermal Resources Council Transactions*, 29, (2005), 203-208.

Carmichael, I.S.E., Lange, R.A., Hall, C.M., Renne, P.R. “Faulted and tilted Pliocene olivine-tholeiite lavas near Alturas, NE California, and their bearing on the uplift of the Warner Range.” *GSA Bulletin*, 118, 9–10, (2006) 1196–1211.

Colgan, J.P., Shuster, D.L., Reiners, P.W. “Two-phase Neogene extension in the northwestern Basin and Range recorded in a single thermochronology sample.” *Geology*, 36, 8, (2008), 631–634.

Curewitz, D., and Karson, J.A. “Structural settings of hydrothermal outflow: Fracture permeability maintained by fault propagation and interaction.” *Journal of Volcanology and Geothermal Research*, 79, 3-4, (1997), 149-168.

DeAngelo, J., Burns, E.R., Lindsey, C.R., and Mordensky, S.P. “Detrending Great Basin elevation to identify structural patterns for identifying geothermal favorability.” *Geothermal Rising Conference Transactions*, 47, (2023), 1694-1702.

Duffield, W.A., and Fournier, R.O. “Reconnaissance study of the geothermal resources of Modoc County, California.”, *USGS Open-File Report*, 74-1024, (1974), 20 p.

Earney T.E., and Glen, J.M.G. “Characterizing Structure in southern Summer Lake Valley, Oregon using ground- and sUAS-based potential field geophysics.” *Proceedings, 49th Workshop on Geothermal Reservoir Engineering*, Stanford University, Stanford, California, (2024), 16 p.

Egger, A.E., and Miller, E.L., “Evolution of the northwestern margin of the Basin and Range: The geology and extensional history of the Warner Range and environs, northeastern California.” *Geosphere*, 7, 3, (2011), 756-773.

Egger, A.E., Glen, J.M.G., and McPhee, D.K. “Structural controls on geothermal circulation in Surprise Valley, California: A re-evaluation of the Lake City fault zone.” *Geological Society of America Bulletin*, 126, (2014), 523–531, doi: 10.1130 /B30785 .1.

Egger, A.E., Glen, J.M.G., and Ponce, D.A. “The northwestern margin of the Basin and Range province part 2: Structural setting of a developing basin from seismic and potential field data” *Tectonophysics*, 488, (2010), 150–161, doi: 10 .1016 /j .tecto .2009 .05 .029.

Esri, ArcGIS Map Service, accessed from: https://services.arcgisonline.com/ ArcGIS/rest/services/Reference/World_Reference_Overlay/MapServer, (accessed, 7/2024).

Faulds, J.E., Coolbaugh, M.F., Bouchot, V., Moek, I., and Oguz, K. “Characterizing Structural Controls of Geothermal Reservoirs in the Great Basin, USA, and Western Turkey: Developing Successful Exploration Strategies in Extended Terranes.” *Proceedings World Geothermal Congress*, (2010), 11.

Faulds, J.E., and Henry, C.D. “Tectonic influences on the spatial and temporal evolution of the Walker Lane: An incipient transform fault along the evolving Pacific – North American plate boundary.” *Arizona Geological Society Digest*, (2008), 22, 437-470.

Glen, J.M.G., and Earney T.E. “GeoDAWN: Airborne magnetic and radiometric surveys of the northwestern Great Basin, Nevada and California.”, *U.S. Geological Survey data release*, (2024), https://doi.org/10.5066/P93LGLVQ.

Glen, J.M.G., Egger, A.E., Ippolito, C., and Athens, N. ”Correlation of geothermal springs with sub-surface fault terminations revealed by high-resolution, UAV-acquired magnetic data.”, in Proceedings of the 38th Workshop on Geothermal Reservoir Engineering: *Stanford Geothermal Program Workshop*, Report SGP-TR-198, (2013), 1233–1242.

Glen, J.M.G., Peacock, J., Earney, T., Schermerhorn, W., Siler, D., Faulds, J.E., and DeAngelo, J. “A Geophysical Characterization of Structure and Geology of the Northern Granite Springs Valley Geothermal System, Northwestern Nevada.” *Geothermal Resources Council Transactions*, 46, (2022), 22p.

Glen, J.M.G., Egger, A.E., Ponce, D.A. “Structural control of hot springs in a developing basin-and-range setting, Surprise Valley, California, NW Great Basin,.” *Geothermal Resources Council Transactions*, 32, (2008), 8p.

Google Earth Pro: Google Earth 7.3.6.9750, Accessed from: https://earth.google.com/web/ (accessed 7/2024).

Hammond, W.C., Thatcher, W. “Northwest Basin and Range tectonic deformation observed with the Global Positioning System, 1999–2003.” *Journal of Geophysical Research*, 110, B10405, (2005), 12 pp.

Hammond, W.C., Thatcher, W. “Crustal deformation across the Sierra Nevada, northern Walker Lane, Basin and Range transition, western United States measured with GPS, 2000–2004. “*Journal of Geophysical Research*, 112, B05411, (2007), 26 pp.

Hedel, C.W. “Maps showing geomorphic and geologic evidence for late Quaternary displacement along the Surprise Valley and associated faults, Modoc County, California (1:62,500).” *U. S. Geological Survey. Miscellaneous Field Studies Map* MF-1429, Reston, VA., (1984),

Holt, R., Kuscu, L., Rose, C., Mink, R., and Kuscu, I. “Resource Evaluation Case Study for Surprise Valley, California.” *Proceedings, 48th Workshop on Geothermal Reservoir Engineering, Stanford University, Stanford, California* (2023), 14 p.

Kennedy, B.M., and van Soest, M.C. “A helium isotope perspective on the Dixie Valley, Nevada, hydrothermal system.” *Geothermics*, 35, 1, (2006), 26-43.

Lerch, D.W., Klemperer, S.L., Egger, A.E., Colgan, J.P., and Miller, E.L. “The northwestern margin of the Basin-and-Range Province, part 1: Reflection profiling of the moderate-angle (~30°) Surprise Valley Fault.” *Tectonophysics*, 488, 1-4, (2010), 143-149.

Lerch, D.W., Miller, E., McWilliams, M., and Colgan, J. “Tectonic and magmatic evolution of the northwestern Basin and Range and its transition to unextended volcanic plateaus: Black Rock Range, Nevada.” *Geological Society of America Bulletin*, 120, 3-4, (2008), 300-311.

Lund Snee, J.E., and Zoback, M. “Multiscale variations of the crustal stress field throughout North America.” *Nature Communications*, 11, 1951, (2020) 10.1038/s41467-020-15841-5, 1-9.

Marrett, R., and Allmendinger, R.W. “Amount of extension on “small” faults: An example from Viking graben.” *Geology*, 20, (1992), 47–50.

Personius, S.F., Crone, A.J., Machette, M.N., Mahan, S.A., and Lidke, D.J. “Moderate rates of late Quaternary slip along the northwestern margin of the Basin and Range Province, Surprise Valley fault, northeastern California.” *Journal of Geophysical Research*, 114, B09405, (2009), 17.

Ritzinger, B.T. “Paleomagnetic mapping of Late Miocene-Pliocene basalt flows in the northwestern basin and range: determining structural and topographic controls on the distribution of volcanic activity.” Master Thesis, Central Washington University, (2014), 44p.

Sawyer, M.E. “Potential role of dikes in damaging rock to support hydrothermal fluid flow, Surprise Valley California, USA: Implications for geothermal development.” *Master Thesis, Temple University*, (2022), 273p.

Scholz, C.H., Dawers, N.H., Yu, J.Z., Anders, M.H., and Cowie, P.A. “Fault growth and fault scaling laws: Preliminary results.” *Jour. Geophys. Res.*, 98, B12, (1993), 21951-21961.

U.S. Geological Survey: 3D Elevation Program 10-Meter Resolution Digital Elevation Model, accessed from URL https://www.usgs.gov/the-national-map-data-delivery, (accessed, 7/2024).

U.S. Geological Survey: Quaternary Fault and Fold Database for the United States, accessed from: https://www.usgs.gov/natural-hazards/earthquake-hazards/faults, (accessed, 7/2024).

Wesnousky, S.G., Bormann, J.M., Kreemer, C., Hammond, W.C., and Brune J.N. “Neotectonics, geodesy, and seismic hazard in the Northern Walker Lane of Western North America: Thirty kilometers of crustal shear and no strike-slip?” *Earth and Planet. Sci. Lett.*, 329-330, (2012), 133-140.

White, D.E. “Violent mud-volcano eruption of Lake City Hot Springs, northeastern California.” *Geological Society of America Bulletin*, 66, (1955), 1109–1130.

Mitigating Induced Seismicity in Geothermal Energy Production: The Application of the Traffic Light System (TLS) and Global Case Studies

Zeming Hu[1], Cesar Vivas[1], Orkhan Khankishiyev[1], Vagif Mammadzada[1], Salehi Saeed[2], Runar Nygaard

[1]University of Oklahoma, [2]Southern Methodist University

Keywords

Seismicity, Geothermal Energy, Traffic Light System, Mitigation Plan

ABSTRACT

This review paper focuses on applying the Traffic Light System (TLS) in managing induced seismicity, particularly geothermal energy development. Induced seismicity, a consequence of human activities such as geothermal energy production, poses significant challenges to the environment and surrounding communities. Inspired by its conventional use in road traffic management, the TLS offers a promising approach to mitigate these risks by categorizing seismic events based on their magnitudes and dictating operational responses.

This paper presents a comprehensive workflow for implementing the TLS in geothermal projects, starting with the initial seismic monitoring and ending with the application of operational controls based on predefined seismic thresholds. This workflow emphasizes the importance of continuous monitoring, real-time data analysis, and adaptive management of geothermal operations to minimize the risk of significant seismic events.

Further, the paper reviews several case studies from around the world, showcasing the effectiveness of the TLS in diverse geological settings. These case studies highlight the system's flexibility and potential to be tailored to specific project needs and seismic risk profiles.

This review argues that the TLS enhances the safety and sustainability of geothermal energy production and serves as a crucial tool for gaining public trust and regulatory approval. By systematically managing the risk of induced seismicity, the TLS contributes to the responsible development of geothermal resources, aligning with global efforts to transition to renewable energy sources.

1. Introduction

Geothermal energy has seen a steady increase in electricity generation, expanding at an average rate of 3.5% per year, culminating in a global installed capacity of roughly 15.96 gigawatts electric (GWe) by 2021. Despite this growth, geothermal energy only constitutes about 0.5% of the total installed capacity for renewable electricity and heating/cooling systems worldwide. Conversely, the use of geothermal energy for heating and cooling applications has experienced more robust growth. From 2015 to 2020, it expanded by an average of 9% annually, achieving an installed capacity of 107 gigawatts thermal (GWth) 2020. However, this rapid expansion has also brought increased attention to the challenge of induced seismicity associated with geothermal operations. According to recent studies, pore-fluid pressure in rocks weakens and reactivates existing faults, and the injection of wastewater and stress perturbations lead to earthquakes (Ellsworth, 2013; Grigoli et al., 2017). Figure 1 shows a distribution of the induced seismicity caused by these factors. Twenty-one events are from exploration for geothermal energy. These seismic events, ranging from small tremors to moderate quakes, have posed considerable challenges to the sustainability and public acceptance of geothermal energy.

In some cases, induced seismicity has caused damage to local infrastructure, disrupted project operations, and heightened concerns among affected communities about geothermal development's safety and environmental impacts (Majer et al., 2007). To address this issue, the geothermal industry, in collaboration with researchers and policymakers, has been actively exploring various technological solutions, including advanced seismic monitoring systems (i.e., traffic light systems) (Braun et al., 2020; Cesca & Grigoli, 2014; Chang & Yoon, 2021). The adoption of these mitigation approaches has shown promising results in various geothermal projects around the world. Still, ongoing efforts are needed to refine and standardize best practices for managing induced seismicity risks in the growing global geothermal sector (Wang et al., 2023).

This review paper focuses on applying the Traffic Light System (TLS) to manage induced seismicity risks, particularly in worldwide geothermal energy development. The objective is to comprehensively assess the TLS workflow to mitigate the challenges of induced seismic events associated with geothermal operations. The scope of the review covers the mechanisms and impacts of induced seismicity, the importance of effective risk management for the continued growth of the geothermal industry, and the current best practices and case studies demonstrating the application of the TLS. This paper presents a detailed workflow for implementing the TLS, emphasizing the system's flexibility and potential to be tailored to diverse geological settings and project-specific seismic risk profiles. By examining real-world case studies from various countries, the review highlights the effectiveness of the TLS in enhancing the safety, sustainability, and public acceptance of geothermal energy production. The findings aim to guide geothermal practitioners, policymakers, and researchers on the responsible development of this renewable energy technology.

2. Principles and Conceptual Framework of the Traffic Light System

The TLS has been widely used to manage reduced seismicity activity, risk, and hazards and develop a seismicity mitigation plan (Bommer et al., 2006). It is a site-specific, real-time, and multi-level seismic risk management system.

The TLS has failed in the past. For example, in May 2006, the first critical TLS was utilized in a

geothermal energy project at Basel, involving the injection of approximately 11,500 cubic meters of water into a 5 km deep well at high pressure (up to 30 MPa). The injection triggered significant seismic activity recorded by local and regional monitoring networks. A magnitude 2.6 earthquake occurred during peak injection, exceeding the safety threshold of a four-level "traffic light" system designed to prevent dangerous seismic events. Consequently, the infusion was halted (Häring et al., 2008). Similar events occurred at Blackpool and St. Gallen. The effectiveness of the traffic light systems utilized in Basel, Blackpool, and St. Gallen was not high. In 2014, an advanced TLS was developed by Evans et al. (2014) and is currently in development. However, this system could not suit micro-seismicity events. In 2023, Wang et al. (2023) the Gutenberg-Richter law was applied as a parameter in the TLS system, and it was confirmed that the optimized TLS system could work for either large or small magnitudes.

2.1 Definition and Critical Components of the TLS

A basis of TLS consists of three thresholds for governing the level of risk:

- Red means stop. The injection/operation should be stopped.
- Yellow means caution. The process should be reviewed and watched, and injection/related activities, such as injected pressures, may need to be reduced.
- Green means normal. The operation/activities/injection can be continued as planned.

These thresholds should be determined based on different input parameters, such as peak ground velocity (PGV), peak ground acceleration (PGA), and the frequency of induced seismicity. Another critical parameter in this system is ground-motion prediction equations (GMPEs) for ground-motion amplitude. Those parameters can be used to assess the potential impacts of induced seismic events and inform mitigation strategies and operation adjustments to minimize the risk of damaging seismic events (Bommer et al., 2015; Grigoli et al., 2018; van Thienen-Visser & Breunese, 2015; Verdon & Bommer, 2021).

PGA refers to the maximum acceleration experienced by a particle at the ground surface during an earthquake. It is a critical parameter for evaluating the potential damage to structures and infrastructure. Due to gravity, PGA is typically measured in acceleration units and is an essential input for the seismic hazard and risk analysis (Bommer, 2015; Crowley and Pinho, 2015).

GMPEs, also known as attenuation relationships, are mathematical models that predict the expected ground motion parameters, such as PGA and PGV, at a site based on various factors, including earthquake magnitude, source-to-site distance, and site-specific characteristics (Douglas, 2003). These equations are essential for estimating the potential ground shaking and associated risks in seismic hazard and risk assessments.

The three thresholds of TLS were typically determined differently by area. In the UK, the red light was set at 0.5 (Clarke et al., 2019). In Finland, TLS thresholds were based on acceptable ground motion levels and associated probabilities, triggering Amber alerts for a PGV of 1 mm/s with an ML $\geq$ 1 event and Red alerts for a PGV of 7.5 mm/s with an ML $\geq$ 2.1 event (Verdon & Bommer, 2021). In the Western Canadian Sedimentary Basin (WCSB), hydraulic fracturing set the red-light threshold much higher at an ML of 4.0 (Roy et al., 2021). In Canada, the Alberta Energy Regulator (AER) and BC Oil and Gas Commission established five Traffic Light Protocols (TLPs) for hydraulic fracturing (HF) operations at various locations. These included a TLP near Fox Creek,

Alberta, with a red-light threshold at a magnitude (ML) of 4.0; near Red Deer, Alberta, at an ML of 3.0; near Brazeau Dam, Alberta, at an ML of 2.5; near the community of Pink Mountain, British Columbia, at an ML of 4.0; and near Dawson Creek, British Columbia, at an ML of 3.0 (Kao et al., 2018; Yaghoubi et al., 2024). In Oklahoma, US, the red-light threshold was an ML of 2.0 (Johnson et al., 2021).

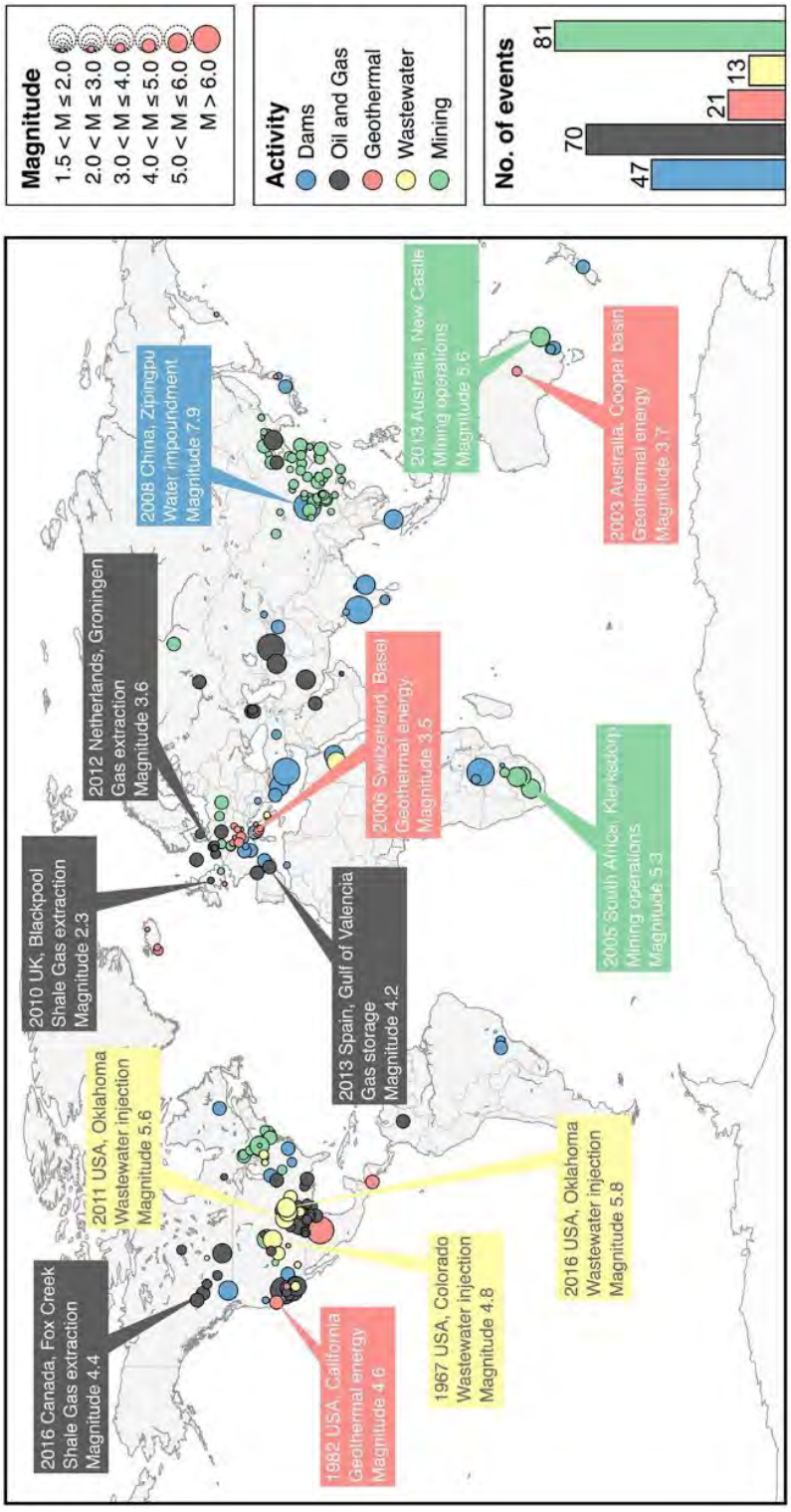

Figure 1: The Distribution of The Induced Seismicity Caused by Industrial Activities (Grigoli et al., 2017)

3. Review of Global Case Studies on TLS Application in Geothermal Energy Production

3.1 Finland

The dataset collected during the simulations contained location, magnitude levels, hypocenters, etc. The authors establish thresholds based on the ground motion. The authors selected PGV as the main parameter to estimate the ground motion. They analyzed the historical PGVs and preliminary screening of the 3 thresholds:

Green: PGV = 0.3mm/s or 0.13mm; Yellow: PGV = 1mm/s; Red: PGV = 7.5mm/s.

However, they considered two additional parameters for addressing false positives and negatives: Joint PGV and Magnitude. A false positive is that high vibrations not caused by induced earthquakes at the geothermal well could be recorded. These vibrations might result from surface blasting, road traffic, equipment malfunction, distant natural earthquakes, or other unanticipated sources. A false negative is that PGV can only be measured at specific locations where instruments are installed. As a result, PGV thresholds could be exceeded at locations without instruments, leading to missed recordings of such events.

The authors calculated the magnitudes and negotiated with regulators. Finally, they set up:

Yellow: PGV >= 1mm/s and M >= 1; M>1.2

Red: M >=2.1

The method provided the benefit of requiring agreement with the regulator on only two parameters: the PGV thresholds and the acceptable probability levels to reach these thresholds.

In Figure 2, they used this system in the well OTN-3, which started on 4 June 2018 and ended on 22 July 2018. A total of 18,160 m^3 of drinking-quality water was injected through five stages in the open-hole section of the well, inducing 1,357 seismic events with $\mathbf{0} \geq \boldsymbol{M} \geq \mathbf{1}$, shown in Fig.3. The injection rate typically ranged from 400 to 600 liters per minute. Still, during stage 2, it was increased to approximately 800 liters per minute for a couple of hours, rapidly increasing seismic activity.

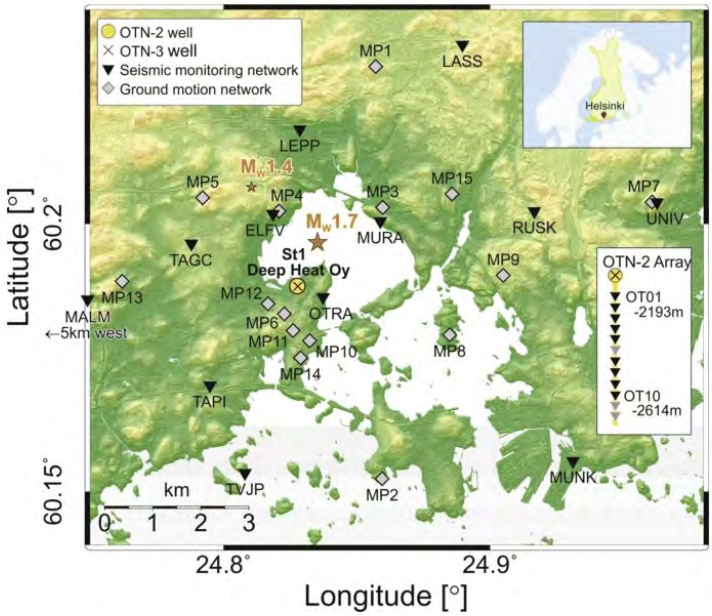

Figure 2: The Location Of The Seismicity Network And Geothermal Wells (Ader et al., 2020)

Stage	Start date	Net injected volume (m^3)	Max injection pressure (bars)	Mean depth (m)	Number of events $M_L \geq 0$	$M_L \geq 1$	$M_L \geq 1.2$	$M_L \geq 2.1$
1	4 June 2018	3783	890	6056	173	5	3	0
2	16 June 2018	4023	900	5973	280	11	6	0
3	23 June 2018	1537	850	5884	131	8	4	0
4	1 July 2018	4411	860	5771	361	14	9	0
5	12 July 2018	4406	870	5625	412	18	14	0
Total	22 July 2018	18,160	-	-	1357	56	36	0

Figure 3: The Table Of The Seismic Events During Injection And Stimulations (Ader et al., 2020)

During stimulations, the events shifted horizontally and vertically slightly, as shown in Figure 4. The yellow light was clearer around the depth of 500 meters on the horizon and 1000 meters in the vertical hypocenters, as shown in Fig.5.

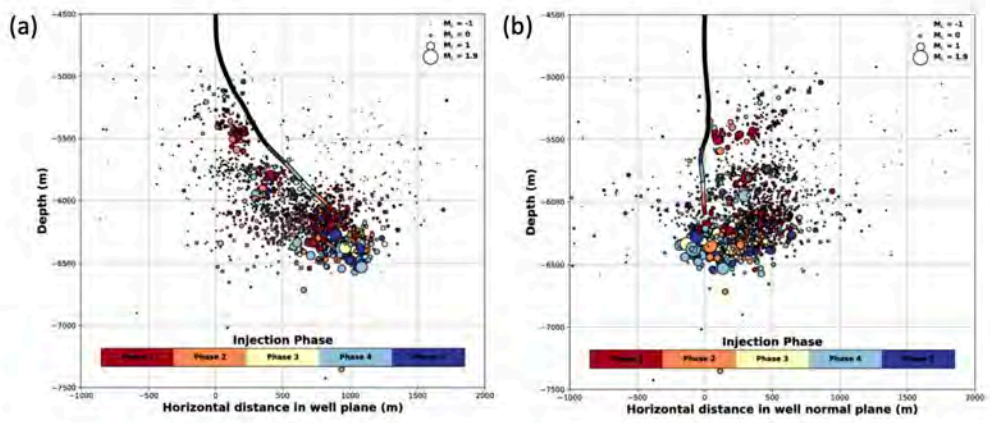

Figure 4: The Map for Micro-Seismicity Using TLS Implementation. (A) The Shift Is Horizontal, And (B) The Shift Is Vertical. (Ader et al., 2020)

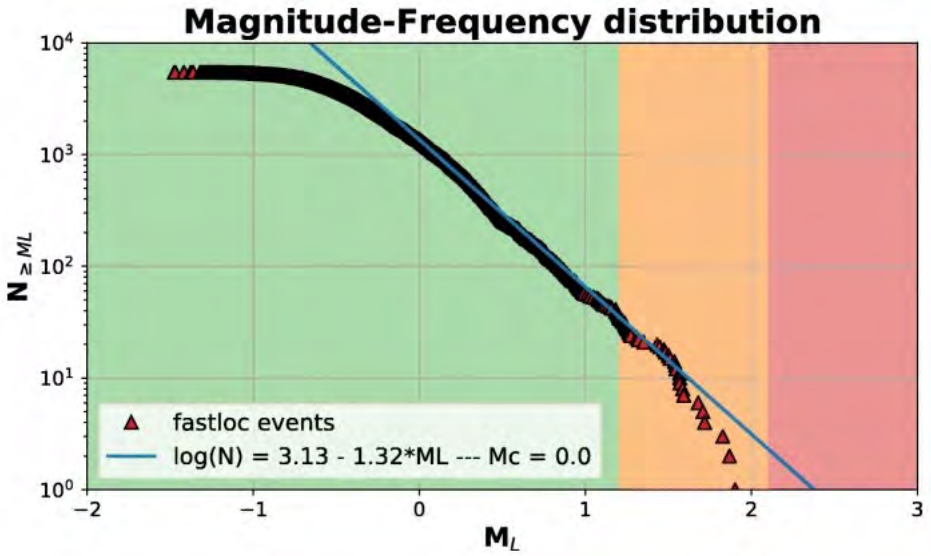

Figure 5: The Map For Magnitudes In The Traffic Light System (Ader et al., 2020)

They obtained 37 alters in green, 36 in yellow, and 0 in red during the stimulations. Of the 36 yellow alters, only 6 of the yellow events reached a PGV >1mm/s, as shown in Fig.6. The most minor event generating a PGV ≥ 1 mm/s was an ML 1.55 event, which caused a maximum PGV of 1.19 mm/s. The highest PGV recorded during stimulation was 2.99 mm/s, following an ML 1.87 event. Events started to trigger alerts at magnitudes lower than those required to exceed the PGV threshold of 1 mm/s. This suggests that the magnitudes associated with the PGV thresholds were reasonably conservative.

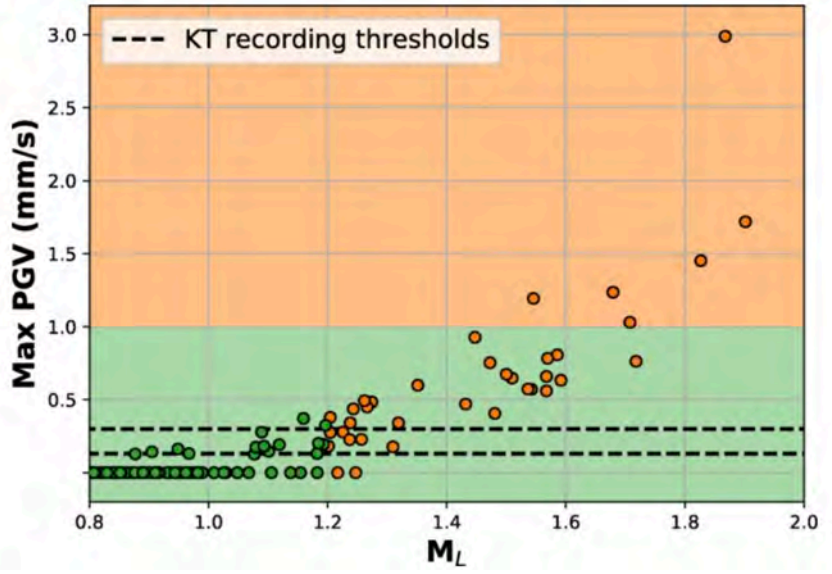

Figure 6: The PGV Events in Green And Yellow Lights (Ader et al., 2020)

3.2 Alberta, Canada

The Alberta No.1 Geothermal Project study area is highlighted in a red box in Figure 7. Colored circles represent reported earthquakes, with their magnitudes indicated by a scale bar. Major induced earthquake focal mechanisms are shown. Green triangles mark seismic stations. Several

identified faults are depicted by thick black lines, shown in Figure 7.

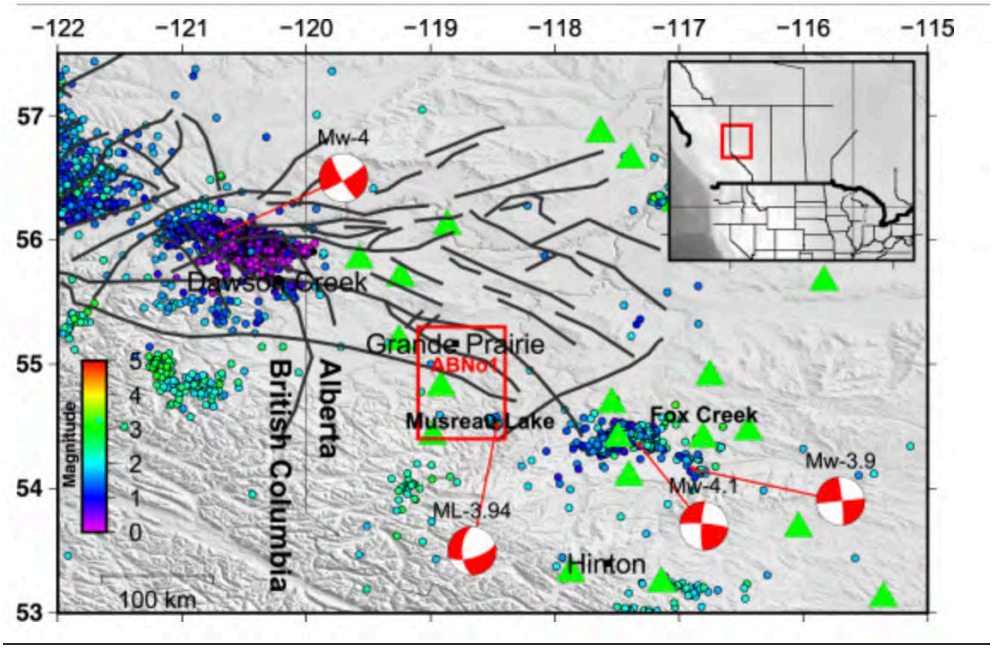

Figure 7: The Map Of The Seismicity Network And Well Locations (Yaghoubi et al., 2024)

They integrated formation depth, site amplification, ground motion prediction equations (GMPEs), fragility functions, nuisance functions, and population distributions to establish red-light thresholds. Additionally, they performed numerical simulations to estimate risk metrics like potential damage, nuisance impacts, and local personal risk (LPR) related to injection-induced earthquakes, using a method like estimating fatalities in significant seismic events.

3.2.1 Data Collection and Workflow for Determining the Thresholds

The risk-based framework determines the red-light threshold by integrating datasets that include spatial population distributions, earthquake ground motion prediction equations (GMPEs), details on the location, depth, size, and frequency of induced seismic events, site amplification factors, nuisance and fragility functions, and geological characteristics. Three key risk metrics are considered: Local Personal Risk (LPR), damage risk, and nuisance risk.

Local Personal Risk (LPR) assesses the likelihood of a person experiencing a fatal building collapse, which is crucial for community safety during induced seismicity. Nuisance impacts, which involve disturbances and discomfort caused by ground shaking, have significant social and economic implications, making their minimization vital for securing public acceptance for geothermal or injection activities. Damage impacts are directly linked to financial consequences, such as building damage and repair costs; minimizing these impacts helps protect infrastructure, property values, and overall economic stability.

The importance of each metric varies based on stakeholders' priorities, the nature of the community, and the built infrastructure. In some cases, prioritizing human life (LPR) may be paramount, while others may focus on minimizing social disturbances (nuisance) or economic losses (damage).

T_{DS1} and T_{DS2} are two parameters used to construct the damage maps, as shown in Fig.8. The combination map, displayed in Figure 8c, shows that the iso-damage red-light magnitude threshold ranges from 3.0 to 4.0 ML. The assessment also evaluates the iso-LPR risk, which measures the probability of a fictional person inside a building experiencing a fatal collapse. To determine the tolerances for LPR, we adopt a likelihood of 10^{-6}, representing the highest value from Figure 8c and commonly used for this specific risk metric.

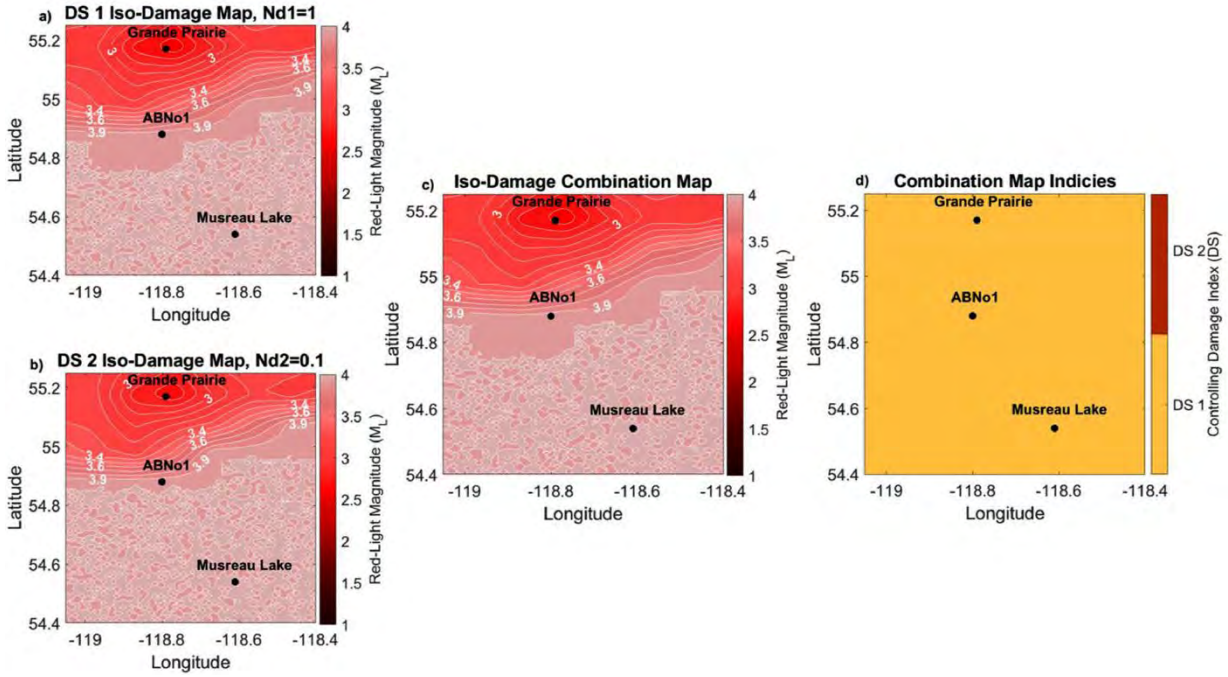

Figure 8: Damage maps (Yaghoubi et al., 2024)

Fig 9 shows a magnitude of 3.55, representing the red-light threshold for nuisance risks, indicating the level of ground shaking that causes disturbances. The LPR (Local Personal Risk) threshold is set at an ML of 4, indicating the risk of fatal building collapses. The damage risk threshold is an ML of 4.1, signifying potential economic consequences such as building damage and repair costs.

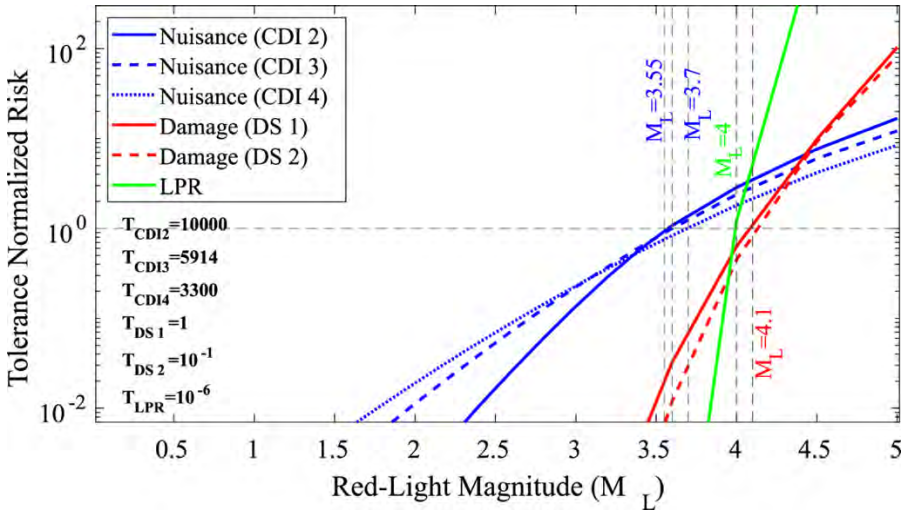

Figure 9: The Determination of Red-Light System (Yaghoubi et al., 2024)

Based on the analysis in Figures 9 and 10, this project's risk-based traffic light protocol suggests a red-light threshold of ML 3.5. This indicates the seismic activity level at which induced seismicity poses a significant risk to infrastructure or public safety, requiring immediate mitigation actions. To allow operators sufficient time to respond, yellow-light thresholds are two magnitudes lower than red-light thresholds. For the ABNo1 site, the yellow-light threshold is suggested at ML 1.5 to prevent sudden jumps from green to red scenarios that bypass the mitigation plan (Schultz et al., 2021). Operators can adjust the yellow-red gap size based on their risk tolerance, with a more significant gap being more conservative and a smaller gap indicating a less conservative approach with a potentially higher level of risk.

> 3.5 ML	Immediately report the event to AER (communication).Assess potential damage (communication).AER must receive real-time seismic waveform monitoring data (communication).Stop injection, pump fluids out of the well, and bleed off (operational action).Return the well to a safe state (operational action).Determine the hypocenter of the earthquake. Is it in the basement rock or nearby the injection zone? (seismic analysis).Analyze spatial and temporal connections between the event and the ABNo1 operation. Determine if the event connects to HF or wastewater disposal operations in the immediate vicinity of ABNo1 (seismic analysis).
> 1.5 ML	Immediately report the event to AER (communication).AER must receive real-time seismic waveform monitoring data (communication).Increase real-time earthquake monitoring and analysis; intensify observations (operational action).Use tracer and chemical monitoring to assess fluid balance between injector and producer wells (operational action).Monitor fluid recovery if fluid lost circulation is occurring; intensify observations (operational action).Reduce the injection rate, pressure, and volume, and pump fluids out of the well until seismicity remains below a certain threshold (operational action).Determine the hypocenter of the earthquake (seismic analysis)
< 1.5 ML	Pumping operations proceed as planned

Figure 10: The Proposed TLS (Yaghoubi et al., 2024)

4. Integrated Workflow from Cases

Seismic activity is monitored in real-time, and hydraulic data is collected alongside historical seismic catalogs. These datasets are integrated to perform seismic forecasting calculations using GMPEs. Probabilistic seismic hazard metrics such as PGV, PGA, potential damage, nuisance impacts, and LPR are computed. These metrics are assessed against predefined thresholds to determine the appropriate alert level. The traffic light system indicates low risk (green) for normal operations, moderate risk (yellow) for preparation, and high risk (red) for immediate mitigation, ensuring an effective and scientifically informed response to seismic events.

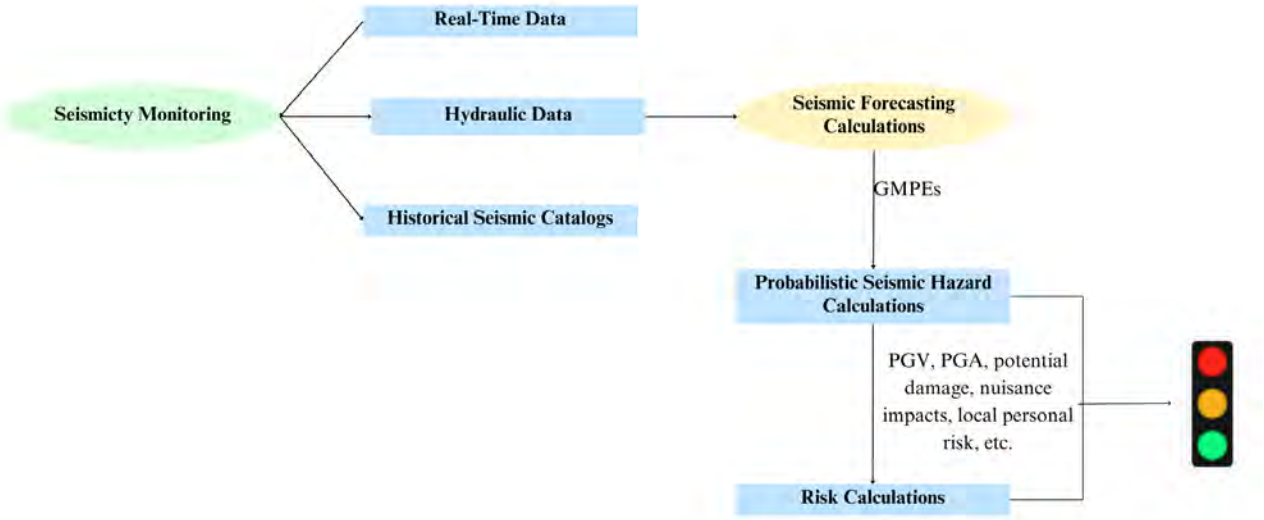

Figure 11: The Summary of Workflow of TLS

5. Benefits and Challenges of Implementing the TLS

Implementing a Traffic Light System (TLS) in seismicity management offers several significant benefits. It facilitates real-time monitoring and immediate response to seismic events, mitigating risks and enhancing public safety. By providing clear and actionable alerts, TLS helps maintain public confidence and acceptance of projects, particularly in sensitive urban areas. It enables operators to make informed decisions regarding the continuation, modification, or halting of activities based on the severity of seismic events, ensuring regulatory compliance and minimizing legal and financial risks. The TLS also enhances the ability to analyze and respond to seismic data, improving the overall understanding and management of induced seismicity. Furthermore, it helps distinguish between actual seismic events and other sources of vibrations, preventing false alerts and unnecessary interruptions. Lastly, the system protects infrastructure, reduces the risk of injuries or fatalities from seismic events, and promotes community safety.

However, the low levels of seismicity sometimes resulted in limited seismic data for calibrating and designing the Traffic Light System (TLS). Stimulation occurred under a large urban area with many sensitive receptors and high vibration noise from activities like construction blasting, posing a risk of false alerts. Additionally, the population's high sensitivity to earthquakes risked negative public perception, historically leading to the shutdown of geothermal projects.

6. Conclusions and Future Directions

After reviewing several cases, a workflow for implementing Traffic Light Systems (TLS) has been designed. The thresholds should be determined by considering various parameters and conditions. Several risk metrics, including population density, Local Personal Risk (LPR), and nuisance impacts, should be factored into risk-based assessments. Peak Ground Velocity (PGV) and magnitude levels are critical foundational parameters for evaluating seismicity risk.

The Canadian case successfully established the red threshold based on its risk analysis and developed a framework to manage seismicity during stimulation. The Finnish case designed its TLS using PGV

and magnitude levels derived from historical earthquake catalogs and real-time seismic events.

In the future, monitoring measures such as tracer and chemical tests can delineate subsurface fluid pathways and rock-fluid geochemical interactions. This information could help identify potential areas with a higher probability of induced seismicity, guiding actions to mitigate their occurrence. Additionally, tracer and chemical tests can monitor the effectiveness of mitigation measures and ensure the safety of surrounding communities by providing detailed insights into subsurface processes and the impact of operational activities.

Acknowledgment

This material is based upon work supported by the U.S. Department of Energy's Office of Energy Efficiency and Renewable Energy (EERE) under the Geothermal Technologies Office Award Number DE-EE0009962. Finally, I thank the University of Oklahoma for accessing all the resources and laboratories to develop this study.

REFERENCES

Ader, Thomas, Michael Chendorain, Matthew Free, Tero Saarno, Pekka Heikkinen, Peter Eric Malin, Peter Leary, et al. 2020. "Design and Implementation of a Traffic Light System for Deep Geothermal Well Stimulation in Finland." *Journal of Seismology* 24 (5): 991–1014. https://doi.org/10.1007/s10950-019-09853-y.

Bommer, Julian J., Helen Crowley, and Rui Pinho. 2015. "A Risk-Mitigation Approach to the Management of Induced Seismicity." *Journal of Seismology* 19 (2): 623–46. https://doi.org/10.1007/s10950-015-9478-z.

Bommer, Julian J., Stephen Oates, José Mauricio Cepeda, Conrad Lindholm, Juliet Bird, Rodolfo Torres, Griselda Marroquín, and José Rivas. 2006. "Control of Hazard Due to Seismicity Induced by a Hot Fractured Rock Geothermal Project." *Engineering Geology* 83 (4): 287–306. https://doi.org/10.1016/j.enggeo.2005.11.002.

Braun, Thomas, Stefania Danesi, and Andrea Morelli. 2020. "Application of Monitoring Guidelines to Induced Seismicity in Italy." *Journal of Seismology* 24 (5): 1015–28. https://doi.org/10.1007/s10950-019-09901-7.

Cesca, Simone, and Francesco Grigoli. 2014. "Full Waveform Seismological Advances for Microseismic Monitoring." *Advances in Geophysics* 56 (November). https://doi.org/10.1016/bs.agph.2014.12.002.

Chang, K. W., and H. Yoon. 2021. "Mitigating Injection-Induced Seismicity Along Basement Faults by Extraction: Application to 2016–2018 Pohang Earthquakes." *Journal of Geophysical Research: Solid Earth* 126 (4): e2020JB021486. https://doi.org/10.1029/2020JB021486.

Clarke, Huw, James P. Verdon, Tom Kettlety, Alan F. Baird, and J-Michael Kendall. 2019. "Real-Time Imaging, Forecasting, and Management of Human-Induced Seismicity at Preston New Road, Lancashire, England." *Seismological Research Letters* 90 (5): 1902–15. https://doi.org/10.1785/0220190110.

"Direct Use of Geothermal Energy, World, 2012-2024 – Charts – Data & Statistics." n.d. IEA. Accessed June 17, 2024. https://www.iea.org/data-and-statistics/charts/direct-use-of-geothermal-energy-world-2012-2024.

Douglas, J. 2003. "Earthquake Ground Motion Estimation Using Strong-Motion Records: A Review of Equations for the Estimation of Peak Ground Acceleration and Response Spectral Ordinates." *Earth-Science Reviews* 61 (1): 43–104. https://doi.org/10.1016/S0012-8252(02)00112-5.

Ellsworth, William L. 2013. "Injection-Induced Earthquakes." *Science* 341 (6142): 1225942. https://doi.org/10.1126/science.1225942.

Grigoli, F., S. Cesca, A. P. Rinaldi, A. Manconi, J. A. López-Comino, J. F. Clinton, R. Westaway, C. Cauzzi, T. Dahm, and S. Wiemer. 2018. "The November 2017 Mw 5.5 Pohang Earthquake: A Possible Case of Induced Seismicity in South Korea." *Science* 360 (6392): 1003–6. https://doi.org/10.1126/science.aat2010.

Grigoli, Francesco, Simone Cesca, Enrico Priolo, Antonio Pio Rinaldi, John F. Clinton, Tony A. Stabile, Bernard Dost, Mariano Garcia Fernandez, Stefan Wiemer, and Torsten Dahm. 2017. "Current Challenges in Monitoring, Discrimination, and Management of Induced Seismicity Related to Underground Industrial Activities: A European Perspective." *Reviews of Geophysics* 55 (2): 310–40. https://doi.org/10.1002/2016RG000542.

Häring, Markus O., Ulrich Schanz, Florentin Ladner, and Ben C. Dyer. 2008. "Characterisation of the Basel 1 Enhanced Geothermal System." *Geothermics* 37 (5): 469–95. https://doi.org/10.1016/j.geothermics.2008.06.002.

Hu, Zeming, Cesar Vivas, Orkhan Khankishiyev, and Saeed Salehi. 2024. *Machine Learning-Based Rock Facies Prediction Using Geothermal Data: A Comparative Analysis of Algorithms*.

Johnson, Eric G, Ryan Haagenson, Abbie B Liel, and Harihar Rajaram. 2021. "Mitigating Injection-Induced Seismicity to Reduce Seismic Risk." *Earthquake Spectra* 37 (4): 2687–2713. https://doi.org/10.1177/87552930211008479.

Kao, Honn, Ryan Visser, Brindley Smith, and Stuart Venables. 2018. "Performance Assessment of the Induced Seismicity Traffic Light Protocol for Northeastern British Columbia and Western Alberta." *The Leading Edge* 37 (2): 117–26. https://doi.org/10.1190/tle37020117.1.

Khankishiyev, Orkhan, Saeed Salehi, Gurban Hasanov, and Zeming Hu. 2024. *Application of Distributed Temperature Sensing (DTS) in Geothermal Wells*.

Khankishiyev, Orkhan, Saeed Salehi, Cesar Vivas, Runar Nygaard, and Danny Rehg. 2023. "Techno-Economic Investigation of Geothermal Development in Sedimentary Basins." *ASME Open Journal of Engineering* 2 (021030). https://doi.org/10.1115/1.4062412.

Lebedys, Arvydas, Dennis Akande, and Nicolas Coënt. 2022. "Renewable Energy Statistics 2022." *International Renewable Energy Agency*, July.

Majer, Ernest L., Roy Baria, Mitch Stark, Stephen Oates, Julian Bommer, Bill Smith, and Hiroshi Asanuma. 2007. “Induced Seismicity Associated with Enhanced Geothermal Systems.” *Geothermics* 36 (3): 185–222. https://doi.org/10.1016/j.geothermics.2007.03.003.

Roy, Corinna, Andy Nowacki, Xin Zhang, Andrew Curtis, and Brian Baptie. 2021. “Accounting for Natural Uncertainty Within Monitoring Systems for Induced Seismicity Based on Earthquake Magnitudes.” *Frontiers in Earth Science* 9 (May). https://doi.org/10.3389/feart.2021.634688.

Schultz, Ryan, Gregory C. Beroza, and William L. Ellsworth. 2021. “A Risk-Based Approach for Managing Hydraulic Fracturing–Induced Seismicity.” *Science* 372 (6541): 504–7. https://doi.org/10.1126/science.abg5451.

Thienen-Visser, K. van, and J. N. Breunese. 2015. “Induced Seismicity of the Groningen Gas Field: History and Recent Developments.” *The Leading Edge* 34 (6): 664–71. https://doi.org/10.1190/tle34060664.1.

Verdon, James P., and Julian J. Bommer. 2021. “Green, Yellow, Red, or out of the Blue? An Assessment of Traffic Light Schemes to Mitigate the Impact of Hydraulic Fracturing-Induced Seismicity.” *Journal of Seismology* 25 (1): 301–26. https://doi.org/10.1007/s10950-020-09966-9.

Vivas, Cesar, Zeming Hu, and Saeed Salehi. 2023. “Texture-Dependent Thermal Properties of Sandstone Rocks Examined by Scanning Electron Microscopy for Thermal Energy Storage Applications.” *ASME Open Journal of Engineering* 2. https://asmedigitalcollection.asme.org/openengineering/article/doi/10.1115/1.4064030/1173193.

Wang, Rui, Ying Chang, Peng Han, Miao Miao, Zhiyi Zeng, Haixia Shi, Danning Li, Lifang Liu, and Youjin Su. 2023. “Optimized Traffic Light System with AIC and Application to the 2021 M6.7 Yangbi Earthquake Sequence.” *Entropy* 25 (5): 759. https://doi.org/10.3390/e25050759.

Yaghoubi, Ali, Ryan Schultz, Catherine Hickson, Andrew Wigston, and Maurice B. Dusseault. 2024. “Induced Seismicity Traffic Light Protocol at the Alberta No. 1 Geothermal Project Site.” *Geothermics* 117 (February):102860. https://doi.org/10.1016/j.geothermics.2023.102860.

Integrating Geophysics Into Geothermal Workflows: Example of DAS-Acquired Microseismic Monitoring and a Few Other Fiber Optic-Based Applications

Joël Le Calvez, Takashi Mizuno, Pierre Bettinelli

SLB

Keywords

Geophysics, Fiber Optics, Distributed Temperature Sensing, Distributed Acoustic Sensing, DxS, Microseismic, Geophysics, Injection, Leak Detection, Fracture

ABSTRACT

From a high-level point of view, a geothermal project lifecycle covers several steps such as initial scoping (quick-look screening), evaluation (initial subsurface and surface evaluation), detailed design (e.g., plant, pipeline and well design, as well as subsurface static, dynamic, and geomechanical models), construction, operations (real-time updating and optimization for safe injectivity and production). Focusing on operations, the main objectives are to verify operations and assure the various stakeholders that all concerns are monitored and addressed as needed. Design of a monitoring system calls for understanding what is to be monitored (e.g., fluid injection, well integrity, leakage, fracture initiation, fracture network propagation, etc.), what are the changes in formation properties (e.g., temperature, resistivity, density, velocities, attenuation, seismicity, etc.) and how will those variations occur (e.g., over time, within a specific range (time and space); thus, what sensors need to be deployed (e.g., seismic, electromagnetic, temperature, pressure, etc.) and what specificities they need to meet (e.g., accuracy, precision, resolution, robustness, etc.) over what period of time for what frequency of interrogation.

Looking at real-time microseismic monitoring using DAS data, we deploy a system that consists in (a) “optimized data” issue from edge computation, (b) automated geophysical processing for continuous data stream from edge to office, (c) data connectivity between field and remote location. The “optimized data” includes depth-windowed enhanced data as well as mask traces containing probability information of seismic phase arrivals in continuous data stream. Taking advantage of data redundancy in densely sampled DAS data, we perform signal enhancement at the edge. Subsequently, we reduce the trace amount leveraging depth windowing to meet bandwidth limitations between wellsite and office. Such signal enhancement and data volume reduction enable real-time data inspection by a geophysicist sitting in a remote location. The

office-based multi-well simultaneous processing includes traditional migration-based event location followed or not by Geiger relocation (and/or any other processing scheme) as well as magnitude computation with intuitive QC visualization.

To achieve our energy needs, geothermal-focused efforts need to increase significantly over the next 20 years. Fiber optic is a cost-effective and easy-to-deploy monitoring system that can deliver on several answer products across several domains.

1. Introduction

Distributed acoustic sensing (DAS) has been widely applied to several areas of seismology. Passive seismic monitoring is one of the areas considering versatile deployment options and long aperture of one or more seismic arrays. Several successful passive seismic monitoring case studies have been reported by research organisms, academia and the industry at large with more recently a focus on new energy and geothermal-focused applications. However, there are several practical challenges associated to the utilization of a DAS-based network to perform real-time passive seismic monitoring. This is coming from the nature of DAS geophysics including its single component and strain response, redundant but relatively low signal-to-noise ratio (S/N) measurement, and high throughput of data from the acquisition system. We introduce our recent attempts to address those challenges and highlight key technology components.

2. Simulation in planning and preparation

Simulation has an important role to play in a real-time passive seismic monitoring campaign in terms of the survey design and system testing. Survey design is a critical step to plan field deployment of the sensor network. It is a recommended step in the conventional geophone area, and similarly when using DAS. We simulate the amplitude of passive seismic data and estimate signal to noise ratio using the ray theory with assumptions in terms of (1) area of interest, (2) placement of the fiber optics cable, and (3) its noise level (Mizuno and Le Calvez, 2023). A DAS response model is considered as single component strain measurement. We evaluate the limitation of sensitivity in terms of the magnitude of the passive seismic events. The uncertainty of event location could also be assessed. Figure 1 shows the example of the minimum magnitude distribution along the vertical DAS cable. Although each strain sensing point presents the anisotropic nature of sensitivity, distributed sensing along the fiber brings adequate detectability performance: minimum magnitude increases with distance from the cable.

The simulation technology is also critical to measure how reliable are the processing and reporting systems. There are two reliabilities issues to be concerned about. One is stability of the overall system under the high throughput of the data from the interrogator box. The other is the accuracy of the processing result. The real-time simulator presented in Mizuno et al. (2024) is developed to suite the afore mentioned considerations (Figure 2). The simulator outputs continuous DAS waveforms at real time speed assuming a statistical seismicity model (magnitude distribution, spatial-temporal distribution). Figure 3 shows am example of the data generated by the simulator. The system outputs a total of 4 Tb of continuous data for a dual well monitoring scenario per day. The data contains about 17,000 events.

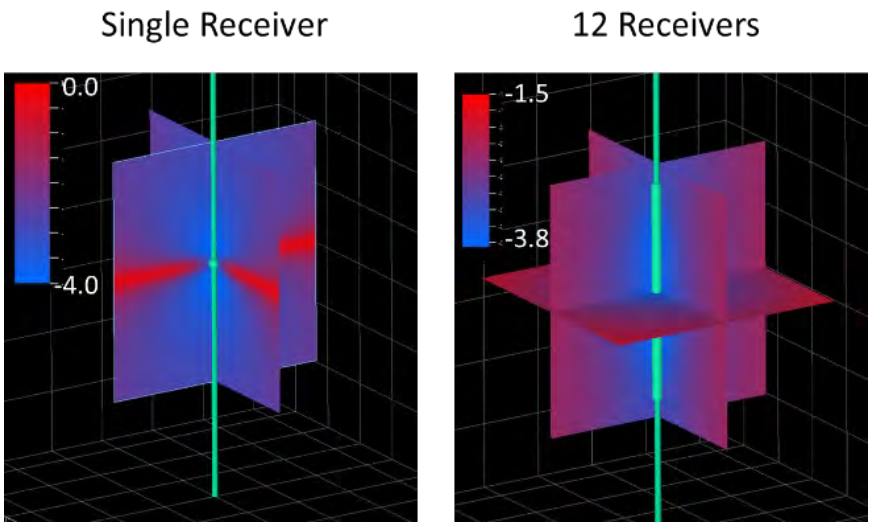

Figure 1: Detectability map comparison (minimum magnitude threshold in space) in single DAS receiver (left) and 40 'point' DAS receivers (right). The monitoring well is vertical (green trajectory) and receiver positions are represented as disks. Noise level is assumed to be of one nano strain.

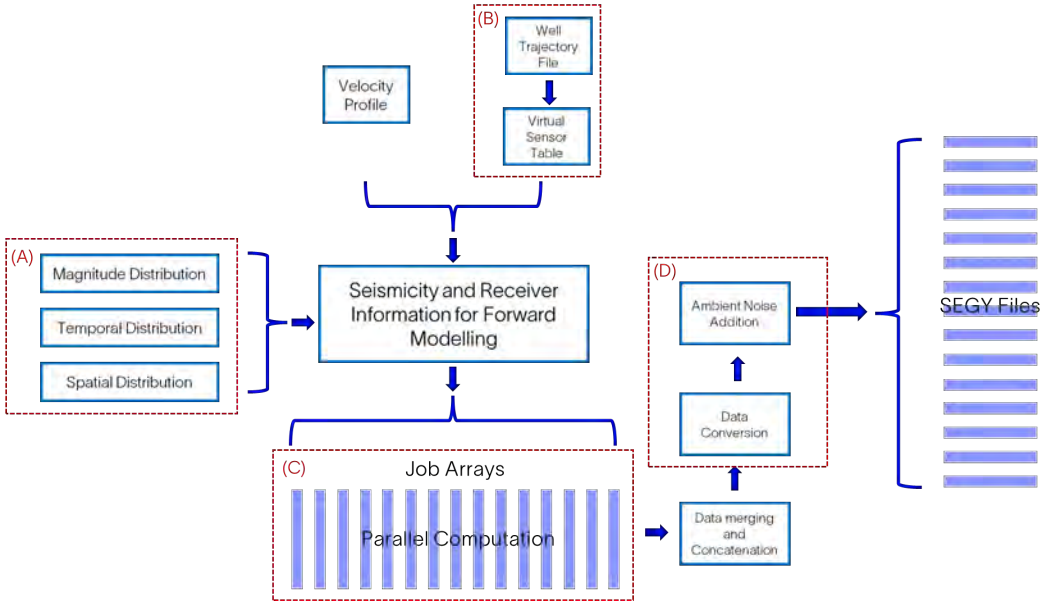

Figure 2: Real-time microseismic DAS simulator elements.

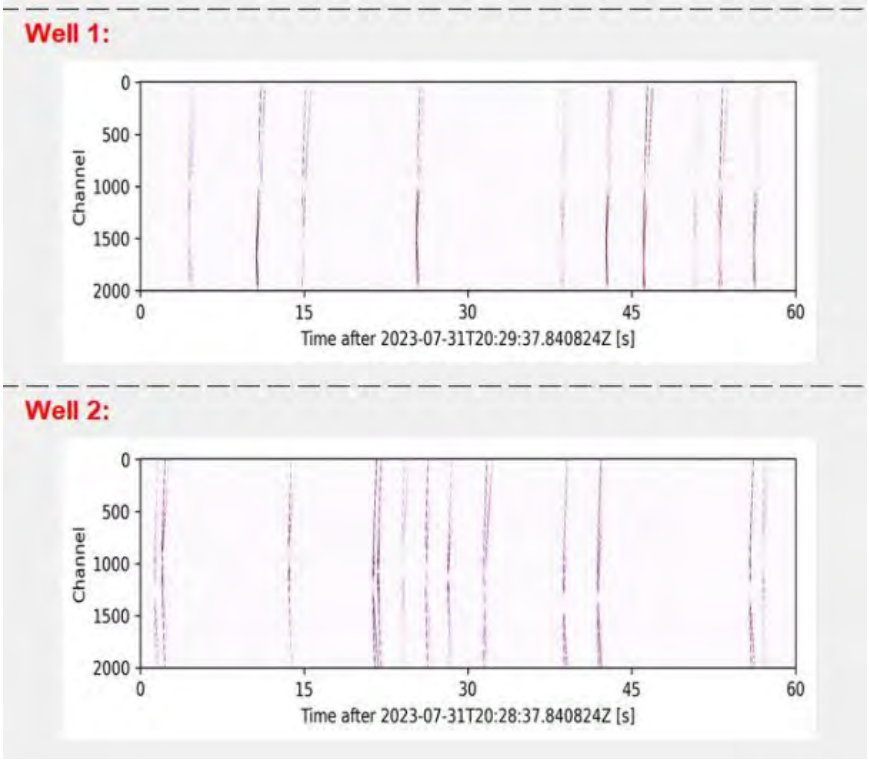

Figure 3: DAS synthetic example showing continuous waveforms as generated by the real-time simulator over a one-minute-long time window). Due to their hypocenter positions respective to the DAS arrays and their magnitudes, some events can be seen by both arrays (partially or in their entirety) while others are not.

3. Real-time DAS microseismic monitoring

Real-time geophysics is critical to perform passive and active induce seismic monitoring. During active and passive seismic monitoring, data should be recorded continuously. Therefore, the data volume could take terabytes of storage space each day for a DAS array. Processing should start as soon as acquisition is initiated to reduce lead time of processing. Additionally, data quality is to be monitored on a regular basis since the acquisition cannot be repeated as one an event has occurred, the same event will not occur again. A large volume of data is hard to review relying on human eyes only and is therefore difficult to QC. We need to implement robust processing for large volume of DAS data.

To reduce the data volume and to enhance the signal are two key elements to achieve. Those objectives are to be performed at the well site in real-time while acquisition is taking place. Figure 4 shows an example of a dataset prepared by the well site processing system. The data consist of two parts (1) strain waveforms which are depth-windowed and locally stacked. (2) the “mask” waveform which represents the probability of the phase arrival of the passive seismic signal in the original data. Comparing to the original continuous data generated from the interrogator box, this data take less volume and more information is available for the geoscientists for QC. The resulting dataset is adequate for further event location and magnitude computation at either the wellsite or the remote office.

Hypocenter and magnitude are to be estimated automatically in real time. We use a migration-based approach to determine the hypocenter without time picks needed. This approach is useful even if the network consists of a combination of geophone and DAS arrays (e.g., Mizuno et al. 2021). Several migration-based methods are proposed depending on the data to be migrated. One may use the "mask" trace prepared at the well site in the step above (Figure 5). In terms of moment magnitude estimation, we revised the geophone-based algorithm to support DAS data. To estimate moment magnitude, we need the signal moment defined in terms of a displacement spectrum. Because a DAS system measures the strain, we estimate the displacement spectrum from the DAS data through data conversion from DAS to 1C geophone. Having the event location estimated from the migration-based method described above, the algorithm applies a timing window for the P and S signal part of the DAS data to extract the P and S signals. Then, we invert the signal moment and corner frequency of the displacement spectrum for the P- and S-wave of each event assuming an omega-squared spectrum model which is commonly observed in passive seismic events. The magnitude distribution follows the Gutenberg – Richter law, which is often seen as characteristic of passive seismic events.

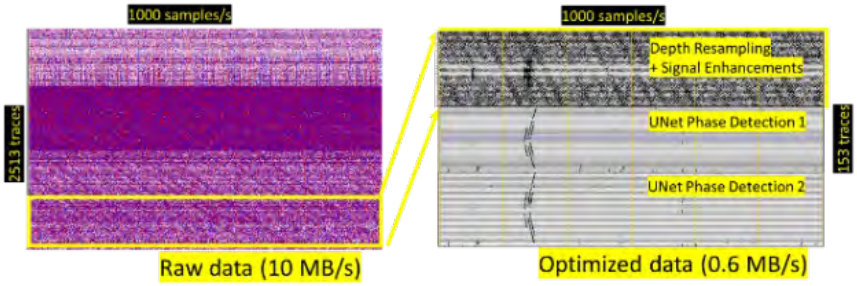

Figure 4. Example of (left) raw continuous seismic data from the DAS interrogator box and (right) waveform processing result at the well site. The depth trimming and signal enhancements are applied so that easily QC data and process using DAS waveform in the right. The "mask" trace is also computed at the well site and attached to the data to present probability of passive seismic arrivals in waveform.

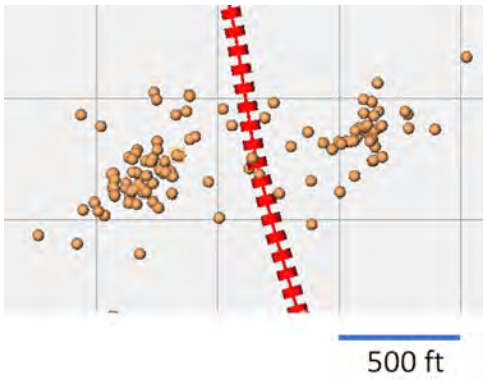

Figure 5. Example of the map view of the event location estimated from the migration-based method using the mask trace in Figure 3. Note that because this DAS is deployed only in a single borehole (red trajectory) and data at the horizontal section are processed (DAS sensing points are presented as red disks), events are assumed in the same depth as the borehole in this processing.

4. Distributed Temperature Sensing (DTS) and Distributed Acoustic Sensing (DAS) for geothermal fields

Integrated use of borehole and surface geophysics tools allow us to provide an end-to-end monitoring solution that can streamline and accelerate the vast expansion of site characterization and monitoring tasks needed for the success of geothermal-focused applications.

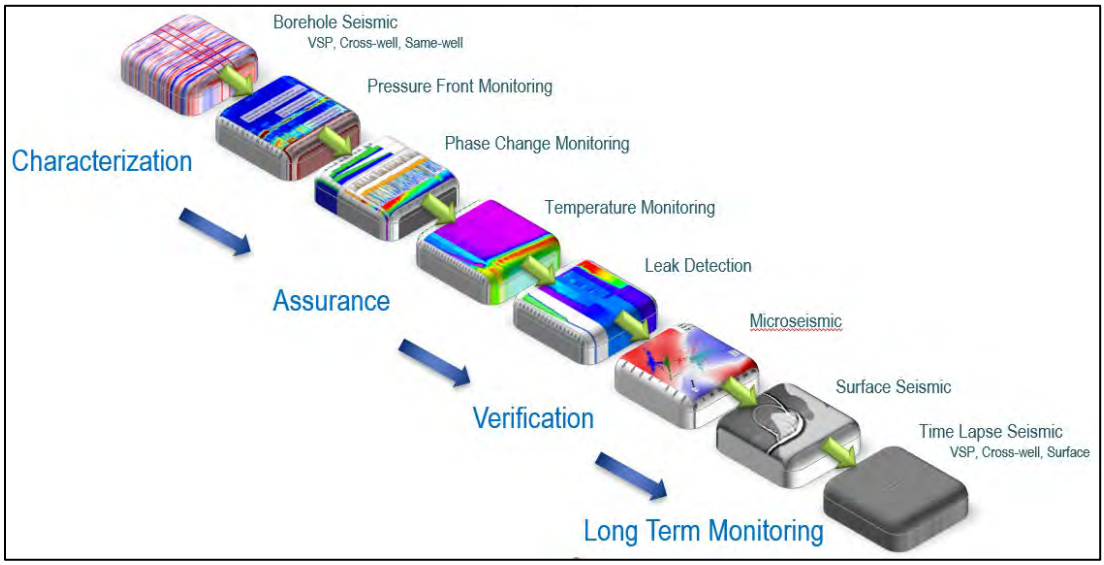

Figure 1: Fiber optic for life of geothermal field

Acknowledgement

We thank our SLB and Sintela colleagues for discussions throughout the technology development cycle. We are grateful to the operators involved to allow us to present the data.

REFERENCES

Mizuno, T., Le Calvez, J., and Raymer, D. "Coalescence microseismic mapping for distributed acoustic sensing (DAS) and geophone hybrid array" *in* Y. Li, M. Karrenbach, and J.B., Ajo-Franklin, eds., Distributed acoustic sensing in geophysics: methods and applications, American Geophysical Union and Wiley, San Franciso, CA (2021).

Mizuno, T., and Le Calvez, J. "Quantitative evaluation of DAS passive seismic monitoring: theory and case studies" *Proceedings: 84th Annual Conference and Exhibition, European Association and Geoscientists and Engineers*, Vienna, Austria (2023).

Mizuno, T., and Le Calvez, J. "Real-time microseismic data simulator for the qualification of DAS passive seismic CCUS monitoring systems" *CCUS2024*, Houston, Texas (2024).

Repeat Microgravity Measurements in Beppu Geothermal Area, Japan

Yohei Morifuji[1,2], Jun Nishijima[2], Kensho Ota[2], Kenji Kubota[1], Hiroshi Suenaga[1] and Shunichi Okamoto[1]

1. Central Research Institute of Electric Power Industry, Chiba, Japan

2. Department of Earth Resources Engineering, Faculty of Engineering, Kyushu University, Fukuoka, Japan

Keywords

Repeat Microgravity Measurements, Reservoir Monitoring, Reservoir Simulation, Gravity Change Forward Calculation

ABSTRACT

Repeat microgravity measurements were conducted to elucidate the long-term gravity changes in the Beppu geothermal area, one of the most famous hot spring areas in Japan, where the use of geothermal energy remains prevalent. The gravity values in (2023) showed a decrease of 20 μgal to 40 μgal from 2015, mainly at the western survey points (D1, TERUYU, and B3). To examine the relationship between the gravity changes and behavior of reservoir, the reservoir model was created based on existing geological information and gravity basement elevations, and forward calculations of the gravity changes associated with production were performed. The current reservoir model did not fully reproduce the measured gravity changes, primarily around TERUYU and B3. It is thought to be due to the low permeability of the model on the north side and insufficient supply for the reservoir model. The measured gravity values must be explained by adding a structural survey on the north side, revising and/or optimizing parameters such as permeability. Although there is room for improvement in the current reservoir model in terms of reproducing the measured values, it was shown that the gravity change can be utilized for reservoir model evaluation by comparing the forward gravity calculation with the measured values.

1. Introduction

For the sustainable utilization of geothermal resources, understanding the geothermal model of the target area and the appropriate amount of production and reinjection is necessary. Continuously monitoring subsurface conditions, such as fluid increase/decrease is also crucial. As changes in density caused by increases or decreases in fluid appear as gravity changes at the surface, repeated microgravity measurements can be used to estimate changes in subsurface conditions. Compared with other monitoring methods, repeated microgravity measurements are advantageous because

they are low-cost, require minimal personnel, and provide information as a two-dimensional distribution. In this study, the Beppu geothermal area, where geothermal activity is active, and hot springs and small-scale geothermal power generation are still being actively conducted, was selected as the target area. We conducted repeated microgravity measurements starting in 2021 and compared the gravity values with those of the past to elucidate the long-term trends in gravity changes. Repeated microgravity measurements have been conducted in some areas (e.g. Oka et al., 2012; Nishijima et al., 2016), but few studies have combined reservoir analyses. Gravity change is one of the few observed values that reflect reservoir changes other than wellbore information and can be used to validate reservoir models. To utilize gravity changes for reservoir model evaluation, we constructed a reservoir model of the Beppu area and attempted forward calculation of gravity changes caused by production.

2. Beppu Geothermal Area

The Beppu geothermal area is one of the largest hot spring areas in Japan, with more than 2,000 sources. Geothermal energy is mainly harnessed from in hot springs. Several small-scale binary power plants have been in operation in Beppu area since 2014. The geology of the Beppu area is characterized by a Quaternary volcanic group consisting of Tsurumi-dake (Mt. Tsurumi) and Garan-dake (Mt. Garan), located at the northeastern end of the Beppu-Shimabara rift, and an alluvial fan area extending from the foot of these mountains to Beppu Bay (Figure 1). The Kannawa and Asamigawa faults are located on the northern and southern margins of the fan, respectively. The tuff, lava and pyroxene andesite are deposited in the lower part of the fan deposits, which are several hundred meters thick (Hoshizumi et al., 1988). Compositional analysis of hot spring water has revealed that fluid flows in multiple pathways from the upstream side where Mt. Tsurumi and Mt. Garan are located downstream to where the coast is located (Osawa et al., 1994; Osawa and Yusa 1996). The flow paths are largely divided into two parts on the north and south sides of the Beppu area, flowing along the Kannawa Fault on the north margin and the Asamigawa Fault on the south side. Hot springs are mainly distributed in the fan area. In particular, hot springs in the Myoban, Kannawa, Shibasaki, Kamegawa, Horita, Kankaiji, Beppu, and Hamawaki areas are known as representative hot springs in the city and are called Beppu Hattou. Nishijima and Naritomi (2017) conducted a gravity structure survey and mentioned the relationship between the gravity base elevation and Na-Cl hot spring flow paths (Figure 2).

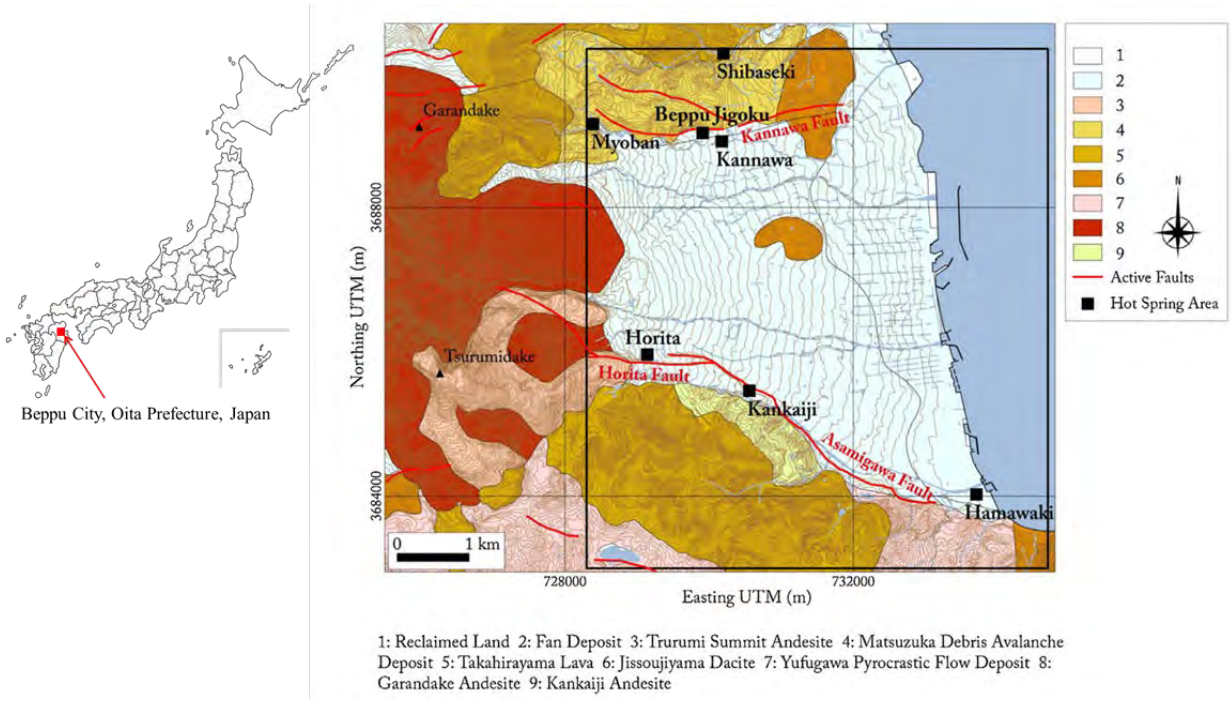

Figure 1: Geology map of Beppu geothermal field (Geological Survey of Japan, 2014). The red lines are active faults (Chida et al., 2000)

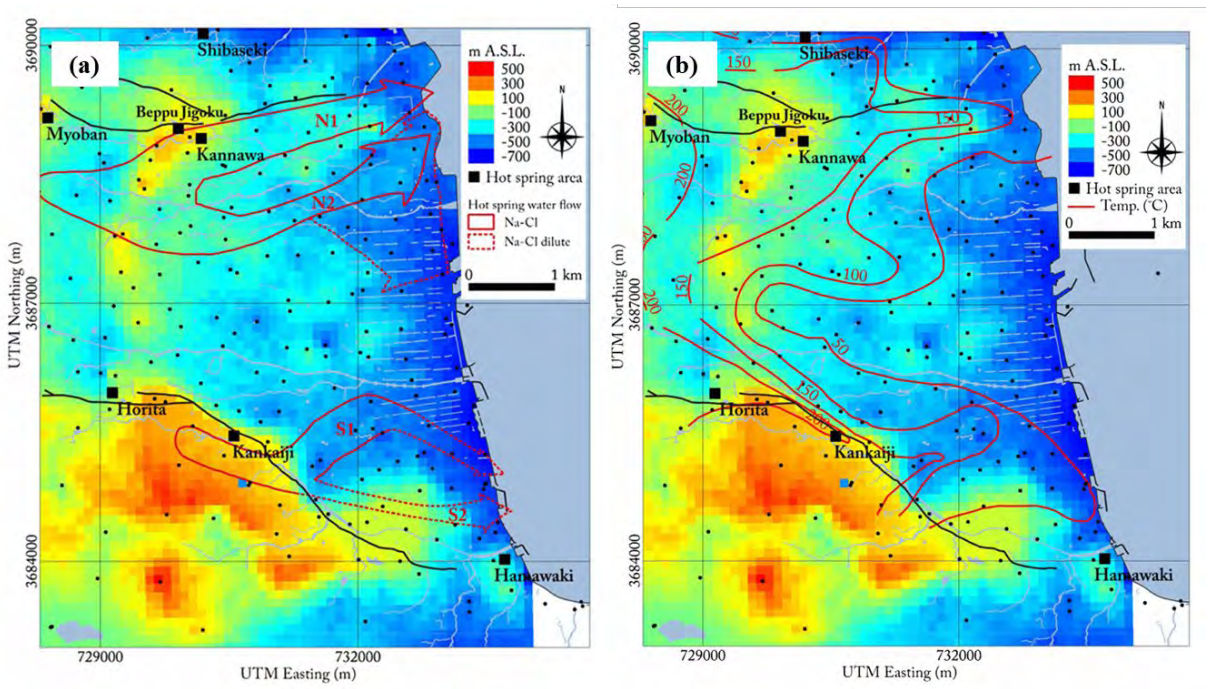

Figure 2: Comparison between the gravity basement and hot spring data (Nishijima & Naritomi, 2017) (a) The gravity basement and the subsurface flows of the Na-Cl type hot spring water, modified from Ohsawa et al. (1994) and Osawa and Yusa (1996). (b) The gravity basement and the isotherm at 100 m below sea level, modified from Allis and Yusa (1989).

3. Repeat Micro-gravity Measurements

In this study, repeat microgravity measurements were conducted, starting from October 2021, in the Beppu area. The measurement points were the same as those used in a previous study, which was conducted from 2014 to 2016, (Nishijima et al., 2018) to investigate long-term trends (Figure 3). A CG5 relative gravimeter (Scintrex, Ontario, Canada) was used until June 2022, and CG6 (Scintrex, Ontario, Canada) was used after September 2022, 3–4 times a year. Closed loops were formed with multiple measuring points and round-trip measurements were performed to effectively detect and analyze microgravity changes. In each of the outbound and return measurements, gravity values were measured multiple times until they settled within 10 μgal at each measurement point. After applying tide, machine height, and drift corrections to the obtained data, the relative gravity differences from a reference point were calculated. The reference point was C1, which was the closest to the sea and was considered to have the smallest change in groundwater saturation.

Figure 4–6 show the changes in gravity over time at each station. The measurement errors were large in March and June 2022, but the variation in the values for the subsequent measurement cycles was small. To observe the long-term trend, the time reference was April 2014, the start of monitoring by Nishijima et al. (2018), and the value at each time was shown as the gravity change from April 2014, the reference time. Many of the measurement points show repeated irregular fluctuations in the range of +-40 μgal (Figure 4, 5). The gravity values of C2, D1, TERUYU, and B3, in 2023 are decreasing from -20 μgal to -40 μgal compared to 2016, the year before the interruption of the measurement. Seasonal variations were observed for the BGRL stations, with gravity values increasing from November to December and then decreasing. Differences between the BGRL and other measurement points were noted during the 2014–2016 measurements. The BGRL reflects the shallow groundwater level in the unconfined aquifer, and gravity values in areas with active geothermal use, such as C3 and TERUYU, are influenced by saturation changes in both the unconfined aquifer and the hot spring aquifer.

Figures 7 and 8 show the distributions of gravity changes between the measurement periods of the previous study (2014–2016) and the present study (2022). To minimize impact of seasonal variations, differences were recorded for the same month each year and a two-dimensional distribution map of gravity change was obtained. The gravity values decrease at D1, TERUYU, and B3, which are located west of C3, compared to the area directly under the Kannawa area, which has the largest amount of production.

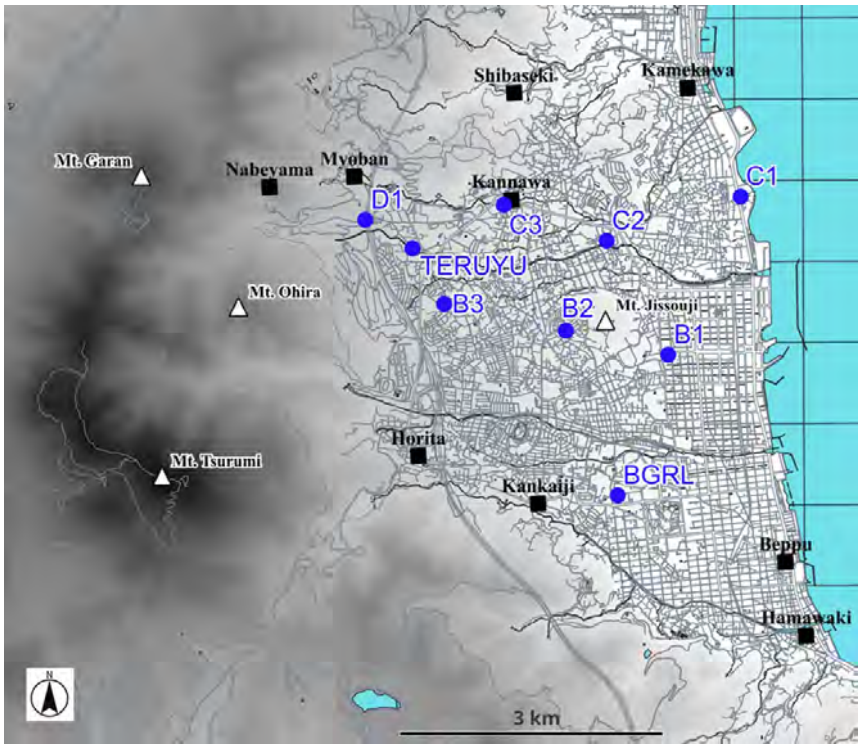

Figure 3: Gravity measurement points (blue plots)

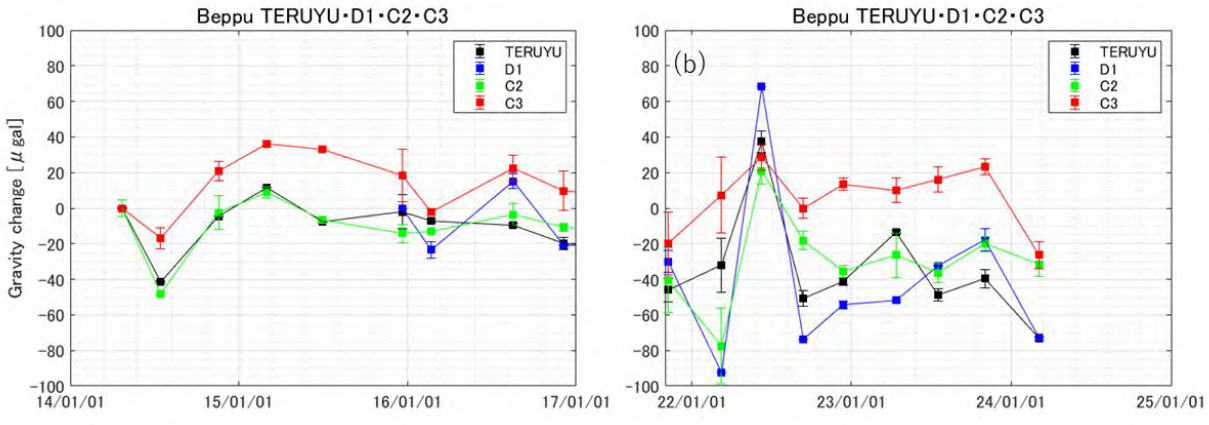

Figure 4: Gravity changes at TERUYU, D1, C2, and C3. Error bars are the difference between the outward and return drift-corrected gravity values, and the average value is plotted as a square.

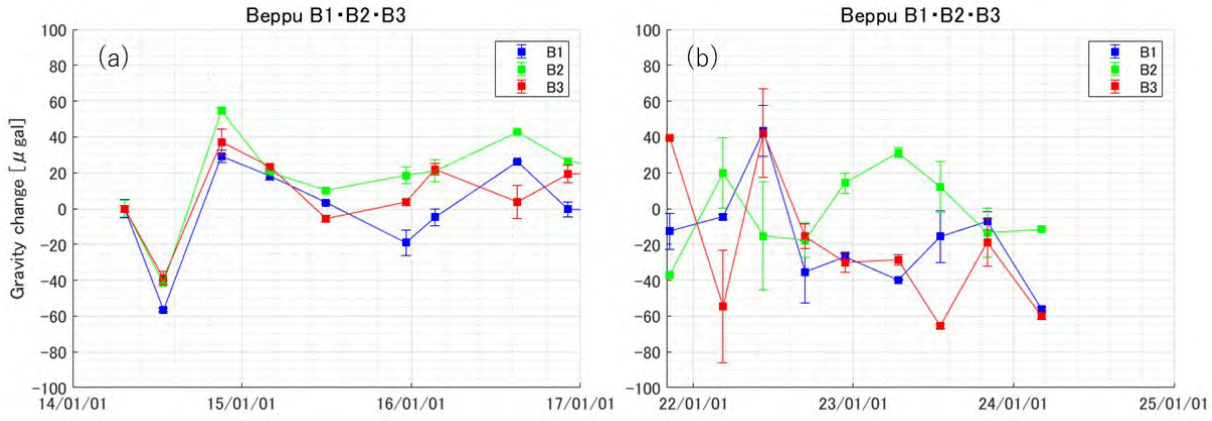

Figure 5: Gravity changes at B1, B2 and B3. Error bars are the difference between the outward and return drift-corrected gravity values, and the average value is plotted as a square.

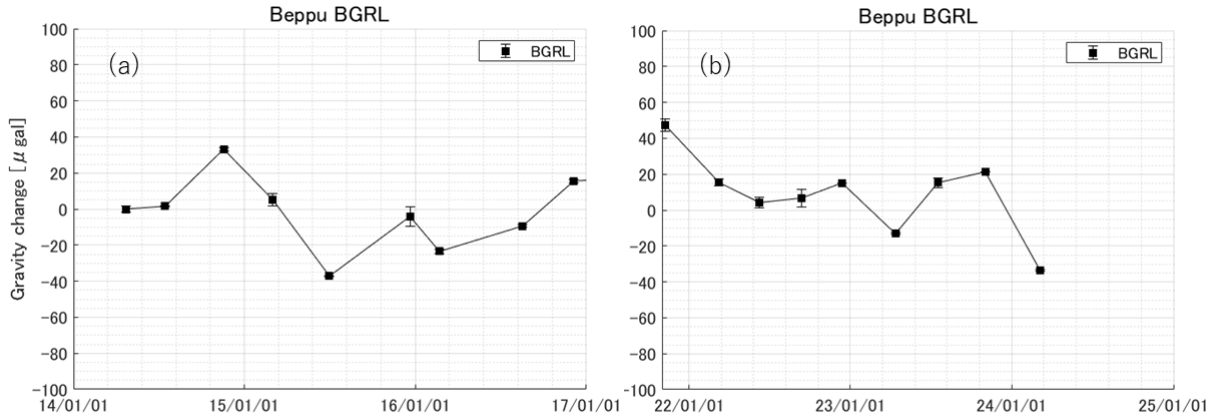

Figure 6: Gravity changes at BGRL Error bars are the difference between the outward and return drift-corrected gravity values, and the average value is plotted as a square.

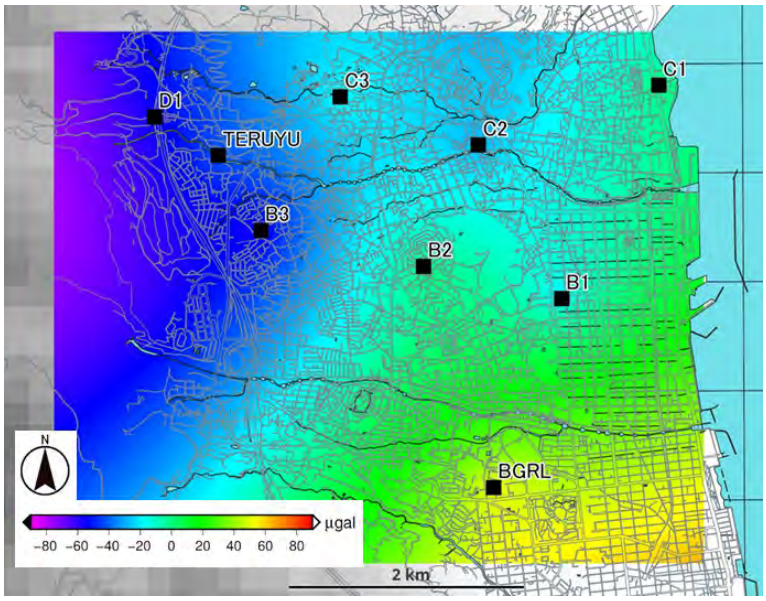

Figure 7: Distribution of gravity changes from July 2015 to July 2023

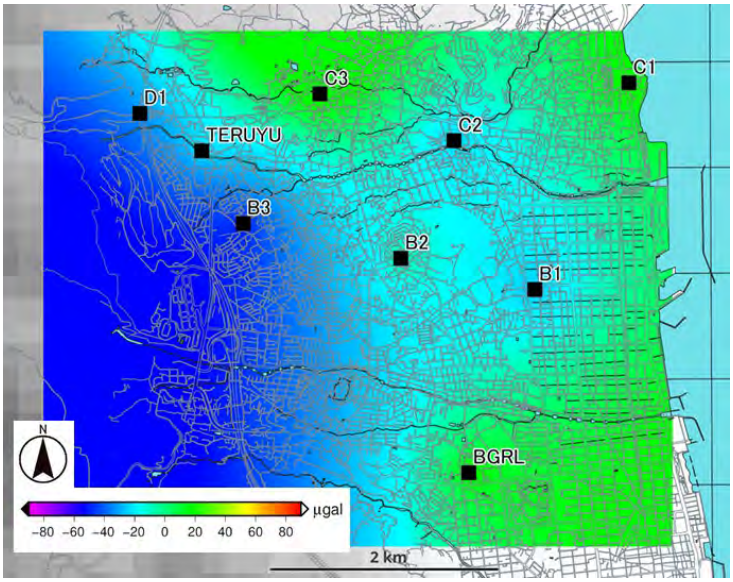

Figure 8: Distribution of gravity changes from December 2016 to December 2022

4. Forward Calculation of Gravity Change Using Reservoir Simulation

First, to understand the geothermal fluid flow regime before production, a geothermal reservoir model was constructed based on the results of geophysical surveys of the Beppu area, including geological and gravity base elevations. We conducted a natural-state simulation using the reservoir model in TOUGH2. Next, a production simulation was conducted based on the natural state model, and the gravity changes caused by the production were calculated by forward calculations using the Volsung simulator.

4.1 Natural-State Model

A region of interest was enclosed by a square of 8 km (200 m × 40) on each side, with a 1 km buffer region on the outside, making the entire model area 10 km × 10 km (Figure 9). The depth of the model was set at an elevation of -2000 m as the bottom and 1000 m elevation as the top of the model (100 m × 20 at the top and 200 m × 5 at the bottom). The geological model (Figure 1) and gravity base structure (Figure 2) were reflected in the model, and rock properties were determined based on Murata et al. (1991) and Yahara et al. (1994) (Table 1). Because the model was assumed to be porous, highly permeable geological domains such as the fault structure were assigned to high permeability (Figure 10). The fault structures are based on Chida et al. (2000) (Figure 1). Boundary conditions were fixed at atmospheric pressure and 17 °C for surface grids. The eastern side (bay) was set as permeable, whereas the other sides (watershed) were set as adiabatic or impermeable. A heat flux of 0.25 W/m^2 was given from entire bottom grids as the crustal heat flux, and a mass flow velocity with a specific enthalpy of about 300 °C was given at 15 kg/s to the bottom about 1.5 km southeast of Mt. Garan and 23 kg/s to the bottom about 1 km northeast of Mt. Tsurumi as heat fluid sources. Because the age of the hot spring system, calculated from the potassium concentration of the hot spring water, was estimated to be 50,000 years (Yusa, 2000), the calculated results at the age of 50,000 years were used as the natural state. Figure 11 shows the temperature distribution and fluid flow at elevations of -200 m and -100 m after 50,000 years. In the geochemical analysis of the hot spring water flow shown in Figure 2, the flow path is divided into two large channels on the north and south sides and high-temperature regions of 100 °C or higher are distributed along each channel. In the natural state model, the water flows from the west side of the source to the east in two separate north and south directions, and high-temperature regions of 100°C or higher are distributed along each flow path (Figure 11).

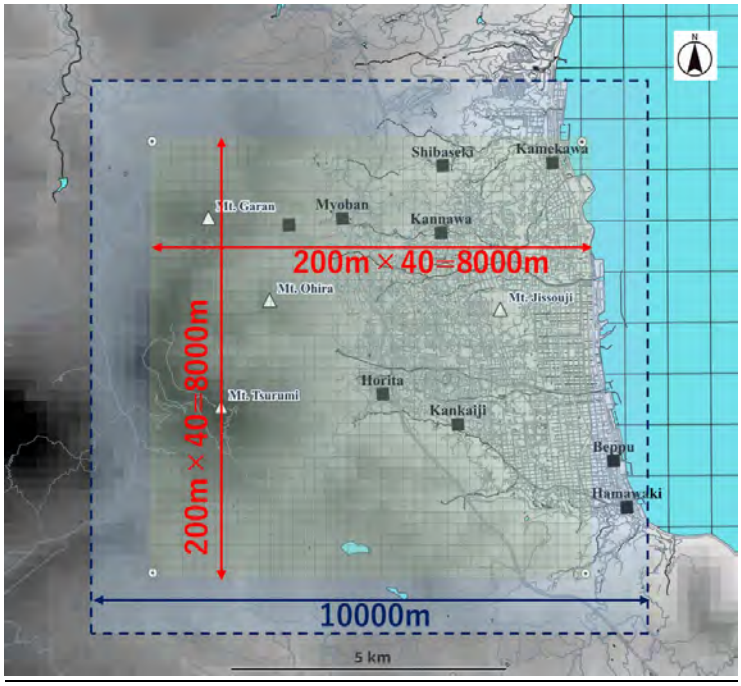

Figure 9: Area of reservoir simulation.

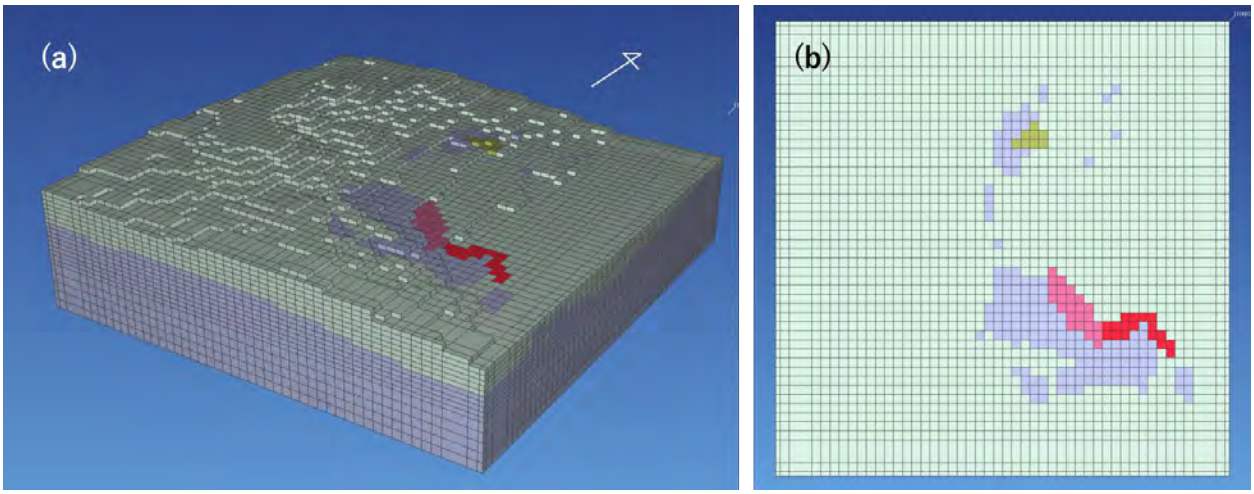

Figure 10: Geothermal reservoir model (a) 3D View and (b) Surface grid

Table. 1: Rock properties used in simulation (Colors are the same as shown in Figure 10)

	Materials	Porosity	Heat conductivity [W/m・K]	Density [kg/m^3]	Specific Heat [J/kg・K]	Permeability [m^2]
	Fan deposit	0.15	1.8	1900	1000	10^{-14}
	Cap rock	0.15	1.8	1900	1000	10^{-17}
	Fault structure	0.09	2.1	2100	1000	10^{-13}
	Fracture in Andesite	0.02	2.4	2100	1000	10^{-15}
	Andesite (Bed rock)	0.02	2.4	2300	1000	10^{-16}

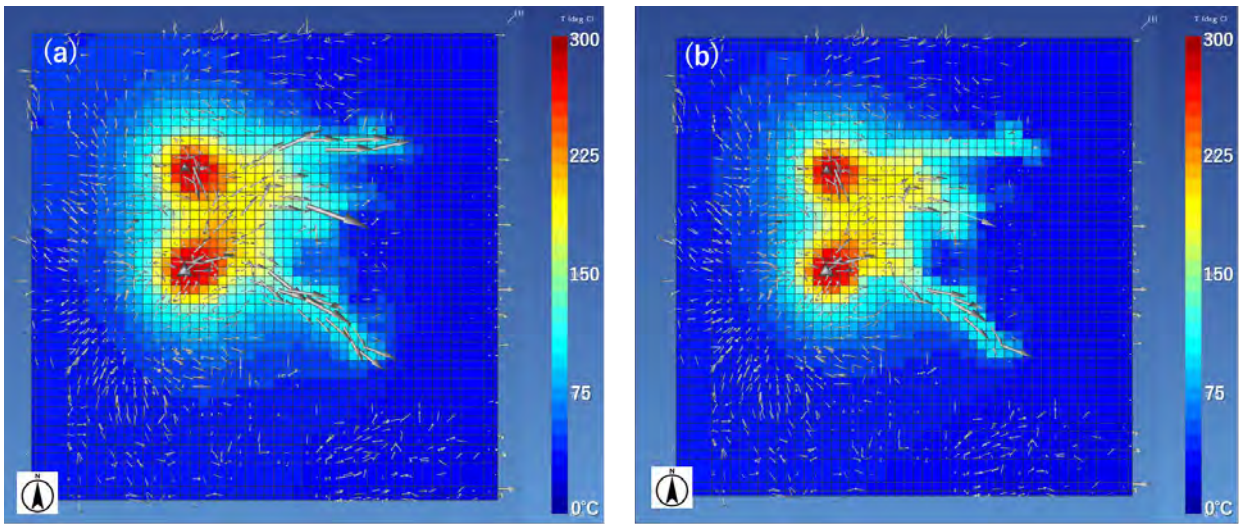

Figure 11: Temperature distribution and fluid flow over 50,000 years (a) Elevation -200m (b) Elevation -100m.

4.2 Production Simulation and Gravity Change

Possible causes of gravity changes during the measurement period in this study include changes in shallow groundwater levels and reservoir saturation associated with production. The annual shallow groundwater level fluctuation is about 2 m in Beppu area, and the corresponding gravity change is about 12.5 μgal (calculated with a porosity of 0.15). The observed gravity changes in Beppu were higher than this value (Figure 4–5), suggesting that a large proportion of gravity changes was associated with changes in saturation in the reservoir due to production. The simulation in this study reproduced the gravity changes associated with the saturation change in the reservoir due to production.

Hot spring water has long been used in the Beppu area, and the amount of hot spring water collected from 1949 to 1987 varied between 431 and 656 kg/s (Yusa et al., 2000). Currently, there are more than 2000 sources, because it is difficult to reflect all wells in the mesh, approximately 70 wells were placed based on the production distribution shown by Yusa (2012) (Figure 12). Each well produced 5–10 kg/s (432–864 ton/day), resulting in a production rate of 498 kg/s (43027 ton/day) for the entire simulated area. The volume produced was equivalent to the middle of the production volumes in 1949 and 1987, as documented by Yusa et al. (2000). Induction wells were not set because most of the hot-spring operators were not reduced. The production period was assumed to be approximately 70 years from 1950 to the present (2023), and production simulations were conducted. Changes in gravity with respect to July 2015 were obtained by the forward calculation (Figure 13).

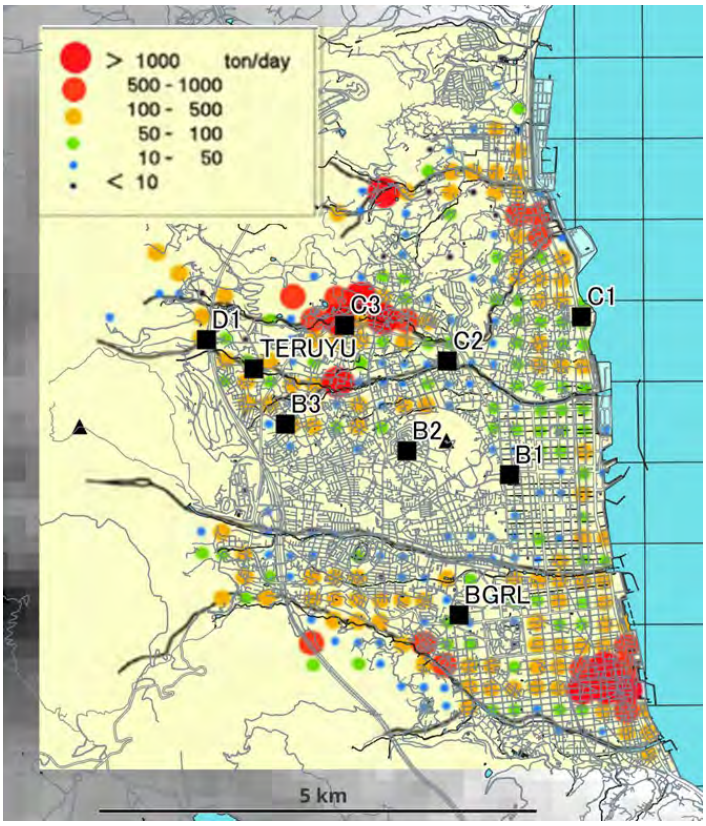

Figure 12: Distribution of production rate (Yusa, 2012)

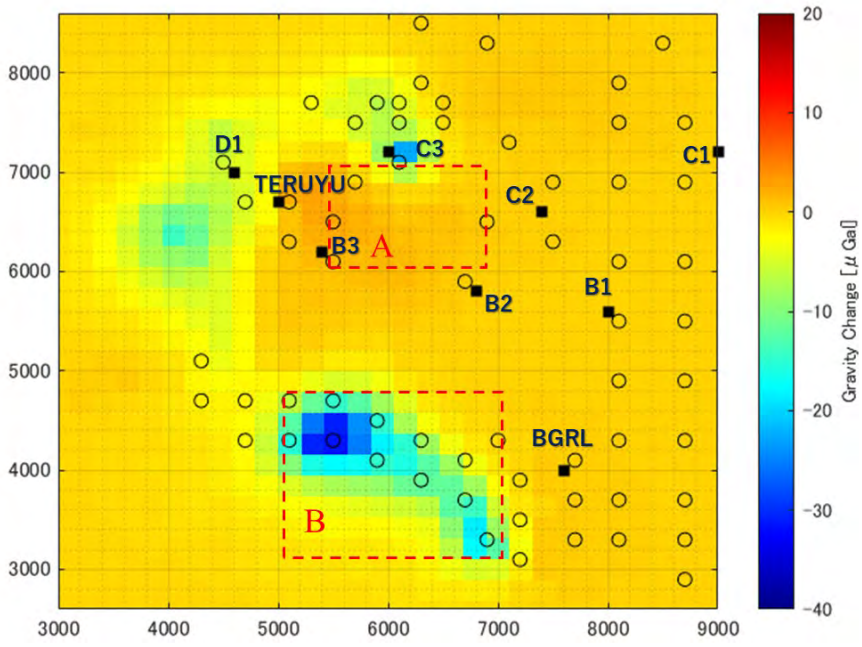

Figure 13: Gravity forward calculation result. Black circles indicate well locations.

5. Discussion

Comparing the two-dimensional distributions of the measured and forward calculation, the measured gravity decreases extended to the TERUYU and B3 measurement points, whereas the forward calculation showed no gravity decrease at TERUYU and B3 measurement points (Figure 7 and 13). One possible reason for this is that production wells could not be set in Region A on the southern side of Kannawa (C3). In the current production simulation, 43,000 tons/day were produced from the entire Beppu area, but the current model does not allow for further production, which is thought to be due to the low permeability of the model on the north side centered on the Kannawa area and insufficient supply for the reservoir model. The measured gravity values must be explained by adding a structural survey on the north side, revising and/or optimizing parameters such as permeability, and revising the supply (source mass flow rate) to the overall model to reproduce a more realistic production rate. Although there is room for improvement in the current reservoir model in terms of reproducing the measured values, the gravity change can be utilized for reservoir model evaluation by comparing the forward gravity calculation with the measured values. The gravity decrease observed in Region B (west of the BGRL) in the forward calculation did not fit the observations. Because there are no observation points in Region B, it is necessary to set the new measurement points over a wider area to capture gravity changes.

6. Conclusion

Repeat microgravity observations were conducted in the Beppu area, and the long-term trend of gravity was clarified by comparison with historical gravity values, showing that gravity has been decreasing mainly at the western survey points, such as D1, TERUYU, and B3. In addition, a reservoir model was developed based on existing geological information and basement elevations,

and forward calculations of gravity changes associated with production were performed. By comparing the forward gravity calculations with the measured values, it was shown that repeated microgravity measurements can be used to evaluate the reservoir model.

Acknowledgement

We thank the people of Beppu City, the Geothermal Research Facility of Kyoto University, and the Flower Group of the Agricultural Research Department of the Oita Prefectural Agriculture, Forestry, and Fisheries Research and Guidance Center for their cooperation in setting up the measurement points.

REFERENCES

Allis, R.G. and Yusa, Y. “Fluid flow processes in the Beppu geothermal system, Japan.”, *Geothermics*, 18, (1989), 743–759.

Chida, N., Ikeda, Y., Nakada, T., Okada, A., Une, H., “1:25000 Active Fault Map in Urban Area, Beppu.”, *Geographical Survey Institute of Japan*, (2000), (in Japanese).

Geological Survey of Japan, AIST, “Seamless Digital Geological Map of Japan 1: 200,000. Jan 14, 2014 Version.”, *Geological Survey of Japan, National Institute of Advanced Industrial Science and Technology*, (2014).

Hoshizumi, H., Mimura, K., Ono, K., and Noda, T. “Geology of the Beppu district with geological sheet map of 1:50,000.”, *Geological Survey of Japan*, (1988), (in Japanese with English abstract).

Nishijima, J., Umeda, C., Fujimitsu, Y., Takayama, J., Hiraga, N. and Higuchi, S. “Repeat Absolute and Relative Gravity Measurements for Geothermal Reservoir Monitoring in the Ogiri Geothermal Field, Southern Kyushu, Japan”, *IOP Conf. Series: Earth and Environmental Science, 42, 5th ITB International Geothermal Workshop*, (2016).

Nishijima, J., and Naritomi, K. “Interpretation of gravity data to delineate underground structure in the Beppu geothermal field, central Kyushu, Japan.”, *Journal of Hydrology: Regional Studies*, 11, (2017), 84–95.

Nishijima, J., Naritomi, K., Sofyan, Y., Ohsawa, S., and Fujimitsu, Y. “Monitoring Hot Spring Aquifer Using Repeat Hybrid Micro-gravity Measurements in Beppu Geothermal Field, Japan.”, *The Water-Energy-Food Nexus*, (2018), 55–68.

Murata, Y., Suda, Y. and Kikuchi, T. “Rock physical properties of Japan: Density, magnetism, P-wave velocity, porosity, thermal conductivity.”, *Geological Survey of Japan Report*, 276, (1991), (in Japanese).

Oka, D., Fujimitsu, Y., Nishijima, J., Fukuda, Y. and Taniguchi, M. “Evaluation of geothermal reservoir mass change from the gravity change at the Takigami geothermal area, Ōita Prefecture, Japan”, *Proceedings Thirty-Seventh Workshop on Geothermal Reservoir Engineering Stanford University, Stanford, California*, (2012).

Ohsawa, S., Yusa, Y., and Kitaoka, K. “Flow paths of thermal groundwaters in the southern part of Beppu, Japan.”, *J. Hot Spring Sci. Japan*, 44, (1994), 199–208, (in Japanese with English abstract).

Ohsawa, S., and Yusa, Y. “Flow paths of thermal ground water inferred from the chemical composition of hot spring water in the northern part of Beppu, Japan”, *Report of a Study on Geothermal Fluid Flow Processes and Subsurface Structure*, (1996), 103–114, (in Japanese).

Yahara, T., Shimada, K. and Yusa, Y. “Thermal Fluid Flow System in the Southern Part of the Beppu Field, Japan.”, *Journal of the Japan Geothermal Energy Association*, (1994), 114-129, (in Japanese).

Yusa, Y. “Natural Scientific Factors of Hot Spring Hot Springs”, *Beppu City Cultural Landscape Preservation Plan for Beppu's Hot Spring Scenery*, 3, (2012), (in Japanese).

Yusa, Y., Ohsawa, S., and Kitaoka, K. “Long-term changes associated with exploitation of the Beppu hydrothermal system, Japan.”, *Geothermics*, 29, (2000), 609–625.

Detailed Airborne Magnetic Survey of the Puna Geothermal Venture and the Lower East Rift Zone, Island of Hawai‘i

Zach Reynolds, Drew Spake, Derek Caro, Nick Prina, Danny Feucht, Kelly Blake, Ryan Libbey, and Ben Delwiche

Ormat Technologies, Inc.

Keywords

Geophysics, Aeromagnetic Survey, Pahoehoe, A'a, Puna Geothermal Venture, Lower East Rift Zone, Hawaii

ABSTRACT

A recently collected high-resolution airborne magnetic survey provides insight into the structural setting of the Puna Geothermal Venture (PGV) on the Island of Hawai’i. Previous magnetic investigations of the eastern flank of Kīlauea predominantly relied on the ‘Puna Forest’ airborne magnetic survey conducted by the United States Geological Survey in 1978. Those data revealed that the Lower East Rift Zone (LERZ) of the Kīlauea volcano is characterized by a magnetic high anomaly extending from Kīlauea’s summit down its southeastern flank. That feature makes a notable left step near PGV in an area with enhanced permeability in the geothermal system. Ormat’s 2024 airborne magnetic survey improves on that legacy survey by utilizing denser line spacing (100 m flight lines), as well as advanced magnetic detection equipment and processing techniques, to delineate smaller-scale fissures and fractures in and around PGV. The new magnetic data have been correlated, where applicable, with magnetic intensity measurements, lithologic interpretations from drilling, and paleointensity data previously collected across the area of interest.

The magnetic signatures captured by this survey reveal pronounced positive magnetic anomalies along the major N63°E LERZ trend, as well as with cross-cutting features that strike perpendicular to this regional LERZ trend. The N63°E-trending fissures and fractures have been well-characterized by drilling and can host permeability associated with production, however the location, orientation, and size of the cross-cutting geologic structures are not well understood. These structures were first hypothesized as an explanation for results from reservoir tracer studies which showed rapid tracer returns from certain production and injection wells. This implies permeable pathways trending approximately perpendicular to the structural grain of the LERZ. The existence of NW-SE trending fractures was recently confirmed by an acoustic borehole image log, but additional studies are required to quantify their contribution to field permeability (Spake

et al., 2024). In a geologically homogeneous environment, a largely uniform magnetic signature would be expected. However, the basalts deposited across the LERZ present a contrast of strong magnetic highs flanked by broad magnetic lows (±6000 nT). This paper discusses the results of the recently acquired magnetic survey and the implications to the magnetic and structural environment at PGV.

1. Introduction

The Island of Hawai'i is part of the Emperor-Hawaiian volcanic chain and is formed by a group of five shield volcanoes, each shaped by lava accumulations from eruptive events. Our understanding of the island's subsurface geology is largely derived from geophysical data and sparse drill hole data (Hildebrand et al., 1993). At Ormat's Puna Geothermal Venture, a dense cluster of drilling allows for the testing and refinement of magnetic interpretations.

Magnetic surveys can be effective at measuring magnetic variations in volcanic regions like Hawai'i (Gudmundsson et al., 1997). This is due, in part, to significant variations in rock magnetization across the island (Hildebrand et al., 1993). Previous magnetic studies on the island have demonstrated the effectiveness of magnetic surveys and have been able to identify rift features, volcanic vents, conduits, and areas of alteration. The United States Geological Survey (USGS) conducted magnetic surveys over Hawai'i's volcanic regions in the 1960's (Malahoff & Woollard, 1966), revealing correlations between magnetic anomalies and volcanic structures. The 1978 'Puna Forest' survey provided a comprehensive magnetic dataset fundamental in understanding the island's magnetic features (Godson et al., 1981).

This paper analyzes the results of a detailed airborne magnetic survey conducted over PGV and part of the Lower East Rift Zone (LERZ). The goal of this survey was to map lateral variations in magnetic intensity to better understand subsurface geologic structure and strengthen the conceptual model for the geothermal system. This detail-oriented survey, like its regional predecessors, demonstrates that airborne magnetic mapping can effectively image intrusive dike complexes as well as areas of complicated deposition or alteration. There is good correlation between anomalies detected in the survey and geologic observations from the geothermal field. Magnetic intensity measurements indicate strong variations in rock magnetization, which likely represents conditions during deposition or changes that the rock has undergone over time. We have utilized various transformation and filtration techniques to help visualize and analyze the total magnetic intensity of the project area.

2. Geologic Setting

The Puna Geothermal Wellfield lies within the Lower East Rift Zone of the Kīlauea volcano (Figure 1). The LERZ hosts volcanic vents, craters, fissures, and fractures along a N63°E regional trend, mapped by Moore and Trusdell, in 1991. These volcanic features can act as conduits for both magma and hydrothermal fluids (Kenedi et al., 2010; Moore and Trusdell, 1991; Tilling & Dvorak, 1993). The PGV site is located in an area where eruptive vents appear to shift northward, suggesting the presence of north-south trending transform faulting (Moore, 1992; Spielman et al., 2006). This area is characterized by a magnetic high anomaly extending from Kīlauea's summit down its southeastern flank, with a notable left step in the magnetic field near PGV. This magnetic discontinuity may be an indicator of left-step transform faulting (Trusdell et al., 2009; Neal et al., 2019).

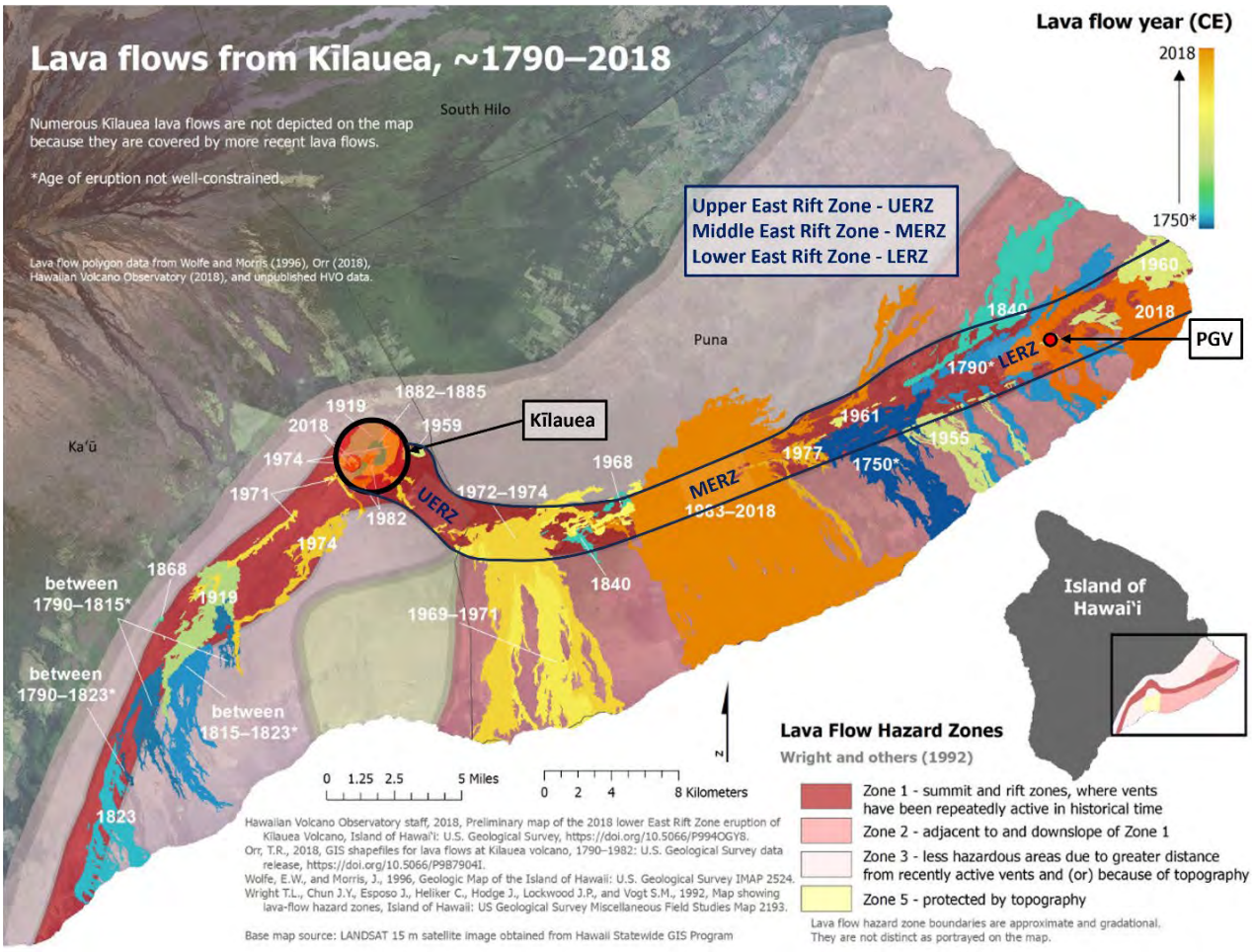

Figure 1: Annotated map showing the subaerial extents of lava flows and explosive deposits from Kīlauea, 1790–2018. Lava flow hazard zones, districts of the County of Hawai'i, the Upper, Middle, and Lower East Rift Zones are also depicted. Modified from Mulliken et. al, HVO (2024).

Tholeiitic basalts make up the overwhelming majority of the rock volume on the Island of Hawai'i and dominate the geology around PGV (Clague and Dalrymple, 1989). Notably, 80% of the LERZ is covered by basalt flows erupted within the last 500 years (Teplow et al., 2009). Most of the flows visible at the surface were deposited by eruptions in 1790, 1955, and 2018, all sourced from Pu'uhonuaula and Ahu'ailā'au craters (Figure 2). These events have resulted in ground deformation and changes in the subsurface, including fracture dilation, contraction, and reactivation of previously sealed fractures (Kauahikaua & Trusdell, 2020). The 2018 eruption was impactful, producing substantial changes in the landscape of the LERZ (Neal et al., 2019).

Subsurface lithology at PGV consists of four main units: subaerial basalts, a transitional sequence dominated by hyaloclastites, submarine basalts, and dike complexes intruded into basaltic host rock. Steeply dipping dacitic and diabase dikes associated with fissure eruptions have been linked to areas of high permeability (Teplow et al., 2009). The reservoir's permeability is influenced by en echelon, fracture systems oriented N63°E and dipping 85° to the NW. The intricate and long-lived nature of the geothermal system is evident from mineralogic studies of the reservoir rock (e.g., Iovenitti and D'Olier, 1985), which identify alteration due to contact metamorphism, low-temperature interaction with magma, and hydrothermal processes.

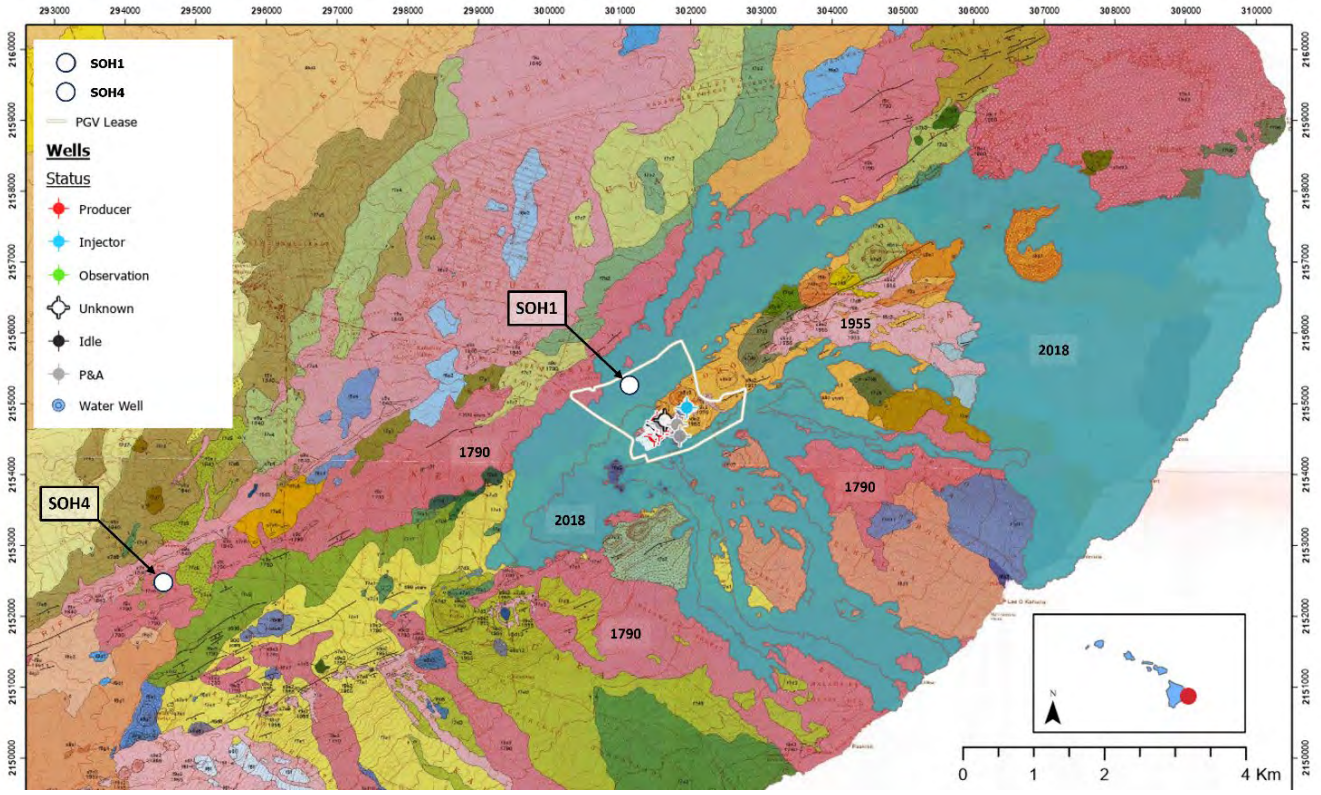

Figure 2: Annotated Map of the LERZ highlight recent impactful depositional events and Scientific Observation Holes SOH1 and SOH4. Modified geologic map from Moore and Trusdell, (1991). 2018 flow geospatial data from Zoeller et al, 2019.

Inflated pāhoehoe sheet flows, as found on the island and in the LERZ, can form when lava is injected beneath an existing, solidified crust (Self et al., 1998). Often, inflated sheet flows form in low-relief areas and can be the result of fluid pressure building within a cooling shell, as lava is injected into the interior of the flow (Holcomb, 1980; Hon and Kauahikaua, 1991). These flows cool relatively slowly, which likely has an effect on the quantity, distribution, and grain size of magnetic material within the flows (Audunsson et al., 1992). During the prolonged cooling process, ferromagnetic minerals like titanomagnetite have more time to align with the paleomagnetic field. This results in higher measured magnetic intensities compared to surrounding rocks.

‘A’ā lava flows, as characterized by MacDonald in 1953, form fragmented, rough surfaces, with clinkers often overlying an auto-brecciated base. The lava cools quickly and clasts topple along the flanks of the flow forming clinkers as a result of differential motion and shearing of the molten interior (Harris et al, 2016). This flow behavior results in a surface morphology that transitions from spiny fragments near volcanic conduits to loose, rubbly flow-breccia as the flow moves further away from the source (MacDonald, 1953). The irregularity and fragmented nature of these flows may affect the distribution, direction, and grain size of magnetic minerals, potentially leading to more variable magnetic signatures compared to other flow types (Hildebrand et al., 1993). ‘A’ā clasts that have tumbled and have varying magnetic orientation could lead to a mixed or suppressed measured magnetic intensity compared to pāhoehoe flows. The magnetic minerals

in these clasts may not have sufficient time to align with the magnetic field before rapidly cooling, creating a mixed domain state within the rock (Bücker et al., 1999).

3. Magnetic Data

The 'Puna Forest' airborne magnetic survey, (Figure 3), was conducted in 1978 by the USGS and has been integral to the design and justification of this survey. The USGS survey was predominantly flown at a height of 305m with 1600m spacing with lines oriented N27°W (Godson et al., 1981) and perpendicular to the main rift trend, at N63°E (Flanigan et al., 1986). The data provide a total magnetic intensity map suitable for regional analysis.

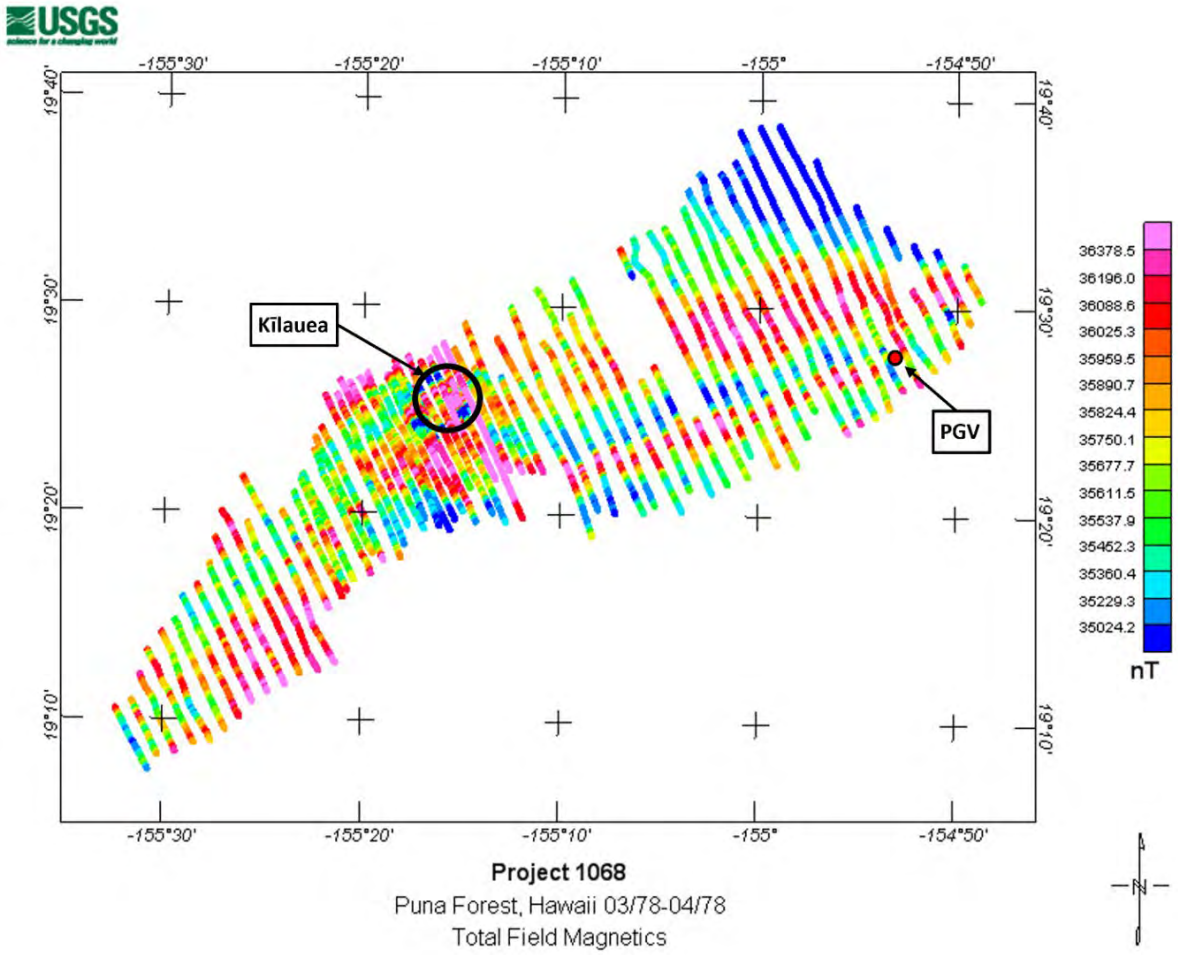

Figure 3: Map of the 1978 USGS 'Puna Forest' airborne magnetic survey with flight lines overlain with Total Field Magnetics.

In 2024, Ormat Technologies contracted MWH Geo-Surveys to collect an unmanned aerial system (UAS) magnetic survey covering 36 km² over PGV and the surrounding area (Figure 4). Total magnetic field data were collected using the Geometrics MagArrow, a laser-pumped cesium magnetometer specifically designed for UAS surveys with a sensitivity of 0.0005 nanotesla (nT).

Main flight lines for this survey, spaced 100 m apart and bearing N27°W, were flown perpendicular to the main LERZ trend, totaling 344 line-km. Tie-lines, flown perpendicular for

leveling and enhancing possible rift-perpendicular structures (Figure 4), covered 88 line-km, bearing N63°E and spaced 400 m apart. Flights were conducted at 140 m above ground level (AGL) to minimize localized magnetic effects from anthropogenic sources and highly magnetic fresh lava flows prevalent in the LERZ. Flight line drape was planned using a 1 m DEM model from the USGS, in an attempt to minimize terrain effect on the data.

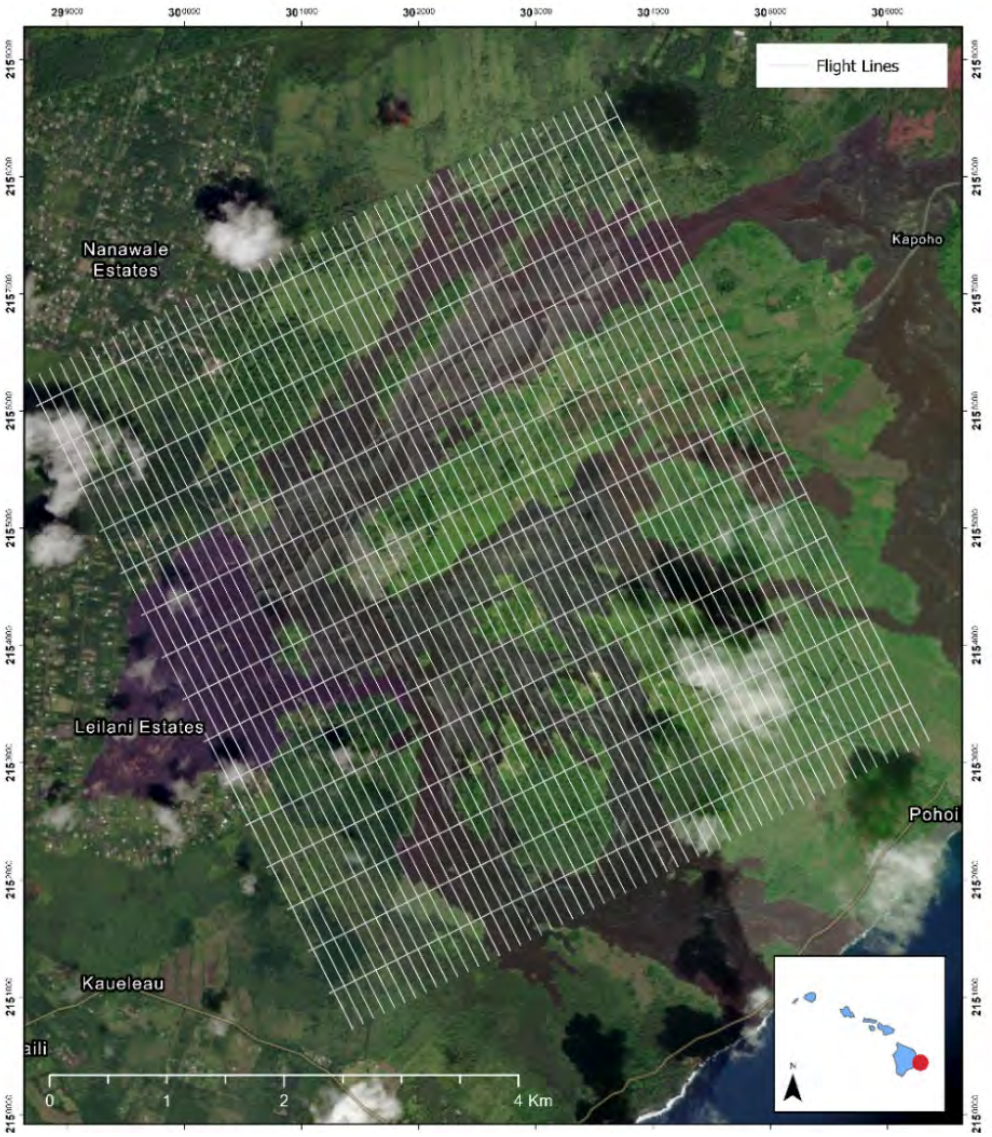

Figure 4: Flight lines from the 2024 Ormat UAS magnetic survey, spaced 100 m, with tie-lines every 400 m.

Total magnetic intensity (TMI) data were processed using minimum curvature gridding and reduced to the pole (RTP) (Figure 5) with a magnetic inclination of 36.5° and a declination of 9.5°. A map of total magnetic intensity, reduced to the pole reveals distinct magnetic anomalies interpreted to be associated with intrusive dike complexes, slowly cooled pāhoehoe basalt flows, ‘a’ā flows, and areas of possible alteration.

4. Data Analysis

Total Magnetic Intensity (TMI) was calculated for the high-resolution magnetic dataset by adding the International Geomagnetic Reference Field (IGRF), approximate value 34,302 nanotesla for the survey date and location, to the diurnally corrected magnetic data. Standard line-to-line leveling resolved herringbone effects, while tie-line leveling adjusted data values based on mis-tie values at line/tie-line intersections, ensuring consistency in the final maps.

At Hawai‘i’s low magnetic latitude, total magnetic intensity anomalies can present as dipolar in shape, with circular intrusions manifesting as magnetic highs closely flanked by magnetic lows, often in a north-south orientation. This can result in east-west oriented gradients that can be misleading in interpretation. The Reduction-to-Pole (RTP) transformation (Figure 5a) corrects for this by shifting positive anomalies over their sources (Bhattacharyya, 1965). For visualization and interpretation, magnetic data were gridded at 40 m intervals and contoured at 200 nT increments to accommodate high-quality data with very steep magnetic gradients.

5. Results

The magnetic data collected in this survey offer valuable insights into the magnetic and structural characteristics of the LERZ and PGV. The UAS magnetic survey highlights N63°E trending fissures and fractures as intermediate to low magnetic anomalies, which correlate well with the fissures and fractures mapped by Moore and Trusdell (1991). Cross-cutting anomalies are also apparent in this dataset, with the most significant rift-perpendicular lineament located east of PGV. Broad magnetic low anomalies are more common to the south of PGV and the highest amplitude magnetic low anomalies coincide with mapped craters (Figure 5b).

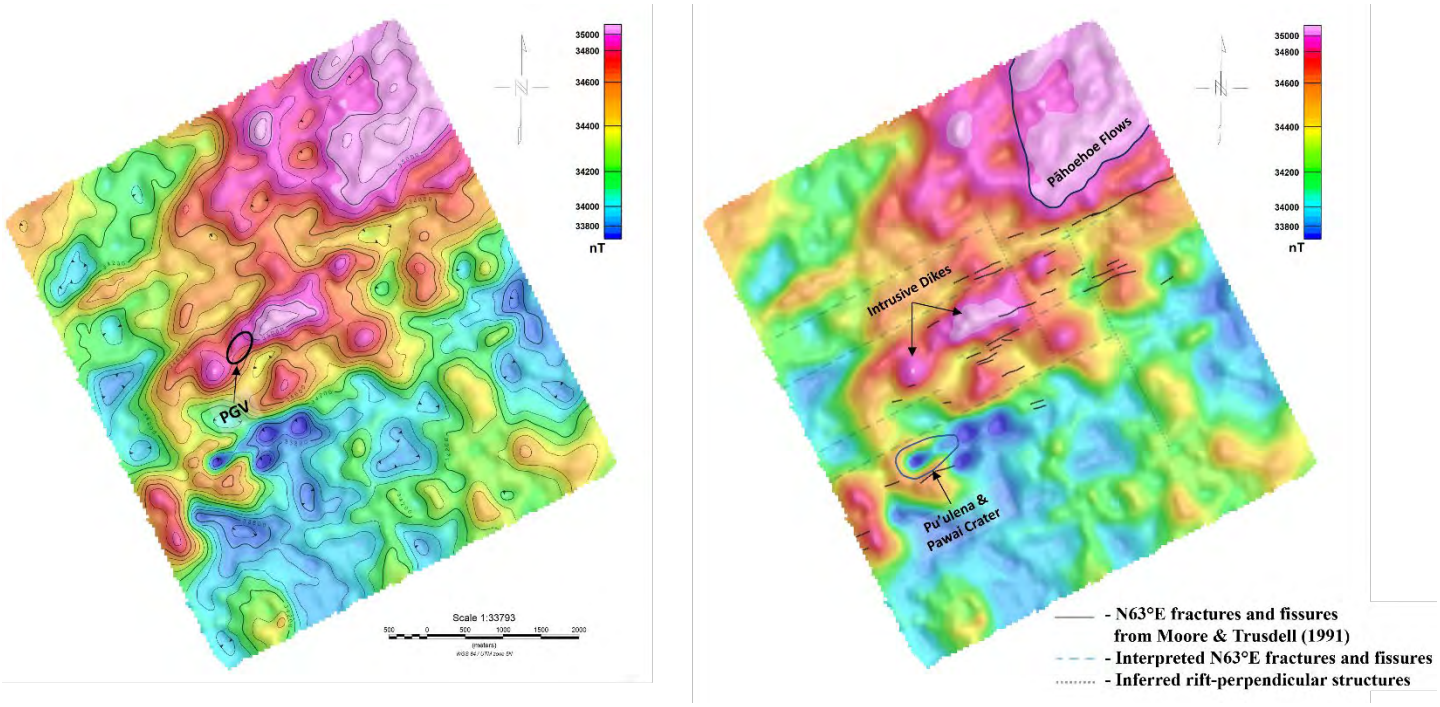

Figure 5: a.) Reduced-to-Pole (RTP) magnetic data with contours every 200 nT. b.) RTP magnetics with interpreted and inferred fissures and fractures based on Moore & Trundell (1991). Both figures have been color shaded to enhance structure.

There are areas in the dataset that may have a positive correlation with topographic relief. In some regions, a positive magnetic anomaly is observed near or over an area with elevated topography. Two strong, spherical magnetic low anomalies are imaged to the southwest of PGV and appear to correlate with the Pu‘ulena and Pawai craters. These magnetic low anomalies may be due to terrain effects, as flying an accurate flight drape over such steep gradients would be challenging. These anomalies may also be the result of alteration occurring in an area of increased permeability or may be areas of lowered magnetic intensity derived from complicated depositional processes.

The 1978 USGS survey and the 2024 Ormat survey show good agreement when sampled over a profile. To facilitate this comparison, the 2024 RTP data were upward continued to a height of 300 m and plotted against the more regional survey. The magnetic intensity profiles are in good agreement, showing the two datasets are generally consistent with each other.

6. Discussion

A key objective of this survey was to capture images of buried structures perpendicular to the LERZ. The apparent offset in the magnetic signature suggests that we may have effectively imaged such rift-perpendicular structures. It is also plausible that magnetic discontinuities in the datasets may be imaging subsurface heterogeneity, variations in dike structure and deposition. Alternatively, we may be measuring highly magnetic intrusive dike complexes that have formed along the rift trend, flanked by relatively lower magnetic intensity material. This juxtaposition in intensity may be creating lineaments that closely correlate with mapped fractures and fissures.

Intermediate to low magnetic lineaments align with mapped fissures and fractures. These geologic features may project into the deep reservoir and are interpreted as potential influencing structures within the geothermal system. However, it is unlikely that the magnetic lows observed in this data set can be directly attributed to hydrothermal alteration from the geothermal system. The geothermal reservoir is overlain by a clay cap, ~1000 m of subaerial basalt and hyaloclastite sequences and a pervasive cold-water aquifer. These are all factors likely to limit hydrothermal alteration near the surface. Given the uncertainty in the depth of investigation, it is highly unlikely that airborne magnetics can image the deep hydrothermal alteration occurring within the reservoir at depths of 1000 m and below. The anomalous magnetic lineaments imaged by this survey correspond with mapped geologic features (Hoversten et al., 2022). Apparent offset in rift-parallel magnetic highs may indicate a NW/SE trending structural fabric, manifesting as a localized left-step structure near PGV (Figure 6). NW/SE-trending structures likely intersect the main N63°E fissures and fractures, potentially acting as additional geothermal fluid pathways and enhancing reservoir connectivity at PGV (Kenedi, 2010).

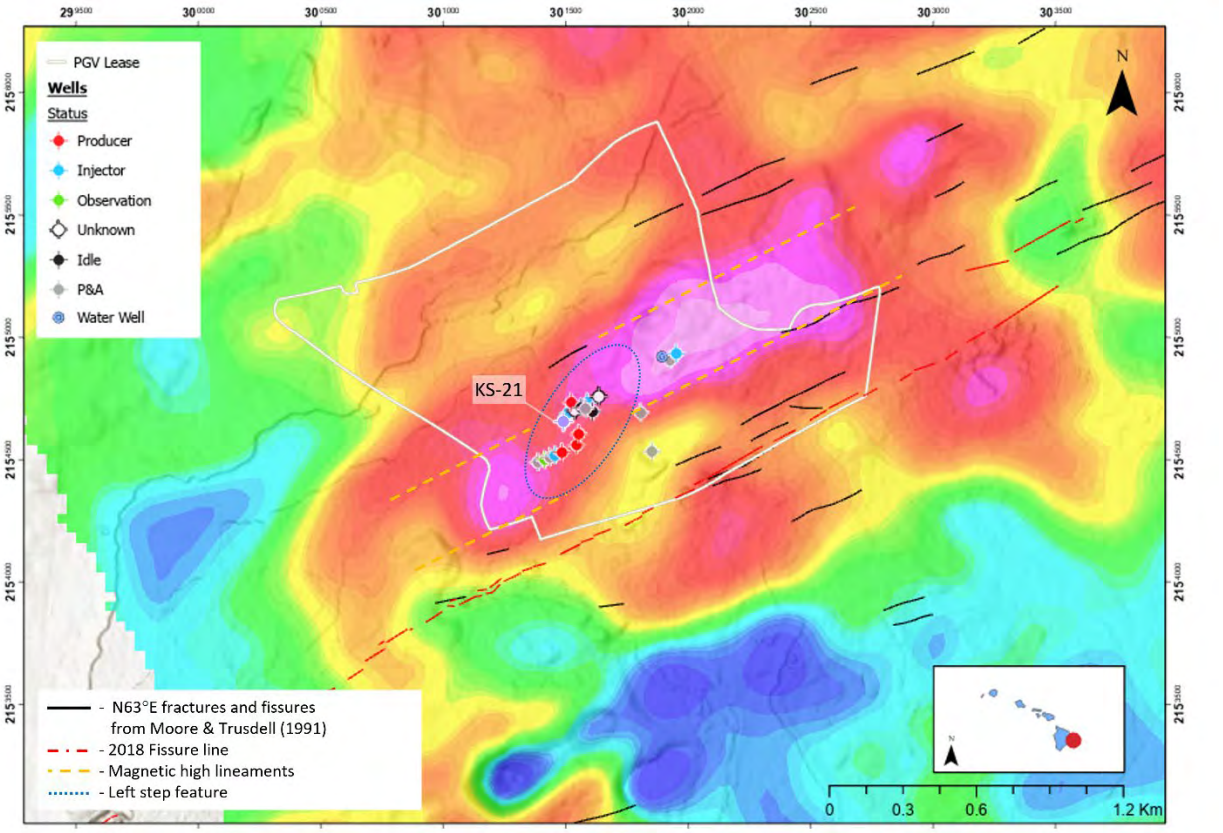

Figure 6: RTP magnetic map highlighting the left-step feature along with interpreted and inferred fractures and fissures.

Strong magnetic high anomalies have been interpreted to result from slower cooling, often associated with in-situ deposition. Intrusive dike complexes and inflated sheet flows share similar mechanisms of emplacement where lava has more time to cool, allowing ferromagnetic minerals to align more effectively with the ambient magnetic field (Audunsson et al., 1992). In contrast, broad intermediate to low magnetic anomalies may be caused by terrestrial flows like ‘a’ā or by weathering alteration processes. The rapid cooling and varying orientation of clasts in ‘a’ā flows do not allow magnetic crystals to align as consistently with the magnetic field, yielding an intermediate to anomalously low response (Harris et al., 2016; Bücker et al., 1999).

The likelihood of encountering reversely magnetized rocks on the Island of Hawai’i is low, and the probability is even lower in the Lower East Rift Zone (LERZ). The oldest rocks on the island have been dated to approximately 0.70 ma, which is younger than the last geomagnetic field reversal that occurred around 0.78 ma. All radiometric ages for rocks in the LERZ are significantly younger than the last geomagnetic reversal, and no reversely magnetized rocks have been documented on the Big Island (Langenheim and Clague, 1987; Doell and Cox, 1965).

Paleomagnetic data collected by Rosenbaum et al. (2009) from boreholes SOH1 and SOH4 (Figure 2) help us understand the magnetic properties of the geology in the LERZ and PGV. Measurements show that shallow dikes have the highest total magnetization compared to other rock types encountered (Table 1). This suggests that shallow dikes are significant sources of short-wavelength magnetic high anomalies associated with the LERZ, while deep dikes likely present as longer wavelength, intermediate magnetic values. These results are consistent with the finding

of this study, that high-amplitude magnetic anomalies are often flanked by broader magnetic low anomalies, likely representing mixed domain terrestrial flows or rock may have been altered in the LERZ (Rosenbuam et al., 2009). Over time, weathering or other forms of alteration may reduce the magnetization of these rocks, explaining the lack of magnetic high anomalies in older areas of the rift zone and in exposed terrestrial flows (Garnier et al., 1996).

Rock Type	**Total Magnetization (Am^{-1})**
Terrestrial flow	5.4 ± 0.6
Hyaloclastites	3.7 ± 2.1
Pillow basalt	9.4 ± 2.8
Shallow dikes (<800 m)	12.6 ± 2.5
Deep dikes	8.4 ± 1.4

Table 1: Total Magnetization values measured by Rosenbaum et al. (2009)

An acoustic borehole image log and Pressure/Temperature/Spinner (PTS) data were collected and analyzed from well KS-21. Despite overall low image log quality, 248 fractures were picked over the 3,266 ft log interval. Most fractures identified are sub-vertically dipping and NE-SW striking, consistent with the trend of the LERZ (Figure 7), and combined analysis of image and PTS surveys supports rift-parallel fractures controlling permeability over imaged feedzones. In addition to the NE-SW striking fractures, there is a minor, but significant, population of WNW- to NNW-trending features distributed throughout the image log. These features are broadly consistent with the attitude of rift-cutting fractures expected from interpretation of magnetic lineaments, however, they do not appear to be major contributors to permeability in the imaged interval and evidence for large, throughgoing NW-trending fractures has so far not been encountered.

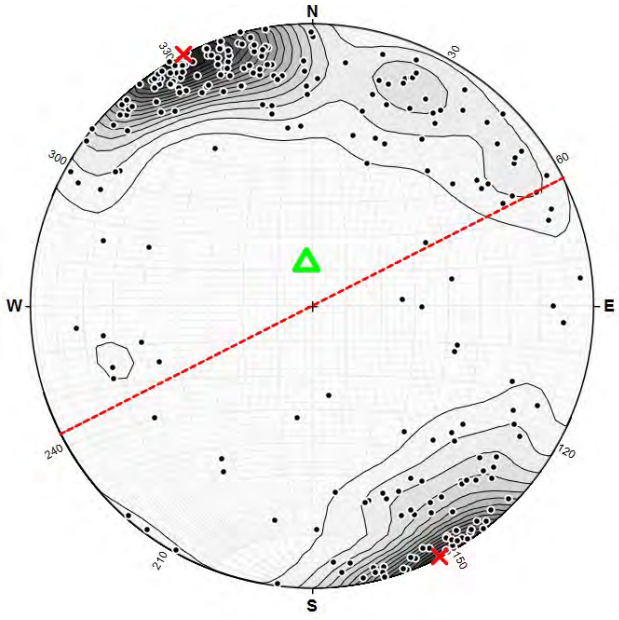

Figure 7: Lower hemisphere stereonet with all fractures identified in the image log (n=248) plotted as black dots representing poles to planes. The trend of the LERZ (063°/243°) is represented by the dashed red great circle, with poles to that vertically dipping plane indicated by red X's. The average attitude of the borehole through the logged interval is plotted as a bold green triangle.

Several tracer studies both pre- and post-eruption have been conducted within the PGV resource to gain a better understanding of potential fluid pathways and the connectivity between production and injection wells. Most notably, tracer studies show a high degree of connectivity within the N63°E-trending rift parallel structures which are well characterized by downhole data including fluid losses during drilling, image logs, and pressure and temperature (PT) surveys.

However, results from multiple tracer studies have also suggested that injection into the northern rift-parallel fractures return to production wells in the southern portion of the reservoir. A cross-cutting structure may explain the connected pathway to allow for the tracer returns. With more recent drilling, additional tracer studies are required to further investigate these potential pathways.

6. Conclusion

The 2024 airborne magnetic survey of the Puna Geothermal Venture within the LERZ has provided a new perspective into the area's magnetic characteristics and structural complexities and has provided a solid foundation for future geophysical interpretation. This survey has identified high magnetic anomalies interpreted as intrusive dikes and thick inflated sheet pāhoehoe flows. In contrast, intermediate and low magnetic anomalies in some areas may be the result of alteration or weathering along mapped fissures and fractures.

Utilizing a multi-disciplinary approach to incorporate the interpretations from this airborne magnetic survey has proven valuable to understanding the geologic structure at PGV. Pairing interpretations from paleointensity data, image logs, and reservoir tracer tests bolsters the interpretation that there are rift-perpendicular structures may exist in the geothermal reservoir and could be conduits for fluid flow. Further integration of these data with existing datasets will improve the geologic conceptual model and inform future resource management decisions.

Further investigation may include additional geophysical investigations, additional injection testing through tracer studies and production data, and geologic mapping. Ground-based electromagnetic geophysics, particularly magnetotellurics (MT), may be helpful in mapping subsurface alteration and understanding the structural controls of the geothermal system, including the geometry clay cap overlying the geothermal reservoir.

Acknowledgement

The authors would like to express our gratitude to our colleagues at Ormat Technologies for their support and encouragement throughout this project. We would like to thank the MWH team for executing this survey in a safe, efficient manner while collecting excellent data. Special thanks to the PGV on-site operational team for their assistance and commitment to safety throughout the duration of the survey. We are very appreciative of our fellow scientists Robin Zuza and Simon Webbison for their insightful feedback and valuable contributions to this study. I would like to express my heartfelt gratitude to my father, John Reynolds, whose passion for geophysics and support have inspired my career path.

REFERENCES

Audunsson, H., Levi, S., & Hodges, F. "Magnetic property zonation in a thick lava flow." Journal of Geophysical Research: Solid Earth, 97(B4), 4349-4360 (1992).

Baranov, Vladimir, and Henri Naudy. "Numerical calculation of the formula of reduction to the magnetic pole." Geophysics, 29(1), 67-79 (1964).

Bhattacharyya, B. K. "Two-dimensional harmonic analysis as a tool for magnetic interpretation." Geophysics, 30(5), 829-857 (1965).

Bücker, C. A. J., K. V. Cashman, and S. Planke. "Data Report: Physical and magnetic characterization of aa and pāhoehoe flows: Hole 990A." Proc. Ocean Drill Program Sci. Results. Vol. 163. (1999).

Clague, D. A., & Dalrymple, G. B. "Tectonic, geochronology, and origin of the Hawaiian-Emperor volcanic chain." In E. K. Winterer, D. M. Hussong, & R. W. Decker (Eds.), The Eastern Pacific Ocean and Hawaii, The Geology of North America (Vol. N, pp. 188-217). Geological Society of America, Boulder, CO (1989).

Cherkasov, S., & Kapshtan, D. "Unmanned Aerial Systems for Magnetic Survey." In Drones - Applications. InTech. https://doi.org/10.5772/intechopen.73003 (2018).

Doell, R. R., & Cox, A. "Paleomagnetism of Hawaiian lava flows." Journal of Geophysical Research, 70, 3377-3405 (1965).

Doell, R. R. "Paleomagnetism of the Kau volcanic series, Hawaii." Journal of Geophysical Research, 74, 4857-4868 (1969).

Harris, Andrew JL, et al. "Pāhoehoe,'a'ā, and block lava: an illustrated history of the nomenclature." Bulletin of Volcanology 79 (2017): 1-34.

Hoversten, G. M., et al. "Magnetotelluric investigations of the Kīlauea Volcano, Hawaii." Journal of Geophysical Research: Solid Earth, 127(8), e2022JB024418 (2022).

Garnier, F., et al. "Geomagnetic field intensity over the last 42,000 years from core SOH-4, Big Island, Hawaii." Journal of Geophysical Research: Solid Earth, 101(B1), 585-600 (1996).

Godson, R. H., Zablocki, C. J., Pierce, H. A., Frayser, J. B., Mitchell, C. M., & Sneddon, R. A. "Aeromagnetic map of the Island of Hawaii, scale 1:250,000." U.S. Geological Survey Geophysical Investigations Map, GP-946, 1 p. (1981).

Gudmundsson, Magnús T., and John Milsom. "Gravity and magnetic studies of the subglacial Grímsvötn volcano, Iceland: Implications for crustal and thermal structure." Journal of Geophysical Research: Solid Earth 102.B4 (1997): 7691-7704.

Flanigan, V.J., Long, C. K., Rohret, D. H., & Mohr, P. J. "Aeromagnetic map of the rift zones of Kīlauea and Mauna Loa volcanoes, Island of Hawaii, Hawaii." U.S. Geological Survey Miscellaneous Field Investigations Map, MF-1845A (1986).

Hon, K., & Kauahikaua, J. P. "The importance of inflation in formation of pāhoehoe sheet flows." Eos Transactions AGU, 72, 557 (1991).

Holcomb, R. T. "Kīlauea volcano, Hawaii—Chronology and morphology of the surficial lava flows." Ph.D. dissertation, Stanford University, Stanford, CA, 321 pp. (1980).

Iovenitti, J. L., & D'Olier, W. L. "Preliminary results of drilling and testing in the Puna geothermal system, Hawaii." Stanford University, Stanford, CA, SGP-TR-84; CONF-850107-18 (1985).

Kauahikaua, J. "Geophysical characteristics of the hydrothermal systems of Kīlauea volcano, Hawaii." Geothermics, 22(4), 271-299 (1993).

Kauahikaua, J. P., & Trusdell, F. A. "Have humans influenced volcanic activity on the lower East Rift Zone of Kīlauea Volcano? A publication review." US Geological Survey, No. 2020-1017 (2020).

Kenedi, C. L., Shalev, E., Lucas, A., & Malin, P. "Microseismicity and 3-D mapping of an active geothermal field, Kīlauea lower east rift zone, Puna, Hawaii." In Proceedings of the World Geothermal Congress 2010 (pp. 1-6) (2010).

Langenheim, V. A. M., & Clague, D. A. "Stratigraphic framework of volcanic rocks of the Hawaiian Islands." In R. W. Decker, T. L. Wright, & P. H. Stauffer (Eds.), Volcanism in Hawaii (pp. 55-84). U.S. Geological Survey Professional Paper 1350 (1987).

Macdonald, Gordon Andrew. "Pāhoehoe, aa, and block lava." American Journal of Science 251.3 (1953): 169-191.

Malahoff, A., & Woollard, G. P. "Magnetic surveys over the Hawaiian Islands and their geologic implications." Geophysical Research, 71, 2493-2510 (1966).

Mohamed, Ahmed, et al. "Geometry of the magma chamber and curie point depth beneath Hawaii Island: Inferences from magnetic and gravity data." Frontiers in earth science 10 (2022): 847984.

Moore, R. B., & Trusdell, F. A. "Geologic map of the lower east rift zone of Kīlauea Volcano, Hawaii." U.S. Geological Survey, Map No. 2225 (1991).

Moore, R. B. "Volcanic geology and eruption frequency, lower east rift zone of Kīlauea volcano, Hawaii." Bulletin of Volcanology, 54(6), 475-483 (1992).

Nabighian, M. N., et al. "The historical development of the magnetic method in exploration." Geophysics, 70(6), 33–61. https://doi.org/10.1190/1.2133784 (2005).

Malehmir, A., Dynesius, L., Paulusson, K., Paulusson, A., Johansson, H., Bastani, M., & Marsden, P. "The potential of rotary-wing UAV-based magnetic surveys for mineral exploration: A case study from central Sweden." The Leading Edge, 36(7), 552-557 (2017).

Neal, C. A., et al. "The 2018 rift eruption and summit collapse of Kīlauea Volcano." Science, 363(6425), 367-374 (2019).

Rosenbaum, J. G., et al. "Magnetic properties from the East Rift Zone of Kīlauea: Implications for the sources of aeromagnetic anomalies over Hawaiian volcanoes." AGU Fall Meeting Abstracts (2009).

Spielman, P., W. Rickard, and W. Teplow. "Puna geothermal venture, Hawaii—2005 drilling program." GRC Transactions 30 (2006).

Teplow, W., Marsh, B., Hulen, J., Spielman, P., Kaleikini, M., Fitch, D., & Rickard, W. "Dacite melt at the Puna Geothermal Venture wellfield, Big Island of Hawaii." Geothermal Resources Council Transactions, 33, 989-994 (2009).

Tilling, R. I., & Dvorak, J. J. "Anatomy of a basaltic volcano." Nature, 363(6425), 125-133 (1993).

Thomas, D. M. "Hydrothermal systems in Hawaii." Geothermics, 18(1), 45-70 (1989).

Zoeller, M.H., Perroy, R.L., Wessels, R.L., Fisher, G.B., Robinson, J.E., Bard, J.A., Peters, J., Mosbrucker, A.R., and Parcheta, C.E., 2020, Geospatial database of the 2018 lower East Rift Zone eruption of Kilauea Volcano, Hawai'i: U.S. Geological Survey data release, https://doi.org/10.5066/P9S7UQKQ.

Geological Causes for Deep Electrical Conductors under Volcanic High-Enthalpy Geothermal Systems

Friedemann Samrock[1], Wolfgang Soyer[1], Stefano Garanzini[1], Randall Mackie[1], Chevy Iskandar[2], Elfina[2], Inusa Pamusyawara Fauzi[3], Aditya A Juanda[3], Nasradin-Ahmed Ibrahim Ahmed[4], Steven Sewell[6], Hjalmar Eysteinsson[7], Stephen Hallinan[1]

[1]Viridien Group, CGG Electromagnetics, Italy
[2]PT Geo Dipa Energi, Indonesia
[3] Pertamina Geothermal Energy
[4] Djiboutian Office of Geothermal Energy Development (ODDEG), Djibouti
[6]JACOBS, New Zealand
[6]Reykjavik Geothermal Iceland

Magnetotellurics, 3D inversion, volcanic geothermal systems, deep conductors

ABSTRACT

Elevated temperatures in volcanic geothermal systems result from high heat flow caused by shallow intrusion of magma, driving hydrothermal convection. Understanding the nature and location of magmatic heat sources is therefore relevant for characterizing the geothermal system. Magnetotelluric studies around the world have revealed numerous occurrences of deep electrical conductors below volcanic geothermal prospects. Interpretations of such deep conductors often invoke the presence of magmatic melt and magma derived fluids. However, the architecture of magmatic systems is rather complex and strongly depends on the degree of solidification, residual melt, and volatile content. We describe a selection of scenarios and their impact on geothermal reservoir formation: Under favorable conditions magmatic mush reservoirs in the upper crust can remain stable over long geological timescales thereby providing a constant heat supply for a geothermal system. Undesirable situations are encountered when H_2S from degassing magma combines with water to form sulfuric acid brine, a fluid with exceptional high electrical conductivities. Such acidic hydrothermal plumes can form above largely cooled intrusions and make geothermal drilling unattractive. In cases where volcanic eruption happened through sedimentary overburden, deep conductors may also represent buried fluid-bearing sediments, hence being unrelated to magmatic systems and potential heat sources. Therefore, conclusive interpretations of deep conductors require a comprehensive geoscientific approach. First, a detailed understanding of the geological setting, eruptive history and magma evolution is required and, second, integration of various types of geophysical observables is key to understand the internal structure and fundamental petrophysical properties of deep electrical conductors under volcanic geothermal prospects. Here we present a surface to depth hypothetical model of a volcanic high-temperature geothermal system and a classification or grouping for deep conductors based on the geological setting, volcanic history and experience from well data. As representative examples we

show seven case studies from geothermal prospects in East Africa and Indonesia where deep conductors have been encountered in 3D models.

1. Introduction

Since the beginnings of industrial-scale development of geothermal resources, electrical sounding methods have played an important role in geothermal exploration and for siting drilling targets (Wright et al., 1985). It was recognized early that high-temperature volcanic geothermal reservoirs are often overlain by a pronounced low resistivity layer that is composed of electrically conducting clay minerals, which are produced through hydrothermal alteration (Moskowitz and Norton, 1977). Consequently, electrical resistivity methods became popular in geothermal exploration due to their capability to identify and map the extent of the electrically conductive clay "cap". The clay cap is not only a product of hydrothermal processes and hence a strong indicator for geothermal activity, but it also seals the reservoir top, due to the properties of clays, which swell when in contact with water and form an impermeable layer (Gunderson et al., 2000).

Amongst a variety of active and passive geophysical electromagnetic (EM) sounding techniques, the magnetotelluric (MT) method established itself as a widely used tool in geothermal exploration. MT relies on natural electric and magnetic field variations that originate from global lightning activity and the interaction of the Earth's geomagnetic field with the solar wind (e.g. Vozoff, 1991). The EM source fields are always present, allowing a short deployment time of measurement systems in the field, and MT covers penetration depths relevant for clay cap imaging, reservoir characterization and beyond (e.g. Berktold, 1983; Cumming, 2016; Muñoz, 2013).

In early applications of the MT method in geothermal exploration MT data were generally interpreted using 1D modeling and focused on delineating the clay cap atop the geothermal reservoir (Pellerin et al. 1992, Anderson et al., 2000). 1D imaging of the clay cap is an established application and remains a common method (e.g. Árnason et al. 2010) even after 3D interpretations became feasible with increasing computational capacities. The reason why 1D modelling of MT responses to image the clay cap produces valuable models can be attributed to the strong electrical conductivity signature of the clay cap, which is essentially 1D. Therefore, cross-sections stitched from 1D inversions of the MT responses are still common in geothermal exploration and often used as an initial quality assurance check. Anderson et al. (2000) pointed out that clay cap topography delineated by 1D MT modelling enables the reliable location of geothermal reservoirs, which are encountered under regions of clay cap updoming. 1D models of geothermal areas and prospects often imaged deep electrical conductors below the clay that typically extend from below the clay cap and the geothermal reservoir to greater depths. These deep conductors have been found as early as in studies by Hermance et al. (1976), who interpreted a deep low-resistivity zone beneath Icelandic volcanic prospects as small fractions of basaltic melt. However, quantitative interpretations of deep conductors were hampered by limitations of 1D interpretations of MT data, which provide only a valid approximation for the shallow part near the surface of a volcanic geothermal system. Only in rare cases do MT data obey 1D or even 2D conditions down to larger depths. Owing to their geological nature, volcanic geothermal prospects exhibit strong 3D features that extend from the surface to the lower crust. Deep seated magmatic melt sources feed vertically extensive magmatic pathways that crosscut geological strata and feed shallow melt reservoirs that drive localized hydrothermal fluid flow often hidden under heavily faulted terrain with strong surface topography and steep slopes.

The 3D nature of volcanic geothermal prospects became apparent when 3D MT interpretations of volcanic geothermal prospects provided full-featured 3D images that revealed lateral resistivity variations below the clay cap with vertically extensive transcrustal anomalies raising question about their nature (e.g. Newman et al. 2008, Heise et al. 2015, Hill et al. 2015).

2. Methods

The MT method is an inductive EM sounding technique especially sensitive to electrical conductors (e.g. Vozoff, 1992). MT relies on measuring time series of the natural electric (**E**) and magnetic (**H**) field variations at a specific location (**r**) at the Earth's surface. In the frequency domain (ω) the electric and magnetic field are related through a complex-valued second-rank tensor Z:

$$\boldsymbol{E}(\boldsymbol{r},\omega) = \begin{pmatrix} C_{11}(\boldsymbol{r}) & C_{12}(\boldsymbol{r}) \\ C_{21}(\boldsymbol{r}) & C_{22}(\boldsymbol{r}) \end{pmatrix} \begin{pmatrix} Z_{xx}(\boldsymbol{r},\omega) & Z_{xy}(\boldsymbol{r},\omega) \\ Z_{yx}(\boldsymbol{r},\omega) & Z_{yy}(\boldsymbol{r},\omega) \end{pmatrix} \boldsymbol{H}(\boldsymbol{r},\omega) \quad (1)$$

The impedance Z contains the full 3D information about the electrical resistivity distribution of the subsurface, and is a function of the location (**r**) and frequency ω, which relates to depth. MT electric field data are commonly subject to frequency-independent amplitude changes known as galvanic distortions (e.g. Jiracek, 1990). Distortion is described by a real-valued frequency-independent distortion matrix C. In the ideal case of no distortion present C has the form of the identity matrix and can be omitted from eq. (1).

3D interpretation of MT data requires 3D inverse modelling of the full impedance tensor. In contrast, 1D interpretations of the impedance tensors typically interpret a rotationally invariant of the tensor such as the determinant (Berdichevsky, 1999). For 2D interpretations the impedance tensor is rotated into the direction of geoelectrical strike and only the two modes TE (Z_{xy}) and TM (Z_{yx}) are interpreted. The impedance tensor (eq. 1) can also be affected by galvanic and inductive distortions, which are either caused by small-scale near surface electrical scatterers below the resolution of the data, by pronounced topography (Stark et al., 2013; Käufl et al. 2018), or by a superimposition of both. Concepts to correct for distortions exist for underlying 1D and 2D assumptions (Groom and Bailey, 1989), however, they are strictly speaking not valid for 3D data.

3D inversions can be performed inverting simultaneously for 3D resistivity structure and distortion matrices, with a control parameter that suppresses deviations from the identity matrix, which represents the a priori condition of no distortion (Soyer, 2020). Topographic distortions are addressed by the accurate implementation of topography in the 3D resistivity model (Käufl et al. 2018; Soyer at al., 2019). Another method to bypass distortions is to invert for magnetotelluric phase tensors (e.g. Samrock et al. 2018), a quantity that is unaffected by distortions (Caldwell et al., 2004). 3D inversion of MT data and concepts to address distortion without simplifying assumptions have led to an increasing number of 3D electrical resistivity models of volcanic geothermal prospects that allow for interpretations consistent with theoretical concepts of the architecture of volcanic geothermal systems and geological models. In the following we present a surface to depth hypothetical model of a volcanic hydrothermal system that builds upon existing models with a stronger focus on deep electrical conductors.

Besides geological causes for deep conductors, non-geological sources must be considered as a possible reason. Data distortion, cultural noise and systematic bias in the MT dead band can lead

to geological misinterpretations (Miensopust, 2017; Sato et al. 2017; Hennessy and Macnae, 2018).

3. Comprehensive hypothetical model of volcanic high-temperature geothermal systems

Magma is primarily generated through partial melting processes in the Earth's mantle (Grove and Till, 2015). Melt is generated through two main processes: First, by decompression melting at extensional settings such as continental rifts, in the backarc of subduction zones, at midoceanic ridges and by mantle plume activity. The second melt generation process is through a change of composition in the Earth's mantle that lowers its solidus temperature.

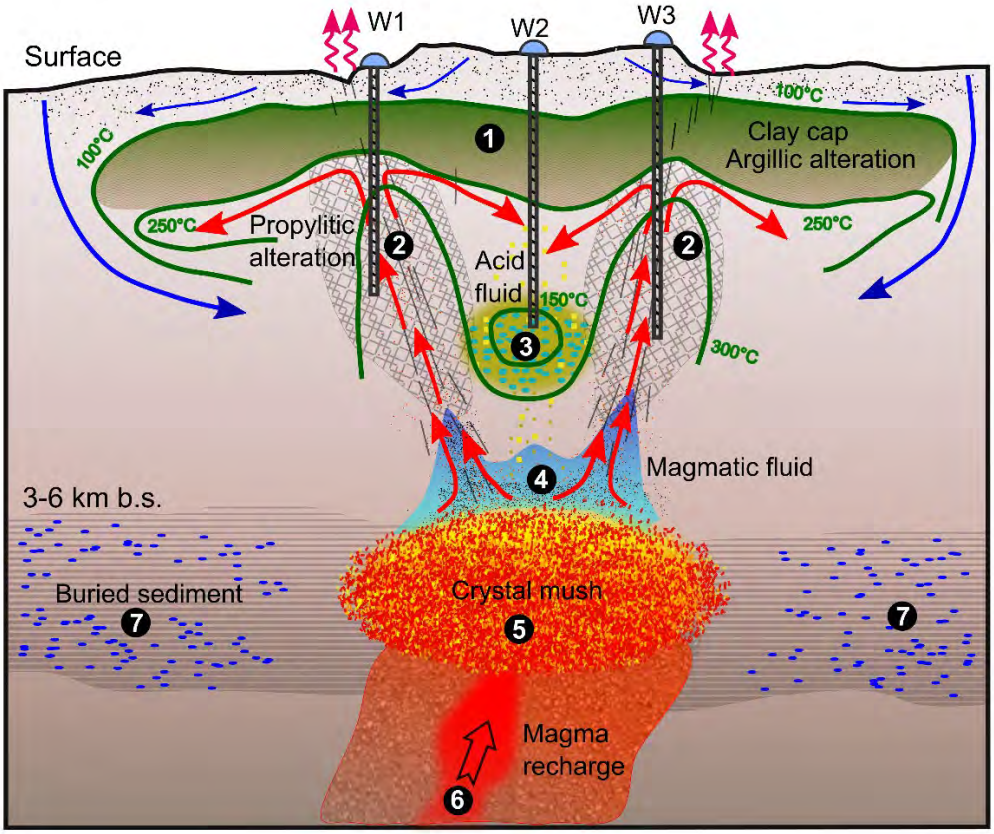

Figure 1: Surface to depth hypothetical model of a volcanic high-temperature geothermal system. The sketch shows the main features of a geothermal system and possible causes for conductive zones below the clay cap. 1) Clay cap: Argillic hydrothermal alteration zone with sealing function atop the reservoir. 2) Propylitic alteration zone below the clay cap, major target for drilling. 3) Acidic hydrothermal plume and formation of pyrite, both form through reaction of sulfur from magmatic degassing with fluids and host rock. 4) Liquid magmatic brine lens with high concentration of dissolved solids. 5) Magmatic reservoir with well interconnected partial melt fraction. 6) Magmatic recharge channel. 7) Buried sedimentary layer.

This process happens e.g. in subduction zones. Magmatic systems are dynamic transcrustal features (Cashman et al., 2017) with a highly complex architecture (Edmonds et al. 2019). Melt eventually reaches the Earth's surface where it erupts in volcanoes or is stored at mid-crustal depths in highly crystalline magmatic mush reservoirs.

Crystal mush reservoirs have relatively small melt fractions and can be in a rheologically locked-up rigid state forming ephemeral systems that undergo increasing solidification through fractional crystallization and degassing (Sparks et al. 2019). Re-melting of crystal mush can be initiated through emplacement of new magma from below at the base of the crystal mush reservoir (Huber at al. 2011). Magma storage in the upper crust drives hydrothermal convection, ultimately leading to the formation of a high-temperature geothermal system (Scott et al. 2015). The architecture of such a system is shown in Figure 1. In the following we will describe the individual geological features and their electrical characteristics. The hypothetical model (Fig.1) builds up and expands work by Berktold (1983), Pellerin et al. (1992), Ussher et al. (2000), Andersson et al. (2000), Cumming (2016) and Samrock et al. (2023) amongst others.

Starting from the surface, the shallow depths of volcanic geothermal prospects are typically composed of fresh volcanic material including pumice, ash, and lava flows. This material is mostly dry and characterized by high resistivity. Going deeper, circulating geothermal fluids lead to the formation of the clay cap (feature 1 in Fig. 1). The clay cap forms through alteration along the flow paths of hot circulating fluids that hydrothermally alter the volcanic host rock producing clay minerals such as smectite (Ussher et al. 2000). These clays are characterized by very low electrical resistivities leading to a pronounced electrically conductive layer atop the geothermal reservoir. The clay cap has also a sealing function due to the tendency of clay minerals to hydrate and swell forming an impermeable layer when exposed to water. Hydrothermal alteration is temperature dependent and with increasing temperature clays produced in the argillic alteration regime become hydrothermally unstable. At higher temperatures propylitic alteration takes place with different alteration products such as chlorite and epidote. These minerals are characterized by much higher resistivities leading to an increase in bulk resistivity in the hotter propylitic alteration zone (feature 2 in Fig. 1) below the clay cap. Its bottom is therefore marked by a pronounced gradient to higher resistivity. Whereas absolute resistivities at the clay cap bottom may vary from place to place, Gíslason et al. (2015) suggest the 10Ωm isoline as a proxy. Observed temperatures at the clay cap bottom vary substantially from prospect to prospect. Ardid et al. (2021) analyzed numerous prospects and inferred an average formation temperature of 198°C at the bottom of the clay cap with a broad range of +48 and -69°C. For the illustration in Figure 2 we use the values reported in Gíslason et al. (2015). Temperatures are hotter in the propylitic alteration zone and in upflow zones that form preferably along geological discontinuities such as faults (Wallis et al. 2017). Since the temperature pattern follows the upflow zones, temperature isosurfaces and hence the argillic alteration front are pushed closer to the land surface leading to the characteristic clay cap updoming above upflow zones (Fig.1; Anderson et al. 2000, Samrock et al. 2023). For a comprehensive database with petrophysical properties, including electrical resistivity of rocks from volcanic geothermal systems, see e.g. Scott et al. (2023).

In the following, low resistivity features below the clay cap and below or within the propylitic alteration zone are referred to as *deep conductors*. Deep conductors can have various origins of which several are described here:

- One reason can be the formation of an acidic hydrothermal plume and a high pyrite concentration. Hydrothermal acid plumes (feature 3 in Fig. 1) form through chemical reactions of sulfur-rich volcanic degassing and water (Byrdina et al. 2018). Byrdina et al. (2018) observed resistivities of acid fluids from Indonesian volcanoes below 0.1Ωm and decreasing resistivities with decreasing pH. Low pH environments also promote the

formation of electrically conductive pyrite (FeS_2) by reaction between H_2S-rich fluids and Fe-rich volcanic rock (Levy et al. 2020).

- Magma-derived fluids that are exsolved from crystallizing melt tend to migrate upwards due to buoyancy forces and may accumulate in the upper part of an active or cooled magmatic intrusion (feature 4 in Fig. 1). Such magmatic brine lenses can be composed of vapor and brine or even supercritical fluids. Romero-Mujalli et al. (2022) analyzed dissolved solutes in hydrothermal end-member fluids from Aso volcano, Japan, and report fluid resistivites as low as 2Ωm. Watanabe et al. (2021) presented an empirical model to calculate the electrical conductivity of H_2O-NaCl fluids for pressures up to 200 MPa and temperatures up to 525°C. Their model shows that magmatic brine lenses have low electrical resistivities at the expected temperature and pressure conditions of a high-temperature geothermal system. Tseng et al. (2020) interpreted a deep conductor with resistivities less than 1Ωm below Kusatsu–Shirane volcano, Japan, as pressurized magmatic brine lens, sealed by an impermeable layer of precipitated silica and halite above.

- Magmatic brine lenses are sourced from deeper magma reservoirs that may exist in form of crystal mush reservoirs (feature 5 in Fig. 1). Crystal mushes have a crystal fraction of minimum 50 to 60 vol.% which is the mechanical threshold when crystals start touching each other and the melt crystal mixture becomes too viscous to flow and erupt (Bachmann and Bergantz, 2008). Samrock et al. (2021) coupled laboratory inferred melt electrical conductivity models and thermodynamic modelling of melt evolution and crystal fractionation to constrain electrical conductivities within crystal mush reservoirs. Their models provide interpretations of deep conductors under volcanic geothermal prospects in the Ethiopian rift that agree with thermodynamic equilibrium conditions and consider crystal mush reservoirs as three phase systems that consist of melt, crystals, and a fluid phase. Cordell et al. (2022) used a similar approach to interpret deep conductors and to constrain magma reservoir conditions by integrating thermodynamic petrological models and resistivities within deep conductors.

- The upper crustal melt reservoir is fed from deeper parental melt sources. Recharge of melt might have ceased or still be ongoing if active magmatic melt channels between the upper crustal melt reservoir and the deeper source region of the melt exist (feature 6 in Fig. 1). Active magmatic pathways will appear as deep rooted conductors below the volcanic geothermal prospect. As an example, Dambly et al. (2023) presented a multiscale magnetotelluric model of a section in the Ethiopian Rift that shows melt generation and transport from the lower crust up to the near surface below the producing Aluto-Langano geothermal field.

- In cases where volcanic eruption happens through deep buried sedimentary layers, deep conductors can be related to fluid bearing sediments under volcanic cover having no volcanic origin (feature 7 in Fig. 1). This situation is encountered in Sumatra where Tertiary transgressive sediments are embedded between older Mesozoic volcanic units and younger Quaternary volcanic overburden (Barber et al., 2005; Mussofan et al., 2016). Despite not having a volcanic origin, deep sedimentary conductors might be falsely interpreted as magmatic heat source. However, if the geological context is known, deep

sedimentary conductors under volcanic prospects might be target zones for drilling since they are often characterized by high permeabilities and provide good reservoir conditions (Ikhwan et al., 2023).

Figure 1 shows a simplified surface to depth sketch of a volcanic geothermal system including its magmatic heat source and shallow clay cap, which is one of the key components of a geothermal system that appears as pronounced shallow low resistivity zone in geophysical models. However, a common mistake is to generally interpret shallow low resistivity zones at volcanic geothermal prospects as clay cap of an active geothermal system. Shallow conductors can also represent clay caps of formerly active geothermal systems, palaeo-outflow zones or sediment basins with smectite-rich volcaniclastics surrounding volcanoes (see e.g. history of exploration at Aluto volcano by Hochstein et al. (2017) and recent geophysical model by Samrock et al. (2023)). The reliable identification of potential target zones for drilling requires holistic conceptual geothermal models that integrate geophysics, geology, geochemistry, and petrology.

4. Examples of deep conductors imaged under geothermal prospects

In our long experience in the field of 3-D MT imaging of volcanic high-temperature geothermal systems, deep conductors appear under about half of volcanic geothermal prospects, whereas other geothermal fields show no indications for deep conductors (e.g. Soyer at al., 2018). In the following we present vertical sections of 3-D magnetotelluric models from volcanic geothermal fields, where deep conductors have been encountered. Note, all presented models have a very good data fit and a small rms misfit value. In addition, multiple modelling and inversion tests demonstrated the sensitivity of the data to the deep conductors.

Figs. 2 to 4 show three examples of deep conductors encountered below volcanic geothermal prospects in Indonesia. A detailed interpretation is beyond the task of this work and data availability is limited; however, all three prospects have a long eruptive history and active geothermal surface manifestations. The conductor below Sibayak (Fig. 2) is clearly deep rooted, which is indicative of an intrusive origin.

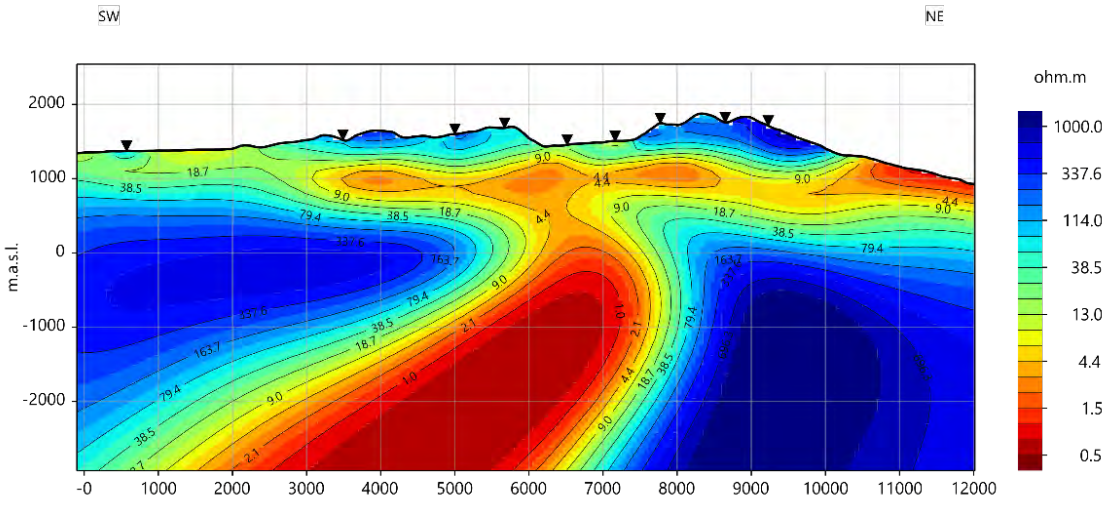

Figure 2: Deep conductor imaged below Sibayak, Indonesia.

Geochemical analyses of aqueous fluids from Sibayak reveal a dominant magmatic volatile contribution and components of quenched magmatic gases (Fahmi et al., 2020). Sibayak belongs to the Singkut caldera from which Forni et al. (2024) report eruption of crystal-rich magmas and geochemical evidence for long-lived large cumulate crystal mushes.

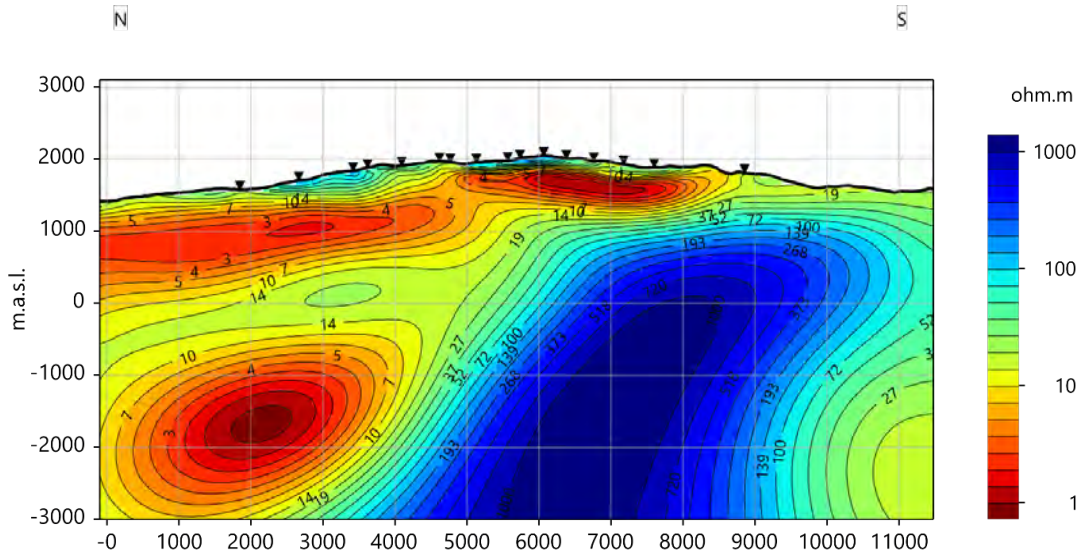

Figure 3: Deep conductor imaged below Patuha, Indonesia.

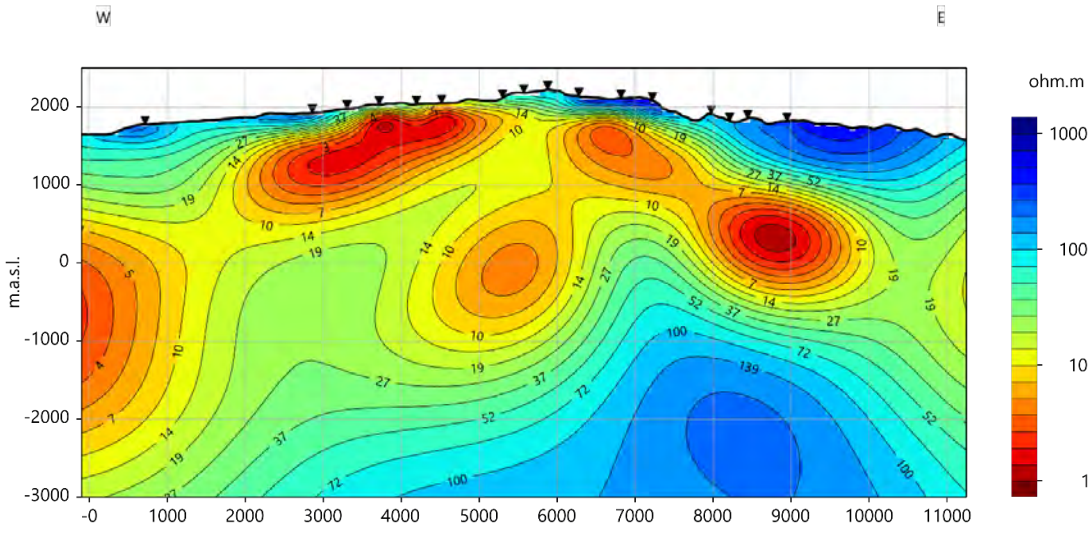

Figure 4: Deep conductor imaged below Dieng, Indonesia

Not enough data are available from Patuha (Fig. 3) and Dieng (Fig. 4) to provide a conclusive interpretation of the deep conductors. In view of the absence of deep roots and considering the isolated shapes of the deep conductors it could be argued that they represent fluid-rich zones, magmatic brine lenses, or hydrothermal fluid plumes with end-member compositions.

Figures 5 to 7 show cross-sections through 3-D MT models from geothermal prospects in the East African Rift. Corbetti (Fig. 5) is a volcanic geothermal prospect in the Main Ethiopian Rift. Geodetic and gravimetric studies proposed ongoing magmatic intrusion below Corbetti (Gottsmann et al. 2020). The location of the deep conductor agrees well with the location of the intrusion proposed by Gottsmann et al. (2020) and was confirmed in an independent MT study by Dambly et al. (2024). Dambly et al. (2024) interpreted the deep conductor in Fig. 5 as crystal mush and inferred 20 to 35 vol. % rhyolite melt in its upper part. Their melt estimates are based on empirical conductivity models for melt and consider temperature and melt composition consistent with thermodynamic equilibrium conditions of rhyolite melt (Cordell et al. 2022).

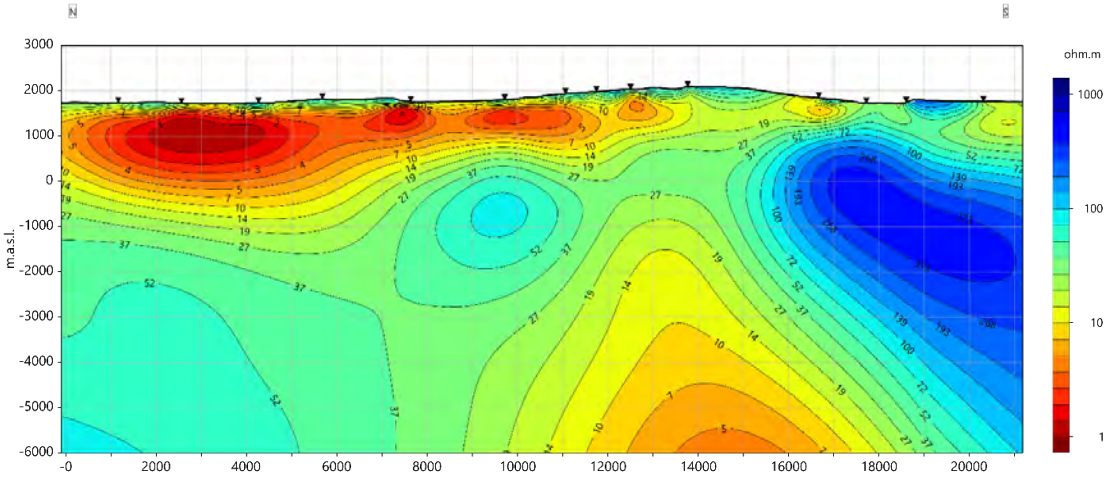

Figure 5: Deep conductor imaged below Corbetti, Ethiopia.

Samrock et al. (2021) presented models from the Aluto and Tulu Moye geothermal prospects in the Ethiopian rift (Fig. 6). They invoke magmatic causes for imaged deep conductors and the presence of upper crustal crystal mush reservoirs with deep-routed magmatic recharge channels. In their studies they combine modelling of phase equilibria in cooling magma and laboratory measurements of electrical properties of melt to derive the evolution of electrical conductivity in a crystallizing silicic magmatic system. Their study considers magma reservoirs as three-phase systems composed of crystals, melt and fluids and shows that different resistivities in the interpreted deep conductors can be interpreted to reflect different stages of melt evolution, temperature, and composition. A detailed discussion of the electrical resistivity model of Aluto and well data can be found in Samrock et al. (2023). The existence of the imaged deep conductor was confirmed by Dambly et al. (2023), who presented a multi-scale cross-rift model of the area that images the extend of the deep conductor down to a magma ponding zone at the base of the crust in agreement with other geoscientific models and the conceptual understanding of magma-assisted rifting in the Ethiopian Rift.

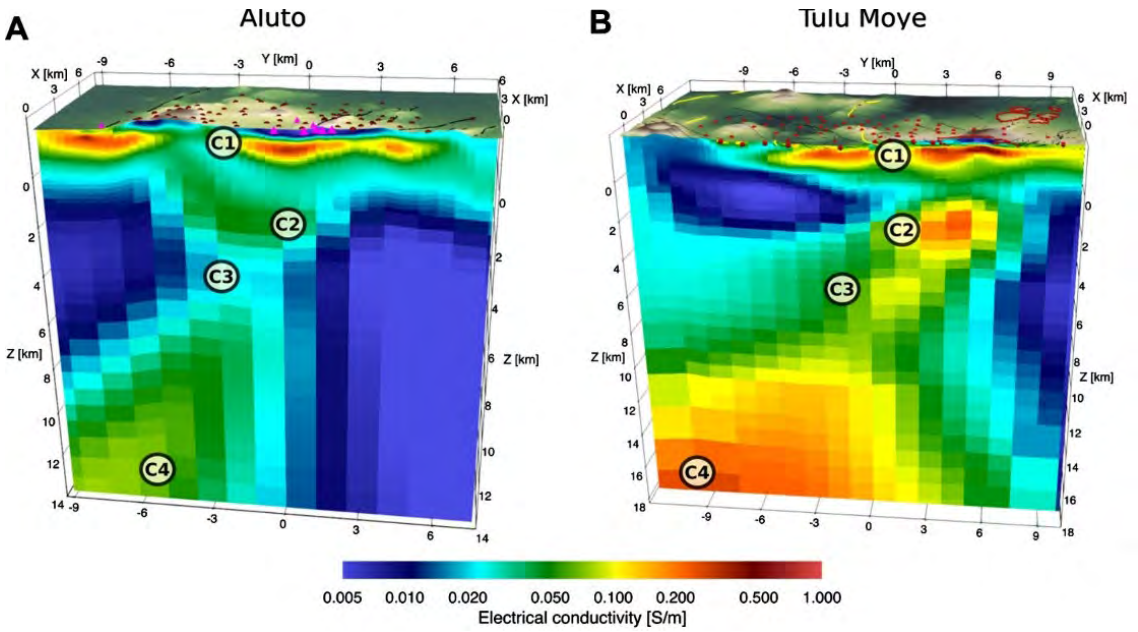

Figure 6: Deep conductors imaged below Aluto (A) and Tulu Moye (B) geothermal prospects in the Ethiopian Rift. Figure taken from Samrock et al. (2021). The two volcanoes are about 50km apart. The authors interpret C1 as clay cap, C2 as gas-rich crystal mush reservoir, C3 as magmatic recharge channel and C4 as deep parental melt region. The differences in electrical resistivity are interpreted in terms of different stages of melt evolution. For details see Samrock et al. (2021) and Dambly et al. (2023).

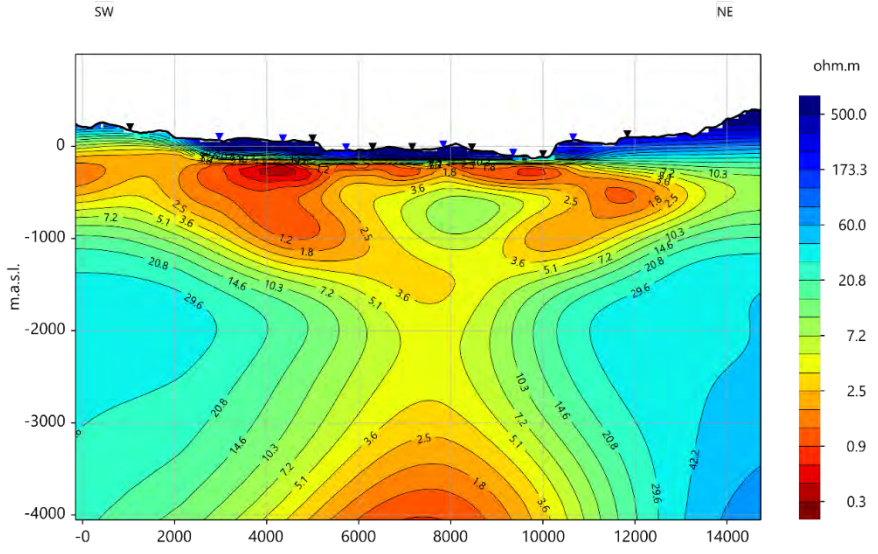

Figure 7: Deep conductor imaged below Asal Fiale, Djibouti.

Asal (Fig. 7) is a geothermal field in Djibouti and lies at the northern end of the East African Rift where continental rifting is in its final stages. The volcanic geothermal prospect is located between the bay of Ghoubbet and Lake Asal and it is characterized by seafloor type hydrothermal activity. The last volcanic eruption occurred in 1978 (e.g. Sakindi, 2015). Varet et al. (2014) report several

events of abrupt heating of the geothermal reservoir that occurred between 1991 and 2001 subsequent to magma injection. The MT model of Asal shows a pronounced deep conductor at depths below 3km b.s.l. (Fig. 7). A magmatic origin of the deep conductor is likely considering ongoing volcanic activity in the area. The interpretation of low electrical resistivities being related to presence of melt at depths below 3km b.sl. agrees with studies by Pasquet et al. (2023) and their presented geological model of the area.

5. Conclusions

Deep conductors under volcanic high-temperature geothermal systems can have many origins that range from magma-related processes and favorable conditions like stable crystal mush reservoirs that represent powerful heat sources, to unfavorable conditions like acidic hydrothermal plumes that cause corrosion of geothermal wells and facilities. Even amagmatic causes are possible in cases where volcanic eruption happens through sediments. The described causes for deep conductors provide only a selection, and thus, an incomplete overview. Interpretation of deep conductors requires detailed knowledge of the geological context and eruptive history of the volcanic geothermal prospect. More work is required in the field of melt electrical conductivity models to provide more complete models for composition-dependent melt resistivities. More research is also required to understand bulk resistivities of reactive multiphase magmatic systems that consist of melt, solid, and fluids in different states from liquid to vapor and supercritical. In reactive systems traditional multi-phase mixing laws to derive bulk resistivities do not apply. Finally, yet importantly, the quality of MT data used to derive 3D resistivity models must be critically evaluated and the robustness of imaged deep conductors must be tested. It must be considered and investigated whether deep conductors might be artifacts with no geological explanation caused by poor data quality and systematic data bias. Currently, there is a lack of examples where deep conductors under volcanic geothermal prospects were identified as false structure and evidently caused by noise, data gaps or inversion limitations. Future studies should also present such cases and address the identification of corrupted data, statistical biases and resulting artifacts in 3D models.

Acknowledgement

The authors would like to express their gratitude to PT Geo Dipa Energi, Pertamina Geothermal Energy, Reykjavik Geothermal, ODDEG and Jacobs for the permission to publish results from the 3D inversion modeling of MT data from Patuha and Dieng (PT Geo Dipa Energi), Sibayak (Pertamina Geothermal Energy), Corbetti (Reykjavik Geothermal) and Asal Fiale (ODDEG, Jacobs). We thank the two reviewers Karen Christopherson and William Cumming for their valuable comments, which helped to improve the manuscript. FS thanks Reykjavik Geothermal, the Geological Survey of Ethiopia and colleagues from Addis Ababa University and ETH Zurich for their essential contributions to the Ethiopian studies.

REFERENCES

Anderson, Errol, Daryl Crosby, and Greg Ussher. "Bulls-eye! Simple resistivity imaging to reliably locate the geothermal reservoir." Proceedings World Geothermal Congress. 2000.

Ardid, A., Archer, R., Bertrand, E., Sepulveda, F., Tarits, P., & Dempsey, D. (2021). Heat transfer through the Wairakei-Tauhara geothermal system quantified by multi-channel data modeling. Geophysical Research Letters, 48(8), e2020GL092056.

Árnason, Knútur, Hjálmar Eysteinsson, and Gylfi Páll Hersir. "Joint 1D inversion of TEM and MT data and 3D inversion of MT data in the Hengill area, SW Iceland." Geothermics 39.1 (2010): 13-34.

Bachmann, O., & Bergantz, G. (2008). The magma reservoirs that feed supereruptions. Elements, 4(1), 17-21.

Barber, A.J., Crow, M.J., and Milsom, J.S., Sumatra: Geology, Resources and Tectonic Evolution. Geological Society, London, Memoirs, 31 (2005), 290 pp.

Berdichevsky, M. N. "Marginal notes on magnetotellurics." Surveys in Geophysics 20 (1999): 341-375.

Berktold, A. "Electromagnetic studies in geothermal regions." Geophysical surveys 6.1 (1983): 173-200.

Byrdina, S., Grandis, H., Sumintadireja, P., Caudron, C., Syahbana, D. K., Naffrechoux, E., ... & Vandemeulebrouck, J. (2018). Structure of the acid hydrothermal system of Papandayan volcano, Indonesia, investigated by geophysical methods. Journal of Volcanology and Geothermal Research, 358, 77-86.

Caldwell, T. Grant, Hugh M. Bibby, and Colin Brown. "The magnetotelluric phase tensor." Geophysical Journal International 158.2 (2004): 457-469.

Cashman, K. V., Sparks, R. S. J., & Blundy, J. D. (2017). Vertically extensive and unstable magmatic systems: a unified view of igneous processes. Science, 355(6331), eaag3055.

Cordell, D., Naif, S., Troch, J., & Huber, C. (2022). Constraining magma reservoir conditions by integrating thermodynamic petrological models and bulk resistivity from magnetotellurics. Geochemistry, Geophysics, Geosystems, 23(9), e2022GC010455.

Cumming, W. (2016). Resource conceptual models of volcano-hosted geothermal reservoirs for exploration well targeting and resource capacity assessment: Construction, pitfalls and challenges. GRC Transactions, 40, 623-638.

Dambly, M. L. T., Samrock, F., Grayver, A. V., & Saar, M. O. (2023). Insights on the interplay of rifting, transcrustal magmatism and formation of geothermal resources in the central segment of the Ethiopian Rift revealed by 3-D magnetotelluric imaging. Journal of Geophysical Research: Solid Earth, 128(7) .

Dambly, M. L., Samrock, F., Grayver, A., Eysteinsson, H., & Saar, M. O. (2024). Geophysical imaging of the active magmatic intrusion and geothermal reservoir formation beneath the Corbetti prospect, Main Ethiopian Rift. Geophysical Journal International, 236(3), 1764-1781.

Edmonds, M., Cashman, K. V., Holness, M., & Jackson, M. (2019). Architecture and dynamics of magma reservoirs. Philosophical Transactions of the Royal Society A, 377(2139), 20180298.

Fahmi, F.L., Giriarso, J.P, Mulyanto, A. P., Thamrin, M. H., Pasaribu, F. (2020). Geochemistry Monitoring of Surface Thermal Manifestation in Sibayak, North Sumatra, Indonesia. Proceedings World Geothermal Congress. 2020.

Forni, F., Phua, M., Bernard, O., Fellin, M. G., Oalmann, J., Maden, C., ... & de Maisonneuve, C. B. (2024). Remobilization and eruption of an upper crustal cumulate mush at the Singkut caldera (North Sumatra, Indonesia). Journal of Volcanology and Geothermal Research, 445, 107971.

Gíslason, G., Eysteinsson, H., Björnsson, G., & Harðardóttir, V. (2015, April). Results of surface exploration in the Corbetti Geothermal Area, Ethiopia. In World Geothermal Congress, Melbourne, Australia (pp. 19-25).

Gottsmann, J., Biggs, J., Lloyd, R., Biranhu, Y., & Lewi, E. (2020). Ductility and compressibility accommodate high magma flux beneath a silicic continental rift caldera: Insights from Corbetti caldera (Ethiopia). Geochemistry, Geophysics, Geosystems, 21(4), e2020GC008952.

Groom, Ross W., and Richard C. Bailey. "Decomposition of magnetotelluric impedance tensors in the presence of local three-dimensional galvanic distortion." Journal of Geophysical Research: Solid Earth 94.B2 (1989): 1913-1925.

Grove, T. L., & Till, C. B. (2015). Melting the Earth's Upper Mantle. In The Encyclopedia of Volcanoes (pp. 35-47). Academic Press.

Gunderson, Richard, et al. "Analysis of smectite clays in geothermal drill cuttings by the methylene blue method: for well site geothermometry and resistivity sounding correlation." Proceedings World Geothermal Congress. 2000.

Heise, W., Caldwell, T.G., Bertrand, E.A., Hill, G.J., Bennie, S.L., and Palmer, N.G., 2015, Imaging the deep source of the Rotorua and Waimangu geothermal fields, Taupo Volcanic Zone, New Zealand: Journal of Volcanology and Geothermal Research, v. 314, p. 39–48.

Hennessy, L., & Macnae, J. (2018). Source-dependent bias of sferics in magnetotelluric responses. Geophysics, 83(3), E161-E171.

Hermance, J. F., Thayer, R.E. and Bjornsson. "The telluric-magnetotelluric method in the regional assessment of geothermal potential." Proc. Second UN Symposium on the Development and Use of Geothermal Resources. Vol. 2. Washington, DC.: US Government Printing Office, 1976.

Hill, Graham J., et al. "Structure of the Tongariro Volcanic system: Insights from magnetotelluric imaging." Earth and Planetary Science Letters 432 (2015): 115-125.

Hochstein, M. P., Oluma, B., & Hole, H. (2017). Early exploration of the Aluto geothermal field, Ethiopia (History of discovery well LA-3). *Geothermics*, *66*, 73-84.

Huber, C., Bachmann, O., & Dufek, J. (2011). Thermo-mechanical reactivation of locked crystal mushes: Melting-induced internal fracturing and assimilation processes in magmas. Earth and Planetary Science Letters, 304(3-4), 443-454.

Ikhwan, M., Prasetyo, I. M., & Suryanto, S. (2023) The Role of The Hulusimpang Formation in Well-Scale Permeability of The Central-Southern Sumatra Geothermal Fields. Proceedings World Geothermal Congress 2023

Jiracek, George R. "Near-surface and topographic distortions in electromagnetic induction." Surveys in geophysics 11.2 (1990): 163-203.

Käufl, Johannes S., Alexander V. Grayver, and Alexey V. Kuvshinov. "Topographic distortions of magnetotelluric transfer functions: a high-resolution 3-D modelling study using real elevation data." Geophysical Journal International 215.3 (2018): 1943-1961.

Lévy, L., Maurya, P. K., Fiandaca, G., Bording, T. S., Madsen, L. M., Gailler, L., ... & Árnason, K. (2020). Geo-electrical monitoring of H2S mineralization into pyrite, upon re-injection in basalts at Nesjavellir Geothermal site, Iceland. In World Geothermal Congress (Vol. 1).

Matsushima, N., Utsugi, M., Takakura, S., Yamasaki, T., Hata, M., Hashimoto, T., & Uyeshima, M. (2020). Magmatic–hydrothermal system of Aso Volcano, Japan, inferred from electrical resistivity structures. Earth, Planets and Space, 72, 1-20.

Markússon, S. H., & Stefánsson, A. (2011). Geothermal surface alteration of basalts, Krýsuvík Iceland—Alteration mineralogy, water chemistry and the effects of acid supply on the alteration process. Journal of Volcanology and Geothermal Research, 206(1-2), 46-59.

Moskowitz, B., and Dennis Norton. "A preliminary analysis of intrinsic fluid and rock resistivity in active hydrothermal systems." Journal of Geophysical Research 82.36 (1977): 5787-5795.

Miensopust, M. P. (2017). Application of 3-D electromagnetic inversion in practice: challenges, pitfalls and solution approaches. Surveys in Geophysics, 38, 869-933.

Munoz, Gerard. "Exploring for geothermal resources with electromagnetic methods." Surveys in geophysics 35 (2014): 101-122.

Mussofan, W., Sutrisno, L., Ramadhan, I., & Aulia, N. (2016). Geological aspects to constrain geothermal conceptual model: Gunung Rajabasa case study. In Proceedings The 4th Indonesia International Geothermal Convention & Exhibition (Vol. 1).

Newman, Gregory A., et al. "Three-dimensional magnetotelluric characterization of the Coso geothermal field." Geothermics 37.4 (2008): 369-399.

Pasquet, G., Idriss, A. M., Ronjon-Magand, L., Ranchou-Peyruse, M., Guignard, M., Duttine, M., ... & Moretti, I. (2023). Natural hydrogen potential and basaltic alteration in the Asal–Ghoubbet rift, Republic of Djibouti. BSGF-Earth Sciences Bulletin, 194(1), 9.

Pellerin, Louise, Jeffrey M. Johnston, and Gerald W. Hohmann. "Evaluation of electromagnetic methods in geothermal exploration." SEG Technical Program Expanded Abstracts 1992. Society of Exploration Geophysicists, 1992. 405-408.

Romero-Mujalli, G., Hartmann, J., Hosono, T., Louvat, P., Okamura, K., Delmelle, P., ... & Böttcher, M. E. (2022). Hydrothermal and magmatic contributions to surface waters in the Aso caldera, southern Japan: Implications for weathering processes in volcanic areas. Chemical Geology, 588, 120612.

Samrock, Friedemann, et al. "Geophysically guided well siting at the Aluto-Langano geothermal reservoir." Geophysics 88.5 (2023): WB105-WB114.

Samrock, Friedemann, et al. "Magnetotelluric image of transcrustal magmatic system beneath the Tulu Moye geothermal prospect in the Ethiopian Rift." Geophysical Research Letters 45.23 (2018): 12-847.

Samrock, F., Grayver, A. V., Bachmann, O., Karakas, Ö., & Saar, M. O. (2021). Integrated magnetotelluric and petrological analysis of felsic magma reservoirs: Insights from Ethiopian rift volcanoes. Earth and Planetary Science Letters, 559, 116765.

Sakindi, G. (2015). Three-Dimensional Inversion of Magnetotelluric Data: Geological/Geothermal Interpretation of Asal Geothermal Field, Djibouti (Doctoral dissertation).

Sato, S., Goto, T. N., Kasaya, T., & Ichihara, H. (2017, September). Noise-reduction method of magnetotelluric data based on frequency-domain independent component analysis. In SEG International Exposition and Annual Meeting (pp. SEG-2017). SEG.

Scott, S., Driesner, T., & Weis, P. (2015). Geologic controls on supercritical geothermal resources above magmatic intrusions. Nature communications, 6(1), 7837.

Scott, S. W., Lévy, L., Covell, C., Franzson, H., Gibert, B., Valfells, Á., Newson, J., Frolova, J., Júlíusson, E., and Guðjónsdóttir, M. S. (2023). Valgarður: A database of the petrophysical, mineralogical, and chemical properties of Icelandic rocks, Earth Syst. Sci. Data, 15, 1165–1195,

Soyer, W., F. Miorelli, and R. L. Mackie. "On the Effects of Finite Dipoles in 3-D Magnetotelluric Modeling." 81st EAGE Conference and Exhibition 2019. Vol. 2019. No. 1. European Association of Geoscientists & Engineers, 2019.

Soyer, Wolfgang, et al. "Geophysics over High Enthalpy Fields: Lessons from RLM-3D Magnetotelluric and Joint Inversions." Proceedings World Geothermal Congress. 2020.

Soyer, W., Mackie, R., Hallinan, S., Pavesi, A., Nordquist, G., Suminar, A., ... & Nelson, C. (2018). Geologically consistent multiphysics imaging of the Darajat geothermal steam field. First Break, 36(6), 77-83.

Sparks, R. S. J., Annen, C., Blundy, J. D., Cashman, K. V., Rust, A. C., & Jackson, M. D. (2019). Formation and dynamics of magma reservoirs. Philosophical Transactions of the Royal society A, 377(2139), 20180019.

Stark, M. A., et al. "Distortion effects on magnetotelluric sounding data investigated by 3D modeling of high-resolution topography." GRC Transactions 37 (2013): 521.

Tseng, K. H., Ogawa, Y., Nurhasan, Tank, S. B., Ujihara, N., Honkura, Y., ... & Kanda, W. (2020). Anatomy of active volcanic edifice at the Kusatsu–Shirane volcano, Japan, by magnetotellurics: hydrothermal implications for volcanic unrests. Earth, Planets and Space, 72, 1-11.

Ussher, G., Harvey, C., Johnstone, R., & Anderson, E. (2000, May). Understanding the resistivities observed in geothermal systems. In proceedings world geothermal congress (pp. 1915-1920). Japan: Kyushu.

Varet, J. (2014, October). Asal-Fialé geothermal field (Djibouti republic): a new interpretation for a geothermal reservoir in an actively spreading rift segment. In Proceedings 5th African Rift geothermal Conference (Vol. 9).

Vozoff, K. "The Magnetotelluric Method." Electromagnetic Methods in Applied Geophysics: Volume 2, Application, Parts A and B. Society of Exploration Geophysicists, 1991. 641-712.

Wallis, I. C., Rowland, J. V., Cumming, W., & Dempsey, D. (2017, November). The subsurface geometry of a natural geothermal reservoir. In Proceedings 39th New Zealand Geothermal Workshop (Vol. 21, p. 25). New Zealand: Rotorua.

Watanabe, N., Yamaya, Y., Kitamura, K., & Mogi, T. (2021). Viscosity-dependent empirical formula for electrical conductivity of H2O-NaCl fluids at elevated temperatures and high salinity. Fluid Phase Equilibria, 549, 113187.

Wright, Phillip M., et al. "State-of-the-art geophysical exploration for geothermal resources." Geophysics 50.12 (1985): 2666-2696.

Aerial Thermal Infrared to Assess Surface Heat Loss at High Temperature Geothermal Fields, Taupo Volcanic Zone, New Zealand.

Anya Seward, Robert Reeves, Chris Bromley, Samantha Alcaraz, Nick Macdonald, Thomas Brakenrig, Fiona Sanders

GNS Science, Wairakei Research Centre, Private Bag 2000, Taupo 3352, New Zealand

Keywords

Heat Flow, Thermal Infrared, Calorimetry, Taupo Volcanic Zone,

ABSTRACT

Assessing the surface heat loss in geothermal areas can provide information and insight into the size and character of underlying geothermal resources. It also provides a means to monitor changes at the surface of a geothermal system and assess geothermal hazards in response to natural and/or development of the geothermal system over time.

Aerial thermal infrared methods provide a quick, easy and safe means to identify heated areas (including water bodies and steaming ground). Over the last decade we have developed methods which relate ground-based measured heat flow to aerial thermal infrared measurements. Empirical relationships are derived which relate thermal infrared measurements to ground-based calorimetry measurements. These are then used to calculated heat loss from thermal infrared data for field-wide heat-loss assessments.

This method has been developed and applied to several geothermal fields within the Taupō Volcanic Zone, located in the central North Island, New Zealand. Each geothermal field has its own unique characteristics which need to be taken into consideration when assessing heat loss. The Karapiti area, part of the Wairakei Geothermal Field, is dominated by steam heated ground while Waiotapu Geothermal Field has a lot of water features and very little heat loss through the ground. These areas require slightly modified approaches to estimate heat loss. For fields with springs and/or thermal streams, ground-based assessments of flow rate and water temperature are also needed to assess the convective heat loss through mass flow.

This paper will overview the approach taken in developing the method, and comparisons between aerial and terrestrial based heat loss assessment at different geothermal fields in the Taupō Volcanic Zone. The true benefit of this method is that field-scale heat flow assessments can be made relatively rapidly with reduced uncertainties compared to ground-based estimates. The techniques also remove a high level of health and safety concerns associated with conducting fieldwork within active geothermal areas.

1. Introduction

Geothermal pools, springs and areas of steaming ground originate from discharges of geothermal fluids and vapour through the subsurface (Figure 1). Accurately quantifying and monitoring surface heat-loss is difficult and can be time-consuming and expensive. However, heat-loss data is becoming ever more important for calibrating and informing geothermal reservoir models and understanding geothermal heat use potential. This paper describes research undertaken over the last decade to improve the quantification of heat-loss assessments using remote TIR techniques and ground-based temperature and calorimetry measurements.

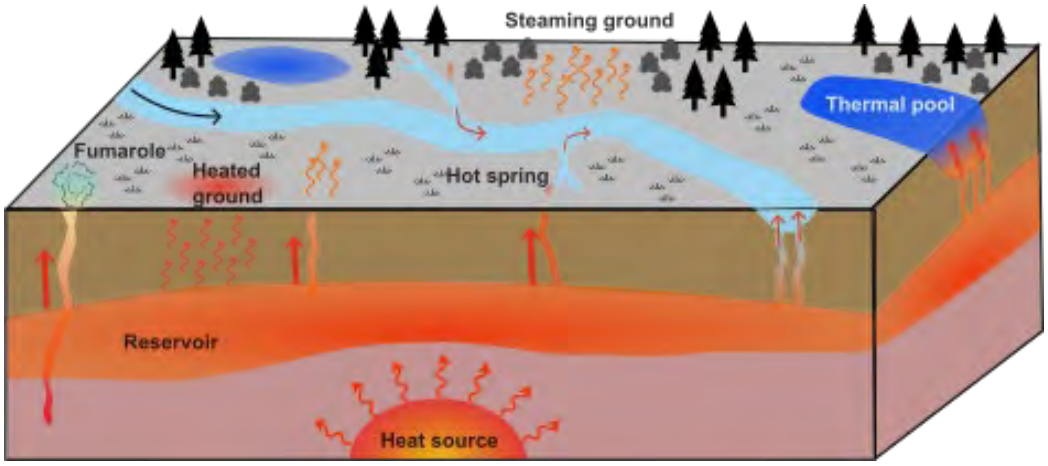

Figure 1: Typical setting of the geothermal area, adapted from Wang and Pang 2023

Investigations into heat flux from geothermal and volcanic areas can be traced back to 1950s (e.g. Bensemen, 1959), with improvements in techniques, approaches and technologies developed over the years (Wang and Pang, 2023; Hochstein and Bromley, 2005; Seward et al, 2023). Documented methods include: calorimeter measurements to determine the total heat flux through the surface of the ground (e.g., Benseman, 1959; Hochstein and Bromley, 2005); the ground temperature-depth profile method (e.g., Hurwitz et al., 2012; Wang et al., 2019); the thermal infrared remote sensing (TIR) method based on the radiative heat loss (e.g., Allis et al., 1999; Eneva et al., 2006; Vaughan et al., 2012; Bromley et al., 2015; Seward et al, 2018a); Satellite infrared (e.g. Andres and Rose, 1995; Mia et al, 2012; 2013; Vaughan et al, 2012; Ramirez-Gonzalez et al., 2019); the chloride content balance method using the concentration of chloride in run off and streams (e.g., Ellis and Wilson, 1955; Ingebritsen et al., 2001); CO_2 surface emissions (e.g., Fridricksson et al, 2006; Yang et al, 2023), and a combinations of two or more approaches (e.g., Bouligand et al., 2019; Favorito et al., 2021; Seward et al, 2018a).

Early assessments of heat loss in New Zealand focused on the heat output of individual surface features, however, this assessment can be unreliable as natural fluctuation and changes in subsurface flow paths can result in cyclic or changing behavior of springs and flowing fluids (e.g., Fisher, 1964; Thompson et al., 1961). Other methods have included chloride flux analysis of discharging fluids (e.g. Nairn and Findlayson, 1981; Bibby et al., 1995; Glover, 1992; Seward and Kerrick, 1996), relationships between the measured ground temperature at 15 cm depth and surface

heat flux (Dawson 1964; Allis, 1981; Fridriksson et al., 2006), surface heat flux based on shallow (1 m deep) temperature-depth profiles (Bromley and Hochstein, 2000; 2005; Hochstein and Bromley, 2001, 2005; Bromley et al., 2011), and aerial and/or satellite thermal infrared (TIR) imagery (e.g. Mongillo and Bromley, 1990; Mongillo, 1994; Mongillo et al., 1995; Mia et al., 2013; Reeves and Rae, 2016; Seward et al., 2018a).

1.1 New Zealand Geothermal setting

New Zealand's land mass lies on the plate boundary between the Pacific and the Australian Plates. Beneath the North Island, the Pacific Plate subducts under the Australian Plate, resulting in a rift system, known as the Taupō Volcanic Zone (TVZ). Twenty-two active high temperature (> 225°C / 435°F) geothermal systems are present within the TVZ, of which seven generate electricity from the resource (Figure 2). Other geothermal fields have varying amounts of utilization, with others having little or no utilization because they are classified as protected.

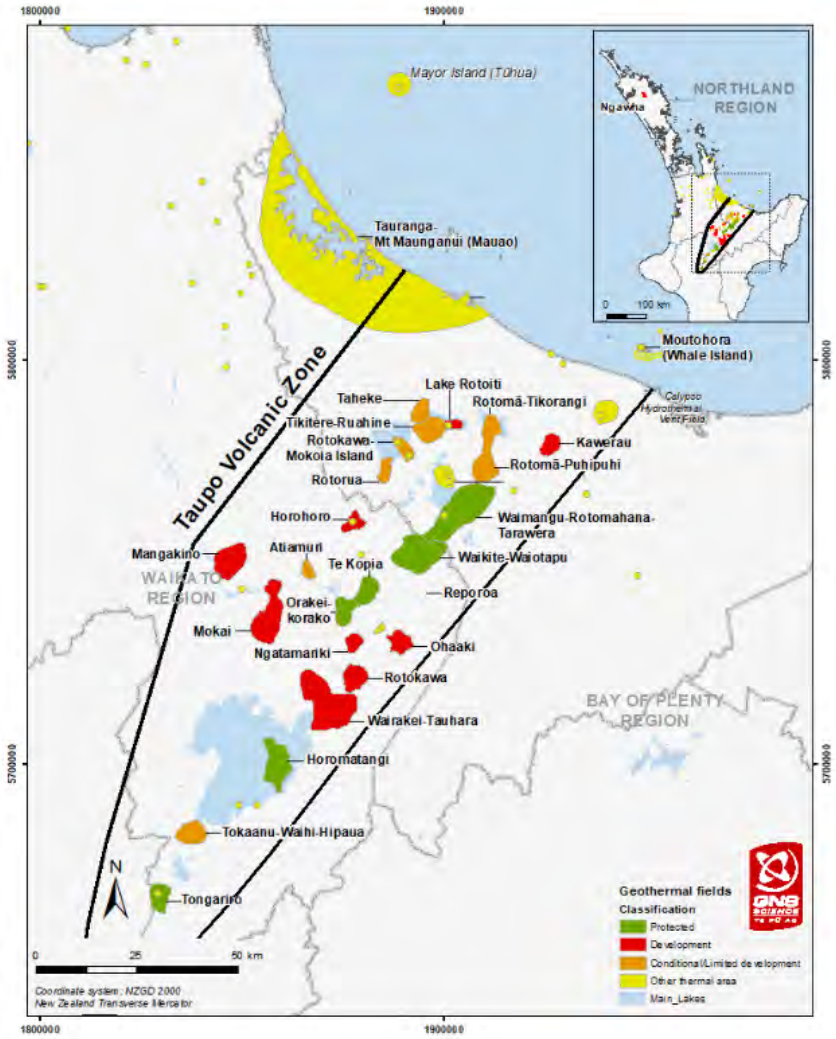

Figure 2: High temperature geothermal fields in the Taupo Volcanic Zone, North Island, New Zealand. Insert shows the location of Ngawha high temperature field, outside of the Taupo Volcanic Zone.

Many of the geothermal systems contain geothermal surface features, including, areas of heated or steaming ground, hot pools, springs and seeps, and fumaroles. The heat lost through these features provide insight into the geothermal resource and can provide a means to identifying changes to the geothermal system. Additionally, these features are of great cultural and economic importance. Geothermal waters are considered Taonga (treasure) by New Zealand's indigenous Māori, with many early settlements located in the proximity of natural geothermal surface features. The protection of these surface features is not only culturally important but also provide a great source of income to local communities with geothermal recreation in the Bay of Plenty estimated to be valued between NZ$90-120M per annum (Bay of Plenty Regional Council, 2018), and Waikato estimating geothermal tourism providing between NZ$63-120M per annum (Barns and Luketina, 2011). These published figures are both out of date, however numbers are thought to be similar today (*pers comm* WRC & BOPRC). It is therefore vital that the use of the geothermal resources is done so in a sustainable and environmentally friendly way so that cultural values and community values are maintained.

2. Methods:

The objective of this study is to assess surface heat loss using remote sensing methodologies. We explore and compare heat loss assessments from both terrestrial based datasets and methodologies, with aircraft collected TIR data.

Heat is lost to the atmosphere within geothermal environments through varying surface manifestations, including hot springs, geysers, hot pools, mud pools, heated and steaming ground, and fumaroles (Figure 1). The heat output from these surface phenomena is often difficult and hazardous to measure.

2.1 Terrestrial based methods

There are several components to consider in determining heat loss for a geothermal area. They include heat loss to the atmosphere from heat transferred through heated ground (section 2.1.1), and from geothermal water bodies, including surface hot pools, and springs (section 2.1.2), and also heat transferred into streams through subsurface seeps, and springs, and also surface flows accumulated in streams (section 2.1.3). The follow sections describe methods for data collection and analysis for each component.

2.1.1 Heat loss through the ground

Two methods have been used to calculate a surface heat flux from the ground, one using a water-based calorimeter, and the other using temperature depth profiles. To get a total heat loss for a geothermal area, sites are selected to represent a predefined ground-cover type, following the assumption that different vegetation types grow in different shallow subsurface thermal regimes (Dawson and Dickenson, 1970; Allis, 1981; Smith, 2013). An average heat flux for each ground-cover class is determined and assigned to the area of like groundcover to determine a surface heat loss for a field.

2.1.1.1 Calorimeter method

One technique for determining surface heat flux is using a water-based calorimeter (Hochstein and Bromley, 2005; Seward et al 2018a). The calorimeter records linear increases in temperature of water (starting from near-ambient conditions), caused by steady ground heat transfer over a set amount of time (e.g. 5 minutes), while covered by the calorimeter. This allows a total heat flux from the surface to be determined. Increase in water temperature while the calorimeter is slightly elevated (on a 2 cm ring) over a similar period of time (e.g., 5 minutes) allows the radiation and convection heat flux from the surface to be determined. Before, after, and in-between ground and elevated measurements, the calorimeter is insulated from the ground to measure "background" atmospheric influences (e.g. air temperatures). Figure 3 shows an example of the recorded temperature in the water-filled calorimeter over a total site occupation period of about 30 minutes.

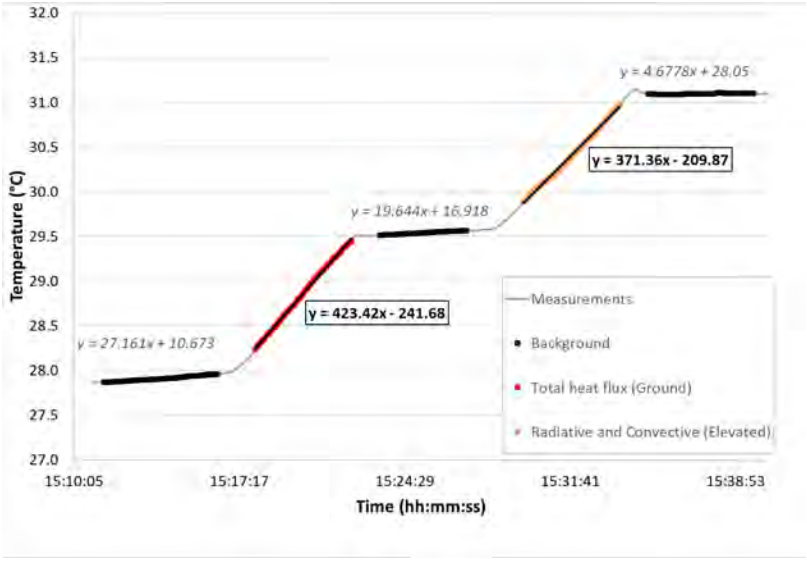

Figure 3: Example of calorimeter data measurements used to calculate heat flux at a measurement site.

The total heat flux is determined using EQ 1:

$$q_{tot} = \frac{mc\left(\frac{\Delta T_g}{\Delta t} - \frac{\Delta T_{lid}}{\Delta t}\right)}{A} \quad \textbf{(EQ 1)}$$

Where, $\frac{\Delta T_g}{\Delta t}$, is the temperature gradient determined while the calorimeter is placed on the ground, $\frac{\Delta T_{lid}}{\Delta t}$, is the change in atmospheric temperature (lid sensor), *m* is the mass of the water within the calorimeter, *c* is the specific heat capacity of water and *A* is the footprint area of the calorimeter. This equation can also be used to determine the radiative and convective heat flux components by substituting $\frac{\Delta T_E}{\Delta t}$ (thermal gradient measured when the calorimeter is elevated) for $\frac{\Delta T_g}{\Delta t}$ into the equation.

2.1.1.2 Temperature-depth Profiles

An alternative approach to determine ground heat flux is from ground temperature-depth profiles (e.g. Hochstein and Bromley 2005; Seward et al., 2018a), where the depth (Z_{BP}) at which boiling temperatures are reached are determined (EQ 2) and converted into heat flux (EQ 3). The depths to boiling points are either measured directly when Z_{BP} is less than 1 m or inferred from extrapolating a fitted exponential function to the temperature-depth data.

$$Z_{BP} = exp[c_1(T_{BP} - T_z)] \quad \textbf{(EQ 2)}$$

Where T_z is the temperature at depth z, T_{BP} is the temperature at which boiling occurs (i.e. T = 98.8°C in the Taupo area), and c_1 is a constant derived by Hochstein and Bromley (2005) at the Karapiti geothermal area (–0.025).

Heat flux is then calculated from the boiling point depth using the following power-law relationship (Hochstein and Bromley 2005).

$$q_{ZB} = a\left[\frac{Z_{BP}}{Z_0}\right]^{-b} \quad \textbf{(EQ 3)}$$

Where a and b are empirically derived constants determined through comparisons of temperature-depth profiles with calorimeter measurements at the same locations. For the Taupo area, a = 148 Wm^{-2} and b = 0.84 (Seward et al. 2018a), and Z_0 is a normalised depth (1 m).

2.1.2 Heat loss from water features (pools and streams)

We use the methods developed by Dawson (1964) and converted to SI units by Sorey and Colvard (1994), to calculate a heat loss from water bodies. Although other methods for deriving heat loss from heated pools have been developed by many (e.g. Lund 2000; Ryan et al, 1974; Shanahan, 1984), Bloomer (2012) suggests Dawsons (1964) method is the most applicable for a variety of temperatures and pool sizes. There are four key mechanisms for heat loss from water bodies to consider when assessing total heat loss. They are evaporation (Q_E), conduction (Q_C), radiation (Q_R) and direct mass flow (Q_S). Dawson (1964) developed the following set of empirical equations to determine each component (in kW).

$$Q_E = 0.001 * A\left(h_{s,Tp} - h_{w,Tp}\right)(0.0065 + 0.0029w)\frac{\left(P_{H2O,tp} - P_{H2O,atm}\right)}{P_{atm}} \quad \textbf{(EQ 4)}$$

Where A is the surface area of the pool (m^2), $h_{s,Tp}$ is the enthalpy of the steam at pool temperature (T_p) (Jkg^{-1}), $h_{w,Tp}$ is the enthalpy of water at pool temperature (Jkg^{-1}), w is the wind speed (ms^{-1}), $P_{H2O,tp}$ is the vapour pressure of water at T_p (bar), $P_{H2O,atm}$ is the atmospheric vapour pressure (bar) and P_{atm} is the average annual atmospheric pressure in bar.

The heat loss by conduction and molecular diffusion, Q_C, is related to Q_E by the Bowen ratio, RB (Sutton 1953).

$$RB = \frac{Q_C}{Q_E} = 6.1 \times 10^{-4} P_{atm}\frac{\left(T_p - T_{atm}\right)}{\left(P_{w,tp} - P_{w,atm}\right)} \quad \textbf{(EQ 5)}$$

where T_{atm} is the atmospheric temperature (°C).

$$Q_R = 0.001 * A\varepsilon\sigma(T_P^4 - T_{atm}^4) \quad \textbf{(EQ 6)}$$

where ε is emissivity (0.955 for water), σ is the Stefan-Boltzmann constant (5.67 x 10^{-8} $Wm^{-2}K^{-4}$), and T_P and T_{amt} refer to the temperature of the pool (*P*) and ambient air (*amt*) temperature (°K).

Heat loss through mass discharge of flowing springs and overflow of pools can be determined by:

$$Q_S = M_w(h_w - h_{atm}) \quad \textbf{(EQ 7)}$$

where M_w is the mass flow of heated water in kgs^{-1}, h_w is the enthalpy of the discharging water in $KJkg^{-1}$ and h_{atm} is the enthalpy of water at the atmospheric temperature in $KJkg^{-1}$ (Sorey and Colvard 1994).

Therefore, the total heat loss (Q_{WB} (MW)) is represented by:

$$Q_{WB} = 0.001 \times (Q_E + Q_C + Q_R + Q_S) \quad \textbf{(EQ 8)}$$

2.1.3 Assessment of geothermal heat loss into streams

Two methods for determining the heat flow within a stream are compared to determine heat loss through surface discharges into streams. The first method below is a similar approach to that described above (EQ 7), where heat loss (MW) is determined from the enthalpy of stream water (calculated from stream temperatures) and flow rate (*V*)

$$Q_T = 0.001 \times H_T V \quad \textbf{(EQ 9)}$$

Where H_T is the enthalpy of the stream at measured temperature (*T*) (KJ/kg) and *V* is the measure flow rate of the stream (kg/s).

In the second approach, heat loss (MW) is calculated from chloride flux (F_{Cl}) and the enthalpy of the deep geothermal water associated with chloride (Glover 1992; Bibby et al 1995).

$$Q_{Cl} = 0.001 \times F_{Cl}H_{Cl} \quad \textbf{(EQ 10)}$$

This second method assumes that the chloride content of surface water provides a direct measure of amount of deep geothermal fluid reaching the surface (Ellis and Wilson, 1955; Hochstein, 1988; Giggenbach et al 1994). The chloride flux method assumes that the ratio of enthalpy to chloride concentration from deep reservoir fluid is constant and that all chloride in the up flowing geothermal water is discharged at the surface (Bibby et al, 1995).

2.2 Aerial Thermal Infrared

Thermal Infrared data are collected by mounting a TIR camera to an aircraft (either a helicopter or a fixed wing plane), and flying survey lines at a known elevation over a survey area. The collected images are mosaicked and geo-registered to aerial photography. Inferred surface temperatures are

calculated per pixel by applying a calibration equation derived from measured water temperatures at known locations collected at the time of the flight. Heat loss through the ground and through water bodies are determined separately, as the emissivity's of the surfaces are different (Seward et al 2018a).

Heat loss (q (m^2)) through ground surfaces is determined using a direct empirical relationship between TIR inferred surface temperatures ($T_{(inferred)}$) and measured heat flux, and is given in EQ 11:

$$q_{TIR} = 50.3 \times \left(T_{(inferred)} - T_{(ambient)}\right) - 148 \quad \textbf{(EQ 11)}$$

Where $T_{(ambient)}$ is the measured ambient air temperature at the time of the TIR data collection, and a is the pixel area (m^2). The empirical equation was determined by Bromley et al (2011), from 8 years of measurement at the Tauhara Geothermal Field and was further tested at the Wairakei Geothermal Field (Bromley et al., 2015).

An average heat flux per image pixel is calculated from the inferred surface temperatures and summed to get a fieldwide heat loss value.

$$Q_{totTIR} = \sum q_{TIR} \times a \quad \textbf{(EQ12)}$$

Equations EQ4 - EQ8 are used, to determine the heat loss from non-flowing water bodies (i.e. pools and lakes). The surface areas (A) of the features are determined from the TIR image, and inferred surface temperatures per pixel are used for T_w. While enthalpy (H), and vapour pressure (P) are determined from the inferred surface temperatures.

3. Results and discussion:

This approach has been tested and developed over several different active geothermal fields, with the initial investigation being undertaken in areas within the Wairakei and Tauhara Geothermal Fields (Figure 2; Hochstein and Bromley, 2005; Bromley et al, 2011; Seward et al., 2018a). These thermal areas are now largely steam driven features, consisting predominately of heated and steaming ground. Seward et al. (2018a) applied the relationship (EQ3) developed by Hochstein and Bromley (2005) and revised the empirically derived constants using 85 Q_{tot} and Z_{BP} data collected between 2001 and 2014 at the Karapiti geothermal site, within the Wairakei Geothermal Field. Results using the revised values showed close correlation between the two terrestrial heat loss methods and the aerial TIR assessment (Table 1).

Table 1: Results from heat loss assessments at Karapiti (Seward et al 2018a). The 18°C cut off for Q_{TIR} reflects the ambient temperature at the time of the TIR survey.

	Heat loss (MW)
TIR Results	
Q_{TIR} for land pixels T>18°C only	49
Terrestrial Results	
Q_{tot}	47.6
Q_{ZB}	58.2

This method was further developed at Rotorua (Seward et al., 2018b), Waimangu (Seward et al, 2023) and Waiotapu Geothermal Fields (Seward et al., 2024), where pools, lakes and flowing streams also contribute to the surface heat loss from these geothermal systems.

At the Waimangu Geothermal Field, comparisons between using the terrestrial based measurements and aerial TIR inferred temperatures to calculate evaporative surface heat loss from large lake surfaces show that the methods provided very different results (Seward et al 2023; Table 2).

Table 2: Comparisons between heat loss values determined from terrestrial measurement and remote TIR data (Seward et al 2023).

Lake	Measured temperature at outlet (°C)	Q_E (MW)	Inferred pixel temperatures (°C)	$Q_{E\text{-}TIR}$ (MW)
Frying Pan Lake (surface area = 35800m^2)	48.7	49.5	23-85	83.8
Inferno Crater Lake (surface area = 6650m^2)	51.3	10.6	20-78	22.3

The key observations from the comparison in Table 2, is that the temperature measured at the outflow or edge of a large water body is not representative of the whole lake (Figure 3). Using terrestrial based measurements alone results in an underestimated heat loss over large surface areas of geothermal lakes, were evaporation and cooling of lake fluids occur between the source and outflow.

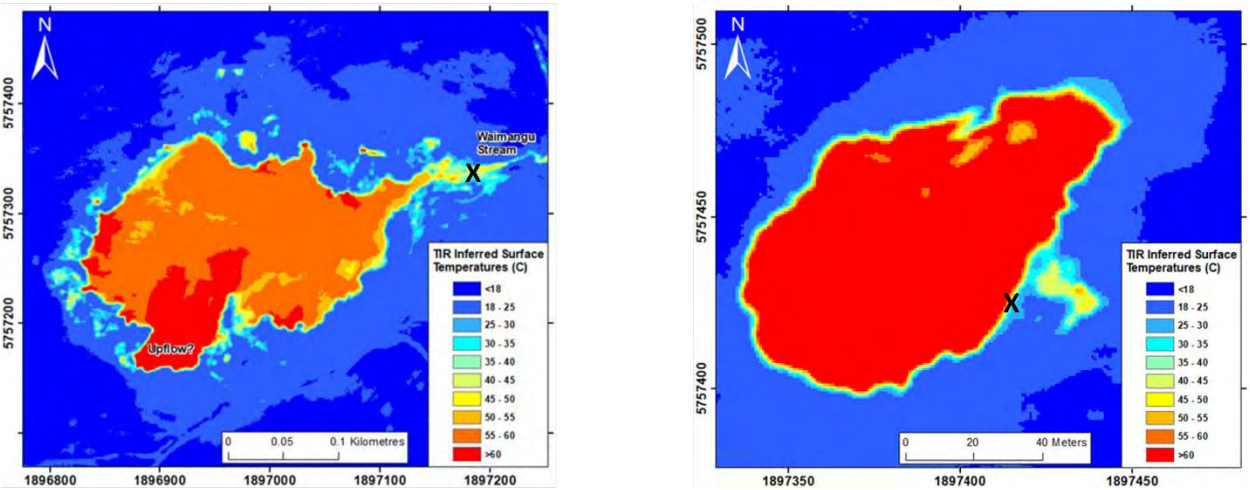

Figure 3: TIR image of (a) Frying Pan Lake and (b) Inferno crater Lake. "X" mark the indicative location of terrestrial based measurement (Seward et al, 2023).

Additionally, further considerations into the effects of varying wind speeds across the surface of large water bodies needs to be considered. For all field assessments, we have assumed an average windspeed of 1ms^{-1}. We are aware that this is likely to result in an underestimation of heat loss in exposed areas and water bodies with large surface areas. Using the TIR data may reduce this effect, by detecting the resulting changes in water surface temperatures (Seward et al, 2018a).

For smaller water bodies, we believe that terrestrial based water temperatures combined with surface areas derived from visual or thermal aerial images provide the best estimations, particularly, for those features with water temperatures > 60°C (Seward et al, 2022). At these elevated temperatures steam is often produced which can mask the thermal signature of the water body, often resulting in cooler than measured inferred surface temperatures (derived from TIR data; e.g Figure 4). As steam is often transient, it is very hard to quantify and account for this effect.

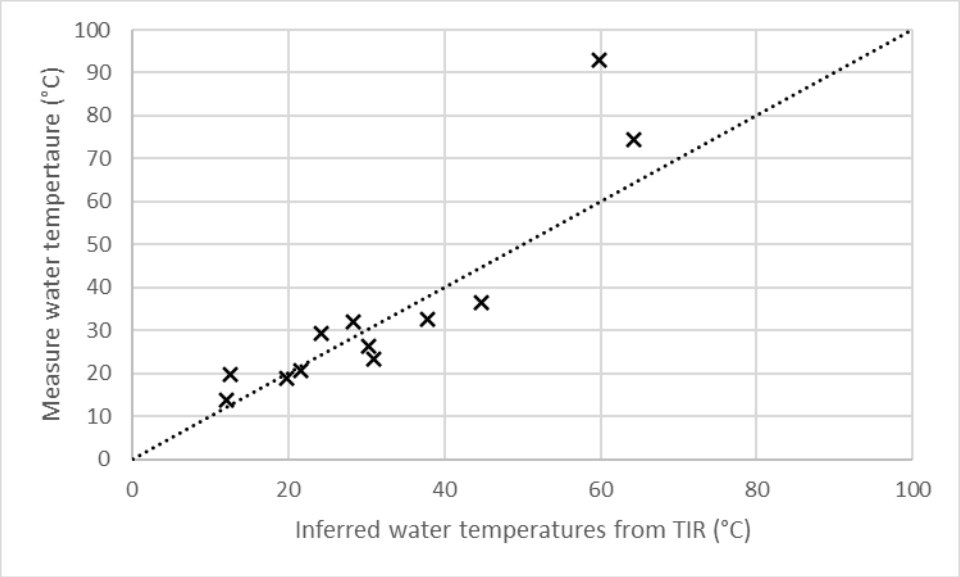

Figure 4: Comparisons of measured water temperatures and inferred surface temperatures from water features located at the Waiotapu Geothermal Field (Reeves and Sanders, 2019).

The effect of steam and evaporation can also affect the results of heat loss from mass discharge to streams. Equations 7 and 9, use the measured water temperature to determine an enthalpy of the flowing water. At higher temperatures, evaporation can result in cooler surface water temperatures, and this suggests that the chloride flux method may be more accurate for estimating advective heat loss from a geothermal system, provided a chloride content of the deep geothermal parent water is known and the chloride concentration in the discharge waters can be measured with sufficient accuracy.

Further complexities were identified at the Waiotapu Geothermal Field, where large difference between heat losses calculated from calorimeter measurements (q_{tot}) and depth-to-boiling point (q_{ZBP}) were measured. Seward et al, (*under review*) discussed the possible causes of these results and concludes potentially two key reasons for the differences. The first of which was related to the measurements made by the calorimeter. At the time of data collection, air temperatures were high (28-40°C) resulting in little temperature change measured during the measurement as the air temperature was very close to the ground surface temperature. The second potential cause is related to the structure of the subsurface. Temperature-depth profiles indicated elevated heat flux compared to the surface measurements, suggesting that there is high heat in the shallow subsurface (< 1m) that is not reaching the surface. Seward et al (*submitted*) suggest that it could potentially be caused by a small scale “heat pipe”-like mechanism, where heat in the form of steam is rising from depth but reaches an impermeable structure (e.g. clay or sinter), resulting in condensation of

steam, which then descends, due to gravity, back to depth. This interpretation of the differences between the terrestrial measurements is supported with TIR data (Figure 5), that identifies very little heat loss from the ground surface. The majority of heat loss at the Waiotapu Geothermal Field appears to be reaching the surface through the water features (Seward et al, 2024; Rodrigues-Gomez et al., 2023).

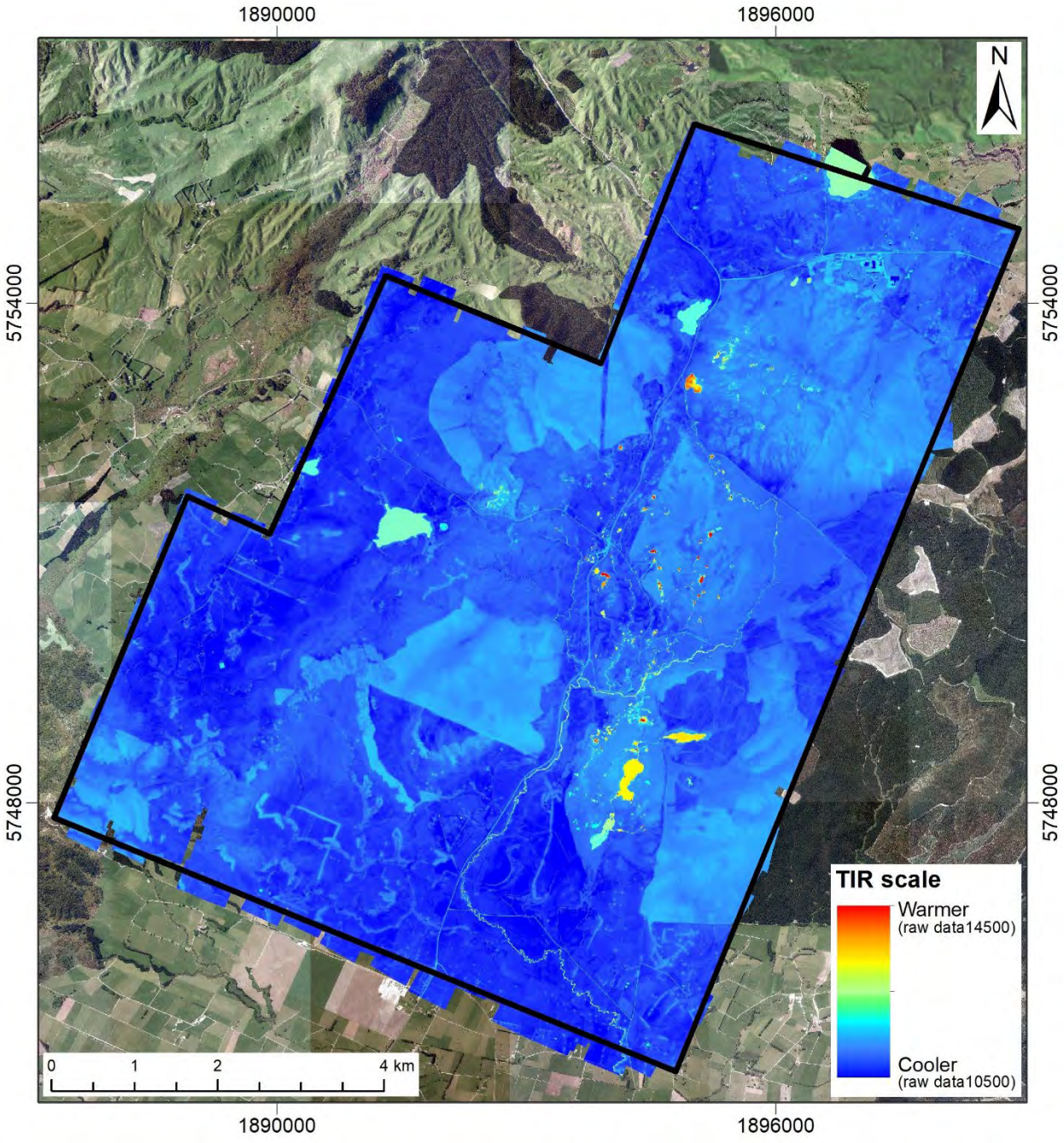

Figure 5: Thermal infrared image over the Waiotapu Geothermal Field. Blue colours show the ambient cooler surface temperatures, while yellows and reds show the area of high surface temperatures. These higher temperatures are generally associated with geothermal water bodies at Waiotapu (Reeves and Sanders, 2019; Seward et al., *2024*).

There are clear benefits to using aerial thermal infrared to determine surface heat loss from a geothermal field. The largest of which is the ability to gather a large amount of data relatively quickly. Remote data collection also allows data to be collected in areas that are not accessible on the ground, it also can be easily replicated, with flight plans, and data collection points set. However, care needs to be taken when interpreting heat loss results, as illustrated above. There are several key components of heat loss that can not be collected remotely, and need terrestrial measurements to be made, namely, mass discharge into streams. Additionally, ground-based measurements of ground temperatures at the time of aerial data collection, allows for inferred surface temperatures to be calculated which are crucial for determining heat loss.

Although there are many sources of uncertainties and errors associated with measuring heat loss, through using a combination of approaches, interpretation of data can be made easier, providing gains on historic approaches.

4. Summary and Conclusions:

This paper has presented methods developed over the last decade to improve estimations of surface heat losses at several New Zealand geothermal fields. It has compared remote sensing techniques with labor-intensive ground-based data collections. Derived empirical relationships to infer heat flux from subsurface temperature gradients, and inferred surface temperatures from TIR data are presented.

The approaches have been applied to several geothermal fields across the Taupō Volcanic Zone, New Zealand. Initial investigations compared two terrestrial approaches and aerial TIR data in a steam-dominated setting (Bromley et al., 2015; Seward et al, 2018a). Results showed close correlations between the 3 methods. Then, the approaches were applied and developed further in mixed- and fluid-dominated geothermal fields (Seward et al., 2023; 2024). In these settings, methods for interpreting and comparing heat loss from water bodies were developed. Although there are benefits for using inferred surface temperatures from aerial data is clear for larger water bodies, the interpretation of results was more complicated for smaller water bodies and stream flows. These geothermal settings emphasized the importance of having terrestrial based measurements for streams and outflow channel, as remote sensing methods cannot capture these mass heat flows.

Discrete terrestrial direct measurements of heat flux (using a calorimeter) are complicated and time-consuming. Time can be reduced through temperature-depth measurements at each site, however, as results collected at Waiotapu Geothermal Field have shown, heat transfer in the shallow subsurface (<1m) does not necessarily result in anomalous convective heat loss at the surface (Seward et al, 2024). Therefore, care must be taken when interpreting these results.

Discrete terrestrial measurements are amalgamated to estimate a field-wide total heat loss through the use of ground-cover classifications. Unquantifiable uncertainties are introduced through this method. This is where the benefits of using aerial TIR data greatly reduce uncertainties.

Conclusions from, particularly, Seward et al. (2024) suggest that the best approach for determining the most accurate surface heat loss for mixed- or water-dominated geothermal systems is through using aerial TIR data, combined with spot terrestrial heat-flux (calorimeter) measurements, and

surface temperatures. For streams and outflow channels, terrestrial measurements of flowrates, water temperatures and chloride concentrations are necessary.

Acknowledgement

The data presented in this paper were collected as part of the 'New Zealand Geothermal Futures' research programme (C05X1702), with additional support from the Waikato Regional Council, the Bay of Plenty Regional Council, and Contact Energy. We would like to acknowledge Ngati Tahu - Ngati Whoa Runanga Trust, Wai-O-Tapu Geothermal Wonderland (WGW), Craters of the Moon trust, Te Puia, Whakarewarewa, Waimangu Geothermal Valley, Department of Conservation, and the other landowners for permission to access land for the surveys, and Chris Bromley for his insight and foundational work.

REFERENCES

Allis, R. G.,1981, Changes in heat flow associated with exploitation of Wairakei geothermal field, New Zealand. *New Zealand Journal of Geology and Geophysics*, *24*(1), 1-19.

Allis, R., Nash, G.D., Johnson, S.D., 1999. Conversion of thermal infrared surveys to heat flow: Comparisons from Dixie Valley, Nevada, and Wairakei, New Zealand. Trans.-Geothermal Resource. Council 23, 499–504.

Andres, R.J., and W.I. Rose, 1995, Description of thermal anomalies on two active Guatemalan volcanoes using Landsat Thematic Mapper Imagery, *Photogrammetric Engineering and Remote sensing*, 61 (6), 775-782

Barns, S., and Luketina, K., 2011, Valuing uses of the Waikato regional geothermal resource, Waikato Regional Council Technical Report 2011/15,

Bay of Plenty Regional Council, 2018, Valuing geothermal attributes in the Bay of Plenty region, Strategic Policy Publication 2022/02,

Benseman, R.F., 1959, The calorimetry of steaming ground in thermal areas. *Journal of Geophysical Research*. 64 (1), 123–126. https://doi.org/10.1029/JZ064i001p00123.

Bibby, H.M., Caldwell, T.G., Davey, F.J., Webb, T.H., 1995, Geophysical evidence on the structure of the Taupo Volcanic Zone and its hydrothermal circulation. *Journal of Volcanology and Geothermal Research* 68 (1), 29–58. https://doi.org/10.1016/0377-0273(95)00007-H.

Bloomer, A., 2012, Heat loss from high temperature ponds, In Proceedings New Zealand Geothermal workshop 2012.

Bouligand, C., Hurwitz, S., Vandemeulebrouck, J., Byrdina, S., Kass, M.A., and Lewicki, J.L., 2019, Heat and mass transport in a vapor-dominated hydrothermal area in Yellowstone National Park, USA: inferences from magnetic, electrical, electromagnetic, subsurface temperature, and diffuse CO2 flux measurements. *Journal of Geophysical Research: Solid Earth* 124 (1), 291–309. https://doi.org/10.1029/2018JB016202

Bromley, C.J., and Hochstein, M.P., 2000, Heat transfer of the Karapiti fumarole field (1946-2000). p. 87-92 IN: Dunstall, M.G.; Morgan, O.E.; Simmons, S.F. (eds.) *Proceedings of the 22nd New Zealand Geothermal Workshop 2000.* Auckland: University of Auckland.

Bromley, C.J., and Hochstein, M.P., 2005, Heat discharge of steaming ground at Karapiti (Wairakei), New Zealand. 7 p. IN: *Proceedings of the World Geothermal Congress 2005, Antalya, Turkey, 24-29 April 2005.* [Reykjavik, Iceland]: International Geothermal Association

Bromley, C.J., van Manen, S.M., and Mannington, W., 2011, Heat flux from steaming ground: reducing uncertainties. In proceeding of Stanford Geothermal Reservoir Engineering Workshop, Stanford University.

Bromley, C., Ashraf, S., Seward, A., Reeves, R., 2015. Monitoring and quantifying heat loss from significant geothermal areas via remote sensing, In Proceedings of New Zealand Geothermal Workshop

BOPRC *pers comm*, email received on 5 June 2024, from Penny Doorman

Dawson, G.B., 1964. The nature and assessment of heat flow from hydrothermal areas. *New Zealand Jounrnal of Geology and Geophysics*. 7 (1), 155–171. https://doi.org/10.1080/00288306.1964.10420167.

Dawson, G. B., and Dickinson, D. J.,1970, Heat flow studies in thermal areas of the North Island of New Zealand. *Geothermics, 2*, 466-473.

Ellis, A. J., and Wilson, S. H., 1955, The heat from the Wairakei-Taupo thermal region calculated from the chloride output. *The New Zealand Journal of Science and Technology*. B.36, 622-631.

Eneva, M., Coolbaugh, M., and Combs, J., 2006, Application of satellite thermal infrared imagery to geothermal exploration in east central California. *GRC Transactions*, *30*, 407-412.

Favorito, J.E., Harris, R.N., Sohn, R.A., Hurwitz, S., and Luttrell, K.M., 2021, Heat Flux From a Vapor-Dominated Hydrothermal Field Beneath Yellowstone Lake. *Journal of Geophysical Research: Solid Earth*, 126(5): e2020JB021098. DOI:https://doi.org/10.1029/2020JB021098

Fisher, R.G., 1964, Geothermal heat flow at Wairakei during 1958. *New Zealand Journal of Geology and Geophysics*, 7 (1) pp. 172-184, 10.1080/00288306.1964.10420168

Fridriksson, T., Kristjánsson, B.R., Ármannsson, H., Margrétardóttir, E., Ólafsdóttir, S., and Chiodini, G., 2006, CO2 emissions and heat flow through soil, fumaroles, and steam heated mud pools at the Reykjanes geothermal area. SW Iceland. *Applied Geochemistry*. 21 (9), 1551–1569. https://doi.org/10.1016/j.apgeochem.2006.04.006.

Giggenbach, W.F., Sheppard, D.S., Robinson, B.W., Stewart, M.K. and Lyon, G.L., 1994, Geochemical structure and position of the Waiotapu geothermal field, New Zealand. *Geothermics*, *23*(5-6), pp.599-644.

Glover, R.B., 1992, Integrated heat and mass discharges from the Rotorua Geothermal System *Geothermics*, 21 (1–2), pp. 89-96

Hochstein, M.P., 1988, Assessment and modelling of geothermal reservoirs (small utilization schemes) *Geothermics*, 17 (1), pp. 15-49, 10.1016/0375-6505(88)90004-1

Hochstein, M.P. and Bromley, C.J., 2001, Steam cloud characteristics and heat output of fumaroles. *Geothermics, 30(5):* 547-559

Hochstein, M.P., and Bromley, C.J., 2005, Measurement of heat flux from steaming ground, *Geothermics*, 34, 133-160

Hunt, T.M., Glover, R.B., Wood, C.P., 1994, Waimangu, Waiotapu, and Waikite Geothermal Systems, New Zealand: Background and history. *Geothermics*, 23 (5/6), pp. 379-400

Hurwitz, S., Harris, R.N., Werner, C.A., Murphy, F., 2012. Heat flow in vapor dominated areas of the Yellowstone Plateau Volcanic Field: Implications for the thermal budget of the Yellowstone Caldera. *Journal of Geophysical Research: Solid Earth* 117 (B10). https://doi.org/10.1029/2012JB009463.

Ingebritsen, S.E., Galloway, D.L., Colvard, E.M., Sorey, M.L., and Mariner, R.H., 2001. Time-variation of hydrothermal discharge at selected sites in the western United States: implications for monitoring. *Journal of Volcanology and Geothermal Research*, 111 (1– 4), 1–23. https://doi.org/10.1016/S0377-0273(01)00207-4

Lund JW, Design Considerations for Pools and Spas (Natatoriums), GHC Bulletin (September 2000).

Mia, M.B., Bromley, C.J., and Fujimitsu, Y., 2012, Moniroting heat flux using Landsat TM/ETM+ Thermal infrared data - A case study at Karapiti ('Craters of the moon') thermal area, New Zealand, *Journal of Volcanology and Geothermal Research*, 235-236, 1-10, https://doi.org/10.1016/j.jag.2018.08.027

Mia, M.B., Bromley, C.J., and Fujimitsu, Y., 2013, Monitoring Heat losses using Landsat ETM + Thermal Infrared Data: a case study in Unzen Geothermal Field, Kyushu, Japan. *Pure and Applied Geophysics* 170. 2263-2271

Mongillo, M. A., and Bromley C.J., 1990, Thermal infrared video imagery over the Rotorua geothermal field. *Proceedings 12th NZ Geothermal Workshop*. University of Auckland, 1990.

Mongillo, M.A., 1994, An aerial thermal infrared survey of the Waimangu-Waiotapu Geothermal Region, New Zealand, *Geothermics* 23(5-6), 511-526

Mongillo, M.A., Cochrane, G.R., Wood, C.P., Shibata, Y., 1995, High resolution aircraft scanner mapping of geothermal and volcanic areas. In: Hochstein MP, Brotheridge J, Simmons SF, editors. *Proceedings of the 17th New Zealand Geothermal Workshop 1995*. Auckland (NZ): University of Auckland. p. 13-18.

Nairn, I.A., and Finlayson, B.F., 1981., Chloride flux measurements in the Tarawera River system DSIR, Wellington, *Geothermal Circular*, IBF2, IAN3

Ramirez-Gonzalez, L.M., Aufaristama, M., Jonsdottir, I., Hoskuldsson, A., Thordarson, T., Proietti, N.M., Kraft, G., and McQuilkin, J., 2019, Remote sensing of surface hydrothermal alteration, identification or mineral and thermal anomalies at Sveifluhals-Kryuvik high-temperature geothermal field, SW Iceland. *IOP Conference Series: Earth and Environment Science.*

Reeves, R., and Rae, L., 2016, Changes in aerial thermal infrared signature over the Rotorua Geothermal Field, New Zealand: 1990–2014. *Geothermics*, *64*, 262-270.

Reeves, R., and Sanders, F., 2019, 2019 Thermal Infrared survey of the Waiotapu Geothermal Field. Wairakei (NZ): GNS Science. 22p. GNS Science Report 2019/57/ doi:10.21420/ZD6D-GD88

Rodriguez-Gomez, C., Kereszturi, G., Whitehead, M., Reeves, R., Rae, A., Pullanagari, R., 2013, Point pattern analysis of thermal anomalies in geothermal fields and its use for inferring shallow hydrological processes, Geothermics, 110, doi.org/10.1016/j.geothermics.2023.102664

Ryan PJ, Harleman DRF, Stolzenbach KD, Surface Heat Loss from Cooling Ponds, Water Resources Research Vol 10 No 5, (Oct 1974).

Seward, T. M., and Kerrick, D. M.,1996, Hydrothermal CO2 emission from the Taupo Volcanic Zone, New Zealand. *Earth and Planetary Science Letters*, *139*(1-2), 105-113.

Seward, A.M., Ashraf, S., Reeves, R., and Bromley, C., 2018a. Improved environmental monitoring of surface geothermal features through comparisons of thermal infrared, satellite remote sensing and terrestrial calorimetry. *Geothermics* 73, 60–73. https://doi.org/10.1016/j.geothermics.2018.01.007.

Seward AM, Sanders F, Mroczek EK, Reeves RR, Bromley CJ, Brakenrig T, Macdonald N, Graham DJ, Lor S. 2018b. Rotorua heat flow survey 2018. Wairakei (NZ): GNS Science. 63 p. (GNS Science consultancy report; 2018/94).

Seward A.M., Brakenrig T., Macdonald N., and Shanks, J., 2022, Collection and initial assessment of terrestrial heat flux of the Waiotapu Geothermal Field. Lower Hutt (NZ): GNS Science. 79 p. (*GNS Science report; 2022/07*). doi:10.21420/ECCP-E459.

Seward, A.M., Reeves, R., Alcaraz, S., 2023, Assessment of the surface heat loss from Waimangu Geothermal Valley: Comparison of terrestrial based assessment techniques with remote sensing, *Journal of Volcanology and Geothermal Research*, 430, https://doi.org/10.1016/j.jvolgeores.2022. 107630

Seward, A.M., Reeves, R., Mroczek, E., Macdonald, N., and Brakenrig, T., 2024, Surface heat loss assessment at the Waiotapu Geothermal Field, Taupo Volcanic Zone, New Zealand, *Geothermics*

Shanahan P, Water Temperature Modelling: A Practical Guide, Proceedings of Stormwater and Water Quality Model Users Group Meeting, (1984)

Seward, T. M., and Kerrick, D. M.,1996, Hydrothermal CO2 emission from the Taupo Volcanic Zone, New Zealand. *Earth and Planetary Science Letters*, *139*(1-2), 105-113.

Sorey, M. L., & Colvard, E. M., 1994, *Measurements of heat and mass flow from thermal areas in Lassen Volcanic National Park, California, 1984-93* (p. 35). Menlo Park, CA: US Geological Survey.

Sutton, P. M., 1953, The variation of the elastic constants of crystalline aluminum with temperature between 63 K and 773 K. *Physical Review*, *91*(4), 816.

Thompson, G.E.K., Banwell, C.J., Dawson, G.B., and Dickinson, D.J., 1961, Prospecting of Hydrothermal areas by Surface thermal surveys, *United Nations Conference on New Sources of Energy*, Paper 35/G/54

Vaughan, R.G., Keszthelyi, L.P., Lowenstern, J.B., Jaworowski, C., and Heasler, H., 2012, Use of ASTER and MODIS thermal infrared data to quantify heat flow and hydrothermal change at

Yellowstone National Park. *Journal of Volcanology and Geothermal Research*, 233–234, 72–89. https://doi.org/10.1016/j.jvolgeores.2012.04.022.

Wang, Y., and Pang, Z., 2023, Heat flux in volcanic and geothermal areas: Methods, principles, applications and future directions, *Gondwana Research* 122, 260-278, https://doi.org/10.1016/j.gr.2022.09.010

Wang, Y., Pang, Z., Hao, Y., Fan, Y., Tian, J., and Li, J., 2019. A revised method for heat flux measurement with applications to the fracture-controlled Kangding geothermal system in the Eastern Himalayan Syntaxis. *Geothermics* 77, 188–203. https://doi.org/10.1016/j.geothermics.2018.09.005.

WRC *pers comm,* email on 30 May 2014 from Katherine Luketina

Yang, T. H. J., Chambefort, I., Rowe, M., Mazot, A., Seward, A., Werner, C., Fischer, T., Seastres, J., Siega, F., Macdonald, N., Brakenrig, T., Coup, L., and Sander, F., 2024, Variability in surface CO2 flux: Implication for monitoring surface emission from geothermal fields. *Geothermics*, *120*, 102981.

Low-Temperature / Direct Use

U.S. DOE Community Geothermal Heating and Cooling Design and Deployment Status

Arlene Anderson[1], Alexis McKittrick[2], Lindsay Morse[3]

[1,2] Geothermal Technologies Office, U.S. Department of Energy (DOE)

1000 Independence Ave. SW

Washington D.C. 20004

[3]Boston Government Services

105 Mitchell Road, Suite 101

Oak Ridge, TN 37830

Keywords

Community Geothermal, ComGeo, Geothermal District Heating and Cooling, Thermal Energy Networks, Disadvantaged Communities, Geothermal Heat Pumps, U.S. DOE Geothermal Data Repository, GDR

ABSTRACT

Community Geothermal Coalitions across the United States are nearing completion of their first phase of work focused on expanding community-scale geothermal systems. The work began on October 1, 2023, and is funded through U.S. Department of Energy (DOE), Geothermal Technologies Office (GTO) Community Geothermal Heating and Cooling Design and Deployment Initiative Cooperative Agreements.

A main goal of the initiative is to support the formation of U.S.-based community coalitions that will develop, design, and install community geothermal heating and cooling systems that supply at least 25% of the heating and cooling load in communities. The coalitions describe how switching to a geothermal district heating and cooling system would result in greenhouse gas emission reductions for the community where the system is installed.

In total, the selected coalitions comprise more than 60 partners across the U.S. and include one or more partners that: represent the community, are expert geothermal designers, focus on geothermal workforce development and training needs and include a deployment focused coalition partner such as a gas utility.

The eleven coalitions are designing their heating and cooling systems in close partnership with, and many led by, the communities in which the geothermal projects would be deployed. The

coalitions are based in urban, suburban, rural, and remote communities each developing innovative community scale systems.

Anticipated community benefits include addressing: environmental justice conditions, such as cumulative environmental pollution and other hazards; underserved and disadvantaged communities; and community members who have historically experienced vulnerability due to climate change impacts.

Preliminary case studies developed in the first phase will help illustrate how Community Geothermal Coalitions can be replicated throughout the U.S. followed by the development of more complete case studies by coalitions whose projects move to the deployment phase.

1. Introduction

On July 12, 2022, the U.S. Department of Energy (DOE) announced the Community Geothermal Heating and Cooling Design and Deployment Funding Opportunity Announcement (FOA), for projects that will help communities design and deploy geothermal district heating and cooling systems, create related workforce training, and identify and address environmental justice concerns. Widespread adoption of geothermal heating and cooling systems will help decarbonize the building and electricity sectors, reduce energy costs for families, and boost resilience.

The eleven Community Geothermal (ComGeo) Coalitions funded in Phase 1 are helping to expand community-scale geothermal by supporting new systems and developing preliminary case studies to be replicated throughout the country.

1.1 U.S. DOE Community Geothermal Heating and Cooling Initiative Background

On April 25, 2023, the U.S. DOE Geothermal Technologies Office (GTO) announced the selection of 11 projects in the first phase (Phase 1) of the ComGeo Heating and Cooling Design and Deployment Initiative. In the second phase, following a down select, GTO will support multiple projects to deploy their systems. Under this initiative, GTO is funding U.S.-based urban/suburban, rural, or remote/islanded ComGeo Coalitions to develop, design, and install ComGeo heating and cooling systems.

1.1.1 Community Geothermal Heating and Cooling Design and Deployment Project Locations

The Phase 1 projects are in Nome, AK; Seward, AK; Carbondale, CO; Shawnee, OK; Hinesburg, VT; Wallingford, CT; Chicago, IL; Framingham, MA; Ann Arbor, MI; Duluth, MN; and New York City; NY

1.1.2 Community Geothermal Coalition Role Definitions

Each ComGeo Coalition features representatives in four key roles (Figure 1) including:

- Community Voice: Understand & communicate community needs
- Analysis & Design: Design geothermal district heating/cooling system
- Deployment: Obtain permits & build
- Workforce: Develop & implement training/apprenticeships

Entities in the "Community Voice" role understand and can communicate the energy, environmental, economic, social, and/or other relevant needs that the proposed system would address, as well as local development and regulatory requirements. ComGeo Workforce entities know the community labor market and can help the coalition with apprenticeship opportunities, job placement, and developing training or lesson plans for the applicable trades. Analysis and design entities have the experience designing geothermal systems as well as analyzing the economic and technical aspects of such systems. Deployment entities, although not developing the community systems in Phase 1, have experience building new or retrofitting existing energy systems and can assist or learn from other ComGeo Coalition partners.

To assist coalition formation, GTO provided a Teaming Partner List where interested parties could provide contact information and areas of expertise and search for other entities interested in partnering on an application.

Figure 1: Graphic describing the four types of partners each ComGeo Coalition is required to include in their project team.

1.1.3 Objectives

GTO set five primary goals for the ComGeo initiative as follows:

- Deploy new or retrofitted geothermal, or geothermal-hybrid, district heating and cooling systems in U.S. districts, neighborhoods, and communities;

- Identify solutions for environmental justice conditions, such as cumulative environmental pollution and other hazards; underserved and disadvantaged communities; and community members who have historically experienced vulnerability due to climate change impacts;
- Assist U.S. communities to develop career and technical education and workforce transition initiatives to design, install, inspect, operate, and maintain new energy systems such as geothermal heating and cooling;
- Develop U.S. case studies about projects, including technical and economic data, to illustrate how projects can be replicated by communities throughout the United States; and
- Publish data and information about U.S. community-scale geothermal heating and cooling system deployment to demonstrate the success of such systems in a range of environments and geographies.

1.2 U.S. DOE Community Geothermal Heating and Cooling Initiative Project Requirements

The 11 ComGeo Coalitions are working in American communities with partners from local and state governments, nonprofits, educational institutions, national labs, tribal government entities, utilities, industry, and unions. While there are more than a few terms and conditions that must be adhered to as part of the ComGeo Coalition Cooperative Agreements with DOE, several important requirements are highlighted below.

1.2.1 Coalition and Resources

Since achieving broad community support for a proposed ComGeo heating and cooling system is key, the entity representing the community where the geothermal system is planned to be located is a critical part of the overall project. Thus, each ComGeo Coalition (the project team) is required to include qualified leaders with appropriate expertise and sufficient time committed to each required role in community representation, workforce planning, geothermal analysis and design, and project deployment.

1.2.2 Project Planning, Community Research, and Data Availability

For the ComGeo systems to produce the desired community benefits, plans for system adoption including workforce training require community research and data gathering. To measure the community benefits and impacts, community baseline conditions are assessed including greenhouse gas emissions reduction or prevention, fuel use, electricity use, and/or environmental contamination that can be reduced or avoided. To prepare for geothermal system deployment, regulations, codes, and standards must be included in a permit plan.

2. ComGeo Project Status as of March 30, 2024

Since the ComGeo projects began on October 1, 2023, all eleven teams shared information with each other pertaining to how their community members are being included and how their workforce training and design plans are proceeding. In the final quarter of Phase 1, teams will meet with DOE to review the data they plan to make public and will discuss sharing important lessons learned in preliminary case studies. A generalized status of the ComGeo team activities during the first two quarters is provided below.

2.1 Community Geothermal Engagement and Workforce Training

The Ann Arbor, MI. ComGeo team engaged more than 50 stakeholders using resident-centered success metrics. The City of Chicago "Blacks in Green" ComGeo team is facilitating community conversations to make decarbonization, electrification, and beneficial electrification meaningful and accessible to Chicago communities in their "Sustainable Square Mile" area. The Duluth, MN. ComGeo team is providing outreach to their top 50 natural gas consumers. The Framingham, MA. ComGeo team is conducting a pilot recruitment and training program for geothermal drillers with planned 4–6-week summer internships. In addition, the team is partnering with the GHP trade associations on curriculum development. Union forums were conducted with electrical, utility, operating engineers, plumbing and pipefitting trades. The New York City ComGeo team scheduled site visit with their community stakeholder organizations and are researching NYC workforce entities including technical and vocational schools and local trade unions. The Wallingford, CT. ComGeo team met with their town government, school board, and residents and surveyed four stakeholder groups about employees, barriers, capacities, and other workforce needs. The Carbondale, CO ComGeo team shared preliminary design and modeling at a community open house. The Hinesburg, VT. ComGeo team obtained community input on priorities, concerns, and perspectives on the feasibility of geothermal projects and met with the non-profit "Habitat for Humanity" regarding housing for under-resourced populations. The Seward, AK. ComGeo team receives strong support from the City Manager. The Seward team is also supporting demonstration-related training where residential CO2 heat pump equipment for hands-on training is being provided. The Shawnee, OK ComGeo team gained approval from their tribal (Potawatomi Nation) partner. The Nome, AK ComGeo team conducted community planning meetings to help inform their design options.

2.2 Community Geothermal Design

Several of the ComGeo Coalitions are designing innovative community-scale geothermal heating and cooling systems (GDHC). These preliminary designs contemplate GDHC systems that flow ambient temperature water through a single distribution pipe, loop, or network to Geothermal Heat Pumps (GHPs). This type of design is also referred to as a Thermal Energy Network (TEN) or one that includes several generations of district heating and cooling technology capable of operating as a modular, installed network.

GDHC systems and TENs are more common outside of the United States, although U.S. interest in such systems is growing. GDHC systems leverage commercially available geothermal direct use and GHPs. Conventional direct use systems take advantage of naturally hot water from deep underground, which is pumped to the surface and through a heat exchanger for heating, while GHPs use the naturally occurring difference between the above-ground air temperature and the shallow subsurface soil temperature to create a heat sink in warmer temperatures and a heat source in cooler temperatures.

Unless innovative engineering techniques are used, direct use systems are limited to regions where naturally occurring, hydrothermal resources can be located and brought to the surface for heating. Innovation is needed to add cooling to a direct use system. In contrast, where there is electricity, GHP technology can be used anywhere in the United States for both heating and cooling. In a GHP-based system, an above-ground electric-powered heat pump moves water or another fluid

through a series of buried pipes or ground loops that are generally located tens to hundreds of feet below the surface, where heat is exchanged with the earth.

When either direct use or GHP systems are used to heat or cool water using common piping (or a district loop), GDHC systems can be efficiently designed to heat and cool multiple buildings. The degree of innovation and planning used in the system design can result in more efficient energy distribution taking advantage of heat sources and sinks to the greatest extent possible. Borehole design and spacing to correctly size a system requires innovation.

Early district energy systems, referred to as "1G" or first-generation systems, shown in Figure 2, mostly required fossil fuels to heat water to high temperatures conducive to making steam. As district energy systems evolved, the required water supply temperature significantly dropped. As such, in "4G" or fourth-generation district energy systems, renewable energy such as GHPs can circulate low-temperature—even ambient temperature—water to heat and cool buildings.

Innovative GDHC systems can be roughly classified as either fourth or fifth generation. Fourth-generation systems contain two separate pipe loops, one that acts as a source of hot or cold water, and a second that acts as a sink. In these systems, hot or cold water is delivered directly to buildings, where it is used for heating or cooling. In a fifth-generation system, pipe loop(s) containing ambient temperature (50–60°F) water can act as a source or sink for multiple buildings. An important innovation is the way heat is used throughout the system. For example, discarded heat from one building can be transported and used in another. Buildings connected to this type of system often contain their own heat pump. GDHC systems may also include non-geothermal components. Supplemental boilers and chillers can provide additional heating and cooling on very hot or cold days. Electricity is needed to operate the heat pump(s), and solar panels or another renewable could provide all or some energy.

	1G	2G	3G	4G	5G
Piping Configuration	Pipe acts only as source Only provides heating	Pipe acts only as source Only provides heating	Pipe acts only as source Only provides heating	Two different pipe loops (one loop as source, other loop as sink) Provides heating and cooling	Single "ambient temperature" pipe loop can simultaneously act as source or sink for various buildings, thus enabling "prosumers" Provides heating and cooling Can take discarded heat from one building and transport it for use in another building
Temperature of Supply Pipe	~400 °F	~250 °F	~190 °F	~140 °F for heating ~45 °F for cooling	~60 °F
Fluid in Supply Pipe	Steam	Pressurized Hot Water	Water	Water	Water

Source: Dana Levy, NYSERDA

Figure 2: District Energy Technology Advancements

GHP systems can use several different ground heat exchanger configurations (e.g., closed-loop horizontal and vertical, standing-column wells, open- and closed-loop pond). The analytical model used in the GeoVision (The Distributed Geothermal Market Demand Model, known as dGeo) considered only the most common and widely applicable of these configurations: closed-loop

horizontal (field loops) and vertical (borehole) systems. Data and information from innovative ComGeo systems will be an important addition to future analysis to estimate the potential for geothermal district heating and cooling systems. Although GHP and GDHC technologies are commercially available, innovation is necessary to develop new systems in regions and communities that have been underserved in this technology space and to transition existing district-scale systems from fossil fuels to geothermal. Successful innovation can be measured by the degree to which a new or an existing system can transition to geothermal heating or heating and cooling.

2.3 Community Geothermal Deployment

Planning for potential system deployment, various ComGeo ownership options are under review by each ComGeo Coalition. The Ann Arbor, MI. team is in conversations with utilities and regulators about municipal ownership. Chicago team ownership options include the City of Chicago as a municipal entity owner or ownership through a private entity. The Duluth, MN. team is assessing business models for construction, ownership, maintenance, and operations. The Framingham, MA. team will decide whether to adopt the ownership model currently in place at an adjacent ComGeo system. The New York City Housing Authority would own their system as would the Wallingford, CT. Housing Authority own theirs. The Carbondale, CO. team is developing a plan that includes project finance, construction, retrofitting, ownership, and operation. The Hinesburg, VT. team is considering a joint development / utility ownership model where all-electric systems are made available to as many utility rate payers as possible and where it is easy for the customer to participate. The City of Seward, AK. would own their system. In Nome, AK. a consortium of five indigenous-led organizations would own their system, and in Shawnee, OK. the Citizen Potawatomi Nation would own theirs.

3. Community Geothermal Data Submissions to the U.S. DOE Geothermal Data Repository

The U.S. DOE Geothermal Data Repository (GDR) is the repository and catalog for data generated by projects funded by GTO (Weers et al., 2022). The GDR provides public access to geothermal datasets, which are increasing in variety, size, and complexity. GTO funds recipients are required to upload their project data to the DOE GDR as the project data is generated in its final form. ComGeo data sets uploaded as of the date of this writing include:

- GDR Submission 1594: “Ann Arbor Electricity and Gas Usage Data” describes hourly electric and gas data for a single-family home type: Worst, Mid, Best. Both the existing system type and replacement geothermal system is simulated.
- GDR Submission 1997: “Connecticut Workforce Needs Assessment Report and Data” provides a geothermal industry workforce needs assessment report for Connecticut.
- GDR Submission 1598: “Final Thermal Conductivity Test Report and Data Logs - Carbondale, CO.” includes the final thermal conductivity test report, a drilling log, and a heat rejection log from Carbondale, CO.
- GDR Submission 1590: “Thermal Conductivity Test and Data Analysis Report” from Wallingford CT. includes a report on a formation thermal conductivity test that was performed on the geothermal test bore at Ulbrich Heights in Wallingford, CT.

Additional details about data uploaded to the GDR is available at GDR: All Submissions (openei.org).

GTO looks forward to sharing additional data helpful to low-temperature geothermal development, including thermal conductivity and drilling datasets, across the country. To facilitate the submission of larger datasets, future ComGeo Coalition project data submissions may utilize a recently developed GDR tool known as an automated data pipeline. The first automated data pipeline implemented within the GDR is for drilling data. This pipeline currently supports and is capable of processing data from Pason (Pason Systems Corp., 2023) and RigCloud (Nabors Industries Ltd., 2021) drilling data platforms in Excel and CSV formats and may in the future be amended to standardize drilling data from other sources and in other formats as well. The pipeline recognizes the platform-specific field names and units and converts them to the standard field names and units in CSV format. The standard additionally includes the RIMBase drilling data platform (Infostat, 2023) field names (Taverna et al., 2023).

4. Community Geothermal Preliminary Case Studies

Case studies of different type of communities (Remote/Islanded, Urban/Suburban, Rural) are an important component of the overall ComGeo initiative. In Phase 1, preliminary case studies are anticipated from ComGeo Coalitions and final case studies at the end of the deployment phase are anticipated from those down selected to continue to Phase 2. During the last quarter of Phase 1 work, ComGeo Coalitions will decide which community, design, workforce or deployment related lessons or best practices to include in their preliminary case studies.

5. Conclusion

While GTO can fund only a subset of the 11 ComGeo Coalition projects to proceed to the deployment stage, the work accomplished by all the teams in Phase 1 is already making an impact on the future of geothermal heating and cooling. The 11 Phase 1 projects are enabling community-scale deployment of GDHC systems in a diverse set of communities by coalitions comprised of technical experts, community leaders, workforce innovators, and deployment professionals. The objective to support the formation of U.S. community coalitions that will develop and design ComGeo heating and cooling systems is more than halfway accomplished. In 2025, ComGeo Coalitions that deploy their systems are poised to supply at least 25% of their overall community heating or heating and cooling demand. Many of the communities are hoping to supply most of their heating or heating and cooling from deployed ComGeo systems.

REFERENCES

GDR. “DOE Geothermal Data Repository.” OpenEI: Open Energy Information. National Renewable Energy Laboratory (NREL), 12 June 2024. Web. https://gdr.openei.org/

Taverna, N., Weers, J., Huugins, J., Porse, S., Anderson, A., Frone, F., Scavo, R.J. 2023. “Improving the Quality of Geothermal Data Through Data Standards and Pipelines Within the Geothermal Data Repository.” *Proceedings of the 48th Workshop on Geothermal Reservoir Engineering*, Stanford University, Stanford, CA (2023).

Weers, J., Anderson, A., and Taverna, N. “The Geothermal Data Repository: Ten Years of Supporting the Geothermal Industry with Open Access to Geothermal Data.” *GRC Transactions, Vol. 46* (2022).

GeoVision: Harnessing the Heat Beneath Our Feet, 2019. (Section 4.2.1). U.S. Department of Energy, Geothermal Technologies Office).

A Preliminary Investigation on the Performance of a Dual-Source Heat Pump using both the Air and the Ground

Fady Anees[1, 2], Jyothis Anand[1], Bo Shen[1], Xiaobing Liu[1, *]

[1] Buildings and Transportation Science Division, ORNL, TN, USA

[2] University of Tennessee-Oak Ridge Innovation Institute, TN, USA

*** Corresponding author: liux2@ornl.gov (X. Liu)**

Keywords

dual-source heat pumps, integrate air- and ground-source, borehole length, energy efficiency

ABSTRACT

Air source heat pumps (ASHPs) and ground source heat pumps (GSHPs) are the two most common types of electric-driven heat pumps in the marketplace to replace fossil fuel-based heating systems. However, the performance and efficiency of ASHPs depend on the ambient air conditions. Therefore, ASHPs usually are equipped with electric resistance heaters to provide supplemental heating when the ambient temperature is low, and the heating demand is high. The electric resistance heaters could result in high power draws when they are turned on. On the other hand, due to the relatively steady temperature of the ground, GSHPs are more energy efficient than ASHPs when providing space heating and cooling to the buildings. However, the adoption of GSHP is hindered by its high initial cost, mostly due to the cost of drilling boreholes for installing ground heat exchangers (GHE). To solve the above issues, our study investigates the performance of dual-source heat pumps (DSHPs) with respect to that of ASHPs and GSHPs. The DSHP will use ambient air when its temperature is favorable for the efficient operation of the heat pump. When the ambient temperature is too hot or too cold, the ground source will be utilized to retain the high-efficiency operation of the heat pump. Because the cumulative thermal load of the GHE is shared with the ambient air, the size of the GHE could be smaller than those of the conventional GSHPs. The study will model the DSHP and simulate its performance in providing heating and cooling for a typical single-family house in regions with hot, mild, or cold climates. In addition, the required GHE size of the DSHP system will be determined through annual simulations and compared with that of conventional GSHPs.

1. Introduction

In the U.S., residents spend 90% of their time indoors, thereby resulting in a substantial sum of money on building energy costs—upwards of $370 billion annually (Langevin et al., 2024), as heat related mortality is considerably correlated with indoor air temperature (Sailor et al., 2021). Therefore, switching to clean energy sources for buildings and cutting back on total energy use

will not only mitigate climate concerns but also improve everyone in America's health and financial security. Moreover, replacing fossil fuel-based heating systems with electric-driven heating systems can improve indoor air quality (Kelly et al., 2016). The current U.S. administration aims to reduce carbon emissions from U.S. buildings by 65% by 2035 and 90% by 2050 compared with 2005 while enabling net-zero emissions economy-wide (Langevin et al., 2024). Building decarbonization is the key to these targets. Currently, natural gas-based space heating accounts for 52% of the U.S. residential buildings (EIA, 2020). Air source heat pumps (ASHPs) and ground source heat pumps (GSHPs) are the two most common types of electric-driven heat pumps in the marketplace to replace fossil fuel-based heating systems.

A recent modeling study shows that a majority of Americans (at least 62% of households, depending upon the heat pump efficiency) would observe a reduction in their energy bills by upgrading to ASHPs. Moreover, the study shows that ASHP could be cost-effective without subsidies in 59% of households (Wilson et al., 2024). However, another numerical study shows that, whole-house electrification with ASHPs may raise aggregated peak loads in the US by 70% and in 23 US states by more than twice as much (Waite & Modi, 2020). This is mostly because the efficiency and heating/cooling capacity of ASHPs depend on outdoor conditions when they are in use. Therefore, lower outdoor air temperature results in lower efficiency and capacity of ASHPs while heating and vice versa for cooling. As a result, ASHPs are equipped with electric resistance heaters to provide supplemental heating. These electric resistance heaters are turned on when the outdoor temperature is low, and the heating demand is high, thereby resulting in high power draws during peak hours.

Considering the relatively steady temperature of the ground, GSHPs are more energy efficient than ASHPs when providing space heating and cooling to the buildings. Therefore, employing GSHP technology is one workable way to reduce the need for US electric power systems to have their capacity and transmission increased. For instance, GSHPs require 30–50% less than the seasonal average power usage for supplying the same amount of cooling or heating using air-to-air heat pumps, which use the outdoor air as a heat sink/source (Ahmadi et al., 2018). Moreover, mass deployment of GSHP in the U.S. can reduce 26% of carbon emissions from the building sector (Liu et al., 2023). However, the high initial cost of GSHPs is impeding its adoption (Liu et al., 2022). This is primarily because installing GSHP requires drilling boreholes in the ground for installing ground heat exchangers (GHE). The amount of energy released to the ground during cooling and the quantity of energy gained during heating affect a GHE's size and cost. Given the immense thermal storage capacity of the ground, the heat transfer process of a GHE is nearly transient all the time, and thus both the total thermal loads and peak demand of a GHE need to be accounted for when sizing a GHE.

The current numerical study proposes a novel way to use ground and air as heat pump’s source/sink based on the demand. The proposed dual source heat pump (DSHP) will use outdoor air when its temperature is favorable for the efficient operation of the heat pump. When the ambient temperature is too hot or too cold, the ground source will be utilized to retain the high-efficiency operation of the heat pump. The proposed DSHP will have an additional heat exchanger that enables switching between air and ground sources based on the intensity of the energy demand for every timestep. Therefore, DSHP will not potentially raise the regional scale peak demand capacity and transmission needs as that of mass deployment of ASHPs. Since the cumulative thermal load of the GHE is shared by the ambient air, the length of the borehole for the GHE of DSHP can be

smaller than the conventional GSHPs. Thereby, reducing the initial cost of GHE and operational cost by switching between air source and ground source, and possibly shortening the payback period.

The study will model the DSHP using a whole building energy simulation tool coupled with a Python plug-in to enable DSHP simulation and evaluate its performance in providing heating and cooling for a typical single-family home in regions with hot, mild, or cold climates. In addition, the required GHE size of the DSHP system will be determined through annual simulations and compared with that of conventional GSHPs. In the end, a lifecycle cost analysis will be conducted to compare ASHP, GSHP, and the DSHP. The findings from this study can be used as a guideline for homeowners, designers, and builders for new and existing building electrification applications.

2. Methodology

The study uses the whole building energy simulation tool, EnergyPlus v9.5, coupled with a Python plug-in for conducting the numerical analysis. EnergyPlus is a widely used and extensively validated whole building energy analysis software tool. It is an open-source platform developed by the U.S. Department of Energy's Building Technologies Office, as part of their building energy modeling program portfolio. The individual features of the tool and the modeling package as a whole have been validated in several previous studies. Each EnergyPlus simulation requires hourly weather data. The weather files used in this study are typical meteorological year files, which contain data for a specific location, listing hourly values of solar radiation and meteorological elements for one year. These values are obtained by combining previous weather data observations. The latest typical meteorological year (TMY3) weather files. The current study used TMY3 weather files of a hot city, moderate city, and cold city to evaluate the performance and lifecycle cost analysis of DSHP over ASHP and GSHP.

2.1 Single family prototype building models

This study utilizes the U.S. Department of Energy's prototype building models, created following the 2006 edition of IECC, for single-family detached houses (Mendon & Taylor, 2014), which represent a set of identical 221 m^2 two-story houses that use various heating systems and foundation types. ASHP and slab-on-grade foundation are used as the ASHP models for this study, see Figure 1. The prototype building model for ASHP has a nominal heating coefficient of performance of 3.69 and 4.07 that of cooling. The model has supplementary resistance heater which turns on when the temperature is below 7.2°C (45°F) and it works along with the heat pump till the temperature reaches -17.78°C (0°F). Once the temperature goes below -17.78°C (0°F), the compressor of the ASHP is automatically shut off, only electric resistance is the only source for heating. The characteristics of these prototype buildings, such as the insulation level of building envelopes are in compliance with one of the several editions of the International Energy Conservation Code (IECC) for each climate zone (CZ).

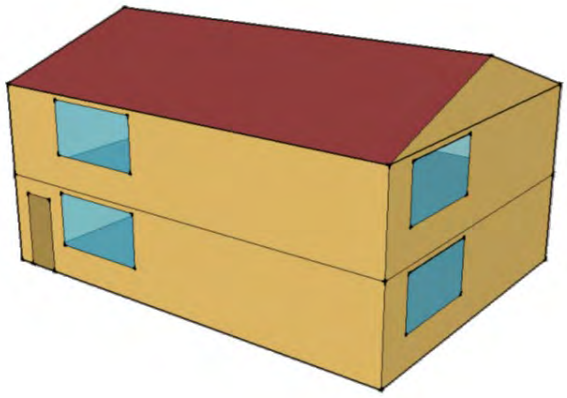

Figure 1. Single family prototype building model used in this study.

2.2 Modeling ground source heat pumps

The original ASHP system of the prototype building model is replaced with a GSHP system. The developed GSHP system includes an extended range water-to-air heat pump, a vertical bore GHE, and a circulation pump. The heating and cooling coefficients of performance of the GSHP system are kept as 4.0 and 6.5, respectively, at the rating conditions for the ground loop application mentioned in the ANSI/AHRI/ASHRAE/ISO Standard 13256-1 Water-to-Air and Brine-to-Air Heat Pumps — Testing and Rating for Performance. The design parameters of the default vertical borehole GHE used in this study can be seen in Table 1. The undisturbed ground temperatures are based on a dataset created by (Xing et al., 2017).

Table 1. Vertical borehole GHE design parameters

Parameter	Default value	Parameter	Default value
Borehole radius (m)	0.0762	Grout heat capacity (kJ/m3-K)	3,900
U-tube pipe thickness (m)	0.0024	Ground conductivity (W/m-k)	1.3
U-tube pipe outer dia. (m)	0.0267	Ground heat capacity (kJ/m3-K)	2,347
U-Tube distance (m)	0.025	Design flow rate (m3/s)	0.000689
Pipe conductivity (W/m-K)	0.3913	Bore spacing (m)	6.5
Pipe heat capacity (kJ/m3-K)	1,770	Maximum GHE supply temp. (°C)	35
Grout conductivity (W/m-k)	1.3	Minimum GHE supply temp. (°C)	-3

The building models used in this study use design day cooling and heating loads to auto-size the capacity of the water-to-air heat pump. This method may not always size the heat pump system with sufficient capacity. In certain cases, the unmet hours (i.e., the hours when the room temperature is not maintained at the set point) could be more than 300 hours, which is the maximum unmet hours recommended by ANSI/ASHRAE/IES Standard 90.1-2010's Performance Rating Method Reference Manual (Goel & Rosenberg, 2016). To ensure the total unmet hours in our study are always less than 300 hours, the auto-sized heat pump capacity is corrected, by increasing heat whenever it is necessary.

The design parameters of the vertical borehole GHE, including the undisturbed ground temperature, and thermal loads of the GHE predicted with an initial simulation of the GSHP

system, which uses a roughly sized GHE, are used to more accurately size the GHE using GHEDesigner (v 1.3). The sized GHE, including the number of boreholes, the layout of the borehole field and the depth of each borehole, and the associated g-functions are used to revise the building energy simulation model to perform the final simulation.

2.3 Modeling dual source heat pumps

The dual source heat pump (DSHP) is modeled by dynamically connecting the EnergyPlus simulation model with Heat Pump Design Model (HPDM) through an EnergyPlus Python plugin as shown in the Figure 2.

Figure 2. Co-simulation using EnergyPlus, Python Plugin, and Heat Pump Design Model

EnergyPlus model includes building information, weather data, schedules, loads, loops, plants, branches, GHE, heat pump, and reports the required outputs. HPDM is a research software designed by Oak Ridge National Laboratory under sponsorship of the U.S. Department of Energy (https://hpdmflex.ornl.gov/hpdm/wizard/welcome.php) for detailed physics-based modeling of various heat pumps. It predicts performance, including heating/cooling capacity and power consumption) of heat pumps in the four different modes (air-source heating, air-source cooling, water-source heating, and water-source cooling) in response to given operating conditions (e.g., ambient air temperature or supply water temperature of the ground heat exchanger). The predicted performance is compared with the performance at reference conditions (i.e., the Air-Conditioning, Heating, and Refrigeration Institute rating conditions for ASHP and GSHP). The calculated ratios at each simulation time step are sent through Python Plugin to the EnergyPlus model to replace the ratios determined using the default performance curves of heat pump in the EnergyPlus model. Python plugin works as a connector between EnergyPlus and HPDM and includes a control strategy to decide the needed operation mode and apply corresponding heat pump mode in HPDM. By coordinating the EnergyPlus model, Python plugin, and HPDM at each simulation time step, the performance of a DSHP is predicted. In this study, a simply control strategy is implemented in the Python plugin to automatically run the DSHP. For cooling operation, if the outdoor air is hotter than 80 °F (26.67°C) and the GHE outlet water is cooler than the outdoor air, then the GSHP system is used to meet the space cooling demands, otherwise, ASHP will meet the space cooling demand. In the case of space heating, the model uses ASHP when the outdoor air temperature is above 42°F (5.5°C), otherwise GSHP is used. Below 42°F (5.5°C), the chance for frosting will be higher (Wang et al., 2018), and therefore, the use of GSHP is more energy efficient than ASHP.

The DSHP simulation is done in the following steps as shown in Figure 3:

1. The initial simulation of DSHP uses the GHE details from the GSHP model.

2. If needed, the DSHP heat pump capacity is adjusted to ensure total unmet hours are less than 300 hours.
3. GHE heat transfer load data is used as input for the GHEDesigner to update the GHE size for the DSHP model.
4. If needed, GHE size is adjusted manually to ensure total unmet hours are less than 300 hours.
5. Conduct the final simulation of DSHP using the updated heat pump size and GHE design details.

2.4 Building Energy Simulations

The simulation is conducted for 3 U.S. climate zones, based on ASHRAE. The study considers one representative city for each climate zone, Minneapolis, MN for a cold climate (ASHRAE climate zone 6A), Albuquerque, NM for a moderate climate (ASHRAE climate zone 4B), and Miami, FL for a hot climate (ASHRAE climate zone 1A). The undisturbed ground temperatures used for DSHP and GSHP building models for 24℃, 16.4℃, and 9.1℃ are Miami, Albuquerque, and Minneapolis, respectively, based on the dataset created by (Xing et al., 2017). The study uses a Python module, Eppy, for conducting the parametric simulation (Glazer, 2016). The default options[1] of the prototype building models are modified slightly to conduct this simulation.

Result and Discussion

3.1 Heat pumps capacities

Table 1 shows the heat pumps capacities for GSHP, DSHP and ASHP systems. GSHP and DSHP capacities are represented in ton refrigeration (ton) while ASHP capacities are represented in (ton) and (kW) for their auxiliary heaters. The table shows that DSHP systems have capacities that are equal or less than those of GSHP systems, as DSHP uses ground source during the peaks hours (when outdoor air condition is extreme). The capacities of ASHP are always lower than DSHP and GSHP, as auxiliary heaters play an important role while meeting peak heating demand.

Table 1. GSHP, DSHP and ASHP capacities

Climate zone	GSHP (ton)	DSHP (ton)	ASHP (ton + kW)
1A	3.13	3.13	3 Ton + 5kW
4B	2.87	2.87	2.5 Ton + 15kW
6A	5.93	5.67	4 Ton +25 kW

[1] The default prototype building models need EnergyPlus preprocessing software to execute "GroundSlabPreprocessorAverage", unfortunately, the current versions of Eppy don't support EnergyPlus preprocessing software while running the simulations, therefore, the outside boundary condition is changed to "Ground". For modeling outdoor infiltration, the prototype building models use the airflow network, which is replaced with an effective leakage area method for this study. The effective leakage area is kept at 0.142 m^2, estimated based on a correlation developed by a previous study (Chan, 2013), to represent 0.8 ACH in the buildings (representing a typical residential construction (Margaret et al., 2022).

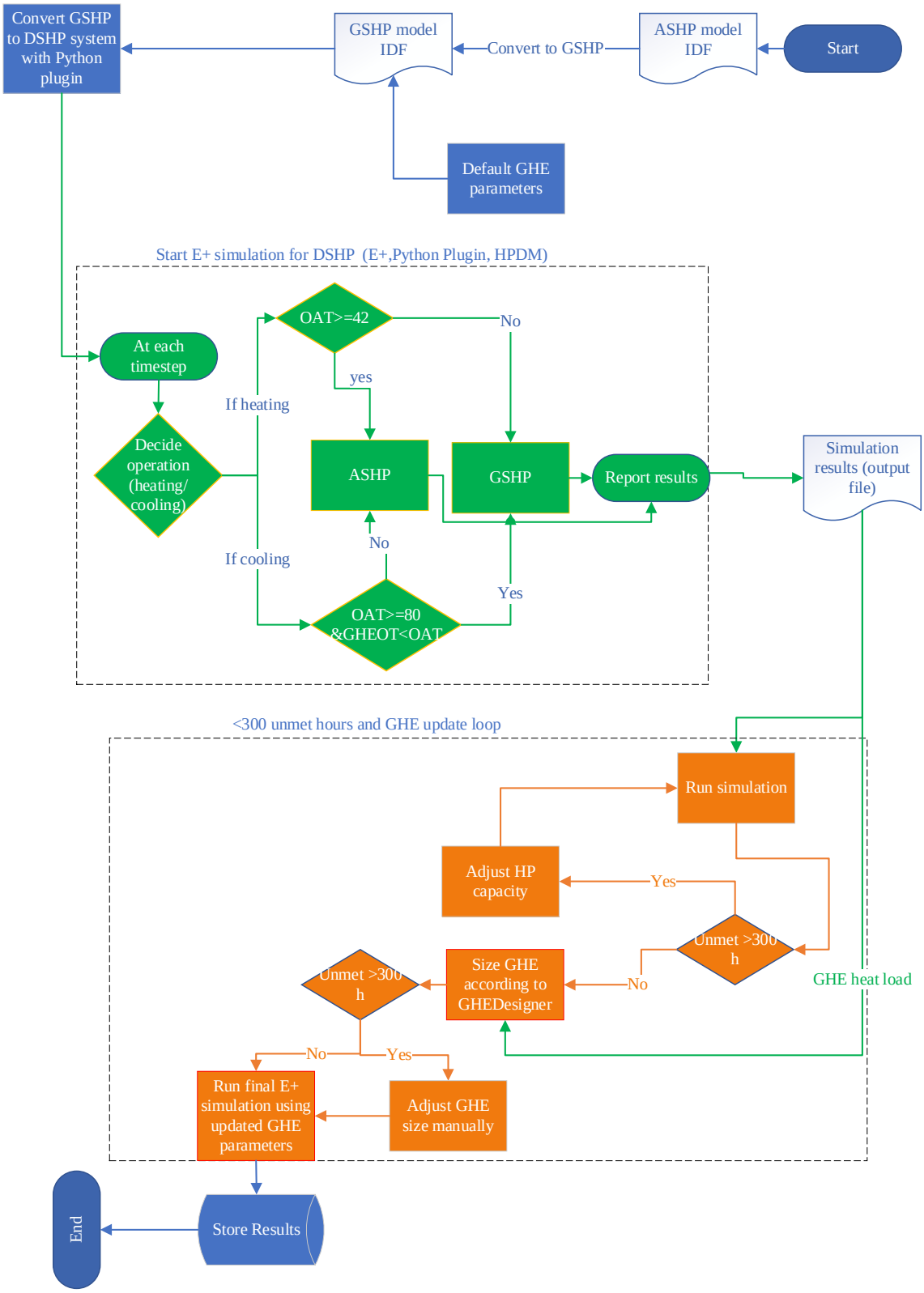

Figure 3. DSHP simulation process

3.2 Cooling and heating energy consumption

Figure 4 compares the cooling and heating electricity consumption for ASHP, GSHP, and DSHP for the three selected regions. The results from the study show that ASHP consumes more electricity than both GSHP and DSHP to meet the same thermal loads for space heating and cooling. For space cooling in Miami (1A), the electricity consumption of GSHP and DSHP is 36% and 7%, respectively, lower than that of ASHP, see Figure 4a. In the case of DSHP, it uses air-source cooling mode more frequently than ground-source cooling mode given the control strategy described before. In Albuquerque (4B), the space cooling electricity consumption is almost similar for the ASHP, DSHP, and GSHP, due to mild summer weather. In Minneapolis (6A), both DSHP and GSHP use less electricity for cooling than the ASHP because of the low ground temperature in this cold climate, see section 2.4.

On the other hand, for space heating, electricity consumption of GSHP and DSHP are ~40% and ~50% lower than ASHP in Albuquerque (4B) and Minneapolis (6A), respectively. Both GSHP and DSHP consumed about the same amount of electricity for meeting the heating demand. It indicates that DSHP runs in ground-source heating mode more frequently than in air-source heating mode. In Miami (1A), electricity consumption is almost the same for all due to warm weather there, even in the winter months.

Figure 5 shows the combined electricity consumption for space heating and cooling in the three locations. The results show that, the combined electricity consumption of DSHP lies between that of ASHP and GSHP. In Miami (1A), the combined electricity consumption of DSHP is closer to that of ASHP due to mild winter weather and the DSHP operates in air-source cooling mode more frequently than ground-source cooling mode. In moderate and cold regions, Albuquerque (4B) and Minneapolis (6A), the combined electricity consumption of DSHP is closer to that of GSHP.

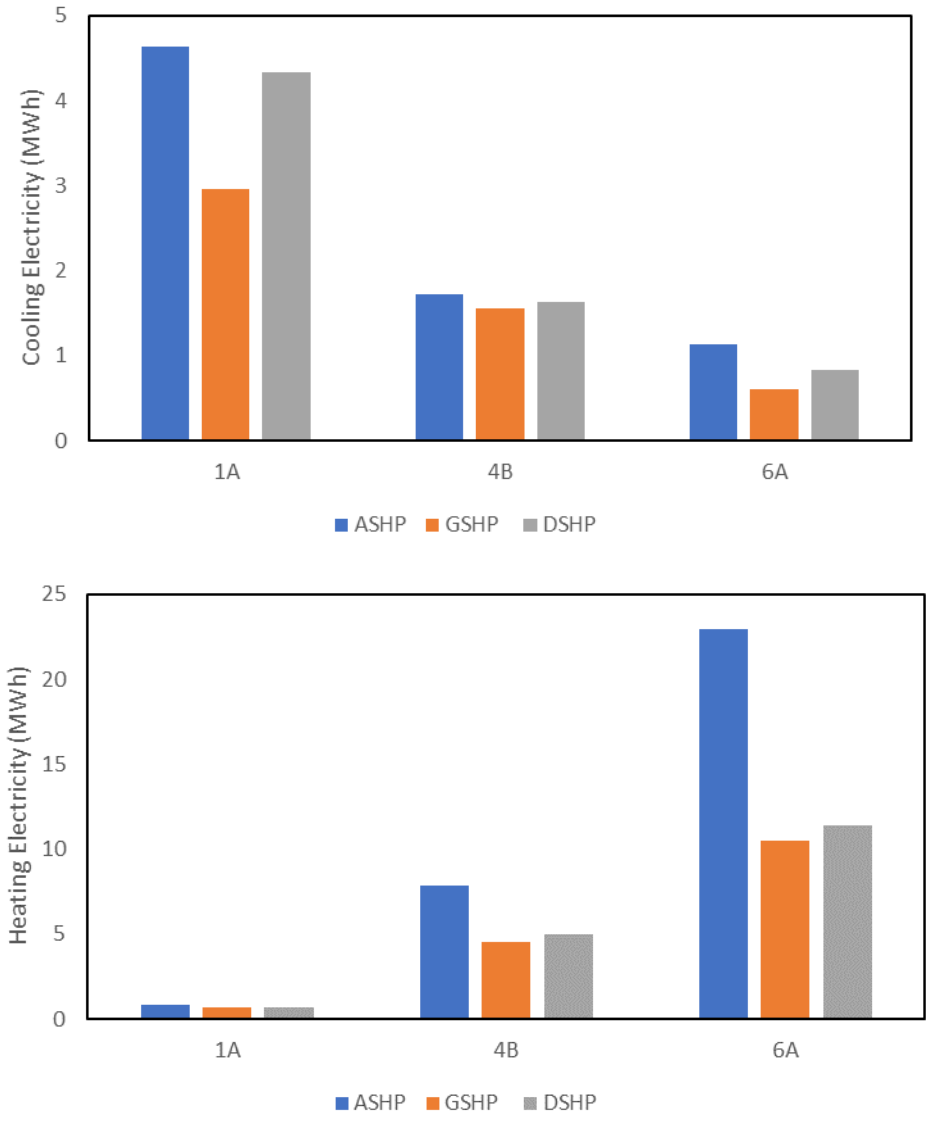

Figure 4. Comparison of a) cooling and b) heating electricity usage for 3 selected regions when electrifying the single-family houses with ASHP, GSHP, and DSHP.

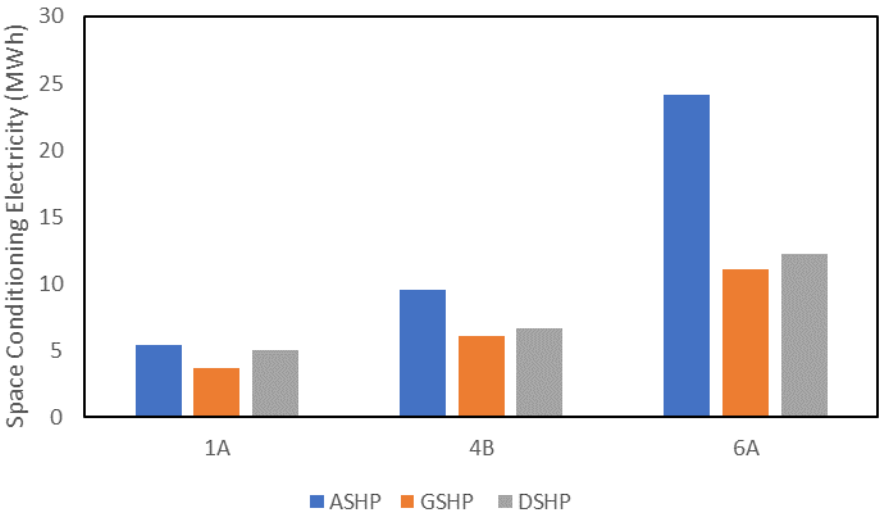

Figure 5. Combined electricity consumption for space heating and cooling in 3 selected cities when electrifying the single-family houses with ASHP, GSHP, and DSHP.

3.3 Borehole length

Figure 6 shows the required borehole length for both GSHP and DSHP in the three locations. The results show that the required total borehole length for DSHP is significantly smaller than that of GSHP. The reason for this reduction is because DSHP does not solely depend on GHE as a heat source/ heat sink. It utilizes air whenever the ambient air temperature is favorable, which reduces the load on the GHE and hence reduces the required borehole length. Interestingly, the reduction in borehole length is significant in extreme climatic locations, therefore it can largely reduce the initial cost for implementing GSHP there. For instance, in Miami (1A), the required total borehole length of DSHP is 325 m shorter than that of GSHP. In Minneapolis (6A), the reduction is 250 m. In Albuquerque (4B), the reduction is 49 m because the required total borehole length of GSHP is low compared with that in the other two cities.

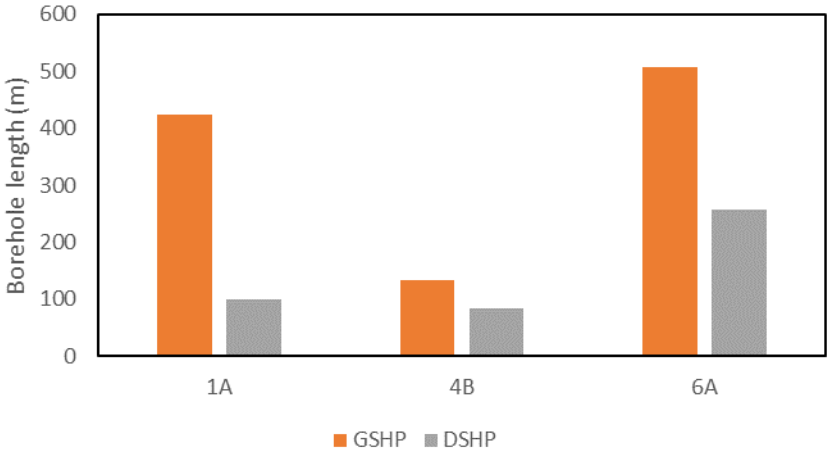

Figure 6. Required borehole length for the selected 3 cities.

3.4 Comparison of DSHP and GSHP

Figure 7 shows the change in the required total borehole length and the combined electricity consumption for space cooling and heating in the three locations when comparing the DSHP system to the GSHP system. The results show that, in Miami (1A), using DSHP instead of GSHP system can cut the required total borehole length by 77%, but it will increase the combined electricity consumption by 38%. In Minneapolis (6A), the required total borehole length is shortened by almost half, and the total electricity consumption is increased only by 10%. Similarly, in Albuquerque (4B), the required total borehole length was reduced by 37% and the total electricity consumption only increases by 8%. In case of hot city, Miami (1A), even though penalty in electricity percentage increase when comparing DSGP system to the GSHP is higher (38%), as shown in Figure 7, their absolute increase in electricity consumption is considerably smaller than moderate or cold regions, as their overall space cooling and heating requirement is lower, see Figure 5.

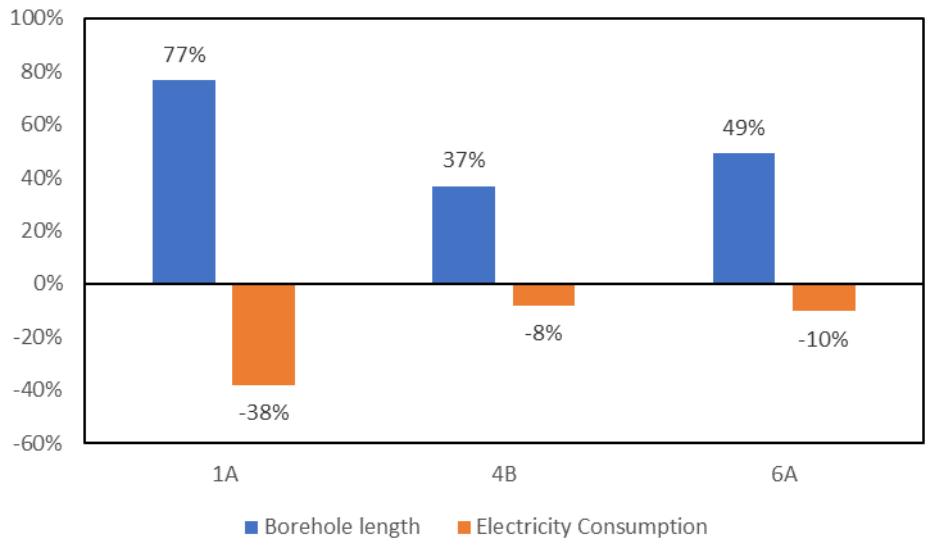

Figure 7. The change in the required borehole length and electricity consumption for meeting the heating and cooling demand of the SHF after converting the GSHP system to the DSHP system.

Conclusions

The results from this study show that deployment of GSHP consumes the lowest electricity for space heating and cooling for single-family houses in hot, moderate, and cold climatic regions. For all the considered regions, DSHP consumes less electricity than ASHP for both space heating and cooling but more electricity than GSHP. However, the borehole length requirement for meeting the thermal demands of DSHP is significantly lower than that of the GSHP, thereby showing the ability to significantly reduce the initial cost for GHE deployments. Therefore, lifecycle cost analysis is to be conducted to compare ASHP, GSHP, and the DSHP to investigate their economic feasibilities. The next step of this study is to conduct an economic analysis accounting for the

added cost of the DSHP unit, reduced cost for GHE, and the lifecycle operating cost. This economic analysis is expected to answer whether the deployment of the DSHP system is more cost-effective than that of GSHP and ASHP for different climates.

Acknowledgement

This study is a part of a project funded by the US Department of Energy (DOE) Office of Energy Efficiency and Renewable Energy, Geothermal Technologies Office. This manuscript has been authored by UT-Battelle, LLC, under contract DE-AC05-00OR22725 with the US Department of Energy (DOE). The US Government retains and the publisher, by accepting the article for publication, acknowledges that the US government retains a nonexclusive, paid-up, irrevocable, worldwide license to publish or reproduce the published form of this manuscript or allow others to do so, for the US government purposes. DOE will provide public access to these results of federally sponsored research in accordance with the DOE Public Access Plan (http://energy.gov/downloads/doe-public-access-plan).

REFERENCES

Ahmadi, M. H., Ahmadi, M. A., Sadaghiani, M. S., Ghazvini, M., Shahriar, S., & Alhuyi Nazari, M. (2018). Ground source heat pump carbon emissions and ground-source heat pump systems for heating and cooling of buildings: A review [https://doi.org/10.1002/ep.12802]. *Environmental Progress & Sustainable Energy*, *37*(4), 1241-1265. https://doi.org/https://doi.org/10.1002/ep.12802

Chan, W. (2013). *Analysis of Air Leakage Measurements from Residential Diagnostics Database*.

Glazer, J. (2016). Using python and Eppy for a large national simulation study.

Goel, S., & Rosenberg, M. I. (2016). *ANSI/ASHRAE/IES Standard 90.1-2010 Performance Rating Method Reference Manual*.

Kelly, J. A., Fu, M., & Clinch, J. P. (2016). Residential home heating: The potential for air source heat pump technologies as an alternative to solid and liquid fuels. *Energy Policy*, *98*, 431-442. https://doi.org/https://doi.org/10.1016/j.enpol.2016.09.016

Langevin, J., Wilson, E., Snyder, C., Narayanamurthy, R., Miller, J., Kaplan, K.,…Geyer, J. (2024). *Decarbonizing the US Economy by 2050: A National Blueprint for the Buildings Sector*.

Liu, X., DeGraw, J., Malhotra, M., Forman, W., Adams, M., Accawi, G.,…New, J. (2022, 2022-12-01). Development of a web-based screening tool for ground source heat pump applications. United States.

Liu, X., Ho, J., Winick, J., Porse, S., Lian, J., Wang, X.,…Prem Anand Jayaprabha, J. A. (2023). *Grid Cost and Total Emissions Reductions Through Mass Deployment of Geothermal Heat Pumps for Building Heating and Cooling Electrification in the United States*. https://www.osti.gov/biblio/2224191https://www.osti.gov/servlets/purl/2224191

Margaret, P., Natalie Mims, F., Eric, W., Andrew, P., & Elaina, P. (2022). *End-Use Load Profiles for the U.S. Building Stock: Practical Guidance on Accessing and Using the Data*.

Mendon, V. V., & Taylor, Z. T. (2014). *Development of Residential Prototype Building Models and Analysis System for Large-Scale Energy Efficiency Studies Using EnergyPlus* ASHRAE/IBPSA-USA Building Simulation Conference, Atlanta, Georgia. https://www.osti.gov/biblio/1194327

Sailor, D. J., Anand, J., & Kalkstein, L. (2021). Potential overall heat exposure reduction associated with implementation of heat mitigation strategies in Los Angeles. *International Journal of Biometeorology*, *65*(3), 407-418. https://doi.org/10.1007/s00484-020-01954-5

Waite, M., & Modi, V. (2020). Electricity load implications of space heating decarbonization pathways. *Joule*, *4*(2), 376-394.

Wang, Z., Wang, F., Ma, Z., Song, M., & Fan, W. (2018). Experimental performance analysis and evaluation of a novel frost-free air source heat pump system. *Energy and Buildings*, *175*, 69-77. https://doi.org/https://doi.org/10.1016/j.enbuild.2018.07.031

Wilson, E. J. H., Munankarmi, P., Less, B. D., Reyna, J. L., & Rothgeb, S. (2024). Heat pumps for all? Distributions of the costs and benefits of residential air-source heat pumps in the United States. *Joule*, *8*(4), 1000-1035. https://doi.org/https://doi.org/10.1016/j.joule.2024.01.022

Xing, L., Spitler, J. D., & Bandyopadhyay, A. (2017). Prediction of undisturbed ground temperature using analytical and numerical modeling. Part III: Experimental validation of a world-wide dataset. *Science and Technology for the Built Environment*, *23*(5), 826-842.

Galleries-to-Calories (G2C): An International Collaboration Evaluating Thermal Energy Storage in Abandoned Mines for District Heating

Trevor Atkinson[1], Travis McLing[1], Robert Egert[1], Wencheng Jin[1], Christine Doughty[2], Patrick Dobson[2], Curtis Oldenburg[2], Yingqi Zhang[2], Tim Kneafsey[2], Christopher McDermott[3], Samuel Graham[3], Alejandro Perez Silva[3], and Pablo Rodriguez Salgado[4]

[1]Idaho National Laboratory

[2]Lawrence Berkeley National Laboratory

[3]The University of Edinburgh

[4]University College Dublin

Keywords

Thermal energy storage, District heating, Mines, Coupled process modeling, Waste heat

ABSTRACT

With the increasing focus on sustainable energy solutions and national net-zero emissions goals, repurposing of abandoned underground mines for thermal energy storage has the potential to make significant impacts. The international Geothermica consortium, Galleries to Calories (G2C), is investigating the potential for storing waste heat from a supercomputing facility in abandoned, flooded coal mines southeast of Edinburgh, Scotland. The system termed the Geobattery or GeoTES involves injecting heat into mine workings, conveying it using regional groundwater flow, and then using the stored thermal energy for district heating and cooling via heat pumps. The Edinburgh site is unique due to the connection of three individual collieries that are linked by underground roadways and hydraulically conductive coal seams, thus enabling heat to be readily stored and transported over several kilometers.

The internal structure of collieries poses challenges due to their partially unknown internal structure, involving fully excavated seams, partially mined pillars, open and collapsed tunnels, and unmined rock formations. To address these uncertainties, we propose to use a multi-level stochastic modeling approach using the open-source Multiphysics Object-Oriented Simulation Environment (MOOSE). Our team has developed a preliminary and geometrically simplified numerical model that focuses on the main coal seams. These seams are further subdivided into multiple subdomains so that they can be discretized individually. Initially, a stochastic analysis involving many thermo-hydraulic simulations is conducted to identify promising bulk parameter combinations that replicate field observations. Once these parameter combinations are determined, the model is extended in a second phase to incorporate the geomechanical effects associated with

various operational conditions of the Geobattery. This extension facilitates the necessary evaluation of heat plume migration and stress field changes, critical for assessing the mechanical stability of the collieries and heat losses that may occur during the operation of the Geobattery.

1. Introduction

The energy transition towards net-zero emissions will require viable long-term energy storage solutions that support communities formerly dependent on fossil fuels. An important application of subsurface energy storage is direct-use heating and cooling. Globally, heating and cooling represents almost half of energy consumption (IRENA, 2023). Repurposing of underground infrastructure including abandoned mines for thermal energy storage and district heating offers a promising avenue to address widespread energy storage challenges. Abandoned flooded coal mines commonly have relatively stable temperatures throughout the year, rendering them ideal candidates for thermal energy storage. The water in the extensive flooded workings is available as a working fluid for thermal energy transport. Moreover, their pre-existing interconnections, often across kilometers of lateral distance, minimize the need for costly drilling, which is a major expense in traditional geothermal energy endeavors involving heat pumps. This system, called the Geobattery or GeoTES, involves injecting heated water into mine workings, conveying it using regional groundwater flow, and then using the stored thermal energy for district heating and cooling via heat pumps as shown in Figure 1.

Internationally, abandoned coal mines have been effectively repurposed into district heating and cooling systems, exemplified by initiatives in Heerlen, the Netherlands (Roijen et al., 2007; Bazargan Sabet et al., 2008; Verhoeven et al., 2014; Adams et al., 2019), Springhill, Canada (Jessop et al., 1995), Asturias, Spain (Jardón et al., 2013; HUNOSA, 2019), and Bochum, Germany (Hahn et al., 2023). In the United Kingdom, ongoing research at the Glasgow Geothermal Energy Research Center (Adams et al., 2019; Monaghan et al., 2022) explores the feasibility of utilizing abandoned Scottish mines for thermal energy storage and district heating applications. Additionally, the utilization of subsurface reservoirs for data center cooling is a current interest of the United States Department of Energy with analyses having been completed in Colorado, Texas, and Virginia (Zhang et al., 2023, Zhang et al., in review).

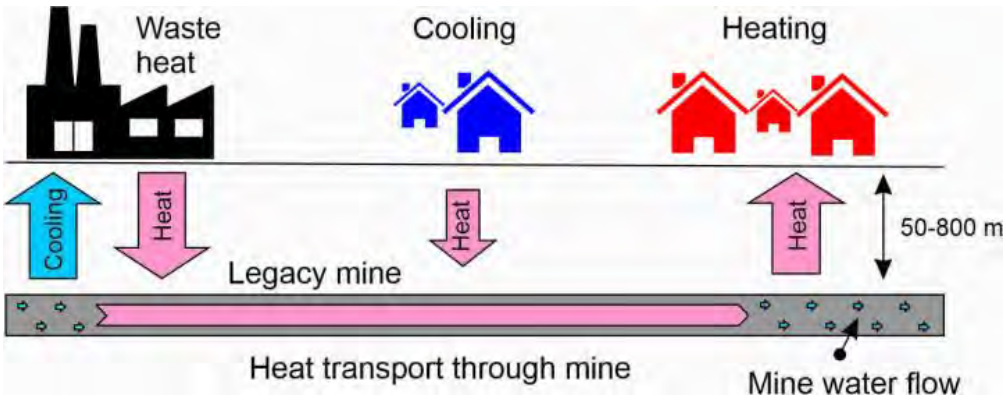

Figure 1: Schematic diagram showing the G2C Geobattery concept with waste heat injected in the mine that is recovered downgradient for heating.

Galleries to Calories (G2C) is an internationally supported Geothermica project led by industry and researchers from the University of Edinburgh and Townrock Energy as well as University of

Strathclyde-Glasgow, University College Dublin, Sandown Ltd, Scene, Idaho National Laboratory, and Lawrence Berkeley National Laboratory. The team aims to demonstrate heat storage and transport in legacy mine workings for recycled heat utilization via heat pump extraction near Edinburgh, Scotland. The specific application is to store waste industrial heat from a university data center in flooded abandoned coal mine workings and use that heat downgradient for community heating during winter months. Repurposing these mines presents technical and commercial challenges due to their intricate and unpredictable nature. We plan to employ advanced modeling methodologies to forecast the system's long-term performance, inform decision making, and conduct risk assessments. Presently, our efforts entail simplified modeling approaches pending the acquisition of more comprehensive field data. This paper provides an overview of the G2C field site, synthesizes pertinent literature, elucidates our initial modeling strategies, and outlines our forthcoming research agenda.

2. Site Description

2.1 Overview

The project site is located approximately 9 km south of Edinburgh, Scotland near the towns of Roslin, Bilston, Straiton, and Loanhead. The abandoned mine workings and their mine water in the Midlothian Coalfield (Figure 2) will serve as both the thermal storage and transport medium. The depth of these mine workings ranges from 50-800 m below the surface, but this project is focused on the upper 150 m to minimize drilling and future operational costs. The heat source for the project is the University of Edinburgh's Advanced Computing Facility (ACF) near the Easter Bush Campus. This facility will provide between 3-9 MW of waste heat to the subsurface. Adjacent communities located approximately 5 km downgradient of groundwater flow will be the main beneficiaries of the heat stored in the mines.

2.2 Geology and Hydrology

Southwest of Edinburgh lies the Pentland Hills rising to an elevation of approximately 578 m above sea level (masl). These hills consist of Devonian and Silurian sedimentary formations of the Old Red Sandstone and North Esk Group as well as extrusive volcanics of the Pentland Hills Volcanic Formation with basaltic and andesitic compositions (Tulloch and Walton, 1958). The Pentland Hills Fault forms the southeast edge of the hills with substantial downthrow to the southeast. Parallel to the Pentland Hills and approximately 13 km to the east of the Pentland Hills lies an unnamed set of hills extending from the coast at Prestonpans stretching towards D'Arcy Farm. Between these two prominent topographic features lies the Midland Valley and the Midlothian Coalfield (Figure 2, British Geological Survey, 2003).

The geology of the Midlothian Coalfield consists of basin-fill sandstones, siltstones, mudstones, ironstones, marine limestones, and coal-bearing units (Figure 3). The main units of interest for this study include the Upper Limestone, Limestone Coal, and Lower Limestone Formations, which contain various coal seams (Figure 4) including the Peacock and Kittlepurse Coals. These coals seams are semi-parallel and highly inclined with thicknesses of approximately 1 m (Figure 5).

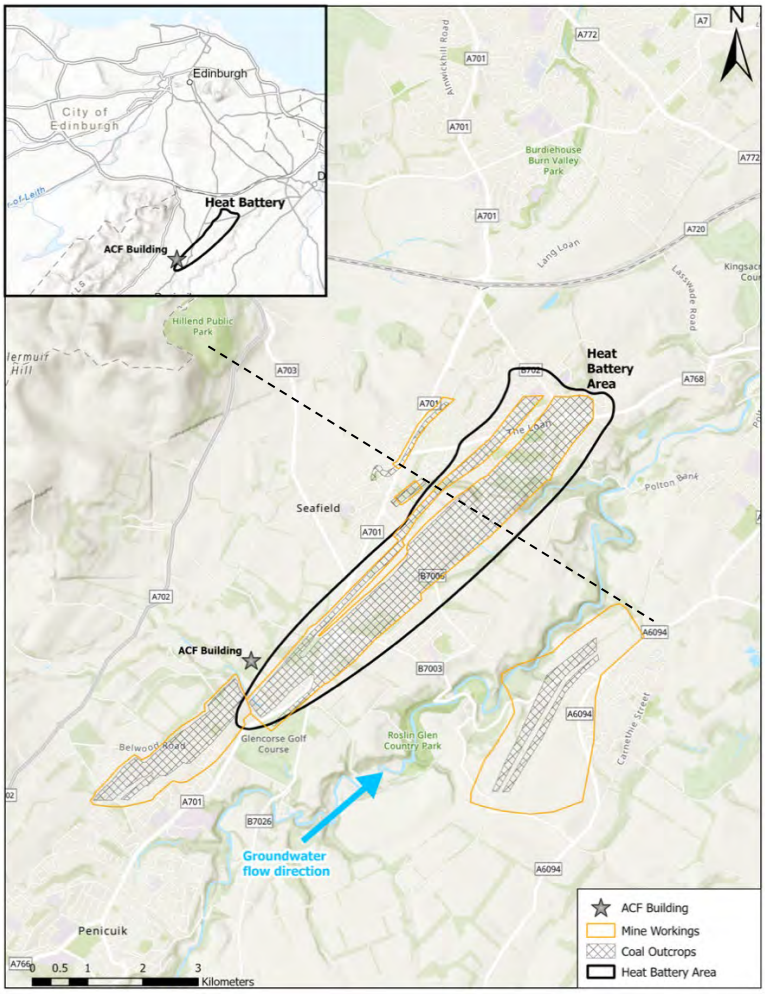

Figure 2: A regional map of the project location south of Edinburgh. Advanced Computing Facility (ACF) is the cooling-waste-heat source indicated by the green star. Hatched pattern represents portions of the legacy mine workings that will be utilized for the Geobattery. Dashed line represents the approximate location of the cross section in Figure 3.

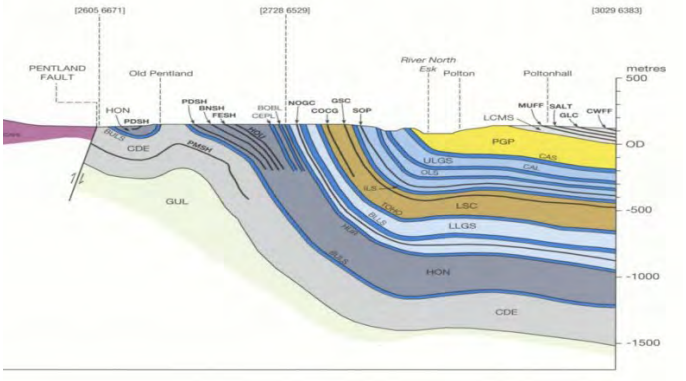

Figure 3: Cross section of the Midlothian Coalfield highlighting the edge and flat coals. Note the Pentland Hills Fault forming the western boundary of the field. Relevant geologic units include Lower Coal Measures (LCMS) Passage Formation (PGP), Upper Limestone Formation (ULGS), Limestone Coal Formation (LSC), and the Lower Limestone Formation (LLGS). (modified after British Geological Survey, 2003)

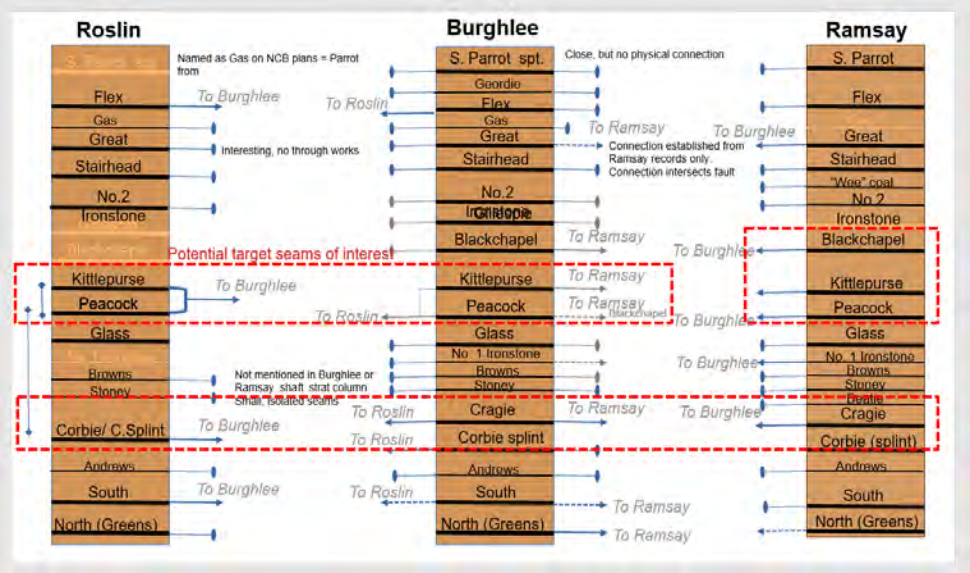

Figure 4. Named coal seams in each of the three collieries. The red dashed lines indicate seams that are hydraulically connected between collieries. Courtesy of Dr. Samuel Graham, University of Edinburgh.

The coalfield area is drained by the North and South Esk Rivers and their tributaries. After coal mining ceased in Scotland in the late 20th century, natural groundwater began filling voids left behind flowing from the southwest to the northeast. Groundwater is recharged by precipitation runoff from the surrounding Pentland Hills. Ambient groundwater temperatures can vary in the mines across Scotland ranging from 12-21° C with a mean of 17° C (Gillespie and Crane, 2013) but measurements from the Bilston Glen Colliery show 15° C. These temperatures can vary due to a variety of factors including the sampling location, the recharging source, the depth of the formation, and the local geothermal gradient, which can range from 17-34 °C/km in similar coal fields in Britain (Farr et al., 2020). Groundwater flow rates can vary widely due to the complex hydrogeological systems created from legacy mine workings and the result of decades of groundwater flow re-entering a system that had been modified for mining for so many years.

2.3 Legacy Mine Workings

For 200+ years coal mining in the UK was performed at differing intensity due to various supply and demand scenarios (Todd, 2023). Older mines utilized manual labor, employing the 'pillar and room' technique. Here, support props sustained the structure while explosives were employed to extract coal manually. Variations of this method were referred to as 'stoop and room' in Scotland (Younger and Adams, 1999). Typically, certain portions of coal, termed stoops or pillars, were intentionally left intact to ensure the stability of the workings (Figure 5). A series of these rooms and pillars would exist and be interconnected with tunnels containing mining rails and other equipment associated with coal extraction. These workings and all associated infrastructure are referred to as a colliery.

Within the proposed Geobattery area, there are three distinct collieries: Roslin, Burghlee, and Ramsay. Groundwater flow and mine water flow from the southwest to the northeast from Roslin to Ramsay, approximately 5 km away (see Figure 5). Vertical shafts at each colliery intersect various coal seams, as depicted in Figure 4. At Roslin, the coal seams are separated by distances ranging from 17 m to 55 m, with an average separation of around 35 m, and the pit bottom reaches

a depth of 280 m. Many of these coal seams are present in all three collieries, and some exhibit hydraulic connectivity, as indicated by the red dashed lines in Figure 4. These connected seams serve as the main pathways for fluid flow within the Geobattery.

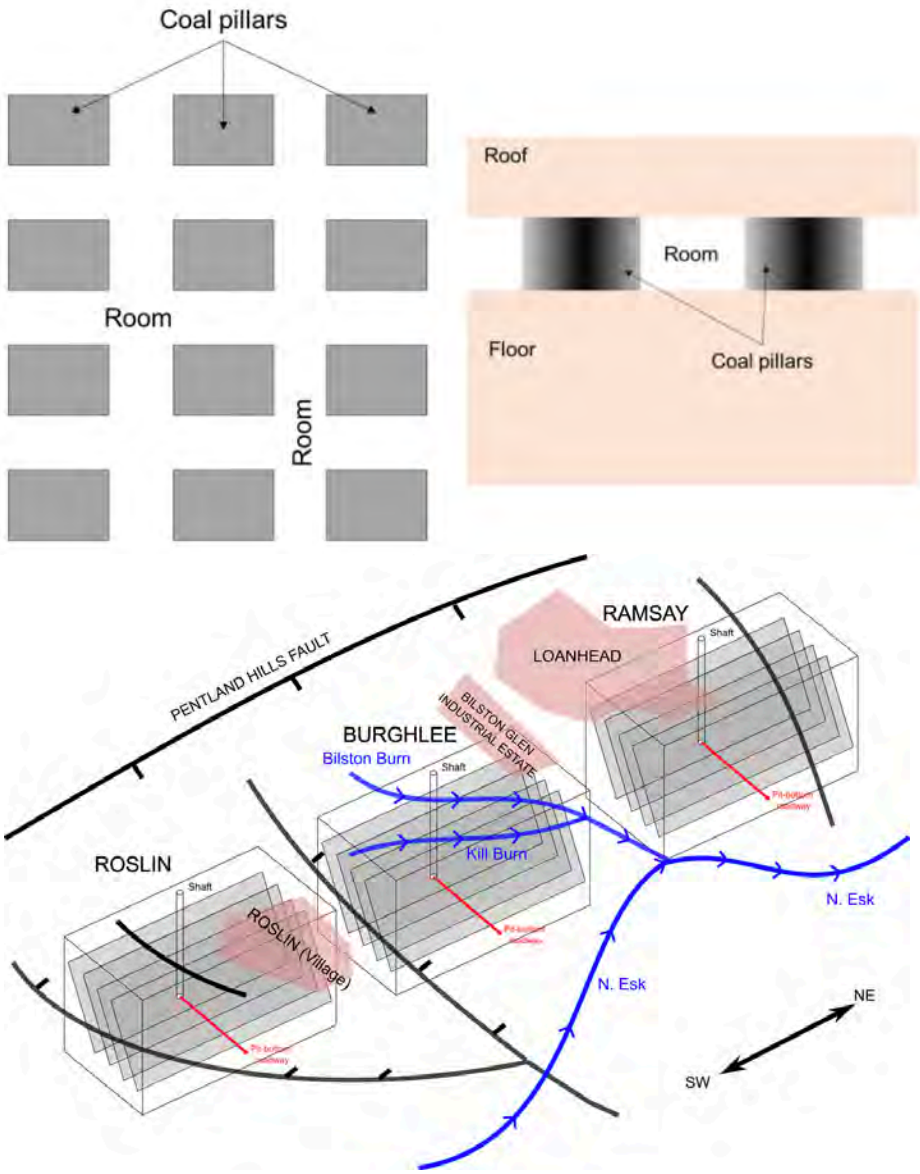

Figure 5: Top-Plan view and cross section view (left) of a simplified layout of a pilar and room working adapted from Younger and Adams (1999). Bottom-Schematic diagram of the tilted planar mined-out coal seams separated by low-permeability rock in the three collieries making up the Geobattery. The pit-bottom roadway connecting the coal seams at the bottom of the mine workings (~300 m deep) is also shown in red (Todd, 2023). Black curves are fault surface traces and blue lines are surface water courses.

3. Preliminary Modeling

Based on the geology described in Section 2, the project team has built a geological model with details on faults, fractures, and formation layers (Figure 6a). It is challenging to create a robust mesh considering all these features for multiphysics coupled simulation. The uncertainties related

to formation parameters (e.g., hydraulic conductivity) as well as the legacy mine working (i.e., pillar versus room) may lead to misinformed predictions of the system. Consequently, we focus on a simplified subset of the original large-scale structural mode while preserving essential geometric information concerning the extent of three collieries, the identified primary conduits for heat storage and transfer (i.e., the Kittlepurse and Peacock coal seams), the primary fault zone between the Roslin and Burghlee collieries, and the associated dip and thickness for each feature as shown in Figure 6b. Note that the team is using two distinct modeling approaches to represent the mine system: one involves a deterministic model implemented in the TOUGH code (Doughty et al., 2024), and the second employs a stochastic approach, using the MOOSE simulator. The initial results of the MOOSE simulations are described below.

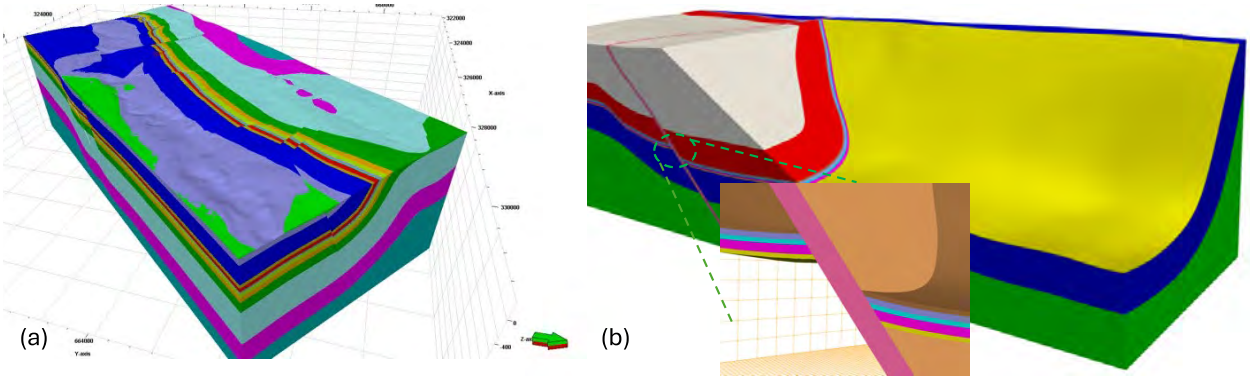

Figure 6. (a) A geological model with detailed structural features. (b) A simplified geological model with key features (i.e., heat transfer conduit – the Kittlepurse and Peacock coal seams and the fault between the Roslin and Burghlee collieries).

The site-specific initial distribution of temperature, effective stress, as well as pore pressure are all unknown at this stage. A 2D regional groundwater flow model at steady-state is used to approximate the pore pressure distribution. We used the open-source Multiphysics Object-Oriented Simulation Environment (MOOSE, Giudicelli et al. 2024) and performed hydraulic simulations using the parameters in Table 1. For boundary conditions, we applied no-flux boundaries for the two sides perpendicular to the ground water flow directions, while a hydraulic static pore pressure is applied at the downgradient surface. A ground water flow flux of 10^{-4} m/s is applied to the upgradient surface based on work done by Doughty et al. (2024). 15 L/s of water is injected into each of the targeted three coal seams (i.e., 45 L/s total water injection). Within this simulation, we used tracers to show the convective thermal plume distribution, excluding heat conduction. Figure 7 shows the tracer plume that reaches the fault and then continuously travels through the conductive coal seams to the downstream Burghlee and Ramsay collieries. The modeled tracer plumes show that the ground water flow difference across different coal seams within the Roslin colliery affects the tracer distribution. However, this impact is negligible once the plume passes through the fault.

Table 1: Parameters of coal seams and limestone bedrock used in initial modeling simulations.

Model component	Permeability (m^2)	Porosity
Coal Seam	10^{-12}	0.20
Fault	10^{-13}	0.05
Limestone bedrock	10^{-18}	0.01

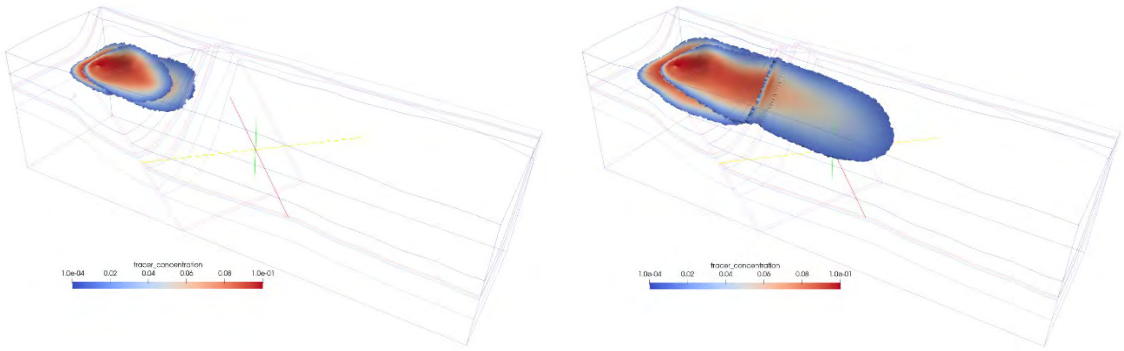

Figure 7. Tracer plume evolution after ½ year (left) and two years (right) of continuous water injection into the targeted Kittlepurse and Peacock coal seams.

The above hydraulic simulation will be expanded into thermo-hydraulic (TH) and thermo-hydro-mechanical (THM) coupled simulations with more *in-situ* data of effective stress and thermal gradient to constrain the model. In addition, we will subdivide the three coal seams into a suite of blocks and statistically assign material properties (e.g., Young's modulus, porosity, permeability) for those blocks so the pillars and rooms shown in Figure 5 can be represented. These statistical simulations will be used to reduce uncertainty by comparing and matching against future *in-situ* testing and monitoring data. Eventually, the THM models with reduced uncertainty will be used to predict performance, design operation, and quantify impacts of the Geobattery.

5. Conclusions and Future Work

The overall concept of storing waste heat in abandoned mine workings for seasonal district heating and cooling is of interest on the domestic and international scale. The mines beneath Edinburgh offer great a opportunity to explore the feasibility of mine thermal energy storage because of established flow paths, favorable groundwater flow magnitude, direction, and temperature, and interconnected mine workings. Initial modeling efforts show that flow is impacted by the fault separating the Roslin and Burghlee collieries. The plume of heated water then travels through the fault downstream, passing through the Kittlepurse and Peacock coal seams.

Over the next year, drilling will commence leading to data collection of key information to better constrain TH and THM simulation efforts. Once data are obtained on the various formations, the team will conduct more sophisticated modeling to ensure safe and efficient operations can be planned and executed for the project. The work being undertaken by the G2C consortium will be instrumental in evaluating this technology and in offering a solution for waste heat storage in mine workings and downstream utilization in community heating and cooling systems.

Acknowledgements

We are thankful for important discussions, data, and other support from the entire G2C team, including University of Edinburgh, TownRock Energy Ltd., University of Strathclyde, University College Dublin, Scene Connect Ltd., and Sandown Ltd. This material was based upon work supported by the U.S. Department of Energy (DOE), Office of Energy Efficiency and Renewable Energy (EERE), Geothermal Technologies Office, Low-Temperature Geothermal Program, under

Award Number DE-AC02-05CH11231 with LBNL and under Contract Number DE-AC07-05ID14517 with INL. The views expressed herein do not necessarily represent the views of the DOE or the U.S. Government. The G2C project is funded through the GEOTHERMICA consortium by several national funding agencies: Scotland (Scottish Enterprise), Ireland (Geological Survey Ireland), and USA (DOE). We are grateful for their support.

REFERENCES

Adams, C., Monaghan, A., and Gluyas, J.: Mining for heat, Geoscientist, 29(4), (2019), 10–15, https://www.geolsoc.org.uk/Geoscientist/Archive/May-2019/Feature-1.

Bazargan Sabet, B., Demollin, E., and Van Bergermeer, J.J.: Geothermal use of deep flooded mines, post-mining, Nancy, France, (2008), 11 p.

British Geological Survey, 2003, Edinburgh, Scotland Sheet 32E, Bedrock, 1:50,000, Keyworth, Nottingham, British Geological Survey, https://largeimages.bgs.ac.uk/iip/mapsportal.html?id=1002357

Doughty, C., Dobson, P., Oldenburg, C., Zhang, Y., Kneafsey, T., Egert, R., McLing, T., Atkinson, T., and Jin, W.: Thermohydrogeologic modeling for the Geothermica project G2C (Galleries to Calories). Proceedings, 49th Workshop on Geothermal Reservoir Engineering, (2024), Stanford University.

Farr, G., Busby, J., Wyatt, L., Crooks, J., Schofield, D.I. and Holden, A. 2020. The temperature of Britain's coalfields. Quarterly Journal of Engineering Geology and Hydrogeology.

Gillespie M.R., Crane E.J., B.H.F. 2013. Study into the Potential for Deep Geothermal Energy in Scotland. Volume 2 of 2. British Geological Survey, 2, 125.

Giudicelli, G., Lindsay, A., Harbour, L., Icenhour, C., Li, M., Hansel, J. E., ... & Permann, C. (2024). 3.0-MOOSE: Enabling massively parallel multiphysics simulations. SoftwareX, 26, 101690.

Hahn, F., Klein, S.,Güldenhaupt, J., ., Seidel, T, and König, T.: The high temperature-mine thermal energy storage (HT-MTES) project in Bochum Germany. 57th US Rock Mechanics/Geomechanics Symposium, (2023), ARMA 23-443.

HUNOSA: Barredo Colliery district heating, (2019), https://www.districtenergyaward.org/wp content/uploads/2019/09/19GDECADesc-DHeating-BarredoColling-Spain.pdf

Jardón, S., Ordóñez, A., Álvarez, R., Cienfuegos, P., and Loredo, J.: Mine water for energy and water supply in the central coal basin of Asturias (Spain), Mine Water Environ. 32, (2013), 139–151.

Jessop, A., Macdonald, J.K., and Spence, H.: Clean energy from abandoned mines at Springhill, Nova Scotia, Energy Sources, 17(1) (1995): 93–106.

Monaghan, A.A., Starcher, V., Barron, H.F., Shorter, K., Walker-Verkuil, K., Elsome, J., Kearsey, T., Arkley, S., Hannis, S., and Callaghan, E.: Drilling into mines for heat: geological synthesis of the UK Geoenergy Observatory in Glasgow and implications for mine water heat resources. Quarterly Journal of Engineering Geology and Hydrogeology, 55, (2022), qjegh2021-033.

Roijen, E., Op'tVeld, P., and Demollin-Schneiders, E.: The Minewaterproject Heerlen - Low exergy heating and cooling in practice, 2nd PALENC Conference and 28th AIVC Conference on Building Low Energy Cooling and Advanced Ventilation Technologies in the 21st Century, September 2007, Crete, Greece, (2007), 839–844.

Todd, F: Modelling the Thermal, Hydraulic and Mechanical Controlling Processes on the Stability of Shallow Mine Water Heat Systems, PhD Thesis, The University of Edinburgh, (2023).

Tulloch, W. and Walton, H.S., 1958. The Geology of the Midlothian Coalfield. Edinburgh: Her Majesty's Stationery Office, Department of Scientific and Industrial Research. Memoirs of the Geological Survey Scotland.

Verhoeven, R., Willems, E., Harcouet-Menou, V., De Boever, E., Hiddes, L., Op't Veld, P., and Demollin, E.: Minewater 2.0 project in Heerlen the Netherlands: Transformation of a geothermal mine water pilot project into a full-scale hybrid sustainable energy infrastructure for heating and cooling, Energy Procedia, 46, (2014), 58–67.

Younger, P.L. and Adams, R., 1999, Predicting Mine Water Rebound Research and Development, United Kingdom, DOI:10.13140/2.1.4805.5681

Zhang, Y., Acero-Allard, D., Atkinson, T., Beckers, K., Dobson, P., Jin, W., Lei, N., Oh, H., Peng, P., Sartor, D., & Sickinger, D., 2023, Addressing Data Center Cooling Needs through the Use of Subsurface Thermal Energy Storage Systems. In SPE Energy Transition Symposium. SPE-215746-MS.

Technical Feasibility of a Novel Geothermal-Solar Thermal Hybrid Plant

Carl Belmonte

Mapúa University

Keywords

Single-flash geothermal power plant, Solar parabolic dish, Hybrid power generation, Thermodynamic analysis, HelioFocus

ABSTRACT

Coal plants are more efficient than geothermal plants since thermal efficiency is proportional to temperature. When geothermal steam comes out of the well, the temperature is around 180°C compared to coal plants with steam temperatures greater than 500°C. This is why typical coal plants have a thermal efficiency of 36%, whereas geothermal has about 18%. In this work, a novel hybrid system was designed to control the temperature and pressure of geothermal steam to approximate the steam conditions and thermal efficiency of coal plants using solar thermal technology. The thermodynamic model of the hybrid system was developed wherein heat transfer was modified by directly using steam as the heat transfer fluid instead of air to eliminate heat loss in the heat exchanger resulting in more efficient use of solar energy. The results showed that the hybrid plant produced a net additional power output of 26% compared to a standalone geothermal plant due to increased thermal efficiency from 17% to 34%. The hybrid plant also performed better than geothermal and solar thermal plants operating separately. The novel design proved technically feasible and more efficient than all current hybrid designs. Detailed engineering design and economic feasibility of the proposed system are recommended for future studies.

1. Introduction

Geothermal energy is a renewable resource that is virtually unlimited much like solar and wind energy. However, its advantage over the latter is that it provides sustained thermal energy 24 hours a day and 7 days a week. Geothermal wells continuously produce steam because the Earth's magma will remain hot for billions of years. The disadvantage of geothermal energy is the geographic limitation. It is found in the boundaries of tectonic plates such as the Circum-Pacific Belt. The Philippines has access to geothermal steam resources because it is a part of this region. Another disadvantage is that the quality of geothermal steam is beyond the control of engineers. Steam

quality can be controlled in a coal power plant because it is produced in the boiler. In contrast, in a geothermal power plant, the quality of the steam depends on the characteristics of the geothermal reservoir. Geothermal steam loses energy as it goes up the well due to pressure loss, friction, and turbulence. In power generation, the temperature is above 150°C (Li et al., 2020) when the steam comes out of the well compared to the steam in coal plants which is superheated at much higher temperatures. This is why coal power plants are more efficient than geothermal power plants because thermal efficiency is proportional to temperature. Generally, the higher the temperature, the higher the efficiency. If the temperature and pressure of geothermal steam can be controlled in such a way that it approximates the steam in coal power plants, then the thermal efficiency of geothermal power plants will significantly increase. Solar thermal energy systems, particularly concentrated solar power (CSP), can be utilized to achieve this improvement in power plant performance. If the two systems are combined in such a way that they produce a common steam output, then the hybrid system will be more efficient than the two separate systems. In solar energy, CSP is falling behind solar photovoltaic (PV). As of 2020, the global installed capacity of solar PV and CSP is 707 and 6 GW, respectively, according to the International Renewable Energy Agency (*Renewable Capacity Statistics*, 2021). One reason for this large gap in installed capacity is that PV is a simpler system with no moving parts. It directly converts solar energy to electricity without needing conversion to mechanical energy such as a rotating turbine and electric generator. Solar thermal energy plants need a thermodynamic cycle to convert heat to electricity. It also requires more equipment and has a higher capital cost than PV. Another reason is that PV costs have dropped due to economies of scale in manufacturing and low production costs in China. Despite the disadvantages, solar thermal energy systems have one important advantage. Combined with a geothermal power plant, it can improve the overall thermal efficiency of the combined Rankine cycle. It has a synergy with geothermal energy that PV cannot offer.

Several hybrid designs for geothermal-solar thermal systems have been proposed in the literature. Cardemil et al. (2016) analyzed the performance of single and double-flash geothermal power plants integrated with parabolic trough collectors (PTC) for various reservoir conditions. The results showed that a greater increase in power output was observed when solar thermal energy was used in superheating the steam compared to evaporating the brine for both single and double-flash hybrid plants. The 2nd law efficiency also increased by at least 3% when the steam temperature increased. Similarly, Assad et al. (2021) investigated the hybridization of a single-flash geothermal power plant and a PTC system. The steam temperature increased by 50°C due to the additional heat provided by the PTC, effectively increasing the steam temperature from 200°C to 250°C and improving the power output and efficiency of the system. McTigue et al. (2018) evaluated different methods for adding solar heat to a double-flash geothermal power plant. It was found that reheating the brine was the best approach to reduce the risk of scaling and the cost of retrofitting. Bonyadi et al. (2018) proposed a novel hybrid solar geothermal power plant by adding a solar topping steam Rankine cycle to a binary geothermal power plant and assessed its performance. The hybridization scheme led to a higher solar-to-electricity conversion efficiency without affecting the binary bottoming cycle. The power output also increased during the summer days and consumed fewer geothermal resources than a stand-alone binary geothermal power plant.

This paper presents some key differences in the design of the proposed hybrid geothermal-solar thermal system compared to other hybrid systems in the literature. The main difference lies in the type of solar collectors used in the solar thermal system. Solar parabolic HelioFocus dishes are selected in this work because they can produce higher heat transfer fluid temperatures, higher

topping cycle steam temperatures, and higher thermal efficiencies than PTCs or other CSP technologies (Keck et al., 2015). The innovation in the novel hybrid system is implementing all these improvements in a single system. The study is needed to prove in principle that the proposed geothermal-solar thermal hybrid plant is different from and superior in some measures to other hybrid systems found in the literature.

This study aims to design a system to control the temperature and pressure of geothermal steam to approximate the steam conditions in coal power plants using HelioFocus or similar technology. The objectives are: (1) to develop a thermodynamic model of the proposed hybrid geothermal-solar thermal system; (2) to modify the heat transfer between the geothermal steam and the hot air; and (3) to evaluate the performance of the proposed hybrid system.

The long-term plan is to develop this novel technology by conducting further research, building a small prototype plant, and eventually commercializing the technology. Only after making the technology available to the industrial market will society benefit from it. Geothermal power producers will benefit from increased thermal efficiency and power output if the commercialization is successful. The benefits will reach consumers through lower electric costs and less carbon dioxide emission than fossil fuel plants. This will also mitigate the public's grave concern about climate change.

This study covers the basic design, specifications, and thermodynamic model of a hybrid single-flash geothermal-solar thermal power plant. It aims to demonstrate the technical feasibility and increase in thermal efficiency and electrical energy output of the proposed hybrid geothermal-solar thermal system. The data in this paper are gathered from technical literature on hybrid geothermal-solar thermal systems and interviews with an engineer with working experience in geothermal power plant operations. The thermodynamic and heat transfer model is theoretical. It is based on specialized software modeling and manual computations. Assumptions in the model are based on either data gathered or extrapolation of data. The solar thermal system is based on HelioFocus solar dish technology. Data from HelioFocus is used when available. This study does not cover the detailed engineering design of the equipment and components of the proposed hybrid geothermal-solar thermal system. It is limited to available technical data from HelioFocus. Since the thermodynamic and heat transfer model is theoretical, it does not include experimental testing or empirical and operational data. This paper aims for technical feasibility by demonstrating consistency with thermodynamic and physical laws. It does not include economic feasibility because this would require cost data and price quotations from HelioFocus and other equipment suppliers. Since the proposed hybrid plant is not yet in existence, equipment with matching specifications may not be available in the market. In such cases, the equipment suppliers must conduct internal studies before providing cost estimates and price quotations.

2. Review of Related Literature

This paper proposes a novel hybrid geothermal-solar thermal power plant by combining a single-flash steam geothermal power plant with a solar thermal system based on HelioFocus technology to improve plant thermal efficiency and power output. The HelioFocus system uses large solar parabolic dishes to transfer solar thermal energy to the steam to increase its temperature and pressure and attain similar steam conditions found in coal power plants.

2.1 Geothermal Energy

Geothermal energy is the thermal energy produced within the earth used for either electric power generation or heat generation depending on the enthalpy of the resource (Li et al., 2020). The former employs equipment akin to coal power plants including steam generators, steam turbines, and condensers in a thermodynamic Rankine cycle (Martín-Gamboa et al., 2015). However, instead of a steam generator, production wells drilled into the geothermal reservoir supply the steam, which powers a turbine and generator set to produce electricity (*GeoVision*, 2019). Then the energy-depleted fluids are injected back into the earth to recover heat for continuous energy extraction.

2.2 Types of Geothermal Power Plants

The three basic types of geothermal power plants are dry steam, flash steam, and binary cycle as shown in Fig. 1. Low-temperature resources are used in binary cycle power plants (*Geothermal Rising*, 2016). Conversely, high-temperature resources are used in dry steam and flash steam power plants. Binary cycle systems can operate at temperatures as low as 85°C (Barbier, 2002). However, conventional electric power generation is restricted to fluid temperatures above 150°C, as for dry and flash steam systems. In flash steam power plants, the brine is flashed and throttled, and the steam is extracted from the brine. In contrast, dry steam power plants do not need a flashing process because the resource is already steam. Binary cycle power plants employ an organic Rankine cycle (Greenhut, 2010), wherein the brine supplies heat to an organic working fluid through a heat exchanger.

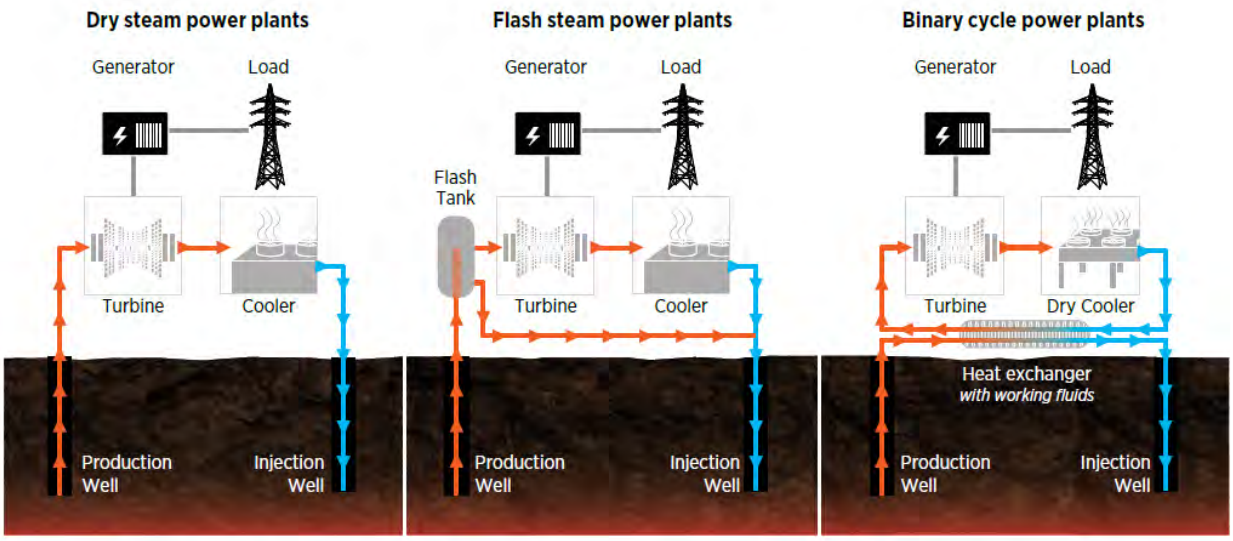

Figure 1: Geothermal power plant technologies (*GeoVision*, 2019).

2.3 Efficiency of Geothermal Power Plants

According to Barbier (2002), geothermal power plants only achieve about a third of the electricity generation efficiency of coal power plants due to the low temperatures of geothermal steam. The

efficiency of geothermal power plants ranged from 10% to 17% with steam temperatures of less than 250°C. Zarrouk and Moon (2014) conducted a worldwide review to determine the conversion efficiencies of geothermal power plants based on the reservoir enthalpy. The results showed that the average conversion efficiency of geothermal power plants was around 12%. The efficiencies were as low as 1% in binary power plants and as high as 21% in dry steam power plants. Fig. 2 shows the geothermal power plant efficiency as a function of the reservoir enthalpy. Dry and flash steam power plants are more efficient than binary plants because they utilize higher working fluid temperatures corresponding to higher enthalpies. Besides plant design, many other factors affect the efficiency of geothermal power plants such as energy losses from the well, non-condensable gas content, parasitic load, heat losses, and turbine and generator efficiency (Zarrouk and Moon, 2014).

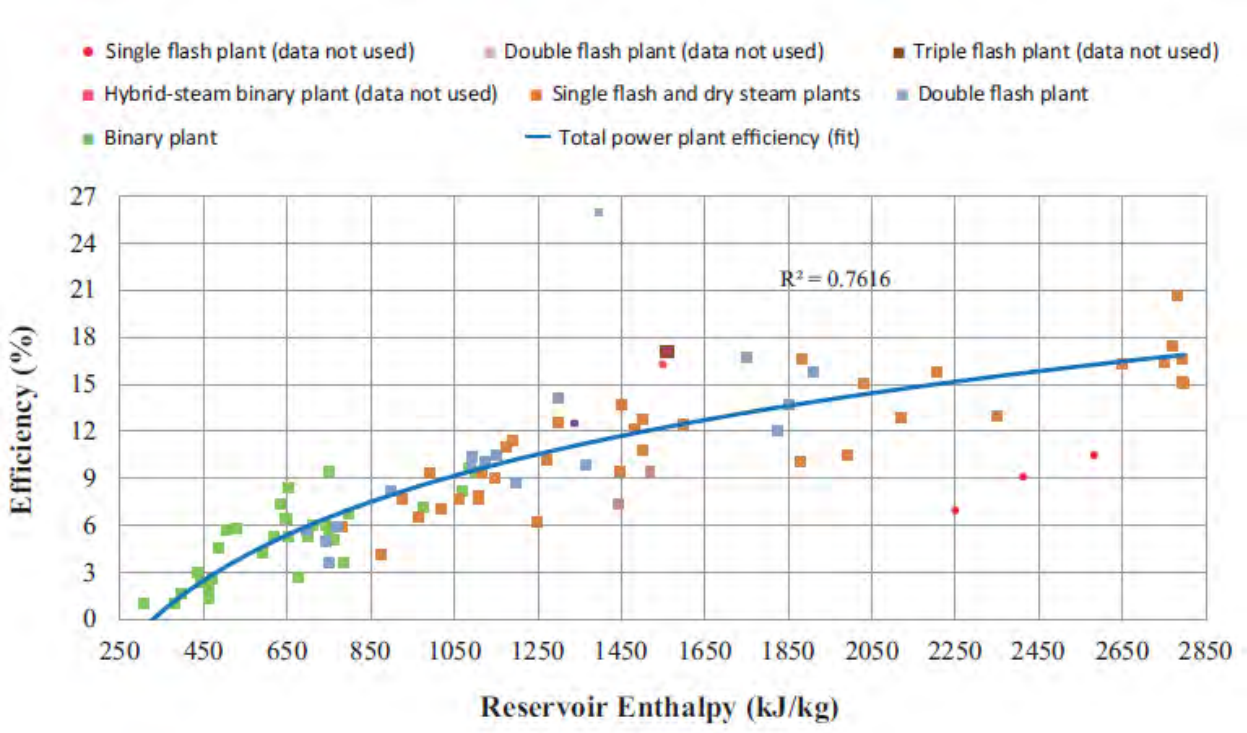

Figure 2: Geothermal power plant efficiency (Zarrouk and Moon, 2014).

2.4 Solar Thermal Energy

Solar thermal technology indirectly converts solar energy into electrical energy using a thermodynamic cycle (Desideri et al., 2013). In high-temperature applications, CSP plants focus solar energy onto special receiving surfaces using reflecting mirrors to achieve the necessary temperatures for electric power generation. Solar energy is captured by the solar field and converted into thermal energy which can be stored (Li et al., 2020). The power block then uses mechanical work to convert heat into electricity.

2.5 Types of Solar Thermal Power Plants

The four main types of concentrated solar power plants are parabolic trough collectors, solar power towers, linear Fresnel reflectors, and solar parabolic dishes as shown in Fig. 3. Parabolic trough collector plants use parabolic reflectors that direct sunlight onto an absorber tube positioned in the parabola's focal line, moving in tandem with the sun (Zhang et al., 2013). Power tower plants consist of distributed mirrors that track the sun independently and direct its rays onto the tower top (Müller-Steinhagen and Trieb, 2004). Similarly, linear Fresnel reflector plants consist of linear mirror strips that reflect and focus the sun rays onto a cylindrical receiver on a linear tower (Islam et al., 2018). Lastly, solar parabolic dish plants consist of parabolic point-focus concentrator dishes that track the sun on two axes and reflect solar radiation onto a Stirling engine receiver at its focus to generate electricity.

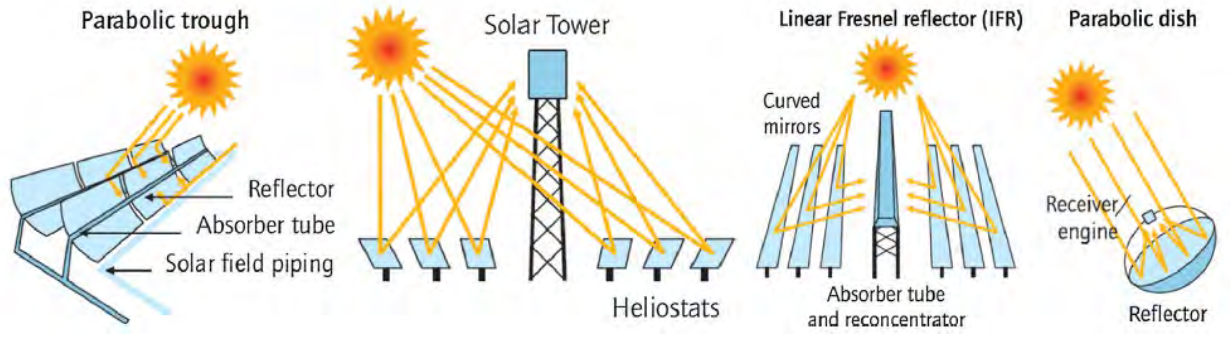

Figure 3: Concentrated solar power technologies (Gonzalo et al., 2019).

3. Methodology

This study demonstrates the technical feasibility of a novel hybrid geothermal-solar thermal power plant by developing a thermodynamic model and conducting a thermodynamic analysis to determine the increase in thermal efficiency and power output of the system compared to (1) a standalone geothermal power plant and (2) a geothermal and solar thermal power plant operating separately. The proposed hybrid system consists of a single-flash steam geothermal power plant and a solar thermal dish system based on HelioFocus technology. The thermodynamic model of the hybrid system is developed in the Engineering Equation Solver software. Manual calculations are also done to highlight important results.

3.1 Hybrid Geothermal-Solar Thermal System

The hybrid plant employs a single-flash steam Rankine cycle integrated with solar thermal energy. The schematic diagram in Fig. 4 shows the components of the hybrid plant. The geothermal fluid from the production well undergoes flashing through the expansion valve and then enters the separator where the saturated vapor and liquid are separated from the mixture. Before reaching the steam turbine, the saturated vapor is directed to the solar field, receiving heat from the solar dishes to superheat the steam. Then it expands in the steam turbine and travels to the condenser where the steam condenses into saturated liquid. Next, another separator removes the non-condensable gases from the saturated liquid and releases them into the atmosphere. Finally, the saturated liquid is pumped back into the reinjection well and the cycle repeats.

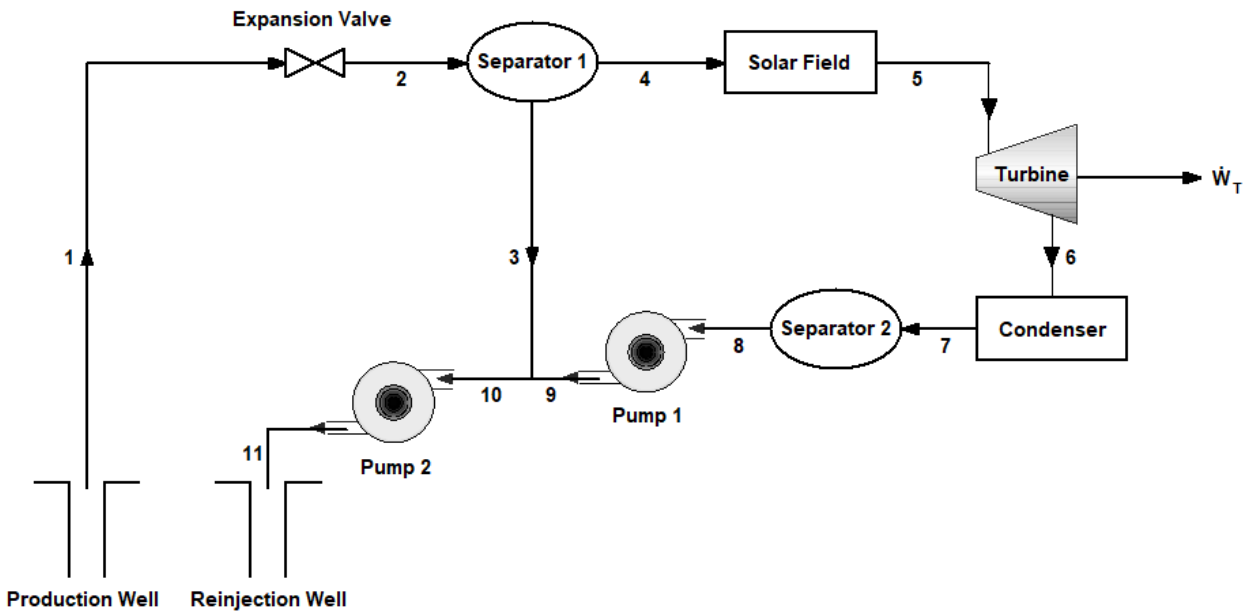

Figure 4: Schematic diagram of the hybrid geothermal-solar thermal power plant.

3.2 Solar Thermal System

The HelioFocus solar thermal system consists of a solar field of parabolic dishes, a heat transmission system, and a heat exchanger (Keck et al., 2015). A volumetric receiver is mounted at the focal point of each dish. It absorbs solar radiation reflected by parabolic mirrors and heats the air to 1000°C. Heat transfer between the hot air and geothermal steam is modified by using geothermal steam directly as the heat transfer fluid instead of air to eliminate the need for a heat exchanger. Heat transfer occurs directly at the receiver of the solar dishes. This reduces the equipment cost and eliminates the heat loss in the heat exchanger resulting in more efficient use of solar energy. From the steam pipe, geothermal steam is distributed to multiple pipes going to the solar dishes. After the solar dishes heat the steam, the steam pipes converge into a single pipe going to the turbine.

The HelioFocus system is selected as the solar thermal system to be integrated with geothermal energy because it has the highest steam temperature and solar efficiency among all CSP technologies. Table 1 shows some of the differences between CSP technologies. The dual axis tracking mechanism of parabolic dishes allows the curved mirrors to always point directly at the sun (Islam et al., 2018). This makes them more efficient than parabolic trough collectors and solar power towers, which have smaller receiving areas for sunlight. Each dish has a receiver installed near the mirrors, resulting in more efficient heat collection, higher concentration ratios, and minimal land use. The modular design also gives flexible installation capacities.

Parameter	Parabolic Trough Collector	Linear Fresnel Reflector	Solar Power Tower	Solar Parabolic Dish	HelioFocus Dish
Capacity (MWe)	10-200	10-200	10-150	0.01-0.4	10-100
Concentration ratio	25-100	70-80	300-1000	1000-3000	2000
Solar efficiency max. (%)	20	21	20	29	30
Land requirement	Large	Medium	Medium	Small	Small
Operating temperature of the solar field (°C)	290-550	250-390	250-650	800	1000
Heat transfer fluid	Synthetic oil, water/steam	Water/steam	Water/steam, molten salt	Air, hydrogen, helium	Air
Steam conditions (°C/bar)	380-540/100	260/50	540/100-160	Not applicable	620/160

Table 1: Comparison of CSP technologies (Keck et al., 2012, 2015, Shi, 2015, Islam et al., 2018).

3.3 Model Assumptions

In this study, the solar dishes in the hybrid system heat the geothermal steam directly to increase its temperature and pressure from 180°C to 500°C and 7 bars to 160 bars, respectively. Steam conditions are typical for coal plants. Consequently, the hybrid plant is expected to achieve the same thermal efficiency. Unless otherwise stated, the solar dishes are assumed to operate based on the available design parameters provided by the manufacturer. The pump work is assumed to be negligible, and the condenser temperature is set to 40°C. The following are the assumptions for each plant model:

3.3.1 Hybrid Model

- The steam quality at the turbine exhaust is 0.85.
- The steam temperature at the turbine inlet is 500°C.
- The steam pressure at the turbine inlet is 160 bars.

- The thermal efficiency of the steam turbine is 35%.
- The heat loss in the solar receiver is 10%.

3.3.2 Geothermal Model

- The steam quality at the turbine exhaust is 0.9.
- The steam temperature at the turbine inlet is 180°C.
- The steam pressure at the turbine inlet is 7 bars.
- The thermal efficiency of the steam turbine is 18%.

3.3.3 Solar Thermal Model

- The steam temperature at the turbine inlet is 500°C.
- The steam pressure at the turbine inlet is 160 bars.
- The thermal efficiency of the steam turbine is 36%.
- The water temperature at the heat exchanger inlet is 40°C.
- The water pressure at the heat exchanger inlet is 1 bar.

3.4 Thermodynamic Model

The thermodynamic model of the proposed hybrid system is developed using mass and energy balance equations based on the laws of thermodynamics to determine the thermal efficiency and power output.

3.4.1 Mass Balance

The following equations give the mass flow rates for each state in the hybrid system (Assad and Rosen, 2021):

$$\dot{m}_1 = \dot{m}_2 = \dot{m}_{10} = \dot{m}_{11} \quad (1)$$

$$\dot{m}_2 = \dot{m}_3 + \dot{m}_4 \quad (2)$$

$$\dot{m}_4 = x_2\dot{m}_2 = \dot{m}_5 = \dot{m}_6 = \dot{m}_7 = \dot{m}_8 = \dot{m}_9 \quad (3)$$

$$\dot{m}_{10} = \dot{m}_3 + \dot{m}_9 \quad (4)$$

where ṁ and x are the mass flow rate and the steam quality of the geothermal fluid, respectively.

3.4.2 Energy Balance

The following equations give the energy rate balance for each state and component in the hybrid system (Assad, 2021, Assad and Rosen, 2021):

State 1: Saturated Liquid

$$h_1 = h_f \quad (5)$$

where h and h_f are the specific enthalpy of the geothermal fluid and the saturated liquid, respectively.

Expansion Valve:

$$h_1 = h_2 \tag{6}$$

State 2: Two-Phase

$$h_2 = h_f + x_2 h_{fg} \tag{7}$$

where h_{fg} is the phase change-specific enthalpy of the geothermal fluid.

Separator 1:

$$\dot{m}_2 h_2 = \dot{m}_3 h_3 + \dot{m}_4 h_4 \tag{8}$$

State 3: Saturated Liquid

$$h_3 = h_f \tag{9}$$

State 4: Saturated Vapor

$$h_4 = h_g \tag{10}$$

Solar Field and State 5: Superheated Vapor

$$Q_{solar} = \dot{m}_4 (h_5 - h_4) \tag{11}$$

where $\dot{Q}_{solar}$ is the solar heat addition rate.

Steam Turbine:

$$W_T = \dot{m}_5 (h_5 - h_6) \tag{12}$$

where $\dot{W}_T$ is the steam turbine power output.

State 6: Two-Phase

$$h_6 = h_f + x_6 h_{fg} \tag{13}$$

Condenser:

$$Q_{cond} = \dot{m}_6 (h_6 - h_7) \tag{14}$$

where $\dot{Q}_{cond}$ is the condenser heat rejection rate.

State 7: Saturated Liquid

$$h_7 = h_f \tag{15}$$

Separator 2 and State 8: Saturated Liquid

$$\dot{m}_8 h_8 = \dot{m}_7 h_7 \tag{16}$$

Pump 1:

$$W_{P1} = \dot{m}_8 (h_9 - h_8) \tag{17}$$

where $\dot{W}_P$ is the pump power.

State 9: Sub-Cooled Liquid

$$h_9 - h_8 = v_8(P_9 - P_8) \quad (18)$$

where v and P are the specific volume and pressure of the geothermal fluid, respectively.

State 10: Sub-Cooled Liquid

$$\dot{m}_{10}h_{10} = \dot{m}_3h_3 + \dot{m}_9h_9 \quad (19)$$

Pump 2:

$$W_{P2} = \dot{m}_{10}(h_{11} - h_{10}) \quad (20)$$

State 11: Sub-Cooled Liquid

$$h_{11} - h_{10} = v_{10}(P_{11} - P_{10}) \quad (21)$$

3.4.3 Net Power Output

$$W_{net} = W_T - (W_{P1} + W_{P2}) \quad (22)$$

3.4.5 Thermal Efficiency

$$\eta_{th} = \frac{W_{net}}{\dot{m}_1(h_1 - h_{ref}) + Q_{solar}} \quad (23)$$

where h_{ref} is the specific enthalpy of the geothermal fluid at the reference temperature (25°C).

3.5 Theoretical Calculation of Heat Loss

The HelioFocus parabolic dish uses a volumetric solar receiver. Solar radiation passes through a transparent window to transfer energy to the volumetric solar receiver inside a pipe where the heat transfer fluid flows. The transparent window allows solar radiation to come in and light and infrared radiation from the solar receiver to come out. Hence, radiation travels both ways: in and out of the pipe through the transparent window. The outgoing radiation is a heat loss because it exits to the atmosphere outside the thermodynamic system of the hybrid plant. The heat loss can be theoretically estimated using the Stefan-Boltzmann law. The HelioFocus solar receiver can heat air to 1000°C. This is assumed to be the equilibrium temperature.

Assuming that the incoming solar irradiance is equal to the outgoing radiant emittance of the solar receiver,

$$E = M \quad (24)$$

where E and M are the incoming solar irradiance and outgoing radiant emittance, respectively.

From the Stefan-Boltzmann law,

$$M = eoT_e{}^4 \quad (25)$$

where e, o, and T_e are the emissivity of the solar receiver, the Stefan-Boltzmann constant, and the equilibrium temperature, respectively.

Combining Equations (24) and (25),

$$E = eoT_e{}^4 \tag{26}$$

In the proposed hybrid plant, geothermal steam is heated to 500°C by the incoming solar irradiance. The outgoing radiation is heat loss. Again, this can be calculated from the Stefan-Boltzmann law:

$$J = eoT^4 \tag{27}$$

where J is the radiant emittance of the solar receiver at T = 500°C.

The heat loss is given by:

$$q = \frac{J}{E} = \frac{e\,o\,T^4}{e\,o\,T_e{}^4} \tag{28}$$

where q is the heat loss percentage.

Simplifying Equation (28),

$$q = \left(\frac{T}{T_e}\right)^4 \tag{29}$$

However, this assumes that the incoming solar irradiance equals the outgoing radiant emittance. In reality, the incoming solar irradiance is greater than the outgoing radiant emittance because not all the heat energy is radiated out. Some heat energy is used to heat the air to 1000°C. Hence, the equilibrium temperature must be higher than 1000°C and the true value of the heat loss must be less than the upper bound of the heat loss.

The lower bound of the heat loss can be obtained by calculating a higher equilibrium temperature:

$$E_h = eoT_h{}^4 \tag{30}$$

where E_h and T_h are the higher incoming solar irradiance and higher equilibrium temperature, respectively.

Since the heat loss is equal to the radiant emittance of the solar receiver at T_e = 1000°C,

$$qE_h = M \tag{31}$$

Substituting the Stefan-Boltzmann formula and simplifying,

$$qeoT_h{}^4 = eoT_e{}^4 \tag{32}$$

$$T_h = \frac{T_e}{\sqrt[4]{q}} \tag{33}$$

Let the lower bound of the heat loss = q'

q' is obtained by substituting T_h for T_e in Equation (29),

$$q' = \left(\frac{T}{T_h}\right)^4 \tag{34}$$

4. Results and Discussion

4.1 Thermal Efficiency

4.1.1 Hybrid Geothermal-Solar Thermal Plant vs. Standalone Geothermal Plant

Thermal efficiency increases from 17% to 34% when a geothermal power plant is converted into a hybrid geothermal-solar thermal system. The calculation of thermal efficiency is based on specific enthalpy. The analysis starts at the steam turbine instead of the production well to obtain the useful energy input of the geothermal plant. This is the thermal energy of the extracted steam per unit mass. In the case of the hybrid plant, an additional solar energy input is added to the total energy input to account for the solar energy provided by the solar dishes. The useful energy output is expressed as the specific work of the turbine on a unit mass basis. Thermal efficiency is simply the ratio of the total energy output to the total energy input. The results agree with the thermal efficiencies typically found in coal plants.

4.1.2 Hybrid Geothermal-Solar Thermal Plant vs. Separate Geothermal and Solar Thermal Plants

Thermal efficiency increases from 24% to 34% when a separate geothermal and solar thermal plant is converted into a hybrid geothermal-solar thermal system The separate geothermal and solar thermal plants each produce their own steam to generate electricity. Consequently, they have different steam turbines and thermal efficiencies because of the differences in steam temperatures and pressures. The thermal efficiency of the solar thermal plant is 30%, whereas the geothermal plant is 18%. Thus, the average efficiency of the two plants is 24%. However, the hybrid system combines the two plants to produce a common steam output. As a result, the thermal efficiency of the hybrid plant is 34% which is higher than the two plants.

4.2 Power Output

4.2.1 Hybrid Geothermal-Solar Thermal Plant vs. Standalone Geothermal Plant

Power output increases by 136% when a geothermal power plant is converted into a hybrid geothermal-solar thermal system. The power output is expected to improve significantly because the energy input has increased with the addition of the solar thermal system that collects solar energy. However, overall thermal efficiency has also increased, contributing to a higher power output. The solar energy input is deducted from the total power output to quantify the incremental power output due to the improved efficiency. The increase in power output due to improved thermal efficiency is 26%. Additionally, the calculated lower and upper bounds of the heat loss in the solar receiver are 2% and 13%, respectively. The assumed heat loss value in the hybrid model is within the computed range.

4.2.2 Hybrid Geothermal-Solar Thermal Plant vs. Separate Geothermal and Solar Thermal Plants

The power output has increased by 261% when a separate geothermal and solar thermal plant is converted into a hybrid geothermal-solar thermal system. The solar thermal plant is given the same solar energy input used in the hybrid plant to determine the energy output of the solar thermal plant compared to the additional energy output of the hybrid plant. The big advantage of the hybrid plant over a solar thermal plant is that the former applies solar energy to heat geothermal steam further which is already in a gaseous state. The latter uses solar energy to turn water into steam. The latent heat of vaporization is much higher than the specific heat of steam. Thus, the hybrid plant can produce a greater steam mass than a solar thermal plant given the same solar energy input. The results are summarized in Table 2.

Parameter	Geothermal	Geothermal & Solar Thermal	Hybrid
Thermal Efficiency (%)	17	24	34
Increase in Power Output with Hybrid (%)	136	261	-
Net Increase in Power Output with Hybrid (%)	26	-	-
Steam Temperature (°C)	180	180/500	500
Steam Pressure (bar)	7	7/160	160

Table 2: Power Plant Performance.

5. Conclusion

A novel hybrid system was designed to control the temperature and pressure of geothermal steam to approximate the steam conditions and thermal efficiency of coal power plants by integrating solar thermal energy with geothermal energy. The thermodynamic model was developed for the hybrid system wherein the heat transfer process was modified by directly heating the geothermal steam with solar dishes instead of using the air-to-steam heat exchanger to reduce equipment costs and eliminate heat loss in the heat exchanger. The hybrid system was analyzed to evaluate its performance compared to a standalone geothermal plant and separate geothermal and solar thermal plants. The novel design is technically feasible and capable of generating an additional 136% power output compared to a standalone geothermal plant due to additional solar energy input and increased thermal efficiency from 17% to 34%. It is also superior to a separate geothermal and solar thermal system as it can generate 261% more power output given equal solar energy inputs. Moreover, it achieves a higher thermal efficiency than all current hybrid designs in the literature. Further studies may be done on the detailed engineering design of the equipment and components of the proposed hybrid geothermal-solar thermal system. An economic feasibility study may also be recommended when the required equipment with matching specifications becomes available in the market.

REFERENCES

2016 Annual US Global Geothermal Power Production | Geothermal Rising :: Using the Earth to Save the Earth. (2016, March 1). https://geothermal.org/resources/2016-annual-us-global-geothermal-power-production

Assad, M. E. H., Ahmadi, M. H., Sadeghzadeh, M., Yassin, A., and Issakhov, A. "Renewable hybrid energy systems using geothermal energy: hybrid solar thermal–geothermal power plant." *International Journal of Low Carbon Technologies*, 16(2), (2021), 518–530.

Assad, M., and Rosen, M. A. (Eds.). (2021). *Design and performance optimization of renewable energy systems*. Academic Press.

Barbier, E. "Geothermal energy technology and current status: an overview." *Renewable & Sustainable Energy Reviews*, 6(1–2), (2002), 3–65.

Bonyadi, N., Johnson, E., and Baker, D. "Technoeconomic and exergy analysis of a solar geothermal hybrid electric power plant using a novel combined cycle." *Energy Conversion and Management*, 156, (2018), 542–554.

Cardemil, J. M., Cortés, F., Díaz, A. J., and Escobar, R. "Thermodynamic evaluation of solar-geothermal hybrid power plants in northern Chile." *Energy Conversion and Management*, 123, (2016), 348–361.

Desideri, U., Zepparelli, F., Morettini, V., and Garroni, E. "Comparative analysis of concentrating solar power and photovoltaic technologies: Technical and environmental evaluations." *Applied Energy*, 102, (2013), 765–784.

GeoVision. (2019). Energy.gov. https://www.energy.gov/eere/geothermal/geovision

Gonzalo, A. P., Marugán, A. P., and Márquez, F. P. G. "A review of the application performances of concentrated solar power systems." *Applied Energy*, 255, (2019), 113893.

Greenhut, A. D. "Modeling and analysis of hybrid geothermal-solar thermal energy conversion systems." (2010). Master's thesis, Massachusetts Institute of Technology. https://dspace.mit.edu/handle/1721.1/58087

Islam, T., Huda, N., Abdullah, A., and Saidur, R. "A comprehensive review of state-of-the-art concentrating solar power (CSP) technologies: Current status and research trends." *Renewable & Sustainable Energy Reviews*, 91, (2018), 987–1018.

Keck, T., Balz, M., and Blumenthal, Y. "Large is Beautiful – Progress of HelioFocus 500 m2 Dish." *Energy Procedia*, 69, (2015), 1597–1602.

Keck, T., Balz, M., Schiel, W., Zlatanov, H., Blumenthal, Y., and Gadot, O. "The HelioFocus Large Dish Prototype." *Proceedings: 18th SolarPACES Conference*, Marrakech, Morocco (2012).

Li, K., Liu, C., Jiang, S., and Chen, Y. "Review on hybrid geothermal and solar power systems." *Journal of Cleaner Production*, 250, (2020), 119481.

Martín-Gamboa, M., Iribarren, D., and Dufour, J. "On the environmental suitability of high- and low-enthalpy geothermal systems." *Geothermics*, 53, (2015), 27–37.

McTigue, J. D., Castro, J. R., Mungas, G., Kramer, N., King, J., Turchi, C., and Zhu, G. “Hybridizing a geothermal power plant with concentrating solar power and thermal storage to increase power generation and dispatchability.” *Applied Energy*, 228, (2018), 1837–1852.

Müller-Steinhagen, H. and Trieb, F. “Concentrating solar power, - A review of the technology.” *Ingenia*, 18, (2004), 43-50.

Renewable Capacity Statistics 2021. (2021, April 1). https://www.irena.org/publications/2021/March/Renewable-Capacity-Statistics-2021

Shi, M. “Market Analysis of Israeli CSP Technologies in the Chinese Market.” (2015). Master’s project, Duke University. https://hdl.handle.net/10161/9602

Zarrouk, S. J., and Moon, H. “Efficiency of geothermal power plants: A worldwide review.” *Geothermics*, 51, (2014), 142–153.

Zhang, H. L., Baeyens, J., Degrève, J., and Cáceres, G. “Concentrated solar power plants: Review and design methodology.” *Renewable & Sustainable Energy Reviews*, 22, (2013), 466–481.

Low-Temperature Geothermal Play Fairway Analysis for the Denver Basin

Estefanny Davalos Elizondo[1], Nicole Taverna[1], Abra Gold[1]

[1]National Renewable Energy Laboratory, Golden, CO

Keywords

Denver Basin, Play Fairway Analysis, Geothermal Direct Use, Combined Heat and Power, Sedimentary Basin Geothermal Play Type, Python Code, Favorability Map

ABSTRACT

This project is part of a national initiative to showcase the benefits of incorporating low-temperature geothermal resource assessment into the deployment of geothermal heating, combined heat and power (CHP), and geothermal direct-use (GDU) technologies. The initiative was established to accelerate the country's decarbonization efforts by identifying potential for low-temperature geothermal resource utilization (<150°C, e.g., CHP and GDU) in selected sedimentary basins with numerous population centers.

The play fairway analysis (PFA) methodologies in this study were adapted from previous PFA investigations of sedimentary basin geothermal play types (SBGPTs) that evaluated the potential for low-temperature resources (<150°C). Workflows, relevant datasets, a new Python library, and common and composite geological criteria maps are utilized to develop low-temperature geothermal resource favorability maps for the Denver Basin, a sedimentary basin spanning Colorado, Nebraska, and Wyoming. The replication of these methodologies in other SBGPTs can evaluate potential for low-temperature resources. To facilitate future assessment of low-temperature geothermal resources in SBGPTs, this project provides PFA workflows, data, tools, and favorability maps that will ultimately support the utilization of low-temperature geothermal resources in sedimentary basins.

1. Introduction

Sedimentary basins often have numerous layers of highly porous rocks and can have elevated fracture permeability, depending on the stress regimes affecting each basin. Candidate fluids for low-temperature geothermal utilization (<150°C) readily accumulate in these naturally porous, fractured rocks at depth. Nearly half of the United States is underlain by sedimentary basins that have been widely uninvestigated for low-temperature geothermal resource potential (USGS 2022).

A sedimentary basin geothermal play type (SBGPT) is influenced by its historical development and current tectonic and geological conditions. Crucial elements of an SBGPT include heat sources, the presence of circulating fluids (either natural or injected) for heat transport, reservoir porosity and permeability as well as storage attributes (both natural and induced), and reservoir

seals. These characteristics differ from hydrocarbon play systems, which are characterized by their source rock, reservoir traps, and trapping mechanisms (Doughty et al. 2018).

Most hydrothermal plays dominated by conduction in sedimentary basins occur in deep aquifers with a nearly normal thermal gradient (Moeck 2014). Variations in porosity and permeability are dictated by lithology, faulting, diagenetic patterns, and stress fields (Wolfgramm et al. 2009; Hartmann and Beaumont 2000), all of which are significantly shaped by the evolution, subsidence rates, and contemporary tectonics. Previous research focusing on geothermal resources in sedimentary formations emphasized those with high porosity/high permeability (~100 mD) for effective convection (Augustine 2014) or high porosity/low permeability at elevated temperature gradients, typically found at depths greater than 3 km (Moeck 2014). SBGPTs with low permeability may harbor petrothermal resources, which can be accessed by enhancing permeability through various reservoir stimulation techniques (Zimmermann et al. 2007). The storage capacity related to the host rock's porosity could critically affect the performance of Enhanced Geothermal Systems (EGS) in hot sedimentary aquifers (Rybach 1981).

It is imperative that more research be conducted to evaluate the potential for low-temperature geothermal resources in highly permeable and porous rocks of sedimentary basin geothermal play types (SBGPTs). This study centers on implementing a geothermal play fairway analysis (PFA), adapted from the hydrocarbon industry for low-temperature resources in SBGPTs, with a specific focus on the Denver Basin. The workflow is based on the forthcoming Geothermal Play Fairway Analysis Best Practices report (Pauling et al. 2023) and the Low-Temperature Geothermal Play Types assessment (Davalos-Elizondo et al. 2023), which identified a general geothermal PFA process (Figure 1).

PFA methodologies should be adapted to each geothermal play type individually. To classify this SBGPT, we used the scheme suggested by Coleman and Cahan (2012) based on a simple geological setting (Figure 2): (1) intracratonic basins created within the boundaries of a craton; (2) pericratonic basins formed near or accreted to the margins of the craton; (3) intercratonic basins formed between cratons and extend onto oceanic crust; and (4) oceanic basins that developed independently of cratons, primarily on oceanic crust.

Identification of areas with low-temperature geothermal potential in SBGPTs is a multicriteria geospatial decision problem. We suggested three essential criteria for the evaluation of low-temperature resources (Figure 1):

- Geologic criteria (e.g., heat, accessible fluid, permeability, and seal).
- Economic criteria (e.g., population, infrastructure, heating and cooling demand, levelized cost of heat).
- Risk criteria (e.g., exclusion areas, and environmental/natural disaster regions).

The focus of this paper is exclusively on the geological criteria, our goal is to identify potential locations for more detailed geological data collection. Further work has been conducted to effectively integrate other criteria in the future.

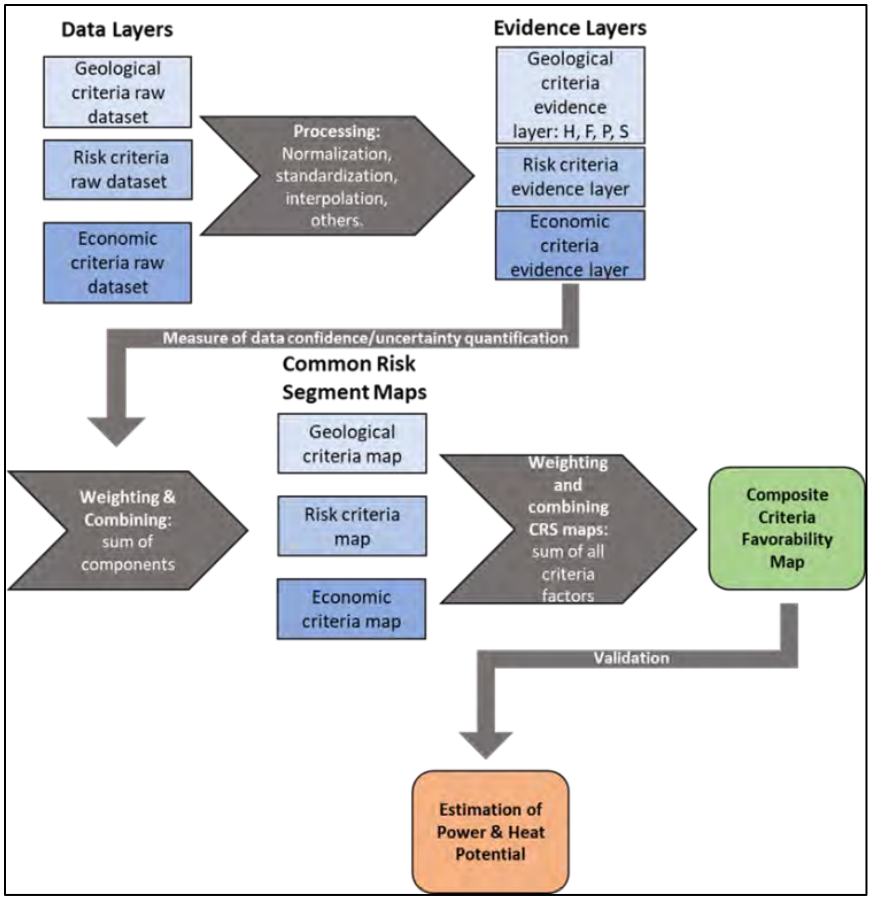

Figure 1: Flow chart outlining a generalized methodology for low-temperature assessment resources modified from Pauling et al. (2023) by Davalos-Elizondo et al. (2023)

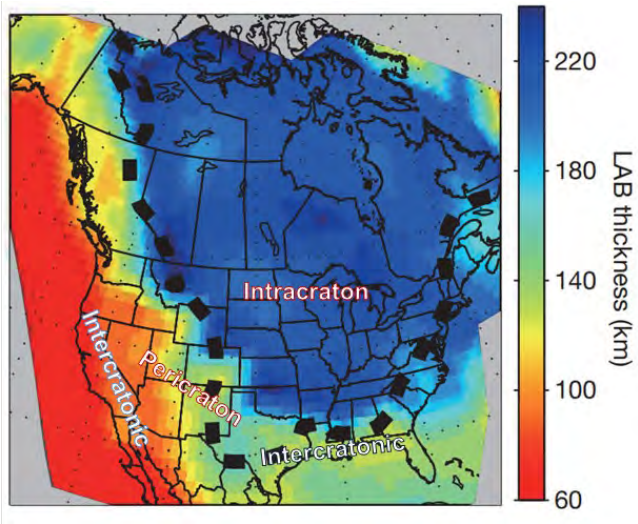

Figure 2: Present lithospheric-asthenospheric boundary thickness of North American continent from Yuan and Romanowicz (2010). A thick black dashed line indicates the borders of the craton

2. Background

The Denver Basin is characterized as a geothermal sedimentary foreland basin play type (Figure 3). This foreland basin is located on the eastern side of the Rocky Mountain orogenic belt in a pericratonic setting. Foreland basins are sedimentary basins that form between an orogenic belt and a craton, characterized by thick sedimentary deposits and asymmetric shape (Allen et al. 1986). They develop due to the weight of thickened crust and deposited sediments, causing the lithosphere to bend downward and create zones of extension and normal faulting. The formation of foreland basins is driven by factors such as horizontal compression, slab pull, lateral asthenospheric push, and delamination of the retreating mantle lithosphere (Garcia-Castellano and Cloetingh 2011). The rigidity of the plates also plays a key role in controlling the geometry and drainage history of foreland basins.

The Denver Basin is asymmetric, with suspected granite basement rocks underneath the sedimentary cover. It becomes much deeper as it stretches towards the Front Range in the western direction, reaching depths of around 3.5 km, while it is approximately 1.6 km deep in the eastern part (Dixon 2002). It spreads across more than 82,000-km^2 area, primarily in Colorado, followed by smaller portions in Wyoming and Nebraska (Fishman 2005). This basin is renowned for its petroleum extraction, with thousands of wells drilled for oil and gas production in various reservoir formations, providing data that describes the subsurface conditions.

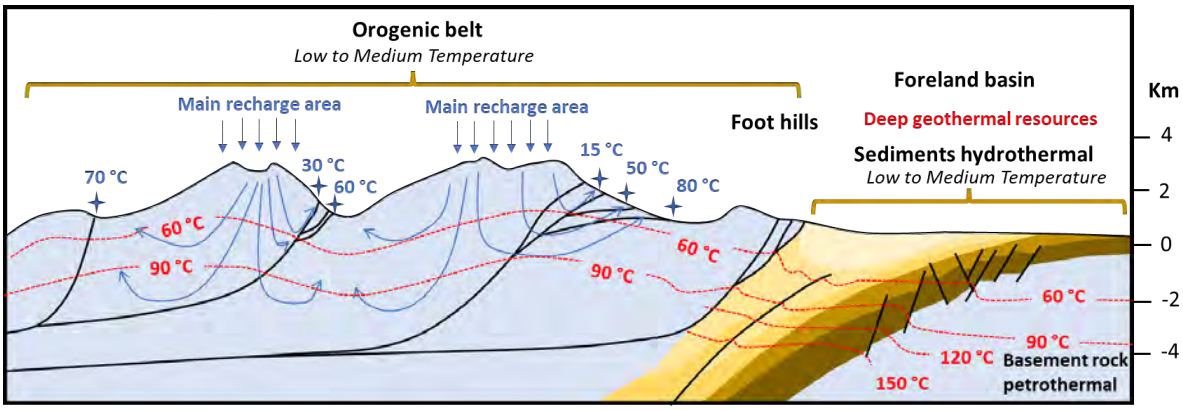

Figure 3: Orogenic Belt Geothermal Play Type and related SBGPT foreland basin. Modified from Moeck (2014)

3. Methodology

A classification of the Denver Basin geothermal play type as a foreland basin was established to outline the specific scope of work. Our approach includes: 1) identifying relevant data; 2) developing python code to combine multiple relevant data into PFA for geological criteria; and 3) rendering favorability or common criteria maps for low-temperature geothermal resources.

The PFA workflow was adapted accordingly (Figure 2) allowing overlaying of multiple geological criteria layers (see Table 1) to evaluate resource potential. We created favorability maps to identify suitable regions for CHP and GDU technologies. Moreover, the Python library titled “geoPFA” was developed and utilized to generate a workflow for producing common and composite maps

(Section 5). This Python library and its implementation are updated as the project and related work evolve, and it is expected to be released as an open-source toolset when it is robust enough.

QGIS, an open-source geographic information system from OSGeo, was used in combination with the geoPFA Python library to combine and process (e.g., interpolate, standardize, transform) different sets of geographic data related to the geological criteria from the raw data layers (e.g., heat, fluid, permeability).

The relevant data for this PFA workflow is outlined in Table 1, but may vary depending on data availability, region, and new discoveries.

Table 1. Relevant data suggested for PFA of low-temperature geothermal resources in the Denver Basin

GPT and Combination Method	Criteria	Component	Data
Pericratonic Foreland basin Modified Voter Veto	Geological	Heat	Bottom-Hole Temperatures
			Gradient Temperatures
			Thermal Conductivity
			Heat Flow
		Accessible Fluid	Hot Springs
			Co-production Water (BBL) Per Year
			Groundwater Wells
		Permeability	Faults and Shear Zone
			Earthquake Data

4. Relevant Data

4.1 Geological Criteria

Choosing optimal locations for low-temperature GHC and GDU opportunities involves the consideration of multiple factors. Suitability of sites is determined, in-part, based on geological criteria, such as heat, fluid, and permeability components (Section 3, Table 1). Combining these criteria into favorability maps suggests viable domains for low temperature geothermal resource utilization, without consideration for other important factors like risk and economic criteria.

4.1.1 Heat Component Analysis

Analyzing the temperature at the bottom of oil and gas wells, along with navigating limited certainty of reported bottom-hole temperature (BHT) accuracies, forms the basis for evaluating geothermal resources, according to Spicer (1964) and Whealton (2015, 2016). The end goal of our assessment is to determine the heat flow throughout the Denver Basin, suggesting areas of high heat flow that may be suitable for low-temperature geothermal resource utilization. There is a wealth of temperature data Python from oil and gas wells in the Denver Basin; decades of historic oil and gas production has provided many datapoints in the western and central regions of the Denver Basin. The basis for our heat component evaluation relies on BHT datasets as reference points for temperature at depth.

We identified three BHT datasets (Figure 4A): (1) Southern Methodist University (SMU); (2) Association of American State Geologists (AASG); and (3) Colorado Geological Survey (CGS). BHT data from Wyoming, Nebraska, and Colorado was gathered and narrowed down to focus specifically on the Denver Basin region. Despite abundance of BHT data, measurements can be distorted by heat changes caused by drilling and errors during data collection; for instance, if BHT data comes from a survey conducted a week after drilling, mud circulation could cause the BHT measurement to be falsely lower than if the data point were collected from a thermally stable shut-in well. Several correction methods have been created to estimate equilibrium conditions for BHTs in sedimentary basins (e.g., Harrison et al. 1983; Förster & Merriam 1995; Blackwell & Richards 2004).

To estimate heat flow and temperature distribution at depth, understanding the thermal conductivity of thousands of boreholes was necessary. It involves assigning lithologic units, unit thicknesses, and thermal conductivities from the surface to the basement for each borehole that had BHT data in the analysis. We utilized the lithology charts and thermal conductivity values used by the SMU data from AAPG COSUNA in the Denver Basin. To complete this assessment, an interpolation was performed, which estimated the likely distribution of thermal conductivity throughout the basin (Figure 4B). Higher thermal conductivities are associated with the southwest Denver Basin, while a nearly static thermal conductivity of 1.6 W/m/K is consistent in the northeast.

This project generated a uniformly corrected set of BHT datapoints from the SMU, AASG, and CGS datasets. Applying a generalized correction scheme was required. If a prior BHT correction scheme had been applied to the constituent datasets, that correction was reversed to obtain the original uncorrected BHT datapoints (i.e., AASG). We used the Förster correction to unify the datasets. The Förster correction has been suggested as the best correction scheme tailored for Denver Basin based on equilibrium data by Crowell et al. (2012; Equation 1):

$$Tcf = 0.0124\,x + 7.8825 \quad (1)$$

where Tcf is the temperature correction factor, and x is the depth at which the BHT measurement was reported. It is important to mention that this correction formula is only suitable for the Denver Basin and potentially other basins that have comparable stratigraphy (Crowell et al. 2012). For this reason, the Förster equation was applied to the Wyoming portion of the Denver Basin to the limited BHT datapoints in that region, as the stratigraphy is not drastically different from the Colorado and Nebraska portions (which the Förster correction scheme had been applied to previously in Crowell et al. 2012). The BHT data of SMU, AASGS, and CGS were corrected with the Förster equilibrium factor (Figure 5). Overall, the improved unified BHT dataset offered a more thorough evaluation of BHTs, reducing uncertainty and navigating potential errors in the datasets via tailored correction scheme for the Denver Basin. This unified BHT data will be available in the Geothermal Data Repository.

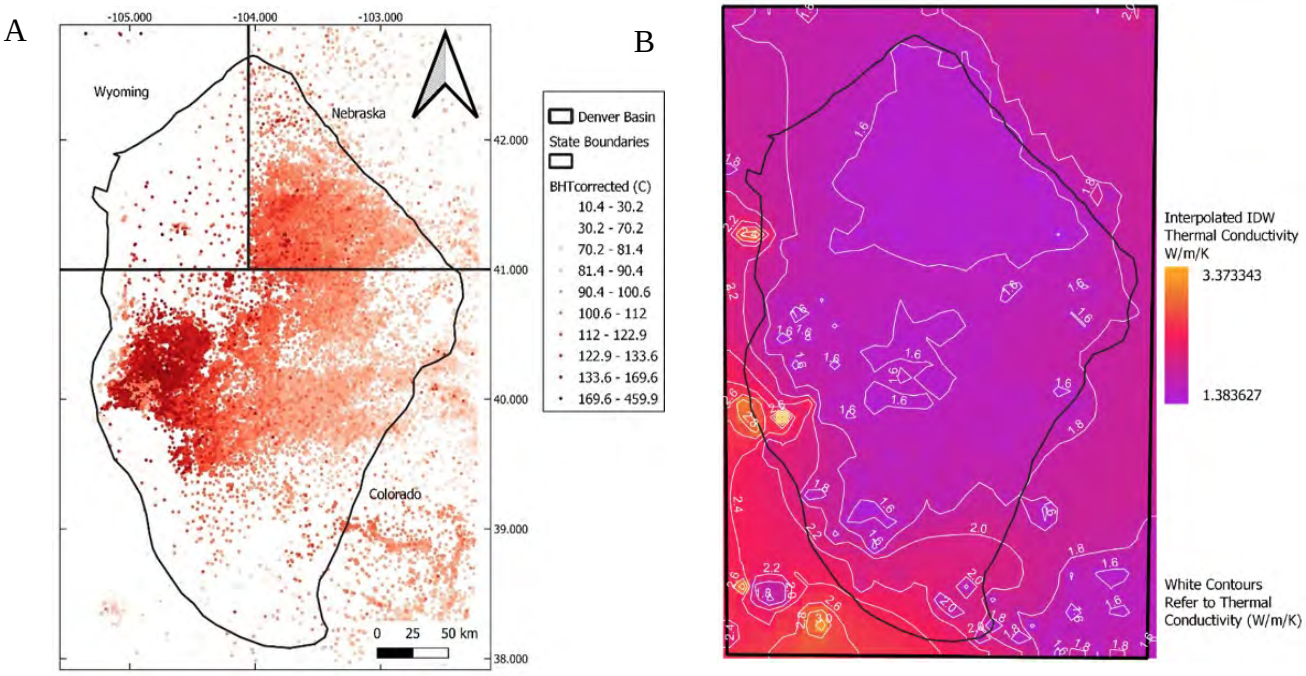

Figure 4: A. Bottom-hole temperatures of oil and gas wells in the Denver Basin from three different datasets: SMU, AASG, and CGS. Depth increases to the western side and decreases towards the eastern side of the basin. B. Thermal conductivities interpolation of rock across the Denver Basin

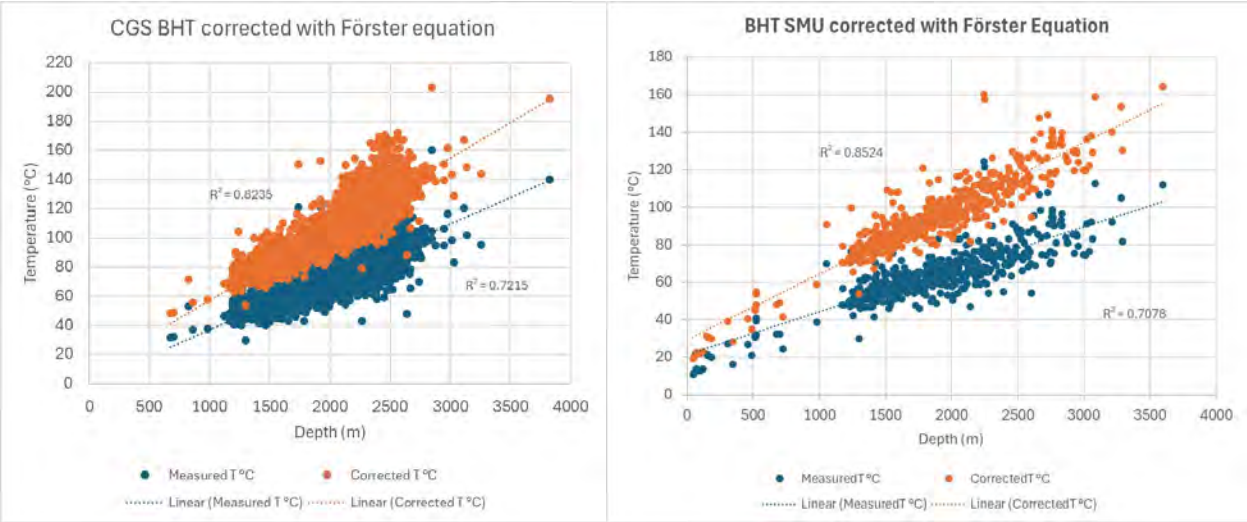

Figure 5: Bottom-hole temperature data of SMU and CGS corrected with the Förster equilibrium factor suggested by Crowell et al. (2012)

Heat transfer is also an essential factor in assessing the potential of geothermal resources, as the heat discharge data linked to Earth's heat flow is a vital indicator of potential. Heat flow maps are valuable tools for pinpointing regions of high geothermal resource potential in a specific area or country (Blackwell et al. 2007). The geothermal gradient plays a vital role in determining heat flow. Therefore, the uniformly corrected BHT dataset was used to estimate a temperature-depth profile (Figure 6A) in equilibrium developed by Crowell et al. (2012). We estimated the geothermal gradient as follows (Equation 2):

$$dT/dZ = [\text{corrected BHT datapoint} - \text{Surface temperature (°C)}]/ \text{depth (m)} \quad (2)$$

where dT/dz is the geothermal gradient (°C/Km).

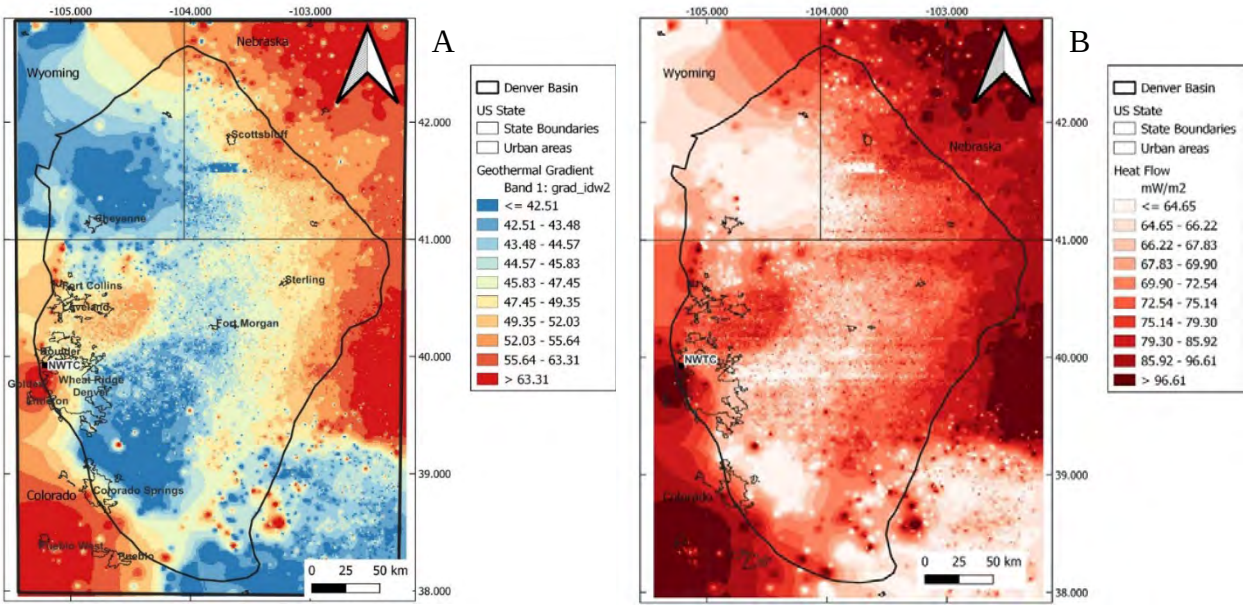

Figure 6: A. Geothermal gradient estimated from BHT data at 1 km. The average gradient temperature in the Denver Basin ranges around 42°C/km to 63°C/km. B. Heat Flow map of the Denver Basin calculated from geothermal gradient and thermal conductivities from SMU data. The heat flow map shows ranges around 64 to 96 mW/m^2. NWTC: National Wind Technology Center facility

We calculated heat flow as a function of depth (mW/m^2; Figure 6B). The uniform BHT dataset is required to estimate a geothermal gradient in conjunction with the lithology-dependent thermal conductivity. The following equation was used to estimate the heat flow:

$$Q = dT/dz * K \quad (3)$$

where Q is the heat flow (mW/m^2), dT/dz is the geothermal gradient (°C/Km), and K is thermal conductivity (W/m/ K), see Figure 4B.

The 1D heat flow model contains the following input assumptions and simplifications:

1. The model assumes that the generation of radiogenic heat is consistent and evenly spread throughout sedimentary rocks.
2. Input data was spatially interpolated to estimate the average and standard error of the average data values for the resource, producing maps depicting thermal quality in a GeoTIFF format (Figure 6).

In the Denver Basin, BHT data are concentrated in regions containing oil and gas reserves, such as central Colorado, while data are scattered in areas lacking exploration, such as southeastern Wyoming and southern Colorado. Sparsity of data in areas of the basin necessitates interpolation algorithms that can accurately predict nonexistent datapoints in both sparse and clustered datasets.

The intended application of the heat component is to suggest areas with a high geothermal resource potential based on temperature gradient as a proxy of heat flow, with high-temperature resources above 150°C typically used for generating electricity, while lower-temperature resources (<150°C) can be utilized for various direct applications such as heating buildings, industrial processes, agriculture, and recreational purposes.

4.1.2 Fluid Component Analysis

This first analysis was focused on the presence of coproduction water in oil and gas wells. Water production data can be used to provide information about where flowing water exists in the basin. It also indirectly provides a proxy for permeability aquifers and/or geothermal reservoirs, which is a key factor in hydrothermal resource and direct-use assessment. This type of data indicates reservoir quality of rocks by showcasing their capacity to uphold fluid flow rates needed for extracting heat from the rocks.

The main source for this water coproduction data from O&G wells in the Denver Basin is the USGS database that collates drilling and production records in the United States. The USGS dataset offers a comprehensive summary of the production records of U.S. wells spanning from 1817 to 2020. It was constructed using information gathered by IHS Markit, a commercial database provider. The production figures are consolidated in increments ranging from 2 to 10 square miles, detailing the cumulative output of oil, gas, and water volumes. In this study we used water production aggregated in 2 miles square that sum production per year in Barrels (BBL; Figure 7A).

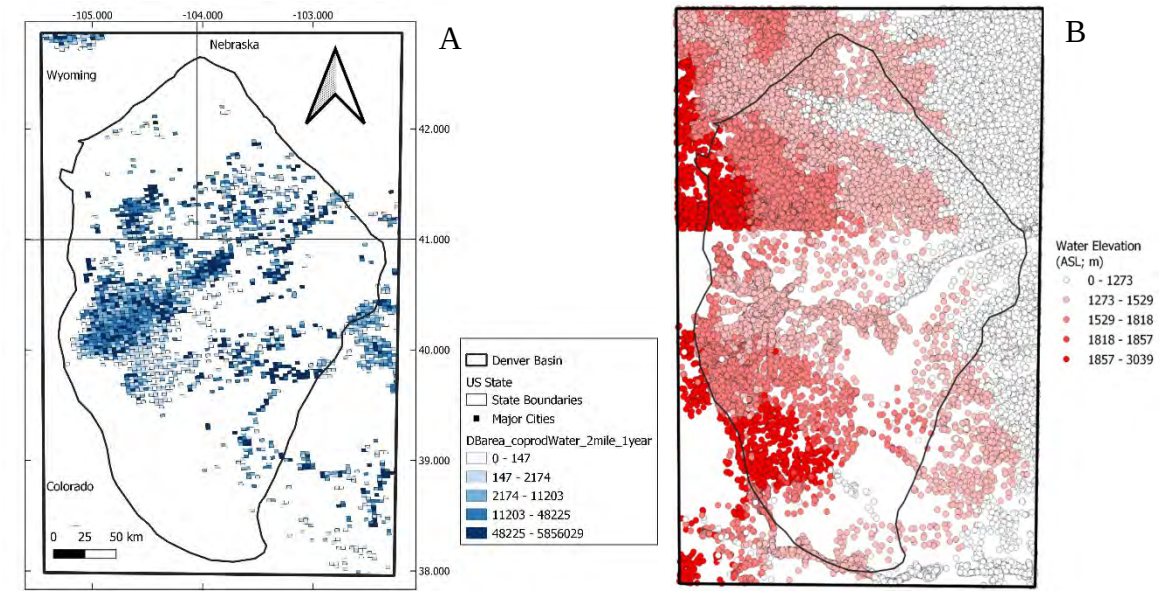

Figure 7: A. Water coproduction volumes (BBL) per year from oil and gas wells in the Denver Basin. B. Well water levels for Colorado, Nebraska, and Wyoming

The data quality information mentioned that comparing the annual production numbers with the total production figures revealed a discrepancy likely stemming from wells with unspecified production years. To ensure accuracy, the consistency between the original and processed total production values was verified. Moreover, a cross-check of well counts in various categories was

performed to confirm alignment, with the disparity between annual and total figures attributed to wells lacking spud dates.

Deeper reservoirs in the Denver Basin are well explored; for instance, over 8,000 wells have been drilled across the basin into the top of the Terry ("Sussex") sandstone alone (Fishman 2005). When investigating potential for direct-use geothermal energy (range of 50 m to 1,000 m vertical depth; minimum 80°C), grasping the potential volume of fluid available in shallower reservoirs is crucial. To achieve an estimation of shallow fluid availability, the elevation of static water level for all available groundwater wells in the Denver Basin area was calculated in Equation 4:

$$WL=GL-SWL \quad (4)$$

where WL (ft) is the water elevation in the well above sea level, GL (ft) is the ground surface elevation, and SWL (ft) is the reported static water level measured in the well. The datasets used to create an estimated water elevation in the Denver Basin were: SEO groundwater wells, where the depth to water (static water level) and well depth was reported in feet (WWDC 2024) and the ground elevation was obtained from USGS DEM files and converted to feet; CDSS wells, where the water elevation was reported as field 'WLElevation' in feet; and DNR for Nebraska, where Static Level was reported in feet. Well water elevation availability is visualized in Figure 7B.

4.1.3 Permeability Component Analysis

The permeability component analysis was simplified using structural geology data (e.g., faults and shear zones) and earthquake data due to a lack of accessibly data and short time frame to find, collect, and organize porosity, thickness, and other permeability data of reservoirs rock in the Denver Basin.

Most of the structural data in the region (Figure 8A) is inferred from surface fault features predominantly located in the western and southwestern parts of the Denver Basin. In the western section, the prevailing fault structures are primarily high-angle reverse faults that trend northwest and dip northeast, as documented by Erslev and Selvig in 1997. On a more specific level within the Wattenberg area, north of Denver, smaller but important structural characteristics are evident. These include ENE-trending wrench strike-slip faults and related listric normal faults with NNE, N, and NNW trends, as highlighted in works by Fishman (2005), Weimer (1996), and Weimer & Davis (1996). Research from multiple sources, such as Fishman (2005) and Weimer (1996), suggests the existence of five significant wrench faults in the Denver Basin within right-lateral movement along vertical planes, extending from the basement to the sedimentary cover (Weimer 1996). The intricate patterns of faulting indicate that the region is predominantly experiencing compressive stress, with the highest horizontal stress oriented towards the NNW, as noted by Heidbach et al. (2018).

Secondary permeability in the Denver Basin was assessed by distance from geologic structures in the Denver Basin. In a study conducted by Filina et al., structures in Nebraska were interpreted from a filtered magnetic field (2018). The structures identified in the study were digitized and included in the assessment of Denver Basin secondary permeability. Colorado structures were obtained from the USGS Geologic Map Database, and Wyoming structures were obtained from the Wyoming State Geological Survey. Primary permeability data of aquifers and rock formations were not accessible.

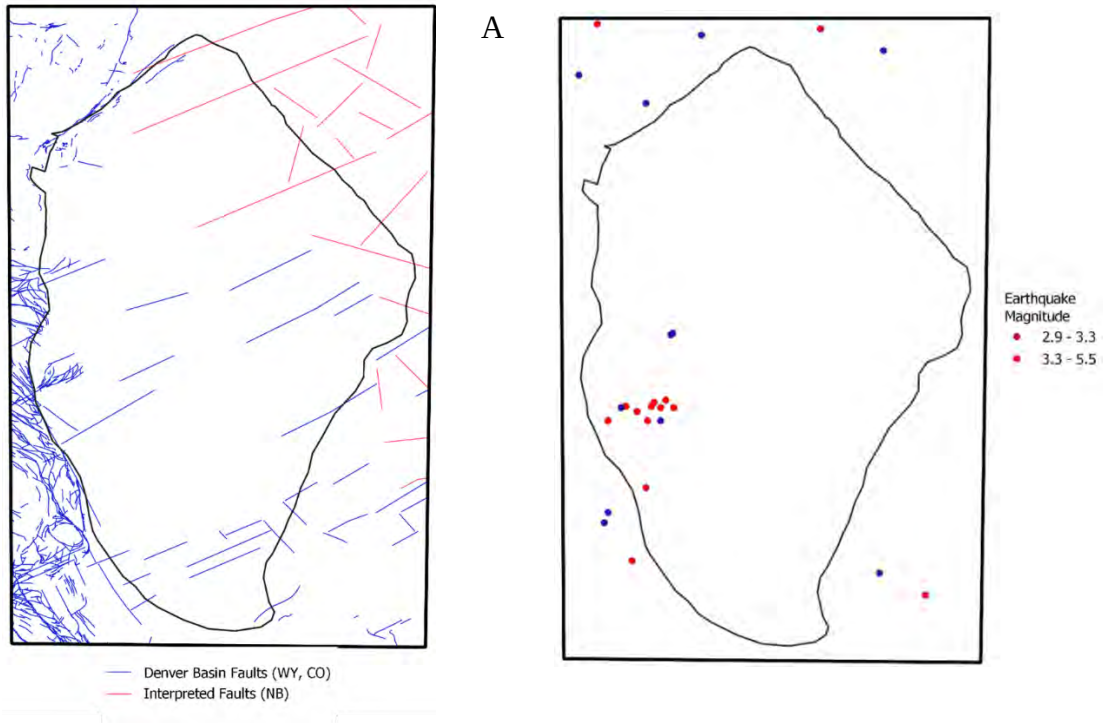

Figure 8: A. Faults and filtered magnetic lineaments and structures in the Great Basin area. B. Earthquakes greater than 2.9 magnitude in the Denver Basin from USGS earthquake catalog

To project secondary permeability of active faults, earthquake data from the 1950s to present day that was equivalent to or exceeded 2.9 magnitude was obtained from the USGS earthquake database presented in Figure 8B to identify Quaternary Faults and permeability of fluid pathways.

5. PFA Methodology

The Python library geoPFA was built with extensibility and reusability in mind, in the hopes that it may eventually be developed further and released as an open-source Python library. It is technologically agnostic and is modelled after the workflows described in the PFA Best Practices report. The library includes tools for:

- Reading in geospatial data in various formats (i.e., shapefile, TIFF, CSV).
- Cleaning the data (i.e., projecting onto the same CRS and grid, changing geometry type).
- Processing the data (i.e., distance function, various interpolation methods).
- Transforming the data (i.e., standardization, various methods for going from data values/data layers to favorability values/evidence layers).
- Weighting and combining the evidence layers (i.e., Voter-Veto method).
- Plotting the data and ouputs.

Throughout this section, examples of how the geoPFA Python library can be used to conduct PFA will be provided. The geoPFA is expected to be released as an open-source toolset in the future.

5.1 Configuration

There are several required inputs for each criterion and each component in the PFA process. These include component weights, component prior probabilities, evidence layer weights, and data layer transformation methods. In the full PFA, we will also add in criteria weights since there will be multiple criteria.

Component weights and component prior probabilities were assigned using expert opinion. Transformation methods were assigned based on a simple understanding of which relative relationship between data values and favorability (e.g., high values are more favorable = No transformation, or vice-versa = Negate). This could also be done more intelligently in the next PFA iteration. Evidence layer weights were also assigned using expert opinion and are set to 1.0 when there is only one evidence layer within a component (i.e., heat). Below are these parameters in tabular format for the geologic criteria only (Table 2).

geoPFA is built to be extensible to any possible combination of criteria, associated components, and data layers. It does so through requiring a configuration file that specifies the relationship between the data layers, respective components, and respective criteria. It also specifies the weights, units, data column names, and required transformation method for each data layer, and the prior probabilities associated with each component. Figure A.1 in the Appendix shows the configuration file for the geologic criteria only, in json format, compiling the information from Table 2 into a machine-readable format. Note that additional criteria may be added to the configuration file and formatted in a similar way.

Table 2: Table of component weights, component prior probabilities, evidence layers, evidence layer weights, and transformation methods applied. This table provides the basis for the configuration file shown in Figure A.1 in the Appendix.

Criteria	Component	Component weight*	Component Prior Probability	Evidence Layer Name	Evidence Layer Weight**	Transformation method
Geologic	Heat	0.40	0.65	Temperature Gradient	1.0	None
Geologic	Permeability	0.30	0.50	Structures (Faults)	0.50	Negate
Geologic	Permeability	0.30	0.50	Earthquakes	0.50	None
Geologic	Fluid	0.30	0.50	Hot Springs	0.5	Negate
Geologic	Fluid	0.30	0.50	Groundwater	0.2	Negate
Geologic	Fluid	0.30	0.50	Coproduced Fluid	0.3	None

*Note that the Voter-Veto method, as published in Ito et al. 2017, does not allow use of component weights. We have created a modified version of the Veto equation for combining component and criteria probabilities using weights.
**Note that the data layer weights are set to 1 when there is only one layer associated with a component.

It is also important that the data directory follows this same structure: there is a directory for each criteria, which contains subdirectories for each component, which each contain their respective data layers. The temperature gradient shapefile is named as described in the configuration file. Everything is also named as it is in the configuration file. This structure is demonstrated in Figure A.2 in the Appendix.

The configuration file is read into a Jupyter Notebook and stored as a Python dictionary named ‘pfa.’ This ‘pfa’ dictionary is updated throughout the process so that the entire PFA process is stored in a single data structure. This allows users to reference different parts of the PFA process throughout the workflow, for example, by comparing the original data layer to the final resulting favorability map or comparing the component favorability maps to the criteria favorability map.

5.2 Read in Data

The configuration and setup make it straightforward to read in the data (see Appendix: Figure A.3). Figure A.3 in the Appendix is a screenshot of the code which uses the ‘gather_data’ function from the ‘GeospatialData’ class in the geoPFA Python library. In this code snippet, we limit the data gathering only to shapefiles, but this can be adjusted to other formats, or all compatible geospatial data formats (currently shapefile, TIFF, and CSV). You can see from the text output that three data layers were read in–one for each component of the geologic criteria.

We can plot the raw data layers and see that they include various geometries (from left to right: point, line, and polygon), different CRSs, and different data spacing. The data need to be converted into point geometries, interpolated and/or processed to represent a feature of interest (e.g., distance from faults instead of fault traces), and projected onto the same CRS and the same grid (Figure 9). They also require some cleaning of outliers to show the trends more clearly in the data. These raw data layers are stored in Pandas GeoDataFrames (a type of dataframe that stores geospatial metadata and geometry) and added to 'data’ keys within their associated layer/component/criteria path within the ‘pfa’ dictionary so that they can be plotted at any point throughout the process.

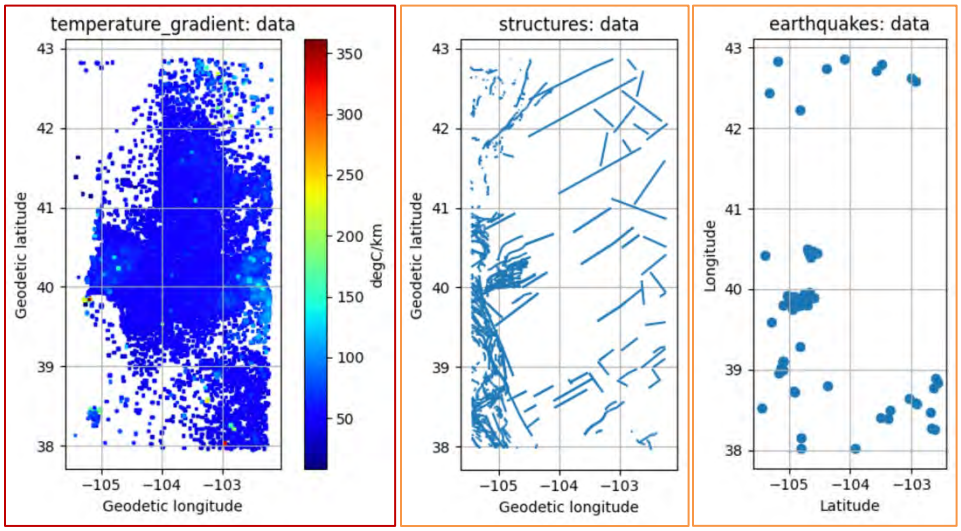

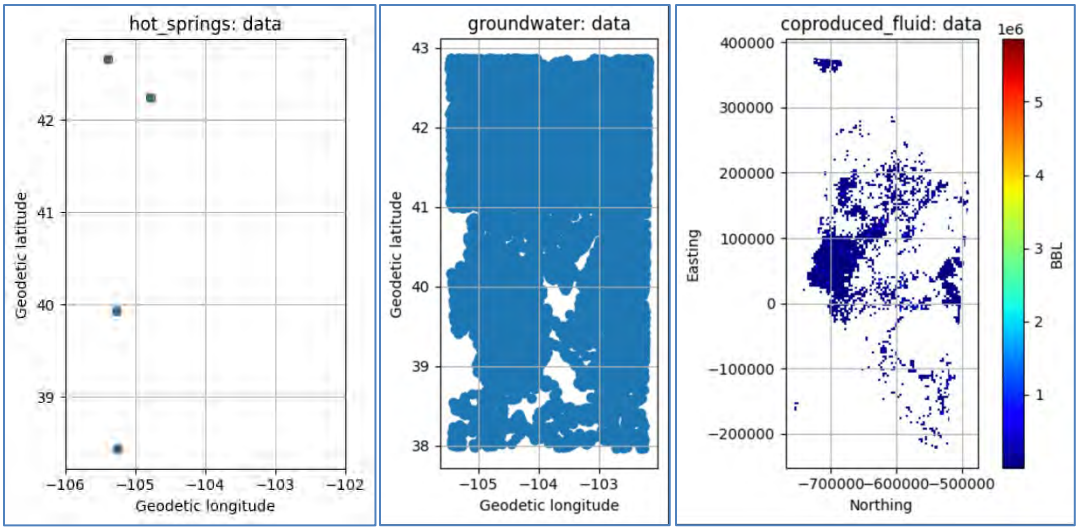

Figure 9: Raw data layers input into geoPFA for geologic criteria favorability mapping, including layers associated with the heat (red border), permeability (orange border), and fluid (blue border) components

5.3 Cleaning and Processing

Cleaning is done in just a few lines of code (Appendix: Figure A.4). This includes projecting everything onto the same CRS and filtering out outliers in some datasets by setting everything above the 0.9 quantile to the value associated with the 0.9 quantile. Particularly, the coproduced fluid and temperature gradient datasets included anomalously high values that masked the trends in the data. Outliers above the 90th percentile were filtered out and set to the value at the 90th percentile. Next, all the datasets were projected onto the same CRS. WGS 84 (EPSG:3857) was used because it is a common projected coordinate system. A projected coordinate system is a requirement for the interpolation and distance function to be accurate.

Linear interpolation is applied to temperature gradient and coproduced fluid data to produce 2D maps from these point datasets. A Euclidean distance function is used to calculate distance from faults, converting this line dataset into a 2D map. All three of the resulting 2D maps are on the same grid with the same CRS.

This is done using functions built into the ‘Cleaners’ class in the geoPFA. Currently the code requires somewhat manual cleaning of the data, but this could be automated in the future through allowing the user to specify cleaning methods for each layer within the configuration file.

Next, the data layers are interpolated/processed into maps (Appendix: Figure A.5). This process also puts all the layers onto the same grid through setting the ‘nx,’ ‘ny,’ and ‘extent’ variables. In addition, since the ‘interpolate_points’ function in the ‘Processing’ class of geoPFA requires point geometry, the polygon geometry of the produced fluid data layer is converted to point geometry by calculating the centroid of each grid square and applying the values for each grid square to its associated centroid. We have built this functionality into the ‘interpolate_points’ function. Currently, this function includes options for linear, cubic, or nearest-neighbor interpolation, and the linear option is selected.

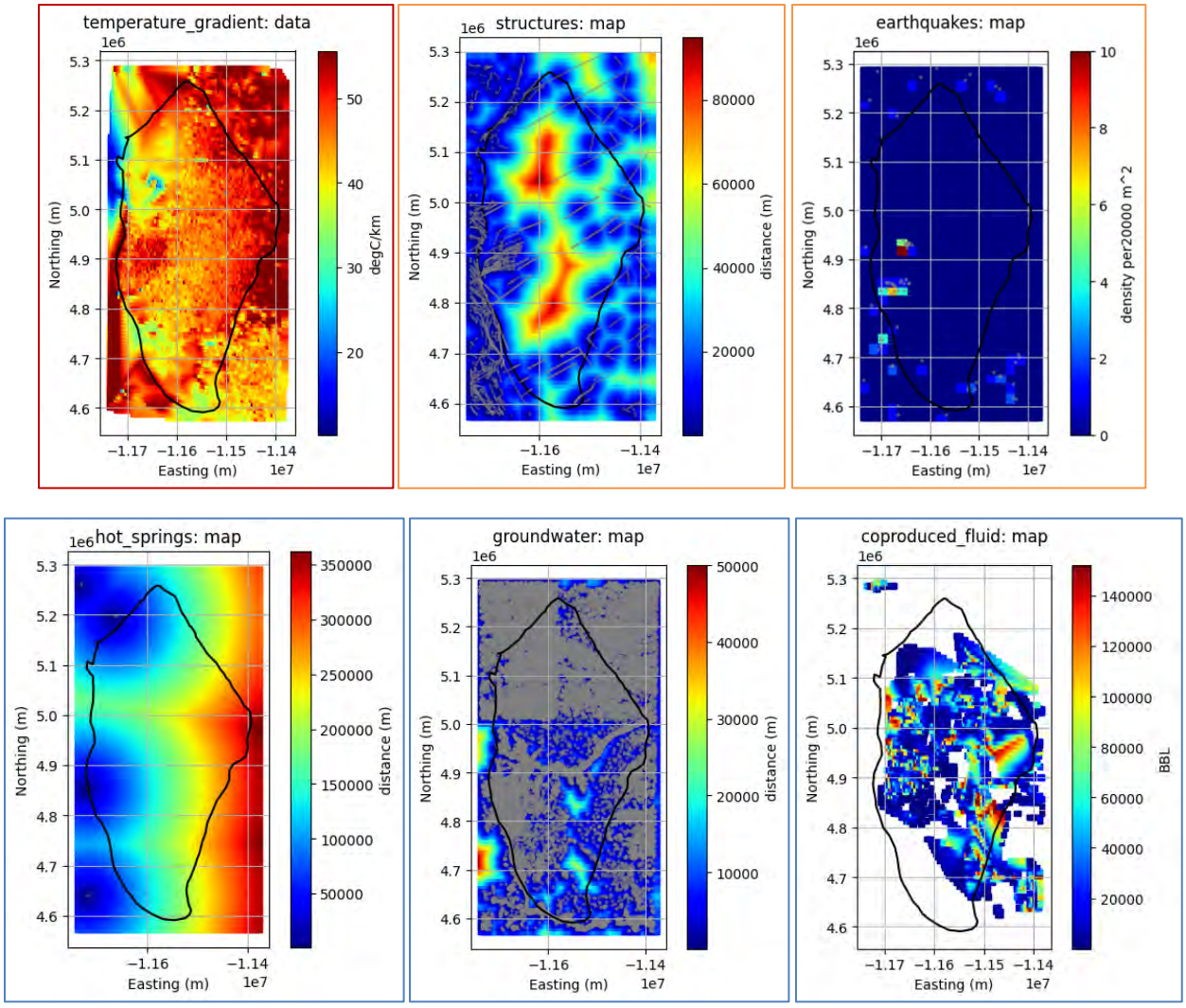

Figure 10: Processed data layers (or maps) input into geoPFA for geologic criteria favorability mapping, including layers associated with the heat (red border), permeability (orange border), and fluid (blue border) components Note that gray lines and dots represent data locations. Data locations are not labelled in the temperature gradient and coproduced fluid maps because the data points are dense and hide the trend in the interpolation

The fault location data is easily converted into a 'distance from faults' map using the 'distance_from_lines' function, and the hot springs and groundwater datasets are converted into 'distance from hot springs' and 'distance from groundwater observations' maps using the 'distance from points' function. The earthquake location data is converted into an 'earthquake density map' using the 'point_density' function. All three of these functions are in the 'Processing' class of the geoPFA. Similar to the cleaning functionality, geoPFA requires somewhat manual processing of the data, but this could also be automated in the future through allowing the user to specify processing methods for each layer within the configuration file.

The resulting maps are added to 'map' keys within their associated layer/component/criteria path within the 'pfa' dictionary so that they can be plotted at any point throughout the process. Above are the resulting maps produced from the processed data layers (Figure 10).

5.4 Transformation and Layer Combination

Next, all the data layers need to be converted into evidence layers. This involves normalizing and transforming (mapping data values to favorability values) each of the data layers. The evidence layers are then weighted and combined using the Voter-Veto method (Ito et al. 2017).

These steps are all built into the 'do_voter_veto' function in the VoterVeto class because transformation methods are specific to a given layer combination method. Transformation methods are additionally specific to a given data layer and are therefore specified in the configuration file for each data layer (Appendix: Figure A.6). For example, lower distance from faults is more favorable than higher distance from faults, so the evidence layer is produced by multiplying the fault distance map by –1 ('negate' method). No transformation methods are applied to the temperature gradient and coproduced fluids data layers because higher values are more favorable. In the future, transformation methods will be improved to better represent probability distributions associated with data layers as they pertain to their respective components and criteria. This will enable mapping of probabilities rather than just relative favorability.

Each data layer is normalized using min-max normalization. This puts all datasets on the same, positive, scale so that datasets with higher magnitudes do not dominate the results. Normalization may be done using either 'min-max' or mean absolute deviation ('mad').

Figure A.6 in the Appendix shows that we are able to normalize, transform, weight, and combine all of the data layers using just one line of code and the information (i.e., prior probabilities, transformation methods) stored in the configuration file. This uses the 'do_voter_veto' function from the 'VoterVeto' class in the geoPFA.

The 'do_voter_veto' function is written to complete the following steps:

1. Converts the data from a Pandas GeoDataFrame into a rasterized array to allow linear algebra/matrix math.
2. Transforms the data layers ('map') into evidence layers ('pr') using the transformation method specified for each data layer in the configuration file (if any) and then normalizing.
3. Weights and combines evidence layers into component favorability maps using the 'voter' method with the evidence layer weights in the configuration file.
4. Combines component favorability maps using the 'veto' method.
5. Combines criteria favorability maps using the 'veto' method.
6. Converts the rasterized favorability maps back into Pandas GeoDataFrames with the original geometry.

In other words, the weights and prior probabilities described in Table 2 are used in a modified version of the Voter-Veto equation (Ito et al., 2017). Within the Voter-veto method proposed by Ito et al, the Voter method (generalized linear model) is used to combine data layers into component favorability maps. Then, the modified Veto equation (element-wise multiplication) is used to combine component favorability maps into a geologic criteria favorability map, and to combine criteria maps into combined overall favorability maps, vetoing areas where any component criteria have a favorability value of 0. The original equations for this methodology are

described in Section 2.1 of Ito et al., 2017, and our modified version of the Veto equation is as follows:

$$\Pr(R) = \frac{\sum^c w_c \Pr(X_c)}{\max[\sum^c w_c \Pr(X_c)]} \times \max[\prod^c \Pr(X_c)] \quad (5)$$

where PrR is the probability of a resource, w_c is the weight of a given component or criteria, and Pr(X_c) is the probability of a given component or criteria. In written language, the equation produces a weighted some of the components or criteria, depending on which level the probability mapping is occurring on, normalizes by dividing by the maximum value, and scales using the product of the individual component or criteria probability maps to ensure that the resulting probability map represents a valid probability distribution. The veto portion of the equation is optional, but when desired, resulting indices in Pr(R) are set to zero if the associated indices in any Pr(X_c) are zero. In the methodology presented here, the veto option is used when combining criteria, but not when combining components.

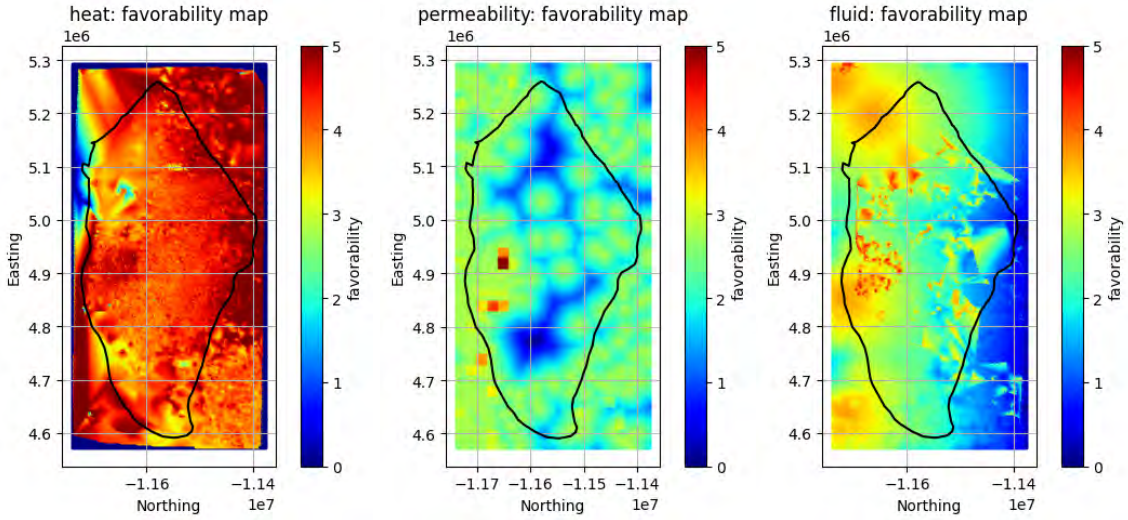

Figure 11: Geologic criteria component favorability maps, including heat, permeability, and fluid components, produced using geoPFA

The resulting evidence layers and component favorability maps are added to 'fav' keys within their associated criteria/component/layer and criteria/component paths, respectively, within the 'pfa' dictionary so that they can be plotted at any point throughout the process. The resulting component favorability maps are shown in Figure 11. Note that since we only are inputting one data layer to map the heat component, the temperature gradient evidence layer is equivalent to heat component favorability map, but typically this is not the case. The resulting criteria favorability maps are added to 'fav' keys within their associated criteria paths (in this case 'geologic') within the 'pfa' dictionary, and the resulting combined favorability map (not yet generated) is stored under a 'fav' key at the top level of the 'pfa' dictionary. The draft geologic criteria favorability map produced by geoPFA is shown in Figure 12.

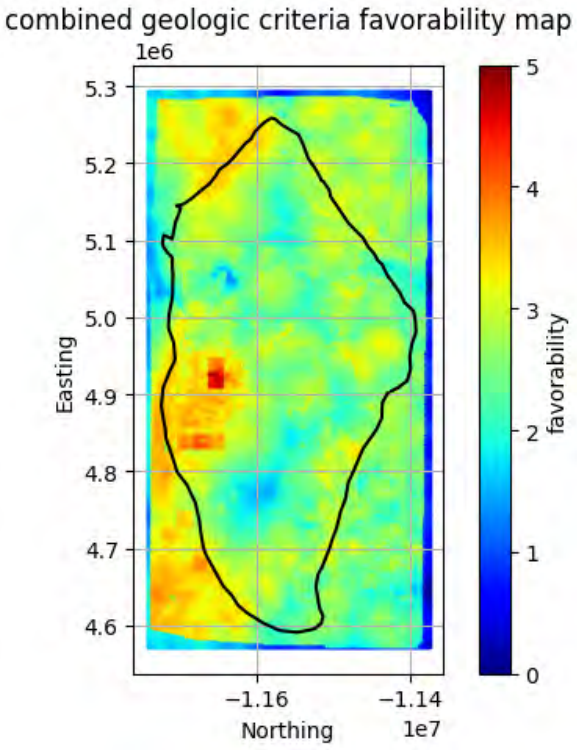

Figure 12: Combined geologic criteria favorability map of the Denver Basin, produced using geoPFA

6. Geological Criteria Favorability Map

The resulting favorability map is shown below in Figure 13. In the future, more robust data transformation methods will be implemented to more realistically map data values to probability values.

The map appears to validate the methodology thus far. The map highlights the area to the west end of the Denver Basin (e.g., Wattenberg area) where there appears to be intersection between faults, some seismic activity, elevated temperature gradient values, ground water presence, a hot spring, and relatively high volumes of coproduced fluids. It also highlights some other smaller areas that are not as obvious to the human eye, within the northwest (in southeast Wyoming) and southwest areas (near Colorado Springs) of the Denver Basin.

However, the significant reliance on earthquake density as a component of permeability in the geothermal favorability map raises concerns about potential artifacts, as the highest probability area coincides with multiple back-to-back earthquakes in very close proximity to each other. This suggests that the earthquake component may need to be weighted lower in our future analyses to avoid artifacts in the resulting favorability maps.

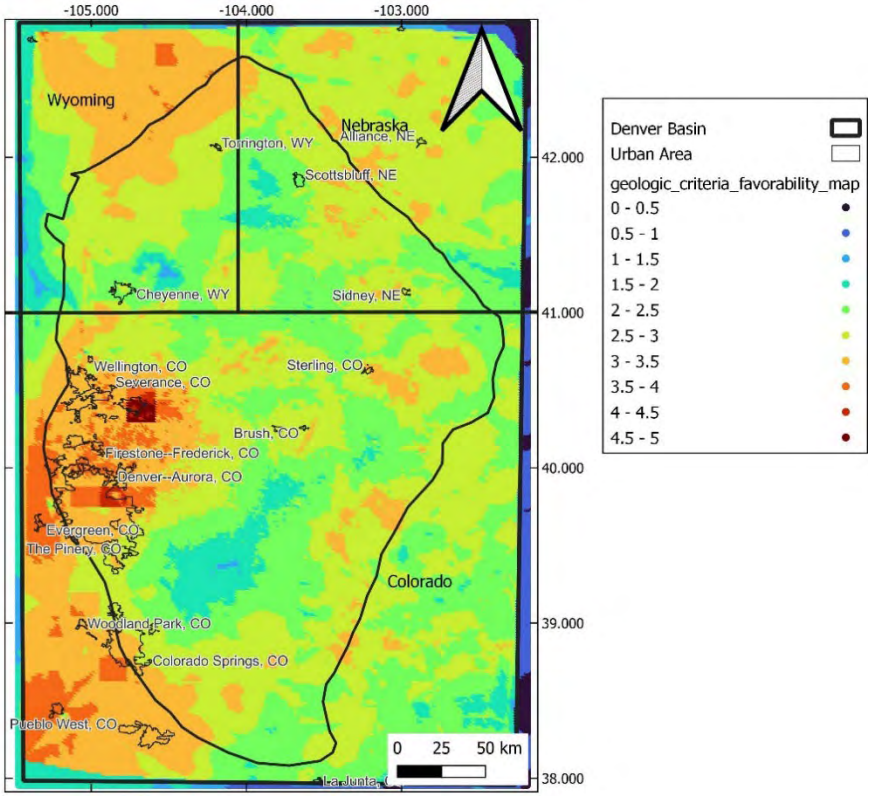

Figure 13: Geological Criteria Favorability Map for the Denver Basin

7. Conclusions

The study adapted PFA methodologies from previous studies to SBGPT to assess the potential of low-temperature resources in the Denver Basin. The resulting favorability map highlights areas with high potential for geothermal technology opportunities. While the map is still uncertain, it suggests promising areas, particularly in the western part of the Denver Basin.

To improve the accuracy and uncertainty quantification of the geological resource maps, future steps include: (1) incorporating additional high-quality data that provide enough information to create confidence layers; (2) adding more layers to the permeability component, particularly those that provide information about primary permeability in the geological formations rather than only secondary permeability; (3) improving interpolations and implementing more intelligent transformation methods; (4) refining prior probabilities and weights for each component (e.g., earthquakes will be weighted lower); and (5) building other layer combination methods into the geoPFA library, such as weights of evidence. The geoPFA Python library is expected to be released as an open-source tool in the future to enable others to use this code for their own PFA studies.

Furthermore, identifying potential areas for geothermal direct uses, and combined heat and power is a complex geospatial decision-making problem that requires consideration of multiple criteria. This paper was focused on the geological criteria, including heat, accessible fluid, and permeability, as essential factors for evaluating low-temperature resources. However, it is recognized that other critical criteria such as risk (seismicity, exclusion areas, and environmental/natural disaster) and economic factors (population, infrastructure, heating and

cooling demand, and levelized cost of heat) must also be considered in the evaluation process in this project. Future work will integrate these additional criteria to provide a comprehensive assessment of potential areas for geothermal applications.

In conclusion, this project aims to accelerate the country's decarbonization efforts by identifying opportunities for utilizing low-temperature geothermal resources (<150°C) in sedimentary basins with numerous population centers geothermal direct uses, and combined heat and power applications. The project has provided PFA workflows, data, tools, and favorability maps to support the utilization of low-temperature geothermal resources in the Denver Basin. Future improvements will focus on refining the methodology to ensure accurate and reliable results, ultimately facilitating future assessment of low-temperature geothermal resources in sedimentary basins and supporting the country's transition to a low-carbon economy.

Acknowledgement

This work was authored by the NREL operated by Alliance for Sustainable Energy, LLC, for the U.S. Department of Energy (DOE) under Contract No. DE-AC36-08GO28308. Funding and feedback provided by the U.S. Department of Energy Office of Energy Efficiency and Renewable Energy Geothermal Technologies Office. The views expressed herein do not necessarily represent the views of the DOE or the U.S. Government. The U.S. Government retains and the publisher, by accepting the article for publication, acknowledges that the U.S. Government retains a nonexclusive, paid-up, irrevocable, worldwide license to publish or reproduce the published form of this work, or allow others to do so, for U.S. Government purposes.

REFERENCES

Allen, P. A., Homewood, P. and Williams, G. D. 1986. Foreland basins: an introduction. In: Foreland Basins. Eds: P. A. Allen and P. Homewood, Special Publication of the International Association of Sedimentologists, 8, 3-12.

Augustine, C., 2014. Analysis of sedimentary geothermal systems using an analytical reservoir model. Geothermal Resources Council Transactions, 38, pp.641-647.

Blackwell, D. D., and Richards, M., 2004, Calibration of the AAPG Geothermal Survey of North America BHT Data Base: American Association of Petroleum Geologists Annual Meeting 2004, Dallas, Texas, Poster session, paper 87616.

Blackwell, D.D., Negraru, P.T. and Richards, M.C., 2007. Assessment of the enhanced geothermal system resource base of the United States. Natural Resources Research, 15, pp.283-308.

Coleman Jr, J.L. and Cahan, S.M., 2012. Preliminary catalog of the sedimentary basins of the United States.

Crowell, A.M., Ochsner, A.T. and Gosnold, W., 2012. Correcting bottom-hole temperatures in the Denver Basin: Colorado and Nebraska. GRC Transactions, 36(GRC1030229).

Davalos-Elizondo, E., Kolker, A., Taverna, N. and Holt, E., 2023. Assessing Low-Temperature Geothermal Play Types: Relevant Data and Play Fairway Analysis Methods (No. NREL/TP-5700-87259). National Renewable Energy Laboratory (NREL), Golden, CO (United States).

Dixon, J. M. (2002). Evaluation of Bottom-Hole Temperatures in the Denver and San Juan Basins of Colorado: Colorado Geological Survey.

Doughty, C., Dobson, P.F., Wall, A., McLing, T. and Weiss, C., 2018. GeoVision analysis supporting task force report: exploration.

Erslev, E.A. and Selvig, B., 1997. Thrusts, backthrusts and triangle zones: Laramide deformation in the northeastern margin of the Colorado Front Range.

Filina, I., Searls, M., Guthrie, K. and Burberry, C.M., 2018. Seismicity in Nebraska and adjacent states: The historical perspective and current trends.

Fishman, N. S. (2005). Energy Resource Studies, Northern Front Range, Colorado: US Geological Survey.

Förster, A., Merriam, D.F., and Davis, J.C., 1996, Statistical analysis of some bottom-hole temperature (BHT) correction factors for the Cherokee Basin, southeastern Kansas: Tulsa Geol. Soc. Trans., pp. 3-9.

Garcia-Castellanos, D. and Cloetingh, S.I.E.R.D., 2011. Modeling the interaction between lithospheric and surface processes in foreland basins. Tectonics of Sedimentary Basins: Recent Advances, pp.152-181.

Harrison W. E., Luza, K.V., Prater, M. L., and Chueng, P. K., 1983, Geothermal resource assessment of Oklahoma, Oklahoma Geological Survey, Special Publication 83-1.

Hartmann, D.J., Beaumont, E.A. and Coalson, E., 2000. Prediction sandstone reservoir system quality and example of petrophysical evaluation. Search and discovery, 40005.

Heidbach, O., Rajabi, M., Cui, X., Fuchs, K., Müller, B., Reinecker, J., . . . Xie, F. (2018). The World Stress Map database release 2016: Crustal stress pattern across scales. Tectonophysics, 744, 484-498.

Ito, G., Frazer, N., Lautze, N., Thomas, D., Hinz, N., Waller, D., Whittier, R., Wallin, E. (2017) "Play fairway analysis of geothermal resources across the state of Hawaii: 2. Resource probability mapping." Geothermics, Volume 70, 2017, Pages 393-405, ISSN 0375-6505, https://doi.org/10.1016/j.geothermics.2016.11.004.

Moeck, I.S., 2014. Catalog of geothermal play types based on geologic controls. Renewable and Sustainable Energy Reviews, 37, pp.867-882.

Moghaddam, M.K., Noorollahi, Y., Samadzadegan, F., Sharifi, M.A., Itoi, R., (2013) "Spatial data analysis for exploration of regional scale geothermal resources." Journal of Volcanology and Geothermal Research, Volume 266, Pages 69-83, ISSN 0377-0273, https://doi.org/10.1016/j.jvolgeores.2013.10.003.

Pauling, H., Taverna, N., Trainor-Guitton, W., Witter, E., Kolker, A., Warren, I., Robins, J., and Rhodes, G. (2023). "Geothermal Play Fairway Analysis Best Practices. Golden, CO: National Renewable Energy Laboratory." NREL/TP-5700- 86139. https://www.nrel.gov/docs/fy23osti/86139.pdf.

Rybach, L., 1981. Geothermal systems, conductive heat flow, geothermal anomalies. Geothermal Systems: Principles and case histories, pp.3-36.

Skinner, C.C., Miller, R.F., Kinney, S.A., Gianoutsos, N.J., Gunther, G.L., and Shorten, C.M., 2022, Aggregated Oil and Natural Gas Drilling and Production History of the United States (ver. 1.1, April 2023): U.S. Geological Survey data release, https://doi.org/10.5066/P9UIR5HE.

Spicer, H. C. (1964). A compilation of deep earth temperature data, U. S. A. 1910-1945. Open-File Report 64-167, U.S Geological. Survey.

USGS (2022) USGS CO2Viewer. Accessed from: https://co2public.er.usgs.gov/viewer/%0A

Weimer, P. and Davis, T.L. eds., 1996. Applications of 3-D seismic data to exploration and production (Vol. 5). Published jointly by the American Association of Petroleum Geologists and the Society of Exploration Geophysics.

Weimer. (1996). Guide to the petroleum geology and Laramide Orogeny, Denver Basin and Front Range, Colorado: Colorado Geological Survey Bulletin 51. Two miners inside the Black Diamond Mine (2).

Whealton, C. (2015). Statistical Correction of Temperature Data for New York and Pennsylvania Wells. M.S. Thesis, Cornell University, Ithaca. Retrieved from http://hdl.handle.net/1813/40609

Whealton, C. A. (2016). Statistical Data Analysis, Global Sensitivity Analysis, and Uncertainty Propagation Applied to Evaluating Geothermal Energy in the Appalachian Basin, in Ithaca, NY, USA, Cornell University, Ph.D. dissertation, p. 250

Wolfgramm, M., Obst, K., Beichel, K., Brandes, J., Koch, R., Rauppach, K. and Thorwart, K., 2009. Produktivitätsprognosen geothermischer aquifere in Deutschland. Der Geothermiekongress, pp.17-19.

Wyoming Water Development Commission, 2024. Groundwater water wells database. Accessed from: https://water.geospatialhub.org/pages/wwdc-gis-standards

Yuan, H. and Romanowicz, B., 2010. Lithospheric layering in the North American craton. Nature, 466(7310), pp.1063-1068.

Zimmermann, G., Reinicke, A., Blöcher, G., Milsch, H., Gehrke, D., Holl, H.G., Moeck, I., Brandt, W., Saadat, A. and Huenges, E., 2007, January. Well path design and stimulation treatments at the geothermal research well GtGrSk4/05 in Groß Schönebeck. In Proceedings Thirty-Second Workshop on Geothermal Reservoir Engineering (pp. 22-24). Stanford University Stanford, California.

APPENDIX A. Screenshots of code using geoPFA Python library

```
"criteria": {
    "geologic": {
        "weight": 0.35,
        "components": {
            "heat": {
                "weight": 0.4,
                "layers": {
                    "temperature_gradient": {
                        "weight": 1,
                        "units": "degC/km",
                        "data_col": "Gradient",
                        "transformation_method": "none",
                        "processing_method": "interpolate"
                    }
                },
                "pr0": 0.65
            },
            "permeability": {
                "weight": 0.3,
                "layers": {
                    "structures": {
                        "weight": 0.5,
                        "units": "NA",
                        "data_col": "None",
                        "transformation_method": "negate",
                        "processing_method": "distance"
                    },
                    "earthquakes": {
                        "weight": 0.5,
                        "units": "NA",
                        "data_col": "None",
                        "transformation_method": "none",
                        "processing_method": "density"
                    }
                },
                "pr0": 0.5
            },
            "fluid": {
                "weight": 0.3,
                "layers": {
                    "hot_springs": {
                        "weight": 0.5,
                        "units": "NA",
                        "data_col": "None",
                        "transformation_method": "negate",
                        "processing_method": "distance"
                    },
                    "groundwater": {
                        "weight": 0.2,
                        "units": "NA",
                        "data_col": "None",
                        "transformation_method": "negate",
                        "processing_method": "distance"
                    },
                    "coproduced_fluid": {
                        "weight": 0.3,
                        "units": "BBL",
                        "data_col": "SUM_WATER_",
                        "transformation_method": "none",
                        "processing_method": "interpolate"
                    }
                },
                "pr0": 0.5
            }
        }
    },
```


Figure A.1: Configuration file used to map criteria to components, components to data layers, and additional information to data layers. This configuration file is part of the required setup for geoPFA

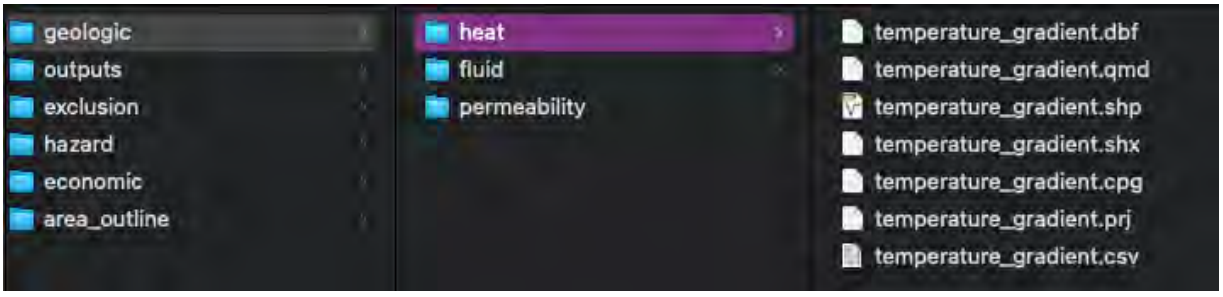

Figure A.2: Example directory structure for input data layers for geoPFA

Read in Data

```
file_types = ['.shp']
pfa = GeospatialDataReaders.gather_data(DATA_DIR,pfa,file_types)
```

```
criteria: geologic
        component: heat
                reading layer: temperature_gradient
        component: permeability
                reading layer: structures
                reading layer: earthquakes
        component: fluid
                reading layer: hot_springs
                reading layer: groundwater
                reading layer: coproduced_fluid
criteria: economic
        component: demand
                reading layer: population
                reading layer: infrastructure
        component: site_accessibility
                reading layer: roads
criteria: hazard
        component: natural_disaster
                reading layer: flood_plains
```

Figure A.3: Screenshot of code to read in data using geoPFA

Cleaning

```
pfa = Cleaners.set_crs(pfa, target_crs=3857)
```

```
data = pfa['criteria']['geologic']['components']['fluid']['layers']['coproduced_fluid']['data']['SUM_WATER_']
filtered_data = Cleaners.filter(data,quantile=0.9)
pfa['criteria']['geologic']['components']['fluid']['layers']['coproduced_fluid']['data']['SUM_WATER_'] = filtered_data
```

```
•••
```

```
data = pfa['criteria']['geologic']['components']['heat']['layers']['temperature_gradient']['data']['Gradient']
filtered_data = Cleaners.filter(data,quantile=0.9)
pfa['criteria']['geologic']['components']['heat']['layers']['temperature_gradient']['data']['Gradient'] = filtered_data
```

```
•••
```

```
gdf = pfa['criteria']['economic']['components']['demand']['layers']['population']['data']
clipped_gdf = Cleaners.set_extent(gdf,extent)
pfa['criteria']['economic']['components']['demand']['layers']['population']['data'] = clipped_gdf
```

```
gdf = pfa['criteria']['economic']['components']['demand']['layers']['population']['data']
col = pfa['criteria']['economic']['components']['demand']['layers']['population']['data_col']
filtered_gdf = Cleaners.filter_geodataframe(gdf,col,quantile=0.9)
pfa['criteria']['economic']['components']['demand']['layers']['population']['data'] = filtered_gdf
```

Figure A.4: Screenshot of code to clean data using geoPFA, including setting the CRS and filtering datasets

Figure A.5: Screenshot of code to process data using geoPFA, including interpolation, distance, and density functionalities

Figure A.6: Screenshot showing code to transform and combine data layers in one line of code using geoPFA

Shallow Geothermal Resources for Cooling Applications at the University of Hawai‘i

Christine Doughty[1], Nicole Lautze[2], Patrick Dobson[1], Craig Ulrich[1], Jianjun Hu[3], Sean Murphy[3], Donald Thomas[2], and Mike Campton[4]

[1]Earth and Environmental Sciences Area, Lawrence Berkeley National Laboratory, Berkeley, CA

[2]Hawai‘i Institute of Geophysics and Planetology, University of Hawai‘i at Mānoa, Honolulu, HI

[3]Energy Technologies Area, Lawrence Berkeley National Laboratory, Berkeley, CA

[4]National Renewable Energy Laboratory, Golden, CO

Keywords

Geothermal heat exchanger, building cooling, Hawai‘i, favorability map, numerical modeling

ABSTRACT

Scientists at Berkeley Lab have teamed up with The University of Hawai‘i at Manoa (UH Manoa) through the U.S. Department of Energy’s (DOE’s) Energy Transitions Initiative Partnership Project (ETIPP) to evaluate the technological and market feasibility of shallow geothermal heat exchanger (GHE) technology for building cooling, energy efficiency, and emissions reduction applications in Hawai’i. The team is assessing the data necessary to model the feasibility of deploying this technology, the actual models that will be used, and what hurdles need to be overcome to install a demonstration case. UH has an abundance of geologic and geothermal data and is looking to the national labs’ expertise to execute this analysis. UH is also interested in investigating policy, regulatory, and business conditions advantageous for implementation of a pilot project, and more broad deployment of this technology in Hawai‘i.

In many locations around the world, the demands for heating and cooling are roughly balanced over the course of the year, so GHEs do not cause significant long-term changes in subsurface temperature. This is not the case in Hawai’i, where the demand for heating is very small, meaning that over time, GHEs will add heat to the subsurface. If temperatures increase significantly, GHE systems will not work as designed. Regional groundwater flow has the potential to sweep heated water away from boreholes, thereby maintaining the functionality of the GHE system. Significant regional groundwater flow requires two things: a sufficiently large driving hydraulic head gradient

(usually closely related to surface topography), and sufficient porosity and permeability to enable groundwater to flow in large enough quantities to enable near-borehole temperatures to be maintained at ambient values. Hawai‘i’s volcanic terrain offers ample surface topographic variation. The lava itself shows an extremely large range of porosity and permeability, making it crucial to select sites with large enough values of these properties. Numerical modeling of coupled groundwater and heat flow can be used to determine how large is large enough. Both closed-loop and open-loop systems are being investigated. Another option being considered is using cool seawater as the source of chill.

Currently work is progressing on two fronts. A hydrogeologic model for a closed-loop system is being developed for the Stan Sheriff Center at the UH Manoa campus, where a subsurface karst system immediately downgradient of the borefield may provide efficient removal of heated groundwater. The team will also develop a technoeconomic model for this site to compare the cost of cooling using a GHE system with the costs of operating the current air conditioning system. At the state scale, geographic information system (GIS) layers of various attributes relevant for GHE are being combined to develop an overall favorability map for employing GHE in Hawai‘i.

1. Introduction

This study is a DOE Energy Transitions Initiative Partnership Project (ETIPP), which seeks to partner DOE national laboratory scientists with remote, coastal, and island communities looking to transform their energy systems and increase energy resilience. The overall goals of this project with the University of Hawai‘i include analyzing the potential for geothermal cooling in buildings across its 10 campuses by modeling shallow geologic conditions and building heating and cooling loads and evaluating potential geothermal technologies that could improve energy efficiency and significantly increase sustainability for these communities. This could contribute to decarbonizing building energy requirements throughout the United States (e.g., Liu et al., 2023).

This project builds upon an earlier assessment by Dores and Lautze (2020), who evaluated a variety of scenarios relating to the applicability of ground source heat exchangers for space cooling in Hawai‘i. They examined a number of important parameters for six of the Hawaiian Islands, such as shallow geology, depth to water table, and groundwater and measured air temperatures. These datasets were then projected onto GIS maps of each of the studied islands. For effective cooling to occur using GHE technology, a threshold maximum water table depth of 80 m was assigned. The groundwater temperature was used as a proxy for subsurface ground temperature at the same depth as the groundwater measurement, and a comparison was made between air and subsurface temperatures throughout the year for the major population areas on the four most populated islands. Using literature values for the thermal conductivities of the four main rock types—alluvium and fill, basalts and other volcanic rocks, sand and dune deposits, and limestone and reef deposits—the basalts and limestones were identified as having the most prospective thermal properties for deploying GHE systems. Both seasonal and yearly operational scenarios were evaluated. The study concluded that space cooling would be feasible using GHE systems in Hawai‘i, and that more detailed modeling would be needed to assess the impacts of advective heat transfer.

The current project has two primary objectives: 1) expanding the GIS-based screening methodology of Dores and Lautze (2020) to further assess the feasibility of deploying GHE

technology in Hawai‘i, and 2) conducting a more detailed technical and economic assessment of the potential for developing such a system for cooling of the Stan Sheriff Center athletic complex at the UH Manoa campus. This involves developing a detailed 3-D geologic model of the area that can be used to create a hydrogeologic framework for numerical modeling. One of the key concerns for applying GHE in tropical environments is that heat is continually added to the subsurface with only cooling being used, and that lateral flow of groundwater is required to sweep the heat away so that the system can continue to operate.

2. GIS-based Screening Criteria for GHE in Hawai‘i

As noted earlier, Dores and Lautze (2020) used the shallow geology, depth to water table, and groundwater and air temperatures to help identify prospective areas within six of the Hawaiian Islands where GHE might be feasible. Our team expanded this list of parameters to include additional screening criteria that would be useful in evaluating the suitability of a particular location for installing a closed-loop GHE system. We also looked at the potential of using open-loop systems as well as seawater cooling systems (e.g., Leraand and Van Ryzin, 1995), but this evaluation is confined to closed-loop GHE applications. The criteria consist of a variety of physical (i.e., geographic, geologic, hydrologic), ecological/environmental, and cultural factors that would influence the viability of deploying a GHE system. Two examples of these GIS screening criteria (soil permeability and the locations of schools and Department of Defense (DOD) land) on O‘ahu are displayed in Figure 1. Table 1 summarizes these features and provides some suggestions as to what might constitute favorable versus unfavorable conditions for each of these parameters. Many of these parameters can be mapped using corresponding GIS layers, so that multiple factors can be examined and areas that have favorable or unfavorable conditions can be easily identified using this approach.

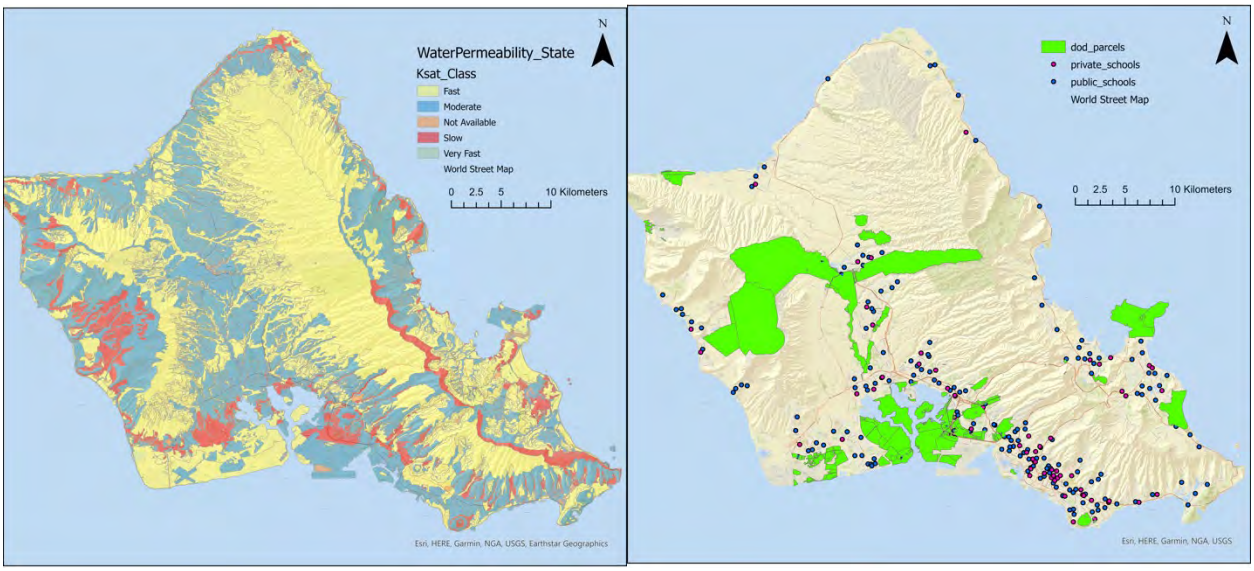

Figure 1: Left – GIS map of O‘ahu depicting different soil permeability zones: slow = <3μm/s; moderate = 3 – <10 μm/s; fast = 10 – <100 μm/s; very fast = ≥100 μm/s. Right – Locations of DOD lands and public and private schools on O‘ahu. See Table 1 for data sources.

2.1 Key Physical Parameters

A number of physical parameters are important for GHE installations. To meet the needs of cooling, the groundwater temperature needs to be low enough to be able to effectively cool buildings. Given that the GHE system will not be balanced between heating and cooling, there needs to be sufficient groundwater flow so that heat can be swept away from the boreholes. Having a sufficiently sloped piezometric surface and hydraulic head will promote higher lateral water flow rates needed to remove the heat, but it's also important to consider the ground surface slope (i.e. from the Digital Elevation Model), as it will add complexity to siting the GHE. The subsurface geology needs to have high enough permeability to facilitate a high flux of groundwater flow through the area where the borefield will be situated. Finally, the boreholes need to be located in an area with a fairly shallow water table, as the bulk of the boreholes need to be located in the saturated zone to allow for effective heat transfer between the closed-loop boreholes and the surroundings.

2.2 Key Ecological and Environmental Parameters

The siting of a GHE will require drilling numerous boreholes. This may not be possible in densely vegetated and forested lands, and in areas that have endangered species. There are areas with restricted watersheds that might not permit GHE deployment. There may be conflicts with existing use of the subsurface for freshwater production or water injection. The use of a closed-loop system may minimize such conflicts. Areas with existing wells will be better characterized with respect to their hydrogeology, which can help develop better constrained models that can be used to predict long-term GHE performance and estimate the cost effectiveness of such systems.

2.3 Key Cultural Parameters

There are a variety of cultural factors that may promote or restrict the deployment of GHE systems. Areas with an elevated community heat index and high cooling needs may be good candidates for such a system. Disadvantaged communities often lack access to housing with resilient and inexpensive cooling systems, so developing such systems within those neighborhoods could have very beneficial impacts. Some organizations, such as schools and the U.S. military, have prioritized decarbonizing their facilities and making them more climate resilient, so they may be good candidates for GHE cooling systems. There are some locations, such as national parks and sites of cultural and archeological sensitivity, where such systems cannot be deployed.

Table 1: Summary of key screening parameters for siting GHE installations

Parameter	Importance	Data range	Favorable	Acceptable	Unfavorable	Comments	GIS data source
Physical parameters							
Elevation	Useful	0 to >3,000 m	0-20 m	20-100 m	> 100 m	Proxy for depth to water table	https://planning.hawaii.gov/gis/download-gis-data-expanded/
Slope	Useful	0 to 90°	2-5°	0-2°, 5-10°	>10°	Higher slope harder to build on, but provides steeper hydrologic gradient	Calculated from Elevation model
Depth to water table	Critical	0 to >100 m	0-10 m	10-80 m	> 80 m	GHE needs to be deployed within saturated zone for heat to be dissipated effectively via advection	Dores and Lautze, 2020 https://waterdata.usgs.gov/hi/nwis/gw/
Geology	Critical	Basalt lava flows, breccia, tuff, limestone, alluvium	Fractured basalt, limestone		Unfractured basalt (dike-rich zones)	Fractured basalts typically have good horizontal permeability. Caverns in limestone may be problematic for drilling and well completion.	https://ngmdb.usgs.gov/Prodesc/proddesc_111883.htm
Soil moisture	Useful	Arid to very wet (7 classes)	Wet zones	Intermediate zones	Arid zones	Wet zones likely have higher subsurface flow, arid zones may have deeper water table	https://www.sciencebase.gov/catalog/item/57a902e8e4b05e859bdf3c83

Permeability	Critical	Ksat classes (fast, moderate, slow, very fast)	High permeability	Intermediate permeability	Low permeability	High permeability zones more likely to effectively dissipate heat	http://gis.ctahr.hawaii.edu/SoilAtlas
Groundwater temperature	Critical		< 20°C	20-25°C	>25°C	Warm water less favorable for cooling applications	https://www.higp.hawaii.edu/hggrc/projects/hi-play-fairway/pf-project-data/
Tsunami zone	Useful		outside		inside	Borehole installations are below ground surface, so this should be less critical	https://www.honolulugis.org/apps/39a9e07068a14d01a85b437adcf50beb/explore
Ecological and environmental parameters							
Vegetation cover	Useful	Bare ground, sparse vegetation, forested	Bare ground	Sparse vegetation	Forested	Densely forested areas would be impacted by developing a GHE borefield	https://planning.hawaii.gov/gis/download-gis-data-expanded/
Critical species habitat	Critical		No critical species present		Critical species present	It may be possible to install a GHE system and not disturb critical species habitat	https://planning.hawaii.gov/gis/download-gis-data-expanded/
Restricted watersheds	Useful/Critical		Unrestricted		Restricted	With a closed-loop system, deployment of a GHE system might be permitted in a restricted watershed	https://planning.hawaii.gov/gis/download-gis-data-expanded/
Underground injection zones	Useful		Distant		Proximal	There may be competing uses to the subsurface, injection may perturb	https://planning.hawaii.gov/gis/download-gis-data-expanded/

						subsurface temperatures; these areas may have better subsurface characterization	
Recycled water management zones	Useful		Unrestricted	Conditional	Restricted	There may be competing uses to the subsurface, water recycling may perturb subsurface temperatures; these areas may have better subsurface characterization	https://planning.hawaii.gov/gis/download-gis-data-expanded/
Water quality	Useful	Water to be left in natural state, discharge allowed, water known to be toxic/corrosive	Discharge allowed	Water to be left in natural state	Water known to be toxic/corrosive	For closed-loop system, main concern would be corrosion to underground installation. Heating of subsurface over time would perturb natural state conditions.	https://planning.hawaii.gov/gis/download-gis-data-expanded/
Existing wells	Useful					Existing wells may provide useful information regarding subsurface conditions, but may also indicate competing uses of the subsurface	https://www.higp.hawaii.edu/hggrc/projects/geothermal-digital-collection/groundwater-collections/

Cultural parameters							
Land ownership	Useful	Private and public lands	DOD, UH lands		Some private land, protected land	Landowner needs to provide access to site, some landowners are motivated to decarbonize operations	https://planning.hawaii.gov/gis/download-gis-data-expanded/
Schools	Useful	Public and private	School sites			Schools often have significant cooling load, interest in developing renewable energy resources, GHE system provides educational opportunities	https://planning.hawaii.gov/gis/download-gis-data-expanded/
Parks	Useful		No parks	Urban, multi-use parks	National parks and preserves	Parks often restrict or prohibit development. Also, parks may not have a need for cooling nearby.	https://planning.hawaii.gov/gis/download-gis-data-expanded/
Archeology/cultural site	Critical		No identified sites		Identified sites	Presence of archeological or cultural features would likely preclude GHE deployment	https://planning.hawaii.gov/gis/download-gis-data-expanded/
Community heat index	Useful		High heat index – greater need for resilient cooling		Low heat index – lesser need for resilient cooling	Linked to cooling demand	https://www.arcgis.com/apps/View/index.html?appid=ff1b73d836074cf6b2aca420fffbd930 (for O‘ahu)
Population density	Useful		High density	Intermediate density	Low density	Greater cooling demand with more concentrated	https://files.hawaii.gov/dbedt/op/gis/maps/

						population density, impact of urban heat island effect	2010_pop_density.pdf
Cooling demand	Critical		High cooling demand		Low cooling demand	GHE systems in greater need where cooling demand is higher	https://www.honolulugis.org/
Disadvantaged communities			Areas with disadvantaged communities		Areas with affluent communities	Deployment of GHE in disadvantaged communities can address energy poverty	https://screeningtool.geoplatform.gov/en/#6.3/20.657/-157.697

3. Evaluation of the Stan Sheriff Center at UH Manoa

The UH team members identified the Stan Sheriff Center at the UH Manoa campus as an ideal candidate to evaluate for cooling using GHE technology. It has a very high cooling load and is surrounded by open space and athletic fields where GHEs could be deployed. The following sections describe our efforts to characterize the local geology, develop a 3-D hydrogeologic model, create a numerical grid, and conduct some scoping simulations with different lateral groundwater flows to evaluate the potential for this area to sustainably provide cooling using GHE.

3.1 Geologic Model of the Stan Sheriff Center Site

A variety of data sources were used to create a 3-D geologic model of the area surrounding the Stan Sheriff Center at the UH Manoa campus (Wolf, 1975; Finstick, 1996; Holliday, 1998; Clague et al., 2016; Okuhata, 2017; Sherrod et al., 2021). The campus is partially located in an old quarry within the 76 ka Sugarloaf melilite nephelinite flow, which is reported to have a thickness of 15 m (Clague et al., 2016), and a series of limestone underground caves have also been reported in the area (Halliday, 1998); limestone reef deposits outcrop just seaward of the campus, on south side of H1 (Figure 2). Just to the north is Waʻahila Ridge, representing a series of older lava flows from the Koʻolau volcano. A number of engineering geology borings in the area help constrain the shallow subsurface geology as well as the depth to the water table, which is generally around 2.4 m to 3 m (8 ft to 10 ft) depth below ground surface. All of this information was georectified and imported into the Leapfrog 3-D geologic modeling tool. Figure 3 displays the plan view image of the study site, as well as a cross-sectional view of the area. For simplicity, six geologic units were identified: the older Koʻolau basalt (which forms the basement rock of this area), the younger Sugarloaf lava flow, limestone, coralline sand, alluvium, and fill. The locations of identified shallow limestone caves are also represented in this geologic model.

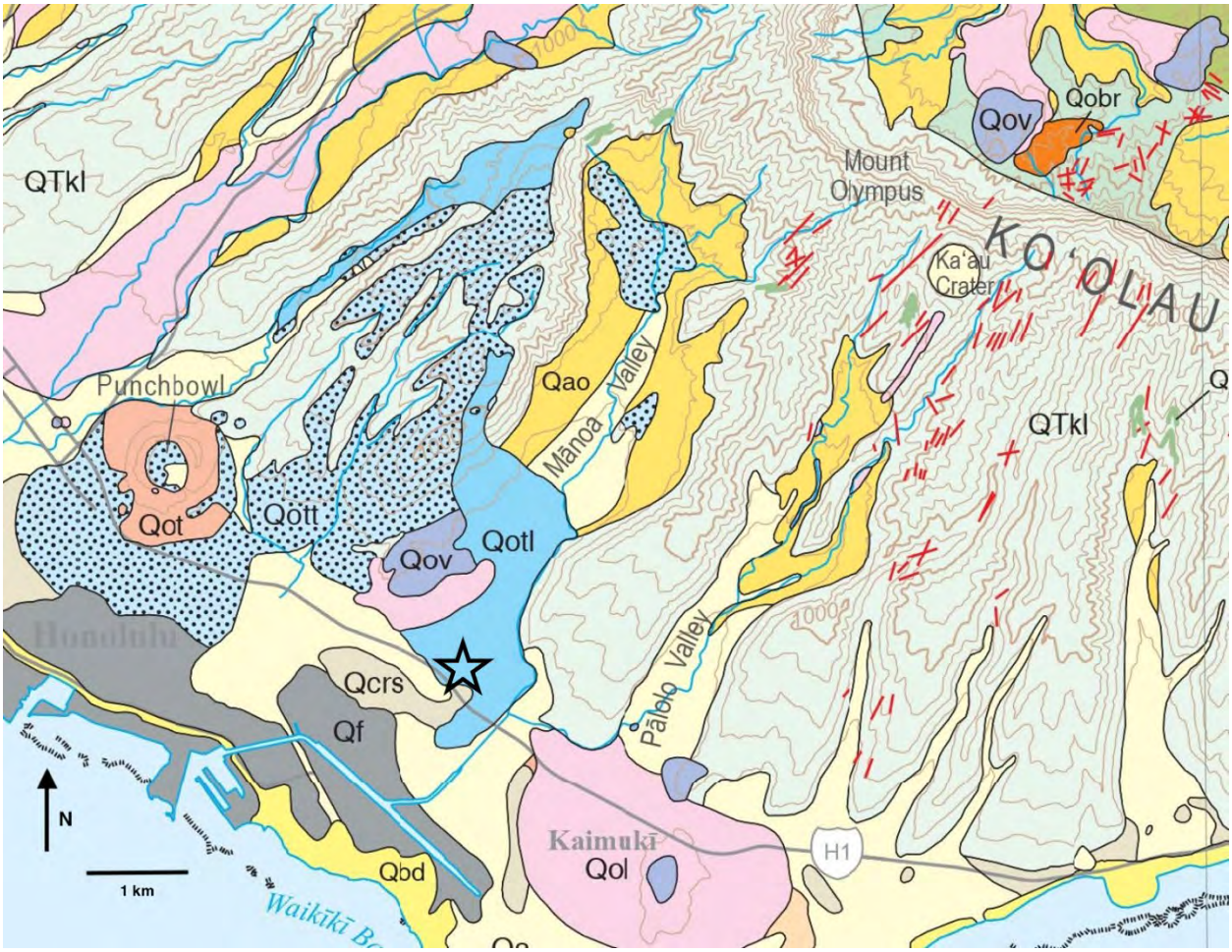

Figure 2: Portion of the geologic map featuring southern Oʻahu, from Sherrod et al. (2021). Depicted geologic units are as follows: Qf - Fill (Holocene); Qa - Alluvium (Holocene and Pleistocene); Qao - Older alluvium (Pleistocene); Qbd - Beach deposits (Holocene); Qcrs - Calcareous reef rock and marine sediment (Pleistocene); Qol - Lava flows, Honolulu Volcanics (Pleistocene); Qov - Cinder vent deposits, Honolulu Volcanics (Pleistocene); Qot - Tuff cone deposits, Honolulu Volcanics (Pleistocene) Qotl - Lava flows from Tantalus Peak and Sugarloaf vents, Honolulu Volcanics (Pleistocene); Qott - Tuff from Tantalus Peak and Sugarloaf vents, Honolulu Volcanics (Pleistocene); QTkl - Lava flows from Koʻolau Basalt (Pleistocene and Pliocene). The star denotes the location of the Stan Sheriff Center at the UH Manoa campus.

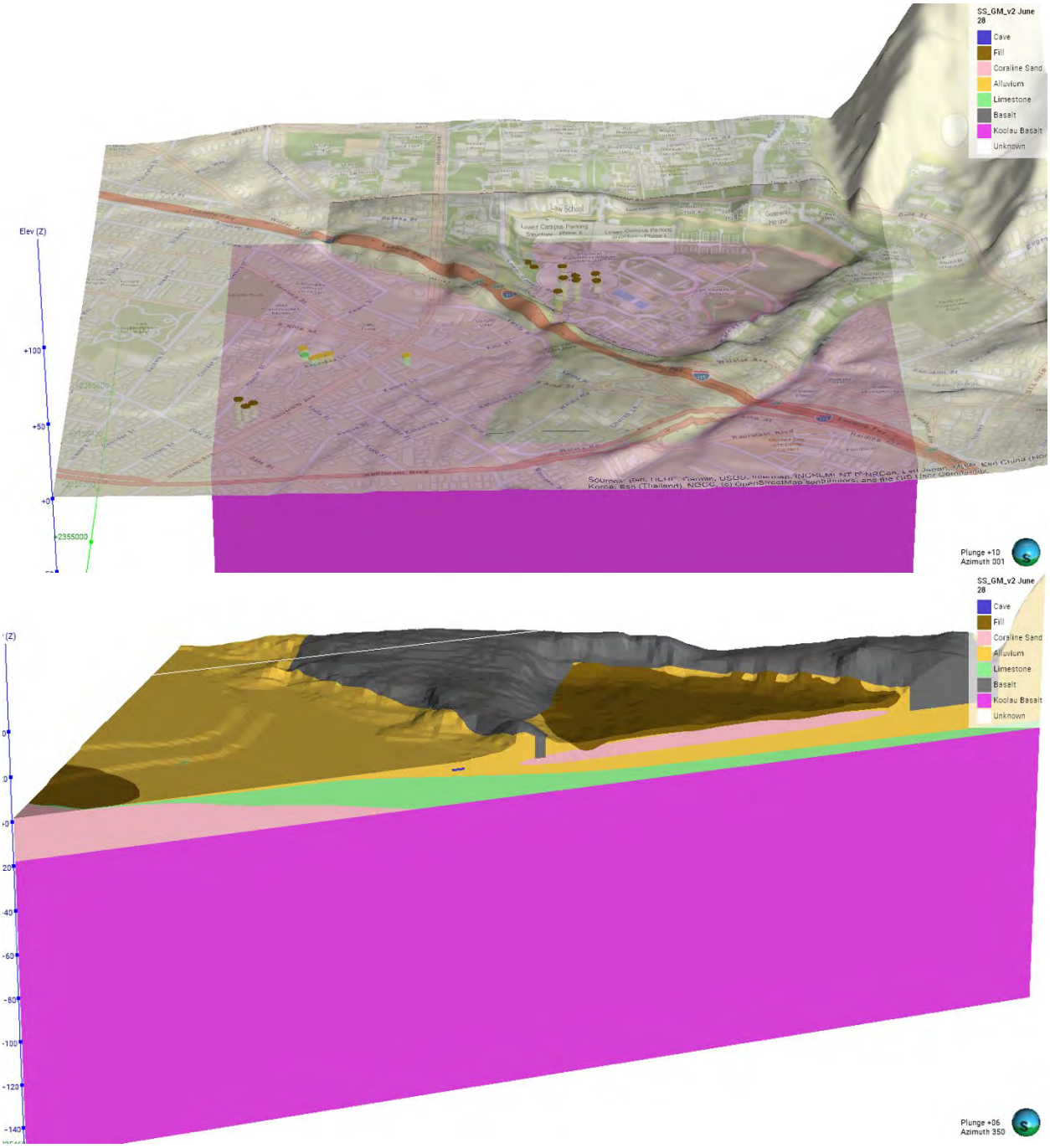

Figure 3: Three-dimensional images from the geologic model of the UH Manoa Stan Sheriff Center. Upper figure shows the excavated quarry in the Sugarloaf lava flow where the athletic complex is located, along with locations of engineering boreholes. The lower figure depicts a cut section through the 3-D geologic model, with the exposed cross section parallel to the main hydrologic flow direction (from right to left). Note that the majority of the geologic section is comprised by the older Ko'olau basalt flows.

3.2 Hydrogeologic Model and Heat Exchange Model of the Stan Sheriff Center Site

One of Leapfrog's capabilities is to convert the 3-D geologic model into a grid for the numerical simulations, where the grid blocks are assigned the appropriate petrophysical, thermal, and hydrologic properties corresponding to those pertaining to the units in the geologic model (e.g., Milicich et al., 2015). The grid was oriented so that the grid blocks would be parallel to the primary groundwater flow direction, which flows down from the crest of the Ko'olau Range towards the coastline in a southwesterly direction (Nichols et al., 1996) (Figure 4).

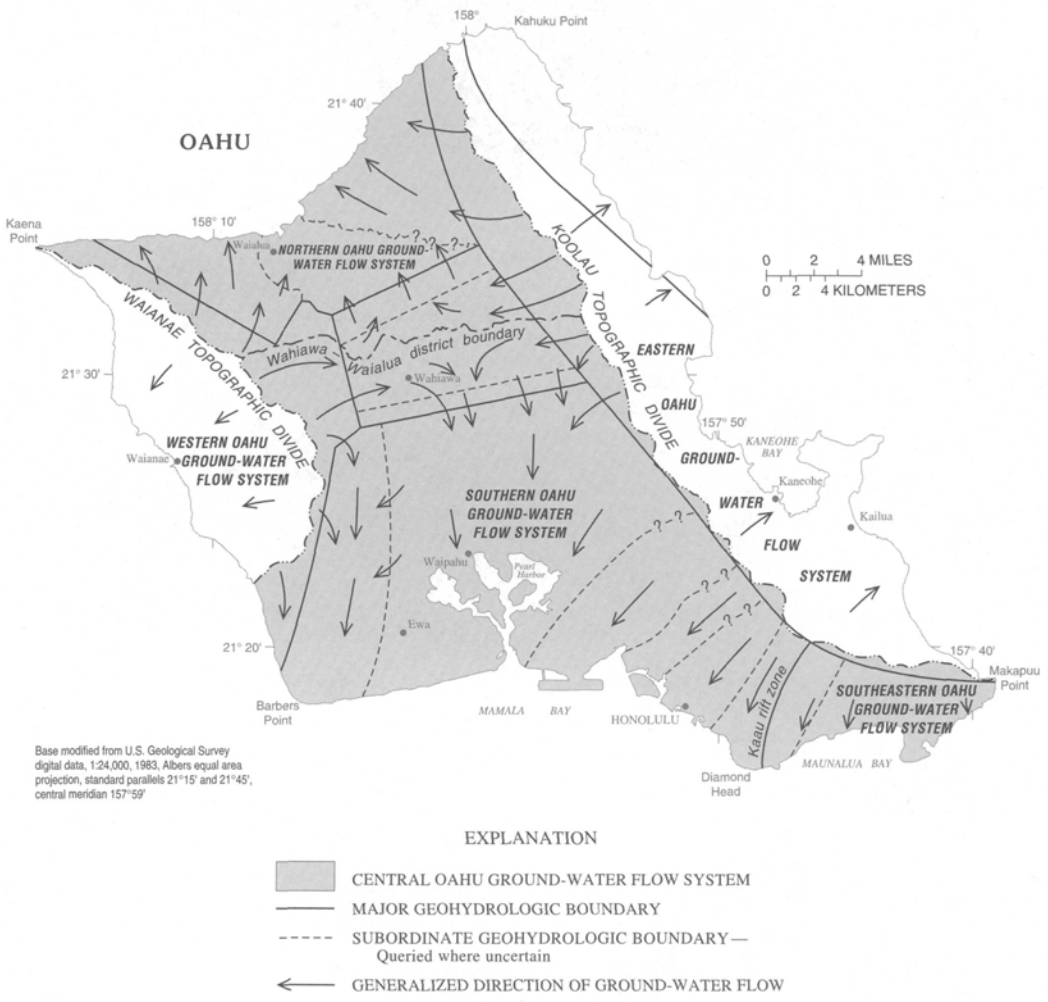

Figure 4: Groundwater flow systems for O'ahu (Nichols et al., 1996). The UH Manoa campus is located within the southern O'ahu groundwater flow system, just west of the Kaau rift zone.

The grid extent and thickness were designed to contain the potential region where a GHE system would be potentially deployed for cooling the Stan Sheriff Center. The grid extends from the ground surface to a depth of about 150 m. It contains 21 layers, with each layer thickness about 10 m. The upper five layers are incomplete, representing the variable surface elevation. The lower 16 layers all contain 2771 grid blocks. The total number of grid blocks in the model is about 46,000. Lateral grid spacing is 25 m, but the central portion of the grid is refined to 12.5 m, to better resolve

caves and the borefield. The lateral extent of the model is about 1.3 km in the east-west direction and 1 km in the north-south direction. Although the model itself is oriented east-west/north-south, the grid is rotated laterally to align with the regional groundwater flow direction. Figure 5 shows the grid. The numerical simulator being used is Transport of Unsaturated Groundwater and Heat (TOUGH) (Jung et al., 2018), a multi-phase, multi-component simulator for fluid flow and heat transport through porous or fractured geologic media.

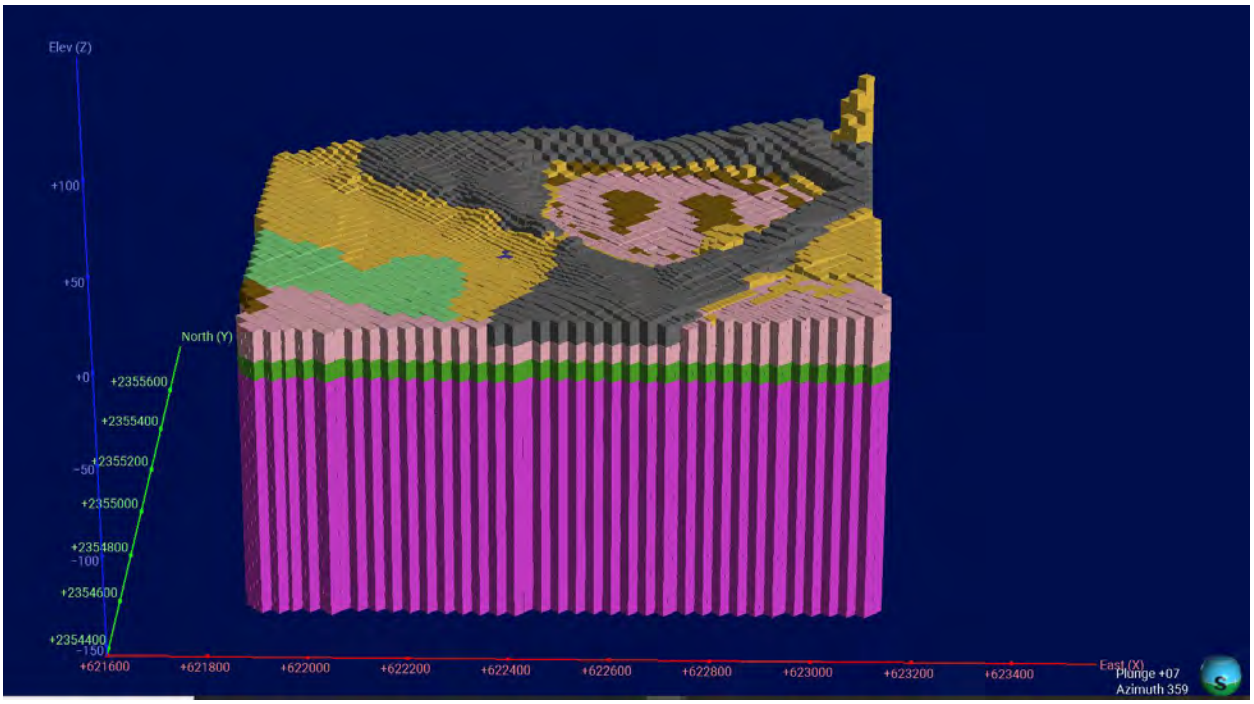

Figure 5: TOUGH grid used for the preliminary simulations.

There have been a number of hydrogeologic studies that have modeled groundwater flow in southern O‘ahu (e.g., Finstick, 1996; Nichols et al., 1996; Hunt, 1996; Lau and Mink, 2006; Rotzoll and El-Kadi, 2008; Okuhata, 2017; Izuka et al., 2018; Izuka and Rotzoll, 2023); they have summarized the hydrologic properties of the main geologic units of this area. In addition, Dores and Lautze (2020) have reported representative thermal conductivity values of the main lithologic units; these have been supplemented by data from Clark (1966) and Robertson (1988). Tables 2 and 3 present a summary of these properties, which are needed to properly simulate the groundwater flow and heat exchange of a GHE system. It is important to note that if 100 m closed loop borehole heat exchangers are to be used, then the Ko‘olau basalt unit will be the primary hydrogeologic unit controlling the heat exchange (the geologic model depicted in Figure 3 suggests that this unit will be present at depths greater than 20 m).

Table 2: Summary of key hydrologic properties of primary geologic units

Rock type	Hydraulic conductivity (m/d)	Effective porosity (%)	Comments	Sources
Koʻolau basalt (dike-free lava)	600 (horizontal – longitudinal); 150 (horizontal – transverse); 0.75 (vertical)		HC values used in our simulations	Okuhata (2017)
	152-1524			Hunt (1996)
	457, 305-1524	5	Porosity value used in our simulations. Vertical permeability estimated to be much lower than horizontal	Lau & Mink (2006)
	401-550		Based on Fig. 8a for study area	Rotzoll & El-Kadi (2010)
Honolulu volcanics	3 (horizontal – longitudinal); 1 (horizontal – transverse); 0.05 (vertical)		HC values used in our simulations	Okuhata (2017)
	0.3-152			Hunt (1996)
Limestone	100 (horizontal – longitudinal); 100 (horizontal – transverse); 0.5 (vertical)		HC values used in our simulations	Okuhata (2017)
	30-6096			Hunt (1996)
	0.43-53 (13)	15-45 (35)	Used average porosity value in our simulation. Coral ledge	Finstick (1996)
Alluvium	0.05 (horizontal – longitudinal); 0.05 (horizontal – transverse); 0.05 (vertical)		HC values used in our simulations	Okuhata (2017)
	0.0009-2.9 (0.9)	38-71 (54)	Used average porosity value in our simulations	Finstick (1996)
	0.006 – 0.113	46.4-62.4	Values for older alluvium	Lau & Mink (2006)

	0.3-152			Hunt (1996)
Fill	0.015-86 (43)	28-69 (46)	Used average HC and porosity values in our simulations	Finstick (1996)

Average values shown in parentheses

Table 3: Summary of thermal properties of primary geologic units

Rock type	**Thermal conductivity (W m^{-1} K^{-1})**	**Specific heat (10^3 J/kg K)**	**Comments**	**Sources**
Basalt	2.0		TC value used in our simulations	Dores & Lautze (2020)
	2.1-3.1		TC mean values for 2 different lavas measured at 20°C	Clark (1966)
	2.1	1.03	TC determined for non-porous rock with 10% mafic phenocryst content at 300 K; SH value for Dresser basalt at 20°C	Robertson (1988)
Limestone	3.1		TC value of 3.0 used in our simulations	Dores & Lautze (2020)
	2.18-3.05		TC mean values for 3 different limestones measured at 20°C	Clark (1966)
	2.7	1.01	TC determined for non-porous rock at 300 K; SH value for Bedford limestone at 20°C	Robertson (1988)
Alluvium	0.8		TC value used in our simulations	Dores & Lautze (2020)

As noted in Table 2, permeability in the basalt is anisotropic, with horizontal permeability much greater than vertical permeability, and longitudinal permeability (i.e., in the direction of the lava flow) higher than transverse permeability. In basalts, permeability is dominated by the presence of fractures. The TOUGH code is able to independently model fracture and matrix permeability by employing a dual continua model, where grid blocks are subdivided into fracture and matrix grid blocks by using the multiple interacting continua (MINC) approach (Pruess, 1992). The orientation and spacing of the fracture network can be specified using this approach. For these preliminary simulations, only a single continuum was used, but by orienting the grid with the direction of groundwater flow, we also align it with the orientation of the major fractures, enabling the code to model anisotropic fracture permeability effectively.

Another important input for this model is the initial temperature distribution in the subsurface. There are a number of deep groundwater monitoring wells in southern O‘ahu, including three (Kaimuki High School (HS), Kaimuki Station, and Waahila) that are fairly close to the UH Manoa campus. As part of the groundwater monitoring effort, multi-parameter sensors that measure fluid electrical conductivity, temperature, and pressure are regularly run in these wells to detect changes in the fresh water-brackish water interface (Rotzoll et al., 2010). The temperature information from these wells can be used to constrain the general temperature-depth gradient that can be expected for the Stan Sheriff site. For these preliminary simulations a uniform initial temperature of 21.5°C is used – Dores and Lautze (2020) report an average groundwater temperature of 21.36°C for Honolulu. These temperatures are consistent with the thermal profiles from the nearby monitoring wells mentioned above that were shared by the Honolulu Board of Water Supply.

The details of the vadose zone and heat and moisture transfer to the ground surface are not addressed in these preliminary simulations, but they are within the TOUGH simulator capabilities and will be included in future modeling. Here, the entire model domain is water-saturated and the top model boundary is closed.

Initially, all lateral boundaries of the model are closed, and a gravity-equilibration simulation is done to create a hydrostatic pressure distribution throughout the model. Next, columns at the upgradient and downgradient extremes of the model are held fixed with a given pressure difference, and the model is run to steady state, to create a regional groundwater flow. Finally, heat sources are specified to represent five 100-m long boreholes, with a total heat source strength of 400 kW, roughly comparable to the cooling load for the Stan Sheriff arena, and the model is run for 20 years.

3.3 Preliminary Heat Exchange Simulations of the Stan Sheriff Athletic Complex Site

Where the heating and cooling loads of a geothermal heat exchange system are unbalanced, it is important that heat that is discharged into the subsurface is dissipated through advective flow caused by groundwater flow to the sea so that the GHE system retains its efficiency over time. Such a system operates more like a radiator (such as the Verona ground source heat exchange (GHX) system, which has over 6000 GHX boreholes (Hart et al., 2022)), where heat dissipation is needed to maintain the heat balance of the subsurface reservoir over time. Thus, capturing the impact of lateral groundwater flow and its ability to sweep heat out of the system is critical in developing numerical models to help design and predict the system performance. Most GHE models utilize a simple g-function to represent heat exchange between the closed loop system and the subsurface, which does not capture the thermal impact of lateral groundwater flow, as it only

captures the effects of conductive heat transfer. A more rigorous representation of subsurface heat and flow processes can be realized using the TOUGH simulator, which can accurately model the effects of both advective and conductive heat flow. This simulator has been used to model geothermal district heating and cooling systems, and has been adapted to connect with the Modelica Buildings library (Wetter et al., 2014) developed by Lawrence Berkeley National Laboratory (LBNL), which includes dynamic simulation models for building and district energy and control systems (e.g., Doughty et al., 2021; Hu et al., 2022). Building upon these past efforts, our initial models examine the heat dissipation that can be achieved using a range of reasonable lateral groundwater flow rates based on reported transmissivity values.

Figure 6 shows some results of the preliminary modeling. Three cases were considered: no regional groundwater flow, small regional groundwater flow, and large regional groundwater flow. The plots show plan views of the temperature field at the top of the central portion of the model surrounding the borefield, after 20 years of heat injection. It is clear that the magnitude of regional groundwater flow has a significant effect on the long-term temperature in the borefield, with the maximum temperature decreasing as the magnitude of groundwater flow increases. The five injection boreholes are each separated by 12.5 m, and are arranged in a square.

Figure 7 shows an alternative suite of cases where the same load is distributed between 25 boreholes, also with 12.5 m separation, arranged in a square. It is apparent that the maximum temperature is much smaller in this case.

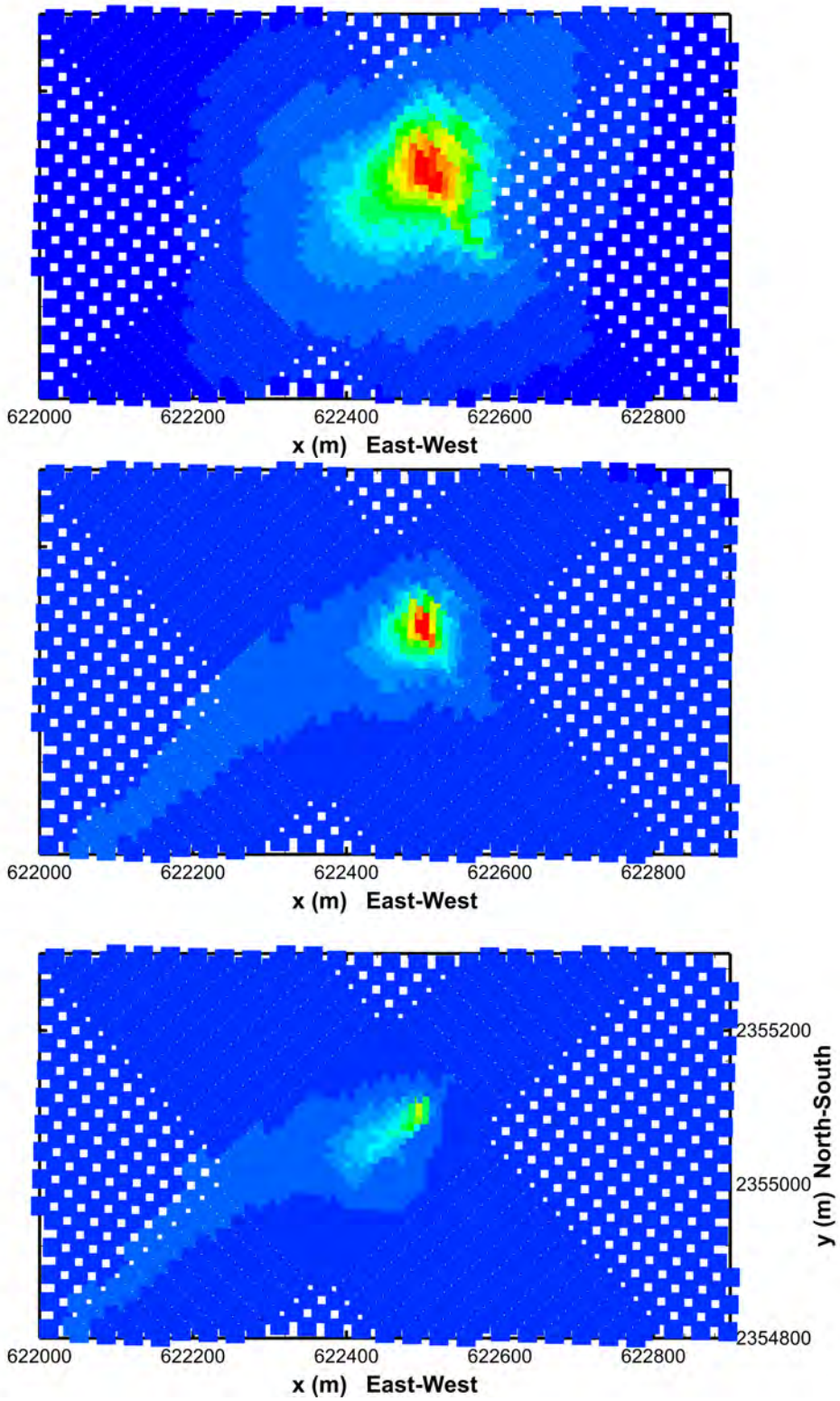

Figure 6: Preliminary TOUGH simulation results for a borefield with five boreholes. Temperature distributions at the top of the model after 20 years of heat injection. Top to bottom: increasing groundwater flow. Warmer colors indicate higher temperatures.

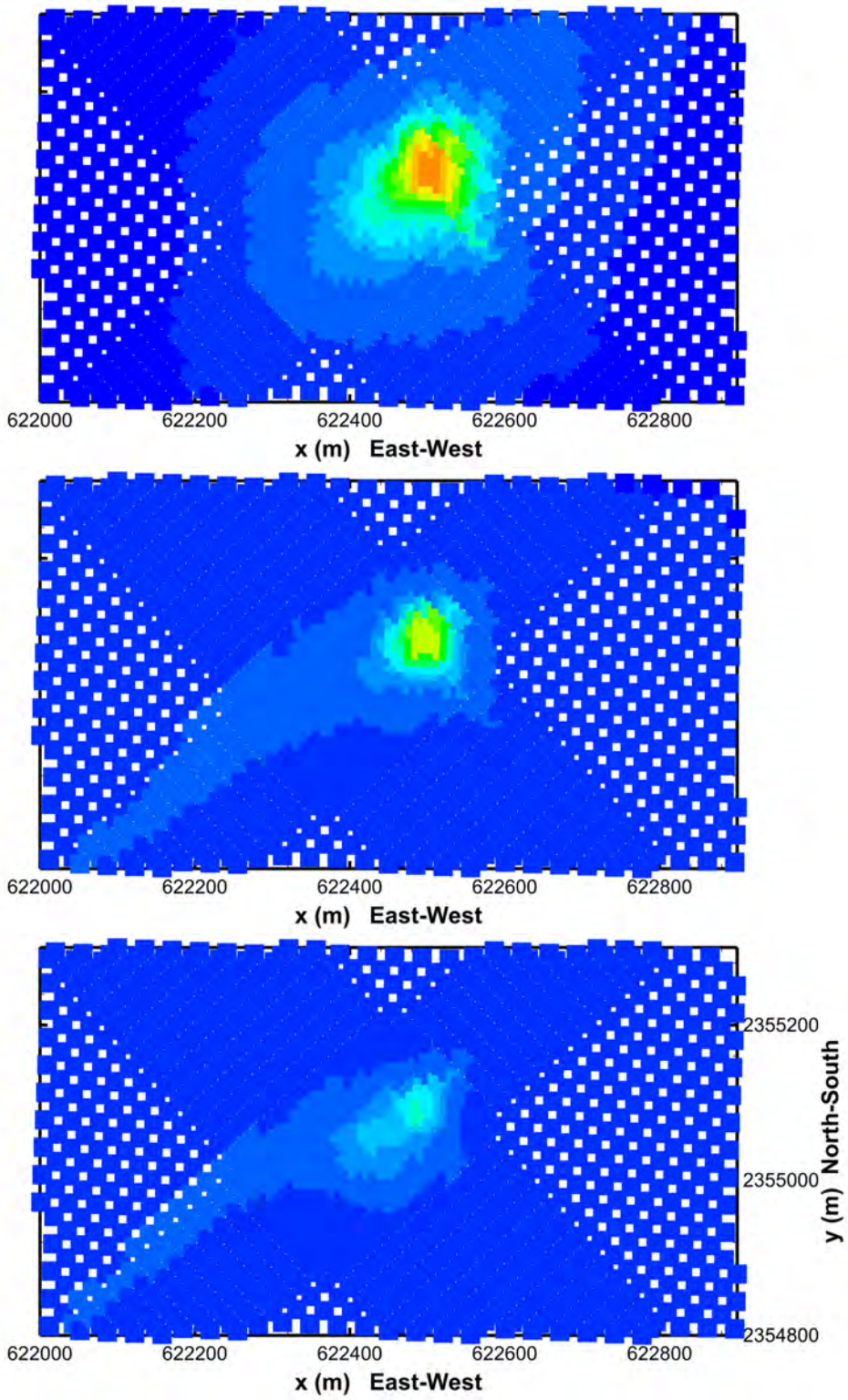

Figure 7: Preliminary TOUGH simulation results for a borefield with 25 boreholes. Temperature distributions at the top of the model after 20 years of heat injection. Top to bottom: increasing groundwater flow. Warmer colors indicate higher temperatures.

4. Next Steps

The preliminary TOUGH model can be improved in several ways to improve representation of the hydrogeologic setting: (1) the model can be reoriented in the direction parallel to groundwater flow to allow better assignment of pressure boundary conditions, (2) the vadose zone (with a smaller thermal conductivity due to drier conditions) can be represented, (3) moisture and heat transfer to the atmosphere, including evaporation and infiltration, can be included. Double-porosity or MINC methods can be used to better represent heat transfer in fractured rock. More accurate representation of the borehole heat exchangers can be implemented (e.g., Falta et al., 2023).

The results of the initial TOUGH simulations will then be coupled with Modelica runs to evaluate the effectiveness of a GHE system in providing sustained seasonal cooling to the Stan Sheriff Center. We will build a mechanical and thermal model of the Stan Sheriff Center's heating, ventilation, and air-conditioning (HVAC) system to assess the energy and demand impacts of transferring heat to the geothermal resource. We will then calculate the electricity bill savings associated with those energy and demand impacts. Finally, we will calculate the net present value of the geothermal exchange system, accounting for the capital costs of its installation, the lifecycle electricity bill savings, and tax credits made available in the Inflation Reduction Act (IRA).

There are several key economic incentives that could support the development of a GHE project such as the one described in this paper. The IRA includes the Clean Energy Investment Tax Credit, which applies to geothermal heat pumps, and includes a monetization pathway for non-taxable entities, such as universities. Eligible projects can claim up to 40% of the project cost as a credit. The base credit is 6%, but is increased 5 times to 30% if the system is less than 1 MW, or if the project meets prevailing wage and apprenticeship requirements. An additional 10% credit can be obtained if the project meets domestic content requirements. In addition, Hawaiian Electric Company offers incentives for custom energy efficiency project of up to 50% of incremental project costs–this effort would need to be coordinated with the utility, requiring an application that includes the energy savings calculations.

Acknowledgments

This project was supported by DOE's Energy Transitions Initiative Partnership Project (ETIPP) with the University of Hawai‘i and under the U.S. Department of Energy Award Number DE-AC02-05CH11231 with LBNL. We thank our colleagues Kendal Leonard, and Miles Topping at the University of Hawai‘i, Mark Glick, and Dora Nakafuji (formerly of Kamehameha Schools) for their contributions to this project. The geologic model output for this paper was generated using Leapfrog Software. Copyright © Seequent Limited. Leapfrog and all other Seequent Limited product or service names are registered trademark or trademarks of Seequent Limited. We thank Jay Egg for sharing his insights with our team on deploying geothermal heat pumps in tropical environments. We also thank Nancy Matsumoto from the Honolulu Board of Water Supply for generously sharing measured thermal profiles from three deep monitoring wells near the Stan Sheriff study area.

REFERENCES

Clague, D.A., Frey, F.A., Garcia, M.O., Huang, S., McWilliams, M., and Beeson, M.H. "Compositional heterogeneity of the Sugarloaf melilite nephelinite flow, Honolulu Volcanics, Hawai'i." *Geochimica et Cosmochimica Acta*, 185, (2016), 251-277.

Clark, S.P., Jr. (ed.) "Handbook of Physical Constants – Revised Edition" Geological Society of America, Memoir 97, (1966).

Dores, D., and Lautze, N. "Preliminary assessment of ground-source heat exchangers for cooling in Hawai'i." *Sustainable Energy Technologies and Assessments*, 37, (2020), 100579.

Doughty, C., Hu, J., Dobson, P., Nico, P., and Wetter, M. "Coupling subsurface and above-surface models for optimizing the design of borefields and district heating and cooling systems in the presence of varying water-table depth." Proceedings, 46th Workshop on Geothermal Reservoir Engineering, Stanford University, Stanford, CA, (2021).

Falta, R., L. Murdoch, C. Hammock, K. Bicknell, J. McDaniel, J. Horvath, "Simulation of high temperature subsurface thermal energy storage using closed-loop borehole heat exchangers." TOUGH Symposium 2023, Berkeley, CA, September 18-20, (2023).

Finstick, S.A. "Subsurface geology and hydrogeology of downtown Honolulu with engineering and environmental implications." Ph.D. Thesis, Department of Geology and Geophysics, University of Hawaii at Manoa, (1996).

Halliday, W.R. "History and status of the Moiliili Karst, Hawaii." *Journal of Cave and Karst Studies*, 60(3) (1998), 141-145.

Hart, D.J., Tinjum, J.M., Fratta, D., Thomas, L.K., and Carew, E.L. "Radiators or reservoirs: Heat budgets in district-scale ground-source geothermal exchange fields." Proceedings, 47th Workshop on Geothermal Reservoir Engineering, Stanford University, (2022).

Hu, J., Doughty, C., Dobson, P., Nico, P., and Wetter, M. "Coupling subsurface and above-surface models for optimizing the design of borefields and district heating and cooling systems in the presence of moving groundwater." Proceedings, 47th Workshop on Geothermal Reservoir Engineering, Stanford University, (2022).

Hunt, C.D., Jr. "Geohydrology of the Island of Oahu, Hawaii." U.S. Geological Survey Professional Paper 1412-B, (1996).

Izuka, S.K., Engott, J.A., Rotzoll, K., Bassiouni, M., Johnson, A.G., Miller, L.D., and Mair, A. "Volcanic aquifers of Hawai'i – Hydrogeology, water budgets, and conceptual models." U.S. Geological Survey Scientific Investigations Report 2015-5164, version 2.0, (2018).

Izuka, S.K., and Rotzoll, K. "Volcanic aquifers of Hawai'i – Contributions to assessing groundwater availability on Kaua'i, O'ahu, and Maui." U.S. Geological Survey Professional Paper 1876, (2023).

Jung, Y., G.S.H. Pau, S. Finsterle. C. Doughty, "TOUGH3 User's Guide, Version 1.0", Rep. LBNL-2001093, Lawrence Berkeley Laboratory, Berkeley, Calif., (2018).

Lau, L.S., and Mink, J.F. "Hydrology of the Hawaiian Islands." University of Hawaii Press, (2006).

Leraand, T.K., and Van Ryzin, J.C. “Air conditioning with deep seawater: A cost-effective alternative for West Beach, Oahu, Hawaii.” Proceedings of the IEEE Oceans 1995 Conference, (1995), 1100-1109.

Liu, X., Ho, J., Winick, J., Porse, S., Lian, J., Wang, X., Liu, W., Malhotra, M., Li, Y., and Anand, J. “Grid cost and total emissions reductions through mass deployment of geothermal heat pumps for building heating and cooling electrification in the United States.” Oak Ridge National Laboratory Report ORNL/TM-2023/2966, (2023).

Nichols, W.D., Shade, P.J., and Hunt, C.D., Jr. “Summary of the Oahu, Hawaii, regional aquifer-system analysis.” U.S. Geological Survey Professional Paper 1412-A, (1996).

Milicich, S.D., Alcaraz, S., and Pearson-Grant, S.C. “An integrated approach to geological and fluid flow modelling: From a 3D geological model to TOUGH2.” Proceedings, 37th New Zealand Geothermal Workshop, 18-20 November 2015, Taupo, New Zealand, (2015).

Okuhata, B. “Development of a model to identify local hydrogeology and simulate groundwater injection in Nuuanu and Kalihi aquifer systems, Oahu, Hawaii.” Masters Report, Department of Geology and Geophysics, University of Hawaii at Manoa, (2017).

Pruess, K. “Brief guide to the MINC-method for modeling flow and transport in fractured media.” Lawrence Berkeley National Laboratory Report LBL-32195, (1992), https://escholarship.org/uc/item/38r1c71c

Robertson, E.C. “Thermal properties of rocks.” U.S. Geological Survey Open-File Report 88-441, (1988).

Rotzoll, K., and El-Kadi, A.I. “Estimating hydraulic conductivity from specific capacity for Hawaii aquifers, USA.” *Hydrogeology Journal*, 16, (2008), 969-979.

Rotzoll, K., Oki, D.S., and El-Kadi, A. “Changes in freshwater-lens thickness in basaltic island aquifers overlain by thick coastal sediments.” *Hydrogeology Journal*, 18, (2010), 1425-1436.

Sherrod, D.R., Sinton, J.M., Watkins, S.E., and Brunt, K.M. “Geologic map of the State of Hawaii.” U.S. Geological Survey Scientific Investigations Map SIM-3143, (2021).

Wolf, J.E. “Map location and dimensional definition of subsurface caverns.” Senior Thesis, Department of Geology and Geophysics, University of Hawaii, (1975).

How 5th Generation Energy Networks Can Be The Source Of Energy To Supply High Temperature Water to Decarbonize Buildings Using High Temperature Distribution Loops

Jay Egg

Egg Geo, LLC

Keywords

Geothermal, Micro Districts, Infrastructure, Natural Gas, GeoMicroDistrict, Beneficial Electrification, Health and Safety, Heat Pump, How To, Engineering, Architecture, Codes and Standards, Green Building, Hydronics, HVAC, Health Care, Legionnaires Disease, IAPMO

ABSTRACT

A challenge of decarbonization and electrification of buildings has been the expense associated with converting the buildings to 130° piped heating networks for radiators and perimeter induction heating. New technologies in high temperature heat pumps can deliver 180°F plus temperatures to these buildings from 5th generation thermal energy networks.

1. High Temperature Building Heating Loops

Throughout the heating ventilation and air conditioning industry, building loops have Ben designed for perimeter induction heaters and radiators at temperatures from 150 to 200°F or more. This has posed challenges for the conversion to heat pump technologies. Until recent years, heat pumps have been limited to about 140°F delivery temperatures. With more robust technologies being introduced to the industry, we are finding success with high temperature heat pumps delivering hot water at temperatures of up to 240° or more.

This presents a remarkable solution for industry. Previously, groups have had to B retrofitted for lower temperature heating delivery devices. With these new high temperature heat pumps, buildings may be left as is as far as infrastructure, significantly reducing the construction costs for decarbonization and electrification of these buildings using heat pumps.

2. High Temperature Heat Pumps

Heat pumps such as the Oilon ChillHeat are providing solutions that allow building extra fits from combustion boilers that typically deliver 160°F plus temperatures to building systems. With high temperature delivery, building mechanical systems can be left intact.

Figure 1: The Oilon ChillHeat Heat Pump is providing temperature lift of 100F or more (Oilon)

Performance of these heat pumps is remarkable in both the heating and cooling mode. With combustion heat boilers, cooling is not typically possible. This opens another dimension to building decarbonization and electrification. When considering the need for cooling becoming increasingly important to sustain health and safety of building occupants, this provides solution to a growing problem of heat stress in our built environment.

ChillHeat	P	S	RE
Heating capacity EN 14511 0/35	30 - 450 kW	180 - 2000 kW	210 - 420 kW
Max. temperature of heat produced *	120 °C	85 °C	62 °C
Min. temperature of cooling produced *	-7 °C	-12 °C	-15 °C
ChillHeat product suitability for various applications			
Combined heating and cooling	●●●	●●	●●
Heat recovery at refrigeration plants	●●●	●●●	●
Heat recovery from waste water	●●●	●●●	●●
Ground source heating	●	●●	●●●
Heat recovery from flue gases	●●●	●●●	●
Heat extraction from outdoor air	●	●●	●●●
Heat recovery from industrial processes	●●●	●●●	●
Water chiller applications	●	●●●	●●●
Refrigeration applications	●	●●	●●●

Figure 2: Performance of a heating and cooling heat pump for high temperature applications (248F) (Oilon Specifications)

Using Heat Pump and the Stable Earth Temperature (Background taken from GRC Transactions, Vol. 45, 2021)

Ground Source Heat Pumps have been used throughout the world for generations, one example is Tampa's Church of Christ Scientists that was initially installed in 1949 (EggGeo 2014). Combining a ground source heat pump and the stable temperature of the earth is a proven technology that continues to provide the most energy efficient cooling and heating available. This is attributed to the steady temperature of the heat source and heat sink, being the earth and its stable temperatures.

Installation at a building requires excavation and /or drilling to access the earth's ambient temperatures, which drives the cost of the technology. The outside ground source pipe and work can be responsible for 60% or more of the total cost.

The costs for excavation are brought down by creating a geothermal pipeline that is installed in place of or into already existing typical natural gas pipeline, like a water main. Each home and building are connected to the District Geothermal Energy Network, just as they are to City or County Water. They will pay a connection and / or an energy fee just as they would for electricity or water.

3. Ambient Geothermal Distribution Pipelines

Eversource, has applied to do geothermal districts for multifamily buildings, dense urban or mixed-use, and purely residential. (Hasan 2020). The system will use ground-source heat pump technology, which uses electricity to transfer heat from the ambient temperature GeoMicroDistrict

(in the ground) to a network of geothermal heat pumps to provide clean heating and cooling for the buildings within each district.

In this case, the pipelines will be buried in place of or into the existing natural gas pipelines, providing the heat exchange needed for each of the buildings on the circuit. Some buildings need heating, and others need cooling at the same time; normally wasted energy is harvested for use in the pipeline. An example of this is the Stanford Energy System Innovations (SESI). The project illustrates the capability to combine waste heat from cooling operations with the heat needed for heating operations, reducing energy consumption by sharing as much as 80% of the energy moved on campus (Stagner 2015). (See Table 1)

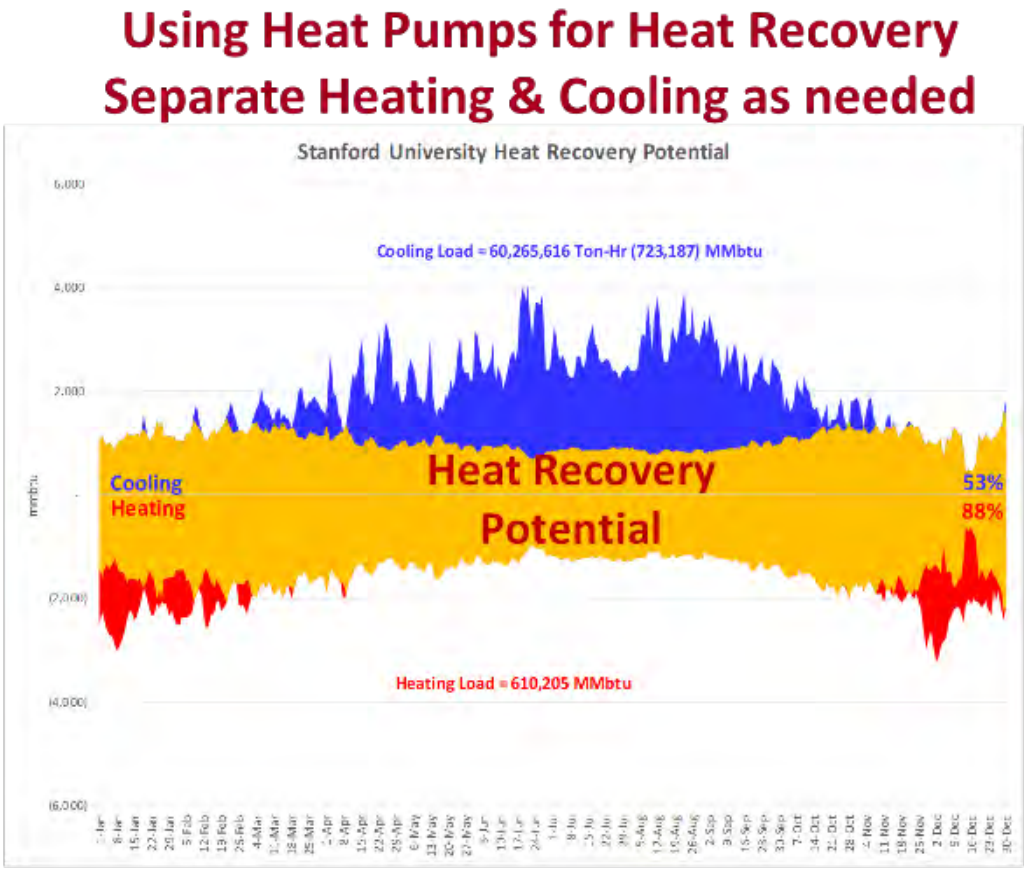

Figure 3: Stanford Energy System Innovations (SESI) shows the shared energy from buildings needing heat, and those rejecting heat.9

Similarly, District Geothermal Energy Networks will enable energy access for all of buildings in a community to tap into one central exchange source, without the added cost of onsite excavation and drilling [Figure 3].

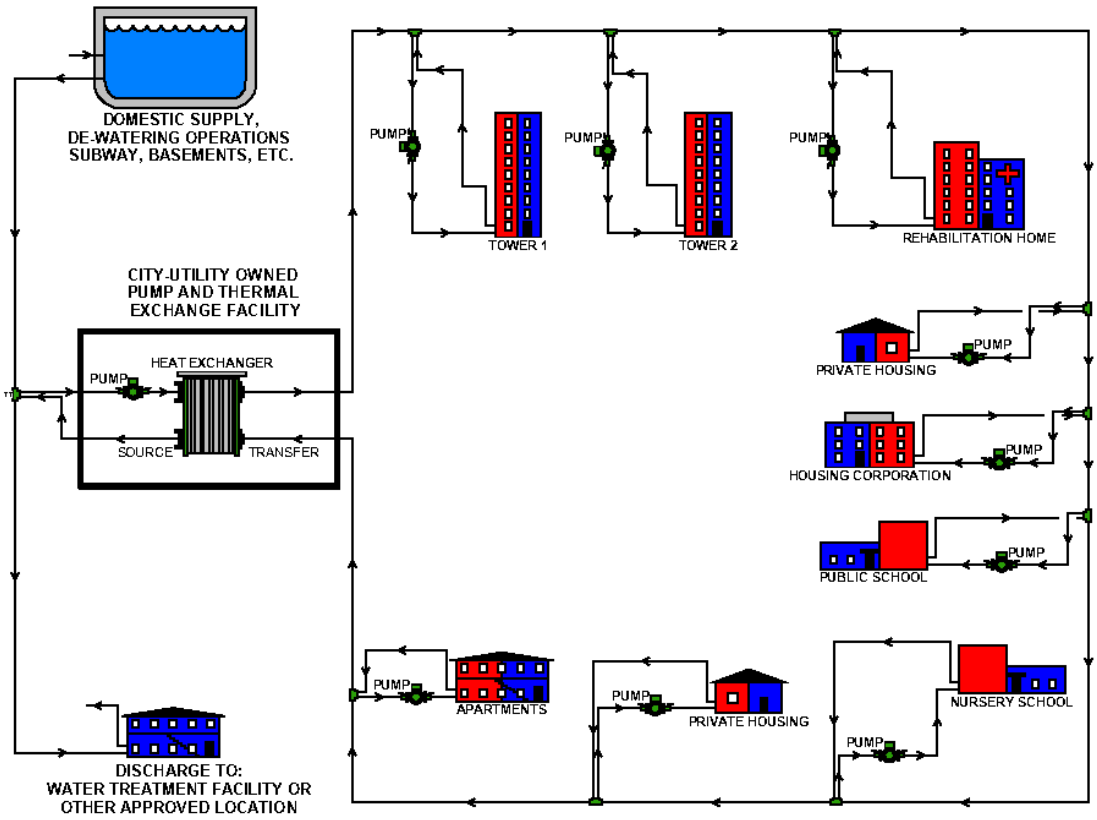

Figure 4: A District Geothermal Energy Network has many different buildings served, and many different heat sources and heat sinks

4. Ambient Temperature Surface Water & Aquifer Exchange

There are dozens of variations for earth-coupled heat exchange. The possibilities are wide and varied. Some of the solutions have a lower first cost than others for a variety of reasons. Some are listed below and depicted in Figure 4.

- **Closed loop vertical exchange:** Can be configured in 2-pipe, 4-pipe, concentric and many more adaptations.
- **Closed loop horizontal exchange:** Can be configured in many various ways to apply open-trench based exchangers.
- **Closed loop pond/lake/ocean:** These can be configured to use fabricated plate exchangers, or polyethylene pipe arranged in the body of water.
- **Closed loop energy piles:** Like closed loop vertical exchange, these can be adapted in many different ways.
- **Open standing column wells:** Primarily allows for reduction in boreholes, allowing for a smaller footprint. Needs specific geology (competent bedrock).

- **Open Class V well doublets:** Primarily allows for reduction in boreholes, allowing also for a smaller footprint. Needs a specific geology (abundant aquifer). Great for large-scale applications in hot and humid climates (cooling dominant).

Figure 5: Some of the variations for heat sources and heat sinks in a District Geothermal Energy Network (Egg 2014)

Efforts are underway to prepare a heat map like that which has been created in the UK for the Department of Energy & Climate Change. Surface water thermal exchange includes rivers, ponds, lakes, aqueducts, and water features. Surface water exchange can consist of plate exchangers or pipe in the water, water extraction and rejection, or any variations of submerged exchangers.

The UK Department of Energy and Climate Change commissioned a study of surface water exchange potential. The study shows 6 GW of thermal capacity, enough to heat and cool 7 million homes (Department of Energy & Climate Change 2015). Though the United States has no such research, it is reasonable to suppose U.S. capacity would be greater.

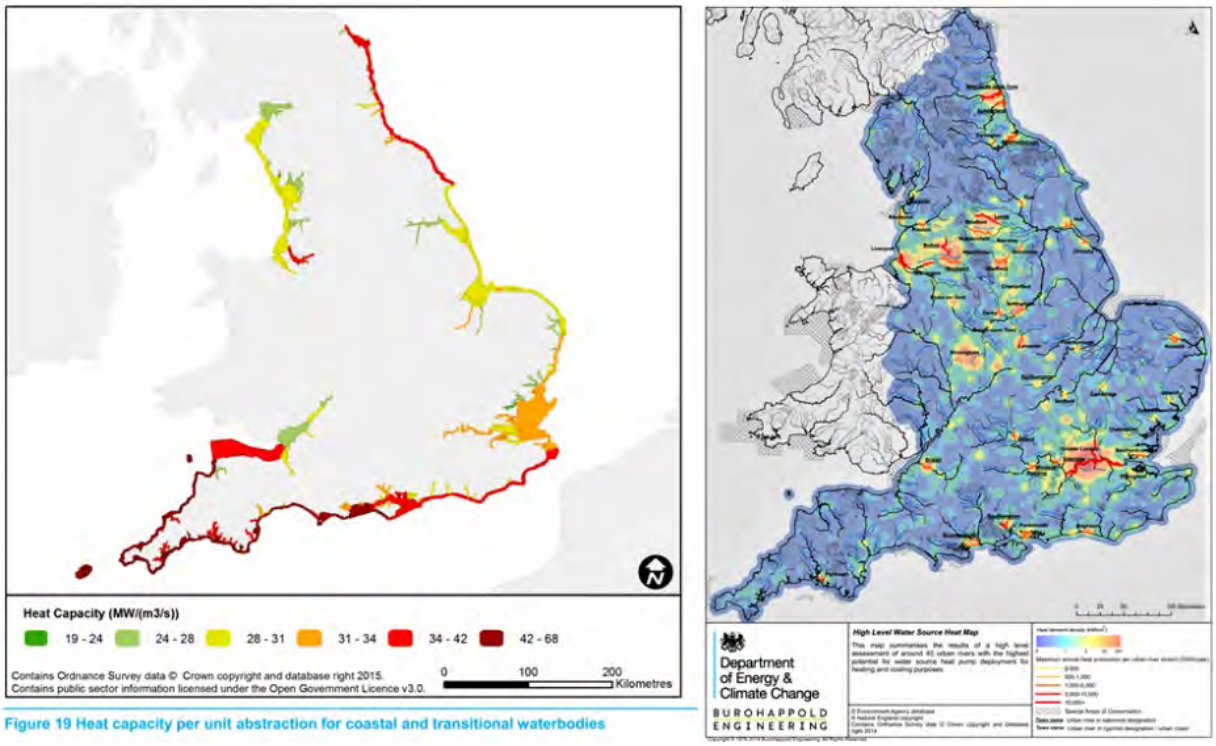

Figure 6: UK National Heat Map for Surface Water (Department of Energy & Climate Change 2015)

Infrastructure dewatering thermal exchange includes ongoing efforts for low-lying cities and infrastructure, subways and conduits that need to be kept dry and, of course, the need for current and future efforts to handle ocean rise. Where relative sea-level rise occurs, it amplifies near-term vulnerability to storm surge and increases long-term flood and inundation risk.

Well Water Thermal Energy Exchange is another of the technologies identified along with surface water energy exchange that can significantly reduce first cost. It is depicted in the Figure 6a and is identified as either “Aquifer or “Well Water” Thermal Energy Exchange. Water is pumped from one well, used for thermal exchange, then injected into another. This method is considered environmentally friendly and a good use of resources.

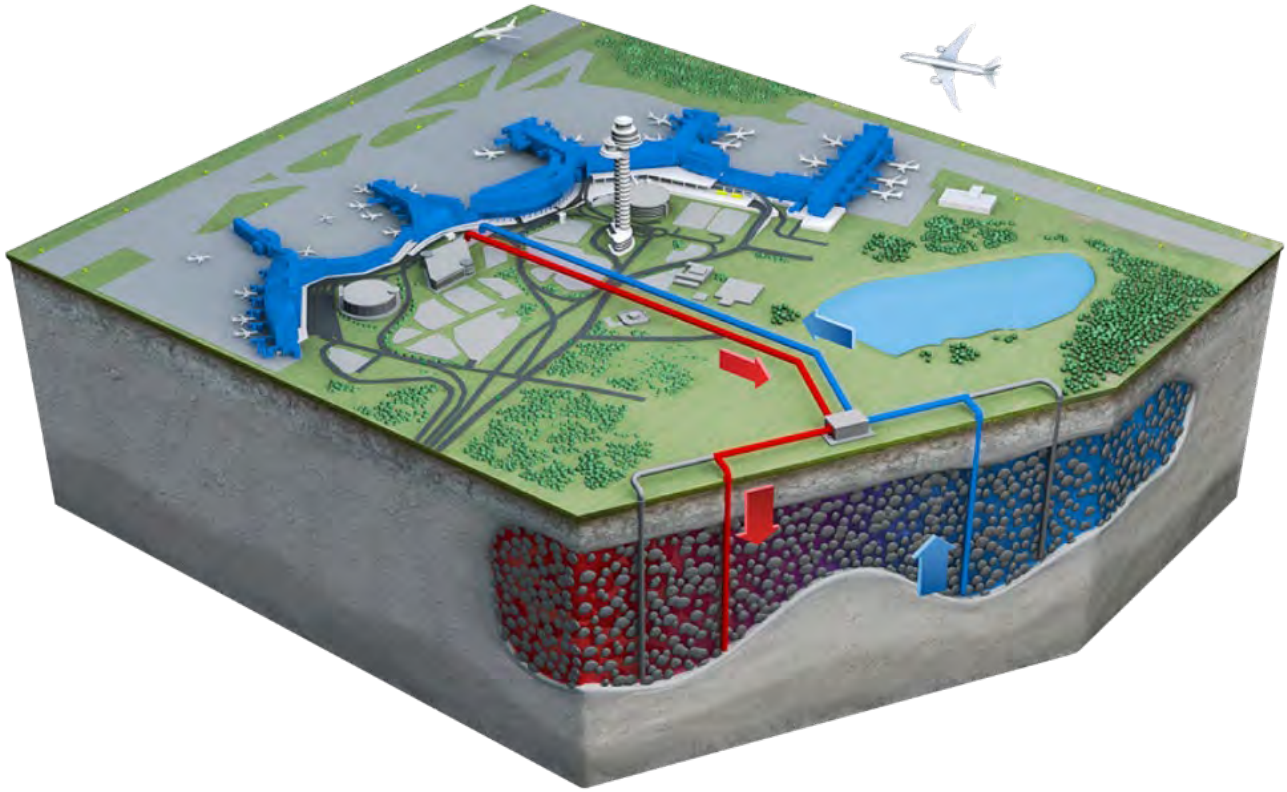

Figure 7a: Depiction of Aquifer Thermal Exchange

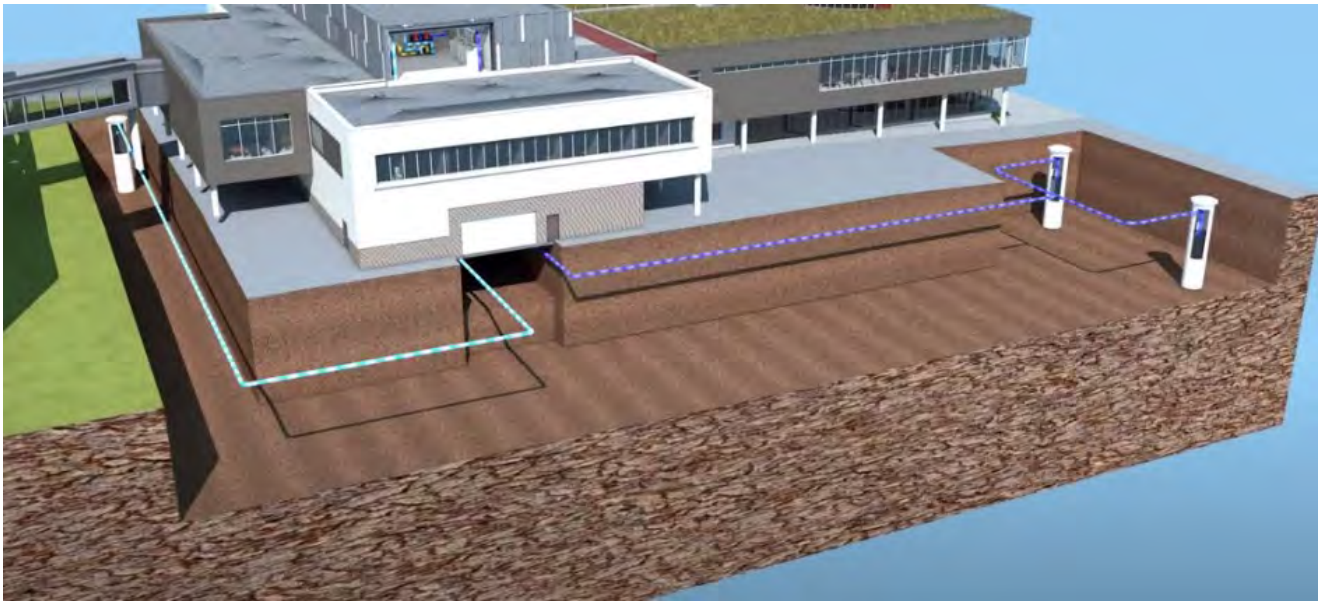

Figure 7b: Another depiction of Well Water Thermal Exchange

We have the means of heat transfer already in the ground, which can eliminate the need for much of loop infrastructure that is normally identified as prescribed by the ground source heat pump

industry. Tapping existing pipe infrastructure for thermal exchange helps to reduce the first cost well below that of single geothermal systems, and adds load sharing and diversity, significantly reducing energy consumption beyond stand-alone systems, once again as in the Stanford example. The water/energy utility can own the exchange facilities and sell the energy.

With the advent of high temperature heat pumps, building retrofits and utility thermal energy networks may be done without re-piping the building hydronic systems. The existing radiators and heat distribution equipment can remain in place.

*Note: The terminology **Thermal Energy Networks**, **GeoMicroDistrict, Ambient Geothermal Networks, Pipelines, or Distribution** as applied to geothermal systems are used interchangeably. These all have the common thread of an ambient, or an earth temperature fluid pipeline used as a utility to provide energy exchange for geothermal heat pump systems in homes and buildings.*

Ground Source Heat Pump (GSHP) and Geothermal Heat Pump (GHP) mean the same thing.

WORKS CITED

GRC Transactions, Vol. 45, 2021. “Cooling Technology Integration with Communities Using Waste Heat from Geothermal Electric Generating Facilities

Cross, Colleen. 2018. "Talking Geothermal." *Groundwater Canada.* April 25. Accessed 2018. https://www.groundwatercanada.com/talking-geothermal-4261/.

Department of Energy & Climate Change. 2015. "National Heat Map: Water source heat map layer." *www.gov.uk/decc.* Accessed 2021.

Department of Energy. 2017. *Absorption Chillers for CHP.* Fact Sheet, Washington DC: Energy Efficiency & Renewable Energy. Accessed 04 20, 2021. https://www.energy.gov/sites/prod/files/2017/06/f35/CHP-Absorption%20Chiller-compliant.pdf.

Egg, J. 2014. *www.EggGeo.com.* Accessed 2021.

EggGeo. 2014. *First Church of Christ Scientists Tampa Florida.* Accessed 02 20, 2020.

Hasan, N. 2020. "Geothermal Microdistricts & the FUTURE: A renewable alternative to gas heating." *https://www.takebackthegrid.org.* April 04. Accessed 01 24, 2021.

Lowenstein, A. I., A. S. Slayzak, E. Kozubal 2006. A zero carryover. 2006. "A Low-Flow, Zero Carryover Liquid Desiccant Conditioner." Edited by DOE. *International Sorption Heat Pump Conference Proceedings.* Interlocken: NREL. 1-11.

Stagner, J. 2015. *Stanford Energy System Innovations.* Fact Sheet, Stanford: Office of Sustainability.

City-scale Thermal Energy Network Design for Utility Decision Makers

Nicholas Fry[1], Catherine Roy[1], Jason Willeford[1], Shellie Jober[1], and Joseph Jebamalai[2]

[1]Jacobs Engineering Group

[2]IQGeo

Keywords

Ground-source heat pumps, District heating and cooling, Decarbonization, Urban planning

ABSTRACT

Building heating and cooling took center stage in the European Union's 2023 Energy Efficiency Directive update, released in September of the same year. There were more than 350 mentions of heat, largely relating to the decarbonization of current combustion processes, including those in individual building systems. One of the pillars of decarbonizing building stock in the plan calls for a near doubling of existing district heating and cooling networks by 2050. The same calls for building stock decarbonization are being heard in North America, though the organization of regulation is much more disparate. Lessons from similar European initiatives suggest that local utility planning for city-scale projects is an effective way to attract investments in sustainable heat. In the context of geoexchange heating and cooling, that using the earth as a modulating mechanism for stable fluid temperatures, 5th generation district heating and cooling systems are useful in every geologic province of the continent. These 5th generation district heating and cooling systems are more frequently referred to as thermal energy networks (TEN) in North America, with the ability to operate at ambient or near-ambient ground temperatures using a spectrum of centralized through distributed water-source heat pumps (WSHP). While front-end engineering and design of the systems rely on detailed transient simulation, prefeasibility is an important first step in providing sufficient technical and economic data to support the development of networks that may contain a few dozen, or even a few thousand, structures. City-scale sustainable heat planning, therefore, requires city-scale simulation capabilities. In this desktop study, a downtown section of Boulder, Colorado serves as an exploratory example of which metrics are important to consider before proceeding with production level engineering on a TEN. Geographic information system simulation tools enable the designer to quickly iterate through optimal pipe routing pathways, bills of materials, and electrical ramping requirements of heat pumps, among other technical outputs, creating a method of global sensitivity analysis in the earliest stages of design while respecting the variable entering and exiting fluid temperatures of closed loop borehole arrays.

1. Introduction

Over the last year Europe took a strong step towards building stock decarbonization with a revision of the Energy Efficiency Directive (EU/2023/1791). As a result, energy policy from the European Union (EU) now implements a principle of energy efficiency first (Directorate-General for Energy, 2023). Full decarbonization of district energy systems is a 2050 requirement, with public buildings to receive similar envelope renovations no later than 2040. All buildings with floorspace greater than 750 m^2 (>8000 ft^2) must renovate or consider the use of performance-based contracts from energy service companies to decarbonize their heating and cooling systems within the same timeframe (European Commission, 2023).

In the United States the Inflation Reduction Act of 2022 (IRA) offers provisions for home and commercial building energy efficiency tax credits (Internal Revenue Service, 2024a, 2024b). The IRA itself does not codify sustainable heating and cooling like the EU Energy Efficiency Directives do. Instead, the US Department of Energy (US DOE) recently released their first-ever building sector decarbonization blueprint, targeting a national 90% emissions reduction by 2050. The report cites building energy consumption costs of $370 billion dollars, annually (US Department of Energy, 2024a, 2024b).

Both the EU Energy Efficiency Directive and the US DOE building sector decarbonization report suggest such conversions of predominately combustion-driven heating and cooling may put the most vulnerable low-income persons across society at risk of energy cost increases (European Commission, 2023; US Department of Energy, 2024a). These would be the people across society unable to afford individual building system upgrades or building envelope improvements on their own. A community- or city-scale sustainable heating and cooling plan is, therefore, necessary to avoid inequities brought about by the energy transition. One system type that may offer city-scale decarbonization of building stock heating and cooling with the same utility-like economies of scale as gas distribution grids is the thermal energy network (TEN).

The modern TEN is a 4th or 5th generation district heating and cooling system, typified by its ability to perform waste heat recovery, leverage lower-temperature resources, temper hydronic distribution systems with heat pumps or passive heat transfer equipment, and maximize performance by minimizing electricity inputs (Buonocore et al., 2022; Lund et al., 2021; Zeh et al., 2021). During the intervening decades since the 1800's installation of 1st generation of district energy steam distribution, greater efficiencies have been found with decreasing source and sink temperature regimes. Lowering temperature regimes reduces the requirements for zone heating and cooling within a building and mitigates heat losses or gains to the soil along a district distribution network (Collins, 1959; Lund et al., 2014). Some of the sources and sinks that can tie to those distribution networks now include conventional geothermal resources of a relatively high temperature, and closed loop borehole arrays of a near ambient ground temperature (Hirsch & Paepcke, 2022; Wirtz et al., 2022; Zeh et al., 2021).

Regulators across several states are recognizing the importance of finding utility-scale replacement options for gas distribution systems, with many beginning to lean into TEN concepts. The landscape of law requiring gas utilities to implement TEN options across their service territories is growing. As of this writing, laws or proposed bills mentioning TENs exist in Colorado, Illinois, Massachusetts, Maryland, Minnesota, Vermont, Washington, and New York, among others. This

number is likely to grow as policymakers realize the only sustainable heat solution is one accessible to everyone.

Therefore, policymakers, energy service companies, and utilities need designers that offer accessible solutions for city-scale planning and TEN prefeasibility. The remainder of this paper addresses design implementation approaches that apply to TEN implementation studies and their eventual construction. Further, to demonstrate the initial steps a section of the downtown core for Boulder, Colorado serves as a basis for the desktop investigation.

2. Approaches to TEN Design

District heating and cooling design relies on several requirements. These requirements include the available sources and sinks across a community, the initial and projected demand by building, and the intended configuration. As mentioned, sources and sinks for TENs are more efficient at lower temperature regimes. It is also true, however, that the policymakers and designers must take advantage of waste heat resources across their community. These waste heat resources may dictate the eventual system configuration. Building energy modeling is another non-trivial task in the design, representing the initial and projected demand across the system. Some preliminary demand information may be available from gas utility operators, but the operation of the TEN can become sophisticated to the extent that city-scale modeling and simulation becomes a better characterization method. There are many different configurations of a TEN which impact design, performance, ease of installation, and construction risk, among other variables. Generally, the topology of thermal networks is either radial, meshed, or ringed (von Rhein et al., 2019). Radial and ringed topologies are often most appropriate for centralized or hybridized TENs while a mesh represents a complicated hydraulic design with potentials for efficiency gains on a case-by-case basis (Figure 1).

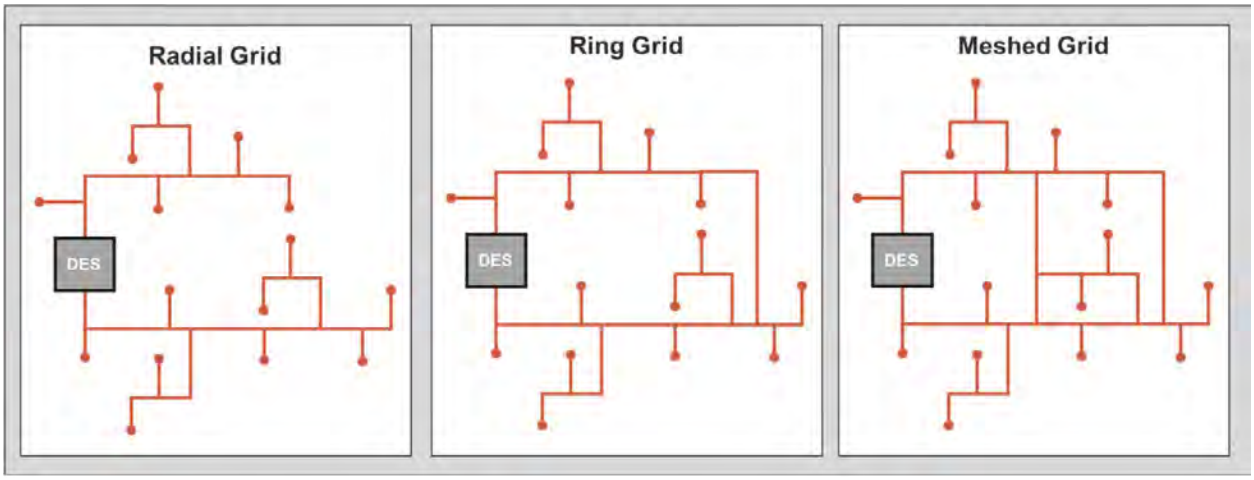

Figure 1 Network topologies for community-scale heating and cooling systems (von Rhein et al., 2019).

Before the advent of most low-temperature networks with heat recovery, district energy relied mostly on steady state calculations to dimension the systems. These dimensioning techniques are still important for transient systems, such as borehole heat exchange supported networks, but they now represent only one of several steps. The system dimensions are assembled in such a way that they can meet the transient operational constraints of maximum and minimum temperature responses. Maximum and minimum temperature responses are a function of design

parameterization – for example, the choice in sizing a closed loop borehole array – and stochastic climatic inputs, waste heat recovery cyclicity, and the incident heat losses or gains.

While many more details exist across other resources on the dimensioning of TEN inputs, such as thermal energy storage (TES) (Jebamalai et al., 2020), pipe configurations (Averfalk & Werner, 2018), supply equipment (Manente et al., 2019; Schifflechner et al., 2023), and primary side equipment (Postnikov et al., 2019), among others, this paper focuses on the new logistics of dynamic design implementation. (IQGeo, 2023) suggests there are three levels of design technique maturity (Figure 2). In the first tier, designers are pushing approximate numbers through spreadsheets that may or may not address the complexities of other subsurface utilities and artifacts that the distribution system installers may encounter during the roll-out. When encountering a tier three design, the integration of geospatial mapping and automation provides the necessary accuracy that would-be TEN providers should expect from their engineering consultancies. Comsof Heat is one such software that enables that automation with pipe routing based on heuristic clustering algorithms, approaching a near cost optimization for right-of-way use cases (Jebamalai et al., 2019).

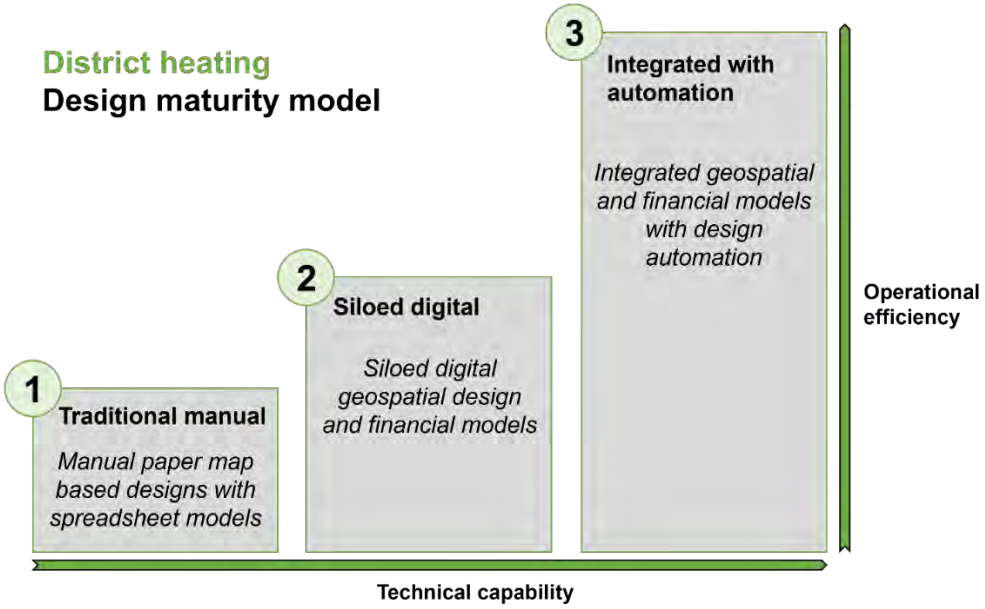

Figure 2 Three design technique maturities for thermal energy networks (IQGeo, 2023).

The following section will explain Comsof Heat as an important steady-state system dimensioning tool which integrates with a transient system ground response on a desktop study of a hybrid TEN for Boulder, Colorado.

3. Case Study Methodology

There are four primary steps to the analysis of a TEN for Boulder, Colorado. They include:

- Geospatial reconstruction of the service area
- Building energy modeling
- Borehole array modeling and simulation
- TEN dimensioning

Geospatial construction of the service area requires building footprints and geometries. Previous analysis from states other than Colorado recommends gathering occupancy, floorspace, and other parameters of the structures from cadastral data (Fry, 2021). After gathering the appropriate building information, each structure undergoes energy modeling to extract annual hourly load profiles for heating, cooling, and domestic hot water (DHW) consumption. These load profiles are fed into thermal response functions with a central heat pump performance curve. Finding the borehole array dimensions to meet the demand using an average, near-ambient, distribution temperature, we use Comsof Heat to dimension the pipe network.

This system prefeasibility demonstration uses a hybrid TEN configuration. Hybrid configurations for the network include a central heat pump at the central utility building with distributed heat pumps across the district. This limits unnecessary heat losses as the fluids make their way to 150 buildings across Boulder, Colorado. Each of the 150 heat pumps range in cost from $15,000 - $90,000, depending on peak demand size. These 150 buildings include retail storefronts, multifamily housing, and offices. Each receives various construction sets typified by US DOE building benchmarks, sorted by climate zone (“Commercial Reference Buildings,” n.d.). The predominate years of construction for the structures are before 2000. These years of construction will dictate the building standards and, therefore, the building envelopes. To minimize computational time, only the building geometries and types for the service area of interest are run through simulation (Figure 3).

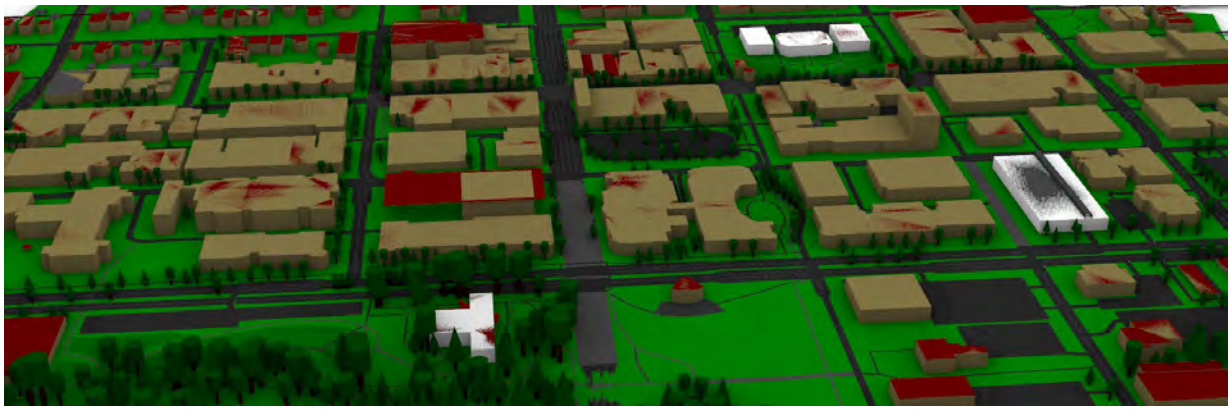

Figure 3 Isolated building geometries for building energy modeling of the Boulder, Colorado downtown district.

System dimensioning of both the borehole array and the pipe distribution grid requires several iterations. These iterations account for the simultaneity of demand (Eq. 1 and Eq. 2), and the incident peak heat transfer necessary across the closed loop borehole array. The simultaneity of demand is a principle advantage of district energy that reduces the average pipe diameters of the network and decreases costs. A coincidence factor is taken which suggests that demand for space heating or DHW across the district heating network does not occur at the same time. For example, as more structures of varying types connect with the network, the simultaneous demand will decrease. The peak of heating or cooling demand is multiplied by the coincidence factor to determine the simultaneous demand. It is generally good practice, even in single-building systems, to remove the simultaneous load when considering sizing of geothermal or geoexchange sources or sinks. This concept is, therefore, extended to the city scale to dimension component parts of a TEN. General engineering parameter assumptions for the pipe network appear in Table 1. A plastic pipe catalog is also part of the simulation, with the material having unique thicknesses, roughness,

maximum pressure gradients, and thermal conductivities. The burial depth is set to a minimum 36 inches (0.91 m), as regulated by Boulder County (Boulder County, 2017).

$$C_{SHC} = x + \frac{(1-x)}{n} \quad \text{Eq. 1}$$

$$C_{DHW} = \frac{1}{\sqrt{n}} \quad \text{Eq. 2}$$

Where:

x is the simultaneity factor[1]

n is the number of consumer nodes

C_{SHC} is the coincidence factor for space heating or cooling

C_{DHW} is the coincidence factor for domestic hot water

Table 1 Engineering parameter assumptions for the distribution system.

Parameter Type	Value
Ground thermal conductivity (W/(m.K))	1.1
Wet ground thermal conductivity (W/(m.K))	2
Near surface ground temperature (ºC)	9.44
Ground-to-air transition insulance (m^2.K/W)	0.0685
Ground water depth (m)	1
Elevation head (m)	2
Working fluid specific heat (kJ/(kg.K))	4.186
Pump efficiency (%)	60
Distribution temperature (ºC)	15
Target differential temperature (ºC)	5
Seasonal coefficient of performance (COP) for DHW, distributed heat pumps	2.8
Seasonal COP for space heating, distributed heat pumps	3.5
Seasonal COP for space cooling, distributed heat pumps	6.1

Closed loop borehole arrays serve as a modulating thermal storage device, where heat can both be extracted or rejected to the borehole array. This study uses software based on the conduction-only

[1] In this study a simultaneity factor of 0.62 is taken, aligning with several European empirical standards.

thermal response from the borehole. This is generally derived or modified from the infinite line source (ILS) method, as originally described by Ingersoll et al., 1954, p. 146. This collection of equations describes the heat released from a point along a continuous line, where the heat released at the point is divided by the thickness to get the heat released per unit length of the line. Ingersoll describes this as appropriate for "subterranean sources and sinks," with an example for closed loop boreholes tied to heat pumps (Ingersoll et al., 1954, p. 151). Several modifications to the Ingersoll work are generally incorporated into modern engineering software, such that the long-response limitation (hours or days for temperatures to change) of the ILS becomes relevant for short-response thermal impacts (minutes for temperatures to change) (Nian & Cheng, 2018). One of the earliest and most well-known modifications to the ILS approach for borehole thermal response is the finite line method, described by Eskilson (1987) – also in use for this case study. The general engineering parameter assumptions for individual boreholes appear in Table 2. In practice, these parameters are refined through the study of well logs, predictive models, and in-situ testing and define the boundary conditions of the borehole thermal response.

Table 2 General engineering parameter assumptions for the closed loop boreholes in simulation.

Parameter Type	Value
Effective borehole thermal conductivity (W/(m.K))	1.7
U-tube diameter (inches)	1.5
Grout thermal conductivity (W/(m.K))	1.5
Borehole separation (m)	7.62
Borehole thermal resistance (m.K/W)	0.16
Initial borehole ground temperature (ºC)	9.44
Peak flow rate ($(m^3/hr)/kW$)	0.195
Borehole depth	183
Propylene Glycol (% by weight)	20

Finally, Comsof Heat features economic parameterization to estimate the costs of the construction roll-out period, revenue during TEN operations, and net present value, among others. The general economic parameters for the techno-economic calculations appear in Table 3.

Table 3 General economic parameter assumptions for the Boulder, Colorado TEN simulations.

Parameter Type	Value
Network lifetime (years)	50
Network deployment time (years)	3
Discount rate (%)	7
Cost of electricity ($/kWh)	0.06
Annual electricity price escalation (%)	1.0
Subsidy for project capital costs (%)	30
Fixed annual O & M costs (% of asset value)	0.75
Variable annual O & M costs ($/MWh$_t$)	1
Borefield capital costs ($)	$30,000 per borehole
Central energy transfer station costs ($)	$500,000
Distributed heat pump costs ($/kW)	225 – 600 depending on unit size
Relative pipe cost ($/(mm.m))	4
Tariff ($/kWh)	0.10
Service connection fee ($)	2,200
Fixed monthly fee per user account ($)	60

4. Results

The load profile of the downtown district will dictate the size of sources and sinks which connect with a thermal energy network. The peak load for heating and DHW is 11,998 kW_t while the peak load for cooling is 7,954 kW_t (Figure 4). There are 556 equivalent full load hours (EFLH) for cooling and 1437 EFLH for heating. The EFLH is a ratio for the annual heat delivery divided by the peak of the hourly demand. This indicates a heating dominant district, based on the non-rigorous building envelope assumptions for simulation inputs.

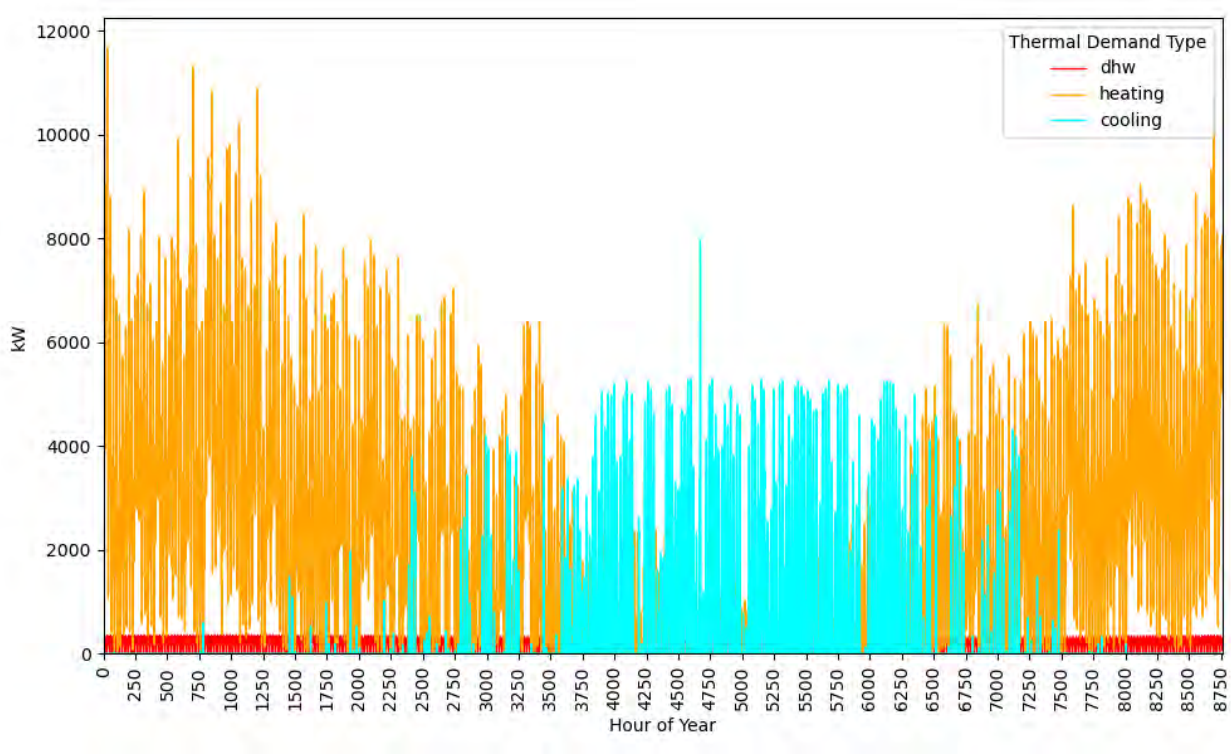

Figure 4 Annual load profile for the simulated downtown district of Boulder, Colorado.

To accommodate the demand for both heating and cooling over a 50-year planning period while also maintaining a minimum entering water temperature (EWT) to heat pump equipment above 0ºC, the ground loop heat exchanger (GLHE) requires more than 5,000 boreholes without hybridization. Such a system would cost more than $150,000,000 before subsidy, for drilling and completions alone.

A hybrid approach using supplemental distributed heat pumps decreases simultaneous demand to 5,505 kW_t. That is 44% of the sum of all peaks for heating. Standardization of the load profile and reiteration of the borehole array simulation indicates the need for 2,500 boreholes. The scale of this system would cost $75,000,000 for drilling and completions.

Since the seasonal heat transfer imbalance from the load profile cannot be resolved through diversity alone, a final iteration assumes a 50-year project lifetime with a run-of-the-river heat exchange with Boulder Creek to pre-charge the borehole array for the heating season. Extracting 37% of the total heating demand from the creek, the borehole array size drops to 1,000 boreholes. The pre-subsidy cost of the drilling and completions would then be $30,000,000. The minimum EWT for the equipment is 0.1ºC across 50 years (Figure 5). The central heat pump seasonal COP for cooling is 6.0 and 3.6 for heating, resulting in a central utility cooling production cost of $10.00/$MWh_t$ and heating production cost of $16.67/$MWh_t$.

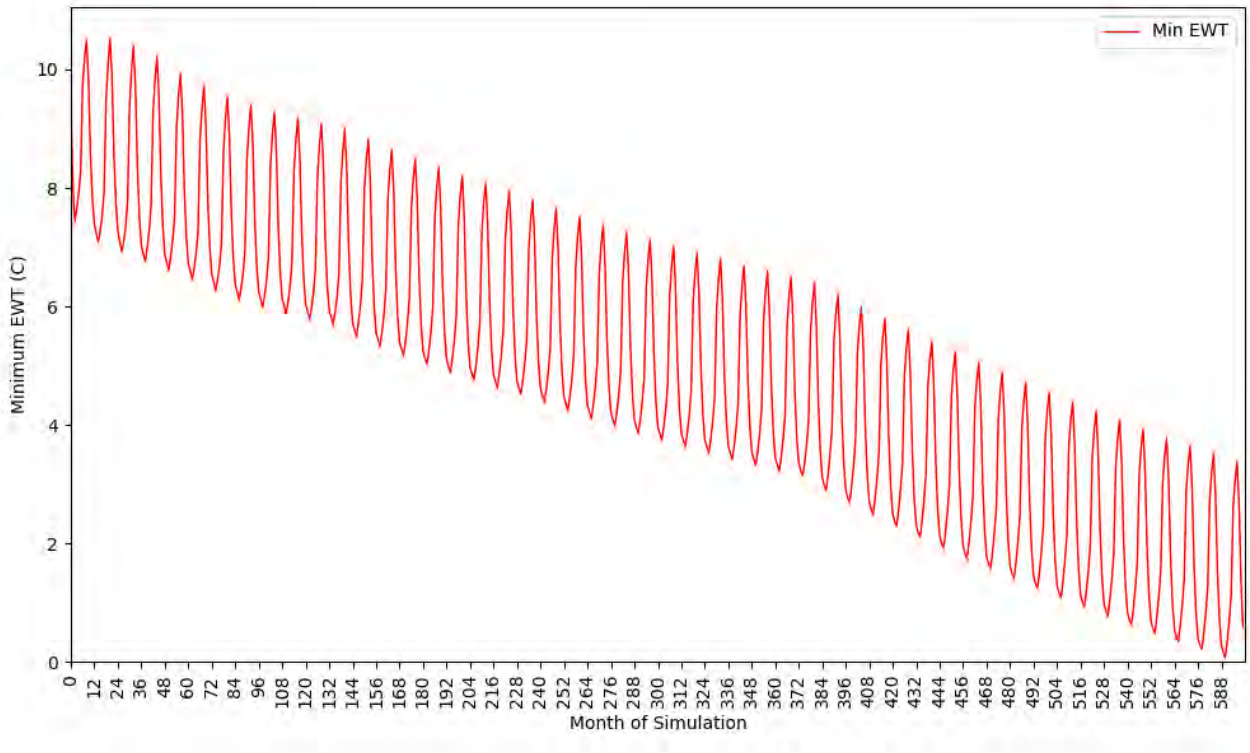

Figure 5 Minimum EWT for central heat pumps from 1000 borehole array, over 50 years. This figure demonstrates that the system meets the minimum temperature constraints over the project lifetime.

Assuming the borehole array position along Boulder Creek, on what is largely public property, a simulation of the thermal energy network routing seeks a near optimum pipe placement (Figure 6). Comsof Heat routing algorithms indicate the need for 8,415m of pipe, ranging in size from a nominal diameter of 100 – 400mm (4 – 16 inch). The peak mass flow rate for the system ranges from 1 – 260 kg/s, depending on zone (Figure 7). For an enhanced dimensioning value in the planning stage, the material selection can be made with the appropriate manufacturer's pipe catalog characteristics as inputs (constraints).

Figure 6 Thermal energy network routing with proposed energy sources in Boulder, Colorado.

Figure 7 Mass flow rate at peak operating conditions for the thermal energy network in Boulder, Colorado.

The unsubsidized total project cost is $40,381,248. That results in a deployment cost per commercial customer in the service area of $237,536. Clustering algorithms for the construction roll-out phasing across a 3-year period suggest 2.5km, 2.3km, and 3.6km of network pipe will be put into operation over year 1, year 2, and year 3, respectively. With the borehole array constructed in year 1, that correlates with a subsidy schedule of $13,565,229, $1,112,586, $1,474,683 for the corresponding years of construction.

Other commercial metrics include the simple payback period, levelized cost of heat, and the internal rate of return. The thermal energy network, in this conceptual design, pays back in 17 years. The internal rate of return is 5.76% and the levelized cost of heat is $0.158/kWh$_t$.

5. Discussion

Thermal energy networks are assemblages of district energy systems. The component parts of these networks can complement each other in a variety of ways. The design in this desktop demonstration uses a radial network pattern to maintain a 15ºC supply temperature from a heat-pump-equipped central energy plant connected to distributed heat pumps. These central-distributed hybrid networks offer the flexibility for expansion and the option to introduce thermal energy storage as a more impactful demand side management tool.

In other configurations of a thermal energy network, the topology may appear as a ring. Those instances can leverage more load sharing, where it is available. The heating dominance from the building energy modeling in Boulder, Colorado makes it challenging to balance a closed loop borehole array or provide load sharing. Hybridization of the sources and sinks is highly advantageous, and the demonstration area is conveniently situated near a creek. This and other sources, such as low flow groundwater doublets or data center waste heat, may condition the borehole array on a seasonal basis, providing a performance boost. Cities themselves could use the potential to attract desirable tenants, such as commercial operators who reject more heat over the year than they consume.

In the context of utility-scale heating and cooling network deployment, an operator having leverage over multiple sources and sinks will maximize their ability to conduct energy arbitrage. Such energy arbitrage can be optimized through time as the behavior of the closed loop borehole array varies. This behavior of the closed loop borehole array is the supply temperature variation across time. While the ILS and finite line methods of conduction-only modeling do provide designers with trends to expect at the decadal scale, operators will find a great deal of difference from these simulations in practice.

Some of the likely reasons to expect variation in the study area include the presence of Boulder Creek, and the accompanying alluvial sediments. These unconsolidated zones, and those lithologies influenced by them, will induce movement of the thermal plume that would otherwise accumulate during a given heating or cooling season. For this reason and others, all commercial systems should be equipped with the appropriate measurement, monitoring, and verification devices.

All the values in this desktop demonstration are fictitious. It is likely with better market survey and building energy modeling practice that more commercially viable scenarios may be found.

This preliminary design methodology would also benefit from a preceding site suitability analysis, for example.

With the completion of these initial plan iterations, the designer now has appropriate starting dimensions for their system. Field testing remains a requirement. These preliminary dimensions undergo even more rigorous modeling and simulation in the detailed design phase to validate the expected transient thermal performance of the borehole array when coupled to the thermal energy network.

6. Conclusion

Thermal energy networks have varying temperature regimes (Hirsch & Paepcke, 2022; Wirtz et al., 2022; Zeh et al., 2021). Those with higher geothermal and geoexchange uptake generally offer greater energy efficiency, resulting in lower electricity consumption. Ambient temperature networks have lower parasitic heat losses or gains than previous generations of district energy systems (Lund et al., 2014; Zeh et al., 2021). In some cases, this makes them a good commercial opportunity for gas and electric utility companies wishing to participate in the energy transition while reducing peak electricity consumption from a community's soon-to-be electrified heating and cooling demand.

This work demonstrates the steps necessary to conduct the initial design of a thermal energy network with an expandable radial topology, using a desktop study of a district in Boulder, Colorado. The preliminary design uses assumptions of ground thermophysical properties to size a borehole array. This borehole array size is then reduced in size with source hybridization and considerations for load diversification. A 1,000-borehole array meets the requirements for 150 commercial and multifamily structures across the service area. Using several iterations to dimension the network, the design is ready for more rigorous analysis. Preliminary techno-economics for the system suggest it has a 17-year simple payback with an internal rate of return of 5.76%.

While the parameters for the system design in this desktop demonstration are fictitious, this paper offers insights that are often not readily available to the would-be utility or municipal planner, entering the thermal energy network business for the first time. There are many ways to design, model, and simulate these systems. While there is no one-size-fits-all approach, the history of district energy operators dating back more than 100 years suggests that multi-scenario planning is a critical first step in designing a system that is modular, expandable, and long lasting.

Acknowledgement

The authors wish to thank Comsof Heat for authorizing a license to perform analysis of subsurface-supported sustainable heating and cooling in the case study region.

REFERENCES

Averfalk, H., & Werner, S. (2018). Novel low temperature heat distribution technology. *Energy*, *145*, 526–539. https://doi.org/10.1016/j.energy.2017.12.157

Boulder County. (2017, March). Building form B07: Utility burial depths. Boulder, Colorado. Retrieved from https://assets.bouldercounty.gov/wp-content/uploads/2017/03/b07-utility-burial-depths.pdf

Buonocore, J. J., Salimifard, P., Magavi, Z., & Allen, J. G. (2022). Inefficient building electrification will require massive buildout of renewable energy and seasonal energy storage. *Scientific Reports*, *12*(1), 11931. https://doi.org/10.1038/s41598-022-15628-2

Collins, J. (1959). The history of district heating. *District Energy OnSite*, (June, 2009). Retrieved from http://www.verenum.ch/Dokumente/1959_Collins_History.pdf

Commercial Reference Buildings. (n.d.). Retrieved June 1, 2024, from https://www.energy.gov/eere/buildings/commercial-reference-buildings

Directorate-General for Energy. (2023). Energy efficiency directive. Retrieved June 1, 2024, from https://energy.ec.europa.eu/topics/energy-efficiency/energy-efficiency-targets-directive-and-rules/energy-efficiency-directive_en

Eskilson, P. (1987). *Thermal analysis of heat extraction boreholes* (Doctoral Thesis (compilation)).

European Commission. Energy efficiency directive (EU/2023/1791), 231 OJ L § (2023). Retrieved from http://data.europa.eu/eli/dir/2023/1791/oj/eng

Fry, N. A. (2021). Building-level heat demand mapping of commercial-residential areas for simulated district heating assessments in Montana, Idaho, and Washington. *Energy and Buildings*, *245*, 111075. https://doi.org/10.1016/j.enbuild.2021.111075

Hirsch, H., & Paepcke, A. (2022). Detailed modelling of large district heating and cooling network coupled to ground heat exchanger (Vol. 9, pp. 0–0). Presented at the BauSim Conference 2022, IBPSA-Germany and Austria. https://doi.org/10.26868/29761662.2022.38

Ingersoll, L. R., Zobel, O. J., & Ingersoll, A. C. (1954). *Heat conduction with engineering, geological, and other applications*. Madison, Wisconsin: University of Wisconsin Press.

Internal Revenue Service. (2024a, May 29). Home energy tax credits. Retrieved June 1, 2024, from https://www.irs.gov/credits-deductions/home-energy-tax-credits

Internal Revenue Service. (2024b, June 10). Credits and deductions under the Inflation Reduction Act of 2022. Retrieved June 1, 2024, from https://www.irs.gov/credits-and-deductions-under-the-inflation-reduction-act-of-2022

IQGeo, K. M., Head of Innovation at. (2023, March 17). Three levels of district energy network design maturity. Retrieved June 1, 2024, from https://www.iqgeo.com/blog/three-levels-of-district-energy-network-design-maturity

Jebamalai, J. M., Marlein, K., Laverge, J., Vandevelde, L., & Van Den Broek, M. (2019). An automated GIS-based planning and design tool for district heating: Scenarios for a Dutch city. *Energy*, *183*, 487–496. https://doi.org/10.1016/j.energy.2019.06.111

Jebamalai, J. M., Marlein, K., & Laverge, J. (2020). Influence of centralized and distributed thermal energy storage on district heating network design. *Energy*, 117689. https://doi.org/10.1016/j.energy.2020.117689

Lund, H., Werner, S., Wiltshire, R., Svendsen, S., Thorsen, J. E., Hvelplund, F., & Mathiesen, B. V. (2014). 4th generation district heating (4GDH): Integrating smart thermal grids into future sustainable energy systems. *Energy*, *68*, 1–11. https://doi.org/10.1016/j.energy.2014.02.089

Lund, H., Østergaard, P. A., Nielsen, T. B., Werner, S., Thorsen, J. E., Gudmundsson, O., et al. (2021). Perspectives on fourth and fifth generation district heating. *Energy*, *227*, 120520. https://doi.org/10.1016/j.energy.2021.120520

Manente, G., Lazzaretto, A., Molinari, I., & Bronzini, F. (2019). Optimization of the hydraulic performance and integration of a heat storage in the geothermal and waste-to-energy district heating system of Ferrara. *Journal of Cleaner Production*, *230*, 869–887. https://doi.org/10.1016/j.jclepro.2019.05.146

Nian, Y.-L., & Cheng, W.-L. (2018). Analytical g-function for vertical geothermal boreholes with effect of borehole heat capacity. *Applied Thermal Engineering*, *140*, 733–744. https://doi.org/10.1016/j.applthermaleng.2018.05.086

Postnikov, I., Stennikov, V., & Penkovskii, A. (2019). Prosumer in the District Heating Systems: Operating and Reliability Modeling. *Innovative Solutions for Energy Transitions*, *158*, 2530–2535. https://doi.org/10.1016/j.egypro.2019.01.411

von Rhein, J., Henze, G. P., Long, N., & Fu, Y. (2019). Development of a topology analysis tool for fifth-generation district heating and cooling networks. *Energy Conversion and Management*, *196*, 705–716. https://doi.org/10.1016/j.enconman.2019.05.066

Schifflechner, C., Kuhnert, L., Irrgang, L., Dawo, F., Kaufmann, F., Wieland, C., & Spliethoff, H. (2023). Geothermal trigeneration systems with Organic Rankine Cycles: Evaluation of different plant configurations considering part load behaviour. *Renewable Energy*, *207*, 218–233. https://doi.org/10.1016/j.renene.2023.02.042

US Department of Energy. (2024a). *Decarbonizing the U.S. Economy by 2050: A national blueprint for the buildings sector*. Retrieved from https://www.energy.gov/eere/decarbonizing-us-economy-2050-national-blueprint-buildings-sector

US Department of Energy. (2024b, April 2). DOE releases first ever federal blueprint to decarbonize America's buildings sector. Retrieved June 1, 2024, from https://www.energy.gov/articles/doe-releases-first-ever-federal-blueprint-decarbonize-americas-buildings-sector

Wirtz, M., Schreiber, T., & Müller, D. (2022). Survey of 53 fifth-generation district heating and cooling (5GDHC) networks in Germany. *Energy Technology*, *10*(11), 2200749. https://doi.org/10.1002/ente.202200749

Zeh, R., Ohlsen, B., Philipp, D., Bertermann, D., Kotz, T., Jocić, N., & Stockinger, V. (2021). Large-scale geothermal collector systems for 5th generation district heating and cooling networks. *Sustainability*, *13*(11). https://doi.org/10.3390/su13116035

Developing Geothermal District Heating in Lakeview, Oregon

Nicholas Fry, Shellie Jober, Casey Lavigne, Julian McDowell

Jacobs Engineering Group

Keywords

District heating, direct-use, energy savings, space heating, hydrogeology

ABSTRACT

Geothermal district heating (GDH) in North America has a history dating back to the 1800s. Although North American GDH systems have been around almost as long as the steam networks of New York, they have not enjoyed large scale commercial expansion. There are several reasons for this. Low enthalpy geothermal systems historically develop around surface manifestations. Early production from these surface manifestations is often a matter of trial and error. Few low enthalpy geothermal systems undergo rigorous exploration, geologic investigation, or wellfield planning prior to drilling. In many cases, this leads to unnecessary contamination of distribution lines in the GDH, decreases in equipment lifetimes, and overall declines in reservoir temperatures and pressures. Despite the lack of deliberate development procedures for most North American GDH systems, they tend to save communities millions of dollars over the lifetime of operation, decrease the carbon footprints of building space conditioning, and provide jobs in sustainable energy. This paper explores the direct uses of geothermal energy, including GDH, in the Town of Lakeview, Oregon, highlighting early exploration, recent development activity, and recommendations for the future. To other GDH system operators, or those considering development, the case of Lakeview can serve as a lesson, a tale of continuous improvement, and a success story.

1. Introduction

Geothermal resources have been at the heart of the Town of Lakeview since its founding in 1869. The town of 2,326 people sits in a Known Geothermal Resource Area (KGRA), with surface manifestations - hot springs - to the north and south of the downtown core. Commercial development of the geothermal resources began in 1923, with bathing or balneology as the primary application (Coury and Associates, Inc., 1980).

In recent decades, various geothermal exploration programs have taken place in Lakeview, leading to new developments and pilots ranging from greenhouse operations to small modular power

plants. Lakeview's community pool is fed by geothermal waters from a depth of 2300 feet and has been since 1938. The earliest GDH system (no longer operational) supplied 15 single family homes in the Goldmohr Terrace neighborhood. Magma Power began wildcat drilling for geothermal in 1960. The resulting well had an initial production temperature of 217ºF, which later fed greenhouse operations (Sifford, 2010). Between 1982 and 1983, Wood & Associates of California owned and operated modular Ormat Technologies Inc. (Ormat) and Solar Power System (now defunct) organic Rankine cycle (ORC) power plants in a canyon in the adjacent Warner Mountain Range, with a total stamped capacity of 2.1 MW_e (Wood & Ram, 1983).

Today, Lakeview is home to two of North America's 23 operating GDH systems (Lund & Toth, 2021; Robins et al., 2021; Thorsteinsson, 2008). These geothermal heating systems support agencies within the State of Oregon, the regional hospital campus, public schools, and emergency service facilities, among others. Both systems are foundational for the community, serving as critical infrastructure and a consistent draw for businesses throughout the region.

The production well feeding the northern GDH, serving Warner Creek Correctional Facility, began producing from a completion depth of 602 feet in December of 2004. Slotted liners, at a diameter of 10 inches, are in place from 181 – 601 feet. The well itself is capable of producing between 200 – 500 gallons per minute. From a line shaft pump house (Figure 1), the field gathering system arrives at a heat exchange substation, several hundred feet west, where a gauge read 192ºF in December 2023. An initial fluid temperature of 204ºF at the wellhead, has held steady since 2004. All fluids are reinjected.

Figure 1: Production wellhead for the northern GDH in Lakeview, December 2023.

The production well feeding the southern GDH, which serves the remainder of GDH customers across Lakeview, has a completion date of September 2013. The well, having a total depth of 900 feet and liners from 242 – 900 feet, was originally capable of producing 190 gallons per minute with a fluid temperature of 191ºF. During a site visit in December 2023, sustainable flow rates were as low as 80 gallons per minute with a production temperature of 158ºF. All fluids are reinjected.

Maintaining both GDH systems is important to Lakeview for several reasons. The customers subscribing to the heating service from the municipal utility collectively avoid fuel expenditures, saving in the hundreds of thousands of dollars each year. These savings allow more money to stay in the community, contributing to economic growth. Many of the customers are using the heat to support critical infrastructure, including emergency services, living quarters, and medical care departments. The importance of these critical services is emphasized due to the relative remoteness of Lakeview. If local emergency medical services became unavailable, residents in an emergency situation would be left with a choice between an unfeasibly long ground transport or an unfeasibly expensive air transport.

2. Lakeview Geothermal Resource Area Characterization

The Oregon Department of Geology and Mineral Industries (DOGAMI) maintains a well database and geothermal information layer in a web map service. Some of the geothermal data for Lakeview originates from geothermal gradient well surveys that took place in the late 1970s (Brown et al., 1980). These data sources, along with previous consulting engineer reports, served as the basis of desktop review for a more recent geothermal resource characterization in Lakeview, performed by Jacobs (Fry et al., 2024).

There are more than a dozen low enthalpy wells in Lakeview with fluid temperatures above 100ºF. Two predominate surface manifestations in Lakeview include Hunters Hot Springs to the north, and Barry Hot Springs to the south of the downtown district. Of those, the highest temperature wells are in, or west of, Hammersley Canyon, near Hunters Hot Springs. Both GDH production wells are in close proximity to the respective north and south surface manifestations (Figure 1).

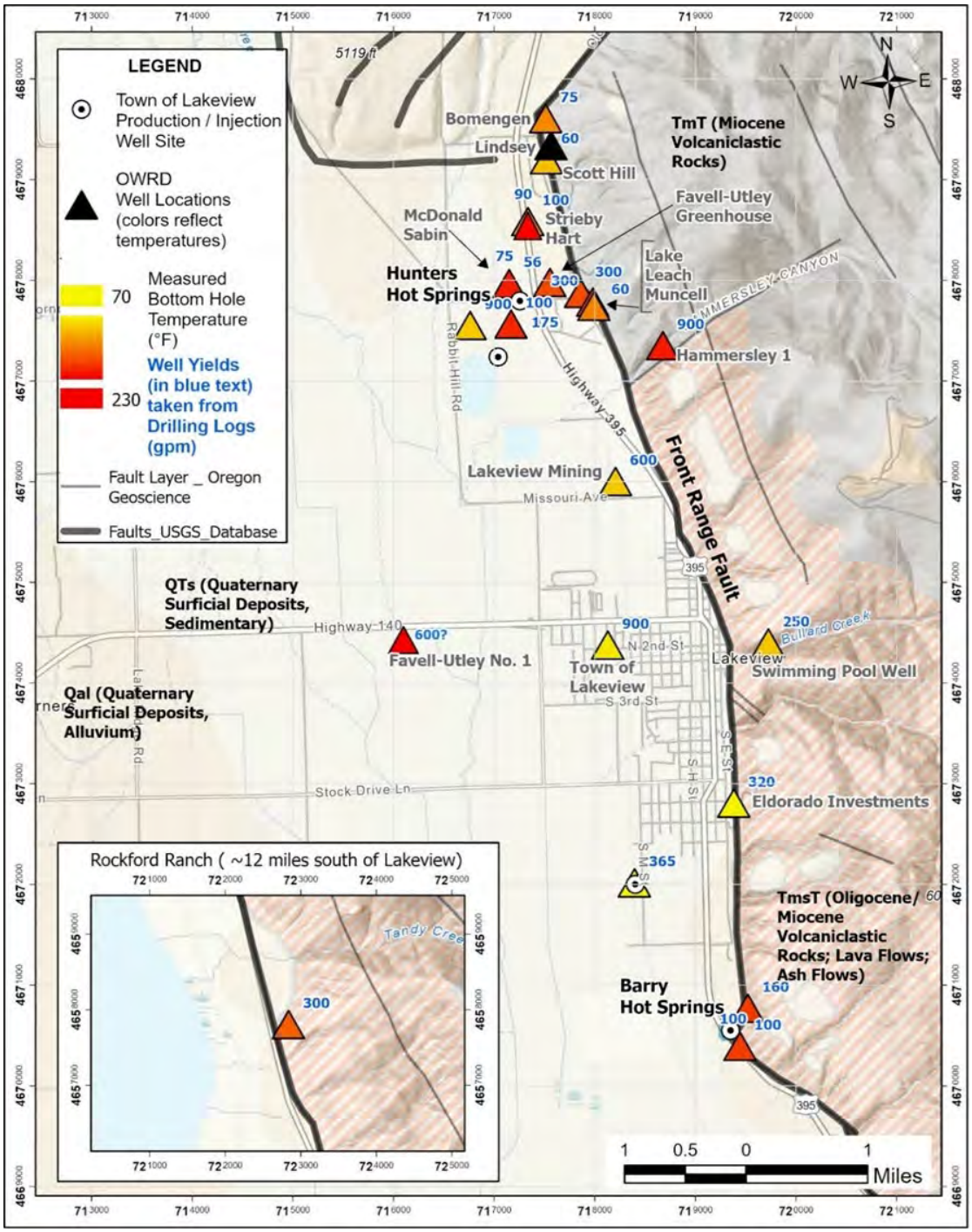

Figure 2: Plan map showing some of the geothermal wells from the Oregon Water Resources Department (OWRD), and other features from DOGAMI databases (Fry et al., 2024).

The surface manifestations coincide with other higher temperature wells and, although there is limited west to east and vertical spread in well and temperature data, this suggests the presence of two distinct upflow zones surrounding Hunters Hot Springs and Barry Hot Springs. These upflow zones occur along the western side of a north-south running front range fault, evident in a cross-

section interpolation from well logs (Figure 2). To the east of the front range fault is the Warner Mountain Range. To the west of the fault are the alluvial plains and the Town of Lakeview.

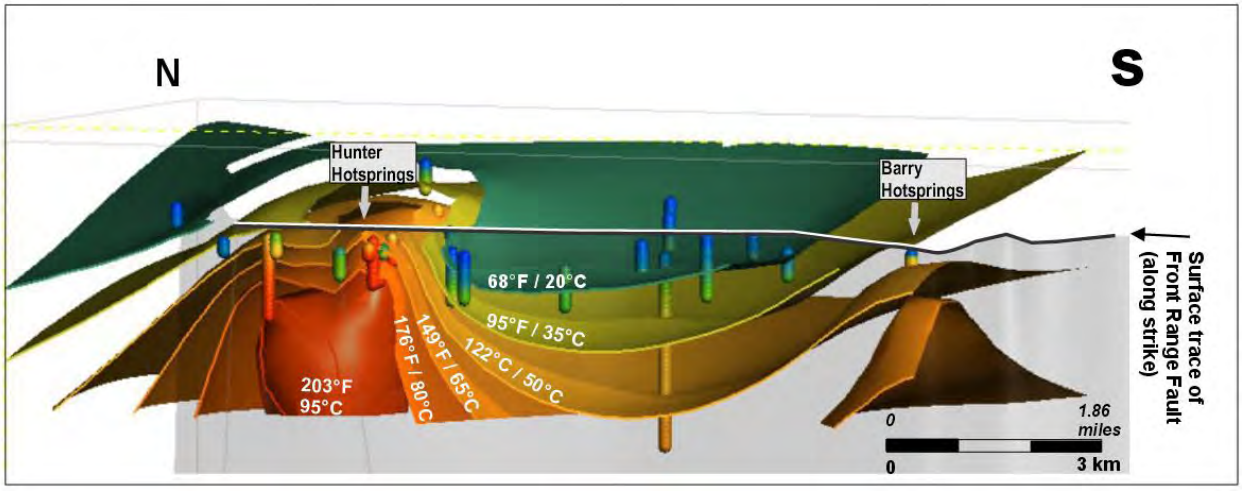

Figure 3: Cross section view of inferred interpolated temperature isotherms (Fry et al., 2024) from well gradient data (Brown et al., 1980).

The upflow zones of Lakeview's geothermal resource lie within a typical Basin and Range geological setting, with characteristic block faulting and deep sediment basin fill – in Goose Valley, a structural basin west of the Warner Range. The dominant influence on upflow and outflow is the front range fault, where lateral migration of hot fluids travels through permeable clastic horizons of the valley basin away from the fault. There is, therefore, interlayering of permeable and low permeability deposits in the plain, variably affecting the geothermal system beneath Lakeview (Figure 3).

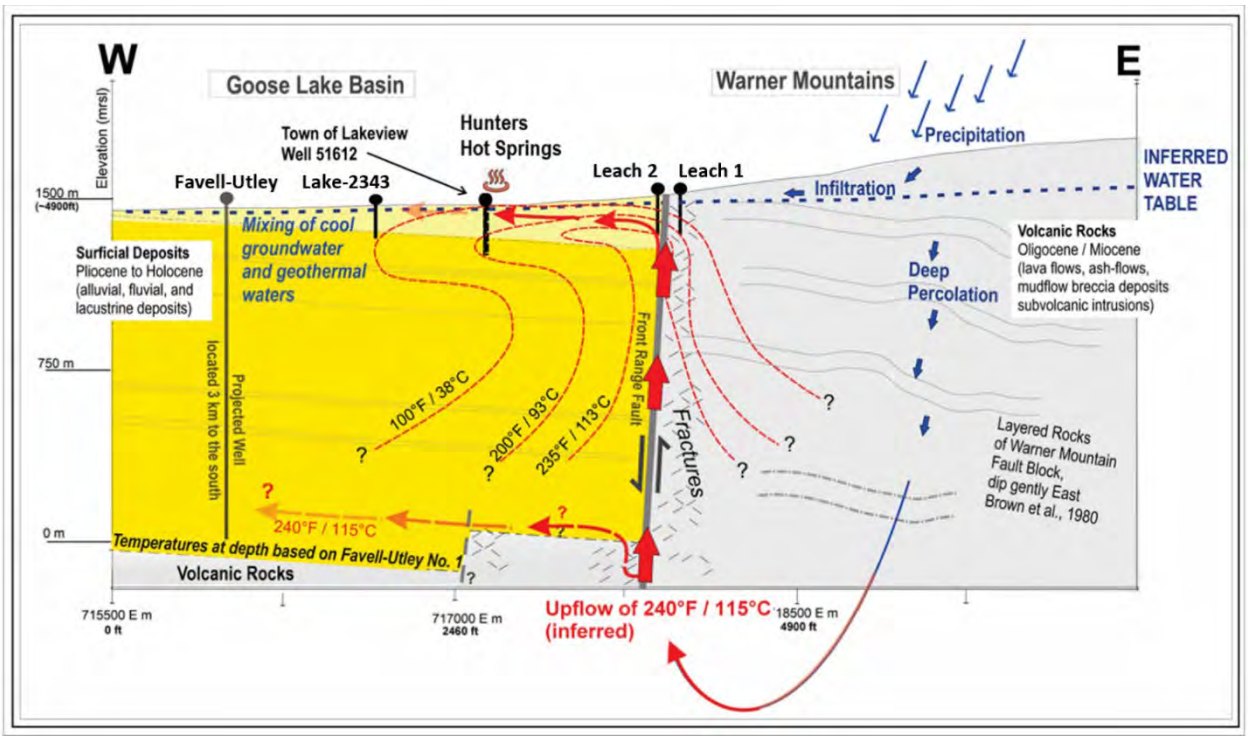

Figure 4: Idealized conceptual cross section of the geothermal area at Lakeview (Fry et al., 2024).

Poor data integrity in the DOGAMI database does not allow for adequate characterization of the geothermal resource in Lakeview. During investigation by Jacobs, it became evident that future iterations of exploration and study must include field surveys to update existing DOGAMI datasets. Some current data only shows well locations by the closest quarter section, with rare descriptions of proximate locations in available well logs and geoscientific reports.

3. Historic Design and Operation of Geothermal Facilities

The US Geological Survey (USGS) put Lakeview on the list of Known Geothermal Resource Areas in 1971, in accordance with the Geothermal Steam Act of 1970 (Godwin et al., 1971). Most of the projects for geothermal power and heating surface facilities in Lakeview included front end engineering design studies. These studies, however, only rarely attempt to characterize the subsurface system. In practice, since 1970 – and throughout the history of geothermal development in Lakeview – it appears most drilling continues to take place near the surface manifestations. Further, for the current GDH systems under ownership by Lakeview, the planning reports for the facilities do not match systems in place.

The mismatch between study and practice in the GDH systems is not exclusive to Lakeview. The 23 operating GDH systems in North America have largely been the result of drilling success by chance, near surface manifestations. When that is the approach taken for GDH implementation for municipal operators, the system sustainability becomes a risk.

During the recent investigation, Lakeview undertook a well remediation effort for the south GDH producer. In February 2024, Blue Spark Energy of Calgary performed hydraulic pulse stimulation to remove scale. As of this writing, the flow rates are back to 2014 volumes, but the temperatures remain the same.

Sustaining design temperatures for GDH systems is important for several reasons, one of which involves end-user equipment. End-user equipment may require a minimum entering fluid temperature to achieve a differential temperature high enough to meet space conditioning (heating) and domestic hot water (DHW) preparation needs. Where this differential temperature becomes insufficient, the end-users may need to supplement the GDH supply with peaker equipment – such as a boiler. This operation becomes costly where, following a production well temperature decline curve, additional fuel purchases become the norm.

Some ways to prevent temperature declines in GDH operations include rigorous hydrogeologic investigations, geothermal resource assessments, and system design that emphasizes energy efficiency. Rigorous hydrogeologic investigation can provide insights into regional groundwater flow directions, and seasonal regimes which might affect shallow production in outflows – like those found in Lakeview. Drilling into the fractured upflow zone – such is the case with the southern GDH production well in Lakeview – may be contraindicated by good geothermal resource assessment before drilling. Fractured upflow zones may result in successful production wells for a short period, but the fluid pathways may change over the life of the operations or new influences from cold feedzone flow may decrease system performance. Designing a GDH for energy efficiency means thinking holistically about the temperature regimes of the end-users, not simply designing to a given peak demand or seeking to develop around the hottest well. In the case of Lakeview, the south GDH has become susceptible to unplanned increases to the end-user demands, creating conditions which require more pumping from the geothermal resource. Accounting for these factors in design and ongoing operations for GDH systems may mitigate resource temperature declines.

In the northern GDH system, serving the Warner Creek Correctional Facility, a review of piping and instrumentation diagrams suggests that the original end-user design temperature for fluids entering the substation is 210ºF. As of February 2024, the entering fluid temperature at the Facility is 160ºF, with the production wellhead temperature at or near 210ºF. The difference between the design temperature and the current entering fluid temperature results in greater boiler cycling and, therefore, additional fuel expenditures. This is particularly costly in a place like Lakeview, where delivery of fuel is expensive, forcing unit rates for gas and fuel oil well above hub averages.

To date, no evidence has been found indicating delivery temperatures from the heat exchange substation (Figure 4) were ever intended to reach 210ºF. There are several reasons why this design flaw might occur in GDH development, and they may serve as lessons for future engineering practice. In discussions with facility operating engineers at Warner Creek Correctional Facility and Lakeview, two or potentially three different engineering firms were designing the whole geothermal well, heat exchange substation, transportation pipelines, and in-facility hot water distribution system at the same time. Heat losses through the system were likely underestimated. Design temperatures for each section of the system, whether it was production, heat exchange, distribution, or in-facility portions, were not communicated correctly.

Figure 5: Heat exchange substation for the northern GDH, taken December 2023, serving the Warner Creek Correctional Facility.

Communication between geothermal system engineering and development firms serving multiple clients across the same GDH network is paramount. The Warner Creek Correctional Facility design flaw is not a problem of GDH operations, rather it is an apparent problem of communication during the design stages. Some ways in which multi-stakeholder GDH developments may unfold with more design risk mitigation includes the use of different contract vehicles, employment of an owner's engineer, or provision of single source engineering design. In GDH, and district heating more broadly, multiple stakeholders may contribute funding to the design of the initial operations. This may mean that multiple procurement systems overlap each other from multiple institutions. To mitigate risk, a standalone operations, development, and design agreement can serve as an important delivery vehicle. Owner's engineers may serve as a single source of truth to review multiple engineering design firm works across the different sections of the GDH system - wellfield, heat exchange substations, transportation pipelines, and in-facility connections, among others. Employing a single design firm for all of the different sections of the GDH system will drastically reduce miscommunication risk. Very few firms, however, have experience in the exploration of geothermal resources, well targeting, wellfield design, surface facilities design, and in-facility mechanical systems, to offer single source options. Some combination of the contract vehicles, owner's engineering services, and design team procurement strategies are likely necessary to implement and efficient GDH while mitigating design risk.

Similar strategies are applicable to the relatively small power generation capacity that may be possible from Lakeview's geothermal resources. In historic review, it appears that the Ormat modular power generation equipment in operation at Lakeview during the early 1980's was

susceptible to very large parasitic loads, waning demand for higher cost electricity sources following the oil crises of the 1970s, and short-term contract vehicles (Sifford, 2010; Wood & Ram, 1983). Modern power generation equipment may offer a more economical model to develop the resource for electricity production. A holistic approach to geothermal systems development, therefore, remains the necessary norm for small operators at the peripheries of the grid – such is the case with Lakeview.

4. Development Opportunities

Lakeview is a place rich in natural resources, while also located to the greater California market. The premiums for sustainable materials and low- or no-emission power and fuels in the California market attract many manufacturers to Lakeview.

Lakeview has a long history in the wood products industry, including milling services, engineered wood, cabinetry, and door manufacturing, among others. Mining operations are ongoing in the nearby Warner Mountain Range. Greenhousing and agriculture are staple industries for the community. Recently, biofuels and low-emission cement production facilities have begun construction in Lakeview. These facilities alone will require more than 30MWe, preferably no-emissions electricity. Limitations in the interconnection of Lakeview to distant electricity generation plants provides a new opportunity for geothermal heat and power development in or around the town. For those developers willing to invest in the proper exploration, design, and construction of geothermal heat and power facilities, adjacent industry presents a primary business development opportunity for heat and power purchase agreements.

5. Recommendations and Findings

In a summary strategy report for Lakeview, Jacobs provides a detailed discussion of recommendations for policymakers and city engineering officials (Fry et al., 2024). In this section we offer some recommendations and findings to private geothermal resource developers and would-be low-enthalpy geothermal system engineers or geoscientists.

- At the outset of a geothermal development project, implement a communications plan for all design teams that is commensurate with experience, past performance, and operational expectations.
- Low-enthalpy system development may not be as attractive as higher margin power systems, but it nonetheless may serve critical infrastructure.
- When developing low-enthalpy geothermal systems, a subsurface sustainability study is just as important at the outset of a project as any medium- or high-enthalpy venture.
- Contract vehicles and rate base agreements are an important component of long-term sustainability of the geothermal resource for GDH and the overall performance of mechanical systems.

6. Conclusion

The Town of Lakeview is a place with abundant natural resources, one of which being geothermal. Geothermal development has been a foundation of the community, dating back to the earliest native American presence in the region. Today, Lakeview is home to 2 of the continent's 23 GDH systems (Lund & Toth, 2021), saving end-users tens of thousands of dollars every year. As new

industries arrive in Lakeview, greater and more sustainable uses of the geothermal resources may reduce combustion fuel consumption, save businesses and homeowners money, and contribute to greater economic growth for the community.

Developing these low-enthalpy geothermal resources for Lakeview in a sustainable manner will require more rigorous exploration of the subsurface, thoughtful design of the surface facilities, and communications. Low-enthalpy geothermal development, including the GDH systems in Lakeview, can and do serve critical infrastructure. This critical infrastructure is vital for life, economy, and community sustainment. These multiple stakeholders across a community like Lakeview are often also the financiers of such systems, and designers must support their needs by clearly communicating what is and is not possible to know at the outset of a geothermal engineering program. Engineering design of low-enthalpy geothermal resources is, therefore, a serious task requiring thoughtful communications plans to mitigate design flaws. A firm supporting these community geothermal system developments should also describe to the stakeholder group the role of contract vehicles and base rate agreements which mitigate unplanned changes to demand and, therefore, risks to geothermal resource and mechanical systems' sustainability.

Acknowledgement

The authors wish to thank the entire Town of Lakeview for embracing geothermal as a viable resource for improving their community. We would like to thank the executive, administrative, and engineering staff of the Town of Lakeview for providing ongoing data updates and an openminded nature during development strategy discussions. We would also like to acknowledge Shiela Strubel – Community and Economic Development – and Scott Langum – Special Projects Manager – for their tireless commitment to understanding the geothermal systems in place and expansion potential.

REFERENCES

Brown, D. E., Peterson, N. V., & McLean, G. D. (1980). *Preliminary geology and geothermal resource potential of the Lakeview area, Oregon* (No. 0-80–9) (p. 114). Portland, Oregon: State of Oregon Department of Geology and Mineral Industries.

Coury and Associates, Inc. (1980). *A feasibility analysis of geothermal district heating for Lakeview Oregon* (No. DE81030003). Denver, Colorado: Northwest Geothermal Corporation.

Fry, N., Jober, S.-A., Lavigne, C., & McDowell, J. (2024). *Commercial-industrial geothermal energy strategy* (p. 75). Lakeview, Oregon: Town of Lakeview.

Godwin, L. H., Haigler, L. B., Rioux, R. L., White, D. E., Muffler, L. J., & Wayland, R. G. (1971). *Classification of public lands valuable for geothermal steam and associated geothermal resources* (Report No. 647). https://doi.org/10.3133/cir647

Lund, J. W., & Toth, A. N. (2021). Direct utilization of geothermal energy 2020 worldwide review. *Geothermics*, *90*, 101915. https://doi.org/10.1016/j.geothermics.2020.101915

Robins, J. C., Kolker, A., Flores-Espino, F., Pettitt, W., Schmidt, B., Beckers, K., et al. (2021). *2021 U.S. geothermal power production and district heating market report*. United States. https://doi.org/10.2172/1808679

Sifford, A. (2010). Geothermal energy in Oregon. In *World Geothermal Congress 2010*. Bali, Indonesia: International Geothermal Association.

Thorsteinsson, H. H. (2008). *U.S. geothermal district heating: Barriers and enablers*. Massachusetts Institute of Technology, Cambridge, MA. Retrieved from http://hdl.handle.net/1721.1/42932

Wood, J., & Ram, H. (1983). Binary power plant tested at Lakeview, Oregon. *Geothermal Resource Council Bulletin*. Retrieved from https://publications.mygeoenergynow.org/grc/7000189.pdf

Advancing District Energy Geoexchange Solutions in Single Family Home and Mixed-Use Communities: Strategies and Real-World Insights

Carson Gemmill, Cameron Leitch, Neeraj Raghuram, and King Tung

Enwave Energy Corporation

Keywords

District Energy, Geoexchange, Ambient Loop, Thermal Energy Network (TEN), Thermal Networks, Geothermal Heat Pumps, Hybrid Geoexchange Systems, 4-Pipe Systems, Ground Source

ABSTRACT

District energy geoexchange systems are emerging as a promising solution for efficient, low-carbon heating and cooling in communities. This paper explores the implementation strategies and real-world applications of these systems, focusing on 4th and 5th generation district energy (DE) configurations. We present a comprehensive comparison of these two generations, highlighting their respective benefits and drawbacks in various contexts.

Two case studies are examined in detail: the Etobicoke Civic Centre Precinct, utilizing a 4th generation DE geoexchange system, and the Springwater Single Family Home community, using a 5th generation system. These cases illustrate the practical considerations and decision-making processes involved in selecting and implementing district energy geoexchange solutions.

Our analysis reveals that the choice between 4th and 5th generation systems depends on factors such as load aggregation benefits, operational complexity, space constraints, and end-user preferences. The 4th generation systems excel in scenarios where centralizing thermal energy generation offers significant advantages, while 5th generation systems prove beneficial in distributed, smaller-scale applications.

This research contributes to the growing interest in sustainable community energy systems and provides valuable insights for planners, developers, and policymakers considering district energy geoexchange solutions.

1. Introduction

Buildings account for 30% of global final energy consumption and 26% of global energy-related emissions(Delmastro & Chen, 2023). Electric heat pumps have become an increasingly effective way for buildings to reduce energy consumption and emissions due to operating, equipment, and installation costs becoming more competitive in certain markets, as well as their high efficiencies relative to other forms of heating production (Bolin, et al., 2022). When applied in a jurisdiction with a low carbon grid (or when leveraging renewable power) this decarbonization benefit can be further enhanced to achieve near zero emissions.

Geothermal heat pumps (or geoexchange systems as referred to in this paper) are regarded as one of the most efficient means of providing heating and cooling energy to buildings (U.S. Energy Information Administration (EIA), 2022). This is due to the relatively stable temperature of the ground used as a heat source and sink driving superior system Coefficients of Performance (COPs) compared to other heating and cooling technologies.

The application of geoexchange has been common for single buildings and is now becoming more popular for communities (Wiltshire, 2015). District energy (DE) is the centralizing of thermal energy production and shared distribution of this thermal energy through a network of buried piping. DE systems have been in use across North America for over a century but have typically been limited to college campuses or central business districts (Fulton & Thomas, 2023). In Europe, their adoption is more widespread. According to a report published in 2021 by the European Union (EU), 12% of heat for space heating and hot water in the EU was supplied through district energy systems (Kranzl, et al., 2022).

The appeal of DE systems is growing, and the role they have to play in the global energy transition has been building momentum. A recent study in Europe singles out district heating and cooling as one of Europe's most efficient measures to reduce fossil fuel imports over the next decade (Mathiesen BV, 2023). The United Nations refers to DE as "a secret weapon for climate action and human health" and DE systems are recognized for their ability to assist in connecting heat pumps to renewable energy sources using thermal grids (UN Environment Programme, 2019). Consistent with this sentiment, geoexchange systems when applied at the DE scale offer a number of benefits to the communities they serve. Recently, the term Thermal Energy Network (TEN) has emerged to describe the next generation of district energy systems that focus on the use of low-carbon energy sources such as geo-exchange (The Building Decarbonization Coalition (BDC), 2024).

2. District Energy Geoexchange Systems Overview

This paper will focus on implementing district energy geoexchange systems in 4th generation and 5th generation DE systems, and the benefits and drawbacks to be considered when evaluating when system to implement. Refer to Figure 1 for an overview of the major development stages in the evolution of district energy systems, including the 4th and 5th generations.

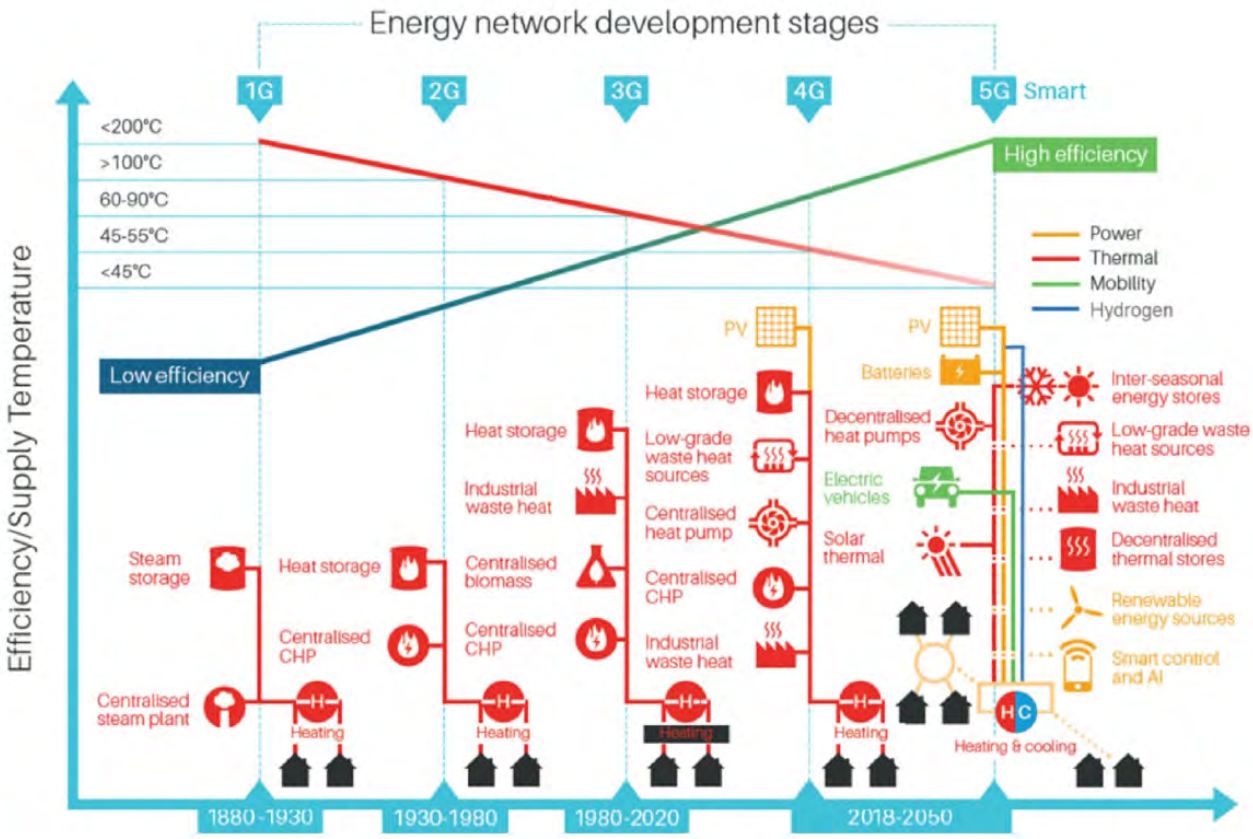

Figure 1: Energy network development stages including 5G concept (Revesz, et al., 2020).

2.1. 4th Generation DE Geoexchange System – 4-Pipe Systems

A 4th Generation DE system, also known as the "modern 4-pipe system", is characterized by low temperature hot water distribution (ranging from 30 – 70ºC) that enables the use of centralized plants featuring heat pumps, as well as other renewable or waste heat resources (Lund H, 2014). These systems deliver hot water and chilled water (4 pipes) at temperatures adequate to provide space heating, space cooling, and domestic hot water, often via a local building heat exchanger system. When integrating geoexchange into a 4th Generation DE system, supplemental heating and cooling sources (such as dry coolers, cooling towers, or supplemental boilers) are usually implemented to improve overall system economics and these systems are often referred to as hybrid geoexchange systems (Gudmundsson, et al., 2022).

2.2. 5th Generation DE Geoexchange System – Ambient Loop Systems

A 5th Generation DE system, also known as an Ambient Loop system, is characterized by maintaining temperature in the loop at near ambient conditions (below 45ºC) to maximize the ability to share energy amongst the network and to maximize the ability to integrate waste heat sources (Revesz, et al., 2020). These systems deliver thermal energy via supply and return pipes (2 pipes) and require the use of distributed heat pumps to "upgrade" the thermal energy from the Ambient Loop to be used for heating and cooling application at each thermal end-user.

Geoexchange systems integrate well with these types of systems as they provide the heat source (or sink) necessary to maintain the Ambient Loop temperatures in the necessary range.

3. Comparing 4th Generation & 5th Generation Systems

The main distinction between 4th and 5th Generation system has to do with where useful thermal energy is generated. In 4th generation systems, this is done at central plants; in 5th generation systems, this is done at the end-user site (Gudmundsson & Thorsen, 2021).

While 5th Generation DE Systems are regarded as having the potential to be the most energy efficient system given their ability to share energy between end-users and to leverage waste heat sources, this may not be the case in every application (Gudmundsson & Thorsen, 2021; Revesz, et al., 2020). Furthermore, 4th Generation systems offer other qualitative benefits that may be desirable to the end user, and therefore in certain applications may be deemed more attractive. Table 1 outlines these key considerations and the potential benefits and drawbacks to be considered.

Table 1: Comparing the Benefits and Drawbacks of 4th and 5th Generation DE Geoexchange Systems

	4th Generation DE Geoexchange System	5th Generation DE Geoexchange System
Generation		
Geoexchange Field		
Benefit		- Allows for simpler integration of geoexchange systems distributed throughout the network (given heat pumps are located at the end-user site)
Drawback	- Typically requires geoexchange to be implemented into the central plant(s), requiring distributed fields to be piped back to this central distribution	
Central Heat Pump Plant		
Benefit	- Aggregating loads into central heat pump plants can allow for the greatest value add in employing operational optimization strategies, driving greater system COPs - Depending on the jurisdiction, central heat pumps can allow for leveraging time-of-use rate or demand management structures for greater economic value	N/A

	4th Generation DE Geoexchange System	5th Generation DE Geoexchange System
	- Diversity of end-user load profiles can permit construction of a smaller overall central plant capacity relative to the sum of the end-user peak demands that are required by a 5th generation system.	
Drawback	- Requires significant space to site a central plant	N/A
Supplemental Systems		
Benefit	- Central plants allow for the greatest value add hybridizing the geoexchange field with supplemental systems given their ability to optimize both installed geo capacity and delivery temperatures	
Drawback		- Challenging to integrate and add value given useful thermal energy production occurs at the customer site

Distribution

Piping System	**4-Pipe Distribution:**	**2 Pipe (or Single Pipe) Distribution:**
Benefit	- Relatively simple and predictable system hydraulics	- Reduced network piping and capital costs - Lower system distribution losses
Drawback	- Increased network piping and capital costs - higher system distribution losses	- Can result in more complicated system hydraulics - Temperature control is not centralized which can add complexity to manage - Smaller system temperature differentials drive significantly larger pipe sizes

	4th Generation DE Geoexchange System	5th Generation DE Geoexchange System
End-Use		
Thermal Exchange	**Energy Transfer Station:**	**Distributed On-Site Heat Pumps:**
Benefit	- End-user benefits from simple, passive on-site heat exchangers to access the thermal energy (highest value thermal product delivered) - Requires no further thermal "upgrade" to deliver heating and cooling energy - Least energy intensive for the end-user on-site - Smallest space requirement for the end-user - Low and infrequent maintenance requirements	- Ability to design the heat pumps to meet the specific temperature needs of each end-user
Drawback		- End-user requires an on-site heat pump to produce useful thermal energy (lowest value thermal product delivered) - Adds operational complexity and maintenance requirements for the end-user - Added space requirement for the end-user

4. Case Studies

To date, Enwave has developed two major geoexchange based district energy systems – each of which employs a different system design approach. This section will provide an overview of each of these projects and explain the rationale behind the design approach that was taken in each case. The case studies include the Etobicoke Civic Centre Precinct and the Springwater Single Family Home Community.

5. Etobicoke Civic Centre Precinct – 4th Generation DE Geoexchange System

5.1.Development Overview

The Etobicoke Civic Centre (ECC) Precinct is a mixed-use redevelopment located in Toronto, Canada. The redevelopment consists of 6 development blocks, with a total floor area approaching 300,000 m^2. The building use types across the precinct include commercial office, community space, retail, and significant residential development. Refer to Figure 2 for a conceptual plan of the redevelopment area.

The ECC Precinct is being master planned by the City of Toronto, and therefore is adhering to ambitious building standards with a heavy focus on low carbon energy systems.

Enwave worked in partnership with the City of Toronto under a Joint Development Agreement (JDA) signed in 2018 to develop a new low carbon district energy system to be built alongside the new ECC development. The precinct is recognized by the City of Toronto as the City's first Net Zero community.

Figure 2: ECC Precinct Conceptual Plan (Mirabelli, 2021)

5.2. Technical Solution Overview

A 4th Generation DE Geoexchange System was selected as the solution of choice to serve the ECC precinct. The ECC District Energy System consists of a central district energy (DE) plant, a connected geoexchange system, distribution piping system (DPS) and energy transfer stations

(ETS) at each end-user site. Refer to Figure 3 for a conceptual diagram of the DE system. Table 2 summarizes the major equipment components and capacities.

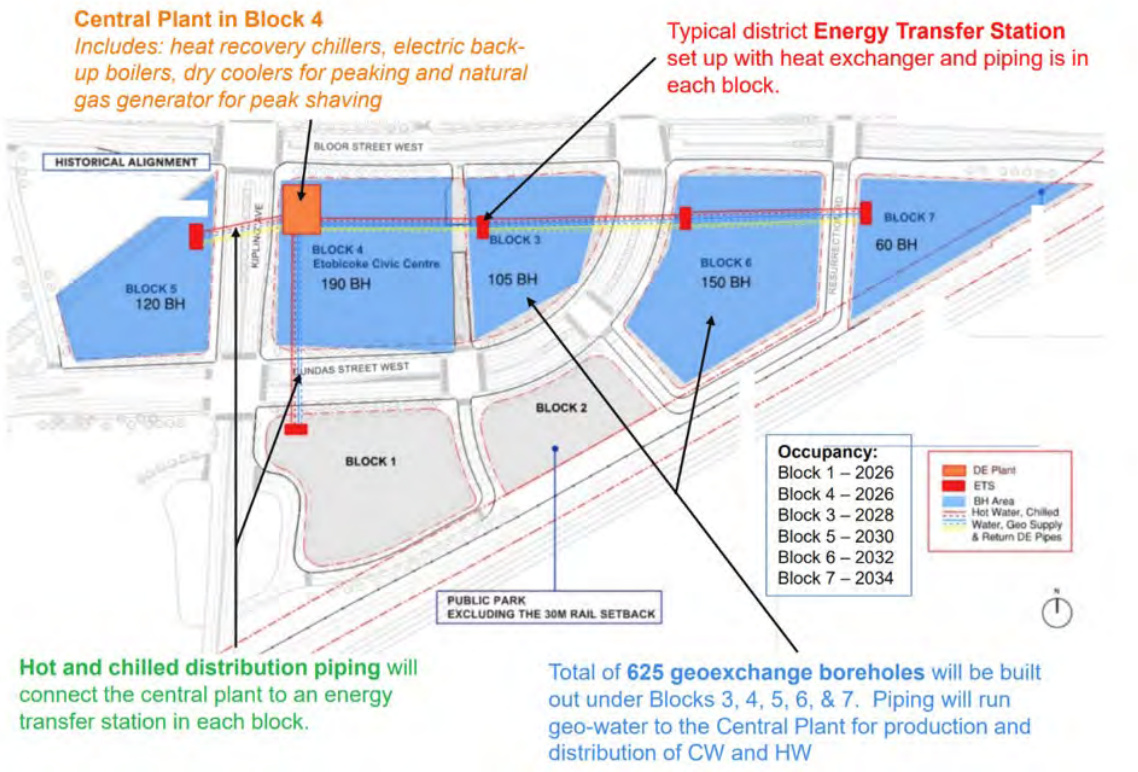

Figure 3: ECC Precinct District Energy Conceptual Plan.

Table 2: ECC Precinct DE System – Component Capacity Summary

Component	**Details**
Geoexchange Boreholes	625 at 244 m
Heat Pump Capacity	11.25 MW(th)
Supplemental Heating Capacity Installed	1.90 MW(th) – Electric Boiler
Supplemental Cooling Capacity Installed	1.40 MW(th) – Dry Cooler
% of Annual Heating Energy Source from Geoexchange	100%
% of Annual Cooling Energy Source from Geoexchange	75%

5.2.0.Generation - Geoexchange & Supplemental Systems

The Central DE plant, located within the ECC “Block 4” building, includes heat pumps integrated with a geoexchange system that will serve the base heating, domestic hot water, and cooling loads and be supplemented with electric boilers and dry coolers for peak heating and cooling loads,

respectively. The system will also consist of natural gas generators to facilitate electrical peak load shedding and enhance system resiliency.

The boreholes of the geoexchange system are located underneath the footprints of each of the buildings. The geoexchange bore field will be phased to meet the demands of the district and installed in alignment with development construction timelines. To date, two buildings in the community have been designed and are under construction, totaling over 100,000 m^2 of floor area. Enwave has built the first phase of the geoexchange system totaling 190 boreholes. At full build-out, the project is expected to require a total of 625 boreholes.

5.2.1.Distribution – 4-Pipe System (5th Generation DE)

The project consists of a 4-pipe DPS comprised of hot water and chilled water supply and return piping. The distribution piping delivers thermal energy to the end-users via an ETS in each building.

The system also has an additional pair of distribution pipes, geoexchange supply and return lines, to connect the geoexchange borefields installed below each building throughout the precinct. This brings the total distribution to 6 pipes – hot water supply/ return, chilled water supply/ return, and geoexchange supply/ return.

5.2.2.End-Use – Energy Transfer Station

Each end-user site interfaces with the DE system through an ETS. The ETS consists of heat exchangers for space heating, space cooling and domestic hot water (DHW), metering, valves, controls and other ancillaries. Each building's space heating and cooling will be served by fan coil systems with larger units serving the corridors and common spaces. The building thermal loads will be connected by a four-pipe system that connects to the ETS, which receives/rejects heat to the central DE plant via the DPS.

5.3. Rationale for a 4th Generation DE System

A 4th Generation DE Geoexchange System was selected for the ECC Precinct for the following reasons:

- The partnership with the City of Toronto motivated a willing host for the central plant. Centralizing thermal energy production at end-use temperatures allowed for thermal energy to be delivered via customer ETSs, driving significant space savings and operational simplicity for the end-user.

- The central plant allowed for the ability to take full advantage of the diversity in loads in selecting equipment sizes, resulting in a ~20% reduction in installed cooling capacity and a ~10% reduction in installed heating capacity based on design loads. This benefit grows further when considering the total heat pump capacity that would be required for the alternative 5th generation solution with in-suite heat pumps installed at each site.

- The central plant facilitated the ability to integrate supplemental capacity (such as dry coolers and electric boilers) to centrally manage any geoexchange load imbalance over the life of the system. This allowed for the geoexchange system to be "right sized" to optimize

energy and emission performance with operating and capital costs, as the supplemental equipment was designed to address the system redundancy needs.

- Economies of scale were realized through purchasing fewer, large capacity units.
- Centralized operations offered increased operational flexibility to optimize system efficiency.
- Reduced operations and maintenance costs by procuring contracts at scale.
- Central plant operation allowed for the ability to integrate generators for electrical load shed. Through this, an operational strategy was developed to participate in demand response programs through the electrical system operator which drove significant operating cost savings for the plant.
- Provides enhanced redundancy to the community as back-up power for the thermal energy system can be provided centrally.

6. Springwater Single Family Home Community – 5th Generation DE Geoexchange System

6.1. Development Overview

The Springwater is a single-family home community located in Markham, Canada. The development consists of 312 single family homes, including townhomes and detached homes and ranging in size from 170 m^2 to 290 m^2. Refer to Figure 4 for a conceptual plan of the Springwater development.

The Springwater geoexchange system was developed collaboratively between Mattamy homes Canada, Enwave Energy Corporation, and the City of Markham. For the City of Markham, the project offered an opportunity to demonstrate that near net-zero emission heating and cooling for single family homes was possible at no additional cost compared with the business-as-usual HVAC.

6.2. Technical Solution Overview

A 5th Generation DE Geoexchange System was selected to serve the Springwater community. The novel system consists of a single-pipe, low-temperature ambient system with distributed vertical geoexchange boreholes and ground-source heat pumps (referred to as in-suite heat pumps) installed at each end-user site, thereby eliminating the need for a central plant. The result is a system that achieves over a 90% reduction in greenhouse gas emissions compared to traditional in-home heating and cooling systems. Refer to Table 3 for a summary of the system component capacity, and Figure 5 for an overview of the system components.

Figure 4: Springwater Community Concept Plan. (CondoNow, 2024)

Table 3: Springwater DE System – Component Capacity Summary

Component	**Details**
Geoexchange Boreholes	144 at 244 m
Heat Pump Capacity	312 in-suite heat pumps ranging from 5kW to 10kW (Estimated total of 2.3MWth)
Supplemental Heating Capacity Installed	In-suite heat pumps include 100% resistance back up
Supplemental Cooling Capacity Installed	N/A
% of Annual Heating Energy Source from Geoexchange	100%
% of Annual Cooling Energy Source from Geoexchange	100%

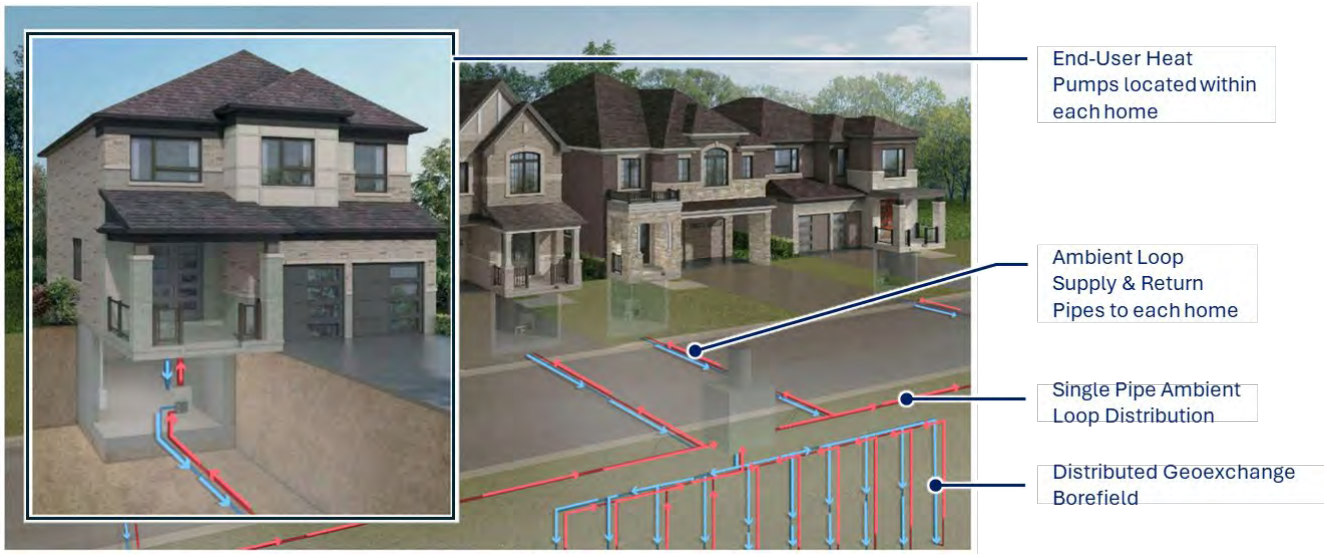

Figure 5: Springwater Geoexchange DE System – Components Diagram

6.2.1. Generation - Geoexchange overview

Heating and cooling energy for the Springwater community is provided exclusively from the distributed geoexchange system. Geoexchange boreholes are installed throughout the public right-of-way, in arrays of 12 boreholes drilled to a depth of 259 m each. Each borehole array collects in a buried vault that houses pumps for circulation within each array. In total, there are 12 borehole arrays and pump vaults, making up a total of 144 boreholes throughout the system. Each borehole array injects/ rejects thermal energy at strategic locations throughout the ambient loop distribution in order to maintain sufficient temperature throughout the loop.

6.2.2.Distribution – Single Pipe Ambient Loop System (5th Generation DE)

The single pipe ambient system runs in a loop throughout the community, spanning over 2.9 km. There are four distribution pumping vaults distributed throughout the system that maintain sufficient flow and pressure throughout. The loop temperatures vary annually between -3 and 32 ºC depending on the time of year. Refer to Figure 6 for the Ambient Loop Distribution diagram.

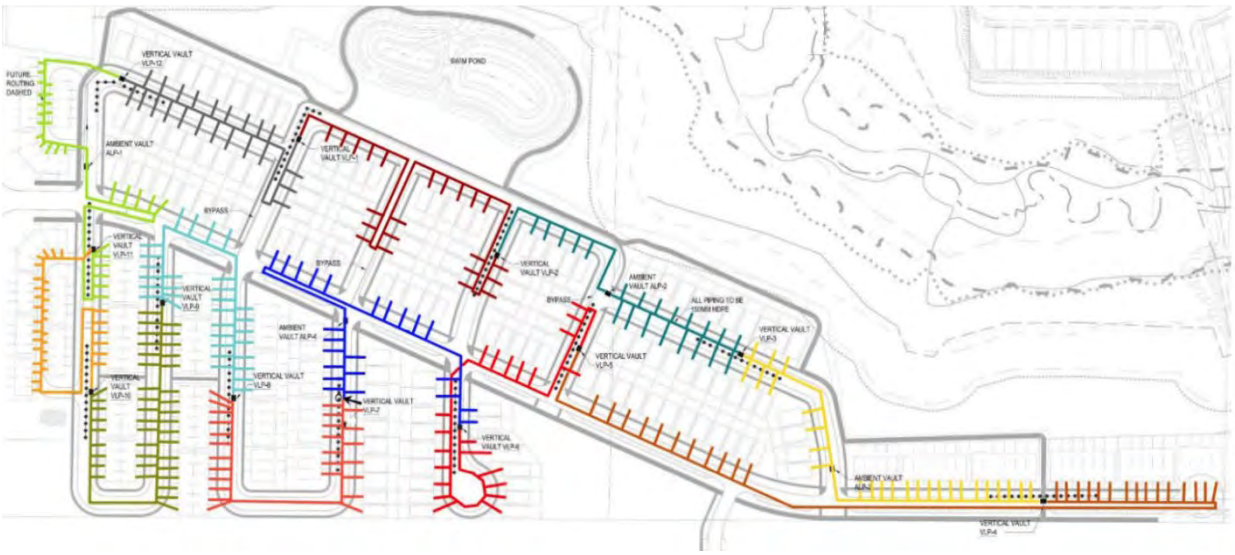

Figure 6: Springwater Geoexchange DE System – Ambient Loop Distribution Diagram

6.2.3.End-Use – Water-to-Air Heat Pumps

Water-to-Air heat pumps located within each home provide space heating and cooling throughout the year. Each home has its own circulation pump to pull in water from the distribution loop as required. This gives each end-user full flexibility to control their own setpoint and operate the system in heating and cooling mode as they see fit.

6.3. Rationale for a 5th Generation DE System

A 5th Generation DE Geoexchange System was selected for the Springwater Community for the following reasons:

- The distributed heat pump system allowed for the elimination of a central plant. The pumping system was installed in buried vaults located in the public right-of-way. This strategy ensured all system infrastructure was installed below grade, allowing the developer to maximize sellable land.

- Partnership with the City of Markham facilitated the coordination of the DE system with other utilities in the public write-of-way. Given the city's support, all system infrastructure was able to be located in the public right-of-way, including distribution, the geoexchange bore field, and pumping vaults. Once again, this maximized the developer value proposition to ensure no sellable land was impacted by the DE system development.

- Geoexchange was used as the only source/ sink of thermal energy for space heating and cooling. This maximized the value associated with an ambient loop system – removing all noisy and visible equipment above grade.

- Given the small size of each end-user served, space savings associated with centralizing thermal energy generation would be immaterial if any. This further supported the case for an ambient loop system.

- The development electrical service was planned at 208V, typical of a residential community. This added further cost and space requirements to aggregating loads into a central plant, once again supporting the case for a distributed ambient loop type system.

- The developer did not want any geoexchange infrastructure located within the private parcels slated for sale. This forced all geoexchange borefield arrays to be located within the public right-of-way. Given this constraint, it naturally led to a distributed system with multiple geoexchange injection points through the ambient loop system compared to "home running" long geoexchange distribution piping back to a central plant for thermal distribution.

- The single-pipe ambient loop system facilitated through the distributed geoexchange concept drove capital cost savings compared to a 4-pipe system required in a 4th generation DE system.

- Given the smaller scale of the system, significant operating and capital cost benefits would not be realized that would justify centralizing thermal energy production.

7. Conclusion

This paper aims to bring to light the practical considerations when considering the use of 4th generation and 5th generation DE systems integrating geoexchange. Much like most of the conversation the exists around the energy transition today, there is no one-size-fits-all approach. Each project context needs to be reviewed and the benefits and drawbacks of each type of system considered to determine the highest value approach. Further, there are more things to consider beyond just the quantifiable techno-economics of each system, but also the often hard to quantify, qualitative aspects of each system such as their impact on space, operational complexity, and resiliency.

In summary, the factors favoring the installation of a 4th Generation DE Geoexchange System over a 5th Generation system are driven primary by the value proposition associated with centralizing thermal energy generation. In our experience, 4th Generation systems win out when realizing high value in aggregating loads to reduce overall system capacity size, achieving scale where operating strategies can be implemented that justify the added cost and complexity, and where providing significant end-user benefits such as space savings and operational simplicity are perceived as high value.

Acknowledgement

The case studies presented in this paper are based on the experience and insights gained by the Enwave team in working with our many developer, municipal, consultant, and contractor partners who supported us in the development of these next generation DE systems. A big thank you to the municipalities whose low carbon ambitions have been the catalyst for the development of these systems, and to the developers who are taking action and leading the way by adopting these systems into the communities they build.

REFERENCES

Bolin, G. et al., 2022. *Building decarbonization: How electric heat pumps could help reduce emissions today and going forward.* [Online] Available at: https://www.mckinsey.com/industries/electric-power-and-natural-gas/our-insights/building-decarbonization-how-electric-heat-pumps-could-help-reduce-emissions-today-and-going-forward

CondoNow, 2024. *Springwater Markham.* [Online] Available at: https://condonow.com/Springwater-Markham

Delmastro, C. & Chen, O., 2023. *Buildings.* [Online] Available at: https://www.iea.org/energy-system/buildings

Fulton, M. R. & Thomas, A. R., 2023. *Overview, Facilitation, and Strategies Involving Municipal Geothermal District Energy systems in Ohio,* s.l.: Maxine Goodman Levin School of Urban Affairs.

Gudmundsson, O., Schmidt, R.-R., Dyrelund, A. & Thorsen, J. E., 2022. Economic comparison of 4GDH and 5GDH systems - Using a case study. *Energy.*

Gudmundsson, O. & Thorsen, J. E., 2021. *THE GENERATION BATTLE – 4th versus 5th generation of District Heating.* [Online] Available at: https://dbdh.dk/the-generation-battle-4th-versus-5th-generation-of-district-heating/

Kranzl, L. et al., 2022. *Renewable space heating under the revised Renewable Energy Directive,* s.l.: European Union.

Lund H, W. S. W. R. S. S. T. J. H. F. M. B., 2014. 4th Generation District Heating (4GDH): Integrating smart thermal grids into future sustainable energy systems. *Energy,* pp. 1-11.

Mathiesen BV, W. C. N. S., 2023. *Heat Matters: The Missing Link in REPowerEU,* s.l.: Aalborg University.

Mirabelli, J., 2021. *Housing Now Bringing Over 1,000 Affordable Units to Etobicoke Centre.* [Online] Available at: https://urbantoronto.ca/news/2021/02/housing-now-bringing-over-1000-affordable-units-etobicoke-centre.44164

Revesz, A. et al., 2020. Developing novel 5th generation district energy networks. *Energy.*

The Building Decarbonization Coalition (BDC), 2024. *Thermal Energy Networks.* [Online] Available at: https://buildingdecarb.org/initiatives/tens

U.S. Energy Information Administration (EIA), 2022. *Geothermal explained: Geothermal heat pumps.* [Online] Available at: https://www.eia.gov/energyexplained/geothermal/geothermal-heat-pumps.php

UN Environment Programme, 2019. *District energy: a secret weapon for climate action and human health.* [Online] Available at: https://www.unep.org/news-and-stories/story/district-energy-secret-weapon-climate-action-and-human-health

Wiltshire, R., 2015. *Advanced District Heating and Cooling (DHC) Systems.* s.l.:Elsevier Science & Technology.

Rangárveita - Small District Heating in the South Part of Iceland - Future Master Plan

Heimir Hjartarson, Egill Maron Thorbergsson and Thráinn Fridriksson

Veitur

Keywords

Heating, Geothermal, Rangarveita, Master Plan, Roadmap, Veitur

ABSTRACT

Rangárveita District Heating Utility (RDHU) harnesses geothermal energy from four main production wells—LL-04 and LL-06 in Laugaland, boasting temperatures around 96°C, alongside KH-36 and KH-37 in Kaldárholt at approximately 67°C. Additionally, GN-01 at Laugaland serves both as a reinjection well and occasionally as a producer. This infrastructure supports heating for homes in Ásahreppur, Hella, Hvolsvöllur, Gunnarsholt, and areas along its 35 km main supply pipeline, delivering about 3 million cubic meters of hot water annually. With demand growing by roughly 1.3% each year the RDHU has a challenge to support regional heating needs.

As communities expand, Veitur is tasked with ensuring the scalability of its district heating systems to meet increasing demands. Accurate forecasting and strategic planning for resource expansion and pipeline enhancements are crucial. To this end, Veitur has launched "Resource for the Future" projects for each of its district heating systems, aiming to assess and plan for future needs effectively.

Investment decisions, particularly those concerning geothermal exploration and capacity expansion, are based on comprehensive analyses of potential hot water sources and their integration into the existing network. These long-term plans, spanning over 50 years, are informed by detailed evaluations, including AHP (Analytic Hierarchy Process) analysis. This process helps pinpoint optimal geothermal resource development opportunities and their alignment with current infrastructure, thereby guiding strategic investments.

The project presents a systematic exploration of geothermal resource development options for Rangárveita, assessed through AHP analysis to ensure their compatibility with existing transport pipelines. The findings serve as a crucial foundation for Veitur's investment strategies, ensuring that the utility's capacity to meet future heating demands remains robust and sustainable.

1. Introduction

Rangárveita District Heating Utility (RDHU) is owned by Veitur ohf., a subsidiary of Reykjavík Energy. The RDHU was established by the municipalities in Rangárvallasysla, South Iceland, in 1981 to serve, mainly the small towns of Hella and Hvolsvöllur and also the rural areas in the vicinity of the main pipeline. Reykjavík Energy acquired the RDHU in 2005 and Veitur has been responsible for the operation of the RDHU since 2014.

Initially, the RDHU was run on a single production well at Laugaland í Holtum, located about 10 km NW of Hella and 22 km NW of Hvolsvöllur. In 2000 a second geothermal resource, at Kaldárholt, was taken into production and connected to the RDHU via a 12 km long pipeline. After the addition of the Kaldárholt field a number of users in the rural areas in Rangárþing ytra and Ásahreppur were connected. As of today, there are two production wells at each geothermal area, LL-04 and LL-06 in Laugaland and KH-36 and KH-37 in Kaldárholt. Overview of the RDHU is shown in Figure 1 (Kristjánsson and Tómasdóttir 2024).

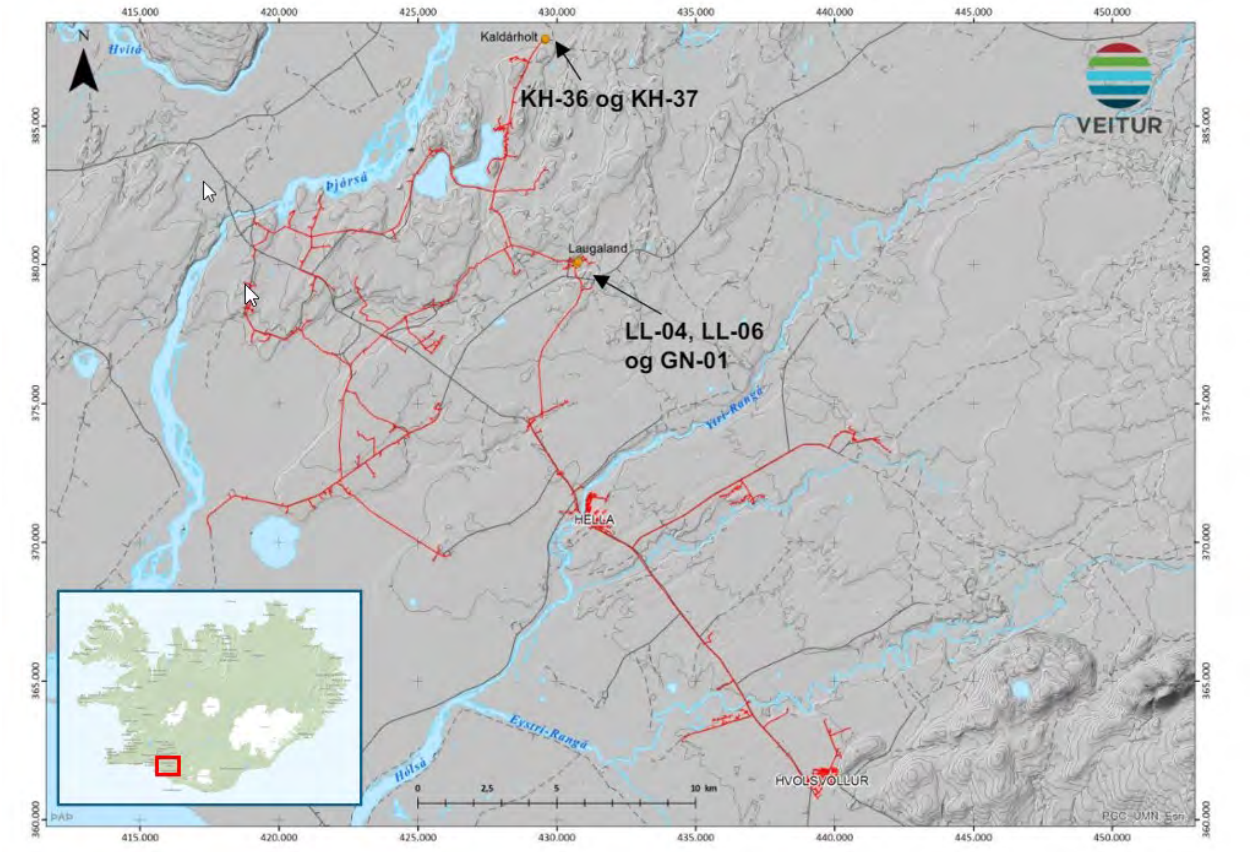

Figure 1: Overview of RDHU network. Red lines are district heating pipes. Grey lines are roads. Wells KH-36 and KH-37 in Kaldárholt are shown as wells LL-04, LL-06 and GN-01 in Laugaland

2. Current status and challenges

One of the main challenges of the RDHU are the relatively long distances between the production areas and the load centers. This was already a challenge in the beginning when production started at Laugaland. The length of the main and secondary transport pipelines further increased when the

Kaldárholt field was connected. Long pipelines pose a challenge for district heating utilities where demand is growing because if the pipes are too large heat loss will be a problem and if the pipes are too small, they will need to be scaled up frequently as demand grows, which is very costly.

To further complicate things for the RDHU, neither of the two geothermal resources used for the system are optimal production fields. While the Laugaland field is hot, 95 to 97°C, the productivity of the field is limited resulting in massive drawdown in response to production and long-term water level drop if annual production exceeds some 15 l/s on average. The Kaldárholt field, on the other hand, is very productive with very little drawdown in the reservoir at annual production levels in excess of 80 l/s but there the problem is relatively low temperature of only ~65°C (Kristjánsson and Tómasdóttir 2024).

The RDHU has been operated at close to full capacity for the last few years. As demand grows in Hella and Hvolsvöllur it is critical to add more capacity in the near future. At this time no additional geothermal resources in the vicinity of the RDHU have been confirmed through deep drilling but several prospective resources have been explored with surface investigations and shallow, temperature gradient drilling. The purpose of this project is to define a road map for the expansion of the RDHU in the next decades. While this project has a strong up-stream focus, i.e. the main objective is to identify the most feasible geothermal resources, it also must consider the necessary expansions of the transport capacity in the system needed for each potential resource.

In Figure 2 is a simplified schematic of RDHU network which show how two production fields and the temperature and transmission capacity restrictions. The western area of the utility in Ásahreppur relies solely on water from Kaldárholt, which is relatively cold (65°C) and cools considerably before reaching customers. Laugaland mixes Kaldárholt water with hotter water from Laugaland (95°C), but due to limited production capacity, the output temperature remains relatively low (73°C). During cold spells, the transmission capacity is fully utilized between Kaldárholt and Laugaland, as well as between Hella and Hvolsvöllur, leading to unmet demand and the closure of swimming pools.

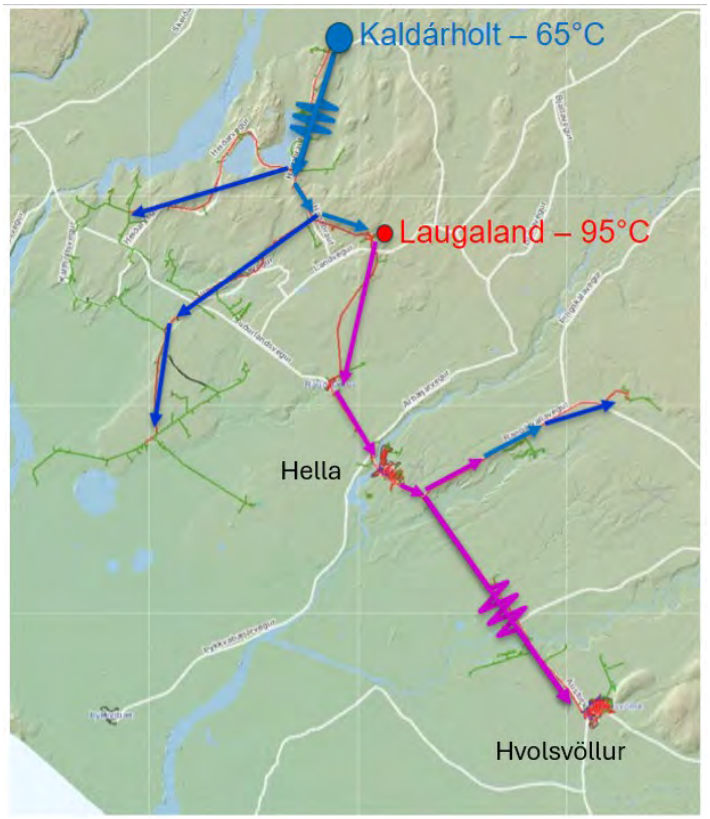

Figure 2: Simplified Schematic of RDHU distribution network, the temperature in the system is indicated with color change and transmission capacity restrictions indicated with zik zak line

3. Purpose and scope

The Rangárveita Future Master Plan (Roadmap) is a strategic initiative aimed at evaluating the current state of resources and predicting future hot water demand for the RDHU from 2023 to 2070. This project aims to prioritize actions to improve the resource status of the utility and provide support for further strategic planning.

The primary goal is to assess the resource status of Rangárveita, estimate future demand for hot water, and identify the most suitable energy supply options. This information will guide the prioritization of actions to enhance the resource status of the utility. The project does not aim to fix decisions or exact timelines but rather to support further strategic planning for the district heating system's infrastructure development.

In order to prioritize the financial resources of the RDHU it is important to compare the potential additional geothermal resources before Veitur invests in costly deep exploration drilling. The most important parameters to consider for that comparison include the expected properties of the geothermal system in terms of temperature and productivity and the location of the geothermal fields with respect to the pipelines of the RDHU. The location will affect the feasibility of utilization in two ways; a) it will have direct bearing on the cost of connection to the RDHU main pipeline and b) the location of the connection point with the main pipeline will determine how the diameter of the main pipeline needs to be scaled up.

The project described in this paper involved the development of a demand forecast for the RDHU and AHP analysis of different additional heat resources for the utility. Below we briefly describe the methodology used for the demand forecast, the AHP analysis of the 12 to 15 options considered and the resulting strategic plan for geothermal exploration, capacity addition and scaling up of transport pipelines for the RDHU.

3.1 Past Strategic Projects

Previous strategic projects identified urgent resource shortages and recommended increasing production capacity. Efforts included installing deep pumps and improving electrical infrastructure for borehole pumps. However, these measures have only temporarily increased production capacity without fully resolving the transportation constraints.

Efforts to secure additional resources for Rangárveita have been ongoing since the utility's inception. Various strategies have been proposed over the years, including deep drilling at Kaldárholt and linking to geothermal fields on Skeið. The most recent strategic project in 2020 suggested several actions, such as utilizing excess water from existing privately owned wells and exploring new geothermal sites. These historical efforts provide a foundation for current and future initiatives aimed at enhancing the utility's resource base.

3. Future Demand Scenarios

Predicting the future is challenging. Demand forecasts estimate potential demand development. Veitur regularly update short- and long-term demand forecasts. This project looks 50 years ahead to ensure sufficient hot water for customers. Since most resource-enhancing actions take many years or even decades, timely forecasts are crucial.

Forecasts for future demand are based on historical data and population growth trends. These projections help identify potential future demand increases, ensuring timely implementation of resource-enhancing actions. The forecasts consider various factors, including historical usage patterns, population growth, and planned development in residential and tourism sectors. Key limitations include:

- High system complexity and missing data in some areas.
- Many meters have only about 5 years of data, too short to analyze trends reliably.
- In areas with longer usage history, population and peak power usage are less stable.
- Population forecasts and municipal scenarios conflict with each other and historical growth.
- Demand exceeds production and transportation capacity during cold spells, meaning historical peaks may not reflect actual demand, potentially leading to underestimated forecasts.

To simplify the problem future demands scenarios where only produced for the RDHU after Laugland where mixed water from Kaldárholt and Laugland is distributed to the larger municipalities of Hella and Hvolsvöllur. In Figure 3 is presented historic demand peaks and predictions for future demands in the RDHU after Laugaland and the result show that the RDHU needs to get more geothermal resources to cover increased demand for hot water in the coming years.

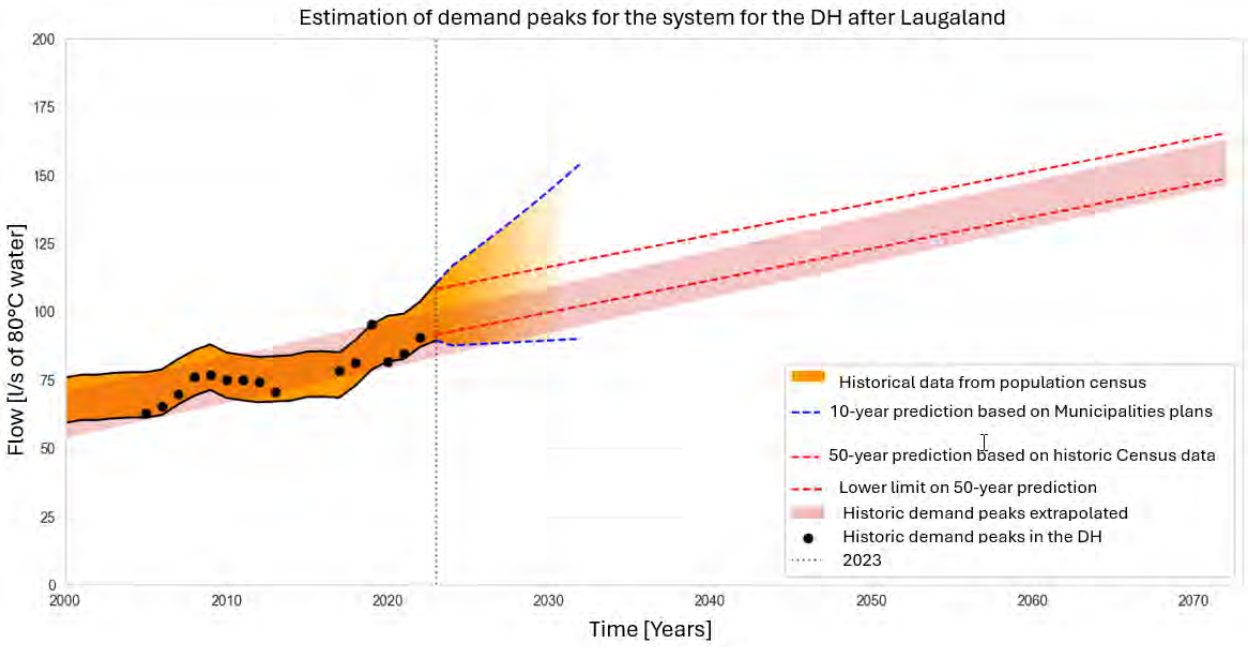

Figure 3: Historic demand peaks and predictions for future demands in the RDHU after Laugaland in standard liters per second. The red shaded area is linear extrapolation prediction based on historic census and demand peaks. The blue dotted lines show possible future utilization based on municipalities plans. The flow of geothermal fluid is standardized to 80°C thermal equivalent of 80°C for easier comparison.

In Figure 3 the flow data is standardized to represent flow of thermally equivalent amount of 80°C hot water, called "standard liters per second" or sl/s. The temperature of the hot water in the RDHU varies by location, day, and season. To standardize the flow time series, the thermal power that users can obtain from the water is calculated, assuming they return it at 30°C. The equation used is following:

$$R_{80°C} = R * \frac{T - T_{\text{return}}}{80 - T_{\text{return}}} \quad (1)$$

were $R_{80°C}$ is the equivalent flow of same thermal power if the actual water temperature were 80°C, R is the measured flow, T is the actual water temperature and T_{return} is the estimated temperature of the return water, or 30°C.

4. Transmission Capacity Issues

Transmission capacity is a critical challenge for Rangárveita. The main bottlenecks are the pipelines between Kaldárholt and Laugaland and between Hella and Hvolsvöllur, as is presented in Figure 2. Simulations indicate that the maximum flow from Kaldárholt is nearing its limit, and similar constraints exist between Hella and Hvolsvöllur. Enhancing transmission capacity involves significant investment, and any increase in resource acquisition must consider these transmission limitations to avoid further bottlenecks.

5. Geothermal Resource Options

The strategic project evaluated 13 potential geothermal/thermal resources for the RDHU shown on Figure 4 and presented in Table 1. These resources were assessed based on cost, resource risk, expected temperature, and potential benefit to users. The analysis aimed to identify the most feasible options for increasing resource availability.

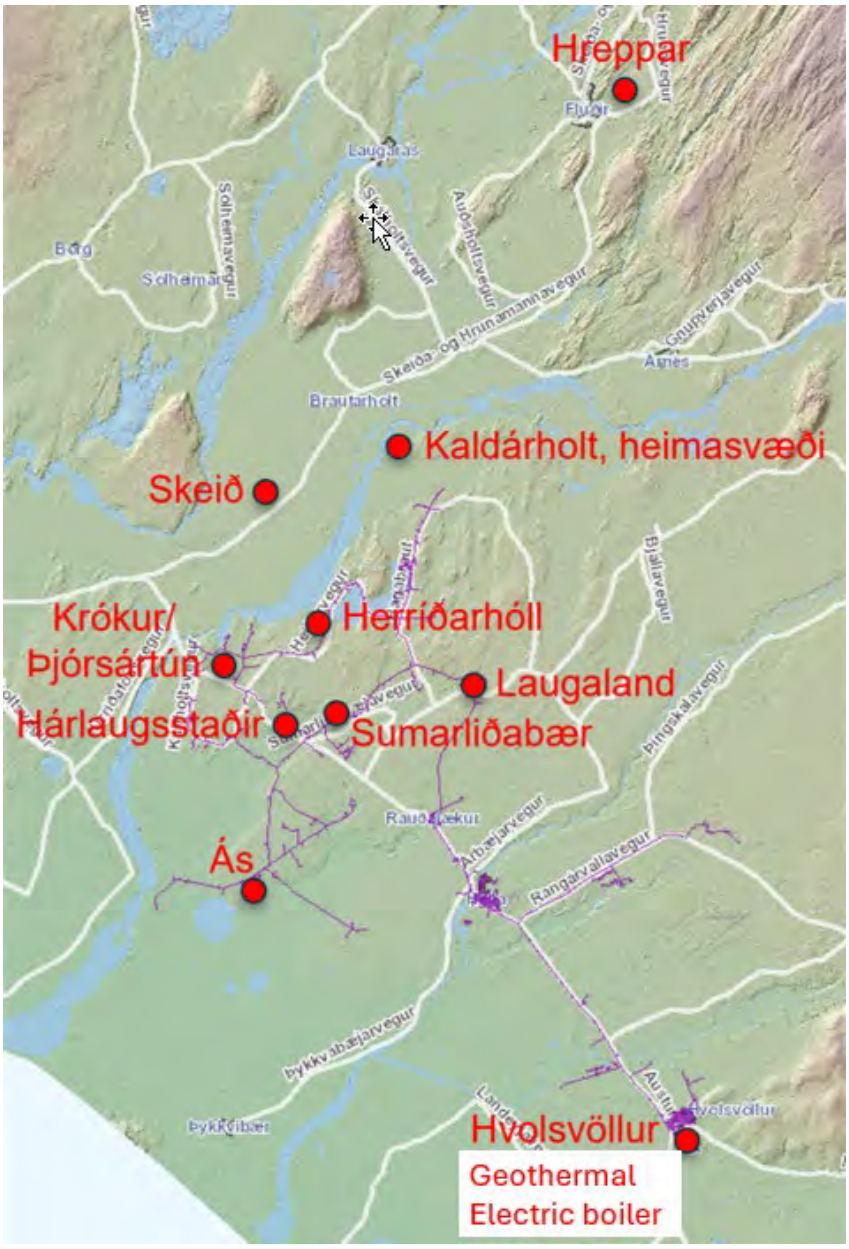

Figure 4: Overview of potential Geothermal options for Rangárveita District Heating Utility (RDHU).

Table 1: Geothermal Resource options that were evaluated and assumptions

Geothermal resource option	Potential capacity (l/s)	Probable temperature (°C)	Distance from DHS (km)	Next steps (excluding Connection to DH)
Hreppar	>50	100	22	Drilling and commissioning
Skeið	25	80	12	Exploration, drilling and commissioning
Kaldárholt, heimasvæði	25	70	3	Drilling and commissioning
Herríðarhóll	25	70	0,2	Exploration, drilling and commissioning
Krókur/Þjórsártún	25	70	1,3	Exploration, drilling and commissioning
Hárlaugsstaðir	25	70	1,8	Exploration, drilling and commissioning
Sumarliðabær and well SB-19	6	72	0,2	Commissioning
Sumarliðabær and new well	20	72	0,2	Exploration, drilling and commissioning
Ás	25	70	1	Exploration, drilling and commissioning
Laugaland, reinjection well	12,5	95	1	Drilling and commissioning
Laugaland, production well	25	95	1	Drilling and commissioning
Hvolsvöllur new geothermal field	25	70	2,5	Extensive exploration, drilling and commissioning
Hvolsvöllur electric boiler	10	80	0	Install electric boiler and connect return water

6. AHP Analysis

The Analytic Hierarchy Process (AHP) was used to rank the geothermal resources and heating options presented in Table 1. This analysis considered cost, resource risk, expected temperature and capacity, user benefit and interest in collaboration. The weight for each factor is presented in table Table 2 and then further explained.

Table 2: The weight for each factor used in the AHP analysis

Factor	Weight
Cost	10
Resource Risk	3
Expected Temperature	2
Estimated Capacity	2
User Benefit	2
Interest in Collaboration	1

6.1 Cost

Highest score (1) for the option with the cheapest cost per liter per second and lowest score (0) for the option with the most expensive cost per liter per second. Linear scaling between highest and lowest scores for all other options. All costs for geothermal exploration, development, and transportation are spread over the depreciation period of investments, with operating costs calculated as a fixed percentage of investment. Additional electricity costs for electric heating options are based on heating 10 l/s for 30 days per year. For a new geothermal field near Hvolsvöllur, the cost of upgrading the transport pipeline needed to handle more flow is deducted. This does not apply to electric heating options, which are considered temporary solutions.

6.2 Resource Risk

Highest score (1) where temperature and capacity are proven by drilling (and for electric heating options). 0.75 if geothermal resources are confirmed by drilling but further drilling is needed to verify additional capacity. 0.5 if surface activity provides strong indications of a usable resource. 0.25 if surface activity provides weak indications of a usable resource. 0 for areas with no surface activity.

6.3 Expected temperature

The score for expected temperature is presented in Table 3.

Table 3: Expected temperature scoring system

Temperature Range	Score
≥90°C	1.0
80-90°C	0.75
70-80°C	0.5
<70°C	0.0

6.4 Estimated Capacity

Highest score (1) for options that cover half of the expected increase in demand for the utility by 2070 (30.5 l/s at 80°C), with linear scaling down to a score of 0 for 0 l/s. All options with expected capacity over 30.5 l/s receive a score of 1.

6.5 User Benefit

The proportion of users benefiting from the thermal option in the utility, multiplied by the difference between the expected temperature and 65°C, multiplied by the expected capacity up to 30.5 l/s. The highest value receives a score of 1, scaled linearly down to 0.

6.6 Interest in Collaboration

Highest score (1) for resources managed by the utility; 0.75 for options where responses have been positive towards RDHU collaboration requests; 0.5 for options where geothermal rights are held by RDHU but the landowner is unwilling to collaborate; 0.25 for options where collaboration has not been sought; 0 for negative responses to RDHU collaboration requests.

6.7 AHP results

The AHP results is presented in Table 4. The most feasible option is to increase production capacity in Laugaland, either through increased sustainable production (ranked 1st) or enhanced reinjection (ranked 3rd). Utilizing excess water from the production well at Sumarliðabær also ranks very high (2nd place) due to the absence of risk and low connection costs, despite the landowner's lack of interest in collaboration. The next ranks include four low-temperature areas in the western part of the service area: Kaldárholt heimasvæði, Herríðarhóll, Sumarliðabær, and Ás. The unknown geothermal potential near Hvolsvöllur ranks 8th, despite complete uncertainty about its existence, primarily because of the significant benefits if the transmission line between Hella and Hvolsvöllur does not need to be upgraded. Following this are the expected low-temperature areas in the western region at Hárlaugsstaðir and Krókur/Þjórsártún, then connections to geothermal areas in Hreppar and Skeiðar, with electric heating options in Hvolsvöllur ranking last.

Table 4: Results from the AHP analysis. Flow data is standardized to represent flow of thermally equivalent amount of 80°C hot water, called "standard liters per second" or sl/s

Geothermal Resource Option	Weighted AHP score	USD/sl/s	KUSD
Laugaland production well	16.0	650	3,065
Sumarliðabær and well SB-19	14.4	200	145
Laugaland reinjection well	14.3	1,000	2,471
Kaldárholt, heimasvæði	12.6	1,170	3,500
Herríðarhóll	10.5	1,050	3,022
Sumarliðabær new well	10.3	1,250	3,022
Ás	10.1	1,160	3,377
Hvolsvöllur new geothermal field	10.1	850	2,377
Hárlaugsstaðir	9.7	1,280	3,732
Krókur/Þjórsártún	9.4	1,200	3,507
Hreppar 50 l/s	9.3	2,750	29,913
Skeið	8.5	2,310	8,783
Hvolsvöllur electric boiler	7.3	2,490	725

7 The Future Master plan and Recommendation

For the RDHU multiple efforts are needed to improve the resource situation. Test drilling is under preparation at Laugaland aimed at increasing the sustainable production capacity from the system and/or improving the reinjection process into the system. It is essential to explore geothermal resources closer to Hvolsvöllur because if successful, costly measures to upgrade the transmission line between Hella and Hvolsvöllur can be avoided. While this exploration is ongoing, it is necessary to set up temporary electric heating of return water in Hvolsvöllur. Additionally, it is crucial to seek more reserves for the utility since the current reserve shortage is a fact and it is not viable to wait for the results of geothermal exploration in Hvolsvöllur or exploratory drilling in Laugaland. Investing in geothermal exploration in the western area of the utility is not a waste, as any usable resources found there will benefit the utility's future plans, even if they are not

immediately developed. An improved long-term resource outlook for the utility benefits both the utility and the municipalities it serves. In Figure 5 a proposed roadmap is presented for the next years to addressee the RDHU hot water shortage and in Figure 6 is more specific roadmap for Hvolsvöllur.

- Meet peak power demands for the winter of 2023 to 2024 by increasing the supply temperature from Laugaland. This means increased production in Laugaland over the winter without the need to increase production in Kaldárholt.
- Procure electric heating equipment that can be installed for the winter of 2024/2025. Once this equipment is operational, production in Laugaland can be slightly reduced, but the supply temperature can remain higher than it is now (73°C). It should be noted that production in Laugaland might be aggressive in the coming years.
- Continue geothermal exploration in the western area of the utility:
    - Continue geothermal exploration in Laugaland. The next step is to drill an 800-meter-deep exploratory well in 2024. If successful, it may serve as a production well or otherwise as a reinjection well.
    - Conduct temperature gradient drilling in west area Ás, Hárlaugsstaðir, Herríðarhóll and in Krókur/Þjórsártún. If landowners are willing to cooperate in geothermal exploration and utilization, proceed with temperature gradient drilling in these areas and subsequently select the most promising sites for exploratory drilling.
    - Make every effort to obtain permission from landowners in Kaldárholt heimavæði for exploratory drilling. If this is not successful, expropriation may be necessary to obtain drilling authorization.
- Utilities should seriously investigate how much water is available in Hreppar and at what temperature. Subsequently, a detailed feasibility study, preliminary design, and cost estimate for such a connection need to be conducted. It is essential to know with greater certainty what is available and what it costs if geothermal exploration in the western area of the utility is unsuccessful, so that a connection to Hreppar can be compared with other, less expensive options.
- In the years 2026 to 2027, after geothermal exploration in the western area is completed, a decision can be made on which geothermal area in the western part of the utility is best suited to add more reserves to the utility. If none of the areas we are targeting prove usable, a connection to Hreppar may be the only option. The development and connection of a new area to the utility must be completed by 2030, allowing production in Laugaland to return to sustainable levels.
- Since none of the above measures will solve the transmission problem to Hvolsvöllur permanently, it is recommended to begin geothermal exploration near Hvolsvöllur in 2024. The timeline for these actions is shown in Figure 6.
    - Temporary electric heating of return water in Hvolsvöllur will begin in 2024
    - Apply for exploration permits in the area around Hvolsvöllur (3-5 km radius) with the aim of conducting temperature gradient drilling in the area. If temperature anomalies are found, follow up with exploratory drilling and development if usable geothermal resources are found. These studies must be completed by the end of 2027.

- If geothermal exploration near Hvolsvöllur is unsuccessful, the transmission problem to Hvolsvöllur needs to be solved, whether by upgrading, adding a parallel line, or installing more pumping stations between Hella and Hvolsvöllur.

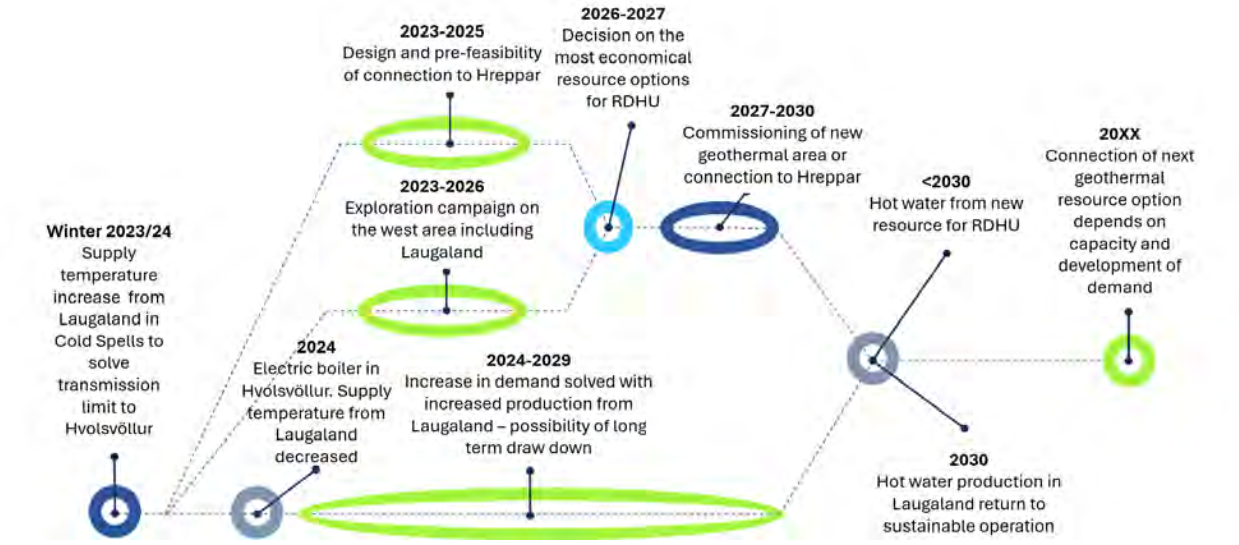

Figure 5: Proposed roadmap for research and actions to support increased demand in the RDHU

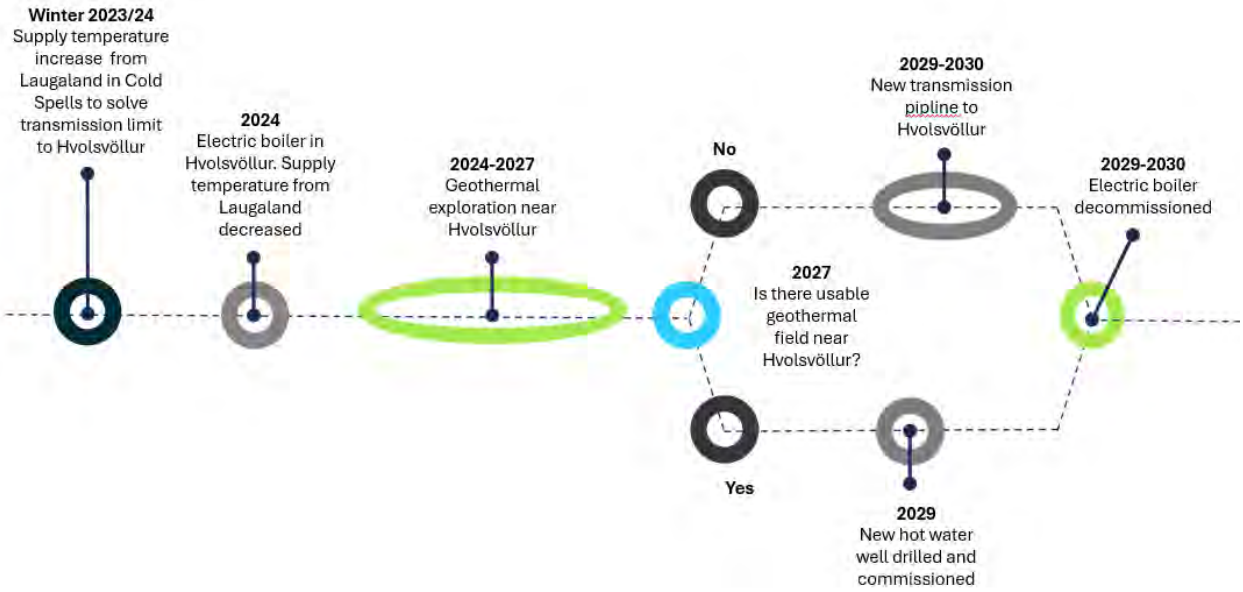

Figure 6: Proposed roadmap for research and actions to support increased demand in Hvolsvöllur

8. Conclusion

The RDHU future master plan provides a strategic framework for addressing the utility's current and future resource challenges. By prioritizing a mix of immediate and long-term actions, the roadmap aims to ensure a reliable and sustainable supply of hot water for the communities served by Rangárveita. Continued research, investment in infrastructure, and strategic planning will be crucial to achieving these goals and securing the utility's future.

The following are short-term actions:

- Increase Production at Laugaland: Implement measures to enhance sustainable production and improve resource stability.
- Geothermal Exploration at Hvolsvöllur: Conduct temperature gradient studies to identify potential geothermal resources.
- Temporary Heating Solutions: Install electric boiler systems to heat return water to address immediate shortages.

The following are the long-term actions:

- Resource Exploration: Continue exploring geothermal resources in the western region and other potential areas.
- Infrastructure Improvements: Upgrade transportation infrastructure to increase capacity and ensure reliable distribution.
- Strategic Partnerships: Engage with stakeholders and landowners to secure agreements for resource development.

REFERENCES

Kristjánsson, B.R., Tómasdóttir, S. "Rangárveita – Vatnavinnsla 2023" *Report No. 2024-016,* Reykjavik Energy/Veitur, Reykjavík (2024) https://eu-assets.contentstack.com/v3/assets/blt5bf0023ca96cf071/blt4ae6518174f57c06/66717f5b37b8d01c5da996ec/2024-016_Rang%C3%A1rveita_-_Vatnsvinnsla_2023.pdf

Grid Value Analysis of Geothermal Systems for End-Use Applications

Jonathan Ho, Hyunjun Oh, Geoffrey Mibei, Matthew Mowers, and Joseph Mowers

National Renewable Energy Laboratory

Keywords

Geothermal Heat Pump, Electrification, Power System Model, Externalities, Valuation, Direct Use, Manufacturing, Decarbonization

ABSTRACT

Fuel based end-uses for residential, commercial, and industrial consumers require a technology change to achieve economy-wide decarbonization. Space heating accounts for 42% of residential and 32% of commercial energy demand, much of which is currently met through carbon emitting fuels. Industrial energy use is heavily fuel based with electricity currently representing 13% of energy demand. Geothermal heat pumps (GHPs) and geothermal direct use can eliminate the need for CO_2 emitting and simultaneously allow for more efficient electrification of end uses. Past work has assessed the impact on total energy costs and generation investments but did not identify specific grid services benefited. Energy usage in residential and commercial structures was assessed by leveraging data from ComStock and ResStock models. These models utilize housing attributes, occupancy patterns, weather data, and sophisticated energy simulations to generate hourly load profiles for individual buildings identified by unique IDs associated with their locations. Industrial sector energy use was evaluated using information from the Manufacturing Energy Consumption Survey (MECS) as well as plant utilization data from the US Census to estimate hourly plant operations. The change in end-use demand for electricity, natural gas, and other fuels was calculated for different technologies that could meet this need. Using the ReEDS capacity expansion model, we produce regional price profiles that capture the grid benefit associated with the amount and timing of energy shifts in the power system from the adoption of geothermal systems relative to other technologies that could meet space heating, space cooling, and process heat requirements. We find that geothermal systems for meeting end-use demand add value to the energy system. In buildings where geothermal systems increase grid costs, these values are offset by reduced fuel costs and benefits to externalities, including emissions and health impacts.

1. Introduction

Decarbonizing energy systems is a key goal for mitigating the impacts of climate change by reducing greenhouse gas emissions. A transition to a net zero carbon electric power system representing 34% of U.S. total energy consumption is a vital component of this strategy having both a substantial amount of existing zero emissions generation and rapid growth in wind and solar. Carbon free electric power can be utilized to support the decarbonization of other sectors that today are heavily dependent on fossil fuels. Electrification plays a pivotal role in this transition by adopting end-use technologies that use electricity directly rather than fuels.

For residential and commercial buildings, space conditioning (heating and cooling) represents the majority of energy consumption. Space heating in the U.S. is primarily met through natural gas furnaces, although the distribution of heating energy sources varies regionally. Space heating accounts for 42% of residential and 32% of commercial energy consumption and is a ripe opportunity for electrification. Industrial energy use is heavily fuel based with electricity currently representing 13% of energy demand. These sectors, including space heating, cooling, and manufacturing process heat, are substantial contributors to U.S. greenhouse gas emissions. Electrification of these end-use applications has broad benefits for which there exist a range of technology solutions.

Geothermal systems offer a promising solution for electrifying these end uses. Geothermal heat pumps (GHPs) can efficiently electrify buildings while maintaining a stable coefficient of performance (COP) even at low temperatures since heat exchange occurs in the subsurface as opposed to ambient air. Cooling with GHPs can also realize efficiency gains over air conditioning (AC). In addition to space conditioning, process heat for manufacturing could be provided through deep direct use and high-temperature heat pumps. These solutions utilizing geothermal systems, are not the only electrification options for end uses. Understanding the relative benefits is important for determining the right solution for a given building end use.

Metrics like the reduced energy consumption and change in CO_2 emissions provide useful comparisons but do not provide a complete picture of a technology's benefits. Applying flat energy prices helps to convey the costs a consumer sees and the net economic value but has similar drawbacks to examining change in energy consumption alone. The cost of operating them is not equally distributed, given small periods of high system stress potentially reflecting a disproportionate share of costs. Reflecting the value to grid considering the timing and quantity of energy shifts is important for providing a comprehensive measure of the grid costs and benefits of an electrification measure. Focusing on energy costs alone excludes the negative externalities associated with CO_2 emissions and health impacts from criteria pollutants.

To address this, there is a need for valuation methods that incorporate a broader range of factors mentioned. Through the inclusion of grid costs, fuel costs, and externalities, we can develop a more comprehensive understanding of the relative value of end-use technologies, leading to more informed decisions and policies that support sustainable and efficient energy systems.

2. Methods

In order to evaluate the relative value of applying geothermal systems we needed to quantify the changes in hourly end use energy consumption for consumers as well as develop a comprehensive measure of value. This section first describes the methods and data sources developed for

quantifying residential and commercial space heating load changes with GHPs. Next, we describe the approaches used to measure manufacturing process heat demand that could be met through heat pumps or direct use. Finally, we describe a method that incorporates changes in electric power costs, fuel costs, and the cost of externalities, including in building CO_2 emissions and health impacts.

2.1 Development of End Use Load Profiles for Geothermal Systems

2.1.1 Residential and Commercial Space Conditioning

ResStock and ComStock are modeling tools that provide hourly end-use load profile information considering the intricacies of the U.S. building stock.

- **ResStock** represents residential buildings (Present 2024)
- **ComStock** represents commercial buildings (Parker 2023)

The tools utilize OpenStudio and EnergyPlus to perform physics-based building energy simulations to generate hourly end use load profiles specific to end use and energy source. Building energy consumption is broken down by specific end use (e.g., space heating) and energy source for meeting that end use (e.g., electricity, natural gas).

A key feature of these tools is the inclusion of upgrades compared to a base building stock representation. An upgrade case models how energy consumption changes with different home improvements. Critically for this analysis these modeling tools include cases where buildings upgrade to air source heat pumps as well as geothermal heat pumps.

For our analysis we identified upgrade scenarios that changed only the building heating and cooling type, making no alterations building envelope improvements. This allows us to directly compare the changes in energy consumption patterns attributable to changing the end use technology used to provide building space conditioning.

In this analysis we compared the base building configuration against a ground source heat pump upgrade.

- Residential: Energy Star geothermal heat pump
- Commercial: Comprehensive geothermal heat pump package (Hydronic GHP, Packaged GHP, or Console GHP)

ResStock and ComStock include end-use load profile (EULP) results for the 2018 actual meteorological year (AMY) as well as a typical meteorological year (TMY). To integrate the data into our power system valuation method, the data needed to be concurrent with a 2012 (AMY). Aligning weather years is important as meteorology impacts the balance of electric power supply through variable renewable energy sources (solar and wind) and the demand through requirements for building space conditioning.

The computational intensity and workload required to run ResStock and ComStock prohibited full simulations specific to 2012 AMY. We developed, in collaboration with developers to the building stock simulation tools, a regression tool using random forest, that could train on available hourly space conditioning end use demand profiles and generate predictions for alternate weather years.

A strength of random forest is that it is well suited to modeling non-linear relationships between inputs (meteorological conditions) and outputs (end use energy demand).

We validated the quality of the random forest-based tool by training it on a prior elease of ResStock which included simulations for both 2012 and 2018 meteorological years. Using 2018 data to train the random forest model we then predicted 2012 space heating and cooling end use energy demand. Comparing the predictions from the regression against the actual ResStock hourly building simulation results, we found a close alignment between the two datasets.

2.1.2 Geothermal Systems for Manufacturing

The U.S. Energy Information Administration (EIA) defines the industrial sector as an energy-consuming sector consisting of any facilities and equipment used for producing, processing, or assembling goods. In 2022, the industrial sector consumed primary energy sources amounting to 28.1 exajoules (EJ) accounting for approximately 35% of the U.S. primary energy consumption (EIA 2021). A total of 76% of the energy consumption in the industrial sector was consumed in the manufacturing sector (mining = 12%, construction = 7%, agriculture = 4%) (EIA 2022). In this section, the manufacturing end-use energy consumption data was analyzed to develop time-varying thermal demand profiles, particularly using the 2018 Manufacturing Energy Consumption Survey (MECS) released in 2021.

The EIA periodically surveys and analyzes the end-use energy consumption in the manufacturing sector (e.g., 2018 MECS, 2014 MECS, 2010 MECS). The end-use fuel consumption database in MECS consists of end-use energy consumptions by 1) net demand for electricity, 2) residual fuel oil, 3) distillate fuel oil and diesel fuel, 4) natural gas, 5) hydrocarbon gas liquids (HGL), and 6) coal for various end-use categories (e.g., process heating, process cooling and refrigeration, conventional boiler) in 82 manufacturing subsectors ranging from Food categorized by the North American Industry Classification System (NAICS) as 311 to Miscellaneous (NAICS = 339). In this study, 65 subsectors were selectively analyzed while duplicated sectors were excluded to avoid any uncertainties. For example, although 3112 Grain and Oilseed Milling category includes seven sub-categories from 311211 Flour Milling to 311230 Breakfast Cereal Manufacturing, the MECS data only includes 311221 Wet Corn Milling among the seven sub-categories. This study therefore excluded 3112 Grain and Oilseed Milling and analyzed 311221 Wet Corn Milling. Among the different end-use categories, this study focused on any energy consumptions for process heating and conventional boiler end-use categories where geothermal heat pump (GHP) and deep direct-use (DDU) applications may supply extensively energy needs. Future research on additional end-use categories, including process cooling and refrigeration and facility HVAC, is recommended to extend potential opportunities the decarbonizing the energy demand using geothermal applications.

As discussed in Oh and Beckers (2023), the end-use energy consumption data is not always allocated to the thermal demand with 1:1 efficiency (i.e., the actual thermal demand can be higher or lower than the energy consumption depending on the system efficiency). To estimate thermal demand, in this study, the end-use energy consumption data was incorporated with different coefficients of performance (COP) in terms of the type of energy sources: COP = 1 for net demand for electricity, COP = 0.8 for natural gas, and HGL, and COP = 0.7 for residual fuel oil, distillate fuel oil and diesel fuel, and coal. For example, energy consumptions for conventional boilers in the 311221 Wet Corn Milling subsector were 1 TBtu by electricity, 8 TBtu by natural gas, and 1

TBtu by coal. However, the estimated thermal demand total was 8.1 TBtu, instead of total energy consumption of 10 TBtu when the different COP factors are taken to account.

Even though the MECS and the U.S. Environmental Protection Agency (EPA) Greenhouse Gas Reporting Program (GHGRP) database have been analyzed for the annual thermal demand in the manufacturing sector by previous researchers (e.g., McCabe et al. 2015; McMillian et al. 2016; McMillan et al. 2021; Oh and Beckers 2023), there are limited resources and publicly available data for hourly- thermal demand profiles based on standardized facility operation hours. This study estimated the hourly thermal demand profiles using average plant operation hours per week data obtained from 2018 Census Quarterly Survey of Plant Capacity Utilization (QPC) data where quarterly statistics on utilization rates and average plant operation hours per week data are available for manufacturing subsectors based on the NAICS codes. As a first step, the number of shifts and operating days were defined for each manufacturing subsector in terms of the weekly average operation hours in the QPC database. The assumptions included one shift represents an 8-hour operation at full capacity from 8 am to 4 pm, and one day can consist of up to three shifts (i.e., full operation during the whole day). There was a one-hour transitional operation at 60% full capacity before and after the operation at full capacity (i.e., the weekly operation hours are allocated to fit one-and two-shifts, or three-shift with five or six operating days per week), and a 20% of full capacity was assumed for non-operating hours. For example, the 2018 QPC for Quarter 1 demonstrates that the average weekly operation hours for the 3112, 5, 6 Grain and oilseed milling, dairy, and animal slaughtering and processing sector was 99.6. In the analysis, the 96 hours were allocated in six operating days (from Monday to Saturday) with two shifts (from 8 am to 12:00 am) for operations at full capacity, while the rest of 3.6 hours was allocated for operations at the 60% transitional and 20% non-operating hours. This process allows us to estimate the time-varying demand shape from 20% to 100% capacity of the facility (Figure 1(a)). Then, the annual total thermal demand estimated for process heating and conventional boiler end uses was incorporated into the demand shape (Figure 1(b)).

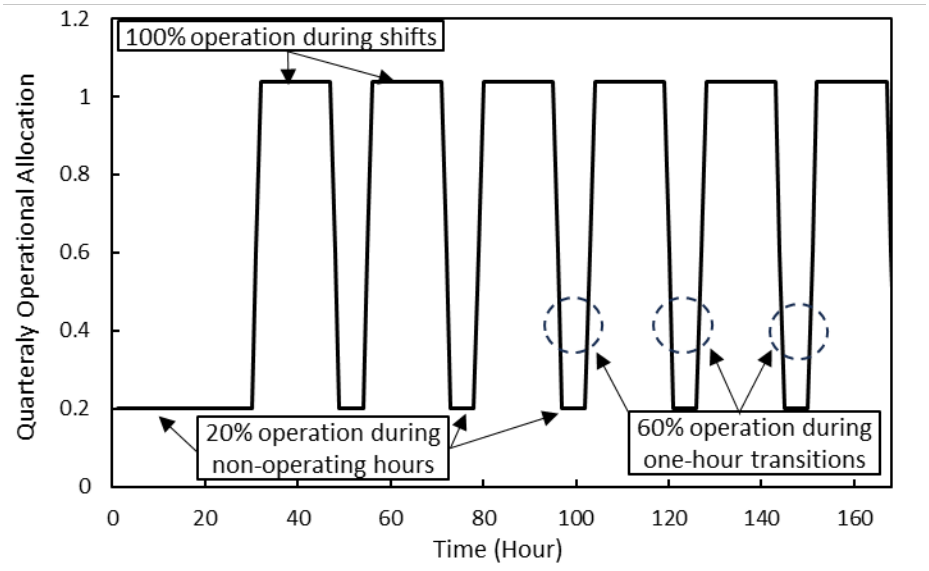

(a)

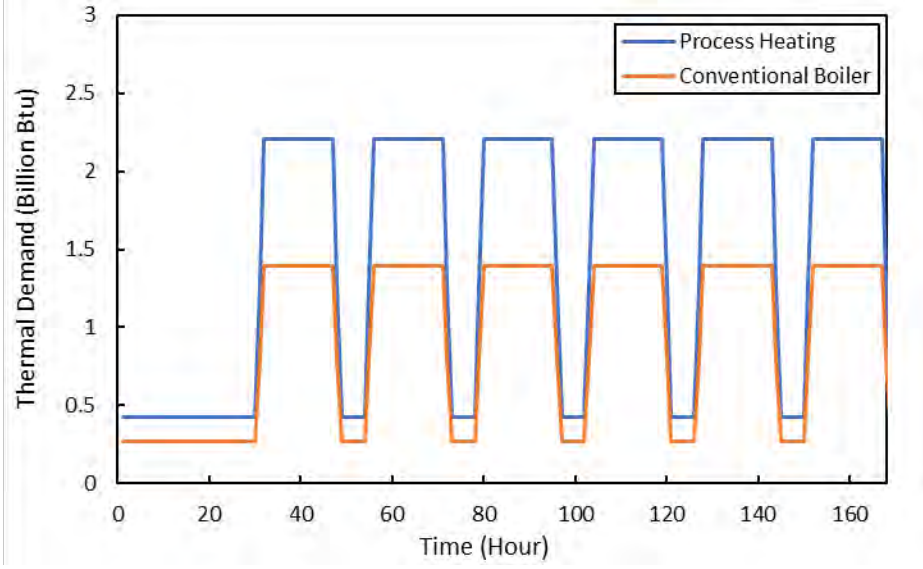

(b)

Figure 1. Manufacturing thermal demand profile for 311221 Wet Corn Milling example subsector: (a) quarterly operational allocation from 20% to 100% and (b) thermal demand profile for process heating and conventional boiler end uses.

In the second step, the thermal demand profiles for each of the 65 manufacturing subsectors analyzed in this study (e.g., Figure 1(b)) were then divided by the number of establishments obtained from 2018 MECS to normalize the demand profiles per establishment, assuming there is no significant difference in energy consumptions among the facilities in the same NAICS categories. For the final step, the electricity consumption by GHP and DDU to supply the manufacturing thermal demand (i.e., normalized hourly thermal demand profile in each subsector) was estimated to generate electric consumption profiles in kWh (hourly electric loads). The DDU estimation was based on correlation models by Oh et al (2024) for the GHP estimates were based on the PANYNJ project (While electricity consumed in the DDU system was assumed as the pumping power to circulate water throughout the deep boreholes at 2.1 km or 3.3 km depth (Oh et al. 2024), those consumed in the GHP system were estimated as a combination of the GHP operational and water circulating pumping power. Figure 2 represents example electricity consumption profiles to supply the estimated thermal demand total in 311221 Wet Corn Milling subsector by GHP and DDU applications.

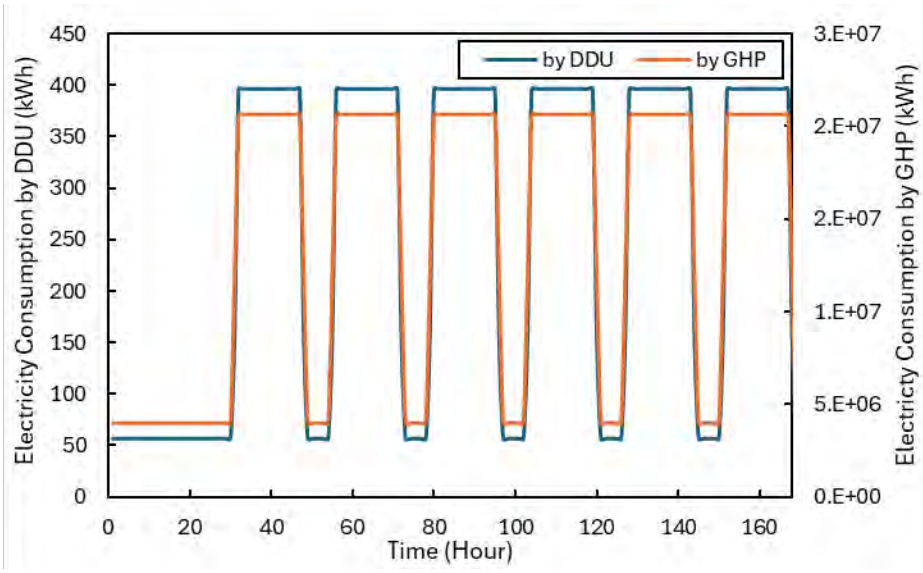

Figure 2. Electricity load profiles by GHP and DDU applications to supply the total thermal demand in 311221 Wet Corn Milling per establishment

2.2 Quantifying Relative Value

2.2.1 ReEDS Background

The Regional Energy Deployment System (ReEDS), developed by NREL, is a capacity expansion model that simulates the evolution of the U.S. power system (Ho 2021). ReEDS considers the electric power demand along with the cost and characteristics of generation and storage technologies that could meet this demand, selecting a mix of technologies that minimizes total system costs. The unique topology of demand, available resources, and transmission infrastructure are included in ReEDS and play a significant role in what decisions are made within the model.

2.2.2 Power System Cost/Value: reValue

Power system simulation tools produce prices that are a direct reflection of resource utilization, and necessary investments support the needs of the system. The prices, composed of energy prices and resource adequacy prices, represent wholesale prices within restructured power markets, and can communicate periods of increased system stress when changes in energy consumption have significant cost or value to the system.

Energy prices in power system models are analogous to Locational Marginal Prices (LMP) a pricing mechanism used in wholesale energy markets to determine the cost of electricity at specific locations within the power grid. It represents the marginal cost of supplying an additional unit of electricity at a particular node or location on the grid at a specific time, taking into account factors such as generation costs, transmission constraints, and demand patterns. LMPs vary across the topology of the power system and time periods based on supply and demand dynamics.

Resource adequacy refers to the ability of an electric power system to reliably meet the electricity demand of its customers at all times, ensuring there are sufficient resources available to avoid shortages or interruptions. Capacity markets are a mechanism where sufficient capacity from

eligible participating generators is procured in excess of a defined margin above peak demand in compliance with NERC guidelines. A competitive capacity price is paid to participating generation and storage technologies for committing to a specified fraction of their generating capacity required to generate during periods of high system stress. These prices provide financial incentives for generators to invest in and maintain sufficient capacity to support resource adequacy, thus ensuring the reliability of the power system. These are analogous to capacity markets that exist in restructured power markets in the U.S. Payments for participating resources occur on an annual basis but the time periods that govern the need for this resource can be mapped to specific periods of high system stress. This enables the price signal for resource adequacy to be allocated to specific periods along with the previously discussed energy prices.

Cambium is an NREL analysis product that utilizes the combined analysis for ReEDS capacity expansion modeling with PLEXOS production cost modeling to generate key metrics relevant to power system planners and decision-makers. Region specific hourly prices of electricity that incorporate the price of energy and capacity for resource adequacy are one included metric. The hourly price generated can be utilized to evaluate the expected revenue of a participating power generator or storage asset. It can also be utilized to understand the costs to the grid of supplying energy for a specific end use load profile.

While Cambium is a powerful analysis tool, there is a high degree of computation and modeling effort required to generate the necessary outputs. This effort is performed for a limited number of cases as part of the annual ReEDS Standard Scenario results, which are released and available for use in other analysis efforts. For analysis of future power systems that differ substantially from the preexisting scenario assumptions included in Standard Scenarios, the Cambium workflow is not feasible.

A new development to ReEDS is an analysis tool called reValue, which generates hourly prices analogous to those produced by Cambium. The capability works by allocating ReEDS prices for energy and capacity requirements in each ReEDS time period to the full hourly dataset. While using ReEDS alone limits the understanding of how operational constraints like ramping and unit commitment impact energy prices, its prices are a direct reflection of the economics that govern ReEDS decision making. Utilizing ReEDS with revalue has a much lower computational intensity and is feasible to run quickly for bespoke scenarios required for an analysis effort.

For this effort features were added to reValue to support analysis of the grid value of hourly electric power changes associated with the adoption of geothermal systems. Combining the hourly electric power prices with end-use load shapes allows for a calculation of the annual cost to the grid of supplying that end-use. The end-use load shapes and magnitudes change based on the application of geothermal systems to meet that need. Calculating the difference between annual cost by specific end use determines the relative cost or value to the grid of adopting a geothermal system as compared to alternatives.

Building sizes can differ substantially by end user and reValue includes metrics that normalize the annual costs to a comparable floorspace equivalent. The valuation tool scales and can be quickly applied to value any number of specific end-use energy profiles and locations. Grid valuation calculated using reValue reflects wholesale prices with an option to include a price escalator to estimate retail prices.

2.2.3 Quantifying Non-Electric Power Values

While an important metric examining only the power system value of a geothermal system applied to a building end-use is important, it does not consider the larger system of impacts. As an example, were a building to electrify a natural gas furnace used for heating, the increase in electric power consumption would appear as an increase in cost relative to maintaining an existing heating system. This would omit the direct financial benefits of reduced fuel consumption as well as the benefits of reduced in building emissions for climate and health impacts.

The fuel consumption associated with an end-use technology is utilized and calculated against wholesale natural gas prices in ReEDS. These natural gas prices are aligned with those used in AEO 2023 and can optionally include price elasticity if required for a ReEDS simulation. The use of wholesale natural gas prices keeps the calculation of fuel price consistent with the quantification of power system value, although applying an escalator to reflect retail gas prices is an available option.

To calculate benefits of changes to in-building emissions we consider these impacts as externalities in order to calculate them in terms of a value equivalent. For the cost of CO_2 emissions associated with an end-use emissions we applied a $51/ton social cost of carbon consistent with a moderate value proposed by the Whitehouse Interagency Working Group (IWG 2021). In addition to CO_2 we estimated costs associated with air pollutants including fine particulates, NOx and SOx using emissions intensity factors specific to the modeled end use. The impacts of air pollution depend on both the type and location of emissions relative to downwind populations. We utilized a linkage to ReEDS regions of a reduced complexity air pollution model (RCM) based upon data available from the Center for Air, Climate, & Energy Solutions, which provides information to apply three possible integrated air assessment models (AP3, EASIUR, and InMAP) with two concentration-response function studies (American Cancer Society and Harvard Six Cities Study). The RCM is used to calculate the cost of health damages associated with emissions which can be included in the externalities of an associated end use (Kim 2020).

3. Results

3.1 Selected Buildings

As an illustrative example of this approach, we applied the valuation described in the prior section to residential and commercial buildings in Washington State. The selected profiles were obtained from ResStock 2024.2 and ComStock 2024.2. The selected residential and commercial buildings all fall into a common region sharing climate and energy prices, and all had available GHPs upgrades to constraint valuation.

The selection of representative residential buildings, shown in Table 1, was made to allow for a comparison in the change of value on the basis of the initial building heating type and whether the building possessed air conditioning. For building heating, the selected buildings either utilized resistive electric heating or a natural gas furnace. For space cooling, buildings either possessed a conventional air conditioner or had no existing cooling system. When the GHP upgrade is applied to the selected buildings, it is utilized both for building heating and cooling regardless of whether the building had cooling in its base configuration.

Table 1 Residential Building Base Characteristics

Building ID	Heating Fuel	Heating System	Cooling System
25	Natural Gas	Natural Gas Furnace	None
249	Natural Gas	Natural GasFurnace	AC, SEER 10
311	Electricity	Electric Furnace	None
500	Electricity	Electric Furnace	AC, SEER 13

Commercial buildings, shown in Table 2, were selected to allow a comparison in the change of value for buildings depending on their base heating system. In contrast to the selected residential buildings all commercial buildings have installed cooling. For heating systems, it includes gas and electric furnaces similar to the residential buildings but also includes an air source heat pump. This allows a contrast between two types of building heat pumps and the associated annual benefits.

Table 2 Commercial Building Base Characteristics

Building ID	Building Type	Heating Fuel	Heating System	Cooling System
333469	Warehouse	Natural Gas	Furnace	DX
333463	Warehouse	Electricity	ASHP	ASHP

3.2 Analysis of Residential Buildings

Using the method discussed in the prior section we calculated the comprehensive cost of meeting the building space conditioning for the selected residential buildings, shown in Figure 3. For all the selected buildings the application of GHPs had a lower annualized cost compared to meeting the same requirements with the base HVAC equipment. This pattern held for buildings 25 and 331 which lacked air conditioning in their base configuration.

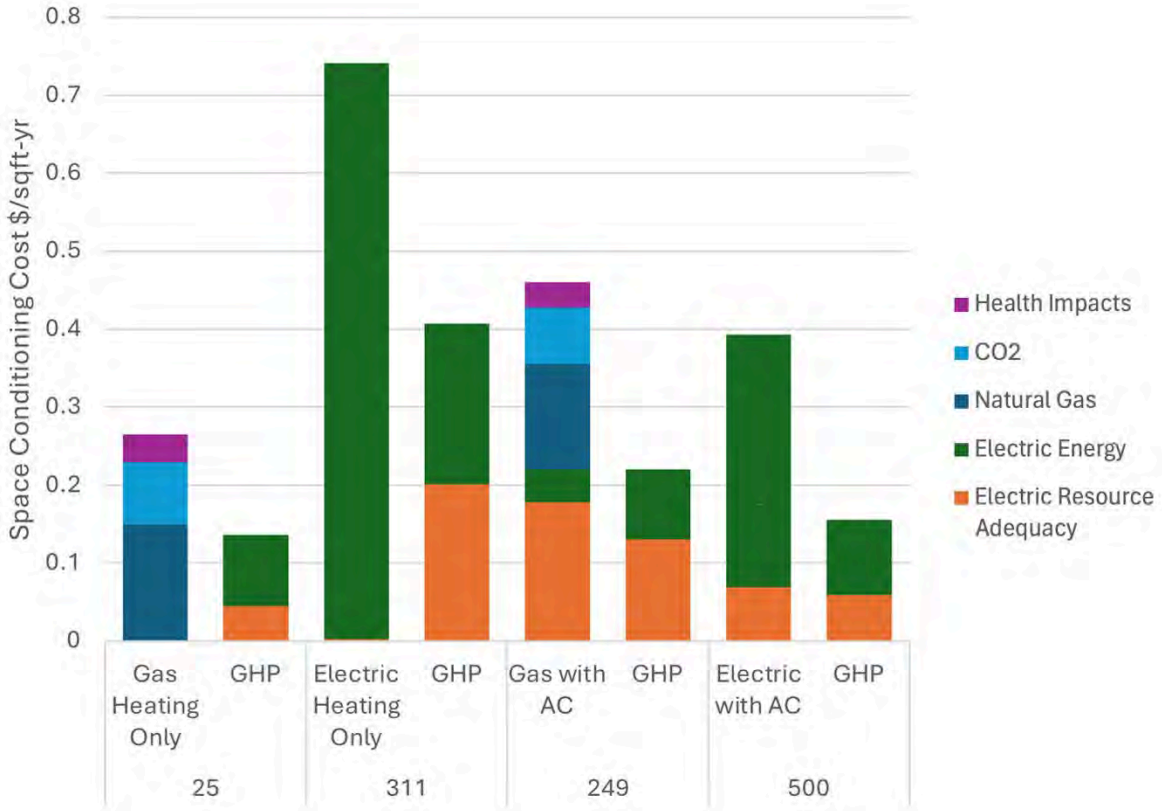

Figure 3. The annualized cost per square foot of meeting space conditioning needs for residential buildings with and without GHPs.

The electric power costs are separated into energy and resource adequacy requirements. The addition of GHPs altered the distribution of these two components. Building 331 with a resistive electric furnace and no AC was dominated by energy component, with the addition of GHPs combined electric power costs fall. The addition of summer electric power demand to meet cooling results in an increase in the cost to meet resource adequacy, which tends to be governed by summer peaking time periods. For buildings 249 and 500, which included AC, the upgrade to GHP reduced the resource adequacy component of electric power costs due to improved summer cooling efficiencies, shown in Table 3.

Table 3 Reduced Cost of GHP Upgrade for Residential Buildings by Component

Building ID	HVAC Type	Net Value of GHP Upgrade ($/sqft-yr)				
		Electricity	Fuel	Externalities	Electricity + Fuels	Combined
25	Gas Only	-0.136	0.149	0.116	0.013	0.129
331	Electric Only	0.334	0.000	0.000	0.334	0.334
249	Gas with AC	0.000	0.135	0.105	0.135	0.240
500	Electric with AC	0.237	0.000	0.000	0.237	0.237

The value of a building upgrading to a GHP is indicated by the difference between the cost of heating using the original system and a GHP upgrade. Buildings 25, which electrified natural gas with a GHP, showed an increase in electricity costs, which were offset by a greater reduction in avoided fuel costs. Building 249 showed no net change in electric power costs, as the electric costs incurred to electrify heating were coincidentally offset by savings through greater cooling efficiency relative to the base AC system. The value of the externalities from CO_2 emissions and health impacts from criteria pollutants were at a similar magnitude to the calculated natural gas costs.

The total combined benefits were greatest for the buildings with electric resistive heating (buildings 331 and 500) due to the energy and cost intensity of this end-use. Buildings using natural gas as a heating fuel had a smaller benefit, still showing net savings for electricity and fuel costs. The savings were further bolstered when the externalities of CO_2 and health impacting emissions were included.

3.3 Analysis of Commercial Buildings

In contrast to the analysis of residential buildings commercial warehouses with substantially larger floor area showed lower costs for space conditioning. For the selected buildings costs are lower with GHP applied compared to the base heating and cooling technologies. In building 333469, with natural gas as a primary heating, the GHP upgrade allows for a reduction but not complete elimination of natural gas for heating based upon the assumed size of the geothermal system. This has a small increase in electric costs of 0.007 $/sqft-year, which, when combined with the substantial fuel cost reduction, shows a 0.037 $/sqft-year savings, shown in Figure 4. Factoring in externalities grows the savings from GHP to 0.068 $/sqft-year.

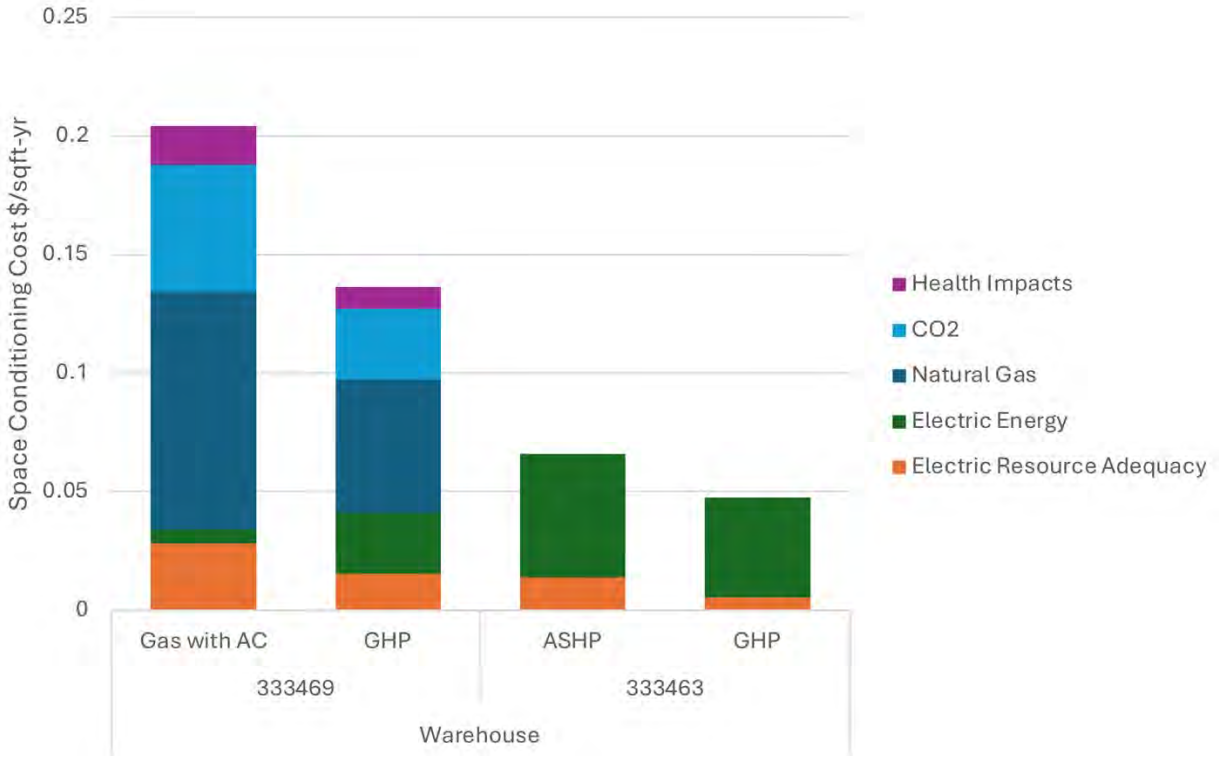

Figure 4. The annualized cost per square foot of meeting space conditioning needs for commercial buildings with and without GHPs.

Building 333463 differs from the base building electric heating comparison in the prior section as it utilizes more efficient air source heat pumps to provide space conditioning. The addition of GHPs have a comparably smaller 0.018 $/sqft-year or 28% of baseline costs. These benefits were obtained from an equal cost reduction between resource adequacy costs and energy costs. Proportionally this has a visibly greater effect on the resource adequacy costs which are halved primarily due to substantially higher summer cooling efficiencies.

4. Conclusions

As part of our analysis, we identified a method to evaluate the comprehensive benefits of applying geothermal systems to meet end use demand. By leveraging ReEDS prices through reValue we can quantify the hour specific impacts to grid prices from associated electric power consumption. The inclusion of externalities, including CO_2 and health impacts from air pollution, provides a more comprehensive valuation of electrification through geothermal systems. The combination of these measures provides an improved measure of comparison between end use technologies.

To enable this analysis, we identified data sources and work flows to allow analysis of space conditioning for residential and commercial buildings as well as applications in the manufacturing sector. We applied this method to a selection of residential and commercial buildings in Washington state to compare how and where savings were realized and how focusing on the combined impacts creates a more comprehensive understanding of the relative benefits of applying GHPs.

The next steps in our work are to apply the calculated residential, commercial, and manufacturing end-use load impacts at a national scale. For space heating and cooling we will be shifting to county aggregates based upon original heating and cooling type to compare both upgrades from base end use technology as well as comparisons across space conditioning upgrades. This will capture substantial differences in the climate, building configuration, and preference for space conditioning technologies that are extraordinarily regionalized. County aggregations address computational challenges and keep the overall data size to an interpretable level. The health impacts of emissions will also vary substantially depending on the location and downstream effects with other regions having much higher marginal impacts than in the region selected.

We plan to report results highlighting regions where geothermal systems are best suited on the basis of their net operating value. This will provide important context for comparing the benefits to the energy system of a whole of end-use technology upgrades including geothermal systems. For manufacturing energy, which in part uses DDU, which is dependent on suitable conditions, an analysis will be done to determine the regional feasibility of applying DDU.

REFERENCES

Denholm, Paul et al. “The Challenge of Defining Long Duration Energy Storage.” NREL/TP-6A40-80583. National Renewable Energy Laboratory, Golden, CO, (2021). https://www.nrel.gov/docs/fy22osti/80583.pdf.

EIA. “U.S. energy facts explained.” U.S. Energy Information Administration, (2021), Available from: https://www.eia.gov/energyexplained/us-energy-facts.

EIA. “Use of energy explained – Energy use in industry.” U.S. Energy Information Administration, (2022), https://www.eia.gov/energyexplained/use-of-energy/industry.php

Ho, Jonathan, et al. “Regional Energy Deployment System (ReEDS) Model Documentation (Version 2020)”. NREL/TP-6A20-78195 National Renewable Energy Laboratory, Golden, CO (United States).. (2021).

IWG. “Technical Support Document: Social Cost of Carbon, Methane, and Nitrous Oxide”, Interagency Working Group on Social Cost of Greenhouse Gases, United States Government, (2021).

Kim S., et al. “Concentrations of criteria pollutants in the contiguous U.S., 1979 – 2015: Role of prediction model parsimony in integrated empirical geographic regression.” PLoS ONE 15(2), e0228535. (2020). https://doi.org/10.1371/journal.pone.0228535

McCabe, K., Gleason, M., Reber, T., and Young, K. R. “Characterizing U.S. heat demand for potential application of geothermal direct use.” *Proceedings: 40th Geothermal Rising Conference Annual Meeting*, Sacramento, CA, (2016).

McMillan, C., Boardman, R., McKellar, M., Sabharwall, P., Ruth, M., and Bragg-Sitton, S. “Generation and use of thermal energy in the U.S. industrial sector and opportunities to reduce its carbon emissions.” Technical Report, INL/EXT-16-39680, NREL/TP-6A50-66763, Idaho National Laboratory, Idaho Falls, ID, (2016).

McMillan, C., Schoeneberger, C., Zhang, J., Kurup, P., Masanet, E., Margolis, R., Meyers, S., Bannister, M., Rosenlieb, E., and Xi, W. “Opportunities for solar industrial process heat in the

United States." Technical Report, NREL/TP-6A20-77760, National Renewable Energy Laboratory, Golden, CO, (2021).

Oh, H. and Beckers, K. "Geospatial characterization of low-temperature heating and cooling demand in the United States." *Proceedings: 48th Workshop on Geothermal Reservoir Engineering*, Stanford University, Stanford, CA, (2023).

Oh, H., Akar, S., Beckers, K., Bonnema, E., Vivas, C., and Salehi, S. "Techno-economic feasibility of geothermal energy production using inactive oil and gas wells for district heating and cooling systems in Tuttle, Oklahoma." *Energy Conversion and Management*, 308, (2024), 118390.

Parker, Andrew, et al. "ComStock Reference Documentation." NREL/TP-5500-83819. National Renewable Energy Laboratory Golden, CO, (2023). https://www.nrel.gov/docs/fy23osti/83819.pdf

Present, E., et al. "ResStock Dataset 2024.1 Documentation." NREL/TP-5500-88109. National Renewable Energy Laboratory (NREL), Golden, CO (United States), (2024). https://www.nrel.gov/docs/fy24osti/88109.pdf

Exploring the Open Loop Geothermal Potential of the Penn South Neighborhood, NY, Using Numerical Modeling

Carter Johnson and Justin Mariniak

Egg Geo LLC

Keywords

Numerical Modeling, ATET, Open Loop Geothermal, New York City, Geoexchange

ABSTRACT

This study aims to assess the feasibility of utilizing open loop aquifer exchange for the Penn South Neighborhood of Manhattan, New York City. This neighborhood energy system will serve over 6.5 million square feet (60,400m2) of heated and cooled space. Aquifer thermal energy storage (ATES) was originally considered as part of a larger thermal energy network (TEN) to provide high peak load capacities to meet extremes and to ameliorate saltwater intrusion. However, initial investigation produced serious concern that the shallow unconfined glacial till was not deep enough to avoid mixing oxygenated and anoxic waters. In particular, iron dissolved in anoxic water precipitates into iron oxide in oxygenated water. The Penn South neighborhood subsurface, however, does have favorable aquifers with high transmissivity for a properly designed open loop system. This study aims to build on the work done previously for the ATES model but focuses on the utilization potential of an open loop geothermal and its associated risks, challenges, and benefits in the heavily populated New York neighborhood.

A 3D geologic model was developed to represent the phreatic glacial aquifer formation, weathered bedrock, and other minor sedimentary formations in the area. The simulations were conducted using TOUGH2 (EOS1) and visualized in PetraSim. Injection and extraction rates and accompanying enthalpies were matched and calculated to a preliminary load profile of the surrounding residential and commercial buildings to ensure that the model was representative and accurate.

Some of the challenges with developing a geoexchange system of this magnitude include the depth to bedrock in the project area, management of the thermal plume, the presence of nearby dewatering wells, and building foundations that extend through the entirety of the target formation and into the bedrock. The depth to bedrock across the service area varies from about 20m to 92m. Since the thermal plume size is also a function of the screen length or thickness of the target formation, careful planning for well separation is necessary when storing the system's heat in the

subsurface of a dense urban area. While many recharge zones for the phreatic aquifer are cut off because of civil engineering practices, there is still some recharge from the higher elevations to the north and a large volume of water arises from fractured bedrock. Nearby dewatering wells are common for building basement areas, subways, and utility corridors.

As New York City continues to push towards the electrification of all building heating and cooling, groundwater as an energy resource must be prioritized. The heat capacity of groundwater or ground-source fluids is about 4 times that of air and should become the primary choice for policymakers, utility companies, and building managers in the energy transition. Administering groundwater as an energy resource at an urban scale requires careful study and engineering. The results of this study will help to quantify the potential for open aquifer exchange in the Penn South Neighborhood aquifers and inform the feasibility of implementing similar systems in other areas that target phreatic glacial aquifers in dense urban areas.

1. Introduction

Geothermal and geoexchange systems for heating and cooling are increasingly recognized as the most efficient decarbonization application for buildings. Building heating and cooling makes up in excess of 50% of community emissions in many locales throughout the world. This is also true of places like New York City where importation of fuel oil for building heating seasons causes a high concentration of emissions for the metro area.

The New York State Utility Thermal Energy Networks and Jobs Act of 2022 (UTENJA) continues to make a significant impact. While conventional gas and electric utilities are now proposing demonstration projects for geothermal and geoexchange district energy, other organizations are taking notice. To comply with Climate Mobilization Act, passed by the New York City Council in 2019, building portfolio managers are turning to engineering firms specializing in subsurface energy exploitation. One such building portfolio manager is Penn South, also known as Mutual Redevelopment Houses Incorporated.

Like all buildings, Penn South must decarbonize their heating and cooling, fed by a $7MW_e$ combined heat and power plant (CHP). To stop the combustion of fuels on-site, Penn South sponsored a community-based geoexchange district energy investigation. Neighboring building owners, including Amtrak's Penn Station, the State University of New York's Fashion Institute of Technology, Tishman Speyer's historic Morgan North Postal Facility, and community faith groups sent in supporting letters. With a groundswell of community engagement, grants became available from the New York State Energy Research and Development Authority. The contributions of the investigation led by Egg Geo LLC will provide lessons learned and guide future industry best practices for wide-scale building stock decarbonization in the challenging urban environment.

Challenges for the neighborhood geoexchange district energy system include space limitations, retrofit costs, equipment, capitalization policies, among others. Usually geothermal and geoexchange is touted as having smaller footprints than the typical power plant, for example. In Manhattan's dense urban setting, even the small drill rig footprint can be difficult to permit and deploy. Equipment in place varies widely across organizations involved. There are more than 30 structures and 6 million square feet of conditioned floorspace that would be affected by HVAC conversions. Some partner building operators face organizational capitalization policies that will

force them to use combustion equipment in place, even as the TEN becomes a connection option across the neighborhood.

1.1. Site Plan

Chelsea is a neighborhood on the West Side of Manhattan, New York City. The neighborhood's boundaries are roughly 30th Street to the north, Sixth Avenue to the east, 14th Street to the south, and the Hudson River/West Street to the west (Figure 1Figure 2Figure 3). Notable buildings in this area include Penn South (15 housing buildings), Amtrak Penn Station (1 building), Patrick Moynihan Train Hall (1 building), SUNY Fashion Institute of Technology (9 buildings), Tishman Speyer's Morgan North (1 building), Saint Eleftherios (1 building), Holy Apostles (3 buildings), among others.

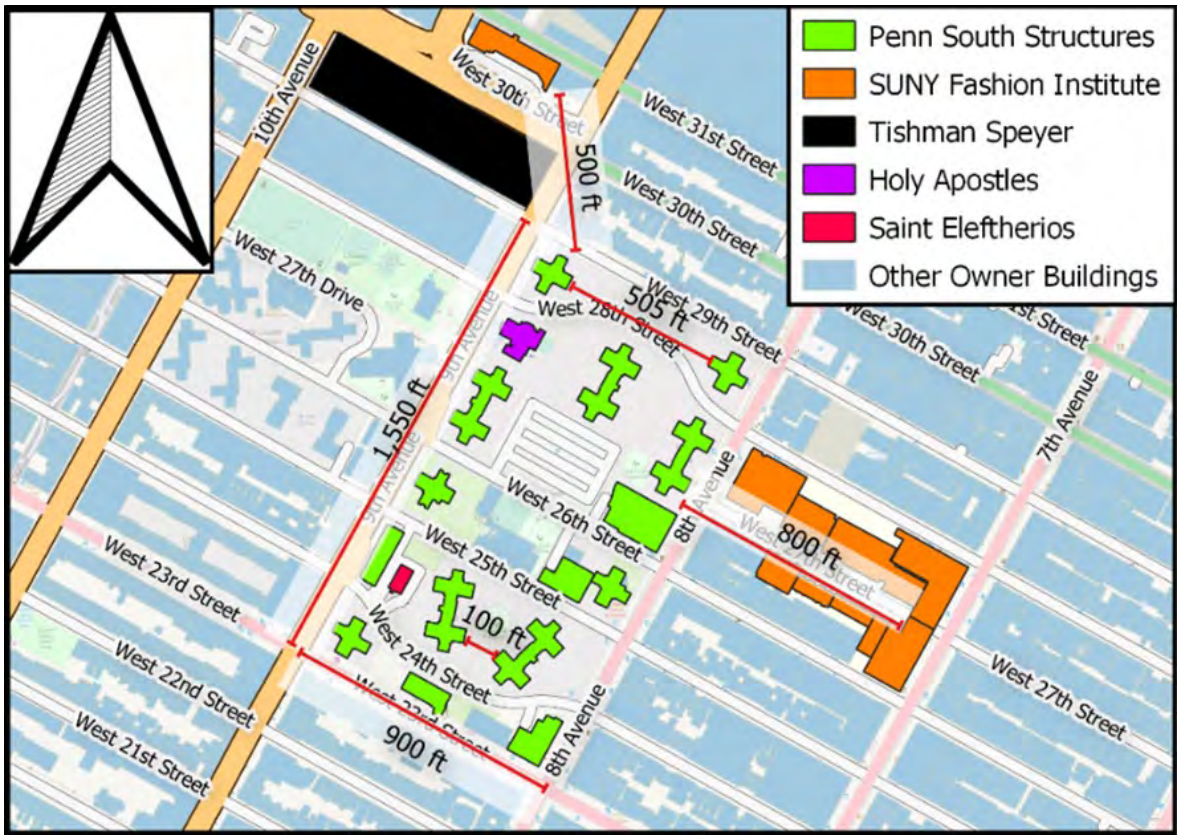

Figure 1: Site plan of the Chelsea neighborhood including the Penn South structures and other nearby buildings that are part of the study

Figure 2: Aerial view of the site obtained from Google Earth

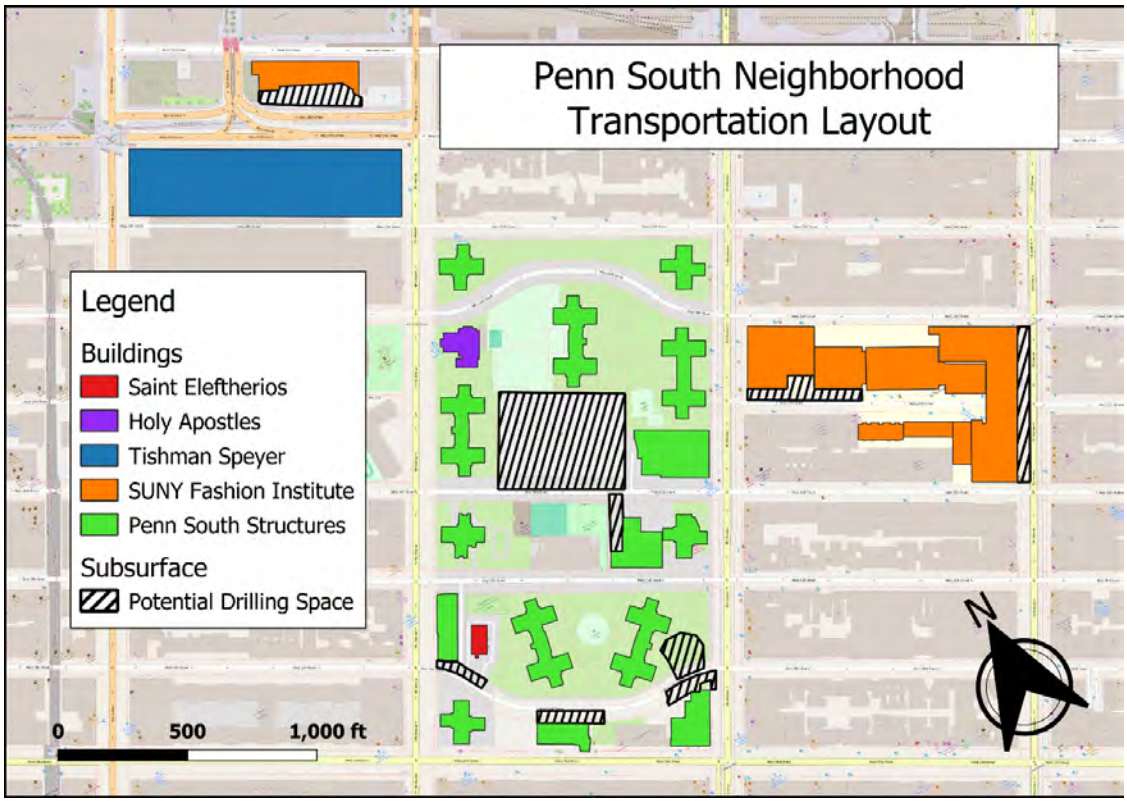

Figure 3: Site plan with the potential drilling space (~250,000 sq ft)

1.2. Open Loop Aquifer Exchange

An open loop doublet system consists of a series of supply and return (or injection) wells that draw ambient temperature groundwater from an aquifer for heat exchange in the building, then return the thermally-altered water back into the aquifer. Commercial doublet systems require high-producing aquifers, such as the glacial sand and gravel aquifer and bedrock aquifers beneath the project site. The water table around a pumping supply well is drawn down into the shape of a cone and mounds up around the return wells. The return groundwater is warmer than the ambient temperature during the summer, as heat is extracted from the building and transferred to the groundwater injected back into the ground. In the winter, the process is reversed; heat is extracted from the groundwater and transferred to the building for heating, so the return water is colder than the ambient temperature.

The supply wells should be located on the upgradient side of a site, relative to natural groundwater flow direction, and the return wells on the downgradient side. In this manner, the thermally-altered return water enters the natural groundwater flow and moves away from the project site. The return wells must also be separated from the supply wells such that their respective areas of influence do not overlap, i.e., the re-injected water is not drawn back into the supply well, a condition known as thermal “short circuiting”.

2. Methods

2.1. Geologic Modeling

The first step in estimating the available capacity of an open loop exchange system in the Penn South Neighborhood is to achieve a high level of detail on the geologic and hydrologic characteristics of the subsurface. The southern portion of Manhattan Island consists of unconsolidated glacial deposits ranging from just a few feet thick to more than 250 feet in some areas. These deposits host an aquifer system that is rich in quartz and has very low percentages of fine materials such as silts and clays. Aquifer tests indicate a wide range of aquifer hydraulic conductivity in the glacial deposits. The highest values were found on the western and northern sides of the island near the study area (Figure 4) with small, localized exceptions in stream channels to the north where bedrock outcrops are present. Values used in this analysis, derived from local well data is presented in Table 1 and Table 2.

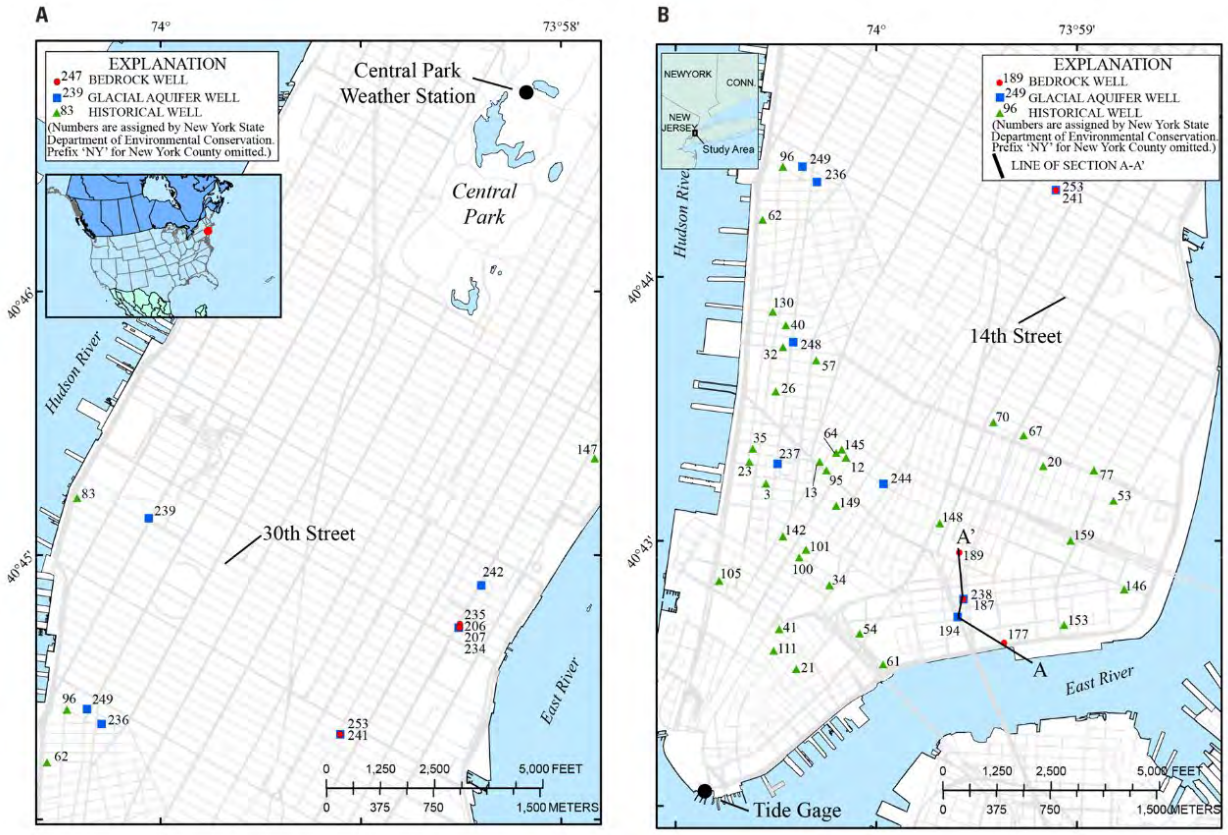

Figure 4: Wells surrounding the thermal energy network study area in Manhattan, New York City (Stumm & Como, 2017)

Table 1: Existing well characteristics in the study area (Stumm & Como, 2017)

Hydrogeologic Unit	New York State ID Number	Land Surface Elevation (m)	Bottom Depth of Well (m)	Casing Length (m)	Water Level (m) above Mean Sea Level	Chloride in Glacial Aquifer (mg/L)	Hydraulic Conductivity (m/Day)	Transmissivity (m^2/Day)
bedrock	NY 241	8	183	15	3.41	NA	NA	NA
	NY 206	6	155	7	NA	NA	NA	NA
	NY 207	6	183	8	NA	NA	NA	NA
	NY 234	6	162	9	NA	NA	NA	NA
	NY 189	13	183	71	NA	NA	NA	NA
	NY 187	11	171	88	NA	11,800 **	NA	NA
	NY 177	2	182	69	NA	7000 **	NA	NA
glacial aquifer	NY 239	6	8	6	1.16	641	6	48
	NY 248	5	12	11	−0.09	240	550	13,470
	NY 237	5	12	11	−0.04	1080 *	12	297
	NY 253	8	18	14	3.31	357	NA	NA
	NY 235	6	8	6	0.95	1440 *	0.05	0.10
	NY 242	11	20	18	4.47	405	0.04	0.20
	NY 236	6	25	24	0.28	672 *	39	660
	NY 244	8	20	19	0.30	217	52	670
	NY 194	9	65	62	NA	15,250 *	0.9	53
	NY 238	11	11	9	2.64	277	22	1660
	NY 249	5	9	8	0.25	560	92	409

Table 2: Rock types used in the analysis and their hydrological values

Rock Type	Glacial Till	Bedrock
Density	2200 kg/m^2	2700 kg/m^2
Porosity	0.3	0.01
Permeability	1.5E^{-09}m^2	0 m^2
Wet Heat Conductivity	1.8 W/(m*K)	3.2 W/(m*K)
Specific Heat	1300 J/(kg*K)	740 J/(kg*K)

Across the project service area, the unconsolidated gravels are thickest on the Penn South Campus, where more open green space appears as potential urban drilling locations. The Penn South affordable housing community has a campus at the center of the study area with a length of 465m by 265m. The property constraints define the possible well locations of the open aquifer geothermal system.

Additional geologic data including surface land elevation, and depth to bedrock was gathered from the United States Geological Survey and the New York State Department of Environmental Conservation with the goal of producing an accurate geologic model that could be used to produce reliable numerical simulations to produce data on necessary well separation ("USGS Groundwater Data for the Nation," n.d.) ("Downloadable Well Data - NYSDEC," n.d.). TOUGH 2 (EOS1) was used as the modeling software for this analysis. TOUGH 2 is a numerical simulation program used for multi-dimensional, multiphase, and multicomponent fluid flow and heat transfer through porous and fractured media. Petrasim was the graphical user interface to visualize the simulations and results. The data described above was imported to PetraSim for model creation before the initialization of the numerical model. This data was interpolated and used to create geologic layers that represent the unconsolidated glacial deposits and bedrock across the entire length of Manhattan Island (Figure 5Figure 9). It was important to start with a geologic model for the entire region first to interpolate data on the Penn South site as there exists very limited data immediately surrounding the neighborhood.

Figure 5: The well data (red dots) displayed were imported into PetraSim and used to create a geologic model of the entire Manhattan Island

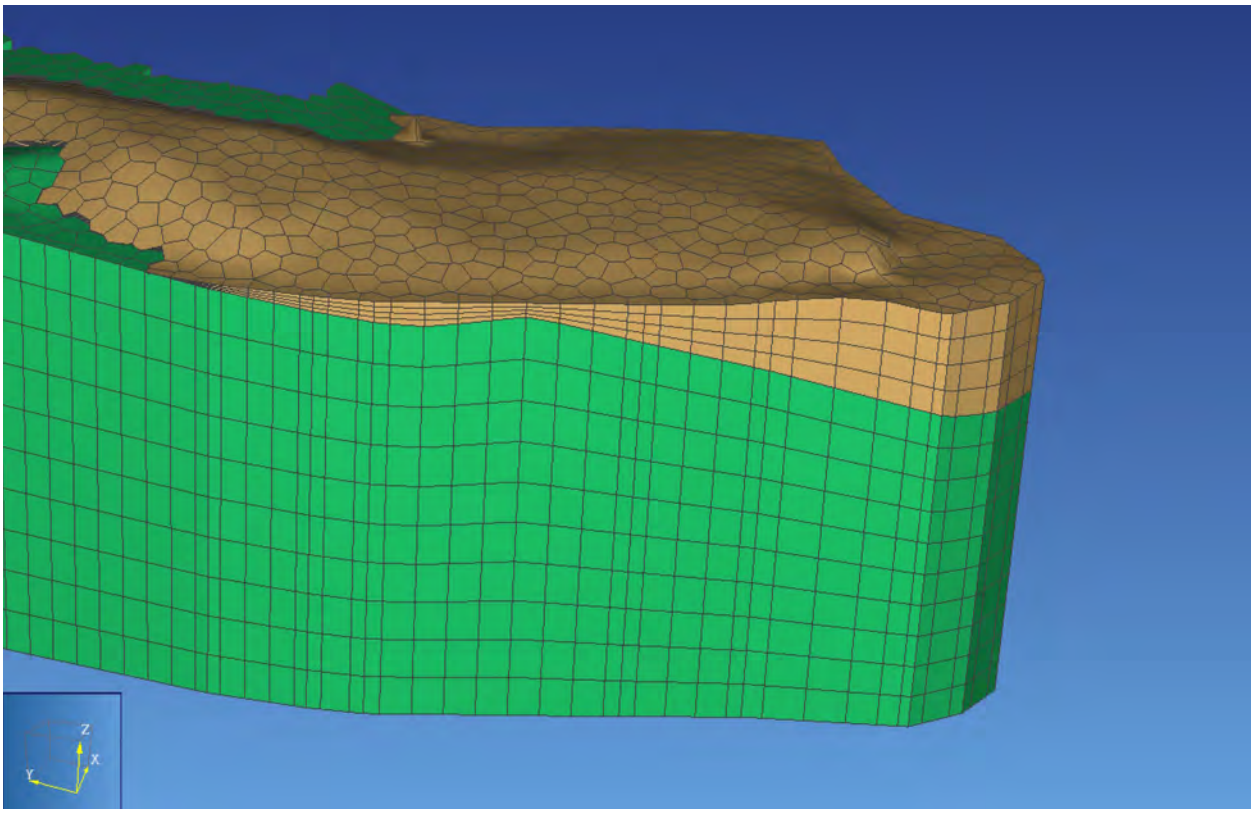

Figure 6: A sideview of the completed geologic model. Glacial till is represented by the tan cells and bedrock is represented by the green. Vertical distance (Z axis) has been exaggerated by 8x

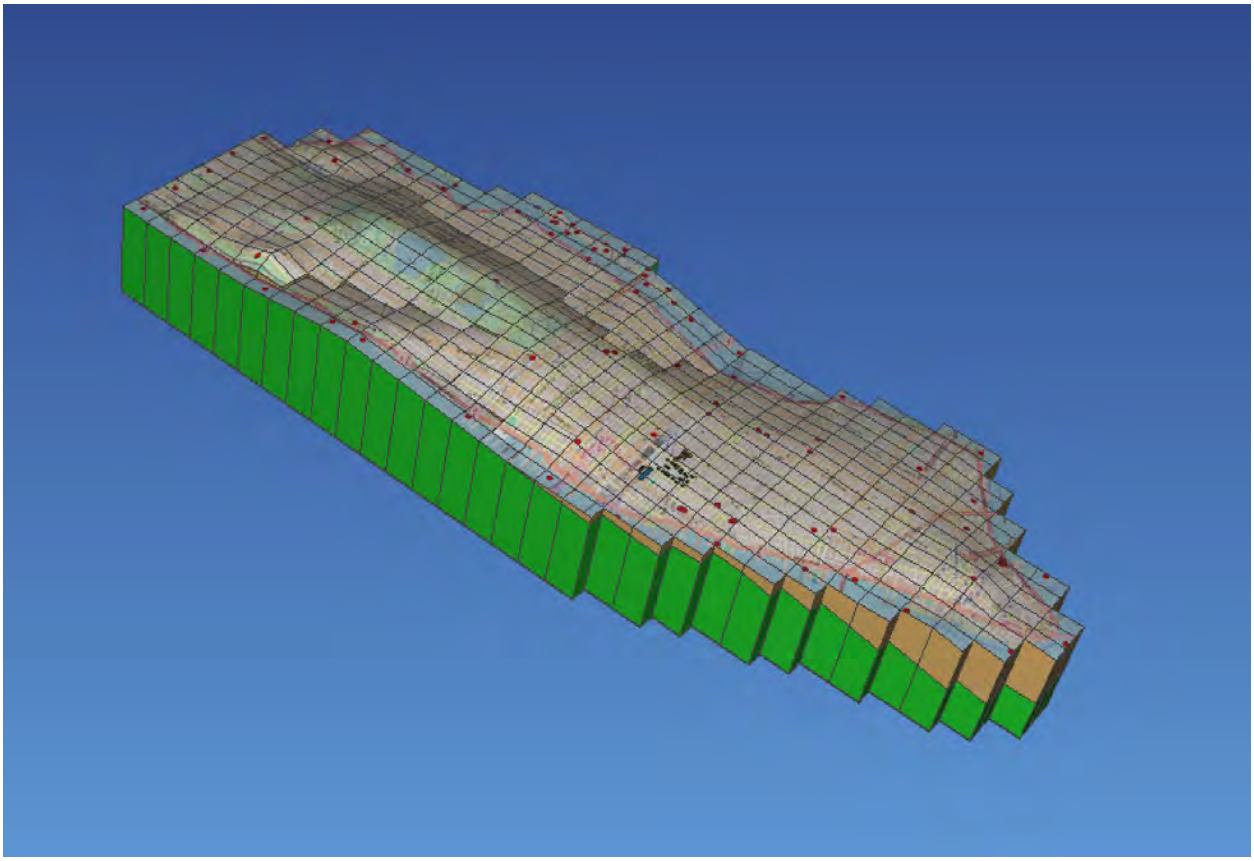

Figure 7: A screenshot of the Manhattan Island geologic model. The site is displayed as a small cluster of buildings on the western side of the peninsula

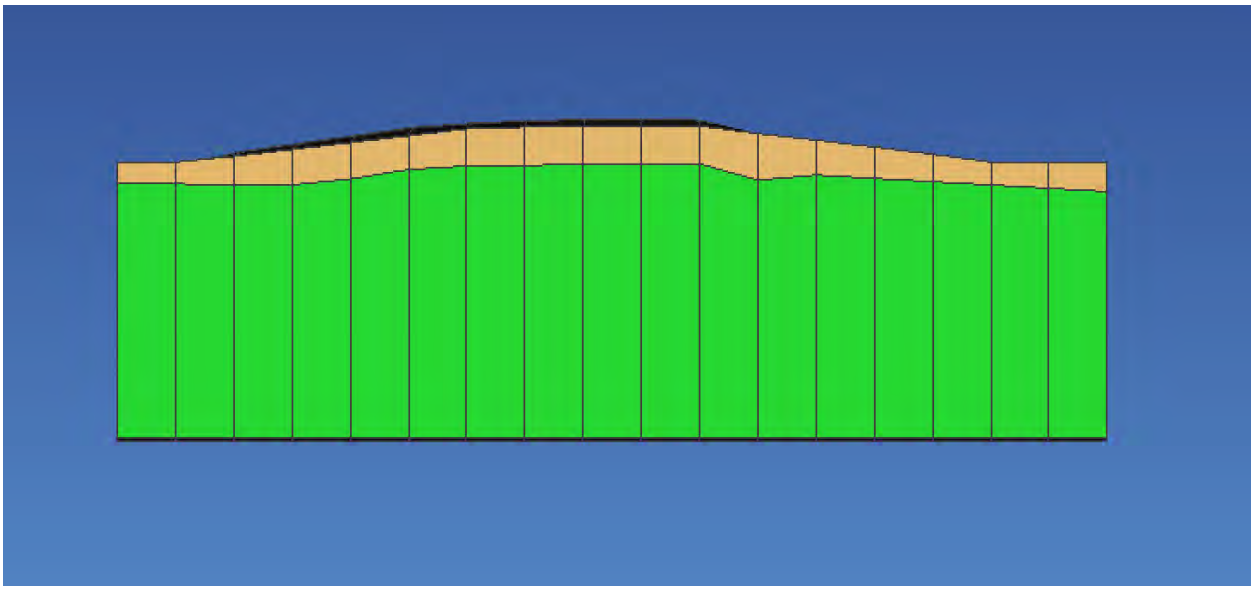

Figure 8: Cross section of the Manhattan Island geologic model from east to west through the Penn South site

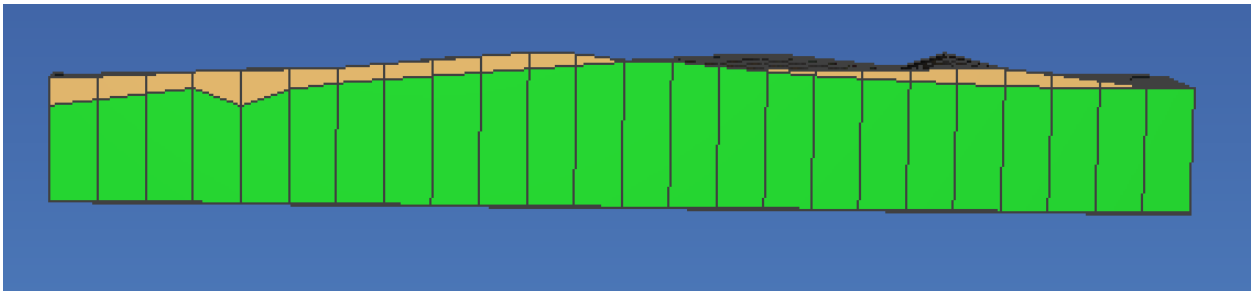

Figure 9: Cross section of the Manhattan Island geologic model from south to north through the Penn South site

The next step was to crop the model down to just the project site (Figure 10). This allows for a more detailed look at the geologic conditions directly beneath the project site. The glacial deposits overlay a bedrock with varying degrees of metamorphism, weathering, and composition. Schist, gneiss, and occasional marble make up the majority of the bedrock encountered under Manhattan Island. For simplicity we will refer to any rock beneath the glacial deposits as bedrock and assume an average permeability. Although some areas of bedrock have higher permeability due to metamorphism and heavy weathering, the majority is intact gneiss with very low permeability and conductivity compared to glacial deposits above.

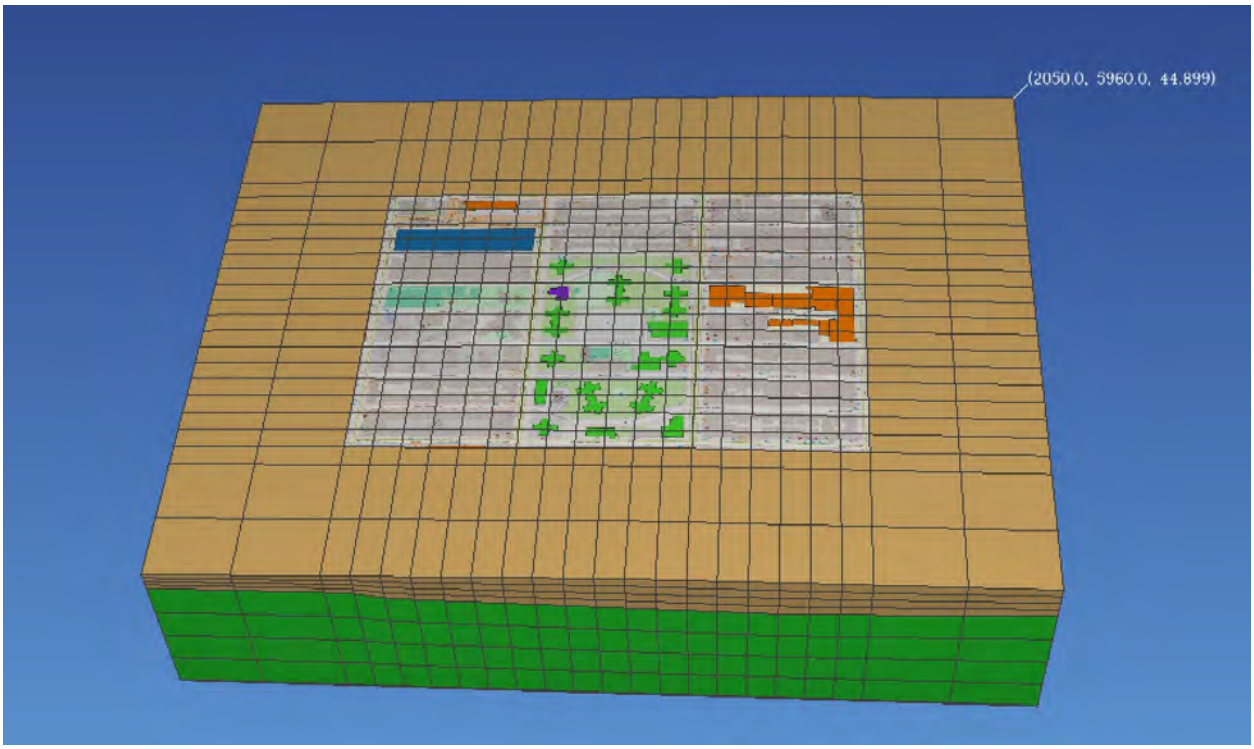

Figure 10: The geologic model of the Penn South site cropped down from the larger Manhattan Island model

Because the target aquifer is so shallow, many of the building foundations in the neighborhood extend at least halfway through the aquifer and some into the bedrock, creating an interesting element when modeling the flow of fluids through the glacial till during simulated production. Foundation depths for each of the neighborhood buildings were gathered and integrated into the

model using detailed region functions included in the Petrasim software (Figure 11). For simplicity, an average depth of 25 ft was assigned for the concrete foundations.

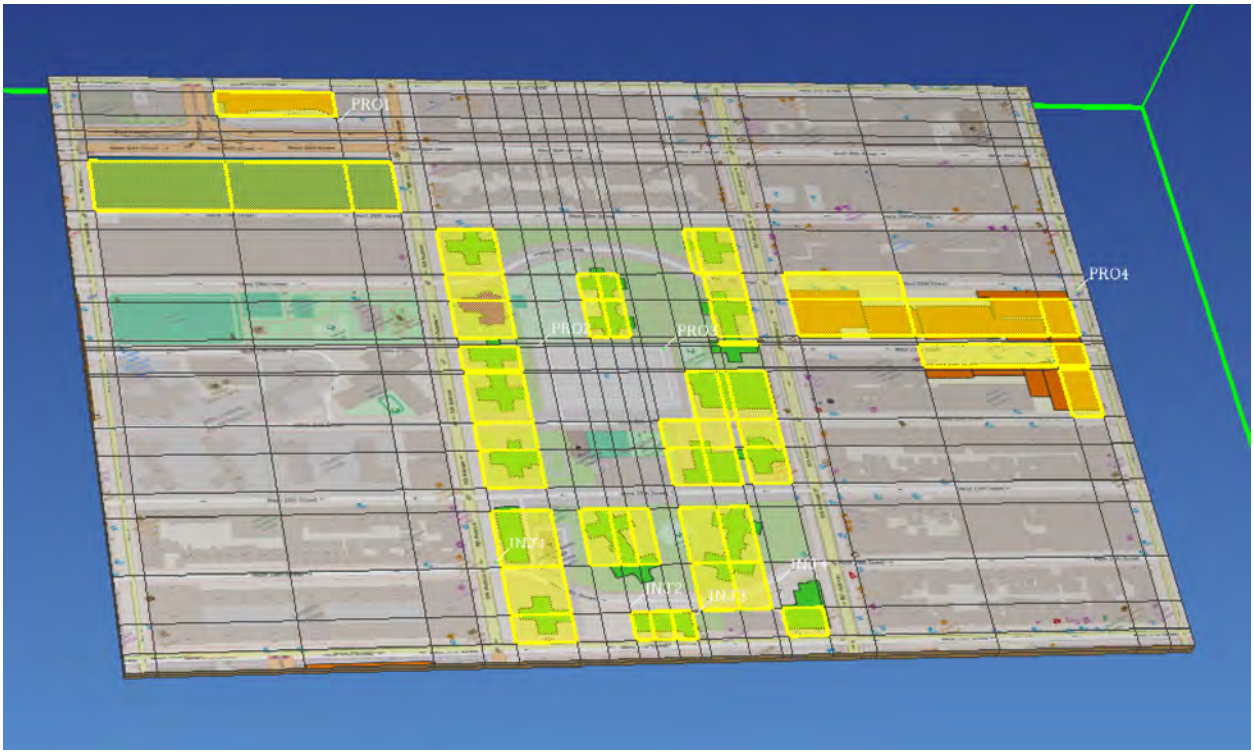

Figure 11: The cells highlighted in yellow were selected to represent the concrete foundations of the buildings. Each cell was selected and assigned to the concrete material down to 25 feet

These cells associated with building foundations are assigned the geologic characteristics below (Figure 12). The hydrological characteristics of concrete can be hard to estimate, especially if it has been buried under the water table for decades. Most concrete used for foundations has a porosity of under 10% but is usually considered impermeable if it has been poured recently (reference). However, the concrete's porosity/permeability values may increase over time due to erosion. These factors led to the decision to assign porosity/permeability values slightly higher than standard concrete, but still less permeable than the surrounding glacial till. Additionally, other values such as the specific heat and wet heat conductivity can vary widely depending on the type of concrete and its age/condition. These values were also chosen from an average (Skutnik et al., 2020).

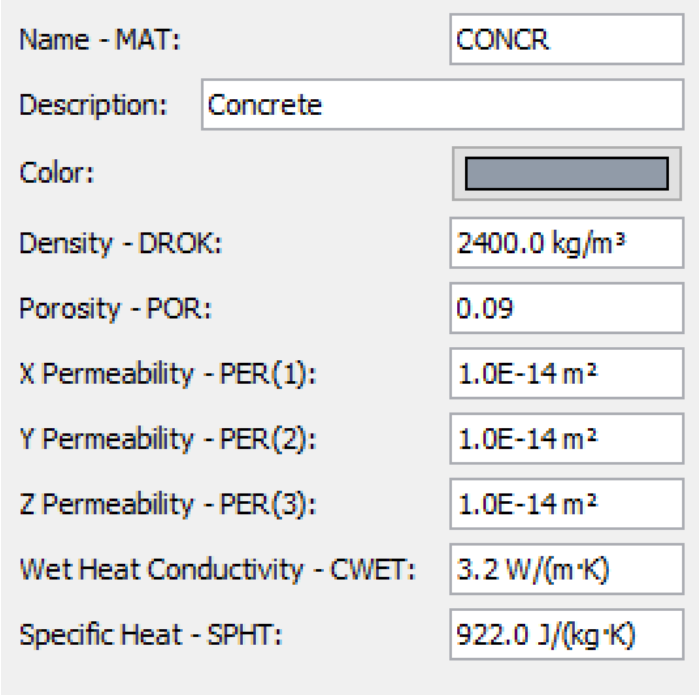

Figure 12: Geologic properties of the building foundations on site

2.2. Hydrologic Investigation

Next, local well data was analyzed to assist in determining the highest possible yield from the formations beneath the project site. This task proved to be difficult, and a test well will be required to obtain reliable numbers. Although there are dozens of wells in the area producing from the glacial aquifer, no production data could be obtained because they are privately owned. Despite this, a preliminary study of the glacial aquifers in the area was conducted. A report prepared by the Geological Survey titled "Properties of Aquifers on Long Island, New York" published estimated aquifer yields for a variety of glacial aquifers nearby the project site. These values varied greatly (between 25 and 300 gpm) due to varying rock characteristics (thickness of glacial till, clay and silt content, formation permeability etc) (McCymonds & Franke, 1972). To gain a better understanding of the possible yields at the project site, a very similar aquifer on Shelter Island of Suffolk County was studied (Soren, 1978). The glacial till in this area has very similar characteristics to that of Manhattan Island and the average thickness of the formation is very similar to the site as well (~50ft) (Figure 13). Measured water extraction from this aquifer average around 130 gal/min, but the report also states that the "highest possible yields and specific capacities were not obtained". The same publication also suggests that the highest yields in the area could be hundreds of gal/min higher than those recorded. Additionally, other aquifers with similar characteristics across Minnesota (Zhang, n.d.) have sustainable aquifer yields between 1,000 and 2,000 GPM. With this research in mind, two scenarios were considered in the sensitivity analysis – one that assumes a maximum yield of 300 gal/min and one of 600 gal/min as the best-case scenario. Sustainable yield rates on site will need to be determined by a test well and pump test.

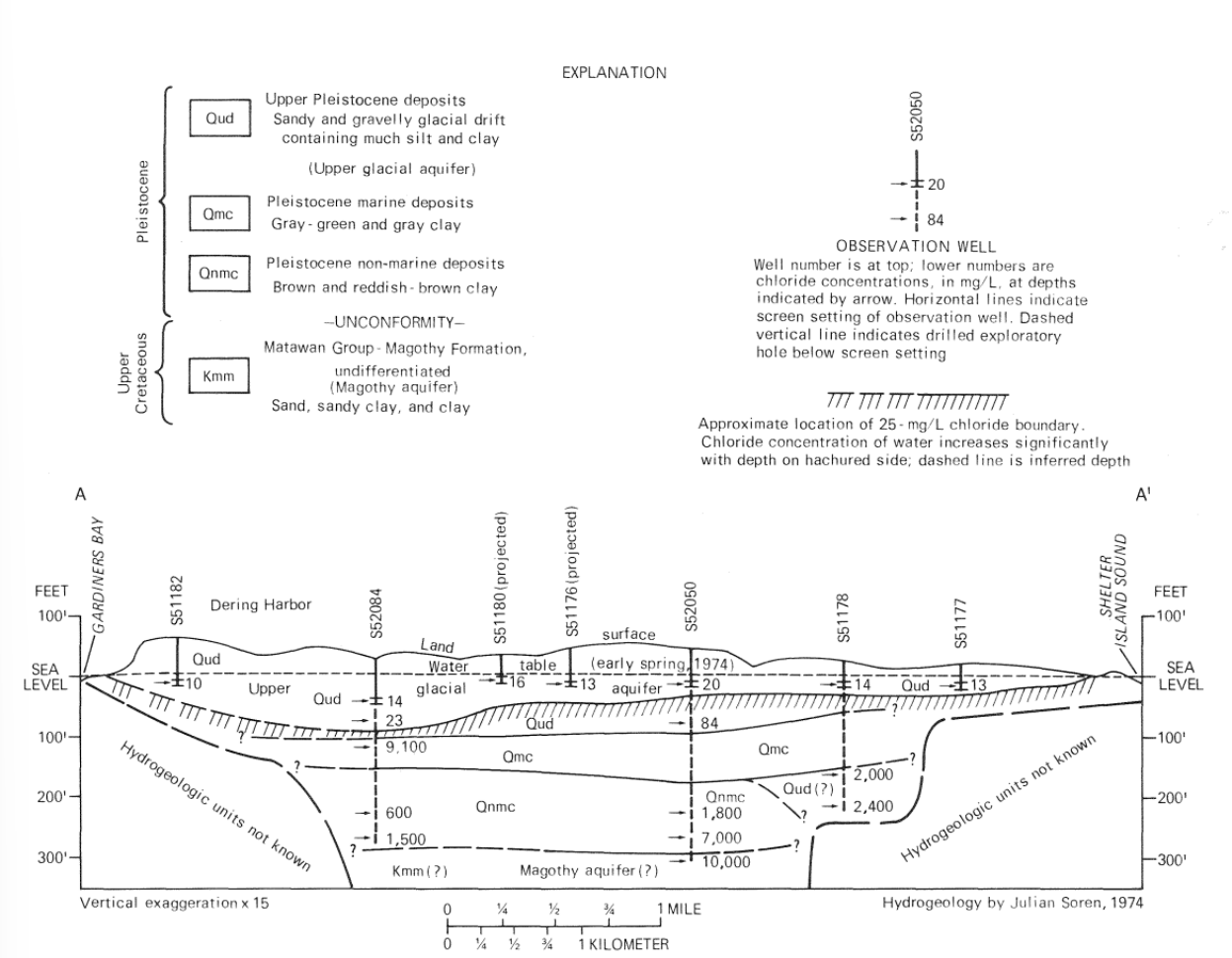

Figure 13: Geologic vertical slice of Shelter Island in Suffolk County (Soren, 1978)

2.3. Advective Flow Modeling

To accurately model the effects of an open loop geothermal configuration, the advective flow under the project site must first be understood and modeled. On Manhattan Island, the majority of the recharge zones are north of the site. From here, the flow of the subsurface water follows the topography of the island (NNE to SSW). There is a small ridge that runs down the center of the island that also contributes to the flow by forcing much of the water to either the east or west coasts to either the Hudson River or the East River (Figure 14). For the Penn south project site, this means that the flow will run slightly diagonally from the north boundary of the site to the south boundary (Figure 15).

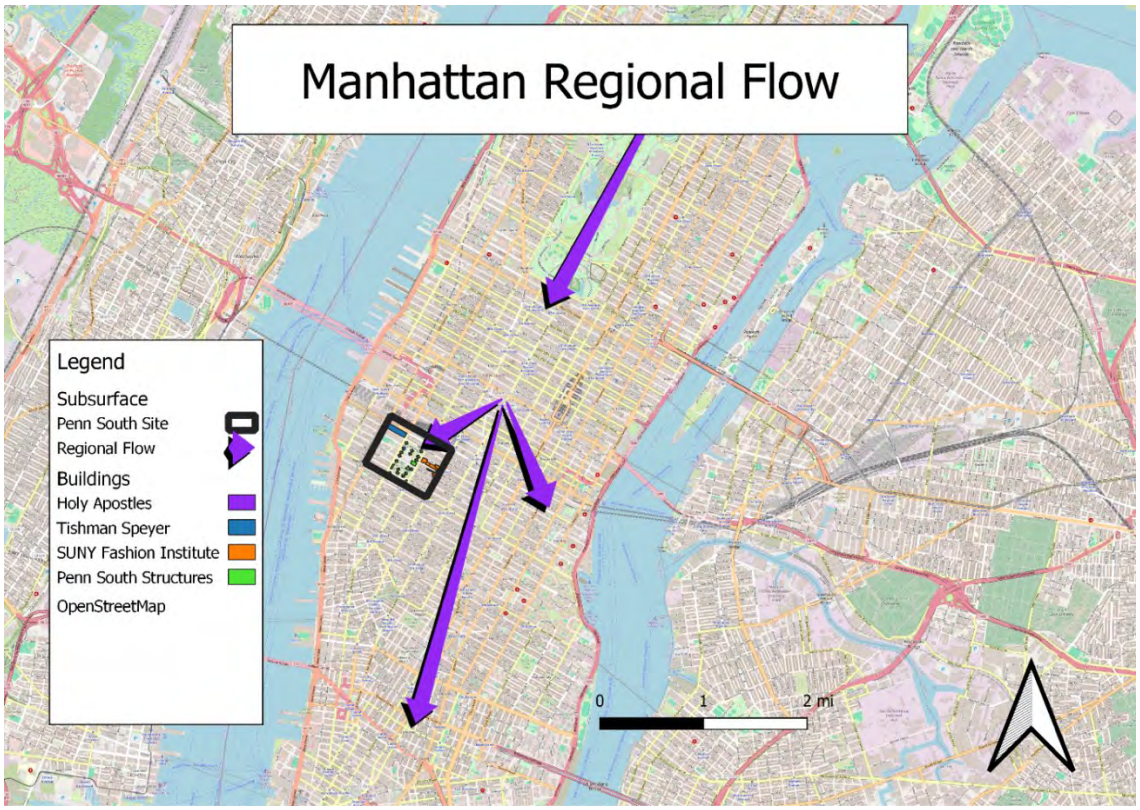

Figure 14: General regional flow of groundwater on Manhattan Island and across the site

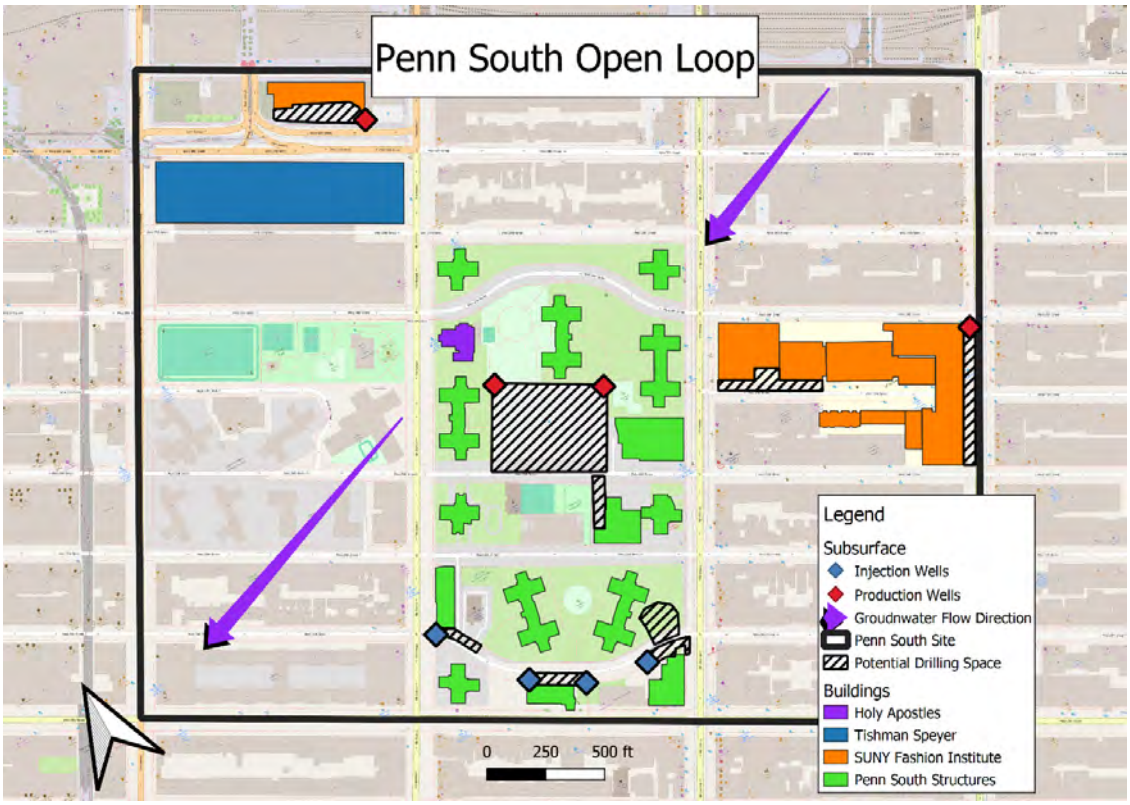

Figure 15: Regional flow across the Penn South site

To model the advective flow in PetraSim, a technique was used that requires multiple save files that build on top of each other. First, the depth to water was obtained for the north and south sides of the site. Using some simple math, the pressures at the bottom of the glacial till were estimated for each side (Table 3). To obtain pressure values for the rest of the depths on the north and south sides, all the cells but those immediately bordering the north and south sides were disabled, the pressure at the bottom of the glacial till was set to a fixed state, and the model was allowed to run for 1000 years. This produced an accurate prediction of the pressure at all depths of the model boundaries (Figure 16).

Table 3: Pressures at each side of the model used to drive the regional groundwater flow (high to low)

Depth to Water (ft)	
North Elev	31
South Elev	24
North Water Elev	24
South Water Elev	3.8
North Depth to Water	7
South Depth to Water	20.2
Average Depth to Water	13.6
Average Depth to Bedrock	50

Pressure at Depth (Pa)	
North Pressure @ 50ft	128573.784
South Pressure @ 50 ft	89104.6224

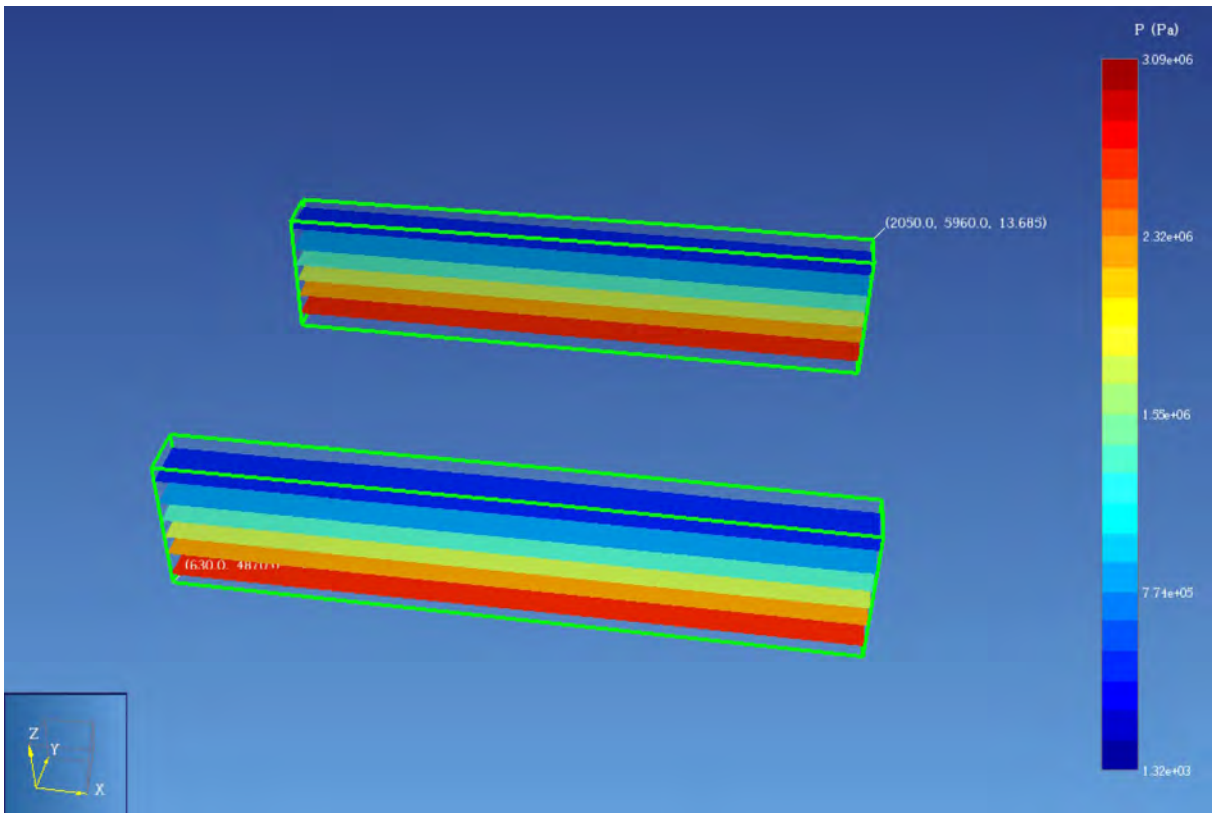

Figure 16: Pressure (Pa) displayed in the cells on the north and south edges of the site model after the 1000-year simulation

Next, the north and south boundary cells at all depths were set to a fixed state with infinite volume to simulate the extent of the subsurface north and south of the site. The disabled cells between the two zones of differing pressure were enabled, and the model was again allowed to run for 1000 years to obtain equilibrium between the two zones (Figure 17). The result is an accurate model of the advective flow beneath the project site (Figure 18). This process is called natural state modeling, and the output will be used as a base to run production scenarios on top of the simulated advective flow.

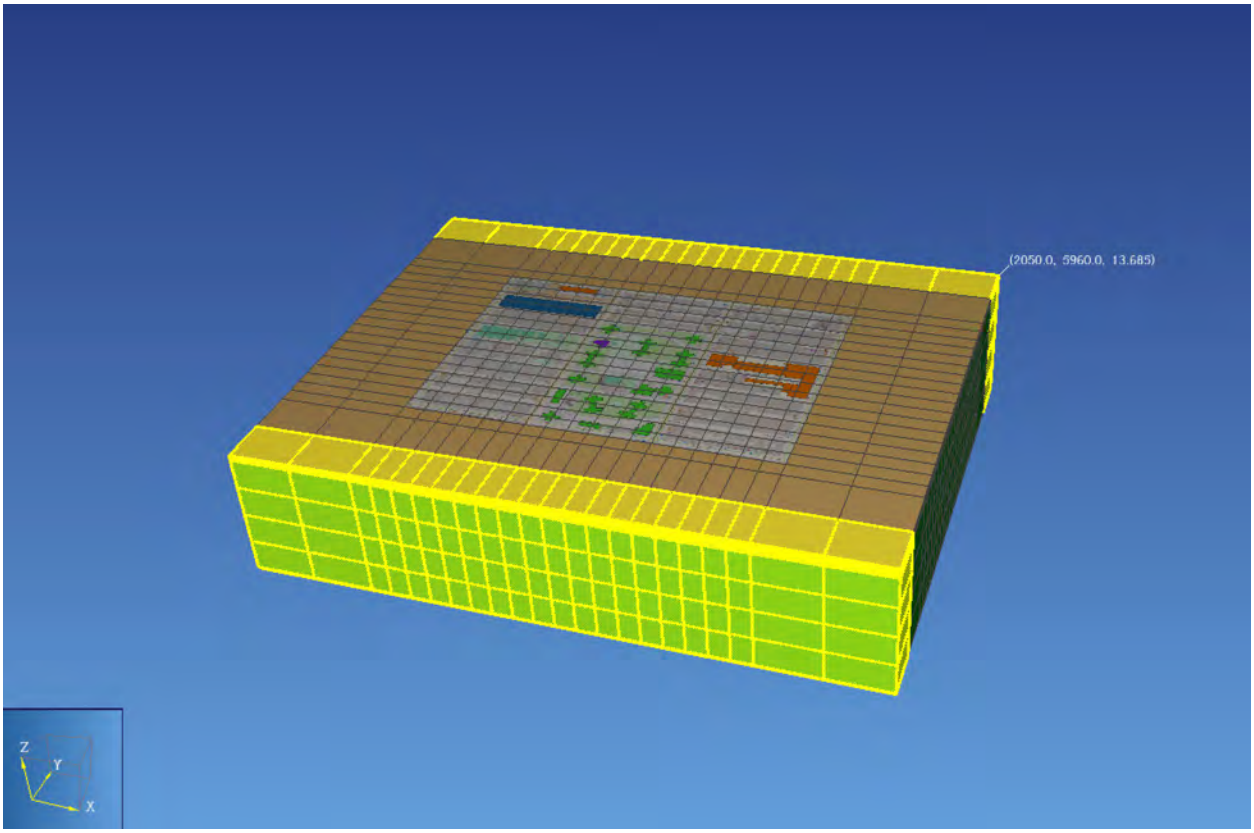

Figure 17: A screenshot of the site model before the natural state (advective flow) modeling. The cells highlighted in yellow with their varying pressures were set to a fixed state

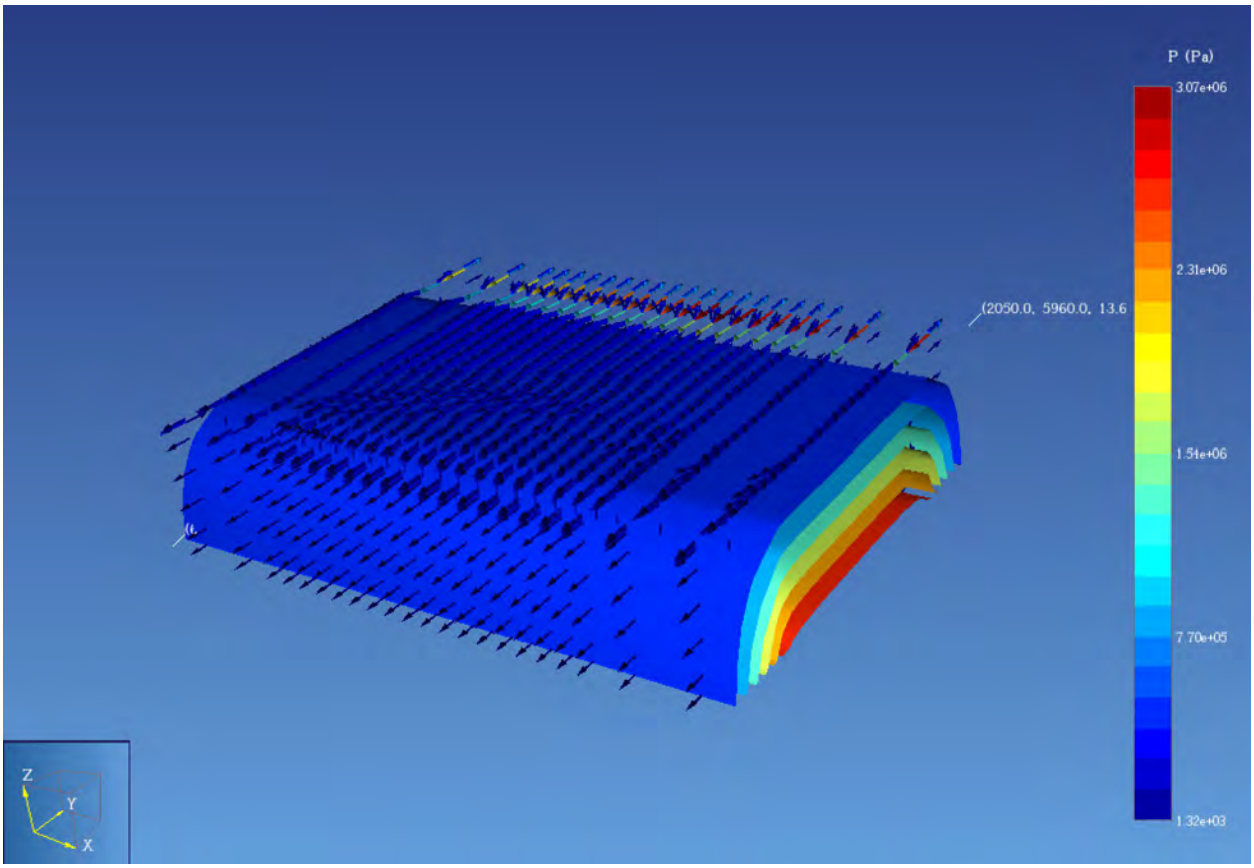

Figure 18: Pressure (Pa) displayed across the site model and vectors indicating the groundwater flow across the site

2.4. Simulations

Two scenarios (A and B) were considered to simulate the thermal performance of a doublet system at this project site and to inform on well spacing. As noted previously, two pumping flow rates were simulated, one low (300 gpm) and one high case (600 gpm). An additional two scenarios (C and D) were also simulated with the building foundations included for each flow rate to compare the reach of the thermal plumes. All four scenarios simulated the baseline condition of ~seven months of cooling (5170 hours) alternating with ~five months of heating (3590 hours), which would be the anticipated case for buildings in this geographic region. Additionally, for all four scenarios, the heating and cooling system is anticipated to run on a 12F delta T for heating months and 18F delta T for cooling months. Because the groundwater is projected to be about 52F, it is estimated that 40F water will be injected during heating months and 70F water will be injected in the cooling months. Each of the four production simulations ran for 25 years (Table 4).

Industry norms generally require at least 1000 ft of separation between injection and production wells, and at least 200 ft between wells of the same likeness. At first glance, and considering these industry norms, four production well locations and four injection well locations were chosen. More specific well locations and varying layouts will be explored in future studies, but it suffices the scope of this study to gain a better understanding of potential well yield, necessary separation estimates, the effect of building foundations, and an estimated load to be met by an open loop

configuration in this neighborhood. The example well layout used for this experiment is displayed in Figure 19.

Table 4: Modeled Scenarios

	Flow Rate / Well (GPM)	Total Flow Rate (GPM)	Foundations Included (Y/N)
Scenario A	300	1200	N
Scenario B	600	2400	N
Scenario C	300	1200	Y
Scenario D	600	2400	Y

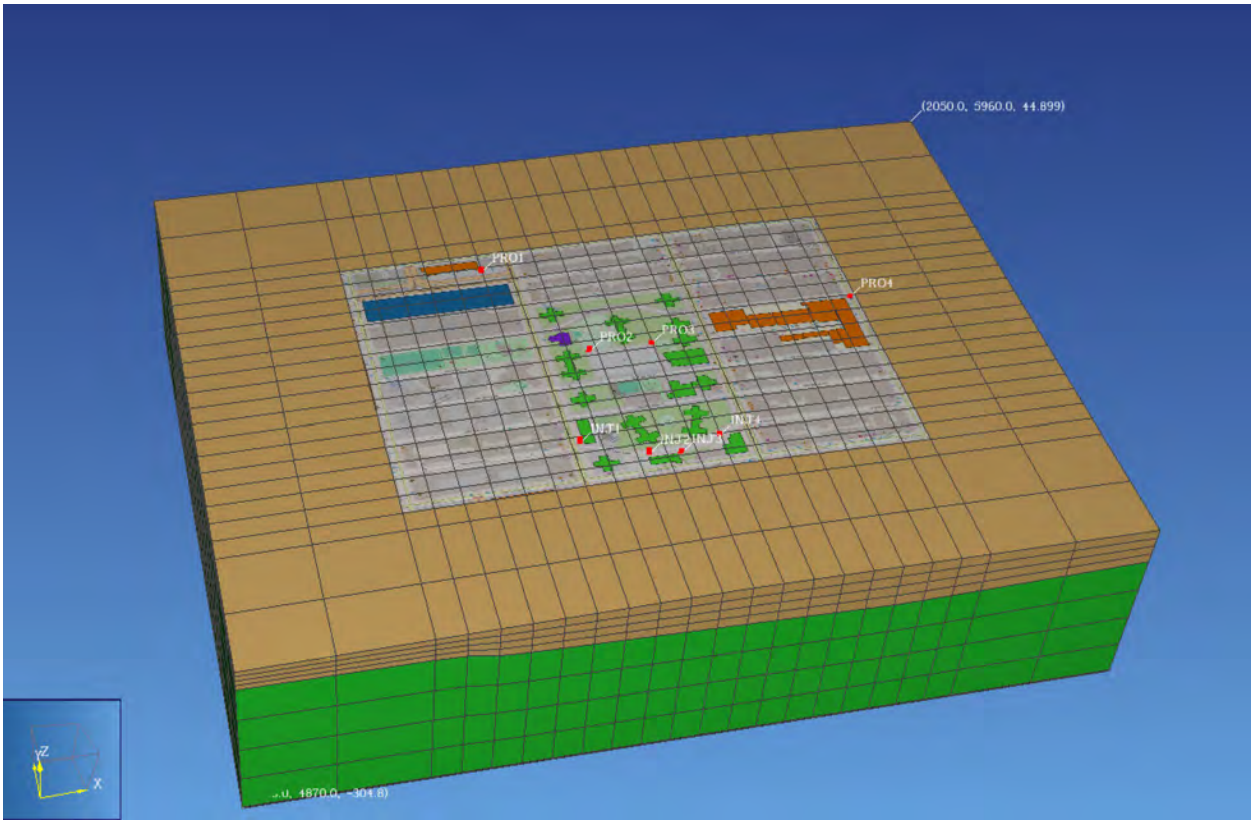

Figure 19: Well locations for the simulations. The 4 wells to the north (PRO1-4) extract water from the formation and the 4 to the south (INJ1-4) inject water after it has been used for heat exchange

3. Results

The results for each scenario are displayed and discussed below. To help visualize the flow of heat and fluid (groundwater) through the aquifer, three screenshots were used to display the results after 25 years of operation for each scenario. The first figure presents temperature as isosurfaces across the site and displays the injection and production wells. A horizontal slice at a depth of 45’ is also included. This depth was chosen because it is the average middle depth of the open hole sections of all 8 wells. It represents the most likely depth for thermal short-circuiting to occur (Figure 20). Additionally, a temperature log across 25 years for production well 2 and 3 has been included. These two wells were chosen because they are the closest geographically to the injection wells and most likely to be influenced by the plume from the injection wells. Because the well temperatures

for the scenarios with and without foundations included did not change, well temperature screenshots were not included for scenarios C and D.

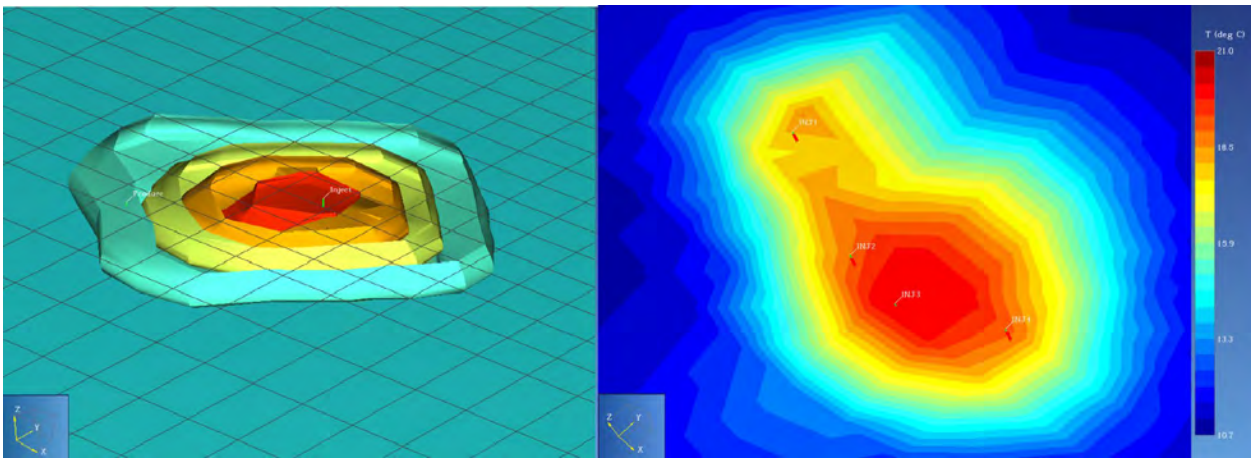

Figure 20: Example results displaying the temperature isosurfaces in the narrative to visualize the most important output from an otherwise large and complex 3-dimensional model (Left).). An example result of a horizontal slice is also included (Right) Temperature in Fahrenheit across 25 years is also computed at the production wells and plotted below (not pictured here).

3.1. Scenario A

This scenario simulated 300 gpm per well or 1200 total gpm for 25 years under the alternating seasons of heating and cooling cycle described above. Advective flow was considered in this scenario using the natural state modeling described above. The output (SAVE) file from the natural state modeling was used as the initial conditions file (INCON) for the following production scenarios. The aquifer displayed no hydraulic stress in yielding this rate. Additionally, after 25 years, the temperature at the production wells increased by less than 0.01F. This shows virtually zero thermal short-circuiting and no thermal saturation despite a heating dominant load profile.

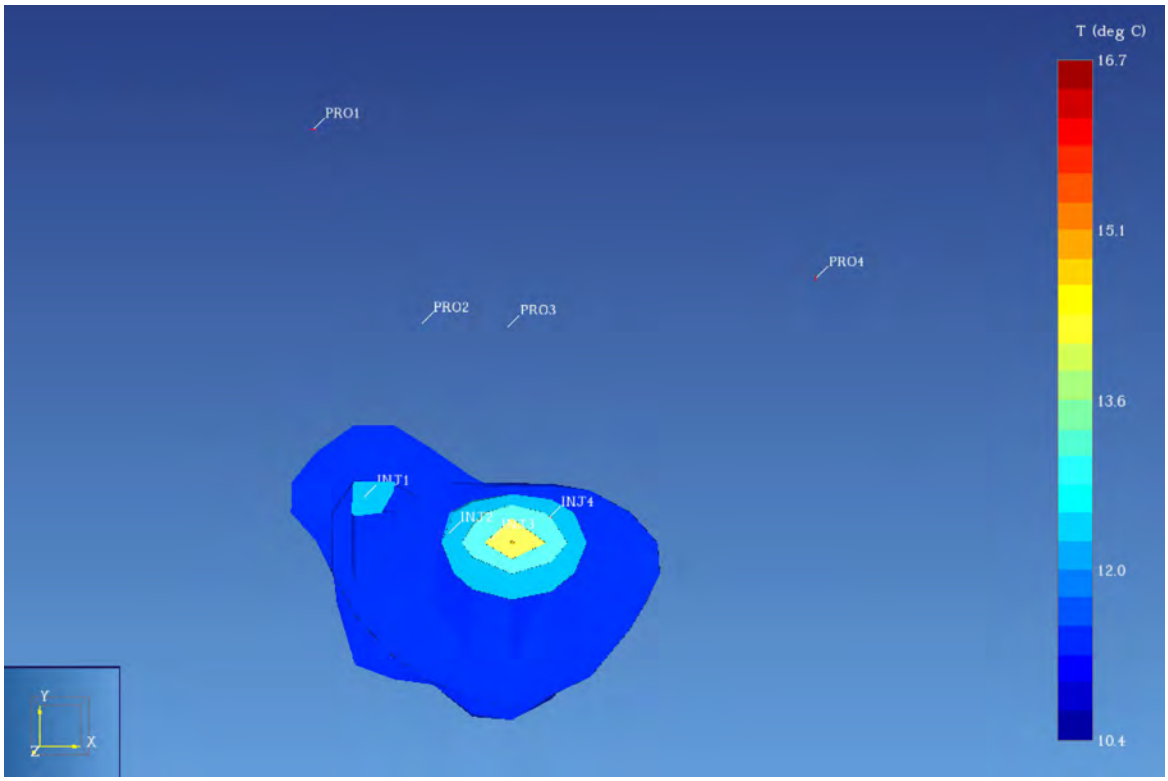

Figure 21: Scenario A - Temperature isosurface results after 25 years of pumping at 300 gpm

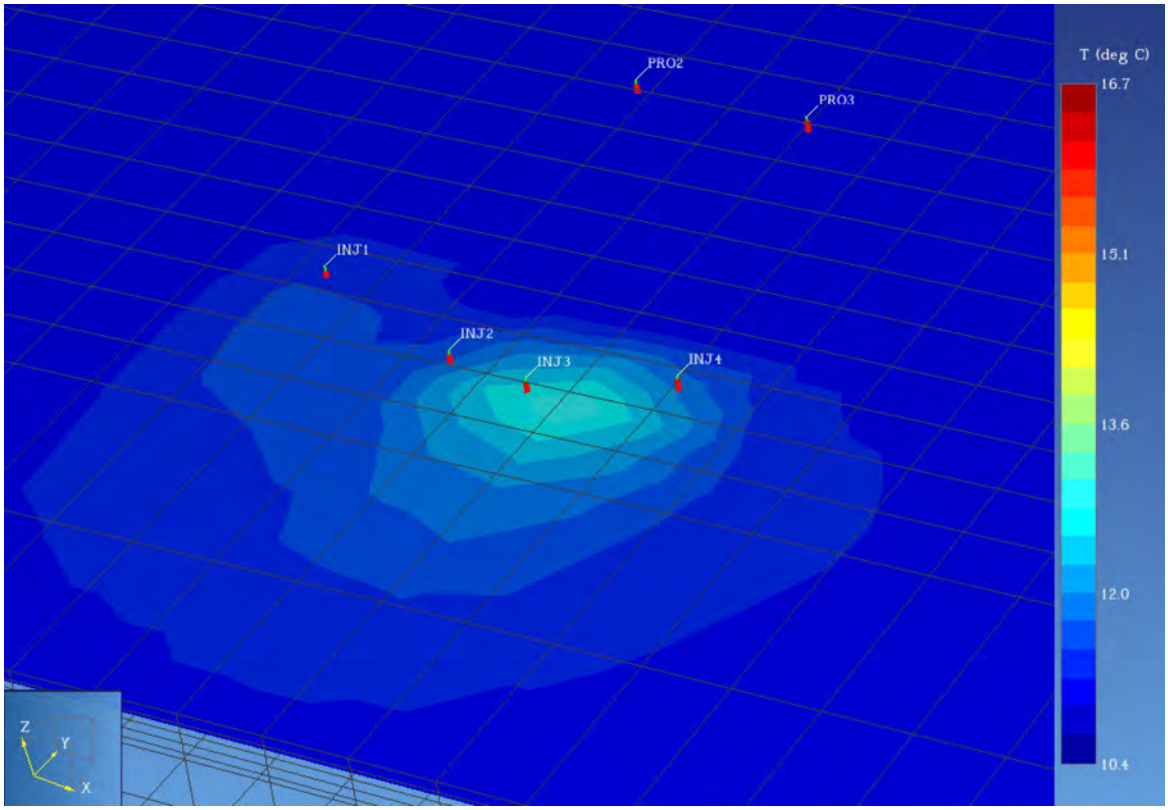

Figure 22: Scenario A - Horizontal temperature slice at 45' below surface after 25 years of pumping at 300 gpm

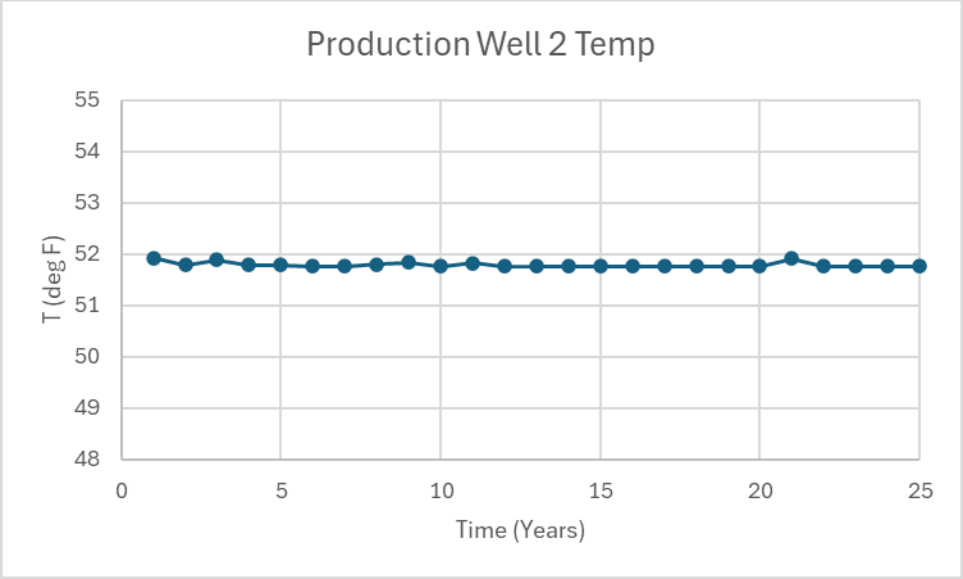

Figure 23: Scenario A - Temperature results at production well 2 plotted across 25 years of pumping at 300 gpm

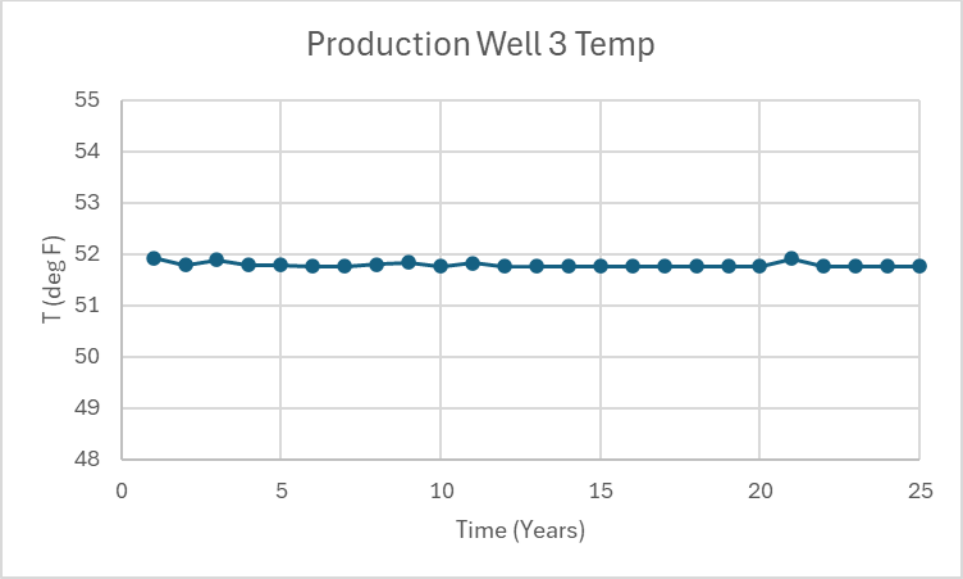

Figure 24: Scenario A - Temperature results at production well 2 plotted across 25 years of pumping at 300 gpm

3.2. Scenario B

This scenario simulated 600 gpm per well or 2400 total gpm for 25 years under the alternating seven months of heating and five months of cooling cycle described above. Advective flow was considered in this scenario using the natural state modeling described above. The aquifer displayed no hydraulic stress in yielding this rate. Additionally, after 25 years, the temperature at the production wells increased by less than 0.01F. This shows minimal thermal short-circuiting and no thermal saturation despite a heating dominant load profile. Despite the increased production, there was little change in temperature at the production wells. This is likely due to the advective flow that flushes thermally altered injection fluid away from the site. This result indicates that the

limiting factor for this system will likely be the aquifers ability to sustainably yield water, not the constrictions of the site boundaries.

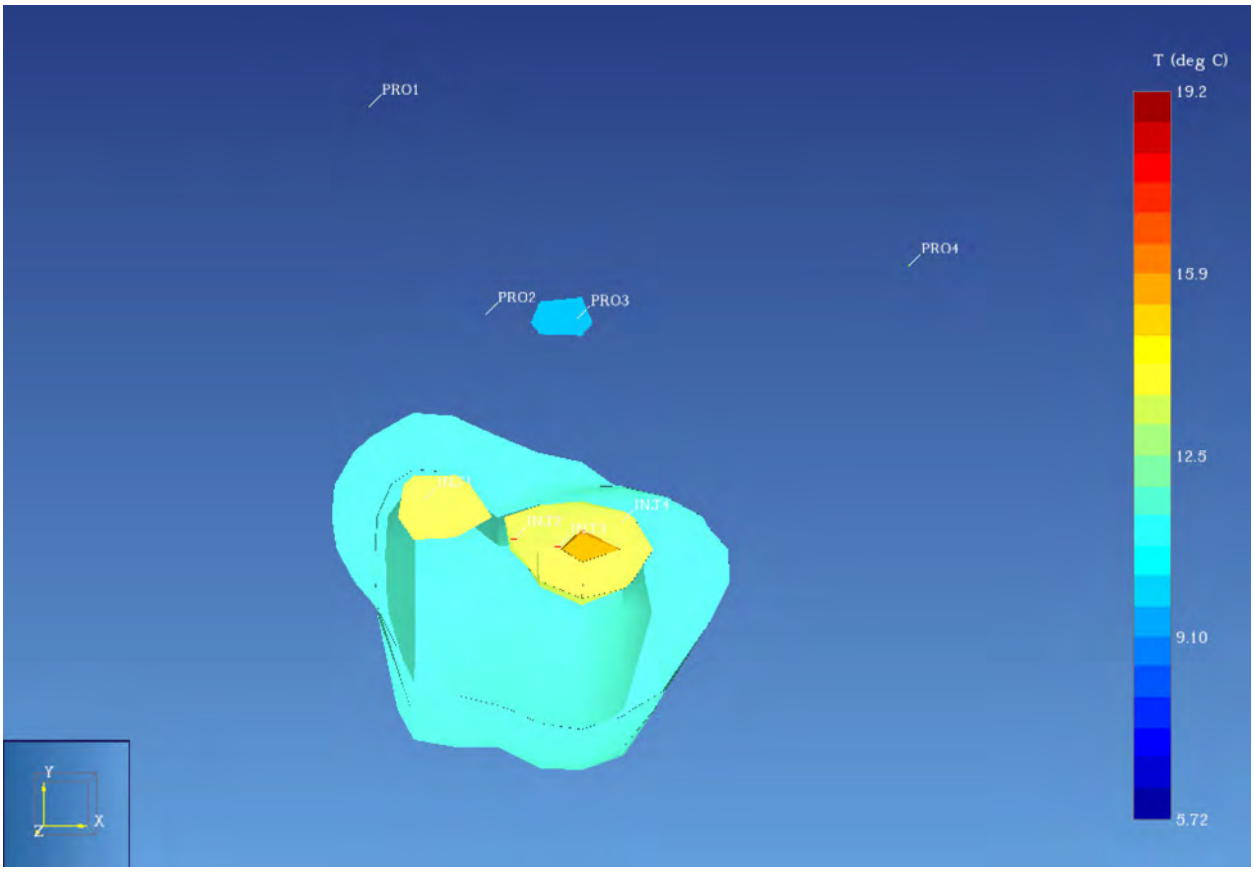

Figure 25: Scenario B - Temperature isosurface results after 25 years of pumping at 600 gpm

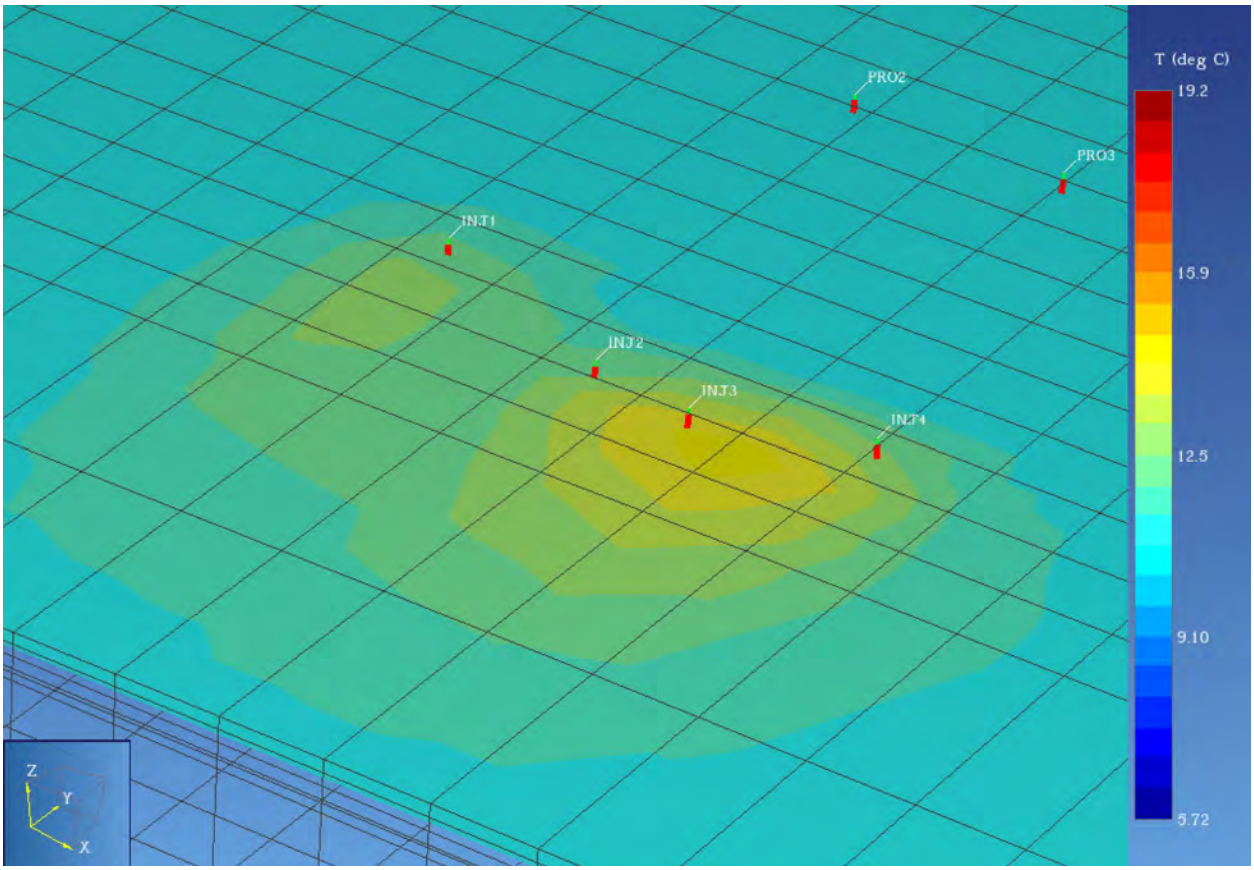

Figure 26: Scenario B - Horizontal temperature slice at 45' below surface after 25 years of pumping at 600 gpm

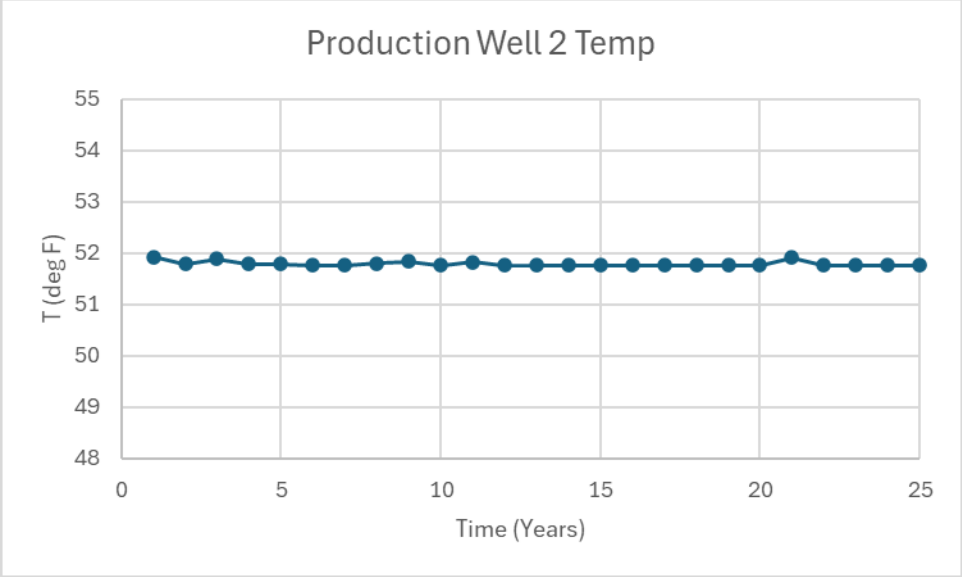

Figure 27: Scenario B - Temperature results at production well 2 plotted across 25 years of pumping at 600 gpm

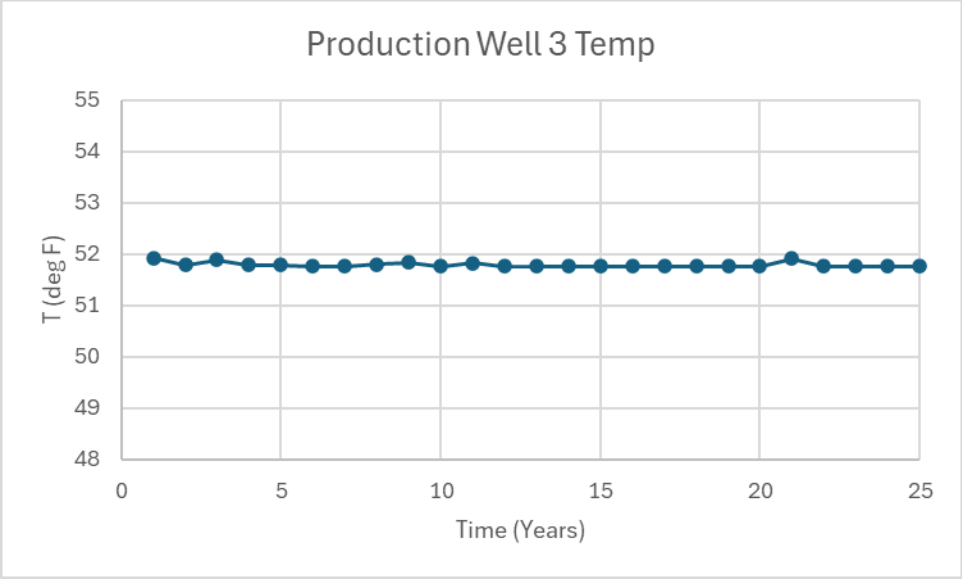

Figure 28: Scenario B - Temperature results at production well 3 plotted across 25 years of pumping at 600 gpm

3.3. Scenario C

This scenario simulated 300 gpm per well or 1200 total gpm for 25 years under the alternating seasons of heating and cooling cycle described above. Advective flow was considered in this scenario using the natural state modeling described above. Building foundations were included in this model to an average depth of 25 ft below the surface. Results were very similar to Scenario A.

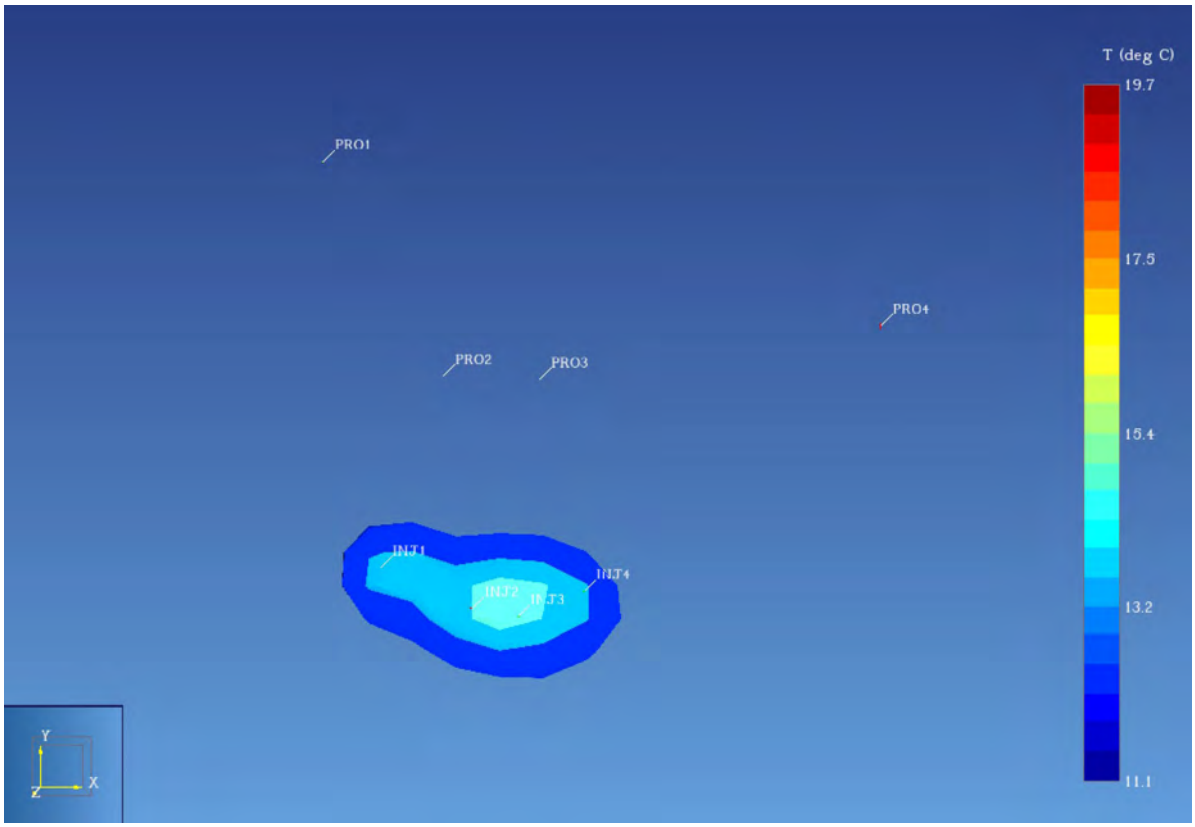

Figure 29: Scenario C - Temperature isosurface results after 25 years of pumping at 300 gpm with building foundations added to the model

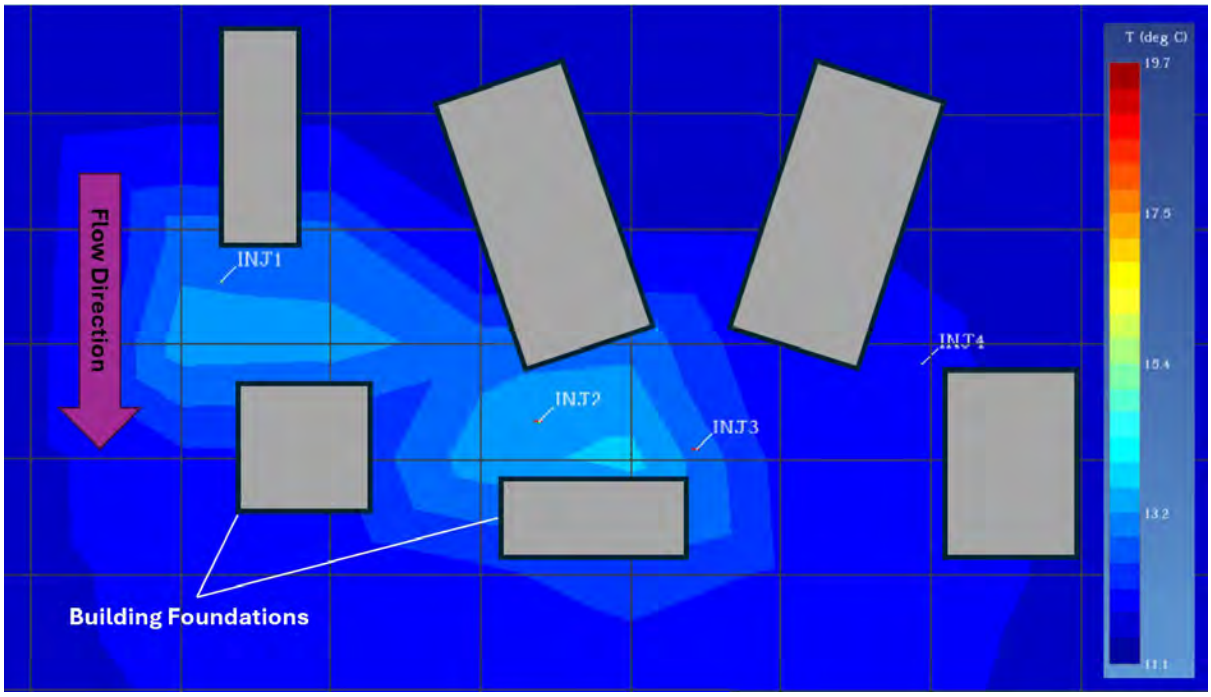

Figure 30: Scenario C Horizontal temperature slice at 45' below surface after 25 years of pumping at 300 gpm with building foundations visualized

3.4. Scenario D

This scenario simulated 600 gpm per well or 2400 total gpm for 25 years under the alternating nine months of heating and three months of cooling cycle described above. Advective flow was considered in this scenario using the natural state modeling described above. Building foundations were included in this model to an average depth of 25 ft below the surface. Results were very similar to Scenario C.

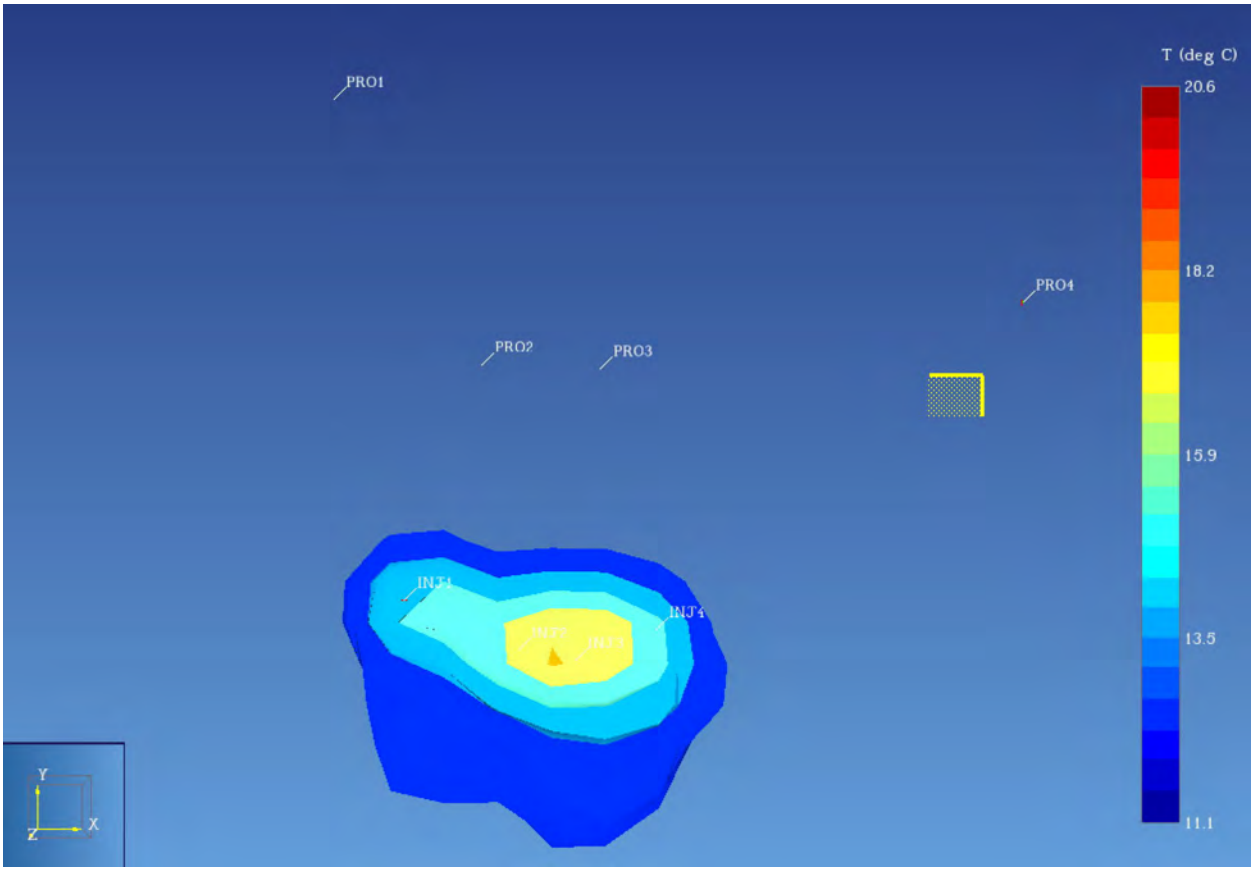

Figure 31: Scenario D - Temperature isosurface results after 25 years of pumping at 600 gpm with building foundations added to the model

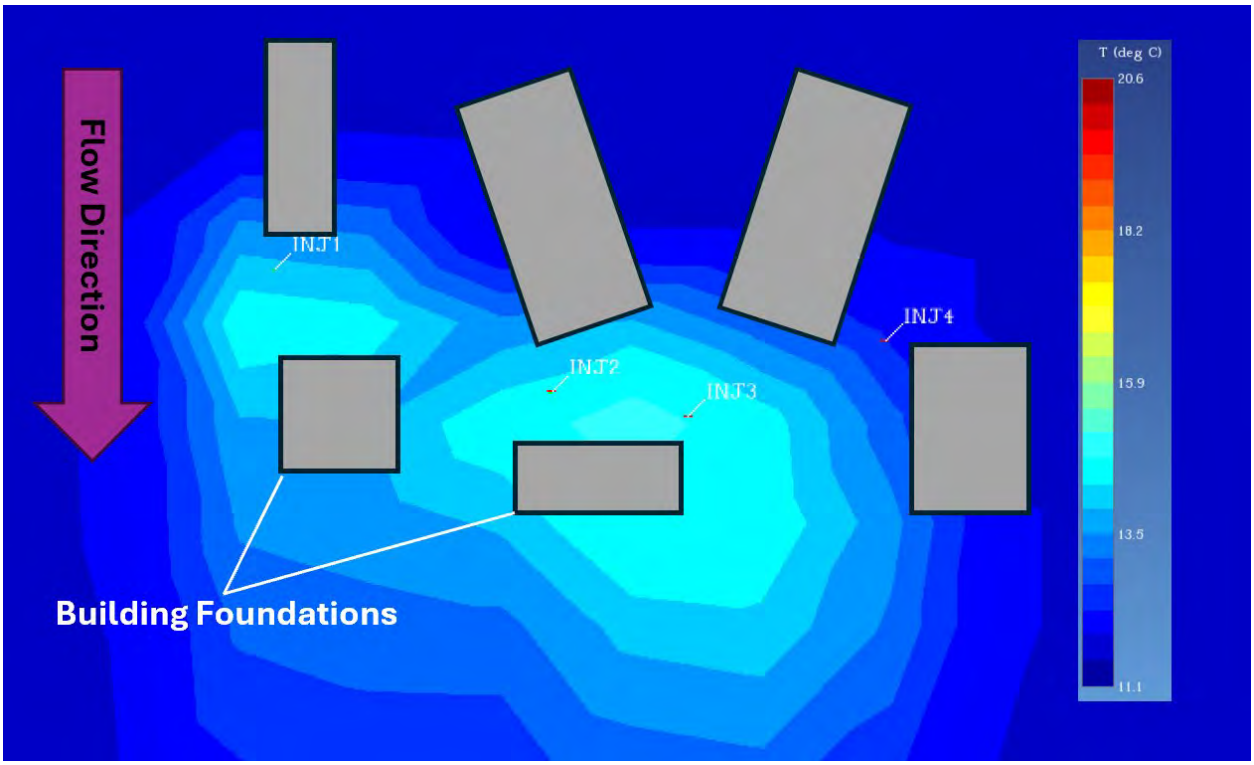

Figure 32: Scenario D Horizontal temperature slice at 45' below surface after 25 years of pumping at 600 gpm with building foundations visualized

4. Conclusion

Originally, a closed loop array had been considered for this site. An early system design was conducted, and it was estimated that there was enough green space to meet 15% of the peak with a closed loop system. The open loop array estimates were combined with the original closed loop estimates. The separate performance of each of these systems is displayed in Figure 33. The combined systems (closed and open loop) have the potential to meet the heating and cooling loads about 51% of the time (Scenario B & D). This number is initial and approximate and will change depending on the results of a test well. It should also be noted that although the system only meets the heating and cooling loads around half the time, the percent of BTUs met is over 70% (Table 5). Additionally, more work should be done in future studies to determine the optimal well layout. This was not explored fully in this study because a full design relies on the results of a test well. Instead, a realistic example layout was chosen to test the well separation needs. The results suggest that, due to the high advective flow in the area, the necessary well separation between production and injection can be far closer than the industry standard if needed. The closest distance between a production and injection well in this example is the 1085 ft between INJ1 and PRO2. Even in Scenario B, after 25 years there was still over 800 ft between the two wells with no thermal influence.

Table 5: Best case scenario combined system results

System Heating and Cooling for 15% of Peak Closed Loop and High Yield Open Loop				
Sum of Total Heating Met (BTUs)	Sum of Total Cooling Met (BTUs)	Sum of Unmet Heating(BTUs)	Sum of Unmet Cooling (BTUs)	% of BTUs Met
210,132,856,571.91	(71,042,600,726.35)	77,374,610,698.80	(36,331,933,501.47)	71.20
% of Total Heating Met	% of Total Cooling Met	% of Heating Time Met	% of Cooling Time Met	% of Time Heating & Cooling Met
73.09	66.16	65.97	85.71	51.68

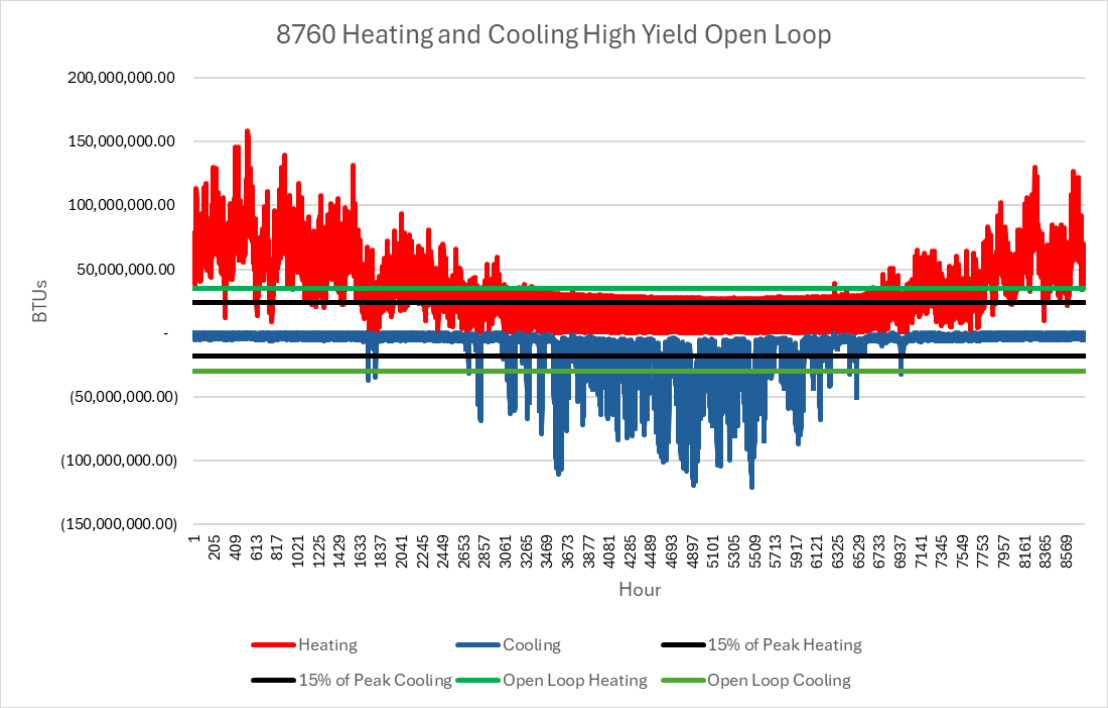

Figure 33: Separation of the closed loop system (15% heating/cooling) and the open loop system (green horizontal lines) compared to the overall 8760 heating and cooling loads.

Figure 34 and Figure 35 were prepared for comparison between the scenarios with and without concrete foundations. Generally, the thermal plumes were obstructed by the foundations. In scenarios that included the foundations, the fluid was forced between or under the building foundations. This contributed to lower temperatures immediately down gradient from the wells. Obstruction of groundwater flow around and under the foundations is easily observed in Figure 34, but the shapes of the high temperature portions of the plumes in Figure 35 are still very indicative of a shift groundwater flow either laterally or beneath the foundations. Although the inclusion of foundations didn't have an effect on the temperature of the production wells for this well layout, we learned that it has the potential to affect the results of other simulations. These results suggest that subsurface elements not usually included in groundwater modeling may have dramatic effects on the results of simulations and should be considered if we are to produce accurate subsurface models in dense urban areas and for systems that exploit shallow aquifers.

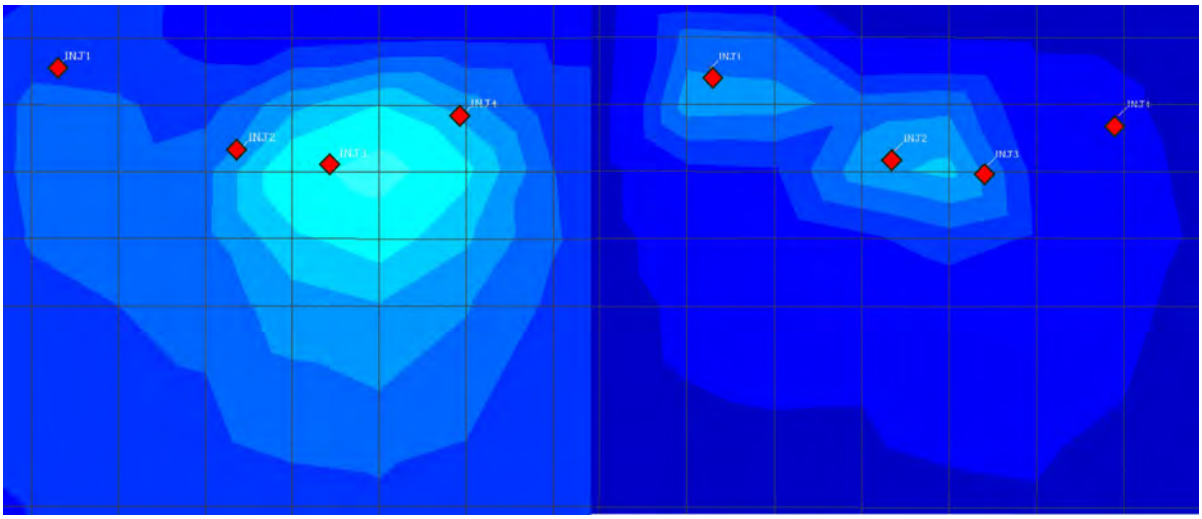

Figure 34: (Left) Temperature isosurface (45 ft deep) from Scenario A (300 GPM) with wells displayed in red. (Right) Temperature isosurface from Scenario C (300 GPM) with building foundations included in the model

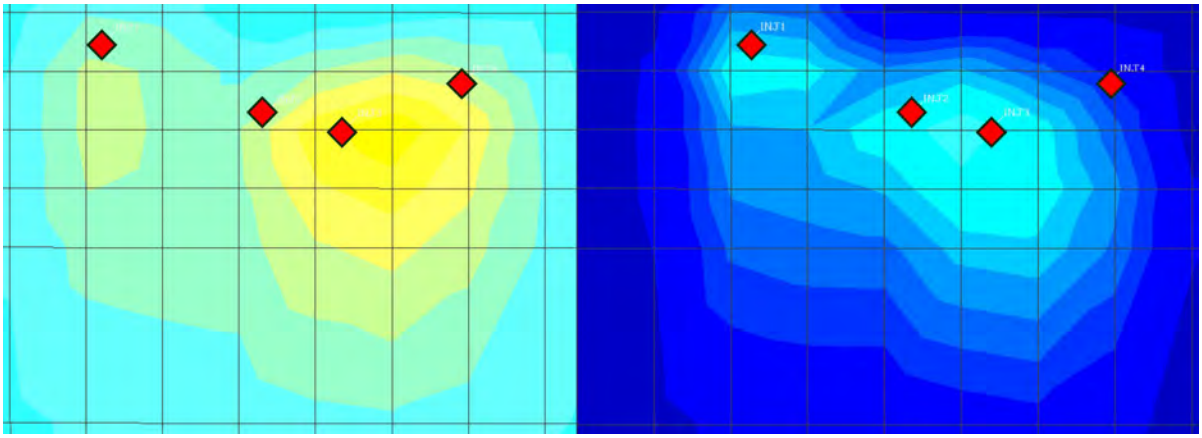

Figure 35: (Left) Temperature isosurface (45 ft deep) from Scenario B (600 GPM) with wells displayed in red. (Right) Temperature isosurface from Scenario D (600 GPM) with building foundations included in the model

Decarbonization in urban areas, such as New York City, presents a tremendous engineering challenge. The regulatory environment created by the UTENJA and the Climate Mobilization Act promote the application of geothermal and geoexchange technologies in New York State and New York City. Geothermal and geoexchange technologies offer building portfolio managers a responsible electrification technique that can reduce their operational costs over the long term wherever the appropriate sources and sinks are available. Aquifer thermal energy transfer is one of several subsurface exploitation methods that can provide engineering firms, building managers, and policymakers with city-scale decarbonization. Future studies will be necessary to fully ensure the success of a potential geothermal system in the Penn South neighborhood. To achieve the transition to clean energy, the Penn South neighborhood will need to optimize the open loop well layout, but also consider implementing additional clean energy sources including wastewater energy transfer and closed loop geothermal techniques. Understanding the geologic conditions and the surface system engineering necessary to utilize those conditions is absolutely essential to maximize heating and cooling performance. Special care should be taken to understanding the

depth of glacial till, the permeabilities of shallow bedrock, regional advective flow, and other elements that may influence the flow of groundwater including building foundations, subway dewatering, and localized stream channels that increase the depth to bedrock.

REFERENCES

Bedrock-Surface Elevation and Overburden Thickness Maps of the Five Boroughs, New York City, New York. (2023). (Data Report).

Downloadable Well Data - NYSDEC. (n.d.). Retrieved August 27, 2024, from https://dec.ny.gov/environmental-protection/oil-gas/wells-data-geographical-information/downloadable-data

McCymonds & Franke. (1972). Water-Transmitting Properties of Aquifers on Long Island, New York (Professional Paper).

Skutnik, Z., Sobolewski, M., & Koda, E. (2020). An Experimental Assessment of the Water Permeability of Concrete with a Superplasticizer and Admixtures. *Materials*, *13*(24), 5624. https://doi.org/10.3390/ma13245624

Soren, J. (1978). HYDROGEOLOGIC CONDITIONS IN THE TOWN OF SHELTER ISLAND, SUFFOLK COUNTY, LONG ISLAND, NEW YORK.

USGS Groundwater Data for the Nation. (n.d.). Retrieved August 27, 2024, from https://waterdata.usgs.gov/nwis/gw

Water | Free Full-Text | Delineation of Salt Water Intrusion through Use of Electromagnetic-Induction Logging: A Case Study in Southern Manhattan Island, New York. (n.d.). Retrieved August 27, 2024, from https://www.mdpi.com/2073-4441/9/9/631

Zhang, H. (n.d.). HYDROGEOLOGY OF THE QUATERNARY WATER-TABLE SYSTEM.

A Definitional Taxonomy for (Geo)Thermal Energy Networks

Zeyneb Magavi[1], Angie Alberto-Escobar[1] and Isabel Varela[1]

[1]Home Energy Efficiency Team (HEET)

Keywords

Geothermal energy, taxonomy, heat pumps, thermal energy networks, geothermal networks, district heating and cooling, 5GDHC, community geothermal

ABSTRACT

Geothermal technologies can all provide the stable, dispatchable, non-intermittent energy that our energy system needs, yet the challenge of differentiating among these technologies and clearly defining them for the public and decision-makers is impeding progress. Even within the scope of district-scale geothermal technologies, there are multiple naming systems which are not always clearly linked to the specific designs and outcomes. In order to scale the provision of the different types of technologies that tap geothermal energy, technically accurate, clear, and standardized terminology needs to be adopted. This study proposes a taxonomy for geothermal energy networks (GENs), within the context of definitional clarity for geothermal technologies, district energy systems, and thermal energy networks (TENs). We introduce a taxonomy rubric that connects nomenclature and design choices to expected system outcomes. The proposed taxonomy is the product of extensive interviews and stakeholder engagement, with members of the geothermal and ground source heat pump communities, as well as academic, industry, advocacy, workforce, customer, policy and environmental justice groups. Across these industry stakeholders, the link between technology components, system design, performance, and terminology is desired and seen as necessary to industry success. One state regulatory leader referred to TENs as the first new utility in a hundred years. As multiple states and countries create policy to enable geothermal and thermal energy networks at the utility-scale, this proposed taxonomy rubric is intended to provide a clear nomenclature upon which to build statutory language and regulatory frameworks.

1. Introduction

The greek root of the word geothermal is a reasonable descriptor, ‘earth heat’, and we further define *geothermal energy as all thermal energy that is generated or stored at or below the surface of the earth, including in soil, rock, and water*. Near to the surface the majority of this energy is stored solar thermal energy accumulated across millenia and replenished at an increasing rate due

to global warming. Deeper geothermal energy comes from the core of the earth which is similar to the surface temperature of the sun and is replenished by radioactive decay. Both of these energy sources are considered both renewable and a large enough reservoir to be functionally inexhaustible. According to the U.S. Department of Energy's *GeoVision: Harnessing the Heat Beneath Our Feet* (2019), these thermal resources have been largely untapped in the US.

Despite the scale of this non-intermittent renewable energy source, none of the technologies that tap this energy have yet scaled to match the opportunity. One consistent hurdle to scaling is a limited understanding of geothermal energy among policy experts and decision makers in part driven by inconsistent, and therefore confusing, use of terminology to describe the technologies that tap this energy.

Unlike many renewable energy technologies such as solar and wind, all geothermal technologies can offer non-intermittent baseload renewable energy that is dispatchable, stable, and reliable. Beyond this, geothermal technologies are varied in their depth (from shallow to deep), temperature (from super hot to ambient), distribution (from a few spots to everywhere), application (from power to heating and cooling) and scale (from single buildings to regional utilities). This diversity is one source of the definitional challenge which the authors propose to address through the following geothermal energy nomenclature. There are many more possible combinations and exceptions to this categorization, however the simplicity of these four main categories depicted in **Figure 1** has proven useful to a wide range of stakeholders.

(1) Geothermal Power: Uses high temperature geothermal energy for electricity generation. Temperatures are typically higher than 120℃ / 245℉. However, lower temperatures can be used with binary power plants (Febrianto et al. 2019).
(2) Geothermal Direct-Use: Uses temperatures in the range of 30 ℃ / 85℉ to 120℃ / 245℉ (Østergaard and Svendsen 2017) for direct use of hot water to provide space heating and domestic hot water for one or more (usually multiple) buildings.
(3) Geothermal Heat Pump*: Uses ambient temperatures to provide thermal energy for heating and cooling for individual buildings, and can provide domestic hot water.
(4) Geothermal Networks: Uses ambient temperatures interconnecting to provide heating and cooling for multiple buildings, and can provide domestic hot water.

* Geothermal heat pumps will be referred to in this study interchangeably as ground source heat pumps, and are also sometimes referred to as water-source heat pumps.

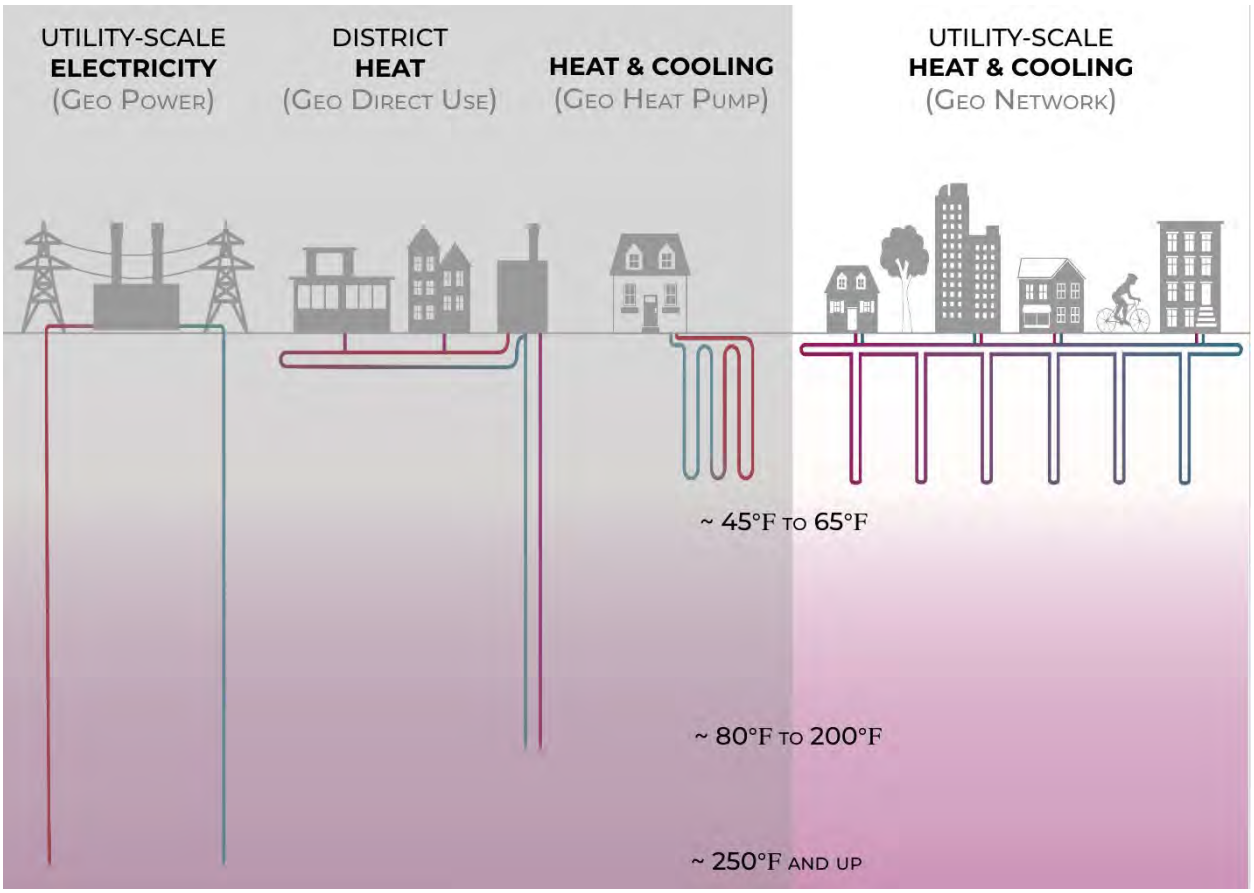

Figure 1. Geothermal Energy: Geothermal technologies by temperature harvested and applications. Includes geothermal power for electricity generation, geothermal direct-use for district heating, geothermal heat pump for heating and cooling of individual buildings, and geothermal networks for heating and cooling multiple buildings.

This study focuses on the terminology used to describe the newest of this geothermal technology family, the geothermal networks, which this publication will also refer to interchangeably as geothermal energy networks (GENs). Geothermal energy networks are generally understood to be thermal energy networks that access shallow geothermal energy - with thermal energy networks understood to be distribution infrastructure interconnecting heat pumps in multiple buildings together with distributed thermal resources.

In order to clarify terminology for GENs, this study first clarifies the word geothermal, as above, and next defines these GENs through first a consideration of district energy system nomenclature, then a consideration of the emerging thermal energy networks nomenclature, and finally followed by the integration of each of these into one consistent proposed taxonomy.

The district heating and cooling (DHC) system nomenclature and the thermal energy networks (TENs) nomenclature have largely evolved in different contexts. DHC systems have developed most in societies with a centralized planning of the energy supply, with many examples in Europe. In the U.S. such DHC systems are most common on campuses. The TENs and GENs subset of these DHC systems have emerged only in the past decade within the context of building decarbonization.

As Buffa et al. (2019) argue, even within the scope of district-scale technologies, there are multiple naming practices that are not clearly linked to the specific designs. To enable optimized scaling of this relatively novel technology there is a clear need for accurate, consistent, and standardized terminology to link designs to outcomes. This work is an effort to meet this need and is organized into six main sections: (1) introduction, (2) methodology, (3) background on existing terminology, (4) risks of ambiguous terminology, (5) proposed taxonomy and (6) conclusions.

2. Methodology

The methods used to inform the taxonomy rubric proposed include an extensive stakeholder engagement process, a literature review and learnings from ongoing pilot projects in Massachusetts.

2.1. Stakeholder Engagement

The stakeholder engagement process which informed the proposed taxonomy consists of three main initiatives including community charrettes, open reporting and informing policymakers.

2.1.1. Community Charrettes.

Community charrettes are a gathering of multiple stakeholders to discuss a common challenge or opportunity (Condon 2012) and have been used by HEET for this purpose since January of 2020. They are designed to ensure all stakeholder groups are represented in the development of a concept with the shared purpose of resolving conflicts and mapping solutions. Many community charrettes abide by Chatham House Rules, to encourage the sharing of information and minimize any perceived risks.

One of the early charrettes for GENs was conducted to develop site selection criteria and included collaborators from the following stakeholder groups: New York and Massachusetts state energy offices, gas utilities, geothermal solution providers, academics, municipalities, building developers, climate advocates and environmental justice advocates. The HEET charrette series for GENs has been ongoing since 2020 and spans a range of topics intended to share knowledge and methodology on how to install and grow these systems across the country. The HEET charrette series represents an inclusive and iterative approach to designing parameters and defining desired outcomes of a thermal energy transition.

2.1.2 Transparent Reporting

Charrette reports are published open source through Creative Commons CC-BY-SA licensing so that the public has access to methods, data and findings for each discussion. Progressive reporting is a key element of stakeholder engagement, allowing for a broader range of stakeholders to track progress and contribute their own ideas. By centering transparency and accountability, HEET developed trust and credibility with many stakeholder groups which led to enhanced collaborations. This active approach to stakeholder engagement has resulted in the formation of several national networks of stakeholders including groups focused on geothermal network policy, regulation, advocacy and system modeling. The access to many experts across multiple disciplines through both the charrettes and the national networks has informed the understanding that led to the proposed taxonomy rubric.

2.1.3 Informing Policymakers

HEET is actively engaged in informing policy makers to drive progress within the thermal sector. The stakeholder engagement process described coupled with HEET's research and innovation efforts enables the systematic investigation and analysis of issues yielding evidence-based insights and recommendations for policymakers and stakeholders.

The ongoing charrette series is also responsive to policymakers, frequently addressing topics informed by the needs, concerns or opportunities in the thermal transition policy landscape. This fosters policy relevant collaboration among government, industry, and academia through the charrettes. Common threads and concerns across stakeholders influenced the development of the taxonomy rubric proposed and the clear need for such an effort emerged in part from policymakers' request for clear links between technology, nomenclature, and outcomes.

2.2 Literature review

A literature review of academic journals, books and policy documentation was performed on current terminologies being used to describe conventional district heating and cooling systems (DHC) and fifth generation or 5GDHC installations. This review focuses on clarifying the technologies more commonly referred in the U.S. to as thermal energy networks and geothermal networks. The literature review results are summarized in section 3 below.

3. Background on Existing Taxonomy

The nomenclature for district heating and cooling systems has matured in Europe. The adoption of district-scale heating and cooling systems has been more prevalent in Europe than in the United States and has been primarily driven by the high demand for space and water heating in cold climates in Europe (Gjoka et al. 2023). The evolution of current district energy terminology began with district heating and expanded to encompass district heating and cooling systems. This terminology system has evolved to categorize district systems into distinct generations, reflecting changes in their characteristics and applications. This generational classification system provides a framework for understanding the development and refinement of district-scale heating and cooling systems in Europe and elsewhere, evolving generation after generation towards simultaneously lower temperatures and higher efficiencies.

Generations based DHC terminology is used in the U.S. within the district energy community and on college campuses but does not have widespread recognition or adoption in policy. This is perhaps how a parallel terminology evolution occurred, rooted in the geothermal and ground source heat pump industry, resulting in geothermal networks and thermal energy networks (TENs). The ground source or geothermal heat pump industry and the district energy industry language practices intersect in this new and rapidly emerging space of 5G, TENs, and GENs.

In this section we review: a) the terminology of district heating and cooling systems, b) the evolution towards fifth generation (5G), and c) the geothermal network and thermal energy network terminology that is mainly used in US policy manuscripts.

3.1 District Heating and/or Cooling

District heating systems are clearly defined by Woods (2023) as the distribution of heat to multiple buildings from one or more heat production facilities. Similarly, district cooling or coolth, is the distribution of chilled water to multiple buildings from a main chiller plant (Woods 2023). As

Woods (2023) clarifies, district heating and cooling systems are methods for transporting energy, but are not tied to a specific energy source. Additionally, Woods (2023) emphasizes that this definition encompasses a broad range of scales, going from small housing complexes to large district developments that could reach city-wide deployments.

Most existing district heating systems use fossil fuels as the supply method. Werner (2023) provides a global review of district heating and cooling systems from 1990 to 2014, for which the dominant heat supply was mainly powered by fossil fuels to heat water that was then utilized for direct use. As Werner (2023) describes, the fuel sources were recycled heat from combined heat and power (CHP) plants that use fossil fuels, as well as from boilers that burn fossil fuels to heat water for direct usage. In Europe 72% of the fuel in DHC systems is from recycled heat from combined heat and power plants, and 27% is from renewable sources. Globally the proportion of fossil fuels is larger, thus the recycled and renewable heat is lower, at 56% and 9% respectively.

District systems do not necessarily provide both heating and cooling, most are for heating only. Werner (2023) estimates that there are about 80,000 district heating systems globally, with about 6,000 of those in Europe. By contrast, Werner (2023) estimates that there are only about 150 district cooling systems in Europe, and mentions that there is a lack of data to estimate the global amount of cooling systems.

Societies with more central planning have more district systems. District systems have been implemented at larger scales in countries where the energy system is centrally planned and not driven solely by the market. Several European countries with high heating demands have adopted district systems to a large extent. Russia, Denmark and Sweden have high proportions of residential homes connected to DH, with 75%, 65% and 59% respectively (Woods 2023). Finland and Germany follow them, with penetrations at 38% and 14% (Woods 2023).

Conventional DHC systems can experience significant energy loss. Even though district systems are a more efficient way to heat and cool buildings than individual solutions, there are several disadvantages related to their use of energy. Traditional district heating and cooling systems (2G - 4G) experience significant thermal losses because they operate at relatively high temperatures of 25 C to 90 C. Additionally, to reach those high temperatures, most use fossil fuel sources that produce greenhouse gas (GHG) emissions. Furthermore, DHC systems require separate infrastructure in the form of combustion plants or chillers to be able to provide both heating and cooling. The markedly different fifth generation or 5GDHC heating and cooling systems address these concerns.

3.2 Nth Generation District Heating and Cooling systems

In recent years, 5GDHC systems have found a common definition in numerous academic studies. 5GDHC systems are described thoroughly by Buffa et al. (2019), Boesten et al. (2019), Sulzer et al. (2021) and Lund et al. (2018). They define 5GDHC systems as having the following characteristics: non-linear, bi-directional energy flow, and decentralized. They provide ambient temperature fluid to decentralized water-source heat pumps in the buildings on the loop, which deliver the required thermal energy for heating and cooling the building space (Gjoka 2023).

Bi-directional energy flow results in more efficient systems. Because of this, 5G systems are more efficient than previous generations of DHC systems. The bi-directional energy flow from the main

loop to the buildings and vice-versa makes 5GHDC systems well suited for urban environments with a high diversity of thermal load profiles. The bidirectional nature and diversity of building loads enables them to effectively "cancel" thermal loads between buildings, increasing the efficiency of the system. Furthermore, this bidirectional feature allows each building on the loop to be not only a consumer, but also a producer of heat. Systems with a single pipe as the main loop enable immediate recycling of low-grade waste heat or coolth. The authors refer to this phenomena as synchronous load canceling.

Integration of 5GHDC with thermal storage and advanced controls could result in further efficiencies. Due to the ultra-low or ambient temperature loop, 5G systems have the ability to integrate thermal storage infrastructure for different time scales (Boesten et al. 2019). This would allow the development of synergies with other energy sectors and optimisation of the use of energy (Gjoka 2023). Although currently underutilized, the use of artificial intelligence (AI) for prediction of thermal loads and optimization of thermal energy could make 5G systems even more efficient (Buffa et al. 2019).

Systems that use a single-pipe at ambient temperature are not explicitly described in the 5G systems. The work of Buffa et al. (2019), Boesten et al. (2019), and Lund et al. (2018) describe 5G systems as having two pipes that are near ambient temperature, with one pipe for circulating colder fluids and the other pipe for hotter fluids. Even though there is a lack of literature references to single-pipe ambient-temperature 5G systems, they share many of the characteristics described in the 5G literature, and the authors conclude should be considered within their broader definition.

DHC systems are common in Europe, but implementation of 5G is progressing slowly. Buffa et al. (2019) evaluate 40 geothermal 5G networks in Europe that provide heating and cooling to buildings using heat pumps installed at customers' substations. Boesten et al. (2019) outlines a case study of a 5GDHC system in Mijnwater, Hareen, Holland as an example of a two-pipe 5G system that has been implemented at a city wide scale. So when Garcia-Cespedes et al. (2023) examine the use of 5G systems with geothermal heat pumps in Europe, they identify two main barriers that explain their current limited deployment: 1) high capital costs for ground-source heat pumps and the ground heat exchangers (boreholes) and, 2) limited awareness in the general public, investors, public and academic institutions.

3.3 Geothermal Energy Network Policy Terminology

Legislation mandating climate action such as the Climate Leadership and Community Protections Act (2019) enacted by New York State, and the Massachusetts Global Warming Solutions Act (2008), have structured a policy environment open to novel approaches to greenhouse gas reduction. One such solution, the geothermal network, has spread rapidly since its first appearance in a Massachusetts regulatory proceeding at the Department of Public Utilities (DPU) Docket No. 19-120 in 2019. The following section reviews the terminology used by policymakers in Massachusetts, New York State, Colorado, Vermont, Minnesota, Washington State, and Maryland.

3.3.1 Terminology in Regulation

The *geothermal network* term and the concept in general were introduced into the U.S. policy space in regulatory filings in the Commonwealth of Massachusetts. In the Department of Public Utilities (DPU) Docket No. 19-120 (2019), Eversource Gas proposed to implement a geothermal

demonstration project to study the effectiveness and scalability of providing low-carbon heating and cooling in Massachusetts (43). The term used in the proposal and subsequent proceedings were *geothermal networks* and *networked geothermal*, used interchangeably, the latter of which went undefined. While the ruling for this proceeding did not include a definition for geothermal networks, a report released by HEET shortly before the docket (Buro Happold 2019) and submitted to the department did describe the technology as decentralized, bi-directional, and consisting of a single-pipe ambient temperature loop with heat pumps in buildings and borefields. This proposal to investigate this renewable and carbon-free alternative to natural gas networks was approved by the Massachusetts Department of Public Utilities in 2020.

Since 2019, the term *geothermal network* has been continuously used in MA in regulatory documents by gas utilities and by the DPU. The term appears in a 2019 settlement with Columbia Gas Massachusetts (Massachusetts DPU 2019) and in a 2020 National Grid Gas regulatory request to pilot geothermal networks (Massachusetts DPU 2020). More recently in July 2024, this term was used by the Massachusetts DPU Pipeline Safety Division as it issued the first safety guidelines for networked geothermal projects (Massachusetts DPU 2024).

In New York State, the emerging fusion between geothermal heat pumps and district energy was identified as a vital technology to meet the state's climate goals. To accelerate its adoption, in 2021, NYSERDA launched Program Opportunity Notice (PON) 4614, a multi-round funding initiative to support the development of *Community Heat Pump Systems*. The definition of these systems allowed for two configurations: 1) a centralized heat pump system, or 2) decentralized heat pumps located at every building. The centralized electric heat pump would produce hot water which would then be used in the buildings via radiators for hydronic heating. The decentralized system would use water at ambient temperature as a thermal source for space comfort and for domestic hot water. Thus, the program allowed for systems that fit within district energy definitions for both 4G and 5G technologies. Through this program, 48 feasibility studies, and over 50 projects, have received funding.

To date no federal regulation is relevant to this discussion, however it is of note that the federal Department of Energy uses the term Geothermal Heat Pump to describe the heat pump technology inclusive of the borehole or geothermal energy exchange. In addition the DOE's Geothermal Technology Office released in 2022 a first-in-nation FOA (0002632) titled Community Geothermal Heating and Cooling Design and Deployment which is inclusive of any district solution that includes geothermal energy.

3.3.2 Terminology in Legislation

In 2021, the Commonwealth of Massachusetts passed An Act Creating a Next Generation Roadmap for Massachusetts Climate Policy (2021), which among many other things is the first law in the US to allow gas utilities to pilot geothermal networks. It did not, however, use the term from earlier regulatory filings but instead used the phrase 'utility-scale renewable thermal energy' and permitted gas companies to bill for thermal energy within these permitted demonstration projects. In 2022, An Act Driving Clean Energy and Offshore Wind (2022), defined "clean energy" and "clean energy research" as inclusive of geothermal energy including *networked geothermal* and deep geothermal energy, and further repeated the term networked geothermal in listing data collection efforts. This 2022 legislation also allowed such projects to be paid for with funds from the gas pipe replacement program.

In 2022, New York State (NYS) pioneered the term *Thermal Energy Networks,* choosing not to use the phrase Community Heat Pump Systems from other state efforts. New York State enacted the Utility Thermal Energy Networks and Jobs Act (UTENJA) (2022), mandating the seven largest gas utilities to propose *thermal energy network* pilot projects for review and approval by the NY Public Service Commission (PSC). UTENJA introduced the term *Thermal Energy Networks, abbreviated as TENs* to the policy landscape. TENs were defined as a utility-scale system that provides thermal energy with pipes carrying water at ambient temperature that is used by heat pumps at every building. The heat pumps allow thermal energy to be used for heating and cooling and for hot water. This definition is consistent with both 5G district energy and with Massachusetts' description of networked geothermal.

The TENs terminology proposed by UTENJA indicates the intent to transition existing gas utilities to deliver thermal energy instead of gas. However, despite the TENs definition used, gas utilities in New York proposed 3G and 4G systems for projects in their initial submissions to the PSC, some of which included fossil-fueled central plants. Thus the TENs terminology, despite its definition, gets misinterpreted in NYS to include fossil fuels spurring an effort to name fossil fuel free TENs as clean thermal energy networks, or CTENs.

Other states followed NYS in the use of the term TENs. In 2023, Vermont and Colorado passed bills using the TENs terminology, and in 2024 Washington State followed. The bills were An Act Relating to Thermal Energy Networks (2023), and An Act Concerning the Implementation of Measures to Advance Thermal Energy Service (2023) and An Act Relating to Promoting the Establishment of Thermal Energy Networks (2024), respectively. However, the bills from Vermont and Washington define TENs only as utility-scale infrastructure that supplies thermal energy, and does not define the technology further. Nevertheless, Washington legislation specifies that the commission should approve projects based on whether it is a distributed system with ambient temperature fluid and high efficiency heat pumps, making them 5G compliant. Notice that geothermal heat pumps are not clearly specified as a requirement in any of these states.

Colorado, clearly aware of the growing nomenclature challenge, actually lists a variety of competing terms to refer to the geothermal district systems. Colorado defines the technology as assisting to reduce greenhouse gas emissions by supplying thermal energy to two or more buildings that are not a campus. They also mention that the technology should consist of pipe loops between buildings that carry noncombustible fluids at a desired, but unspecified, thermal temperature. Unlike Washington and Vermont, Colorado includes the word geothermal in its bill. Specifically, it refers to these systems as a "*geothermal exchange district, networked geothermal system, geoexchange system, geogrid system, community geothermal heating and cooling district,* or a *geothermal heating district"*. Despite the variety in the *geo* terms included, the definitions provided by the Colorado legislature do not explicitly indicate the generation source of this type of district heating and cooling.

Nevertheless the examples from NY, VT, WA and CO exemplify the proliferation of the now more common terminology in the US policy landscape, *thermal energy networks.* The inconsistent definition of this terminology across these states and the lack of technical clarity has resulted in TENs being an ambiguous term that is approached differently in each state.

Maryland and Minnesota added more options, with some specificity to the mix. Maryland's Working for Accessible Renewable Maryland Thermal Heat (WARMTH) Act, introduced the term

geothermal heating and cooling system and defined it as a system that uses one or more geothermal heat pumps that can be either closed loop or open loop.

Some states, such as Minnesota, use more traditional terminology. The Minnesota legislature passed a relevant amendment in Natural Gas Utility Innovation Plans (2023), using the term *District Energy* defined as a heating and cooling system powered by solar thermal, the constant temperature of the Earth or aquifers to heat or cool multiple buildings via a network of pipes.

No federal legislation has been passed directly naming this technology yet, however a bill filed in August 2024 by Senator Markey, title the 'Pipeline Accountability, Safety, and Environmental Standards (PASES) Act' uses the term *networked geothermal systems*.

4. Risks of Ambiguous Terminology

The proliferation of ambiguous terminology in the US policy landscape has created uncertainty and hindered the adoption of this technology. The term 5GDHC was not explicitly mentioned in policy documents reviewed, highlighting the disconnect between terminology evolution in Europe versus in the United States. Outside of the policy space the term is used in the U.S. among district energy providers, researchers, and the district energy community, primarily to describe the increasing use of fifth generation on campuses. Within the district energy community there was a recent debate around definitional differences between 4G and 5G, another sign that this emerging technology remains in the definitional process.

Community and stakeholder groups agree on the need for a clear and concise term that stakeholders can universally understand. There are a number of risks that arise from the use of ambiguous terminology in policy documents, including:

A. Misleading impact expectations – Ambiguous terminology may lead to benefit expectations for one design getting misallocated to a different design. Key examples:
    a. A Thermal Energy Network with no boreholes or other forms of thermal storage may not deliver the benefits to the electric grid of a Geothermal Energy Network.
    b. Without specifying ambient-temperature loops, cooling benefits could be lost together with the efficiency of bidirectional energy exchange.
B. Greenwashing possible – Ambiguous terms can be exploited to exaggerate environmental benefits, misleading stakeholders and hindering genuine progress. For example, in New York some preliminary proposals under UTENJA did not eliminate reliance on fossil fuel combustion. The authors are not weighing in on those projects merits but are instead highlighting the gap between the intent of the UTENJA legislation not matching some of the proposed projects.
C. Optimization and Scalability hampered – Without clearly linking terminology to design, maximizing favorable outcomes such as ultra high efficiency design of 5G systems may not be easily achieved and modularity may be lost leading to unintended limits on regional interconnectability to improve efficiency and resilience.
D. Stakeholder Confusion – Unclear terminology can confuse stakeholders, including policymakers, industry professionals, and the public, hindering effective communication and collaboration, increasing the sense of risk, and reducing trust, and therefore action.

A common language is needed for policy and technical clarity in order to minimize risk and maximize trust in decisions. The International Energy Agency (IEA) emphasizes the importance of clear and consistent terminology in energy policy, stating that "a common language is essential for effective communication among policymakers, industry stakeholders, and the public" (IEA 2020). Future policy frameworks should prioritize precise terminology to facilitate the transition to renewable energy sources and avoid perpetuating ambiguity. Furthermore, in terms of technical outcomes, the authors agree with Buffa et al. (2019), who argue that the nomenclature used for lower temperature networks compared to traditional direct use district heating systems, can lead to misinterpretations.

5. Proposed Taxonomy

In appreciation of the enormous potential of the recently emerged ambient-temperature single-pipe bi-directional thermal energy infrastructure with decentralized geothermal heat pumps and centralized management of thermal resources, this proposed taxonomy focuses on clarifying the nomenclature for such a system within all other possible similar systems. It is the single-pipe ambient-temp distributed geothermal heat pump system that initially sparked the recent rapid spread of policy actions due to the potential to multi-solve the policy challenge of decarbonization and specifically the equitable transition beyond gas networks. Other district energy systems and designs are excellent as well and may be the ideal choice for a given location, so this taxonomy is not intended to select a winner but instead to clarify the names of the competitors - or the team of competitors.

Given the clear step change from centralized to decentralized district energy when moving from 4G to 5G, and incidentally also the challenge of 5G being actively used and understood to be a cell phone network in the U.S., we see value in the rise of novel terminology overlapping with the term 5G. We further appreciate the value of the word network rather than the word district as stakeholders of all backgrounds more readily understand network to be bi-directional and decentralized with the word district indicating the presence of a central plant.

Given the growing public preference for the pithy TENs abbreviation based on the term thermal energy network, we then consider the various boundaries on this term. The original TENs definition in New York's UTENJA legislation established it as single-pipe and ambient-temperature, which connects directly to the public expectations of a scalable utility technology and places it as a subset of 5G and thus not duplicative terminology. Subsequent evolutions have moved the boundary to include less easily scalable designs and 4G systems. This substantially increases the risks outlined in section 4, so we conclude that the definition of a thermal energy network should return to, in clear relationship with the district energy nomenclature, an ambient-temperature bi-directional 5G system of a single-pipe design. This differentiates TENs as an efficient subset of the 5G system with an interconnectability-based growth model - a technology that shifts the scale potential from district to utility. Should there be a need, particularly in the U.S. where 5G is so strongly associated with cellular service, to use a name other than 5G for a two-pipe ambient system we suggest distinct language be developed.

All such ambient-temperature networks feature the ability to connect to multiple and diverse thermal energy sources, sinks, and storage - or resources. The thermal resources can include not only geothermal boreholes which tap bedrock thermal but also other thermal exchange systems including those tapping aquifers and thermal reservoirs such as ponds, lakes, rivers and the ocean - all of which fit within the definition of geothermal energy. In addition, thermal resources can

include heat from other industrial sources and processes such as data centers, brewing, and waste water or sewers. Furthermore, infrastructures such as swimming pools, irrigation and snowmelt systems can be used as thermal resources, the former as storage and the latter as mechanisms to balance a system increasing the needed cooling or heating capacity. There has been much discussion in New York of TENs which use no geothermal at all and there are excellent examples such as a wastewater based TEN in Denver Colorado.

Given the need to differentiate the impact of geothermal heat pumps on outcomes, including grid impacts, we further specify the term geothermal energy networks (GENs) to refer to a subset of TENs systems that includes some baseload geothermal energy. It is critical to understand that with these definitions TENs and GENs are potentially interconnectable and part of a vision of a new thermal utility infrastructure. We further appreciate that the geothermal energy differentiator results in an acronym, GENs, that implies to many stakeholders an energy generation capacity, which matches the technology described.

Thus, in conclusion, we reinforce the well-established and existing district energy generational nomenclature and see value in further specifying, within the ambient-temperature 5G category, the single-pipe TENs, and within TENs, the geothermal energy based GENs. A taxonomy or classification rubric that links key design parameters to the performance and main characteristics of any thermal energy network is presented in this section. The classification rubric used divides any thermal energy networks into three main components, (1)Thermal resources, (2)Distribution, and (3)End-users. This classification is highly relevant to regulatory, ownership, and finance models and is depicted in Figure 3 and also described in Varela and Magavi (2024).

Figure 3. The geothermal energy networks or thermal energy networks can be subdivided into three main components: thermal resources, distribution and end-users with typical examples of each pictured. Figure modified from Varela and Magavi (2024).

5.1 Thermal Resources

The choice of thermal resources define key features of any DHC system. 5GDHC systems, including TENs and GENs can have a wide variety of thermal sources. Traditional DHC systems use sources from fossil fuels and combined heat and power (CHP) plants that generate high temperatures leading to higher thermal energy losses during the distribution. Table 1 shows how key thermal networks features vary depending on the type of fuel used for the supply of energy

into the system. For example, high temperature primary thermal sources means the system is likely a centralized system and only provides heating.

Table 1 also shows that geothermal networks are a subset of thermal networks that include geothermal energy sources. Other renewable energies such as solar thermal can also be used as thermal sources and connected to the thermal network.

The capture of thermal energy resulting from industrial or civil processes can include heat recovered from waste-water treatment facilities, sewer lines, subway tunnels, and more. Capture of excess or waste heat where available can be more cost effective than boreholes as a heat supply. It is of note that boreholes or other forms of geo-exchange, however, also provide cooling and sufficient energy storage to provide electric grid load flattening and shifting capacity.

Inclusion of boreholes can make the system more efficient by increasing short and longer term thermal storage. If a majority of buildings connected to a loop reject heat during the summer, this thermal energy can be stored in the subsurface and a portion can be leveraged months later during the winter when most buildings will be heating dominant. The subsurface dissipation rate together with the borehole spacing, design, and management drives the percentage stored at different time intervals. Geothermal heat pump designers have worked for decades to minimize long duration storage - avoiding system ‘thermal drift’ - however a managed thermal network provides the opportunity to design some borefields or thermal exchange to maximize this long duration storage.

5.2 Distribution

The number of pipes used in the distribution system is a key design parameter affecting the performance of the system. Conventional DH systems often operate with a four pipe design, using high temperatures for direct use of hot water without providing cooling. Because there is no load cancellation, if a heat pump is used, the COP of the system is equal to the COP of the heat pump as shown in Table 2. Buffa et al. (2019) define the 5G systems as having two pipes and highlight the increased efficiencies encountered by using ambient temperatures. TENs and GENs or differentiated as a subset of 5G with a single pipeline for the distribution system.

The TENs and GENs distribution system design consists of a single pipe circular ‘loop’ with both end-users and thermal resources distributed anywhere around the loop. This design allows for reduced infrastructure costs, efficient bidirectionality, and adaptable interconnectability at any point on the loop to both add and subtract end-users and thermal resources. This design also requires thermal management to ensure the loop does not shift outside the design temperature range and may require strategic addition of thermal resources. As these loops can interconnect, becoming thermal resources to each other while increasing efficiency and load predictability, this system design provides a growth model for the managing thermal utility.

Single Pipe Design Notes:

1. While the diameter of the main pipe is often a cost consideration, the costs of using a pipe with a larger diameter should be balanced with the potential gains. Including that having a pipe with a larger diameter enables the addition of future thermal loads to the loop and allows lower power pumping. Pumping energy use follows the affinity laws, so slower is disproportionately less power used. A slower loop speed may further reduces pumping power required by shifting the loop into laminar flow.
2. The thermal storage capacity of the volume of water - or water with glycol - filling the loop is calculable and can cover some demand from building heat pumps without drawing on the borefields or other thermal resources. At the Colorado Mesa University installation the five interconnected loops met all heating and cooling demands of the buildings without calling on the borefields during the shoulder seasons nearly 40% of the hours of the year.
3. That this thermal storage tank is in motion has led the lead author (who has an affection for flywheels) to describe the behavior of these single-pipe distribution loops as 'thermal flywheels'. The author's hypothesis, shared with one of the designers of Colorado Mesa, Cary Smith, is that a large diameter and slow moving main loop could aggregate hourly building loads over the duration of time it takes to complete a loop rotation, thus reducing the peak demand calculations from a hourly load to a multiple hour aggregation of loads. This is supported by findings that a larger pipe diameter provides more thermal inertia, and even short-term thermal storage along the distribution pipe (Guelpa and Verda 2019) resulting in more thermal mixing and simultaneous balancing of thermal loads - making the system more resilient and also smoothing spikes in thermal demand.

5.3 End-User

The end-user or customer has traditionally been solely a consumer of energy in DHC systems. However, in 5G systems and in TENs and GENs, the buildings or end-users are not only consumers but also producers (or prosumers) of heat. The simultaneous connection of consumers and prosumers to the same loop results in the total or partial cancellation of their thermal loads.

Diversity in both type and timing of load profiles is optimal to allow for cancellation and reduction of loads in 5G systems. Load profiles are usually associated to building typology, so ensuring a variety of building typologies to be connected in the thermal networks increases the overall efficiency of the system.

For 5G systems a heat pump or array of heat pumps is needed at every building. These heat pumps are known as ground source heat pumps or a water source heat pumps or geothermal heat pumps. We have chosen to use the term used by the U.S. Department of Energy, the geothermal heat pump or GHP, however we acknowledge that water source is the most accurately descriptive term. Regardless of the name these are more efficient, longer lasting, and have less refrigerant leakage than the more widely known air source heat pump (AHSP).

To minimize energy losses in the building, a weatherized building with an optimal building envelope is a modern necessity. Sizing public infrastructure and private heat pumps and distribution systems for an inefficient building is a waste of resources, though it can be done in the case of an unalterable historic building for example. As for the building typology, all types of residential and commercial buildings are eligible to be connected to geothermal energy networks.

Finally, balancing the aggregated end-user loads drives optimal long term performance of the system. Thermal management can address excess demands or loads and is the purview of the thermal utility. Balanced annual loads ensure that the subsurface temperature does not increase - nor decrease- after multiple years of operation. If the thermal loads are not balanced and subsurface temperatures are drifting up or down over years, additional boreholes or other thermal sources/sinks or strategies for thermal management such as dissipation of excess heat may be needed for the system to operate optimally over a long duration. This thermal management and optimization is the obligation of the managing thermal utility.

A conceptual representation of a GENs with diverse thermal resources and end-users is depicted in **Figure 2**.

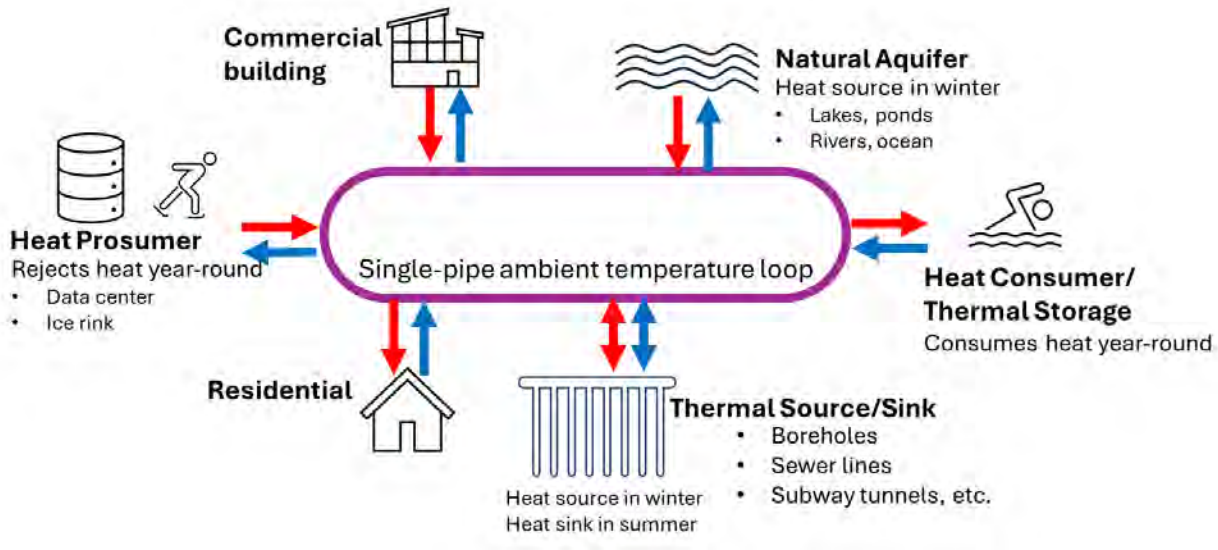

Figure 2. Conceptual representation of a geothermal energy network: a system for heating and cooling using interconnected heat pumps with a single-pipe ambient-temperature loop. Buildings and thermal resources connected to the system have the ability to be both a consumer and a producer of heat.

A schematic representation that summarizes the concept of geothermal networks and thermal energy networks and how they relate to 3GDHC, 4GDHC and 5GDHC is depicted in **Figure 3.** This schematic representation shows that geothermal networks as defined in this work, are a subset of the 5GDHC systems that use a single pipeline with ambient temperature for the main loop.

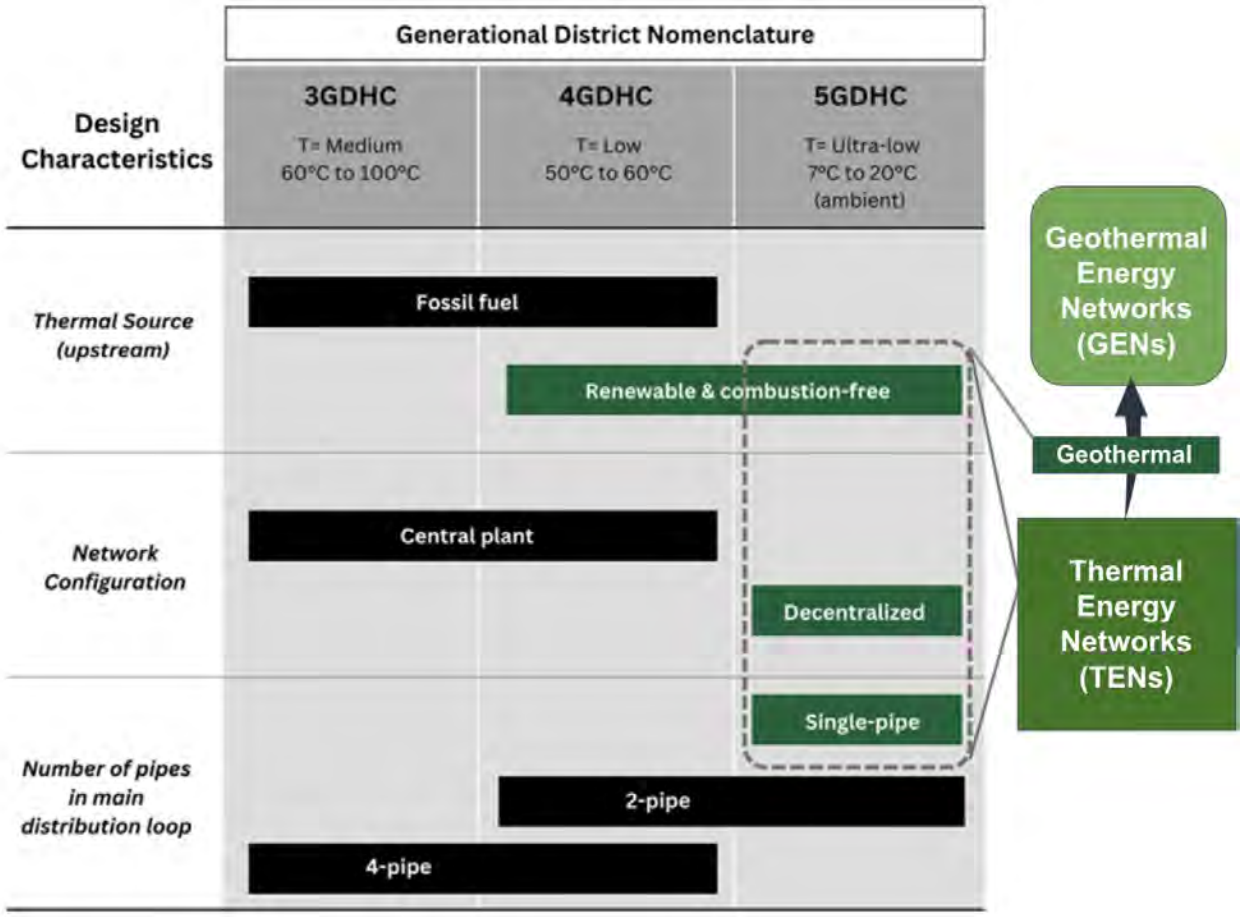

Figure 3. Schematic diagram of district energy characteristics for 3GDHC, 4GDHC and 5GDHC. GENs are shown in green and are a subset of the 5GHDC systems and, by tapping geothermal energy, are a further subset of TENs.

6. Conclusions

This study aimed to improve clarity for all stakeholders on terminology related to geothermal energy networks, with the purpose of supporting the growth of these technologies as a tool to decarbonize the built environment. Stakeholders from widely varying industries and sectors report that the greatest barrier to maximizing impacts of geothermal heat pumps and energy networks is a lack of knowledge and understanding among both decision makers and the public. A clear nomenclature can greatly reduce confusion and increase trust, leading to more widespread understanding of the ground-breaking potential of geothermal energy networks.

Yet geothermal energy networks exist at the intersection of multiple technology communities including the district energy community, the geothermal energy community, and the ground source heat pump community. Each has their own naming and language norms. As do policy experts, academics, and engineers. This work did not attempt to meet the needs of any one group but rather to find the common ground between them. Furthermore, this work did not address language appropriate to engineering docs or technical specifications, which requires an additional rigor in definitional clarity, but rather addressed the more public-facing policy terminology.

Addressing widespread language use necessarily requires acceptance that the public or key stakeholders may not accept or adopt this work. If our clarification of geothermal technologies, our division of a thermal network into three parts, our introduction of the GENs term, or any other part of this work is not yet used and useful then this work will need to evolve again until the terminology and categorizations in use are clearly defined and linked to operational outcomes and impacts. It is that potential impact - an energy system that meets the needs of our shared future - that is, after all, the end game.

Acknowledgement

This study and the work that informed it at HEET was funded by grants from the Massachusetts Clean Energy Center, Barr Foundation, The Energy Foundation, Liberty Mutual Foundation, E4TheFuture, and other generous donors. HEET accepts no funds from those industries our work directly effects, including the gas and geo industries.

Table 1 Thermal energy networks taxonomy rubric for parameters related to thermal resources.

Function	Parameter	Parameter Option	Temperature	Features	Network Configuration	Combustion	Operational GHG Emissions	Taxonomy
Thermal Resources	Renewable	Geothermal (deep)	High temperature 60C - 120C	Deeper boreholes higher risks and costs. Requires high geothermal gradient	Centralized	No	Low (closed loop binary system)	Geothermal District
		Geothermal (shallow)	Low temperature 7C - 20C	Local, feasible in most geologies.	Decentralized	No	Low*	Geothermal Energy Network
		Water bodies (lakes, ponds, rivers, ocean)	Low temperature 7C - 20C	Lowers cost compared to drilling boreholes	Both	No	Low*	Geothermal Energy Network
		Solar thermal	High temperature	Can be integrated at the building or loop level	Both	No	Low	Thermal Energy Network
		Concentrated solar	High temperature 60C - 120C	Requires large land area and only feasible in certain climate zones	Centralized	No	Low	Thermal Energy Network
		Biomass	High temperature 60C - 120C	Requires industrial process	Centralized	Yes	Low	District Energy
	Waste Heat	Waste-water treatment facilities		Generally used for low temperatures	Centralized	No	Low	Thermal Energy Network
		Sewer lines		Distributed geographically	Decentralized	No	Low	Thermal Energy Network
		Rejected heat		Can be rejected heat from industrial processes or commercial buildings	Both	No	Low	Thermal Energy Network
	Non-renewable	Fossil fuel plant (coal, gas)	High temperature 60C - 120C	Requires	Centralized	Yes	High	District Energy
		Combined heat and power	High temperature 60C - 120C	Leverages the by-product of power production	Centralized	Yes	Medium to high	District Energy

Table 2 Thermal energy networks taxonomy rubric for parameters related to the distribution system or main loop.

Function	Parameter	Parameter Option	System Features	Network configuration	Main Pipe Diameter	Main Pipe Temperature Range	Load Canceling	Generation
Distribution	Number of Pipes in Main Loop	Single pipe • Ambient temperature loop	• More efficient in canceling thermal loads between buildings	Decentralized	Larger (6 inch to 12 inch)	Ultra-low, near ambient	Yes	5G
		Two-pipe loop • Supply and return	• More efficient than 4-pipe • Generally is either heating or cooling • Can have a heat pump to do cooling	Centralized	Small systems: 4 to 12 inches Large systems: 12 to 36 inches	low (50-60°C) or ultra-low	Not bidirectional	4G/5G
		Four-pipe loop • Two inlet temperatures • Two outlet temperatures	Direct use of high temperatures • No heat pump • No cooling	Centralized	Small systems: 2 to 12 inches Large systems: 12 to 24 inches	low (50-60°C)	No	4G
	Heat Exchange Medium	Water	• Cost efficient • Environmentally friendly	Both	NA			
		Water & food grade glycol	• Antifreeze • Higher cost • Low environmental risk	Decentralized				
		Water vapor	• Inefficient, high heat loss during distribution • Requires central plant • Likely dependent on fossil fuels	Centralized				
		CO2	High pressure (135 to 435 psi)					

Table 3. Thermal energy networks taxonomy rubric for parameters related to the end-user or customer.

Function	Parameter	Parameter Option	System Features	Network Configuration	Energy Usage
End-user	HVAC Equipment	• Heat pumps at every building • HVAC at every building	Space heating and cooling, and domestic hot water	Decentralized	Buildings are consumers and prosumers
		HVAC in every building	Space heating and cooling, and domestic hot water	Centralized	Buildings are consumers only • Primarily unidirectional (from central source to consumers)
	Building Envelope	Energy efficient	Optimal use of energy	NA	Consumes less energy
		Not energy efficient	Needs weatherization	NA	Consumes more energy
	Building Typology	Commercial	Peak energy use: 9 am - 5 pm	NA	Likely anchor tenant
		Residential	Peak energy use: 7 am - 9:30 am, 4 pm - 8 pm	NA	Likely consumer
		Industrial	Peak energy use: variable	NA	Likely prosumer and anchor tenant
	Thermostat Control	Yes - active load management	Optimization of consumption: • Responds to system peak electric consumption	NA	Reduced energy consumption based on high demand periods
		No - preset	No thermostat-based optimization of consumption	NA	No thermostat-based optimization of energy consumption
	Heat Exchanger at Every Building	Yes	• Clear delination of distribution vs. behind the meter infrastructure • Increases cost of system per customer	Isolation of building supply from those in the main loop	Impacts efficiency of the system
		No	• No separation of fluids between main loop and buildings	Fluids from main loop circulate to the building	

REFERENCES

Boesten, S., Ivens, W., Dekker, S. C., and Eijdems, H. "5th generation district heating and cooling systems as a solution for renewable urban thermal energy supply." *Advances in Geosciences*, 49, (2019), 129-136.

Buffa, S., Cozzini, M., D'Antoni, M., Baratieri, M., and Fedrizzi, R. "5th generation district heating and cooling systems: A review of existing cases in Europe." *Renewable & Sustainable Energy Reviews*, 104 (2019), 504–522.

Colorado General Assembly. Concerning the implementation of measures to advance thermal energy service. House Bill 23-1252. (2023).

Condon, P. M. "Design charrettes for sustainable communities." *Island Press*, Washington, DC (2012).

Febrianto, R., Bydder, J., Hochwimmer, A., Ussher, G. and Libbey, R. "Developing low temperature geothermal projects in Indonesia using pumped well technology." *IOP Conference Series Earth and Environmental Sciences*, 254 (2019), 012021.

García-Céspedes, J., Herms, I., Arnó, G., and De Felipe, J.J. "Fifth-generation district heating and cooling networks based on shallow geothermal energy: a review and possible solutions for Mediterranean Europe." *Energies*, 16, no. 1 (2022), 147.

Gjoka, K., Rismanchi, B., and Crawford, R. H. "Fifth-generation district heating and cooling systems: A review of recent advancements and implementation barriers." *Renewable & Sustainable Energy Reviews*, 171 (2023), 112997.

Guelpa, E. and Verda, V., "Thermal energy storage in district heating and cooling systems: A review" *Applied Energy*, 252, (2019), 113474.

International Energy Agency. "Energy technology perspectives 2020. Annex C: glossary of terms." *International Energy Agency*, Paris, France (2020).

Lund, H., Østergaard, P. A., Chang, M., Werner, S., Svendsen, S., Sorknæs, P., and Thorsen, J. E. "The Status of 4th Generation District Heating: Research and Results." *Energy,* 164, (2018), 147–59.

Maryland General Assembly. Working for accessible renewable Maryland thermal heat act. House Bill 397. (2024).

Massachusetts Department of Public Utilities. Docket No. 19-120: Approval of General Increases in Base Distribution Rates for Gas Service. (2019).

Massachusetts Department of Public Utilities. Networked geothermal safety guidelines. (2024).

Massachusetts General Assembly. An act establishing the global warming solutions act. Chapter 298. (2008).

Massachusetts General Assembly. An act driving clean energy and offshore wind. House Bill 5060. (2022).

Massachusetts State Senate. An act creating a next generation roadmap for Massachusetts climate policy. Senate Bill 2995. (2021-2022).

Minnesota State Statutes. Natural gas utility innovation plans. Chapter 216B Section 2427. (2023).

New York State Assembly. Climate leadership and community protections act. Senate Bill 6599. (2019).

New York State Assembly. An act to amend the public service law. Amendment 10493. (2021).

New York State Energy Research and Development Authority. "Community heat pump systems program opportunity notice (PON) 4614." *New York State Energy Research and Development Authority*, Albany, New York (2021).

New York State Senate. An act to amend the public service law. Senate Bill 9422. (2021).

Østergaard, D., and Svendsen S. "Space heating with ultra-low-temperature district heating–a case study of four single-family houses from the 1980s." *Energy Procedia*, 116, (2017), 226-235.

Simpson, J. and Zhu, G. "An efficient annual-performance model of a geothermal network for improved system design, operation, and control". *Proceedings, 49th Workshop on Geothermal Reservoir Engineering*, Stanford University, Stanford California (2024).

Sulzer, M, Werner, S., Mennel, S., and Wetter, M. "Vocabulary for the Fourth Generation of District Heating and Cooling." Smart Energy 1 (C): 100003. https://doi.org/10.1016/j.segy.2021.100003 (2021).

U.S. Department of Energy. "Geovision: harnessing the heat beneath our feet." *U.S. Department of Energy*, DOE/EE-1766, Oakridge, TN (2019).

Varela, I., and Magavi, Z. "The first open-source database for geothermal networks". *Geothermal Rising Conference (GRC) Transactions*, Waikoloa, HI 48 (2024).

Vermont General Assembly. House. An act relating to thermal energy networks. House Bill 242. (2024).

Washington State Assembly. An act relating to promoting the establishment of thermal energy networks. House Bill 213. (2024).

Washington State Legislature. Concerning community heat pump systems. House Bill 1589. (2023).

Werner, S. "International review of district heating and cooling." *Energy*, 127, (2017), 617-631.

Woods, P. "An introduction to district heating and cooling : low carbon energy for buildings." *IOP Publishing*, Open University, Kents Hill, UK (2023).

Development and Preliminary Analysis of a U.S. Geothermal Heat Pump Installation Database

Hannah Pauling, Slater Podgorny, and Dayo Akindipe

National Renewable Energy Laboratory (NREL)

Keywords

Geothermal heat pumps (GHP), data collection, market analysis, geospatial analysis

ABSTRACT

This paper seeks to addresses the significant gap in the literature regarding the installation and adoption of geothermal heat pump (GHP) systems in the United States. While the "2021 U.S. Geothermal Power Production and District Heating Market Report" published by the National Renewable Energy Laboratory (NREL) focused on direct-use geothermal district heating systems, it did not include an analysis of GHP installations (Robins et al. 2021). To bridge this gap, NREL has compiled a novel database currently containing 70,470 records of GHP installations, primarily sourced from state well permits and small-scale studies.

Our methodology emphasizes the collection, cleaning, and standardization of data, addressing challenges such as inconsistent reporting formats and privacy concerns. Despite limitations in data on capacity, costs, and performance, our preliminary geospatial analysis reveals insights into the distribution of GHP systems across urban and rural areas and climate zones.

The paper highlights the importance of publicly accessible data for advancing GHP technology adoption with a discussion of existing data sources and their limitations, advocating for improved collaboration between NREL and industry stakeholders.

1. Introduction

Geothermal heat pump (GHP) technology offers significant potential for sustainable heating and cooling in the United States, yet comprehensive data on GHP installations remains scarce. The National Renewable Energy Laboratory (NREL) aims to address this gap through the development of a detailed database of GHP installations across the country. This effort builds on the foundation laid by the "2021 U.S. Geothermal Power Production and District Heating Market Report" (Robins et al. 2021), which focused on direct-use geothermal systems but did not include GHPs.

So far, the newly compiled database contains 70,470 records, primarily sourced from state well permits and supplemented by small-scale studies. This collection of data provides a foundational resource for analyzing the spatial distribution and adoption trends of GHP technology. However, key metrics such as capacity, costs, and performance are sparsely populated, presenting challenges for comprehensive analysis.

This paper details the methodology used in the creation of the database, including data collection, cleaning, and standardization processes. It also discusses the initial findings from geospatial analysis, offering insights into the distribution patterns of GHP installations across various regions and climate zones. The importance of publicly accessible data for policy development, market analysis, and strategic planning in the renewable energy sector is emphasized, highlighting the need for ongoing collaboration between NREL and industry stakeholders.

2. Database: Description, Metrics, and Main Sources

The GHP database compiled by NREL predominantly consists of records derived from state well permits. These permits often provide detailed location information but lack other key metrics such as installed capacity, costs, and performance data. Within the 70,470 records, geographic coordinates are available for 98.4% of the entries, while metrics such as capacity and costs are sparsely populated and present in less than 1.5% of entries. These additional metrics are primarily sourced from specialized studies focusing on specific GHP systems and cannot be universally applied.

Because of its reliance on well permits, the database does not capture installations using horizontal configurations, which are common in residential applications because of lower installation costs. This omission underscores the need for more comprehensive data collection practices that include all types of GHP installations.

GHP reporting practices vary widely among states, with disparities in the accessibility of drilling permits that specify well usage. At the federal level, GHP manufacturers report annual heat pump unit sales to Energy Star, providing a broad overview of industry trends but offering limited insights into capacity, costs, and performance metrics. Analysis often necessitates assumptions based on established benchmarks, such as the 12 kW per heat pump unit guideline used by Lund et al. (2020).

Installation costs are heavily influenced by drilling expenses and site-specific subsurface conditions, while performance metrics exhibit variability because of a wide range of utilization factors, even among identical GHP units. Despite these challenges, existing studies, such as Cox et al. (2022), enable scenario-based analysis incorporating factors such as drilling costs, thermal conductivity, and utilization rates to present a range of costs and performance metrics. In addition, various modeling tools facilitate the modeling of geothermal market demand, including GHPs, despite limited data availability on GHP demand itself.

These insights emphasize the necessity for improved and standardized data collection and reporting practices to better understand and optimize GHP system performance, costs, and deployment across various regions.

3. Methodology

3.1 Data Collection

Our approach to compiling data on GHP installations primarily relied on state well permits as the primary data source because of challenges encountered with other data collection methods. Initial attempts to gather information from heat pump manufacturers and distributors proved unsuccessful, leading us to prioritize state well permits for their availability and detailed location information.

Permitting practices vary widely from state to state. Drilling permits may be managed by various departments within a state, including Environmental Protection, Water Rights, Natural Resources, the Engineer's Office, and in some cases, the Department of Health. This diversity in management can complicate data collection, because each department may have different reporting standards and data accessibility.

Even when well permits are publicly available and easy to find, they may lack specific end-use identifiers that include heat pumps. For this reason, any well permits without clear end-use identification were excluded from our analysis to ensure accuracy and relevance.

Despite these challenges, the reliance on state well permits provided a substantial dataset, offering valuable insights into GHP installations across various regions. However, the absence of end-use identifiers in many permits suggests a need for more standardized reporting practices to facilitate comprehensive data collection.

3.2 Data Cleaning and Consolidation

Each permit provided valuable location data, though variations in reporting formats necessitated significant standardization efforts to streamline the analysis. Some states require a separate permit for each well, while others only require one permit per property. This inconsistency required extensive consolidation to ensure that each system in the database is represented by a single entry. For instance, a system with 40 boreholes should be associated with one entry, not 40, to avoid redundancy and ensure accurate analysis.

The database will be made publicly available upon completion, so efforts are being made to address privacy concerns. Many well permits include sensitive information such as the owner's name, address, and phone number. To protect privacy, these details will be excluded from the public release of the database. Additionally, discussions are underway to identify and mitigate other potential privacy issues.

To enhance the utility of the database, we are implementing a robust data cleaning and standardization process. This involves normalizing location data to a consistent format, ensuring that all entries adhere to a uniform structure, and cross-referencing permits to eliminate duplicates. These steps are crucial to maintaining the integrity and usability of the database for researchers, policymakers, and industry stakeholders.

4. Geospatial Analysis

While the database represents only a fraction of total U.S. GHP installations, its rich location data supports preliminary geographic analysis. Despite the gaps in data on capacity, costs, and performance, geospatial analysis can provide valuable insights into the current state and potential growth areas for GHP technology.

4.1 Climate Zones

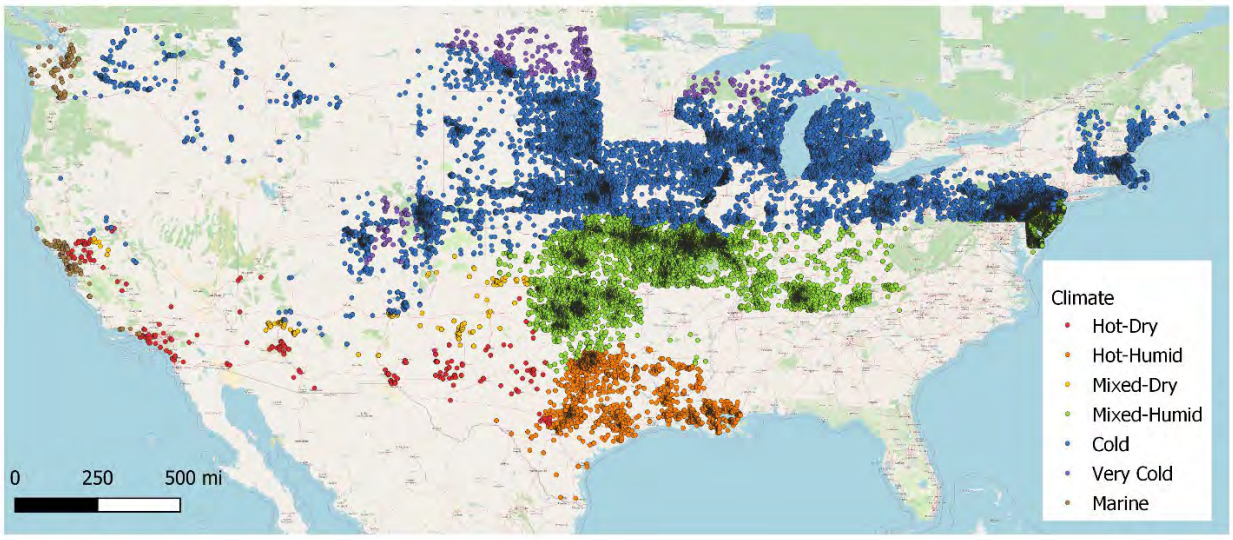

Figure 1: Geographic distribution of GHP installations across the United States, color-coded by climate zone. The Building America climate zones are described in Baechler et al. (2015).

The map in Figure 1 illustrates the concentration of GHP installations across different regions, highlighting variations in adoption patterns influenced by climate. The vast majority of systems in the database are found within Mixed-Humid and Cold climate zones. Notably, several states, particularly in the southeastern United States (Hot-Humid region), are still missing from the database. Despite this gap, valuable insights can still be drawn from the existing distribution.

GHP systems are highly efficient in both heating and cooling, making them particularly attractive in regions with significant seasonal temperature variations. Mixed-Humid and Cold climates experience such variations, allowing GHP systems to provide substantial energy savings and comfort. Cold climates, in particular, have a higher demand for heating during the winter months, further enhancing the appeal of GHP systems in these areas.

Even with the exclusion of the southeastern United States, the data shows that significantly more systems are located in humid climates compared to dry ones. One potential explanation is that the eastern half of the United States, which primarily encompasses humid climates, has a significantly higher population density compared to the western, drier regions. Higher population density leads to more residential and commercial buildings, thereby increasing the demand for heating and cooling solutions.

Additionally, the soil and ground conditions in humid climates are often more favorable for GHP installations. Moist soil conditions improve the thermal conductivity of the ground, enhancing the efficiency and effectiveness of GHP systems.

4.2 Urban Areas

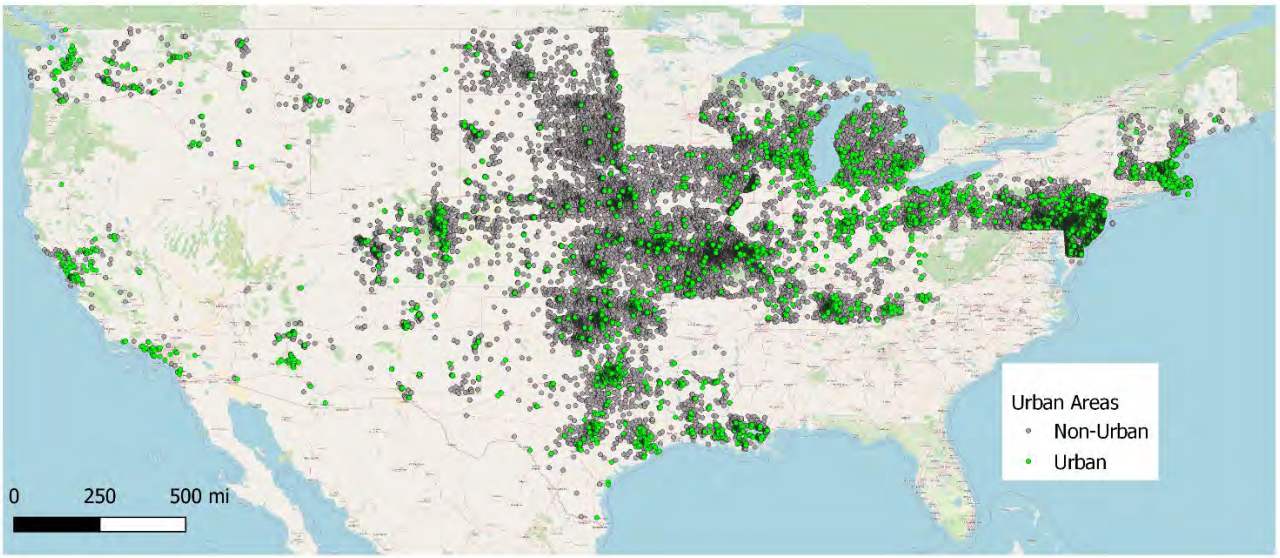

Figure 2: Geographic distribution of GHP installations across the United States, color-coded by urban areas. Urban area outlines from U.S. Census (2020).

The map in Figure 2 shows the nationwide distribution of urban areas and nonurban areas (suburban and rural). Currently, only 34.64% of GHP systems in the database are located in urban areas, despite the typically higher population density in these regions. In contrast, a significant 65.36% of installations are situated in rural and suburban areas.

Urban areas tend to have a higher concentration of multifamily housing, which could partially explain the lower number of systems. Instead of having many small systems for single-family housing, there could be a tendency toward fewer, larger installations.

As previously noted, the database primarily relies on well permits as its data source. Consequently, horizontal GHP configurations, which do not require well permits, are largely absent from the database. If included, these horizontal systems would likely be found predominantly in nonurban areas because of their larger space requirements compared to vertical systems. This absence of horizontal system data suggests that the actual disparity in distribution between urban and nonurban installations may be even more pronounced than the data currently reveals.

5. GHPs in the United States

Publicly accessible data on GHPs is crucial for accurate assessment, strategic planning, and informed decision-making in the energy sector. However, the current availability of such data is sparse and fragmented, posing significant challenges to stakeholders. Comprehensive and detailed

data collection, including information on various installation types and their performance, is necessary to support the broader adoption and optimization of GHP technology. This would enable more accurate market analysis, better policy development, and enhanced efficiency in energy use and management.

The U.S. Energy Information Administration Residential Energy Consumption Survey (RECS) offers some insights, but only lists ~250 GHP sites. GHP manufacturers report annual shipment numbers to Energy Star, but these figures are aggregated at the national level, making state-by-state data unavailable. This lack of granularity complicates efforts to understand regional market dynamics and deployment patterns.

The 2022 International Energy Agency geothermal report (GTO 2024) estimates a nationwide capacity of 20.2 GWth, derived from the U.S. Energy Information Administration data and incremental shipment data. However, this report also lacks state-specific information, limiting its utility for localized analysis.

The U.S. Energy Information Administration's nationwide capacity estimates from 1989 to 2011 were based on data from the Oregon Institute of Technology's Geo-Heat Center. Since the center ceased operations, the U.S. Energy Information Administration has assumed annual estimates from 2012 onward to be static, equal to those of 2011. This methodology results in outdated and potentially inaccurate data. These data limitations highlight the need for more detailed and disaggregated reporting to better support the growth and optimization of GHP technologies across various states and regions.

7. Conclusion

Creating a database for GHP installations in the United States is a critical step toward understanding and optimizing the use of geothermal energy. While significant progress has been made in compiling location data, there remains a pressing need for more detailed and consistent reporting on key metrics such as capacity, costs, and performance. Improved data collection practices and ongoing collaboration between NREL and industry stakeholders are essential to support the broader adoption of GHP technology. By leveraging detailed geospatial analysis and making data publicly accessible, we can enhance public awareness, drive market growth, and inform strategic decisions in the renewable energy sector.

Acknowledgement

Funding for this work was provided by U.S. Department of Energy, Office of Energy Efficiency and Renewable Energy, Geothermal Technologies Office to the National Renewable Energy Laboratory, operated by Alliance for Sustainable Energy, LLC, for the U.S. Department of Energy (DOE) under Contract No. DEAC36-08GO28308. The views expressed herein do not necessarily represent the views of the DOE or the U.S. Government.

REFERENCES

Baechler, M.C., Gilbride, T.L., Cole, P.C., Hefty, M.G., and Ruiz, K. “Guide to Determining Climate Regions by County.” *Building America Best Practices Series*, 7.3, (2015).

Cox, J., Campos, G., Armatis, P., Belding, S., Lowder, T., Kristensen, L., Zourellis, A., Bless, F., Arpagaus, C., and Baldwin, S. “Low-Carbon District Heating: Performance Modeling of Hybrid Solar, Heat Pump, and Thermal Storage Systems for District Thermal Energy in the United States.” *19th International Refrigeration and Air Conditioning Conference*, Purdue, Indiana (2022).

Lund, J.W., Sifford, A., Hamm, S.G., and Anderson, A. “The United States of America Direct Utilization Update 2019.” *Proceedings World Geothermal Congress 2020*, Reykjavik, Iceland (2020).

Robins, J., Kolker, A., Flores-Espino, F., Pettit, W., Schmidt, B., Beckers, K., Pauling, H., and Anderson, B. “2021 U.S. Geothermal Power Production and District Heating Market Report.” *National Renewable Energy Laboratory*. (2021).

United States Census. “2020 Census Urban Area TIGER/Line Geodatabase.” (2020).

United States Department of Energy Geothermal Technologies Office (GTO). “2022 United States Country Report.” *IEA Geothermal*, (2024).

United States Energy Information Administration (EIA). “Commercial Buildings Energy Consumption Survey (CBECS).” (2018).

United States Energy Information Administration (EIA). “Residential Energy Consumption Survey (RECS).” (2020).

United States Energy Information Administration (EIA). “Table 10.2a: Renewable Energy Consumption: Residential and Commercial Sectors.” (2024).

National Modeling of Geothermal District Energy Systems with Ambient-Temperature Loops Using dGeo

Juliet G. Simpson, Koenraad F. Beckers, Diana Acero Allard, Yunzhi Chen, Paritosh Das, Jonathan Ho, Hyunjun Oh, Ashreeta Prasanna, Shashwat Sharma

National Renewable Energy Laboratory, Golden CO, USA

Keywords

Ambient-temperature loop, thermal energy network, district energy system, heating and cooling, geothermal boreholes, spatial modeling, dGeo

ABSTRACT

Geothermal district energy systems (DES) with ambient-temperature loops, also known as thermal energy networks, are one option for decarbonizing space heating and cooling loads. Geothermal fifth-generation DES include an “ambient” temperature thermal loop that connects heat pumps at each building with thermal balancing sources such as geothermal borehole fields. Heating and cooling are provided via a water-source heat pump at each end-user.

This project seeks to analyze the nationwide potential for ambient-temperature loop districts by creating a new module within the Distributed Geothermal Market Demand Model (dGeo). dGeo is an agent-based modeling tool for distributed geothermal resources; it can investigate potential on a nationwide or statewide scale using geospatial data for all 50 states and thermal demands for existing buildings. This process allows for high-level estimates of technical and economic potential for ambient-temperature loop districts across the United States.

A lookup table was created using GHEDesigner to size borehole fields for different thermal loads and ground conditions experienced across the country. A cost and financing structure, along with incentives, were applied. Cost estimates include costs for the distribution network, borehole field installation and operation, and circulation pump operation, while savings are calculated based on energy bills for building owners (agents). This newly developed module can be used for assessing which areas of the country have the highest potential for agent benefits from ambient-temperature loop installation and assess the impact of future cost and price scenarios.

Initial results for statewide analysis (for Vermont) and nationwide (for United States) are provided. Future work includes expanding the module to consider mixed residential and commercial districts as well as evaluating multiple cost scenarios.

1. Introduction

Decarbonizing heating and cooling is a critical step to achieve carbon reduction goals, as traditional heating has significant on-site carbon emissions (often from burning natural gas or fuel oil). Even traditional district heating and cooling systems which utilize steam or chilled water often use fossil-fuel-based systems in the central plant. In 2020, commercial and residential building energy consumption accounted for 40% of the United States' primary energy consumption (U.S. Energy Information Administration 2020). In the European Union, heating and cooling of buildings accounted for more than half of the energy consumption in 2020 (International Energy Agency (IEA) 2023). It is critical to decarbonize heating and cooling loads in ways that are economical, equitable, and compatible with a renewable electric grid.

District energy systems connect buildings in a community with a thermal network (generally one or several pipes running under the street) to provide heating and cooling. Ambient-temperature loops (ATL) are a specific subset of district systems which provide water at near-ambient temperatures (generally in the range 10°C to 25°C) to localized water-source heat pumps located in each building to meet heating and cooling loads. The water in the loop may exchange heat with multiple buildings and other energy sources (such as boreholes, waste heat from refrigeration, or heat from a sewer heat exchange system). One common way of moderating the loop's temperature is to run the fluid in the loop through geothermal boreholes in a borehole field. This allows the ground to act as a heat exchanger and transfer heat to or from the loop. These shallow closed loop geothermal systems, also known as geo-exchange, can be used to provide consistent low-temperature energy streams.

District systems enable a thermal resource with a relatively high capital cost (such as a geothermal borehole system) to be shared among a large number of users and amortized over a long period of time (30 or more years). Distributing costs in this manner may increase equitable access to decarbonization and reduce energy bills.

A recent study by Liu et al. (2023) found that converting existing HVAC systems to individual geothermal heat pumps reduced loads, energy prices, transmission requirements, and emissions. Ambient-temperature districts are thought to have equal or greater potential to reduce load on the electrical grid compared to individual geothermal heat pumps, resulting in significant grid cost savings.

A diagram for an ambient-temperature loop system is shown in Figure 1. The main thermal loop carries water (or a glycol-water mixture) between loads in the community and exchanges heat with the ground via the geothermal borehole field. These systems have various names in the literature including thermal energy networks and fifth generation district energy systems.

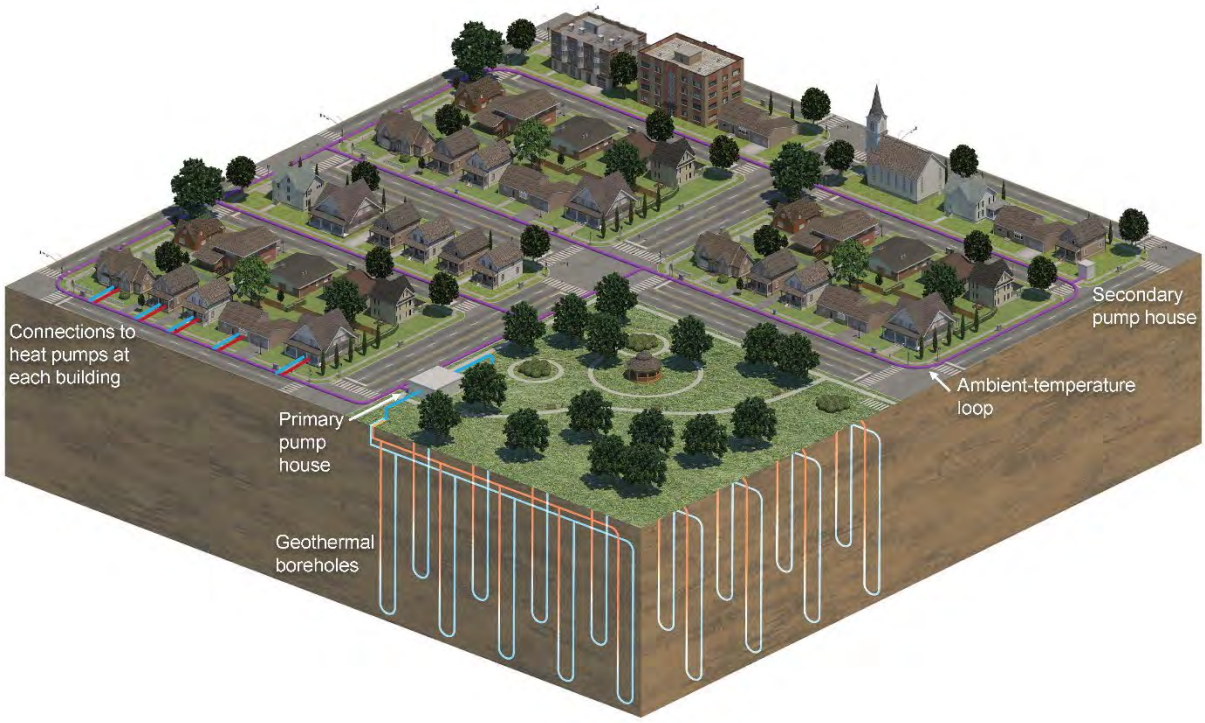

Figure 1. Example ambient-temperature loop district system with a single pipe thermal loop (purple line). This loop connects with heat pumps at each building to meet heating and cooling loads and exchanges heat with the ground via geothermal boreholes, under a park. *Graphic by Besiki Kazaishvili, NREL.*

The major components covered in this project, shown in Figure 1, include buildings with heat pumps, a single-pipe thermal loop, a geothermal borehole field, and a pump house. The pump house contains the pumps for the borehole field, the circulation pumps for the main thermal loop, any auxiliary heating or cooling, and the control system.

These systems have been deployed on campuses and in communities with promising results. Examples include Colorado Mesa University (Woodruff 2022; Schulman 2020; Oh and Beckers 2023; Electric Power Research Institute, n.d.), Minewater (Brummer and Bongers 2019; Verhoeven et al. 2014; Boesten et al. 2019), and Whisper Valley (Marin 2022; Wolfson and Mapel 2020; "Whisper Valley," n.d.). Unlike most previous examples, the Eversource DES in Framingham, Massachusetts is retrofitting an existing community in the United States through a utility-led installation (Eversource, n.d.; HEET 2022), which provides a clear example for how district systems can be installed in existing communities.

The National Renewable Energy Laboratory developed the Distributed Geothermal model (dGeo) as part of its Distributed Generation Market Demand Model (dGen) to explore the technical, economical, market, and adoption potential for geothermal heating and cooling technologies in the United States (Liu et al. 2019; McCabe et al. 2019; Beckers and Young 2017; Gleason et al. 2017). dGeo is an agent-based modeling framework that uses geospatial-based data on geothermal resources, thermal demand, building characteristics, and energy prices to evaluate technical performance, cost-competitiveness, and potential adoption of geothermal heating and cooling systems. While dGeo does not model each building in the United States, it simulates "a *synthetic*

population of commercial and residential buildings that is statistically representative of the true population" (McCabe et al. 2019).

Given the potential benefits to the electrical grid, decarbonization, and energy justice, this study investigated the potential of ambient-temperature districts for national deployment. The initial focus of dGeo was geothermal heat pumps and geothermal direct use for district heating. In this project, a new capability was added to dGeo for modeling ambient-temperature loop district energy systems using geothermal boreholes. This module investigates high-level techno-economic performance of ambient-temperature loops across the United States.

2. dGeo Ambient-Temperature Loop Methodology

The new ambient-temperature loop module uses the same dGeo agent-based modeling framework as previously documented (Liu et al. 2019; McCabe et al. 2019; Beckers and Young 2017; Gleason et al. 2017). Geospatial data layers for dGeo modeling include:

- Building type count for the residential (such as single-family detached and single-family attached) and commercial (such as restaurant, hotel, and office) sectors at the census block level based on the Federal Emergency Management Agency's HAZUS 6.1 dataset (FEMA 2023).
- County heating and cooling load in the residential and commercial sectors based on statewide and regional data and county level building counts from the U.S. Energy Information Administration's Residential Energy Consumption Survey and Commercial Buildings Energy Consumption Survey.
- Residential Energy Consumption Survey /Commercial Buildings Energy Consumption Survey microdata by climate zone to allow sampling of current building HVAC system types, HVAC lifetimes, and housing square footages.
- National and state incentives (such as rebates or tax credits) for geothermal technologies.
- Shallow ground thermal conductivity ranges by climate zone.
- Current and projected future regional energy prices for electricity, propane, natural gas, and distillate fuel oil, collected from the U.S. Energy Information Administration's Annual Energy Outlook datasets.
- Neighborhood road lengths by census tract.

Non-geospatial inputs include:

- Current and future costs for well drilling, heat pump and baseline HVAC systems.
- Project financing inputs.
- Current and future HVAC system performance.

2.1 Creating Borehole Field Look-up Tables

While ambient-temperature loops can be designed to use a variety of thermal sources and sinks, this study only considered the use of geothermal borehole fields. Sizing a borehole field for every potential district across the United States would have prohibitively high computational costs.

Instead, a look-up table was created to represent the different thermal loads and ground conditions across the country. This table was then used to size borehole fields.

For each set of inputs in the look-up table, GHEDesigner (a ground heat exchanger design tool) was used to size the number of boreholes and length needed to meet the thermal load (Jeffery Spitler et al., n.d.; Jeffrey Spitler, West, and Liu 2022; Mitchell et al. 2023). The recorded metric was the total borehole length required per gross building load (sum of absolute value of annual heating and cooling loads in the district). Thus, the output can be used to scale the size of the borehole field based on the total load in each district.

A multi-dimensional look-up table of 540 scenarios (= 15 × 3 × 3 × 4) was developed by independently varying climate zone, ground thermal conductivity, number of buildings and ratio of annual heating to cooling load (see Table 1).

Table 1. Lookup table inputs

Variable	Inputs
Climate zone*	1A, 2A, 2B, 3A, 3B, 3C, 4A, 4B, 4C, 5A, 5B, 6A, 6B, 7A, 7AK
Ground thermal conductivity quartile	25^{th}, 50^{th}, 75^{th}
Number of buildings	3 options (between 25-300, range varied by climate zone)
Ratio of annual heating to cooling loads	4 options (from 0.002 – 12, range varied by climate zone)

**ResStock building loads were not available for climate zones 7B or 8A. Those loads were thus excluded from this analysis.*

Within the United States, there are eight climate zones and three moisture regimes (A, B, C), using the categories designated by the Internation Energy Conservation Code (IECC). For each climate zone, a representative city was selected and ResStock (National Renewable Energy Laboratory, n.d.) timeseries building data was retrieved. Building data from actual meteorological year 2012 was used to be compatible with ReEDS for future grid impact analysis. For each climate zone, the average ground temperature (Xing 2014) and each of the three quartiles for ground thermal conductivity (Liu, Warner, and Adams 2016) were used as inputs for the geothermal borehole modeling.

The number of buildings and ratio of heating to cooling loads specified as inputs for the look-up table (as described in Table 1) were determined based on analyzing loads across each climate zone. The goal was to create three different district sizes by specifying a number of buildings, while maintaining district borehole field size between 200 and 1000 total boreholes. Climate zones with more balanced loads can hold more buildings in each district within these bounds, while climate zones with highly unbalanced heating and cooling loads use fewer buildings. Additionally, the ratio of heating to cooling was varied to capture differences between different building types and load profiles. While the heating and cooling loads may be scaled up or down to capture a specific

ratio, the hourly variations are still present. This allowed the lookup table to capture a wide variety of potential district building compositions.

Once the buildings were selected for a given climate zone and the loads scaled to match a given ratio, the building loads were summed for each hour of the year across all the buildings in the district and then converted into ground loads via the heating and cooling coefficient of performance (COP). The resulting timeseries ground load values were then input into GHEDesigner to size the appropriate borehole field.

The general model settings for GHEDesigner were:

- 30-year design period
- Minimum entering temperature of 0°C and maximum entering temperature of 35°C for the heat pump
- Initial COP values of 4 for heating and 6.5 for cooling (Liu et al. 2023), then iterated to find new COP values based on fluid temperature leaving borehole field during simulation and a residential heat pump COP curve
- Maximum borehole depth of 175 m
- Borehole spacing of 6.1 m
- 20% glycol mixture
- 1.25-inch single U-tube pipe

2.2 Other Pre-processing and Inputs

Before running dGeo, the distribution network (the length of thermal loop piping to be installed) was sized for each census tract based on road lengths and land area. First, the distribution system was sized to be 75% of the road lengths in each census tract, excluding major roads (based on (Reber 2013)). Then, upper and lower limits were applied to cap distribution network sizing based on a study of European district energy systems (Sánchez-García et al. 2023).

Additionally, the census tract was flagged for potential space constraints if the land area required for the borehole field is greater than 5% of the tract's total land area. These census tracts may require a more in-depth assessment of land availability and heat exchange options. Borehole locations underneath roads or deeper concentric boreholes may increase the chances of installing borehole fields in dense urban areas.

The HEATNETS model (Simpson and Zhu 2024) was used to estimate operational energy and cost. Given load cancelling, loop thermal inertia, and heat exchange between the thermal loop and the surrounding soil, borehole field heat exchange may not be required at all times, with the working fluid instead circulating only in the thermal loop. The borehole fields may operate less in the shoulder seasons, which reduces pumping power needed to operate the system. HEATNETS was used to choose reasonable parameters for the dGeo system estimates, including a borehole capacity factor of 50%. Thus, for operational energy, the borehole field pumps are only considered to run 50% of the year.

2.3 District Costs

Estimating the capital and operational cost for these district energy systems is critical to determining their economic feasibility. In addition to costs, the potential incentives and financing structures must be considered.

Because district geothermal system adoption is limited in the United States, the financing structures are still to be determined. The study team assumed that the district-level components—including the borehole field installation, control system, distribution piping, and operation costs—are all covered by a commercial entity. Those costs are then passed on to agents through monthly bill payments based on each building's annual heating and cooling load. Agents are then responsible for heat pumps and building retrofits, as well as a portion of the district cost.

The potential economic benefits are quantified by the net present value for the agent. This value is based on the annual energy savings from the new system compared to baseline HVAC energy consumption, the agent's annual costs for the upgrades, and the agent's portion of the district cost.

Cost assumptions are highly uncertain due to the technology's early development stage. Cost estimates were gathered from the literature and publicly available financial data on utility installations. However, a range of values will be assessed to look at the impact of different values on economic potential.

The structure for building the cost estimate is as follows:

- District cost (assumed by commercial entity):
    - Borehole field:
        - Drilling cost per foot of depth (per borehole).
    - Distribution system:
        - Horizontal thermal loop pipe installation under community streets, cost per meter.
        - Central pump house or plant with controls, piping, and auxiliary systems, cost per kW of pumping power (to scale with system size).
        - Pump cost (for circulation of thermal loop and operation of borehole fields), cost per kW or HP.
    - Engineering, procurement, and construction, as a percent of installed cost before incentives.
    - Operations and maintenance, as a percentage of total installed cost before incentives.
- Agent cost (assumed by building owner):
    - Heat pump cost per ton.
    - Hook-up cost per building to connect to distribution network.
    - Retrofit cost per ton (only applied if the current HVAC system is not ducted).
- Incentives:
    - Federal investment tax credit (ITC) applied to district costs.
    - Federal tax incentive and state and local incentives (if available) applied to agent costs.

- Additional assumptions:
    - Pump operation costs assume borehole fields are run 50% of the time, with commercial electric rates applied.

2.4 Simulation Steps

An ambient-temperature loop simulation in dGeo begins with the same initial process documented previously (Gleason et al. 2017; McCabe et al. 2019; Liu et al. 2019), including referencing spatial databases and creating agents. Agents are assigned heating and cooling loads and HVAC system types, ages, and costs. After this general set-up, the ambient-temperature loop module in dGeo performs the following tasks:

1. Performs district sizing calculations for district energy systems within each census tract:
    - Ground thermal conductivity is randomly assigned as either 25^{th}, 50^{th}, or 75^{th} percentile of thermal conductivity for that climate zone.
    - Imports ground heat exchanger (borehole field) sizing lookup table, discussed in Section 2.1.
    - Sums the agent thermal heating and cooling loads in the census tract and scales to a reasonable size for a single district.
    - From the look-up table, assigns to the census tract a ratio of total length of borehole heat exchanger needed to gross heating and cooling load (m/kWh) based on the total thermal load, ratio of heating to cooling load, climate zone, and ground thermal conductivity of the district.
    - Assigns the distribution length needed to connect all agents in the census tract into districts based on pre-processed data (discussed in Section 2.2).
2. Sizes the heat pumps and calculates energy savings based on the geothermal heat pump module (Liu et al. 2019).
    - Compares current baseline capital and energy costs to proposed heat pump costs.
3. Calculates district sizing and costs for each census tract:
    - Sizes the borehole field based on the total gross load within the census tract (representing a total borehole field size that would likely be distributed amongst multiple borehole fields supporting multiple districts).
    - Estimates district system cost by applying the cost structure defined in Section 2.3, and then applies commercial financing and incentives.
    - Applies district costs to agents in each census tract based on $/kWh of total demanded thermal load.
4. Calculates agent financials:
    - Applies residential incentives and financing.

- Converts agent costs and energy savings into cashflows and then calculates net present value.
- Marks agents with positive net present value as economic potential.

5. Repeats every 2 years.

Note that district sizing and cost calculations are done at a census tract scale. Most census tracts will need to include multiple districts. The study team assumed that each district in a given census tract has the same mix of buildings and the required costs are scaled up to the census tract level.

In the dGeo geothermal heat pump module, the market potential and adoption over time are calculated using adoption data and Bass diffusion curves. However, there is limited data available on district systems in general and no clear adoption data available at this time. Therefore, the ambient-temperature loop analysis will only go as far as economic potential and will not calculate market potential or adoption rates as was done previously for geothermal heat pump (Liu et al. 2019).

3. Initial Results and Discussion

Many geospatial data layers are used as inputs for dGeo. Figure 2 provides examples for the road lengths and thermal demand density spatial data for Vermont (chosen arbitrarily).

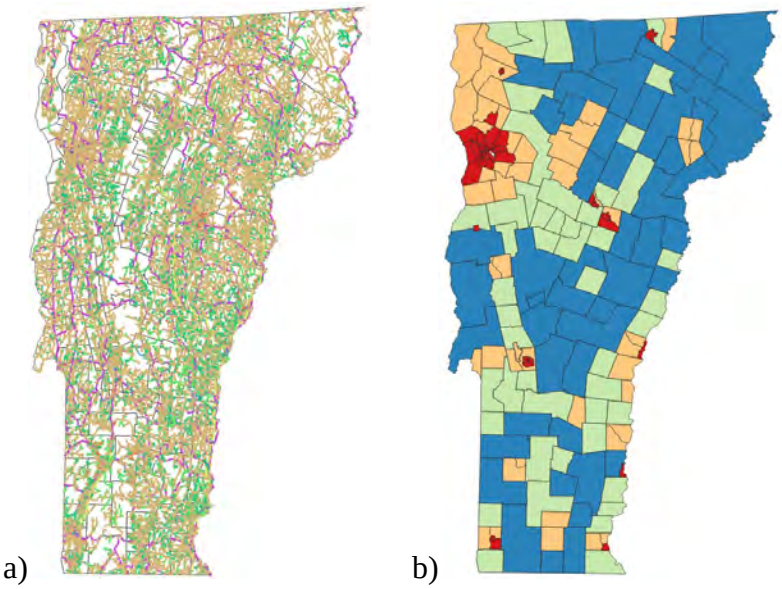

a) b)

Figure 2: a) Roads (different colors represent different road types), and b) thermal demand density (warmer colors represent higher thermal demand density) in Vermont.

To demonstrate dGeo's potential, a state-wide run was completed for Vermont, followed by a nationwide run for the entire United States, with results for 2032 shown in Figures 3 and 4. An advanced costing scenario was used, with cost values for well drilling, distribution system, etc. at

the lower end of current estimates. The median relative favorability of ATL for each census tract is shown, with darker colors representing a more economically favorable median agent net present value and lighter colors representing a less economically favorable median.

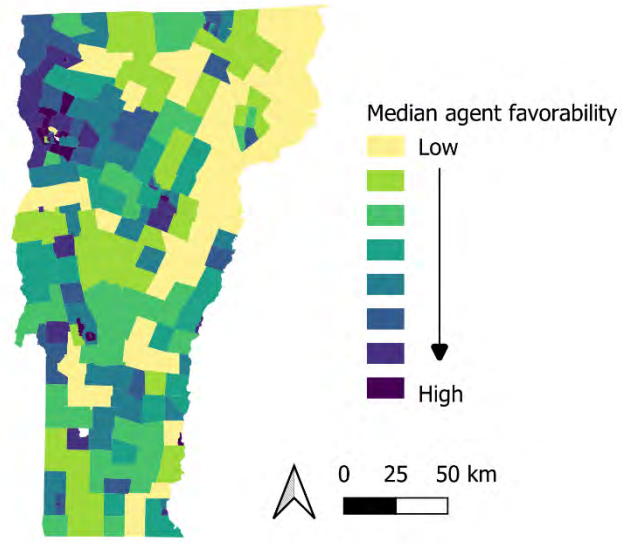

Figure 3: Vermont census tract median agent economic favorability in 2032.

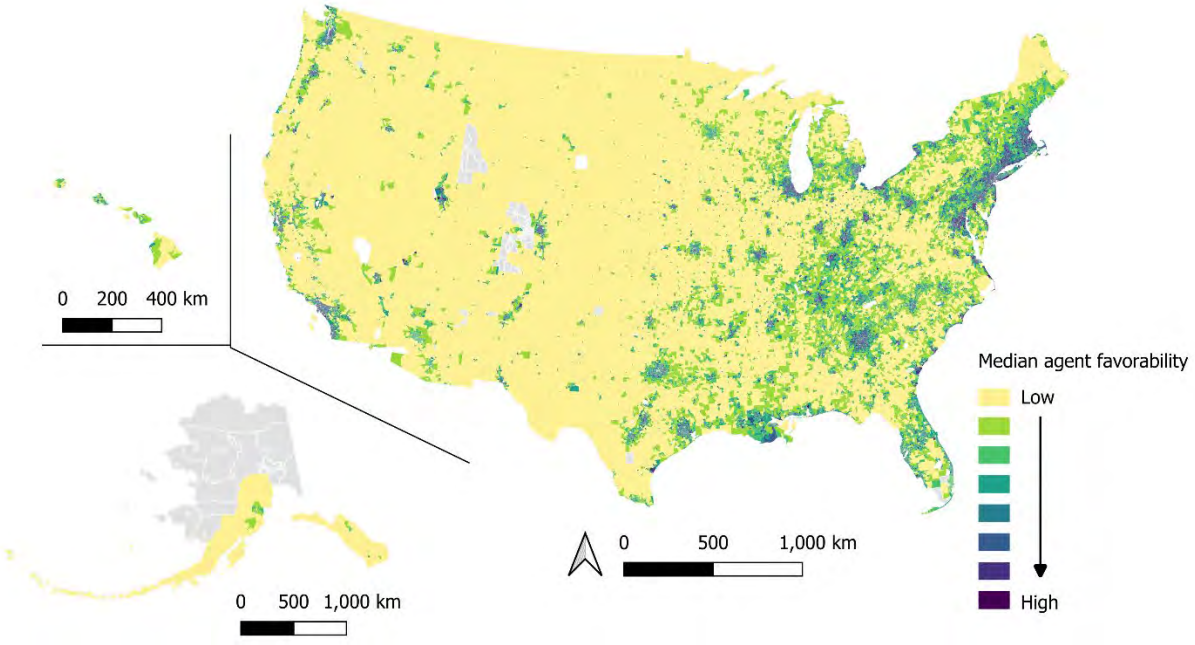

Figure 4: United States census tract median agent economic favorability in 2032. (Representative building models were not available for regions shaded in grey.)

To create the maps in Figures 3 and 4, the net present value for each agent was calculated for 2032. These net present values account for the additional capital costs of the heat pump installation,

shared ambient-temperature loop capital costs, and each agent's potential energy savings from switching from an original HVAC system to a geothermal heat pump. The year 2032 was used because the federal investment tax credit is still in place at this time, significantly decreasing capital costs. As expected, cities in each state tend to have higher favorability. More urban settings are likely to have reduced transmission costs per load, which can be a significant factor in the total capital costs. There are also differences in favorability seen among tracts in individual cities.

Figure 5 shows the ATL economic potential (given an advanced costing scenario) for Vermont, defined as the sum of the HVAC system size for all agents with a positive net present value when switching from their baseline HVAC to an ATL system. Every two years, dGeo adds new agents, updates HVAC costs and ages, adjusts energy costs, and generates new results. The number of agents with positive net present value generally increases over time until the federal investment tax credit expires at the end of 2034, after which the economic potential decreases significantly.

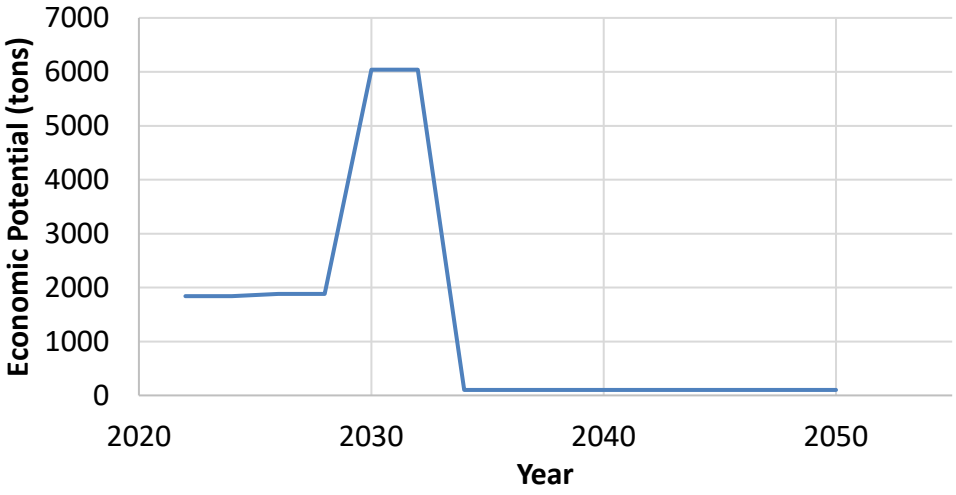

Figure 5: Vermont economical potential for agents with positive net present value over time.

The preliminary economic potential shown in Figure 5 accounts for most current incentives and rebates, but it does not account for any additional value to the electric grid or benefits for retiring natural gas infrastructure. These benefits to utilities are expected to be significant and may influence future adoption of ambient-temperature loop systems. Additionally, these initial results only consider residential buildings, and it is expected that performance would be improved when residential and commercial buildings are considered on the same loop.

These results are based on the economic potential for each individual agent. For district systems to work effectively, a critical mass of agents would need to agree to join a network. The study did not consider this aspect of district adoption, instead focusing on determining which agents would find district systems economically viable if district systems were an option in their community.

4. Conclusions and Future Work

In this project, dGeo was expanded with a new module to consider economic potential for ambient-temperature loop systems in the residential sector. A methodology was created for building a look-up table to size borehole fields for ambient-temperature loop districts across the United States. Cost correlations and financial structure assumptions were added to the module. The developed methodology compares the costs and benefits of ambient-temperature loop systems against baseline HVAC systems for agents in each census tract in the United States.

This new module can be used for assessing which areas of the country have the highest economic potential for ambient loop installations and what the impact is of different futures cost and price scenarios.

This research is ongoing, with additional improvements planned for the dGeo code. National simulations are still being processed, and the cost models continue to be updated as additional information becomes available. Future work includes expanding the module to consider mixed residential and commercial districts and considering multiple cost scenarios.

Acknowledgments

This work was authored by the National Renewable Energy Laboratory, operated by Alliance for Sustainable Energy, LLC, for the U.S. Department of Energy (DOE) under Contract No. DE-AC36-08GO28308. Funding was provided by the U.S. Department of Energy Geothermal Technologies Office. The views expressed in the article do not necessarily represent the views of the DOE or the U.S. Government. The U.S. Government retains and the publisher, by accepting the article for publication, acknowledges that the U.S. Government retains a nonexclusive, paid-up, irrevocable, worldwide license to publish or reproduce the published form of this work, or allow others to do so, for U.S. Government purposes.

References

Beckers, Koenraad F, and Katherine R Young. 2017. “Performance, Cost, and Financial Parameters of Geothermal District Heating Systems for Market Penetration Modeling Under Various Scenarios.” In *42nd Workshop on Geothermal Reservoir Engineering*. Standford, California.

Boesten, Stef, Wilfried Ivens, Stefan C. Dekker, and Herman Eijdems. 2019. “5th Generation District Heating and Cooling Systems as a Solution for Renewable Urban Thermal Energy Supply.” *Advances in Geosciences* 49 (September):129–36. https://doi.org/10.5194/adgeo-49-129-2019.

Brummer, Nichol, and Joyce Bongers. 2019. “Mijnwater Heerlen: Roadmap to 2040.” www.guidetodistrictheating.eu.

Electric Power Research Institute. n.d. “Efficient Electrification.” Accessed May 5, 2023. https://publicdownload.epri.com/PublicAttachmentDownload.svc/AttachmentId=70746.

Eversource. n.d. “Geothermal Pilot Project Updates.” Accessed June 13, 2023. https://www.eversource.com/content/residential/about/transmission-distribution/projects/massachusetts-projects/geothermal-pilot-project.

FEMA. 2023. “Hazus Inventory National Database.” https://msc.fema.gov/portal/resources/hazus.

Gleason, Michael, Kevin McCabe, Meghan E Mooney, Benjamin O Sigrin, and Xiaobing Liu. 2017. “The Distributed Geothermal Market Demand Model (dGeo): Documentation.” NREL/TP--6A20-67388, 1408285. https://doi.org/10.2172/1408285.

HEET. 2022. “Eversource Gas Breaks Ground on First Networked Geothermal Installation.” November 23, 2022. https://heet.org/2022/11/23/eversource-gas-breaks-ground-on-first-networked-geothermal-installation/.

International Energy Agency (IEA). 2023. “Renewables 2022.” https://iea.blob.core.windows.net/assets/ada7af90-e280-46c4-a577-df2e4fb44254/Renewables2022.pdf.

Liu, Xiaobing, Jonathan Ho, Jamie Lian, Xiaofei Wang, Weijia Liu, Mini Malhotra, Yanfei Li, Jyothis Anand Prem Anand Jayaprabha, and Frangxing Li. 2023. “Grid Cost and Total Emissions Reductions Through Mass Deployment of Geothermal Heat Pumps for Building Heating and Cooling Electrification in the United States.” ORNL/TM-2023/2966, 2224191. https://doi.org/10.2172/2224191.

Liu, Xiaobing, Patrick Hughes, Kevin McCabe, Jeffery Spitler, and Laura Southard. 2019. “GeoVision Analysis Supporting Task Force Report: Thermal Applications—Geothermal Heat Pumps.” ORNL/TM--2019/502, 1507876. Oak Ridge National Laboratory. https://doi.org/10.2172/1507876.

Liu, Xiaobing, Joseph Warner, and Mark Adams. 2016. “FY16 Q3 Milestone Report for Geothermal Vision Study Thermal Application (Geothermal Heat Pump): Complete Simulations of GHP Installations for Representative Buildings.” ORNL/LTR-2016/344, 1324190. Oak Ridge National Laboratory. https://doi.org/10.2172/1324190.

Marin, Carey. 2022. “Austin’s Whisper Valley GeoGrid™ Proves to Be Resilient Sustainable Energy Solution After Extreme Weather and Grid Events.” *Business Wire*, February 3, 2022. https://www.businesswire.com/news/home/20220203005848/en/Austin%E2%80%99s-Whisper-Valley-GeoGrid%E2%84%A2-Proves-to-be-Resilient-Sustainable-Energy-Solution-After-Extreme-Weather-and-Grid-Events.

McCabe, Kevin, Koenraad J Beckers, Katherine R Young, and Nathan J Blair. 2019. “GeoVision Analysis Supporting Task Force Report: Thermal Applications. Quantifying Technical, Economic, and Market Potential of Geothermal District Heating Systems in the United States.” NREL/TP-6A20-71715, 1524767. https://doi.org/10.2172/1524767.

Mitchell, Matt, Edwin Lee, Jeffrey Spitler, Ishraque Borshon, Jonathan Cook, Xiaobing Liu, and Timothy West. 2023. “GHEDesigner [SWR-23-33].” Oklahoma State Univ., Stillwater, OK (United States); National Renewable Energy Laboratory (NREL), Golden, CO (United States). https://doi.org/10.11578/dc.20230406.4.

National Renewable Energy Laboratory. n.d. “ResStock.” https://resstock.nrel.gov/.

Oh, Hyunjun, and Koenraad Beckers. 2023. “Cost and Performance Analysis for Five Existing Geothermal Heat Pump-Based District Energy Systems in the United States.” NREL/TP-5700-86678, 1992646, MainId:87452. National Renewable Energy Laboratory. https://doi.org/10.2172/1992646.

Reber, Timothy J. 2013. “Evaluating Opportunities For Enhanced Geothermal System-Based District Heating In New York And Pennsylvania.” Master’s Thesis, Cornell University.

Sánchez-García, Luis, Helge Averfalk, Erik Möllerström, and Urban Persson. 2023. "Understanding Effective Width for District Heating." *Energy* 277 (August):127427. https://doi.org/10.1016/j.energy.2023.127427.

Schulman, Audrey. 2020. "Pipes or Wires?" RMI. January 23, 2020. https://rmi.org/pipes-or-wires/.

Simpson, Juliet G, and Guangdong Zhu. 2024. "An Efficient Annual-Performance Model of a Geothermal Network for Improved System Design, Operation, and Control: Preprint." In *49th Stanford Geothermal Workshop*. Stanford, California.

Spitler, Jeffery, I Borshon, J Cook, E Lee, X Liu, M Mitchell, and T West. n.d. "GHEDesigner." https://ghedesigner.readthedocs.io/en/latest/.

Spitler, Jeffrey, Timothy West, and Xiaobing Liu. 2022. "Ground Heat Exchanger Design Tool with Rowwise Placement of Boreholes." In *Proceedings of the IGSHPA Research Track 2022*. International Ground Source Heat Pump Association. https://doi.org/10.22488/okstate.22.000016.

U.S. Energy Information Administration. 2020. "Monthly Energy Review." 0035. http://www.eia.gov/totalenergy/data/monthly.

Verhoeven, René, Eric Willems, Virginie Harcouët-Menou, Eva De Boever, Louis Hiddes, Peter Op't Veld, and Elianne Demollin. 2014. "Minewater 2.0 Project in Heerlen the Netherlands: Transformation of a Geothermal Mine Water Pilot Project into a Full Scale Hybrid Sustainable Energy Infrastructure for Heating and Cooling." *Energy Procedia* 46. https://doi.org/10.1016/j.egypro.2014.01.158.

"Whisper Valley." n.d. EcoSmart. Accessed April 24, 2023. https://www.whispervalleyaustin.com/ecosmart/.

Wolfson, Greg, and Michelle Mapel. 2020. "The Importance of Nanogrids in Low-Carbon Residential Communities." Whisper Valley. September 29, 2020. https://www.whispervalleyaustin.com/the-importance-of-nanogrids-in-low-carbon-residential-communities/.

Woodruff, Chase. 2022. "Gov. Polis Pitches Geothermal Energy as Clean-Heating Solution in Western Governors' Initiative." *Colorado Newsline* (blog). October 7, 2022. https://coloradonewsline.com/2022/10/07/gov-polis-pitches-geothermal-energy-as-clean-heating-solution-in-western-governors-initiative/.

Xing, Lu. 2014. "Estimations of Undisturbed Ground Temperatures Using Numerical and Analytical Modeling." PhD Dissertation, Oklahoma State University.

The First Open-Source Database for Geothermal Networks

Isabel Varela[1] **and Zeyneb Magavi**[1]

[1]**Home Energy Efficiency Team (HEET)**

Keywords

Heat pumps, geothermal heat pump, ground source heat pump, geothermal network, thermal energy network, database, heating and cooling, 5GHCD

ABSTRACT

Geothermal networks, defined as networked ground-source heat pump systems, are a clean energy alternative to fossil fuels for heating and cooling buildings, and a scalable solution with the potential to decarbonize entire neighborhoods. The individual components used in these networks are well developed technologies, such as pipes, pumps, and geothermal heat pumps. Nevertheless, there is a knowledge gap regarding how to optimize design parameters for performance and costs for the entire system, to account for region-specific conditions and localized heating and cooling needs for the buildings within the network. Additionally, there is a current lack of standardized methods for comparing these systems.

This study introduces a systematic and quantitative approach to comparing geothermal networks and provides the first open-source database where the datasets can be accessed and analyzed. In the US, geothermal networks have been most commonly adopted in university campuses. Recently, geothermal networks gained widespread attention from gas utility companies, cities, and states, as a strategy to reach net-zero emissions goals. Massachusetts is one of the leaders in this space, with five approved demonstration projects, each at different stages. In order to facilitate the optimized adoption of these systems, it is necessary to compare them and apply lessons from existing installations to those in earlier feasibility or planning stages.

This paper selects and examines key parameters to be systematically measured and recorded before and after the installation of geothermal networks, allowing for a quantitative comparison of these systems, as well as optimization of future ones. These recorded parameters fall into three categories: thermal resources (borefields, boreholes, etc.), distribution (main pipe system), and end-users (buildings, weatherization, etc.). This categorization of parameters, paired with cost data, will allow for fair comparison of geothermal networks with other heating systems. The creation of this open-access database for geothermal networks will therefore inform and facilitate the development of these projects, enabling decarbonization of buildings on a wider scale.

1. Introduction

By shifting from distributing gas to delivering emissions-free heat, gas utilities are becoming unexpected actors in effecting a decarbonization of heating systems in the Northeastern US. A network of geothermal (or ground-source) heat pumps, connected at a neighborhood scale, is at the heart of this transformation. These systems, that will be referred to in this study as geothermal networks, are also known as thermal energy networks (TENs), geothermal energy networks (GENs) or 5GDHC systems (Magavi et al., 2024). Geothermal networks have three main parts:

1. The **thermal resources** (sources, sinks, and storage) which are most frequently boreholes

2. The "**end-users**," or the buildings and customers which receive heating and cooling

3. The **distribution** system, which consists of the horizontal piping connecting the thermal resources and the end-users

Together, these form a closed-loop system, with water circulating through the boreholes, the main loop in the street and the service loop that connects to the buildings. In the winter, that water primarily carries heat from the boreholes to the buildings, and with the use of a heat pump at the building, that water can then be used for space (and water) heating. In the summer, this process is reversed, and the water primarily carries heat from the building to the boreholes. Systems such as these can facilitate a clean thermal market on a societal scale, where buildings that reject heat year-round, like data centers or ice rinks, could be connected to those that constantly require heat, like swimming pool facilities. Sharing heating and cooling loads into a common network makes the overall system more energy efficient. Because we are at the very initial stage of this transformation, capturing and disseminating lessons and data from these geothermal networks will be an important factor in supporting their growth. In order to facilitate this growth, this study is focused on creating a database of geothermal networks that can be used to inform the feasibility and design of future networks, as well as support data-driven policy for these systems.

Heating buildings accounts for 4 gigatons of CO2 nationwide, or 10% of global annual emissions (International Energy Agency [IEA], 2022). Within Massachusetts, for example, emissions from buildings account for 45% of the state's greenhouse gas emissions, and most of these emissions come from space and water heating systems (Mass.gov, n.d). Gas is currently the most commonly used fuel for heating in the state; 52% of households use natural gas, followed by 22% relying on fuel oil and kerosene. Electricity is used to heat 18% of the homes in the state. The electrification of heating and cooling systems is an important step in the US' journey towards net-zero in 2050. Installing heat pumps for heating and cooling, instead of relying on fossil fuel-based systems, will significantly reduce greenhouse gas (GHG) emissions related to the building sector. Networked geothermal heat pumps (GHP) are not only a highly efficient way of decarbonizing the building sector, but can also be implemented at scale while addressing equity in the energy transition. Furthermore, geothermal networks provide a path for decarbonizing high-emission industries, including gas utility companies.

Even though geothermal networks employ technologies that have been used for decades and mechanical equipment that is widely commercially available, there is a lack of standardized methods for quantitatively comparing the cost, efficiency, and design parameters between different

geothermal networks. Furthermore, there is debate on best practices for how to design these systems to maximize efficiency and cost. Generally, there is also a lack of research and data regarding the performance projections of these networks, their energy storage capacity, and optimal network parameters (Schulman and Magavi, 2022). This is largely because, until recently, geothermal networks were mainly implemented on university campuses in the US. It is only in the past three to five years that they have been considered as a societal scale decarbonization pathway, following the "Gas To Geo" proposal by HEET (2024) in Massachusetts seven years ago. This lack of information represents an obstacle to the wider expansion and implementation of these systems. It impedes not only the technical comparison of these systems, but it makes it difficult to leverage lessons from existing installations for others that are in earlier feasibility or planning stages. To fill this critical gap, this research project is focused on producing the first open-source database for geothermal network systems, in order to allow for a systematic comparison between these systems. This database will also support the development of data-driven legislation and regulation for geothermal networks that will enable a rational path to wider implementation of these systems.

1.1 Research Questions

The three central research questions that drive this project are:

1. How can lessons learned from the few existing networked ground-source heat pumps be leveraged to optimize the coefficient of performance and cost of future installations of these systems, and enable wider adoption to support decarbonization?

2. What are the optimal parameters that should be systematically measured and recorded before and after the installation of a geothermal network, to allow for a quantitative comparison amongst existing systems, as well as optimization of future ones?

3. How can the parameters be categorized and grouped in such a way that they allow for a fair and systematic comparison between different heating and cooling systems?

1.2 Goals of the Database

Creating an open access database for geothermal networks can inform and facilitate the development of these projects, enabling a societal-scale decarbonization of buildings. Systematically recording and assessing properties from existing geothermal networks into a database will be beneficial for a variety of reasons, including:

1. Enabling the quantitative comparison of these systems by identifying parameters that may be significantly influencing the overall coefficient of performance and costs;

2. Contributing to prediction models that estimate the future performance of existing installations;

3. Informing the planning and optimization of parameters for future installations through analyses made possible by this database;

4. Recording costs related to heating and cooling of buildings with the legacy systems versus the geothermal network system, which will allow quantification of cost differentials;

5. Identifying costs and energy use by stages, such as thermal resources, distribution, and buildings, which will allow for fair comparison with other heating systems.

6. Catalyzing the adoption of geothermal network technology through increased knowledge of their efficiency or coefficient of performance and costs;

7. Demonstrating impacts on emissions, environment, and human health, by recording emissions and air quality effects before and after the installation of geothermal network;

8. Supporting the development of data-driven legislation and regulation related to the proliferation of geothermal network systems;

1.3 Sustainability Framing

By creating a database for networked ground-source heat pumps, this project will contribute to the advancement of several of the UN's Sustainable Development Goals (SDGs). The UN SDGs are 17 global objectives that aim to achieve sustainable societies by addressing current global problems such as hunger, poverty, human health, pollution, and climate change, as well as many others. At its core, this project supports the transition of heating and cooling of buildings to renewable and clean energy for the communities involved. Thus, this work furthers SDG7, which focuses on affordable and clean energy. The potential scalability of these systems means that this project also has the potential to contribute to the transformation of the communities involved in these pilots into sustainable cities and communities, contributing to SDG11. Because the installation of these systems will require a skilled workforce that includes drillers, pipefitters, HVAC installers, and engineers, it will also spur job creation and economic growth, contributing to SDG8. Furthermore, when deployed at scale, these networked geothermal systems will contribute to the reduction of GHG emissions by replacing heating systems based on gas and oil with ground-source heat pump technology, thus contributing to SDG13, which promotes climate action. Lastly, there are clear benefits to human health. Natural gas has been shown to contain small amounts of non-methane gasses that can be detrimental to human health and air quality (Michanowicz et al., 2022). The use of gas stoves for cooking or heating without ventilation has been shown to result in an increased risk of asthma, wheezing, and bronchitis in children (Kile et al.,2014). Thus, reducing or eliminating the need for gas in buildings also has the potential to contribute to SDG3, which focuses on good health and well-being.

1.4 Organization

This study is organized into five main sections: introduction; background; methods; results and discussion; and conclusion and further work. The background section provides a brief overview of ground-source heat pumps and compares them to air-source heat pumps. This section also introduces the concept of geothermal network systems, as well as their benefits and challenges. Additionally, it describes the current momentum of these systems, reflected by the interest from utility companies, the number of states that have passed legislation supporting their growth, and the feasibility and pilot projects which are already underway. It is this momentum that has sparked the need for the database proposed by this study.

The methods section explains the process used for creating this database. A key aspect of this project was to collect a set of parameters that captures the main characteristics of the system while remaining simple to record and report. The methods section describes the process of gathering

input from various stakeholders regarding what parameters should be recorded and how they were categorized.

The selected parameters are presented in the results and discussion section. This results section presents the classification of the parameters into thermal resources, distribution, and end user or buildings. It also describes the categorization of the parameters into two further groupings: an essential or basic collection, and an enhanced, in-depth or case study collection.

This study ends with the conclusion and future work section. This segment describes how this database can be used and how it may further evolve. This part also discusses the expected growth of the database, the challenges it faces, and the impact it can have.

2. Background

This section aims to provide the background context for the creation of the database. In order to do this, three main questions are addressed: 1) Why use geothermal heat pumps? 2) Why use geothermal networks? and 3) Why do this now?

2.1 Why Use Geothermal Heat Pumps?

The wider implementation of heat pumps can contribute to GHG reduction, as well as improving air quality which affects human health. The use of heat pumps instead of fossil fuel-based systems will significantly reduce GHG emissions, even taking into account the current electricity generation mix (IEA, 2022). As the electric grid transitions to cleaner generation, this advantage will further increase. Additionally, moving away from the use of natural gas for heating and cooking in residential homes will improve the air quality and is expected to have a positive effect on health. This is important because negative impacts to air quality have been documented resulting from natural gas leaks in residential homes in the larger Boston area (Michanowicz et al., 2022). Additionally, outdoor air quality is impacted by pipeline gas leaks, which can pose disproportionate burdens on marginalized populations (Luna and Nicholas, 2022).

Heat pumps also have the benefit of being very energy efficient. A metric used to evaluate the efficiency of heat pumps is the coefficient of performance (COP), which is a ratio of the useful heat output by the system, divided by the energy consumed. Because heat pumps move heat from a source (ground, air, water) to a sink (indoor location), the temperature difference between the source and the sink strongly influences the COP. However, even in climates where the average winter temperatures are above -10 °C, air-source heat pumps have an average annual COP above 2.4, which is equivalent to an efficiency of 240%, as demonstrated by Gibb et al. (2023). Gibb's team composed of members of the Regulatory Assistance Project in Belgium and Oxford, Exeter, and Ulster Universities, set out to study the COP of air-source heat pumps throughout 17 European countries. They also found that in colder climates with winter temperatures above -30 °C the average COP of air source heat pumps was 1.5, equivalent to an efficiency of 150%. Interestingly, they report that heat pumps are more common in countries with colder winters such as Finland, Norway, and Sweden, compared not only to warmer countries like Portugal, Spain, and Italy, but also to countries such as France, Germany, Switzerland, and the UK.

Importantly, geothermal heat pumps (GHPs) have a higher COP than air-source heat pumps. This is because the subsurface temperature remains relatively constant throughout the year compared to air temperature, as well as the fact that GHPs do not have to spend energy on defrosting (Gibb

et al., 2023). Which means that GHPs are not only more efficient, but also better suited for colder weather.

Additionally, there is a large innovation potential for improving the COP of a GHP system. This can be via thermal exchange innovations or interactions with environmental factors. For example, a modeling study by Wołoszyn and Golas (2017), faculty members from the department of Mechanical Engineering and Robotics from the AGH University of Science and Technology in Krakow, found that the coefficient of performance of a horizontal ground heat exchanger is strongly influenced by the soil moisture. This is due to water increasing the thermal conductivity, which influences the COP. Wołoszyn and Golas (2017) proposed using a water irrigation system to increase the COP in their system.

In addition, GHPs are not only more efficient than air-source heat pumps, but a life cycle assessment by Violante et al. (2022) showed that they also have a lower overall long-term environmental impact. The study by Violante et al. (2022), from the Italian National Agency for New Technologies, Energy and Sustainable Economic Development, showed that GHPs are more beneficial, with lower impacts on three of the four categories studied, including human health, climate change, and resources. For the fourth category, ecosystem quality, ASHPs showed lower impact. Nevertheless, the study concluded that because the lifespan of the geothermal source or borefield can be estimated at 100 years, the resulting impact of the vertical U-bends in the borefield is reduced. Furthermore, the study suggested that GHP systems be connected to photovoltaic systems so that the electricity required by the heat pumps is generated using renewable energy.

GHPs have the further benefit of functioning as base load dispatchable energy. Currently, the strong seasonal fluctuation in the energy demand of buildings is largely being met by fossil fuels (Buonocore et al., 2022). As buildings are decarbonized and electrified, this will shift the energy demand to be highest in January (heating season), followed by a second peak in July (cooling season), which results in the so called “falcon curve” (Buonocore et al., 2022). Due to the baseload and dispatchable nature of GHPs, they are one of the technologies that can address the seasonal increases in energy demands, thus contributing to the reduction of seasonal peaks in electricity demand.

2.2 Why Use Geothermal Networks?

Geothermal network systems have further advantages over individual building GHP systems, including higher system COP, lower costs of installation, and scalable solutions to decarbonizing entire neighborhoods. Critically, they also provide a path for high emitting industries, including gas utility companies, to have a pathway to decarbonization and thus buy-in to the state’s net-zero targets.

The system COP of existing geothermal network systems is larger than that of individual buildings with GHP. The COP of the geothermal network system increases as buildings with diverse energy needs are connected to the same thermal network. For example, if the network consists of a data center (which even in the winter rejects heat), this heat can then be used by the other residential or commercial buildings that are connected to the geothermal network. Because of this, the heating and cooling needs of buildings in the geothermal network can be partially met even without tapping into boreholes. Colorado Mesa University has a geothermal network system that has been operating since 2008, and the average annual COP of the entire system has been calculated at 5.6,

with a winter season COP of 8.9 (Xcel Energy, 2023). This means that during the winter season the system has an efficiency of 890%. For every unit of energy (or electricity) input into the system, 8.9 units of energy (or heat) are put out. These efficiencies are very high, and they are higher than the efficiency that can be achieved by individual geothermal heat pumps.

Unlike air-source heat pumps, geothermal networks represent a utility-scale approach to decarbonization, providing an evolutionary new business model for gas utility companies. In order to reach 2050 net-zero emissions targets, gas utility companies must adopt new business models to decarbonize their operations.

The initial cost barrier to ground-source heat pumps can be overcome by geothermal network systems. These costs can be integrated as part of the utility infrastructure in new developments (Liu et al., 2017), or the up front infrastructure costs can be covered by the gas utilities installing and operating these systems using existing utility financing models.

2.3 Why Now?

A confluence of recent studies on GHPs, combined with the net-zero decarbonization targets of numerous states, the installation of pilot projects by gas utility companies in MA, and a nascent but favorable regulatory environment, make the present a particularly promising moment for the expansion of geothermal networks.

2.3.1 Research on GHP Impacts

Research findings show that if deployed at a national scale, GHP coupled with weatherization can offer significant savings on the electrical grid in terms of transmission lines and electrical capacity needed. Recent work led by the Oak Ridge National Laboratory and commissioned by the Department of Energy shows that if GHP are installed in 68% of residential and commercial buildings in the US, they could reduce the nationwide electricity generation capacity by 410 GW and eliminate the need for the construction of 43,500 miles of transmission lines by 2050 (Liu et al, 2023). The US' current electricity capacity is 1,300 GW, so eliminating 410 GW of future capacity generation is significant, representing about 32% of the current electricity capacity. For further reference, 43,000 miles of transmission lines would be equivalent to crossing the US 16 times from east to west. Even though Liu et al. (2023) do not consider the additional energy savings that would be accrued if networked GHP were installed, the benefits of GHP are significant. While the energy savings of installing geothermal networks at scale are expected to be even more compelling than those of GHP, there is a current lack of research in this area.

2.3.2 Gas Utilities Pilot Projects in Massachusetts

In 2017, the Home Energy Efficiency Team (HEET), a non-profit climate solutions organization, proposed the idea of geothermal network systems as an alternative business model to gas utility companies in Massachusetts. There are multiple benefits to this approach, including:

1. Gas utility companies have the technology and know-how to install new energy distribution systems, particularly subsurface pipes in public rights of way,

2. Utilities would benefit from the decarbonization journey, allowing their business to grow while still meeting Massachusetts' net-zero decarbonization target,

3. Utilities would be able to retain their customers and billing systems, minimizing disruption to their customers,

4. Utilities are uniquely positioned to install these systems at a societal scale, as they have already engaged in, and financed, this process in the past, through the creation of the current gas distribution system,

5. This approach incentivizes the elimination of emissions from an industry that is difficult to decarbonize in a way that can provide equitable access to clean energy,

6. Compared to other electrification methods geothermal network installed at scale by utilities ensures equitable access to heating and cooling, while avoiding rising costs of the gas system burdening those that cannot afford to electrify their homes,

7. Utilities are required by regulators to collect data from their systems with an emphasis on safety, affordability and reliability. Regulators could also require utilities to share their data with this proposed database, with the intention of improving outcomes for the public.

Massachusetts has an aging gas infrastructure, with a quarter of the piping in need of being replaced in the next 20 years, which would incur an estimated cost to gas customers of $34 billion (Seavey, 2023). But such a large investment in gas infrastructure is not in keeping with the Massachusetts 2050 Decarbonization Roadmap. In light of this issue, HEET and Buro Happold (2019) undertook a feasibility study for networked geothermal systems in MA. They found that for low-density residential areas and medium-density mixed use areas individual geothermal networks would meet 100% of the heating and cooling needs of these street segments. Thus, the large capital investment needed to replace Massachusetts' aging gas infrastructure could instead be used towards geothermal networks. Additionally, interconnected geothermal networks could expand beyond the locations with gas infrastructure in need of repair or replacement.

Massachusetts is advanced in piloting utility-led, neighborhood-scale retrofits of geothermal network systems (Smith, 2024). Over the past seven years regulators have approved six installations in the state, five of which will be installed by gas utility companies (Schulman and Magavi, 2022). The positive results from the HEET and Buro Happold (2019) study led to the commissioning of the first utility-owned neighborhood-scale retrofit geothermal network system in Framingham, with the project led by Eversource Gas. While this first pilot is currently in commissioning and is expected to begin operations in the fall of 2024 (Eversource, 2023a). The Framingham project will serve 36 buildings and 125 individual customers, including commercial buildings, public housing from the Framingham Housing Authority, a school, a fire station, a gas station, and single-family homes (Eversource, 2023). This geothermal network system is being financed entirely through Eversource Gas, using the same ratepayer-based financial structure established by gas utility companies to deliver gas.

Gas utility companies have spent a significant amount of capital to build the gas distribution network in place today. They can recover that cost by amortizing it in a longer timeframe (30 or 50 years) and distributing it amongst their customers on their monthly bills. This model could also be used to finance the networked geothermal system. Similarly, all of the Eversource Gas customers in Massachusetts are contributing to the installation of the geothermal network system in Framingham, just as all of them are contributing to every new gas pipe that goes in the ground.

There are also three other geothermal network projects at different stages within the state. National Grid completed the design phase of a geothermal network system in Lowell and is expected to start construction in 2025. HEET won an award from the DOE to design a second loop, as an expansion to the Framingham first loop. The design of the second loop in Framingham will be finished in the fall of 2024. Additionally, Mayor Michelle Wu together with National Grid announced that the first geothermal network for the City of Boston will be installed in the Franklin Field community (Wu, 2024) and will start the design in the fall of 2024.

In the state of Massachusetts, regulatory mandates support the expansion of geothermal network pilots. The recent regulatory order by the Massachusetts Department of Public Utilities is expected to propel the expansion of geothermal network systems by gas utility companies. The order requires utility companies to evaluate the use of non-gas options, such as geothermal networks, as alternatives to expanding the gas system or making additional investments in gas infrastructure (DPU, 2023).

Throughout the state, communities are interested in these pilot projects; 13 communities in Massachusetts are currently undertaking feasibility or site selection studies for the development of a geothermal network in their localities, as depicted in Figure 1. These studies are being sponsored by HEET through the Learning from the Ground Up (LeGUp) research project, funded by the Massachusetts Clean Energy Center. Communities conducting feasibility studies are Arlington, Deerfield, Gloucester, Lexington, Lowell, Salem, Somerville, and Worcester. The communities engaged in site selection and community engagement are Acton, Ashland, Melrose, New Bedford, and Newton (Heet.org, n.d.).

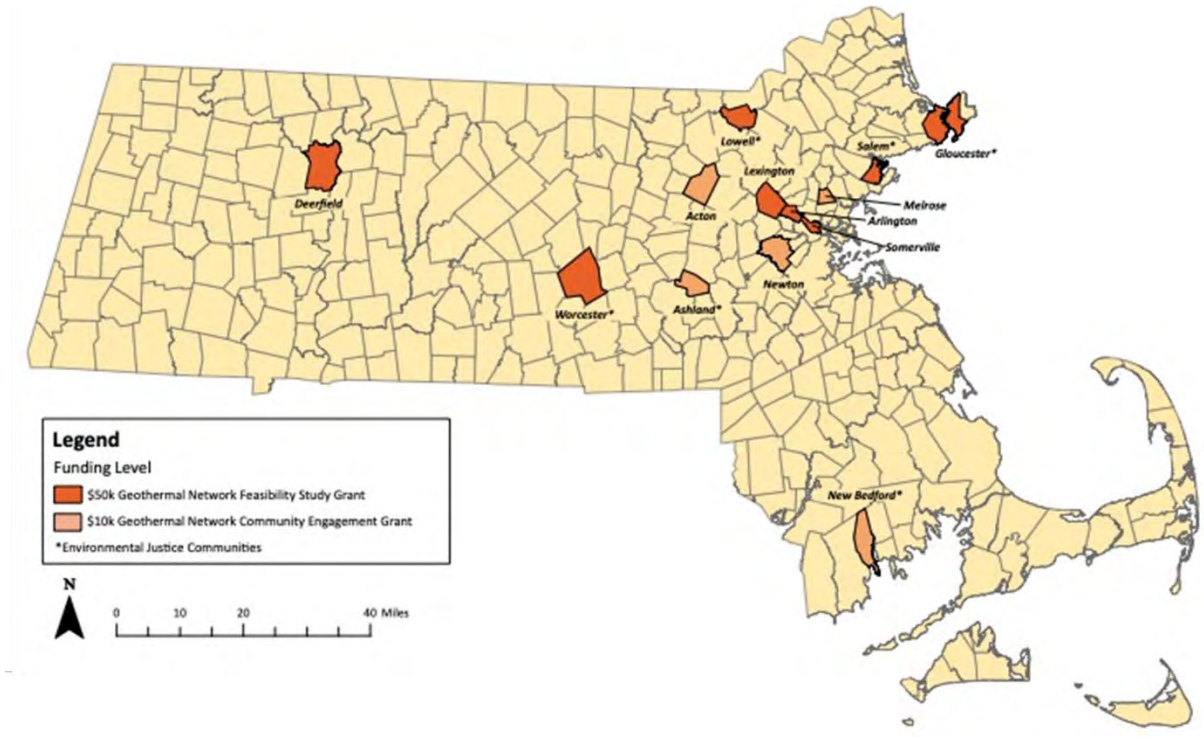

Figure 1: Massachusetts communities undertaking geothermal network feasibility or site selection studies. Figure modified from Heet.org, (2024).

2.3.3 National Landscape for Geothermal Networks

Even though Massachusetts is a leading state in the type of utility-led neighborhood-scale geothermal network systems that would ideally populate the database for this project, only the first Framingham project will have sufficient data to be input into the database in the first year of its launch. However, networked geothermal systems have existed for many years on university campuses (Oh and Beckers, 2023). Colorado Mesa University has a network geothermal system that has been operating since 2008, and Xcel Energy recently published a study on its performance (Xcel, 2023). Another system that has been operating for several years is Whisper Valley, TX which started operations in 2016. Whisper Valley is a newly built residential community, with the geothermal system planned since the design phase of the community. Given data availability, this project aims to populate the database with data from Colorado Mesa University, Whisper Valley, TX and other existing networks in addition to the Framingham, MA project in the first year after its launch.

On a national level, there is increasing support for geothermal networks that points to a future expansion of these systems. The Department of Energy granted $13 million to support community geothermal heating and cooling solutions (Department of Energy , 2023). As part of this funding, 11 projects were awarded grants for the design phase of geothermal projects. The states where these projects are being designed include AK, CO, OK, VT, CT, IL MA, MI, MN, and NY, as shown in Figure 2. A subset of these projects will receive further funding from the DOE for construction in 2025.

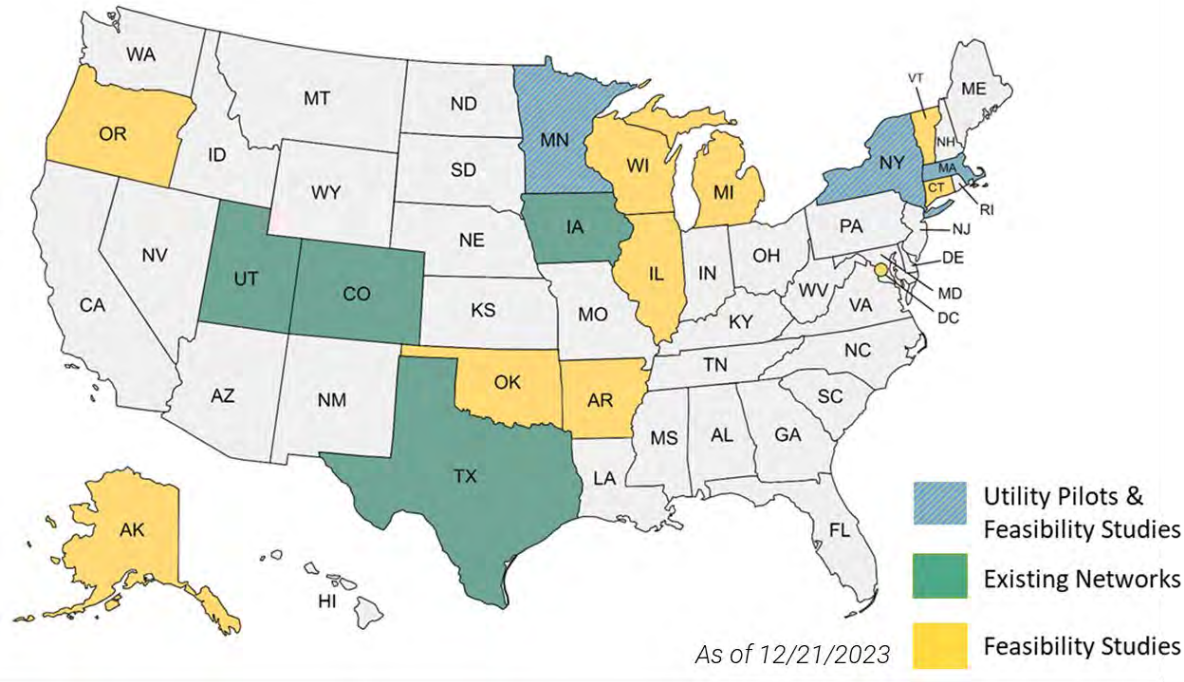

Figure 2 Map showing states with geothermal network installations and feasibility studies. Figure modified from Building Decarbonization Coalition and HEET (2024).

Changes in legislation are happening state by state, to support the growth of geothermal networks by gas utilities. Traditionally, gas utilities have been restricted by law to only provide gas to their

customers. In order for gas utilities to undertake geothermal networks as pilot projects or as a new business line, legislation must be changed to support this. As mentioned previously, in Massachusetts, the DPU approved the development of geothermal networks as pilot projects and encouraged the expansion of these. However, it still needs to approve the installation of geothermal networks as regular business for the gas utilities and not just as pilot projects. Other states have also filed legislation for the support of geothermal networks, as shown in Figure 3. To date six states have passed legislation enabling the gas to geo transition pathway, including NY, CO, MD, WA, MN, and VT.

Gas utility companies are becoming increasingly interested in geothermal networks. Gas utilities interested in geothermal networks have formed the Utility Networked Geothermal Coalition (UNGC), a group of gas utilities that have come together to share their collective knowledge in this area. This coalition includes 28 gas utilities, and together they serve nearly 50% of the gas customers in the US (Building Decarbonization Coalition and HEET, n.d.). The states that this coalition serves are depicted in Figure 4. In December of 2023, 15 of these utilities visited the pilot project in Framingham, MA.

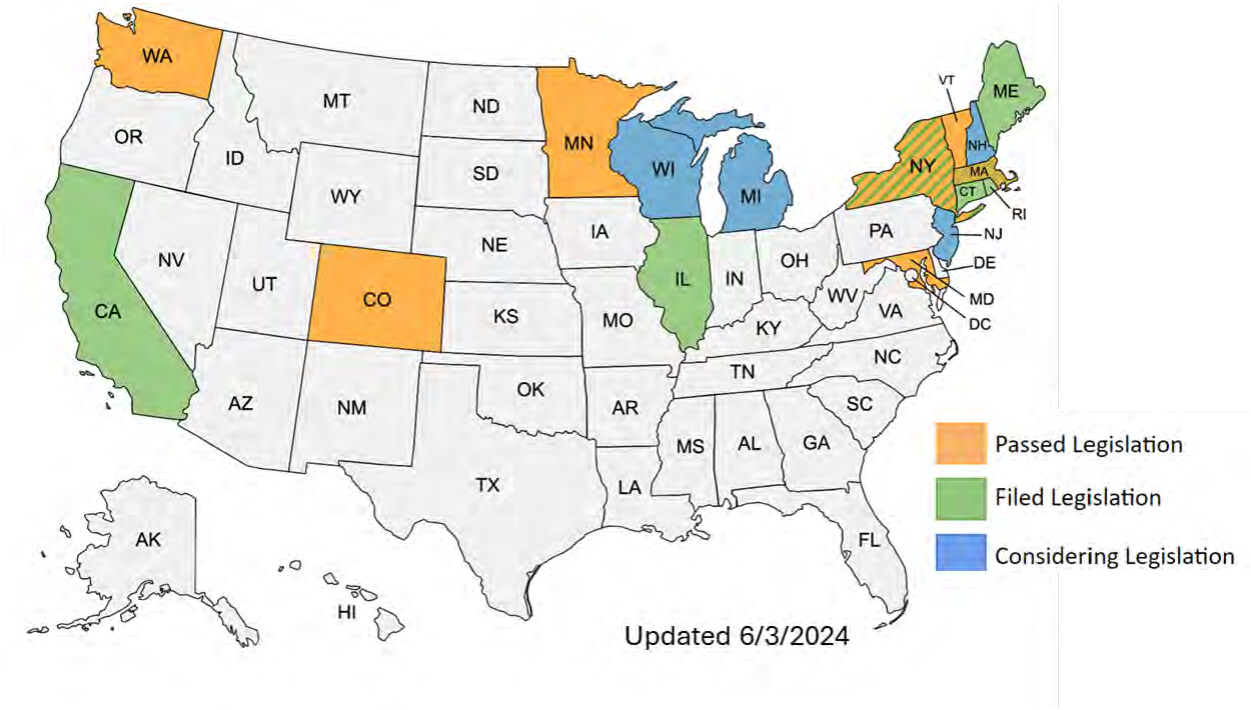

Figure 3 Map of geothermal networks legislation landscape. Figure modified from Building Decarbonization Coalition and HEET (2024).

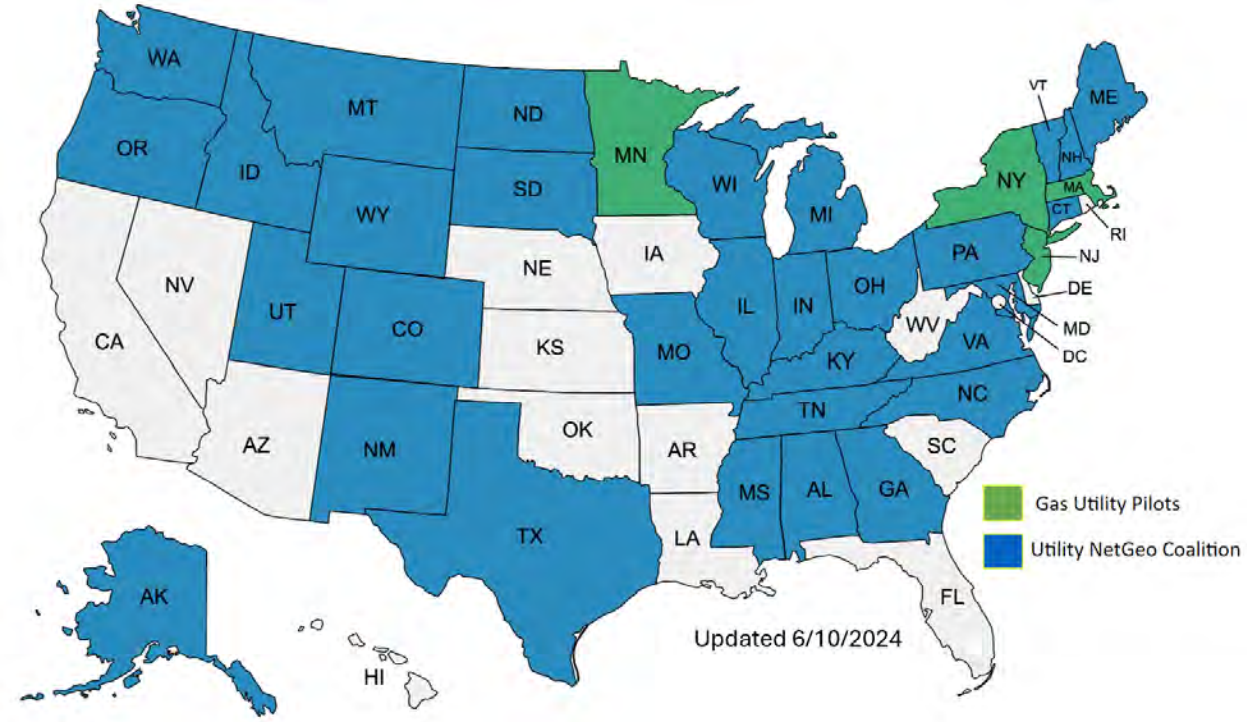

Figure 4 Map of the Utility Networked Geothermal Coalition (UNGC). Figure modified from Building Decarbonization Coalition and HEET (2024).

2.4 Why Do We Need a Database of Geothermal Networks?

While the database for geothermal networks would be the first open-source database of its type, there are other databases and tools related to GHPs that are relevant to this project. These include a geothermal data repository by the DOE and a feasibility tool and database from New York City.

The Geothermal Data Repository (GDR), hosted by the US Department of Energy, is a vast database that collects data from research projects funded by the US Department of Energy Geothermal Technologies Office (GTO), including projects on geothermal networks. This database has a broad focus; the data collected includes not only studies on ground-source heat pumps, but also any studies related to geothermal energy funded by the GTO (DOE, 2024). Most importantly, this database is limited in that it excludes all projects that have not been funded by the GTO, even if they are related to geothermal networks. This means that existing projects, such as the CMU and Whisper Valley systems, cannot be included. Furthermore, even for the geothermal network systems that are funded by the GTO and that can be included in their database, there is no standardization as to what parameters should be collected. Thus, there is also no systematic way to compare one case study of these networked geothermal systems to another.

Although New York City has developed a localized database and tool for geothermal heat pump information, it focuses only on projects within the city, and only on GHPs installed in individual businesses. New York City has a Pre-Feasibility tool for GHPs that includes a database of existing geothermal wells. The tool is very comprehensive, combining the geological, technical, and economic aspects required by the different types of geothermal heat pumps into a pre-feasibility assessment (New York City Major Office of Sustainability [NYCMOS] and USGS, 2018).

However, the database aspect of the tool is not set up to record networked geothermal systems (NYCMOS, 2024).

The creation and open accessibility of a database for geothermal networks can inform and facilitate future developments of these projects, enabling the pursuit of decarbonization. Communities doing feasibility studies can use the database to inform their choice of parameters and calculate prediction models (Simpson and Zhu, 2024) for their own systems. The potential beneficiaries of this database include consumers, utility companies, and regulators, among others. Building occupants, and, in a more indirect manner, the state residents are also beneficiaries of this database, as it would help enable state 2050 decarbonization goals (Executive Office of Energy and Environmental Affairs [EOEEA], 2020). Other states, beyond New York, Colorado, Washington, Minnesota and Maryland are also following Massachusetts' lead in the implementation of geothermal networks, some by receiving grants from the DOE (DOE, 2023) or through clean energy funding such as in Washington, D.C. Ultimately, the database will enable decarbonization efforts, as it will inform communities, developers, and regulators that are considering installing geothermal networks for heating and cooling as an alternative to gas and other fossil fuels.

3. Method

The methodological approach followed in this study consisted of collecting a large set of parameters related to geothermal networks, classifying them according to different criteria, and prioritizing them into an essential group and an enhanced group. The methodological approach is explained in more detail in the following steps,

3.1 Collected Input from Stakeholders

An initial list of parameters was collected from stakeholders, including gas utilities with geothermal pilots, modelers, academics, and engineers.

3.2 Identified Categories of Parameters

The initial set of parameters was classified into groups related to their commonality or functionality. Nine functional groups were identified. These functional groups were further classified into three groups, depending on where they fit in the stages of the system.

3.3 Grouping of Variables by Described Feature

Grouped variables by the feature they described, stage, and attribute. The parameters were classified by the feature described, as well as by their location in the overall geothermal network system and a single qualifying attribute. The data was arranged as a relational database, with seven tables that are related to each other via a key.

3.4 Defined Essential Mode and Enhanced Mode

In order to increase participation in the database, two modes of input were selected: an essential and an enhanced version. The essential mode contains fewer parameters that can at a high level describe the system. The enhanced version contains a larger set of parameters, which can be used for a more in-depth study of the geothermal network. These enhanced parameters will allow for a quantitative comparison of the energy usage by building for at least one year before and one year

after the start of operations of the geothermal system. The initial parameter list, which contained around 200 parameters, was revised and classified into the categories listed above. Additionally, parameters that were deemed unnecessary in both the essential and enhanced versions were flagged.

3.5 Consulted Experts

This step involved reaching out to experts and requesting their input on the proposed parameters for inclusion in the database. The expert group was composed of professionals in the field, such as energy consultants, designers of geothermal network systems, and utility companies that have geothermal network pilot projects, as well as researchers and modelers of these systems.

3.6 Selected Datasets

This step involved identifying the first datasets that can be used to populate the beta version of the database. These datasets were drawn from the Colorado Mesa University System, which has been in operation since 2008, and the Framingham, MA pilot project, which is currently in the commissioning stage and is set to start operations in fall of 2024. These datasets were selected based on the longevity of the system (CMU) and the likelihood of obtaining comprehensive datasets to populate the database (Framingham and CMU).

3.7 Defined Final Parameter List

With input from stakeholders and experts in the field, the parameter list to be included in the first beta-version of the database was selected. The selection was performed by considering the list of ideal parameters in comparison with those that are easier and more cost-effective to measure.

Getting geothermal network owners to share their data and populate the database is critical for the database to be useful. The state of Maryland has stipulated in their regulations that any geothermal network system in their state must share their data with this database (WARMTH Act 397, 2024). The implementation of similar regulations in other states would ensure that the database is comprehensive and remains up to date.

4. Results and Discussion

Many stakeholders contributed to the initial stage of parameter collection. The engagement process for this resulted in a comprehensive list composed of more than 200 parameters. One of the challenges of this study was to find a balance between identifying a comprehensive list of parameters, while still incorporating those that can be measured in a cost-effective way. Additionally, the data included in the database must be reported in such a way that individual buildings —and therefore customers— cannot be identified. This restriction must be followed so that utility companies do not violate customer privacy when reporting geothermal network data to this database.

4.2 Classification of Parameters

A high-level understanding of the data collected was acquired through a first categorization. More than 200 parameters were collected through the engagement of different stakeholders. The data

was interpreted, organized, and classified into nine categories related to their functionality. These categories include borefield, system, system performance, environment, subsurface, buildings, energy usage and demographics, as shown in Figure 5. Each of these categories will include a set of parameters that affect how the geothermal network system will perform.

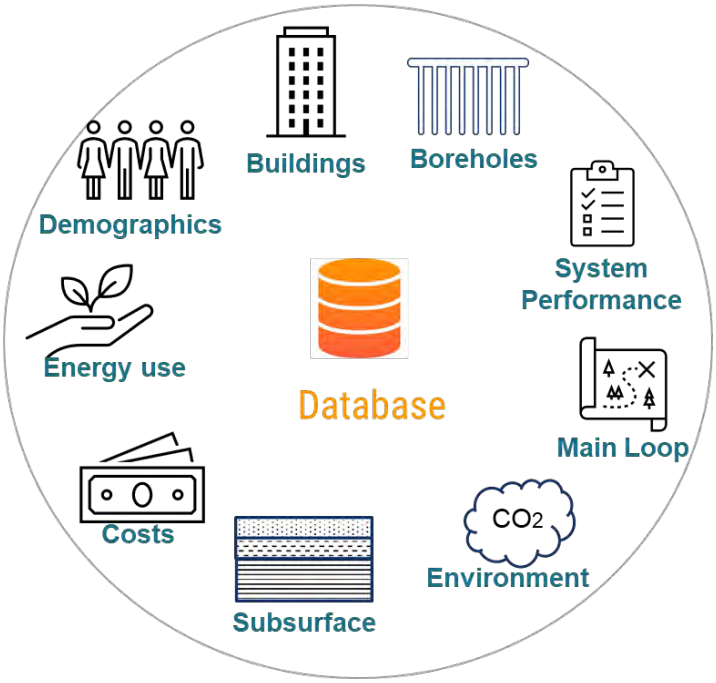

Figure 5 Categories of Parameters by Functionality. The parameters are grouped into nine categories including boreholes, system, system performance, environment, subsurface properties, costs, energy usage, demographics, and buildings.

The borefield category includes data related to the ground-heat exchanger (i.e. boreholes). For example, the borefield category will include information such as number of boreholes, geometry of boreholes, and length or depth of boreholes. This category also includes design parameters related to the borefield, such as borehole and U-tube diameters, material of the U-tube, type of grout, grout conductivity, and configuration of the ground-heat exchanger. Future versions of the databank will add other thermal resources such as dedicated thermal energy storage, solar thermal, etc.

In order to compare the geothermal network system to the gas distribution system, the parameters were also grouped in terms of where they are in the cycle of the system: upstream, distribution, and end-user. For the geothermal network system, upstream refers to thermal resources. The distribution refers to the single pipe or main loop that connects the thermal resource to the buildings and the end-user refers to the individual buildings, as shown in Figure 6.

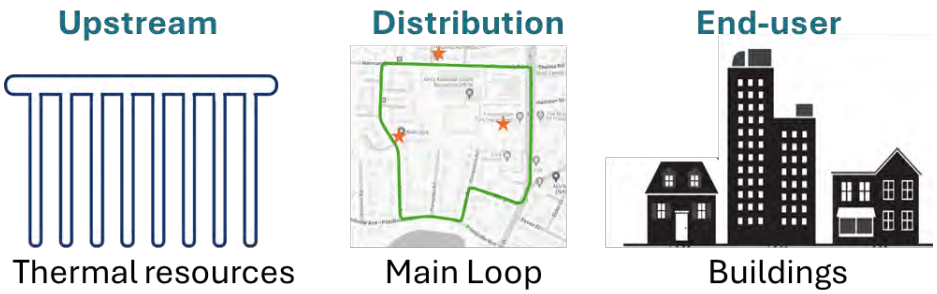

Figure 6 Category of Parameters by Position in System Stage. Parameters are grouped according to where they are in the energy value chain.

4.2 Essential Parameters

This section presents the list of parameters that were selected for inclusion in the essential mode. These are a high level set of parameters that describe the system while making it easier for owners and operators of geothermal networks to include their systems in the database.

4.2.1. Main Loop

The complete list of parameters that refer to the general system are listed in Table 1. These include a subset of non-technical parameters grouped as general information, and a set of technical parameters about the distribution system or main loop. The non-technical parameters capture basic information about the location of the loop, the ownership model, the designer company, and provide a narrative of key learnings on efficiency, design, and operation of the system. With the purpose of shedding light on the beneficiaries of these projects, this section also records whether the community where the loop is located is an environmental justice community as defined in the Justice 40.

The so-called ‘just energy transition’ refers not only to the residents or businesses on the loop, but also to the workforce employed in the construction and maintenance of the loop. Because of this, this section also captures whether the workforce employed in the construction of the loop meets federal prevailing wage standards.

In acknowledgment that the lessons learned in the design, construction, and operation of each system are valuable knowledge for other geothermal network systems, Table 1 has an option where these learnings can be uploaded in a narrative form.

The technical parameters for the main loop include the number of buildings that are in the loop and whether they are an existing or a new construction. This includes the number and type of thermal sources and sinks, which most commonly will be borefields. Information about the main pipe is key, such as the inner diameter and material of the pipe and length and location of the main loop. Note that the larger the diameter of the main pipe, the larger the thermal inertia, thermal storage, and capacity that the system has for expansion. Larger pipe diameters have only an incremental increase in cost and may allow for future buildings to be connected to the same geothermal network system. This section also captures the design flow rate of the system and the temperature range in which it is designed to operate. Table 1 also records the number of pumps

that are needed for the fluid to reach the desired flow rate and the type of fluid that circulates through the system. Water or water mixed with glycol are common fluids used as working fluids. Although there are examples of systems in northern climates such as Canada where the working fluid is 100% water, a percentage of glycol of up to 25% is often added to avoid pipes freezing and increase the system's thermal capacity. Additionally, costs are an important aspect of this database, and for the main system the compound cost of installing the main pipe per linear foot is recorded.

4.2.2. Thermal Resources

The complete list of parameters captured for boreholes are listed in Table 2. While future versions of this database will capture thermal sources that are different from boreholes, such as ponds and lakes, this first beta version of the database is set up to only capture thermal sources and sinks that are vertical or deviated closed-loop boreholes. For each borefield, the average characteristics of the boreholes are captured without providing detail on each one of them. For example, the database records the number of boreholes, the geometry of the boreholes (vertical or deviated), the geometry of the heat exchanger inside the borehole: concentric or U-bend, distance between boreholes and average borehole length.

Because test boreholes are important for gauging the subsurface properties and performance of the system, the database captures the thermal conductivity, thermal diffusivity, and borehole thermal resistance measured in the test boreholes. The database also includes the type of grout and the thermal conductivity of the grout. A basic geological description of the geological column encountered is captured.

Average costs are captured per borefield in the form of average cost per unit of drilled length and average cost per unit of lateral lengths trenched. Trenching is needed to connect the piping from the boreholes to the main loop and is often costly especially if it is in a paved area.

4.2.3. Buildings

Parameters are recorded per building and per unit in the building, as listed in Table 3. For each building it is recorded whether it is a new or existing construction, the year of construction, and the total square footage. It also records the number of individual units in the building and whether cooling will also be installed. This is because some buildings may choose to use the GHP system only for space heating. The database also records the number of heat pumps per building and number of additional heat sinks or sources that it may have, such as cooling towers. The database also asks whether a heat exchanger was placed outside the building. A heat exchanger is sometimes placed between the main loop and the building HVAC, to isolate the fluid in the main loop from the fluid circulating in the pipes inside the building. While this can have advantages in terms of resilience or thermal isolation of unique buildings, having a heat exchanger as a default for every building can lower the overall system performance.

In this building section, parameters related to building occupancy are also recorded, including the average occupancy of the building and the building peak occupancy.

4.2.4. Building Units

At the building unit level, the database captures the previous heating system type, including the previous heating system distribution type and fuel type. Weatherization and retrofit upgrades are captured at the building unit type as well. Costs for weatherization and building retrofit changes can vary significantly, depending on the specific upgrades performed. In this section, a multiple-choice option is provided with numerous weatherization and retrofit options that are often performed for energy efficiency and electrification of heating systems. In Massachusetts, weatherization plans usually strive to meet the MassSave standards.

Different geothermal network systems aim for different levels of electrification in the buildings. Because of this, the database captures whether the system aimed for full electrification of the building or if only certain appliances were substituted for electrical options. The cost of the new electric appliances is also recorded. It is also important to capture whether there is another source of heating that will remain in the building apart from the GHP, and determine the source of fuel that it uses.

4.2.5. Pumps, Heat Pumps and Other Sinks

Specificity about the number, type and size of every pump used is important to determine the total amount of energy going into the system. Table 4 captures the pump parameters for the pumps located in the main loop, at the borefields, and in the buildings. Note that these are pumps which are used to circulate the fluid in the pipes.

Table 4 also captures the type, size, and number of heat pumps in every building unit, as well as their seasonal energy efficiency rating (SEER) and their heating seasonal performance factor (HSPF). The cost of every heat pump is also recorded.

4.3 Enhanced Parameters

The enhanced parameter set builds upon the essential set. The number of additional parameters included in the enhanced parameter is smaller as shown in Table 5. However, each parameter itself has a high density of information about the system. At the system level the enhanced set includes a design schematic for the geothermal network. In the general information section, it includes a description of the community engagement strategies as well as more detailed information about workforce demographics involved in designing, building, and maintaining the system.

At the borefield level, the enhanced set includes a map with a layout of the boreholes, drilling logs when available. In terms of temperature, Table 5 records the temperature of the circulating fluid entering and exiting each borefield, as well as downhole temperature measurements (when available) in producing and non-producing boreholes one to three years after the start of operations. These downhole temperature measurements are key in assessing whether there is a temperature drift in the subsurface year-on-year, and how large that drift is. For the geothermal heat pumps to function optimally, they need to stay within a temperature range that depends on their manufacturing. If the subsurface temperature is outside that range, then the geothermal heat pumps will not function optimally, and the system COP will decrease. If a drift in subsurface temperature is recorded, initiatives can be taken to modify the controls of the system such that the subsurface temperatures stay within the optimal operation range. Ground water flow can affect the thermal conductivity of the boreholes. Because of this, the ground water flow rate, if known, is recorded.

At the building unit level, the enhanced set captures monthly or daily energy consumption and their associated costs one to three years before and after system startup. This involves electricity and gas or other fuel bills. In terms of design, the enhanced set asks for a schematic of how the building is connected to the main loop. Temperature measurements of the fluid entering and exiting each building throughout the year are also recorded.

Table 1 Parameters describing the overall geothermal network System. Selected list of parameters to be included in the database from the geothermal network describing the overall geothermal network system. The subcategories include general information about the system and the distribution stage

	Category	Attribute	Variable Name	Input Type	List Name
System	General Info	Site	System Name (Input string)	Unique string	
		Site	Year that system began operatiing (YYYY)	Select from pull-down menu	YEAR
		Site	Country (Select from pull-down menu)	Select from pull-down menu	COUNTRY
		Site	City (Input string)	Unique string	STATE (US only)
		Site	US State (Select from pull-down menu)	Select from pull-down menu	STATE (US only)
		Site	Ownership (Select from pull-down menu)	Select from pull-down menu	OWNERSHIP MODEL
		Site	List other main stakeholders engaged in planing or implemetnation and their respective roles	Unique string	
		Site	Contact Name(Input string)	Unique string	NEW OR EXISTING CONSTRUCTION?
		Site	Contact email(Input email)	Unique string	
		Site	Designer Company Name	Unique string	
		Site	Key learnings (on efficiency, design or operation of system)	Unique string	
		Demographics	Is this an Environmental Justice community? Based on Federal Justice 40 definition.(yes/no)	Select from pull-down menu	EJ 40 COMMUNITY (YES,NO, MIXED)
		Demographics	Workforce involved in construction of geothermal network(Select from pull-down menu)	Select from pull-down menu	WORKFORCE (Union, non-union, mixed)
	Distribution	Buildings	Type of buildings on network (Select from pull-down menu)	Select from pull-down menu	TYPE OF BUILDINGS ON NETWORK
		Buildings	New or existing construction?	Select from pull-down menu	NEW OR EXISTING CONSTRUCTION?
		Buildings	Number of buildings (#)	Number value	
		Design	POLYGON OF SITE	Upload link	
		Design	Number of thermal sources/sinks or borefield sites(#)	Number value	
		Design	Main pipe type(Select from pull-down menu)	Select from pull-down menu	MAIN PIPE CONFIGURATION
		Design	Length of main pipe	Number value	
		UNITS	Length of main pipe. UNITS	Select from pull-down menu	UNITS. Length (ft, m)
		Design	Main pipe depth	Number value	
		UNITS	Main pipe depth. UNITS	Select from pull-down menu	UNITS. Length (ft, m)
		Design	Main pipe inner diameter (inches)	Number value	
		UNITS	Main pipe inner diameter. UNITS	Select from pull-down menu	UNITS. Length (in, cm)
		Design	Main pipe design flow rate	Number value	
		Design	Main pipe minimum design flow rate. UNITS	Number value	
		Design	Main pipe maximum design flow rate. UNITS	Number value	
		UNITS	Main pipe design flow rate. UNITS	Select from pull-down menu	UNITS. Flow rate (gpm, l/s, ft3/s)
		Design	System minimum design temperature	Number value	
		Design	System maximum design temperature	Number value	
		UNITS	System design temperature. UNITS	Select from pull-down menu	UNITS. Temperature (F, C)
		Design	System circulating fluid(Select from pull-down menu)	Select from pull-down menu	CIRCULATING FLUID
		Design	Percentage of glycol (%)	Number value	
		Costs	Cost of main pipe distribution ($/ft)	Number value	
		Design	Number of main pipe pumps (#)	Number value	

Table 2 Table 2 Parameters Describing the Borefield. Selected list of parameters to be included in the database from the geothermal network describing the borefields. The subcategory is related to thermal resources.

	Category	Attribute	Variable Name	Input Type	LIST NAME
Borefield	Thermal Resources	Site	Borefield Name	Unique string	
		Design	Number of boreholes(#)	Number value	
		Design	Type of heat source/sink	Select from pull-down menu	TYPE OF HEAT SOURCE/SINK
		Design	Borehole Geometry(Select from pull-down menu)	Select from pull-down menu	BOREHOLE GEOMETRY (vertical, deviated, horizontal)
		Design	Connection between boreholes (series or parallel)	Select from pull-down menu	CONNECTION BETWEEN BOREHOLES (parallel, series)
		Design	Average Borehole Max Length	Number value	
		UNITS	Length. UNITS	Select from pull-down menu	UNITS. LENGTH (ft, m)
		Design	Test borehole max length	Number value	
		UNITS	Length. UNITS	Select from pull-down menu	UNITS. LENGTH (ft, m)
		Subsurface Property	TRT Thermal Conductivity from Test Borehole	Number value	
		UNITS	Thermal Conductivity. UNITS	Select from pull-down menu	UNITS. Thermal Conductivity (Btu/hr*ft*F)
		Subsurface Property	Thermal Difussivity	Number value	
		UNITS	Thermal Difussivity. UNITS	Select from pull-down menu	UNITS. Thermal Difussibity (ft2/day)
		Design	TRT Thermal Borehole Resistance	Number value	
		Subsurface Property	TRT Average Ground Temperature	Number value	
		UNITS	Temperature. UNITS	Select from pull-down menu	UNITS. Temperature (F, C)
		Design	Inner Diameter of Borehole	Number value	
		UNITS	Length. UNITS	Select from pull-down menu	UNITS. Length (in, cm)
		Design	Type of Heat Exchanger	Select from pull-down menu	TYPE OF HEAT EXCHANGER (co-axial, single U-tube, double U-tube)
		Design	Inner Diamter of U-tube	Number value	
		UNITS	Length. UNITS	Select from pull-down menu	UNITS. Length (in, cm)
		Design	U-tube material	Select from pull-down menu	TYPE OF PIPE MATERIAL IN U-TUBE (HDPE, PEX, PE-RT)
		Subsurface Property	Simplified geological column(upload file, csv, pdf, etc)	Upload file	
		Subsurface Property	Most common lithologies (list of to three if necessary)	Unique string	
		Costs	Cost of drilling ($) per unit length	Number value	
		UNITS	Cost/length. UNITS	Select from pull-down menu	COST OF DRILLING ($/ft, $/m)
		Costs	Cost of laterals ($) per unit length	Number value	
		UNITS	Cost/length. UNITS	Select from pull-down menu	COST OF LATERALS ($/ft, $/m)
		Design	Total Laterals Length	Number value	
		UNITS	Length. UNITS	Select from pull-down menu	UNITS. LENGTH (ft, m)
		Design	Number of Pumps (#)	Number value	
		Design	Type of grout	Select from pull-down menu	TYPE OF GROUT (bentonite, bentonite/sand, cement-based, granite-based)
		Design	Thermal conductivity of grout	Number value	
		Site	Location Latitude(Decimal)	Number value	
		Site	Location Longitude(Decimal)	Number value	
		Site	Google Maps (Link to Borefield Site)	Unique string	

Table 3 Table 3 Parameters Describing the Buildings and Building Units. Selected list of parameters to be included in the database from the geothermal network describing the buildings and building units.

	Category	Attribute	Variable Name	Input Type	List Name
Buildings	Buildings	Buildings	Building ID	Select from pull-down menu	
		Buildings	Buildng Type(Select from pull-down menu)	Select from pull-down menu	BUILDING TYPE
		Buildings	New or Existing/retrofit	Select from pull-down menu	NEW OR EXISTING
		Buildings	Year of Building Construction	Select from pull-down menu	YEAR
		Buildings	Number of Individual Units	Number value	
		Design	Will cooling be installed	Select from pull-down menu	YES/NO option
		Costs	Total Cost/building ($)	Number value	
		Design	Number Heat pumps/ Building	Number value	
		Design	Heat exchanger at building?	Select from pull-down menu	HEAT EXCHANGER OPTIONS (NA, outside vs inside building, per unit vs per building)
		Design	Heat Pump Size	Number value	
		Buildings	Square Footage(ft^2)	Number value	
		Demographics	Building average occupancy(# of people)	Number value	
		Demographics	Building peak occupancy (# of people)	Number value	
		Buildings	Number of additional heat sinks (e.g. cooling towers)	Number value	
Building Units	Buildings	Buildings	Building Unit ID	Select from pull-down menu	
		Buildings	Previous heating system	Select from pull-down menu	PREVIOUS HEATING SYSTEM (furnace, boiler,electric, etc)
		Buildings	Previous heating system distribution system (select from pull-down menu)	Select from pull-down menu	PREVIOUS HEATING SYSTEM DISTRIBUTION SYSTEM (forced air, steam radiant, randiant heating, etc)
		Buildings	Previous heating system fuel (select from pull-down menu)	Select from pull-down menu	PREVIOUS HEATING SYSTEM FUEL (oil, natural gas, propane, electricity, etc)
		Design	Weatherization features (select from pull-down menu)	Select from pull-down menu	WEATHERIZATION FEATURES (insulation, air sealing, etc)
		Costs	Weatherization cost. ($)	Number value	
		Design	Retro-fit features (select from pull-down menu)	Select from pull-down menu	RETROFIT FEATURES (duct installation, weatherization, full electrification, etc)
		Costs	Retrofit cost ($) (includes upgrade electrical box, install duct work, etc)	Number value	
		Design	Type of appliances replaced (e.g. stove, fireplace, DHW)	Select from pull-down menu	TYPE OF APPLIANCES REPLACED
		Costs	Cost of new appliances. ($)	Number value	
		Design	Type of new Domestic Hot Water (DHW)	Select from pull-down menu	
		Buildings	Is there another source of heating? (apart from the NGSHP)	Select from pull-down menu	YES/NO option
		Buildings	Specify additional source of heating? (apart from the NGSHP)	Unique string	
		Water	Annual water use before system startup	Number value	
		Water	Annual water use after system startup	Number value	

Table 4 Parameters Describing the Pumps, Heat Pumps and Other System Sinks. Selected list of parameters to be included in the database from the geothermal network describing pumps, heat pumps and other thermal sinks. Pumps can be located in the main loop, borefields and buildings.

	Category	Attribute	Variable Name	Input Type	List Name
Pumps	Distribution	Design	Main loop pump type	Select from pull-down menu	PUMP TYPE (at boreholes and buildings)
		Design	Pump capacity	Number value	
	Thermal Resources	Design	Borefield pump type	Select from pull-down menu	PUMP TYPE (at boreholes and buildings)
		Design	Pump capacity	Number value	
	Buildings	Design	Building pump type	Select from pull-down menu	PUMP TYPE (at boreholes and buildings)
		Design	Pump capacity	Number value	
Heat Pumps	Buildings	Design	Heat Pump Type (Select from pull-down menu)	Select from pull-down menu	HEAT PUMP COMPRESSOR TYPE
		Design	Heat Pump Size	Number value	
		Design	Heat Pump Size. UNITS	Number value	UNITS. HEAT PUMPS SIZE (tons, Btu/hr)
		Design	Heat pump Seasonal Energy Efficiency Rating (SEER)	Number value	
		Design	Heat pump Heating Seasonal Performance Factor (HSPF)	Number value	
		Costs	Cost of heat pump. ($)	Number value	
Other Heat Sinks	Buildings	Design	Type of heat sink (e.g. cooling tower)	Unique string	
		Design	Temperature difference of water entering and leaving the cooling tower (F)	Number value	

Table 5 Table 5 Additional Parameters proposed for the Enhanced version. Selected list of parameters to be included in the enhanced version of the database. These additional parameters describe the system, borefield, buildings and building units.

	Category	Attribute	Variable Name	Input Type
System	Distribution	Design	System design schematic	Upload file
	General Info	Design	Describe the community engagement approach (nature and frequency of cc	Unique string
		Demographics	Demographic information about workforce (e.g., race and ethnicity, age, ge	Upload file
Borefield	Thermal Resources	Subsurface Property	Average groundwater flow rate	Number value
		Subsurface Property	Main groundwater flow direction	Number value
		Subsurface Property	Temperature data in selected producing boreholes (DFOS) for 1 to 3 years	Upload file
		Subsurface Property	Temperature data of undisturbed ground (DFOS) for 1 to 3 years after insta	Upload file
		Design	Borehole layout map	Upload file
		Subsurface Property	Drilliing logs	Upload file
		Design	Temperature of circulating fluid entering and exiting each borefield	Number value
Buildings	Buildings	Demographics	Start time of peak occupancy	Number value
		Demographics	Duration of peak occupancy (hours)	Number value
Building Units	Buildings	Energy	Monthly (or daily) consumption of gas. Data going back 1-3 years before in	Upload file
		Costs	Cost of monthly consumption of gas. Data going back 1-3 years before inst	Upload file
		Energy	Electric use (hourly for 1-3 years before and after system startup). Data fr	Upload file
		Costs	Cost of electric use (for 1-3 years before and after system startup). Data fi	Upload file
		Design	Configuration schematic of how the Building system connecting to the distri	Upload file
		Design	Temperature of circulating fluid entering and exiting each building	Number value
		Energy	Electric demand at each building or sub-building serviced by separate H/C p	Upload file

4.4 Output Parameters

Apart from collecting needed data, the database will also perform basic calculations, as listed in Table 6, that are based on the input data. The main calculation related to the overall system performance is the system Coefficient of Performance (COP). This measurement will account for the overall system, including the boreholes, main loop, and buildings.

The database will also calculate the impacts on the environment and human health. Specifically, the database will compute the amount of CO2 and methane emissions eliminated due to electrification of heating as shown in Table 6. For existing constructions, the baseline scenario refers to the emissions before installing the geothermal network that replace the existing HVAC system. For new constructions, the baseline is defined and simulated with a standardized approach. Furthermore, the database will estimate the impact on human health using the disability adjusted life years (DALY) approach.

Table 6 Database outputs

Variable Name
Average annual efficiency of the system
Climate zone
Eliminated CO2 emissions
Eliminated methane emissions
Impact on human health
Impact on electricity consumption

5. Conclusions and Further Work

Geothermal networks are a highly efficient way of electrifying heating and cooling in buildings, and have the potential to do this at scale if this model is adopted by the gas utility companies beyond the pilot projects currently being pursued in Massachusetts and other states.

This project provides the basis for the creation of the first open-source database for geothermal network systems. It argues for the proposed set of parameters that should be collected to allow for a quantitative comparison between these systems as well as optimization of future ones. Furthermore, this study presents a categorization of parameters into three groups: thermal resources, main loop, and end-users. This grouping allows for the comparison of geothermal networks with other heating and cooling systems.

The creation of this database will support the growth of geothermal networks by allowing for a quantitative comparison between different systems and informing the planning and optimization of future ones. Recording costs and calculating the overall system efficiency will highlight the energy efficiency of these systems and help catalyze further adoption. Moreover, this database can serve as a reference point for policy makers as they develop regulations for these systems.

5.1. Further Work

While the main purpose of this study was to set the standard for the parameters that need to be reported to the database, there are other steps that need to be completed to launch the database,

including setting up a graphical user interface (GUI) for inputting data into the system and creating a data architecture for the database.

The GUI for collection of the parameters is currently being built. The interface aims to be simple and easy to use. Additionally, the database architecture is being carefully planned so that the database can be managed as the number of systems that report to it grow. The database is being stored at the Harvard Dataverse (Harvard Dataverse Support, 2020), as this is an open-source platform that commits to maintain the data in perpetuity.

HEET is now in the process of collecting and collating data from two systems to launch the beta version of the database with the geothermal network information available for CMU and Framingham.

Ultimately, for the database to be successful, it needs participation from the data owners of these systems, such as utilities, municipalities, co-ops, and university or industrial campuses. Dissemination of the existence of this database at professional conferences and in technical journals will help emphasize the legitimacy of the database. The preliminary plan for the database was presented as part of an invited panel at the annual conference of the International Ground-Source Heat Pump Association (IGSHPA) on Dec 5, 2023 (Magavi et al., 2023).

As the database becomes populated it will provide benefits for communities interested in geothermal networks. Whether the interested communities are in the pre-feasibility, feasibility, design, construction or operational phases, the populated database is expected to be beneficial. It will enable quantitative comparisons between systems, and contribute to prediction models and optimization. Additionally, it can provide cost comparisons by stages and demonstrate the impacts on emissions, environment and human health.

For geothermal networks to become mainstream and affect societal scale building decarbonization, they will need support from multiple key stakeholders, including regulatory entities, cities, states, utilities, private developers and a skilled workforce. This database is a tool that can inform and connect these different entities with their varying perspectives. In aligning stakeholders around delivering decarbonization through geothermal networks, this database supports global sustainable development goals, national decarbonization goals, and the transition of heating and cooling of buildings to renewable energy for the communities involved.

Acknowledgement

This study is part of the Learning from the Ground Up (LeGUp) project run by HEET and funded by a grant from the Massachusetts Clean Energy Center (MassCEC).

The authors would like to acknowledge the contributions of Angie Alberto-Escobar, Eric Juma, Elizabeth Nigh, Mark Kleinginna from HEET and Juliet Simpson from NREL. Thanks to Michaela Thompson from MIT and Xiaobing Liu from ORNL for editorial revisions and to the numerous stakeholders involved.

REFERENCES

Building Decarbonization Coalition and HEET. “National Landscape for Geothermal Networks”. 2024. https://buildingdecarb.org/resource-library

Buonocore, J. J., P. Salimifard, Z. Magavi, and J. G. Allen. "Inefficient Building Electrification Will Require Massive Buildout of Renewable Energy and Seasonal Energy Storage." *Scientific Reports* 12, no. 1 (2022): 11931. https://doi.org/10.1038/s41598-022-15628-2.

Department of Energy. "DOE Announces $13 Million to Support Community Geothermal Heating and Cooling Solutions." April 25, 2023. https://www.energy.gov/articles/doe-announces-13-million-support-community-geothermal-heating-and-cooling-solutions.

Department of Energy. “Geothermal Data Repository”. Accessed June 17, 2024. https://gdr.openei.org/.

Department of Public Utilities. "Investigation by the Department of Public Utilities on Its Own Motion into the Role of Gas Local Distribution Companies as the Commonwealth Achieves Its Target 2050 Climate Goals." The Commonwealth of Massachusetts, Department of Public Utilities. December 6, 2023. https://fileservice.eea.comacloud.net/FileService.Api/file/FileRoom/18297602.

Eversource. "Decarbonized Heating and Geothermal Energy." Eversource. Accessed June 17, 2024. https://www.eversource.com/content/residential/about/sustainability/renewable-generation/decarbonization-geothermal.

Eversource. "Geothermal Pilot Project in Framingham." Accessed June 17, 2024. https://www.eversource.com/content/residential/about/transmission-distribution/projects/massachusetts-projects/geothermal-pilot-project.

Executive Office of Energy and Environmental Affairs. “Massachusetts 2050 Decarbonization Roadmap”. Massachusetts Executive Office of Energy and Environmental Affairs, 2020. https://www.mass.gov/doc/ma-2050-decarbonization-roadmap/download.

Gibb, D., J. Rosenow, R. Lowes, and N. J. Hewitt. "Coming in from the Cold: Heat Pump Efficiency at Low Temperatures." *Joule* 7, no. 9 (2023): 1939–1942. https://doi.org/10.1016/j.joule.2023.08.005.

Harvard Dataverse. "Harvard Dataverse Support." 2020. https://support.dataverse.harvard.edu/about.

HEET. “Gas to Geo”. Accessed August 22, 2024. https://www.heet.org/gas-to-geo-transition

HEET. "Who We Are." Accessed June 17, 2024. https://heet.org/who-we-are/.

HEET and BuroHappold. “Geothermal Networks 2019 Feasibility Study”. *HEET*, 2019. https://assets-global.website-files.com/649aeb5aaa8188e00cea66bb/656f8ad67bbc7df081e3fe17_Buro-Happold-Geothermal-Network-Feasibility-Study.pdf.

Kile, M. L., E. S. Coker, E. Smit, D. Sudakin, J. Molitor, and A. K. Harding. "A Cross-Sectional Study of the Association Between Ventilation of Gas Stoves and Chronic Respiratory Illness in U.S. Children Enrolled in NHANESIII." *Environmental Health* 13, no. 1 (2014): 71. https://doi.org/10.1186/1476-069X-13-71.

Liu, X., P. Hughes, J. Spitler, and A. Anderson. "Updated Assessment of the Technical Potential of Geothermal Heat Pump Applications in the United States." 2017. https://doi.org/10.22488/okstate.17.000538.

Liu, X., Ho, J., Winick, J., Porse, S., Lian, J., Wang, X., Liu, W., Malhotra, M., Li, Y. and Anand, J. "Grid Cost and Total Emissions Reductions Through Mass Deployment of Geothermal Heat Pumps for Building Heating and Cooling Electrification in the United States". *Oak Ridge National Laboratory* (2023). https://info.ornl.gov/sites/publications/Files/Pub196793.pdf

Luna, and D. Nicholas. "An Environmental Justice Analysis of Distribution-Level Natural Gas Leaks in Massachusetts, USA." *Energy Policy* 162 (2022): 112778. https://doi.org/10.1016/j.enpol.2022.112778.

Mass.gov. "Massachusetts Clean Energy and Climate Metrics." Accessed. https://www.mass.gov/info-details/massachusetts-clean-energy-and-climate-metrics.

Magavi, Z., A. Alberto-Escobar, H. Braun, I. Varela, and A. McKittrick. "Changing the System: Scaling to Meet This Historic Moment." *Conference panel presentation at the IGSHPA* 2023 Annual Meeting, Las Vegas, AZ, United States, December 5-7, 2023. https://igshpa.org/wp-content/uploads/IGSHPA-Dec-2023-Scaling-Panel.pdf.

Magavi, Z., Alberto-Escobar, A. & Varela, I. "A Definitional Taxonomy for (Geo)Thermal Energy Networks". *Geothermal Rising Conference Transactions*, Waikoloa, HI Vol 48, (2024).

Michanowicz, D. R., A. Dayalu, C. L. Nordgaard, J. J. Buonocore, M. W. Fairchild, R. Ackley, J. E. Schiff, A. Liu, N. G. Phillips, A. Schulman, Z. Magavi, and J. D. Spengler. "Home is Where the Pipeline Ends: Characterization of Volatile Organic Compounds Present in Natural Gas at the Point of the Residential End User." *Environmental Science & Technology* 56, no. 14 (2022): 10258–10268. https://doi.org/10.1021/acs.est.1c08298.

National Grid. "Introducing Our Geothermal Network Program." *National Grid US*. Accessed June 17, 2024. https://www.nationalgridus.com/Geothermal-Energy-MA.

New York City Mayor's Office of Sustainability and New York City Department of Design and Construction. "Geothermal Pre-Feasibility Tool." *New York City Mayor's Office of Sustainability* Accessed June 17, 2024. https://www.nyc.gov/assets/ddc/geothermal/geothermalTool.html.

New York City Mayor's Office of Sustainability and USGS. "Geothermal Screening Webtool Pre-Feasibility." *New York City Mayor's Office of Sustainability*. 2018. https://www.nyc.gov/assets/ddc/geothermal/Geothermal%20Screening%20Webtool%20Pre-Feasibility.pdf.

Oh, H., and K. Beckers. "Cost and Performance Analysis for Five Existing Geothermal Heat Pump-Based District Energy Systems in the United States." National Renewable Energy Laboratory, 2023. https://www.nrel.gov/docs/fy23osti/86678.pdf.

Schulman, A., and Z. Magavi. "Learning from the Ground Up – A Proposal for Performance and Potential Assessment for Networked Geothermal Demonstration Projects." *HEET*, 2022.

Seavey, D. "GSEP's Cumulative Costs as Derived from the 'Future of Gas' Independent Consultant Reports." *GroundworkData.org*. 2023. https://www.mass.gov/doc/seavey-gsep-cost-presentation/download.

Simpson, J. and Zhu, Guangdong. “An Efficient Annual-Performance Model of a Geothermal Network for Improved System Design, Operation, and Control”. *Proceedings, 49th Workshop on Geothermal Reservoir Engineering,* Stanford University, Stanford California (2024). https://pangea.stanford.edu/ERE/db/GeoConf/papers/SGW/2024/Simpson.pdf

Smith, J. "Utilities Dig into Geothermal Systems in Race to Decarbonize." *CommonWealth Beacon*. 2024. https://commonwealthbeacon.org/energy/utilities-dig-into-geothermal-systems-in-race-to-decarbonize/.

Violante, A. C., F. Donato, G. Guidi, and M. Proposito. "Comparative Life Cycle Assessment of the Ground Source Heat Pump vs Air Source Heat Pump." *Renewable Energy* 188 (2022): 1029–1037. https://doi.org/10.1016/j.renene.2022.02.075.

WARMTH Act. 397. (2024). Public Utilities – Thermal Energy Network Systems – Authorization and Establishment (Working for Accessible Renewable Maryland Thermal Heat (WARMTH) Act) https://mgaleg.maryland.gov/mgawebsite/Legislation/Details/hb0397

Wołoszyn, J., and A. Gołaś. "Coefficient of Performance Stabilization in Ground Source Heat Pump Systems." *Journal of Sustainable Development of Energy, Water and Environment Systems* 5, no. 4 (2017): 645–656. https://doi.org/10.13044/j.sdewes.d5.0173.

Wu, Michelle. "Mayor Wu’s 2024 State of the City Address." January 9, 2023. https://www.boston.gov/news/state-city-2024.

Xcel Energy. "Evaluating a Community Ground Source Heat Pump System at Colorado Mesa University." Xcel Energy Report, 2023.

Towards Accurate Geothermal Mapping: Analyzing BHT Correction Approaches and Impact on Project Economics

Bissett Young[1], Mohamed Shafik Khaled[1,2], Ken Wisian[1],

Malcolm Ross[1], Shuvajit Bhattacharya[1]

[1] Bureau of Economic Geology, The University of Texas at Austin

[2] Petroleum Engineering Department, Colorado School of Mines

Keywords

Bottom hole temperature correction, Presidio County, heat flow mapping, geothermal resource assessment

ABSTRACT

The reliability of heat flow maps and techno-economic models for geothermal energy projects are significantly influenced by the accuracy of bottom hole temperatures (BHTs) derived from oil and gas drilling operations. However, BHT measurements are often influenced by the cooling effect of drilling fluids, necessitating the application of correction methods to develop an approximation of the rock's equilibrium temperature. Previous methodologies, including those developed by Harrison, Förster, and Kehle, rely on correlating unadjusted BHTs with high-quality, equilibrated temperature logs within specific basins in the United States to determine a generalized offset suitable for each study area.

This research evaluates the efficacy of established correction methods and highlights their significant impact on project economics. We applied these methods to raw BHT data from Presidio County, Texas—a region lacking high-quality equilibrated temperature logs. Using the GEOPHIRES tool, we conducted an in-depth analysis of the thermal regime and the economic feasibility of developing a geothermal plant based on corrected BHT values. Our findings reveal a significant discrepancy of up to 16% between the Harrison method and the other two correction methods, translating to over a kilometer difference in the estimated depth to reach temperatures of 250°C. This variability becomes even more pronounced at higher temperatures, impacting the depth estimation and, consequently, the project's feasibility. Moreover, the techno-economic analysis demonstrates that the choice of correction method can substantially affect the project's economic outlook, with a variance exceeding $10 million in project net present value among the methods for an enhanced geothermal systems (EGS) project scenario in Presidio County. These results underscore the critical need for high-quality temperature logs from abandoned wells to

validate temperature corrections or develop a new correction method tailored to regional conditions.

1. Introduction

Accurate geothermal resource assessment and subsequent development require high-quality depth-to-temperature data. Several sources are commonly used to determine temperature, heat flow, and geothermal potential. The most reliable types of temperature measurements come from tests conducted after enough time has passed for the well temperature to return to equilibrium. However, most available temperature data come from measurements of bottom-hole temperatures (BHT). During drilling, fluid is circulated to cool the drill bit, consequently cooling the surrounding rock in the well. Temperatures recorded immediately following circulation will be cooler than the equilibrium rock temperature. Subsequently, the measured values of bottom hole temperature must be corrected to account for this cooling effect, requiring a reliable correction method. Several correction methods have been developed with a specific data set and/or study area in mind. These correction methods may not be appropriate for broader applications. Here, we compare three common correction methods: Kehle, Harrison, and Förster, as applied to data for Presidio County, Texas.

In an AAPG geothermal survey for data in North America from 1970, Kehle et al. (1970) postulated that surface temperature and time since circulation are the two critical factors for explaining the difference between BHT and the true equilibrium temperature. They presented a mathematical method for correcting BHTs from well headers based on those factors, but this approach relies on knowing the time since circulation, a factor that is commonly not recorded or reliable if recorded in an older well. The correction was later modified by Gregory et al. (1980) to remove the time variable. We have adjusted the equation from Gregory et al. (1980) from feet to meters, resulting in the following correction factor (Tcf_K):

$$Tcf_K(℃) = -3.112 \times 10^{-10}x^3 - 2.307 \times 10^{-7}x^2 + 1.435 \times 10^{-2}x - 1.018 \quad (2)$$

Where x is depth in meters.

While the Kehle correction is widely cited as providing the original method and rationale for correcting BHTs, it is not a commonly used correction method (Crowell et al., 2014; Shalev et al., 2013; Bédard et al., 2017).

Following Kehle, Harrison et al. (1983) devised a correction method for the Oklahoma Geological Survey to compare bottom-hole temperatures and more reliable temperatures obtained from pressure tests from shut-in wells and high-quality temperature logs. They calculated the average temperature for each township in Oklahoma with sufficient data. Due to a lack of high-quality data for comparison in over half of the townships, the state was subdivided according to the underlying geological structures of basin and shelf. Using a correction curve to compare BHTs and high-quality logs, they calculated the following temperature correction factor (Tcf_H):

$$Tcf_H(℃) = -16.512 + 0.0183x - 0.00000234x^2 \quad (1)$$

Where x is depth in meters.

The Harrison correction has since been used in multiple studies for Texas, around North America, and elsewhere around the world (Batir & Richards, 2020; Blackwell, 2011; Blackwell & Richards, 2004; Shalev et al., 2013; Bédard et al., 2017).

The Förster correction method was developed to adjust temperatures from southeastern Kansas (Forster et al., 1996). The study compares hundreds of BHTs to temperatures taken during drill stem tests. Drill stem tests (DST) are taken during a temporary completion of a well, when a portion of the well is sealed off from the rest, and sensors are used to test pressure and temperature, among other things. Since the measurements are taken after a period of quiescence, DST are considered to be closer to actual equilibrium formation temperatures. The correction coefficients are defined using regression analysis to compare BHT and DST, resulting in the following correction factor:

$$Tcf_F\ (℃) = \ 0.012x - 3.68 \tag{3}$$

Where x is depth in meters.

Though the method used to define this equation is similar to what was done to define the Harrison correction, the Förster correction method is not widely used. Compared to the Harrison correction, the equation's simplicity questions whether any correction methods are genuinely appropriate to be broadly applied outside their original study areas.

Fundamentally, these are all empirical corrections. The underlying reason behind the differences in correction curves is primarily due to differences in geological structure, rock type, and/or thermal regime. Further comparison between high-quality temperature logs and BHTs over a broader range of geological settings would enhance our understanding of the relationship between the two measurement types.

Note that these corrections were developed in the last century and only depend on depth. This is a significant handicap and limits BHT correction accuracy. This limit is mainly because the next level of essential information that would allow for a better correction, such as mud temperature, drilling time, time since last circulation, etc., is generally unavailable, particularly for older wells. Given the wealth of data recorded during drilling today, a new standard of well information recording is now feasible and needed. This would allow for much more accurate BHT corrections, reducing development risk.

In this study, we apply each correction method to data for Presidio County, TX, and compare how the differences in corrected temperature can impact the viability of a geothermal project. With more reliable temperature data, even for a small number of wells in the county, we could test the correction methods above and possibly devise a better correction curve. A correction curve designed for a region outside a production basin may be useful across southwest Texas and other areas with similar geology.

2. Methodology

2.1 Geological Setting

Presidio County is in west Texas, along the Rio Grande River, west of Big Bend National Park, and bordering the Mexican state of Chihuahua. The generalized geology of the county consists of three stratigraphic units: Precambrian granite, Paleozoic-Mesozoic sedimentary deposits, and Tertiary volcanics (Figure 1). Overlying Tertiary volcanic tuff and mixed breccia layers thin from ~1,457 meters in the northeastern part of Presidio to ~793 meters in the southwest. The average porosity of the tertiary layers varies widely, which can impact thermal conductivity. The Paleozoic-Mesozoic section, primarily comprised of carbonates with some mixtures of shale and sandstone, reaches a depth of ~6,000 meters in the northeast, which tapers to a depth of ~2,438 meters to the southeast. The shallower occurrence of the basement along the border, supported by geophysical data and drilled wells, may contribute to a greater radiogenic heat flow. The county also has several warm springs in the Rio Grande Valley. The structure is dominated by basin and range-style extensional faulting along the border, including the Bolson graben (Wisian et al., 2024).

Presidio County leadership, the Presidio Municipal Development District (PMDD), the West Texas Economic Development District (WTEDD), and the Rio Grande Council of Governments (RGCOG) are invested in the county's economic development. A recent report authored by WTEDDD and the RGCOG identified energy (particularly renewable energy) as a critical strategy for investment and development (West Texas Economic Development District, 2021).

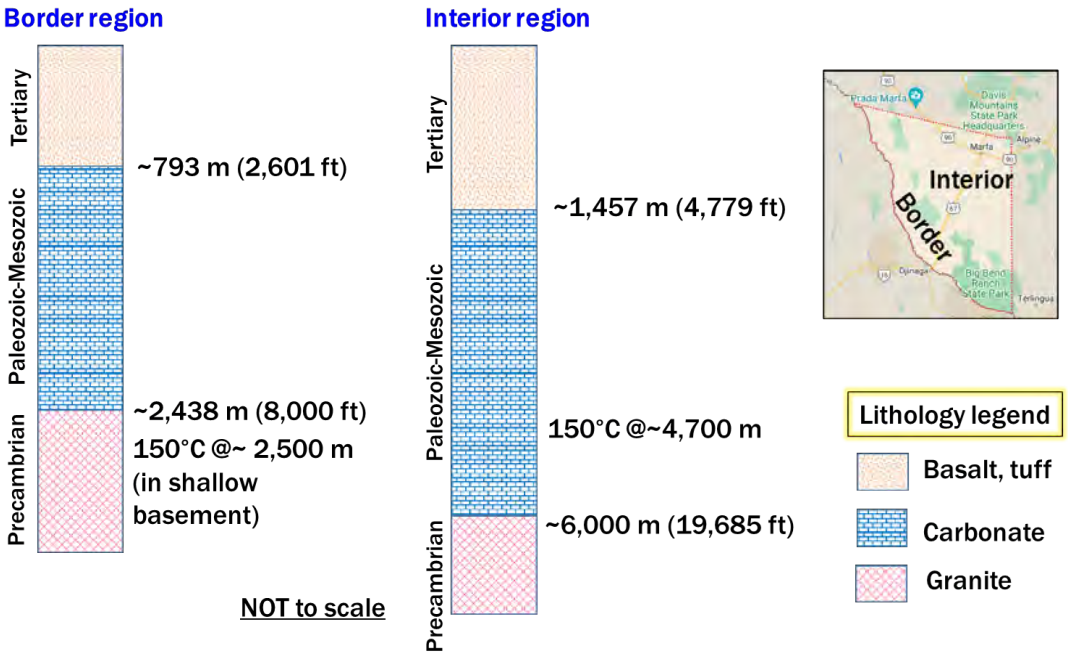

Figure 1: Simplified litho-stratigraphy of the Border and Interior regions, with the inset map of Presidio County (after Wisian et al., 2024).

2.2 Temperature Data

The temperature data for this study consist of BHTs collected from the Southern Methodist University (SMU) node of the National Geothermal Data System (NGDS), using the Borehole Temperature in Content Model Formula and Heat Flow data files, the Bureau of Economic Geology (BEG) comprehensive well database and log library, as well as data points from the Standard and Poor's Enerdeq Browser managed by Information Handling Services (IHS), for data ranging from January 2016 to May 2023.

From the databases listed above, we extracted 120 unique BHTs from 101 wells (Figure 2). The data are somewhat heterogeneously distributed across the county; more data needs to be collected in the county's southeast corner. More than half of the temperature measurements in this data set are from wells less than 1 km deep.

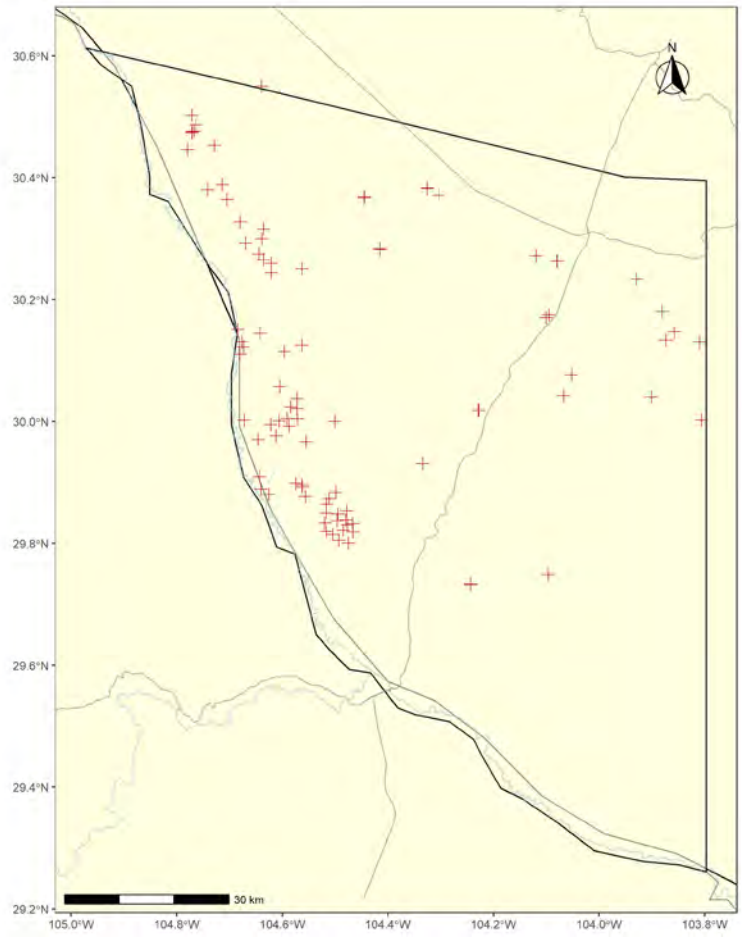

Figure 2: Map of well locations with bottom hole temperatures in Presidio County, TX. The data set includes 120 BHTs from 101 wells. More than half of the BHTs were taken at depths < 1km. The shallow data are mainly concentrated along the border. Data is lacking for the southeastern portion of the county.

We applied each correction method to the data, as shown in Figure 3. We fit each set of points using linear regression, with a top anchor point at 15°C for the average surface temperature. Many

of the shallow wells appear to show a steeper gradient curve than illustrated by the regression. Due to the shallow depth of these points, the high temperatures seen may result from groundwater movement carrying warmer temperatures up through fractures rather than being reflective of an actual high gradient.

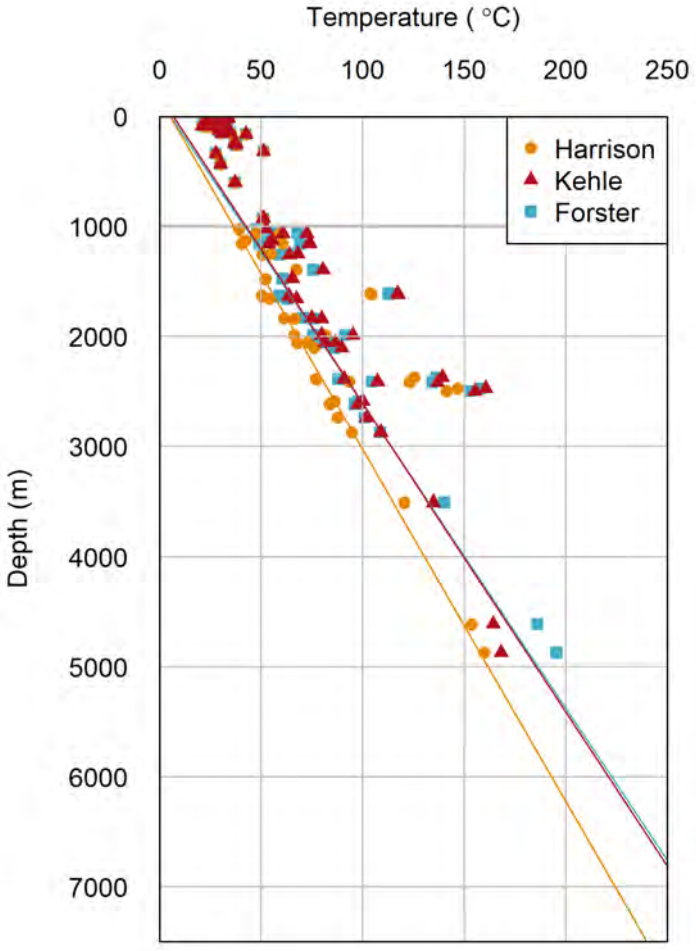

Figure 3: Harrison, Kehle, and Förster corrected temperatures versus depth of data points for Presidio County. The top of the linear regression curve is fixed to an average surface temperature of 15°C. Many of the shallow temperature records show higher-than-expected temperatures. We attribute those temperatures to shallow groundwater movement.

We use the linear regression method above to calculate an average gradient for each correction method and use that gradient to calculate the depth to 150°, 200°, and 250°C for each correction method (Table 1). The difference of close to 1 km between Harrison and Kehle/Förster corrections to reach the same reservoir temperatures has a marked impact on the techno-economic modeling.

Table 1: Resulting depth to temperatures 150, 200, and 250° calculated for Presidio County with Harrison, Kehle, and Forster temperature correction methods.

Correction Method	*Depth to 150°C (km)*	*Depth to 200°C (km)*	*Depth to 250°C (km)*
Harrison	4.31	5.91	7.51
Kehle	3.78	5.18	6.58
Förster	3.73	5.11	6.49

2.3 GEOPHIRES

The potential to advance geothermal energy projects heavily relies on accurate site characterization, which includes understanding the local geology, infrastructure availability, and the region's specific energy demands. This study examines the impact of temperature correction methodologies on the financial viability of geothermal energy initiatives in Presidio County, as highlighted in the recent geothermal study (Wisian et al., 2024).

Our analysis encompasses two primary methods of geothermal energy extraction: Enhanced Geothermal Systems (EGS), which rely on enhanced permeability of rock formations, often facilitated by hydraulically stimulated fractures (Beard et al., 2023), and Advanced Closed-Loop Geothermal System (AGS), which operates by circulating a working fluid through a closed-loop system in the wellbore, harnessing heat through conduction. AGS mainly creates a long path in the ground to transfer heat from the rock into the wellbore and, as with EGS, does not produce formation fluids but instead continuously recirculates its own fluids. Note that the heated fluid can then be used directly for heating or, more commonly, for generating electricity (GeoVision, 2019).

The economic evaluations of these geothermal systems are conducted using the updated GEOPHIRES model (Beckers et al., 2019; Ross and Beckers, 2023)., which integrates a wide array of up to 150 input variables. This comprehensive model facilitates a nuanced economic analysis, calculating essential economic indicators such as Net Present Value (NPV), Value Investment Ratio (VIR), and Internal Rate of Return (IRR). These metrics are pivotal in guiding investment decisions. Furthermore, GEOPHIRES calculates the Levelized Cost of Electricity (LCOE) as well as for heating, cooling, and carbon sequestration—known respectively as LCOH, LCOC, and LCOCS—which provide a standardized metric for comparing the cost efficiency of various energy projects.

To illuminate the implications of different temperature correction methods—specifically, those developed by Harrison, Kehle, and Förster, various simulations were performed across EGS and AGS scenarios for power generation and direct heat use. These simulations are meticulously documented in Table 2, providing a clear comparative analysis of the economic outcomes for each method. Note that for all electricity-producing scenarios, the financial model assumes a sale of the electricity at a price starting at $0.15/kWh and rising with 2% inflation after plant completion

Crucially, our financial models consider incentives from the Inflation Reduction Act (IRA), such as the Investment Tax Credits (ITC) and Production Tax Credits (PTC), which significantly influence project economics. An ITC of 50%, applicable upon project completion, can substantially reduce the LCOE. For example, if an initial LCOE is 15 cents/kWh, applying a 50% ITC could lower it to about 7.5 cents/kWh, thus transforming a marginally viable project into a robustly feasible one.

For all case scenarios in Presidio County, the CAPEX (Capital Expenditure) and OPEX (Operational Expenditure), estimated using the Harrison correction method, were higher than those calculated using the Kehle and Förster methods. This discrepancy is primarily attributed to the geothermal gradient adjustments. The Harrison method predicts a geothermal gradient approximately 14% and 16% lower than those calculated by the Kehle and Förster methods, respectively. Consequently, reaching the desired reservoir temperatures necessitates drilling significantly deeper wells, thereby increasing the initial and ongoing costs associated with the project. For instance, to achieve a reservoir temperature of 150 °C, the required well depths are estimated to be 4.3 km, 3.8 km, and 3.7 km for the Harrison, Kehle, and Förster methods, respectively.

Table 2. Techno-economics scenarios utilized by the GEOPHIRES model

Scenario	CAPEX, M$	OPEX, M$	NPV, M$
EGS for Power Generation			
Harrison	27.1	1.3	17.3
Kehle	24.7	1.3	22.5
Förster	24.5	1.3	22.9
AGS for Power Generation			
Harrison	27.6	1.9	3.5
Kehle	25.6	0.9	6.1
Förster	25.4	0.9	6.3
AGS for Direct Heat			
Harrison	29.1	1.7	36.9
Kehle	27.1	1.7	39.6
Förster	27.0	1.7	39.9

3. Results

The Enhanced Geothermal Systems (EGS) scenarios are conventionally considered the most cost-effective option for electricity production in Presidio County (Wisian et al., 2024). These scenarios involve drilling four wells—two producers and two injectors—to access a reservoir with an in-situ formation temperature of 150 °C. Additionally, the construction of an energy production plant with a projected operational lifespan of 30 years is planned.

Figure 3 illustrates the cumulative revenue over the 30-year project lifespan for the EGS case study, using different temperature correction methods. The estimated net power from this project is around 3.3 megawatts (MW), with a net cash flow estimated. The Kehle and Förster methods are notably similar, contrasting sharply with the more conservative estimates derived from the Harrison method. The latter consistently yields the lowest net cash flow projections for the EGS project. It is worth noting that the Harrison method remains widely used in recent literature for temperature correction, heat flow mapping, and subsequent techno-economic analysis.

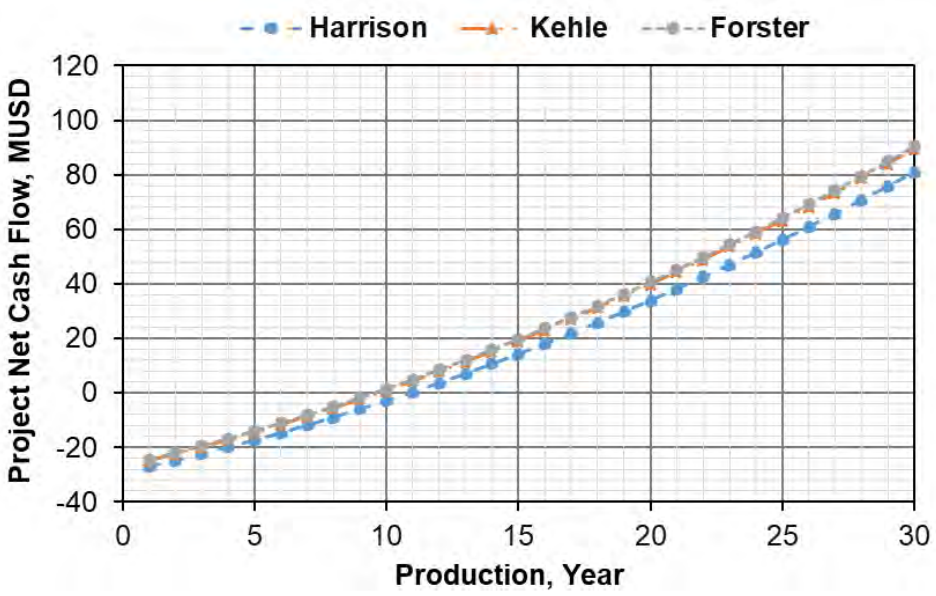

Figure 4: Project Net cash flow over the EGS project lifetime of 30 years based on different temperature correction methods.

Figure 4 illustrates the payback period for the Advanced Closed-Loop Geothermal System (AGS), comparing project economics with and without considering incentives provided by the Inflation Reduction Act (IRA). The AGS design adopted for this scenario is inspired by the innovative approach detailed by Yuan et al. (2021), featuring an 8.5-inch horizontal open-hole with five 3 km laterals each and a 90 kg/sec production flow rate. The vertical depth of the wellbore in each scenario is determined based on the temperature gradient corrections provided by the Harrison, Kehle, and Förster methods.

In scenarios where the downhole reservoir temperature targets 150°C, the estimated average net electricity equals 2.2 MW with a payback period for the AGS system that is initially lengthy, spanning 24.4 years for Harrison, 22.7 years for Kehle, and 22.6 years for Förster correction methods. However, the payback times are significantly reduced when incorporating the financial benefits of the IRA, specifically through the Investment Tax Credit (ITC) or the Production Tax Credit (PTC). With a 50% ITC applied across all AGS scenarios, the revised payback periods are 14.1, 13.0, and 12.9 years for Harrison, Kehle, and Förster methods, respectively. This dramatic reduction highlights the profound impact of IRA incentives on enhancing the financial attractiveness of renewable energy projects.

Furthermore, it is important to note that the NPV for AGS projects, while robust, tends to be lower than that observed for Enhanced Geothermal Systems (EGS) within the same region. The EGS systems, benefiting similarly from IRA incentives, exhibit even shorter payback periods of 10.9, 9.7, and 9.5 years for Harrison, Kehle, and Förster methods, respectively. This discrepancy underscores the greater efficiency and economic viability of EGS systems in Presidio County, likely due to their ability to harness natural subsurface heat more effectively than AGS's engineered solutions. This observation about NPV needs to be tempered by the incorporation of risk–projects move forward when the risk-reward relationship is well understood. It is generally understood that AGS projects have a substantially lower risk (since their subsurface approach is so simple). The lower NPVs of AGS projects will be more acceptable for some investors, given the lower risk.

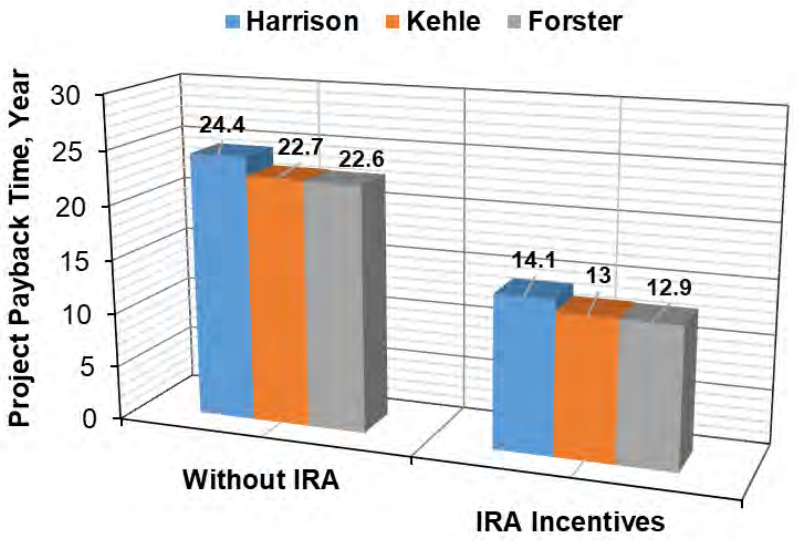

Figure 4: AGS project payback period with and without IRA incentives for Harrison, Kehle, and Förster temperature correction methods.

Geothermal direct heat use presents substantial advantages over geothermal power generation, particularly in terms of efficiency and economic benefits. Direct heat applications, such as space heating, industrial processes, and agricultural uses, typically achieve thermal efficiencies that often exceed 70%, while electricity generation projects at 150 C have efficiencies of <15%, a five-fold improvement. The higher efficiency in direct heat use is due to the lower temperatures required and minimal energy conversion losses, which means more of the extracted thermal energy is

directly utilized rather than lost in conversion processes (Lund and Boyd, 2016). From an economic perspective, direct heat systems demand lower capital investments and operational costs, making them more accessible and cost-effective. This is especially true in regions with lower geothermal gradients where the cost of accessing suitable temperatures for power generation may be prohibitively high (DiPippo, 2018). In such scenarios, the direct use of geothermal energy can provide a practical alternative with a more rapid return on investment.

In the specific case of AGS, direct heat applications can significantly outperform power generation projects. For example, an AGS project focusing on direct heat could yield an average production of 33.4 MWth, whereas a similar project for power generation might only produce about 2.2 MWe. Figure 5 compares AGS projects' cumulative net cash flow geared towards power generation and direct heat use. When incentives are considered in the Inflation Reduction Act (IRA), the economic benefits of direct heat use become even more pronounced. The net cash flow for direct heat use projects is nearly three times higher than that for power generation. Furthermore, the payback period for direct heat use projects decreases to 6 years, compared to 13 years for power generation projects (utilizing Kehle and Förster correction methods).

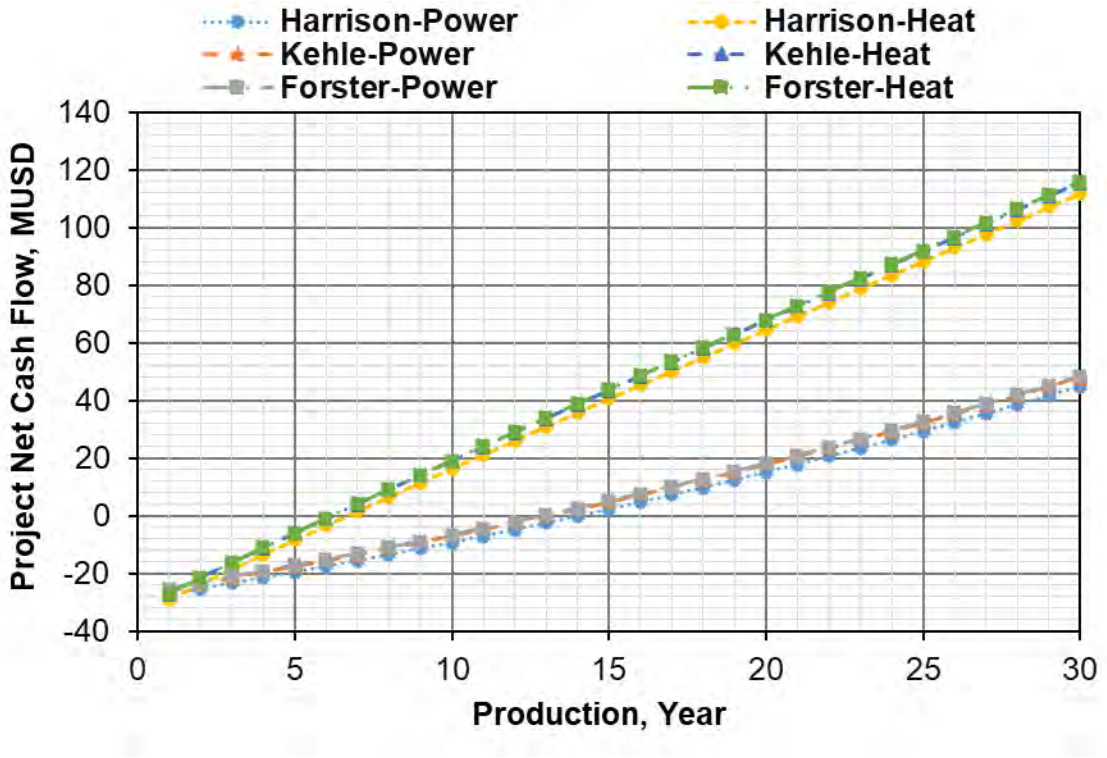

Figure 5: AGS project cumulative cash flow for power and heat generation based on Harrison, Kehle, and Förster BHT correction methods.

Additionally, selecting the BHT correction method can significantly influence the economic outcomes of these projects. For instance, the AGS project's predicted NPV for direct heat use, utilizing the Förster correction method, is approximately $3 million higher than that using the Harrison method. This variance is even more substantial in Enhanced Geothermal Systems (EGS), where the difference can reach up to $5.6 million, highlighting how critical the choice of BHT

correction method can be in determining the economic viability and investment attractiveness of geothermal projects.

4. Conclusion

This study has demonstrated the profound impact that different BHT correction methodologies can have on the techno-economic assessments of geothermal projects in Presidio County, Texas. Specifically, the Harrison method predicts a geothermal gradient approximately 14% and 16% lower than those calculated by the Kehle and Förster methods, respectively. This variance in gradient predictions means that using the Harrison method requires drilling to significantly greater depths to reach the desired reservoir temperatures, thereby increasing both the initial investment and ongoing operational costs.

Our analysis with the GEOPHIRES model shows that these discrepancies can alter the estimated project net present value by as much as $10 million, underscoring the crucial role of selecting an appropriate temperature correction method in geothermal resource evaluation. The study suggests a pressing need for adopting more localized correction methods and highlights the limitations of using generalized empirical models outside their original study regions.

By refining these methodologies through integrating comprehensive datasets, including high-quality temperature logs and advanced data recording techniques, the accuracy and reliability of geothermal assessments can be significantly enhanced, thereby improving the economic viability and reducing the risks associated with geothermal energy projects.

5. Recommendation

The use of current BHT corrections, while cost-effective for preliminary assessments, introduces significant uncertainties when applied outside their calibration areas, impacting the economic feasibility of geothermal projects. To mitigate these risks:

1. Risk Awareness: Stakeholders need to understand the uncertainties and economic risks of BHT-based corrections.

2. Data Quality: Prioritize acquiring high-quality, equilibrated temperature logs to improve correction accuracy and reduce dependency on empirical methods.

3. Data Recording Standards: Enhance recording practices during drilling to capture all relevant variables, supporting the development of physics-based corrections.

4. Targeted Thermal Logging: Conduct thermal logging in a deep well within the study area to refine regional BHT corrections and contribute to broader correction methodologies.

These steps will enhance the reliability of geothermal assessments and reduce the development risks associated with these projects.

Acknowledgment

The authors thank the Bureau of Economic Geology, the Presidio Municipal Development District, the State of Texas Advanced Resource Recovery program and the HotRock consortium at the Bureau of Economic Geology, Jackson School of Geoscience, The University of Texas at Austin, and its sponsors for supporting this work.

REFERENCES

Batir, J., and Richards, M. “Analysis of Geothermal Resources in Three Texas Counties.” Dallas, (2020).

Beard, J.C.E. and Jones, B.A.,. “The Future of Geothermal in Texas: Contemporary Prospects and Perspectives.” *UT Faculty/Researcher Works*, (2023).

Beckers, K.F. and McCabe, K. “GEOPHIRES v2.0: updated geothermal techno-economic simulation tool.” *Geothermal Energy*, 7(1), pp.1-28. (2019).

Bédard, K., Comeau, FA., Raymond, J., Malo, M. and Nasr, N. “Geothermal Characterization of the St. Lawrence Lowlands Sedimentary Basin, Québec, Canada.” *Natural Resources Research* **27**, 479–502, (2018).

Blackwell, D.D. and Richards, M. “Calibration of the AAPG Geothermal Survey of North America BHT database” *AAPG Annual Meeting*, Dallas, TX, paper 87616 (2004a).

Blackwell, D.D., and Richards M. “Geothermal Map of North America.” *AAPG Tulsa, OK* (2004b).

Blackwell, D.D.. “Heat flow map of the continental U.S in 2011.” Retrieved 1 28, 2024, from SMU Geothermal Lab: https://www.smu.edu/-/media/Site/Dedman/Academics/Programs/Geothermal-Lab/Graphics/SMUHeatFlowMap2011_CopyrightVA0001377160_jpg, (2011).

Crowell, A.M., Oschner, A.T., and Gosnold, W. “Correcting Bottom-hole temperatures in the Denver basin: Colorado and Nebraska.” *GRC Transactions*, Vol 36, (2012).

DiPippo, R., "Geothermal Power Plants: Principles, Applications, Case Studies, and Environmental Impact," *Elsevier*, (2018).

Forster, Andrea, Merriam, Daniel F., Davis, John C. "Statistical Analysis of Some Bottom-Hole Temperature." *Transactions of the 1995 AAPG Mid-Continent Section Meeting (Tulsa Geological Society)*, (1996).

Gregory, A. R.; Dodge, M. M.; Posey, J. S. & Morton, R. A. "Volume and accessibility of entrained (solution) methane in deep geopressured reservoirs - tertiary formations of the Texas Gulf Coast. Final report", report, University of North Texas Libraries; Austin, Texas. https://digital.library.unt.edu/ark:/67531/metadc1072529/, (1980).

Geothermal Technologies Office, US DOE., “GeoVision: Harnessing the Heat Beneath Our Feet - Analysis Inputs and Results.” The USA. https://doi.org/10.15121/1572361, (2019).

Harrison W.E., Luza K.V., Prater, M.L., and Chueng P.K. n.d. "Geothermal resource assessment of Oklahoma." *Oklahoma Geological Survey Special Publication 83-1*, (1983).

Kehle, R.O., Schoeppel, R.J., and Deford R.K. 1970. "The AAPG geothermal survey of North America." *Geothermics* (Elsevier BV) Volume 2, Part 1 (Special Issue 2): 358-367. doi:https://doi.org/10.1016/0375-6505(70)90034-9, (1970).

Lund, J.W., Boyd, T.L., "Direct utilization of geothermal energy 2015 worldwide review", *Geothermics*, vol. 53, pp. 467-507, (2016).

Ross, M. and Beckers, K. "GEOPHIRES-X: An object-oriented update to GEOPHIRES2.0", *GRC Transactions*, Vol. 40, (2023).

Shalev E., Lyakhovsky V., Weinstein Y., and Ben Avraham, Z. "The thermal structure of Israel and the Dead Sea fault." *Tectonophysics*, Vol 602, pages 69-77, (2013).

West Texas Economic Development District. *Economic Development*. Retrieved 01 02, 2024, from Rio Grande Council of Governments: http://www.riocog.org/wp-content/uploads/2022/09/2021thru2025.WTEDD_.CEDS_.pdf, (2021).

Wisian, K., Ross, M., Bhattacharya, S., Khaled, M., Young, B., Chapman, D., Turan, A. "Presidio County Geothermal Assessment." *Report for the Presidio Municipal Development District*, Bureau of Economic Geology, University of Texas at Austin (2024).

Yuan, W. C. "Closed-loop geothermal energy recovery from deep high enthalpy systems." *Renewable Energy*, 976-991, (2021).

ABBREVIATIONS

AGS – Advanced Closed-Loop Geothermal System

BEG – Bureau of Economic Geology

BHT – bottom-hole temperature

CAPEX – Capital Expenditure

DST – drill stem test

EGS – Enhanced Geothermal System

IHS – Information Handling Services

IRA – Inflation Reduction Act

IRR – Internal Rate of Return

ITC – Investment Tax Credits

LCOE – Levelized Cost of Electricity

LCOC – Levelized Cost of Electricity for Cooling

LCOCS – Levelized Cost of Electricity for Carbon Sequestration

LCOH – Levelized Cost of Electricity for Heating

MW – megawatts

NGDS – National Geothermal Data System

NPV – Net Present Value

OPEX – Operational Expenditure

PMDD – Presidio Municipal Development District

PTC – Production Tax Credits

RGCOG – Rio Grande Council of Governments

SMU – Southern Methodist University

VIR – Value Investment Ratio

WTEDD – West Texas Economic Development District

Case Studies of Borehole Thermal Energy Storage System Design and Operating Schedules

Haiyan Zhou[1], Matthew Minnick[1], Dan Hoyer[1], Kevin Kitz[2]

[1] RESPEC Company, LLC

[2] KitzWorks LLC

Keywords

Geothermal Heat Pump (GHP), borehole thermal energy storage (BTES), Grid Amplified Building Energy Seasonal Storage (GABESS), underground thermal energy storage (UTES), thermal battery, borehole field design and optimization, FEFLOW, grid energy storage, grid cost reduction, air source heat pump (ASHP), water source heat pump (WSHP), thermal network.

ABSTRACT

Underground thermal energy storage (UTES) systems behave like a thermal battery, which preheats or pre-cools the ground to later heat/cool buildings. Borehole thermal energy storage (BTES) is a UTES system in which fluid is circulated in closed-loop pipes installed in a closely spaced borehole array. BTES is gaining popularity over the world because of its wide adaptability in various climates, limited surface area, lower total borehole length compared to traditional geothermal heat pump (GHP) installations, and ability to efficiently provide seasonal energy storage. To maximize the economic value of the cost of drilling and operating a BTES, modeling and optimizing the BTES for the site, climate, building energy loads, available energy sources, and the time-of-day pricing from the electric utility is critical. The round-trip efficiency of a BTES is influenced by factors such as borehole spacing, the way boreholes are connected, and the operating schedules. In the work presented in this paper, we optimize the design of BTES using the numerical simulator FEFLOW coupled with various charge/discharge algorithms.

In the BTES optimization, the following factors are considered: (1) BTES borehole quantity, spacing, and length; (2) method for connecting the boreholes (e.g., radial flow versus independent rings); (3) options for hot and cold storage included seasonal switching of the entire BTES, separate zones within the same BTES, and physically separate hot and cold BTES; and (4) charging and discharging schedules.

This paper presents two types of GHP-based multi-building thermal network BTES case studies. The first type is the storage of diesel engine waste heat to serve an Arctic community's heating needs. The second type is the use of a particular energy storage concept called GABESS (Grid Amplified Building Energy Seasonal Storage). GABESS is a combination of air source heat pump

(ASHP), BTES, and water source heat pump (WSHP), in which ASHP provides warm/cold water during off-peak time to heat or cool the BTES. The heat/cold is later extracted by WSHP to heat or cool the buildings on the thermal network.

1. Introduction

Renewable energy development has increased significantly in recent years because of greenhouse gas emission concerns. Among various renewable energy sources, such as solar and wind, geothermal resources play a critical role in heating and cooling buildings that account for a large part of the greenhouse gas emissions (Dascalaki et al., 2010). A UTES system is one method that takes advantage of shallow geothermal energy. UTES behaves like a thermal battery, which preheats or pre-cools the ground. In the case studies presented in this paper, that stored energy in the UTES is later used to heat or cool buildings. For example, in summer, heat is stored in the underground, and in winter, the heat is extracted to warm buildings with low carbon emissions. Similarly, the cold stored in winter (pre-cooling the ground) can be used to more efficiently cool buildings in summer. Different types of UTES are available—aquifer thermal energy storage (ATES), BTES, pit thermal energy storage (PTES), and tank thermal energy storage (TTES). Akhmetov et al. (2016) reviewed and compared different types of thermal energy storage systems. The U.S. Department of Energy and others have published papers on reservoir thermal energy storage (RTES) for power generation (e.g., Amiri et al. [2024] and McLing et al. [2022]).

BTES is one of the UTES systems in which fluid is circulated in closed-loop pipes installed in a closely spaced borehole array. BTES is gaining popularity all over the world because of its wide adaptability in various climates and subsurface conditions, limited surface footprint, and ability to efficiently provide seasonal energy storage. Moreover, BTES can be combined with other energy generation and storage systems. For example, Euros Energy recently published a system that combines PTES, BTES, and hybrid solar panels for a district heating system. Drake Landing Solar Community, Okotoks, Alberta, Canada consists of BTES, solar collectors, and short-term thermal storage tanks.

One of the design challenges for BTES systems is how to maximize BTES performance considering factors like specific site and climate conditions, energy loads, and the time-of-day pricing from the electric utility. Parameters that can affect the performance of BTES systems include borehole layout (borehole spacing and length), inlet temperature, borehole connection method, and the operating schedules. A variety of research has been devoted to optimizing such parameters (e.g., Ekmekci et al. [2023]; Nilsson and Rohdin [2019]; Olabi et al. [2023]). In this paper, we present two BTES applications illustrating the optimization schemes we performed. One case study is in Baker Lake, Nunavut, Canada, and the other in Vernal, Utah. The numerical simulator FEFLOW (Diersch et al., 2011a, 2011b) was used to model the BTES simulating heat transport to predict outlet temperatures and evaluate system performance. FEFLOW was chosen based on the built-in borehole heat exchanger (BHE) model, which serves as a boundary condition to the finite element grid and the Python scripting API, allowing the team to quickly model complex flow paths and operational constraints.

2. BTES in Subarctic Climate in Baker Lake, Canada

Baker Lake is located in Nunavut, one of the three territories that are not connected to Canada's energy grid. In Nunavut, electricity is produced by diesel generators, and most communities rely

only on fossil fuels for heating, which causes problems such as high cost in fuel transportation, health issues, and air pollution, including emission of greenhouse gases. Previously, a high-temperature thermal energy network was proposed to heat a few community buildings. The system had limitations based on the amount of heat the generators could deliver at any time. Adding a heat storage system to capture waste heat year-round and using a lower temperature thermal energy network increased deliverability and efficiency, expanding the thermal energy network to heat more of the community and meet peak demand loads. The feasibility of introducing BTES at Baker Lake was investigated. The Baker Lake BTES would store waste heat from the diesel generators in summer and other periods when less heating is required and recover the heat in winter to warm buildings, reducing the need to burn heating oil.

2.1 Model Setup

The BTES modeled for Baker Lake was a cylindrical shape with a diameter of 100 meters (m) and a total of 280 boreholes. The length of the boreholes varies from 90 m near the center to 110 m at the outside ring, as shown in Figure 1. Longer boreholes at the outside ring are intended to help capture the heat that conducts out from the bottom of the inner hotter boreholes. To reduce computational time, only an eighth of the BTES is simulated using symmetry with 35 boreholes. The piping is divided into seven radial flow paths with five boreholes in each connection, as shown in the left plot of Figure 2. Spacing between boreholes ranges from 3.5 m to 7 m. Double-U shape BHE is applied in this case (right plot in Figure 2). In summer, hot water (45 degrees Celsius [^{o}C]) that represents waste heat from diesel generators flows through the BHE in the center boreholes of the BTES radially outward along each connection. This creates a thermal gradient, from the hotter center toward the cooler outer edge. In winter, the flow path is reversed, and the water (1^{o}C) flows through the BHE in the outermost boreholes first and then radially inward toward the center to efficiently heat the cold water to as high a temperature as possible. A flow rate of 10 cubic meters per day (m^3/d) is assigned to each connection except for those on the edge, which are assigned to 5m^3/d to account for symmetry representing a total flow rate of 480 m^3/day in the whole BTES system.

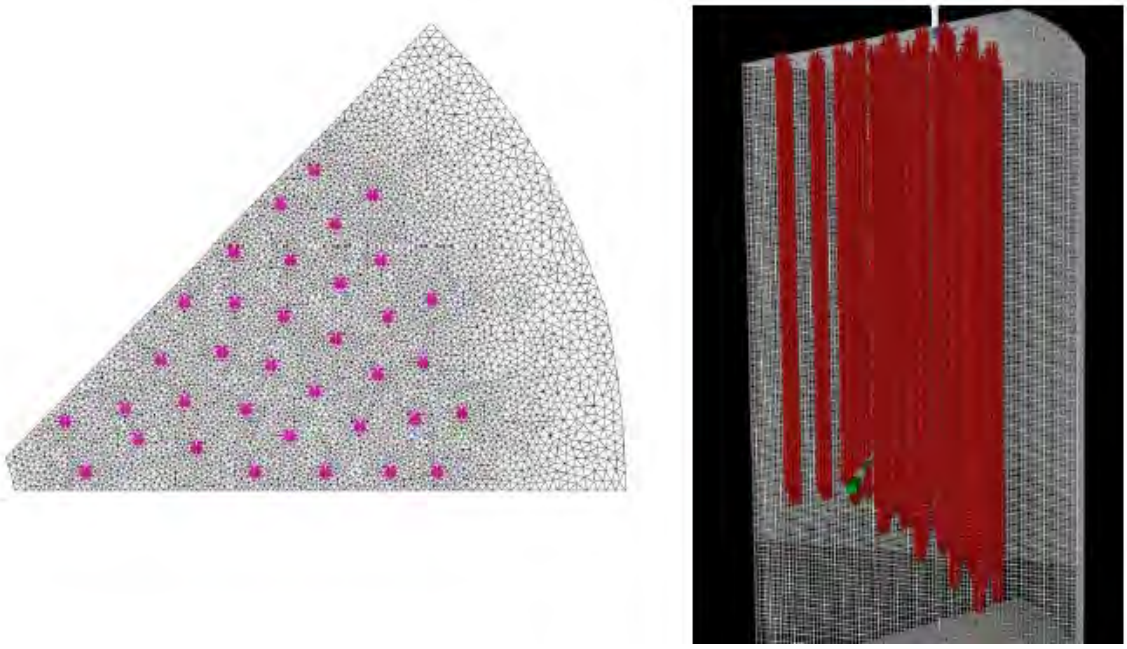

Figure 1: Borehole locations (left plot: top view; right plot: side view).

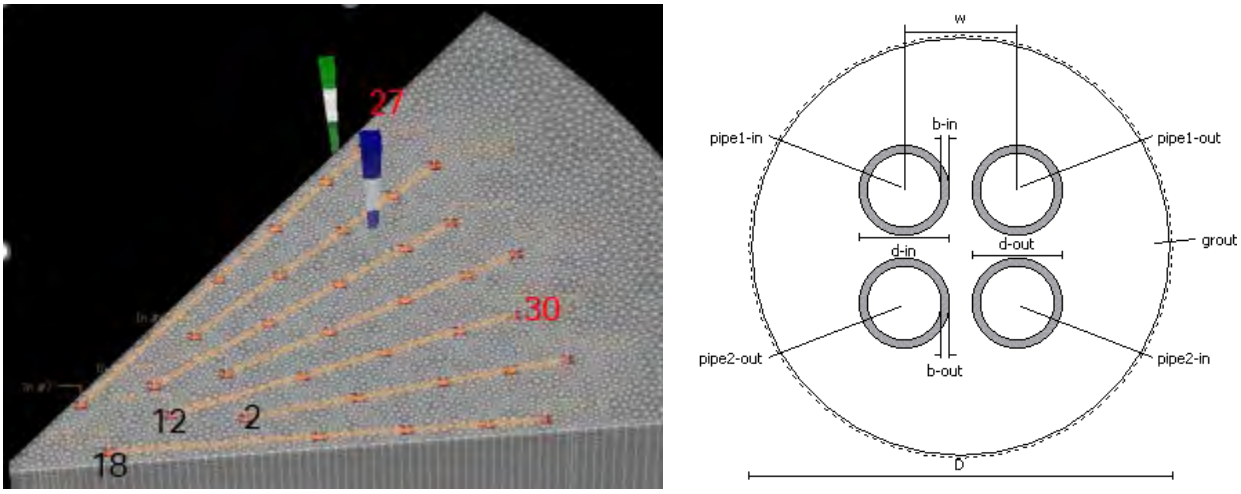

Figure 2: BTES connections (left plot) and Double-U shape BHE (right plot) (Diersch et al., 2011a). The numbering in the left plot indicates some of the boreholes referred to in the outlet fluid temperature discussion in Section 2.2.

2.2 Simulation Results

A script using the Python FEFLOW API was created to run a 7-year cycle simulation. The BTES is designed to operate for several decades; however, the model simulation is run for 7 years at which the BTES cycles reach a steady state. The simulation starts in summer, when hot water created from the diesel generator waste heat charges the BTES, forming a hot central core. In winter, the flow direction is reversed, and cool water flows from the edge of the BTES to the center. By the end of winter, much of the heat has been extracted from the BTES core, which has cooled.

Figure 3 shows the temperatures at the end of the seventh summer and the seventh winter. The fact that the temperatures are still high at the end of winter may imply that much higher heat extraction rates are possible with the initial BTES design. The outlet fluid temperature at the start and end of each connection show similar trends, as shown in Figure 4. After a rapid rise in the initial years, the outlet temperatures at winter's end nearly stabilize between 15°C and 20°C after 7 years. Some of the wells are indicated in the left plot of Figure 2. For example, well 30 (highlighted with a thick purple curve in Figure 4) is the outside end borehole of the third connection from the bottom, and well 2 (highlighted with a thick blue curve in Figure 4) is the inside end borehole of the second connection from the bottom. Well 2 shows a higher temperature because it is in the center of the BTES, which receives hot water in summer.

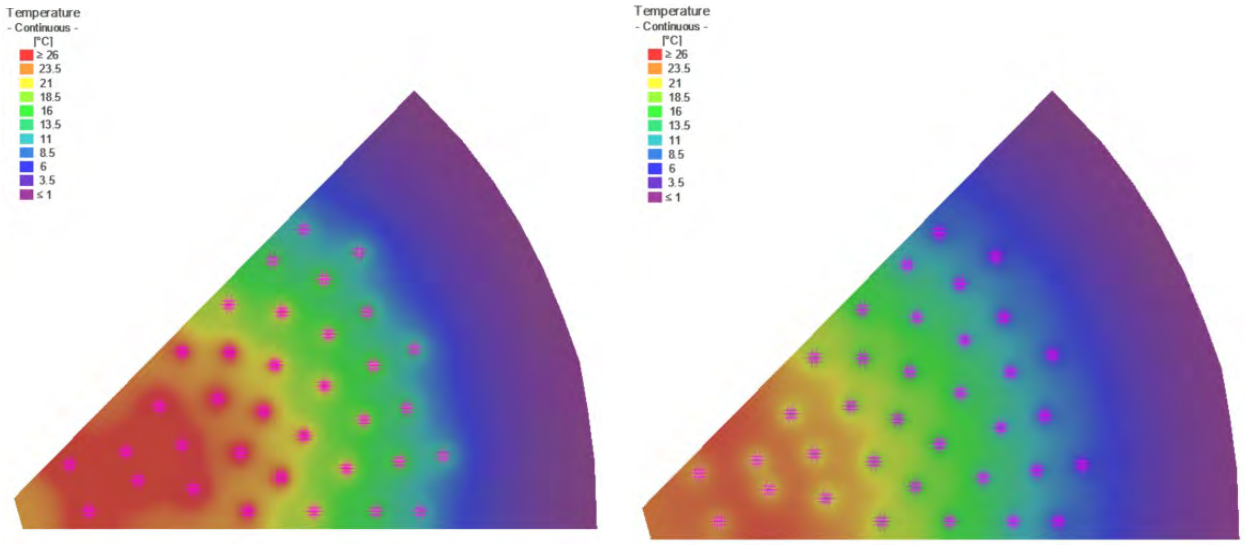

Figure 3: Temperature field at the end of the seventh summer (left plot) and winter (right plot).

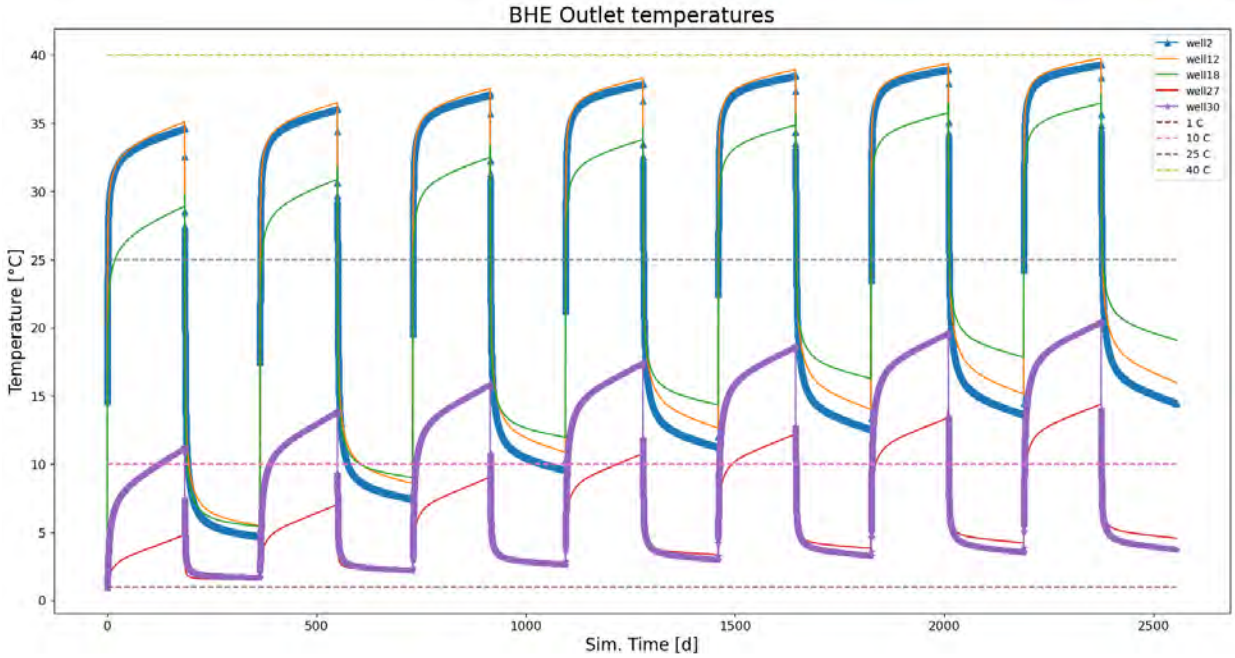

Figure 4: Outlet fluid temperature at both ends of each connection.

2.3 Implementation

The Baker Lake project has been modeled at the conceptual level. Additional detailed modeling has been proposed, along with distribution piping and building retrofit planning.

3. BTES Combined With GABESS in Vernal, Utah

Kitz (2021) proposed the concept of GABESS, which is a combination of three existing technologies in a new arrangement that delivers large grid value. The three technologies are WSHP, ASHP, and BTES, in which ASHP provides warm/cold water during off-peak time to heat or cool the BTES. The heat/cold is later extracted by WSHP to heat or cool the buildings on the thermal network. With the new arrangement in GABESS, we are able to take advantage of the extra heat/cool in off-peak periods and extract the energy during peak load periods. A feasibility study was performed in Vernal, Utah, to evaluate the performance of GABESS system for district heating and cooling.

3.1 Borehole Layout

Figure 5 shows one-fourth of the full-size BTES system with a diameter of 60 m and a depth of 80 m. The one-fourth-size model of the system consists of 103 boreholes with an inside “peaking” zone (34 boreholes) and outside “off-peak” zone (69 boreholes), for a total of 412 boreholes in the full-size system. All boreholes in both zones are connected in parallel, so that flow direction does not have to change between storing heat and cold. According to the sensitivity analysis at the site by Kumawat et al. (2024), the borehole spacing in this case is determined to be 3 m.

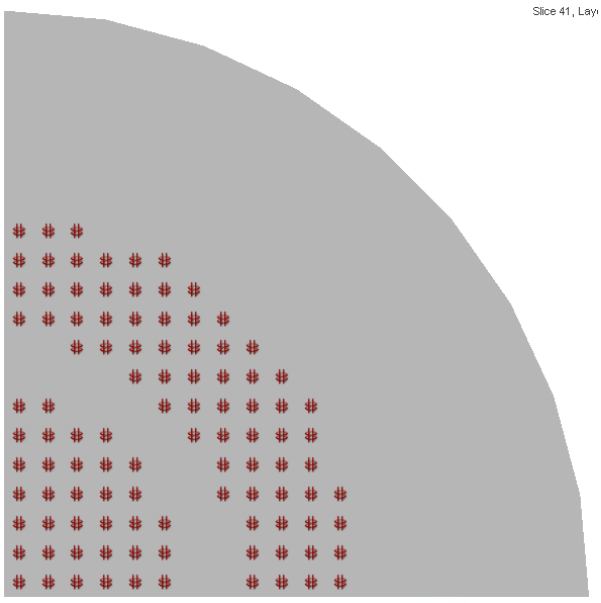

Figure 5: One-fourth of the BTES system. The 103 boreholes are divided into two groups: the central hot zone (peaking zone) and the outside cold zone (off-peak zone).

3.2 Single-Year Simulation

In summer, heat is stored in the BTES system, and in winter, the heat is extracted, which results in different charging and extraction schedules. Diurnal heat demand varies; for example, more heat is required from 5 a.m. to 11 a.m. based on energy demand data. A flexible schedule is proposed to meet energy demand that varies seasonally and diurnally. Table 1 shows an example of the operating schedule of BTES over a year. The "last 2 days" schedule is used to evaluate the capacity of the BTES to meet the peak demand. Input and output of the BTES is constrained by temperature difference (dT in ^{o}C) and flow rate (m^3/d). Working zones for specific time range and ASHP/WSHP are also defined in the schedule. For example, from April 20 to May 19 (except for the last 2 days), ASHP is used to provide heat from 9 p.m. to 6 a.m. and 6 a.m. to 1 p.m. From 1 p.m. to 9 p.m., the outside zone (69 boreholes) of BTES will work with the dT of 4^{o}C and flow rate of 10 m^3/d. A single zone or multiple zones can work independently because of the ring connection of the boreholes. For example, from October 26 to November 24, from 5 p.m. to 5 a.m., only the outside zone is supplying heat, whereas from 11 a.m. to 5 p.m., the center zone is providing heat to the district energy system while the outside zone is being charged by an ASHP.

The temperature fields at the end of the winter and summer seasons are shown in Figure 6. At the end of the winter season, the BTES has cooled by extraction of the heat. The BTES is further cooled by running an ASHP to pre-cool the ground when power is inexpensive and lower carbon. At end of the summer season, the BTES has been warmed by heat from the buildings, and in early fall, the BTES is further charged with heat from the ASHP. Figure 7 shows a time series of inlet/outlet fluid temperature at the cold and hot zones in a single-year simulation. When inlet fluid temperature (shown in blue) is greater than outlet fluid temperature (shown in orange), the BTES is recharged (heat storage), and when the inlet temperature is less than the outlet fluid temperature, the BTES is discharged (heat extraction). The effect of different schedules can be observed in the temperature history, that is, the vibration of inlet/ outlet indicates changing schedule both seasonal and diurnal.

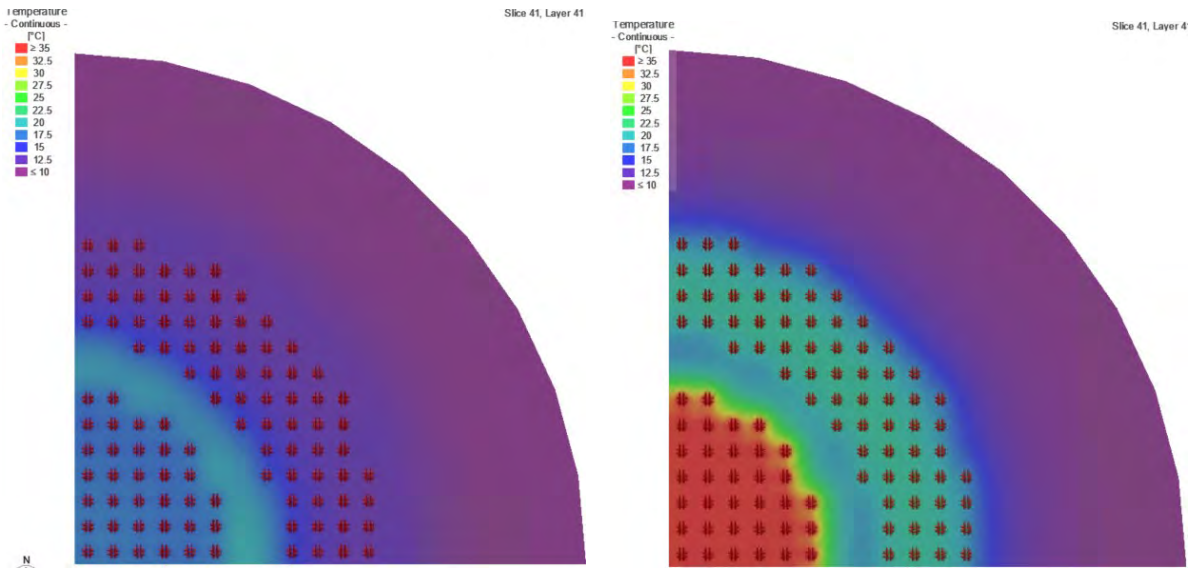

Figure 6: Temperature field at the end of the winter season (left) and at the end of the summer season (right).

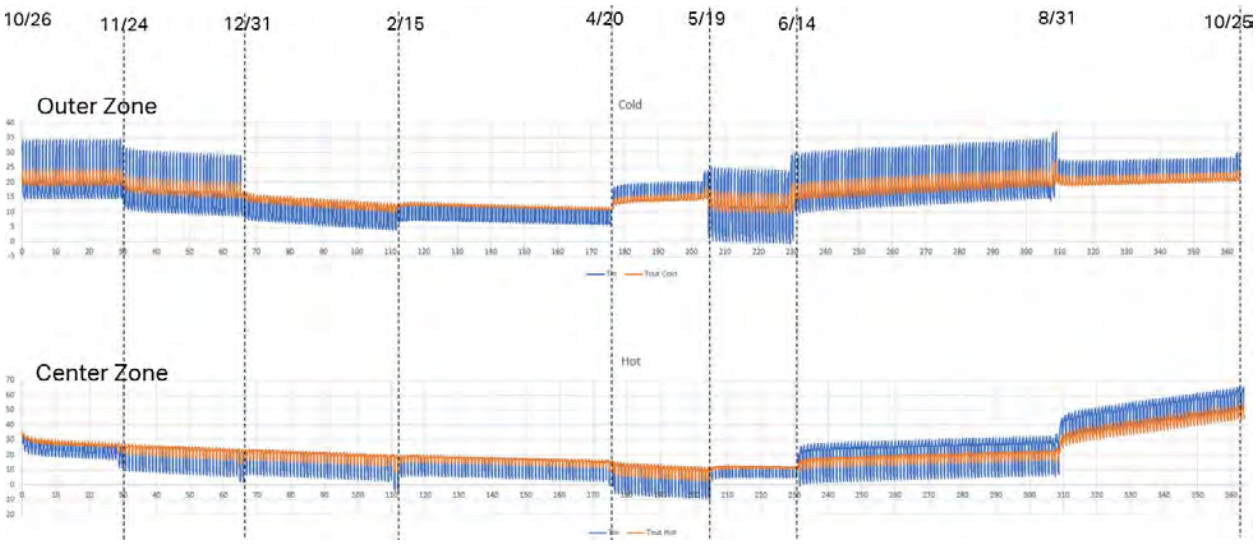

Figure 7: Inlet/outlet fluid temperature of the outer zone (upper) and center zone (lower). Blue represents the inlet fluid temperature and orange represents the outlet fluid temperature.

Figure 8 compares the simulated energy capacity and the actual energy demand (summer and winter separately). The solid dots are the energy demand colored to correspond to periods of a day. For example, blue dots show energy demand from 11 a.m. to 5 p.m. in winter and 9 p.m. to 6 a.m. in summer. The triangles represent heat storage/extraction to/from BTES, and the cross stands for the heat from ASHP. As an example, during the first period of the winter season (October 26 to November 24), heat extraction from BTES between 11 a.m. and 5 p.m. (blue triangles) corresponds to the heat demand (blue solid dots) very well; orange triangles match the orange dots (5 p.m. to 5 a.m. heat needs); and green triangles coincide with the green dots (5 a.m. to 11 a.m.), which is the time that needs most heat in this season. The two green triangles at the end of the period are simulated heat energy in the “last 2 days” described in the running schedule (Table 1), which is used to evaluate the system’s capability to meet peak demand.

Table 1: BTES running schedules in winter (October 26 through April 19) and summer (April 20 through October 25). (Page 1 of 2)

Start Date	End Date	Time Range	Target (MMbtu/ hr)	dT (in to out) (°C)	Flow (m^3/day)	Boreholes (#)	Actual (MMbtu/ hr)	Excess (% of target)	Center Zone (136)	Outside Zone (276)	ashp Q, not btes (run?)	ashp Q to center (run?)	ashp Q to outside (run?)
Winter													
26-Oct	24-Nov	5 p.m. – 5 a.m.	-1.4	-5	6	276	-1.37	-2%	No	Yes	No	No	No
		5 a.m. – 11 a.m.	-2.4	-8	13	136	-2.34	-3%	Yes	No	No	No	No
		11 a.m. – 5 p.m.	-0.7	-6	5	136	-0.67	-4%	Yes	No	No	No	—
		11 a.m. – 5 p.m.	5	10	11	276	5.02	0%	No	Yes	No	No	Yes
	(last 2 days)	5 a.m. – 11 a.m.	-3.5	-10	16	136	-3.60	3%	Yes	No	No	No	No
25-Nov	31-Dec	5 p.m. – 5 a.m.	-2.7	-6	10	276	-2.74	1%	No	Yes	No	No	No
		5 a.m. – 11 a.m.	-3.7	-11	16	136	-3.96	7%	Yes	No	No	No	No
		11 a.m. – 5 p.m.	-2.5	—	—	0	0.00	-100%	No	No	Yes	No	—
		11 a.m. – 5 p.m.	2.5	10	5.5	276	2.51	0%	No	Yes	No	No	Yes
	(last 2 days)	5 a.m. – 11 a.m.	-5	-12	18	136	-4.86	-3%	Yes	No	No	No	No
1-Jan	15-Feb	5 p.m. – 5 a.m.	-2.6	-6	10	276	-2.74	5%	No	Yes	No	No	No
		5 a.m. – 11 a.m.	-3.7	-10	16	136	-3.60	-3%	Yes	No	No	No	No
		11 a.m. – 5 p.m.	-2.4	—	—	0	0.00	—	No	No	Yes	No	No
		11 a.m. – 5 p.m.	0	—	—	0	0.00	—	No	No	No	Y	No
	(last 2 days)	5 a.m. – 11 a.m.	-5.5	-12	20	136	-5.39	-2%	Yes	No	No	No	No
16-Feb	19-Apr	5 p.m. – 5 a.m.	-1.1	-5	5	276	-1.14	4%	No	Yes	No	No	No
		5 a.m. – 11 a.m.	-2.3	-9	12	136	-2.43	6%	Yes	No	No	No	No
		11 a.m. – 5 p.m.	-0.5	—	—	0	0.00		No	No	Yes	No	No
	(last 2 days)	5 a.m. – 11 a.m.	-3.5	-10	15	136	-3.37	-4%	Yes	No	No	No	No
Summer													
20-Apr	19-May	9 p.m. – 6 a.m.	-0.4	—	—	0	0.00	-100%	No	No	Yes	No	No
		6 a.m. – 1 p.m.	-0.3	—	—	0	0.00	-100%	No	No	Yes	No	No
		1 p.m. – 9 p.m.	1.8	4.0	10.0	276	1.82	1%	No	Yes	No	No	No
	(last 2 days)	1 p.m. – 9 p.m.	3.0	6.0	11.0	276	3.01	0%	No	Yes	No	No	No

Table 1: BTES running schedules in winter (October 26 through April 19) and summer (April 20 through October 25). (Page 2 of 2)

Start Date	End Date	Time Range	Target (MMbtu/ hr)	dT (in to out) (°C)	Flow (m^3/day)	Boreholes (#)	Actual (MMbtu/ hr)	Excess (% of target)	Center Zone (136)	Outside Zone (276)	ashp Q, not btes (run?)	ashp Q to center (run?)	ashp Q to outside (run?)
Summer													
20-Apr	19-May	9 p.m. – 6 a.m.	0.1	-0.1	0.1	276	0.00	-100%	No	Yes	No	No	Yes
		6 a.m. – 1 p.m.	-4.0	-12.0	15.0	136	-4.05	1%	Yes	No	No	Yes	No
20-May	14-Jun	9 p.m. – 6 a.m.	0.3	—	—	0	0.00	-100%	No	No	Yes	No	No
		6 a.m. – 1 p.m.	0.9	—	—	0	0.00	-100%	No	No	Yes	No	No
		1 p.m. – 9 p.m.	3.9	8.0	11.0	276	4.01	3%	No	Yes	No	No	No
	(last 2 days)	1 p.m. – 9 p.m.	7.0	10.0	16.0	276	7.30	4%	No	Yes	No	No	No
		9 p.m. – 6 a.m.	-4.7	-10.0	10.0	276	-4.56	-3%	No	Yes	No	No	Yes
		6 a.m. – 1 p.m.	-2.0	-6.0	7.0	136	-0.94	-53%	Yes	No	No	Yes	No
15-Jun	31-Aug	9 p.m. – 6 a.m.	1.3	6.0	10.0	136	1.35	4%	Yes	No	No	No	No
		6 a.m. – 1 p.m.	2.6	—	—	0	0.00		No	No	Yes	No	No
		1 p.m. – 9 p.m.	7.1	10.0	10.0	136	2.25	-68%	Yes	No	No	No	No
		1 p.m. – 9 p.m.	7.1	10.0	11.0	276	5.02	-29%	No	Yes	No	No	No
	(last 2 days)	1 p.m. – 9 p.m.	10.0	10.0	15.0	136	3.37	-66%	Yes	No	No	No	No
		1 p.m. – 9 p.m.	10.0	10.0	15.0	276	6.84	-32%	No	Yes	No	No	No
		9 p.m. – 6 a.m.	-1.0	-5.0	5.0	276	-1.14	14%	No	Yes	No	No	Yes
		6 a.m. – 1 p.m.	-2.4	-10.0	11.0	136	-2.47	3%	Yes	No	No	Yes	No
1-Sep	25-Oct	9 p.m. – 6 a.m.	-0.2	-5.0	5.0	0	0.00	-100%	No	No	No	No	No
		6 a.m. – 1 p.m.	-0.1	-9.0	12.0	0	0.00	-100%	No	No	No	No	No
		1 p.m. – 9 p.m.	2.5	5.0	11.0	276	2.51	0%	No	Yes	No	No	No
	(last 2 days)	1 p.m. – 9 p.m.	3.0	6.0	11.0	276	3.01	0%	No	Yes	No	No	No
		9 p.m. – 6 a.m.	5.0	12.0	15.0	136	4.05	-19%	Yes	No	No	Yes	No
		6 a.m. – 1 p.m.	5.0	12.0	18.0	136	4.86	-3%	Yes	No	No	Yes	No

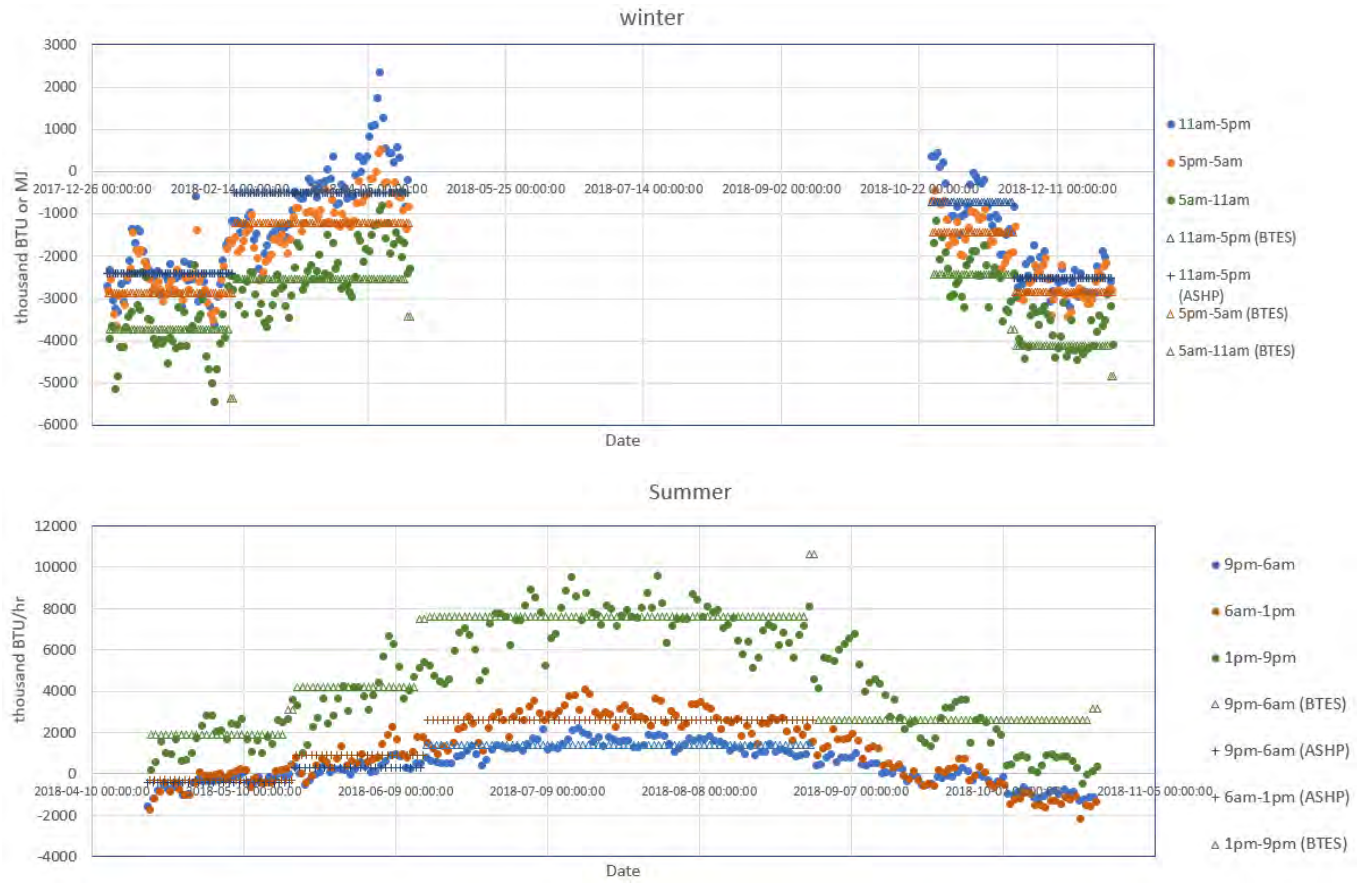

Figure 8: Comparison between simulated heat capacity and energy demand (top: winter season, bottom: summer season). Solid dots are from actual energy demand, triangles from BTES simulation, and cross from ASHP. Different colors correspond to different time ranges within each day.

3.3 Multiple-Year Simulation

Section 3.2 shows simulation results of 1 year, after which we ran 3 years to better evaluate the robustness of the BTES system. Figure 9 shows an underground temperature series at five observation points (obs1 to obs5 from the hot core to the outside cold zone). The temperature at obs5 slightly rises with time, confirming heat loss at the boundary of the BTES system. Obs1 and obs2 show significant seasonal variation (i.e., the underground temperature decreases in winter because of heat extraction and increases in summer from heat injection). Seasonal variation at obs3 and obs4 can also be observed but is not as significant as points close to the hotter core (obs1 and obs2).

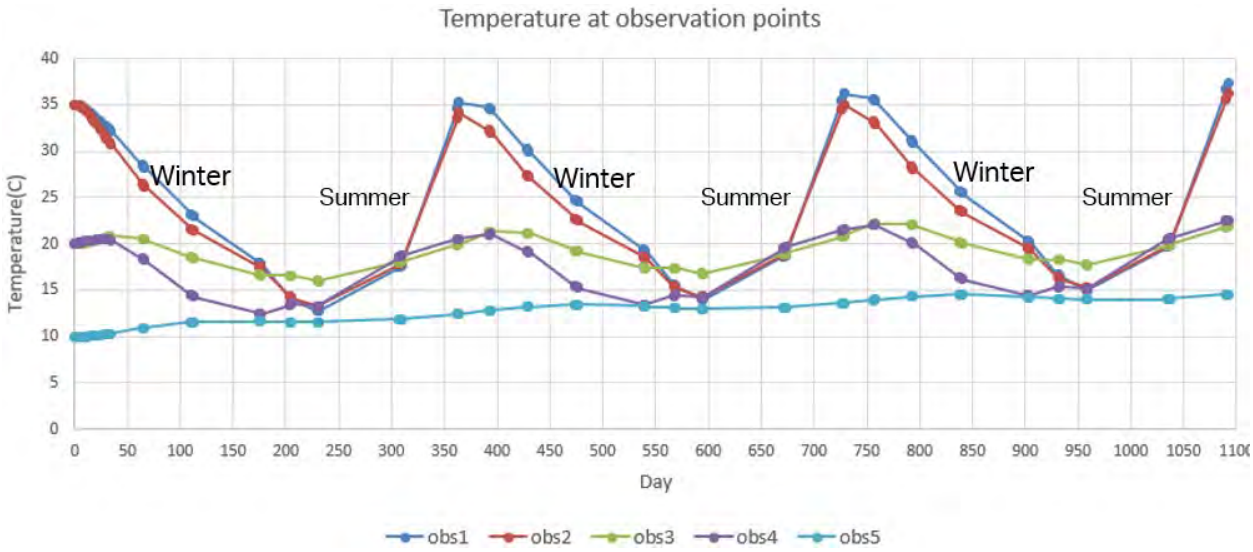

Figure 9: Temperature history at five observation points (obs1 to obs5 from the center to the border).

4. Discussions and Conclusions

Subsurface thermal energy storage systems combined with heat pumps are gaining recognition around the world. Our paper presents two BTES case studies that differ in number of boreholes, borehole spacing, length, borehole connection, and operating schedules. Table 2 summarizes the design and operating parameters of the two case studies: Baker Lake, Nunavut, Canada, and Vernal, Utah.

Table 2: Summary of the parameters in the two BTES case studies.

Parameter	Baker Lake, Nunavut, Canada	Vernal, Utah
Number of boreholes	280	412
Borehole length (m)	90 – 110	80
Borehole spacing (m)	3.5 – 7	3
Borehole connection	Serial	Parallel
Independent zone	No	Yes
Heat source	Diesel engine waste heat	Stored energy from previous season, plus ASHP
Temperature constraint	Inlet temperature	Temperature difference

In Baker Lake, a radial connection with multiple boreholes in each connection is applied in which the boreholes are not as dense as in the Vernal case. The length of the boreholes in Baker Lake, however, is longer and the extended length near the outside of the BTES system is tested and confirmed. In Vernal, we combined a flexible operating schedule with GABESS to shift heat/cold from off-peak time to meet the peak load demand. Results indicate the GABESS is able to meet the high thermal energy deliverability and seasonal storage demands with a small surface footprint.

Acknowledgement

We acknowledge the support of Qulliq Energy Corporation and the community of Baker Lake, Nunavut along with the municipality of Vernal, Utah.

REFERENCES

Akhmetov, B., Georgiev, A.G., Kaltayev, A., Dzhomartov, A.A., Popov, R., and Tungatarova, M.S. "Thermal energy storage systems–review." *Bulgarian chemical communications*, 48(Special Issue E), (2016), 31-40.

Amiri, L., Ermagan, H., Kurnia, J.C., Hassani, F., and Sasmito, A.P. "Progress on rock thermal energy storage (RTES): A state of the art review." *Energy Science & Engineering*, 12(2), (2024), 410-437.

Dascalaki, E.G., Droutsa, K., Gaglia, A.G., Kontoyiannidis, S., and Balaras, C.A. "Data collection and analysis of the building stock and its energy performance—An example for Hellenic buildings." *Energy and Buildings*, 42(8), (2010), 1231-1237.

Diersch, H.J., Bauer, D., Heidemann, W., Rühaak, W., and Schätzl, P. "Finite element modeling of borehole heat exchanger systems: Part 1. Fundamentals." *Computers & Geosciences*, 37(8), (2011a), 1122-1135.

Diersch, H.J., Bauer, D., Heidemann, W., Rühaak, W., and Schätzl, P. "Finite element modeling of borehole heat exchanger systems: Part 2. Numerical simulation." *Computers & Geosciences*, 37(8), (2011b), 1136-1147.

Ekmekci, E., Ozturk, Z.F., and Sisman, A. "Collective behavior of boreholes and its optimization to maximize BTES performance." *Applied Energy*, 343(121208), (2023).

Kitz, K. "Grid Energy Storage in Shallow Geothermal Boreholes as a Higher-Performing and Lower-Cost Solution to Grid and Building Decarbonization." *GRC Tranactions*, 45, San Diego, CA (2021).

Kumawat, P.K., Zhou, H., Kitz, K., McLennan, J., Powell, K., Deo, M., and Panja, P., "Sensitivity Analysis of Borehole Thermal Energy Storage (BTES): Examining Key Factors for System Optimization." *Energy Storage and Saving*, 3(3), (2024), 218-230.

McLing, T.L., Dobson, P., Jin, W., Spycher, N., Doughty, C., Neupane, G.H., Smith, R.W., and Atkinson, T.A. "Dynamic Earth Energy Storage: Terawatt-year, Grid-scale Energy Storage Using Planet Earth as a Thermal Battery (GeoTES): Phase I Project (No. INL/RPT-22-66762-Rev001)." Idaho National Lab., Idaho Falls, ID (2022).

Nilsson, E., and Rohdin, P. "Performance evaluation of an industrial borehole thermal energy storage (BTES) project–Experiences from the first seven years of operation." *Renewable energy*, 143, (2019), 1022-1034.

Olabi, A.G., Abdelghafar, A.A., Maghrabie, H.M., Sayed, E.T., Rezk, H., Al Radi, M., Obaideen, K., and Abdelkareem, M.A. "Application of artificial intelligence for prediction, optimization, and control of thermal energy storage systems." *Thermal Science and Engineering Progress*, 39(101730), (2023).

Machine Learning / Computing

Unsupervised Machine Learning For Assessing Geothermal Heat Exchanger Performance

Paul Michael B. Abrasaldo[1,2*], Sadiq J. Zarrouk[1] and Andreas W. Kempa-Liehr[1]

[1] Department of Engineering Science and Biomedical Engineering, The University of Auckland, 70 Symonds Street, Auckland, New Zealand

[2] Contact Energy Ltd., Wairakei Power Station, Taupo, New Zealand

***pabr612@aucklanduni.ac.nz**

Keywords

clustering, unsupervised learning, feature engineering, time-series analysis, geothermal, heat exchangers

ABSTRACT

Artificial intelligence and machine learning applications for above-ground geothermal energy operations are limited despite volumes of data being generated in real-time by facilities all over the world. There is a need to extensively annotate operational data before it is ready for tasks such as condition monitoring, fault detection, and performance forecasting.

In this study, we propose the application of unsupervised machine learning to automatically label fifteen (15) years of operational data for a geothermal heat exchanger. The framework implemented in this study relies on well-established techniques in systematic time-series feature engineering, feature selection, and cluster analyses. Nine clustering algorithms were trained using the extracted time-series features as inputs and were able to identify data groups that represented periods before and after a cleaning activity was done on the heat exchangers. The resulting data labels can be used to assess the effectiveness of different heat exchanger cleaning methods and the development of an optimal maintenance plan. The labels generated automatically are now primed for use in more machine learning applications that rely on a supervised learning approach. The developed framework can also be applied in other parts of the geothermal value chain, such as using unsupervised machine learning to create an effective maintenance plan for scaled-up production wells.

1. Introduction

The quality and amount of operational geothermal data have been consistently advancing. Research indicates that standardising and integrating datasets throughout the geothermal value chain is crucial for maximising value from existing facilities (Krieger et al., 2022; Okoroafor et al., 2022). Digitising monitoring systems and adopting data governance practices have significantly enhanced the interoperability and accessibility of operational data for engineers and scientists focusing on performance improvements. Progress in sensor technology has further broadened the scope of monitoring systems, driving innovative changes in the operation, monitoring, and maintenance of geothermal power plants.

Interest in data science, artificial intelligence (AI), and machine learning (ML) applications within the geothermal energy sector has surged significantly over the past decade (Abrasaldo et al., 2024; Okoroafor et al., 2022). The vast availability of time-series operational data and affordable computing power has enabled real-time, data-intensive analysis. While most AI and ML applications in geothermal energy have concentrated on subsurface reservoir characterisation, recent studies have also explored their use for surface facilities. These studies have utilised simulated, experimental, and actual operational data to create models that help scientists and engineers optimise power plant design, enhance performance, monitor conditions, and make data-driven decisions in the geothermal field (Abrasaldo et al., 2024). Notably, supervised learning has been the predominant approach researchers employ in AI and ML studies within the geothermal energy discipline.

A major challenge in many AI and ML studies in geothermal and other industries is the necessity for extensive annotation of operational data (Buster et al., 2021; Taverna et al., 2022). Sensor data is less useful for supervised machine learning without labelling by domain experts. In applications like condition monitoring and fault detection, these annotations are vital for accurately defining various power plant operation regimes. However, efforts to fully annotate operational data in geothermal energy operations lag behind the vast amount of data generated across facilities, as most operators are already busy with the plant's daily operations.

1.1 Study motivation and objective

This work presents a proposed workflow to automatically generate data labels designed to help operators assess and monitor the performance of heat exchangers in geothermal binary power plants. Potential fouling in heat exchangers significantly hinders the broader adoption of geothermal energy as a reliable electricity source despite the abundance of accessible low to medium-enthalpy reservoirs (Ann Candido & Zarrouk, 2017; Ledésert et al., 2021; Mroczek et al., 2017; Zarrouk et al., 2014). In geothermal settings, fouling primarily arises from the deposition or precipitation of materials as mineral-rich geothermal brine passes through the heat exchangers to vaporise the motive fluid in a binary cycle power plant (Brown, 2011; Ledésert et al., 2021; Mroczek et al., 2017; Yanagisawa, 2015; Zarrouk et al., 2014). The performance reduction of heat exchangers and overall power plants due to fouling has prompted researchers to develop proactive and reactive measures to mitigate the effects of mineral scaling (Ann Candido & Zarrouk, 2017; Penot et al., 2023).

Chemical treatment of geothermal brine before it enters binary plants is a standard method to prevent scale deposition within surface facilities. However, when chemical treatment is not cost-

effective or existing scale buildup in heat exchangers impedes effective chemical cleaning, operators resort to mechanical methods to remove the scale. Mechanical removal of mineral deposits in heat exchangers can be accomplished using boring technology or high-pressure water blasting. Both methods require significant downtime, incurring high costs for operators beyond the labour and material costs of mechanical cleaning. Accurately assessing heat exchanger conditions is critical to determining the optimal timing for mechanical cleaning (Zarrouk et al., 2014).

Given the various factors affecting heat exchanger performance, reliable evaluation is challenging. This study employs a workflow based on unsupervised machine learning algorithms, trained on time-series features extracted from sensor data, to annotate the operational history of heat exchangers in a geothermal binary power plant. These annotations can be used to assess the effectiveness of different cleaning methodologies and identify system and environmental conditions that may impact the success of these interventions. Successfully implementing this workflow could also lead to developing an optimal cleaning and maintenance plan for heat exchangers based on their current condition and performance. The following sections discuss the proposed approach and its applicability in studying heat exchanger performance at the Wairakei geothermal binary power plant in New Zealand.

1.2 Wairakei Geothermal Binary Power Plant

The Wairakei geothermal project, situated north of Taupo in New Zealand, hosts an active geothermal reservoir projected to support the current 353 MW of electricity generation for another four decades (Ciriaco et al., 2022). The Warakei geothermal power plant was inaugurated in 1958 with a 132 MWe conventional geothermal power plant, later expanding to a capacity of 187 MWe following the addition of the 55 MWe Poihipi power station (Thain & Carey, 2009). Subsequently, in 2005, a 14-MW Organic Rankine Cycle (ORC) power plant, comprising two generating units, was commissioned in Wairakei. It was designed to intake 2800 tons per hour of geothermal fluid at a nominal temperature of 127°C (Zarrouk et al., 2014).

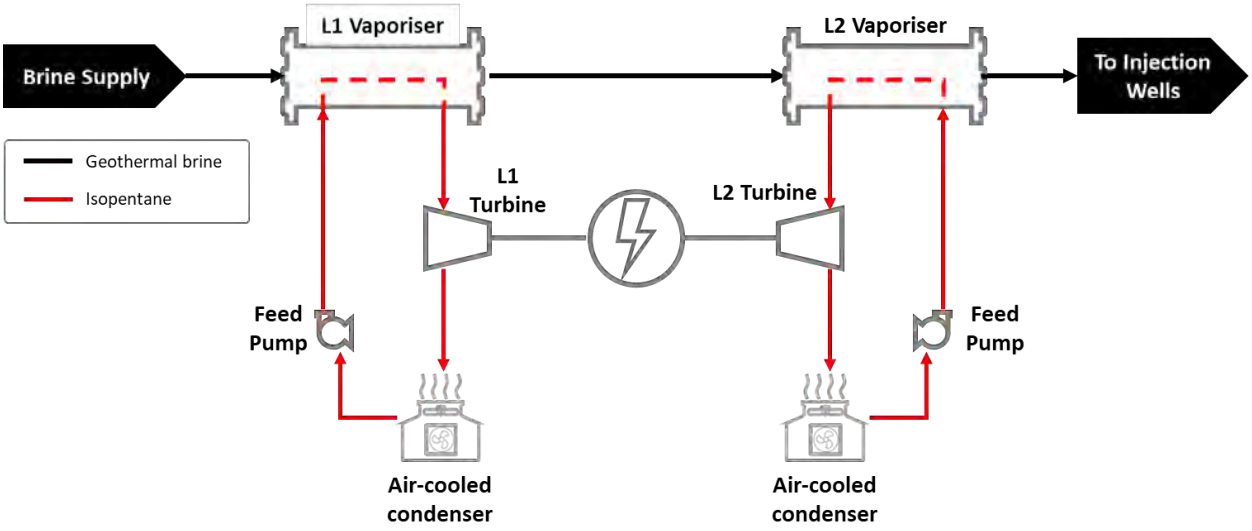

Figure 1. Schematic diagram illustrating one of the two multi-level Ormat generating units forming the Wairakei binary power plant. Note that pre-heaters and recuperators are omitted for brevity.

The Wairakei binary power plant operates on an Organic Rankine Cycle (ORC) using isopentane as the working fluid (Thain & Carey, 2009). Separated geothermal fluid from the Wairakei production wells supplies the binary power plant, where approximately 130 MW of thermal power is transferred from the geothermal brine to vaporise and superheat the working fluid. The superheated isopentane drives the turbines to generate electricity, which is then cooled back to its liquid state using forced-draft air condensers. A feed pump in each generating unit circulates the working fluid to maintain the cycle during regular operation (Zarrouk et al., 2014). In each generating unit, heat exchangers are connected to extract heat from the source fluid in two stages (Figure 1). The lower temperature fluid exiting the second vaporiser level flows through another set of heat exchangers to preheat the working fluid in the individual isopentane circuits. The heat exchangers at the Wairakei binary power plant are shell and tube types, with the geothermal fluid passing through the tube side and the isopentane travelling through the shell side. This configuration facilitates easier cleaning when scaling occurs on the tube side, where the mineral-rich geothermal fluid flows.

1.3 Heat-exchanger scaling and cleaning

Geothermal fluids contain high concentrations of minerals that can precipitate on the surface facilities of a geothermal project when left untreated. Fouling of heat exchangers in the geothermal industry is a well-documented issue (Ann Candido & Zarrouk, 2017; Brown, 2011; Ledésert et al., 2021; Mroczek et al., 2017; Muller et al., 2015; Penot et al., 2023; Yanagisawa, 2015; Zarrouk et al., 2014), with minerals like silica and metal sulfides commonly depositing along the tube side of binary plant heat exchangers. To prevent significant scaling within the heat exchangers, it is standard practice to chemically dose the source geothermal fluid with anti-scalants or pH modifiers before it enters the vaporisers (Ann Candido & Zarrouk, 2017; Johnston et al., 2020; Muller et al., 2015; Zarrouk et al., 2014). When chemical dosing cannot wholly prevent scaling, mechanical cleaning of mineral deposits becomes necessary. Standard methods for mechanical cleaning include drilling out the scale from the heat exchanger tubes or using high-pressure water-blasting. These methods require substantial financial and human resources and result in significant power plant downtime. Chemical cleaning is also an option but has been found to cause undue corrosion in surface pipelines and injection wells (Penot et al., 2023; Zarrouk et al., 2014). Therefore, an accurate assessment of the condition of geothermal heat exchangers and understanding the effectiveness of various cleaning methods are essential to develop an optimal, condition-based maintenance program for geothermal heat exchangers.

2. Methodology

The workflow proposed in this study involves systematically extracting time-series features from operational sensor data and using these engineered features to train several unsupervised clustering algorithms, which generate labels for the input time series. A crucial component of this workflow is an automated feature selection process conducted in two stages to ensure only statistically relevant features are included in model training and to minimise collinearity among the features. The filtered time-series feature matrix is then normalised and used as input to train several clustering algorithms. These trained models are evaluated using clustering metrics that do not depend on ground truth labels. Additionally, a comparison and initial interpretation of the labels generated by the various clustering algorithms are performed as part of the model validation

process. An overview of the approach taken in this study is illustrated in Figure 2. The following subsections briefly summarise the techniques used in the proposed workflow.

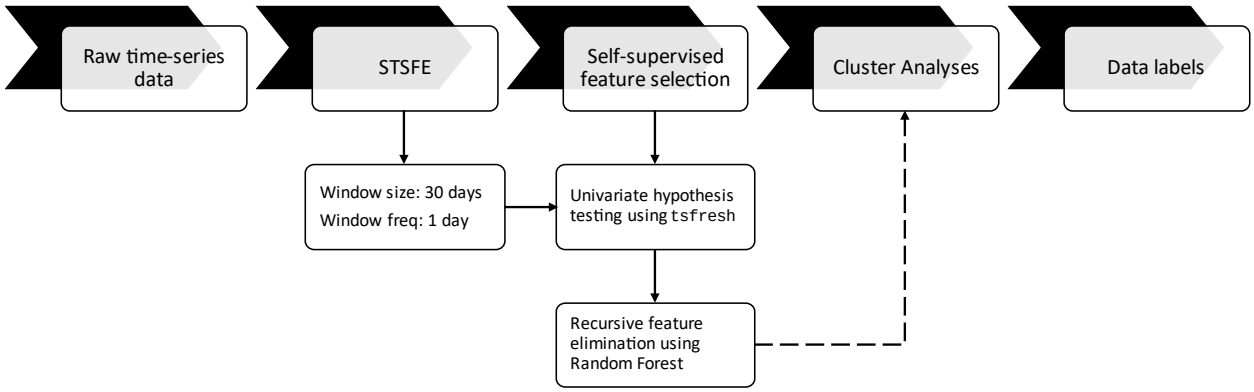

Figure 2. A high-level flowchart of the approach applied in this study combines systematic time-series feature engineering (STSFE), self-supervised feature selection and unsupervised machine learning to annotate the historical performance of geothermal heat exchangers. The generated data labels can be used for further domain-specific analysis and standard supervised machine learning applications.

2.1 Heat exchanger sensor data

Geothermal operators worldwide use various forms of centralised platforms where data collected from sensors are stored, processed, visualised, and archived. The data gathered from these sensors are processed by several control systems to ensure the safe and normal operation of the various equipment in the power plant. This study focuses on data captured by sensors used to monitor and assess the condition and performance of the heat exchangers in the Wairakei binary power plant.

In this study, the two generating units in the Wairakei binary power plant are considered a single system due to the absence of individual pressure sensors and flow meters at each generating unit's inlet. Line pressures measured by sensors at the inlet and outlet of the binary system, along with metered flow rates at the inlet, are used to calculate the flow resistance parameter. This metric, as reported by Zarrouk et al. (2014), is a better measure of the impact of mineral scaling on heat exchanger performance. The temperature difference of the geothermal brine upstream and downstream of the binary plant is also included in the analysis to represent the heat transfer efficiency of the heat exchangers. The monitored parameters are measured in real-time but vary in magnitudes and sampling rates over the periods covered (Figure 3). The various time series used in this study cover fifteen years, amounting to about 7.9 GB of data files.

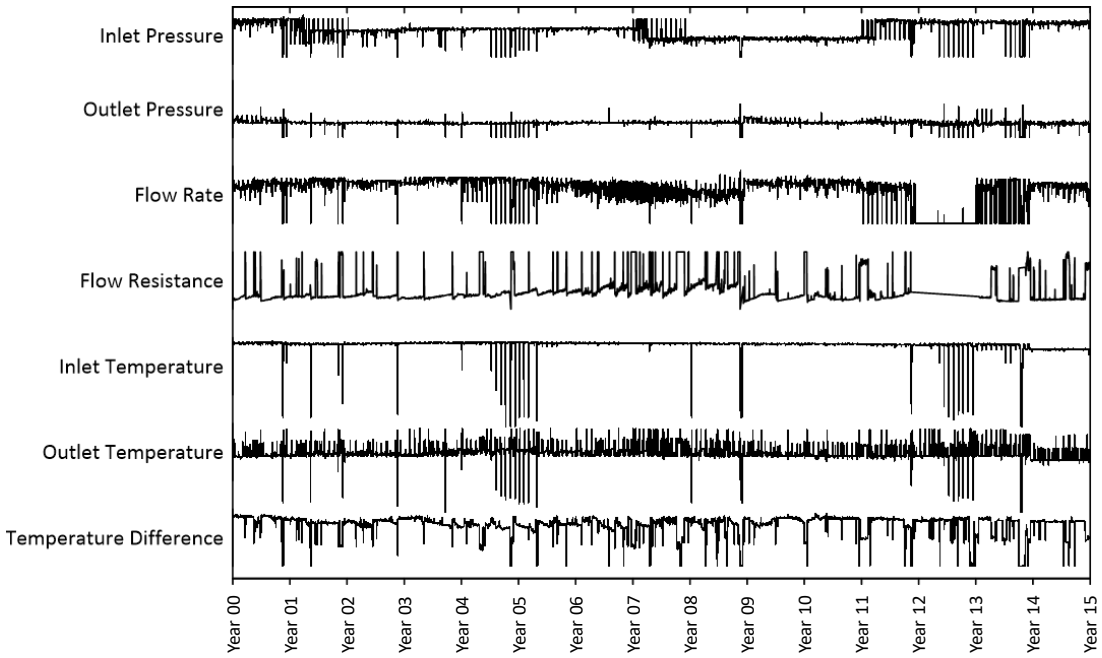

Figure 3. Sparklines of the time series raw values showing changes in relative magnitude across the covered period.

2.2 Systematic time-series feature engineering and self-supervised feature selection

This study proposes a feature-based approach to time-series modelling wherein quantified characteristics of the input time series are used to train the algorithms instead of the raw data values. Directly using raw values can be sufficient in some cases (Box et al., 2016) but is significantly impacted by noise and redundancies due to the large volume of data. Emerging research indicates that utilising appropriate time series features as model inputs improves model performance and interpretability (Fulcher, 2017; Kennedy et al., 2021; Simmons et al., 2021; Teh et al., 2021). The dimensionality reduction achieved by identifying relevant time series features for machine learning also enhances computational efficiency and reduces the risk of overfitting in the resulting models.

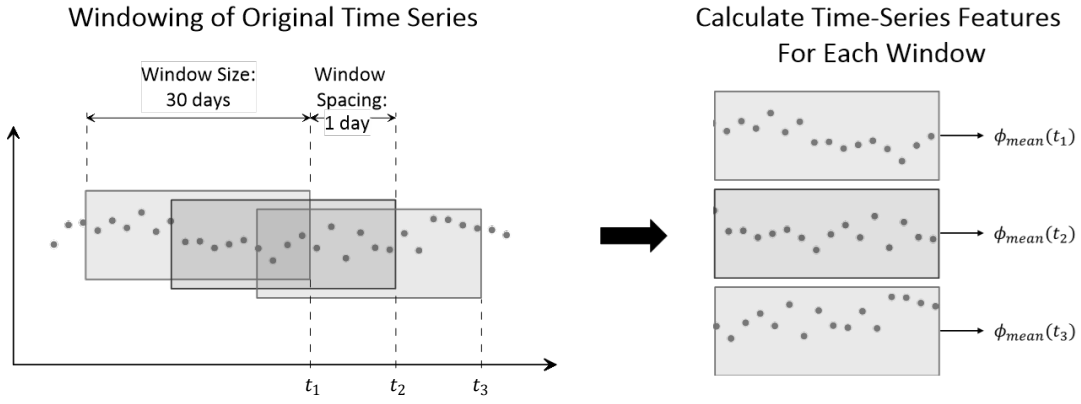

Figure 4. Diagram illustrating the rolling window method: A window of a set size is moved across the original time series at regular intervals. The resulting subsets of time series are then analysed using feature calculators to extract important statistics and characteristics, such as the mean.

In this study, a sensor-specific feature selection process is implemented, similar to the approach described by Teh et al. (2021). Each sensor's time series $\vec{s} = [x_1, \dots, x_t, \dots, x_T]$ undergoes systematic time-series feature extraction and two stages of feature selection. The main difference lies in the target variable used for the self-supervised feature selection process, where the last value of the subsequent window is forecasted rather than a specific statistic of the next window. Initially, a rolling window is applied to all sensor time series, resulting in a matrix of windows $\boldsymbol{W} = [\vec{w}_1, \dots, \vec{w}_n, \dots \vec{w}_N]$, where n indexes each window and N is the total number of windows (Figure 4). Each rolling window is bounded by two timestamps, referenced by the right-most timestamp. A window size of thirty (30) days and a window frequency of one (1) day are utilised, ensuring each window $\vec{w}_n$ contains sensor readings for the last thirty days, overlapping by 29 days with the adjacent windows.

The rolled time series window matrix $\boldsymbol{W}$ undergoes systematic feature extraction using the `tsfresh (v0.19.0)` Python package (Christ et al., 2018). This Python library employs highly parallelisable and efficient algorithms to systematically apply a set of feature calculators $\phi(\vec{w})$ on the window matrix $\boldsymbol{W}$ to extract $Q = 794$ characteristic time series features for each time-series window. The resulting feature matrix $\boldsymbol{W}_\phi$ has N number of rows corresponding to the number of time series windows and Q number of columns:

$$\boldsymbol{W}_\phi = \begin{bmatrix} \phi_1(\vec{w}_1) & \cdots & \phi_q(\vec{w}_1) & \cdots & \phi_Q(\vec{w}_1) \\ \vdots & \ddots & \vdots & \ddots & \vdots \\ \phi_1(\vec{w}_n) & \cdots & \phi_q(\vec{w}_n) & \cdots & \phi_Q(\vec{w}_n) \\ \vdots & \ddots & \vdots & \ddots & \vdots \\ \phi_1(\vec{w}_N) & \cdots & \phi_q(\vec{w}_N) & \cdots & \phi_Q(\vec{w}_N) \end{bmatrix}. \quad (1)$$

In many applications, not all extracted features are relevant or crucial for a specific machine learning task, and some may even be redundant, which can adversely affect model performance. Therefore, the next step in the proposed workflow is a two-stage selection process to retain only the statistically important features during model training. The target vector $\vec{y}$, which includes future values of the time series relative to a specific window, serves as the basis for feature selection. The initial selection phase utilises univariate hypothesis tests integrated into the `tsfresh` library. This step filters out irrelevant features for predicting future time series values, ensuring that only properties capturing the dynamics of future values are retained in the feature matrix. Following this, a second round of feature selection employs recursive feature elimination (RFE) to reduce the feature set further and eliminate collinear variables. RFE is executed using a Random Forest regressor from the `scikit-learn` (Pedregosa F. et al., 2011) machine learning library, which ranks the most influential parameters for predicting future time series values.

2.3 Unsupervised machine learning

Machine learning has garnered significant attention across various research disciplines, encompassing applications in the four primary paradigms: supervised, semi-supervised, unsupervised, and reinforcement learning (Cook, 2016; Murty & Devi, 2015). While the other approaches require full or partial labelling of the input data, unsupervised learning represents the opposite end of the spectrum, relying solely on unlabelled data to reveal hidden patterns and structures within the input data. In this study, various clustering algorithms are trained on the filtered and normalised time-series feature matrix to identify potentially distinct operating

conditions of the studied geothermal heat exchangers. Detailed descriptions of each clustering algorithm (Figure 5) used in this study can be found in the `scikit-learn` library documentation.

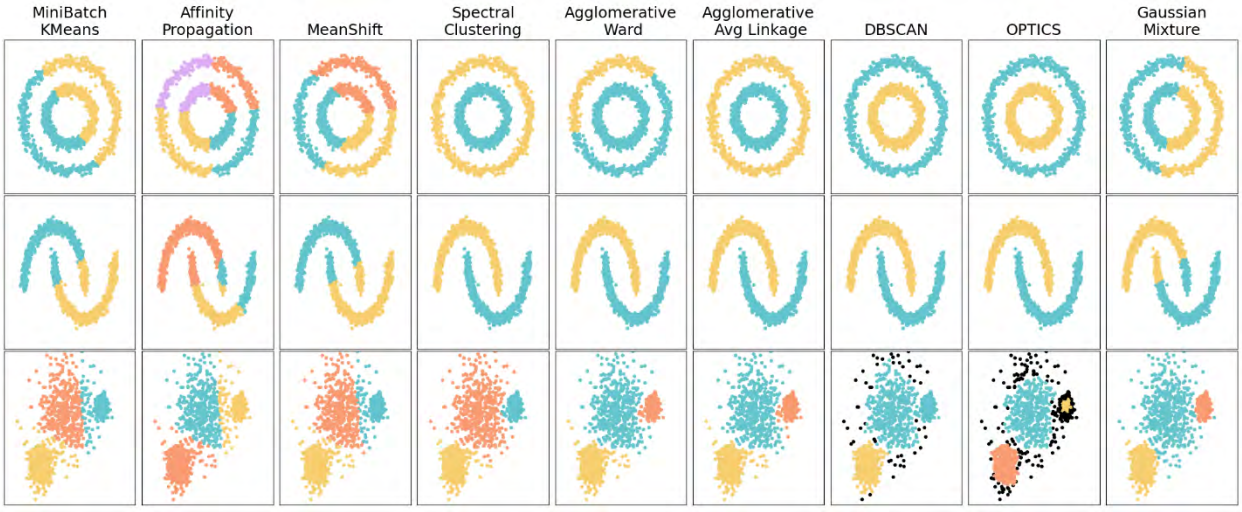

Figure 5. Exemplary behaviour of the different clustering algorithms used in this study on sample datasets with various structures. Adapted from the scikit-learn [33] documentation.

Three evaluation metrics for cluster analyses that do not depend on ground-truth class assignments are chosen: the Silhouette Coefficient (SIL), the Calinski-Harabasz index (CHI), and the Davies-Bouldin index (DBI). These metrics are straightforward to calculate for each clustering algorithm using their implementation in the `scikit-learn` library. The SIL of a partitioning task compares the tightness of each resulting cluster and the separation of each cluster from the other clusters (Rousseeuw, 1987). The CHI, also known as the variance ratio criterion, is calculated as the ratio of the sum of inter-cluster and intra-cluster dispersion, where the sum of distances squared is used as the dispersion metric (Calinski & Harabasz, 1974). Lastly, the DBI measures the clusters' similarity by comparing the separation between clusters and the size of the individual clusters (Davies & Bouldin, 1979).

3. Results

The workflow described in the previous section was applied to 15 years of operational data gathered at the Wairakei binary power plant (Figure 6). Temperature data of the geothermal fluid was also utilised as an indicator of the heat transfer efficiency of the binary unit, as previously mentioned. The flow resistance data displayed a sawtooth pattern, indicating the periods when cleaning and maintenance were performed on the heat exchangers.

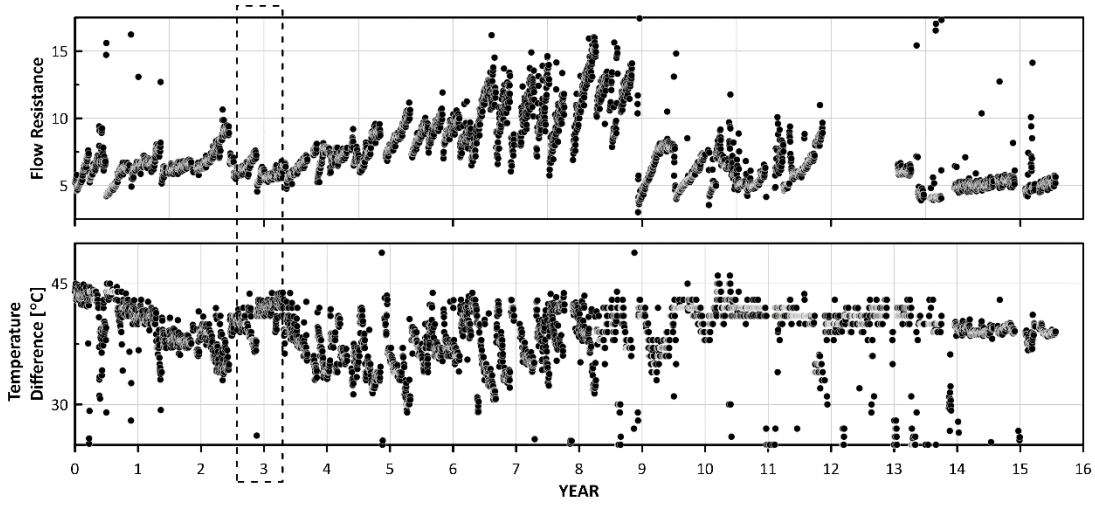

Figure 6. A sawtooth pattern is observed in the historical performance metrics of the heat exchangers where mineral scaling causes the flow resistance to increase over time while successful cleaning activities instantaneously reduce the flow resistance parameter.

3.1 Self-supervised feature selection

The flow resistance and temperature difference time series were subjected to the rolling window process described in section 2.2 and underwent systematic time-series feature extraction and selection using `tsfresh`. A reference target vector, composed of the last value of the succeeding window, was used to conduct univariate hypothesis testing to identify the time series features relevant to the desired task. This first feature selection phase resulted in a high-dimensional time series feature matrix with 539 statistically relevant features at the default false discovery rate of 0.05. Therefore, these relevant features underwent a second selection stage using a recursive feature elimination algorithm with a Random Forest regressor, utilising the same reference target vector as in the previous step. The second feature selection step identified an optimal feature count of fewer than ten for both input time series (Figure 7). After normalisation, the time series feature matrix is ready for training unsupervised learning models.

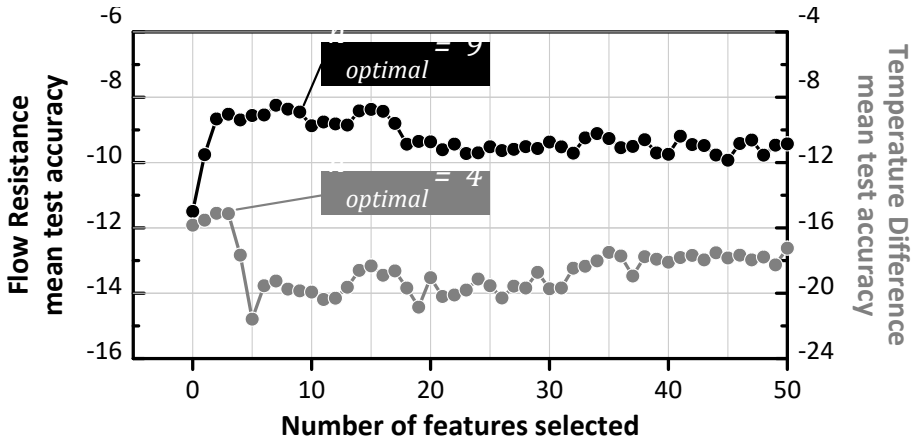

Figure 7. Recursive feature elimination results showed that the optimal feature count for both input time series is less than ten (10).

3.2 Cluster analysis and hyperparameter optimisation

One of the main tasks in cluster analysis is determining the optimal number of clusters for algorithms that require this information at the start of model fitting. This optimal cluster count can be identified by examining how the performance metrics of the clustering algorithms change with different cluster counts. The sensitivity analysis results (Figure 8) indicate a general decrease in the SIL for most algorithms when the cluster count exceeds two. However, the CHI and DBI offer counterindications, with some clusters showing increasing CHI and decreasing DBI values as the cluster count rises. Additionally, it is observed that for cluster counts greater than or equal to four, there is no significant change in performance for most clustering methods, regardless of the metric used.

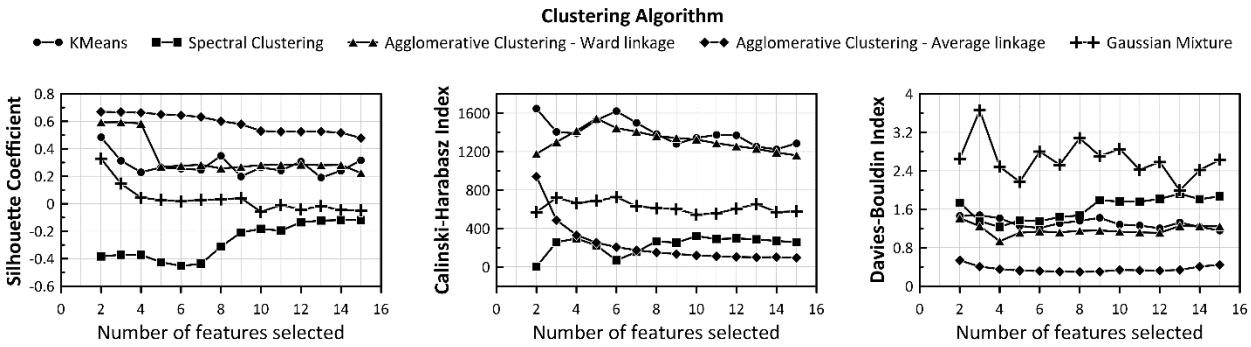

Figure 8. The elbow curve shows SIL, CHI, and DBI trends for clustering algorithms that require the cluster number to be defined prior to model fitting.

After selecting an initial value for the number of clusters, hyperparameter optimisation was conducted on various clustering algorithms using the `Optuna` Python library (Akiba et al., 2019). A multi-objective function was employed to tune the algorithm parameters, aiming to maximise the SIL and CHI and the inverse of the DBI. An overall model performance metric was calculated using the magnitude of the vector created by the SIL, CHI, and inverse DBI values for each trained model, with the best model ideally having the largest value of this metric. However, when overlaying clustering results on the raw time series, models with higher indicative overall performance did not always yield good clustering results, such as trial #41 in Figure 9B. Visual inspection indicated that clusters generated by models with a relatively lower SIL but higher CHI were more reasonable (e.g., trial #52 in Figure 9C). The tuned clustering algorithms were trained on the final input matrix of time-series features to annotate the performance history of the heat exchangers in the binary unit.

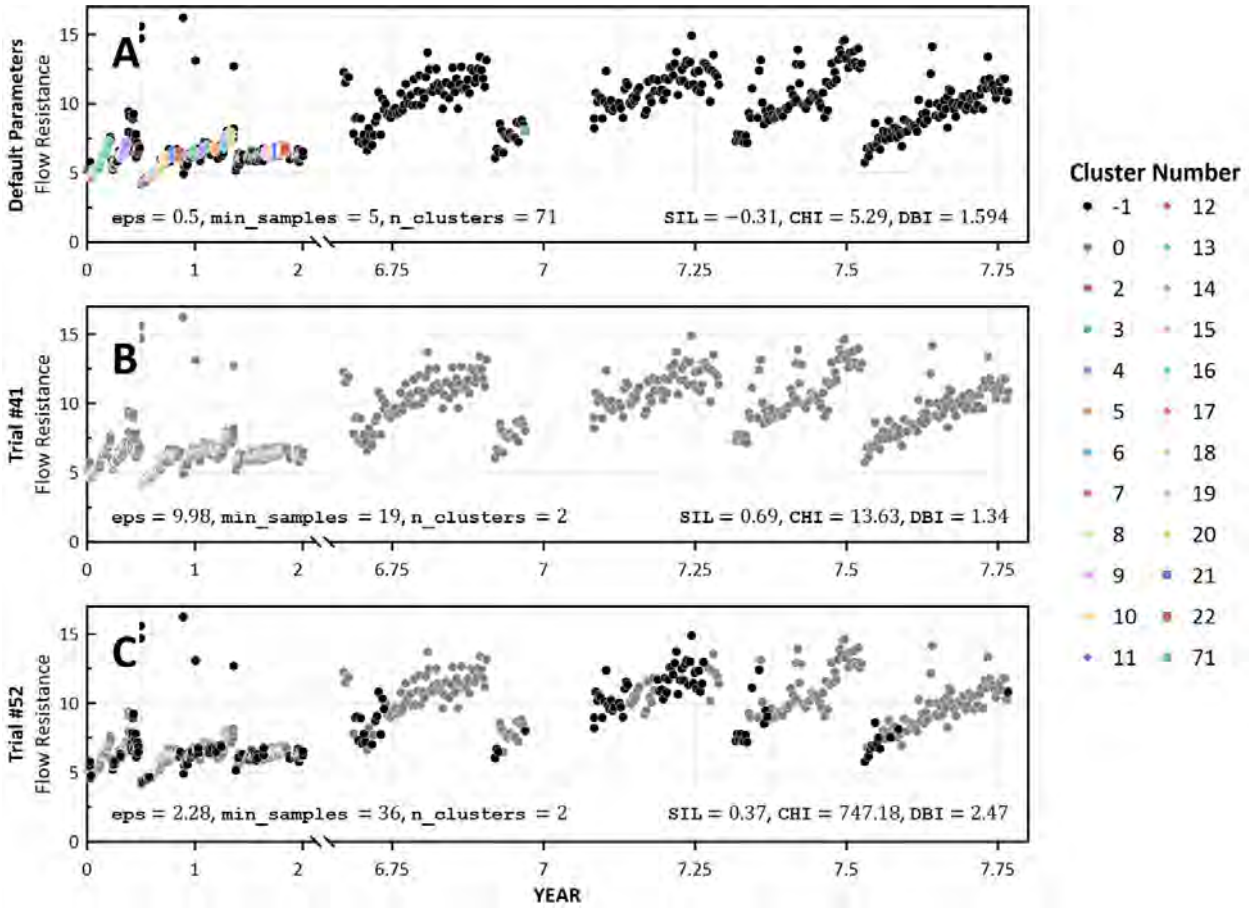

Figure 9. Exemplary clustering results comparing DBSCAN models trained using (A) default hyperparameters, (B) hyperparameters of models with the highest overall performance metric, and (C) hyperparameters of the optimal model.

The cluster labels produced by the optimised algorithms match up well with the maintenance history of the heat exchangers. One cluster group is observed to group the data points after a recent cleaning job, and another cluster is associated with data points before a cleaning activity (Figure 10). Furthermore, because of the distinction produced by the cluster groups, the data points clustered after a cleaning activity can be considered the “effective duration” of the said maintenance job. This information is vital for operators to evaluate the effectiveness of various cleaning methods and assess the environmental and operating conditions under which a particular method may be less effective than at other times. Ideally, a successful heat exchanger cleaning activity should reduce frictional losses in the piping system, leading to a sharp decrease in the flow resistance parameter and an improvement in heat transfer efficiency, indicated by an abrupt increase in the values of the temperature difference time series. Cleaning jobs A, C, and D from Figure 10 exemplify effective interventions that led to a decrease in flow resistance, an increase in temperature difference, and an observed change in cluster labels. Cleaning job B, on the other hand, is an example of an unsuccessful cleaning activity with no significant improvement in the heat exchanger performance and no changes in the cluster label after the activity.

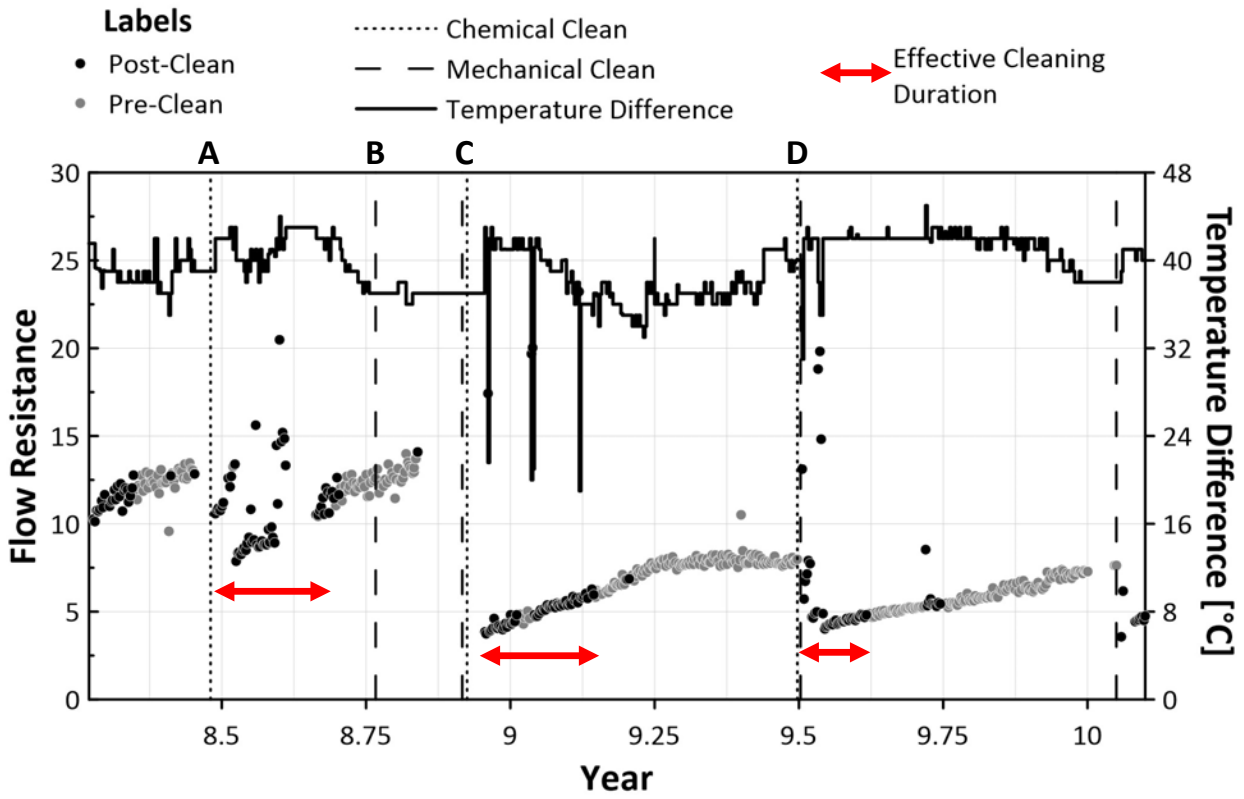

Figure 10. Subset of the labelled performance history of the heat exchangers based on the clustering results of the optimised Gaussian Mixture model.

4. Conclusion

This study introduced a novel method for annotating the performance history of geothermal heat exchangers based on a workflow consisting of efficient, systematic time-series feature engineering, self-supervised feature selection, and cluster analysis. After extracting time-series features from flow resistance and temperature difference data of the Wairakei binary power plant, thirteen (13) features were selected through univariate hypothesis testing and self-supervised feature selection. These final features were then used to train and optimise nine (9) clustering algorithms.

The promising clustering algorithms successfully differentiated between the “clean” and “scaled-up” state of the geothermal heat exchangers. Data points recorded right after a cleaning activity were typically grouped, while another cluster represented data points preceding a cleaning job. The cluster labels reveal that not all cleaning activities are equally effective. Further analysis could quantitatively compare the effectiveness of mechanical versus chemical cleaning of the heat exchangers. Nonetheless, developing a maintenance plan that combines both cleaning methods appears beneficial.

The proposed framework is effective in automatically labelling time-series data from geothermal facilities and can allow scientists and engineers to develop a data story that can enrich the vast amount of data recorded in power plants worldwide. These data annotations can open up more applications of machine learning and other data-driven methods in the geothermal industry, promoting a more efficient and safe production of renewable energy.

Acknowledgement

This work was possible through the New Zealand Ministry of Business, Innovation and Employment (MBIE) through the Reversing Carbon Emissions in Geothermal Energy Industry – Template for Emissions – Intensive Industries project funds (UOAX2211).

The authors wish to acknowledge the use of New Zealand eScience Infrastructure (NeSI) high-performance computing facilities, consulting support and training services as part of this research. New Zealand's national facilities are provided by NeSI and funded jointly by NeSI's collaborator institutions and through the Ministry of Business, Innovation & Employment's Research Infrastructure programme. URL https://www.nesi.org.nz.

REFERENCES

Abrasaldo, P. M. B., Zarrouk, S. J., & Kempa-Liehr, A. W. (2024). A systematic review of data analytics applications in above-ground geothermal energy operations. Renewable and Sustainable Energy Reviews, 189, 113998. https://doi.org/10.1016/j.rser.2023.113998

Akiba, T., Sano, S., Yanase, T., Ohta, T., & Koyama, M. (2019). Optuna. Proceedings of the 25th ACM SIGKDD International Conference on Knowledge Discovery & Data Mining, 2623–2631. https://doi.org/10.1145/3292500.3330701

Ann Candido, C. S., & Zarrouk, S. J. (2017). Scaling Mitigations for the Binary Plant Vaporizer: Upper Mahiao, the Philippines. Proceedings 39th New Zealand Geothermal Workshop. https://www.geothermal-energy.org/pdf/IGAstandard/NZGW/2017/123_Zarrouk-Final_.pdf

Box, G. E. P., Jenkins, G. M., Reinsel, G. C., & Ljung, G. M. (2016). Time Series Analysis : Forecasting and Control (5th ed.). John Wiley & Sons, Inc.

Brown, K. (2011). Antimony and Arsenic Sulfide Scaling in Geothermal Binary Plants. Proceedings International Workshop on Mineral Scaling, 103–106. https://www.geothermal-energy.org/pdf/IGAstandard/WPRB/2011/15_Brown.pdf

Buster, G., Siratovich, P., Taverna, N., Rossol, M., Weers, J., Blair, A., Huggins, J., Siega, C., Mannington, W., Urgel, A., Cen, J., Quinao, J., Watt, R., & Akerley, J. (2021). A New Modeling Framework for Geothermal Operational Optimization with Machine Learning (GOOML). Energies, 14(20), 6852. https://doi.org/10.3390/en14206852

Calinski, T., & Harabasz, J. (1974). A dendrite method for cluster analysis. Communications in Statistics - Theory and Methods, 3(1), 1–27. https://doi.org/10.1080/03610927408827101

Christ, M., Braun, N., Neuffer, J., & Kempa-Liehr, A. W. (2018). Time Series FeatuRe Extraction on basis of Scalable Hypothesis tests (tsfresh – A Python package). Neurocomputing, 307, 72–77. https://doi.org/10.1016/j.neucom.2018.03.067

Ciriaco, A. E., Zarrouk, S. J., Downward, A., McDowell, J., & Mannington, W. (2022). Experimental design for estimating the power potential of the Wairakei geothermal field, New Zealand: A retrospective analysis. Geothermics, 104, 102443. https://doi.org/10.1016/j.geothermics.2022.102443

Cook, D. (2016). Practical machine learning with H2O (1st ed.). O'Reilly Media, Incorporated.

Davies, D. L., & Bouldin, D. W. (1979). A Cluster Separation Measure. IEEE Transactions on Pattern Analysis and Machine Intelligence, PAMI-1(2), 224–227. https://doi.org/10.1109/TPAMI.1979.4766909

Fulcher, B. D. (2017). Feature-based time-series analysis. Feature Engineering for Machine Learning and Data Analytics, 87–116. https://doi.org/10.48550/arxiv.1709.08055

Johnston, J. H., Borrmann, T., Schweig, M., Cairns, M. J., Fraser, H. P., & Aljohani, S. (2020). INTEGRATION OF THE CALCIUM SILICATE (CASIL) TECHNOLOGY INTO GEOTHERMAL POWER GENERATION TO PREVENT SILICA DEPOSITION. Proceedings 42nd New Zealand Geothermal Workshop. https://www.geothermal-energy.org/pdf/IGAstandard/NZGW/2020/076.pdf

Kennedy, A., Nash, G., Rattenbury, N. J., & Kempa-Liehr, A. W. (2021). Modelling the projected separation of microlensing events using systematic time-series feature engineering. Astronomy and Computing, 35. https://doi.org/10.1016/j.ascom.2021.100460

Krieger, M., Kurek, K. A., & Brommer, M. (2022). Global geothermal industry data collection: A systematic review. Geothermics, 104, 102457. https://doi.org/10.1016/j.geothermics.2022.102457

Ledésert, B. A., Hébert, R. L., Mouchot, J., Bosia, C., Ravier, G., Seibel, O., Dalmais, É., Ledésert, M., Trullenque, G., Sengelen, X., & Genter, A. (2021). Scaling in a Geothermal Heat Exchanger at Soultz-Sous-Forêts (Upper Rhine Graben, France): A XRD and SEM-EDS Characterization of Sulfide Precipitates. Geosciences, 11(7), 271. https://doi.org/10.3390/geosciences11070271

Mroczek, E., Graham, D., Siega, C., & Bacon, L. (2017). Silica scaling in cooled silica saturated geothermal water: Comparison between Wairakei and Ohaaki geothermal fields, New Zealand. Geothermics, 69, 145–152. https://doi.org/10.1016/j.geothermics.2017.05.006

Muller, L., Gill, J. S., Rodman, D., Brown, K., & Robinson, R. (2015). Control of Metal Sulfide Deposits in Geothermal Binary Plants. Proceedings World Geothermal Congress. https://www.geothermal-energy.org/pdf/IGAstandard/WGC/2015/27046.pdf

Murty, M. N., & Devi, V. S. (2015). Introduction to Pattern Recognition and Machine Learning (Vol. 5). Co-Published with Indian Institute of Science (IISc), Bangalore, India. https://doi.org/10.1142/8037

Okoroafor, E. R., Smith, C. M., Ochie, K. I., Nwosu, C. J., Gudmundsdottir, H., & (Jabs) Aljubran, M. (2022). Machine learning in subsurface geothermal energy: Two decades in review. Geothermics, 102, 102401. https://doi.org/10.1016/j.geothermics.2022.102401

Pedregosa F., Varoquaux, G., Gramfort, A., Michel, V., Thirion, B., Grisel, O., Blondel, M., Prettenhofer, P., Weiss, R., Dubourg, V., Vanderplas, J., Passos, A., Cournapeau, D., Brucher, M., Perrot, M., & Duchesnay, E. (2011). Scikit-learn: Machine Learning in Python. Journal of Machine Learning Research, 12, 2825–2830. http://jmlr.org/papers/v12/pedregosa11a.html

Penot, C., Martelo, D., & Paul, S. (2023). Corrosion and Scaling in Geothermal Heat Exchangers. Applied Sciences, 13(20), 11549. https://doi.org/10.3390/app132011549

Rousseeuw, P. J. (1987). Silhouettes: A graphical aid to the interpretation and validation of cluster analysis. Journal of Computational and Applied Mathematics, 20(C), 53–65. https://doi.org/10.1016/0377-0427(87)90125-7

Simmons, S., Jarvis, L., Dempsey, D., & Kempa-Liehr, A. W. (2021). Data Mining on Extremely Long Time-Series. IEEE International Conference on Data Mining Workshops, ICDMW, 2021-December, 1057–1066. https://doi.org/10.1109/ICDMW53433.2021.00137

Taverna, N., Buster, G., Huggins, J., Rossol, M., Siratovich, P., Weers, J., Blair, A., Siega, C., Mannington, W., Urgel, A., Cen, J., Quinao, J., Watt, R., & Akerley, J. (2022). Data Curation for Machine Learning Applied to Geothermal Power Plant Operational Data for GOOML: Geothermal Operational Optimization with Machine Learning. PROCEEDINGS, 47th Workshop on Geothermal Reservoir Engineering. https://pangea.stanford.edu/ERE/pdf/IGAstandard/SGW/2022/Taverna.pdf

Teh, H. Y., Wang, K. I.-K., & Kempa-Liehr, A. W. (2021). Expect the Unexpected: Unsupervised Feature Selection for Automated Sensor Anomaly Detection. IEEE Sensors Journal, 21(16), 18033–18046. https://doi.org/10.1109/JSEN.2021.3084970

Thain, I. A., & Carey, B. (2009). Fifty years of geothermal power generation at Wairakei. Geothermics, 38(1), 48–63. https://doi.org/10.1016/j.geothermics.2008.12.004

Yanagisawa, N. (2015). Case Study of Calcium Carbonate Scale at EGS and Hot Spring Binary System. Proceedings World Geothermal Congress. https://www.geothermal-energy.org/pdf/IGAstandard/WGC/2015/27013.pdf

Zarrouk, S. J., Woodhurst, B. C., & Morris, C. (2014). Silica scaling in geothermal heat exchangers and its impact on pressure drop and performance: Wairakei binary plant, New Zealand. Geothermics, 51, 445–459. https://doi.org/10.1016/j.geothermics.2014.03.005

FORGE Geothermal Project Modeling using Phase Field Finite-Element

Ahmed G. Almetwally*, Mary F. Wheeler*, and Robert K. Podgorney[#]

***Center of Subsurface Modeling, The University of Texas at Austin, Austin, Texas, USA**

[#] Idaho National Laboratory, Idaho Falls, Idaho, USA

Keywords

FORGE, EGS, Phase Field, Enriched Galerkin, Fracture Modeling

ABSTRACT

Modeling field-scale Enhanced Geothermal Systems (EGS) is challenging due to complex fluid flow, heat transfer, and rock mechanics interactions. Existing numerical methods like finite difference (FD), Discrete Fracture Network (DFN), and coupled Finite Element Method (FEM) with finite volume (FV) simulators fall short in accurately capturing EGS complexities. This paper introduces a phase-field model for fracture initiation and propagation in EGS, coupled with the enriched Galerkin method for flow and energy equations. Implemented in the MOOSE (Multiphysics Object Oriented Simulation Environment) framework, this approach is validated through analytical, laboratory, and field-scale simulations, notably for the FORGE geothermal project, showcasing improved accuracy and computational efficiency in EGS modeling.

1. Introduction

Numerical simulation plays a critical role in understanding and optimizing Enhanced Geothermal Systems (EGS) (Figure 1). Complex 3D models are routinely used to simulate these systems, with ongoing research continuously improving modeling techniques (Pardalos et al., 2001). However, EGS presents unique challenges. Simulators need to explicitly represent fractures, account for stress-induced changes in fracture aperture, and model the interplay between fluid flow and thermal effects within fractures (Sanyal et al., 2000). Researchers are actively developing advanced tools to address these complexities. For instance, Xing et al. (2015) present a supercomputer simulation tool that can visualize microseismic events and integrate geological data for detailed fluid flow simulations (H. Xing et al., 2015). The importance of accurate fracture representation is further emphasized by Ilyasov et al. (2009), who highlight recent advancements in seismic processing and fluid/thermal flow simulations for fractured systems (Ilyasov et al., 2009). These advancements underscore the need for integrating various modeling approaches to capture the multifaceted dynamics of EGS.

The Department of Energy's FORGE initiative aims to revolutionize Enhanced Geothermal Systems (EGS) technology by utilizing a dedicated field laboratory near Milford, Utah (Allis et al., 2019; Moore, 2019). This site, characterized by crystalline granitoid rocks overlaid with sedimentary and volcanic deposits, presents an ideal environment for developing and testing EGS

in hot, dry rock formations (Nielson et al., 1986). The Utah FORGE project represents a critical effort in EGS development (R. K. Podgorney et al., 2020). Here, hydraulic fracturing is used to create reservoirs within granite formations for geothermal energy extraction (Nadimi et al., 2020). Accurately simulating these complex fracture networks is essential for optimizing well stimulation strategies and predicting reservoir performance. The referenced studies (Janiga et al., 2022; Xing et al., 2021; Mindygaliyeva et al., 2023; Kumar et al., 2023; Cao and Sharma, 2023; McClure et al., 2024; Riahi et al., 2019; Wu et al., 2020) showcase a range of numerical methods, each with its strengths and limitations (Cao et al., 2023; Janiga et al., 2022; Kumar et al., 2023; M McClure et al., n.d.; Mindygaliyeva et al., n.d.; Riahi et al., 2019; Wu et al., 2020; P. Xing et al., 2021). A key challenge lies in finding the right balance between computational efficiency and the ability to capture the intricate details of the fracture network. Discrete Fracture Network (DFN) approaches (Cao and Sharma, 2023; Riahi et al., 2019) offer detailed representations, potentially exceeding 7,000 fractures, but struggle with scalability, especially for large-scale Utah FORGE simulations lacking extensive pre-existing fracture network data (Cao et al., 2023; Riahi et al., 2019). Additionally, DFN methods may require substantial supporting geological data for robust predictions. While Distinct Element Methods (DEM) like Xing et al.'s (2021) XSite™ offer exceptional accuracy in simulating fracture interactions, their computational demands can be prohibitive for large-scale reservoir simulations (P. Xing et al., 2021).

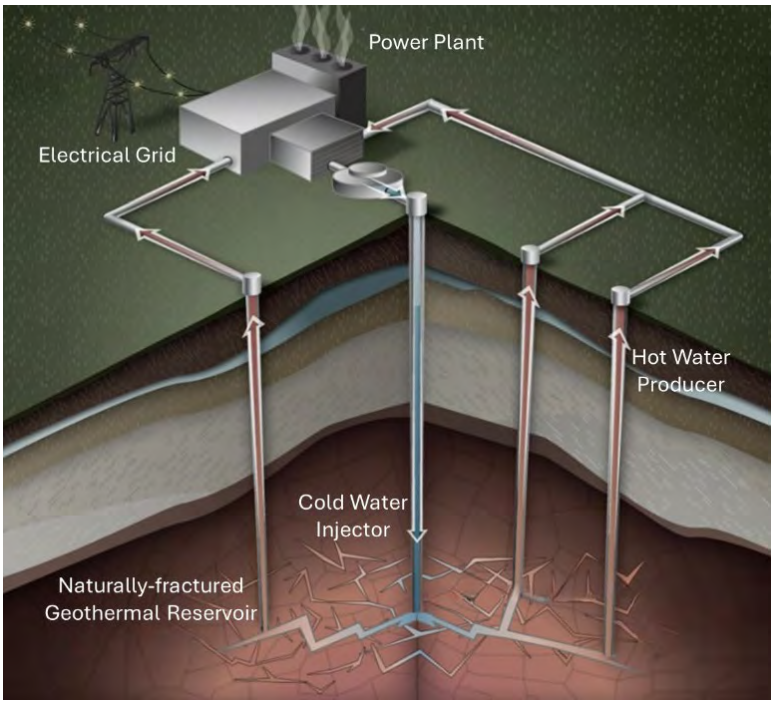

Figure 1: Schematic representation of EGS (U.S. Department of Energy, 2016)

Conversely, computationally efficient finite difference methods (Mindygaliyeva et al., 2023) may struggle to accurately represent the complex geometries of these fractured systems (Mindygaliyeva et al., n.d.). McClure et al.'s (2024) work, aiming for a fully integrated approach, highlights the challenges of model calibration, particularly when dealing with complex systems like the Utah FORGE reservoir (M McClure et al., n.d.). Here, extensive field data integration, beyond planar fractures, might be necessary to achieve reliable results that match recorded microseismicity data. Figure 2 illustrates two limitations encountered when applying numerical methods to simulate the

complex fracture network of the FORGE geothermal project. (a) Highly Detailed DFN Model: This image depicts a Discrete Fracture Network (DFN) model (Cao and Sharma, 2023) with a potentially excessive number of fractures (Cao et al., 2023). (b) Planar Fracture Model with Limited Applicability: This image represents a coupled planar mechanics model with a reservoir model used for stage 3 of the fracturing job (McClure et al., 2024) (Mark McClure, 2023). This method may not be applicable to earlier stages (stages 1 & 2) due to its limitations in capturing complex fracture geometries. Additionally, calibrating such models can be challenging, particularly when attempting to match observed microseismic data beyond planar fractures.

This paper introduces a phase-field finite-element framework for modeling field-scale EGS that addresses the aforementioned challenges. The framework employs a diffusive formulation for thermoporoelasticity to model changes in petrophysical properties based on fracture propagation, ensuring smoother mass and energy transfer (A G Almetwally et al., 2023b). We utilize enriched Galerkin discretization for flow and energy to accurately capture sharp discontinuities at fracture-matrix interfaces with improved computational efficiency with fewer degrees of freedom (Ahmed G Almetwally et al., 2023). By enriching the continuous Galerkin (CG) basis functions with discontinuous piecewise-constants, the enriched Galerkin (EG) discretization effectively captures these discontinuities while ensuring local mass and energy conservation. The framework also incorporates field-scale phase-field finite element modeling, eliminating the need for complex mesh manipulation and enabling seamless representation of fracture evolution (A G Almetwally et al., 2023a). Additionally, a fixed-stress split decoupling technique, combined with specialized solvers, significantly accelerates simulation times (Wheeler et al., 2020). Finally, the framework employs localized mesh refinement around evolving fracture zones, reducing computational costs for large-scale simulations (Ahmed G Almetwally et al., 2024).

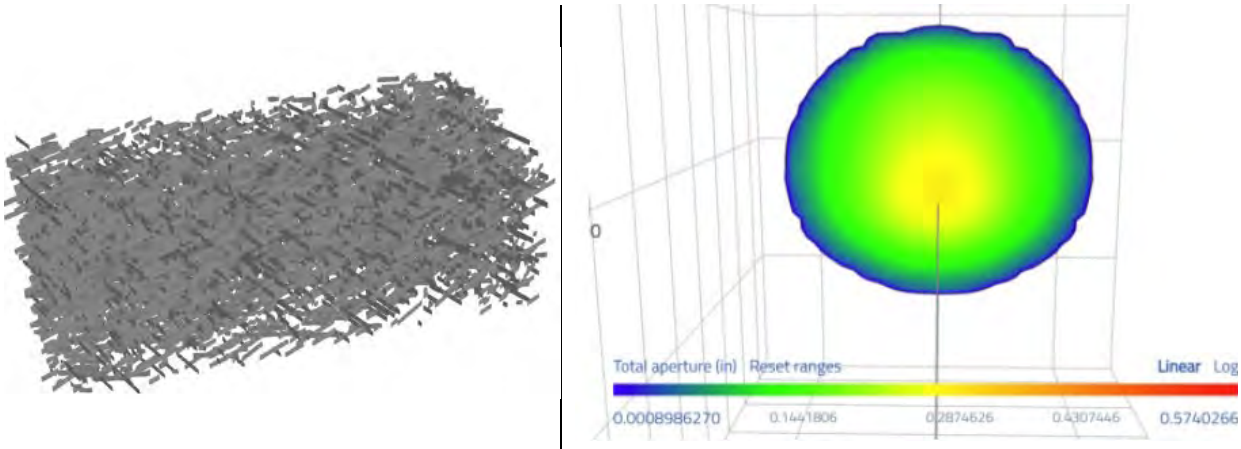

a. Highly Detailed DFN Model (Cao et al., 2023): offers high detail but may not scale for large domains with limited fracture data.

b. Planar Fracture Model with Limited Applicability (Mark McClure, 2023): struggles with complex geometries and early-stage calibration.

Figure 2: Challenges in numerical modeling of the Utah FORGE reservoir: a trade-off between complexity and scalability

2. Model Formulation

The mathematical formulation represents a dynamic fracture model for porous media, integrating thermo-poroelasticity theory and phase-field finite-element model (Li et al., 2021; Noii et al., 2019). This approach captures the coupled effects of fluid flow, heat transfer, deformation, and fracture initiation/propagation, enabling simulation under multiple physical processes (Kolesov et al., 2017; Mikelic et al., 2014). Building upon incremental thermodynamically consistent phase-field models (Amor et al., 2009; Francfort et al., 1998; Griffith et al., 1921; C Miehe et al., 2010; Christian Miehe et al., 2010), displacement (u) and phase-field (φ) variables are incorporated into the Mechanics framework for fracture modeling. We validated the model, in reference (A G Almetwally et al., 2023b)(Ahmed G Almetwally et al., 2023), through comparison with analytical thermoporoelasticity problems and experimental EGS observations. The model was validated against the KGD model for fracture length evolution and the Sneddon solution for fracture aperture under varying fluid pressure. Additionally, the model's capability to simulate EGS reservoir creation in granite was confirmed through comparison with a laboratory experiment by Frash et al. (2014), demonstrating an accurate prediction of breakdown pressure and fracture growth patterns.

2.1. Fracture Propagation Model

A coupled mechanics and phase-field energy functional (Equation 1) is employed to calculate the energy, ($E_\varepsilon(\mathbf{u}, p, \varphi)$), associated with displacement ($\mathbf{u}$), pressure (p), and phase-field (φ) variables (Wheeler et al., 2020). This function incorporates terms for elastic strain, surface energy, and fracture energy, accounting for internal forces (stress tensor), pressure-displacement coupling (Biot's coefficient), volumetric plastic dissipation, and work done by fluid pressure and thermal loading. The regularization parameter (ε) controls the fracture zone width, while the fracture energy (G_c) represents the energy required for crack surface creation. The phase-field variable influences the model through factors such as elastic property degradation and volume change. A degradation function ($g_D(\varphi)$) governs the impact of the crack on material elasticity. The stress tensor ($\sigma(\mathbf{u})$) and strain tensor ($e(\mathbf{u})$) model internal forces and deformation, respectively. Biot's coefficient (α) quantifies pressure-displacement coupling, while constants relating temperature to displacement are estimated based on reference (Noii et al., 2019). Fracture width is determined in relation to the phase field using a method proposed in (Wheeler et al., 2020). This involves computing the jump in normal displacements at the fracture boundary using an estimated normal vector derived from level set values of a specific fracture isoline. The fracture width is then calculated using the equation:

$$-\Delta w = \beta \left\| -2\mathbf{u} \cdot \frac{\nabla \varphi_{LS}}{\|\nabla \varphi_{LS}\|} \right\|_{L^\infty(\Lambda)}$$

where Δw is the Laplacian of w, β is a constant chosen to ensure a smooth profile, and $\nabla \varphi_{LS}$ refers to the gradient of the level set function defining the fracture boundary.

$$\underbrace{E_\varepsilon(\mathbf{u},p,\varphi)}_{Energy\ Functional} = \underbrace{\int_\Lambda \frac{1}{2} g_D(\varphi)\sigma(\mathbf{u}):e(\mathbf{u})dx}_{Strain\ Energy} - \underbrace{\int_{\partial A} \tau\cdot\mathbf{u}dS}_{External\ Load} + \underbrace{-\int_\Lambda (\alpha-1)\varphi^2 p\nabla\cdot\mathbf{u}dx + \int_\Lambda (\varphi^2\nabla p)\mathbf{u}dx}_{Hydraulic\ Work} + \underbrace{-\int_\Lambda (\alpha_T+\mathrm{C})\varphi^2 T\nabla\cdot\mathbf{u}dx + \int_\Lambda (\varphi^2\,\mathrm{C}\,\nabla T)\mathbf{u}dx}_{Thermal\ Work} + \underbrace{G_c\int_\Lambda \left(\frac{1}{2\varepsilon}(1-\varphi^2)+\frac{\varepsilon}{2}|\nabla\varphi^2|\right)dx}_{Fracturing\ Energy} \quad (1)$$

2.1. Fluid Flow and Energy Balance Model

The cracked reservoir body, denoted as Λ, is divided into three distinct domains for computational fluid flow analysis: the reservoir, fracture, and transition domains (Wheeler et al., 2020). These domains, identified by $\Omega_R(t)$, $\Omega_F(t)$, and $\Omega_t(t)$ respectively, are distinguished based on the phase-field value φ, corresponding to $\varphi \le 0$, $\varphi \ge 1$, and $0< \varphi <1$. To standardize the material parameters, auxiliary quantities χ_r and χ_f are introduced as follows:

$$\begin{cases} \chi_r = 1, \chi_f = 0 & \text{in } \Omega_R(t) \\ \chi_r = 0, \chi_f = 1 & \text{in } \Omega_F(t) \\ \chi_r = \frac{1-\varphi}{1-0}, \chi_f = \frac{\varphi-0}{1-0} & \text{in } \Omega_t(t) \end{cases} \quad (2)$$

Material constants (density ρ, permeability κ, viscosity η, Biot coefficient α_p, thermal expansion coefficient α_T, Biot modulus reciprocal c_p, heat capacity c_T, hydrothermal-coupling coefficient β, hydraulic conductivity k_p, thermal conductivity k_T) are then expressed uniformly as: $(\cdot) = (\cdot)_r\chi_r + (\cdot)_f\chi_f$.

Conservation of mass and momentum for fluid flow within the system is given by:

$$c_p\frac{\partial p}{\partial t} - \beta\frac{\partial T}{\partial t} + \alpha_p\,\chi_r\frac{\partial \mathrm{div}\,\boldsymbol{u}}{\partial t} - \mathrm{div}\left(k_p \mathrm{grad}\ p\right) = q_p \quad (3)$$

Conservation of energy is represented by:

$$c_T\frac{\partial T}{\partial t} - \beta T_0\frac{\partial p}{\partial t} + \alpha_T T_0\,\chi_r\frac{\partial \mathrm{div}\,\boldsymbol{u}}{\partial t} - \mathrm{div}\left(k_T\,\mathrm{grad}\,T + \alpha_c\,T\,k_p\,\mathrm{grad}\ p\right) = q_T \quad (4)$$

where α_c is the fluid heat convective capacity, T_0 is the initial temperature, f represents body forces, and q_p and q_T are fluid and heat sources, respectively. Coupling between energy, fluid flow, and solid mechanics is achieved through equations of state, source terms, the effective stress tensor, and changes in porosity, permeability, and thermal strains. The thermoporoelasticity system coupled with the phase field for fracture propagation is solved using the Enriched Galerkin scheme for energy/mass conservation and the Continuous Galerkin scheme for the mechanics' momentum balance, coupled with the flow problem through an iterative fixed-stress split scheme (Ahmed G Almetwally et al., 2023; Lee et al., 2016, 2017, 2018).

3. FORGE Project Field-Scale Simulation

Extensive subsurface data collection through deep exploratory wells has facilitated the development of a static finite-element model using the FALCON code; a MOOSE-based code for

modeling EGS (Gwynn et al., 2019) (R. Podgorney et al., 2021). This model integrates detailed 3D petrophysical properties (Table 1) and insitu equilibrium boundary conditions to simulate thermal, hydraulic, and mechanical behavior of the geothermal reservoir.

Table 1: Reservoir Rock Properties at the FORGE Site

Permeability	1.00E-18 m^2	Young's Modulus	6.50E+10 Pa
Porosity	1.00E-03	Drained Poisson's Ratio	0.3
Rock Grain Density	275 kg/m^3	Biot Coefficient	0.3
Specific Heat Capacity	790 J/kg K	Thermal Expansion Coefficient	6.00E-06
Grain Thermal Conductivity	3.05 W/m K	Fracture Toughness	0.72E6 Pa $m^{0.5}$

In April 2022, the FORGE team implemented a 3-stage fracture stimulation program (Forbes et al., 2019) (McLennan, 2022):

1. **Stage 1:** Involved identifying potential fracture initiation sites through jagged pressure patterns and microseismic event analysis, indicative of fracture activity.
2. **Stage 2:** Employed slickwater at a maximum rate of 35 bpm (5.56 m^3/min), monitored formation breakdown pressure, and conducted a hard shutdown to evaluate fracture behavior. This stage included flowback analysis at 4 bpm (0.64 m^3/min), with wellhead pressure dropping to 0 psi.
3. **Stage 3:** Utilized crosslinked polymer fluid at similar pump rates to Stage 2, introduced microproppant to enhance fracture geometry and sustain fracture conductivity. Microseismicity data from this stage provided critical insights into the fracture network's behavior.

The simulations, focusing on hydraulic fracture growth across all three stages, employed the EG-phase-field framework within the MOOSE platform to accurately capture the dynamic evolution of the fracture network. Figures 3 to 6 offer insights into the simulation of the fracture propagation and pressure responses during the hydraulic stimulation stages of the FORGE geothermal project. Figure 3 illustrates the refined finite element mesh used in the simulations, which captures the complexity of fracture propagation, particularly around the injection points, ensuring an accurate representation of the evolving fracture network. It shows how modeling FORGE reservoir mesh (multiple kilometers scale) is refined to capture the natural fracture network (sub-meter scale). Figures 4 and 5 compare simulated and observed pressure responses during the three-stage hydraulic stimulation program. The simulations accurately capture the pressure step-up and step-down responses, despite an acceptable degree of misalignment.

Noting that the recorded shut-in pressure is set to be zero after each stage and concatenated for simpler visualization versus a stabilized simulated reservoir pressure after each stage. The pressure misalignment is caused by grid resolution (the finer the mesh, the better the match) and operational differences such as the sudden pump shut-in during Stage 2 also. This misalignment is also referred to the idealized injection schedules used in simulations versus the actual injection procedure. The simulated pressure data are colored with the phase field variable, in Figure 4, indicating the extent of fracture opening at the injection nodes, providing a clear visual correlation between pressure

changes and fracture propagation. Figure 5 provides a 3D representation of the fracture initiation at Stage 1, the activation of natural fractures during Stage 2, and the development of a purely hydraulic fracture in Stage 3. Figure 6 showcases the correlation between the simulated fracture propagation and the recorded microseismic events for each stimulation stage. The fracture mesh propagating in the yellow grid aligns precisely with the locations of the recorded microseismicity for the three stages, validating the model's ability to predict fracture growth patterns accurately. In Stage 1, the initiation and final extension of fractures are clearly depicted, while Stage 2 shows the extension of fractures activated during Stage 1. Stage 3 demonstrates further hydraulic fracture propagation, closely matching the microseismic data. This rigorous validation against microseismicity and pressure data confirms the model's accuracy in predicting reservoir behavior under field-scale operational scenarios. By providing a reliable predictive tool, this model significantly enhances the efficiency and effectiveness of EGS development, enabling informed decision-making and optimization of stimulation strategies.

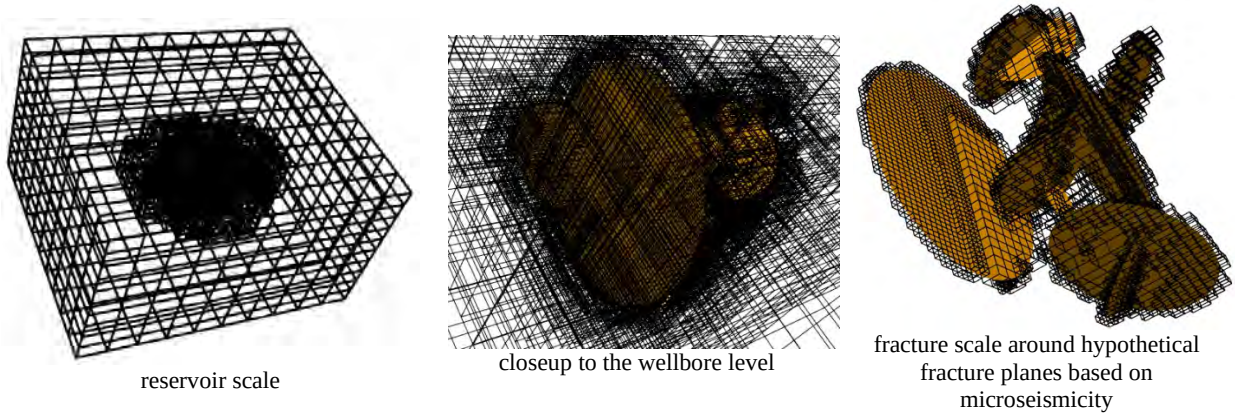

Figure 3: Refined finite element mesh from reservoir-scale to fracture-scale employed for the coupled thermo-hydro-mechanical modeling of the FORGE EGS reservoir.

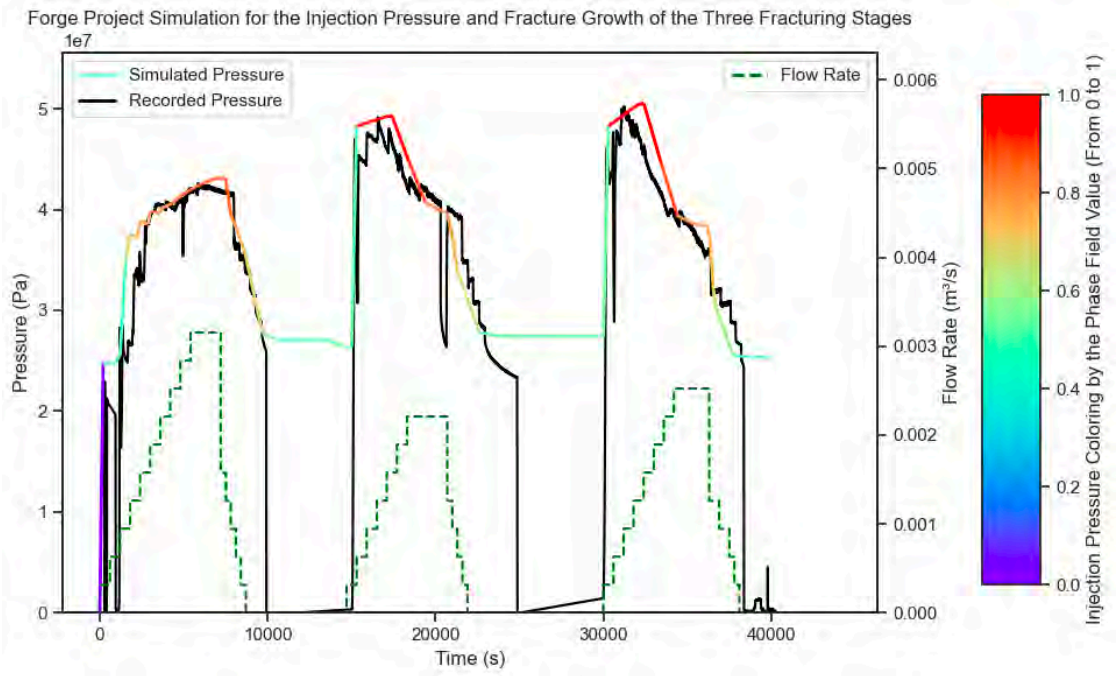

Figure 4: Comparison of simulated and observed wellhead pressure responses during the three-stage hydraulic stimulation program at the FORGE site

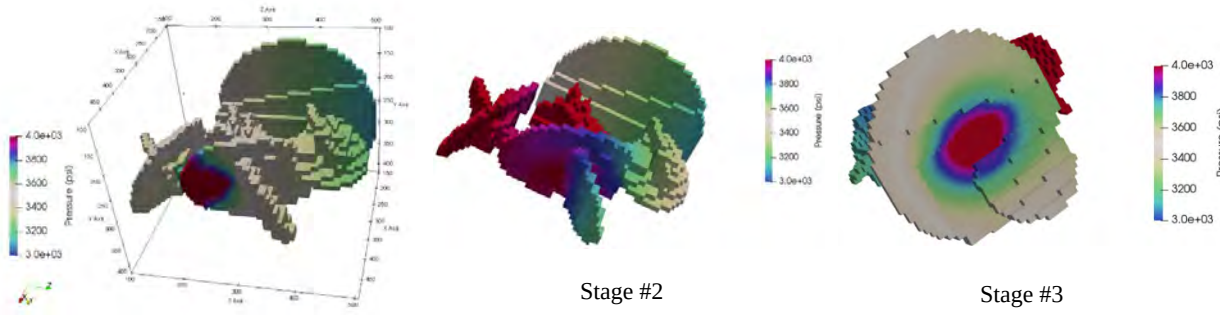

Stage #1 Stage #2 Stage #3

Figure 5: propagation pressure modeled using the EG-phase-field framework during the three stimulation stages at the FORGE site..

Microseismicity is represented for the three stages as follows: stage #1 in blue, stage #2 in green, and stage #3 in red.

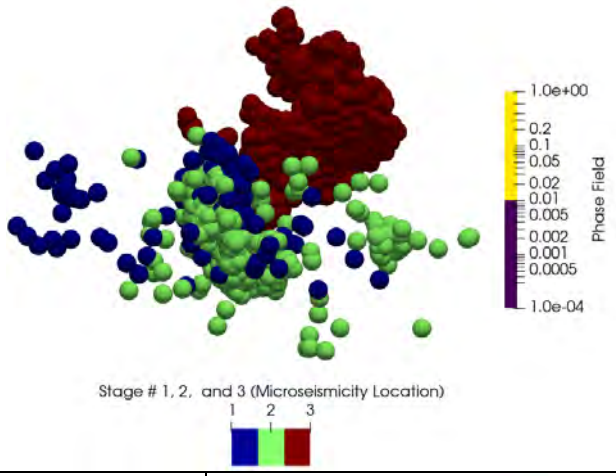

Stage #1

fracture initiation

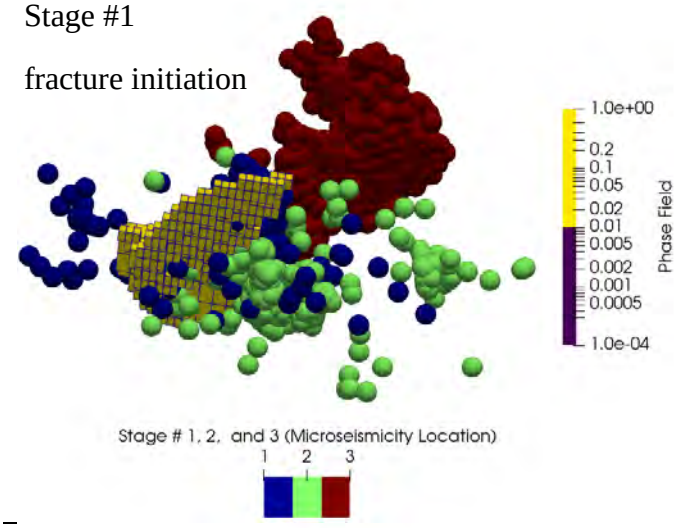

Stage #1

final extension

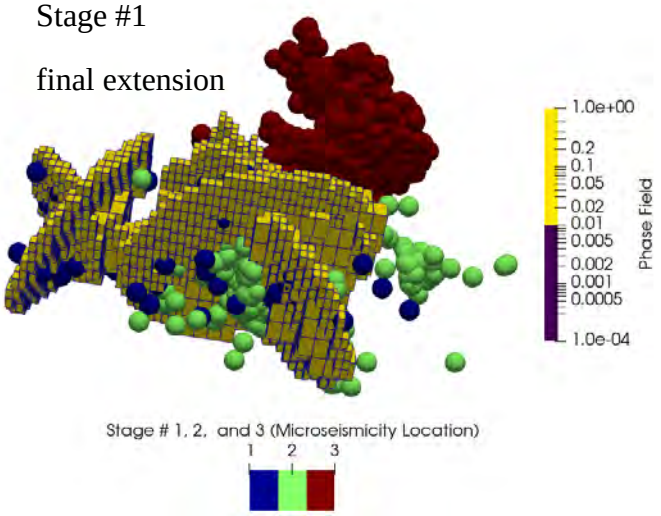

Stage #2 extension for activated fractures through stage #1

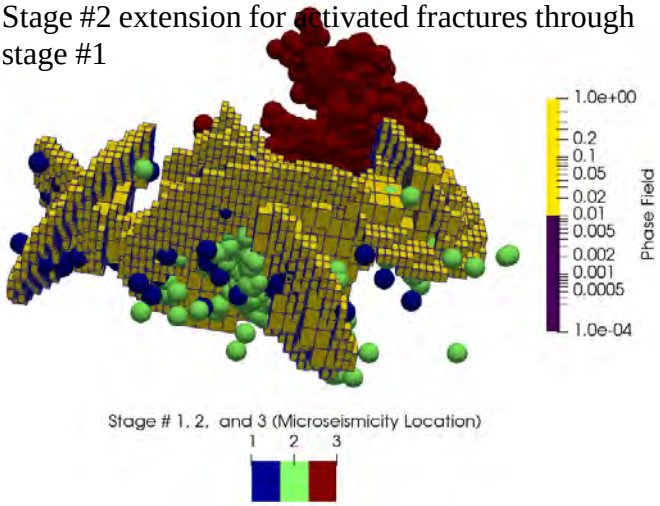

Stage #3

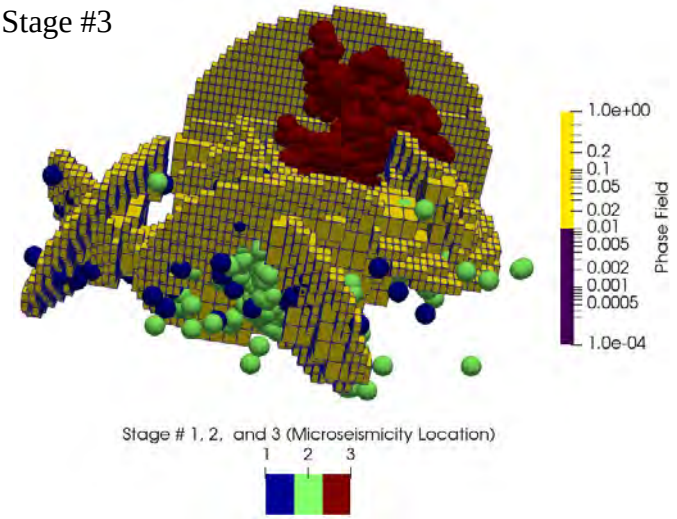

Figure 6: Sequential images showing fracture propagation (yellow grids) and recoded microseismic events: (1) initial fracture initiation (Stage 1, blue), (2) final fracture extension (Stage 1, blue), (3) activated fractures (Stage 2, green), (4) purely hydraulic fractures (Stage 3, red), and (5) overlay of all stages.

4. Conclusion

This study presents a novel phase-field finite-element framework for modeling field-scale Enhanced Geothermal Systems (EGS), addressing the challenges of complex fluid flow, heat transfer, and rock mechanics interactions. By incorporating a diffusive thermoporoelasticity formulation, enriched Galerkin discretization, and field-scale phase-field modeling, the framework accurately captures fracture propagation and its impact on reservoir behavior. The successful application to the FORGE geothermal project, validated against analytical solutions, laboratory experiments, and field data, demonstrates the framework's effectiveness in simulating fracture initiation, propagation, and interaction. The integration of a fixed-stress split decoupling technique and localized mesh refinement further enhances computational efficiency, making it a valuable tool for large-scale EGS simulations. This research contributes to advancing EGS technologies by providing a robust and efficient modeling approach for optimizing reservoir performance and geothermal energy extraction.

Acknowledgment

This work is supported through the Idaho National Laboratory Directed Research & Development Program (LDRD) under the Department of Energy Idaho Operations Office contract no. 23A1070-117FP. The U.S. Government retains and the publisher, by accepting the article for publication, acknowledges that the U.S. Government retains a nonexclusive, paid-up, irrevocable, worldwide license to publish or reproduce the published form of this manuscript or allow others to do so, for U.S. Government purposes.

REFERENCES

Allis, R. G., Gwynn, M., Hardwick, C., Kirby, S., & Moore, J. (2019). Thermal characteristics of the Roosevelt Hot Springs system, with focus on the FORGE EGS site. In R. Allis & J. N. Moore (Eds.), Geothermal characteristics of the Roosevelt Hot Springs system and adjacent FORGE EGS site, Milford, Utah. Utah Geological Survey Miscellaneous Publication 169 (p. 24). Utah Geological Survey. doi: https://doi.org/10.34191/MP-169-D

Almetwally, A G, & Wheeler, M. (2023a). Modeling Frac-hits Using Reservoir Geomechanics and Phase Field Finite Element. In 57th U.S. Rock Mechanics/Geomechanics Symposium (p. ARMA-2023-0869).

Almetwally, A G, & Wheeler, M. (2023b). 3D Modeling of Fracture Propagation Using Coupled Variational Phase Field and Porous Media Multiphysics. In 57th U.S. Rock Mechanics/Geomechanics Symposium (p. ARMA-2023-0872).

Almetwally, Ahmed G, Podgorney, R., & Wheeler, M. F. (2023). Using Enriched Galerkin as an Energy and Mass Conservative Scheme for Simulating Thermoporoelasticity Problems. In SPE Reservoir Simulation Conference (p. D011S003R004). doi: 10.2118/212240-MS

Almetwally, Ahmed G, Wheeler, M. F., Gaston, D., & Podgorney, R. (2024). Physics-based Mesh Adaptivity and Independent Finite Element Discretization for Multiphysics Simulation. *Under Review*.

Amor, H., Marigo, J.-J., & Maurini, C. (2009). Regularized formulation of the variational brittle fracture with unilateral contact: Numerical experiments. *Journal of the Mechanics and Physics of Solids, 57*(8), 1209–1229. doi: https://doi.org/10.1016/j.jmps.2009.04.011

Cao, M., & Sharma, M. M. (2023). Geomechanical Modeling of Fracture Growth in Naturally Fractured Rocks: A Case Study of the Utah FORGE Geothermal Site. *Proceedings of the 11th Unconventional Resources Technology Conference*. doi: 10.15530/urtec-2023-3864731

Forbes, B., Moore, J. N., Finnila, A., Podgorney, R., Nadimi, S., & McLennan, J. D. (2019). Natural fracture characterization at the Utah FORGE EGS test site—discrete natural fracture network, stress field, and critical stress analysis. In R. Allis & J. N. Moore (Eds.), Geothermal characteristics of the Roosevelt Hot Springs system and adjacent FORGE EGS site, Milford, Utah. Utah Geological Survey Miscellaneous Publication 169 (p. 11). Utah Geological Survey. doi: https://doi.org/10.34191/MP-169-N

Francfort, G. A., & Marigo, J.-J. (1998). Revisiting brittle fracture as an energy minimization problem. *Journal of the Mechanics and Physics of Solids*, *46*(8), 1319–1342. doi: https://doi.org/10.1016/S0022-5096(98)00034-9

Griffith, A. A., & Taylor, G. I. (1921). VI. The phenomena of rupture and flow in solids. Philosophical Transactions of the Royal Society of London. Series A, Containing Papers of a Mathematical or Physical Character, 221(582–593), 163–198. doi: 10.1098/rsta.1921.0006

Gwynn, M., Allis, R., Hardwick, C., Jones, C., Nielsen, P., & Hurlbut, W. (2019). Compilation of Rock Properties from FORGE Well 58-32, Milford, Utah. In A. R. & J. N. Moore (Eds.), Geothermal characteristics of the Roosevelt Hot Springs system and adjacent FORGE EGS site, Milford, Utah: Utah Geological Survey Miscellaneous Publication 169 (p. 38). Utah Geological Survey. doi: https://doi.org/10.34191/MP-169-L

Ilyasov, M., Ilyasov, M., Ostermann, I., Ostermann, I., Punzi, A., Punzi, A., & Punzi, A. (2009). Modeling Deep Geothermal Reservoirs: Recent Advances and Future Problems. *Null*. doi: null

Janiga, D., Kwaśnik, J., & Wojnarowski, P. (2022). Utilization of Discrete Fracture Network (DFN) in Modelling and Simulation of a Horizontal Well-Doublet Enhanced Geothermal System (EGS) with Sensitivity Analysis of Key Production Parameters. *Energies*. doi: 10.3390/en15239020

Kolesov, A., & Vabishchevich, P. (2017). *Numerical Solution of Thermoporoelasticity Problems*. doi: 10.1007/978-3-319-57099-0_47

Kumar, D., Liu, B., & Ghassemi, A. (2023). 3D Modeling of the Utah Forge Reservoir Stimulation with Proppant Transport and Deposition. *Day 2 Tue, October 17, 2023*. doi: 10.2118/214865-ms

Lee, S., Mikelić, A., Wheeler, M. F., & Wick, T. (2016). Phase-field modeling of proppant-filled fractures in a poroelastic medium. *Computer Methods in Applied Mechanics and Engineering*, *312*, 509–541. doi: https://doi.org/10.1016/j.cma.2016.02.008

Lee, S., & Wheeler, M. F. (2017). Adaptive enriched Galerkin methods for miscible displacement problems with entropy residual stabilization. *Journal of Computational Physics*, *331*, 19–37. doi: https://doi.org/10.1016/j.jcp.2016.10.072

Lee, S., & Wheeler, M. F. (2018). Enriched Galerkin methods for two-phase flow in porous media with capillary pressure. *Journal of Computational Physics*, *367*, 65–86. doi: https://doi.org/10.1016/j.jcp.2018.03.031

Li, P., Li, D., Wang, Q., & Zhou, K. (2021). Phase-field modeling of hydro-thermally induced fracture in thermo-poroelastic media. *Engineering Fracture Mechanics*, *254*, 107887. doi: https://doi.org/10.1016/j.engfracmech.2021.107887

McClure, M, Irvin, R., England, K., Mclennan, J., Petro, E.-K., & Llc, C. (n.d.). Numerical Modeling of Hydraulic Stimulation and Long-Term Fluid Circulation at the Utah FORGE Project. *Null*. doi: null

McClure, Mark. (2023). Calibration parameters required to match the Utah FORGE 16A (78)-32 stage 3 stimulation with a planar fracturing model. *Proceedings*.

McLennan, J. (2022). *Utah FORGE Well 16A (78)-32 Stimulation Data (April, 2022)*. USDOE Geothermal Data Repository (United States); Energy and Geoscience ….

Miehe, C, Welschinger, F., & Hofacker, M. (2010). Thermodynamically consistent phase-field models of fracture: Variational principles and multi-field FE implementations. *International Journal for Numerical Methods in Engineering*, *83*(10), 1273–1311. doi: https://doi.org/10.1002/nme.2861

Miehe, Christian, Hofacker, M., & Welschinger, F. (2010). A phase field model for rate-independent crack propagation: Robust algorithmic implementation based on operator splits. *Computer Methods in Applied Mechanics and Engineering*, *199*(45), 2765–2778. doi: https://doi.org/10.1016/j.cma.2010.04.011

Mikelic, A., Wheeler, M. F., & Wick, T. (2014). Phase-field modeling of pressurized fractures in a poroelastic medium. *ICES Report*, 14–18.

Mindygaliyeva, B., Uzun, O., Amini, K., Kazemi, H., & Fleckenstein, W. W. (n.d.). Assessment of Two Recent Hot Dry Rock Thermal Energy Production Projects. *Available at SSRN 4675948*.

Moore, J. (2019). *Utah FORGE: Phase 2C Topical Report*. Energy and Geoscience Institute at the University of Utah. doi: 10.15121/1578287

Nadimi, S., Forbes, B., Moore, J., Podgorney, R., & McLennan, J. D. (2020). Utah FORGE: Hydrogeothermal modeling of a granitic based discrete fracture network. *Geothermics*, *87*, 101853.

Nielson, D. L., Evans, S. H., & Sibbett, B. S. (1986). Magmatic structural, and hydrothermal evolution of the Mineral Mountains intrusive complex, Utah. *Geological Society of America Bulletin*, *97*, 765–777.

Noii, N., & Wick, T. (2019). A phase-field description for pressurized and non-isothermal propagating fractures. *Computer Methods in Applied Mechanics and Engineering*, *351*, 860–890. doi: https://doi.org/10.1016/j.cma.2019.03.058

Pardalos, P. M., O'Sullivan, M., O'Sullivan, M., Pruess, K., Pruess, K., Lippmann, M. J., & Lippmann, M. J. (2001). State-of-the-art of geothermal reservoir simulation. *Geothermics*. doi: 10.1016/s0375-6505(01)00005-0

Podgorney, R., Finnila, A., Simmons, S., & Mclennan, J. (2021). A Reference Thermal-Hydrologic-Mechanical Native State Model of the Utah FORGE Enhanced Geothermal Site. *Energies*, *14*, 4758. doi: 10.3390/en14164758

Podgorney, R. K., Simmons, S., Finnila, A., McLennan, J., Neupane, H., O'Brien, J., Elliott, J., Williams, B., & Poux, B. (2020). A Framework for Coordinated Earth and Numerical Modeling and Simulation of the Utah FORGE Site. *Proceedings World Geothermal Congress*, 1.

Riahi, A., Riahi, A., Pettitt, W., Pettitt, W., Damjanac, B., Damjanac, B., Varun, _, Varun, Blanksma, D., & Blanksma, D. (2019). Numerical Modeling of Discrete Fractures in a Field-Scale FORGE EGS Reservoir. *Rock Mechanics and Rock Engineering*. doi: 10.1007/s00603-019-01894-6

Sanyal, S. K., Sanyal, S. K., Butler, S. J., Butler, S. J., Swenson, D., Hardeman, B., Swenson, D., & Hardeman, B. (2000). REVIEW OF THE STATE-OF-THE-ART OF NUMERICAL SIMULATION OF ENHANCED GEOTHERMAL SYSTEMS. *Null*. doi: null

U.S. Department of Energy. (2016). *Enhanced Geothermal System (EGS) Fact Sheet.* Retrieved from https://www.energy.gov/sites/default/files/2016/05/f31/EGS Fact Sheet May 2016.pdf

Wheeler, M. F., Wick, T., & Lee, S. (2020). IPACS: Integrated Phase-Field Advanced Crack Propagation Simulator. An adaptive, parallel, physics-based-discretization phase-field framework for fracture propagation in porous media. *Computer Methods in Applied Mechanics and Engineering*, *367*, 113124. doi: https://doi.org/10.1016/j.cma.2020.113124

Wu, Y., Yu, X., Wang, S., Wang, C., & Winterfeld, P. (2020). Modeling Thermal-Hydrologic-Mechanical Processes for EGS Collab Thermal Circulation Tests Using Embedded Discrete Fracture Model. *Null*. doi: null

Xing, H., Xing, H., Liu, Y., Liu, Y., Gao, J., Gao, J., Chen, S., & Chen, S. (2015). Recent development in numerical simulation of enhanced geothermal reservoirs. *Journal of Earth Science*. doi: 10.1007/s12583-015-0506-2

Xing, P., Damjanac, B., Radakovic-Guzina, Z., Finnila, A., Podgorney, R., Moore, J. M., John, & McLennan. (2021). Numerical Simulation of Injection Tests at Utah FORGE Site. *Null*. doi: null

Separating Signals in Elevation Data Improves Supervised Machine Learning Predictions for Hydrothermal Favorability

Pascal D. Caraccioli[1,2,5], Stanley P. Mordensky[3], Jacob DeAngelo[4], Erick R. Burns[4], John J. Lipor[1]

[1]Contractor to the U.S. Geological Survey, Portland, OR, 97201, USA

[2]Portland State University, Portland OR 97201, USA

[3]U.S. Geological Survey, Spokane, WA 99201, USA

[4]U.S. Geological Survey, Moffet Field CA 94035, USA

[5]Cornell University, Ithaca NY 14853, USA

Keywords

Machine learning, Geothermal, Nevada, XGBoost, Play fairway analysis, Feature engineering, Geothermal favorability

ABSTRACT

A recent study identified topography (land surface elevation above sea level) as an important input dataset (feature) for predicting the location of hydrothermal systems in the Great Basin in Nevada. Yet, topography is generally a result of more than one geological process and may consequently contain multiple distinct signals. For example, the geologic evolution of the Great Basin has produced both crustal thickening (i.e., regional-scale trends in elevation) and thinning via Basin and Range extensional faulting (i.e., valley-scale topographic relief). We postulate that these geologic processes may affect the occurrence of hydrothermal systems differently. Therefore, we separate the regional trend from the valley-scale signal in the Great Basin, and then use them separately to evaluate the importance of each as predictors for hydrothermal favorability.

Our prior work applying supervised machine learning (ML) using the data from the Nevada Machine Learning Project demonstrated that employing a training strategy that randomly selects negative training sites produces better performing models for predicting hydrothermal favorability than a training strategy that used expert-selected negatives. The models created using both training strategies exhibited a west-east geographic trend in the predictions for the favorability of hydrothermal resources. These models generally predicted higher favorability in western Nevada

and lower favorability in eastern Nevada. This west-east trend in predicted favorability correlates with elevation across the Great Basin, which trends higher from west to east.

By separating the original elevation feature into distinct features for *elevation trend* (i.e., regional-scale topography) and *detrended elevation* (i.e., valley-scale or local relative topography), we find that models using the separated topographic signals consistently outperform competing models that use the original elevation feature. Although western Nevada still exhibits higher favorability than eastern Nevada, using separated signals for regional elevation and local structure reduces the west-east prediction trend in the region and emphasizes structures associated with hydrothermal upflow. This work emphasizes how carefully engineering features to represent geological conditions relevant to hydrothermal systems allows ML algorithms to detect important patterns for predicting hydrothermal resource favorability and leads to better model performance.

1. Introduction

Hydrothermal systems in the Great Basin, a prominent extensional province in the western United States, are generally controlled by basin-bounding faults located in actively subsiding basins (Faulds et al., 2011; Faulds and Hinz, 2015) with many systems having no easily identifiable surface manifestations (i.e., many systems are *blind*; Coolbaugh et al., 2007). Yet, changes in valley-scale topography (i.e., relative positions of basins and adjacent mountain ranges) serve as an indicator of geologic structures that may be associated with hydrothermal upflow.

The Nevada Machine Learning Project (NVML; Brown et al., 2020; Faulds et al., 2021a; Smith, 2021; Faulds et al., 2024), aimed to identify hidden geothermal resources in the Great Basin. Using datasets compiled under the Nevada Play Fairway Analysis (Faulds et al., 2017; Faulds et al., 2021b) as well as data collected specifically for NVML, NVML fit an artificial neural network (ANN) to predict the presence or absence of hydrothermal resources. The NVML research team labeled 83 of the 1,728,000 250-m square cells as positive (i.e., as having a known hydrothermal system) and 62 cells as negative (i.e., as not having a hydrothermal system). The remaining cells were unlabeled (i.e., the presence or absence of a hydrothermal system was and remains unknown). Eleven 250-m resolution evidence layer grids were used as input features (i.e., predictors or unassociated datasets) to the NVML ANN. Ten of these 11 input features consisted of quantitative data (e.g., elevation, strain rate, heat flow, and gravity). One of the 11 input features was engineered by experts as ellipses that were drawn around favorable structural settings. By using expert-knowledge to address fundamental challenges (e.g., selecting known sites without hydrothermal systems), the NVML project demonstrated that machine learning methods can be successfully used in geothermal resource evaluation.

Mordensky et al. (2023) conducted a similar study to predict hydrothermal favorability in the western United States, using data-driven ML approaches and data from the most recent U.S. Geological Survey (USGS) Geothermal Resource Assessment (Williams et al., 2008). Of the approximately 700,000 2-km square cells, 278 were known positives, but there were no known negatives provided in the Williams et al. (2008) data. Because hydrothermal systems are inherently sparse (i.e., < 99.9% of the study area), Mordensky et al. (2023) recognized that a random sample of the unlabeled cells could be labeled as negative with high confidence; therefore, they implemented a training strategy that treated a random sample of the unlabeled cells as negatives during the training process. The random selection of negative cells from unlabeled cells also addressed the mathematically problematic condition of severe class imbalance (i.e., having many

more sites without hydrothermal systems than with hydrothermal systems) that mired the ML algorithms. Mordensky et al. (2023) estimated the natural positive-negative ratio as approximately 1:700, thereby identifying the number of randomly selected negatives needed during fitting. Mordensky et al. (2023) demonstrated that data-driven ML algorithms could be used successfully to remove or minimize the need for expert feature-weighting decisions used previously in Williams et al. (2008).

Recent work by Caraccioli et al. (2023) compared the results of the NVML ANN to other less-complicated ML models (logistic regression and eXtreme Gradient Boosting [XGBoost; Chen and Guestrin, 2016]) using different strategies for selecting negatives (i.e., NVML versus Mordensky et al., 2023) and nearly the same input features. The single difference between the input features used in NVML compared to those in Caraccioli et al. (2023) is that Caraccioli et al. (2023) did not use the ellipses that were drawn around favorable structural settings. Caraccioli et al. (2023) elected not to use these expert-crafted ellipses which tended to dominate ML models because the NVML team had drawn the ellipses around the majority of the positives, arguably engineering each ellipse as a fuzzy (i.e., mathematically vague or imprecise) positive. The influence of the ellipses on the NVML ANN can be seen in Fig. 1.

By comparing the NVML strategy of expert-selected negatives to the strategy of randomly selecting negatives from Mordensky et al. (2023), Caraccioli et al. (2023) demonstrated that employing a training strategy that randomly selects negative training sites consistently produces better-predicting models when using the XGBoost algorithm, which is mathematically simpler than an ANN. Caraccioli et al. (2023) hypothesized that using only expert-selected negative sites may impart bias towards one or two types of negatives while there are really many conditions that can cause hydrothermal systems to be absent. Central to the work described herein, Caraccioli et al. (2023) identified elevation as the most important feature in the best-performing model; however, a low-high, west-east trend in elevation dominated the signal of that feature and contributed to similar favorability predictions at the tops of mountain ranges in the west as in the valley floors in the east. This finding seemed contrary to the geologic interpretation that proximity to relative valley-scale structure controls deep circulation pathways. As a result, Caraccioli et al. (2023) postulated that the contribution of the valley-scale topographic signal in the elevation feature was negligibly small compared with the regional signal. To allow for the possibility that valley-scale topography contains an important signal, we herein use the separate regional trend and valley-scale topographic data from DeAngelo et al. (2023) as separate features to test the importance of local topographic relief when predicting hydrothermal systems.

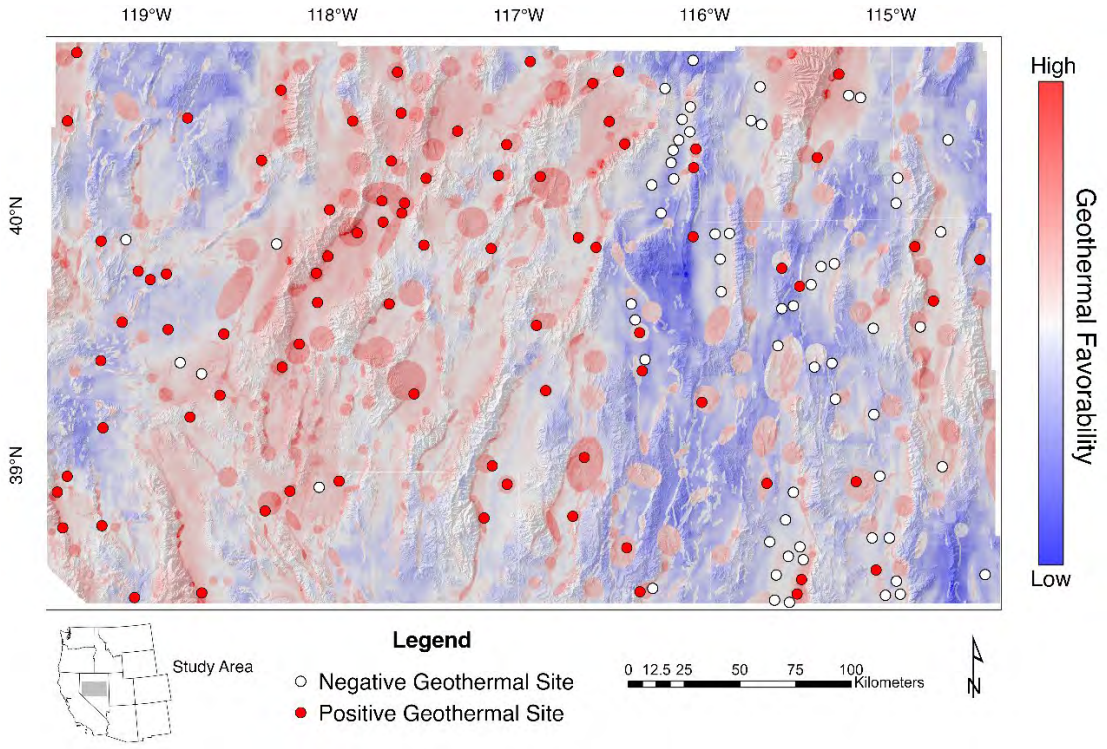

Figure 1: Nevada Machine Learning project (NVML) favorability map from Faulds et al. (2021a). White points are negative training/testing sites defined through expert selection. Red points are the positive sites (i.e., known hydrothermal systems). Favorability scores from the artificial neural network (ANN) have been normal score transformed for easy comparison with the results below from our study. Hillshade from USGS 3D Elevation Program (U.S. Geological Survey, 2019).

2. Methods

We compare XGBoost ML models using the original NVML features with models that replace the original elevation feature with two separate features (i.e., *elevation trend* and *detrended elevation* from DeAngelo et al., 2023). That is, although *elevation trend* and *detrended elevation* sum to the original elevation feature, we consider these two topographic features as two unique signals that we separate to inspect their value as predictors.

XGBoost is a boosted decision-tree ML algorithm in which a series of decision trees (i.e., estimators) predict probabilities for a cell being a positive or negative site (Chen and Guestrin, 2016). The cells are then formally classified as positive or negative by specifying a probability decision threshold. We use the commonly chosen decision threshold of 0.5 (see generally Fernández et al., 2018). ML algorithms (e.g., XGBoost, ANNs) calculate probabilities differently. Therefore, to allow the comparison of the new models with the NVML ANN, all favorability maps presented herein are the normal score transform (see generally Pyrcz and Deutsch, 2018) of the model predictions. Because the normal score transform preserves quantiles, the transformed prediction values are plotted as hydrothermal favorability, allowing for an easy comparison of regions of highest and lowest favorability.

In the remainder of this section, we briefly describe the data processing, exploratory data analysis, training strategies, hyperparameter optimization, and our method for comparing model performance.

2.1 Feature Selection

We use the features from the original NVML project and the separated regional and valley-scale elevation features engineered in DeAngelo et al. (2023). The original NVML ANN used 11 features. Ten of the 11 features were derived from interpolated maps of the following geologic properties: elevation, strain rate, slip rate, fault recency, gravity, slip and dilation tendency, seismic density, heat flow, magnetics, and distance to the nearest fault (Fig. 2). The eleventh feature was created by defining ellipses that contain geologic structures deemed by experts to be favorable for the occurrence of hydrothermal systems (i.e., known favorable structural setting; Fig. 3). Because the experts drew ellipses around known positives, the ML algorithms associate all areas within the ellipses with the occurrence of a hydrothermal system; therefore, the structural ellipses impart an implicit bias. The goal of this study is to predict favorable structural settings where a geologist has not had occasion to draw an ellipse, thus we remove the dataset with the structural ellipses.

Using the features from NVML and then by replacing the original elevation feature with the two separated elevation features from DeAngelo et al. (2023), we create two feature sets that can be compared. The first feature set (the Original Elevation Signal feature set) contains the same input features used in Caraccioli et al. (2023), corresponding to the 10 interpolated maps from NVML (i.e., original elevation, strain rate, slip rate, fault recency, gravity, slip and dilation tendency, seismic density, heat flow, magnetics, and fault). The second dataset (the Separated Elevation Signal feature set) replaces the original elevation feature with *elevation trend* and *detrended elevation*.

2.2 Exploratory Data Analysis

As part of exploratory data analysis, we inspect the linear correlation of the features using the Pearson correlation coefficient (see generally Lee Rodgers and Nicewander, 1988). Comparison of correlation allows us to see the pairwise linear relationships of the features (i.e., if the feature is unique or strongly correlated with one or more other features) and establish if two features represent similar signals. The Pearson correlation is a statistical measure that quantifies the linear relationship between two variables by providing values between -1 and 1, where -1 indicates a strong negative correlation, 1 indicates a strong positive correlation, and 0 indicates no correlation.

For each input feature, we compare the distributions of feature values for the NVML-labeled (i.e., positive and negative) sites to the full range of input-feature values to see if labeled sites mostly have low, intermediate, or high values relative to the unlabeled sites. To allow for an evaluation of whether labeled data are in discrete intervals within the larger range of the input feature values, we plot a cumulative distribution function (CDF) for every combination of features and labels (Fig. 4). When randomly sampling negatives and handling class imbalance, the CDF of the randomly sampled negatives should look similar to the CDF of all values of the input feature, because we are sampling most of the map area except the sparse positives.

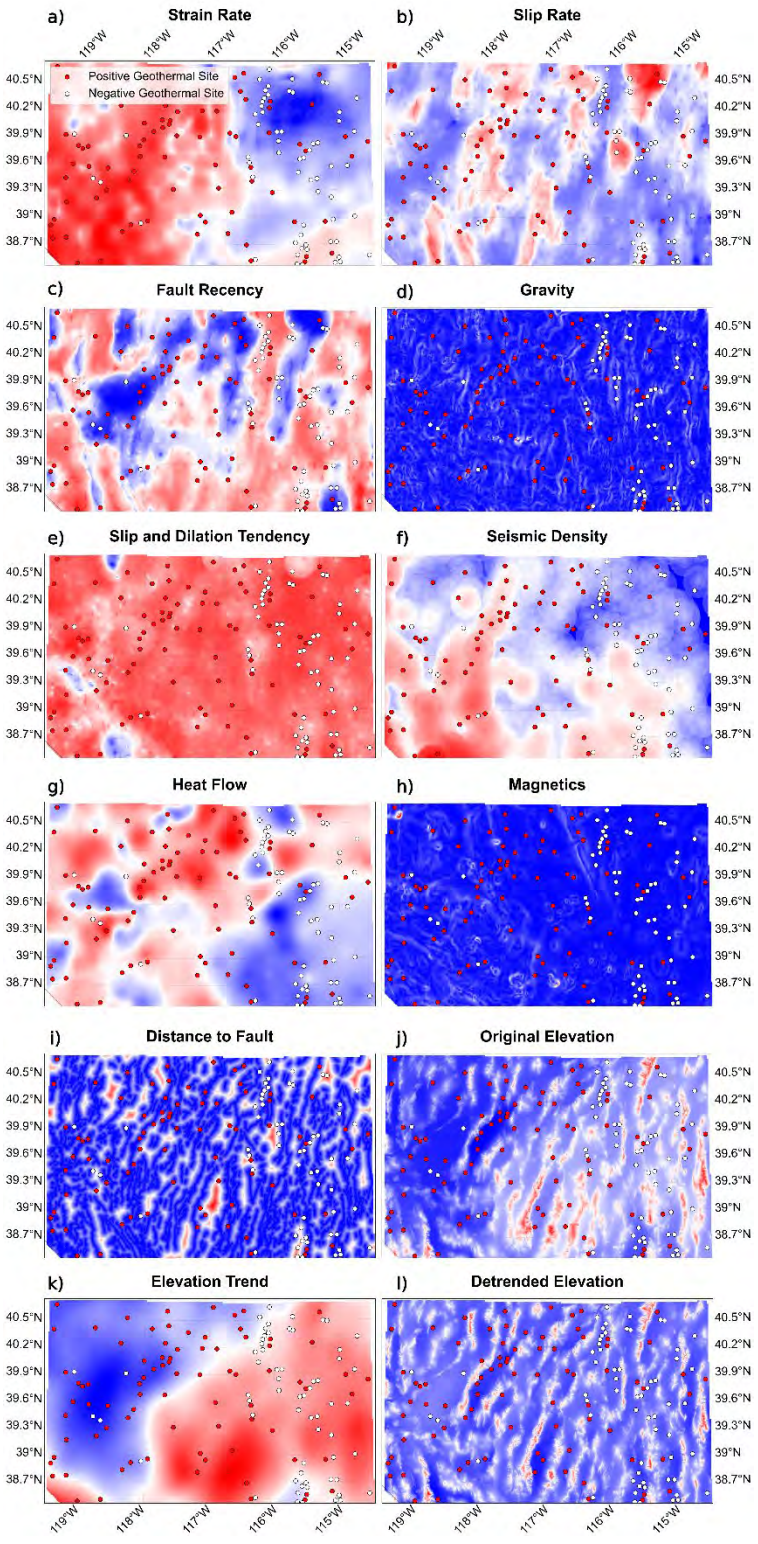

Figure 2: Maps of the ten standardized (i.e., unitless) Nevada Machine Learning project (NVML; Faulds et al., 2021a) features (a-j) and the DeAngelo et al. (2023) separated elevation input features (k, l) used for analysis herein. Blue depicts low values in the unitless scale. Red depicts high values in the unitless scale. White points are negative training/testing sites defined through expert selection. Red points are the positive sites (i.e., known hydrothermal systems).

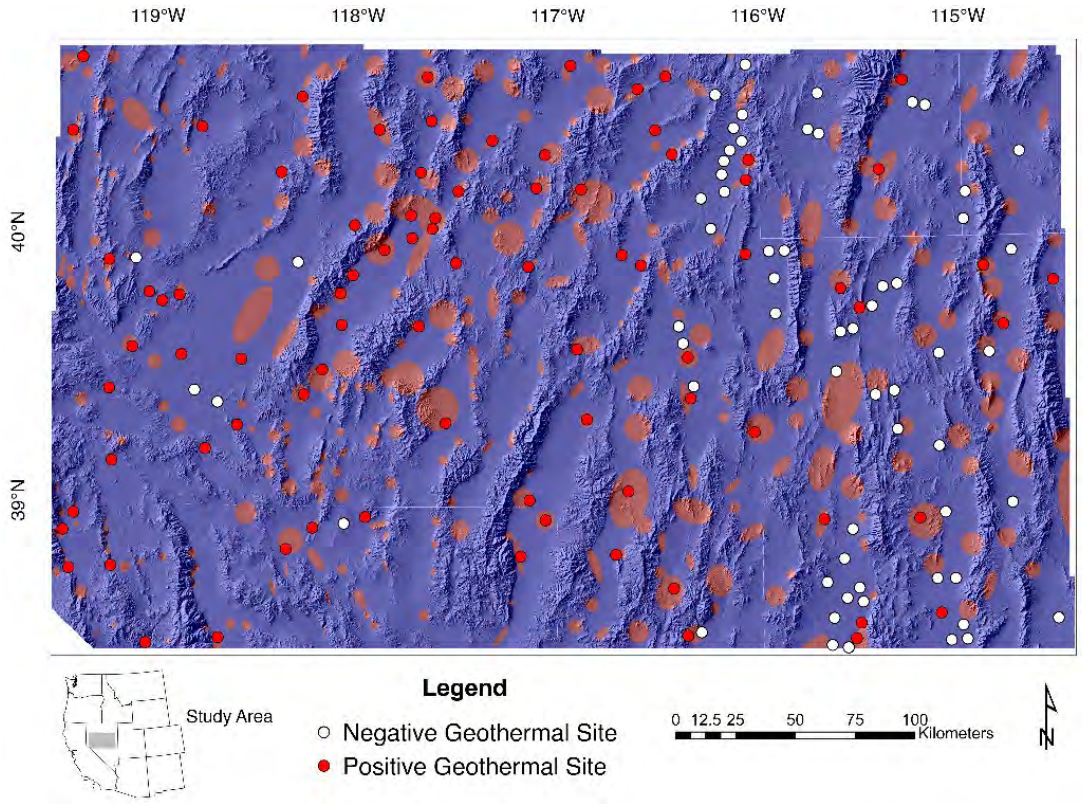

Figure 3: Map of the eleventh Nevada Machine Learning project (NVML) feature (favorable structural setting ellipses [red areas] from Faulds et al., 2021a) used for the artificial neural network (ANN) model (Fig. 1), but not used as an input feature for analyses herein. For strategy subsampling negative sites from unlabeled sites, negative sites were selected from areas outside of ellipses (i.e., blue area). White points are negative training/testing sites defined through expert selection. Red points are the positive sites (i.e., known hydrothermal systems). Hillshade from USGS 3D Elevation Program (U.S. Geological Survey, 2019).

2.3 Training Strategies

We implement two strategies for each training dataset: 1) the NVML training strategy; and 2) the training strategy from Mordensky et al. (2023) that implements random subsampling of negatives from unlabeled sites and accounts for class imbalance (the Natural Class Imbalance training strategy). The NVML strategy uses the same negative and positive sites from NVML (i.e., 62 negative sites and 83 positive sites). The Natural Class Imbalance strategy uses the same known positives as the NVML strategy, but randomly selects negative sites. Because we would like to minimize the possibility of randomly sampling and labeling an unlabeled positive site as negative, we choose to only select negatives from outside the favorable structural ellipses delineated by NVML (blue area in Fig. 3). We do this under the assumption that the highly sparse systems are less likely to occur without a favorable structural setting. Following Mordensky et al. (2023), we estimate that one in four hydrothermal systems have already been discovered in the study area, thereby approximating a roughly 1:5,100 positive-negative ratio. Although this estimate is approximate, Mordensky et al. (2023) demonstrated that the corresponding model predictions are insensitive within the expected range of uncertainty (see Mordensky et al. [2023] for complete details).

2.4 Hyperparameter Optimization

We optimize prediction performance by tuning four hyperparameters: class weight, number of estimators, maximum depth of estimators, and learning rate. Class weight is a way to correct for class imbalance. The greater the class weight, the greater the emphasis the model imparts on correctly identifying positive labels (i.e., the minority class) as positives at the expense of predicting negative labels as negatives (i.e., the majority class). The number of estimators specifies the number of decision trees (i.e., estimators). The maximum depth of estimators determines the number of levels in the estimators. The learning rate controls the amount of information communicated from a previous estimator to a new estimator. We leave the other parameters on XGBoost at the default settings found in the Python XGBoost, version 1.7.3 module as they have only a modest impact on performance (Chen and Guestrin, 2016).

We optimize the hyperparameters using the F1 score (Equation 1), a recommended metric for binary positive-unlabeled classifications (Bekker and Davis, 2020). We minimize bias resulting from any singular train-test split by conducting 60 80:20 train-test splits with five-fold cross-validation. For the Natural Class Imbalance strategy, we select new random negatives with each train-test split. We fit a final model using all the labeled data, the median optimal hyperparameters from the 60 train-test splits, and one last random sample of negative sites for the Natural Class Imbalance strategy.

$$F1\ Score = \frac{True\ Positives}{True\ Positives + \frac{1}{2}(False\ Positives + False\ Negatives)} \quad (1)$$

To test and prevent overfitting, we impose generalization loss early stopping (see generally Prechelt, 2002) in the validation subset of the training data during the five-fold cross-validation. With generalization loss early stopping, the fitting of new estimators stops immediately after the loss (a function that is penalized by decreased model performance) increases. We train a final model for each approach using the median estimator at which early stopping is engaged from the 60 train-test splits.

2.5 Measures of Feature Importance

For every modeling approach, we measure the relative importance of each input feature in making predictions using three measurements of feature importance: 1) sensitivity analysis using an F1 score; 2) sensitivity analysis using the area under the receiver operating characteristic curve (i.e., ROCAUC), and 3) Shapely Additive exPlanation (i.e., SHAP) values (see Mordensky et al. [2023] for a more detailed summary). To allow comparison between the different measures, each measure is min-max normalized to a zero-to-one scale. Using three different measures allows us to explore the variability between the measures.

2.6 Comparing Model Performance

To compare model performance, we perform a normal score transform on the predictions for each approach and compare the transformed distribution of predictions for the known positives with the transformed distribution of predictions for the unlabeled sites (see Mordensky et al. [2023] for additional details). Approaches with greater overlap in the distributions of predictions for known

positives and unlabeled sites indicate lower predictive skill than approaches with distinct distributions of predictions for the known positive and unlabeled sites.

3. Results

In this section, we briefly describe the input feature data, present favorability maps, and plot feature importance. We provide the median optimal hyperparameter values in Appendix A.

3.1 Exploratory Data Analysis

CDFs of feature values for the positive, NVML negative, and remaining unlabeled sites (essentially the distribution of a random sample of negatives) are shown in Fig. 4. The separation of cumulative distribution functions show that distributions are markedly different. The CDFs for the positive and negative sites generally bound that for the unlabeled sites with strain rate, seismic density, heat flow, fault distance, and slip rate, indicating that the corresponding features may have more value for separating positives from NVML negatives when used as predictors. Conversely, the CDFs for positive and unlabeled data show a greater difference in distribution for fault recency, fault distance, original elevation, *elevation trend*, and *detrended elevation*.

The Pearson correlation coefficient (Fig. 5) shows various degrees of correlation among the features with values from 0.78 to -0.59. Overall, strain rate is the feature most correlated with the greatest number of other features (e.g., *elevation trend* and seismic density; -0.59 and 0.64, respectively). *Elevation trend* and *detrended elevation* are minimally correlated. *Elevation trend* has similar correlation to the original elevation. *Detrended elevation* has poor correlation with all other datasets other than the original elevation.

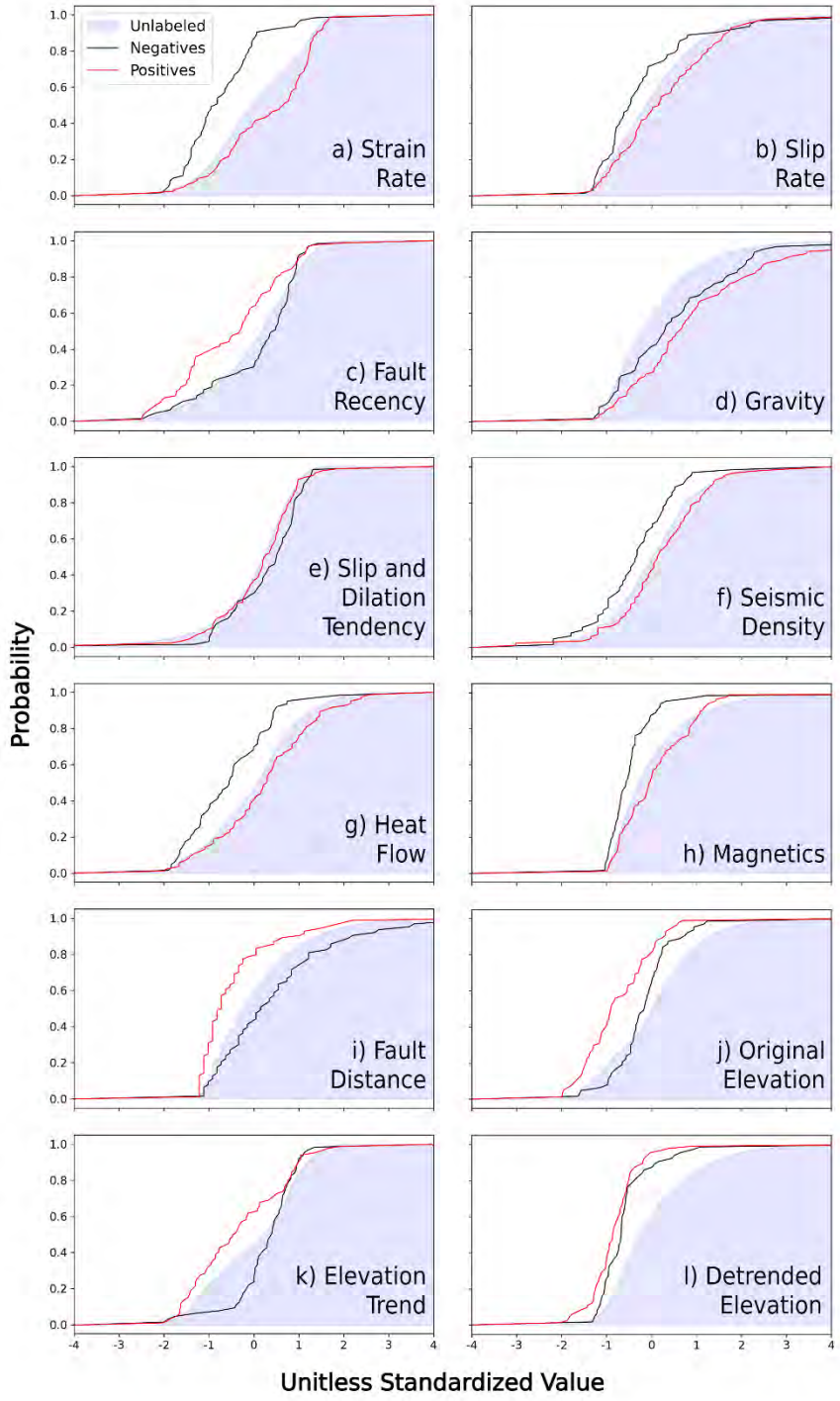

Figure 4: Cumulative distributions of the standardized features for the ten Nevada Machine Learning project (NVML) features (a-j) and the DeAngelo et al. (2023) separated elevation features (k, l). The shaded blue area corresponds to the unlabeled sites in NVML. The red line corresponds to positive-labeled sites in NVML. The black line corresponds to the negative-labeled sites in NVML. Separation of cumulative distribution functions show that distributions are markedly different, so a difference between the positive and negative lines implies the feature may be useful for discriminating between the positive and negative training sites.

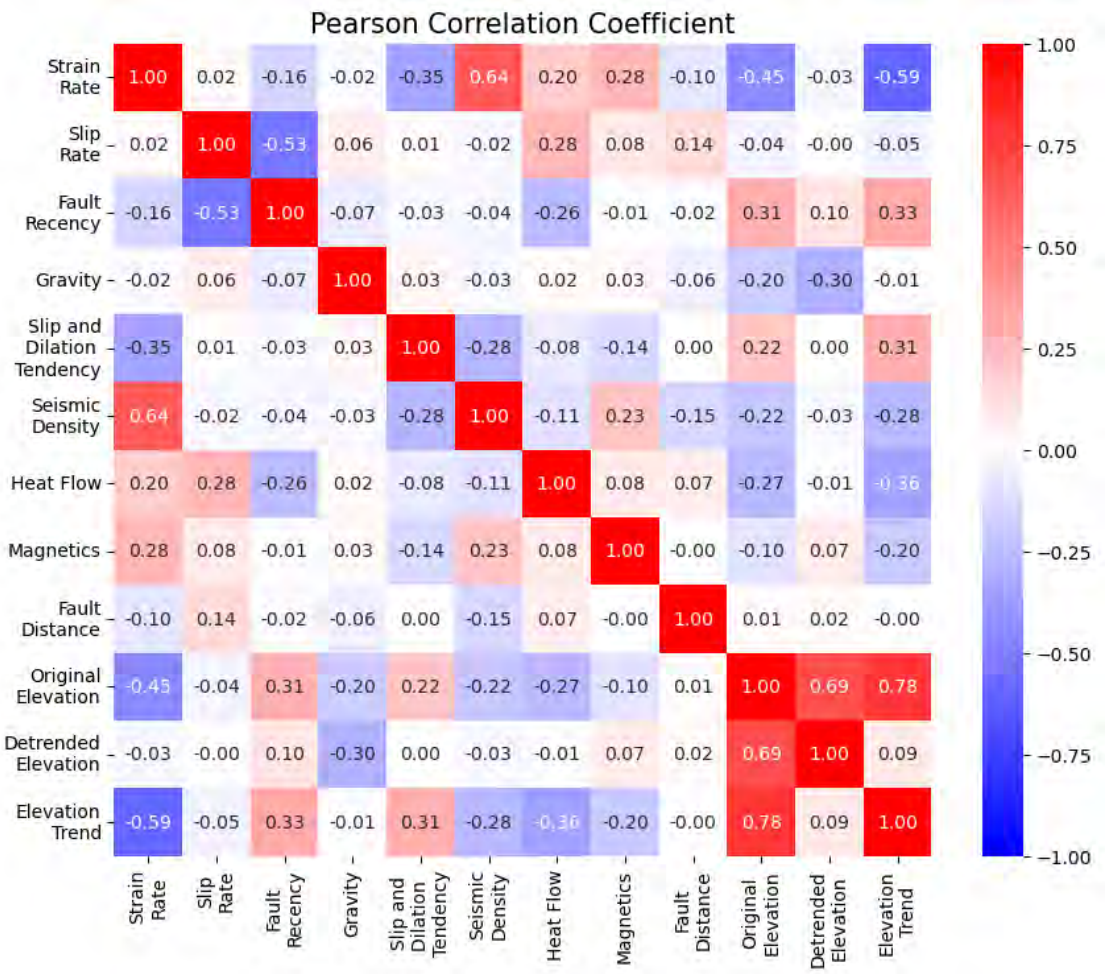

Figure 5: Pearson correlation matrix of the different features for all examples (i.e., sites or cells). Brighter colors indicate a higher absolute correlation between feature pairs. Blue indicates a negative correlation, and red indicates a positive correlation.

3.2 Favorability Maps

When using the Original Elevation Signal feature set there is a greater west-east trend between high and low favorability (compare Fig 6a to 6b, and 7a to 7b) in the models produced by both the strategy that used expert-selected negatives (i.e., NVML; Fig. 6) and the strategy that used randomly selected negatives (i.e., Natural Class Imbalance; Fig. 7). The model using the Separated Elevation Signal feature set and the randomly selected negatives (Fig. 7b) places greater emphasis on low relative topography (i.e., basins) when predicting high favorability.

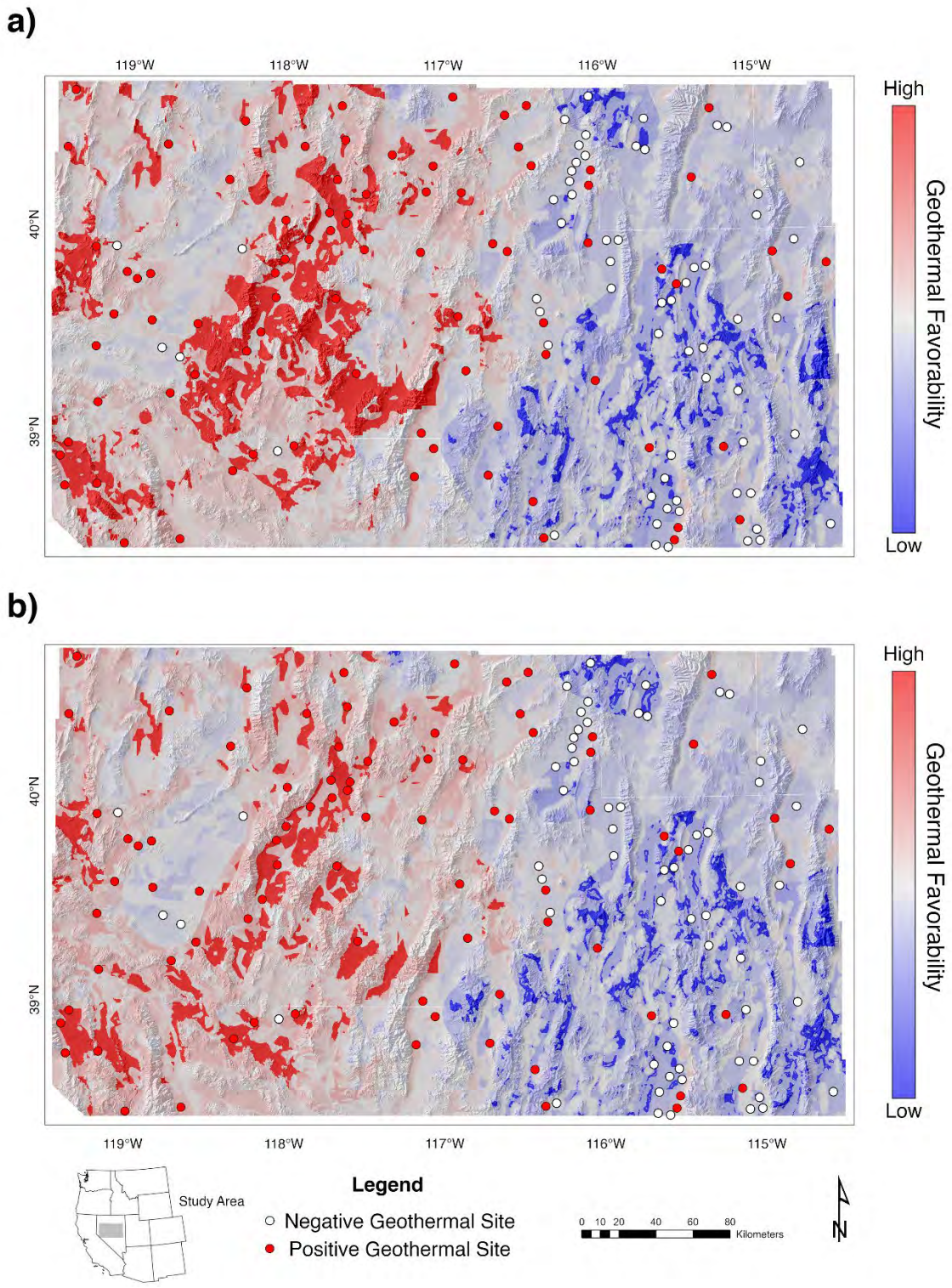

Figure 6: Geothermal favorability maps using the NVML negatives with a) the Original Elevation Signal feature set; and b) the Separated Elevation Signal (separated regional-scale and valley-scale elevation) feature set. Geothermal favorability is the normal score transform of XGBoost-computed probability. Hillshade from USGS 3D Elevation Program (U.S. Geological Survey, 2019).

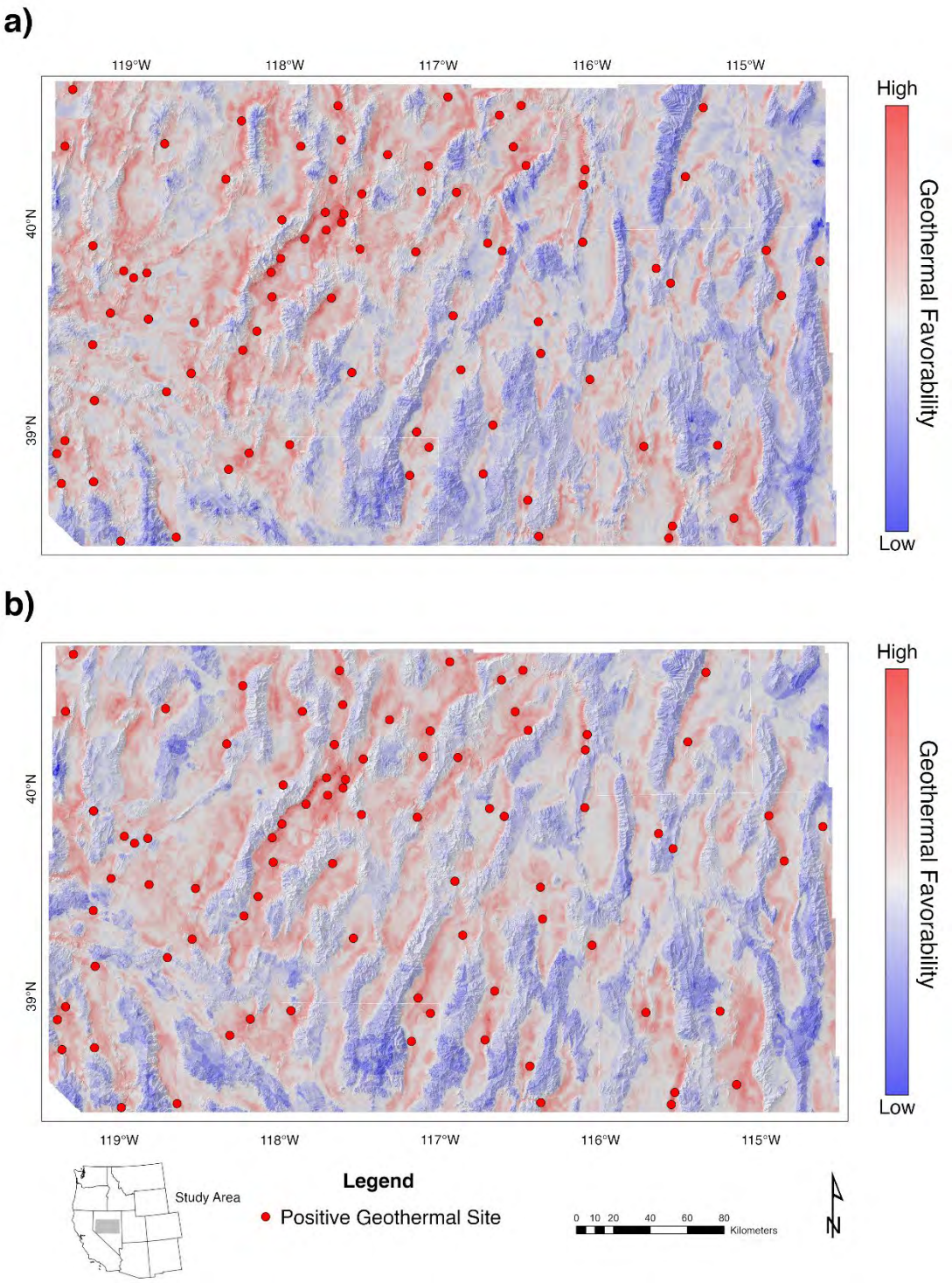

Figure 7: Geothermal favorability maps using random negatives and accounting for Natural Class Imbalance with a) the Original Elevation Signal feature set; and b) the Separated Elevation Signal (separated regional and valley-scale elevation) feature set. Because each random sampling produces different negatives, negatives are not shown. Geothermal favorability is the normal score transform of XGBoost-computed probability. Hillshade from USGS 3D Elevation Program (U.S. Geological Survey, 2019).

3.4 Feature Importance

The relative ranking of feature importance by different measures (Fig. 8) shows that models are primarily dominated by five features (i.e., strain rate, original elevation or *detrended elevation,* fault distance, and heat flow). For the NVML strategy (Figs. 8a, 8c), strain rate is the dominant feature for both models, regardless of the topographic dataset used. For the Natural Class Imbalance strategy (Figs. 8b, 8d), the most important feature varies depending on the input features used. If the model is trained using the feature set containing the original elevation, then the original elevation is the most important feature. Similarly, if the model is trained using the dataset containing *detrended elevation*, then *detrended elevation* ranks as the most important feature.

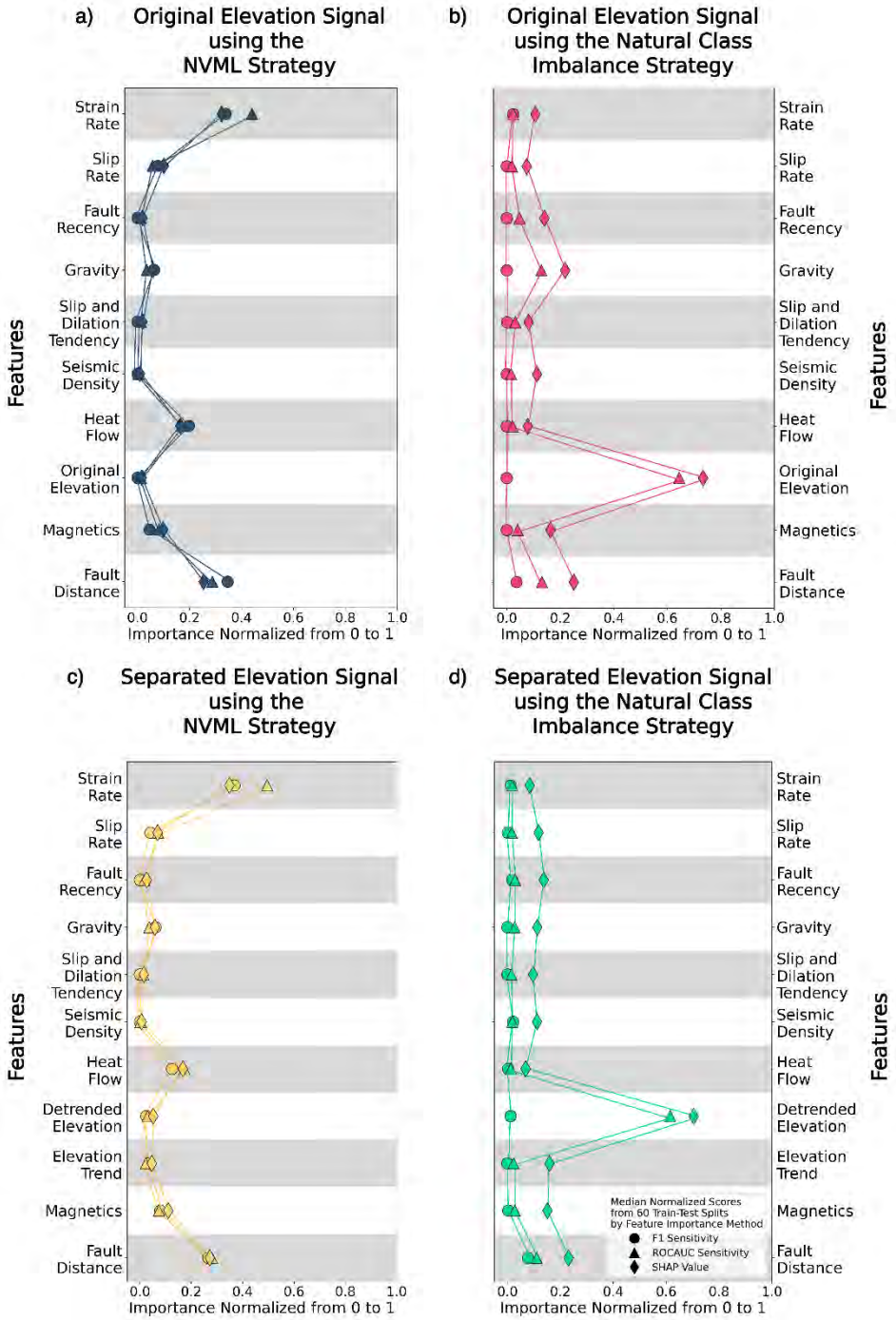

Figure 8: Median normalized feature importance values from the 60 train-test splits using a) the Original Elevation Signal feature set using the Nevada Machine Learning (NVML) strategy (blue); b) the Original Elevation Signal feature set using the Natural Class Imbalance strategy (red); c) the Separated Elevation Signal feature set using the NVML strategy (yellow); d) the Separated Elevation Signal feature set using the Natural Class Imbalance strategy (green). Abbreviation: ROCAUC (triangle) – Area Under the Receiver Operating Characteristic Curve; SHAP (diamond) – Shapely Additive explanation. The legend shown in 8d also applies to 8a, 8b, and 8c.

4. Discussion

All the resulting resource favorability maps (Figs. 6, 7) exhibit some degree of a west-east trend in favorability predictions, but the models using the separated signals for regional elevation and valley-scale elevation (Figs. 6b, 7b) fit models with spatially narrower predicted zones of high hydrothermal favorability that correspond to low relative topography and reduce the west-east trend in predicted favorability regardless of the dominant signal in the model (i.e., Fig. 8c, 8d). In the context of resource assessments, these narrower highly favorable areas minimize exploration efforts to smaller regions.

Recognizing that hydrothermal systems are sparse, we postulate that the models with the most known positives in the smallest area with the highest favorability are the best-performing models. A CDF of predictions for known positives serves as a summary of this information, such that CDF curves of predictions for known positives further to the right indicate that the predictions for the positives have higher favorability scores (Fig. 9). The models from each training strategy using the separated topographic features (i.e., *detrended elevation* and *elevation trend*) consistently outperform the models using the same respective training strategy and the original elevation. Despite the increased model performance when using separated topographic signals, utilizing a training strategy that randomly selects negatives (i.e., the Natural Class Imbalance strategy) rather than using expert-selected negatives (i.e., the NVML strategy) has a greater impact on improved model performance than using the Separated Elevation Signal feature set rather than the Original Elevation Signal feature set. The improvement in performance when using the Separated Elevation Signal feature set may be because adding a *detrended elevation* feature (i.e., valley-scale topographic signal) isolates relevant basin and range structural patterns and may contribute to the algorithm capturing patterns indicative of hydrothermal upflow (Faulds et al., 2011; Faulds and Hinz, 2015). We note, however, that in systems where basin and range faulting is not a controlling feature for hydrothermal circulation, detrending elevation may not be necessary or the scale of the trend may need to be tuned.

The models using the Natural Class Imbalance training strategy outperform NVML ANN regardless of which version of the feature is used, even though XGBoost is mathematically simpler than an ANN. The most important feature in the top-performing approach (i.e., *detrended elevation* in the approach using the Separated Elevation Signal feature set and the Natural Class Imbalance training strategy) shows that the most important signal for predicting hydrothermal systems we use is valley-scale topography. That signal is partially obfuscated when in the original elevation feature because of the inclusion of the signal for regional trend. The second-best performing model (i.e., the approach using the Natural Class Imbalance with the Original Elevation Signal feature set), assigns greater importance to the original elevation and gravity features compared to the top-performing model. This difference may arise from the higher pairwise correlation between gravity and *detrended elevation* (-0.3; Fig. 5) used in the top-performing model compared to the correlation between gravity and original elevation (-0.2; Fig. 5) used in the second-best performing model. Because *detrended elevation* better partially captures the signal for gravity than the original elevation feature, the model using the separated topographic signals lessens the overall contribution of gravity to the model. As the importance of gravity decreases when going from the approach using detrended elevation to the approach using original elevation, the importance of fault distance increases in two of the three metrics of feature importance, emphasizing the importance of local structure for predicting hydrothermal systems (Fig. 8b vs 8d). Hence, the mixed signal in the feature for original elevation with higher elevation in the east and lower

elevation in the west combined with the geospatial distribution of known positives (being primarily in the west) biases the model, causing the model to fail at identifying local topographic signals and predict high favorability at high local elevation (on ranges; Fig. 7a).

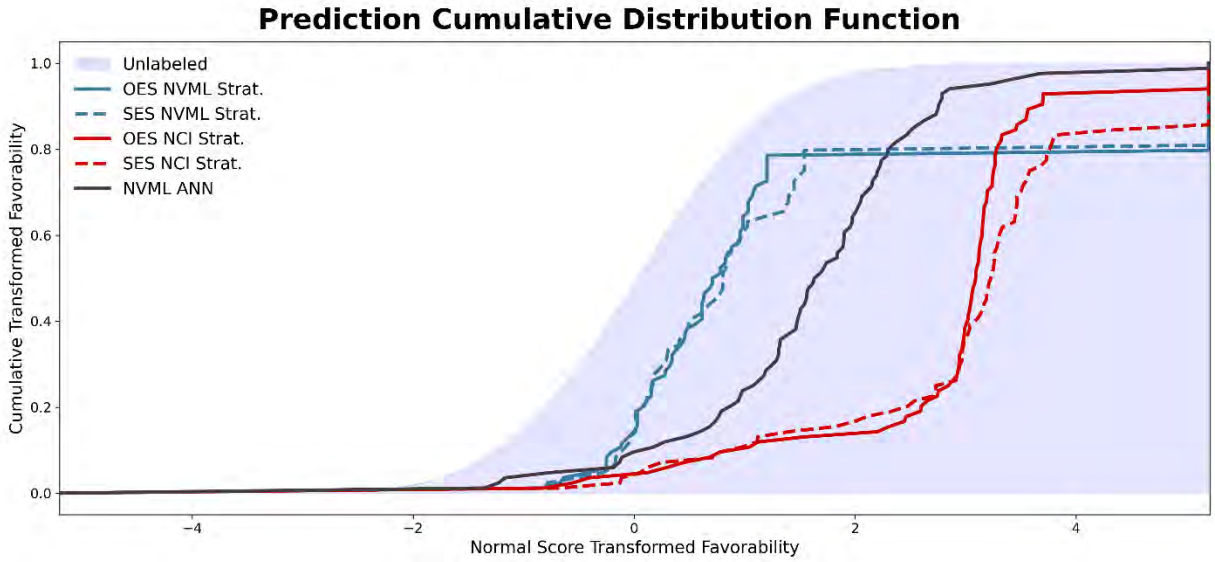

Figure 9: Cumulative distribution function (CDFs) of favorability scores for known geothermal systems relative to other map locations (i.e., unlabeled sites). Shaded blue provides the cumulative distribution of predictions for unlabeled sites. Lines represent the cumulative distributions of predictions for positive-labeled sites from the different approaches. Abbreviations: OES NVML Strat. (solid blue line) – Original Elevation Signal feature set using the Nevada Machine Learning strategy; SES NVML Strat. (dashed blue line) – Separated Elevation Signal feature set using the Nevada Machine Learning Strategy; OES NCI Strat. (solid red line) – Original Elevation Signal feature set using the Natural Class Imbalance; SES NCI Strat. (dashed red line) – Separated Elevation Signal feature set using the Natural Class Imbalance; NVML ANN (solid black line) - Nevada Machine Learning Artificial Neural Network.

The most important feature in the models using the NVML training strategy is strain rate, but adding the *detrended elevation* feature lessens the intensity of the west-east trend in the predicted hydrothermal favorability (Fig. 6). Although both models using the NVML training strategies rank last (Fig. 9), adding the *detrended elevation* feature improves model performance, demonstrating the importance of engineering input features that emphasize relevant geological information.

5. Conclusion

In this study, we evaluate the importance of regional-scale and valley-scale topographic relief as separated input features used to fit models that predict hydrothermal favorability. Separating the topographic signals allows the machine learning (ML) algorithm to fit better to the geological structures associated with hydrothermal systems in the Great Basin as evidenced by the models fit using the separated topographic signals consistently outperforming the models fit using the original topographic feature with the combined signals. Separating the topographic signals into two features also lessens the intensity of a west-east trend in the hydrothermal favorability maps. Hence, careful feature engineering through domain expertise with geothermal ML can deconvolute signals in geologic datasets and consequently improve model performance when predicting

favorability for hydrothermal resources. We explore the impact of separated topographic signals using two training strategies: 1) using expert-selected sites with no hydrothermal systems; and 2) using randomly selected sites from unlabeled sites as having no hydrothermal system. As is consistent in our prior works, the approach using randomly selected sites as having no hydrothermal system vastly outperforms the approach using expert-selected sites with no hydrothermal systems.

Acknowledgments

This work was done under contract to the U.S. Geological Survey. This work was supported by the Portland State University Louis Stokes Alliance for Minority Participation Program, Portland State University Institute for Sustainable Solutions Program, and the U.S. Geological Survey-Portland State University Partnership. Additional support for John Lipor was provided by the National Science Foundation award NSF CAREER CIF-2046175. This work was also supported by the U.S. Department of Energy's Office of Energy Efficiency and Renewable Energy (EERE), Geothermal Technologies Office (GTO) under Contract No. DEAC02-05CH11231 with Lawrence Berkeley National Laboratory, Conformed Federal Order No. 7520443 between Lawrence Berkeley National Laboratory and the U.S. Geological Survey (Award Number DE-EE0008105), and Standard Research Subcontract No. 7572843 between Lawrence Berkeley National Laboratory and Portland State University. This study was funded by the U.S. Geological Survey Energy Resources Program and the U.S. Department of Energy - Geothermal Technologies Office under award DE-EE0009254 to the University of Nevada, Reno for the INnovative Geothermal Exploration through Novel Investigations Of Undiscovered Systems (INGENIOUS). Any use of trade, firm, or product names is for descriptive purposes only and does not imply endorsement by the U.S. Government.

Appendix A: Hyperparameters and Early Stopping

The median optimal hyperparameters from the 60 train-test splits (Table A1) are used to fit the final models using all the data. We use the median estimator for early stopping in the 60 train-test splits in the final models to prevent overfitting.

Table A1: Median optimal hyperparameters (± one standard deviation) from the 60 train-test splits. Abbreviations: OES: Original Elevation Signal feature set model, SES: Separated Elevation Signal feature set model, NVML Strat: Nevada Machine Learning Strategy, NCI: Natural Class Imbalance Strategy

Strategy & Algorithm	Class Weight	Learning Rate	Maximum Depth	Number of Estimators
OES NVML	2 ± 0.8	0.10 ± 0.06	4 ± 1.0	13 ± 15.8
SES NVML	2 ± 0.8	0.11± 0.05	4 ± 1.0	11 ± 13.9
OES NCI	1790 ± 94.0	0.14 ± 0.10	4 ± 0.5	76 ± 30.3
SES NCI	1815 ± 95.0	0.15 ± 0.06	4 ± 0.4	80 ± 26.8

REFERENCES

Bekker, J., and Davis, J. (2020). Learning from positive and unlabeled data: A survey. *Machine Learning*, *109*(4), 719-760.

Brown, S. R., Coolbaugh, M. F., DeAngelo, J., Faulds, J. E., Fehler, M., Gu, C., Queen, J., Treitel, S., Smith, C., and Mlawsky, E. (2020). Machine learning for natural resource assessment: An application to the blind geothermal systems of Nevada. *Geothermal Resources Council Transactions*, *44*, 920-932.

Caraccioli, P. D., Mordensky, S. P., Lindsey, C. R., DeAngelo, J., Burns, E., and Lipor, J. (2023). Don't Let Negatives Hold You Back: Accounting for Underlying Physics and Natural Distributions of Hydrothermal Systems When Selecting Negative Training Sites Leads to Better Machine Learning Predictions. *Geothermal Resources Council Transactions*, *47*, 1672-1693. https://pubs.usgs.gov/publication/70251035

Chen, T., and Guestrin, C. (2016). *XBGoost: A Scalable Tree Boosting System*. KDD '16: Proceedings of the 22nd ACM SIGKDD International Conference on Knowledge Discovery and Data Mining, San Francisco, California, United States.

Coolbaugh, M. F., Raines, G. L., and Zehner, R. E. (2007). Assessment of exploration bias in data-driven predictive models and the estimation of undiscovered resources. *Natural Resources Research*, *16*, 199-207.

DeAngelo, J., Burns, E., Mordensky, S. P., and Lindsey, C. R. (2023). Detrending Great Basin elevation to identify structural patterns for identifying geothermal favorability. *Geothermal Resources Council Transactions*, *47*, 1694-1702. https://pubs.usgs.gov/publication/70250639

Faulds, J. E., Brown, S. R., Smith, C. M., Queen, J., and Treitel, S. (2021a). *Machine Learning Model Geotiffs-Applications of Machine Learning Techniques to Geothermal Play Fairway Analysis in the Great Basin Region, Nevada*. https://doi.org/https://doi.org/10.15121/1897036

Faulds, J. E., and Hinz, N. H. (2015). *Favorable Tectonic and Structural Settings of Geothermal Systems in the Great Basin Region, Western USA: Proxies for Discovering Blind Geothermal Systems*. Proceedings of the World Geothermal Congress, Melbourne, Australia.

Faulds, J. E., Hinz, N. H., Coolbaugh, M., Ayling, B., Glen, J., Craig, J. W., McConville, E., Siler, D., Queen, J., and Witter, J. (2021b). *Discovering Blind Geothermal Systems in the Great Basin Region: An Integrated Geologic and Geophysical Approach for Establishing Geothermal Play Fairways: All Phases* (DOE-UNR-06731-01).

Faulds, J. E., Hinz, N. H., Coolbaugh, M. F., Cashman, P. H., Kratt, C., Dering, G., Edwards, J., Mayhew, B., and McLachlan, H. (2011). Assessment of Favorable Structural Settings of Geothermal Systems in the Great Basin, Western USA. *Geothermal Resources Council Transactions*, *35*, 777-783.

Faulds, J. E., Hinz, N. H., Coolbaugh, M. F., Sadowski, A., Shevenell, L. A., McConville, E., Craig, J., Sladek, C., and Siler, D. (2017). *Progress Report on the Nevada Play Fairway Project: Integrated Geological, Geochemical, and Geophysical Analyses of Possible New Geothermal Systems in the Great Basin Region*. Proceedings of 42nd Workshop on Geothermal Reservoir Engineering, Stanford University, Stanford, California, United States.

Faulds, J. E., Smith, C. M., Brown, S., Coolbaugh, M., DeAngelo, J., Glen, J., Ayling, B., Siler, D., Mlawsky, E., and Queen, J. (2024). *Final Technical Report-Applications of Machine Learning Techniques to Geothermal Play Fairway Analysis in the Great Basin Region, Nevada*.

Fernández, A., García, S., Galar, M., Prati, R. C., Krawczyk, B., and Herrera, F. (2018). *Learning from imbalanced data sets* (Vol. 10). Springer.

Lee Rodgers, J., and Nicewander, W. A. (1988). Thirteen ways to look at the correlation coefficient. *The American Statistician*, *42*(1), 59-66.

Mordensky, S. P., Lipor, J. J., DeAngelo, J., Burns, E. R., and Lindsey, C. R. (2023). When less is more: How increasing the complexity of machine learning strategies for geothermal energy assessments may not lead toward better estimates. *Geothermics*, *110*, 102662.

Prechelt, L. (2002). Early stopping-but when? In *Neural Networks: Tricks of the trade* (pp. 55-69). Springer.

Pyrcz, M. J., and Deutsch, C. V. (2018). Transforming data to a gaussian distribution. *Geostatistics Lessons*.

Smith, C. M. (2021). *Machine Learning Techniques Applied to the Nevada Geothermal Play Fairway Analysis* University of Nevada, Reno]. Reno, Nevada. https://scholarworks.unr.edu//handle/11714/7940

U.S. Geological Survey. (2019). *3D Elevation Program 1-Meter Resolution Digital Elevation Model*. https://www.usgs.gov/the-nationalmap-data-delivery

Williams, C. F., Reed, M. J., Mariner, R. H., DeAngelo, J., and Galanis, S. P. (2008). Assessment of Moderate-and High-Temperature Geothermal Resources of the United States. *U.S. Geological Survey Fact Sheet 2008-3082*, 1-4.

Hard Rock Drilling Efficiency Mapping Using Machine Learning

Shaolin Jahan Eidee, Dionne Mayibeki, Geir Hareland, Mohammed F. Al Dushaishi

Oklahoma State University, Stillwater, Oklahoma, USA

Keywords

Drilling Optimization, Confining Pressure, Machine Learning in Drilling, Hard Rock ROP Model, Geothermal Drilling

ABSTRACT

It is crucial to comprehend how drilling efficiency changes as operating parameters and confining pressure environment change since this can enable improved drilling performance and optimization. The rate of penetration (ROP) and torque (T) required to penetrate hard rock significantly impact the efficiency of the cutting action of the Polycrystalline Diamond Compact (PDC) cutters. As the incremental weight of bit is applied, the drilling process undergoes three different distinct drilling efficiency phases, Phase 1, inefficient drilling, Phase II, efficient drilling where weight on bit (WOB) and rotation per minute (RPM) are strongly correlated to ROP and T, and Phase III where ROP and T are limited with incremental weight on bit and rotation per minute. This study analyzed the different efficiency phases for a PDC bit design under different pressure environments and applied parameters with resulting T and ROP. An in-house rig was utilized for the testing, with the capability of collecting data at frequencies of 200 Hz. Tests were performed in Sierra White Granite (SWG) with a 3 ¾" bit design. The operating parameters applied were rotation per minute (80-160 RPM), weight on bit (0-6 klbs), and confining pressure (0-2,000 psi). The rotation per minute was set constant during all the tests, and the weight on bit was incrementally increased stepwise for data collection at each step. For each weight on bit range and step, heat maps were created showing the correlations between all the different parameters (applied and resultant) to inform the machine learning (ML) feature selection method. Distinct correlations between applied and resultant parameters were seen in the different drilling efficiency phases and within the different phases for different applied parameters. The potential application of this method in a real-time drilling environment shows promising results in identifying the most efficient drilling parameters to obtain optimal drilling.

1. Introduction

It is widely accepted that confining pressure plays a substantial role in determining the mechanical properties of rocks during drilling. It affects the efficiency, cost-effectiveness, and bit wear of drilling operations. Increasing confining pressure increases the lateral stress around the drill bit, resulting in greater resistance and the required force. Evidence shows that higher confining pressure significantly impacts rock energy variation, with higher pressures resulting in increased energy transmission and reduced energy release (Zhou et al., 2021). With the increase of rock's stress, the rock becomes more resistant to being fractured and cut by the drilling equipment. Moreover, specific energy and rate of penetration of laser-perforated (a non-explosive technology) oil and gas wells are significantly affected by confining pressure, with disparities observed between 8 and 16 MPa (Ahmadi et al., 2012). Therefore, higher thrust forces, torque, and penetration depths are necessary to remove the rock material effectively. It is noted that higher confining pressures lead to reduced cutting tool performance, particularly with a diamond bit impregnated with titanium. Drilling efficiency can be significantly improved by incorporating the effects of confining pressure into drilling models and operational strategies (Zhou et al., 2021).

It is typical for the geothermal energy sector to drill through hard rock such as igneous and metamorphic rock formations (Akhtarmanesh et al., 2021). Properly selecting a bladed bit significantly enhances hard rock drilling efficiency by reducing drilling costs, enhancing penetration rates, and minimizing non-productive time (Kouzaiha et al., 2022). A polycrystalline diamond compact bit (PDC) excels in hard rock drilling due to its superior cutting structure and enhanced performance capabilities. It is designed with strategically arranged cutters, alternated back rake angles, and innovative cutter configurations. This bit type helps to manage the depth of cut (DOC) effectively, reduce torsional instability, limit torque fluctuations, and increase the rate of penetration (ROP) (Hababi et al., 2023). PDC bits offer high wear resistance, making them ideal for challenging formations and enhancing drilling efficiency (Yang et al., 2022). To achieve a higher efficiency and ROP in drilling operations, numerical simulations are conducted to optimize the interaction model between PDC cutters and rock (Ahmad et al., 2023). It is also important to note that PDC bits are designed to reduce vibrations caused by torsional vibrations, thereby ensuring maximum penetration speed and drilling efficiency in hard rock. PDC bits can be made more productive and durable by implementing improvements such as cone-shaped or rotating cutters in hard rock drilling applications (Hareland et al., 2009).

Drilling hard rock, especially in geothermal reservoirs, is challenging due to low penetration rates and high bit wear. Advanced bit technology is required to work with hard and abrasive rocks at high confining pressures. Because geothermal drilling poses unique challenges, developing a model capable of predicting the ROP of these types of rocks is imperative. Several ROP models have been developed for PDC bits for various sedimentary rock formations. Based on the geometry of single-cutter rock interaction, the lithology coefficient, and bit wear, Hareland and Rampersad (1994) developed a model for drag bits. To scale up the ROP model from a single cutter to a full bit, they introduced the concept of equivalent bit radius and dynamic cutter action. (Hareland and Rampersad, 1994). The ROP model developed by Motahhari et al. (2010) calculates how a single PDC cutter interacts with rock. In 2014, another ROP model incorporated operational parameters, cutter back and side rake angles, bit hydraulic function, and bit wear function (Kerkar and Hackbarth, 2014). A PDC hybrid drill bit was developed by Wang et al. (2020) to navigate hard and abrasive formations. Wear flat area and interfacial friction angle concepts were incorporated into Atashnezhad et al. (2020) ROP model for PDC bits in hard rocks.

The two phases of drilling efficiency were defined by Akhtermanesh et al. (2021) focusing on the rate of penetration (ROP) in relation to the weight on bit (WOB). This study was conducted particularly for drilling with PDC bits. Phase 1 is marked by insufficient WOB. Due to low WOB, the depth of cut (DOC) is minimal, increasing friction and reducing the ROP. This scenario results in a less effective drilling process with scraping mechanism with low ROP, where the bit does not penetrate deeply with each rotation. On the contrary, phase 2 occurs when WOB is adequately increased (a more efficient drilling process). Higher WOB enables multiple cutting mechanisms, including chipping, crushing, and scraping. These mechanisms effectively reduce and allow for a deeper penetration. ROP is high in this phase, indicating effective operation compared to Phase 1. Phase 3 occurs when WOB exceeds Phase 2's optimal range. There may even be a decline in ROP in this phase. Identifying the transition between phase 1 and phase 2 is critical. Operating within Phase 2 ensures optimal drilling efficiency, reduced operational cost, and minimum bit wear (Akhtarmanesh et al., 2021).

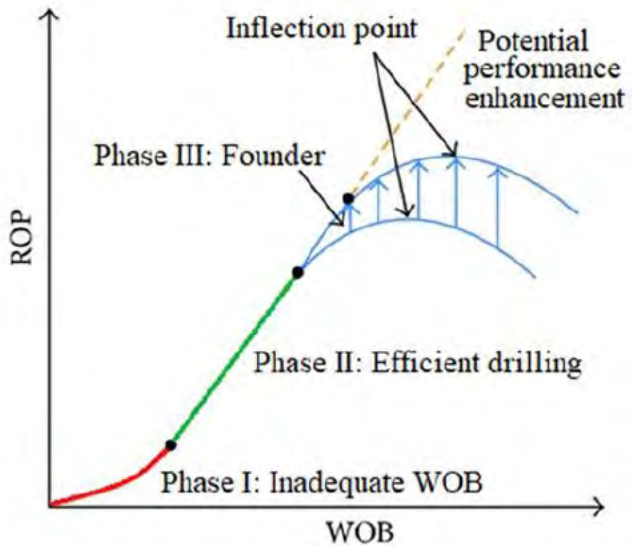

Figure 1: Different phases of drilling (Akhtarmanesh et al. 2021)

Various research papers indicate that machine learning plays a significant role in optimizing Rate of Penetration (ROP) models in drilling operations. ROP predictive models have been successfully constructed using a variety of machine learning algorithms, including Random Forest, Gradient Boosting, Extreme Gradient Boost, and Adaptive Boosting in Southern Iraq oil field (Al-Sahlanee et al., 2023). Machine learning techniques such as Support Vector Regression and Gradient Boosting Regression have also been evaluated for predicting ROP in areas such as Troll West (Liu et al., 2023). Global ROP optimization utilizing deep neural networks for ROP modeling also emphasizes the importance of machine learning concerning making real-time decisions for drilling operations (Brenjkar and Biniaz Delijani, 2022). Tests conducted in areas like Northeastern British Columbia, Canada, and offshore drilling operations in West Africa and Malaysia have demonstrated that machine learning can optimize ROP, reduce drilling costs, and improve operational efficiency (Robertson et al., 2023; Al-Riyami et al., 2023). In this study, machine learning techniques have been applied to understand the transition from the inefficient drilling phase to the efficient one under myriad key operating conditions.

Although significant advancements have been made by the above-mentioned researchers in developing ROP models for PDC bits, it is crucial to create a specifically designed model dedicated to geothermal drilling applications. The impact of confining pressure on rock deformation has been previously extensively studied. Still, the effect of confinement on hard rock drilling efficiency phase change and ROP had not been fully examined. This research aims to understand how changes in confining pressure alter the forces required for efficient drilling. The transition point, where Phase I shifts to Phase II in Figure 1, of WOB and ROP between phases was accurately determined. The detection of the transfer point is complex and is affected by some key drilling parameters, bit design, and cutter geometry. However, the transition point is fundamental to optimizing drilling in hard rock. This is the first attempt to determine this point using laboratory data which could potentially be used in a real-time automated system. This will lead to enhancing operational decision-making in geothermal drilling applications. This work is crucial for optimizing parameters such as drilling speed and bit design to increase drilling efficiency.

2. Methodology

2.1 Experimental Test

An indoor full-scale rig was used to test the Sierra White Granite (SWG) rock sample. The rig consisted of an 8-foot (2.45 m) long hydraulically driven drill string with an outer diameter of 6 inches (15.24 cm). A 559 kW (750 hp) direct-current electric motor was used to supply hydraulic power to rotate the drill string. The SWG core with a diameter of 9 inches (22.86 cm) was inserted inside the pressure cell. The sample's unconfined compressive strength (UCS) was 193,053 kPa (28,000 psi), its Young's Modulus was 4.14×10^7 kPa (6×10^6 psi), and its bulk density was 2650 kg/m^3. The permeability and porosity of SWG are negligible. Drilling parameters and wellbore pressures were reproduced using the drilling system. As the drilling fluid, water was used at a rate of 6.3×10^{-3} m^3/s (100 gal/min) at 15.6 °C (60 °F). The fluid was circulated through the drill string and bit, under the drill bit and out of the pressure cell until the desired confined back pressure was achieved. Sensors placed in the drill string monitored the weight on bit (WOB) and the rotational speed of the bit in a feedback loop. The bit ROP was recorded and analyzed with the drilling parameters controlled.

Figure 2: Drilling facility with rock sample (Reza et al. 2021)

PDC bit with a diameter of 95 mm (3-3/4" inches) was utilized for the experiments. As shown in Figure 2, the bit has four blades and 11 face cutters with a 13 mm cutter diameter.

Figure 3: 4 bladed PDC bit

Three confining pressures were tested: 0 kPa, 6895 kPa, and 13,790 kPa (0 psi, 1000 psi, and 2000 psi). The tests were conducted at 8.4 rad/s and 15.7 rad/s (80 RPM and 150 RPM), with the WOB gradually increasing. In the atmospheric tests, samples were taken at 100 Hz, whereas in the confined tests, samples were taken at 200 Hz. Figure 4 depicts a sample of raw measurement data for the 4-bladed PDC bit at 8.4 rad/s (80 RPM). The ROP was calculated based on the penetration range and measured time for each WOB step (Mayibeki et al., 2023)

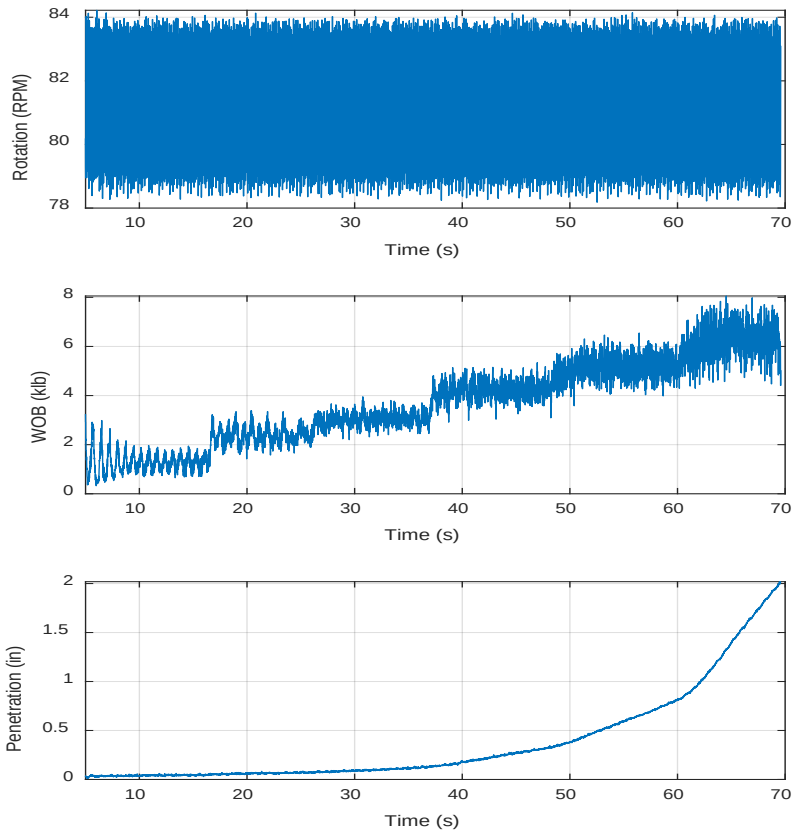

Figure 4: Raw measured drilling data with 4-bladed PDC bit at 80 RPM under atmospheric conditions

2.2 Phase-Driven Variability in Drilling Parameter Correlations Model

Using a comprehensive methodology, this study analyzes the efficiency of a four-bladed PDC bit across two distinct drilling phases. Figure 5 illustrates the method for developing the phase-driven variability model. Initially, the methodology involved loading data followed by rigorous preprocessing, including standardization and splitting. It is crucial to standardize the feature scales to minimize bias caused by varying scales and normalize the influence of each parameter. With this preprocessing step, the subsequent analytical techniques operate optimally, improving accuracy and reproducibility. Based on the standardization of our drilling data, a Random Forest regression model was developed, which was fine-tuned specifically for the drilling data. The decision was based on the model's ability to handle non-linear relationships and its robustness against over fitting, making it an ideal choice for our complex geological data. As the model's evaluation metrics, MAE (Mean Absolute Error), MSE (Mean Squared Error), and R squared score were determined. The MAE represents the average magnitude of the errors in a set of predictions, without considering their direction. The MSE measures the average of the squares of the errors, thereby giving more weight to larger errors. The R^2 score indicates the proportion of the variance in the dependent variable that is predictable from the independent variables. This random forest model provided a baseline predictive framework, crucial for subsequent analyses. To increase the granularity of our analysis, a Cubic Spline interpolation was used to transform the discrete dataset into a continuous one, ensuring smooth transitions. A practical application of the PELT algorithm,

a Pruned Exact Linear Time algorithm that identifies significant shifts in operational efficiency, required this interpolation. Based on the PELT algorithm's sensitivity and efficiency in detecting these change points, the critical transitions in drilling performance were identified. These were then quantitatively analyzed to determine their effects on overall drilling efficiency. Additionally, this methodology provided a robust statistical basis for assessing the impact of different drilling parameters on the efficiency of the 4-bladed PDC bit.

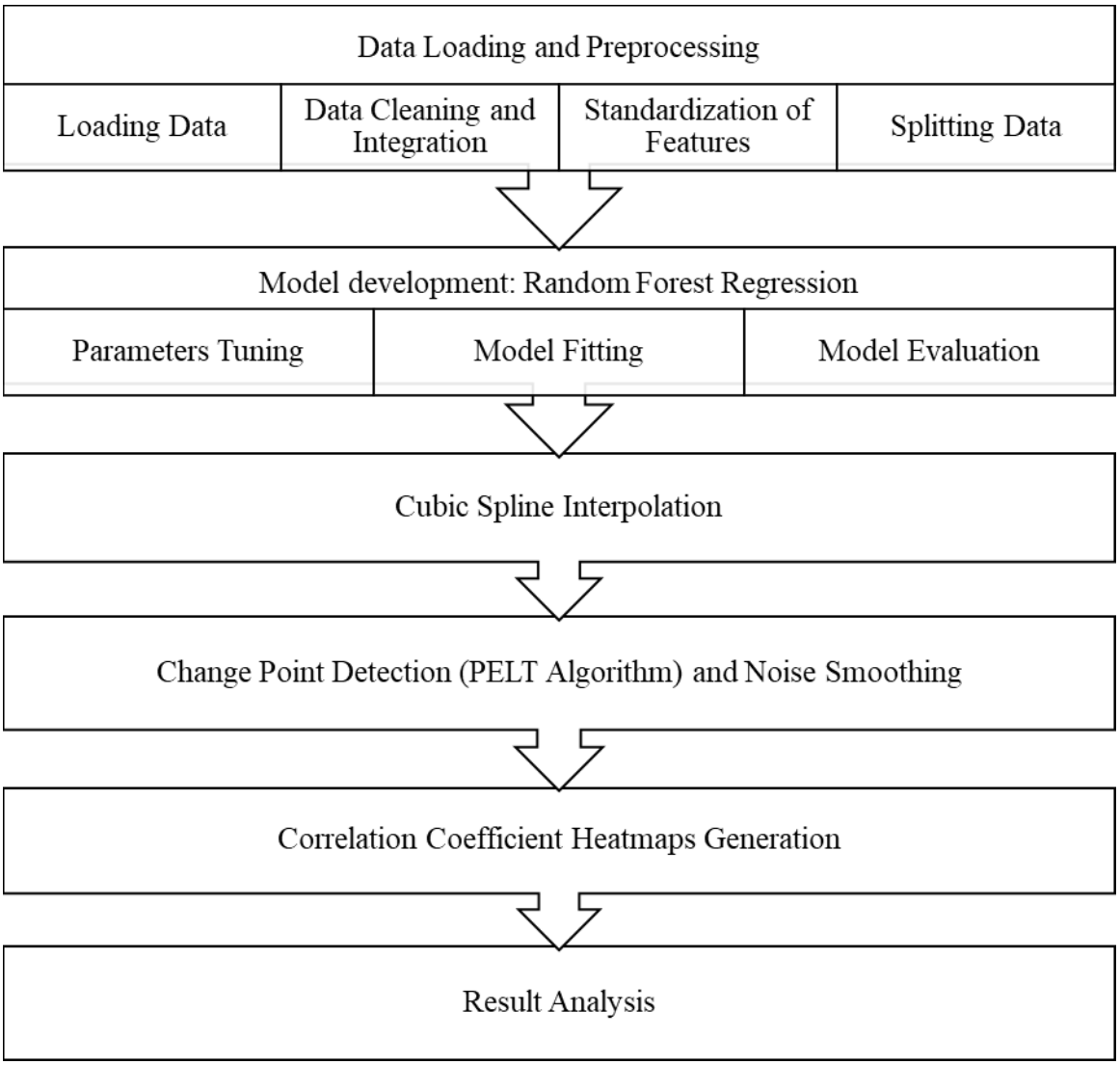

Figure 5: Methodology of the phase-driven variability of the drilling parameters model

3. Result and Discussion

3.1 Transition point of WOB and RPM measurement

For a 4-blade drill bit configuration, a Random Forest regression approach was utilized in conjunction with Cubic Spline interpolation and PELT change point detection. The relation of

WOB and ROP at various confining pressures at various RPM settings was studied. The model captures significant shifts in drilling performance across different operational settings. Figure 6 illustrates the model's effectiveness in capturing ROP behavior. The 4-bladed drill bit is presented operating at 80 RPM under varying confining pressures. Panels (a) through (f) depict actual versus predicted ROP values against the weight on the bit and interpolated data that identifies critical change points. This structured visualization facilitates the understanding of the relationship between WOB, ROP, and operational efficiency under different subsurface pressure conditions.

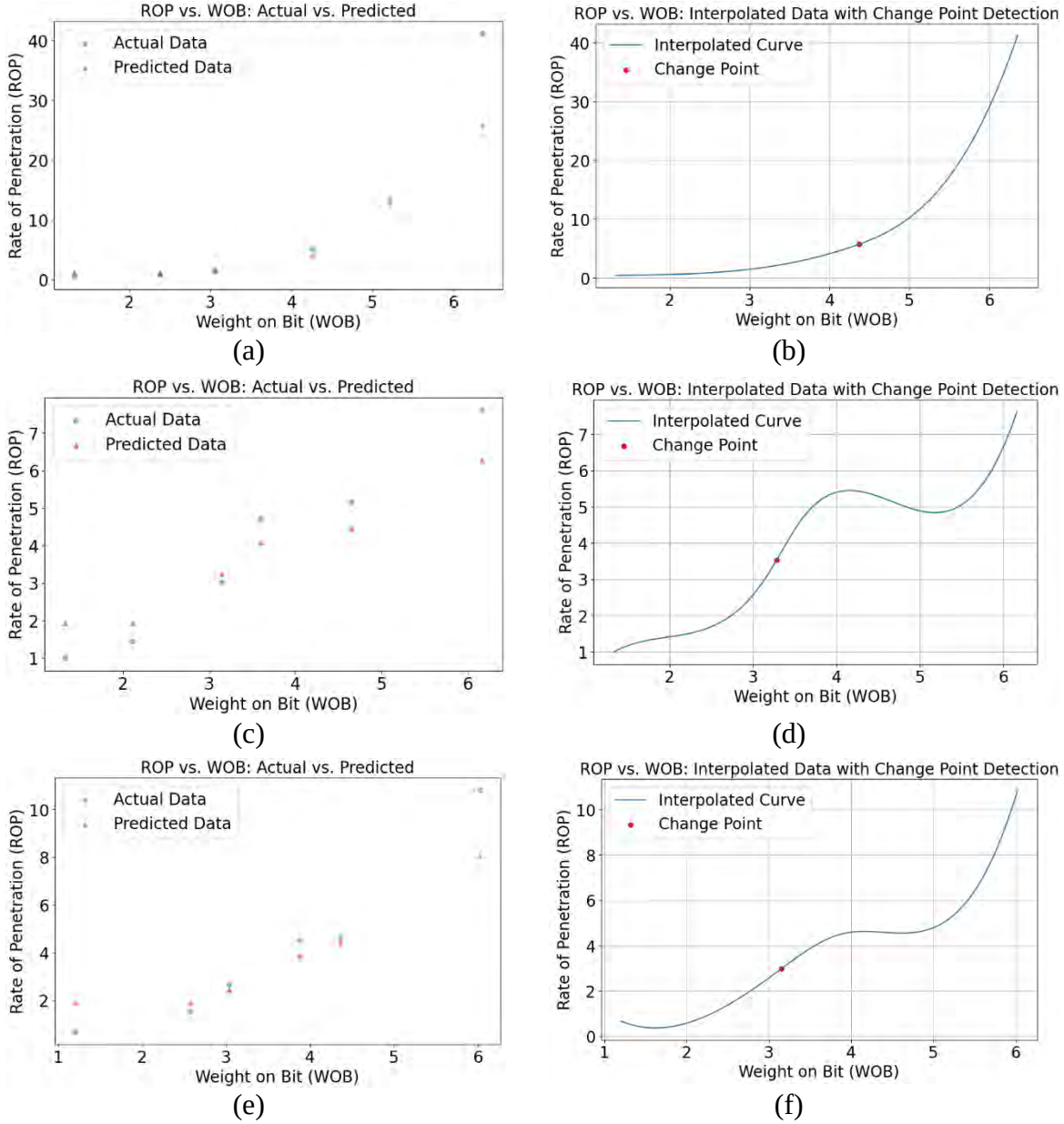

Figure 6: Random Forest model fit on the data to determine the transitional (or change) WOB and ROP point for 4 bladed bit at 80 RPM (a) Actual vs. predicted data at 0 psi confining pressure (b) Change point at 0 psi confining pressure (c) Actual vs. predicted data at 1000 psi confining pressure (d) Change point for at 1000 psi confining pressure (e) Actual vs. predicted data at 2000 psi confining pressure (f) Change point at 2000 psi confining pressure

Table 1 depicts the evaluation metrics of the random forest model at different confining pressures running at 80 RPM. This table provides information regarding the accuracy and goodness-of-fit of the model. The metrics include Mean Absolute Error (MAE), Mean Squared Error (MSE), and the R-squared (R^2) score. It offers a comprehensive assessment of the model's performance.

Table 1: Model evaluation metrics for 80 RPM

Confining Pressure	MAE	MSE	R^2 Score
0 psi	0.79	0.64	0.98
1000 psi	0.82	0.69	0.84
2000 psi	0.70	0.77	0.80

The MAE of the developed model is lowest at 2000 psi (0.70), suggesting that predictions are most accurate at this pressure level. In terms of penalizing larger errors, the model exhibits the lowest MSE at 0 psi (0.64), indicating that the model performs best under these conditions. The model occasionally produces larger errors than predictions made at lower pressures, with the MSE slightly higher at 1000 psi (0.69), and highest at 2000 psi (0.77). Lastly, the model shows excellent fit at 0 psi, with an R^2 of 0.98, which indicates it explains 98% of the variance. As confining pressure increases, the R^2 drops to 0.84, and 0.80 at 2000 psi, suggesting the model's explanatory power decreases. Even though the MAE is not the lowest at 0 psi, the combination of high R^2 and low MSE demonstrates superior accuracy and consistency. It is evident from the R^2 scores that the model has an impaired ability to explain variance at 1000 and 2000 psi, with the highest predictive accuracy (lowest MAE) at 2000 psi despite a higher MSE. According to this discrepancy, while the model predicts more accurately on average at 2000 psi, it is more susceptible to errors.

Figure 7 shows that the random forest model is developed and applied to detect the change points at a range of confining pressures at a speed of 150 RPM. The figure shows the actual data compared to the predicted data for each case. Then, the change point on the interpolated curve of the dataset is pointed out as well.

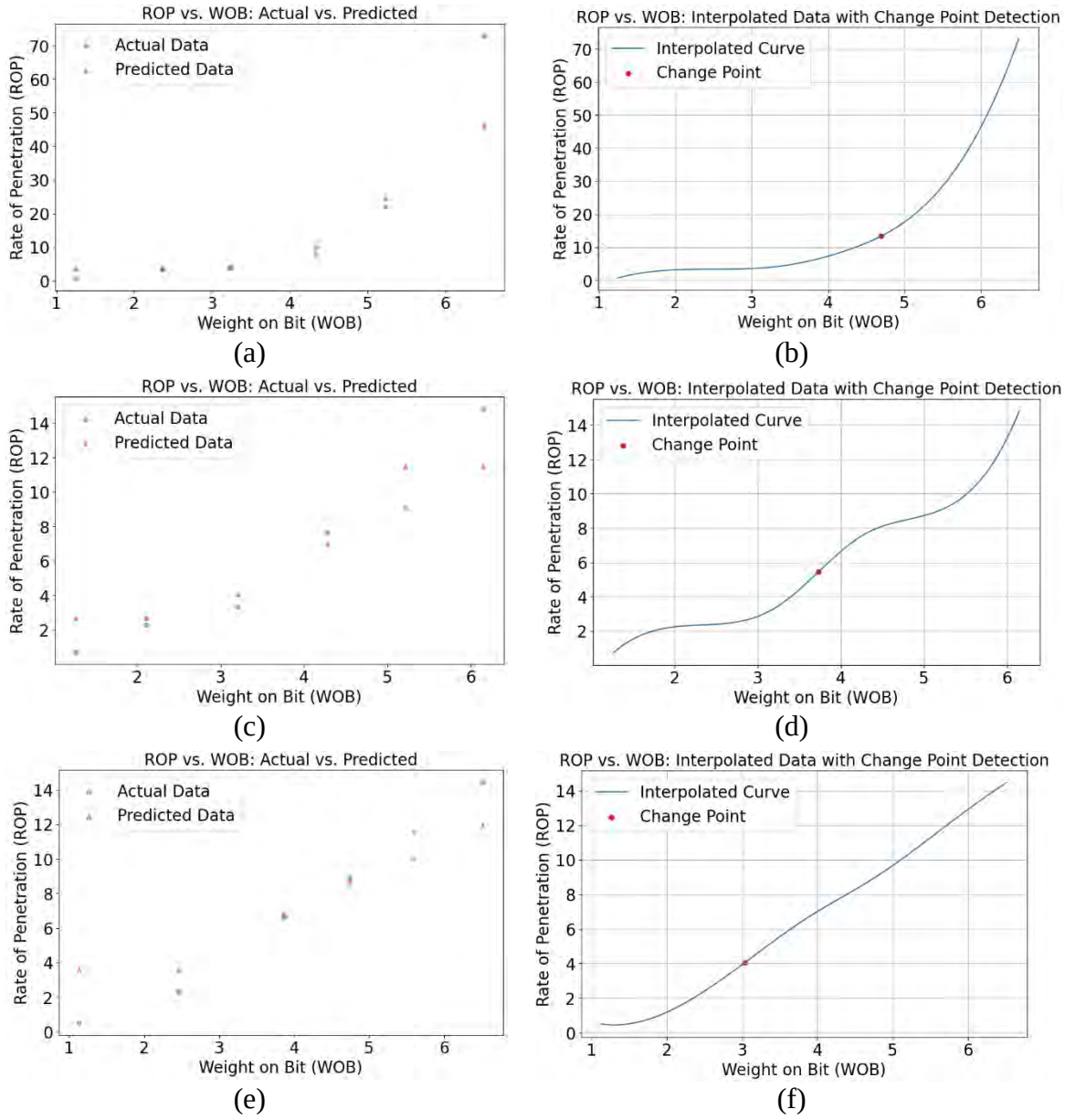

Figure 7: Random Forest model fit on the data to determine the transitional (or change) WOB and ROP point for 4 bladed bit at 150 RPM (a) Actual vs. predicted data for at 0 psi confining pressure (b) Change point at 0 psi confining pressure (c) Actual vs. predicted data at 1000 psi confining pressure (d) Change point at 1000 psi confining pressure (e) Actual vs. predicted data at 2000 psi confining pressure (f) Change point at 2000 psi confining pressure

Table 2 shows that the random forest model is evaluated at a speed of 150 RPM. The same metrics (MSE, MAE, and R^2 score) as the 80 RPM model are calculated based on a range of confining pressures. This table is indicative of the performance of the model.

Table 2: Model evaluation metrics for 150 RPM

Confining Pressure	MAE	MSE	R Squared Score
0 psi	2.75	7.59	0.93
1000 psi	2.19	4.84	0.72
2000 psi	2.29	5.88	0.81

At 0 psi, the model has the highest R^2 score (0.93), indicating excellent explanatory power. However, the MAE (2.75) and MSE (7.59) are the highest. Thus, while the model fits the overall data well, its predictions are less accurate and prone to larger errors on average. At 1000 psi, the model achieves the lowest MAE (2.19) and MSE (4.84), indicating the highest predictive accuracy and the smallest average errors. Despite this, the R^2 score is the lowest (0.72). This suggests that while the individual predictions are more accurate, the overall fit is not as strong. At 2000 psi, the model balances predictive accuracy and explanatory power. The MAE (2.29) and MSE (5.88) are moderately low, and the R^2 score (0.81) is relatively high, indicating a good compromise between fitting the data and maintaining predictive accuracy. In short, at 150 RPM, the model performs best in terms of predictive accuracy (lowest MAE and MSE) at 1000 psi, but it explains the most variance (highest R^2) at 0 psi. The results suggest a trade-off between the accuracy of individual predictions and the model's overall fit, with 2000 psi providing a balanced performance.

Table 3 provides a summary of the transition points between ROP and WOB for a wide range of rotational speeds and confining pressures. Based on the results, it is evident that transition points vary suggestively with fluctuating operating conditions. A thorough understanding of these insights is crucial to drilling performance in diverse drilling operations.

Table 3: Transition point of ROP and WOB for varying RPMs and confining pressures

4 Blade Bit			
RPM	**Confining Pressure**	**$WOB_{transition}$**	**$ROP_{transition}$**
80	0 psi	4.37 klbs	5.73 ft/hr
80	1000 psi	3.28 klbs	3.53 ft/hr
80	2000 psi	3.15 klbs	2.97 ft/hr
150	0 psi	4.69 klbs	13.34 ft/hr
150	1000 psi	3.73 klbs	5.43 ft/hr
150	2000 psi	3.03 klbs	4.05 ft/hr

Firstly, from Table 3, it is noticed that, at 80 RPM, the WOB transition decreases from 4.37 klbs at 0 psi to 3.15 klbs at 2000 psi. Whereas, at 150 RPM, the WOB transition shows a similar trend, decreasing from 4.69 klbs at 0 psi to 3.03 klbs at 2000 psi. At both 80 RPM and 150 RPM, the WOB transition decreases with increasing confining pressure. Higher confining pressures require lower WOB to transition, possibly due to increased resistance from the surrounding rock formation.

Secondly, at 80 RPM, the ROP transition decreases from 5.73 ft/hr at 0 psi to 2.97 ft/hr at 2000 psi, as seen in Table 3. At 150 RPM, the ROP transition is significantly higher at 0 psi (13.34 ft/hr)

compared to 5.43 ft/hr at 1000 psi and 4.05 ft/hr at 2000 psi. It concludes that the ROP transition also decreases with increasing confining pressure for both RPM levels. Higher confining pressures seem to slow down the rate of penetration, indicating more resistance to drilling.

Finally, at 0 psi, increasing the RPM from 80 to 150 results in a higher WOB transition (from 4.37 klbs to 4.69 klbs) and a significantly higher ROP transition (from 5.73 ft/hr to 13.34 ft/hr) as noted in Table 3. Higher RPM improves the drilling rate significantly in the absence of confining pressure. At 1000 psi and 2000 psi, the trends are consistent but less pronounced. For instance, at 1000 psi, WOB transition increases from 3.28 klbs to 3.73 klbs and ROP transition increases from 3.53 ft/hr to 5.43 ft/hr with higher RPM. At 2000 psi, the WOB transition decreases from 3.15 klbs, while the ROP transition is at 4.05 ft/hr. This suggests at higher RPM, the drill bit performs slightly better. This is due to the improved cutting action of the bits against the hard rock formation.

3.2 Efficiency mapping of Phase 1 and Phase 2

The distance correlation coefficient analysis provides a robust quantitative framework to evaluate the interdependencies among drilling parameters. By comparing the coefficients across two efficiency phases, the key variables that contribute to enhanced drilling performance can be identified. Figure 8 shows the distinct correlation coefficient heat-maps for Phase 1 and Phase 2 of drilling efficiency. These heat maps describe the strength of the correlations between several drilling parameters: ROP, RPM, WOB, Torque, and Confining Pressure. The phases have been distinguished based on the change point detected listed in Table 3.

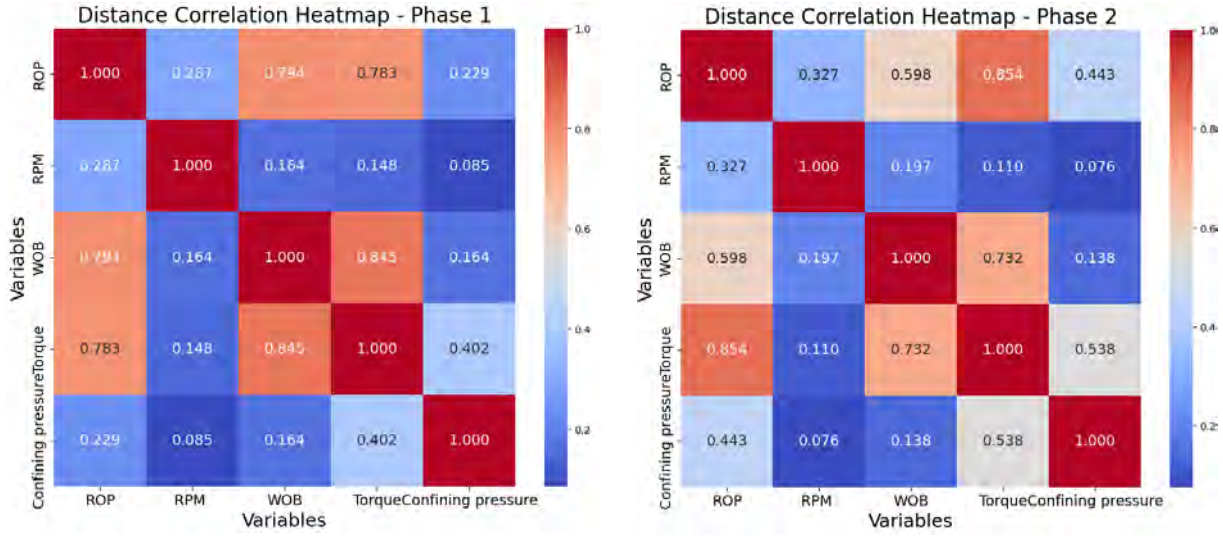

(a) (b)

Figure 8: Distance correlation heat map of 4 bladed bit (a) inefficient drilling phase: Phase 1 (b) efficient drilling phase: Phase 2

In Phase 1 (Figure 8a), WOB and ROP showed a moderate correlation (0.794), indicating a role for WOB in influencing ROP. As a result of this sub-optimal correlation score, the WOB was not effectively translated into penetration efficiency. This could be the result of poor bit-to-rock

interaction. WOB and torque correlate more strongly (0.845) than ROP and torque (0.883). A higher WOB generally results in a deeper cut per revolution, which typically requires a higher torque. According to the correlation between RPM and torque (0.148), there is little to no synchronization between bit rotation speed and mechanical torque. The reason for this is often a mismatch between the drilling parameters and the rotary system, which results in inefficient energy transfer. A minimal correlation was observed between confining pressure and torque (0.402), indicating that changes in confining pressure did not significantly alter torque requirements, possibly due to insufficient hydraulic power.

In Phase 2 (Figure 8b), WOB and ROP correlation significantly strengthened (0.598), indicating effective transmission of WOB to penetration through the rock. This improvement was observed due to the increase in drilling efficiency. The strongest relationship of ROP is with Torque (0.854) in this phase. Higher torque means better engagement of the bit's cutting elements with the rock, increasing the ROP. The confining pressure also strongly affects the ROP in this phase (0.443 compared to 0.229), as confining pressure makes the rock more resistant to the mechanical force applied by the bit. The WOB and torque demonstrate a similar relationship to Phase 1. RPM and torque demonstrated a similar correlation to Phase 1, suggesting no efficiency improvements in the rotary drive system. Confining pressure and torque show an increased correlation (0.538), which could reflect better adaptation to varying geological pressures.

Table 4 shows the difference in the distance correlation coefficients of Phase 1 and Phase 2. The heat maps reveal higher correlation coefficients in Phase 2 than in Phase 1. This suggests that the operational parameters are more interdependent and possibly better optimized in Phase 2. The stronger correlations indicate more cohesive interactions among variables such as WOB, RPM, Torque, and Confining Pressure. These parameters could contribute to improved drilling performance. Changes in the drilling environment (more precisely, applying more confining pressure) affect the efficient phase more than the inefficient phase. The slight changes in correlations involving RPM indicate that RPM's role remained relatively consistent across phases. As seen from the differences of ROP-torque and torque-confining pressure in Table 4, torque became a more critical factor in the drilling process in Phase 2. A possible explanation for this is the changes in bit design, drilling fluid properties, or formation characteristics.

Table 4: Distance Correlation Differences between Phase 1 and Phase 2 (Phase 2 - Phase 1)

	ROP	**RPM**	**WOB**	**Torque**	**Confining Pressure**
ROP	0	0.04	-0.195	0.071	0.214
RPM	0.04	0	0.033	-0.038	-0.009
WOB	-0.195	0.033	0	-0.112	-0.026
Torque	0.071	-0.038	-0.112	0	0.136
Confining Pressure	0.214	-0.009	-0.026	0.136	0

Parameters showing significant correlation increases from Phase 1 to Phase 2 might be targeted for specific adjustments to enhance efficiency. From Table 4, the pairs of ROP-WOB (-0.195), ROP-confining pressure (0.214), WOB-torque (-0.112) and torque-confining pressure (0.136)

are key combinations here that need to be optimized while drilling under varying confining pressure and RPMs. Synchronizing these parameters more closely leads to better performance outcomes. For example, WOB and ROP show a strong correlation in Phase 2. Maintaining or optimizing WOB settings could be crucial for maximizing ROP under similar conditions.

3.3 Discussion

It is important to note that, this model was designed to identify a single detection point. It performs well under atmospheric confining conditions (0 psi). In contrast, for confining pressures of 1000 psi and 2000 psi, there is evidence of an intermediate transition zone as the drilling efficiency phase transitions from Phase 1 to Phase 2. The observed sinusoidal shape of the interpolated line in the graphs for these pressures supports this hypothesis. Figure 9 shows where this transition zone from Phase1 to Phase 2 could exist. In this area, the drilling is not yet efficient, rather transitioning into the efficient phase.

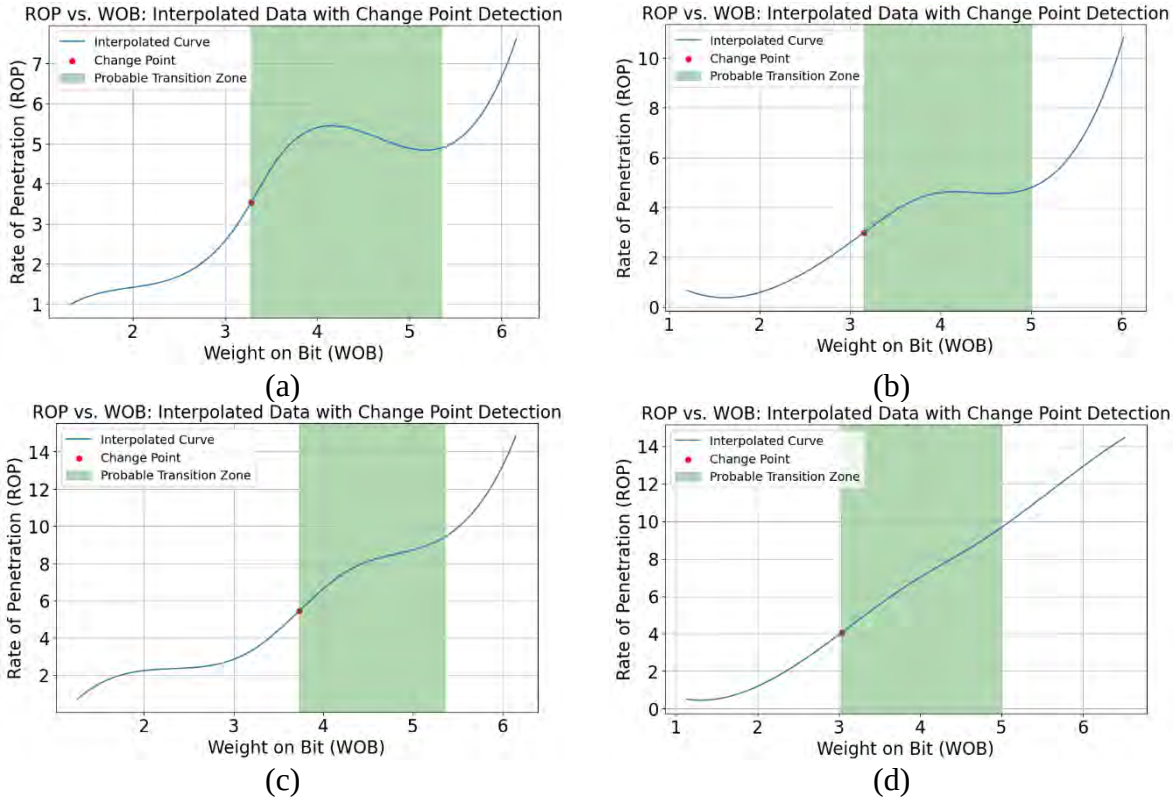

Figure 9: Probable intermediate transition zone from phase 1 to phase 2 for 4 bladed bit (a) 80 RPM at 1000 psi confining pressure (b) 80 RPM at 2000 psi confining pressure (c) 150 RPM at 1000 psi confining pressure (d) 150 RPM at 2000 psi confining pressure

The exact magnitude of this intermediate transition zone remains unknown within the scope of our current study. The authors are precisely detecting and characterizing this region through ongoing research.

4. Conclusion

- This study identified three distinct phases of drilling efficiency for geothermal drilling using a PDC bit under varying confining pressures and operational parameters. During Phase 1, the drilling is inefficient with a low depth of cut and high friction. During Phase 2 the drill is efficient with optimal WOB and RPM leading to effective rock penetration. The correlations between drilling parameters exhibit significant phase-driven variability. As a result of this variability, it is possible to identify which parameters need to be adjusted to improve performance. It also emphasizes the need for synchronized WOB, RPM, and torque adjustments.
- ROP correlation with WOB and confining pressure and torque relationship with WOB and confining pressure are the most significant combinations that can convert the inefficient drilling phase into an efficient phase under increasing confining pressure.
- Random forest regression, cubic spline interpolation, and PELT change point detection, were utilized to analyze the relationship between WOB and ROP. In particular, this approach highlights the model's ability to capture significant changes in performance across various settings. Additionally, it gives a nuanced understanding of how operational parameters affect drilling efficiency.
- The random forest model demonstrated high predictive accuracy, as indicated by low MAE and MSE values and high R-squared scores under various operational conditions. The predictive capability of this system will enable proactive adjustments to be made to drilling performance.
- The distance correlation coefficient heat maps were generated for Phase 1 and Phase 2, considering the change points detected as the transition point. However, in future research works, if the intermediate transition zone between these phases is detected, the heatmaps would be different for Phase 2 (efficient phase). That might also reveal other striking correlations among the drilling parameters leading to an optimized drilling operation.
- Confining pressure had a significant impact on drilling operations. High confining pressures increase resistance around the drill bit, requiring higher thrust and torque forces to remove rock effectively. ROP and torque are affected the most due to confining pressure in the efficient drilling phase. Incorporating confining pressure effects into drilling models could significantly improve drilling efficiency.
- The transition points of ROP and WOB were quantitatively determined for different RPM settings, which provides an essential benchmark for optimizing drilling operations. However, with little to no effect of RPM on transitioning the drilling phase in efficient one concludes that changing RPM is of the least importance to get better results. To maintain drilling within the efficient phase, this insight is crucial for making real-time adjustments to operations.

5. Limitation and Future Recommendation

In this study, we employed Random Forests (RF), which typically assume independent and identically distributed inputs (IID). Due to the temporal dependencies inherent in drilling operations, adjacent data points tend to be correlated based on the input data, which is a time-series measurement. Therefore, the model may be affected by the violation of the IID assumption. A potential improvement would be to incorporate lag features or hybrid approaches (e.g., to combine RF with time-series models, such as Long Short-Term Memory (LSTM) networks).

Furthermore, this modeling effort is based solely on a single rock type, whereas in practice, drilling operations often encounter varying formations, which may have an impact on parameters such as weight on bit (WOB), torque, and rate of penetration (ROP). These changing formations should be incorporated into the model in future work. Finally, although adjusting WOB in real-time can offer insights, drastic changes to WOB for model training could pose risks such as bit failure. It is important to consider controlled, incremental changes, along with historical data from different WOB levels, in order to avoid damage to the equipment.

A broader range of confining pressures and RPM settings should be considered for future studies to refine efficiency models and better understand the limits of PDC bit performance under extreme conditions. Implementing the machine learning models developed in this study into real-time drilling operations will enhance decision-making processes. It will allow for dynamic adjustments based on immediate feedback from the drilling parameters. Moreover, it would be useful to investigate the impact of other bit materials and designs (apart from 4 bladed PDC bit) on drilling efficiency, particularly in hard rock geothermal drilling. Furthermore, the authors are developing more complex machine learning algorithms and incorporating additional prediction factors such as bit wear and specific energy.

Acknowledgement

The authors acknowledge the support of the U.S. Department of Energy, DOE EERE –Geothermal Technologies Program under Award Number EE0008603.

REFERENCES

Ahmad, F., Al-Kayiem, H.H., and King Soon, W.P. "Lecture Notes in Mechanical Engineering." *ICPER 2020: Proceedings of the 7th International Conference on Production, Energy and Reliability*, Springer Nature Singapore, Singapore (2023). https://doi.org/10.1007/978-981-19-1939-8

Ahmadi, M., Erfan, M.R., Torkamany, and M.J., Sabbaghzadeh, J. "The effect of confining pressure on specific energy in Nd:YAG laser perforating of rock." *Optics & Laser Technology 44, 57–62* (2012). https://doi.org/10.1016/j.optlastec.2011.05.017

Al-Riyami, N., Revheim, O., Robinson, T.S., Batruny, P., Meor Hakeem, M.H., and Tze Ping, G. "Drilling in the Digital Age: Case Studies of Field Testing a Real-Time ROP Optimization System Using Machine Learning." *Presented at the SPE/IADC Middle East Drilling Technology Conference and Exhibition*, SPE, Abu Dhabi, UAE (2023). https://doi.org/10.2118/214521-MS

Al-Sahlanee, D.T., Allawi, R.H., Al-Mudhafar, W.J., and Yao, C., 2023. "Ensemble Machine Learning for Data-Driven Predictive Analytics of Drilling Rate of Penetration (ROP) Modeling: A Case Study in a Southern Iraqi Oil Field." *Presented at the SPE Western Regional Meeting*, SPE, Anchorage, Alaska, USA (2023). https://doi.org/10.2118/213043-MS

Atashnezhad, A., S. Akhtarmanesh, S. Sleeper, and G. Hareland. "Rate of Penetration (ROP) Model for PDC Drill Bits based on Cutter Rock Interaction." *In ARMA US Rock Mechanics/Geomechanics Symposium*, pp. ARMA-2020. ARMA (2020).

Akhtarmanesh, S., Atashnezhad, A., Hareland, G., and Al Dushaishi, M., "ROP model for PDC bits in geothermal drilling." *In ARMA US Rock Mechanics/Geomechanics Symposium, pp. ARMA-2021. ARMA* (2021).

Brenjkar, E., and Biniaz Delijani, E. "Computational prediction of the drilling rate of penetration (ROP): A comparison of various machine learning approaches and traditional models." *Journal of Petroleum Science and Engineering* 210, 110033 (2022). https://doi.org/10.1016/j.petrol.2021.110033

Hababi, A., Omar, M., Alqunais, D., Teasdale, P., Case, M., and Casad, C. "Unique PDC Bit Design Significantly Improves Drilling Efficiency Across Several Interbedded Formations." *Presented at the Gas & Oil Technology Showcase and Conference*, SPE, Dubai, UAE (2023). https://doi.org/10.2118/214240-MS

Hareland, G., and Rampersad, P.R., 1994. "Drag - Bit Model Including Wear." *Presented at the SPE Latin America/Caribbean Petroleum Engineering Conference* (1994). https://doi.org/10.2118/26957-MS

Hareland, G., Yan, W., Nygaard, R., and WiSe, J.L. "Cutting Efficiency of a Single PDC Cutter on Hard Rock." *Journal of Canadian Petroleum Technology* 48 (2009).

Kerkar, P.B., Hareland, G., Fonseca, E.R. and Hackbarth, C.J., "Estimation of rock compressive strength using downhole weight-on-bit and drilling models." In *International Petroleum Technology Conference*, pp. IPTC-17447. IPTC (2014).

Kouzaiha, R., Sayyaleh, S., Khalil, A., Borayek, A., Reyad, M., and Al Otaibi, A. "Using In-Bit Data Capturing Sensors to Identify and Reduce Dysfunctions Using a Higher Drilling Efficiency Shaped Cutter Solution." *Presented at the ADIPEC*, SPE, Abu Dhabi, UAE (2022). https://doi.org/10.2118/211535-MS

Liu, W., Fu, J., Tang, C., Huang, X., and Sun, T. "Real-time prediction of multivariate ROP (rate of penetration) based on machine learning regression algorithms: Algorithm comparison, model evaluation and parameter analysis." *Energy Exploration & Exploitation* 41, 1779–1801 (2023). https://doi.org/10.1177/01445987231173091

Mayibeki, D., G. Hareland, M. Al Dushaishi, and S. Blaylock. "The Effect of Confinement on Rate of Penetration (ROP) in Hard Rock." *Paper presented at the 57th U.S. Rock Mechanics/Geomechanics Symposium* (2023)

Motahhari, H.R., Hareland, G., and James, J.A. "Improved Drilling Efficiency Technique Using Integrated PDM and PDC Bit Parameters." *Journal of Canadian Petroleum Technology* 49 (2010).

Robertson, R., Deans, A., Singh, K., Braga, D., Kamyab, M., Cheatham, C., and Borges, T., 2023. "Field Test Results for Real-time ROP Optimization Using Machine Learning and Downhole Vibration Monitoring - A Case Study" *Presented at the SPE/IADC International Drilling Conference and Exhibition*, SPE, Stavanger, Norway (2023). https://doi.org/10.2118/212568-MS

Wang, B., Li, J., and Zou, D. "Design & Application of a PDC Hybrid Drill Bit with Impregnated --Diamond Cutter（IDC）for the Hard and Strong Abrasive Formations." *In ARMA US Rock Mechanics/Geomechanics Symposium* (pp. ARMA-2020). ARMA. (2020).

Yang, D., Song, X., Wang, Z., Pei, Z., and Zhu, Z. "PDC Bit Wear Detection Based on YOLO V5 and OpenCV." *Presented at the 56th U.S. Rock Mechanics/Geomechanics Symposium*, ARMA, Santa Fe, New Mexico, USA (2022). https://doi.org/10.56952/ARMA-2022-0351

Zhou, B., Zhang, M., Wang, L., and Ma, G. "Experimental study on mechanical property and microstructure of cement mortar reinforced with elaborately recycled GFRP fiber." *Cement and Concrete Composites* 117, 103908 9 (2021). https://doi.org/10.1016/j.cemconcomp.2020.103908

Predicting Steam Production in Water-Dominant Geothermal Reservoirs affected by Reinjection rate Using Recurrent Neural Networks

Magnus Thor Jonsson and Lilja Magnusdottir

University of Iceland, HS-Orka

Keywords

Recurrent Neural Network, Geothermal Reservoir, Pressure Drawdown, Reinjection

ABSTRACT

This research explores the use of Recurrent Neural Networks (RNNs) to predict pressure drawdown in both water-dominant and shallow steam wells within geothermal reservoirs affected by reinjection practices. Reinjection, a common technique to maintain reservoir pressure and extend the lifespan of geothermal systems, introduces complexities due to the interaction between reinjected and native fluids, significantly impacting steam production rates.

The study aims to develop a RNN model that utilizes historical data on water and steam production, reservoir characteristics, and injection practices to accurately forecast pressure drawdown in both the water part of the reservoir as well as in the steam zone. RNNs, with their capability to retain past information and predict future events in time-series data, provide a promising approach to modeling the non-linear and dynamic behavior of geothermal reservoirs influenced by reinjection.

A dataset generated using a 3D numerical reservoir model, including pressure in water-dominant and steam-dominant wells, as well as fluid, steam, and injection rates, forms the basis for training and validating the RNN model. The model's performance is compared against both measured data and predictions from a lumped parameter model to highlight its forecasting accuracy and reliability.

The results demonstrate that the RNN model outperforms the lumped parameter model in predicting pressure drawdown in water-dominant wells. It also effectively predicts steam pressure drawdown, accounting for the transient effects of reinjection on reservoir behavior.

1. Introduction

Geothermal energy, a sustainable and renewable resource, has the potential to play a significant role in meeting global demands for sustainable energy. Geothermal reservoirs, especially those dominated by water, are essential sources of geothermal energy. In these systems, the production of steam plays a crucial role in energy generation. One common method to sustain reservoir pressure and extend the lifespan of these resources is reinjection. Reinjection involves the process of reintroducing fluids back into the geothermal reservoir after energy extraction. While this practice helps maintain reservoir pressure, it also introduces complexities due to the interaction between reinjected and native fluids. Understanding and predicting the effects of reinjection on steam production in shallow wells is essential for optimizing the management of geothermal energy extraction.

Traditional methods of predicting steam production in geothermal reservoirs often rely either on complex 3D numerical models with many unknown parameters that are difficult to calibrate or on lumped parameters models that may not adequately capture the intricate dynamics of reinjection and its effect on the steam zone in the reservoir. As a result, there is a need for more advanced and accurate predictive tools. Recent advancements in Artificial Intelligence (AI) and machine learning offer promising solutions to address these challenges.

Recurrent Neural Networks (RNNs) have demonstrated their capability to model time series data and complex temporal relationships, making them suitable for predicting steam production in geothermal reservoirs influenced by reinjection practices. Production and injection management is important for optimizing the geothermal resource. Although it is crucial, only limited research on using machine learning has been published in this area. Siler et al. (2022), did a study where machine learning (ML) models were utilized to enhance performance predictions for geothermal reservoirs by combining reservoir modeling with ML to produce accurate predictions of temperature and pressure timeseries for productions wells. More commonly, AI techniques have been used for geothermal potential assessments such as extracting hidden features from hydrological data, generating geothermal potential maps, and identifying production-associated geologic factors (Song et al., 2021; Zhou et al., 2020; Lai et al., 2019; Garcia et al., 2018; Noh et al., 2018).

This research focuses on the application of RNNs to predict pressure drawdown, especially in shallow steam wells, in water-dominant geothermal reservoirs where a steam cap has formed. Shallow wells are particularly challenging due to their susceptibility to changes in reservoir dynamics and reinjection impacts on the steam zone. By leveraging the strengths of RNNs, this study aims to develop a predictive model that can accurately forecast pressure in both the water and steam parts of the reservoir, taking into account the complex interactions between reinjected and native fluids. The objective is to evaluate the impact of reinjection practices on steam production , thereby aiding in the optimization of reinjection strategies.

Integrating advanced AI techniques with geothermal reservoir management, this research aims to enhance the efficiency and sustainability of geothermal energy production. The findings are expected to improve the understanding of reinjection dynamics and boost predictive capabilities for steam production, thereby optimizing extraction processes. This predictive tool can help optimize operational strategies, ensure sustainable reservoir management, and enhance the economic viability of geothermal projects. By offering a novel approach to managing the

complexities of reinjected reservoirs, this study contributes significantly to advancing the field of geothermal energy production.

This paper is structured as follows: Section 2 provides an overview on geothermal energy production, reinjection practices, and the application in geothermal reservoir modeling. Section 3 details the data collection and preprocessing. Section 4 discusses the architecture of the Long Short-Term Memory (LSTM) RNN model. Section 5 presents the results of the study, highlighting the performance of the RNN model in predicting steam production. Finally, Section 6 concludes the paper with a summary of key insights.

2. Geothermal Energy Production

Geothermal energy production harnesses the Earth's internal heat to generate electricity and provide heating. This sustainable energy source is derived from the natural thermal energy contained within the Earth's crust. The process begins by drilling wells into geothermal reservoirs, which are typically located in regions with high tectonic activity. These reservoirs contain hot water and steam, which are brought to the surface through production wells as shown in Figure 1.

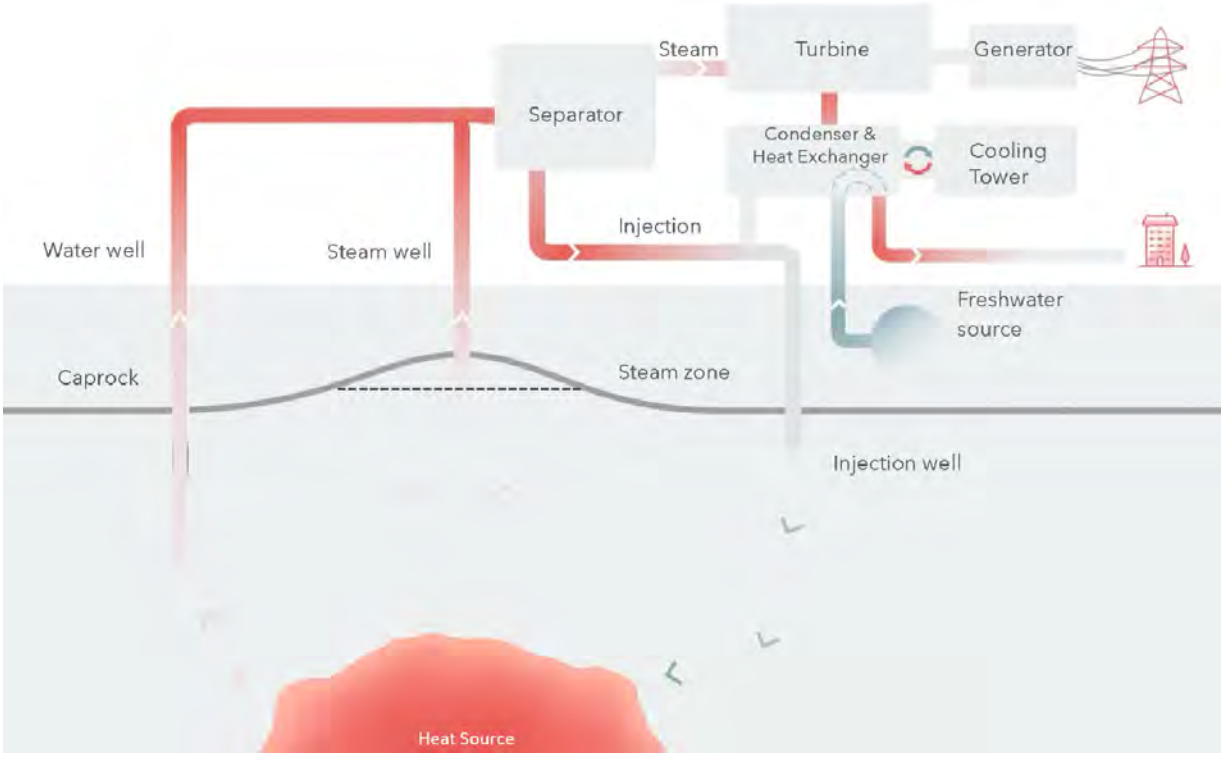

Figure 1: A geothermal power plant producing electricity and hot water from both water and steam wells.

Once at the surface, the hot water and steam are directed to a geothermal power plant. There are three main types of geothermal power plants: dry steam, flash steam, and binary cycle. Dry steam plants take steam directly from fractures in the ground and use it to drive a turbine that generates electricity. Flash steam plants pull deep, high-pressure hot water into cooler, low-pressure water, causing the rapid vaporization or "flashing" of the water into steam, which is then used to drive a turbine. Binary cycle plants transfer the heat from geothermal hot water to another liquid that boils at a lower temperature than water; this secondary liquid is vaporized and used to turn a turbine.

One of the primary advantages of geothermal energy is its low environmental impact. Geothermal plants emit very low levels of greenhouse gases compared to fossil fuel-based power plants. Additionally, geothermal energy provides a stable and reliable power source, unlike solar and wind energy which are intermittent. The continuous availability of geothermal resources allows for consistent base-load power generation, making it a valuable component of the renewable energy mix.

The efficiency of geothermal energy production depends significantly on the characteristics of the geothermal reservoir, including its temperature, pressure, and fluid composition. The energy production involves managing the extracted fluids, which may contain various minerals and gases. The re-injection of cooled geothermal fluids back into the ground helps to sustain the pressure in the reservoir and mitigate environmental impacts. This system ensures the long-term sustainability of the geothermal resource.

Effective management of a geothermal reservoir involves precise control over various operational parameters, such as the wellhead valve openings, production rates for each well site or area, and the injection rates. The complexity of these tasks is compounded by the diversity of wells within the reservoir. Some wells penetrate deep into water-dominated layers at high pressure, while others extend just below the caprock to capture steam, as illustrated in Figure 1.

In conclusion, geothermal energy production is a sustainable and reliable method of harnessing the Earth's internal heat for power generation and heating. With its low environmental impact and potential for continuous energy supply, geothermal energy plays a vital role in the renewable energy landscape. The future of geothermal energy production lies in improving the efficiency of extraction and utilization processes, reducing costs, and expanding the geographical reach of geothermal projects. Ongoing research and technological innovations are essential to overcoming the challenges associated with geothermal energy production and realizing its full potential as a major contributor to global energy needs.

3. Data Pipeline

Effective machine learning relies heavily on the quality and preparation of the input data. Thus, a robust data pipeline is crucial. It encompasses the entire process of collecting, processing, and transforming raw data into a form suitable for use by a machine learning model. This process involves several critical steps: data collection, data preprocessing, data transformation, storage, and workflow management. Effective data preprocessing is essential as it ensures the data is clean, normalized, and formatted correctly, which significantly enhances model performance and generalization. Without proper preprocessing, models may learn from noise rather than meaningful patterns, leading to poor predictions.

In this study, historical data spanning 43 years from various sources, including water wells, steam wells, and injection wells, serves as the foundation for the analysis. Key variables such as date, reservoir pressure, and flow rates were organized in a time-series format. To model the reservoir's response to these operational conditions, a comprehensive dataset is essential. This dataset forms the backbone for training and validating the Recurrent Neural Network (RNN) model, enabling accurate predictions and informed decision-making.

The primary components of this dataset include mainly the production rate, pressure data and injection rates generated using a 3D reservoir model of a geothermal reservoir in Iceland. However, production and injection rates used in the model to simulate the pressure drawdown, were synthetically generated as laws in Iceland prevent geothermal companies from sharing that data. Pressure data is vital for monitoring the reservoir's pressure dynamics, which are influenced by production and reinjection activities, as shown in Figure 2. Records of injection volumes are necessary to quantify the amount of fluid being reinjected into the reservoir. Monitoring injection volumes also aids in assessing the effectiveness of reinjection in maintaining reservoir pressure and prolonging the reservoir's productive life. By correlating steam production records with other dataset components, the RNN model can be trained to predict future pressure and production trends and optimize operational decisions.

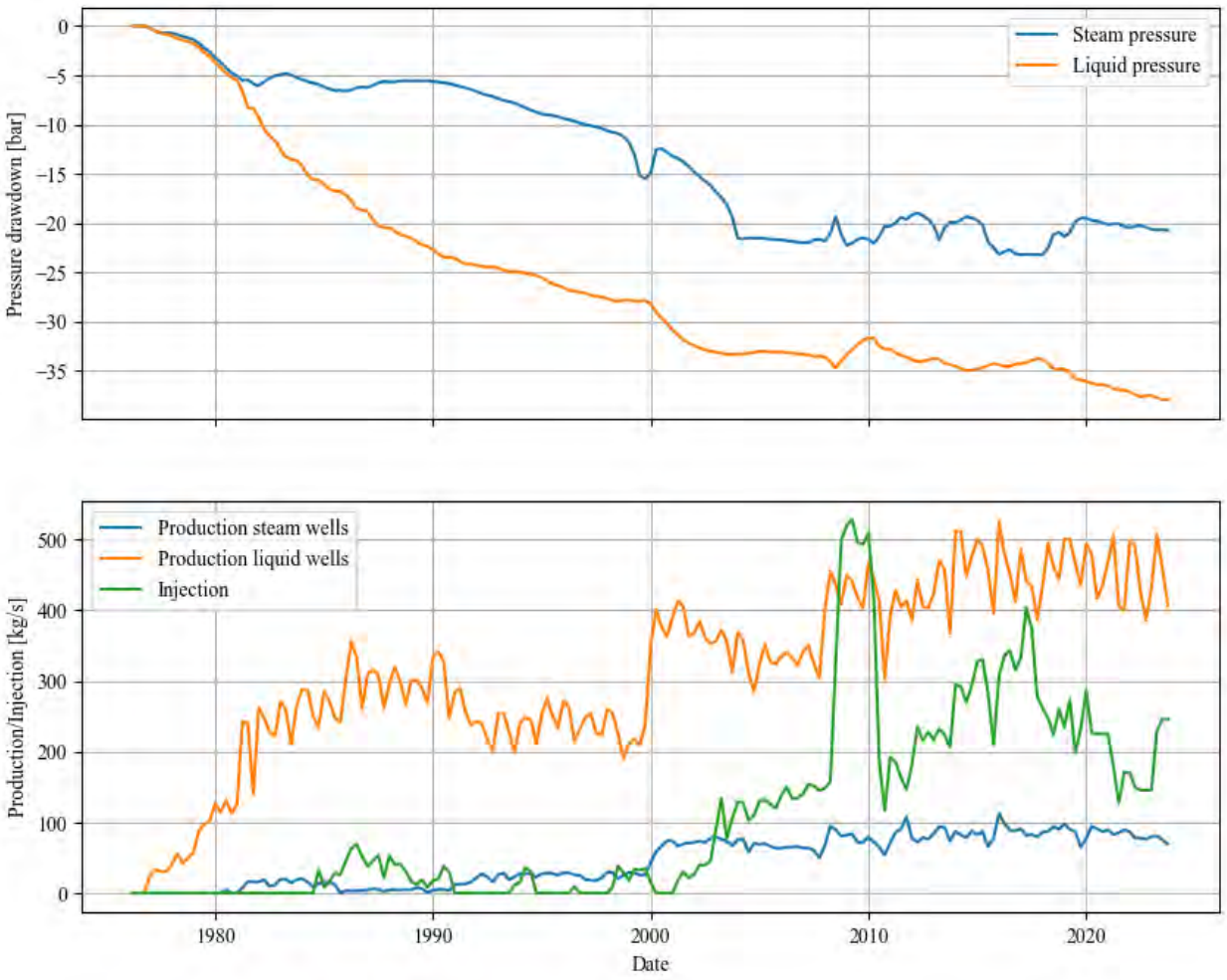

Figure 2: Production and injection rates, and pressure drawdown in both water and steam wells.

The data collection process entails ongoing monitoring and recording of the specified parameters through a network of sensors and measurement devices positioned at various well sites. These devices are calibrated regularly to ensure data accuracy and reliability. The data is then transmitted to a central database for storage and further analysis.

Preprocessing involved handling missing values through interpolation or forward-filling methods, differencing to remove trends, and normalization to ensure the data values were within a suitable range for model convergence. The following subsections will explain the preprocessing steps used to prepare the data for training.

3.1 Differencing

Differencing is the first process in the data pipeline. This procedure not only centers the data but also smooths out fluctuations during model training, resulting in a more stable training process. First-order differencing involves subtracting each data point from the previous one, centering the data and eliminating trends.

3.2 Normalization

Normalization is essential when dealing with multivariate time series of different scales. It involves scaling the data so that the standard deviation of the training data is set to unity and its mean to zero. This is achieved by dividing each value by the standard deviation of the training set and subtracting the mean. To prevent data leakage, the mean and standard deviation are calculated only from the training set. The same normalization transformation is then applied to the test set to ensure comparability.

The normalization formula is:

$$\boldsymbol{X}_{norm} = \frac{\boldsymbol{X} - \mu_{Xtrain}}{\sigma Xtrain} \tag{1}$$

where $\boldsymbol{X}$ is the original time series, $\boldsymbol{X}_{norm}$ is the normalized version, μ_{Xtrain} is the mean of the training set, and σ_{Xtrain} is the standard deviation of the training set. If $\boldsymbol{X}$ is also the training set, then it will be normalized to have a mean of zero and a standard deviation of one.

3.3 Batching

For batch learning with time series data, it is necessary to create fixed-length sequences using a sliding window approach. This involves sliding two side-by-side windows over the dataset, one step at a time. The points inside the first window are collected and stored as a sequence, maintaining their temporal order. This sequence serves as the input for the models. The second window, positioned one step to the right, contains the target data that the model must predict based on the input sequence.

Figure 3 illustrates the sliding window method, where circles represent data points, marked with the first letter of the variable and a subscript denoting their time step. An input window of size I_s and a target window of size T_s are shown side by side, with their subsequent shifted windows.

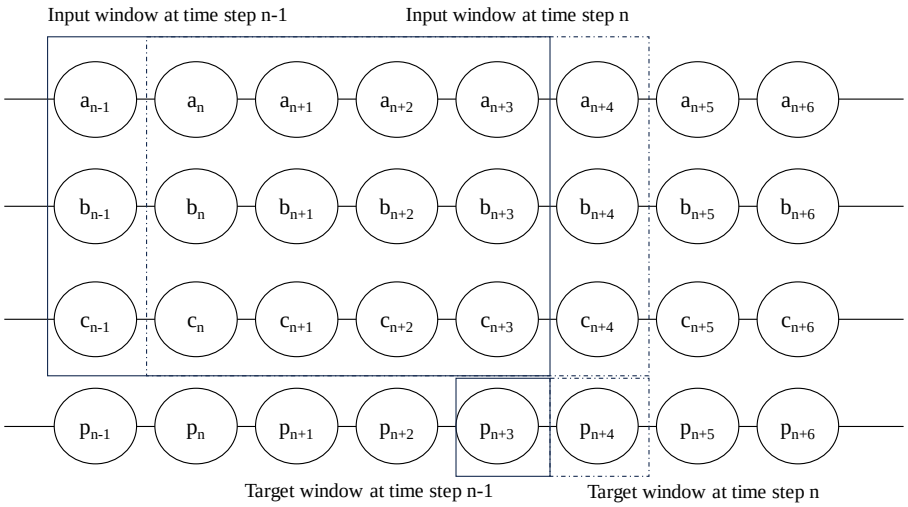

Figure 3: Diagram showing sliding window method

The length of the input sequence, I_s, is a hyperparameter that needs tuning. The ideal input size captures the most significant features of the data while providing the model with the temporal context necessary for accurate long-term predictions.

3.4 Splitting

Evaluating a model's performance requires testing it on unseen data. Typically, data is split into three sets: a training set, a validation set, and a test set. The training set is used for model training, the validation set for tuning hyperparameters, and the test set for evaluating performance on unseen data. Initially, only the train and test sets are necessary. Once the model achieves acceptable performance, a validation set can be introduced to further assess its generalization ability.

For time series data, it is crucial to split the data chronologically to ensure the model is not trained on future data, which could leak information and result in overfitting. This approach ensures the model learns to predict future trends based solely on past data, maintaining the integrity of the predictive process.

In summary, the data pipeline for this study involves careful preprocessing, including differencing, normalization, batching, and proper splitting, to prepare the data for LSTM network training. These steps are essential for ensuring the model can effectively learn and generalize from the historical data, leading to accurate predictions of reservoir pressure drops.

4. Long Short-Term Memory Neural Network Model

Long Short-Term Memory (LSTM) is a specialized architecture within the realm of Recurrent Neural Networks (RNNs), renowned for its ability to address the vanishing gradient problem, as outlined in Pattern (2006). RNNs are designed to handle sequential data by maintaining a hidden state that captures information about the sequence seen so far, effectively serving as a memory matrix. LSTMs enhance this capability by introducing a more sophisticated internal structure compared to standard RNNs.

From a high-level perspective, an LSTM network resembles an ordinary neural network, such as a Multi-Layer Perceptron (MLP), but each neuron is replaced with an LSTM cell, the fundamental building block of an LSTM model. Each LSTM cell contains internal mechanisms called gates that regulate the flow of information in and out of the cell, allowing it to remember or forget information over long periods. This gating mechanism includes three types of gates: the input gate, the forget gate, and the output gate. These gates control how much of the current input and the previous cell states should be updated, retained, or discarded, making LSTMs particularly well-suited for time series data where long-term dependencies are crucial.

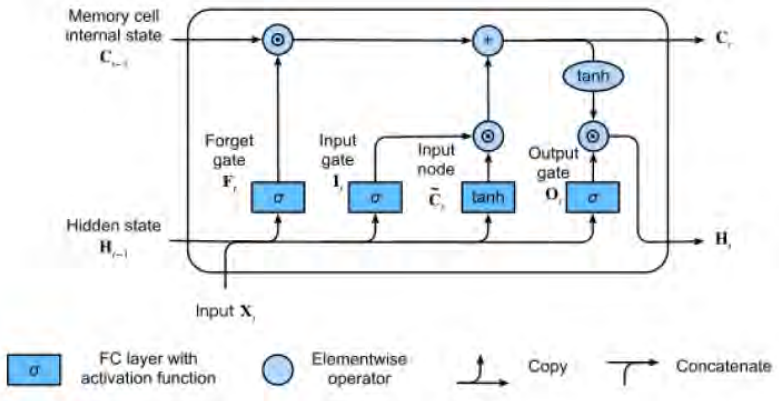

Figure 4: LSTM cell

The input to each LSTM cell at time step t is the concatenated values of the time series at that step, denoted as $x_t = [a_t, p_t, s_t]$, where a_t, p_t, and s_t are individual components of the input series as shown in Figure 4. Additionally, each cell receives the hidden state (h_{t-1}) and the cell state (C_{t-1}) from the previous time step. Each LSTM cell processes this information through its gates:

- Forget Gate: Determines which information from the cell state should be discarded.

- Input Gate: Decides which new information should be added to the cell state.

- Output Gate: Determines the output of the cell, which is based on the cell state.

The internal operations involve matrix multiplications and activation functions, which modulate the inputs through the gates, updating the hidden state and cell state accordingly. These updated states are then passed to the next cell in the sequence.

LSTM cells can be organized in different configurations. In single-layer configurations, cells are aligned horizontally, forming a single chain where the output of one cell becomes the input for the next. In stacked layer configurations, multiple layers of LSTM cells are stacked vertically, allowing the network to learn more complex representations of the input data. In these configurations, the hidden states ($h_i^{(k)}$) of the cells in different layers and time steps interact, with each cell in a layer having recurrent connections to itself over time.

The output from each LSTM cell can be extracted directly from the output gate and typically passes through a fully connected layer to match the desired output shape. This output can be used in

various ways, such as direct prediction for the current time step, as input to the next layer of cells in a layer-wise passing fashion, or for sequence generation tasks where future values in a sequence prediction task are generated.

While theoretically, a sufficiently complex MLP could model any function that an LSTM can, in practice, LSTM networks are more efficient for sequential data due to their recurrent structure and shared weights across time steps. This recurrent nature allows LSTMs to capture temporal dependencies more effectively, making them a preferred choice for tasks involving time series prediction, natural language processing, and other sequence-related applications.

In summary, LSTM networks provide a robust solution for modeling time series data. By leveraging their unique gating mechanisms, they can effectively learn long-term dependencies, address the vanishing gradient problem, and provide accurate predictions. Their architecture, combining hidden states and cell states, allows them to maintain and update information across time steps, making them particularly suitable for complex sequential data analysis.

5. Results

In this study, we employed Recurrent Neural Networks (RNNs), specifically Long Short-Term Memory (LSTM) networks, to predict steam production in water-dominant geothermal reservoirs affected by varying reinjection rates. The dataset used for training and validation encompassed 43 years of historical data, including variables such as reservoir pressure, water and steam flow rates, and reinjection rates. Our model aimed to capture the complex temporal dependencies and interactions within the data to provide accurate predictions of steam production.

The LSTM network was trained on 80% of the data and validated on the remaining 20%. The model's performance was evaluated using standard metrics such as Mean Squared Error (MSE) and Mean Absolute Error (MAE), and Table 1.1 shows the hyperparameters used for the prediction.

Table 1: RNN's model hyperparameters.

Parameter	Symbol	Value
Activation function	*A*	*Relu*
Training loss function	*MSE*	*MSE*
Input length	*I*	*16*
Hidden layers	*K*	*3*
Hidden layers size	*h*	*64*
Learning rate	α	$4\ 10^{4}$
Batch size	*B*	*64*
Number of epochs	*E*	*230*

Figure 5 shows the predicted steam pressure versus the actual values for the validation set. The close alignment of the predicted values with the actual values indicates that the LSTM model effectively captures the underlying patterns and temporal dependencies in the data.

Figure 5: Predicted vs actual steam pressure in a water dominated well.

A lumped parameter model was also set up for this research for the geothermal system in Iceland using the LUMPFIT program to predict the drawdown in the system. In lumped parameter models, two or more tanks are used to simulate the water capacity of the rock layers, and flow resistance is used to simulate their permeability. The models are calibrated based on pressure history and cumulative mass production. Lumped parameter models are much simpler than three-dimensional numerical models and are based on different assumptions. For instance, they do not consider the properties of individual rock layers and cannot simulate phase boundaries or thermal fronts. They are also not useful for determining well locations, such as for reinjection. However, for simple systems, they can be powerful for predicting drawdown trends based on estimated mass extraction.

In the lumped parameter model (LPM) for this research, data from the 3D reservoir model on pressure measurements and mass extraction from 1983 to 2019 were used to calibrate the LPM and calculate the drawdown prediction from 2019 to 2023. The best fit for the data was obtained using a 2-tank closed model. Although the LPM showed an adequate fit to the historic data, the results for the predicted pressure were more accurate using the RNN model, as shown in Figure 6.

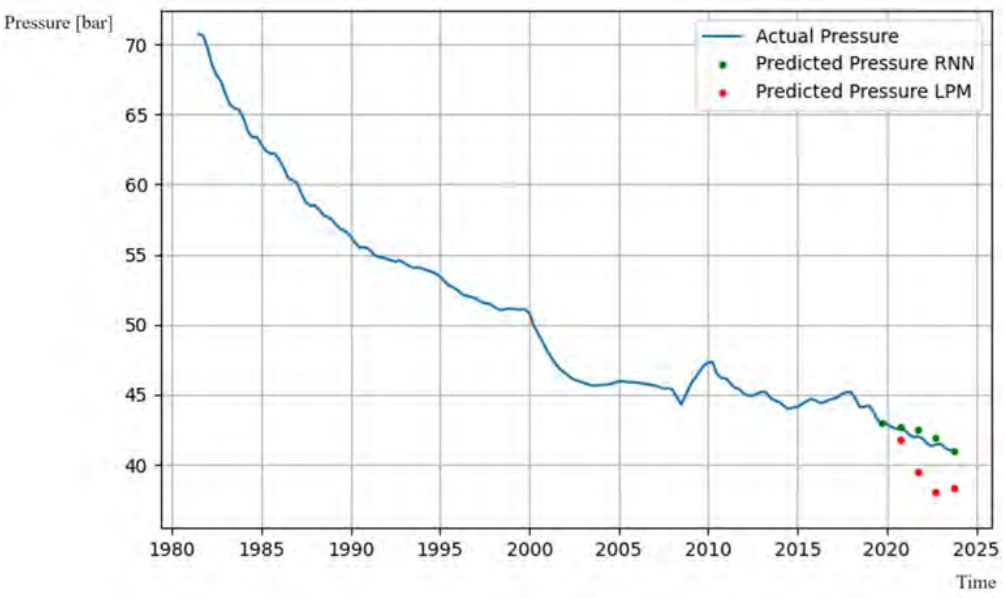

Figure 6: Predicted pressure drawdown using Lumped parameter model and RNN model.

The LPM does not have the capability of simulating the steam zone, only the liquid part of the reservoir. However, the RNN was trained for predicting the pressure drop in a steam dominated well. The fit to the measured stream pressure was good, as seen in Figure 7.

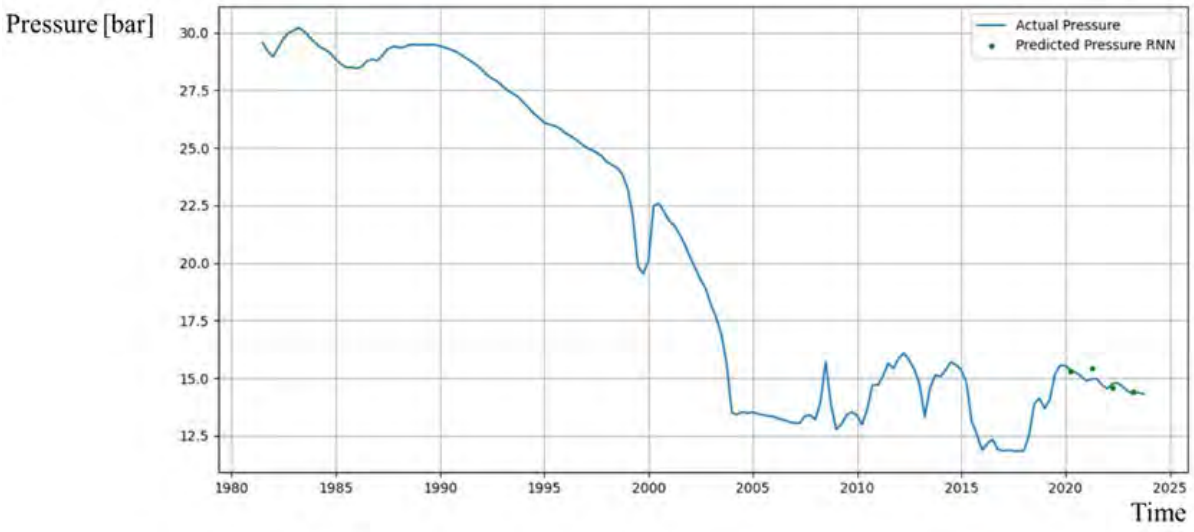

Figure 7: Predicted vs Actual Steam Pressure in steam dominated well

Overall, the LSTM model achieved an MSE of 0.002 and an MAE of 0.015 on the validation set, indicating high accuracy and reliability in steam production forecasting. The possibility of predicting the pressure in the steam zone is crucial to optimize injection strategies and ensuring long-term production from the steam wells.

6. Conclusions

This research demonstrates the efficacy of Long Short-Term Memory (LSTM) networks in predicting steam production in water-dominant geothermal reservoirs influenced by reinjection rates. The ability of LSTM models to capture long-term dependencies and complex temporal patterns makes them well-suited for this application.

The results indicate that the LSTM model provides accurate predictions, closely aligning with the actual steam production values and showing no significant bias. The model's robustness is further validated by its consistent performance across varying reinjection rates, underscoring its potential as a reliable tool for geothermal reservoir management.

The successful implementation of LSTM networks in this study opens up new avenues for predictive modeling in geothermal energy production. By providing accurate forecasts, these models can aid in optimizing operational strategies, enhancing the efficiency of resource utilization, and improving overall energy production management. Future work can explore integrating additional variables and using more advanced neural network architectures to further enhance prediction accuracy and model robustness.

In conclusion, LSTM networks represent a powerful and versatile approach for forecasting pressure drawdown in the steam zones of geothermal reservoirs, offering significant advantages over traditional methods. Their ability to handle complex, sequential data and adapt to varying operational conditions makes them an invaluable asset in the field of geothermal energy management.

REFERENCES

Box, G.E.P, Jenkins, G.M. and Reinsel, G.C. "Time Series Analysis". 3rd ed. Upper Saddle River, NJ: Pearson, Feb. 1994.

Garcia Gonzalez, C., Ledesma-Ramirez, D., & Tejeida-Padilla, R. (2018). "Predicting geothermal energy potential using a combination of machine learning algorithms and GIS." *Energy Procedia*, 154, 409-414.

Glorot, X. and Bengio, Y. "Understanding the difficulty of training deep feedforward neural networks. " *AISTATS. Ed. by Yee Whye Teh and D. Mike Titterington. Vol. 9. JMLR Proceedings*. JMLR.org, 2010, pp. 249–256. url: http : / / dblp . uni - trier . de / db / journals / jmlr /jmlrp9.html#GlorotB10.

Hochreiter S. and Schmidhuber, J. "Long Short-term Memory". Neural computation 9 (Dec. 1997), pp. 1735–80. doi: 10.1162/neco.1997.9.8.1735.

Kingma D.P. and Adam J.B."A Method for Stochastic Optimization". 2017. arXiv: 1412.6980 [cs.LG].

Lai, J., & Dzunic, M. (2019). "Geothermal resource assessment using deep learning algorithms: A case study in the Great Basin, USA." *Renewable Energy*, 140, 101-112.

Noh, J., Kim, S., & Lee, K. (2018). "Application of artificial neural networks for geothermal potential mapping in South Korea." *Renewable and Sustainable Energy Reviews*, 92, 649-660.

Pattern C.M. "Recognition and Machine Learning". 1st ed. New York, NY: Springer, 2006.

Siler, D. L., Martin, M. J., & Johnston, H. E. (2022). Modeling subsurface performance of a geothermal reservoir using machine learning. *Energies*, 15(3), 967. https://doi.org/10.3390/en15030967

Song, W., Hu, J., & Lu, Z. (2021). "Using convolutional neural networks to assess geothermal potential based on remote sensing data." *Journal of Geophysical Research: Solid Earth*, 126(5), e2020JB021017.

Williams, R.J. and Zipser, D. "A Learning Algorithm for Continually Running Fully Recurrent Neural Networks". Neural Computation 1.2 (1989), pp. 270–280. doi: 10.1162/neco.1989.1.2.270.

Zhou, X., He, L., Li, X., & Xu, G. (2020). "A machine learning approach to estimate geothermal potential from geological and geophysical data." *Geothermics*, 87, 101876.

Development of Artificial Neural Networks for Estimating Static Formation Temperature

Shunsuke Kaneko, Shigemi Naganawa and Elvar K. Bjarkason

Graduate School of International Resource Sciences, Akita University, Japan

Keywords

Formation temperature, estimation, machine learning, neural networks, geothermal wells

ABSTRACT

This study looks at using artificial neural networks (ANNs) for estimating the static formation temperature (SFT) in geothermal wells. SFTs are conventionally estimated from temperature recovery data using some form of linear regression, such as the Horner method. However, there are a multitude of regression models to choose from, and the optimal one is not settled and may be situation specific. Moreover, commonly used linear regression methods, like the Horner method, require suitably long shut-in periods for their linearization assumptions to apply. As an alternative, machine learning methods have been considered previously to some extent for estimating SFTs. Nevertheless, the development of machine learning alternatives has been limited by available field data and especially accurate SFT data. In this study, we look at using ANNs for estimating the SFT in geothermal wells based on transient temperature recovery data. For training the ANNs, a large set of synthetic temperature recovery data was generated using a wellbore simulator called GEOTEMP2. The GEOTEMP2 simulations describe the temperature in a wellbore during drilling and the following recovery period after drilling. The developed ANN model was evaluated by comparing its estimation accuracy with the Horner method for synthetic validation data. On average, the ANN model provided SFT predictions of comparable quality to the standard Horner method.

1. Introduction

Accurate knowledge of static formation temperatures (SFTs) is important to ensure efficiency and safety when drilling wells in geothermal fields, as well as to determine whether development is possible (Sasaki, 1987). Furthermore, SFT estimates are used to understand the temperature distribution in geothermal fields and as reference data when calibrating geothermal reservoir models. SFTs can only be measured or estimated reliably by drilling wells and measuring temperatures down the wells. Logging equipment is lowered into the wellbore after drilling is completed or paused, and the formation temperature is determined based on temperature data

obtained from the logging. However, wellbore fluid circulation required during drilling shifts the wellbore temperature considerably below the formation temperature. Therefore, since it typically takes many days for the wellbore temperature to equilibrate with the surrounding formation temperature, multiple well logs are generally needed to understand how the wellbore temperature rebounds over time. Assuming negligible internal flow within the wellbore, the wellbore temperature can be expected to gradually rebound towards the SFT state that existed before drilling the well.

To estimate SFTs, analytical methods that are based on physical theory have been used in the past as well as simple empirical equations. The well-known Horner method is one of those methods that is commonly used in practice to estimate SFTs. The Horner method uses an approximate theoretical description of the thermal recovery of the temperature in the wellbore after the completion of drilling. The method requires an estimate of the time that fluid was circulated at the well depth of interest, and multiple bottom-hole temperatures measured at different times after shut in. Until now, the Horner method has been widely used for SFT estimation because of its simplicity, but this method requires sufficient shut-in time and an appropriate number of logging runs, which use up time and resources. A multitude of other SFT estimation methods have also been developed. However, it is not clear from the literature which methods should be preferred as the results appear to be generally inconclusive.

In response to these problems, this study proposes developing a new estimation method that applies machine learning as an alternative approach to SFT estimation. Previously, Bassam et al. (2010) developed an artificial neural network (ANN) model with one hidden layer to estimate SFTs. Their model used only three input values, including a bottom-hole temperature observation, the observation shut-in time, and an estimate of the derivative of the temperature with respect to time. A drawback of their neural network development approach was that the field data they used for training did not include reliable measurements for the SFTs. Because of that issue, they used multiple pre-existing SFT estimation methods to derive the reference SFT values used for training their neural network. Based on that, the training process could have been negatively impacted by inaccurate SFT training data.

As the Bassam et al. training procedure reflects, it is generally difficult to find reliable temperature data for training and validating SFT estimation methods. Therefore, the present study used a wellbore simulator to generate synthetic temperature recovery data to train neural networks. Differently to Bassam et al. (2010) we looked at developing deep neural networks containing multiple hidden layers to achieve better SFT estimates.

2. Methods

2.1 Horner Method

Figure 1 shows a schematic diagram of temperature recovery in a wellbore. The graph shows how the bottom-hole temperature is lowered when drilling fluid is circulated through the well. After fluid circulation ceases and the well is shut in, the well gradually warms up towards the SFT. As it can take a long time for the well temperature to equilibrate, the SFT is usually extrapolated from a series of well temperature logs recorded after shut in.

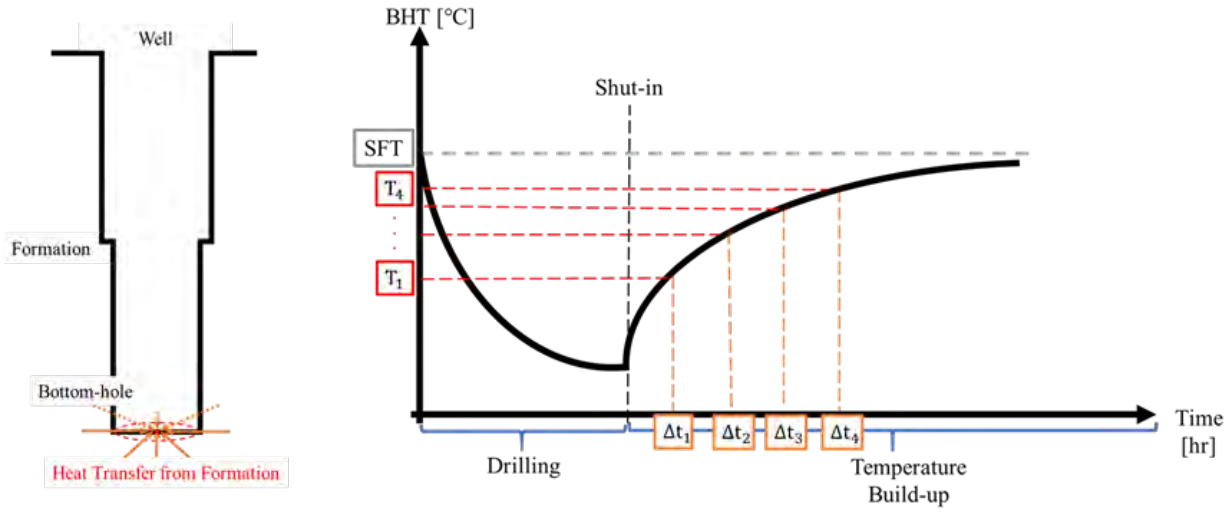

Figure 1: Recovery of bottom-hole temperature (BHT) after shutting in a well.

The Horner method has been widely used to estimate formation temperatures in geothermal wells. In the Horner approach, the SFT is estimated through linear regression by matching the following equation to the recorded temperature history.

$$T_{\mathrm{BHT}} = T_{\mathrm{SFT}} + m \times \log \frac{t_c + \Delta t}{\Delta t} \tag{1}$$

Here T_{BHT}, T_{SFT}, m, t_c, and Δt are the bottom-hole temperature, the SFT, slope, the fluid circulation time at bottom hole, and the elapsed time after shut in, respectively. The assumption is that the downhole temperature changes follow (1) when a sufficiently long time has elapsed.

The Horner plot equation (1) can be derived by describing the well as a line heat-sink drawing in a constant heat flux while the drilling fluid is circulating (see, e.g., (Kutasov and Eppelbaum, 2018)). However, that is a simplification of reality since the temperature conditions and heat flux across the well wall vary during operation. Similar simplifications have been used to derive various other analytical equations for SFT extrapolation. As a result, the applicability of those methods can be limited. Instead of using some of the standard analytical equations, we consider using ANNs to derive an empirical relationship between wellbore temperature recovery data and the SFT.

2.2 Neural Network Approach to SFT Estimation

2.2.1 Neural Network Architecture

This research aimed to develop an SFT estimation model using an ANN algorithm. The neural network model was developed using TensorFlow in Python. The ANN model in this study is a supervised learning model, in which the parameters of the model were adjusted so that it can estimate SFT values by learning hidden relationships between the ANN input data and the SFT values to be estimated.

Figure 2 shows a diagram of the multi-layered feed-forward neural network model developed in this study. The figure shows that the neural network outputs an SFT prediction based on nine model inputs: the circulation time, four observation times, and four corresponding bottom-hole

temperature observations. Figure 1 provides an example illustration of the four pairs of observation times (Δt_i) and temperatures (T_i) that are used as model inputs. In practice, available logging data can be limited and SFT estimation is sometimes carried out based on as few as three or even (with difficulty) two temperature observations. For reliability, however, we suspect that at least four observations might be needed to reveal useful information about the nonlinearity of the temperature transient. The number of temperature inputs were chosen based on that expectation and for the purpose of generating a simple neural network algorithm that would be applicable to cases with observations from only a few well logging runs.

A linear activation function was applied after the output layer of the model and a ReLU (rectified linear unit) activation function was used between all the layers. The number of nodes and hidden layers are not specified in Figure 2 since we tested out different combinations to optimize the ANN design. However, the tested neural networks were constructed with an equal number of nodes in each hidden layer. The following section describes the optimization of the network design.

2.2.2 Optimization of the Neural Network

To optimize the ANN model structure, we trained multiple neural networks using different combinations of layer and node numbers. Those hyperparameters were optimized using simple grid search with the number of hidden layers varied from one to five, and the number of nodes (neurons) in a layer varied from ten to a hundred at intervals of five nodes. The RMSProp (Root Mean Square Propagation) optimization algorithm was used to fit each ANN model to the training data. We chose to minimize the mean squared error (MSE) of the match to the SFT training data while monitoring the MSE of the SFT test data for early stopping. Each optimization run was stopped when the test MSE did not improve for 500 consecutive epochs. The maximum number of epochs was set to 5,000. The combination of network weights, biases, and hyperparameters (number of nodes and layers) that resulted in the lowest mean absolute error for the test data was adopted for the final ANN model. The final model obtained through this optimization process was a network with 3 hidden layers and 30 neurons in each layer. This model was subsequently tested on validation data to check its prediction performance.

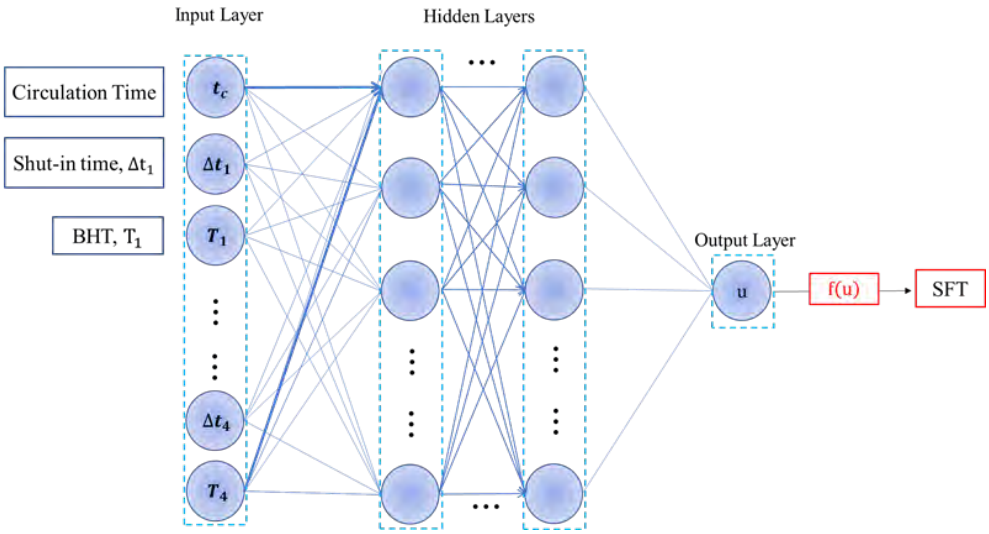

Figure 2: Conceptual diagram of the neural network used in this study.

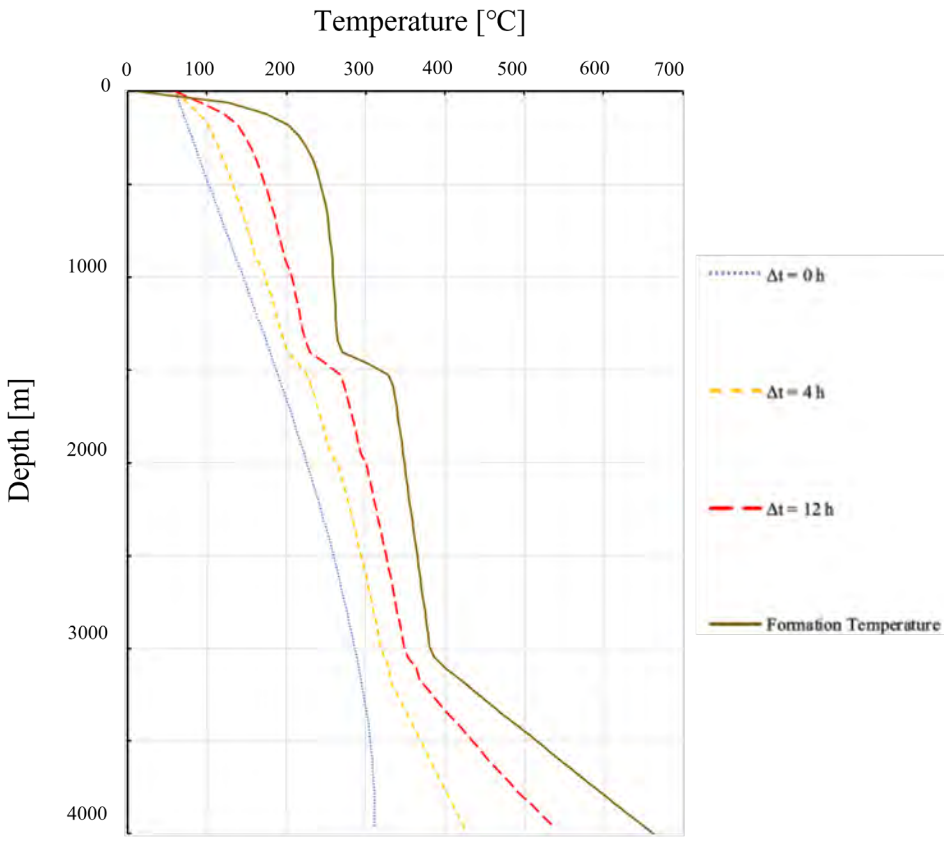

Figure 3: Example GEOTEMP2 simulation results for temperature recovery in a wellbore. Shut in is at $\Delta t = 0$. The static formation temperature shown is based on well WD-1a in the Kakkonda geothermal field, Japan.

2.3 Training Data

2.3.1 Creation of Training Data Using the GEOTEMP2 Well Simulator

The training data used to train the SFT estimation model was generated using a wellbore temperature simulation program called GEOTEMP2 developed at Sandia National Laboratories in the U.S. (Mondy et al., 1984). We used the simulator to model thermal transport within the wellbore for both the drilling period where the well is cooled by drilling fluid circulation and the warmup period when the well is shut in. GEOTEMP2 numerically solves the temperature distribution in a wellbore using a finite volume method for the heat transfer between the downhole fluids and rock formations surrounding the wellbore.

We note that the simulator describes thermal transport caused by both convection and conduction within the wellbore. However, the heat transport within the formation is limited to conduction. As a result, neural networks developed based on the GEOTEMP2 simulations are expected to be mainly applicable for conduction dominated formations.

Figure 3 shows examples of GEOTEMP2 simulated temperature profiles for a well warming up after halting fluid circulation. In this study, GEOTEMP2 was used to assemble a dataset containing multiple series of bottom-hole temperature recovery data. In total, we generated 20,000 instances of thermal recovery data from wellbore simulations. That dataset was used to develop the presented

neural network with 70% of the dataset used as training data and the remaining 30% of the data used as test data. Distinct data series were generated by randomly allocating the formation temperature and well operation conditions.

2.3.2 Range of Input Values for Well Simulations

The performance of a machine learning model depends largely on the quantity and quality of the training data used for the model development. In particular, the ANN generalization ability is expected to be improved by using data obtained from a variety of cases. Therefore, we diversified the training data by randomly allocating input values for the GEOTEMP2 simulations. Variable drilling parameters include the target drilling depth, the fluid circulation time (t_c) after reaching the target depth, and the fluid circulation rate. The target drilling depth varied between 100 and 4,000 m, while the drilling rate was set to a constant 50 m/day for all simulations. Similar drilling rates can be expected for typical geothermal wells. In fact, according to Ong'au (2012), the average drilling rate for wells in Kenya and Iceland is around 50 m/day. The circulation time was allowed to range from 2 to 48 hours, and the flow rate was randomly set to a value between 1,000 and 4,000 L/min (see, e.g., (Ajima et al., 2023; Ishikawa and Naganawa, 2022)).

The drilling fluid was assumed to be injected down the drill string from the surface at a constant temperature of 30°C. In addition, the formation temperature conditions were randomly assigned for each simulation. For simplicity, the temperature with depth profile was assumed to be linear. Thus, we only varied the temperature gradient and the ground surface temperature. This was achieved by randomly varying the surface temperature between 5 and 30°C, and the temperature at a 4 km depth was allowed to range between 100 and 800°C (Figure 4). Note that this SFT-depth profile assumption does not cover all field conditions since actual underground temperature profiles are often nonlinear—influenced by geological structures and groundwater flow. The thermal conductivity of the reservoir formation used in all cases the default value of 1.73 W/m·K in GEOTEMP2. However, we plan to vary the formation thermal conductivity in future work.

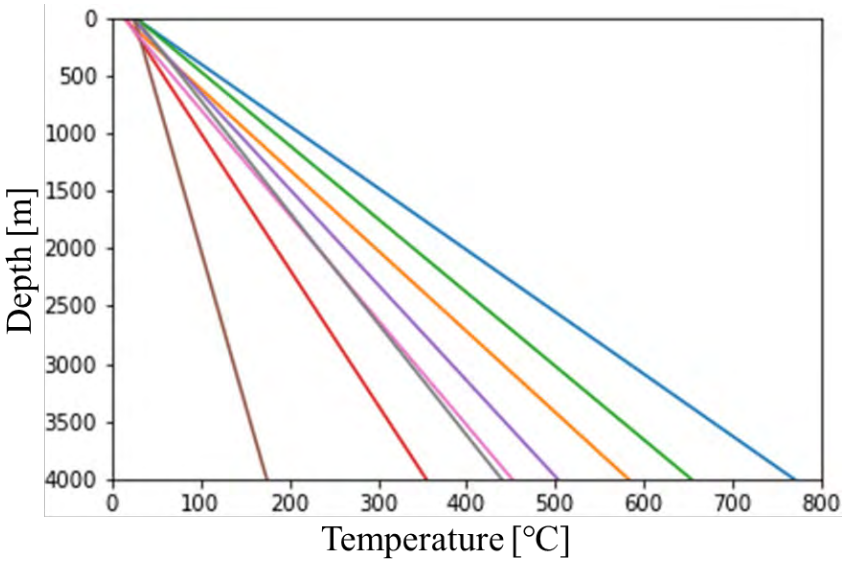

Figure 4: Example formation temperature gradients used for generating training data.

For the temperature observations, the constructed ANN model assumes that data from four logging runs are available. When generating the training dataset, the fourth observation time, Δt_4, was randomly varied from 10 to 250 hours, and the values for Δt_1 to Δt_3 were randomly selected within the range from one to Δt_4 hours. The temperature data obtained at those observation times was used as input into data for training the ANN model. The range of observation times was set to encompass the validation data used in this study.

2.4 Validation Data

The accuracy of the developed ANN static formation temperature estimation model was evaluated using data that is independent of the training data. In this study, the validation data includes synthetic data based on well WD-1a, a super-hot geothermal well drilled in the Kakkonda area of Iwate prefecture, Japan (Ikeuchi et al., 1998). The Kakkonda validation data was generated using the GEOTEMP2 simulator. However, unlike the formation temperature profiles used for training, the shallow Kakkonda temperature profile is characteristic of a convective, high-temperature geothermal field (Figure 3).

Table 1: Synthetic Kakkonda validation data for different bottom-hole depths.

2,000 m Depth		3,000 m Depth		3,700 m Depth		4,000 m Depth	
T_{SFT} = 349.3℃		T_{SFT} = 380.6℃		T_{SFT} = 580℃		T_{SFT} = 670℃	
Δt [h]	T_{BHT} [℃]	Δt [h]	T_{BHT} [℃]	Δt [h]	T_{BHT} [℃]	Δt [h]	T_{BHT} [℃]
46	304.7	5.2	295.8	73.1	561	70.5	647.9
64.3	310.9	24	353.7	75.7	561.5	78.8	649.7
74.7	313.77	113.4	368.9	145.1	568.1	104.9	653.2
86.3	316.33	163.4	371.4	180.6	569.8	132.1	655.7

Table 2: Validation data from the literature (Bassam et al., 2010).

Shen and Beck (1986)		Cao et al. (1988)		Iglesias et al. (1995)		Steingrimsson and Gudmundsson (2006)	
T_{SFT} = 80°C t_c = 5 h		T_{SFT} = 120°C t_c = 5 h		T_{SFT} = 169°C t_c = 5 h		T_{SFT} = 240°C t_c = 2.5 h	
Δt [h]	T_{BHT} [℃]	Δt [h]	T_{BHT} [℃]	Δt [h]	T_{BHT} [℃]	Δt [h]	T_{BHT} [℃]
15	69.6	24	115.8	12	94	30	125
20	71.7	30	117.1	26.57	122	52	158
30	74.1	40	118.4	47.1	139	96	184
40	75.5	50	119.1	95.27	152	242	218

Table 1 summarizes the temperature recovery data generated using GEOTEMP2 based on the temperature profile of well WD-1a in Kakkonda. The fluid circulation time was commonly set to 48 hours for the cooling operation after the target drilling depth was reached, and the simulations were run for four different bottom-hole depth cases. The flow rate was set to 2,000 L/min for all four cases.

Moreover, we also considered validation data used previously by Bassam et al. (2010). Table 2 summarizes this additional validation data. It includes synthetic warmup data reported by Shen and Beck (1986) and Cao et al. (1988). Those datasets have known SFT values that are useful for validation. For real geothermal field examples, we considered well tests reported by Iglesias et al. (1995) for well CH-A in El Salvador and Steingrimsson and Gudmundsson (2006) for well KJ-21 in Iceland. The values reported in Table 2 for those two wells are taken directly from (Bassam et al., 2010). We note, however, that we have not been able to confirm the reliability of those reference values and we consider that the reference SFT values reflect plausible values.

For the datasets taken from the literature, we selected the last four reported temperature observations. An exception is the data from well KJ-21 reported by Steingrimsson and Gudmundsson (2006). For well KJ-21, we ignored data recorded at 556 hours of shut in.

3. Results

The newly developed ANN model was evaluated using the validation data presented in Tables 1 and 2. Figure 5 shows the results of SFT estimation using the newly developed ANN model and the Horner method. The SFT estimates are compared against the reference SFT values for the validation data. The straight line drawn in the figure has a slope of 1, indicating that the closer the data points are to the straight line, the smaller the estimation error. The figure shows for both the ANN model and the Horner method that the estimation errors are within or close to ±5% for all validation data.

Table 3 summarizes the results of Figure 5 in more detail. From left to right, there are the reference SFT values for the test data, the estimated values by the ANN model, the estimated values by the Horner method, the deviation (error) between the ANN model and the reference (true) values, and the deviation (error) between the Horner method and the reference (true) values. The maximum estimation errors of the ANN model and Horner method for all validation data are respectively 8.0% and 6.8%. The average error is 3.2% for the ANN model and 2.7% for the Horner method. The ANN approach, therefore, performed nearly as well as the standard Horner method for the presented test cases.

The maximum estimation error of the ANN model is 0.6% for the Kakkonda synthetic data, which assumes a super-hot geothermal well. This indicates that the developed model can estimate formation temperatures above 400°C, which is considered to be in the high-temperature range, with good accuracy. On the other hand, the ANN approach showed larger errors for the low-temperature data, with a particularly high error for the synthetic dataset from Shen and Beck (1986). The error for the Cao et al. (1988) synthetic dataset is surprisingly high considering that the last temperature observation is within 1% of the true SFT. The Horner method gave considerably better estimates for those two datasets. However, the ANN model markedly outperformed the Horner method for the Kakkonda data. These results suggest that there might be

some features in the Shen and Beck, and Cao et al. datasets that are not reflected in the training dataset. This aspect needs to be explored further in future work.

The ANN estimates for the two geothermal wells (CH-A and KJ-21) appear to be plausible, which is an encouraging result considering that the field measurements are affected by measurement errors. Furthermore, the temperatures in those wells are affected by fluid flow through the surrounding formations, unlike the temperature simulations that generated the training data. Therefore, the ANN approach could potentially be robust to measurement errors and some conceptual differences between the heat transport governing the training data and field data.

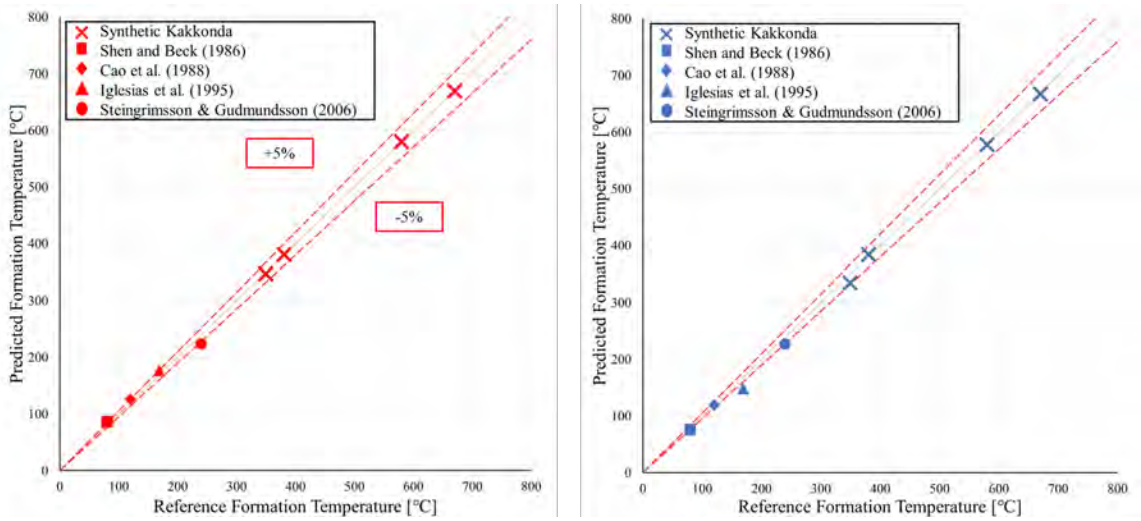

Figure 5: Comparison between reference static formation temperature data and estimated values using the developed ANN model (Left) and the Horner method (Right). The solid diagonal line indicates perfect agreement, while the red dashed lines signify errors of 5%.

Table 3: Results for estimated static formation temperature (SFT).

		Estimated SFT [°C]		Estimation error [%]	
	Reference SFT [°C]	ANN model	Horner method	ANN model	Horner method
Kakkonda 4 km	670	669.7	667.1	0.0	0.4
Kakkonda 3.7 km	580	580.0	577.5	0.0	0.4
Kakkonda 3 km	380.6	380.6	384.1	0.0	0.9
Kakkonda 2 km	349.3	347.3	334.6	0.6	4.2
Steingrimsson and Gudmundsson	240	223.5	223.59	6.9	6.8
Iglesias et al.	169	177.0	158.93	4.7	6.0
Cao et al.	120	126.3	122.5	5.3	2.1
Shen and Beck	80	86.4	79.5	8.0	0.6

4. Conclusions

In this study, we aimed to develop a new method for estimating the SFT in geothermal wells using an ANN algorithm. The neural network method estimates the SFT from transient temperature recovery data recorded while the well warms up after halting fluid circulation. The neural network was trained using a synthetic temperature recovery dataset generated using a wellbore simulator that describes temperature changes caused by fluid circulation during drilling and the following warmup period after the well is shut in.

The ANN estimation errors were found to be within 1% for synthetic validation data generated using the same wellbore simulator as was used to create the training data. However, the ANN errors were around 5–8% for synthetic validation data reported elsewhere in the literature. Moreover, when applied to field data from two geothermal wells influenced by natural convection, the ANN predictions deviated by about 5–7% from the expected reference values. On average, the performance of the ANN approach was similar to the standard Horner plot method. The Horner method resulted in an average percentage error of 2.7% while the average was 3.2% for the ANN approach. A more detailed comparison shows that the ANN method outperformed the Horner method for synthetic datasets generated using the GEOTEMP2 wellbore simulator used in this study. For the synthetic GEOTEMP2 validation data, the average error was 0.2% and 1.5% for the ANN approach and the Horner method, respectively. The ANN errors were noticeably worse for synthetic validation data generated by other means in the literature. This indicates that the data used to train the ANN model may lack relevant features and there is room to improve the training dataset.

Although additional testing is needed, these results indicate that this machine learning approach holds promise for estimating SFTs in geothermal wells. However, improvements are needed to make the presented ANN approach widely applicable. Future work should consider extending the training dataset and other ways of improving the optimization of the ANN model parameters and possible enhancements of the model architecture. The neural network presented here uses a fixed number of temperature inputs. In future work, it may therefore be worth considering extending this approach to allow more flexibility in the number of inputs. Furthermore, we are interested in exploring the potential advantages of this approach for short observation histories for which traditional methods, such as the Horner method, usually fail to deliver good predictions. We also think it is necessary to examine more field data for validation purposes.

REFERENCES

Ajima, K., Naganawa, S., and Bjarkason, E. K. "Application of insulated drill pipe to supercritical/super-hot geothermal well drilling." *Proceedings, ASME 2023 42nd International Conference on Ocean, Offshore and Arctic Engineering,* (2023).

Bassam, A., Santoyo, E., Andaverde, J., Hernández, J. A., and Espinoza-Ojeda, O. M. "Estimation of static formation temperatures in geothermal wells by using an artificial neural network approach." *Computers & Geosciences*, 36(9), 1191–1199, (2010).

Cao, S., Lerche, I., and Hermanrud, C. "Formation temperature estimation by inversion of borehole measurements." *Geophysics*, 53(7), 979–988, (1988).

Iglesias, E. R., Campos-Romero, A., and Torres, R. J. "A reservoir engineering assessment of the Chipilapa, El Salvador, geothermal field." *Proceedings, World Geothermal Congress*, Florence, Italy, 1531–1536, (1995).

Ikeuchi, K., Doi, N., Sakagawa, Y., Kamenosono, H., and Uchida, T. "High-temperature measurements in well WD-1a and the thermal structure of the Kakkonda geothermal system, Japan." *Geothermics*, 27(5/6), 591–607, (1998).

Ishikawa, S., and Naganawa, S. "Development of downhole cooling charts to prevent drilling problems in geothermal wells through wellbore temperature simulation." *Proceedings, 44th New Zealand Geothermal Workshop*, (2022).

Kutasov, I. M., and Eppelbaum, L. V. "Utilization of the Horner plot for determining the temperature of frozen formations—A novel approach". *Geothermics*, 71, 259–263, (2018).

Mondy, L. A., and Duda, L. E. "Advanced Wellbore Thermal Simulator GEOTEMP2 User Manual." Sandia Report SAND-84-0857, Sandia National Laboratories, Albuquerque, NM, (1984).

Ong'au, M. T. "Controlled directional drilling in Kenya and Iceland (time analysis)." *GRC Transactions*, 36, (2012).

Sasaki, S. " A reliability of Horner-plot method for estimating static formation temperature from well log data." *Journal of the Japanese Association for Petroleum Technology*, 52(3), 243–252, (1987).

Shen, P. Y., and Beck, A. E. "Stabilization of bottom hole temperature with finite circulation time and fluid flow." *Geophysical Journal of the Royal Astronomical Society*, 86, 63–90, (1986).

Steingrimsson, B., and Gudmundsson, Á. "Geothermal borehole investigations during and after drilling." *Presented at Workshop for Decision Makers on Geothermal Projects in Central America*, El Salvador, 10 pages, (2006).

Fostering Geothermal Machine Learning Success: Elevating Big Data Accessibility and Automated Data Standardization in the Geothermal Data Repository

Nicole Taverna[1], Jon Weers[1], Scott Mello[1], Adrienne Lowney[1], Amber Mohammad[1], and Sean Porse[2]

[1] National Renewable Energy Laboratory

[2] U.S. Department of Energy, Geothermal Technologies Office

Keywords
data, data standard, data pipeline, data lake, user experience, accessibility, gdr, data science, gis, geospatial, das, distributed acoustic sensing

ABSTRACT

The Department of Energy's (DOE's) Geothermal Data Repository (GDR) has implemented improvements to both its data lakes and its data standards and automated data pipelines. The GDR data lakes have reduced storage and compute-related barriers to using large geothermal datasets, enabling these large datasets to be accessed by anyone with a modern computer and internet access. More recently, the GDR has been working to further reduce barriers through streamlining the data intake process, educating users on the process and requirements, and helping users access data from the data lakes. These improvements have augmented the quantity of datasets the GDR is able to accept into its data lakes and have enabled users who are new to cloud tools to access these datasets more easily, overall increasing the accessibility of big geothermal data for use in machine learning and other projects. In addition, the GDR now has built-in data standards and pipelines for drilling data, geospatial data, and distributed acoustic sensing (DAS) data. These standardization efforts aim to enhance the real-world applicability of geothermal machine learning outcomes by improving the quality of training data. Specifically, through standardizing high-value datasets, the GDR is reducing project-specific data curation requirements, thus allowing more time for actual research. By automating this process, the burden of standardization is lifted from the user, ultimately increasing the availability of standardized data.

This paper provides an update on recent improvements made to the GDR's data lakes and automated data pipelines, including: (1) streamlining the data lake intake process, (2) better educating users on the process and requirements through a new data lakes page, (3) adding data lake direct access links to GDR data lake submission pages, (4) implementing a DAS data pipeline to convert DAS data uploaded in SEG-Y format to a standardized hierarchical data format v5 (HDF5), (5) extending this pipeline to encompass data in the GDR data lake, (6) adding metadata

requirements for geospatial data, (7) making user interface/user experience (UX) enhancements to the data pipelines' documentation pages, and (8) improving the GDR's data standards and pipelines pages to better guide users in ensuring that their data is standardized by the GDR's automated data pipelines.

1. Introduction

The U.S. Department of Energy's (DOE's) Geothermal Data Repository (GDR) serves as the repository and catalog for data generated by projects funded by the DOE Geothermal Technologies Office (GTO) (Weers et al. 2022). The GDR provides public access to geothermal datasets, which are consistently increasing in variety, size, and complexity. These datasets are becoming increasingly valuable for geothermal machine learning projects. To accommodate this, the GDR is improving its data lakes, implementing new robust data standards, and refining its data pipelines (Taverna et al. 2023(a,b), Weers et al. 2021). Additionally, improvements in user experience (UX) aim to make submitting, accessing, and utilizing datasets more convenient and efficient for researchers. These efforts collectively ensure that the GDR remains a crucial resource for advancing geothermal machine learning and data science projects.

1.1 GDR Data Lakes

As research datasets increase in size, the classic access model of downloading a dataset to a local compute resource becomes less feasible and can result in barriers to access and inefficiencies. Data lakes are a modern approach to data storage and access that provide a solution to these challenges. In the data lake model, especially large or complex (i.e., hierarchical) datasets are housed in a central, public-facing, cloud-based data store (Weers et al. 2021). The GDR data lakes not only enable users to parse or access data without needing to download the full dataset, but they also allow submitters to upload data without needing to rely on the traditional method of uploading data to the GDR submission form. Cloud-based data lakes have made big GDR data accessible to anyone with cloud access, eliminating the need for collaborators to have their own high-performance computing and big data storage solutions (Weers et al. 2021).

The GDR data lakes are currently home to more than 700 TB of public data, including distributed acoustic sensing (DAS), big geospatial data, raw magnetotellurics binary files, and more. Hosting the GDR's big data in the GDR's data lakes has greatly improved accessibility of these datasets and therefore the potential to use them in machine learning and data science workflows. Despite this, there have been challenges surrounding user understanding of data lake access, the data lake intake process, and data lake submission requirements. We have attempted to mitigate some of these challenges through streamlining the dataset intake process, better educating users on the process and requirements, and providing tools on the GDR submission page to ease access of GDR data lake data.

1.2 Data Standardization and Automated Data Pipelines

High-quality data is another key component of machine learning applications. High-quality geothermal datasets are characterized by reliable sensors or devices, frequent measurements, sufficient data points, comprehensive metadata, secure data storage, and effective data curation. Another aspect contributing to data quality is reusability, which can be improved through standardization. Standardizing data ensures consistency in formatting and content across similar

datasets, reducing preprocessing requirements and ensuring that the dataset provides adequate information (Taverna et al. 2023(b)). Currently, the GDR has developed data standards for drilling data in its most common formats (Taverna et al. 2023(a)), DAS data in SEG-Y format (Taverna et al. 2023(b)) using PRODML (PRODML Work Group 2022) and the DAS RCN's metadata standard (IRIS DAS RCN Metadata Working Group 2022), and geospatial metadata. Each standard has an associated page on the GDR to provide additional information on how the standards work. These pages have recently undergone a UX review to improve their usability and accessibility.

The GDR has begun implementing automated data pipelines for certain high-value data types in order to take the burden of data standardization off of the user and ensure that the benefits of data standardization are felt more widely across the GDR (Taverna et al. 2023(b)). These data pipelines align with the data standards. The GDR previously only had one automated data pipeline for drilling data (Taverna et al. 2023(a)) but has since expanded this to include DAS and geospatial data.

2. Streamlining the Data Lake Intake Process

Previously, the GDR data lake submission process was characterized by a lack of consistency, with only a few individuals possessing partial knowledge of the process, confusing conditional and inconsistent requirements, and a heavy reliance on ad hoc communication from curators. This resulted in a lack of standardization in UX and requirements, as well as an outward lack of clarity on how long the process takes and what it entails. The GDR has worked to remedy this problem through streamlining the data lake submission process.

As a reminder, regular datasets should be submitted as normal via the GDR submission form. However, especially large or complex datasets should follow these steps, which are also condensed into the graphic in Figure 1:

1. Create a GDR catalog entry with associated metadata and supporting files. Supporting files may include related publications, readme files, GitHub repositories, a few sample files, or any other information that may help to give context to our curators. Do not try to upload the entire dataset to the submission form. Instead, contact our curation team at GDRHelp@ee.doe.gov and request a data lake resource.
2. Assist GDR curators with public datasets program application requirements. Some data lake datasets may be eligible for free hosting and/or registration in the data catalogs of our cloud partners, such as the Amazon Sustainability Data Initiative. This may include filling out an additional questionnaire to justify the value of your dataset, helping to create a tutorial Jupyter notebook with examples for accessing and using the data, and providing any additional requested resource metadata.
3. Wait to hear back about approval from third-party public datasets programs. The review process is currently quarterly, so please be patient and plan on a few months for this step.
4. Assist data curators with the data transfer process either by making the data available via Globus, FTP, Google drive, or another web-based file-sharing service or by moving the data directly into our staging bucket.
5. When the data have been properly staged and organized, the GDR curation team will ask you to review the data one more time for organization, naming, and completeness. Data will be considered permanent and final after this step unless stated otherwise.

6. Assist curators with any final metadata tweaks. If you are publishing a journal article related to the data, share a preprint with the GDR Team and follow up when the article is published.

Please note that the GDR does not validate or peer review datasets. **All data should be finalized, validated, and peer reviewed by the project team prior to submission to the GDR.** Datasets published to the GDR are considered scientific records, and their data resources are expected to remain unchanged in the same location permanently. Incremental additions can be easily added to existing datasets, including the addition of new versions of previously published data. However, publishing changes to existing data or other major updates to datasets—including data in data lakes—often requires creating an entirely new version of the dataset.

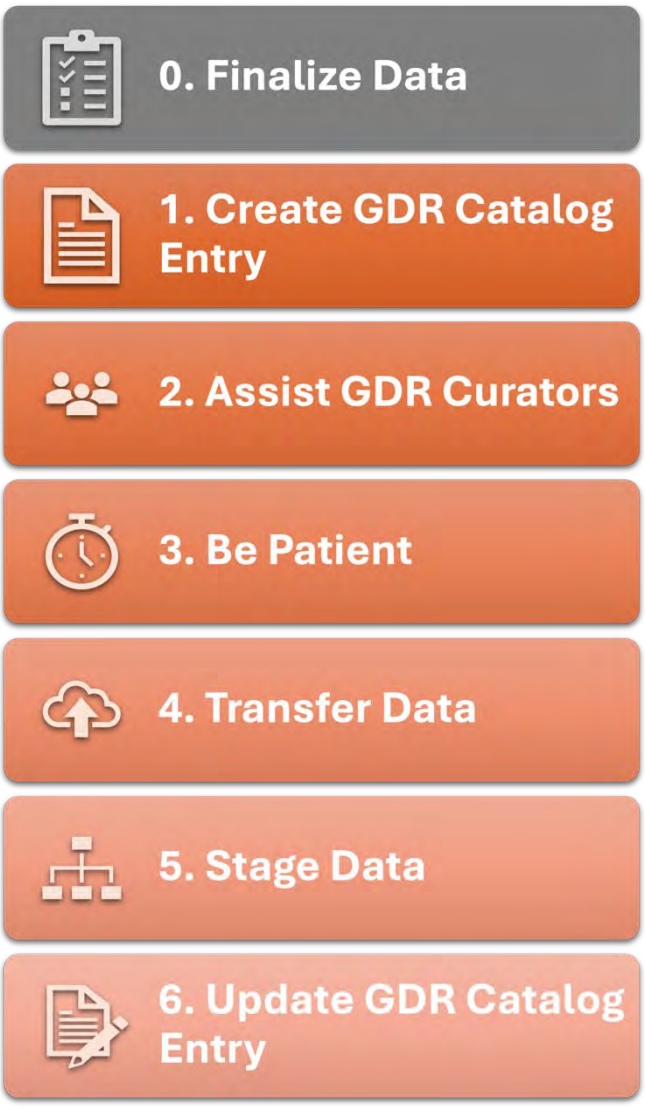

Figure 1: Graphical representation of the streamlined data lake intake process.

This new streamlined process standardizes the UX and makes the intake process more efficient. This has been evident in our ability to scale up data lake data intake to meet the growing demands

of big geothermal data storage. The 475 TB of DAS data currently available through the GDR is a great example of this achievement.

3. User Education and Support

In addition to lacking consistency, the data lake intake process has also lacked transparency. User feedback has relayed that there is a lack of understanding surrounding the submission requirements, the submission timeline, and the GDR's data posterity requirements. To mitigate this issue, the GDR has decided to focus on more proactive education and support. This has included creating a new page on the GDR to describe the data lake intake process in detail, including the graphic in Figure 1, along with more in-depth information about what to expect during the data lake intake process. This has also included work to publish and present on these requirements—including this paper. These steps allow the GDR to clearly communicate the requirements and expectations to potential submitters prior to initiating the submission process.

The impact of this proactive education approach has been observed through an overall decrease in requests that conflict with our policies, an improvement in organization of new submissions, and a reduction in proliferation of largely duplicative versions of data in our data lakes. These factors combined result in higher quality data lake submissions overall.

4. Direct Access Links for Data Lake Data

Users have frequently asked questions surrounding how to efficiently access data from GDR data lakes. In order to make this information more readily discoverable, the GDR has added direct access links to the submission form for data lake resources. These direct access links allow users to easily copy and paste access commands for accessing the data using the Amazon Web Service Command Line Interface (AWS CLI). An example of a direct access link is shown in Figure 2.

Figure 2: Example of a direct access link associated with a GDR data lake resource. Users can use the icon to the right to quickly copy the command so that they may paste it into their terminal for AWS CLI access to the data.

Additionally, the GDR has listed multiple ways to interact with data in data lakes on the Data Lakes page, accessible from the Data drop-down at the top of every page. This list, complete with examples, illustrates how to access GDR data through:

- Jupyter notebooks
- Native cloud query engines like Athena (AWS) and Google Earth Engine
- Native cloud access direct to the public data lakes
- The GDR Data Lake Viewer, a simple user interface that allows users to explore data lakes through their web browser

- Native cloud command line tools, such as the AWS CLI example above
- Mounting the data as a local read-only drive in a cloud-built computer cluster (requires a cloud account in the same availability zone as the data lake.)

5. Implementation of DAS Data Pipeline

To maximize the utility of the large quantity of DAS data stored in the GDR, a data pipeline has been implemented to convert DAS data in nonstandard SEG-Y format to a standardized hierarchical data format (HDF5). The data standard combines aspects of the PRODML raw DAS data format (PRODML Work Group 2022) with the DAS RCN Metadata Working Group's metadata standard (IRIS DAS RCN Metadata Working Group 2022).

This hybridized approach is described in Figure 3 and is described in more detail in Taverna et al. 2023(b). The file structure is hierarchical, broken into two main groups: one for raw DAS data, and one for DAS metadata. The DAS raw data group includes two datasets—one containing a time array, and another containing a raw data array. The metadata group includes two types of subgroups: one for each cable's metadata that contains subgroups for each fiber's metadata, and one for each interrogator's metadata, which is further broken down into acquisition and channel-specific metadata. While the DAS RCN recommends that metadata be stored in a separate JSON file, the GDR standard attempts to store as much of it as possible within the HDF5 file to keep the metadata packaged with the data. Channel location information, however, is stored in a separate channel map file to allow for simplified updates.

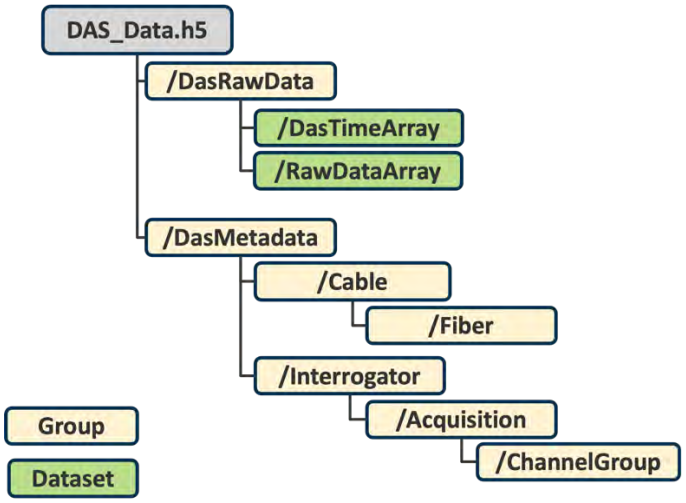

Figure 3: GDR DAS data standard file structure. The GDR standard is HDF5-based, combining aspects of the PRODML format with the DAS RCN Metadata Working Group's metadata standard.

The DAS data pipeline generally operates as described in Figure 4. Metadata are stored in three main locations within a SEG-Y file: The text header, trace header, and binary headers. Because metadata in the text header are not standardized by nature, fuzzy matching is used to identify keywords in the text header, and these keywords are used to extract desired information. Metadata are standardized by nature in the trace and binary headers, so direct translation may be used to extract this information. Extracted metadata are then stored in the associated attributes of an HDF5 file's groups and datasets. This pipeline is not fully automated yet because of the massiveness of

DAS datasets, the diverse ways that GDR DAS datasets are organized, and the frequently incomplete DAS metadata packages.

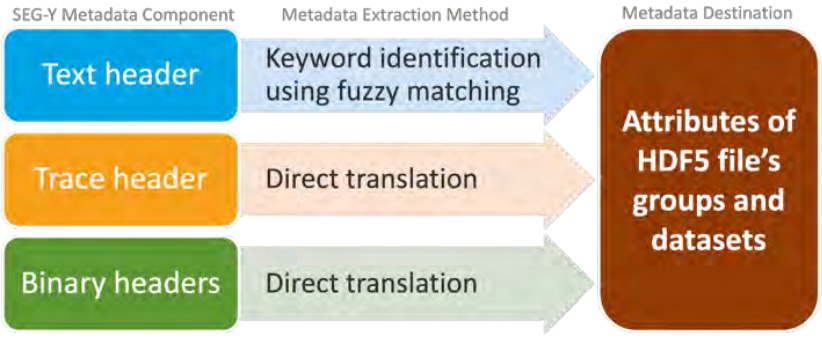

Figure 4: Graphic depicting the general process followed by the DAS data pipeline. Metadata are extracted using a combination of direct translation and fuzzy matching and stored in the associated attributes of the standardized HDF5 file's groups and datasets.

While we are retroactively applying this data pipeline to existing DAS datasets in the GDR, many of these existing datasets have incomplete metadata packages. This is because the most common GDR DAS data format, SEG-Y, is a file format intended for conventional seismic data, not DAS data, meaning that it is not compatible with all of the metadata required for robust DAS data analysis. On top of that, there was no universally agreed on DAS metadata standard until the recent work of the DAS RCN Metadata Working Group (2022). In an attempt to maximize the amount of metadata added to the standardized DAS data files, a metadata template was created to allow data owners to provide additional metadata. GDR curators are actively reaching out to legacy DAS data owners requesting additional metadata via this form.

At the time of this publication, 16.5% of the approximately 287 TB of DAS data in the GDR has been standardized using this method. The remaining data are in formats (non-standardized HDF5, TDMS, and zipped directories) that are not yet compatible with our data pipeline. Future work will investigate the merit of adapting our pipeline to additionally standardize one or more of these formats.

6. Extension of Data Pipelines for GDR Data Lake

The DAS data pipeline is the first to be adapted to work for data in the GDR data lakes. Because DAS data are often on the order of tens of terabytes in size (Trainor-Guitton et al. 2022), they are almost exclusively stored in the GDR data lakes. This means that, in order to be of maximum utility, the data pipeline needed to be adapted to work on data in the data lakes. This necessitated adjustment of the data detector script to detect DAS data files in specific directories in the cloud as opposed to on the GDR servers.

This adaptation will streamline the development of future data pipelines that are compatible with big data in the data lake, which is arguably where data standardization provides the most value. Big datasets require more time-consuming data curation; therefore, standardization of big data results in more significant time savings through reducing the curation requirements (Taverna et al. 2023(a)).

7. Added Metadata Requirements for Geospatial Data

Current storage models often lack the necessary metadata for enabling thorough analyses and reproducibility. Consequently, GDR submissions of geospatial data from GIS nonexperts have frequently lacked complete geospatial metadata (Taverna et al. 2023(b)). To address this problem, a comprehensive review was conducted of proper metadata to be archived alongside geospatial datasets (Taverna et al. 2023(b)). It was decided that the most crucial piece of geospatial metadata is the coordinate reference system (CRS), and hence a required input for CRS has been added to the resource-specific metadata for files with geospatial file extensions (Figure 5). This required input ensures that the CRS is added for every geospatial data file added to the GDR and recommends additional CRS-specific metadata to add to the resource description.

Beyond the CRS, the GDR geospatial metadata standard provides suggestions of which other geospatial metadata is useful to include in your GDR submission, and where to include it in the GDR submission form. These suggestions may be found in Taverna et al. 2023(b) or on the GDR's new geospatial data standard page: https://gdr.openei.org/geospatial_data_standard. The GDR has already seen an improvement in the quality of its geospatial datasets in the short time since this standard and the additional required input have been implemented.

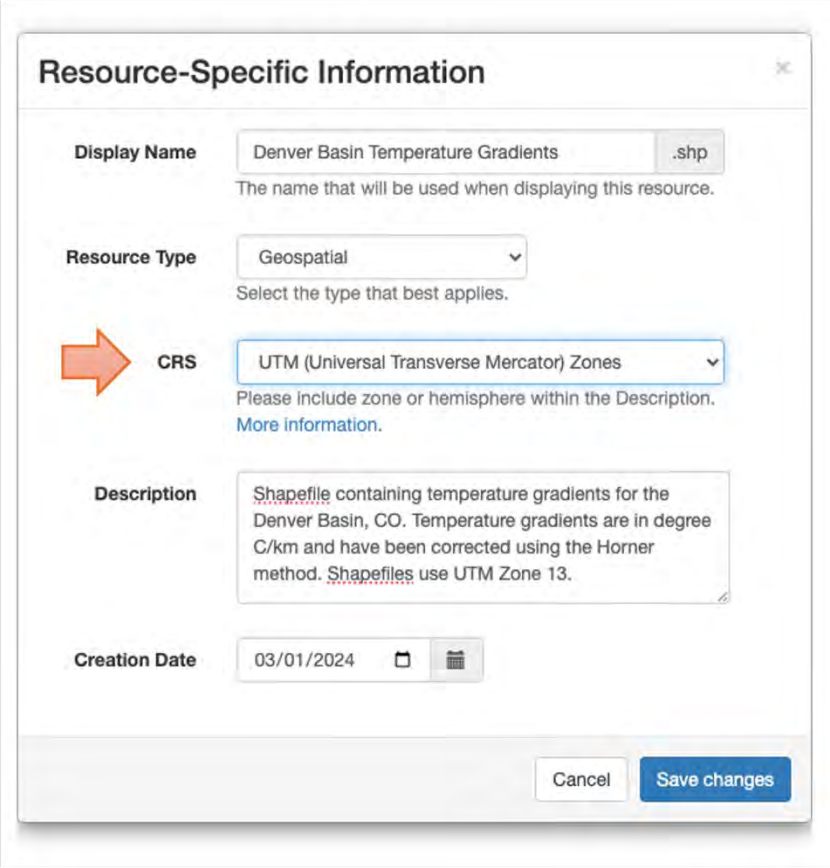

Figure 5: Image of new CRS requirement for geospatial data files uploaded to the GDR. Note the additional CRS-specific metadata suggestion that appears below the CRS field.

8. UX Enhancements

In order to improve the UX associated with the GDR data standards and pipelines, a UX review was conducted on the existing GDR data standard and pipeline pages. This heuristic review primarily focused on the following user-centric design principles: user needs and goals, accessibility, simplicity and clarity, responsive design, feedback and performance, and trust and credibility. This was achieved through revisiting the GDR's data standard and pipeline pages, identifying bugs, confusing wording, and non-intuitive designs; and providing suggestions on how to improve functionality, clarity of information, intuitiveness of navigation, and more.

In this heuristic review, several design principles are recommended to enhance the user interface and functionality of a data table. Key principles include improving navigation by making table headers sticky to reduce scrolling lag and adding a keyword search feature for efficient data filtering. Clear organization is suggested by adding distinct headers for different data sections and creating separate columns for specific data categories. To improve readability, long descriptions should be truncated with an option to expand for more details, and sorting capabilities should be added for key columns. User interaction can be enhanced with icons indicating required fields and maintaining row highlights on hover. Accessibility improvements include ensuring color contrast.

9. Improvements in Data Standards and Pipelines Pages

The input gathered from the UX review was then combined into new and improved data standard and pipelines pages. The key takeaways were then applied to the new data standard and pipeline pages to ensure that they adhered to the same design principles. This included enhancements to design and layout, in addition to pipeline guides and user instructions (i.e., tips to make sure your data are standardized, compatible formats, helpful resources, and how it works). These updates may be found on the data standards and pipeline pages here: https://gdr.openei.org/standards. While it is too soon to tell, the GDR team anticipates that these new pages will have positive impacts on the amount of data that can be automatically standardized, the use of standardized data, and the overall support for the GDR data standards and pipelines.

10. Discussion: Real-World Applicability and Impact on Research

The Geothermal Operational Optimization with Machine Learning project exemplifies how emphasizing data quality through best practices in data curation can significantly enhance the success of a machine learning project (Taverna et al. 2022). Having access to structured and standardized data streamlines data handling by reducing time spent on dataset preparation, enabling efficient assembly of multiple datasets. Having access to especially large or complex datasets through data lakes eases data access, reducing barriers surrounding downloading, uploading, and working with the data. Combined, these features lessen the data curation requirements associated with a project, preserving more time for machine learning and data science experiments.

While it is too soon to see the scale of the impact of the GDR's data standardization efforts, we hope to see growth in the number of geothermal projects using standardized GDR data in their machine learning and data science workflows. We have observed the impact of the GDR data lakes through the sheer number of downloads of our data lake resources.

Table 1 lists the top ten most downloaded datasets of all time, with six of them being data lake resources. This trend is partly due to the nature of data lakes, which often contain especially large and complex datasets comprising numerous files accessed directly from the data lake (i.e., using files in situ instead of a one-time download). Additionally, this highlights the popularity of GDR data lake resources, which significantly enhance the accessibility of extremely large datasets. Notably, the first data lake resource was introduced nine years after the first conventional data resource, which was submitted in 2012.

Table 1: Top 10 most downloaded data submissions of all time as of August, 2024, including information on number of downloads, year published, and dataset storage type.

Rank	Downloads	Year Published on GDR	Title	Dataset storage type
1	5,845,469	2021	PoroTomo Natural Laboratory Horizontal and Vertical Distributed Acoustic Sensing Data	Data lake
2	1,561,471	2021	Brady's Geothermal Field - March 2016 Vibroseis SEG-Y Files and UTM Locations	Data lake
3	1,089,412	2021	Brady's Geothermal Field Nodal Seismometer Data	Data lake
4	728,186	2014	Evaluation Data of a High Temperature COTS (Commercial Off-the-Shelf) Flash Memory Module (TI SM28VLT32) for Use in Geothermal Electronics Packages	Conventional
5	434,950	2021	Brady's Geothermal Field DASH Resampled in Time	Data lake
6	309,362	2023	EGS Collab Experiment 1: Continuous Active-Source Seismic Monitoring (CASSM) Data	Data lake
7	28,441	2014	Project HOTSPOT: Kimama Well Borehole Geophysics Database	Conventional
8	22,472	2023	Imperial Valley Dark Fiber Project Continuous DAS Data	Data lake
9	18,126	2014	Project HOTSPOT: Kimberly Well Borehole Geophysics Database	Conventional
10	12,807	2013	Newberry EGS Demonstration Well 55-29 Stimulation Data	Conventional

This statistic also gives context to the plot in Figure 6, which shows cumulative GDR downloads per fiscal year since the GDR was rolled out more than 10 years ago. Because data lake downloads make up most of the FY24 downloads, it is apparent that the exponential growth in downloads over time would not be possible without the implementation of GDR data lakes.

Figure 6: Cumulative GDR downloads over time, by fiscal year, as of August 2024. This graph demonstrates exponential growth in the number of downloads per fiscal year, enabled by the GDR data lakes (*Graphic by Joelynn Schroeder and Dominique Barnes, NREL, 2024)*.

11. Conclusion

In conclusion, the GDR has made significant advancements in its data lakes, data standards, automated data pipelines, and associated pages to educate users. These enhancements have reduced barriers related to storage, access, and computation, enabling broader access to large geothermal datasets. Recent efforts to streamline the data intake process, educate users, and improve data accessibility have increased the number of datasets the GDR can accept into its data lakes and made it easier for new users to access the data using cloud tools. Introducing standardized pipelines for drilling, geospatial, and DAS data has improved the quality of training data, thereby enhancing the real-world applicability of geothermal machine learning outcomes. Automating

these processes has increased the availability of standardized data, reducing the burden of project-specific data curation on users and allowing more time for research. Overall, these improvements have significantly increased the accessibility and usability of big geothermal data for various projects.

We encourage geothermal data users to leverage the GDR's enhanced data lakes, standardized datasets, and streamlined data pipelines; and to provide feedback on their experience, including both success stories and shortcomings. Your active participation and feedback are crucial for driving innovation and ensuring that future improvements to the GDR align with the needs and wants of the geothermal community and stakeholders. We would love for you to join us in this initiative to make geothermal data more accessible, efficient, and impactful for the entire community.

Acknowledgement

This work was authored in part by the National Renewable Energy Laboratory (NREL), operated by Alliance for Sustainable Energy, LLC, for the U.S. Department of Energy (DOE) under Contract No. DEAC36-08GO28308 with funding provided by U.S. Department of Energy Office of Energy Efficiency and Renewable Energy (EERE) Geothermal Technologies Office (GTO). The views expressed in the article do not necessarily represent the views of the DOE or the U.S. Government. The U.S. Government retains, and the publisher, by accepting the article for publication, acknowledges that the U.S. Government retains a nonexclusive, paid-up, irrevocable, worldwide license to publish or reproduce the published form of this work, or allow others to do so, for U.S. Government purposes.

We'd like to recognize the National Geothermal Data System content models as the catalyst for the work on data standardization. We'd also like to acknowledge Aleksei Titov, Kurt Feigl, Herb Wang, Kathleen Hodgkinson, Rob Porritt, and the rest of the DAS RCN Metadata working group for their input on and inspiration for our DAS data standard. In addition, we thank Meghan Mooney at NREL for her review of and suggestions around the geospatial metadata and data standards proposed in this paper. And lastly, we acknowledge OpenAI's ChatGPT 4 for its assistance in brainstorming and proofreading.

REFERENCES

The Geothermal Data Repository (GDR). https://gdr.openei.org/home.

IRIS DAS Research Coordination Network (RCN) Metadata Working Group. "Distributed Acoustic Sensing (DAS) Metadata Model." Whitepaper (2022). https://github.com/DAS-RCN/DAS_metadata.

PRODML Work Group, "PRODML Technical Reference Guide." Energistics, v2.2 (2022). https://www.energistics.org/prodml-data-standards.

Taverna, N., Weers, J., Porse, S., Anderson, A., Frone, F., Holdt, E. 2023. "An Update on the Geothermal Data Repository's Data Standards and Pipelines: Geospatial Data and Distributed Acoustic Sensing Data" *GRC Transactions, Vol. 47* (2023).

Taverna, N., Weers, J., Huggins, J., Porse, S., Anderson, A., Frone, F., Scavo, R.J. 2023. "Improving the Quality of Geothermal Data Through Data Standards and Pipelines Within the Geothermal Data Repository." *Proceedings of the 48th Workshop on Geothermal Reservoir Engineering*, Stanford University, Stanford, CA (2023).

Taverna, N., Buster, G., Huggins, J., Rossol, M., Siratovich, P., Weers, J., Blair, A., Siega, C., Mannington, W., Urgel, A., Cen, J., Quinao, J., Watt, R., and Akerley, J. "Data Curation for Machine Learning Applied to Geothermal Power Plant Operational Data for GOOML: Geothermal Operational Optimization with Machine Learning." *Proceedings of the 47th Workshop on Geothermal Reservoir Engineering*, Stanford University, Stanford, CA (2022).

Trainor-Guitton, W., Martin, E. R., Rodríguez Tribaldos, V., Taverna, N., and Dumont, V. "Distributed sensing and machine learning hone seismic listening." *Eos, 103* (2022).

Weers, J., Anderson, A., and Taverna, N. "The Geothermal Data Repository: Ten Years of Supporting the Geothermal Industry with Open Access to Geothermal Data." *GRC Transactions, Vol. 46* (2022).

Weers, J., Porse, S., Huggins, J., Rossol, M., and Taverna, N. "Improving the Accessibility and Usability of Geothermal Information with Data Lakes and Data Pipelines on the Geothermal Data Repository." *GRC Transactions, Vol. 45* (2021).

Empowering Geothermal Research: The Geothermal Data Repository's New AI Research Assistant

Jon Weers[1], Slater Podgorny[1], Nicole Taverna[1], Arlene Anderson[2], Sean Porse[2], and Grant Buster[1]

[1] National Renewable Energy Laboratory (NREL)

15013 Denver West Parkway

Golden, CO 80401-3305

[2] U.S. Department of Energy (DOE)

1000 Independence Ave. SW

Washington D.C. 20004

Keywords

Geothermal, data, repository, management, community, engagement, enhancements, open, access, GDR, OpenEI, DOE, ELM, NREL, discoverability, usability, accessibility, innovation, metadata, artificial intelligence, AI, machine learning, ML, large language model, LLM

ABSTRACT

The Department of Energy's (DOE) Geothermal Data Repository (GDR) team has integrated a Large Language Model (LLM) with the metadata and supporting documents associated with GDR datasets to create an Artificially Intelligent (AI) research assistant. By leveraging work done to make GDR metadata machine-readable and an open-source LLM integration model called the Energy Language Model, developed by the National Renewable Energy Laboratory, AskGDR serves as a virtual research assistant to GDR users. It provides answers to a variety of user-provided questions using natural language processing and generative machine learning. Users can get answers to questions about specific datasets, including inquiries about the equipment, assumptions and methodologies used in the origination of the data; or more abstract questions, such as the applicability of data to specific research fields. AskGDR improves the discoverability of geothermal data by helping guide users to datasets beyond simple keyword searches. It enables users to find data based on properties of the data, discover information contained within supporting documents, and explore data from projects related to their research objectives.

This paper will outline the development, integration, output, and efficacy of the AskGDR LLM, including adherence to scientific rigor through improvements designed to increase the accuracy of generated answers, avoid speculation, and provide proper references for all resources used.

1. Introduction

The U.S. Department of Energy's Geothermal Data Repository (GDR) is currently home to 1,209 datasets containing over 5,900 individual resources totaling more than 147 TB of geothermal data. (GDR 2024). Searching on the GDR was previously limited to keyword associations with the provided metadata, facilitating queries analogous to "Show me all the of the seismic data from the PoroTomo project" by executing searches on keywords "PoroTomo" or "seismic", but these types of searches are inherently limited. At best they match all datasets containing those keywords at a superficial level while fundamentally failing to understand the depth of contextual associations in the query itself. Fortunately, as part of the GDR's effort to maximize the utility and discoverability of geothermal data through adherence to FAIR data principles (Wilkinson et al, 2016), each dataset on the GDR includes a comprehensive set of metadata designed to increase the discoverability, accessibility, interoperability, and utility of geothermal data. Furthermore, the GDR strives to adhere to FARR data principles, which combine FAIR with machine readability and AI-readiness, to make geothermal data accessible not only to researchers, but also to machine learning algorithms and artificial intelligence (FARR 2024). These principles laid the foundation for the adaptation of a Large Language Model (LLM) that now powers an Artificially Intelligent (AI) research assistant called "AskGDR", which allows users to ask and receive answers to questions beyond simple keyword searches.

1.1 Adherence to FAIR and FARR Data Principles

A core tenet of the GDRs mission is to make geothermal data universally accessible (Weers et al, 2023). For over a decade, the GDR has strived to achieve the guiding principles of the FAIR data standards: to make data Findable, Accessible, Interoperable, and Reusable. (Wilkinson et al, 2016; Weers et al, 2022). These principles align directly with the U.S. Department of Energy's 2011 Strategic Plan, which states, "Success should be measured not when a project is completed or an experiment concluded, but when scientific and technical information is disseminated." (DOE 2011). Put simply, data and information which cannot be found, accessed, or reused effectively has no value. Previous work done by the GDR team to maximize the value of data submitted to the GDR has laid the foundation for innovation in machine learning (Weers et al, 2022). The GDR team has expanded upon these efforts through the adoption of FARR data principles, which build upon FAIR data principles. FARR data principles include all those in FAIR, plus AI Readiness and Reproducibility. To meet FARR data standards, the GDR team has worked to make GDR metadata machine-readable, rendering it comprehensible by modern AI platforms in addition to meeting FAIR data standards. These efforts enabled AI and Machine Learning (ML) platforms, including Large Language Models (LLMs), to incorporate GDR metadata into their respective knowledge bases to develop smarter search algorithms.

2. Developing a Smarter Search

Building upon recent innovations in LLM research and the GDR's adherence to FAIR and FARR principles, the GDR team began exploring AI-assisted search capabilities with two primary goals:

1) Help users get quick answers to contextual questions about data
2) Help guide users to insights beyond simple keyword searches

2.1 Helping Users Get Quick Answers to Contextual Questions About Data

Every dataset in the GDR contains metadata describing dataset. Good metadata contains sufficient information to understand and properly use the data, including any assumptions, anomalies, and errors incurred while collecting the data (Taverna et al, 2022). Submitters of data to the GDR and the curators who evaluate their submissions each work vigilantly to ensure users of the data have access to all the information they need to properly use and comprehend the included data, it is not always possible to cover every conceivable use of the data. To ensure data reusability in accordance with FAIR data principles, GDR data is curated to promote as many future uses as possible, including potentially unforeseen, novel applications to promote innovation (Weers et al, 2022). However, it's not always possible to anticipate what questions innovators of the future will be asking of the data generated today. As a result, the points of contact listed for GDR datasets often receive unforeseen questions about their data, assumptions, and anomalies incurred during the acquisition of the data. Examples include: "What assumptions were made in the development of this dataset?" or "Does this dataset include an assumption, such as curtailment, in its output?"

The answers to these questions are often buried in supporting documents, published papers, and other materials associated with the dataset. Previously, users had to either read through the supporting materials looking for their answer, or email the Point of Contact (POC) listed on the dataset landing page and wait for a response, sometimes just to find out if the dataset they were interested in would work for them and their research or not. And POCs for popular datasets would often receive the same question(s) over and over, despite having included the answer in the supporting materials. AskGDR instantly devours all the metadata and supporting information associated with a dataset and can provide insight into the assumptions made, equations used, and anomalies detected, saving the dataset POC valuable time and providing the data user with real-time answers to deep technical questions (Sample Question 1 below).

2.2 Helping Guide Users to Insights Beyond Simple Keyword Searches

The primary search interface on GDR relies solely upon keyword matching to produce search results and can quickly find answers to questions like, *"Which datasets include EGS stimulation data?"* through a simple search for "EGS" data, but it cannot answer abstract queries such as, *"Which geothermal technologies have the potential to reduce carbon in the atmosphere?"* (Sample Question 2 below). AskGDR can make the connection between a dataset's characteristics and the potential impact of associated research by incorporating related papers, publications and other supporting documents into the contextual knowledge associated with each dataset.

2.3 Sample Questions

The following questions were input into AskGDR and its responses have been copied here verbatim. Note that some of the links included lead directly to the download of cited resources (i.e., clicking the links may initiate a download).

2.3.1 Sample Question 1: "How was the PoroTomo seismic data recorded?"

Response generated by AskGDR (including format, and cited hyperlinks):

> The PoroTomo seismic data was recorded using a combination of instruments and techniques. The seismic instrumentation included 238 Zland 3-component sensors manufactured by FairfieldNodal, which operated autonomously and continuously with a sampling interval of 0.002 seconds for the entire two-week deployment. The seismic network also included six 3-component seismic stations from the national instrumentation program named Portable Array Seismic Studies of the Continental Lithosphere (PASSCAL). Each station included an L28 model, 4.5-Hertz, 3-component geophone, Reftek RT130 seismograph, and a GPS timing clock.
>
> Additionally, Distributed Acoustic Sensing (DAS) was used, which was the first such deployment in a geothermal field in North America. The "intelligent" Distributed Acoustic Sensing (iDAS) system used a continuous length of fiber-optic cable as an array of seismic sensors. At Brady, the instrumentation included 8700 meters of DAS cable buried horizontally in a shallow trench and 400 meters of DAS cable hanging vertically in Well 56-1. The DAS data were recorded continuously, archived in 30-second files in SEG-Y format.
>
> Sources used in this answer:
>
> - PoroTomo: Horizontal Distributed Acoustic Sensing (DAS) Measurements During an M 2.3 Explosion
> - Brady's Geothermal Field - March 2016 Vibroseis SEG-Y Files and UTM Locations
> - Feigl et al. 2018 Stanford Paper from GDR dataset: PoroTomo Natural Laboratory Horizontal and Vertical Distributed Acoustic Sensing Data
> - README_GDR from GDR dataset: DASH Slow Strain Rates from Brady Hot Springs Geothermal Field during PoroTomo Deployment Period
> - Final Seismic Data Processing Report from GDR dataset: Three-Component Long Offset Surface Seismic Survey Data Used to Find Large Aperture Fractures in Geothermal Resources - San Emidio Geothermal Resource Area

(End of Sample Question 1 Response)

2.3.2 Sample Question 2: “Which geothermal technologies have the potential to reduce carbon in the atmosphere?”

Response generated by AskGDR (including format, and cited hyperlinks):

> Geothermal technologies that have the potential to reduce carbon in the atmosphere include:
>
> 1. Geothermal power generation: This technology involves tapping into the Earth's natural heat to generate electricity. Geothermal power plants emit significantly less carbon dioxide (CO2) and other pollutants compared to fossil fuel-based power plants, making them a cleaner energy source.

2. Geothermal heating and cooling (GHC): GHC technologies, also known as direct use or geothermal heat pumps (GHP), utilize the Earth's stable temperatures to provide heating and cooling for buildings, agriculture, industrial processes, and other applications. By replacing conventional heating and cooling systems that rely on fossil fuels, GHC technologies can help reduce greenhouse gas emissions.

3. Hybrid systems: These systems combine geothermal energy with other renewable energy sources, such as solar or wind power, to further reduce carbon emissions and increase the overall efficiency of the energy system.

4. Enhanced Geothermal Systems (EGS): EGS involves the artificial stimulation of geothermal reservoirs to increase their permeability and heat extraction capabilities. By expanding the potential for geothermal energy production, EGS can help displace more carbon-intensive energy sources.

By increasing the adoption of these geothermal technologies, it is possible to reduce carbon emissions and contribute to the global efforts to mitigate climate change.

Sources used in this answer:

- Final Report from GDR dataset: Technoeconomics of Transported Geothermal Energy
- Final Report from GDR dataset: Baseline System Costs for a 50 MW Enhanced Geothermal System 2012
- Salton Sea Geothermal Development - Nontechnical Barriers to Entry - Analysis and Perspectives - Final 6.28.22 from GDR dataset: Salton Sea Geothermal Development - Nontechnical Barriers to Entry - Analysis and Perspectives
- Low-Temperature Geothermal Geospatial Datasets from GDR dataset: Low-Temperature Geothermal Geospatial Datasets: An Example from Alaska
- Phase I Final Report from GDR dataset: Dynamic Earth Energy Storage: Terawatt-year, Grid-scale Energy Storage Using Planet Earth as a Thermal Battery (GeoTES): Phase I Project Final Report

(End of Sample Question 2 Response)

3. Implementation

By leveraging work done to make GDR metadata machine-readable and a prototype LLM called the Energy Language Model (ELM) developed by Pinchuk et al (2024) at the National Renewable Energy Laboratory (NREL), AskGDR serves as a virtual research assistant to GDR users. AskGDR leverages OpenAI's ChatGPT framework to analyze and derive insight from the metadata and supporting documentation associated with GDR datasets. Whenever possible, included ReadMe files and publications are incorporated, along with other metadata provided during the submission process, to create a corpus of knowledge associated with each dataset in the GDR. This corpus is then used to generate AskGDR's response, along with certain limitations put in place to enforce scientific rigor, encourage citation, and promote data provenance.

3.1 Constrained for Scientific Rigor

Unlike conventional LLMs, many of which have knowledge bases that include internet content of unknown or questionable origin, the GDR development team has limited the AskGDR knowledge base to only the data and information provided in GDR data submissions. These data have been curated by the GDR data curation team and vetted for appropriateness, completeness, and relevance. As a starting point, the application has been instructed to act as a librarian maintaining a collection of documents and datasets related to energy and to generate responses using only the context provided. The AskGDR algorithm has been instructed not to deviate from these constraints and will not go to the internet at large in search of answers. AskGDR will not speculate. If the GDR knowledge base does not provide sufficient information for AskGDR to answer a question, it has been instructed to reply that it could not find an answer.

AskGDR has also been instructed to always cite its sources. The datasets and associated publications used to generate an answer are cited below each answer and include links to the relevant datasets and resources on the GDR (see Example Questions 1 and 2). This is important for establishing credibility and a reproducible audit trail of calculated answers in accordance with FARR data principles.

3.2 An AI Research Assistant, Not a Chat Bot

In early planning stages the GDR teams weighed the potential for two very different LLM implementation paradigms: a more traditional, conversational chatbot similar to ChatGPT, and a more constrained, scientific model, which we referred to as an AI Research Assistant. After consulting with industry professionals, potential users, and subject matter experts, we opted for the latter. We determined that adherence to a controlled corpus of knowledge coupled with scientific rigor superseded the conversational aspects of a true chatbot and provided greater value to the geothermal community. As a result, AskGDR is not fully conversational. Each question asked of it is independent of the last. This helps guarantee scientific rigor but limits a user's ability to ask follow-on questions in a natural language syntax. Context can, however, be carried from question to question through careful question engineering, i.e., by embedding the necessary context into subsequent questions.

3.3 Architecture and Flow

AskGDR is an extension of NREL's ELM, which uses Retrieval Augmented Generation (RAG) based on a predefined corpus of knowledge to provide deep insights into text contained within its knowledge base. For AskGDR, NREL's ELM framework has been used to integrate an LLM with the metadata associated with each GDR dataset in addition to supplemental documents including README files, publications, and other PDFs. These documents are parsed into pure text files (AskGDR cannot currently process images or other non-text elements) and then chunked into manageable fragments to optimize information retrieval and the natural language processing (NLP) used to create broader contextual understanding from the text fragments. The chunks are then fed into Amazon Bedrock, a cloud-based framework for building and scaling generative AI applications, which allows for the fine tuning of RAG techniques. Automated build agents in Bedrock convert the text fragments into embedding vectors stored in AskGDR's vector database. When a user asks a question, it is embedded using the AWS Titan model and compared against vectors in the database using cosine similarity. This process returns text chunks from the corpus

that are most relevant to the question and provides that information as context to OpenAI's ChatGPT to produce answers to GDR users' questions.

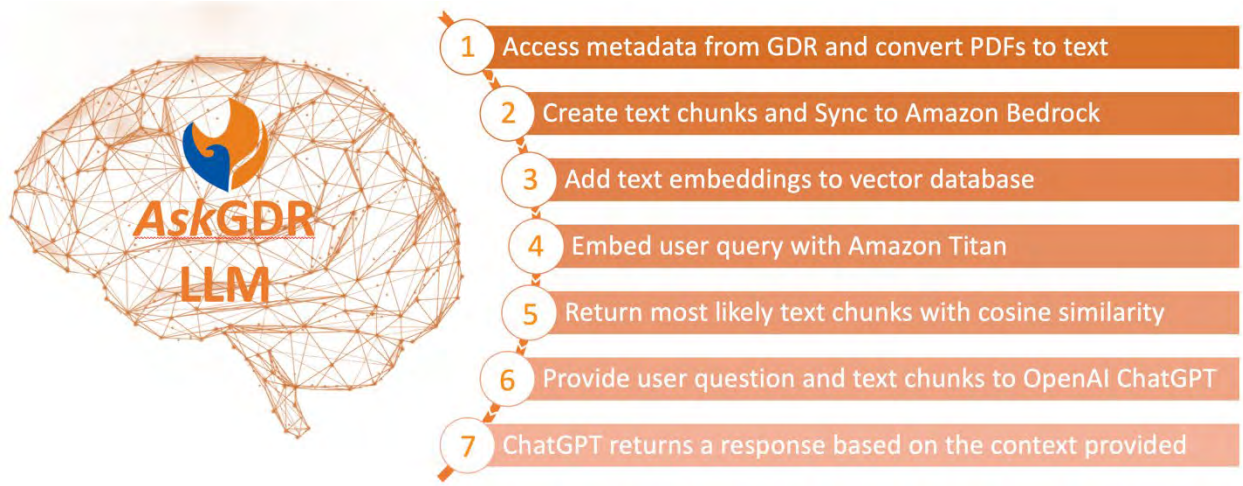

Figure 1 Flow of information from GDR metadata to AskGDR answers.

3.4 Limitations

AskGDR is currently based on ChatGPT 4.0, which produces answers based on the probability of generative text tokens, and not mathematical calculations. As a result, it is not reliable for answering mathematical questions. Similarly, basic ChatGPT implementations are not great at interpreting figures, images, maps, or other visual media. While many extensions exist for ChatGPT that vastly improve its capabilities in these areas, AskGDR has not been programed with any extended capabilities and cannot interpret nor derive insight from images or other visual media within the GDR.

By design, AskGDR is limited to the knowledge and information contained within the GDR. It will not go out to the greater internet nor consult any unapproved sources for answers to user-provided questions. It has intentionally been constrained to the corpus of knowledge that is the metadata and supporting documents associated with curated GDR data submissions. That said, AskGDR can only correctly respond to questions that are answered within the metadata provided by submitters.

Lastly, AskGDR responses are not perfect. Some answers draw upon connections between two datasets that are not actually related, especially when project acronyms are involved. For example, Sample Question 1 above cites a source from the submission titled "Three-Component Long Offset Surface Seismic Survey Data Used to Find Large Aperture Fractures in Geothermal Resources - San Emidio Geothermal Resource Area," which is a seismic dataset not related to the PoroTomo project. This is likely related to the fact that PoroTomo is an acronym, not a real word, and that the project cited has similar text associated with it. Therefore, it is always recommended to fact check responses given by LLMs and chat bots.

3.5 User Interface (UI) Integration

Understanding that the need to ask questions can arise at any time during an exploration of data, the GDR team has devised a UI for AskGDR based on a modal "pop up" that allows it to be accessible from anywhere in the GDR. The AskGDR button (Figure 2, left) opens the AskGDR modal window on any GDR page, allowing users to ask questions without navigating away from their current location.

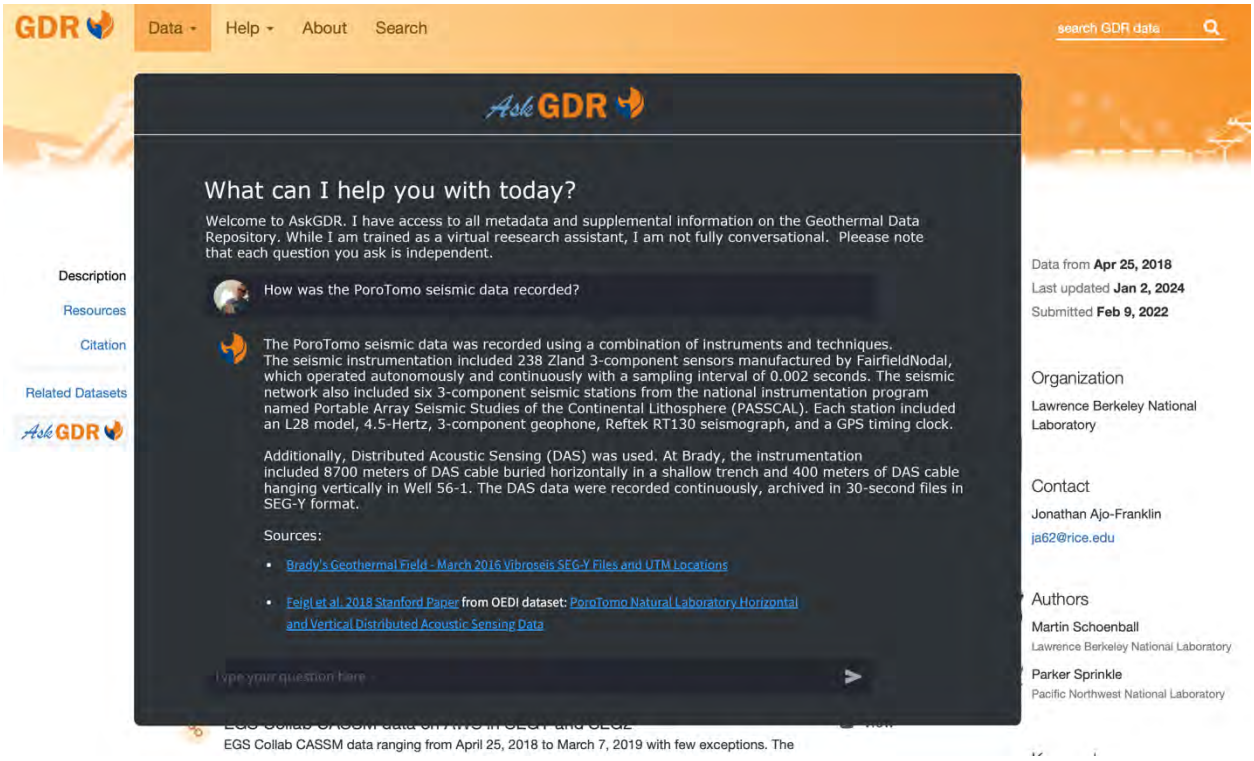

Figure 2 Screenshot showing the AskGDR button (middle left) and the AskGDR pop up (center, black)

The AskGDR button is featured prominently on the GDR homepage, each dataset landing page, and is included under Help in the main navigation.

4. Risks and Uncertainties

AskGDR uses a novel approach that includes several new technologies, some of which come with their own risks and uncertainties, such as cost and quality of generated answers. Additionally, concerns over the legality of AI-generated content have been raised by numerous communities. GDR will continue to monitor these risks and uncertainties and act accordingly to ensure that AskGDR benefits the geothermal community overall.

4.1 Cost

AskGDR utilizes several modern cloud-based technologies, including managed services for its vector database, Amazon Bedrock, and Titan, and OpenAI's API for ChatGPT. Each of these services comes with their own cost, and while the costs of hosting AskGDR have been negligible to date, some of these expenses (e.g. the ChatGPT API) are transactional and will scale linearly with the number of questions asked. Rate limits have been added to AskGDR to prevent users

from asking an unreasonable number of questions per day or mischievously driving up costs for the GDR. These limits are still being fine-tuned by the GDR team in an effort to find an optimal balance between utility and cost but are set high enough that the average user will likely never encounter them.

Other expenses are related to the size of the underlying knowledge base and the computational power required to convert it into a vector database for the LLM to use. These expenses are expected to benefit from economies of scale and should decrease over time. The GDR team is keeping a close eye on these expenses and has already identified several efficiencies that could be implemented to reduce costs, should they become necessary and economical.

4.2 Legality

Concerns have been raised over the legality of AI-generated answers; specifically whether or not these answers constitute plagiarism (Murugesan 2023). These concerns were a factor in our decision to develop AskGDR to function more as an AI Research Assistant than a fully conversational chat bot. AskGDR has been instructed to always cite its sources and will link back to the original source material within each answer, helping to create data provenance and attribute proper credit to the original authors. AskGDR is fully compliant with current DOE and NREL policies on the use of generative AI and the GDR team will continue to monitor these policies as they evolve.

4.3 Quality of Generated Content

One of the greatest risks of generative AI tools like AskGDR is the ability of the underlying LLM to "hallucinate," i.e. recognize patterns in language that result in the generation of inappropriate, nonsensical, or inaccurate outputs (IBM 2024). The GDR team has greatly reduced this risk by instructing AskGDR not to speculate. Rather than attempting to generate an answer from nothing, or reaching out to the internet at large, AskGDR will remain confined to the predetermined, curated GDR knowledge base and will inform the user if insufficient information is available to generate an answer. This reduces the risk of hallucinations but does not eliminate it. The GDR team is keeping track of questions asked by users to monitor the use of AskGDR and the quality of its answers. Questions asked are stored anonymously and are not associated with any user or individual data.

The GDR team is keeping close watch on all of these concerns, collecting data on usage and expenditure, to evaluate the efficacy and impact of AskGDR.

5. Conclusion

AskGDR increases the utility and discoverability of geothermal data by providing the geothermal community with the means to quickly interrogate the methods used to collect data and any assumptions made while also providing the ability to link datasets to abstract concepts aligned with specific research objectives. This new functionality not only saves time for researchers looking to investigate datasets on the GDR, but it also reduces the number of repetitive questions received by data owners and dataset POCs, increasing efficiency and saving time for more critical research activities.

Furthermore, the foundational work necessary to make AskGDR possible, including the prerequisite that GDR datasets adhere to both FAIR and FARR data principles, helps ensure that GDR data is accessible to other LLMs and machine learning efforts. AskGDR enables valuable research done by the geothermal community to be included in the answers generated not only by AskGDR, but also by other generative AI applications, and helps to set a precedent for the availability of scientific information in the world of AI-generated answers.

The GDR provides universal access to data and information and AskGDR helps to further that mission by provide equity in access across diverse communities. It simplifies the interrogation of complex datasets and the insights it provides are free to use for everyone.

Acknowledgement

This work was authored by the National Renewable Energy Laboratory, operated by Alliance for Sustainable Energy, LLC, for the U.S. Department of Energy (DOE) under Contract No. DE-AC36-08GO28308 with funding provided by U.S. Department of Energy Office of Energy Efficiency and Renewable Energy (EERE) Geothermal Technologies Office (GTO). The views expressed in the article do not necessarily represent the views of the DOE or the United States Government. The United States Government retains and the publisher, by accepting the article for publication, acknowledges that the United States Government retains a nonexclusive, paid-up, irrevocable, worldwide license to publish or reproduce the published form of this work, or allow others to do so, for United States Government purposes.

REFERENCES

Department of Energy (DOE). “Strategic Plan”. *DOE/CF-0067*. Washington, DC (2011). 43-44.

FARR. “FARR: FAIR in ML, AI Readiness, & Reproducibility.” FARR Research Coordination Network (RCN), 12 June 2024. Web. https://www.farr-rcn.org/

Feigl, K. “PoroTomo Natural Laboratory Horizontal and Vertical Distributed Acoustic Sensing Data.” [data set]. University of Wisconsin, Madison, WI (2017). Web. https://dx.doi.org/10.15121/1778858

GDR. “DOE Geothermal Data Repository.” OpenEI: Open Energy Information. National Renewable Energy Laboratory (NREL), 12 June 2024. Web. https://gdr.openei.org/

IBM. “What are AI hallucinations? Think: IBM. 12 June 2024. Web. https://www.ibm.com/topics/ai-hallucinations

Murugesan, S. “The Rise of Ethical Concerns about AI Content Creation: A Call to Action.” *Tech News*, IEEE Computer Society, 24 April 2023.

Pinchuk, P., Buster, G., Podgorny, S. “Energy Language Model (ELM).” 12 June 2024, GitHub repository, https://github.com/NREL/elm

Pinchuk, P., Buster, G., and Podgorny, S. “NREL/ELM: NREL Research Hub Example, API Handling, and Vector DB Querying”. Zenodo, June 4, 2024. https://doi.org/10.5281/zenodo.11476365

Taverna, N., Buster, G., Huggins, J., Rossol, M., Siratovich, P., Weers, J., Blair, A., Siega, C., Mannington, W., Urgel, A., Cen, J., Quinao, J., Watt, R., and Akerley, J. “Data Curation for Machine Learning Applied to Geothermal Power Plant Operational Data for GOOML: Geothermal Operational Optimization with Machine Learning.” *Proceedings*, 47th Workshop on Geothermal Reservoir Engineering, Stanford University, Stanford, CA. 2022.

Weers, J., Anderson, A., and Taverna, N. "Connecting People to Data: Enabling Data Connected Communities through Enhancements to the Geothermal Data Repository." *GRC Transactions*, Vol. 47, 2023.

Weers, J., Anderson, A., and Taverna, N. “The Geothermal Data Repository: Ten Years of Supporting the Geothermal Industry with Open Access to Geothermal Data” *GRC Transactions*, Vol. 46, 2022.

Wilkinson, M., Dumontier, M., Aalbersberg, I. et al. “The FAIR Guiding Principles for scientific data management and stewardship.” Scientific Data 3, 160018 (2016). https://doi.org/10.1038/sdata.2016.18

Prediction of Formation Properties Based on Drilling Data from Multiple Wells at Utah FORGE Site Using Machine Learning

Pengju Xing[1], Palash Panja[1], John McLennan[2], Joseph Moore[1]

[1] Energy & Geoscience Institute, University of Utah, Salt Lake City, UT, USA

[2] Department of Chemical Engineering, University of Utah, Salt Lake City, UT, USA

Keywords

Machine learning, Drilling, Formation Properties, Enhanced Geothermal System, Utah FORGE

ABSTRACT

In this study, machine learning methods have been employed to establish relationships between drilling parameters and the formation properties – confined compressive strength (CCS) – in geothermal wells at the Utah FORGE (Frontier Observatory for Research in Geothermal Energy) site. CCS can be considered as a proxy for the ability to comminute rock during drilling. At Utah FORGE, the logging data is available to provide a continuous measurement of CCS, which is then calibrated against the core testing results. Drilling data from four deep wells that used PDC (polycrystalline diamond compact) bits were used to train the machine learning model. The dataset from multiple wells mitigates the risk of overfitting associated with using data from a single well, leading to improved prediction results, especially for the Random Forest (RF) model. For the RF models used to predict CCS, the top four important features are: 1) true vertical depth (TVD), 2) top drive torque, 3) rate of penetration (ROP), and 4) standpipe pressure. Trained by the four-well dataset, the R-squared score of RF model for the training dataset is 0.95 and for the testing dataset is 0.91. RF models are also trained by the three-well dataset (part of the whole dataset). The trend of predicted CCS – by the three-well RF model using the unseen drilling data (the fourth well) – along TVD matches well with the actual value, with a Root Mean Squared Error (RMSE) of 0.10. Thus, the machine learning models are not limited to a single well and hold potential for application to any future wells drilled in this region. This work showcases the utilization of machine learning models to predict formation properties, reducing costs and complexity associated with traditional methods like well logging or core testing.

1. Introduction

Formation properties, e.g. compressive strength, can be obtained through well logging or core testing. However, these procedures are expensive, and implementation can be complex, especially in geothermal wells with high-temperature conditions. Alternatively, predictions of formation properties can be derived from bit-rock interactions without additional operational costs, utilizing machine learning models. To train machine learning models effectively, substantial data is required. Fortunately, at the Utah FORGE (Frontier Observatory for Research in Geothermal Energy) site, five deep wells have been drilled (refer to Figure 1), and each of these wells has well-documented drilling data, a comprehensive suite of well logs, and core testing data. Utah FORGE

is a U.S. Department of Energy funded project for Enhanced Geothermal System (EGS) development (Moore et al., 2019). This rich dataset from Utah FORGE is invaluable in training a machine learning model for predicting material properties in situ.

In this study, machine learning methods are employed to establish relationships between drilling parameters and the formation properties, particularly focusing on the confined compressive strength (CCS). The logging data provides a continuous measurement of CCS (bit face compressive strength under the local effective confining stress regime – mean effective stress), which is then calibrated against the core testing results. CCS reflects the ability to comminute rock during drilling. Phelan et al. (2022) showed the prediction of CCS from a single well, 16A(78)-32 at Utah FORGE. In this study, the dataset from multiple wells that used PDC (polycrystalline diamond compact) bits is investigated. It is beneficial to use multiple wells because it can mitigate the risk of overfitting associated with using data from a single well and increase the overall prediction accuracy for any future wells drilled in this region of Utah FORGE.

The paper first shows how to obtain the "label" – CCS and its calibration. The second part of the paper details the data preprocessing and feature evaluation. Finally, different machine learning models are evaluated, and their performances are discussed.

2. Data Collection

The information of the four wells that used PDC bits at Utah FORGE is listed in Table 1 (Dupriest and Noynaert, 2024). There is only one well, 58-32, which was drilled with tri-cone bits. In this study, only the drilling data from the four wells drilled with PDC bits is used to train the machine learning model. For the machine learning model, the features (input data) are from the drilling data, which include weight on bit, top drive torque, differential pressure, standpipe pressure, top drive rotary, bit RPM, flow rate, and rate of penetration (ROP). True vertical depth (TVD) is also a feature because the rock properties could be different at different depths. The label (output data) is one of the rock properties, CCS. The drilling data (features) can be directly obtained. However, the label, CCS, has to be inferred from the logging data and calibrated by the core testing results.

Figure 1. Utah FORGE site (adapted from Moore et al., 2023).

Table 1. Deep wells drilled with PDC bits at Utah FORGE site

Well Name	Well Type	Drill Bit	MD (ft)	TVD (ft)	Logs	Core testing
16A(78)-32	Deviated	PDC	10987	8559	Sonic log	Yes
16B(78)-32	Deviated	PDC	10947	8391	Sonic log	No
78B-32	Vertical	PDC	9500	9500	Sonic log	Yes
56-32	Vertical	PDC	9145	9145	ThruBit Dipole	No
*58-32	Vertical	Tri-cone	7536	7536	Sonic log	Yes

*Well 58-32 is excluded from the machine learning training because PCD bits were not used.

2.1 CCS Calculation

Continuous CCS along the measured depth (MD) of the four wells was first estimated from analysis of the sonic logs. The method of calculating CCS using logging data is detailed in Phelan et al. (2022). There are core testing results available from three wells, 58-32, 16A(78)-32, and 78B-32, which are used to calibrate the parameters inferred from sonic logs. It is important to note that even though the drilling data of well 58-32 is not used due to different drill bit types, its core testing results can still be used for the CCS calibration. The compressive strength of the core samples under different confining pressure from multiple Utah FORGE wells is shown in Figure 2.

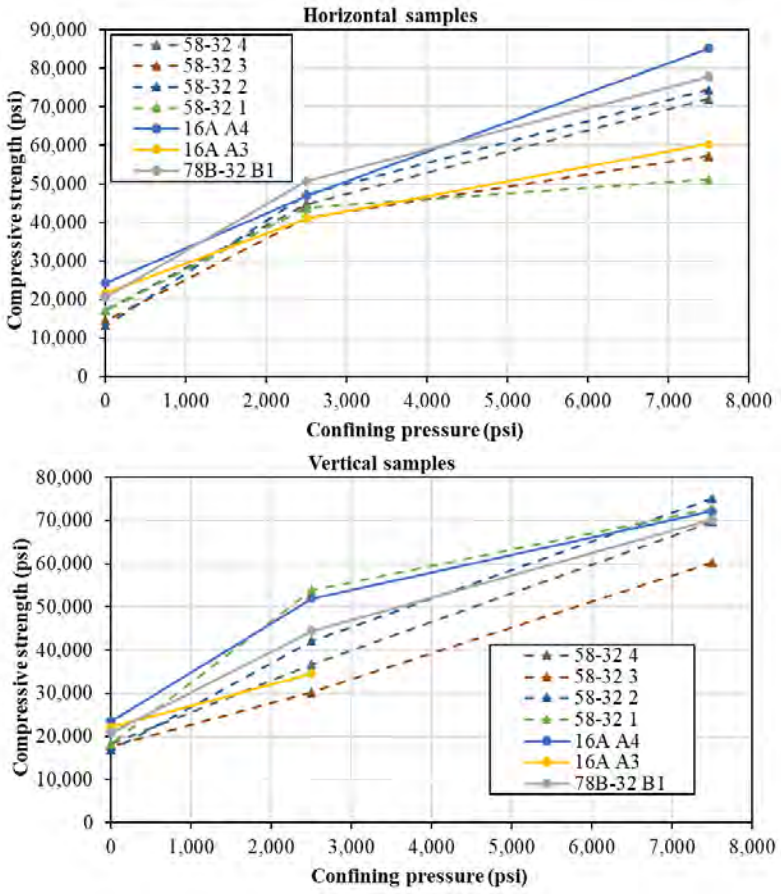

Figure 2. Compressive strength under different confining pressure of the cores from Utah FORGE wells.

During the writing of our previous article (Phelan et al., 2022), the core testing results of well 16A(78)-32 were not available. Consequently, core testing results of well 58-32 were used to calibrate the relevant parameters calculated by logging data for well 16A(78)-32. During this study, core testing results are available from three wells including well 16A(78)-32, 58-32, and 78B-32. Figure 3 shows the comparison of unconfined compressive strength (UCS) and internal friction angle between the inferred values from logs in well 16A(78)-32 and core testing results (including all three wells), which are in good agreement.

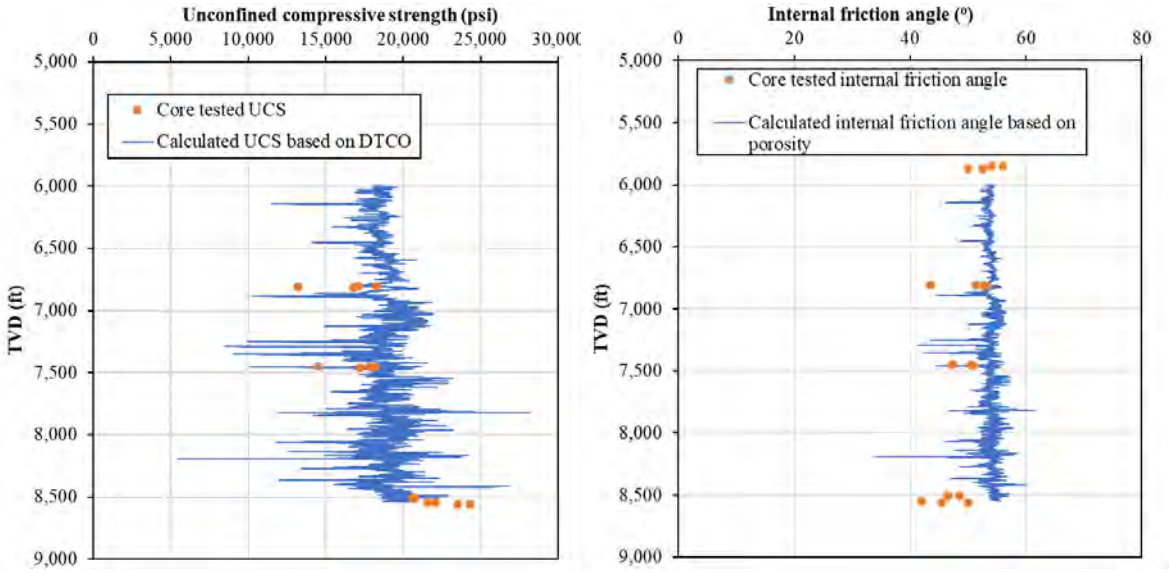

Figure 3. Comparison of UCS and internal friction angle between core testing results and calculated results. The calculated results are from the interpretation of the sonic logs from well 16A(78)-32. Please note the core testing results include wells 16A(78)-32, 78B-32 and 58-32.

The calculated and calibrated UCS and CCS along MD for well 16A(78)-32 are shown in Figure 4. The mud weight is 0.54 psi/ft and the reservoir pressure is 0.433 psi/ft.

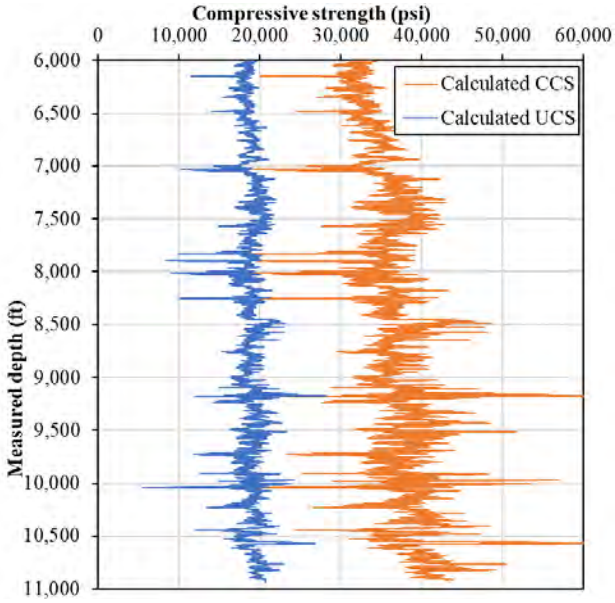

Figure 4. Calculated UCS and calculated CCS along MD for well 16A(78)-32.

3. Data Preprocessing

3.1 Data Filtering

For this research, the area of interest is focused on the reservoir rock, i.e., granitoid and metamorphic rock. Therefore, the data that belongs to the overlying alluvium is deleted. Then, the base filter shown in Table 2 is applied to the features. The data out of the range shown in this table was not reasonable and hence removed and not used. The data with low bit RPM was also removed because its volume is small, and its clustering is different from that of large bit RPM.

For well 16B(78)-32, the available data started from 6000 ft MD, but the selected data for machine learning started from 7600 ft MD (6934 ft TVD). That is because from 6000 ft MD to 7600 ft MD, a Halo Rotary Steerable System was used, which is different from the deeper section and the other wells.

Table 2. Base filter applied to the features

Parameter	Base filter min	Base filter max
Weight on Bit (klbs)	0	200
Top drive torque (kft_lb)	0	100
Differential Pressure (psi)	-8000	N/A
Standpipe Pressure (psi)	0	10000
Top Drive Rotary (RPM)	0	500
Bit RPM (RPM)	0	500
Flow (flow percent)	0	100

3.2 Sliding Section Deletion

The drilling can be classified as rotating and sliding. Rotating is drilling with top drive or rotary table, and the drill string is rotated in order to gouge the hole. Rotary drilling will be used when a straight hole direction is needed. Sliding (orienting or steering) is drilling with downhole steerable mud motor, which does not rotate drill pipe because it uses hydraulic power to drive down the motor and bit. Sliding is used in order to control well direction (DrillingFormulas.Com). When it is sliding, top drive rotary is 0, while there is still a bit RPM.

The purpose of this study is to infer the rock properties from the rock-bit interaction. Rotating is much more reflective of the rock-bit interaction than sliding. Therefore, the sliding section was removed from the dataset. Most of the sliding section is from well 16A(78)-32.

After the data processing (filtering, outliers removal, and sliding section deletion), the maximum and minimum magnitude of the features and label of each well are listed in Table 3.

Table 3. Maximum and minimum value of parameters for each well after pre-processing

Parameter	Max				Min			
	16A(78)-32	16B(78)-32	56-32	78B-32	16A(78)-32	16B(78)-32	56-32	78B-32
Weight on Bit (klbs)	66	82	54	78	0	0	0	0
Top Drive Torque (kft_lb)	15	37	17	22	0	1	3	6
Differential Pressure (psi)	755	1249	1006	999	-364	-396	-174	-413
Standpipe Pressure (psi)	4678	3132	4277	3614	2328	1415	2119	1508
Top Drive Rotary (RPM)	74	128	107	72	21	21	21	21
Bit RPM (RPM)	339	266	235	205	109	157	170	114

Flow (flow percent)	85	82	93	40	39	38	59	13
Calculated ROP (ft/hr)	144	339	270	247	9	3	10	23
TVD (ft)	8553	8339	9036	8400	6062	6934	4275	4021
CCS (psi)	58833	59063	53323	52423	12841	18821	15045	15584

3.3 Feature Evaluation and Selection

The pair plots of features and label after data preprocessing are shown in Figure 5. The pair plot provides a direct view of the relationship between different parameters for different wells. Obviously, bit RPM changes linearly with top drive rotary.

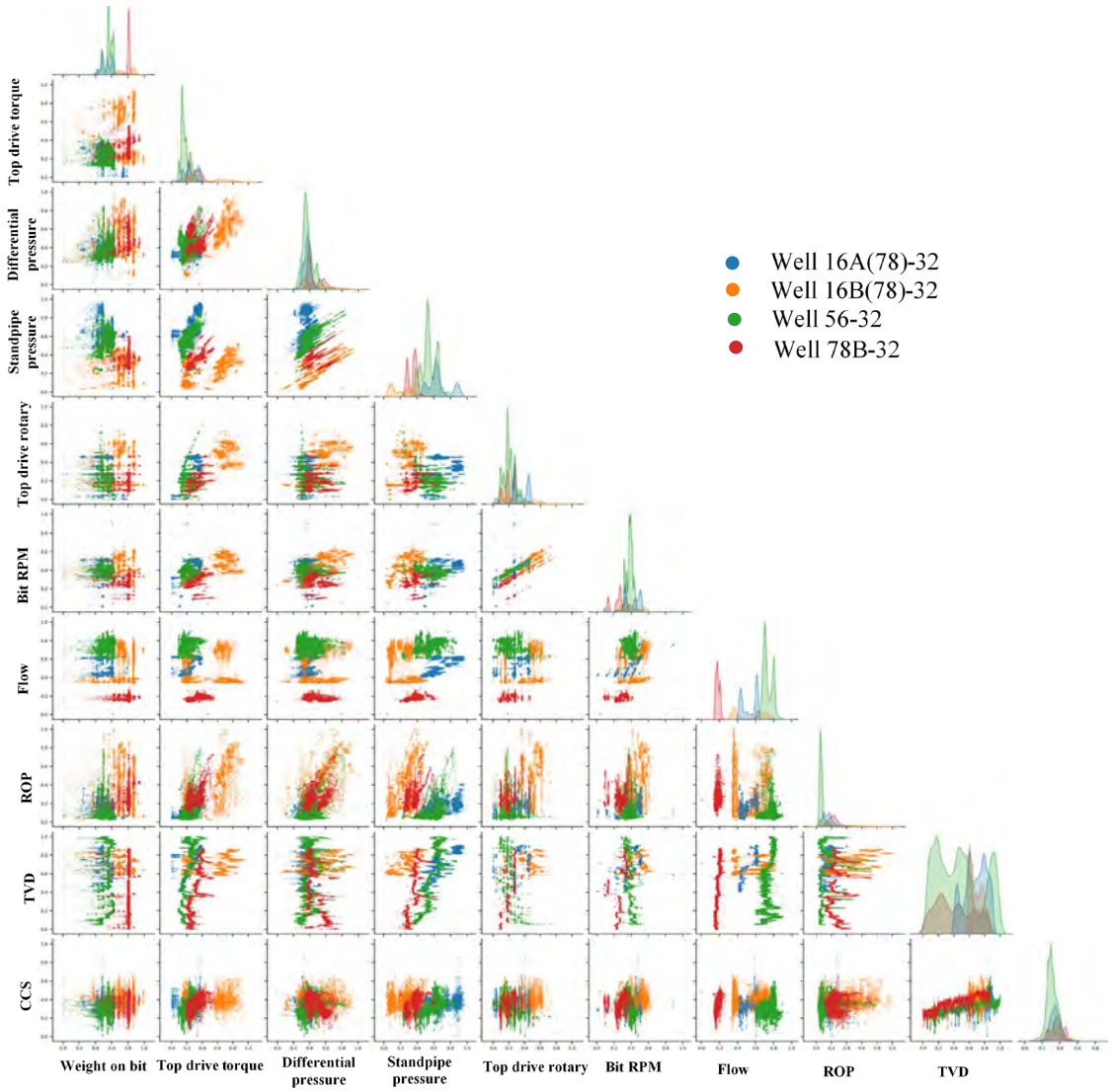

Figure 5. Pair plot of the drilling parameters for the four wells.

Figure 6 shows the correlation coefficients among features and label. The top three parameters that have a high correlation coefficient with CCS are 1) TVD, 2) top drive torque, and 3) ROP.

The top three pairs with a high correlation coefficient are ROP vs. top drive torque, CCS vs. TVD, and Bit RPM vs. top drive rotary. Considering the results of both pair plots (Figure 5) and correlation heat map (Figure 6), bit RPM and top drive rotary are highly correlated, and only the

feature – top drive rotary – is kept. Therefore, the features that are selected for the machine learning model training are: weight on bit, top drive torque, differential pressure, standpipe pressure, top drive rotary, flow rate, and ROP. In addition, to investigate the influence of TVD, the machine learning models are trained with two scenarios: one with TVD as a feature, and the other one without TVD.

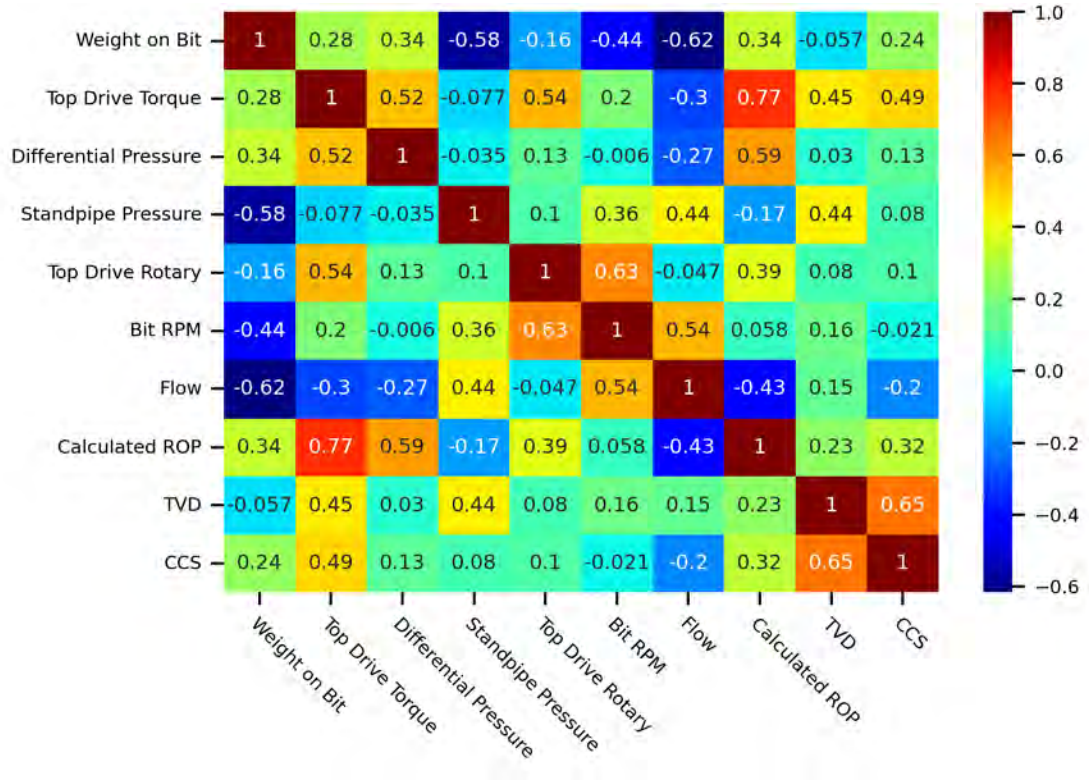

Figure 6. Correlation heat map showing correlation coefficients of the drilling parameters for the four wells.

4. Model Training and Performance Evaluation

After data preprocessing, two types of machine learning models – Random Forest (RF) and Artificial Neural Network (ANN) – are used to build the relationship between drill data (features) and rock CCS (label). Different datasets containing a combination of different wells are used to train the machine learning models. During the training of the dataset containing multiple wells, the features are normalized to the maximum and minimum values of the total dataset (multiple wells together), not to each well. For the prediction of the unseen data, the unseen data was filtered not to exceed the maximum and minimum range of both the features and labels of the "seen" data during the training.

4.1 Machine Learning Model – RF

RF is an ensemble learning method that operates by constructing a multitude of decision trees at training time. For regression tasks, the mean or average prediction of the individual trees is returned. An advantage of the RF model is that it can give feature importance after training.

We first investigate the performance of RF model without TVD and then evaluate its performance with TVD as a feature. In order to reduce the overfitting of RF model, 5-fold cross validation, limiting the maximum tree depth as 20, and setting a minimum number of samples at a leaf node as 5 are applied.

4.1.1 TVD not as a feature

Here TVD is not considered as a feature. Two RF models were trained with different datasets. The two different datasets are: 1) four wells including 16A(78)-32, 16B(78)-32, 78B-32, 56-32; 2) three wells including 16B(78)-32, 78B-32, 56-32 [no well 16A(78)-32]. The four-well model is used to evaluate the performance of the whole dataset, while three-well model is used to test the prediction accuracy of the unseen data, the fourth well. When training the model, the dataset is split into 80% of training and 20% of testing.

The top three important features for the four-well model are: 1) top drive torque, 2) standpipe pressure, 3) ROP, which are the same with the three-well model without 16A(78)-32.

The unseen data set (data from well 16A(78)-32) for the three-well RF model excluding well 16A(78)-32 is also tested. The number of rows in the three-well dataset without well 16A(78)-32 is 76712. 40% of well 16A(78)-32 (7593 rows) was used to test the model trained by the three-well dataset without well 16A(78)-32 is, which is 7593 rows. All of the performance metrics i.e., R^2 (R-squared), RMSE (Root Mean Squared Error), MAE (mean absolute error) are good for the "seen" dataset, including both training (80%) and testing (20%). The RMSE and MAE for the unseen dataset from well 16A(78)-32 for the three-well RF model is good, but R^2 is relatively low (refer to Table 4). Nevertheless, the predicted CCS along TVD matches the actual CCS for well 16A(78)-32 (refer to Figure 9).

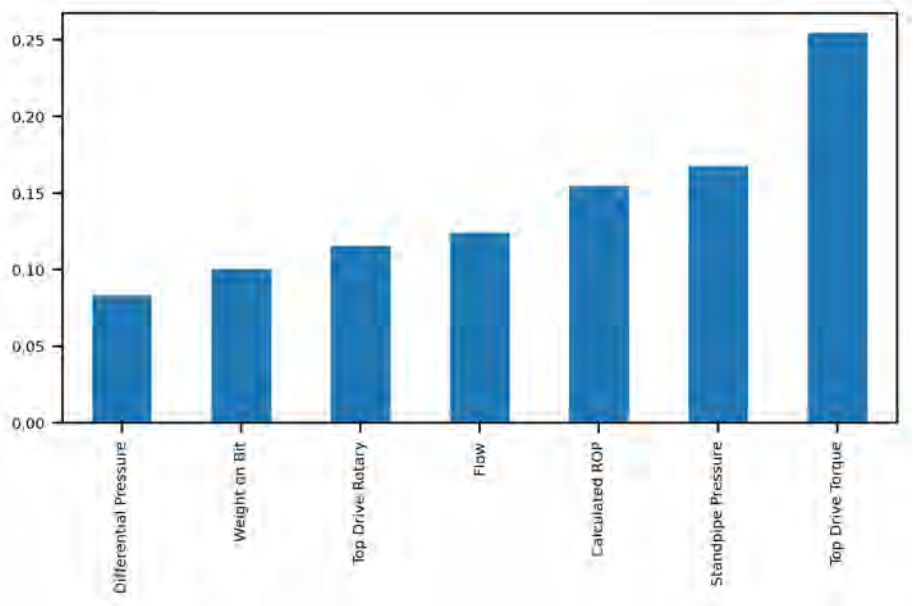

Figure 7. Feature importance of the RF model for the dataset of four wells [16A(78)-32, 16B(78)-32, 78B-32, and 56-32]. TVD is not a feature.

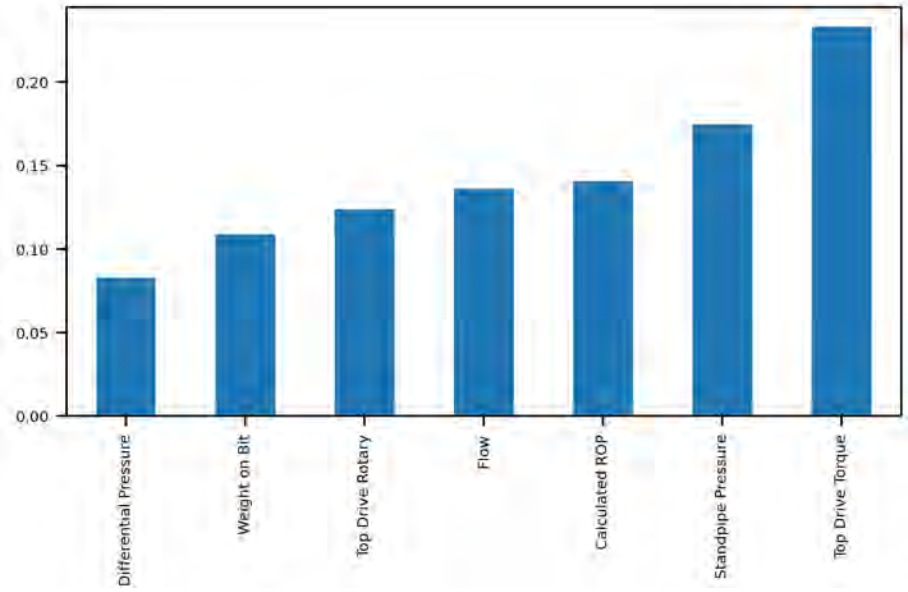

Figure 8. Feature importance of the RF model for the dataset of three wells [excluding 16A(78)-32, including 16B(78)-32, 78B-32, and 56-32]. TVD is not a feature.

Table 4. RF model performance of different datasets (TVD not as a feature)

Model	Train data metrics			Test data metrics			Test new dataset	Test new dataset metrics		
	R^2	RMSE	MAE	R^2	RMSE	MAE		R^2	RMSE	MAE
4 wells	0.91	0.02	0.01	0.84	0.03	0.02	N/a	N/a	N/a	N/a
3 wells (excluding 16A(78)-32)	0.93	0.03	0.02	0.88	0.04	0.02	40% of 16A (7593 rows of 16A)	0.16	0.08	0.06

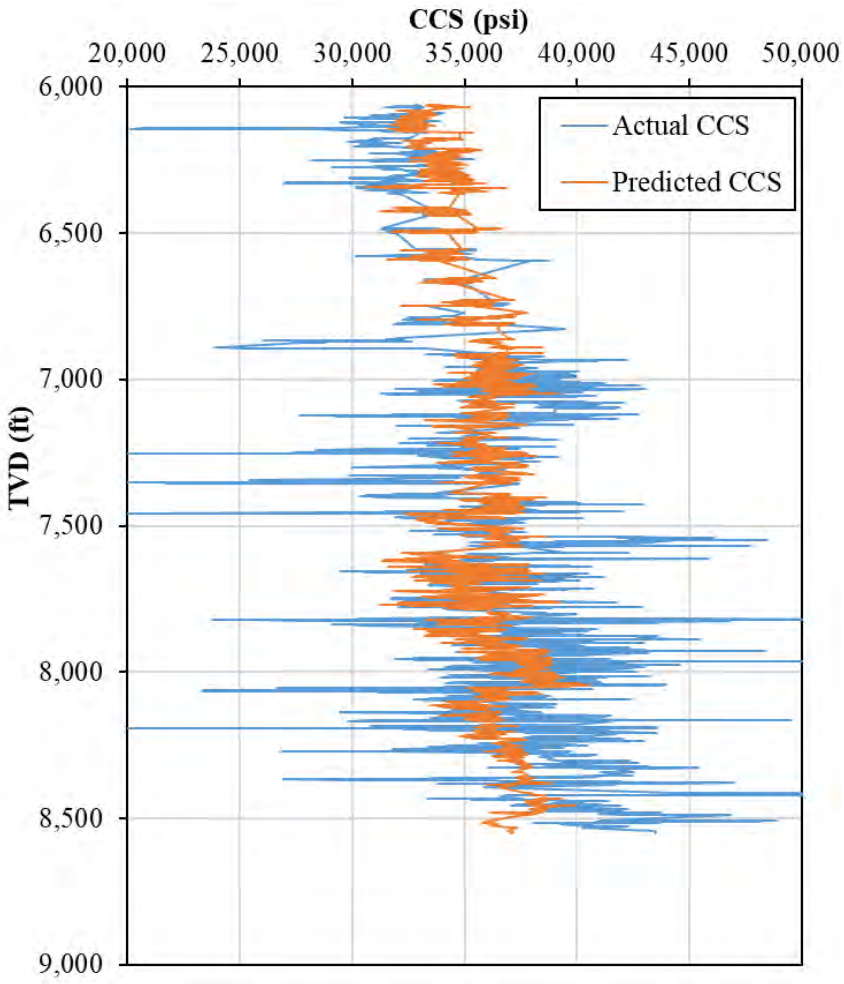

Figure 9. Comparison between predicted value from the three-well RF model and actual value of CCS for well 16A(78)-32. The RF model is trained with the dataset of three wells excluding 16A(78)-32 [including 16A(78)-32, 16B(78)-32, 78B-32, and 56-32]. TVD is not a feature.

4.1.2 TVD as a feature

TVD is added as a feature to investigate its influence. For model training, the datasets are split into 80% training and 20% testing. The feature importance of the four-well RF model is shown in Figure 10. The top three important features are 1) TVD, 2) top drive torque, and 3) ROP, which is the same as the top three features with a higher correlation coefficient with CCS (refer to Figure 6).

The RF models trained with three-well datasets are also investigated. Their feature importance is shown from Figure 11 to Figure 14. For almost all the three-well RF models, the top four important features are the same: 1) TVD, 2) top drive torque, 3) ROP, and 4) standpipe pressure. Only for the model excluding 56-32, flow ranks as the third important feature. This feature importance ranking is aligned with the ranking of correlation coefficient with CCS. Even though standpipe pressure has a very low correlation coefficient (0.08) with CCS, it ranks as third or fourth important feature. Obviously, after adding TVD as a feature, the TVD becomes the first important feature in the RF model. There are two reasons from the point of view of physics: the confining pressure increases with TVD and the rock properties change with TVD.

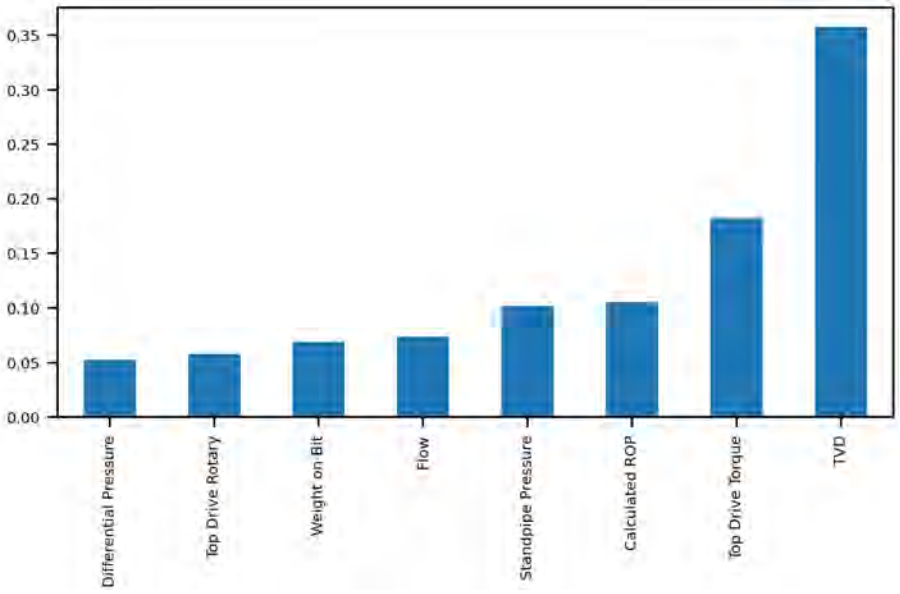

Figure 10. Feature importance of the RF model for the dataset of four wells [16A(78)-32, 16B(78)-32, 78B-32, and 56-32]. TVD is a feature.

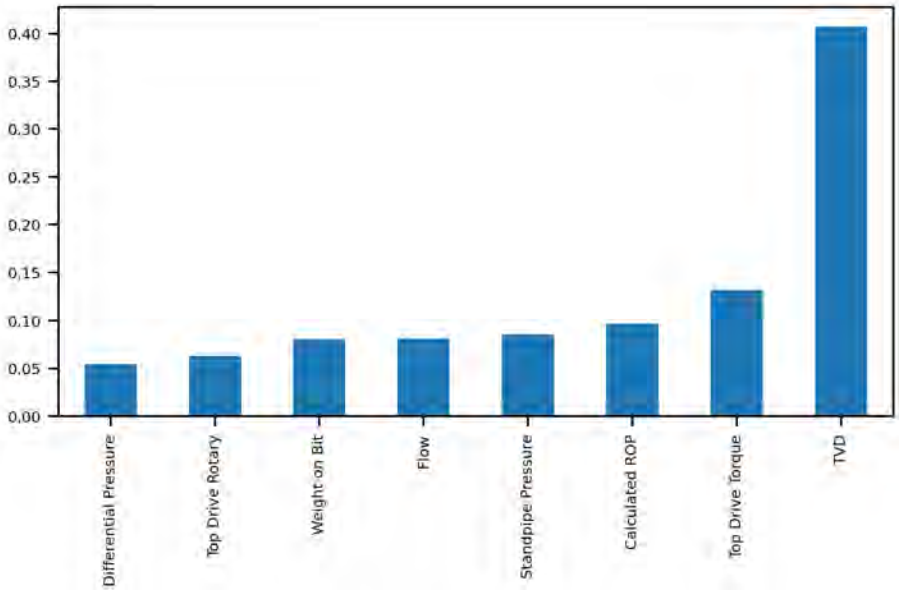

Figure 11. Feature importance of the RF model for the dataset of three wells excluding 16A(78)-32 [including 16B(78)-32, 78B-32, and 56-32]. TVD is added as a feature.

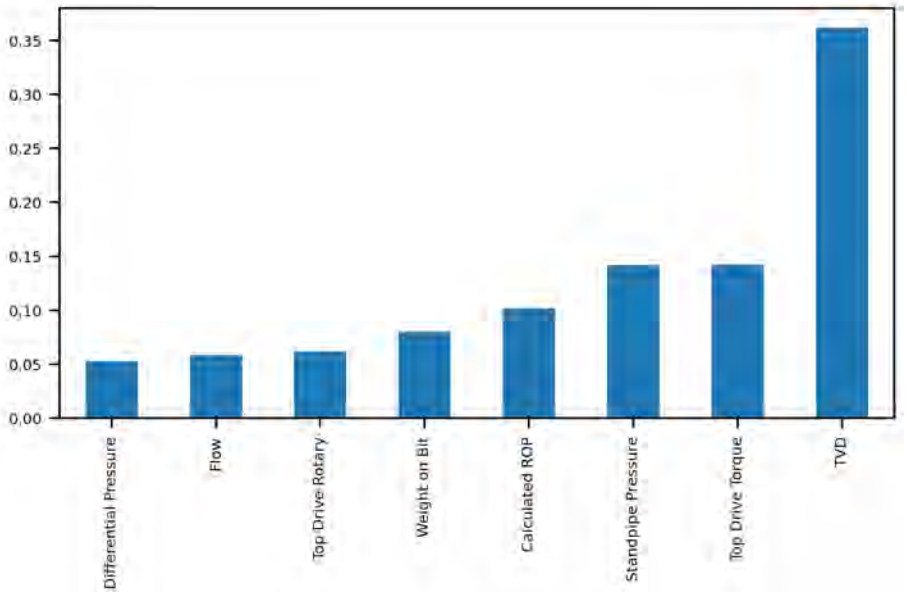

Figure 12. Feature importance of the RF model for the dataset of three wells excluding 78B-32 [including 16A(78)-32, 16B(78)-32, and 56-32]. TVD is added as a feature.

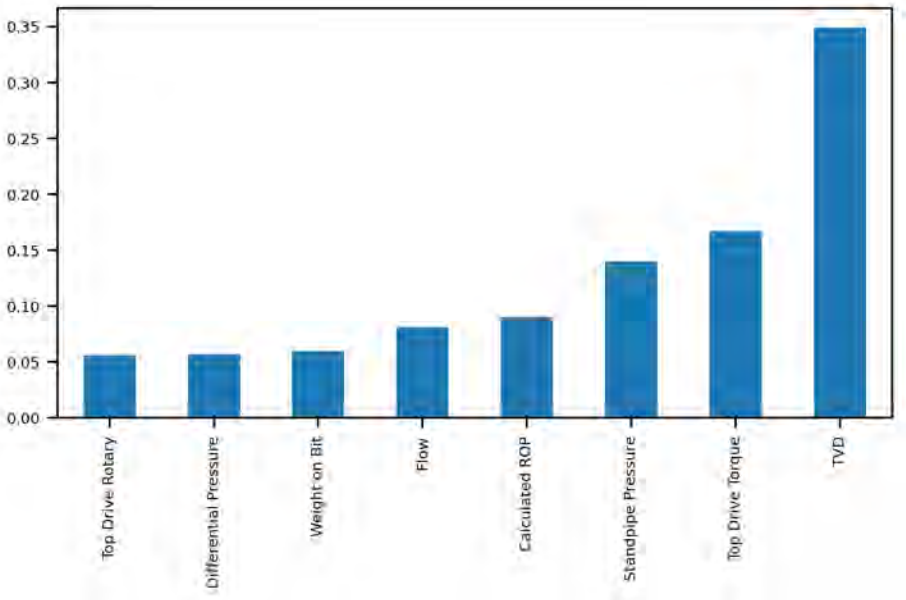

Figure 13. Feature importance of the RF model for the dataset of three wells excluding 16B(78)-32 [including 16A(78)-32, 78B-32, and 56-32]. TVD is added as a feature.

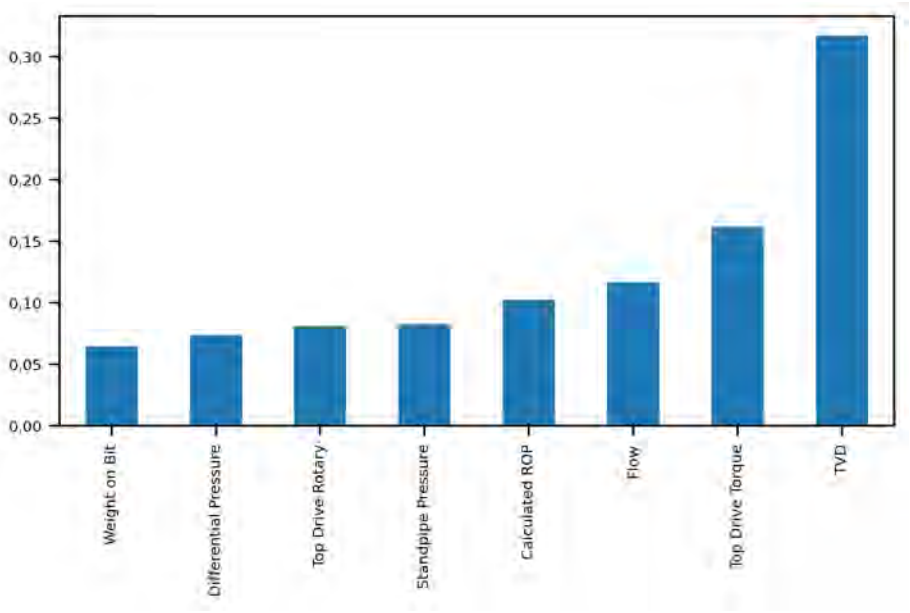

Figure 14. Feature importance of the RF model for the dataset of three wells excluding 56-32 [including 16A(78)-32, 16B(78)-32, 78B-32]. TVD is added as a feature.

The models' performance is shown in Table 5. The R-square score of the four-well RF model for the training dataset is 0.95 and for the testing dataset is 0.91. The overall RMSE, MAE, and R-squared for prediction using three-well RF models from unseen data are not improved compared to those models without TVD.

Table 5. RF model performance of different datasets with TVD as a feature

Model	Train data metrics			Test data metrics			Test new dataset	Test new dataset metrics		
	R^2	RMSE	MAE	R^2	RMSE	MAE		R^2	RMSE	MAE
4 wells	0.95	0.02	0.01	0.91	0.02	0.01	N/a	N/a	N/a	N/a
3 wells (excluding 16A(78)-32)	0.95	0.02	0.01	0.93	0.03	0.02	40% of 16A	0.20	0.08	0.06
3 wells (excluding 78B-32)	0.95	0.02	0.01	0.91	0.03	0.02	50% of 78B-32	-0.17	0.11	0.10
3 wells (excluding 16B(78)-32)	0.96	0.02	0.01	0.94	0.03	0.02	90% of 16B(78)-32	-0.10	0.12	0.09
3 wells (excluding 56-32)	0.91	0.03	0.02	0.85	0.04	0.03	49762 vs 43292	0.35	0.07	0.05

However, as shown in Figure 15, the trend of CCS predicted by the model with TVD has a much better match for well 16A(78)-32. Similarly, we also plot the predicted CCS vs. TVD for well 78B-32 and 56-32, and their trends generally match the actual data (refer to Figure 16 and Figure

17). For well 16B(78)-32, since its top drive torque is much larger than that of the other three, and top drive torque is an important impacting factor, the predicted CCS vs. TVD trend is not well aligned with the actual values. It is important to note that in all of these predicted and actual value comparisons, the predicted data is obtained from input drilling data, which is not seen by the corresponding machine learning models before.

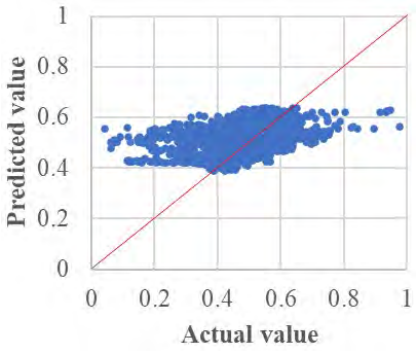

(a)

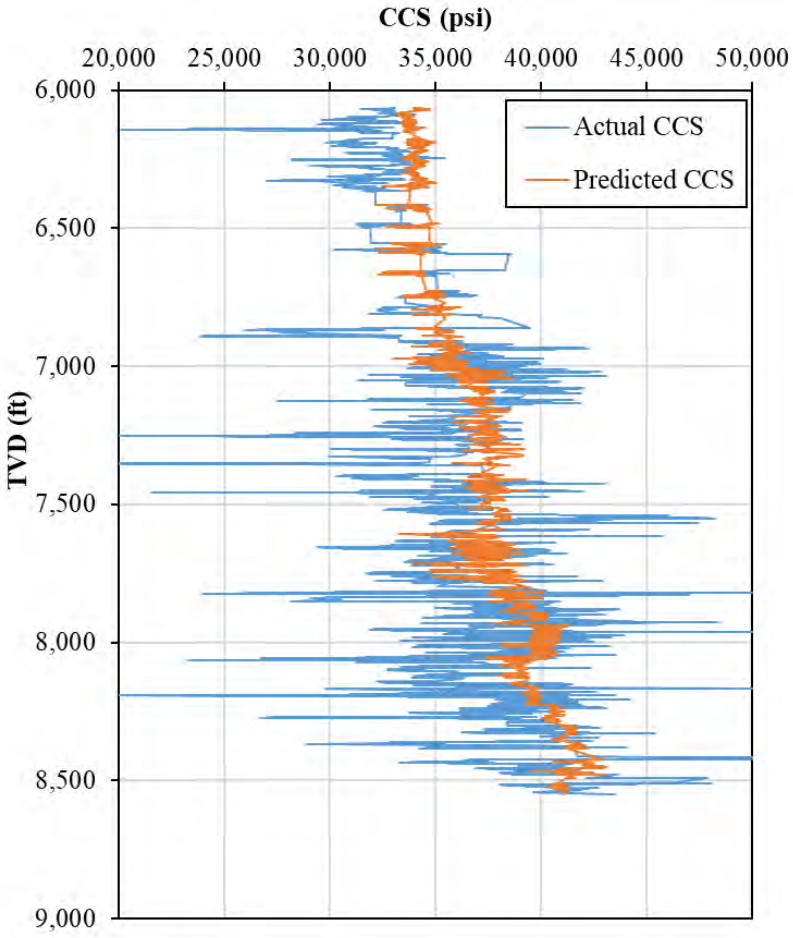

(b)

Figure 15. Comparison between predicted value and actual value of CCS for well 16A(78)-32: (a) normalized predicted value vs normalized actual value, (b) predicted and actual value along TVD. The RF model trained with the dataset from three wells [excluding 16A(78)-32, including 16B(78)-32, 78B-32 and 56-32]. TVD is added as a feature.

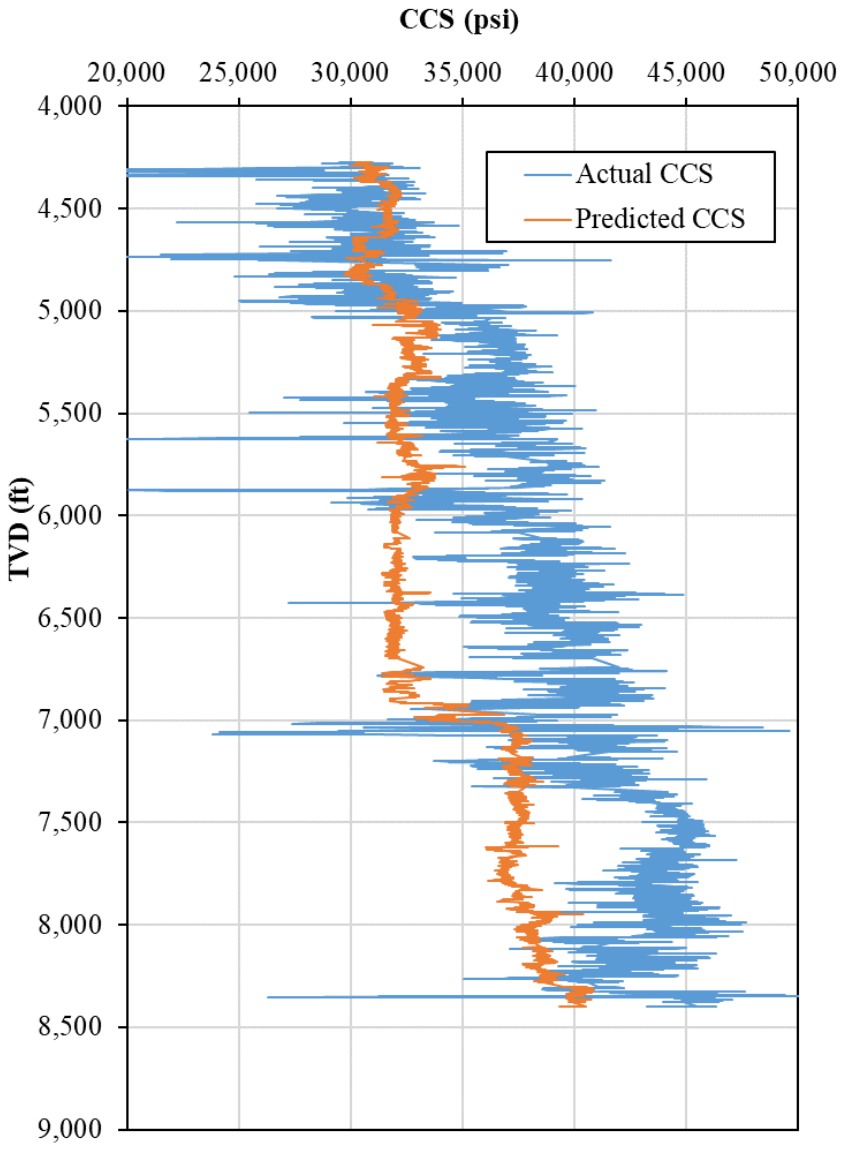

Figure 16. Comparison between predicted value and actual value of CCS for well 78B-32. The predicted value is predicted from the RF model trained with the dataset from three wells [excluding 78B-32, including 16A(78)-32, 16B(78)-32, and 56-32]. TVD is a feature.

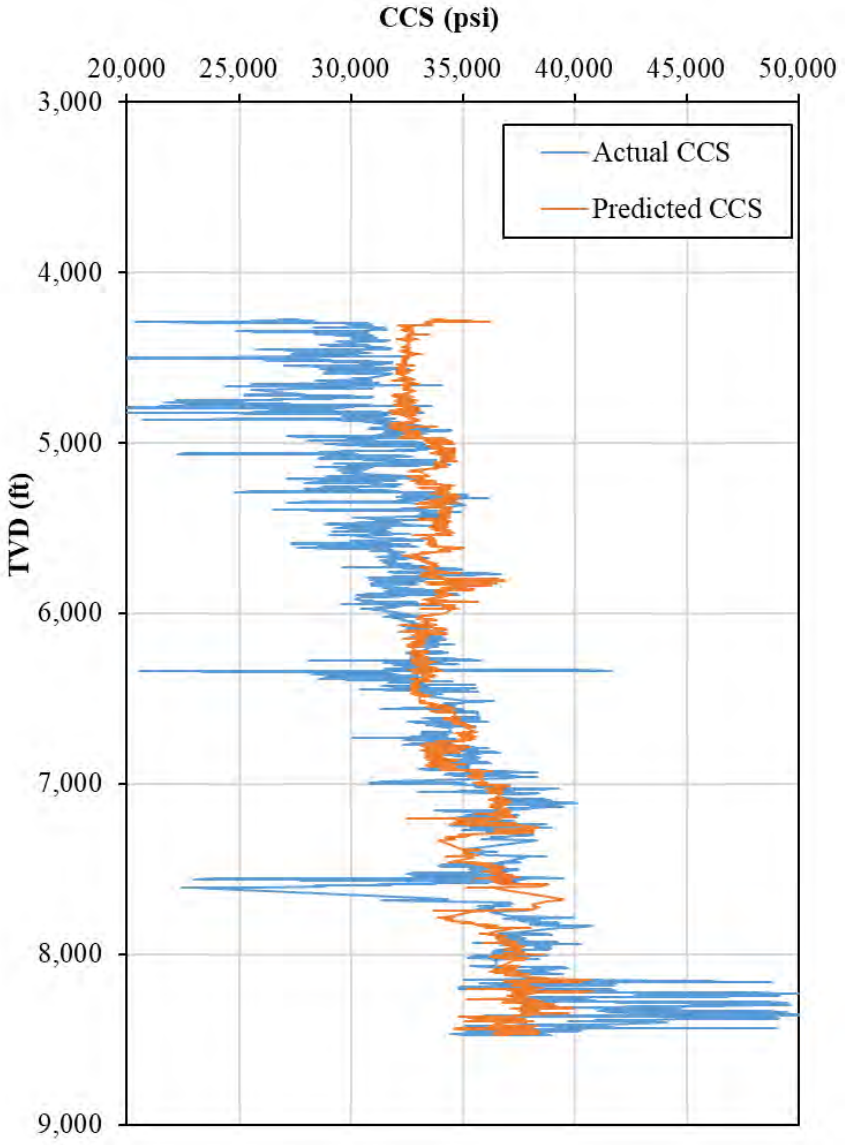

Figure 17. Comparison between predicted value and actual value of CCS for well 56-32. The predicted value is predicted from the RF model trained with the dataset from three wells [excluding 56-32, including 16A(78)-32, 16B(78)-32, and 78B-32]. TVD is a feature.

4.2 Machine Learning Model – ANN

Here we tested the performance of another machine learning model – ANN model. ANNs consist of interconnected neurons, organized in layers. The connections between neurons have associated weights that determine the strength of the signal passing through them. ANNs are typically composed of three types of layers: input layer, hidden layer, and output layer (LeCun et al., 1998).

Table 6 shows the performance of two ANN models trained with 4 wells dataset and 3 wells dataset excluding well 16A(78)-32. TVD is added as a feature during the training of ANN models. The dataset is split into 80% of training and 20% of testing. The overall performance of the RF model is better than the ANN model. The RMSE and MAE of the ANN model are slightly larger than the RF model, but R^2 of the ANN models is much smaller than the RF model. From Figure 18, we can

also see that the variation of predicted CCS vs. TVD for the ANN model is worse than that of the RF model (see Figure 15).

Table 6. ANN model performance of different datasets (TVD as a feature)

Model	Train data metrics			Test data metrics			Test new dataset	Test new dataset (unseen) metrics		
	R^2	RMSE	MAE	R^2	RMSE	MAE		R^2	RMSE	MAE
4 wells	0.66	0.04	0.03	0.66	0.04	0.03	N/a	N/a	N/a	N/a
3 wells (excluding 16A(78)-32)	0.71	0.06	0.04	0.71	0.06	0.04	40% of 16A (7593 rows of 16A)	-0.09	0.09	0.07

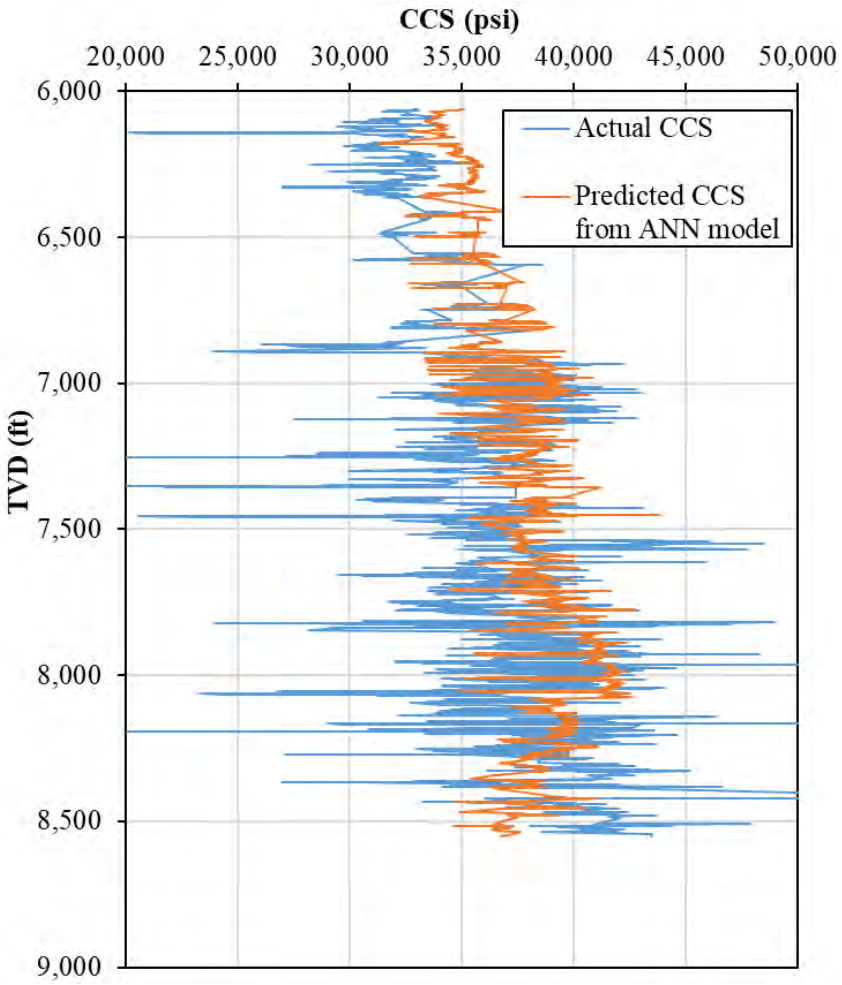

Figure 18. Comparison between predicted value from the ANN model and actual value of CCS for well 16A(78)-32. The ANN model trained with the dataset of three wells excluding 16A(78)-32 [including 16B(78)-32, 78B-32 and 56-32]. TVD is added as a feature.

4.3 Discussion

Based on the above analysis, the performances of the RF model are better than those of the ANN model, both for the training data and unseen data. We also compared the performances between the models with TVD as a feature and those without TVD: the metrics (R^2, RMSE and MAE) are similar, but the trend of CCS vs. TVD for the model trained with TVD as a feature has a better match. The predictions of unseen data have a low RMSE but also a low R^2, which means the models might make accurate predictions but fail to explain much of the variability in the data. Nevertheless, the trend of predicted CCS along TVD by unseen drilling data matches well with the actual value.

The reasons for low R^2 could be due to overfitting, high variance, or inadequate features. During the training of the RF model, K-fold cross validation, was employed along with setting maximum tree depth and minimum number of samples at a leaf node to reduce the overfitting.

In the development of predictive models, particularly in the context of drilling activities, the selection and refinement of features are critical to achieving high accuracy and reliability. One strategy to enhance model performance is the incorporation of additional relevant features. For instance, including the condition of drill bits as a feature may prove advantageous. The state of drill bits can significantly influence drilling efficiency and outcomes, and by capturing this information, the model can better reflect the complexities of the drilling process.

Conversely, the presence of irrelevant or redundant features in a model can lead to high variance. This condition is characterized by the model's excellent performance on training data but poor generalizability to new, unseen data. To address this, it may be beneficial to streamline the model by identifying and removing features that do not contribute meaningfully to the predictive accuracy. Simplifying the feature set not only helps in reducing the risk of overfitting but also enhances the interpretability of the model.

Moreover, expanding the dataset with more comprehensive drilling data from the region could further refine the model’s performance. Additional data can provide a more robust foundation for training and testing, allowing the model to capture a wider array of scenarios and variations within the data. This, in turn, can help in building a model that is both more accurate and generalizable across different drilling conditions and environments.

5. Conclusions

In this study, machine learning methods were employed to establish the relationship between drilling data and CCS of the rock at Utah FORGE site. The training dataset comprised data from four deep wells that used PDC drill bits. The CCS is calculated from sonic logs by empirical formula and calibrated by core testing results.

Initially, data preprocessing involved the removal of outliers, such as exceptionally large values, and sliding sections (where the top drive rotary was zero but the bit RPM was non-zero), ensuring that only rotating sections indicative of bit-rock interactions were analyzed. The analysis identified three parameters—TVD, top drive torque, and ROP—as having the highest correlation with CCS. A further refinement based on pair plots and a correlation heatmap showed a high correlation between bit RPM and top drive rotary, leading to the exclusive use of the "top drive rotary" feature.

The selected features for training the machine learning models included TVD, weight on bit, top drive torque, differential pressure, standpipe pressure, top drive rotary, flow rate, and ROP.

Two types of models, Random Forest (RF) and Artificial Neural Network (ANN), were developed to predict CCS. The RF model outperformed the ANN, consistently showing TVD, top drive torque, ROP, and standpipe pressure as the most influential features. The RF model demonstrated robust predictive ability, with an R-square score of 0.95 for the training set and 0.91 for the test set. The predictions of UCS using three-well RF models using unseen drilling data have a low RMSE (around 0.10). Despite a lower R^2 score indicating limited explanation of variability in unseen data, the model effectively predicted CCS trends along TVD, aligning closely with actual values.

These results suggest that the refined RF model is highly effective for predicting CCS based on specific drilling parameters and can be confidently applied to forecast CCS in new wells within this region. This capability underscores the potential of machine learning in enhancing the precision of geological predictions based on drilling data, thereby supporting more informed decision-making in geological and drilling operations.

Acknowledgements

Funding for this work was provided by the U.S. DOE under grant DE-EE0007080 “Enhanced Geothermal System Concept Testing and Development at the Milford City, Utah FORGE Site.” We thank the many stakeholders who are supporting this project, including Smithfield, Utah School and Institutional Trust Lands Administration, and Beaver County, as well as the Utah Governor’s Office of Energy Development.

REFERENCES

Dupriest, F.E. and Noynaert, S.F. “Continued Advances in Performance in Geothermal Operations at FORGE Through Limiter-Redesign Drilling Practices.” In SPE/IADC Drilling Conference and Exhibition (p. D031S024R002). SPE, February (2024).

LeCun, Y., Bottou, L., Bengio, Y., & Haffner, P. “Gradient-based learning applied to document recognition.” Proceedings of the IEEE, 86(11), 2278-2324 (1998).

Moore, J., McLennan, J., Allis, R., Pankow, K., Simmons, S., Podgorney, R., Wannamaker, P., Bartley, J., Jones, C., Rickard, W. “The Utah Frontier Observatory for Research in Geothermal Energy (FORGE): An International Laboratory for Enhanced Geothermal System Technology Development.” In Proceedings of the 44thWorkshop on Geothermal Reservoir Engineering, Stanford University, Stanford, CA, USA, 11–13 February (2019).

Moore, J., McLennan, J., Pankow, K., Finnila, A., Dyer, B., Karvounis, D., Bethmann, F., Podgorney, R., Rutledge, J., Meir, P. and Xing, P. “Current activities at the Utah Frontier Observatory for Research in Geothermal Energy (FORGE): A laboratory for characterizing, creating and sustaining Enhanced Geothermal Systems.” In ARMA US Rock Mechanics/Geomechanics Symposium, Atlanta, Georgia, USA, 25-28, June (2023).

Phelan, Z., Xing, P., Panja, P., Moore, J. and McLennan, J. “Prediction of Formation Properties Based on Drilling Data of Wells at Utah FORGE Site Using Machine Learning.” In ARMA US Rock Mechanics/Geomechanics Symposium (pp. ARMA-2022), Santa Fe, New Mexico, June (2022).

Mineral Extraction

Quantifying the Impact of Water Needs for Lithium Production from Geothermal Brines in the Salton Sea KGRA

Shaily Gupta[a] and Margaret M. Busse[a,b]

[a]Pennsylvania State University, [b]Lawrence Berkeley National Laboratory

Keywords

Water Use, Direct Lithium Extraction, Geothermal Energy, Renewable Energy, Salton Sea, Known Geothermal Resource Area

ABSTRACT

Geothermal brines from the Salton Sea Known Geothermal Resource Area (SS-KGRA) are highly saline and contain high concentrations of lithium. These brines are currently brought to the surface, used to produce geothermal energy, and then reinjected into the subsurface to maintain pressure in the geothermal reservoir. Before reinjection, there is an opportunity to extract the lithium. This is promising for securing a domestic supply chain of lithium to help meet energy storage needs for transition to a renewable energy grid. Previous analyses of how much water these processes will require in the region are limited by the lack of data available on freshwater use for both geothermal energy production and direct lithium extraction (DLE) processes. In this work, we develop improved estimates for water use in geothermal energy production and DLE processes. Our findings indicate that the water requirements for geothermal facilities may be higher than previously reported, potentially reaching 46.3 acre-feet per year per megawatt (AFY/MW) in some cases, compared to the average of 16 AFY/MW. For DLE, the ion exchange method is identified as potentially more water-intensive than liquid-liquid extraction. Additionally, the need to reallocate agricultural water to support these processes could strain local water resources and lower the water level of the Salton Sea.

1. Introduction

The surge in demand for energy storage devices has been fueled, in large part, by the rapid progress and widespread integration of renewable energy technologies in recent years. Lithium is highly valued as an optimal battery metal because it is the lightest, naturally occurring metal (Zeng et al. 2024). Lithium is primarily sourced from two types of deposits: hard rock, such as spodumene and lepidolite, and brine deposits. These sources contribute 34% and 66% of the global lithium supply, respectively. Extraction from brine is generally more cost-effective and energy-efficient compared to hard rock mining (Boroumand and Razmjou, 2024).

In the SS-KGRA, there are significant levels of lithium in the geothermal brine, and this brine is already being brought to the surface to produce energy. This provides a readily available source of lithium that can be extracted before the brine is reinjected into geothermal wells. As with any mineral extraction, the processes required consume other valuable resources such as freshwater. For the SS-KGRA, this is important because the region is already experiencing water shortages.

Previous studies have used public data to assess the environmental impacts of geothermal and lithium extraction in the region. These studies found that the growing geothermal/lithium industry would have a minor effect on regional water availability compared to the expected reductions in water allocation from the Imperial Irrigation District (IID). The expected IID reductions are a result of declining Colorado River levels (Busse et al. 2023; Dobson et al. 2023).

In this work, we improve the previous analysis with more up-to-date and detailed understanding of regional water use for geothermal and DLE processes. We collected data from the literature, industry, and patents to create water use ranges for regional geothermal energy production. We also synthesized data on potential DLE unit processes. This approach allowed us to scale potential water use to existing, planned, and maximum geothermal capacities.

2. Methods

2.1 Geothermal Production Overview

A geothermal power plant is typically comprised of a geothermal resource production facility, a power generation facility, and various ancillary installations. In Figure 1, these are indicated by the dashed boxes, and the ancillary installation shown in this instance is a DLE facility for producing lithium hydroxide monohydrate (Figure 1c). High-, standard-, and low-pressure steam is directed from the geothermal resource production facility (Figure 1b) to the power generation facility (Figure 1a) to operate the turbine generator system, producing electricity.

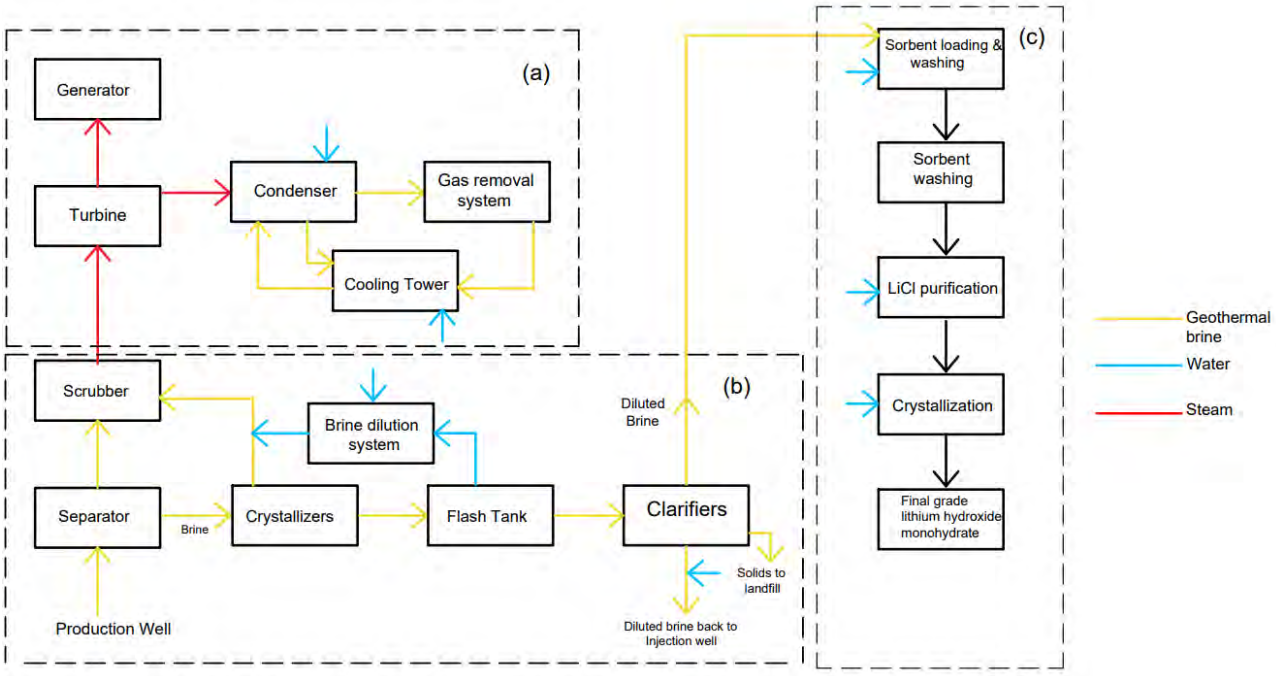

Figure 1. General flow of freshwater (blue lines), geothermal brine (yellow lines), and steam (red lines) through the flash geothermal process in the SS-KGRA.

The resource production facility (Figure 1a) comprises two types of wells: production wells and injection wells. During standard operations, the production fluids are channeled from production wells to the high-pressure separator. The high-pressure separator system divides the production fluid into steam and residual production fluid. The high-pressure steam is sent to the high-pressure scrubber and demister before it reaches the steam turbine. The remaining fluid moves through these same processes at standard-pressure and low-pressure to extract all possible steam for energy production (Figure 1b). The remaining fluid is processed to produce additional steam for energy production and prepare the remaining production fluid for reinjection (Black Rock Geothermal LLC 2023, Featherstone et al., 2020).

2.1.1 Geothermal Freshwater Use

Freshwater is mainly used for dilution and cooling throughout these processes. 29% of the total operating water, is introduced into the system as dilution water for geothermal brine moving from the crystallizer to the scrubber. This water flows through a condenser, mixing with fluid from the flash tank before joining the stream to the scrubber. Remaining production fluid from the flash tank is directed to clarifiers to remove solids before reinjection. This process has two stages: the first removes solids in slurry form, and the second dewaters the slurry. After passing through the secondary clarifier, spent geothermal fluid is directed to the injection wells, and freshwater is added before reinjection to prevent precipitation of solids.

Steam exiting the turbine is condensed in a shell-and-tube condenser, where freshwater is added to support the cooling process. The resulting condensate is piped to the biological oxidizer for hydrogen sulfide removal. The non-condensable gas (NCG) removal system uses ejectors and vacuum pumps to extract gases from the condenser and directs them to the cooling tower basin. Water circulates through the cooling tower, cooled by evaporation and air heat exchange, and is then pumped back to the condenser to condense the steam. This circulating water, which constitutes 70% of the plant's operating water, is managed by vertical wet-pit pumps for both turbine condensers and plant auxiliary cooling needs.

To quantify the amount of water required for geothermal energy production, we extracted information from Environmental Impact Reports (EIRs) that have been submitted by companies in the SS-KGRA. Water use data for construction and operation of geothermal facilities was provided in documentation from Controlled Thermal Resources, Energy Source Minerals, and Berkshire Hathaway (BHER) (Energy Source, 2012; Black Rock Geothermal LLC, 2023; Elmore North Geothermal LLC, 2023; Morton Bay Geothermal LLC, 2023; Controlled Thermal Resources, Inc., 2024).

2.2 Lithium Extraction Process

The conventional method for extracting lithium from brine involves pumping the lithium-rich brine into expansive surface ponds that can cover thousands of acres. In these ponds, lithium and other salts are concentrated through passive solar evaporation over the course of a year or more to increase the lithium concentration to about 6,000 mg/kg (Khalil et al., 2022).

DLE is emerging as a more efficient, alternative to this approach. DLE approaches offer distinct advantages over conventional evaporation ponds and Hard rock mining methods, such as reduced land and overall water usage (fossil and freshwater), faster time-to-market for lithium products,

and lower carbon emissions during operations (Warren, 2021). In broad terms, DLE techniques can be categorized into three main classes: adsorption, ion exchange, and solvent extraction. Regardless of the specific DLE technique employed, either alone or in combination with additional processing steps, these methods must be capable of selectively extracting lithium from chemically complex brines containing high concentrations of various ionic species like sodium, potassium, calcium, magnesium, borates, sulfates. Moreover, for geothermal brines, silica as well as potentially elevated levels of iron, manganese, and other dissolved components, must be considered (Warren, 2021). To quantify freshwater use for various lithium extraction processes, we conducted a literature search and evaluated industry and patent data.

2.3 Local Water Cuts Proposed

In December 2023, the Imperial Irrigation District (IID) (local water authority in the Imperial Valley) with other local water authorities, signed an agreement for water conservation into 2026. The water districts, in return, receive funding from the Inflation Reduction Act to support water conservation efforts. IID plans to focus on agriculture and fund an irrigation efficiency program (Saegert, 2023). In 2023, IID agreed to conserve 100,000 AF. IID is expected to conserve 800,000 AF between 2024 – 2026 (U.S. Department of the Interior, 2023). These additional cuts will be in exchange for $175 million in federal funds for projects at the Salton Sea (IID, 2024b). Conservation measures are to be determined by IID (Garcia, 2024). In previous analysis, we considered at 10% and 40% cut to water allocation for the region (Busse et al., 2023; Dobson et al., 2023). The proposed 800,000 AF over 3 years (Garcia, 2024), if divided equally between each year, represents a 8.6% cut to the 3.1 million AF annual entitlement (IID, 2024a), which is what we will consider herein.

3. Results and Discussion

3.1 Geothermal Water Use in the SS-KGRA

In the United States, there are more than 90 operational geothermal power plants, many of which have been running for over three decades (Robins et al., 2021). The common types of geothermal plants include dry-steam, flash-steam, and binary cycle, with flash-steam plants being the most prevalent in the SS-KGRA. According to historical and estimated water use data, geothermal facilities in the SS-KGRA typically require an average of 16 acre-feet (AF) of water per megawatt (MW) of net generation capacity annually (Dobson et al., 2023). However, water needs can vary significantly across different facilities, ranging from as low as 0.4 AF to as high as 32 AF per MW each year (Dobson et al., 2023).

Here we provide a breakdown of the water use for geothermal facilities in the SS-KGRA that have reported water use for construction (Table 1) and operation (Table 2). Freshwater in this analysis is water purchased from IID. Freshwater required for construction is minimal compared to the freshwater required for operation over the lifespan of the facilities. Operational freshwater use from these facilities ranges from 4 – 46 AFY/MW (Table 2), higher than what was previously reported. It is important to note that the total required water for operation is higher than the freshwater requirement. For example, Elmore North and Morton Bay require twice as much water, but the plant to use steam condensate for the additional water (Elmore North Geothermal LLC

2023; Morton Bay Geothermal LLC 2023). Black Rock Geothermal plans to use 80% steam condensate to meet their total required water need (Black Rock Geothermal LLC 2023).

Table 1. Summary of the construction freshwater use for proposed geothermal facilities in the SS-KGRA.

Geothermal Unit	Phase of Water Use	Source	Quantity of water used (Reported Units)	Duration (months)	Total Freshwater Use (AF)	Net Energy Output (MW)	Citations
Hudson Ranch (HR-2)*	Well Drilling	IID	73.7 AF	2	128.7	49.9	Energy Source, 2012
	Facility Construction	IID	55 AF	28			
Hell's Kitchen PowerCo 1	Dust Control	IID	50,000 gallons/day	10	87	49.9	Imperial County Planning & Development Services Department (2022); Controlled Thermal Resources, Inc. (2024)
Black Rock Geothermal	Dust suppression, concrete prep, hydrostatic testing of pipelines, potable	IID	150 AFY	29	363	77	Black Rock Geothermal LLC, 2023
Morton Bay	Dust suppression, concrete prep, hydrostatic testing of pipelines, potable	IID	150 AFY	29	363	140	Morton Bay Geothermal LLC, 2023
Elmore North	Dust suppression, concrete prep, hydrostatic testing of pipelines, potable	IID	150 AFY	29	363	140	Elmore North Geothermal LLC, 2023

* Facility was never constructed.

Table 2. Summary of the operational water use for proposed geothermal facilities in the SS-KGRA.

Plant Name	Phase of Water Use	Source of Water	Quantity of Water (AFY)	Total Freshwater (AFY)	Net Energy Output (MW)	Water Use (AFY/MW)	Citations
Hudson Ranch (HR-2)*	Cooling	Steam Condensate	2,740	1200	49.9	24.0	Energy Source, 2012
		IID	44				
	Brine Dilution	IID	1,124				
	Freshwater Pond Evaporation	IID	20				
	Miscellaneous	IID	12				
Hell's Kitchen PowerCo 1	Cooling tower makeup, other uses	IID	200	200	49.9	4.01	Imperial County Planning & Development Services Department (2022); Controlled Thermal Resources, Inc. (2024)
Black Rock Geothermal	Well Maintenance	IID	6.95	1132	77	14.61	Black Rock Geothermal, LLC (2024)
	RO, plant wash down, cooling tower makeup	IID	1125				Black Rock Geothermal LLC, 2023
		Steam Condensate	4500				
Morton Bay	Plant water, dilution water, plant wash down, cooling tower makeup	IID	5560	5560	140	39.71	Morton Bay Geothermal LLC, 2023
		Steam Condensate	5560				
Elmore North	Plant water, dilution water, plant wash down, cooling tower makeup	IID	6480	6480	140	46.29	Elmore North Geothermal LLC, 2023
		Steam Condensate	6480				

* Facility was never constructed.

The average geothermal water use from the analysis in Dobson et al. (2023) was used as a comparison to the water use scenarios identified in Table 2. Figure 2 illustrates this impact across the geothermal production scenarios in the region. The current capacity is 400 MWe, the projected capacity of facilities proposed across the next 3 – 4 years is an additional 520 MWe, and the total possible capacity of the resource is 2950 MWe (Kaspereit et al. 2016).

The maximum water use was identified for Elmore North at 46.3 AFY/MW (57110 m^3/MW) compared to the 16 AFY/MW (19735 m^3/MW) average. If all facilities operated at this water use rate, it would almost triple the impact of geothermal in the region, representing a non-negligible increase in regional water use for geothermal energy production.

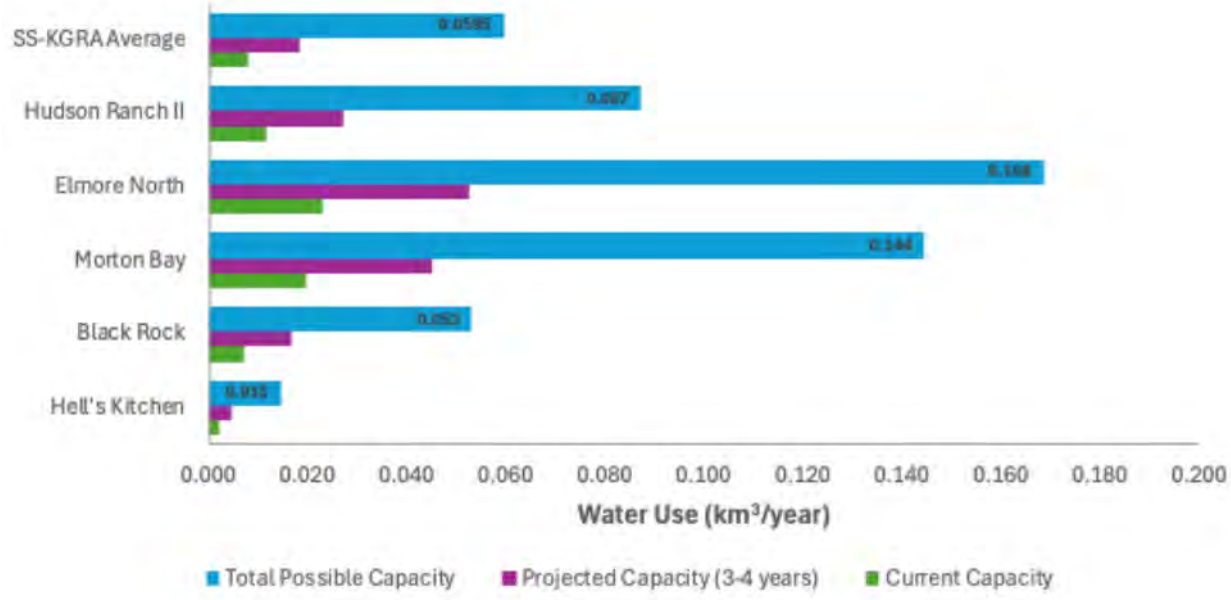

Figure 2. Comparison of how different facility water use projections for geothermal production would compare to the SS-KGRA average water use projections from Dobson et al. (2023).

3.2 Lithium Extraction Water Use

As mentioned previously, the main DLE processes can be categorized as adsorption, ion exchange, and solvent extraction processes. In the SS-KGRA the expected processes are adsorption and ion exchange. Unfortunately, most literature studies we identified did not quantify water use of these processes. Moreover, many did not test their proposed method with brines similar to those in the Salton Sea. Table 3 provides a summary of some of the brines studied at bench-scale for DLE in comparison to the brine composition in the SS-KGRA. Studies that evaluated synthetic brines often did not include fluid composition in this form. For example, Zhang et al. (2024) reported NaCl, LiCl, $MgCl_2$, and $CaCl_2$ concentrations of their synthetic brine. The geothermal brine from Suharyanto et al. (2024) is the most similar we have found to the Salton Sea brines, and this study evaluated an adsorption process, but did not report water use.

Table 3. Summary of geothermal brine composition in the SS-KGRA compared to brine compositions from DLE studies in the literature.

	Dissolved Solids (mg/L)					
Type of Fluid	Lithium (Li)	Sodium (Na)	Magnesium (Mg)	Calcium (Ca^{2+})	Boron (B)	Citation
Salton Sea Brine	211	52,000	160	24,000	350	(Gagne et al. 2015)
East Mesa Brine	6.3	2,600	3.4	130	5.4	(Gagne et al. 2015)
Salt Lake Brine	969	77,650	34,010	176	807	(Luo et al. 2021)
Geothermal Brine	27.02	8,834	422.66	1308.3	86.48	(Suharyanto et al. 2024)

Based on these constraints from the bench-scale literature, we have summarized the water use information we were able to obtain for DLE processes from patents and industry EIRs.

3.2.1 Ion-Exchange

Based on a 2020 patent from EnergySource Minerals LLC, we developed a flow diagram of the proposed process that would exist in an ion-exchange-based DLE facility (Figure 2). This flow includes freshwater flows into the system (blue lines), geothermal brine flow (yellow lines), and process water (brown lines) (Featherstone et al., 2020). For this process, EnergySource Minerals LLC reported the anticipated water use for the entire process at 3400 AFY, but specific allocation of this water was not specified. During normal operation, they also identify a water requirement for fugitive dust control at 56 AFY, which sums up to an operational water need of 3456 AFY at the DLE facility. The estimated duration of the project is 30 years, consuming approximately 102,112 AFY water in its entire duration to produce 17,000 tonne of lithium carbonate equivalent (LCE) (Energy Source, 2012). Though, as mentioned in Dobson et al. (2023), EnergySource has indicated that this may be an overestimate of water use.

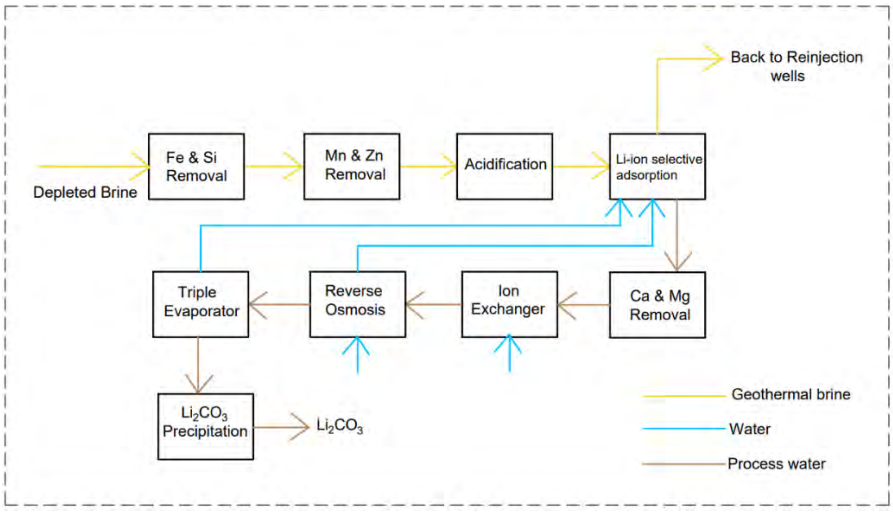

Figure 3. General flow of freshwater (blue lines), geothermal brine (yellow lines), and process water (brown lines) through the ion exchange process as it is often set up in the SS-KGRA (Featherstone et al., 2020).

In their proposed process depleted brine is mixed with limestone to precipitate out iron (Fe) and silicon (Si) compounds, and quicklime is used to remove manganese (Mn) and zinc (Zn) under conditions that do not remove lithium. The addition of these compounds raises the pH of the brine, which is then lowered through the addition of hydrochloric acid (HCl). An aluminum monohydroxide (AlOH)-based cationic resin is used to selectively adsorb lithium ions from the pretreated brine solution. The adsorbed lithium is then stripped from the resin using freshwater, yielding a lithium-enriched solution for further processing. The remaining geothermal fluid is diverted back to the reinjection well (Featherstone et al., 2020).

In the lithium-enriched solution, residual calcium (Ca) and magnesium (Mg) are precipitated out by adding sodium hydroxide and soda ash. An ion exchange step further removes any lingering divalent ion impurities like Ca, Mg and boron (B). To increase the lithium concentration, the solution volume is reduced through reverse osmosis followed by triple-effect evaporation. The triple effect evaporator utilizes steam from geothermal operations and/or a fuel boiler to operate. After processing through the evaporator, the lithium concentration in the product stream is increased from about 5,000 ppm to about 30,000 ppm. Soda ash is introduced to precipitate lithium as lithium carbonate technical grade product.

The precipitated battery-grade lithium carbonate goes through final steps of washing to remove residual impurities, followed by centrifugation to dewater the solid product. The washing fluid is not identified. Finally, the dewatered lithium carbonate is sent to a rotary dryer for complete drying, yielding the final battery-grade lithium carbonate product (Featherstone et al., 2020). A recent study by Schenker et al. (2024) conducted a parameterized life cycle assessment (due to lack of available data) of lithium carbonate production from geothermal brines in the SS-KGRA and Upper Rhine Graben in Germany. They identified that large amounts of freshwater are used in the adsorption process and for regenerating the ion-exchange media. This is in line with where we have identified freshwater inputs in the Featherstone et al. (2020) process.

3.2.2 Liquid-Liquid Extraction

In the liquid-liquid extraction process, impurities are removed from the geothermal brine before lithium is extracted using an adsorption process to selectively bind lithium ions to a solvent. Two streams result from the adsorption process: one returns to the reinjection well, while the purified liquid containing LiCl undergoes further purification. The pH of the lithium chloride stream drops from 5 to about 2.5 before entering solvent extraction process, which occurs in tall, pulsed columns. Here, extraction separates impurity ions in the aqueous phase from lithium ions in the organic phase. Sulfuric acid is used to strip the lithium from the organic phase back into an aqueous solution. The organic phase is then able to be reused. The final purification step involves electrolysis and crystallization to produce dried lithium hydroxide crystals.

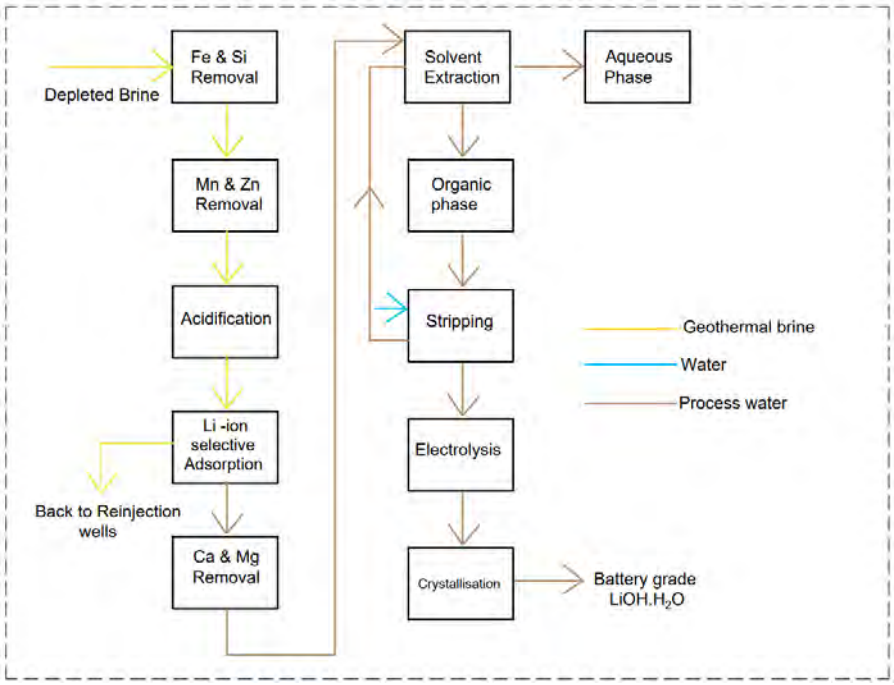

Figure 4. General flow of freshwater (blue lines), geothermal brine (yellow lines), and process water (brown lines) through the liquid-liquid extraction process for DLE (Featherstone et al., 2020; Sun et al., 2021).

We attempted to extract data for freshwater use in liquid-liquid extraction processes from the literature, but we did not find quantitative values for water use. We were able to extract some information on where water is used in the process. This analysis indicated that liquid-liquid extraction may reduce freshwater consumption compared to ion exchange, as it eliminates the need for resin desorption and regeneration, which are major freshwater consumers. Only the stripping step in this DLE process consumes freshwater, as indicated in Figure 4.

3.3 Impact on Regional Water Resources

Due to the lack of quantified water use from applicable DLE processes in the literature, water use for lithium extraction in this analysis remains the same as what was estimated in the Dobson et al. (2023) report. This value is the average estimated water use from three companies – EnergySource Minerals, Berkshire Hathaway, and Controlled Thermal Resources – at 328 m^3/tonne of lithium carbonate equivalent (Paz et al., 2022; Controlled Thermal Resources, Inc., 2024). Based on the agreed upon cuts to water resources in the SS-KGRA (8.6% of the 2022 allocation), we evaluated the possible impacts of geothermal expansion under average and high water use conditions and a scenario of average water use for lithium extraction on the regional water supply (Figure 5).

If the full geothermal field was utilized, the high geothermal water use estimate would require 1.4 times the water allocation for renewable energy compared to the average water estimate. For the planned geothermal expansion, the higher geothermal water estimate would only increase 1.2 times. For context, this additional water equates to a reduction in 2025 acres of land irrigation in the region.

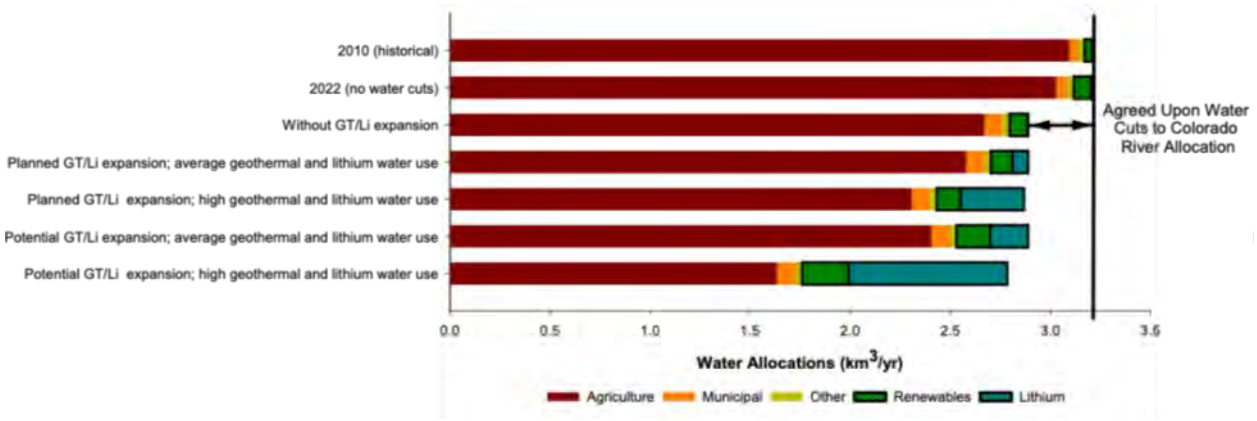

Figure 5. Summary of expected impact of water cuts, geothermal expansion, and DLE on local water availability.

4. Conclusion

This study provides a preliminary analysis of the unit process water requirements for both geothermal energy production and direct lithium extraction (DLE) processes at the SS-KGRA. By developing more detailed water use information, we were able to quantify potential water use scenarios and their impact on the region. Our results show that geothermal facilities in the SS-KGRA may require as much as 46.3 AFY/MW, even though the average reported use in the region is 16 AFY/MW. For DLE processes, we expect the ion exchange method to be more water-intensive than liquid-liquid extraction, with the latter eliminating water needs for resin desorption and regeneration. But from the patents submitted by companies in the region, ion-exchange is likely the process that will be used. Further, we evaluated the potential impacts of the agree upon water cuts (8.6%) along with scenarios for geothermal and lithium production expansion in the region. This analysis indicates that maximizing geothermal and DLE capacity could strain local water resources.

Reducing the available agricultural water in the region by reallocating it to geothermal energy expansion and lithium production has the potential to impact the water level of the Salton Sea, and thus the toxins released to the air because of this decline. This will be exacerbated by current regional efforts to improve irrigation efficiency, which will reduce runoff to the sea. This impact was outside the scope of this work, but it should be evaluated further.

REFERENCES

Black Rock Geothermal LLC, “Black Rock Geothermal Project Application for Certification Volume 1,” 2023 (BHER).

Black Rock Geothermal, LLC, “Black Rock Geothermal Project CURE Data Response Set 2 (Responses to Data Requests 100 to 242),” (2024).

Boroumand, Yasaman, and Amir Razmjou, “Adsorption-type aluminium-based direct lithium extraction: The effect of heat, salinity and lithium content,” *Desalination*, 577 (2024), 117406.

Busse, Margaret M, Jennifer Stokes-Draut, Mary Kay Camarillo, Dev Millstein, Margaret Slattery, Michael McKibben, Patrick Dobson, and William Stringfellow, “Environmental

Impact Assessment of Lithium Recovery from Geothermal Brines in the SS-KGRA: An Overview," 2023.

Controlled Thermal Resources, Inc., "Appeal #23-0004 of the December 13, 2023, Planning Commission Decision's of Approval for the Hell's Kitchen Power and Lithium Projects," 2024 (Imperial County Planning & Development Services Planning/Building).

Dobson, Patrick, Naod Araya, Maryjo Brounce, Margaret Busse, Mary Kay Camarillo, Lauren English, Jennifer Humphreys, Boriana Kalderon-Asael, Michael McKibben, Dev Millstein, Nori Nakata, John O'Sullivan, Noah Planavsky, Joris Popineau, Theo Renaud, Jeremy Riffault, Margaret Slattery, Eric Sonnenthal, Nicolas Spycher, Jennifer Stokes-Draut, William Stringfellow, and Malcolm White, "Characterizing the Geothermal Lithium Resource at the Salton Sea," LBNL Report, 2023.

Elmore North Geothermal LLC, "Elmore North Geothermal Project Application for Certification Volume 1," 2023 (BHER).

Energy Source, "Hudson Ranch Power II Geothermal Plant/Simbol Calipatria II Plant Project," Draft EIR, 2012 (Imperial County).

Featherstone, John L., Paul J. Hanson, Michael Garska J., and Charles R. Marston, "System and Process for Recovery of Lithium from a Geothermal Brine," 2020.

Gagne, Douglas, Scott Haase, Brett Oakleaf, David Hurlbut, Sertac Akar, Anna Wall, Craig Turchi, Philip Pienkos, Jennifer Melius, and Marc Melaina, "The Potential for Renewable Energy Development to Benefit Restoration of the Salton Sea. Analysis of Technical and Market Potential," 2015.

Garcia, Eduardo, "AB-2610 Protected species: authorized take: System Conservation Implementation Agreement," 2024.

IID, "Water Conservation," <https://www.iid.com/water/water-conservation> (May 28, 2024a)., "IID Applauds Garcia Bill to Support Water Conservation Efforts," *News & Resources*, <https://www.iid.com/Home/Components/News/News/1168/793> (May 28, 2024b).

Imperial County Planning & Development Services Department, "Initial Study & Environmental Analysis For: Hell's Kitchen PowerCo 1 and LithiumCo 1 Project," 2022.

Kaspereit, Dennis, Mary Mann, Subir Sanyal, Bill Rickard, William Osborn, and Jeff Hulen, "Updated conceptual model and reserve estimate for the Salton Sea geothermal field, Imperial Valley, California," *Geotherm. Res. Council Trans*, 40 (2016), 57–66.

Khalil, Abdullah, Shabin Mohammed, Raed Hashaikeh, and Nidal Hilal, "Lithium recovery from brine: Recent developments and challenges," *Desalination*, 528 (2022), 115611.

Luo, Qinglong, Mingzhe Dong, Guoliang Nie, Zhong Liu, Zhijian Wu, and Jun Li, "Extraction of lithium from salt lake brines by granulated adsorbents," *Colloids and Surfaces A: Physicochemical and Engineering Aspects*, 628 (2021), 127256.

Morton Bay Geothermal LLC, "Morton Bay Geothermal Project Application for Certification Volume 1," 2023 (BHER).

Paz, Silvia, Ryan E. Kelley, Steve Castaneda, Rod Colwell, Roderic Dolega, Miranda Flores, James C. Hanks, Arthur Lopez, Luis Olmedo, Alice Reynolds, Frank Ruiz, Manfred Scott, Tom Soto, and Jonathan Weisgall, "Report of the Blue Ribbon Commission on Lithium Extraction in California," 2022 (California Energy Commission).

Robins, Jody, Amanda Kolker, Francisco Flores-Espino, Will Pettitt, Brian Schmidt, Koenraad Beckers, Hannah Pauling, and Ben Anderson, "2021 U.S. Geothermal Power Production and District Heating Market Report," 2021.

Saegert, Rhiannon, “Officials commit to deals to conserve Colorado River water,” *Las Vegas Sun*, <https://lasvegassun.com/news/2023/dec/13/officials-commemorate-deal-to-conserve-colorado-ri/> (May 28, 2024).

Schenker, Vanessa, Peter Bayer, Christopher Oberschelp, and Stephan Pfister, “Is lithium from geothermal brines the sustainable solution for Li-ion batteries?,” *Renewable and Sustainable Energy Reviews*, 199 (2024), 114456.

Suharyanto, Ariyo, Miftakhur Rohmah, Latifa Hanum Lalasari, and Mohammad Zaki Mubarok, “Lithium Adsorption Behaviour from Ciseeng Geothermal Brine Water onto Amberlite Resin,” (2024).

Sun, Ying, Qi Wang, Yunhao Wang, Rongping Yun, and Xu Xiang, “Recent advances in magnesium/lithium separation and lithium extraction technologies from salt lake brine,” *Separation and Purification Technology*, 256 (2021), 117807 (Elsevier).

U.S. Department of the Interior, “Biden-Harris Administration Announces New Agreement with Imperial Irrigation District to Save 100,000 Acre-Feet of Water in Colorado River System | U.S. Department of the Interior,” Press Release, <https://www.doi.gov/pressreleases/biden-harris-administration-announces-new-agreement-imperial-irrigation-district-save> (May 28, 2024).

Warren, Ian, “Techno-Economic Analysis of Lithium Extraction from Geothermal Brines,” 2021.

Zeng, Yiwen, Wanpeng Li, Zhixin Wan, Shaoyi Qin, Qinlin Huang, Wenlong Cai, Qian Wang, Meng Yao, and Yun Zhang, “Electrochemically Mediated Lithium Extraction for Energy and Environmental Sustainability,” *Advanced Functional Materials*, (2024), 2400416.

Zhang, Lingjie, Tingting Zhang, Shuaike Lv, Shaoxian Song, Hiram Joazet Ojeda Galván, Mildred Quintana, and Yunliang Zhao, “Adsorbents for lithium extraction from salt lake brine with high magnesium/lithium ratio: From structure-performance relationship to industrial applications,” *Desalination*, 579 (2024), 117480.

Initial Simulations of Lithium Production from Geothermal Brines

Richard Holt[1], William Rickard[2] and Mary Mann[2]

RESPEC Company LLC

Geothermal Resource Group, Inc.

Keywords

Lithium, Reservoir Simulation, Recovery Factor, Coproduction

ABSTRACT

New methods for extraction of Lithium from Lithium-rich geothermal brines, combined with the increased industrial demand for Lithium for batteries has caused significant interest in using geothermal brine as an economically viable domestic source of Lithium. In initial simulations of co-production of geothermal energy and lithium it was found that well pattern (production and injection well layout) can significantly affect lithium production. A simplified numerical model was constructed that simulates the production of lithium rich brine and injection of lithium depleted brines under several configurations, with the aim of understanding the effect of well patterns on lithium recovery factors. While the interactions of Lithium with rocks and brine are highly simplified pending further research, this numerical model provides a preliminary tool to quantitatively compare lithium production under various scenarios. It was found that lithium production was far more sensitive to well patterns than geothermal.

1. Introduction

In anticipation of making commercial simulation forecasts for the co-production of geothermal energy and lithium, a general non-specific numerical model was developed in TETRAD. The model doesn't represent a particular field or use propriety data and is only intended to provide insight and sensitivity analysis. It is known lithium extraction is being implemented in a geothermal field where the production and injection wells have already been drilled using patterns and concepts applicable to geothermal-only production, and those can't be changed. In that case this preliminary modeling can be used to gain insight into lithium recovery factors. It is also possible that some new projects will start as co-production from the start, and in those cases, the preliminary model can provide insight into the types of well layouts that are advantageous.

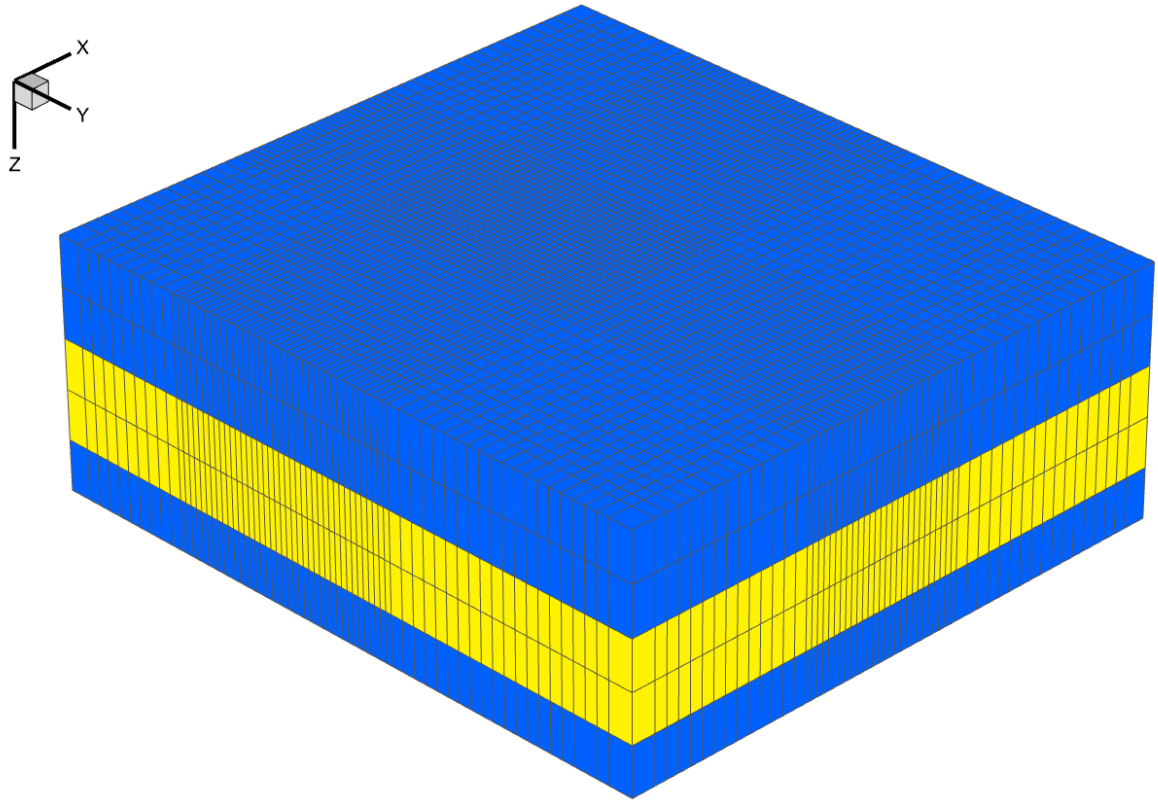

Figure 1: 3-Dimensional view of the model grid

2. Overview of Preliminary Modeling

The model's grid divides each one square mile section into equal sized grid blocks (4x4) and the entire grid covers an area more than 10 by 10 km (Figure 1). The model has the ability after making a run to "blank" peripheral areas and to visualize a focus area Figure 2. This modeling technique allows the model to include simulated interaction with the surrounding resource, which is necessary to properly model effects over time, such as recharge into or outflow from a focus area and adjacent areas.

Figure 2 is the model grid showing the focus at the model's layer 3, which is at an elevation of 1500 meters below sea level. Shown in Figure 3 is the well layout for Scenario as shown in a sample development plan. This plan has three production wells (PW1, PW2, and PW3) and three injection wells (IW1, IW2, and IW3). This figure shows a 2-dimensional representation of two sample parameter distributions (horizontal permeability and estimated lithium concentration). The lithium concentration contours are hypothetical and not based on data.

The model was used to make sample test runs to quantify the effects of different well layouts. The test run supposed three production wells each at 1200 tph for a total production rate of 3600 tph (7920 kph). Within the model the production flows into a separator at 17.2 barg (250 psig) which calculates the flash percentage continuously based on the inflow parameters. The model supposes that injected fluid is the post-flash brine, which is cooled and enriched in chloride with all lithium

removed. This is an assumption because lithium extraction process will remove all the lithium, for the purposes of reservoir engineering and prediction of the possible decline of produced lithium over time, this is the conservative approach

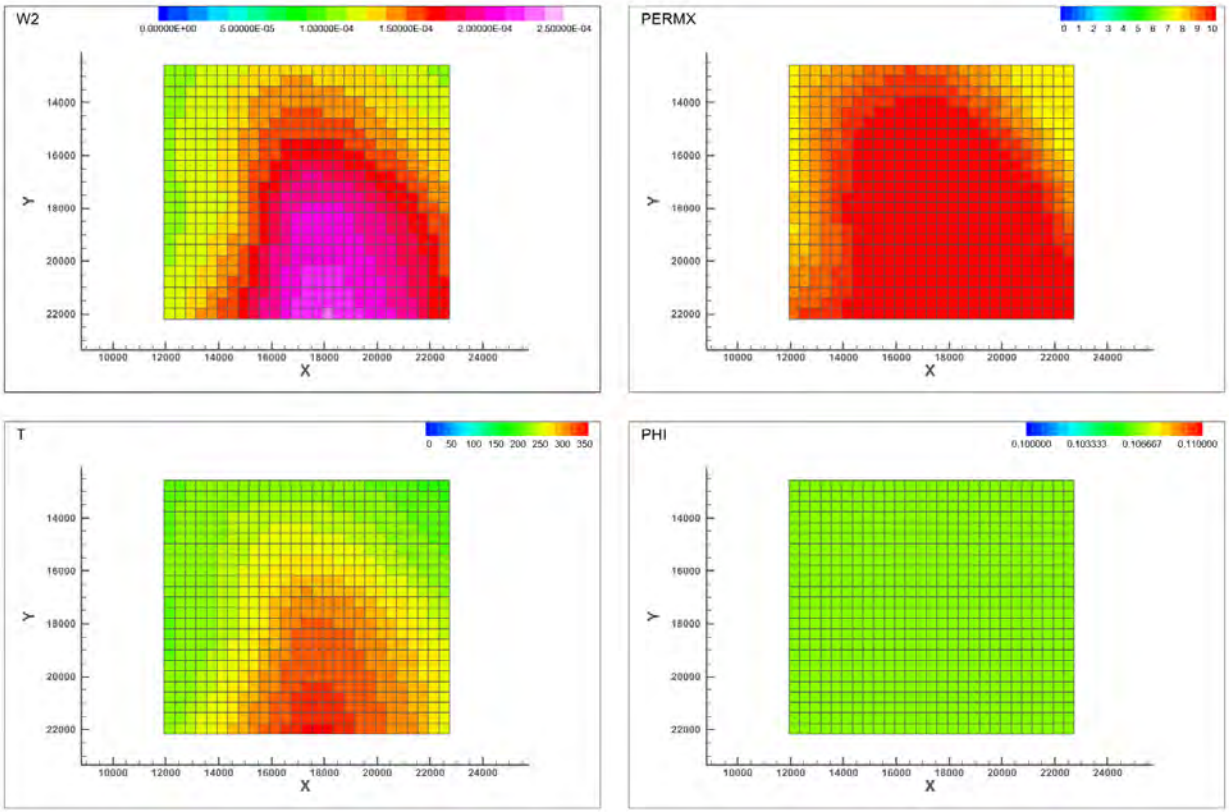

Figure 2: 3-Dimensional view of the model grid

3. Simulation of Full-Field Production with Preliminary Model

The preliminary model was used to model a hypothetical 55 Mwe development as known from published cases. For the simulation, it was assumed that each plant was single flash at 250 psig and required 1100 kph of steam (at 250 psig), which equates to 55 MWe at a consumption rate of 20 kph/MWe. In the model, each plant was configured with 3 production wells and 3 injection wells. In the model, each plant's three production wells were flowed into a simulated separator at 250 psig which automatically calculated the flash at each timestep.

The production flowing into the separators contained TDS including lithium. The result of the simulated flash was steam and brine (with TDS including lithium). The mass of the flashed steam was removed from the model. We assumed that the brine with TDS (including lithium) was then sent through a lithium extraction process which removed the entirety of the lithium and the remaining brine at 210 deg C (with enriched TDS and no lithium) was split into three streams to be reinjected. Note the injection brine is higher in TDS than the produced brine but is devoid of lithium. The assumption that all lithium is removed from the brine creates "worst case" scenario for lithium decline as the injectate has zero lithium. It was found that regarding the forecasted enthalpy, there was low sensitivity to well locations, thus for a geothermal-only development well placement is less important. For lithium production well location was much more important

because relatively small adjustments in well layout can lead to much different lithium recovery versus time, while those same small adjustments had a negligible effect on the geothermal performance (steam flow and enthalpy).

Figures 6, 7, and 8 show the well layout in the simulation grid for Layer 3 (1500mBSL) with respectively; the interpreted initial temperature, horizontal permeability, and lithium concentration. There is some correlation of permeability, temperature, and lithium concentrations but it was not possible to use one overall correlation to generate contours. . Figure 4 shows the results of the test run described above for lithium concentration decline (shown as the percentage of initial concentration) and the average flowing downhole temperature from the production wells over time. This was a 30-year simulated forecast (2025 to 2055). The results show that lithium concentration to be nearly constant in the first 5 years of production, then predicts a gradual decline such that the lithium concentration is 75% of its initial concentration in 2055. The predicted slow downhole temperature decline is near linear and the temperature reduction in 2055 is less than 4 deg C from the initial resource temperature.

The well configuration used was the most optimal plan investigated, especially for lithium production, out of seven tested layouts, the design of which was guided by waterflooding techniques. Further changes may provide better results, and the final layout should be planned in part by the actual parameter distribution found through drilling. Thus, the presented layout and its resulting performance is a favorable layout considering currently known data and current best estimates of the distribution of parameters in the absence of drilling results. Figure 9 shows that with the current interpretation of parameter distribution the full 1100 kph of steam at 250 psig is maintained on all nine of the units over a 30-year period. This is consistent with the historical performance of the Salton Sea geothermal field that has seen long-term production with only minor (or negligible) declines in enthalpy.

Figure 10 shows the forecasted field-wide lithium production versus time expressed as a fraction of initial concentration, assuming that the reinjected fluid is devoid of lithium making the forecast a “worst case” scenario for the given well layout. For the parameter distribution and well layout, the field-wide lithium concentration declines to 62% of its initial concentration after 30 years. As was noted above, lithium production is sensitive to well layout. The lithium production may improve with further changes in the well layout. In general, for geothermal production, most reasonable layouts give a good result. However, for lithium production better results were found with injection wells far away from production wells configured as “injection islands” or as “line drive” configurations like waterflood design in oil reservoirs.

Figure 11 shows the simulated enthalpy of all the production separators on a mass weighted basis. While minor enthalpy decline is forecasted over 30 years full steam flow is maintained in the simulation by gradually increasing the production rate to add 6-7% more flow by the end of the 30-year period to make up for the minor temperature decline. Thus, a 6-7% increase in total flow from the production wells fully counteracts the enthalpy decline and maintains constant full capacity of steam flow.

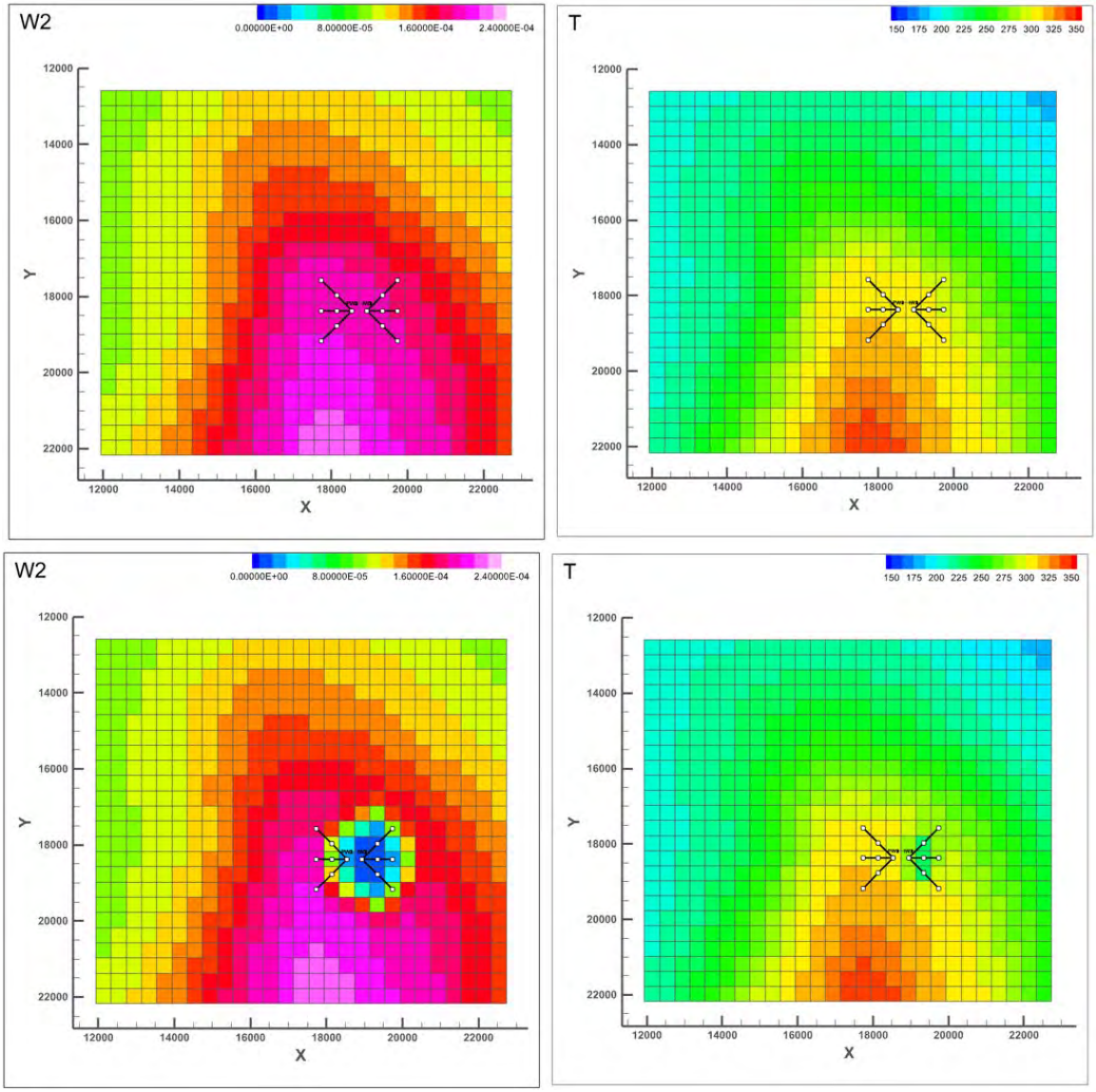
W2
0.00000E+00
8.00000E-05
1.60000E-04
2.40000E-04
T
150 175 200 225 250 275 300 325 350
12000
14000
16000
18000
20000
22000
X
Y

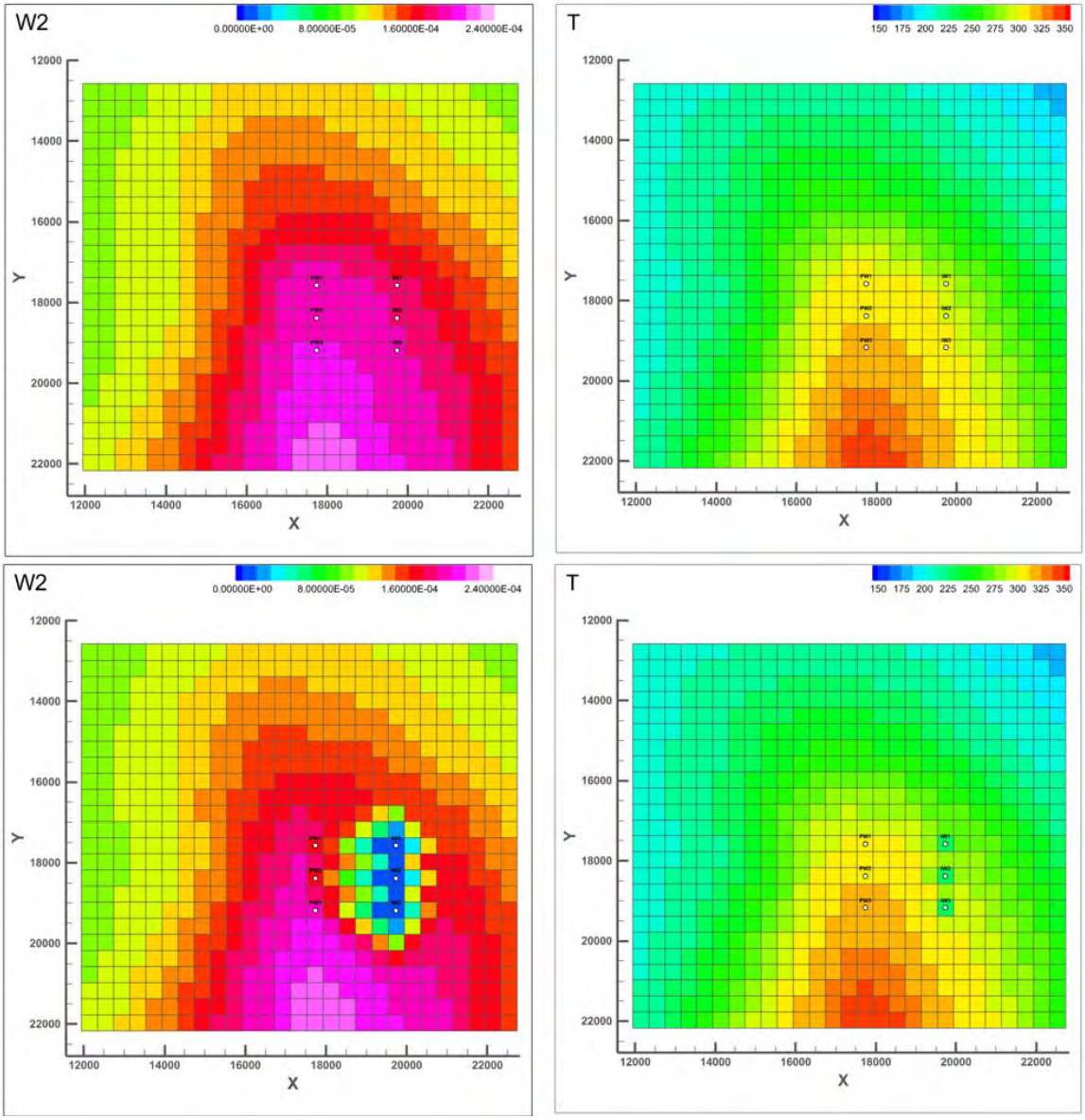

4. Conclusions

We have full confidence that the field, with the well layout as configured in the simulation, will support full geothermal production and over 70% of the initial lithium production over a 30-year period. Lithium production was found to be more sensitive to well layout than geothermal production. Within limits, the lithium recovery could be enhanced by further experimenting with additional well layouts guided by waterflood techniques in a more detailed reservoir numerical model. Maintaining and continually updating a reservoir model will allow an operator to optimize field development decisions throughout the life of the project.

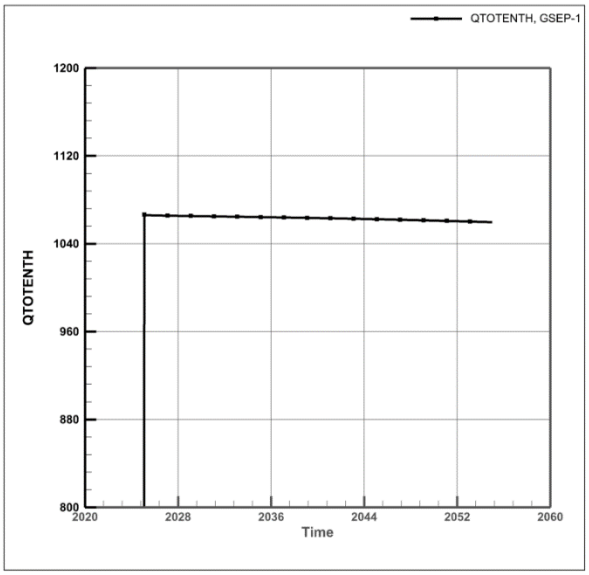
QTOTENTH, GSEP-1
QTOTENTH
1200
1120
1040
960
880
800
2020
2028
2036
2044
2052
2060
Time

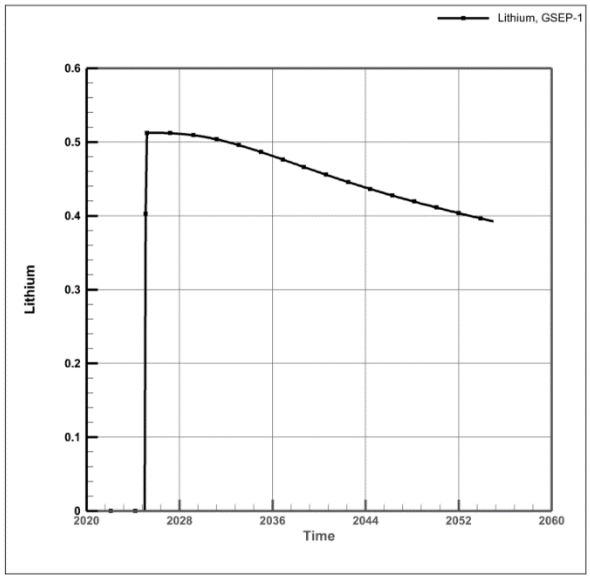
Lithium, GSEP-1
Lithium
0.6
0.5
0.4
0.3
0.2
0.1
0
2020
2028
2036
2044
2052
2060
Time

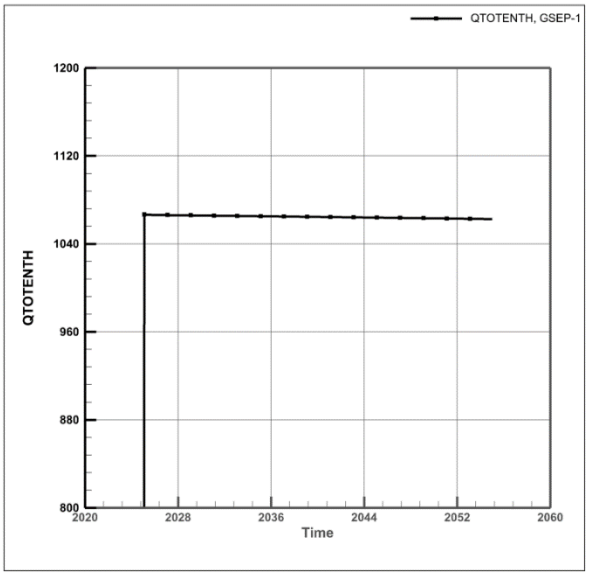
QTOTENTH, GSEP-1
QTOTENTH
1200
1120
1040
960
880
800
2020
2028
2036
2044
2052
2060
Time

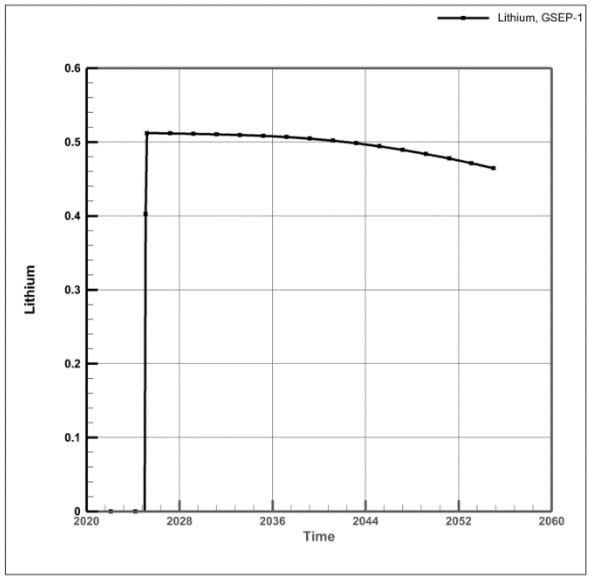
Lithium, GSEP-1
Lithium
0.6
0.5
0.4
0.3
0.2
0.1
0
2020
2028
2036
2044
2052
2060
Time

What's in Your Brine - a Case for Critical Minerals Co-production from Geothermal Brines

Kim Mohler

GLJ Ltd., Calgary, Alberta, Canada

Keywords

Geothermal, Lithium, Brine, Direct lithium extraction, Critical minerals

ABSTRACT

The global demand for production of critical minerals to supply the energy transition away from fossil fuels has been increasing at a fast pace. The cost to produce these critical minerals is typically high, with technology testing and development required to produce critical minerals like lithium with a lower carbon footprint.

Lithium is one of the critical minerals that is required for battery manufacturing, driven mainly by electric vehicle demand increasing globally. The global market for lithium is currently supplied primarily by Australia, China, Chile and Argentina from hard rock mining and evaporation ponds (salars). The current production methods for lithium are environmentally destructive with large surface land impacts and have high operating costs.

The advent of Direct Lithium Extraction technologies has opened the opportunity to produce lithium from deep subsurface brines. The processing technology is being piloted for production of lithium hydroxide and lithium carbonate from deep subsurface brines in Germany, Canada, and the USA. Commercial DLE projects are in development utilizing deep subsurface brines that are from reservoirs that have proven oil and gas production or geothermal heat and power production.

Understanding what is in your geothermal brine through geochemical analysis will define the available concentration of lithium in the brine, but also other potential recoverable minerals and metals. The composition of the brine is important to understand as the DLE process is sensitive to geochemical composition, including components or attributes that can make the lithium extraction process less effective or uneconomic. Equally important to understand are the reservoir conditions including pressure and temperature, in order to define the well network plan, production forecast, and operating plan.

Production of lithium from geothermal brines offers a clean green energy solution utilizing a binary Organic Rankine Cycle geothermal power plant design. The extraction of lithium is an energy intensive process and the use of geothermal energy to power the process provides cost savings, emissions reduction, and a renewable energy source. Many geothermal projects produce brines from the deep subsurface that may have sufficient lithium concentrations to warrant further

investigation and potential development for lithium extraction processes co-produced as a value stream.

This paper will describe the considerations for co-production of lithium from geothermal brines. The paper will include a case study of a lithium enriched geothermal brine project in Germany that is currently in progress. The author is a Competent Person for the Germany project.

1. Introduction

The economies of the largest nations are caught in a wave of energy transition activities, resulting from climate change policies that target reduction of greenhouse gases (GHG). “Energy Transition” is a term used since the 1970’s but more popularized in the last decade, to describe the move away from fossil fuels as primary heating and power generation sources to renewable low carbon intensity sources. Technology development has been underway for many decades to bring renewable power sources like wind and solar to the forefront as options to offset high GHG emission electricity. The market share from renewables has been slow to increase, reported in 2023 to represent 30% (IEA Publications, 2024) of global electricity supply. Geothermal power generation is part of the future for renewable energy sources that have low carbon intensity, however the supply from geothermal is still low at 0.5% of global electricity capacity in 2023 (IEA Publications, 2024).

As part of the global energy transition, the shift to electric vehicles is growing at a rapid pace. The International Energy Association (IEA) estimates that almost one in five vehicles sold globally in 2023 were electric (IEA Publications, 2024), which was up by 14% from 2022. A challenge for the growth of the electric vehicle (EV) sector is supplying all the critical minerals needed for battery manufacturing and other electric vehicle components. One of the critical minerals needed is lithium as the lithium-ion battery is still the main rechargeable battery type used in EV’s, with different chemistries being tested to optimize performance, safety and cost.

Lithium is primarily sourced today from hard rock mining and evaporation ponds (salars) from the top producing countries Australia, Chile, and China. These countries are expected to maintain supplies along with growth in lithium production from Argentina and Zimbabwe in the coming years. The current production methods have large environmental impacts. Hard rock mining of spodumene requires open pit mining methods that cause large land disturbances and require many steps to process a marketable product. Similarly, the large evaporation ponds (salars) used in South America create environmental disturbances which require long periods of time to achieve the desired lithium concentrations before processing. The operating costs for these current extraction technologies are high and with lithium prices softening in recent years, the profit margins are shrinking.

2. Lithium from Deep Subsurface Brines

There is an opportunity for more environmentally friendly lithium production via wells from deep subsurface reservoirs and lithium enriched brines. Several developments are underway utilizing this production method in North America and Europe, applying Direct Lithium Extraction (DLE) technologies for extraction. DLE technologies include sorption, ion exchange, solvent extraction, membranes, and a few other emerging processes, which selectively remove the lithium ions from the brine. The DLE technologies provide a more sustainable and faster method of producing

lithium for feedstock to battery manufacturing and have also been piloted at some salar operators in South America to improve the production timelines.

Deep subsurface brines can be sourced from geothermal aquifers, and oil and gas reservoirs, which in many cases are already delineated so the well data and reservoir rock data can be leveraged for reservoir modeling for lithium enriched brine production. The key factors that need to be understood for development of an economic lithium brine play from deep subsurface reservoirs are rock formation data, fluid data, and flow deliverability.

The geologic characterization of the target formation is key in determining the size and extent of the rock hosting the brine, and then to understand the petrophysical qualities to define the flow characteristics. As well, data on the potential source rock, caprock, and other formations bounding the reservoir are important to understand and include in the modeling. The data required for the static geomodel are comparable to data needed for geothermal or oil and gas evaluations, including porosity, pay thickness, fluid and gas saturations, shale content, and permeability. Further, subsurface pressure and temperature data is needed for flow modeling. In all cases, starting with data from existing wells is a lower cost way of defining the mineral resource and prioritizing for new reservoir data capture through drilling or testing wells, or acquiring and interpreting seismic data.

When existing wells are available, and the target formation for lithium brine production is already producing for geothermal or oil and gas, it is easier to capture produced fluid for geochemical analysis providing the ability to measure the lithium concentrations and other components of the brine. Typically, fluid analysis for these plays includes only standard analysis of trace elements, which may not include lithium and may not provide a full measurement of all ions. In recent years sampling and analytical programs have been undertaken to determine the lithium concentrations in the brines. In Canada and the United States of America (USA), efforts have been made to document the lithium concentrations from geothermal and oil and gas wells, with resulting data shown below for oil and gas field brines in Alberta, Canada, and the Western USA for geothermal brines (Figure 1, Figure 2).

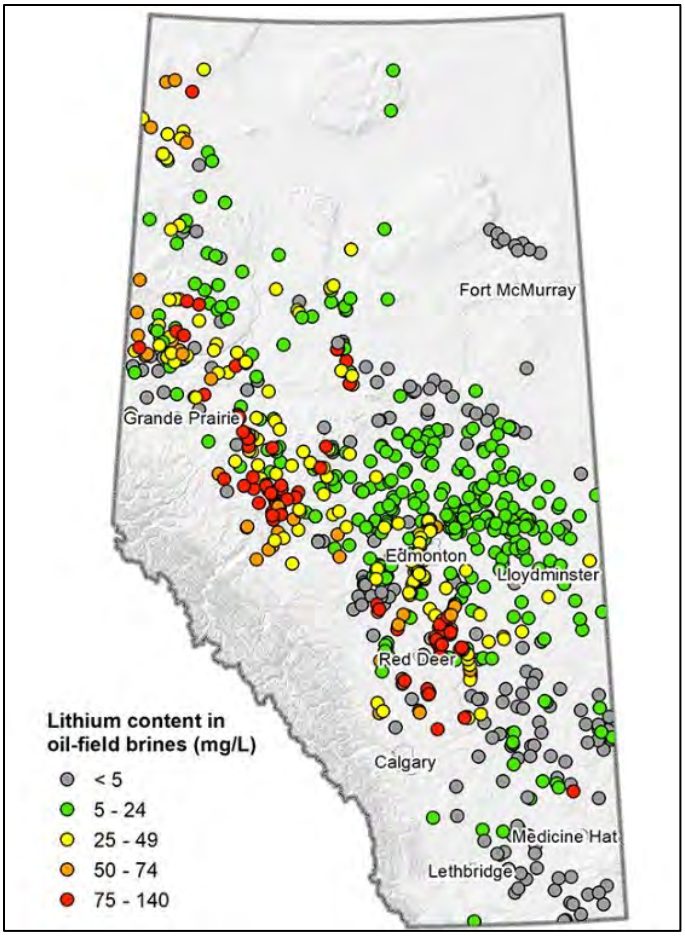

Figure 1: Province of Alberta, Canada, lithium content in existing oil and gas wells in milligram per litre (2024, Alberta Geological Survey, https://ags.aer.ca/research-initiatives/critical-minerals-potential)

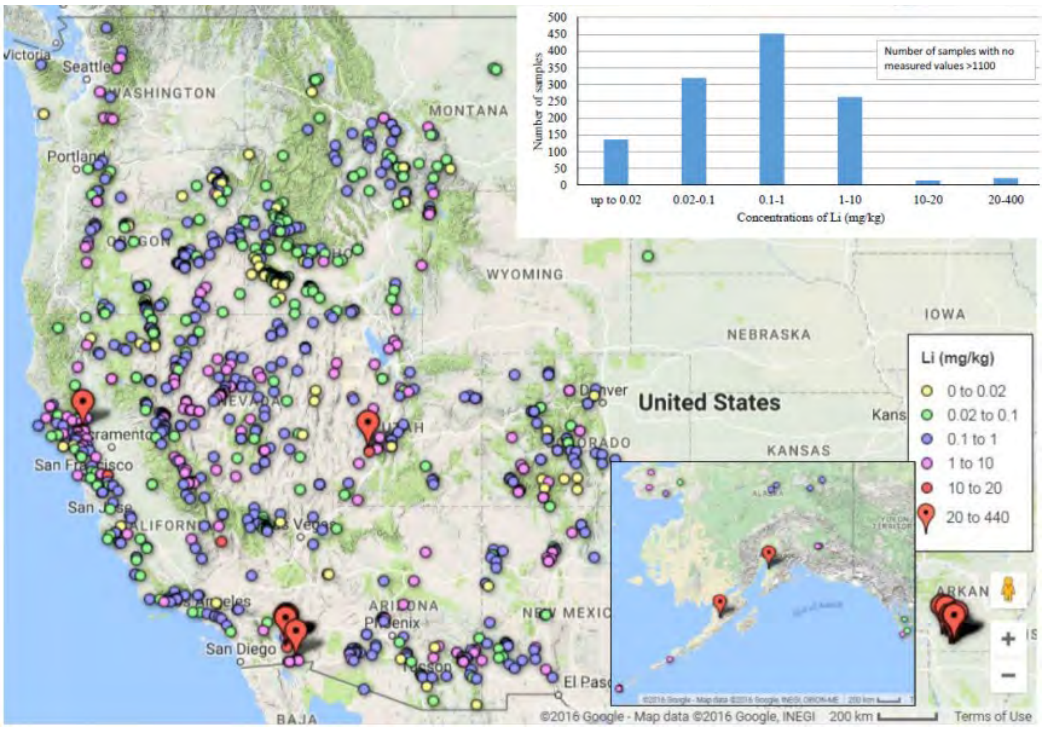

Figure 2: Lithium concentrations in geothermal fluids of Western USA, in milligram per kilogram (NREL Technical Report/TP-5700-79178, May 2021 – Reference: Nupane and Wendt – 2017)

A full geochemical analysis of the brine is required to define the economic potential of the play, and the appropriate DLE technology and other processing that might be required such as pre-treatment. It is possible that other producible minerals are identified in economic quantities like magnesium or bromine, which may require separate extraction and processing equipment and costs.

The geochemical analysis of the brine will provide insights into other physical and geochemical water properties that can impact the efficiency of the DLE process. Some common issues encountered that require pretreatment are high levels of calcium, magnesium, or dissolved organic carbon, which are impurities for most DLE processes. For oilfield brines, any oil and gas must be removed prior to lithium extraction to meet acceptable levels of TOC (total organic carbon) for the DLE technology. For geothermal brines, the issues can be related to the high fluid temperatures and the resulting challenges from dissolved minerals like iron and silica, high TDS (total dissolved solids), and salinity.

Pretreatment is an added cost and large consideration for the project design and economics. As part of the derisking process it is recommended to have an early understanding of the fluid chemistry and metallurgy, which will provide a higher level of certainty early in the project design.

The flow deliverability of the brine is another critical piece of data required to understand the economic viability of the project. Typically, artificial lift, through pumps like line shaft pumps (LSP) or electrically submersible pumps (ESP), will be installed to lift the fluid to surface from the deep subsurface formation for production. The reservoir must have sufficient flow potential to deliver the fluid over the long term to the well, which requires a minimum permeability and porosity in the rock to allow for flow. Each rock and play type will have different minimums,

depending on many factors like well depth, pump type, pump placement, surface infrastructure, areal extent of reservoir, and project costs.

The well network typical for lithium brine projects from deep subsurface reservoirs is similar to conventional geothermal, where production will come from a well or set of wells, and the depleted brine will be reinjected into the same reservoir at a distance away from the production wells (Figure 3). This setup is done to provide pressure maintenance in the reservoir and to avoid brine disposal at surface. The play should be extensive enough to not suffer drawdown from the brine production and allow for the reinjection of the depleted lithium brine to occur at a distance from the production well to mitigate early breakthrough.

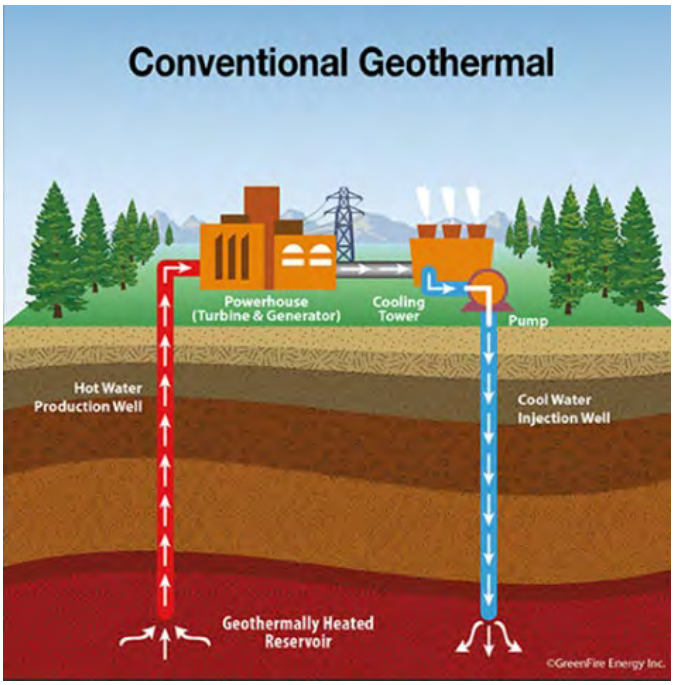

Figure 3: Diagram showing typical conventional geothermal well network with production well and injection well (Greenfire Energy Inc. 2024, https://www.greenfireenergy.com/geothermal-energy/how-does-geothermal-energy-work)

An example is shown below (Figure 4) of a lithium brine project in Alberta Canada, operated by E3 Lithium. They plan to have an array of production wells in one area of the reservoir with reinjection of lithium depleted brine occurring 15 km away from the production well array. They will be using multi-lateral long well drilling techniques to access large areas of the subsurface reservoir with many wells drilled from one well pad.

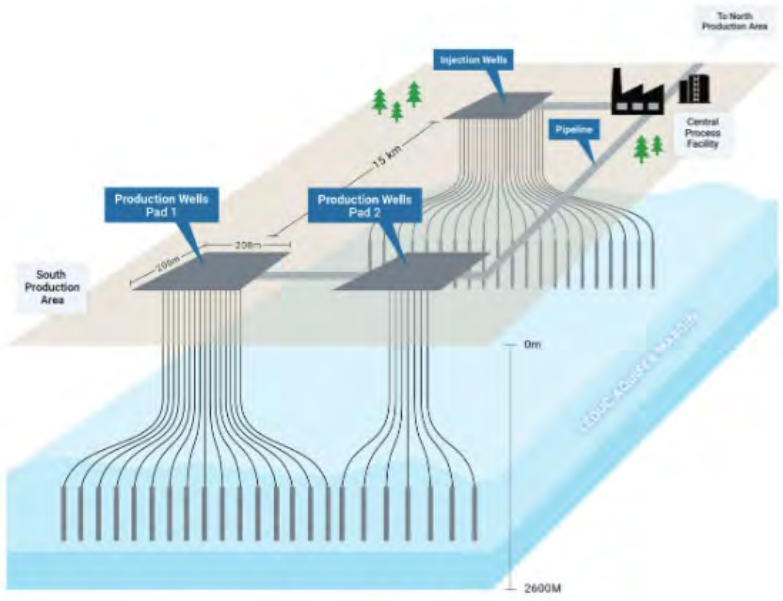

Figure 4: E3 Lithium Conceptual well network layout from report "NI 43-101 Technical Report Preliminary Economic Assessment Clearwater Lithium project Alberta, Canada" dated 12/21/2020 amended 09/17/2021 (E3 Lithium https://e3lithium.ca/our-assets/resources/)

For a geothermal lithium brine project, the spacing between the production and injection wells will have to take into consideration both the temperature breakthrough and lithium depletion. This can be done with detailed reservoir flow models, to optimize the bottomhole spacing for co-production of both products.

3. Reporting of Lithium Mineral Resources and Reserves

The regulatory framework is well established for oil and gas projects and for hard rock mining of critical minerals like lithium from pegmatites, however the regulatory processes for deep subsurface brine projects are still in catch up as regulations for these projects address fluid flow from reservoirs to wells to surface processing facilities. In most jurisdictions, lithium from oilfield or geothermal brines from deep reservoirs is treated as a mineral, under mining industry disclosure standards. The international standards are from CRIRSCO (Committee for Mineral Reserves International Reporting Standards) 2012 (ICMM, 2019). See below for relationship between exploration results, mineral resources, and mineral reserves (Figure 5). This roadmap for transition from mineral resources to mineral or ore reserves is commonly used amongst country standards such as Canada in the NI 43-101 (National Instrument), and in Australia in the JORC Code 2012 (Joint Ore Reserves Committee).

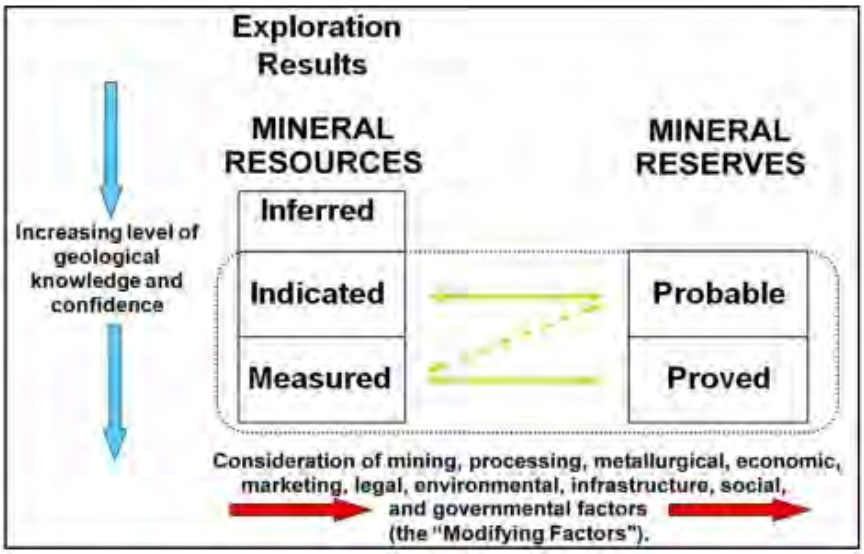

Figure 5: General relationship between Exploration Results, Mineral Resources and Mineral Reserves, CRIRSCO 2019

In the United States the disclosure regulations are established and governed by the Securities Exchange Commission (SEC) under Regulation S-K 1300, where the CRIRSCO framework is applied for applying modifying factors to determine economic viability of a project.

A similar framework and resource reporting process is in place in many jurisdictions for geothermal projects. Below (Figure 6) is the framework from the Australian Code for Reporting of Exploration Results Geothermal Resources and Geothermal Reserves, The Geothermal Reporting code 2010, under the Joint Committee of the Australian Geothermal Energy Group (AGEG) and the Australian Geothermal Energy Association (AGEA) (AGRCC, 2010).

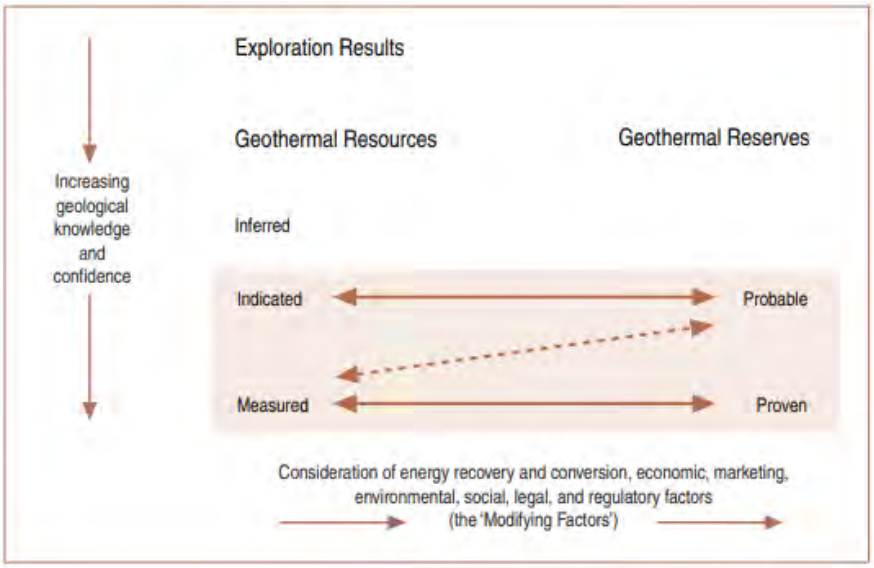

Figure 6: Geothermal Reporting relationship between Exploration Results, Geothermal Resources and Geothermal Reserves, AGEA 2010

In the case of lithium and geothermal resource and reserve reporting, several terms are common, such as “modifying factors” which describe the considerations to convert from resource to reserve and to determine technical and economic viability. They can include mining, processing, metallurgical, infrastructure, economic, marketing, legal, environmental, social, and governmental factors.

4. Geothermal Lithium Brine Project Opportunities, Risks and Challenges

A geothermal lithium brine project from a deep subsurface reservoir may be subject to many risks and challenges, along with the opportunities.

The opportunities to consider may include the following:

- Geothermal reservoir may be characterized and have historical production which reduces project risks and reservoir understanding when adding co-production of lithium.
- Directional drilling techniques of multi-lateral long wells have improved the ability to drill more wells from one wellsite, which allows for smaller surface footprint for the geothermal lithium wells.
- Operating costs can be reduced with geothermal power generation to support the lithium co-production.
- Using geothermal power generation is a low GHG emissions renewable power source.
- Communities could use district heating from the geothermal plant, which may improve stakeholder support of the project.
- It might be possible to produce other critical minerals if they are present in sufficient quantities and can be economically co-produced.

The risks and challenges to consider may include the following:

- Reservoir and Wells:
    - Lithium concentration data might not be available from existing wells within the play area and require drilling and testing of a new well(s), which is expensive.
    - Dissolved gas in the brine may contain toxic gases like hydrogen sulfide (H2S), so well and facility design will require detailed gas and fluid testing.
    - Parasitic load of brine production and injection pumps can be high and should be considered in the net power capacity estimation.
    - Reservoir may not be as extensive as estimated, which can affect long term flow deliverability, where mitigation can be new data from wells and seismic and improved reservoir modelling.
    - Early depletion of heat or lithium if communication between the production and injection wells occurs early, where optimal well spacing at reservoir depth requires good data and reservoir modeling.
    - Corrosion issues due to brine chemistry can impact wells and infrastructure, which can be mitigated with corrosion integrity programs.
- Surface Facility:
    - High geothermal temperatures can result in brine chemistry and physical properties that require additional treatment and processing, increasing capital and operating costs.

    - DLE, lithium polishing, and lithium refining are energy intensive and need to be considered in net power capacity estimation.
    - Operating uptime can be impacted by challenged brine chemistries and well pumping systems.
    - Matching the best DLE technology to the brine and conducting sufficient benchscale and pilot testing before commercial design to optimize cost and operating performance.
    - Location of play with good lithium concentrations and geothermal temperatures may not be proximal to existing power infrastructure or offtake users.
- Market:
    - Lithium pricing has suffered a decline and project may not be as profitable as predicted from studies in last 3 years.
    - Defining the desired end product early in alignment with pricing differentials and possible offtake users for each product type - LiCl (lithium chloride), LCE (lithium carbonate equivalent), or LHM (lithium hydroxide monohydrate) and taking into consideration extra processing to get to more refined products like LHM.
    - EV batteries may move away from lithium as critical component.
- Stakeholders:
    - Community and stakeholders may not support a geothermal lithium project and associated facilities, infrastructure, and operations.
    - Regulatory framework may not provide incentives for geothermal lithium projects.

5. Example of Geothermal Lithium Brine Project

Several geothermal lithium brine projects are in the early development and pilot stages in Canada, the USA and Germany. Notably, Vulcan Energy Resources Limited (Vulcan) has progressed their Zero Carbon Lithium™ project in Germany past the pilot stage to a Lithium Extraction and Optimisation plant (LEOP) scaled up stage. The Vulcan Phase One project is located in the Upper Rhine Valley in south central Germany (Figure 7) and is considered a brownfield development around existing geothermal brine production and geothermal power generation.

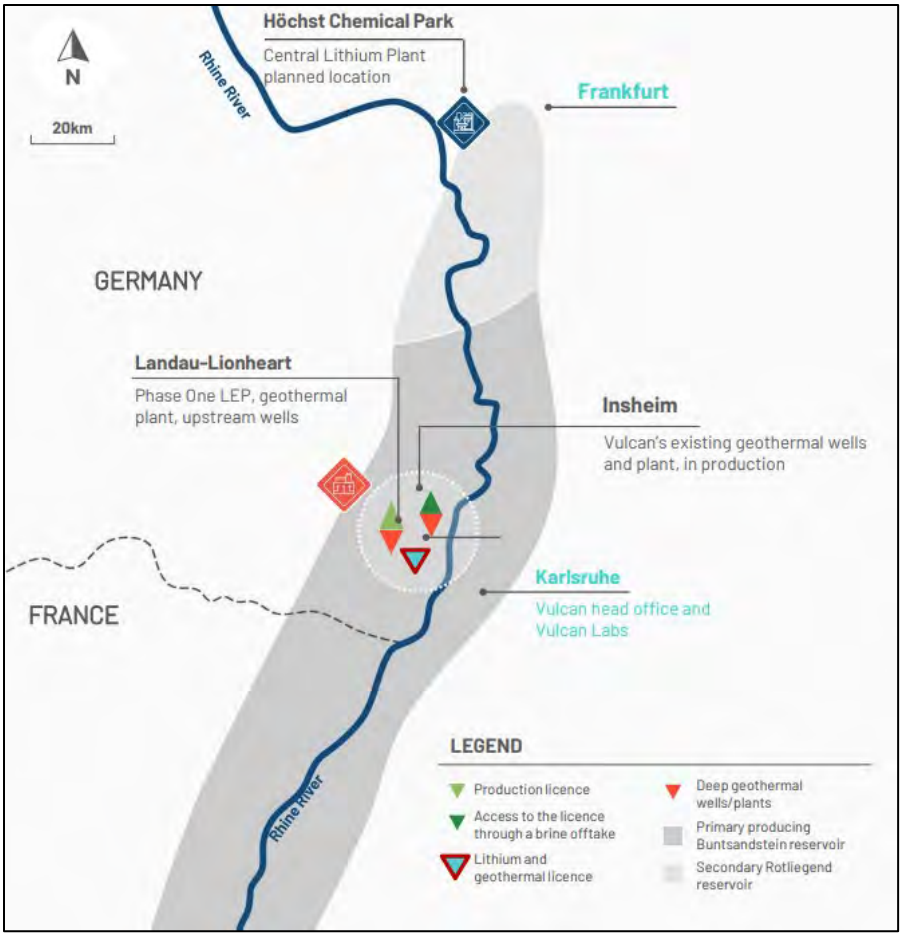

Figure 7: Vulcan Phase One Zero Carbon LithiumTM project location, Upper Rhine Valley, Germany (Vulcan, 2024, https://www.investi.com.au/api/announcements/vul/1e22d4df-e78.pdf)

Vulcan is an Australian based company founded in 2018 that is publicly traded on the Australian Stock Exchange (ASX) and Frankfurt Stock Exchange (FSE). The purpose of the company is to empower a carbon neutral future through the co-production of lithium, heat, and renewable energy from geothermal brine. (Vulcan, 2024). They own and operate a geothermal power plant at Insheim, Germany, called Natürlich Insheim, with capacity of 4.2 MW (Megawatt) that has been in operation for over 10 years. This plant utilizes a binary Organic Rankine Cycle (ORC) for power generation from geothermal brine.

The Phase One development, focused on the Lionheart area, is planned to co-produce the lithium from the geothermal brine, adding new wells to the existing wells in operation at the Natürlich Insheim facility, and adding new facilities to support additional geothermal heat and power, and lithium extraction. See Figure 8 below that shows a representation of the full production process. The Phase One development is targeting a capacity of 24,000 tpa (tonnes per annum) LHM production. The conversion from LiCl to LHM will occur at the planned Central Lithium Plant (CLP) located in Höchst Industrial Park near Frankfurt, Germany, through an electrolysis process.

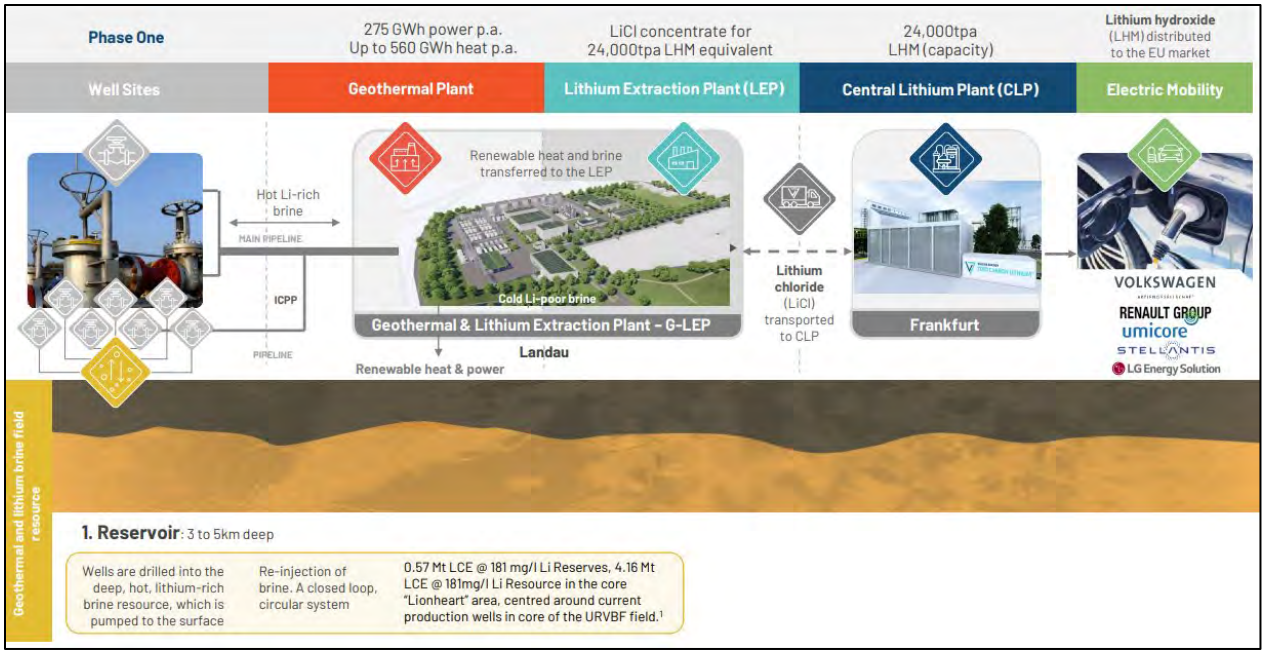

Figure 8: Representation of Vulcan's Phase One development plan (Vulcan, 2024, https://www.investi.com.au/api/announcements/vul/1e22d4df-e78.pdf)

The deep subsurface geothermal reservoir supporting this Vulcan Phase One development is part of the larger Upper Rhine Graben in the aquifers of the Permo-carboniferous Rotliegend Group sandstone, the Triassic Buntsandstein Group sandstone, and the Middle Triassic Muschelkalk formation. The strata are laterally heterogeneous within a structurally complex rift basin (Vulcan, 2023). A high degree of faulting and fracturing exist in the strata which results in some degree of hydrogeological communication with the granitic basement.

The typical depth of the aquifers in the Phase One area is 3,000 m (metre), with bottomhole temperatures of 165°C (Celsius). The geochemical analysis of the producing Vulcan geothermal brines indicates there is a good distribution of lithium enrichment in the brine. The average lithium concentration in the Phase One area is 181 mg/L (milligrams per litre) based on extensive long-term analysis of the brine produced from the six geothermal wells in the region.

Vulcan has reported Mineral Resources (Measured and Indicated) in the Phase One area at 4.16 Mt LCE at 181 mg/L lithium concentration, reported in accordance with Joint Ore Reserves Committee's Australasian Code for Reporting of Mineral Resources and Ore Reserves (JORC Code). They have Proved Reserves of 0.318 Mt LCE and 0.252 Mt LCE Probable Reserves reported for Phase One. The development is based on five new well sites and using two existing well sites, where production and injection wells will be situated. (Vulcan, 2024)

A new geothermal power plant is going to be added to the existing one at Natürlich Insheim, with combined total power capacity of 32 MW and heat capacity of 80 MW, utilizing an ORC plant design.

Vulcan is using an Adsorption-type DLE system where an alumina-based sorbent is used to extract the lithium from the geothermal brine and purify and concentrate in the form of LiCl. Vulcan is using its own tailored sorbent technology referred to as Vulsorb®. The facility where this is conducted is called the Lithium Extraction Plant (LEP). Vulcan has been testing the performance and optimizing with pilot plant operations from 2021 – 2023. In April 2024 they started operation and production from their LEOP located in Landau, Germany. This facility is being used to train staff in a pre-commercial facility to be ready for full commercial operation. This facility produces LiCl, which is to be sent to the Central Lithium Electrolysis Optimisation Plant (CLEOP) to make battery grade LHM. The CLEOP and commercial scale CLP are located near Frankfurt at the Höchst Industrial Park. The CLEOP is expected to start operation in mid-2024 to train staff and optimize before commercial operation of three key processes 1) electrolysis of LiCl to LHM solution, 2) LHM crude and pure crystallization, 3) LHM drying, to deliver battery grade LHM at the 24,000 tpa commercial rate for Phase One, which is planned to start-up in 2026.

The economics of the Vulcan Phase One development have been reported as robust based on an operating cost of €4,022/t LHM and Initial Capital cost of €1.39 B (Billion), with a pre-tax IRR (internal rate of return) of 27.8% and NPV8 (net present value at discount rate of 8%) of €3.9B. The payout period is estimated to be 4 years. See Figure 9 below which summarizes the financial metrics of the project.

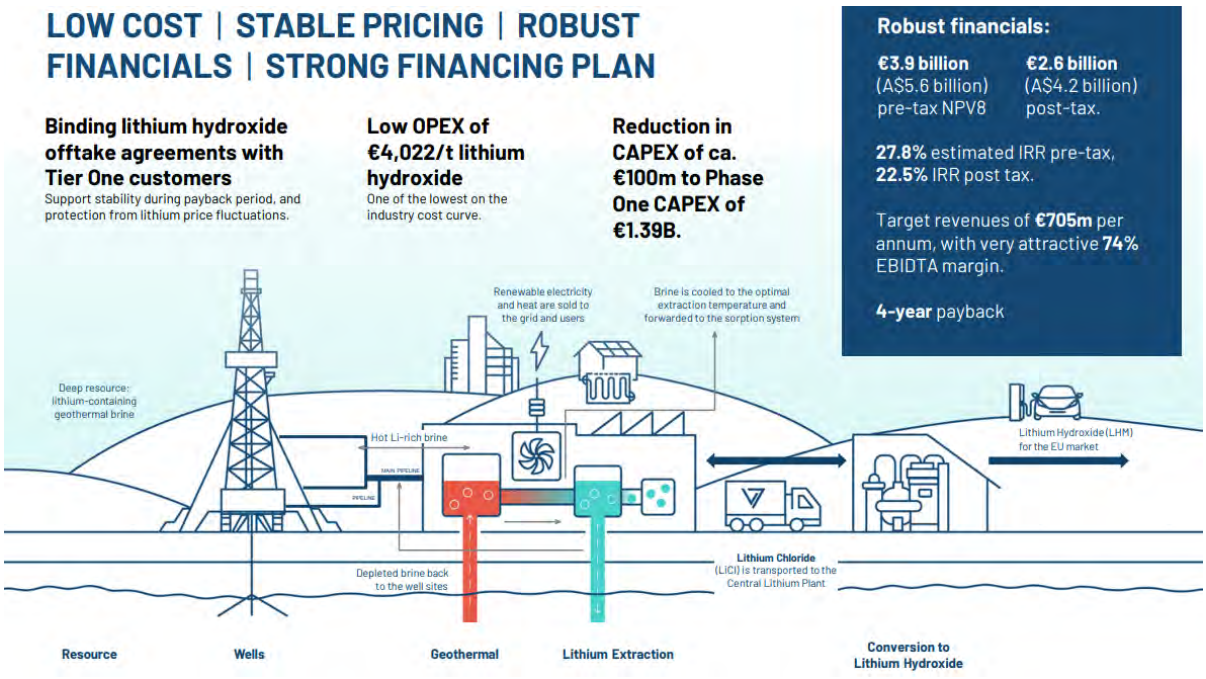

Figure 9: Summary of Vulcan Phase One project plan and economics (Vulcan, 2024, https://www.investi.com.au/api/announcements/vul/1e22d4df-e78.pdf)

What makes this project so unique is the ability to leverage the historical data from long term geothermal production and brine analysis data from the geothermal brine in the Phase One area of development. With the development planned as a brownfield construction, it enables a lower cost solution than many new projects would face. Vulcan is also located near established infrastructure

that supports delivery of the LiCl to the Central Plant in Frankfurt and then access by rail, road, and sea to markets for battery manufacturing. Vulcan has established offtake agreements already with major auto manufacturers, and established strategic supply partners, which allows for improved risk management for pricing.

6. Conclusion

The technical and economic potential for geothermal lithium brine projects is gaining momentum with recent technological improvements in exploration of appropriate aquifers and reservoirs, multi-lateral long well drilling, extraction/refining processes, and battery manufacturing. The increasing demand for lithium is not expected to wane in the upcoming decades with the energy transition to lower GHG emissions. As countries target domestic production of critical minerals and EV manufacturing, the opportunity to develop these projects is improving with potential for government grants and incentives.

In the global market today, ensuring your project considers environmental, social and governance (ESG), is critical to securing stakeholder approvals and financing. The co-production of geothermal brine with lithium extraction not only provides for a green energy solution that has low greenhouse gas emissions, but also reduces operating costs with geothermal power generation. The added benefit to the community of providing district heating can be an additional revenue stream, but also provide an incentive for community involvement and support.

A geothermal lithium brine co-production project from deep subsurface reservoirs is developed with a much smaller surface footprint and environmental impact than the traditional methods of lithium production through hard rock mining and evaporation ponds. Identification of more locations for geothermal lithium projects is possible through leveraging of existing well and seismic data, or supplementing data with new well tests or seismic reprocessing.

Though no commercial scale geothermal lithium brine project exists today from deep subsurface reservoirs, there are several pilots in operation with commercial production to start within 2 to 5 years in Germany, USA, and Canada. These will represent a small portion of the lithium production worldwide but are a step toward critical mineral self-sufficiency for the countries they are located in, and greener approaches to critical mineral production.

Acknowledgement

The author would like to thank Vulcan Energy Resources for the ongoing work relationship with GLJ Ltd. as Competent Persons for the JORC reporting of Mineral Resources and Ore Reserves for their Zero Carbon Lithium™ project. The data contained in this paper is from publicly available sources.

REFERENCES

AGRCC, A. G. (2010). *The Geothermal Reporting Code, Second Edition 2010.* Joint Committee of the Australian Geothermal Energy Group and the Australian Geothermal Energy Association.

ICMM, I. (2019). *International Reporting Template for the public reporting of Exploration Targets, Exploration Results, Mineral Resources and Mineral Reserves.* Committee for the Mineral Reserves International Reporting Standards (CRIRSCO).

IEA Publications. (2024). *Global Critical Minerals Outlook 2024.* International Energy Agency. Retrieved from https://www.iea.org/

Vulcan. (2023, November 16). *Vulcan Positive Zero Carbon LithiumTM Project Bridging Study Results.* Retrieved from Australian Stock Exchange: https://cdn-api.markitdigital.com/apiman-gateway/ASX/asx-research/1.0/file/2924-02740777-6A1180852

Vulcan. (2024, April). *Delivering – Europe's Green Energy and Mobility Transition | Corporate Presentation April 2024.* Retrieved from https://www.investi.com.au/api/announcements/vul/1e22d4df-e78.pdf

Review of Lithium Extraction Suitable for Indonesia Geothermal Brine

Esty Mustika Suud[1], Suryantini[1,2], and Herbert Lubis[3]

[1]Geothermal Master Program, Faculty of Mining and Petroleum Engineering, ITB, Bandung, Indonesia

[2]Applied Geology Research Group, Faculty of Earth Science and Technology, ITB, Bandung, Indonesia

[3]Alumnus Sarulla Geothermal Project and Member of Indonesia Renewable Energy Society, Indonesia

Keywords

Lithium, energy transition, net zero emissions, geothermal brine, traditional brine extraction, direct lithium extraction (DLE), adsorption, ion exchange, solvent extraction, CAPEX/OPEX, operating pilot plant

ABSTRACT

Lithium is the cornerstone of energy transition for Indonesia to achieve Net Zero Emissions by 2060 or earlier. This energy transition will drive the Indonesia demand projection for Electric Vehicle Battery and Energy Storage System and in turn will demand much more lithium for this transition effort. Many studies have been conducted to find the sources of lithium, one of them is geothermal brine. Indonesia has enormous geothermal resources, some fields have lithium content that can potentially be extracted. Various methods in the extraction process of lithium from the geothermal brine have been developed, both on laboratory and pilot projects. The geothermal brine is typically pumped to the surface by a geothermal power plant, used for energy generation, and then returned to the underground reservoir via an injection well. Prior to reinjection the geothermal brines contain in the temporary ponds whereas the lithium extraction points may occur here or at any point suitable for the extraction technology. Typically there are three phases in the lithium extraction, like end- to-end process technology solutions, namely **1)** Lithium Brine Extraction- depending on the geothermal brines field compositions, pre-treatment may be employed to remove any contaminants or unwanted constituents from the brines, then selective absorbents are used to separate lithium from other elements **2)** Concentration with membrane system to concentrate lithium at a desired concentration **3)** Deposition using chemical precipitation and purification for

saleable lithium production. This paper reviews traditional brine extraction and direct lithium extraction (DLE) in general and specifically in geothermal brine. The study is based on a desktop study and aims to summarize the knowledge, method, technology, and techniques of lithium extraction from geothermal brine that has already been used and to find out which extraction method is suitable for the Indonesian geothermal field. Our finding indicates the adsorption end-to-end technology process includes pretreatment, lithium extraction, purification, and lithium product production steps such as electrodialysis (a form of ion exchange) and reverse osmosis to yield high recovery rates. The adsorption DLE solution has been used on a commercial scale, in Argentina and China and it has a fifty-year development and implementation history, higher lithium recovery, lower water and chemicals consumption, shorter lead time to production, minimal footprint, potential for no carbon emissions, and an additional revenue stream from unused brine resources for geothermal power producers. The authors have not researched that far for the issue of scaling when the extracted fluid is injected. An important issue that needs to be added to the paper for further research. There is unlikely a one size fits all solution, hence a complete operating pilot plant to simulate the real condition of geothermal field brines is important. The other important points are to keep the project commercial operation date punctuate with faster, cheaper, better and rapid speed of technology implementation.

1. Introduction

Lithium is the cornerstone of energy transition because of the following two reasons, the first reason is that it has the key ingredient in batteries for electric cars and renewable power storage, making it a critical commodity for the energy transition to reduce emissions of greenhouse gases. And the second reason is that Lithium is a big enabler of the energy transition from a battery perspective as we move to electric vehicles and add energy storage to electricity grids, allowing for greater penetration of renewables. As a result, lithium is increasingly being seen as a critical mineral by governments, where they want to secure supplies for that transition, and that has made it an increasingly important commodity. In line with this cornerstone of energy transition, Indonesia is committed to achieve Net Zero Emissions by 2060 or earlier and is beginning to put in place the policies and frameworks that can help reach this target while moving towards advanced economy status.

Lithium is a light and highly reactive metal that offers excellent heat and electrical conductivity. Because of its high reactivity, pure elemental lithium is not found in nature but is instead present as a constituent of salts or other compounds. Lithium is found in three main types of deposits: pegmatites (crystalline hard rock), saline subsurface waters (lithium brines) and sedimentary deposits. The primary commercial sources of lithium are hard rock deposits in Australia and China approximately 60%, and brine deposit in Argentina, Chili, China, and the rest of the world approximately 40%. The three main types of lithium brine deposits include salt-lakes or salt-flats (salars), geothermal, and oil field deposits. Future potential for geothermal brine to supply demand is recognized as an important brine sources of lithium.

For both geothermal and conventional lithium resources, there is interest in developing technology, and processes for the direct extraction of lithium from brines. Unlike conventional methods for producing lithium, the so-called **Direct Lithium Extraction (DLE)**, a potential game changing technology, uses filters, membranes or resin materials to extract mineral from brine water. And as such DLE may significantly increase the supply of lithium, nearly doubling production from same

resource and improving project returns through a process that may be more sustainable. A number of proven DLE technologies are emerging and being tested at scale, with a handful of projects already in commercial construction. While there may still be challenges around scalability and water consumption/brine reinjection. With the ongoing efforts, DLE could be implemented between 2024-2030 in USA and Europe, and between 2025-2030 in both Chile and Argentina.

2. Technology For Lithium Extraction Methods

The following table summarizes the processes for hard rock, traditional brine ponds, and key DLE technologies and their detailed comparisons [1].

Table 1: Lithium Extraction Methods in Hard Rock, Evaporation and Direct Lithium Extraction in Brine [1]

Lithium Extraction Methods	Hard Rock	Brine	
	Mining	Evaporation	DLE
Production Times (Extraction to Production	Weeks to Months	Months to Years	Hours to Days
Lithium Recovery Rates	~60-80% (processing)	~40-60%	~70-90%
Costs Capex Opex	Varied on Grade/ Chemical Conversion	~US$23-34,000tpa LCE ~US$3,300-4,900t LCE	~US$26-34,000tpa LCE ~US$2,800-3,600t LCE
Lithium Product	Spodumene (~5-6% Li_2O)	Lithium Carbonate (Li_2CO_3) Lithium Chloride (LiCl)	Lithium Carbonate (Li_2CO_3) Lithium Chloride (LiCl)
Process	Heating, Cooling, Crushing, and Roasting	Staged Atmospheric Evaporation, Plant Processing	Adsorption (Ad), Ion Exchange (IX), Solvent Extraction (SX), Membrane
Further Process Requirements	Yes	No (subject to end use)	No (subject to end use)
Land Area Requirement	High	High	Low
Weather Dependence	Yes	Yes	No
Water Consumptions	High	Medium-High	Low-Medium
Energy Consumption	High	Low (free solar evaporation)	Medium
Emissions	High	Low	Low

The traditional lithium extraction method from well-established producing countries like from hard rock (Australia & China) and from brines (Chile, Argentina, and China), to countries with recently mapped resources and reserves such as the United States, Europe, Mexico, Canada, Bolivia, and Ukraine, to locations typically not associated with lithium such as United Kingdom, Peru, Siberia, and Thailand, exploration for traditional deposits of “white diamond pearl” is happening globally.

From the nontraditional brines deposits (geothermal, oilfield brines) will come additional brines with grades of 100 to 200 part per million (ppm). The first option focuses on providing both clean geothermal energy and lithium supply. Although nothing has been proven on a commercial scale as yet, there are already financially confirmed projects in Europe and North America sites. With technology development and proof of concepts, more geothermal lithium-brine operations will appear on the global map, with some automotive companies supports like General Motors, Renault, and among others.

2.1 Traditional Evaporation versus Brine Direct Lithium Extraction

Traditionally, lithium produced from brine water is stored in evaporation ponds. As the water evaporates, the other elements of the brine such as magnesium or calcium precipitate out, leaving the brine more concentrated to produce lithium carbonate. The evaporation process, however, yields only 40% to 60% of the potential lithium in the brine. DLE has the potential to yield 80% to 90% or more. It's also much faster. The evaporation process can take nine to 18 months depending on the type of project and weather conditions. With DLE, that process can be shortened to days or even hours. And you do not need all the land for the pond evaporation process. What is more, you can potentially reinject the remaining brine water after the process, which further reduces the environmental impact.

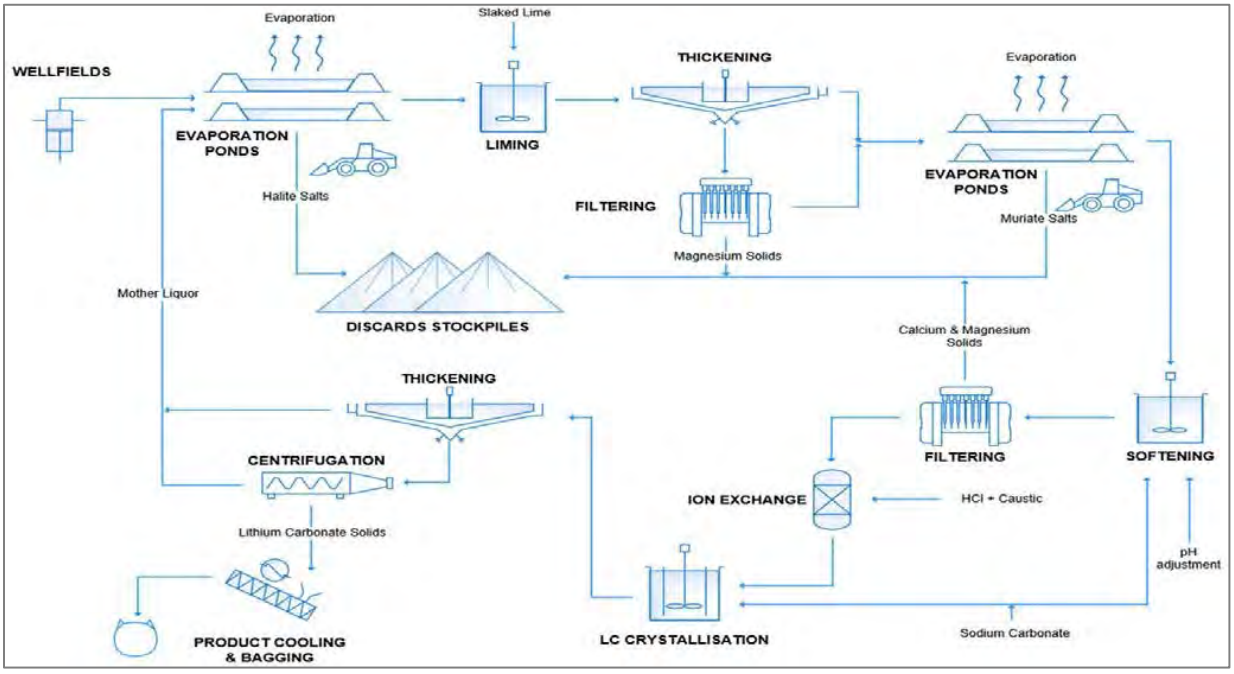

Figure 1: Traditional Brine Pond Flowchart [1]

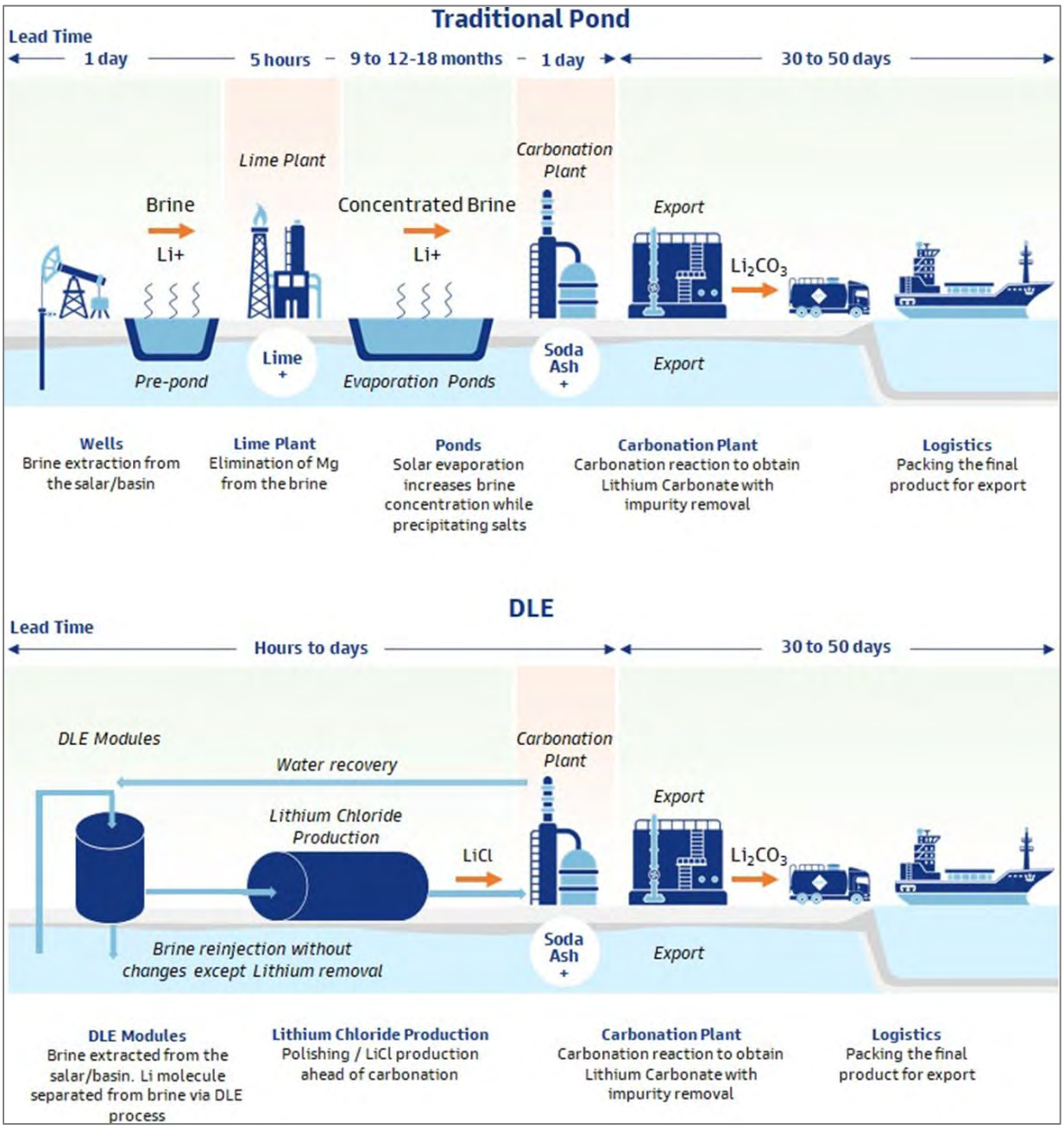

Figure 2: Traditional Process Brine Extraction vs DLE, and Timing of Each stage [1]

Indicative pond process flowsheet based on Sal de Vida flowsheet
Source: Company data, Goldman Sachs Global Investment Research

The following table above outlines 27 global lithium projects that are using or plan to implement DLE, along with a further nine advancing third-party technology developers.

Table 2: 27 Global Lithium Projects That Are Using or Plan To Implement DLE, Along With A Further Nine Advancing Third-Party Technology Developers [1]

Company	Project	Country	DLE Project stage	DLE technology provider	Lithium extraction technology	Tech Origin	Geothermal	Resource (Mt LCE)	Start date	Capacity (ktpa LCE)
Lithium project developers/operators										
Eramet/Tsingshan	**Centenario-Ratones**	Argentina	Construction	Proprietary	Sorption	-	-	10	2024	~24+50 (P1+P2)
Livent	**Fenix (Hombre Muerto)**	Argentina	Production	Proprietary	Sorption	USA	-	12	1998	~80 (3 expansions)
RIO	**Rincon**	Argentina	Pilot	Proprietary	Sorption	-	-	12	2024	30
Lake Resources	**Kachi Project**	Argentina	Pilot	Lilac Solutions	IX	USA	-	4	2024	25
Allkem	**Olaroz enhanced recoveries**	Argentina	Study	TBD (in testing phase)	TBD	TBD	-	-	-	-
Tibet Summit Resources	**Angeles**	Argentina	Construction	SunResin	Sorption	China	-	2	2024	25 (P1)
Eon Minerals	**Amanecer**	Argentina	Pilot	Proprietary	Sorption	Argentina	-	-	-	-
Albemarle	**Atacama**	Chile	Pilot	Proprietary LiET / Third party testing	TBD	TBD	-	11	2023	-
SQM	**Atacama**	Chile	Pilot	Proprietary / Third party testing	TBD	TBD	-	68	2024	220-250
CleanTech Lithium	**Laguna Verde**	Chile	Pilot	SunResin	Sorption	China	-	2	2026	20
CleanTech Lithium	**Fransisco Basin**	Chile	Pilot	TBD (in testing phase)	TBD	TBD	-	1	-	-
Lanke Lithium	**Yiliping Lake**	China	Production	SunResin	Sorption	China	-	-	2017	20
Zangge lithium	**Chalkhan Lake**	China	Production	SunResin	Sorption	China	-	-	2018	20
Jintai Lithium	**Mahai Lake**	China	Production	SunResin	Sorption	China	-	-	2019	7
Tibet National	**Qinghai**	China	Commissioning	SunResin	Sorption	China	-	-	-	-
Yiwei Lithium	**Qinghai Salt Lake**	China	Construction	SunResin	Sorption	China	-	-	-	-
Anson Resources	**Paradox Lithium**	USA	Pilot/DFS	SunResin	Sorption	China	-	-	-	-
Compass Minerals	**Great Salt Lake**	USA	Pilot	Energy Source Minerals (ILiAD)	Sorption	USA	-	2	2025	35
Berkshire Hathaway	**Salton Sea**	USA	Pilot	Proprietary	Sorption	USA	Yes	-	-	90
Energy Source Minerals	**Salton Sea (Project ATLIS)**	USA	Pilot	Proprietary (ILiAD)	Sorption	USA	Yes	-	2024	20
Controlled Thermal Resources	**Salton Sea**	USA	Pilot	Lilac Solutions	IX	USA	Yes	-	-	25
Controlled Thermal Resources	**Hell's Kitchen**	USA	Offsite Pilot	Lilac Solutions	IX	USA	Yes	3	2024	25
Standard Lithium	**Smackover (Lanxess Project)**	USA	Demonstration	Proprietary (LiSTR)	IX	USA	-	3	-	22
American Battery Materials	**Lisbon Lithium Project**	USA	Pilot	TBD (in testing phase)	TBD	USA	-	-	-	-
E3 Metals Corp	**Clearwater**	Canada	Pilot	Proprietary	IX	Canada	-	7	2025	20
LithiumBank	**Boardwalk**	Canada	Pre-PEA	Conductive Energy	IX	Canada	-	6	-	-
Vulcan Energy	**Upper Rhine Valley**	Germany	Pilot	Proprietary (VULSORB)	Sorption	Germany	Yes	16	2024	48
Technology developers										
Summit Nanotech	-	-	Pilot/Demo	Proprietary (denaLi)	Sorption	Canada	-	-	-	-
SunResin	-	-	Commercial (growing scale)	Proprietary	Sorption	China	-	-	-	-
International Battery Metals (IBAT)	-	-	Demo/Commercial	Proprietary	Sorption	USA	-	-	-	-
Koch Technology Solutions	-	-	Lab/Pilot	Proprietary (Li-Pro)	Sorption	USA	-	-	-	-
Lilac Solutions	-	-	Demo/Commercial	Proprietary	IX	USA	-	-	-	-
Conductive Energy	-	-	Pilot/Demo	Proprietary	IX	Canada	-	-	-	-
EnergyX	-	-	-	Proprietary (LiTAS)	Membrane	USA	-	-	-	-
Geo40	-	-	Lab	Proprietary (GeoSieve)	Membrane	NZ	Yes	-	-	-
Solvay	-	-	Pilot	Proprietary (CYANEX 936P)	SX	Belgium	-	-	-	-

For geothermal or oilfield brines to succeed as a source of lithium supply, a proven process for DLE will be required. There are a number of companies testing various DLE approaches. While their ideas differ, the concept remains the same: letting the brine flow through a lithium-bonding material using adsorption, ion-exchange, membrane-separation, or solvent-extraction processes (Figure 3), followed by a polishing solution to obtain lithium carbonate or lithium hydroxide (Figure 4).

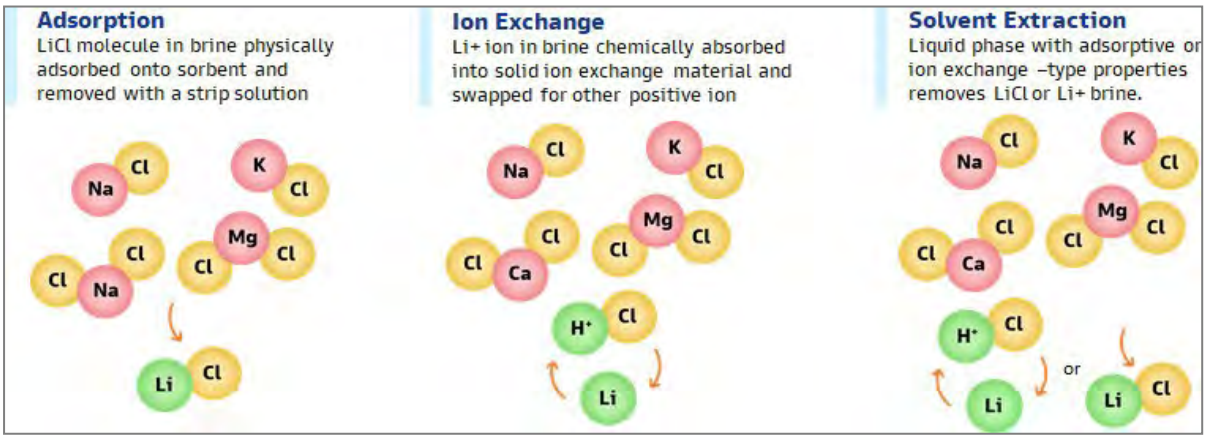

Figure 3: Details of the 3 Different Types of DLE Processes [1]

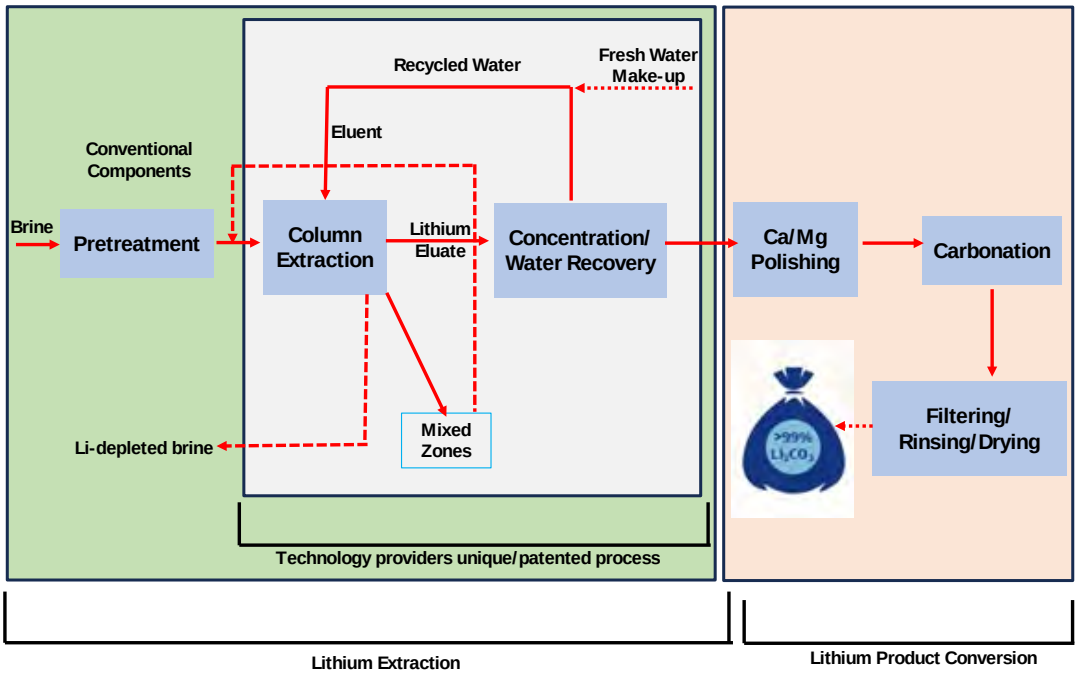

Figure 4: DLE Flow Chart [1]

Adsorption

Adsorption is the most developed DLE technology globally, using adsorbents to adhere to the lithium for selective removal. Some sorbents developed can recover >90% of the lithium present, including recently tested lithium aluminium layered double hydroxide chloride sorbent, or LDH (Lithium-Aluminium Double Hydroxide Chloride). During more recent testing, the LDH sorbent was made by intercalating (inserting) aluminium hydroxide with lithium chloride, which made several $[LiAl_2(OH)_6]$+layers in the sorbent. These layers were separated by water molecules and hydroxide ions that created spacing requirements to allow lithium chloride to enter more readily than other ions, such as sodium and potassium. After the sorbent was loaded with the lithium chloride, it was washed with a diluted lithium chloride stream to remove unwanted ions, then washed a second time to unload the lithium chloride.

The Pros of Adsorption: (i) does not require reagents or solvent extraction, instead water is used to recover lithium chloride with soda ash to convert to carbonate (ii) less impacted by brine composition, weather conditions, with lower waste generation (iii) lithium extraction efficiency of greater than 90% (iv) may combine processing steps such as electrodialysis (a form of ion exchange) and reverse osmosis to yield high recovery rates (v) produce high quality lithium chloride/carbonate.

The Cons of Adsorption: (i) requires temperature lower than 40^0 C (ii) lower eluate (extracting a substance process) LiCl concentration than ion exchange (iii) some implementation may difficult to prevent contamination with the brine (iv) the adsorption equipment can be expensive (high upfront cost).

Ion Exchange

Ion exchange systems separate ionic contaminants from solution through a physical-chemical process where undesirable ions are replaced by other ions of the same electrical charge. This reaction occurs in an IX (ion exchange) column or vessel where a process or waste stream is passed through a specialized resin that facilitates the exchange of ions.

The Pros of Ion Exchange: (i) simple process (ii) high selectivity for lithium and reduced risk of impurity contamination in the product stream (iii) high capacity and high concentration of lithium in the strip solution, can be suitable for low lithium concentration brines (iv) low energy/water consumption (v) continuous operation.

The Cons of Ion Exchange: (i) high upfront cost (ii) high opex due large amount of base and acid inputs (iii) some IX material may degrade in acidic conditions.

Solvent Extraction (SX)

Solvent extraction uses an organic solution containing solvent and extractant to extract lithium from brines. The organic solution comprises of kerosene (or similar material) and an extractant that very high selectivity toward lithium over sodium and magnesium.

The Pros of Solvent Extraction (SX): (i) high concentration of lithium can be produced from brine with high recovery rate, and not effected by weather conditions (ii) low opex costs (iii) lithium solvent extraction is essentially a stand-alone process.

The Cons of Solvent Extraction: (i) less applicable with higher impurity (ii) organic solvents are environmentally challenging (iii) fire risk with high temperature brines (iv) expensive relative to other technologies (v) the residual brine that remains after lithium extraction may require post-treatment to remove leached solvent.

The following figure shows the effectiveness and readiness of direct lithium extraction technologies.

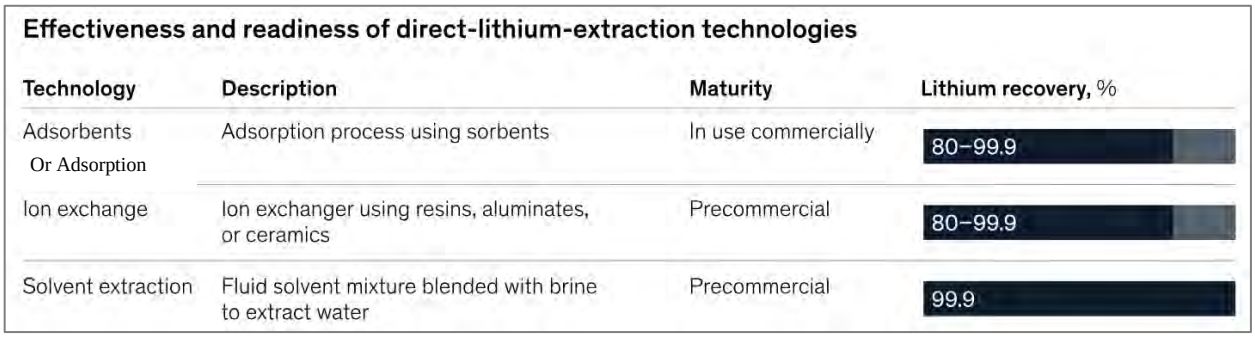

Figure 5: Effectiveness and Readiness of DLE Technologies [2]

Promising DLE technology is currently being considered not only by unconventional players but also by companies that traditionally develop “typical” brine assets. DLE has several potential benefits, including:

1. eliminating/reducing the footprint of evaporation ponds

2. decreasing production times compared with conventional brine operation
3. increasing recoveries from around 40 percent to over 80 percent
4. lower usage of fresh water, which can be one of the deciding factors when applying for a mining concession in a region with scarce water resources
5. lower reagents usage and increased product purity (in terms of magnesium, calcium, and boron) compared with conventional brine operations

To date only adsorption DLE has been used on a commercial scale, in Argentina and China. If DLE can be scaled up and spread across brine assets, it will boost existing capacities via increased recoveries and lower operating costs, while also improving the sustainability aspects of operations.

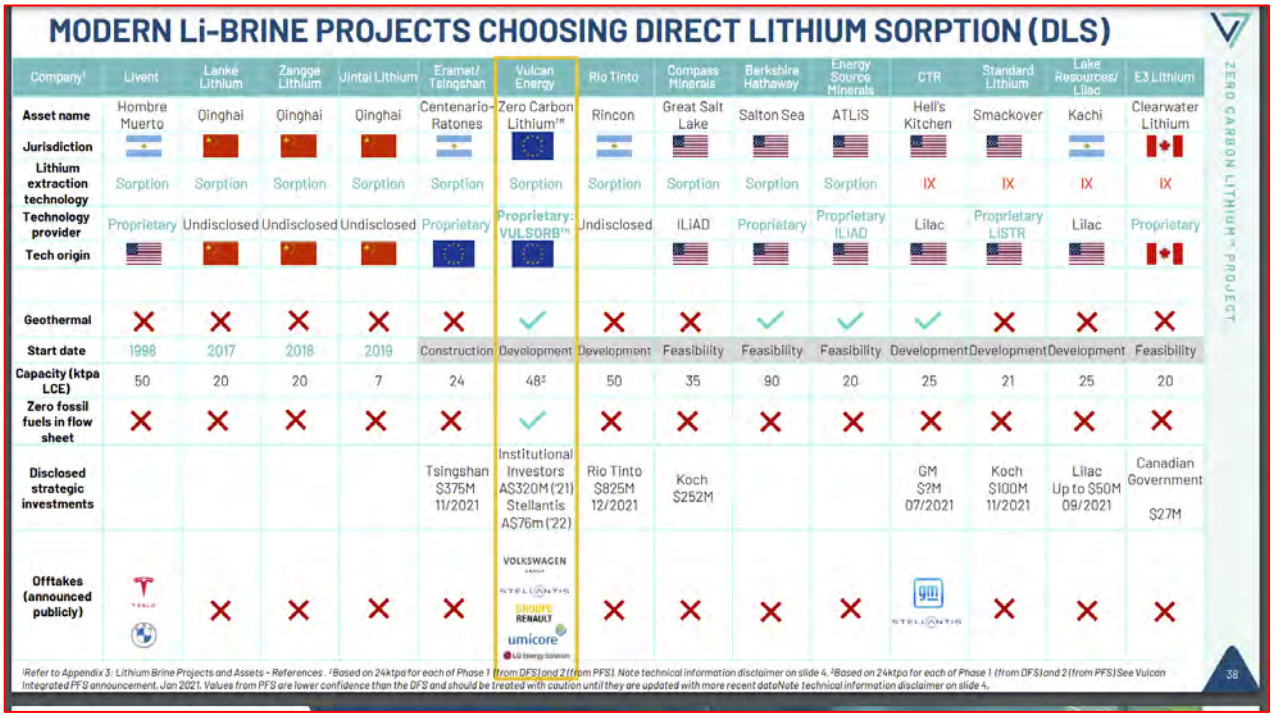

Company[1]	Livent	Lanke Lithium	Zangge Lithium	Jintai Lithium	Eramet/ Tsingshan	Vulcan Energy	Rio Tinto	Compass Minerals	Berkshire Hathaway	Energy Source Minerals	CTR	Standard Lithium	Lake Resources/ Lilac	E3 Lithium
Asset name	Hombre Muerto	Qinghai	Qinghai	Qinghai	Centenario-Ratones	Zero Carbon Lithium™	Rincon	Great Salt Lake	Salton Sea	ATLiS	Hell's Kitchen	Smackover	Kachi	Clearwater Lithium
Jurisdiction														
Lithium extraction technology	Sorption	Sorption	Sorption	Sorption	Sorption	Sorption	Sorption	Sorption	Sorption	Sorption	IX	IX	IX	IX
Technology provider	Proprietary	Undisclosed	Undisclosed	Undisclosed	Proprietary	Proprietary: VULSORB™	Undisclosed	ILiAD	Proprietary	Proprietary ILiAD	Lilac	Proprietary LiSTR	Lilac	Proprietary
Tech origin														
Geothermal	✗	✗	✗	✗	✗	✓	✗	✗	✓	✓	✓	✗	✗	✗
Start date	1998	2017	2018	2019	Construction	Development	Development	Feasibility	Feasibility	Feasibility	Development	Development	Development	Feasibility
Capacity (ktpa LCE)	50	20	20	7	24	48[2]	50	35	90	20	25	21	25	20
Zero fossil fuels in flow sheet	✗	✗	✗	✗	✗	✓	✗	✗	✗	✗	✗	✗	✗	✗
Disclosed strategic investments					Tsingshan $375M 11/2021	Institutional Investors A$320M ('21) Stellantis A$76m ('22)	Rio Tinto $825M 12/2021	Koch $252M			GM $?M 07/2021	Koch $100M 11/2021	Lilac Up to $50M 09/2021	Canadian Government $27M
Offtakes (announced publicly)		✗	✗	✗	✗		✗	✗	✗	✗		✗	✗	✗

[1]Refer to Appendix 3: Lithium Brine Projects and Assets - References. [2]Based on 24ktpa for each of Phase 1 (from DFS) and 2 (from PFS). Note technical information disclaimer on slide 4. [3]Based on 24ktpa for each of Phase 1 (from DFS) and 2 (from PFS) See Vulcan Integrated PFS announcement, Jan 2021. Values from PFS are lower confidence than the DFS and should be treated with caution until they are updated with more recent dataNote technical information disclaimer on slide 4.

Figure 6: Modern Li-Brine Projects Choosing Direct Lithium Sorption (DLS) [3]

DLE Adsorption is a commercial technology adapted to the local resource for the following reasons:

1. DLE using sorption has a fifty-year development and implementation history;
2. DLE Adsorption practiced commercially in South America for 26 years by Livent. More recently DLE Adsorption has been commercially deployed in China;
3. Large investment in DLE projects have recently been made in Argentina by Rio Tinto and Eramet;
4. DLE Adsorption includes several key advantages compared to traditional brine evaporation such as higher lithium recovery, lower water and chemicals consumption, shorter lead time to production, minimal footprint;
5. DLE Adsorption associated with geothermal brine adds the following no need to heat the brine with natural gas, potential for no carbon emissions, additional revenue stream from energy.

2.2 Early Review of Indonesia Geothermal Brine Lithium Extraction

The paper written by Suud et al [4] reviewed the lithium extraction from the geothermal brine by direct extraction methods using solvent extraction, adsorption and ion exchange, membrane, and electrodialysis. Multiple-stages solvent extraction from geothermal brine well in one of Indonesian Geothermal working areas performed by Suud et al demonstrated an extraction efficiency of 94% and indicated an opportunity to be further investigated for lithium extraction from one of the Indonesian geothermal brine.

3. Case Study To Implement Direct Lithium Extraction in Geothermal Brines

Lithium is an alkali metal that typically occurs in brine as LiCl. This LiCl solution is concentrated and purified through various processes and is then converted to high-purity Lithium Carbonate Li_2CO_3 and/or Lithium Hydroxide Monohydrate $LiOHH_2O$ commercial products. In the produced geothermal brines as shown in the following figure, consisted of the following chemical components such as Li, Fe, Si, Ca, Mg, and Na and may include additional components such as K, B, Al, Sr, Mn, Cu, Ba, Zn, Ni, Cr.

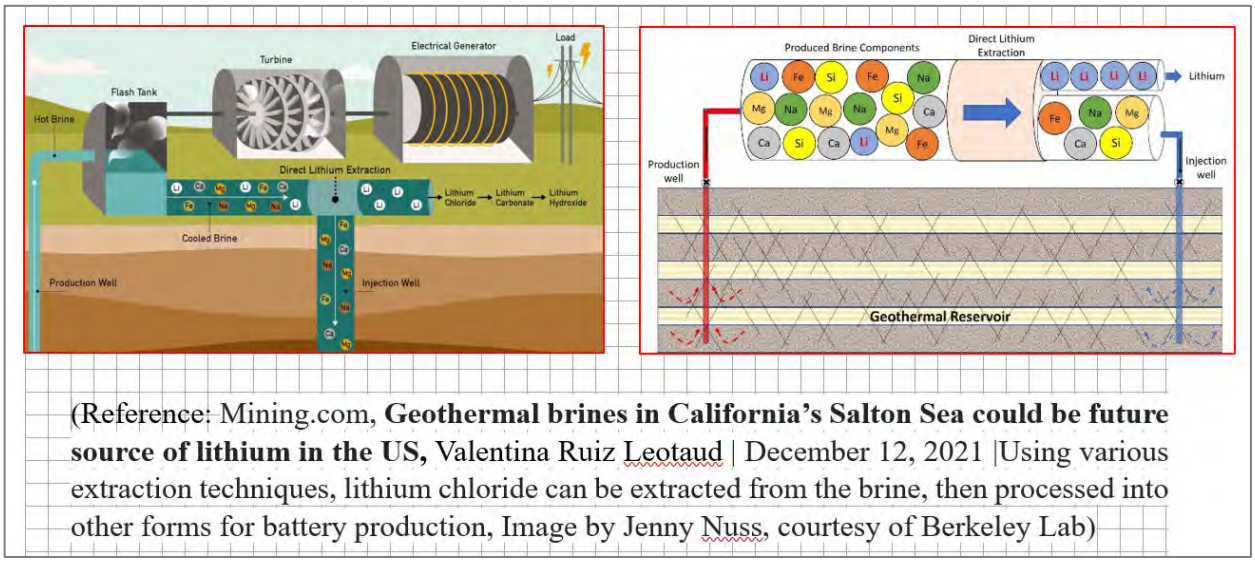

(Reference: Mining.com, **Geothermal brines in California's Salton Sea could be future source of lithium in the US,** Valentina Ruiz Leotaud | December 12, 2021 |Using various extraction techniques, lithium chloride can be extracted from the brine, then processed into other forms for battery production, Image by Jenny Nuss, courtesy of Berkeley Lab)

Figure 7: Geothermal Brines in California's Salton Sea [5]

To refresh our memory on these geothermal brine components the following Periodic Table is presented here to comprehend where those brine components located in the Table from US National Institute of Standards & Technology [https://www.nist.gov].

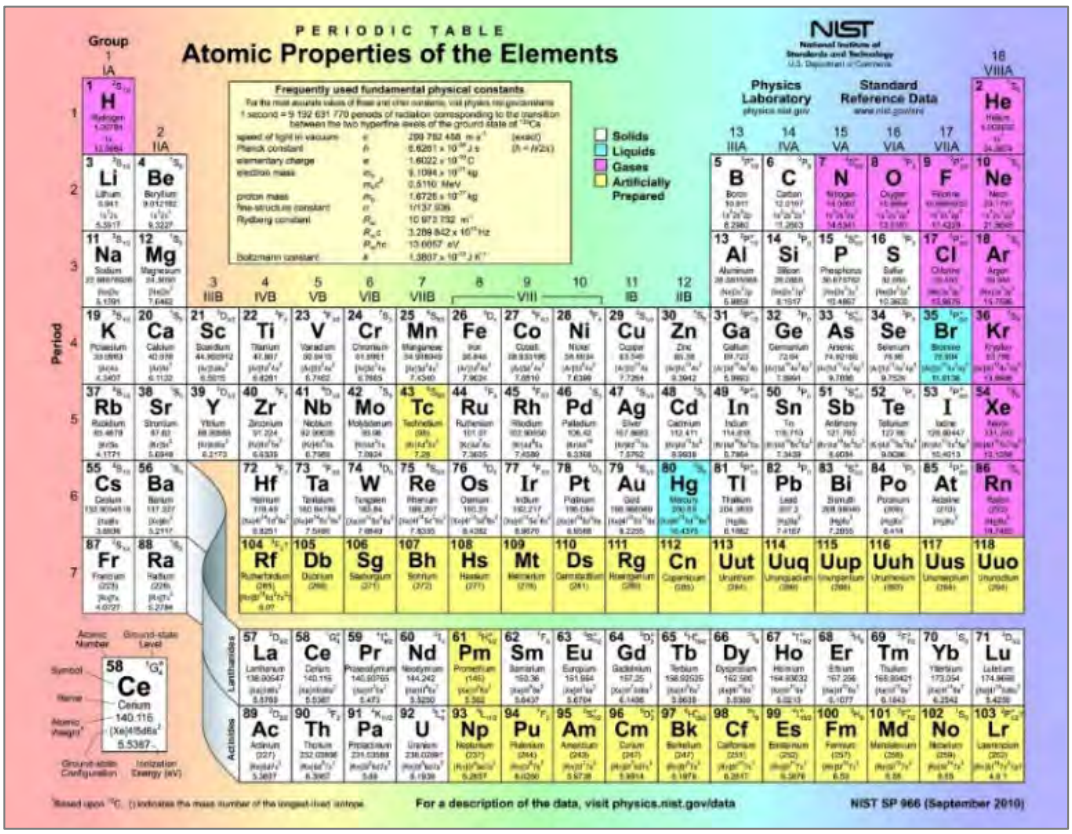

Figure 7A: Periodic Table [https://www.nist.gov]

The most well-investigated and technologically advanced method for direct lithium extraction from geothermal brines from the Salton Sea, with information available in the public domain, is **ILiAD (Integrated Lithium Adsorption Desorption)** [6]. The Iliad process includes pretreatment, lithium extraction, purification, and lithium product production steps. In the ILiAD process, removal of zinc and manganese precedes the lithium extraction process. Iron, silica, and manganese are removed and recovered in sequential steps before lithium extraction. Lithium is removed with AlOH or AlO_x sorbents using continuous bed process. According to the patent, the lithium chloride selective adsorbent may be a resin-based alumina imbibed adsorbent, a lithium alumina intercalate adsorbent, an alumina imbibed ion-exchange resin, or an alumina-based adsorbent. Iron and silica are removed by precipitation and zinc and manganese are removed by solvent extraction with Cyanex 272 or similar solvents using counter-current contactor. Post-extraction purification and processing include processes for removal of calcium and magnesium by ion exchange and further purification of the lithium chloride stream by precipitation and solvent stripping reactions. Lithium hydroxide is produced by electrolysis and lithium carbonate is produced by the addition of sodium carbonate and purified by cycles of crystallization and dissolution. The process is designed to be modular, with each process module sized for production of approximately 3,000 metric tons LCE (Lithium Carbonate Equivalent) per year, depending on brine lithium concentrations. Pilot trials demonstrated the ability to produce high-purity lithium products (>99.9% pure) at a 90% lithium recovery rate.

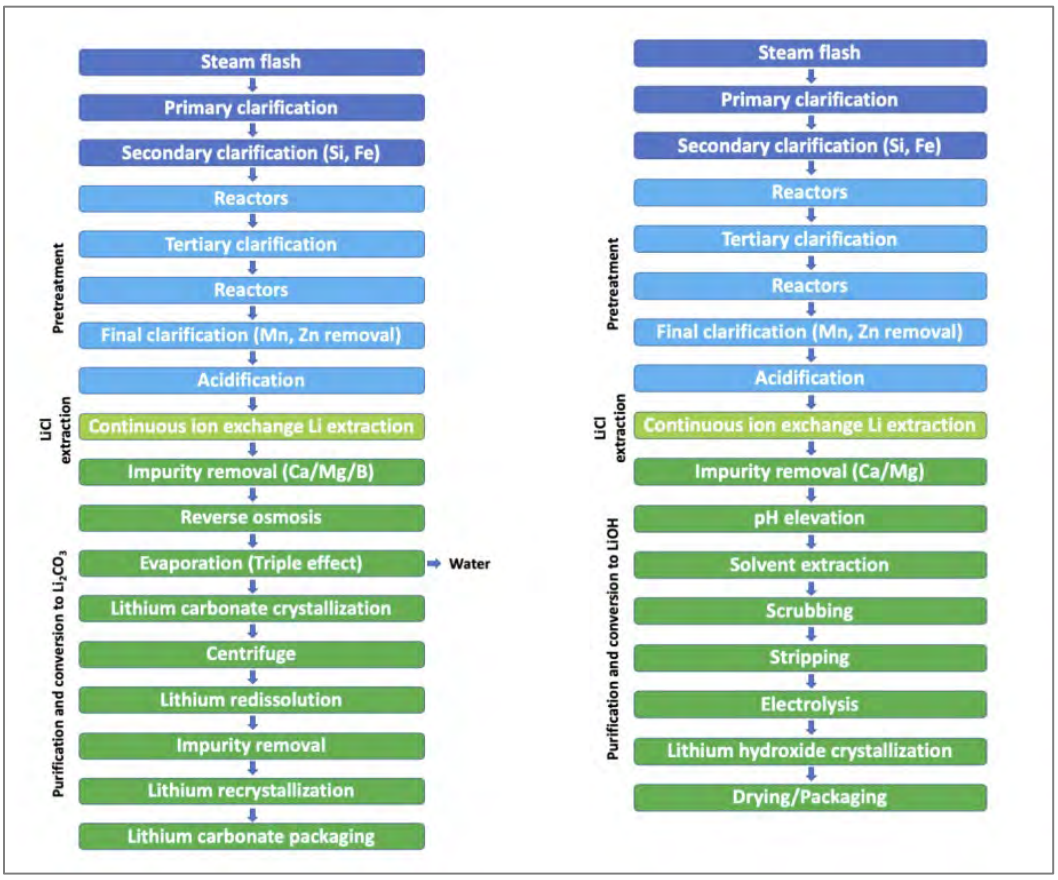

Figure 8: The ILiAD (Integrated Lithium Adsorption Desorption) Process [6]

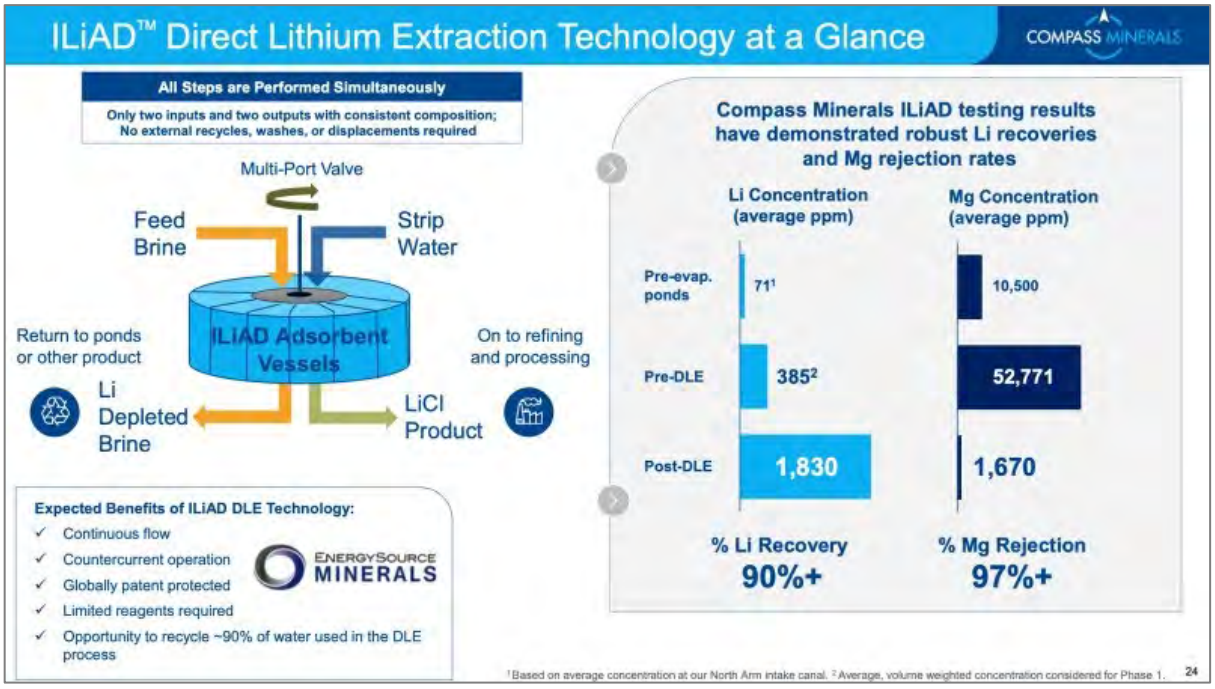

Figure 9: ILiAD Direct Lithium Extraction Technology at a Glance [7]

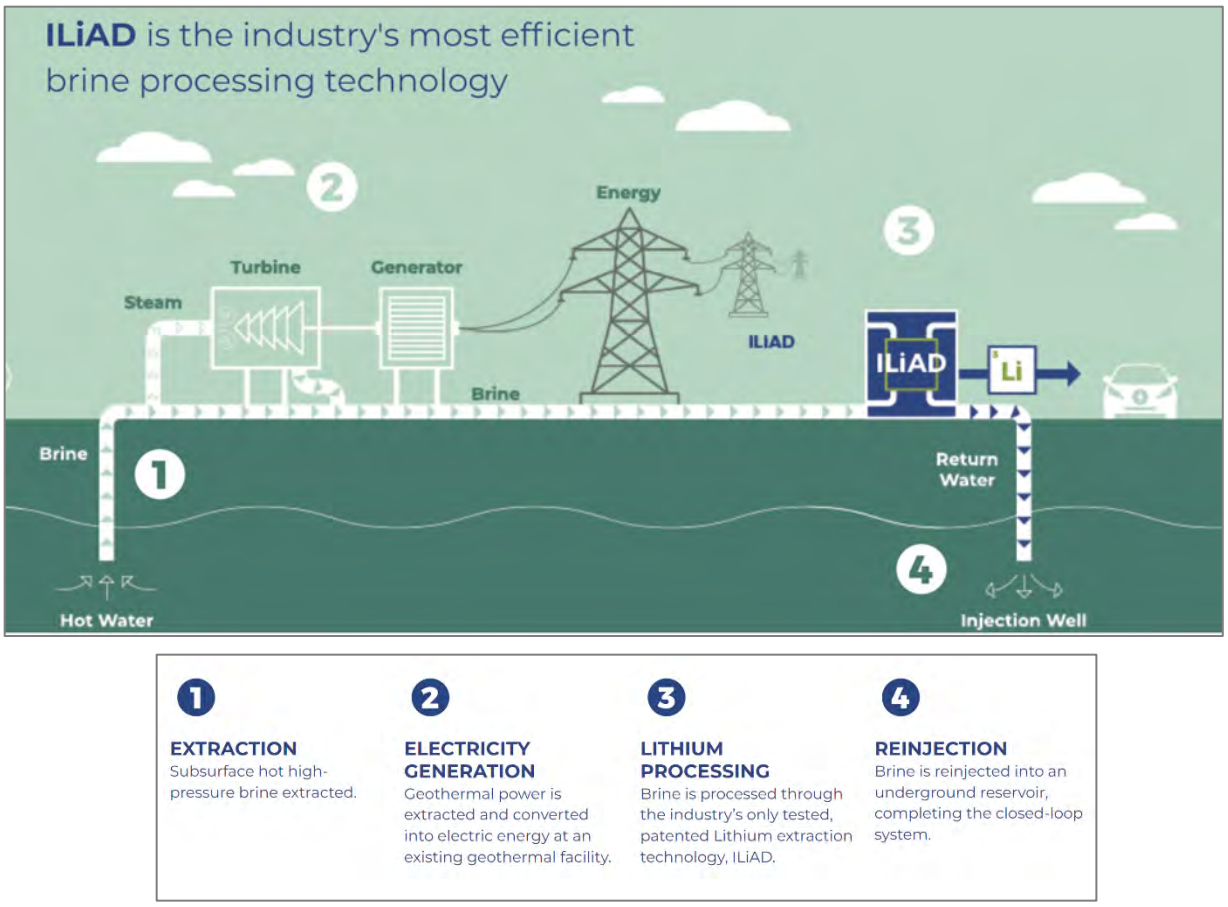

Figure 10: ILiAD Processing Technology [7]

4. Supply/Demand Implication of New Direct Lithium Extraction Supply From 2025+

The following table shows the global production lithium and in 2022 (Reference: 8) the total global production was 130,400 tonnes. The largest lithium producers are Australia, Chile, and China. The need for lithium has increased significantly due to the growing demand for electric vehicles. The demand forecast for lithium is expected to reach 1.5 million tonnes of lithium carbonate equivalent by 2025 and over 3 million tonnes by 2030 [9].

Table 3: Lithium Production and Reserves [8]

Lithium production and reserves
Thousand tonnes of Lithium content

													Reserves				
												Growth rate per annum		Share	at end of		
Thousand tonnes	2012	2013	2014	2015	2016	2017	2018	2019	2020	2021	**2022**	2022	2012–22	2022	2022	Share	R/P ratio
Argentina	2.7	2.5	3.2	3.6	5.8	5.7	6.4	6.3	5.9	6.0	**6.2**	3.9%	8.7%	4.8%	2700	11.7%	435
Australia	12.7	10.1	12.4	11.9	14.0	21.3	57.0	45.0	39.7	55.3	**61.0**	10.3%	17.0%	46.8%	6200	26.9%	102
Brazil	0.2	0.4	0.2	0.1	0.2	0.3	1.0	2.2	1.4	1.7	**2.2**	29.4%	30.8%	1.7%	250	1.1%	114
Chile	12.3	10.5	10.8	9.8	13.6	14.2	17.0	19.2	21.6	28.3	**39.0**	37.8%	12.2%	29.9%	9300	40.4%	238
China	4.5	4.7	2.3	2.0	2.3	6.8	7.1	10.8	13.3	14.0	**19.0**	35.7%	15.5%	14.6%	2000	8.7%	105
Portugal	0.3	0.3	0.3	0.3	0.4	0.8	1.2	0.9	0.3	0.9	**0.6**	-33.3%	6.8%	0.5%	60	0.3%	100
US	1.0	0.9	0.9	0.9	0.9	0.9	0.9	0.9	0.9	0.9	**0.9**	–	-0.6%	0.7%	1000	4.3%	1065
Zimbabwe	1.1	1.0	0.9	0.9	1.0	0.8	1.6	1.2	0.4	0.7	**0.8**	12.7%	-2.8%	0.6%	310	1.3%	388
Rest of World	–	–	^	–	^	0.1	3.0	0.4	0.1	0.1	**0.6**	420.8%	–	0.5%	1204	5.2%	1892
Total World	**34.7**	**30.4**	**31.0**	**29.5**	**38.2**	**50.9**	**95.1**	**86.9**	**83.7**	**107.9**	**130.4**	**20.8%**	**14.1%**	**100.0%**	**23024**	**100.0%**	**177**

Sources: includes data from US Geological Survey, British Geological Survey ©UKRI and World Mining Data.
^ less than 0.05.
Rest of World is the sum of only recorded reserves.

The new technologies for lithium extraction, such as DLE which extracts lithium from brine, has the potential to revolutionize the production, timing and environmental impact of lithium extraction. While there may still be challenges around scalability and water consumption/brine reinjection. With the ongoing efforts, there will be more brine supply if DLE could be implemented between 2024-2030 in USA and in Europe, and between 2025-2030 in both Chile and Argentina.

5. The Techno-Economic Analysis

Pre-Feasibility Study and/or Pilot Scale in the Technical Feasibility Study of Direct Lithium Extraction (DLE), with reasonable assumptions, can provide guidance for estimating costs of lithium extraction from geothermal brines. The following table summarizes report in National Renewable Energy Laboratory (NREL) US Department of Energy in May 2021 [10] on DLE Project Economics. The main focus of this present study was limited to understanding techniques and costs made publicly available by companies with projects advanced to stages of development and investment that require formal reporting to pertinent institutions. These projects were focused on geothermal, salar (brine from salt-flat or lakebed), oilfield, and evaporite brines, all of which were informative for estimating costs of lithium extraction from geothermal brines. Eventually, a specific geothermal fluid will require a best-lithium extraction processes, or combination of processes, based on fluid composition and physical and chemical requirements related to power generation and reservoir management. The estimated lithium production cost of $ 3,485/mt Lithium Carbonate Equivalent LCE using ion exchange technology.

Table 4: Summary of DLE Project Economics [10]

Company	SRI International	Vulcan Energy Resource	Standard Lithium	E3 Metals Corp	Anson Resources	Pure Energy Minerals	Lake Resources
Project	Salton Sea	Upper Rhine Valley	Lanxess Smackover	Clearwater	Paradox Stage 3 (Li)*	Clayton Valley	Kachi
Location	California, USA	SW Germany	Arkansas, USA	Alberta, Canada	Utah, USA	Nevada, USA	Argentina
Document	DOE, CEC reports	PFS	PEA	PEA	PEA	PEA	PFS
Brine type	Geothermal	Geothermal	Evaporite (Br tail brine)	Oilfield	Evaporite	Evaporite	Salar
Resource (1,000 kg LCE)	NA	15,850,000	3,140,000	2,200,000	192,000	217,700	1,010,000
Lithium concentration (mg/L)	400	181	168	74.6	100–500	65–221	289
Production (mt/yr)	20,000**	40,000	20,900	20,000	15,000	11,500	25,500
Production cost ($/mt)	3,845	3,217***	4,319	3,656****	4,545	3,217*****	4,178
CAPEX ($1,000)	52,300	1,287,600	437,162	602,000	120,000	358,601	544,000
OPEX ($1,000/yr)	76,900	128,688	90,259	73,200	68,180	36,516	106,539
Modeled product price ($/mt)	12,000	14,925	13,550	15,160	13,000	12,267	11,000
Pre-tax IRR (%)	268	31	41.8	32	106	24	25
Technology	Ion exchange	Adsorption	Ion exchange	Ion exchange	Ion exchange	Solvent extraction******	Ion exchange
Lithium recovery	90%	90%	90%	>90%	75%	90%	83.20%
Product	Li2CO3	LiOH·H2O	Li2CO3	LiOH·H2O	Li2CO3	LiOH·H2O	Li2CO3
Comments	Bench-scale testing and ASPEN modeling of hybrid sorbent with nanostructured manganese oxide embedded within Li-imprinted polymer beads using synthetic brine.	Known geothermal resource with measured chemistry and temperature. Bench-scale testing of two commercially available adsorbents using Upper Rhine Valley brine.	Bench- and mini-pilot-scale confirmation of process using ceramic adsorbent and crystallization process to convert concentrated LiCl into high-purity Li2CO3.	Bench-scale testing demonstrated high Li selectivity and recovery. Full process yet to be tested.	Multi-stage development with stage 3 producing 60,000 mt/yr NaBr and 15,000 mt/yr Li2CO3. Production cost reported as All-in Sustaining Cost.	Bench-scale testing of brine and synthetic equivalents informed the solvent extraction process developed by Tenova.	Nano-coated, porous ion exchange beads, tailored composition, and continuous column process.

*Estimated based on lithium component of operations; Phase 3 PEA retracted in June 2020 due to amounts of inferred resources. This does not affect estimates of CAPEX and OPEX.
**Estimated commercial production with costs and performance informed by bench-scale experiments and ASPEN modeling (Ventura et al. 2020).
***Euro to USD exchange rate 1.2; $3,656/mt Li2CO3.
****$4,155/mt Li2CO3

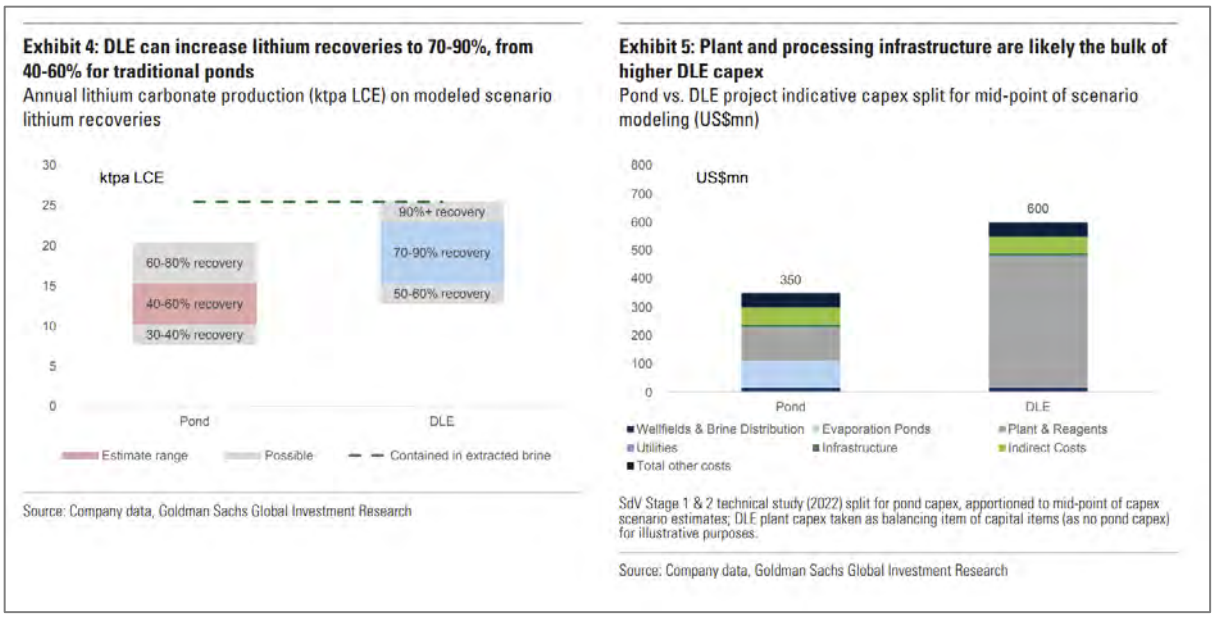

Figure 11: Scenario Economics & Real World Asset Benchmarking [1]

The scenario economics [1] assume a hypothetical brine resource is extracted at the same grade and volume at ~25ktpa contained LCE over a 20-yr production life to produce and sell the same quality of lithium carbonate product, both as a DLE (which ramps up 18 months faster vs. traditional ponds though with higher nominal Capex/Opex) and a traditional evaporation pond project.

The DLE project achieves recoveries of ~70-90% producing ~18-23ktpa LCE, while a traditional brine pond achieves recoveries of ~40-60% producing ~10-15ktpa LCE . The plant and processing infrastructure drive a higher upfront Capex for a DLE project, which more than offsets the lack of traditional pond infrastructure.

6. The Issue of Scaling When The Extracted Fluid Is Injected

The silica scaling can caused a significant cost to the geothermal producer and as such it reduces generation efficiency, and prevents further generation. By removing silica prior to lithium extraction process is beneficial, and in turn it will lower operating costs and generate more power from the same fluid. in the extraction process is beneficial before lithium extraction. Mroczek et.al [11] investigated the potential for extraction of lithium by electrodialysis from the brines at the Wairakei Geothermal Field in New Zealand. The necessitated removal of silica prior to extraction of lithium is beneficial for the extraction process; in particular, lower silica concentrations may decrease pre-treatment costs. Electrodialysis, like Nanofiltration (NF) and Reverse Osmosis (RO), are membrane processes that have been used as an end-to-end technology solution increasingly for the production of "pure" waters from fresh water and seawater. Membrane processes are also being applied in process and wastewater systems. The authors have not researched that far and there have not been any case studies from companies that have researched it to date. It is all still under research. And as such that is an issue that needs to be added to this paper for further research.

7. Lithium Extraction Method Suitable For Indonesia Geothermal Field

The extraction methods for mining geothermal brine for lithium has been recognized for decades, yet many methods and technologies, which are still being tested and have yet to break through commercially, can be inefficient or costly. So which method is suitable for geothermal brine sources in Indonesia? The variations between brine resources such as concentrations of lithium and any other elements or impurity ratios mean there is unlikely a one size fits all solution; however solutions may still offer some transferability of successful direct lithium extraction technologies between resources. There are still some concerns on type of end products (lithium carbonate or chloride), project finishing capacity, scalability, and brine reinjection not dilutive to the resource; in short the implementation of DLE technologies has the potential game changing technology to significantly increase the supply of lithium from brine projects.

One of the methods project and technology providers continue to pursue such as adsorption end-to-end process includes pretreatment, lithium extraction, purification, and lithium product production steps. Adsorption method may combine processing steps such as electrodialysis (a form of ion exchange) and reverse osmosis to yield high recovery rates. To date only adsorption DLE has been used on a commercial scale, in Argentina and China. If DLE can be scaled up and spread across brine assets, it will boost existing capacities via increased recoveries and lower operating costs, while also improving the sustainability aspects of operations.

DLE Adsorption is a commercial technology possibly could be adapted and suitable to Indonesia Geothermal Fields for the following reasons it has a fifty-year development and implementation history, practiced commercially in South America for 26 years and recently in China, higher lithium recovery, lower water and chemicals consumption, shorter lead time to production, minimal footprint, potential for no carbon emissions, and an additional revenue stream from unused brine resources for geothermal power producers.

Lithium extraction from geothermal brines requires complex technologies and systems. The question probably will be: How much does it cost to extract lithium from geothermal brine? Estimating the complicated cost of end-to-end process such as pretreatment, lithium extraction (may combine processing steps such as electrodialysis, a form of ion exchange and reverse osmosis to yield high recovery rates), purification, and lithium product production is difficult. So what are the main factors of lithium extraction system cost?

The main factors of geothermal extraction cost will depend at least on the following twelve (12) factors such as brine contaminants (to remove these impurities first and lithium second, other front-end contaminants such as silica, sulfate, iron, calcium, magnesium, hardness, and any suspended solids), lithium concentration (the less concentration in the liquid stream the more cost to concentrate it), flow rates (the higher the flow rate for lithium extraction and polishing the bigger equipment the more capital cost), up-front planning (concepts, designs, and regulatory requirements), space requirement (the footprint will affect cost), installation rates (installation rates in geothermal fields or consider prepackaged modules vs build-in-facilities), level of system automation needed (higher level of automation with less operators and less human errors or lesser automation with less capital cost), turnkey and prepackaged systems (save time in construction time with about the same cost or less), shipping the system to the plant (factor in freight cost where the system can be constructed near the field), operation cost (factor in system operating costs over

time), other possible costs and fees (hidden costs and fees might be), and treating costs of secondary waste produced by the system.

The bottom line is a complete pilot plant to simulate the real condition of geothermal field brines. A complete operating pilot plant installed may run for 1/10 to 2/10 of the lithium extraction facilities. The most important point is to keep the project commercial operation date punctuate with faster, cheaper, better and rapid speed of technology implementation.

8. Conclusion

Lithium is a big enabler of the energy transition from a battery perspective as we move to electric vehicles and add energy storage to electricity grids, allowing for greater penetration of renewables. That is why lithium is increasingly being seen as a critical mineral by governments, where they want to secure supplies for that transition, and that has made it an increasingly important commodity.

Traditionally, lithium produced from brine water is stored in evaporation ponds and the process can take nine to 18 months depending on the type of project and weather conditions. With Direct Lithium Extraction DLE, that process can be shortened to days or even hours. And you do not need all the land for the pond evaporation process. What is more, you can potentially reinject the remaining brine water after the process, which further reduces the environmental impact.

Various DLE technology consists of the following three (3) methods such as adsorption, ion-exchange, membrane-separation or solvent-extraction processes. The next step is a polishing solution to obtain lithium carbonate or lithium hydroxide. To date only adsorption DLE has been used on a commercial scale, in Argentina and China. DLE Adsorption is a commercial technology possibly could be adapted and suitable to Indonesia Geothermal Fields for the following reasons it has a fifty-year development and implementation history, practiced commercially in South America for 26 years and recently in China, higher lithium recovery, lower water and chemicals consumption, shorter lead time to production, minimal footprint, potential for no carbon emissions, and an additional revenue stream from unused brine resources for geothermal power producers.

How much does it cost to extract lithium from geothermal brine? Estimating the cost of end-to-end process lithium extraction from geothermal brine is difficult but manageable. The main factors of lithium extraction system cost will be depending of the following factors such as brine contaminants, lithium, flow rates, up-front planning, space requirement, installation rates, level of system automation needed, turnkey and prepackaged systems, shipping the system to the plant, operation cost, other possible costs and fees, and treating costs of secondary waste produced by the system.

The authors have not researched that far for the issue of scaling when the extracted fluid is injected.

An important issue that needs to be added to the paper for further research. The bottom line is a complete pilot plant to simulate the real condition of geothermal field brines. A complete operating pilot plant installed may run for 1/10 to 2/10 of the lithium extraction facilities. The most important point is to keep the project commercial operation date punctuate with faster, cheaper, better, and rapid speed of technology implementation.

REFERENCES

[1] Goldman Sachs, Equity Research, Global Metals & Mining, Direct Lithium Extraction: A Potential Game Changing Technology, April 27, 2023.

[2] McKinsey & Company, Lithium mining: How new production technologies could fuel the global EV revolution, April 22, 2022.

[3] Vulcan Energy, Zero Carbon Lithium, Phase One DFS Presentation 2023.

[4] Esty Mustika Suud *et al* 2023 *IOP Conf. Ser.: Earth Environ. Sci.* **1159** 012011, Lithium Extraction Method from Geothermal Brine to Find Suitable Method for Geothermal Fields in Indonesia: A Review.

[5] Geothermal brines in California's Salton Sea could be future source of lithium in the US, MINING.COM, December 12, 2021.

[6] William T. Stringfellow and Patrick F. Dobson, Technology for the Recovery of Lithium from Geothermal Brines, Energy Geoscience Division, Lawrence Berkeley National Laboratory, October 18, 2021.

[7] Energy Source Minerals Website: https://www.esminerals.com/

[8] Statistical Review of World Energy, 2023.

[9] World Economic Forum, This Chart shows which countries produce the most lithium, January 5, 2023.

[10] Ian Warren, National Renewable Energy Laboratory (NREL), Techno-Economic Analysis of Lithium Extraction from Geothermal Brines, May 2021.

[11] Ed Mroczek, Gaetano Dedual, Duncan Graham, and Lew Bacon, Lithium Extraction from Wairakei Geothermal Fluid using Electrodialysis, GNS Science, Wairakei Research Centre, Private Bag 2000, Taupo 3352, New Zealand, 19-25 April 2015.

Non-Technical

Advancing Understanding of Geothermal Representation in the Power Sector to Accelerate Deployment

Laura Chiaramonte[1], Whitney Trainor-Guitton[2], Anahi Molar Cruz[1], Diana Acero Allard[2], Nils A. Johnson[1], Jonathan Ho[2], Sean Porse[3], and Andrew Coleman[1]

[1]EPRI, [2]NREL, [3]DOE-GTO

Keywords

Resource planning, Power Generation, Capacity Expansion Models, Grid Decarbonization, Utilities

ABSTRACT

Driven mostly by decarbonization goals, geothermal interest in the US power sector has grown considerably, gradually evolving from being considered a niche technology, to being recognized as a viable source of clean, baseload, grid-balancing power, and renewable electric power generation. Furthermore, recent technical advances that could greatly accelerate deployment in the near future, and US federal incentives for low-carbon generation technologies, including geothermal, can enable opportunities for integrating geothermal into utilities resource planning portfolios.

However, in general, utilities do not have in-house expertise to evaluate geothermal technologies and its potential role in helping decarbonize the grid as well as help them achieve their individual decarbonization goals. To date, geothermal is rarely included in Capacity Expansion Models (CEM) which utilities use in their planning activities and resource/technologies prioritization.

To this end, EPRI and NREL are working together in a DOE-GTO funded research project to improve geothermal understanding (opportunities, value, risks) among the power industry to help accelerate geothermal deployment.

In the present paper we describe the approach and preliminary findings of this work, focused on two topics: 1) Expand the degree of understanding on the value, opportunity, and risk of geothermal technologies among utilities and related companies/groups, specifically around geothermal for power generation. 2) Improve representation of geothermal power technologies in capacity expansion models (CEM).

1. Introduction

Given recent studies (Blankenship et al., 2024) and advancements (Fercho et al, 2024), geothermal has become a viable, secure, and flexible clean resource to a much broader geographic area than

previously possible. Given state and utility decarbonization targets as well as federal incentives for low-carbon generation technologies, including geothermal, it is important that power utilities understand the value and risks of geothermal power and its potential role in helping to decarbonize the power sector.

However, utilities often lack in-house expertise to assess geothermal technologies and their potential impact on grid decarbonization. Furthermore, geothermal energy is seldom incorporated into most energy system models, including Capacity Expansion Models (CEM) that utilities employ for resource planning and prioritization.

To address this issue, and help with the overarching goal of accelerate geothermal deployment, EPRI and the National Renewable Laboratory (NREL) are working together in a one-year, Department of Energy (DOE)-Geothermal Technology Office (GTO) funded research project to engage with the power sector, to transferer knowledge (on the opportunities and value of geothermal technologies and how to evaluate and handle risks) as well as to increase geothermal representation in utilities resource planning process. Having a common understanding of how geothermal energy technologies are currently represented in CEM used by U.S. electric and gas utilities and how CEM results inform utility planning activities and priorities will enable opportunities for integrating geothermal energy technologies into a broad range of plant operation and investment decision planning.

2. Approach

The current one-year project is focus on two main topics:

1. Expand the degree of understanding on the value, opportunity, and risk of geothermal technologies among utilities and related companies/groups, specifically around geothermal for power generation, through a “Utilities Engagement Workshop” and the delineation of strategies and best practices for utilities to plan for geothermal build out. The target audience for the workshop are:

    a) utilities’ Resource Planning Groups, which are in charge of evaluating the full range of options (including new generating capacity) for their medium- to long-term planning based on financial, and other considerations, such as decarbonization goals;
    b) utilities’ Technology-Centered Groups, which perform more in-depth technical assessments of emerging or alternative technologies that can be integrated into their portfolio;
    c) other companies/groups that could benefit from geothermal power generation.

2. Implement improved representations of geothermal resources and technologies in EPRI’s capacity expansion model, the U.S. Regional Economy, Greenhouse Gas, and Energy (US-

REGEN), which EPRI[1] utilizes to undertake numerous power sector analysis for their utility members.

This second effort aims at generating guidance for realistic representation of geothermal resources and technologies in utility models since accurate geothermal representations are critical for economic comparisons and valuations. This will be achieved through a phased approach that includes:

a) Assess how/if geothermal is represented in other capacity expansion models used by the power industry in their regional utility planning processes.
b) Generate best practices and guidance for realistic representation of geothermal resources.

3. Utility Engagement

In the past two years, EPRI launched a Geothermal Interest Group (GIG), to engage utilities and other members that would be considering geothermal for replacing their fossil fuel power plants and diversifying their portfolio. In the context of this project, a virtual workshop has been organized to provide opportunities to exchange ideas, challenges and prospects between EPRI, GTO and NREL with participant utilities/companies (particularly those previously engaged in the GIG) to identify barriers and a path forward. The workshop will be centered on geothermal for power generation, which includes Hydrothermal, Enhanced Geothermal Systems (EGS) and Advanced Geothermal Systems (AGS).

The target audiences for this effort are two main groups within the EPRI membership that would have interest in geothermal power:

- Resource Planning Groups in charge of higher-level analysis with financial modeling focus, considering future portfolio including decarbonization goals.

- Technology-Centered Groups in charge of more technical assessments of emerging technologies and R&D efforts.

As part of the workshop planning a Survey was sent out to EPRI and GIG members to understand their knowledge and interest in geothermal technologies and with their input structure the workshop to their needs. The survey questions are presented in Table 1.

[1] EPRI is an independent non-profit energy research, development, and deployment organization, whose membership consist of hundreds of organizations around the world, including the energy sector, academia, and government. In particular in the US, it serves over 100 utilities.

Table 1: Survey Questions

Survey Questions to EPRI members
1. Name 2. Organization 3. Contact Email where you would like to receive updates regarding this workshop. 4. Of the following, what best describes your role in your company. *Business and Strategy, Technical and Operations* 5. Is your organization actively operating, considering or planning geothermal projects? *Yes, No* *Box: If you answered YES please specify, if you answered NO why did you select NO?* 6. What is the level of familiarity you have with geothermal technologies *a. Not at all familiar* *b. Slightly familiar* *c. Moderately familiar* *d. Very familiar* *e. Extremely familiar* 7. If applicable, which activity describes your largest commitment/investment in geothermal thus far *a. Participation in EPRI's Geothermal Interest Group (GIG)* *b. Funding of feasibility studies (internal or contracted)* *c. Partnering in projects* *d. Operating geothermal power plant* *e. Other (Please Specify)* 8. Do you use US-REGEN or other capacity expansion models (e.g. ReEDS)? *Yes, No, Other (Please Specify)* 9. Are you familiar with geothermal costs or resource data? *a. Do you use NREL's geothermal ATB (annual technical baseline) geothermal technology cost data: Yes/No* *b. Do you use proprietary geothermal technology cost data: Yes/No* *c. Other: [fill in]* 10. Are you aware of the incentives that exist for geothermal development? *Yes, No* 11. When evaluating technologies what value has the highest importance? Please select Highest, Medium, Lowest Importance for each of the options below. *a. Resilience* *b. Cost*

c. Capacity
d. Decarbonization
e. Incentives
f. Other: please comment

12. Would you or your organization be interested in participating in a workshop addressing geothermal power production integration in utilities portfolios? (to be held second half of August 2024)
Yes, No, Maybe

13. What would you like to see in this workshop. Your input will help better target the content to current needs.
Fill in

3.1 Survey Results

The survey was delivered to approximately 50 organizations (more than 170 individuals) of which 35 responses were received. A list of the engaged organizations is presented in Table 2.

Table 2: List of survey answering organizations

US-Canada Utilities/Companies	International Organizations
Calpine	CELEC EP
Con Edison	Empresa de Pesquisa Energética
Constellation Energy	Eneva
CPS Energy	Petrobras
CRC	
Fervo Energy	
Hawaiian Electric Company	
Manitoba Hydro	
National Grid	
New York Power Authority	
Southern Company	
SRP	
Tri-State Generation & Transmission Assn. Inc	
Vistra Corp	
Xcel Energy	

3.1.1 Summary of relevant survey information (Questions 4-13, see Table 1)

- 94% of survey participants stated their organizations are actively evaluating the long-term cost effectiveness of geothermal.
- 69% of survey participants stated their organizations are actively operating, considering or planning geothermal projects.

- The average level of familiarity with geothermal technologies of the survey participants is Moderately Familiar, 35%, while 26% are very familiar.
- Almost 80% of participants stated not using capacity expansion models in their planning process.
- Regarding geothermal cost or resource data, 19% indicated the use of NREL's geothermal ATB technology cost data and 26 % indicated the use of proprietary geothermal technology cost data.
- When asked about incentives awareness for geothermal development, participants split almost equally. 48% yes, 52% no. But when considering US only responses, 65% indicated awareness.
- The value that has the highest importance, for participants, when evaluating geothermal technologies is cost, following by decarbonization, resilience, capacity, and incentives. From all the attributes, incentives have a largest range between high to low importance.
- Some organizations (see Table 3) provided multiple responses and in some cases from different type of groups (Business and Strategy and Technical and Operations).

Table 3: Organizations with multiple responses and from different type of groups.

	CELEC EP	**Con Edison**	**Fervo Energy**	**Manitoba Hydro**	**National Grid**	**PETROBRAS**	**Xcel Energy**
Business and Strategy	1	1	2	1	0	0	2
Technical and Operations	2	2	0	2	2	6	0

3.1.2 Full Survey Responses:

The graphics below represent all the answers to the survey (except questions 1-3), including the individual comments that were required in some questions:

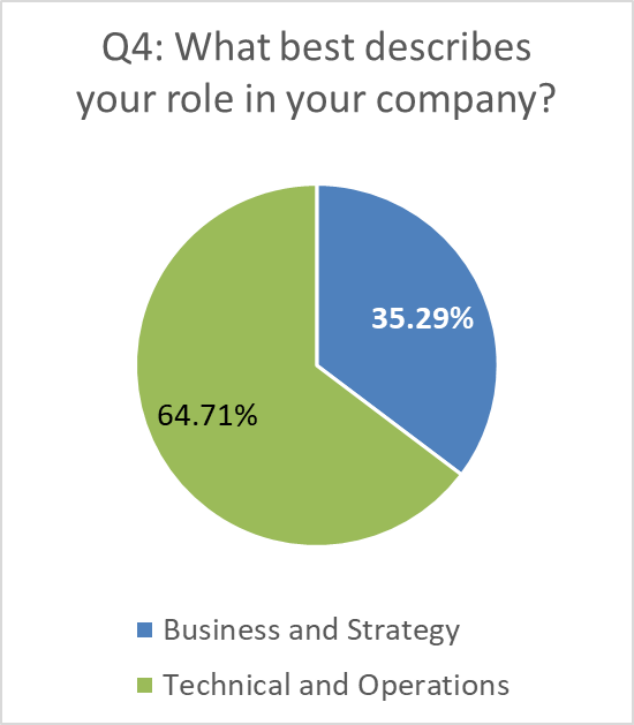

Figure 1.- Distribution of roles among survey participants.

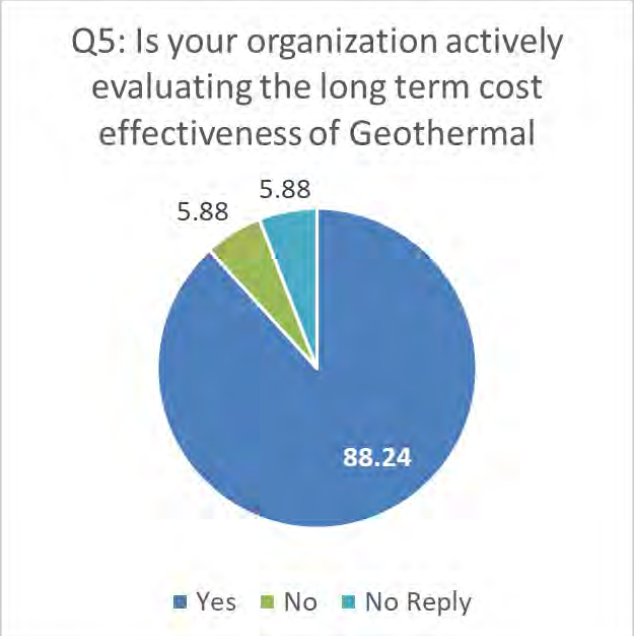

Figure 2.- The survey discussed in this paper was distributed to a diverse group of utilities and companies, primarily EPRI members. Over 88% of respondents indicated they are evaluating the long-term cost effectiveness of geothermal energy; those not considering geothermal were likely not to respond to the survey.

Figure 3.- The percentage of companies that are actively considering, planning, or operating geothermal projects. Additional details about these companies' activities were provided by respondents in some of the comments included in the text.

Participants were asked to provide additional information whether their organization was actively operating or considering planning geothermal projects. Below is the list of provided answers. Specific individual/company information has been removed and comments were grouped by themes:

Monitoring geothermal developments:

- We are a load service entity in CA and will comply with the California clean baseload energy generation requirements.
- We consider geothermal in our long-range planning but it is not economic.
- We aren't yet, but we hope to be
- […] I work for the [an international] government doing research to support energy policies development
- Considering funding feasibility studies

Actively study and/or planning geothermal projects:

- Our organization is in charge of the development of geothermal projects for electric generation. We have around 5 prospects in a study stage.
- Research project with NREL
- We are working on a geothermal plan, an also we are studying (feasibility) the first geothermal project in Ecuador.
- Every energy source and technology is considered in the long term energy planning process.
- We are planning projects across the WECC.

- Planning geothermal projects
- We have done resource studies, waiting for drilling costs to come down to be practical.
- Considering. We are in a phase of diagnosing the possibility of the business, particularly from a geologic evaluation.
- There are a few initial studies in progress about this theme
- We are evaluating the geothermal potential but geothermal projects are not yet part of our Strategic Plan.
- Due to the resource location(s), we do PPAs. We have 167 MW spread over 6 PPA projects.
- I am a venture investor in a closed loop geothermal company.
- As explained in question 7, we have PPAs, all of which were from bi-lateral deals. We do get developers that bid on geothermal projects that could be competitive project pricing, but the transmission wheeling or existing transmission constraint usually makes these projects uneconomical compared to other resources that bid into our RFPs.
- Development of pilot projects

Active developing geothermal projects:

- My company is actively involved with the operation of a geothermal field and looking into opportunities to grow
- Our organization is now in the field development phase with a geothermal project
- We are building a 400 MW next-generation geothermal project in southwest Utah

Thermal Energy Networks/ Direct use: Although the survey is focused on Electricity Generation, several participants highlighted their interest in heating uses.

- We are currently developing three utility thermal energy network pilot projects
- We are keeping an eye on geothermal technology. District heating is of particular interest. In my role, we are assessing how to incorporate district heating with geothermal into capacity expansion modelling.
- 4 Projects under the Utility Thermal Energy Networks and Jobs Act
- We are implementing pilot proposal demonstrations on geothermal based district heating.
- Geothermal heating projects in multiple outlying buildings at existing power plant facilities. No geothermal electrical generating projects at this time.
- Proposed three utility-owned thermal energy network projects in New York State

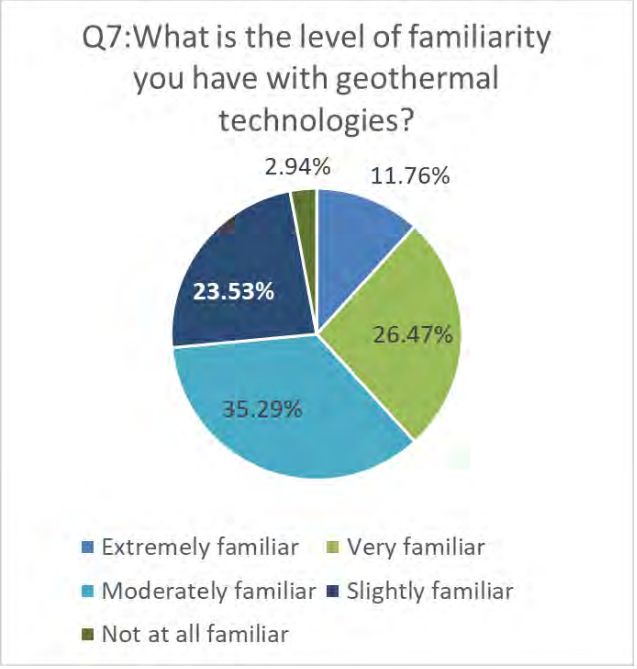

Figure 4.- Level of familiarity with geothermal energy among survey respondents.

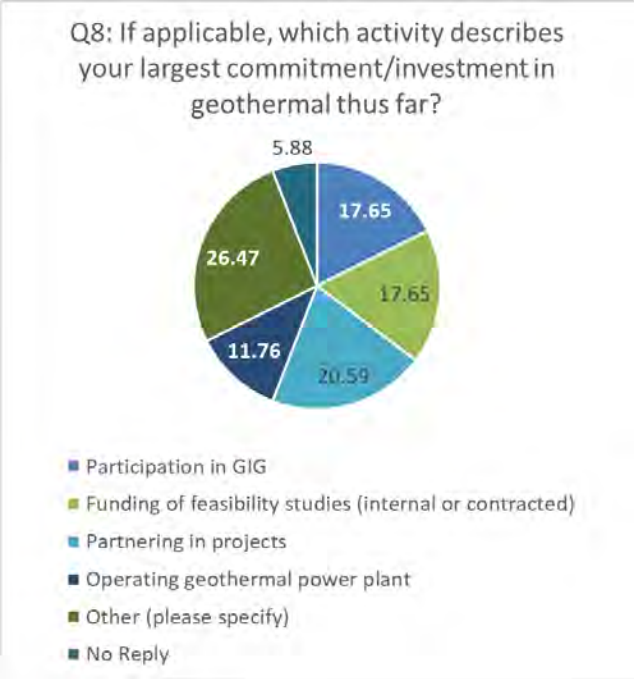

Figure 5.- The distribution of companies' commitment and investment in geothermal energy. Specifically, 17.65% are involved in EPRI's Geothermal Interest Group (GIG) without economic commitment, 17.65% have funded feasibility studies, 20.59% are partnering in projects, and 11.76% operate geothermal power plants. Additionally, 26.47% selected 'other' (with comments provided in the text below), and 11.76% did not respond.

In the case of selecting “Other” participants specified the following:

- Proposed three utility-owned thermal energy network projects in New York State
- I am a venture investor in a closed loop geothermal company.
- [,,,] I work for the [an international] government doing research to support energy policies development
- Participate in EPRI 178B (invite extended through that program) [*note: 178B program is EPRI’s Resource Planning for Electric Power Systems program]
- Development of pilot projects
- Exploration of potential areas.
- Internal evaluations of potential for geothermal
- As explained in question 7, we have PPAs, all of which were from bi-lateral deals. We do get developers that bid in geothermal projects that could be competitive project pricing, but the transmission wheeling or existing transmission constraint usually makes these projects uneconomical compared to other resources that bid into our RFPs.
- considering funding feasibility studies

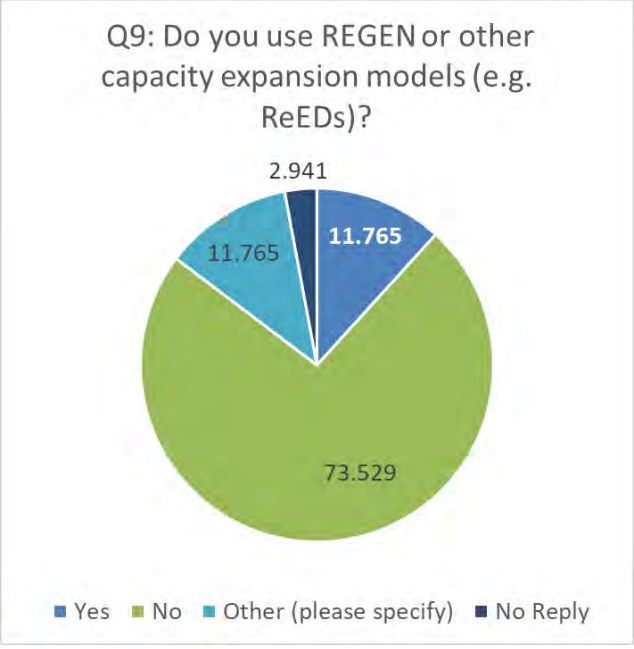

Figure 6.- The percentage of respondents that use and/or know about capacity expansion models (CEM) which is approximately 23.5 %. Of those, half indicated the use of REGEN or ReEDs while the rest mentioned other CEM as listed in the text below.

In the case of selecting “Other” participants specified the following:

- We know about REGEN through EPRI but our company uses PSR software SDDP, OptGen, and NCP.
- Aurora LTC
- Aurora
- Matriz/Encad, developed by Cepel (www.cepel.br)

Q10: Are you familiar with geothermal costs or resource data?

	Yes	No	No. of Responses
Do you use NREL's geothermal ATB (annual technical baseline) geothermal technology cost data?	6	26	32
Do you use proprietary geothermal technology cost data?	8	23	31
No Reply			2
Other			5

Other (please specify):

- It is done by someone else, in another area of my company.
- Still sourcing cost information
- I know the technical-feasibility tool from innerspace
- Not familiar
- Old TAGWeb cases and recent developer RFP pricing proposals.

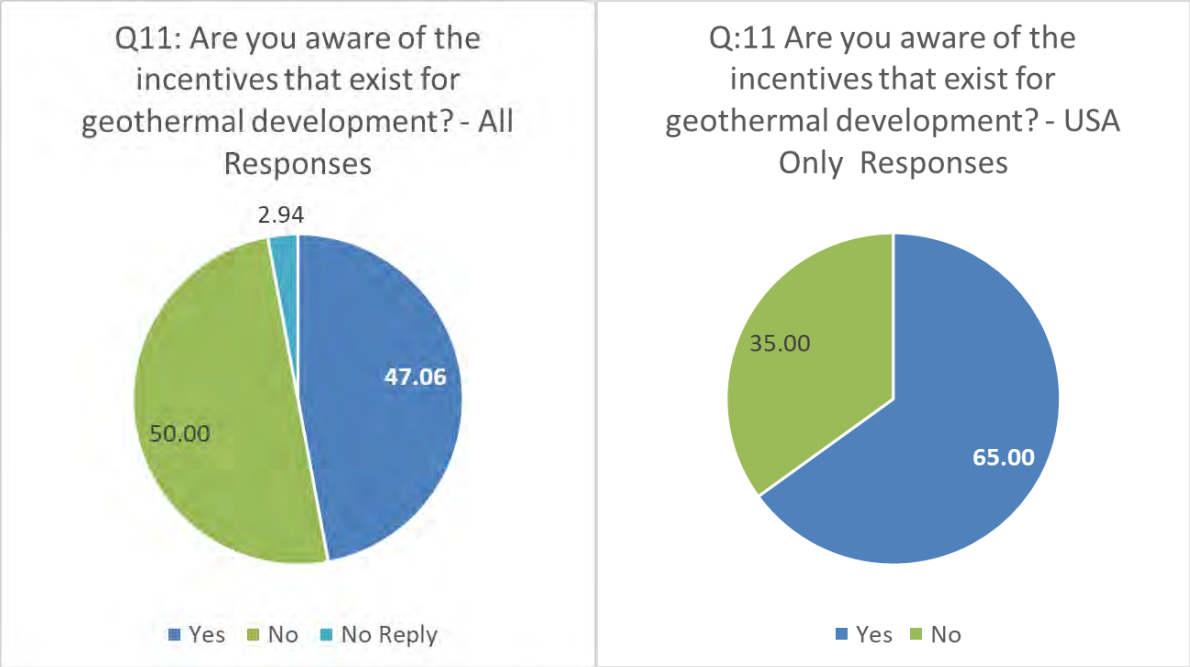

Figure 7.- Percentage of respondents that are aware of incentives for geothermal development. In the USA 65% of respondents indicated awareness.

Q12: When evaluating technologies what value has the highest importance?

	Highest Importance	Medium Importance	Lowest Importance
Resilience	17	15	1
Cost	25	8	0
Capacity	15	16	2
Decarbonization	17	14	1
Incentives	10	15	7

Figure 8.- Distribution of respondents' interest in participating on a workshop on geothermal power production integration in utilities portfolios. The input of the following questions (as described in the text below) was intended to help in the design of such workshop.

Q14: What would you like to see in this workshop. Your input will help better target the content to current needs.

- Utilities and ISOs
- Funds availability for geothermal studies.
- The overview of the entire project phases from scoping through funding approval and permit process thermal conductivity test and test drill safety and EH&S consideration,

drilling process, operation and maintenance, end of life ? Capacity limitation. What could go wrong .... maybe case studies

- My area is focused on networked geothermal systems, also referred to as neighborhood district geothermal. My group is not evaluating geothermal at the power production level.
- I would like to have an open discussion of the many forms of geothermal power coming into the market, including advanced closed loop geothermal, which the DOE's GTO often ignores in favor of enhanced geothermal.
- Technology development, actual costs, incentives.
- We would be interested in understanding opportunities for Geothermal energy in Texas and how to conduct technoeconomic research and analysis.
- Equipment manufacturers, resource assessment, regulations and policies
- Novel applications for geothermal heat
- Would love to see how hourly compliance requirements (for example, slice of day in California) affect planning decisions.
- Challenges in developing geothermal. Community outreach. study/survey potential geothermal site and evaluation of project development
- Technical performance and cost information for district geothermal to support incorporating into a capacity expansion planning model, as well as strategies for modelling.
- Capital costs, O&M, and reasonable cost declines especially with respect to drilling.
- Looking to see what is out there and how to optimize geothermal load balancing for networking purposes.
- Enabling and scaling geothermal based space heating/cooling. Optimization of technology.
- The use of geothermal heating in areas of the country with low potential for use geothermal energy.
- Performance of low-enthalpy geothermal systems.
- Repurposing abandoned oil/gas field to geothermal energy production.
- News about recent years developments in this subject, especially Abou next-generation technologies to enable geothermal exploration at places with medium and low enthalpy
- -The role of O&G industry on that -Possible applications in medium and low enthalpy areas like in Brasil - Estimates of the value of having an increase in Geothermal use in a country that already has an energy matrix with a high percentage of renewables (such as in Brazil) -Regulations (suggestions/examples on how to advance on that subject)
- I'd like to understand the state of the technology emphasizing the recent developments in: - advanced geothermal - geothermal resource assessment - geothermal system configurations and related costs (investment and LCOE) - Operational information: recommended modes of operation and related efficiencies; ramping capabilities; start-up/shut-down characteristics and constraints. - Environmental impacts
- How geothermal can be harnessed in regions with sub-optimal geothermal resources like the southeast USA
- I would like to see deeper dives into the drilling process, derisking of identifying location(s) to drill, specific deep dives into Fervo's technology and their project(s), identify how much potential additional geothermal there is in the Salton Sea region, and closer look into advanced future technologies that will eventually evolve and assimilate into standard designs.

- Ways to help our regulators allow for cost recovery to assess, explore, and build geothermal power plants.
- How to get through the plant development risk/cost portion of a project

4. US-REGEN

The second objective of this project is to develop guidance for improving the representation of geothermal resources and technologies in utility models. This will be achieved by enhancing the geothermal resources and technologies representation in EPRI's US-REGEN model, leveraging NREL's geothermal resource supply curves, technology costs, and modeling approaches from the Regional Energy Deployment System (ReEDS) capacity expansion model (Ho et al., 2021; Pinchuk et al., 2023). US-REGEN is the CEM which EPRI utilizes to undertake numerous power sector analysis for their utility members.

US-REGEN is an economy-wide model developed and maintained by EPRI, that combines a detailed dispatch and capacity expansion model of the United States electric sector with a technologically detailed consumer choice model of end-use service and energy demand as well as a fuel supply model representing alternative primary resources and conversion technologies for non-electric fuels. The three models are solved iteratively to convergence, allowing analyses of policy impacts on the electric sector taking into account electricity demand responses, and conversely allowing analysis of how end-use energy policies and technological improvements impact electric and non-electric demands and load shapes. US-REGEN considers 16 sub-regions of the continental U.S., to account for differences in resource endowments, energy demand, costs, policies, and policy impacts. EPRI has used US-REGEN to undertake numerous analyses for their utility members, including a wide range of environmental and energy policies in both the electric and non-electric sectors. A list of highlighted analyses using US-REGEN can be found at https://esca.epri.com/models.html.

US-REGEN electric sector model is an intertemporal capacity expansion model and can be run separately with higher regional and temporal resolution, or for a single year with hourly resolution and unit commitment constraints. The power generation technologies considered in the electric model are described in (EPRI, 2021: Electricity Generation section). The electric model can be extended to include additional sub-state detail for other states based on the boundaries of independent system operators (ISOs) and regional transmission operators (RTOs). By default, it solves in five-year time steps from 2015 through 2050, but can be configured to use other time-steps and base years. Full documentation of the US-REGEN model can be found in (EPRI, 2021).

Geothermal energy in US-REGEN (Version 2021A) includes only hydrothermal flash technology for power generation; EGS technologies are not considered. New additions of hydrothermal power capacity are constrained based on estimates of discovered and undiscovered conventional sites in the western regions by the U.S. Geological Survey (USGS) in 2008 with total new potential additions amounting to 39 GW (USGS, 2008) by 2050. US-REGEN also assumes an improving capacity factor for geothermal power over time as a result of technical progress, from roughly 50% today to roughly 80% by 2050 with capital costs for new geothermal capacity around $5000/kW today and slightly declining over time.

4.1 Improved representation of geothermal resources and technologies in capacity expansion models

The model structure and complexity determine the level of detail to represent primary resources and power generation technologies. However, general guidelines for the accurate representation of geothermal resources and technologies can be drawn from the enhancement of geothermal energy in EPRI's US-REGEN model, leveraging NREL's ReEDS model. These include:

- *Consistent definition of geothermal resources and technologies across models.* Having a consistent definition of geothermal resources and technologies across different models is crucial for ensuring comparability and coherence in data analysis and decision-making. NREL's definition of geothermal resources, used in this project, include:
    - Hydrothermal
    - EGS-NF (Enhanced Geothermal Systems near hydrothermal fields)
    - Deep EGS
- *Temperature-based representation of geothermal resources*. Geothermal resource quality is directly related to temperature. Adding temperature to geothermal resource classification aligns it with potential assessment structures of other renewables like wind and solar.
- *Disaggregation of supply curves by region, technology type and resource classes*. Breaking down of supply curves by region, technology, and resource class allows for localized insights. However, the model structure, complexity and computational time ultimately define the level of detail for geothermal technologies. For example, ReEDs currently represents 3 geothermal technologies (hydrothermal, EGS-NF and EGS), 10 temperature-based resource classes and 134 regions; the updated US-REGEN represents 3 geothermal technologies, 6 temperature-based resource classes and 48 regions (state-level).
- *Inclusion of range of technology costs and performance*. Modeling several cost scenarios provides a comprehensive economic outlook, helping stakeholders assess risks and opportunities for geothermal technologies more accurately. Based on NREL's ATB, conservative, moderate, and advanced cost scenarios can be included.
- *Integration of discovery rate*. Accounting for the discovery rate reflects potential future resource availability, making models dynamic and forward-looking. This factor ensures realistic projections of geothermal energy expansion, aiding in strategic and sustainable energy planning.

4.2 Next steps

The first phase in this project consisted in updating guidelines and geothermal representation in US-REGEN. A second phase is ongoing, where a series of scenario will be developed to better understand the role and system value of geothermal technologies, particularly in deeply decarbonized futures.

An outcome of this second phase aims at generating guidance for realistic representation of geothermal resources and technologies highlighting system conditions where geothermal becomes attractive and highlight data gaps to achieve a more realistic representation.

Summary

EPRI and NREL are working together in a DOE-GTO funded research project to improve geothermal understanding (opportunities, value, risks) among the power industry to help accelerate geothermal deployment. This one-year project focuses on engagement with national and international utilities/organizations to deepen their comprehension of the value, opportunities, and risks associated with geothermal technologies, particularly in the context of power generation. As well as to enhance the representation of geothermal power technologies within capacity expansion models (CEM) with the objective of facilitating better planning and decision-making in the energy sector.

By collecting input via a 13 question survey, key topics of interest from the surveyed utilities and energy companies were identified: Resource assessment, de-risking, technology innovations (drilling, completion, new technologies), cost, financial incentives, technoeconomic analysis, grid integration and planning, regulation, compliance and policies. This input helped designed the engagement workshop to take place on September 4th, 2024. The key objectives for the workshop include: knowledge transfer, Utilities' experience transfer, and identification of challenges, and opportunities for EPRI-NREL-GTO to help accelerate geothermal technologies in the power sector.

Furthermore, an updated geothermal representation has been implemented in EPRI's US-REGEN model in collaboration with NREL's ReEDS team and leveraging NREL's resource supply curves and technology costs inputs for geothermal power generation technologies. In the second phase of this project, a series of scenario are being developed to better understand the role and system value of geothermal technologies, particularly in deeply decarbonized futures, highlighting how model formulation and assumptions impact geothermal deployment projections in capacity expansion models.

Acknowledgement

This paper was prepared as an account of work sponsored by the U.S. Department of Energy (DOE) and the National Renewable Energy Laboratory (NREL) under Contract No. DE-AC36-08GO28308. Funding provided by the U.S. Department of Energy Office of Energy Efficiency and Renewable Energy Geothermal Technologies Office. The views expressed herein do not necessarily represent the views of the DOE or the U.S. Government. The U.S. Government retains and the publisher, by accepting the article for publication, acknowledges that the U.S. Government retains a nonexclusive, paid-up, irrevocable, worldwide license to publish or reproduce the published form of this work, or allow others to do so, for U.S. Government purposes.

REFERENCES

Blankenship, D., Gertler, C., Kamaludeen, M., O'Connor, M., Porse, S. (2024). Pathways to Commercial Liftoff: Next-Generation Geothermal Power. DOE Report. https://liftoff.energy.gov/wp-content/uploads/2024/03/LIFTOFF_DOE_NextGen_Geothermal_v14.pdf

EPRI. "US-REGEN Model Documentation" Palo Alto, CA: EPRI, 2021.

https://us-regen-docs.epri.com/v2021a/assumptions/electricity-generation.html

Fercho, S., Matson, G., McConville, E., Rhodes, G., Jordan, R., and Norbech, J. (2024). Geology, Temperature, Geophysics, Stress Orientations, and Natural Fracturing in the Milford Valley, UT Informed by the Drilling Results of the First Horizontal Wells at the Cape Modern Geothermal Project. In In Proceedings of the 49th Workshop on Geothermal Reservoir Engineering.

NREL Regional Energy Deployment System. https://www.nrel.gov/analysis/reeds/

USGS. "Assessment of Moderate- and High-Temperature Geothermal Resources of the United States." Menlo Park, CA: U.S. Geological Survey, 2008. https://pubs.usgs.gov/fs/2008/3082/pdf/fs2008-3082.pdf.

U.S. Regional Economy, Greenhouse Gas, and Energy (US-REGEN) https://esca.epri.com/models.html

Ho, J., Becker, J., Brown, M., Brown, P., Chernyakhovskiy, I., Cohen, S., & Cole, W. (2021). Regional Energy Deployment System (ReEDS) Model Documentation: Version 2020. . National Renewable Energy Lab.(NREL), Golden, CO (United States), 2021. (NREL/TP-6A20-78195). National Renewable Energy Lab.(NREL).

Pinchuk, P., Thomsen, S.-M., Trainor-Guitton, W., Buster, G., & Maclaurin, G. (2023). Development of a Geothermal Module in reV: Quantifying the Geothermal Potential while Accounting for the Geospatial Intersection of the Grid Infrastructure and Land Use Characteristics. Geothermal Resources Council Transactions, 47, 2564–2586. https://www.geothermal-library.org/index.php?mode=pubs&action=view&record=1034921

Navigating Geothermal Permitting under HEPA: The PGV Repower Project

Mike Kaleikini, Erica Freese, and Alissa Sanchez

Ormat Technologies Inc.

Keywords

Puna Geothermal Venture, environmental permitting, geothermal, Environmental Impact Statement (EIS), Hawaii Environmental Policy Act (HEPA), Hawai'i Public Utilities Commission (HPUC), State of Hawaii Department of Health (DOH), State of Hawaii Department of Land and Natural Resources, Office of Planning and Sustainable Development (OPSD)

ABSTRACT

The Puna Geothermal Venture Repower Project includes the commissioning of three new efficient generating units and the decommissioning of the old twelve generating units, allowing for an increase of generation up to 46 megawatts. The Repower Project required an environmental analysis and multiple environmental permits to be reviewed and approved by various agencies. The environmental review process began with the Hawaii Public Utilities Commission requiring the review as a condition of the approval of the Amended and Restated Power Purchase Agreement. With no permits to construct the project requiring discretionary review by an agency, the County of Hawaii Planning Department was designated as the authorizing agency. Ormat requested to have the project reviewed under an Environmental Impact Statement, thus maximizing the opportunity for the public to participate in the process. The EIS process took just over two years to complete, including two public involvement periods, with in-person meetings held in Puna. Other environmental permits needed for a successful Project include the Noncovered Source Permit from the State of Hawaii Department of Health (DOH), the Underground Injection Control Permit approvals from the U.S. Environmental Protection Agency and DOH, the Geothermal Resource Permit from the Planning Department, and the Plan of Operations for drilling with the State of Hawaii Department of Land and Natural Resources.

1. Introduction

Puna Geothermal Venture (PGV), a subsidiary of Ormat Technologies, Inc., has operated a geothermal facility on the Big Island of Hawai'i for over three decades. On March 16, 2022, the

Hawai'i Public Utilities Commission (HPUC) approved an Amended and Restated Power Purchase Agreement (ARPPA) between PGV and Hawaiian Electric to provide an additional eight megawatts (MW) of geothermal energy with the PGV Repower Project (Repower Project). The ARPPA would allow for an increase of up to 46 MW. The Project includes the commissioning of new efficient generating units and the decommissioning of the old generating units, allowing for an increase in generation (Figure 1).

Figure 1. Project location and proposed facilities.

As part of the approval of the ARPPA, the HPUC required an environmental review under the Hawaii Environmental Policy Act (HEPA) (Chapter 343, Hawaii Revised Statues, and Title 11, Chapter 200.1, Hawaii Administrative Rules) to be completed before the commencement of construction for the Project. The HPUC, the Department of Land and Natural Resources and the Department of Health Clean Air Branch all declined to be the authorizing agency for the environmental review; therefore, a request was made to the Office of Planning and Sustainable Development (OPSD) to determine the approving agency. OPSD determined that the County of Hawaii Planning Department be designated as the accepting authority for the environmental review because they are responsible for supervising the project through compliance with county

permits that govern the Project. At Ormat's request and after much discussion with agency staff, PGV, and the county, it was determined that an Environmental Impact Statement (EIS) would be the appropriate level of environmental review and would provide the most opportunity for public input.

The PGV facility requires authorization from several federal, state, and county governments to operate. There are six main permits for development. At the county level, construction authorizations for grading and building are required from the Department of Public Works. To comply with the Hawaii ambient air quality standards, amendments to the Noncovered Source Permit (NSP) from the State of Hawaii Department of Health (DOH) must be submitted. The Geothermal Resource Permit (GRP) from the Hawaii County Planning Department is the primary permit, focusing on local land use requirements. In addition, a Plan of Operations (POO) for geothermal well drilling with the State of Hawaii, Department of Land and Natural Resources (DLNR) is also required. Wellfield operations include permits authorized under the Underground Injection Control (UIC) Permit from the U.S. Environmental Protection Agency (EPA) and DOH.

2. Environmental Impact Statement

The EIS analyzed the potential impacts of the Repower Project, which included the replacement of the existing 12 operating power-generating units with four, much more efficient power-generating units. The Repower Project would increase renewable energy production at the existing facility (within the current site fence line) using new, more efficient Ormat Energy Convertor (OEC) units on a co-located smaller land footprint compared to the existing units. The Repower Project would increase power production from 38 to 46 MW in Phase 1, and may further increase production to 60 MW in Phase 2. The overall property size would remain the same, and most of the existing infrastructure and buildings would remain, including administration buildings, the control room, maintenance areas, well pads, and the gathering system. The new OEC units would continue safely supplying reliable power from renewable geothermal resources with more efficient and quieter equipment.

In coordination with the County, Ormat contracted Stantec Consulting Services Inc. (Stantec) to be the third-party consultant preparing the EIS. During the entire EIS process, PGV made all documents available on the project's website (https://punageothermalproject.com/eis/) to keep the public informed of upcoming meetings and the status of the EIS.

The Project's EIS Prep Notice (EISPN) was published on July 23, 2022, which began a 30-day public scoping period. The EIS analyzed the ARPPA-approved Repower Project, which increased power production up to 46 MW (Phase 1). The EIS also analyzed a potential increase from 46 to 60 MW (Phase 2). During the scoping period, the public could submit written comments anytime. As a Hawaii Environmental Review Program requirement, PGV hosted a community meeting during the scoping period. The community meeting was held on August 17, 2022, at the Pahoa Neighborhood Center in Pahoa, HI, with a link for virtual attendance. A one-hour informational open house was held during this meeting, followed by a two-hour period for oral comments. During the scoping period, 29 comments (written or oral) were received regarding the Repower Project.

Once the scoping period was over, Stantec began preparing the Draft EIS document. The public scoping comments were reviewed, with substantial comments received during the scoping period

being addressed in the Draft EIS. The Draft EIS analyzed potential impacts to the following resources: geology, hydrology, air quality and climate change, noise, biological resources, socioeconomics and environmental justice, historic resources, cultural practices, aesthetics, hazardous materials and solid waste, public health and safety, transportation and access, and cumulative effects. The Draft EIS was published on May 8, 2023, beginning a 45-day public comment period. While not required by statute, PGV hosted an open house and public comment meeting on June 1, 2023, where information on the Draft EIS was presented, and the public could provide written and oral comments. The meeting was again held at the Pahoa Neighborhood Facility Center in Pahoa, HI. During the public comment period, 90 comments (written or oral) were received, with more than 1000 individual comments. Comments mainly related to the following issues (not an all-inclusive list): existing operations, hydrology, air quality, cultural impacts, hazardous materials and waste, noise, emergency response, and geologic hazards.

During the preparation of the Final EIS, each comment received during the public comment period was reviewed and responded to, and any necessary changes were made to the final document. The Planning Department accepted the Final EIS on January 22, 2024 and the document was submitted to the HPUC on February 8, 2024; finalizing a two year process from start to finish of the EIS.

3. Operational Permits

Ormat has operated PGV for over 20 years and is committed to providing safe, reliable renewable energy to the grid by operating safely and sustainably. This includes protecting our employees, our environment, and our neighboring communities. PGV recognizes the need to maintain and comply with environmental regulations, and from its inception, the facility has maintained the appropriate environmental permit approvals for operation.

The following section details the types of permits and lead agencies required for the operation of a geothermal facility in Hawai'i. With the completion of the EIS, the timeframe to construct the Repower Project was established by the HPUC at 36 months. This timeframe includes completing the required operational permits and updates. The environmental permits necessary for the operation of PGV are managed at the federal, state, and county levels. Several types of permits are currently needed for operation from these agencies. The Repower Project will require an update to the County GRP, the DLNR POO, and the State and Federal UIC permits. Additionally, an amended permit will be sought for air quality under the NSP program. For construction of the Repower Project, grading, grubbing, and building permits will be acquired from the County Department of Public Works.

3.1 Geothermal Resource Permit

The GRP is managed by the County of Hawai'i Planning Department, with permit approval authority with the East Hawaii Planning Commission. This permit focuses on local land use requirements maintaining home rule. The current GRP allows PGV to increase the power output up to 60 MW, and thus the reason for Phase 2 being analyzed in the EIS. The GRP was initially approved in 1989 and was amended in 2001. Informational updates have been provided to the Planning Department, coincident with changes to PGV's operation.

3.2 Plan of Operation

PGV operates a geothermal wellfield comprised of production and injection wells, which is regulated by DLNR. The POO is PGV's living document that oversees geothermal well development and allows drilling of up to 30 wells and electrical generation up to 60 MW. The geothermal well program is an iterative process that is fit-for-purpose based on geology, resource constraints, land holdings, and regulatory requirements. The Repower Project's new electrical generation units will use geothermal fluid from existing geothermal wells. New wells that are eventually designated as injection wells are also regulated by the DOH and EPA.

3.3 Underground Injection Control

The UIC program at PGV is regulated by both the EPA and DOH. Both agencies have their respective UIC permits for the PGV facility. Well operations are continuous and include testing for integrity and reservoir monitoring programs. The UIC permits include injection pressure limits that are based on formation testing to reduce the potential for the creation of fractures and well construction requirements so that injected fluids do not intersect potential underground sources of drinking water. Continuous monitoring and systematic testing requirements are in place for each injection well, including mechanical integrity tests. Groundwater is monitored to ensure no impacts to groundwater quality occurs from the geothermal operations. The DOH UIC permit is renewed every five years, and the EPA UIC permit is renewed every ten years.

3.4 Noncovered Source Permit

The State of Hawai'i Clean Air Branch manages air quality regulations for PGV by issuance of the NSP for the operation of the wells and geothermal facility. The NSP allows PGV to generate up to 41 MW. The NSP will be amended to add the Repower Project's new electrical generation units and additional MW.

Fugitive hydrogen sulfide emissions at PGV are controlled by capture and treatment with a series of two reactors for chemical abatement. The combustion emissions for current and future drilling are covered in the PGV's existing NSP. No greenhouse gases are emitted from PGV operations. The State NSP is renewed every five years.

4. Conclusion

The PGV facility and the Repower Project demonstrate how environmental conservation and technological advancement can coexist successfully. Currently, all the necessary environmental and government permits to operate the PGV facility are active without any interruptions, ensuring the continuous production of 38 MW of renewable power.

However, as PGV progresses toward the 46 MW Repower Project, and as the State of Hawaii's 2045 mandate to be at 100% renewable energy looms near, everyone is facing complex regulatory challenges involving local, state, and federal authorities. For example, the HPUC's requirement for environmental review of the proposed 46 MW Repower Project, BEFORE any construction could commence, added an unprecedented layer of complexity that is unique in its nature. The Repower Project ARPPA was negotiated and approved between Ormat and Hawaii Electric Light Company (HELCO) in 2019. On December 31, 2019, HELCO submitted the ARPPA to the HPUC for review and approval. The HPUC opened a docket, which followed the PUC procedural

schedule for information requests and responses by all parties from January 2020 through March 2021. On March 31, 2021 the HPUC suspended the docket, pending the completion of an environmental review. The suspension by the HPUC was ordered, AFTER the DOH and DLNR both informed the HPUC that an environmental review was not required. With the docket for the Repower Project in limbo, PGV reached out to the Office of Planning and Sustainable Development for guidance. The result was that PGV was able to designate Hawaii County to be the Accepting Authority for the environmental review. The County's position was that an environmental review was not required, but, to assist with completing the HPUC review and approval of the ARPPA, the County accepted the designation. The EIS took two years to complete, and PGV submitted the Final EIS on December 27, 2023. On February 8, 2024, HELCO filed a copyof the EIS with the HPUC. This filing concluded the conditional approval of the ARPPA, and now allows construction to begin on the Repower Project. For a State in high demand for renewable energy, this process took over four years to get an approval from the HPUC for an additional eight MWs.

PGV's Repower Project is not just about expansion—it symbolizes a commitment. A commitment to responsibly harness geothermal energy, provide reliable and sustainable power, and honor the people and traditions of Hawai'i. By aligning our operations with the regulatory expectations from county, state, and federal agencies, PGV is positioned to enhance its capacity while preserving the delicate balance between progress and conservation.

Creating a Universal Pitch for Geothermal: A Declaration of Communication

Kristina Hagström Ilievska

Baseload Capital

Keywords

Geothermal energy, geothermal industry, geothermal associations, geothermal communications, geothermal messaging

ABSTRACT

Geothermal energy is both a renewable reality and the source of tremendous untapped potential. The energy resource offers an off-ramp for the oil and gas workforce to transition into the clean energy economy and is an essential solution to draw down the climate crisis. Its benefits are clear: stable, baseload power, capable of offsetting regional energy needs through direct use applications and geothermal ground source heat pumps as well as generating electricity on a much larger commercial scale. Yet geothermal is rarely mentioned alongside its renewable counterparts like wind and solar.

Lack of external awareness about the important role that geothermal must play in the transition to a sustainable, green energy future is one of the biggest issues facing the industry. This disconnect between industry knowledge and public perception has been the subject of multiple panels and roundtable discussions at international geothermal gatherings over the past four years. The common theme that emerged from these events was the importance of replacing confusing and disjointed messaging with clear, concise, and cohesive communication.

In late 2023, multiple members of the geothermal community, representing geothermal developers, investors, and associations, convened several workshops to collect data from the industry on how to address geothermal's specific communication challenges. This paper analyzes, categorizes, and distills those insights into a series of actionable recommendations, including:

- Establish one common definition of geothermal energy;
- Tell a simplified story about geothermal in its many applications;
- Employ consistent wording and imagery that focuses on geothermal as a stable, sustainable, and safe source of energy that allows end users to live their normal life;
- Focus on geothermal as a community rather than a group of competitors; and
- Align and coordinate global and regional geothermal events.

1. Introduction

Geothermal energy is an important source of renewable and clean firm energy that has the potential to provide a significant portion of the world's electricity, thermal, and air conditioning needs.[1] Despite its many benefits, geothermal energy has not yet achieved the same level of awareness nor widespread adoption as other renewable energy sources like wind and solar.[2]

One major challenge facing the geothermal industry is the lack of worldwide community alignment on messaging about the merits, benefits, and potential of geothermal energy. This is evident when surveying the websites of international and regional geothermal associations, with each organization employing different terminology, numbers, and even facts. The lack of alignment results in confusion about the definition and uses of geothermal among the general public. For example, the following three questions were posed to the general public via a social media poll in 2023:

1. *What is geothermal?*

   The top three answers: heat, energy, earth

2. *What comes to mind when you think about geothermal?*

   The top three answers: Iceland, volcanoes, hot springs

3. *How could you use geothermal?*

   The top three answers: “no idea,” power, hot water[3]

The disconnect between the real and potential benefits of geothermal and the public perception (or lack thereof) about the technology has been a topic at several international gatherings of the geothermal community. Following the World Geothermal Congress 2021, the International Geothermal Association (IGA),[4] ThinkGeoEnergy,[5] Baseload Capital,[6] the International Renewable Energy Administration (IRENA),[7] and Geothermal Rising[8] agreed that crafting a clear, cohesive, and compelling message that communicates the uses and benefits of geothermal to a global audience was a key step to telling the story of geothermal and garnering increased support.

In 2023, in an effort to address this challenge, they convened communication workshops at two of the world’s largest geothermal industry conferences: the World Geothermal Congress in Beijing, China, and the Geothermal Rising Conference in Reno, Nevada, United States. These workshops brought together leaders in the geothermal energy sector from across the globe to discuss and align on messaging around geothermal energy.

This paper analyzes the data from these workshops to identify patterns, gaps, and opportunities in communication strategies. From these, the authors worked to distill actionable insights, draw conclusions, and present recommendations to be shared with participants and the broader industry.

2. Methodology

2.1 Research questions

At the World Geothermal Congress 2021, held in Reykjavik, Iceland, the issue of communication was raised in a panel discussion. Following that discussion, Baseload Capital convened a communications roundtable with IGA and Think GeoEnergy to discuss data collection. The social media poll and subsequent two workshops in 2023 were the result of that roundtable. Geothermal Rising and IRENA joined the initiative to help further develop a workshop with four specific questions:

1. Where can geothermal associations improve alignment/partnerships?
2. Where can geothermal companies/industry improve alignment and build partnerships?
3. What keywords and images should we use to discuss geothermal?
4. What are the myths and misconceptions around geothermal that we need to dispel?

2.2 Research design

The research questions were deliberately presented in an open-ended manner, in order to a) allow for flexibility and creativity in participant responses and b) generate new ideas and meaningful insights that might not otherwise be captured by close-ended survey data. A thematic analysis was then undertaken to discover and interpret patterns in the data.[9]

This qualitative approach provides more complexity and depth to our understanding of *why*, particularly from sociology and psychology perspectives. As sociologist Kristin Luker argues, "[canonical researchers] are doing a logic of verification study, and [qualitative researchers] are doing a logic of discovery."[10]

Qualitative research complements more abundant quantitative and geoscientific research exploring geothermal energy. It seeks to fill an empirical data gap around how the geothermal ecosystem utilizes marketing and communication to engage and familiarize external audiences about geothermal technologies and applications. This study joins a growing segment of qualitative research that can help us to better understand the energy transition and the role of geothermal in this transition.

Qualitative research scholar Sarah Tracy argues, "Many people erroneously assume that formal generalizability is the only way to achieve resonance."[11] "Resonance" is important because it invites the audience of a study to recognize and apply elements of the study to other academic research and provides practitioners with a practical guide to implement findings from qualitative research. This study seeks to achieve what Tracy calls a "naturalistic generalization," whereby findings from this study aim to influence and affect readers' understanding, routines, and future decision-making and, therefore, produce transferable findings.[12]

2.3 Participants

Participants were attendees of communication workshops held at two of the largest gatherings of the geothermal community. These gatherings, which both took place in late 2023, brought together leaders from industry, academia, finance, government, indigenous communities, research organizations, media, non-governmental organizations (NGOs), and the global community to share scientific and technological achievements and collaborate on solutions to build a sustainable

society. Participants included representatives from the entire geothermal ecosystem, including geothermal ground source heat pumps, direct use and thermal energy networks, and power production.

World Geothermal Congress 2023, Beijing, China

The theme of the 7th World Geothermal Congress (WGC) was "Clean Geothermal, Green Earth." Held at the China National Convention Center in Beijing from September 15-17, 2023, it was China's first time hosting an international geothermal event of this kind. The WGC was attended by more than 1,400 guests from 54 countries and regions. The event consisted of 88 forums and seminars in parallel with a technology and equipment exhibition.

Sixty individuals participated in the communication workshop at the WGC.

Geothermal Rising Conference, Reno, Nevada, USA

With more than 1,700 attendees from 32 countries descending on the western U.S. city of Reno, Nevada, from October 1-5, 2023, the Geothermal Rising Conference (GRC) was the largest annual gathering of the geothermal industry. The event consisted of more than 500 technical, policy, and market sessions, educational seminars, panels, workshops, tours of geothermal and renewable energy projects, and an exhibition hall.

Eighty individuals participated in the communication workshop at the GRC.

2.4 Data collection and analysis

The two workshops were conducted and facilitated in the same manner. The WGC workshop was facilitated by staff from Geothermal Rising and IRENA. The GRC workshop was facilitated by staff from Geothermal Rising and Baseload Capital. Participants at both communication workshops were presented one question at a time and then broken into working groups composed of approximately seven members. They had 10 minutes to discuss each question and record team answers on flip charts prior to reporting back to the larger group. In some cases, groups voted or otherwise indicated support for suggestions with which they agreed by placing a colored sticker "dot" next to the answer.

Recorded answers were photographed by workshop organizers to be compiled and analyzed. The authors of this paper transcribed each written answer into a spreadsheet, along with the question, conference location, group number, and votes received (if any). Results were then coded into broad thematic categories using a bottom-up, or inductive, approach. In other words, the authors had no preconceived notions nor preset categories, but instead allowed the codes to emerge based on what the raw data revealed.

2.5 Limitations

Some participants were invited and others self-selected into the communication workshops. Invitations were issued in an effort to capture a breadth of individuals who otherwise may not have participated and to avoid skewing to one type of perspective, group, or demographic. Those who self-selected to participate likely did so because they had a vested interest in the topic of marketing and communication.

There are not firm non-probabilistic sample size guidelines in a qualitative study such as this, and qualitative research methods suggest study continue until the researchers achieve a point of saturation, meaning no new information or themes are discovered or observed in the data. After two workshops, new findings were still emerging, which suggests there is more data to be uncovered. The authors of this report encourage future studies, perhaps even conducting more workshops using the same process and methodology employed in the two used for this study.

There can be subjectivity in the interpretation and coding of the data. When transcribing the results, every effort was made to decipher the handwritten answers. Approximately 1 percent of the time, this was not possible, either because the answers were illegible, or the photos did not fully capture the data. In some instances – approximately 6 percent of responses – it was not clear to the authors which question was being answered, and thus the data was not coded to a specific question for consideration in the final analysis.

Finally, workshop responses were coded to identify data as it links to, or represents, unique phenomena or "synthesizing concepts."[13] A code is a word or short phrase that symbolically assigns a summative, salient, essence-capturing attribute. In several cases, responses could have fit into multiple, overlapping thematic categories – e.g. "collaboration" and "communication" or "danger" and "environmental damage." Every effort was made to capture the spirit of the responses and acknowledge recurring themes.

3. Overview and Analysis of Data

The communication workshops yielded a data set of over 300 suggestions, including keywords, phrases, questions, and, in some cases, images. Each question was thematically coded independent of the other questions and is considered separately in the analysis below.

3.1 Where can geothermal associations improve alignment/partnerships?

Every group responded to this question, resulting in over 70 suggestions. Participants consistently indicated three overlapping areas where geothermal associations could improve alignment and partnerships:

Collaborate with one another and with outside partners.

There are "many associations, alliances, etc.," wrote one WGC group. "Who do we listen to?" Another WGC group mentioned a need for "global alignment of organizations," including by region and country, and a GRC group suggested "shared memberships between organizations."

Likewise, many groups referenced the importance of coordinating event schedules. "Don't schedule conferences on top of each other," said a group at the Geothermal Rising Conference. This sentiment was echoed by several others, one of whom bemoaned the "cadence of events."

At the same time, participants suggested that geothermal associations should focus on creating partnerships with universities, other renewables, and influencers to help spread the word about geothermal energy.

Establish common definitions and vocabulary for the industry.

Every group mentioned that industry associations should help to better define geothermal. “Define what we are,” wrote one group at the Geothermal Rising Conference. “Align on definitions,” urged a group at the World Geothermal Congress. Several groups suggested developing a glossary of streamlined geothermal vocabulary.

Engage in simplified storytelling.

“K.I.S.S.,”[14] wrote one GRC group, which was immediately followed up by an all-caps demand for “NO NEW ACRONYMS.” Multiple groups used the word “simplify” when talking about messaging and communication with the general public and external audiences. “Improve storytelling (simple illustrations/animations),” wrote one GRC group. Likewise, a WGC group suggested creating simple “models [to] help understand” and communicating at the “grassroots level – how you convey to children/community.”

Participants also thought geothermal associations should “help with framing the message (turn setbacks into positive story – [e.g. a] well with insufficient yield = new data/knowledge)” as well as “share successful stories and policies.”

3.2 Where can geothermal companies/industry improve alignment and build partnerships?

Only groups attending the Geothermal Rising Conference recorded answers to this question, resulting in approximately 50 suggestions. One common theme emerged:

Choose cooperation over competition.

Multiple groups even used similar phrasing when urging industry cooperation; some version of “Bake a bigger pie; don’t fight over the slices,” and “A rising tide lifts all boats,” appeared multiple times.

“Eliminate zero-sum mindset,” wrote one GRC group, and embrace the “mentality that geothermal is for the greater good.” When people do that, it should follow that “what you do in your day-to-day business needs to also promote geothermal.”

To that end, participants also said it was important to “share technical data” and “if you aren’t doing it, give it to another company (the jobs, leads, seismic data).”

3.3 What keywords and images should we use to discuss geothermal?

Every group at both conferences recorded answers to this question. For coding purposes, responses were broken into two separate categories: keywords and images.

There were over 100 responses that fit into the category of keywords; of these responses, approximately one-third were hashtags, and the rest were typically one or two words long. They most commonly focused on three areas:

Stability/reliability/energy security

The clear favorite was #alwayson. Some version of “always on” and “24/7” appeared on nearly every group’s sheet. This also received the largest number of sticker “votes” of any hashtag,

garnering 34 votes from participants at the GRC and eight votes at the WGC. The words “reliable,” “stable,” and “resiliency” also appeared over and over.

Sustainability

Here, #carbonfreeenergy, along with the words clean, green, and renewable appeared in multiple groups’ answers.

Identity

Simply using the hashtag #geothermal or #geothermalenergy (in one case, the “o” was stylized as the earth) also proved popular, showing up in most groups’ recorded answers. Similarly, “geowatt,” “geowhat,” “wearegeo” and “whatisgeothermal” were all suggestions that garnered multiple votes within several groups.

There were 20 “image” suggestions, both descriptive and illustrative. They were primarily – but not exclusively – recorded by groups at the GRC. The plurality focused on the daily, positive experience of end users – “people laughing,” “home showing heat/power/cooking,” “warm house/family dinner, etc.” One group paired a series of images with its own hashtag: “kitchen/light/fridge/family/people – #poweredbygeothermal” or “#energyfromgeothermal.”

The second largest tranche of images focused on the fact that geothermal is earth-friendly and unobtrusive – “beautiful land, nothing to see,” and “invisible” wrote one group. “No steam (except sometimes, maybe),” hedged other participants. Still another group drew earth with a tree, house, and person. “Healthy world,” they wrote.

3.4 What are the myths and misconceptions around geothermal that we need to dispel?

There were approximately 45 responses to this question, with answers clustered relatively tightly around two categories.

Danger and/or negative environmental impact

While the authors initially coded these responses separately, there was sufficient overlap between the two to merit a combined category. “Earthquakes,” “groundwater pollution” and/or “drain[ing] out underground water,” and “steam is often mistaken as pollution,” were the most commonly cited misconceptions, in that order.

Economic feasibility (or lack thereof)

Less commonly cited than myths about environmental impact, but still appearing several times, was the idea of cost. This concern was expressed only in groups attending the WGC, who used words such as “profitability,” “subsidies,” and “economic failure.” “Expensive against wind, gas, solar,” received seven votes from one group. “Expense (high capital cost),” stated another.

4. Conclusions and Recommendations

Data from communication workshops held at the 2023 World Geothermal Congress and Geothermal Rising Conference provide a clear indication that participants would like to see increased alignment among geothermal associations, including coordinating membership and

conferences, standardizing vocabulary across technologies and regions, and taking the lead in communicating the benefits of geothermal to the public and other stakeholders. They want geothermal companies and associations to focus on growing the industry rather than competing with one another. They believe that messaging should emphasize geothermal's reliable, stable, and sustainable nature, with a focus on showcasing the normal, everyday activities made possible by energy from the earth. And they wish to counter the idea that geothermal is somehow dangerous, damaging to the environment, or too expensive to pursue.

Based on these results, there are several opportunities for action, as well as further study. Five recommendations are presented:

- Improve partnerships and share resources;
- Promote a unified industry taxonomy and apples-to-apples comparison;
- Develop a messaging architecture for geothermal;
- Update the visual identity of geothermal to match the messaging architecture; and
- Develop a strategic plan to dispel myths and misconceptions.

4.1 Improve Partnerships and Share Resources

National and international geothermal associations could take this opportunity to reach out to one another when establishing conference schedules to ensure they don't overlap. They could then examine objective data, including attendance numbers, and measure attendee satisfaction by administering surveys after with specific, detailed questions about scheduling. Based on this data, they could consider co-hosting conferences and offering dual memberships.

Likewise, they could collaborate to expand the financial pie. IGA and GR, as the two most impactful and well-known associations, should seek to fundraise and partner in ways that will increase philanthropic funding opportunities. This could be achieved through a joint fundraising position that seeks out donations for the two organizations.

4.2 Promote a Unified Taxonomy and Apples-to-Apples Comparison

The same associations could also take the lead in establishing common definitions, vocabulary, keywords, and images to be used across communication channels. The suggestions provided by participants here could serve as the basis for an industry-wide survey to determine how to best promote geothermal energy in different regions and how these strategies can be replicated and scaled globally.

Additionally, developing a uniform dataset and clear comparison methodology could facilitate apples-to-apples comparison with other renewable energy sources.Transparent and fair methods of comparison could increase industry credibility and attractiveness for investors and partners.

4.3 Develop a Messaging Architecture for Geothermal

In the endeavor to expand the geothermal industry and attract the right investors and partners, it is necessary to redefine the communication strategy and/or create a communication strategy that cuts through the noise.

Instead of relying on traditional sales pitches from individual companies or organizations, associations representing the geothermal industry should consider a common pitch that focuses on solving the problems and meeting the needs of their audience. “Audience” in this context refers primarily to the general public, but could also include more targeted audiences, such as global investors. Creating a strong messaging architecture can guide the entire industry’s communication and allow for increased resonance with a variety of audiences. A potential strategy to achieve this goal is outlined below:

- Understand the audience’s problems: It is vital to first clarify the target audience and carefully research the challenges that the target audience faces. Identifying and addressing these problems allows geothermal to position itself as part of the solution and create a strong connection with the audience.
- Develop a messaging architecture: A common messaging architecture is crucial to deliver tailored messages that are relevant to each stage in the buyer’s journey. (A buyer’s journey describes a buyer’s path to purchase, including awareness, consideration, evaluation, and eventually adoption). Focusing on audience needs instead of company benefits can create resonance and increase industry influence.
- Deploy a common pitch for the industry: Agreeing on a common message around change drivers, choice of category, and choice of subcategory (see Figure 1) could increase geothermal’s visibility and impact in debate and in media. Collaborating with other renewables and including oil and gas in the discussion could also create a stronger position for the geothermal industry.
- Use of Megadeals methodology: Applying the Megadeals methodology and creating a buyer’s journey specific to the chosen audience could optimize communication and increase the geothermal industry’s chances of successful business opportunities. Communicating the right messages at the right time could help build trust and establish long-term relationships with potential investors and partners.

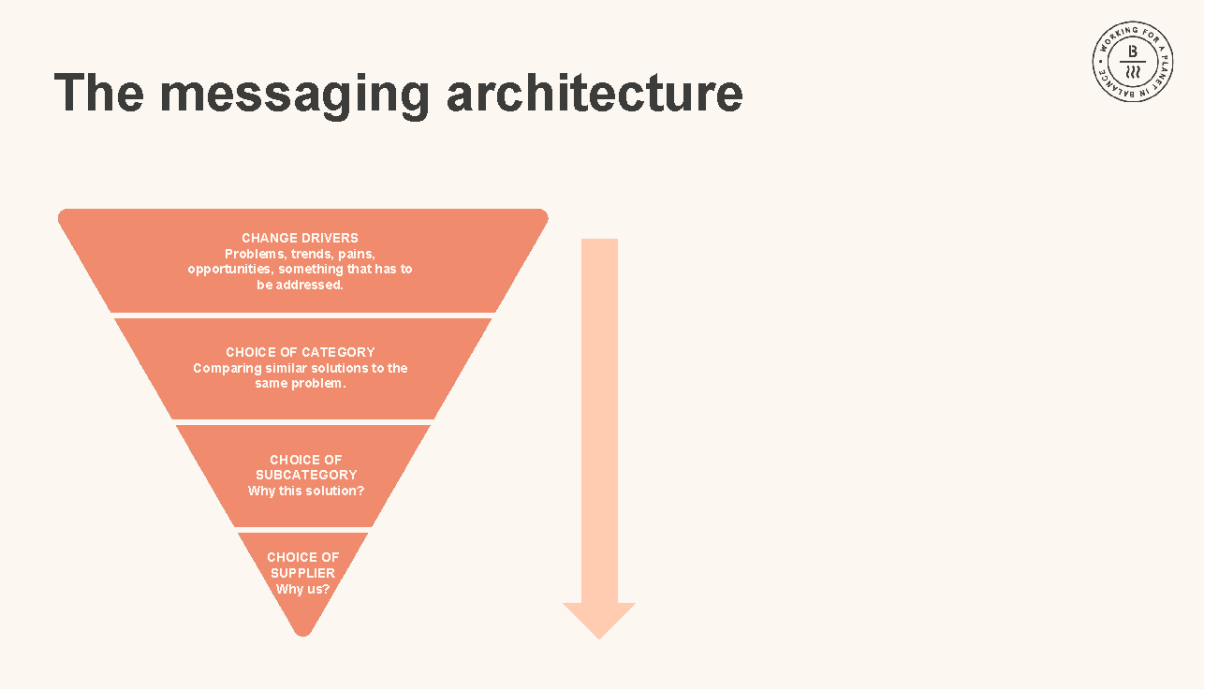

Figure 1: The reverse pyramid shape of messaging architecture demonstrates how focusing on the audience's needs when it comes to energy allows for more salient, persuasive communications on the path from awareness about the benefits of geothermal to eventual adoption.

4.4 Update the Visual Identity of Geothermal to Match the Messaging Architecture

The end user should be the focus of social media and geothermal narratives. Too often the images and marketing employed by geothermal companies, associations, and other organizations are internally focused. Images of cooling towers, piping, boiling mud pots, and geysers appeal to the geoscientists, drillers, reservoir managers, and geologists who make up the geothermal workforce. However, the main audience of images and narratives should be end users – the people who switch on the lights at night or cool down their house in the heat of summer. End users don't understand that the white puffs of smoke coming from a cooling tower are just water vapor. To the external audience, it represents pollution, greenhouse gas emissions, carbon, and climate change.

Other end users are the passionate and well-intentioned advocates of environmental and climate NGOs, policymakers and their staff who change laws, educators who teach the next generation of engineers and marketing professionals, and editors of textbook publishers, to name a few target audiences that the geothermal industry should keep in mind when developing brands, narratives, and marketing strategies.

A good example of a geothermal company taking into consideration the end user are the marketing campaigns of WaterFurnace, owned by the Swedish company NIBE Group and one of the largest manufacturers of geothermal heat pumps. WaterFurnace promotes the individual, the environment, and impacts of policy in its marketing and communications strategies with less focus on infrastructure, geology, and engineering.

4.5 Develop a Strategic Plan to Dispel Myths and Misconceptions

Geothermal associations should develop a high-level strategic communications plan that can be used by the entire geothermal ecosystem. A strategic communications plan could include:

- A geothermal industry public affairs manual;
- Media monitoring and rapid response;
- A daily geothermal clip report;
- A media relations and editorial board/op-ed/letter-to-the-editor strategy;
- A geothermal media-trained member speakers' bureau (expert geothermal talking heads) that can be made available for broadcast opportunities (BBC, DW, CNN, MSNBC, Fox News, VOA, etc.); and
- A crisis communications plan.

This paper's findings demonstrate that the time has come for geothermal associations, companies, and other stakeholders to coalesce around a common message to ensure a global understanding of the important role geothermal has to play in transitioning to a green energy economy and drawing down the effects of climate change.

By working together, using clear, consistent vocabulary and messaging architecture, the geothermal industry can position itself as the preferred solution for investment and partnership. Reshaping the communication strategy for the geothermal industry, focusing on understanding and solving the chosen audience's problems, and dispeling pervasive myths can increase visibility, attract investors and partners, and drive continued growth within the industry.

ACKNOWLEDGMENT

Gathering the research for this paper was truly a team effort and could not have been achieved without the dedication and enthusiasm of many partner organizations, companies, and individuals. The authors wish to acknowledge the members and staff of Baseload Capital, Geothermal Rising, the International Geothermal Association, the International Renewable Energy Administration, and ThinkGeoEnergy for recognizing the importance of this topic and working to convene discussions around the issue of communication within the geothermal industry. Thank you to companies like Baker Hughes, Ormat Technologies, and GeothermEx, which supported the idea from the start. The authors would also like to recognize all the participants who attended the communication webinars, panels, and workshops – your time, energy, and thoughtful insights are most appreciated. And a special thank you goes to Peter Tait, who inspired many conversations along the way.

REFERENCES

1. *World Energy Resources: Geothermal*. (World Energy Council, 2013), 9.2. https://www.worldenergy.org/assets/images/imported/2013/10/WER_2013_9_Geothermal.pdf.
2. "Geothermal Energy." International Renewable Energy Agency, accessed January 29, 2024, https://www.irena.org/Energy-Transition/Technology/Geothermal-energy.
3. Kristina Hagström Ilievska. "Geothermal Communications & Marketing Workshop" (presentation, 2023 Geothermal Rising Conference, Reno, NV, October 4, 2023).
4. Headquartered in The Hague, The Netherlands, the International Geothermal Association's mission is to advocate for and promote the sustainable utilization and development of geothermal resources worldwide.
5. ThinkGeoEnergy is a business-to-business organization focused on the international geothermal energy market. Its services include online news, market research, communications strategy, and event promotion in the geothermal industry.
6. Baseload Capital is a specialized investment entity that leads partnerships to scale up geothermal power deployment worldwide. Based in Stockholm, Sweden, it has established operating companies in the U.S., Japan, Taiwan, and Iceland under the name Baseload Power.
7. The International Renewable Energy Administration is an agency of the United Nations and is headquartered in Abu Dhabi, United Arab Emirates. The international government organization contains the Global Geothermal Alliance, which seeks to familiarize geothermal technologies and applications to national governments.
8. Geothermal Rising is the oldest geothermal association in the world founded in 1972. A 501(c)3 nonprofit organization based in the United States, its mission is to align the geothermal ecosystem, empower the geothermal community, conduct and promote geothermal research, and champion geothermal energy in the U.S. and across the globe.
9. See the Data Collection and Analysis section for further discussion of this method.
10. Kristin Luker, *Salsa Dancing into the Social Sciences* (Cambridge, MA: Harvard University Press, 2008), 39.
11. Sarah J. Tracy, *Qualitative Research Methods: Collecting Evidence, Crafting Analysis, Communicating Impact* (UK, John Wiley & Sons, 2013), 238.
12. Tracy, *Qualitative Research Methods*, 230.
13. Tracy, 28.
14. K.I.S.S. is an acronym for "keep it simple, stupid."

A Social Science of the Subsurface: Advances in EGS Communication and Engagement Research

Catherine Lambert, Dominic Balog-Way, and Katherine McComas

Cornell University

Keywords

Enhanced geothermal, communication, public acceptance

ABSTRACT

While enhanced geothermal technology is a potentially powerful source of renewable heating and power, it also poses unique challenges for public acceptance. Understanding how the public assesses the risks, benefits, and tradeoffs of EGS projects is crucial for successful development; at the same time, the growth of EGS projects in multiple countries allows for critical comparisons of how public support develops across settings. We present novel findings from a series of studies in Switzerland, the United Kingdom, and the United States on EGS risk perception and public attitudes, with implications for best practices in communication and public engagement. First, a cross-national survey in Switzerland and the United States illuminates how people make sense of an unfamiliar technology like EGS, relying on associations with other technologies, beliefs about the underground, and perceptions of EGS technology as "tampering with nature." Second, a series of qualitative case studies of EGS projects in the UK and the US investigate the role of context-sensitive communication strategies from geothermal developers, in a comparison of projects in the UK and the US. This body of research includes ongoing work as part of the GEOHUB trans-Atlantic collaboration to examine the impact of public attitudes on energy development efforts and how they evolve in real time. A better understanding of critical factors that underlie beliefs and attitudes towards EGS informs evidence-based approaches to the challenge of public engagement, allowing development efforts to better align with societal values and priorities while underscoring the value of social science in global efforts to transition to renewable energy systems.

1. Introduction

The development of Enhanced Geothermal Systems (EGS), a form of deep geothermal energy that relies on creating engineered reservoirs within low permeability rock layers, could potentially expand the use of geothermal resources well beyond the traditional geographic reach of conventional hydrothermal systems. As such, EGS technology could play a critical role in

decarbonizing both heat and power and achieving low-carbon energy transitions. EGS has been described as one of the most benign and low impact options for renewable energy, particularly when comparing issues such as visual impact with wind and solar energy (Stephens & Jiusto, 2010). However, EGS is not without risks, including induced earthquakes, a major source of potential disruption to nearby communities, as well as impacts on water use and potential changes related to traffic, noise and the infrastructure of seismic exploration and drilling (e.g., Ellsworth, 2013; Porter, Striolo, Mahgerefteh, & Faure Walker, 2018; Trutnevyte & Ejderyan, 2018). While addressing the risks of EGS development requires significant technical considerations, successful development also requires the recognition that "a technology's license to operate depends on public acceptance" (Hoşgör, Apt, & Fischhoff, 2013, p.1032).

Public responses to EGS as an emerging renewable energy option have been relatively unstudied, despite calls for increased insight into the risks and social impacts of geoenergy (Giardini, 2009; Knoblauch & Trutnevyte, 2018; Pellizzone & Allansdottir, 2019). Existing research has demonstrated that key concerns often center on seismic risk (Cousse et al., 2021; Dowd et al., 2011; Knoblauch et al., 2019; Stauffacher et al., 2015). Knoblauch et al. (2019), for instance, found that potential earthquakes exerted the strongest influence on acceptance of both EGS and shale gas. Other concerns that have been identified include economic and technological uncertainty (Romanach et al., 2015), as well as procedural fairness (McComas et al., 2016; Song et al., 2021).

Though relatively little research has examined EGS directly, decades of research on risk perception and public acceptance have highlighted a wide range of critical factors, including trust, fairness, and perceptions of risks and benefits (e.g., Balog-way et al., 2020; Siegrist & Árvai, 2020; Wüstenhagen et al., 2007). Research on effective risk communication recognizes the need to move from a one-way communication model to a multi-directional engagement model emphasizing early involvement of stakeholders in the decision-making process (Fischhoff, 1995; Trench, 2008). An engagement-based model recognizes social, cultural and psychological factors shaping lay attitudes and behaviors, and emphasizes engagement through dialogue and deliberation. Through upstream engagement efforts, communicators may define a baseline of public concerns, and perceptions of risks early in the process (Kasperson & Ram, 2013). This allows communicators to stay ahead of problems, demonstrate competence, fairness and openness, and, critically, establish relationships with communities that are built on trust (Besley & McComas, 2014).

Understanding why people support or oppose deep geothermal development requires moving past the dismissal of local concerns as "NIMBYism" (Not In My Backyard) and addressing the underlying drivers of individuals' perceptions of geothermal technologies. Because EGS allows geothermal development outside of areas with conventional hydrothermal resources, it is likely unfamiliar to many in potential target areas. As a result, people are likely to rely on pre-existing associations with comparable industries and technologies to make sense of the new technology. Below, we identify several critical conceptual directions based on the unique characteristics of EGS as a subterranean renewable energy technology. As part of an emerging body of work, we present key findings and implications from two studies of attitudes towards geothermal energy development across three countries. In Study 1, a cross-national Swiss/US survey illuminates how respondents make sense of EGS through associations with the underground and perceptions of EGS as "tampering with nature." In Study 2, case studies of two current EGS projects in the UK and the US investigate the impact of place, culture, and local legacies of extractive industries on stakeholder responses to actual EGS projects in context.

2. Study 1

2.1 Motivation

Prior research has suggested that drivers of attitudes towards EGS may include associations with other subterranean technologies as well as the perceptions that the public has of the deep underground itself. Members of the public have been shown to associate EGS production with fracking and other extractive industries, leading to potentially negative impacts on acceptance (Cuppen et al., 2020, Westlake et al., 2023). The underground nature of geothermal resources, in comparison with more visible renewable energy sources aboveground, may increase this association (Gross, 2013).

Also relevant is the perception of "tampering with nature" (TWN) the belief that humans influence nature in a negative manner through behaviors or use of technologies (Hoogendoorn et al., 2021). Feelings of discomfort with tampering in natural systems can create resistance to technological developments and have been shown to be a strong predictor of public acceptance and risk perceptions for a variety of technologies and behaviors (Sjoberg, 2000; Fritz et al., 2004; Meisenberg, 2009; Corner et al., 2013; Stewart and Lewis, 2017).

The extent to which EGS is perceived as TWN is unclear and may be closely related to whether the underground is viewed as part of nature or not. While underground spaces may be linked with a range of cultural, religious, and spiritual meanings like burial and the underworld (Kearnes & Rickards, 2017), other depictions are of an artificial, inorganic space accessed only through technological interventions (Williams, 1990). Subterranean spaces may be viewed as mysterious and inscrutable (Kinchy et al., 2018; Stewart & Lewis, 2017), or may elicit primordial fears of what lurks in the depths (Giardini, 2009; Gross, 2013) – beliefs which may figure in individuals' assessments of EGS development and whether it constitutes "tampering." Given the associations of EGS with induced seismicity and fracking, it seems plausible that similar associations may apply to EGS.

Drawing on these concepts, Study 1 explores the following research questions:

RQ1: How do individuals perceive the deep underground with respect to EGS development?

RQ2: To what extent do individuals consider EGS to be TWN?

RQ3: To what extent do beliefs about TWN and perceptions of the underground relate to support for EGS development?

2.2 Methods

Survey data collection was conducted in Switzerland and the US in November 2021, with a total sample of 2,031 responses. The sample was nationally representative of age, gender, and education in both countries and by race in the US, and was recruited by two market research agencies, Qualtrics (US) and Intervista AG (Switzerland), using online panels and quota sampling. The questionnaire was translated for Swiss respondents from English into German and French.

2.2.1 Perceptions of the deep underground

We first asked respondents to estimate their familiarity with geothermal energy. Participants then read a one-age vignette about EGS in order to ensure similar baseline knowledge. To address RQ1, we measured perceptions of the underground (i) in general, (ii) with respect to human activities, and (iii) regarding its safety, controllability, and utility for storing. First, we used a free association exercise (Leiserowitz, 2006; Peters & Slovic, 1996; Slovic et al., 1991), in which participants were asked to type the first thought, association, or image that came to their mind when they thought of "the deep underground." They then ranked each association as positive or negative.

Second, a series of semantic differential scales were used to assess what properties respondents associated with the deep underground. These items were developed from prior theoretical and qualitative work on the underground (Gross, 2013; Kearnes & Rickards, 2017; Kinchy et al., 2018; Partridge et al., 2019; Williams, 1990) and consisted of the word pairs shown in Table 1.

Third, respondents indicated agreement with statements about human activity in the deep underground. Two sets of statements were designed to capture 1. whether respondents believed the deep underground was a place for human use and 2. whether respondents believed that the deep underground should be left alone. These items were combined into the scales labelled "Underground as a resource for human use" (α =.87)[1] and "Underground should be left alone" (α = .81). Table 2 lists the items that comprise each scale used in the regression model.

2.2.2 Tampering with nature

To assess perceptions of EGS as TWN (RQ2), we measured whether respondents perceived EGS as (i) unnatural, (ii) disturbing the order of nature, and (iii) contrary to nature. As a comparison, we included the same measures for technologies that previous research has shown are seen as TWN: chemical pesticides and genetically modified organisms (GMOs) (Hoogendoorn et al., 2021; Raimi et al., 2021). Lastly, we measured whether respondents perceive human-induced seismicity as TWN. For each technology, we averaged the three items to form scales labeled "EGS-as-tampering-with-nature" (α = .87), "pesticides-as-tampering-with-nature" (α = .85), GMOs-as-tampering-with-nature"(α=.87), and "induced-seismicity- as-tampering-with-nature" (α = .83).

2.2.3 Support for EGS and related factors

Respondents were asked their general feeling about the implementation of an EGS project in the proximity of where they live on a 7-point scale from "very negative" to "very positive." In addition, we measured factors that previous research has shown as important predictors of technology support: perceived risks and benefits, trust in risk managers, attitudes towards climate change and renewables, and demographics.

2.3 Findings

Results indicate low levels of familiarity with geothermal energy; overall, about 40% of the sample indicated they knew almost nothing or nothing at all about geothermal, and another 40% said they knew just a little about it, with no significant differences between the US and Swiss (CH)

[1] Removing the item "the deep underground is a place to store things" increased the reliability (Cronbach's α) of the "Underground as a resource for human use" scale from .81 to .87, so we removed that item from the final scale.

respondents. We note, however, that responses to the "support for EGS" item indicate generally positive feelings towards EGS (M=4.85, SD=1.75), with no significant differences between the US and Swiss samples.

2.3.1 Perceptions of the deep underground

When rating their free associations, 42% of respondents rated their associations as positive, 28% neutral, and 30% negative. US respondents were more likely than Swiss respondents to rate their associations with the deep underground as positive (M_{US}=4.44, SD_{US}=1.70 versus M_{CH}=4.02, SD_{CH}=1.74, p<.001). In the semantic differential scale regarding perceived characteristics of the underground (Table 1), respondents were more likely to consider the underground as part of nature, mysterious, tangible, clean, bright, controllable, static, predictable, safe, and familiar than the opposing quality (e.g., invisible, dirty, etc.). Swiss respondents tended to perceive the underground as more a part of nature and cleaner than their US counterparts. In comparison, US respondents perceived the underground as more controllable, tangible, and brighter than their Swiss counterparts.

Table 1

Perceptions of the underground – semantic differential items

	M (SD)		t (df=2,029)
	United States	Switzerland	
Separate from nature – Part of nature	3.79 (1.28)	4.09 (1.1)	-5.62*
Comprehensible – Mysterious	3.53 (1.26)	3.34 (1.16)	3.52
Dirty – Clean	3.20 (1.28)	3.40 (1.12)	-3.61
Unstable – Stable	2.92 (1.31)	3.00 (1.19)	-1.43
Uncontrollable – Controllable	2.94 (1.31)	2.61 (1.15)	5.92*
Dangerous – Safe	2.74 (1.34)	2.58 (1.1)	2.97
Unpredictable – Predictable	2.74 (1.35)	2.54 (1.16)	3.65
Unfamiliar – Familiar	2.72 (1.35)	2.52 (1.16)	3.61
Dynamic – Static	2.81 (1.21)	2.61 (1.13)	3.87
Grim – Bright	3.06 (1.26)	2.75 (1.08)	6.05*
Invisible – Tangible	3.34 (1.26)	2.77 (1.17)	10.51*

Note: We used a 5-point scale, anchored at each end by the different items. All of the differences were significant at p<.005, with the exception of dynamic vs. static. We used Cohen's d to examine effect size: * = small effect size (.20 - .45).

Table 2

Perceptions of human use of the underground: Scale items, means, standard deviations, and reliabilities

	M (SD)		t (df=2,029)
	United States	Switzerland	
Underground: Leave alone (α = .81)			
Whatever is below us belongs to the Earth and should be left untouched	3.93 (1.85)	3.7 (1.81)	2.83
Humans should not interfere with Earth's fundamental processes (n.s.)	4.35 (1.78)	4.28 (1.73)	.90
Because processes like EGS are hidden from sight, we won't know about problems until it's too late	4.60 (1.67)	4.33 (1.61)	3.74
The deep underground is a sacred place	4.06 (1.82)	3.25 (1.84)	9.96*
Drilling wells is an invasive way to take something from the Earth (n.s.)	4.38 (1.75)	4.22 (1.66)	2.11
We have no control over what happens in the deep underground (n.s.)	4.64 (1.77)	4.69 (1.65)	-.68
Scale	4.38 (1.36)	4.25 (1.25)	2.36
Underground: Human use (α = .87)			
Exploring the underground is a pathway for new knowledge and discovery (n.s.)	5.27 (1.48)	5.19 (1.47)	1.09
The deep underground below us exists as a resource for humans to use	4.82 (1.63)	4.56 (1.65)	3.52
Using resources from the deep underground can be done safely	4.76 (1.59)	4.14 (1.57)	8.79*
The deep underground is a new frontier for humans to explore	5.05 (1.65)	4.77 (1.63)	1.09
Scale	4.97 (1.38)	4.67 (1.31)	5.15*
The deep underground is a place to store things.ǂ	3.49 (1.83)	3.1 (1.83)	4.83*

Note: Scales ranged from 1=strongly disagree to 7=strongly agree. All items except those marked with n.s. are significantly different between countries at p<.005. We used Cohen's d to examine effect size: * = small effect size. ǂ "The deep underground is a place to store things" did not load on either factor, reduced the Underground: Human Use scale reliability from .87 to .81, and was excluded from further analysis.

2.3.2 Human use of the deep underground

Respondents tended overall to view the underground as a resource for humans to use, with general similarity between the US and Swiss respondents, with two exceptions (Table 2). US respondents were significantly more likely to perceive the underground as "a sacred place," a "place to store things," and that "using resources from the deep underground can be done safely." Comparing the "underground as a resource for human use" and "underground should be left alone" scales between countries, US respondents were significantly more likely to give higher ratings to the items in the "underground for human use" scale at a meaningful level.

2.3.3 EGS as tampering with nature

RQ2 examined whether respondents viewed EGS as TWN. Respondents generally rated the individual tampering-with-nature dimensions slightly above the mean, while US respondents tended to consider EGS as more "contrary to nature" (M_{US}=4.14, SD_{US}=1.85, M_{CH}=3.77, SD_{CH}=1.76), "unnatural" (M_{US}=3.98, SD_{US}=1.91, M_{CH}=3.77, SD_{CH}=1.76), and "disturbing the order of nature" (M_{US}=4.26, SD_{US}=1.88, M_{CH}=4.04, SD_{CH}=1.77) than their Swiss counterparts. Although the differences were significant, only "contrary to nature" had a small but meaningful effect size (d=.21). In comparison with items on pesticides, GMOs, and human-induced seismicity (Figure 1), respondents were more likely to perceive pesticides and GMOs as TWN than EGS and induced seismicity. Induced seismicity was also viewed as TWN more than EGS. While the differences between countries in views about TWN were significant at p<.005, only perceptions of pesticides were meaningfully different (d=-.34).

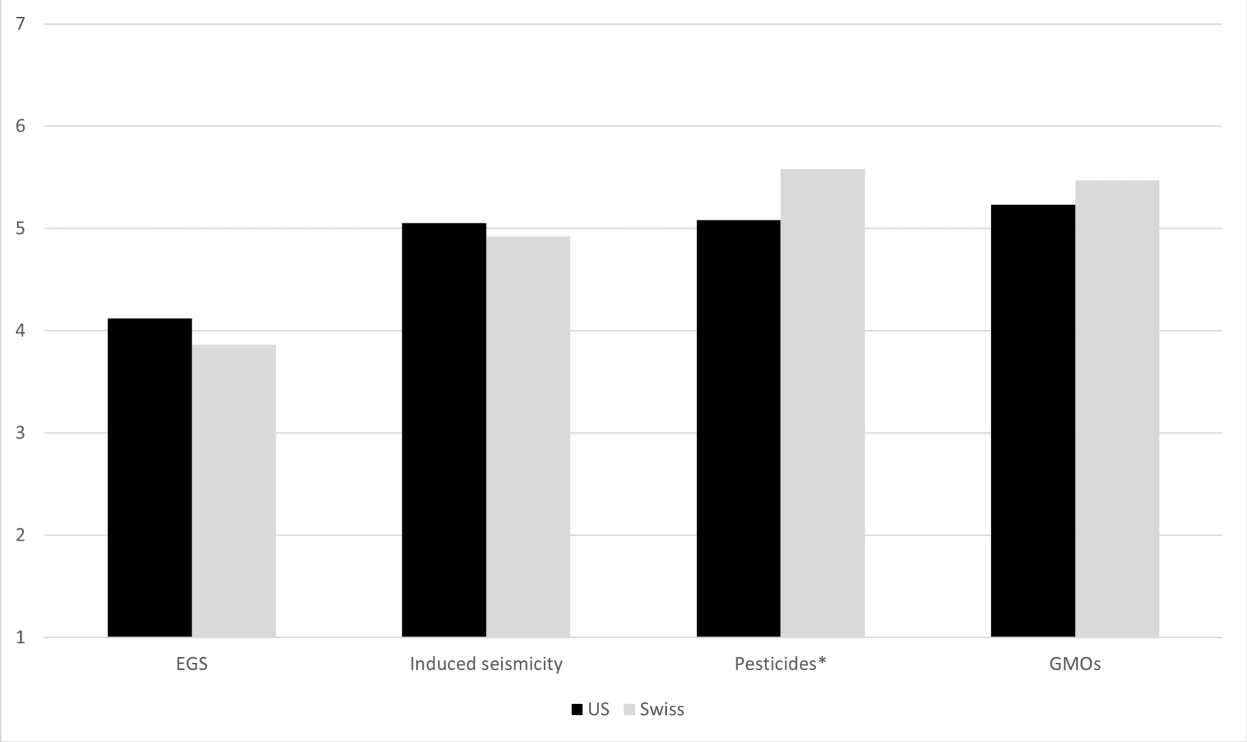

Figure 1. Bar chart showing the mean of perceptions of different technologies as "tampering with nature." While there were significant differences between countries for each technology, an examination of effect size using Cohen's d suggests only the variable *pesticides* was meaningful (-.34).

2.3.4 Factors relating to EGS support

A linear regression was used to measure the influence of different sets of variables on respondents' support for a hypothetical EGS project. We entered four different blocks in order to examine the R square change, i.e., the incremental change of the new addition. Tables 3 and 4 present the final block results for each country.

Table 3

Regression analysis for "What is your general feeling about the implementation of an EGS project in the proximity of where you live?" for US sample (N=989)

						95% Confidence Interval for B	
Variables	B	SE	Beta	t	p-value	Lower Bound	Upper Bound
(Constant)	-.707	.371		-1.905	.057	-1.435	.021
Education (low to high)	-.078	.072	-.026	-1.078	.281	-.219	.064
Gender (female=1)	.029	.081	.008	.357	.721	-.131	.189
Political leaning (Left à Right)	.086	.026	.088	3.320	.001	.035	.138
Age	-.009	.002	-.094	-3.858	.001	-.014	-.005
Location of residence (urban à rural)	.020	.039	.012	.524	.601	-.056	.097
Adjusted R Square .011	ANOVA F(5, 949)=3.019), p=.010						
Underground: Human Use	.301	.041	.243	7.291	.001	.220	.382
Underground: Leave Alone	-.049	.039	-.039	-1.264	.207	-.125	.027
Cum. Adjusted R Square .364	ANOVA F(7, 942)=78.602, p<.001						
Risk-benefit perceptions	.676	.062	.356	10.822	.001	.553	.798
Trust in government regulators	.001	.037	.001	.033	.974	-.071	.074
Trust in private industry	.087	.035	.090	2.452	.014	.017	.156
Climate change concern	.082	.032	.076	2.552	.011	.019	.145
Support for moving to renewables	.205	.033	.185	6.264	.001	.141	.270
Cum. Adjusted R Square .514	ANOVA F(12, 937)= 84.760, p<.001						
EGS as tampering with nature	-.023	.031	-.022	-.758	.449	-.084	.037
Induced seismicity as tampering with nature	.052	.031	.044	1.683	.093	-.009	.112
Cum. Adjusted R Square .515	ANOVA F(14, 935)=72.962, p<.001						

Note: Listwise deletion of missing values.

In both countries, whether respondents perceived the deep underground as a place for humans to use was positively associated with EGS support. However, belief that the underground should be left alone did not significantly influence EGS support in the US or Switzerland at the p<.005.

The third block added risk-benefit perceptions, trust in government and private industry, climate change concerns, and support for moving to renewable energy. Risk-benefit perceptions were significantly related to EGS support, as was support for transitioning to renewable energy. Trust in private industry was significantly related to EGS support for those in Switzerland, but not for the US. Lastly, the fourth block examined the relationship between TWN and EGS support. For Swiss respondents, perceiving EGS as TWN was significantly related to decreased support for EGS projects, which was not the case for US respondents.

Table 4

Regression analysis for "What is your general feeling about the implementation of an EGS project in the proximity of where you live?" for Swiss sample (N=1,027)

						95% Confidence Interval for B	
Variables	B	SE	Beta	t	p-value	Lower Bound	Upper Bound
(Constant)	1.585	.465		3.406	.001	.672	2.498
Education (low to high)	-.117	.073	-.036	-1.601	.110	-.261	.026
Gender (female=1)	-.059	.083	-.016	-.707	.480	-.222	.104
Political leaning (Left Right)	-.030	.032	-.023	-.955	.340	-.092	.032
Age	-.013	.003	-.118	-5.297	.001	-.018	-.008
Location of residence (urban rural)	.005	.034	.003	.139	.889	-.061	.071
Adjusted R Square .024	ANOVA F(5, 1022)=6.151, p<.001						
Underground: Human Use	.157	.043	.114	3.661	.001	.073	.241
Underground: Leave Alone	-.110	.041	-.077	-2.690	.007	-.191	-.030
Cum. Adjusted R Square .341	ANOVA F(7, 1020)=76.844, p<.001						
Risk-benefit perceptions	.803	.074	.346	10.860	.001	.658	.948
Trust in government regulators	-.002	.042	-.002	-.054	.957	-.084	.080
Trust in private industry	.152	.040	.128	3.783	.001	.073	.230
Climate change concern	-.040	.032	-.033	-1.244	.214	-.103	.023
Support for moving to renewables	.232	.037	.175	6.250	.001	.159	.305
Cum. Adjusted R Square .489	ANOVA F(12, 1015)= 83.009, p<.001						
EGS as tampering with nature	-.139	.031	-.126	-4.449	.001	-.200	-.077
Induced seismicity as tampering with nature	-.017	.016	-.025	-1.079	.281	-.047	.014
Cum. Adjusted R Square .499	ANOVA F(14, 1013)=74.032, p<.001						

Note: Listwise deletion of missing values

2.4 Study 1 Discussion

Addressing RQ1, respondents tended to perceive the deep underground as a "part of nature." While respondents, on average, have a neutral to positive affective response to the deep underground in relation to the use of EGS, Swiss responses were generally less positive than in the US. This could be linked to two prior EGS projects in Switzerland that caused felt earthquakes in the past and attracted attention nationwide (Stauffacher et al., 2015). Another potential explanation may lie in the US's greater familiarity with industries involving underground extraction.

Respondents tend to perceive the underground as a resource for humans to use, though results are mixed regarding support for specific activities, with low support for the use of the underground to store things, for instance. US respondents are more likely than Swiss respondents to agree that the underground is a space for exploration and a resource for humans, but notably are also significantly more likely to view the underground as sacred, showing that one does not exclude the other.

With respect to RQ2, respondents viewed EGS as somewhat disturbing the order of nature, but perceptions of EGS as TWN were relatively neutral, especially when compared with GMOs and pesticides. Induced seismicity was more likely to be viewed as TWN than EGS itself, despite being a consequence of the technology. Respondents' perceived benefits of EGS may compensate for the perceived negative impacts of induced seismicity. Alternatively, the difference between EGS and induced seismicity perceptions may also be a further consequence of the complexity of "nature" as a construct. TWN can be seen as negative either because nature is vulnerable and needs to be protected, or because nature is threatening and "tampering" with it may lead to unintended consequences. Induced seismicity may suggest a sense of nature "biting back" after being disturbed.

RQ3 investigated how beliefs about EGS as TWN compared with other antecedents in explaining support for EGS development. Beliefs about TWN were associated with EGS support in Switzerland but not the United States. The Swiss results align with past research on resistance to technological developments driven by discomfort with TWN (Corner et al., 2013; Wolske et al., 2019), and support findings from the risk perception literature for technologies such as geoengineering (Siegrist & Árvai, 2020). In addition, that beliefs about human use of the underground greatly matters in explaining support for EGS suggests that pre-existing beliefs about the underground and with subterranean endeavors may be an important contextual factor in responses to deep geothermal development.

In general, support for EGS development was high in both countries, in contrast with numerous case studies which have highlighted oppositional issues with deep geothermal projects (Chavot et al., 2018; Ejderyan et al., 2019). Within our sample, EGS was generally viewed as a positive, renewable form of energy technology, though there are some differences between the US and Swiss samples. Specifically, Swiss respondents who perceived EGS as TWN were much less supportive of the technology, whereas this was not the case for US respondents. Overall, however, there were more similarities than differences between the two countries in the patterns of factors relating to EGS support.

3. Study 2

Study 2 aimed to investigate how public attitudes towards EGS are influenced by contextual elements like sense of place, local histories, and legacies of extractive industries, as well as how geothermal developers adapt to context in their outreach and communication efforts. In comparison to Study 1, which examined attitudes towards EGS technology with reference to a hypothetical project in the respondents' area, Study 2 presents data on community attitudes towards two EGS projects currently in development in the UK and the US, using qualitative case study methods.

3.1 Motivation

Study 2 further examines the role of perceptions of the underground and associations with geothermal energy through the lens of place theory, a conceptual area drawn from human geography and social psychology. The importance of place in shaping responses to energy has received increasing attention in energy acceptance research, particularly as an alternative to the reliance on NIMBY language (Boudet, 2019). A place-based perspective on energy acknowledges that how people interpret new technologies reflects their relationships with place, involving both the physical landscape and the identities, relationships, events, experiences, and history embedded there. Attachment to place can help to reinforce the social construction and amplification of risk, providing a spatial explanation for differences in responses to risky technologies (Masuda & Garvin, 2006). Energy developments that introduce land-use changes and new risks may instigate abrupt disruptions to place attachment, leading to loss of identity and sense of stability (Brown & Perkins, 1992). Disruption itself as well as the perceived risk of future disruption can drive oppositional attitudes towards the cause of the changes (Jacquet & Stedman, 2014).

Place meanings – of place as area of natural beauty or as a community, for example – serve as foundations for the bonds that people feel, and when important symbolic meanings are threatened, people are more likely to take protective action (Stedman, 2002). Perceived contradictions between the interpretations of place and technology lead to opposition, while a perception of "fit" between the place and technology results in support (Devine-Wright & Howes, 2010; McLachlan, 2009). Actors involved in development may attempt to influence perceptions of a project and its impacts by deliberately framing it in ways that emphasize the project's consistency with local place meanings and identities (Jacquet & Stedman, 2014).

Meanings of, and attachment to, place develop over time through the accumulation of experiences, memory, and interaction. Prior research has shown that past experiences with energy industries both contribute strongly to sense of place, and also provide an interpretive lens that shapes perceptions of new energy technologies (Bugden et al., 2017). In the Marcellus Shale, for instance, responses to unconventional oil and gas development were strongly influenced by past experiences with extractive industries (e.g., Brasier et al., 2011; Bugden et al., 2017; Jacquet et al., 2018; Stedman et al., 2012). Regional history with coal mining provided a way for residents to express concerns about the possibility of a similar legacy of environmental problems (Brasier et al., 2011). Given the shared characteristics of EGS development with other subterranean technologies, it seems plausible that community responses to EGS may draw heavily on place identities related to legacies of extractive industries like oil and gas or mining.

In addition, the role of perceptions of the underground and whether the underground is considered a valued part of nature, as explored above, also raises the question of how the underground figures in residents' senses of place. Proponents of geothermal often highlight its underground nature by referring to invisible but limitless "heat beneath our feet" from a featureless and empty territory waiting to be exploited – in essence, positioning the underground as a space rather than a place. As Tuan (1977) describes, "What begins as undifferentiated space becomes place as we get to know it better and endow it with value" (p. 6). Given the findings of Study 1, which suggest that the meanings and interpretations attributed to the underground are varied and potentially strongly value-laden, it seems reasonable to ask whether the underground is considered part of, or separate from, what people consider their "place."

Drawing on these concepts, Study 2 addresses the following research questions:

RQ4: How are residents' evaluations of EGS projects influenced by perceptions of place and the underground?
RQ5: To what extent is "the underground" part of place?
RQ6: How do geothermal developers navigate these dimensions when communicating about EGS?

3.2 Methods

To capture the contextual variables of interest, Study 1 uses a comparative case study approach to understand how contemporary EGS projects have unfolded in real-life contexts, using the comparison of international cases to analyze differences in underlying social and cultural factors. The Cornell Earth Source Heat (ESH) Project in Ithaca, New York is located in the Finger Lakes region of New York and aims to provide district heating to Cornell University's Ithaca campus. A test borehole was drilled in 2022 and feasibility studies are underway. The United Downs Deep Geothermal Project (UDDGP) in Redruth, Cornwall, UK, is being developed by Geothermal Engineering Limited (GEL), aiming to provide 10MW of electricity and 55MW of local heating. Drilling of a well pair was completed in summer 2019 and testing was deemed successful in summer 2022. Each case represents a project in the early stages of development, located within or in close proximity to a host community in a rural region, while allowing comparison between cultural contexts.

Data collection used qualitative methods to evoke attitudes towards EGS and elicit people's embedded experiences with place and energy (Sovacool et al., 2018; Tuck, 2014).These methods consisted of interviews with key actors (local officials, project managers, researchers, and community stakeholders), thematic analysis of publicly available documents (public relations materials, social media content, policy and planning documents, and news coverage), and site and participant observations; community focus groups were also used in the ESH case. Data collection efforts are summarized in Tables 5 and 6.

Table 5. Summary of Cornell Earth Source Heat data collection

Methods	Cornell Earth Source Heat
Document analysis	News articles (n=39) *National publications (n=6)* *Local publications (n=33)* Policy documents (n=32) Press releases (n=31) YouTube channel Project websites
Interviews	Experts (n=9) Students (n=19)
Focus groups	5 groups, N=42
Site observations	2018-2023 Town hall meetings Visitors' center

Table 6. Summary of UDGP data collection

Methods	United Downs Deep Geothermal
Document analysis	News articles (189): *National (n=60)* *Regional (n=59)* *Local (n=70)* Policy documents (n=36) Press releases (n=4) Facebook account Twitter account Project website YouTube channel Planning Register public comments
Interviews	Experts (n=8) Informal community interviews (n=~10)
Site observations	June 13-19, 2022 Visitors' center Local events, museums, and landmarks

3.3 Findings

3.3.1 Cornell Earth Source Heat

Public discourse surrounding the Earth Source Heat project (ESH) drew on place in four distinct themes, relating to different scales of place. The project was closely linked to the university's identity as a research institution and land-grant university; rhetoric throughout news coverage,

public relations materials, and planning documents connected the project to an idealized vision of the campus as a "living laboratory," a place for innovation, curiosity, and exploration. Regional and national place identities were also consistently used to frame the project and its projected benefits – for instance, with frequent references to using geothermal heat to defeat the Northeast's cold winters, or embracing EGS as a means to maintain the United States' identity as a technological leader.

A local vision of place was evident primarily in local news coverage, where a sense of identity as a place of sustainability and progressive values was used to promote adoption of EGS: "If New York State is going to [decarbonize], Tompkins County should really be in a leadership position to show how it's done." However, discussion of the project also drew on past experiences, sense of local character, and concerns about impacts to place. This was evident in the interviews and focus groups, where residents' attitudes towards ESH were mixed. For those more positive towards the project, there was a clearly expressed sense of fit with their sense of Ithaca and Cornell as places of innovation and sustainability leadership. As one participant stated, "if it's going to be done anywhere, it should be here."

In contrast, oppositional attitudes emerged from a perceived lack of fit with the area. Participants' views of Ithaca as a place of urgent, pragmatic sustainability leadership were rooted in their experiences with the anti-fracking movement in New York State. As such, some were opposed to an emerging technology that uses fracking and drilling techniques. The uncertain nature of a developing technology was also a major contributing factor; there was considerable concern that ESH did not support local goals for urgent climate action due to the uncertainty of success based on one new technology with high financial costs and technical uncertainty: "all your eggs are in one basket."

An unease with ESH based on similarities with fracking was underscored by perceptions of the underground. Some focus group participants felt protective of the underground as part of Mother Earth: "the image that came out to mind was that Earth is a living organism and we're drilling into it, and the Earth is screaming in pain." Others expressed feelings of unease or dread associated with the general depth of the drilling required, making references to disaster films or joking about the possibility of awakening sleeping threats.

Efforts by university communicators recognized and adapted to these concerns in several ways. In outreach efforts including town hall meetings, visitor hours at the drill site, and online materials, messages were deliberately focused on distinguishing EGS from fracking. This included both technical descriptions and an emphasis on the motives of ESH as a demonstration project generating new knowledge. The framing of the project's test borehole as a "data mine" that only produces information was frequently repeated. As one speaker stated, "We're not producing oil and gas here. We're producing information. The stimulation here is intellectual. There is no [hydraulic] stimulation. There's no fracking." While this approach addresses concerns about similarities with fracking, it overlooks the related concern from residents about the uncertainty of testing a new technology, creating additional dissonance for audience members.

Another prominent communication strategy successfully addressed the challenge of visualizing and contextualizing the project given its invisibility from the surface. To aid visitors in understanding the spaces and depths involved, materials drew comparisons to local settings and landmarks to put the depth of the borehole into perspective. When explaining the different rock

layers that the borehole is passing through, for instance, videos referenced surface contexts like the rock layers visible in the many gorges surrounding the ESH site.

3.3.2 United Downs Deep Geothermal

In Cornwall, discourse surrounding UDDGP drew closely on local and regional place identities rooted in Cornwall's long history of hard rock mining. Rhetoric promoting the project emphasized the revival of the mining industry in the form of geothermal development. At the national level, the project was incorporated into a broader narrative of a "green industrial revolution" in the UK, while regional and local narratives of EGS emphasized the historical identities of Cornwall and the Redruth area as homes of science and invention. News and promotional materials directly connected UDDGP to themes of Cornish leadership, identity, and heritage, with repeated mentions of "a 4,000-year history of mineral extraction and innovation." Cornwall's long history with mining and underground extraction also positions the underground as both a resource for prosperity and as a source of knowledge and discovery.

Residents' responses to UDDGP strongly reflected this sense of fit with place identity, with many participants expressing strong support due to viewing it as an updated form of mining. As one participant stated, "They say, 'Where there's a mine or a hole in the ground, you'll find a Cornishman.'…that's part of our cultural identity. It was born out of the mining industry, and we know the ground very well…So geothermal was built on that, it's mining for heat." However, some negative responses to EGS development in the area included concerns about disruption to the rural character of the area, with potential noise and traffic from drilling viewed as a threat to the historic landscape. For some, this stemmed from concerns about the fragility of the underground given the extensive mining works; one commenter noted "the potential damage both to subterranean and above-ground features" from drilling and induced earthquakes.

Communications from the developer relied on a strong emphasis on geothermal as "heat mining," representing the project as an embodiment of Cornwall's mining heritage, expertise in underground matters, and identity as a home of technology and scientific development. In displays at the visitors center and in social media posts, for instance, the achievements of UDDGP were compared to the work of Cornish historical figures and inventors. This theme was supported with social media and online messaging emphasizing regional themes and imagery like the Cornish flag and the iconic mining landscape surrounding the drill site.

Similarly to ESH, UDDGP materials also use visuals of the local geology and mining infrastructure to contextualize the project; in one video, a staff member is filmed within a mine shaft where water is visibly flowing through fractures in the rock, demonstrating the characteristics of the EGS target reservoir. Another staff member was filmed in front of the surface expression of a fault in the area, explaining what the target fault zone for UDDGP looks like. These tactics both emphasize the localized nature of the resource and provide a concrete model for audiences to understand remote and unfamiliar geological frameworks.

3.4 Study 2 Discussion

In both cases, residents consider the fit of EGS with their conceptions of place, drawing on prior experiences with energy and extractive industries. In ESH, residents evaluated EGS as one option among many for the future of energy in their community, with some finding the ESH project to be

incompatible with the local focus on urgent climate action, due to EGS's emergent nature and perceived similarity with fracking. In Cornwall, UDDGP is evaluated through the lens of local place character and an identification with subterranean expertise and technological innovation, with a strong perception of fit with the mining identity of Cornwall. Perceptions of the underground contributed to residents' perceptions of fit between place and technology, informing whether human use of the underground was viewed as extractive and exploitative, or a source of prosperity and pride in cultural heritage.

Addressing RQ6, communication efforts from Cornell and from GEL drew heavily on place-based rhetoric. In the ESH case, communicators emphasize the campus-level identity of innovation and the pursuit of knowledge to distance the project from comparisons to fracking, while UDDGP emphasizes the alignment between the project and the local, regional, and national visions of EGS. In both cases, geothermal developers made persuasive appeals that are based on local relationships with extractive industries: as "data mining" or as "heat mining."

This research demonstrates the role of place in shaping responses to energy infrastructure and new energy technologies. Perceptions of "fit" between EGS technology and place depend on the nuances of place characteristics; persuasive efforts from each project developer deliberately confront these contextual dimensions, linking the projects to different place-based energy visions and addressing local legacies of extractive technologies. However, the success of these tactics may depend on understanding the importance of competing visions of place in driving opposition, including whether the underground is considered a valued and threatened part of place.

4. Conclusion

In an engagement-based model for geothermal communication efforts, it is critical to understand what the underlying drivers of concern are for public stakeholders, rather than relying on assumptions or assuming a simple lack of knowledge. In this set of studies, we highlight several key findings that inform sources of concern towards EGS.

The results of both studies indicate that people may often view the underground as part of nature, and as such, part of the environment deserving consideration. In some cases such as Cornwall, people may view the underground as part of their "place," attributing value and meaning to subsurface spaces. While the low surface impact of geothermal installations is often emphasized as a benefit, it does not necessarily follow that it is "out of sight, out of mind." Communicators should assess and understand meaningful place characteristics in a community and address potential disruptions beyond simply the visual.

Issues may arise through both concern about the underground itself as a valued part of nature, and concern about the underground as a source of threat not to be interfered with. We recommend that communicators take steps such as focus groups, deliberative workshops, or other participatory engagement methods to understand the prior experiences that a community has with underground extraction and related technologies, such as histories with fracking or mining. Alongside the impact on perceptions of the underground, different contexts with respect to extractive histories may be an important factor in determining the impact of perceived TWN on EGS support, as Study 1 showed.

Study 1 also highlights the fact that people view the deep underground, in and of itself, as more dangerous and unfamiliar than EGS. As such, risk communication about EGS projects could seek to familiarize individuals with current activities in the deep underground before trying to address fears around the use of EGS (e.g., induced seismicity). Contextualizing underground structures and settings using more familiar surface comparisons may also be an effective approach. In addition, although the results found that the US and Swiss public were largely in favor of the underground as a resource for humans to use, respondents also expressed concerns about exploitation (e.g., drilling, storage), as did US and UK participants in Study 2, suggesting that risk communication messages should convey what geothermal managers are doing to mitigate risks and subsurface impacts.

This body of work is part of the GEOHUB trans-Atlantic collaboration between Cornell University, King's College London, University of Edinburgh, and University of Stirling, a research and policy network focusing on deep geothermal energy risk communication. Future work will continue to expand on a "social science of the subsurface," seeking to augment the currently limited literature on the social acceptance of deep geothermal energy projects as well as other subsurface technologies.

REFERENCES

Balog-way, D., Mccomas, K., & Besley, J. (2020). The Evolving Field of Risk Communication. *Risk Analysis*, *0*(0). https://doi.org/10.1111/risa.13615

Besley, J., & McComas, K. (2013). Fairness, public engagement, and risk communication. In *Effective risk communication* (pp. 108-123). Routledge.

Boudet, H. (2019). Public perceptions of and responses to new energy technologies. *Nature Energy*, *4*(June), 1. https://doi.org/10.1038/s41560-019-0399-x

Brasier, K., Filteau, M., McLaughlin, D., Jacquet, J., Stedman, R., Kelsey, T., & Goetz, S. (2011). Residents' Perceptions of Community and Environmental Impacts From Development of Natural Gas in the Marcellus Shale: a Comparison of Pennsylvania and New York Cases. *Journal of Rural Social Sciences*, *26*(1), 32.

Brown, B., & Perkins, D. (1992). Disruption in place attachment. In I. Altman & S. M. Low (Eds.), *Place Attachment* (pp. 279–304). Springer.

Bugden, D., Evensen, D., & Stedman, R. (2017). A drill by any other name: Social representations, framing, and legacies of natural resource extraction in the fracking industry. *Energy Research and Social Science*, *29*(April 2018), 62–71. https://doi.org/10.1016/j.erss.2017.05.011

Chavot, P., Heimlich, C., Masseran, A., Serrano, Y., Zoungrana, J., & Bodin, C. (2018). Social shaping of deep geothermal projects in Alsace: politics, stakeholder attitudes and local democracy. *Geothermal Energy*, *6*(1), 1–21. https://doi.org/10.1186/s40517-018-0111-6

Corner, A., Parkhill, K., Pidgeon, N., & Vaughan, N. (2013). Messing with nature? Exploring public perceptions of geoengineering in the UK. *Global Environmental Change*, *23*(5), 938–947.

Cousse, J., Trutnevyte, E., & Hahnel, U. (2021). Tell me how you feel about geothermal energy: Affect as a revealing factor of the role of seismic risk on public acceptance. *Energy Policy*, *158*(September), 112547. https://doi.org/10.1016/j.enpol.2021.112547

Cuppen, E., Ejderyan, O., Pesch, U., Spruit, S., Van de Grift, E., Correljé, A., & Taebi, B. (2020). When controversies cascade: Analysing the dynamics of public engagement and conflict in the Netherlands and Switzerland through "controversy spillover". *Energy Research & Social Science*, *68*, 101593.

Deichmann, N., & Giardini, D. (2009). Earthquakes Induced by the stimulation of an enhanced geothermal system below Basel (Switzerland). *Seismological Research Letters*, *80*(5), 784–798. https://doi.org/10.1785/gssrl.80.5.784

Devine-Wright, P., & Howes, Y. (2010). Disruption to place attachment and the protection of restorative environments: A wind energy case study. *Journal of Environmental Psychology*, *30*, 271–280. https://doi.org/10.1016/j.jenvp.2010.01.008

Dowd, A.-M., Boughen, N., Ashworth, P., & Carr-Cornish, S. (2011). Geothermal technology in Australia: Investigating social acceptance. *Energy Policy*, *39*(10), 6301–6307. https://doi.org/10.1016/j.enpol.2011.07.029

Ejderyan, O., Ruef, F., & Stauffacher, M. (2019). Geothermal energy in Switzerland: Highlighting the role of context. In A. Manzella, A. Allansdottir, & A. Pellizzone (Eds.), *Geothermal Energy and Society* (pp. 239–257). Springer International Publishing. https://doi.org/10.1007/978-3-319-78286-7

Ellsworth, W. (2013). Injection-induced earthquakes. *Science*, *341*(6142), 1225942. https://doi.org/10.1126/science.1225942

Fischhoff, B. (1995). Risk perception and communication unplugged: twenty years of process. *Risk Analysis*, *15*(2), 137–145.

Fritz, S., Ward, S., Byrne, P., Namuth, D., & Egger, V. (2004). Short and Long-Term Impacts of Biotechnology Education on Professionals Who Communicate Science to the Public. *Journal of Natural Resources and Life Sciences Education*, *33*(1), 111–116.

Giardini, D. (2009). Geothermal quake risks must be faced. *Nature*, *462*(7275), 848–849. https://doi.org/10.1038/462848a

Gross, M. (2013). Old Science Fiction, New Inspiration: Communicating Unknowns in the Utilization of Geothermal Energy. *Science Communication*, *35*(6), 810–818. https://doi.org/10.1177/1075547012469184

Hoogendoorn, G., Sütterlin, B., & Siegrist, M. (2021). Tampering with Nature: A Systematic Review. *Risk Analysis*, *41*(1), 141–156. https://doi.org/10.1111/risa.13619

Hoşgör, E., Apt, J., & Fischhoff, B. (2013). Incorporating seismic concerns in site selection for enhanced geothermal power generation. *Journal of Risk Research*, *16*(8), 1021–1036. https://doi.org/10.1080/13669877.2013.788058

Jacquet, J., Junod, A., Bugden, D., Wildermuth, G., Fergen, J., Jalbert, K., Rahm, B., Hagley, P., Brasier, K., Schafft, K., Glenna, L., Kelsey, T., Fershee, J., Kay, D., Stedman, R., & Ladlee, J. (2018). A decade of Marcellus Shale: Impacts to people, policy, and culture from 2008 to 2018

in the Greater Mid-Atlantic region of the United States. *The Extractive Industries and Society*. https://doi.org/10.1016/J.EXIS.2018.06.006

Jacquet, J., & Stedman, R.(2014). The risk of social-psychological disruption as an impact of energy development and environmental change. *Journal of Environmental Planning and Management*, *57*(9), 1285–1304. https://doi.org/10.1080/09640568.2013.820174

Kasperson, R., & Ram, B. (2013). The public acceptance of new energy technologies. *Daedalus*, *142*(1), 90-96.

Kearnes, M., & Rickards, L. (2017). Earthly graves for environmental futures: Techno-burial practices. *Futures*, *92*, 48–58. https://doi.org/10.1016/j.futures.2016.12.003

Kim, K.-H., Ree, J.-H., Kim, Y., Kim, S., Kang, S. Y., & Seo, W. (2018). Assessing whether the 2017 Mw 5.4 Pohang earthquake in South Korea was an induced event. *Science*, eaat6081. https://doi.org/10.1126/SCIENCE.AAT6081

Kinchy, A., Phadke, R., & Smith, J. (2018). Engaging the Underground: An STS Field in Formation. *Engaging Science, Technology, and Society*, *4*, 22–42. https://doi.org/10.17351/ests2018.213

Knoblauch, T., & Trutnevyte, E. (2018). Siting enhanced geothermal systems (EGS): Heat benefits versus induced seismicity risks from an investor and societal perspective. *Energy*. https://doi.org/10.1016/j.energy.2018.04.129

Knoblauch, T., Trutnevyte, E., & Stauffacher, M. (2019). Siting deep geothermal energy: Acceptance of various risk and benefit scenarios in a Swiss-German cross-national study. *Energy Policy*, *128*, 807–816. https://doi.org/10.1016/J.ENPOL.2019.01.019

Leiserowitz, A. (2006). Climate change risk perception and policy preferences: The role of affect, imagery, and values. *Climatic Change*, *77*(1–2), 45–72. https://doi.org/10.1007/s10584-006-9059-9

Masuda, J., & Garvin, T. (2006). Place, Culture, and the Social Amplification of Risk. *Risk Analysis*, *26*(2), 437–454. https://doi.org/10.1111/j.1539-6924.2006.00749.x

McComas, K., Lu, H., Keranen, K., Furtney, M., & Song, H. (2016). Public perceptions and acceptance of induced earthquakes related to energy development. *Energy Policy*, *99*, 27–32. https://doi.org/10.1016/j.enpol.2016.09.026

McLachlan, C. (2009). "You don't do a chemistry experiment in your best china": Symbolic interpretations of place and technology in a wave energy case. *Energy Policy*, *37*(12), 5342–5350. https://doi.org/10.1016/j.enpol.2009.07.057

Meisenberg, G. (2009). Designer babies on tap? Medical students' attitudes to pre-implantation genetic screening. *Public Understanding of Science*, *18*(2), 149–166.

Partridge, T., Thomas, M., Pidgeon, N., & Harthorn, B. (2019). Disturbed Earth: Conceptions of the Deep Underground in Shale Extraction Deliberations in the US and UK. *Environmental Values*, *28*(6), 641–663. https://doi.org/10.3197/096327119X15579936382482

Pellizzone, A., & Allansdottir, A. (2019). Drawing the Picture: Public Engagement Experiences as Tools Towards an Emerging Framework. In A. Manzella, A. Allansdottir, & A. Pellizzone (Eds.), *Geothermal Energy and Society*. Springer.

Peters, E., & Slovic, P. (1996). The Role of Affect and Worldviews as Orienting Dispositions in the Perception and Acceptance of Nuclear Power1. *Journal of Applied Social Psychology*, *26*(16), 1427–1453. https://doi.org/10.1111/j.1559-1816.1996.tb00079.x

Porter, R., Striolo, A., Mahgerefteh, H., & Faure Walker, J. (2018). Addressing the risks of induced seismicity in subsurface energy operation. *Energy and Environment*. https://doi.org/10.1002/wene.324

Raimi, K. T., Wolske, K. S., Hart, P. S., & Campbell-Arvai, V. (2020). The Aversion to Tampering with Nature (ATN) Scale: Individual Differences in (Dis)comfort with Altering the Natural World. *Risk Analysis*, *40*(3), 638–656.

Romanach, L., Carr-cornish, S., & Muriuki, G. (2015). Societal acceptance of an emerging energy technology: How is geothermal energy portrayed in Australian media? *Renewable and Sustainable Energy Reviews*, *42*, 1143–1150. https://doi.org/10.1016/j.rser.2014.10.088

Siegrist, M., & Árvai, J. (2020). Risk Perception: Reflections on 40 Years of Research. *Risk Analysis*, *40*(S1), 2191–2206. https://doi.org/10.1111/risa.13599

Sjöberg, L. (2000). Perceived risk and tampering with nature. *Journal of Risk Research*, *3*(4), 353–367. https://doi.org/10.1080/13669870050132568

Slovic, P., Flynn, J., & Layman, M. (1991). Perceived risk, trust, and the politics of nuclear waste. *Science*, *254*(5038), 1603–1608.

Song, H., Lu, H., & McComas, K. (2021). The Role of Fairness in Early Characterization of New Technologies: Effects on Selective Exposure and Risk Perception. *Risk Analysis*, *41*(9), 1614–1629. https://doi.org/10.1111/risa.13633

Sovacool, B., Axsen, J., & Sorrell, S. (2018). Promoting novelty, rigor, and style in energy social science: Towards codes of practice for appropriate methods and research design. *Energy Research and Social Science*, *45*(July 2018), 12–42. https://doi.org/10.1016/j.erss.2018.07.007

Stauffacher, M., Muggli, N., Scolobig, A., & Moser, C. (2015). Framing deep geothermal energy in mass media: the case of Switzerland. *Technological Forecasting and Social Change*, *98*, 60–70. https://doi.org/10.1016/j.techfore.2015.05.018

Stedman, R. (2002). Toward a Social Psychology of Place: Predicting Behavior From Place-Based Cognitions, Attitude, and Identity. *Environment and Behavior*, *34*(5), 561–581.

Stedman, R., Jacquet, J., Filteau, M., Willits, F., Brasier, K., & McLaughlin, D. (2012). Marcellus shale gas development and new boomtown research: Views of New York and Pennsylvania residents. *Environmental Practice*, *14*(4), 382–393. https://doi.org/10.1017/S1466046612000403

Stephens, J., & Jiusto, S. (2010). Assessing innovation in emerging energy technologies: Socio-technical dynamics of carbon capture and storage (CCS) and enhanced geothermal systems (EGS) in the USA. *Energy Policy*, *38*(4), 2020–2031. https://doi.org/10.1016/j.enpol.2009.12.003

Stewart, I., & Lewis, D. (2017). Communicating contested geoscience to the public: Moving from ‘matters of fact’ to ‘matters of concern.’ *Earth-Science Reviews*, *174*(September), 122–133. https://doi.org/10.1016/j.earscirev.2017.09.003

Trench, B. (2008). Towards an analytical framework of science communication models. *Communicating science in social contexts: New models, new practices*, 119-135.

Trutnevyte, E., & Ejderyan, O. (2017). Managing geoenergy-induced seismicity with society. *Journal of Risk Research*, *21*(10), 1287–1294. https://doi.org/10.1080/13669877.2017.1304979

Tuan, Y. F. (1977). *Space and Place: the Perspective of Experience*.

Tuck, E. (2014). Place in Research. In *Place in Research* (Issue January). https://doi.org/10.4324/9781315764849

Westlake, S., John, C., & Cox, E. (2023). Perception spillover from fracking onto public perceptions of novel energy technologies. *Nature Energy*, *8*(2), 149–158. https://doi.org/10.1038/s41560-022-01178-4

Williams, R. (1990). *Notes on the Underground: An Essay on Technology, Society, and the Imagination*. MIT Press.

Wolske, K., Raimi, K., Campbell-Arvai, V., & Hart, P. S. (2019). Public support for carbon dioxide removal strategies: The role of tampering with nature perceptions. *Climatic Change*, *152*(3), 345–361.

Wüstenhagen, R., Wolsink, M., & Bürer, M. (2007). Social acceptance of renewable energy innovation: An introduction to the concept. *Energy Policy*, *35*(5), 2683–2691. https://doi.org/10.1016/j.enpol.2006.12.001

Embracing a Circular Model in the Management of Cooling Tower Fill Packs. A Case Study of a Pilot Project Rolled out in Partnership Between Kengen and 'Jua Kali' Entrepreneurs

Rose Mathenge

Keywords

Cooling tower fill packs, circular economy, sustainability, Jua Kali

Entrepreneurs

ABSTRACT

Cooling tower fill packs are an integral part of geothermal power plants cooling tower system systems. The purpose of the cooling tower fill packs is to increase the surface area to allow for maximum contact between air and water to hasten the cooling process. All the power plants and wellheads in the Olkaria geothermal field utilize fill packs which form one of the major wastes generated. During annual inspections of power plants, enormous amounts of cooling tower fill and pack waste are generated. Disposal of the fill packs waste has been a challenge because the waste is mainly hardened plastic and, therefore, could not be disposed of in dump sites. Similarly, efforts to dispose of through incineration proved costly and unsustainable given the accelerated development envisaged in Olkaria. The cost stood at two hundred thousand USD as of the year 2016. Given the above background, since the commissioning of the Olkaria II power plant in 2003, no disposal of the said waste had been undertaken up to the year 2019. Before conducting this study, a large volume of cooling tower waste had been stored at one of the well pads posing a fire risk and halting well monitoring activities for over ten years. To address the problem of disposal of the fill packs, a joint study was conducted between KenGen and" Jua Kali" entrepreneurs. From this study, a potential market for the waste was established. The process entailed shredding the waste at the site to facilitate transport given the bulk nature of the waste, heating and mixing the waste with other additives to produce various products from the waste. The processing was undertaken at the Jua Kali entrepreneurs' sheds in Nairobi.

Establishing a market for the cooling tower fill pack waste is a major milestone as it has created a circular model in managing the waste through reuse to produce products. This is a win-win situation for all: the environment, KenGen, and the entrepreneurs. The breakthrough has reduced the environmental footprint, spurred a secondary market for SMEs, and reduced the disposal cost.

During the pilot study over twenty tonnes of waste were recycled for manufacturing products. The pilot study has saved KenGen about USD Five Hundred Thousand (500,000) and is expected to derive a saving of USD Seventy-Two Thousand (72,000) annually.

1. Introduction

Globally, corporate leadership teams face unprecedented difficulties, including unsustainable natural resource consumption rates. Embracing circularity in value chains in place of a linear model presents an opportunity to create an additional natural resource to address high global natural resource consumption rates.

Circularity means a decoupling of economic growth from resource consumption. It entails reusing, repairing, refurbishing, and recycling existing materials and products. According to Maj et al. (2022), for organization, circularity entails conserving materials, extending a product's lifetime through repair and reuse, and ultimately recycling. According to Zhang et al. (2010), the circularity model's overarching goal is to mimic the natural mechanism of the "producer-consumer-decomposer" system to obtain closed material circulation, multilevel utilization, and the minimum output of waste. Industrial symbiosis can present one of the pathways to achieving the circular economy (CE) and achieving green growth. Industrial symbiosis is a particular kind of synergy, that "engages traditionally separate industries in a collective approach to competitive advantage involving physical exchange of materials, energy, water, and/or by-products" (Chertow, 2000). It proposes to create a system for trading material, energy, and water by-products among companies, usually within a park, neighborhood, or region" (Lowe, 2001). Governments play a key role in rolling out a circular economy model by setting technical guidelines, creating appropriate market conditions, policy, and Institutional and regulatory frameworks. To steer the country towards a circular model, the Government of Kenya has enacted the Sustainable Waste Management Act, of 2022. The Act presents a major milestone, and the expected inherent regulations will offer clarity along this journey. The Act mandates the National Environment Management Authority to develop a database of different waste streams generated by various industries as a focal point for creating industrial symbiosis. Further, the Act obligates producers to bear extended producer obligations to reduce pollution and environmental impacts of their products and waste arising thereof.

To address unsustainable natural resources utilization, circularity represents a strategic issue, which presents an opportunity to cut costs, boost growth, and build resilience. The merit of circularity in any organization is clear. However, the trajectory to a circular business model requires setting up a robust system including building the right cross-functional team to implement a circular strategy and establish measurable goals and target levels of recycled content, reuse, and recycling. In addition to supportive legislation, regulatory framework, and industry standards to help change behavior and strengthen circular economies, establishing partnerships with suppliers and key stakeholders.

Normally, embracing circularity in a process offers several benefits including addressing environmental challenges by reducing material consumption, increasing efficiency, and cutting greenhouse gas emissions, and can set up a strong commercial foundation that is scalable. In addition, it addresses SDGs no 9, 12, and 17 on Industrial, innovation &infrastructure, Sustainable consumption& production, and partnership for the goals which are key pillars in achieving sustainable development.

The current pilot project sought to address five objectives, which were to explore possibilities of recycling cooling tower fill packs, establish a partnership to roll out the pilot research study, demonstrate potential economic and environmental benefits for undertaking the pilot study, document successes experienced along the way and distill lessons learned in the process.

The pilot research study seeks to embrace circularity models in managing cooling tower fill packs instead of linear models to convert cooling tower fill waste into raw materials. The waste forms a major waste from geothermal power plants. It seeks to convert the waste into raw material for other industrial processes. The pilot study seeks to expand the list of materials being recycled in Kenya as the country embarks on the journey to embrace the circular economy model. Currently, there are initiatives underway on recycling and circularity, but it's still not enough to provide the amount of recycled material that the industry will need. In addition, stringent laws are in place to minimize environmental pollution associated with plastics, which the company is required to comply with. For instance, the Sustainable Waste Management Act of 2022 requires NEMA to develop a database on input and type of industrial waste generated countywide as a step towards creating industrial synergies and minimizing environmental risks. Further, KenGen is in the process of setting up a green energy park in Olkaria as a special economic zone, which seeks to create industrial symbiosis for enhancing efficiency in material utilization. The study, therefore, is a step towards embracing industrial synergies to minimize environmental risk and increase resource utilization efficiency. In addition, the study is aligned with international priorities such as the Sustainable Development Goals and climate change mitigation.

To address the four objectives a joint pilot project between KenGen and" Jua kali" entrepreneurs was conducted in the years 2020, and through to February 2024. From this study, a potential market for waste was established. The process entailed shredding the waste at the site to facilitate, heating, and mixing the waste with other additives to allow to produce various products from the waste. The processing was undertaken at the Jua Kali entrepreneurs' sheds.

2. Initial Research and Product Development Process

The research to develop a circularity model in managing cooling tower fills commenced in 2012 and registered a breakthrough in 2020. The research commenced by engaging cooling tower fill manufacturers in discussions on available options for managing the waste. The discussions did not yield any results as manufacturers seemed unaware or rather sent a silent message implying the organization just needs to use the product and then figure out how best to deal with the waste along the way. This was followed by holding discussions with recyclers to explore options for recycling the waste. The first step was marked by holding discussions with water tank manufacturers in the Export Processing Zone Authority zone in Kitengela area in Kenya. This was followed by discussions with Finlays LTD on the possibility of manufacturing recyclable fencing posts from the waste, which proved unsuccessful. This was mainly because the waste exhibits the characteristics of hardened plastic, which charges on being subjected to heat instead of melting. This was followed by visiting the Naivasha Sub County Environmental Office for advice on possible disposal mechanisms. This too was unsuccessful as the county handles mainly the Municipal solid waste category. From the discussion, it was clear that KenGen was therefore obliged to develop a disposal mechanism for any industrial waste related to geothermal development. This was followed by seeking incineration firms to dispose of the waste. However, this though a feasible option turned out to be unsustainable given that KenGen was accelerating

geothermal development in Olkaria. The lowest bidder put a figure of Two Hundred Thousand dollars to dispose of the waste that had been accumulated up to the year 2015. This was followed by a successful step of engaging Jua Kali entrepreneurs to partner in creating reuse of the waste in manufacturing construction industry products. Upon reaching out to the entrepreneurs, it took about two months to make a breakthrough in researching different chemical processing to facilitate the recycling of waste.

2.1 Cooling tower waste generating information

The Olkaria Geothermal field is home to five conventional power plants and seven wellheads. The cooling tower fill packs are estimated at One Thousand Six Hundred tonnes and fourteen tonnes from the conventional power plants and the wellheads, respectively. The replacement frequency of the cooling tower fills is guided by the condition of the fill packs and normally takes about two to four years, with manufacturers recommending three years. In 2023, a new initiative was put in place whereby the removal of cooling tower fill packs is being done per cell while the power plant is operational. This implies that there will be continuous production of waste.

2.2 Initial research and product development process

The research to develop a circularity model in managing cooling tower fills commenced in 2012 and registered a breakthrough in 2020. The research commenced by engaging cooling tower fill manufacturers in discussions on available options for managing the waste. The discussions did not yield any results as manufacturers seemed unaware or rather sent a silent message implying the organization just needs to use the product and then figure out how best to deal with the waste along the way. This was followed by holding discussions with recyclers to explore options for recycling the waste. The first step was marked by holding discussions with water tank manufacturers in the EPZA zone in Kitengela. This was followed by discussions with Finlays LTD on the possibility of manufacturing recyclable fencing posts from the waste, which proved unsuccessful. This was mainly because the waste exhibits the characteristics of hardened plastic, which charges on being subjected to heat instead of melting. This was followed by visiting the Naivasha Sub County Environmental Office for advice on possible disposal mechanisms. This too was unsuccessful as the county handles mainly the Municipal solid waste category. From the discussion, it was clear that KenGen was therefore obliged to develop a disposal mechanism for any industrial waste related to geothermal development. This was followed by seeking incineration firms to dispose of the waste. However, this though a feasible option turned out to be unsustainable given that KenGen was accelerating geothermal development in Olkaria. The lowest bidder put a figure of Two Hundred Million dollars to dispose of the waste that had been accumulated up to the year 2015. This was followed by a successful step of engaging Jua Kali entrepreneurs to partner in creating reuse of the waste in manufacturing construction industry products. Upon reaching out to the entrepreneurs, it took about two months to make a breakthrough in researching different chemical processing to facilitate the recycling of waste.

2.3 Product processing processes

Upon removal of the cooling tower fills from the power plants, the waste is ordinarily stored in an open area within the Olkaria field. The entrepreneurs shred the waste and put it in gunny bags for ease of transportation to Jua Kali industries. At the industries, the shredded raw material undergoes filtration to remove dust. Secondly, the raw material is put in a fine crusher to crush the material

further. Thirdly, the fine material is put in a drier where additives are added to facilitate chemical processing. This is followed by adding heating and compression. This is followed by a tooling process, whereby the product is shaped to the desired shape. The final processes entail cutting the terrazzo strip to the desired size and stacking them into bundles for storage.

2.4 Research approach and methodology

The methodology applied entailed deploying a joint pilot research undertaken by KenGen and "Jua Kali" entrepreneurs. It entailed visiting "Jua Kali" sheds for test running the possibility of recycling the materials and undertaking market surveys. Upon establishing the feasibility of recycling the packs. The approach entailed crushing the waste, chemical processing, heating, compression, and tooling process to facilitate the desired shape of the product.

2.5 Challenges experienced

Just like any new process, diverse challenges were encountered during the joint pilot research study. This included determining the right crushing machine. At first, some of the partners commenced with air-cooling crushing machines, which proved ineffective as they experienced overheating. The team finally settled for water-cooled riser engines to give motion to the machine. Secondly, determining the right licensing requirements for entrepreneurs to facilitate partnerships was a major challenge. This was a critical component to ensure control of the waste from the source to the final site. The team finally settled for licensing from the Association of Recyclers and National Environment Management Authority. Thirdly, the dust accumulated in the cooling tower fills over the years is quite significant, approximately half a tonne for every four tonnes of crushed waste. This meant that the entrepreneurs had to engage more staff to remove soil particles to ensure acceptable quality of raw materials to the recyclers. Fourth, frequent breakdown of crushing machines, which necessitated transportation of the machine to Naivasha town for repair as the site is in a remote area. Fifth, during transportation, the traffic police would impound the waste as they were unfamiliar with the waste. Lastly, the rigidity of clearance at the KWS gate requires that the vehicles transporting waste be cleared in advance, this meant that the entrepreneurs were unable to utilize return trips for general transport vehicles and had to have a dedicated vehicle to transport the waste. This meant a reduced profit margin on their side and increased CO_2 footprint for the transportation of the waste.

2.6 Successes

The pilot study presented varying economic, environmental, and social benefits by turning an environmental problem into business solutions. The project registered numerous successes, Firstly, by creating a circular model for managing waste, created an opportunity to put the materials back into the supply chain, rather than disposing of them as waste. This meant the creation of new a secondary resource for the Small Medium Enterprises (SMEs). Secondly, it has created an employment opportunity for non-skilled and semi-skilled workers in the Jua Kali Industries and at the crushing site. Thirdly, it has created an income for the entrepreneurs, thus improving their livelihood. Fourth, it presented a quality product to the construction industry. In addition, the partnership offers SMEs an opportunity to grow in line with the government's commitment to spurring the growth of SMEs through the Bottom-up Economic Transformation agenda (BETA). Fifth, KenGen has realized cost savings in the form of foregone waste disposal and avoided GHG

emissions to the tune of 2.125 tonnes Co_2e annually. Further, commencing March 2024 the waste will be sold competitively in the market implying a further income to KenGen.

2.7 Lessons learnt

The cooling tower fill pack generation far outstrips the SME market. This is compounded by the slow economic downturn being experienced currently. This saw some of the SMESs closing shops in the year 2023. To address the issue, carrying out market surveys and conducting joint research efforts is critical to create more markets for the waste. Secondly, to reduce operation costs efforts should be geared toward creating linkages with manufacturers to explore options for procuring reusable cooling tower fills. Thirdly, KenGen needs to procure a crushing machine to crush the waste at the generation point. This would reduce the storage area required, transportation costs, and littering experienced during the transportation phase. Lastly, there is a need to identify three storage areas to minimize transportation costs.

3. Discussion

A joint KenGen and Jua Kali entrepreneurs' joint research journey has been presented in this paper. According to this study's results, the research journey was a success marked by leveraging various partners' strengths and a shared vision and goal of a healthier environment, creating a product from waste. The pilot research aligns with KenGen's vision of embracing a circular economic model in the management of the resources at the upcoming Olkaria Green Energy Park. In addition to aligning with the global SDGs particularly SDG no 9, 12, and 17 on Industrial, innovation &infrastructure, Sustainable consumption& production, and partnership for the goals which are key pillars in achieving sustainable development.

The study results demonstrate that the partnership model is a critical aspect in managing various sustainability aspects in geothermal development. Indeed, partnerships can open doors to different business models for organization and stakeholders. Thirdly, to scale up circularity in geothermal development in a strategic manner, there is a need to scan the whole value chain identify opportunities and prioritize as a route to sustainably managing geothermal development. In addition, this can assist in identifying different industrial sectors that have the potential to set up at the green energy park. This can play a critical role in ensuring a wide variety of resource input and output flows available for inter-industry exchanges. Similarly, having companies of varied sizes (including SMEs) can facilitate the development of symbiosis, by offering opportunities for adding value to different volume streams from geothermal processes.

4. Conclusion

The purpose of the paper was to showcase successful joint research between KenGen and Jua Kali entrepreneurs, which created a market for cooling tower fills by converting waste into a product. In addition to offering a platform for piloting a symbiotic link between KenGen and relevant Jua Kali entrepreneurs. The pilot study has demonstrated environmental and economic benefits to the company, community, and entrepreneurs. The research is a story of resilience and applying innovation in managing waste sustainably. Secondly, it is a step in the operationalization of industry symbiosis envisaged in the upcoming Olkaria Green Energy Park. Third, the research

demonstrates the need to embrace partnerships to derive value for various processes in geothermal development. Fourth, the research is a major win for the environment as it allows the waste back to the value chain instead of disposing of the waste. Finally, to optimize circularity in the processes, it is critical to map the potential for circular flows in the company's existing value chain, select the options that create the most value, and start scaling a circular business.

5. Recommendations

Based on the research findings and the evolving regulatory framework requiring the country to embrace a circular model in managing waste, KenGen needs to set up a multi-disciplinary team to identify possible waste that can move to the circular economy, serve structures, and roll out the circular economy for the company different categories of waste.

REFERENCES

Government of the Republic of Kenya, 2022: Sustainable Waste Management Act, 2022

Government of the Republic of Kenya, 2020: The Nakuru County Waste Management Act, 2021

Government of the Republic of Kenya, 2007: The Constitution of Kenya, 2010

Maj, M., Erick, O., Lourenço, G., 2022: Green economic change in Africa – green and circular innovation trends, conditions and dynamics in Kenyan companies, Innovation and Development

Zhang, L., Yuan, Z., Bi, J., Zhang, B., Liu, B. 2010: *Eco-industrial parks: National pilot practices in China*. Journal of Cleaner Production

Regional Updates

The Deep Geothermal Energy Potential of Baker Lake (Nunavut, Canada): Initial Resource Assessment from Monte Carlos Analysis

Ysaline Bacon[1,2], Mafalda M. Miranda[1], Jasmin Raymond[1], Juliet Newson[2], Andrew Wigston [3], Matthew Minnick[4]

[1] Institut national de la recherche scientifique, Québec, Canada

[2] Reykjavik University, Reykjavík, Iceland

[3] Natural Resources Canada, Ottawa, Canada

[4] RESPEC, Rapid City, USA

Keywords

Enhanced Geothermal System (EGS); Heat flow estimation; Monte Carlo analysis; Northern Canada; Renewable energy; Sensitivity analysis; Resource assessment

ABSTRACT

Diesel generators and oil-fired boilers are the main energy systems for many remote communities in Canada and worldwide. This unsustainable energy framework has been creating a cycle of energy insecurity and poverty that communities have a desire to break. Geothermal energy resources, due to their base-load nature, versatility, and the fact that they are produced locally, could be one of the options for improving the energy sovereignty of remote communities. To find out whether geothermal energy is an option for remote communities, the first step is to carry out a resource assessment. The objective of this study was to evaluate the geothermal resource potential of Baker Lake, Nunavut, a typical remote community located in the northern Canadian Shield region where heat flow is usually low (<50 mW m^{-2}). The results of this study indicate, however, that Baker Lake has a greater heat flow, ranging from 68 to 78 mW m^{-2}. This suggests that geothermal resources could be exploited for space heating applications, and our analysis indicates that a depth of 4 km is required to have a high probability (>90%) of meeting the community's ~77 GWh annual heat demand. A depth of 8 km is required to have a high probability of generating electricity. Cogeneration potential also suggests that waste heat from electricity production can significantly support heating needs. Although these results are promising, exploiting geothermal resources in remote areas is particularly risky due to the scarcity of geothermal data. A way to de-risk geothermal projects at an early stage is to identify the sources of uncertain information that have the greatest impact on resource evaluation. The Monte Carlo-based sensitivity analysis carried out as part of this work revealed that, given the existing information, the recovery factor and reservoir volume are the main sources of uncertainty. Future research should focus on reducing the uncertainty of these sources to fully assess the potential for geothermal energy use at Baker Lake.

1. Introduction

Off-grid communities, characterized by their lack of connection to national electricity grids or natural gas networks (Royer, 2011), are prevalent in remote regions such as northern Canada. These communities face major energy challenges due to their isolation and reliance on diesel for space heating and power generation (Pinto and Gates, 2022).

Baker Lake, located in the hinterland of Nunavut (Figure 1.1), is a pertinent case study of the difficult energy situation faced by these northern communities. Reliance on diesel presents environmental risks, including greenhouse gas emissions and the risk of fuel spills, which can have detrimental effects on the Arctic ecosystem (Byrne, 2018). Aware of the need to find sustainable energy solutions, various levels of government, energy companies and research institutions have launched efforts to explore alternative energy sources (QEC, 2018).

Geothermal energy has gained attention as a promising option, offering several benefits for off-grid communities (Minnick et al., 2018). Unlike fossil fuels, geothermal energy offers a renewable, local, and environmentally friendly alternative with minimal carbon emissions. Additionally, geothermal power plants operate continuously, providing a stable and predictable source of electricity and heating regardless of weather conditions.

Enhanced geothermal systems (EGS) offer the potential to develop geothermal energy for electricity and/or heat use in locations without conventional hydrothermal (i.e., convective) resources (Sircar et al., 2022). An EGS is a technology for harnessing geothermal energy from subsurface reservoirs that require artificial stimulation methods such as hydraulic fracturing to enhance the permeability of the reservoir host rocks (Sircar et. al, 2022). For example, the Rittershofen EGS Project (Baujard et al., 2016) in the French Upper Rhine Graben has provided heat for industrial proposes with an installed capacity of 24 MW_{th} to the Beinheim Starch plant since 2005. The system has a depth of 2500 m and utilizes fractured sandstone and carboniferous granite where the 3-well bottom-hole temperature is 177°C. The Soultz-sous-Forêts EGS power project, operational since 2009, can generate 2 MW of electricity via a binary cycle power plant from heat produced from crystalline basement rocks at 5000 m depth (Koelbel and Genter, 2017). Challenges associated with this technology include efficiently stimulating reservoirs without causing significant microseismic activity, managing injected fluids, and developing accurate simulations for reservoir characterization and description (Sircar et al., 2022).

The Government of Nunavut and Nunavut's power utility company, Qulliq Energy Corporation (QEC), are committed to exploring the potential of EGS to provide a sustainable energy alternative for remote communities such as Baker Lake, Nunavut (QEC, 2018). In this framework, Minnick et al. (2018) conducted a preliminary study to assess the regional geothermal potential of Nunavut. The study determined there was insufficient data to accurately assess Nunavut's geothermal potential and recommended more data be collected, including drilling boreholes in a few targeted communities, including Baker Lake.

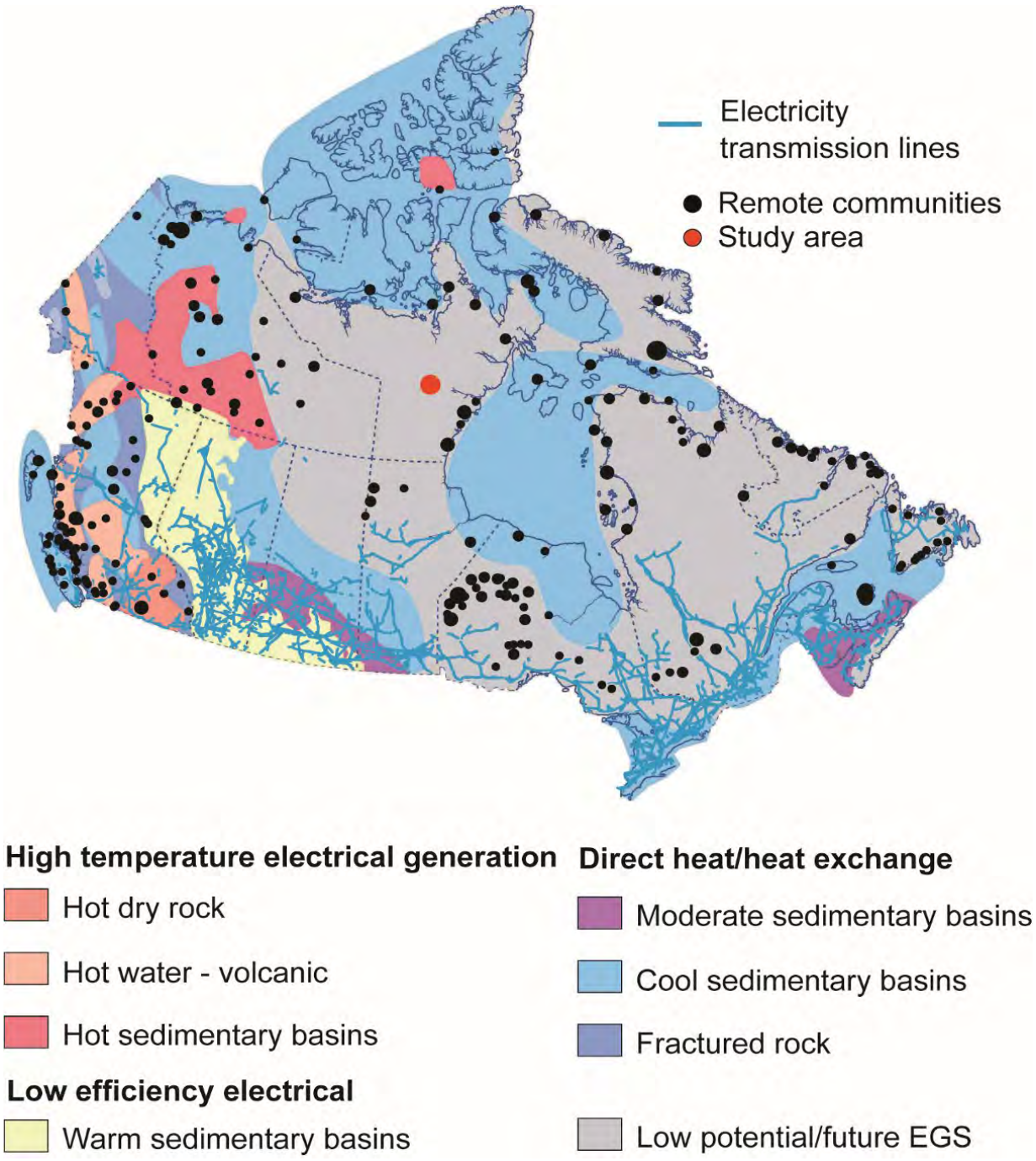

Figure 1.1: Geothermal potential of Canada estimated by Grasby et al. (2012) with location of remote communities taken from Arriga et al. (2017) and modified by Miranda (2021). The red dot represents the municipality of Baker Lake, which is the geographic center of Canada.

In support of this recommendation, a 500 m-deep borehole was cored in Baker Lake in late 2022 and instrumented with a thermistor logging cable. Gold et al. (2023) previously used this data to evaluate various technologies to mitigate the melting of permafrost considering the development of a borehole thermal energy storage system. Using available rock and temperature data, this study builds on the work of Minnick et al. (2018) with the objective of evaluating the deep geothermal

potential of Baker Lake. An EGS would most likely be required to develop geothermal energy in the region given the relatively low geothermal gradient and low permeability of the crystalline bedrock found at depth. As such, our study employed a data-driven Monte Carlo-based approach to assess the feasibility of generating electricity and producing heat at depths from 1 to 10 km. The EGS Resource Assessment Protocol, or Beardsmore Protocol (Beardsmore et al., 2010), was adapted to the arctic context of the region in this study to estimate the thermal energy available to the end user. Additionally, this study aims to rigorously assess the uncertainties associated with the input parameters. By taking these uncertainties into account, this study aims to provide a more robust understanding of Nunavut's theoretical deep geothermal potential.

2. Geological Setting

The community of Baker Lake lies on the Precambrian basement (Figure 2.1) of the Western Churchill Province in the Canadian Shield. Although in close proximity to the Baker Lake Basin (Figure 2.2), the lithology beneath the community of Baker Lake is Archean meta-granite gneiss, and some intercalation of rhyolite and granite rock types. The overburden is thin (0.2 to 2.0 m thick) and mostly composed of gravel to silty sand.

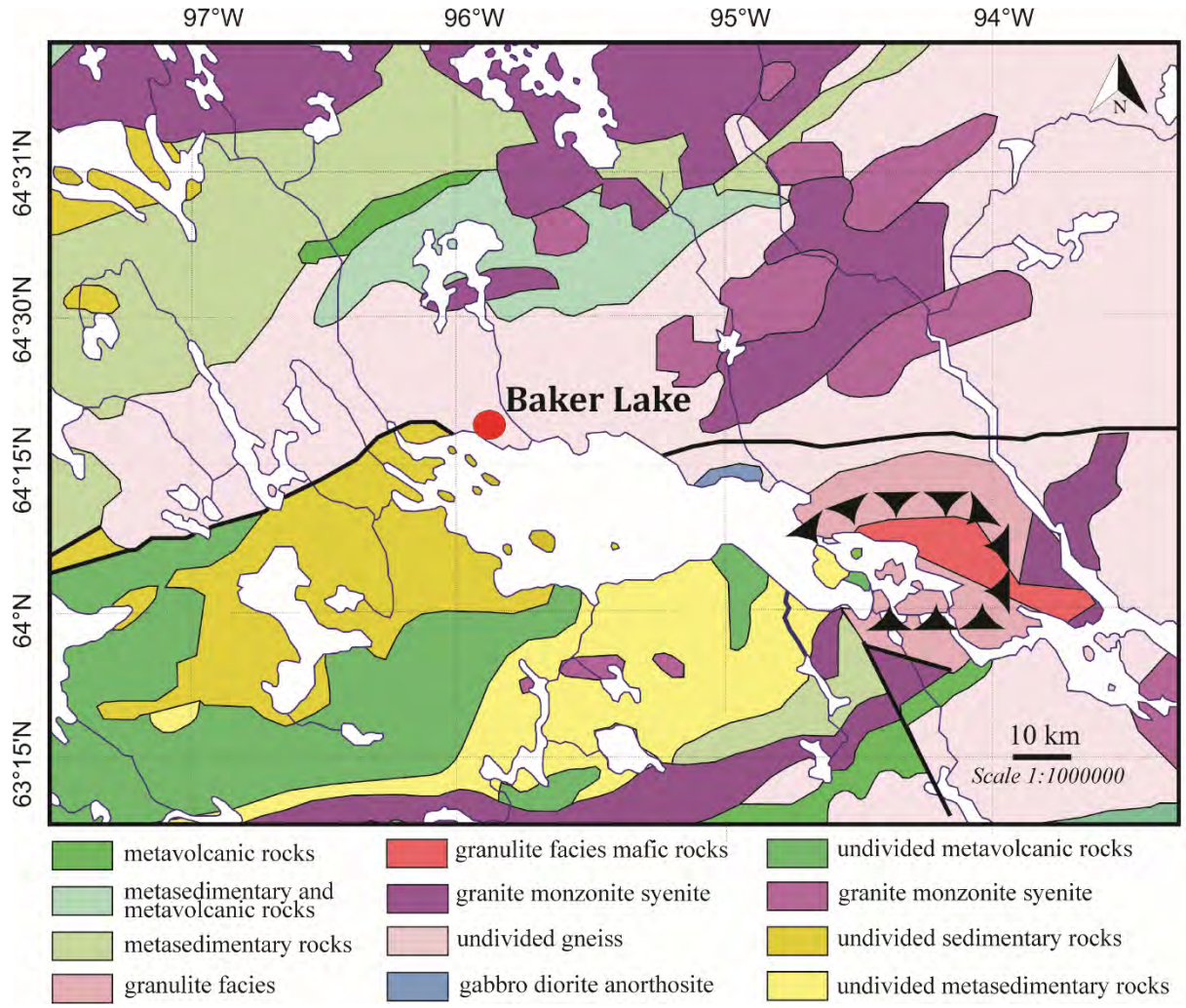

Figure 2.1: Extract of the regional geological map of Nunavut, focusing on the surface geology surrounding Baker Lake. (adapted from Kemp et al., 2006).

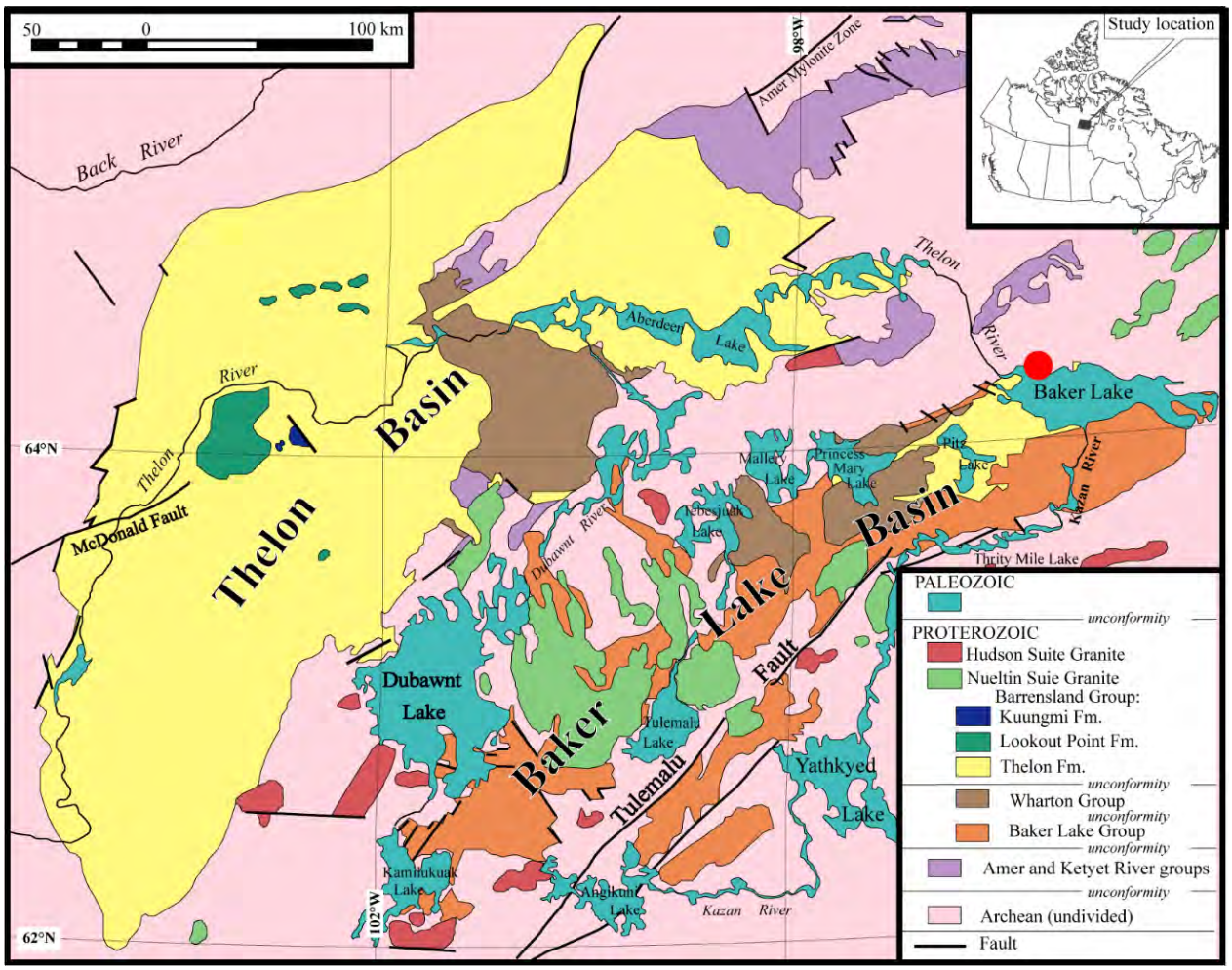

Figure 2.2: Geological map of the Thelon and Baker Lake basins (modified from Rainbird et al., 2003). Baker Lake community is represented by the red dot. The lithostratigraphy of the Baker Lake is composed of the Dubawnt Supergroup. This supergroup comprises the Baker Lake, Wharton, and Barrensland formations (Rainbird et al., 2003; Hadlari et al., 2006). Among these stratigraphic units, the Wharton Group is characterized by the presence of sub-arkosic sandstones, volcaniclastic sandstones, volcaniclastic conglomerates, and rhyolite flows, thus illustrating an advanced phase of basin development. The Barrensland Group is represented by quartzose sandstones of the Thelon Formation. Finally, the Baker Lake Group consists primarily of various sedimentary and volcanic rocks. Concerning the specific lithology of the Baker Lake Basin, it is primarily characterized by the presence of siliciclastic and volcanic rocks. The Hudson granitoids (1850-1810 Ma) are voluminous late to post-orogenic monzonites to granites, while the Nueltin granite (around 1750 Ma) is a rapakivi granite accompanied by porphyritic rhyolite, formed after the Hudson granitoids (Peterson, 1999). The Amer Group is correlated with the Ketyet River Group, which consists of thin metaconglomerate overlain by orthoquartzite and gray pelitic schist (McEwan, 2012). The Archean basement is primarily composed of undivided gneiss, representing the oldest rocks of the continental crust.

3. Materials and Methods

The Beardsmore protocol et al. (2010) is a systematic method for assessing the deep geothermal energy potential of a region to a depth of 10 kilometers and the feasibility of producing heat and or electricity via an EGS.

The protocol begins by modeling the vertical temperature distribution based on thermal properties (conductivity and heat generation), surface heat flow, and average surface temperature as starting points. Next, the protocol evaluates the theoretical and technical potential for energy production at various depths. The theoretical potential assumes that all available heat can be converted into energy. The technical potential considers practical constraints such as terrain accessibility and drilling depth limitations and is thus less than the theoretical potential.

In this article, we used the Beardsmore protocol to assess the deep geothermal potential of Baker Lake and the feasibility of developing a deep EGS for heat and/or power generation. We incorporated paleoclimatic events in the model we used to determine the vertical temperature distribution and heat flow to generate realistic results. This approach is detailed in this section, along with an explanation of our resource assessment method.

As the input parameters are uncertain, the resource assessment relied on the Monte Carlo method. The software @Risk was used for this purpose. The goal is to assess the probability of meeting the community's demand, assessed at 14 GWh for electricity and 77 GWh for space heating. Sensitivity analyses based on the Monte Carlo method were conducted to identify key geological and technical uncertainties.

3.1 Temperature Survey

A digital temperature cable with thermistors was installed in the borehole after drilling was completed. The sensors operate within a range of -55°C to +125°C, with an accuracy of ±0.1°C from -10°C to 30°C, and a resolution of ±0.063°C. Temperature recordings began on December 14, 2022, and ended on April 23, 2023. The last temperature profile recorded was used for the vertical temperature profile model to ensure that the temperature was in equilibrium and not affected by the drilling operations.

3.2 Thermal Properties and Radiogenic Heat Production

Twenty-six core samples were collected throughout the drilling process. The thermal properties of these samples, such as thermal conductivity, diffusivity, and heat capacity, were measured using a thermal conductivity scanner (TCS; Popov et al., 2016). The radiogenic heat production (A) was calculated based on Rybach’s (1998) empirical function, using concentrations of uranium (U), thorium (Th), and potassium (K) obtained through ICP-MS/OES analyses.

Given the lack of more detailed geological information at greater depths, we assume that the reservoir is a heterogeneous rock medium with properties equivalent to those observed in this 500-meter core sample characteristic of basement rocks. Although individual samples exhibit varying properties, these differences contribute to the overall variability of the reservoir's properties. Monte Carlo simulations were employed to incorporate this variability into our calculations.

3.4 Heat Flow Estimation

The heat flow in Baker Lake was estimated through an optimization simulation utilizing the subsurface temperature distribution. To account for the Arctic condition of the study area, a method that incorporates paleoclimate influence has been adopted. The shallow subsurface had been affected by paleoclimate events, which was reflected in the logged temperature profiles in boreholes. Consequently, this data could not be directly used to calculate the heat flow. To address this challenge, we developed a heat conduction analytical model that integrates the thermal properties of the roc and uses historical surface temperature steps. The simulated temperature profile was matched with the measured temperature profile by adjusting the basal heat flux under a given surface temperature scenario based on the understanding of the region's climatic history.

The general mathematical formulation of the 1D inverse heat conduction problem (ICHP) to estimate heat flow is:

$$\frac{\partial}{\partial z}\left(\lambda\frac{\partial T}{\partial z}\right)+A=\rho c\frac{\partial T}{\partial t} \quad \text{in} \quad 0<z<z_{\mathrm{n}}\ 0<t\leq t_{\mathrm{n}} \tag{1}$$

$$-\lambda\frac{\partial T}{\partial z}=Q=\text{unknow} \quad \text{at} \quad z=z_{\mathrm{n}} \quad t=t_{\mathrm{n}} \tag{2}$$

$$T=T(t) \quad \text{at} \quad z=0\ 0<t\leq t_{\mathrm{n}} \tag{3}$$

$$T=T(z)=T_0\ \frac{Q_0}{\lambda}z\ -\ \frac{A}{2\lambda}z^2 \quad \text{for} \quad t=0 \quad 0\leq z\leq z_{\mathrm{n}} \tag{4}$$

where T (°C) is temperature, Q (W m^{-2}) is the heat flow, ρc (J m^{-3} K^{-1}) is the volumetric heat, z (m) is the spatial variable and t (s) is time. The thermal conductivity λ (W m^{-1} K^{-1}) and the radiogenic heat production A (W m^{-3}) were assumed uniform and constant with the time.

The analytical solution of the 1D ICHP stated above is:

$$T\,(\,z\,)=\ T_0\ +\ \frac{Q_0}{\lambda}z\ -\ \frac{A}{2\lambda}z^2+T_t(z) \tag{5}$$

where $T_t\,(z)$ represents the variation of the surface temperature in time by considering a literature-based paleoclimate history (Table 3.1), and is defined as (Birch, 1948):

$$T_t(z)=\sum_i(T_v)\times(\mathrm{erf}\left(\frac{z}{\sqrt{4\alpha t_{i_1}}}\right)-\mathrm{erf}\left(\frac{z}{\sqrt{4\alpha t_{i_1}}}\right)) \tag{6}$$

where T_{v} (°C) is the average temperature variation between the climatic event and today, *erf* is the error function, α (m^2 s^{-1}) is the thermal diffusivity of the rocks, and t_{i1} and t_{i2} (s) are the end and beginning of the climatic event.

T_0 represents the initial temperature condition, which was assumed to be equal to the ground surface temperature T_{g} (°C) (Ouzzane et al., 2015):

$$T_{\mathrm{g}}=17.898+0.951T_{\mathrm{amb}} \tag{7}$$

where T_{amb} (K) refers to the surface air temperature. Using the surface air temperature from the 1981-2010 climate normal period (-11 ºC; ECCC, 2022), the reference ground surface temperature was calculated to be -6 ºC.

Table 3.1: Literature-based paleoclimate history and uncertainty (Miranda et al., 2020 and references therein).

Epoch	Climate event	Time step (years B.P.)	Temperature scenario		
			Cold	Average	Warm
Late Pleistocene	Nebraskan (glacial period)	300,000 – 265,000	-10	-5	-1
	Aftonian (interglacial)	265,000 – 200,000		0	
	Kansan (glacial period)	200,000 – 175,000	-10	-5	-1
	Yarmouth (interglacial)	175,000 – 125,000		0	
	Illinoian (glacial period)	125,000 – 100,000	-10	-5	-1
	Sangamonian (interglacial)	100,000 – 75,000		0	
	Wisconsinan (glacial period)	75,000 – 11,600	-10	-5	-1
Holocene	Holocene (interglacial)	11,600 – 7,000		0	
	Holocene Thermal Maximum	7,000 – 5,800	+1	+1.5	+2
	Holocene (interglacial)	5,800 – 3,200		0	
	Roman & Medieval warm periods	3,200 – 1,000	+1	+1.25	+1.5
	Holocene (interglacial)	1,000 – 500		0	
	Little Ice Age	500 – 270		-1	
	Pre-Industrial & Industrial Revolution	270 – 77	+1.4	+1.7	+2
	1946-2022	77 – 0	+3	+3.5	+4

The heat flow in equation (9) was adjusted to minimize the sum of squared differences (RSS) between the measured and simulated temperatures. This was accomplished using the least squares method in conjunction with a Generalized Reduced Gradient (GRG) solver (Lasdon et al., 1974).

$$RSS = \sum[T_{measured} - T_{simulated}]^2 \quad (8)$$

As literature-based paleoclimate history is uncertain, three scenarios were established to evaluate heat flux and assess the imposed uncertainty.

3.5 Temperature In-Depth

Once heat flow was found, the temperature profile to 10 km depth was estimated using the analytical solution of the 1D heat conduction equation (5).

A Monte Carlo-based sensitivity analysis was used to calculate the in-depth temperature distribution, taking into account the uncertainties and variability of the parameters. While assuming that the thermal properties are consistent with depth due to lithologic coherence, variations in the analyzed values along the column are observed. To model this variability, a triangular distribution is used, encompassing the minimum and maximum values found in all samples, along with the average of the entire column. Additionally, the heat flow value is estimated using a triangular distribution, accounting for warm, cold, and mean climate scenarios (Table 3.2). This approach provides a probabilistic solution, yielding the most probable outcome and two least probable outcomes (minimum and maximum).

The choice of distribution type for each parameter is based on its variability and uncertainty. For T_0, a single value is used because it depends on a linear equation whose unknown has a unique value found in the literature. A triangular distribution best represents the variability in λ and A with the minimum, average and maximum values measured in the laboratory. Q_0 is also represented by a triangular distribution, considering the uncertainty of the calculations related to the paleoclimatic correction, with a warm, cold, and average scenario giving the minimum, average, and maximum Q_0 values. Finally, a single value for the depth z is used because the objective is to calculate the temperature at specific depths.

Table 3.2: Distribution of variables in IHCP equation

Symbol	Description	VariableType	Distribution
T_0	Surface temperature		Single value
λ	Thermal conductivity	Continuous	Triang(min,mean,max)
Q_0	Surface heat flow	Continuous	Triang(min,mean,max)
z	Depth		Single value
A	Radiogenic heat production	Continuous	Triang(min,mean,max)

3.6 Resource Assessment

The available thermophysical data along with Monte Carlo simulations were utilized to estimate the geothermal potential beneath Baker Lake (Table 3.3). First, the available thermal energy for space heating and electricity generation was estimated with the volume method (Beardsmore et al., 2010).

$$H = V \ \rho c \ (T_{\text{res}} - T_{\text{ref}}) \ R \quad (9)$$

where H (J) is the thermal energy, V (m³) is the volume of the reservoir, T_{res} (°C) is the reservoir temperature, T_{ref} (°C) is the abandonment temperature of the reservoir, and R (%) is the recovery factor representing the fraction of thermal energy in a reservoir that can be feasibly extracted for power generation.

For space heating, a reservoir abandonment temperature between 30 and 50 °C was defined (Lindal, 1973; Sarmiento et al., 2013). The potential for electricity generation was assessed using a binary geothermal power plant technology suitable for Arctic conditions, and assuming a reservoir abandonment temperature of 120 to 140 °C (Tomarov & Shipkov., 2017).

Using the waste heat from the power plant for heating purposes is termed cogeneration, or combined heat and power (CHP), and this scenario was also considered in our study using the same electrical system and parameters as described above.

The recovery factor was defined to be between 2 and 20%. The conversion of thermal energy to potential heat and power output P (GWh) was calculated with (Miranda et al., 2020 and references therein):

$$P = \frac{H\,\eta_{\mathrm{th}}}{F_{GPP}\,t} \tag{10}$$

where P ($W_{th,\,e}$) represents the power, F_{GPP} (%) is the geothermal power plant or surface facilities factor related to its availability throughout the year, t (years) represents the project lifetime, and η_{th} (%) is the cycle efficiency calculated as follows (Miranda et al., 2020 and references therein):

$$\eta_{\mathrm{th}} = 0.0935T_{\mathrm{res}} - 2.3266 \tag{12}$$

Table 3.3: Distributions of Variables in Power Output Equation

Symbol	Description	Variable Type	Distribution
V	Reservoir volume	Continuous	Uniform(min,max)
c_p	Heat capacity	Continuous	Triang(min,mean,max)
T_{res}	Reservoir temperature	Continuous	Triang(min,mean,max)
T_{ref}	Reservoir abandonment temperature	Continuous	Uniform(min,max)
R	Recovery factor	Continuous	Uniform(min,max)
F_{GPP}	GPP factor	Continuous	Uniform(min,max)
η_{th}	Thermal efficiency		f(T)
t	Project lifetime	Continuous	Trinag(min,most,max)

4. Results

4.1 Thermal Conductivity and Radiogenic Heat Production

The data obtained from the analysis of samples from the 2022 drilling program reveal that the meta-granite gneiss samples analyzed have a thermal conductivity varying between 2.1 and 2.9 W m^{-1} K^{-1} while the rhyolite samples have a thermal conductivity ranging between 2.2 and 2.4 W m^{-1} K^{-1}. The granite sample analyzed has a thermal conductivity of 2.3 W m^{-1} K^{-1}. The average thermal conductivity of the core samples is 2.4 W m^{-1} K^{-1} (Figure 4.1). The thermal

diffusivity of the meta-granite gneiss samples was evaluated to vary between 1.2 and 1.9 $mm^2 s^{-1}$, while the thermal diffusivity of the rhyolite samples ranges between 1.2 and 1.3 $mm^2 s^{-1}$. The granite sample revealed a thermal diffusivity of 1.3 $mm^2 s^{-1}$. Volumetric heat capacity, defined by dividing thermal conductivity by thermal diffusivity, varied between 1.3 and 2.0 MJ $^{-3} K^{-1}$. The rhyolite samples had a volumetric heat capacity of 1.8 to 1.9 MJ $m^{-3} K^{-1}$, and the granite sample was 1.8 MJ $m^{-3} K^{-1}$.

The meta-granite gneiss samples are characterized by a Th concentration ranging between 2.14 and 8.31 mg kg^{-1}, a U concentration varying between 1. 24 and 9.79 mg kg^{-1}, and a K concentration of 1.88% and 5.43%. The radiogenic heat production in these samples spans from 0.734 to 1.604 µW m^{-3}. For rhyolite samples, Th concentrations vary between 1.71 and 16.1 mg kg^{-1}, U between 1.38 and 9.69 mg kg^{-1}, and K between 1.19% and 4.91%. The radiogenic heat production of the rhyolite samples ranges from 3.384 to 4.198 µW m^{-3}. The single granite sample analyzed has a Th concentration of 3.03 mg kg^{-1}, a U concentration of 0.95 mg kg^{-1}, and a K concentration of 2.49%, with a radiogenic heat production of 1.204 µW m^{-3}.

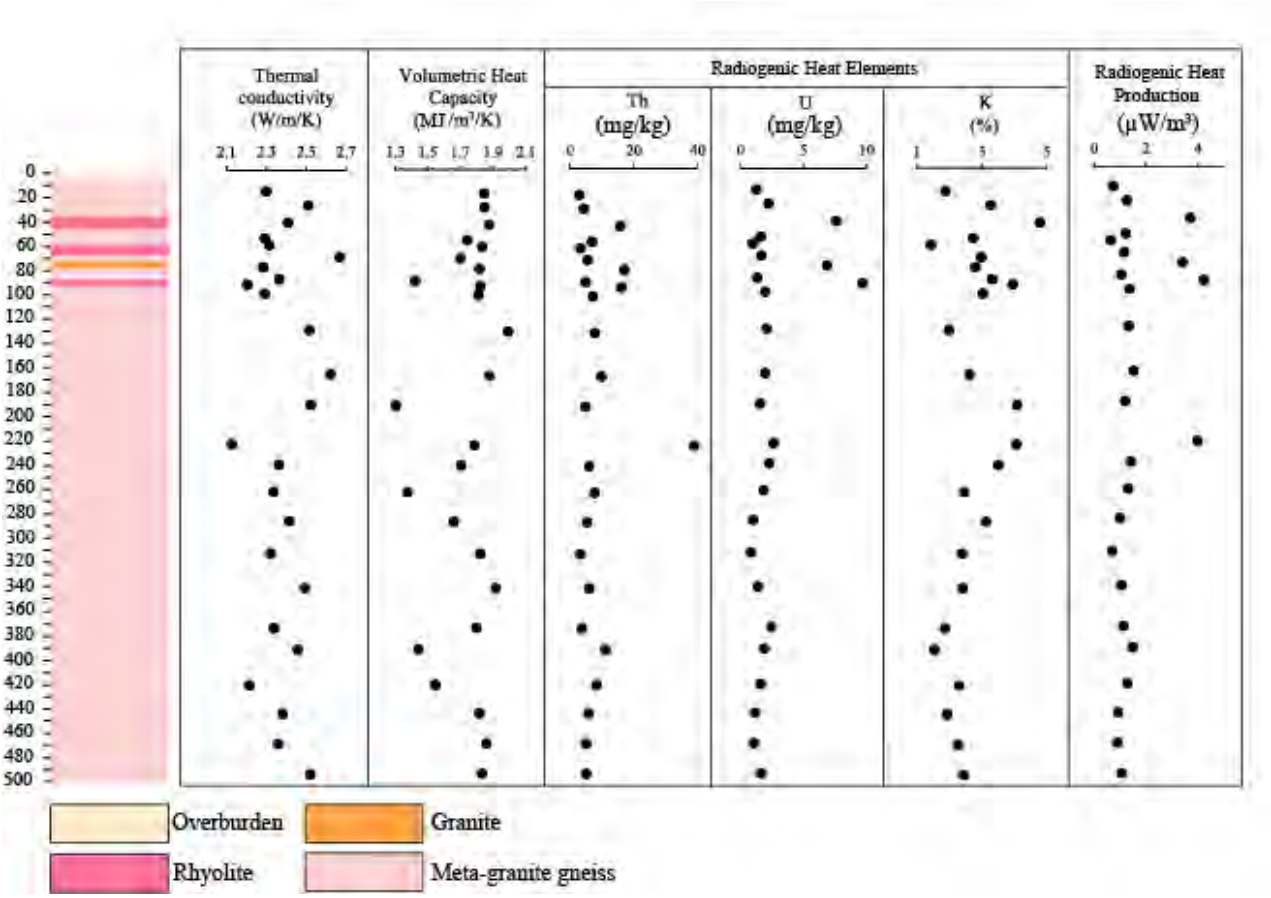

Figure 4.1: Graphical well log illustrating the lithologies observed, and the laboratory data profiles.

4.3 Heat Flow

The temperature profile measured in the Baker Lake well reveals the typical gradient inversion caused by paleoclimate events (Figure 4.2). Below a depth of approximately 100 m, the temperature profile shows a consistent linear temperature increase with depth, suggesting a conduction-dominated heat transfer medium.

The optimization approach used to estimate the heat flow took into account past climatic variations and assumed homogeneous thermal conductivity and radiogenic heat production. As previously mentioned, three probabilistic climate scenarios were defined—cold, average, and warm scenarios. The heat fluxes estimated for the cold, average, and warm climate scenarios are 78 Mw m^{-2}, 73 mW m^{-2}, and 68 mW m^{-2}, respectively (Table 4.1). The RSS values, which measure the deviation or error in the data and indicate the model's fit, are 0.53 for both the cold and average scenarios and 0.52 for the warm scenario. These RSS values are very similar across all scenarios, indicating a consistent level of fit or error among the different probabilistic scenarios.

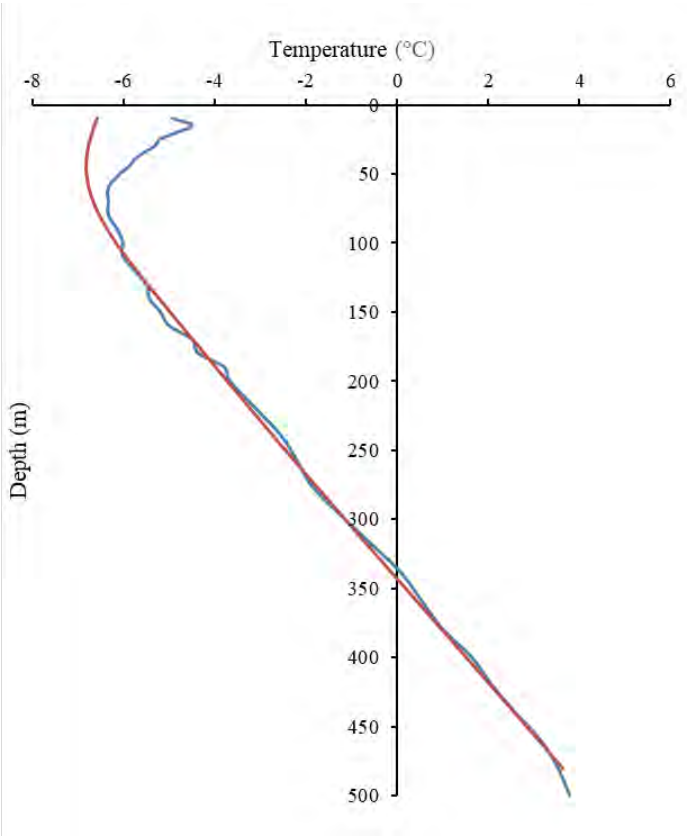

Figure 4.2: Observed temperature (in blue) compared to compute temperature (in red) after optimization.

Table 4.1: Comparison of heat flow and sum of squared residuals across cold, mean, and hot scenarios.

	Cold scenario	Mean Scenario	Hot scenario
Heat Flow (mW m^{-2})	78	73	68
RSS	0.53	0.53	0.52

4.4 Subsurface Temperature Predictions

According to the estimates carried out, minimum temperatures suitable for direct use of the geothermal resource (i.e., 40 °C), may be found starting at a depth of 2 km (Figure 4.3). For electricity production, and assuming that temperatures above 100 °C would be needed, the conditions are met at a depth starting at 5 km. At this depth, the temperature ranges from a minimum of 109°C to a maximum of 170°C, with a most likely value of 139°C.

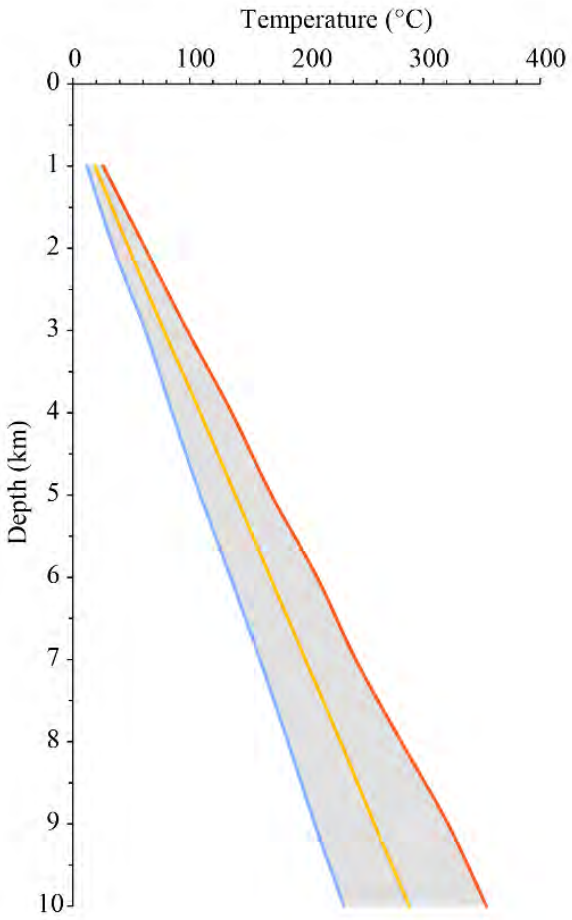

Figure 4.3: This figure shows the average (orange), minimal (blue), and maximal (red) temperatures at depths between 1 and 10 kilometers.

4.5 Resource Assessment and Risk Analysis

4.5.1 Heat Production

The data-driven Monte Carlo-based approach used in this study suggests that at a depth of 1 km, there is a 0% probability of meeting the community's estimated annual average heating needs (i.e., 77 GWh; Figure 4.4.a). However, as the depth increases, the likelihood of achieving the energy target rises significantly. At 2 km depth, this probability increases to 15% (Figure 4.4.b). At 3 km depth, the probability is 76%, and at 4 km, it increases to 91% (Figure 4.4.c,d). At 5 km depth, the probability climbs to 96%. The probability reaches a 100% chance of fulfilling the community heating needs at depths of 6 km and below (Figure 4.4.f-i).

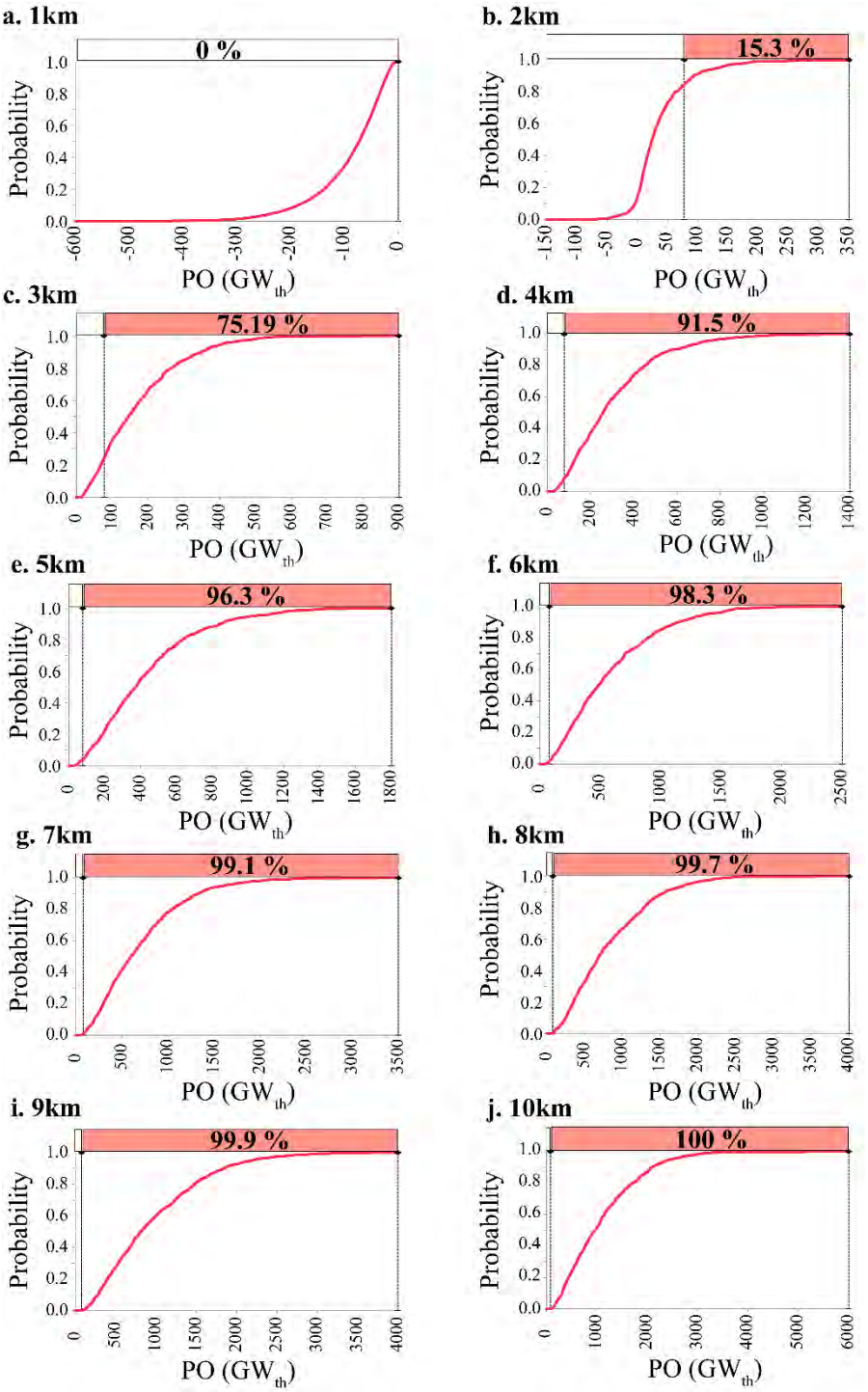

Figure 4.4: Probabilities of meeting the community's thermal energy demand, evaluated at 77 GWh, as a function of heat power in GWh between 1 and 10 km deep. The ten graphs feature an ascending curve, with the x-axis adjusted based on the increasing probability, ranging from 0 to 100%. As the depth increases, each graph illustrates how the probability of meeting the thermal energy demand evolves based on the available heat power at that specific depth. The probability of meeting the 77 GWh demand is indicated in the top right portion of each graph, expressed as a percentage. This approach visually analyzes the impact of depth on the probability of meeting the community's thermal energy demand, providing a detailed understanding of the potential variation in geothermal availability with depth.

4.5.2 Electricity Generation

The estimates for electricity generation are less promising. There is a 0% probability of meeting the community's estimated annual electricity needs (i.e., 14 GWh) up to 5km depth (Figure 4.5.a-c). At 5 km depth, the probability increases to 11% (Figure 4.5). As the depth continues to increase, the likelihood of achieving the energy target rises significantly. At 6 km depth, the probability is 61.5%, and at 7 km, it increases to 87.6% (Figure 4.5.d,e). At 8 km depth, the probability reaches 96.2% (Figure 4.5.f). Finally, at 9km depth and below, the probability of achieving 14 GWh is more than 99% (Figure 4.5.g,e).

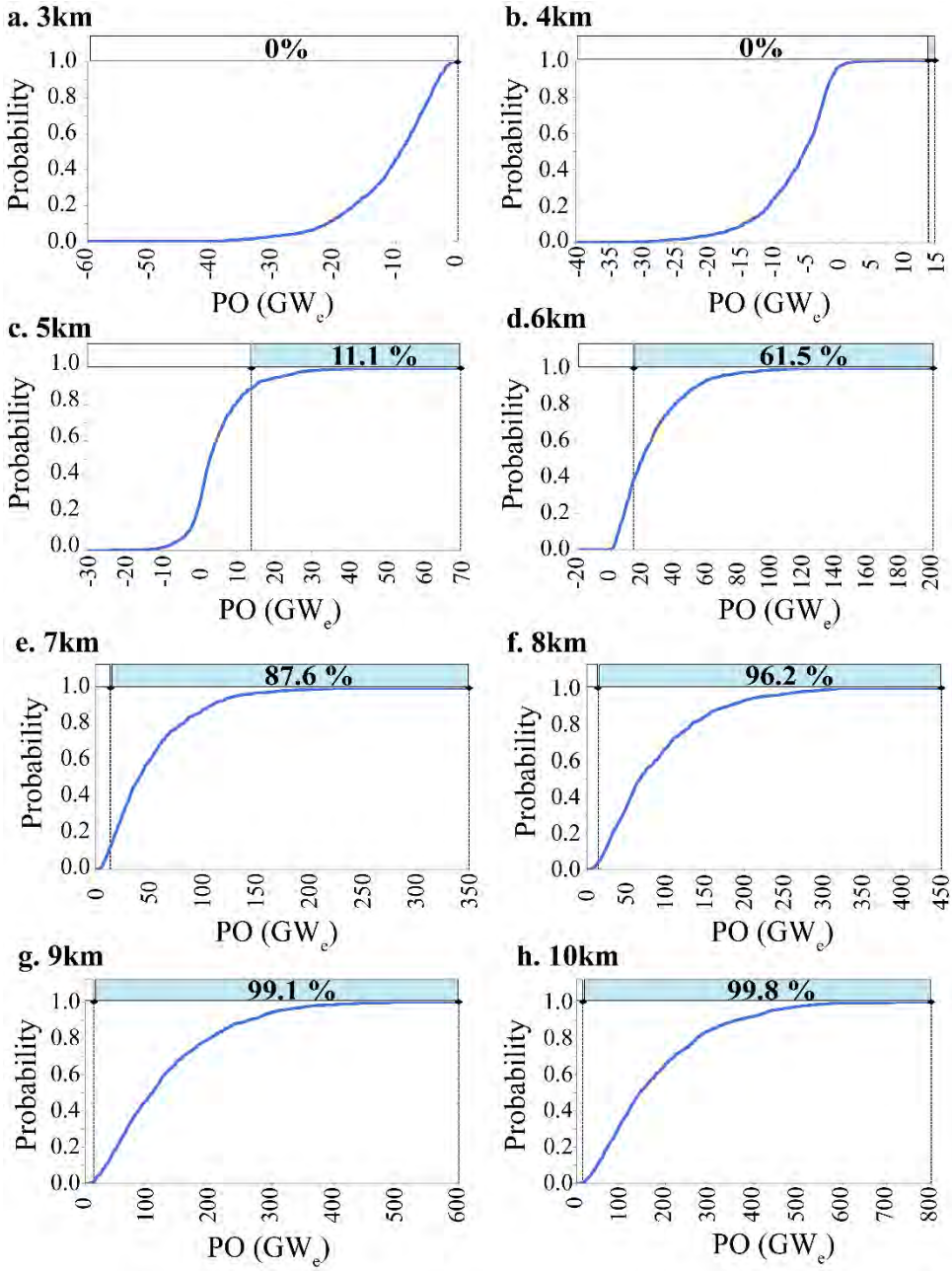

Figure 4.5: Probabilities of meeting the community's electric energy demand, evaluated at 14 GWh, as a function of heat power in GWh between 3 and 10 km deep; Depths under 3 km were excluded due to zero probability.

4.5.3 Cogeneration

In the context of improving the sustainability of a geothermal power plant, cogeneration of heat and power could be an option. Waste heat from the electricity generation process could be used for space heating instead of being released to the atmosphere. The results suggest probable depths between 6 and 10 km (Figure 4.6), although the residual heat production may not suffice to meet all heating needs (i.e., 77 GWh/year) but significantly contribute to addressing them (Figure 4.6).

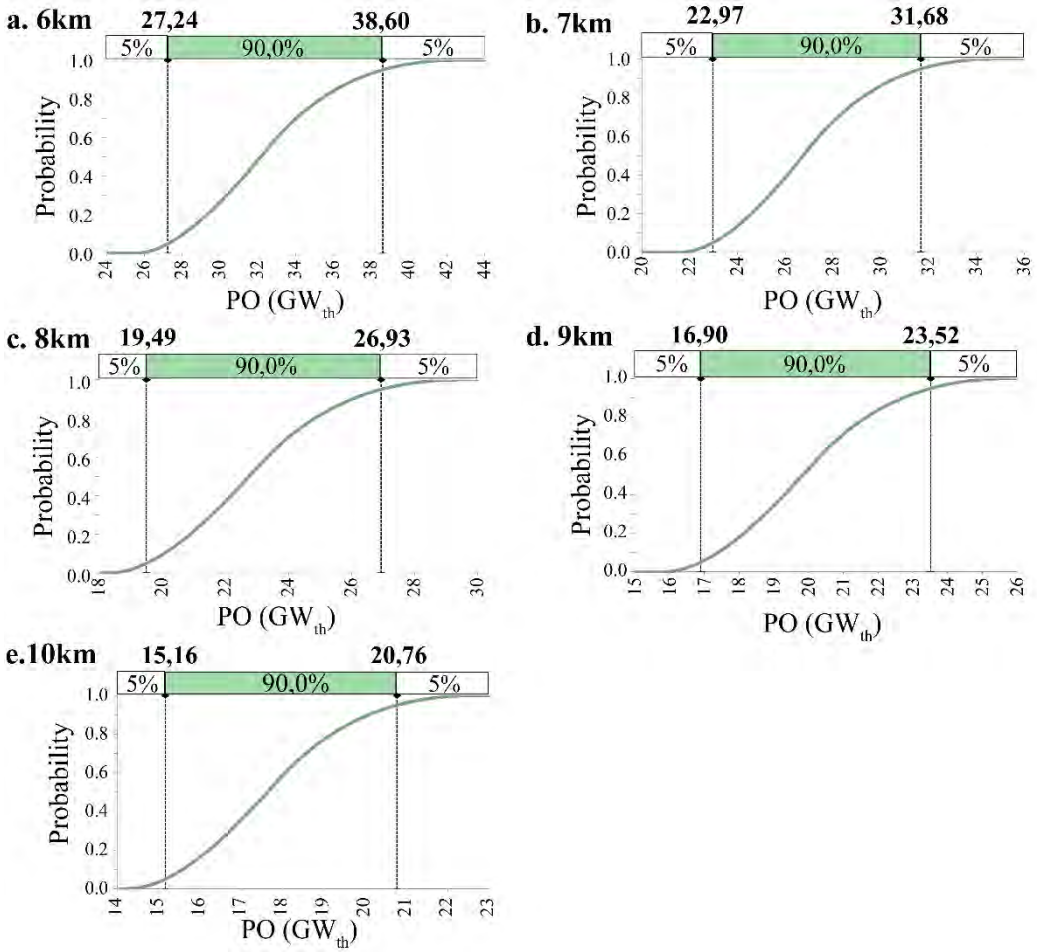

Figure 4.6: Probabilities of meeting the community's thermal energy demand, evaluated at 77 GWh, as a function of heat power in GWh between 6 and 10 km deep.

4.6 Sensitivity Analysis

The Monte Carlo-based sensitivity analysis carried out suggests that, for heat production, the recovery factor and the reservoir volume are the most important parameters, strongly influencing the quantity of thermal energy that can be provided to the end user (Figure 4.7) while project lifetime has a lower impact (Figure 4.7). The least influential parameters are the subsurface temperature distribution, the heat capacity of the reservoir host rocks, the reservoir abandonment temperature, and the availability of the surface facilities throughout the year (Figure 4.7). For electricity generation, on the other hand, the main influential parameters are subsurface temperature distribution and cycle efficiency up to 7 km depth (Figure 4.8.a,b). Below this depth, the recovery factor gains importance (Figure 4.8.c-f).

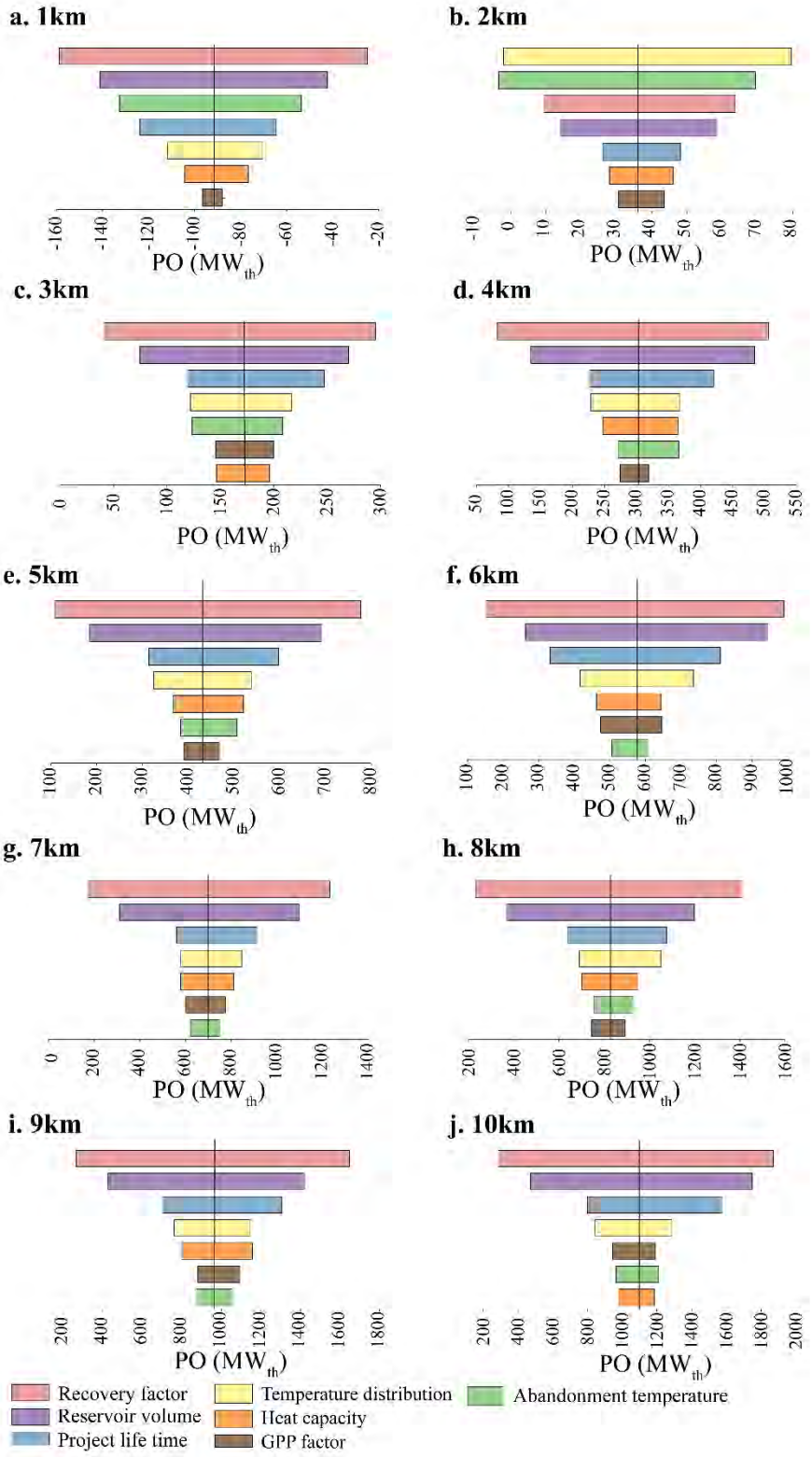

Figure 4.7: Potential impacts on heat output between 1 and 10 km deep. Longer bars indicate greater influence on heat production potential.

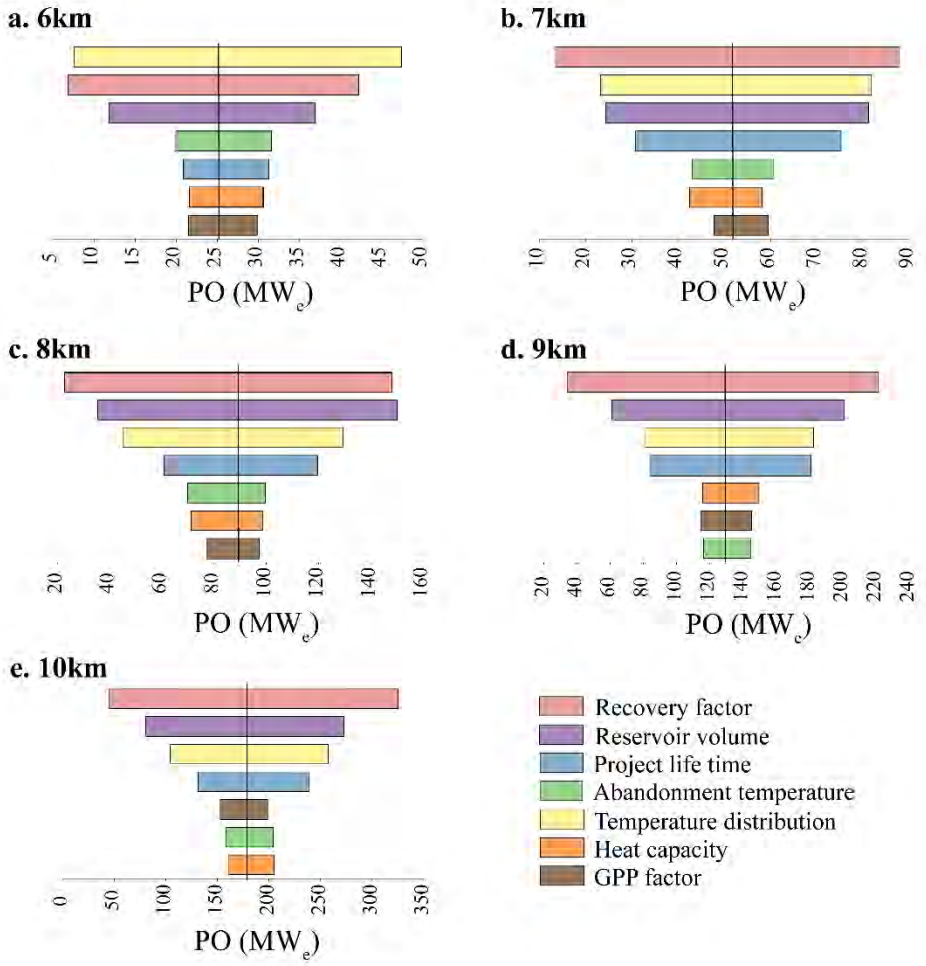

Figure 4.8: Potential impacts on heat output between 6 and 10km. Longer bars indicate greater influence on electric generation potential.

5. Discussion

The isolation from the national energy grid is a major challenge for Canada's northern communities. The search for an alternative solution to diesel is a crucial mission (Pinto and Gates, 2022), supported by QEC (QEC, 2018) and the community themselves. In fact, the desire to create an affordable, sustainable, reliable and environmentally responsible energy system has been expressed by Nunavut residents, and in 2007, the Government of Nunavut launched the Government of Nunavut Energy Strategy called Ikummatiit (Government of Nunavut, 2007). Although developing renewable energy sources is a key component of Ikummatiit, reducing dependence on diesel not only involves harnessing different forms of energy, but also making more efficient use of energy and strengthening energy system management. Another important aspect is energy literacy. Educating the public to promote energy conservation and inform the citizens about the different energy sources will help them make better, well-informed decisions about their energy use.

The key findings of the previous study made by Minnick et al. (2018) to estimate geothermal resources beneath Baker Lake revealed a low potential that would be suitable for heat or electricity generation using an EGS. However, extrapolation of data from scarce and sparse wells, on a regional scale, is a method associated with major uncertainties. Thus, Minnick et al. (2018) called for an in-depth study of the community's potential to be achieved via the drilling and evaluation of data from a 500 m-deep geothermal prospecting well. This study presents the findings of that evaluation based on a well that was drilled in December 2022.The following sections discuss the contributions of this work in terms of improving conventional resource assessment methods, and in terms of the potential use of geothermal energy to offset diesel consumption in Baker Lake via an EGS. Next steps to de-risk geothermal potential evaluation in this community are further discussed.

The heat flux calculation method used in this study, although it was based on the optimization method of Miranda et al. (2021), was modified to simplify the evaluation protocol. The new heat flux methodology uses an Excel solver instead of a numerical simulation software such as COMSOL multiphysics. This reduces complexity and calculation time, while maintaining a stochastic approach to quantify risk. The results obtained by Miranda et al. (2023) for Baker Lake following different analytical methods suggest heat flux varying between 68 and 75 mW m^{-2}. The optimization method used here results in a heat flux of 68 to 78 mW m^{-2} for cold to warm paleoclimate scenarios. These results show the importance of considering various paleoclimate scenarios in heat flow assessment.

In addition, compared to the subsurface temperature estimates of Miranda et al. (2023), the paleoclimatic correction term was added to the analytical solution of the 1D heat conduction equation to improve the accuracy of the vertical temperature profile. This term allows the influence of paleoclimatic conditions to be taken into account, the effect of which was to reduce the estimated temperatures at shallow depths. This avoids an overestimation of subsurface temperatures and energy potential in the first kilometers.

Regarding resource estimation, the methodology used in this study integrates the recovery factor in the calculation of available thermal energy, unlike the original Beardsmore et al. (2010) protocol. This adjustment was done to better reflect the nature of porous and/or fractured reservoirs, and the fraction of thermal energy that can realistically be extracted depending on the reservoir permeability. In addition, the calculation of potential production capacity included a surface facilities factor, $F_{GPP,}$ which represents the percentage of time during which the surface facilities can operate each year and accounts for periods when the facility is not operational due to issues such as maintenance. The Beardsmore protocol does not include this factor, which can lead to an underestimation of the production capacity by assuming continuous and uninterrupted operation. Finally, the reference temperature used in the calculation of energy potential is specific temperatures found in the literature, representing the minimum temperatures at which resource extraction stops. The Beardsmore protocol uses, generally, the ambient air surface temperature. In this work, we decided to use reservoir abandonment temperatures to make a more realistic assessment of the resource. The minimum reservoir abandonment temperature of 30°C and 50°C were set for space heating, and a minimum required temperature of 120°C to 140°C was set for electricity production with a binary geothermal plant. This approach ensures that the chosen temperatures are relevant in the geological and climatic framework, especially in Arctic conditions.

The preliminary study of Minnick et al. (2018) expected a heat flux of about 50 and 60 mW m^{-2}, with temperatures of 120°C reached at depths of 6 to 7.5 km. However, the present study, with reduced uncertainties, shows a heat flux ranging from 68 to 78 mW m^{-2}, and temperatures of 120°C reachable at depths starting at 5 km depth. In fact, the most likely value is 139°C at 5 km depth.

Similarly, Miranda's et al. (2021) study focused on assessing the deep geothermal potential of the Kujjuaq community in Nunavik without the use of deep borehole data. Miranda's et al. approach involved a numerical model to simulate the impact of paleoclimate events and infer heat flow by reproducing a temperature profile at 80 m depth. Due to the lack of deep well data, the uncertainties in their studies were higher. The uncertainty in heat flow in Miranda et al. (2021) was 40%, and the uncertainty in subsurface temperature distribution in Miranda et al. (2020) was greater than 75%. In contrast, our study used data from a 500 m-deep well, significantly reducing uncertainties in heat flow and subsurface temperature distribution. This access to deeper data allowed for a reduction in uncertainties in our final heat flux assessment. The uncertainties in heat flux and subsurface temperature in this study are 13% and less than 50%, respectively.

The Monte Carlo-based sensitivity analysis carried out allowed us to rate the parameters in terms of their uncertainties and their impact on the estimation of the geothermal energy potential. The recovery factor is the most decisive, and its uncertainty could be reduced by carrying out flow tests in deep wells. However, this is only done at later stages of geothermal projects, when the risk has been reduced. At early stages, characterizing the reservoir permeability through an analysis of the fracture network in the field is a valuable option. The information collected can be used to parameterize numerical models and simulate the geothermal reservoir behavior. This can help the project moving forward to justify the cost of exploration drilling. The reservoir volume is another important factor influencing heat production. The uncertainty associated with the reservoir volume can be reduced with large-scale hydraulic stimulation and microseismic monitoring. Again, this can only be done at the later stages of the project. At early stages, numerical models to optimize well locations considering the fracture network observed in the field can be a helpful option. Finally, the reservoir abandonment temperature also has a significant influence on the estimates, and its improvement will require innovations in the technology of EGS and the development of their use.

6. Conclusions

This study demonstrates the significant potential of geothermal energy as an alternative to meet the energy needs of the Baker Lake community. Analysis of a 500 m-deep well drilled in Baker Lake provided new data allowing the assessment of heat flow and temperature distribution at depth. The corrected geothermal gradient of 28 °C/km and a terrestrial heat flux of 73 mW/m^2 suggest that geothermal energy can be realistically exploited for space heating at a depth of 4 km and for electricity generation at a depth of 8 km. The feasibility of geothermal cogeneration, using waste heat from electricity generation, is a technology that can boost the efficiency of an EGS project. The estimates of this work suggest that although the waste heat is insufficient to meet all of the community's heating needs, it can partially meet them. Sensitivity analysis based on the Monte Carlo method showed that the recovery factor and reservoir volume have the most uncertainty and are the most impactful. Reducing their uncertainty at an early stage of the project would require detailed fieldwork focused on fracture and geostructure characterization, combined with numerical modeling.

This study provides a foundation for transitioning from diesel to renewable energy in Nunavut, highlighting geothermal energy as a viable and environmentally friendly alternative. This study supports the broader goal of energy independence for northern communities.

ACKNOWLEDGMENTS

This study was funded by a discovery grant from the Natural Sciences and Engineering Research Council (NSERC) and additional INRS revenues awarded to Jasmin Raymond. The authors express their gratitude to Philipe Girard, Félix-Antoine Comeau, Xavier Leveillee-Dallaire, and Maria Jose Oviedo Valencia for their invaluable support during the analyses of the thermophysical properties. We also thank the laboratory teams at INRS and RESPEC for assisting with sample analysis, and Qulliq Energy Corporation for providing access to the drilling cores.

REFERENCES

Arriaga, M., Nasr, E., & Rutherford, H. (2017). Renewable energy microgrids in northern remote communities. IEEE potentials, 36(5), 22-29.

Baujard, C., Genter, A., Dalmais, E., Maurer, V., Hehn, R., & Rosillette, R. (2016). Temperature and hydraulic properties of the Rittershoffen EGS reservoir, France. In Proceedings of the European Geothermal Congress. Strasbourg, France, pp. 1-8.

Beardsmore, Graeme & Rybach, Ladislaus & Blackwell, David & Baron, Charles. (2010). A Protocol for Estimating and Mapping Global EGS Potential. Transactions - Geothermal Resources Council. 34. Sacramento, CA, 271-282.

Birch, A. F. (1948). The effects of Pleistocene climatic variations upon geothermal gradients. American Journal of Science, 246(12), 729–760. https://doi.org/10.2475/ajs.246.12.729

Byrne, D. L. (2018). Exploring renewable energy opportunities for Nunavut. Master's thesis, University of Calgary, Calgary, Canada, 71p. https://doi.org/10.11575/PRISM/33094

Gold, A., Miranda, M. M., Raymond, J., & Asbjornsson, E. J. (2023). Minimizing permafrost thaw and maximizing thermal heat storage in Baker Lake, Nunavut: an investigation on energy storage in permafrost, Final Report, Rapport de recherche (R2178). INRS, Centre Eau, Terre et Environnement, Québec.

Government of Nunavut. (2007). Ikummatiit: An Energy Strategy for Nunavut. Governemental report, the Government of Nunavut Energy Strategies, Nunavut, 24 p https://climatechangenunavut.ca/en/content/ikummatiit

Grasby, S. E., Majorowicz, J., & Fiess, K. (2020). Geothermal Energy Potential of Northwest Territories, Canada. In Proceedings, World Geothermal Congress, 1. Reykjavik, Iceland

Hadlari, T., & Rainbird, R. H. (2011). Retro-arc extension and continental rifting: a model for the Paleoproterozoic Baker Lake Basin, Nunavut Geological Survey of Canada Contribution 20100436. Canadian Journal of Earth Sciences, 48(8), 1232–1258. https://doi.org/10.1139/e11-002

Hadlari, T., Rainbird, R. H., & Donaldson, J. A. (2006). Alluvial, eolian and lacustrine sedimentology of a Paleoproterozoic half-graben, Baker Lake Basin, Nunavut, Canada. Sedimentary Geology, 190(1–4), 47–70. https://doi.org/10.1016/j.sedgeo.2006.05.005

Kemp, E. A., Gilbert, C., & James, D. T. (2006). Geology of Nunavut, Canada. Map. Nunavut Geoscience. https://nunavutgeoscience.ca/

Koelbel, T., Genter, A. (2017). Enhanced Geothermal Systems: The Soultz-sous-Forêts Project. Uyar, T. (Ed.) Towards 100% Renewable Energy. Springer, Berlin, pp 243–248. https://doi.org/10.1007/978-3-319-45659-1_25

Lasdon, L. S., Fox, R. L., & Ratner, M. W. (1974). Nonlinear optimization using the generalized reduced gradient method. Revue française d'automatique, informatique, recherche opérationnelle. Recherche opérationnelle, 8(3), 73-103.

Li, S., Wang, S., & Tang, H. (2022). Stimulation mechanism and design of enhanced geothermal systems: A comprehensive review. Renewable and Sustainable Energy Reviews, 155, 111914.

Lindal B (1973) Industrial and other Application of Geothermal Energy, Armstead HCH (Ed.) Geothermal Energy, UNESCO, Paris, pp. 135-148.

Lu, S. M. (2018). A global review of enhanced geothermal system (EGS). Renewable and Sustainable Energy Reviews, 81, 2902-2921. https://doi.org/10.1016/j.rser.2017.06.097

McEwan, B. J. (2012). Structural style and regional comparison of the Paleoproterozoic Ketyet River group in the region north-northwest of Baker Lake, Nunavut. Master Thesis, Faculty of Graduate Studies and Research, University of Regina, Regina, 160 p.

Minnick, M., Schewfelt, D., Hickson, C., Majorowicz, J., Rowe, T. (2018). Nunavut Geothermal Feasibility Study. Topical Report RSI-2828. RESPEC Consulting Inc, Saskatoon, 42 p.

Miranda, M. A., Márquez, M. I. V., Raymond, J., & Dezayes, C. (2021). A numerical approach to infer terrestrial heat flux from shallow temperature profiles in remote northern regions. Geothermics, 93, 102064. https://doi.org/10.1016/j.geothermics.2021.102064

Miranda, M. A., Raymond, J., & Dezayes, C. (2020, b). Uncertainty and risk evaluation of deep geothermal energy source for heat production and electricity generation in remote northern regions. Energies, 13(16), 4221. https://doi.org/10.3390/en13164221

Miranda MM, Bacon Y, Raymond J.(2023) Deep geothermal energy potential of Baker Lake (Nunavut, Canada): Thermal properties characterization and surface heat flow estimation. Research report R2217, Institut national de la recherche scientifique, Centre Eau Terre Environnement, Québec, 64 p.

Pinto, H., & Gates, I. D. (2022). Why is it so difficult to replace diesel in Nunavut, Canada? Renewable & Sustainable Energy Reviews, 157, 112030. https://doi.org/10.1016/j.rser.2021.112030

Popov, Y., Beardsmore, G., Clauser, C., & Roy, S. (2016). ISRM Suggested Methods for Determining Thermal Properties of Rocks from Laboratory Tests at Atmospheric Pressure. Rock Mechanics and Rock Engineering, 49(10), 4179–4207. https://doi.org/10.1007/s00603-016-1070-5

Peterson, T. D., & vanBreemen, O. (1999). Review and progress report of Proterozoic granitoid rocks of the western Churchill Province, Northwest Territories (Nunavut). https://doi.org/10.4095/210177

Qulliq Energy Corporation (2018). Website page, Qulliq Energy Corporation, Iqaluit. Accessed on April 30, 2024. https://www.qec.nu.ca/about/missionvision-values

Rainbird, R. H., Hadlari, T., Aspler, L. B., Donaldson, J. A., LeCheminant, A. N., & Peterson, T. D. (2003). Sequence stratigraphy and evolution of the Paleoproterozoic intracontinental Baker Lake and Thelon basins, western Churchill Province, Nunavut, Canada. Precambrian Research, 125(1–2), 21–53. https://doi.org/10.1016/s0301-9268(03)00076-7

Royer, J. (2011). Status of Remote/Off-Grid communities in Canada. Accessed on April 30, 2024. https://natural-resources.canada.ca/maps-tools-and-publications/publications/energy-publications/energy-reports-and-publications/status-remoteoff-grid-communities-canada/11916

Rybach L (1988) Determination of heat production rate. Hänel R, Rybach L & Stegena L (Eds.) Handbook of Terrestrial Heat Flow and Density Determination, Springer, Dordrecht, pp. 125-142.

Sircar, A., Solanki, K., Bist, N., & Yadav, K. (2022). Enhanced Geothermal Systems–promises and challenges. Int. J. Renew. Energy Dev, 11(2), 333-346. 10.14710/ijred.2022.42545

Sarmiento, Z.F., Steingrímsson, B. and Axelsson, G.: Volumetric resource assessment. Proceedings, Short Course V on Conceptual Modelling of Geothermal Systems, UNU-GTP, Santa Tecla, El Salvador, (2013).

Tomarov GV & Shipkov AA (2017) Modern geothermal power: Binary cycle geothermal power plants. Thermal Engineering, 64(4), 243–250. 10.1134/S0040601517040097

Fort Wainwright Army Installation Geothermal Prototype Initiative: Initial Results

Joseph Batir[1], Emilie Gentry[1], Michael Jones[2]

[1]Teverra LLC, [2]Army OEI

Keywords

Greenfield, Exploration, Alaska, DoD

ABSTRACT

Motivated by a Department of Defense directive to reduce coal consumption and guided by the 2022 United States Army Climate Strategy, the Army Office of Energy Initiatives began pursuing geothermal energy opportunities for various locations throughout the United States, carried out through the Defense Innovation Unit (DIU). One of these projects was awarded to Teverra, to explore, quantify, and design a geothermal prototype energy utilization system for Fort Wainwright (FWA) in Fairbanks, Alaska. Fairbanks is within the Tanana Valley in interior Alaska. The Tanana Valley has no significant hydrocarbon or geothermal exploration but may have geothermal potential because of the regional tectonic setting and limited far field heat flow data. As such, the FWA geothermal initiative is a greenfield exploration project located within a favorable regional tectonic setting. To date, existing datasets have been collated and used to build a simplistic 3D geologic model, and new data were collected during Summer 2024, which are being incorporated into the existing model. Here, we present a review of the project goals, existing data, and new data that were collected that will be used for defining next steps in the exploration and development process.

1. Introduction

As part of the Department of Defense (DoD) directive to reduce coal consumption, Fort Wainwright (FWA) is the location of a new opportunity through the Defense Innovation Unit (DIU), a geothermal protype that is meant to provide geothermal energy directly to a DoD facility. FWA is located within the Tanana Basin of central interior Alaska. This area and the adjacent Nenana Basin are one of the most seismically active regions in North America, associated with the Denali Fault System. This area is also known to have significant Cenozoic coal-bearing formations which is of interest to energy and mining industries. Previous research in the basin that loosely encompasses Fort Wainwright includes geophysical studies and geological studies to define the tectonics and energy resource geology in the area (Dixit and Hanks, 2021).

The Alaska Department of Geological and Geophysical Surveys (DGGS), the US Army Corps of Engineers, Alaska Department of Natural Resources, and University of Alaska Fairbanks have all produced various reports, datasets, and maps that provide data and analysis to determine the basin structure. These data sources were collected and collated to use for further analysis in this geothermal feasibility study.

2. Existing Data

As part of this work, existing data were collected and combined into a single geologic model for the Tanana Valley – Fairbanks area. Data collected includes common greenfield geothermal exploration data as well as examination of public databases for any additional data within the general study area that may then help interpretation in the specific area of interest (AOI). Data examined are reported in Table 1. Because there are limited existing geothermal studies for the AOI, data needed to be collated to find all the necessary elements for a traditional geothermal system: heat, fluid, and fluid flow pathways. Data were mapped individually as well as collectively to examine total data coverage as well as data value for geothermal exploration. Below, the most abundant data sources are discussed.

Table 1. Summary of Data Collated for Fort Wainwright Geothermal Exploration.

Category	Data Available	Data Use	Sources
Geophysical	Low-quality magnetics maps Gravity data points Earthquake locations	Identify sedimentary thickness and potential subsurface structures	DGGS, USGS Dixit and Hanks, 2021
Structural	State Geologic Map Mapped Faults	Fluid pathways and structures that may alter the depth of thermal resource	DGGS, public database
Lithological	Regional Stratigraphic columns and cross sections	Stratigraphic column development for thermal mapping and identification of key rock formations	DGGS GMC 446 report Dixit and Hanks, 2021
Thermal	Shallow water well data Heat flow data points	Temperature characterization	Alaska Department of Natural Resources, SMU heat flow database
Geochemistry	Shallow water well data Rock samples		Alaska Department of Natural Resources DGGS
Hydrology	Reports	Permafrost and aquifer studies	DGGS Army Corps of Engineers report

2.1 Well Data

Within the Fairbanks area, there is no deep oil and gas or geothermal exploration. The nearest deep wells are at Eielson Air Force Base, oil and gas exploration wells in the Nenana Basin, and Chena Hot Springs geothermal wells. The Eielson deep well is approximately 30 km away, and both the Nenana Basin and Chena Hot Springs wells are approximately 75 km away from the AOI. These are too far away for local exploration relevance but do provide potential regional thermal regime context. These wells have surface heat flow values of approximately 90 – 100 mW/m² (Batir et al., 2016). These values, while sparse, suggest there is a regional elevated thermal regime.

The local water well database was examined through the Alaska Department of Natural Resources Mining, Land & Water Well Log Tracking System (WELTS). The database was searched for deep water wells which are opportunities to collect regionally relevant thermal data and water chemistry information (Figure 2). There are more than 3,000 water wells within the Fairbanks area, with a large number also on FWA; however, only 70 wells are greater than 500 ft (152 m) deep. Past research shows that climatic warming is visible in temperature logs in Alaska to a depth of approximately 80 m (Batir et al., 2017). Here, a minimum well depth of 150 m is used to provide the opportunity to collect temperature logs that may be deeper than the recent climatic warming signal, and as such, be at thermal equilibrium. These 70 wells are actively being examined for temperature logging opportunities. Water chemistry data is available for major components; however, many of the common geothermal constituents, such as those for the various geothermometry estimations, were not recorded.

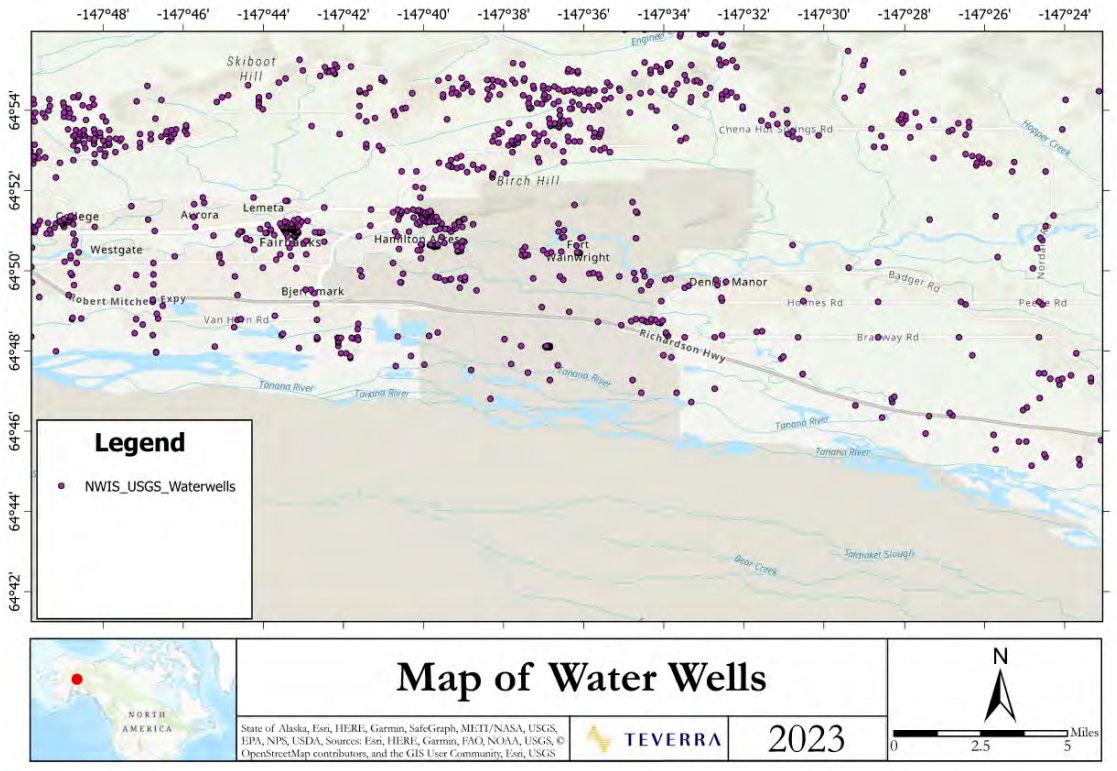

Figure 1. Water wells near the Fort Wainwright AOI, extracted from WELTS (Alaska DNR, 2023).

2.2 Geophysical Data

Previous work produced regional cross sections of the Nenana Basin and Tanana Valley utilizing only gravity and magnetic surveys for inversion modeling (Dixit and Hanks, 2021). As such, geophysical datasets were expected to be abundant and directly applicable to geothermal exploration. Processed gravity and magnetic data points (as opposed to gridded maps) were searched for, and where available, collated (Figure 3 and Figure 4, respectively). Because of the limited data from past studies directly crosscutting the AOI, it was determined that the individual data points, if available should be collated, combined with new data, and then used to perform gridding and inversion modeling. In addition to gravity and magnetic field data points, earthquakes were collected to infer potential for active faults on or near the AOI (Figure 5). To our dismay, data coverage for the AOI is subpar. Gravity stations for the AOI are low in number and not evenly distributed. There is a recent high resolution aeromagnetic survey, however, the survey only covers a portion of the AOI, and individual flight lines are still being converted to a usable format. Earthquake data is an exception to the poor data coverage in that there are sufficient earthquakes that can be used to infer seismically active areas.

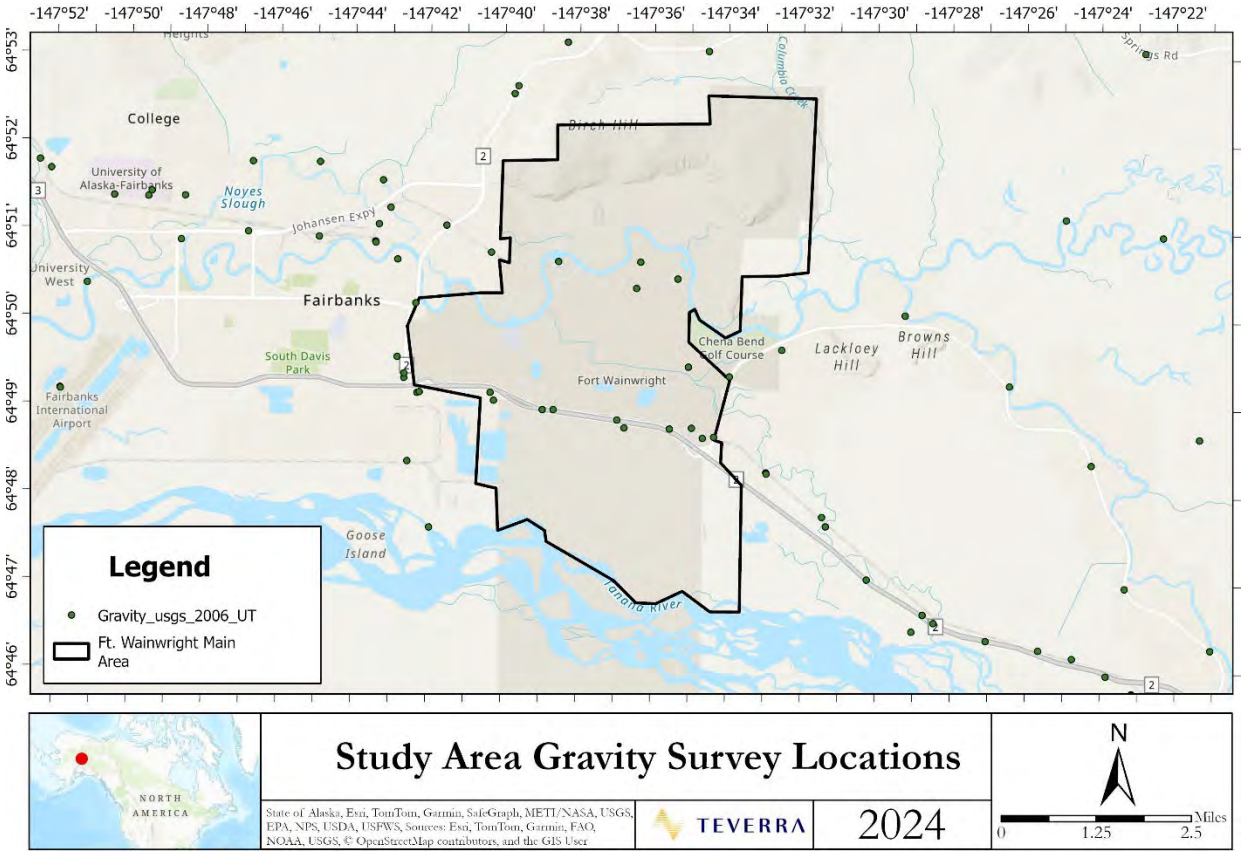

Figure 2. Location of gravity data points near the AOI (USGS, 2006).

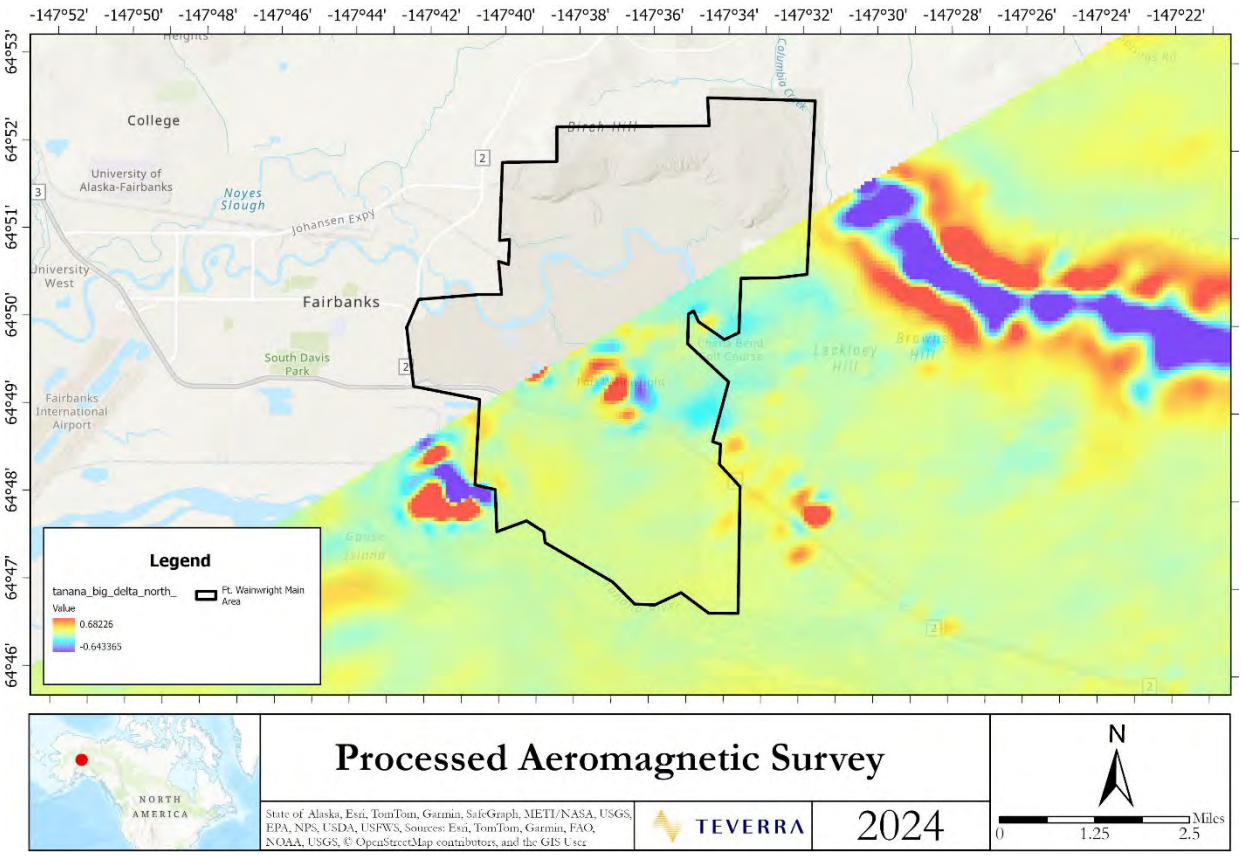

Figure 3. Regional magnetic anomaly map of AOI (Emond and MPX Geophysics LTD, 2022). Note that this is shown as a gridded map surface, but the raw data are available and were collected.

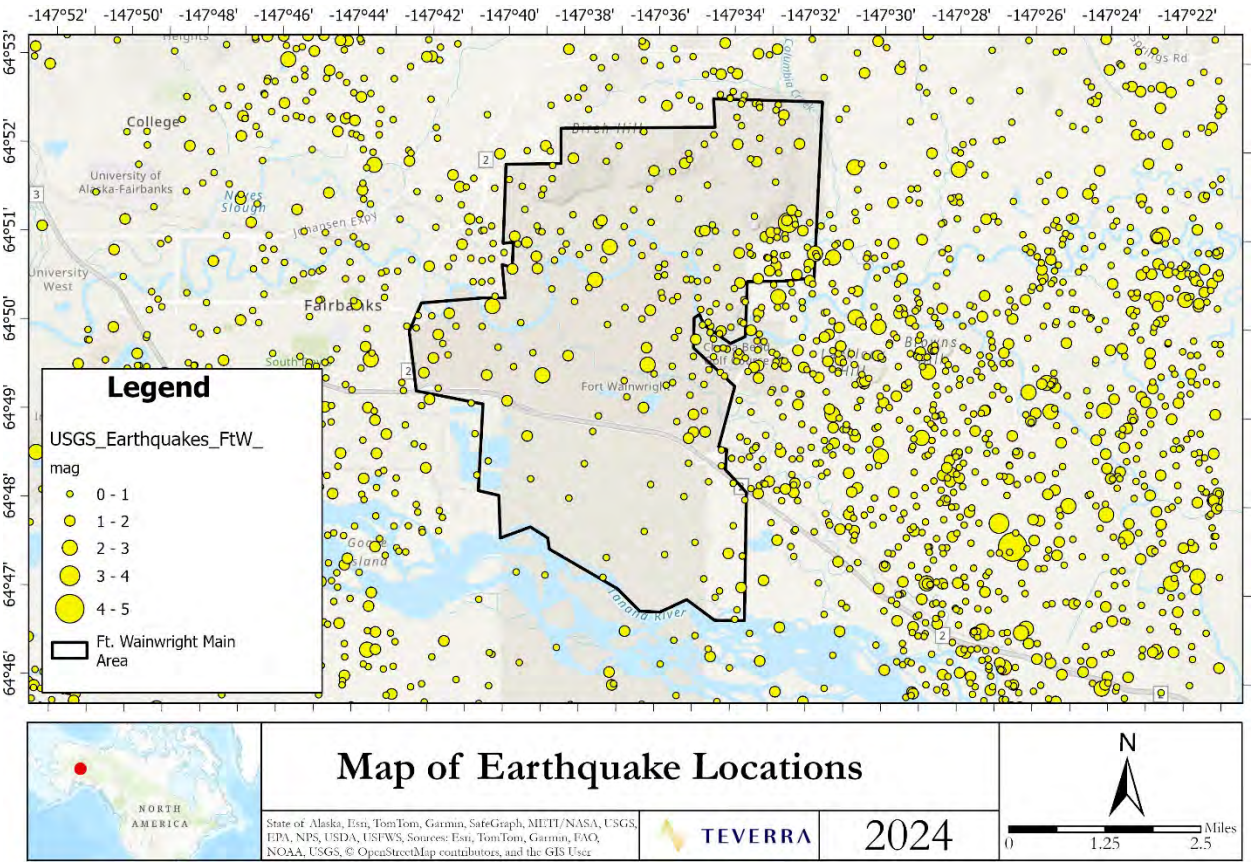

Figure 4. Location map of USGS earthquake catalog for the AOI, 1973 - 2023 (USGS, 2023).

2.3 Geologic Data

As stated previously, there are no regionally relevant deep wells within the AOI. As such, regional stratigraphy and structural trends are interpreted from regional surface mapping and limited, shallow water well drilling. In general, there is a package of Cenozoic sedimentary formations overlying Mississippian and older metamorphic rocks, which are labeled as basement. Depending on location, basement rocks outcrop at surface, including within the AOI (Figure 6). Additionally, surface mapping identified strike-slip faults within outcrops that are projected to crosscut the AOI. Previous models show there can be significant sedimentary sequences where there is vertical offset along faults, which could then be a target for geothermal exploration (Dixit and Hanks, 2021).

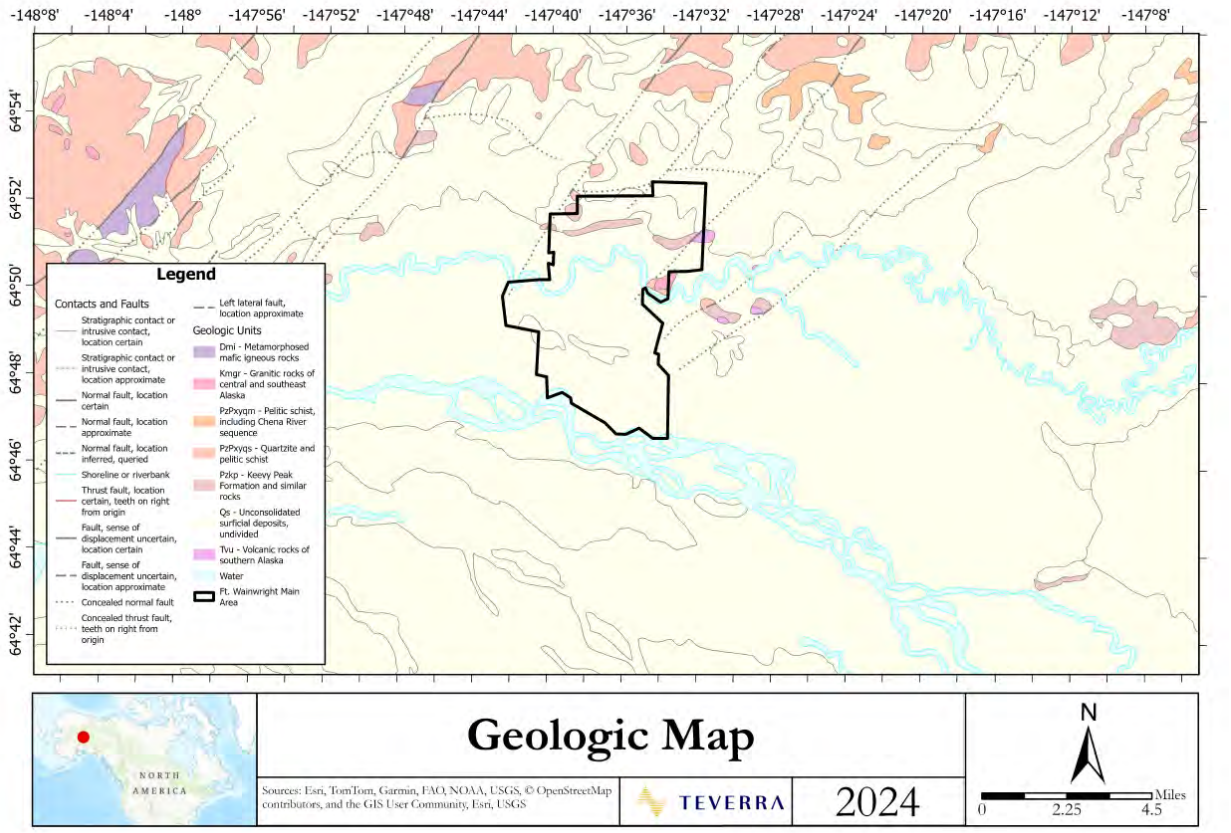

Figure 5. Geologic map of the Fort Wainwright region, with the AOI indicated as the thick black bordered polygon (Wilson et al., 2015). The map shows potential faults crosscutting the installation as well as several formation outcrops in the northern portion of the installation.

3. Interpretation

While there is limited data, there is sufficient data to begin interpretation and geothermal exploration.

One of the previous geophysical inversion model cross sections produced by Dixit and Hanks (2021) intersects the Tanana Valley west of the AOI, while all others are south and west. Still, the Dixit and Hanks (2021) cross sections are used to project subsurface formation thickness from the nearby cross section to the AOI. This projection shows that there is potential for the sedimentary package to be approximately 750 ±300 m (2500 ±1000 ft) thick, at which point the metamorphic rocks would begin. This thickness is heavily dependent on fault location and total fault offset, which were previously interpreted from the sparse and low-resolution gravity and magnetic field data.

Based on the existing far field heat flow data points, heat flow should be 75 ±20 mW/m² and hypothesized to be on the higher end based on the nearby data. Using this estimated heat flow, the subsurface should be approximately 45 ±5 °C (115 ±15 °F) at the base of the sediment 750 ±300 m (2500 ±1000 ft). This temperature may be further elevated if one of the extrapolated faults is acting as a fluid flow pathway that enables deep circulation of fluids and upflow of elevated

temperature water. While there is no surface indication of deep-seated fluid circulation, this is the primary target for this exploration.

3.1 Key Challenges

There are several identified challenges associated with the limited data available. First, the heat flow and estimated thermal regime is calculated from far field data. These data points are not directly relevant to the local AOI and as such may not be representative of the thermal regime within the AOI. Second, there are limited data points to build new inversion models for estimating basement depth. Both of these uncertainties are reflected in the large error estimations within the heat flow and basement depth.

4. New Data Collection

New data collection will have taken place during summer 2024, before the GRC 2024, but after the writing of this paper. New data collection is planned to fill in these two key uncertainties of sediment thickness and thermal regime. Sediment thickness will be estimated by collecting a ground-based gravity survey, an aeromagnetic survey, and a passive seismic survey. The gravity and passive seismic will be collected in a grid pattern similar to the example grid below (Figure 7). The goal of the grid style data collection will be to produce a complete gravity survey and passive seismic survey, centered on the AOI. Additionally, an aeromagnetic survey will be conducted, and data collected over approximately the same area to complete the magnetic anomaly map over the AOI. By combining these three geophysical datasets, we anticipate producing a higher resolution inversion model to estimate sediment thickness as well as potential regional variation in the sediment formations (i.e., structural features such as faulting or formation dip). A secondary goal of the multiple geophysics data collection will be imaging/interpretation of faults underlying the AOI. This goal will be more difficult to achieve because of the still limited resolution that will be able to be collected, but processing will be completed to attempt imaging of faults within the AOI.

Similar to the geophysical data collection, temperature logs will be attempted to be collected throughout the Fairbanks region. As stated previously, there are 70 wells that are deeper than 500 ft (152 m). These wells are the highest opportunity wells to measure the thermal regime of the Fairbanks region. While there is an abundance of wells, these may be a challenge to get final permission for logging.

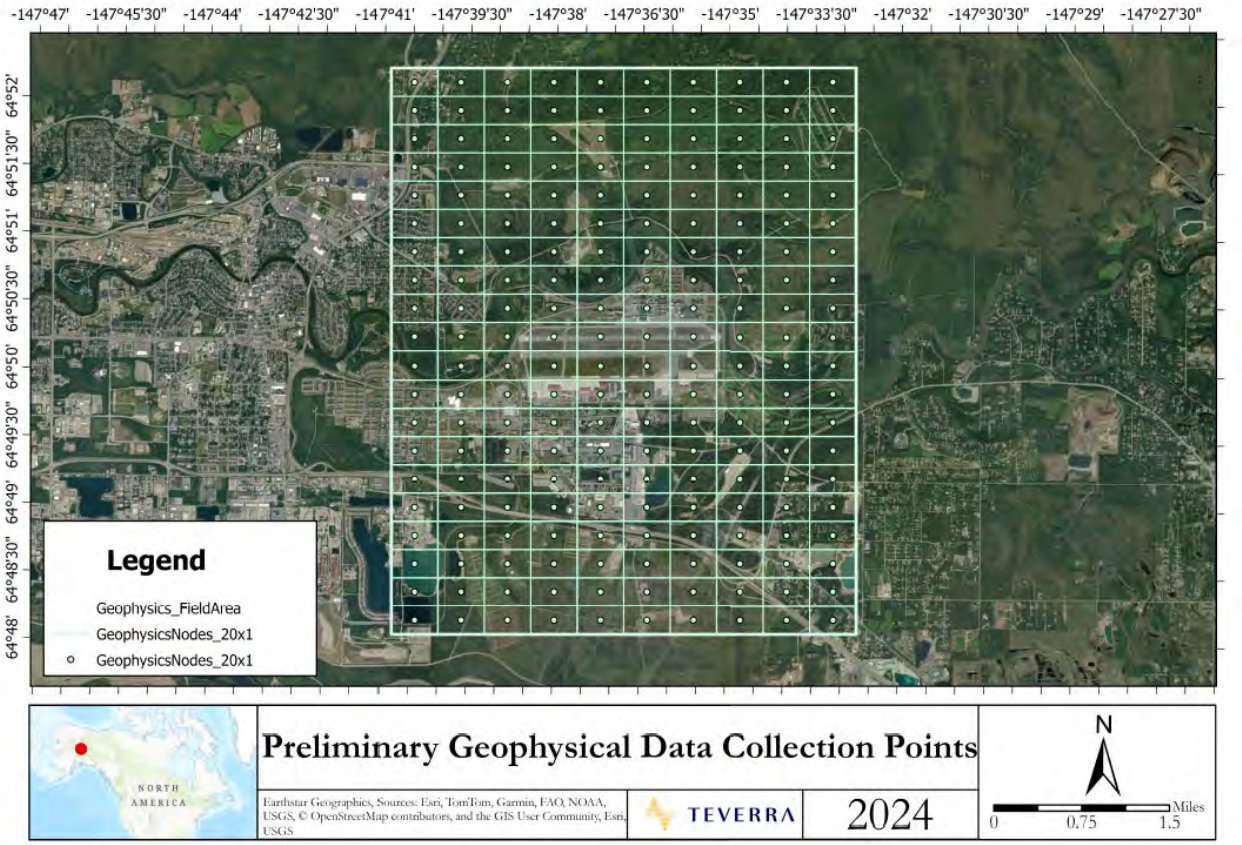

Figure 6. Preliminary data collection plan. Each point will be a location for a geophone and a gravity station. The aeromagnetic survey will cover nearly all of this area.

5. Conclusions

Fort Wainwright has a clear desire for more power and is pursuing options for lower carbon fuel sources, as evidenced by this project. While there is a clear demand, the understanding of the potential resource is lacking because of a lack of proper geothermal exploration data. Still, there is sufficient evidence to support further exploration, taking place Summer 2024. The Summer 2024 data collection campaign will consist of gravity stations, a passive seismic survey, an aeromagnetic survey, temperature logging, and rock sample collection. With successful collection of these data, we anticipate being able to provide better estimates of the local thermal regime and sediment thickness.

Acknowledgements

Effort sponsored by the U.S. Government under Other Transaction Agreement number HQ00342390015 between Teverra and the Government. The U.S. Government is authorized to reproduce and distribute reprints for Governmental purposes not withstanding any copyright notation thereon. The views and conclusions contained herein are those of the authors and should not be interpreted as necessarily representing the official policies or endorsements, either

expressed or implied, of the U.S. Government. The authors also acknowledge the additional staff and collaborators who are making this project successful.

REFERENCES

Alaska DNR, 2023. “Alaska Department of Natural Resources Mining, Land & Water”, *WELTS - Home,* dnr.alaska.gov/welts/. Accessed 14 Nov. 2023.

Batir, J., Blackwell, D., and Richards, M., 2016. “Heat flow and temperature-depth curves throughout Alaska: finding regions for future geothermal exploration”, *Journal of Geophysics and Engineering*, 13(3). doi: 10.1088/1742-2132/13/3/366

Batir, J., Hornbach, M., Blackwell, D., 2017. “Ten years of measurements and modeling of soil temperature changes and their effects on permafrost in Northwestern Alaska”, *Global and Planetary Change*, 148.

Dixit, N.C. and Hanks, C., 2021. “Basement structure and styles of active tectonic deformation in central interior Alaska”, *Geosciences*, 11(3), p.127.

Emond, A.M., and MPX Geophysics LTD, 2022. “Tanana River and Big Delta airborne magnetic and radiometric survey: Alaska Division of Geological & Geophysical Surveys Geophysical Report 2022-1”, https://doi.org/10.14509/30899

USGS, 2006. “USGS Gravity Stations UTM 2006”, *Personal Communication*, 26 October 2023.

USGS, 2023. “USGS Earthquake Catalog”, *U.S. Geological Survey*, https://earthquake.usgs.gov/earthquakes/search/. Accessed 11 Nov. 2023.

Wilson, F.H., Hults, C.P., Mull, C.G, and Karl, S.M, comps., 2015, Geologic map of Alaska: U.S. Geological Survey Scientific Investigations Map 3340, pamphlet 196 p., 2 sheets, scale 1:1,584,000, http://dx.doi.org/10.3133/sim3340.

Canadian Expertise and Financing in Global Geothermal Exploration and Development

Catherine Hickson and Brian Fairbank

Alberta No. 1

Keywords

Canada, Geothermal Exploration, International, financing

ABSTRACT

Canadian companies and Canadian experts have made a mark in the global exploration and development of all types of mineral and hydrocarbon resources including geothermal energy. Most of the worlds exploration funds are raised on the Toronto Stock Exchange (TSX and TSX-V) that fuels the global search for mineral wealth. This is also true of the geothermal sector. But Canada's global ambitions came after focus on Canadian geothermal resources starting in 1975. The early 1970's worldwide oil crisis spurred increased interest in geothermal resources globally. The crises fostered an increased interest in both the USA and Canada, major oil producing nations, in geothermal resources. In 1973, a small group of energy professionals, scientists and academics came together in California to explore potential synergies and research projects that might help their countries combat the coming fuel shortages with another way to produce power. This was the nascent beginnings of the US-based Geothermal Resources Council (now Geothermal Rising). Several Canadians attended that meeting and upon returning to Canada, established the Canadian Geothermal Association as a not-for-profit technical association to bring together Canadians interested in geothermal energy both domestically and globally. The association is still active today, 50 years later, after rebranding as Geothermal Canada in 2018. During these 50 years Canadians have been active globally in all aspects of geothermal development from green-field exploration to brown-field development, to building and operating plants, to reservoir management. Canadian drilling expertise was also sought after based on the drilling of 1000's of wells since the early 1940s. Canadian drillers and engineers found themselves involved in geothermal exploration projects in Japan, USA and elsewhere. Research also included exploration technologies such as the development of electromagnetic geophysical methods. These methods were developed and first used in Canada at Mount Meager, supported by funding from Canada's Federal Government Natural Resources Canada (Geological Survey of Canada and the Earth Physics Branch).

1. Introduction

Canadians first became interested in geothermal energy resources in the early 1970's when a global oil crisis spurred increased interest in geothermal resources globally (Figure 1). The crises fostered an increased interest in both the USA and Canada (Hintz 2023). In 1973, a small group of energy professionals, scientists and academics came together in California to explore potential synergies and research projects that might help their countries combat the coming fuel shortages with another way to produce power. This was the nascent beginnings of the US-based Geothermal Resources Council, now known as Geothermal Rising.

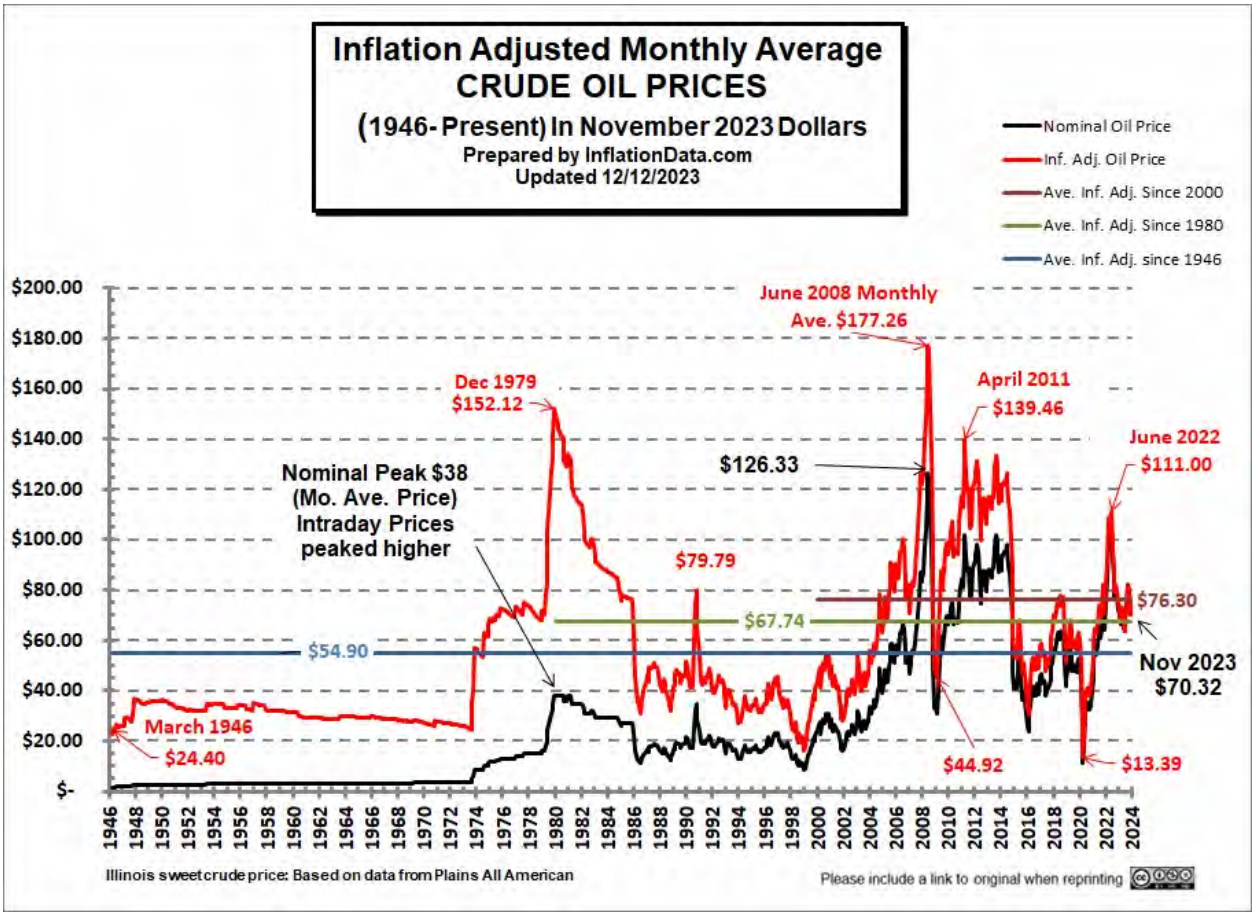

Figure 1: Inflation adjusted crude oil prices (https://inflationdata.com/articles/inflation-adjusted-prices/historical-oil-prices-chart/), showing the rise and fall of crude oil prices that fueled and cooled geothermal investments globally.

Three Canadians attended that meeting, Dr. Jack Souther, Geological Survey of Canada, Tim Sadlier Brown, and Andrew Nevin, both from Nevin-Sadlier Brown-Groodbrand and Associates. Upon returning to Canada, they established the Canadian Geothermal Association as a not-for-profit technical association to bring together Canadians interested in geothermal energy both domestically and globally. The association is still active today, 50 years later, after rebranding as Geothermal Canada in 2018. During these 50 years Canadians have been active globally in all aspects of geothermal development.

Canadians have been involved in everything from green-field exploration to brown-field development, to building and operating plants, to reservoir management. For more details on the efforts by Canadians in Canada see Jessop (2008) and Jessop et al. (2024). These papers chronical the significant investment made by the Canada Government between 1975 and 1985, to support geothermal research and development in Canada. In addition to the efforts at home in the 1980s and 1990's Canadian drilling expertise was sought after globally. Canadian drillers, well known from oil and gas exploration in the Western Canada Basin where 1000's of wells had been drilled since the early 1940s, found themselves involved in geothermal exploration projects in Japan, USA and elsewhere.

Canadian expertise in mineral exploration using geophysical methods was directed at the exploration for geothermal resources in the mid-1070's. Early R&D efforts by Greg Shore, Premier Geophysics, in the use of electromagnetic methods for exploration of high temperature systems, were first used in Canada at Mount Meager, supported by funding from Canada's Federal Government, Dept of Natural Resources (Shore 1978). These methods were soon being tested and deployed globally.

It was these early efforts and the training of a cadre of young geologists, geophysicists and engineers that led to expansion of the involvement of Canadian's in geothermal development efforts globally. Throughout the decades these investments have been largely financed by the Toronto Stock Exchange (TSX) and TSX Venture Exchange (TSX-V). These exchanges are home to 42% of the world's public mining companies. In 2021, 203 mining firms were listed on the TSX and 967 firms listed on the TSX-V. These firms had a combined market capitalization of $558 billion and raised $10 billion in equity capital in 2021.

2. Global Efforts

In the early 1980's Toronto based Polaris Renewable Energy became active in Nicaragua, developing an operating asset there (Tiffer et al. 1988). In Nevada, Vancouver based Nevada Geothermal explored and developed the Blue Mountain Geothermal field (Fairbank et al. 1999, Fairbank 2024). The mid-2000's saw several Canadian companies entering the scene, among these Western Geothermal, Siera Geothermal, and Magma Energy Corp. The capital investment in these companies was bolstered by the steady rise in crude oil prices noted from the early 2000s to the 2008 financial crises (Figure 1) (Helleiner 2011).

Western Geothermal focused on assets in Canada such as Meager Mountain, and Siera Geothermal was involved in exploration in Canada and the USA. In 2007 Magma Energy Corp was formed and commenced a global exploration program as well as purchasing operating assets in Nevada (Soda Lake) USA and Iceland (HS Orka Svartsengi and Reykjanes). Headquarters were in Vancouver, Canada in addition to offices in Lima, Peru; Reno, Nevada; Santiago, Chile; Sienna, Italy; and Keflavik, Iceland, they also established additional subsidiary companies in Chile (Hickson 2011), Italy, Nicaragua, and Peru. The company merged in 2011 with Plutonic Power Corp, becoming Alterra Power Corp. Eventually the company was bought by Innergex Renewable Energy, who continues developing renewable energy projects, but is no longer actively engaged in geothermal development, despite holding key geothermal assets in Italy and Chile.

The 2008 financial crises left many companies struggling to raise capital. Publicly traded Magma Energy Corp. was the first Canadian company of any type to go to the markets post-crises with an

"initial public offering." In June 2009, they raised just over $CDN120MM on the TSX. By 2013, many geothermal companies were again challenged to raise capital as crude oil prices fell (Figure 1) and the geothermal value proposition for electrical generation vs natural gas declined.

By the early 2020s, most of the financial and development emphasis for Canadians was on home grown projects (Huang et al 2023). With time the focus in Canada has shifted from low-cost Natural Gas and coal power generation to renewable energy projects, geothermal energy for power production is slowly gaining momentum in Canada (Huang and Hickson 2024). However, wind, solar and run-of-river hydro, still make up the bulk of renewable electricity projects in Canada.

Of note, is the 2023 achievement of Calgary based, Futera Energy Corp to produce the first geothermal electrons in their co-production facility in the Swan Hills of Alberta (https://www.globenewswire.com/news-release/2023/03/22/2632687/0/en/Canada-s-First-Co-Produced-Geothermal-Power-Project-is-Operational.html) , 40 years after the 250 kw generator produced power at Mount Meager, British Columbia in 1983. Additionally, Parex Resources Inc, based in Calgary, Alberta and operating in the Llanos Basin, Colombia, installed and operates two ORC units powered by a high temperature water cut from their hydrocarbon operations (Figure 2). Generation began in 2021, as the second only geothermal power plant operating in South America. Polaris continues to develop the geothermal resources of Nicaragua and has also expanded into solar and hydro projects in Latin America.

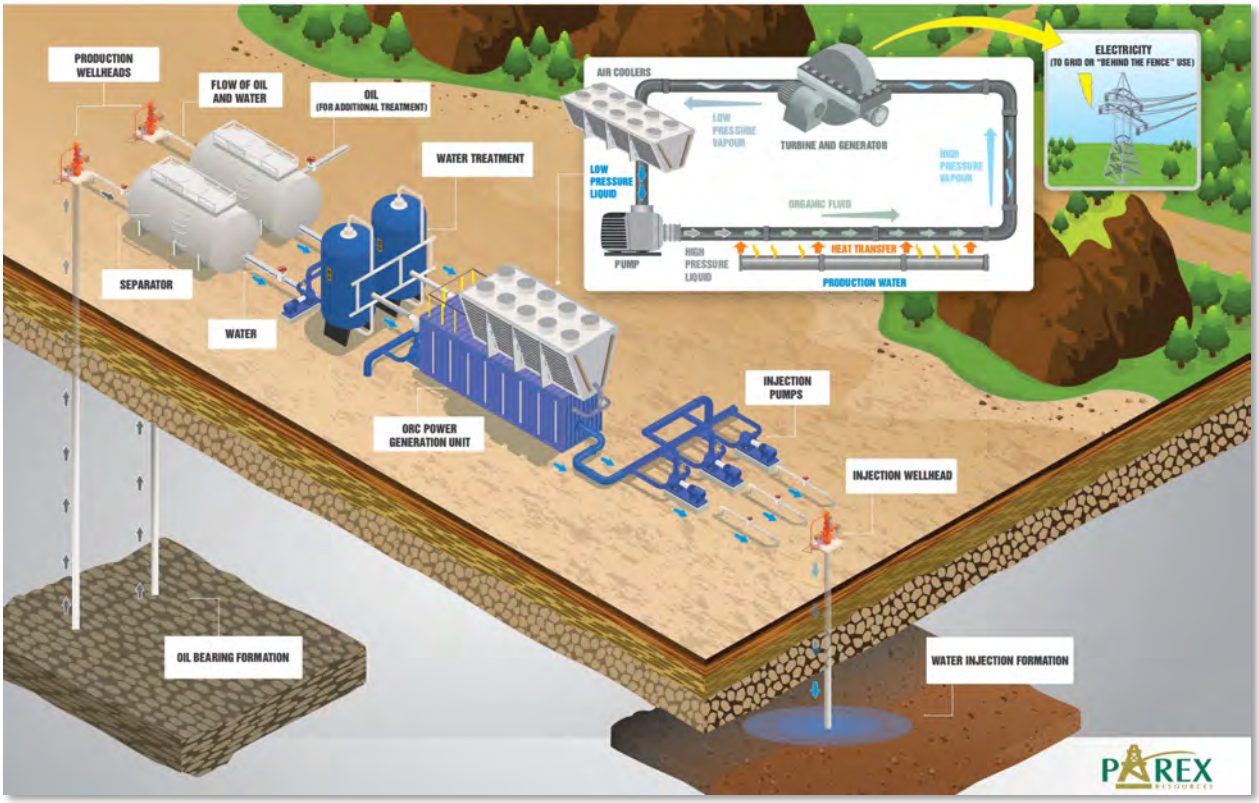

Figure 2: Parex Resources Ltd. operating ORC unit in the Llanos Basin, Colombia, utilizes a high temperature water cut to produce electricity then used in the field operations.

Acknowledgement

The Canadian pioneers who laid the groundwork for the current cohort of geothermal geoscientists and engineers are thanked for their perseverance and fortitude. Innovation and advances in the oil and gas sector have fueled new ways of looking at geothermal development, these pioneers are thanked for their contributions over the decades. The authors apologize for projects and developments where Canadian's have been instrumental and have been missed in this brief review. The mention of any specific project is not an endorsement of that project or the development team. We welcome updates and additions.

REFERENCES

Fairbank, B. P. Blue Mountain "Faulkner 1" 49.5 MW Geothermal Power Plant, Humbolt County, Nevada – A Canadian Story. GeoConvention, Calgary, AB. (2024)

Fairbank, B. and H. Ross. "Geology and Temperature Gradient Surveys - Blue Mountain Geothermal Discovery, Humboldt County, Nevada." TRANSACTIONS-GEOTHERMAL RESOURCES COUNCIL: 513-518. (1999)

Gutiérrez-Negrín, C.A. "Evolution of worldwide geothermal power 2020–2023." Geothermal Energy (2024) 12:14 https://doi.org/10.1186/s40517-024-00290-w (2023)

Helleiner, Eric. "Understanding the 2007 – 2008 Global Financial Crises: Lessons for Scholars of International Political Economy." Annual Review of Political Science, Volume 14:67-98 https://doi.org/10.1146/annurev-polisci-050409-112539 (2011)

Hickson, C. J. F., F.; Rodriquez, C.; Sielfeld, G.; Henriquez, R.; Gislason, T.; Selters, J.; Benoit, D.; White, P.; Southon, J.; Ussher, G.; Charroy J.; Smith, A.; Lovelock, B.; Lawless, J.; Quinliven, P.; Smith, L.; Yehia, R. "The Mariposa Geothermal System, Chile." Geothermal Resources Council Annual Meeting, San Diego, CA, GRC. (2011)

Hintz, E. "Looking Back on the 1973 Oil Crisis, New Perspectives on Energy Innovation." Lemelson Center for the Study of Invention and Innovation. (2023)

Huang, K and Hickson, C.J. "Geothermal Energy Solutions for Canada's Geological Provinces" GRC Transactions, Vol 48 (2024).

Huang, K., Dehghani-Sanij, A., Hickson, C., Grasby, S.E., Smejkal, E., Miranda, M.M., Raymond, J., Fraser, D., Harbottle, K., Torres, D.A. "Canada's Geothermal Energy Update in 2023." *Energies*, 17, (2024), 1807.

Jessop, A. "Review of National Geothermal Energy Program, Phase 2 – geothermal potential of the Cordillera." Geological Survey of Canada, Open File 5906, (2008), 86.

Jessop, A., S. Grasby and C. J. Hickson. "The history of geothermal research in Canada." GeoConvention, Calgary, AB, CEGA. (2024)

Shore, G. Meager Creek Geothermal System, British Columbia, Part III: Resistivity Methods and Results. Geothermal Resources Council Annual Meeting. 2: 593-596. (1978)

Tiffer, E. M., R. A. Lacayo and G. Sabatino. "Geothermal development in Nicaragua." Geothermics 17(2): 333-354. (1988)

Geothermal Energy Technology Solutions Based on Canada's Geological Provinces

Katherine Huang, Catherine Hickson

Alberta No. 1

Keywords

Canada, Conventional, Unconventional, AGS, EGS, GSHP, Borehole Heat Exchanger, Heat Capture and Storage

ABSTRACT

The increased demand for energy, commitment to develop more renewable energy, and need for baseload renewables has pushed geothermal energy development in Canada in recent years. The country's geological diversity, as well as population distribution and infrastructure, require a variety of geothermal systems. Conventional geothermal systems need heat, fluid, and permeability, however, only portions of Canada's orogen and platform provinces have all 3 parameters. Unconventional methods and shallow geothermal systems have been/are being developed to produce geothermal energy in areas that lack one or more of the conventional requirements. As well, new innovations allow for re-purposing existing end-of-life wells and creating heat storage and utilization for use in conjunction with intermittent renewables. This paper outlines seven classes of geothermal energy systems and suggests where each class is suitable for development in Canada. Geologically, Canada is made up of a number of geological "provinces", the most aerially extensive is the Canadian Shield. The Shield, which is comprised of crystalline Precambrian rock and characterized by lower temperatures and low permeability, cannot produce geothermal energy from conventional means; alternative technology is required. This region is potentially suitable for ground source heat pumps south of the permafrost zone (and possibly with heat augmentation within permafrost zones), shallow subsurface hydrological systems, Advanced Geothermal Systems (AGS), Enhanced/Engineered Geothermal Systems (EGS), and heat capture and storage. On the other hand, conventional geothermal development is possible in some sedimentary basins within the platform geological provinces, and there are already several projects being developed. In Canada's orogenic geological provinces, conventional geothermal projects are possible in fault-hosted systems, especially within the volcanic belts that have been shown to have high subsurface temperatures. In both the platform and orogen provinces, AGSs and EGSs are options in areas that lack permeability and/or subsurface fluid, and can also support the shallow systems, borehole heat exchangers, and heat capture and storage.

1. Introduction

The geothermal landscape in Canada continues to be shaped by both challenges and successes, emulating many similar setbacks that projects have faced over the past several decades, such as regulatory hurdles, limited funding, and geological challenges. Despite this, the geothermal industry in Canada is still growing as commercial projects in several provinces and territories continue to develop, while new projects are entering planning phases. Research in many fields of geothermal energy, such as direct heat use, co-production, Enhanced/Engineered Geothermal Systems (EGS), and more, is also very strong across universities and research groups. The continual increase in interest and drive to develop the industry shows strong promise as geological and energy conferences grow their focus on geothermal energy. This is a strong preparation for Calgary, Alberta to host the World Geothermal Congress in 2026.

Development of geothermal energy projects is especially critical since the announcement of the 2030 Emissions Reduction Plan which pledges to reduce emissions of 40% below levels from 2005 and reach net zero greenhouse gas emissions by the year 2050. This plan includes reducing emissions from oil and gas development, lowering energy costs for homes and buildings, and investing in renewable electricity. The Government of Canada plans to invest $600 million for renewable electricity support and grid modernization through the Smart Renewables and Electrification Pathways Program as well as $250 million to support predevelopment work of large-scale, clean electricity projects (Environment and Climate Change Canada, 2022).

The increasing need for renewable energy has in part driven companies and researchers to develop novel technologies, including geothermal energy systems that generate electricity and heat, collaborate with the oil and gas industry, and work with other existing renewables like solar and wind. As well, the variation in geology across the country, the population distribution, infrastructure, and climate lends itself to different requirements and needs. The country's 14 onshore geological provinces (plus 3 offshore) can be divided into orogens (which include mountain and volcanic belts), platforms (hosting sedimentary basins), and the Canadian Shield (Precambrian rock) (Figure 1). These provinces generally outline which technologies may be suitable for development.

This paper provides an overview of the geological provinces in Canada, outlines seven different geothermal classes, attributes which technologies are being used and could be used in each area, and provides examples of each class.

2. Regions and Provinces of Canada

Canada is comprised of 17 geological provinces based on their general rock type, age, and history (Geological Survey of Canada, 1981; Figure 2). The Canadian Shield, characterized by crystalline Precambrian rocks, includes seven geological provinces. Extending beyond the Canadian Shield are platforms where these Precambrian rocks are overlain by younger strata; these are known as the Interior, Arctic, Hudson, and St. Lawrence Platforms, and there are several sedimentary basins within them. At the western, northern, and eastern edges of Canada are the Cordilleran Orogen, Innuitian Orogen, and Appalachian Orogen, respectively. These geological provinces are comprised of mountains, volcanic belts, and other sequences that have undergone significant metamorphism, folding, faulting, and uplift. Finally, there are three continental shelves (not shown on Figure 1).

The use of varying classes of geothermal energy is dependent on many factors. Where favourable geology is present, population density plays a role. The population distribution map of Canada shows that the majority of the country's population lives within the Interior Platform, St. Lawrence Platform, Appalachian Orogen, and Cordilleran Orogen, which has led to progress of several conventional geothermal projects (applicable mostly in platforms or orogens) and ground source heat pumps (GSHPs) (Figure 2). Smaller populations within the Canadian Shield not only have geological challenges, but also limited infrastructure, requiring innovative solutions.

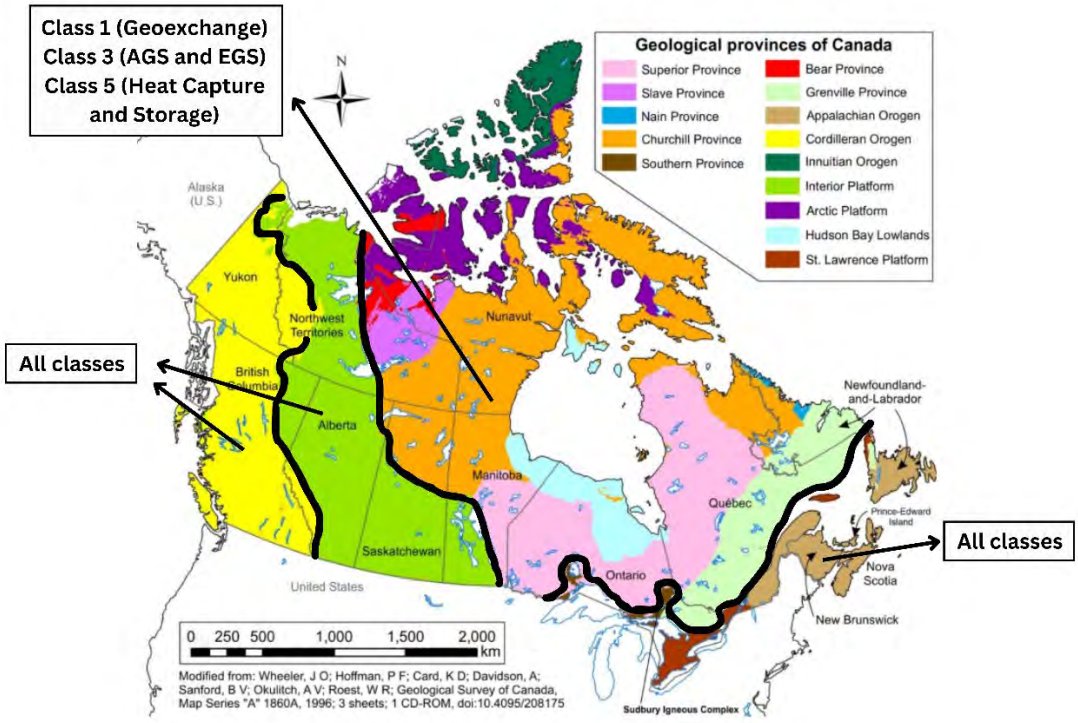

Figure 1: Geological provinces of Canada with suggestions of each geothermal class that could be developed in each (modified from Mercier-Langevin, 2017 and Wheeler et al., 1996).

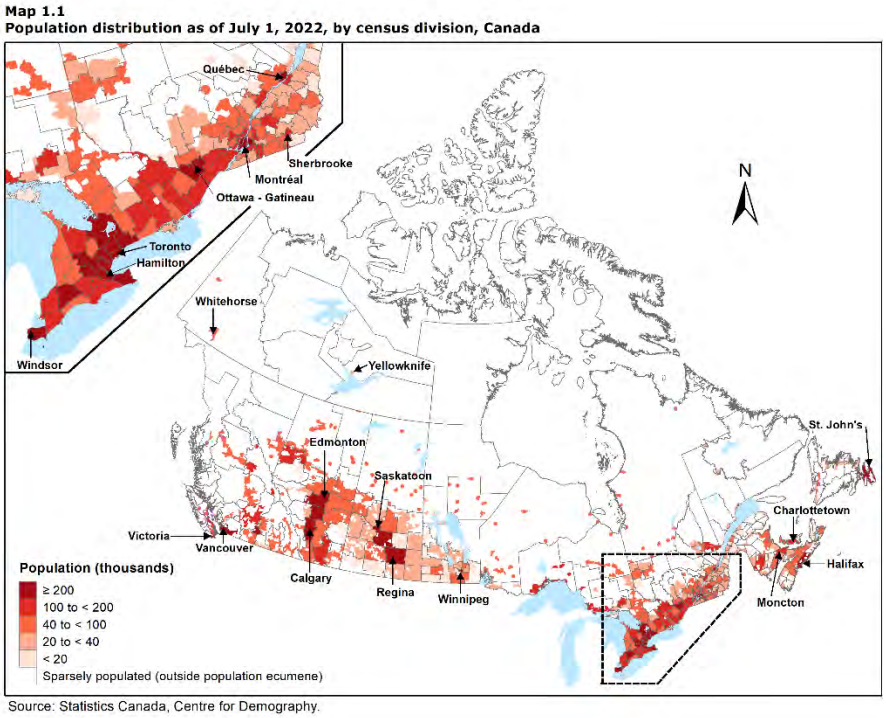

Figure 2: Population distribution map of Canada (Statistics Canada, 2022). The Canadian population reached 40 million in 2023.

3. Classes of Geothermal Systems

This paper divides the potential available geothermal systems into seven classes (Figure 3; Hickson and Smejkal, 2024). Class 1 utilizes the shallow ground/water as a battery for heating and cooling and is divided into 2 subclasses: Class 1 A: Ground Source Heat Pumps (GSHP) and Class 1 B: Shallow Subsurface Hydrological Systems. The most widely known system is Class 2: Conventional Geothermal, which uses a hydrothermal system. Class 3 encompasses 2 types of unconventional geothermal system technology. Unconventional systems are gaining traction in both research and utilization in many areas globally because they provide a solution to "geothermal anywhere". Class 3 systems are defined here as Advanced Geothermal System (AGS) and Enhanced Geothermal System (EGS). Both of these classes have also been referred to as Petrothermal Systems (Hickson et al., 2022) because they are well suited for reservoirs with insufficient permeability and/or fluid volumes for conventional geothermal. Class 4: Deep Borehole Heat Exchangers utilize similar technology to GSHP systems but are deployed down hole into deeper wells. Finally, Class 5 G: Heat Capture and Storage describes an emerging technology which use a subsurface reservoir for artificial heat storage much like those in Class 1, but is capable of storing excess heat at higher temperatures from other energy sources.

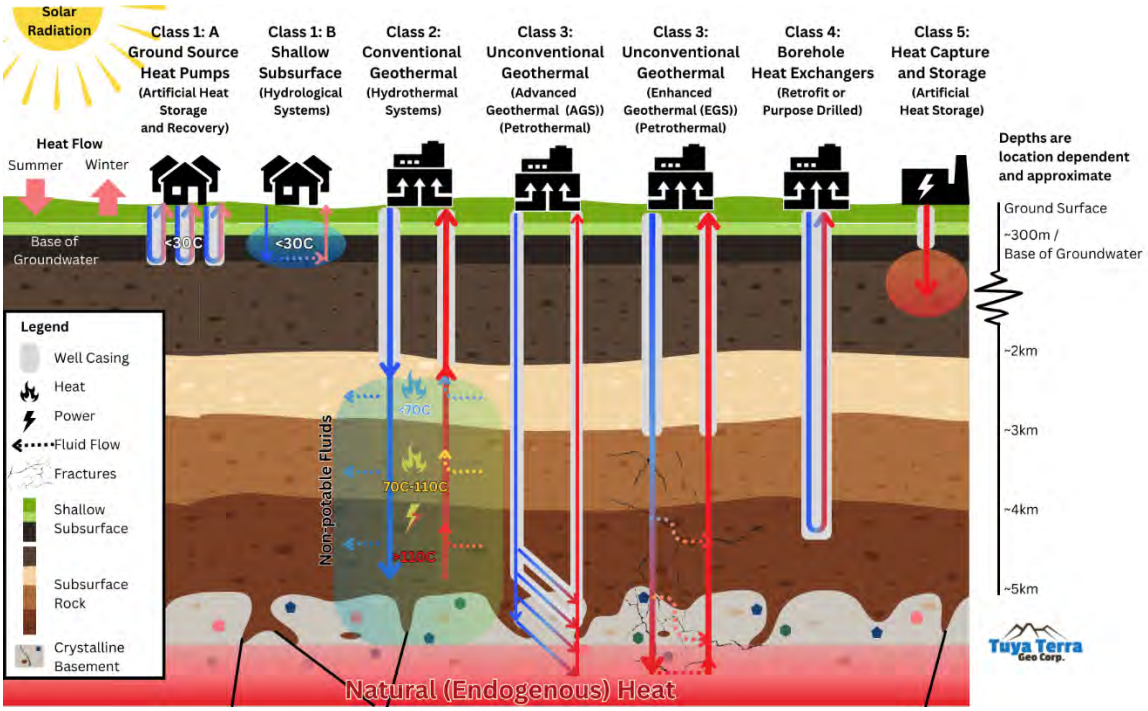

Figure 3: The 7 classes of geothermal systems that are described in this paper as possible solutions in various geological provinces and areas in Canada (Hickson and Smejkal, 2024).

3.1 Class 1: Ground Source Heat Pumps (Artificial Storage and Recovery)

3.1.1 Overview

Ground Source Heat Pumps (GSHP), also called GeoExchange®, are HVAC (heat, ventilation, and air conditioning) systems which use the ground temperature at shallow depths (generally above the base of groundwater) for heating and cooling. The technology extracts temperatures from the soil through closed-loop pipes, a borehole heat exchanger, and a ground source heat pump (Khodayar and Björnsson, 2024). These systems can also be used for artificial heat storage and recovery by storing heat in the shallow ground through heat pumps, then extracted at a later time (Khodayar and Björnsson, 2024).

3.1.2 Potential Areas in Canada

GSHPs can be used anywhere in Canada and have particular importance within the Canadian Shield where the geology limits use of other geothermal systems. However, permafrost zones in Canada's north create challenges for use of GSHPs due to permanently frozen ground and challenges balancing of the heat requirements in the winter months with the ability to store heat in the summer at shallow depths. In general, GSHPs can be easily utilized within the 'No Permafrost' zone (yellow-brown in Figure 4) and may be feasible within the permafrost zone by using heat augmentation and careful load balancing.

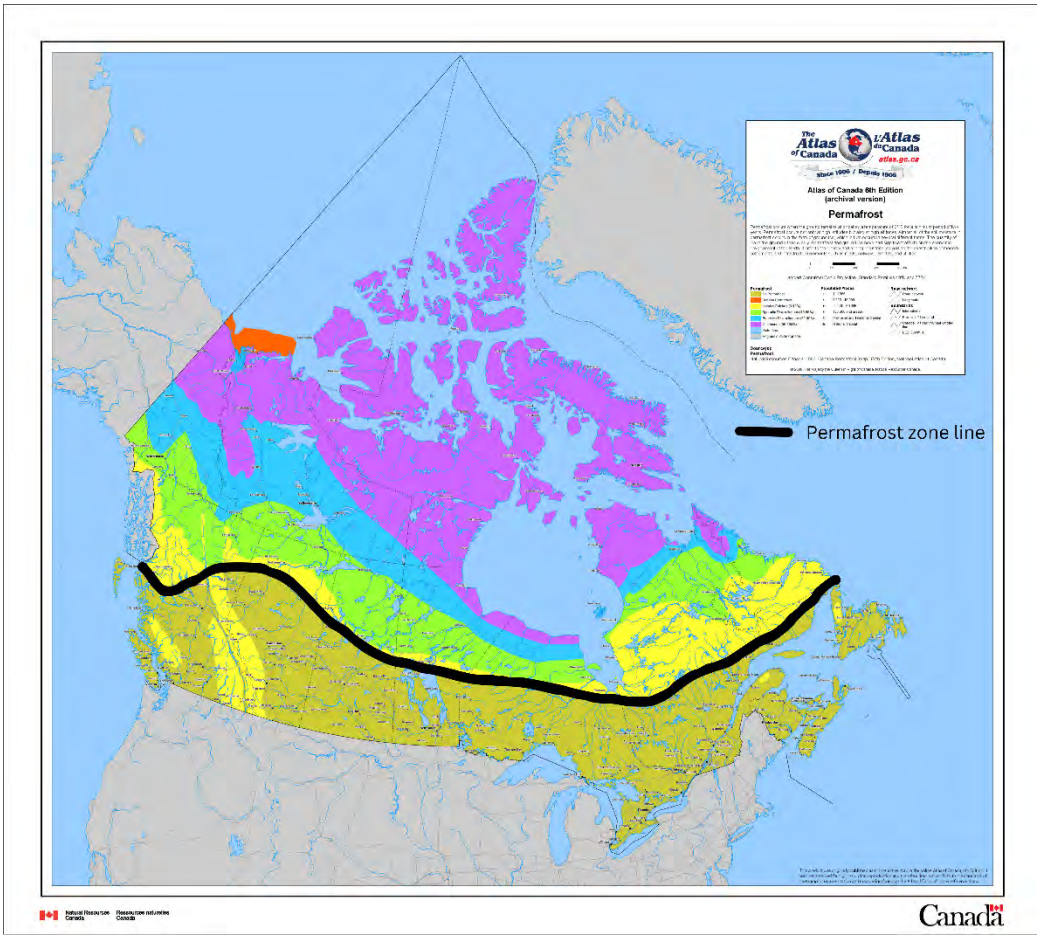

Figure 4: Canada's permafrost zones. The black line separates the zone of no permafrost (yellow-brown region) and zones of isolated patches, sporadic, and continuous permafrost zones to the north of the line. GSHPs can be used below this line but require heat augmentation for use to the north of the line (modified from Natural Resources Canada, 1993).

3.1.3 Examples

There are many GSHP operations in Canada. In Northern Quebec, within the Canadian Shield, the town of Kuujjuak has installed a 30-kW horizontal GSHP system for the community's swimming pool facility (Giordano and Raymond, 2020). A 240-m deep slim hole has also been drilled with the goal of installing a 145-m deep vertical closed-loop GSHP (Geothermal Solutions Inc, 2022). GSHP use is not limited to the Canadian Shield- in the St. Lawrence Platform, for example in Toronto and surrounding towns, GSHPs are becoming popular for district energy systems. The University of Toronto is constructing a large GeoExchange® system on its St. George campus for heating and cooling (University of Toronto, 2022). GeoExchange® systems are already constructed and utilized for select buildings at University of Toronto Mississauga and University of Toronto Scarborough campuses. Additionally, companies like Subterra Renewables partnered with Enercare Inc. plan to provide heating and cooling systems to homes in Canada through GeoExchange® systems.

3.2 Class 1:B Shallow Subsurface (Hydrogeological System)

3.2.1 Overview

Class 1 B systems are very similar to Class 1 A but instead of the ground being used to store heat captured by the GSHP, these systems utilize water sources at shallow depths such as aquifers, lakes, ponds, seas, or even flooded mines (Khodayar and Björnsson, 2024). Generally, these systems work more efficiently for cooling than heating, for example, Toronto's Deep Water Lake Cooling (DWLC) system, but are currently operational in Canada for both uses.

3.2.2 Potential Areas in Canada

In Canada, Class 1 B systems can be installed anywhere with shallow water sources with temperatures that remain relatively consistent throughout the year. They are not suitable for areas of permafrost, but there may be some limited energy gains using deep large lakes or ocean water. Deep mine shafts in areas of permafrost are also potential sources of energy (see below).

3.2.3 Examples

There are several operations in Canada which use shallow hydrogeological systems for heating and cooling. In Nova Scotia, which lies within the Appalachian Orogen, the abandoned coal mines of Springhill are flooded with approximately 4,000,000 m^3 of water. The system pumps this water to the surface (recovered at around 18°C) and through heat pumps where it is used for heating and cooling of many buildings in the nearby geothermal business park (Jessop, 1995; Saltwire, 2019).

Within the Canadian Shield, the City of Yellowknife, Northwest Territories is home to the Con Mine, an abandoned and flooded gold mine. A 2019-2021 study by the Northwest Territories Geological Survey concluded that the thermal energy within the water in the Con Mine contains thermal energy sufficient for heating and cooling buildings for several decades (Huang et al., 2024).

3.3 Class 2: Conventional Geothermal (Hydrothermal Systems)

3.3.1 Overview

Conventional geothermal (hydrothermal) systems utilize the heat and fluid from relatively deep in the earth to create electricity and/or for direct heat use. These systems require permeability and as such do not involve stimulation of the reservoir like EGSs (Khodayar and Björnsson, 2024). As well, conventional geothermal uses open loop technology, in contrast to Advanced Geothermal Systems (AGSs).

3.3.2 Potential Areas in Canada

Conventional geothermal energy production has potential in the sedimentary basins within Canada's platform provinces as well as in the Cordilleran Orogen through fault-hosted and volcanic settings. Several projects are being developed within the Interior Platform, while research is being conducted for potential within the St. Lawrence Platform. Potential for development within the Arctic Platform is also being assessed (Figure 1).

3.3.3 Examples

Conventional geothermal projects in the Interior Platform throughout British Columbia, Alberta, and Saskatchewan are pushing forward. Examples include the Deep Earth Energy Project (DEEP) in southern Saskatchewan that targets the Williston Basin. In the Western Canada Sedimentary Basin (WCSB), Alberta No. 1 near Grande Prairie, Alberta, and Tu Deh Kah outside Fort Nelson, British Columbia, are in various development stages. Near Swan Hills, Alberta, Futura Power has begun operations on their geothermal and natural gas co-production plant where geothermal energy powers approximately 30% of the 21 MWe power plant (Huang et al., 2024).

In the Arctic Platform, several studies have been conducted to assess the geothermal potential in Nunavut. In 2018, a feasibility assessment by the Qulliq Energy Corporation indicated that power could be produced within the sedimentary basins of the northern Arctic Islands (Minnick et al., 2018), but noted major data gaps that still must be addressed. In 2023, researchers from the University of Alberta assessed the potential for geothermal energy development in Resolute Bay and Cambridge Bay (both within the Arctic Platform) as data from oil wells drilled in the 50s and 60s suggest slightly higher than average temperatures; they also found that heat might be sufficient to generate electricity (The Weather Network, 2023). As all communities in Nunavut rely on diesel for power generation, geothermal energy could drastically change the territory's energy usage.

In the Cordilleran Orogen, Geoscience BC is studying the Kootenay Lake, British Columbia area for direct heat use potential within a deep-seated fault system. The 2023 summer and fall research phase found evidence of a geothermal reservoir of over 70 °C within the fractured rock (Geoscience BC, 2024). The Kitselas project is also assessing for potential for direct heat use near Lakelse Lake, British Columbia and has recently received funding. Within the Garibaldi Volcanic Belt of British Columbia, Mount Meager has seen multiple rounds of geothermal investigations, including drilling of several wells in the 1990s. These wells discovered high-temperature resources exceeding 250 °C but found that permeability was insufficient for economic geothermal energy production (Jessop, 2008; Witter, 2019; Grasby et al., 2022). The Garibaldi Volcanic Belt has recently been the focus of a geothermal study by GeoscienceBC, with Phase 1 focusing on developing methods to more accurately map high permeability zones in the reservoir (Grasby et al., 2022).

3.4 Class 3: Unconventional Geothermal (Advanced Geothermal (AGS), Petrothermal)

3.4.1 Overview

Unconventional geothermal describes systems that utilize technology to extract heat from the subsurface in geological settings that lack fluid and/or permeability. This paper describes two sub-classes of unconventional systems- Advanced Geothermal Systems (AGS), and Enhanced (or Engineered) Geothermal Systems (EGS). These systems have also been referred to as "petrothermal" (Hickson et al., 2022).

AGSs utilize long drilled wells that are connected and closed to the formation rocks into which they are drilled. Heat is extracted by proprietary fluids (working fluids) circulating through the radiator like system of connected wells. Heat is transferred by conductive heat transfer from the surrounding rocks into the working fluid (IRENA 2023). Because these systems rely on conductive heat transfer, long and/or many well bores are required which can increase drilling and total project

cost, however, they have the potential to successfully extract heat in almost any location globally, fulfilling the dream of “geothermal anywhere” (IRENA 2023).

3.4.2 Potential Areas in Canada

These systems are most efficient in areas of high rock conductivity, high heat flow and tight crystalline rocks that do not require casing or synthetic “rock pipe” to prevent escape of the working fluid. They can potentially be installed anywhere depending on how the technology develops and the investment limits. The deeper and cooler the system the more expensive the installation due to drilling costs. Within Canada, there is potential within the platforms and orogens where local permeability and fluid volumes are limited, and especially within the Canadian Shield where outcrop and subsurface is Precambrian granite.

3.4.3 Examples

Canada-based company, Eavor, has developed two AGSs- Eavor Loop 1 for sedimentary rocks and Eavor Loop 2 for igneous rocks. Eavor Loop 1 includes vertical production and injection wells drilled 50 – 100m apart to around 4.5 km depth. At this depth, the wellbores bend and 24 lateral wells are drilled to maximize surface area for conductive heat transfer (Khodayar and Björnsson, 2024). If the temperatures are high enough, water is circulated then heat is converted to power at the surface using an Organic Rankine Cycle (ORC); otherwise the system operates to provide thermal energy through a heat exchanger system. Eavor Loop 2 is very similar but the wellbores are drilled deeper to reach hotter temperatures. Their demonstration project for Eavor Loop 1 near Hinton, Alberta (in the Interior Platform) is operating at a thermal output of approximately 800 kWth (Huang et al., 2024; Toews et al., 2020).

3.5 Class 3: Unconventional Geothermal (Enhanced Geothermal (EGS), Petrothermal)

3.5.1 Overview

EGSs utilize stimulation, either by hydraulic, chemical, or thermal means, to increase the permeability of a geothermal reservoir (IRENA 2023). They are viable options in reservoirs with limited permeability and/or subsurface fluid. They generally require elevated temperatures but can be drilled very deep to access hot, deep rocks.

3.5.2 Potential Areas in Canada

Almost all areas in Canada are potentially viable for EGS development. There are reservoirs within the platform and orogenic provinces where subsurface temperatures are sufficient for conventional geothermal, but permeability in the target formations have been shown to be too low, such as in the Liard Basin of the Northwest Territories, which lies within the Interior Province (Huang et al., 2024). EGSs also have potential within the Canadian Shield if drilled deep enough. EGSs have advantages over AGSs in that they require significantly less drilling and thus have a much lower CAPEX compared to AGSs. However, the CAPEX for EGSs is still higher than conventional Class 2 systems. Currently there is significant research funding being directed towards these systems in jurisdictions such as the US as they are seen as the most likely solution to “geothermal anywhere”, notably, the Utah Frontier Observatory for Research in Geothermal Energy (FORGE) initiative.

3.5.3 Examples

U.S.-based company Fervo Energy has developed and tested an EGS technology which uses pairs of horizontal injection and production wells (Norbeck et al., 2023). In 2023, they announced the completion of “Project Red”, a 3.5 MW test plan in Nevada which now delivers power to the local grid (Fervo Energy, 2023). They have also begun development of a 400 MW power plant in Utah which plans to be operational by 2026 (Fervo Energy, 2024). In Canada, E2E Energy Solutions is planning to use a new technology called Enhanced Geothermal Reservoir Recovery System (EGRRS) to provide power and heat in the community of Rainbow Lake, Alberta, which lies within the Interior Platform. The EGRRS plans to combine conventional and EGS technologies by injecting the reservoir fluid into a deeper, stimulated reservoir to increase the temperature (E2E Energy Solutions, 2024). Utah FORGE, sponsored by the US Department of Energy, is an ‘underground field laboratory’ dedicated to developing and testing EGS technologies. The research and development initiatives are focused on basement fracture networks and how they can be initiated and sustained (Office of Energy Efficiency and Renewable Energy; Utah FORGE, 2024). The goal is to understand and develop EGS technologies and resources to make geothermal development possible anywhere.

3.6 Class 4: Borehole Heat Exchangers (Retrofit or Purpose Drilled)

3.6.1 Overview

Borehole heat exchangers are a part of GSHP systems, however, this class refers to installation of borehole heat exchangers in deep wells to extract the heat from circulating fluids. A borehole heat exchanger is comprised of a heat exchanger inside a borehole where fluids are heated up through conductive heat transfer from the rock and circulated. This is a closed-loop system that does not involve production of fluid to the surface (Toth, 2017). As well, they are drilled to shallower depths than conventional geothermal and generally only used for direct heat purposes. Two possibilities with this technology are to repurpose existing wellbores and/or to drill purposed-drilled new wells. The former option is attractive because it has the potential to utilize dry, unsuccessful or end-of-life wells, however, most existing oil and gas wellbores lack the diameter to allow for sufficient heat transfer.

3.6.2 Potential Areas in Canada

Deep borehole heat exchangers can be utilized almost anywhere with sufficient thermal conductivity and have high potential in areas with high heat flow. One example is in the Dehcho Region near Nahanni Butte, Northwest Territories in the Interior Platform, as the thin sedimentary cover overlaying the rocks of the Canadian Shield in the area make conventional geothermal development challenging, but its elevated heat flow suggests potential for deep borehole heat exchangers (Grasby et al. 2021; Smejkal et al., 2023).

3.6.3 Examples

One example of this developing technology is the GreenLoop Closed Loop Geothermal system, developed by Greenfire Energy, which consists of several closed-loop borehole pipes in a single well with various working fluids to produce either electricity or heat. Their 2019 field test in Coso, California indicated that their technology installed in an idle well could produce approximately 1.2 MWe (Scherer et al., 2023).

3.7 Class 5: Heat Capture and Storage (Artificial Heat Storage)

3.7.1 Overview

Class 5 describes a heat capture and storage system that creates an artificial reservoir to store excess heat from other energy sources for later use. In the cases of wind and solar power, the power would be stored as hot water or steam, then brought to the surface for electricity production when wind and solar are not producing (World Economic Forum, 2022). This emerging technology has potential to provide a storage solution for excess wind and solar energy as Canada looks to decarbonize its grid with intermittent renewable power sources.

3.7.2 Potential Areas in Canada

In Canada, heat capture and storage systems can be used anywhere that there is excess heat and/or power production. Based on results of pilot projects and new studies (described below), there is potential for storage in EGS reservoirs and depleted oil and gas reservoirs.

3.7.3 Examples

Vantaa Energy is planning the construction of an innovate heat storage system in Finland. The project plans to build underground caverns to store hot water. When renewable electricity production is cheap or production is in excess of load, it will power electric boilers to heat water which will then be stored in the underground caverns (pv magazine, 2024).

U.S.-based company Sage Geosystems has developed a system called EarthStore™ for heat capture and storage. The pilot project in Texas involved initially creating a large vertical reservoir (over 3 km deep) using fracturing technology then pumping and storing water in the 3,200-foot vertical reservoir deep underground using its novel fracturing technology. Demonstrating long-term and short-term storage capabilities, the pilot produced 200 kWe for over 18 hours and 1 MWe for 30 minutes (Sage Geosystems, 2023).

In 2023, the National Renewable Energy Laboratory (NREL) announced a new project to evaluate the potential of heat capture and storage systems. This will involve a case study to assess using depleted oil and gas reservoirs for solar thermal storage in California, and another case study for storage of excess wind power into water reservoirs in Texas to explore using legacy oil/gas reservoirs with solar thermal hybridization in California (NREL, 2023).

4. Conclusions

The increasing global demand for renewable energy has birthed innovations within geothermal energy systems, making geothermal energy production possible in reservoirs with limited permeability, low heat flow, and inadequate fluid volume. Geothermal energy is a viable solution to help meet Canada's emissions reductions goals, however, unconventional methods must be considered for energy production within many of the country's geological provinces. The seven different classes of geothermal systems described in this paper include two types of shallow, GeoExchange® systems (GSHPs and hydrological systems; Class 1), conventional geothermal (Class 2), two types of unconventional systems (AGS and EGS; Class 3), borehole heat exchangers (Class 4), and heat capture and storage (Class 5). While many areas within Canada's interior platform and orogenic provinces host reservoirs capable of producing conventional geothermal

energy (in both sedimentary basins and fault-hosted volcanic systems) at lower cost, the geology of the rest of the country lacks one or more of permeability, heat flow, and fluid volume. In the Canadian Shield, where Precambrian rock outcrops, geothermal energy production is possible through AGS, EGS, GeoExchange®, and heat capture and storage, although environmental implications in zones of permafrost must be considered for GeoExchange®.

Acknowledgement

This work is based on the learning and experience gained by both authors while being supported by the Alberta No. 1 project, partially funded under the Emerging Renewable Power Program, under Canada's ministry of energy, Natural Resources Canada.

REFERENCES

Canada. Environment and Climate Change Canada, issuing body. "2030 Emissions Reduction Plan." (2022). Available from https://publications.gc.ca/collections/collection_2022/eccc/En4-460-2022-eng.pdf (accessed on 26 April 2024).

Canada. Natural Resources Canada. "Canada-Permafrost." [map]. Fifth Edition, National Atlas of Canada. (1993).

E2E Energy Solutions. (2024). https://e2eenergysolutions.com/ (accessed on 25 April 2024).

Fervo Energy. "Fervo Energy Raises $244 Million to Accelerate Deployment of Next-Generation Geothermal." (2024). https://fervoenergy.com/fervo-energy-raises-244-million-to-accelerate-deployment-of-next-generation-geothermal/ (accessed on 25 April 2024).

Fervo Energy. "Well test results at Fervo Energy's commercial pilot project confirm record production of 24/7 carbon-free enhanced geothermal energy." (2023). https://fervoenergy.com/fervo-energy-announces-technology-breakthrough-in-next-generation-geothermal/ (accessed on 25 April 2024).

Geological Survey of Canada. "Geology and Canada". (1981). Adapted from Prospecting in Canada 4th edition by A.H. Lang, published in 1970. Geological Society of America. The Geology of North America, 1988-1997. 11 vol. Wheeler, J.O. 1996. About the Geology of Canada. Geological Survey of Canada.

Geoscience BC. "Geoscience BC Geothermal Study Zooms-in on Kootenay Lake Area Geothermal Potential." (2024). https://www.geosciencebc.com/geoscience-bc-geothermal-study-zooms-in-on-kootenay-lake-area-geothermal-potential/ (accessed on 26 April 2024).

Geotherma Solutions Inc. "Thermal response test and assessment of the shallow geothermal potential at the Kuujjuaq Forum, Nunavik, Québec." (2022).

Giordano, N., and Raymond, J. "Field report and monitoring plan of the ground source heat pump system for the community swimming pool in Kuujjuaq (Nunavik, Canada)." (2020). *Institut national de la recherche scientifique - Centre Eau Terre Environnement, Québec,* Rapport de recherche R2007,

Grasby, S. E., J. Majorowicz and K. Fiess. “Geothermal Energy Potential of Northwest Territories, Canada.” *Proceedings: World Geothermal Congress 2020+1*, Reykjavik, Iceland (2021).

Grasby, S.E., Calahorrano-Di Patre, A., Chen, Z., Dettmer, J., Gilbert, H., Hanneson, C., Harris, M., Leiter, S., Liu, J., Muhammad, M., et al. “Geothermal resource potential of the Garibaldi volcanic belt, southwestern British Columbia (part of NTS 092J): Phase 2.” In Geoscience BC Summary of Activities 2021: Energy and Water; Report 2022-02; Geoscience BC: Vancouver, BC, Canada, (2022).

Hickson, C.J., Smejkal, E.J. and Rathbone, J. “A Geoexchange to Deep Conventional Geothermal Energy Extraction Technology Spectrum Comparison - Simplified.” *GeoConvention*, Calgary, AB, Canada (2022).

Hickson, C.J. and Smejkal E.J. “The Spectrum of Geothermal Technologies - Updated.” *GeoConvention*, Calgary, AB, Canada (2024).

Huang, K., Dehghani-Sanij, A., Hickson, C., Grasby, S.E., Smejkal, E., Miranda, M.M., Raymond, J., Fraser, D., Harbottle, K., Torres, D.A., et al. “Canada’s Geothermal Energy Update in 2023.” *Energies*, 17, (2024), 1807.

IRENA and IGA “Global geothermal market and technology assessment.” International Renewable Energy Agency, Abu Dhabi; International Geothermal Association, The Hague. (2023).

Jessop, A. “Geothermal energy from old mines at Springhill, Nova Scotia, Canada.” *Proceedings: World Geothermal Congress*, Florence, Italy (1995).

Jessop, A. “Review of National Geothermal Energy Program, Phase 2 – geothermal potential of the Cordillera.” Geological Survey of Canada, Open File 5906, (2008), 86.

Khodayar, M. and Björnsson, S. “Conventional Geothermal Systems and Unconventional Geothermal Developments: An Overview.” *Open Journal of Geology*, 14, (2024), 196-246.

Mercier-Langevin, P. “Mineral Deposits of Canada: A Compilation: 1905-2016.” Society of Economic Geologists, 13 (2017).

Minnick, M., Shewfelt, D., Hickson, C., Majorowicz, J., Rowe, T. “Nunavut Geothermal Feasibility Study.” Report No.: Topical Report RSI-2828; Qulliq Energy Corporation: Iqaluit, NU, Canada. (2018).

Norbeck, J., Latimer, T., Gradl, Ch., Agarwal, S., Dadi, S., Eddy, E., Fercho, S., Lang, C., McConville, E., Titov, A., Voller, K. and Woitt, M. “A Review of Drilling, Completion, and Stimulation of a Horizontal Geothermal Well System in NorthCentral Nevada.” *Proceedings: The 48th Workshop on Geothermal Reservoir Engineering*, Stanford University, CA (2023).

NREL. “NREL-Led Team Explores Potential of Underground Geothermal Energy Storage for All Seasons.” (2023). Available from https://www.nrel.gov/news/program/2023/nrel-led-team-explores-potential-of-underground-geothermal-energy-storage-for-all-seasons.html (accessed on 24 April 24).

Office of Energy Efficiency & Renewable Energy. “FORGE Geothermal Technologies Office.” (No Date). Available from https://www.energy.gov/eere/geothermal/forge (accessed on 17 June 2024).

pv magazine. “Finland to host 90 GWh thermal energy storage system.” (2024). Available from https://www.pv-magazine.com/2024/04/09/finland-to-host-90-gwh-thermal-energy-storage-system/#:~:text=Vantaa%20Energy%20plans%20to%20construct,standards%20upon%20completion%20in%202028 (accessed on 18 April 2024).

Sage Geosystems. “Sage Geosystems Raises $17 Million in Series A, Announces World’s First Commercial Geopressured Geothermal System (GGS) Facility.” (2023). Available from https://www.sagegeosystems.com/sage-geosystems-raises-17-million-in-series-a-announces-worlds-first-commercial-geopressured-geothermal-system-ggs-facility/ (accessed on 24 April 2024).

SaltWire. “Concept Design for Springhill Geothermal Business Park Underway.” (2019). Available from https://www.saltwire.com/atlantic-canada/federal-election/concept-design-for-springhill-geothermal-business-park-underway-336905/ (accessed on 23 April 2024).

Scherer, J., Golla, G., Chandrasekar, H., Amaya, A., Chin, H., Brown, S., Sonnenthal, E., Rutqvist, J., and Oldenburg, C. “The GreenLoop Closed-Loop Geothermal (CLG) System: Optimizing Power Generation and Evaluating Its Impact on the Reservoir.” *Proceedings: The 9th Indonesia International Geothermal Convention & Exhibition (IIGCE)*, Jakarta, Indonesia (2023).

Smejkal, E., Hickson, C., Collard, J. (2023). “Revisiting the geothermal potential of the Dehcho Region in NWT: New data from old wells.” *Proceedings: Geoconvention*, Calgary, AB (2023).

Statistics Canada, Centre for Demography, “Map 1.1 Population distribution as of July 1, 2022, by census division, Canada.” (2022).

The Weather Network. “Exploring the possibility of geothermal energy in Nunavut.” (2023). Available from https://www.theweathernetwork.com/en/news/climate/solutions/exploring-the-possibility-of-geothermal-energy-in-nunavut (accessed on 26 April 2024).

Toews, M., Riddell, D., Vany, J., and Schwarz, B. “Case Study of a Multilateral Closed-Loop Geothermal System.” *Proceedings: World Geothermal Congress*, Reykjavik, Iceland (2020).

Toth, A. “Chapter 13 - Borehole Heat Exchangers.” Flow and Heat Transfer in Geothermal Systems, Elsevier, Aniko Toth, Elemer Bobok, (2017), 287-298.

University of Toronto. “'He’d be thrilled to see this': U of T's massive geoexchange project built on pioneering work of late prof.” (2022). Available from https://www.utoronto.ca/news/he-d-be-thrilled-see-u-t-s-massive-geoexchange-project-built-pioneering-work-late-prof (accessed 24 April 24).

Utah FORGE. “UTAH FORGE.” (2024). Available from https://utahforge.com/ (accessed 17 June 2024).

Wheeler, J.O., Hoffman, P.F., Card, K.D., Davidson, A., Sanford, B.V., Okulitch, A.V., and Roest, W.R., Geological map of Canada / Carte géologique du Canada; Geological Survey of Canada, Map 1860A. (1996).

Witter, J. “South Meager geothermal project – new perspectives from recently unearthed data.” Geoscience BC, Report 2019-07, (2019), 5.

World Economic Forum “Here's why geothermal systems could be better for storing renewable energy than batteries.” (2022). Available from

https://www.weforum.org/agenda/2022/11/geothermal-renewable-energy-storage/ (accessed on 24 April 2024).

GRC Transactions, Vol. 48, 2023

Geothermal Development and Use, 1995-2024

John W. Lund[1], Gerald W. Huttrer[2], Aniko N. Toth[3]

[1]Geo-Heat Center, Oregon Institute of Technology, Klamath Falls, OR, USA

[2]Post Office Box 2425, Frisco, CO, USA

[3]University of Miskolc, Miskolc, Hungary

Keywords

Geothermal, Electric power, Direct use, Bathing, Space heating, District heating, Aquaculture, Greenhouses, Heat pumps, Industrial uses, Agricultural drying, Cooling/snow melting, World-wide uses, Future trends.

ABSTRACT

Geothermal power generation started at Lardarello, Italy in 1904, resulting in the first commercial plant of 250 kW being installed in 1913. New Zealand came on-line in 1958 with a 1.2 MWe plant at Wairakei followed by Mexico in 1959 with a 3 MWe plant at Pathe. The first plant in the USA was at The Geysers in northern California at 11 MWe in 1960. All these plants were of the flash steam type. The first binary power plant was at Paratunka, in Kamchatka, Siberia, Russia (1967), followed by binary plants in Japan and Iceland in 1966, and China in 1970. Today (2023), 29 countries produce electricity from geothermal resources for a total estimate of 18,000 MWe generating 108,000 GWh of electricity. Geothermal direct use is one of the oldest, most versatile, and most common forms of utilizing geothermal energy. Direct use has been documented for over 2000 years throughout the world. Today (2023), it is estimated the installed capacity is 126,000 MWt and the annual energy use is 1,280,000 TJ (355,600 GWh) in over 88 countries. The average worldwide capacity factor over the past 25 years for direct use is 0.327, indicating 2,866 full-load equivalent capacity hours per year. Direct uses include bathing and swimming, space heating including district heating, greenhouse and aquaculture pond heating, industrial applications, and snow melting and cooling. Geothermal (ground-source) heat pumps using ground or ground-water temperatures between 5 and 30 degrees C for both heating and cooling are found throughout the world and are the largest direct use application. The leading countries for geothermal direct use are China, United States, Sweden, Germany, Turkey, France, Japan, Iceland, Finland, and Switzerland (>2000 MWt). In summary, lower temperature resources (<90 degrees C) are becoming more economical for greenhouses, aquaculture and drying aquacultural products such as fruit and

vegetables. Lower temperatures are now possible down to 90 degrees C for power generation with units less than 1 MWe becoming economical. Geothermal heat pumps are becoming more popular and economic with over 6.5 million units presently installed worldwide.

1. Introduction

This paper presents a review of world-wide applications and uses of geothermal energy for both electric power generation and direct utilization, including geothermal (ground-source) heat pumps, for the last 25 years (1995-2020). These data are summarized from world geothermal congresses (WGC) held every five years. These include chronologically, congresses held, in Italy, Japan, Turkey, Indonesia, Australia, and Iceland. The data included in this paper for 2020 are from 88 countries/regions; however additional areas most likely exist, but unfortunately have not been documented. We have estimated the data for 2023. See Table 1 for data from 1995 to 2023.

Table 1: Summary of geothermal capacity of production 1995-2023

Year	Installed Electric Capacity MWe	Produced Electric Energy GWh/yr	Installed Thermal Capacity MWt	Produced Thermal Energy TJ/yr
1995	6.832	38,035	8,664	112,441
2000	7,972	49,261	15,145	190,699
2005	8,933	55,709	28,269	273,372
2010	10,897	67,246	48,493	423,830
2015	12,635	73,549	76,885	592,638
2020	15,950	95,098	107,727	1,020,887
2023*	18,000	108,000	126,000	1,280,000

*Estimated

The resource temperature along with a sustainable flow rate and fluid chemistry will determine the best and most economical use of the resource. The following temperatures are general guidelines for the use of a geothermal resource. However, for these cases the temperature range can vary depending on the location.

- >175°C (350°F) – dry steam and flash steam electric power generation
- 100 to 175°C (212 to 350°F) - binary electric power generation
- 100 to 150°C (212 to 300°F) – industrial process heating/cooling
- 60 to 100°C (140 to 212°F) – space heating
- 30 to 60°C (90 to 140°F) – greenhouse and aquaculture pond heating
- 5 to 30°C (40 to 90°F) - geothermal (ground-source) heat pumps

2. Geothermal Electric Power Generation

The first geothermal power generation was from a reciprocating steam engine powered by geothermal steam at Larderello, Italy on 4 July 1904 under the supervision of Prince Piero Ginori Conti. It lit four light bulbs. By 1905 the power had been increased to 20 kWe and the first commercial power plant of 250 kWe was built there in 1913. By 1916 it distributed 2,750 kWe of electricity to the surrounding cities. Italy was the world's only industrial producer of geothermal electricity until 1958.

In 1958 New Zealand became the second country to produce geothermal electricity at Wairakei on North Island using wet steam to generate 11.2 MWe. This was followed by the first geothermal power plant in Mexico at Pathė, Acambay in 1959 at 3 MWe. In the USA, Pacific Gas and Electric began operation of the first geothermal power station in the country located at The Geysers in northern California in 1960 at 11 MWe.

The first binary cycle power plant was demonstrated in 1967 at Paratunka, in Kamchatka, Siberia, Russia at 750 kWe. Binary geothermal power was introduced in the USA in 1981 at Heber in southern California at 45 MWe. These were followed by geothermal binary plants in Japan and Iceland in 1966 and China in 1970. These plants use a secondary working fluid, a hydrocarbon, heated by low temperature geothermal fluid producing a vapor used to turn the generator for electricity (Figure 1).

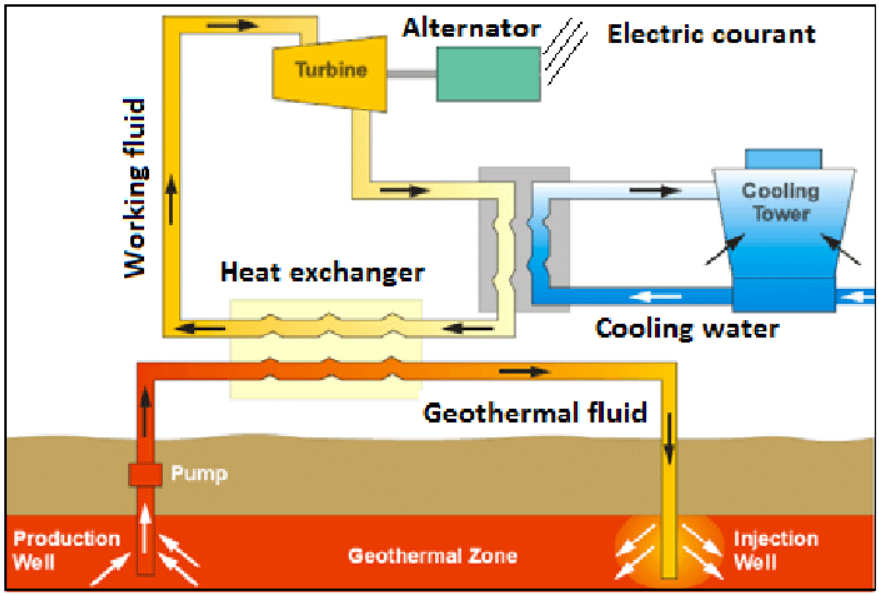

Figure 1: Binary power cycle diagram.

In 2020, 29 countries produced electricity 95,098 GWh/yr from geothermal resources, from an installed capacity of 15,950 MWe. From 2015 to 2020 geothermal electricity had the highest growth rate compared to other periods, amounting to 26.2% in MWe and 29.3% in GWh/yr. By 2023, it is estimated that geothermal power and generation has increased to 108,000 GWh/yr and 18,000 Mwe and 108,000 GWh/yr. See Table 2 for a summary of data from 2020 for countries producing greater than 100 MWe.

Table 2: Installed and generating capacity for geothermal worldwide >100 MWe in 2020

Country	MWe	GWh/yr
USA	3,700	18,366
Indonesia	2,289	15,315
Philippines	1,918	9,893
Turkey	1,549	8,168
Kenya	1,193	9,930
New Zealand	1,064	7,728
Mexico	1,006	5,375
Italy	916	6,100
Iceland	755	6,010
Japan	550	2,409
Costa Rica	262	1,559
El Salvador	204	1,442
Nicaragua	159	492
Total*	**15,950**	**95,098**

*29 countries

Electricity produced is a better measure of the geothermal contribution than installed capacity, since geothermal plants usually operate at a higher capacity factor, around 95%, than other types of power plants. Unfortunately, geothermal energy only contributes less than 0.4% of the world's electricity.

3. Geothermal Direct Utilization

Direct utilization (direct use) of geothermal energy is one of the oldest, most versatile, and most common form of utilizing this resource (Dickson and Fanelli, 2003/2013). The early history of geothermal direct use was reviewed from over 25 countries in: *Stories from a Heated Earth – Our Geothermal Heritage* (Cataldi et al., 1990). The information presented here is based on country update papers submitted to the various World Geothermal Congresses that are held every five years from 1995 to 2020. Data has been estimated to 2023 by the authors. The number of countries reporting direct use has increased from 28 in 1995 to 88 in 2020. The thermal capacity and produced thermal energy in these years have increased from 8,664 MWt and 112,441 TJ/yr to the present figure of 107,727 MWt and 1,020,887 TJ/yr (283,580 GWh/yr) with annual increases of 10.61% and 9.23% respectively. This is estimated to have increased by 2023 to 126,000 MWt and 1,280,000 TJ/yr. The average worldwide capacity factor over the past 25 years is 0.327, indicating 2,866 full-load equivalent capacity hours per year. More detailed information on geothermal direct use can be found in *Geothermics Volume 90* by Lund and Toth, 2021.

The authors have relied on country update reports from World Geothermal Congress (1995-2020), as well as from five *Geothermics* publications (Lund and Freeston, 2001; Lund et al., 2006; 2011; Lund and Boyd, 2016; Lund and Toth, 2021) along with reports from the European Geothermal Congresses in 2007, 2013, and 2019, together with information gained from personal communications.

The worldwide leaders in direct use of geothermal energy including geothermal heat pumps for 2020 are shown in Tables 3 and 4. Tables 5 and 6 show data by various categories and by regions.

Table 3: Leading countries in 2020 in terms of installed capacity including geothermal heat pumps (>2,000 MWt)

Country	MWt	Major uses
China	40,610	Bathing, district heating
United States	20,713	Heat pumps, bathing
Sweden	6,680	Heat pumps, district heatings
Germany	4,806	District heating, heat pumps
Turkey	3,488	District heating, bathing
France	2,597	Heat pumps, district heating
Japan	2,570	Bathing, heat pumps
Iceland	2,373	Bathing, district heating
Finland	2,300	Heat pumps
Switzerland	2,197	Heat pumps, space heating

Table 4: Leading countries in 2020 in terms of annual energy use including geothermal heat pumps (>12,000 TJ/yr)

Country	TJ/yr	Major uses
China	443,492	Bathing, district heating
United States	152,110	Heat pumps, bathing
Sweden	62,400	Heat pumps, district heatings
Turkey	54,584	District heating, bathing
Iceland	33,598	Bathing, district heating
Japan	30,723	Bathing, heat pumps
Germany	29,139	District heating, heat pumps
Finland	23,400	Heat pumps
France	23,280	Heat pumps, district heating
Canada	14,512	Heat pumps, bathing
Switzerland	13,292	Heat pumps, space heating
Norway	12,610	Heat pumps

Table 5: Summary of direct use by various categories for 2020

Utilization	Capacity MWt	Utilization TJ/yr	Capacity Factor
Geothermal heat pumps	77,547	599,981	0.245
Space heating/district heating	12,768	162,979	0.405
Bathing and swimming	12,253	184,070	0.472
Greenhouse heating	2,459	35,826	0.462
Aquaculture pond heating	950	13,573	0.463
Industrial uses	852	16,390	0.610
Agriculture drying	257	3,529	0.435
Cooling/snow melting	435	2,589	0.189
Others	106	1,960	0.584
Total	**107,627**	**1,020,897**	**0.300**

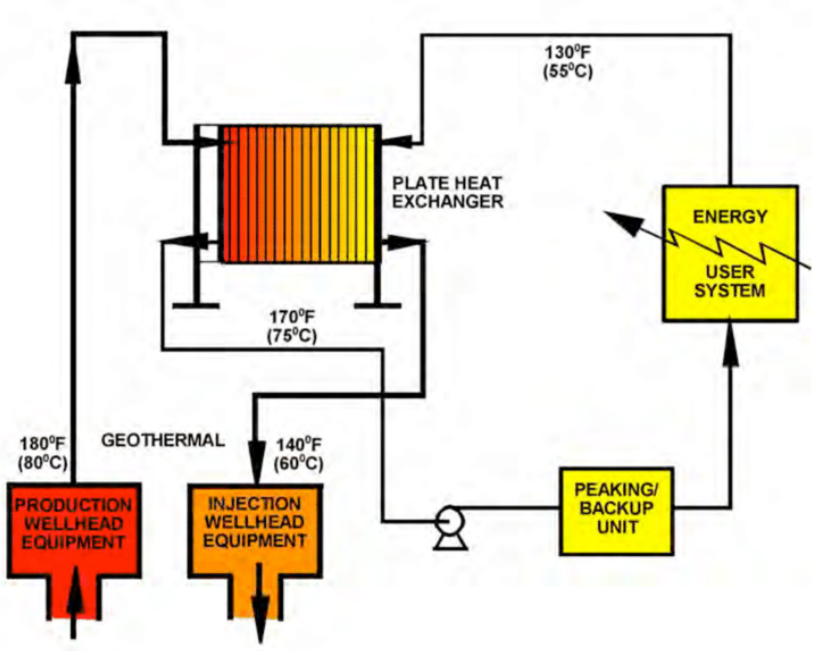

Figure 2. Geothermal direct use diagram.

Table 6: Summary of direct use data worldwide by region and continent for 2020 (Indicates number of countries)

Region/Continent	MWt	TJ/year	GWh/year	Capacity
Africa (11)	198	3,730	1,036	0.597
Americas (17)	23,330	180,414	50,115	0.245
Central America and	9	195	54	0.687
North America (4)	22,700	171,510	47,642	0.24
South America (8)	621	8,709	2,419	0.445
Asia (18)	49,079	545,019	151,394	0.352
Commonwealth of	2,121	15,907	4,419	0.238
Europe (34)	32,386	264,843	73,568	0.259
Central and Eastern Europe	3,439	28,098	7,805	0.259
Western and Northern	28,947	236,745	65,762	0.259
Oceania (3)	613	10,974	3,048	0.568
Total (88)	**107,727**	**1,020,887**	**283,580**	**0.300**

Based on data from the European Geothermal Congress (EGC) (Sanner et al, 2022), the geothermal power generation capacity of the 32 European countries, totaled about 3,496 MWe, while the geothermal heating from medium to low temperature sources exceeded 11,600 MWt. About half of that is used for district heating. Regarding shallow geothermal energy, including ground source heat pumps (GSHP) and Underground Thermal Storage (UTES), direct use capacity of at least 30,300 MWt was achieved by the end of 2021, distributed over about 2.1 million installations. In Europe, Turkey is a new leader, having very dynamic developments with 17 geothermal district heating systems in operation serving the equivalent of 116,000 residents. There are also six major greenhouse areas covering 4.3 million square meters, mainly growing tomatoes, most of which are sold internationally. In addition, twenty million local and 20,000 foreign visitors annually enjoy the balneological uses of Turkey's geothermal waters.

The former Soviet Union dominated countries in eastern Europe, comprising of Bulgaria, the Czech Republic, Hungary, Lithuania, Macedonia, Poland, Romania, Servia, Slovakia, Slovenia, and Ukraine, have never been energy independent. They have always had to import the energy they needed, mainly from Russia. Thus, these countries' overall energy consumption has dropped to levels not seen since the 1970s due to lack of funding and leadership. However, more recently, the shallow geothermal direct use sector has grown steadily, but very slowly in Eastern Europe with Poland in the lead. Hungary has shown some strong direct use development, especially in the district heating and agricultural sectors. A summary of the former Soviet Union countries in eastern Europe using ground source (geothermal) heat pumps is based on the Summery of EGC 2022 Country Update Reports on Geothermal Energy in Europe by Sanner et al, 2022. It is shown in Table 7.

Table 7: Ground Source Heat Pumps use in the leading former Soviet Union Countries in 2022 (Sanner et al, 2022)

Country	Number GSHP	Capacity MWt	Production GWh/yr
Poland	78,480	900	1,200
Czech Republic	22,740	320	472
Slovenia	14,818	237	329
Lithuania	10,647	140	314
Hungary	7,353	81	161
Slovakia	10	2	14
Ukraine	43,700	1,600	1,316
Serbia	2,850	53	117
Macedonia	1,000	3	21
Romania	600	40	100
Bulgaria	n/a	n/a	1,174

4. Summary and Conclusions

Although the number of countries now using geothermal energy to generate electricity is still small in comparison to the many countries that use geothermal resources for direct use such as for space and district heating, agricultural, aquaculture, and industrial processes, there are new nations producing geothermal electricity since 2015. These include Belgium, Chile, Honduras, and Hungary. By 2023 we may see small geothermal power on-line in Argentina, Australia, Canada, China, Dominica, Ecuador, Greece, Iran, Montserrat, Nevis, Saint Lucia, Saint Vincent, and Taiwan. In the East African Rift Zone, Malawi, Rwanda, Tanzania, and Uganda, are also trying to bring electric plants on-line. In the last five years, there has also been increased attention shown to the possibility of developing Engineered Geothermal Systems (EGS) to tap the vast thermal energy resources trapped in rocks of low natural permeability. This work is proceeding in the USA, Iceland, Great Britain, Germany, China, Portugal, Denmark, and The Netherlands.

Overall, it appears that the initial, high-risk phases of new and expanded uses of geothermal resources are being funded by federal government agencies, quasi-federal entities, and international multilateral lending banks rather than private industry. Turkey, the Philippines, and the USA appear to be the only exception to this trend. The early-stage involvement of public funds is a way to mitigate the risks perceived by private investors. Once suspected resources have been discovered, characterized and, their extent preliminarily delineated, projects can be transferred to the private sector for the necessary confirmation, development and production as the risk has been reduced.

The countries that stand out as major producers and consumers of geothermal fluids for direct use are listed in Table 3. In most countries, however, development has been slow as fossil fuels are a major competitor. Another obstacle is the high initial investment costs for geothermal projects. Countries where geothermal direct use provides a significant contribution to their energy needs are summarized in Table 8. The distribution of geothermal use by continent is shown in Table 9, indicating that Asia and Europe are the leaders, with 57 of the 88 countries reporting that they provide 77.5 % of the world's installed capacity (MWt) and 80.8% of the direct uses (TJ/yr).

Table 8: Significant contributions of direct use geothermal energy to a country's economy

Iceland	90% of buildings space heated
Japan	2,000 onsens, 5,000 public baths, 1,500 hotels serving 15 million guest/year
Sweden	40% of buildings heated using geothermal heat pumps
Switzerland	110,000 geothermal heat pumps installed (~3.7 units/sq. km)
Tunisia	244 ha of heated greenhouses
Turkey	116,000 apartments/residences heated in 17 cities
USA	Approximately 1.685 million geothermal heat pumps (4.0% growth/year)

Table 9: Distribution of direct use geothermal energy utilization by continent

Continent	Countries	%MWt	%TJ/year
Africa	11	0.2	0.4
Americas	17	21.7	17.7
Asia	19	45.6	53.4
Europe*	38	31.9	27.4
Oceania	3	0.6	1.1

* Includes CIS Countries (Georgia, Russia and Ukraine)

With the increased interest in geothermal deep drilling for direct use and ground-source heat pumps, it is now evident that geothermal energy can be developed anywhere for both heating and cooling. Heat pumps now make up 72.0% of the installed capacity (MWt) and 58.5% of the annual energy use (TJ/yr). This use has increased since 2015 by 54% of installed units reported. Low-to-moderate temperature geothermal resource are also being used in combined heat and power plants (CHP), where hot water, often with temperatures below 100^{o}C, is first run through a binary (organic Rankine cycle) power plant, then cascaded for direct uses, before being injected back into the aquifer. GHP projects can maximize resource use, while improving the return on investment. This has been shown in Iceland, Austria, Germany, as well as on the Oregon Institute of Technology Campus in the USA.

Approximately US$ 22.262 billion was reported as invested in geothermal energy by 53 countries during the period 2015-2019 for both electric power (64%) and direct use (36%). The average was US$ 420 million per country, with countries investing over US$ 500 million being Indonesia, Turkey, China, Taiwan, Kenya, Republic of Korea, Mexico, Chile, and Italy (in descending order). Investments were 27.9% for electric power utilization in 16 countries, 15.4% for direct use in 30 countries, 32.4% for field development including production drilling and surface equipment in 33 countries, and 24.3% for R&D including surface exploration and exploratory drilling in 47 countries. The following are the percentages of the worldwide geothermal investments and funding by continents (total US$22.262 billion). The world summary by country of ground source (geothermal) heat pumps ≥ 15.000 units are shown in

Table 10. A total of 54 countries/regions report using geothermal heat pumps, with a average unit size of 12 kW.

- 6.3% in Africa by 7 countries (US$1.412 billion)
- 10.2% in the Americas by 11 countries (US$2.275 billion)
- 74.2% in Asia by 11 countries (US$16.506 billion)
- 8,7% in Europe by 22 countries (US$1.926 billion)
- 0.6% in Oceania by 2 countries (US$0.143)

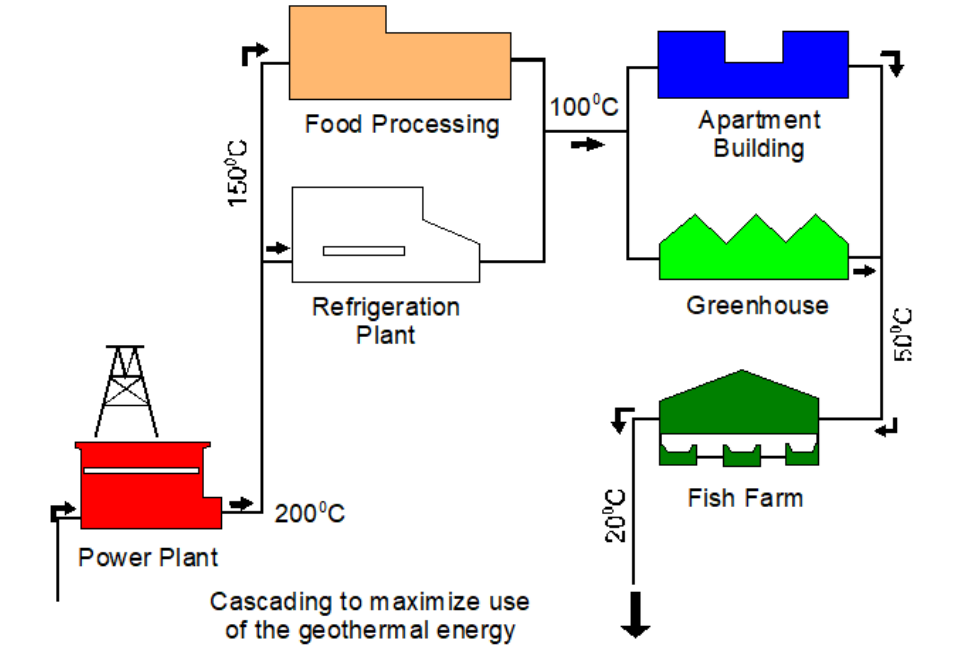

Figure 3. Cascading of geothermal power and direct use.

Table 10: Worldwide leaders in geothermal (ground-source) heat pumps in 2020 (≥15,000 units)

Country	Units	MWt	TJ/yr	GWh/yr	L.F.
United States	1,686,000	20,230	145,460	40,406	0.23
China	1,000,000	26,450	246,212	68,392	0.30
Sweden	591,000	6,680	62,400	17,333	0.30
Germany	382,000	4,400	23,760	6,600	0.17
Canada	200,000	1,831	14,512	4,031	0.25
France	174,800	2,015	12,600	3,500	0.20
Norway	150,000	1,700	10,800	3,000	0.20
Finland	140,000	2,300	23,400	6,500	0.32
Brazil	110,000	1,300	6,622	1,839	0.16
Netherlands	60,354	1,400	10,860	3,017	0.25
Poland	56,000	700	3,500	972	0.16
Denmark	40,000	350	3,500	972	0.32
Ireland	18,092	201	937	260	0.15
Austria	15.000	1,000	6,309	1,752	0.20
Worldwide total	**4,608,261**	**70,557**	**570,872**	**158,574**	**0.23**

As oil and gas supplies dwindle and increase in price, geothermal energy becomes a more economically viable alternative energy source. Even though the initial cost of developing a geothermal resource is high (exploring, drilling well, constructing pipelines and plants), the long-term cost is low. Compared to 2015, geothermal direct use has doubled its contribution to the world's annual energy mix from about 0.13 to 0.27%. As geothermal energy becomes more competitive with fossil fuels, especially if carbon penalties are applied to the price, and the environmental benefits are better understood and accepted, development of this natural "heat from the earth" should accelerate. An important task for all of us in the geothermal community is to spread the word about geothermal energy, its various applications, and the many environmental benefits that can accrue from its use.

5. The Future of Geothermal Energy.

Geothermal energy use is trending as follows (Lund et al., 2006, 2021).

- Lower temperature down to 90°C is now possible for economic power generation
- Electrical units less than 1 MWe becoming economical.
- Lower temperature resources can be made economical such combined uses as:
  - power generation and space heating
  - power generation and industrial applications
- Lower temperature resources <90°C, are becoming more economical for green-houses, aquaculture, and drying agricultural products such as fruit and vegetables.
- Geothermal ground-source heat pumps are becoming more popular and economic with over 6.5 million units presently installed worldwide. These units provide both heating and cooling and only need a 5° to 30°C temperature resource, which are typical ground temperatures in most of the world.

6. References

Dickson, M. H., Fanelli, M. Geothermal Energy: Utilization and Technology, UNESCO, Paris, 2003. 205 p.

Cataldi, R., Hodgson, S.F., Lund, J.W., 1999. Storied from a Heated Earth – Our Geothermal Heritage, Geothermal Resources Council, Davis, CA, 569 p.

European Geothermal Congress 2007, Unterhaching, Germany, Proceedings.

European Geothermal Congress 2013, Pisa, Italy, Proceedings.

European Geothermal Congress 2019, The Hague, The Netherlands, Proceedings.

European Geothermal Congress 2022, Berlin, Germany, Proceedings.

Lund, J.W., Boyd, T.J., 2016. Direct Utilization of Geothermal Energy 2015 Worldwide Review, *Geothermics* 60, Elsevier, pp. 66-93.

Lund, J.W. and Freeston, D.H., 2000. World-Wide Direct Uses of Geothermal Energy 2000, Proceedings World Geothermal Congress 2000 Kyusu, Japan, May 28-June 10 2000.

Lund, J.W. and Freeston, D.H., 2001. World-Wide Direct Uses of Geothermal Energy 2000, *Geothermics*, 30, Elsevier, pp.29-68.

Lund, J. W., Freeston, D. H., Boyd, T. J., 2006. Direct Applications of Geothermal Energy, 2005, Worldwide Review. *Geothermics*, 34, Elsevier, pp. 691-727.

Lund, J. W., Freeston, D. H., Boyd, T. J., 2010. Direct Utilization of Geothermal Energy 2010 Wordwide Review, Proceedings World Geothermal Congress 2010 Bali, Indonesia, 25-29 April 2010.

Lund, J.W., Freeston, D.H., Boyd, T.J., 2011. Direct Utilization of Geothermal Energy, 2010 Worldwide Review. *Geothermics*, 40, Elsevier, pp. 159-180.

Lund, J.W., Bertani, R. Boyd, T.J., 2015. Direct Utilization of Geothermal Energy 2015 Worldwide Review, Proceedings World Geothermal Congress 2015 Melbourne, Australia 19-24 April 2015.

Lund, J. W., Toth, A.N., 2021. Direct Utilization of Geothermal Energy Worldwide Review. *Geothermics*, 90, Elsevier, pp. 1-31.

Sanner, B., Antics, M., Baresi, M., Urchuegula, J.F., and Dumas, F.: Summary of EGC 2022 Country Update Report on Geothermal Energy in Europe, European Geothermal Congress 2022, Berlin, Germany, 13 p.

World Geothermal Congress 1995, Roma, Italy, Proceedings.

World Geothermal Congress 2000, Kyushu-Tohoku, Japan, Proceedings.

World Geothermal Congress 2005, Antalya, Turkey, Proceedings.

World Geothermal Congress 2010, Bali, Indonesia, Proceedings.

World Geothermal Congress 2015, Melbourne, Australia, Proceedings.

World Geothermal Congress 2020+1, Reykjavik, Iceland, Proceedings.

Exploring the Past, Present, and Future: Geothermal Energy on the 100th Anniversary of the Turkish Republic

Orhan Mertoglu[1], Sakir Simsek[2], Nilgun Basarir[1] and Aysegul Turan[3,4]

[1] Turkish Geothermal Association, (TGA) And Sokak 8/2, Çankaya/Ankara, Türkiye

[2] Hacettepe University UKAM/Beytepe-Ankara, Türkiye

[3] Technische Universität Darmstadt, Institute of Applied Geosciences, Group of Geothermal Science and Technology, Schnittspahnstrasse 9, 64287 Darmstadt, Germany

[4] HotRock Geothermal Consortium, Bureau of Economic Geology, The University of Texas at Austin

Keywords

country update Türkiye

ABSTRACT

This paper provides a comprehensive overview of the geothermal energy landscape in Türkiye on the occasion of the 100th anniversary of the Turkish Republic. The study examines the country's progress and internationally recognized applications in geothermal energy, highlighting key milestones and the impact of the founding vision that underscores the central role of geosciences in economic development. The use of legislation and feed-in tariff mechanisms to promote the use of indigenous energy resources is discussed in the context of cause-and-effect relationships, highlighting the dynamics of geothermal development.

MTA (The Institute of Mineral Research and Exploration) started geothermal exploration in Türkiyein the 1960s. From the drilling of the first geothermal well in 1963 to the centenary celebration in 2023, Türkiye has made its name in the global rankings and secured a pioneering position in the field. There are currently over 2000 thermal springs and wells, with drilling depths of up to 5 km, and direct use applications have resulted in 6300 MWt. This includes district heating (1422 MWt), greenhouse heating (2417 MWt), heating for thermal facilities, hotels, etc. (680 MWt), balneological use (1763 MWt), agricultural drying (9.5 MWt), cooling (0.35 MWt) and geothermal heat pump applications (8.5 MWt). The total installed capacity has reached 1710 MWe and the carbondioxide that is produced is used in the production of 400,000 tonnes of dry ice per year.

In 1982, the first Turkish-Italian seminar on geothermal energy was held. The first geothermal electricity was produced in 1984. In 1999, the Izmir-Balçova geothermal heating system was

selected as a best practice by the European Geothermal Energy Council (EGEC). The World Geothermal Congress (IGA-TGA) was held in 2005 and the European Geothermal PhD Days were held in Türkiye for the first time in February 2020. In April 2023, with the inauguration of the first geothermal-solar hybrid power plant, Türkiye has reached another significant milestone, demonstrating its commitment to innovative and sustainable energy solutions as it looks to the future.

1. **Introduction**

Geothermal is a domestic, renewable, environmentally friendly, base-load resource with multiple integrated uses such as electricity generation, district heating, greenhouse heating, spa and thermal tourism, liquid CO_2 and dry ice production, fruit and vegetable drying, production of various minerals, and aqua fishing. It is technically and economically attractive. If appropriate technology is used and reinjection is carried out, there is no discharge of uncondensed gas.

In Türkiye geothermal areas are mainly located along the main grabens in Western Anatolia, along the North Anatolian Fault Zone, and in volcanic regions in Central and Eastern Anatolia (Figure 1).

The utilization of geothermal potential in Türkiye extends far beyond the foundation of the Republic. For example, the ancient city of Hierapolis, recognized as a UNESCO World Heritage Site, was spa town and the use of geothermal resources here dates to the Roman Empire. In these lands, geothermal resources were used by Hittites, Romans, Seljuks, Ottomans and Turks for health and cooking purposes in BC and AD, and some of them were built spas, some of which are still in use. This study focuses on the utilization of geothermal resources in the first hundred years of Turkish Republic starting from 1923 to 2023.

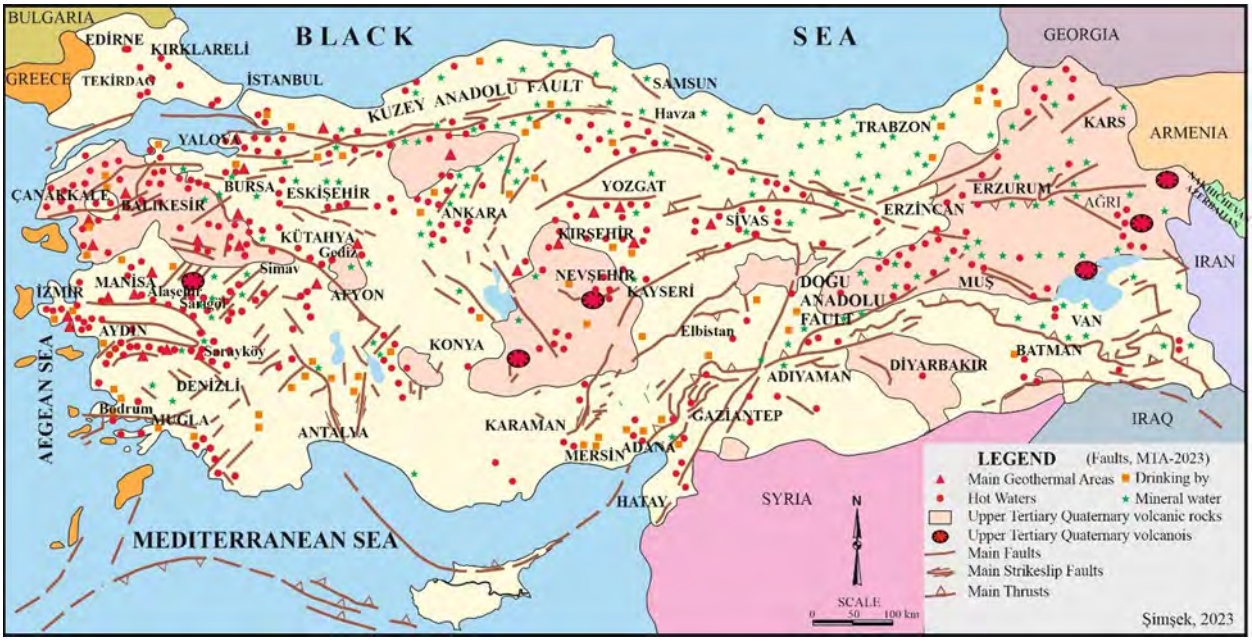

Figure: Türkiye map showing the main geothermal sites with main neotectonic lines, hot spring distribution, and volcanic areas (Şimşek, 2023).

2. Past

In the early years of the Republic, geothermal hot springs were used for spa, treatment and health purposes. The first law on the exploitation of hot springs was passed in 1926, just three years after the foundation of the Turkish Republic, reflecting the founder's vision of the vital role of earth sciences. This foresight led to the establishment of the Institute of Mineral Research and Exploration (MTA) in 1935, when the Republic was only 12 years old. The vision also included sending the country's youth abroad for higher education and training cadres with a strong belief in science (Law No. 1416). The MTA, as one of the institutions employing these cadres, carried out surveys and inventory studies throughout the country.

In some regions, natural springs continued to be used in traditional spas, and in the 1970s they were also used for simple greenhouse heating. The first geothermal borehole was drilled by MTA in 1963 in Izmir-Balcova. The well-bottom temperature of the 40-meter deep well was measured at 124°C. The well was in production for a few days but was closed due to scaling and then abandoned as it was considered unviable.

In 1968, with the financial and technical support of the United Nations, drilling was started in the Denizli Sarayköy-Kızıldere geothermal field as part of the geothermal exploration for electricity generation under the United Nations - UNDP project of MTA. A 200ºC reservoir was discovered and 2-decare geothermal greenhouse was heated as a pilot application. A 0.5 MWe pilot geothermal power plant was designed, built and commissioned using MTA facilities. Fundamental information and experience on geothermal scaling, corrosion, non-condensable gases (NCG), etc. were gained from this power plant. This power plant provided free electricity to the villages of Kızıldere, Karatas and Savcılı for 7 years. The work carried out at these stages are all exploration investments and geothermal services of MTA.

In the following years, exploration and drilling continued and in the light of these developments, the first commercial power plant with a gross capacity of 20 MWe was established by the Turkish Electricity Authority (TEK in Turkish initials) in 1986. Subsequently, an integrated liquid carbon dioxide-dry ice (CO_2) factory was established by the private sector. This factory cleaned and liquefied the carbon dioxide released into the air by the geothermal power plant and distributed it all over Türkiye. In those years, this factory was a first in the world. Today, its total capacity is 400.000 tonnes/year.

Subsequently, MTA carried out geothermal survey and exploration drillings in hundreds of places such as Afyonkarahisar, Gönen, Simav. In 1983, the downhole heat exchanger was applied in Izmir-Balcova and the heating of Dokuz Eylül University hospitals, campus and thermal facilities was provided. It paved the way for the heating of Afyonkarahisar city centre by conducting heat exchanger tests. In 1974, a 1000m deep well was drilled in Afyonkarahisar. Under the conditions of the time, 1000m was an important depth for geothermal energy.

In addition to electricity generation, district heating, central heating, CO_2 production, the use in spas and thermal facilities has gained momentum and the first 5-star thermal touristic facility of the private sector was established in Afyonkarahisar. Gönen became the first town geothermally heated in 1986 and it was followed by Simav, Kırsehir, Balcova, Narlıdere, Edremit, Kızılcahamam, Kozaklı, Sarayköy, Sandıklı and Bigadic. District heating has been achieved using 55-60°C geothermal fluids and this has had a global effect. In 1999, İzmir-Balcova geothermal

heating system was selected as the best practice by the European Geothermal Energy Council (EGEC). District heating has been an investment that has made great contributions to the benefit of the people, the environment and raising the standard of living. However, it has slowed down after the 2000s.

The Turkish Geothermal Association (TGA), which was established in 1992, has organized congress and conference trips to various countries of the world such as Germany, France, Italy, Japan, Japan, USA, Iceland for the promotion of geothermal, ensured the participation of ministers, members of parliament, governors, mayors, bureaucrats and engineers in these countries, organized technical trips and carried out promotional activities. All these expenses were covered by TGA and its sponsors.

MTA continued exploration, discovered geothermal fields by taking risks and started the preparation of geothermal law through the commissions established. However, the biggest development came after the World Geothermal Congress (WGC2005), organized by the International Geothermal Association (IGA) and the Turkish Geothermal Association (TGA) in Antalya in 2005. 2000 people from Türkiye and the world attended this congress. In addition, the participation of ministers, member of parliaments, scientists and bureaucrats was ensured and the importance of geothermal was understood. Thereupon, the Law No. 5686 on Geothermal Resources and Natural Mineral Waters was enacted as a stimulus law. In addition, the model of leasing the geothermal sites, explored and discovered by MTA, to the private sector for 30 (+10) years with 1 or 2 wells drilled was accepted and appreciated by the Turkish private sector. As a result, MTA has leased the fields for very large amounts (up to $109 million). Additionally, MTA has conducted hundreds of tenders and leased low temperature fields to the private sector.

The Turkish private sector has acted swiftly, drilled additional production and reinjection wells, prepared feasibility studies and projects, started investment, and constructed and commissioned a power plant in record time. Congratulations and thanks are due to the State and Government of the Republic of Türkiye, the Ministry of Energy and Natural Resources, the universities, the private sector and, of course, MTA.

The milestones in Turkey's geothermal history are presented in chronological order in Table 1.

3. Present

After the Law No. 5686 on "Geothermal Resources and Natural Mineral Waters" entered into force in 2007, significant developments have been achieved and investments have started as mentioned in the previous chapter. Power plants have started to be established rapidly and the adventure that started with 0.5 MWe pilot power plant and 20 MWe commercial power plant has reached 1710 MWe of installed capacity today, ranking 1st in Europe and 4th in the world. 3-4% of country's electricity production is met from geothermal resources. Table 2 presents the full list of geothermal power plats active in Türkiye.

Geothermally heated greenhouses have gained momentum and importance in the last 10 years due to the importance of food security, economic use of geothermal heat, export and employment. Today it has exceeded 10400 acres and ranks 1st in the world.

Table 1: Year-based development in Turkish geothermal sector.

Year	Development
1926	A law was enacted regarding hot springs.
1935	The General Directorate of Mineral Research and Exploration (MTA) was established.
1947	'Türkiye Mineral Waters' book was prepared (Çağlar, 1947).
1948	'Tectonics of Aegean Region, Hot Springs, Mineral Water Sources' was published (Pınar,1948).
1960s	MTA General Director Dr. Sadrettin Alpan emphasized geothermal research.
1962	The first geological surveys were conducted in Balçova.
1963	The first geothermal drilling was carried out in Balçova.
1966	Several studies including thermal mineral resources were published (Erentöz and Ternek, 1966).
1967	The Western Anatolia and Kızıldere geothermal exploration project was initiated by MTA-UNDP.
1968	The first high-T reservoir was discovered at 198°C at a depth of 540 meters in Kızıldere.
1974	The first geothermal power test plant with a capacity of 0.5 MWe was established in Kızıldere.
1975	The book 'Türkiye Mineral Waters' was published by Istanbul University Faculty of Medicine.
1979	The first draft geothermal law was prepared by MTA.
1982	The Germencik (232°C) and Tuzla (174°C) fields were discovered through drilling.
1982	The first Turkish-Italian seminar on geothermal energy took place.
1982	The first geothermal regulation was included in the Mining Law.
1983	The first geothermal heating system with an in-well heat exchanger was established in Balçova.
1984	The first GEPP with single flash steam technology was commissioned in Kızıldere (15 MWe) by TEK.
1986	The first CO_2 factory was established in Kızıldere.
1987	The first centralized geothermal district heating system was initiated in Gönen.
1990	The scaling problem was resolved, leading to increased investments in heating applications.
1990s	Heating became widespread, started in Afyon, Kırşehir, Balçova, Narlıdere, Edremit, Bigadiç, Salihli.
1999	Balçova geothermal heating system was selected as a best practice by EGEC.
2000	After earthquakes in 1999, TÜBİTAK, universities, MTA monitored field (Simsek&Yildirim, 2000).
2002	The first reinjection studies were carried out in the Kızıldere.
2003	The Bank of Provinces (İller Bankası) began research and credit support for geothermal projects.
2005	The World Geothermal Congress (WGC-2005) was held in Antalya. MTA inventory was published.
2006	The first private sector plant (Mege) and binary system power plant were established in Salavatlı.
2007	The Geothermal Resources and Natural Mineral Waters Law was published, and the related regulation
2008	Kızıldere was privatized.
2009	The first double flash steam power plant was established in Germencik (47.4 MWe).
2011	MTA auctioned off the fields it had discovered to allow private sector exploration and operation.
2013	A new 80 MWe power plant was commissioned in the Kızıldere.
2014	The total installed capacity of geothermal power plants reached 400 MWe by the end of 2014.
2015	The installed capacity in Ömerbeyli reached 162 MWe.
2016	Türkiye's heat flow data were added to IRENA Atlas.
2017	Türkiye joined 1 GW country club. OrmaTürk started domestic manufacturing.
2020	11th European Geothermal PhD Days was hosted for the first time in Türkiye.
2022	awarding of WING Türkiye with the WING Global Operations role.
2023	inauguration of the first geothermal-solar hybrid power plant by Zorlu Energy

Approximately 40000 houses in İzmir-Balcova, 30000 houses in Afyonkarahisar, hotels, greenhouses and university campuses have started to be heated with geothermal energy. The total residential heating capacity has increased to 158000 housing equivalents.

According to the type of evaluation of geothermal resources in direct applications (non-electricity), it is in the 2nd - 4th position in the world. This success of Türkiye has been the subject of all conferences, aroused curiosity and appreciation.

Türkiye started to be a part of international projects such as GEOCOND, GECO, GEOENVİ, GEORISK, GEOSMART, REFLECT Horizon 2020 projects. For Horizon Europe projects, Türkiye signed an agreement to participate with same conditions as EU members (Directorate for EU Affairs, 2021).

Therefore, the biggest driving forces in the development of geothermal in the country can be listed as the organization of the World Geothermal Congress in 2005, followed by the introduction of a geothermal law and incentive system, scientific and technical monitoring of geothermal developments in the world by scientists in Türkiye, and organizing seminars, summer schools, national symposia and training courses. In addition, the fact that MTA took the risk of exploring and discovering the fields and opening them up to the Turkish private sector through competitive bidding has ensured progress and development.

The economic activity contribution of geothermal to the Turkish National Economy through electricity generation, geothermal district heating, greenhouse heating, carbon dioxide production, thermal tourism and others has been calculated as approximately 172 billion TL per year by 2023 (October 2023 in US$). Total (direct/indirect) employment in the sector is 240.000 people.

In addition, according to the separate calculation of all existing geothermal assessments according to the electricity tariff and state-supported heating tariff, it is approximately 78 billion TL natural gas equivalent (October 2023). In addition, if all existing assessments are made with natural gas, it will be approximately 5 billion m^3/year natural gas equivalent. (Note: October 2023 average US dollar value is taken as 28 TL.)

In Türkiye, as of 2023, a depth of 5000m has been reached. The number of thermal resource outputs and wells has exceeded 2000. As a result, as of 2023, 100th anniversary of Turkish Republic, Türkiye has reached an important position in the world with the studies carried out by the government, technical staff, engineers, employees and investors for the development of geothermal resources in the country. However, due to the size of the geothermal potential, it is of great importance to accelerate and support continuous exploration and development activities in order to meet the energy needs of the country and to benefit from these domestic resources socially and economically.

Here is the Türkiye's geothermal technical potential according to various estimations:

- The geothermal technical heat potential is 107000 MWt. This potential is equivalent to approximately 13 million house heating or 400 thousand acres of greenhouse heating or approximately 90 billion m^3/year natural gas equivalent.
- Technical economic electricity potential is 9000 MWe.

- EGS/HDR (Enhanced Geothermal System/Hot Dry Rock) technical economic potential is 40000 MWe.

Now, a new geothermal law regulating exploration, operations and increasing non-electricity geothermal incentives has been initiated by MENR (ETKB in Turkish initials) and is expected to be finalized.

Table 2: Full list of geothermal power plants active in Türkiye and their characteristics.

Region	Plant - Company	Start Year	Number of Units	Unit Type	Total Installed Capacity (MWe)
Denizli	Kızıldere (Zorlu)	1984/2003	2	1F, 2F+B	80 + 15
Aydın	Salavatlı Dora 1,2,3 (MeGe)	2006/2013	3	B	50.86
Aydın	Germencik (Gürmat)	2009	1	2F	47.4
Çanakkale	Tuzla (Enda)	2010	1	B	7.5
Aydın	Hıdırbeyli (Maren)	2011/2013	3	B	92
Aydın	Pamukören (Çelikler)	2013	1	B	45
Denizli	Kızıldere (Bereket)	2007	1	B	6.85
Manisa	Alaşehir (Türkerler)	2014	1	B	24
Aydın	Gümüşköy (BM)	2014	1	B	6.6 + 6.6
Denizli	Gerali (Değirmenci)	2014	1	B	2.52
Aydın	Germencik (Gürmat)	2014	1	B	22.5
Denizli	Tosunlar (Akça)	2015	1	B	3.5
Aydın	Pamukören (Çelikler)	2015	1	B	22.5
Aydın	Germencik (Gürmat)	2015	3	2B + 2F	22.5 + 22.5 + 47.4
Manisa	Alaşehir (Zorlu)	2015	1	B	45
Aydın	Umurlu (Kar-Key)	2015	1	B	12
Denizli	Tekkehamam (Greeneco)	2015	1	B	12.8
Manisa	Alaşehir – Kemaliye (Enerjeo)	2015	1	B	25
Aydın	Germencik 2 (Gürmat)	2016	1	2F	25
Aydın	Sarayköy (Zorlu)	2016	1	2F	50
Denizli	Sarayköy 2 (Zorlu)	2017	1	2F	65
Manisa	Alaşehir 2 (Zorlu)	2018	1	B	40
Aydın	Efeler (Gürmat)	2018	1	2F	162
Manisa	Salihli (Zorlu)	2019	1	2F	60
Aydın	Kızıldere 3 (Zorlu)	2020	1	2F	165
Total					**1710.03**

Legend: 1F = Single flash, 2F = Double flash, B = Binary

4. Future

Table 3 represents the 2030 projections in the country.

Table 3: Türkiye's 2030 projection for geothermal applications and the additional investment required to reach this target

Geothermal Application	Estimated Targets for 2030	Additional Investment Required (USD) (2024 to 2030)
Electricity Production	3000 MWe (24 billion kWh)	5.4 billion
Heating (residential, hotel, etc.)	5000 MWt (Equivalent to 500000 Households)	1.2 billion
Greenhouse Heating	5600 MWt (Equivalent to 24,000 Acres)	2.5 billion
Drying, etc.	80 MWt (Equivalent to 300000 tons/year)	30 million
Thermal Tourism (Renovation and Development)	2000 MWt (520 Facilities including Thermal Springs, Health Tourism Facilities)	1.0 billion
Cooling	350 MWt (Equivalent to 20000 Households)	140 million
Fishing and Other Uses (Mineral Extraction, etc.)	400 MWt	100 million
Total Investment		10.37 billion

Natural Gas Equivalent of All Geothermal Uses (additional): 6.8 billion USD/Year

Economic Impact of Geothermal Electricity Production, Heating (residential, thermal facilities, etc.), Thermal Tourism (thermal springs), Greenhouses, Drying, Fishing, and Other Applications by 2030: 420 billion TL/Year (as of October 2023)

Direct and Indirect Employment Created by 2030: 420000 People

Further suggestions to pursue the development in the country can be listed as follows:

- Strengthen Public-Private Partnerships: Encouraging collaboration between government agencies, private companies, and research institutions can drive innovation and increase investment in geothermal projects. Public incentives and subsidies can be used to attract private sector participation.
- Invest in Research and Development: Supporting R&D initiatives focused on improving geothermal technologies, such as enhanced geothermal systems (EGS) and resource assessment methods, can help unlock new resources and increase efficiency.
- Expand Workforce Training: Developing specialized training programs and educational initiatives to build a skilled workforce will ensure that the sector has the expertise needed for advanced geothermal projects.

- Promote International Collaboration: Engaging in international partnerships and knowledge exchange with countries. Türkiye can be an international hub for geothermal energy as it enables in-situ learning, observation of different geological settings and different utilization ways and holds a geopolitical position between Europe and the rest of the world.
- Explore Hybrid Energy Solutions: Integrating geothermal with other renewable energy sources, such as solar or wind, can create more resilient and efficient energy systems, maximizing the potential of available resources.
- Establish a 'National Data Repository and Processing Center for Geothermal Resources' in Türkiye (Turan, 2019) while making subsurface data older than 10 years open to public (i.e. Germany).

5. Conclusion

The Turkish geothermal sector has evolved significantly from its early exploration phases in the 1970s to becoming a global leader in geothermal energy production by the 2020s. This growth has been driven by strategic regulatory changes, increased investment, and a strong emphasis on sustainable practices. Moving forward, Turkey's focus on innovation and efficiency will likely further enhance its position in the global geothermal market.

References

Çağlar, K. Ö. (1947) Mineral Water and Hot water Spring in Turkey, (Mineral Research and exploration of Türkiye (MTA) Publications, Ankara) (in Turkish).

Erentöz, C. and Ternek, Z. (1966). Thermo Resources and Geothermic Energy Studies in Turkey, (Mineral Research and exploration of Turkey (MTA) Publications, Ankara) (in Turkish).

Pınar, N. (1948). Tectonics and Hot and Mineral Water Springs of Aegean Area, (Ist. Univ.Science Fac Press, Istanbul) (in Turkish).

Simsek, S. and Yildirim, N. (2000). Geothermal activity at 17 August and 12 November 1999 Eastern Marmara earthquake region, Turkey, International Geothermal Association, Board of Directors Meeting, 6-7, pp. 1-15, Antalya.

Şimşek, Ş. (2015). Dünya'da ve Türkiye'de jeotermal gelişmeler. In III. Jeotermal Kaynaklar Sempozyumu Bildiriler Kitabı (pp. 1-17). 4-6 Kasım 2015, Ankara.

TJD. (2024). Türkiye Cumhuriyeti'nin 100. Yılında Jeotermal Kaynaklarda Başarı Öyküsü, Türkiye Jeotermal Derneği (TJD), Ankara (Unpublished).

Turan, A. (2019). National Data Repository and Processing Center for Geothermal Resources, LinkedIn, [April 19, 2021].

Directorate for EU Affairs. (2021). Agreements on Turkey's association to Horizon Europe, Erasmus+, and European Solidarity Corps (ESC) programmes for the period 2021-2027 signed. Republic of Turkey Ministry of Foreign Affairs. Retrieved from https://www.ab.gov.tr/agreements-on-turkeys-association-to-horizon-europe-erasmus-and-european-solidarity-corps-esc-programmes-for-the-period-_52756_en.html on January 2023.

Evaluation of the Precambrian Basement Temperature Below Four South Slave Communities, Northwest Territories, Canada

Michaël Thibault[1,2], Félix-Antoine Comeau[1], Jasmin Raymond[1], Mirah Rajaobelison[1],Viktor Terlaky[3], Juliet Newson[2]

[1]Institut national de la recherche scientifique (INRS)

[2]Iceland School of Energy (ISE), Reykjavik University

[3]Northwest Territories Geological Survey (NTGS)

Keywords

Regional update, Western Canada Sedimentary Basin, Energy ressource, Remote communities, Thermal conductivity, Heat flow, Laboratory analyses

ABSTRACT

Fort Providence, Kakisa, Hay River, and Enterprise are four South Slave communities located in the Northwest Territories (Canada). These communities rely on fossil fuels for space and water heating, and could benefit from geothermal systems. The South Slave Region is estimated to have the highest heat flow (>100 mW m^{-2}) in the Western Canadian Sedimentary Basin (WCSB), therefore is a target for geothermal exploration. However, an analysis of the deep geothermal resources has not been undertaken in this region. This research project objective is to fill this knowledge gap by providing a Precambrian basement temperature assessment below the sedimentary basin, around the four communities.

The Devonian sedimentary rock sequence on which the communities lie is thin (500 to 750 m) and has relatively low permeability (on average $<10^{-14}$ m^2). The lack of information on the Precambrian basement below Devonian sedimentary rocks limits the development of deep geothermal energy resources due to high uncertainty and risk. Deep borehole heat exchangers (DBHE) could be an appealing technology for direct use of heat in this geological context. However, a comprehensive assessment requires a detailed understanding of the thermal properties of the rocks. This information is mandatory to model such systems and provide accurate temperature estimates at depth.

A rock sampling campaign focusing on the Precambrian basement rocks was made in summer 2023, during which 91 outcrops and drilling cores were sampled to analyze their thermal properties. A range of thermal conductivity expected in the Precambrian basement was determined for the location of each community. Then, the results were used to extrapolate the subsurface temperature in the Precambrian basement until 10 km depth. The newly available information confirmed the presence of a significant geothermal potential in these communities.

In the more likely scenario (the normal one), the temperature at the top of the Precambrian basement ranges from 30.5 to 36.5 °C, with a basement surface heat flow of 99 mW m^{-2} to 157.7 mW m^{-2}. At 3 km depth, the temperature ranges from 100.4 to 156 °C; at 10 km depth, the temperature ranges from 303.6 to 511.6 °C for each community. Hay River has the highest values and most promising geothermal potential for deep closed-loop systems.

1. Introduction

Energy costs in northern Canada, populated by several indigenous communities, are higher than in the rest of the country. For example, electricity rates in the Northwest Territories (NWT) are more than twice the national average (Canada Energy Regulator & Government of Canada, 2023). The NWT, like many other northern regions, mainly relies on carbon-intensive fossil fuels such as oil to meet its electricity, space heating, and water heating needs. The Government of the NWT aims to ensure a balance between energy security, affordability, and reduction of greenhouse gas emissions in its 2030 Energy Strategy (Government of Northwest Territories, 2018). Key initiatives include replacing diesel with renewable energy solutions by exploring the potential of technologies such as deep geothermal resources in areas that have been identified as having high geothermal potential (EBA Engineering Consultants Ltd., 2010). These areas have yet to be defined and characterized.

This research project focuses on the geothermal potential of four communities in the southern part of the NWT with the intent of characterizing its deep geothermal resources. The communities (Figure 1) are located within the South Slave administrative region, part of the Dehcho First Nations: Hay River (Xátł'odehchee, K'atlodeeche First Nation and Ts'ueh Nda, West Point First Nation), Fort Providence (Zhahti Kų́ę́, Deh Gáh Got'îê First Nation), Enterprise, and Kakisa (K'ágee, Ka'a'gee Tu First Nation). Due to their close vicinity, Hay River Town and Hay River Dene (Katlodeeche First Nation Reserve) are referred to as "Hay River" in the study.

These four communities are situated within the largest high heat flow anomaly in Canada, known as the Northern Plains Heat Flow Anomaly (NPHFA) or Northern Anomaly (Majorowicz, 1996; Majorowicz & Weides, 2014). This anomaly is approximately 300 km wide and stretches 500 km from north to south. The geothermal gradient and heat flow in the research areas are significantly higher compared to other Precambrian platform locations worldwide (Majorowicz & Jessop, 1981). Several hypotheses have been proposed to explain the thermal anomalies in this region. Bachu (1993) suggested that the unusually high temperatures measured could be related to hydrogeological effects which can disturb heat flow patterns. Majorowicz (1996) suggested the presence of an increased mantle upflow beneath the region which aligns with other heat flow anomalies along the western margin of the North American Craton. Despite these hypotheses, Majorowicz (2018) concluded that the exact cause of the heat flow anomaly remains speculative.

Rajaobelison et al. (In press) measured thermophysical properties on the NWT South Slave's sedimentary rocks. Then, Rajaobelison et al. (2024) created 1D temperature models based on temperature data from vintage oil and gas wells to evaluate the geothermal potential in the sedimentary sequence of NWT South Slave's communities.

Due to the generally low permeability and porosity inferred for the matrix of the sedimentary rocks analyzed in these studies and the shallow depth of the basement (525 to 729 m), the potential technologies that can be envisioned to produce geothermal energy are closed-loop DBHE relying on conduction to extract heat from rock formations and/or enhanced geothermal systems (EGS) requiring stimulation of potential reservoir formation to extract heat by forced convection.

A temperature model for the Precambrian basement, which lies below the sedimentary sequence, could not be made in previous studies due to a lack of information on the basement thermal properties. Very little information and data exist about the basement below the communities, representing a limitation when it comes to understanding and assessing the geothermal resources of the region. To reach higher temperatures below the sedimentary cover (>37 °C, Rajaobelison et al., 2024), Precambrian basement depth must be considered.

Therefore, this study objective is to assess the temperature at depths within the basement rock beneath the communities. To achieve this goal, we intend to determine a range of thermal properties for each tectonic domain (i.e., the Precambrian bedrock underlying each community). Additionally, we wish to extend previous work on sedimentary sequences (Rajaobelison et al., 2024) by incorporating new data from previously unsampled formations. This will help reduce uncertainties related to the rock thermal properties and temperature calculation at depth.

2. Geological Settings

The four NWT communities are located on the eastern edge of the WCSB. It is positioned between the Cordilleran Orogen to the west and the Canadian Shield to the east (Figure 2). Significant oil and gas exploration activities have taken place since the 1950s, with over 400 exploration wells drilled, most of which are now abandoned (OROGO, 2024) but has contributed to the identification of the high geothermal potential in the area (Figure 1).

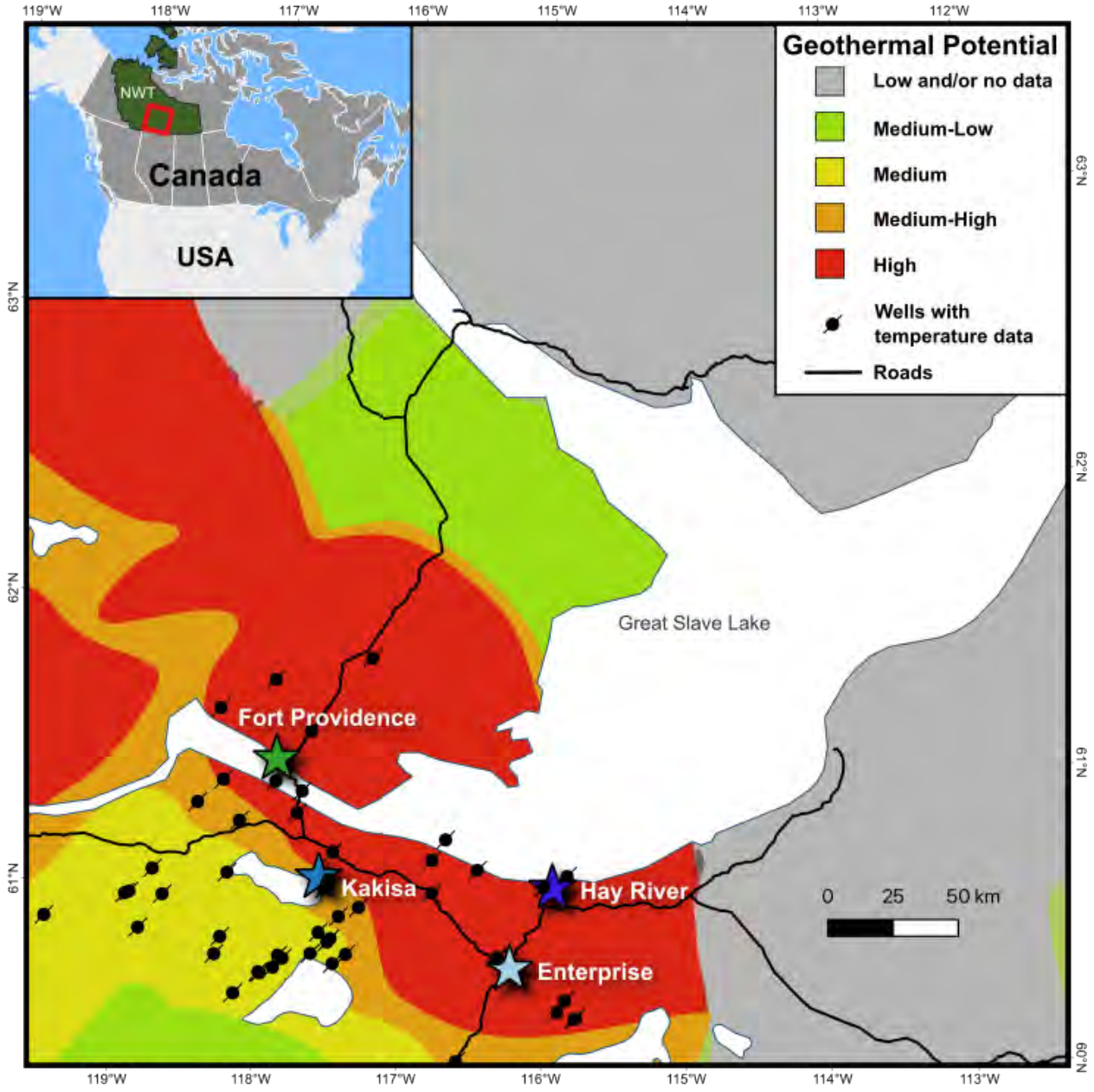

Figure 1: Geothermal potential map based on temperature (adapted from EBA Engineering Consultants Ltd., 2010) showing wells (abandoned) with temperature data and community locations.

The Quaternary glacial sediment, often called soil or alluvium, is between 4 m and 20 m thick at the community's location. It was deposited unconformably over the Paleozoic-Cenozoic sedimentary rock formations.

The sedimentary rocks lie on the top of a Precambrian crystalline basement that is part of the Canadian Shield. The sedimentary strata gradually thicken from east-northeast to west-southwest, ranging from about 500 m to 715 m in thickness at the community's locations. Furthermore, the geological formations in the region exhibit low porosity and permeability, implying a limited

potential for hot sedimentary aquifers, as noted by Rajaobelison et al. (In press). The anticipated permeability is expected to be mostly influenced by fault and fracture networks rather than the intrinsic porosity of the formations. Conduction is the dominant mechanism for geothermal heat flow in the region (Bachu, 1993; Gray et al., 2012; Majorowicz et al., 1999; 2012), which is the focus of the present study.

The Precambrian basement underlying the sedimentary cover consists of a poorly known mix of igneous and metamorphic rocks. It is characterized and subdivided by tectonic domains (Figure 2). The domains in the study area, listed from east to west and in chronological order of age are; Slave Craton, Great Bear Magmatic Zone, and Hottah Terrane that is part of Wopmay Orogen accreted terranes (Ootes et al., 2015). All tectonic domains of the Precambrian basement have various compositions, ages and tectonic histories, as well as different thermal properties that are critical for geothermal assessment. Thus, we employ tectonic domain terminology in this study to address basement classification. Hay River and Enterprise are part of the Slave Craton tectonic domain. Fort Providence and Kakisa, on the other hand, are located in Hottah Terrane.

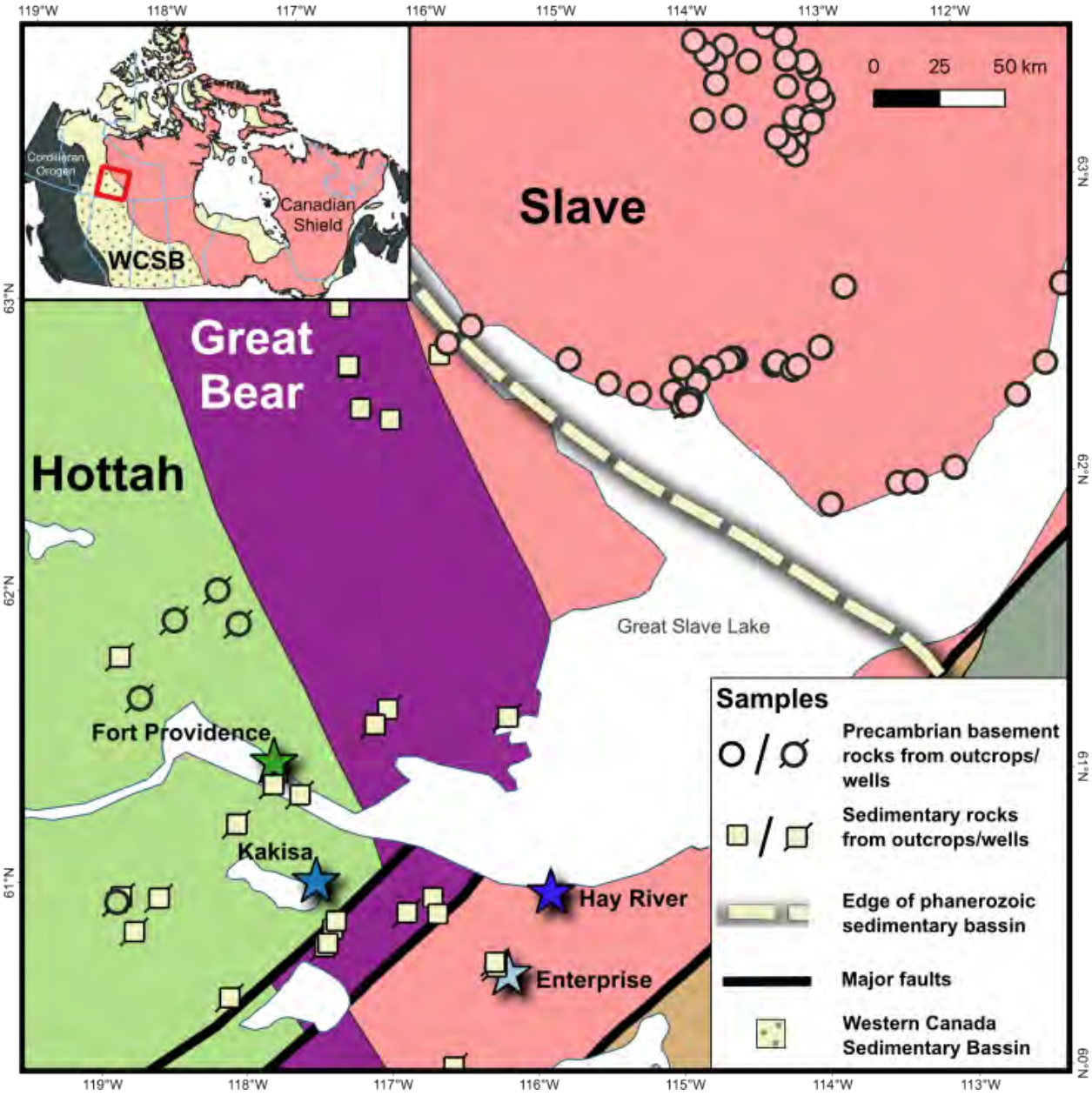

Figure 2: Tectonic domain map (based on Ootes et al. (2015) domain division), with samples and community locations.

3. Material, Methods and Input Data

To accurately predict temperature at different depths, it was essential to use representative input data that accurately reflected the geological characteristics of the location. Due to the lack of information on thermal properties for geological materials in this area, we conducted extensive sampling and laboratory measurements. Collected data was used as input and is the foundation of subsequent analyses and thermal assessment. We therefore present below an updated

thermostratigraphic assessment, providing a new comprehensive dataset for the Precambrian bedrock and enhancing the previous sedimentary rocks sequence data.

This section gives an overview of the sampling process, thermal property analysis, undisturbed ground temperature assessment, input data and scenario examination, and a comprehensive thermostratigraphic assessment. All this information was used to create temperature profiles until the basement's top, 3 km and 10 km depths, which are the main results of this research.

3.1 Sampling overview

In 2022, we sampled 84 split core samples from 43 vintage oil and gas exploration wells of the South Slave region. Related descriptions and laboratory results are presented in Rajaobelison et al. (In press). Some sedimentary formations under the communities remained unsampled and thermal conductivity values from literature were assigned based on their lithologic content.

A rock sampling campaign in 2023 allowed the collection of 91 Precambrian basement rock samples, for which we think to have recovered a variety of geological units of each tectonic domain related to each community that could give us a good approximation of the material that can be encountered under these communities (Table 1). Sedimentary rocks sampling was partial and had to be interrupted due to forest fires and an evacuation order in the area (Figure 3).

Table 1: Sampling overview.

Geological material			Number of samples		
Alluvium					3
Sedimentary Rocks					112
Precambrian Basement Rocks	Igneous	Plutonic	54	66	91
		Volcanic	12		
	Metamorphic	Sedimentary	16	25	
		Plutonic	5		
		Volcanic	4		

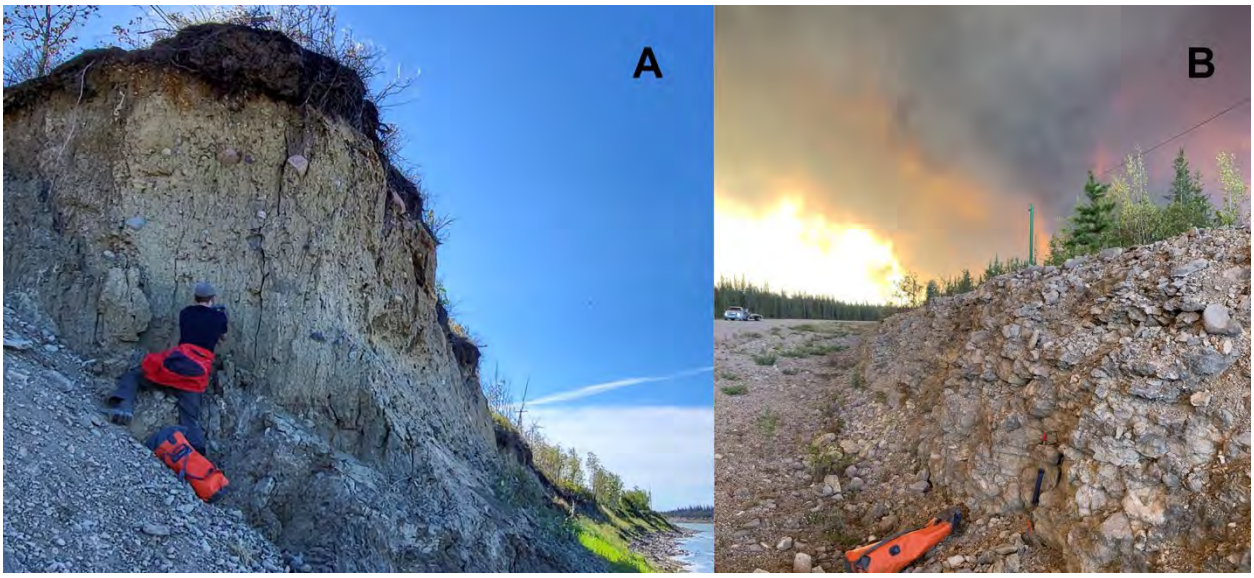

Figure 3: A) Soil sampling in Fort Providence on a glacial till cliff along the DehCho Dr road. B) Sedimentary rock outcrop sampling on the roadside of Highway 1 between Kakisa and Enterprise, one of the last samples before the evacuation order.

3.2 Thermal Properties

3.2.1 Thermal Conductivity

All sedimentary and basement rock samples collected (Table 1) were analyzed for thermal conductivity. The methodology follows that of Rajaobelison et al. (In press). Transient measurements were made using an optical scanning instrument developed by Popov et al. (2023) under dry conditions (Figure 4).

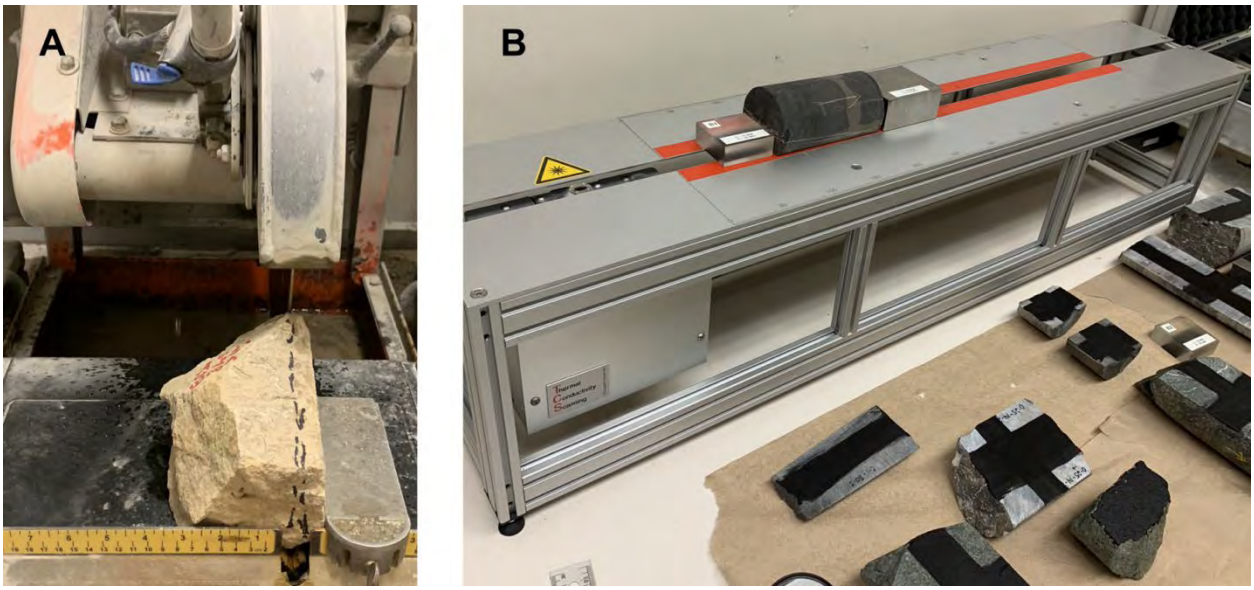

Figure 4: Sample preparation and analyses. A) Rock sample saw cutting. B) Thermal property measurement on the optical scanning instrument developed by Popov et al. (2023).

The average thermal conductivity values for all the measured samples, presented by types of material are shown in Figure 5. The classification of rocks according to their insulating to conductive potential indicated on Figure 5 and 6 is based on Rajaobelison et al. (In press), Sass & Götz (2012) and Sass et al. (1992).

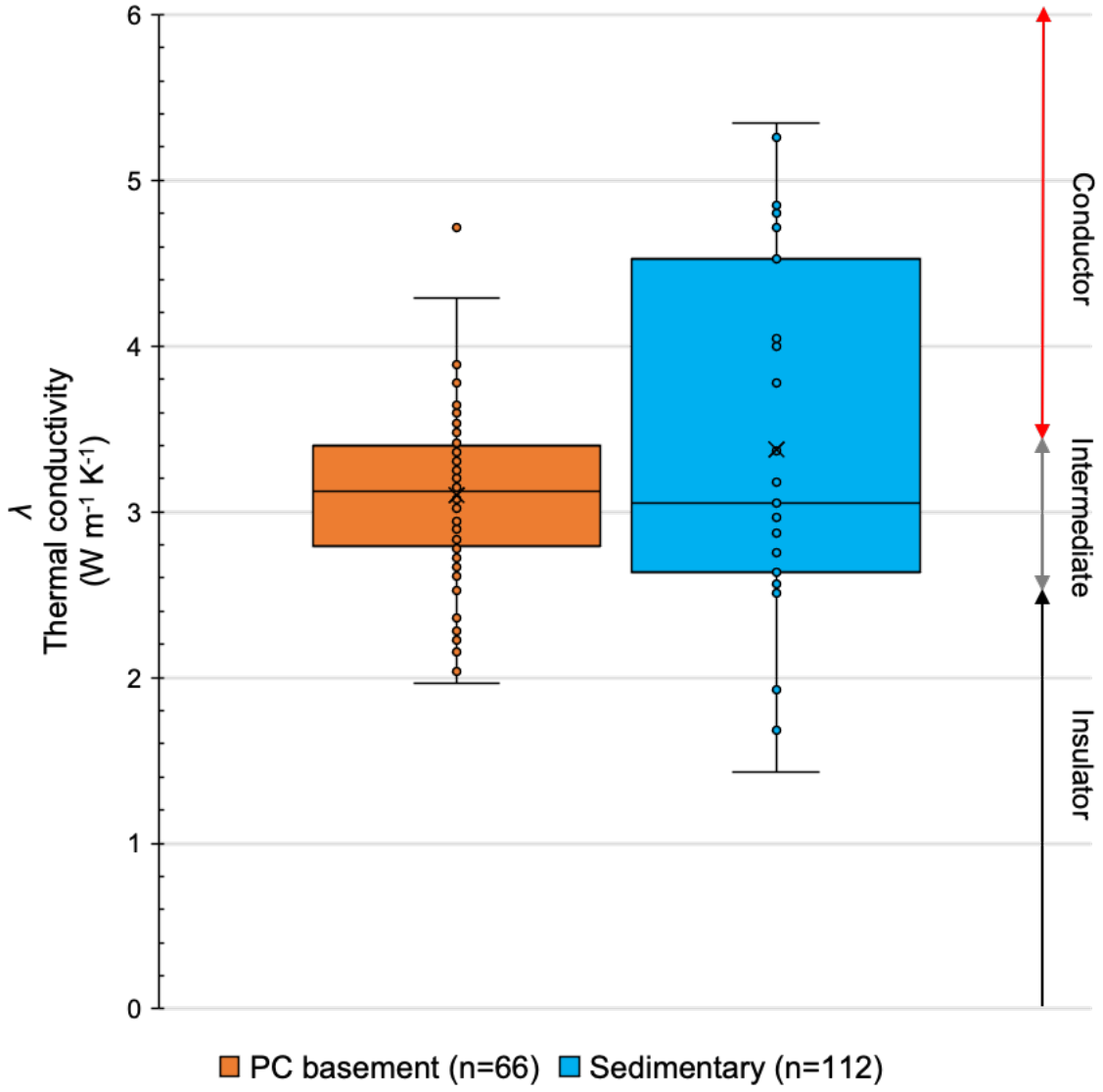

Figure 5: Thermal conductivity for the overall sampled Precambrian (PC) basement and sedimentary rocks.

In this study, we treat each tectonic domain (Figure 2) as a uniform thermal unit. Sixty-six samples from the outcropping Slave Province were analyzed for the Slave Craton tectonic domain, which is associated with the Hay River and the Enterprise Precambrian basement. For the Hottah Terrane tectonic domain (Fort Providence and Kakisa), we sampled eleven core cuttings and surface rocks. We added ten additional previously measured core cuttings from other locations in our data set, which came from Majorowicz et al. (2014). Figure 6 shows the corresponding thermal conductivity ranges.

The values attributed to the Slave Craton account for a wide range of lithologies that represent practically all geological units visible at the surface of the Slave Province, from which these Precambrian structures extend beneath the sedimentary layer (Ootes et al., 2015). The Hottah Terrane has slightly higher thermal conductivity values, a broader spread, and fewer samples.

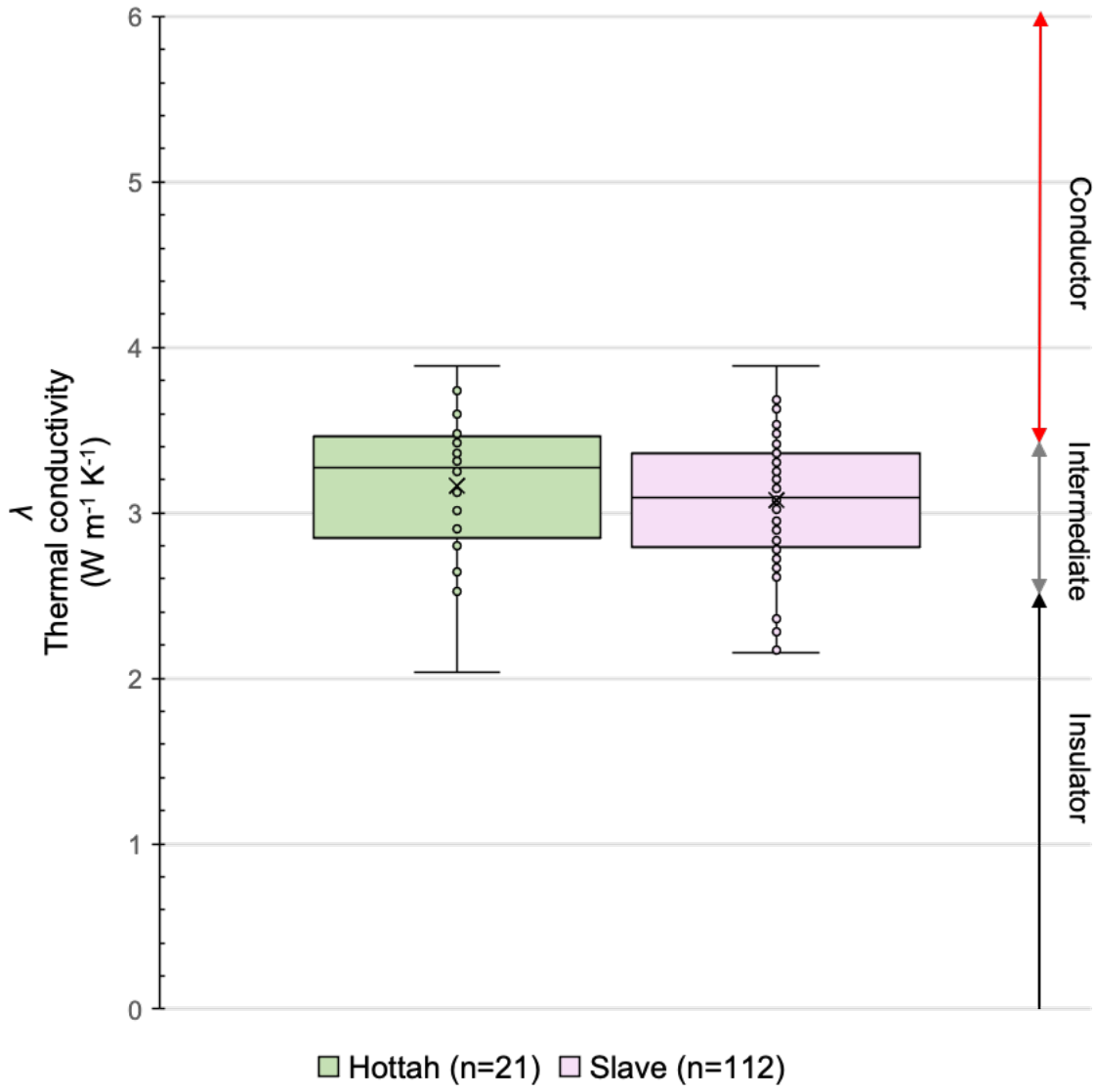

Figure 6: Thermal conductivity for basement domain related to each community.

3.2.2 Heat Generation Rate

Table 3 shows the heat generation rate expected for sedimentary units and basement domain. The sedimentary formations values were obtained from Rajaobelison et al. (2024). The basement heat generation rate was determined according to literature values specific to each tectonic domain, including Jessop (1992) for the Hottah Terrane and Perry et al. (2010) for the Slave Craton.

3.3 Undisturbed Ground Temperature

The undisturbed ground temperature T_s (K) was estimated using the equation proposed by Ouzzane et al. (2015):

$$T_s = 17.898 + 0.951 T_{amb} \quad (1)$$

where T_{amb} (K) is the ambient air temperature, which is considered to be -2.5 °C based on the mean annual air temperature from the Hay River-A weather station (Government of Canada & Environment and Natural Resources, 2024). T_s is thus estimated to be 2.1 °C in the South Slave region.

3.4 Input Data and Scenarios

In this study, various scenarios were proposed based on the probabilistic distribution of thermal properties. This provides for a normal, pessimistic, or optimistic outlook. These are presented in Table 2 as input for thermal properties and in Table 3 as results.

The normal scenario employs the 50th percentile (P_{50}) values of basement thermal conductivity, heat generation rate, as well as the heat flow and geothermal gradient acquired from the corrected well temperature measurements, resulting in a neutral approach. The pessimist scenario uses the 25th percentile (P_{25}) value of heat flow and temperature gradient, the minimum heat generation rate value and the 75th percentile (P_{75}) percentile values for the thermal conductivity, embodying a cautious approach. In contrast, the optimist scenario utilizes P_{75} values for heat flow and temperature gradient, the maximum heat generation rate, and P_{25} values for the thermal conductivity, providing insight into best-case scenarios. These diverse perspectives allowed for a comprehensive analysis of potential outcomes across different scenarios.

Table 2. Thermal properties (thermal conductivity and heat generation rate) values assigned to each scenario (normal (N), pessimist (P) and optimist (O)) for each community in the sedimentary sequence and the Precambrian (PC) basement (Hottah Terrane and Slave Craton tectonics domain). The number of samples is denoted by *n*.

			λ Thermal Conductivity ($W\ m^{-1}\ K^{-1}$)				***A*** Heat Generation Rate ($\mu W\ m^3$)			
			n	N P_{50}	P P_{75}	O P_{25}	*n*	N P_{50}	P min	O max
Sedimentary		Fort Providence	80	2,5	2,8	2,4	80	0,5		
		Kakisa		2,3	2,7	2,2		0,4		
		Hay River		2,8	3,1	2,5		0,4		
		Enterprise		2,6	2,8	2,4		0,4		
PC basement	Hottah	Fort Providence	21	3,3	3,4	2,9	7	2,1	1	3,6
		Kakisa								
	Slave	Hay River	66	3,1	3,4	2,8	20	2,3	1	4,8
		Enterprise								

3.5 Thermostratigraphic Assessment

Temperature was calculated at the base of each sedimentary rock units and at each 500 m intervals in the basement. To be consistent with previous work, we used for each community the same well temperature data listed in the assessment of Rajaobelison et al. (2024), where well temperature measurements from drill-stem tests (DST) and borehole temperature (BHT) were corrected for drilling disturbance and paleoclimate effects. This temperature assessment of the sedimentary basin served as inputs for the present temperature assessment in the Precambrian basement.

3.5.1 Paleoclimate corrections

Past glaciations in Canada lowered subsurface temperatures at shallow depths, due to both the cooling effects of lower surface temperatures and crustal compression induced by the weight of ice sheets that covered the land. These paleoclimate effects persist today to consideradable depth, necessitating paleoclimate corrections in temperature assessments for accurate deep geothermal estimations out of shallow wells temperature measurements (Jessop, 1992). The effects of past glaciations in Canada can be significant to the depth of two kilometres or more (Bédard et al., 2016; J. Majorowicz, Chan, et al., 2014; J. Majorowicz et al., 2012). While this influence diminishes with depth, it's essential to account for paleoclimate corrections, particularly for this area where temperature measurements from old oil and gas exploration wells are mainly less than a thousand metres deep. Beyond a certain depth, temperatures tend to reach equilibrium, reflecting the long-term geothermal gradient of the region. In this study we consider a depth of 3 km, from which climatic variations no longer have a significant impact on temperature and that we consider as equilibrium temperature. The 3 km cut-off value for the South Slave region seems reasonable, considering that northern Alberta estimates are 2200 m based on the first heat flow measurement in a well that reached the basement under the WCSB below the depth of the paleoclimatic influence (Majorowicz, Chan, et al., 2014; Majorowicz et al., 2012). In areas where paleoclimates have a deeper influence, such as the St. Lawrence Lowlands sedimentary basin in Quebec (Bédard et al., 2016; Chapelet, 2022), the influence on temperatures and heat flow are minimal below 3 km depth. The equilibrium temperature at depth $T_{z\,(\mathrm{eq})}$ is calculated with the following paleoclimate correction equation (Jessop, 1990; Rajaobelison et al., 2024):

$$T_{z(\mathrm{eq})} = T_{\mathrm{m}} + \sum_{\mathrm{i}}(T_{\mathrm{i}}) \left[erf\left(\frac{z}{2\sqrt{\alpha\, t_1}}\right) - erf\left(\frac{z}{2\sqrt{\alpha\, t_2}}\right)\right] \quad (2)$$

where T_{m} (°C) represents the temperature measured at a certain depth z (m), corrected from drilling disturbance and T_{i} (°C) is the temperature step between glaciations. The error function is represented by *erf*, α ($\mathrm{m^2\ s^{-1}}$) is the mean thermal diffusivity of the rocks, t_1 (s) represents the end of the ice age, while t_2 (s) represents the beginning of the ice age. Specific information regarding the values employed can be found in the laboratory and thermostratigraphic studies conducted by Rajaobelison et al. (2024).

Thus, to estimate the actual subsurface temperature at a depth of less than 3 km, the paleoclimatic correction (equation 2) was removed such that temperature is characteristic of the value that can be measured (i.e., affected by glaciation). However, the paleoclimate correction was applied to calculate temperature until 10 km depth since glaciations are expected to have a low impact at great depth.

3.5.2 Geothermal Gradient

The geothermal gradient g (°C m^{-1}) refers to the rate at which temperature increases with depth below the Earth's surface. It can be stated by the following:

$$g = \frac{\Delta T}{\Delta z} = \frac{T_z - T_s}{z} \quad (3)$$

where ΔT (°C) is the difference between the temperature at the depth being assessed T_z (corrected measured temperature are from Rajaobelison et al., 2024) and the undisturbed ground temperature (T_s = 2.14 °C), and z (m) is the depth of the corrected temperature assessed.

3.5.3 Surface Heat Flow

Heat flow in the context of geothermal energy refers to the movement of thermal energy from the Earth's interior toward the surface, often used to assess the potential for geothermal energy extraction. Surface heat flow Q_0 (W m^{-2}) quantifies the rate at which this heat energy is transferred per unit area over the Earth's surface. The following equation (Bédard et al., 2016; Jessop, 1990; Rajaobelison et al., 2024) is used to compute surface heat flow in a sedimentary basin:

$$Q_0 = \lambda_{sed} g + A_{sed} \frac{z}{2} \quad (4)$$

λ_{sed} (W m^{-1} K^{-1}) denotes the effective thermal conductivity of the sedimentary sequence, determined by calculating the weighted harmonic mean of the λ for the different lithologic units that make up the sedimentary rock cover at each location, g (°C km^{-1}) refers to the geothermal gradient determined from temperature measurements as described previously, A_{sed} (W m^{-3}) is the effective heat generation obtained from the weighted arithmetic average in the sedimentary rock sequence and z (m) is the rock sequence thickness between the measured temperature depth and the ground surface.

3.5.4 Basement Heat Flow

The basement top heat flow Q_{PC} (W m^{-2}) is defined here as the heat flow at the boundary between the sedimentary layers and the underlying Precambrian basement rocks. It is calculated by removing the heat generation effects A_{sed} within the sedimentary rocks from the surface heat flow through the sedimentary sequence, according to the following equation (Bachu, 1993; Bédard et al., 2016; Majorowicz, Nieuwenhuis, et al., 2014; Majorowicz & Grasby, 2010b):

$$Q_{PC} = Q_0 - A_{sed} \frac{z_{sed}}{2} \quad (5)$$

where z_{sed} is the thickness of the sedimentary rocks sequence, which is the depth between the top of the Precambrian basement and the ground surface.

3.5.5 Temperature at Depth in the Sedimentary Rocks Sequence

Each sedimentary rock formation has a distinct effective thermal conductivity λ, hence the temperature at depth $T_{z(sed)}$ (°C) was calculated at their boundaries. It was computed analytically under steady-state condition, taking into account conductive heat transfer using a one-dimensional approach (Rajaobelison et al., 2024; Stein, 1995):

$$T_{z(sed)} = T_s + \frac{Q_0 z}{\lambda} - A \frac{z^2}{2\lambda} \quad (6)$$

where *T*s (°C) is the temperature at the base of the sedimentary formation, *z* (m) the formation thickness and λ (W m^{-1} K^{-1}) the formation effective thermal conductivity.

3.5.6 Temperature at Depth in the Precambrian Basement

The temperature at any depth in the Precambrian basement $T_{z(\mathrm{PC})}$ was calculated at each 500 m intervals, using the same relationship mentioned above for $T_{z(\mathrm{sed})}$:

$$T_{z(\mathrm{PC})} = T_{PC} + \frac{Q_{\mathrm{PC}}\, z_{\mathrm{PC}}}{\lambda_{\mathrm{PC}}} - A_{PC}\, \frac{{z_{PC}}^2}{2\lambda_{\mathrm{PC}}} \quad (7)$$

where T_{PC} (°C) is the temperature at the top of the basement, Q_{PC} (W m^{-2}) is the basement heat flow, z_{PC} (m) is the depth from the top of the basement, λ_{PC} (W m^{-1} K^{-1}) the thermal conductivity of the basement and A_{PC} (W m^{-3}) is the heat generation of the basement rocks.

4. Results

4.1 Input data

Table 3 presents the calculated geothermal gradient and surface heat flow for the sedimentary sequence, which were used in the temperature calculations.

Table 3: Geothermal gradient and heat flow assigned to each scenario (normal (N), pessimist (P) and optimist (O)) for each community (Fort Providence (FP), Kakisa (K), Hay River (HR) and Enterprise (E)) in the sedimentary sequence.

		g Geothermal Gradient (°C km^{-1})			***g*$_{eq}$** Equilibrium (°C km^{-1})			***Q*$_0$** Surface Heat Flow (W m^{-2})			***Q*$_{0(eq)}$** Equilibirum (W m^{-2})		
		N	P	O	N	P	O	N	P	O	N	P	O
		P_{50}	P_{25}	P_{75}	P_{50}	P_{25}	P_{75}	P_{50}	P_{25}	P_{75}	P_{50}	P_{25}	P_{75}
Sedimentary	FP	53	43	56	56	47	58	133	104	158	141	112	166
	K	43	39	44	45	41	46	99	85	118	105	90	125
	HR	56	46	61	59	50	64	158	115	186	167	124	195
	E	41	37	43	44	39	46	106	88	120	113	93	129

4.2 Temperature in the Sedimentary Rocks Sequence

Each temperature point used for calculations in the sedimentary rock sequence corresponds to the top of each sedimentary formation (fm.; Figure 7). The calculated temperature is based on heat flow assessed in wells near the communities. The profiles represent an estimate of the current temperature found in the sedimentary rocks, thus affected by glaciations and uncorrected for paleoclimates.

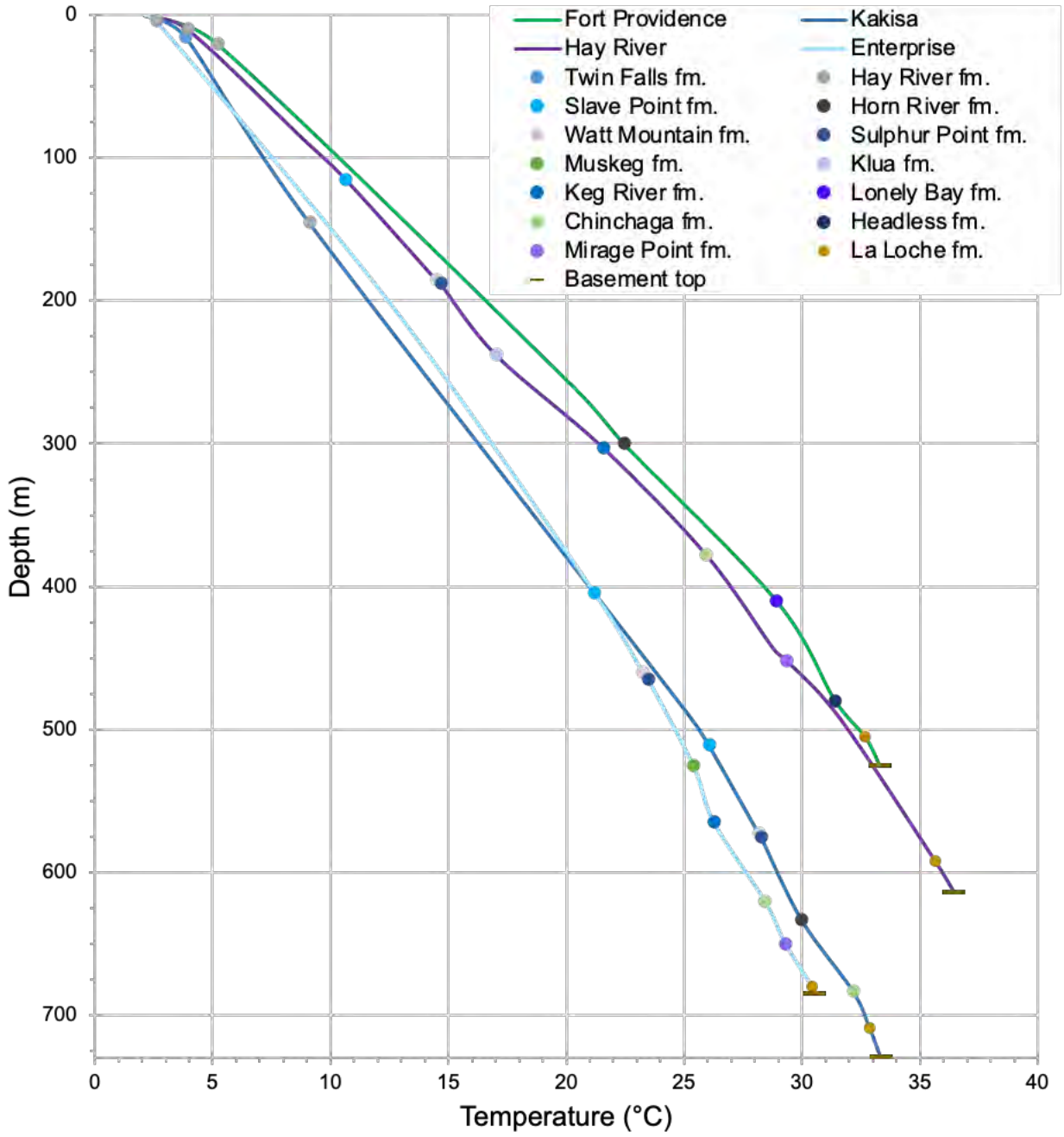

Figure 7: Temperature at depth in the sedimentary sequence, with normal scenarios, considering heat flow uncorrected for paleoclimates. Each community is represented by a distinct coloured line, and each geological formation (fm.) top is represented by a specific coloured circle.

4.3 Temperature in the Basement until 3 km depth

The temperature calculated until 3 km depth (Figure 8, 9, 10, 11, 12) incorporates uncertainty scenarios. The calculated temperatures represent an estimate of expected and current temperatures found in the basement, thus affected by glaciations and uncorrected for paleoclimates.

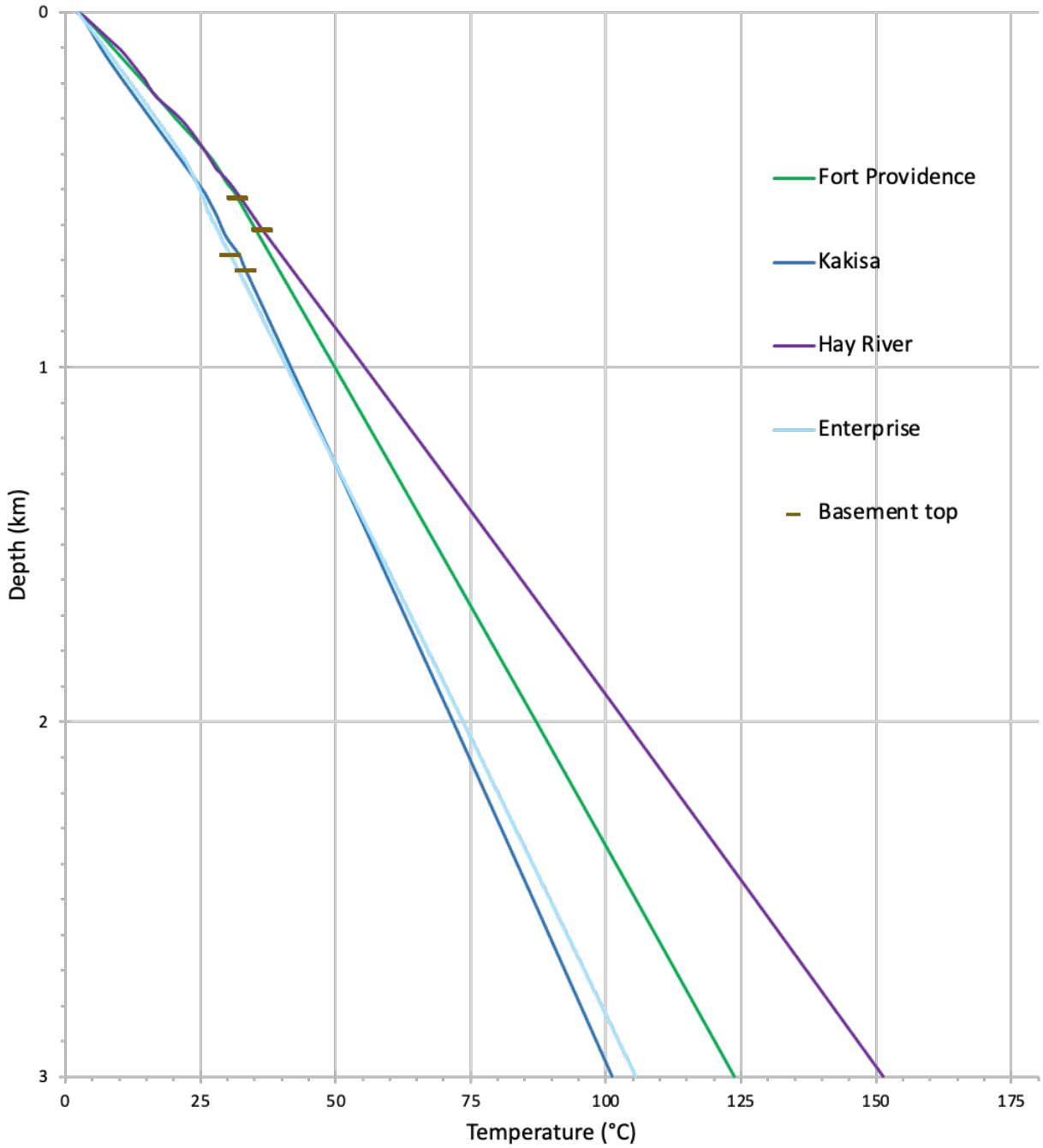

Figure 8: Temperature until 3 km depth, with normal scenarios, considering heat flow uncorrected for paleoclimates. Each community is represented by a distinct coloured line.

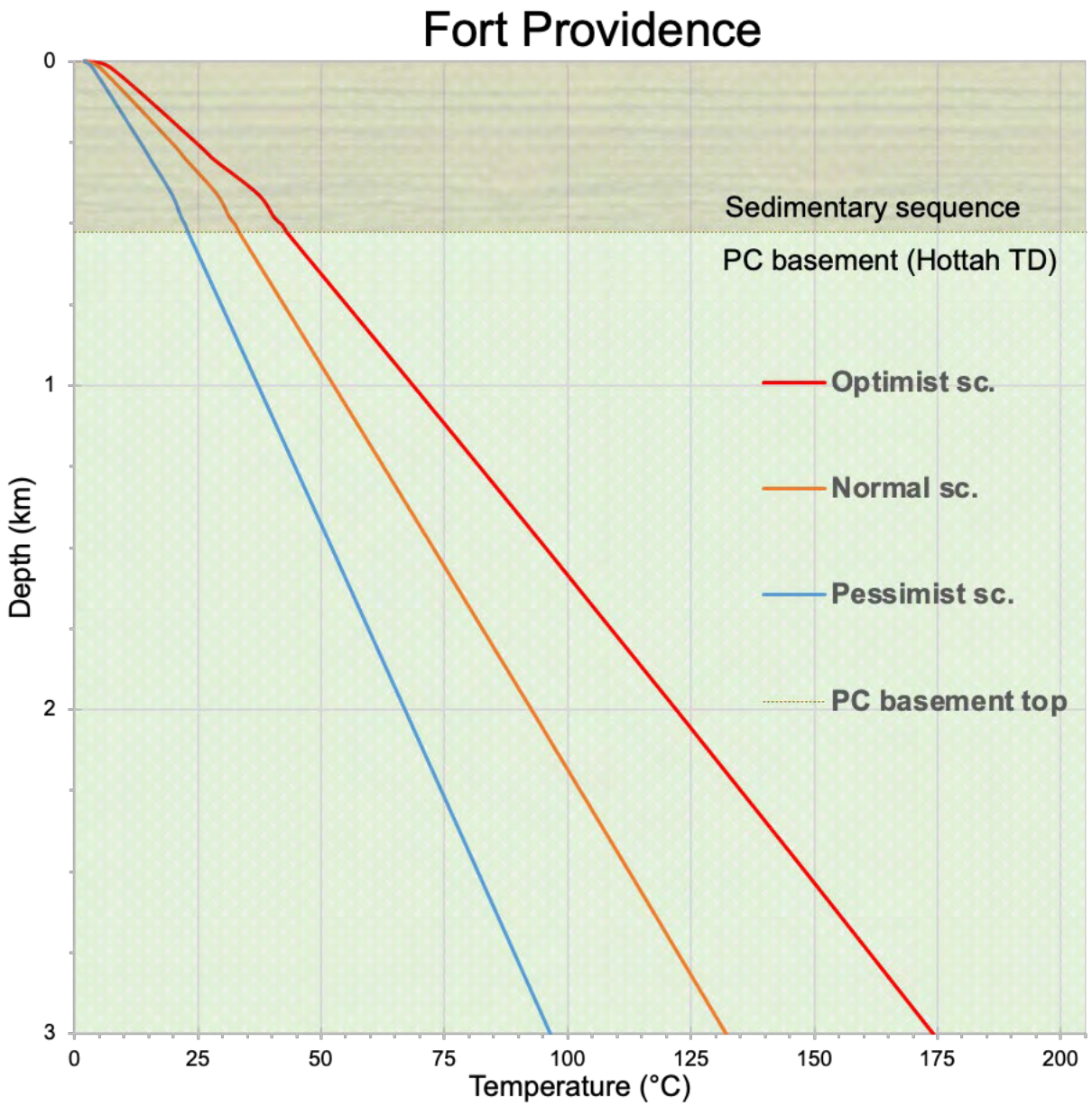

Figure 9: Temperature until 3 km depth for Fort Providence, with optimist, normal and pessimist scenarios, considering heat flow uncorrected for paleoclimates.

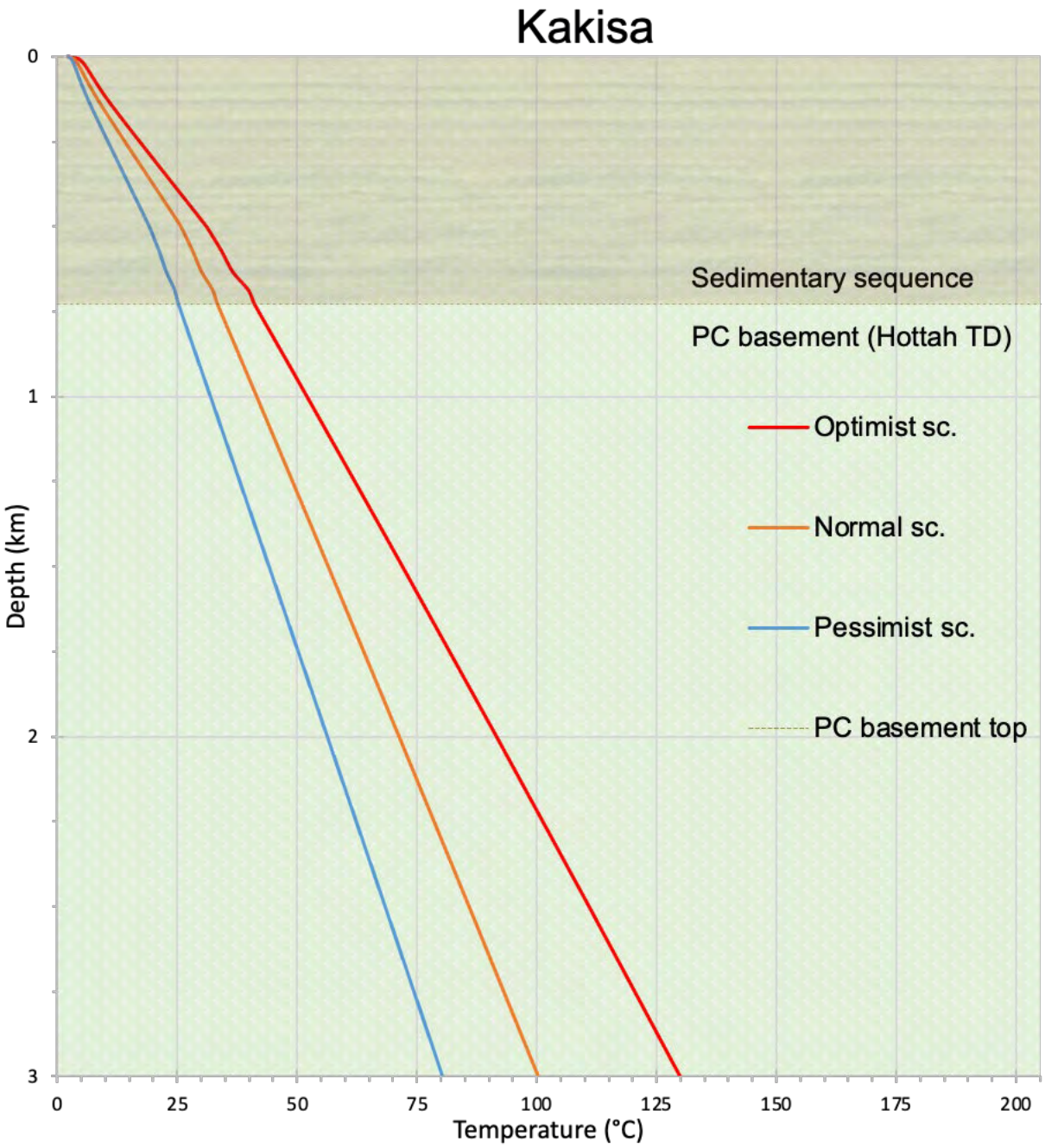

Figure 10: Temperatures at depth until 3 km depth for Kakisa, with optimist, normal and pessimist scenarios, considering heat flow uncorredted for paleoclitates.

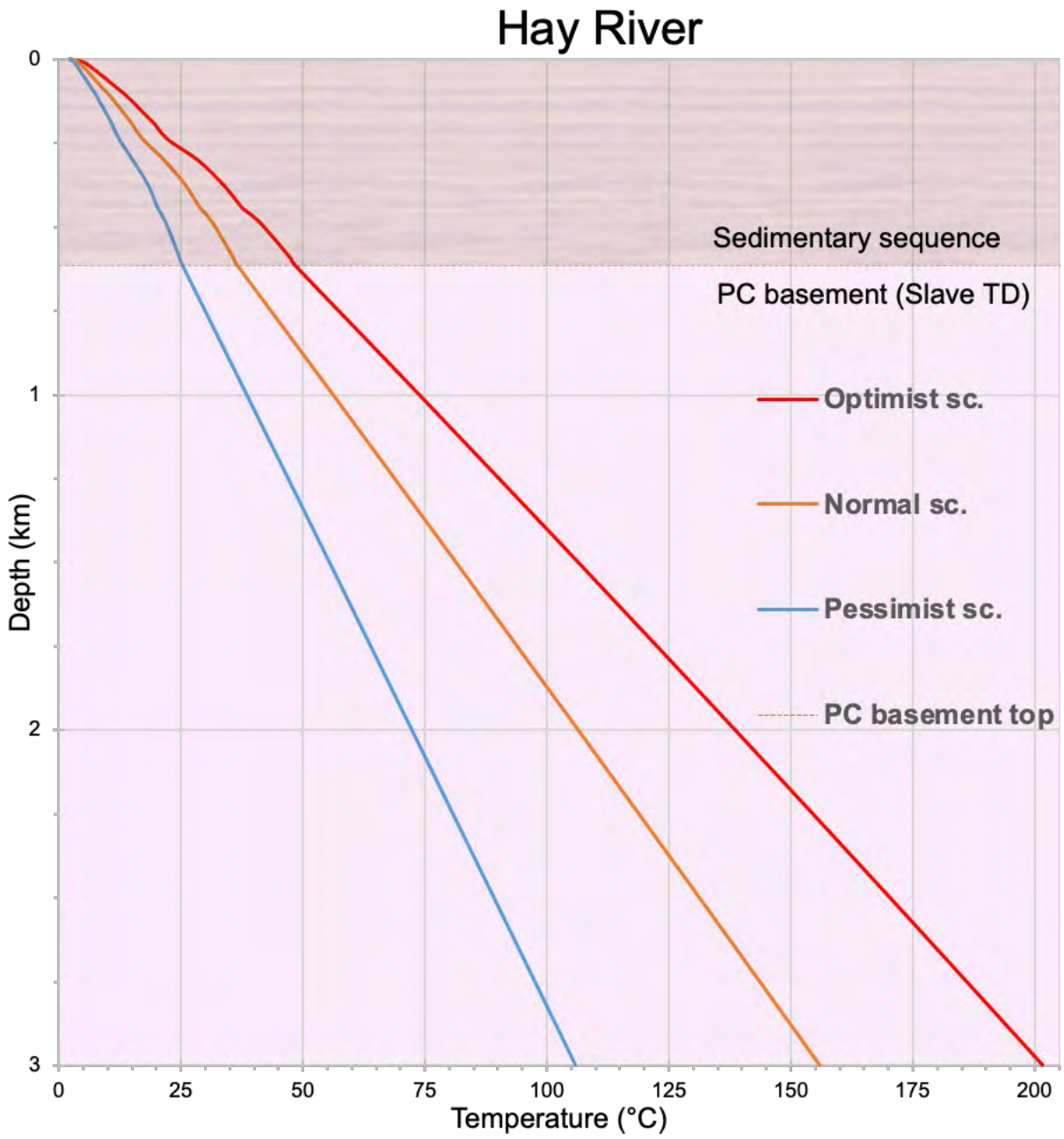

Figure 11: Temperatures at depth until 3 km depth for Hay River, with optimist, normal and pessimist scenarios, considering heat flow uncorrected for paleoclimates.

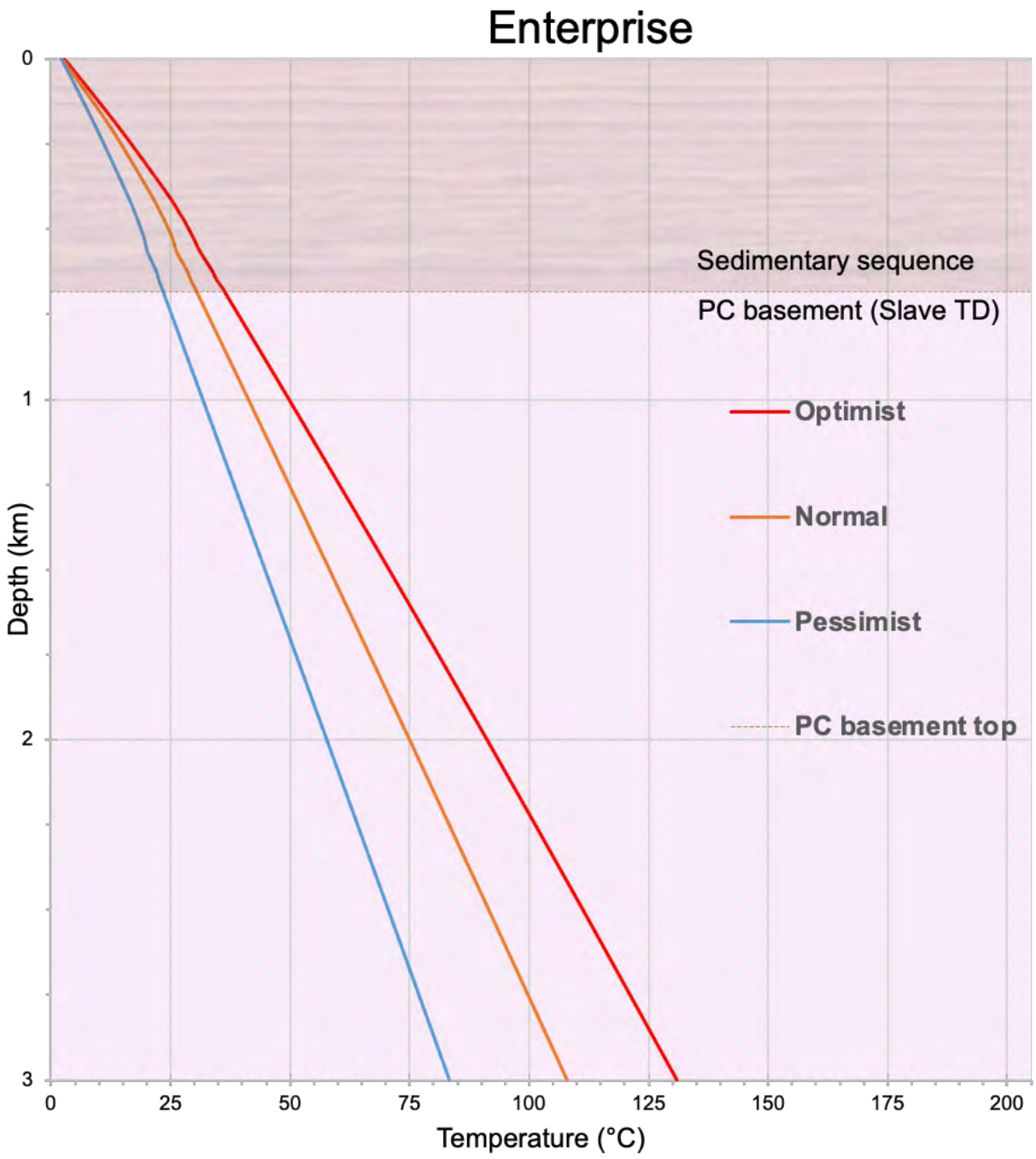

Figure 12: Temperatures at depth until 3 km depth for Enterprise, with optimist, normal and pessimist scenarios, considering heat flow uncorrected for paleoclimates.

4.4 Temperature in the Basement until 10 km depth

For the sake of clarity, only the normal scenario is considered for the temperature calculated until 10 km depth below each community (Figure 13). The calculated temperatures represent an estimate of the equilibrium temperature, considering heat flow corrected for paleoclimates.

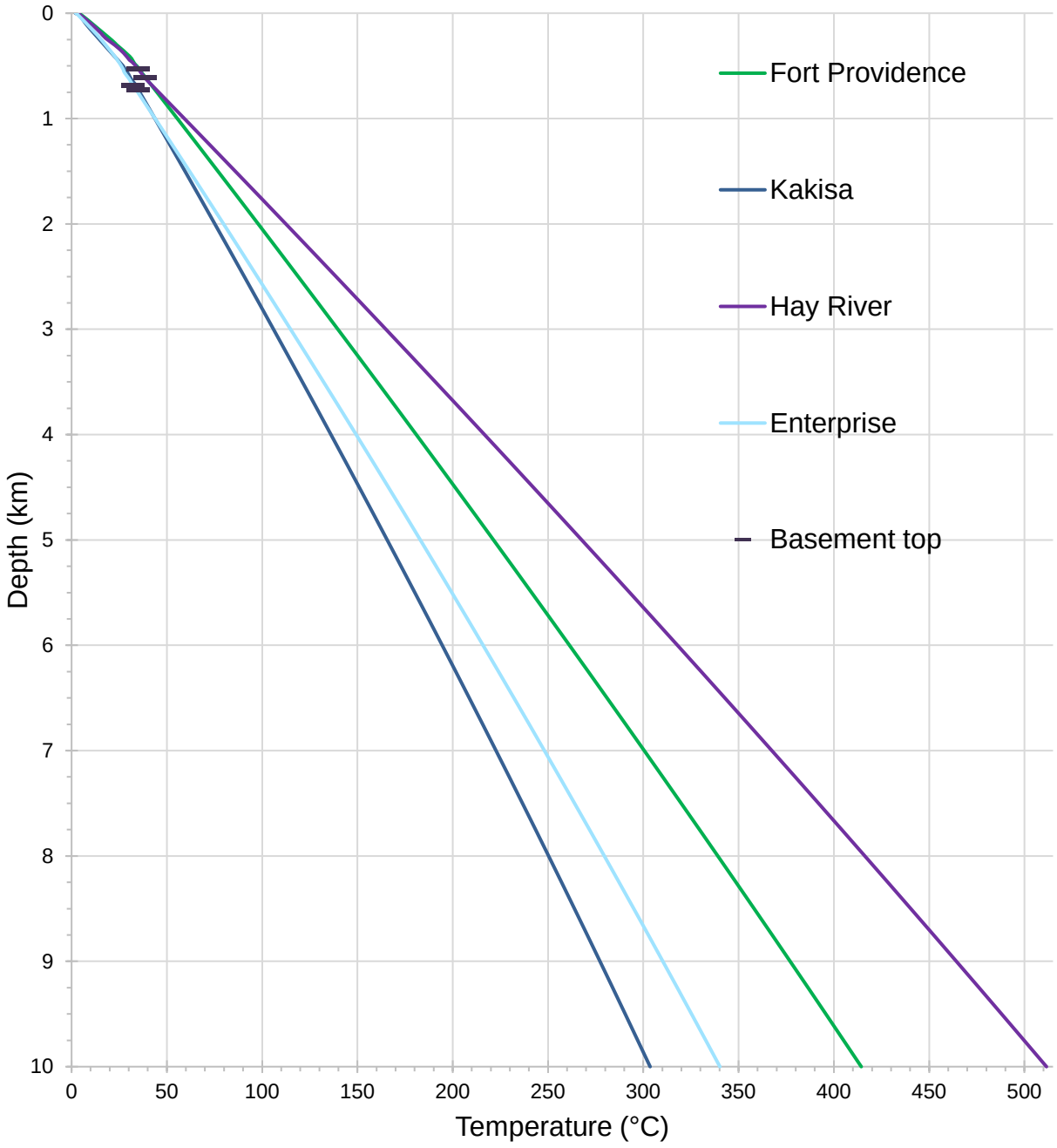

Figure 13: Temperature until 10 km depth, with the normal scenario, considering equilibrium heat flow, corrected from paleoclimate effects. Each community is represented by a distinct coloured line.

5. Discussion

This basement thermal property assessment allowed to predict temperature at depth below the sedimentary rock cover for the NWT communities of Hay River, Fort Providence, Enterprise, and Kakisa. The new thermal properties data present in this study will be publicly available and can be used for additional subsurface studies in other regions of the WCSB and the Slave Province.

This research builds upon previous studies that focused on the shallow sedimentary sequence (<730 m) (Rajaobelison et al., 2024, In press) by extending the assessment to the deeper Precambrian basement, further demonstrating how oil and gas exploration data can be used for early stage deep geothermal resource assessment.

Thermal conductivity values significantly influence the geothermal gradient. Precambrian basement rocks exhibit higher thermal conductivity than sedimentary rocks, resulting in a slower temperature increase within the basement. In contrast, the sedimentary sequence, with its lower effective thermal conductivity, act as a 'thermal blanket', trapping heat and causing a higher temperature increase with depth.

Our findings indicate that the highest geothermal gradient is expected below Hay River, with temperature increasing more rapidly than in other communities. Conversely, Kakisa has the lowest geothermal gradient, followed closely by Enterprise. The variation in subsurface temperature among these communities, despite their proximity within a 120 km radius, highlights the importance of localized resource assessments rather than relying on extrapolated values from a regional scale assessment.

Temperature at depth for Hay River and Fort Providence reveal a similar profile within the sedimentary sequence, but is significantly different in the Precambrian basement. This disparity can be explained by a lower thermal conductivity and a higher heat flux inside the Slave Craton for Hay River. These factors contribute to a faster increase in temperatures at depth. Similar observations can be made for Enterprise and Kakisa.

Although we would have expected similar temperature due to their proximity, Hay River and Enterprise (approximately 30 km apart and part of the same tectonic domain) show a notable temperature difference at depth. This discrepancy is primarily due to the different heat flow values used in calculations and originating from well temperature measurements that can enclose a high uncertainty (Rajaobelison et al., 2024).

Upon comparing our findings with those of other studies (Grasby et al., 2011; Majorowicz & Grasby, 2010b, 2010a), notable disparities in temperature estimations emerge, particularly in Hay River. Majorowicz & Grasby (2010b) estimate a temperature of approximately 85 °C at 3 km and around 250 °C at 10 km for Hay River. On the other hand, we estimate temperatures slightly above 150 °C at 3 km and 500 °C at 10 km. Moreover, Grasby et al. (2011) report a depth of 3.5 km to reach 150 °C in that region. Also, Majorowicz & Grasby (2010a) estimate a temperature slightly below 350 °C at 10 km for the community locations. However, the temperatures we calculated at depth in Hay River and Fort Providence are much higher than those reported in previous studies. Enterprise and Kakisa values are also higher albeit slightly lower than the other two communities. This is mostly attributed to the utilization of a larger heat flow estimate in our calculations. For example, when using a lower heat flow value, similar to these studies, 95 ± 5 mW m^{-2}, our results align more closely with those of previous studies.

Input temperature is the most influential factor in the estimation of the geothermal gradient and heat flow; therefore, its variability directly affects the results. Noisy or poor-quality data can significantly bias geothermal gradient assessments. The reliability and accuracy of temperature measurements can be influenced by factors such as the method of measurement, quality, depth, season, and the age of the data, as discussed by Majorowicz et al. (1999, 2014b). In this region, the availability of high-quality thermal data is limited, with most drilling reports dating from the 1960s to the 1980s. Also, wells are limited in depth, with only four boreholes exceeding 1000 m and situated at a reasonable distance (<50 km) from the communities. Reconsidering the input values, particularly for unusually high heat flows such as those observed in Hay River and Fort Providence, which may have been overestimated, could lead to more consistent results between communities and with literature values.

Another limitation of the study is that the 1D analytical temperature models do not account for expected decreases in thermal conductivity with increasing temperature and pressure at depth (Clauser, 2011; J. Majorowicz, Nieuwenhuis, et al., 2014). These factors could influence the values obtained by increasing our temperature values at greater depths, especially those predicted to 10 km. Additionally, our results are theoretical predictions that should be interpreted with caution. They heavily depend on the inputs used in calculations, and the uncertainty increases with depth, as highlighted by the optimistic and pessimistic scenarios and in comparison to the literature.

This study is not intended as a regional or large-scale analysis and does not evaluate three-dimensional resource distribution. It does not focus on potential aquifers or consider structural geology impacts, such as faults and fractured patterns on localized resources.

However, one of the strengths of our study is the use of representative thermal properties for the geological formations under the communities. These were obtained from laboratory measurements on the same geological formation rocks that we expect to be found below the communities, rather than from broad literature values, as was done in previous studies. Furthermore, our localized approach ensures relevance to community end users, making our findings directly applicable and reliable for the community's geothermal resource assessment.

Geothermal resources within the sedimentary sequence (<37 °C) could be used for heating applications, most likely requiring the use of a heat pump system. However, for applications requiring temperatures above 40 °C, which can support a wide range of geothermal energy uses, drilling into the Precambrian basement would be necessary to reach such temperature. Specific applications, such as electricity production, necessitate temperatures above 80°C, below which it becomes uneconomical. However, a high temperature above 150°C is more commonly employed for power generation (Ahmadi et al., 2020). Based on our 1D models, such temperature is expected at depths about 1500 m and 3000 m for the community of Hay River and around 2250 m and 4500 m for Kakisa. Low permeability crystalline rocks are expected at such depth, which would either require EGS or DBHE.

While our results indicate a great geothermal potential for the South Slave communities, with high temperature at depth, these are theoretical estimates. This potential can only be validated through exploration drilling to confirm the geothermal potential.

6. Conclusions

This study provides critical insights into the thermal properties of the Precambrian basement rocks beneath the sedimentary basin in the South Slave communities of the NWT. It was combined with previous temperature assessment in the sedimentary rock cover.

The calculated temperature profiles highlight the importance of local resource assessments for the community's end user, from which geothermal development could potentially contribute to energy independence, reduce greenhouse gas emissions, and promote regional economic development.

The temperature profiles presented in this work can be used as input for future work, focusing on numerical simulations aimed at evaluating the efficiency of heat extraction for each community considering DBHE. Such systems, when coupled with heat pumps, present a promising technology for heating applications in the South Slave Region. Numerical modelling will further assist in defining the thermal output of these systems in locations without deep aquifers. These efforts will provide important information for future decision-making about energy supply in that region as well as any further geoscience study in the area.

Acknowledgement

We would like to thank the Office of the Regulator of Oil and Gas Operations and the Geological Survey of Canada Core Repository in Calgary for providing access to the drilling cores and assistance with sampling, Northwest Territories Geological Survey (NTGS) staff to provide access and assistance with archive samples and Dr. Jacek Majorowicz and Rod Smith for constructive discussions. This research was funded by a scholarship from the Natural Sciences and Engineering Research Council of Canada to the first author as well as research grants given to INRS under the Northern Scientific Training Program, GEM-GeoNorth program of Natural Resources Canada and the NTGS. The Centre d'études nordiques is also acknowledged for help with logistics.

REFERENCES

Ahmadi, A., Assad, M. E. H., Jamali, D. H., Kumar, R., Li, Z. X., Salameh, T., Al-Shabi, M., & Ehyaei, M. A. (2020). Applications of geothermal organic Rankine Cycle for electricity production. *Journal of Cleaner Production*, *274*, 122950. https://doi.org/10.1016/j.jclepro.2020.122950

Bachu, S. (1993). Basement heat flow in the Western Canada Sedimentary Basin. *Tectonophysics*, *222*(1), 119–133. https://doi.org/10.1016/0040-1951(93)90194-O

Bédard, K., Comeau, F.-A., Millet, E., Raymond, J., Malo, M., & Gloaguen, E. (2016). *Évaluation des ressources géothermiques du bassin des Basses-Terres du Saint-Laurent.* (Rapport de recherche 1659; Issue R1659). Institut national de la recherche scientifique, Centre Eau Terre Environnement. https://espace.inrs.ca/id/eprint/4845/

Canada Energy Regulator & Government of Canada. (2023, November 28). *Market Snapshot: Explaining the high cost of power in northern Canada* [Governmental website]. Canada Energy Regulator. https://www.cer-rec.gc.ca/en/data-analysis/energy-markets/market-snapshots/2017/market-snapshot-explaining-high-cost-power-in-northern-canada.html

Chapelet, M. (2022). *Chapelet, M. (2022). Évaluation du potentiel des anomalies géothermiques du bassin sédimentaire des basses-terres du Saint-Laurent (Québec, Canada)* [Master's thesis, Institut national de la recherche scientifique]. https://www.proquest.com/openview/3ffdbacd59fcde3cdc69e7c98d58fd28/1?pq-origsite=gscholar&cbl=18750&diss=y

Clauser, C. (2011). Thermal Storage and Transport Properties of Rocks, I: Heat Capacity and Latent Heat. In H. K. Gupta (Ed.), *Encyclopedia of Solid Earth Geophysics* (pp. 1423–1431). Springer Netherlands. https://doi.org/10.1007/978-90-481-8702-7_238

EBA Engineering Consultants Ltd. (2010). *Geothermal Favourability Map Northwest Territories Report* (Governmental Report Y22101146; Northwest Territories Environment and Natural Resources., pp. 1–59). Northwest Territories Environment and Natural Resources. https://www.enr.gov.nt.ca/sites/enr/files/reports/geothermal_favorability_report.pdf

Government of Canada & Environment and Natural Resources. (2024). *Historical Climate Data* [Governemental Website]. Weather, Climate and Hazard. https://climate.weather.gc.ca/

Government of Northwest Territories. (2018). *2030 Energy Strategy* (Governmental Report 7272; p. 46). Government of Northwest Territories. https://www.inf.gov.nt.ca/en/services/energy/2030-energy-strategy

Grasby, S. E., Allen, D. M., Bell, S., Chen, Z., Ferguson, G., Jessop, A., Kelman, M., Ko, M., Majorowicz, J., Moore, M., Raymond, J., & Therrien, R. (2011). *Geothermal energy resource potential of Canada* (Open File 6914; p. 322). Geological Survey of Canada. https://doi.org/10.4095/291488

Gray, A. D., Majorowicz, J., & Unsworth, M. (2012). Investigation of the geothermal state of sedimentary basins using oil industry thermal data: Case study from Northern Alberta exhibiting the need to systematically remove biased data. *Journal of Geophysics and Engineering*, *9*(5), 534–548. https://doi.org/10.1088/1742-2132/9/5/534

Jessop, A. M. (Ed.). (1990). Chapter 3—Analysis and Correction of Heat Flow on Land. In *Developments in Solid Earth Geophysics* (Vol. 17, pp. 57–85). Elsevier. https://doi.org/10.1016/B978-0-444-88309-4.50007-5

Jessop, A. M. (1992). Thermal input from the basement of the Western Canada Sedimentary Basin. *Bulletin of Canadian Petroleum Geology*, *40*(3), 198–206. https://doi.org/10.35767/gscpgbull.40.3.198

Majorowicz, J. (1996). Anomalous heat flow regime in the Western margin of the North American Craton, Canada. *Journal of Geodynamics*, *21*(2), 123–140. https://doi.org/10.1016/0264-3707(95)00020-2

Majorowicz, J. A. (2018). Heat flow–heat production relationship not found: What drives heat flow variability of the Western Canadian foreland basin? *International Journal of Earth Sciences*, *107*(1), 5–18. https://doi.org/10.1007/s00531-016-1352-x

Majorowicz, J. A., Garven, G., Jessop, A., & Jessop, C. (1999). *Present Heat Flow Along a Profile Across the Western Canada Sedimentary Basin: The Extent of Hydrodynamic Influence* (A. Förster & D. F. Merriam, Eds.; pp. 61–79). Springer US. https://doi.org/10.1007/978-1-4615-4751-8_3

Majorowicz, J. A., & Jessop, A. M. (1981). Regional heat flow patterns in the Western Canadian Sedimentary Basin. *Tectonophysics*, *74*(3), 209–238. https://doi.org/10.1016/0040-1951(81)90191-8

Majorowicz, J., Chan, J., Crowell, J., Gosnold, W., Heaman, L. M., Kück, J., Nieuwenhuis, G., Schmitt, D. R., Unsworth, M., Walsh, N., & Weides, S. (2014). The first deep heat flow determination in crystalline basement rocks beneath the Western Canadian Sedimentary Basin. *Geophysical Journal International*, *197*(2), 731–747. Geophysical Journal International. https://doi.org/10.1093/gji/ggu065

Majorowicz, J., Gosnold, W., Gray, A., Safanda, J., Klenner, R., & Unsworth, M. (2012). Implications of Post-Glacial Warming for Northern Alberta Heat Flow—Correcting for the Underestimate of the Geothermal Potential. In *GRC Transactions* (2012th ed., Vol. 36, pp. 693–698).

Majorowicz, J., & Grasby, S. E. (2010a). Heat flow, depth–temperature variations and stored thermal energy for enhanced geothermal systems in Canada. *Journal of Geophysics and Engineering*, *7*(3), 232–241. https://doi.org/10.1088/1742-2132/7/3/002

Majorowicz, J., & Grasby, S. E. (2010b). High Potential Regions for Enhanced Geothermal Systems in Canada. *Natural Resources Research*, *19*(3), 177–188. https://doi.org/10.1007/s11053-010-9119-8

Majorowicz, J., Nieuwenhuis, G., Unsworth, M., Phillips, J., & Verveda, R. (2014). High Temperatures Predicted in the Granitic Basement of Northwest Alberta—An Assessment of the EGS Energy Potential. *Thirty-Ninth Workshop on Geothermal Reservoir Engineering*, 12.

Majorowicz, J., & Weides, S. (2014). Large Scale Geothermal High in the Westernmost North American Covered Craton–Can Heat Flow Vs. Basement Heat Production Be a Reliable Tool in Predicting Deep EGS Geothermal Resource? *Thirty-Ninth Workshop on Geothermal Reservoir Engineering*, 9.

Ootes, L., Davis, W. J., Jackson, V. A., & Van Breemen, O. (2015). Chronostratigraphy of the Hottah terrane and Great Bear magmatic zone of Wopmay Orogen, Canada, and exploration of a terrane translation model. *Canadian Journal of Earth Sciences*, *52*(12), 1062–1092. https://doi.org/10.1139/cjes-2015-0026

OROGO. (2024). *Well Status* [Well list; Excel sheet]. OROGO. https://www.orogo.gov.nt.ca/en/resources-0

Ouzzane, M., Eslami-Nejad, P., Badache, M., & Aidoun, Z. (2015). New correlations for the prediction of the undisturbed ground temperature. *Geothermics*, *53*, 379–384. https://doi.org/10.1016/j.geothermics.2014.08.001

Perry, H. K. C., Rosieanu, C., Mareschal, J.-C., & Jaupart, C. (2010). Thermal regime of the lithosphere in the Canadian Shield. *Canadian Journal of Earth Sciences*, *47*, 389–408. https://doi.org/10.1139/E09-059

Popov, Y., Lippmann, E., & Rauen, A. (2023). *TCS-Manual. Thermal conductivity (TC) and thermal diffusivity (TD) Scanner. Version 15.11.2023.* https://www.schwartech.de/index_en.html#/tcs_en

Rajaobelison, M., Thibault, M., Comeau, F.-A., Raymond, J., Smejkal, E. J., & Terlaky, V. (2024). Thermostratigraphic and Heat Flow Assessment of the South Slave Region in the Northwest Territories, Canada. *Energies*, *17*(16), Article 16. https://doi.org/10.3390/en17164165

Rajaobelison, M., Thibault, M., Comeau, F.-A., Raymond, J., & Terlaky, V. (In press). *Laboratory analyses on split core samples from wells to assess the geothermal potential of the South Slave Region, Northwest Territories, Canada* (Open Report 2023–015). Institut national de la recherche scientifique & Northwest Territories Geological Survey.

Sass, I., & Götz, A. E. (2012). Geothermal reservoir characterization: A thermofacies concept. *Terra Nova*, *24*(2), 142–147. https://doi.org/10.1111/j.1365-3121.2011.01048.x

Sass, J. H., Lachenbruch, A. H., Moses Jr., T. H., & Morgan, P. (1992). Heat flow from a scientific research well at Cajon Pass, California. *Journal of Geophysical Research: Solid Earth*, *97*(B4), 5017–5030. https://doi.org/10.1029/91JB01504

Stein, C. A. (1995). Heat Flow of the Earth. In T. J. Ahrens (Ed.), *Global earth physics: A handbook of physical constants* (pp. 144–158). American Geophysical Union. https://doi.org/10.1029/RF001p0144

Geothermal Resource and Transmission Planning in the Western United States:

A Review of Recent Results and a Roadmap for Continued Expansion

Paul Thomsen and Kayla Dowty

Ormat Technologies

Keywords

Geothermal, electric power, resource planning, transmission planning, decarbonization, planning assumptions and models, regional coordination, Western U.S. states

ABSTRACT

Long-term electric power resource planning is a primary mechanism for driving geothermal procurement in the western United States. At the same time, transmission expansion is required to further unlock the region's abundant geothermal resources. In a prior paper, Thomsen (2021) described the regulatory processes and analyzed geothermal selection across various resource plans and other resource procurement decisions issued from 2019 to mid-2021. A key finding was that geothermal selection was highly variable from year to year, and, among other things, the paper recommended several revisions in resource modeling and proposed enhanced regional coordination. Since the paper's publication, the geothermal sector has received significant boosts from 2021 and 2023 procurement decisions by the California Public Utilities Commission (CPUC), which have resulted in new projects and contracts, and California planning scenarios which include large capacities of geothermal over the next 10-20 years. With a few exceptions, the rest of the West has been less proactive in supporting the geothermal industry, but there are new developments which reflect increased federal and state support (as well as a new interest in corporate procurement). This paper updates the prior findings, evaluates whether the recommendations have been addressed, and provides suggestions for further resource and transmission planning improvements. In addition, the paper proposes development of a planning roadmap to support high geothermal scenarios across the region.

1. Introduction

Resource planning is a primary input into clean energy procurement decisions by load-serving entities (LSEs) in Western U.S. states and transmission planning to support rapidly changing resource portfolios. Almost all the larger LSEs in the region conduct integrated resource planning (IRP), and in some cases, state agencies and regional entities also conduct such planning. These resource plans guide subsequent resource procurements and transmission expansion options. This

paper elaborates on two earlier papers,[1] which are starting points for an updated survey of how geothermal is evaluated in resource planning and extended to include some developments in transmission planning.

Geothermal energy has received significant commercial interest in the past 2-3 years due in large part to the California Public Utilities Commission's (CPUC) 2021 and 2023 Mid-Term Reliability (MTR) decisions requiring buyers to procure geothermal or other clean firm energy resources (CPUC 2023a, 2021). These decisions actually reversed the CPUC's lack of consistent support for geothermal in its prior planning processes, and led to new geothermal contracting by almost all LSEs in California and interest in more significant geothermal development. There has also been an increase in procurement associated with industry innovation and federal and state government support elsewhere in the region.[2] Overall, this new direction for geothermal energy reflects many of the recommendations that were made in the earlier papers and by the geothermal industry.

Additionally, commercial and industrial customers have a strong interest in geothermal energy seeking clean, firm baseload energy. A common application is for data centers, which typically have relatively firm loads but also some capability to shift load during operations to reduce costs or emissions. Load growth due to these uses is being reflected in utility resource planning. Some corporate customers are also entering directly into clean energy contracts with developers.

Transmission development is required to facilitate any significant growth in regional geothermal development. Since geothermal resources must be located at particular sites, transmission availability can limit geothermal development—several utility resource plans reviewed in this paper note that further geothermal procurement will require transmission availability. In the western U.S., a number of new transmission lines are being energized over the next few years and others are in advanced planning for operations in the early 2030s. For geothermal development to meet demand, it is necessary to identify specific transmission upgrades and be ready to utilize the new transmission capability before it is contracted for other resources. The geothermal industry needs to create its preferred long-term transmission plan for the West; otherwise, geothermal access to transmission could be an afterthought of the planning for other resources.

2. Regulatory Framework and Methods for Resource Planning

IRP is conducted by almost all LSEs in the western U.S., with different types of regulatory oversight. Since the last rounds of IRPs in the western states reviewed in the prior paper (Thomsen 2021), most of the planning entities have continued to conduct resource planning using variants of the same methodologies. As discussed below, California seems to be the state in the region with the most changes in the past few years, both in terms of state policies and planning methods as they pertain to geothermal energy.

[1] These include Thomsen's (2021) survey of geothermal in Western resource planning, which provided a framework for analysis of trends and identified the need for certain planning improvements, while in an earlier paper, Thomsen (2018) demonstrated how a resource planning model used by the California Public Utilities Commission (CPUC) could be tested for geothermal selection.

[2] See, e.g., the Department of Energy's (DOE), Pathways to Commercial Liftoff: Next-Generation Geothermal Power (DOE 2024) and the Western Governors' Association (WGA), The Heat Beneath Our Feet (WGA 2023).

No standard method or set of analytical tools is used in resource planning, making comparative analysis of trends in geothermal selection more difficult (Thomsen 2021, Warren *et al*., 2021). Additionally, the ongoing changes in state clean energy policies and programs, and in utility strategic objectives, have required almost continuous adaptation of both methods and tools. This has resulted historically in variations in geothermal selection in the planning studies reviewed in the prior surveys and, to some degree, this continues to the present day.

In our observation, the challenge is not so much in how geothermal is represented operationally in planning models since it is typically analyzed relatively simply as a flat (or firm) block of power, possibly with some shaping throughout the year and by the time of day. Usually, geothermal is assigned a capacity factor[3] of 80-90% and a capacity value[4] in that same range; actual assumptions used by different planners are discussed below. Whether these models select geothermal as a desirable resource has to do with various factors specific to geothermal, including the estimated regional resource potential for geothermal and geothermal cost assumptions and operational attributes, but as importantly, how the costs, profiles and operations of the competing resources, wind (onshore and offshore) and solar, and more recently batteries (stand-alone or hybrid), are captured, as well as their assumed capacity value. Most resource planners have not yet modeled geothermal power as a dispatchable generator (Warren *et al*., 2021). However, operational flexibility was examined in some studies discussed below, and has been incorporated into some recent geothermal contracts.

The following sections turn to specific results from each region's resource and transmission planning processes, which help illustrate some of the findings on models and methods.

3. California

Over the past few years, California has been the leading state for geothermal procurement, building on the MTR orders by the CPUC to support reliability in response to the 2020 blackouts and subsequent scarcity events during peak net load hours. These orders have re-set the resource planning process, setting a floor but not a ceiling for geothermal procurement. At the same time, subsequent long-term resource planning simulations for the state suggest that geothermal selection could dramatically increase over the coming decade if the geothermal industry can deliver at forecasted costs.

[3] Capacity factor is the percentage (%) of total possible output based on nameplate capacity (MW), typically calculated annually or monthly. Hence, a 100 MW generator which operates at an average of 90 MW production for a year has a capacity factor of 90%.

[4] Capacity value refers to the capacity (MW) or the percentage of capacity (%) which is available during the subset of peak load or net peak load hours being evaluated for resource adequacy. Hence, if a 100 MW generator is expected to operate at 75 MW during those hours (as identified by the planning entity), its capacity value is 75 MW or 75%. Capacity value thus typically focuses on a subset of hours, and may take into account hourly variability during those hours and expected forced outage rates, whereas capacity factor is an average of production in all hours.

California has the most resource plans running in parallel of all the states in the region, and geothermal is present in all of them.[5] Table 1 lists California's critical resource planning processes and indicates their timing and relationship.

Table 1 – California primary resource planning processes

Resource planning process	Recently Completed	Forthcoming
CPUC Integrated Resource Planning proceeding (CPUC and jurisdictional LSEs)	2018-19, 2020-21, 2022-23	2024-25
CPUC Mid-Term Reliability (MTR) procurements	2021, 2023	
Joint state energy agencies - SB 100 decarbonization scenarios	2021	Ongoing process
CPUC resource portfolios for CAISO Transmission Planning Process (TPP)	Annual	Annual
State agency resource portfolios for CAISO 20-Year Transmission Outlook	2022, 2024	2026
Los Angeles Department of Water and Power (LADWP)	2017, 2022, 2023	2025
Other publicly owned utility (POU) integrated resource plans (CEC oversight)	2018-2019, 2023-2024	2028-2029 (every 5 years)

3.1 CPUC Procurements to Address Mid-Term Reliability in the 2020s

Even though the CPUC IRP proceeding pre-dates the CPUC's Mid-Term Reliability (MTR) decisions (CPUC 2021, 2023a), for this survey, we begin with the MTR decisions since these are so influential to geothermal planning and procurement. The MTR decisions corrected the CPUC IRP proceeding's early failures (over the first two planning cycles in 2018 and 2020) to properly value geothermal in resource planning, which caused several years of stagnation in geothermal procurement.[6]

The first MTR procurement decision in 2021 (CPUC 2021), established a target for jurisdictional LSEs to procure 1 GW of geothermal power by 2026-2028.[7] This target was then incorporated and increased in the CPUC's subsequent IRP decision, determining a final 2020 Preferred System Plan (PSP) (also issued in 2021). These decisions were motivated by the heatwaves and blackouts in September 2020 and the strong reliability contribution of geothermal energy, which was not reflected in the prior IRP results. This procurement process has been underway and is reflected in the results shown in the figures and tables below. The CPUC's Supplemental Mid-Term Reliability

[5] In some years, when planning cycles for the CPUC-jurisdictional LSEs and the publicly owned utilities (POUs) roughly coincide (such as 2022-2023) this results in over 100 different studies for individual LSEs and regional entities, such as CAISO. This includes about 70 integrated resource plans for CPUC jurisdictional LSEs and about 20 plans for publicly owned utilities.

[6] Thomsen (2018, 2021) provide many details about why the CPUC IRP proceeding did not select geothermal consistently.

[7] The CPUC 2021 MTR defined the procurement to require 1 GW of “firm resources with zero on-site emissions” with a capacity factor of at least 80% (and hence not subject to use limitations or weather dependence) by 2026 or at latest 2028. The CPUC 2020 IRP final decision explicitly named geothermal.

procurement decision (2023a) then identified a resource planning need for up to 1,863 MW of new geothermal by 2033. Figure 1 below summarizes the results of these two CPUC decisions. The response to the MTR decisions by jurisdictional LSEs was to commit to new geothermal procurement, reversing years of inactivity in the geothermal market.

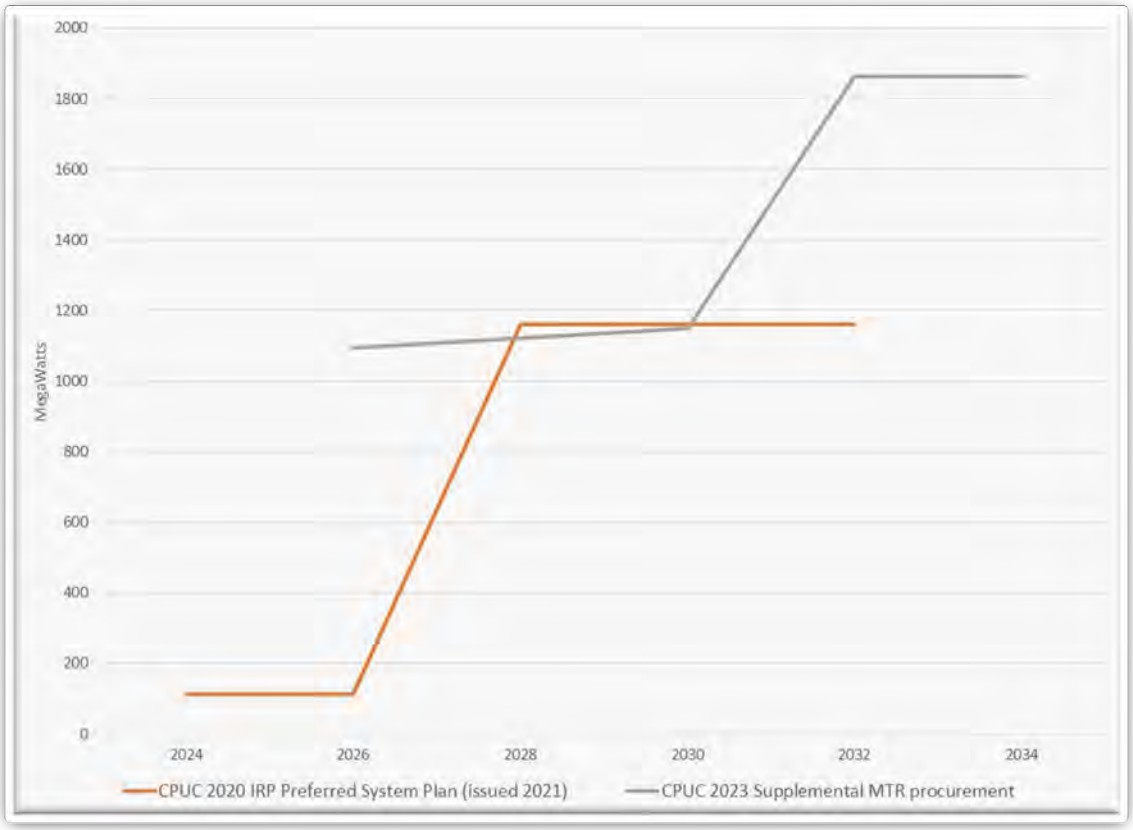

Figure 1: CPUC resource planning and procurement recommendations on geothermal, 2021 and 2023

3.2 CPUC 2022 IRP Results and Trends

The MTR procurement decisions became the baseline for the subsequent IRP cycles. The 2022 IRP PSP (CPUC 2024) increased the geothermal selected in the 2023 MTR and includes 2 GW of new geothermal by 2035 in the core scenario (which targets 25 million metric tons of carbon emissions). This is shown in Figure 2, below.

Although not the preferred case, the 2022 IRP includes a High Gas Retirement Sensitivity Case, which will retire about 16 GW of natural gas plants (including combined heat and power) by 2040. As also shown in Figure 2, in response to the progression of gas retirements, the model builds 4.6 GW of new geothermal by 2035 and up to 5.1 GW by 2045. None of this geothermal is

characterized as EGS, due to the high assumed cost.[8] The CAISO will study the high gas retirement case in its 2024-25 Transmission Planning Process (TPP).

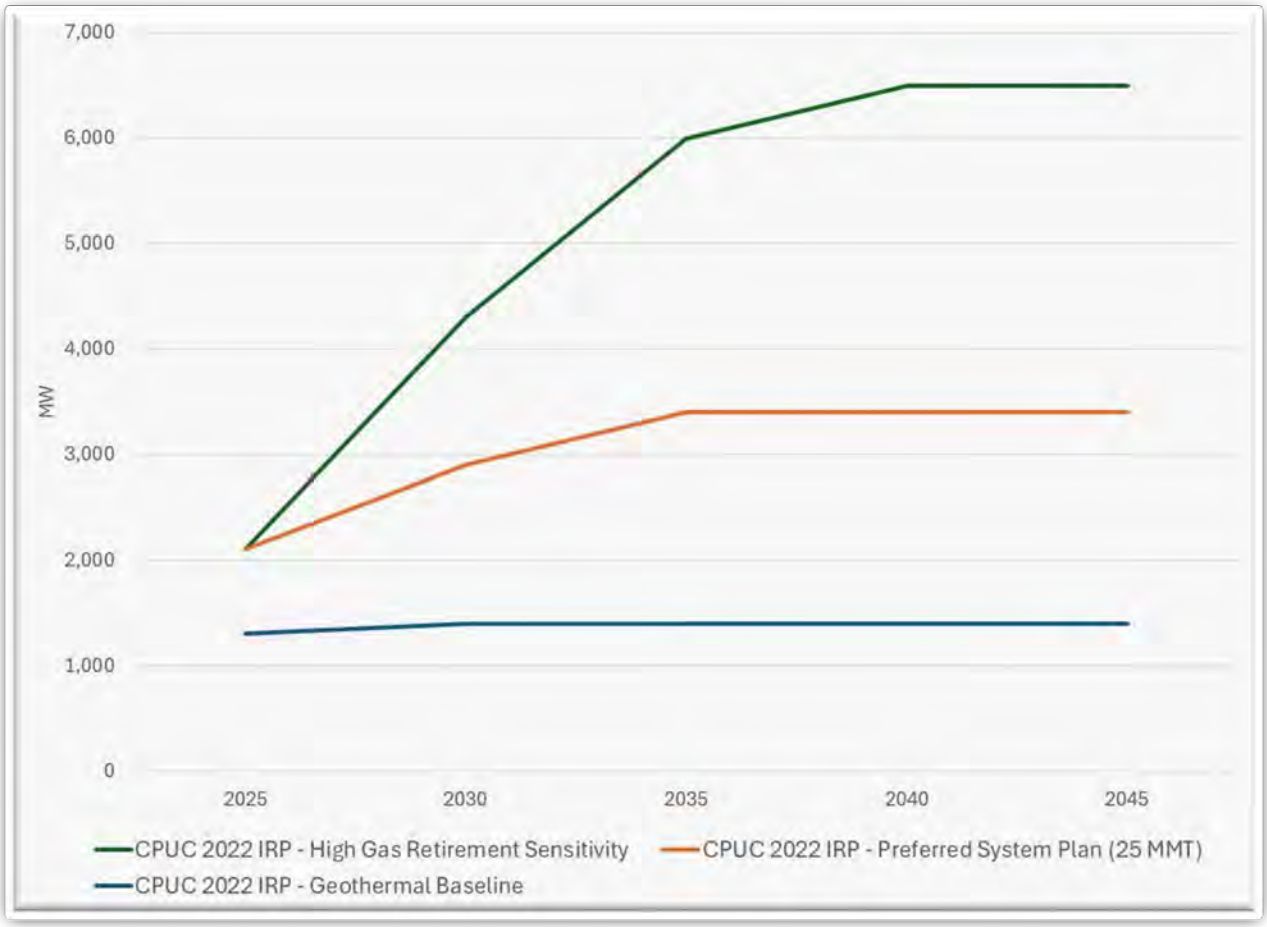

Figure 2: CPUC 2022 IRP selection of geothermal

While the CPUC 2022 IRP portfolios establish the benchmark for associated LSE resource planning and procurement, each LSE can determine an equivalent resource portfolio that suits their needs. Moreover, the LSE can open a procurement to meet CPUC requirements but determine that offers are not cost-effective. Hence, the LSE planning and procurement decisions can be tracked to assess the accuracy of the CPUC planning forecasts.

Table 2 provides data on geothermal selection by some of the larger CPUC-jurisdictional LSEs in their 2020 and 2022 IRPs; we have not tracked all actual procurements. The planning results show that in almost all cases, LSEs selected more geothermal in their 2022 IRPs than in their 2020 IRPs (but in a few cases, lower selection in 2022 reflected procurement concluded since 2020). In

[8] The CPUC is contemplating specific procurement targets for EGS, which will not be finalized prior to publication of this paper.

addition, some LSEs have begun additional planning initiatives to support geothermal development.

Table 2 – Geothermal selection by selected CPUC-jurisdictional LSEs, 2020-2022 IRPs

LSE	Type of LSE	Aggregate geothermal in preferred scenarios (MW)	
		2020 IRP	2022 IRP
Southern California Edison (SCE)	IOU	180	379
Pacific Gas & Electric (PG&E)	IOU	None, existing contracts to expire	Not specified
San Diego Gas & Electric (SDG&E)	IOU	None	42
Clean Power Alliance (CPA)	CCA	175	228
Clean Power SF	CCA	50	49.3
East Bay Community Energy (EBCE)	CCA	78	40
San Diego Community Power (SDCP)	CCA	100	100
Pomona Choice Energy	CCA	0	5.73
San Jose Clean Energy	CCA	0	59
Sonoma Clean Power Authority (SCPA)	CCA	31	85.52

3.3 Geothermal in Resource Planning by the POUs

The California Publicly Owned Utilities (POUs) in southern and northern California include several utilities with long experience with geothermal resources, both through ownership and contracts. They comprise about 20 percent of California load. Each POU conducts an IRP, with oversight by the California Energy Commission (CEC).[9]

3.3.1 Los Angeles Department of Water and Power (LADWP)

LADWP has been a leading buyer of geothermal in the western U.S., and its resource plans in recent years have examined scenarios for significant geothermal expansion. At the same time, similar to some other planning entities, LADWP has issued different results over time, reflecting revised modeling and the availability of new geothermal resources to procure.

Until 2017, LADWP issued an annual IRP, which is now called the *Power Strategic Long-Term Resource Plan*. The annual planning process was suspended for 2-3 years while a very detailed, scenario-based planning study called LA100 was conducted jointly with the National Renewable Energy Laboratory (NREL) and issued in 2021 (Cochran and Denholm, eds., 2021). In 2022, the utility issued a new IRP (LADWP 2022), which took some of the LA100 results into account and then submitted a version of the results to the CEC as its 2023 IRP (LADWP 2023).

[9] The recent IRPs cited in this section can all be found in one location on the CEC website and are not listed in the paper references.

As summarized in Table 3, LADWP planners have typically forecasted the need for around 500 MW of geothermal over the next 10-15 years.[10] As of 2022-23, LADWP has contracts for 223 MW with nine geothermal plants, which is around 10% of annual energy (LADWP 2023). At the same time, the 2022 and 2023 resource plans have reduced the forecast for potential new geothermal compared to the prior studies.[11] Although the discussion isn't clear, the 2023 IRP supply tables suggest that 52 MW of additional geothermal are under consideration as "Planned Utility-Scale Geothermal."

Table 3 – LADWP geothermal portfolios in recent IRPs

IRP year	Existing geothermal capacity in starting year (MW)	Total geothermal capacity in final planning year (MW)
2022, 2023	223 operational + 52 planned	52
2021 (LA100)	230	500 - 1,600
2017	106	445
2016	108	498
2015	69	293

* For 2015-2017, 20 years, for 2022-23, 2045; Sources: Cochran and Denholm, 2021; LADWP 2023, 2022, 2017, 2016, 2015

3.3.2 Other POUs

Table 4 summarizes geothermal results in the other recent POU IRPs, and incorporates the results from their prior IRPs for easy comparison. Similarly to other western resource plans, these POUs have increased the selection and procurement of geothermal energy, typically through the collective procurement under the Southern California Public Power Authority (SCPPA), and similar to other planners, their resource forecasts for geothermal energy are higher in more rapid decarbonization scenarios. It is worth noting that while the POUs are not CPUC-jurisdictional, they are influenced by the CPUC's current emphasis on firm resources to support resource adequacy.[12]

A few results stand out:

- since the 2018-19 IRPs, several POUs have already procured more geothermal than they envisioned over the next 20 years in those prior IRPs (e.g., Pasadena Power and Light, SVP);
- similarly to other LSEs reviewed in this paper, the POUs would have to dramatically increase their resource capacity to achieve clean energy goals;

[10] In its 5 scenarios, the LA 100 study adopted a baseline target for geothermal of around 500 MW, which reflected internal LADWP judgement rather than independent modeling. In addition, the study examined sensitivity cases which accelerated decarbonization and added some constraints on other technologies. Those sensitivity cases resulted in 1,500-1,600 MW of geothermal in the solution, amounting to around 10% of LADWP's peak load.

[11] Unfortunately, the data presentation in these recent IRPs isn't clear. In several figures, geothermal is bundled with biofuels in a category which is called "long-duration renewable capacity."

[12] For example, City of Anaheim's 2023 IRP (pg. 88) observes that "Firm resources refer to geothermal, biomass, biogas, nuclear, gas and coal generation, and are considered preferable under the CPUC reliability evaluations. While APU is not a CPUC-jurisdictional entity, CPUC considerations are considered for potential future impacts to the CAISO Resource Adequacy accounting rules."

- geothermal is selected more often than in the prior submissions, and is almost always selected for full decarbonization scenarios;
- In some cases where geothermal is not selected, planning assumptions may play a role. For example:
    - SVP's 2023 IRP, the quantity of available geothermal is limited to 350 MW by assumptions about the available resource potential;[13]
    - City of Redding's 2024 IRP, very little geothermal is selected, but this may be because the model uses a geothermal price of $109.38/MWh in 2031

In 2021, SMUD issued a 2030 decarbonization plan which was subsequently adopted as a 2022 update to its prior IRP. This plan aims to develop portfolios which could achieve decarbonization on an accelerated time-frame, by 2030. This plan selects 100-220 MW of geothermal, out of a total 6,400 MW in the 2030 clean energy portfolio.

City of Anaheim's 2023 IRP Update only selects new geothermal in its Zero Emissions Portfolio (with procurement beginning in 2025), where it ultimately comprises 26% of total capacity, but does not select geothermal in its other higher carbon portfolios.

Table 4 – Geothermal selection in selected California publicly-owned utilities (POUs) resource plans, 2018-2024

POU IRP	Planning scenarios for geothermal
City of Anaheim	**2023 IRP** – Twenty year forecast. Zero Emission Portfolio – 100 MW geothermal (775 MW new resources), Reliability Portfolio – no geothermal (575 MW new resources); RNG Portfolio – no geothermal (475 MW new resources) (currently 39 MW of geothermal)
	2018 IRP – Small adjustments to existing geothermal contracts
City of Redding	**2024 IRP** – Three major scenarios - Low "Base Case" (current portfolio, does not meet mandates), Mid "Net-Zero Carbon 2045" (meets mandates and targets), High "100% Zero Carbon 2045" (exceeds mandates and targets). Geothermal was only selected in a sensitivity case of the Net-Zero scenario, requiring resource diversity, under which 25 MW were selected in the late 2030s. Model uses a very high cost of geothermal, beginning at $109.38/MWh in 2031. Final Preferred Plan maintains gas generation and adds 315 MW of solar and 55 MW of 8-hour batteries.
	2019 IRP – Geothermal not specifically evaluated
Pasadena Power and Light	**2024 IRP** – Scenario 1: 100% Carbon-Free by 2030 (No Limit on Internal Resources) – 46 MW of geothermal by 2040 under existing contracts beginning in 2027, no "new" geothermal; Scenario 2: 100% Carbon-Free by 2030 – Maximum Limit on Internal Resources – 10-20 MW of new geothermal in 2030s; Scenario 3: 100% Carbon-Free by 2030 (Maximum Limit on Internal Resources and Doubled Distributed Resources) – 10-20 MW of new geothermal in 2030s; plan assumes that geothermal prices in 2027 will be in the range of $70.00/MWh – $110.00/MWh. Current resource portfolio is around 700 MW, clean energy scenarios need up to 1,500 MW by 2040.

[13] SVP observes that "… the CPUC Mid-Term Reliability order requires CPUC-jurisdictional LSEs to procure approximately 1,000 MW long lead-time clean firm resources by 2028, and geothermal is one of the best available candidates to meet that order. An assumption of this IRP is that SVP may not be able to procure that 1,000 MW tranche. SVP would then be limited to a maximum of about 350 MW, which is approximately 15% of the remaining potential. The three scenarios in this IRP build to, or slightly below that limit."

Table 4 – Geothermal selection in selected California publicly-owned utilities (POUs) resource plans, 2018-2024

POU IRP	Planning scenarios for geothermal
	2018 IRP – Multiple scenarios; existing geothermal contracts to expire in most scenarios, but considers 15 MW of additional geothermal in some scenarios for purposes of diversification, with online dates in 2023, 2033 and 2038
Sacramento Public Utilities District (SMUD)	**2030 Zero Carbon Plan (2021)** – To achieve a zero carbon power system by 2030, SMUD would accelerate procurement of geothermal to achieve 100 to 200 MW (currently 52 MW)
	2019 Resource Planning Report - Resource plan estimates 650 MW of geothermal resource potential in WECC. New geothermal in addition to 51 MW of existing geothermal capacity under contract is currently not anticipated until after 2030, but may be reconsidered if baseload power needs change.
Silicon Valley Power (SVP)	**2023 IRP** – Available new geothermal to SVP is capped at 347 MW in 2028. By 2035, "Scenario 1: Base SB 100" – 290 MW of geothermal, out of ~2.5 GW total capacity; "Scenario 2: Accelerated SB 100" – 330 MW of geothermal out of ~2.7 GW; Scenario 3: Zero Emissions with Emerging Technology – 350 MW of geothermal out of ~2.5 GW; Additional sensitivity case on "Geothermal Limitations and Hydrogen Challenges" which limits new geothermal to 50 MW in 2028. (SVP is currently contracted for 58.4 MW of geothermal in operations; 70 MW planned to be available in 2025-2027, increased to 100 MW by 2036)
	2019 IRP – Decline forecast in geothermal production by about 20% from 2020 to 2030 (from 350 GWh to 282 GWh)

3.4 California SB 100 Modeling

California Senate Bill (SB) 100 (2018) committed the state to achieve electricity decarbonization by 2045. In addition, the legislation required statewide planning studies, the first of which was released in 2021 (CEC, CPUC, CARB 2021), and introduced the concept of geothermal as one type of "zero-carbon firm resources."[14] The second phase of this modeling is currently underway (CEC 2023). In addition, the study results are being used to inform other planning processes, such as the CAISO's 20-Year Transmission Outlook discussed below, which requires the geothermal industry to remain involved in scenario development.

3.5 Geothermal in CAISO Transmission Planning

CAISO conducts regional transmission planning to support the CPUC-jurisdictional LSEs and the POUs located in its footprint. Each year since 2021, the CPUC selects a resource portfolio from its IRP proceeding to recommend to the CAISO for its annual Transmission Planning Process (TPP), a 10-year plan. Over the past few years, the geothermal selection has fluctuated, reflecting some of the evolution of the IRP modeling noted above. For the CAISO 2023-2024 TPP, the CPUC

[14] Thomsen (2021) provided a review of the results of the first SB 100 study mentioned above, which will not be extensively repeated here. The study included the analysis of "zero-carbon firm resources," for which geothermal was one eligible technology, priced at $60/MWh, which was selected at 15-20 GW in sensitivity cases. In addition, while the model didn't select much geothermal priced at $85/MWh for its core scenarios, it did select up to 2.3 GW of geothermal at this price in accelerated decarbonization scenarios.

recommended two 2035 scenarios: a Base Portfolio, which included 2,037 MW of geothermal, and an Offshore Wind sensitivity case, which included 1,149 MW of geothermal.

The CAISO 20-Year Transmission Outlook was started in 2021 to complement the state's SB 100 resource planning discussed above. The first report was released in 2022 (CAISO 2022) and the second version in 2024 (CAISO 2024). For the first report, the core "Starting Point scenario" includes 2.3 GW of geothermal, which the agencies adopted from the first SB 100 report (CEC, CPUC, CARB 2021), most located in the Imperial transmission zone and some in southern Nevada.[15] The subsequent 20-Year Transmission Outlook study, developed over 2023-2024, used the same geothermal assumptions but increased the planning horizon to 2045 and also included a 5 GW allocation for "generic clean firm/long-duration energy storage," a category for which geothermal would be eligible. The key observation about the CAISO's latest 20-Year Outlook is that there is no explicit transmission planning for geothermal outside the identified zones, but some of the other new inter-regional transmission lines could facilitate geothermal development.[16] The geothermal industry needs to continue to inform this long-term transmission planning process based on a collective expectation about the transmission needed to meet and exceed the 2.3 GW of new geothermal which the California state agencies are planning towards.

3.6 Conclusions About California

Over the last few years, California has set the pace for geothermal selection in resource planning and procurement. This was due primarily to policy decisions to authorize the 2021 and 2023 MTR geothermal procurements. This approach has had the benefit of stabilizing the geothermal market and stimulating geothermal contracting. It also provided the geothermal industry with a development path to much higher potential geothermal procurement, which is forecast for California's scenarios with more rapid decarbonization. The state agencies have converged on a forecast of at least 2.3 GW of geothermal by the 2030s, and possibly up to 5-6 GW in some recent 2045 scenarios (CPUC 2024).[17]

4. Other Western States

Since the prior paper (Thomsen 2021), there has been little advancement in geothermal resources planning and procurement in the other western states, with the exception of Nevada. Most buyers in the region will consider geothermal energy through their procurement processes, but they mostly screen it out or limit it otherwise in resource planning models. However, there are planning scenarios with high geothermal development in some states and utilities. These need support from the geothermal industry and to be considered within a western regional planning vision and roadmap. This section provides a brief review organized by subregion, with additional data from

[15] This scenario had 2,332 MW of geothermal, essentially the full geothermal resource potential in California and southern Nevada which the CPUC has used since the start of its IRP, of which 2,012 MW was assigned to the Imperial transmission zone and 320 MW to southern Nevada. The study noted that geothermal assumptions should be updated with stakeholder input.

[16] In stakeholder comments, Fervo Energy observed that CAISO needed to account for EGS resources which may be located in other regions which can supply California buyers, such as Fervo's Cape Station plant in Utah (see discussion below), and which is planned to become operational before 2030.

[17] We note that the modeling in Thomsen (2018) was able to calculate modeled results for geothermal in California of 5-6 GW when CPUC model constraints on geothermal expansion were relaxed.

the resource plans provided in Table 5, below. In the conclusions, we also turn to some potential lessons learned for these states from the California experience.

4.1 Southwestern States

After California, the southwestern states of Nevada, Arizona, New Mexico, and Colorado appear to present the most significant opportunity for geothermal commercial activity in the West in the coming decade.

Nevada has a large existing geothermal resource portfolio serving customers within the state as well as in California. With sufficient transmission availability, further resource development could serve additional buyers across the southwest and the northwest. NV Energy has the largest geothermal portfolio outside California, but geothermal typically is not selected through the utility's integrated resource plans (NV Energy 2020, 2023) but rather negotiated through bilateral contracts, which includes some recent portfolio procurements and contracts with individual new projects (PUCN 2023). NV Energy has also facilitated significant corporate geothermal contacts in recent years (NV Energy 2023, PUCN 2023).

Arizona has growing electricity demand and advanced clean energy goals. The state is not considered to have significant conventional geothermal resource potential. In general, the major utility IRPs consider geothermal as a marginal addition and dependent on transmission availability to access imports (APS 2023, TEP 2023, SRP 2023). Salt River Project (SRP) has the most existing geothermal capacity, with around 167 MW contracted with the plants in the Salton Sea area, but there is only limited expectation of additional procurement. SRP allowed for up to 1 GW of new geothermal power in its 2023 Integrated System Plan (SRP 2023), but only 50 MW was selected by 2035. Arizona could soon be served by new transmission lines interconnecting to New Mexico (such as Sunzia and several others in advanced development) and between the other neighboring states, potentially allowing increased transfers to and from Nevada and the Pacific Northwest. Additional transmission upgrades could improve transmission transfer capability to California and geothermal development in the Salton Sea region. For Arizona utilities, transmission is the key to further geothermal procurement.

New Mexico has a history with geothermal research, and since 2023, state legislation and workshops have sought to advance geothermal development.[18] There is only one small commercially operating geothermal plant in the state, contracted with Public Service Company of New Mexico (PNM). PNM has not selected additional geothermal resources through its 2023 IRP but will accept offers in its all-source RFPs. El Paso Electric Company evaluated geothermal in its 2021 IRP but did not select any through the modeling. A successful geothermal expansion in New Mexico could serve both the LSEs in the state and even export to the other states in the region. The new transmission projects under construction or planned to connect New Mexico to its western neighbors were developed mostly to export wind generation. These lines could also present an opportunity for any new geothermal projects in the state to have export opportunities.

Finally, Colorado does not yet have any operating geothermal projects. Still, the state has undertaken ambitious recent initiatives to advance geothermal energy through legislation to support research and financial incentives, which were implemented through the Colorado Energy

Office (CEO). As such, there are new projects in the planning stage. Xcel's most recent IRPs for Colorado (Xcel 2022, 2024) did not select any geothermal through the planning scenarios, but subsequent RFOs have received some offers for geothermal projects.

In 2024, the CEO released a simulation study of decarbonization in the state by 2040, which included new geothermal in several scenarios (CEO 2024). The "Optimized 100" scenario is intended to be the least cost pathway, and selects 800 MW of geothermal by 2040. A sensitivity case on Accelerated Geothermal Adoption selects 2 GW of geothermal by 2040, which represents 10% of annual electric energy.

4.2. Pacific Northwest States

The Pacific Northwest has consistently been estimated to have significant potential for geothermal development (Northwest Council 2020), and will have increased access in the future to expanded transmission connections across the region and in the southward direction, which could either facilitate geothermal exports from the region or geothermal imports, including from Nevada. As of early 2024, there are only about 50 MW of operational geothermal resources in the region (28.5 MW in Oregon), but several new hydrothermal and EGS projects underway. Among the drivers of a potential geothermal expansion will be state clean energy policies and resource adequacy requirements. However, most resource planners in the region have not included significant geothermal in their recent planning scenarios, in part due to a lack of geothermal offers in renewable energy procurements.

Among the few utilities that has recently selected new geothermal through planning, Idaho Power (Idaho) evaluated up to 150 MW of new geothermal resources in its 2023 IRP, assuming a price of $78/MWh and with 2030 as the first available year. The preferred portfolio selected 30 MW of geothermal in 2030. More geothermal was selected in sensitivity cases.[19]

Interest in geothermal is currently more tentative elsewhere in the region, given the limited resource development and policy support. PacifiCorp (Utah, Oregon, Washington, Wyoming, Idaho, and California) has significant potential as a buyer of new geothermal generation due to its large footprint and access to other regional resources and transmission. The utility is also engaged in significant transmission expansion, which will facilitate renewable development across the region. However, its recent IRPs have evaluated, but not selected new geothermal, while allowing geothermal offers in its (recently suspended) clean energy procurement processes (PacifiCorp 2023, 2024).

Most other utilities in the region are following this approach. The most recent IRPs by Portland General Electric (Oregon), Puget Sound Energy (Washington), Avista (Washington, Idaho), and Northwest Energy (Montana) do not select any geothermal (see Table 5). Despite these results, several of these utilities have indicated interest in new offers by geothermal through their RFOs.

There is also continued interest from out-of-state buyers. Notably, the CPUC remains potentially interested in geothermal from these states. The CPUC's estimate of geothermal resource potential in the Pacific Northwest for its resource planning has been reduced from 850 MW in the previous

two IRP cycles (2018, 2020) to 520 MW in the 2022-2023 cycle (CPUC 2023). This reduction was due to several factors, including a review of transmission availability by CPUC staff during the planning period. As in prior planning cycles, the CPUC modeling did not select any Pacific Northwest geothermal in its preferred portfolio, despite authorizing an increasing amount of out-of-state wind from the region. Despite these planning results, new contracts have been signed between geothermal companies with projects in the region and California buyers. If these new resources can be developed, new transmission projects linking California and Nevada to the Northwest region such as SWIP-North, may also facilitate additional geothermal contracting.

Table 5 – Assumptions and attributes of geothermal resources in recent selected western planning studies

Planning Entity	Resource Plan	Existing geothermal resources	Geothermal as candidate resource	Assumed geothermal costs, as presented	Other selected financial assumptions	Other attributes mentioned	Selection in IRP preferred portfolio and/or other scenarios	Other geothermal procurements
A. California								
CPUC	Integrated Resource Planning proceeding, 2022-2023	1,397 MW by 2027	Yes	NREL ATB		Capacity value of 80-90%, depending on location	See Figure 2 above	See LSE IRP and procurement results above
LADWP	2022 Power Strategic Long-Term Resource Plan	223 MW	Yes	NREL ATB 2021			52 MW	
B. Southwestern states								
NV Energy	2024 IRP and PUCN (2023)	448.1 MW operational, ~534 MW including existing contracts	Yes	As reported in PUCN (2023): Avg. contract price of portfolio: $75/MWh; Eavor Valmy project contract price: $70/MWh; Fervo contract price with corporate customer: $107/MWh		Geothermal ELCC of 41%; geothermal candidate hourly production profile	No, but IRP references geothermal procured through bilateral contracts; see PUCN (2023)	Bilateral contract for 105-135 MW through portfolio contract; new 20 MW contract; add'l 115 MW contracted for corporate client (PUCN, 2023)
	2021 IRP	385 MW (15 projects), 150 MW	Yes				No, but 500 MW of add'l geothermal evaluated in one	140 MW procured through bilateral contracts

Table 5 – Assumptions and attributes of geothermal resources in recent selected western planning studies

Planning Entity	Resource Plan	Existing geothermal resources	Geothermal as candidate resource	Assumed geothermal costs, as presented	Other selected financial assumptions	Other attributes mentioned	Selection in IRP preferred portfolio and/or other scenarios	Other geothermal procurements
		add'l under contract					scenario (Net-Zero with GEO ("Geo") Plan) from 2030	
Arizona Public Service (APS)	2023 IRP	10 MW (Salton Sea, contract ends 2030)	Yes	Capital cost $6,226/kW (note increase from 2020)	Book life - 30 yr; Tax life - 5 yr	Capacity factor – 80%	No	
	2020 IRP	10 MW	Yes	Capital cost $3,034/kW	Book life - 30 yr; Tax life - 5 yr		Not specified	
Tucson Electric Power (TEP)	2023 IRP	No	Yes	$91/MWh, 2024 LCOE (Lazard)			No	
Salt River Project (SRP)	2023 Integrated System Plan	Yes	Yes, up to 1 GW	NREL ATB 2022		90% capacity factor	No	Eligible for 2024 all-source RFPs
	2017-18 IRP, 2019-2021 updates	105 MW existing and recently contracted	Yes				Selected in most scenarios	No
Public Service of New Mexico (PNM)	2023 IRP	11 MW	No	Not specified		47% or 77% capacity value, depending on table	No	No
C. Pacific Northwestern states								
Northwest Power and Conservation Council (NPCC)	Seventh Northwest Conservation and Electric Power Plan (2016), Interim	Yes, in region	Yes, significant regional potential identified; opportunities for enhanced	PPA cost $85/MWh (2016); Geothermal reference plant (2021): Capital Cost,	Geothermal reference plant (2016, 2020): Economic life – 30 yr;	80% - 90% capacity factor, depending on technology	Identifies up to 475 MW of resource potential (2016, 2020)	

Table 5 – Assumptions and attributes of geothermal resources in recent selected western planning studies

Planning Entity	Resource Plan	Existing geothermal resources	Geothermal as candidate resource	Assumed geothermal costs, as presented	Other selected financial assumptions	Other attributes mentioned	Selection in IRP preferred portfolio and/or other scenarios	Other geothermal procurements
	Assessment (2019), Eighth Plan in development (2021)		geothermal systems	$5,400/kW; fixed O&M, $150/kW-yr, var. O&M Cost, $5/MWh (see also Geothermal reference plant, 2016 version)				
Avista	2023 IRP	No	Yes	PPA $54.03/ MWh in 2023			None in preferred portfolio; 20 MW selected in several scenarios.	
	2021 IRP	No	Yes	PPA $81/MWh in 2022			None in preferred portfolio; 20 MW selected in several scenarios.	
Northwestern Energy	2019 IRP, 2020 Supplement	No	Yes	Geothermal Flash Steam, 20 MW, $2,800/kW, $123.98/kW-yr fixed O&M, $9.88/MWh var. O&M	Project life – 30 yr	95% capacity factor	No	
PacifiCorp	2023 IRP (suspended), 2019 IRP	34 MW owned and operated; 3.65 MW under contract	Yes	Greenfield Binary: $5,973/kW, $103.85/kW-yr fixed O&M, $1.16/MWh var. O&M; generic	Greenfield plant – 40 yr PPA – 20 yr	90% capacity factor	No	Eligible for renewable procurements

Table 5 – Assumptions and attributes of geothermal resources in recent selected western planning studies

Planning Entity	Resource Plan	Existing geothermal resources	Geothermal as candidate resource	Assumed geothermal costs, as presented	Other selected financial assumptions	Other attributes mentioned	Selection in IRP preferred portfolio and/or other scenarios	Other geothermal procurements
				geothermal PPA: $77.34/MWh				
Portland General Electric	2023 IRP	Yes	Yes, hydrothermal flash and EGS	NREL 2021 ATB	10% cost reduction, 2026-2040	80-90% capacity factor	No	
	2019 IRP	Yes	Yes	Flash steam plant $6,216/kW, 30 MW, $120/kW-yr fixed O&M, $2.39/MWh var. O&M		92.2% capacity factor	No	

5. Conclusions and recommendations

As in previous years, the geothermal sector must continuously be proactive in analyzing resource and transmission planning methods and models to ensure that geothermal resources are appropriately valued.

5.1 General findings and recommendations

5.1.1 Targeted policy support for geothermal

The CPUC MTR decisions in 2021 and 2023 provided a needed planning target for geothermal in California, creating a floor for subsequent CPUC planning scenarios and stimulating the geothermal market. While the California market now has sufficiently high geothermal planning forecasts to maintain commercial momentum, some other states and regions in the West feel similar to California before 2021, with fluctuating interest by LSEs and a lack of consistency across the state or region in how they treat geothermal in resource planning. Even a modest policy target of a few hundred MW could help to organize the geothermal markets in the other states in the region. In addition, such targets could help encourage transmission planners and developers to consider geothermal appropriately as a major Western clean and reliable energy resource.

5.1.2 Geothermal in higher renewable energy and more rapid decarbonization scenarios

The opportunity for geothermal expansion since 2020, is due to several factors. Still, two stand out: (1) shorter-term power system reliability needs arising in the 2020s as conventional generation is replaced by variable energy resources, combined with higher summer temperatures, and (2) the high value for clean firm energy in longer-term decarbonization scenarios which address the 2030s and after. This updated survey finds that, at least in some resource plans, the opportunities for high geothermal selection on scales of several GW is correlated with higher decarbonization objectives. We find this particularly in the California resource plans and elsewhere in the Western region (most recently, in Colorado).

5.1.3 Advanced geothermal technologies

Compared to 3-4 years ago, there is more mention of advanced geothermal technologies, such as EGS, in resource plans. Still, resource planning models will typically not select these technologies at current known prices. Hence, while EGS contracts are being signed (DOE 2024), for these next few years, these technologies will continue to seek procurement primarily through bilateral negotiations rather than through modeled resource planning portfolios. We noted above that even the CPUC's most aggressive recent geothermal scenario to support gas plant retirement does not select any EGS among the almost 8 GW of new geothermal (CPUC 2024). The geothermal sector thus needs to coordinate efforts to establish how these technologies are considered in regional resource planning.

5.2 Recommendations on IRP and capacity expansion models

Resource planners use a wide diversity of methods and tools and a range of inputs and assumptions about geothermal resources. In the past few years, there have been efforts by government and national laboratories to advise on these processes (e.g., Warren *et al*., 2021, DOE 2024). The WGA (2023) recommends further that "DOE should develop guidance on how to incorporate the full

value of geothermal projects into resource planning." As discussed below, there does seem to be some convergence among planners on certain inputs, such as using the NREL ATB geothermal costs. The geothermal industry must continue to evaluate these planning processes and provide advice where possible to ensure that the results for geothermal are not simply artifacts of model inputs, assumptions, and structures.

5.2.1 Geothermal costs

Many resource planners have adopted the NREL ATB costs for geothermal, which helps with coordination and transparency. At the same time, actual geothermal contract prices are a function of specific project costs and market conditions. Further, because of the variation in locations and technologies and the companies involved, there has been a wide range of contract prices in recent years, ranging from $67/MWh to $107/MWh, as noted above from public sources (e.g., some utility IRPs, NREL ATB survey and DOE 2024). As such, resource planners should continue to test a wider range of geothermal cost assumptions in their planning models so that the industry can understand how sensitive geothermal selection is to cost (see, e.g., Thomsen 2018).

5.2.2 Geothermal attributes

Similarly to what was found in Thomsen (2021), resource planners mostly assume capacity factors of 80%-90% for new geothermal resources and similar ranges for capacity value (for resource adequacy). As reviewed in Table 5 above, there are still a few exceptions where utilities with existing geothermal plants have assigned lower capacity factors or capacity values, which reflect older plants sometimes operating well below their original rated installed capacities. As such, the geothermal sector needs to provide clear guidance on calculating capacity factors and capacity value, distinguishing between plant vintages and individual plant and fleet averages. Geothermal plants can also offer operational flexibility (e.g., Nordquist *et al*., 2013, Warren *et al*., 2021, DOE 2024), and there have been some recent examples of contracts which allow for system operator dispatch control. However, flexible geothermal is typically not evaluated explicitly in resource planning.

5.2.3 Geothermal development timelines

The CPUC MTR procurement decisions have smoothed the development pathway for geothermal projects that can sell into California and instigated growth in exploration. There is still substantial work to be done between the geothermal industry and resource planners to conceptualize how the geothermal expansion will continue and what reasonable milestones are for resource development, including possibilities for significant expansion in the 2030s to meet decarbonization needs. Similar issues would arise in other states that determine to pursue higher geothermal scenarios.

5.3 Geothermal in the context of zero carbon firm and flexible resources

The concept of a generic category of "zero carbon firm/flexible resources" was introduced most notably in California's SB 100 decarbonization analysis (CEC, CPUC, CARB, 2021), which showed that at sufficiently low costs, such a resource could become a significant component in the state's resource portfolio; it remains a component in the state's procurement and planning processes (CPUC 2024). Given the limitations that most planners place on geothermal resource potential, this category remains a useful placeholder while geothermal development continues and newer

geothermal technologies such as EGS demonstrate whether they can expand the number of viable geothermal sites.

5.4 A regional vision and roadmap for geothermal expansion

Building on the progress achieved over the last 3-4 years, policymakers, planners and the geothermal industry need to develop a conceptual plan for the region that could tie together resource and transmission planning to 2045. As done in this paper, a preliminary step is reviewing the current set of resource plans and scenarios. But this must be followed by the analytical work to create a roadmap to geothermal power providing as much as 5-10% of the western region's power at the end of this planning period. This pathway needs to identify the geothermal resource costs that are needed to justify this buildout, as well as the attributes of the expanded geothermal fleet.

Of the transmission plans we have reviewed, the CAISO's 20-Year Outlook (2022) offers the most analysis of a transmission buildout to address increased geothermal needs, although still limited in regional scope. The CPUC's 2024 sensitivity case using an over 5 GW increase in geothermal by 2045 to support natural gas plant retirement (CPUC 2024) could go further in driving additional transmission upgrades and should be reviewed carefully by the geothermal industry. However, for most of the new regional transmission projects in advanced development, geothermal energy is very much a secondary consideration after wind and solar energy. To address these shortcomings, a western regional plan for transmission development to support geothermal expansion should aim to study two topics. First, the existing and advanced planned transmission network needs to be analyzed with respect how it would facilitate geothermal development and contracting, with appropriate upgrades identified. Second, conceptual transmission planning is needed to identify additional transmission needs for high geothermal scenarios.

REFERENCES

Arizona Public Service (APS), "2023 Integrated Resource Plan," June 2023.

Arizona Public Service (APS), "2020 Integrated Resource Plan," June 2020.

Avista, Integrated Resource Planning [Online]. Available: https://myavista.com/about-us/our-company/integrated-resource-planning

CAISO, 20 Year Transmission Outlook (2023-2024), June 2024 [Online]. Available: https://stakeholdercenter.caiso.com/RecurringStakeholderProcesses/20-Year-transmission-outlook-2023-2024

CAISO, 20 Year Transmission Outlook (2021-2022), May 2022 [Online]. Available: https://stakeholdercenter.caiso.com/RecurringStakeholderProcesses/20-Year-transmission-outlook

CEC, Webpage on "Integrated Resource Plan" [2023 POU submissions], Docket 18-IRP-01, Accessed May 2024a [Online]. Available: https://efiling.energy.ca.gov/Lists/DocketLog.aspx?docketnumber=18-IRP-01

CEC, Webpage on POU Integrated Resource Plan Public Events and Activities," Accessed May 2024b [Online]. Available: https://www.energy.ca.gov/rules-and-regulations/energy-suppliers-reporting/clean-energy-and-pollution-reduction-act-sb-350-1

CEC, "RFP-22-805 SB 100 Technical Support," 2023 [Online]. Available: https://www.energy.ca.gov/solicitations/2023-02/rfp-22-805-sb-100-technical-support

CEC, CPUC, CARB, "2021 SB 100 Joint Agency Report Achieving 100 Percent Clean Electricity in California: An Initial Assessment," March 2021, CEC-200-2021-001 [Online]. Available: https://www.energy.ca.gov/sb100

CPUC, Decision Adopting 2023 Preferred System Plan and Related Matters, and Addressing Two Petitions for Modification, Rulemaking 20-05-003, January 10, 2024.

CPUC, Decision Ordering Supplemental Mid-Term Reliability Procurement (2026-2027) and Transmission Electric Resource Portfolios to California Independent System Operator for 2023-2024 Transmission Planning Process, February 28, 2023a. [Online]. Available: https://docs.cpuc.ca.gov/PublishedDocs/Published/G000/M502/K956/502956567.PDF

CPUC, Inputs & Assumptions, Inputs & Assumptions, 2022 - 2023 Integrated Resource Planning (IRP), June 2023b [Online]. Available: https://www.cpuc.ca.gov/-/media/cpuc-website/divisions/energy-division/documents/integrated-resource-plan-and-long-term-procurement-plan-irp-ltpp/2023-irp-cycle-events-and-materials/draft_2023_i_and_a.pdf

CPUC 2022 LSE IRPs [Online]. Available: https://www.cpuc.ca.gov/industries-and-topics/electrical-energy/electric-power-procurement/long-term-procurement-planning/2022-irp-cycle-events-and-materials/lse-2022-integrated-resource-plans

CPUC, "Decision Requiring Procurement to Address Mid-Term Reliability (2023-2026)" Proceeding, June 30, 2021, R2005003, D2106035 [Online]. Available: http://docs.cpuc.ca.gov/PublishedDocs/Published/G000/M389/K603/389603637.PDF

CPUC, "Decision 20-03-028, 2019-2020 Electric Resource Portfolios to Inform Integrated Resource Plans and Transmission Planning," April 6, 2020a, Rulemaking 16-02-007. [Online]. Available: http://docs.cpuc.ca.gov/PublishedDocs/Published/G000/M331/K772/331772681.PDF

CPUC, "Inputs & Assumptions: 2019-2020 Integrated Resource Planning," February 2020b.

Cochran, Jaquelin, and Paul Denholm, eds. 2021. The Los Angeles 100% Renewable Energy Study. Golden, CO: National Renewable Energy Laboratory. NREL/TP-6A20-79444. [Online]. Available: https://maps.nrel.gov/la100/

Colorado Energy Office (CEO), Pathways to Deep Decarbonization in Colorado's Electric Sector by 2040, 2024 [Online]. Available: https://energyoffice.colorado.gov/about-us/reports

Hawaiian Electric, 2023 Renewable Portfolio Standard Status Report, February 2024 [Online]. Available: https://www.hawaiianelectric.com/documents/clean_energy_hawaii/rps_report_2023.pdf

Hawaiian Electric Companies, Power Supply Improvement Plan (PSIP), Update Report: December 2016, December 23, 2016. [Online]. Available: https://www.hawaiianelectric.com/about-us/our-vision-and-commitment.

Los Angeles Department of Water and Power (LADWP), 2023 Power Integrated Resource Plan, https://efiling.energy.ca.gov/Lists/DocketLog.aspx?docketnumber=18-IRP-01

Los Angeles Department of Water and Power (LADWP), 2022 Power Strategic Long-Term Resource Plan [Online]. Available:https://www.ladwp.com/sites/default/files/2023-08/2022%20LADWP%20Power%20Strategic%20Long-Term%20Resource%20Plan_0.pdf

Los Angeles Department of Water and Power (LADWP), 2017 Power Strategic Long-Term Resource Plan, December 2017.

Los Angeles Department of Water and Power (LADWP), 2016 Power Integrated Resource Plan, December 2016.

Los Angeles Department of Water and Power (LADWP), 2015 Power Integrated Resource Plan, December 2015.

New Mexico Bureau of Geology & Mineral Resources [Online]. Available: https://geoinfo.nmt.edu/index.html

Nordquist, J., Buchanan, T., and Kaleikini, M. 2013. "Automatic Generation Control and Ancillary Services." *GRC Transactions,* v. 37, p. 761–766.

Northwest Power and Conservation Council (NPCC), " Summary of Recent Resource Development and Comparison to 2021 Power Plan Recommendations," January 2024. [Online]. Available: https://www.nwcouncil.org/fs/18611/2024_02_3.pdf

Northwest Power and Conservation Council (NPCC), 2021 Northwest Power Plan, March 10, 2022 [Online]. Available: https://www.nwcouncil.org/2021-northwest-power-plan/

Northwest Power and Conservation Council (NPCC), "Seventh Northwest Conservation and Electric Power Plan," February 2016. [Online]. Available: https://nwcouncil.org/energy/powerplan/7/plan/.

Northwest Power and Conservation Council (NPCC), "Conventional Geothermal Reference Plant for the 2021 Plan," Presentation by Gillian Charles, Power Committee, February 11, 2020 [Online]. Available: https://www.nwcouncil.org/sites/default/files/2020_02_p4.pdf

Northwest Power and Conservation Council (NPCC), "The 2024 Northwest Power Plan," Accessed 2021 [Online]. Available: https://www.nwcouncil.org/2021-northwest-power-plan.

National Renewable Energy Laboratory (NREL), Annual Technology Baseline. [Online]. Available: https://atb.nrel.gov/

NV Energy, 2024 IRP, May 2024. [Online]. Available: https://www.nvenergy.com/about-nvenergy/rates-regulatory/recent-regulatory-filings

NV Energy, 2021 IRP, 2021. [Online]. Available: https://www.nvenergy.com/about-nvenergy/rates-regulatory/recent-regulatory-filings

NV Energy, 2018 IRP, June 1, 2018. [Online]. Available: https://www.nvenergy.com/about-nvenergy/rates-regulatory/recent-regulatory-filings

PacifiCorp, 2023 Integrated Resource Plan, 2023 [Online]. Available: https://www.pacificorp.com/energy/integrated-resource-plan/public-input-process.html

PacifiCorp, 2019 Integrated Resource Plan, 2019 [Online]. Available: https://www.pacificorp.com/energy/integrated-resource-plan/public-input-process.html

Pacific Gas & Electric (PG&E), 2020 Integrated Resource Plan, access through Rulemaking 20-05-003, [Online]. Available: www.cpuc.ca.gov

Pacific Northwest Utilities Conference Committee (PNUCC), "Northwest Regional Forecast of Power Loads and Resources August 2024 through July 2034," May 2024 [Online]. Available: https://www.pnucc.org/system-planning/northwest-regional-forecast/

Portland General Electric, 2023 Integrated Resource Plan, [Online]. Available: https://portlandgeneral.com/about/who-we-are/resource-planning

Portland General Electric, 2019 Integrated Resource Plan, July 2019 [Online]. Available: https://portlandgeneral.com/about/who-we-are/resource-planning

Public Service of New Mexico (PNM), 2023 IRP [Online]. Available: https://www.pnmforwardtogether.com/irp

Public Utilities Commission of Nevada (PUCN), Order, May 12, 2023, Docket No. 22-11032.

Sacramento Municipal Utility District (SMUD), 2019 Resource planning report (IRP) ([Online]. Available: access through https://www.energy.ca.gov/rules-and-regulations/energy-suppliers-reporting/clean-energy-and-pollution-reduction-act-sb-350-1

Salt River Project, 2023 Integrated System Plan [Online]. Available: https://www.srpnet.com/grid-water-management/future-planning/integrated-system-plan

San Diego Gas & Electric, 2020 Integrated Resource Plan [Online]. Available: access through Rulemaking 20-05-003, Retrieved from www.cpuc.ca.gov

Southern California Edison, 2020 Integrated Resource Plan [Online]. Available: access through Rulemaking 20-05-003, Retrieved from www.cpuc.ca.gov

Thomsen, Paul, Geothermal in Western U.S. resource planning: a review of recent results, *GRC Transactions*, Vol. 45, 2021.

Thomsen, Paul, Geothermal selection in California resource planning: Preliminary results from the CPUC's IRP tools and recommendations for future development and analysis, *GRC Transactions*, 2018.

Tucson Electric Power, 2023 Integrated Resource Plan, November 1, 2023 [Online]. Available: https://www.tep.com/2023-irp/

Warren, Ian, Sean Porse and Jeff Winick, "Geothermal Representation in Power System Models," *GRC Transactions*, Vol. 45, 2021.

Western Governors' Association (WGA), The Heat Beneath Our Feet, 2023 [Online]. Available: https://westgov.org/images/files/2023_HBOF_Initiative_Report_for_web.pdf

U.S. Department of Energy (DOE). Pathways to Commercial Liftoff: Next-Generation Geothermal Power, March 2024 [Online]. Available: https://liftoff.energy.gov/wp-content/uploads/2024/03/LIFTOFF_DOE_NextGen_Geothermal_v14.pdf

U.S. Department of Energy (DOE). GeoVision: Harnessing the Heat Beneath our Feet. DOE/EE-1306. U.S. Department of Energy, Washington, D.C., June 17, 2019 [Online]. Available: https://www.energy.gov/eere/geothermal/geovision.

Xcel, Colorado Clean Energy Plan, Phase II, January 2024 [Online]. Available: https://corporate.my.xcelenergy.com/s/sustainability/plans/colorado-plan

Xcel, Colorado Clean Plan, Phase I, 2021 [Online]. Available: https://corporate.my.xcelenergy.com/s/sustainability/plans/colorado-plan

How Can the EU's Post-Communist Countries Use Geothermal to Achieve Energy Independence?

Aniko N. Toth[1], David K. Fenerty[2], Orsolya L.Sztermen[1]

[1]University of Miskolc, Miskolc, Hungary

[2]Post Office Box 2425, Boulder, CO, USA

Keywords

EU, geothermal funding, legislation, projects, climate neutral, obstacles

ABSTRACT

At the forefront of the effort to resist climate change, the European Union (EU) is one of the first major regions to have proposed binding greenhouse-gas (GHG) emission reduction targets. In particular, the EU has set its sights on cutting GHG by at least 55% by 2030, as so to become the first climate-neutral continent by 2050. To meet these ambitious targets, the EU has instituted a number of public funding instruments. These are designed to support proposed investments in renewables and energy efficiency projects, to include but not limited to geothermal projects. Envisaged are a wide range of projects are, from some which are innovative to other more mature, well-established technologies, and ranging from small-scale Research, Development and Innovation (RD&I) to large-scale plants. This article tries to take a closer look at a representative sample of the post-communist EU members – Lithuania, Poland, Slovakia, Croatia, Slovenia, Hungary and Bulgaria – so as to assess how well they are equipped to take advantage of these new geothermal-development opportunities from a legislative, administrative and legal point of view. The analysis therefore necessarily applies to Renewable-energy (RE) law, a particular subset of energy law. RE relates primarily to transactional legal and policy issues involved in the development, implementation, and commercialization of such renewable-energy sources as solar, wind, geothermal and tidal.

1. Introduction

In the EU, a group of 27 European countries, the Covid pandemic and the war in Ukraine resulted in price volatility and supply disruptions of fossil fuels. This prompted the EU to intensify its focus on geothermal and other renewable energy systems. The Renewable Energy Directive, introduced in 2009, provides the legal framework for developing clean energy across all sectors of the EU

economy, supporting cooperation between EU countries towards this goal. In 2022, the highest penetration of renewables occurred in the power sector, with renewable energy accounting for 40.7% of all electricity generated in the EU. Next came the heating and cooling sector, with a Renewable Energy Source (RES) share of 23.2%. The RES share in transport was 9.6 % (data from the European Environment Agency EEA, 2023).

Renewable energy made up 24.8 % of total energy use for heating and cooling in the EU, up from 11.7 % in 2004. Developments in the industrial sector, services and households contributed to this growth. Also playing a role was the ambient energy captured by heat pumps used in heating and cooling.

Geothermal energy accounted for 9.6% of the total renewable energy supplied, and investment in heat pump installations was up by 12% in 2020 (data from the International Energy Agency IEA, 2023).

According to the European Environment Agency (EEA), the share of renewable energy sources in EU energy consumption has gone from 12.5% in 2010 to 22.5% in 2022, a share which is expected to continue growing. To meet the EU's new target of 42.5% for 2030, however, the entire European energy network will have to undergo a much more profound transformation.

2. Renewable energy legislation in The EU

EU decision-makers have the right to legislate on different issues affecting the geothermal energy sector, however deep beneath the surface the resource's location, or whether the resource is adapted to heating/cooling, electricity or combined heat and power (CHP). The EU has passed specific legislation aiming to increase renewable energy use by, among other efforts, incentivizing the use of geothermal energy technologies. In the EU as elsewhere, environmental-protection measures may restrict a new geothermal project's placement, which could affect the procedures required and perhaps increase implementation costs.

EU legislation on energy was long based on various provisions scattered throughout the EC Treaty, relating to the EU's authority over its internal market and environment. After the inclusion of a dedicated chapter in the 2009 Lisbon Treaty, energy officially become a subject of shared competence between the EU institutions and its member states. The Treaty on the Functioning of the European Union (TFEU) included energy policy among the shared competences.

The energy market regulation in its current form was developed step by step in the EU's legislative process over the last few decades. The rules created for each energy source vary significantly, and are still evolving in response to technological developments and global challenges. In its 2000 Green Paper, the European Commission stated that growing energy demand meant that new supplies and routes must be found and also that the use of renewable resources must be increased.

It was recognized at the time that energy security depended on diversifying Europe's energy sources. To that end, the 2006 Green Paper highlighted three objectives: sustainability, competitiveness, and security of supply. The Commission prioritised certain topics to support these three objectives. These topics included energy efficiency, energy saving, and the development of new renewable energy sources. The European Commission presented "Clean Energy for All Europeans" in 2016, a package of measures to address the EU's energy policy

The package was designed to meet the EU's 2030 climate and energy policy objectives. by emphasizing 3 main objectives: prioritizing energy efficiency, ensuring fair treatment of consumers, and making the EU a global leader in renewable energy. Considering the specificities of renewable energy production and electricity consumption, i.e., that much renewable energy production is weather-dependent, not consumed when or where it is produced, and difficult or expensive to store, it is understandable that the EU would also try to reward systems that have flexible capacity.

In 2014, the Council set itself an ambitious target, and decided that the share of renewable energy in terms of gross final consumption within the EU should reach 27%. EU member states are encouraged to contribute to this EU-wide binding target. One difference between the 2020 and the 2030 goals is that the 2020 target (based on the 2009 Renewable Energy Directive) was broken down into binding targets for Member States, whereas the 2030 target is not binding – it was only posited as a contribution to the EU target.

High levels of electricity transmission require an optimum uptake of renewable energy, with an extensive distribution grid structure and good interconnectivity between the EU's national and regional grids. To this last point, the 2014 Council Decision provides for a legislative package to help achieve the 15% interconnection target. One of the packages's main features is the Governance Regulation for the Energy Union. This seeks to harmonize member states' diverse planning and reporting bodies by consolidating and standardizing both climate and energy policy reporting into 1-year and 2-year reports. To that end, member States are required to submit Integrated Energy and Climate Plans based on the Table of Contents in the Annex to the Regulation.

Renewable energy legislation varies significantly from country to country and even within regions. In their current form, EU laws and regulations are designed to promote the development, integration, and utilization of renewable energy sources. These laws' key components frequently include targets for renewable energy deployment, financial incentives, grid access, and environmental standards. It is crucial to note that renewable energy legislation is dynamic and subject to change. EU governments occasionally update or revise policies based on technological advancements, economic considerations, and environmental goals.

2.1 How Geothermal Fits into Community Energy (CE) Development in Post-Socialist Europe

The EU plays a leading role in financing thousands of ongoing projects of small to medium size, but those projects are unevenly distributed over the continent. The majority of such CE projects are in northwest and central Europe. In the formerly communist nations of Eastern Europe, projects like those are much more rare. This paper gives an overview of the geothermal CE situation in a representative sample of post-socialist countries (PSECs): Bulgaria, Croatia, Hungary, Poland, Slovakia and Slovenia. Croatia stands out in this groupd as a positive example. The other countries are farther behind, although Hungary actually has far superior geothermal resources, since it enjoys the geographic advantage of being located mostly in the Pannonian Basin, a region blessed with abundant low-enthalpy and medium high enthalpy geothermal reservoirs. One generally valid explanation for this lack of development, true especially for Hungary and for other countries to differing degrees, is the widespread distrust of 'community projects' -- of which there have been few positive examples since the communist-system collapse over 30 years ago. Compared with the rural communities which could most benefit from CE projects, politically well-connected elites

in the PSECs usually have more access to investment capital or the expertise needed to prepare an EU-funded CE proposal. Those groups, however, are often less interested in geothermal CE projects, which do not entail any rapid profit for investors. This can pose a real problem, since a geothermal project's upfront exploration and drilling costs greatly exceed what a typical small village can scrape together.

2.2 Renewable in the Post-Socialist European Countries

Renewable energy usage conditions are critical in effecting an ambitious local energy transition in the post-socialist renewable energy policy environment that constrains local initiatives. Nonetheless, outliers can also be observed, e.g., the island of Krk in Croatia, a unique case of a shared vision of 100 % renewable energy. In spite of political commitments, RES potential, advanced technologies, and decreasing production costs, ongoing energy transition remains a challenge. The following representative survey of PSECs is presented in alphabetical order, and looks at the general energy situation and the renewable and/or geothermal CE situation.

2.1.1 Bulgaria

The main local energy source in Bulgaria is still lignite coal. Another local energy source is nuclear energy, which significantly contributes to energy independence. Bulgaria has a high solar-energy potential, especially in the south. From a total of 100 MW of solar power installed capacity in 2011, Bulgaria has raised that figure to more than 2,400 MW as of 2023, with 600 MW added in 2022 alone. The Energy from Renewable Sources Act regulates the establishment of citizen energy communities. They are becoming market participants, able to sell any surplus electricity they produce and legally entitled to sign bilateral contracts with suppliers.

There are more than 170 geothermal fields in the Republic of Bulgaria. They represent the main sources of geothermal energy in the country. These are spread all over the country. The temperature of the thermal water varies between 25-100 ^{o}C, and about 72 % of thermal water sources have low enthalpy, with water temperature below 50 ^{o}C. Geothermal water as a source of geothermal energy is used in local heating systems and greenhouses. This usage represents only 1.8 % of the total thermal water use. Regulatory change is one of the planned steps forward, which will result in better utilization and management of the geothermal resources (Deneva et al, 2022).

2.1.2 Croatia

Croatia has promising natural potential for the exploitation of RES, especially in the northern (Pannonian) part. As part of the Euro-integration process, the whole concept of the energy sector reforms through the legal and institutional frame- work was accepted, and conforms to EU requirements. Such official national documents as the National Action Plan, along with with the 2013/18/EU Directives, stipulate that the 19.6% gross share of RES will be used for direct heating and cooling consumption by year 2020.

The Croatian part of the Pannonian basin area has long been known as a high potential geothermal area. Deep geothermal energy is covered by the Mining Act if it is used for energy purposes, or by the Water Act. The commissioning of the first geothermal power plant, Velika 1, with a capacity of 10 MW at the Velika Ciglena site in 2018, triggered new developments in the geothermal sector.

Croatian investors with their partners started to develop Croatia's second geothermal power plant in 2022. The exploration work of Bukotermal indicates a geothermal resource of about 142 C at a depth of 2.4 kilometers .The proposed project site in the northern Varazdin County in Croatia can support a 16-MW geothermal power plant. Aew incentive for additional geothermal exploration has also recently come from Croatia's recovery and resilience plan, which funds the Croatian Hydrocarbons Agency with almost €30 million intended for confirmation of geothermal potential. This includes geophysical surveys and the drilling of two exploration wells for geothermal energy to be used in district heating.

Furthermore, Norway Grant's Energy and Climate Change Programme funds four calls for geothermal developments in Croatia that are currently being implemented. (Note: Norway has been a generous contributor of funds in PSECs, but recently suspended all such activities in Hungary after it decided that the grants it made there where not properly used.) All these funding opportunities triggered increased interest in geothermal exploration from private investors and local communities, resulting in more exploration licenses being issued. Consequently, 14 exploration and 7 exploitation licenses for geothermal waters are now active, promising new developments in the following years. Even though private investors are mostly interested in electricity generation projects, local communities and agricultural entrepreneurs have expressed their interest in geothermal heat production to reduce dependency on fossil fuels and to increase the security of supply. There is also a financial component of the heat projects, where users can save up to 30% on energy bills (Zivković et al, 2022).

2.1.3 Hungary

Hungary published its renewed Energy Strategy and National Energy and Climate Plan (NECP) in 2020. These documents highlight the role of geothermal energy especially in the heating/cooling sector, in agriculture and in making district heating more environmentally friendly.. Although the foreseen growth of geothermal in the heating-cooling sector is 58% (84.6 ktoe by2020, 116.6 ktoe by 2030), this would barely increase the overall share of geothermal within the total RES, which will stay around 5 %. The Hungarian NECP foresees 59 MWe installed capacity in geothermal power production, but only after 2040.

To foster geothermal project development, the Ministry of Innovation and Technology announced a Call for bids, promising to support geothermal heating by assuming the geological risks for the first wells. This Call supports only projects with reinjection, i.e., drilling doublets, or drilling only reinjection wells to complete already existing systems. The target depth is 1000-2500 m. The total budget is 6 billion Hungarian forints (approx. €16.6 million). The Call was open until December 31, 2023. The reimbursement rate is 30 % in case of success, 40 % in case of partial success and 60 % in case of unsuccessful projects. Due to institutional reorganizations at the end of 2021, the former program operator (Mining and Geological Survey of Hungary) has been replaced by the Western Balkan Green Center, which caused a temporary suspension of the application and evaluation procedures (Nador et al, 2022).

The Hungarian Ministry of Innovation and Technology National Energy Strategy 2030, looking ahead to 2040, has set very ambitious targets for the expansion of domestic renewable, mainly as regards photovoltaic capacity. The strategy thus seeks to contribute to meeting Hungary's EU commitments, promoting sustainable consumption, and providing financial market players with a stable portfolio. Taking into account the renewable energy currently being installed in Hungary

and the 2030, 2040- and 2040- targets for the EU, the EU is in a position to provide a more sustainable energy source. Given the ambition of its targets, and the investment costs of the renewable technology, Hungary will find it a challenge to achieve these goals in the current domestic regulatory and financing environment.

2.2.4 Lithuania

Lithuania depends on energy imports, as domestic production in 2022 covered only one-quarter of total energy supply (TES). Two-thirds of TES comes from oil and natural gas and a quarter from renewable such as wind, biomass and hydro. The Law of the Republic of Lithuania on Renewable Energy (the 2021 consolidated version) defines RECs as non-profit-making legal entities who own and develop renewable energy production facilities and have the right to produce, consume, store and/or sell energy in installations.

Lithuania has rich low-enthalpy geothermal resources. The first geothermal investigations was initiated in the periods of 1987-1989. From 1992 to1994 the government of Denmark financed the Baltic Geothermal Energy Project, covering Lithuania and Latvia. Based on this and other projects, Klaipeda Geothermal Demonstration Plant was engineered (prospective capacity 49MW, production of heat 598 TJ/year). The plant aimed to meet about 25% of yearly Klaipeda City heat demands. The main legal basis for geothermal energy growth is the new act “National Energy Independence Strategy of the Republic of Lithuania”, approved in 2018. The Baltic Geothermal Energy Project begun in 1992 was finally completed in 2000, when the geothermal plant in Klaipeda started producing heat. Various technical problems occurred, but by 2002 KGDP was producing 189000MWh of heat. The Klaipeda plant has also had to solve problems related to reaching the market and obtaining a profitable fixed minimum heat fee (Zinevicius, 2022).

2.2.5 Poland

Dependence on domestic coal has locked Poland into the carbon trap. Coal constitutes around 80% of the country's energy production and around 50% of the total primary energy supply. This makes Poland the EU-27 country with the highest emission intensity relative to its energy production Capellán-Pérez (2020). This context translates into very challenging conditions for RES deployment in general and for cooperatives and community initiatives in particular. Nevertheless, there are still some fragile projects to be found. The co-operative Spółdzielnia Nasza Energia in the district of Zamość, initiated in 2014 by a local company and several municipalities, has a democratic one-member-one-vote structure and operates a network of biogas stations. According to the Central Statistical Office (data source: GUS, 2021; 2) in 2020 the RES share in total primary energy acquisition was estimated at 16.3 % (499’338 TJ), then given by Eurostat as 16.1 % 3. The contributions of particular RES were as follows: solid biofuels 71.61 %, wind 10.85 %, liquid biofuels 7.79%, biogas 2.58%, heat pumps 2.38%, solar 1.99 %, municipal wastes 1.15 %, geothermal 0.20 % Kepinska and Hajto (2022).

Poland’s geothermal roadmap was published in May 2022. This is a comprehensive approach targeting geothermal in key sectors such as residential buildings and across its vast array of fossil-powered district heating systems. Heat reservoirs with temperatures between 30-90°C can be found across 40-55% of Poland’s land mass. The roadmap identified 491 localities with heating plants greater than 1 MW and 78 localities with 5 MW situated within the heat reservoir range. Around 114 geothermal plants have been identified by the plan. The next steps are to construct 78 test

holes to construct 78 geothermal installations with a combined capacity of 290 MW and 9,949.6 TJ generated by 2040.

2.2.6 Slovenia

Slovenia generated 68.8% of its electricity with zero carbon or carbon neutral sources in 2019, dominated by nuclear power and hydroelectricity. Indigenous energy sources – in the form of domestic coal, nuclear power, hydropower, and renewables —satisfy slightly more than half of Slovenia's energy needs. For 2030 the target is 27 %, to be reached mainly through solar and hydro power, and through the use of wood biomass Tsagarakis et al (2020).

Geothermal energy is considered to be a natural resource, owned by the Republic of Slovenia. Research and exploitation of SGE are regulated by two basic laws: the Mining Act and the Water Act. The Mining Act regulates the research and exploitation of geothermal energy without ground water, whereas the Water Act applies when thermal water extraction occurs. The Water Act regulates the management of surface and groundwater, which are a natural resource owned by the Republic of Slovenia. If there is a water temperature above 20 C (thermal water), a grant must be obtained by the Ministry of Agriculture and Environment. For boreholes deeper than 300 m, a revised mining project needs to be obtained and treated as a system that is not shallow (Tsagarakis et al, 2020). So far only direct use of geothermal energy is effective in the country with emphasis on exploitation of low temperature resources for district and individual space heating, for greenhouses and thermal spas. During the last 20 years direct use showed only slight and changing increase and more recently has remained stagnant. The reasons depend on the locality. Overexploitation of geothermal resources in some localities of the north-eastern part of the country is one of the problems, but there have also been some occasional technical difficulties, and weak incentives for efficient use of the resources. Total installed capacity and annual energy use (both deep and shallow geothermal) in 2021 are 298.45MWth, respectively. Installed capacity and energy use at all 31 users of thermal water from deep sources amounted to 60.70MWth, Rajver et al, (2022).

2.2.6 Slovakia

Slovakia’s is still an economy oriented towards fossil fuels, where RES contribute with roughly 29 % on heat production, whilst geothermal energy yields only a 2 % share. In power production, fossil fuels account for a 21 % share, renewables (including small to large hydro) are over 25 %, and nuclear power has the largest share. The Slovak National Energy and Climate Plan was approved by the Slovak Government in 2019. The planned total share of RES for 2030 is 19,2%, which is lower than the EU 2030 goal of 32%. Share of RES in transport is projected to be 14% by 2030.

Geothermal resources contribute exclusively as direct use in Slovakia. A total of 31 geothermal water bodies have been defined to date, responding to The Water Framework Directive No. 2000/60/EC of the EU Parliament and the European Council. Geothermal resources have already been proven with 282 wells, drilled in 30 out of the 31 geothermal water bodies (GWBs), yielding a proven 436 MWth of reserves Fričovský et al, (2022).

3. Renewable enery Share in EU

In 2022, renewable energy represented 23.0 % of energy consumed in the EU, up from 21.9% in 2021. The share of energy from renewable sources used in transport in the EU reached 9.6 % in 2022, up from 9.1% in 2021 (EUROSTAT, 2023).

Figure 1. shows the renewable energy production by percent of gross final energy consumption in 2004 and in 2022. The former socialist countries were close to each other in terms of renewable energy sources at the start. Initially, the use of renewables was not a priority in any of the countries, thanks to cheap Soviet energy sources, and EU quotas were not initially in place with regard to the energy use of the states. But there were clearly differences due to geography. In terms of renewable energy use, the Baltic states of Latvia, Estonia and Lithuania lead the pack. Serbia and Slovenia approached the EU average. The rest -- Bulgaria, Czechia, Slovakia, Poland, and Hungary -- fall below the EU average. For the EU as a whole, the share of renewable electricity increased from 38 % to 39 % between 2021 and 2022, whilst fossil fuels still represented 38 % of the EU's electricity production. In 2021, fossils produced 36% of the EU's electricity EGEC, (2023).

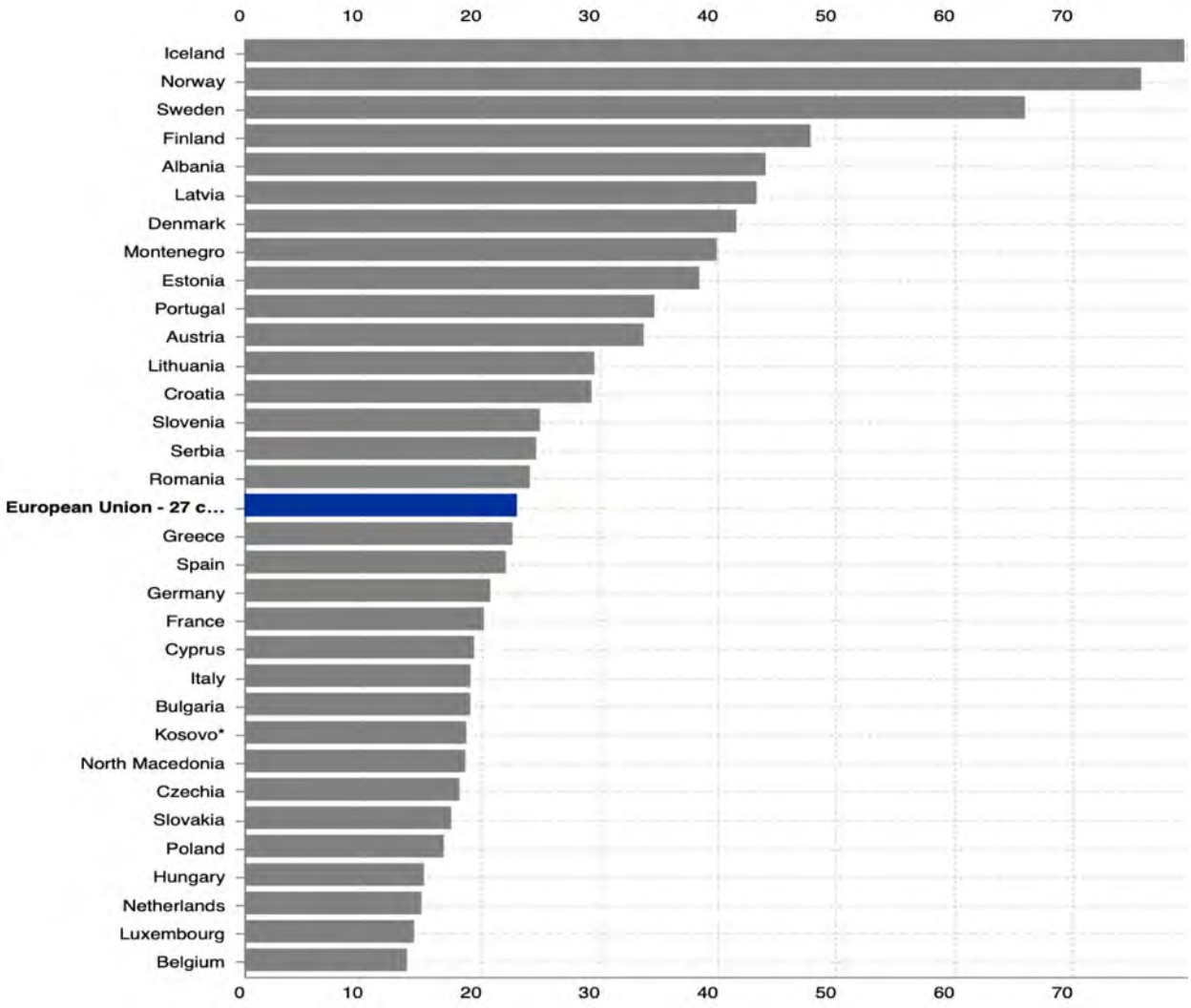

Figure 1: Renewable energy's share of gross final energy consumption

On Jan. 18, 2024, the European Parliament approved a resolution, led by Prof. Krasnodebski of the European Conservatives & Reformist Group (ECR), to support a common European geothermal energy strategy.

3.1 A Brief History of Geothermal in Europe

The geothermal energy situation varies from country to country according to the geological background and the geothermal technology that best suits the available natural resource. Figure 2 shows the geothermal heat-flow in Europe. The spectrum varies, led by power generation derived from high enthalpy resources in Iceland, Italy, Greece and Turkey – and in Italy, where the first geothermal electricity plant started its operation in Larderello, in 1913, and is still operating. It was composed of an alternator Ganz 250 kW, three-phase 50 Hz, and a voltage of 4500 volts coupled with a Tosi Parsons turbine of 350 horsepower.

A handful of geothermal power plants were installed in Europe in the 1970s, in Turkey, Italy, Iceland and French Guadalupe (which is European legally if not geographically). They were all high temperature plants using flash/dry steam turbine technology. The development of new turbine technologies, such as the binary cycle (i.e., Kalina and Organic Rankine Cycle-ORC), was a game changer as it allowed low and medium temperature geothermal power plants to be commissioned. Countries such as Austria, Germany, Portugal, Croatia, and Hungary have installed geothermal power plants over the last 20 years using these technologies. Figure 2 shows the significant difference between the high enthalpy and low enthalpy resources. In 2022, 142 geothermal power plants were in operation with an installed capacity of about 3,5 GWe and generating more than 22 TWh. The average capacity factor last year was 79% Sanner et al, (2022).

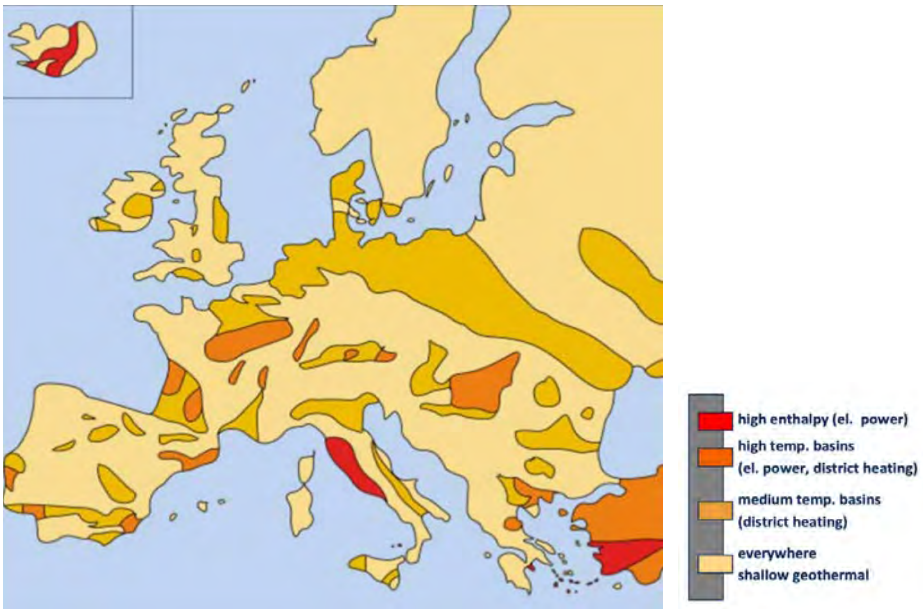

Figure 2: Heat-flow map of Europe

3.2 Geothermal Electricity Market in Europe

Demand in Europe has stagnated. This is an important issue when considering power decarbonization and possible demand for new geothermal power plants!

- 1923-2023: 100 years of geothermal power
- Oldest continually operating geothermal power plant has run since 1987.
- 4 plants operational since the 80's, 17 from the 90's, 32 from the 2000's.
- 21 power plants are more than 25 years old, 53 more the 15 years old.
- The geothermal electricity market is now entering a new development phase, with many plants to about to begin operating in the next 5-7 years.
- In total, 43 projects are currently being developed, and 140 are being considered.

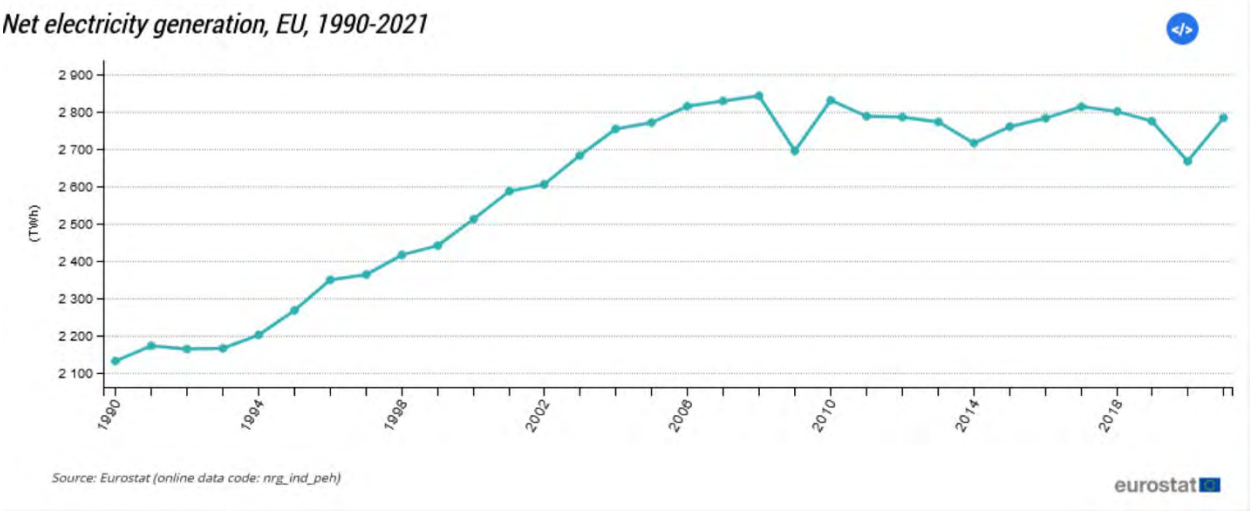

Figure 3: Electricity Demand in Europe (EGEC, 2023)

In 2022, the wholesale average electricity price in Europe was €230/MWh. This was 121% higher than in 2021. Italy had the highest wholesale electricity price at €304/MWh. From 2021 to 2022, renewable electricity's share increased from 38% to 39%. Fossil fuel's share of EU electricity production increased from 36% in 2021 to 38% in 2022.

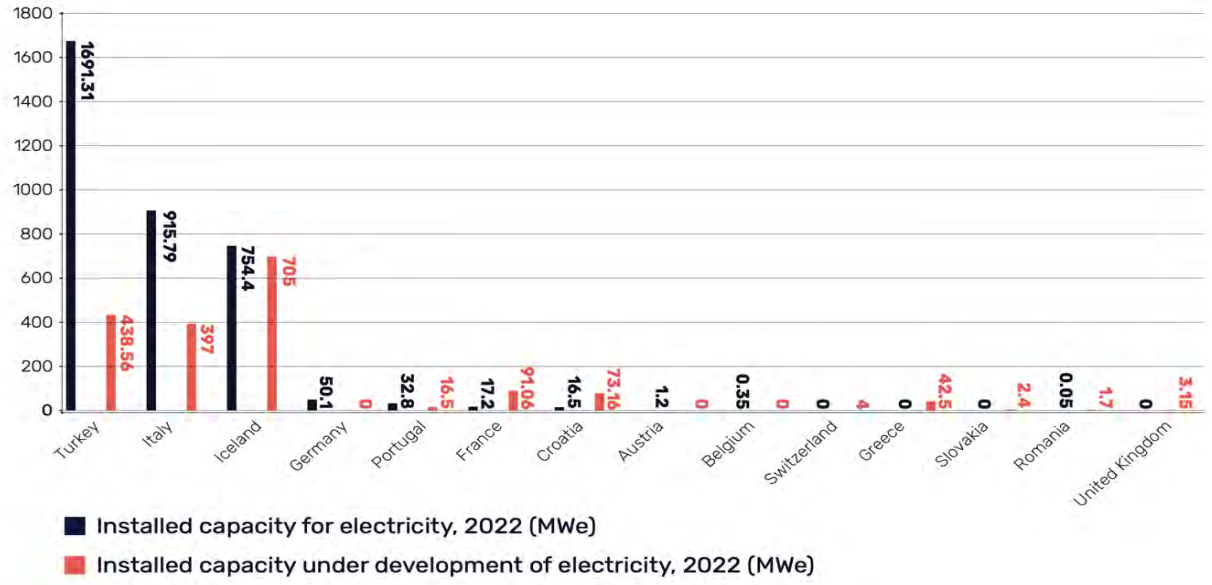

Figure 4: Installed capacityfor electricity (EGEC, 2023)

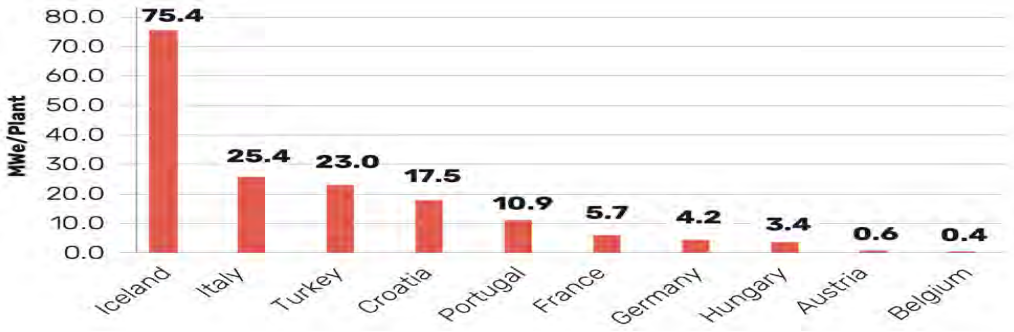

Figure 5: Average size of geothermal power plant (EGEC, 2023)

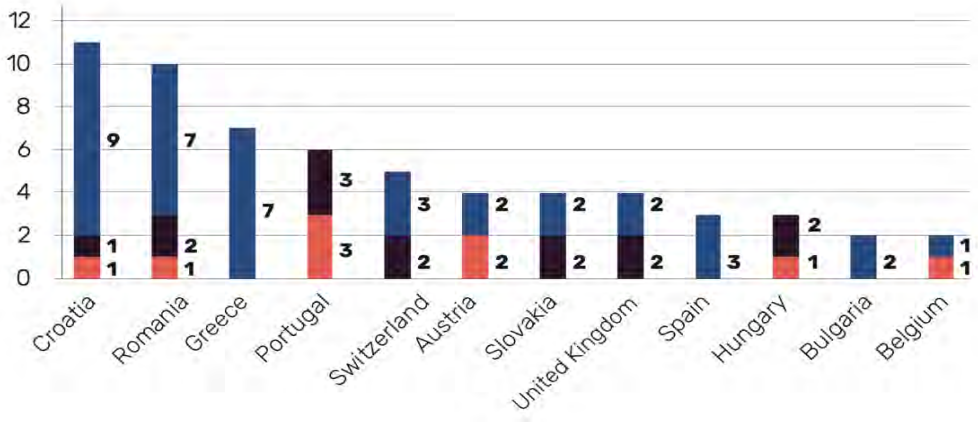

Figure 6: Number of geothermal power plants installed, planned, or being considered (EGEC, 2023)

For direct use of hydrothermal resources in sedimentary basins such as in France, Germany, Poland, Italy, Hungary, and Romania. Heat supply from geothermal energy in Europe is primarily achieved by using hot water from deep aquifers for district heating. Figure 7 shows geothermal direct uses in the EU countries. Figure 8 shows main geothermal reservoirs with existing DH systems In Europe.

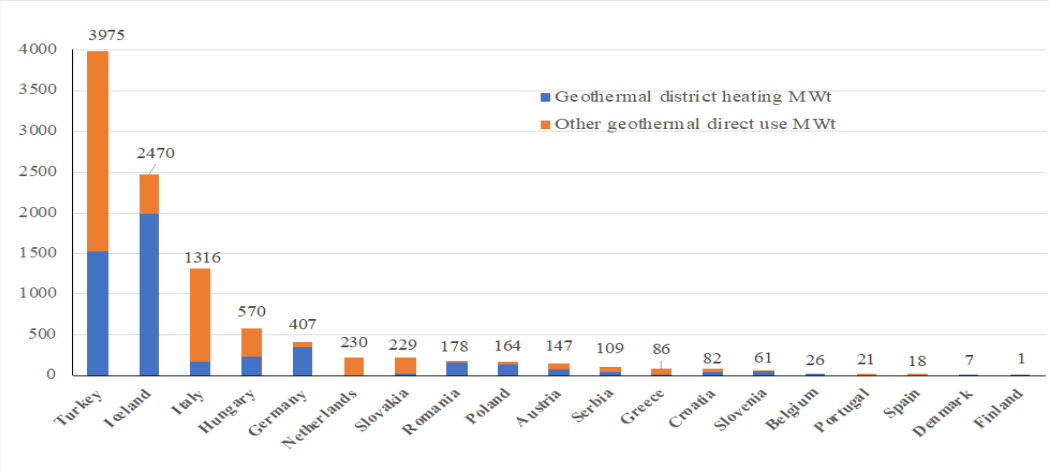

Figure 7:Geothermal direct uses (Sanner et al, 2022)

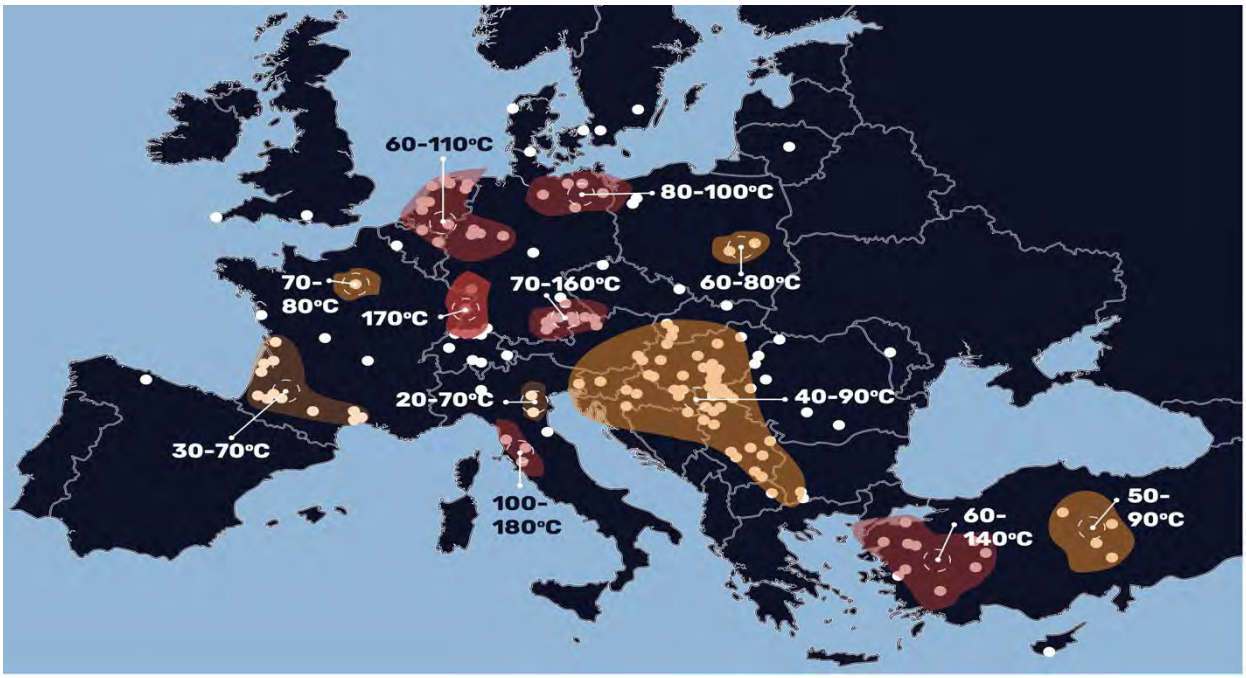

Figure 8: Mapping of main geothermal reservoirs with existing DH systems (EGEC, 2023)

Geothermal heat pumps represent by far the largest sector of geothermal energy use in Europe in terms of the number of facilities, installed capacity and produced energy. The shallow geothermal share accounts for more than 66% of the installed energy. The total number of geothermal heat pumps installed in Europe is more than 2.1 Mio units. The leader by far is Sweden; Germany, with a population more than eight times larger, comes in second. France is still in the 3rd rank, but due

to a relatively low annual number of new installations might lose that rank soon to Finland. Figure 9. shows the numbers of installed heat pumps per country for countries with at least 1000 existing units reported, compared to annual sales. In this regard, the post-socialist European countries lag far behind the European average.

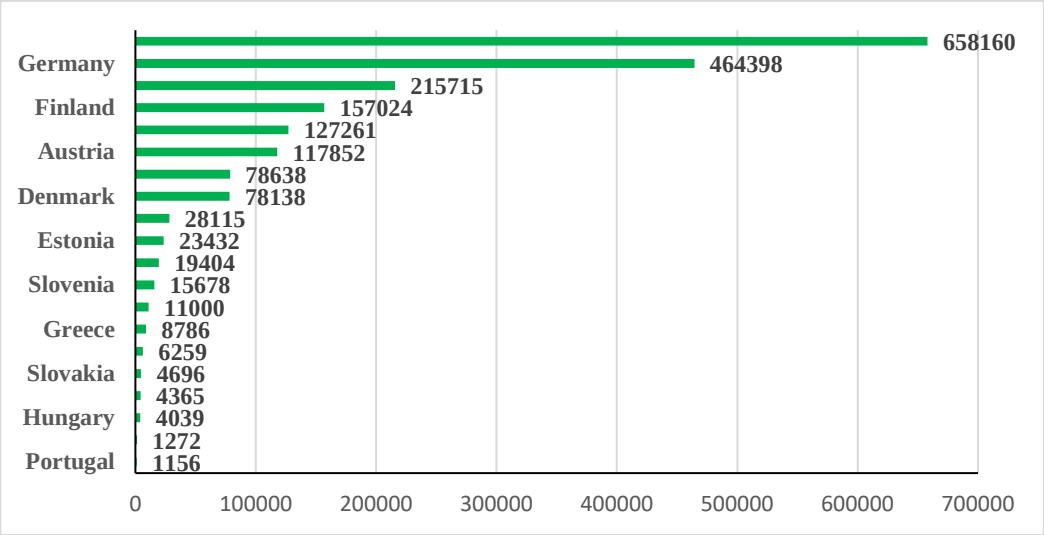

Figure 9: Number of geothermal heat pumps (Sanner et al, 2022 and Zinevicius, 2022)

4. How the EU Funds Geothermal opportunities

The EU supports research and development in geothermal technologies, funding projects for both direct use of heat and the use of extracted heat to generate electricity. EU support also focuses on reducing costs in exploration and drilling, because geothermal installations have high capital costs.

4.1 European Energy Efficiency Fund (eeef)

In the era of climate change and fossil fuel depletion, renewable energy sources (RES) also offer a key transformative potential from a social point of view due to their modularity and capacity to generate energy at a local level, allowing for the development of local, democratic and participative bottom-up initiatives.

EEEF aims to support the climate goals of the European Union (EU 2030 framework for climate and energy, and the climate-neutral objectives of the European Green Deal) to promote a sustainable energy environment and to foster climate protection by enabling projects in European cities, regions and communities so as to build resilient infrastructure. The final beneficiaries of eeef are municipal, local and regional authorities as well as public and private entities acting on behalf of those authorities such as utilities, public transportation providers, social housing associations, energy service companies etc. Investments can be made in Euros, or local currencies, although the latter is restricted to a certain percentage.

4.2 Horizon

Horizon Europe is the largest transnational program ever, supporting research and innovation, and will be implemented by the EU. The new EU research and innovation program will have a budget

of around €95.5 billion for 2021-2027 (current prices). This includes €5.4 billion (current prices) from Next Generation EU to boost Europe's recovery and make the EU more resilient for the future, as well as an additional reinforcement of €4.5 billion (current prices).

As of January 17, 2024, there are 17 ongoing funding and tender opportunities for the Innovative applications/integration of geothermal heating and cooling in industry (HORIZON-CL5-2024-D3-01-06), where the topic is high integration of geothermal heating and/or cooling in different industry sectors, with operation flexibility taking into account start-up time and ramp-up rate, and maximum cascaded use of thermal energy. Activities related to geothermal heat for industry and agriculture, underground thermal energy storage (UTES) including high-temperature storage, innovative and multiple uses for geothermal energy and side-products, balneological systems, and design and operation of geothermal doublets can be considered. Activities are expected to achieve TRL 5 by the end of the project.

4.3 European Climate Infrastructure and Environment Executive Agency (CINEA)

CINEA manages the Horizon Europe work program, which includes Energy Use, Energy Supply, Transport and Mobility and Climate Action areas. In total, it is expected that CINEA just for Horizon Europe will manage a budget of up to €15 billion for Horizon Europe under the 2021-2027 Financial Framework.

4.4 Life

The LIFE program began in 1992 and has co-financed thousands of projects in the field of environmental protection. It is the EU's funding instrument for environment and climate action. The budget of the LIFE Programme increased to €5.4 billion between 2021 and 2027. The LIFE Clean Energy Transition sub-program has a budget of nearly €1 billion over the period of 2021-2027 and aims at facilitating the transition towards an energy-efficient, renewable energy-based, climate-neutral and -resilient economy by funding coordination and support actions (Other Action Grants) across Europe.

4.5 NER 300 program

Renewable energy technologies are the focus of NER 300. It is a funding program pooling together about €2 billion for innovative low-carbon technology, focusing on the demonstration of environmentally safe Carbon Capture and Storage (CCS) and innovative renewable energy technologies on a commercial scale within the EU. The NER 300 program involving all EU Member States, was set up to support the demonstration of a wide range of renewable energy technologies, namely bioenergy, concentrated solar power, photovoltaics, geothermal, wind, ocean, hydropower, and smart grids.

4.6 European structural and investment funds (ESIF)

Over the period 2014-2020 more than half of EU funding was channeled through the 5 European structural and investment funds (ESIF). They were jointly managed by the European Commission and the EU countries. The Cohesion fund (CF) is of particular importance for Eastern European countries, because it funds transport and environment projects in countries where the gross national income (GNI) per inhabitant is less than 90% of the EU average. For the 2021-2027 period, the Cohesion Fund is providing support for 15 Member States: Bulgaria, Croatia, Cyprus, Czechia,

Estonia, Greece, Hungary, Latvia, Lithuania, Malta, Poland, Portugal, Romania, Slovakia and Slovenia. Over the period of 2021-2027, EU funds allocated to Cohesion Policy will have amounted to €392 billion.

5. Conclusion

Clearly, the EU as a whole has the expertise and political will to achieve the ambitious renewable- and geothermal-energy goals it has announced for itself. Even before the war in Ukraine made independence from Russian hydrocarbons an obvious priority, EU leadership had committed itself to a renewable energy as a way to protect against global warming and make each EU member more energy-independent. The problem comes when community-energy projects fail to take root in post-communist countries where the political and administrative disadvantages outweigh the projects' apparent advantages. In these cases, it might be helpful for the EU to 'twin' each project, by making sure there is a more experienced western European manager/advisor to guide the local managers and keep the project on track. Examples of this are the HORIZON-WIDERA 2023 Twinning Green Deal Calls. It would also help if, when evaluating bids for EU geothermal research project bids, the EU evaluators provided more detailed justifications to show why they accepted or rejected specific bids.

REFERENCES

Capellán-Pérez, I., Johanisova, N., Young, J., and Kunze, C.: Is community energy really non-existent in post-socialist Europe? Examining recent trends in 16 countries, Elsevier, Energy Research & Social Science 61, (2020).

Deneva, B., Kolev, S., Valtchev, S. and Toteva, A.: Geothermal Energy Use, Country Update for Bulgaria, Proceeding of European Geothermal Congress 2022, Berlin, Germany (2022)

Fričovský, B., Marcin, M., Benková,K., Černák, R., Fordinál, K. and Pelech, O.: Geothermal Energy Use, Country Update for Slovakia, Proceeding of European Geothermal Congress 2022, Berlin, Germany (2022)

Nádor, A., Kujbus, A. and Tóth, A.: Geothermal Energy Use, Country Update for Hungary, Proceeding of European Geothermal Congress 2022, Berlin, Germany (2022)

Rajver, D., Lapanje, A., Rman, N. and Prestor, J.: Geothermal Energy Use, Country Update for Slovenia, Proceeding of European Geothermal Congress 2022, Berlin, Germany (2022)

Sanner, B., Antics,M., Baresi, M., Urchueguía, J. and Dumas, P.: Summary of EGC 2022 Country Update Reports on Geothermal Energy in Europe, Proceeding of European Geothermal Congress 2022, Berlin, Germany (2022)

Tsagarakis, K. P., Efthymiou, L., Michopoulos, A., Mavragani, A., Andelkovic, A. S., Antolini, F., Bacic, M., Bajare, D., Baralis, M., Bogusz, W., Burlon, S., Figueira, J., Genc, S. M., Javed, S., Jurelionis, A., Koca, K., Ryzynski, G., Urchueguia, J. F. and Zlender B.: A review of the legal framework in shallow geothermal energy in selected European countries: Need for guidelines, Elsevier, Renewable Energy 147 (2020)

Zinevicius, F.: Geothermal Energy Use, Country Update for Lithuania, Proceeding of European Geothermal Congress 2022, Berlin, Germany (2022)

Živković, S., Kolbah, S., Tumara1, D., Škrlec, M., Bilić, T. and Vajdić, M.: Geothermal Energy Use, Country Update for Croatia, Proceeding of European Geothermal Congress 2022, Berlin, Germany (2022)

Young, J., and Brans, M.: Fostering a local energy transition in a post-socialist policy setting, Environmental Innovation and Societal Transitions, Elsevier, Volume 36. (2020)

Article 4(2) TEU, 12008E004 - EUR-Lex.europa.eu. - European Union

European Geothermal Energy Council (EGEC) Market Report, 12th Edition (2023)

World Energy Outlook, International Energy Agency IEA, 2023, https://iea.blob.core.windows.net/assets/86ede39e-4436-42d7-ba2a-edf61467e070/WorldEnergyOutlook2023.pdf,

European Parliament, Fact Sheets on the European Union: The Treaty of Lisboa, https://www.europarl.europa.eu/factsheets/en/sheet/5/the-treaty-of-lisbon

COMMISSION OF THE EUROPEAN COMMUNITIES: GREEN PAPER
A European Strategy for Sustainable, Competitive and Secure Energy, Brussels, 8.3.2006 COM(2006) 105 final,
https://europa.eu/documents/comm/green_papers/pdf/com2006_105_en.pdf

COMMISSION OF THE EUROPEAN COMMUNITIES: Clean energy for all Europeans package, https://energy.ec.europa.eu/topics/energy-strategy/clean-energy-all-europeans-package_en

Improving Geothermal Representation in Energy Analysis Tools to Quantify Geothermal's Role in Decarbonization

Whitney Trainor-Guitton[1], Amanda Kolker[1], Sean Porse[2], Jeff Winnick[2], Jonathan Ho[1], Dayo Akindipe[1], Koenraad Beckers[1], Tom Harris[1], Estefanny Davalos Elizondo[1], Marlena Praprost[1], An Pham[1] & Matt Mitchell[1]

[1]National Renewable Energy Laboratory

[2]Geothermal Technologies Office, Department of Energy

Keywords

Geothermal power, geothermal heating and cooling, modeling and analysis

ABSTRACT

Geothermal energy technologies have sometimes been excluded from large-scale renewable energy analysis efforts because of deficient geothermal representation in energy analysis models. Beginning in 2022, National Renewable Energy Laboratory (NREL) launched a 3-year effort supported by the Geothermal Technologies Office in the Department of Energy (DOE) to address this problem. The first phase consists of enabling geothermal representation in flagship NREL analysis tools and models with the same fidelity as solar and wind technologies. These tools and models are key in future-grid scenario studies that identify pathways to meeting U.S. goals for widescale electrification and decarbonization.

This paper summarizes Phase 1 progress, addressing expanded functionality of eight existing NREL modeling tools and data collection. This includes: (1) Updating the Regional Energy Deployment System (ReEDS) capacity expansion model and examining future scenarios to understand how the value and competitiveness of geothermal power is represented (e.g., grid decarbonization, emergent technologies, resource availability). (2) Updating the Geothermal Electricity Technology Evaluation Model (GETEM) with geothermal energy system costs and learning curves. (3) Enabling the Renewable Energy Potential (reV) geospatial platform to interface with GETEM for the entire continental United States, providing geothermal supply curves that account for conventional and emerging technologies. (4) Integrating ambient temperature loops in the Distributed Geothermal Market Demand Model (dGeo) and coupling dGeo with the GEOPHIRES tool. (5) Developing a template for binary geothermal power plants via the GEOPHIRES techno-economic model to derive cost-capacity relationships for Engage, a flexible web-based energy planning model for district energy to national scales. (6) Updating the ground source geothermal heat pump (GHP) model in ResStock and ComStock, which are a probabilistic representation of the U.S. national building stock. (7) Expanding the GHP module of

the Renewable Energy Integration and Optimization (REopt®) platform for energy system integration and optimization by including more technology diversity and techno-economic optimization of GHP systems. (8) Updating and integrating the Urban Renewable Building and Neighborhood optimization (URBANopt™) model (campus- to building-scale energy model) with robust, validated, and extensible open-source software that enables the computational analysis for designing community-scale district GHP systems.

In addition to these model updates, large data collection efforts include analysis of heating and cooling demand in the United States for residential, commercial, industrial, and data center sectors; and inventorying, classifying, and analyzing low-temperature datasets in Alaska, Hawai'i, and the contiguous United States.

1. Introduction

Execution of the GeoVision study (Hamm et al., 2019) revealed a few shortcomings of National Renewable Energy Laboratory (NREL) modeling tools in accurately representing geothermal technologies. These shortcomings are related to three main areas: (1) insufficient resource supply data for geothermal energy relative to other renewable energy resources; (2) lack of, or incomplete, representation of geothermal technologies in tools used for capacity expansion modeling; and (3) lack of, or incomplete, representation of geothermal technologies in building heating and cooling models. To address these gaps, NREL kicked off a 3-year portfolio of data, modeling, and analysis projects in 2022 aiming to improve baseline geothermal resource supply data for use in models, update geothermal tools with current technology and resource information, and improve representation of geothermal technologies in a variety of NREL software tools. This paper presents results to-date from the first half of this 3-year effort.

Many of the models referred to in this paper have interdependencies. In parallel with the improvements described above, efforts were also made to align baseline datasets, inputs, and assumptions across models when possible and to streamline the outputs and inputs for better model coupling.

2. Geothermal Electricity Generation: Modeling Tool Updates

This section of models only considers geothermal power. The upgrades described here allow for more robust and spatially finer supply curves of geothermally powered electricity compared to the estimates utilized in GeoVision.

2.1 ReEDS: Regional Energy Deployment System

Capacity expansion models forecast how the future electrical grid can evolve by representing climate policies and balancing the investment costs and values of different power sources. The common result from capacity expansion models includes the total capacity and the amount of power produced, but sometimes it is not apparent why the model selected certain electricity generation sources to invest in. The Regional Energy Deployment System (ReEDS) is an NREL capacity expansion model.

Since 2009, ReEDS has been the primary analytical tool in several studies, including the Hydropower Vision (DOE, 2016), Wind Vision (DOE, 2015), SunShot Vision (DOE, 2012), Geothermal Vision (Hamm et al., 2019), and Renewable Electricity Futures (NREL, 2012). The annual *Standard Scenarios* report, which provides a U.S. electric sector outlook under a wide range of possible futures, utilizes ReEDS (Cole et al., 2020). ReEDS has also been used to examine the impacts of a range of existing and proposed energy policies (Gagnon et al., 2017; Lantz et al., 2014; Mai et al., 2012). The ReEDS website (https://www.nrel.gov/analysis/reeds/) includes an up-to-date list of publications that use ReEDS.

As part of this effort, ReEDS researchers aligned how geothermal is represented in ReEDS with other renewable energy resources. Geothermal resource classes are now binned using a 10-class resource definition with the geothermal resource directly related to the reservoir temperature (Table 1). This is consistent with the approach used for wind, photovoltaics, and concentrated solar resources.

Table 1: Technical Resource Potential (GW)

Resource Class	Reservoir Temperature (°C)	Hydrothermal	Near-Field EGS	Deep EGS
Class 1	> 325		0.2	
Class 2	300–325	1.8	0.2	
Class 3	275–300	9.3	0.1	1.2
Class 4	250–275	0.7	0.1	8.2
Class 5	225–250	1.1	0.1	74
Class 6	200–225	2.4	0.2	320
Class 7	175–200	0.2	0.3	709
Class 8	150–175	2.6	0.3	995
Class 9	125–150	1.1	0.03	1270
Class 10	< 125	4.7	-	-
Total		23.9	1.4	3,375

EGS = enhanced geothermal system

With these improvements, ReEDS was used to evaluate value streams and competitiveness of geothermal electricity generation. Value streams include revenue obtained from all grid services, including energy, operating reserves, planning reserves, and reserved planning services. These value streams represent a more comprehensive picture compared to the more standard levelized cost of energy (LCOE) metric, which only considers the energy value of a plant and does not consider the interactions during operations between technologies. Competitiveness is a measure of

how much additional revenue or how much costs would need to be reduced to develop a specific resource.

Three types of future uncertainty were explored to understand how the value and competitiveness of geothermal power evolve in ReEDS: 1) Grid decarbonization, 2) Uncertain availability of emergent technologies, and 3) Limited resource availability for land-intensive renewables. Results suggest that while all the future uncertainties could improve the value proposition for geothermal power, the size and exact effects varied significantly. In the event of all three occurring simultaneously, the value of geothermal improves by 33%, and there is an order of magnitude greater geothermal capacity.

With decarbonization policies alone, the ReEDS model predicted no strong impact to the total geothermal electrical generation revenue, although the capacity value represented a higher fraction of revenues. Reduced cost metrics had more impact: a substantial divergence between a 95% and 100% decarbonization was observed, especially after $1,500/kW. Reduced resource availability showed small increases in geothermal revenue in scenarios such as drought and limited land access, with the reduced cost cases also showing small impacts. The most substantial change was observed in the technology availability grouping, where a restricting carbon capture and storage scenario increased value stream revenue by 7% and a restricting of carbon capture and storage, H_2, and nuclear small modular reactor increased revenue by 33% (Figure 1).

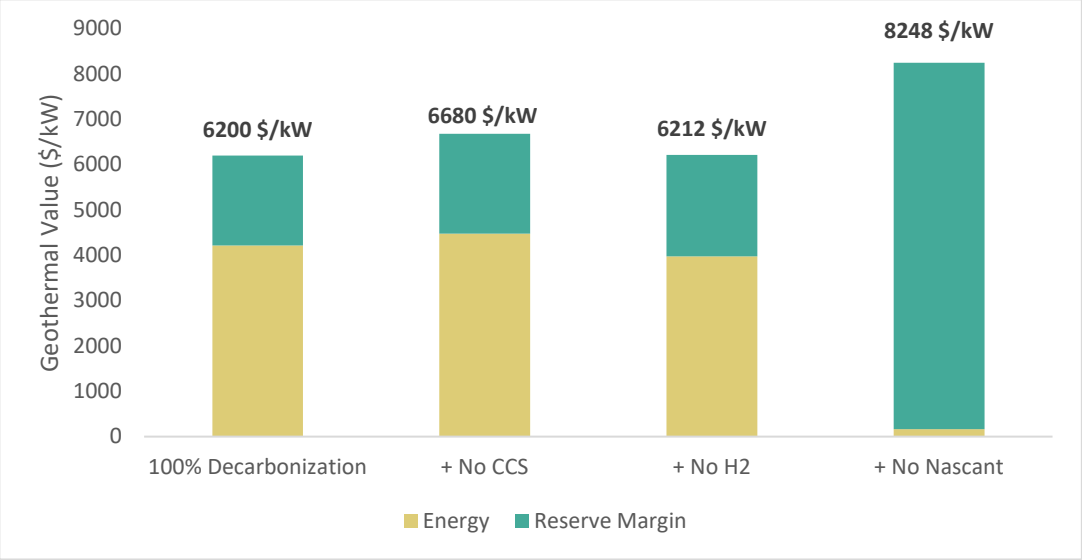

Figure 1 Value composition for geothermal power under select scenarios in 2050.

We found that the interactions in the assumptions of an uncertain future had substantial value implications for how the model predicted geothermal electricity generation to deploy with respect to other technologies. The change in value metrics within geothermal and among technologies in ReEDS provided useful insight into model behavior and useful context for consumers of capacity expansion model results to help them interpret the results by indicating the exact services provided by an invested grid technology and the economic value of those services, which are not well captured by metrics such as LCOE. Reduced cost metrics show how close undeveloped geothermal technologies are to deployment. These metrics allow decision makers to consider economic

viability of geothermal alongside other values and planning priorities not considered in a capacity expansion model.

2.2 reV: Renewable Energy Potential model

The Renewable Energy Potential (reV) model is a geospatial platform for estimating technical potential and developing renewable energy supply curves, initially developed for wind and solar technologies. The model evaluates deployment constraints, considering land use, environmental, and cultural factors, and estimates the distance to existing grid features to connect future plants (Maclaurin et al., 2021). Until last year, representation of geothermal electricity generation technologies was a pressing deficiency in the reV model.

In FY23, the reV Geothermal project brought representation of geothermal electricity generation closer to parity with wind and solar technologies in reV, and thus in downstream bulk power system models for the contiguous United States. The new geothermal module in reV relies on the U.S. Department of Energy's (DOE's) Geothermal Electricity Technology Evaluation Model (GETEM) implemented in the System Advisor Model (Blair et al., 2018). Both hydrothermal and enhanced geothermal systems (EGS) with binary and flash power plants are implemented. We developed the module to be flexible and extensible such that geothermal supply curves can rely on different geothermal resource datasets, support a wide range of deployment assumptions, and accommodate future improvements to data and modeling approaches.

This novel geothermal generation module in reV allows for representation and analysis at the same level of detail as other renewable technologies. We released the geothermal module as part of the open-source reV model to enable public access and encourage external collaboration. The process for evaluating data sources for the modeling and the initial reV geothermal results using two resource data sets were presented at the Geothermal Rising Conference (Pinchuk et al., 2023). Several sensitivity runs were presented. The results are encouraging, showing competitive LCOE values utilizing 2023 annual technology baseline (ATB) hydrothermal and EGS drilling costs.

The supply curves and LCOE results, which are posted on the DOE Geothermal Data Repository and NREL Geospatial Data Science pages for easy access, should be considered preliminary because of the uncertainty in geothermal resource potential data. We present median LCOE values for the contiguous United States for three scenarios: one hydrothermal (3.5 km depth) and two EGS (4.5 km—see Figure 2—and 6.5 km depth). The capital and operating costs for each respective technology are modeled. The reV supply curves are compatible with the ReEDS model. Understanding the relative technical potential for geothermal will better inform policy and planning for a high penetration of renewable energy. This first year of the project established the modeling foundation for additional functionality and further innovation in modeling geothermal electricity generation for the bulk power system. We have already seen industry interest in these data and look forward to further engaging with the private sector and external collaborators.

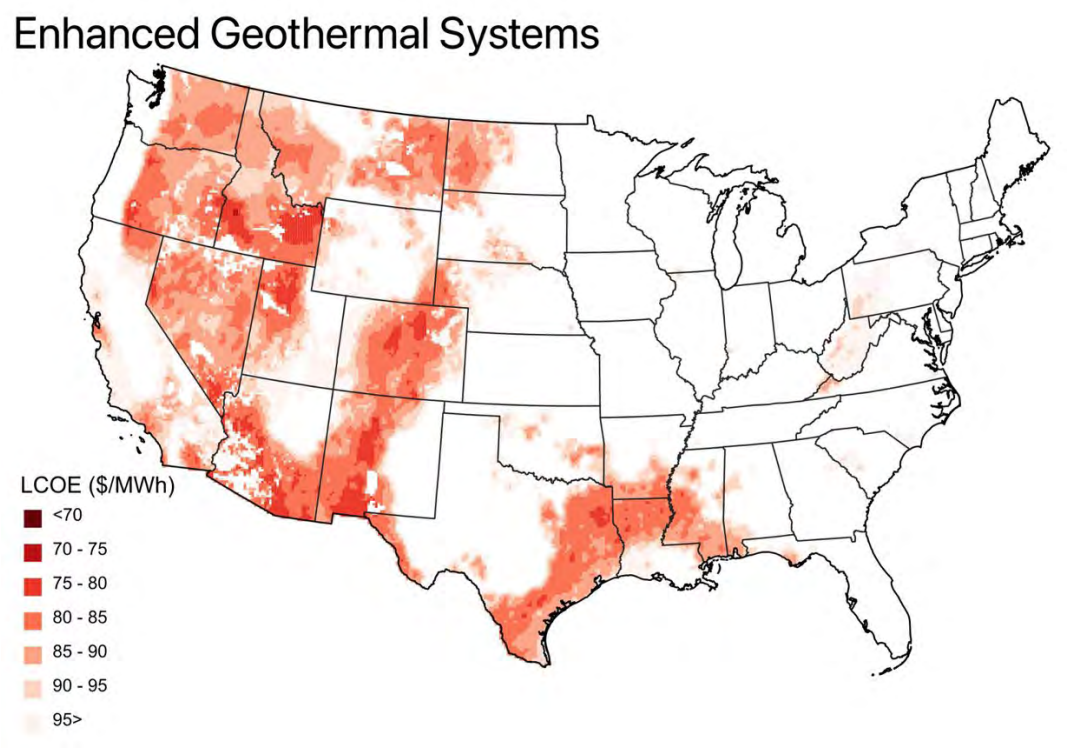

Figure 2: Projected LCOE using 2030 ATB Geothermal EGS Costs for 4.5 km depth

2.3 GETEM: Geothermal Electricity Technology Evaluation Model

The Geothermal Electricity Technology Evaluation Model (GETEM) is the prime techno-economic calculator for geothermal electricity for DOE. GETEM underwent several improvements to ensure accurate analysis of geothermal energy system costs, including a modification of the existing learning curve methodology used in the ATB projections. These costs were used for the geothermal inputs for NREL's ATB for 2023. Lastly, improvements to GETEM's functionality and user interface in the System Advisor Model were made.

Using data from industry and the Frontier Observatory for Research in Geothermal Energy (FORGE), EGS technology performance in the ATB is represented with reduction in exploration well requirements, increased exploration drilling success, and higher stimulation success rates resulting in a base year (2021 dollar) cost reduction from 41.3 c/kWh (in 2022) to 32.0 c/kWh (in 2023) for near-field EGS. NREL developed a new learning curve methodology to estimate future cost declines with respect to anticipated geothermal capacity deployments. The learning curve methodology, applied to the Moderate and Advanced ATB cases, is a single-factor model that accommodates historical "learning-by-doing" rates and learning rates experienced by the unconventional oil and gas industry (particularly for EGS). The learning-by-doing rate accounts for improvements in the cost of hydrothermal field development and plant construction that have driven historical capacity additions. For hydrothermal technologies, learning rates of 13% and 30% were defined for the Moderate and Advanced cases, respectively. For EGS technologies, the learning rates were 18% and 30%, respectively. This resulted in a better representation of cost reduction scenarios, especially for the Moderate ATB case.

NREL, the Geothermal Technologies Office, and industry stakeholders collaborated to ensure that the GETEM model assumptions for the 2023 ATB were aligned with current industry trends. Specific updates were made to delineate near-field EGS from deep EGS by treating the former as a brownfield that adjoins a producing hydrothermal resource. This resulted in a substantial reduction in the exploration costs for near-field EGS relative to deep EGS. Other significant changes to the GETEM input spreadsheets are listed in Table 2 and relate to those that characterize reservoir performance, drilling success, and plant contingency. We also aligned reservoir performance for hydrothermal resources with those encountered in real systems based on well flow and productivity data compiled by (Snyder et al., 2017).

Table 2: Updated GETEM input assumptions for EGS technologies

GETEM Input		**Near-Field EGS**			**Deep EGS**		
		Conservative	**Moderate**	**Advanced**	**Conservative**	**Moderate**	**Advanced**
ECONOMIC	Contingency	10%	10%	10%	10%	10%	10%
EXPLORATION	Successful Full-Size Wells	5	3	2	5	3	2
DRILLING AND COMPLETION	Success Rate (Exploration)	76%	76%	90%	52%	52%	90%
	Success Rate (Development)	76%	76%	90%	76%	76%	90%
	Success Rate (Stimulation)	75%	81%	90%	75%	81%	90%
RESERVOIR PERFORMANCE	Well Flow Rate	40 kg/s	80 kg/s (Binary) 60 kg/s (Flash)	110 kg/s (Binary) 80 kg/s (Flash)	40 kg/s	80 kg/s (Binary) 60 kg/s (Flash)	110 kg/s (Binary) 80 kg/s (Flash)
	Well Productivity	250 lb/hr-psi	1,365 lb/hr-psi	6,370 lb/hr-psi	250 lb/hr-psi	1,365 lb/hr-psi	6,370 lb/hr-psi
	Well Injectivity	300 lb/hr-psi	1,650 lb/hr-psi	7,645 lb/hr-psi	300 lb/hr-psi	1,650 lb/hr-psi	7,645 lb/hr-psi

2.4 GEOPHIRES tool

GEOPHIRES is a techno-economic simulation tool for analyzing geothermal technologies. GEOPHIRES stands for GEOthermal energy for Production of Heat and electricity IR Economically Simulated; “IR” represents electric current and resistance and refers to the electricity mode. GEOPHIRES is distinct from GETEM in that it can analyze both geothermal electricity generation as well as geothermal heating and cooling technologies (Beckers & McCabe, 2019). In FY23, GEOPHIRES, like GETEM, updated both the costs for the surface power plant and drilling

costs. Additionally, GEOPHIRES was used as the foundational code for two other modeling tool improvements: Engage (described next) and the Distributed Geothermal Market Demand Model (dGeo) (described in Section 3.2).

2.5 Engage

Engage is a flexible web-based energy planning model for scenario exploration from district energy to national scales. In FY23, the Engage team focused on allowing modelers to easily represent complex technologies such as geothermal bulk electricity generation technologies via Engage Technology Templates and invoking physics-based and techno-economic models for parameterized runs to derive cost-capacity relationships. The team implemented the new capabilities into Engage by building general purpose facilities in the database, user interface, and computational infrastructure (to invoke other physics-based models such as GEOPHIRES) along with new programmatic data exchange and translation capabilities to translate the physics-based model outputs to inputs appropriate to the Engage model.

The Engage model paradigm relies on archetype technologies that can be composed and configured to simulate real-world technologies such as solar photovoltaic, wind turbines, thermal power plants, etc. The compositions of these archetype technologies required to represent real-world technologies can be complex and require externally derived data to characterize their cost and performance characteristics. Engage Technology Templates allow for templating archetype technology compositions of any level of complexity and the automated translation of simulation and cost data into appropriate constraints in the Engage model via user-driven workflows.

Having developed the template and workflow capability, the Engage team developed a template for a Binary Cycle Subcritical Organic Rankine Cycle geothermal power plant relying on the GEOPHIRES techno-economic model to derive linearized cost-capacity relationships for Engage based on modeler input to the Engage template input forms. After the Engage inputs are derived from GEOPHIRES runs, the modeler can then instantiate the technology into the Engage model at the click of a button in the user interface. The new capability also implements application logic to allow the modeler to manage various components of the instantiated technology in ways that prevent inadvertent deletion of instantiated template technology components but facilitates reopening the template to edit and re-instantiate the technology.

The development of the template's capability was tightly integrated with other Engage development efforts including new carriers functionality allowing association of appropriate units of measure with each carrier in the model. Carriers in an Engage model refer to flows of energy or commodities. Engage models can now represent energy flows in, for example, kWh or MMBTU as desired and, for example, water flows in gallons or cubic meters with the capability to convert among compatible units of measure throughout the application seamlessly. This unit of measure functionality is fully integrated with Engage templates to facilitate unit of measure flexibility in template definitions, allowing modelers to think in familiar ways about the flows they are modeling and inherently document their models in terms of units of measure associated with their data sources, minimizing unit of measure errors. These combined features were tested and deployed to the live NREL-hosted Engage web application and are now accessible and usable by the general public and NREL modelers alike (https://engage.nrel.gov/en/login/?next=/en/).

3. Geothermal Heating and Cooling Model Updates

3.1 Geothermal Heating and Cooling (GHC) Geospatial Datasets and Analysis

Prior to evaluating the potential role of geothermal heating and cooling (GHC) in decarbonization strategies at different scales, better and more accessible baseline data and characterization for low- and medium-temperature geothermal resources is required. GHC is defined as "the utilization of geothermal energy underground or naturally arising at the surface of the ground for any purpose other than electricity generation" (International Geothermal Association, 2022). Some of the technologies associated with GHC are geothermal heat pumps (GHPs), geothermal direct use, and combined heat and power. The two aims of the "GHC geospatial datasets and analysis" project were: (1) establish baseline geospatial datasets for low-temperature resources (<150°C) relevant for evaluating GHC potential; and (2) establish a methodology for better geospatial analysis of low-temperature geothermal resources.

In the first phase of this project, we placed particular focus on the states of Alaska and Hawai'i because these states were excluded from prior geothermal potential evaluations because of a lack of data (e.g., GeoVision). We compiled baseline geospatial datasets for low-temperature geothermal resources including new data from oil and gas wells. Several low-temperature data inventories were submitted to the Geothermal Data Repository including Alaska, Hawai'i, and the contiguous United States (https://gdr.openei.org/submissions/1553 and https://gdr.openei.org/submissions/1518). Based on these compiled datasets, NREL's GeoRePORT Resource Size Assessment Tool was implemented to estimate the low-temperature resource base in Alaska (Figure 3).

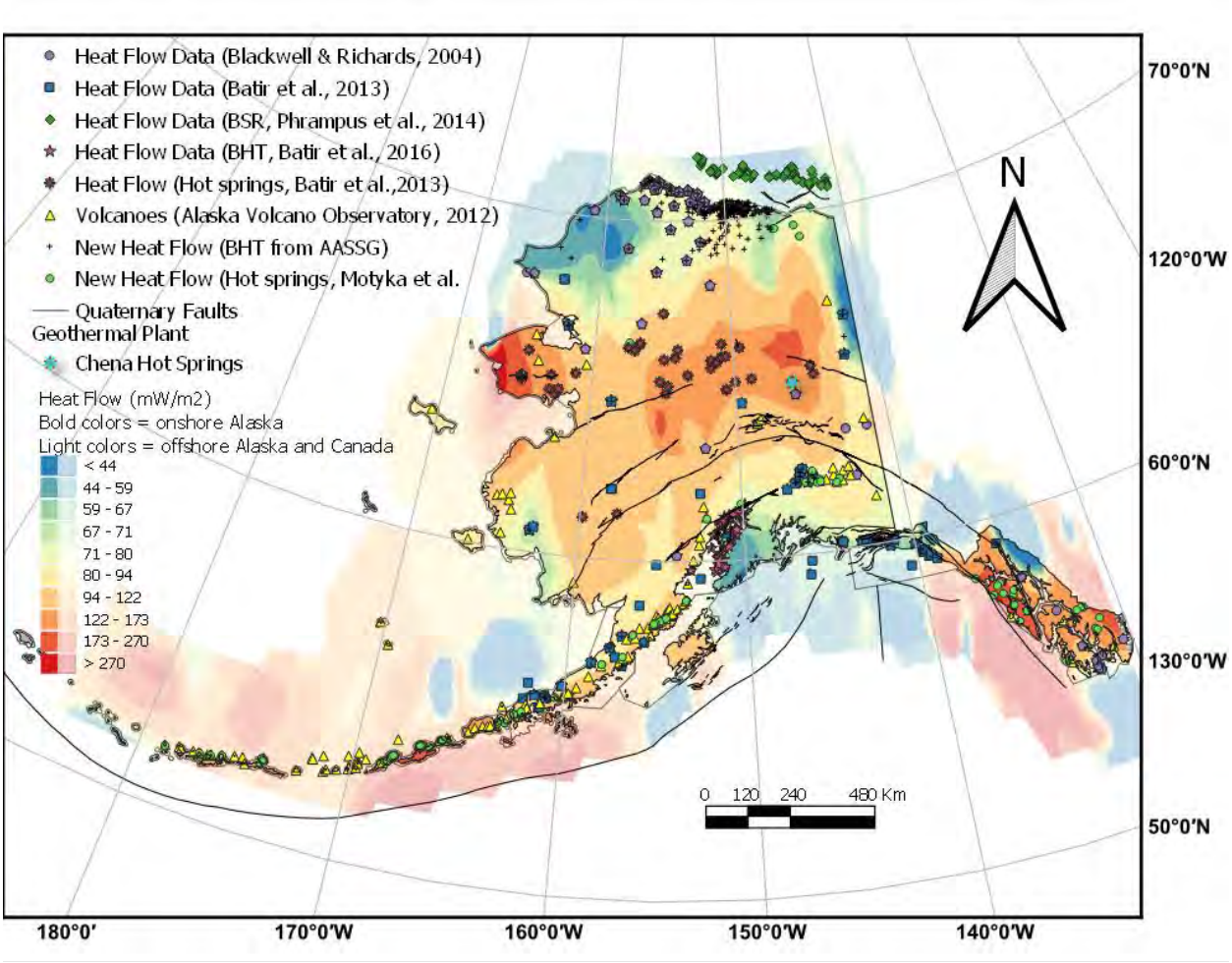

Figure 3: Updated heat flow map of Alaska modified from Batir et al. (2016). New heat flow values from 311 bottom-hole temperature data points by Association of American State Geologists and 72 hot springs by Motyka et al. (1983) were added to this version.

To establish a methodology for better geospatial analysis of low-temperature geothermal resources for GHC applications, a workflow based on prior work in geothermal Play Fairway Analysis was developed. A classification and characterization of low-temperature geothermal play types (sedimentary basins, orogenic belts, and radiogenic play types) and the identification of relevant data for exploration most suited to prospecting for these types of resources were presented at Geothermal Rising 2023 (Davalos-Elizondo et al., 2023).

Ongoing work includes compiling relevant data and Play Fairway Analysis workflows to the assessment of sedimentary basins for combined heat and power and direct uses, using the Denver Basin as an example. The goal of this project is to facilitate GHC analysis at multiple scales (e.g., national deployment analysis as well as community-scale planning). Additionally, a python code, geoPFA, was generated to create favorability maps, and it will be updated during the evolution of this and other projects at NREL. T The geoPFA Python library is expected to be released as an open-source tool in the future to enable others to use this code for their own PFA studies.

3.2 dGeo: Distributed Geothermal Market Demand Model

The Distributed Geothermal Market Demand Model (dGeo) was developed by NREL in 2016–2017 for use in the Geothermal Technologies Office-funded Geothermal Vision Study, with a primary objective of simulating the techno-economics of geothermal district heating systems and the adoption of GHPs. The tool is consistent with others in the family of Distributed Generation Market Demand models (Das et al., 2020), including the Distributed Solar Market Demand and Distributed Wind Market Demand models that explore the potential role of distributed energy resources in meeting energy demands in the United States. dGeo simulates the potential for deploying geothermal distributed energy resources in the residential and commercial sectors of the United States. Originally, GHPs and geothermal direct use for district heating could be simulated. Recently, an ambient temperature loop module was integrated in dGeo. To quantify the opportunity space for these technologies, dGeo leverages a highly resolved geospatial database and robust bottom-up, agent-based modeling framework. It can simulate the technical potential, economic potential, market potential, and technology deployment of geothermal technologies through the year 2050 under a variety of user-defined input scenarios. Through these capabilities, dGeo can provide substantial analytical value to various stakeholders interested in exploring the effects of various techno-economic, macroeconomic, financial, and policy factors related to the opportunity for GHP, geothermal direct use, and ambient temperature loop in the United States (McCabe et al., 2017).

The original model used simplified calculations to model the various aspects of a district heating system and, importantly, did not consider any physics-based representation to model the subsurface conditions. In this effort, dGeo was upgraded by integrating the updated GEOPHIRES v3 tool as the techno-economic engine that calculates surface plant considerations, subsurface conditions, and project economics. Coupling the more detailed modeling aspects of GEOPHIRES with the established, agent-based framework of dGeo enables more reliable, robust results for district heating system viability. In addition, GEOPHIRES has a built-in absorption chiller module and can be used to assess geothermal cooling. Further, the updated thermal demand maps for heating and cooling have been made available to use as input in dGeo.

To facilitate the coupling of the two models, we first updated the original source code for dGeo from Python 2 to Python 3. This enables the new model to use the latest capabilities from Python and to have longevity for future analyses. The new model also retains the original dGeo capability of simulating district heating systems for a comprehensive set of regions across the United States. The user can, for example, run dGeo for all counties of a single state for a more detailed analysis or can configure a scenario analysis for the entire United States, all while utilizing GEOPHIRES as the detailed techno-economic engine. Data input and output considerations are still handled based on the legacy GEOPHIRES setup—that is, dGeo will create a text file for the case considered, pass the file to GEOPHIRES for simulation, and then output results into dGeo for postprocessing needs (e.g., plotting, mapping).

We recently implemented several additional upgrades to dGeo including:

- Expanding the tool to Alaska and Hawai’i

- Upgrading the GHP module by leveraging ResStock and ComStock load profiles and the GHEDesigner tool for sizing the borehole field (Mitchell et al., 2023; Spitler, West, & Liu, 2022)
- Implementing a new module to simulate ambient temperature loops
- Updating the incentives database including accounting for the Inflation Reduction Act
- Incorporating the latest releases of the EIA thermal demand, building growth, and energy cost data.

An example dGeo simulation result for ambient temperature loops is shown in Figure 4.

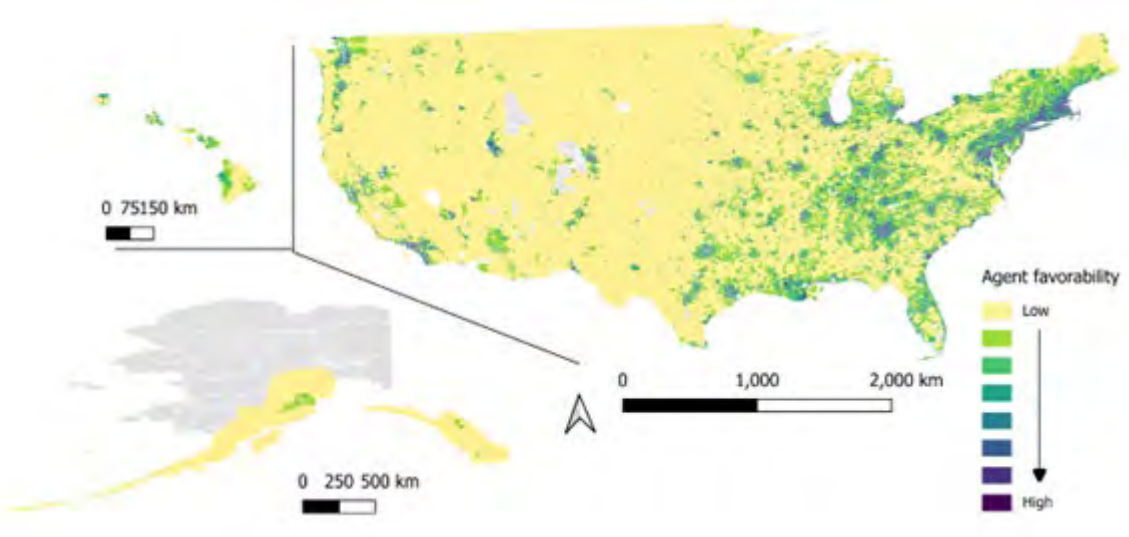

Figure 4: Example dGeo nationwide simulation run for ambient temperature loop, a new module recently integrated into dGeo (Simpson et al. 2024).

3.3 ComStock and ResStock: Commercial and Residential Building Stock

The ComStock and ResStock analysis tools developed and maintained by NREL help states, municipalities, utilities, and manufacturers identify which building stock improvements save the most energy and money. ComStock is a DOE model of the commercial building stock.

ComStock is a highly granular, bottom-up model that uses multiple data sources, statistical sampling methods, and advanced building energy simulations to estimate the annual subhourly energy consumption of the commercial building stock across the United States. ComStock asks and answers two questions: **(1) How is energy used in the U.S. building stock?** and **(2) What are the impacts of energy-saving technologies?**

ResStock leverages DOE's open-source building energy modeling ecosystem of OpenStudio® and EnergyPlus™. The model is a versatile tool that takes a new approach to large-scale residential energy analysis by combining large public and private data sources, statistical sampling, detailed subhourly building simulations, and high-performance computing to

accurately model the diversity of the housing stock and the distributional impacts of building technologies in different communities.

As part of this 3-year effort, the NREL ComStock and ResStock teams established a technical advisory group (TAG) of 15 academics, national laboratory researchers, and industry-leading companies, associations, and advocate groups. The TAG convened three meetings to solicit feedback and approval of the modeling methodologies and implementation. The TAG also conducted five focused interviews with specific technical advisory group members. TAG inputs, insights, and data were crucial to developing GHP functionality in the ComStock and ResStock tools, as well as others (e.g., Urban Renewable Building and Neighborhood optimization (URBANopt^{TM})).

3.3.1. Commercial GHP Modeling

During FY23, the ComStock team conducted research on the state of commercial-scale GHP systems through literature reviews, focus meetings with subject matter experts, and input from TAG members. Ultimately, the team selected three GHP configurations for modeling: central hydronic water-to-water, packaged water-to-air, and console water-to-air. The team developed extensive documentation explaining the applicability criteria, modeling methodology, and technical assumptions for each of these three systems. Three measures were developed in OpenStudio, which replace the existing system with the most compatible GHP configuration. The measures leverage an in-the-loop call to the GHEDesigner python package, which designs ground heat exchanger systems based on the time series of annual building loads and other borefield assumptions. The key output of GHEDesigner is the g-function, which are commonly used to simulate ground heat exchangers used with ground-source heat pump systems. The g-function is then imported back into the model and used in the final building simulation. Several output variables were added to the simulation that will inform the stock modeling results and analysis, including number of boreholes, borehole depth, ground heat exchanger flow, and GHP capacities. The team acquired real performance data representing the GHPs from Trane and Carrier and will integrate that data in the modeling in FY24 pending required OpenStudio capability upgrades.

3.3.2. Residential GHP Modeling

The major accomplishment of the residential GHP modeling in FY23 was updating the more than 10-year-old model of GHPs in OpenStudio-HPXML. To achieve this accomplishment, the team reviewed residential GHPs in the U.S. residential building stock. The team quantified the number of residential GHP systems and where they were located, identified correlations to various housing characteristics using U.S. Energy Information Administration's 2020 Residential Energy Consumption Survey (RECS), investigated installed mechanical equipment types and efficiencies, and reviewed the prevalence of geothermal loop configurations in the residential building stock. The team made numerous updates to the OpenStudio-HPXML GHP models including:

- Integrating a more complete and up-to-date published library of g-functions (Spitler et al., 2021; Spitler, West, Liu, et al., 2022) that support additional borefield configurations
- Updating ground thermal conductivity and undisturbed ground temperatures

- Expanding the input schema for HPXML
- Improving the borefield sizing methodology
- Providing fan and pump assumptions consistent with ISO 13256-1
- Updating GHP performance curves based on a newer GHP system.

3.4 REopt: Renewable Energy Integration and Optimization

REopt® (Renewable Energy Integration and Optimization) is NREL's techno-economic decision support model that evaluates the economic viability of grid-connected distributed energy resources at commercial and small industrial sites. A mixed-integer linear program, REopt optimizes distributed energy resource sizes and dispatch by minimizing system costs (and/or other energy goals such as resilience or emission reductions) over the analysis period, subject to system- and unit-level constraints. The GHP module of REopt has been expanded to increase its flexibility in configuring GHP, including hybrid vs. non-hybrid geothermal heat exchange system (Figure 5 and Figure 6) and central plant water-to-water GHP vs. distributed water-to-air GHP. The REopt help manual has been updated with details of these new capabilities, which are available in both the REopt Julia Package (REopt.jl) and web tool. Both the REopt Julia Package and web tool are open-source and can be accessed at https://github.com/NREL/REopt.jl and https://reopt.nrel.gov/tool, respectively.

In the web tool, when choosing GHP as one of the technology options, users now have access to four new inputs:

1) "Heat pump configuration" with the option to select "Central plant water-to-water heat pumps (WWHP)" in addition to the already available "Distributed water-to-air heat pumps (WAHP)"

2) "GHX configuration" with the option to select "hybrid" or "non-hybrid"

3) "GHX useful life (years)" with a default value of 50 years, which is used to calculate a residual value of the GHX if its useful life is longer than the analysis period

4) "Avoided HVAC upgrades ($)" with a default value of $0, which users can adjust if there are possible needed upgrades to their existing HVAC equipment, e.g., a chiller replacement, that could be avoided if a GHP retrofit is undertaken.

These new GHP configurations aim to improve the versatility of the REopt GHP module and the accuracy of its life cycle cost analysis.

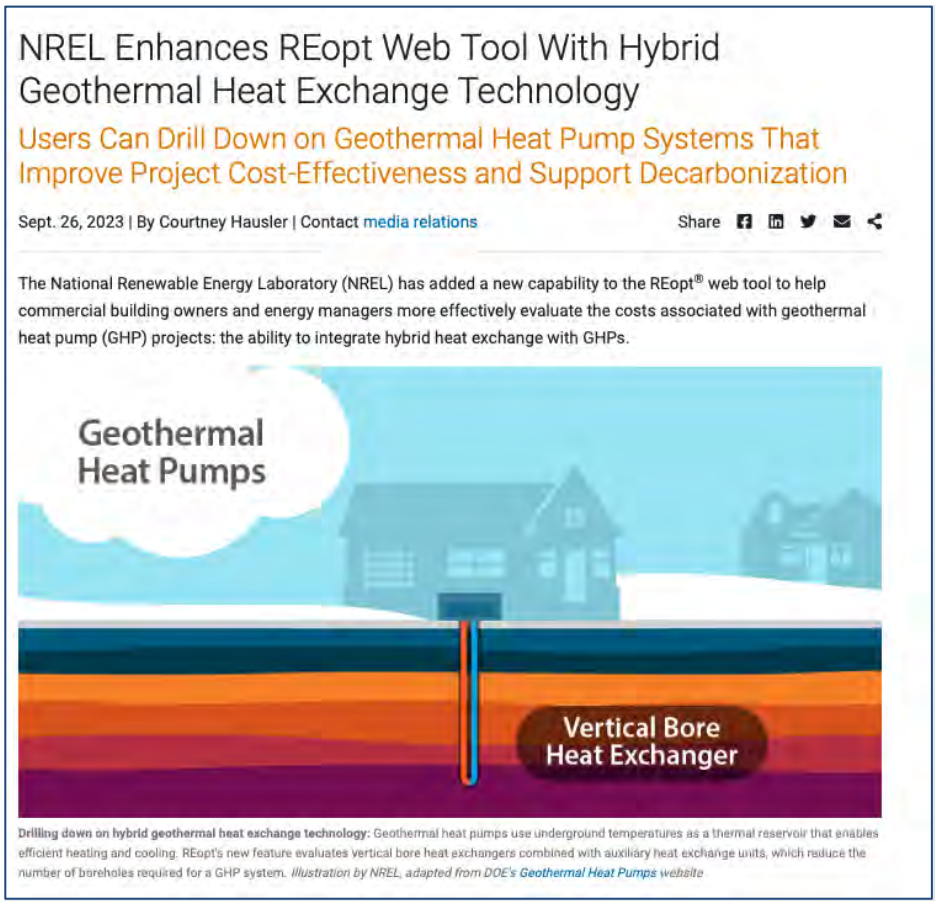

Figure 5: NREL news release of GHP inclusion to REopt web tool

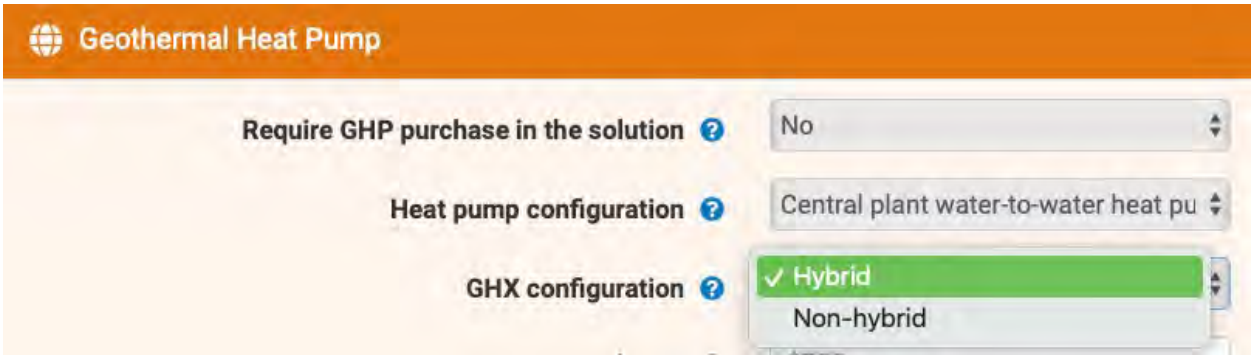

Figure 6: New GHP/GHX configurations in the REopt web tool

3.5 URBANopt™: Urban Renewable Building and Neighborhood optimization

Urban Renewable Building and Neighborhood optimization (URBANopt™) is an advanced analytics platform for high-performance buildings and energy systems within one geographically cohesive area in a city (e.g., a city block or district). URBANopt was developed by NREL to investigate:

- Detailed energy tradeoffs between building locations and geometry
- Building energy efficiency features

- Building and district energy storage strategies and technologies
- Aggregated grid services such as dynamic and responsive loads
- District energy system locations
- District energy system performance characteristics to identify best approaches for reaching site-wide energy goals.

URBANopt modeling capabilities leverage the DOE's open-source building energy modeling ecosystem of OpenStudio and EnergyPlus. The underlying URBANopt workflows and measures are open-source such that the broader urban energy modeling community can leverage them. Active partnerships to apply URBANopt for specific districts or neighborhoods, utility distribution feeders, and technology solutions are currently underway.

Updates for adding district-connected GHP systems were implemented to allow the tool to automatically calculate the size of GHEs (geothermal heat exchangers) given the campus thermal demand. In addition, URBANopt was updated to dynamically generate network models that represent the thermal pipe network and district energy systems with GHPs. The platform uses geometric and nongeometric user inputs related to the buildings, borefield, and district energy loop to generate these models that users can then apply to study the geothermal district GHP system. A case study was published to demonstrate the workflow and simulation result plausibility of the proposed platform (Wang et al., 2024).

4. Conclusions and Future Work

The DOE Geothermal Technologies Office is supporting a broad effort to demonstrate the multi-faceted value of integrating geothermal power and GHC technologies into national decarbonization plans and community energy plans. This paper presents a progress report on work performed by NREL to-date in updating flagship modeling tools and baseline data sets to better represent the state of the art in geothermal resource data, technologies, costs, and other key information. Model development is expected to continue, and future work will leverage these updated modeling tools to perform robust analyses of the role of geothermal power and heating and cooling technologies in decarbonization strategies across multiple scales.

Acknowledgement

This work was authored by the National Renewable Energy Laboratory, operated by Alliance for Sustainable Energy, LLC, for the U.S. Department of Energy (DOE) under Contract No. DE-AC36-08GO28308. Funding was provided by the DOE Office of Energy Efficiency and Renewable Energy Geothermal Technologies Office. The views expressed herein do not necessarily represent the views of the DOE or the U.S. Government. The U.S. Government retains, and the publisher, by accepting the article for publication, acknowledges that the U.S. Government retains a nonexclusive, paid-up, irrevocable, worldwide license to publish or reproduce the published form of this work, or allow others to do so, for U.S. Government purposes.

REFERENCES

Beckers, K. F., & McCabe, K. (2019). GEOPHIRES v2.0: Updated geothermal techno-economic simulation tool. *Geothermal Energy*, *7*(1). https://doi.org/10.1186/s40517-019-0119-6

Blair, N., DiOrio, N., Freeman, J., Gilman, P., Steven Janzou, Neises, T., & Wagner, M. (2018). *System Advisor Model (SAM) General Description (Version 2017.9.5)* (NREL/ TP-6A20-70414. .). National Renewable Energy Laboratory. https://www.nrel.gov/docs/fy18osti/70414.pdf

Cole, W., Gates, N., Mai, T., Greer, D., & Das, P. (2020). *2019 Standard Scenarios Report: A U.S. Electric Sector Outlook* (NREL/PR-6A20-75798). NREL. https://www.nrel.gov/docs/fy20osti/75798.pdf

Das, P., Sigrin, B., & Stanley, T. (2020). *Open Source dGen: Beta Release.* https://www.nrel.gov/docs/fy20osti/77705.pdf

Davalos-Elizondo, E., Kolker, A., & Taverna, N. (2023). Low- Temperature Geothermal Resources: Relevant Data and PFA Methods to Reduce Development Risk. *2023 Geothermal Rising Conference*. Preprint. Golden, CO: National Renewable Energy Laboratory. NREL/CP-5700-86889. https://www.nrel.gov/docs/fy24osti/86889.pdf

DOE. (2012). *SunShot Vision Study* (Technical Report DOE/GO-102012-3037). U. S. Department of Energy. http://www.nrel.gov/docs/fy12osti/47927.pdf

DOE. (2015). *Wind Vision: A New Era for Wind Power in the United States* (Technical Report DOE/GO-102015-4557). U. S. Department of Energy. http://energy.gov/sites/prod/files/2015/03/f20/wv_full_report.pdf

DOE. (2016). *Hydropower Vision: A New Chapter for America's 1st Renewable Electricity Source* (Technical Report DOE/GO-102016-4869). U. S. Department of Energy. http://energy.gov/eere/water/articles/hydropower-vision-new-chapter-america-s-1st-renewable-electricity-source

Gagnon, P., Cole, W. J., Frew, B., & Margolis, R. (2017). The impact of retail electricity tariff evolution on solar photovoltaic deployment. *Electricity Journal*, *30*(9). https://doi.org/10.1016/j.tej.2017.10.003

Hamm, S., Augustine, C., Tasca, C., & Winick, J. (2019). *An Overview of the U.S. Department of Energy's GeoVision Report: Preprint.* (NREL/CP-5500-74378). National Renewable Energy Laboratory. https://www.nrel.gov/docs/fy20osti/74378.pdf

International Geothermal Association. (2022). *Geothermal Heating & Cooling Data*. https://www.lovegeothermal.org/wp-content/uploads/IGA-Geothermal-Heat-Data.pdf

Lantz, E., Steinberg, D., Mendelsohn, M., Zinaman, O., James, T., Porro, G., Hand, M., Mai, T., Logan, J., Heeter, J., & Bird, L. (2014). *Implications of a PTC Extension on U.S. Wind Deployment* (Technical Report NREL/TP-6A20-61663). National Renewable Energy Laboratory. http://www.nrel.gov/docs/fy14osti/61663.pdf

Maclaurin, G., Grue, N., Lopez, A., Heimiller, D., Rossol, M., Buster, G., & Williams, T. (2021). *The Renewable Energy Potential (reV) Model: A Geospatial Platform for Technical Potential and Supply Curve Modeling*. https://www.nrel.gov/docs/fy19osti/73067.pdf.

Mai, T., Wiser, R., Sandor, D., Brinkman, G., Heath, G., Denholm, P., Hostick, D. J., Darghouth, N., Schlosser, A., & Strzepek, K. (2012). *Exploration of High-Penetration Renewable Electricity Futures. Vol. 1 of Renewable Electricity Futures Study* (NREL/TP-6A20-52409-1). National Renewable Energy Laboratory.

McCabe, K., Mooney, M. E., Sigrin, B. O., Gleason, M., & Liu, X. (2017). *The Distributed Geothermal Market Demand Model (dGeo): Documentation* (NREL/TP--6A20-67388, 1408285; p. NREL/TP--6A20-67388, 1408285). https://doi.org/10.2172/1408285

Mitchell, M., Lee, E., Spitler, J., Borshon, I., Cook, J., Liu, X., & West, T. (2023). *GHEDesigner [SWR-23-33]* [Computer software]. Oklahoma State University. https://doi.org/10.11578/DC.20230406.4

NREL. (2012). *Renewable Electricity Futures Study*. National Renewable Energy Laboratory. http://www.nrel.gov/analysis/re_futures/

Pinchuk, P., Thomsen, S.-M., Trainor-Guitton, W., Buster, G., & Maclaurin, G. (2023). Development of a Geothermal Module in reV: Quantifying the Geothermal Potential while Accounting for the Geospatial Intersection of the Grid Infrastructure and Land Use Characteristics. *Geothermal Resources Council Transactions, 47*, 2564–2586. https://www.geothermal-library.org/index.php?mode=pubs&action=view&record=1034921

Snyder, D. M., Beckers, K., & Young, K. (2017). Update on Geothermal Direct-use in the U.S. *Proceedings, 42nd Workshop on Geothermal Reservoir Engineering*. Stanford Geothermal Workshop, Stanford, CA.

Spitler, J., Cook, J., West, T., & Liu, X. (2021). *G-Function Library for Modeling Vertical Bore Ground Heat Exchanger.* [Dataset]. https://doi.org/10.15121/1811518.

Spitler, J., West, T., & Liu, X. (2022). Ground heat exchanger design tool with rowwise placement of boreholes. *Proceedings of the IGSHPA Research Track 2022*. International Ground Source Heat Pump Association. https://doi.org/10.22488/okstate.22.000016

Spitler, J., West, T., Liu, X., & Borshon, I. (2022). Open library of g-functions for 34,321 configurations. *Proceedings of the IGSHPA Research Track 2022*. International Ground Source Heat Pump Association. https://doi.org/10.22488/okstate.22.000040

Wang, J., Mitchell, M., Charan, T., Ball, B., Moore, N., & Haleem, S. A. (2024). *Development of a Sizing and Modeling Platform for District Energy Systems with Geothermal Heat Pumps*. https://www.nrel.gov/docs/fy24osti/87975.pdf.

Reservoir / Production

Temporal Evolution of Kamojang Reservoir Pressure: Unraveling Upflow Dynamics in a Dry Steam Geothermal System Through Multidisciplinary Analysis

Fathan Hamim Abdurachman, Sendy Hendriana, Baiq Lolla Riandari, Imam Muhammad Prasetyo, Cedric Cease, Pudyo Hastuti and Fernando Pasaribu

Pertamina Geothermal Energy, Grha Pertamina, Jl. Medan Merdeka Timur, Gambir, Jakarta 10110

Keywords

Kamojang, Dry Steam Reservoir, Reservoir Process, Conceptual Model, Upflow Dynamics, Reservoir Engineering, Geoscience

ABSTRACT

A geothermal conceptual model reflects our understanding of reservoir processes and is continuously refined and updated as the reservoir evolves over time. Since the commencement of its commercial production in 1982, Kamojang geothermal field has been gathering numerous static and dynamic data from new well drilling and continuous monitoring of the reservoir's responses to various development scenarios. Changes to the interpreted reservoir boundaries, structures, and reservoir interconnectivity are examples of what have been made to Kamojang conceptual model over the course of its exploration and development phases.

Reservoir pressure is one of the most important dynamic data to have to interpret the fluid flows and permeability in a geothermal reservoir. Furthermore, in dry steam reservoirs such as Kamojang with currectly low observable superheat, reservoir pressure is directly related to enthalpy and potential for steam production. This paper presents the effort of data processing and analysis of Kamojang reservoir pressure distribution that was mapped from 66 wells distributed throughout Kamojang geothermal field over the time span of about 42 years. The observed reservoir pressure behavior shows multiple pressure regions exists in Kamojang and each differs in pressure magnitude that is increasing from the West to the East part of Kamojang with all the regions sharing similar reservoir pressure decline. This pressure behavior implies effective lateral permeability between each pressure region and fluid flows from the East toward the West of the reservoir.

As the East side of Kamojang is characterized with high reservoir and shut in pressure suggesting that the area is connected to the upflow, interpreting the location of the upflow in a dry steam reservoir requires multidisciplinary analysis. Therefore this analysis is still needed to be integrated with other disciplines to validate this finding and further refine the Kamojang conceptual model.

1. Introduction

The development of a geothermal resource conceptual model is an information organizing principle that depicts those aspects of the geothermal reservoir that are most relevant to high value economic decisions like well targeting and capacity assessment and provides a scientific hypothesis that a well will confirm or refute [Cumming, 2016]. A geothermal conceptual model reflects our understanding of reservoir processes and, to build it properly, several main components have to be placed, namely; heat source, fluid phase, isotherm, hydrology, thermal manifestation, reservoir boundaries, structures and permeability distribution.

Interpreting the hydrology of a geothermal reservoir plays a vital role in determining the flow of hot fluids from the bottom of reservoir to the the upper part of the reservoir that is accessible for further utilization. An upflow zone in a geothermal reservoir is a near vertical flow zone of which occurs the major flow coming from the heat source to the commercial reservoir zone. For dry steam reservoirs the upflow can represent most of the mass entry and a significant fraction of heat entry into the reservoir. Generally the temperature in an upflow zone is the highest and it increases with depth along the upflow path. As the flow reaches the reservoir cap rock, the upflow zone transition to the outflow zone where the flow become horizontal and the temperature declines with distance and depth. For most geothermal reservoirs a recharge zone, as the name suggest is the zone where cold water enter the reservoir and recharges the reservoir fluid. Most recharge zones in a geothermal reservoir comes in permeable pathways crossing into the reservoir. This cold water can enter the reservoir from the side boundary due to pressure difference or it may also enter from the overlying aquifer at higher elevation than the water level in the geothermal reservoir. Again for dry steam reservoirs these are usually very small leaks that can increase steam condensation where they occur.

These fluid flows in the reservoir along with the mass and heat transfer in a geothermal reservoir can be interpreted from multidisciplinary analysis. This paper will focus on the reservoir engineering role to the extent of available surface and downhole pressure trend data in unravelling the upflow dynamic in Kamojang, a dry steam geothermal reservoir located about 42 km Southeast of Bandung, West Java, Indonesia. An upflow in a volcano hosted geothermal reservoir is likely to be associated with recent magmatic activity or deep fluid circulation that enables the flow upward from the heat source. Certain geologic settings needs to exist that creates vertical permeability on an otherwise impermeable rock deposition and act as a conduit to the commercial reservoir zone. In a dry steam reservoir, the reservoir cap rock is completely sealed from the surrounding aquifers keeping the reservoir fluid in the steam phase. Steam from the upflow will be redirected laterally once it hits the cap rock and flow beneath the cap toward the lower pressure part of the reservoir.

2. Geoscience

2.1 Background

Kamojang field lies in a Quaternary Volcanic complex of Mounts Guntur-Rakutak in the Southern West Java volcanic chain. Several volcanic edifices and caldera structures are recognized within the prospects. Geothermal features are also manifested within the volcanic complex and marks its resource area.

Mt. Rakutak-Guntur is a volcanic chain that trends West-Southwest to the East-Northeast where the volcanic activity was believed to take place since the Pleistocene along the axis. The volcanic activity moved away from Mt. Rakutak (1.02 ± 0.02 mA) towards East-Northeast where Mt. Sanggar-Gandapura and Mt. Sigit-Guntur erupted in 0.425 ± 0.015 mA and (0.025 ± 0.1 mA) respectively. Another prominent volcanic feature in this area is the Pangkalan caldera where it erupted prior to the Mt. Masigit-Guntur eruption. Major geothermal activity is located within the Pangkalan caldera and Masigit-Guntur areas. The magmatic composition of this volcanic chain is predominantly Andesitic to Basaltic Andesite. Although there is also an indication of a compositional evolution to be more basaltic towards the eastern volcanoes such as Mt. Guntur.

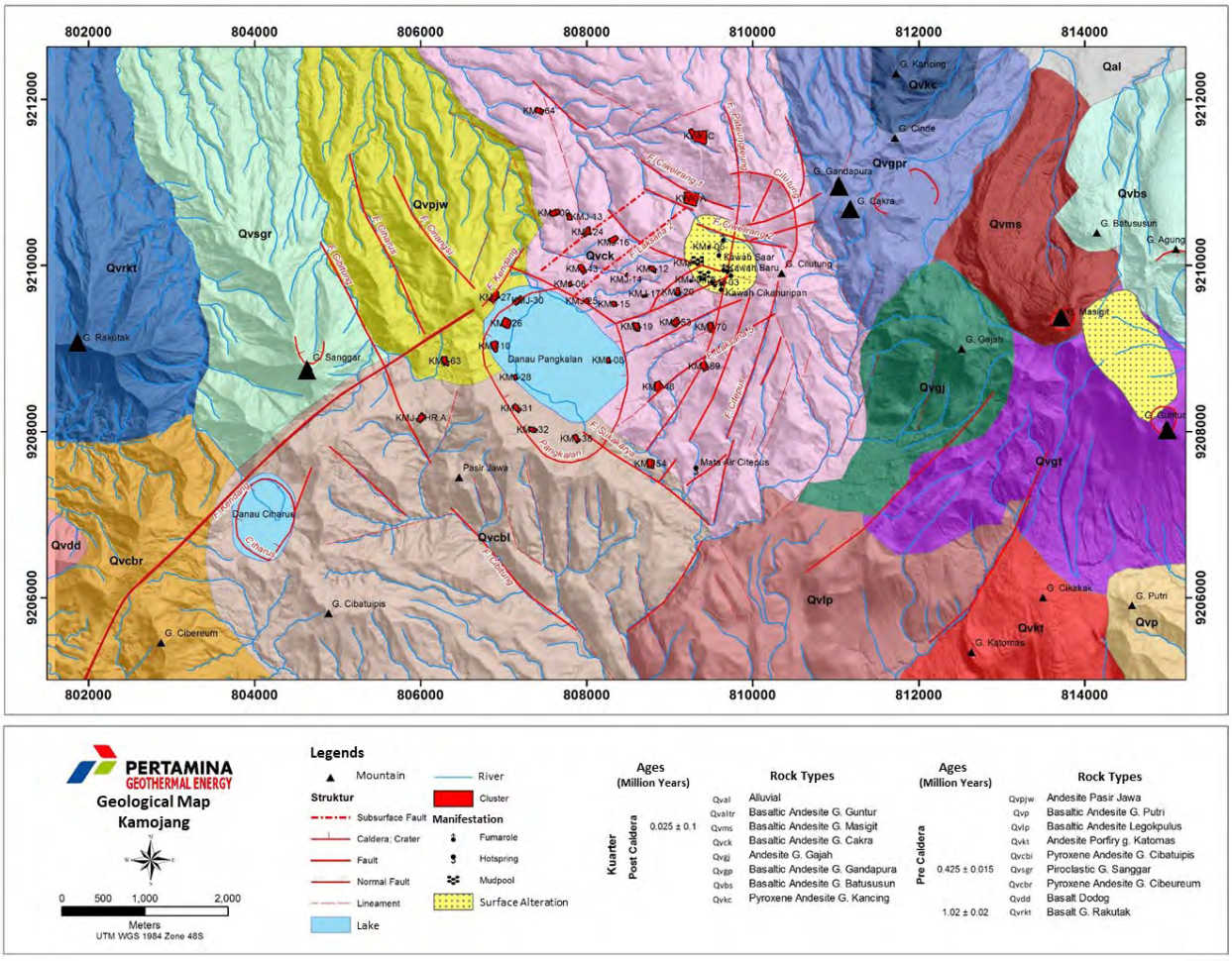

Figure 1: Geological Map of Kamojang

The main structural trends in the area are Northeast-Southwest and Northwest-Southeast where the most notable faults are the Kendang and Pateungteung-Citepus in the West and east respectively. Both faults act as the prospect boundaries on the West and East parts of the area. The Kendang fault extends to the Southwest where the neighboring vapor dominated field is situated, Darajat field. Kendang is a tensional fault that may have constructed the graben-like structure along the West part of the volcanic axis. Upon the extension of this fault zone, volcanic edifices developed. Another prominent structure is the Rim of Pangkalan caldera. The rim is about 2 km wide. The structure is shaped like a half circle and the scarp can be seen on the West to South. The North-Eastern side is unclear due to deposits of younger Cakra volcanics covering the area.

Distribution of geothermal manifestations mainly occur in the North-Eastern part of the area at the slope of the Gandapura volcanic complex. The type of manifestations found are predominantly steam heated features such as fumaroles, steaming ground, solfatara, acid sulphate hot springs and mud pools covering an area about 14 km2. Warm bicarbonate springs seeps to the surface on the creek along the Citepus fault in the North part of the area. The characteristics of the fluids are the following; the temperature of the springs are about 93-95^{o}C, close to the local boiling point, discharging large volumes of steam, the hot springs are typically acid (pH 2) and contains 1000-2000 ppm sulphate with small amounts of chloride (< 5 ppm). Isotope studies suggests that the water is of local meteoric origin. It has been heated by steam containing hydrogen sulphide which oxidises to sulphuric acid to give the waters a high sulphate concentration and low pH. The gas concentration in the vapor phase from the earliest exploration wells indicates a low content (less than 1%wt) with no significant amounts of magmatic contribution in the samples.

2.2 Existing Upflow Postulation

Geologically, the Kamojang geothermal model is controlled by a depressed structure named Pangkalan “caldera collapse” and Kamojang Crater, fault structure of Kendang Fault in the West, and Citepus-Pateungteung in the East. These structures in combination, was presumed to control the alterations and manifestations distribution, including the pattern of the MT resistive layer in the Kamojang area. The boundaries of Kamojang field laterally are limited to the West by the Kendang Fault, to the East by the Citepus fault, to the Northeast by the Gandapura-Cakra volcanic complex (which has not been delineated yet) and to the Southwest by the Ciharus volcanic crater.

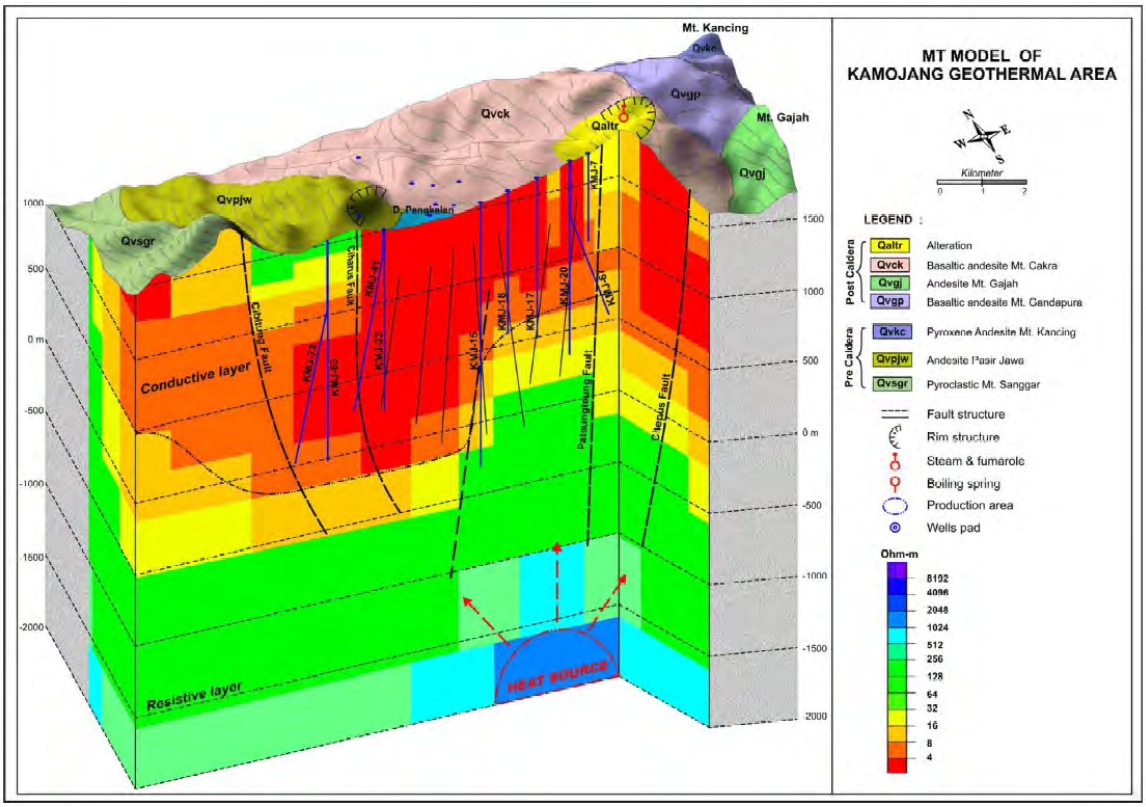

Figure 2: The thickness of the conductive and resistive zones of the Kamojang area based on MT data Geological Map of Kamojang

The Southwest and Northeast oriented sections of the geothermal tentative model were based on the integration of recent geoscience data as shown in Figure 2. Based on the gravity model, a high gravity anomaly occurs beneath the Gandapura-Cakra complex and a low anomaly beneath the Pangkalan area. Thus, it shows that a shallow intrusion is located beneath the Gandapura-Cakra that may act as a potential heat source. However, wells drilled inside and around the Pangkalan caldera rim reveal the extent of the dry steam reservoir with saturated temperatures. Consequently, the heat source may extend from Gandapura-Cakra to the Pangkalan area. The existing upflow zone interpretation is also supported by the previously observed geochemistry. The magmatic input was found on gas samples from wells located more to the Northeastern area. This is understandable since the evolution of young volcanoes are trending towards the Northeast. The wells drilled on the Northeast also shows higher temperature, pressure and productivity. The vapor fluid flowing laterally, creating a condensate layer on top of the cap rock. This condensate may move laterally and interact with shallow groundwater. One of the outflow evidence are found on the Citepus hotsprings, diluted HCO_3 water in the Southeast, away from the center of the Kamojang field. The marginal recharge from isotope data may originate from an elevation of about 1300-1700 masl.

2. Production Monitoring

Kamojang, similar with other geothermal reservoirs are monitored by observing mainly well parameter such as well pressures, flow rates, and enthalpies. Other valuable data that can be observed are the chemistry of produced fluids and micro-seismic monitoring. All monitoring data are incorporated into a geothermal reservoir management approach that continues to develop our understanding of the reservoir through all phases of its development.

2.1 Production History

The exploration of Kamojang field dates back to 1926. The initial phase of non-direct geothermal development was the generation of 0.25 MW from a mono-block unit in 1978, followed by the construction of power plant Unit 1, which went online with a capacity of 30 MW. The following years, multiple drilling campaigns were carried out to continue field expansion. Units 2 & 3 (2 x 55 MW) went online in 1987utilizing wells in the Western part of Kamojang then were followed by Unit 4 (60 MW) in 2008 and Unit 5 (35 MW) in 2015, each utilizing wells in the Southeastern and Eastern part of Kamojang respectively. After more than 40 years of development, there are currently 61 active production wells that and 6 wells active as injectors. There are also 27 other wells that are currently inactive with few acts as monitoring wells. The field is now producing 235 MW at full generation capacity from about 515 kg/s of steam production and giving an excess of 95 kg/s of condensate to reinject [Abdurachman, 2022].

2.2 Reservoir Monitoring

Since the first power plant unit deployment, a set of surveillance programs were set up to monitor the reservoir response. This paper presents the effort of data processing and analysis of the Kamojang reservoir pressure distribution that was mapped from 66 wells distributed throughout the Kamojang geothermal field over the time span of about 42 years as part of the ongoing collective works to characterize the Kamojang Reservoir and update its conceptual model. The wells used in this study are wells that are known to be free of wellbore damage or obstructions to ensure the pressure data used are representative of the normal reservoir response. The reservoir pressure data was taken from the downhole pressure and temperature survey of each well from its initial fully heated up condition together with the routine monitoring surveys. These pressure profiles taken from the selected wells are then normalized to 500 masl, the average main feedzones depth of kamojang reservoir to represent reservoir pressure. The next step is to ensure the pressure data quality by comparing the individual pressure data points with the overal pressure trend of each well within the time period and note if there is any specific well related activity that may compromise the quality of the data recorded. For example, a static downhole pressure and temperature survey that was done without the well reaching its pseudo-steady state pressure condition. Reaching the pseudo-steady state condition in a dry steam well can vary depending on the well and reservoir characteristics. Specifically in kamojang, on average, the production well requires about a month to reach steady state condition. While it is not ideal to do a downhole static pressure and temperature survey on a well still in its transient state, more than often, steam supply requirements take priority over reservoir monitoring.

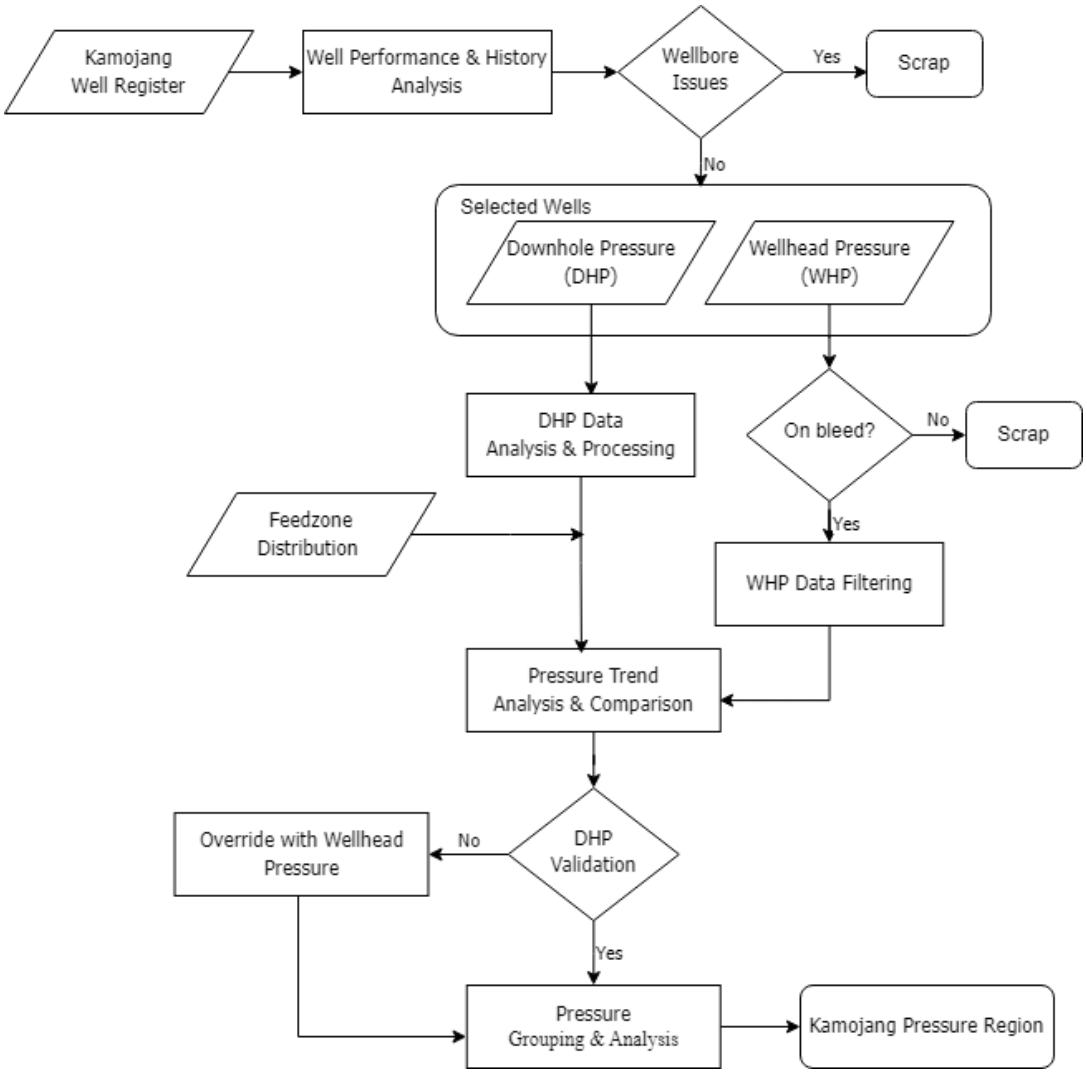

Figure 3: Workflow for Kamojang reservoir pressure data processing and analysis

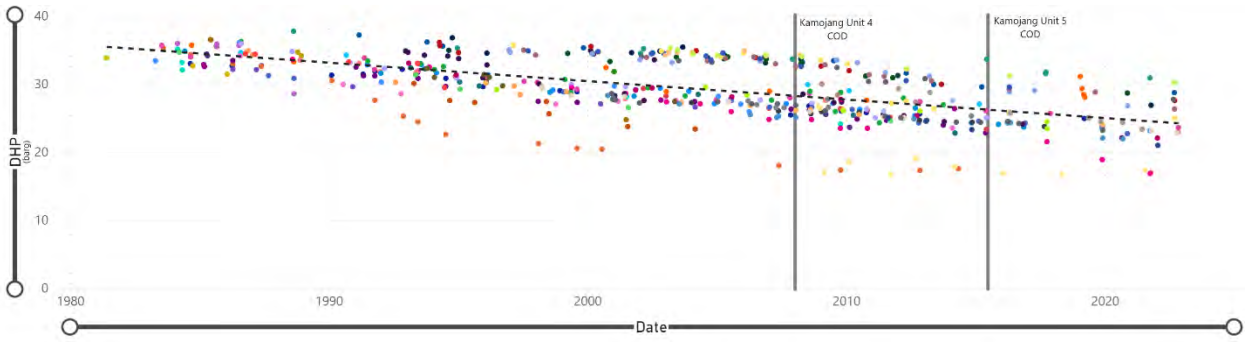

Figure 4: Kamojang collective downhole pressure in barg normalized to 500 masl depth

The last step of processing the collective pressure data is employing well head pressure data to help validate the downhole pressure. Since its a full length dry steam column inside every Kamojang well, well head pressure, adjusting for the vapor static gradient, can also be used as reservoir pressure. It has to be noted that the well head pressure used were only for wells on bleed condition. In Kamojang field, or any other dry steam reservoir field, it's a common practice to apply a very small bleed to inactive producer wells as a safety measure to vent the non-condensable gas coming from the reservoir. Furthermore, similar with the downhole static pressure and temperature survey conditions, care has to be taken to ensure that the well head pressure of the well already reached its pseudo steady state.

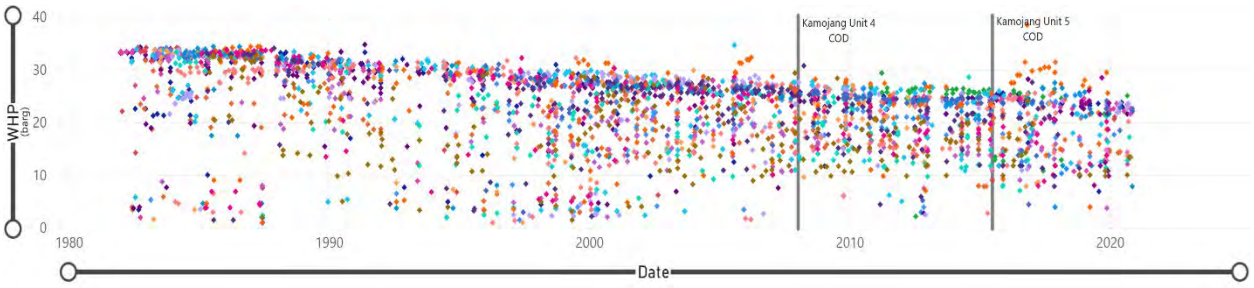

Figure 5: Kamojang Collective Well Head Pressure on Bleed in barg

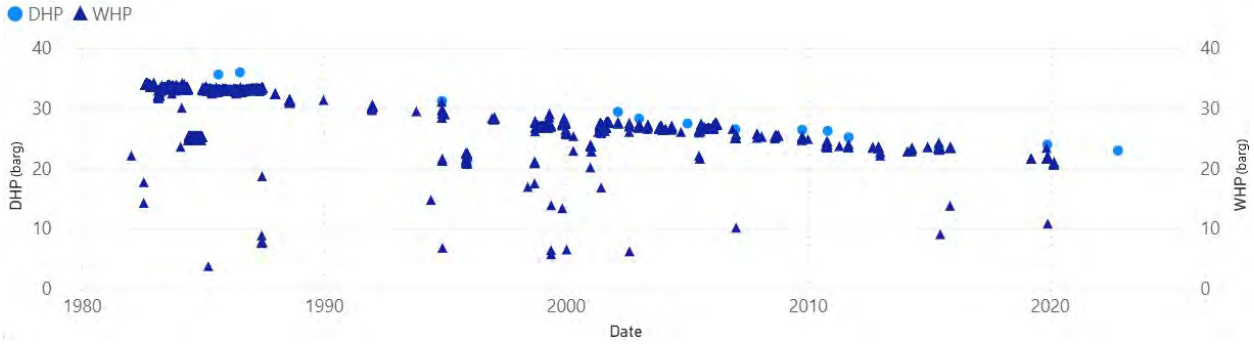

Figure 6: Comparing Downhole Pressure and Well Head Pressure in barg

Analysis of the processed reservoir pressure data set suggest there are multiple pressure regions in Kamojang. These regions are grouped by pressure trend line characteristics and simply named; high, medium and low pressure regions. The high pressure region as the name suggest is the region with the highest average reservoir pressure with 28 barg as observed in 2023 and includes most wells in the Eastern with all the wells in the Southeastern part of Kamojang. The medium pressure region has an average reservoir pressure of 24 barg in 2023 and include some wells in the central and Eastern part of Kamojang. The lower pressure region is the region with the smallest reservoir pressure of 22 barg in 2023 and includes the greatest number of wells compared to the other regions. Those wells are mainly located in the Western part of Kamojang with a couple wells in the Northern part of the field.

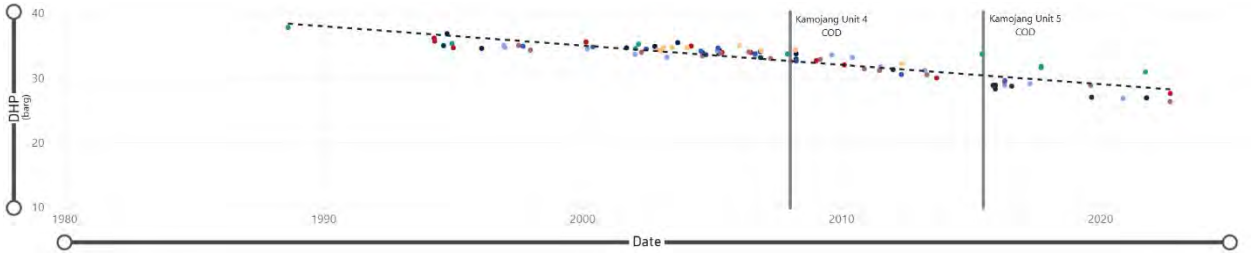

Figure 7: High Pressure Wells Grouping in barg

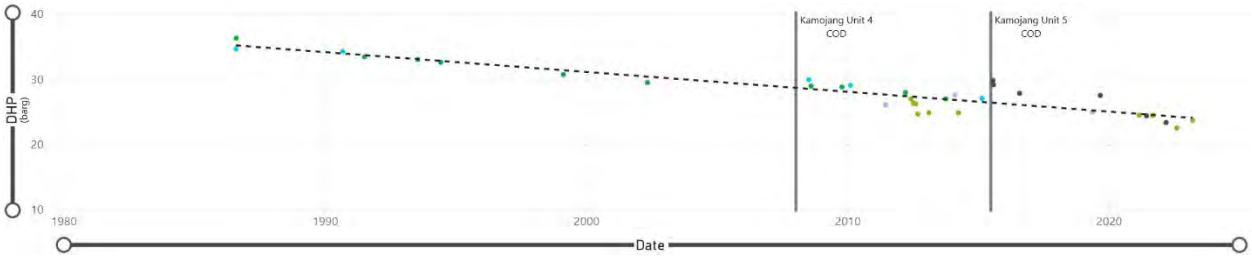

Figure 8: Medium Pressure Wells Grouping in barg

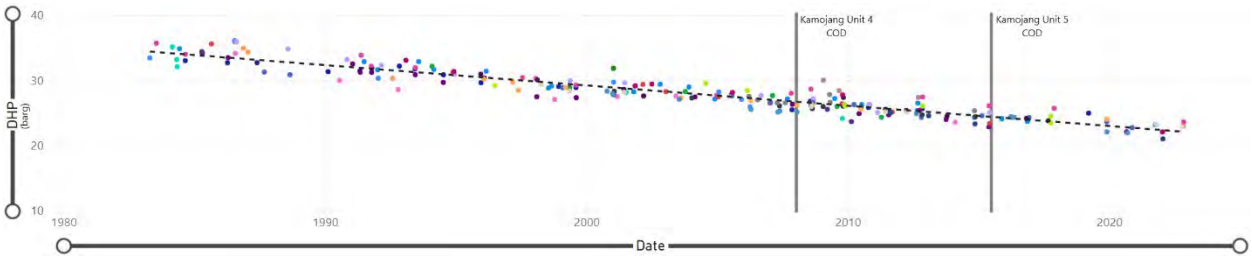

Figure 9: Low Pressure Wells Grouping in barg

Excluding wells with wellbore or reservoir issues, all the above mentioned pressure regions in Kamojang are sharing similar reservoir pressure declines ranging from 0.28 to 0.31 bar/year. While some transient declines were also observed in some of the wells due to initial production phase or power plant coming online, the observed pressure trends showshow the pressure of some wells merging with their each pressure group by the end of their transient period. Few clear examples on this phenomena were able to be observed in wells in North Kamojang that were initially deemed as high pressure wells, but are currently grouped in the low pressure region after their transient period ends. The uniform pressure decline behavior throughout Kamojang field implies two possible reasons; First is the effectiveness of reservoir lateral permeability and, second, that no subsurface structures inside the reservoir act as barriers between the defined Kamojang pressure regions.

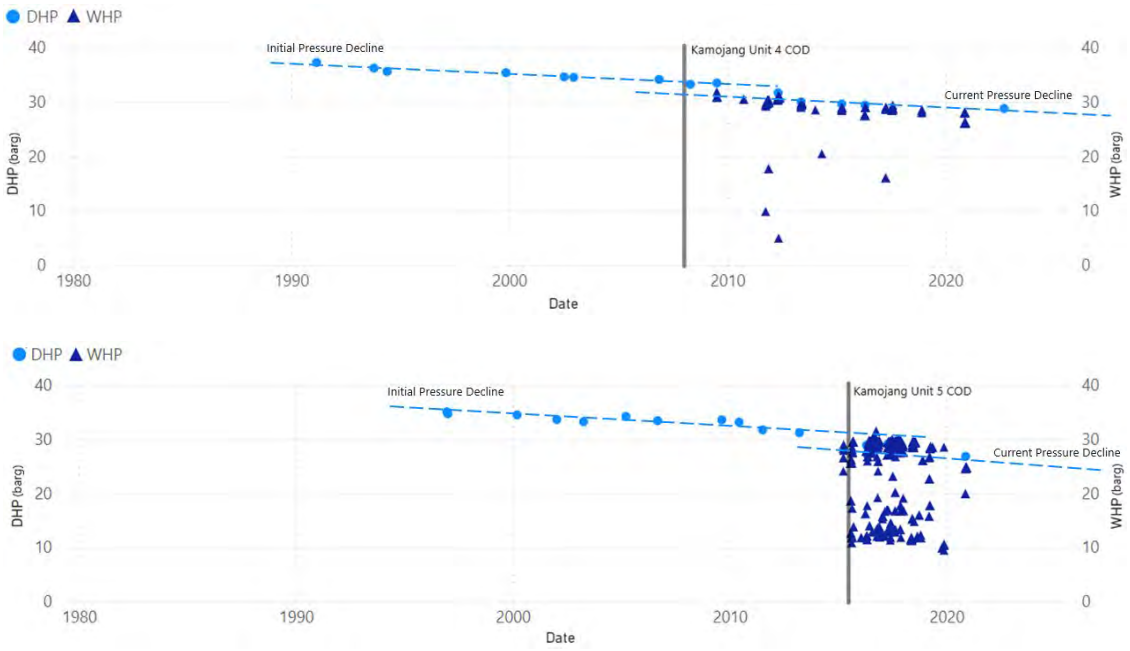

Figure 10: Transient Period During New Unit Commencing. Unit 4 (above) and Unit 5 (below) Timeline

Additional datasets were also analyzed to further test the above mentioned implication of the pressure data. Individual production rates were summed based on their respective pressure groups and observations were made to see the correlation between the cumulative production rates with the pressure decline of each pressure region. The result shows that field production changes with time does not correspond with the pressure decline trend. Pressure decline in Kamojang remain steady throughout the exploitation phases. This further supports the reasoning above on the effectiveness of the lateral permeability with no reservoir compartmentalization .

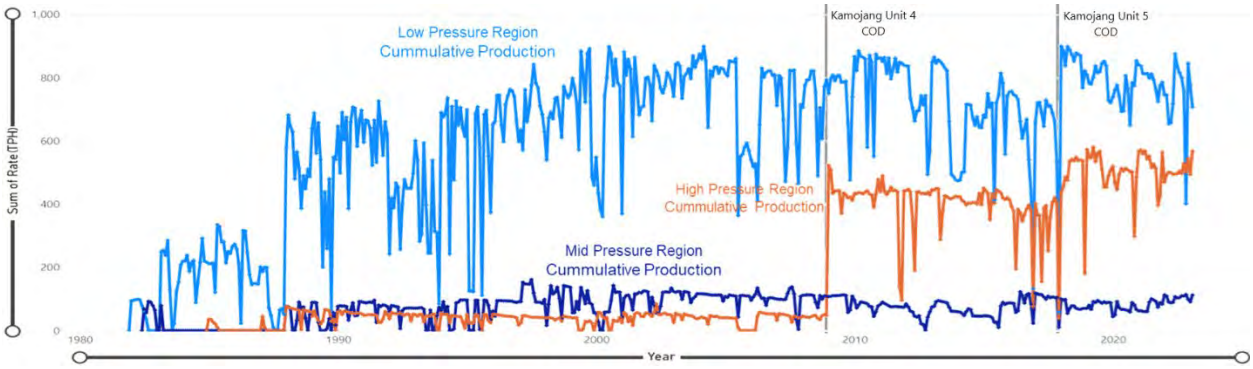

Figure 11: Kamojang Cumulative Production Rate in ton/hour per Pressure Region

2.3 Geochemistry Monitoring

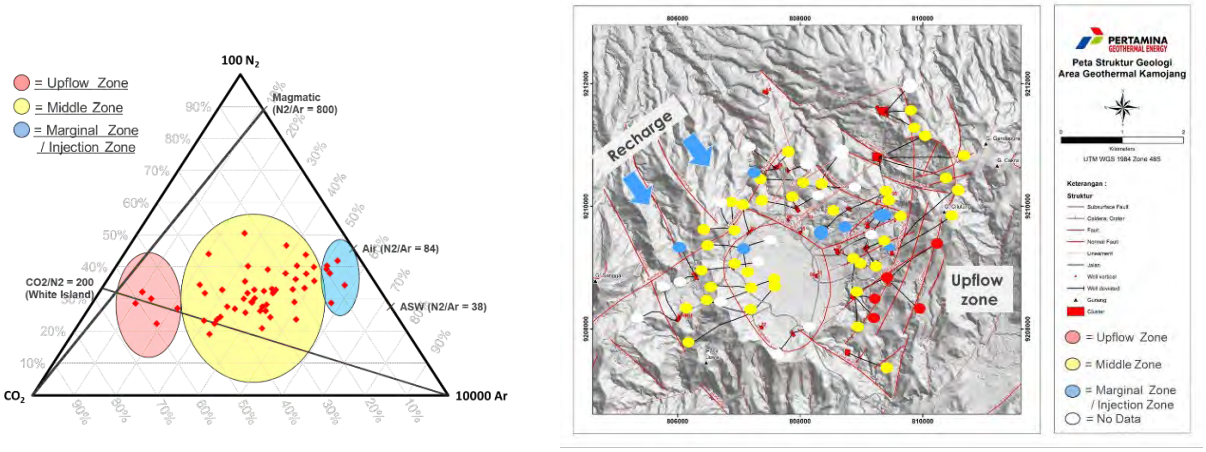

Figure 12: Kamojang Distribution Map of N2-CO2-Ar Trilinear Diagrams Plot

To determine the upflow based on geochemical data, the use of ternary diagrams is a common practice. Plot positions that are close to the magmatic line or peak of CO2 indicate that these wells are nearer to the upflow. In contrast, other wells are closer to the air point, indicating proximity to the outflow or being affected by injection, while the wells plotted in between indicate the middle zone. Geochemical gas data from Kamojang in this plot shows that wells in the upflow zone are situated in the Eastern part, while wells around Ciharus (SW area) indicate a marginal zone signature with high Ar concentration. Confirmation of the upflow and outflow positions in the Kamojang area is also supported by the CAR-HAR gas geothermometer, where wells in the upflow (Eastern part) area exhibit the highest temperatures, while wells in the Southwest area tend to have lower temperatures.

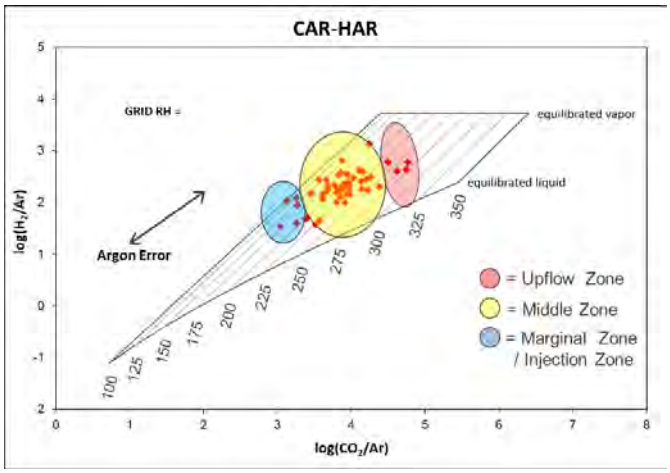

Figure 13: Gas Geothermometer CAR-HAR Shows High Temperatures For Wells in The Upflow Area

In addition to the two points above, in a steam-dominated geothermal system, NCG is also used to determine the upflow area and the edge area affected by condensation, marked by high NCG and CO2/H2S gas ratios. However, in Kamojang, these two indicators cannot be used. This is because the high NCG and the high CO2/H2S gas ratio in this area are more influenced by the high CO2 values than by a decrease in H2S values due to condensation. The CO2 values in these wells are

exceptionally high, exceeding 20,000 ppmw when compared to other wells, which have average values of 1,000-4,000 ppm. The area with this anomaly includes wells in the Eastern part and is assumed to be caused by a consistently high supply of CO2 gas in these wells, which is characteristic of the upflow zone. This is consistent with the results of the N2-CO2-Ar ternary diagram plot and the gas geothermometer, which also provide similar results, thus strengthening the hypothesis that the Kamojang upflow is located in the Eastern area.

In addition to determining upflow and outflow, the recharge zone in the Kamojang area is also identified using Oxygen-18 ($\delta^{18}O$) and Deuterium ($\delta^{2}H$) isotope data. Isotope data is collected from manifestations, wells, and shallow groundwater in the Kamojang area. These stable isotopes are commonly used in hydrology to trace the origin and movement of water, providing information about the sources and pathways of groundwater recharge. Based on isotope data in Kamojang, it is known that the recharge area is located at an elevation of 1300 masl in the SW and SSE, while the Kendang Fault is interpreted as a conduit, the entry point for marginal recharge into the Kamojang reservoir. This data is then integrated with other geochemical data and supports the hypothesis of the Kamojang outflow area being in the Southwest region

3. New Upflow Postulation

Referring to the reservoir and new geochemistry findings presented in this paper, it changes how the upflow dynamics are intepreted in the reservoir. From the previously interpreted upflow in Northeast Kamojang, beneath the Gandapura-Cakra complex, analysis and mapping of the pressure region shows that the Eastern and Souteastern parts of Kamojang is characterized with the highest reservoir pressure suggesting a new hypothesis that these are the areas with the most steam recharge likely to be interpreted as an area near the upflow. The drop of reservoir pressure from the Eastern to the Western parts of Kamojang also suggest that the steam flow is getting weaker with distance from the East of Kamojang. A similar hypothesis also comes from the new geochemistry interpretation by the N2-CO2-Ar ternary diagram and CAR-HAR geothermometer suggesting that the Kamojang upflow is located in the Eastern part of the field. However strong this hypothesis, it still needs to be integrated with the ongoing revisit of the geological and geophyisical studies to validate the new interpretation and further refine the Kamojang conceptual model.

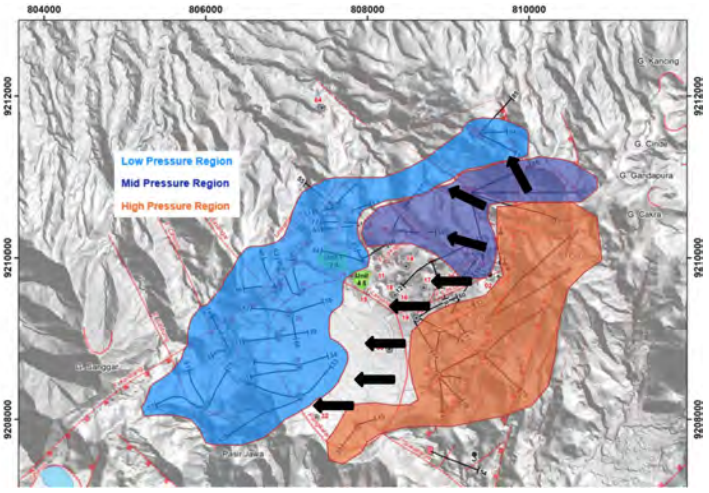

Figure 14: Reservoir Pressure Grouping of Kamojang & Suggested Lateral Steam Flow

4. Impact to Resource Assessment

Updating the Kamojang conceptual model is a continuous process, even after more than 40 years worth of data. It is a primary component in understanding the reservoir for which the upflow dynamic is still being unraveled. The newly postulated upflow will bring new constraints to the reservoir process uncertainty and ultimately affecting the resource capacity. Re-assessing Kamojang resource requires multiple stages. The first stage is the ongoing PGE effort to redefine the conceptual model where it serves as a guide in setting up the next stage. The second stage is numerical simulation. Numerical reservoir simulation has been proven as the most reliable option for geothermal resource assessment. It is a more advanced tool that models the physics of fluid flow and heat transfer and the complex nature of reservoir geometry [Ciriaco, 2020]. The existing reservoir model owned by PGE needs to be updated and re-calibrated to its natural state condition and production history following the interpreted reservoir process in the revised conceptual model. The first two stages will be fundamental to assess the Kamojang resource and support its future business decision as the last stage will be to generate production forecasts from the reservoir model to optimize the development plan further.

5. Conclusion

Processing and analyzing reservoir pressure data from the Kamojang wells suggests there are multiple pressure regions existing in the field. These regions are each grouped using pressure trend line characteristics and simply named; High, Medium and Low pressure regions. Each pressure region has its own pressure magnitude with the highest reservoir pressure in the Eastern and Southeastern Part of Kamojang and the lowest in the Western part of Kamojang. All the pressure regions are sharing similar reservoir pressure declines throughout the exploitation period.

The mapping of the pressure regions suggests a new hypothesis that the Eastern part of Kamojang is the area with the most steam recharge likely to be interpreted as an area near the upflow. The drop of reservoir pressure from the Eastern to the Western part of the field also suggests that the steam flow is getting weaker with distance from the East of Kamojang. The lateral steam flow from Eastern to the Western direction is also supported by the pressure decline characteristics. The uniform pressure decline throughout the pressure regions implies the effectiveness of the reservoir lateral permeability and that there are no subsurface structures in the reservoir acting as barriers between the defined pressure regions. Similar conclusions were also coming from the new geochemistry study suggesting that the Kamojang upflow is located in the Eastern part of the field and replaces the previous interpretation that it is located beneath the Gandapura-Cakra complex in the Northeast.

However, these newly combined hypothesis from reservoir engineering and geochemistry still needs to be integrated with the ongoing review of both geological and geophyisical studies to validate the new interpretation of the upflow dynamics and further refine the Kamojang conceptual model. The new conceptual model will be fundamental to fully assess the field resource and support its future business decision to optimize the development plans in the future.

Acknowledgement

We extend our sincerest gratitude to all those in Pertamina Geothermal Energy Reservoir and Geoscience team who have contributed to the completion of this paper. We also thank our families for their unwavering encouragement.

REFERENCES

Fathan H. Abdurachman et al. “Kawah Kamojang Pilot Injection Test: Production Monitoring Evaluation and Numerical Reservoir Modelling Study to Support Kamojang Injection Optimization Program”. *45th New Zealand Geothermal Workshop* (2023).

John O’Sullivan et al. “Numerical Modelling of the Kamojang Geothermal Field” *Internal Report Pertamina Geothermal Energy*, Jakarta, Indonesia (2022).

Imam M. Prasetyo, Sardiyanto et al. “Kamojang Geothermal Field Conceptual Update” *Internal Report Pertamina Geothermal Energy*, Jakarta, Indonesia (2020).

Anthony E. Ciriaco, Sadiq J. Zarrouk, Golbon Zakeri. “Geothermal resource and reserve assessment methodology: Overview, analysis and future directions.” *Renewable and Sustainable Energy Reviews* (2020)

William Cumming (2016). “Resource Conceptual Models of Volcano-Hosted Geothermal Reservoirs for Exploration Well Targeting and Resource Capacity Assessment: Construction, Pitfalls and Challenges.” *Geothermal Resources Council Transactions* (2016)

Suryadarma, Dwikorianto, T., Zuhro, A. A., Yani, “Sustainable Development of the Kamojang Geothermal Field.” Geothermics 39 (2010), 391–399.

Suryadarma, Azimuddin T Dwikorianto et al. “The Kamojang Geothermal Field: 25 Years Operation.” *Proceedings World Geothermal Congress*, Antalya, Turkey (2005).

Mammoth Casa Diablo IV: A Case Study for Cooperative Baseline Analysis to Mitigate Environmental Impacts

John Akerley, Mark Hanneman, John Murphy, Adam Johnson, Drew Spake, Erica Freese, Derek Caro, Danny Feucht, Lu Lee

Ormat Technologies, Inc., Reno NV

Keywords

Casa Diablo, groundwater monitoring, case study, Long Valley, Mammoth, cooperative monitoring

ABSTRACT

The Mammoth Geothermal Complex has been in operation since 1984, and during this timeframe it underwent several expansions and repowers prior to the 2022 commissioning of the Casa Diablo IV station (CDIV). Due to its proximity to population centers, groundwater wells, hot springs, and thermal creeks, a fit-for-purpose monitoring network was installed ahead of field expansion to understand potential environmental impacts. Ormat cooperated with the Bureau of Land Management, the U.S. Forest Service, the U.S. Geological Survey, and the Mammoth Community Water District to collect and analyze baseline data prior to drilling new production and injection wells to support the CDIV project. During the CDIV commissioning, this monitoring network was reviewed as output from the new geothermal production wells was ramped up in incremental steps over a four-week period. The combination of strategic downhole pressure monitoring, geochemical monitoring, temperature monitoring, and ground leveling provided confidence that there would be no measurable impacts to nearby water resources, including thermal features and municipal water supply wells from CDIV operations. Now two years into operation, the water monitoring network continues, and no impacts have been identified.

1. Introduction

Ormat operates four binary geothermal power plants located about three miles east of the town of Mammoth Lakes, California and near the Casa Diablo hot springs. The binary cycle works by using hot geothermal fluid to vaporize a secondary working fluid like isobutane, which then powers a turbine. This process not only allows an efficient extraction of energy from the lower temperature geothermal resource compared to the steam turbine design but also allows 100 percent reinjection of geothermal brine. The first power plant at the site (G-1) began operating in 1985. Binary plants G-2 and G-3 were constructed in the early 1990s. In 2022, the fourth unit, the 30

megawatt (MW) Casa Diablo IV (CDIV) binary unit began commercial operation, bringing total production to 65 MW. Figure 1 shows the total production history of the Casa Diablo/Mammoth complex from 1985 to present, highlighting periods of increase in the early 1990s with expansion of two additional binary units and again in 2022 with the CDIV expansion. Throughout this timeframe, the total thermal-water discharge into Hot Creek, located east of the geothermal operations, has not changed (Evans et al, 2018).

Exploration drilling by the United States Geologic Survey (USGS), Ormat and others determined that the geothermal system's source area was west of the original Casa Diablo development in an area known as Basalt Canyon. Deeper wells drilled in the area in 2006 (57-25 and 66-25) were higher enthalpy (up to 375° F) than the lower Casa Diablo producers, highly permeable, and hydraulically connected to the Casa Diablo area. Further drilling at the western end of Basalt Canyon in 2010 (wells 12-25 and 14-25) also encountered the resource, leading to project release of CDIV.

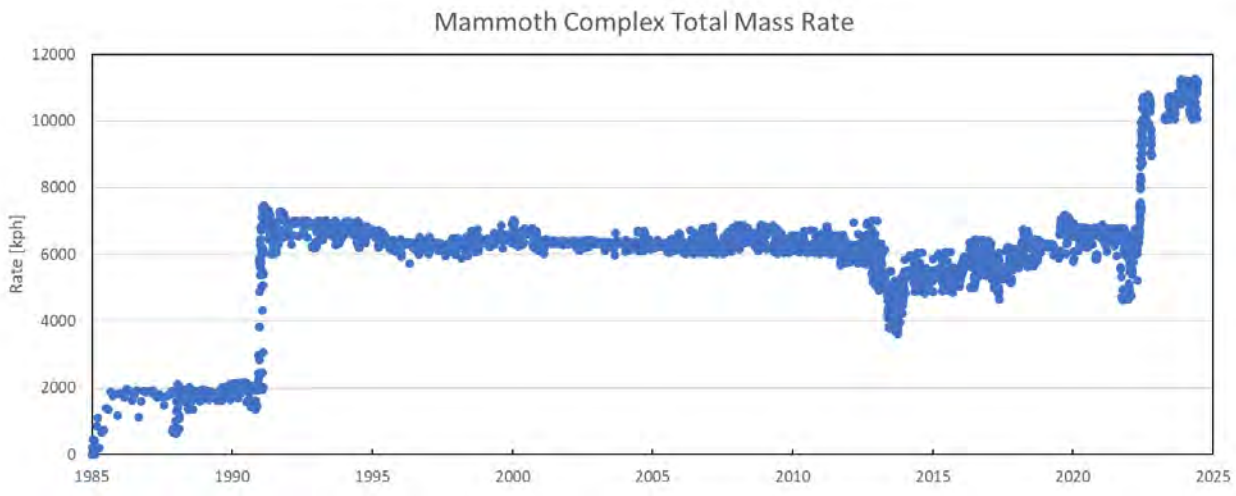

Figure 1: Total mass rate from the Mammoth geothermal complex since installation of the first binary unit in 1985 through June 2024. Flow unit is thousands of pounds per hour (kph).

A combined Environmental Impact Statement/Environmental Impact Report (EIS/EIR) was completed in 2013 that evaluated the potential impacts from CDIV development. All of the new production well sites were to be located in Basalt Canyon, closer to the town of Mammoth Lakes and to municipal water supply wells operated by the Mammoth Community Water District (MCWD). Since the community relies on these wells for drinking water and there are many stakeholders near the development, a special emphasis was placed on assessing potential impacts to that groundwater resource. Although geologic and hydrologic modeling indicated that the two systems were hydraulically disconnected and that impacts would not occur, it was decided that a fit-for-purpose groundwater monitoring and mitigation program would be implemented prior to initiating production in order to ease concerns around the development.

The CDIV Geothermal Development Project, Groundwater Monitoring and Response Plan (GMRP) was developed cooperatively by the BLM, Ormat, USGS, MCWD and the other agencies and finalized in January 2018. The purpose of this GMRP was to *"establish a monitoring program to detect any direct or indirect effects on the municipal water supply for the Town of Mammoth*

Lakes that may occur from geothermal production and injection associated with the CD-IV Project."

The objectives of the GMRP were to:

1) Identify and implement shallow groundwater aquifer, surface water resource, and deep geothermal reservoir monitoring strategies and protocols necessary to achieve this purpose, and

2) Establish a framework for determining and implementing appropriate response actions if, and when, needed to avoid, minimize, and/or mitigate potential adverse effects to the Town of Mammoth Lakes municipal water supply based on review and analysis of the monitoring data collected.

To meet these objectives, the GMRP outlined: 1) monitoring strategies, 2) data management, data reporting and plan evaluation strategies, and 3) response action strategies.

The GMRP is a cooperative, adaptive effort. An adaptive management approach was preferred because the committee recognized that hydrologic systems are dynamic and many factors can impact groundwater quality and quantity outside of geothermal production including climate, annual precipitation and its effect on aquifer recharge, variable groundwater production, regional seismic activity, and other natural source areas of geothermal fluid. As data is collected and analyzed, the monitoring strategy is reassessed, and new or refined approaches, methods or frequency are developed or optimized to ensure that the plan remains effective and practicable.

2. Geologic Setting

The Casa Diablo geothermal resource is present within a large volcanic feature known as the Long Valley Caldera. The geology of the caldera and the geothermal resources have been extensively studied and described over the past 35 years by Hildreth (2004, 2014, 2017), Bailey (1976), Sorey (1985, 1991, 1998), Suemnicht (1988), Evans (2017), and others. The following briefly summarizes these reports.

2.1 The Geothermal Resource

The geothermal resource wraps around the south and southwest margin of the resurgent dome in a hydraulically interconnected, highly-permeable zone of fractured welded tuffs belonging to two main units known as the Early Rhyolite and the underlying Bishop Tuff. The system's source area is believed to originate at great depth north of the town of Mammoth Lakes and near the Inyo Craters, another 3.5 miles northwest of Basalt Canyon. Due to difficult terrain and the depth needed to reach the resource, few wells have been drilled west of Basalt Canyon, so the exact source area remains uncertain. Figure 2 shows the regional geology and resurgent dome from Hildreth (2017).

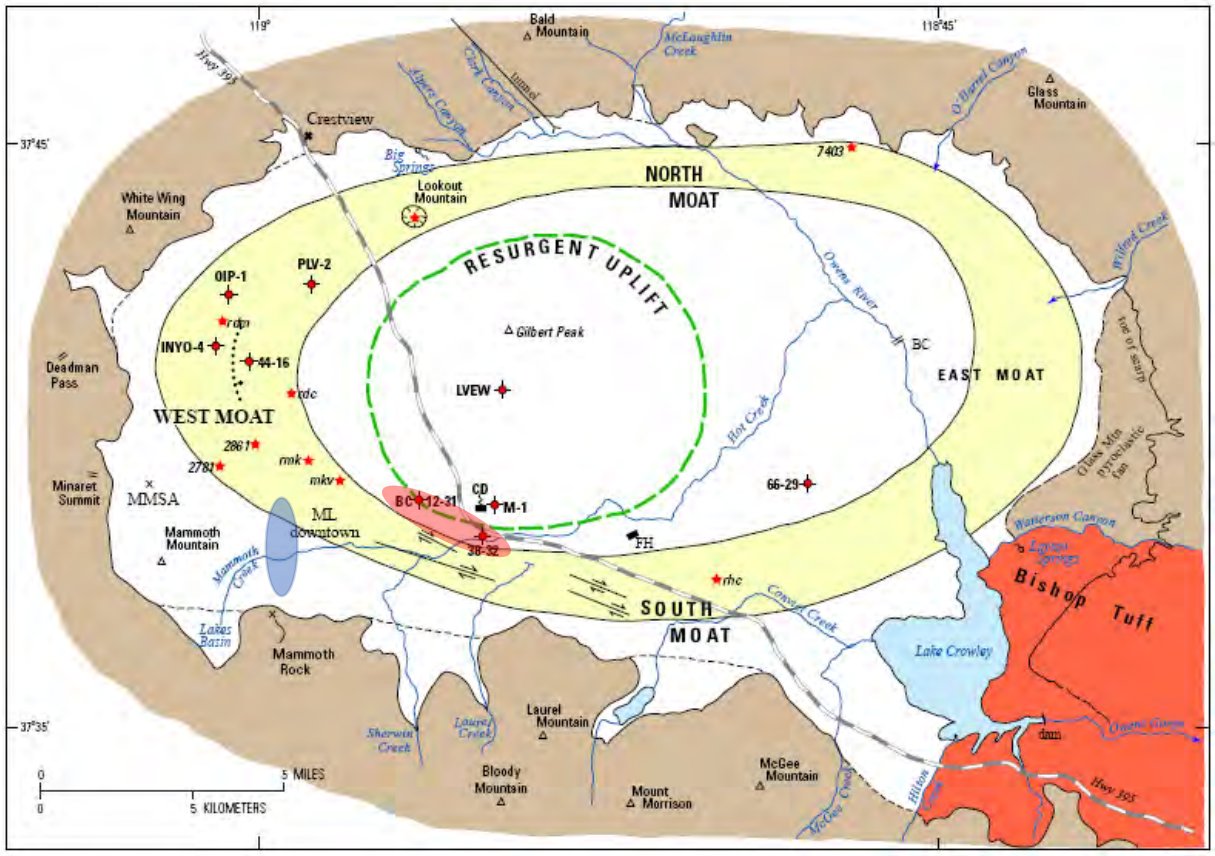

Figure 2: Figure from Hildreth (2017). The resurgent dome is comprised of Early Rhyolite, while basalt flows infill the south and west moat. General location of Ormat geothermal wells highlighted in the red oval, and groundwater municipal wells highlighted in blue oval. Legend: structural ring-fault zone (yell), Precaldera rocks (brown), Bishop Tuff ignimbrite outflow (red), dashed lines crossing caldera-wall embayments suggest continuity of basement rocks concealed beneath modern surficial deposits.

The geothermal production wells in Basalt Canyon include 57-25 and 66-25 drilled in 2005; 14-25 in 2010; 12-25 in 2011; and 47-25 (drilled next to 57-25), 14B-25 and 14C-25 (both drilled adjacent to 14-25) drilled in 2022. The wells have been drilled right up to the eastern edge of the West Moat Coulee where the system was first encountered in wells 14-25 and 12-25.

The system flows eastward through Basalt Canyon, beyond Casa Diablo, to Hot Creek where it ultimately discharges to the surface in a series of hot springs. Total system flow is reportedly 370 kg/s (about 5,500 gpm) at 220° C. The system has a relatively flat horizontal gradient due to its high permeability. In Basalt Canyon, the static water level in the production wells is about 450 feet below the surface and within the Early Rhyolite tuffs. As topography drops from west to east, the water level slowly approaches the land surface, until the system discharges into Hot Creek several miles east of Casa Diablo.

Basalt Canyon wells typically encounter high enthalpy fluids at a depth of about 1,000 ft in a moderately permeable zone in the Early Rhyolite. Below this is a thick section of tuff breccias, and clastic/lacustrine sediments and conglomerates that are essentially impermeable. These materials are underlain by the Bishop Tuff. Total lost circulation in the Bishop Tuff is limited to specific fractured zones, and is encountered at depths ranging from 1600 to 2100 ft. This lower

zone is highly productive but is generally cooler than the upper zone in the Early Rhyolite. The high permeability is likely a combination of open fractures along steep faults passing through brittle welded tuffs, and possibly along undetermined horizontal surfaces on top of individual welded tuff layers.

Cooled fluids from all production wells are reinjected into the deep Bishop Tuff at Casa Diablo near the G-2 and G-3 power plants. Injection wells 54A-32 and 54B-32 were drilled in 2021 for CDIV. There is little communication of this deep injection with the overlying production wells in the Early Rhyolite, but tracer studies in 1992, 2017, and 2023 have shown eventual migration of injection in Bishop Tuff to the Lower Casa Diablo producers.

The resource is bounded on the south by the ring fault zone which places down-dropped moat basalts against the Early Rhyolite. Geophysics indicates that the rings faults likely underlie Highway 203; however, the fault zone is entirely covered by till and younger basalt flows and is nowhere exposed, nor has it been intercepted by drilling. The mag low may be partially masked by basalt flows north of Highway 203.

A few test wells drilled south of Basalt Canyon within the moat and into the underlying Early Rhyolite have not encountered temperatures greater than 175°F. Magnetic surveys indicate that the resurgent dome forms the northern boundary to the system, but that it extends northward somewhat along the NNW-trending faults (see Figure 3). Hydrothermal alteration and small fumaroles locally extend to the surface along these faults in the vicinity of the known resource.

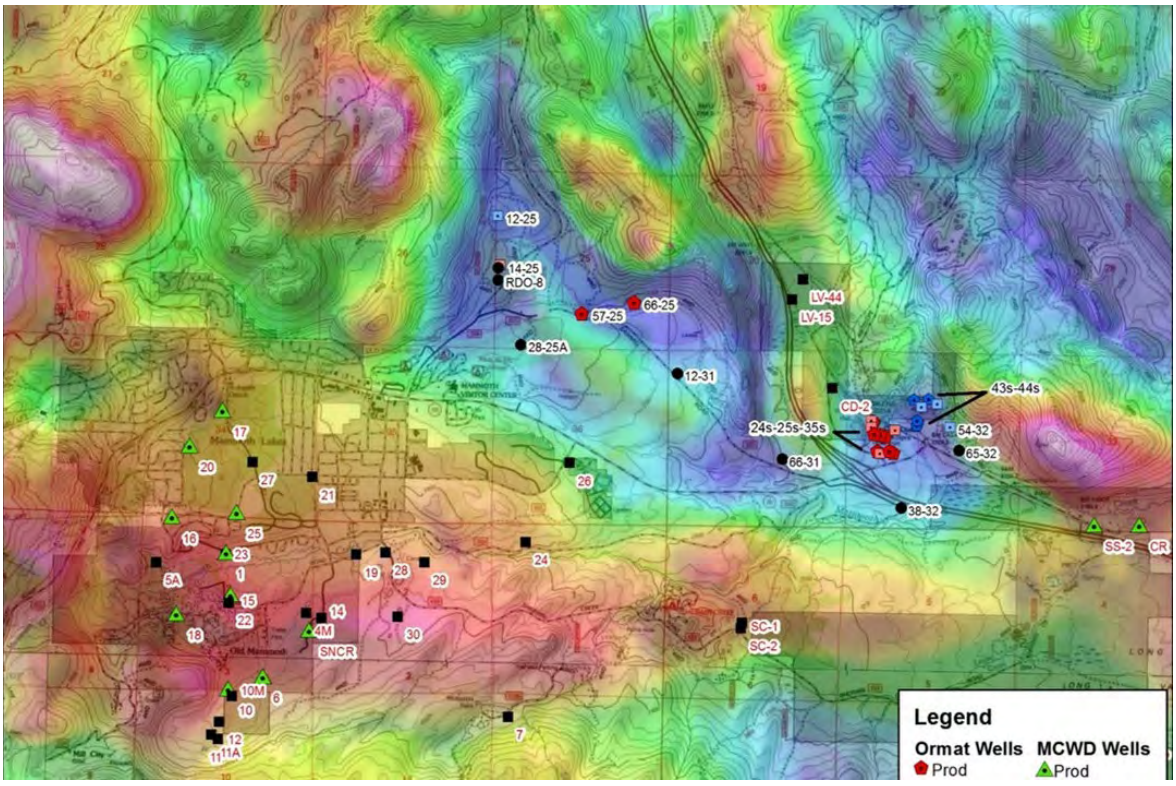

Figure 3: Location of municipal groundwater wells and geothermal wells. Background shading is natural magnetic field intensity from an aeromagnetic survey. Areas of low magnetic intensity (blue shading) map hydrothermal alteration associated with the geothermal system.

2.2 The Groundwater Resource

The municipal groundwater resource is located in the southwest moat and on the east flank of Mammoth Mountain (see Figure 2). Groundwater is produced from nine wells that are oriented in a north-south alignment. All groundwater production wells are located 1.8 miles or more from the closest Basalt Canyon geothermal production well.

The aquifer is hosted by an approximately 1,000-ft-thick sequence of mafic volcanic lavas and cinders that originated from the base of Mammoth Mountain west of the wells. Interflow glacial till is present in some wells. The aquifer is largely recharged by snowmelt and infiltration from Mammoth Creek and Mammoth Mountain. Numerous exploratory wells drilled east of the production wells within the moat had low productivity (Schmidt et al 2018).

The groundwater wells are about 700 ft deep and moderately productive. Water levels decline as pumping increases, but at variable rates due to widely varying transmissivities. Well P17 is the most productive and produces about 800 gpm with about 4 feet of drawdown. Annual operational summaries for all wells are available on the MCWD website.

Four of the wells regularly exceed the arsenic drinking water standard of 10 µg/L; three of the wells occasionally exceed the standard, and two of the wells do not exceed the standard. Well P17 water, on the north end of the field, typically contains between 86 and 150 µg/L arsenic (As). Several wells also exceed the secondary drinking water standard for iron (0.3 mg/L) and manganese (0.05 mg/L). Water temperature is highest in northern and western wells, and generally increases with increasing production and declining water levels. Well P17 is the warmest (up to 81° F), see Figure 4 for location of P17 with respect to geothermal system.

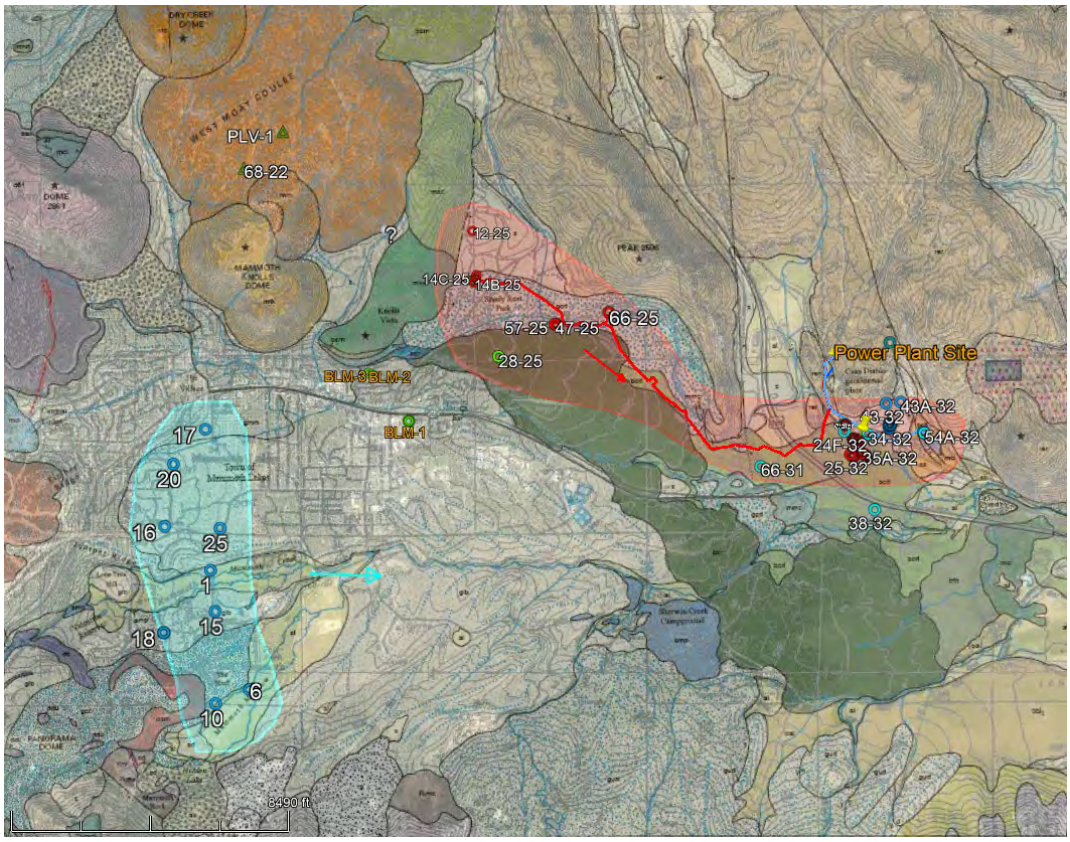

Figure 4: Geologic map showing location of MCWD (blue) and geothermal system (red). Well 17 is closest to geothermal source area and produces water containing elevated temperature and metals.

Chloride is a conservative element that is not normally present in area groundwater but is present in the geothermal fluid. As a result, it has been used to estimate that in P17, which contains the most chloride of the groundwater producers, contains about 2-3% geothermal fluid. Chloride in that well reached an all-time high of about 12 mg/L in late 2016 following three years of drought and regular production pumping. However, melting and infiltration of the large snowpack in the spring of 2017 resulted in significant recharge to the groundwater aquifer that returned chloride concentrations to lower levels by early 2020. Figure 5 shows the chloride trends for seven of the groundwater production wells including this P17 trend. Concentrations again increased during the 2020-2022 drought years. Since geothermal operations were constant during this period (see Figure 1), these responses indicate that the arsenic and chloride content in the groundwater supply wells is unrelated to the Mammoth geothermal complex operations.

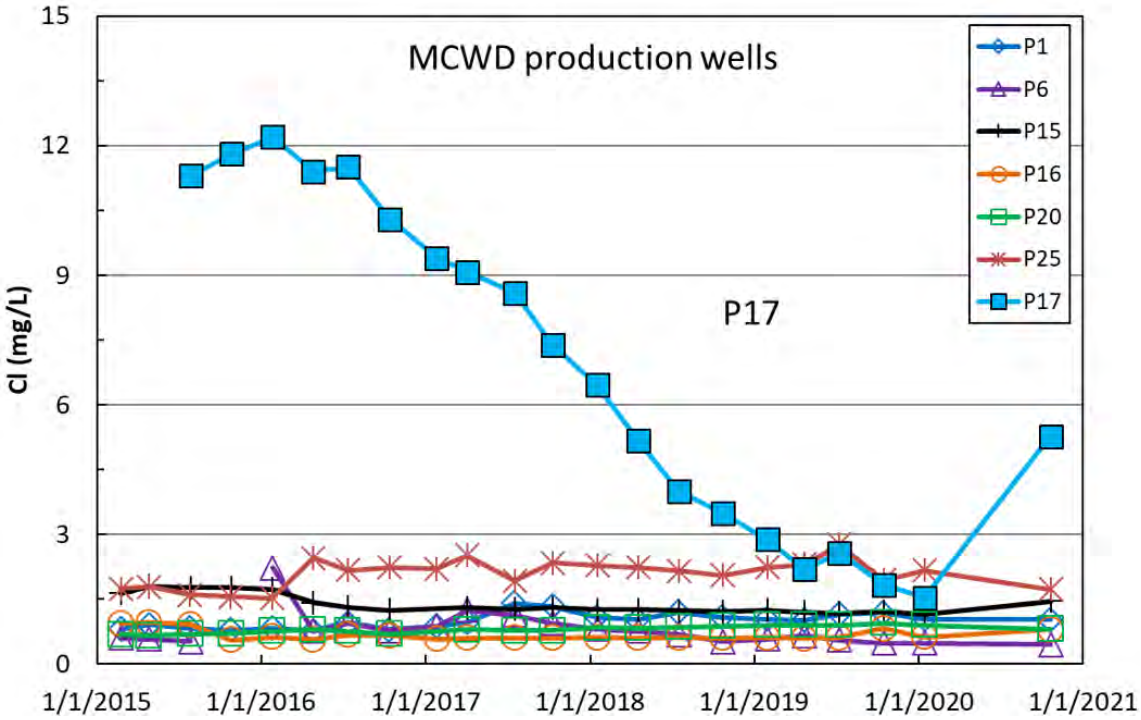

Figure 5: Groundwater production geochemistry chloride (Cl) trends from 2015 to 2021. Note decrease in sampling frequency in 2020 due to Covid-19 restrictions.

3. Monitoring Well Network

The GMRP established a baseline monitoring well network comprised of 28 sites that included a combination of shallow groundwater, dual completion (shallow and intermediate depth), and geothermal reservoir wells to be monitored for temperature, pressure/water level, and geochemical parameters, depending on well type. Tables 2 and 3 outline the types of data collected.

Since 2015, the BLM in coordination with the US Forest Service (USFS), the USGS and MCWD, has approved the installation of several wells dedicated to the CDIV Project. Table 1 summarizes the well constructions.

- 14A-25 is a 600-ft-deep, dual completion monitoring well installed by the USGS in 2015. 14A-25 is located on the well pad that hosts production wells 14B-25 and 14C-25, and standby production well 14-25. 14A-25 monitors fluid in the Early Rhyolite about 400 ft above the upper production zone.

- 28A-25 is a 600-ft-deep, dual completion monitoring well installed by the USGS in 2015. The well is 2,000 feet southwest of production wells 47-25 and 57-25, but still 1.75 miles down-gradient of the closest MCWD well. Both monitoring point are constructed in the Early Rhyolite.

- 28-25 is located next to 28A-25 and is a 1622 ft deep core hole installed by Ormat in 2017. The well measures pressure within the Bishop Tuff.

- BLM-1 is a dual completion monitoring well drilled to 600 ft by USGS in 2017. The well is completed in the moat basalts.
- BLM-2 is a 680-ft-deep dual completion monitoring well drilled by USGS in 2021 to monitor a hypothetical fault running between the MCWD wells and Basalt Canyon. Both wells are completed in the Early Rhyolite.
- BLM-3 is a 1320-ft-deep well installed by USGS in 2021, ostensibly to monitor the Bishop Tuff in a theoretical fault running between the groundwater wells and Basalt Canyon. The well, however, was completed in Early Rhyolite.

The groundwater production well group includes MCWD wells 1, 6, 15, 16, 17, 20, and 25.

Table 1. Monitoring Well Construction Summary (bolded wells indicate Moat basalts vs. Early Rhyolite completion).

Well Number	Installed by	Screen Interval	Filter Pack Interval	Geology of screened interval
14A-25 Shallow	USGS	470-490	446-496	Rhyolite tuff and obsidian. Base of basalt at 196 ft.
14A-25 Deep		575-595	555-600	Altered rhyolite tuff
28A-25 Shallow	USGS	440-460	418-481	Rhyolite xtl tuff
28A-25 Deep		575-595	555-602	USGS incorrectly logged as andesite. Core from adjacent well 28-25, has vuggy, pumiceous, pinkish grey rhyolite at this depth.
28-25	Ormat	Cased to 1322'. Slotted 1407 to 1622'		Monitors pressure in the geothermal reservoir. Bishop Tuff present from 1524ft to bottom. Total loss of circulation at 1620 ft. USGS sinker bar stuck at 1440ft.
BLM-1 Shallow	USGS	415-435	395-455	Vesicular basalt.
BLM-1 Deep		520-540	488-541	Vesicular basalt
BLM-2 Shallow	USGS	440-460	420-480	Early Rhyolite. Well construction uncertain. Base of basalt isat 408'
BLM-2 Deep		640-660	620-680	Early Rhyolite. Base of basalt at 408 ft
BLM-3 Deep	USGS	1190-1300	1180-1320	Early Rhyolite. Base of basalt at 404 ft. Well is screened in Early Rhyolite.
MW-33	USGS for MCWD	610		Basalt

3.1 Monitoring and Sampling Requirements

Table 2 outlines the baseline monitoring well network, including the type of well (target formation) as well as the parameters and frequency of data collection for the wells within the GMRP program.

Table 3 outlines the geochemical constituents that are analyzed at the frequency specified under the "Geochemical" column in Table 2.

Table 2. Baseline monitoring well network and parameters

Well Type	Well Name	Monitoring Entity	Temperature	Pressure	Water Level	Geochemical
Shallow Groundwater Monitoring Wells	MCWD 14	MCWD			D (t)	
	MCWD 19				D (m)	
	MCWD 24				D (t)	
	MCWD 26	MCWD & USGS	D (t)		D (t)	Q
	SC-1	Ormat & USGS	D (t)		D (t)	
	SC-2		D (t)		D (t)	
Shallow Groundwater Production Wells	MCWD 1	MCWD & USGS			D (t)	Q
	MCWD 6				D (t)	Q
	MCWD 15				D (t)	Q
	MCWD 16				D (t)	Q
	MCWD 17				D (t)	Q
	MCWD 18				D (t)	
	MCWD 20				D (t)	Q
	MCWD 25				D (t)	Q
Dual Completion Monitoring Wells	14A-25-Shallow [490 feet] and 14A-25-Deep [595 feet])	USGS	Q (VTP)	D (b)		Q
	28A-25-Shallow [460 Feet] and 28A-25-Deep [595 feet]		Q (VTP)	D (b)		Q
	BLM-1-Shallow [435] and BLM-1-Deep [580]		Q (VTP)	D (b)		Q
Geothermal Reservoir Monitoring Wells	Ormat 12-31	Ormat	D (b)	D (b)		
	Ormat 65-32		D (b)	D (b)		
	Ormat 48-29		D (t)	D (t)		
	Ormat 28-34		D (b)	D (b)		
	Ormat CW-3		D (t)	D (t)		
	USGS CH10B	USGS		D (b)		
	Ormat 28-25		Q (VTP)	D (b)		Q
	BLM Off-Lease 2		Q (VTP)	D (b)		Q
Geothermal Reservoir Production Wells	Ormat 57-25	Ormat & USGS	D (b)	D (b)		Q
	Ormat 66-25		D (b)	D (b)		Q
	Ormat 12-252	Ormat	TBD	D (b)		TBD
	Ormat 14-252		TBD	D (b)		TBD

Notes: D = Daily Average, Q = Quarterly, TBD = To Be Determined, (t) = Transducer, (b) = Bubbler Tube, (m) = Manual, VTP = Vertical Temperature Profile

Table 3. Constituents and parameters in monitoring program

Constituents and Parameters	Units
Chemicals and Parameters	
Alkalinity - Field	Milligrams per liter (mg/l) Field Raw Water Alkalinity
Acid Neutralizing Capacity (ANC)	Milligrams per liter (mg/l)
Arsenic (As)	micrograms per liter (µg/l)
Boron (B)	micrograms per liter (µg/l)
Bromide (Br)	micrograms per liter (µg/l)
Calcium (Ca)	milligrams per liter (mg/l)
Chloride (Cl)	milligrams per liter (mg/l)l
Fluoride (F)	milligrams per liter (mg/l)l
Lithium (Li)	micrograms per liter (µg/l)
Magnesium (Mg)	milligrams per liter (mg/l)
Nitrogen, ammonia (NH_3) as N	milligrams per liter (mg/l)
Nitrogen, as nitrite (NO_3)	milligrams per liter (mg/l)
pH	pH units
pH	pH units
PO_4	milligrams per liter (mg/l)
Potassium (K)	milligrams per liter (mg/l)
Total Dissolved Solids (TDS)[2]	milligrams per liter (mg/l)
Rubidium (Rb)[1]	micrograms per liter (µg/l)
Silica (Si)	milligrams per liter (mg/l)
Sodium (Na)	milligrams per liter (mg/l)
Specific conductance	microseimens per centimeter (µS/cm)
Specific conductance	microseimens per centimeter (µS/cm)
Sulfate (SO_4)	milligrams per liter (mg/l)
Temperature	°C
Temperature	°C
Non-Condensable/Dissolved Gases	
H_2S[1]	
Isotopes	
D/H ratio (Deuterium/Hydrogen)	per mil
$^{18}O/^{16}O$ ratio	per mil
Tritium (^3H)[1]	One-time sample of 14A-25, 28A-25, MCWD 26, and other select MCWD production wells (TBD) to establish existing concentrations; then, annual sampling from select geothermal production wells in Basalt Canyon (TBD); Data not yet available
Additional Constituents and Parameters	Consistent with the adaptive monitoring framework of the GMRP, additional constituents and parameters may be added for specific tests or to improve monitoring effectiveness based on new information

Notes:

[1] H_2S, rubidium, and tritium not yet incorporated into field sampling program.

[2] Laboratory calls total dissolved solids "residue."

4. Mammoth CDIV Stress Test Summary

Prior to full-time facility operations, a production stress test was performed on the new Basalt Canyon wells to demonstrate that CDIV operations would not impact groundwater wells. Data from monitoring wells 14A-25, 28-25 shallow, 28-25 Deep, BLM 1, and BLM 2 were monitored during the test for changes in water level. Four production steps, or test phases, were completed during the testing. Data from each phase was presented to the GMRP committee comprised of Ormat, BLM, MCWD, and the USGS for their review and approval prior to advancing to the next phase. Approval criteria related to the quality of data as well as the change, or lack thereof, in the water levels for each lithology.

This stress test, while instrumental in validating the environmental safety of the geothermal operations, represents a high level of scrutiny that may not be universally applicable or necessary for all geothermal projects. It is recommended that the deployment of such stress tests be considered on a case-by-case basis, taking into account the unique geological, hydrological, and ecological characteristics of each site as well as the size of the geothermal project. For projects in areas with lower sensitivity or established historical data demonstrating minimal risk, a scaled-down version of the stress test or alternative monitoring methods may be more appropriate. This approach ensures that resources are allocated efficiently, focusing intensive testing methods like those used in for CDIV on developments where the potential for environmental impact is greatest.

A full list of activities detailing the four phases of the test are outlined in Table 4. Figures 6 through 11 show the responses in the shallow monitoring wells 14A-25, 28A-25, BLM 1, and BLM 2 during the various phases. These monitoring wells show a primary response to atmospheric pressure conditions and minor, basin-wide water level decline during the summer months. Shallow well 14A-25 is located between production wells 14B-25 and 14C-25 and is constructed in hot Early Rhyolite. The USGS determined that the well exhibits poro-elastic effects on the order of less than 0.5 feet (0.2 psi) during startups of those production wells (Howle 2020). This response was also observed during the 2017 long-term flow test.

Monitoring well 28-25 Deep is completed in the Bishop Tuff geothermal reservoir and shows a direct varying response of drawdown as expected from the increase in flow. 28-25 deep also clearly displays pressure recovery equal to prior state during periods of lesser flow. Table 4 shows various events and dates which occurred during the duration of the test. Table 5 shows the change in depth of water level in ft for 14A-25, 28-25 shallow, 28-25 Deep, BLM 1, and BLM 2. Figure 12 shows the location of production and monitoring wells.

The CDIV stress test was completed in July 2022 after 6 weeks of flow variation and monitoring data analysis.

Table 4. List of events during the 2022 CDIV stress test

Date	**Event**
5/19/2022	47-25 Online
5/27/2022	14C-25 Online
6/1/2022	14C-25 offline and 47-25 online
6/2/2022	14C-25 at full capacity and 47-25 online at reduced capacity **(Phase 1)**
6/3/2022	47-25 online at full capacity; total flow ~5000 gpm
6/4/2022	All wells online, total flow ~5000 gpm
6/6/2022	Only 47-25 online
6/11/2022	All wells online, total flow ~6500 gpm (Nominal flow: **Phase 2**)
6/13/2022	All wells online, total flow ~7000 gpm (Nominal flow)
6/16/2022	CDIV down for 0.5 hours. CDIV unit started at 06:03. Test Energy/Commissioning.
6/17/2022	CDIV down for 2.3 hours. Unit started at 13:27.
6/22/2022	All wells online, total flow ~6000 gpm
6/24/2022	All wells online, total flow ~8400 gpm
6/25/2022	Flow reduced to 4000-4500gpm (50 % of full capacity) (**Phase 3**)
6/28/2022	CDIV down 10 hours. Unit online at 16:25
6/29/2022	Total flow 8700 gpm (**Full capacity**)
6/30/2022	Total flow 8700 gpm (Full capacity)
7/1/2022	CDIV down 3.8 hours
7/6/2022	End of the stress test. Total flow 8700 gpm (Full capacity)

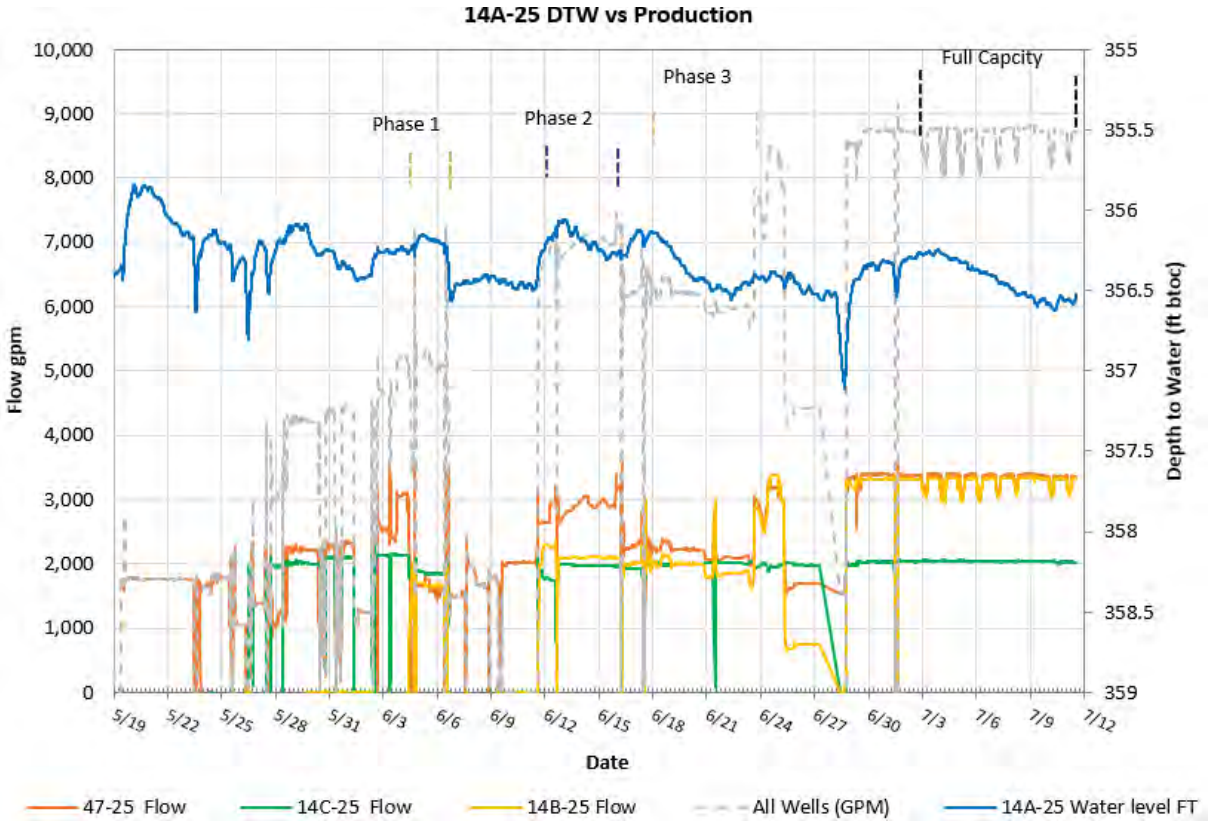

Figure 6: 14A-25 water level and CDIV production flow during four phases of stress test.

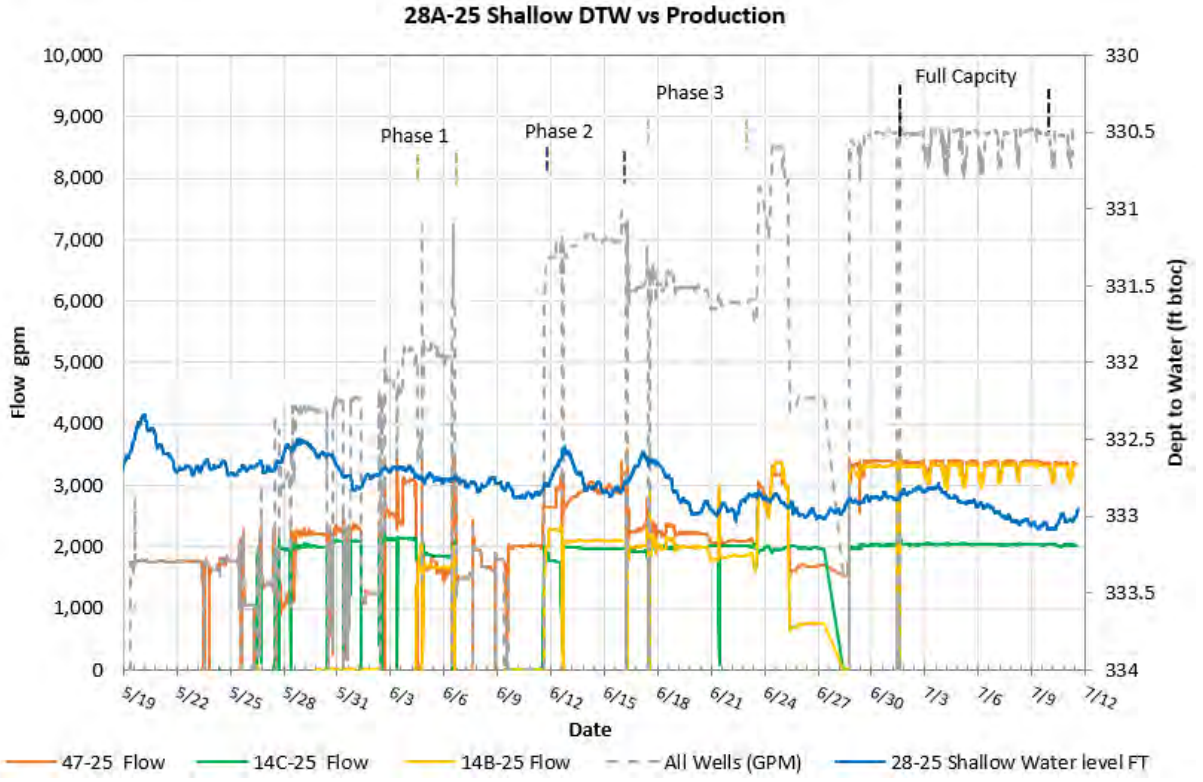

Figure 7: 28-25 Shallow water level and CDIV production flow during four phases of stress test.

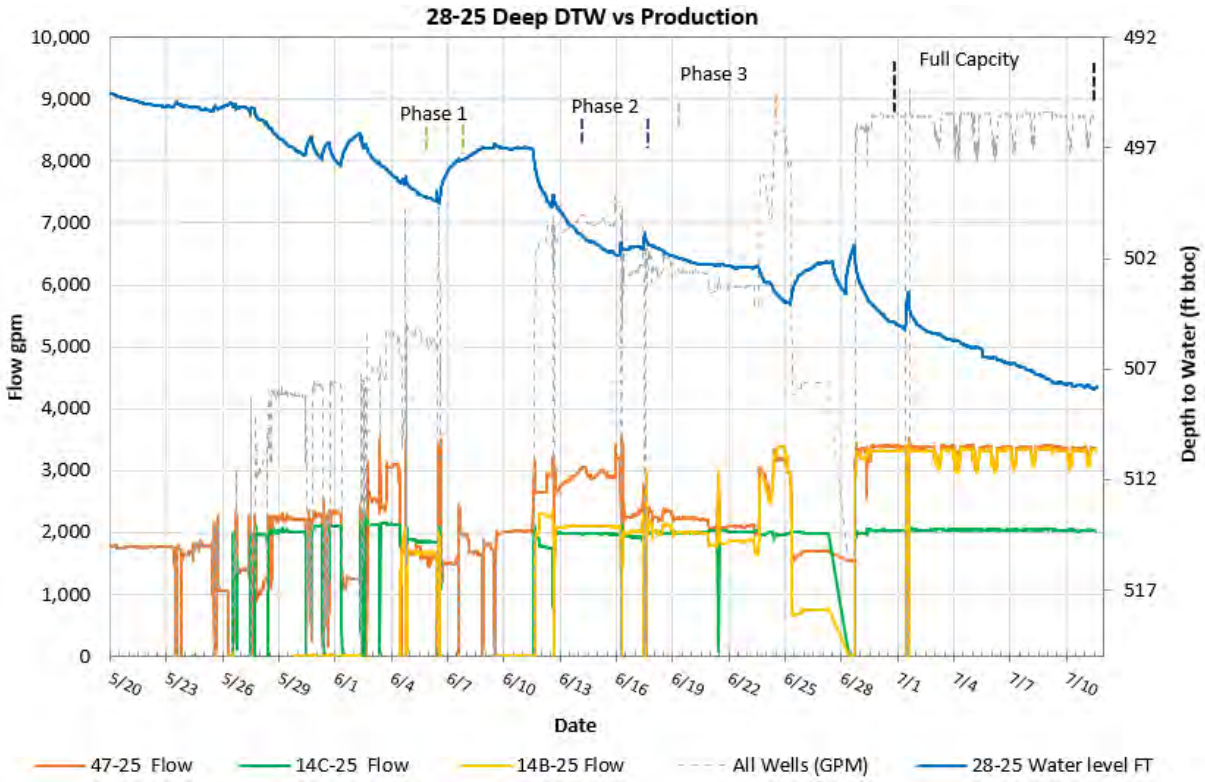

Figure 8: 28-25 Deep water level and CDIV production flow during four phases of stress test.

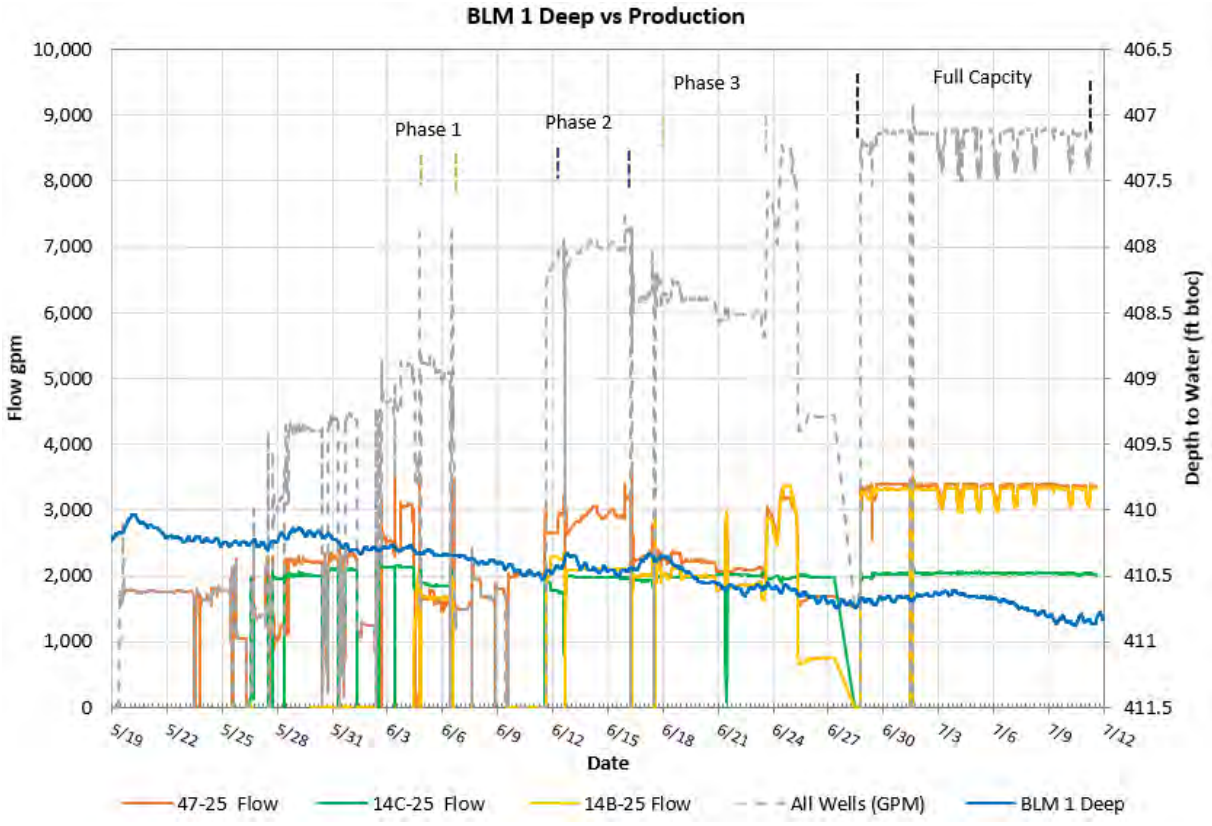

Figure 9: BLM 1 Deep water level and CDIV production flow during four phases of stress test.

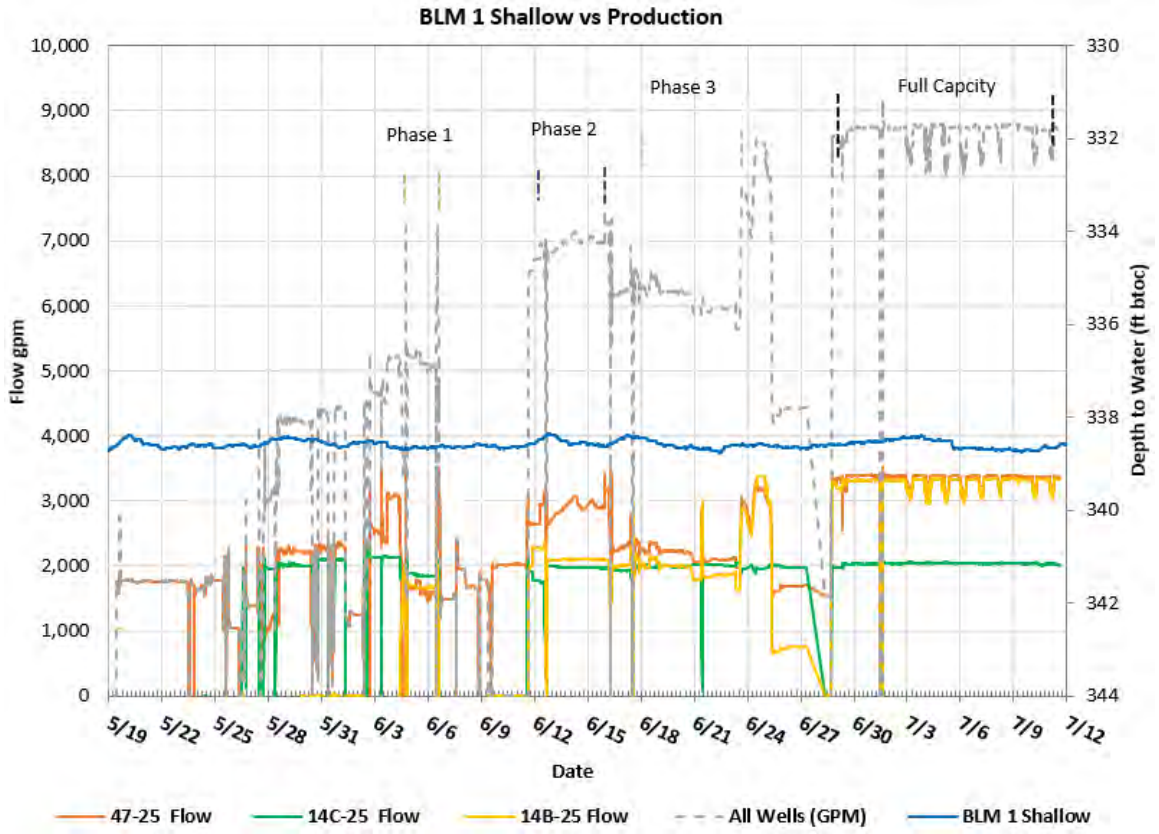

Figure 10: BLM 1 Shallow water level and CDIV production flow during four phases of stress test.

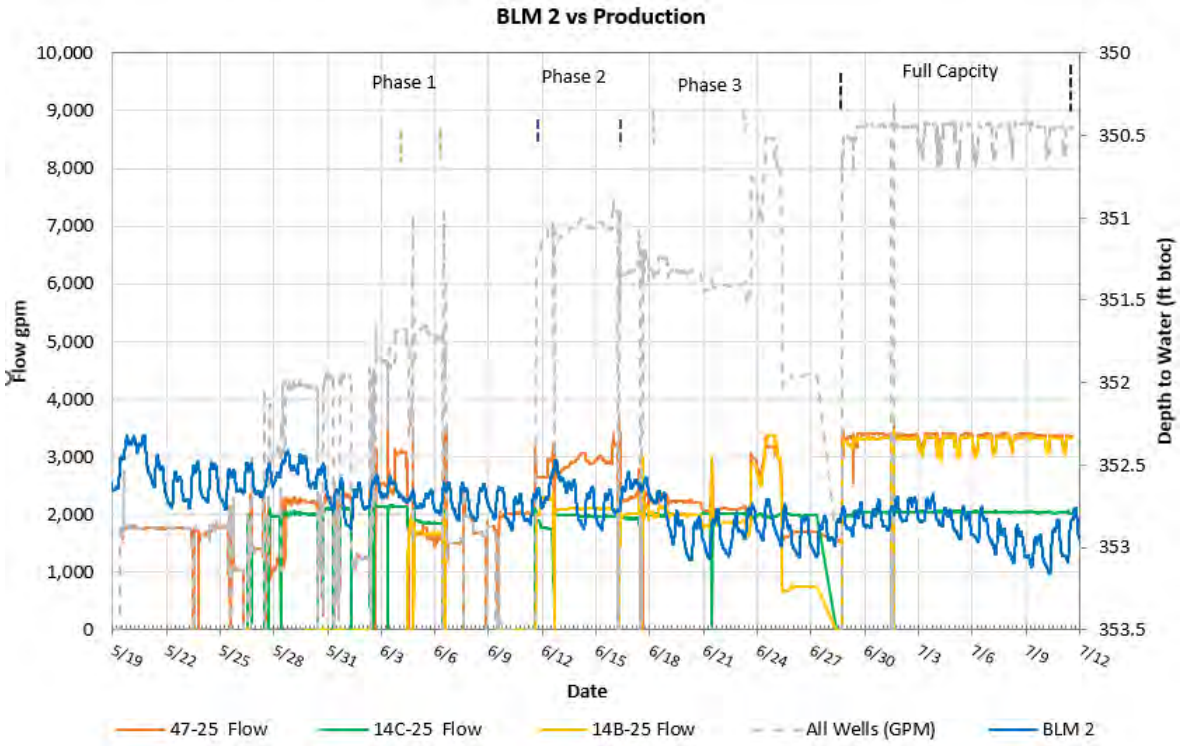

Figure 11: BLM 2 water level and CDIV production flow during four phases of stress test.

Table 5. Depth (ft) to water levels from ground surface before and after the Stress test in each monitoring well. Positive difference indicates a drop in water level.

Depth to Water Level from Ground Surface (ft)						
Date	**Well**					
	14-25	**28-25 shallow**	**28-25 Deep**	**BLM 1 Deep**	**BLM 1 Shallow**	**BLM 2**
5/19/2022 (CDIV Production Flow : 0 gpm)	356.38	332.40	494.53	410.11	338.46	352.37
7/11/2022 (CDIV Production Flow : 8800 gpm)	356.52	332.95	507.82	410.85	338.61	352.93
Difference:	-0.14	0.55	13.29	0.74	0.15	0.56

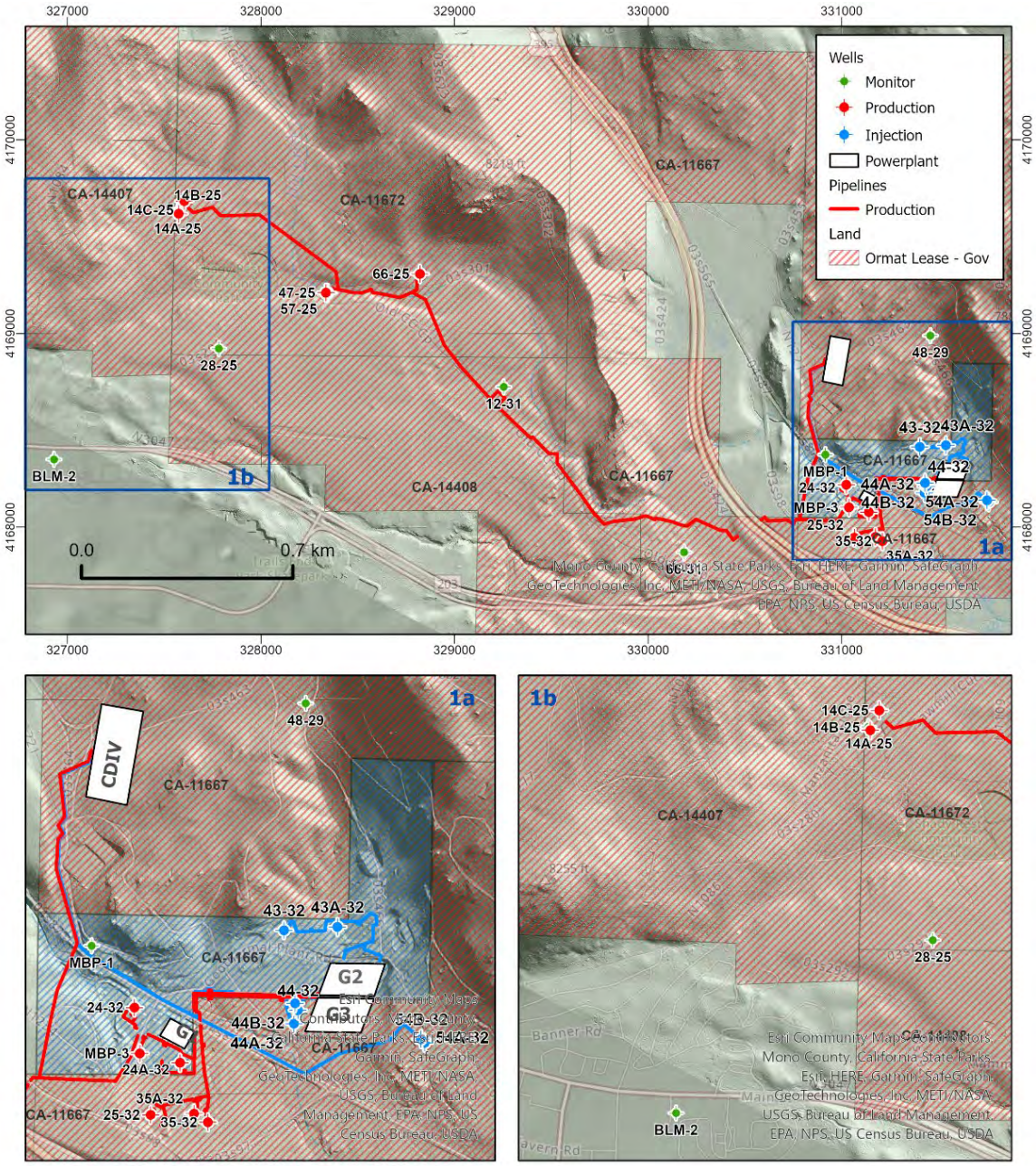

Figure 12: Map showing location of Ormat production (red) and injection (blue) wells along with select monitoring wells (green).

5. Conclusions

Water quality issues, including elevated arsenic, existed in several municipal water production wells that appeared to be of geothermal origin. Previous geologic, hydrologic, and geochemical data indicated that the Basalt Canyon geothermal reservoir and the groundwater aquifer were hydraulically disconnected systems hosted in different rock formations. Because the specific source of the contaminants in these municipal water supply wells had never been identified, some

agencies were still concerned that they were related to Mammoth complex geothermal operations. To allay these concerns and to provide an early warning system should any unforeseen impacts occur, an adaptive but rigorous GMRP was cooperatively developed by Ormat and local, State and Federal agencies. The GMRP was enacted prior to and during startup of the new CDIV production wells.

The monitoring program included a network of shallow groundwater wells, intermediate depth wells, and deep reservoir wells instrumented to track water levels, temperatures, and geochemical parameters. Baseline data were collected for several years leading up to CDIV operations. Once the new production wells were drilled, a carefully designed step-rate stress test was conducted, incrementally increasing flow from the wells while closely monitoring the well network. As expected, the deep monitoring wells within the geothermal reservoir showed a direct response to the changing reservoir pressure during flow variations, but corresponding signals were not observed in either the shallow groundwater monitoring array near the geothermal system or in the municipal water supply wells.

It's important to note that the monitoring program outlined in this case study, while successful in evaluating potential environmental impacts for this development, represents an extensive undertaking that may be prohibitive for geothermal projects in early development or smaller in size. The level of baseline data collection, multi-agency cooperation, and ongoing monitoring was warranted given the proximity to the municipal water supply for Mammoth Lakes and the size of the geothermal project. However, a more streamlined process may be suitable for geothermal developments in less environmentally-sensitive areas or where the risks of groundwater impacts are lower based on preliminary studies. An appropriate balance must be struck between environmental safeguards and enabling cost-effective geothermal energy development.

Now two years into full CDIV operations at a combined complex capacity of 65 MW, the monitoring program continues and has not detected any impacts to the groundwater system to-date, and discussions regarding appropriate reductions to components of the monitoring plan have begun. The cooperative monitoring effort successfully demonstrated that the expanded geothermal operations can be conducted safely without detriment to the community's water resources. The adaptive monitoring program will remain in place going forward to provide long-term tracking and response capability should any future changes occur. This case study highlights the value of establishing comprehensive environmental baselines and monitoring programs through interagency collaboration when developing renewable energy resources in environmentally sensitive areas.

REFERENCES

Bailey, R.A., Dalrymple, G.B., and Lanphere, M.A., 1976, Volcanism, structure, and geochronology of the Long Valley caldera, Mono County, California: Journal of Geophysical Research, v. 81, no. 5, p. 725–744, https://doi.org/10.1029/JB081i005p00725.

Bergfeld, D., Evans, W.C., Howle, J.F., and Farrar C.D., 2006, Carbon dioxide emissions from vegetation-kill zones around the resurgent dome of Long Valley Caldera, eastern California, USA: Journal of Volcanology and Geothermal Research, v. 152, no. 1–2, p. 140–156, https://doi.org/10.1016/j.jvolgeores.2005.11.003.

Bergfeld, D., Vaughan, R.G., Evans, W.C., and Olsen, E., 2015, Monitoring ground-surface heating during expansion of the Casa Diablo production well field at Mammoth Lakes, California: Geothermal Resources Council Transactions, v. 39, p. 1007–1013, https://www.geothermal-library.org/index.php?mode=pubs&action=view&record=1032246.

Brown, S.T., Kennedy, B.M., DePaolo, D.J., Hurwitz, S., and Evans, W.C., 2013, Ca, Sr, O and D isotope approach to defining the chemical evolution of hydrothermal fluids—Example from Long Valley, CA, USA: Geochimica et Cosmochimica Acta, v. 122, p. 209–225, https://doi.org/10.1016/j.gca.2013.08.011.

Bureau of Land Management, 2013, Record of Decision, Casa Diablo IV Geothermal Development Project, Case File Number: CACA 054722: Bishop, California, 19 p., https://openei.org/w/images/7/7c/CD-IV_Final_BLM_ROD_081213.pdf.

Bureau of Land Management, 2018, CD-IV Geothermal Development Project—Groundwater Monitoring and Response Plan, version 1.1 dated January 19, 2018, 29 p.

Evans, W.C., 2017, Overview of the Long Valley hydrothermal system after decades of study, in Hildreth, W., and Fierstein, J., 2017, Geologic field-trip guide to Long Valley Caldera, California: U.S. Geological Survey Scientific Investigations Report 2017–5022–L, p. 99–119, https://doi.org/10.3133/sir20175022L.

Evans, W.C., and Bergfeld, D., 2017, Groundwater resources of the Devils Postpile National Monument—Current conditions and future vulnerabilities: U.S. Geological Survey Scientific Investigations Report 2017–5048, 31 p., https://doi.org/10.3133/sir20175048.

Evans, W.C. et al, 2018, Hot Water in the Long Valley Caldera—The Benefits and Hazards of this Large Natural Resource. U.S. Geological Survey Fact Sheet 2018–3009, 4 p., https://doi.org/10.3133/fs20183009.

Farrar, C.D., Sorey, M.L., Roeloffs, E.R., Galloway, D.L., Howle, J.F., and Jacobsen, R., 2003, Inferences on the hydrothermal system beneath the resurgent dome in Long Valley Caldera, east-central California, USA, from pumping tests and geochemical sampling: Journal of Volcanology and Geothermal Research, v. 127, p. 305–328, https://doi.org/10.1016/S0377-0273(03)00174-4.

Farrar, C.D., DeAngelo, J., Williams, C.F., and Hurwitz, S., 2010, Temperature data from wells in Long Valley Caldera, California: U.S. Geological Survey Data Series 523, https://doi.org/10.3133/ds523.

Galloway, D.L., 2019, Atmospheric-loading frequency response functions and groundwater levels filtered for the effects of atmospheric loading and solid Earth tides for three monitoring wells near Mammoth Lakes, California, 2015–2017: U.S. Geological Survey data release, https://doi.org/10.5066/P9ON8U5U.

Hildreth, W., 2004, Volcanological perspectives on Long Valley, Mammoth Mountain, and Mono Craters—Several contiguous but discrete systems: Journal of Volcanology and Geothermal Research, v. 136, nos. 3–4, p. 169–198, https://doi.org/10.1016/j.jvolgeores.2004.05.019.

Hildreth, W., Fierstein, J., Champion, D., Calvert, A., 2014, Mammoth Mountain and its mafic periphery—A late Quaternary volcanic field in eastern California: Geosphere, v. 10, p. 1315–1365, https://doi.org/10.1130/GES01053.1.

Hildreth, W., Fierstein, J., Champion, D., Calvert, A., 2017, Early postcaldera rhyolite and structural resurgence at Long Valley Caldera, California. Journal of Volcanology and Geothermal Research, v. 335 p. 1-34, http://dx.doi.org/10.1016/j.jvolgeores.2017.01.005.

Hildreth, W., 2017, Fluid-driven uplift at Long Valley Caldera, California: Geologic perspectives. Journal of Volcanology and Geothermal Research, v. 341, p. 269–286, https://doi.org/10.1016/j.jvolgeores.2017.06.010.

Hildreth, W. and Fierstein, J., 2017, Geologic field-trip guide to Long Valley Caldera, California: U.S. Geological Survey Scientific Investigations Report 2017–5022–L, 119 p., https://doi.org/10.3133/sir20175120L

Hill, D.P., Bailey, R.A., and Ryall, A.S., 1985, Active tectonic and magmatic processes beneath Long Valley Caldera, eastern California—An overview: Journal of Geophysical Research, v. 90, no. B13, p. 11111–11120, https://doi.org/10.1029/JB090iB13p11111.

Howle, J.F., 2020. Long Valley Hydrologic Advisory Committee Hydrologic Monitoring Data Unpublished and provisional U.S. Geological Survey Data through December 2019 - Submitted by J.F. Howle. Prepared Jan 30, 2020. 25p.

Peacock, J.R., Mangan, M.T., McPhee, D., and Wannamaker, P.E., 2016, Three-dimensional electrical resistivity model of the hydrothermal system in Long Valley Caldera, California, from magnetotellurics: Geophysical Research Letters, v. 43, no. 15, p. 7953–7962, https://doi.org/10.1002/2016GL069263.

Schmidt, Kenneth D. and Associates, 2018, Annual report on results of Mammoth Community Water District groundwater monitoring program for October 2016–September 2017: Report prepared for Mammoth Community Water District, Mammoth Lakes, California, 87 p.

Schmidt, Kenneth D. and Associates, 2022, Annual Report on Results of Mammoth Community Water District Groundwater Monitoring Program for October 2020-September 2021. April 2022. https://mcwd.dst.ca.us/wp-content/uploads/2022/04/Mammoth-CWD.pdf

Shevenell, L., Goff, F., Grigsby, C.O., Janik, C.J., Trujillo Jr., P.E., and Counce, D., 1987, Chemical and isotopic characteristics of thermal fluids in the Long Valley Caldera lateral flow system, California: Geothermal Resources Council Transactions, v. 11, p. 195–201, https://www.geothermal-library.org/index.php?mode=pubs&action=view&record=1001612.

Sorey, M.L., 1985, Evolution and present state of the hydrothermal system in Long Valley Caldera: Journal of Geophysical Research, v. 90, no. B13, p. 11219–11228, https://doi.org/10.1029/JB090iB13p11219.

Sorey, M.L., Suemnicht, G.A., Sturchio, N.C., and Nordquist, G.A., 1991, New evidence on the hydrothermal system in Long Valley Caldera, California, from wells, fluid sampling, electrical geophysics, and age determinations of hot-spring deposits: Journal of Volcanology and Geothermal Research, v. 48, p. 229–263, https://doi.org/10.1016/0377-0273(91)90045-2.

Sorey, M.L., Evans, W.C., Kennedy, B.M., Farrar, C.D., Hainsworth, L.J., and Hausback, B., 1998, Carbon dioxide and helium emissions from a reservoir of magmatic gas beneath Mammoth Mountain, California: Journal of Geophysical Research, v, 103, no. B7, p. 15303–15323, https://doi.org/10.1029/98JB01389.

Suemnicht, G.A., and Varga, R.J., 1988, Basement structure and implications for hydrothermal circulation patterns in the western moat of Long Valley Caldera, California: Journal of Geophysical Research, v. 93, no. B11, p. 13191–13207, https://doi.org/10.1029/JB093iB11p13191.

Vaughan, R.G., Bergfeld, D., Evans, W.C., Wilkinson, S., Miwa, C., and Diabat, M., 2018, A baseline thermal infrared survey of ground heating around the Casa Diablo Geothermal Plant, Mammoth Lakes, California: Geothermal Resources Council Transactions, v. 42, p. 962–976, https://www.geothermal-library.org/index.php?mode=pubs&action=view&record=1033957.

White, A.F., and Peterson, M.L., 1991, Chemical equilibrium and mass balance relationships associated with the Long Valley hydrothermal system, California, USA: Journal of Volcanology and Geothermal Research v. 48, p. 283–302, https://doi.org/10.1016/0377-0273(91)90047-4.

White, A.F., Peterson, M.L., Wollenberg, H., and Flexser, S., 1990, Sources and fractionation processes influencing the isotopic distribution of H, O, and C in the Long Valley hydrothermal system, California, USA: Applied Geochemistry, v. 5, p. 571–585.

Development and Evaluation of Preformed Particle Gels for Preferential Fluid Flow Control in Geothermal Reservoirs

Baojun Bai[1], Yanbo Liu[1] Caleb Darko[1], Thomas Schuman[1], Philip Winterfeld[2], Sujit Datta[3], Mingzhen Wei[1], Yu-Shu Wu[2], Sara Mccauley[1]

1.Missouri University of Science and Technology, 2. Colorado School of Mines, 3. Princeton University

Keywords

Geothermal, Preferential Fluid Flow, Flow Control, Conformance Control, Heat Recovery Efficiency

ABSTRACT

Enhanced Geothermal Systems (EGS) represent cutting-edge technologies designed to harness clean energy from the Earth's crust. However, the presence of short-circuits in certain geothermal reservoirs poses a significant threat to their sustained viability as reliable sources of clean energy. This issue arises when cold fluids injected into the reservoirs quickly traverse fractures with large apertures and directly communicate between injection and production wells without acquiring sufficient heat from the rock matrix. Effective control of flow dynamics outside the wellbore and within the reservoir is crucial to mitigate undesirable flow patterns. Polymer gels, proven successful in managing preferential flow in oil and gas reservoirs, could be adapted for controlling flow in geothermal reservoirs. Nonetheless, the absence of hydrogel products capable of withstanding the harsh conditions of geothermal reservoirs (>150 ℃) for extended periods has been a limiting factor. In response, our recent efforts have led to the development of innovative high-temperature resistant preformed particle gels (HT-PPG) specifically designed for this purpose. This study provides a comprehensive overview of our research advancements, encompassing the creation of a series of innovative particle gel products. We explore their swelling behavior, rheology, thermal stability, and plugging efficiency to fractures, highlighting their applicability in geothermal contexts, even under elevated temperatures. These products are adaptable for reservoirs with preferential fluid flow paths which have temperatures ranging from 20 to 200 °C (the reservoir could have higher temperature) and can be customized with controllable sizes ranging from micrometers to a few millimeters. Our developed products feature controllable swelling times and demonstrate commendable long-term hydrolytic thermal stability, maintaining their effectiveness for over three months. Additionally, we have designed a micromodel to observe the swelling kinetics and transport mechanisms of a representative particle gel. Furthermore, we employ numerical simulation to model particle gel injection and assess blocking performance. Overall, the HT-PPG developed in this work emerges as a reliable solution for controlling preferential fluid flow in geothermal reservoirs, addressing a critical challenge in the quest for sustainable and efficient geothermal energy extraction.

1. Introduction

Enhanced Geothermal Systems (EGS) represent a promising technology designed to tap into the Earth's vast geothermal energy resources, providing a clean and sustainable source of power. By creating man-made reservoirs in hot rock formations, EGS can potentially generate significant amounts of energy with the total estimated thermal energy above the mean surface temperature to a depth of 10 km being 1.3×10^{27} J (Lund, 2007). However, the efficiency and sustainability of EGS are often compromised by the occurrence of short-circuiting within the reservoir (McClure & Horne, 2014). Short-circuiting refers to the rapid movement of cold fluids through large fractures or direct communication paths between injection and production wells, bypassing the intended heat exchange with the rock matrix. This leads to early breakthrough resulting in the inadequate heating of the injected fluids before they are produced. This affects the thermal production temperatures resulting in suboptimal energy generation (Li et al., 2016; McClure & Horne, 2014; Zhang et al., 2024).

Addressing the issue of short-circuiting is crucial for the viability of EGS as a reliable energy source. Effective control of fluid flow dynamics within the reservoir and outside the wellbore is essential to mitigate undesirable flow patterns. In the oil and gas industry, polymer gels have proven effective in managing preferential fluid flow by blocking high-permeability pathways and diverting fluids into less permeable zones (Bai et al., 2007, 2013; Goudarzi et al., 2015; Seidy Esfahlan et al., 2021; Tongwa & Baojun, 2015). This technology offers a potential solution for controlling fluid flow in geothermal reservoirs. However, the extreme conditions typical of geothermal environments, particularly temperatures exceeding 150°C, pose significant challenges for conventional polymer gels. These gels often degrade or lose their effectiveness under such harsh conditions, necessitating the development of more robust materials (Xiong et al., 2018).

Our research has focused on developing high-temperature resistant preformed particle gels (HT-PPG) specifically designed for geothermal applications (Liu et al., 2024; Song et al., 2023). These innovative gels are engineered to withstand the challenging conditions of geothermal reservoirs, providing a reliable solution for controlling preferential fluid flow. This study offers a comprehensive overview of the development and evaluation of these HT-PPGs, highlighting their potential to improve the performance and sustainability of EGS.

2. Novel Preformed Particle Gel Development

We successfully developed two hydrogel products termed Product-1 (preformed particle gel) and Product-2 (re-crosslinkable preformed particle gel), which can be stable at 200 ^{o}C for over 6 months.

2.1 Synthesis of HT-PPGs:

The HT-PPG/RPPG was synthesized through aqueous free radical polymerization. Then the bulk gel was dried and ground into small particles, as shown in Figure 1.

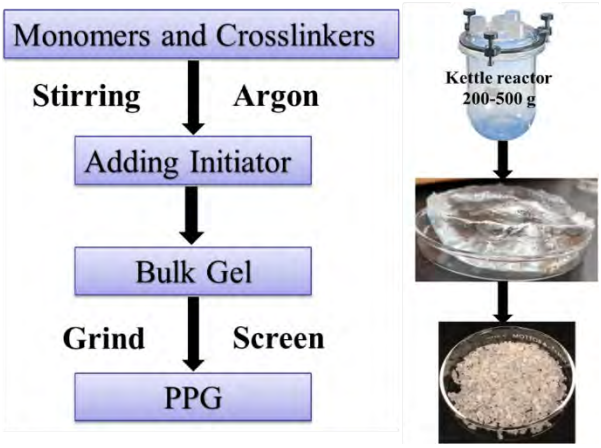

Figure 1. Synthesis procedure of HT-PPG

2.2 Evaluation Methods of PPGs

Swelling Kinetics: PPG dry particles with the size of 1 to 2 mm were used for the swelling kinetics measurements. The swelling kinetics was performed by immersing a weighed dried hydrogel sample in brine. The change in volume with respect to time was studied until the equilibrium swelling ratio was achieved. The swelling ratio of PPG is defined as the ratio of the volume of the hydrated gel to the initial weight.

Rheology Test: The rheology measurements were performed using Haake MARS III rheometer with a parallel plate geometry (PP35L Ti L) with a gap of 1 mm. All sets of rheological measurements were carried out in ambient room temperature conditions. Strain sweep tests were carried out using the oscillation strain-dependent experiment model at a fixed frequency of 1 Hz to determine the linear viscoelastic region over which storage modulus is independent of strain amplitude. The rheology measurements were performed as the oscillation time-dependent experiment model at a fixed frequency of 1 Hz and controlled strain (γ) of 1% to measure storage *modulus (G').*

Thermal Stability: The stability of the PPG was evaluated using high-pressure-resistant glass tubes with thermally stable O-rings and stainless-steel sample cylinders. The dried gel particles were swelled and sealed in anaerobic conditions. After that, the sample cylinder was aged at 150, 200 and 225 ^{o}C oven.

Core flooding tests: Sandstone cores (5 in. length, 2 in. diameter) were used for core flooding experiments, initially dried to remove residual water, vacuumed for 24 hours, and saturated with 2% KCl to calculate porosity. Matrix permeability was determined using the Darcy equation by flooding the cores with 2% KCl at varying flow rates. The cores were then halved and stainless-steel strips were glued on to represent fracture sizes. HT-PPG gel slurry was prepared by swelling dried gel particles in 2% KCl and injected into the fractures at 1 mL/min. After stabilizing the pressure gradient and sealing the cores, a post-water breakthrough test was conducted, measuring breakthrough pressure and recording stable pressures at varying flow rates to calculate the residual resistance factor.

Micromodel swelling kinetics: We designed a micromodel to observe the swelling kinetics and transport mechanisms of a representative particle gel in. In so doing, we experimentally

investigated how gel swelling and deswelling behaviors are influenced by channel size, gel particle properties, and flow conditions under high pressure and high temperature constriction channels.

3. Results

3.1 Results of PPG-1 (HT-PPG)

Product-1 is an enhanced high-temperature resistant superabsorbent hydrogel/ preformed particle gel (HT-PPG) (Buddhabhushan et al., 2021), capable of swelling without dissolving in brine solutions. Our research has demonstrated that this hydrogel remains stable at 150°C for over a year before beginning to degrade. Building on the existing gel formulation, we introduced modifications to improve the stability of the swollen hydrogel at 200°C. The evaluations included tests on swelling kinetics, rheology, and long-term hydrothermal stability.

(1) Swelling Kinetics and Rheology Behavior

Swelling kinetics were employed to measure both the swelling rate and the equilibrium swelling ratio, essential for optimizing field injection (Targac et al., 2020). The elastic modulus, or strength, is a crucial property for plugging fractures or super-K conduits. Figure 2(a) shows the swelling and rheological behavior of Product-1, which requires approximately 2 hours to reach its equilibrium swelling ratio. The equilibrium swelling ratios in 2% KCl and 1% $CaCl_2$ were 55 and 54, respectively. Figure 2(b) depicts the relationship between the swelling ratio and gel strength. The elastic moduli of Product-1 with swelling ratios of 10, half swelling, and full swelling were 960, 451, and 256 Pa, respectively. As the swelling ratio (SR) increased, the elastic modulus (strength) of HT-PPG gradually decreased. This reduction in gel strength is attributed to the absorption of more saline water at higher swelling ratios, which increases the distance between polymer chains, thereby lowering the gel strength.

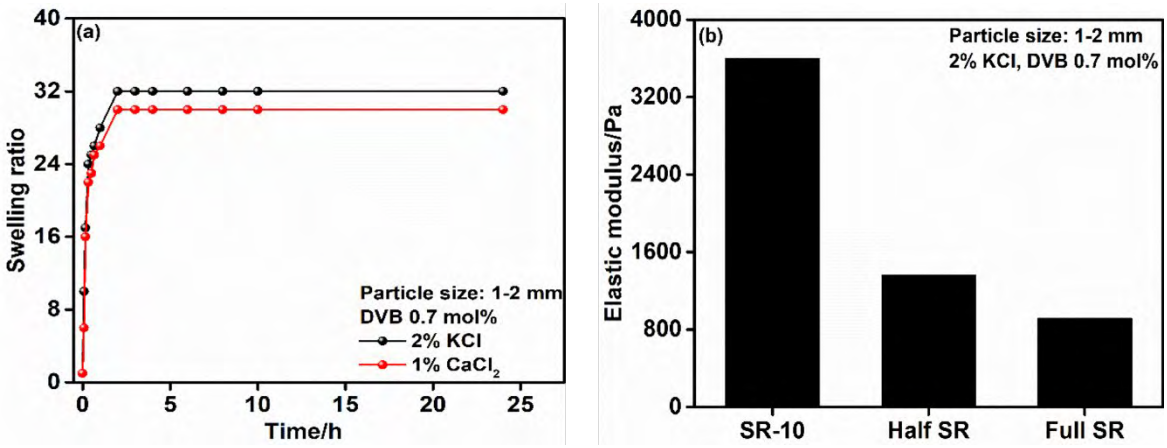

Figure 2. Effect of (a) salinity on the swelling behavior, (b) swelling ratio (SR) on the storage modulus

Figure 3 shows the effect of crosslinker concentration on the maximum swelling ratio. When the ratio of monomer to crosslinker is 996:1, the maximum swelling ratio exceeds 50. As the concentration of the cross-linker decreases, the maximum expansion multiple gradually decreases. Figure 3(b) illustrates the effects of swelling ratio and crosslinker concentration on the gel strength. As the concentration of the crosslinker increases, the strength of the gel also increases.

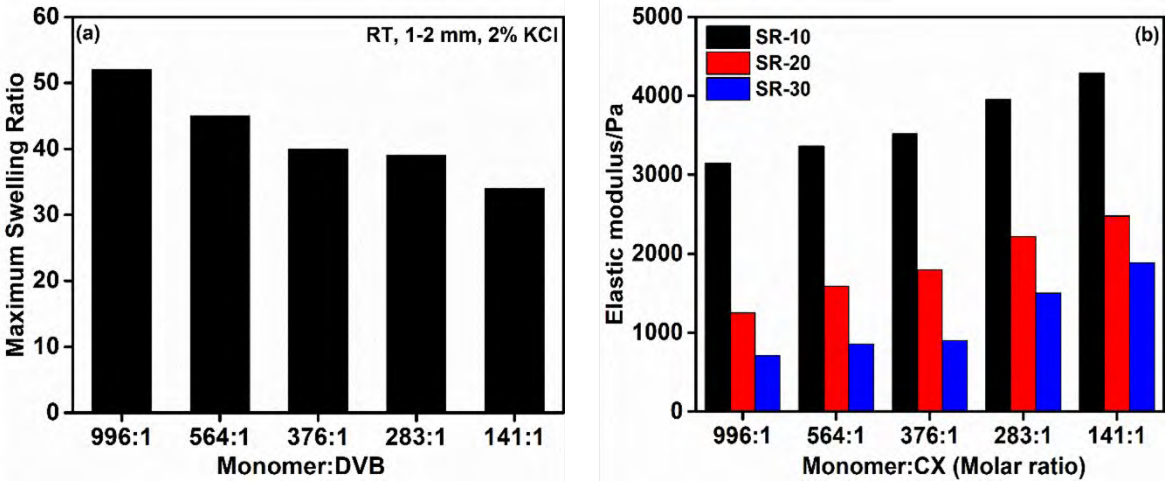

Figure 3. Effect of monomer to crosslinker ratio on the (a) maximum swelling ratio, (b) storage modulus

(2) Thermal Stability of Product-1

Figure 4 shows the stability test result at 200 °C. HT-PPG with swelling ratio 5 and 10 has excellent thermal stability and the volume loss is less than 5% for over 6 months, demonstrating the current product has excellent thermal stability at 200 °C.

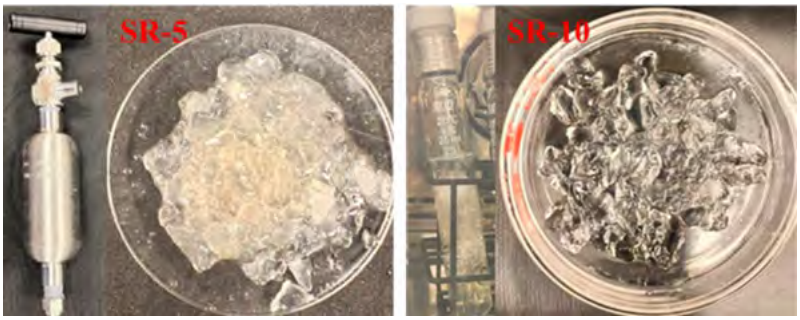

Figure 4. HT-PPG with different swelling ratio after 180 days of aging at 200 °C

3.2 Results of Product-2 (HT-RPPG)

Product-2 is a re-crosslinkable preformed particle gel (RPPG) that can self-heal to form a uniform bulk gel after swelling. This characteristic enhances its blocking performance to fracture and allows it to effectively reduce fluid flow through preferential flow path (Bai et al., 2024). We developed Product-2 by incorporating a specific clay during the synthesis of Product-1. This clay

interacts physically with the polymer backbone, imparting self-healing capabilities to the polymer gels. This method is not only cost-effective but also environmentally friendly, as it eliminates the need for toxic heavy metal ions such as Cr and Zr, as well as toxic organic crosslinkers like phenolic resins and blocked isocyanates, which are typically used in other self-healing mechanisms.

(1) Swelling Kinetics and Rheology Behavior

Figure 5 shows the swelling behavior over time and with varied concentrations of clay, and its the rheological response to swelling ratio and concentration. As shown in Figure 5(a), all HT-RPPGs can reach equilibrium swelling ratios within ten hours. As the clay concentration increases, both the swelling rate and the maximum swelling ratio decrease, with the maximum swelling ratio exceeding 120. In Figure 5(b), the gel strength of HT-RPPG increases with the increase in clay concentration and decreases with the swelling ratio, indicating that clay has a positive effect on improving rheological properties.

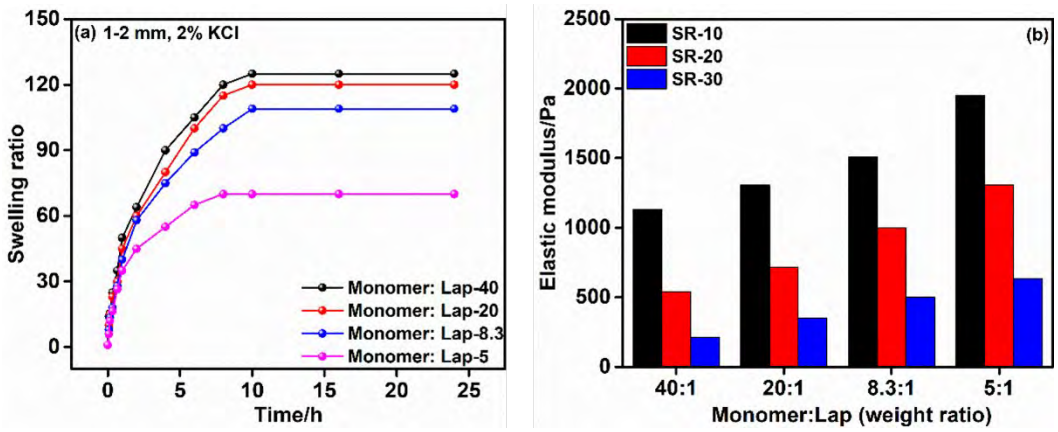

Figure 5. Effect of monomer to clay weight ratio on the (a) swelling kinetics, (b) storage modulus

Figure 6 shows the effect of clay concentration on the gel strength after fully assembling at 200 °C. The gel strength increased with the clay content. Figure 7 shows the gel appearance of HT-RPPG with different clay concentrations. As the clay concentration increases, the boundaries between particles become increasingly blurred, the gel integrity and elasticity gradually increase with clay concentrations.

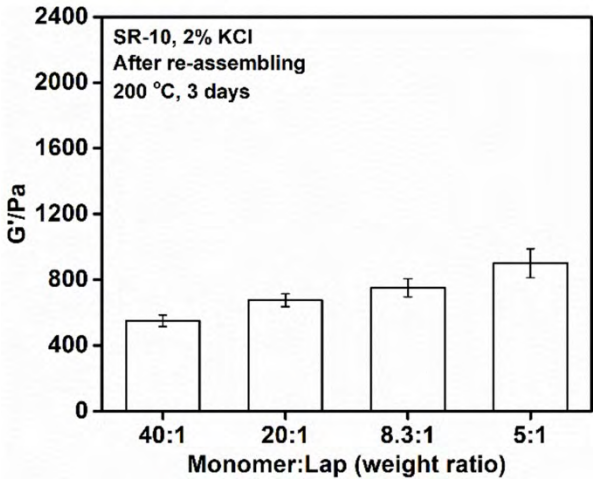

Figure 6. Effect of Clay concentration on the gel strength after fully re-assembling

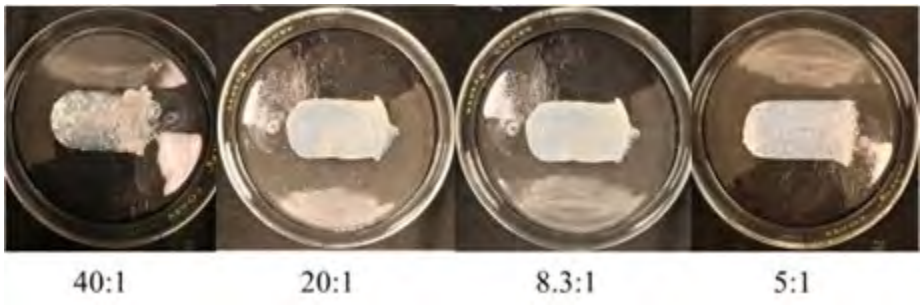

Figure 7. Gel appearance of HT-RPPG with different monomer to clay weight ratio

(2) Thermal Stability of Product-2.

Figure 8 shows the thermal stability of HT-RPPGs at 150 and 200 °C. We use transparent glass sample cylinders to monitor the gel appearance changes during the test. Bulk gel without boundaries was observed without any visible particle and flowing fluid. We also prepared several samples using the stainless-steel sample cylinder to continue studying our samples. The samples (swelling ratio of 10) in stainless-steel cylinders demonstrated excellent thermal stability at 200 °C over 6 months. We observed discoloration, but did not observe any volume loss, and no liquid existed in all cylinders.

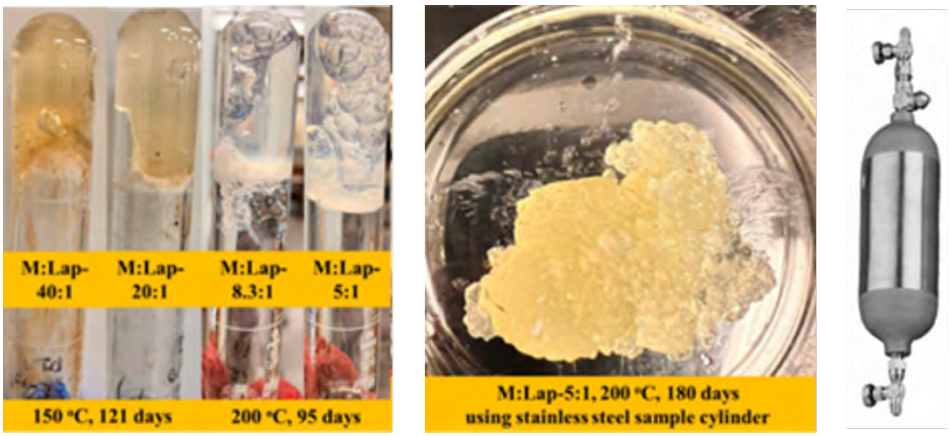

Figure 8. Thermal stability of HT-RPPG at 150 and 200 oC and stainless sample cylinder

3.4 Coreflooding Test

Core flooding tests were conducted to investigate the transport and blocking mechanisms of HT-PPG in fractures. HT-PPG slurry was prepared by swelling the dried gel particles in 2% KCl with various swelling ratios. Once the gel particles had fully absorbed the free water, the gel slurry was injected into the fracture. The core flooding setup, illustrated in Figure 9, includes an ISCO pump, accumulators, a Hassler-type core holder, and a pressure transducer connected to a computer for precise data acquisition and analysis. The test primarily consists of the HT-PPG injection phase followed by a water breakthrough phase.

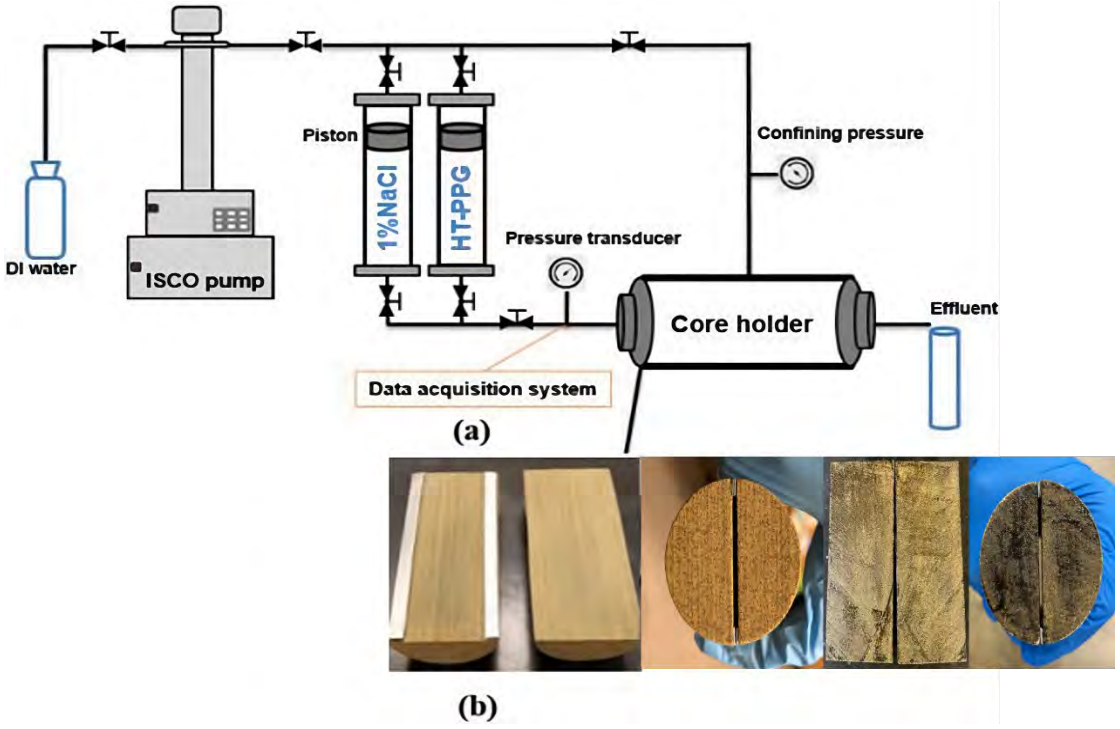

Figure 9. Core flooding setup

HT-PPG Injection: In this experiment, the fractured sandstone model is secured in the core holder, and a confining pressure is applied. The core is first flooded with 2% KCl solution. Next, the swollen HT-PPG is injected into the fracture at a flow rate of 1.0 cc/min to seal it. This injection continues until the pressure stabilizes, as monitored by the acquisition software. Figure 10 illustrates a sample HT-PPG injection profile. Following the injection, the core is sealed and aged in preparation for the breakthrough test.

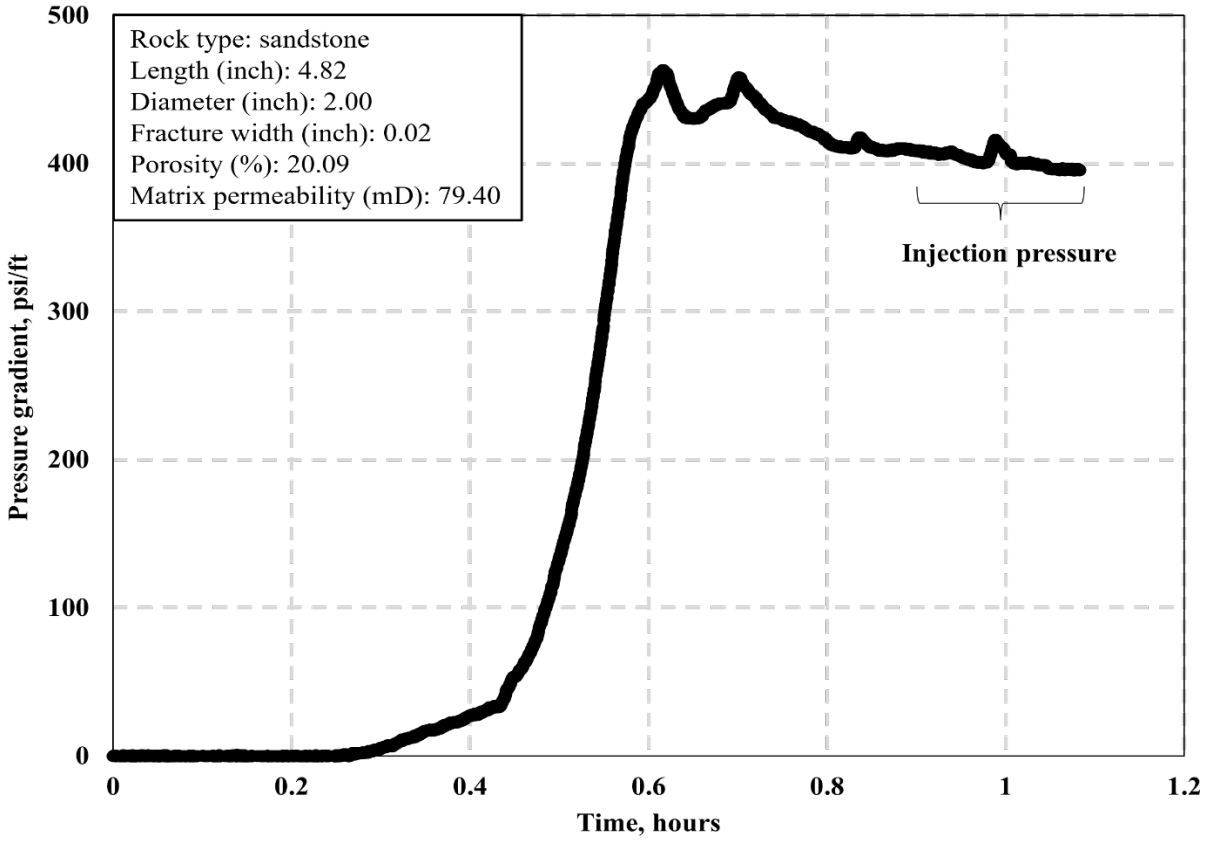

Figure 10. HT-PPG injection profile

Breakthrough pressure and plugging efficiency test: The ability of HT-PPG to reduce fluid flow channels is evaluated by determining threshold pressure and residual resistant factor (Frr). Figure 11 presents an example of the pressure response over the process. After breakthrough, brine was continuously injected at different flow rates of 0.10, 0.25, 0.50, and 1.00 cc/min until pressure reading was stabilized. Figure 12(a) shows the stable pressure readings of a representative sample and the corresponding Frr values are highlighted in Figure 12(b). The initial permeability is determined using Equation 1, while the permeability after water breakthrough is calculated using Equation 2. Frr is then calculated using Equation 3.

$$k_{\text{initial}} = \frac{h^2}{12} \quad \text{Equation 1}$$

$$k_{\text{after}} = \frac{q \times \mu \times L}{A \times \Delta P} \quad \text{Equation 2}$$

$$F_{\text{rr}} = \frac{k_{initial}}{k_{after}} \quad \text{Equation 3}$$

Where $k_{initial}$ is the initial permeability of the fracture and k_{after} is the fracture permeability after gel treatment. $k_{initial}$ and k_{after} were calculated using the above equations, h is the height of the fracture (μm), q is the flow rate (cm^3/s), μ is the viscosity of the liquid (cp), L is the length of the core (cm), A is the cross-sectional area (cm^2) of the fracture, and ΔP is the pressure change (atm).

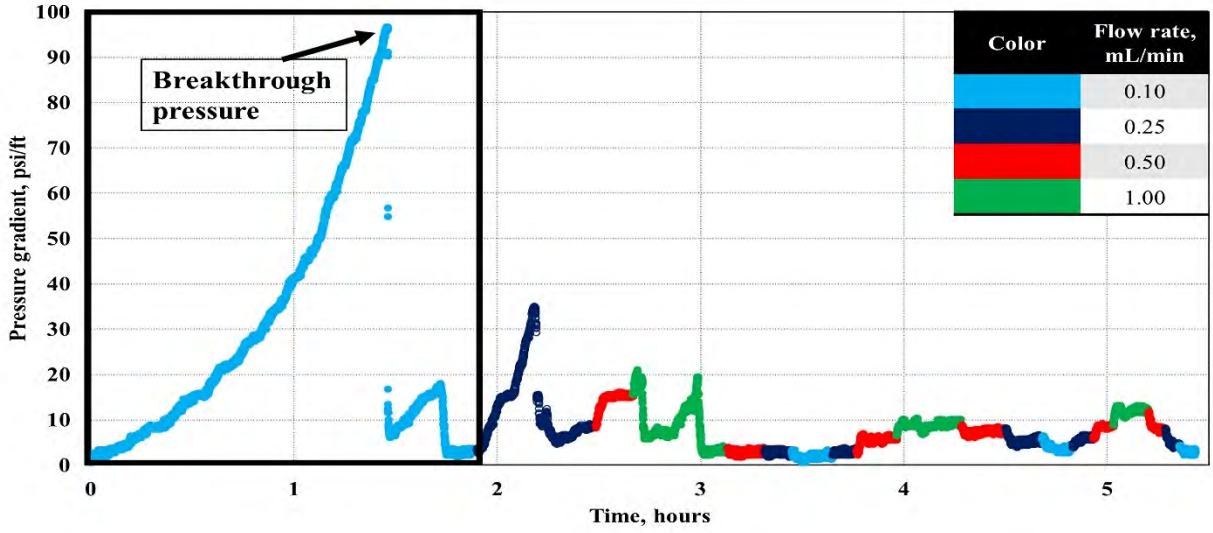

Figure 11. Water breakthrough profile

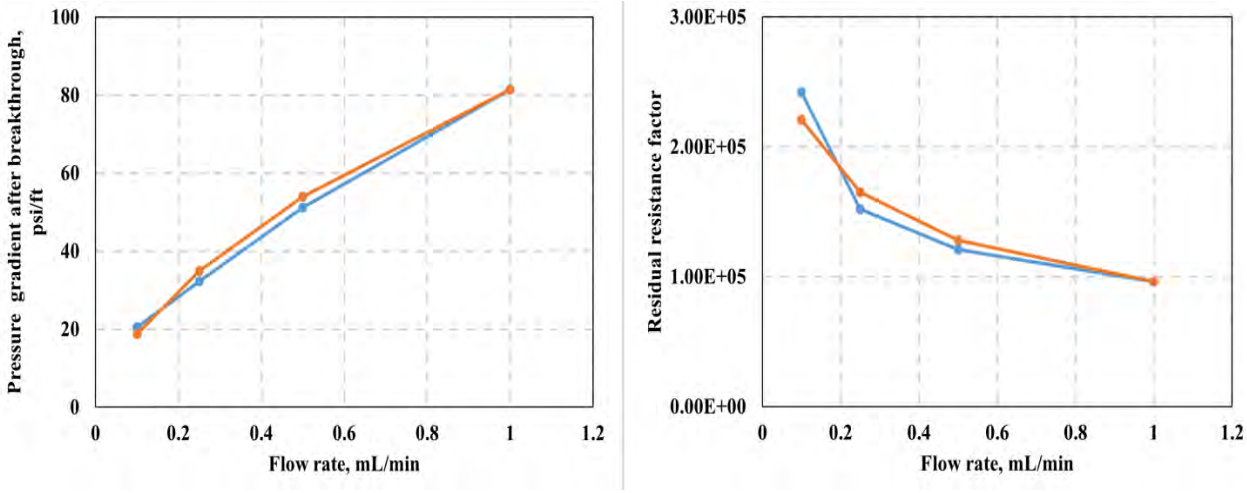

Figure 12. Pressure gradient and Frr against flow rate

We studied the effect of HT-PPG particle size, swelling ratio, and fracture width on injectivity and plugging efficiency. Based on our initial result, we conducted more experiments to further investigate the gel's injection pressure, water breakthrough pressure, and Frr. In doing so, we coated the surfaces of the core with a high temperature epoxy (HT-epoxy) to ensure that the brine used for post flooding is directed toward the HT-PPG in the fracture and not diverted into the core matrix. The HT-epoxy used has a broad service temperature range of -40 to 225 °C (-40 to 437 °F) and has extreme resistance to water and humidity.

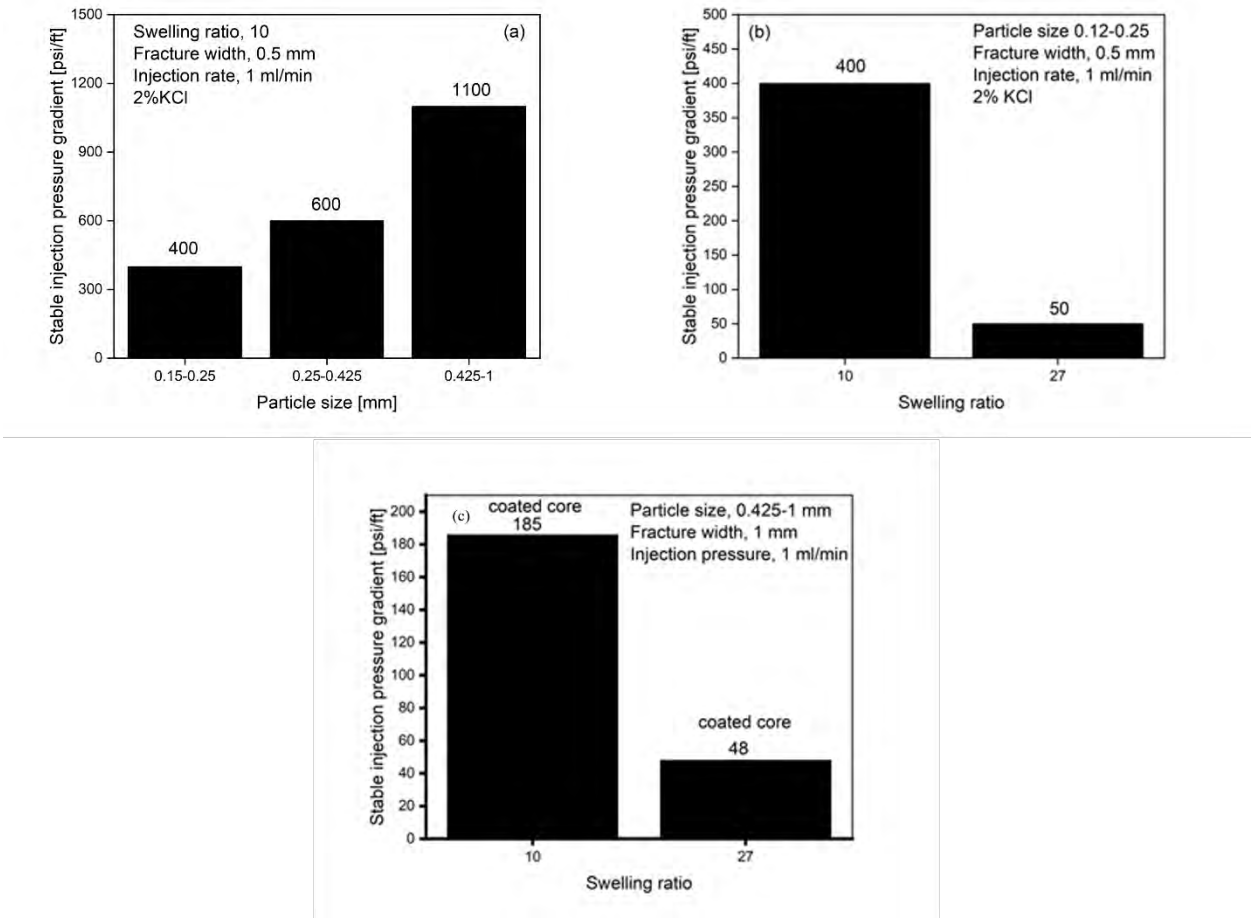

Figure 13. Effect of (a) gel particle size; (b) swelling ratio; and (c) core surface on HT-PPG injection

From our injection results in Figure 13, it is evident that at a constant swelling ratio and fracture width, the injection pressure increases as the particle size increases. It, however, decreases as swelling ratio increases. An increase in swelling ratio requires less pressure for injection into fractures as the soft particles are easier to deforms and penetrate in fractures. The uncoated cores required less pressure for gel placement as adhesion does not play a considerable role as compared to the cores with rough surfaces.

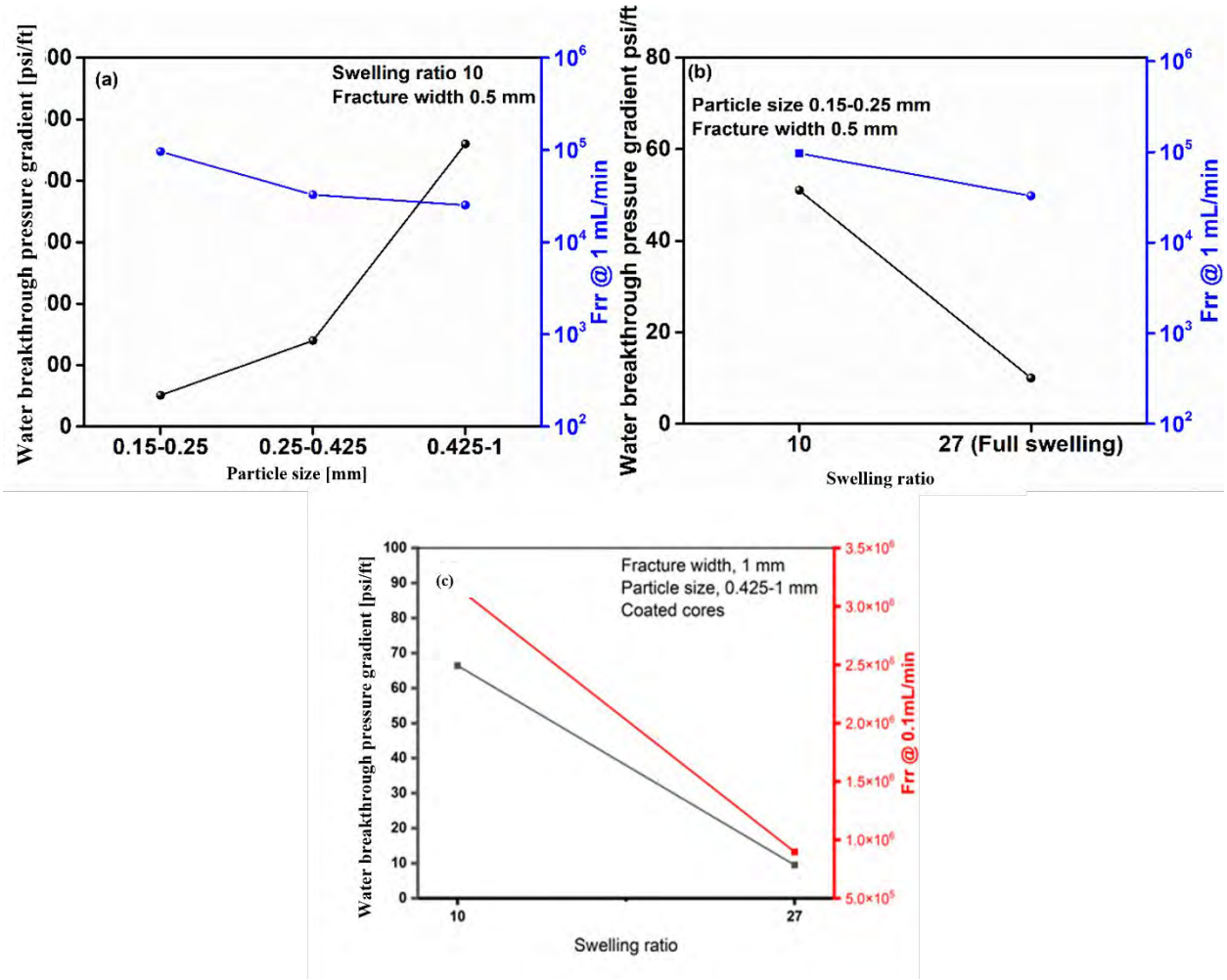

Figure 14. Effect of (a) gel particle size; (b) swelling ratio; and (c) core surface on breakthrough pressure

The effect of gel particle size, swelling ratio, and core surface on HT-PPG breakthrough pressure is summarized in Figure 14. The water breakthrough pressure increases with an increasing particle size but decreases with an increasing swelling ratio. Additionally, there is an increased Frr with the uncoated cores as compared to the coated ones.

3.3 Micromodel swelling kinetics:

We successfully developed a method to print 3D models of fractures and pores for direct visualization of the gel swelling in a confined space. This was to investigate the swelling behavior of our gels under high pressure and high temperature channel constructions. In our experiments, we discovered a novel phenomenon, depicted in Figure 15, where gel particles expand within adequately confined pores and subsequently fracture upon reaching a certain degree of swelling. This results in the formation of smaller fragments capable of blocking the pore space. Our experimental approach has enabled us to methodically investigate the circumstances under which this phenomenon occurs, scrutinize the swelling of gels under varying degrees of porous confinement, and pinpoint the conditions that lead to gel fracturing.

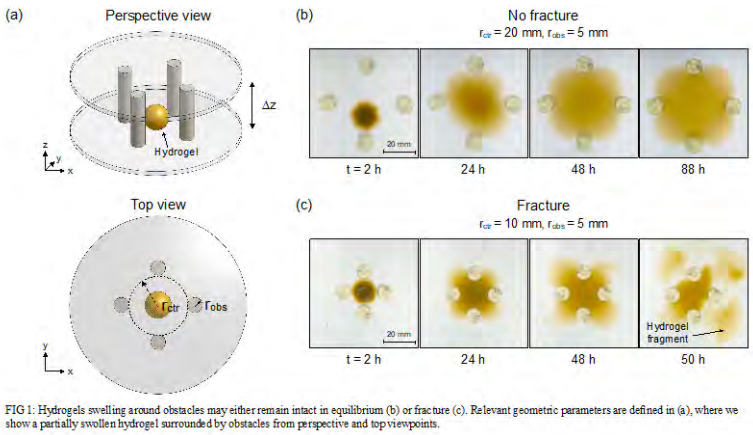

FIG 1: Hydrogels swelling around obstacles may either remain intact in equilibrium (b) or fracture (c). Relevant geometric parameters are defined in (a), where we show a partially swollen hydrogel surrounded by obstacles from perspective and top viewpoints.

Figure 15. Hydrogels swelling around obstacles may either remain intact in equilibrium (b) or fracture (c) relevant geometric parameters are defined in (a), where we show a partially swollen hydrogel surrounded by obstacles from perspective and viewpoints

The outcomes of our study are summarized in Figure 16. Each data point denoted by an 'x' represents a hydrogel experiment that culminated in a fracture, as depicted in Figure 15c. Conversely, data points symbolized by a square indicate experiments where the hydrogel reached equilibrium without fracturing, as illustrated in Figure 15b. The schematics provide a top view of the obstacle geometries corresponding to the specified trials. The shaded region in the upper left corner of the plot denotes parameters that would result in an overlap of the obstacle.

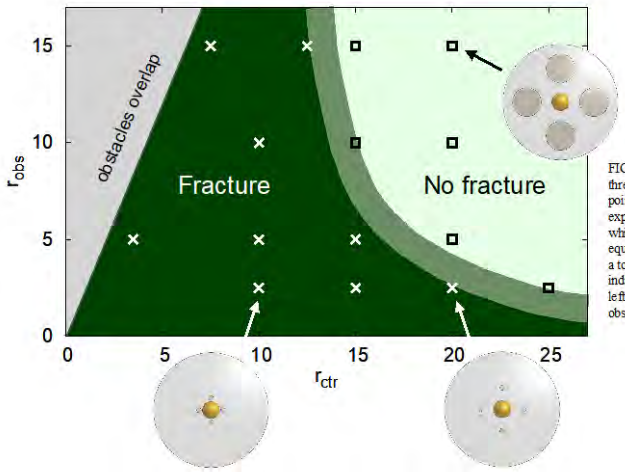

FIG 2: Hydrogel experiments reveal a fracture threshold as a function of obstacle geometry. Each point marked with an x corresponds to a hydrogel experiment that resulted in fracture (as in Fig. 1c), while points marked with a square reached equilibrium intact (as in Fig. 1b). Schematics show a top view of the obstacle geometries for the indicated trials. The grey excluded region in the top left of the plot shows parameters for which the obstacles would overlap.

Figure 16. Hydrogel experiments reveal fracture threshold as a function of obstacle geometry

Based off this finding, we intend to develop theoretical guidelines for gel swelling within confined spaces and to design a computational model for gel placement in fractured media. Additionally, we will experimentally verify how gel placement affects fluid transport pathways, using in situ measurements of pore-scale flow fields and fluid pressures.

3.4 Numerical Simulation to Characterize PPG Transport and Evaluate Gel Treatment Efficiency

We are developing swellable Preformed Particle Gels (PPG) to control preferential fluid and heat flow through fracture networks, thereby enhancing the performance of Enhanced Geothermal System (EGS) reservoirs. Our development includes creating a mathematical model and numerical simulator to simulate PPG treatments, considering coupled thermal-hydraulic-mechanical effects, gel swelling kinetics, and plugging efficiency. This approach aims to achieve an optimized gel treatment design and operation.

Our mathematical model is based on the TOUGH2-CSM formulation and code. The TOUGH2-CSM fluid and heat flow formulation extends the TOUGH2 model for multiphase, multi-component, and multi-porosity systems, incorporating the MINC and EDFM models. The TOUGH2-CSM geomechanical formulation employs the linear theory of elasticity for multi-porosity, non-isothermal media. We have modified this formulation to simulate the injection of PPG into fractures. An equation of state module for gel-water systems was developed, building on a previous TOUGH2 module designed for air and water, as PPGs are primarily water-based. Experimental studies on PPG flow through fractures informed our PPG flow formulation, modeling it as a shear-thinning fluid with yield stress (Herschel-Bulkley fluid). When injected into a permeable fracture, water leaks off through the fracture walls, depositing a more concentrated PPG as a filter cake. Additionally, the transverse pressure gradient during PPG flow can dehydrate the PPG, creating a more concentrated flowing PPG and a separate flowing water phase. These characteristics, along with the PPG's swelling behavior over time, are incorporated into our model.

We verified our simulator's features by matching them with data from experimental studies. These studies included PPG injection into open fractures, used to verify our PPG rheology and longitudinal dehydration models, and PPG injection into closed fractures, used to verify our transverse dehydration model. Finally, we applied our model to a synthetic EGS to evaluate the impact of blocking highly conductive fractures with PPG on energy production. The detail information about the simulation is reported in another paper of this same conference (Winterfeld, Bai and Wu, 2024).

Summary

We have developed a couple of novel particle gels HT-PPGs that exhibit several key properties to make them well-suited for geothermal applications. One of the most critical characteristics is their thermal stability. Unlike conventional polymer gels, HT-PPGs maintain their structural integrity and effectiveness at temperatures ranging from 20°C to 200°C. This makes them adaptable to a wide range of geothermal reservoir conditions. Additionally, the gels can be customized in size, from micrometers to a few millimeters, allowing for tailored solutions to specific reservoir requirements. This adaptability is crucial for addressing the unique challenges presented by different geothermal environments.

The performance of HT-PPGs in geothermal reservoirs is determined by several factors, including their swelling behavior, rheology, and plugging efficiency. Swelling behavior is particularly important, as it affects the ability of the gel to fill and block fractures effectively. Our research has demonstrated that HT-PPGs exhibit controllable swelling times, enabling management of the gel

expansion to optimize its blocking performance. Rheology, or the study of the gel's flow properties, is also critical, as it influences how the gel moves through the reservoir and interacts with the rock matrix. The HT-PPGs developed in our study exhibit favorable rheological properties, ensuring they can be effectively deployed in geothermal reservoirs.

Thermal stability is another crucial aspect of HT-PPG performance. In geothermal environments, where temperatures can exceed 150°C, maintaining the gel's integrity over extended periods is essential. Our HT-PPGs have demonstrated commendable long-term hydrolytic thermal stability, remaining effective for over three months. This long-term stability is vital for ensuring continuous control of fluid flow and maximizing energy production from geothermal reservoirs.

To better understand the behavior and performance of HT-PPGs, we have employed both experimental and micromodel design approaches. With the micromodel, we observe the swelling kinetics and transport mechanisms of a representative particle gel. This allows for detailed visualization and analysis of how the gels interact with the reservoir environment, providing insights into their swelling kinetics. We also developed mathematical models that can simulate PPG transport through factures and optimize PPG treatment parameters.

Overall, our research into HT-PPGs presents a promising solution to one of the major challenges in geothermal energy production. By effectively controlling preferential fluid flow, these gels can enhance the efficiency and sustainability of EGS. The development and implementation of HT-PPG could significantly improve the viability of geothermal energy as a reliable and clean energy source, contributing to a more sustainable energy future.

Acknowledgement
This material is based upon work supported by the U.S. Department of Energy's Office of Energy Efficiency and Renewable Energy (EERE) under the Geothermal Technologies Office (GTO) INNOVATIVE METHODS TO CONTROL HYDRAULIC PROPERTIES OF ENHANCED GEOTHERMAL SYSTEMS Award Number DE-EE0009790.

REFERENCES

Bai, B., Li, L., Liu, Y., Liu, H., Wang, Z., & You, C. (2007). Preformed particle gel for conformance control: factors affecting its properties and applications. *SPE Reservoir Evaluation & Engineering*, *10*(04), 415-422.

Bai, B., Wei, M., & Liu, Y. (2013, March). Field and lab experience with a successful preformed particle gel conformance control technology. In *SPE Oklahoma City Oil and Gas Symposium/Production and Operations Symposium* (pp. SPE-164511). SPE.

Goudarzi, A., Zhang, H., Varavei, A., Taksaudom, P., Hu, Y., Delshad, M., Bai, B. and Sepehrnoori, K. (2015). A laboratory and simulation study of preformed particle gels for water conformance control. *Fuel*, *140*, 502-513.

Li, T., Shiozawa, S., & McClure, M. W. (2016). Thermal breakthrough calculations to optimize design of a multiple-stage Enhanced Geothermal System. *Geothermics*, *64*, 455–465. https://doi.org/10.1016/j.geothermics.2016.06.015

Liu, Y., Song, T., Darko, C. K., Bai, B., & Schuman, T. (2024). Evaluation of Ultra-high Temperature Swelling-Delayed Preformed Particle Gel for the Preferential Fluid Flow Control in Geothermal Reservoirs. *Proceedings, 49th Workshop on Geothermal Reservoir Engineering Stanford University, Stanford, California*.

Lund, J. W. (2007). Characteristics, development and utilization of geothermal resources. Geo-Heat Cent Q Bull 2007;28(2):1–9.

McClure, M. W., & Horne, R. N. (2014). An investigation of stimulation mechanisms in Enhanced Geothermal Systems. *International Journal of Rock Mechanics and Mining Sciences*, *72*, 242–260. https://doi.org/10.1016/j.ijrmms.2014.07.011

Seidy Esfahlan, M., Khodapanah, E., & Tabatabaei-Nezhad, S. A. (2021). Comprehensive review on the research and field application of preformed particle gel conformance control technology. In *Journal of Petroleum Science and Engineering* (Vol. 202). Elsevier B.V. https://doi.org/10.1016/j.petrol.2021.108440

Song, T., Bai, B., & Schuman, T. (2023). Evaluation of Ultra-high Temperature Resistant Hydrogels for the Preferential Fluid Flow Control. *Proceedings, 48th Workshop on Geothermal Reservoir Engineering Stanford University, Stanford, California*.

Tongwa, P., & Baojun, B. (2015). A more superior preformed particle gel with potential application for conformance control in mature oilfields. *Journal of Petroleum Exploration and Production Technology*, *5*(2), 201–210. https://doi.org/10.1007/s13202-014-0136-8.

Winterfeld1, Philip H; Bai, B., Wu, Y. Using Preformed Particle Gels to Control Transport in Geothermal Reservoirs: Mathematical Modeling, a paper to be presented Using Preformed Particle Gels to Control Transport in Geothermal Reservoirs: Mathematical Modeling. GRC Transactions, Vol. 48, 2024

Xiong, B., Loss, R. D., Shields, D., Pawlik, T., Hochreiter, R., Zydney, A. L., & Kumar, M. (2018). Polyacrylamide degradation and its implications in environmental systems. In *npj Clean Water* (Vol. 1, Issue 1). Nature Research. https://doi.org/10.1038/s41545-018-0016-8

Zhang, Q., Dahi Taleghani, A., & Li, G. (2024). Fracture conductivity management to improve heat extraction in enhanced geothermal systems. *International Journal of Heat and Mass Transfer*, *218*. https://doi.org/10.1016/j.ijheatmasstransfer.2023.124725

Enhancing Reservoir Performance Insight: A Comprehensive Monitoring Approach with Steam Allocation Lumut Balai (SALB) Application

Naura T. Fadjar, Teguh Prabowo, Fadiel E. Marastio, Fernando Pasaribu, and Jantiur Situmorang

Pertamina Geothermal Energy

Keywords

Water-dominated, production monitoring, deliverability curve, production decline, steam supply, production variance

ABSTRACT

In the Lumut Balai geothermal field, daily well production flowrates and enthalpy measurement data are not available due to the absence of two-phase flowmeters. This condition complicates quantitative estimations regarding steam availability, steam production decline rates, and subsequently steam supply forecast. Meanwhile, a quarterly Tracer Flow Testing (TFT) has been performed to monitor individual well production flowrates and enthalpy which allows merely a qualitative evaluation of production performance. These uncertainties significantly impact reservoir management strategies.

The Steam Allocation Lumut Balai (SALB) application has been developed to estimate daily individual well production by solving mass and energy balance equations throughout the field process flow diagram and integrating operational data such as wellhead pressure, separator pressure, brine mass flow rate, steam mass flow rate, re-injected mass flow rate, and TFT. This daily monitoring facilitates a nuanced understanding of the wells and the reservoir behavior, expediting the troubleshooting and the resolution of the issues. This paper outlines the methodology employed in the SALB application and details its implementation.

1. Introduction

The Lumut Balai geothermal field is a water-dominated geothermal field located in South Sumatra, ±274 km southwest from the city of Palembang, the capital city of South Sumatra (Figure 1). Currently, it hosts a geothermal power plant with a generation capacity of 55 MWe. A second geothermal power plant unit with an identical generation capacity of 55 MWe is under construction at the Lumut Balai geothermal field. The geothermal field features wells with relatively uniform

specific enthalpy across its expanse from South to North, with reservoir temperatures spanning from 220°C to 250°C.

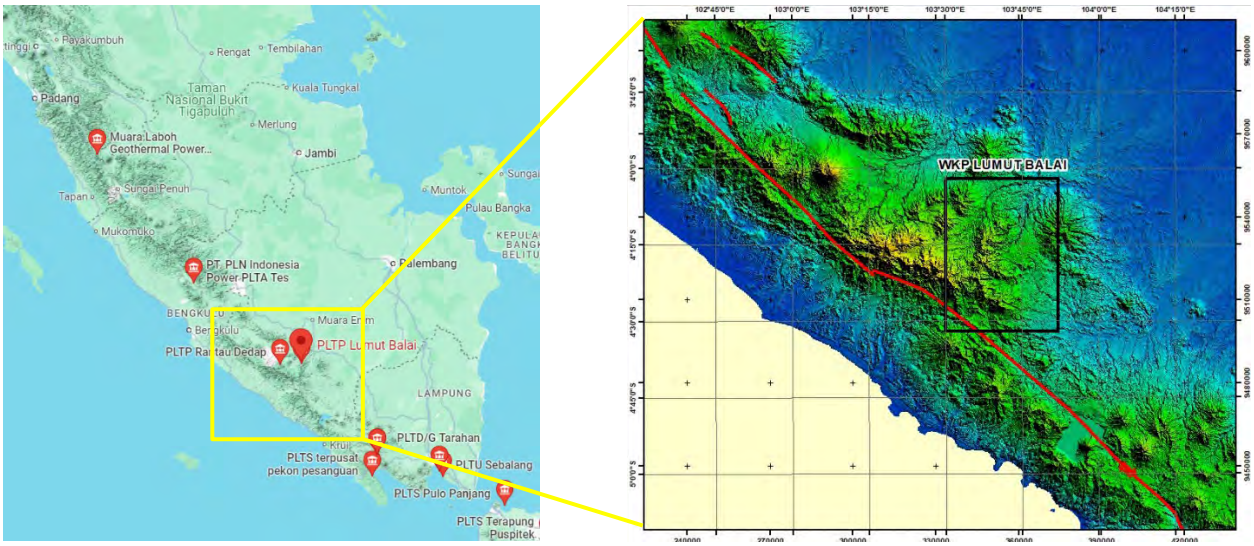

Figure 1: Location map of the Lumut Balai geothermal field.

A quarterly TFT has been employed to monitor individual well production flowrates and enthalpies. Nevertheless, operational constraints typically result in less frequent implementation of TFT. As there are no two-phase flowmeters, the information obtained regarding the reservoir conditions at the Lumut Balai geothermal field is often outdated. This temporal discrepancy between the current state of the reservoir and the most recent data available potentially leads to suboptimal reservoir management strategies.

As the second unit of power plant nearing commercialization, understanding the reservoir performance of the operational Unit 1 is crucial. Unfortunately, daily data for total mass flow rates and production fluid enthalpies from the individual wells in the Unit 1 is not readily available, leading to reliance on the quarterly TFT for steam availability and steam production decline rate calculations. Therefore, developing a technique to estimate daily production data is essential.

2. The Importance of Daily Well Production Estimation

Understanding daily well production is crucial for effective reservoir management. Production wells should provide insights into geothermal reservoir conditions. Changes in well production flow rate and specific enthalpy of well production fluid can reveal significant information about reservoir dynamics. These changes can be analyzed through alterations in deliverability curve from time to time. Figure 2 illustrates how a well deliverability curve shifts over time, indicating different reservoir conditions such as changes in reservoir pressure, temperature, or permeability, as well as well-specific issues like wellbore scaling, as described by Grant and Bixley (2011) and James (1980a). According to Grant and Bixley (2011), Curve A is the basic curve, representing the results from a water-fed well with high permeability. Curve B shows the effect of a decrease in reservoir pressure. Curve C illustrates the effect of an increase in reservoir pressure. Curve D indicates the impact of scaling in the wellbore. Curve E results when the feed is two-phase at the same pressure as for Curve A (Figure 2).

An alteration in deliverability curve of a production well leads to change in the production flow rate at high wellhead pressure, low wellhead pressure, or both. If alterations in a deliverability curve are identified belatedly, subsequent analysis and interventions regarding the conditions within a geothermal well and a reservoir will also be delayed, thereby compromising the effectiveness of reservoir management.

Understanding the most current deliverability curve of a production well is crucial for accurately determining its maximum steam supply. Geothermal wells are frequently operated in a partially open state, or "choked". Therefore, understanding the well deliverability curve enables the assessment of the well production at the maximum opening without fully opening the well, preventing steam wastage and ensuring optimal reservoir exploitation.

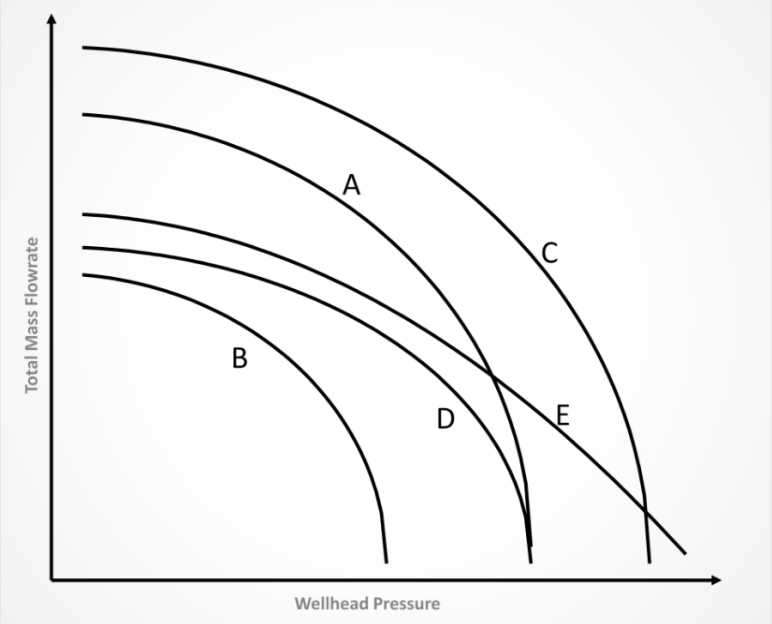

Figure 2: The variations in the shifting of the well deliverability curve over time are caused by different factors. These changes can indicate various reservoir conditions or well-specific issues.

The cumulative steam supply from all production wells within a geothermal field is determined by aggregating the maximum steam output from each production well. Since each production well exhibits a unique alteration in its deliverability curve from time to time, the production decline rate at the maximum opening will differ among production wells. This variability necessitates daily production monitoring of each production well to capture their changes in deliverability curve. The aggregate production decline from all production wells provides an estimate of the overall production decline rate for the geothermal field. The overall production decline rate serves as the basis for calculating the required timeframe to drill a make-up well, ensuring sufficient steam supply to the power plant and maintaining its operational capacity.

3. The Steam Allocation Lumut Balai (SALB) Application

The Steam Allocation Lumut Balai (SALB) application was developed to facilitate the estimation of daily production from each well, despite the absence of two-phase flowmeters in the well production lines at the Lumut Balai geothermal field. This application seeks to mitigate the lack

of well production data that occurs between the quarterly data collection intervals, which currently utilize TFT.

3.1 The Process Flow of The Lumut Balai Geothermal Field

In developing the SALB application, the first necessity is an understanding of the process flow in the Lumut Balai geothermal field. Detailed information on the number of production and reinjection wells, separators, interconnection points, condensate lines, and the availability of brine and steam flowmeters, as well as pressure gauges, is required for the algorithm development.

The Unit 1 is supplied by nine production wells, which direct flow to three separators, while the brine and the condensate from the Unit 1 are re-injected into three reinjection wells (Figure 3). The Unit 2 will receive steam from five production wells, in addition to the steam from the interconnection of wells from the Unit 1. The SALB application is currently operational only for the existing power plant unit, therefore, it does not yet encompass the wells in the Unit 2.

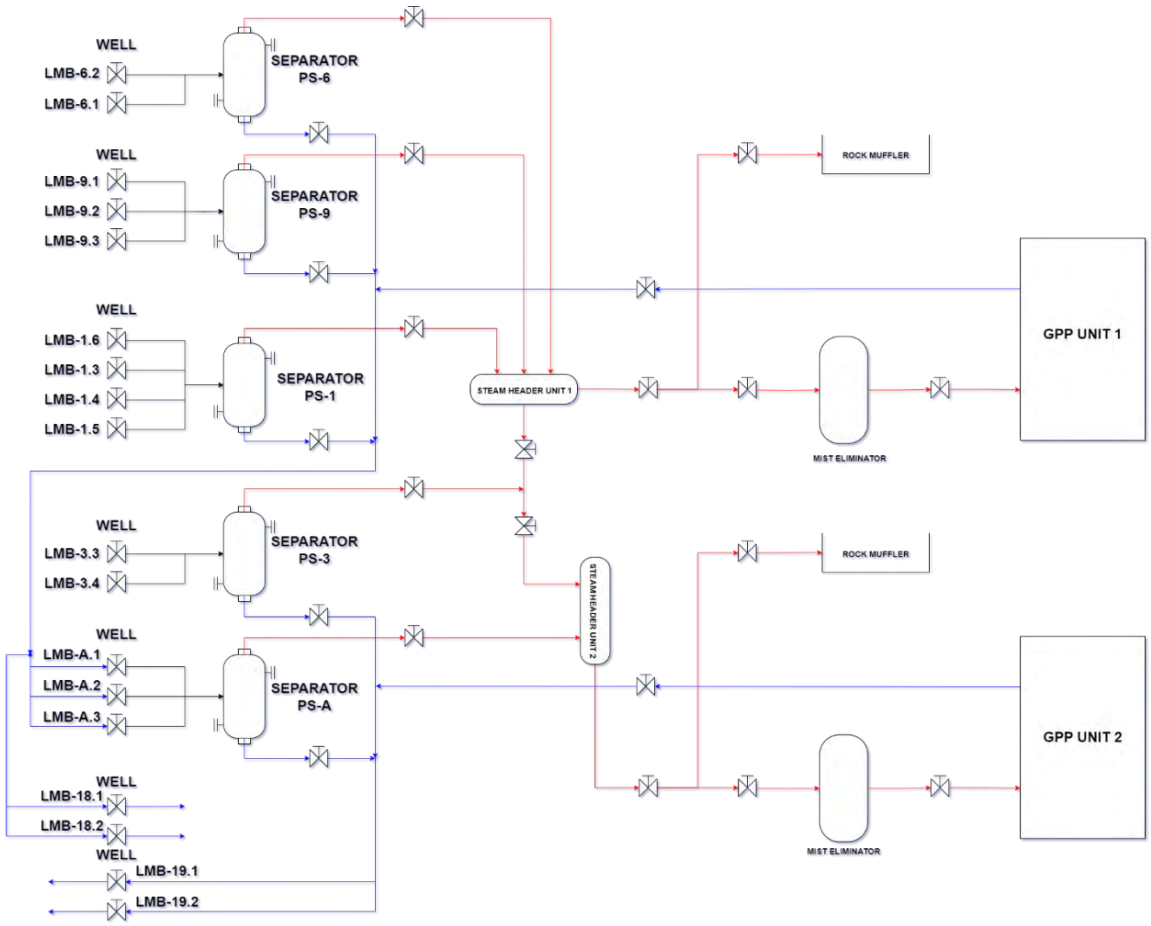

Figure 3: The process flow diagram of the Lumut Balai geothermal field. The SALB application does not yet encompass the wells in the Unit 2.

3.2 Solving Mass and Energy Balance of The Lumut Balai Geothermal Field

The SALB application is developed under the principles of mass and energy conservation. It ensures that the amount of mass and energy exiting the production wells are equivalent to those present in the separators, the steam vessels, and subsequently returned to the reinjection wells.

3.2.1 The Mass and The Energy Balance of The Lumut Balai Geothermal Field

The total mass flow balance equation, aligned with the available flowmeters at the Unit 1 production facility of the Lumut Balai geothermal field, is as follows.

$$\dot{m}_{\text{field}} = \dot{m}_{@\text{reinjector wells}} + \dot{m}_{@\text{scrubber}} + \dot{m}_{@\text{rock muffler}} - \dot{m}_{@\text{condensate line}} \quad (1)$$

Where $\dot{m}_{\text{field}}$, $\dot{m}_{@\text{reinjector wells}}$, $\dot{m}_{@\text{scrubber}}$, $\dot{m}_{@\text{rock muffler}}$, and $\dot{m}_{@\text{condensate line}}$ represent the total mass production flow rate of the field, the measured mass flow rate injected into all reinjection wells, the measured steam mass flow rate in the scrubber, the measured steam mass flow rate in the rock muffler, and the measured condensate mass flow rate in the condensate pump, respectively.

Meanwhile, the steam mass flow balance equation is expressed in the following equation.

$$\dot{m}_{@\text{scrubber}} + \dot{m}_{@\text{rock muffler}} = \dot{m}_{\text{steam}_{@\text{SEP}-6}} + \dot{m}_{\text{steam}_{@\text{SEP}-1}} + \dot{m}_{\text{steam}_{@\text{SEP}-9}} \quad (2)$$

Where $\dot{m}_{\text{steam}_{@\text{SEP}-6}}$, $\dot{m}_{\text{steam}_{@\text{SEP}-1}}$, and $\dot{m}_{\text{steam}_{@\text{SEP}-9}}$ represent the measured steam mass flow rates at the separators of Cluster 6, Cluster 1, and Cluster 9, respectively.

The brine mass flow balance equation is represented by the following equation.

$$\dot{m}_{@\text{reinjector wells}} - \dot{m}_{@\text{condensate line}} = \dot{m}_{\text{brine}_{@\text{SEP}-6}} + \dot{m}_{\text{brine}_{@\text{SEP}-1}} + \dot{m}_{\text{brine}_{@\text{SEP}-9}} \quad (3)$$

Where $\dot{m}_{\text{brine}_{@\text{SEP}-6}}$, $\dot{m}_{\text{brine}_{@\text{SEP}-1}}$, and $\dot{m}_{\text{brine}_{@\text{SEP}-9}}$ are the measured brine mass flow rates at the separators of Cluster 6, Cluster 1, and Cluster 9, respectively.

In addition to the total mass flow balance, energy flow balance is also considered to determine the enthalpy values. The energy flow balance equation, corresponding to the available flowmeters at the Unit 1 production facility of the Lumut Balai geothermal field, is as follows.

$$\dot{m}_{\text{field}} h_{\text{field}} = \dot{m}_{\text{SEP}-6} h_{\text{SEP}-6} + \dot{m}_{\text{SEP}-1} h_{\text{SEP}-1} + \dot{m}_{\text{SEP}-9} h_{\text{SEP}-9} \quad (4)$$

$$h_{field} = \frac{\dot{m}_{SEP-6} h_{SEP-6} + \dot{m}_{SEP-1} h_{SEP-1} + \dot{m}_{SEP-9} h_{SEP-9}}{\dot{m}_{field}} \quad (5)$$

Where h_{field}, $\dot{m}_{SEP-6}$, $\dot{m}_{SEP-1}$, $\dot{m}_{SEP-9}$, h_{SEP-6}, h_{SEP-1}, and h_{SEP-9} represent the weighted enthalpy of the field production fluid, the total mass flow rates at the separators of Cluster 6, Cluster 1, and Cluster 9, and the enthalpy of the production fluid at the separators of Cluster 6, Cluster 1, and Cluster 9, respectively.

3.2.2 The Mass and The Energy Balance of The Separators

In the case of the Lumut Balai geothermal field, the calibration of the total mass flow rate is performed at the separator level to achieve an accurate assessment. Each separator in the geothermal field is equipped with both steam and brine flowmeters, enabling the SALB application to perform history matching using the separator flowmeter data. The following is the total mass flow balance equation for the Cluster 1 separator, which includes four production wells.

$$\dot{m}_{SEP-1} = \dot{m}_{LMB-1.3} + \dot{m}_{LMB-1.4} + \dot{m}_{LMB-1.5} + \dot{m}_{LMB-1.6} \quad (6)$$

Where $\dot{m}_{LMB-1.3}$, $\dot{m}_{LMB-1.4}$, $\dot{m}_{LMB-1.5}$, and $\dot{m}_{LMB-1.6}$ are the total mass flow rates produced from wells: LMB-1.3, LMB-1.4, LMB-1.5, and LMB-1.6, respectively.

Each separator in the Lumut Balai geothermal field is equipped with a pressure gauge, enabling the calculation of the actual enthalpy of production fluid at each separator. Therefore, the calibration of production fluid enthalpy is also conducted at separator level. The energy flow balance equation for the Cluster 1 separator is as follows.

$$\dot{m}_{SEP-1} h_{SEP-1} = \dot{m}_{LMB-1.3} h_{LMB-1.3} + \dot{m}_{LMB-1.4} h_{LMB-1.4} + \dot{m}_{LMB-1.5} h_{LMB-1.5} + \dot{m}_{LMB-1.6} h_{LMB-1.6} \quad (7)$$

$$h_{SEP-1} = \frac{\dot{m}_{LMB-1.3} h_{LMB-1.3} + \dot{m}_{LMB-1.4} h_{LMB-1.4} + \dot{m}_{LMB-1.5} h_{LMB-1.5} + \dot{m}_{LMB-1.6} h_{LMB-1.6}}{\dot{m}_{SEP-1}} \quad (8)$$

Where $h_{LMB-1.3}$, $h_{LMB-1.4}$, $h_{LMB-1.5}$, and $h_{LMB-1.6}$ represent the enthalpies of production fluid from wells: LMB-1.3, LMB-1.4, LMB-1.5, and LMB-1.6, respectively.

3.3 Deliverability Curve and Energy Flow Rate Curve Initial Models

Equations (6), (7), and (8) involve variables for total mass flow rate and production fluid enthalpy from each well in Cluster 1: $\dot{m}_{LMB-1.3}$, $\dot{m}_{LMB-1.4}$, $\dot{m}_{LMB-1.5}$, $\dot{m}_{LMB-1.6}$, $h_{LMB-1.3}$, $h_{LMB-1.4}$, $h_{LMB-1.5}$, and $h_{LMB-1.6}$. The Lumut Balai geothermal field currently lacks instruments to measure these variables directly. Therefore, a method to estimate their values is necessary.

The total mass flow rate of a production well is related to its pressure. Wellhead is the most convenient point for measuring well pressure, as each wellhead in the Lumut Balai geothermal field is equipped with a pressure gauge. The relationship between total mass flow rate and wellhead pressure is represented by a deliverability curve. Since the Lumut Balai geothermal field is water-dominated, the wells have what is known as maximum discharge pressure. Raising the wellhead pressure beyond the maximum discharge pressure results in collapse of the flowing steam-water mixture and closure of the well, as described by James (1970).

A deliverability curve can be represented by an analytical equation that describes an ellipse situated in the first quadrant as discussed by James (1989). The presence of maximum discharge pressure shifts the elliptical axis of a deliverability curve above the x-axis. The optimal solution for this case is by using the offset elliptical equation which was solved by Davila (2017). The alternate expression of the offset elliptical equation by Davila (2017) is as follows.

$$\dot{m}_{@whp} = \dot{m}_{@mdp} + \left[\left(\dot{m}_{@whp=0\ bar} - \dot{m}_{@mdp}\right) \times \sqrt{1 - \frac{whp^2}{mdp^2}}\right] \quad (9)$$

Where $\dot{m}_{@whp}$ is the well total mass flow rate at a given wellhead pressure, $\dot{m}_{@mdp}$ is the well total mass flow rate at the maximum discharge pressure, $\dot{m}_{@whp=0\ bar}$ is the well total mass flow rate at the wellhead pressure of 0 bar, whp is wellhead pressure, and mdp is the maximum discharge pressure. $\dot{m}_{LMB-1.3}$, $\dot{m}_{LMB-1.4}$, $\dot{m}_{LMB-1.5}$, and $\dot{m}_{LMB-1.6}$ are calculated using Equation (9).

The production fluid enthalpy from a well depends on its energy flow rate. This energy flow rate is obtained by multiplying the total mass flow rate by the production fluid enthalpy. The relationship between energy flow rate and wellhead pressure resembles that of total mass flow rate and wellhead pressure (Figure 4). As a result, the equation representing energy flow rate as a function of wellhead pressure forms an elliptical curve in the first quadrant with the elliptical axis above the x-axis due to the presence of maximum discharge pressure. The analytical equation for the energy flow rate as a function of wellhead pressure is as follows.

$$(\dot{m}h)_{@whp} = (\dot{m}h)_{@mdp} + \left[\left((\dot{m}h)_{@whp=0\ bar} - (\dot{m}h)_{@mdp}\right) \times \sqrt{1 - \frac{whp^2}{mdp^2}}\right] \quad (10)$$

Where $h_{@whp}$ represents the enthalpy of the well production fluid at a given wellhead pressure, $h_{@mdp}$ denotes the enthalpy of the well production fluid at the maximum discharge pressure, and $h_{@whp=0\ bar}$ indicates the enthalpy of the well production fluid at the wellhead pressure of 0 bar.

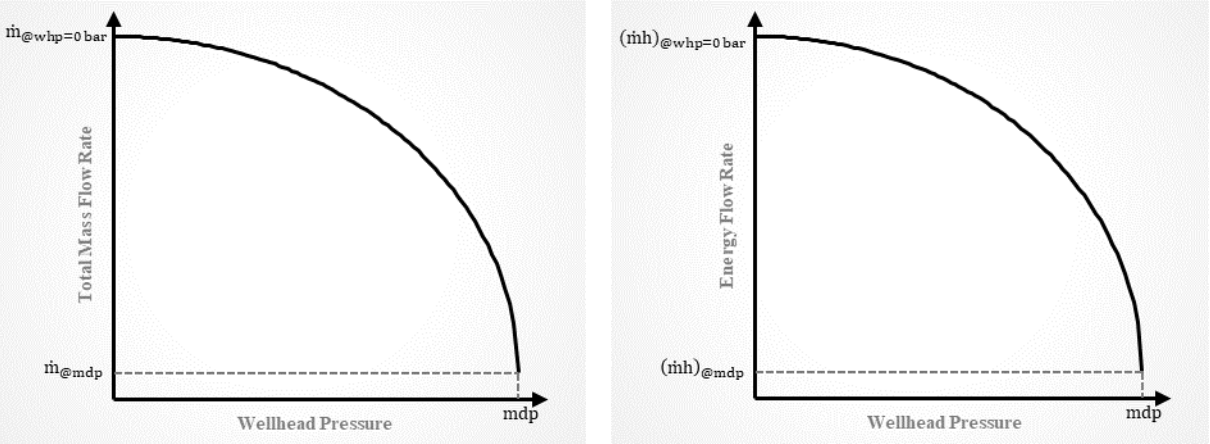

Figure 4: A well deliverability curve (left) and a well energy flow rate curve (right). The relationship between energy flow rate and wellhead pressure resembles that of total mass flow rate and wellhead pressure.

Production fluid enthalpy can be calculated using the following equation.

$$h_{@whp} = \frac{(\dot{m}h)_{@whp}}{\dot{m}_{@whp}} \tag{11}$$

$h_{LMB-1.3}$, $h_{LMB-1.4}$, $h_{LMB-1.5}$, and $h_{LMB-1.6}$ are calculated using Equation (10) and (11). Well production fluid enthalpy is necessary for calculating the dryness fraction of well production fluid using steam tables. This calculation relies on the well production fluid enthalpy value at the separator pressure. The resulting dryness fraction is then used to determine the steam mass flow rate of the production well.

Based on Equations (9) and (10), reservoir engineers will estimate the values of five variables representing the deliverability curve and the energy flow rate curve, namely $\dot{m}_{@mdp}$, $h_{@whp}$, $\dot{m}_{@whp=0\ bar}$, $h_{@whp=0\ bar}$, and mdp. Over time, the values of these five variables undergo changes, which will correspond to the alterations in both the deliverability curve and the energy flow rate curve. Before attempting to estimate changes in the values of these variables, an initial approximation is required. This approximation should reflect the original conditions of the production wells when they were initially producing together to supply electricity according to the power plant capacity. To initially approximate the values of these five variables, it is necessary to utilize production test data collected from these wells before the power plants commence commercial operation. This ensures that the initial approximation of the curve shape maintains a qualitative similarity to the shape derived from the production test data (Figure 5).

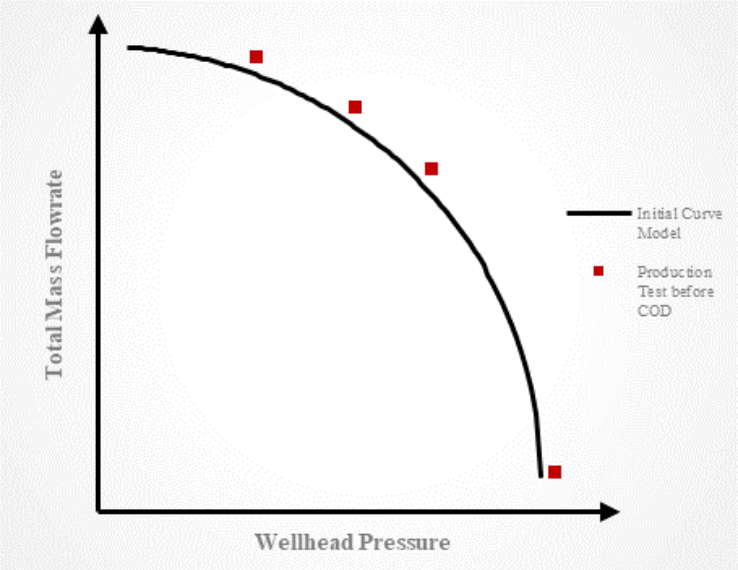

Figure 5: The initial well curve model is created to qualitatively match the shape derived from the well production test data collected before commercial operation date.

3.4 Quantitative History Matching with Separator Flowmeter Data

In the Lumut Balai geothermal field, the smallest scale of mass flow rate measurements is at separator level. Each downstream separator has flowmeters for both brine and steam, which continuously measure using sensors. Data from these flowmeters are utilized for model matching. $\dot{m}_{SEP}$ calculated by summing the mass flow rates from all production wells leading to a separator is compared with $\dot{m}_{SEP}$ obtained by adding the mass flow rates in the brine and steam lines from that separator. Similarly, h_{SEP} calculated using Equation (8) is compared with h_{SEP} obtained from steam tables, utilizing the actual data on the dryness fraction of the production fluid in the separator at the measured separator pressure.

The deliverability curve and the energy flow rate curve models from each well are used to determine the total mass flow rate and the production fluid enthalpy at a given wellhead pressure. Model matching is done daily, so data collected more frequently than daily is averaged to a daily scale.

Flowmeters installed at the separators usually have low margin of error, making it possible to perform a quantitative history matching process using their data. Three parameters will be matched with the flowmeter data at a separator: steam mass flow rate, total mass flow rate, and separator fluid enthalpy (Figure 6). This history matching process is carried out quantitatively, with a cumulative error tolerance of less than 2% for the steam mass flow rate data. Figure 7 depicts the general workflow of using the SALB application for the history matching process.

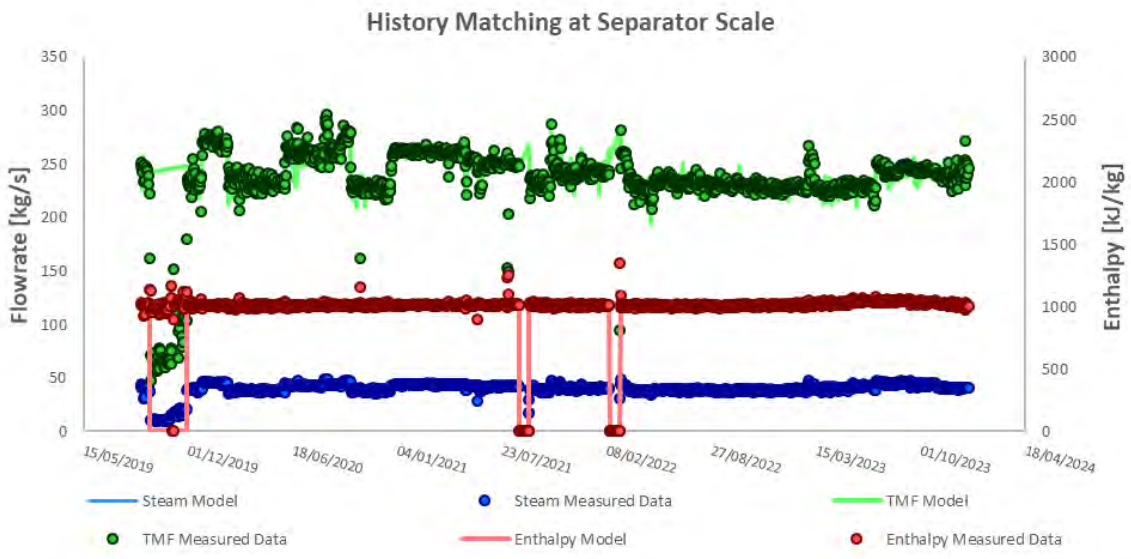

Figure 6: Three parameters are quantitatively matched with the flowmeter data at a separator: steam mass flow rate, total mass flow rate, and separator fluid enthalpy.

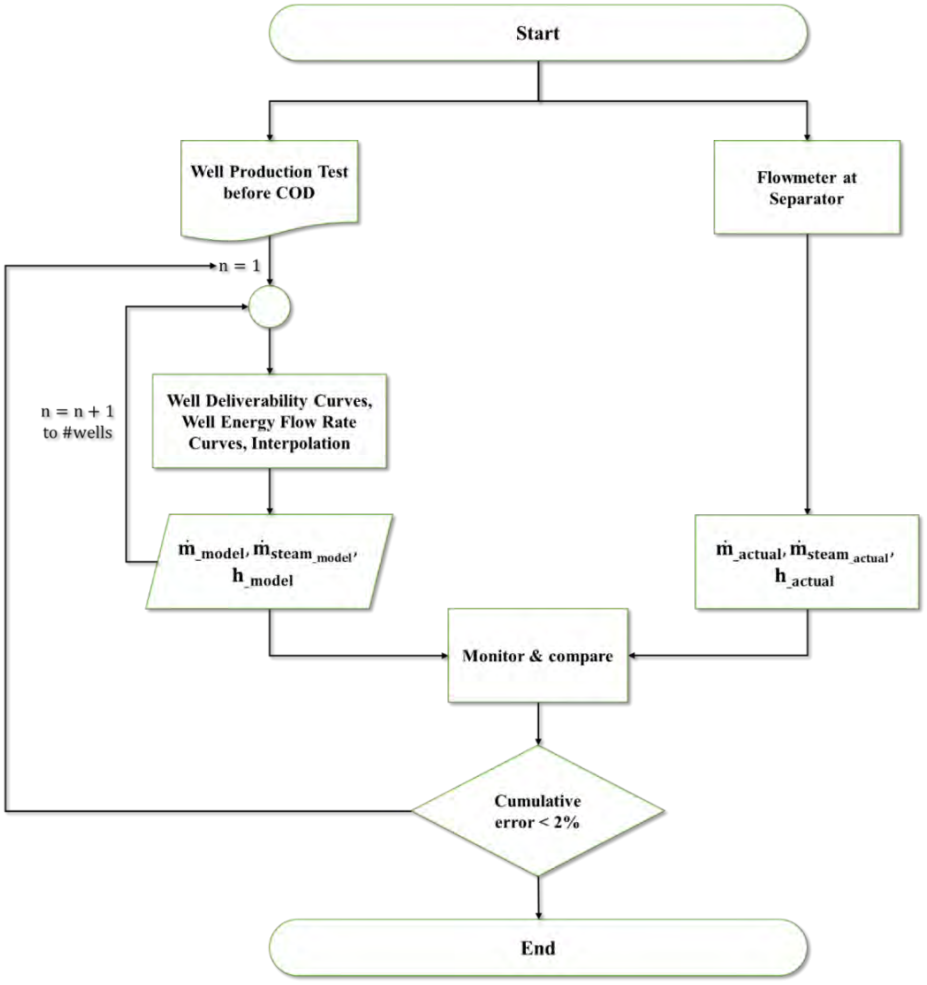

Figure 7: The general workflow of using the SALB application for the history matching process.

Unlike steam mass flow rate, which is highly accurate, total mass flow rate, calculated as the sum of steam mass flow rate and brine mass flow rate, allows for a higher margin of error. This is because brine contains many components that can clog flowmeter, leading to quicker degradation in accuracy. Consequently, since the cumulative error tolerance for the total mass flow rate is relatively large, the cumulative error tolerance for the separator fluid enthalpy values is adjusted accordingly.

3.5 Qualitative History Matching with Tracer Flow Testing Data

History matching with TFT data is qualitatively conducted due to higher error margins in chemical method measurements compared to separator flowmeter. Nevertheless, the chemical method measurements remain crucial for ensuring the credibility of the separator flowmeters. Figure 8 compares the models of total mass flow rate, steam mass flow rate, and production fluid enthalpy over time from LMB-X well alongside the TFT data. Additionally, Figure 9 presents the history matching results of the model against both the flowmeter and the TFT data for Separator-Z.

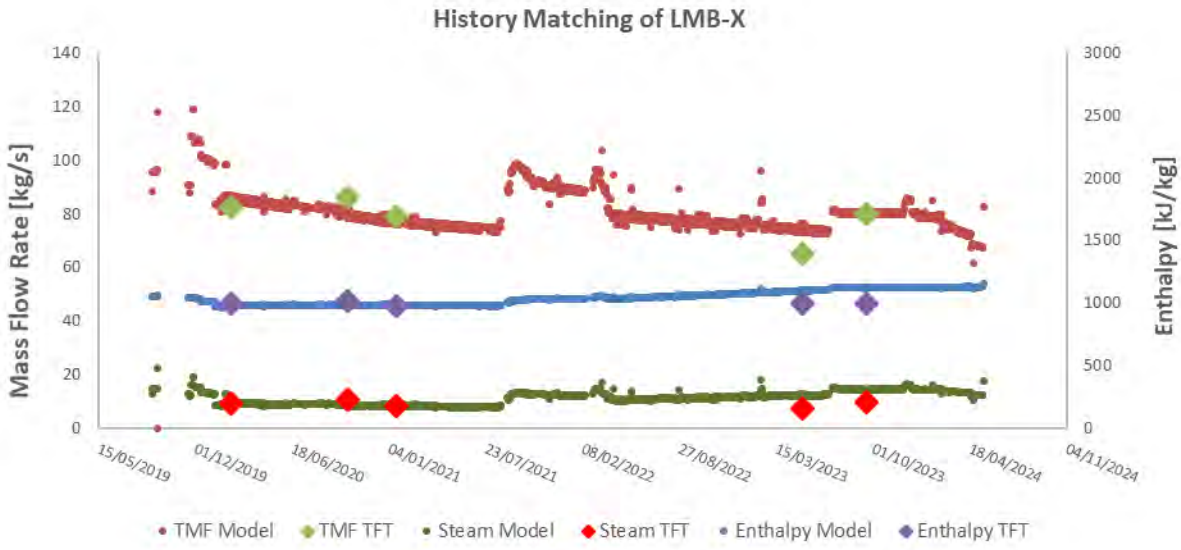

Figure 8: The models of total mass flow rate, steam mass flow rate, and production fluid enthalpy over time from LMB-X well are qualitatively matched with the measurement data obtained using the chemical method.

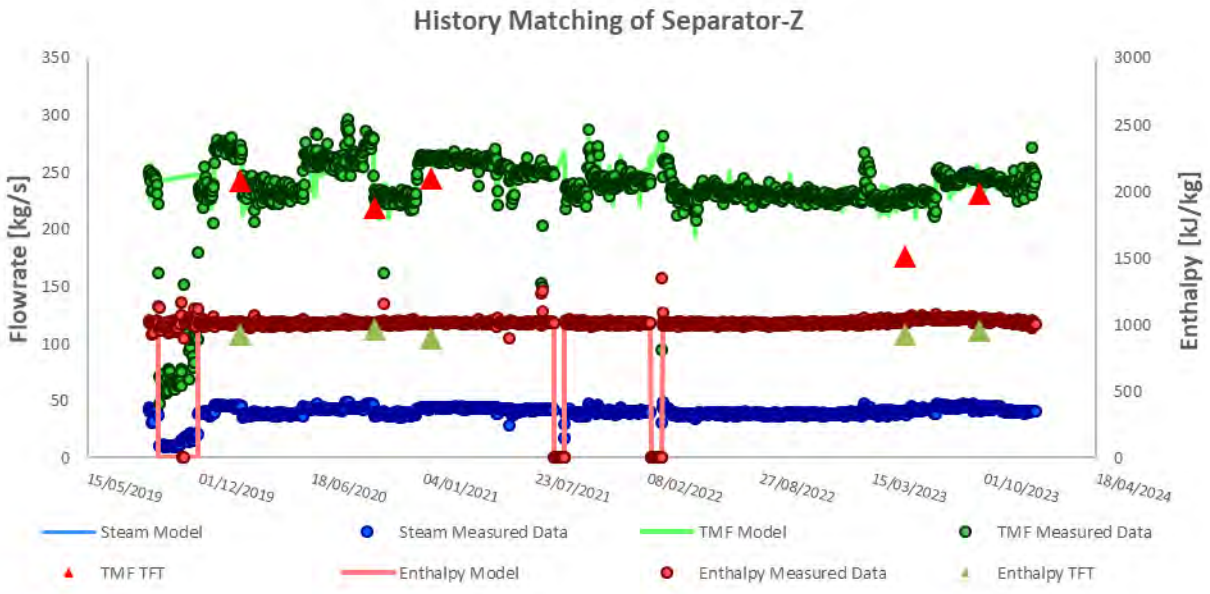

Figure 9: The history matching results of the model against both the flowmeter and the TFT data for Separator-Z.

3.6 Deliverability Curve and Energy Flow Rate Curve Monitoring

The SALB application operates with daily data, necessitating that the model aligns with the actual data on a daily basis. However, creating deliverability curve and energy flow rate curve models daily is not necessary. A critical aspect of using the SALB application is the ability to identify trends in changes to the model curves. The models generated from user input on specific days will be utilized to interpolate models for the days without model input. Therefore, new models are only required when there are significant changes in the shifting trends of the deliverability curve and the energy flow rate curve. Each well has a different timeline for model updates, so monitoring must be conducted on a per-well basis.

The timing for inputting deliverability curve and energy flow rate curve models into the SALB application is variable. Typically, the optimal time for creating a new curve model is during activities such as shutting down a well within a cluster, a major outage of a generation unit, or significantly adjusting well opening. Table 1 shows the example of historical updates for deliverability curve and energy flow rate curve models. Figure 10 illustrates the alterations in the well deliverability curve based on the parameter inputs in Table 1, while Figure 11 illustrates the alterations in the well energy flow rate curve using the same parameter inputs.

Table 1: Well deliverability curve and well energy flow rate curve model parameters inputted in the process of history matching.

Model #	Model Input Date	M_max	H_max	MDP	M_MDP	H_MDP	Remark
1	01-Sep-19	75	980	12	5	960	
2	01-Sep-19	75	980	12	5	960	Well Closed
3	14-Sep-19	75	980	12	5	960	Well Closed
4	08-Feb-20	65	980	11,5	5	960	Reduce Well Opening
5	01-Jan-21	67	980	11	5	960	GPP Shutdown
6	24-Aug-21	85	980	11	5	960	
7	16-Sep-21	85	980	11	5	960	
8	01-Nov-21	85	980	11	5	960	GPP Shutdown
9	13-Feb-22	87	980	11	5	960	
10	03-Mar-22	73	980	11	5	960	Natural Decline
11	01-Jul-23	68	980	11	5	960	Natural Decline
12	08-Jul-23	72	980	11	5	960	
13	01-Jan-24	72	980	11	5	960	
14	22-Jan-24	72	981	11	5	961	
15	09-Feb-24	65	1000	11	5	965	Reservoir Boiling

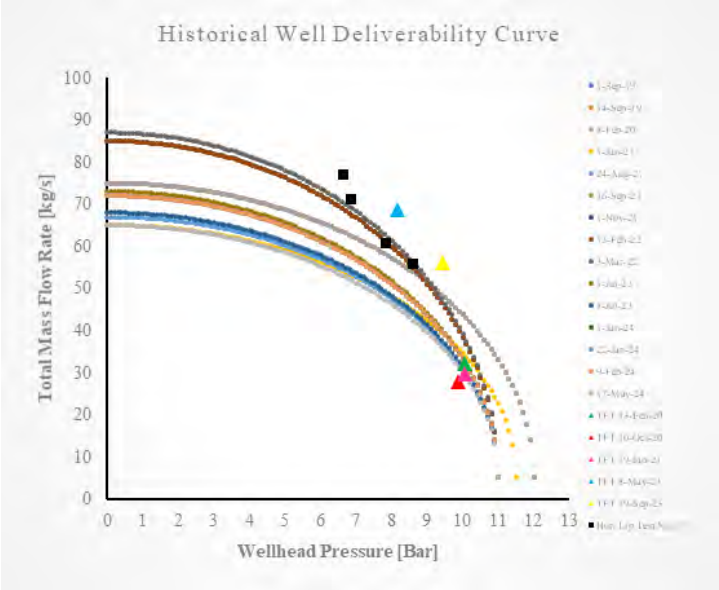

Figure 10: The deliverability curve of a production well shifts over time, leading to changing in the production flow rate at high wellhead pressure, low wellhead pressure, or both.

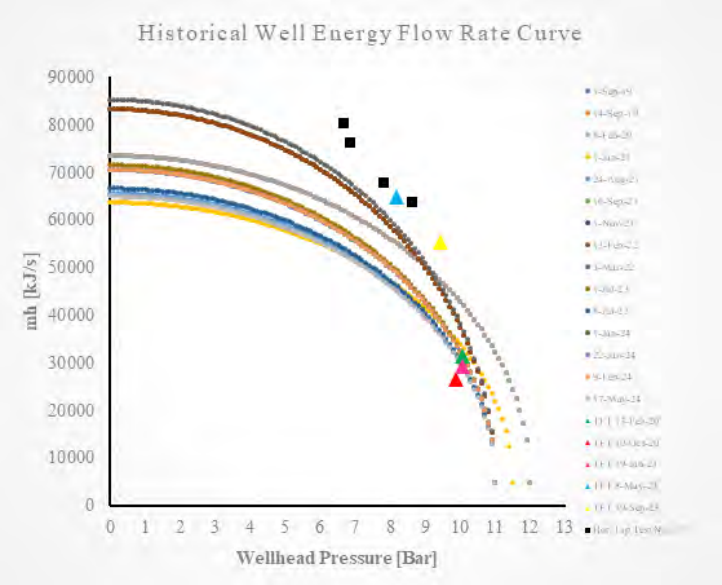

Figure 11: Energy flow rate is obtained by multiplying total mass flow rate by production fluid enthalpy. Consequently, the alterations in the energy flow rate curve qualitatively resemble that of the deliverability curve.

The SALB application inherently involves an element of estimation. The deliverability curve and the energy flow rate curve generated by the SALB application should be validated against periodic production tests data of each well. If the estimated model curves are found to be inaccurate, they can be corrected promptly based the empirical data, ensuring accurate interpretations.

3.7 Production Decline

One purpose of calculating the daily production from all the wells is to determine the field's steam availability. However, optimizing the exploitation rate of the Lumut Balai geothermal field requires choking the production wells, which limits the well production data availability on their maximum opening. This makes it challenging to accurately estimate the field's steam availability.

The SALB application uses Equations (9), (10), and (11) to determine steam production from wells at their maximum opening over time. These calculations rely on the curve models developed over time and the wellhead pressure data at the maximum opening that can be integrated into the production facility system. Figure 12 shows how production from a single well at its maximum opening changes over time, revealing decline trends for total mass flow rate, steam mass flow rate, and production fluid enthalpy. Aggregating the steam production from all the wells determines the steam availability in the Lumut Balai geothermal field. Assessing the current and the historical steam availability in the Lumut Balai geothermal field is crucial for estimating the on-stream time for makeup wells. This ensures a sufficient steam supply to the power plant, thereby maintaining its generation capacity.

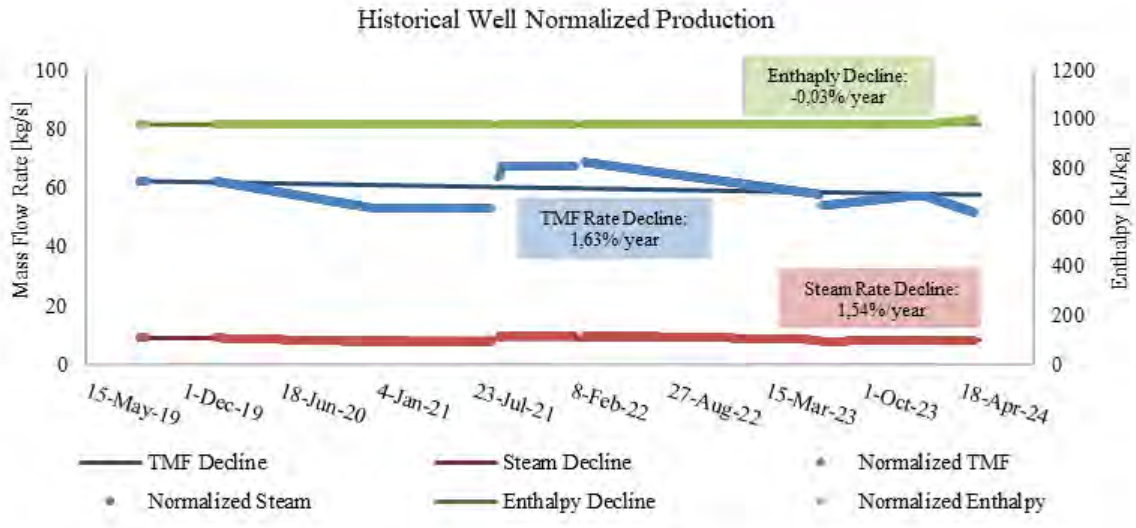

Figure 12: The well steam production at the maximum opening or the normalized condition over time is used to determine the decline rate of the field's steam availability.

3.8 Production Variance

The production variance feature is designed to highlight the disparity between the forecasted and the actual data from separator. It serves two primary functions. First, it acts as an early warning system. When the disparity between the forecasted and the actual data from a separator exceeds 10%, it may indicate abnormal well performance, prompting reservoir engineers to investigate further to identify the specific well and the cause of the high disparity.

The second function is to ensure the accuracy of the history matching models. A daily margin of error below 5% indicates that the last two curve models generated for each well are accurate (Figure 13), thus producing extrapolated curve model that remain relevant to the most recent operational data. Consequently, reservoir engineers only need to update the curve model when there is a shift in the trend for a particular well that diverges from the trend captured by the last two curve models, thereby rendering the existing extrapolated curve model obsolete.

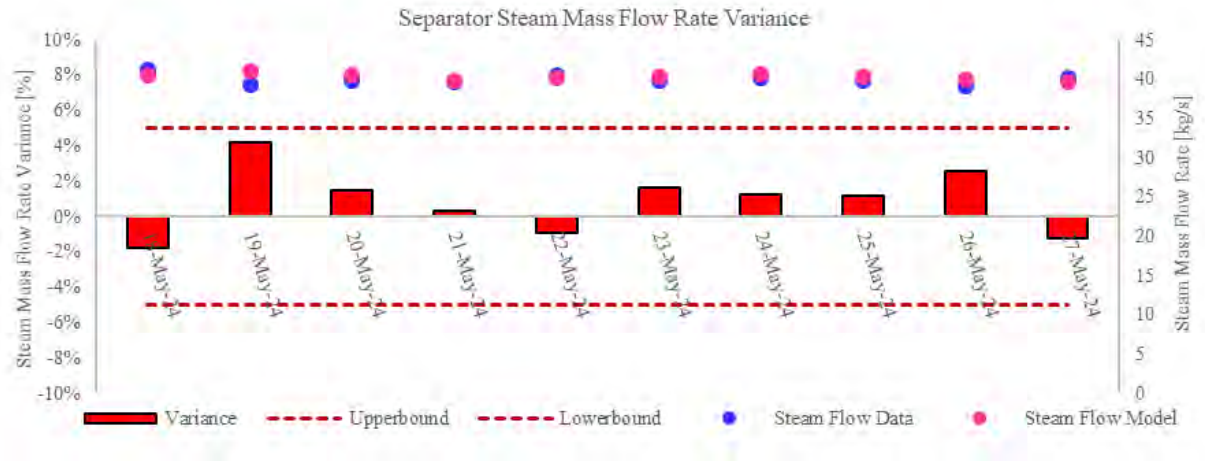

Figure 13: The production variance of Separator-Z depicts daily margin of error below 5%.

4. Conclusion

The SALB application is designed to estimate the daily production output of each production well within the Lumut Balai geothermal field. During the estimation process, the alterations in the deliverability curve and the energy flow rate curve of each well are monitored from time to time, providing insights into the behavior of the individual wells and serving as indicative of the reservoir dynamics. It is essential to validate the alterations in the deliverability curve and the energy flow rate curve of production wells against the periodic well production test data. This validation process enhances the reliability of the SALB application, which inherently relies on estimation.

The SALB application also provides the daily production value of each production well at their respective wellhead pressure at the maximum opening over time. This helps capturing the trends in the decline rate of the steam availability in the Lumut Balai geothermal field. The objective is to estimate the optimal timing for the on-stream time for makeup wells to guarantee a sufficient steam supply to the power plant, thus maintaining its operational capacity.

Acknowledgement

We extend our gratitude to Pertamina Geothermal Energy (PGE) for granting permission to publish this paper. We also highly appreciate the support of Reservoir Function and PGE Lumut Balai Area in the preparation of this paper.

REFERENCES

Davila, H.A. “Deliverability Output Curve Linearization Analysis: Matching the Power Equation with the Offset Elliptical Equation.” Proceedings: 42nd Workshop on Geothermal Reservoir Engineering, Stanford University, Stanford, CA (2017).

Grant, M.A., and Bixley, P.F. “Geothermal Reservoir Engineering - Second Edition.” Academic Press, Burlington, USA (2011).

James, C.R. “Deduction of the Character of Steam-Water Wells from the Shape of the Output Curve.” Proceedings: 2nd New Zealand Geothermal Workshop, The University of Auckland, Auckland, New Zealand (1980).

James, C.R. “Factors Controlling Borehole Performance.” Geothermics Special Issue, 2-2, (1970), 1502-1515.

James, C.R. “One Curve Fits All.” Proceedings: 14th Workshop on Geothermal Reservoir Engineering, Stanford University, Stanford, CA (1989).

NOMENCLATURE

h_{field} = the weighted enthalpy of the field production fluid [kJ/kg]

h_{SEP} = the enthalpy of the production fluid at the separator [kJ/kg]

$h_{@mdp}$ = the enthalpy of the well production fluid at the maximum discharge pressure [kJ/kg]

$h_{@whp}$ = the enthalpy of the well production fluid at a given wellhead pressure [kJ/kg]

$h_{@whp=0\ bar}$ = the enthalpy of the well production fluid at the wellhead pressure of 0 bar [kJ/kg]

$\dot{m}_{brine_{@SEP}}$ = the measured brine mass flow rates at all the separators [kg/s]

$\dot{m}_{field}$ = the total mass production flow rate of the field [kg/s]

$\dot{m}_{LMB}$ = the total mass flow rates produced from a production well [kg/s]

$\dot{m}_{SEP}$ = the total mass flow rates at a separator [kg/s]

$\dot{m}_{steam_{@SEP}}$ = the measured steam mass flow rates at all the separators [kg/s]

$\dot{m}_{@condensate\ line}$ = the measured condensate mass flow rate in the condensate pump [kg/s]

$\dot{m}_{@mdp}$ = the well total mass flow rate at the maximum discharge pressure [kg/s]

$\dot{m}_{@reinjector\ wells}$ = the measured mass flow rate injected into all reinjection wells [kg/s]

$\dot{m}_{@rock\ muffler}$ = the measured steam mass flow rate in the rock muffler [kg/s]

$\dot{m}_{@scrubber}$ = the measured steam mass flow rate in the scrubber [kg/s]

$\dot{m}_{@whp}$ = the well total mass flow rate at a given wellhead pressure [kg/s]

$\dot{m}_{@whp=0\ bar}$ = the well total mass flow rate at the wellhead pressure of 0 bar [kg/s]

mdp = the maximum discharge pressure [bar]

whp = wellhead pressure [bar]

Characterization of Flow in Induced Fractured Networks Using Tracers in Enhanced Geothermal Systems

Sven K. Hartvig, Roy Greig, Christopher N. Fredd, Christopher K. De Cerf, Olaf Huseby

Resman Energy Technology

John McLennan, Energy & Geoscience Institute, University of Utah

Kevin England, E-K Petro Consulting LLC

Keywords

Tracer, Tracer testing, Flow path characterization, Residence time distribution (RTD), Enhanced Geothermal System (EGS)

ABSTRACT

Understanding and characterizing the connectivity through the induced fractured network created between injection and production wells in an Enhanced Geothermal System (EGS) is imperative to maximize enthalpy output from the system. The high temperature controls the requirements for tracer stability, and the high injection rates control the requirements for the tracers' detectability.

In this paper we will present data from a field test with extensive utilization of advanced tracer technology to gain as much understanding as possible from an enhanced geothermal system. Unique tracers were injected during each of 8 stages of fracturing in an EGS well. In addition, several tracers were injected at different times during the fracturing of one of the stages. Tracer responses were established from samples collected during clean-up. Responses from the individual zonal tracer and tracers injected at different times during the individual stage were analyzed and interpreted. After initial clean-up, and fracturing of the production well, the injection well was put into operation and a circulation tracer was added to the injected water. Sampling from the production well was then initiated. Fracture Driven Interaction (FDI) analysis was carried out on the basis of the tracer data, and the fracture communication between individual perforations and fracture networks to the production well was characterized based on the tracer results. Tracer curve analysis based on the multiple tracers injected into one particular fracturing stage was used to further enhance understanding of the fracture network complexity created in the individual stages. Residence time distribution (RTD) analysis and mass balance calculations were used to assess the different stages and characterize the volume created by the induced fracture network.

1. Introduction

Tracer testing is proven as an efficient subsurface surveillance technology and has been used extensively worldwide for applications in oil & gas, hydrology, oceanography as well as geothermal applications. Specialized tracer applications include tracking of injection fluid such as water or gas, stagnant phase quantification using the so-called single well tracer tests (SWCTT) as well as partitioning interwell tracer tests (PITT) to measure oil saturation. Tracers for subsurface applications must fulfil several important characteristics. They must be thermally, chemically and biologically stable under harsh temperature conditions and not adsorb on rock surfaces. In addition, suited tracers must be unique in the subsurface environment, have excellent analytical sensitivity and be environmentally acceptable. Typical chemical tracers are fluorinated benzoic acids for water (Galdiga and Greibrokk, 1998), or perfluorocarbons for gas (Dugstad et al., 1992; Kleven et al., 1996), or naphthalene sulfonates for high-temperature geothermal reservoirs (Rose et. al., 2000). Tracers passively follow any fluids flowing in the subsurface and therefore reflect flow dynamics. An obvious, and important information provided by tracer data is mass transport connectivity. Further interpretation, characterizing the distribution of residence time from tracer production curves, e.g. using so-called residence time distribution (RTD) analysis provide important information of the flow geometry of fractured or porous media. Even the most basic application of RTD – quantifying the produced tracer mass relative to injected at a sampling station give valuable insight of preferential flow paths and can be used to identify flow heterogeneity including fracture hits.

Enhanced geothermal systems (EGS), also sometimes called engineered geothermal systems, offer great potential to significantly expand the production of geothermal energy. Currently, geothermal power is generated from hydrothermal reservoirs. In the U.S., they are found mostly in the West. This restricts the locations of current geothermal energy developments. EGS technology will greatly expand the availability of geothermal energy resources.

The idea behind EGS is to apply methods and tools to extract heat from hot rocks below the surface which lack the same natural permeability that is required for productive hydrothermal reservoirs. This is achieved by enhancing existing fracture systems – the minute fractures and pore spaces between mineral grains so that water can be injected, heated, and produced at very hot temperatures to generate electricity in power plants on the surface.

In EGS development, two or more wells are drilled into the same volume of rock and water circulated through the hot fractured rock heats up. The volume of water injected into an EGS reservoir is very similar to the volume produced. This is different from oil and gas development where the fluids are extracted from one area of the subsurface and injected into another. The balance of water put into and removed from the ground in an EGS system minimizes the environmental impact.

Utah FORGE is a dedicated underground field laboratory sponsored by the Department of Energy (DOE) for developing, testing, and accelerating breakthroughs in EGS technologies to advance the uptake of geothermal resources around the world.

In 2020, the injection well 16A(78)-32 was drilled to a true vertical depth of 8,559 feet and a measured depth of 10,897 feet. Two years later, this well was hydraulically fractured in three stages in intervals towards the toe of the well. Microseismic monitoring mapped these fracture networks.

The production well was subsequently drilled in 2023. The two wells are parallel with lateral sections at 65 degrees to the vertical and spaced apart vertically by 300 feet. The temperature at this vertical depth reaches 225°C (435 F). Immediately following the drilling of the production well, 16B(78)-32, a brief circulation test revealed some connectivity between the two wells.

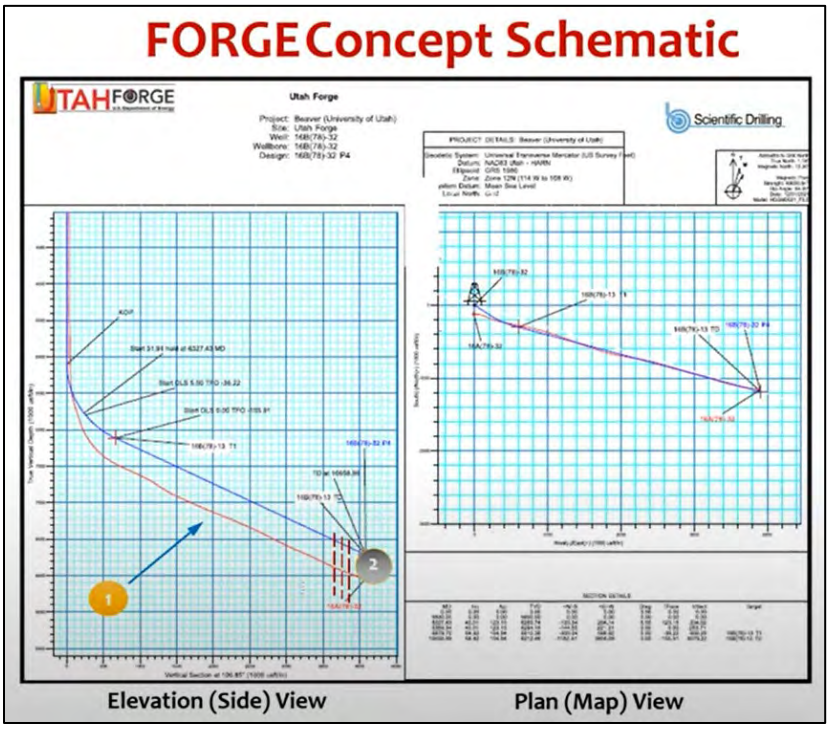

Figure 1: Injection well 16A(78)-32 (bottom) and production well 16B(78)-32 (top).

In the beginning of April 2024, commercial-scale stimulation was conducted on both wells to develop interwell connectivity. Over a period of four days, well 16A(78)-32 was hydraulically fractured in eight different stages. The three intervals previously stimulated in April 2022 were re-fractured and seven new intervals were perforated and hydraulically fractured. The fracturing fluid entering each of the intervals were traced with a unique liquid tracer, enabling increased calculation of the contribution of fluid flowed back during the clean-up of the injection well, and identification and quantification of the connectivity on a stage level. Overall, 118,000 barrels of non-potable water produced from a shallow well on the Utah FORGE site were injected. During the stimulation use of proppant, custom frac plugs, multiple clusters per stage, and different treating fluids were evaluated.

To locate fractures intersecting the production well 16B(78)-32, fiber optic cables run on the outside of the 7” production casing and cemented in place, were monitored during the stimulation of its sister well, 16A(78)-32. The recorded fiber optic signatures highlighted intervals of fracture intersection or proximity. These intervals were selected and perforated for subsequent stimulation stages that were pumped in well 16B(78)-32 (Figure 2). Stimulating both wells ensured connectivity.

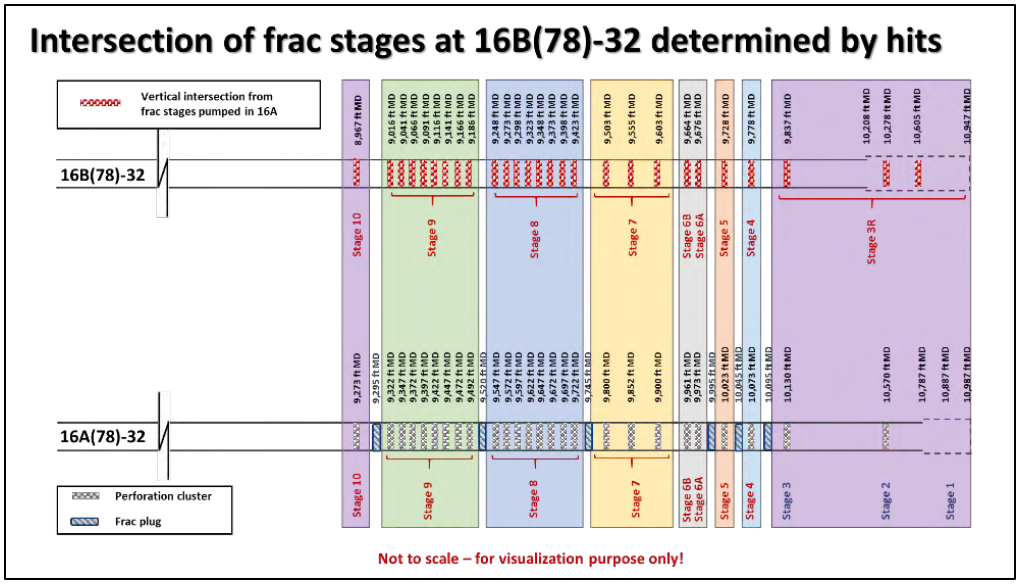

Figure 2: Schematic presentation of injection and production well with located intersections for vertical, planar hydraulic fractures.

Following the stimulation, a short circulation test was conducted. Water was injected into well 16A(78)-32 for nine hours at rates up to 16.5 barrels-per-minute (bpm). The injection led to corresponding production from well 16B(78)-32 of up to 8.2 bpm when the injection rate was 12.4 bpm, resulting in an efficiency rate of around 70% recovery. This reconfirms that conductivity between the wells was established. The temperatures of the outflow water also continually increased to approximately 139° C (282° F). Microseismic events, fiber optics data, spinner logging and tracer data showed that multiple independent flow paths had been created. The latter is described in more detail in this paper.

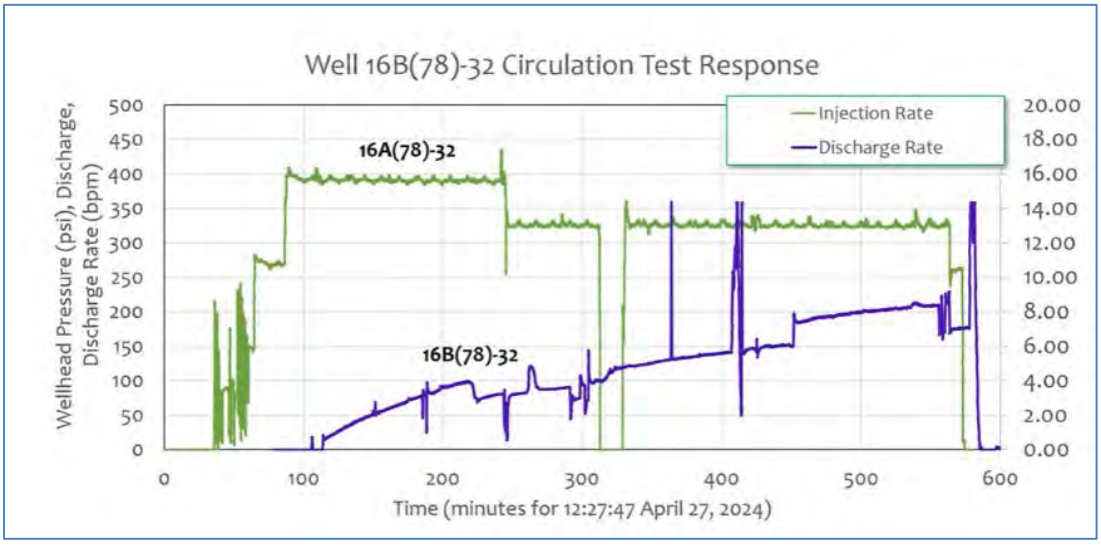

Figure 3: Injection and production rates during the circulation test.

The short circulation test capped this phase of experimentation. Hot water was produced, and the testing confirmed the potential of EGS energy production. These exciting results and the rich sets of data are being analyzed to plan additional fieldwork, including a 30-day circulation test scheduled for July 2024. All data collected are publicly available on the Geothermal Data Repository (GDR) - https://gdr.openei.org/forge.

2. Methodology

2.1 Tracer qualification

An ideal tracer for water must be thermally stable at relevant reservoir temperatures, it has to be chemically and biologically stable under reservoir conditions, the tracer should not experience sorption to rock or steel surfaces. In addition, a qualified tracer must be stable during sample storage, have excellent analytical chemical sensitivity, be environmentally acceptable and be unique in the reservoir environment. Tracer to be utilized in reservoir studies therefore must go through a rigorous testing protocol confirming that all of the above properties are met (Sanni et. al., 2015).

Due to the very high temperatures experienced in geothermal reservoirs, often exceeding 300°C, and in the case of FORGE being 225°C, the temperature-stability of the tracers is the most important parameter. Historically (Rose et. al., 2000) naphthalene sulfonates have proven stability at these elevated temperatures and have been the choice for geothermal reservoirs. Depending on availability and lab quality, the number of available tracers of the naphthalene sulfonate class is in the range of 4 to 8.

However, with the introduction of EGS with multistage hydraulic fracturing, and an objective to confirm communication between all stages of a well-pair, as well as repeated tracer usage during circulation, the required number of unique high-temperature tracers exceed the available number of naphthalene sulfonates and qualification of new geothermal tracers is required.

2.1.1 Stability testing in lab scale

A mixed tracer stock of the tracers listed in Table 1 was prepared in synthetic formation water. The tracer stock contained both newly developed tracers for geothermal as well as accepted naphthalene sulfonate tracers (2,6-NDS and 2,7-NDS) as references. The formation water tracer stock was boiled in a round bottom flask with constant addition of nitrogen gas. The mixed stock (1.5 mL) was added to inert PEEK cylinders inside steel cells and capped with nitrogen gas. All cells were sealed and placed in heating cabinets at 200°C, 220°C and 240°C. Samples were removed after 15, 21, and 34 days. Samples were analyzed and results compared to a refrigerated aliquot of the tracer stock to determine thermal degradation.

The lab scale testing confirmed that all the tested tracers were acceptably thermally stable to be utilized at 225°C.

2.2 Field and tracer operation

2.2.1 Addition of tracers during fracturing

A unique tracer was dosed in constant concentration relative to clean fluid during the fracturing operation for each stage. The same tracer amount was designed for each stage, but due to different clean fluid volumes in each stage and operational on-the-fly changes to the planned pumping program the tracer concentration and total amount injected varied between stages. The data are summarized in Table 1. Stage 4 was extended on-the-fly to a volume larger than the safety factor taken for tracer volume, so the last ~350 bbl of the proppant stage was injected un-traced. For Stage 6 sufficient rate for sand could not be achieved and tracer dosing was stopped for periods due to the prolonged pumping time, further perforations were added (Stage 6B) but sufficient rate could not be achieved. Also, for Stage 7 sufficient rate for sand addition could not be reached. In addition to the mass balance tracers detailed in Table 1, four separate steps of Stage 8 was traced with a pulsed tracer injection according to Table 2.

Table 1 Summary of stage volumes, tracer amounts injected, and corresponding dosage concentrations.

Stage	Clean Volume (bbl)	Total sand (lbs)	Tracer name	Tracer amount (kg)	Tracer concentration (ppb)	Comment
3R	10,319	335,560	WT-17	0.86	560	
4	5,263	127,620	2,6-NDS	1.0	1,409	Minor volume un-traced
5	3,000	136,880	WT-61	0.88	1,417	
6	3,365	0	WT-102/ WT-101	0.12	1,000	Significant volume un-traced
7	12,596	0	2,7-NDS	0.60	344	
8	35,295	981,500	WT-66	0.83	196	
9	27,237	730,632	WT-60	0.67	168	
10	4,550	133,800	WT-109	0.72	1,209	

Table 2 Stage 8 pumping program with detailed information of planned step volumes and tracer amounts injected.

Step	Step name	Clean Volume (bbl)	Sand	Tracer name	Tracer amount (kg)	Comment
1	Pad	6,400	100 mesh	WT-10	1.0	Start injection after 100 bbl (10 min injection time, ~200 bbl)
2	0.5 PPA	3,200	100 mesh	WT-9	1.0	Injected at start (during 2.5 min injection time, ~200bbl)
3	0.75 PPA	3,200	100 mesh	none		
4	1.0 PPA	6,400	100 mesh	none		
5	1.0 PPA	6,400	40/70 mesh	none		
6	1.25 PPA	3,200	40/70 mesh	WT-11	1.0	Injected at end (during 2.5 min injection time, ~200bbl)
7	1.5 PPA	3,200	40/70 mesh	WT-30	1.0	Start injection 700 bbl before end (2.5 min injection time, ~200 bbl)
8	Flush	350		none		

2.2.2 Addition of tracers during circulation test

After the injection and production well had been cleaned up, a 9-hour circulation test was initiated. Water was injected into the injection well 16A(78)-32 and produced from the production well 16B(78)-32. The injection and production rates are given in Figure 3. A unique tracer was added in constant concentration to the injected fluid according to Table 3.

Table 3 Summary of stage volumes, tracer amounts injected, and corresponding dosage concentrations.

Stage	Tracer name	Tracer amount (kg)	Tracer concentration (ppb)
Circulation test	2-NS	0.174	150

2.2.3 Production and Sampling

Both injection and production wells could be routed into a geothermal separator, with a sampling point upstream of the separator. The tracer samples were collected from the upstream sampling point to avoid commingling. Sampling was executed according to a predefined sampling program designed to capture changes in tracer production profiles without the sampling personnel having to be informed on actual operational status continuously. Consequently, a large number of samples were collected, and a sub-set of these samples were selected for analysis based on actual production history. A total of ~200 samples from the clean-up of the injection well, and 23 samples from the 9-hour production test were analyzed.

Figure 4: Picture of geothermal separator and sampling point upstream of the separator.

2.2.4 Chemical Analysis

Highly sensitive and specific analytical chemical methods are needed in order to detect tracer in part per billion (ppb) and part per trillion (ppt) in complex matrixes such as produced water with additives originating from the fracturing fluid. Further, as the injected amount of a tracer is directly proportional to the limit of detection (LOD) of a tracer, a sensitive lab analysis results in a lower environmental burden and a lower carbon footprint.

The tracers listed in Table 1and Table 3 were chromatographically separated utilizing HPLC (High Performance Liquid Chromatography) using a selection of detection methods specific for each of the tracers. The limit of detection achieved in the produced water matrix was 50 part per trillion (ppt).

2.3 Interpretation of tracer signals

A significant advantage of tracer testing stems from tracer's ability to identify the origin of fluids. When unique tracer molecules are introduced and used to track fluids in the subsurface, they provide definite proof of communication based on first principles physics and mass balance considerations. Binary (yes/no) proof of communication from tracers can be expanded to assess the significance of the communication. This can be achieved by calculating the produced amount of a tracer and comparing it with the injected amount. Characterization of flow geometry is also available from tracer signals. This can be realized if we consider that added tracers yield signals containing information of characteristic timescales in a transport process.

A concrete interpretation scheme for tracer signals is to characterize the temporal moments from concentration vs. time. This can typically be done using residence time distribution (RTD) analysis (Danckwerts, 1953; Shook, 2003; Huseby et al. 2014). This analysis requires transforming tracer concentration time series, generated from concentration measurements in the sampled fluid, to a distribution of residence times for the tracers. In practice this requires multiplying concentration, $C(t)$, to fluid rate, $Q(t)$, and normalizing by the injected tracer amount, M. The resulting quantity

$$E(t) = C(t) \cdot Q_p(t)/M \tag{1}$$

is the residence time distribution. Once the residence time distribution is found, its temporal moments,

$$m_n = \int t^n E(t) dt \tag{2}$$

can be used to quantify the flow geometry. As an example, zero-order temporal moment of the residence time distributions ($m_0 = \int E(t)dt$) give the fraction of produced fluids. In a well-to-well setting, m_0 give the fraction of water produced from a specific injector. In a stagewise fracturing application it provides the amount of fluid produced back from a given stage. The first order moment $m_1 = \int t \cdot E(t)dt$ is closely related to average residence time, $\langle t \rangle = m_1/m_0$, that in turn can provide the volume of an inter-well flow geometry by multiplication with injected rate, V=$\langle t \rangle \cdot Q$. Additionally, higher order moments, such as skewness and kurtosis, carry information on the complexity of a flow. Combinations of several temporal moments is also possible. One

example is the comparison of first and second order moments used to characterize the heterogeneity of an inter-well flow, as demonstrated by Shook (2003).

3. Results and discussion

3.1.1 Cleanup of injection well 16A(78)-32

The flowback and cleanup of the injection well 16A(78)-32 was sampled to a) evaluate stage contribution and b) characterize the flow paths after the multistage hydraulic fracturing treatment. Fluid samples were collected periodically and analyzed for tracer concentration to establish tracer response curves for the 13 unique water-based tracers included in the treatment fluids as shown in Figure 5 (left). All tracers were detected at the parts-per-billion (ppb) level, with concentrations impacted by plug milling, shut in, and injection operations during cleanup.

The tracer response data demonstrates stage communication prior to milling of the plugs. At the start of cleanup operations, only stage 10 perforations were accessible due to the plug between stages 10 and 9. Tracers were detected from stages below 10. In particular, stages 9 and 8 give a strong signal, proving flow communication from those stages. However, the frac plugs that were run are, by design, flow-through plugs. This means that higher pressure from below can lift the ball off of the seat and allow flow from stages below the plug. This means that after the initial pressure reduction from the flow of Stage 10, it would be very likely that Stage 9 would start to flow through the frac plug separating stage 9 and 10. With the total amount of fluid flowed back before the start of drilling out the frac plugs in well 16A(78)-32 it is certain that fluid from Stages 8, 9 & 10 (at a minimum) would have been recovered.

This communication could a priori also be caused by flow through a micro-annulus behind casing, and/or flow through fracture connections in the reservoir. However, the strong tracer signal and the consistent observation of tracer across all stages, point to some degree of fracture network communication (e.g., far-field communication) in addition to communication through the plugs. Additional tracer interpretation is ongoing including tracer type curve analysis of the four tracer pulses in stage 8 and additional unique high-temperature tracers included in the various stages. Results of this interpretation are expected to provide additional insights into the flow profiles during cleanup operations.

The recovered masses from the cleanup of the injection well 16A(78)-32 are plotted in Figure 5 (right). Concentrations measured during cleanup were used together with production rates to calculate the amount of tracer recovered per stage and compared to the injected amount of tracer in that stage. Note that for clarity, only the 8 primary tracers added to the stages are displayed in the mass plot in Figure 5 (right).

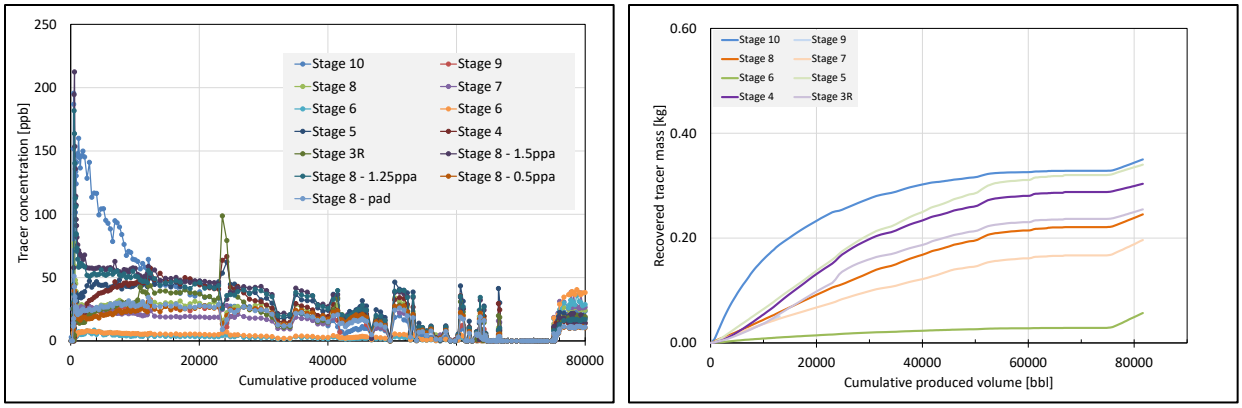

Figure 5: Tracer concentrations profiles (left) and cumulative produced tracer mass (right) during clean-up of well 16A. Eight of the injected tracer are summarized in the mass plot (right) and all 13 tracer are displayed in the concentration plot (left).

Interestingly, the fluid injected in the two unsuccessful stages; Stage 6 and Stage 7 is easily detectable even if no proppant or sand was injected in these stages. Most noticeable is the response when all plugs have been milled and the well is allowed to clean-up from all stages commingled (Figure 6).

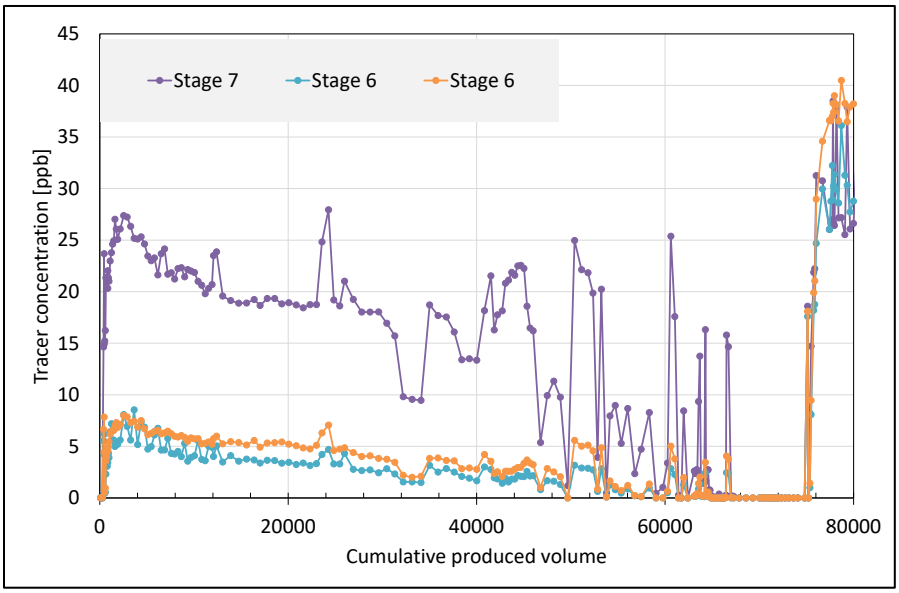

Figure 6: Tracer concentrations profiles from the two unsuccessful stages; Stage 6 and Stage 7. At about 75,000 bbl produced all plugs in the well had been milled and a clear increase in the concentration, especially for Stage 6 tracers can be observed.

3.1.2 Circulation test

Tracer concentration results for tracers injected in each of the stages in the injection well (16A(78)-32) measured in samples from the production well 16B(78)-32 are summarized in Figure 7.

Included are also the concentration profile measured in the offset well (16B(78)-32) for the tracer added to the circulation test used to verify communication and recovery during the circulation test.

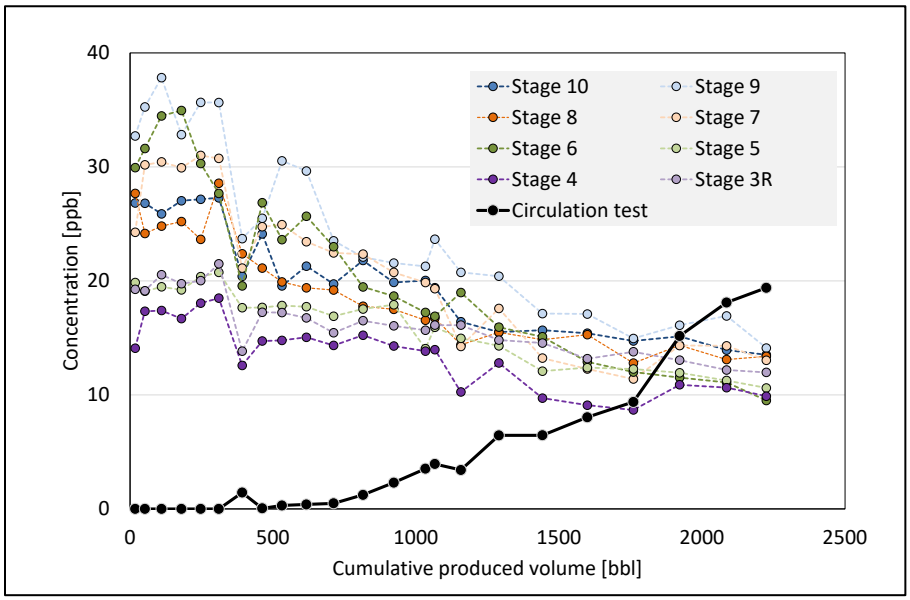

Figure 7: Tracer concentrations observed in the production well 16B(78)-32, originating from individual stages in the injection well. The circulation test tracer is also included.

An important observation from Figure 7 is that all tracers are detected at concentrations well above (~200 times) the detection limits, proving applicability of the tracer chemicals for geothermal operations at this temperature range. From the figure we see that all tracers are detected at significant concentrations at the offset well, proving communication from all stages in 16A(78)-32 towards well 16B(78)-32, even stages without proppant added (Stage 6 and Stage 7).

In Figure 7 we also observe clear correlations in the data, as well as an anticorrelation with the circulation test tracer. The circulation test tracer has a breakthrough at about 700 bbl produced volume and increased gradually after this. At the same time, the tracers from all stages decrease. The reason for this behavior is that the injected stage tracers from 16A(78)-32 are pushed towards the offset well 16B(78)-32 during fracturing and hence are found in significant amounts once the well is open for circulation. As the injected water during the circulation test arrives, the traced water (fracturing fluid) is diluted, and concentrations are declining as the circulation test water is displacing water in the fractured network. A longer duration test (30 days) was carried out in August 2024, and the continued tracer decline that is expected to be observed during that test will enable further characterization of the created fracture network.

In one of the stages (stage 8) four additional tracers were added to the fracturing fluid (Table 2). The resulting tracer profile from these tracers are plotted separately during the circulation test in Figure 8. The detection of the four pulses in the production well indicated good fracture network communication between the injection and production wells.

The concentrations measured in 16B(78)-32, together with the production rates were used to calculate the amounts recovered from each of the tracers injected across all stages (ref Equation

2). These amounts are summarized in Table 4. From the table we see that a fairly consistent amount of tracer (in the order of 0.5-1%) was recovered during the circulation test.

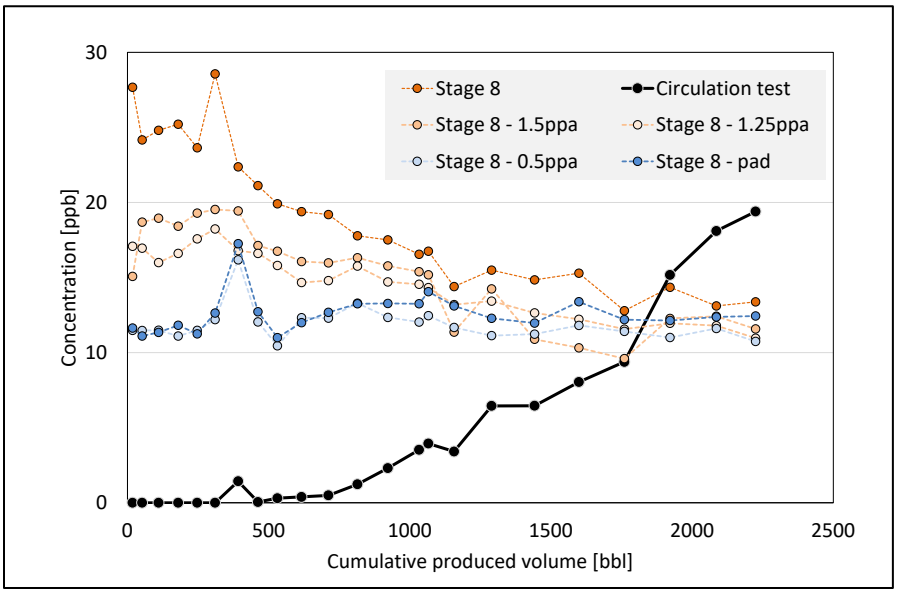

Figure 8: Tracer concentrations observed in the production well 16B(78)-32, originating from individual stages in the injection well. The circulation test tracer is also included.

Table 4 Summary of recovery of the different tracers during the circulation test.

Stage	Tracer	Injected amount (g)	Recovered amount (g)	Relative recovery (% of injected)
3R	WT-17	860	5.5	0.63
4	2,6-NDS	1,000	4.5	0.45
5	WT-61	880	5.3	0.61
6	WT-102 / WT-101	120 / 120	8.0 / 6.6	0.67 / 0.55
7	2,7-NDS	600	6.7	1.1
8	WT-66	830	6.2	0.74
8-pad	WT-10	1,000	4.4	0.44
8-0.50 ppa	WT-9	1,000	4.2	0.42
8-1.25 ppa	WT-11	1,000	4.9	0.49
8-1.5 ppa	WT-30	1,000	5.0	0.50
9	WT-60	670	7.9	1.2
10	WT-109	720	6.6	0.92
Circulation test	2-NS	174	2.0	1.2

4. Conclusions

Precise verification of fracture hits between injector and producer in a geothermal EGS well-pair was demonstrated utilizing tracer technology. Introduction of new high-temperature tracers to geothermal application enabled an increased resolutions compared to what could be achieved by the accepted naphthalene sulfonate tracers.

Calculation of recovered tracer from each stage during both clean-up and circulation enables comparison of different fracture strategies, and further interpretation of the results is expected to yield better characterization of the created fracture network.

Acknowledgement

Funding for the Utah FORGE project is provided by the U.S. DOE under grant DE-EE0007080 “Enhanced Geothermal System Concept Testing and Development at the Milford City, Utah FORGE Site.” The University of Utah thanks the many stakeholders who are supporting this project, including Smithfield, Utah Trust Lands Administration, and Beaver County as well as the Utah Governor’s Office of Energy Development.

Margrete Lie for managing and handling all lab analysis from both stability tests and field samples. Partho Giri for operational coordination and execution of tracer injection and sampling.

REFERENCES

Danckwerts, P. V.; “Continuous Flow Systems, distribution of residence times”, *Chemical Engineering Science*, 2, (No. 1), 1-18 (1953).

Dugstad Ø. Well-to-Well Tracer Tests, Chapter 6 (pp. 651-683), *Petroleum Engineering Handbook, Vol. 5 - Reservoir Engineering and Petrophysics* by Edward D. Holstein (Ed.) SPE, Richardson, Texas, 2007.

Dugstad, Ø., Bjørnstad, T., and Hundere, I.A.: “Measurements and Application of Partition Coefficients of Compounds Suitable for Tracing Gas Injected into Oil Reservoirs”. *Revue de l’Institut Francais du P´etrole, Vol. 47 Num. 2,* pp. 205-215, 1992.

Galdiga, C.U., Greibrokk, T: "Ultra-trace determination of fluorinated aromatic carboxylic acids in aqueous reservoir fluids using solid-phase extraction in combination with gas chromatography-mass spectrometry". *Journal of Chromatography A,* 793 (2), pp. 297-306, 1998.

Huseby O., Hartvig S. K., Jevanord K., Viig S. O. and Dugstad Ø.: “High Quality Flow Information from Tracer Data”. *SPE paper 169183,* Bergen One Day Seminar Bergen, Norway, 2 April 2014.

Jones C.G., England K., Simmons S., Rose, P., Mella M., Barker B., McLennan J. and Moore J.: “Stimulation, Tracers and Geochemistry at Utah FORGE”. P*roceedings 48th Workshop on Geothermal Reservoir Engineering,* Stanford University, Stanford, California, February 6-8 2023. SGP-TR-224.

Kleven, R., Høvring, O., Opdal, S.T., Bjørnstad, T., Dugstad, Ø., and Hundere, I.A.: "Non-Radioactive Tracing of Injection Gas in Reservoirs". *SPE Paper Number 35651*. SPE Gas Technology Symposium, Calgary, Canada, 28 April-1 May, 1996.

Shook, G. M.; "A Simple, Fast Method of Estimating Fractured Reservoir Geometry from Tracer Tests," Trans., *Geothermal Resources Council*, Vol. 27 (2003).

Sanni, M.L, Al-Abbad, M.A., Hartvig, S., Huseby, O. and Jevanord, K.: "A Field Case Study of Inter-well Chemical Tracer Test", *SPE paper 173760-MS*, International Oilfield Chemistry Symposium The Woodlands Texas, 13-15 April 2015.

Rose P., Benoit D., Lee S.G., Tandia B., and Kilbourn P.: "Testing the Napthalene Sulfonates as Geothermal Tracers at Dixie Vally, Ohaaki, and Awibengkok", *Proceedings Twenty-fifth Workshop on Geothermal Engineering*, Stanford University, Stanford, California, January 24-26 2000. SGP-TR-165.

A Wellbore Model Approach for Scaling Prediction and Condition Assessment

Magnus Thor Jonsson

University of Iceland

Keywords

Monte Carlo Particle Filter, Wellbore Model, Scaling, Condition Evaluation

ABSTRACT

This research presents a novel approach to estimating scaling and operational conditions of geothermal wells using a Monte Carlo Particle Filter on a wellbore model. Scaling, the deposition of minerals within the wellbore, significantly impacts the operational efficiency and longevity of geothermal wells. The proposed wellbore model integrates thermodynamic and fluid dynamic principles to predict pressure drop through the well, and, using the Monte Carlo Particle Filter, estimates both scaling and bottom hole pressure.

The study begins with an overview of geothermal wells and the common challenges faced in geothermal operations due to pressure drawdown. A critical operational question is whether the drawdown is due to scaling or bottom hole pressure decrease, which determines whether the well should be cleaned or if a new well needs to be drilled. The paper introduces the Monte Carlo Particle Filter and the wellbore model, detailing their theoretical foundations and computational methodology. The wellbore model simulates the complex interactions between geothermal fluid and the wellbore environment under varying operational conditions, identifying critical factors influencing scaling.

By analyzing data from existing geothermal wells alongside simulations conducted through the model, the research validates its effectiveness in predicting scaling occurrence and bottom hole pressure drawdown. Furthermore, the model offers insights into other well parameters, such as enthalpy, pressure, and flow rate adjustments.

1. Introduction

Geothermal energy is a renewable and sustainable resource with significant potential to contribute to the global energy mix. It harnesses the natural heat generated and stored within the Earth, primarily sourced from the radioactive decay of isotopes in the mantle and crust, as well as residual

heat from the planet's formation. Effective management and utilization of geothermal energy require detailed knowledge of geothermal reservoir conditions and wellbore dynamics.

Monitoring and modeling geothermal wells are crucial for understanding reservoir behavior, optimizing production, and ensuring sustainable operation. Traditional methods of reservoir assessment and wellbore simulation often face challenges in accurately estimating subsurface conditions due to the complex nature of geothermal systems. These complexities include multiphase flow, high-temperature environments, and varying geological formations (Axelsson 2003).

A production well in a geothermal power plant serves as a conduit to the reservoir, transporting geothermal fluid to the plant. When the pressure at the wellhead decreases, it raises questions about whether the cause is pressure drawdown in the reservoir, reduced flow from the reservoir to the well, or scaling (reduced diameter) within the well.

The Monte Carlo Particle Filter (MCPF), also known as Sequential Monte Carlo (SMC), is a statistical method that provides robust solutions for state estimation problems in dynamic systems. By leveraging a set of particles to represent possible states and iteratively updating them based on new observations, the MCPF can handle non-linearities and non-Gaussian noise effectively (Doucet and Johansen 2007). This makes it an ideal candidate for estimating the conditions of geothermal wells, where the system dynamics are often complex and uncertain.

Wellbore modeling is essential for simulating the behavior of fluids within a geothermal well. It involves understanding the interactions between fluid phases, heat transfer, and pressure dynamics. Accurate wellbore models enable the prediction of well performance, identification of potential issues, and optimization of operational parameters. Combining wellbore models with advanced state estimation techniques like the MCPF can enhance the reliability and accuracy of geothermal well assessments.

This paper presents an innovative approach that integrates the Monte Carlo Particle Filter with a wellbore model, Flowell, to estimate the conditions of geothermal wells. The proposed method aims to improve the accuracy of state estimations by incorporating both real-time observational data and sophisticated modeling techniques. The following sections will discuss the theoretical background of the Monte Carlo Particle Filter, the fundamentals of wellbore modeling, and the implementation of the integrated approach. Furthermore, the paper will present case studies demonstrating the effectiveness of this method in various geothermal settings, highlighting its potential benefits for the geothermal industry.

By advancing the methodologies used for geothermal well assessment, this research contributes to the development of more efficient and sustainable geothermal energy management practices. The integration of Monte Carlo Particle Filters with wellbore models represents a significant step forward in accurately understanding and managing geothermal resources, ultimately supporting the broader adoption and optimization of geothermal energy.

This paper is structured as follows: Section 2 provides an overview of geothermal production wells. Section 3 presents the Sequential Monte Carlo or Monte Carlo Particle Filter method. Section 4 discusses the wellbore model Flowell. Section 5 presents the results of the study, highlighting parameter estimation for Flowell with both pressure drawdown and scaling or

diameter reduction. Section 6 discusses the implications of the findings and potential applications of the model. Finally, Section 7 concludes the paper with a summary of key insights and recommendations for future research.

2. Geothermal Production Wells

An important part of geothermal energy production are geothermal production wells, which serve as conduits between subterranean heat sources and surface-level energy conversion systems. Understanding the design, function, and management of these wells is crucial for optimizing geothermal energy extraction and ensuring the sustainability of the resource.

Geothermal production wells are typically drilled into geothermal reservoirs, which are areas of the Earth's crust that contain a high concentration of heat, often in the form of hot fluid or steam. The primary objective of a production well is to transport the geothermal fluids from these reservoirs to the surface, where the heat energy can be converted into electricity or used for direct heating applications as shown in Figure 1.

Once at the surface, the hot fluid and steam are directed to a geothermal power plant. There are three main types of geothermal power plants: dry steam, flash steam, and binary cycle. Dry steam plants take steam directly from fractures in the ground and use it to drive a turbine that generates electricity. Flash steam plants draw high-pressure hot fluid from deep underground into a low-pressure environment, causing the rapid vaporization or "flashing" of the fluid into steam. This steam is then used to drive a turbine. Binary cycle plants transfer the heat from geothermal hot fluid to another liquid that boils at a lower temperature than fluid; this secondary liquid is vaporized and used to turn a turbine.

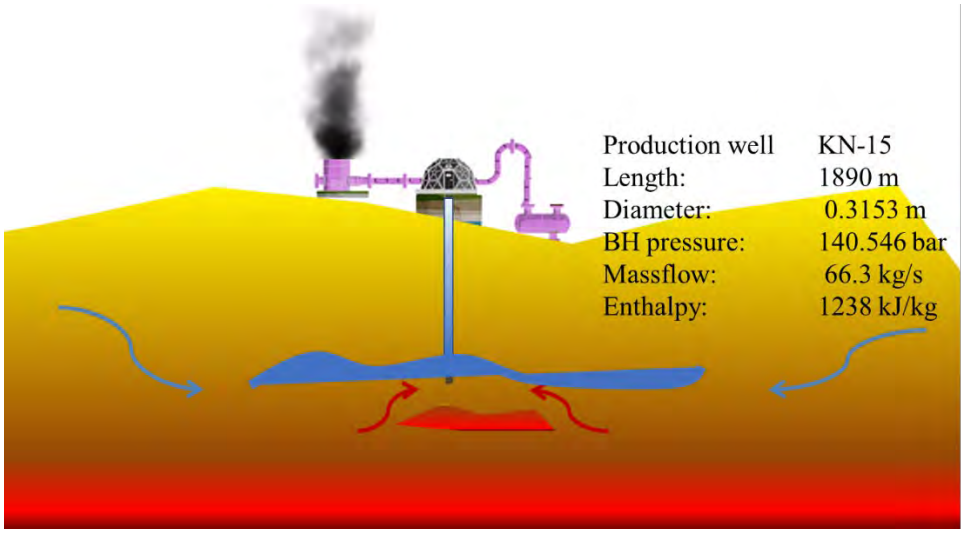

Figure 1: Production well KN-15

The construction of a geothermal production well involves several stages. Initially, exploratory drilling is conducted to locate a viable geothermal reservoir. Once a suitable location is identified, the well is drilled to reach the geothermal resource, often at depths ranging from a few hundred meters to several kilometers. The well is then cased with steel and cement to prevent the walls from collapsing and to protect the surrounding environment from contamination. The wellbore,

the actual hole drilled into the Earth, must be designed to withstand high temperatures and pressures typically found in geothermal systems.

One of the challenges in geothermal production wells is managing the pressure and flow of geothermal fluids. The pressure at the wellhead, the surface point of the well, is a key indicator of the well's performance. A reduction in wellhead pressure can signal various issues, such as pressure drawdown in the reservoir, reduced permeability, or scaling within the well. Scaling refers to the deposition of minerals from the geothermal fluid onto the inner surfaces of the wellbore, which can significantly reduce the well's diameter and impede fluid flow.

Accurate modeling and monitoring of wellbore dynamics are essential for the effective management of geothermal production wells. Traditional methods of wellbore simulation and reservoir assessment often struggle to account for the complex interactions within geothermal systems. These interactions include multiphase fluid flow, heat transfer, and the varying geological characteristics of the reservoir. Advanced modeling techniques, such as wellbore models combined with state estimation methods like the Monte Carlo Particle Filter (MCPF), offer a more robust approach to understanding and predicting well performance under different operational conditions.

Effective management of a geothermal reservoir involves precise control over various operational parameters, such as the wellhead valve openings, production rates for each well site or area, and the injection rates. The complexity of these tasks is compounded by the diversity of wells within the reservoir. Geothermal production wells are a critical component of geothermal energy systems, facilitating the extraction of heat from subterranean reservoirs. Understanding the complexities of wellbore dynamics and employing advanced modeling techniques are essential for optimizing well performance and ensuring the sustainable utilization of geothermal resources.

3. Sequential Monte Carlo

The Sequential Monte Carlo (SMC) or more specific type known as Monte Carlo Particle Filter is a method used for estimating the state of a system that evolves over time. In this study the time or the step is the location or depth of the measuring points for pressure in the well. The method uses a set of particles (samples) to represent the probability distribution of the state and updates these particles over time based on new observations (Doucet and Johansen 2007). The method used in this research is based on following algorithm:

1. Initialization

A set of N particles representing possible states of the wellbore conditions, p, for downhole pressure, $\dot{m}$ for mass flow, h for enthalpy, and d, for diameter is generated. Each particle has an associated weight based on its likelihood.

Let $\left\{p_i^{(0)}, \dot{m}_i^{(0)}, h_i^{(0)}, s_i^{(0)}\right\}_{\{i=1\}}^{N}$ be the initial particles sampled from a prior distribution.

2. Prediction Step

At each time step n ,each particle propagates through the system's model, simulating the physical processes affecting pressure and diameter. This step involves applying the Flowell model to each particle.

For a given particle i at time or step n,

$$y_i^{(n)} = f\left(x_n, p_i^{(n-1)}, \dot{m}_i^{(n-1)}, h_i^{(n-1)}, d_i^{(n-1)}\right) \tag{1}$$

where f is the Flowell function, and x_n is the input or the location, depth at step n.

3. Update Step

Observational data (measured pressure) is used to update the weights of the particles, making more likely particles represent the true state more accurately. The weights of each particle are updated based on how well the particle's prediction matches the observed data. This involves calculating the likelihood of the observation given the particle's state.

For particle i, the weight update equation is,

$$w_i^{(n)} = w_i^{(n-1)} \cdot \mathcal{L}(y_n | y_i^{(n)}) \tag{2}$$

where $\mathcal{L}$ is the likelihood function, and y_n is the observed data at step n.

Assuming Gaussian noise in the observations, the likelihood can be expressed as,

$$\mathcal{L}(y_n | y_i^{(n)}) = \exp\left(-\frac{\left(y_n - y_i^{(n)}\right)^2}{2\sigma^2}\right) \tag{3}$$

where σ is the standard deviation of the observation noise.

The weights are normlized so that they sum to 1,

$$\widetilde{w}_i^{(n)} = \frac{w_i^{(n)}}{\sum_{j=1}^{N} w_j^{(n)}} \tag{4}$$

4. Resampling Step

Particles with higher weights are sampled to form a new set of particles, emphasizing states that better fit the observational data. To avoid particle degeneracy where a few particles have all the weight, the particles are resample based on their weights. This step generates a new set of particles by sampling with replacement from the current set, according to their weights.

The resampling process involves, drawing N new particles $\left\{p_i^{(n)}, \dot{m}_i^{(n)}, h_i^{(n)}, d_i^{(n)}\right\}_{i=1}^{N}$ from the current set $\left\{p_i^{(n-1)}, \dot{m}_i^{(n-1)}, h_i^{(n-1)}, d_i^{(n-1)}\right\}_{i=1}^{N}$ with probabilities $\left\{\widetilde{w}_i^{(n)}\right\}_{i=1}^{N}$.

5. Estimation

The final step is to estimate the parameters based on the particles. The estimate of a parameter θ (e.g., $p, \dot{m}, h$ or d) at time or step n can be computed as the weighted average of the particles,

$$\hat{\theta}^{(n)} = \sum_{i=1}^{N} \tilde{w}_i^{(n)} \theta_i^{(n)} \tag{5}$$

if we use equal weights after resampling, the estimate are:

$$\begin{aligned} \hat{p}^{(n)} &= \frac{1}{N} \sum_{i=1}^{N} p_i^{(n)} \\ \hat{\dot{m}}^{(n)} &= \frac{1}{N} \sum_{i=1}^{N} \dot{m}_i^{(n)} \\ \hat{h}^{(n)} &= \frac{1}{N} \sum_{i=1}^{N} h_i^{(n)} \\ \hat{d}^{(t)} &= \frac{1}{N} \sum_{i=1}^{N} d_i^{(t)} \end{aligned} \tag{6}$$

At time $n = 1$, the algorithm performs three sequential tasks. First new particles are sampled from the initial proposal distribution. Then, the weights are given same value and normalized according to Eq.4. Finally, the particles are resampled, according to a resampling scheme, and all new particles are given equal weight. At time n > 1, the algorithm also performs three sequential tasks. First new particles are sampled from the proposal distribution. The weights are calculated according to Eq. (3) and normalized according to Eq. (4). Finally, the particles are resampled, according to a resampling scheme, and parameter estimated.

4. FloWell Wellbore Model

Flow in geothermal reservoirs, wellbores, and pipelines, involves the interaction of different phases (liquid, vapor, solids). This interaction affects energy, momentum, and mass exchange. The following sections describe the mathematical approaches used in the wellbore simulator FloWell (Gudmundsdottir and Jonsson, 2015), based on the principles of conservation of mass, momentum, and energy.

The governing equations for single-phase flow are as follows:

Continuity Equation (Mass Conservation),

$$\frac{d\rho}{dt} + \rho \nabla \cdot \boldsymbol{u} = 0 \tag{7}$$

Energy Equation,

$$\frac{d}{dt} \left(\frac{1}{2} \rho u^2 + \rho g h + \rho e\right) = 0 \tag{8}$$

Momentum Equation,

$$\rho \frac{d\boldsymbol{u}}{dt} = -\nabla p + \rho \boldsymbol{g} - f \frac{\boldsymbol{u}^2}{d} \tag{9}$$

Where f is the friction factor, calculated using Blasius equation for smooth pipes,

$$f = 0.079\,\mathrm{Re}^{-0.25} \tag{10}$$

and Swamee-Jain equation for rough pipes,

$$f = \frac{0.25}{\left(log_{10}\left(\frac{\epsilon}{3.7d} + \frac{5.74}{\mathrm{Re}^{0.9}}\right)\right)^2} \tag{11}$$

The Reynolds number Re is defined as,

$$\mathrm{Re} = \frac{(\rho\, u\, d)}{\mu} \tag{12}$$

The continuity, energy, and momentum equations for single-phase flow are combined into a single system,

$$\begin{bmatrix} \rho & u\frac{\partial \rho}{\partial p} & u\frac{\partial \rho}{\partial h} \\ \dot{m}u & 0 & \dot{m} \\ \rho u & 1 & 0 \end{bmatrix} \frac{d}{dz} \begin{bmatrix} u \\ p \\ h \end{bmatrix} + \begin{bmatrix} 0 \\ \dot{m}g + \dot{Q} \\ \rho g + \frac{\rho f}{2\,g}\, u\, u \end{bmatrix} = \begin{bmatrix} 0 \\ 0 \\ 0 \end{bmatrix} \tag{13}$$

In two-phase flow, both liquid and vapor phases are considered. Assuming constant pipe diameter and uniform velocity (u), the equations are:

Continuity Equation:

$$\partial \frac{\alpha\, \rho_g}{\partial\, t} + \nabla \cdot \left(\alpha\, \rho_g\, u_g\right) + \frac{\partial\left((1-\alpha)\rho_l\right)}{\partial\, t} + \nabla \cdot \left((1-\alpha)\rho_l\, u_l\right) = 0 \tag{14}$$

Energy Equation:

$$\frac{d}{dt}\left(\frac{1}{2}\rho u^2 + \rho g h + \rho e\right) = 0 \tag{15}$$

Using the mass fraction x and uniform velocity u:

$$\frac{\partial\left(\alpha\rho_g h_g \ + \ (1-\alpha)\rho_l \, h_l\right)}{\partial \, t} + \nabla \cdot (\alpha\rho_g h_g \boldsymbol{u}_g + (1-\alpha)\rho_l \, h_l \, u_l) \ = \ 0 \tag{16}$$

Where γ is:

$$\gamma \ = \frac{u_g - \ u_l}{u} \tag{17}$$

Momentum Equation:

$$\rho \frac{d\boldsymbol{u}}{dt} \ = \ -\nabla p \ + \rho g \ - \Phi^2 \frac{f \boldsymbol{u}^2}{d} \tag{18}$$

where Φ^2 is the frictional correction factor and in this study Friedel's (1979) Correction Factor is used,

$$\Phi^2 \ = \ E \ + \frac{3.24 \, F^{0.045} \, H^{0.035} \left(\frac{\rho_l}{\rho_g}\right)^{0.035} \left(\frac{\mu_l}{\mu_g}\right)^{0.045} \left(\frac{1-x}{x}\right)^{0.035}}{\left(\frac{1}{x} \ + \frac{\rho_l}{\rho_g}\left(\frac{1}{1-x}\right)\right)^{0.9}} \tag{19}$$

The void fraction, which represents the space occupied by gas or vapor, is crucial for predicting pressure behavior.

The Lockhart-Martinelli (1949) correlation:

$$\alpha \ = \frac{1}{1 \ + 0.28 \left(\frac{1-x}{x}\right)^{0.64} \left(\frac{\rho_l}{\rho_g}\right)^{0.36} \left(\frac{\mu_g}{\mu_l}\right)^{0.07}} \tag{20}$$

The continuity (Eq.14), energy (Eq.15), and momentum (Eq.18) equations for two-phase flow are combined into a following system,

$$\begin{bmatrix} \rho_l & u\frac{\partial \rho_l}{\partial p} & 0 \\ \gamma u & \frac{u^2}{2}\frac{\partial \gamma}{\partial p} & 1 + \frac{u^2}{2}\frac{\partial \gamma}{\partial h} \\ \eta \rho_l u & 1 + \rho_l u^2 \frac{\partial \eta}{\partial p} & \rho_l u^2 \frac{\partial \eta}{\partial h} \end{bmatrix} \frac{d}{dz}\begin{bmatrix} u \\ p \\ h \end{bmatrix} + \begin{bmatrix} 0 \\ g + \frac{\dot{Q}}{\dot{m}} \\ ((1-\alpha)\rho_l + \alpha\rho_g)g + \Phi^2 \frac{\rho_l f}{2\,g} \, u^2 \end{bmatrix} = \begin{bmatrix} 0 \\ 0 \\ 0 \end{bmatrix} \tag{21}$$

The one-phase and two-phase systems are solved using numerical integration, either from the bottom of the well to the top or from the top to the bottom.

4. Results

To verify the method, it was applied to well KN-15, where the pressure changes down the well has altered over a 10-year period. Measurements were first taken before the well was connected to the system on February 26, 2003. When the wellhead pressure dropped after 10 years of use, it was decided to take new measurements on June 4, 2013. The results of these measurements are shown in Figure 2.

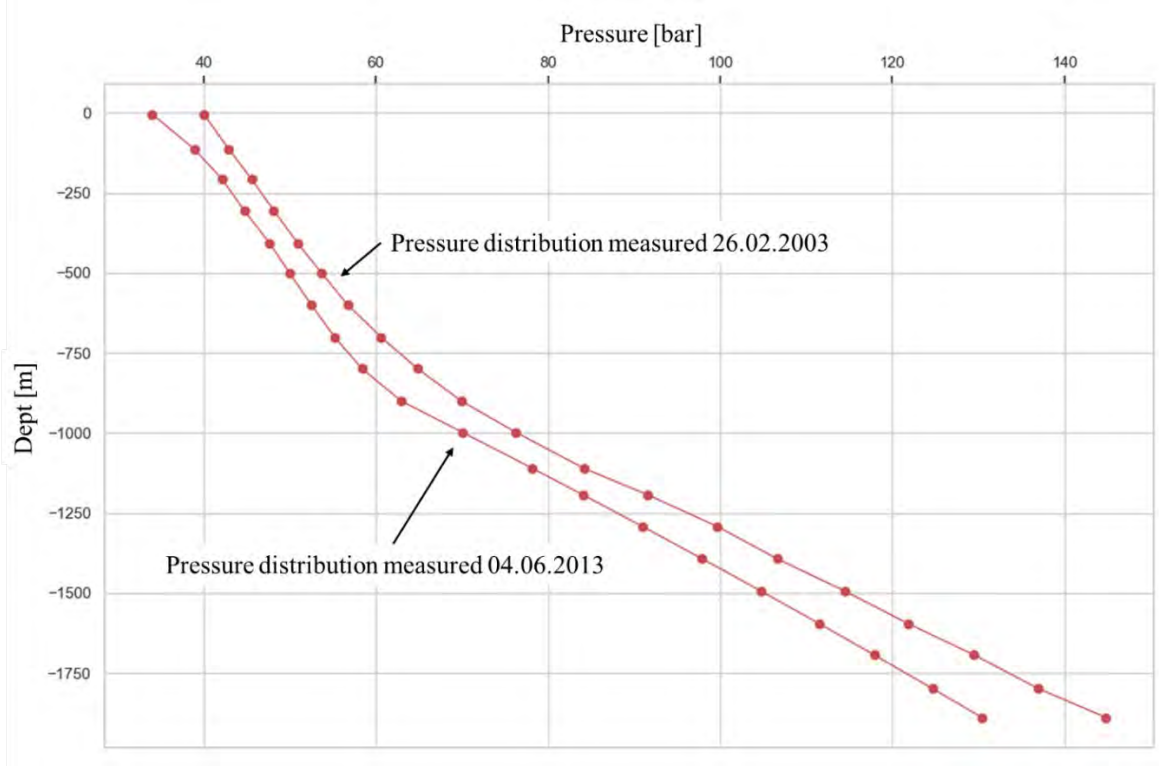

Figure 2: Pressure changes and pressure versus depth for well KN-15 measured 2003 and 2013.

The purpose of the particle filter is to approximate the uncertain values used in the Flowell wellbore model. The particle filter was set up with N = 1000 particles for each undetermined variable. The standard deviation had to be tuned for stable filter performance. If it was too high, the particle filter was unable to converge to any solution; if it was too low, the particle filter made no attempt to explore the solution domain. The pressure measurements presented in this study were obtained using a standard deviation of $\sigma = 2$ bar.

The transition model was fed predefined minimum and maximum allowed values for each particle to ensure the particles stayed within a reasonable expected range. If a particle's value after the random step was outside the range, it was forced to the corresponding boundary value.

For the results presented in this study, the specified ranges for each particle, $(p_i, \dot{m}_i, h_i, s_i)$ with minimum (x_{min}) and maximum (x_{max}) were defined as follows:

x_{max} = (147.50 bar, 69.6 kg/s, 1308.8 kJ/kg, 0.3311 m)

x_{min} = (137.67 bar, 64.9 kg/s, 1221.5 kJ/kg, 0.290 m)

Table 1 presents the key parameters of the well based on the measurement taken on February 26, 2003. To verify these values, the particle filter along with the wellbore model, was used. The corrected values are also shown in the table, and the difference is minimal.

Table 2: KN-15 Well parameters based on measurements 2003 (left) and corrected values (right).

Parameter	Value	Unit	Parameter	Value	Unit
Pressure	140.546	bar	Pressure	140.480	bar
Temp	293.5	^{o}C	Temp	293.5	^{o}C
Enthalpy	1238.0	kJ/kg	Enthalpy	1246.5	kJ/kg
Massflow	66.3	kg/s	Massflow	66.3	kg/s
Diameter	0.3153	m	Diameter	0.3153	m
Depth	1800	m	Depth	1800	m

Figure 3 shows a comparison between the measurement results and the wellbore model with corrected values from the Monte Carlo Particle Filter analysis.

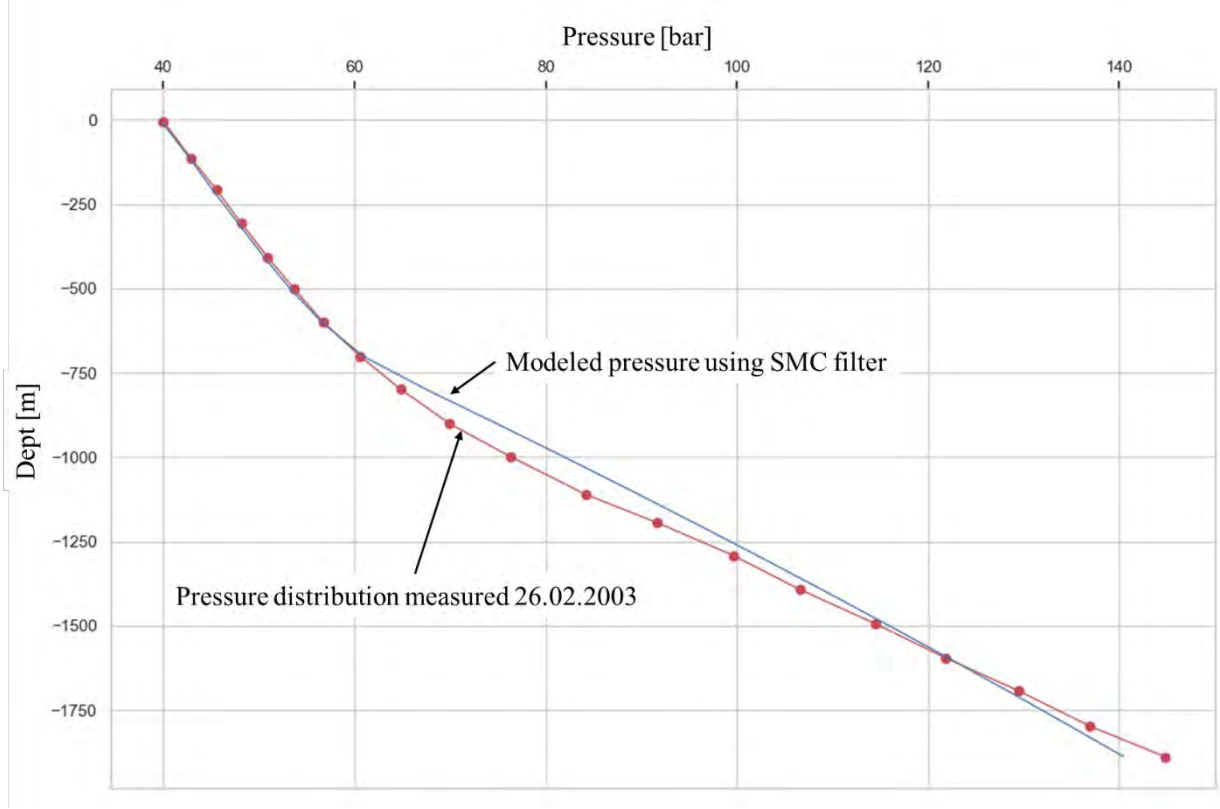

Figure 3: Measured and corrected pressure versus depth in the well KN-15 the year 2003.

Figure 4 illustrates the filter scan connected with lines between particles, showing how well the MCPF covers the area around the pressure line.

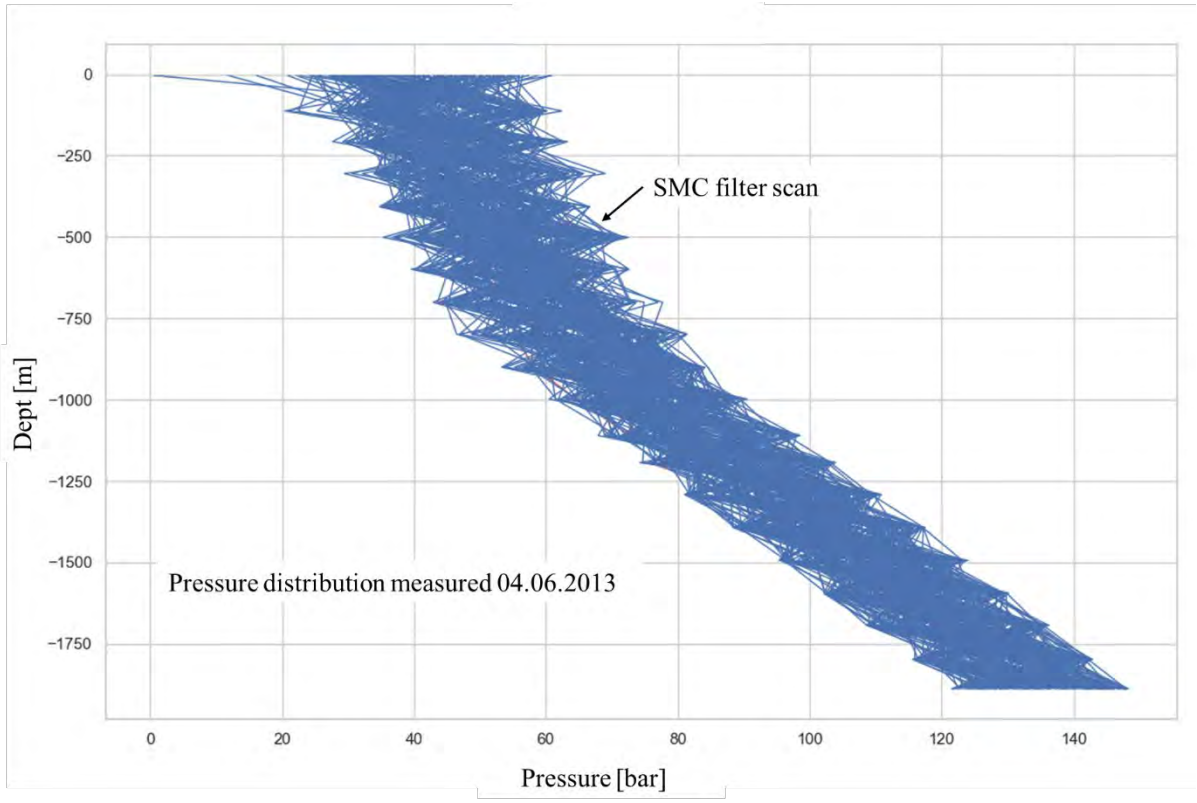

Figure 4: Particles coverage for the measurements in 2013 well KN-15.

Figure 5 presents the results where the parameters for the Flowell wellbore model have been adjusted using the filter. The results indicate that the bottom hole pressure is 137.67 bar, with a drawdown of 9.7 bar over this time period. The diameter is 0.2855 m, showing scaling of 3.5 mm. The results are detailed in Table 2. The mass flow rate is 52.7 kg/s.

Table 2: KN-15 Well parameters corrected 2003 (left) and 2013 (right).

Parameter	Value	Unit	Parameter	Value	Unit
Pressure	140.546	bar	Pressure	130.766	bar
Temp	293.5	°C	Temp	293.5	°C
Enthalpy	1238.0	kJ/kg	Enthalpy	1267.6	kJ/kg
Massflow	66.3	kg/s	Massflow	52.7	kg/s
Diameter	0.3153	m	Diameter	0.2855	m
Depth	1800	m	Depth	1800	m

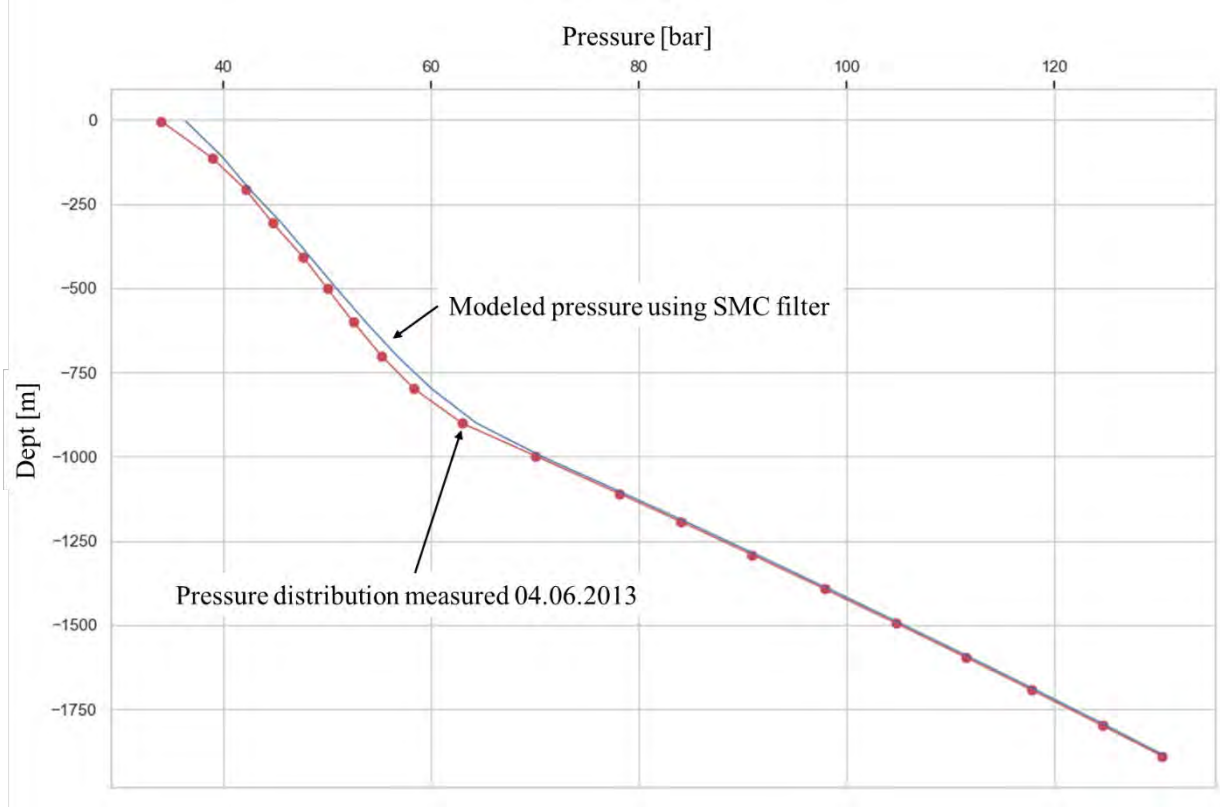

Figure 5: Measured and corrected pressure versus depth in the well KN-15 the year 2013.

5. Discussion

The results highlight the effectiveness of using a Monte Carlo Particle Filter with a wellbore model to predict downhole conditions in a geothermal well. The method successfully estimates the pressure profile and identifies changes in the wellbore diameter due to scaling. This approach provides a robust framework for real-time monitoring and management of geothermal wells.

Key advantages of this integrated method include:

- Improved accuracy in predicting wellbore conditions.

- Enhanced ability to handle non-linearities and uncertainties in the system.

- Capability to incorporate real-time observational data for continuous updating of estimates.

The case study demonstrates that this approach can significantly improve the reliability of geothermal well assessments, aiding in better decision-making for well management and optimization.

6. Conclusion

The application of Monte Carlo Particle Filter combined with a wellbore model provides a powerful tool for estimating downhole pressure and wellbore diameter in geothermal wells. The

case study confirms that this method can accurately predict well conditions and identify scaling, supporting effective and sustainable geothermal energy production.

Future work will focus on validating the approach with more extensive field data or testing the method by doing measurements with calibration before and after a cleaning process of a well. Also refining the method further by incorporating additional factors such as multi-zone scaling or piece wise blocking.

REFERENCES

Axelsson, G. "Sustainable Management of Geothermal Resources.", *Proceedings, the International Geothermal Conference*, Reykjavík, Iceland (2003).

Doucet, A. and Johansen, A.. "A Tutorial on Particle Filtering and Smoothing: Fifteen Years Later". In: *Handbook of Nonlinear Filtering* 12 (Jan.2009).

Gudmundsdottir, H. and Jonsson, M.T. "The Wellbore Simulator FloWell – Model Enhancement and Verification" *Proceedings World Geothermal Congress* 2015, Melbourne, Australia, 19-25 April (2015).

Friedel, J. "Improved Friction Pressure Drop Correlations for Horizontal and Vertical Two-Phase Pipe Flow", *European Two-Phase Flow Group Meeting*, Ispra, Italy (1979).

Lockhart, R.W. and Martinelli, R.C. "Proposed Correlation of Data for Isothermal Two-Phase, Two Component Flow in Pipes", *Chemical Engineering Progress Symposium Series*, 45, (1949), 39-48.

GRC Transactions, Vol. 48, 2024

Gas Lift Production Optimization in Liquid-dominated Geothermal Wells

Orkhan Khankishiyev[1], Elvin Ismayilov[1], Hamidreza Karami[1], Vagif Mammadzada[1], Zeming Hu[1], and Saeed Salehi[2]

[1]Well Construction Technology Center, University of Oklahoma, Norman, Oklahoma, USA

[2]Lyle School of Engineering, Southern Methodist University, Dallas, Texas, USA

Keywords: gas lift, geothermal, production, flow model, thermal model

Abstract

The global consumption of electrical energy is constantly increasing and the demand for sustainable and net-zero energy is more important now than ever. In the context of energy transition, Enhanced Geothermal Systems (EGS) are emerging as a promising solution for renewable and sustainable energy production. The economic efficiency of geothermal wells depends on the production performance, which can be enhanced through various artificial lifting systems such as gas lift and submersible pumps This paper investigates the application of gas lift in liquid-dominated geothermal wells to increase the production rate of hot liquid/steam, eventually improving the enthalpy recovery per well.

A steady-state multiphase flow model is employed to simulate the impact of gas lift on the flow rate within the geothermal well. The model considers various parameters such as fluid properties, wellbore geometry, and operational conditions. Sensitivity analysis is conducted to assess the influence of different gases on gas lift performance under varying reservoir conditions. A comprehensive thermal model is developed using a finite-element modeler to analyze the thermal behavior of the geothermal well during gas lift operations. The model accounts for heat transfer mechanisms, including conduction, convection, and radiation, within the wellbore and the surrounding formation. Factors such as fluid temperature, flow rate, gas injection temperature, and thermal properties of the materials are incorporated into the model to accurately simulate thermal dynamics. Different gas compositions, including compressed air, natural gas, and CO2, are analyzed for their suitability as gas lift agents.

Application of the gas lift results in an up to 30% increase in production rates. Comparative analysis reveals that while compressed air can be utilized with compressors at any geothermal site, natural gas exhibits superior performance as a gas lift agent due to its lower density. Furthermore, the application of CO2 showed potential for commercial use in Carbon Capture, Utilization, and Storage (CCUS) projects, with caution due to the risk of carbonic acid formation, which could lead to corrosion issues in production tubing and processing facilities. Thermal modeling indicates that

an increase in gas to liquid ratio led to higher heat loss through the production tubing. However, the overall enthalpy production of the well increases due to the elevated production rate.

Overall, the combination of multiphase flow and thermal modeling, along with comprehensive sensitivity analyses, provided a robust framework for evaluating the application of gas lift in liquid-dominated geothermal wells. The findings contribute to the optimization of geothermal well performance, highlighting the potential of gas lift systems to play a significant role in the energy transition towards sustainable and renewable energy sources.

1. Introduction

The quest for sustainable and renewable energy sources is critical in addressing the growing global demand for electrical energy. Enhanced Geothermal Systems (EGS) represent a significant advancement in the field of renewable energy, offering a stable and long-term solution for electricity generation. Unlike conventional geothermal systems, which rely on naturally occurring reservoirs, EGS can be implemented in a wider range of geological settings by artificially enhancing the permeability of geothermal reservoirs (Sanyal & Butler, 2005). This innovation broadens the applicability of geothermal energy but also presents new challenges in optimizing well performance to ensure economic viability.

In the context of hydrothermal and enhanced geothermal systems, efficient production from geothermal wells is essential. Artificial lift techniques, such as submersible pumps and gas lift systems, are employed to enhance the production rates of liquid-dominated geothermal wells. Gas lift, a method traditionally used in oil and gas production, involves injecting gas into the well through annulus or coiled tubing to reduce the hydrostatic pressure of the fluid inside the production tubing and improve fluid flow from the reservoir to the surface (Oyewole & Lea, 2008; Takacs, 2005). For the case of injection through the casing-tubing annulus, a gas lift mandrel, equipment that creates a pathway for the injected gas when activated, is assembled with the completion tubular at the desired depth and placed in the well. Depending upon the reservoir deliverability, gas can be injected through the mandrel intermittently or continuously (Guet & Ooms, 2006; Julian et al., 2014). The continuous gas lift method is the most common type used in high reservoir deliverability and high gas-liquid ratio in oil-producing wells. The injected gas which is mostly methane mixes with the reservoir fluid from the point of injection up and reduces the density of the fluid inside the production tubing (Hernandez, 2016; Moffett & Seale, 2017). This assists the reservoir pressure by decreasing the hydrostatic pressure of the fluid column inside the tubing, making the fluid flow to the surface easier. Figure 1 demonstrates the schematic layout of the well with gas lift and pressure profile across the well depth.

When the reservoir pressure declines in geothermal reservoirs due to the years of production, artificial lifting becomes necessary to restore the production rates of low-performance wells. The electric submersible pumps (ESP) have proved to be very useful in oil wells with high production rates but their application in geothermal wells is hindered by the high downhole temperature, scale content, and corrosive nature of the geothermal fluid (Aydin & Merey, 2021; Turnquist et al., 2013). Although high fluid production can be achieved through proper selection and optimization of the ESPs, premature pump failure cases in real-field applications have been reported several times in the literature (Aydin et al., 2021; Aydin & Merey, 2021; Shoeibi Omrani et al., 2021; Xu, 2022). Also, the operating window of those pumps is limited up to 450°F fluid temperature. The

application of the gas lift in liquid-dominated geothermal wells, however, is not limited by the temperature and has minimal to no downhole mechanical components that might fail due to harsh reservoir conditions (Turnquist et al., 2013).

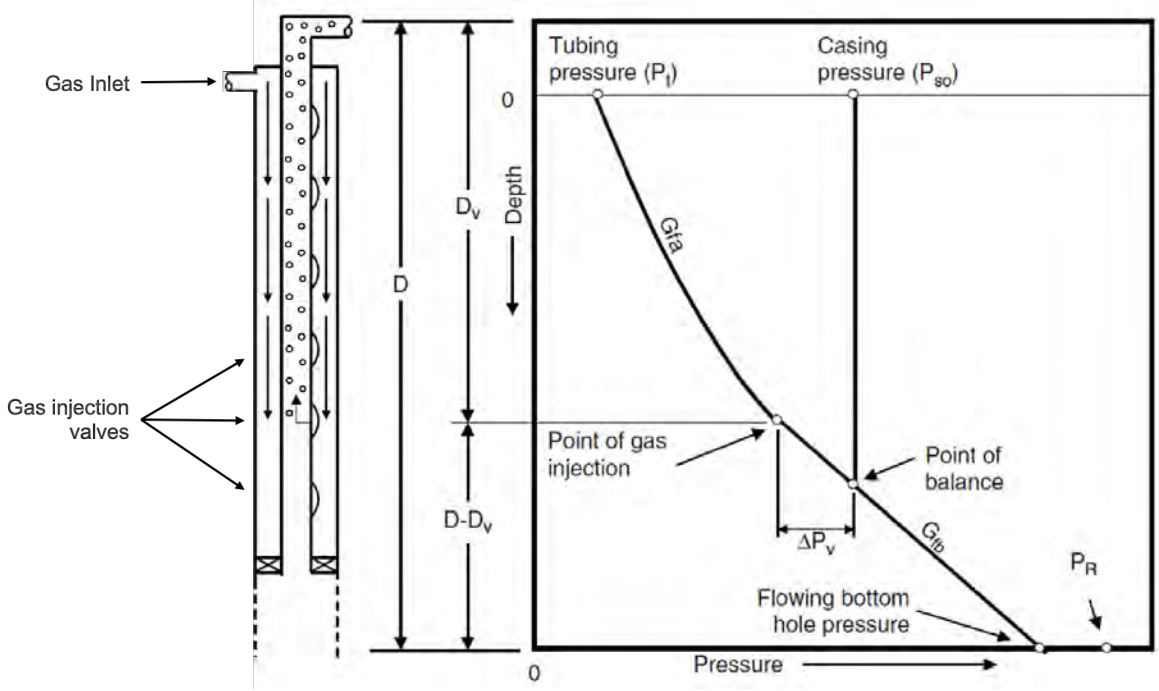

Figure 1: Schematic design of gas lift well and depth-pressure relationship (Guo, 2011). Multiple gas lift valves can be placed in the tubing string, and each can be activated separately to provide an inlet of gas at different depths in the well. At the point of injection, the pressure of the gas (casing pressure) is slightly above the pressure inside the tubing. The pressure profile changes above the gas injection due to density change of producing fluid and it results in positive wellhead pressure and transfer of fluid to the surface.

In liquid-dominated geothermal wells, gas lift production optimization can significantly enhance fluid extraction efficiency and overall system performance (Aydin & Merey, 2024). Implementing gas lift systems involves several key configurations. One common approach involves injecting gas into the annular space, which allows fluid discharge up the tubing. Alternatively, gas can be injected down the tubing to facilitate fluid discharge up the annular space. The third method employs a dual tubing system where gas is injected down one tube, and fluids are lifted in the other (Hernandez, 2016). To achieve higher flow rates without generating too much frictional pressure loss, it is required to keep the tubing diameter as large as possible. Also, producing geothermal fluid has the risk of causing corrosion on the downhole and surface well components. Thus, it is recommended to use production tubing to transfer the reservoir fluid from the well to the surface instead of using the casing alone without any tubing (Wardana & Akhwan, 2023). In the case of corrosion-damaged tubing, it can be retrieved from the well and replaced with a new one, while it is not possible to replace the damaged well casing if they are cemented in place (Song et al., 2023). Also, fiber optic cable can be installed with the tubing to record distributed acoustic and/or temperature survey that enables the producer to continuously monitor the gas lift performance and liquid level inside the tubing, as well as detect any tubing and casing leaks due to heavy corrosion (Khankishiyev et al., 2024 (a)).

The initial steps in designing a continuous-flow gas lift system include determining the optimal gas injection point, calculating the required gas volume, and establishing the necessary injection pressure (Takacs, 2005). This careful planning ensures that the system operates efficiently and effectively. In an intermittent gas lift system, a high-pressure gas bubble or slug expands and ascends to a low-pressure outlet, effectively lifting the geothermal fluid. The control of pressure and volume expansion of gas entering the tubing is managed by a valve with a large port. This valve can regulate the lift of the accumulated fluid head above it with maximum velocity to minimize slippage or control liquid fallback by fully ejecting the fluid to the surface with minimal gas usage. Intermittent gas lift is often complemented by a surface time controller to optimize the injection cycles (Kamari et al., 2014).

Depending on the availability of the gas around the geothermal site, compressed air, methane, nitrogen, and carbon dioxide can be used as injection gas. First proposed by Aqui (1996), nitrogen gas was injected in five geothermal wells in the Sibayak field in Indonesia field from 1993 until 1995 using coiled tubing. Due to its low solubility, non-corrosive, and non-toxic characteristics, nitrogen was preferred as the injection gas in more wells consequently with around 70% success rate (Buñing et al., 1998). However, this method did not prove to be economical due to the cost of coiled tubing service and nitrogen gas (Siega et al., 2006).

Carbon dioxide (CO2) has been previously proposed for use as a working fluid in closed-loop geothermal systems in several modeling studies (Beckers et al., 2022; Khankishiyev et al., 2024 (b); Rajabi et al., 2021). It can also be applied in geothermal well gas lift applications as an injection gas. This creates another commercial use for Carbon Capture, Utilization, and Storage (CCUS) projects. However, carbon dioxide has a higher density compared to air, nitrogen, and methane which limits the hydrostatic pressure reduction through gas lift inside the tubing. Another challenge is the risk of carbonic acid formation from the reaction of CO2 and water under high temperatures, which could lead to corrosion issues in production tubing and processing facilities (Mubarak et al., 2023; Sonke et al., 2022). Thus, careful consideration of every aspect of CO2 as a gas lift agent is necessary.

Air and methane have been used as a gas lift agent in oil production wells for decades. They provide sufficient hydrostatic pressure drop to achieve economic oil production rates when the injection rate and pressure are selected properly (Kamari et al., 2014). Compressed air was injected into the well using coiled tubing to initiate the discharge of geothermal fluid in Philippine geothermal wells in 1998 (Buñing et al., 1998) while there is no published record of the application of methane as a gas lift agent in geothermal wells. Overall, the air can be taken from the atmosphere around the geothermal site, compressed, and injected into the well, while methane and nitrogen must be transported from the provider to the geothermal site. The carbon dioxide can either be transported from the provider or captured around the site if the carbon capturing facility installed nearby the geothermal wells.

Gas lift offers significant advantages in geothermal wells over other artificial lift techniques, primarily due to its cost-effectiveness and operational efficiency. It has low operating costs as it utilizes methane, air, or nitrogen as compressor fuel, which is economical and readily available (Turnquist et al., 2013). Once the injection gas is introduced to the system, the same gas will be separated from the produced fluid in the two-phase surface separator, compressed, and injected back into the well, with very minimal loss during the surface separation process. The system requires minimal downhole equipment, reducing both installation and maintenance costs. With

few moving parts, gas lift systems are easy to maintain and repair, leading to lower overall downtime. Additionally, gas lift valves can be easily and inexpensively replaced without the need for a workover rig, making it a flexible and reliable method for enhancing geothermal production performance (Julian et al., 2014).

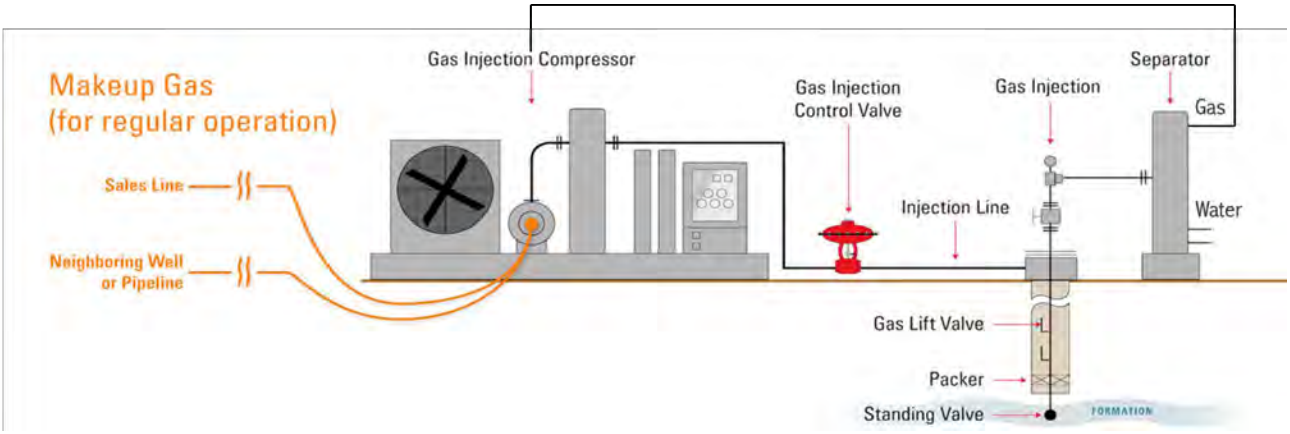

Figure 2: Gas lift well surface equipment (Andrews 2023). The main component of the system is the gas injection compressor. The gas can be provided to the compressor either from neighboring wells and pipelines or transported from the gas provider on the market. The flow of the gas is regulated by the surface control valve. After the injected gas is produced at the surface with geothermal fluid or steam, it is separated from the mixture using a surface separator to be fed into the compressor next.

The surface equipment and process for a gas lift system involve several key components. A compressor is used to pressurize low-pressure gas, which is then injected into the well through a gas injection valve. This valve regulates the flow of gas into the casing-tubing annulus, where it travels down to the gas lift valves. These valves open in response to specific gas pressures, allowing the gas to aerate the fluid column and reduce its density, facilitating easier flow to the surface. Additional equipment such as standing valves and packers ensure the system operates efficiently by maintaining fluid levels and preventing gas from escaping into the formation (Mubarok & Zarrouk, 2017). Figure 2 shows the surface components of the gas injection system.

The application of gas lift in geothermal wells requires specialized modeling and analysis due to the unique thermal and fluid dynamics involved. This study aims to explore the potential of gas lift systems in enhancing the productivity of geothermal wells by developing robust thermal and flow models that simulate the performance of various gas lift scenarios, offering an alternative to downhole pumps. The methodology for gas lift design depicted in this study is described in the subsequent section and includes using inflow performance curves (IPR) and tubing performance curves (TPR) to determine the optimal gas injection rate and liquid production rates, employing well-established methods such as the modified Hagedorn and Brown method for multiphase flow calculations and the Chen method for friction factor determination. The thermal section of the model considers heat transfer through conduction, convection, and radiation within the wellbore and the surrounding formation. Factors such as fluid temperature, flow rate, gas injection pressure, and the thermal properties of the materials are analyzed using sensitivity analysis to find the optimized set of parameters for a given geothermal well design. The results of the simulations are provided in the discussion section and the necessary findings are outlined in the conclusions.

2. Methods, Procedures, Process

This section describes the dynamic flow and thermal modeling details of the geothermal well with gas lift in a commercial steady-state multiphase flow simulation. The well design including casing size, setting depth, and deviation is based on the Well 16B(78)-32 drilled in the Utah Forge site (McLennan et al., 2023). The bottom of the well is at 10208 ft depth, while the completions are placed in 9700-9850 ft intervals. The packer is placed at 9500 ft depth to isolate the annulus from formation fluid and the gas lift inlet point is at 9100 ft. The diagram of the well developed in the model is given in Figure 3 and Table 1 shows the dimensions of the casings and tubing, including setting depth and diameters. The well deviation survey, rock temperature, and thermal conductivity are given in Table 2 below.

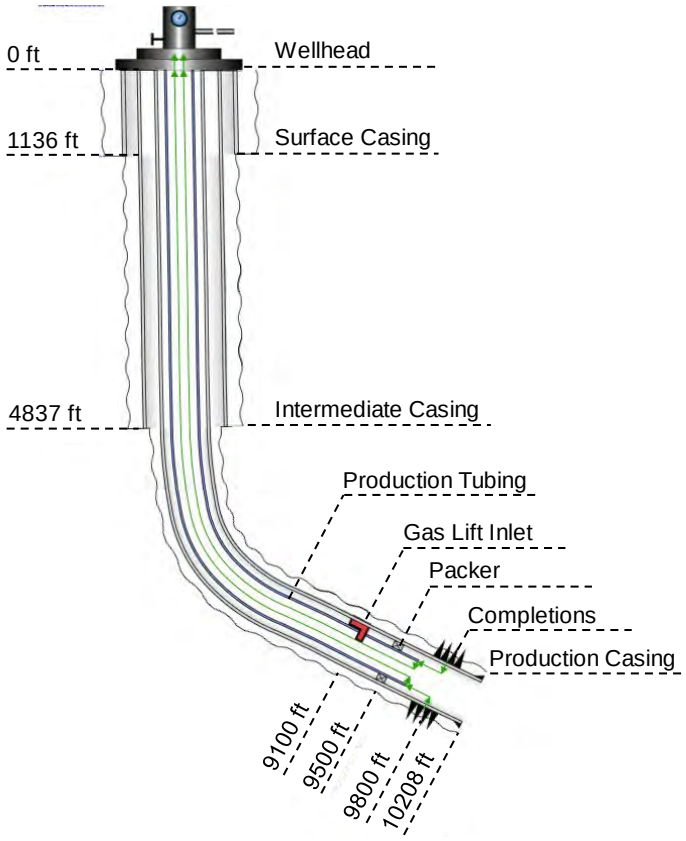

Figure 3: Schematic diagram of the well-developed in the steady-state flow simulator. The given in the diagram is measured depth MD). The green line extending from the completions to the surface is the flow pathway of produced fluid. Surface facilities were not included in the model. Only one well was used for flow and thermal modeling.

The ground temperature at the surface is set to 65°F and the ambient temperature at 8400 ft TVD is set to 425°F. The average thermal gradient and the rock-specific heat capacity are 0.043 °F/ft and 0.2 Btu(lbm.degF) for the whole interval respectively. The thermal conductivity of the rock is set to 1.73 Btu/(h.degF.ft) from the surface to 5000 ft TVD and 2.17 Btu/(h.degF.ft) to 8400 m TVD, which is close to the thermal conductivity of granite. The reservoir pressure was set to 4000 psi and the productivity index was assumed to be 100 lb/(hr.psi) to model the inflow performance relationship. The surface pressure in all simulations was set to 200 psi to consider the pressure losses within the surface facilities and power generation turbines.

Table 1: Dimensions and thermal conductivity of the casing and tubing.

Section type	From MD, ft	To MD, ft	ID, in	OD, in	Roughness, in	Thermal conductivity, Btu/(h.degF.ft)
Conductor	0	60	29	30	0.001	27
Surface Casing	0	1136	15.01	16	0.001	27
Intermediate Casing	0	4837	10.772	11.75	0.001	27
Production Casing	0	10208	5.92	7	0.001	27

Table 2: Well deviation survey, subsurface temperature, and rock thermal conductivity.

MD, m	TVD, m	Horizontal length, m	Angle, deg	Rock temperature, °F	Rock thermal conductivity, Btu/(h.degF.ft)
0	0	0.0	1.06	65	1.73
1000	1000	18.4	1.09	108	1.73
2000	2000	37.4	1.02	151	1.73
3000	2999	55.3	0.68	194	1.73
4000	3999	67.1	1.38	237	1.73
5000	4999	91.2	9.76	280	1.73
6000	5985	260.7	43.62	322	2.17
7000	6709	950.5	67.06	353	2.17
8000	7098	1871.5	62.93	370	2.17
9000	7553	2761.9	64.21	390	2.17
10000	7988	3662.3	64.82	409	2.17
10947	8391	4519.3	64.98	424	2.17

The thermal conductivity of the carbon steel casings and liner are set to 27 Btu/(h.degF.ft). The gas is pumped through the annulus and the gas/fluid mixture is produced through the insulated tubing that has a thermal conductivity of 0.05 Btu/(h.degF.ft). There are several commercially available vacuum-insulated tubing (VIT) products provided by different manufacturers with very low thermal conductivity. The cement around the surface and intermediate casing is two inches thick while it is set to one inch for the production casing. The thermal conductivity value for the cement is set to 0.9 Btu/(h.degF.ft) according to the commonly used H and G class cement in the well construction. Since cement has higher thermal conductivity than water and drilling mud, the annulus between casings is filled with cement up to the surface.

The steady-state multiphase flow simulator incorporates a wide variety of industry-standard multiphase flow correlations that have been developed through decades of research, as well as industrial data collection and analysis. The model enables the calculation of pressure losses, flow

velocities, and flow regimes at any node given in the system. The heat transfer modeling part of the simulator provides an accurate estimation of the heat transfer from the rock to the circulating fluid through cement and casing. The model recalculates the temperature and pressure-dependent fluid properties during the simulation at any given depth in the well to achieve accurate flow and thermal modeling. The simulator carries out comprehensive energy-balance calculations accounting for convection, conduction, Joule-Thomson cooling and heating, and frictional heating (SLB, 2022).

Four gases, air, methane (CH_4), carbon dioxide (CO_2), and Nitrogen (N_2), will be used in the simulations to determine the impact of gas on multiphase flow and thermal performance of the geothermal fluid/steam production. Table 3 provides the properties of each gas. The chemical compositions of the reservoir fluid and injected gas including the names and mole fractions are provided in Table 4. Although geothermal reservoir fluid usually contains a lot of components such as salts, scales, acids, and rare earth minerals, its composition was kept simple during simulations in this study. The H_2S and CO_2 were added to the composition to account for the corrosion taking place during production.

Table 3: Some properties of four gasses used in the multiphase steady-state simulation model as gas lift agents

Property	Air	Methane (CH4)	Carbon Dioxide (CO_2)	Nitrogen (N_2)
Molecular Weight (lb/lbmol)	28.97	~16.04	44.01	28.01
Density at STP (lb/ft³)	0.0765	0.0424	0.1236	0.0727
Specific Heat Capacity (Btu/lb.°F)	0.24	~0.480	0.2	0.248
Thermal Conductivity (Btu/hr.ft.°F)	0.0151	0.0185	0.00845	0.01494
Viscosity at STP (lb/ft.s)	3.78 x 10^-7	~2.30 x 10^-7	3.11 x 10^-7	3.70 x 10^-7
Solubility in Water (lb/ft³)	~0.00181	Very low	0.0906	~0.00125
Non-Corrosive Nature	Yes	Yes	No	Yes
Non-Toxic Nature	Yes	Yes	No	Yes
Inert Nature	No	No	No	Yes
Compressibility Factor (Z)	~1.0	~0.85-0.95	~0.75-0.85	~1.0
Operational Temperature Range	Broad	Broad	Moderate	Broad
Flammability	Non-Flammable	Highly Flammable	Non-Flammable	Non-Flammable

Table 4: Typical chemical composition and mole fractions (%) of the geothermal reservoir fluid and injected gases. The component of the geothermal reservoir fluid changes depending on the location and geology of the field, while it was kept simple during simulations. CO2 and H2S were included in the geothermal fluid to consider for the corrosion evaluation without gas injection.

Chemical Component	Geothermal fluid	Air	Methane (CH4)	Carbon Dioxide (CO_2)	Nitrogen (N_2)
H_2O	99	0	0	0	0
CH_4	0.1	0	100	0	0
CO_2	0.7	0.07	0	100	0
N_2	0	78	0	0	100
O_2	0	21	0	0	0
Ar	0	0.93	0	0	0
H_2S	0.2	0	0	0	0

3. Results and Discussion

3.1 Impact of reservoir pressure and gas injection rate on the operating point

The gas injection method is not recommended to be applied to all types of geothermal wells. In the wells where reservoir pressure is enough to overcome the pressure of the hydrostatic column in the well and provide sufficient pressure at the surface, injecting the gas will provide a very slight increase in production rate, while increasing the temperature loss across the well. To check the impact of reservoir pressure on the Inflow Performance Relationship (IPR) and injection rate Tubing Performance Relationship (TPR) curves, a nodal analysis was performed by setting the reservoir pressure to 2500, 3000, 3500, 4000 psi and gas injection rate to 0, 1, 2 and 3 mmscf/d. The methane was used as a gas lift agent and surface pressure was set to 200 psi. The gas was injected at 9100 ft MD from behind the casing into the production tubing. The productivity index was kept constant at 5 STB/(d.psi). The node was placed at the bottom of the well where the completions are located. The results of the simulation are shown in Figure 4, where negative-slope lines show the IPR curves and positive-slope lines are the TPR curves. The blue dots are the operating point for each scenario that indicates the pressure and flow rate at the bottom of the well.

With increasing reservoir pressure, the inflow curve moves up, and increasing the gas lift injection rate, the outflow curve moves down. When the reservoir pressure is 2500 psi, the well produces only 1350 STB/day liquid without any gas lift, while a 4050 STB/day flow rate can be achieved by injection of 1 mmscf gas per day at 9100 ft MD. Raising the injection rate to 2 mmscf/d provided an additional 150 STB/d and 55 STB/d increase at 3 mmscf/d. A production increase of 35% was estimated for the case of 3500 psi reservoir pressure by injecting 1 mmscf methane per day and an additional 5% can be realized by increasing the injection rate three times. The production rate boosted by the injection rate was relatively smaller at 4000 psi reservoir pressure (20%). The plot indicates that gas lift provides less production rate assistance at high reservoir pressures. In addition, the production rate increase slows down significantly at higher gas lift rates, while causing more heat loss and smaller surface production temperature.

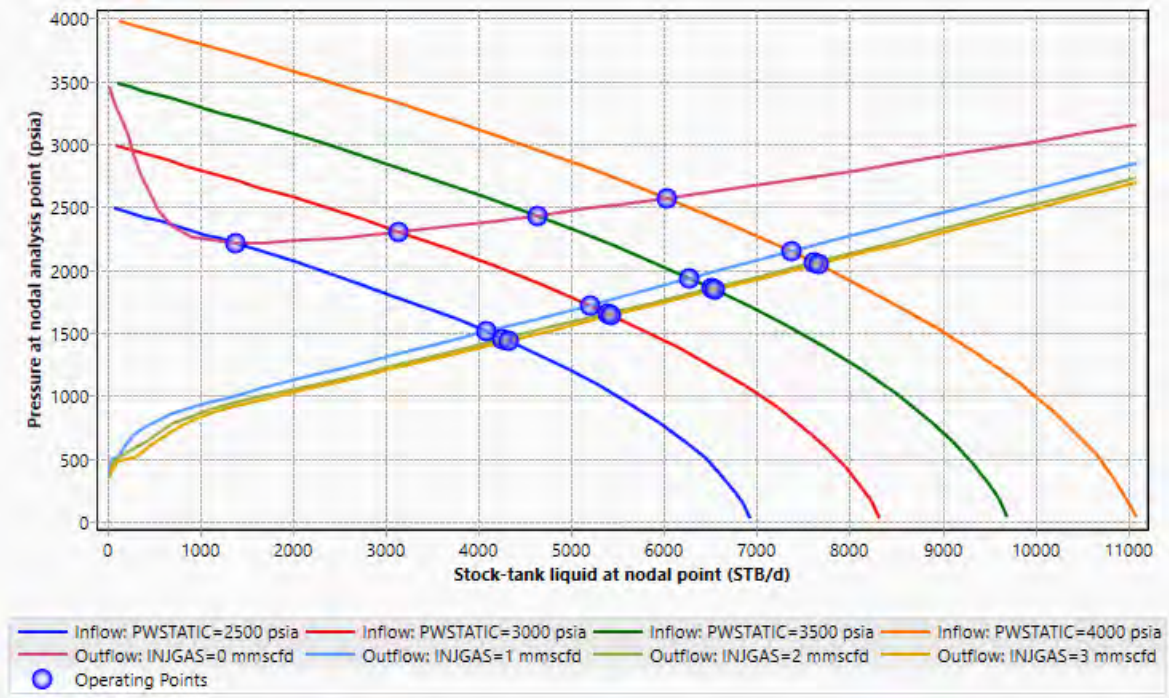

Figure 4: Nodal analysis of Inflow Performance Relationship (IPR) and Tubing Performance Relationship (TPR) curves. The reservoir pressures were set to 2500, 3000, 3500, and 4000 psi which impact the IPR curves. The methane gas injection rates were set to 0, 1, 2, and 3 mmscf/d that impact the IPR curves. At higher rates, the gas lift has minimal influence to increase the production flow rate. The gas injection rate relationship with the production rate increase is not linear and after a certain gas injection rate, the production rate does not increase further.

3.2 Pressure, temperature, and flowrate profiles with different gas injection rates

In this section, pressure, temperature, and flow rate profiles within the wellbore under varying nitrogen gas injection rates are examined. For this analysis, wellhead production pressure is maintained at 200 psi, reservoir pressure at 4000 psi, with an injection point at 9100 ft MD and 7600 ft TVD. The nitrogen injection pressure is set to 2500 psi with an injection temperature of 75°F. It was observed that applying 1 mmscf/day nitrogen injection dropped the bottomhole flowing pressure by around 12% (300 psi). Increasing the injection rate from 1 mmscf/day to 3 mmscf/day resulted in another 3.5% decrease in bottomhole flowing pressure. The surface production temperature dropped by around 10°F as a result of 1 mmscf/day nitrogen injection. Overall, there temperature of the produced liquid drops from around 420°F to 355°F as the heat loss occurs through the tubing. The simulation results are displayed in Figure 5.

The flowing liquid and gas flow rates across the well with varying nitrogen injection rates are shown in Figure 6. The application of gas lift led to a 20% increase in liquid production and up to a 200% rise in gas flow rate, the big majority of which is injected gas. At the bottom of the well, the liquid flow rate is at its maximum while the gas flow rate is at its minimum. As the multiphase fluid moves up the well, the gas expands and accelerates, causing the flowing liquid flow rate to drop by around 10% compared to the bottomhole flow rate.

In Figure 7, the flowing liquid and gas heat capacity of the multiphase fluid flowing inside the production tubing from bottom to top with varying nitrogen injection rates is illustrated. The injection of nitrogen resulted in approximately a 10% drop in the heat capacity of liquid water and

gas, indicating that more temperature drops will occur as the fluid travels up the well. Therefore, insulation of the top part of production tubing is more necessary to prevent heat loss.

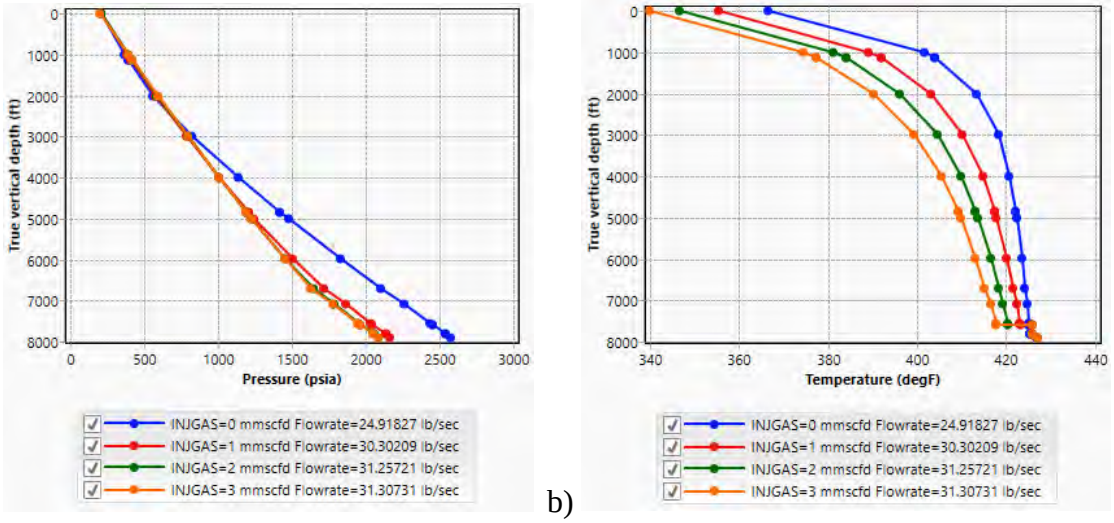

a) b)

Figure 5: Pressure (a) and temperature (b) profiles across the well with varying Nitrogen injection rates. Increasing the injection rate from 1 mmscf/d to 3 mmscf/d decreased the bottomhole pressure by 3.5% and the surface temperature dropped by 4.5%.

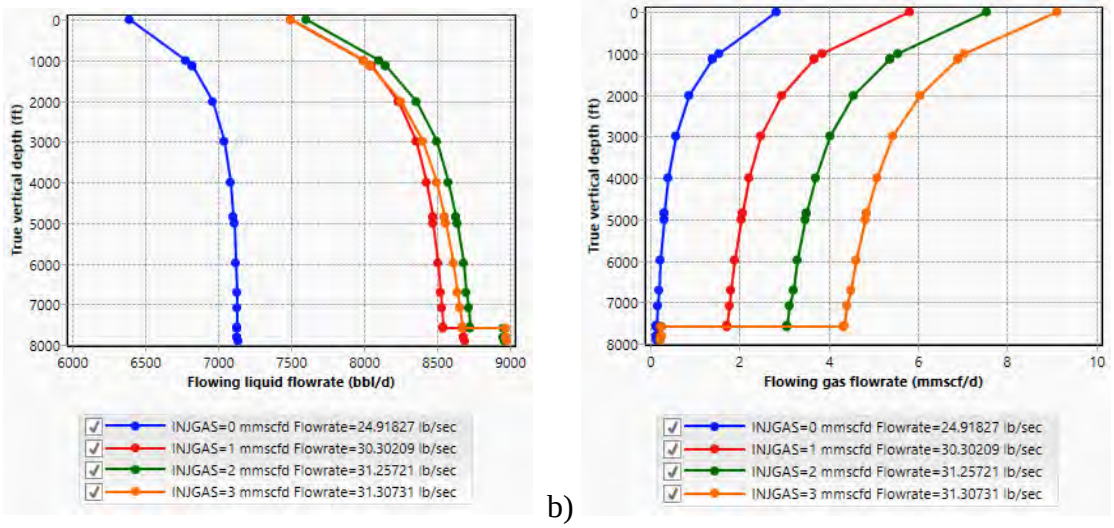

a) b)

Figure 6: Flowing liquid (a) and gas b) flow rates across the well with varying Nitrogen injection rates. Application of gas lift provided 20% increase in liquid production and up to 200% rise in gas flow rate. The liquid flow rate is maximum at the bottom of the well and the gas flow rate is the minimum. As the multiphase fluid moves up the well, the gas expands and speeds up while the liquid flow rate drops by around 10%.

3.3 Impact of injected gas type and rate on production performance

Nitrogen, compressed air, carbon dioxide, and methane were tested as a gas lift agent at different injection rates while keeping the injection pressure and temperature at 2500 psi and 75°F, the injection point at 9100 ft MD, the wellhead production pressure at 200 psi. Figure 8 illustrates the impact of gas injection rate on liquid and gas flow rates at the wellhead for all four gas types. It was observed that the liquid production rate reaches its maximum value at the injection rate of 1.5 mmscf/day, after which it declines. Among the gases tested, methane injection provided the most

support for liquid production, yielding the highest flow rates (max. 7680 bbl/day). The injection of air, primarily composed of nitrogen and oxygen, produced similar results to the injection of nitrogen alone with the highest production rate of 7600 bbl/day, indicating no significant difference between these two gas types in terms of liquid production performance. Carbon dioxide injection exhibited the lowest performance (max. 7420 bbl/day), resulting in the least liquid production. Interestingly, the gas type did not significantly affect the gas flow rate at the wellhead, regardless of the injection rate. As more and more gas enter the tubing above 1.5 mmscf/day injection rate, they expand and prevent liquid from flowing from the reservoir up the tubing. The diminished liquid production rate also decreases enthalpy production. Although gas production seems to be increasing, the majority of it is injected gas and not steam. This means that higher gas lift injection rates do not provide any advantages in terms of power production.

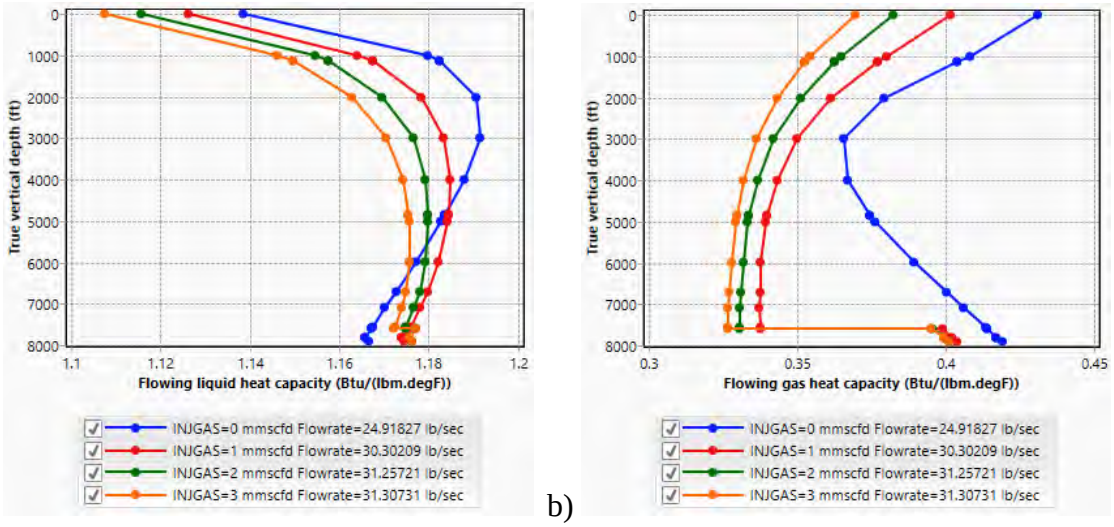

Figure 7: Flowing liquid (a) and gas (b) heat capacity of the multiphase fluid flowing inside the production tubing from bottom to top with varying Nitrogen injection rates. Overall, the injection of nitrogen dropped the heat capacity of liquid water by around 10% which means more temperature drop will occur as the fluid travels up the well.

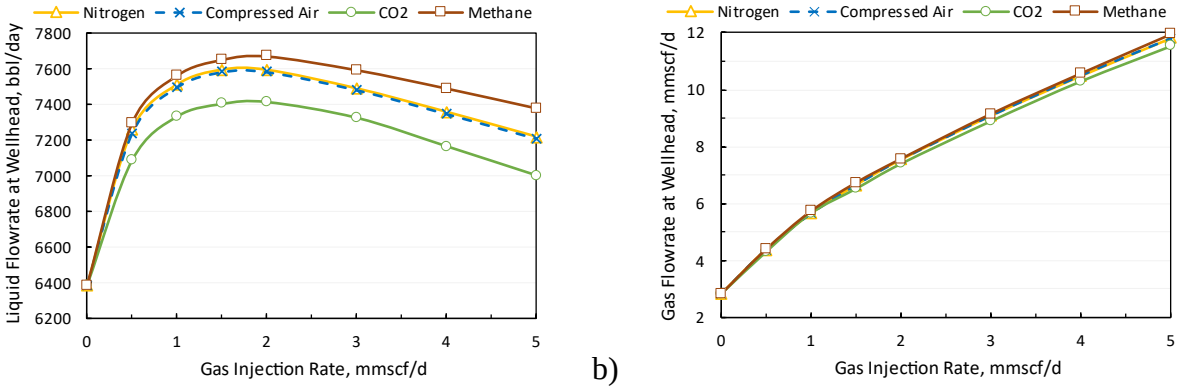

Figure 8: Liquid (a) and gas (b) flow rates at wellhead vs. gas injection rate. The liquid production reaches the maximum value at 1.5 mmscf/d gas injection after which it drops to lower values. Methane injection provided the most support for liquid production. The injection of air that consists mostly of nitrogen and oxygen and the injection of nitrogen alone showed the same results for liquid production. The lowest performance was observed during the injection of carbon dioxide. No considerable difference was observed in the produced gas flow rate at the wellhead no matter which gas type was injected.

The produced heat is a function of the mass production rate, temperature, and heat capacity of the fluid, and it must be considered to find the most effective gas injection rate to achieve the best techno-economic performance. Figure 9 shows the produced heat for different injection rates and gases calculated based on the temperature, flow rate, and liquid and steam heat capacity values taken from the simulation. The produced fluid temperature dropped by around 35°F as the injection rate increased from 0 to 5 mmscf/day. However, the gas type had almost no considerable impact on temperature up to a 2.5 mmscf/day injection rate. The produced heat plot showed that the optimal gas injection rate is around 1.5 mmscf/day, and further increases in the injection rate harmed the production performance. Methane injection resulted in the highest produced heat (13 MW), while air and nitrogen-assisted heat production was slightly lower (12.8 MW). CO2 injection resulted in the lowest heat production (12.6 MW). A reduction of 0.6 MW produced heat was estimated when the gas injection rates increased from 1.5 mmscf/day to 5 mmscf/day. It was concluded that injection above the optimum point not only decreases the produced heat but also increases the capital costs of providing the injection gas and the operating cost of the chiller and compression stations.

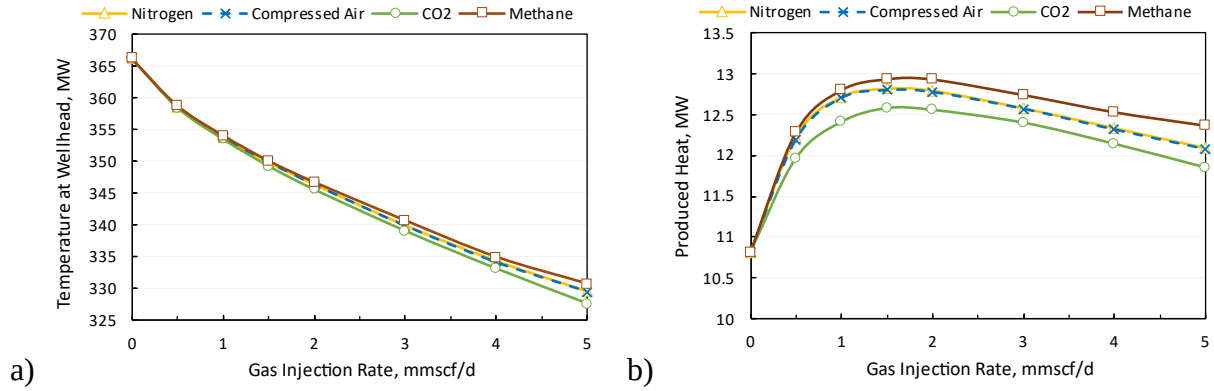

Figure 9: Temperature at the wellhead (a) and Produced heat (b) with varying gas injection rates and types. The produced fluid temperature dropped by around 35°F as the injection rate increased from 0 to 5 mmscf/day. However, the gas type had almost no considerable impact on temperature up to 2.5 mmscf/day injection rate. The produced heat plot showed that the optimal gas injection rate is around 1.5 mmscf/day and further increase of the injection rate had negative impact on production performance. Methane injection resulted in the highest produced heat while air and nitrogen-assisted heat production was slightly under that. CO_2 injection resulted in the lowest heat production.

It is necessary to determine other aspects of the gas lift application to determine which gas is the most suitable. One of such factors is the availability of gas around the geothermal field. Although the methane and nitrogen gases showed superior performance in terms of produced heat, their transportation from the market to the field might be costly. The air and CO_2 on the other hand can be captured from the atmosphere right where the geothermal wells are located and compressed to inject in the well. However, there is a corrosion risk associated with the injection of air and carbon dioxide. The corrosion rate evaluations showed that the injection of air containing 21% oxygen doubled the corrosion rate (Figure 10. a). Without air injection, the corrosion rate was 0.005 in/year on average and after injection of 3 mmscf/day air, the average corrosion rate was estimated to be around 0.01 in/year. The corrosion rate with the CO_2 injected was even more severe (Figure 10. b). Under high pressure and temperature, the CO_2 and water forms carbonic acid that speeds up the corrosion process significantly. The corrosion rate was estimated to increase by at least 150% (from 0.005 in/year to 0.012 in/year) with 1 mmscf/day CO_2 injection by around 8 times with 3

mmscf/day CO_2 injection. Although the application of CO_2 for gas lift in geothermal wells might create commercial use for CCUS projects, the integrity of the geothermal wells would be compromised in the long term.

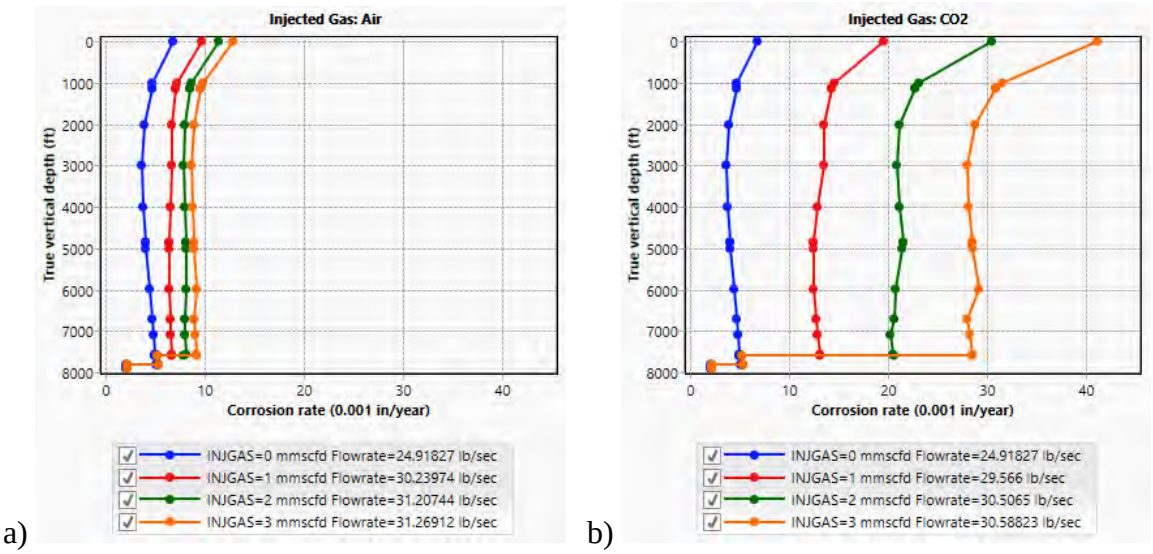

Figure 10: Corrosion rate of production tubing in case of air (a) and CO_2 injection (b) with varying injection rates. Carbon dioxide is estimated to cause three times more corrosion compared to air. To put into perspective, 0.1 inch of the tubing wall would corrode away within 5 years of production using 1 mmscf/day CO2 injection.

These findings highlight the importance of selecting an appropriate gas type and injection rate to optimize geothermal well performance. Although obtaining the air and CO_2 around the geothermal site, injecting them into the well for the long term was estimated to cause irreversible corrosion damage to the tubing and surface facilities. Methane proved to be the most effective gas for maximizing both liquid production and heat output, making it a preferable choice for gas lift operations in geothermal wells. It should also be considered that methane is flammable and any leaks during compression, injection, and production might cause environmental damage and safety hazards. The results also highlight that while increasing the injection rate can initially enhance production, there is a threshold beyond which the benefits diminish and production efficiency declines. Therefore, careful optimization of gas injection parameters is crucial for achieving the best techno-economic outcomes in geothermal energy production.

3.4 Impact of gas injection depth on production performance

Injection pressure does not influence production mass flow rate and wellhead temperature considerably. However, it must be above the pressure of the fluid at the injection point in the well so that it can enter the tubing and mix with the geothermal fluid. The injection depth, on the other hand, impacts the liquid flow rates considerably. To evaluate this impact, gas injection points were set to different depths ranging from 3500 ft TVD to 7500 ft TVD. Air was used as a gas lift agent with an injection rate of 1.5 mmscf/day. The surface injection pressure was kept constant at 2500 psi and the wellhead production pressure was set to 200 psi. The results, illustrated in Figure 11, demonstrate that the deeper the gas lift injection point is installed in the well, the more significant the impact on the mass production rate. This is because a deeper injection point results in a longer hydrostatic column mixing with the gas, which decreases the fluid density and therefore the hydrostatic pressure. Consequently, changing the depth of the injection point from 3500 ft TVD

to 7500 ft TVD resulted in a 13% increase in mass production rate. The temperature of the produced fluid, however, showed very little improvement, only about 2°F. While deeper injection points enhance production rates, they also necessitate higher surface gas injection pressures. This increase in required pressure directly correlates with higher surface gas compression costs, which must be factored into the overall economic analysis of the gas lift system. It is crucial to balance the benefits of increased production with the additional costs associated with deeper gas injection. In practical applications, the selection of the optimal gas injection depth should consider both the technical and economic aspects. The increased production rate and its impact on the levelized cost of electricity (LCOE) must be weighed against the added costs of deeper injection points and higher injection rates. This comprehensive evaluation ensures that the gas lift design maximizes the economic efficiency of geothermal energy production.

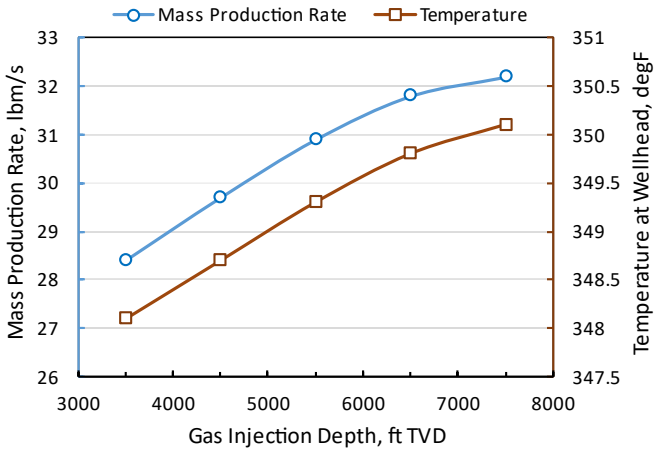

Figure 11: Mass production rate and temperature at the wellhead impacted by the air injection depth. The deeper the gas lift injection point is installed in the well, the longer the hydrostatic column will mix with the gas, decreasing density and therefore the hydrostatic pressure. Changing the depth of the injection point from 3500 ft TVD to 7500 ft TVD resulted in a 13% more mass production rate. It had very little impact on the produced fluid temperature (only 2°F improvement). However, placing the gas lift mandrel deeper means the surface gas injection pressure must be higher and that increases the gas compression costs. The cumulative impact of it on the LCOE needs to be considered.

Conclusion

The comprehensive study on the application of gas lift technology in liquid-dominated geothermal wells yielded significant insights into optimizing geothermal energy production. The following key findings and recommendations are concluded from the analysis:

- Gas lift technology is most beneficial in geothermal wells with lower reservoir pressures. In wells with sufficient natural reservoir pressure to overcome the hydrostatic column pressure, gas lift provides minimal production enhancement and increases temperature losses.
- Optimal gas injection rates must be carefully determined to balance production gains against increased heat loss and operating costs. For methane injection, the production rate benefits were evaluated to diminish beyond an injection rate of 1.5 mmscf/day, and higher rates lead to excessive heat loss and reduced surface fluid temperature.
- Increased nitrogen injection rates resulted in decreased bottomhole pressure and lower surface production temperatures. The maximum liquid flow rate occurs at the bottom of the well, decreasing as the gas expands and accelerates up the well.

- The injection of gases into the tubing reduces the heat capacity of the multiphase fluid, necessitating the insulation of the upper sections of the production tubing to minimize heat loss.
- Methane proved to be the most effective gas lift agent, yielding the highest liquid production and produced heat. The flammability and potential environmental hazards of methane must be considered as well. Nitrogen and air showed similar performance, while CO2 injection was the least effective. CO2 and air injection were estimated to accelerate the corrosion process, compromising the integrity of the well.
- Optimal injection rates (around 1.5 mmscf/day for the case studied in this paper) are crucial for maximizing produced heat and minimizing operational costs. Exceeding this rate results in diminished returns and higher capital expenditures.
- Deeper gas injection points enhance production rates by reducing the fluid density and hydrostatic pressure. However, this requires higher surface gas injection pressures, increasing operational costs.
- The optimal depth for gas injection should balance the production rate benefits against the added compression costs, considering both technical and economic factors.

In summary, the successful implementation of gas lift technology in geothermal wells requires a balanced approach that considers reservoir characteristics, gas type and availability, injection parameters, and long-term economic impacts. The findings of this study provide a solid foundation for optimizing geothermal energy production, contributing to the sustainable and efficient use of geothermal resources.

Acknowledgement

The authors of this paper would like to thank GreenPath Systems for funding this research. The opinions, findings, conclusions, or recommendations presented in this publication are solely those of the authors and do not necessarily represent the views or opinions of the GreenPath Systems.

Declaration of Competing Interest

The authors declare that they have no known competing financial interests or personal relationships that could have appeared to influence the work reported in this paper.

Data Availability

The model files, well design data and simulation results can be provided upon request to the corresponding author at orkhan@ou.edu.

References

Andrews , K. (2023). Gas Lift: How It Works, Why You Should Use It, and Equipment Required.

Aqui, A. (1996). Well discharge stimulation of some geothermal wells in the Philippines by nitrogen gas injection. In *Project for Diploma in Energy Technology*. The University of Auckland New Zealand.

Aydin, H., Akin, S., Tüzen, M. K., & Şentürk, E. (2021). Artificial lifting in liquid dominated high-temperature geothermal fields in Turkey: Lessons learned. 46th Workshop on Geothermal Reservoir Engineering, Stanford University, Stanford, California, USA,

Aydin, H., & Merey, S. (2021). Design of Electrical Submersible Pump system in geothermal wells: A case study from West Anatolia, Turkey. *Energy*, *230*, 120891.

Aydin, H., & Merey, Ş. (2024). Gas lifting design and application in geothermal wells: A case study from West Anatolia, Turkiye. *Geoenergy Science and Engineering*, *233*, 212544.

Beckers, K. F., Rangel-Jurado, N., Chandrasekar, H., Hawkins, A. J., Fulton, P. M., & Tester, J. W. (2022). Techno-economic performance of closed-loop geothermal systems for heat production and electricity generation. *Geothermics*, *100*, 102318.

Buñing, B., Gonzaga, L., Aqui, A., Salera, J., & Sarmiento, Z. (1998). Discharge initiation by gas-lifting: PNOC-EDC experience in Philippine geothermal wells. Proceedings of the 23rd Workshop on Geothermal Reservoir Engineering, Stanford University, Stanford, CA, US,

Guet, S., & Ooms, G. (2006). Fluid mechanical aspects of the gas-lift technique. *Annu. Rev. Fluid Mech.*, *38*, 225-249.

Guo, B. (2011). *Petroleum production engineering, a computer-assisted approach*. Elsevier.

Hernandez, A. (2016). *Fundamentals of gas lift engineering: Well design and troubleshooting*. Gulf Professional Publishing.

Julian, J., Jackson, J., & White, T. (2014). A history of gas lift valve and gas lift mandrel damage and subsequent retrofit gas lift straddle installation in Alaska. SPE/ICoTA Well Intervention Conference and Exhibition,

Kamari, A., Bahadori, A., Mohammadi, A. H., & Zendehboudi, S. (2014). Evaluating the unloading gradient pressure in continuous gas-lift systems during petroleum production operations. *Petroleum science and technology*, *32*(24), 2961-2968.

Khankishiyev, O., Salehi, S., Hasanov, G., & Hu, Z. (2024). Application of Distributed Temperature Sensing (DTS) in Geothermal Wells. *PROCEEDINGS, 49th Workshop on Geothermal Reservoir Engineering*

Khankishiyev, O., Wu, Y., Karami, H., Salehi, S., & Farajli, H. (2024). Potential of Multilateral Closed Loop Geothermal Systems for Power Generation Using Water and Supercritical CO2. *SPE Europe Energy Conference & Exhibition*.

McLennan, J., Mock, B., Swearingen, L., Baldwin, R., Hodder, M., Vetsak, A., Kuhns, A. T., Breland, J., & England, K. (2023). *Utah FORGE: Well 16B(78)-32 Drilling Data* Energy and Geoscience Institute at the University of Utah. https://doi.org/10.15121/1998591

Moffett, R., & Seale, S. (2017). Real Gas Lift Optimization: An Alternative to Timer Based Intermittent Gas Lift. Abu Dhabi International Petroleum Exhibition and Conference,

Mubarak, G., Verma, C., Barsoum, I., Alfantazi, A., & Rhee, K. Y. (2023). Internal corrosion in oil and gas wells during casings and tubing: Challenges and opportunities of corrosion inhibitors. *Journal of the Taiwan Institute of Chemical Engineers*, *150*, 105027.

Mubarok, M. H., & Zarrouk, S. J. (2017). Discharge stimulation of geothermal wells: Overview and analysis. *Geothermics*, *70*, 17-37.

Oyewole, P. O., & Lea, J. F. (2008). Artificial lift selection strategy for the life of a gas well with some liquid production. SPE Annual Technical Conference and Exhibition?,

Rajabi, M. M., Chen, M., Bozorgpour, A., Al-Maktoumi, A., & Izady, A. (2021). Stochastic techno-economic analysis of CO2-circulated geothermal energy production in a closed reservoir system. *Geothermics*, *96*, 102202.

Sanyal, S. K., & Butler, S. J. (2005). An analysis of power generation prospects from enhanced geothermal systems. *Geothermal Resources Council Transactions*, *29*, 131-138.

Shoeibi Omrani, P., Van der Valk, K., Bos, W., Nizamutdinov, E., Van der Sluijs, L., Eilers, J., Pereboom, H., Castelein, K., & Van Bergen, F. (2021). Overview of Opportunities and Challenges of Electrical Submersible Pumps ESP in the Geothermal Energy Production Systems. SPE Gulf Coast Section Electric Submersible Pumps Symposium?,

Siega, C. H., Saw, V. S., Andrino Jr, R. P., & Cañete, G. F. (2006). Well-To-Well Two Phase Injection Using a 10in Diameter Line To Initiate Well Discharge in Mahanagdong Geothermal Field, Leyte, Philippines. 7th Asian Geothermal Symposium,

SLB. (2022). Pipesim steady-state Multiphase flow simulator. In.

Song, X., Li, G., Huang, Z., Shi, Y., Wang, G., Song, G., & Xu, F. (2023). Review of high-temperature geothermal drilling and exploitation technologies. *Gondwana Research*, *122*, 315-330.

Sonke, J., Bos, W., & Paterson, S. (2022). Materials challenges with CO2 transport and injection for carbon capture and storage. *International Journal of Greenhouse Gas Control*, *114*, 103601.

Takacs, G. (2005). *Gas lift manual*. PennWell Books.

Turnquist, N., Qi, X., Raminosoa, T., Salas, K., Samudrala, O., Shah, M., Van Dam, J., Yin, W., & Zia, J. (2013). *High-Temperature-High-Volume Lifting for Enhanced Geothermal Systems*.

Wardana, R., & Akhwan, M. (2023). Geothermal Well Casing Design with High Temperature and Corrosive in Q Field. *Journal of Earth Energy Engineering*, *12*(2s), 74-85.

Xu, Z. (2022). Analysis of common failure causes and optimization suggestions of ESP. In *Advances in Geology and Resources Exploration* (pp. 912-918). CRC Press.

Updates of Numerical Reservoir Model for Sorik Marapi Geothermal Field

Kunhwi Kim[1], Jill Haizlip[1], Nicholas Hinz[1], Jesse Turk[1], Sabodh Garg[1], Zachary Brown[1], Fabiola Pardede[2], Wishnu Triananda[2] and Rivan Tri Yuono[2]

[1] Geologica Geothermal Group, Inc., 75 Caliente St., Reno, NV 89509

[2] PT Sorik Marapi Geothermal Power, Jl. Iskandarsyah Raya No. 1A, Indonesia 12160

Keywords

Sorik Marapi; Numerical Reservoir Model; Conceptual Model; Natural State; History Match

ABSTRACT

The Sorik Marapi Geothermal Field is a volcano-hosted geothermal system, located in North Sumatra, Indonesia. As the field development and operations have expanded over the past several years, the conceptual model has been continuously updated to represent the geologic data from new drilling and well testing results. The numerical reservoir model has also been updated to incorporate the geoscientific understanding from the conceptual modeling work, drilling and well testing results, and field operations. The numerical model was developed within the iTOUGH2 framework for automatic calibration, and a joint inversion of steady-state data (i.e., natural state) and transient production data was performed to adjust model input parameters. The calibrated numerical model demonstrates reasonable matches against the natural state pressures and temperatures and the available monitoring data during wellfield operations. The current numerical model provides a suitable basis for assessing the production capacity of the resource area and will be used to forecast the reservoir response to various development scenarios.

1. Introduction

PT Sorik Marapi Geothermal Power (SMGP), a project of KS Orka Renewables Pte. Ltd. currently has 190 megawatts (MW) installed capacity at Sorik Marapi Geothermal Field (SMGF) adjacent to Sorik Marapi volcano in Northern Sumatra. SMGF was developed in phases: Phase 1 (45 MW) online October 2019, Phase 2 (45 MW) online July 2021, Phase 3 (50 MW) online October 2022, Phase 4 (27 MW) commissioned December 2023, and Phase 5 (23 MW) in planning stage for August 2024. SMGP has confirmed a commercial geothermal resource at ~245 – 320°C by drilling and testing 43 deep exploration and development wells in a 3 km (N-S) × 2 km (E-W) area within the Sumatra Fault System (Figure 1).

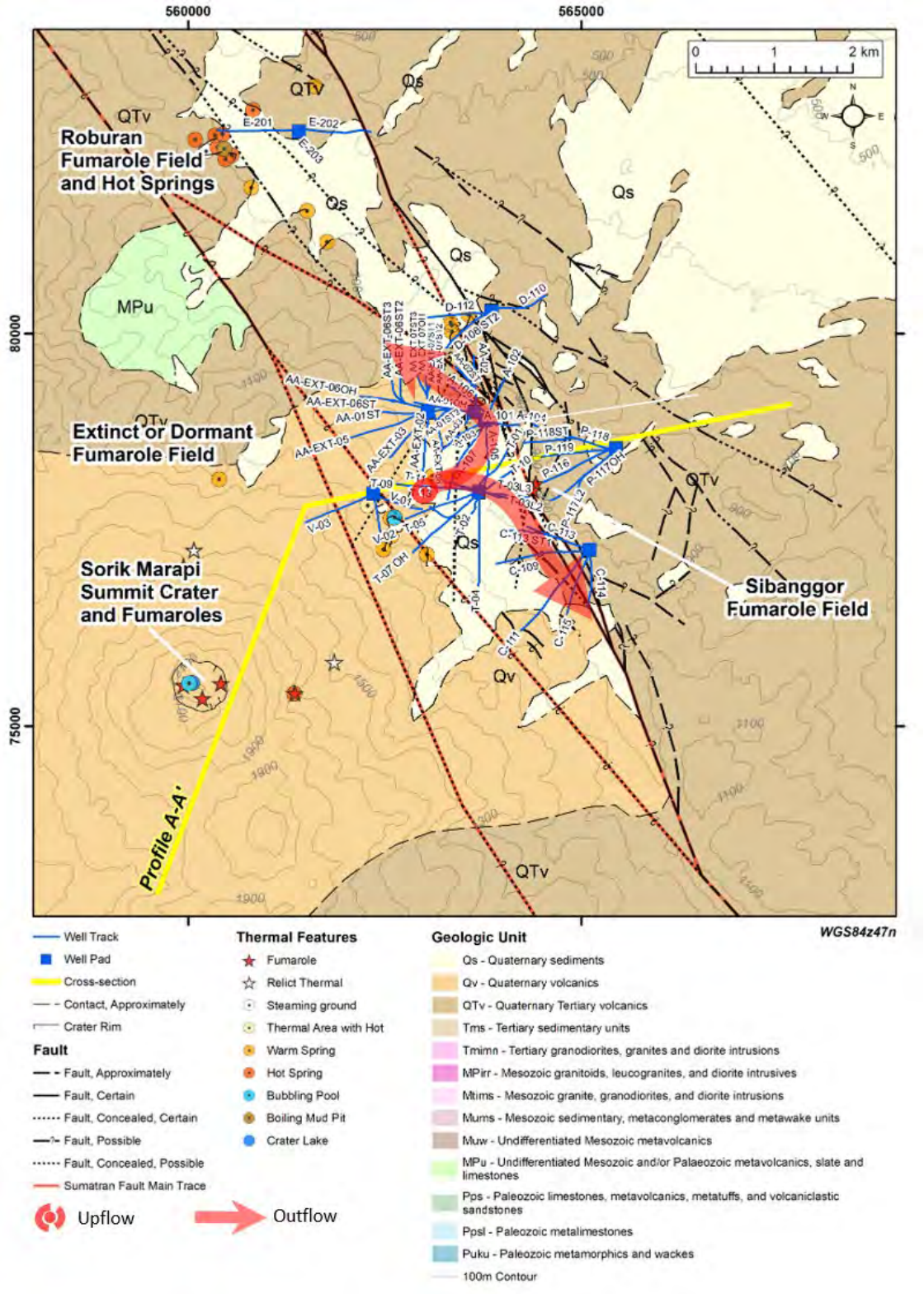

Figure 1: Map of the Sorik Marapi geothermal field. Upflow (red circle) and outflow pathways (red arrows) are shown. The A-A' conceptual model profile line corresponds to the cross-section in Figure 2.

As the field development and operations have expanded over the past years, the conceptual model has been continuously updated to include the geologic data from new drilling and well testing results. The temperature, geologic, geophysical, geochemical, and structural data are integrated into the conceptual model that represents details of upflow, outflow, reservoir rock, and cap. The up-to-date conceptual model shows that the reservoir is elongated along NNW-ESE and is bound on the east by the main strand of the Sumatra Fault System, and a deep ≥320°C upflow is located near the bottom of wells T-05 and T-09, which feeds the shallower productive reservoir to the NE, E and SE (see the arrows in Figure 1). The top of the reservoir (ToR) in the Pad A wells area starts at -50 mASL and deepens to the southwest reaching about -1250 mASL near the TD of T-09 (Figure 2).

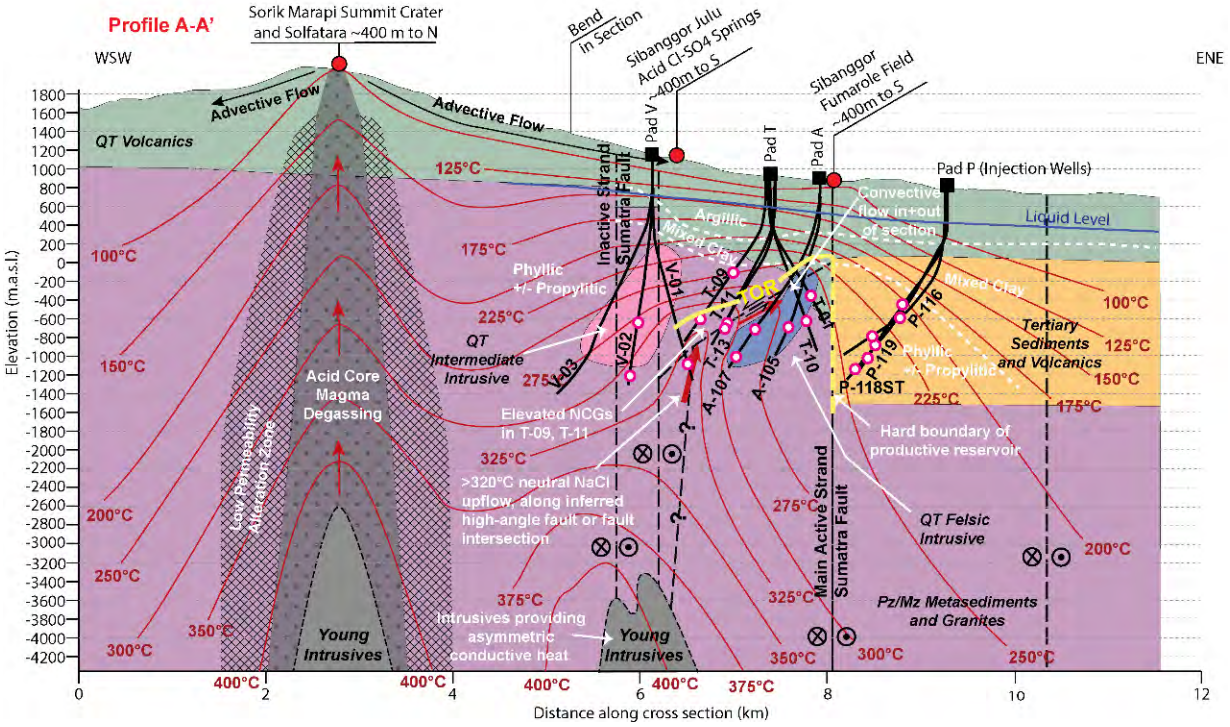

Figure 2: A cross-section of the conceptual model of the Sorik Marapi Geothermal Field along Profile A-A' (ENE-WSW) in Figure 1. The key features of the model include simplified geologic units, temperature isotherms, the top of the reservoir (ToR) shown as a yellow line, major structures (dashed black lines), and hydrothermal alteration (white dashed lines and text). Well courses are solid black lines, and major feedzones are shown as open red circles.

A 3D numerical reservoir model was initially developed using the early-stage conceptual model and calibrated against the pre-production pressure and temperature data (Kim et al., 2021). The updated conceptual model forms the basis for revising the geologic and hydrogeologic setting of the numerical reservoir model, which incorporates lithologic geometry and properties, temperature distribution and fluid flow within the reservoir, and boundary conditions such as upflow and outflow. In addition, natural-state data, field operation (i.e., production and injection history) and reservoir monitoring data are used to constrain the numerical reservoir model.

This paper presents the revised numerical model, model calibration process, and natural-state and history match simulation results compared with the field measurements. The revised and calibrated numerical model provides a suitable basis for assessing the production capacity of the resource area. The calibrated numerical model can be used to forecast the reservoir performance for various development scenarios.

2. Model Description

The computational domain of the numerical model with dimensions of 10 × 11 × 3.5 km is discretized into a three-dimensional structured grid with higher resolution within the well field. The grid origin is at 563,351.73 mE, 70,863.33 mN and -2,500 mASL, and the X-axis is rotated 32.71˚ north of east to be aligned with the orientation of the Great Sumatran Fault zone (Figure 3).

The original numerical model, described in Kim et al. (2021), was constructed based on the iTOUGH2 simulation-optimization framework (Finsterle et al., 2017; Finsterle, 2020), where a single-continuum model set up was employed to perform the natural-state simulation. This paper presents the natural-state and history match simulations, for which the mesh grid has been refined with a dual-continuum (fracture and matrix) model (Pruess and Narasimhan, 1982, 1985) for the elements within the main resource area.

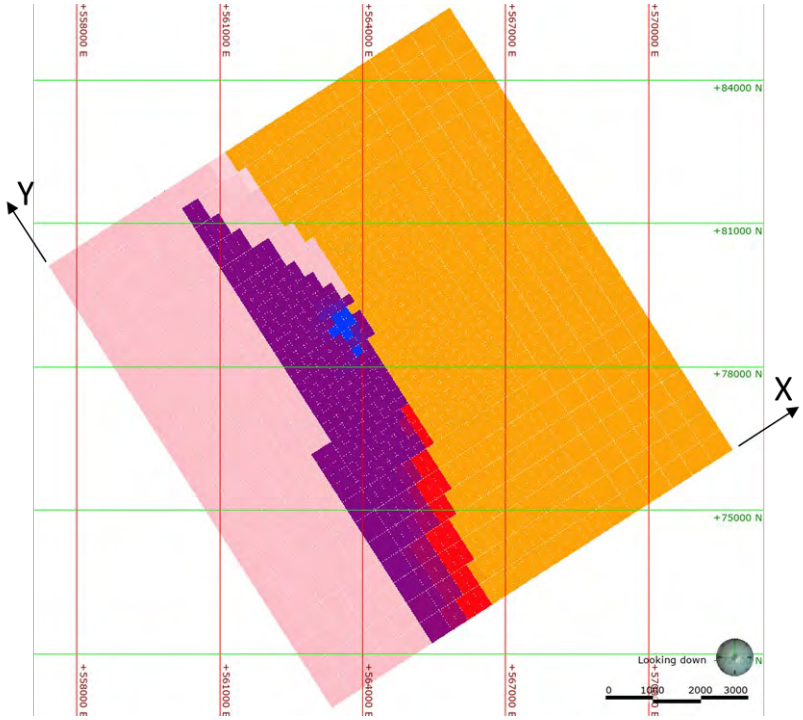

Figure 3: Computational domain and grid orientation.

The updated conceptual model and new drilling and testing data obtained through October 2023 are visualized in the Leapfrog geologic framework, which is adopted as the basis for assigning lithology to the elements of the numerical grid. Further revisions for local element rock types are made to improve the model matches to the observed natural-state and production history data,

which include 1) enhanced local connections to the permeable area; 2) an engineered barrier introduced to weaken the connection between injection and production areas; 3) a uniform lithologic volume subdivided into various rock units; and 4) the upflow chimney extended and inclined towards wells T-09 and T-13 (where the highest static temperature and flowing enthalpy were measured). The revised numerical model has 16 lithologic units. Figure 4 shows map and section views of rock type distributions.

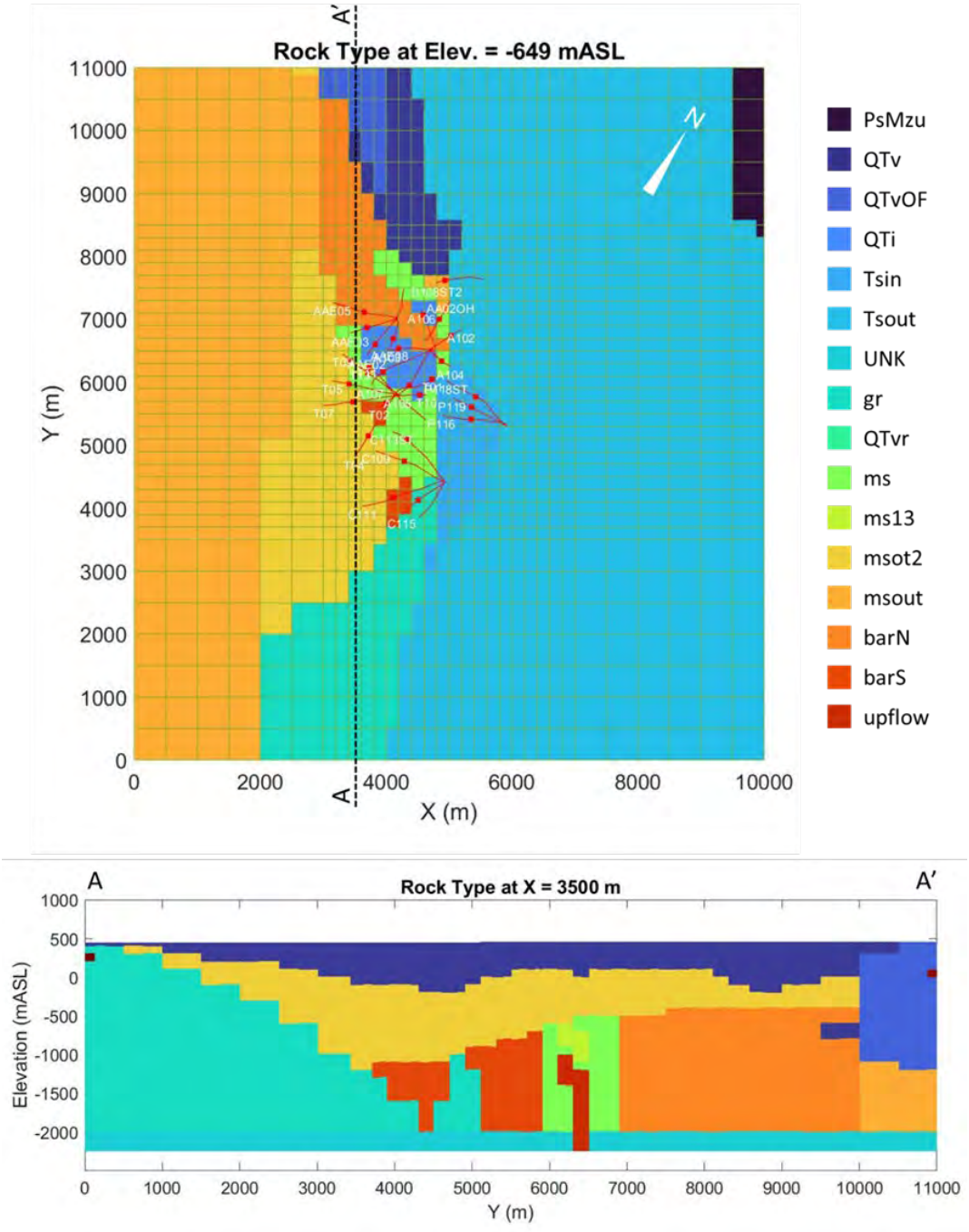

Figure 4: Rock type distributions in the numerical model. Red dots in the map view (upper plot) indicate the intersections of individual well tracks on the plane at the elevation of -649 mASL.

Constant pressure and constant temperature boundary conditions are specified at both the top layer (i.e., water level) at 550 mASL and the bottom layer at -2500 mASL. The boundary pressure and temperature values at these boundaries are determined as part of automatic model calibration. Note that heat flux across these boundaries is conduction-dominated. In addition, hot water flows into a narrow channel at the bottom of the model and connects to the high-permeability upflow chimney west of well T-09. The rate and enthalpy of this mass upflow is determined during model calibration. All side boundaries are impermeable and thermally insulated, except two outflow windows that allow for relatively shallow lateral flow from the center of the reservoir along the major strand of the Sumatra Fault System to the southeast and northwest. The pressures and temperatures at these two outflow windows are adjustable parameters for model calibration.

The revised numerical reservoir model was calibrated via inverse analysis for the natural state and the production history of the well field. A total of 78 parameters, including the rock properties (e.g., thermal conductivities, permeabilities, and porosities) and boundary condition values, are adjustable parameters for the iTOUGH2 automatic inversion. Depending on the importance of a calibration point and the reliability of measured data, the residuals are appropriately weighted in the objective function. The inverse problem solution (i.e., calibrated model results) minimizes the objective function of residuals between measured data and computed values. The following sections present the calibrated model results for the natural-state and history match simulations.

3. Natural-State Model

The numerical reservoir model is run to steady state. The resulting temperature distribution is compared to measured temperature profiles in wells that are considered to have stabilized and to represent natural-state conditions. Moreover, static feedzone pressures in some of the wells are also available for natural-state calibration.

Figure 5 shows the comparison between measured (blue lines) and computed (red lines) static temperature profiles for individual wells, where the measured temperatures are interpolated to the element coordinates for calibration points (indicated by yellow squares). Figure 6 presents the computed pressures compared to the feedzone pressures for the Pad A and Pad C wells from the pre-production period. The computed temperatures and pressures closely fit the measured data; therefore, the model is appraised as a good representation of the natural-state reservoir conditions.

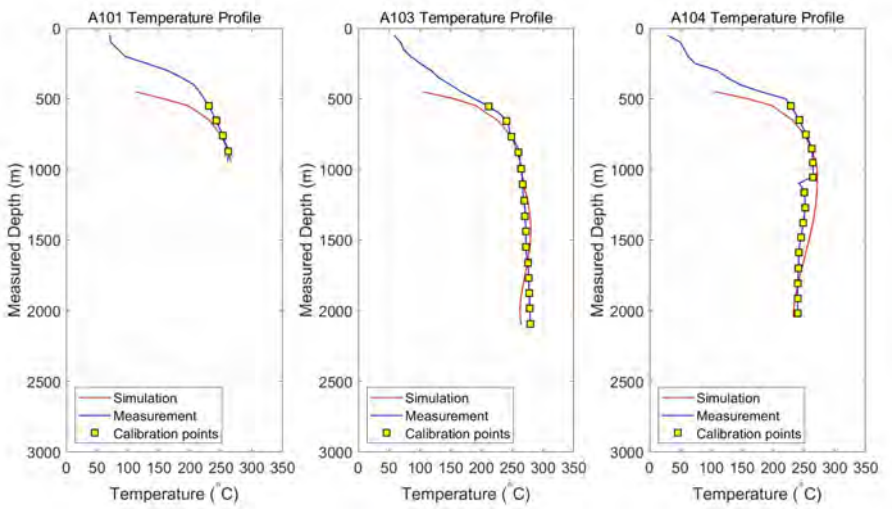

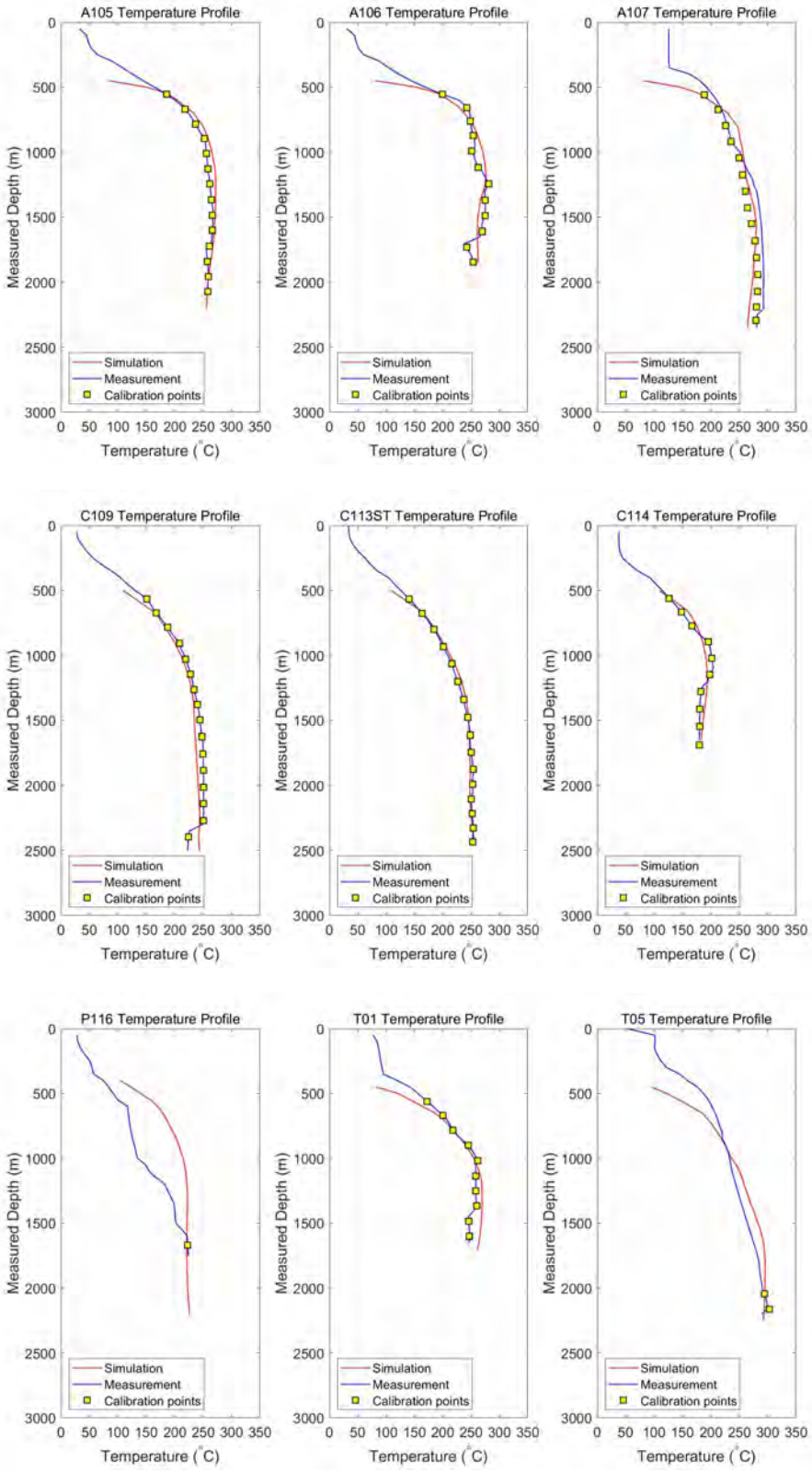
A105 Temperature Profile
A106 Temperature Profile
A107 Temperature Profile
C109 Temperature Profile
C113ST Temperature Profile
C114 Temperature Profile
P116 Temperature Profile
T01 Temperature Profile
T05 Temperature Profile
Measured Depth (m)
Temperature (°C)
Simulation
Measurement
Calibration points

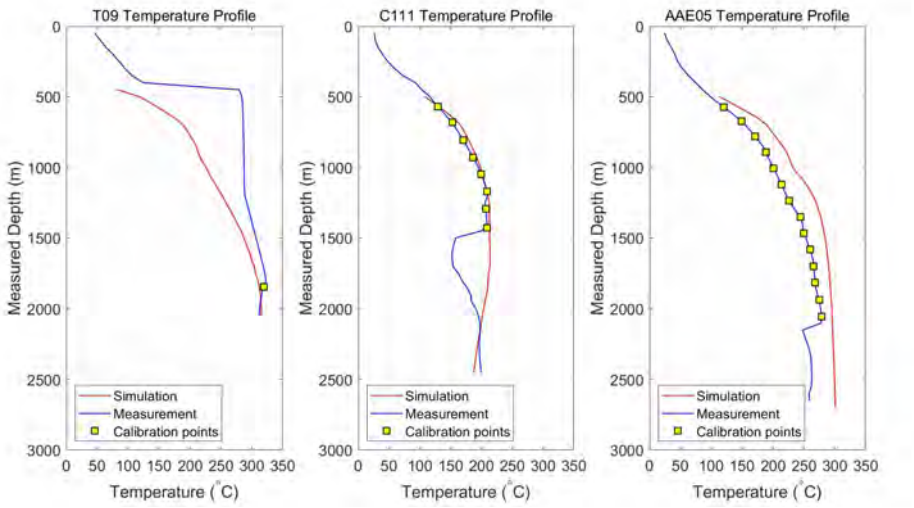

Figure 5: Comparisons between measured and computed temperature profiles for selected wells in natural state conditions.

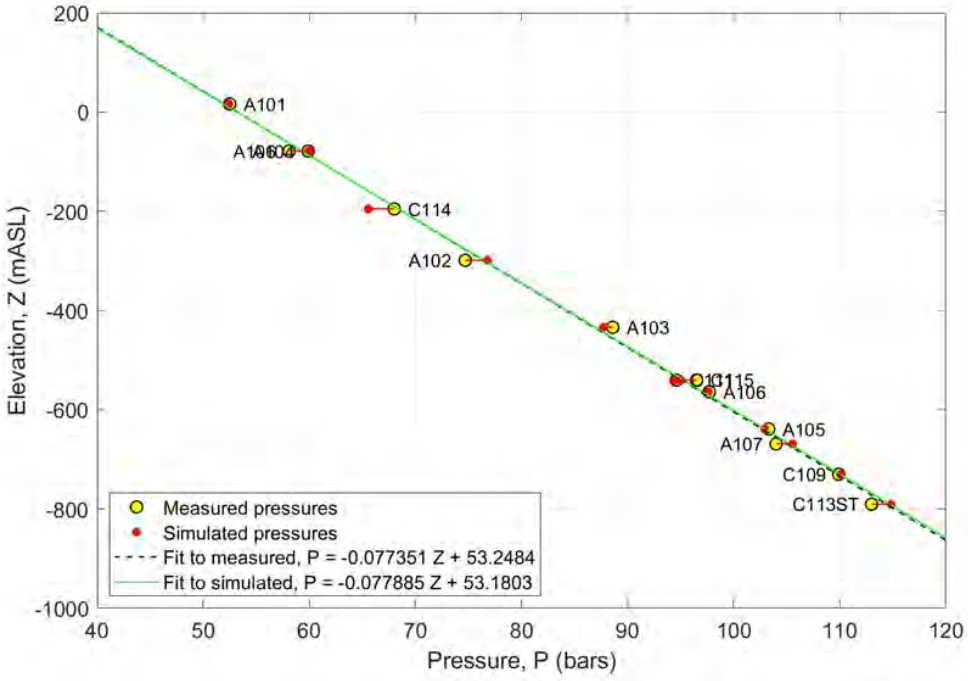

Figure 6: Comparison between measured and computed static feedzone pressures for Pad A and C wells and their correlation with elevation.

4. History Match Simulation

Transient simulations with the numerical model were performed, from which the simulated dynamic behavior of the reservoir was fit to the monitoring data during the field operation (from August 2019 to November 2023). The production and injection rates for individual wells are specified as sink and source terms in the model.

Figure 7 shows the comparison between the computed production enthalpies and the estimated enthalpies based on the tracer flow test (TFT) results for individual production wells. Heat loss from the fluid in the well to the formation is accounted for by adding 25 kJ/kg to the TFT-based enthalpy measured at the wellhead, which is compared to the computed enthalpy at the feedzone grid block. The simulation results show good matches to the field measurements in terms of the overall level of enthalpies in various production wells, and the timing of steam development in well A-101.

Figure 8 compares the computed pressure changes with the observed pressure changes (i.e., shut-in pressures over the production period – natural state pressures) for Pad A, AAE, C, and T wells. While the computed pressure changes are slightly overestimated, the overall trend of pressure changes in the simulation accords with the measurements.

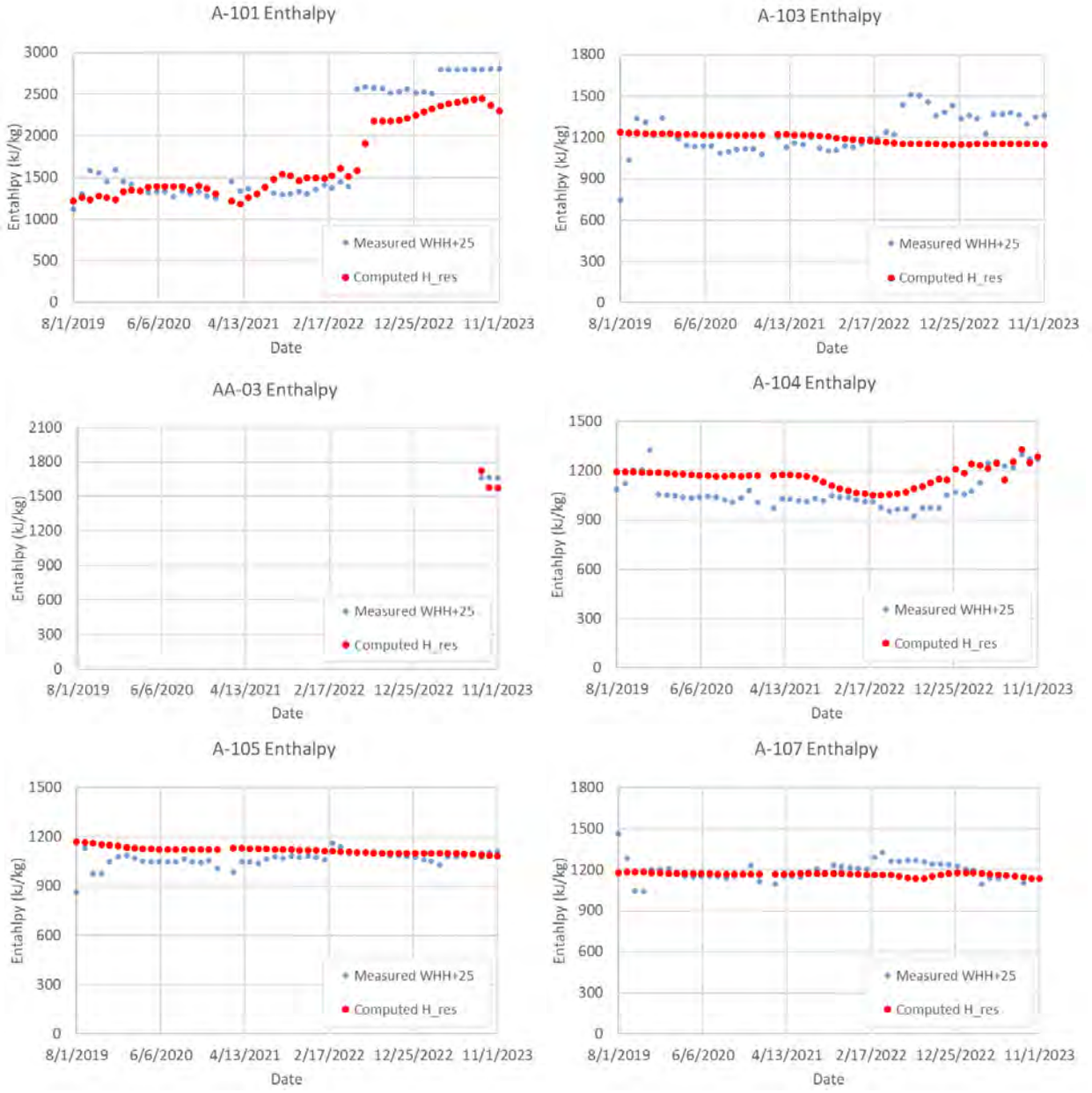

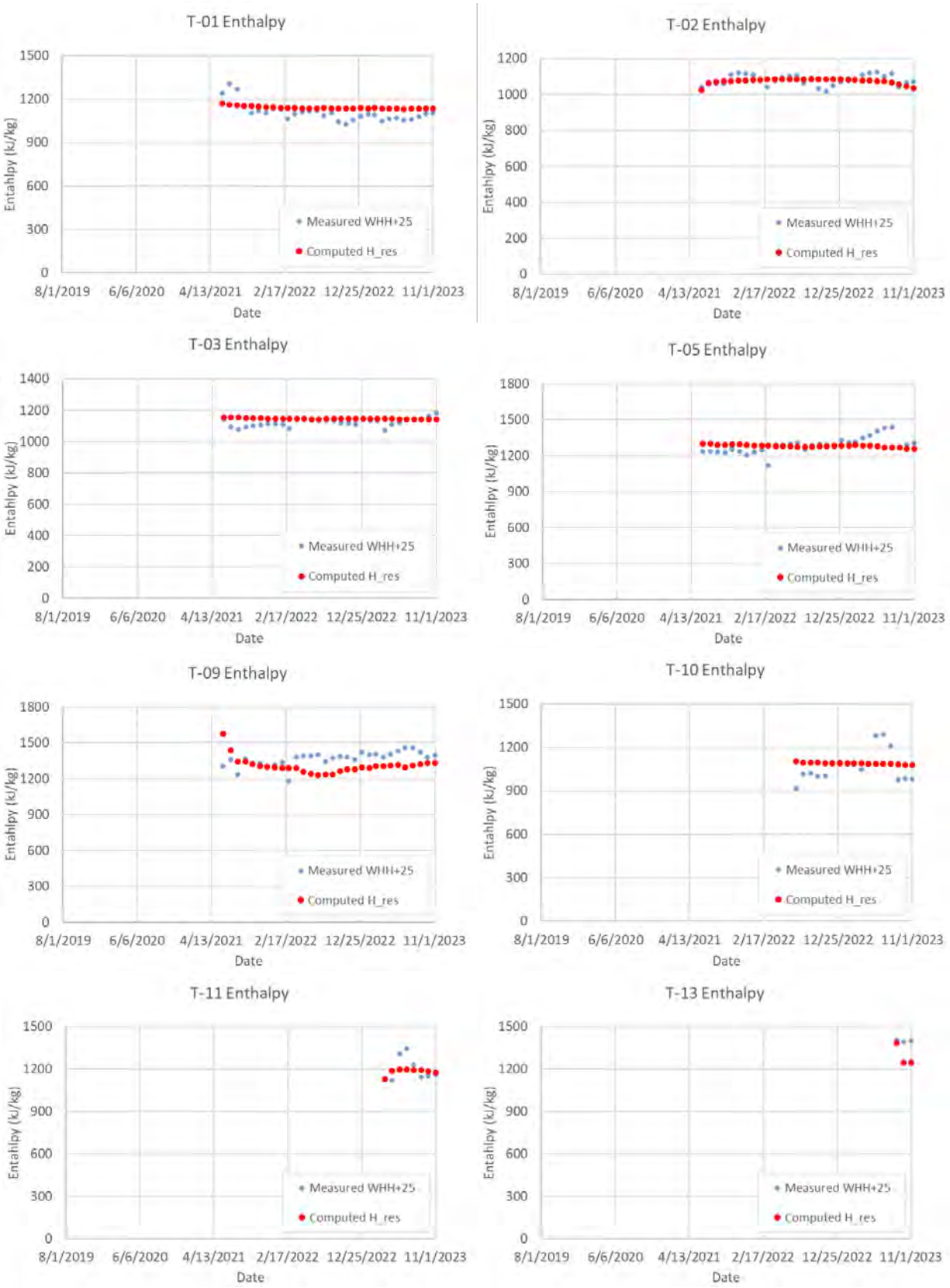
T-01 Enthalpy
T-02 Enthalpy
T-03 Enthalpy
T-05 Enthalpy
T-09 Enthalpy
T-10 Enthalpy
T-11 Enthalpy
T-13 Enthalpy
Entahlpy (kJ/kg)
Date
8/1/2019
6/6/2020
4/13/2021
2/17/2022
12/25/2022
11/1/2023
Measured WHH+25
Computed H_res

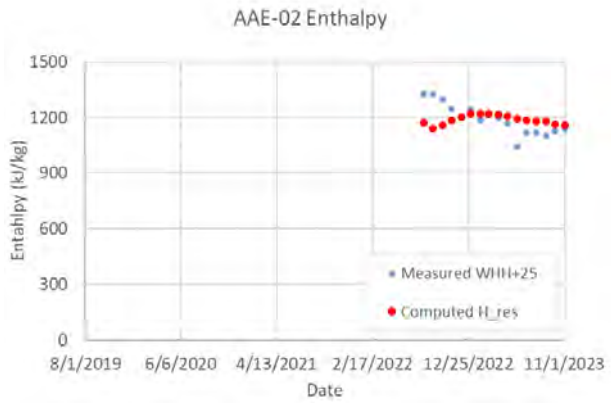

Figure 7: Comparison between measured and computed enthalpy history for individual production wells from August 2019 to November 2023. Note that 25 kJ/kg is added to the measured enthalpy at the wellhead to account for heat loss from the fluid in the well to the formation.

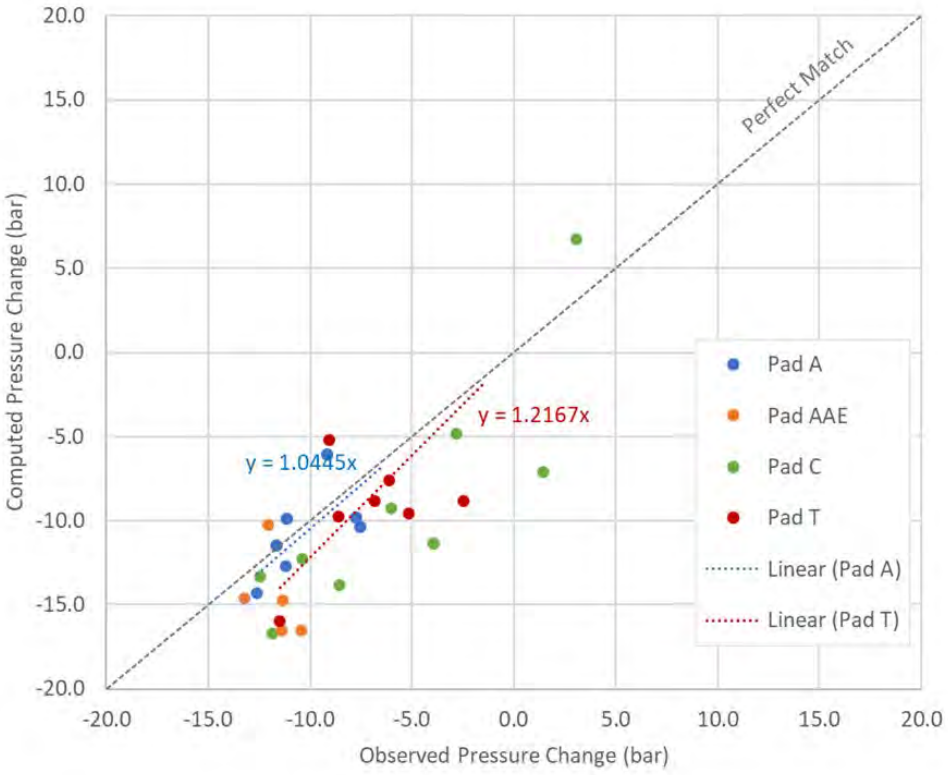

Figure 8: Comparison between observed and computed feedzone pressure changes with respect to natural-state conditions. Points on the diagonal (i.e., y = x) represent a perfect match.

5. Conclusions

The numerical reservoir model of the Sorik Marapi Geothermal Field has been updated to incorporate geologic features from the updated conceptual model and information from new drilling and testing data. In addition, local element rock types are revised to improve the model matches to the observed natural-state and production history data. The updated model with a dual-

continuum (fracture and matrix) set up for the main resource area has been calibrated against the natural-state temperature and pressure and the production enthalpy history and reservoir pressure changes measured over the production period (from August 2019 to November 2023). The simulation results indicate that the calibrated model provides a reasonable representation of the pre-production field condition (i.e., natural state) and the transient reservoir response to the well field operation. The calibrated numerical model will be used to forecast the reservoir performance for various development scenarios and assess the resource and production capacity of the field.

REFERENCES

Finsterle, S., Commer, M., Edmiston, J., Jung, Y., Kowalsky, M.B., Pau, G.S.H., Wainwright, H., and Zhang, Y. “iTOUGH2: A multiphysics simulation-optimization framework for analyzing subsurface systems.” *Computers and Geosciences*, 108, (2017), 8–20.

Finsterle, S., *Enhancements to the TOUGH2 Simulator Implemented in iTOUGH2*, Report FGC-18-02/LBNL-7016E, Finsterle GeoConsulting, Kensington, CA, (2020).

Kim, K., Finstrele, S., Garg, S., Haizlip, J., Hinz, N., Fercho, S., and Tang, Y. “Natural-State Reservoir Model of Sorik Marapi Geothermal Field.” *Proceedings World Geothermal Congress 2020+1*, Reykjavik, Iceland (2021).

Pruess, K., and Narasimhan, T.N. “On Fluid Reserves and the Production of Superheated Steam from Fractured, Vapor-Dominated Geothermal Reservoirs.” *J. Geophys. Res.*, 87(B11), (1982), 9329–9339.

Pruess, K., and Narasimhan, T.N. “A Practical Method for Modeling Fluid and Heat Flow in Fractured Porous Media.” *Soc. Pet. Eng. J.*, 25(1), (1985), 14–26.

Hot Springs and Geysers: Exploring Historical and Modern Impacts of Geothermal Energy Production on Surface Thermal Features and Standardizing Management Practices

Rebecca Kreuzer[1], Mark Rockhold[1], Corey Duberstein[1], Bryan He[1], Stephanie Diraddo[1,] Timothy Steeves[2], and Stuart Simmons[3]

[1] Pacific Northwest National Laboratory

[2] Department of Energy, Geothermal Technologies Office

[3]University of Utah

Keywords

Geothermal Power Permitting Processes, Surface Thermal Feature Management, Hot Springs and Geysers, Standardized Regulatory Protocol, Reducing Barriers to Permitting, Stakeholder Engagement, Social License to Operate, Co-Developing Best Practices

ABSTRACT

Surface thermal features, most notably hot springs and geysers are increasingly being recognized in the U.S. for their importance to ecosystems, indigenous cultures, agriculture, recreation, and tourism. Combined with an unprecedented push to develop renewable energy projects across the U.S., concerns about impacts to these features from geothermal energy projects has resulted in development of tensions, an increase in regulatory scrutiny, and greater stakeholder opposition to geothermal energy development in some locations. Opposition and increased permitting and monitoring requirements have largely resulted from historical examples of negative impacts, most of which were associated with flash steam plants developed prior to 2000 that caused significant fluid/mass and losses from the reservoirs. However, since 2000, nearly all geothermal capacity additions have been binary plants which re-inject 100% of produced geothermal fluids back into the reservoir. With this trend expected to continue, impacts to surface thermal features will be significantly reduced, and possibly eliminated when field development exclusively uses technologies that minimize water losses (e.g., binary cycle power plants), and reinjection strategies that incorporate preservation of surficial flows as a management factor.

Current regulatory requirements for assessing and managing risks to surface thermal features during permitting, exploration, development, and operations are somewhat inconsistent and

unpredictable across different geothermal fields. In some cases, potentially excessive or unnecessary monitoring requirements that may be limited in their ability to provide meaningful insights have led to uncertainty and increases in exploration risk for geothermal energy developers including project delays, cancellations, or hesitation to commit. Varying regulatory requirements can also influence public perception and foster confusion, distrust, and opposition to geothermal projects. This comes at a time when there is an increasing urgency for reliable sources of clean energy, and geothermal can provide a net-zero, renewable solution. Continued integration of geothermal energy into the national energy roadmap can be facilitated through consistent and predictable permitting, providing regulators the framework they need, giving developers a clear path forward, and creating the transparency that the public deserves to feel sure that these resources are being protected.

This project, currently in its beginning phases, seeks to address this important issue by providing a technical basis from which to build a preliminary protocol for assessing and managing potential impacts from new or existing geothermal energy projects to surface thermal features and their associated ecosystems. Development of this preliminary protocol will be informed by (1) literature reviews of well-documented case studies in the western US and internationally to understand the range of conditions that exemplify geothermal-surface thermal systems; (2) development of illustrative conceptual numerical models to quantify, understand, and predict the first-order controls (e.g., pressure and permeability) on surface flows; and (3) additional independent case studies using industry-provided and publicly available data to understand and demonstrate the risk profiles and cause-and-effect relationships between geothermal power production and impacts to surface thermal systems.

Learning from the successes of the process used to develop the Induced Seismicity Management Protocol (ISMP), we ultimately aim to use these initial efforts as a springboard for establishing a surface thermal feature management working group that will collaboratively refine the protocol as well as co-develop recommended best practices for implementation. We envision that the working group will be composed of representatives from diverse stakeholder groups (e.g., regulatory entities, industry, government agencies, Tribes, academia, national laboratories), and will include regular engagement with community organizations and environmental groups to understand and meaningfully incorporate their input into the final protocol and best practices for implementation. This will help ensure broad acceptance and implementation of the protocol, which will facilitate a more consistent, and efficient regulatory process, and ultimately help to ensure that geothermal energy continues to provide a reliable source of clean energy and a pathway to achieving greater energy equity in the U.S.

1. Introduction

Over the last several decades there has been an increasing awareness of the significant importance of hot springs, geysers, and other surface thermal features (Figure 1) to ecosystems, indigenous cultures, agriculture, recreation, and tourism. Combined with an unprecedented push to develop renewable energy projects across the United States (U.S.) this has resulted in development of tensions, an increase in regulatory scrutiny, and greater stakeholder opposition to geothermal energy development in some locations (e.g., Richter, 2019; U.S. BLM, 2022; Newberger, 2023; Coates, 2023; Donnelly, 2023, U.S. DOE, 2024). Opposition to development and increased permitting and monitoring requirements have largely resulted from historical examples of negative

impacts, most of which were associated with flash steam plants developed prior to 2000 that caused significant fluid / mass losses from the reservoir and subsequent pressure and/or groundwater elevation decreases (e.g., White, 1998; Sorey, 2000; Barrick, 2005; White and Hunt, 2005; Allis and Larsen, 2012; Chen et al., 2020; Martinez, 2024). However, since 2000, nearly all new geothermal capacity additions in the U.S. have been binary plants which re-inject 100% of produced geothermal fluids back into the reservoir (U.S. EIA, 2020; Robins et al., 2021). With this trend expected to continue (e.g., Robins et al., 2021), impacts to surface thermal features will be significantly reduced, and may be eliminated when field development exclusively uses technologies that minimize water losses (e.g., binary cycle power plants), and reinjection strategies that incorporate preservation of surficial flows as a management factor (Kagel et al., 2007; Heasler et al., 2009; Kaya et al., 2011; Ratouis et al., 2017; Kamila et al., 2020).

Figure 1. Collection of images depicting examples of surface thermal features. ***Source: Kagel et al., 2007***

Currently, there is a lack of consistency or predictability in permitting and monitoring requirements across different geothermal fields (e.g., U.S. BLM, 2009; U.S. OIG, 2013; Young et al., 2014, 2019; U.S. DOI, 2022; Levine et al, 2013, 2022; U.S. DOE, 2024). Section 3102 of the Energy Act of 2020 requires that the U.S. Secretary of Interior establish a national Renewable Energy Coordination Office (RECO) and State, district, or field offices, as appropriate, to improve federal permit coordination for geothermal, solar and wind projects occurring on federal lands. Section 3102 also allows for the Secretary of Interior to temporarily assign qualified staff to RECOs to expedite the permitting of eligible projects (Levine and Smith, 2023). In response, in 2022 the U.S. Secretary of Interior entered into a memorandum of understanding (MOU) with Secretaries of several other federal agencies, including the U.S. Department of Energy (DOE) to establish RECOs that will:

> *"…implement improved coordination among agencies, help avoid and resolve potential conflicts and bottlenecks, identify best practices, accelerate information sharing, and promote efficient and timely reviews to support smart agency decision-making*." (U.S. DOI, 2022).

For geothermal projects, one of the contributing factors for the inconsistencies in permitting and monitoring requirements is the lack of shared understanding between industry, regulators, and other potentially impacted stakeholders of what general and site-specific conditions drive risk to surface thermal features during exploration and operation, and what mitigative approaches (including characterization, monitoring, and reinjection strategies) are most appropriate for identifying and managing those risks (e.g., Young et al., 2019). This is leading to potentially unsustainable increases in economic risk for geothermal developers (e.g., Neupane and Adhikari, 2022) which derive largely from project delays or potentially excessive or unnecessary site characterization requirements during permitting (i.e., before a developer can drill a single test well to assess economic viability), and during monitoring of operating systems. Importantly, in some cases the additional site characterization or monitoring data being required by regulators may be limited in their ability to provide meaningful insights into the system dynamics or cause-and-effect relationships that exist at a given site. Regulatory inconsistencies may also lead to decreased public trust and increased public opposition which leaves the geothermal industry more vulnerable to legal challenges that can result in project cancellations (e.g., Richter, 2019; U.S. BLM, 2022; Newburger, 2023; Coates, 2023; Donnelly, 2023). This comes at a time when there is a heightened urgency to expand reliable clean energy options that can combat the climate crisis and provide pathways to greater energy equity and environmental justice in the U.S. (U.S. DOE, 2023). Ostensibly, geothermal should be among the best options in the clean energy space, due to its low land use and mineral requirements, as well as the value it adds to the grid in the form of clean, baseload power (e.g., Bromley et al., 2010; U.S. DOE, 2019; Soltani et al, 2021; Vargas et al., 2022).

2. Overview of Regulatory Landscape

Development of geothermal energy must undergo regulatory review similar to other energy resources. If a proposed project may have impacts to human health or the environment and is deemed a federal action (i.e., occurs on federal lands, or federal funds are contributed to the project), then at the highest-level, developers must comply with the National Environmental Policy Act (NEPA). NEPA requires an evaluation of potential impacts from a proposed action and offers a tiered approach that includes a review of the proposed project by an assigned staff member who may either issue a categorical exemption (CX) to the NEPA process or indicate the need to perform an environmental assessment (EA) of the proposed action. The result of the EA may either be issuance of a finding of no significant impact (FONSI), or a finding that the proposed project will significantly affect the quality of human health or the environment. In the latter case, this could then trigger the need for a full environmental impact statement (EIS). For an EA or EIS, compliance with NEPA includes a formal process of public disclosure of potential effects. Importantly, most geothermal energy resources in the U.S. (approximately 90%) are on federally managed land, making NEPA considerations a major factor in present and future geothermal development projects (U.S. BLM, 2005; Young et al, 2014).

Implementation of the NEPA process also includes considerations of various other federal laws, and geothermal development efforts may have to account for many general federal statutes including the, Clean Air Act (42 U.S.C. §7401 et seq.) Clean Water Act (33 U.S.C. §1251 et seq.), Endangered Species Act (16 U.S.C. 1531-1544), National Historic Preservation Act (16 U.S.C. §§470a-470w-6 et seq.), and others as well as resource-specific laws including the

Geothermal Steam Act as amended (30 U.S.C. §23). State and local governments also regulate development and monitoring within their jurisdictional boundaries.

In 2009, the U.S. Department of Interior's (DOI) Bureau of Land Management BLM and U.S. Forest Service issued their final, joint Programmatic EIS (PEIS) for leasing, permitting, exploration and utilization of proposed geothermal projects in the western U.S (U.S. BLM, 2009). The value of a PEIS is to provide early information that can be considered during planning which can be used to inform, and responsibly expedite implementation of site-specific NEPA analyses and permitting. Multiple NEPA analyses are typically required for the development of utility-scale geothermal projects (Young et al., 2014; Neupane and Adhikari, 2022; U.S. BLM, 2023). Figure 2 (modified from Young et al., 2014) provides an example timeline of the multiple NEPA analyses that are or may be required during the stages of geothermal permitting and licensing. However, U.S. federal land and resource management agencies are de-centralized in structure, which has largely left implementation of these NEPA requirements to regional and local offices. Variance, or in some cases, contradiction in agency mission within site offices also contributes to regulation and environmental review process variability, adding another level of complexity to the regulatory landscape that is difficult to anticipate (Levine et al., 2013, 2022).

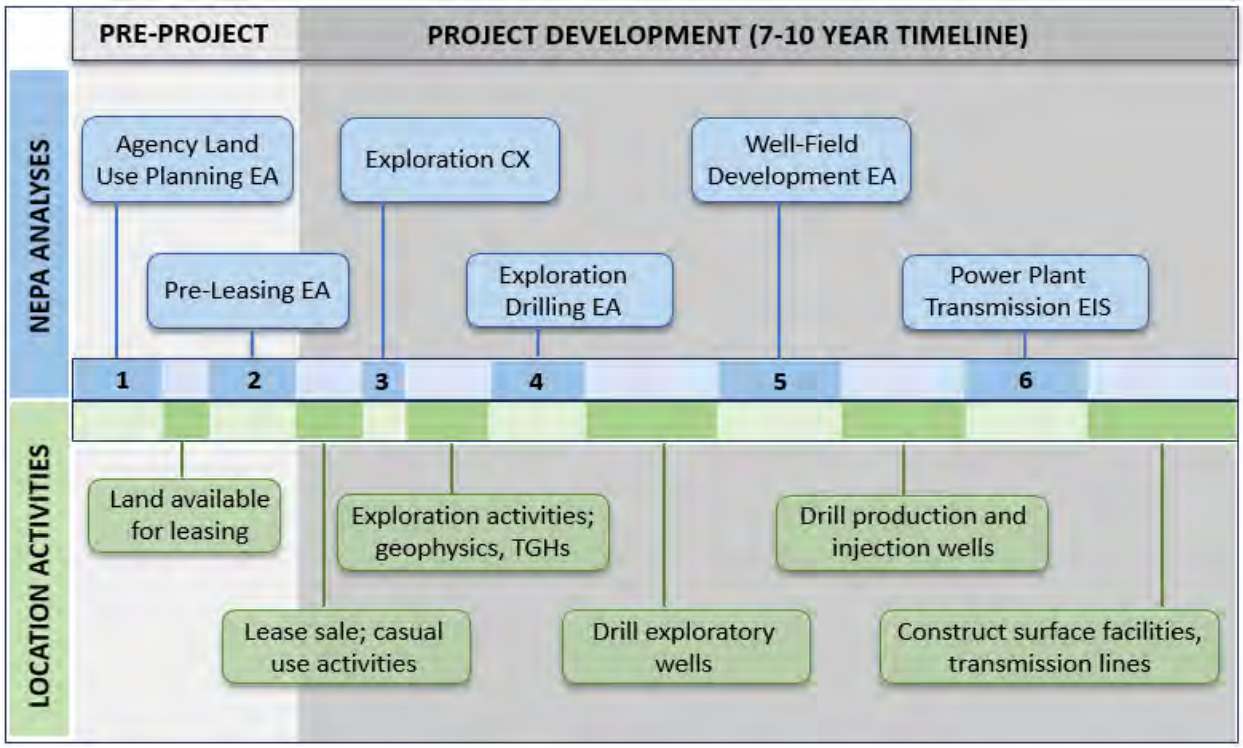

Figure 2. Example of a timeline depicting permitting requirements for geothermal resource project located on federal lands. The example demonstrates that a NEPA analysis (blue timeline) could be triggered as many as six times during permitting benchmarks (green timeline). EA: Environmental Assessment; CX: Categorical Exemption; EIS: Environmental Impact Statement; TGHs: Thermal Gradient Holes *Modified from Young et al., 2014.*

3. Project Goals and Objectives

The *near-term objective* of this project is to establish a preliminary protocol for assessing and monitoring potential impacts to surface thermal features during geothermal permitting and operation. Establishment of this preliminary protocol will be rooted in (1) a review of well-documented case studies in the western U.S. and internationally that are able to illustrate the range of conditions that exist in geothermal-surface thermal systems; (2) development of illustrative conceptual numerical models to quantify, demonstrate, and predict the first-order controls (e.g., pressure and permeability) on surface flows; and (3) conduct additional independent and scientifically rigorous evaluations of geothermal-surface thermal system case studies from the western U.S. that includes analysis of publicly available information as well as data provided by industry through data-sharing agreements.

The *long-term objectives* of this project are three-fold:

1) Establish a working group comprised of individuals representing diverse interests within the geothermal community writ large (e.g., regulatory bodies, industry, academia, government, special interest groups, Tribes, and communities) to collaboratively review stakeholder concerns, technical challenges, and ultimately finalize the preliminary surface thermal feature management protocol and co-create best practices for implementation.
2) Facilitate wide-spread acceptance and adoption of the protocol and best practices throughout the geothermal community.
3) Improve or renew public trust and confidence in geothermal energy projects and establish a strong social license to operate.

Combined, meeting these near-term and long-term objectives will contribute to the realization of *the fundamental goal* of this effort, which is to standardize regulatory requirements associated with understanding and managing impacts to surface thermal features during geothermal energy operations, and to ensure geothermal energy can continue to provide a reliable source of clean energy that the Earth needs, as well as help advance U.S. energy equity and environmental justice goals that underserved communities deserve.

4. Establishing the Technical Foundation for Preliminary Protocol

As illustrated in Figure 3, to meet our near-term objective of establishing a preliminary protocol for managing potential impacts to surface thermal features during geothermal permitting activities and operations, we will perform the following tasks: (1) complete a literature review with key stakeholders to understand the range of domestic and international geothermal circumstances and experiences, both pre- and post-2000; (2) develop a series of illustrative conceptual numerical models to demonstrate the controlling role of pressure and permeability on hot spring and geyser flow; and (3) conduct case study analyses on several additional geothermal systems in the western U.S. using publicly available and industry-provided data. The following sections provide additional information about each of the three near-term objectives.

4.1 Literature review and knowledge capture

The primary overarching objective of this task is to develop a baseline understanding of the range of conditions that might exist in geothermal-surface thermal feature systems, and to assess the known or likely first-order controls on observed or potential impacts to these features from

geothermal development. A literature review will be conducted to collate existing knowledge related to these systems using several well-documented geothermal systems and fields in the U.S. and internationally that are able to clearly demonstrate the relationships. This includes locating and reviewing scientific studies, environmental impact assessments (EISs), industry reports, and regulatory guidelines from around the world. We are also assessing:

- Cases when changes in flow, pressure, temperature, or chemical regime of surface thermal features have resulted in negative impacts to associated ecosystems.
- Impacts to surface thermal features with respect to geothermal plant operational designs.
- The evolution of the geothermal permitting, exploration, and management regulatory requirements, and the potential site-specific drivers behind those requirements.
- Existing mitigation strategies employed to minimize impacts on surface thermal features and associated ecosystems. This may involve wellbore design considerations, pressure monitoring protocols, limitations on water withdrawal, and reinjection strategies.
- Satellite imagery to visually assess the stability of surface thermal features over time, particularly as it relates to industrial or agricultural development.

Importantly, this effort may include interviews with geothermal energy experts, practitioners, regulatory entities, and community organizations, as appropriate, to better understand the diverse perspectives, drivers, and experiences related to assessing and managing potential impacts to surface thermal features. While some of these interviews may only point to anectdotal information or evidence that would not be appropriate to include in any quantitative assessments, this information could provide important qualitative insights that may inform improvements to our quantitative approaches.

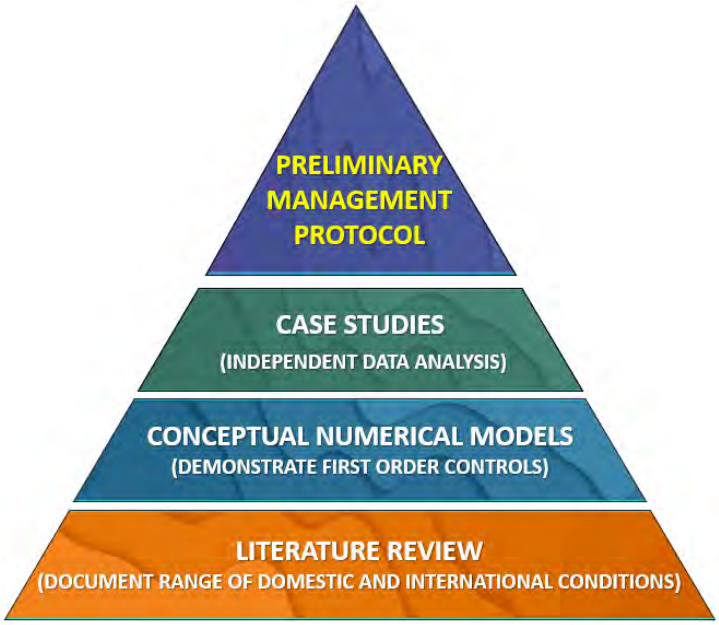

Figure 3. Illustration of the near-term activities that will form the basis for development of a preliminary surface thermal feature management protocol. Future activities include establishment of a surface thermal feature management working group comprised of diverse stakeholders what will co-refine and finalize the preliminary protocol as well as co-create best practices for protocol implementation during permitting and/or monitoring of new or existing geothermal power plants.

4.2 Development of illustrative conceptual numerical models

A series of simple illustrative conceptual numerical models are currently being developed using STOMP-GT (Subsurface Transport Over Multiple Phases-Geothermal) to clearly illustrate first-order cause-and-effect relationships between geothermal field operations and surface flows given a set of basic assumptions about subsurface features. STOMP is a suite of numerical simulators for solving multidimensional, nonlinear problems, including those involving nonisothermal conditions and dual permeability (i.e., fracture-controlled and porous media) using coupled flow and transport processes in variably saturated geologic media (White and Oostrom, 2006; STOMP Online User Guide). The STOMP simulations and models will include parametric evaluations that assume a realistic range of vertical and horizontal permeabilities, with 70% to 100% fluid reinjection, as well as a baseline scenario of 0% reinjection, over a 20- to 50-year period. Depth level of interrogation will initially be constrained to a production-injection depth of >500 to 2000 meters. Examples of models that may be constructed include the following:

- Scenario 0. Isotropic permeability with no fluid reinjection (baseline scenario).
- Scenario 1. Isotropic permeability, 70-100% fluid reinjection.
- Scenario 2. Anisotropic permeability, partial to complete vertical barrier to fluid flow (i.e., a fault), 70-100% fluid reinjection.
- Scenario 3. Anisotropic permeability, partial to complete horizontal barrier to fluid flow (i.e., a fault or low permeability stratigraphic feature), with 70-100% reinjection.

Boundary conditions for these simple scenarios will be established using real-world conditions found in the western U.S. and will be combined with additional assumptions related to permeability, pressures, hydraulic gradients, and heat flow regimes to provide first-order quantification of the effects of pressure drop propagation and on piezometric/water table levels that control hot spring or geyser discharge in a given production/injection regime (e.g., White and Hunt, 2005; Ratouis et al., 2017). We may also conduct sensitivity and uncertainty analyses on each of these scenarios to identify thresholds beyond which geothermal production activities could have significant negative impacts to surface thermal features. These thresholds can then be used to help establish clear guidelines for surface thermal feature management protocol.

4.3 Case studies enabled through publicly accessible and industry-provided data

The project team will evaluate several case studies from the western U.S. using site-specific data that is available in the public domain and that is provided by industry through data-sharing agreements. The intended primary use of these data is to evaluate the time-histories of pressure, temperature, flow rates, and aqueous geochemistry of production/injection fluids and associated surface thermal features, and to assess whether any observed changes in surface thermal feature conditions may be correlated to geothermal energy production. We will also consider the potential influence that natural phenomenon (e.g., seismic activity) or other nearby agricultural or industrial activities may also have on these features. The illustrative conceptual numerical model parameters (refer to Section 3.2) will be updated to be representative of the site-specific conditions at each case study location to improve the correspondence between the simulation results and field observations. This will allow for a greater understanding of the controls on these specific systems as well as identify what information is required to accurately predict observed changes in the geothermal-hydrothermal system. The team has identified four initial case studies and has begun receiving data from industry. To date, industry data received includes:

- Production and injection well coordinates.
- Wireline logs (including image logs, and pressure / temperature flow meter results)
- Raw brine and injectate aqueous chemistry (including pH, conductivity, temperature, pressures, major and minor ion concentrations, isotopic composition of water, dissolved gas concentrations and other gas indicators).
- Underground Injection Control (UIC) O&M manuals.

Additional data that we anticipate receiving from industry or are locating from publicly available sources include:

- Production and injection well depths.
- Permeability of key stratigraphic units.
- Time-series groundwater, surface water, and surface thermal feature data (preferably both before and after geothermal operations) including:
    - Hydrologic parameters (e.g., water levels, photographs, hydraulic gradients, flow rates).
    - Field parameters (e.g., temperature, pH, conductivity).
    - Aqueous chemical composition (e.g., total and dissolved major ion composition, trace metals concentrations, and elemental / molecular and isotopic composition of water and dissolved gases).
    - Visual documentation (photographs or satellite imagery) of changes to surface thermal features and surrounding land.
- Information related to ecosystems that are present and any sensitive flora or fauna that may be dependent on the geothermal/hydrothermal system to thrive.
- Plant permitting, exploration, development, and operational histories.
- Regulatory histories for each plant over time.

Access to these high-quality data from multiple sites expands and diversifies the types of systems we can consider. This provides a more complete understanding of the commonalities and differences in cause-and effect relationships, what conditions pose the greatest risk to surface thermal features, and what the most appropriate approaches are for assessing and managing those risks. This significantly strengthens the quality of the study, enables greater generalizability of the results, and creates a strong, evidence-based foundation for the establishment of preliminary protocol for protection of surface thermal features.

Importantly, a key element of our case studies includes detailed reviews of the regulatory requirements for each site over time, specifically as it relates to assessing or monitoring impacts to surface thermal features. This review will provide an assessment of what is driving the additional requirements, and the degree to which the data requested are able to provide meaningful insights into the risk profile or cause-and-effect relationships. This assessment will build on insights from the literature review, results from the illustrative conceptual numerical models and any findings from the time-history evaluations of geothermal production and flow regimes in the surface thermal features.

4.4 Development of preliminary surface thermal feature assessment and management protocol

The insights gained from the tasks described in sections 3.1, 3.2 and 3.3 will ultimately be integrated to develop a preliminary protocol for assessing and monitoring potential impacts to surface thermal features from geothermal power plant permitting, development, and operation. We envision that this protocol can ultimately be used by geothermal operators, regulators, and other stakeholders to responsibly evaluate and monitor the potential impacts of geothermal development on surface thermal features, without imposing unnecessary regulatory requirements on geothermal developers that may hinder the development of this clean energy resource. We expect that this preliminary protocol will include a clear decision-making framework that will guide geothermal energy developers, regulators, and potentially impacted communities through a more consistent and predictable permitting and monitoring process.

5. Establishing a Surface Thermal Features Management Working Group

One of the long-term objectives of this project is to promote the wide-spread acceptance, adoption, and confidence in these practices and guidelines across the geothermal community. Creation of a surface thermal features management working group will allow diverse stakeholders with unique backgrounds and expertise to collaboratively refine and finalize the protocol and co-create a set of best practices for implementation. We also envision potential co-development of a web-based tool that will allow stakeholders to navigate and implement the protocol and guidance more effectively, which will further optimize implementation of NEPA requirements and reduce barriers to geothermal permitting.

Learning from the process successes of the Induced Seismicity Management Protocol (ISMP) (U.S. DOE, 2012), as well as the Geothermal Interagency Collaboration Task Force (Levine and Smith, 2023), we envision that the surface thermal feature management working group will include representatives from industry, federal and state regulatory entities, other federal agencies (e.g., DOE), Tribes, academia, and national laboratories. It will also engage early and often with local or state governments, community stakeholders and special interest groups (e.g., environmental groups) to ensure that input from these groups is meaningfully incorporated, and issues and concerns are addressed to the greatest extent possible.

Successful co-development of the final protocol and best practices that includes meaningful inclusion of input from many voices offers many important benefits (e.g., Keeys and Huemann, 2017, Rossi and Tuurnas, 2021). First, it helps to ensure that the final products can effectively and equitably address the needs of all impacted or potentially impacted stakeholders. Second, it can lead to development of protocol and procedures that are more comprehensive, practical, and relevant to the real-world context. Third, it can build trust among stakeholders which in turn will foster greater acceptance of the protocol and best practices and increase the probability for wide-spread adoption.

6. Summary and Future Perspectives

The lack of consistency in geothermal permitting, and monitoring requirements, specifically as it relates to assessing and monitoring potential impacts to hot springs and geysers and other surface thermal features has greatly increased exploration risk and permitting costs for geothermal developers. This comes at a time when there is an increased urgency and demand for the clean

energy and renewable power generation that geothermal energy can provide. This paper describes the project team's approach to standardizing regulatory requirements and reducing barriers to permitting and geothermal development. Our near-term objective is to develop a preliminary protocol for assessing and managing potential impacts to surface thermal features using scientifically rigorous and independent analyses that are informed, in part, by site-specific data provided by industry through data sharing agreements. These studies will offer improved understanding of the cause-and-effect relationships that exist in geothermal-surface thermal feature systems, and the primary risk factors to consider when evaluating potential impacts to surface thermal features. Our long-term objectives are to establish a surface thermal features management working group comprised of diverse stakeholders and Tribes from across the geothermal community to refine the preliminary protocol, establish agreed-upon best practices for implementation, promote widespread acceptance and adoption of the protocol and best practices, and build trust within communities. The goal of these efforts is to standardize regulatory requirements associated with mitigation of potential impacts to surface thermal features, and to help ensure that geothermal energy can continue to provide a reliable source of clean energy and a pathway to achieving greater energy equity in the U.S.

Acknowledgement

Funding for this project is provided by the Department of Energy's Geothermal Technologies Office (DOE-GTO). We would like to acknowledge DOE-GTO for their vision, and for their ongoing engagement and support of this project. We would also like to acknowledge Ormat for their willingness to supply site-specific data that will greatly contribute to the team's ability to perform a rigorous and independent study. Finally, we would like to acknowledge Jeff Burghardt for his critical contributions toward establishing project goals and objectives.

REFERENCES

Allis, R., and Larsen, G. "Roosevelt Hot Springs geothermal field, Utah – reservoir response after more than 25 years of power production." Proceedings of the Thirty-Seventh Workshop on Reservoir Engineering, Stanford University, Stanford, California. SGP-TR-194, (2012).

Barrick, K. "Geyser decline and extinction in New Zealand – energy development impacts and implications for environmental management." Environmental Management, 39, (2007), 783-805.

Bromley, C.J., Mongillo, M., Hiriart, G., Goldstein, B., Bertani, R., Huenges, E., Ragnarsson, A., Tester, J., Muraoka, H., and Zui, V. "Contribution of geothermal energy to climate change mitigation: the IPCC renewable energy report." *Proceedings World Geothermal Congress 2010*; April 25-29, 2010, Bali, Indonesia. (2010), pp.1-5.

Chen, S., Zhang, Q., Andrews-Speed, P., and Mclellan, B. "Quantitative assessment of the environmental risks of geothermal energy: A review." Journal of Environmental Management, 276, (2020), 111287.

Coates, P.S., Prochazka, B.G., O'Neil, S.T., Webster, S.C., Espinosa, S., Ricca, M.A., Mathews, S.R., Casazza, M., and Delehanty, D.J. "Geothermal energy production adversely affects a

sensitive indicator species within sagebrush ecosystems in western North America." Biological Conservation, 280, (2023), 109889.

Donnelly, P. "Rare Nevada Butterfly Moves Closer to Endangered Species Protection." Center for Biological Biodiversity Press Release. (16 August 2023). https://biologicaldiversity.org/w/news/press-releases/rare-nevada-butterfly-moves-closer-to-endangered-species-protection-2023-08-16/. Accessed 11 August 2024.

Heasler, H.P., Jaworowski, C., and Foley, D. "Geothermal systems and monitoring hydrothermal features", *in* Young, R., and Norby, L., eds., Geological Monitoring: Boulder, Colorado, Geological Society of America, (2009), 105–140.

Kagel, A., Bates, D., and Gawell, L. E., Smith, C., and Haffner, C. "A guide to geothermal energy and the environment." Geothermal Energy Association. (April, 2007).

Kamila, Z., Kaya, E., and Zarrouck, S.J. "Reinjection in geothermal fields: An updated worldwide review 2020." Geothemics, 89, (2021),101970.

Kaya, E., Zarrouk, S. J., and O'Sullivan, M. J. "Reinjection in geothermal fields: A review of worldwide experience." Renewable and Sustainable Energy Reviews, 15, (2021), 47-68.

Keeys, L. A., and Huemann, M. "Project benefits co-creation: Shaping sustainable development benefits." International Journal of Project Management, 35(6), (2017), 1196-1212.

Levine, A., Young, K.R., and Witherbee, K. "Coordinating Permit Offices and the Development of Utility-Scale Geothermal Energy." GRC Transactions 37, (2013).

Levine, A., Ligia-Smith, E.P., Robins, J., Witter, E., Smith, C., and Haffner, C. "Non-technical barriers to geothermal development in California and Nevada." Golden, CO: National Renewable Energy Laboratory. NREL/TP-6A20-83133, (2022).

Levine, A., and Smith, F. "Geothermal Interagency Collaboration Task Force: Summary of Findings." Golden, CO: National Renewable Energy Laboratory. NREL/TP-6A20-84684, (2023).

Martinez, S. "Land of a Thousand (Steamy) Thrills: Nevada's Lost Hot Spring Geysers." *Flying Nevada Wild*, (2024). https://findingnevadawild.com/land-of-a-thousand-steamy-thrills-nevadas-lost-hot-spring-geysers/. Accessed 11 August 2024.

MOU. "Memorandum of Understanding Between United States Department of the Interior, United States Department of Agriculture, United States Department of Defense, United States Department of Energy, and United States Environmental Protection Agency to Improve Public Land Renewable Energy Project Permit Coordination. (January 6, 2022).

Neupane, G., and Adhikari, B. (2022). "Economic impact of permitting timelines on geothermal power in California, Nevada, and Utah." ID: Idaho National Laboratory. INLEXT-65257.

Newberger, Emma. "Burning Man sues Biden administration over geothermal project." *CNBC,* (January, 2023). https://www.cnbc.com. Accessed 11 August 2024.

Ratouis. T.M.P., O'Sullivan, M.J., Alcaraz, A., and O'Sullivan, J.P. "The effects of seasonal variations in rainfall and production on the aquifer and surface features of Rotorua geothermal field." Geothermics, 69, (2017), 165-188.

Richter, A. “Court decision voids geothermal leases on sacred tribal land in California.” *Think Geoenergy,* (September, 2019). https://www.thinkgeoenergy.com/court-decision-voids-geothermal-leases-on-sacred-tribal-land-in-california/ . Accessed 10 August 2024.

Robins, J.C., Kolker, A., Flores-Espino, F., Pettitt, W., Schmidt, B., Beckers, K, Pailing, H., and Anderson, B. “2021 U.S. Geothermal Power Production and District Heating Market Report.”Golden, CO: National Renewable Energy Laboratory. NREL/TP-5700-78291, (2021).

Rossi, P., and Tuurnas, S. “Conflicts fostering understanding of value and co-creation and service systems transformation in complex public service systems.” Public Management Review, 23, (2021), 254-274.

Soltani, M., Kashkooli, F.M., Souri, M., Rafiei, B., Jabarifar, M., Charali, K., and Nathwani, J.S. “Environmental, economic, and social impacts of geothermal energy systems.” Renewable and Sustainable Energy Reviews, 140, (2021), 110750.

Sorey, M L. "Geothermal Development and Changes in Surficial Features: Examples from the Western United States." *Proceedings World Geothermal Congress 2000*, Kyushu – Tohoku, Japan, (2000).

STOMP Online User Guide. *STOMP*, Pacific Northwest National Laboratory. https://stomp-userguide.pnnl.gov/index.html . Accessed 13 August 2024.

U.S. BLM (Bureau of Land Management).“Comprehensive Strategic Plan for Geothermal Management.” (2005).

U.S. BLM. “Programmatic Environmental Impact Statement for Geothermal Leasing in the Western United States – Volume 1: Programmatic Analysis.” FES-08-44, (2009).

U.S. BLM - Stillwater Field Office. Decision Record: Dixie Meadows 12MW Geothermal Utilization Project. (DOI-BLM-NV-C010-2016-0014-EA). Department of Interior. (December 2022).

U.S. BLM. “BLM Geothermal Training Module.” Geothermal Industry Training. (November 2023), https://www.blm.gov/programs/energy-and-minerals/renewable-energy/geothermal-energy. Accessed 12 August 2024.

U.S. DOE (Department of Energy). “Protocol for Addressing Induced Seismicity Associated with Enhanced Geothermal Systems.” DOE/EE-0662, (January 2012).

U.S. DOE. “Geovision: Harnessing the heat beneath our feet.” (2019).

U.S. DOE. “Equity Action Plan, 2023 Update.” (2023).

U.S. DOE. “Pathways to Commercial Liftoff: Next Generation Geothermal Power.” (2024).

U.S. DOI (Department of Interior). “Establishment of Renewable Energy Coordination Offices.” IB 2022-040, (May, 2022).

U.S. EIA (Energy Information Administration). “Most U.S. utility-scale geothermal power plants built since 2000 are binary-cycle plants.” Department of Energy. Today in Energy (July, 2020). https://www.eia.gov/todayinenergy/ Accessed 11 August 2024.

U.S. OIG (Office of Inspector General). “Bureau of land management’s geothermal resources management.” Department of Interior. Report No. CR-EV-BLM-0004-2012. (2012).

https://www.oversight.gov/sites/default/files/oig-reports/DOI/FinalEvalBLMGeothermalResourecesMgmt030713.pdf. Accessed 05 August, 2024.

Vargas, C.A., Caracciolo, L., and Ball, P.J. “Geothermal energy as a means to decarbonize the energy mix of megacities.” Communications Earth and Environment, 3, (2022), 1-11.

White, D. “The Beowawe Geysers, Nevada, before geothermal development:” United States Geological Survey Bulletin. (1998).

White, P., and Hunt T. “Simple modelling of the effects of exploitation on hot springs, Geyser Valley, Wairakei, New Zealand.” Geothermics, 34, (2005), 187-207.

White M.D., and Oostrom, M. “STOMP - Subsurface Transport Over Multiple Phases, Version 4.0: User Guide.” WA: Pacific Northwest National Laboratory. PNNL-15782, (2006), (UC-2010).

Young, K. R., Witherbee, K., Levine, A., Keller, A., Balu, J., and Bennett, M. “Geothermal permitting and NEPA timelines.” GRC Transactions, 38, (2014), 893-904.

Young, K., Levine, A., Cook, J., Heimiller, D., Ho, J. “GeoVision Analysis Supporting Task Force Report: Barriers—An Analysis of Non-Technical Barriers to Geothermal Deployment and Potential Improvement Scenarios.” Golden, CO: National Renewable Energy Laboratory. NREL/PR-6A20-71641, (2019).

Improving Geothermal Well Production through Scale Removal: A Lakeview, Oregon Case Study

Rochelle Longval[1], Jason Fisher[1], Daniel McCall[2], Scott Langum[3]

Blue Spark Energy[1]

Di Drill Survey Services[2]

Town of Lakeview[3]

Keywords

Geothermal district heating, scaling, wellbore maintenance, wellbore longevity, wellbore integrity

ABSTRACT

Geothermal energy, a sustainable and renewable resource, plays a vital role in the global energy supply. To guarantee peak performance and longevity of geothermal wells, it is essential to implement a wellbore operation and maintenance strategy.

A fundamental component of this strategy is scale management attributed to mineral precipitation from the brine during the reinjection and production process. The accumulation of scale deposits significantly impacts the lifespan and efficiency of geothermal wells by restricting fluid flow, thus reducing wellbore performance. To address these impacts in a geothermal district heating (GDH) system, it is important to administer forward-looking maintenance plans before manageable fluids become unmitigated outages.

The GDH system in the Town of Lakeview, Oregon plays a critical role to heat local schools, the community hospital, the emergency services station, and a dental clinic. By using geothermal energy, Lakeview offsets the expense and environmental impact of traditional fuels like propane, ensuring cost-effective and sustainable heating for the community. The functionality of the GDH was impacted by severe iron oxide-hydroxide scale deposits that had developed over time. In recent years, the scaling drastically reduced the flow rate from 160 gallons per minute (gpm) down to 88 gpm. To efficiently meet the needs of these community buildings, a production rate of 130 gpm is required.

To restore these essential services, various methods for scale removal were considered and electro-hydraulic pulse technology was applied. The targeted pulsing technology in Lakeview achieved

breakthrough results in scale removal, leading to an increased production rate of 206 gpm. The Lakeview case study underscores the importance of regular maintenance and innovative solutions to improve the well production and increase the lifespan of geothermal wells.

1. Introduction

In the global energy portfolio, geothermal energy plays a vital role as a sustainable and renewable resource. As the geothermal industry continues to grow, operators seeking to increase production generally have two primary strategies: embark on capital-intensive drilling campaigns to initiate new wells or optimize and extend the productivity of existing wells. The financial outlay and inherent risks associated with drilling new wells often overshadow the benefits, making it critical for operators to implement a strategic wellbore maintenance plan.

A fundamental component of this strategy is scale management, as geothermal brines typically contain dissolved minerals that can precipitate out of solution during the reinjection and production process. The accumulation of scale deposits significantly impacts the lifespan and efficiency of geothermal wells by restricting fluid flow, thus diminishing wellbore performance. To address these impacts in a geothermal district heating (GDH) system, it is important to administer forward-looking maintenance plans before manageable fluids become unmitigated outages.

A prime example where the fluid flow has been restricted, thus reducing well performance, is the GDH system in the town of Lakeview. The operator’s producer well was severely affected by untreated scale deposits. Given the community's reliance on the geothermal heating system for local schools, the dental clinic, hospital, and emergency services station, it was vital to find an effective and economical solution. By using geothermal energy, Lakeview offsets the expense and environmental impact of traditional fuels like propane, ensuring cost-effective and sustainable heating for the community. When the system was unable to operate to meet the heating demand, buildings had to use propane as the back-up energy source or be shut down until the accumulation of scale deposits were removed through wellbore cleaning treatment.

If an appropriate wellbore maintenance strategy is implemented, then ideal fluid flow can be maintained for improved energy production because of the removal of flow impediments within the geothermal system. A proactive approach for regular wellbore cleaning will extend the operational life of geothermal wells, reduce unplanned downtime, and ultimately enhance the economic viability of a geothermal project.

2. Method

During the utilization of geothermal resources, geothermal wells and surface equipment are susceptible to scale deposition due to various factors that include changes in temperature, pressure, and flow velocity, pH level, degree of supersaturation and presence of ions in solution. Silica, carbonates (calcite, aragonite), and iron-based corrosion products are the most common types of scale in geothermal wellbores.

Developing a wellbore operation and maintenance strategy requires the consideration and evaluation of several factors. These factors include: specific wellbore conditions, operational requirements, regulatory constraints, economic considerations, and various scale removal techniques.

In this case study, the town of Lakeview (operator) initially reviewed conventional chemical and mechanical scale removal techniques. Key considerations for the operator included:

- A rigless operation due to the added mobilization costs to get to their rural locality
- Wellbore integrity by not damaging the completion equipment
- A solution with low health and safety risk

In order to meet these requirements, they decided to pursue, an innovative method, the electro-hydraulic pulsing technology,

The geothermal producer well contained goethite (iron oxide-hydroxide) scale that had been building up over a period of 14 years shown in Figure 1(a) and 1(b). With goethite being a challenging type of scale to remove, the electro-hydraulic technique was important to deploy to ensure an effective cleanout while maintaining the wellbore integrity of their geothermal system.

Figure 1(a): Goethite (Iron Oxide-Hydroxide) scale found in Lakeview producer wellbore. 1(b) SEM photomicrograph of goethite scale particle. Red arrow indicates FeO-OH-rich surface; blue arrow shows black Fe_3O_4 sub-surface (Hudspeth, et al., 2023).

3. Results

Through the strategic maintenance plan for the town of Lakeview, the electro-hydraulic pulse technology was deployed. The technology involved utilizing a small amount of energy that is released over an extremely short timespan to generate powerful electro-hydraulic pulses downhole. The hydraulic pulses propagated outwards (compressional force), reflected off the casing, and traveled back inwards (tensile force). Since scale has high compressional strength and low tensile strength, this push-and-pull motion peeled the scale from the sides of the wellbore.

The pulsing technology targeted specific intervals totaling 105 feet of permeable water-bearing zones that were partially obstructed by scale deposits. The repetition of pulses effectively broke up the goethite scale (iron oxide-hydroxide) in the wellbore to eliminate any flow impediments.

Four years ago, the production rate was 160 gallons per minute (gpm), which had declined to a rate of 88 gpm due to flow impediments. To efficiently meet the needs of the buildings, a production rate of 130 gpm has been recommended. Following the targeted pulsing treatment, the production rate increased to 206 gpm as shown in Figure 2.

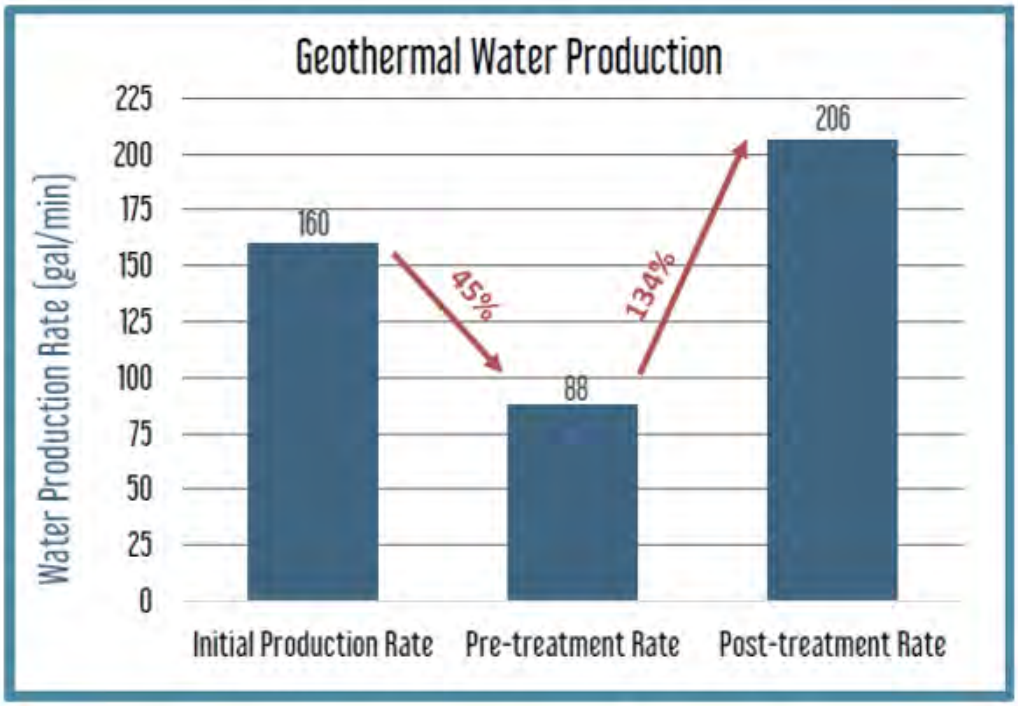

Figure 2: Geothermal production rate of 160 gal/min in 2020, followed by 88 gal/min (pre-treatment) and 206 gal/min (post-treatment) in 2024.

4. Conclusion

The use of this technology in Lakeview achieved breakthrough results in scale removal, leading to increased fluid flow and well productivity. The heat was successfully restored to the town, providing energy security, with a production rate to support the heating of additional buildings as needed. The Lakeview case study underscores the importance of regular maintenance and innovative approaches to managing geothermal wells.

Acknowledgements

The project benefited immensely from the collaborative efforts of the Town of Lakeview, Blue Spark Energy, Jacobs Solutions, and Di Drill Survey Services. The study acknowledges the valuable technical insights from these industry experts, whose contributions have been pivotal in addressing the challenges of scale deposition in GDH systems. Most importantly, the support of the local community and Scott Langum for taking the lead to pursue an innovative approach to scale removal.

REFERENCES

Habibi, A., Fensky, C., Perri, M., Roostaei, M., Mahmoudi, M., Fattahpour, V., Zeng, H., Sadrzadeh, M., and Ghalambor, A. “Unplugging standalone sand control screens with high-power shock waves: an experimental study.” SPE-*199294-MS*, (2020).

Habibi, A., Fensky, C., Roostaei, M., Mahmoudi, M., Fattahpour, V., Zeng, H., and Sadrzadeh, M. “Advances in understanding the scaling potential for thermal wells: a mechanistic study.” *SPE-199937-MS*, (2020).

Zhao. H., Huang, Y., Deng, S., Wang, L., Peng, H., Shen, X., Ling, D., Liu, L., and Liu, Y. “Research progress on scaling mechanism and anti-scaling technology of geothermal well system.” *Journal of Dispersion Science and Technology*, (2022).

Hudspeth, et al. “Analysis of langum south geothermal well scale.” *Hudspeth Land and Water*, (2023).

Optimizing Geothermal Resource Management: Insights from Stock Reservoir Modeling Analysis in Icelandic Fields

Arkaitz Manterola Donoso[1], María Gudjonsdottir[1], Hlynur Stefansson[1], Egill Júlíusson[2]

Reykjavik University[1], Artic Green Energy[2]

Keywords

Sustainable Energy Engineering, Geothermal Utilization, Stock Reservoir Model, Interconnected Production Modeling.

ABSTRACT

It is essential to optimize the sustainable utilization of geothermal resources, considering the current growth trend of the geothermal energy sector, to achieve long-term sustainability and profitability. This involves aligning with market demands, optimizing field management and increasing efficiency, which includes maintaining reservoir pressure, optimizing well production, and minimizing environmental impacts of the utilization.

This study aims to increase the understanding of the production from geothermal reservoirs by using production history data and well characteristic curves to analyze the impacts on the resource by using stock reservoir modeling. This mathematical modeling technique can predict how the reservoir might behave over time in response to production activities. These models can be useful for optimizing production strategies, such as the need for drilling make-up wells, reinjection, and scheduling to ensure energy production and long-term resource sustainability.

The main goals of the research are 1) to apply stock modeling to a variety of wells with different characteristics and production histories to better understand the method's versatility and 2) to analyze the applicability of using stock reservoir modeling for wells with interconnected productions. Specifically, wells from the Þeistareykir geothermal field in North Iceland and the Hverahlið geothermal field in Southwest Iceland are used as case studies to gain insights into their unique characteristics and production histories by applying the model to them.

1. Introduction

Current trends show that most energy sectors, including the geothermal sector, aim to reduce greenhouse gas emissions and enhance sustainability. Geothermal is a renewable energy source that provides relatively clean and reliable electrical and thermal energy. However, although they are closer to being carbon neutral than fossil fuels, there is room for improving geothermal resource utilization to reduce emissions and minimize the impacts on the reservoir.

In this study, a methodology is proposed that uses stock reservoir modeling (SRM) to study the effects of production on geothermal reservoirs. This data-driven approach employs well data to simulate production impacts and characterize each well's production. This modeling tool defines parameters that combine well mass flow rate, thermal output, and wellhead pressure to generate 3D surface diagrams to study production over time. SRM was first presented by Júlíusson E., and Axelsson G., 2018, and was further studied in Manterola Donoso A., et al, 2024; Manterola Donoso A., et al, 2023, Manterola Donoso, A., 2022; which analyzed the technical and financial aspects of geothermal utilization applying SRM.

This study further examines the methodology by applying this mathematical modeling technique to various wells with different characteristics and production histories to understand its versatility and applicability. Specifically, wells from the Þeistareykir geothermal field in North Iceland and the Hverahlið geothermal field in Southwest Iceland are studied to gain insights into their unique characteristics and production histories. Moreover, this study goes further by analyzing the potential of using SRM to study the production of different production wells simultaneously, for wells showing a high interconnection in their output. This method could lead to a novel approach for studying multiple production and reinjection wells using a single SRM.

2. Methodology

Stock reservoir modeling (SRM) is one of the three main geothermal reservoir modeling techniques, together with grid-based numerical reservoir models (Franco A, Vaccaro L., 2014) and lumped parameter reservoir models (LPRM) (Klüpfel S, Gunnarsson G, 2021). These models are important for estimating geothermal resources and understanding production impacts. Each reservoir modeling approach uses different data inputs to generate the models, with numerical models using both physical and operation data, LPRM using mostly physical data, and SRM using only operation data. The models usually also have a different scale and focus. Numerical models and LPRM are usually used to study a whole geothermal field, however, lumped models are usually simpler and have a higher solving speed which comes to the cost of lower accuracy if compared to numerical models, which need more data for their generation, are more complex and provide a more detailed picture of what the geothermal reservoir might look like. SRM, as LPRM, is a faster-solving and simpler modeling approach which, so far, has been used to analyze production impacts on a well-by-well basis instead of studying a geothermal field in its entirety (Júlíusson E., and Axelsson G., 2018, Manterola Donoso A., et al, 2023, Manterola Donoso, A., 2022).

As SRM has yet to be applied more commonly, this study aims to analyze various wells individually in different geothermal systems using the pre-established methodology (Manterola Donoso A., et al, 2023, Manterola Donoso, A., 2022) and to develop further SRM to study production from interconnected wells. This second goal presents a change in formulation, as it requires a more complex stock model than for studying individual wells, which presents a challenge due to the method's reliance on production history data to study well production capacity in geothermal systems.

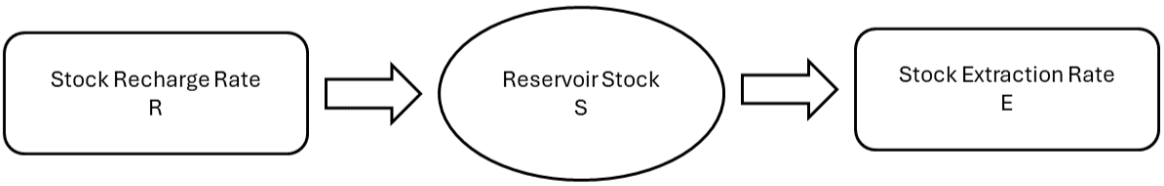

Figure 1: Individual well stock model (Adapted from Júlíusson, E., & Axelsson, G., 2018)

The methodology to study production from additional wells is presented in (Manterola Donoso, A., et al, 2023) where the SRM methodology for individual wells was developed and described. The model minimizes the difference between actual and estimated extraction data by history matching to set stock parameters that characterize a well's production characteristics. These parameters define the maximum energy output of a well (Q_{MAX}) in MW, maximum wellhead pressure (P_{MAX}) in bars, maximum stock (S_{MAX}) in MWyr and maximum recharge (R_{MAX}) in MW of a well. These variables are based on stock changes (S), defining a well's energy availability, calculated based on the model presented in Figure 1, where the geothermal system's extraction (E) and recharge (R) impact the reservoir's energy availability. The model details, including all parameters, equations, and bounds, are described in (Manterola Donoso A., et al, 2023).

The previous SRM methodology must be updated to study the production of interconnected wells. This study considers only the simplest version, where only two production wells are considered, and no reinjection well is in place. This model simulates the production behavior of two different production wells to study the relationship between their production and analyze the possible impacts on the general reservoir they might share. Moreover, this model intends to study how the system is recharged. However, for a more simplistic first look, the authors do not consider that a reinjection well in place. In a future study, reinjection data and tracer test data might help to estimate the connectivity between recharge and production, to compare these estimates with the optimizer's calculations to validate the method and increase its accuracy.

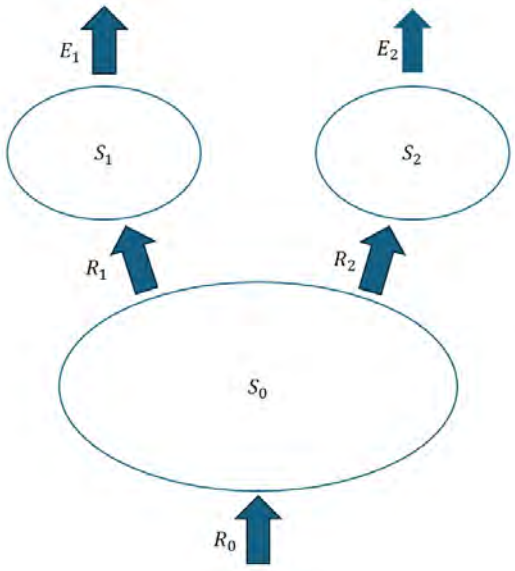

Figure 2: Interconnected stock model for two production wells

Figure 2 shows an interconnected geothermal system with two production wells, each with its stock (S_1, S_2) which will change depending on the extraction (E_1, E_2) and recharge (R_1, R_2) of each well.

This system depicts the simplest possible configuration between interconnected wells to allow for the addition of other wells to study production patterns together. However, as the goal is to study the connection between wells, an additional stock (S_0) must be considered where each well recharges from. This figure also considers the recharge (R_0) of the S_0, which for this simplified model only includes the effects of natural recharge.

To examine the connection between wells, redefining concepts such as reservoir storability and well-to-well transmissibility is essential. These concepts are already used in numerical or lumped parameter modeling, and establishing parallel concepts can be useful in describing and comparing models. Storability defines the total thermal energy the geothermal reservoir or well can produce; transmissibility describes the relationship between well productions. SRM already defines storability using the stock (S) parameter, but transmissibility needs to be added as an additional variable to study the relationship between wells.

The model depicted in Figure 2 uses SRM functions as those defined in a pre-study (Manterola Donoso A., et al, 2023). Said equations define the Extraction (E), Recharge (R), and Stock (S) parameters in Equations 1, 2 & 3 respectively which help analyze the productivity of a well over time. To be able to define the model presented in Figure 1, the model defines said parameters not only for each well in the geothermal system ($\mathrm{E_i}, \mathrm{R_i}, \mathrm{S_i}\ \forall\ i \in N$) but also for the connecting reservoir (S_0). As such, the model includes an additional equation (Equation 4) defining the connecting reservoirs stock (S_0), which is dependent on the recharge ($\mathrm{R_i}\ \forall\ i \in N$) of each production well and the general recharge of the system (R_0). The R_0 parameter could consider both natural recharge and reinjection recharge, but for the simplicity of this study, Equation 5 only considers natural recharge.

$$E_{i,t}\left(P_{i,t}, S_{\mathrm{i,t}}\right) = Q_{i,MAX} \cdot S_{\mathrm{i,t}}/S_{i,MAX} \cdot \sqrt{1 - \left(P_{\mathrm{i,t}}/P_{i,MAX}\right)^2} \forall\ i \in N \tag{1}$$

$$\mathrm{R_{i,t}}\left(S_{\mathrm{i,t}}\right) = R_{i,MAX} \cdot \left(\left(S_{i,MAX} - S_{\mathrm{i,t}}\right)/S_{i,MAX}\right) \forall\ i \in N \tag{2}$$

$$S_{\mathrm{i,t}} = S_{i,(\mathrm{t}-\Delta t)} - \mathrm{E_{i,t}}\left(P_{\mathrm{i,t}}, S_{i,(\mathrm{t}-\Delta t)}\right) \cdot\ \Delta t + \mathrm{R_{i,t}}\left(S_{i,(\mathrm{t}-\Delta t)}\right) \cdot \Delta t\ \ \forall\ i \in N \tag{3}$$

$$S_{0,\mathrm{t}} = S_{i,(t-\Delta t)} - R_1\left(S_{1,(t-\Delta t)}\right) \cdot \Delta t - R_2\left(S_{2,(t-\Delta t)}\right) \cdot \Delta t + R_0\left(S_{0,(t-\Delta t)}\right) \cdot \Delta t\ \forall\ i \in N \tag{4}$$

$$R_0\left(s_{\mathrm{T},t}\right) = R_{0,MAX} \cdot \left(\frac{S_{0,MAX} - S_{0,t}}{S_{0,MAX}}\right) \forall\ i \in N \tag{5}$$

where $E_{i,t}$, $P_{i,t}$, $S_{i,t}$, $R_{i,t}$, $Q_{i,MAX}$, $P_{i,MAX}$, $S_{i,MAX}$, $R_{i,MAX}$, $S_{0,t}$, $R_{0,t}$, $S_{0,MAX}$, $R_{0,MAX}$, t, Δt, i, N represent calculated extraction, wellhead pressure, stock, recharge, maximum output, maximum wellhead pressure, maximum stock, maximum recharge, general tank stock, general tank recharge, general tank maximum stock, general tank maximum recharge, time step, time differential between time steps, well index, and total number of wells respectively.

To better study well transmissibility, the recharge from each well is not independent, but rather connected through the general reservoir stock (S_0). Equation 6 defines the recharge for the non-

primary well, to be selected by the user considering lower well productivity and parametrized using α, which represents well-to-well transmissibility as the connecting factor between wells. Therefore, α connects how each well recharges from the general reservoir considering the other production wells in a system. This equation replaces the definition on Equation 2 for all wells defined as non-primary.

$$R_{2,t}(R_{1,t}) = \alpha \cdot R_{1,t} \tag{6}$$

Where $R_{1,t}$, $R_{2,t}$, α are primary well recharge, secondary well recharge and well-to-well transmissibility, respectively.

The model defines an objective equation (Equation 7) aimed to optimize the well variables that describe the geothermal system ($Q_{i,MAX}, P_{i,MAX}, S_{i,MAX}, R_{i,MAX}, S_{0,MAX}, R_{0,MAX}$). Equation 7 determines the error between the measured values and the extraction estimations made by the model. By comparing and minimizing extraction, the model determines which are the optimal parameters that define each production well, as well as the connecting reservoir.

$$\underset{Q_{i,MAX},P_{i,MAX},S_{i,MAX},R_{i,MAX},S_{0,MAX},R_{0,MAX},}{minimize} \sum_{\tau} \left(Ed_{\mathrm{i},\tau} - E_{\mathrm{i},\tau}(P_{\mathrm{i},\tau}, S_{\mathrm{i},\tau})\right)^2 \ \forall\, i \in N \tag{7}$$

Where $Ed_{i,\tau}$, $E_{i,\tau}$, $P_{i,\tau}$, $S_{i,\tau}$, τ, i, N represent calculated extraction rate, extraction rate data, wellhead pressure, stock, time of measurement, well index and number of wells respectively.

Finally, the variables require at least lower bounds. All variables have a lower bound greater than zero, as all parameters in a geothermal system should be positive. There is no need for an upper bound unless to prevent errors from low recharge or high stock. Upper bounds might need to be applied by the user when required, for example, to reduce local minima errors or if the “optimal” results show, for instance, a seemingly impossible infinite maximum recharge value.

3. Data Collection

Having defined the stock model to characterize production impacts, this section describes the data used in the study. To apply SRM to more wells, the authors study the production data from the Þeistareykir and Hverahlið geothermal fields in Iceland, which include wells with varying outputs and histories. These differences are key for understanding how production patterns and characteristics affect the individual well stock parameters. As aforementioned, the model in Manterola Donoso A., et al, 2024, defines these parameters.

The data used for this study includes information on the wells' measurement date, wellhead pressure, and thermal energy output. Due to confidentiality, the well name, history data, and characteristic curves are not shared, but a short description of each analyzed well is provided. Wells from the Þeistareykir field (wells ÞG-A to D) in the North of Iceland include non-continuous and non-periodical data. They include between 83 and 106 data points, over a period of 4 years. Wells from the Hverahlið field (wells HE-A to D) in Southwest Iceland include daily and/or weekly measurements. They include between 730 and 2922 data points, over 8 years. See below a description of each well:

- Well ÞG-A: Well with a high and continuous production that shows a slow decline through production.

- Well ÞG-B: Well with high and continuous production, with small changes in the operation wellhead pressure, that shows minimal decline through production.
- Well ÞG-C: Well with a high production closed for a year and a half halfway through the studied production period.
- Well ÞG-D: Well with non-constant production, not used in regular production.
- Well HE-A: Well, with fast declining production, only in production for two years.
- Well HE-B: Highly productive with a constant decline in production.
- Well HE-C: Well with a high production. After an initial decline, it was very constant and highly productive.
- Well HE-D: High productivity well, with slight changes to its production and a small output decline.
- Well HE-E: High productivity well, with a high correlation between wellhead pressure and output production.

Moreover, to study well interconnection, two sets of wells with a combined production pattern have been generated instead of using real data to simplify the expected result and to make the model easier to apply. This approach does not validate the model but rather aims to demonstrate whether SRM can be applied to identify, and study impacts between linked production wells. The model is solved using two sets of production wells: one without output decline and another with decline. This comparison aims to highlight the necessary future improvements required in the methodology.

The data for the generated synthetic wells (A-01 to A-04), includes a set of weekly values for wellhead pressures, enthalpies and flows. Wells A-01 and A-03 represent a main production well with continuous production and a short period with reduced production, with A-03 having a decline in production. Wells A-02 and A-04 represent a secondary production well, which is only used for a short period.

Considering the applied wells, an additional constraint (see Equation 8) nullifies the secondary production well's recharge in case its stock is higher than the estimated initial stock. This is applied to negate the unnecessary recharge if production is null.

$$S_{2,t} \geq S_{2,MAX} \rightarrow R_2 = 0 \tag{8}$$

To apply the interconnected model, these wells are first studied individually by applying SRM to each of the wells to characterize the individual stock parameters. Then, these are applied as starting production parameters for the interconnected SRM presented in Section 2.

4. Results

This section presents the study's results on individual and interconnected well analysis using stock reservoir modeling.

First, the results of the individual stock reservoir models are presented in Table 1, which shows all the different stock parameters for the studied wells. The results show the different values for the maximum pressure (P_{MAX}), stock (S_{MAX}) and recharge (R_{MAX}) parameters of each well. To protect sensitive information, the maximum output parameter (Q_{MAX}) is not shown. Table 1 also shows the squared error between the extraction data and the simulated extraction and the corrected error,

which has been adjusted considering the number of data points used to compare results from different fields better.

Table 1. Stock parameters and history match errors for the selected wells.

WELL	P_{MAX} (bar)	S_{MAX} $(MWyr)$	R_{MAX} (MW)	Error	N° of points	Corrected error
ÞG-A	97.17	3656.99	793.97	70.37	87	0.88
ÞG-B	26.87	733.92	1131.53	2887.4	83	34.79
ÞG-C	93.01	182.86	534.77	917.64	65	14.11
ÞG-D	16.18	48.03	133.24	3140.94	106	29.63
HE-A	49.03	125.04	56.59	2987.00	730	4.09
HE-B	66.25	2709.36	38.58	33115.73	2858	11.58
HE-C	83.78	178.91	262.08	72902.93	2922	24.95
HE-D	84.75	5154.04	455.15	193015.22	2893	66.72
HE-E	91.97	570.51	264.28	155374.20	2099	74.02

To support these results, the authors present the following sets of curves to understand better how SRM simulates the production in the studied wells. Figures 3 to 11 show changes in extraction rate, recharge rate, and energy availability or stock. These figures also include a 3D surface diagram that links a well's productivity rate and wellhead pressure with its output, considering the reservoir stock. The figures include data points to show the correlation between the data and the simulation. The output values are shown as a percentual value to protect any sensitive information.

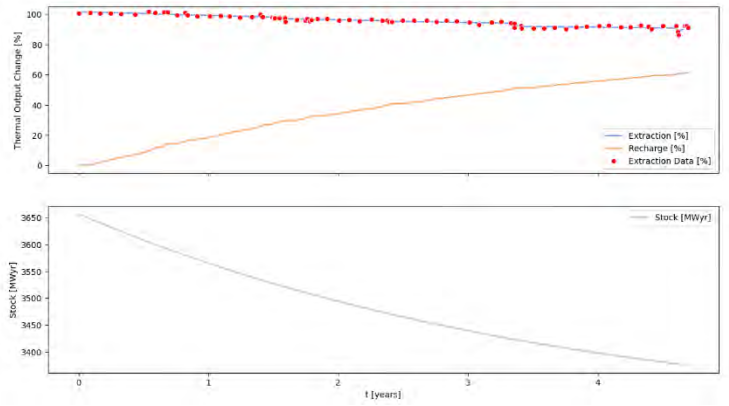

(3a)

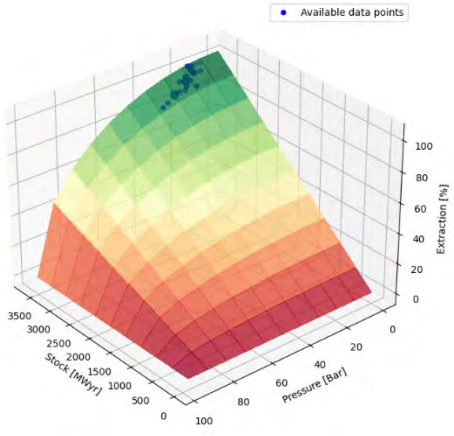

(3b)

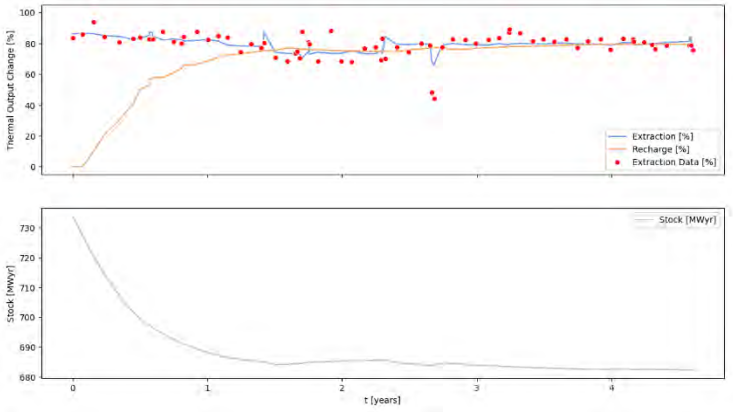

(4a)

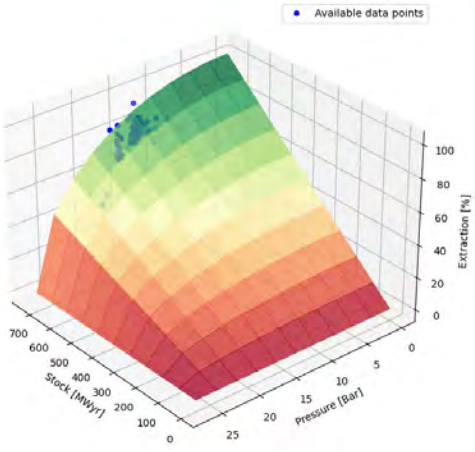

(4b)

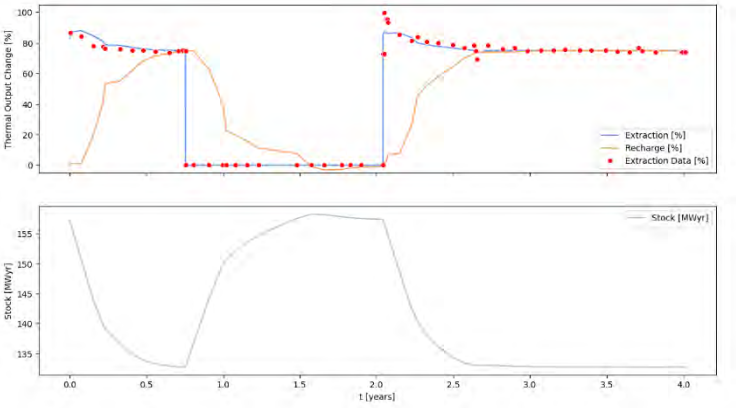

(5a)

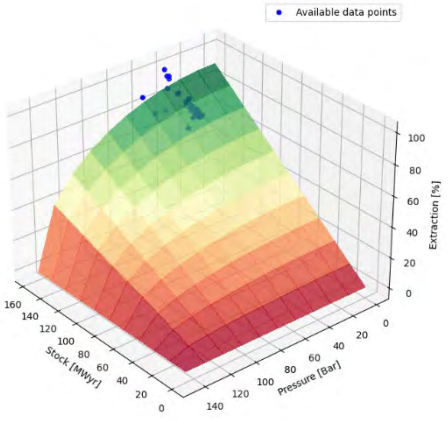

(5b)

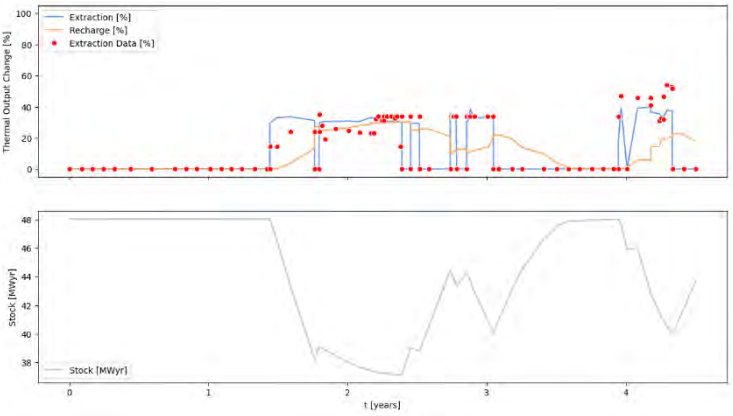

(6a)

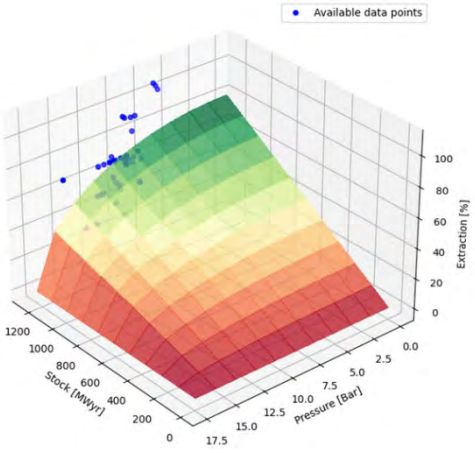

(6b)

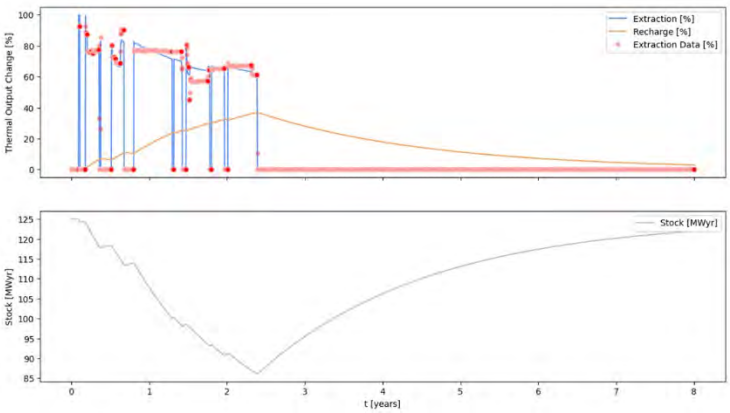

(7a)

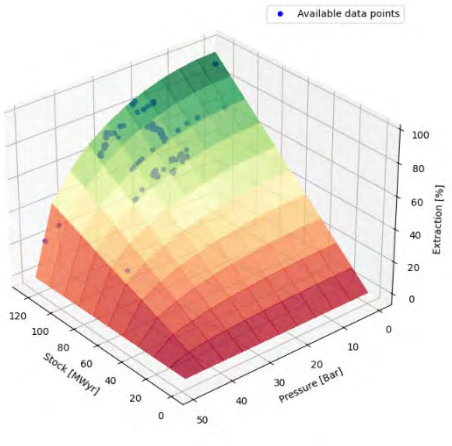

(7b)

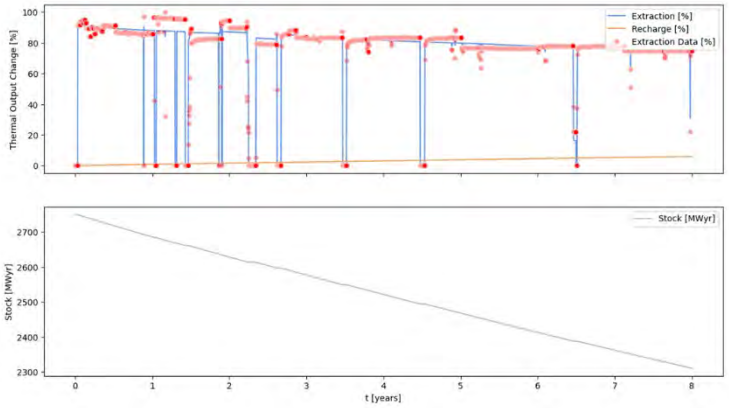

(8a)

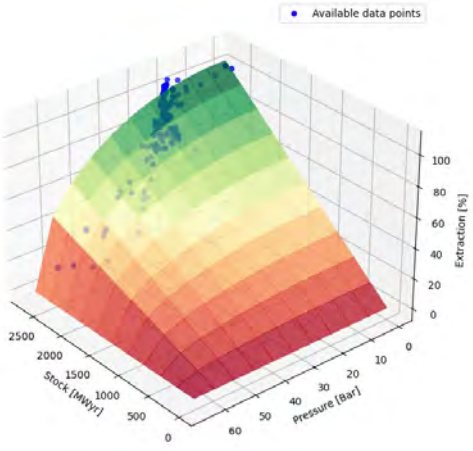

(8b)

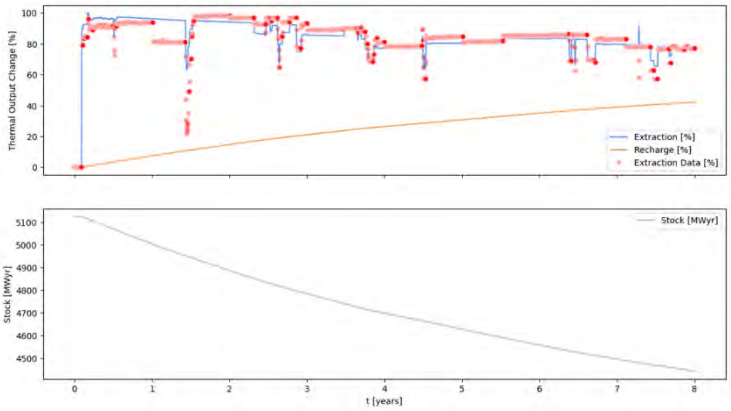

(9a)

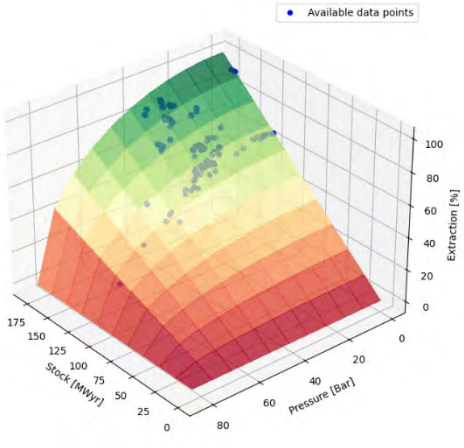

(9b)

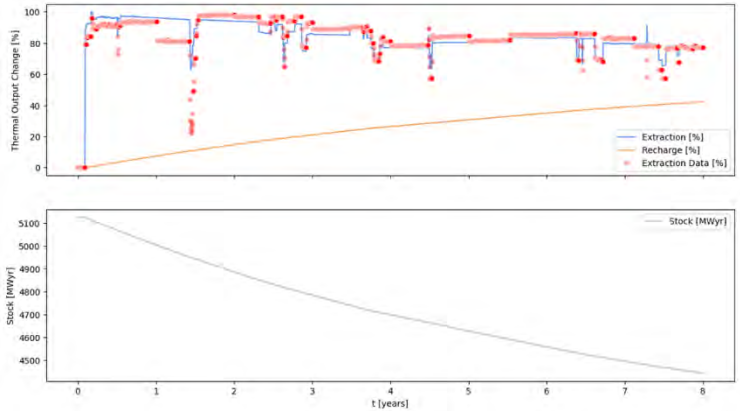

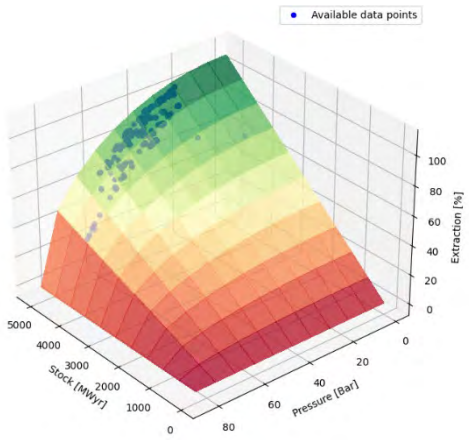

(10a) **(10b)**

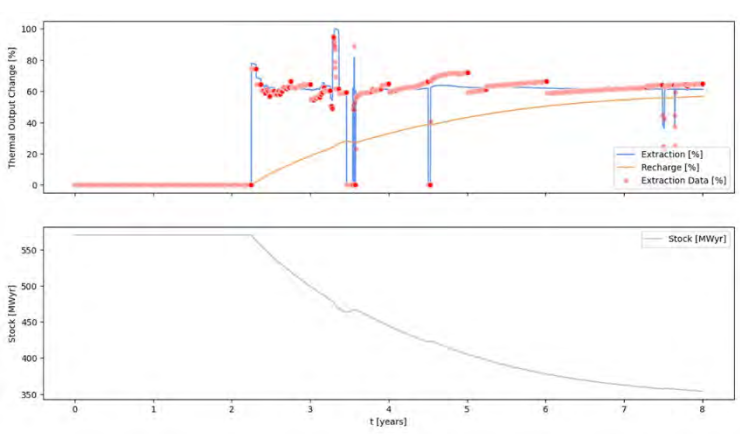

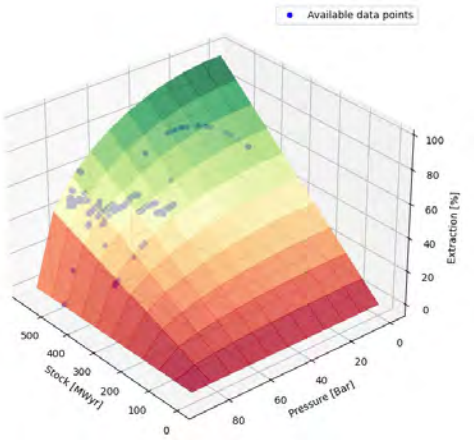

(11a) **(11b)**

Figures 3 to 11: Stock model curves for wells ÞG-A, ÞG-B, ÞG-C, ÞG-D, HE-A, HE-B, HE-C, HE-D, and HE-E, respectively. (a) Upper left: Extraction rate, recharge rate and production data over the studied period. Lower left: Stock of the reservoir over the studied period. (b) 3D surface diagram correlating well stock, wellhead pressure and extraction of well.

Next, the results concerning the interconnected sections are presented. To apply the methodology developed in Section 2, we first apply individual SRM analysis to each well to estimate their stock parameters individually. Table 2 shows all stock parameters and the squared error between the generated values and the model's estimations for each well. Figures 12 to 15 describe the stock, recharge and extraction curves and the extraction data for each set of curves after applying SRM.

Table 2. Stock parameters and history match errors for wells A-01, A-02, A-03 and A-04.

WELL	P_{MAX} (bar)	Q_{MAX} (MW)	S_{MAX} $(MWyr)$	R_{MAX} (MW)	Adjusted Error
A-01	28.91	68.99	3512.40	9584.17	0.029
A-02	20.22	23.09	268.72	7923.31	1.924
A-03	30.58	67.98	1269.39	4425.88	0.9344
A-04	23.09	21.73	934.17	1822.19	0.0642

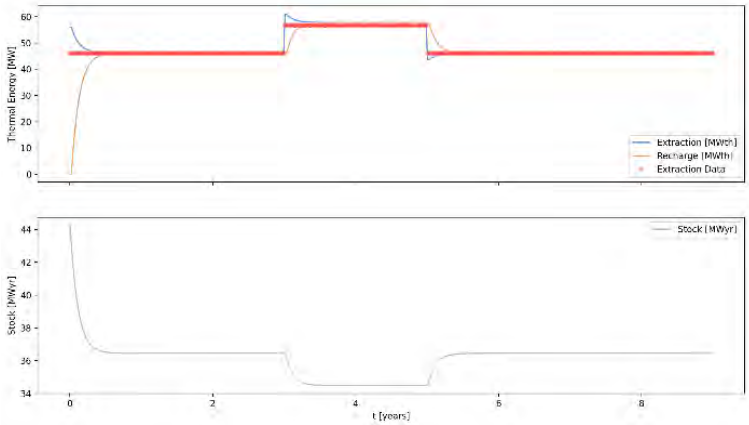
Thermal Energy [MW]
Extraction [MWth]
Recharge [MWth]
Extraction Data
Stock [MWyr]
Stock [MWyr]
t [years]

(12)

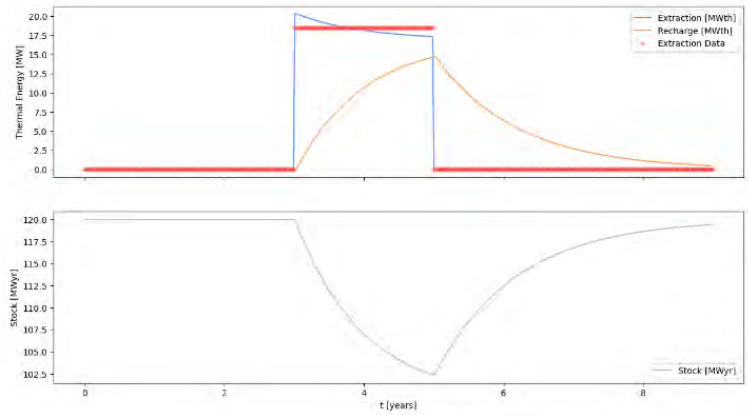
Thermal Energy [MW]
Extraction [MWth]
Recharge [MWth]
Extraction Data
Stock [MWyr]
Stock [MWyr]
t [years]

(13)

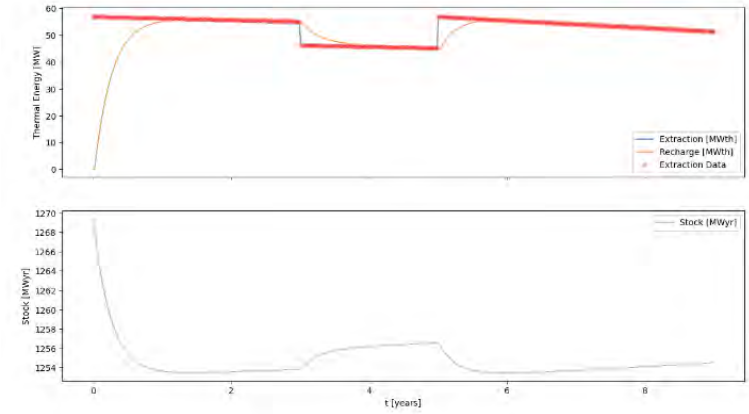
Thermal Energy [MW]
Extraction [MWth]
Recharge [MWth]
Extraction Data
Stock [MWyr]
Stock [MWyr]
t [years]

(14)

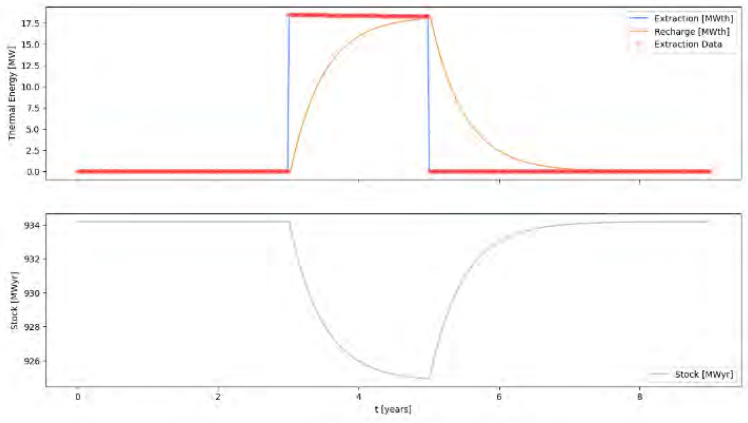

(15)

Figures 12 to 15: Individual stock model curves for wells A-01, A-02, A-03 & A-04, respectively. Upper: Extraction rate, recharge rate and production data over the studied period. Lower: Stock of the reservoir over the studied period.

The interconnected model is solved using the individual SRM parameters as initial values for the interconnected SRM. Tables 3 and 4 present the optimized stock parameters for each set of wells. The model without decline has a square error of 244.06, adjusted to 0.52 considering the number of data points. For the model that accounts for the decline, the square error is 157.16, adjusted to 0.33.

Table 3. Interconnected results for A-01 and A-02.

Wells	P_{MAX}	Q_{MAX}	S_{MAX}	R_{MAX}	α
A-01	29.70	71.91	622.23	895.78	-
A-02	39.45	22.19	115.17	-	0.394
Tank	-	-	500	100	-

Table 4. Interconnected results for A-03 and A-04.

Wells	P_{MAX}	Q_{MAX}	S_{MAX}	R_{MAX}	α
A-03	29.71	72.2	1095.43	911.25	-
A-04	26.77	22.26	219.45	-	0.399
Tank	-	-	500	100	-

For clarity, Figures 16, 17, 19, and 20 compare the extraction, recharge, and stock curves to the well data for both sets of wells. Figures 18 and 21 show the stock and recharge of the general reservoir that connects each set of production wells.

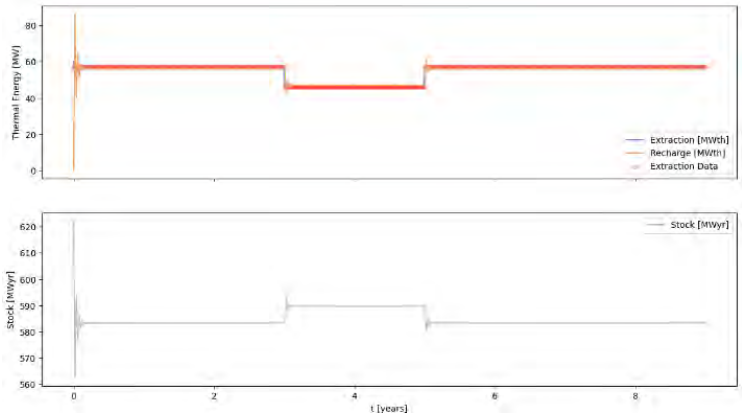

(16)

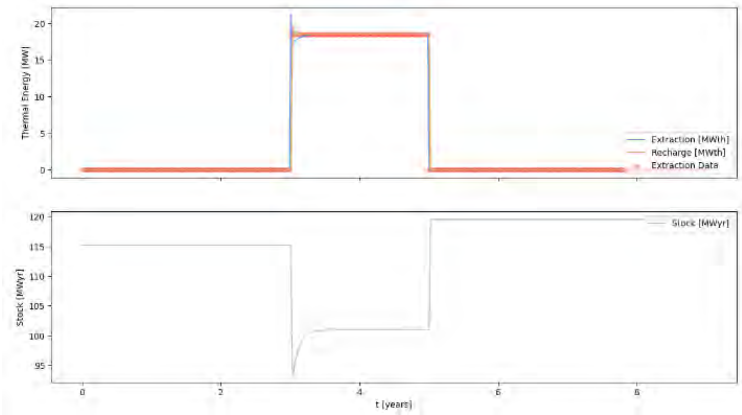

(17)

Figure 16 and 17: Interconnected stock model curves for wells A-01 & A-02, respectively. Upper: Extraction rate, recharge rate and production data over the studied period. Lower: Stock of the reservoir over the studied period.

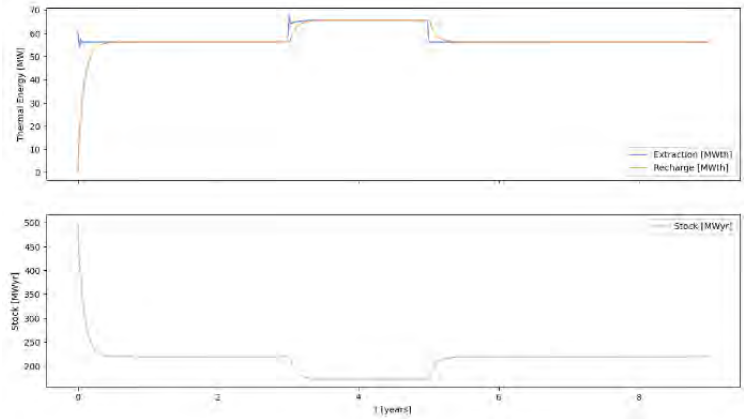

Figure 18: Interconnected stock model curves for the general reservoir linking A-01 and A-02. Upper: Extraction rate, recharge rate and production data over the studied period. Lower: Stock of the reservoir over the studied period.

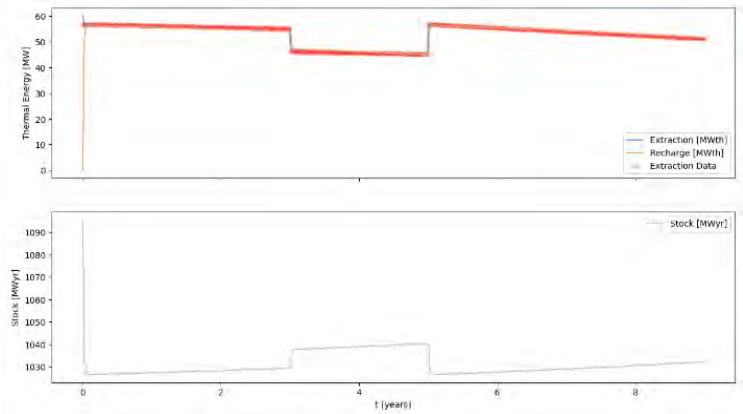

(19)

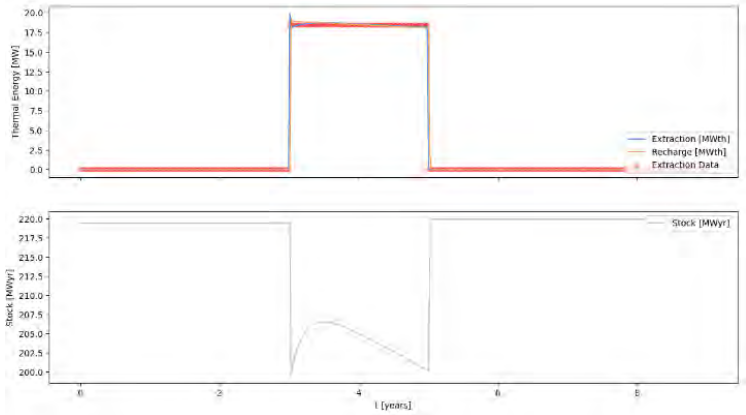

(20)

Figures 19 and 20: Interconnected stock model curves for wells A-03 & A-04. Upper: Extraction rate, recharge rate and production data over the studied period. Lower: Stock of the reservoir over the studied period.

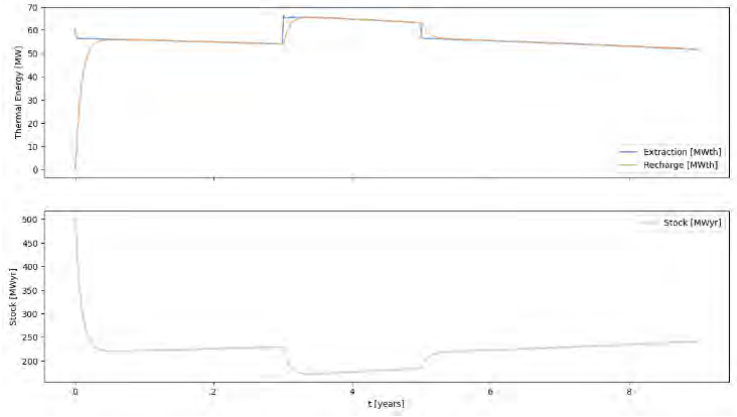

Figure 21: Interconnected stock model curves for the general reservoir linking A-03 and A-04. Upper: Extraction rate, recharge rate and production data over the studied period. Lower: Stock of the reservoir over the studied period.

5. Discussion

The study aimed to apply SRM to a wider range of wells to better understand its versatility and to examine its applicability for studying interconnected well production. The results show the model being applicable to individual wells in different Icelandic geothermal fields and an interconnected synthetic model that considers production from one connected reservoir.

The results show SRM's applicability to many wells with different production patterns, power outputs, and characteristic curves. Overall, wells show a strong correlation between the measured extraction data and the estimated extraction. Generally, more data points result in more reliable results with fewer outlying points. Comparing results from the Þeistareykir and the Hverahlið fields reveals that unless production is highly linear (as in the case of ÞG-A), having more production data increases accuracy.

Wells ÞG-B and ÞG-D show the highest error rates for the Þeistareykir field (see Table 1). Despite having different characteristics, this discrepancy between the model and the data might be due to uneven data distribution. Specifically, well ÞG-B shows minimal output variation over time without any changes in WHP. Consequently, as the estimated extraction correlates with the wellhead pressure change, not having a high correlation between the pressure and output greatly impacts the results. Similarly, well ÞG-D shows two different production stages, each with varying outputs despite comparable wellhead pressures, contributing to a higher error.

In the Hverahlið geothermal field wells HE-A, HE-B & HE-C have an overall low error rate, outlining the benefits of having continuous data when using SRM. However, even then, due to changes in well productivity without pertaining changes in wellhead pressure, slight differences show between the estimated and the measured extraction values for certain periods of the data. This discrepancy is shown more often for wells, HE-D and HE-E, where the adjusted error is higher than the rest. This is believed to be mostly due to the provided data not being consistent in certain time periods where the wellhead pressure does not change while the estimated output changes.

All in all, most wells and their respective 3D surfaces show low error, strong correlation and efficient computation time, as all models were solved in under five minutes. This makes SRM a versatile tool that can assist with successfully analyzing geothermal well production impacts based solely on production data. However, the model can still be improved in future iterations by incorporating additional parameters and constraints. For example, considering the high impact of scaling on a well's output, it would be of high interest to include the decline in production not only by the change in energy availability but also by scaling. This could also help improve the characterization of the stock variable. Moreover, the study's current consideration of one single extraction equation and recharge equation proves to be limiting. Considering the different characteristics of geothermal wells, applying the model using alternative equations could enhance result accuracy.

Regarding the application of interconnected SRM, the study proves successful in further using SRM to study production wells connected via an additional reservoir tank. Despite using synthetic data, the study shows SRM's capability to analyze interconnected wells by minimizing error between estimated and simulated extraction rates for each well. Furthermore, the model successfully defines well-to-well transmissibility consistently, regardless of well decline,

highlighting the connection between these wells. Moreover, it helps establish the minimal initial stock and recharge parameters essential for sustaining the presented production.

Comparing the two sets of wells and their results reveals that considering decline or not does not have much of an impact when calculating the maximum pressure (P_{MAX}) and maximum output (Q_{MAX}) in both individual and interconnected SRM (see Tables 2, 3 and 4). However, this differs for stock (S_{MAX}) and recharge (R_{MAX}) parameters. The individual model highlights how wells with higher decline show a higher stock value and a lower recharge in comparison to those without any decline. In contrast, the interconnected model's understanding of energy availability changes due to having the additional general tank.

Although successful in applying the model, this study represents only the first iteration of interconnected SRM, outlining many areas of improvement required to increase its applicability to more geothermal systems. Currently, the model is not able to appropriately estimate the general tank's stock (S_0), which functions more as an infinite recharge source. This is represented when comparing each well's stock (S_1, S_2) and recharge (R_1, R_2) with the estimated max stock (S_{MAX}) and recharge (R_{MAX}) for the individual models, which have a much higher value. This discrepancy is due to the general tank providing the required energy to maintain a recharge equal to the extraction, as shown in Figures 16, 17, 19 and 20. As long as the general tank's stock remains nonzero, this infinite recharge on wells continues. Future iterations should address these issues by improving the definition of equations 2 and 6 to include the impact that the energy availability in the general stock might have.

This effect is further enhanced by the absence of data on reinjection or recharge. As the recharge of the general tank is not parametrized, the model chooses a suitable recharge parameter to have continuous production. However, if reinjection data was included and the effects of reinjection were compared with how the reinjection might affect the production wells, the model's accuracy in defining energy availability could be improved.

When comparing individual and interconnected models, adjusted error values vary based on the data. Models with continuous data, like those from the Hveralið field or the synthetic data, show more accurate production impacts. Although future work is needed for the interconnected model, it already shows low error, even if helped by synthetic data. Nevertheless, as it considers extraction errors from multiple wells, the total error was expected to be higher. Despite such expectations, the interconnected model's error is comparable to or even lower than some individual SRM results, indicating that, for certain geothermal systems, analyzing well productions together may better assess production impacts.

6. Conclusions

Overall, in this study, SRM was successfully applied both to individual wells and to an interconnected system of wells. Individual SRM results highlight the method's versatility when understanding the production impacts of geothermal wells using 3D surface diagrams, generated by estimating the well characteristics using production history data. Interconnected SRM results show that the proposed method can be applied to systems with more complex production and well configurations. The low error of using interconnected SRM also suggests that analyzing well productions simultaneously for multiple wells can improve the understanding of the production impacts for certain geothermal systems.

These results demonstrate that SRM can be a tool that can consistently help define different types of wells and systems to make more informed decisions in well utilization to further increase the sustainability and good use of geothermal resources. As a fast-solving and easy-to-recalculate method, it allows the operators to include additional data when available or to consider different bounds and constraints that might better recreate the real geothermal system.

Finally, the authors want to outline the challenges that this methodology presents. For instance, regarding individual SRM, the methodology does not consider a changing maximum wellhead pressure for different stock values or the possibility of using different equations to define the extraction and recharge parameters, which could improve the accuracy of the model for certain wells with non-ordinary production patterns. As for the interconnected model, much work still needs to be done when it comes to connecting the production wells between each other and the general tank. Various possibilities arise, such as including reinjection data to simulate the impacts of production in the general reservoir or improving the definition of the system's equation to better simulate the effects of the production.

Acknowledgment

This study received financial support from the Rannis Technology Development Fund (project: 2321574-601) and the Landsvirkjun Energy Research Fund.

The authors also would like to acknowledge Landsvirkjun and Orkuveita Reykjavikur, who provided the required data to perform the work.

Appendix

The repository below has the synthetic data including the flow, enthalpy, and wellhead pressure values used for this study for wells A-01, A-02, A-03, and A-04.

https://github.com/armado11/GeothermalStockModellingInter

REFERENCES

Júlíusson E., and Axelsson G. “Stock models for geothermal resources.” *Geothermics*: 2018. 72:249–57. Available from: https://doi.org/10.1016/j.geothermics.2017.11.006.

Manterola Donoso, A., Guðjónsdóttir, M.S., Júlíusson, E, Stefánsson, H. Optimization of Geothermal Well Control for a Sustainable Utilization Strategy. *Proceedings: Geothermal Rising Conference 2023*, Reno, Nevada, USA. GRC Transactions, Vol. 47, 2023.

Manterola Donoso, A. “Optimization of geothermal well control for a sustainable production strategy using stock reservoir modelling” [Internet] [Thesis]. Reykjavik University; 2022. Available from: https://skemman.is/handle/1946/42384

Franco, A., Vaccaro, L. Numerical simulation of geothermal reservoirs for the sustainable design of 554 energy plants: A review. *Renewable and Sustainable Energy Reviews*. 2014 Feb; 30: 987-1002. 555 Available from: https://doi.org/10.1016/j.rser.2013.11.041. 556

Klüpfel, S., Gunnarsson, G. Flexible Lumped Parameter Modelling for Low-Temperature Reservoir 557 Assessment. *Proceedings World Geothermal Congress 2020+1*, Reykjavik, Iceland. 2021 Apr – Oct. 558 12p.

Permeability and Numerical Modeling of the Puna Geothermal Venture

John Murphy, Nicholas Prina, Paul Spielman, Drew Spake

Ormat Technologies, Inc.

Keywords

Puna Geothermal, Permeability, Numerical Modeling, Well Testing, Reservoir Engineering, Case Study

ABSTRACT

The Puna Geothermal Venture (PGV) power plant was restarted in 2020 following the 2018 Kilauea eruption, providing a unique opportunity to quantify the impacts of this eruption on permeability, temperature, and pressure in the geothermal reservoir. Permeability was quantified using multiple datasets which show reduced permeability in some production fractures but overall good permeability remaining in others.

A numerical model was developed which simulates the pre-eruption and post-eruption reservoir behavior. The numerical model was calibrated to historical reservoir performance and the unique effects of the eruption, including temperature recovery and changes to the permeability distribution. The resulting model accurately matches the post-eruption temperature recovery and the reservoir pressure response to the plant restart under the modified permeability regime.

1. Operational History of the Puna Geothermal Venture

The first exploration wells in Puna were drilled in the early 1960s by Hawaii Magma Power. The Hawaii Geothermal Project conducted federal and state funded research and drilled several wells in the 1970s. The Hawaii Geothermal Project – Abbot (HGP-A), an experimental 3 MW power plant, was completed in 1981 and operated until December 1989 (Kim, 2018).

The Puna Geothermal Venture (PGV) was founded in 1981. Three wells were drilled from 1981 to 1985. A 25 MW power sales contract was signed with Hawaii Electric Light Company (HELCO) in 1986. More wells were drilled in 1991 and power production began in 1993 using steam in a combined cycle (steam turbine with binary condenser) air cooled plant with 100% reinjection of produced fluid. Wells were drilled in 1993, the contract was increased to 30 MW in 1995, and more wells were drilled from 2001 to 2010. The contract was increased to 38 MW in 2012 and a bottoming unit was constructed to generate power from hot water produced with the steam.

The Lower East Rift Zone of Kilauea erupted in May 2018. Earthquakes became frequent on May 1st and the plant was shut down on May 3rd after lava began erupting in nearby Leilani Estates.

Bridge plugs and cement were installed in production wells, piping was removed, and the wellheads were covered with cinders. Lava continued flowing until August 8, 2018. Three wellheads were covered with lava and the substation was destroyed. Recovery work began in 2019 after which a total of six wells were drilled and five pre-eruption wells were worked over. The 2022-2023 drilling campaign consisted of three additional wells after which the plant generated over 32 MW.

2. Reservoir Pressure and Temperature Response to Eruption and Shut-In

During the process of safely securing the wellfield and then preparing for restarting the plant in 2020, downhole surveys were conducted which showed the response to the plant shut-in and eruption. Wellhead pressure observations during the eruption showed increases to over 1840 psig in KS-14 and dissipated to 1100 psig over one day (Spielman et al., 2020). In October 2018 a pressure survey was conducted which showed indications that pressure had reduced significantly, about 3 bar above pre-development conditions; a survey in late April 2020 in KS-18 showed that after two years of no production, the reservoir pressure had returned to pre-development conditions.

Temperature also showed a significant recovery and increase during the eruption. Tracer flow test (TFT) data collected in wells KS-14 and KS-16 prior to the eruption showed enthalpy declines to 1270 kJ/kg, which was interpreted to represent liquid reservoir conditions around 290 °C. This interpretation was supported by a flowing pressure/temperature survey of KS-16ST in 2015 which showed a liquid reservoir feedzone at 292 °C. This section of the reservoir had therefore declined in enthalpy in response to production, as initial reservoir temperatures in the production zones were > 310 °C, based on downhole survey and a flowing enthalpy of 1450 kJ/kg in KS-14. In April 2019, after drilling KS-14RD2, a static survey measured 330 °C in the production reservoir. After plant startup, a survey in KS-18 measured a flowing temperature of 311 °C indicating that the temperature impact of the eruption was to effectively "reset" these temperatures, undoing the temperature declines observed during the first 25 years of operation. Based on a reservoir engineering interpretation of static and flowing temperature surveys and flowing enthalpies, an interpreted post-eruption temperature was compiled for the production reservoir. This compiled temperature is shown in Figure 15 and was used for the numerical model calibration for the production reservoir.

Well KS-15, east of the production area was also impacted by the eruption. While the maximum temperature measured in KS-15 prior to the eruption was 278 °C, a survey in October 2018 showed temperatures as high as 310 °C at the depths of the production reservoir. A subsequent survey in March 2019 measured only 213 °C at these depths, suggesting that although there was a significant heat input, it was not sufficient to permanently alter the temperature distribution beyond the natural conditions observed prior to the PGV development or the impact of long-term injection into KS-15.

The injection area (northwest of production, separated by 200-300 m) was at similar temperatures to the production area prior to the PGV plant startup. Limited equilibrated survey data was able to be obtained in the injection area following the eruption, but the data that was collected did not show a recovery to natural state temperatures in the feedzones. This suggests that the heat input from the eruption was not sufficient to reverse the long-term impact of cool injection in this area. The 2018 eruptive fissures were 200 – 400 meters south of the production area (Lundblad and

Anderson, 2020), and further from the injection area, and the lack of temperature recovery is consistent with the increased distance from the input of magmatic heat.

3. Characteristics of Permeability at the Puna Geothermal Venture Before and After the 2018 Eruption

Permeability in the Puna geothermal reservoir is primarily characterized by discrete fractures in a NE-SW orientation. Wells in the production field are deviated south from the plant area, crossing one to three fractures depending on depth and deviation direction. These fractures are named according to wells that first encountered permeability in those fracture. In the western portion of the production reservoir, these are the KS-8, KS-14, and KS-5 fractures from north to south. Figure 1 shows a map view at surface with the key fractures shown. Further details on the geologic model are provided in Spake et al, this volume. Prior to the 2018 eruption, the KS-14 and KS-5 fractures were the primary sources of production, with the KS-14 hosting very high permeability. Following the 2018 eruption, wells crossing the KS-14 fracture have shown zero to low permeability in that zone. In contrast, well KS-18 (drilled post-eruption), encountered significant permeability in the KS-8 fracture. Deep drilling has also brought significant production success post-eruption, with the majority of production now sourced from the KS-5 fracture at elevations near -1500 mRSL.

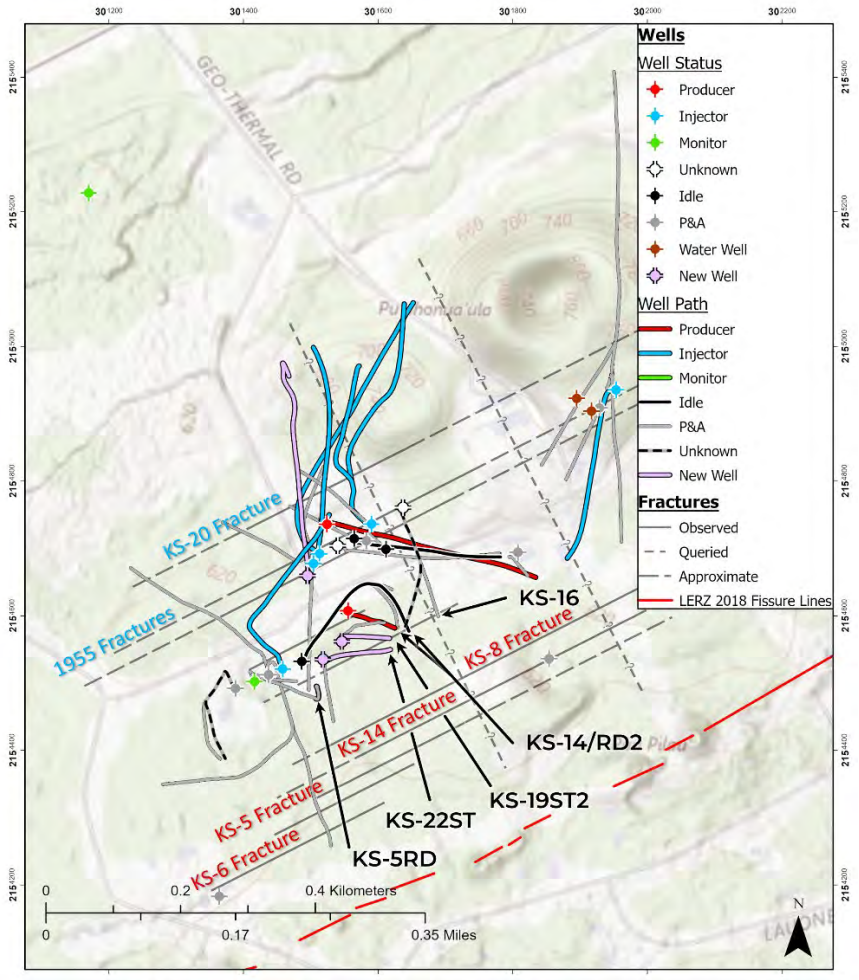

Figure 1: Summary Map of the Puna Geothermal Venture (adapted from Spake et al, 2024)

Four key datasets allow for quantification of permeability in the production reservoir at PGV. Firstly, wells undergo a rig injection test which provides a step-rate injectivity index and a fall-off test on which pressure transient analysis can be conducted. Secondly, interference testing was conducted during a 2023 completion test which gives a supporting dataset for the reservoir permeability. Thirdly, pressure decline over the period of months to years as measured by static downhole pressure surveys measures the bulk reservoir response to production and injection. Productivity index during long-term production provides a fourth dataset. Although complicated by two-phase effects in this high-temperature reservoir, wells with liquid feedzones give a good measure of the productivity index for comparison with other datasets.

3.1 Quantifying Permeability: Injectivity Testing and Productivity

Figure 2 summarizes step-rate injection testing at PGV from six wells drilled into the production reservoir. Conducted after drilling, these tests measure downhole pressure near the primary feedzones while increasing injection rate (although KS-5 pressure was measured at the surface, the measurement is a reasonable proxy for downhole pressure at low rates with negligible frictional effects). Three wells drilled pre-eruption (KS-16, KS-14, and KS-5RD) showed injectivity indexes from 6.5 kg/s per bar to infinite (no change in pressure while injecting). Comparatively, three wells drilled post-eruption (KS-19, KS-22, and a re-drill of KS-14) measured injectivity indexes from 0.9 to 2.5 kg/s per bar, a significant decrease. All post-eruption wells cross the KS-14 fracture which hosted the very high permeability in KS-14 and KS-16. Despite crossing the KS-14 fracture, wells KS-19 and KS-22 primarily feed from the KS-5 fracture. These repeated injection tests show a stark decrease in permeability after the 2018 eruption. Quantifying productivity in a similar way is more complicated, due to the effects of two-phase flow in the reservoir. Using downhole flowing surveys in wells with liquid feedzones, the pre-eruption wells (KS-16 and KS-14) had very high productivity indexes on the order of 25-400 kg/s per bar, with no drawdown observed in flowing surveys, whereas post-eruption wells with liquid feedzones (KS-18 and KS-22) have productivity indexes on the order of 5 to 15 kg/s per bar. Although the post-eruption wells are strong producers, they do not demonstrate the extremely high productivity observed in the KS-14 fracture prior to the 2018 eruption.

An interesting feature of this dataset is the relationship between injectivity and productivity in post-eruption wells tested at PGV wherein the productivity for liquid feedzones is roughly 5-10 times the injectivity during completion testing of those same feedzones. This differs from many geothermal fields where the inverse relationship is observed. A study by Grant et al. (2013) over several high temperature reservoirs found an average 3.5:1 ratio of injectivity from completion testing to productivity. Pressure transient analysis of completion tests and an interference test at PGV give insight to the nature of this relationship and also to the actual permeability of the KS-5 fracture at PGV.

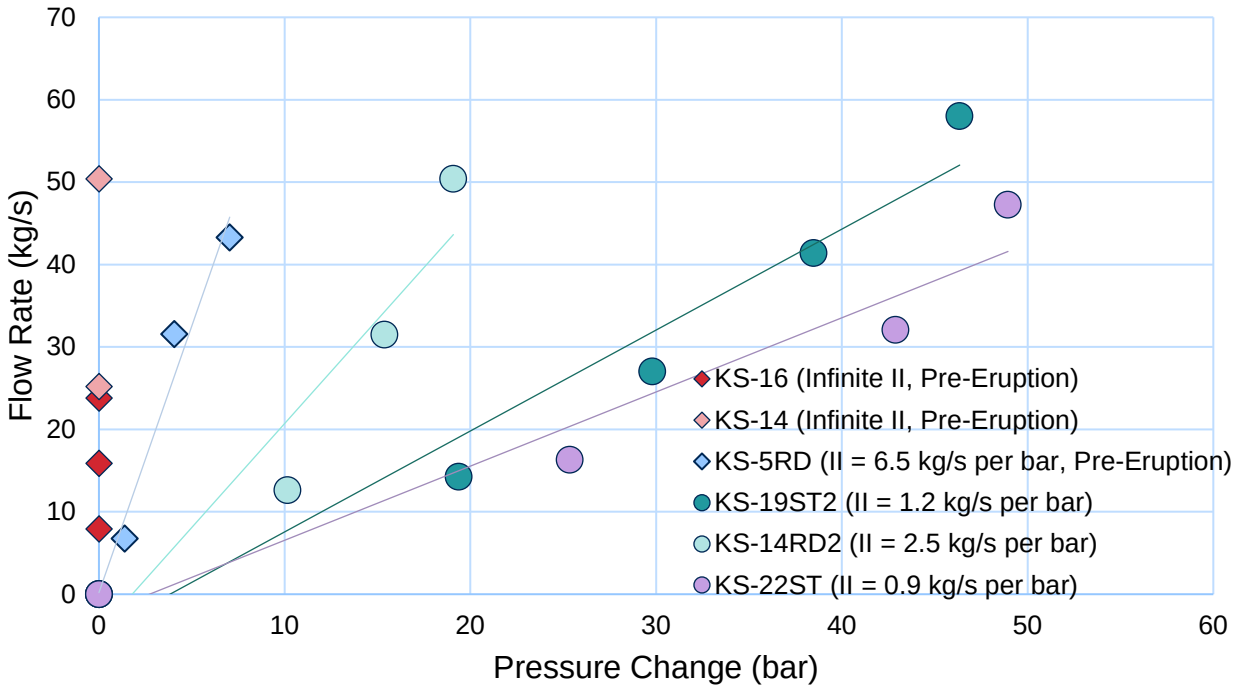

Figure 2: Summary of Injectivity Testing at PGV

3.2 Quantifying Permeability: Pressure Transient Analysis of Fall-Offs and Interference

Figure 3 shows the pressure transient analysis of the fall-off in well KS-19ST2, which is typical of wells at Puna post-eruption. No similar data was available for the pre-eruption wells; with near-infinite injectivity the temperature effects dominate and prohibit meaningful pressure transient analysis. This analysis was conducted using equations for pressure transient type curves which rely on multiple parameters: permeability, thickness, well storage, skin, porosity, and compressibility as described in Kuchuk and Kirwan (1987). The time of pressure transient is corrected using the Agarwal method, appropriate for a fall-off after injecting, and the times are given in Aragwal time (Agarwal, 1980). After shutting injection off, pressure was measured near the feedzone for 1.8 hours, with an overall pressure change of 46 bar. Qualitatively, the majority of the pressure change occurs in the first 0.25 hours (44 bar), after which the pressure nearly stabilizes. This suggests very high skin, and indeed the matching model shown uses a high skin (100), and a moderate permeability-thickness of 17.5 darcy-meters (5.7E-4 md-ft).

During KS-22ST testing, an interference test was also conducted, with downhole pressure measured in KS-19ST at a horizontal spacing of 30 meters in the KS-5 fracture. The fall-off pressure in KS-22ST was similar to KS-19ST2 and very high, 52 bar, whereas the interference measured was small (0.5 bar), suggesting that the permeability of the formation is very high. This data can be matched with a pressure transient analysis using the Theis solution (1935) and the same permeability thickness of 17.5 darcy-m as was estimated from the KS-19ST2 fall-off test (Figure 4). One adjustment was needed: an increase to the compressibility to delay the onset of pressure response slightly. This could be reflecting the impact of colder, high-viscosity injection (discussed below), or a slightly two-phase reservoir. The eventual productivity of KS-22ST is closely predicted by the permeability-thickness; projecting the radial flow pressure response out to one year without skin returns a productivity index of 8.7 kg/s per bar, a good prediction of the

~10 kg/s per bar that has been calculated for these wells from flowing surveys and wellbore simulation (Figure 5).

The high skin is most likely an impact of near-wellbore cooling, a source of skin caused by the higher-viscosity cold fluid surrounding the well in a high-temperature/low-viscosity reservoir. This effect has been demonstrated by numerical modeling of injection tests (McLean and Zarrouk, 2015). Pressure transient analysis can also show the effect, with the same permeability-thickness applied to a reservoir of 49 °C, the long-term pressure response to the same flow rate is 6 times higher, predicting a productivity index of 1.4 kg/s per bar, of similar magnitude to the injectivity and the expected result if the whole reservoir were at the near-wellbore temperature after drilling. One possible explanation for the large skin/temperature effect at Puna is the discrete nature of the permeability. With a single dominant fracture contributing to permeability, the cool fluid circulated while drilling can effectively cool the fracture, whereas in reservoirs with more distributed permeability the cooling should extend less far into the reservoir.

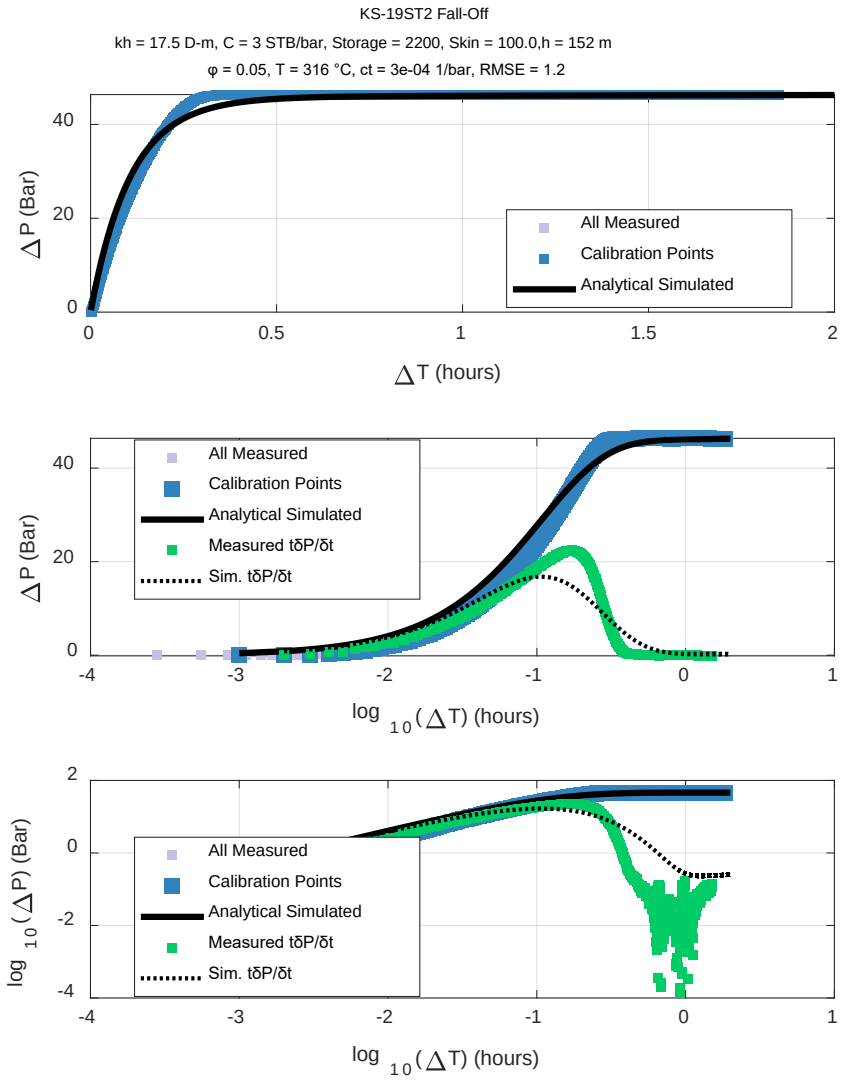

Figure 3: Pressure Transient Analysis for KS-19ST2 Fall-Off from Rig Injection Test

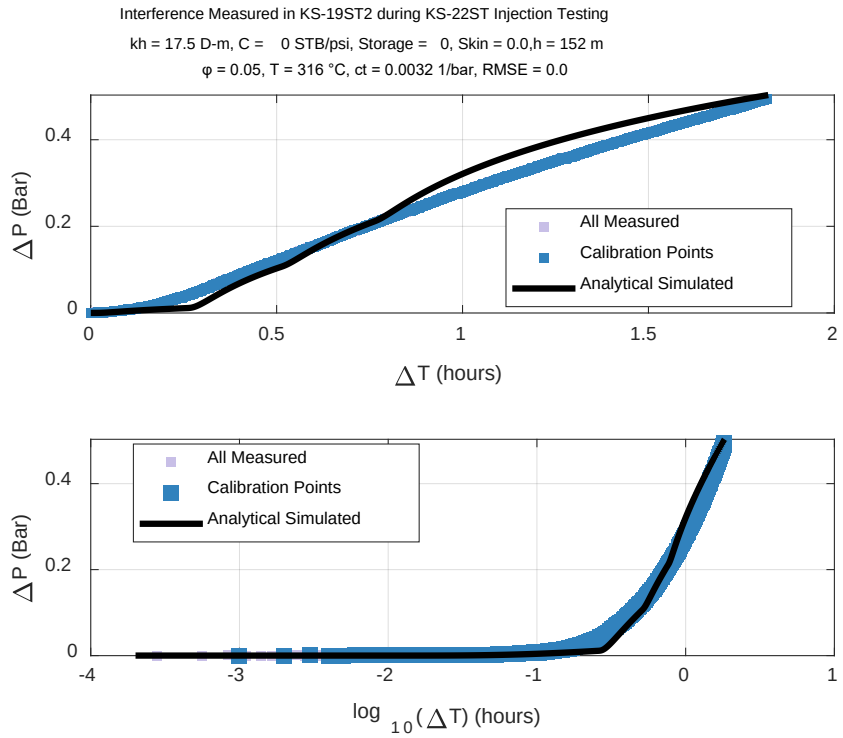

Figure 4: Interference Measured in KS-19ST2 During KS-22ST Injection Testing (30 m spacing)

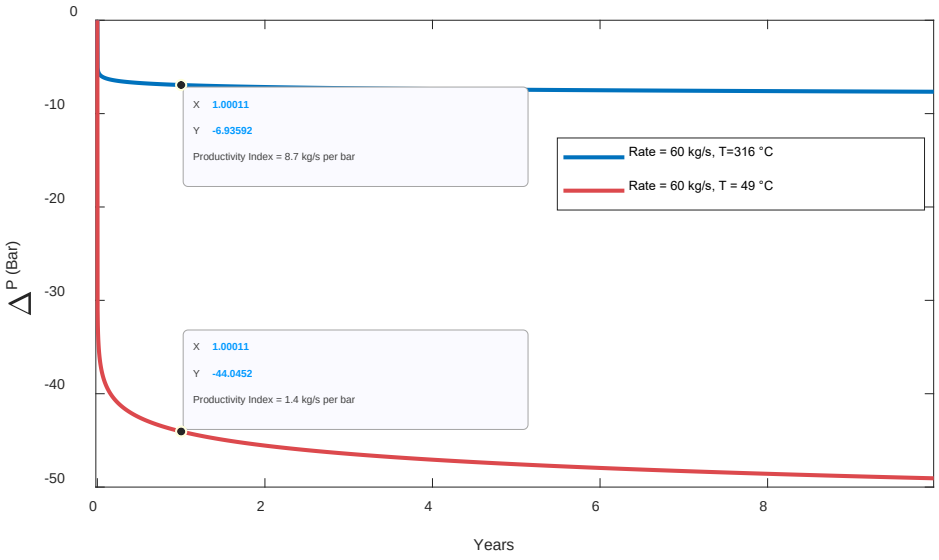

Figure 5: Forecasted Drawdown in KS-22ST Based on Interference Model (60 kg/s flow)

3.3 Quantifying Permeability: Reservoir Pressure Decline

The above tests quantify the short-term pressure responses to flow at PGV, and show that certain fractures in the pre-eruption reservoir hosted extremely high permeability, whereas the key fractures in the post-eruption reservoir host a more moderate but sufficient permeability. The longer-term pressure response to production also demonstrates a reduction in permeability. Figure

6 shows the pressure response at a representative reservoir datum (-1510 mRSL) from static surveys collected over the field history. This figure shows the initial pressure level around 132 bara, declining to a range of 102 to 112 bara as production is ramped up in the pre-eruption configuration, with the range representing operational fluctuations. The last two pre-eruption points measured in KS-14 and KS-16 are the most comparable to current conditions; at this time most of the production was coming from the same area of the PGV reservoir that is also producing post-eruption. During the plant shut-in during and after the eruption, pressure recovered to natural state levels, as discussed in the next section of this paper. In post-eruption operations, the reservoir pressure has declined to a similar range (again impacted by operational fluctuations). Normalizing these pressure changes to flow is instructive. As shown in Figure 7, the pressure change per flow in bar per kg/s was around 0.15 when producing mostly from the prolific KS-14 fracture (pre-eruption), whereas the same reservoir area post-eruption shows a decline of around 0.22 bar per kg/s (about 1.5x the pressure impact for a given total reservoir flow). When the KS-5 area was being produced earlier in the operational history the impact was similar, prior to the discovery and production from the most permeable area (KS-14 fracture) of the production area.

The story of any operating field is complex, with variations in production and injection strategies and production locations. On the whole, the data from PGV shows that the impact of the 2018 eruption was a decrease in individual well productivity and bulk reservoir permeability in the main production area. Key fractures, specifically the KS-8 and KS-5 fractures, remain permeable and highly successful production wells have been drilled post-eruption.

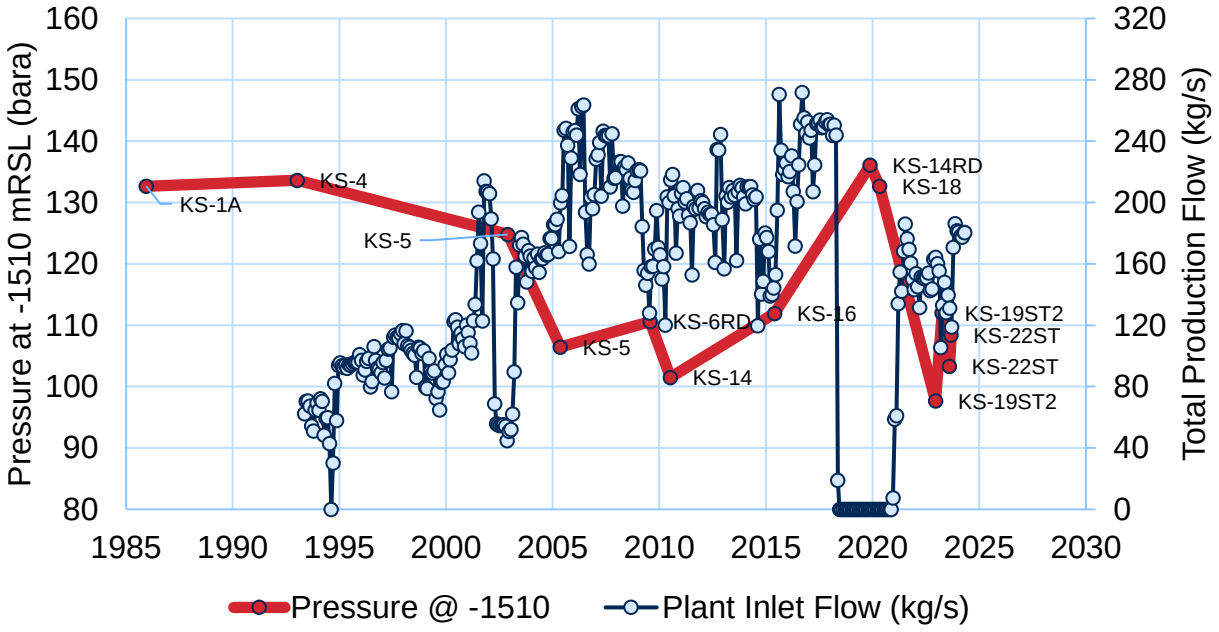

Figure 6: Reservoir Pressure and Total Flow History

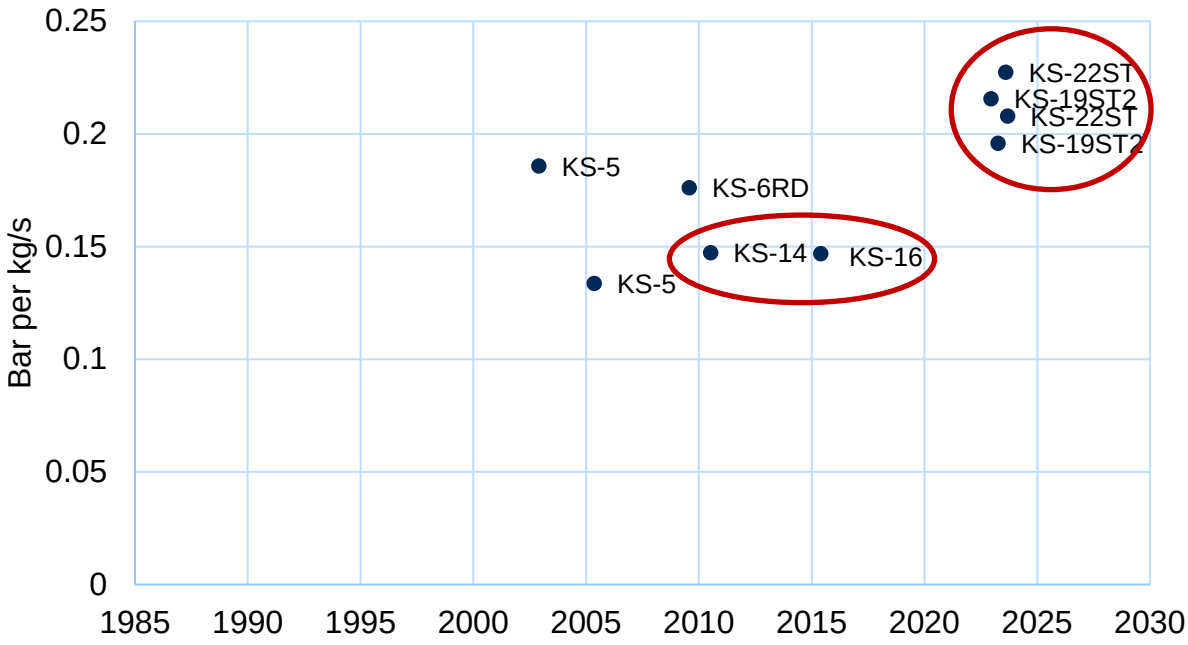

Figure 7: Reservoir Pressure Change Over Total Flow (bar per kg/s)

4. Numerical Reservoir Modeling

Due to the unique history of the PGV field, numerical reservoir modeling was conducted in three phases. (1) Pre-eruption natural state and operations, (2) a transient period of heat and mass input to simulate the impact of magma near the production area during the eruption, and (3) the post-eruption plant startup using an altered permeability structure, reflecting the changes measured in drilling, testing, and operations. Numerical modeling at Puna utilizes a combination of the Tetrad reservoir simulator (Vinsome and Shook, 1993) and the Volsung simulator (Franz et al., 2019).

4.1 Initial State Temperature Model

In the pre-eruption model, the natural state was characterized by a hot upflow centered on these permeable production fractures. Wells KS-1A and KS-3 encountered this upflow most directly, with a maximum temperature of 345-351 °C. KS-5 and KS-4 represent the productive western margin, with maximum temperatures of 337 °C and 325 °C, respectively. The impermeable margins of the system (characterized by conductive temperature gradients below -500 mRSL) are constrained by well SOH-1 to the northwest and Lanipuna 1 to the south. Permeable volcanic rocks overlay the capped geothermal reservoir. Cooler flowing fluid, predominantly a mix of meteoric and altered seawater, effectively sweeps heat leading to cooler temperatures from surface to the reservoir top which is encountered between -500 and -1000 mRSL. Figure 8 shows the natural state temperatures measured in key wells along with the simulated temperature from the calibrated model. Measured data is selected from the available surveys to best represent equilibrated reservoir conditions; in the case of Lanipuna 1, three surveys were used to generate a composite profile. Figure 9 shows the measured and simulated pressure in KS-1A, which has the best dataset to constrain reservoir pressure. In the reservoir at -1510 mRSL, reservoir pressure is 133 bara.

4.2 Permeability Models

The pre-eruption permeability model is shown in Figure 10, with a maximum permeability of 8000 md assigned to the KS-14 fracture. High permeability is used as a damage zone around this feature. As described above, the effect of the 2018 eruption was a significant decrease in the permeability of the KS-14 fracture. The KS-8 fracture hosts a feedzone in KS-18 but has not been successfully targeted again, suggesting a high degree of heterogeneity. The KS-5 fracture is highly permeable, as quantified by well testing in the previous section. The modified permeability distribution is shown in Figure 11. Note NW-SE fractures exist at depth connecting injection to production. The nature of the disconnection between east and west sectors of the production reservoir is uncertain, earlier tracer testing suggested a moderate disconnection, whereas post-eruption testing shows that the east and west are more strongly connected. This may be due to the re-activation of the KS-8 fracture, which was the basis for increasing the permeable connection as shown in Figure 11.

4.3 Temperature Calibration and Heat Input during 2018 Eruption

The evolution of simulated temperature is shown in Figure 12 to Figure 14. The initial state temperature corresponds to the calibrated model in Figure 8. During plant operation, injection wells to the northwest of production cooled those fractures and moderately cooled production. This temperature decline is observable in enthalpy and the resulting subsurface temperature distribution is shown in Figure 13.

Figure 14 shows the same depth slice after the thermal input from the eruption. The impact of the eruption, as described above, was a reset of temperatures in the production area. In the numerical model, this was accomplished using a heat input to the permeable rock types. During the calibration period, it was determined that the heat input was likely sufficient to heat both the fractures and the surrounding matrix, due to the persistent nature of the heat recovery. If the fractures alone had been heated, the remaining low-temperature matrix would have tended to quickly cool the fractures after the end of the eruption, whereas observed enthalpies and flowing temperatures show that the higher temperatures persisted.

There was no clear evidence of significant heat recovery in the injection area. Over two years of plant-shut, the lack of injection did allow for some reheating in this area of the model, from temperatures near the injection temperature up to temperatures in the range 100-200 °C. Such temperature recovery is typical of geothermal systems when injection is shut-off, regardless of eruptive heat input.

Figure 15 shows the interpreted, measured, and simulated temperatures corresponding to the post-eruption conditions. The bold red squares in the production wells represent a composite profile reflecting the best data from downhole static and flowing surveys and flowing enthalpy. This was interpreted to be generally uniform across the production area. Where available, select actual static surveys are shown, although these generally differ from the interpreted composite profile and are impacted by circulation during drilling/workovers, injection, and transient effects.

In the simulated curves, the blue dashed line represents the simulated pre-eruption conditions. This is heavily cooled in the injection feedzones, and moderately cooled in the production feedzones. This cooling was greater in KS-5RD than KS-14 based on observations; as KS-17 and KS-18 were drilled after the eruption, no data was available to constrain the pre-eruption conditions in those

wells. KS-17 is known to have a strong connection to KS-15, so the cooled zone in the simulated blue line for that well shows the effect of long-term injection into KS-15.

The black lines, solid and dashed, represent the simulated fracture and matrix temperatures at the end of the simulated heat input period. These closely match the composite profile for production wells. The profiles for injectors show a small degree of heat-up.

4.4 Pressure Response Calibration

As described in Section 3.3, above, the reservoir pressure history of PGV can be constructed from selected static surveys throughout the operating history. Figure 16 shows the measured and simulated pressure response. Up to plant restart in 2020, the pre-eruption permeability model is used, and a good match is achieved to the measured data. The difference between measured and simulated pressure in KS-5 in 2002 is due to that well's feedzone being located further west than most of the production during that period of operations, whereas the simulated data is taking from the central production reservoir. For the pressure decline observed after plant restart in 2020, the post-eruption permeability model is applied. The good match to the observed data lends support to the modeled permeability distribution and the interpreted impact of the permeability reduction in the KS-14 fracture.

5. Conclusion

With over 31 years of commercial power production at the Puna Geothermal Venture power plant, the field lends itself to robust analyses of permeability and a well-calibrated numerical model. The 2018 Kilauea eruption resulted in a two-year pause in operations, and the data gathered during recovery and restart give unique insights to the impact of the eruption on the geothermal system. The Puna reservoir remains highly productive following the eruption. The KS-14 fracture, previously a source of very high permeability in the production reservoir, has diminished significantly, with the majority of production now coming from the KS-8 and KS-5 fractures. Numerical modeling and calibration to the reservoir performance requires an adjusted permeability model to represent the post-eruption reservoir.

Temperature, which had undergone moderate declines in the production area during the first 25 years of commercial operations, recovered in the production areas during the eruption and plant shut-in. Numerical modeling of this temperature recovery utilized direct heat input of a sufficient magnitude to heat both the fracture and matrix domains of the model. Temperature in the production area remains elevated compared to the pre-eruption conditions, supporting the conclusion that the eruption and shut-in reversed the impact of temperature decline due to production and injection. After an initial period of elevated pressures, as observed from wellhead pressures during the eruption, the reservoir returned to initial (pre-development) pressure following two years without production and injection. The bulk permeability of the reservoir is somewhat lower after the eruption, as quantified by the moderately higher pressure decline in response to production and injection, compared to pre-eruption observations.

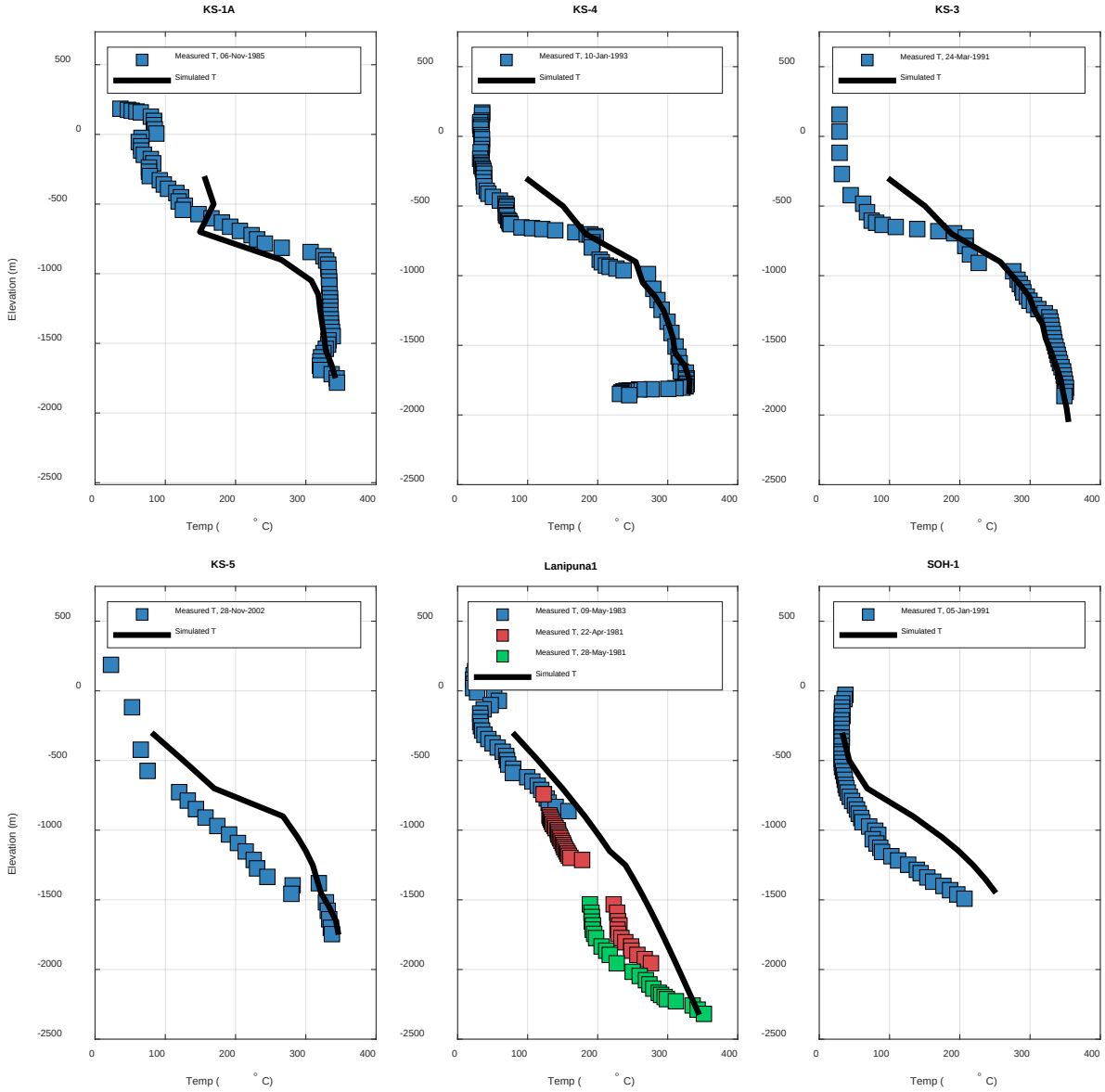

Figure 8: Measured and Simulated Initial State Temperature

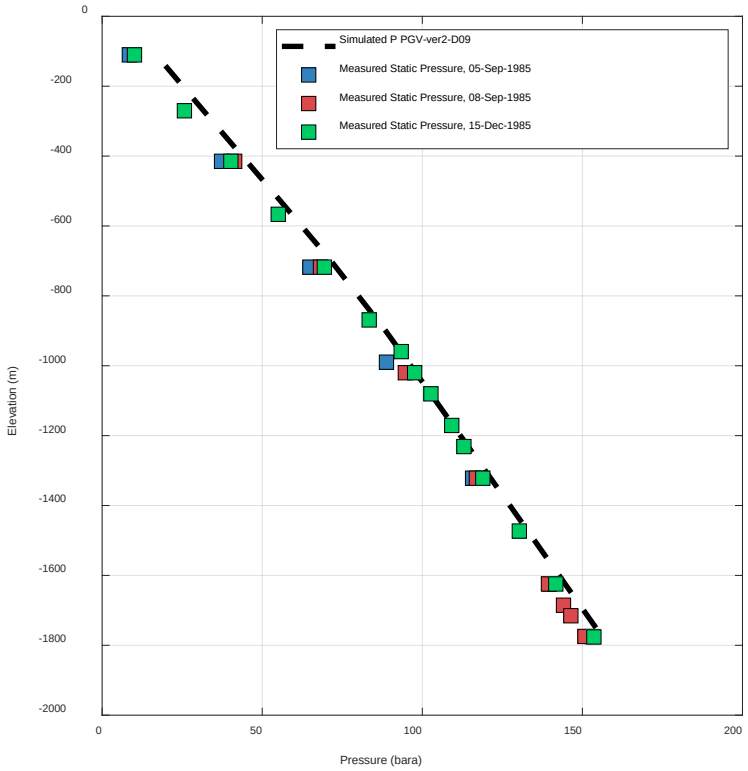

Figure 9: Measured and Simulated Initial State Pressure in KS-1A

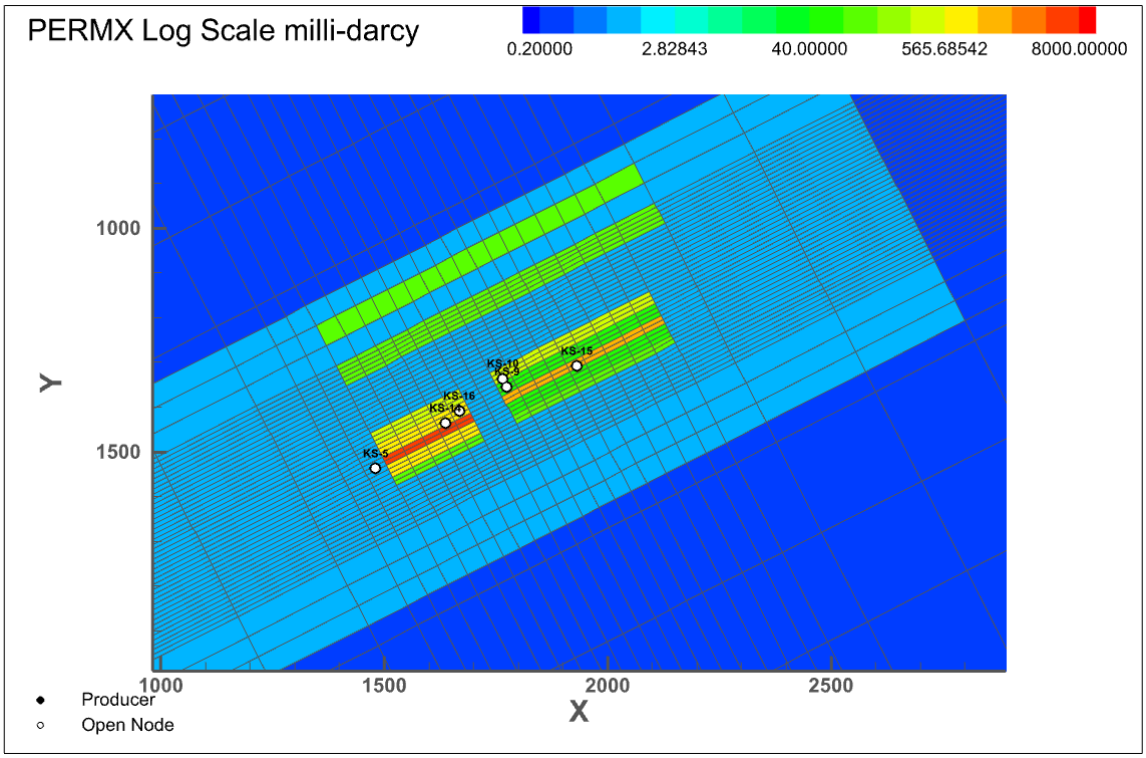

Figure 10: Numerical Model Pre-Eruption at -1350 mRSL

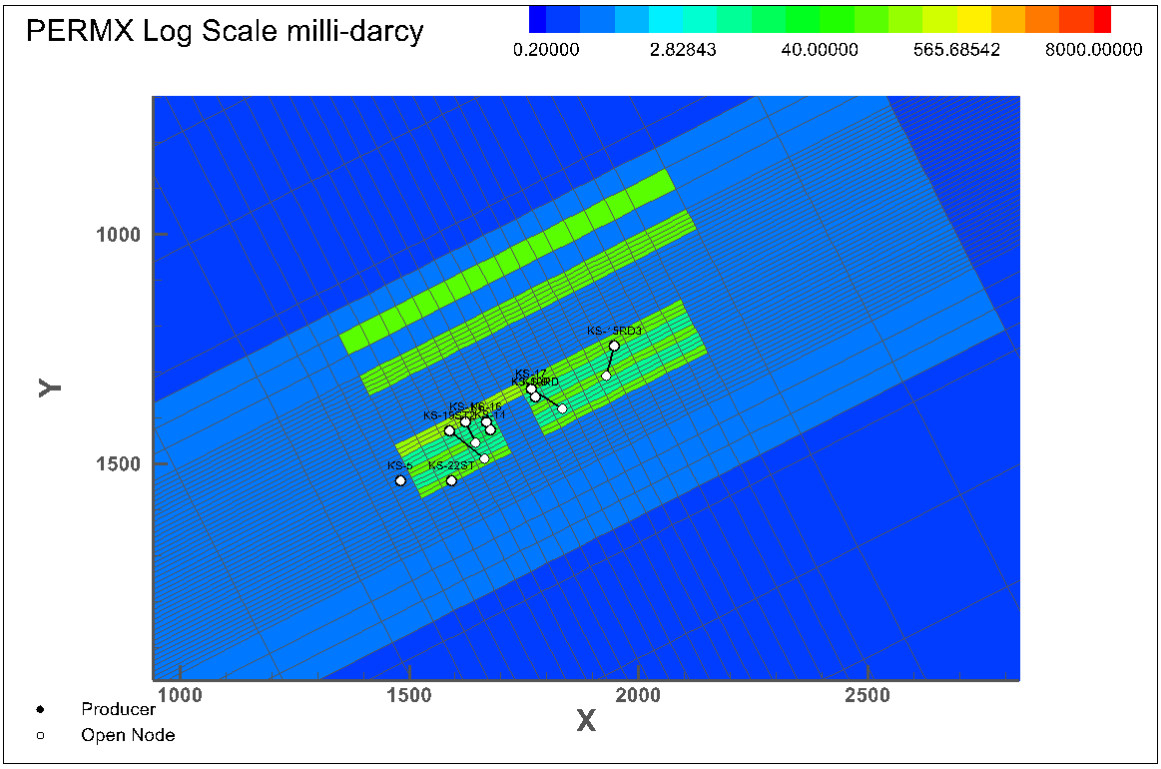

Figure 11: Numerical Model Permeability Post-Eruption at -1350 mRSL

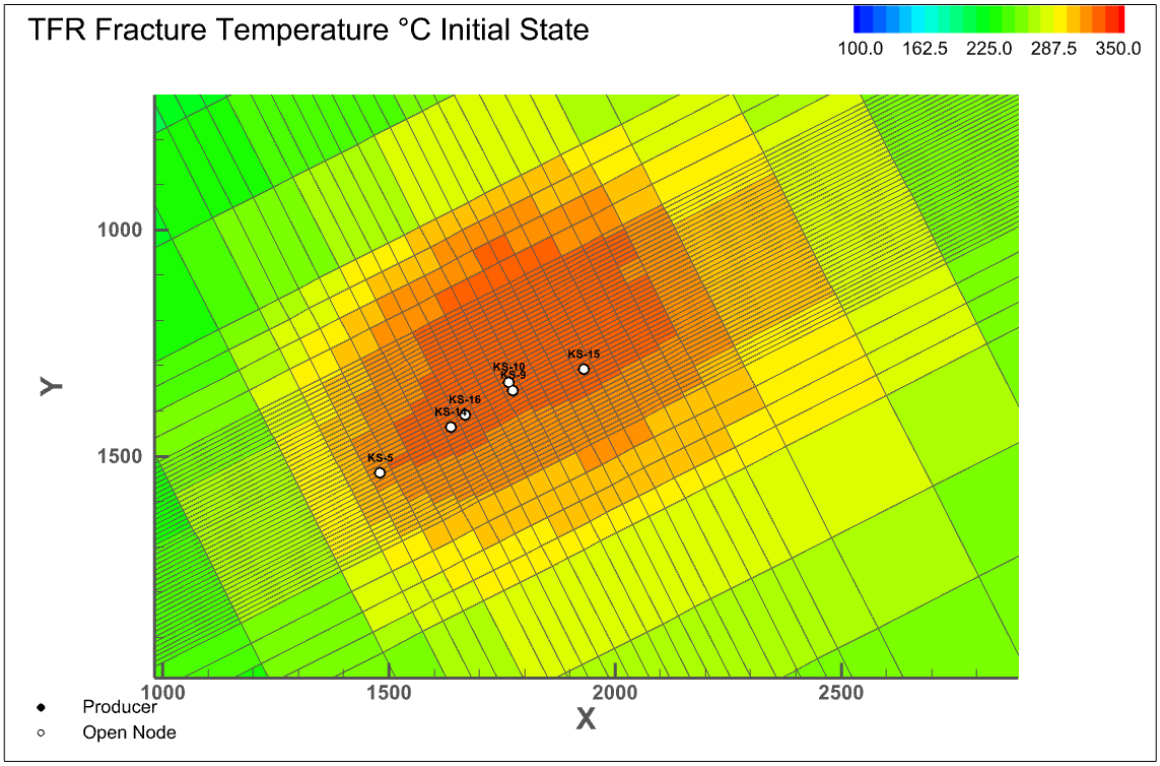

Figure 12: Initial State Simulated Temperature at -1350 mRSL

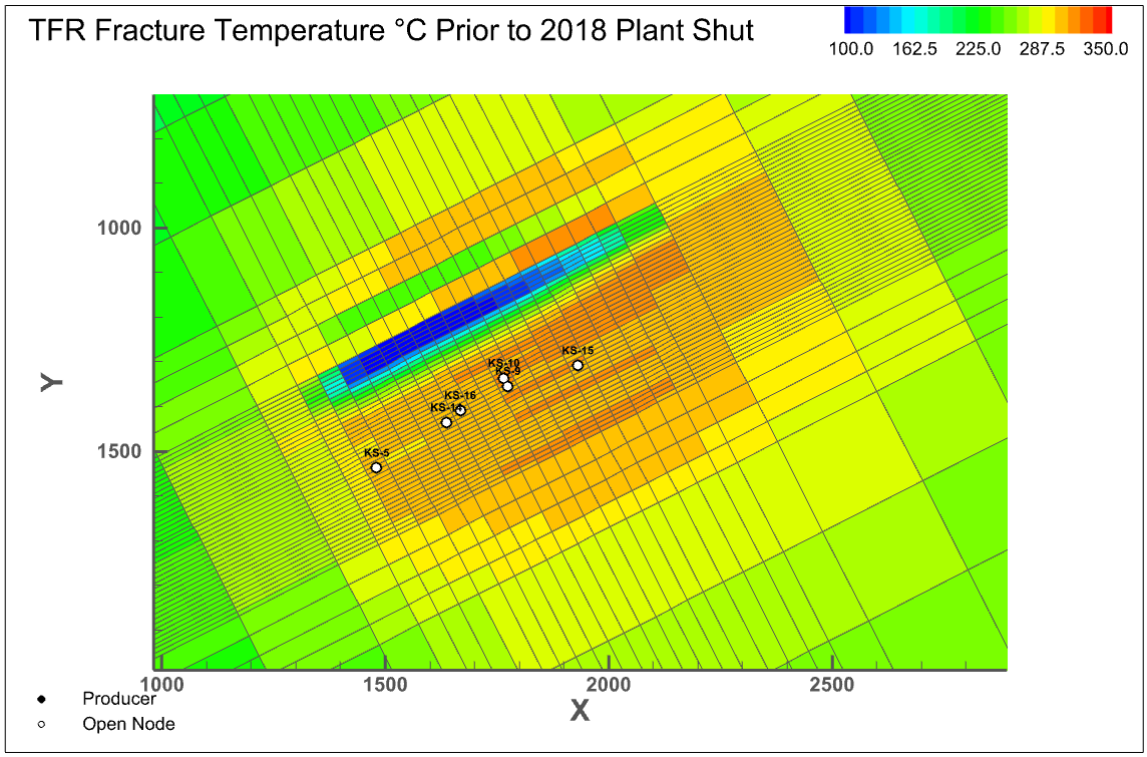

Figure 13: Simulated Temperature Prior to Plant Shut-In at -1350 mRSL

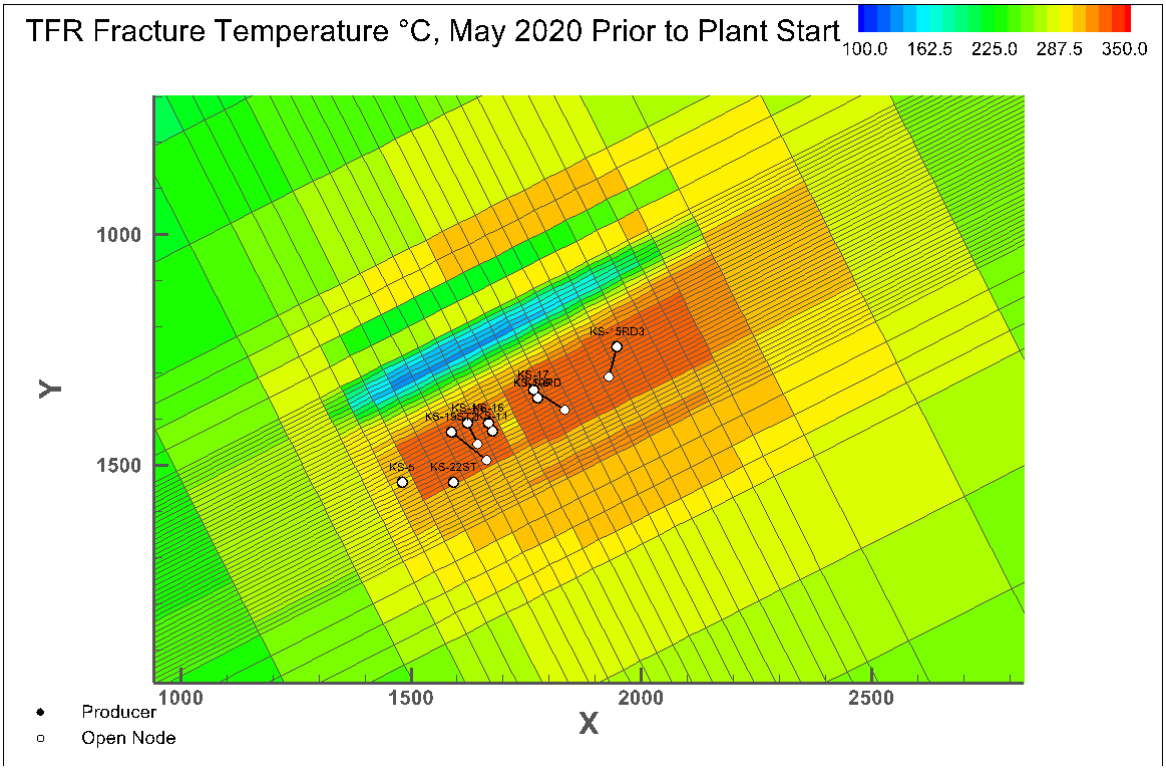

Figure 14: Simulated Temperature after Eruption, Prior to Plant Start

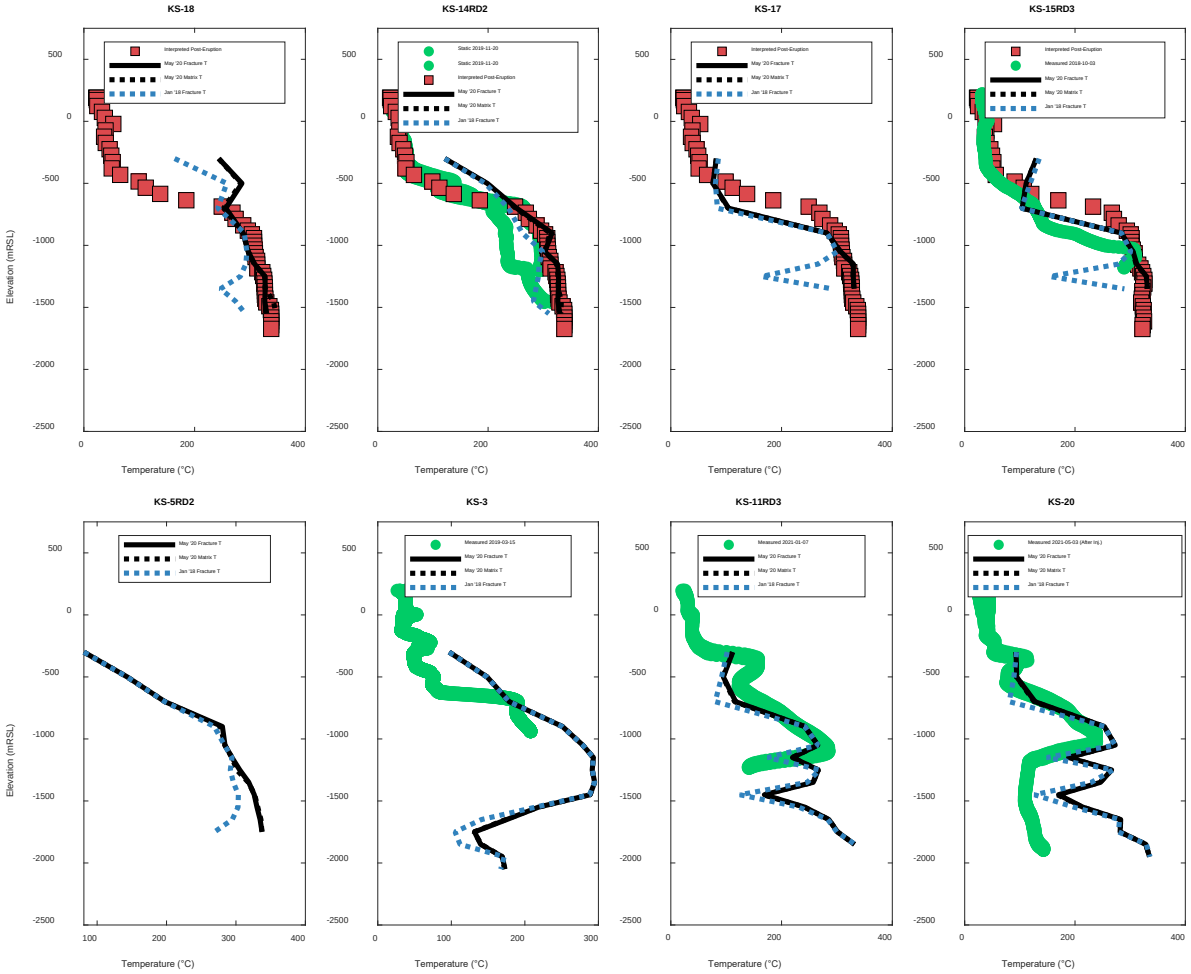

Figure 15: Measured, Interpreted, and Simulated Temperature Post-Eruption

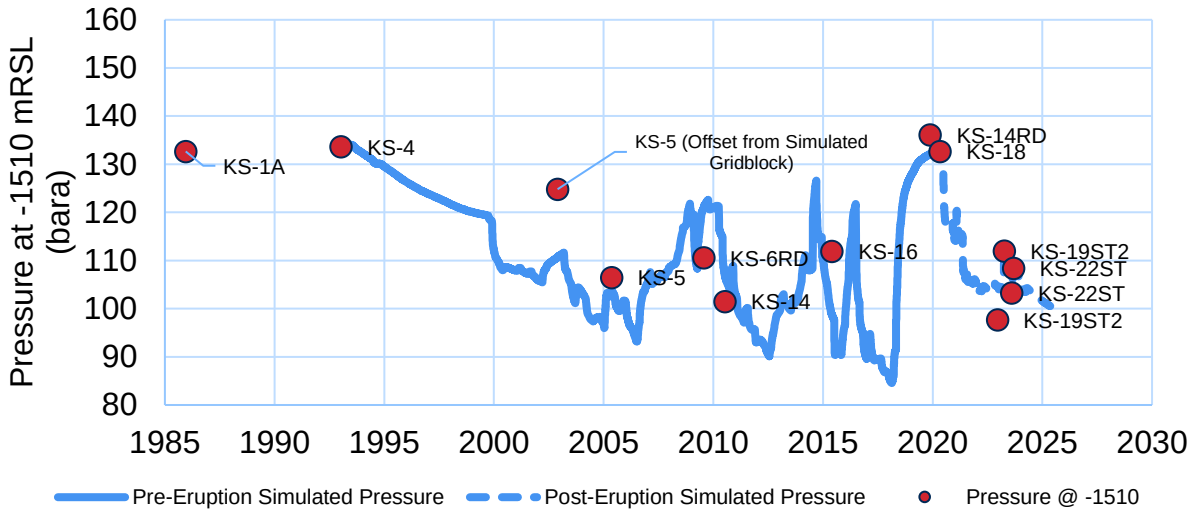

Figure 16: Pressure Matching in Pre- and Post-Eruption Models

REFERENCES

Agarwal, R.G. “A new method to account for producing time effects when drawdown type curves are used to analyze pressure buildup and other test data.” *Proceedings of the 55th Annual Fall Technical Conference and Exhibition of the Society of Petroleum Engineers*, Paper SPE 9289, Dallas, Texas (1980).

Grant, M.A., Clearwater, J., Quinão, J., Bixley, P.F., Le Brun, M. “Thermal Stimulation of Geothermal Wells: A Review of Field Data.” *Proceedings: 38th Workshop on Geothermal Reservoir Engineering*, Stanford University, Stanford, CA (2013).

Franz, P., Clearwater, J., and Burnell, J. “Introducing the Volsung Geothermal Simulator: Benchmarking and Performance.” *Proceedings, 41st New Zealand Geothermal Workshop* (2019).

Kim, Alice. “HGP-A – Hawaii Geothermal Project – Abbott”. *Hawai’i Groundwater & Geothermal Resources Center, University of Hawai’i at Mānoa.* 4 Nov. 2018, https://www.higp.hawaii.edu/hggrc/projects/geothermal-digital-collection/geothermal-collections/geothermal-topic-guides/hgp-a-hawaii-geothermal-project-abbott/

Kuchuk, Fikri J. and Kirwan, Paul A. “New Skin and Wellbore Storage Type Curves for Partially Penetrated Wells.” *Society of Petroleum Engineering Formation Evaluation*, Vol. 2, Issue 4 (1987)

Lundblad, S. P. and Anderson, J. L. “Structural Controls on Early Behavior of the 2018 Kilauea East Rift Zone Eruption Inferred from Geodetic Surveys.” *GRC Transactions*, Vol. 44 (2020), 882-893.

McLean K. and Zarrouk, S. J. “Impact of Cold Water Injection on Geothermal Pressure Transient Analysis: A Reservoir Modelling Assessment”. *Proceedings: 37th New Zealand Geothermal Workshop*, Taupo, New Zealand (2015)

Spake, D., Reynolds, Z., Caro, D., Prina, N., Murphy, J., Johnson, A., Spielman, P., Zuza, R., Webbison, S. “Conceptual Model of the Puna Geothermal System.” *GRC Transactions*, Vol. 48 (2024).

Spielman, P., Drakos, P., Tennison, J., Prina, N., Bakane, P., Dahl, G. “Damage and Repair of Puna Well KS-14.” *GRC Transactions*, Vol. 44 (2020), 894-903.

Theis, C.V. “The relation between the lowering of the piezometric surface and the rate and duration of discharge of a well using groundwater storage”. *Am. Geophys. Union Trans*., Vol. 16, (1935), 519-524.

Vinsome, K.W. and Shook, M. “Multi-Purpose Simulation.” *Journal of Petroleum Science and Engineering*, Vol. 9 (1993), 29-38

Puna Geothermal Venture Flow Testing: Facility Design Upgrades and Results

Nicholas Prina[1], Doug Jung[2], John Akerley[1], Derek Caro[1], Patrick Broderick[3], Charley Wahl[3], Paul Spielman[1], Adam Johnson[1], Ezra Zemach[1], Jordan Hara[4], Gary Dahl[4]

[1]Ormat Technologies, Inc.

[2]Two Phase Engineering & Research, Inc

[3]West Coast Geologic Inc.

[4]Puna Geothermal Venture

Keywords

Puna, Hawaii, flow testing, high enthalpy, flow metering, abatement, atmospheric cleanout flow, hydrogen sulfide, Puna Geothermal Venture, PGV, flow test design

ABSTRACT

Atmospheric cleanout flows and flow tests are standard practices at geothermal projects around the world. These tests are typically conducted after new wells are drilled and act both to cleanout drilling debris from permeable zones and provide initial indications of well performance and reservoir characteristics. However, cleanouts and flow tests have not been conducted at the Puna Geothermal Venture field since 2006 due to complex permit requirements and risks associated with hydrogen sulfide gas and related abatement chemicals. This challenge led to the practice of starting new wells directly to the power plant, which resulted in issues with both well performance and plant equipment. In 2022 an upgraded flow test facility was designed and following completion of two new production wells in 2023, atmospheric cleanouts were safely and successfully conducted using the upgraded facility and improved abatement practices. The tests were completed within permit constraints and ultimately led to increased power generation and improved well performance.

1. Introduction

The Puna Geothermal Venture (PGV) power station is located on the east side of the Island of Hawai'i. The PGV power station began generating power in 1993 with an Ormat-supplied 30 MW capacity plant consisting of 10 nominal 3 MW units utilizing the produced steam only. Ormat

acquired PGV in 2004 and in 2012 added two new plant units with an additional total 8 MW of installed capacity utilizing the brine phase and Ormat Energy Converter (OEC) technology.

The PGV power station was taken offline in May 2018 as a result of the 2018 Kilauea eruption. PGV resumed power generation in late-2020 following the completion of three new geothermal wells and one redrill. Three additional wells were drilled in 2022 and 2023, including new production wells KS-19 and KS-22 which were successfully flow tested utilizing an upgraded flow test facility.

Flow testing is a crucial step in the well completion process for geothermal projects. It involves evaluating the performance and characteristics of a geothermal well by allowing the hot fluid (water or steam) to flow from the reservoir to the surface in a controlled manner. This testing phase provides valuable data on the well's productivity, temperature, pressure, and fluid composition (Hole, 2008). By analyzing this information, engineers can assess the potential energy output of the well, determine the optimal flow rates, and identify potential issues. Flow testing also helps in designing and sizing the surface equipment, such as pipelines, heat exchangers, and power generation facilities, to ensure efficient and sustainable energy production from the geothermal resource (Axelsson, and Steingrímsson, 2012). Additionally, it aids in estimating (and optimizing) the long-term sustainability of the geothermal reservoir and guides future well drilling and field development strategies.

Initial flow testing following drilling completion also assists with well development by cleaning the wellbore and permeable fractures of drilling debris (Grant and Bixley, 2011). This drilling debris typically consists of formation cuttings and remnant drilling fluid which should be cleaned out prior to flowing to power generating facilities. If drilling debris is not properly removed from the wellbore and productive fracture system during flow testing, it can result in negative impacts on both power generating facilities and long-term well performance, both of which have been observed at PGV. To avoid these issues following completion of new wells, PGV worked with Two-Phase Engineering & Research, Inc (TPE) and West Coast Geologic Inc (WCG) to design upgraded testing facilities and implement updated abatement practices. The upgraded facilities and practices were developed with the goals of safely handling the high enthalpy reservoir fluid, safely managing the hydrogen sulfide gas (H_2S) in produced reservoir fluid, minimizing gas emissions, and adhering to unique regulatory requirements.

Use of the upgraded PGV flow test facility proved very effective in achieving desired goals, with brine carryover effectively eliminated and H_2S concentrations in the testing area remaining below 1 part per million by weight (ppmw) for the duration of the flow tests. Total H_2S emissions were more than 17 times below the regulatory limit during the first 2023 test and more than 200 times below the regulatory limit during the second 2023 test. Steam velocity was successfully measured with a constant temperature anemometer designed for wet/condensing gasses, allowing a direct enthalpy calculation.

Overall, the two tests completed in 2023 confirmed atmospheric testing can be safely conducted at PGV with conditions maintained well within the permit limits. Completing atmospheric cleanout flows for new wells provides significant value to the PGV reservoir and power generating facilities. Flow through the upgraded flow test facility allowed the production fracture system to be cleaned of drilling debris prior to initiating flow to the plant, resulting in improved long-term performance of the production wells. The drilling debris was successfully managed by the flow

test facility and later safely disposed of, instead of flowing through the plant gathering system where it can cause equipment fouling and down-time for maintenance. Further, between 2006-2022, prior to the reimplementation of atmospheric cleanouts, starting new wells at PGV was a challenging process requiring generation to be reduced to a minimum as the new wells came online. Use of the upgraded flow test facility allows wells to be put into service seamlessly, with no negative impact on plant generation.

2. Background

Completing atmospheric cleanout flows and flow tests is standard practice at geothermal projects around the world. These tests are typically conducted after new wells are drilled and act to both clean out drilling debris from permeable zones and provide initial indications of well performance and reservoir characteristics (Grant and Bixley, 2011). However, cleanouts and flow tests have not been conducted at the Puna Geothermal Venture field since 2006 due to complex permit requirements and risks associated with hydrogen sulfide gas. As a result, between 2006-2021, new production wells were started directly to the plant. Starting new production directly to a power plant is not common practice for geothermal facilities around the world due to several key risk factors:

1) Drilling debris including cuttings and residual drilling fluid is not fully cleaned out of the wellbore or fracture system. This can result in reduced near-wellbore permeability and impaired production well performance over time.
2) Drilling debris that does flow to the surface during initial well startup is flowed into the gathering system and power plant equipment. This material can cause fouling of plant equipment, specifically in heat exchangers that utilize the separated brine phase.
3) In some cases, the drilling debris can make its way through the surface equipment and damage the permeability of injection wells.
4) Starting new wells directly to the plant typically requires generation to be reduced to a minimum to allow the well to heat slowly and begin production at commercial temperatures and pressures.

Following the 2019-2020 drilling campaign, new PGV production wells were started directly to the power plant without a period of atmospheric cleanout flow. This direct-to-plant startup procedure resulted in all four of the points above being observed to some degree. To avoid these issues in the future, Ormat and PGV completed background research to better understand why flow tests had not been completed in recent years and determine if they could be safely conducted for future wells.

Prior to the 2023 testing, the last atmospheric flow test completed at PGV was in 2006. Atmospheric cleanout flows were not conducted for new wells at PGV post-2006 due to stringent permit regulations that limit the duration of the flow test and require complex installations to abate H_2S in the geothermal fluid. From 2021-2022 Ormat, TPE, and WCG investigated the permit requirements and determined the following key requirements could be met with an upgraded flow test facility design:

1) Total H_2S emissions to be maintained below 2.27 kg/hr (5 lbs/hr).
2) Four-hour maximum duration of flow to atmosphere per day.

3) Hydrogen sulfide concentrations at the local air monitoring stations are not to exceed 10 parts per billion by weight (ppb) on a 24-hour rolling average or 25 ppb on a 1-hour average. Note: local air monitoring stations A1, B1, and C1 are located near the PGV lease boundary between 0.8 km and 1.1 km linear distance from the planned muffler location (Figure 1).
4) Hydrogen sulfide concentrations must be measured upstream and downstream of the abatement location at least twice during the 4-hour flow period to determine the abatement efficiency and ensure emissions remain below the permitted level.
5) Hydrogen sulfide abatement equipment must consist of a cyclonic muffler or other equivalent device designed to minimize particulate and brine aerosol emissions, and direct venting into a vertical direction.
6) A minimum sodium hydroxide (NaOH) treatment mole ratio of four (4) to one (1) ($NaOH/H_2S$) must be used initially and the abatement efficiency monitored.

These requirements are further detailed in PGV's noncovered source permit number 0008-02-N, a publicly available document issued by the Hawaii Department of Health Clean Air Branch. Following review of the flow test permit requirements, Ormat, TPE, and WCG began design work in 2022 with the goal of having equipment ready to test wells completed during the 2022-2023 drilling campaign.

3. Flow Test Facility Design

An upgraded flow test facility was designed by Ormat, TPE, and WCG with the goals of optimizing H_2S abatement and ensuring redundancies for both critical surface equipment (e.g., high pressure abatement pumps) and abatement dosing locations (e.g., primary and secondary ports for adding abatement chemicals). To increase abatement efficiency, ensure the abatement system is comprehensive, and improve collection of testing data, several upgrades were made to the facility design. The relevant upgrades are discussed below.

The Low Emission Atmospheric Metering Separator (LEAMS, Jung and Howard, 2000) was procured from Drill Cool Systems Inc. The LEAMS was designed by TPE in the 1990s and is used in place of a traditional cyclone separator to provide high brine/steam separation efficiency, effectively eliminating carryover of caustic brine in steam. The LEAMS was tested by Sandia in 2000 (Finger et al., 2000) with results indicating superior separation efficiency and minimal brine-carryover compared to a traditional cyclone separator at a similar flow rate and enthalpy conditions. The LEAMS design met the goals of the upgraded design for PGV flow testing.

In place of a James Tube (James, 1962), steam velocity is planned to be measured at the muffler outlet using high-temperature anemometers. Compared to a traditional cyclone muffler, the LEAMS has a relatively constant velocity profile along the muffler outlet. This allows a representative steam exit velocity to be recorded from a point source at the LEAMS outlet. The steam exit velocity can be used together with the brine flow rate from the weir box and atmospheric separation conditions to facilitate a direct calculation of the steam mass flow rate, total mass flow rate, and total flow enthalpy. Two different types of high-temperature anemometers were selected for testing. The first was a mechanical vane anemometer with a temperature rating of 100 ^oC, and the second was a constant temperature anemometer designed for condensing gasses with a temperature rating of 125 ^oC.

Figure 1: The figure above shows the PGV lease boundary as the light-blue line with the air monitoring station locations indicated as A1, B1, and C1. Straight line distances from the planned flow test location to the air monitoring stations are indicated.

A secondary abatement manifold was designed by TPE and installed on the LEAMS. This manifold allows the steam between the two LEAMS demister sections to be treated with NaOH solution (see Figure 2), effectively abating any H_2S remaining in steam following primary abatement of the two-phase flow upstream of the control valve (see reaction equation (1)). The goal of the secondary abatement manifold is to ensure H_2S emissions at the muffler outlet are maintained at a minimum, ideally well below the permit limit of 2.27 kg/hr.

$$H2S(g) + NaOH(aq) \rightarrow NaHS(s) + H2O(aq) \quad (1)$$

A basic schematic of the LEAMS muffler with the secondary abatement port locations and the planned positioning of the high-temperature anemometers is shown in Figure 2.

A static mixer assembly designed by TPE is installed on the 3-inch bypass to increase the abatement efficiency of potential gas slugs that could be encountered during the initial well startup. The static mixer is designed to provide efficient mixing of NaOH solution with dry gas or gas-saturated condensate that may be encountered during initial well discharge through the 3-inch bypass (bleed) line.

Amber HS (a chelated zinc-sulfate solution, Amber Chemical, Inc.) will be pumped into the weir box and weir box drain line to the lined sump to ensure H_2S precipitates out of solution as zinc sulfide, following the reaction shown in equation (2). Precipitation out of solution as zinc sulfide ensures H_2S gas will not break out of solution while brine is stored in the lined sump prior to safe disposal.

$$H2S(aq) + ZnSO4(aq) \rightarrow ZnS(s) + H2SO4(aq) \quad (2)$$

Two real-time H_2S sensors are installed on opposite sides of the LEAMS outlet to allow continuous reading and recording of H_2S concentrations in vented steam. Collection of real time data allows the NaOH pumping rates to be optimized and ensures the emissions remain below the permit limit and are minimized for the duration of the test.

Finally, a portion of the permanent plant piping tie-in will be used as part of the flow test flow line. This ensures the well can be controlled or shut-in by a remote operated control valve and allows all pressure control safety equipment used during long-term operation to be used during the flow test (e.g. two 12-inch 1500 master valves, one 12-inch 1500 side isolation valve, and two 8-inch 1500 remote operated control valves). The full flow line and flow test facility setup are further detailed in Section 4.

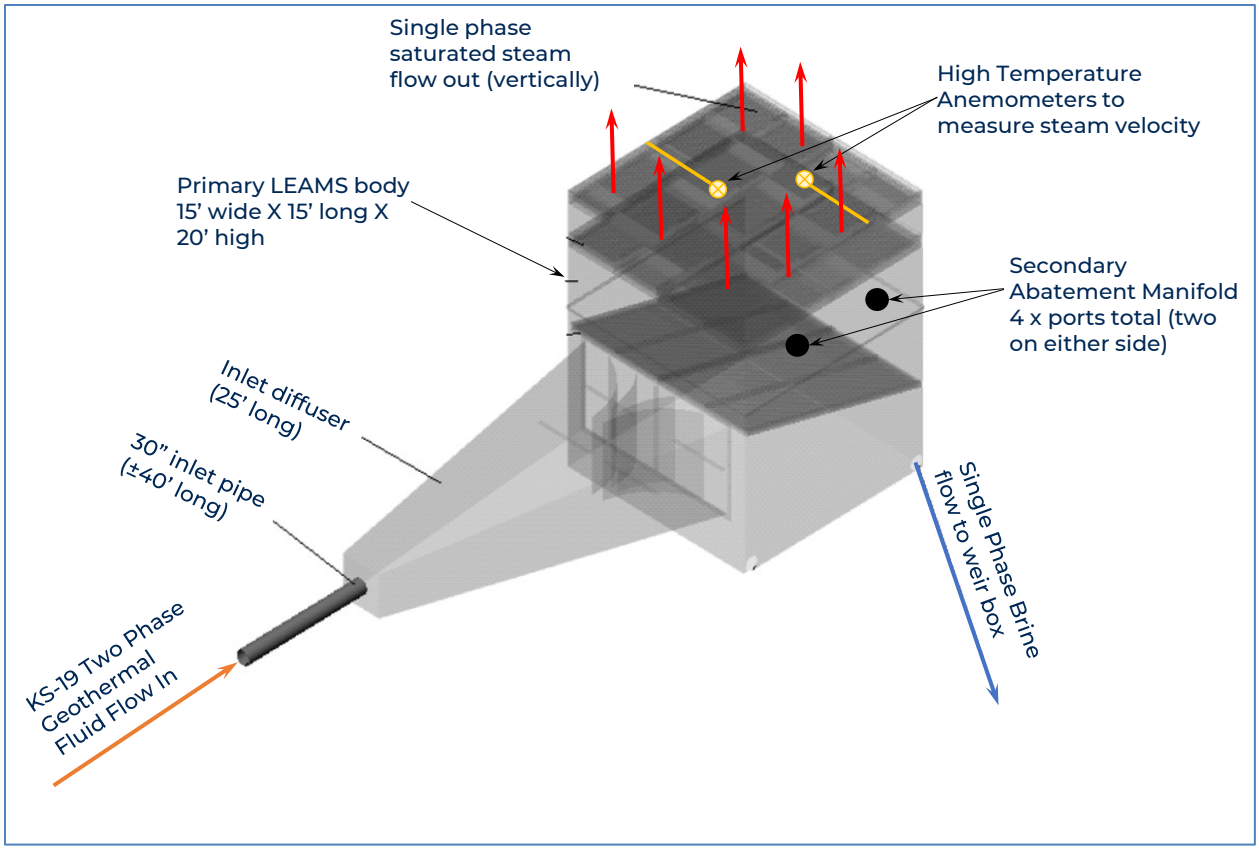

Figure 2. Basic schematic of the Low Emissions Atmospheric Metering Separator (LEAMS) used for PGV flow testing and cleanout flows. Planned locations of the secondary abatement manifold ports and high-temperature anemometers are indicated. Figure modified from Jung and Howard, 2000.

4. Flow Test Equipment Installation

Following completion of KS-19 drilling, Ormat proceeded with installation of the permanent pipeline from the well to the main two-phase production header. At PGV the permanent pipeline from the well to the main header includes two separate branches and four primary 8-inch control valves (CVs), two on each branch (Figure 3). To ensure proper control of the well is maintained during the flow test, the flow test setup is planned to incorporate one of the two permanent branches and two of the four primary control valves. The permanent production wellhead stack is also used during the flow test. This includes a robust design made up of two 12-inch 1500 master valves separated by a 12-inch 1500 kill spool with two 3-inch 1500 side outlets. Above the upper master valve a 12-inch 1500 flow cross is installed with 12-inch isolation valves installed on the two lateral outlets and 1500 class rock catchers attached to the isolations valves. Figure 4 and Figure 5 detail the wellhead arrangement for KS-19, typical of PGV production wells.

The KS-19 flow test setup is detailed in Figure 3, Figure 4, and Figure 5 which identify key valves and abatement injection ports to be used during the flow test. Note that the KS-22 setup is identical, but off the east branch instead of the west. The key valves to be used during KS-19 flow testing include the following:

- Valve #1: Lower 12-inch 1500 master valve (Figure 4)

- Valve #2: Upper 12-inch 1500 master valve (Figure 4)
- Valve #3: West branch 12-inch 1500 Velan Valve (Figure 4)
- Valve #4: 3-inch 1500 gate valve on the bleed line adjacent to the wellhead (Figure 5)
- Valve #5: 8-inch fisher control valve (remote operated). There are redundant 8-inch valves, both may be opened to increase flow following initial well startup (Figure 3).
- Valve #6: The 16-inch 300 gate valve isolating the temporary flow test flowline from the permanent plant flow line (Figure 3).
- Valve #7: The 3-inch 1500 gate valve just upstream of the static mixer (Figure 3)
- Valve #8: The 3-inch 1500 gate valve isolating the static mixer from the downstream plant bleed system (Figure 3).

Valves #1 through #5 are all components of the permanent wellhead installation and flow line to the plant. The CV noted as valve #5 is remotely operated from the PGV control room to ensure the well can be isolated remotely in the case of an emergency. Following the 4-hour testing period of KS-19 through the west-branch, flow will be transitioned to the plant using the east-branch. This allows the west-branch to be isolated with valve #3 so the permanent west-branch flow line and CVs can be cleared of debris produced during the flow test. Also note that a spectacle blind flange is installed on the west-branch just downstream of valve #6. This ensures the dead-leg of the permanent west-branch does not become filled with drilling debris during the flow test period. Once the west-branch is out of service following the test, the spectacle blind is rotated as part of the post-flow test maintenance, so the west-branch can be put in plant service when needed.

The 3-inch static mixer designed by TPE is installed on a tee coming off of the primary bleed line of the well, which is connected to the wellhead below the lower master valve and completely isolated from the primary flow line (see Figure 3 and Figure 5 for additional details).

During the flow testing period, the two-phase geothermal fluid is treated with 50% sodium hydroxide solution (NaOH) through the primary abatement ports located upstream of the CV (ports #1 and #2, Figure 3). Port #2 is to act as a standby backup port in the case there is an issue with injection into port #1. There are also primary and backup high-pressure abatement pumps attached to ports #1 and #2 respectively, providing a fully redundant system to ensure constant NaOH dosing at the primary abatement location for the duration of the testing period. The flow is further treated with NaOH through the secondary abatement manifold installed on the LEAMS muffler to ensure maximum abatement efficiency (ports #5 through #8, Figure 3).

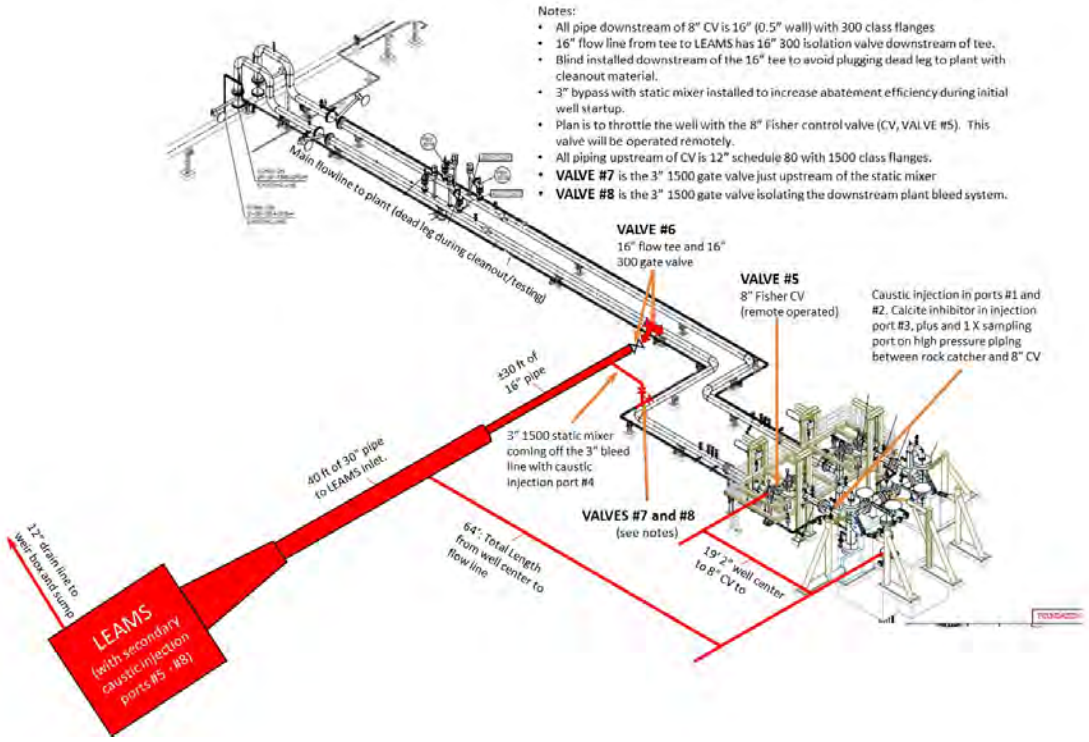

Figure 3. Sketch of the flow test facility as installed for KS-19 testing showing positions of key valves and caustic abatement injection ports.

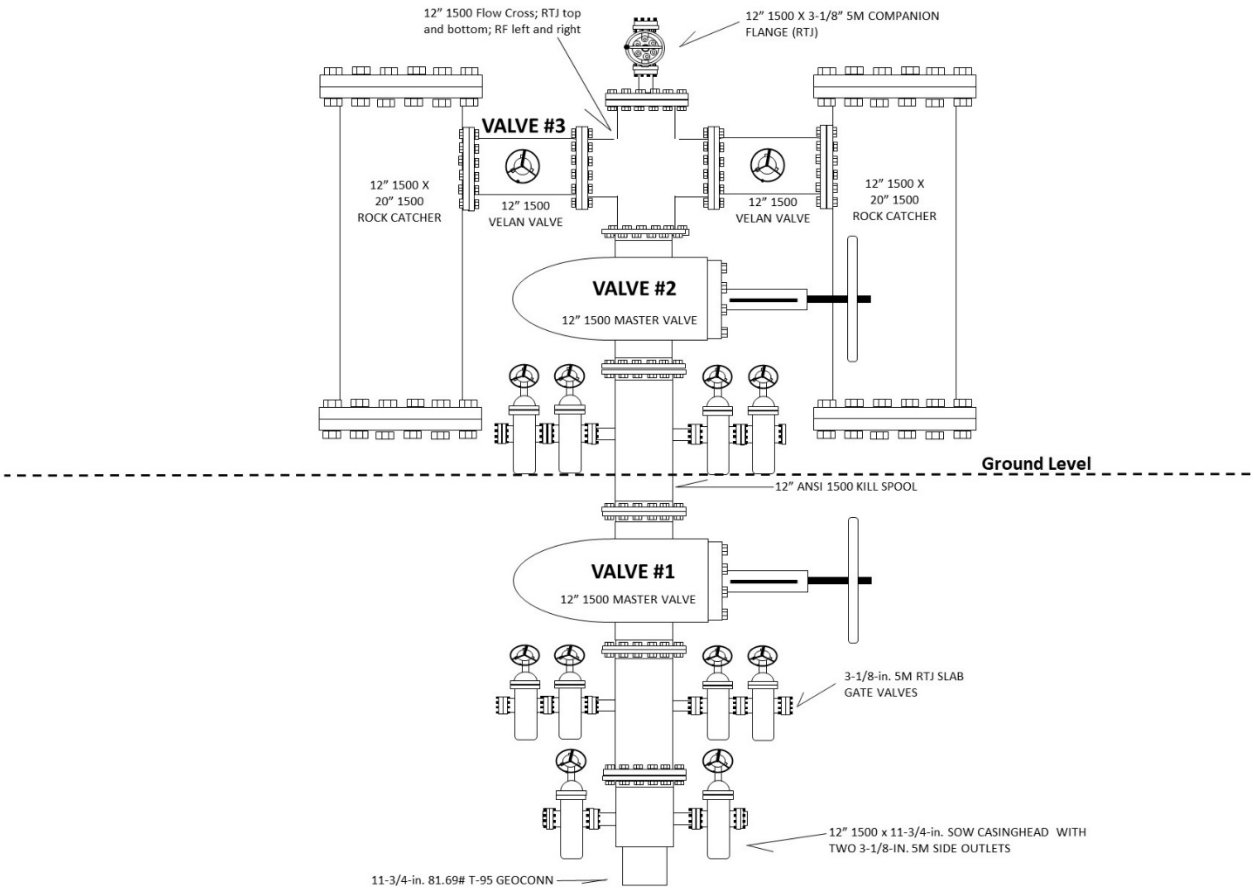

Figure 4. KS-19 wellhead assembly with Velan side-isolation valves and rock catchers included (note: bleed line not shown).

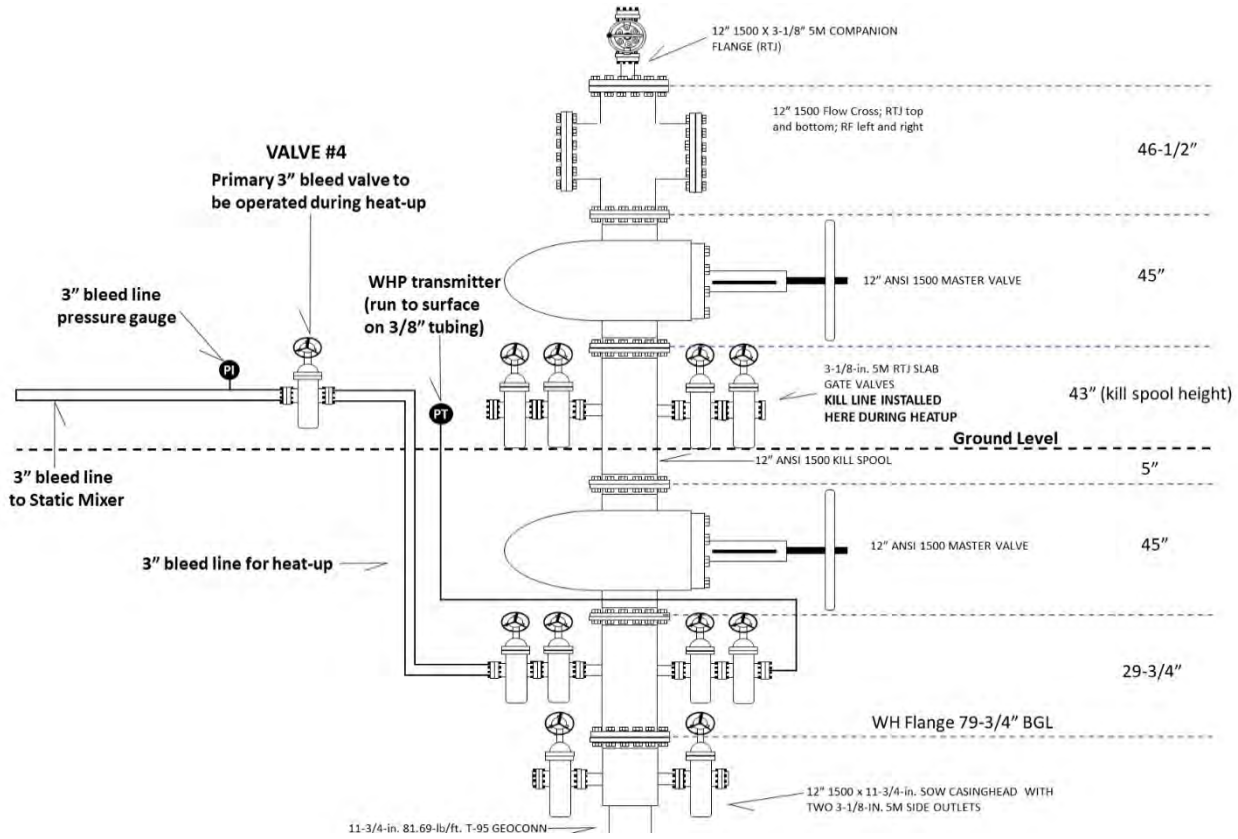

Figure 5. Simplified KS-19 wellhead assembly with bleed line emphasized (note: rock catchers not shown).

5. Hydrogen Sulfide Abatement Calculations

During the four-hour clean-out period, all flow is directed to the LEAMS. The vapor phase is vented to the atmosphere, and the liquid flows through the weir box and into a lined pond, where it is stored until it can be safely disposed. The maximum expected steam flow rate to be vented during the clean-out is approximately 28 kg/s (220 thousand pounds per hour (kph)) based on flow test equipment capacity. The steam phase is assumed to have an initial maximum H_2S concentration of 1000 ppmw based on measured geochemical concentration of other wells at startup. The maximum estimated rate of H_2S production in steam is therefore given by:

$$\frac{220{,}000\ lb\ steam}{hr} * \frac{1000\ ppmw\ H2S}{10^6} = \frac{220\ lb\ H2S}{hr} \quad (3)$$

H_2S abatement efficiency is conservatively estimated to be 98%. Previous test results indicate that efficiencies of 99% or greater are readily achievable using the upgraded abatement equipment designed for the PGV flow testing. The amount of H_2S to be removed based on 98% efficiency is:

$$\frac{220\ lb\ H2S}{hr} * 0.98 = \frac{215.6\ lb\ H2S}{hr} \quad (4)$$

Therefore, at the maximum anticipated flow rate and H_2S concentration, this level of abatement is estimated to result in a maximum emission rate of 4.4 pounds per hour of H_2S to the atmosphere during the clean-out period. This is below the permitted rate of 5 lbs/hr, even based on the most conservative assumptions for maximum steam flow rate, H_2S concentration, and abatement efficiency. Note that average H_2S concentrations in steam during normal operation are typically in the range of 200 – 600 ppmw.

Permit requirements state that a minimum mole ratio of 4 to 1 (NaOH to H_2S) is required for abatement during flow testing to an atmospheric muffler. To be conservative, Ormat, WCG, and TPE determined a mole ratio of 8.4 to 1 (NaOH to H_2S) would initially be used to ensure the required abatement efficiency of 98% is achieved. This mole ratio determines the abatement solution pumping rate required as follows:

$$\frac{8.4 \text{ mole NaOH}}{1\ mole\ H2S} * \frac{40 \text{ lb NaOH}}{1 \text{ mole NaOH}} * \frac{1 \text{ mole H2S}}{34 \text{ lb H2S}} * \frac{1 \text{ gal 50\% NaOH solution}}{5.32 \text{ lb NaOH}} * \frac{220 \text{ lb H2S}}{\text{hr}} = \frac{409\ gal\ 50\%\ NaOH\ solution}{hr} \quad (5)$$

The installed pumping capacities for the two primary pumping units are 500 gallons per hour (gph) each of 50% sodium hydroxide solution for a total capacity of 1000 gph. Therefore, a large excess capacity for abatement is available, including a fully redundant backup system at the primary abatement location to the two-phase flow line upstream of the control valve.

Further, during the 4-hour flow test period, an additional 150 gph of 50% NaOH solution will be added to the secondary abatement manifold to treat the steam phase in the LEAMS and ensure a minimum of 98% abatement efficiency is achieved.

Flow from the well will be initiated through the static mixer on the 3-inch bypass line. Just upstream of the static mixer assembly is port #4 for NaOH injection. 450 gph of 50% NaOH will be added to this port 5-minutes before initiating flow from the well. Flow will be started through the 3-inch bleed line and static mixer assembly to ensure efficient mixing of caustic abatement chemicals with dry gas or gas-saturated condensate that may be encountered during initial well discharge. Flow through the 3-inch static mixer is planned to proceed for roughly 15-min to ensure proper abatement of the initial discharge. Flow will then be transitioned to the primary two-phase flow line once wellhead conditions are stable and saturated steam is observed exiting the top of the muffler and brine observed in the weir box.

6. Procedure for Initiating Flow from Well

Prior to the initiation of flow, the well is to be on back heat from an adjacent active production well. This process is started roughly a week before the planned flow test date with heat being added to the well in a slow, controlled manner to avoid rapid thermal cycling and ensure the wellbore is properly heated before initiating flow. The flow test facility has been installed according to the information presented above and in Figure 3 through Figure 5.

Flow from the well is initiated using the following procedure:

1) All flow for the KS-19 cleanout to the LEAMS is through the west-branch (note: flow initiation procedure is the same for KS-22, but through the east-branch). The KS-19 east-branch Velan should remain closed at all times to keep the branch isolated until flow begins to be transferred to the plant through the east-branch.

2) Valves identified in Figure 3 through Figure 5 should be in the following positions:
    a. Valve #1: OPEN (Lower 12-inch 1500 master valve)
    b. Valve #2: OPEN (Upper 12-inch 1500 master valve)
    c. Valve #3: OPEN (West leg 12-inch 1500 Velan Valve)
    d. Valve #4: OPEN as the well will be on back heat until flow is initiated (3-inch 1500 gate valve on the bleed line adjacent to the wellhead).
    e. Valve #5: CLOSED (8-inch remote operated fisher CV).
    f. Valve #6: OPEN (16-inch 300 gate valve to the LEAMS flow line)
    g. Valve #7: CLOSED (3-inch 1500 gate valve just upstream of the static mixer)
    h. Valve #8: OPEN to allow back heat into the well (3-inch 1500 gate valve for isolation of the static mixer from the downstream plant bleed system).
3) If any leaks in wellhead equipment are encountered during the startup or test operations, shut-in the well and tighten bolts to fix the leaks. Then restart the startup procedure from point #1 above.
4) Ensure that NaOH and abatement pumps are setup to pump at the following rates and ports:
    a. Port #1 (primary caustic port upstream of CV): 50% NaOH at 450 gph
    b. Port #2 (secondary caustic port upstream of CV): 50% NaOH at 450 gph
    c. Port #4: (caustic port on 3-inch bypass line upstream of static mixer) 50% NaOH at 450 gph
    d. Ports #5 through #8 (secondary caustic abatement ports in LEAMS) 50% NaOH at 150 gph total.
5) Make final notification to the control room that test is beginning.
6) Close valve #8 to isolate the back heat flow from adjacent production well.
7) Begin abatement flow into port #4 on the static mixer at 450 gph.
8) Slowly open valve #7 to 20-30% to begin flowing the well through the static mixer and into the LEAMS.
    a. Caustic injection into port #4, should be started 5-minutes before valve #7 is opened. This location will be used for caustic injection until steam flow reaches 2.5-5.0 kg/s and flow is transferred to the primary two-phase flow line.
    b. Caustic injection into ports #5 through #8 will be initiated at this time at 150 gph.
    c. As soon as brine flow begins coming over the weir, begin dosing with Amber HS to complete abatement reaction. Amber HS pumps are rated for 180 gph at pressure up to 40 psi.
9) Well Test Engineer and Geochemist to immediately verify the following parameters before continuing or increasing the by-pass flow:
    a. A pH of 12.0 or more is required for water from weir box.
    b. A temperature at the static mixer of 100 ^{o}C or greater if the temperature at the wellhead is 100 ^{o}C or greater.
    c. A temperature at the static mixer within 10 ^{o}C of the temperature at the wellhead, if the wellhead temperature is less than 100 ^{o}C.
    d. H_2S monitor readings from all stationary and portable devices indicating less than 10 ppm on LEAMS outlet and zero on the ground in the vicinity around the LEAMS. The designated safety supervisor will be roving with a mobile gas sniffer and at this time should be immediately downwind of the muffler and fully masked-up with SCBA working.

e. If any above parameters are not met, immediately close valve #7 and evaluate the cause. Proceed after the situation is fully understood and the process corrected as necessary.

10) If the above parameters are met, slowly increase flow through the 3-inch bleed line to 100% open on valve #7. Continue to monitor the parameters above and close valve #7 if they cannot be maintained.
11) Once stable steam flow has been established through the bleed line, use data from the two H_2S sensors on LEAMS outlet to ensure H_2S emissions are below 2.27 kg/hr (5 lbs/hr).
12) Assuming H_2S emissions are below 2.27 kg/hr, begin injecting 50% NaOH in port #1 at 450 gph.
13) Once the chemical injection rates are established in port #1, change the valve positions in the following order:
    a. Ensure the high-pressure piping has equalized and begin to slowly open valve #5 (8-inch CV) to flow through the primary two-phase flow line into the LEAMS.
        i. Since valve #5 is a remote-operated Fisher CV, coordinate with control room on desired valve position. Flow test engineer to coordinate and confirm all CV position changes.
    b. Valve #6 should already be opened 100% and the well should be controlled and throttled with valve #5.
14) Once flow is established through the main flow line, close valve #7 and stop caustic injection into port #4.
15) Collect fluid samples upstream of the caustic injection ports as needed to determine pre-abatement H_2S concentrations through onsite titration per regulatory requirements.
16) With flow established through the main flowline, continue injection of 50% NaOH at 150 gph into ports #5 through #8 to control H_2S concentrations (i.e. the secondary abatement ports on the LEAMS).
    a. NaOH injection rates into the secondary abatement manifold should be optimized to minimize H_2S concentrations at the muffler outlet.
17) Once stable flow is established through the main flowline, continue to monitor H_2S emissions. Flow test engineer will provide steam flow rate based on available instrumentation to facilitate a running calculation of the hourly emissions.
18) Assuming the H_2S emission rate is 1 kg/hr or less, slowly open valve #5 to a maximum measured steam rate of 28 kg/s (220 kph).
19) If H_2S emissions approach 2.27 kg/hr, reduce flow from the well to stay below this limit. Ensure proper operation of all abatement pumps.
20) Continue the clean-out for a cumulative period of up to 4 total hours. Begin shut-in of the west-branch and transition flow to the plant at 3.5 hours.

7. Results

The upgraded PGV flow test facility was safely and successfully utilized for new production wells KS-19 and KS-22. Both tests stayed well within regulatory limits, with H_2S concentrations remaining below 1 ppmw at the ground-level monitoring stations located in a 5 m radius around the LEAMS. Average H_2S concentrations at the LEAMS outlet briefly reached 5 ppmw during the KS-19 test, though this was due to a temporary issue with an abatement pump which was quickly resolved by transitioning to the standby backup pump. Even considering the temporary abatement pump issue, the maximum hourly H_2S emission during the KS-19 test was 0.32 kg H_2S.

Total emissions for the 4-hour test period were 0.51 kg compared to the maximum allowable 9.1 kg. During the KS-22 testing, abatement pumps functioned properly for the duration of the 4-hour test, and H_2S emissions for the full test were less than 0.041 kg, over 200 times below the regulatory limit of 9.1 kg (i.e. 2.27 kg/hr * 4 hr). Both tests maintained H_2S emissions significantly below the regulatory limit of 2.27 kg/hr. Even KS-19 with slightly higher emissions was more than 17 times below the regulatory limit for the full 4-hour period. Figure 7 shows the total emissions during the flow tests of both KS-19 and KS-22.

Metering of the flow rates during the test went generally according to plan apart from the mechanical vane anemometer failing 15-minutes into the KS-19 test because the wire connecting it to the base station was unintentionally stepped on, removing it from the instrument at the top of the muffler. The constant temperature anemometer successfully measured the steam exit velocity for the duration of both tests, providing values within the expected range of steam flow rates.

At the end of the 4-hour period, the maximum flow rate from KS-19 was 81 kg/s with steam flow rate of 28 kg/s and brine flow rate of 53 kg/s. At PGV atmospheric separation conditions, this provides an enthalpy value of 1200 kJ/kg. This is within the expected range for the well given that the flow test period was only 4-hours. Given the complex reservoir dynamics, PGV production wells typically start production a relatively lower enthalpy than the observed long-term stable enthalpy. Enthalpy increases over-time until the well stabilizes within the first 2-3 months of production. For reference, stable enthalpy for KS-19 after 3-months of production was 1600 kJ/kg.

At the end of the 4-hour period, the maximum flow rate from KS-22 was 72 kg/s with steam flow rate of 28 kg/s and brine flow rate of 44 kg/s. At PGV atmospheric separation conditions this provides an enthalpy value of 1287 kJ/kg. This is within the expected range for the well given that the flow test period was only 4-hours.

Figure 6 shows the flow rate and enthalpy plots for both KS-19 and KS-22.

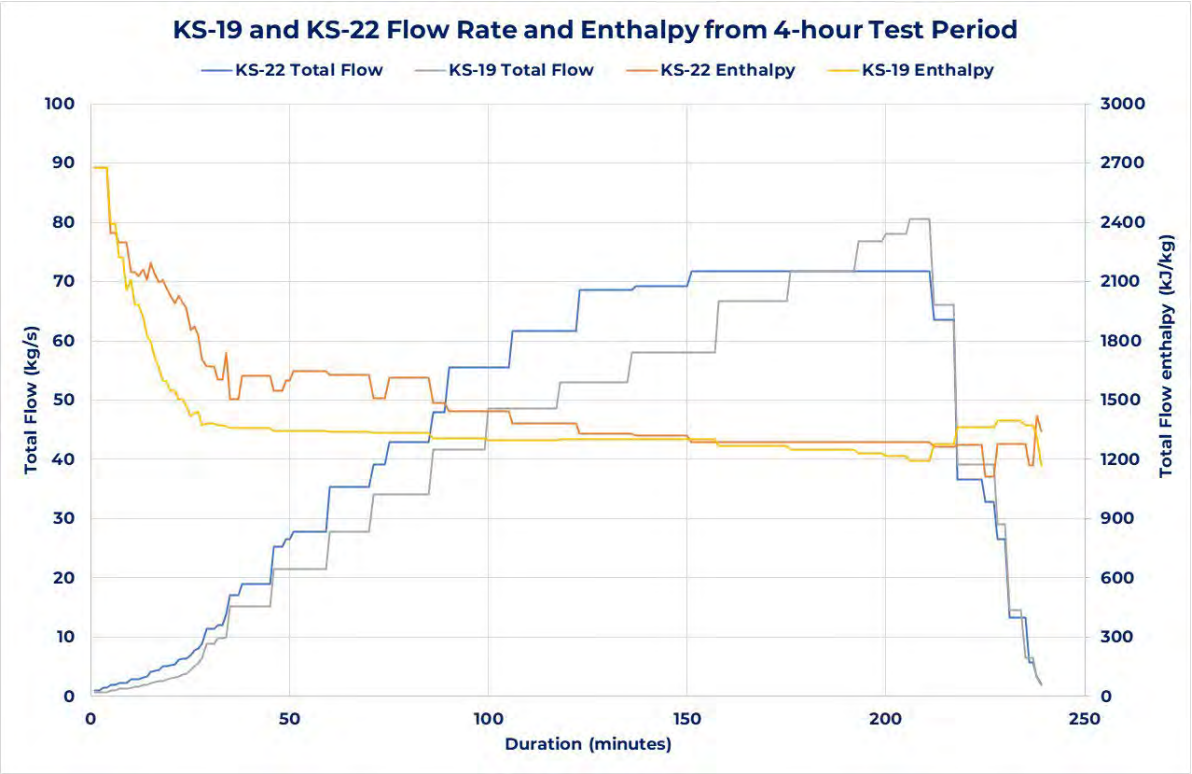

Figure 6: Four-hour flow test measurements of total flow rate and total flow enthalpy for both KS-19 and KS-22 flow tests through the LEAMS.

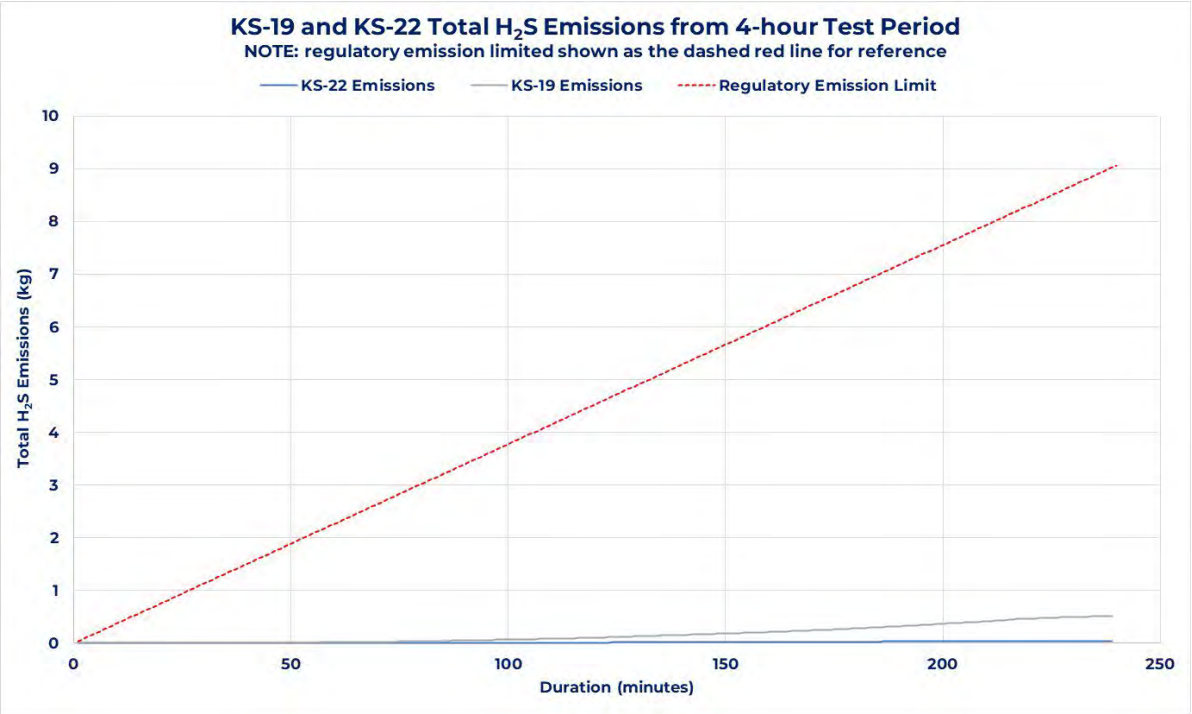

Figure 7: Total emissions of H_2S during the four-hour flow tests for both KS-19 and KS-22 through the LEAMS. For reference, the regulatory emission limit is shown as the dashed red line.

Figure 8: Aerial image of KS-22 flow test in 2023.

7. Conclusions

Overall, the two tests completed in 2023 confirmed atmospheric testing can be safely conducted at PGV with conditions maintained well within the required permit limits. Completing atmospheric cleanout flows for new wells provides significant value to the PGV reservoir and power generating facilities. Flow through upgraded flow test facilities allowed the production fracture system to be cleaned of drilling debris prior to initiating flow to the plant, resulting in improved long-term performance of the production wells. The drilling debris was safely managed by the upgraded flow test facility and later safely disposed of, instead of flowing through the PGV plant gathering system where it has previously been observed to cause equipment fouling requiring down-time for maintenance. Further, between 2006-2022, prior to the reimplementation of atmospheric cleanouts, starting new wells at PGV was a challenging process requiring generation to be reduced to a minimum as the new wells came online. Use of the upgraded flow test facility allows wells to be put into service seamlessly, with no negative impact on plant generation.

Following startup of KS-19, plant generation improved by a factor of roughly 100%, and following startup of KS-22 generation increased by a factor of 150%, indicating significant value in starting new production wells through the upgraded flow test facility. It has now been ten months since KS-22 was started and power generation remains stable with total plant generation 120% higher than observed prior to well start-up, indicating good long-term performance of the new wells.

However, even following the permitted 4-hour clean out flow periods, some fouling of plant equipment from drilling debris was still observed. This indicates the permitted 4-hour flow test period does not provide sufficient time for the well and local fracture system to fully clean out all drilling debris. A longer duration flow test period of up to 12-hours would provide significant value for future PGV production wells and the power generating facilities. Note that at other geothermal projects around the world new wells commonly flow to atmosphere for weeks, or even months at a time during long-term testing (Sanyal et al., 1987; and. Oikawa et al., 2001).

Aside from the duration, the 2023 PGV flow tests met the desired goals of safely conducting the tests within the permit requirements. The upgraded flow test facility and abatement practices further proved that H_2S emissions could be maintained well below the regulatory limit, supporting the idea that a longer testing period could be achievable without any significant modification to the currently permitted emission limits.

Acknowledgment

Special thanks to Doug Jung and Two-Phase Engineering & Research for reviving the LEAMS and providing invaluable insight on the equipment design, setup, and use. Another special thanks to West Coast Geologic for their assistance in preparing for and safely executing the flow tests.

REFERENCES

Axelsson, G., and Steingrímsson, B. (2012). "*Logging, testing and monitoring geothermal wells.*" Proceedings of the "Short Course on Geothermal Development and Geothermal Wells", UNU-GTP and LaGeo, Santa Tecla, El Salvador, 20 pp.

Finger, J., Sattler, A., Whitlow, G., Jacobson, R., Champness, T., Jung, D. B., Howard, W. T., Spielman, P. (2000). "*Field Test of LEAMS Drilling and Well-Test Separator*." Geothermal Resources Council Transactions, Vol. 24.

Grant, M.A., and Bixley, P.F. (2011). "*Geothermal reservoir engineering (2nd Ed.)*." Academic Press, NY, 349 pp.

Hole, H. (2008). "*Geothermal Well Completion Tests*." Petroleum Engineering Summer School Workshop #26. Dubrovnik, Croatia.

James, R. (1962). "*Steam-water critical flow through pipes*." Proceedings of the Institution of Mechanical Engineers 176.1 (1962). 741-748.

Jung, D. B., Howard, W. T. (2000). "*LEAMS Low Emissions Atmospheric Metering Separator for Drilling and Well Testing*." Proceedings of World Geothermal Congress. Beppu, Japan.

Oikawa, Y., Kawasaki, K., Tosha, T., Tenma, N., Satou, Y (2001). "*Long-Term Circulation Test at Hijiori Site, Japan.*" Proceedings 23rd New Zealand Geothermal Workshop.

Sanyal, S., Menzies, E., Granados, E., Sugine, S., Gentner, R. (1987). *Long-Term Testing of Geothermal Wells in the Coso Hot Springs KGRA.* Proceedings, Twelfth Workshop on Geothermal Reservoir Engineering. Stanford University, Sanford, California, SGP-TR-109.

Conceptual Hydrothermal Model of the Salton Sea KGRA

Santiago Rocha[1], Jade Bourdeau-Hernikl[1], D. D. Faulder[2], and Daniel Minguez[1]

[1]Cyrq Energy LLC, [2]Homestead Resources LLC

Keywords

Salton Sea Geothermal Field, conceptual model, high-temperature, high-salinity, double-diffusive convective system, lithium

ABSTRACT

The Salton Sea Geothermal Field (SSGF) is known for its high-temperature, high-salinity brine, the existence of a low-salinity reservoir above the hypersaline reservoir, and complex thermodynamic behavior. Previous conceptual models have generally described homogeneous reservoir architectures with minor variations along known depths (-4,000 to -9,000 ft ASL). This paper presents an alternative view that highlights the interaction of structurally controlled permeability and permeability barriers with the laterally extensive stratigraphically hosted reservoir, while also addressing thermo-chemical barriers that explain the vertical distribution of salinity and temperature in the system.

The model presented here incorporates the key elements of a conceptual model of a hydrothermal system; heat source, permeable pathways, fluid recharge, characterized reservoir, and fluid discharge. Each of these elements are resolved with data sets obtained on the eastern margin of the field, with their implications extended regionally to the rest of the field, informed by observations from previous studies. On the fields' eastern margin, lateral permeability barriers marking the edge of the economic resource are recognized in large offset faults imaged in depth migrated seismic data. Well temperatures from the eastern side of these faults are significantly colder than temperatures encountered in wells on the west side, supporting the demarcation of the resource's edge. The resource top is defined by a thermo-chemical interface where density compensation achieved by a decreasing temperature and salinity gradient gives way to background shallow hydrology. This "brine interface" marks the top of the convecting system and the base of the shallow hydrologic system. The behavior below this interface has been described in other works as a "double-diffusive convective system", and its characteristics in the Salton Sea are discussed at length based on temperature and salinity data presented here.

The conceptual hydrothermal model presented here also accounts for highly permeable zones in transitional metamorphic depths of the Salton Sea reservoir and surface manifestations like mud-pots of the system through discreet vertical pathways (faults and fractures) that rupture the thermochemical cap intact over the rest of the reservoir.

1. Introduction

Different studies, (e.g. Hulen 2002, 2003, and Kaspereit, 2016) have been published to describe the Salton Sea geothermal system. The system exists in a propagating continental rift that has

resulted in divergent sea floor spreading to the south in the Gulf of California while propagating northward along trans-tensional elements stemming from the transform plate boundary to the East and North. The Salton Sea is located at the northern tip of the Gulf of California and hosts extensional and trans-tensional structures that have thinned the crust, elevated the thermal gradient, and enabled intrusive and extrusive magmatism. The permeable structures, (meta-)sedimentary rocks, and heat hosted in this setting provide the basic elements of the geothermal system.

Multiple commercial geothermal projects have come to completion on the southern edge of the Salton Sea in the so-called "Salton Sea Geothermal Field" (SSGF). Data from wells in these fields, as well as regional geologic and geophysical data sets have supported iterations of conceptual hydrothermal models (CHM) described in the literary review section of this paper. The CHM presented here is informed by these previous iterations but is refined by data obtained in the Southeastern margin of the field at the Hudson Ranch Power I project. The model presented here also expands to contemplate interactions between the geothermal system and shallow ground water, as wells as thermal and chemical stratification in the reservoir that results in a perhaps uncommon constant density condition in the main reservoir. This "Double-diffusive convection system (DDCS) was developed by Fournier et al. (1990) and is summarized and applied to our CHM in the sections that follow.

2. Literature review

The CHM outlined in this work builds on key elements previously developed by other authors. The following section highlights the essential geological and hydrothermal findings from previous studies and explains how they are incorporated into our interpretation and proposed model.

2.1 Regional Geology

The SSGF is located in a tectonically active sedimentary pull-apart basin known as the Salton Trough (Kasperit, 2016). Lying at the southern tip of the San Andreas fault system, the Salton Trough borders a continental rift zone between the Pacific and North American plates as the San Andreas fault system steps-over to the right (Figure 1). This zone is dominated by a series of subsiding pull-apart basins, with elevated heat flow, seismicity, and volcanism (McKibben, 1991). The multiple pull-apart basins connect to right-stepping, primarily dextral faults, striking northwest.

The San Andreas fault system, the Imperial fault, and the San Jacinto fault zone play an important role in the formation of the SSGF (Kasperit, 2016). While the step-over from the San Andreas fault to the Imperial fault likely plays a more significant role in the SSGF system, the San Jacinto fault zone runs up the west side of the Salton Sea before joining the San Andreas fault to the north where it impedes northern movement of the Pacific Plate. This northern movement is transferred to the west of the San Jacinto fault zone allowing for rotation to expand over a larger area within the step-over and in turn forming two spreading centers. Extensional forces are the primary control on the location of most active parts of the geothermal field, however, a component of rotation along the faulted blocks may provide additional permeable drilling targets where fault tips intersect. Furthermore, extension creates crustal thinning coinciding with igneous intrusions and volcanism providing a means for the elevated heat flux to support the SSGF (Kasperit, 2016).

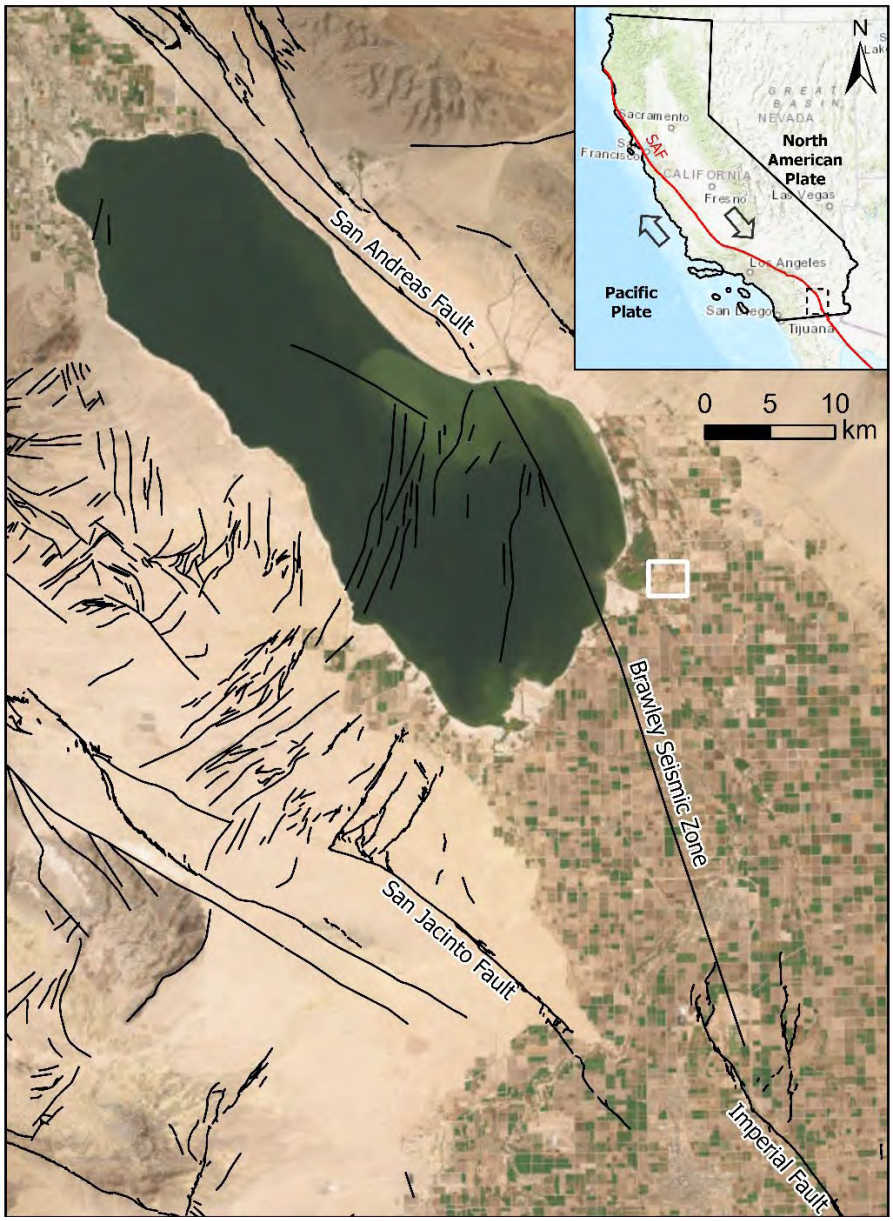

Figure 1: Location of HRP1, outlined in white, in respect to the Salton Sea Geothermal field. Satellite imagery overlain with USGS Quaternary faults. Inset map depicting San Andreas Fault (SAF) with relative sense of motion.

Due to the nature and amount of hydrothermal activity in the SSGF a 'recently' emplaced igneous intrusion is suggested to produce a robust heat source (Norton and Hulen, 2006). A detailed gravity survey of the Imperial Valley conducted in 1971 identified a gravity high extending NW and SE along the axis of the Salton Trough (Biehler, 1971). There are two possible explanations for the anomaly that may not be mutually exclusive; sediment densification through hydrothermal alteration and/or an igneous intrusion at depth (Younker et al., 1981). The intrusion hypothesis also potentially explains a linear magnetic high extending about 18 miles northwest from Calipatria into the Salton Sea (Griscom and Muffler, 1971). Estimates for the intrusions' size are roughly 12,000 ft thick and 15,000-26,000 ft wide. It is suggested that the intrusion was emplaced within ~5km of the surface within the last 50,000 years (Norton and Hulen, 2006). Localized Quaternary

volcanism and upwelling of hydrothermal fluids in the SSGF elevate heat flows to >500mW/m^2 (Sass et al., 1984). High heat flow in the region leads to mineralogical changes at depth that are prolific throughout the Imperial Valley as recorded by numerous boreholes (Norton and Hulen 2006). Within the SSGF greenschist metamorphism can generally be divided into three major zones; chlorite-calcite zone (~190-325°C), biotite zone (325-350°C), and clinopyroxene-amphibole zone (>350°C) (McDowell and Elder, 1980; Han et al., 2016b; Cho et al., 1988).

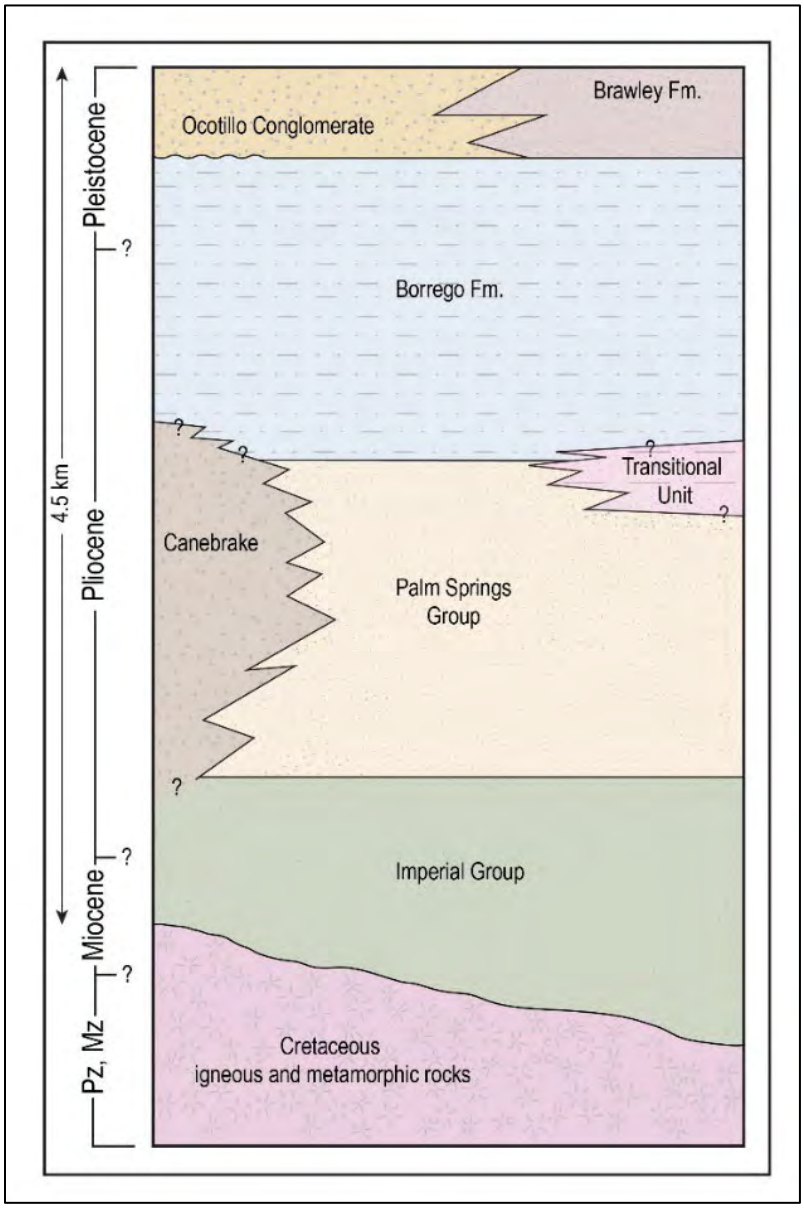

Figure 2: Simplified stratigraphic column of the Salton Trough. Modified from Steely et al., 2009 and Lutz et al., 2006.

The Salton Trough stratigraphy records its tectonic evolution in three main phases: early to late Miocene, Pliocene to early Pleistocene, and early Pleistocene to present (Figure 2). During the Oligocene to Miocene the Farallon Plate began its subduction beneath the North American Plate. The Salton Trough began to rift, and magmatism initiated along the eastern margin (Dorsey,

2006). In the Late Miocene two factors resulted in a marine transgression: a rapid rise in global seal level and accelerated basin subsidence along the western edge of the Salton detachment fault. A thick package of fossiliferous claystone, siltstone, and sandstone sediments of the Imperial Group (Figure 2) were deposited. After sediment deposition, the Colorado River delta developed in the northern portion of the Trough. The delta began to prograde, depositing additional sediment, resulting in the coarsening upward sedimentary sequences in the Imperial Group (Dorsey, 2006). In the Middle Pliocene the Colorado River delta continued to grow until it eventually isolated the Trough from the Gulf of California (McKibben, 1991). The landscape was dominated by a vast delta plain and lush wetlands. Intermittent argillaceous intervals and arkosic sandstone of the Palm Springs Formation were deposited during this period. Eventually a perennial lake basin formed in the northern trough correlating with the lacustrine deposits of claystone, siltstone, and fluvial sandstone of the Borrego Formation (Dorsey, 2006). In the early Pleistocene to Holocene, the Colorado River fluctuated between flowing north or south and as a result, paleolake Chauilla repeatedly flooded and dried (McKibben, 1991). This deposited lacustrine mudstone and evaporitic deposits of the Brawley Formation (Helgeson, 1968). Quaternary age alluvium sediment consisting of unconsolidated gravel, sand, silt, and clay overlies the entire basin (Dutcher et al., 1972).

2.2 Previous conceptual model descriptions

Legacy models of the Salton Sea Geothermal Field (SSGF) have provided insights into the temperature and structural behavior of the reservoir. Hulen et al. (2002 and 2003) highlighted the presence of a still-cooling felsic igneous heat source beneath the geothermal field, estimating it to be 1-10 km^3 in volume and located around 3.6 km below sea level. This source likely fuels the hydrothermal activity observed in the SSGF, which may have started over 100,000 years ago. The permeability of the reservoir is characterized by high vertical permeability through fractures and breccias, as well as sedimentary layers with secondary permeability from calcite dissolution (Hulen, 2002). Although the full extent of the reservoir remains uncertain, the study suggests the presence of deep, permeable zones with significant hydrothermal activity.

Building on the work of Hulen et al. (2002 and 2003), Kaspereit et al. (2016) updated the conceptual model using new geophysical data. Their revised model suggests that the SSGF is compartmentalized by a series of northwest-striking faults, with extensional fractures creating vertical permeability, particularly at the edges of rotated fault blocks. The center of the compartments is interpreted as the thinnest and weakest point for thermal features to form. These interpretations are then correlated with seismic, magnetic, and gravity surveys and with the known rhyolite domes near the Salton Sea, as seen in Figure 3. They serve as the basis for the regional features of this paper's conceptual model.

3. CHM elements and constraining data sets

The CHM proposed in this paper incorporates geoscience data gathered from the HRP1 project to describe this part of the geothermal reservoir (location shown in Figure 3). The key elements of the CHM, defined using geoscience data, include the heat source, permeability structure, temperature model, thermal recharge pathway, characterized reservoir, interactions with shallow hydrology, and a thermochemical description of the salinity distribution of the system. The

geoscience elements are presented individually below and synthesized in Section 5 where the final conceptual model is described.

3.1 Heat source

Estimates of heat flux in the SSGF vary from study to study but converge with a mean of nearly 450 mW/m^2 (Sass, 1988), and with some estimates >500 mW/m^2. Fournier (1990) suggests the heat flow may be greater than 1000 mW/m^2 above the recent intrusives, demonstrating a larger deep conductive zone underneath the Salton Sea and a shallower conductive zone on the periphery to the northwest and southeast.

The shallow heat anomaly was initially generated using data compiled from previous drilling programs in 1982 and 1985 (Newmark et al., 1988). With additional onshore borehole control a revised boundary was compiled in 2002 (Kaspereit, 2016). Both the 1988 and 2002 boundaries were completed using gradient data points only, an analysis of geophysical structure was not included. In 2016 Kaspereit re-contoured the shallow heat anomaly (Figure 3) incorporating the limits of the SSGF extension model. The 2016 northwestern boundary edge was constrained by regional magnetic and gravity data as there are no thermal gradient holes in this area (Kaspereit,2016).

The following geophysical studies further constrained the areal extent of the heat source in the SSGF. In1976 (Meidav et al., 1976) a resistivity survey was conducted by Geonomic, Inc. around the Salton Sea. A zone of high conductance was identified primarily on the known field and ranging along the SE axis of the valley (Araya, 2023). Recently, new marine magnetotelluric technology was applied to provide an integrated approach and discover potential geothermal reservoirs extending beneath the Salton Sea. This 2009 MT survey demonstrated the first combined full field coverage onshore/offshore magnetotelluric survey (Nichols, 2009).

The 2009 Schlumberger onshore/offshore magnetotellurics project provided additional insights for the SSGF (Kaspereit,2016). Four survey profile lines were integrated and interpreted revealing an offshore boundary of the field that is delineated vertically by a deep resistive basement and a thick package of less resistive sediments. These findings are consistent with the assumption that an intrusive basement body would be more resistive than basin sediments. Generally, this boundary aligns with the SSGF extension model, however, towards the northwest there is a slight divergence between the resistivity anomaly and heat anomaly boundary (Kaspereit, 2016).

3.2 Permeability structure

The Salton Trough is situated in a continental rift zone comprised of a series of dextral faults that link the East Pacific Rise to the San Andreas fault system. Recently acquired 2-D seismic at HRPI in 2023 has enabled the identification of fault interactions explaining the vertical permeability and its structural setting on the eastern edge of the reservoir. The seismic interpretation presented here suggests deformation in the reservoir underlying HRP1 consists of a system of almost N-S striking normal faults that steps to the northeast with decreasing displacement. Likely, these faults are not purely dip-slip, and accommodate some kind of oblique motion given the tectonic setting. However, the 2-D seismic does not provide any clear evidence to quantify the oblique or strike-slip, component.

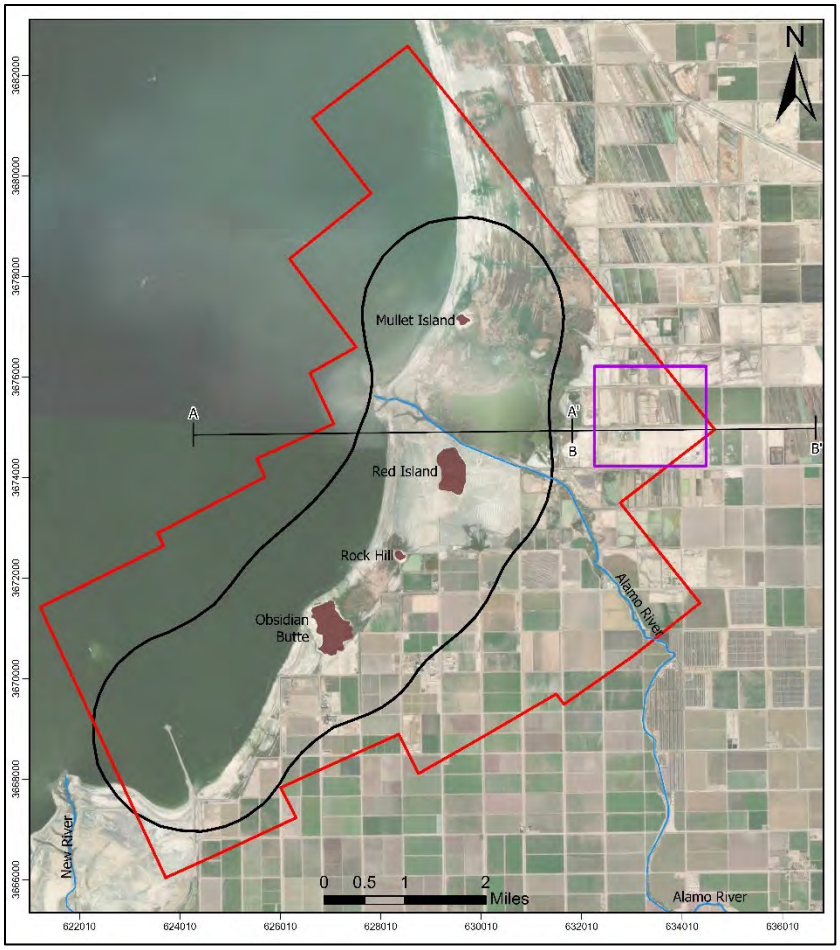

Figure 3: Borehole-controlled reservoir boundaries outlined in red from Kaspereit (2016), with the assumed heat source shape in black, and the Hudson Ranch Wellfield area highlighted in magenta, and conceptual cross section location

The seismic interpretation presented here is an extract from a survey over the HRP1 unit area. Eleven 2D profiles were collected, 6 in the east-west direction and 5 in the north-south direction. The line presented here runs east west, and was acquired along McDonald Road. Six interpreted horizons are presented in our 2D profile (Figure 4). The top white colored horizon marks the based of the youngest, conformable package of reflections which exhibit minor to no evidence of brittle deformation. The next deeper, blue shaded horizon, marks the based of a group of reflections exhibiting regional dip and potential stratigraphic growth or minor extensional folding, suggesting their deposition occurred in the latest stages of deformation along the underlying structures. The next deeper, yellow shaded horizons, marks and important high amplitude reflection that can be regionally correlated, and demonstrates distinct offsets. This horizon marks the top horizon to clearly experience brittle deformation, and is the high confidence seed point for fault tips in our interpretation. The next deeper, orange shaded horizon, was interpreted locally on this line to illustrate growth stratigraphy between it and the deeper green horizon, reflecting a period of significant extensional activity and sedimentary deposition. The green horizon regionally reflects the base of quasi conformable, rotated, high amplitude low frequency reflectors not clearly shown on this line. The package between the orange and green horizon appears to be a depositional package developed before major slip along this fault, that has been rotated down to the east and

south. The final horizon illustrated here is a black dashed line, which marks the last clearly traceable high amplitude reflection in the profile. The fault geometry interpreted here are inferred primarily from offsets visible in the yellow, orange, and green horizons, projected to depth.

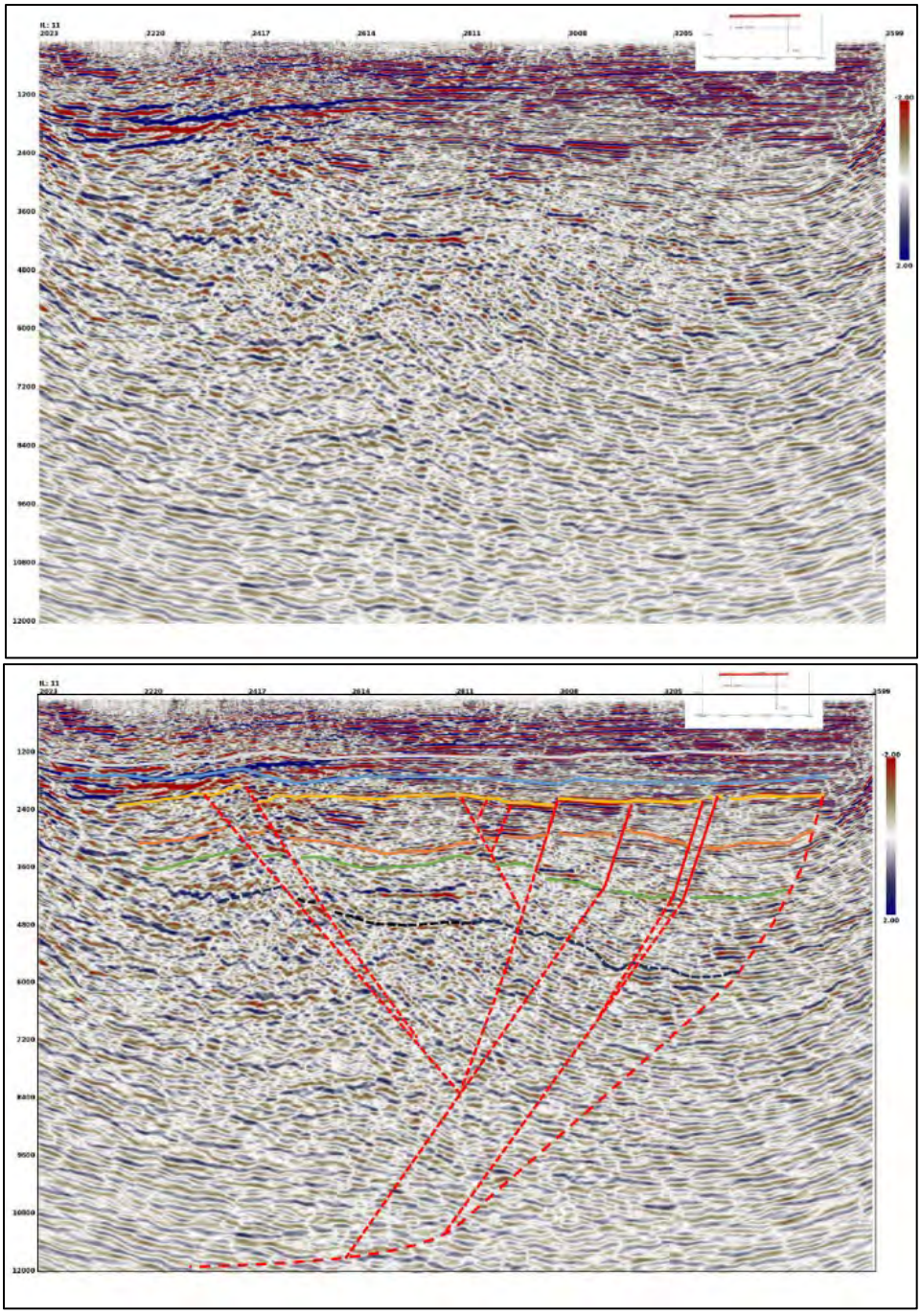

Figure 4: 2-D uninterpreted and interpreted depth migrated seismic survey line taken in the HRP1 wellfield Line orientation shown in inset map at upper right.

Two sources of permeability are probable and may exist either discreetly or simultaneously in the HRP1 reservoir area: a) stratigraphic reservoir permeability that is either primary in shallow units or secondary in deeper units that have undergone metamorphosis and are permeated by brittle

fractures, and b) fault-controlled permeability that allows to a certain degree, some connection between the hot, hypersaline reservoir, and the shallow, low salinity and groundwater reservoir. Shallow drilling losses and some recognized flow zones from temperature and spinner surveys support the presence of permeability in shallow units in HRP1 well 13-1. While core samples and deep production from other wells in the area suggest production from densely fractured meta-sediments, HRP1's wellfield suggest a complex stratigraphic architecture that may challenge the notion of a continuous homogeneous reservoir at depth (Figure 8) but still provides abundant stratigraphic and natural fracture targets in hydrologic communication.

Without image logs, it is difficult to determine the exact differentiation between stratigraphic and structural permeability. Generally, geophysical logs can be used to differentiate between sands and shales in the unaltered portion of the stratigraphy, or above the reservoir at depths greater than -4,000 ft ASL. At greater depths correlations become difficult using geophysical logs as hydrothermal alteration and metamorphism changes the geophysical responses. Additionally, major units are not laterally continuous as is consistent with dynamic fluvial-deltaic environments. Nevertheless, well inflow analysis suggests a mixed permeability contribution. Permeability estimates from the wells analyzed in the HRP1 project indicate values as high as 6,000 mD associated with discreet flow zones. The high permeability value and the narrow distribution of the flowing formation (<100 ft) is consistent with fracture permeability (Bear, 1972). Lower permeability wells were also tested, with permeability values estimated at 20 mD. By using the interpreted geology from the mud logs and the feed zone location, this lower permeability can be attributed to well-sorted sands (Bear, 1972).

3.3 Temperature model

The Salton Sea KGRA is classified as a high-enthalpy, high-salinity geothermal system in an extensional magmatic setting. The well temperature dataset used to interpret the temperature distribution in this study is presented in Figure 5 and was selected due to the vicinity to the HRP1 project. Temperatures for production zones range from 550 °F to nearly 650 °F. The majority of active wells exhibit a similar behavior, with conductive-convective profile boundaries occurring at depths of -3,200 to -4,700 ft ASL (Figure 5).

The temperature anomaly deepens to the northeast, southeast, and east. Wells on these eastern margins display conductive temperature profiles at depths from -5,000 to -9,000 ft ASL. In contrast, wells located to the west and southwest show a conductive-convective boundary as shallow as -3,000 ft ASL, with deep temperatures exceeding 600°F (Figure 5 and Figure 6). The northern edge of the temperature anomaly is poorly constrained, so an extension of the temperature anomaly towards the north is not ruled out. The temperature to the southwest is not well constrained either beyond the geophysical surveys, and no well data was available. The isotherms derived in this study from available well data exhibit a broad, flat shape that appears to terminate in the southeast, indicating a possible reservoir boundary. The isotherms extend towards the west, with a slight increase in shallow temperatures near the *'Old Mud Pots'* as shown in Figure 6.

The isotherm shape is similar to that described by Kaspereit (2016). Temperature mapping at -5,000 ASL and -7,000 ft ASL (Figure 6), shows decreasing temperature from the bottom to the top and from the center to the side of the SSGF corresponding to recent intrusive magma and heat source locations. The lateral extension and termination of the isotherms suggest a flow geometry characterized by a combination of primary high-permeability upflow near the heat source and deep

in the reservoir, with an outflow towards the shallow, matrix-permeable sediments allowing for lateral temperature extension of the system (Wallis, 2017). This interpretation supports Kaspereit's identified compartment in the HRP1 wellfield. The eastern side of the SSGF is cooler than the central thermal anomaly, providing hydrologic support such as a constant pressure boundary at a constant fluid density of ±1.0 g/cm³, meeting a condition for double-diffusive convection, later discussed in this paper.

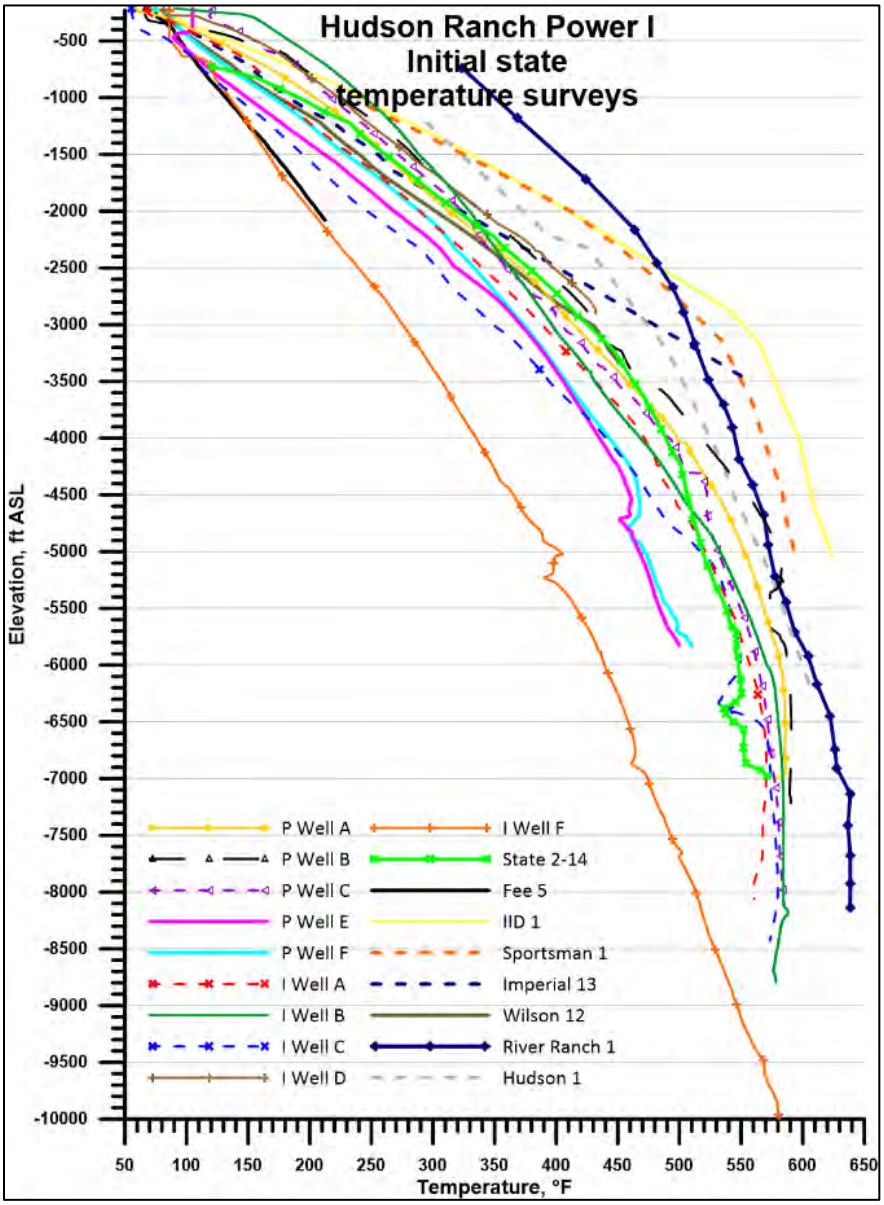

Figure 5: Temperature surveys of some of the wells used in this study. Profiles vary depending on the proximity to the main upflow and/or main heat source. The temperature data used in this study is a combination of legacy surveys conducted before 1990 and more recent surveys conducted after 1990. Most of the surveys in this study were tracked and corrected to better represent the initial state of the reservoir. However, some of the temperature points used in this analysis lacked information on the timing of the surveys, introducing a margin of error in the estimated initial temperatures at depth.

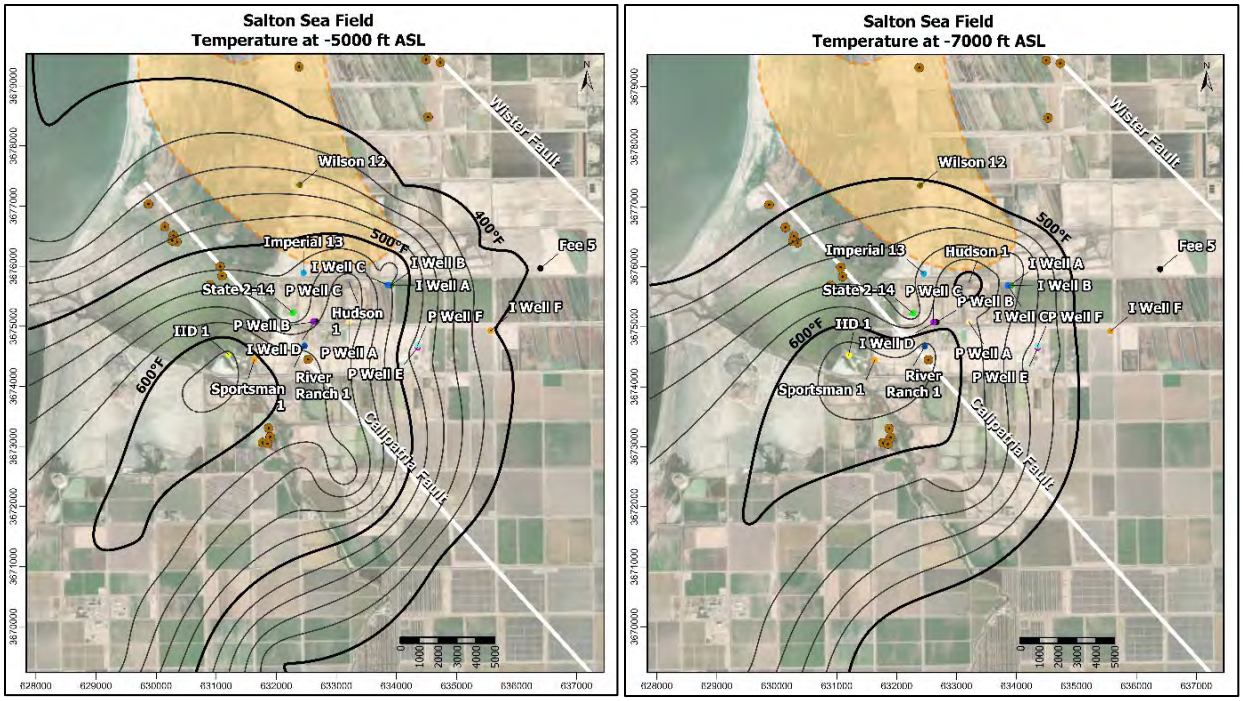

Figure 6: **SSGF temperatures at -5,000 ft and -7,000 ft ASL from thirty-three temperature surveys. Contours are constrained by available data and modified from Faulder (2022). The Imperial carbon dioxide field extent is outlined in orange, production zone from less than 1,000ASL, modified from Hulen and Kaspereit (2002). '*Old Mud Pots*' denoted with brown bullseyes. Calipatria fault originally evidenced by infrared detection (Babcock, 1971) and mud pot fields. Wister fault interpretation by Lynch and Hudnut (2008). Reservoir characterization**

3.4 Recharge pathways

A shallow aquifer system and a deeper hypersaline confined body make up the two aquifers systems for the Imperial Valley (Araya, 2023). The shallow aquifer is relatively stable and recharges primarily from the infiltration of the Colorado, New, and Alamo Rivers, as well as from irrigation seepage and canal leakage. A marginal degree of meteoric discharge is expected given the arid climate. It is theorized that the deeper (<-4,000 ft ASL) aquifer originates from ancient seawater that became isolated when the Colorado River Delta formed (Tompson, et al., 2008). This seawater then began to percolate into the subsurface, forming the deep hypersaline system. The two aquifer systems are generally separated by a lower permeability shale formation (Araya, 2023) and/or due to density differentials between the low and high saline reservoirs interaction that evolve into a stable interface (Oldenburg and Pruess, 2000).

In the HRP1 wellfield, permeable extensional structures (fractures and faults) correlate with the identified upflow, connecting the deep hypersaline reservoir with the known productive zones. The significant downward deflection of isotherms near the footwall of the imaged structure at HRP1 (Figure 6 and Figure 8) suggest the master fault of this structure may be a permeability barrier, with geologic units on its east side being dominated hydrologically by cold downflows from recharge of the shallow hydrology, or simply marginal permeability preventing the incursion of hot geothermal brine. Similar behavior may be achieved within the different compartments of the Salton Sea, where the temperature upflow is closely associated with the rhyolite domes and deep intrusion. The flanks of the reservoir recharge, providing a constant pressure boundary.

Well testing, PTS surveys, and production data. including salinity contribution estimates from production data (Siddique et al., 2024) were used for reservoir characterization of the HRP1 wellfield. The data suggests permeable zones as shallow as -3,200 ft ASL and as deep as -7,700 ft ASL. The average productivity and injectivity indices are 13 and 15 kph/psi, respectively, indicating very permeable wells. There is a significant spread in the estimated indices, ranging from as high as 37 kph/psi to as low as 2 kph/psi, an order of magnitude. This variation in addition to the permeability distribution described earlier suggests that the nature of the permeable productive zones can vary significantly from well to well. This can be explained by the presence of zones with fractured as well and some with matrix permeability.

The top of the high-salinity, high-temperature reservoir can be identified around -4,000 ft ASL, where the temperature profiles switch from conductive to convective. This change also corresponds with the first appearance of epidote in mudlogs. The nature of this boundary is not fully understood, but it can be explained by the double-diffusive effect (discussed later in this paper), where increased density contrast at the top of the plume—resulting from the advance of the brine front—impedes the upward movement of fluid, forming an effective barrier for the thermal and brine plumes (Oldenburg et al., 2000).

Estimating the reservoir bottom is challenging, as many of the wells had convective profiles close to their total depth, suggesting productive zones can also be found at deeper intervals. Well State 2-14 encountered major loss zones at depths as great as -10,000 ft ASL (Paillet, 1986). The only non-productive wells studied (P Well E and P Well F), which were drilled deeper than -9,000 ft ASL, displayed very conductive profiles and over-pressured zones on the last few hundred feet, indicating the possible limit of productive, commercial zones. For this study, the high enthalpy, high salinity commercial reservoir is bounded between -4,000 and -9,000 ft ASL.

Evidence from geochemical sampling and production salinity from Mass Energy Balance (MEB) estimates (Siddique et al, 2024) suggests that production salinity varies from 20-32% with depth in the hypersaline reservoir. The salinity content in each productive zone increases from the shallow to the deep parts of the reservoir and from the core proximal to the heat source toward the flanks where temperature decreases.

3.5 Imperial CO2 field and mud pots as outflow zones

Carbon dioxide was commercially produced in the Imperial Carbon Dioxide Gas Field from 1934 to 1954 (Muffler and White, 1969). Though this CO_2 field has since been abandoned, greater than 54 wells exploited gas reservoirs at depths of -500 to -700 ft ASL and static pressures up to 178psi (Muffler and White, 1968). The legacy Imperial CO_2 field is located north of the current HRP1 geothermal field as shown in Figure 6.

Elevated carbon dioxide levels are likely attributed to volcanic activity and metamorphic reactions at depth. Rook and Williams (1943) conclude that carbon dioxide gas is closely related to volcanic activity. Shallow faulting offers a means of gas migration. Muffler and White (1968) conclude that two hydrothermal metamorphic reactions also affect sediments at depth, destroying original carbonates and liberating additional CO_2. The hydrothermal processes frequently coincide with hydrothermal epidote as the carbonate replacement phases include epidote and other calc-silicate minerals (Norton and Hulen, 2006).Carbon dioxide is released through carbonate dissolution by the hot acid brine at depth and the alteration of calcareous siliciclastic rocks (Norton and Hulen

2006). These processes charged the shallow sandstone/alluvial reservoirs that were exploited in the Imperial carbon dioxide field.

The CO2 field and mudpots are indicative of the natural, low-pressure point where hydrothermal fluid can naturally flow out from the deep hypersaline reservoir. By incorporating the proposed temperature model, surface expressions in the area, seismic data, and the known higher CO_2 content in the legacy Imperial CO_2 field, this zone can be interpreted as a leakage pathway from the deep, hot hypersaline reservoir into the shallow hydrological system, with the fluid migrating northward in response to shallow hydrological forces.

3.6 Salinity distribution

Siddique et al. (2024) proposed a salinity model for the SSGF using data from production wells in the HRP1 project, where a clear thermochemical boundary can be found at -4,000 ft ASL. This model suggests a salinity gradient of 5% per 1,000 ft of total dissolved solids (TDS) in the reservoir brine for the first -4,000 ft ASL in the conductive, low-salinity reservoir. In the convective, highly saline reservoir from -4,000 ft to -8,500 ft ASL, the gradient is reduced to nearly 2.5% per 1,000 ft of TDS in the brine. While the exact salinity of a feedzone can be influenced by a highly permeable zone, the overall behavior of the system is expected to stabilize as a salinity-stratified reservoir, consistent with Fournier (1990).

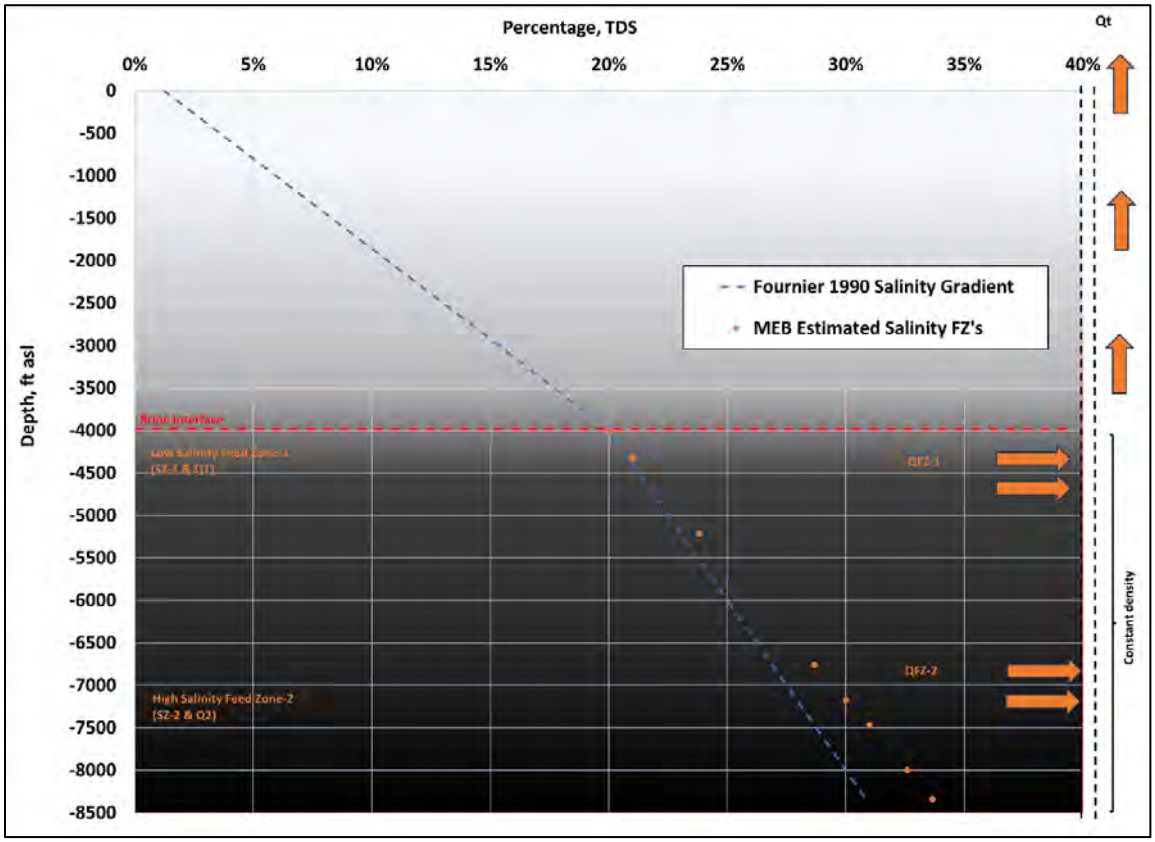

Figure 7: Salinity gradient plot for Salton Sea based on literature and double-diffusive convection model. Feed Zones (FZ) salinity estimated using MEB in orange, compared to Fournier's (1990) salinity gradient in blue. Differences between datasets can be attributed to the distance from the FZ data and the proposed heat source for the SSGF. Modified from Siddique et al. (2024).

The salinity distribution in the SSGF has been theorized and numerically studied using a Double-Diffusive Convective System (DDCS) by Fournier et al. (1990) and Oldenburg et al. (1995 and 2000). Understanding the nature of this salinity distribution is essential for the future development of the SSGF, not only for brine mining but also to effectively prevent scaling in production wells. This is crucial because the SSGF brine tends to precipitate scale based on its composition (Rocha et al., 2023), with significant economic and developmental implications, particularly the potential extraction of metals such as lithium from the brine. Consequently, a separate section is dedicated to describing the DDCS and its application in the proposed conceptual model.

4. Nature of a Double-Diffusive Convective System (DDCS)

Fournier (1990) proposed the possibility of the Salton Sea reservoir behaving as a Double-Diffusive Convective System (DDCS). This concept requires two conditions: the fluid must contain multiple components with different molecular diffusivities, and these components must have offsetting contributions to the fluid density. This leads to a low-salinity and high-salinity brine interface with a density contrast between brines.

Fournier (1990) describes this process as an initially gravity-stable system with heating from below and the sides. Cooler dilute brine lies above hotter, more concentrated brine, both undergoing convection. As the basal heat flow warms the underlying brine, it rises buoyantly into the overlying dilute brine, forming an intermediate layer of gravitationally stable brine with intermediate salinity and temperature. This process continues through the advecting column. The higher density at the top of the plume, caused by the faster movement of the brine front, hinders the upward flow of fluid and creates an effective barrier for the thermal and brine plumes (Oldenburg et al., 1995). Additionally, the medium's porosity and permeability directly affect the transport of mass and heat. Lower velocity systems will produce smaller convective velocities, thereby slowing the flow in a given layer. This process continues through the vertical column, achieving a quasi-steady state temperature, salinity profile, and fluid density (Siddique et al., 2024).

The Salton Sea reservoir high-salinity fluid approaches saturation as temperature increases with depth. This behavior aligns with the double-diffusive convection model, as described by Fournier (1990) and Oldenburg (2000), who identified three key characteristics of the reservoir after performing numerical model simulations of the DDCS:

1. Temperature and salinity decrease from the bottom to the top and from the center to the side of the anomaly.
2. A very high basal heat flow in the center of the thermal anomaly, sometimes exceeding 1000 mW/m^2, enabling significant convective heat flow in a chemically stratified reservoir.
3. A relatively uniform vertical fluid density throughout the hypersaline reservoir under all pressure, temperature, and salinity conditions.
4. A brine interface with a density contrast differentiates the cool, shallow, low salinity reservoir from the hot, deep hypersaline reservoir.

Despite increasing temperature with depth, the fluid density remains constant at approximately 1.0 g/cm^3, a phenomenon first noted by Helgeson (1968). Measurements in the State 2-14 well found the fluid density to be 1.017 ± 0.0023 g/cm^3 with a median of 0.999 g/cm^3. A review of Salton Sea wells by Williams and McKibben (1989) showed that the hypersaline portion of the reservoir, with fluid salinity greater than 20 wt%, had ranging from 0.98 to 1.0 g/cm^3. This requires fluid salinity

to increase with temperature, resulting in a linear increase in salinity with depth, meeting the conceptual requirements of a double-diffusive convective densities system.

Numerical exploration and validation were performed by Oldenburg et al. (1995) supporting this concept by establishing gravity equilibrium in a liquid column with 400°F at the top and 540°F at the bottom, where the heat source was placed, with a constant pressure boundary on the right side of the model. The reservoir parameters were chosen to represent the Salton Sea reservoir. The model equilibrated to a pseudo-steady-state condition over 30 ky, replicating a typical temperature distribution and a uniform brine density of 0.91 to 0.940 g/cm^3, slightly lower than measured. This model exhibits large salinity and temperature gradients in the top -4,700 ft ASL, speculated to result from top no-flow and constant temperature (400°F) boundary conditions, causing vertical convective flow to divert horizontally near the top to the right and the constant pressure boundary, thus forming a convection cell.

5. Proposed Conceptual Hydrothermal Model (CHM)

The model described in this work represents elements similar to those discussed in the literature review, with a particular emphasis on the southeastern section of the SSGF, where the Hudson Ranch Power I project is located. The main differences introduced include the permeability distribution (matrix and fractured permeabilities) in the hypersaline reservoir, a transitional zone, a refined structural framework based on seismic interpretation, the salinity distribution in the system related to the DDCS with a brine interface, and thermal outflow into the shallow reservoir with known surface expressions.

This work conceptualizes the southeastern section of the Salton Sea field, where the Hudson Ranch Power I project is situated, believed to be one of the reservoir's flanks. Lateral temperature extent is lost to the southeast section of the reservoir, while salinity increases due to the stratification described in the DDCS. Non-commercial wells were drilled there in 2013 (Kaspereit, 2016) just outside the commercial reservoir. This conceptual description offers an opportunity to understand the system's behavior on what could be one of the reservoir's flanks.

The following section outlines the main elements of the CHM presented in this work (Figure 8) using a framework for CHM elements described by Faulder (1991).

5.1 Heat Source

The primary heat source for the Salton Sea Geothermal Field in our model is the "still-cooling granitic pluton" located at southern margin of the Salton Sea, as described and invoked in previous works (Hulen, 2002 and Kaspereit et. al, 2016). We adopt the size and locations estimates of previous authors for this body: 2 km in diameter at -3.6 km above sea level providing an estimated heat flux of ~450 mW/m^2.

5.2 Permeable pathways

The permeable pathways in this model are similar to those described by Hulen et. al (2003). High vertical permeability is attributed to fractures, breccias, and veinlets that facilitate the vertical flow of both cooler (recharge) fluid and hot, high-salinity brine heated by the intrusion. These main vertical pathways connect the heat source to the shallow sediments in the basin. The seismic interpretation presented in this paper depicts these high permeable pathways for both, hot and

hypersaline brine, and cool, groundwater hydrology over the HRP1 wellfield. Most of the connection between the two brine systems is conceptualized as flowing from the hot, highly saline reservoir to the cooler, low-salinity reservoir. Although some migration of shallow groundwater into the geothermal system is not ruled out, the stable interface observed on the DDCS suggests only minor percolation of groundwater into the hot, high-salinity reservoir. Nonetheless, groundwater over the sink likely plays a major role for pressure support for the system.

Secondary horizontal permeability is presented by sedimentary and porous (potentially metamorphosed) sandstone layers where calcite is hydrothermally dissolved, creating fluid pathways that explain the lateral extent of the temperature profiles in the Hudson Ranch wellfield. These secondary layers may be difficult to consistently target at depth due to lateral stratigraphic variability, but the permeable heterogeneity of the system can be correlated with sedimentary changes from identified lacustrine and fluvial deposition in the Salton Sink and is expressed in the shallower seismic sections. These productive zones in the Hudson Ranch wells can be identified between -3,400 ft ASL and -7,700 ft ASL, below the low salinity reservoir (brine interface), and is described as the shallow section of the transitional zone, where the rock undergoes metamorphosis and calcite is dissolved from the matrix. Deeper permeability in the transitional zone may be due to brittle fracturing of metamorphosed sedimentary rocks and/or faults and fault associated fractures where present. The combination of these permeable pathways allows for the lateral transport of hot brine away from the intrusion, resulting in the eastern temperature anomaly one mile east of the primary heat source. Inspection of Figure 5 at -5,000 ft ASL shows indications of shallower eastward lateral flow with temperature anomalies to the north and south that may also represent vertical upwelling.

5.3 Thermal recharge

Thermal recharge of the system is facilitated horizontally by the connection between different “compartments” of the reservoir, as described by Kaspereit (2016). Vertical connection between surface water, groundwater and hypersaline water is facilitated by known permeable fractures along the mentioned compartments. Main faults near the heat source facilitate thermal recharge, while faults further away allow cold regional hydrology to recharge the system. Permeable structures west of the primary fault interpreted in the HRP1 seismic appear to be associated with an upflow, linking the deep hypersaline reservoir with the known productive zones and mud-pots at surface. East of the major fault interpreted at HRP1, temperatures quickly fall off, suggesting the fault, which has the highest relative displacement in the area, may be impermeable due to clays or other fine materials generated along the fault during deformation. The porosity east of this boundary, if it exists, is either isolated from the convective system by this permeability barrier and or in stronger communication with the shallow, cooler ground water.

The recharge flow of the system is inferred to be derived from waters following the shallow hydrologic gradient of the basin, reflected by the New and Alamo Rivers, which flow from the Mexicali Valley, towards the Salton Sea. Lateral permeability in the transitional or brine interface layer allows interaction between cold and hot fluids, forming a convective cell. Shallow waters may flow laterally towards the center of the field where they descend, are heated, and are transported laterally and vertically in a convective cell (Figure 8).

5.4 Characterized reservoir

Defining the extent of the reservoir using geophysical data has been challenging because most of the available seismic data is not public. This paper uses Kaspereit's (2016) description, which states that the commercial Salton Sea reservoir is bounded by the NNW Calipatria fault (Figure 6) on the northeast and extends southwest to an unnamed fault parallel to the Calipatria fault along the New River mouth. Perpendicular faults define the southern and northern limits, with rhyolite domes assumed to be compartment centers (see Figure 3).

Commercial reservoir top depths vary around -4,000 ft ASL, where the high and low salinity interface is believed to be located. The reservoir bottom cannot be clearly identified, as there is evidence of producible fluid at greater depths (Paillet, 1986). However, current commercial wells do not exceed -9,000 ft ASL, where over-pressured zones have been found to the southeast. This is the reservoir bottom depth used for this conceptual model.

The salinity of the reservoir varies depending on its proximity to the main heat source and with depth. According to the double-diffusive convection system (DDCS) concept, salinity decreases from the bottom to the top and from the sides to the center of the anomaly. Empirically, the salinity of the system increases gradually at a rate of 2.5% per 1,000 ft over the characterized reservoir from -3,800 ft to -9,000 ft ASL, with slight increases with horizontal distance from the temperature anomaly.

5.5 Outflow into surrounding hydrology

Previous conceptual models describe the deep, highly saline reservoir but often neglect its interaction with the basin's shallow hydrology. Evidence of CO_2 presence is found at both shallow (less than -4,000 ft ASL) and deep (greater than -4,000 ft ASL) levels, evidenced from the HRP1 production brine chemistry. The legacy Imperial CO_2 field indicates the migration direction of CO_2 from the deeper to shallow hydrology, north of the Hudson Ranch Power I (HRP1) wellfield. Surface steam expressions, known as *'Old Mud Pots'*, near the HRP1 project and the legacy Imperial CO_2 field are interpreted to represent the system's outflow, extending north and possibly to the eastern edge of the Salton Sea shoreline. Connectivity of the deep system to the shallow is inferred along the east dipping faults imaged near HRP1, where projections of the fault traces to the surface intersect the mud puts (Figure 8).

6. Conclusions

The proposed conceptual hydrothermal model for the southeastern part of the Salton Sea Geothermal Field, particularly the Hudson Ranch Power I project area, emphasizes the heterogeneous nature of both vertical and horizontal permeability within the hypersaline reservoir. The model provides crucial insights into fluid flow and heat transfer dynamics by distinguishing between matrix and fractured permeabilities. These permeable features described using geoscience data, downhole logs, drilling data, and production history from the HRP1 wells, explains the temperature anomaly on the reservoir's edge and suggests a horizontal extension of the system, even one mile east of the described heat source.

Main permeable structures also highlight the interaction between groundwater recharge and the reservoir's edge, essential for maintaining the reservoir's thermal balance and influencing the overall dynamics of the geothermal system. Additionally, the model describes the potential

outflow of geothermal fluids into the shallow system, explaining the location of the legacy Imperial CO_2 Field and the surface expression of the ‘Old Mud Pots’.

The model addresses salinity distribution within the reservoir as being closely related to the double-diffusive convection system (DDCS). The salinity stratification affects the behavior of the brine and its interaction with surrounding geological formations, with a distinct brine interface between the shallow and deep reservoirs. Understanding brine composition and its distribution is vital for future geothermal development, not only to predict scale precipitation behavior in the wells but also to assess the potential for lithium extraction from the geothermal brine. This aspect underscores the economic viability of geothermal energy projects in the region and its potential for future development.

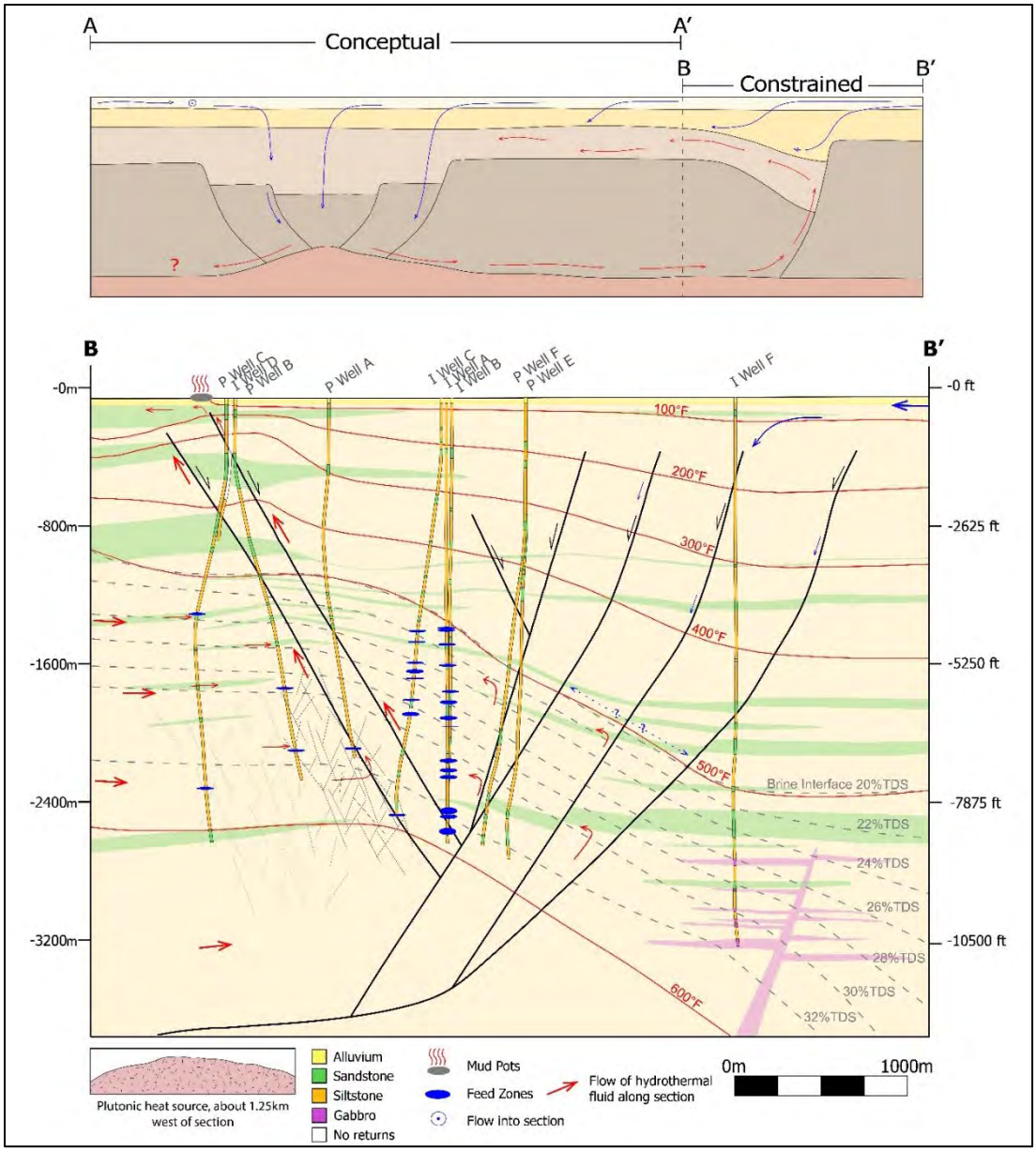

Figure 8: Preliminary conceptual model for the Hudson Ranch Wellfield and location within the Salton Sea Geothermal Field. The following well traces are projected onto the section: I Wells A-C (~2,300 ft due north), and P Wells F and E (~1,300 ft due south). Not depicted, Calipatria fault to the west and Weister fault to the east bounding the HR wellfield. Hot geothermal brine flows from the west into the section, flowing through permeable stratigraphic features, upwelling through faults and fracture dominated damage zones, charging shallow stratigraphic reservoirs in the subsurface. Numerous mud pot surface expressions may indicate outflow of the system. Recharge of the system follows the hydrologic gradient of the basin and flows towards the Salton Sea. Shallow waters descend, are heated, and are transported in a convective cell. The brine interface marks the boundary between the convecting system and the base of the shallow hydrologic system. Salinity contours depict the variation with depth and proximity to the heat source.

Acknowledgement

This study benefited from a seismic reflection survey acquired under the guidance of Luis Navarro. The authors of this paper thank Cyrq Energy's management for the opportunity to present this paper.

REFERENCES

Araya, N., and O'Sullivan J. "A 3D Conceptual and Natural-State Model of the Salton Sea Geothermal Field" *GRC Transactions*, 46, (2022), 2123-2159.

Babcock, E. A., "Detection of active faulting using oblique infrared aerial photography in the Imperial Valley, California." *Geol. Soc. Am.*, 82, (1971), 3189-3196.

Bear, J. "*Dynamics of Fluids in Porous Media"*. Dover, (1988). 764 p.

Biehler, S. "Gravity studies in the Imperial Valley." Cooperative Geological- Geophysical Geochemical Investigation of Geothermal Resources in the Imperial Valley Area of California, (1971), 29-41.

Cho, M., Liou, J.G., and Bird, D.K. "Prograde Phase Relations in the California State 2-14 Well Meta-Sandstones, Salton Sea Geothermal Field." *Journal Geophysics Research, 93,* (1988).

Dorsey, R. "Stratigraphy, Tectonics, and Basin Evolution in the Anza-Borrego Desert Region." In G. T. Jefferson and L. Lindsay, Fossil Treasures of the Anza-Borrego Desert, Sunbelt Publication, (2006), 89-104.

Dutcher, L.C., Hardt, W.F., and Moyle, W.R. "Preliminary Appraisal of Ground Water in Storage with Reference to Geothermal Resources in the Imperial Valley Area, California." Geological Survey Circular 649, (1972).

Faulder, D.D. "Conceptual Geologic Model and Native State Model of the Roosevelt Hot Springs Hydrothermal System", *Proceedings: 16th Workshop on Geothermal Reservoir Engineering*, Stanford University, Stanford, CA, (1991).

Faulder, D. D. "HR Reservoir Model Update Sept 1 2022". Internal report for Cyrq Energy dated 1 Sep 2022, (2022), 50p.

Faulds, J.E., and Hinz, N.H. "Favorable Tectonic and Structural Settings of Geothermal Systems in the Great Basin Region, Western USA: Proxies for Discovering Blind Geothermal Systems", *Proceedings: World Geothermal Congress* (2015), Melbourne, Australia, p.6.

Fournier, R. "Double-Diffusive Convection in Geothermal Systems: The Salton Sea, California, Geothermal System As A Likely Candidate" *Geothermics*, Vol. 19, No. 6, (1990), 481-496.

Griscom, A., and Muffler, L.J.P. "Aeromagnetic Map and Interpretation of the Salon Sea Geothermal Area, California." *United States Geological Survey,* (1971).

Han, L., Hole, J.A., Stock, J.M., Fuis, G.S., Williams, C.F., Delph, J.R., Davenport, K.K., and Livers, A.J. "Seismic imaging of the metamorphism of young sediment into new crystalline crust in the actively rifting Imperial Valley, California." *Geochemistry, Geophysics, Geosystems, 17,* (2016b), 4566-4584.

Helgeson, H.C. “Geologic and Thermodynamic Characteristics of the Salton Sea Geothermal System”, *American J. of Science*, Vol 266, (1968), 129-166.

Hulen, J., Kaspereit, D., Norton, D.L., Osborn, W., Pulka, F.S. “Refined Conceptual Modeling and a New Resource Estimate for the Salton Sea Geothermal Field, Imperial Valley, California.” *GRC Transactions*, 26, (2002), 29-36.

Hulen, J., Norton, D., Kaspereit, D., Murray, L., Van de Putte, T., and Wright, M. “Geology and a Working Conceptual Model of the Obsidian Butte (Unit 6) Sector of the Salton Sea Geothermal Field, California.” *GRC Transactions*, 27, (2003), 227-240.

Kaspereit, D., Mann, M., Sanyal S., Rickard, B., Osborn, W., and Hulen, J. “Updated Conceptual Model and Reserve Estimate for the Salton Sea Geothermal Field, Imperial Valley, California.” *GRC Transactions*, 40, (2016), 57-66.

Lutz, Andrew T. et al. “Stratigraphic Record of Pleistocene Faulting and Basin Evolution in the Borrego Badlands, San Jacinto Fault Zone, Southern California.” Geological Society of America Bulletin, 118, (2006), 1377-1397.

Lynch, D. K., and Hudnut, K. W. “The Wister Mud Pot Lineament: Southeastward Extension or Abandoned Strand of the San Andreas Fault?” *Seismological Society of America.Vol.,* 98, No.4, (2008), 1720-1729.

McDowell, S., Elders, W. “Authigenic layer silicate minerals in borehole Elmore 1, Salton Sea Geothermal Field, California, USA” *Contr. Mineral. and Petrol.,* 74, (1980), 293–310.

McKibben, M.A. “The Salton Trough Rift.” SBCMA Special Publication, 9, (1991), 76-80.

Meidav, T., West, R., Katzenstein, A., and Rostein, Y. “An Electrical Resistivity Survey of the Salton Sea Geothermal Field, Imperial Valley California.” Lawrence Livermore Laboratory, UCRL-13690, (1976).

Muffler, L.J.P., and D.E. White. “Origin of CO_2 in the Salton Sea Geothermal System, Southeastern California, U.S.A.” *XXIII International Geological Congress*, Vol 17, (1968), 185-194.

Muffler, L. J. P., and D. E. White. “Active metamorphism of upper Cenozoic sediments in the Salton Sea geothermal field and the Salton Trough” *Southeastern California, Geol. Soc. Am. Bull.*, 80, (1969), 157–182.Newmark, R. L., P. W. Kasameyer, and L. W. Younker, 1988. Shallow Drilling in the Salton Sea Region: The Thermal Anomaly. J. Geophys. Res., Vol. 93 pp.18.

Nichols, E. “Geothermal Exploration Under the Salton Sea Using Marine Magnetotellurics.” California Energy Commission, PIER Renewable Energy Technologies Program, CEC-500-2009-005, (2009).

Norton, D.L. & Hulen, J.B. Magma-hydrothermal activity in the Salton Sea geothermal field Imperial County, California. *GRC Transactions*, 30, (2006), 991-998.

Tompson, A., Demir, Z., Moran, J., Mason, D., Wagoner, J., Kollet, S et al. “Groundwater Availability Within the Salton Sea Basin Final Report” Lawrence Livermore National Laboratory, 143 p. (2008).

Oldenburg, C. M., Pruess, K., and Lippman, M. “Heat and Mass Transfer in Hypersaline Geothermal Systems.” *Proceedings: World Geothermal Congress,* Florence, Italy, (1995).

Oldenburg, C. M., and Pruess, K. “Thermohaline Convective Mixing At A Brine Interface” *Proceedings: 25th Workshop on Geothermal Reservoir Engineering,* Stanford University, Stanford, CA, (2000).

Paillet, F., Morin, R., Hodges, R., Robison, L. Priest, S., Sass, J., Hendricks, J., Kasameyer, P., Pawloski, G., Carlson, R., Duba, A., Hearst J., and Newmark, R. “Preliminary Report on Geophysical Well-Logging Activity on the Salton Sea Scientific Drilling Project, Imperial Valley, California” U.S. Geological Survey, Open-File Report 86-544, (1986).

Ramirez, G., Zuza, R., Johnson, A., Murphy, J. and Akerley, J., “Integrated Conceptual Model of the Sedimentary Base-Hosted Geothermal Fields in Imperial Valley, CA”, *GRC Transactions*, 47, (2023), 22p.

Rocha, S., Faulder, D., Capuano III, L., Capuano Jr., L., and Walsh, P. “Novel Coiled Tubing Operations in a Hostile Thermo-Chemical Environment”, *Proceedings: 48th Workshop on Geothermal Reservoir Engineering*, Stanford University, Stanford, CA, (2023).

Rook, S. H., and Williams, G. C., “Imperial carbon dioxide gas field”, California Div. Oil and Gas Bull., California Oil Fields-Summ. Operations, v. 28, no. 2, (1942), 12-33.

Sass, J.H., Galanis, S.P., Jr., Lachenbruch, A.H., Marshall, B.V., and Munroe, R.J. “Temperature, Thermal Conductivity, Heat Flow, and Radiogenic Heat Production from Unconsolidated Sediments of the Imperial Valley, California.” USGS Open File Report, 84-490, (1984).

Sass, J.H., Priest, S. S., Duda, L.E., Carson, C.C., Hendricks, J. D. L., and Robison C. “Thermal regime of the State 2-14 well, Salton Sea Scientific Drilling Project”. *Journal of Geophysical Research Solid Earth.* v. 93, (1988).

Siddique, A., Faulder, D., Rocha, S. “Inferring Zonal Contributions and Productivity from a High-temperature, High-salinity Reservoir”, *Proceedings: 49th Workshop on Geothermal Reservoir Engineering*, Stanford University, Stanford, CA, (2024).

Steely, A.N., Janecke, S.U., Dorsey, R.J., and Axen, G.J. “Early Pleistocene initiation of the San Felipe fault zone, SW Salton Trough, during reorganization of the San Andreas fault system.” *Geol. Soc. Am. Bull.*, 121, (2009), 663–687.

Stimac, J., Wilmarth, M., Mandeno, P.E., Dobson, P., and Winick, J. “Review of Exploitable Supercritical Geothermal Resources to 5 km at Geysers-Clear Lake, Salton Sea, and Coso.” *GRC Transactions*, 41, (2017).

Wallis, I., Rowland, J., Cumming, W., and Dempsey, D. “The Subsurface Geometry of a Natural Geothermal Reservoir.” *New Zealand Geothermal Workshop*, Rotorua, New Zealand, (2016).

Williams, A.E., and McKibben, M.A. “A brine interface in the Salton Sea geothermal system, California: Fluid-geochemical and isotopic characteristics.” *Geochimica et Cosmochimica Acta*, v. 5., (1989).

Younker, L.W., Kasameyer, P.W., and Tewhey, J.D. “Geological, Geophysical, and Thermal Characteristics of the Salton Sea Geothermal Field, California.” *Journal of Volcanology and Geothermal Research*, 12, (1981), 221-258.

Power Outputs from the Field Tests of Thermoelectric Generators at Different Temperatures

Yuan Tian[1,2], Yuhao Zhu[1,2], Kewen Li[1,2], Yu-kai Liang[3], and Ji-ping Yang[3]

[1]School of Energy Resources, China University of Geosciences (Beijing), Beijing 100083, China;

[2]Beijing Key Laboratory of Unconventional Natural Gas Geological Evaluation and Development Engineering, Beijing 100083, China;

3. Cnooc (Guangdong) New Energy Engineering Design Co., LTD, China

Keywords

Thermoelectric generators, Field test, Geothermal power generation, Cost.

ABSTRACT

There have been many experimental studies on thermoelectric generators (TEG) for generating electricity using geothermal energy and waste heat from various industries in recent years. TEG power output has been measured at different flow rates of water, different temperatures, and other different conditions. However, there have been few large-scale field tests at geothermal wells and industry sited.

Considering these experimental measurements and field test results, some questions arise. Are there any relationships among the TEG power outputs measured in laboratory and pilot test sites at different temperatures? Can we predict the power output at the field tests (larger scale) using the experimental results with a single TEG module? Does TEG have any advantages in terms of cost compared to solar PV (photovoltaic) panels?

To answer the above questions, we have collected and analyzed the experimental and field test data of the TEG power output at different temperatures and temperature differential (TD). The power output data include those of single TEG module, TEG devices with 6, 10 and 20 layers (the highest number of layers reported) respectively. The 10- and 20-layer TEG devices were tested for power generation using the industrial waste heat from a gas power plant at a temperature of about 80 °C. The field test of the 6-layer TEG device was conducted at a geothermal field with higher temperatures up to 170 °C.

The data analysis demonstrates that the TEG power outputs measured in laboratory and pilot test sites at different temperatures are closely consistent. An equation coupling TEG power outputs and TD has been established. We may predict the power output for large-scale field applications using the experimental results with a single TEG chip at different TD. The cost of TEG is lower than solar PV (photovoltaic) panels when TD is greater than 90o C.

1. Introduction

In recent decades, thermoelectric generators (TEGs) have obtained considerable attention as a sustainable technology for generating electricity from low-grade heat sources. These include geothermal energy and industrial waste heat. As the global demand for renewable energy solutions intensifies, TEGs offer a promising avenue to convert thermal energy directly into electrical energy, using heat to produce power under temperature differentials (TD). This direct conversion process circumvents the need for complex mechanical systems, making TEGs an attractive option for various applications, from remote power generation to enhancing the efficiency of energy utilization during industrial processes.

The principle of thermoelectric generation is based on the Seebeck effect, where a temperature difference across a thermoelectric material induces a voltage, generating an electric current. TEGs have been utilized in various applications, including space missions, remote sensing, and waste heat recovery. The efficiency of TEGs is primarily determined by the material's figure of merit (ZT), which is a function of the Seebeck coefficient, electrical conductivity, and thermal conductivity. Recent advancements in materials science have led to the development of high-performance thermoelectric materials, enhancing the practical applicability of TEGs (Snyder & Toberer, 2008).

Numerous experimental studies have explored the performance of TEGs under different conditions. For instance, Rowe and Min (1998) investigated the effect of temperature gradients on the power output of TEG modules, finding a direct correlation between TD and generated power. Other studies, such as those by Snyder and Ursell (2003), have focused on optimizing the material properties and chip design to maximize efficiency. These laboratory experiments provide a foundational understanding of TEG behavior, but they often lack the complexity of real-world conditions.

Chen et al. (2017) focused on enhancing the efficiency of TEGs through mechanical and electrical structure optimization. Their study in Energies explored how modifications in the mechanical and electrical configurations of TEGs can improve overall performance. By optimizing these aspects, Chen et al. demonstrated enhanced efficiency in converting waste heat to electricity, contributing to advancements in TEG technology.

Li et al. (2020) conducted experimental studies on an expandable thermoelectric power generator, focusing on the power output under different conditions. Their work demonstrated the scalability of TEG systems and provided a foundation for further field tests. Additionally, Li et al. (2021a) provided a comprehensive cost estimation of TEG systems, comparing them to other renewable energy technologies.

Li et al. (2021b) conducted a significant field test of TEGs at the Bottle Rock geothermal power plant. Their study provided critical insights into the challenges and opportunities of deploying TEG

technology in real-world conditions, highlighting the potential for large-scale applications and the need for system optimization to achieve consistent performance.

Field tests of TEGs are less common, but they are crucial for assessing the technology's scalability and practical performance. A notable study by Champier et al. (2010) conducted field tests using TEGs to recover waste heat from biomass boilers, demonstrating the feasibility of TEGs for industrial applications.

Despite the potential of TEGs, much of the research to date has focused on laboratory-scale experiments, investigating the power output of TEG modules under controlled conditions. These studies have provided valuable insights into the performance characteristics of TEGs, examining variables such as temperature gradients, flow rates, and material properties. However, there remains a gap in understanding how these laboratory findings translate to real-world, large-scale applications. Field tests at geothermal wells and industrial sites are limited, leaving critical questions unanswered about the scalability and economic viability of TEG technology.

This research aims to bridge this gap by analyzing experimental and field test data to establish relationships between TEG power outputs measured in laboratory settings and those obtained from larger-scale pilot tests. Specifically, the study seeks to determine whether it is possible to predict the power output of large-scale TEG applications based on single-chip experimental results and to evaluate the cost-effectiveness of TEGs compared to solar photovoltaic (PV) panels under varying temperature conditions.

2. Power output data of TEG from the field tests and the experiments in laboratory

The field test of the 6-layer TEG device, as shown in Figure 1, was conducted at Bottle Rock geothermal field with a temperature of steam up to 170 °C (Li, et al., 2021).

Figure 1: The 6-layer TEG apparatus installed for field test at Bottle Rock geothermal field (Li, et al., 2021).

The total power of the six-layer TEG apparatus measured at Bottle Rock geothermal field is depicted in Figure 2. According the field test results, each layer had 24 TEG chips and each chip could generate a maximum power of around 3.9 W with a temperature difference of 152 °C between the cold and hot fluid manifolds.

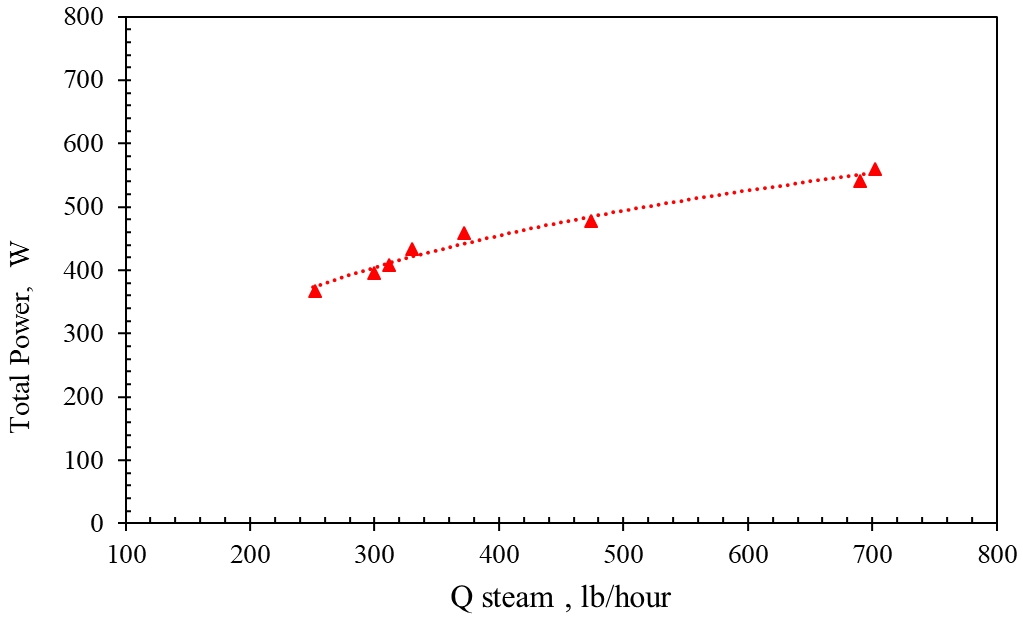

Figure 2: The total power estimated for the six-layer TEG apparatus in field tests at Bottle Rock geothermal field (Li, et al., 2021).

The 10- and 20-layer TEG devices were pilot tested for power generation using the industrial waste heat from a gas (coal bed methane) power plant at a temperature of about 80 °C.

The gas power plant is located at a coal mining area with abundant coal-bed methane resources in Shanxi Province, China. The gas power plant had three gas generators of 1.8 MW with a total installed capacity of 5.4 MW. The waste heat mainly exists in the exhaust gas emissions and the engine cooling closed-loop. The overview of the gas power plant is shown in Figure 3.

Figure 3: Photos of the gas power plant.

As shown in Figure 4, one of the TEG devices (20 layers) was installed nearby the windows. The hot flow channel of TEG was connected to the pipelines via two heat insulated tubes. The valves allowed to control the pressure and flow rate of hot water in the tubes. The cold flow channel was connected to a water tank. Another TEG (10 layers) was connected in the same way in the field tests. The 10-layer TEG contains 24 modules per layer and the 20-layer TEG contains 18 thermoelectric modules per layer.

Figure 4: One of the TEG devices (20 layers) installed for field tests.

The power output of the TEG device at different hot and cold flow rates are depicted in Figs. 5 and 6, respectively. Two times of the power output by the 10-layer TEG matches well with the power of the 20-layer TEG device. This observation implies that the power of the expanded 20-layer TEG device from the 10-layer TEG device was not decreased, which is very important at large-scale industry applications.

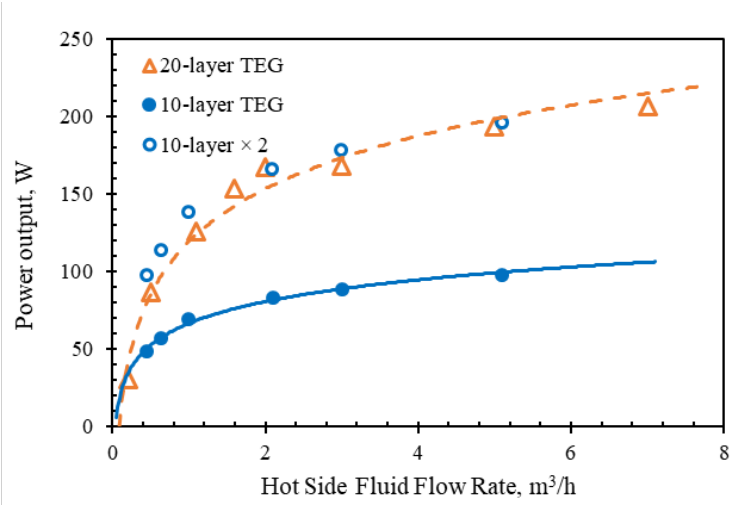

Figure 5: The total power output of the TEG devices at different flow rates on the hot side (water flow rate on the cold side was 3 m^3/h and the temperature difference was 60 °C (Zhu et al., 2024).

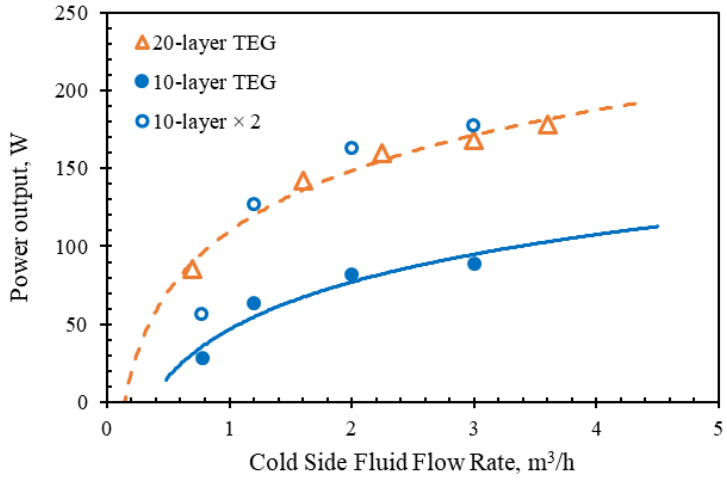

Figure 6: The total power output of the TEG devices at different flow rates on the cold side (water flow rate on the hot side was 3 m^3/h and the temperature difference was 60 °C（Zhu et al., 2024）.

The details of the TEG pilot tests at low temperatures could be found in the paper by Zhu et al., 2024.

Li et al. (2020) conducted the laboratory experiments using a 5-layer TEG apparatus to measure the power output and efficiency at different flow rates of water, different temperature, and different temperature differences between hot and cold sides. The five-layer TEG device could generate about 45.7 W electricity with a temperature difference of 72.2°C between the cold and hot sides. The power of each chip was about 0.51 W at this temperature difference (see Figure 7). Other experimental data could be found in the paper by Li, et al. (2020).

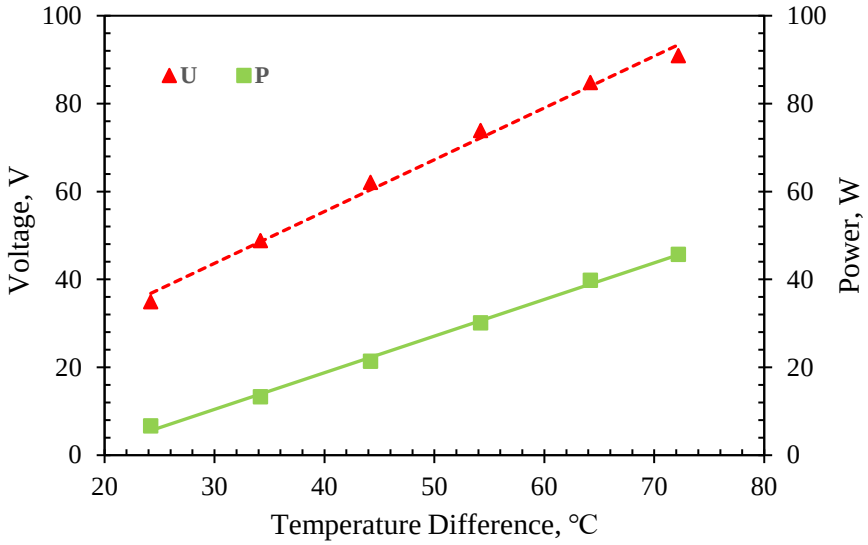

Figure 7: Voltage (U, dashed line) and power output (P, solid line) of the five-layer TEG apparatus at different temperature differences (water flow rates on the cold and hot sides were 654.55 and 1028.57 L/hour, respectively).

Zhu et al. (2023) measured the power output of a single TEG chip in the laboratory at temperatures lower than 100 ºC and the results are depicted in Figure 8. One can see that the power output of a single TEG chip increases with TD almost linearly.

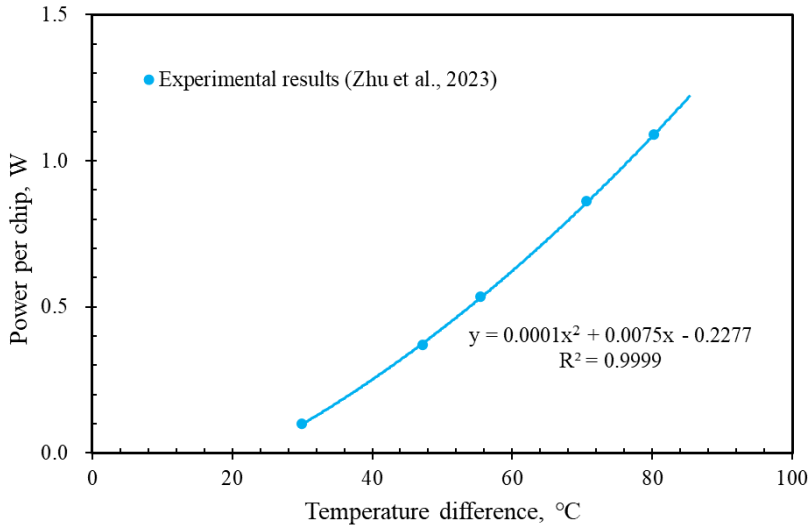

Figure 8: the power output of a single TEG chip in the laboratory vs. TD at temperatures lower than 100 ºC (Zhu et al., 2023).

Zhu et al. (2024) reported that the power output of TEG devices measured at the pilot field test sites increases with TD but not linearly. The reason is discussed in the next section.

3. Results and Discussions

It is useful to predict the power output of large-scale TEG applications based on single-chip experimental results. In order to check such a possibility, we collected all of our previous data of the power output at different TD and converted these data to the power output per TEG chip vs. TD. The results are shown in Figure 9. The red square symbol represents the power data from the geothermal field test reported by Li, et al. (2021). The red triangle symbols represent the power data from the field test reported by Zhu, et al. (2024). The blue circle symbols represent the power data from the lab test reported by Li, et al. (2020). The power output per TEG chip in the above data sets was derived from TEG devices with more than five layers. The green solid circle symbols represent the power data of a single TEG chip from the lab test reported by Zhu, et al. (2023). One can see that all of the data points sit well on a curve characteristic of an exponential function. The matching equation is listed in Figure 9. Note that the value of fitting goodness is over 0.99. This demonstrates that it is possible to predict the power output of large-scale TEG applications based on single-chip experimental results.

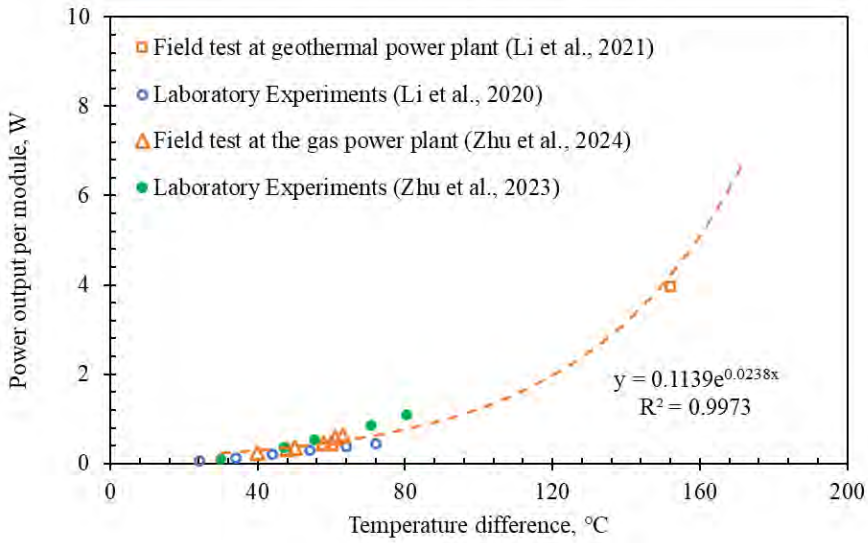

Figure 9: The power output per chip vs. temperature differences.

The power output data of the TEG device with both 10- and 20 layers at different hot and cold flow rates are depicted in Figure. 10. The power output increases with the flow rates on both hot and cold sides and follows the same trend, that is, an exponential function. Note that the power output of the 10-layer TEG device in Figure 10 is multiplied by two in order to compare with the same number of layers.

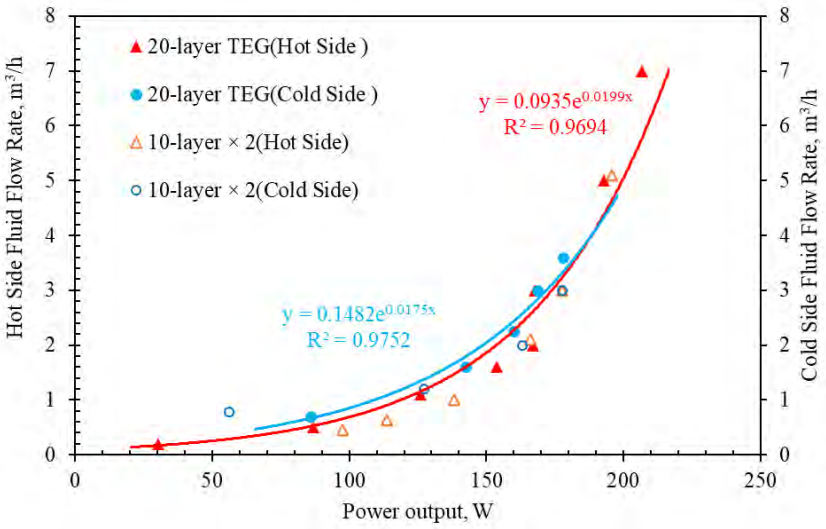

Figure 10: The total power output of the TEG devices at different flow rates on the hot/cold side (water flow rate on the cold/hot side was 3 m^3/h and the temperature difference was 60 °C (± 1 °C)).

Figure 11 shows the efficiency of the TEG devices at different temperature differences and different flow rates. The efficiency of the power generation from heat to electricity increases with temperature difference and decreases with the increase in flow rates at the hot side. The last observation is interesting and the mechanism behind it is not clear yet.

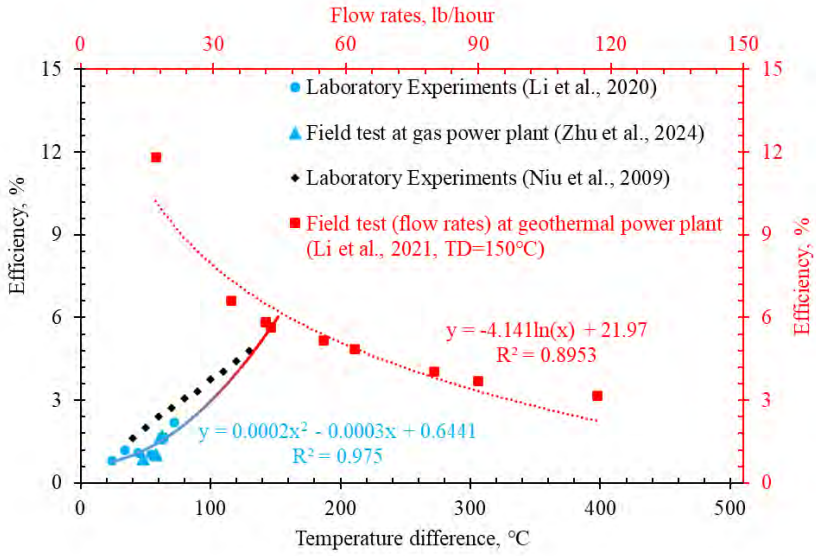

Figure 2: The efficiency of the TEG devices at different temperature differences and different flow rates.

The data of the power per unit area of TEG chips and the power per unit thermoelectric particle area of TEG chips at different temperature differences are shown in Figure 12. Also listed is the power per unit area of PV panels, which is in the range of 150 – 250 W/m^2. The power per unit

area of TEG chips will exceed that of PV panels at temperature differences above 80°C. Interestingly, Lee and Lee (2018) reported a TEG with a very high power density of 233.1 kW/m^2 at a temperature difference of 155 °C.

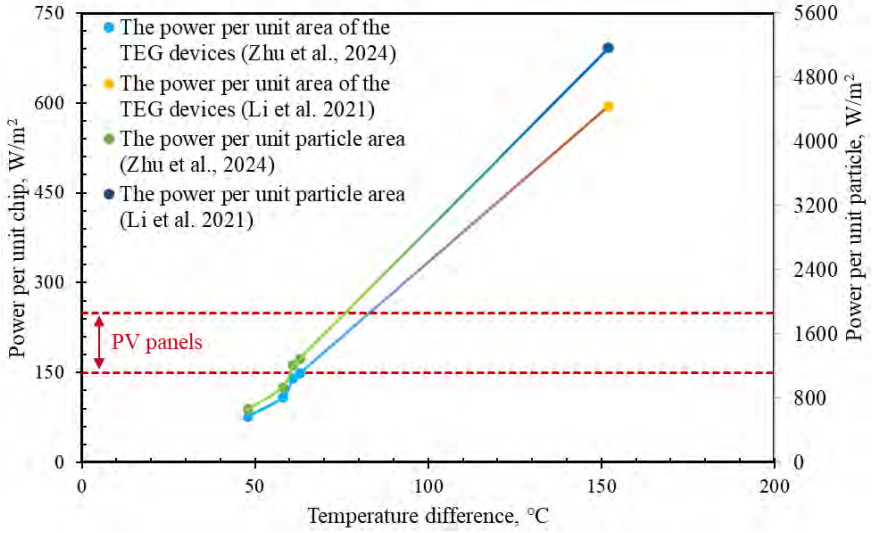

Figure 3: The power per unit area of the TEG devices and per unit particle at different temperature difference.

Figure 13 shows the estimated cost of the TEG devices based on the results of the field tests conducted by Zhu et al.(2024) and the geothermal field tests by Li et al. (2021). The installation cost ($/kW) and the Levelized Cost of Electricity (LCOE) of TEG at different temperature differences were calculated with reference to the cost data of geothermal power generation (from International Renewable Energy Agency). One can see that the relationship between the cost and TD is linear on a single-log coordination plot. As reported by Li et al. (2021), the cost of TEG is also attractive compared with PV panels if the capacity factor were considered.

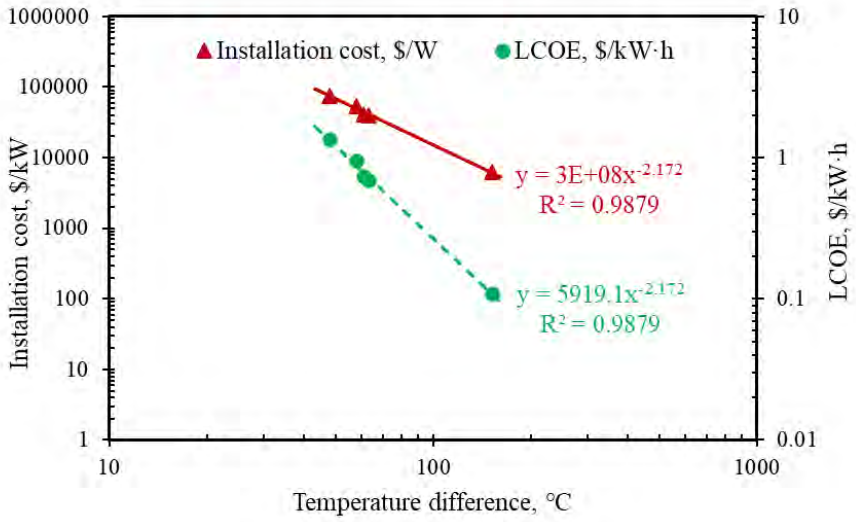

Figure 13: The installation cost and LCOE of TEG at different temperature differences.

4. Conclusions

Thermoelectric generators hold significant potential for sustainable energy generation from low-grade heat sources. Despite the extensive research conducted on TEGs, there remains a critical need to bridge the gap between laboratory-scale experiments and large-scale field applications. According to the field test results, the following conclusions may be drawn:

(1) The TEG power outputs measured in laboratory and pilot test sites at different temperatures are closely consistent. An equation coupling TEG power outputs and TD has been established.

(2) We may predict the power output for large-scale field applications using the experimental results with a single TEG chip at different TD.

(3) The cost of TEG is lower than solar PV (photovoltaic) panels when TD is greater than 90 ℃.

Acknowledgement

This work was partially supported by the specific research fund of “The Innovation Platform for Academicians of Hainan Province” and was partially funded by the Special Science and Technology Innovation Project of Xiong'an New Area, under the task titled "Theoretical and Applied Research on Geothermal Energy Development and Utilization in the Xiong'an Region" (Project Number: 2022XACX0800).

REFERENCES

Champier, D., Bedecarrats, J. P., Rivaletto, M., & Strub, F. (2010). Thermoelectric power generation from biomass cook stoves. Energy, 35(2), 935-942.

Chen, J., Li, K., Liu, C., Li, M., Lv, Y., Jia, L., & Jiang, S. (2017). Enhanced efficiency of thermoelectric generator by optimizing mechanical and electrical structures. Energies, 10(9), 1329.

Lee, W., & Lee, J. (2018). Development of a compact thermoelectric generator consisting of printed circuit heat exchangers. Energy Conversion and Management, 171, 1302-1310.

Li, K., Garrison, G., Moore, M., Zhu, Y., Liu, C., Horne, R., & Petty, S. (2020). An expandable thermoelectric power generator and the experimental studies on power output. International Journal of Heat and Mass Transfer, 160, 120205.

Li, K., Garrison, G., Zhu, Y., Horne, R., & Petty, S. (2021a). Cost estimation of thermoelectric generators. In Proceedings of the 46th Workshop on Geothermal Reservoir Engineering, Stanford, CA, USA (pp. 16-18).

Li, K., Garrison, G., Zhu, Y., Moore, M., Liu, C., Hepper, J., ... & Petty, S. (2021b). Thermoelectric power generator: Field test at Bottle Rock geothermal power plant. Journal of Power Sources, 485, 229266.

Niu, X., Yu, J., & Wang, S. (2009). Experimental study on low-temperature waste heat thermoelectric generator. Journal of Power Sources, 188(2), 621-626.

Rowe, D. M., & Min, G. (1998). Evaluation of thermoelectric modules for power generation. Journal of Power Sources, 73(2), 193-198.

Snyder, G. J., & Toberer, E. S. (2008). Complex thermoelectric materials. Nature Materials, 7(2), 105-114.

Snyder, G. J., & Ursell, T. S. (2003). Thermoelectric efficiency and compatibility. Physical Review Letters, 91(14), 148301.

Zhu, Y., Li, K., Mgijimi, M.B., He, J., Wang, L., Zheng, A., Wang, X., Zhang, H. and Liu, C. (2024) Field Test of Thermoelectric Generators for Power Generation Using Low Temperature Industrial Waste Heat. Proceedings of 49th Workshop on Geothermal Reservoir Engineering, Stanford, California.

Zhu, Yuhao, Li, K., Linghu, J., Yuan, P., Zuo, S., and Weng, Z. "Modeling study on the geometric optimization of thermoelectric modules." Journal of Energy Resources Technology (2023): 1-42.

Dynamic Modeling of Fracture Networks to Optimize Geothermal Reservoir Performance

H. Tounsi[1], E. Nasir[2], B. Damjanac[1], C.A. Barton[2], W.S. Pettitt[2], T. Salter[2], A. Samy[2], P. Vivian Neal[3]

[1] Itasca Consulting Group, Inc., Minneapolis, MN, USA

[2] Baker Hughes, Houston, TX, USA

[3] Kalahari Geo Energy LTD

Keywords

Dynamic Fracture Modeling, Reservoir Modeling, Discrete Fracture Networks, Hydro-shearing, Hydraulic Fracturing

ABSTRACT

Fully coupled high-resolution dynamic modeling of the subsurface is required to optimize geothermal field producibility while ensuring planned operations do not give rise to geohazards. In geothermal settings, understanding the thermo-hydro-mechanical behavior of natural and induced fracture networks is essential to assess the enhancement capacity of target reservoirs. The associated simulation of microseismic locations, magnitudes, and mechanisms is critical for evaluating stimulation success and the risk of induced seismicity.

A Discrete Fracture Network (DFN) hydrostructural approach that incorporates the geometry and properties of discrete features is dynamically calibrated against available reservoir hydrological tests to provide the central component controlling flow and transport through the reservoir. Enhancing the geothermal system through hydro-shearing/hydraulic fracturing is simulated by Dynamic Fracture Modeling (DFM) through the natural fracture network. The DFM was carried out using the numerical software *XSite*, which uses the lattice approach to implement the synthetic rock mass (SRM) method to simulate hydraulic fracturing in naturally fractured rock masses. Fully coupled hydro-mechanical simulation is conducted in the model that explicitly represents pre-existing fractures, and reservoir stimulation is a combination of hydraulic fracture propagation and opening or shear of pre-existing joints (i.e., hydro-shearing). The DFN and DFM-derived fracture permeability distribution was then used in dynamic fluid modeling to explore well-engineering scenarios for optimal production.

This study presents the full link between subsurface characterization and dynamic modeling of natural and induced fracture networks for a geothermal exploration site in Zambia to provide a high-resolution base for reservoir dynamic flow modeling. The results of this full-physics approach reveal the main drivers toward project success.

1. Introduction

Kalahari Geo Energy is undertaking the development of a geothermal power generation project with a minimum of 10 MW and aims for up to 20MW, in the Bweengwa River area at the southern boundary of the Kafue Rift basin. The geothermal resource is represented at the surface as a suite of hot springs clustered along the basin-bounding faults but developed in the subsurface as a deep circulating geothermal system associated with the Karoo age basin-bounding faults.

The resource has been explored in detail over the last 11 years through a combination of geophysics, surface mapping, geochemical sampling and data from twenty-one shallow boreholes (Figure 1).

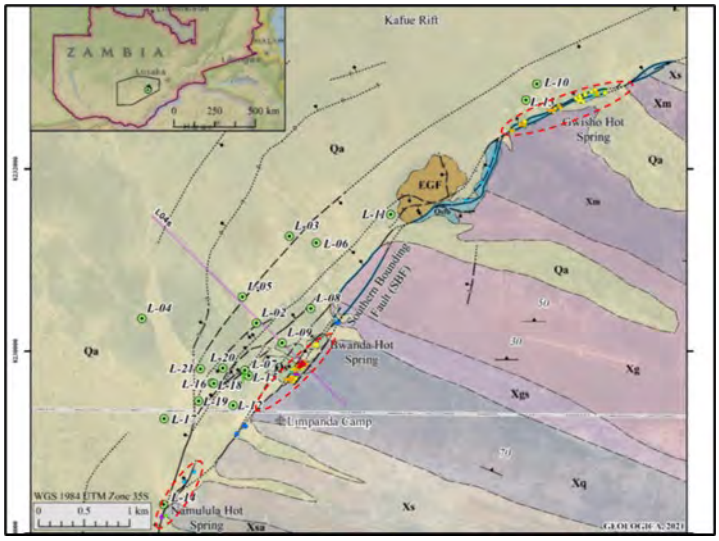

Figure 1. Summary surface geology map showing the Namulula, Bwanda and Gwisho hot springs plus the exploratory LOCH (L) wells focused on the Bweengwa resource (from Geologia Geothermal Group, 2021).

In a recent study (Salter et al., 2024) the productivity hosting fracture system present within the deeper basement was modeled using a discrete fracture network (DFN) with input derived from core review and the faults contained within a newly derived fault framework. Deterministic faults and stochastically generated fracture sets of the DFN were utilized to perform an integrated modeling workflow and deliver 3D models with predictive resource capability. The DFN fracture model was conditioned to well-test transmissivities and calibrated to the thermal model and reservoir rock type. The resulting parameters include directional hydraulic conductivity tensor and fracture porosity, which were upscaled to provide input to dynamic reservoir fluid flow simulation.

In this study, we simulate hydraulic stimulation of the preexisting fracture network by coupling Dynamic Fracture Modeling (Damjanac and Cundall (2016) and Fu et al. (2016, 2019) with Dynamic Reservoir Modeling (Salter et al., 2024) to explore the enhanced permeability and enthalpy achieved through the application of EGS techniques to this field.

2. Base DFN Model

2.1 DFN Fracture Network Model

The fracture conceptual model and the numerical approach used to develop the base DFN model for this study are detailed in Salter et al., 2024. The finite element software used, ConnectFlow™, employs the hydrostructural approach of DFN model generation. This approach involves analysis and modeling which explicitly incorporates the geometry and properties of discrete features as a central component controlling flow and transport. In these DFN models, a stochastic 'pipe' network type algorithm is used to calculate the flow and transport through the fracture network.

Unoriented cores from 17 wells were used to identify fractures' dip magnitude, intensity, and spatial occurrence. The distributions of fracture orientations were divided into five (5) sets (Figure 2b-f) consistent with nine (9) major fault trends (Figure 2a) of the structural model. Fracture set orientations are constrained both by the major faults trends and fracture dips measured from core (Figure 3).

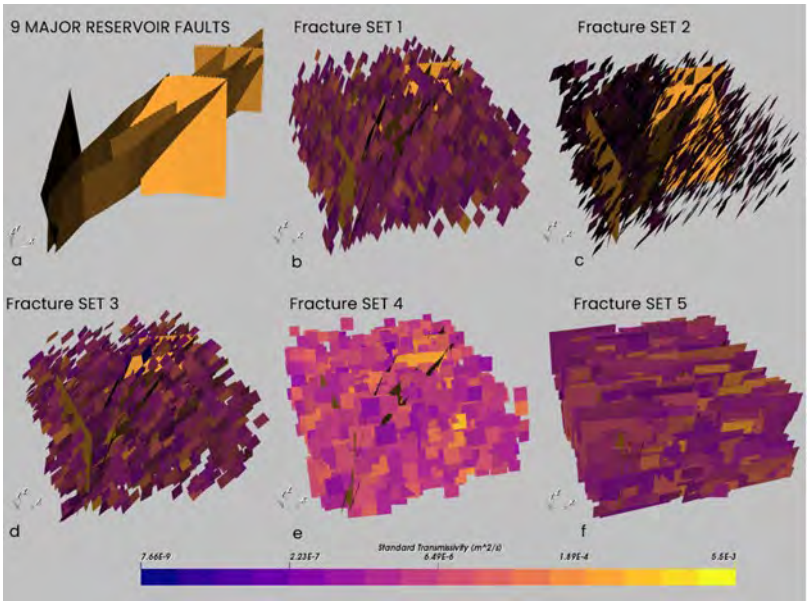

Figure 2. Deterministic faults and stochastically generated fracture sets of the DFN.

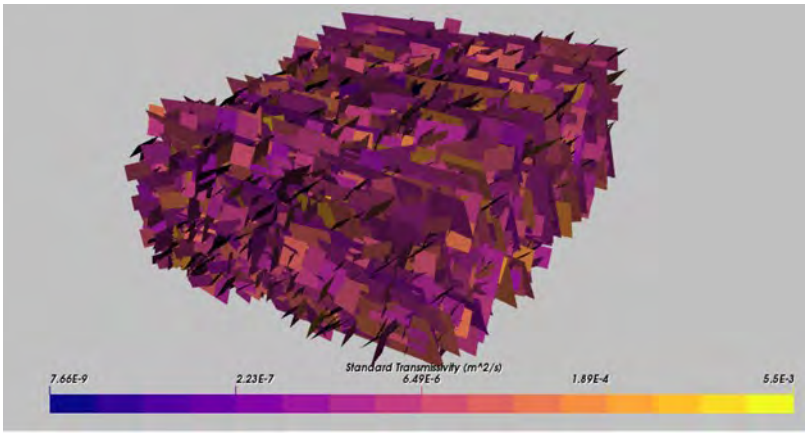

Figure 3. Final DFN realization utilized to calculate the contribution to reservoir permeability of the natural fracture and large-scale faults.

The distribution of fracture intensity was derived by the superposition of reservoir rock type and reservoir temperature-based fracture intensities. An observed characteristic of the Bweengwa fracture system is that although fractures are widespread in the basement rock (in the 17 cored wells, more than one fracture per meter was recorded on average), flow, as evidenced by production or anomalies in PT surveys and drilling information, is dominated by a small number of structures per well. This implies that flow is restricted to a subset of fractures within deformation zones that have sufficient intensity to form extensive interconnected networks.

The DFN was calibrated by matching well-based measurements to the deterministic and stochastically generated fractures intersecting field wells. Matrix permeability was assumed to be negligible for DFN modeling.

2.2 DFN Upscaling

To model flow and transport on the regional scale or over a long time, it is necessary to consider larger-scale bulk properties in the context of an equivalent continuous porous medium (ECPM) continuum concept. Converting the properties of a network of discrete fractures of lengths less than the continuum grid blocks into ECPM grid properties requires upscaling**.** A flux-based upscaling method is used that requires several flow calculations through a DFN model in different directions. In 3D, six directional components characterize the symmetric hydraulic conductivity tensor. Using the DFN flow simulations, the fluxes through each face of each grid cell are calculated for each head gradient direction. The hydraulic conductivity tensor is then derived by a least-squares fit to these flux responses for the fixed head gradients. Figure 4 captures the derived Kx, Ky, and Kz permeabilities within the volume by filtering permeability below 3×10^{-13} m^2.

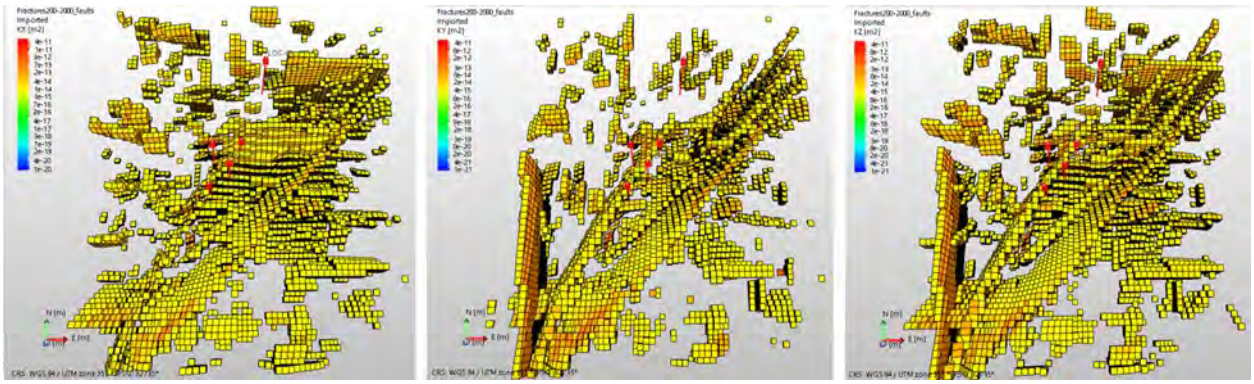

Figure 4. Derived Kx, Ky, and Kz permeabilities within the volume filtered below 3×10^{-13} m^2.

3. Previous Dynamic Reservoir Modeling

In the previous study, the integration of static parameters with dynamic transmissivity enabled a confident initialization of the static model for simulation. Thermal equilibration runs showed stability of the thermal plume, maintaining a suitable balance of conductive and convective heat transfer processes dominating in the Karoo-age sedimentary cap-rock and the resource-hosting metamorphic basement, respectively.

Simulation of prediction cases with existing well doublets highlighted the risk of injection water breakthrough related to permeability anisotropy. Geothermal power output was maximized by injecting into the shallower basement layers whilst producing from the deeper, hotter basement layers. An optimized development scenario of 3 producers plus 3 injectors, with production targeting the deep, hot up-flow and using well rate constraints consistent with the well-test-derived flow rates of up to 2,218 m^3/d, proved to deliver a stable thermal output of 22 MW over a 20-year span.

The dynamic modeling provided optimized well design (insulated tubulars, length of tubing and casing, casing thickness, cement thickness, etc.) to achieve maximized temperature and enthalpy output. Artificial lift assessment was considered for low- and medium-productivity wells using a conceptual ESP design. Although results of this assessment show ESP can allow wells to produce with higher WHFP, the question of achieving higher production rates (or, equivalently, higher injectivity) with stimulation remained unanswered.

In this study, we use the base DFN previously developed for the study area to simulate the creation of an SRV by EGS hydraulic stimulation to enhance permeability and injectivity. The resulting DFN/DFM-derived fracture permeability distribution was then used in dynamic reservoir modeling to explore well-engineering scenarios for optimal EGS production.

4. Reservoir Stimulation Model

4.1 Numerical Model Description

XSite, a Discrete Element Method (DEM) code developed by Itasca Consulting Group (Itasca, 2023), was utilized for simulating fluid injection, hydraulic fracturing of rock masses, and hydro-shearing of natural fractures. Through the implementation of the synthetic rock mass (SRM) method using a lattice numerical approach, *XSite* accurately models deformation, hydraulic fracture (HF) propagation, and related microseismicity in naturally fractured reservoirs. Its capabilities have been extensively verified for both viscosity-dominated and toughness-dominated hydraulic fracturing regimes, as well as for the unrestricted interactions of hydraulic fractures with existing fractures and joints, as demonstrated by Damjanac and Cundall (2016) and Fu et al. (2016, 2019).

4.2 Model Setup

The model consists of a 1 km³ cube, with the top representing a depth of 600 m. At a depth of 1100 m, a horizontal wellbore is placed in the center of the simulation domain, aligned with the horizontal principal stress orientation. The focus of this study is not on accurately representing near-wellbore fracture initiation or the influence of well perforations and casing, so these details are not explicitly included, as in Fu et al. (2024).

The Discrete Fracture Network (DFN) generated for the Kalahari project is explicitly represented, with numerous fractures ranging in length from 200 m to 2000 m intersecting the horizontal wellbore. Two stimulation designs were evaluated: one with the injection well in a dense DFN area (Scenario 1) and another in a sparse DFN area, five times less dense than the dense DFN (Scenario 2).

Scenario 1: Dense DFN (Figure 5a)

In the first scenario, an openhole completion is employed with two stages of reservoir stimulation achieved by injecting fluid directly into natural fractures intersecting the openhole. The objective of the injection strategy for the dense DFN is to stimulate fractures by inducing hydro-shearing. Each stage involves stimulating a section of the openhole with a length of 125 m. The code resolves the partition of the injected rate between the pre-existing fractures intersecting the active segment of the openhole well while maintaining the same pressure within the stage (no pressure drop). The pumping rate is 7.5 bpm (0.02 m³/s) for 1.5 hours per stage.

Scenario 2: Sparse DFN (Figure 5b)

The second scenario uses a cased-hole completion with eight stages of reservoir stimulation. During each stage, fluid is injected at a constant rate of 30 bpm (0.08 m³/s) for 25 minutes into a single spherical perforation. Perforation clusters are spaced at 30 m. The stimulation strategy for the sparse DFN is to propagate hydraulic fractures to connect with the DFN and induce hydro-shearing of the pre-existing fractures. The stages include a single perforation cluster to achieve the best uniformity of stimulation along the well.

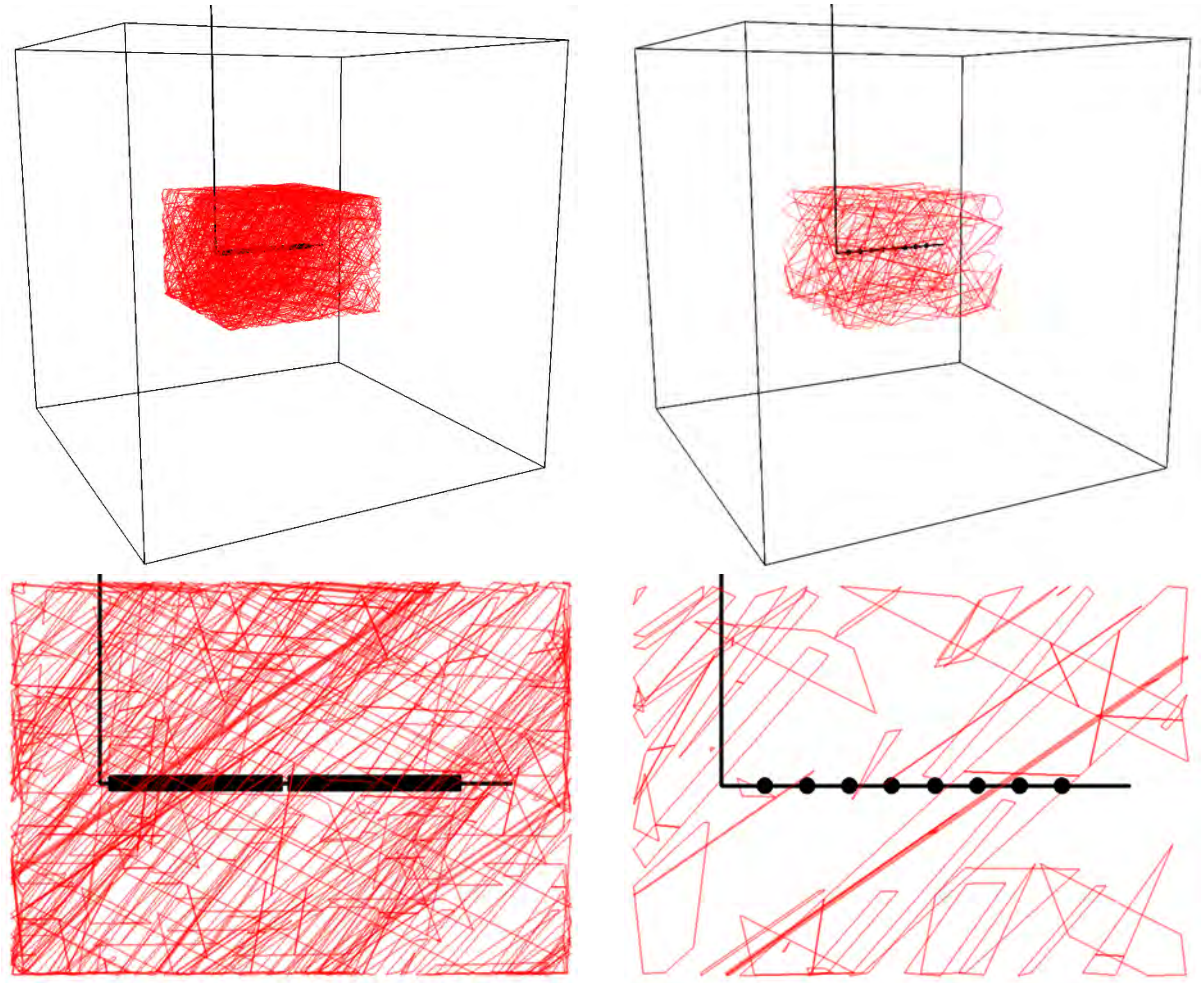

(a) Openhole - Dense DFN (scenario 1) (b) Cased borehole - Sparse DFN (scenario 2)

Figure 1: Stimulation modeling. Top: a) openhole and b) cased borehole simulation domains. Bottom: Zoomed in and trimmed views of the intersection between the DFN and the injection clusters.

The rock mass properties (Schistose Quartzite of the Raduwa Formation as reported by Panthee et al. (2016)), fluid properties, and in-situ stress magnitudes and directions are summarized in Table 1. The properties of the pre-existing fractures are provided in Table 2. The strength properties were determined to ensure that the natural fractures are not in the state of limiting equilibrium under in-situ conditions. Both scenarios assume the in-situ DFN to be permeable initially with a uniform aperture, which is higher in the dense DFN due to the expected greater permeability.

Table 1: Rock properties and initial conditions

Parameter	Schistose Quartzite
Young's modulus, GPa	5
Poisson's ratio	0.25
Fracture toughness, MPa.m$^{1/2}$	1.5
Fluid viscosity, cP	2
Pore pressure, MPa/m	0.00981
Minimum horizontal stress, MPa	0.013 – Dip Direction 135˚
Maximum horizontal stress, MPa	0.018 - Dip Direction 45˚
Vertical stress, MPa	0.025

Table 2: Fracture properties

Parameter	Dense DFN	Sparse DFN
Average aperture, mm	0.05	0.01
Cohesion, MPa	10	
Friction angle, ˚	45	
Tensile strength, MPa	5	

5. Stimulation Results

5.1 Dense DFN

The aperture contours at the end of the two stages of hydro-shearing are shown in Figure 6 in two planes: one perpendicular to the well at its center and the other parallel to the well. As can be seen, this scenario resulted in shear stimulation of existing fractures in a nearly cylindrical domain with an average radius of 90 m centered around the well, contrary to hydraulic fractures that preferentially grow in an upward direction. An aperture increase of four to five times was predicted in the sheared fractures within a 70 m radius from the well. Given the low injection rate occurring directly in the permeable fractures intersecting the well, the resulting pressure increase is minimal, less than 1.2 MPa, as shown in Figure 7.

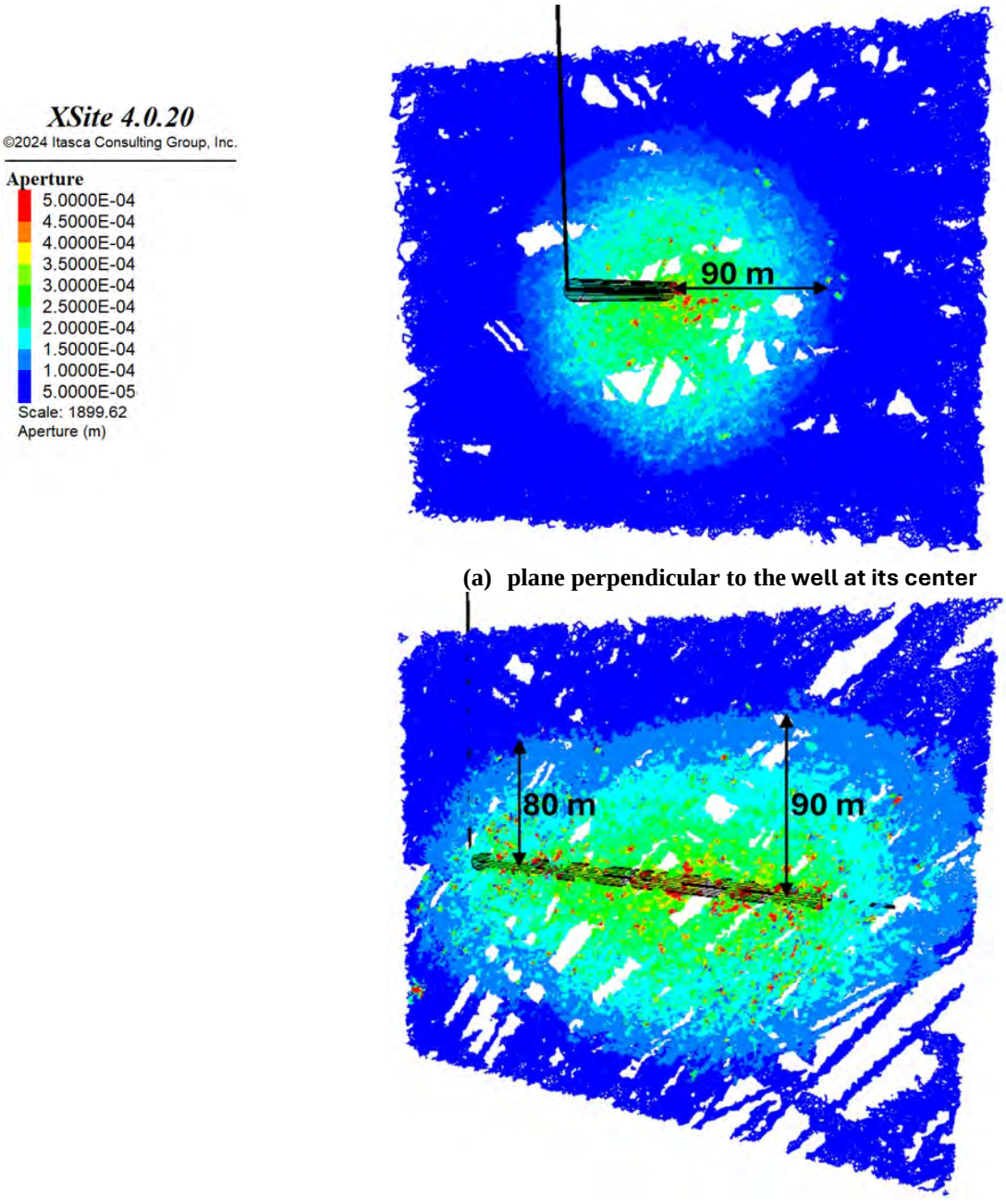

(a) plane perpendicular to the well at its center

(b) plane parallel to the well

Figure 6: Simulated distribution of fracture aperture at the end of the second stimulation stage in Scenario 1 in two planes.

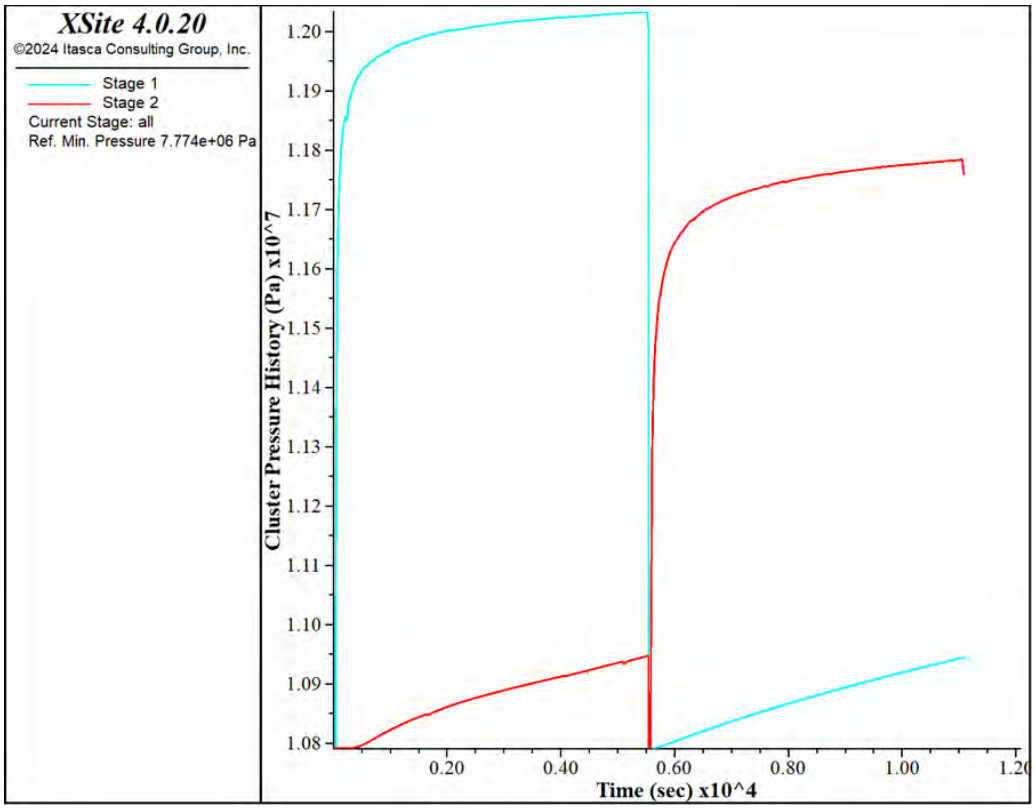

Figure 7: History of pressure in the two stages in Scenario 1.

5.2 Sparse DFN

The fracture geometry and the aperture contours at the end of stimulation of the eight stages are shown in Figure 8. No natural fractures intersect the first cluster. The hydraulic fracture propagates in a planar, penny-shaped manner perpendicular to the well until it intersects one of the natural fractures. At this point, the flow becomes controlled by the sparse network of natural fractures. This same process occurs in Stages 6 and 8, where the natural fractures do not intersect well near the cluster. Otherwise, there is no fracture propagation, and the injection pressure monotonically increases. As expected, Figure 9 shows that high cluster pressures are observed when the perforation cluster does not intersect a natural fracture. As the hydraulic fractures propagate unbounded or when they intersect with the permeable pre-existing fractures of sparse DFN, the pressure drops or stops increasing. Note that cluster pressure here accounts for pressure losses due to the presence of perforations.

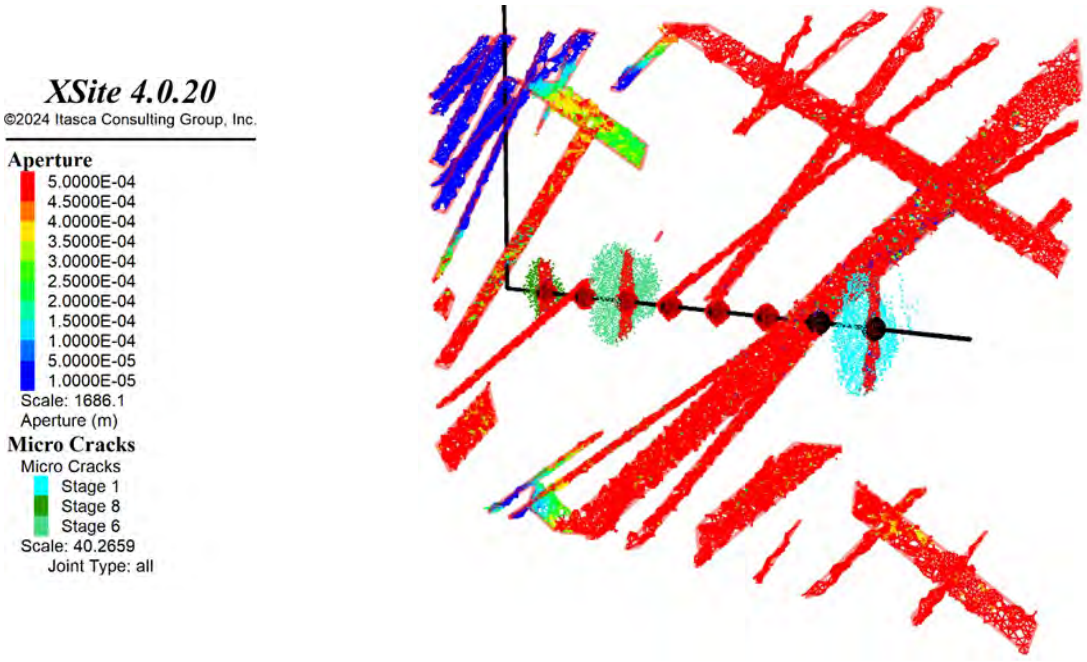

Figure 8: Simulated distribution of microcracks and fracture aperture at the end of Stage 8 in Scenario 2. Sparse DFN is trimmed in the Y direction.

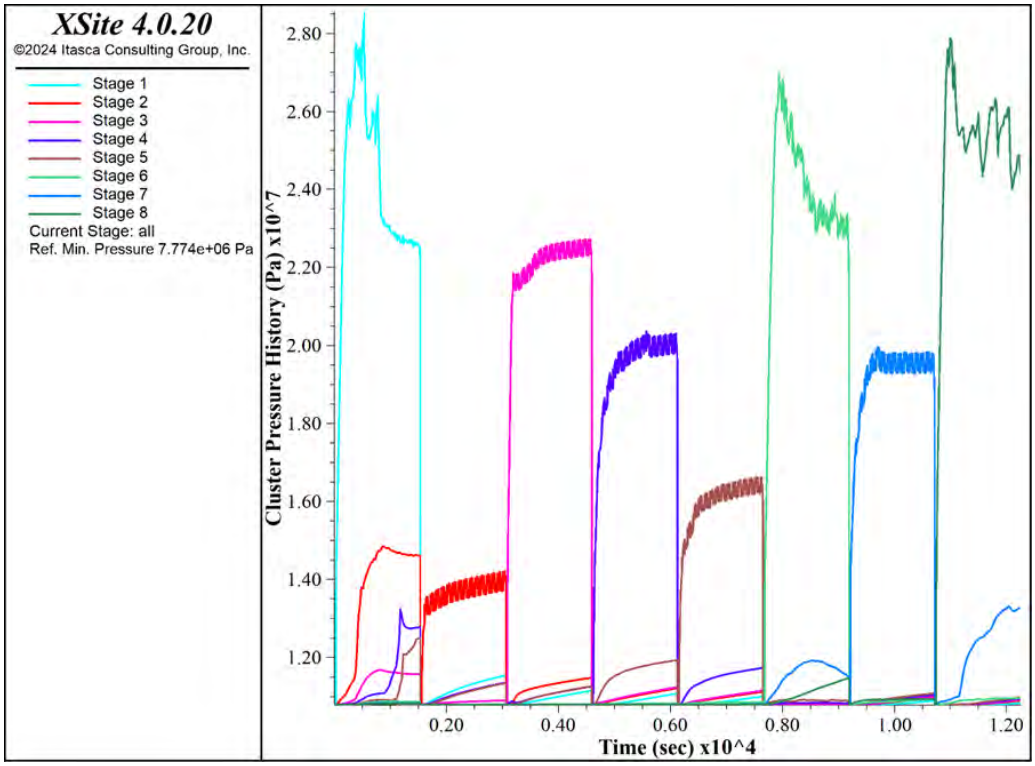

Figure 9: Histories of cluster pressures in the eight stages of hydraulic fracturing in Scenario 2.

6. Dynamic Flow Modeling Results

The 3D static geomodel grid of the stimulated area with the upscaled permeability tensor was exported and incorporated into the base dynamic simulation model. The grid was initially quality checked to optimize dynamic modeling runs. The cell count in IJK (comparable to X, Y and Z) directions was 59 × 66 × 116, respectively. The total number of active grid cells was 188179 after setting cutoffs for cell thickness and volume to avoid numerical instabilities in simulations. Full details of the base equilibrated dynamic model are provided by Salter et. al, 2024.

Multiple forecast scenarios were simulated for SRVs in dense and sparse DFNs, varying well trajectories, well position, well spacing, well stimulation, and injection rates. These parameters and subsequent results are only to highlight the workflow. Additional field data are required to assess the best subsurface characterization for field operations. Well configurations modeled included lateral producers 100 m and 200 m above and below a stimulated lateral injector and a stimulated lateral producer with a vertical injector. The minimum flow rate simulated was 2,218 m^3/d based on the previous study, and a maximum flow rate increase of 3.3 times was assumed based on the average permeability enhancement between the base and stimulation cases along the wellbore. The maximum drawdown was assumed to be 3000 kPa for injectors and producers. The injection temperature was set to 60°C. Forecasts were run for 20 years. Injection enthalpy (enthalpy at 60°C) was subtracted to calculate the net enthalpy gain in kJ/kg. The objective of scenario testing was to determine the optimal injector/producer configuration for sustained heat production at the lowest CAPEX.

Simulation of prediction cases with new well doublets constrained the nominal well spacing for all scenarios to greater than 200 m, again highlighting the risk of injection water breakthrough related to permeability anisotropy. Based on simulations, as anticipated, higher injection rate cases outperformed low-rate cases in maximum heat output and sustainability. Simulated dense DFN cases produce, on average, a higher heat output than sparse DFN simulation cases at equivalent injection rates (Figures 10 and 11). Both sparse and dense DFN cases of a lateral stimulated injector and lower producer do not sustain thermal output over time.

The optimal configuration for both dense and sparse DFN cases is of a stimulated lateral production well (Figure 12 upper) coupled with a vertical injection well at a distance of approximately 500 m perforated above the SRV (Figure 12, lower) injecting at a rate of 7,388 m^3/d. Post-stimulation flow rate testing must be performed to verify the actual maximum injectivity/productivity for this hypothetical configuration.

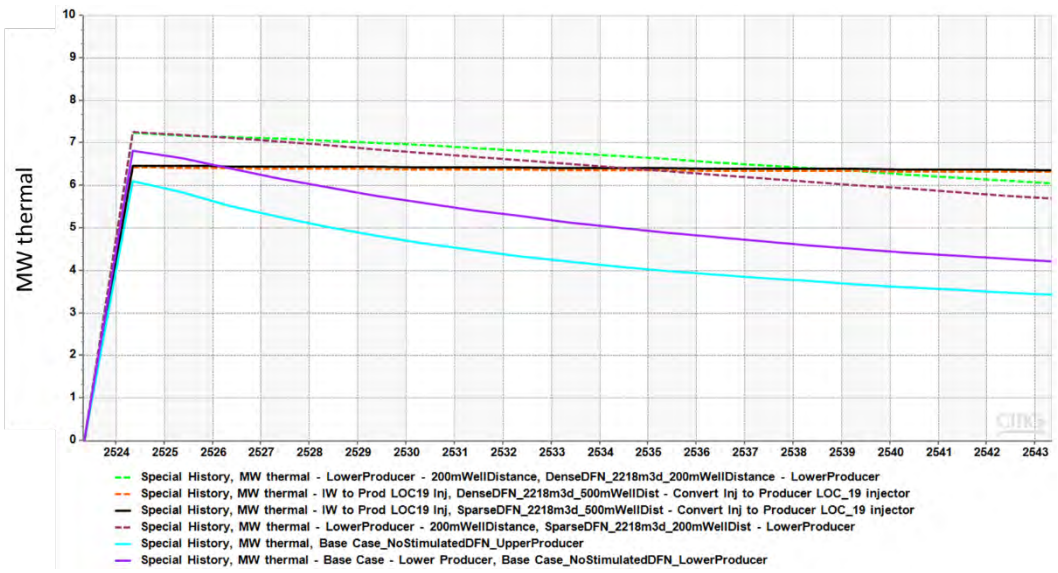

Figure 10. Lower injection rate simulation scenarios compared with the base case of an unstimulated DFN.

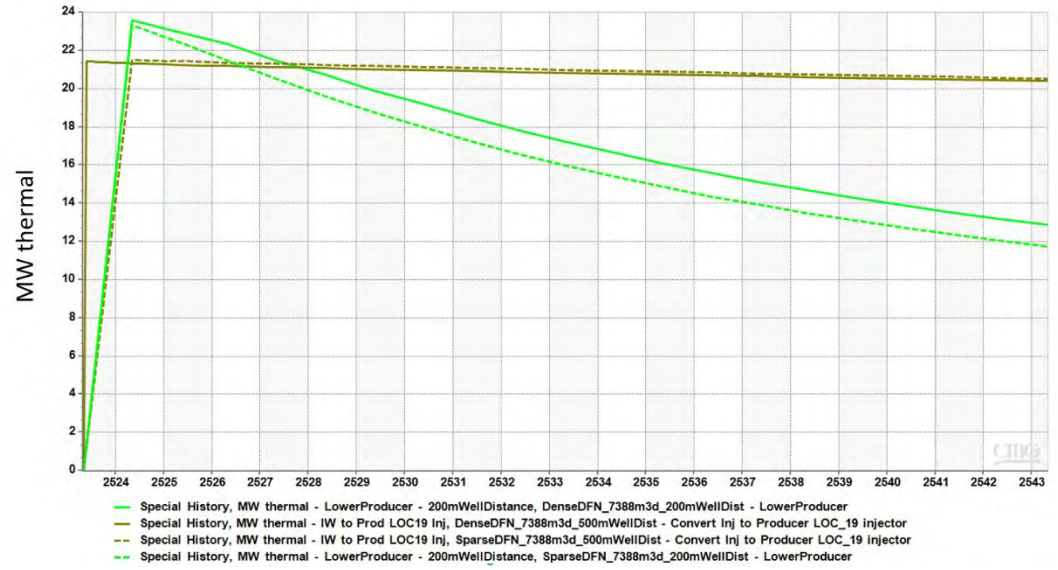

Figure 11. Higher injection rate simulation scenarios comparing vertical unstimulated injector and stimulated lateral producer with stimulated lateral injector and unstimulated lateral producer.

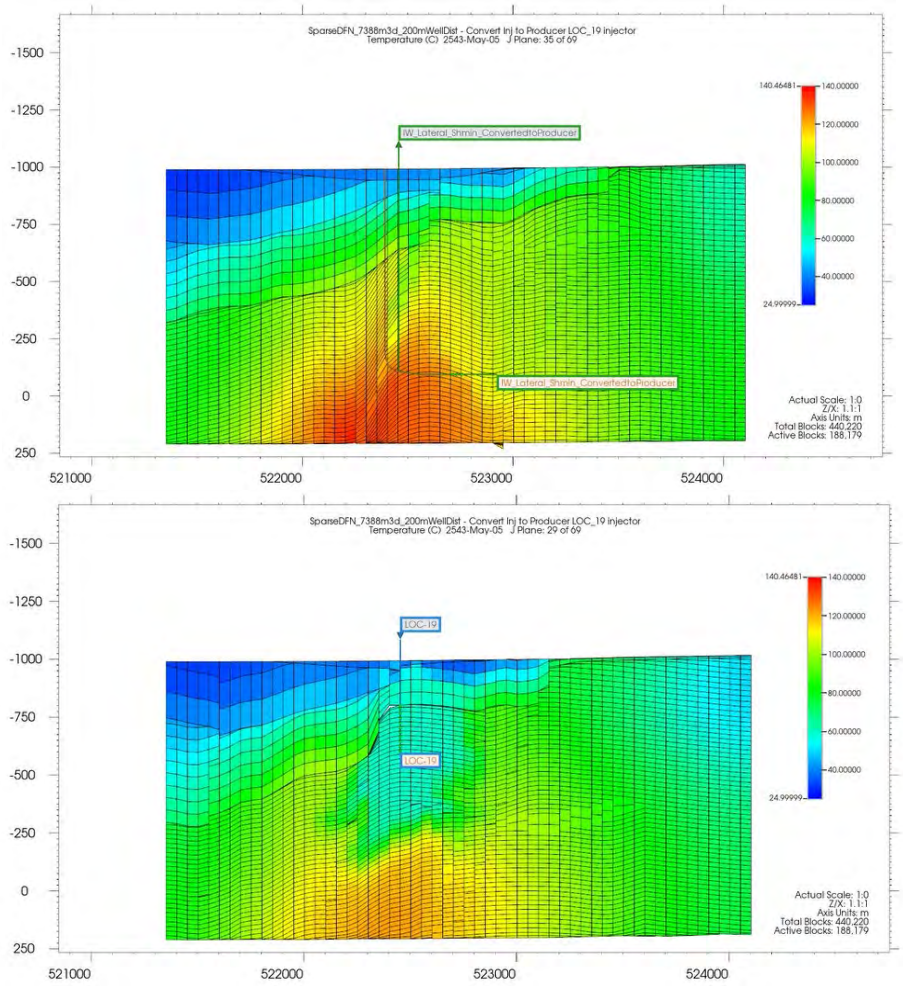

Figure 12. Optimal configuration for a single vertical injector/lateral producer pair. Temperature contours are shown in two vertical cross-sections through the volume (the upper is an E-W section at the location of the lateral producer, and the lower is an E-W section at the location of the vertical injector) at the end of 20 years of injection.

Conclusions

In this paper, we provide a case study example of a full physics-integrated modeling workflow to deliver 3D models with predictive resource capability. Through extensive scenario testing, we conclude for this case study:

- Optimum well spacing depends on the additional fracture permeability created by stimulation.
- Placement of a lateral producer above a lateral injector is not a valid strategy in the presence of a well-connected fracture network due to early breakthrough.
- Placement of a vertical producer above the SRV will limit breakthrough while maintaining reservoir pressure.
- Stimulating lateral producers will maximize contact with DFN, where multiple subsets of fractures at different orientations provide the hydrostructural fracture network.

- The sparse or dense nature of the fracture network can have a significant impact in cases of a stimulated lateral injector and unstimulated lateral producer.

Acknowledgement

The authors would like to thank Kalahari Geo Energy LTD. for permission to utilize the Bweengwa River geothermal resource data for this study and its publication.

REFERENCES

Damjanac, B., & Cundall, P. "Application of Distinct Element Methods to Simulation of Hydraulic Fracturing in Naturally Fractured Reservoirs." *Computers and Geotechnics*, 71, (2016), 283–294. https://doi.org/10.1016/j.compgeo.2015.06.007

Fu, W., Ames, B. C., Bunger, A. P., & Savitski, A. A. "Impact of Partially Cemented and Non-persistent Natural Fractures on Hydraulic Fracture Propagation." *Rock Mechanics and Rock Engineering*, 49(11), (2016), 4519–4526. https://doi.org/10.1007/s00603-016-1103-0

Fu, W., Damjanac, B., Radakovic-Guzina, Z., Finnila, A., Podgorney, R. and Mclennan, J. "Near-Wellbore DEM Model of Hydraulic Fracture Initiation for Utah FORGE Site." *Proceedings of the 49th Workshop on Geothermal Reservoir Engineering Stanford University*, Stanford, California (2024).

Fu, W., Savitski, A. A., Damjanac, B., & Bunger, A. P. "Three-Dimensional Lattice Simulation of Hydraulic Fracture Interaction with Natural Fractures." *Computers and Geotechnics*, 107, (2019). 214–234. https://doi.org/10.1016/j.compgeo.2018.11.023

Geologica Geothermal Group, Inc. "Geothermal Resource Assessment Report: Bweengwa River Geothermal Project", 15 October 2021.

Itasca. XSite — Hydraulic Fracture Simulation of 3D Fracture Networks (4.0). Minneapolis, Minnesota (2023).

Panthee, S., Khanal, M., & Singh, T. N. "Geotechnical and geomechanical characteristics of the rocks along tunnel of Kulekhani III Hydro-electric Project." *Journal of Nepal Geological Society*, 50(1), (2016), 39-50.

Salter, T., Nasir, E, Barton, C., Samy, A., Harper, C., Andrade, H, Vivian-Neal, P, Harrison, P. "Geothermal Reservoir Simulation Workflow for a Low-Enthalpy Fracture Hosted Resource". *PROCEEDINGS, 49th Workshop on Geothermal Reservoir Engineering, Stanford University*, Stanford, California, February 12-14, 2024, SGP-TR-227.

Coupled Multi-Segment Wellbore and Thermal Modeling in a Deep Sedimentary Geothermal Field -- a Case Study for the DEEP Geothermal Project, Saskatchewan, Canada

Minh Tran[1], Logan Hackett[1], Leo Groenewoud[2], Kirsten Marcia[2], Robert Stacey[3]

[1]GeothermEx, [2]Deep Earth Energy Production, [3]Geothermal Analytics

Keywords

Multi-segment wellbore modeling, heat transfer, geothermal

ABSTRACT

Harnessing geothermal energy for power generation in sedimentary basins has traditionally faced significant challenges, primarily due to the lack of prevalent natural fracture network, and the narrow margin of thermodynamically favorable conditions. However, recent technological advancements, particularly those adapted from the oil and gas industry, have made it possible to extract heat from deep sedimentary formations at lower temperatures than previously considered feasible. The Deep Earth Energy Production Corp. (DEEP) geothermal project, located in the Williston Basin of southeastern Saskatchewan, Canada, exemplifies these advancements. To support the development of a 5-MW-gross pilot geothermal project, DEEP has conducted surface exploration and subsurface interrogation activities to characterize the geothermal resource and its ability to support the development of geothermal power. This paper presents an integrated multi-segment wellbore model coupled with a thermal simulation framework in INTERSECT* to assess the geothermal resource performance for the DEEP project.

This approach offers several improvements, including more accurate calculations of wellbore pressure gradients, enhanced crossflow modeling, and improved wellbore storage representation. Importantly, it allows for a precise depiction of heat transfer with surrounding formations and thermal interference between the cased sections of horizontal production and injection doublets. These advancements are critical for validating the feasibility of low-temperature geothermal resources, as even small variations in the pressure and temperature of geothermal brine can significantly impact the long-term viability of the project. The model accurately captures the thermal effects of cold water reinjection and wellbore heat loss on production fluid temperature, enabling the exploration of various production rates, injection temperatures, reservoir permeabilities, wellbore trajectories, and conductive heat transfer rates within the cased sections of the wells. This allows for a detailed quantification of their respective impacts on the thermodynamics of the production fluid.

1. Introduction

DEEP has conducted surface and subsurface resource exploration and characterization activities to understand the geothermal resource in the Williston sedimentary basin of southeastern Saskatchewan, Canada (the Project area) to support the development of a geothermal power project. DEEP's geothermal project is situated about 34 kilometers southwest of Estevan, Saskatchewan, Canada, and 2.4 kilometers north of the border of North Dakota in the United States (**Figure 1**). Prior analyses of this deep basin heat source has led to a strong interest in harnessing geothermal energy to meet the region's green energy needs. DEEP is planning a geothermal power generation project using binary-cycle generation technology, starting with a pilot phase of 5-MW gross, and a project plan to ramp up to 200 MW of power to the grid. This project is targeted to be Canada's first clean, renewable baseload electricity project. The initial pilot development will feature 2 production wells and 2 injection wells (intended to flow at 60 liter/second each), interconnected by a production and injection pipeline system.

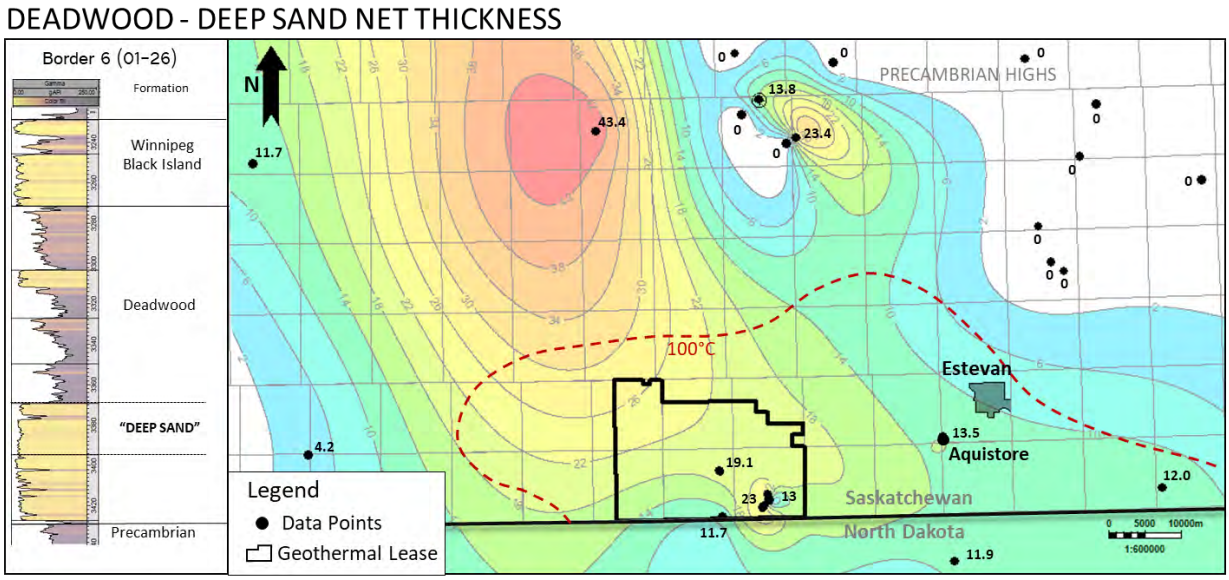

Figure 1: Location of the DEEP Saskatchewan project. The contour of the net sand sand thickness of the Deadwood Formation (porosity greater than 9%) is shown. Solid black boundary is extent of DEEP geothermal license. Dotted red line is 100°C temperature contour.

Cutting-edge horizontal drilling techniques in hot sedimentary geothermal aquifers allow for precise drilling through specific stratigraphic layers (Marcia *et al.*, 2021). Combined with improved cementing and open-hole packer technology for ensuring isolation integrity, these drilling techniques have facilitated access to larger reservoir surface areas for energy extraction. Rock-fluid interaction and heat transfer between the geofluid and wellbore mechanical components (*i.e.*, casing, tubing, etc.) require accurate modeling of heat loss and gain during the circulation of geofluid across the wellbore length and within the reservoir. This paper discusses the application of multi-segment wellbore modeling to improve the characterization of heat transfer of geothermal fluid to inform future decisions on efficient geothermal energy extraction.

2. Resource Characterization

By reviewing publicly available subsurface databases and academic studies, DEEP identified a target area in the Canadian side of the Williston Basin comprised of two geologic units that host with high-temperature brines: the Deadwood and Winnipeg Formations. These two formations are deep in the basin and therefore have the highest temperatures. The development plan focuses on a higher porosity interval within the lower Deadwood Formation to access the hot brine reservoir, named the DEEP Sand (**Figure 1**). The sandstone unit targeted for developing the for geothermal reservoir (the DEEP Sand) is 21.8 to 25.3m thick with an average porosity of 12% and permeability (as measured from core) of 18mD. For these intervals, DEEP's reservoir calculations were developed using a 9% porosity cut-off for the productive intervals, an average thickness of 18.8m, an average porosity of 13%, and an average permeability of 24mD. Stratigraphic correlation and mapping of the basal Deadwood clastics showed a continuous sandstone depositional and temperature fairway capable of supporting multiple arrays of horizontal wells to supply the geofluid to binary-cycle power units.

The successful Border-01 exploration well (which is the deepest well ever drilled in Saskatchewan) reached a depth of 3,530m (**Figure 2**). Recognizing the importance of enhancing fractures in the target lithology, the wellbore was strategically located near the intersection of two significant structural features of the Williston Basin: the Brockton Froid fault zone and the Nesson anticline (Groenewoud and Marcia, 2020). Logging operations recorded temperatures greater than 125°C; the measured temperature gradient within the DEEP Sand is approximately 2°C/100m.

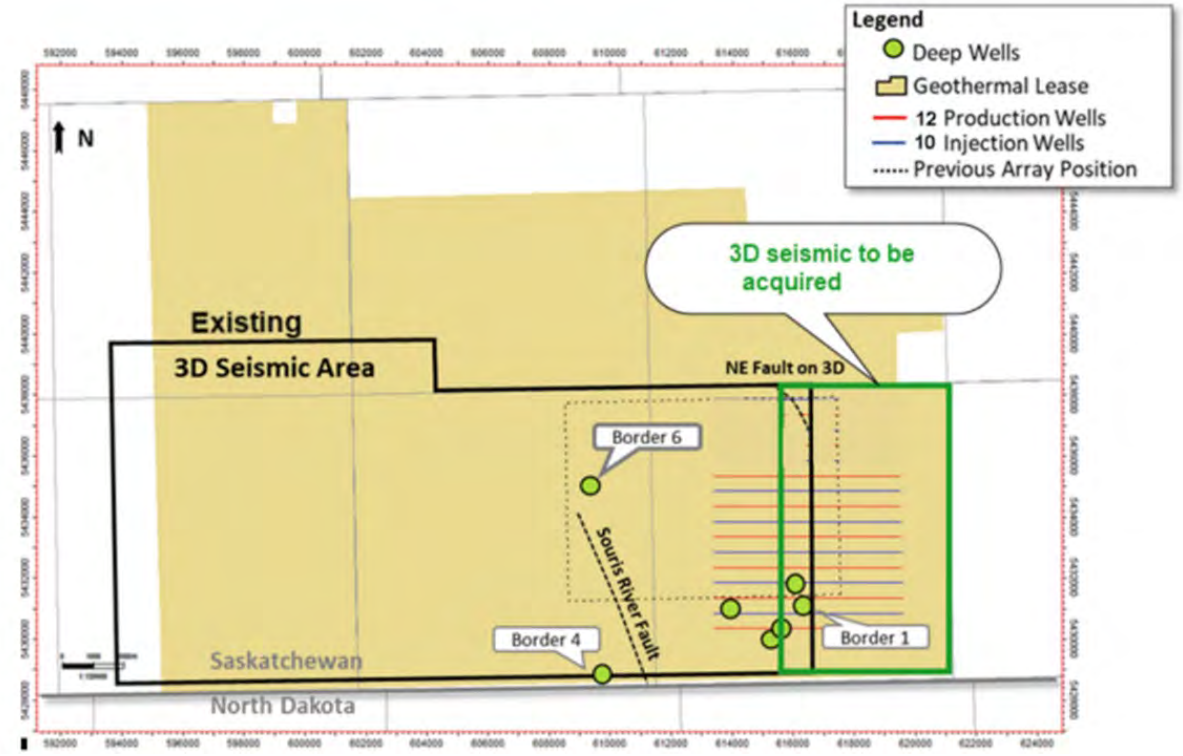

Figure 2: Extent of existing 3D seismic data for the DEEP Saskatchewan Project. Existing Border wells are shown together with the planned development well array.

Between 2018 and 2021, DEEP drilled six vertical and deviated wells in the project area. Data from these wells showed that while the DEEP target sand was productive, it did not have enough thickness to produce hot brine at the required rates using vertical wellbores. The horizontal well Border-5Hz was completed in 2020 as a proof-of-concept test to demonstrate that horizontal wells could achieve the necessary flow rates for a commercial geothermal power project. The Border-5Hz well targeted the main porosity unit of the Cambrian basal clastic (the Deadwood Formation), reaching a total measured depth of 5,672m (3,450m total vertical depth. TVD) with a 2,000m horizontal section. This well proved the viability of horizontal drilling, supported geophysical analyses, and confirmed reservoir continuity, leading to DEEP's geothermal project development plan to focus on drilling horizontal wells within the laterally continuous DEEP Sand for production and injection.

A hydraulic well stimulation was performed at well Border-5Hz to address the reservoir laminations and compartmentalization identified from core samples, which improved overall well productivity. This horizontal well was tested for 53 days in January to March 2021, flowing at an average volume of 1,800 m^3/day (about 330 gal/min or 20.8 L/s) using an Electrical Submersible Pump (ESP), at a production temperature of approximately 114°C. This test provided the necessary data to finalize the development array's design parameters, including lateral length, well spacing, and completion design. The spacing between producers and injectors was optimized to maintain reservoir pressure and minimize thermal breakthrough times. The results of a tracer test confirmed that there was no tracer breakthrough from the injection wells during the production testing period, significantly reducing the risk of early thermal breakthrough during power generation.

3. Coupled Multi-Segment Wellbore Modeling (MSW)

A detailed description of the fluid flow conditions within the well is achieved by dividing the wellbore (and any lateral branches) into several one-dimensional segments (**Figure 3**). Each segment is characterized by its own set of independent variables, such as fluid pressure, total molar flow rate, and flowing molar densities, which describe the local fluid conditions. These variables are evaluated by solving material balance equations for each phase or component, along with a pressure drop equation that considers local hydrostatic, friction, and acceleration pressure gradients. The multi-segment well model offers improved functionalities and greater flexibility, including: enhanced handling of multilateral well topology; more realistic modeling of crossflow; and the capability to simulate complex crossflow regimes in multilateral wells, including branch-to-branch crossflow and crossflow within individual branches.

Each segment includes a node and a flow path to the node of its parent segment. Segments are characterized by specified attributes such as length, diameter, roughness, area, and volume. The volume is used to make wellbore storage calculations, while the other attributes relate to the flow path and are used in friction and acceleration pressure loss calculations. Additionally, the flow rates of water associated with each segment's flow path are determined by the well model calculation. Each segment node is located at a specific depth and has a nodal pressure determined by the well model calculations. Flow from the formation through grid-block-to-well connections also occur at these segment nodes. Heat transfer along the wells was modeled explicitly in INTERSECT using the MSW well modeling tool, which accounts for the pressure and temperature changes along each well in operation (**Figure 4**). This functionality also allows the model to

account for the thermal interaction between injection wells and production wells heating and cooling the formations next to one another above the producing reservoir.

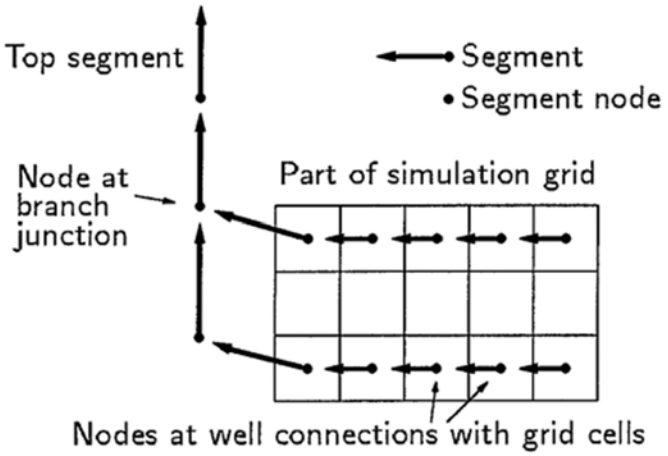

Figure 3: Schematic diagram illustrating the segment structure for an example multilateral well (Holmes *et al.*, 1988).

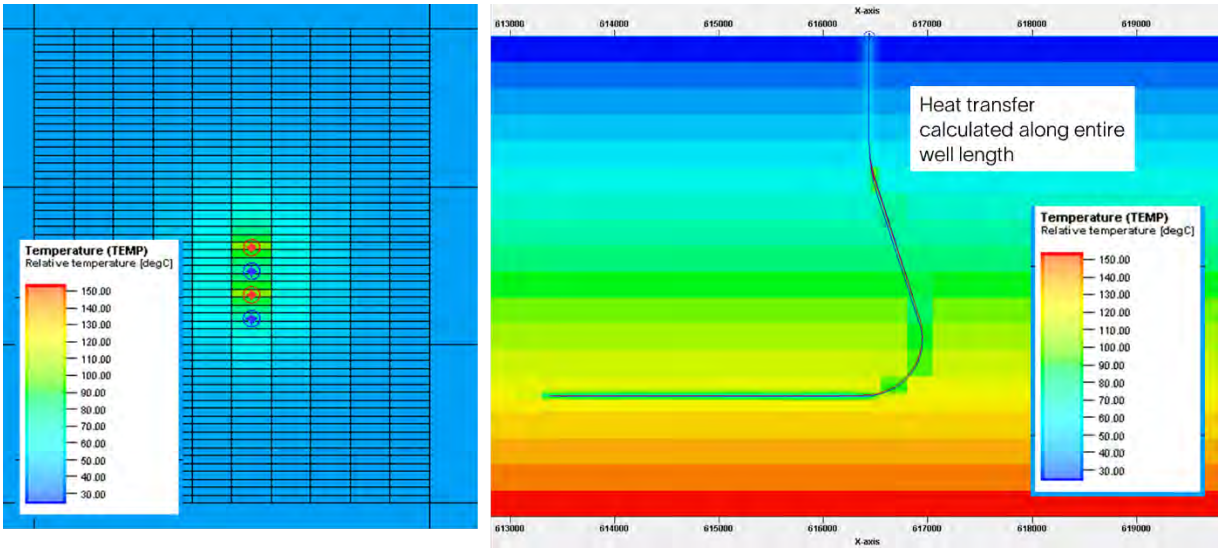

Figure 4: Multi-segment wellbore modeling in the DEEP project. A refined grid was created around the vertical well section to capture the thermal interference between the wells.

4. Numerical Model

To assess the resource's ability to support the project development plan, we utilized a full-field thermal reservoir model to quantify the impact that various uncertainties may have on the long-term sustainability of production from the resource. The numerical model was created in the Petrel* E&P Platform and utilized INTERSECT to perform the numerical flow simulation calculations.

* Mark of SLB

The project has a large set of petrophysical data that has been used to develop, constrain, and calibrate the numerical reservoir model. The petrophysical properties and structure of the reservoir model were created using the structural surfaces identified from completed wells, combined with depth-converted seismic interpretations. The petrophysical properties assigned in the reservoir model were obtained from core data analysis, petrophysical log analysis, and well test analysis.

The final base case design consists of 12 production wells and 10 injection wells to achieve the target flow rate, minimize capital costs, and maintain a reasonable pressure balance. The preliminary subsurface design optimizes well spacing at 500m and enables the configuration to generate ~20 MW of power after the pilot project. Each well will be drilled to a depth of 3.5km with a horizontal length of ~3km (**Figure 5**). The reservoir model was constructed to contain the development's full well array of 22 wells and the surrounding reservoir formation.

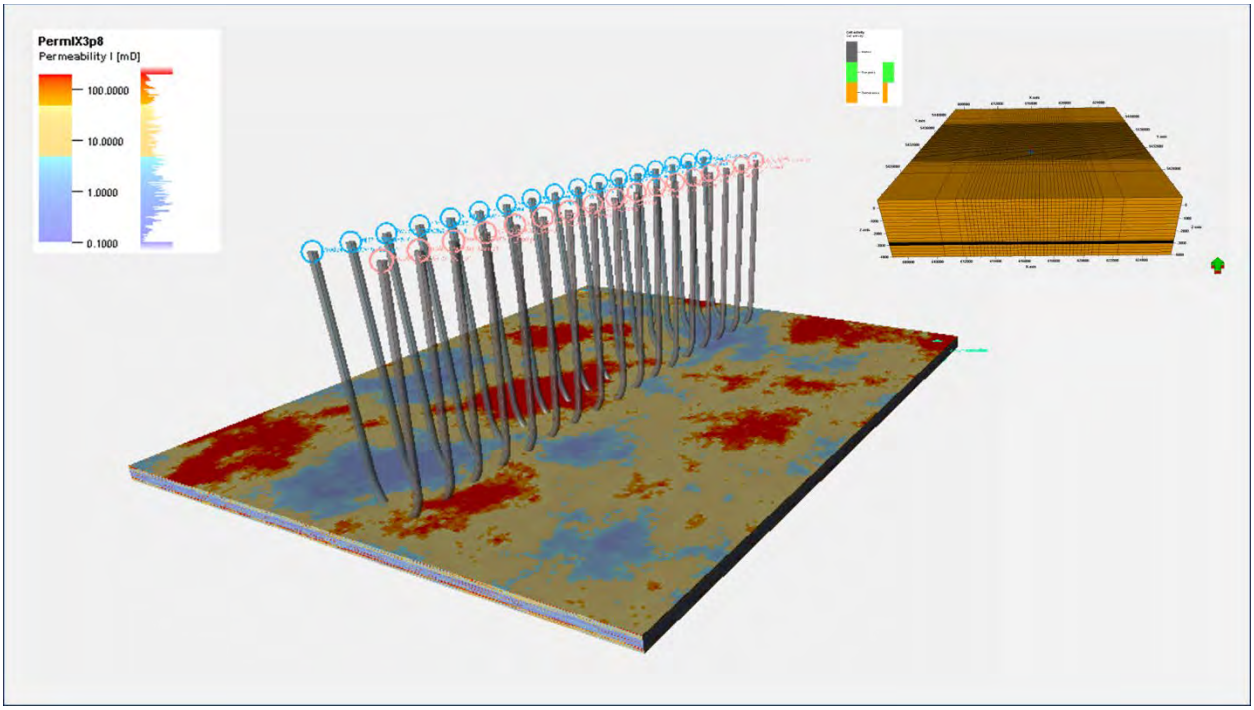

Figure 5: Proposed production and injection well array for the DEEP Saskatchewan project, with extent of reservoir model shown.

4.1 Initial and Boundary Conditions

The model is a single-porosity, single permeability reservoir model, which has been set up to be self-contained, without any thermal or pressure boundary conditions for fluid or heat flow to enter or exit the model (other than through the operating well field). This approach was used so that all fluid and heat content are contained within the grid cells for the forecast; this eliminates any potential influence of boundary condition assumptions on the model forecast. To model the sustainability of the resource during exploitation, the reservoir model was extended 5 km beyond the planned field development to capture the pressure support coming from the region surrounding the reservoir. The formations above and below the target reservoir were also explicitly included in the model to capture the thermal energy available to conductively heat the formation fluids

during project operations. The model was extended to the ground surface to allow it to account for the conductive heat transfer between the cased section of the wells and the overburden formation surrounding them (**Figure 5**). **Figure 6** presents the full-development layout, including the 4 pilot wells.

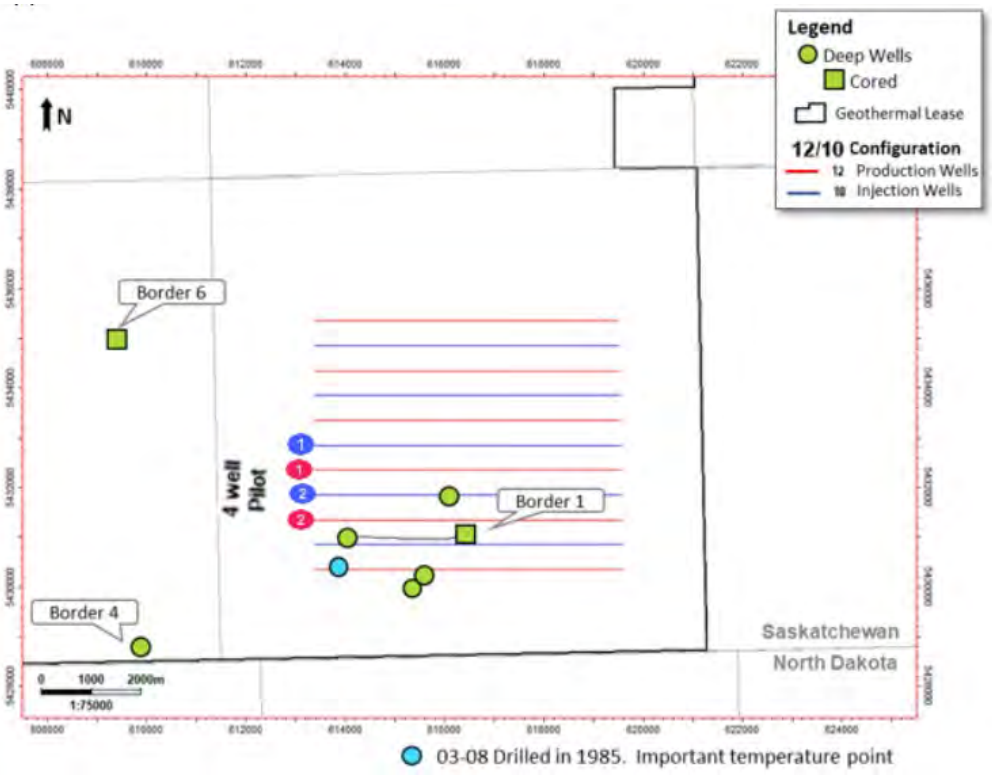

Figure 6: Location map for DEEPs proposed production and injection well array for the full 20 MW project, with 2 production and 2 injection wells identified that would support the 5 MW pilot project.

4.2 Property Assignment

Reservoir permeability was assigned based on well testing and core testing data. The DEEP well 1-26 build-up and fall-off test analysis indicated a formation permeability of 125mD, which is consistent with core data from well 1-26. The arithmetic average permeability of cores collected across the reservoir section was calculated to be 30mD. Appreciating that well testing evaluates the larger-scale permeability structures, while core data sample small-scale permeability, we created a heterogeneous model with permeability ranging from 10mD to 200mD and an average of 65mD. This heterogeneous geologic model was created to capture the expected variability in permeability within the reservoir by accounting for the depositional environment and measured permeability variation in core data. In the modeling study, this heterogeneous permeability model was assessed against a homogeneous permeability model to assess the impact that heterogeneity could have on project operation. **Figure 5** shows the heterogenous permeability of a layer in the DEEP sand unit at the approximate level of the proposed production and injection wells.

4.3 Pilot Development

The base case plan for the 5-MW pilot project is to operate with 4 wells, including 2 injectors (I4 and I6) and 2 producers (P6 and P8), producing 60 L/s and returning the fluid to the reservoir at 60°C (**Figure 6**). The forecast shows that production temperatures will increase over the first year as the near-well region is heated and thermal energy losses diminish. When production starts, hot geofluid flows up the wellbore passing through shallower and cooler surrounding layers and resulting in observable conductive heat loss (**Figure 7**). Gradually, within the first 5 years before the thermal impact of injection becomes significant, hot production fluid heats up the localized region adjacent to the production wellbore. This localized heat up around the production wells diminishes the conductive heat loss, thereby raising the production temperature. The production temperature of the base case reaches ~125°C at its peak after 5 years of production, which is comparable to the reservoir temperature. This is explained by the fact that heat loss due to wellbore friction and conductive heat transfer is balanced by the slight increase in production fluid temperature due to de-pressurization. The reservoir (liquid water) experiences a decompression from ~350 bars at the producing layers to ~40 bars at the production pump. If no conductive heat loss occurred in the adiabatic (constant fluid enthalpy) upward flow, that decompression can yield a 5°C increase in production fluid temperature. Integration of MSW into the modeling workflow helps capture this fine details to ensure proper planning for the project economics.

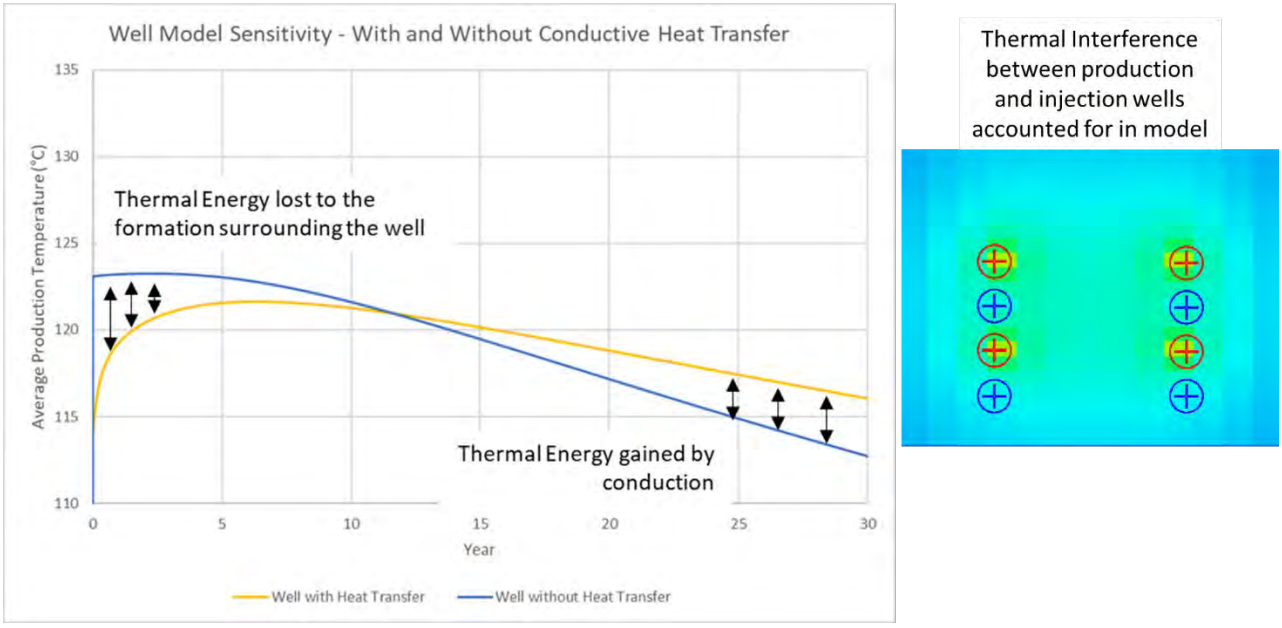

Figure 7: 4-well pilot project forecast – wells with and without heat transfer. Analysis showing the impact of including conductive heat transfer along the well during production. During the initial production period heat is lost to the formation as it heats the upper formation sections, later time heat is recovered by conduction along the well, reducing temperature decline.

The production pressure at the pump intake depth of 650 m-TVD remains above 35 bar (absolute), indicating that the pumps maintain positive suction pressure throughout the life of the project. Similarly, the injection well shows the equivalent of a negative wellhead pressure, indicating that the liquid level is predicted to remain below surface for the forecast period. This indicates that injection pumps will not be required to return the produced fluid to the reservoir given the permeability-thickness achieved by the lateral well completions. Overall, the lower density of the

heated production fluid increases the production intake pressure due to its reduced density, while the cooler fluid sent to the injection wells aids injection because of its greater density. The fluid density changes are advantageous for the project because they reduce injection and production power requirements.

4.3.1 Trajectory Sensitivity

DEEP has proposed several well trajectory configurations to optimize drilling cost and schedule. Two different well configurations are shown in **Figure** 8, where the horizontal separation between the two deviated legs of the new configuration is smaller, contributing to decreased heat loss for this early phase. Because of this trajectory-associated reduction in conductive heat loss, the peak production temperature of the new pilot well trajectories is about 2.5°C higher than for the original trajectories. The shorter length of the lateral results in less conductive heat loss for the production wells and less conductive heat gain for the injection wells (**Figure** 8).

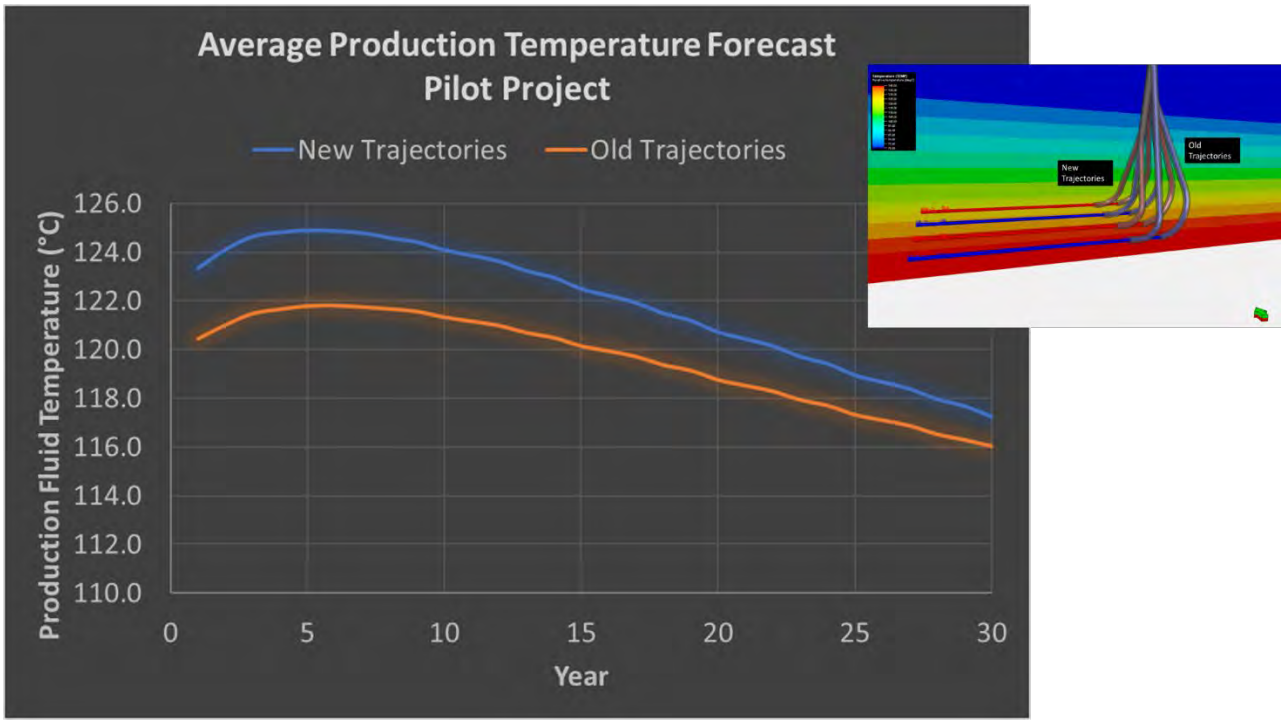

Figure 8: Production temperature at pump depth of different trajectories.

4.3.2 Rate Sensitivity

To evaluate the project's sensitivity to operating flow rates, two additional forecasts were made at average rates of 55 L/s and 65 L/s. **Figure 9** presents the results of this analysis, which show an impact of less than 2°C on production fluid temperatures at the end of a forecast period of 30 years. Production pressures remain adequate to support pumped production at 650 m-TVD, and injection wellhead pressures remain below zero. This indicates that the production and injection can be adjusted without creating a severe impact on the operational sustainability. Higher injection rates produce higher production temperature at first, then lower production temperature is observed toward the end of the forecast (**Figure 9**). Higher injection rate also results in lower average pressure intake at the pump and at higher negative injection pressures.

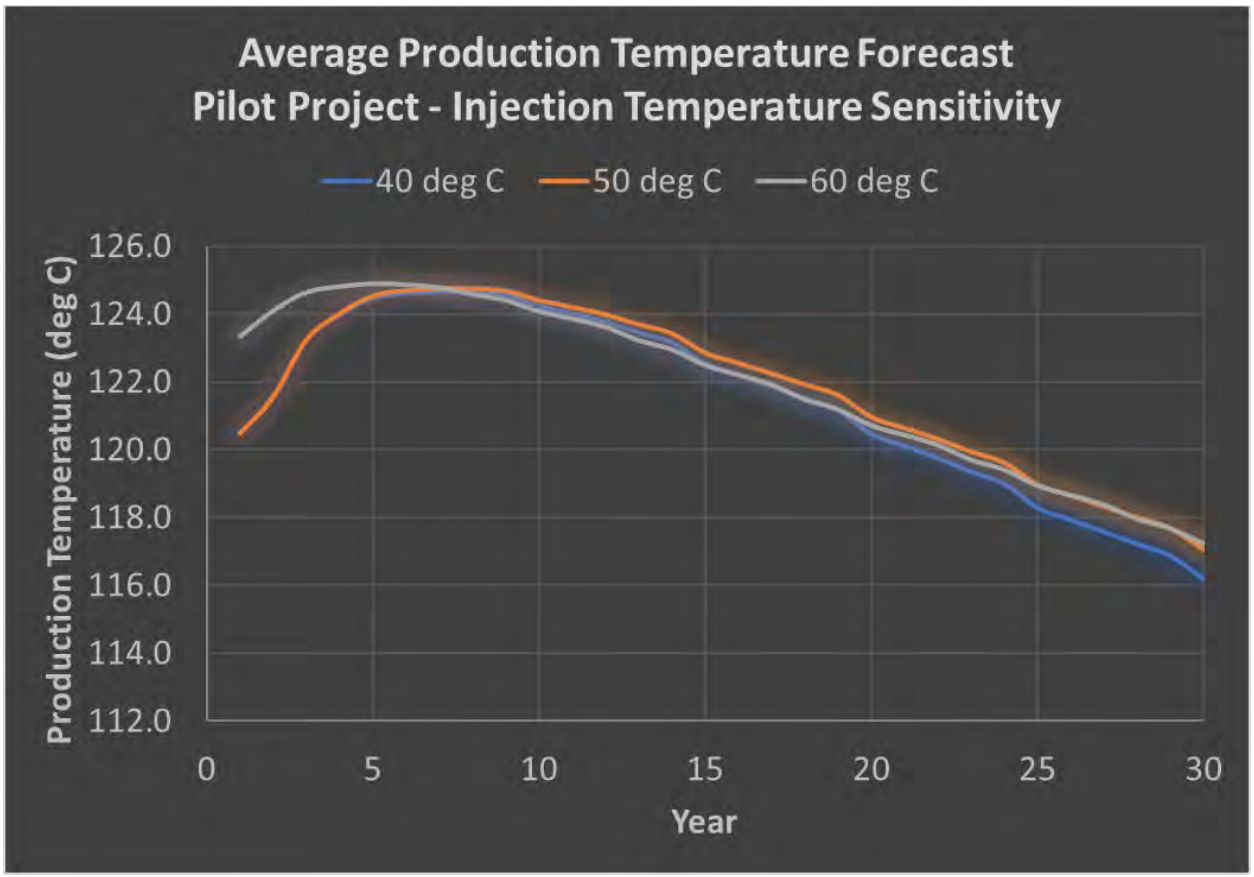

Figure 9: Sensitivity of injection temperature on production temperature at pump depth.

4.3.3 Injection Temperature Sensitivity

To assess the impact of reducing the injection fluid temperature on the production fluid temperature, a sensitivity analysis was performed in which the injection fluid temperature was modeled at 40°C, 50°C, and 60°C. The results show that reducing injection fluid temperature has a minimal impact on the production fluid temperature (**Figure 10**). With a 20°C reduction in injection temperature, the model forecast shows the maximum impact on production fluid temperature is 2°C after 30 years. The injection fluid temperature has a minimal impact on the production temperature because of the advantageous geometry and properties of the DEEP reservoir. The relatively thin DEEP Sand (22 m thick on average) allows conductive reheating from above and below the formation to heat injected fluids. Additionally, the dominance of matrix permeability in the reservoir reduces the fluid velocity, providing sufficient time for the injected fluid to reheat conductively.

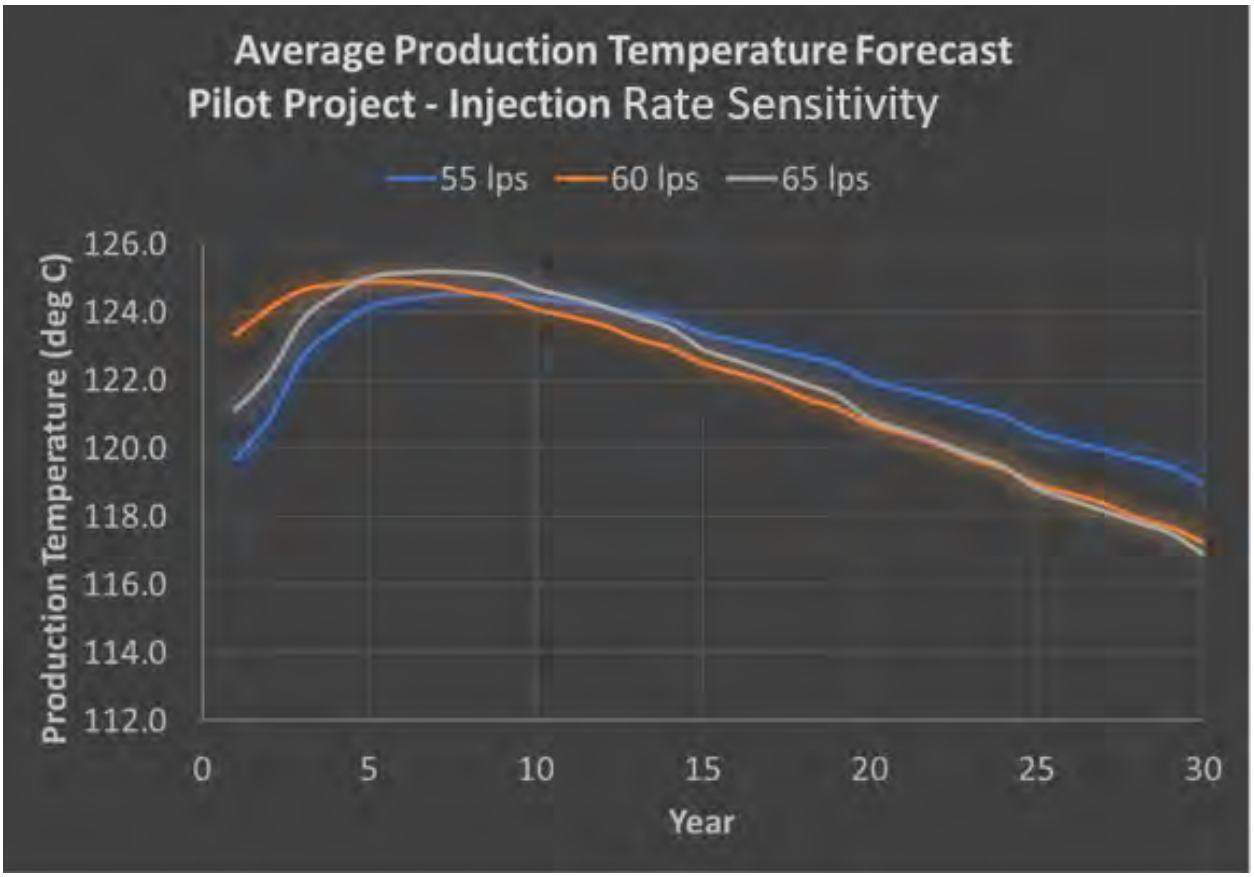

Figure 10: Sensitivity of injection rate on production temperature at pump depth.

5. Conclusion

The project design and well layout enable exploitation of conductive heating from above and below the targeted DEEP Sand to sustain thermal energy production. Employing the latest multi-segment wellbore modeling techniques, the reservoir modeling study has shown that this conductive heating from above and below significantly reduces the impact that heterogeneity could have on sustained thermal energy production. The Project plan targets distributed flow through the formation between the production and injection wells to maintain the production temperature and maximize the thermal energy sweep between the wells. If distributed flow can be maintained, the numerical model predicts that the production temperature will decline by approximately 6-8°C after 30 years. Additionally, the modeling results have shown that the project design takes advantage of changing fluid density gradients to reduce power consumption for pumping. The forecasts indicate that the project can sustain injection with zero wellhead pressure, because the cooled fluid has a higher density gradient, which aids injection. Conversely, the higher-temperature production fluid aids the production pumps by increasing the intake pressure and reducing the pumping power requirements.

REFERENCES

Groenewoud, Leo, and Kirsten Marcia. "The DEEP Geothermal Power Project: Wildcat Drilling For The Earth's Heat, Williston Sedimentary Basin (Canada)." *GRC Transactions* 44 (2020).

Holmes, J. A., T. Barkve, and Ø. Lund. "Application of a multisegment well model to simulate flow in advanced wells." *SPE Europec featured at EAGE Conference and Exhibition*. SPE, 1998.

Marcia, Kirsten, and J. Scott, "Horizontal drilling for geothermal power generation in the Williston Basin (Canada)." *Geoconvention* (2021).

Textural Analysis of Sedimentary Rocks: Implications for Geothermal Reservoir Characterization

Cesar Vivas[1], Zeming Hu[1] and Saeed Salehi[2]

[1]Well Construction Technology Center, University of Oklahoma, Norman, OK, USA
[2]Mechanical Engineering, Southern Methodist University, Dallas, Texas

Keywords

Thermal rock properties, petrophysical properties, mineralogy, reservoir simulation.

ABSTRACT

Understanding sedimentary rocks' mineralogy, petrophysical properties, and thermal behavior is crucial for the effective characterization of geothermal reservoirs. In this study, we investigate the relationship between textural properties, mineralogy, petrophysical properties, and thermal behavior of 30 core samples of sedimentary rocks using scanning electron microscopy (SEM).

The study reveals that well-sorted rocks exhibit superior porosity, permeability, thermal conductivity, diffusivity, and higher quartz content among the samples analyzed. Improved grain sorting enhances the interconnected pore network, facilitating fluid flow and heat transfer within the geothermal reservoir. Moreover, the higher quartz content in well-sorted rocks enhances thermal conductivity and diffusivity. The results provide valuable insights for reservoir characterization and geothermal resource assessment, emphasizing the significance of grain sorting as a controlling factor in the porosity, permeability, and thermal properties of reservoir rocks. Incorporating textural analysis into geothermal reservoir models can improve resource assessments and aid in site selection for geothermal projects.

This study contributes to geothermal energy exploration by highlighting the importance of textural analysis in understanding the geothermal behavior of sedimentary rocks. The findings offer practical implications for enhancing the accuracy of geothermal reservoir models, optimizing resource utilization, and promoting the development of sustainable geothermal energy.

1. Introduction

Geothermal reservoir characterization in sedimentary basins involves understanding the subsurface rock and fluid properties to assess the potential for geothermal energy production. This process is crucial for determining the economic viability of geothermal projects in these environments.

Sedimentary basins offer several advantages for geothermal development, including existing subsurface data from oil and gas exploration, lower drilling costs, and favorable porosity and

permeability conditions compared to traditional geothermal reservoirs (Khankishiyev et al., 2023; Mohamed et al., 2022; Ortiz-Sanguino et al., 2022; Salehi et al., 2022; Vivas et al., 2023a, 2023b). However, identifying suitable reservoirs and their characteristics remains a significant challenge.

Traditional geothermal reservoirs for power generation are typically found in metamorphic or volcanic rock formations. These reservoirs are considered ideal when they possess a network of highly conductive fractures, which facilitate the movement of fluids at high flow rates commonly observed in geothermal fields. In contrast, sedimentary reservoirs exhibit distinct characteristics. In sedimentary porous media, the intrinsic permeability of the reservoir rock plays a crucial role in determining its ability to allow fluid flow. This intrinsic permeability is an inherent property of the material itself. In conventional sedimentary basins, where convective heat transfer is typically dominant, higher temperatures are achieved by drilling deeper wells to access regions with steeper geothermal gradients. As the well depth increases, the temperature also rises. However, it is important to note that deeper reservoirs tend to exhibit lower porosity and permeability. This decrease in permeability becomes particularly significant for power generation projects, as high flow rates are essential for the economic viability of a geothermal power development.

Sedimentary rocks are highly complex, exhibiting both anisotropy and heterogeneity at various scales. Anisotropy arises from the ordered heterogeneities smaller than the seismic wavelength, such as aligned fractures, bedding planes, or preferred mineral orientations (Lynn, 2004). The natural heterogeneity of sedimentary rocks is given by the spatial variations in the porosity, permeability, and lithology within the rock formation. In geothermal systems, these characteristics have significant implications. Anisotropy can lead to preferential fluid flow paths along fractures or bedding planes, influencing heat extraction and reservoir productivity (Panja et al., 2021). Heterogeneities can create localized zones of high or low permeability, affecting the distribution of geothermal fluids and heat transfer efficiency (Goupil et al., 2022). Additionally, anisotropic and heterogeneous rock properties can impact the state of stress and deformation behavior, which is crucial for understanding reservoir stability and potential induced seismicity (Ijeje et al., 2019).

Heterogeneity as well have implication in the rock thermal properties. Sedimentary rocks exhibit significant heterogeneity in their thermal properties due to variations in mineralogy and texture. The thermal conductivity, which governs heat transfer, is strongly influenced by the mineral composition and porosity of the rock (Schön, 2015). Quartz-rich sandstones and siliceous shales tend to have higher thermal conductivities compared to clay-rich mudstones or organic-rich shales (Fuchs et al., 2021; Robertson, 1988). Similarly, the presence of evaporite minerals like halite or anhydrite can substantially increase the thermal conductivity (Jorand et al., 2013). The thermal diffusivity, which determines the rate of heat propagation, is also affected by the rock's mineralogical makeup. Sedimentary rocks with higher quartz and feldspar content generally exhibit higher thermal diffusivities, while clay-rich rocks have lower values (Carmichael & Klein, 2024). Additionally, the anisotropy in sedimentary rocks, arising from features like bedding planes and aligned minerals, can lead to directional variations in thermal properties (Schön, 2015).

In this study, information extracted from experimental research is used to understand the implication of the natural heterogeneity of sandstones, and their petrophysical properties, thermal properties and mineralogy in geothermal reservoir simulations.

2. Materials and Methods

The approach involves examining 30 core samples that exhibit diverse thermal properties. These samples are prepared for scanning electron microscope (SEM) analysis, and detailed SEM images are obtained at a high resolution. Advanced image processing and analysis techniques are utilized to identify and measure various microstructural attributes, including grain size, pore size, and connectivity. Any significant correlations can be determined by comparing the known thermal properties of the core samples with the observed characteristics in the SEM images.

The rock samples used in this study consist of different types of sandstones obtained from formations such as Berea Sandstone, Boise Sandstone, and Kentucky Sandstone. Figure 1 illustrates the workflow and equipment employed for measuring the petrophysical properties, thermal properties, and mineralogy of the samples.

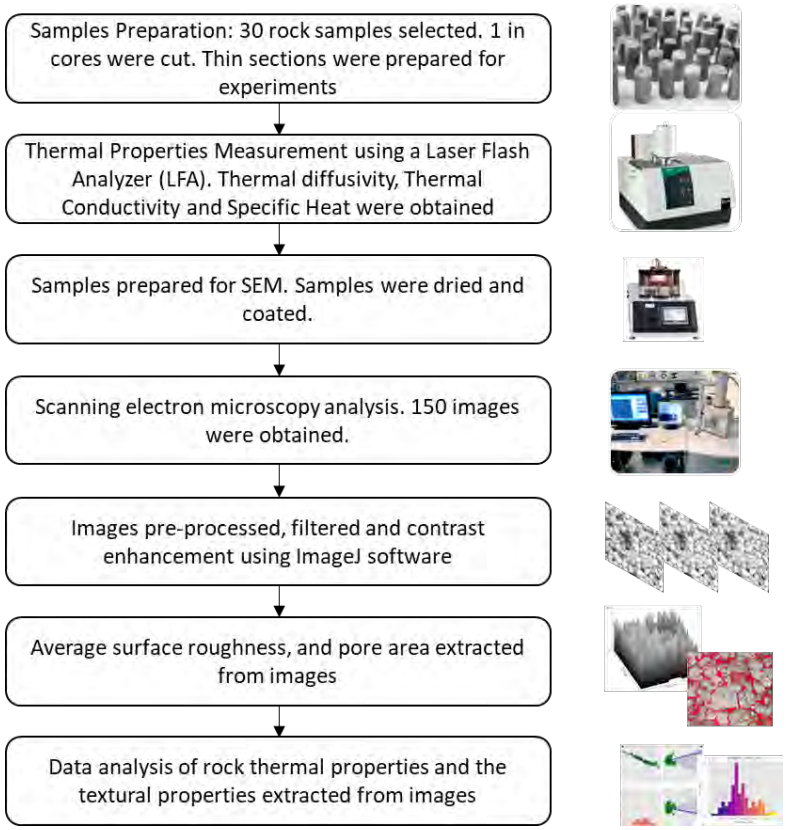

Figure 1: Experimental workflow of this study

2.1 Samples Thermal Properties

The thermal properties of the 30 sandstone samples were obtained experimentally. The thermal properties were measured using the LFA (light flash apparatus) Netzsch LFA 467. The equipment uses a short pulse of energy light to heat up the front surface of a flat sample, which is parallel to a plane. An infrared detector measures the temperature change of the back surface caused by the heat pulse. This measurement allows for the determination of thermal diffusivity and specific heat. When combined with the density of the sample, these thermophysical properties can be used to calculate thermal conductivity.

The variation of equation 3 is used to calculate the thermal conductivity:

$$\lambda = \kappa * \rho * C_P \quad (1)$$

Where λ represents thermal conductivity, κ represents thermal diffusivity, C_P represents specific heat capacity, and ρ represents the density of the samples collected in the laboratory.

2.2 Samples preparation

The 1-inch core samples were cut to expose the surfaces that are going to be analyzed by SEM. This is done to obtain more insight about sample texture. Once the samples were cut to the appropriate size, they were coated with a conductive metal layer to improve conductivity. For this study a carbon coating was applied, to prevent the buildup of electrical charges during SEM analysis. Before performing every experiment, the samples were stored in an oven at 65°C for 24 hours. The objective of this was to have the samples completely dry, prevent moisture from affecting the measurements, and have comparable results.

2.3 SEM Experimental equipment and experiment description

To quantitatively assess the morphological features of the rocks, the samples were prepared and examined using an FEI Quanta 200 Scanning Electron Microscope. A total of 150 SEM images were captured and the magnification considered was 300 times. Micrographs with magnifications of 500, 1000, and 2000, were evaluated, however, the mentioned sizes were discarded since they did not allow to capture textural details that are lost for the higher resolution.

The SEM instrument was then used to scan the surface of the cut section, producing high-resolution images of the rock's texture and structure. To extract the information required to understand how textural features affect the thermal properties of the rocks, the images were analyzed with the Fiji version of the software ImageJ. ImageJ is a widely used open-source image processing software that provides a range of tools and plugins for analyzing and quantifying various properties from SEM images. Image J has been used to analyze SEM rock images for analyzing morphological features, particle size evaluation, or porosity (Bai et al., 2013; Kelly et al., 2016; Nole et al., 2016; Tao et al., 2020; Voutilainen et al., 2019). In this study, the surface roughness and porosity were analyzed.

2.4 Image preparation

Once the SEM images were obtained, a pre-processing process helped to enhance the image features extraction process. Firstly, the images were filtered using the "Median" filter in ImageJ software. This is a type of spatial filter used to reduce noise in digital images. It works by replacing each pixel in the image with the median value of the neighboring pixels within a given radius. For this study, the radius of 2 pixels was sufficient to enhance the images. After the filter, the enhance contrast option in ImageJ software was used to automatically adjust the brightness and contrast of SEM images to improve their visibility. Initially, the color scale of the image is normalized, which scales the pixel values in the image so that the minimum value becomes 0 and the maximum value becomes 255. This ensures that the full range of values is used in the image. Then, the pixels of the images were saturated, which refers to the percentage of pixels in the image that should be saturated (set to either 0 or 255). For this study, this was set to 0.5%, which means that the brightest

and darkest 0.5% of pixels in the image were set to 255 and 0, respectively. An example of SEM preparation result is presented in **Fig. 2**.

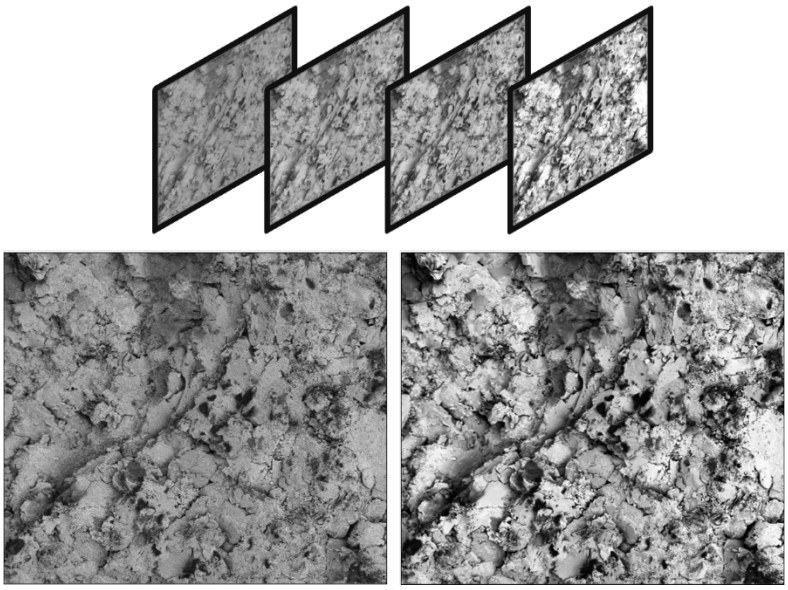

Figure 2: SEM Images, before [left], and after [rigth] pre-processing enhancement.

3. SEM Rock Images Analysis

SEM images were examined to evaluate the feasibility of using them to assess their thermal properties based on textural features. **Fig. 3** shows SEM images of 3 rock samples; they represent samples that have, from left to right, low, medium, and high values of thermal properties from the analyzed dataset.

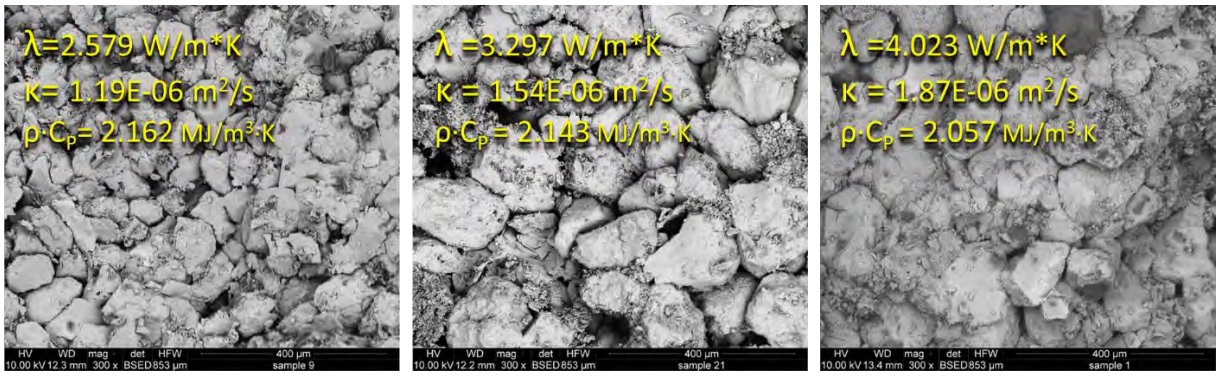

Figure 3: SEM images magnified 300X for samples with high [left] and low [right] thermal properties in the present dataset.

The SEM images showed how different grain sizes, pores and voids, and grains separation affect the rocks' thermal properties. More spaces between grains allow air pockets to form, trapping air that acts as a thermal insulator. The samples with higher porosity, and thus more air pockets, show higher thermal resistance as represented by their higher thermal properties. The software ImageJ was used to extract the morphological characteristics of the rocks.

3.1 Surface Roughness

Surface roughness analysis involves quantifying and characterizing roughness features of a surface profile using various variables obtained from SEM images. These variables play a crucial role in understanding the topographic characteristics of the surface.

In **Fig 3** it is depicted the analysis performed in all images. The average surface roughness is a measure of the height variations in the surface of a material. It is calculated by averaging the absolute values of the deviations of the surface from its mean plane. The average surface roughness is calculated by first subtracting the mean plane from the surface height data. This produces a residual height map that represents the surface roughness.

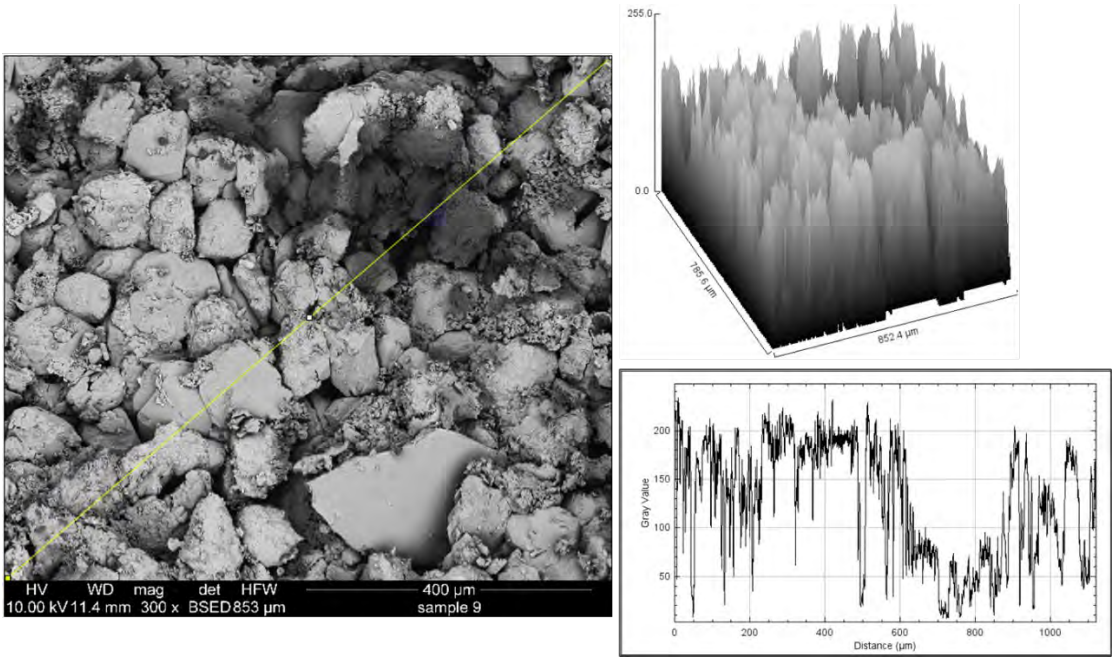

Figure 4: Surface roughness analysis of SEM rock images.

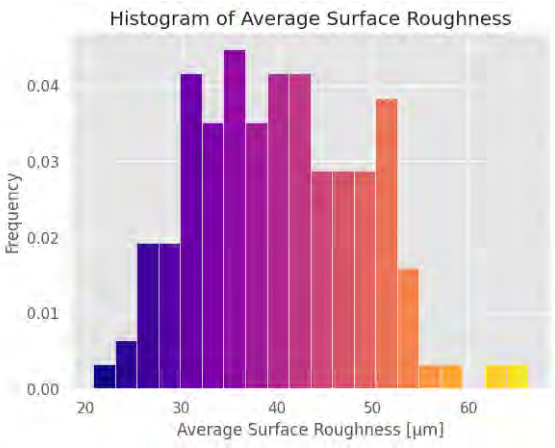

Figure 5: Histogram of the average surface roughness [Ra] values obtained.

3.2 Pore, Voids, and Cracks Area

SEM images of rocks contain complex textures and structures that make it difficult to identify and measure the areas of interest manually. By using the threshold function in ImageJ, the pores and voids in every image were identified and segmented **Fig. 6**. The threshold function in ImageJ was the tool that was used to segment the SEM image into foreground and background based on pixel intensity values. The tool was useful for separating the pores, voids, and cracks of the rock SEM images from the background. The threshold function applies the threshold to the image and generates a binary mask that separates the foreground and background pixels. The mask can then be used for measuring the area of objects in the image that represents the pores, voids, and cracks. **Fig. 7** shows the histogram of the calculated pore in μm^2.

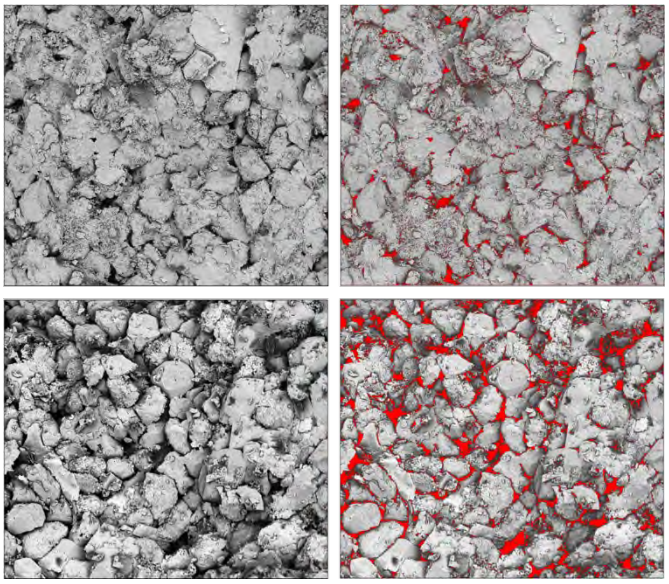

Figure 6: Pore, cracks and voids area analysis of SEM rock images.

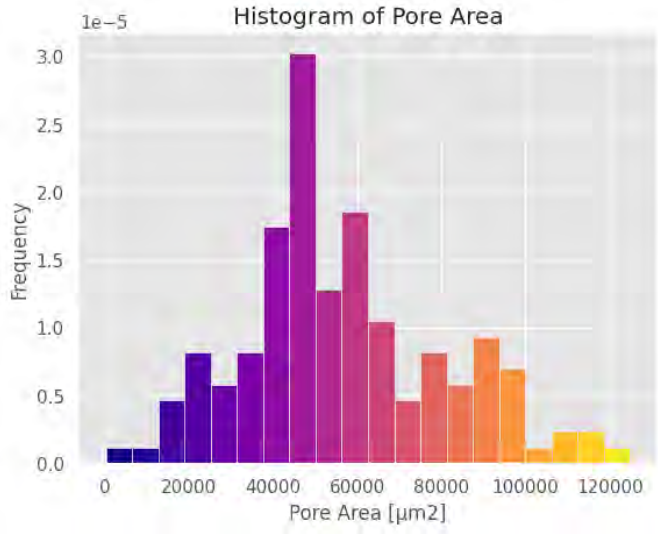

Figure 7: Histogram of pores, cracks, and voids surface area obtained.

4. Results Analysis

The analysis of textural properties in SEM images helps to understand the relationship between the morphologic characteristics of rock samples and the rock's thermal properties. In this section, the average surface roughness and the pores, cracks, and voids surface area extracted from the SEM images are compared with the thermal properties of the rock samples obtained experimentally.

4.1 Surface Roughness Analysis

Fig. 8 presents the relationship between surface roughness (Ra) and thermal properties, specifically thermal diffusivity, thermal conductivity, and volumetric heat capacity for the 150 images. The plot of thermal diffusivity against Ra exposed a trend, indicating that as the Ra values increased, the thermal diffusivity consistently decreased. This suggests that higher surface roughness impedes the efficient conduction of heat, resulting in reduced thermal diffusivity. Similarly, in the plot of thermal conductivity against Ra, as the Ra values increased, indicating greater surface roughness, the thermal conductivity showed a corresponding decrease. When examining the relationship between volumetric heat capacity and Ra, no clear correlation was observed. The plot of volumetric heat capacity against Ra displayed scattered data points, indicating that volumetric heat capacity and Ra are uncorrelated.

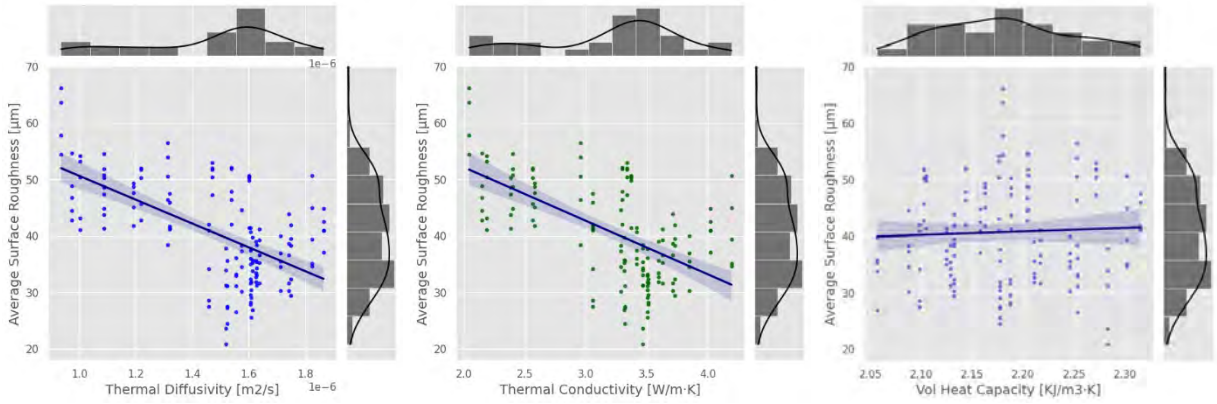

Figure 8: Arithmetic average roughness influence in thermal diffusivity [left], thermal conductivity [middle], and volumetric heat capacity [right].

The surface roughness of the rock is influenced by the grain size and distribution. A smoother surface is indicative of smaller grains that are well-sorted, possessing similar grain shapes. Smaller grains can pack tightly together, while similar grain shapes fit more harmoniously. Consequently, the result is a smoother surface. On the other hand, a rough and irregular surface indicates larger grains that are poorly sorted, with varying grain shapes. The larger grains cannot pack as tightly, and the differing shapes do not align perfectly, leading to a rough and uneven surface.

Additionally, the scale or wavelength of roughness features can provide clues about the grain size. Larger grains produce roughness features on a larger scale, while smaller grains result in smaller-scale roughness. The presence of isotropic or uniform roughness in all directions indicates well-sorted grains with similar sizes and shapes. Conversely, anisotropic roughness, where smoother and rougher areas align in different directions, signifies poorly sorted grains with variable sizes and shapes. Lastly, the texture of roughness features, ranging from smooth to jagged, can offer

insights into the interlocking of grains. Jagged and angular features indicate grains that are not well-interlocked, while smoother undulations suggest grains that are more interfit, demonstrating their interlocking nature. These observations enable a deeper understanding of the geological properties and composition of rocks based on their surface roughness characteristics.

These findings highlight the impact of surface roughness on thermal properties. Higher Ra values lead to decreased thermal diffusivity and thermal conductivity, indicating a hindered ability to conduct and transfer heat. In contrast, the volumetric heat capacity does not exhibit a significant dependence on surface roughness, as indicated by the lack of correlation between volumetric heat capacity and Ra. These findings contribute to our understanding of the intricate relationship between surface roughness and thermal properties, aiding in the design and optimization of materials for efficient heat transfer applications.

4.2 Pore Area Analysis

Fig. 9 shows the relationships between the pore area and the thermal diffusivity, thermal conductivity, and volumetric heat capacity. The plot of pore area versus thermal diffusivity indicates an inverse relationship between the two variables. This means that as the pore area increases, the thermal diffusivity of rocks decreases. Thermal diffusivity is a measure of how quickly heat is conducted through a material, and a lower thermal diffusivity means that heat takes longer to travel through the material. This relationship makes intuitive sense since pores and cracks in rocks are essentially empty spaces that do not conduct heat as well as the solid material. Therefore, as the pore area increases, the proportion of non-conductive material in the rock increases, leading to a decrease in thermal diffusivity.

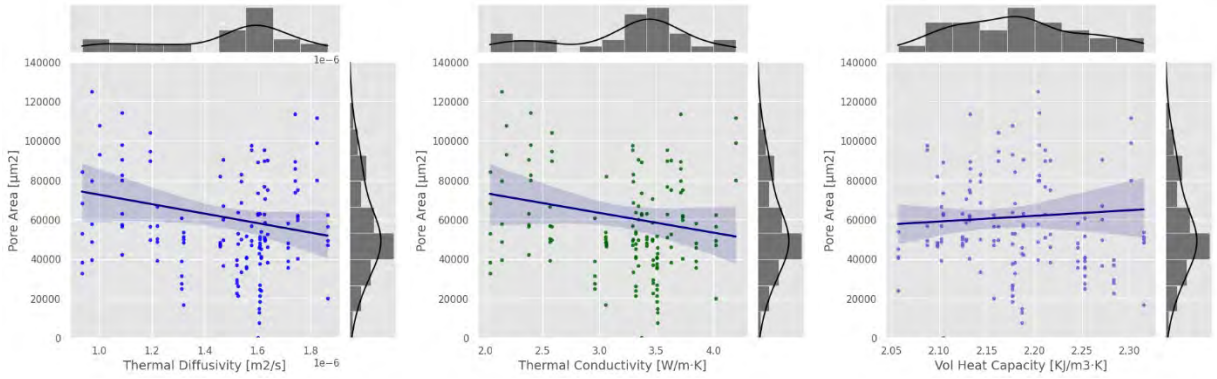

Figure 9: Pores, voids, and cracks area influence in the thermal diffusivity [left], thermal conductivity [middle], and volumetric heat capacity [right].

Similarly, the plot of pore area versus thermal conductivity also shows an inverse relationship between the two variables. This means that as the pore area increases, the thermal conductivity of rocks decreases. Thermal conductivity is a measure of how well a material conducts heat and a lower thermal conductivity means that the material is a poorer conductor of heat. This relationship is also understandable since pores and cracks in rocks act as thermal insulators, reducing the overall thermal conductivity of the rock.

The plot of pore area versus volumetric heat capacity, however, indicates that there is no correlation between the two variables. Volumetric heat capacity is a measure of how much heat a material can absorb before its temperature increases, and in this case, it seems that the presence of

pores and cracks in rocks does not have a significant effect on their volumetric heat capacity. This may be because the amount of solid material in the rock is still the primary determinant of its volumetric heat capacity.

5. SEM Results Discussion

The experimental study surface roughness of rocks can be correlated with their thermal properties. Rocks with rougher surfaces generally exhibit larger, more poorly sorted grain sizes. This leads to a reduced number of grain boundaries per unit volume and inefficient packing, ultimately decreasing the connectivity of the grain network. As a result, heat transfer through the rock becomes more challenging, resulting in lower thermal conductivity and diffusivity.

In contrast, rocks with smoother surfaces tend to have smaller, well-sorted grain sizes. The smaller grain size increases the number of grain boundaries per unit volume, and efficient sorting enables effective packing. This results in a well-connected grain network that facilitates heat transfer. Consequently, rocks with smoother surfaces exhibit higher thermal conductivity and diffusivity.

The presence of grain boundaries can scatter or impede heat transfer. Rocks with smaller, well-sorted grains have a higher density of grain boundaries, providing more opportunities for heat transfer between grains. On the other hand, rocks with fewer, larger grains possess fewer grain boundary sites, limiting heat transfer. Additionally, better packing and grain sorting in rocks minimize the presence of air spaces or pores. This reduces scattering or impedance of heat transfer since air does not conduct heat as efficiently as mineral grains. In contrast, poorer sorting and packing result in more air spaces, creating barriers to heat flow. Smooth grain shapes allow for increased surface contact between grains, enhancing heat transfer. In contrast, angular and irregular grain shapes lack sufficient surface contact, impeding the flow of heat. These insights highlight the significant influence of surface roughness and grain characteristics on the thermal properties of rocks, shedding light on their heat transfer behavior and conductivity.

Fig. 10 displays the correlation between the textural features analyzed, average surface roughness, and the pore, cracks, and voids area extracted from the SEM images, with experimentally obtained thermal properties. Average surface roughness has a strong negative correlation, -0.59 and -0.6 with thermal conductivity and thermal diffusivity respectively. In contrast, the volumetric heat capacity and the average surface roughness are uncorrelated, confirming the results presented in the previous section. The pore, cracks, and void surface area have a less apparent negative correlation, -0.18 and -0.17, related to the thermal conductivity and thermal diffusivity. The reason that the pore, cracks, and voids area values have a less apparent negative correlation with thermal conductivity and thermal diffusivity compared to the average surface roughness could be that these properties affect heat transfer differently. The negative correlation between average surface roughness and thermal conductivity/diffusivity is stronger, as the surface roughness directly affects the connectivity of the grain network and packing efficiency, which are important factors in determining thermal conductivity and diffusivity. On the other hand, the effect of voids on heat transfer is dependent on various factors, and the correlation between pore, cracks, and voids area and thermal conductivity and diffusivity may be weaker due to the complexity of the effect of voids on heat transfer. Factors such as the size, shape, and distribution of the voids affect heat transfer. If the voids are interconnected, they can provide networks for heat to flow through, which can increase the thermal conductivity and thermal diffusivity of the sandstone. Additionally, the

size and shape of the voids can affect the rate at which heat is transferred. Smaller voids, for example, can trap heat more effectively than larger voids.

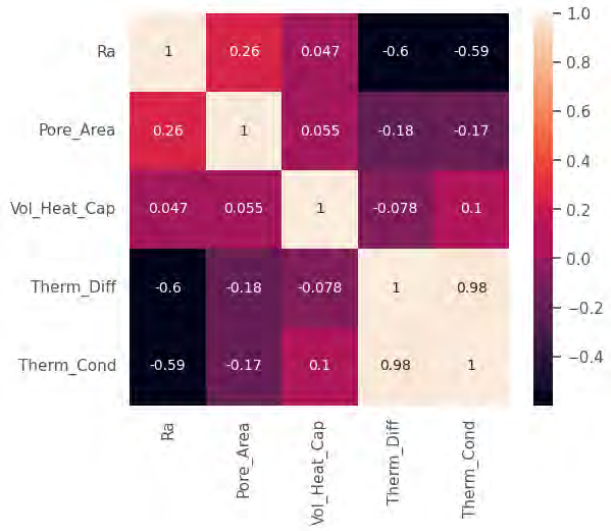

Figure 10: Heat map with the Pearson correlation between thermal properties and textural features where 'Ra' refers to average surface roughness [µm2], 'Pore_Area' refers to the pore area [µm2], 'Vol_Heat_Cap' refers to volumetric heat capacity [KJ/m3·K], 'Therm_Diff' refers to thermal diffusivity [m2/s], and 'Therm_Cond' refers to thermal conductivity [W/m·K].

The thermal properties of rocks are influenced by several factors, including their texture, mineralogy, and porosity. These characteristics can be difficult to discern through visual inspection alone, especially when looking at a two-dimensional image. SEM provides high-resolution, detailed images of the rock's surface, allowing for a more accurate analysis of its texture and other characteristics that can impact its thermal properties.

6. Conclusions

The study aimed to analyze the porosity, permeability, density, and thermal properties of core samples and their correlation with mineral content. In this study, we present the results of the analysis of SEM images obtained from rock samples to investigate various surface roughness properties. The objective was to quantitatively evaluate and characterize the roughness features of the rock surfaces. By utilizing these parameters, we aimed to gain insights into the micro-structural defects, crack types, and other surface characteristics that impact the thermal properties of sedimentary rocks. The analysis of these properties provides valuable information for optimizing the selection of rocks for geothermal energy systems and thermal energy storage applications.

The thermal properties of rocks are affected by their texture, mineralogy, and porosity, which can be difficult to discern through visual inspection alone. The use of SEM images allows for a more accurate analysis of these characteristics, providing insights into the micro-structural defects, crack types, and other surface characteristics that impact the thermal properties of sedimentary rocks. The study found that surface roughness plays a significant role in determining the thermal conductivity and diffusivity of rocks, with smoother surfaces exhibiting higher thermal conductivity and diffusivity. The correlation between pore, cracks, and voids area and thermal conductivity, and diffusivity was found to be weaker than that of surface roughness, likely due to

the complexity of the effect of voids on heat transfer. The findings of this study provide valuable information for optimizing the selection of rocks for geothermal energy systems and thermal energy storage applications. parallel maximum stress to minimize short circuiting in the reservoir

Nomenclature and Acronyms

Symbols

λ	Thermal Conductivity
κ	Thermal Diffusivity
ρ	Density
C_P	Specific Heat Capacity

Nomenclatures:

^oC	Celsius Degrees
K	Kelvin Degrees
m	Meters
MJ	Mega Joules
s	Seconds
W	Watts

Abbreviations:

LFA	Laser Flash Analyzer
SEM	Scanning Electron Microscopy
SRTES	Sedimentary Reservoir Thermal Energy Storage

Acknowledgement <HEADING 5 STYLE>

If you include an acknowledgement(s) section, please use Heading 5 style for the header and Normal style for the text.

REFERENCES

Bai, B., Elgmati, M., Zhang, H., & Wei, M. (2013). Rock characterization of Fayetteville shale gas plays. *Fuel*, *105*, 645–652. https://doi.org/10.1016/J.FUEL.2012.09.043

Carmichael, R. S., & Klein, C. (2024). Rock - Thermal Properties | Britannica. In *Encyclopedia Britannica.* https://www.britannica.com/science/rock-geology/Thermal-properties

Fuchs, S., Förster, H. J., Norden, B., Balling, N., Miele, R., Heckenbach, E., & Förster, A. (2021). The Thermal Diffusivity of Sedimentary Rocks: Empirical Validation of a Physically Based α − φ Relation. *Journal of Geophysical Research: Solid Earth*, *126*(3), e2020JB020595. https://doi.org/10.1029/2020JB020595

Goupil, M., Heap, M. J., & Baud, P. (2022). Permeability anisotropy in sandstones from the Soultz-sous-Forêts geothermal reservoir (France): implications for large-scale fluid flow modelling. *Geothermal Energy*, *10*(1), 1–23. https://doi.org/10.1186/S40517-022-00243-1/FIGURES/13

Ijeje, J. J., Gan, Q., & Cai, J. (2019). Influence of permeability anisotropy on heat transfer and permeability evolution in geothermal reservoir. *Advances in Geo-Energy Research*, *3*(1), 43–51. https://doi.org/10.26804/ager.2019.01.03

Jorand, R., Vogt, C., Marquart, G., & Clauser, C. (2013). Effective thermal conductivity of heterogeneous rocks from laboratory experiments and numerical modeling. *Journal of Geophysical Research: Solid Earth*, *118*(10), 5225–5235. https://doi.org/10.1002/JGRB.50373

Kelly, S., El-Sobky, H., Torres-Verdín, C., & Balhoff, M. T. (2016). Assessing the utility of FIB-SEM images for shale digital rock physics. *Advances in Water Resources*, *95*, 302–316. https://doi.org/10.1016/J.ADVWATRES.2015.06.010

Khankishiyev, O., Salehi, S., Vivas, C., Nygaard, R., & Rehg, D. (2023). Techno-Economic Investigation of Geothermal Development in Sedimentary Basins. *ASME Open Journal of Engineering*, *2*. https://doi.org/10.1115/1.4062412

Lynn, H. (2004). The Winds of Change: Anisotropic Rocks – Their Preferred Direction of Fluid Flow and Their Associate | CSEG RECORDER. *Recorder, Canadian Society of Exploration Geophysicists*, *29*(08). https://csegrecorder.com/articles/view/the-winds-of-change-anisotropic-rocks

Mohamed, A., Ugarte, E., Vivas, C., Wu, Y., Cedola, A., & Salehi, S. (2022). Repurposing Abandoned Oil and Gas Wells for Geothermal Direct Use in Oklahoma: A Case Study. *Geothermal Resources Council Transactions*, *46*(1), 72–82. https://www.geothermal-library.org/index.php?mode=pubs&action=view&record=1034579

Nole, M., Daigle, H., Milliken, K. L., & Prodanović, M. (2016). A method for estimating microporosity of fine-grained sediments and sedimentary rocks via scanning electron microscope image analysis. *Sedimentology*, *63*(6), 1507–1521. https://doi.org/10.1111/SED.12271

Ortiz-Sanguino, L., Vivas, C., Rehg, D., Knight, D., Perry, S., Bradley, A., Bedle, H., Salehi, S., Marshall, S., & cs, G. (2022). Petrophysical Modeling to Improve the Understanding of Geothermal Exploration in a Sedimentary Field on Texas Gulf Coast Basin. *SPE/AAPG/SEG Unconventional Resources Technology Conference*, *2022*. https://doi.org/10.15530/URTEC-2022-3722276

Panja, P., McLennan, J., & Green, S. (2021). Influence of permeability anisotropy and layering on geothermal battery energy storage. *Geothermics*, *90*, 101998. https://doi.org/10.1016/J.GEOTHERMICS.2020.101998

Robertson, E. C. (1988). *Thermal Properties of Rocks*.

Salehi, S., Vivas, C., Nygaard, R., & Rehg, D. (2022). Scalable Geothermal Energy Potential from Sedimentary Basins: Opportunities for Energy Transition and Skilled Workforce Development. *Geothermal Resources Council Transactions*, *46*(1), 964–975.

Schön, J. H. (2015). Thermal Properties. *Developments in Petroleum Science*, *65*, 369–414. https://doi.org/10.1016/B978-0-08-100404-3.00009-3

Tao, R., Sharifzadeh, M., Zhang, Y., & Feng, X. T. (2020). Analysis of Mafic rocks Microstructure damage and failure Process under Compression Test Using Quantitative Scanning Electron Microscopy and Digital Images Processing. *Engineering Fracture Mechanics*, *231*, 107019. https://doi.org/10.1016/J.ENGFRACMECH.2020.107019

Vivas, C., Salehi, S., Nygaard, R., & Rehg, D. (2023a). Scalable Geothermal Energy Potential from Sedimentary Basins and Leveraging Oil and Gas Industry Experience: Case Studies from Texas Gulf Coast. *Proceedings of the Annual Offshore Technology Conference*, *2023-May*. https://doi.org/10.4043/32381-MS

Vivas, C., Salehi, S., Nygaard, R., & Rehg, D. (2023b). Scalable Geothermal Energy Potential from Sedimentary Basins in Oklahoma. *Society of Petroleum Engineers - SPE Oklahoma City Oil and Gas Symposium 2023, OKOG 2023*. https://doi.org/10.2118/213094-MS

Voutilainen, M., Miettinen, A., Sardini, P., Parkkonen, J., Sammaljärvi, J., Gylling, B., Selroos, J. O., Yli-Kaila, M., Koskinen, L., & Siitari-Kauppi, M. (2019). Characterization of spatial porosity and mineral distribution of crystalline rock using X-ray micro computed tomography, C-14-PMMA autoradiography and scanning electron microscopy. *Applied Geochemistry*, *101*, 50–61. https://doi.org/10.1016/J.APGEOCHEM.2018.12.024

Unlocking the Full Production Potential of Geothermal Wells in Indonesia using a Novel In-situ Generated Acid Fluid Technology

Ahmed S. Zakaria, Baker Hughes

Keywords

Geothermal, Non-Corrosive Acid, Stimulation, HSE

ABSTRACT

Global demand continues to grow for a clean and renewable energy source for electricity generation. Geothermal power has the potential to contribute significantly to the global energy mix. However, most of geothermal wells produce below their potential because of the scales deposited around wellbore tubulars or the formation damage that occurs because of drilling fluid invasion, silica plugging, scales deposition in the natural fractures, and fines migration. To restore productivity from geothermal wells, it is often necessary to perform matrix acid stimulation. However, acid treatment fluids under the extremely high temperature environment of geothermal wells are very corrosive to the wellbore tubulars/downhole equipment and spends near-wellbore. This paper presents the next generation acid system that utilizes environmentally friendly non-corrosive fluids to generate acid in situ in the formation for geothermal matrix stimulation.

The non-corrosive deep-penetrating acid is a neutral, non-reactive treatment fluid at the surface and only when it is injected in the formation, it generates acid at a controlled rate in situ under temperature and time. The in-situ generation of acid at a controlled rate allows for safe transport of the acid from the surface to the formation without exposing wellbore tubulars to an acidic fluid and also allows for deep penetration to dissolve deposited materials or scales in the porous formation or along the fractures. A series of solubility testing in HPHT reactor at temperatures above 450°F was first conducted to understand the chemical reactions that generate the acid as a function of temperature, concentration of acid generating components, and time, and to identify the optimum composition that maximize the dissolving of silica and calcite minerals. Coreflow testing was then conducted at 300°F and 475°F using 1.5” in diameter and 6” in diameter Berea sandstone cores to evaluate the penetration of the acid and its capability to provide remarkable permeability improvement.

This paper discusses the laboratory testing results, guidelines for the design of the treatment fluid, and its application in the field to restore the productivity of geothermal wells. The present study explains how the use of the new fluid technology will help to eliminate the need for acid tanks on site, reduce transportation difficulties and logistics, and eliminates HSE concerns associated with acids handling on geothermal sites.

1. Introduction

The potential of many geothermal wells is limited by scales deposition and/or formation damage incurred due to drilling fluid invasion, fines migration, silica plugging, and scaling. To restore productivity from geothermal wells, conventional matrix acid treatments are needed. However, matrix acid treatments for geothermal wells impose many challenges.

Matrix stimulation would involve injecting acid into the formation to remove damaged regions near the wellbore resulting from hydrothermal minerals deposited in fractures and/or the creation of larger aperture fractures via the dissolution of rock forming minerals instead of shear dilation (Portier et al., 2009). At the very high temperature conditions of geothermal wells, acidic fluid would be very corrosive to wellbore tubulars and downhole equipment's. Corrosion can result in a series of undesirable reaction products, which can cause plugging in the formation as iron sulfides, etc. It is very difficult to inhibit acid corrosion as it adds a prohibitive cost of corrosion package to the treatment. Another alternative is to use large water cooldown pads in order to reduce temperature, preferably to the 200 ^{o}F range, where corrosion inhibition can easily last for the duration of the acid treatment. However, this alternative requires sourcing large volumes of water and adds costs related to transposition and logistics.

Another challenge with the matrix acid treatments under high temperature conditions is the rapid reactions of the acid with the rock forming minerals that lead to significant secondary and tertiary precipitations. Furthermore, the acid wouldn't be able to penetrate deep enough to dissolve minerals over long distances or scales along the fractures. The acid reacts with the rock forming minerals throughout three-stage reactions to produce some insoluble precipitates as shown in the following reaction equations.

$$\text{The primary reaction} \qquad \text{aluminosilicates} + HF \rightarrow H_2SiF_6 + 2H_2O$$

Then the produced fluosilicic acid reacts with different aluminosilicates such as potassium feldspars throughout a secondary reaction as follows

$$\text{the secondary reaction}$$
$$SiF_6^{2-} + 6KAlSi_8O_8 + 20H^+ + 10H_2O \rightarrow 6K^+ + 6AlF^{2+} + 18H_2SiO_3 + H_4SiO_4$$

After that, the ratio of fluorine (F)/aluminum (Al) continues to decrease in the aluminum fluoride compounds because of their reaction with aluminosilicate compounds in the presence of HCl. This reaction chelates the aluminum ions from the aluminosilicates leaving silica gel as a precipitate as following

$$\text{The tertiary reaction} \qquad AlF_2^+ + KAlSi_3O_8 + 4H^+ + 4H_2O \rightarrow K^+ + 2AlF^{2+} + 3H_4SiO_4$$

To improve geothermal well stimulation and overcome issues related to corrosion, precipitations, and deep stimulation, a new fluid system has been developed. The new fluid system is neutral (pH around 7) at the surface conditions and only when it is pumped in the formation and under temperature, the fluid system self-generates an acid to dissolve the scales or for formation stimulation. Use of this new fluid system would allow pumping a safe and non-corrosive fluid to the wellbore tubulars, save the prohibitive cost of the corrosion inhibitors needed to inhibit the acid at the very high temperature conditions, and save thousands of gallons of water volumes needed for geothermal wells cooling. The new fluid system is also non-reactive when it is injected

into the formation which would allow for deep stimulation or dissolving scales at long distances before it self-generates acid. In the subsequent sections, the capability of the new fluid system to dissolve different minerals and its stimulation performance at different temperature conditions will be discussed.

2. Experimental Studies

2.1 Solubility Testing

The capability of the new fluid system to dissolve different minerals was assessed in a HPHT reactor cell. Different rock/scales forming minerals were placed in the HPHT reactor cell and heated to a predetermined temperature of 450°F under a pressure exerted by nitrogen gas of 800 psi. The new acid system was also preheated to the same temperature and then transferred to the HPHT reactor to allow for the reaction between the rock and the acid. After the test is completed, the mineral was collected, dried and weighed to identify the dissolution ratio. Fluid samples were also collected from the reactor at specific time intervals and analyzed using ICP-spectroscopy to measure different ions concentration.

2.2 pH Measurements

The new fluid system is neutral (pH is around 7) at the surface conditions and only when it is pumped and under temperature, it self-generates acid for stimulation and scale dissolution. pH measurements were conducted on the fluid system at 75°F at specific time intervals up to 48 hrs to ensure that no acid is being generated at the surface conditions. The fluid system was then heated in a HPHT cell to 450°F and pH measurements were conducted at specific time intervals for up to 4 hours to monitor the acid generation with time.

2.2 Coreflow Experiments

Coreflow experiments were conducted using a high-pressure/high-temperature coreflow setup shown in **Figure 1**. A backpressure of 1,200 psi was set to keep most of the carbon dioxide in solution. An overburden pressure at least 300 psi higher than the inlet pressure was kept while running the experiments to prevent the fluid from bypassing the core. Berea Sandstone plug samples of 1.5” in diameter and 6” in length were used in the coreflow experiments. The plug samples mineralogy is presented in **Table 1**. Berea plug samples were selected since the core samples contain different mineralogies including silica, clays, and calcite. The brine permeability of the plug samples was measured using 5 wt% NH_4Cl and ranged from 10 md to 300 md. In each test, the brine permeability of the plug sample was first measured, followed by predetermined pore volumes of an acid preflush. Then a predetermined pore volumes of main acid treatment was then injected at 2 ml/min. A stage of postflush acid was lastly injected before the regain permeability measurements were conducted using 5 wt% NH_4Cl to assess the stimulation or if any damage is occurred.

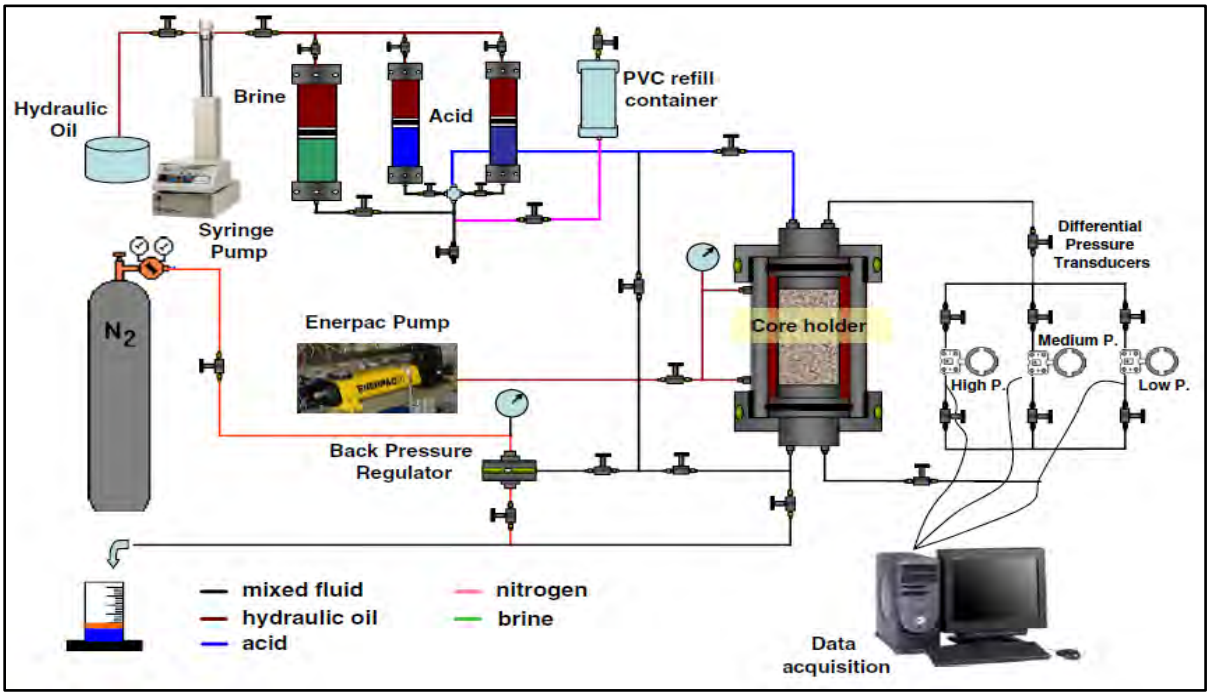

Figure 1: A Schematic of high-pressure/high-temperature coreflow setup

Table 1. Mineralogy of Berea sandstone plug samples.

Mineral	Content (wt%)
Quartz	87
Kaolinite	6
Potassium Feldspar	2
Chlorite	1
Illite	1
Calcite	2
Dolomite	1

3. Results and Discussion

3.1 Solubility Testing

To assess the capability of the new acid to dissolve calcite, a known weight of calcite mineral was allowed to react with 100 mls of the new acid in the HPHT reactor at 450°F for 3 hours. The calcite mineral was collected, dried, and post-reaction weight was measured to identify the calcite dissolution in the new acid. The composition of the new acid was adjusted to generate 5 wt% HCl. The new acid dissolved 51.23% that was similar to the dissolution of calcite in 5 wt% HCl (54.2%)

under same conditions. Increasing the concentration of the components of the new acid by 1.5 increased the generated acid strength to 7.5 wt%.

The composition of the new acid could also be adjusted to generate mud acid of any HF acid strength. Silica particles were placed in the HPHT reactor and allowed to react with the new acid at 450°F to assess the capability of the system to dissolve quartz. After 5 hours of reaction, fluid sample was collected and analyzed by ICP-Spectroscopy to measure Si+ ion concentration. The Si+ ion concentration was 5310 mg/l which is equal to the measured Si+ ion concentration for 1.5 wt% HF mud acid (5010 mg/l). Increasing the concentration of the components of the new acid by 2 dissolved 10,945 mg/l which was very similar to the one measured for 3 wt% HF mud acid (10,221 mg/l). The results showed that the new fluid system can generate HF acid at 1.5 wt% and 3 wt% acid strengths with similar dissolving power.

3.2 Corrosion and pH Measurements

The corrosivity of the fluid is determined primarily by its pH. Fluids with pH from 6.5 to 7.5 is generally considered non-corrosive. Fluids with pH less than 6.5 are considered acidic and corrosive while fluids with pH more than 7.5 are considered alkaline and corrosive. The new acid composition that is designed to generate 5 wt% HCl, was tested for pH changes at different temperatures with time. As shown in **Table 2**, the new acid system was neutral (pH around 7) for the tested time period of 48 hours at surface temperature. This would eliminate the need for acid tanks and all HSE concerns when handling acids on site and allow for easier and safer operations. As shown in **Figure 2**, at a temperature of 450°F, the new fluid system was neutral (pH around 7) for 3 hours and after 3 hours, the fluid system self-generated 5 wt% HCl acid and pH dropped to zero. Pumping the new fluid system in a neutral state would provide a non-corrosive and safe fluid to the wellbore tubulars and downhole equipment's as ESP, etc. and save the prohibitive cost of the corrosion inhibitors needed to inhibit the acid at those very high temperature conditions and for geothermal applications. Only when the fluid system is placed in the formation and under the effect of temperature and time, the fluid system self-generates acid to dissolves calcite and silica scales or for formation stimulation. It is worthy to mention that the triggering time could be controlled to allow for enough pumping time and placement of the new acid system into the formation before an in-situ acid is generated.

Table 2. pH measurements of the new fluid system at surface conditions (75°F).

Time	**4 hrs**	**8 hrs**	**16 hrs**	**20 hrs**	**32 hrs**	**48 hrs**
pH	6.82	7.02	7.15	6.80	6.92	7.05

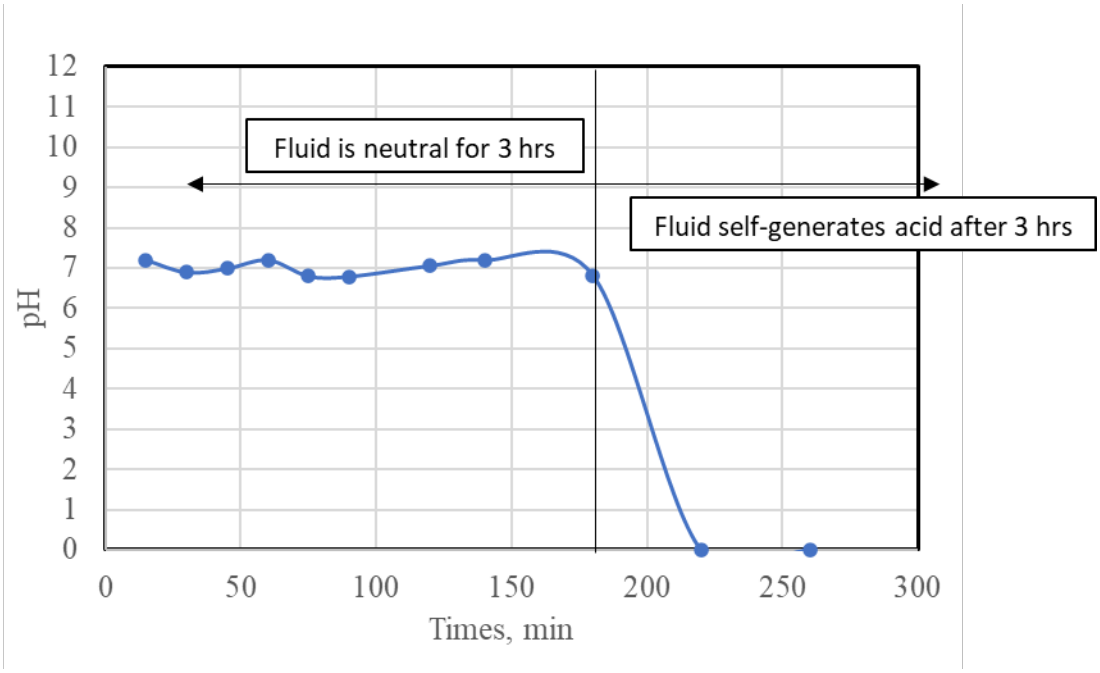

Figure 2: pH measurements of the fluid system during 4 hrs time period at a temperature of 450°F. Fluid system was neutral during the first 3 hrs. Under temperature and time, fluid system self-generated acid after 3 hrs and pH dropped to zero.

3.3 Stimulation Assessment

One coreflow test was first conducted to create a control test to assess the dissolving of silica, clays, and calcites in Berea cores using regular mud acid at very high temperature of 475°F **(Figure 3)**. A 5 wt% NH_4Cl was first injected through the core sample at different flow rates and the corresponding pressure drops were measured. Those pressure drops were used to determine the initial brine permeability. The initial brine permeability was 18 md. A preflush of 4 pore volumes of 10 wt% HCl was then injected followed by 12 pore volumes of 1.5 wt% HF regular mud acid. Then, a postflush stage of 4 pore volumes of 10 wt% HCl was injected before final brine permeability measurements were conducted. All acid stages were injected at 2 ml/min. The final brine permeability after acid treatment was 4.7 md with a regain permeability of 26%. The damage resulted from acid treatment is contributed to the rapid reaction of the regular mud acid with the clays and the precipitations occurred during the secondary/tertiary reactions at these very high temperature conditions.

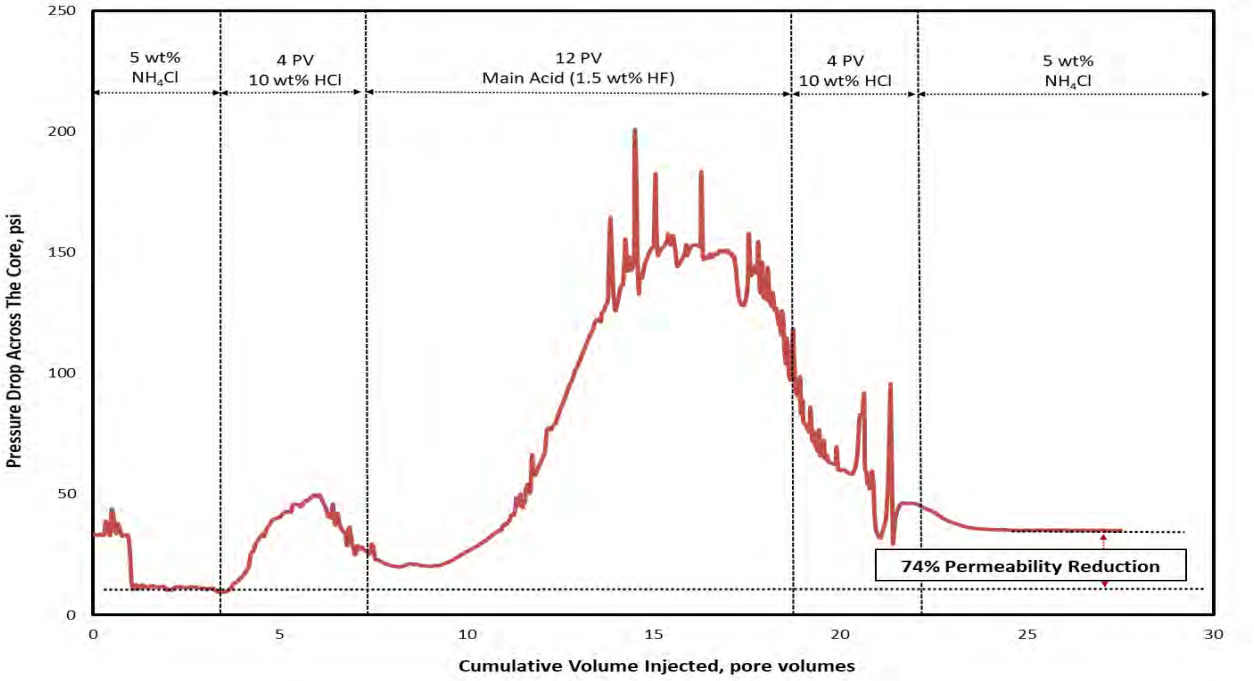

Figure 3: Pressure drop across the plug sample as a function of cumulative pore volume injected. The plug sample was treated with 10 wt% HCl + regular 1.5 wt% HF mud acid + 10 wt% HCl. The test was performed at 475°F and a flow rate of 2 ml/min.

In the second coreflow test **(Figure 4)**, the new non-corrosive deep-penetrating acid was evaluated to stimulate Berea sandstone cores and dissolve different minerals content (calcite, silica, and clays) in those cores at the very high temperature conditions of 475°F. The new acid is a neutral, non-reactive fluid at the surface temperature and when it is injected into the core, the high temperature triggers the in-situ generation of the acid. After the initial brine permeability measurements, a preflush of the new acid of 6 pore volumes was first injected to dissolve calcite content of Berea core. 10 pore volumes of the new acid for the main stage was then injected followed by 6 pore volumes of postflush of the new acid. The new acid composition was designed to generate 10 wt% HCl acid for preflush and postflush stages, and 1.5 wt% HF mud acid for the main stage. Final brine permeability measurements showed 166.7% regain permeability which indicates a remarkable permeability improvement at 475°F and the ability of the new in-situ generated acid to dissolve calcite, clays, and silica. Flow of the new fluid system in a neutral state in the formation before the temperature triggers the in-situ generation of the acid allowed for deeper penetration, uniform dissolution across the penetration depth, and significantly less precipitations from acid/rock reactions. In traditional mud acid, rapid reactions with the various rock mineralogical components, because of the high temperature, leads to significant secondary and tertiary precipitations.

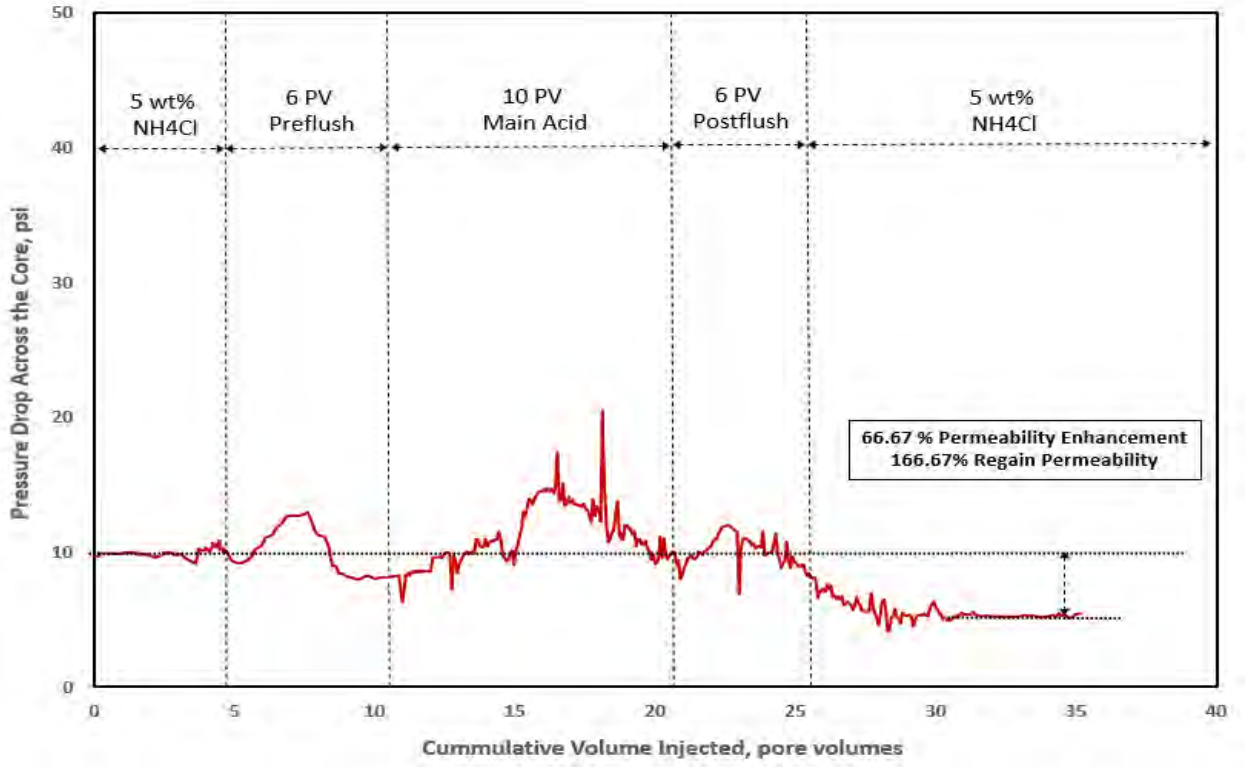

Figure 4: Pressure drop across the plug sample as a function of cumulative pore volume injected. The plug sample was treated with in-situ generated acid. The test was performed at 475°F and a flow rate of 2 ml/min.

In geothermal applications, large stage of water may be injected before acid treatment for cooling. A third coreflow test **(Figure 5)** was then conducted to assess the stimulation efficiency of the new acid at lower temperatures since the in-situ generation of the acid is triggered by temperature. The coreflow test was conducted at a temperature of 300°F. The initial brine permeability is 225 md. After the acid treatment, the permeability increased to 346 md with a regain permeability of 152%. The results showed that the acid was able to significantly improve the permeability which indicates the dissolution of carbonates, clays, and silica.

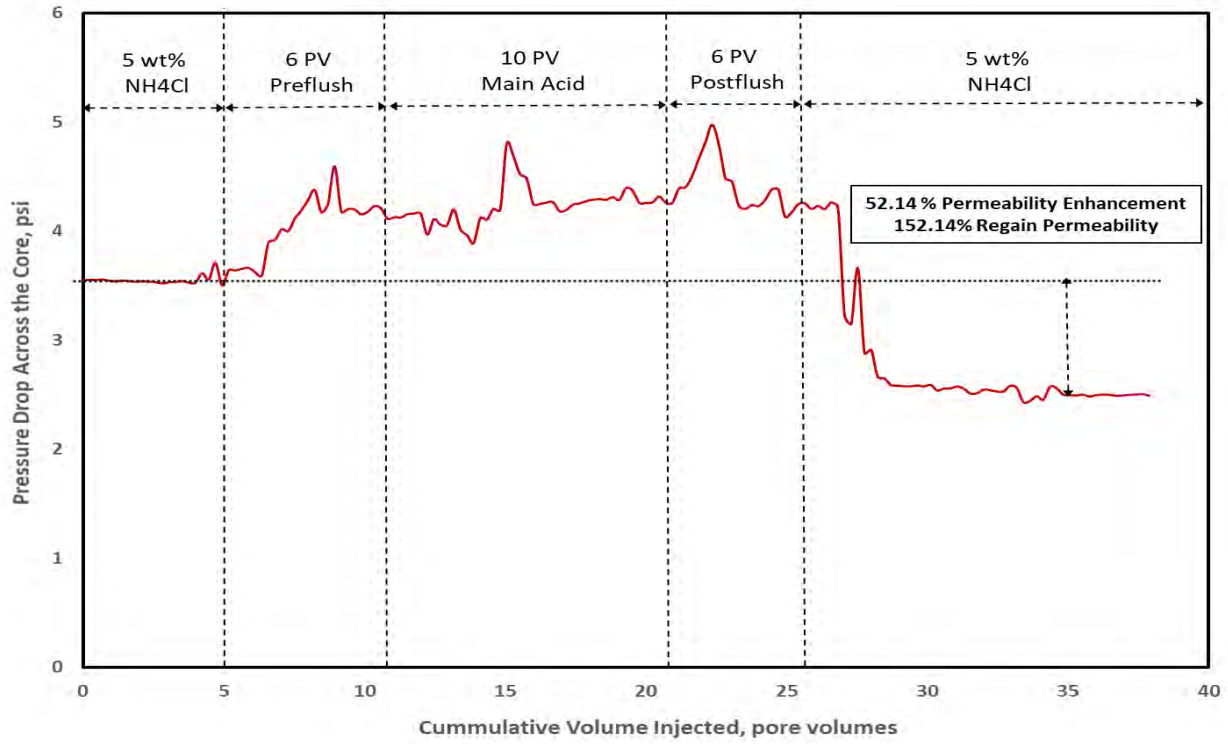

Figure 5: Pressure drop across the plug sample as a function of cumulative pore volume injected. The plug sample was treated with in-situ generated acid. The test was performed at 300°F and a flow rate of 2 ml/min.

4. Conclusions

1. A new non-corrosive, in-situ generated, and deep penetrating acid system has been developed to improve the matrix stimulation for geothermal wells.

2. The solubility testing showed that the new fluid system can self-generate in-situ HCl acid for calcite dissolution and HF acid at any strength for silica dissolution

3. pH measurements showed that the new fluid system is neutral (pH around 7) at the surface conditions and under temperature and with time, it self-generates in-situ HCl or HF acids.

4. The new fluid system was able to significantly improve the permeability and stimulate Berea cores at very high temperature of 475°F as indicated by the coreflow testing.

5. The use of the new fluid system would eliminate the need for acid tanks, and all HSE concerns related to handling acids on site. It also provides safe and non-corrosive fluid for the wellbore tubulars and downhole equipment's

Acknowledgements

The authors would like to thank Robert Comer for their support and guidance throughout the project and gratefully acknowledge all colleagues who directly or indirectly contributed to this paper and would like to thank Baker Hughes management for permission to publish this paper.

REFERENCES

Portier, S., Vuataz, F. D., Nami, P., Sanjuan, B., and Gérard, A. "Chemical stimulation techniques for geothermal wells: experiments on the three-well EGS system at Soultz-sous-Forêts, France." *Geothermics*, 38(4), (2009), 349–359.

McCune C. C., Fogler H. S., Cunningham J. R. "A New Model of the Physical and Chemical Changes in Sandstone During Acidizing." *Soc. Pet. Eng. J.*, 15, (1975), 361–370.

Hill A. D., Lindsay D. M., Silberberg I. H., Schechter R. S. "Theoretical and Experimental Studies of Sandstone Acidizing. " *Soc. Pet. Eng. J.*, 21, (1981), 30–42.

Li Y.-H., Fambrough J. D., Montgomery C. T. "Mathematical Modeling of Secondary Precipitation from Sandstone Acidizing." *Soc. Pet. Eng. J.*, 3, (1998), 393–401.

Super-Hot Geothermal

An Integrated Asset Management Model for Superhot Rock Enhanced Geothermal Systems

Greg Asher and Sriram Vasantharajan

Mazama Energy, Inc., Seattle, WA

Keywords

Superhot Rock (SHR), Enhanced Geothermal Systems (EGS), Engineered Rock Volume (ERV), Supercritical Water, Thermal Lattice, Newberry Volcano, Injection, Production, Power Plant

ABSTRACT

The vision is to build a new clean energy industry to catalyze energy transition globally by creating Enhanced Geothermal Systems (EGS) to harvest heat from Super-Hot Rock (SHR) resources (rocks above 375 °C). The goal is to generate terawatt-scale, carbon-free power from such unconventional resources that will be globally accessible, secure, and cost less than $45 per MWh. Two critical technology areas of focus to achieve sustained power generation from SHR-EGS developments are:

- High integrity well construction: design of reliable, long-life injection and production wells for hostile SHR environments.
- Creation of a thermal lattice: a novel stimulation process to create high-rate pathways that maximize contacted rock volume in SHR. Flow from injection well to production well will be primarily through this Engineered Rock Volume (ERV).

Our internal discussions on how to guide our development of the wells and the thermal lattice led to adopting the use of models. Commercial geothermal models were judged to be not fully applicable for the conditions of the planned implementation. Through an evolutionary process we internally developed an Integrated Asset Management (IAM) model for the full system cycle of injection wells, heat harvesting from the ERV, production wells, and electrical generation. This model, coupled with economic evaluation, has advanced the project well design, stimulation treatment, and operational strategy. It has given greater understanding to unconventional heat harvesting, and it is an enabler towards the goal of cost effective power generation.

The model is based on fundamental physics of heat and mass transfer that includes conduction, convection, and advection for heat harvesting from SHR geothermal wells. It is a transient pressure and enthalpy balance solved as a finite element model with dynamic cells. Water transports through the cells a) down injection wells, b) through the thermal lattice, c) up production

wells, d) through steam turbines for electrical generation, and e) finally, recycled back to the injection wells. The integrated framework solves the entire system to best meet a specified, electrical power target.

A SHR-EGS model must address the operational challenge above 375 °C when water becomes supercritical and its thermophysical properties change dramatically. These supercritical changes affect the production well pressure-temperature characteristics differently compared to conventional geothermal wells. These changes also affect the flow in the wells and in the thermal lattice and guide the needs of the wells and the stimulation treatments to create the reservoir. Finally, an important benefit is that supercritical water has a much higher enthalpy capacity than at conventional temperatures. Therefore, SHR-EGS considerably reduces water requirements while yielding well power capacities substantially beyond conventional EGS.

The goal is reliably assessing and resolving the challenges of SHR-EGS, and it is about addressing the issues need that to be addressed, and that haven't been addressed, in unconventional heat harvesting. A model must be living and learning that will evolve based on data and findings from the field.

1. Introduction

Super-Hot Rock (SHR) is a unique challenge, well beyond conventional geothermal. Our mission is to make the technological and engineering advances to make SHR-EGS reliable and economic, and, as a guide to make these advances, developed an Integrated Asset Management (IAM) model. The model combines an injection well, engineering pathways in the rock, production wells, and a power plant. The goal for this model is to guide business decisions that define a successful economic path forward.

Key requirements for representing the SHR-EGS characteristics are:

1. SHR needs rigorous supercritical water handling because rules-of-thumb from conventional geothermal can lead to erroneous results. Thermophysical properties of water are calculated using the National Institute of Standards and Technology (NIST) Steam (US National Institute of Standards and Technology, 2022) which is built on work of the Internation Association for Properties of Water and Steam (IAPWS).
2. SHR heat harvesting requires an Engineered Rock Volume (ERV) that is economic. Assumptions of negligible decline over decades of harvest are incorrect with an economic ERV. Heat recovery, from this volume via engineered high-rate pathways, is unconventional and will decline significantly faster than conventional geothermal.
3. The injection and production wells influence overall efficiency. The injection well profile will be conventional whereas the production well profile will have water flow as liquid, steam, and/or supercritical that has declining heat recovery and water quality.
4. Power generation should have constant electrical power delivery rather than constant heat delivery. Produced water quality will decline over time, and this will cause a decline in turbine efficiency. This will require managing the water injection rate to have constant power generation.

We reviewed the available literature on geothermal models, and, while we found representations that matched our objectives in part, no model matched our goals in whole.

1.1 Significance of Supercritical Water

SHR heat harvesting occurs at temperatures above the supercritical point of water. Assumptions valid for conventional geothermal can be incorrect for superhot rock. For example, in conventional geothermal, researchers assume that water temperature at the producer wellhead is the rock temperature. It is wrong to extend this assumption and thereby claim that 400 °C rock will produce 400 °C water at the wellhead. Figure 1 shows the pressure temperature response of an ideal production well (fully insulated, adiabatic, and no frictional pressure losses) from bottomhole conditions at Newberry for reservoirs at 200 °C and 400 °C (calculated using NIST STEAM). Note that at 200 °C the temperature at the surface can be the temperature of the rock, but at 400 °C the temperature at surface is 338 °C. For SHR, the temperature at the surface will be less than the rock temperature, because, as the water rises in the production well, the pressure falls causing the temperature to fall per the thermophysical properties of water.

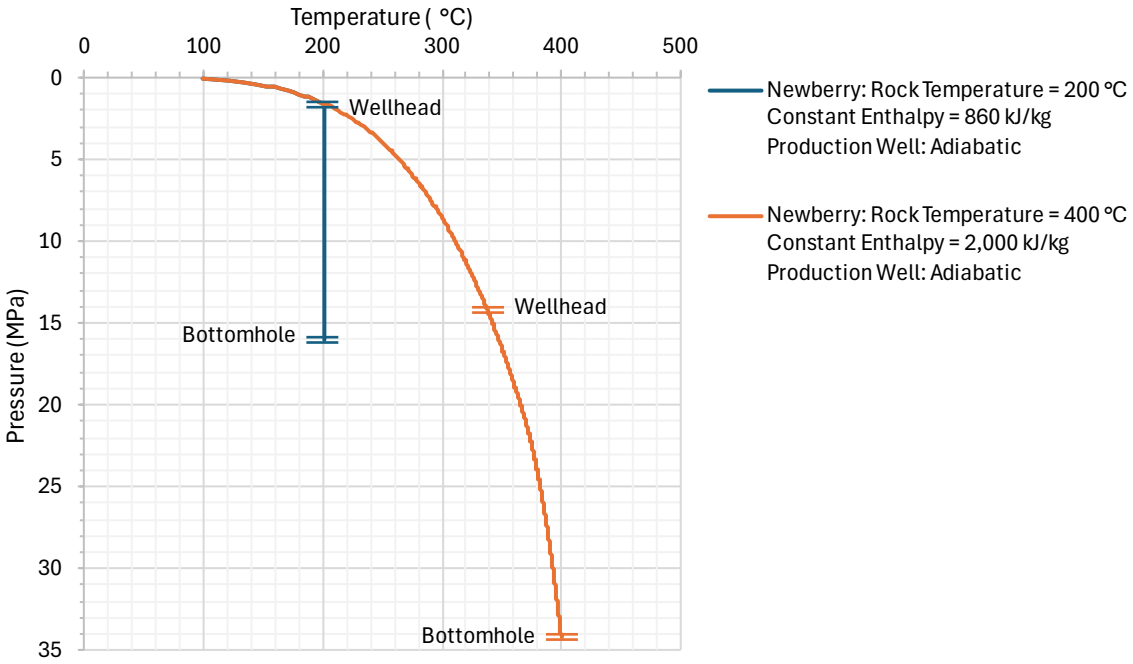

Figure 1: Isenthalpic Expansion of Water by NIST STEAM at Newberry Production Well Conditions

The behavior of water properties at SHR temperatures and pressures is critical. Figure 2 shows the calculated water relative enthalpy, thermal conductivity, product of density and heat capacity, and kinematic viscosity at bottomhole temperatures and pressures for Newberry. This figure shows:

- Water enthalpy at 400 °C is about twice that at 200 °C. Superhot water can carry more heat. But there is no discontinuity in the enthalpy that can occur at constant pressure, because, as the rock temperatures increase with depth, so does the harvest pressure increase with depth.
- Water thermal conductivity at 400 °C is about half that at 200 °C. This is not an issue for harvesting because it is still more than two orders of magnitude greater than the thermal conductivity of rock.

- At conventional temperatures, the product of density and specific heat capacity, ρCp, is constant but not at SHR temperatures. SHR requires variable water thermophysical property modeling.
- The kinematic viscosity, μ/ρ, declines up to supercritical temperatures and then increases. Reynolds number is inversely proportional to kinematic viscosity, and thus, important to maintaining laminar flow in the fractures. Turbulent flow in the fractures yields excessive frictional pressure losses that cause excessive injection pressure requirements causing a parasitic loss of the power generated.

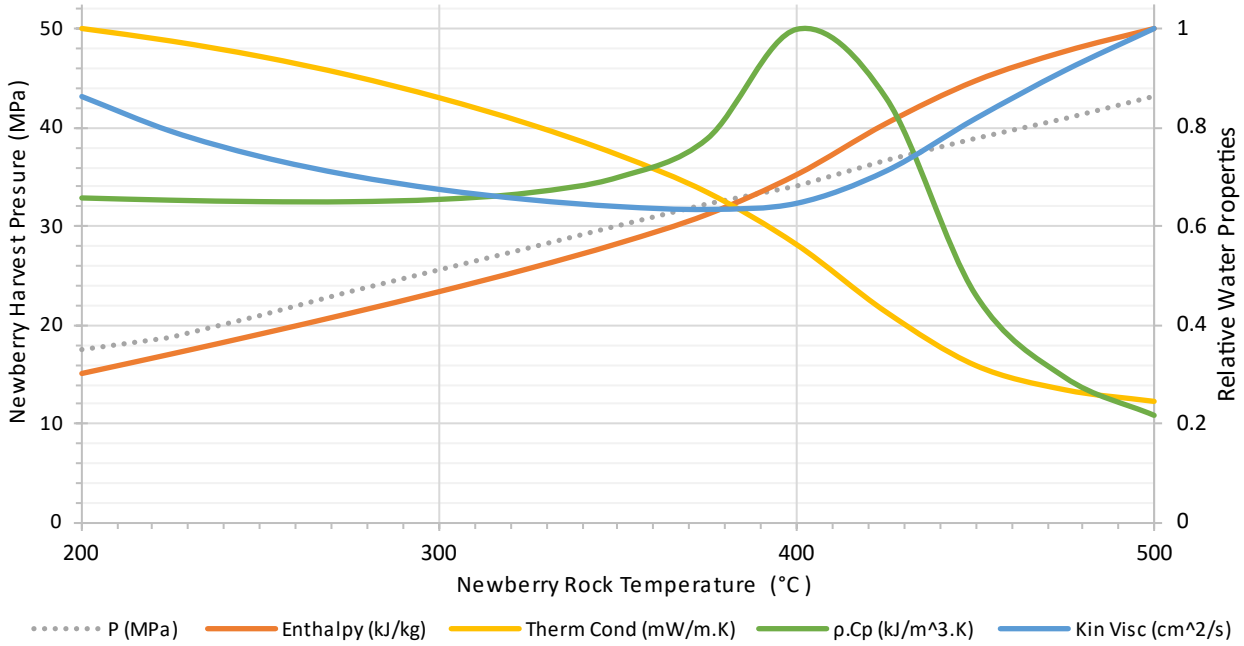

Figure 2: Water Property Behavior at Harvest Conditions for Newberry

1.2 Significance of Engineered Rock Volume (ERV)

Our SHR-EGS pilot targets igneous rock created by the Newberry Volcano in Oregon. In general, there is no heat harvest in SHR without an ERV, and the challenge is how to create an economic volume. Recently, the EGS industry has made significant advances. Fervo's pilot (Norbeck, 2023) produced approximately 50 kg/s at 160 °C, and Forge's pilot (Jacobs, 23 May 2024) produced approximately 40 kg/s at 140 °C. EGS is in progress at lower temperatures, while the challenge of superhot rock remains.

Our pilot plan is ~400 °C. Tensile and shear fracturing will form a thermal lattice of to-be-determined architecture. The heat will be harvested via this reservoir that connects from the injector to the producer. Without a connection, natural fractures activated by the shear fracturing are dead ends that will not contribute to the harvest.

Our ERV, currently, represents the thermal lattice as a tensile planer fracture with multiple, natural, planer fractures. The fractures can be of varying height, length, width, and conductivity, and these fractures are separated by homogeneous and isotropic, impermeable rock. This model is akin to

the concept presented by (Gringarten, 1975) which was an analytical model for an infinite series of identical fractures. The Gringarten representation was a pressure temperature model, with constant volume flow, pressure high enough to hold liquid state, constant product of density and heat capacity, and infinite conductivity fractures. Significant was the statement:

> *"Develop an adequate fracture surface to be used for heat transfer purposes. Because of the low thermal conductivity of rock, a very large heat transfer area must be provided; otherwise, meaningful amounts of energy cannot be extracted at practical rates."* (Gringarten, 1975)

The question becomes how large is large enough? Figure 3 shows "Fig. 6" from Gringarten where 10 fractures have a quite stable heat recovery for rock at 300 °C. Note that this was for 1-km2 fractures for a total fracture face area of 10 * 1000 * 1000 = 10,000,000 m2. Assuming a fracture this size could be pumped and propped, a 3 mm fracture width at a proppant density of 2 g/cc requires 60,000 metric tonnes of proppant. A SHR capable proppant could be ~$600 per metric tonne costing ~$36,000,000. The total upfront SHR fracture treatment costs would be significantly greater, and it would be economically prohibitive to create an ERV that declines a minimal percent per year for decades. An economic ERV is smaller to avoid excessive up-front capital, and this will lead to more rapidly declining thermal recovery.

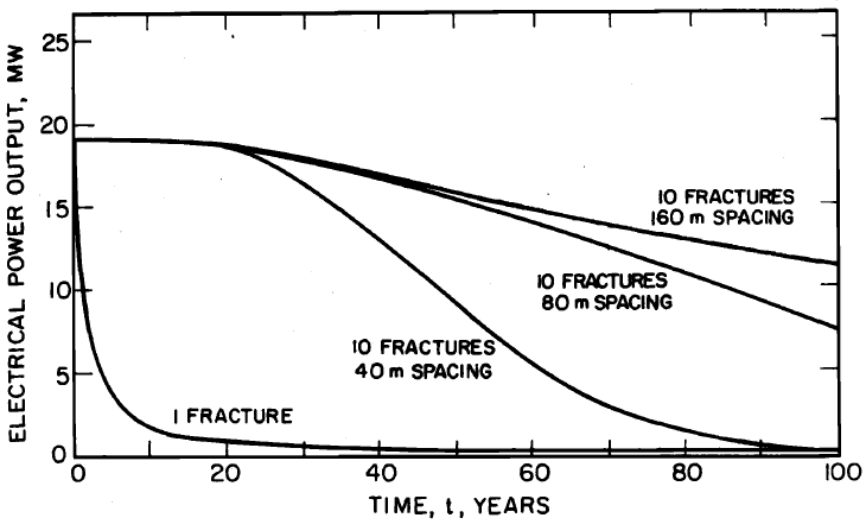

Fig. 6. Electrical power output from 1-km² fractures.

Figure 3: Gringarten Fig. 6. Electrical Power Output from Rock at 300 °C with 1-km2 Fractures

1.3 Significance of Well Models

A SHR asset will have water injection wells and production wells, and the flow regime within each type of well can be different. A single injection well can have a production well for each wing of the fracture. Injection well profiles vary with injection rates but will not experience supercritical conditions during injection. Production well profiles will initially have supercritical flow that diminishes in time as the ERV cools. Details for these well types are:

- Injection well: The control factors for heat recovery are the wellhead injection mass rate, pressure, and temperature. The temperature entering the fractures will be higher than the temperature at the wellhead, and the higher bottomhole temperature will reduce the overall heat recovery compared to the lower wellhead temperature. The injection pressure is set to make sure the water flows to the production wellhead at the minimum pressure required by the steam turbines.
- Production well: Superhot rock flows supercritical water into the production well and the water quality will degrade over time as heat recovery degrades. Depending on well construction and rates, heat harvested from the ERV can be lost in flowing to the surface. Modeling the quality of the water at the production wellhead is critical as that quality controls the efficiency of the power plant. It's more than taking the product of MW harvested from the ERV and multiplying by an efficiency factor to get MWe.

1.4 Significance of Power Plant

Fixed power delivery rates, rather than a fixed heat recovery rate, are essential to the IAM model since a contract is for electricity rather than heat. This presents a challenge given the declining water heat quality over time, caused by economically-size ERV's, that will cause declining efficiency of the stream turbines. Modeling the asset harvest thus requires integrating a power model into the framework.

2 Integrated Asset Management (IAM) Model

The goal of an IAM model is to make business decisions to define a successful economic path forward akin to the use of integrated asset management, or integrated production management, in the petroleum industry. It is a step before rigorous simulations can become possible with data from the pilot projects. It is an evolving model, and it will progress as work toward and beyond the pilot progresses. Figure 4 shows the flow path of the water as down the injection well, through the ERV, up the production well(s), and to the power plant where the heat is converted to electricity.

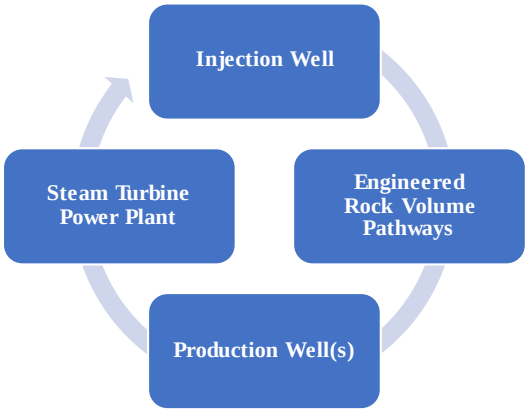

Figure 4: Integrated Asset Management Model Components

The asset model targets SHR bearing supercritical water via a pressure-enthalpy balance model. Pressure balances manage the fluid flow, and enthalpy balances manage the heat flow. The algorithm targets the production life of the asset to enable production decisions through a transient-on-production-scale algorithm built with a pseudo-steady-state finite-element scheme (a general concept used by IPM software in the petroleum industry). The algorithm includes:

- Heat harvesting through ERV pathways built with pressure-enthalpy modeling that includes fluid transfer with conduction, convection, and advection heat transfer. The model begins with an effective set of pathways that will evolve from the learnings of the pilot.
- The injection and production wells use pressure-enthalpy modeling coupled with correlations built on geothermal industry recommendations for flow correlations originally created by the petroleum industry.
- Electrical generation by a SHR power plant uses a multi-stage steam turbine model built on the methods and logic presented by the US Department of Energy (DOE) Energy Efficiency and Renewable Energy (EERE) Steam System Modeling Tool (SSMT) (US Department of Energy EERE, n.d.).

2.1 IAM: Engineered Rock Volume (ERV) Modeling

The integrated model represents the ERV as an effective array of parallel fractures connecting the injector to the producer. This is akin to the Gringarten model with added complexity of flowing supercritical water within fractures that can be of varying height, length, width, and conductivity. Also, the fractures are separated by varying distances of impermeable rock and have a finite fracture face area. The model is for all EGS with pilot SHR application to be at the original Newberry Demonstration Project site and in collaboration with the US DOE (US Department of Energy, 2024).

Davenport Newberry (Waibel, 31 May 2012), in conjunction with DOE Innovative Exploration (IET) Grant 109 program, drilled two deep exploration wells on the western flank of the Newberry Volcano where they found isolated fractures yet no indication of hydrothermal activity. AltaRock Energy assumed operating control of the lease and used hydroshearing to activate the existing fractures (Cladouhos, September 2016). Models of these fractures showed no likely flow from an injector to a producer. Mazama Energy, born from AltaRock Energy and Blade Energy, assumed operating control of the lease and plans to create a thermal lattice by tensile and shear fracturing to connect an injector to a producer.

Table 1 shows the path to formation for the ERV modeling. Column A shows the formation with natural fractures from injector to producer yet without connections amongst the natural fractures to flow from injector to producer. Column B shows the thermal where it is to-be-determined how the natural fractures can be energized to connect the injector to the producer. Column C shows the modeling approach in planning for the demonstration. It represents the thermal lattice as a tensile planer fracture with multiple, natural, planer fractures.

Table 1: Formation of ERV Modeling for the Thermal Lattice

A. Formation w/ Natural Fractures	**B. Formation w/ Thermal Lattice**	**C. Formation Modeled**
Production Well 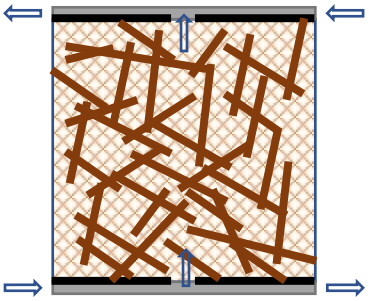 Injection Well	Production Well 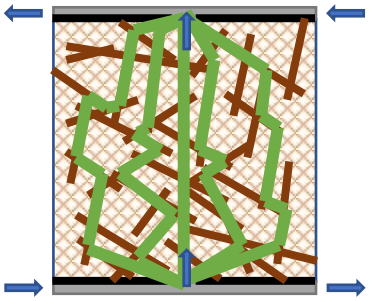 Injection Well	Production Well 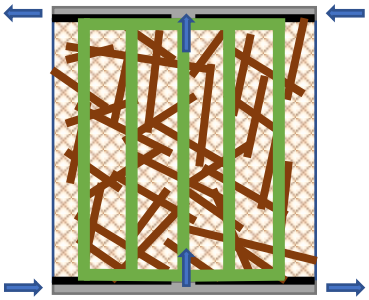 Injection Well
• **No flow** as fractures not open and connected from well to well	• Single tensile fracture from well to well	• Linear pathways to harvest heat from same volume as plausible pathways
	• Multiple pathways through energized natural fractures connecting well to well	• Linear pathways with added pressure loss of longer plausible pathways
	• Mapping actual pathways implausible so consider what is plausible	• Pressure managed by injection pressure—greater pressure drop in pathways requires greater injection pressure
	• Natural fracture pathways of unknown architecture	• Linear pathways used currently from stimulation analysis

Figure 5 shows a planer view of the fracture and surrounding rock volume at points in time.

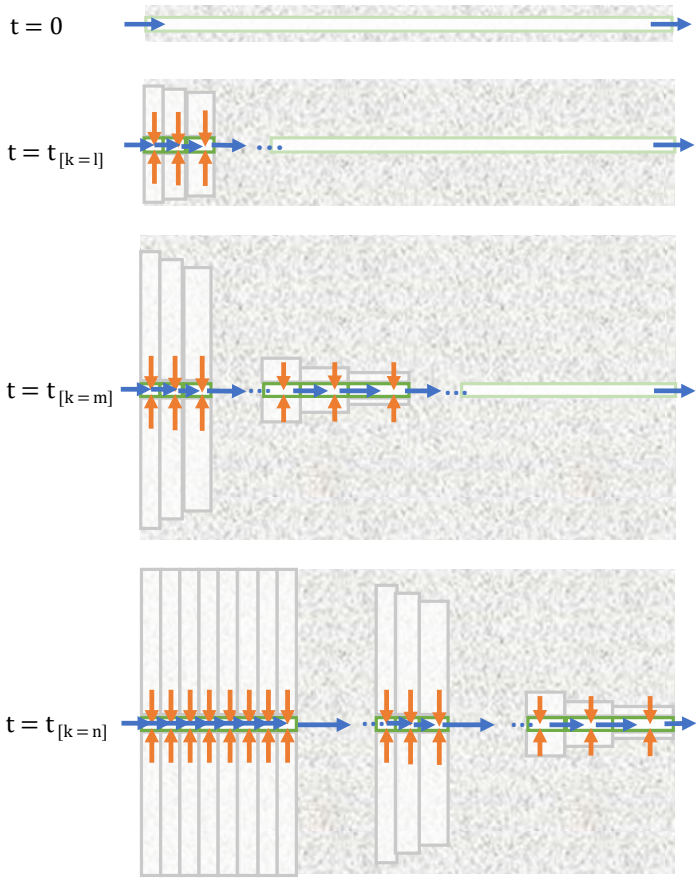

Figure 5: Planer View of Fracture and Rock Volume Elements

1. Initial time, t = 0, where the fracture and the rock are assumed to be in temperature equilibrium with fluid in the fracture remaining from the stimulation treatment.
2. Early time, t = t[k = l], where the water first enters the fracture and quickly comes into equilibrium temperature with the rock. The remaining length of the fracture is near adiabatic, but, at supercritical temperatures as the pressure drops in the fracture from frictional pressure losses due to finite conductivity, the temperature drops that then enables heat flow from the rock. It is important to manage the fracture conductivity and mass rate per fracture to keep the pressure drop minimal and the water not in vapor state.
3. Middle time, t = t[k = m], where the fracture length contributing to heat transfer from the rock continues to lengthen. The elements at the fracture entrance grow until reaching interference with a neighboring fracture. The fluid still exists at maximum enthalpy as there is fresh fracture face to contribute heat to the fluid.
4. Later time, t = t[k = n], the entire fracture length will contribute, and the heat harvested will decline as there is no rock at initial state. Eventually, along the entire fracture length, the thermal penetration distance reaches maximum distance due to neighboring fractures. Decline in the heat harvested is inevitable and becomes a matter of managing the decline.

2.2 IAM: Injection/Production Well Modeling

Well modeling is important to the integrated asset management for the two well types.

- The injection well model takes wellhead injection temperature, pressure, and mass rate and calculates the pressure, enthalpy, and mass rate to each fracture. Through the well model, the wellhead injection conditions translate to the fracture injection conditions. The water gains pressure based on the depth of the ERV, loses pressure due to friction, and gains enthalpy from the surrounding rock before reaching the fractures.
- The production well takes the pressure, enthalpy and mass rate from each fracture to ensure a pressure mass balance from injector to producer. This balance combines injector modeling, fracture flow modeling, and producer modeling. The producer then models the recombined fluid from the last fracture flowing into the well back to the surface. The water loses pressure based on depth of the ERV, loses pressure due to friction, and loses enthalpy to the surrounding rock. This is important to model as the production wellhead water stream is the feed for the power plant.

Flow in the injector well is single phase flow up to the point of entry for each fracture, flow in the fracture is best as single phase liquid or supercritical, flow in the producer changes continuously in time and is single to multi-phase flow.

From the petroleum industry, there are many correlations for water flow in wells. Geothermal researchers have reported the correlations that work for geothermal wells. Although, there are no correlations validated for the flow of supercritical water (outside of the nuclear industry and those are not for well flow). This work built well flow models using correlations validated by geothermal researchers at conventional temperatures using thermophysical properties at supercritical temperatures. The well model employs a finite element well model using a pressure enthalpy balance. The well model works as follows:

- Define the flow regime for Liquid-Bubble-Slug-Transition-Mist-Vapor flow regime map presented by (Ortiz-Ramirez, 1983)
- For single phase flow, the model uses the Fanning liquid and gas correlation as presented by IHS for Harmony (IHS, 2020) and validated using the Petroleum Experts software PROSPER correlation Petroleum Experts 2.
- For two phase flow, the model uses the Ortiz-Ramirez implementation Orkiszewski correlation (Ortiz-Ramirez, 1983), which was based on work presented by (Orkiszewski, Jun 1967) and (Ramey, 1962).

All flow models are pressure enthalpy balances with pseudo-steady-state heat transfer coefficient. Future work will extend the heat transfer to transient conditions.

2.3 IAM: Power Plant Modeling

The plant modeling goal is to study how the changing efficiency of the generator in time affects asset operations to produce fixed electricity rates. At early production life, before the full fracture face contributes to the heat harvest, the harvest is stable, but as the full face contributes the harvest declines in water enthalpy leaving the fracture. And, as the adjacent fractures begin to interfere with each other, the enthalpy declines further. The continual enthalpy decline means, at a constant

mass rate, there is less enthalpy available to generate electricity, and it leads to a declining overall efficiency of the power plant. The power plant in IAM model addresses the changing efficiency effects on asset operations by managing the injector mass rate.

Power plants for geothermal can be steam or binary turbines, and the modeling addresses this by:

- For temperatures above 200 °C, the model use power conversions with a multi-stage steam turbine model built on the thermodynamic methods and logic presented by the US Department of Energy (DOE) Energy Efficiency and Renewable Energy (EERE) Steam System Modeling Tool (SSMT) (US Department of Energy EERE, n.d.).
- For temperatures below 200 °C, the model uses other power plants suitable for lower temperatures based on binary turbine correlations presented by (Moon, 19-21 November 2012). These plants are used for comparison purposes to superhot rock.

3 Integrated Asset Management (IAM) Forecasts

3.1 IAM: Pilot Forecasting

The IAM model guides us in reliably assessing and solving the challenges of SHR-EGS. We began considering vertical and deviated wells, but found the economic answer, regardless of temperature, is that EGS needs long horizontal wells with large numbers of tensile fractures, and that the well spacings be as large as possible to maximize the ERV. The IAM model showed SHR can capture more enthalpy per kg/s of water and therefore make better use of limited water. SHR also yields temperatures where steam turbines are more efficient yielding an even greater MWe per MW of heat harvested. Economic studies showed to have no heat decline for decade upon decade failed to recover upfront capital costs. It showed the harvesting is economically best if accelerated for a given ERV, and this leads to a declining harvest.

A pilot is in development to implement new technologies to drill, complete, and produce SHR successfully at 400 °C. The model forecasts possibilities for the pilot to set reasonable expectations (the actual pilot is currently under review the following is for example purposes only).

- Rock at 400 °C
- Rock thermal conductivity 2.2 W/m.K, density 2,700 kg/m3, and heat capacity 1,000 J/kg.K
- Single injector and single producer with well lengths of 1,000 m and well spacing of 100 m
- Production well not insulated
- Fracture count of 60, height 100 m, width 3 mm, and conductivity of 10 mD.m
- Maximum mass rate = 80 kg/s
- Power harvested = 8, 10, 12, 14, 16, 18, 20 MWe
- Four-stage steam turbine

Figure 6 shows forecasts for the investigative pilot case. The constant power generated is maintained by mass-rate control, shown in Figure 7, and drops in power generated occur when a turbine stage input conditions are no longer met, and a stage is shut down (steam turbine stage design not optimized for this forecast). Figure 8 shows the injection wellhead pressure necessary

to inject the required mass rate. Maintaining the higher injection rates for the high power targets quickly requires excessive injection pressures that are a parasitic pressure loss and could damage the thermal lattice. The wellhead injection pressure must overcome:

- The ERV frictional pressure loss. The tensile/shear fracture treatment design is for a large enough fracture conductivity to control this loss.
- The pressure to lift the fluid in the production well to the surface. As the ERV cools, the production well contains a higher and higher percentage of water thus needing more and more pressure to reach the surface. The production well design must account for time changes of the produced fluid.

For 400 °C, Figure 6, Figure 7, and Figure 8 show that a high power rate is possible, but that rate cannot be sustained given the investigative pilot ERV size. Power targets are set by temperature and the ERV that can be economically put in place.

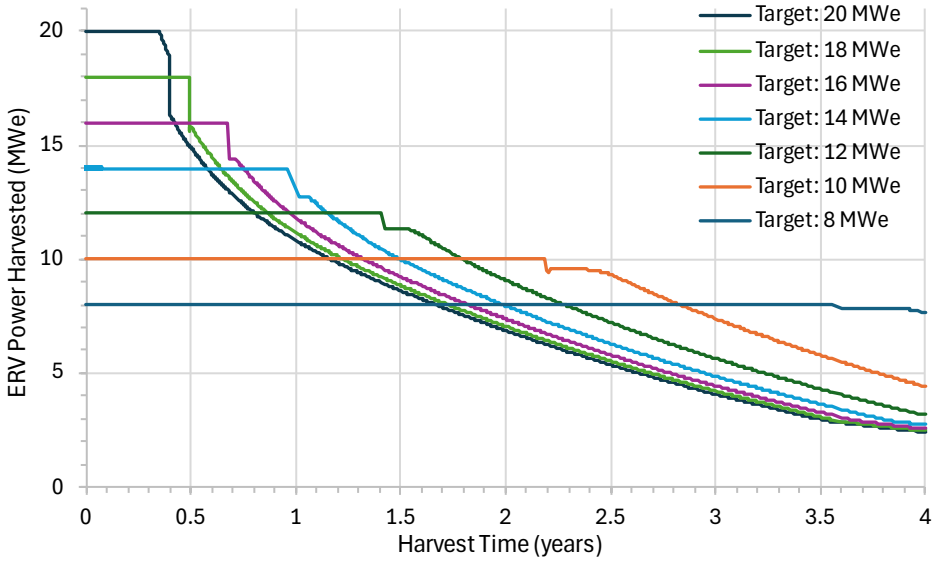

Figure 6: Investigative Pilot Case: Forecast for Power Harvested

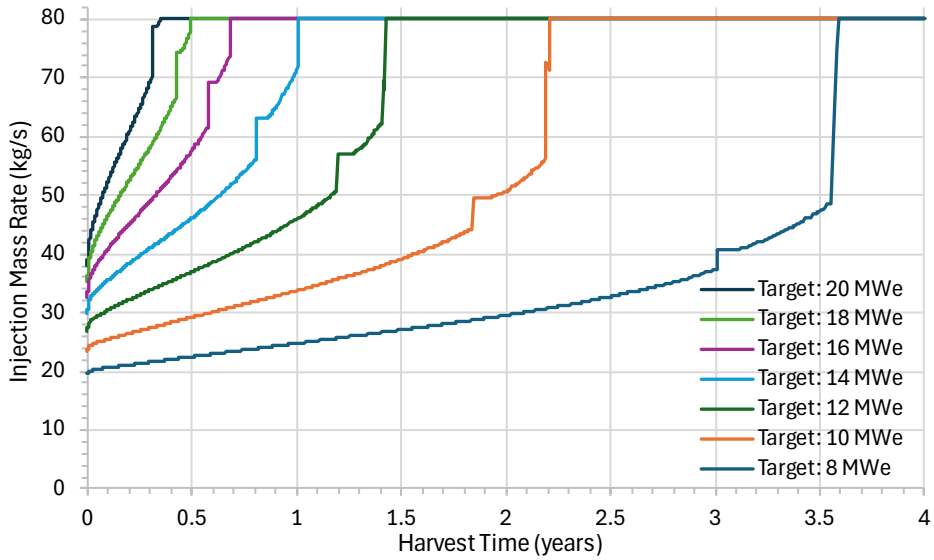

Figure 7: Investigative Pilot Case: Forecast for Injection Mass Rate

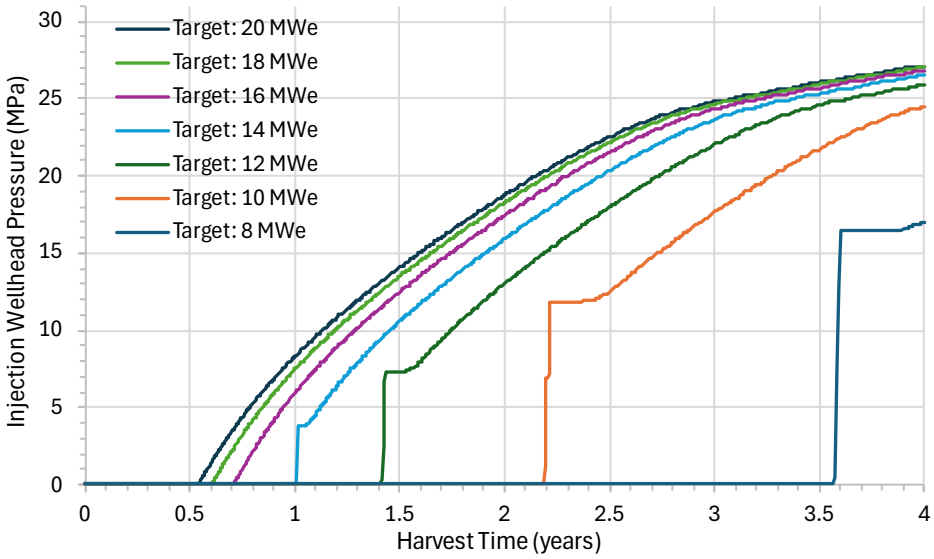

Figure 8: Investigative Pilot Case: Forecast for Injection Wellhead Pressure

Figure 9 shows the fracture pressure for the last fracture on the injection well at various times for the 10 MWe target case. This figure shows two succinct groupings of pressures.

1. Early time. The wellhead injection pump is off and the pressure at the fracture entrance is essentially constant. The fracture outlet pressure as the fracture face cools and the friction pressure increases.

2. Late time. The wellhead injection pressure began to achieve the minimum production wellhead pressure necessary for steam turbine operations. As the ERV continues to cool, the overall density of the fluid in the production well increases and hence the pressure required to lift to surface increases. The continued increase of the injection pressure may cause an issue as the fracture gradient bottomhole pressure is 53 to 61 MPa. For a bottomhole pressure limit of 50 MPa, the pressure is reached at 1008 days, and safe operations would dictate that the injection rate be reduced from 80 kg/s.

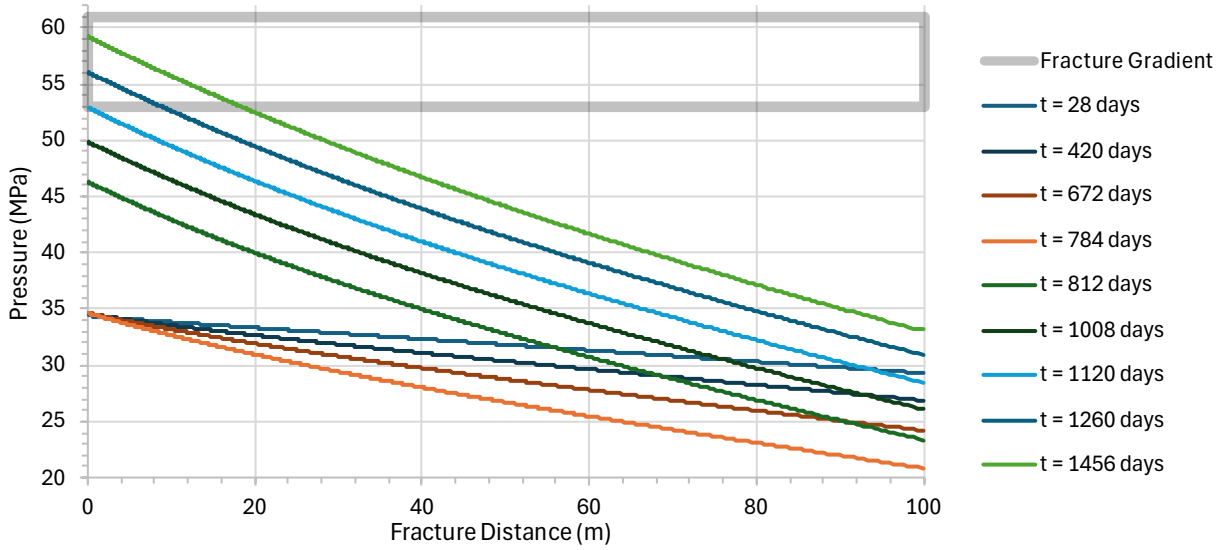

Figure 9: Investigative Pilot Case: Target: 10 MWe Fracture Pressure

Figure 10 shows the bulk enthalpy gradient for the last fracture on the injection well at various times for the 10 MWe target case. At early time most of the enthalpy harvested by the water comes from the fracture as the water enters in fracture. As time progresses the entrance to the fracture contributes a lesser and lesser percentage of the heat harvested. The end of the fracture always has hotter water than the entrance of the fracture, and so the end of the fracture will never be drawn down as far in temperature and hence will always have a lower efficiency. We've considered reversing flow, but unfortunately the injection and production well design differ, and this causes issues in reversing flow. The injection well is always water in liquid state and the producer begins with water in supercritical state. The model, as an IAM model, guides integrated decisions with the wells and fractures combined.

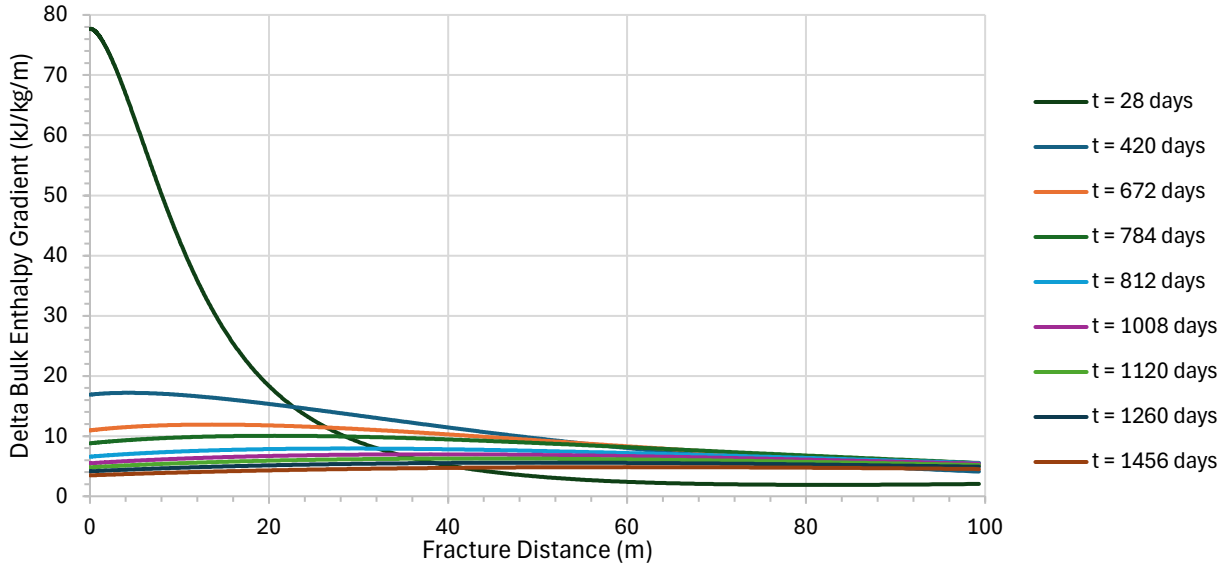

Figure 10: Investigative Pilot Case: Target: 10 MWe Bulk Enthalpy Gradient

There are many conditions to investigate. For example, what are the fracture conductivities that are possible and the range that should be targeted. This work ran multiple fracture conductivity sensitivities and found that a fracture conductivity lower than 10 mD.m significantly reduced the fracture mass rate capacity. These lower mass rates led to a greater residence time in the production well which led to an unacceptable heat loss in the production well per unit of water mass. This set a design goal for the stimulation team to place fractures with a minimum conductivity. Note the fracture conductivity is a function of the ERV, and 10 mD.m for this case may not be the answer for other conditions. Studies of the design and development of an ERV will determine the guidance, and that is the purpose of this modeling work.

3.2 IAM: Post Pilot Constant Mass Rate Forecasting

The following illustrates a case with an identical ERV at depths in the Newberry field corresponding to different temperatures:

- Rock at 200, 350, 400, 425, 450, and 500 °C
- Rock thermal conductivity 2.2 W/m.K, density 2,700 kg/m3, and heat capacity 1,000 J/kg.K
- Single injector and single producer with well lengths of 3,000 m and well spacing of 200 m
- Production well insulated
- Fracture count of 150 equally spaced, height 100 m, width 3 mm, and conductivity of 100 mD.m (approaches infinite conductivity)
- Mass rate = 80 kg/s
- Binary turbine at 200 °C, and a four-stage steam turbine at higher temperatures

The trajectory of the injector and producer at each temperature differs by the depth required for the temperature.

A comparison of this case to Gringarten's Fig. 6 case shown in Figure 3 is:

- Gringarten rock at 300 °C
- Fracture spacing = 20 m—Gringarten 40 m and greater
- Fracture face area = 6 km2—Gringarten = 20 km2
- Mass rate = 80 kg/s—Gringarten = 115 kg/s
- Mass rate / Fracture area = 13.33 kg/s/km2—Gringarten = 5.75 kg/s/km2

Figure 11 shows the model predictions for this case with the power ratio r = {initial power harvested at the given temperature} / {initial power harvested at 200 °C}. The first case where water is supercritical is at rock = 400 °C with r = 4.4, which is a minimal increase from 350 °C with r = 3.5. The first case where water is supercritical at the production wellhead is for rock = 425 °C with r = 6.5, where an additional 25 °C yield a 50% increase in the initial power ratio. Going supercritical is beneficial but it is not an order of magnitude improvement simply being supercritical. To get a tenfold increase in initial power from being supercritical requires rock temperatures above 600 °C, and that is higher than likely with today's technology.

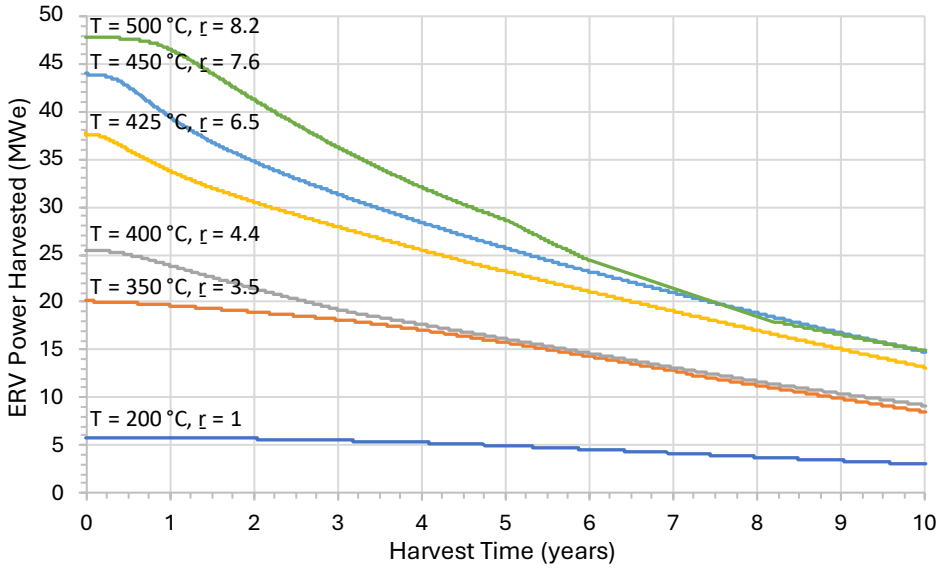

Figure 11: Constant Mass Rate Forecasting: Forecast for Power Harvested

Figure 11 shows that the 200 °C case declines minimally in the first four years while the higher the temperature the greater the decline. This is because all cases are the same mass rate, and the enthalpy of the water increases with temperature to carry more heat per unit mass of water. A simple estimate of the initial power generated is the product of the water mass rate, water enthalpy at the rock temperature, and an efficiency factor. But water is the carrying fluid, not the heat source, and it's the rock's limiting thermal conductivity that determines how the rate of heat

harvesting continues. The higher enthalpy of water at higher temperatures leads to a higher heat harvest rate that the rock cannot maintain, and thus this leads to declining power. To stabilize heat and power recovery, the mass rate should be reduced at higher temperatures to not outpace the rock. This reduces the reduces the power multiplier. This means that the simple estimate to power recovery is not a meaningful estimate for the life of the project.

3.3 IAM: Post Pilot Constant Power Rate Forecasting

The following demonstrates the benefits of constant power rates forecast with managed rates at rock temperature = 425 °C. The model was:

- Rock at 425 °C
- Rock thermal conductivity 2.2 W/m.K, density 2,700 kg/m3, and heat capacity 1,000 J/kg.K
- Single injector and two producers with well lengths of 3,000 m and well spacing of 200 m
- Fracture count of 90 equally spaced, height 100 m, width 3 mm, and conductivity of 100 mD.m (approaches infinite conductivity)
- Production wells not insulated
- Maximum mass rate per producer = 80 kg/s
- Mass rate per producer determined by power target
- Four-stage steam turbine
- Power targets = 25, 33 1/3, and 50 MWe

Figure 12 shows the stable power generation while Figure 13 shows the managed mass rate for a 20 year forecast. Note that the mass rate is held back in time until later achieving the maximum target rate of 80 kg/s. The mass rate is held back to limit the heat recovery (akin to how an oil or gas well is choked control the wellhead pressure and hold production rate at a constant fluid rate). The mass rate increased as the heat recovery potential decreased. Mass rate control is essential to manage a constant power output

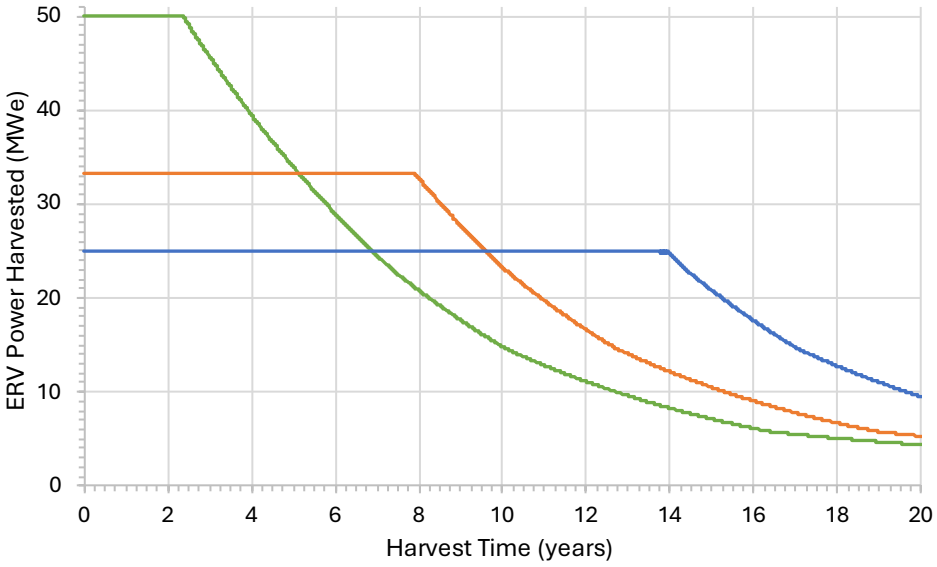

Figure 12: Constant Power Rate Forecasting: Forecast for Power Harvested

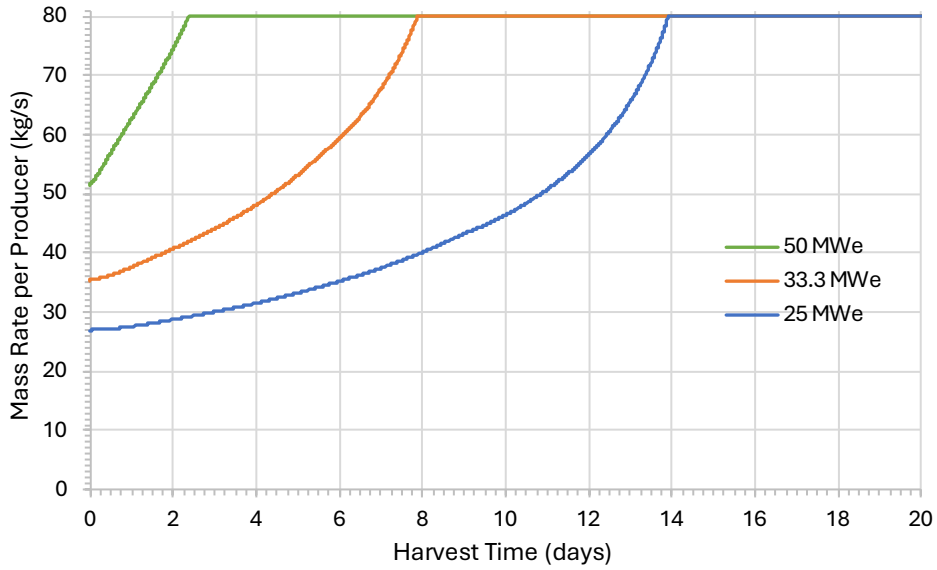

Figure 13: Constant Power Rate Forecasting: Forecast for Mass Per Producer

4 Conclusions

Conventional geothermal models are not applicable for the conditions of SHR-EGS. An Integrated Asset Model which represents the full system cycle of injection wells, heat harvesting from an Engineered Rock Volume (ERV), production wells, and electrical generation is essential to accurately capture the unique characteristics of SHR EGS. Coupled with economics, a model can advance project well design, stimulation treatment, and operational strategy to deliver cost effective power generation outcomes.

Important conclusions for the current work are:

- Heat harvesting potential in time will decline because it is not economically feasible to create an ERV the size required for minimal decline over decades. Studying how to create the optimum ERV is essential.
- Constant power generation requires a managed mass rate and not a constant mass rate to manage the declining heat potential. Studying how to manage the mass rate provides guidance in designing surface facilities.
- Supercritical water temperatures in the ERV does not mean supercritical water temperatures at the production wellhead. In fact, the water temperature will be lower than superhot rock temperature. Supercritical water properties behavior differs from conventional temperatures where that assumption is valid.
- It is a fallacy that supercritical yields tenfold improvement in electricity generated. At initial condition, the fold of improvement comes from the higher enthalpy of super critical water and higher efficiency of the turbines. But water is the enthalpy carrier and not the enthalpy provider. Heat flow by conduction in the low thermal conductivity rock is the bottleneck to heat harvesting, and a higher enthalpy working carrier fluid cannot remove the rock thermal conductivity bottleneck.

SHR-EGS is *unconventional* production when compared to conventional geothermal (hydrothermal) systems. It is akin to unconventional shale gas development, where established assumptions can lead to mismanagement of the asset. This IAM model guides the understanding and management of SHR-EGS.

REFERENCES

Cladouhos, P. S. (September 2016). Results from Newberry Volcano EGS Demonstration, 2010–2014. *Geothermics*, Volume 63, Pages 44-61.

Gringarten, W. O. (1975, March 10). Theory of Heat Extraction From Fractured Hot Dry Rock. *JOURNAL OF GEOPHYSICAL RESEARCH, VOL. 80, NO. 8*, 1120-1124.

IAPWS, R7-97(2012). (2012). *Revised Release on the IAPWS Industrial Formulation 1997 for the Thermodynamic Properties of Water and Steam.* Lucerne, Switzerland: International Association for the Properties of Water and Steam.

IHS. (2020, February 24). *Pressure Loss Calculations*. Retrieved from https://www.ihsenergy.ca/support/documentation_ca/Harmony/content/html_files/reference_material/calculations_and_correlations/pressure_loss_calculations.htm

Jacobs, T. (23 May 2024). Utah FORGE Confirms Good Connectivity Between Enhanced Geothermal Test Wells. *Journal of Petroleum Technology*.

Moon, H. a. (19-21 November 2012). Efficiency of Geothermal Power Plants: A Worldwide Review. *New Zealand Geothermal Workshop 2012 Proceedings*, (pp. 1-13). Auckland, New Zealand.

Norbeck, J. H. (2023). *Commercial-Scale Demonstration of a First-of-a-Kind Enhanced Geothermal System.* Houston, Texas, USA: Fervo Energy.

Orkiszewski, J. (Jun 1967). Predicting Two-Phase Pressure Drops in Vertical Pipe. *Journal of Petroleum Technology*, 829-838.

Ortiz-Ramirez, J. (1983). *SGP-TR-66: Two-Phase Flow in Geothermal Wells: Development and Uses of a Computer Code.* Stanford, California: Stanford Geothermal Program, Stanford University.

Ramey, H. J. (1962). Wellbore Heat Transmission. *Journal of Petroleum Technology, 225*, 427-435.

Stanford University. (June 2015). *Relative permeability for multi-phase flow in CO2 storage reservoirs. Part II: resolving fundamental issues and filling data gaps.* Palo Alto, CA: The Global CCS Institute.

US Department of Energy. (2024, February). *Biden- Harris Administration Invests $60 Million to Expand Clean, Renewable Geothermal Energy*. Retrieved from ENERGY.GOV: https://www.energy.gov/articles/biden-harris-administration-invests-60-million-expand-clean-renewable-geothermal-energy

US Department of Energy EERE. (n.d.). *Advanced Manufacturing Office: Steam Calculators*. Retrieved from US DOE EERE: https://www4.eere.energy.gov/manufacturing/tech_deployment/amo_steam_tool/

US National Institute of Standards and Technology. (2022, July 29). *NIST/ASME Steam Properties Database - SRD 10*. Retrieved from DATA.GOV: https://catalog.data.gov/dataset/nist-asme-steam-properties-database-srd-10-b35bb

Waibel, A. F. (31 May 2012). *Geothermal exploration at Newberry Volcano, central Oregon.* DOE IET Grant 109. Seattle, Washington: Davenport Newberry.

Witherspoon, P. A. (October 1979). *Validity of Cubic Law for Fluid Flow in a Deformable Fracture.* Lawrence Berkeley Laboratory, Berkely California: Water Resource Research.

The Superhot Opportunity for New Zealand- Joining the Ends Together

Isabelle Chambefort[a], Andreas Heuser[b], Mitchell Palmer[b], Daria Rybalka[b], Chris Bromley[a], Brian Carey[a]

[a] GNS Science, [b] Castalia Limited

Keywords

Superhot, super-critical, New Zealand, Geothermal: The Next Generation, inventory, economics

ABSTRACT

Superhot geothermal appears an attractive opportunity for New Zealand (NZ), from 2037 through to at least 2050. It provides a potentially zero-emissions, reliable, and cost-competitive energy source for electricity generation or high-enthalpy direct-use industrial applications. Superhot geothermal, and even conventional geothermal, has been under-represented in the deliberations and consideration of renewable energy sources by energy planners that NZ might utilise in the future. Policy discussed in several planning documents has focused on solar and wind deployment and has under-appreciated the full potential of geothermal in plans for official endorsement.

The NZ research program, "Geothermal - the Next Generation", has been investigating the potential of supercritical geothermal, and has completed two important assessments for NZ. These challenge the current under-representation of geothermal potential by building electricity scenario models to include utilisation of superhot geothermal resources.

The first assessment is a preliminary resource inventory assessed over a depth range of 3.5 to 6 km, and at temperatures between about 375 ^{o}C and 500 ^{o}C. These inferred resources are located in the Taupō Volcanic Zone (Waikato and Bay of Plenty Regions) and at Ngawha (Northland). The cumulative resource potential is determined to be 4.6 GWe (38 TWh/yr at 95% operating capacity factor). If the resource volumes within current regulatory protected geothermal systems are excluded, the assessed total becomes 3.5 GWe (29 TWh/yr).

The second assessment uses electricity market modelling to provide an estimate of the likely commercialisation process for superhot geothermal power plants. The analysis, adopting the grid system operator's assumptions, forecasts that superhot geothermal power plants could contribute an additional 1.4 or 2.1 GWe capacity (depending on whether or not some gas-fired electricity generation is permitted for peak loads) to the NZ grid between 2037 and 2050. Using economically optimised scenarios, the modelling shows that the addition of superhot geothermal power plants

effectively doubles the expected contribution from conventional geothermal power plants, and would still be economical to construct, even if superhot projects prove to be twice the cost of conventional geothermal projects.

1. Introduction

Geothermal has been under-represented in the plans for future renewable energy sources that NZ consumers might utilise. Policy discussed in several recent planning documents has focused on solar and wind deployment and has under-appreciated the full potential of geothermal in policies for official consideration and endorsement. These documents include: a proposed update (currently underway) of the National Policy Statement on renewable electricity generation (MoE, 2011), the NZ government's future energy strategy (MBIE, 2023), and the NZ Climate Change Commission's energy sector modelling (Climate Commission, 2024).

The benefits of geothermal relative to other renewable power generation options are well known. They include sustainability, reliability, efficiency, allowable multiple land uses, security of indigenous energy supply, small surface footprint, and base-load generation, independent of the weather. Superhot developments will have similar advantages and will likely use even less land for well pads, etc., than conventional developments because of expected higher average well productivity, and the more compact and efficient turbines and the reduced cooling system requirements. Newly developed technologies will also enable full reinjection of the non-condensable gas discharges along with the cooled discharge fluids (McLean 2023). Hence CO_2 gas emissions to the atmosphere from NZ geothermal power plants (currently decreasing but still averaging 64 gCO_{2e}/KWh) are not anticipated to be an issue in future superhot geothermal projects. NZ has also benefited from international collaboration through the IEA-Geothermal Technology Collaboration Program in "Deep Roots" (super-critical and superhot) geothermal research and demonstration projects. A summary of these learnings can be found in Bromley & Carey (2023).

As part of five years of effort undertaken through the Geothermal - The Next Generation (GNG) research project, GNS Science has constructed a preliminary inventory of NZ's superhot - supercritical geothermal resources (Bromley et al., 2024; www.geothermalnextgeneration.com). The principal purpose was to assess potential resource availability to inform a costing analysis and economic assessment. The resource inventory uses geophysical data and interpretations, primarily from magneto-telluric 3D models, to assess NZ's superhot geothermal potential. The inventory applies the project-based United Nations Framework Classification for Resources 2019 update (UNFC, 2022) incorporating the Supplementary Specifications for the application of the classification framework to geothermal energy resources (UNECE, 2019). The UNFC methodology categorises projects listed in the inventory; it reflects the level of uncertainty prior to drilling at potential project locations.

An economic assessment of superhot projects using electricity market modelling was undertaken by Castalia Ltd (2023) on behalf of GNS Science. The results are summarised in Section 3 below. The challenge now for NZ is how to attract the needed capital and operational expertise, identify opportunities for landowners to collaborate, and align policies for this significant—and, until now, mostly overlooked opportunity. We consider the challenge to be analogous to that faced by NZ engineers, scientists, regulators, and politicians, during the early decades of NZ's conventional geothermal resource exploration efforts during the 1950's and 1960's. Although the uncertainties

and commercial risks are high at present for superhot geothermal projects, in essence, history points us towards bold action and "if nothing is risked, nothing will be gained".

2. Superhot Inventory for New Zealand

A preliminary quantification (inventory) of New Zealand's supercritical (>374 °C, >220 bar_a) or superhot (>374 °C, <220 bar_a) geothermal resources has been completed (Bromley et al., 2024). These deep resources are predicted to occur at potentially drillable depths of less than 6 km and at temperatures of up to 500°C. The inventory focusses on the Taupō Volcanic Zone (TVZ), and the Northland Region (Ngawha). The assessment has targeted the 'deep roots' of known geothermal systems, combined with possible 'hidden' superhot resources. The resource assessments utilise the 2019 updated UNFC-2009 and its application to geothermal resources using the UNECE-2022 categorisation approach. By way of comparison, a recent application of this assessment methodology has been applied to conventional depth geothermal resources in the Waikato Region of the TVZ (Ussher et al., 2023). The superhot geothermal assessment is based on deep geophysics data and interpretation, and follows the volumetric approach to quantification of the extraction of heat over a project lifetime (Garg & Combs, 2011), rather than the assumed MW_e/km^2 approach in Ussher et al. (2023). The outcome is a preliminary inventory of potential superhot resources for the purposes of long-term energy planning. The identified resources are subdivided according to locations with respect to their current categorisation status under regional geothermal planning regulations (see Table 1 for unprotected systems and Table 2 for protected systems). Figure 1 shows the locations of nine superhot resources that have been identified at the time of writing this paper from 3D geophysical magnetotelluric (MT) models.

The assumptions noted in Table 1 are further explained in Bromley et al. (2024) and informed by: Garg & Combs (2011), Zarrouk & Moon (2014), and Grant (2015). The MT resistivity anomalies are described in Bertrand et al. (2015, 2022). A challenge in constructing this superhot inventory was estimating the unknown parameter of superhot reservoir permeability (both for natural state conditions and for development-modified or stimulated conditions). Permeability will govern the potential economic energy deliverability, and extraction sustainability of such resources (Watanabe et al., 2020). It is also challenging to predict the mineral compositions, and gas contents, of fluid discharges and how these might influence longer term sustainability (Heřmanská et al., 2020, Chambefort and Stefánsson, 2021, Lamy-Chappuis et al., 2022). Analogous fluid properties are inferred from the observed physical and chemical conditions of superhot geothermal fluids that have been encountered in other countries.

Large scale mathematical models (Kissling et al., 2024) and simulations of natural state mass and heat flow through the TVZ using supercritical capable codes (O'Sullivan et al., 2020), provide constraints on likely rock and reservoir properties at the depths of interest. These properties influence the likely productivity and sustainability of superhot fluid resources. Consequently, although currently there are insufficient data to construct robust simulations of individual prospective resources, representative development scenarios of a typical superhot geothermal prospect can be simulated through economically viable extraction lifetimes, informing the preliminary inventory assessment. The scenarios assume lifetimes may vary between 35 and 100 years.

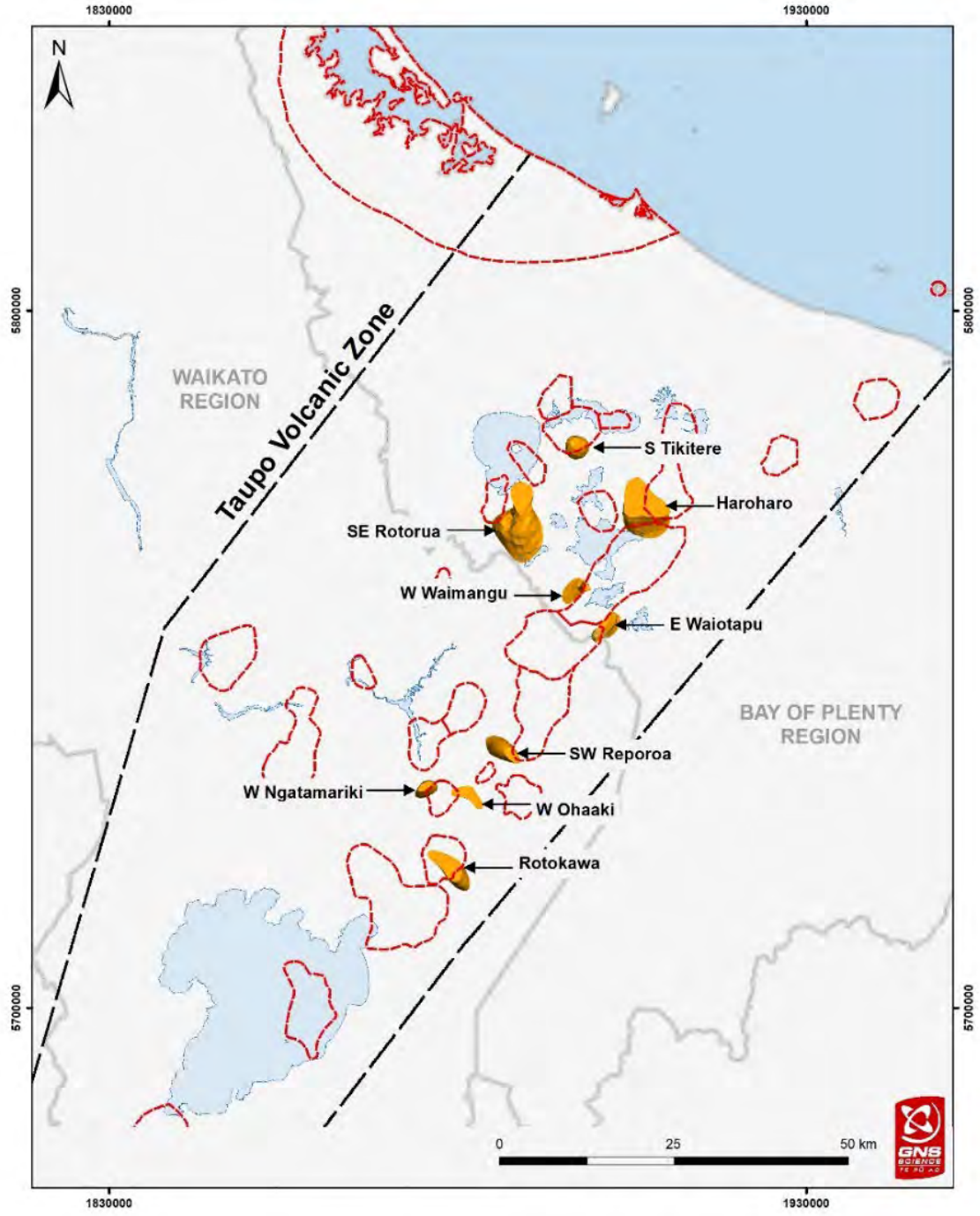

Figure 1: Taupō Volcanic Zone superhot geothermal resources - location and extent of deep, low-resistivity anomalies (shaded relief in orange), 3.5 to 6 km depth, using 3D MT models. Location names are from Tables 1 and 2. Shallow geothermal system boundaries are shown in dashed red contours.

Table 1. Inventory of probable, 3.5 to 6 km deep, superhot resources in New Zealand (excluding protected systems)

Systems	Location	Top Depth	Bottom Depth	Area	Volume	Top Temp.	Bottom Temp.	Stored-Heat*	Capacity	Generat-ion
	TVZ	km (bsl)	km (bsl)	km^2	km^3	°C	°C	EJ	MWe	GWhr/yr
1	Kawerau	3.5	6	15	37.5	375	500	58	412	3428
2	S Tikitere	3.5	6		15.4	375	500	24	169	1408
3	Haroharo-Tikorangi	3.5	6		64.3	375	500	99	706	5877
4	SW Reporoa	3.5	6		23.7	375	500	36	260	2166
5	W Ohaaki	3.5	6		13	375	500	20	143	1188
6	W Ngatamariki	3.5	6		13.6	375	500	21	149	1243
7	Rotokawa	3.5	6		41.1	375	500	63	451	3757
8	Mokai	3.5	6	5	12.5	375	500	19	137	1143
9	Wairakei	3.5	6	5	12.5	375	500	19	137	1143
10	Tauhara	3.5	6	15	37.5	375	500	58	412	3428
11	Tokaanu	3.5	6	10	25	375	500	38	275	2285
	Northland									
12	Ngawha	3.5	6	10	25	375	500	38	275	2285
Vers.	CB 24-7-24	TOTAL:			321			493	3527	29351
*1	assumes rock: 1.3 specific heat capacity, 2700 density									
*2	assumes 2.5% heat recovery (4.6% of usable heat >200°C) over 35 yr life of consents									
	95% capacity factor, 30% turbine energy conversion efficiency									
*3	calculated values from deep Central TVZ geophysics data using MT data, (<10 ohm-m)									
*4	calculated values from deep Okataina geophysics data using MT data, (<15 ohm-m)									
*5	estimated values from geophysics, existing borehole data and reservoir modelling									
*6	excludes resources underlying protected geothermal systems									
*7	default values									

Table 2. Inventory of probable, 3.5 to 6 km deep, superhot resources in protected New Zealand geothermal systems.

Systems	Location	Top Depth	Bottom Depth	Area	Volume	Top Temp.	Bottom Temp.	Stored-Heat*	Capacity	Generat-ion
	TVZ	km (bsl)	km (bsl)	km^2	km^3	°C	°C	EJ	MWe	GWhr/yr
1	SE Rotorua	3.5	6		61.1	375	500	94	671	5585
2	W Waimangu	3.5	6		3.7	375	500	6	41	338
3	E Waiotapu	3.5	6		11.9	375	500	18	131	1088
4	Tongariro	3.5	6	10	25	375	500	38	275	2285
Vers.	CB 24-7-24	TOTAL:			102			156	1117	9296

The assessment for a depth range of 3.5 to 6 km identifies that the potential superhot geothermal energy resources suitable for power generation are the equivalent of about 4.6 GWe. The future utilisation is predicated on the assumption that technical challenges are overcome. If systems currently protected under existing regulatory planning regimes are excluded, the assessed resource reduces to ~3.5 GWe of installed capacity capable of generating 29 TWh/yr of baseload power. This may be compared with the current geothermal generation capacity from conventional depth reservoirs of ~1.1 GWe (8 TWh/yr, or 18% of total NZ generation), rising to an anticipated 1.4 GWe of installed capacity by 2030 and possibly 1.7 GWe (12 TWh/yr) by 2040 to 2050.

The geophysical data set of the Taupō Volcanic Zone and Northland is not yet complete. Consequently, the assessment is not fully comprehensive in terms of areal coverage and on that basis is conservative. The UNFC methodology uses a matrix categorisation of potential projects (Figure 2). All these prospects in the New Zealand superhot inventory are at a low confidence level (G_4 on the matrix degree of confidence axis) reflecting the current high level of uncertainty, prior to any drilling being undertaken to access superhot geothermal conditions in the 3.5 to 6 km depth interval. As data coverage is extended, models refined, and drilling depths increased, the assessed potential can be updated. The UNFC-2019 classifications (currently E3.2, F4.2, G4.1) will be revised over time, as exploratory drilling and pilot studies are undertaken, enlarging the knowledgebase of specific superhot geothermal projects.

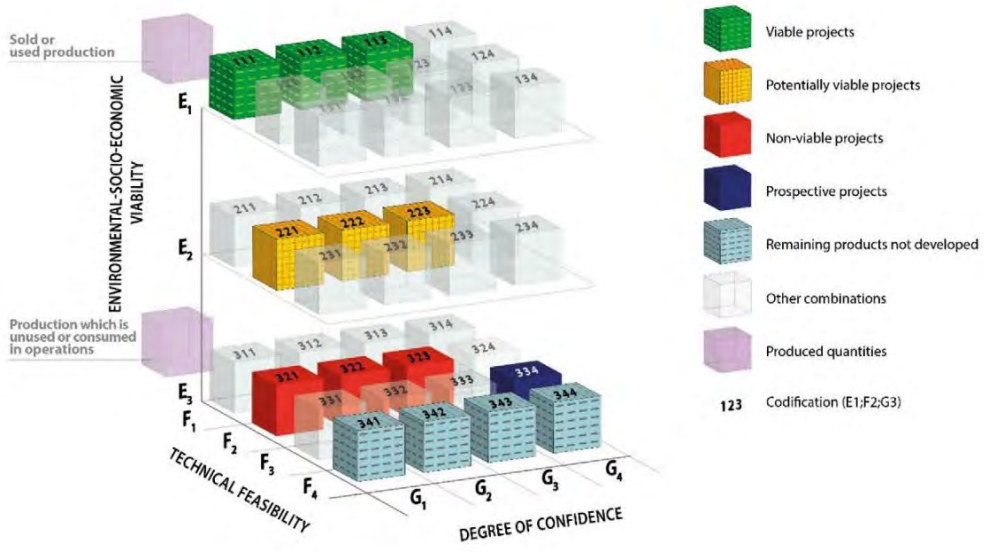

Figure 2: UNFC-2019 Categories and Examples of Classes (Diagram from UNFC-2019). Prior to any deep exploration drilling, NZ superhot projects will remain, for now, categorised as E3.2, F4.2, G4.1.

3. Economic Modelling for the Future NZ Electricity Market

To determine the economic value and potential role of superhot geothermal developments in meeting NZ's future power demand, Castalia (2023) first undertook an economic forecast of the NZ electricity market, considering the NZ Government's climate change commitments regarding use of renewable rather than fossil fuel energy sources. Electricity demand is expected to increase to a value about 19% higher by 2037 and 50% higher by 2050 (based on the NZ Climate Change

Commission's 'demonstration path', (Climate Commission, 2023)). The main drivers for growth are electrification of transport and industry alongside population and economic expansion. The North Island of NZ is forecast to dominate growth in demand (two thirds of the total) like the current split between the North and South Islands (which are linked by a capacity-constrained, DC submarine cable). The seasonal and daily load duration demand curves are expected to retain the same approximate shape in 2050 as in 2023. This affects the relative needs and pricing for baseload and peak generation capacity. The model iteratively calculates the increase in demand distributed across the peak to base load curve for each subsequent year. Wind and solar renewable electricity supplies are de-rated relative to geothermal when calculating a North Island winter-capacity margin to meet demand peaks (that is, variable supplies would require 'over-building' of capacity). The economic model adopts estimates from the grid operator (Transpower) for the peaking role of 'Variable Renewable Energy' to determine the cheapest option, whilst always providing for sufficient capacity.

3.1 Cost analysis

Comparative costs, from the model, for different renewable sources of new generation, and battery storage, as a function of capacity factor, are shown in Figure 3. The costs take into account the need for surplus installed capacity or storage to provide back-up for periods of low supply but high demand (in particular from variable energy sources such as wind and solar). These curves illustrate the cost competitiveness of battery storage and gas-fuelled generation for satisfying short-period peak demand at 10% to 25% capacity factor, but also the cost benefit of building baseload superhot geothermal power plants relative to 'over-built' solar or wind generation for accommodating the full range of capacity factors required to operate the NZ grid. Note that the more expensive battery electric storage capacity would likely substitute for gas peaking if the latter was banned by 2050.

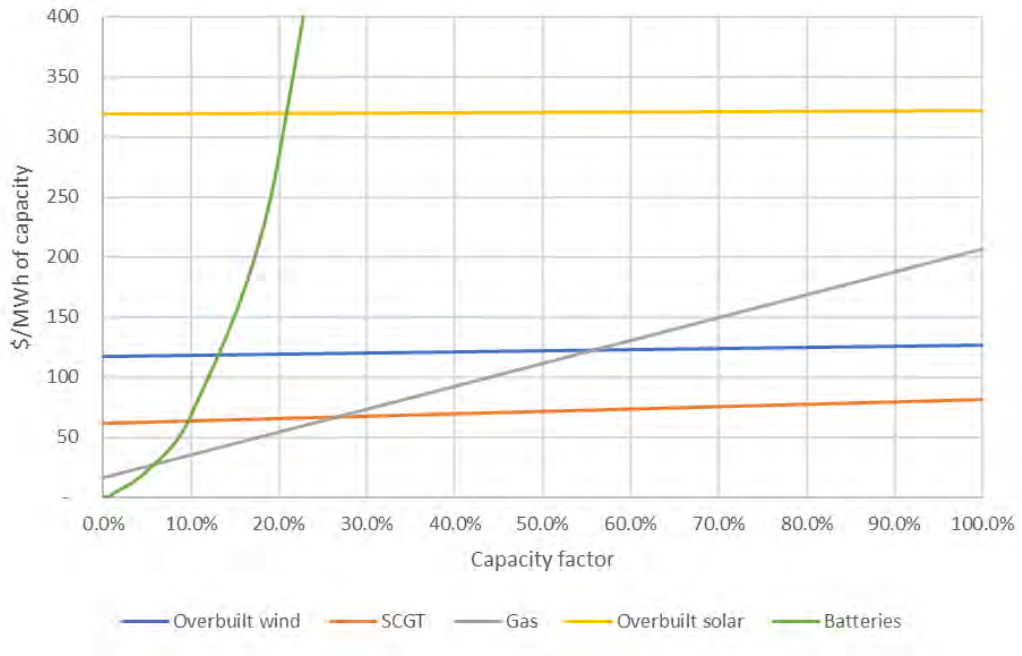

Figure 3: Comparative cost curves ($/MWh) as a function of capacity factor (Peaking 0-20%, Intermediate 20-90%, Baseload 90-100%) for different new-build electricity supply or storage options. (SCGT=superhot geothermal; 'overbuilt' implies some un-used capacity exists during periods of low demand.)

Consequently, the conclusion from the grid capacity modelling is that between 2037 and 2050, about 2 GWe of superhot geothermal capacity would become economic to build (for a 100% renewable scenario, as mandated by the Climate Commission (2023)). A reduced amount of 1.4 GWe would still be economic to build for the alternative scenario where some fossil-fuel (gas) generation is allowed for demand peaks. The 2 GWe scenario would provide about 16 TWh/yr, approximately 55% of the estimated available superhot resource potential from Table 2.2 of 29 TWh/yr. This potential amount is in addition to Transpower's prediction of conventional geothermal capacity by 2035 and beyond, which they expect to plateau at 1.7 GWe (12.5 TWh/yr), based on planned and proposed projects (Transpower New Zealand, 2023). That is, conventional geothermal is expected to grow by about 50% by 2035 compared to the 2023 operating capacity of 1.1 GWe (8 TWhr/yr), then remain stable until at least 2050.

A sensitivity test on varying the cost of superhot geothermal projects (mostly the capital cost of drilling and surface plant) relative to conventional projects, showed that 2.1 GWe of superhot capacity is economic to build if the cost premium is 0%, 2.0 GWe if the cost premium is +20% (the base case scenario), while 1.9 GWe is still economic even if the cost premium is 100% (i.e., costs double). Similarly, if some gas-fired peaking generation is permitted, the economic capacity drops from 1.4 to 1.3 GWe if the relative cost premium for superhot geothermal increases from 0% to 100%.

3.2 Timelines for deployment

Castalia (2023) prepared an ambitious 14-year timeline estimate for NZ superhot projects to reach maturity and become operational. The timeline was informed by the history of previous energy research timelines and learning rates (Our World in Data, 2022), and assumes all conditions will align and barriers will be overcome. The first 10 years (2023-2033) involves continuing geoscientific and engineering research efforts. This is followed by 4 years for design and construction of the first power plant and grid synchronisation (2037). Parallel to these activities, exploratory drilling consents and approvals are predicted to take 1 year, followed by 5 years of drilling. Once technical issues are resolved, the process of site selection, land acquisition, financial and operational approvals are predicted to take another 2 years, prior to commencing the formal design stage for the first power plant and steam gathering system.

Between 2037 and 2050, for deployment to achieve 2 GWe (16 TWh/yr) of new installed superhot capacity (as determined by the economic model), approximately six parallel projects, at about 300 to 400 MWe each, would need to be developed (see Table 1 for the top priority locations). Assuming an average productivity of 40 MWe per well (Rivera & Carey, 2023), one reinjection well per four production wells, and four months to drill each well, this level of new power plant development would require a deep drilling campaign over 10 years (2037 to 2047) using at least two large-capacity drilling rigs.

3.3 Potential value for off-grid and direct industrial energy needs

Off-grid energy needs for industry, in the form of power and/or heat at high enthalpy, could also be met in the future by superhot geothermal resources. Direct use for milk processing, timber drying, wood pellet and paper manufacturing in NZ is already an established and economical

option for conventional geothermal heat. These plants typically use steam or two-phase heat exchangers and are often co-located with electricity generation plants. The opportunity to displace some of the 90 PJ/year of industrial energy still sourced from fossil fuels in NZ is attractive from a carbon emission reduction perspective. A typical application might be a central North Island dairy processing factory which could require about 15 PJ/year of energy. Note that dairy factory demand is inversely correlated with electricity prices because dairy milk supply dries up in winter when power demand is high. In terms of revenue generated, the economics of a co-generation project (dairy factory heat and power), using superhot resources, is comparable to that of an electricity-only plant (see Castalia Ltd, 2023, for more detail).

4. The Next Generation Challenge

The assessment of superhot potential for NZ also identifies the engineering and geoscientific challenges and gaps in technology that require attention and investment to facilitate a smooth transition towards the anticipated renewable energy target by 2050. The challenges include:

- Refine well drilling and completion methods for depths of 3.5 to 6 km, and at superhot temperatures, so that commercial wells can be achieved, and flows maintained.
- Manage scale formation, corrosion, and thermal stress issues so that superhot fluids can be reliably produced from depth.
- Design and construct efficient and cost-effective turbines and related surface infrastructure adequate for the superhot fluids.
- Remove regulatory barriers to help fast-track robust superhot projects.
- Communicate the research findings to key public sector stakeholders, Māori interests, landowners, government agencies, regional councils, potential funding partners and infrastructure investors.
- Coordination among government and private sector parties to mobilise the necessary investment required for exploratory wells and associated scientific and technical research and development.

5. Conclusions

New Zealand's conventional (sub-critical) installed geothermal capacity is currently ~1.1 GW_e generating ~8 TWh/yr (New Zealand Geothermal Association, 2023). This is 18% of the total generation of 43 TWh/yr (2023 data), obtained from a total installed capacity of ~10 GW_e.

Transpower (the NZ grid operator) estimates that about 16 GWe of total capacity will be required by 2037 as NZ decarbonises its energy use. Castalia Ltd (2023) estimates a 50% increase in demand will occur by 2050. Approximately 1.7 GW_e is anticipated by Transpower to be provided by conventional baseload geothermal generation (about 12.5 TWh/yr, or 18% of total demand of 70 TWh/yr, like the current proportion).

The superhot geothermal resource inventory provides, for the first time, additional potential geothermal capacity for the planners to consider. It identifies:

- A total additional capacity of about 4.6 GW_e, or 39 TWh/yr for New Zealand.
- After removing the areas that have protected regulatory planning provisions, this reduces the superhot capacity to ~3.5 GW_e, or 29 TWh/yr of electricity.

Economic assessment shows that 2 GW_e of capacity (15 TWh/yr of generation) would be cost effective to construct between 2037 and 2050 in a fully renewable electricity generation scenario. Alternatively, 1.4 GW_e would be cost competitive if some gas peaking electricity generation is allowed.

The next challenge is how to attract the needed capital, resource the investigative work, identify opportunities for landowners to collaborate, and align policies for this significant renewable energy opportunity for New Zealand to be realised.

Acknowledgement

This work has been the culmination of work by many, especially over the past 5 years, under the umbrella of the 'Geothermal - The Next Generation' (GNG) research project funded by the NZ Government (MBIE contract C05X1904). https://www.geothermalnextgeneration.com/

REFERENCES

Bertrand, E.A., Caldwell, T.G., Bannister, S., Soengkono, S., Bennie, S.L., Hill, G.J., Heise, W. "Using array MT data to image the crustal resistivity structure of the south-eastern Taupo Volcanic Zone, New Zealand." *Journal of Volcanology and Geothermal Research*, 305, (2015), 63–75. https://doi.org/10.1016/j.jvolgeores.2015.09.020

Bertrand, E.A., Kannberg, P., Caldwell, T.G., Heise, W., Constable, S., Scott, B., Bannister, S., Kilgour, G., Bennie, S.L., Hart, R., Palmer, N. "Inferring the magmatic roots of volcano-geothermal systems in the Rotorua Caldera and Okataina Volcanic Centre from magnetotelluric models". *Journal of Volcanology and Geothermal Research*. 431, (2022), 107645. https://doi.org/10.1016/j.jvolgeores.2022.107645

Bromley, C.J., Carey, B. "Ultra hot - supercritical geothermal - IEA Geothermal Collaboration". *Proceedings: World Geothermal Congress 2023;* Beijing, China, (2023).

Bromley, C.J., Rae, A.J., Alcaraz, S.A., Kissling, W.M., Rivera, J.M. "Inventory of New Zealand supercritical resources." GNS Science report SR2023/50, (2024), ISBN: 978-1-99-105857-7. DOI: 10.21420/053X-5618 https://www.geothermalnextgeneration.com/updates/inventory-of-new-zealands-supercritical-geothermal-resources

Castalia Ltd. "Supercritical geothermal in New Zealand: economic opportunity in renewable electricity generation and for off-grid energy." Castalia Limited, Wellington (NZ), (2023), https://www.geothermalnextgeneration.com/updates/supercritical-geothermal-a-potential-economic-opportunity-for-nz

Chambefort, I., and Stefánsson, A. Fluids in Geothermal Systems. Elements 1–5. (2021), https://doi.org/10.2138/gselements.16.6.407

Climate Commission "Modelling and data for our 2024 consultation on the emissions reduction target and emissions budgets." New Zealand Government's Climate Change Commission website (2024), https://www.climatecommission.govt.nz/get-involved/sharing-our-thinking/data-and-modelling/

Garg, S.K., Combs, J. “A re-examination of USGS volumetric ‘heat in place’ method”. *Proceedings: 36th Workshop on Geothermal Reservoir Engineering*, Stanford University, CA, (2011), https://pangea.stanford.edu/ERE/pdf/IGAstandard/SGW/2011/garg.pdf

Grant, M.A. “Resource assessment, a review, with reference to the Australian Code”. *Proceedings: World Geothermal Congress 2015*, Melbourne, Australia, (2015), http://www.geothermal-energy.org/pdf/IGAstandard/WGC/2015/16004.pdf

Heřmanská, M., Kleine, B., Stefansson, A. “Geochemical constraints on supercritical fluids in geothermal systems.” *Journal of Volcanology and Geothermal Research*, 394, (2020), 106824. https://doi.org/10.1016/j.jvolgeores.2020.106824

Kissling, W.M., Ellis, S., Barker, S.J., Caldwell, T.G. “A source-to-surface model of heat and fluid transport in the Taupō Rift, New Zealand.” *Journal of Volcanology and Geothermal Research.* 446, (2024), 107995, https://doi.org/10.1016/j.jvolgeores.2023.107995

Lamy-Chappuis, B., Yapparova, A., Dreisner, T. “Advanced well model for superhot and saline geothermal reservoirs.”, *Geothermics*, 105, (2022), 102529, https://doi.org/10.1016/j.geothermics.2022.102529

MBIE “Advancing New Zealand’s Energy Transition.” New Zealand Ministry of Business Innovation and Employment document (2023), https://www.mbie.govt.nz/building-and-energy/energy-and-natural-resources/energy-consultations-and-reviews/advancing-new-zealands-energy-transition-consultation-document

McLean, K. “Updates from NZGA Emissions Working Group.” New Zealand Geothermal Association seminar 26th July (2023), https://www.nzgeothermal.org.nz/downloads/NZGA-Updates-from-emissions-working-group-2023.pdf

MoE “National policy statement for renewable electricity generation 2011.” New Zealand Ministry for the Environment publication (2011). https://environment.govt.nz/acts-and-regulations/national-policy-statements/national-policy-statement-for-renewable-electricity-generation/

New Zealand Geothermal Association. “Geothermal Electricity Generation Activities Report.”, New Zealand Geothermal Association publication, (2023), https://www.nzgeothermal.org.nz/downloads/NZGA-Geothermal-Electricity-Generation-activities-report-2023.pdf

O’Sullivan, J., Newson, J., Alcaraz, S., Barton, S., Baraza, R., Croucher, A., Scott, S., O’Sullivan, M. “A robust supercritical geothermal simulator.” *Proceedings: 42nd New Zealand Geothermal Workshop*, University of Auckland, (2020), http://www.geothermal-energy.org/pdf/IGAstandard/NZGW/2020/137.pdf

Our World in Data. “Levelized Cost of Energy by Technology.”, 20 October (2022), https://ourworldindata.org/grapher/levelized-cost-of-energy

Rivera, J., Carey, B. “Comparative geothermal well performance – supercritical and subcritical”. GNS Science Report 2023/01, 40 p. (2023), https://doi.org/10.21420/ekkw-d514

Transpower New Zealand. “Transpower transmission tomorrow_2023 Refresh”, (2023), https://static.transpower.co.nz/public/2023-06/Transpower_TransmissionTomorrow_2023_03.pdf

[UNECE] United Nations Economic Commission for Europe. “United Nations Framework Classification for Resources: update 2019.” Geneva (CH): United Nations. 20 p. UNECE Energy Series 61, (2019), https://unece.org/DAM/energy/se/pdfs/UNFC/publ/UNFC_ES61_Update_2019.pdf

[UNFC] United Nations Framework Classification. “Supplementary specifications for the application of the United Nations Framework Classification for Resources (Update 2019) to Geothermal Energy Resources.” Geneva (CH): United Nations Economic Commission for Europe [UNECE], (2022), https://unece.org/sites/default/files/2022-12/UNFC_Geothermal_Specs_25October2022.pdf

Ussher, G., Lebe, J.L., Calibugan, A., Brotheridge, J., Quinao, J., Hendri, R., McLeod, J. “Application of the United Nations Framework Classification for Geothermal Projects in the Waikato Region.” Proceedings: 45th New Zealand Geothermal Workshop Auckland, New Zealand, (2023), ISSN 2703-4275.

Watanabe, N., Saito, K., Okamoto, A., Nakamura, A., Ishibashi, T., Saishu, H., Komai, T., Tsuchiya, N. “Stabilizing and enhancing permeability for sustainable and profitable energy extraction from superhot geothermal environments.” *Applied Energy*, 260, (2020), 114306. https://doi.org/10.1016/j.apenergy.2019.114306

Zarrouk, S.J., Moon, H. “Efficiency of geothermal power plants: a worldwide review.” *Geothermics*, 51, (2014), 142–153, https://doi.org/10.1016/j.geothermics.2013.11.001

Ideal Thermal-Hydraulic Performance of Geothermal Power Systems Above 300 °C

Daniel W. Dichter

Quaise Energy

Keywords

High-temperature, flash, binary, dry steam, cycle, working fluid, exergy, efficiency, supercritical, superhot rock, SHR, utilization

ABSTRACT

Current geothermal power plants are characterized by geofluid production temperatures ranging from about 100-250 °C, with research underway to enable much higher temperatures. The range of 300 °C and above is considered herein, encompassing the region of “superhot rock”, or SHR, defined as exceeding 375-400 °C. To quantify the potential of these systems, the exergetic power of a production well is assessed at its maximum flow capacity, as determined empirically by the onset of erosion. This indicates that at a given temperature, the power output potential is maximized where the geofluid production is most dense. Performance plateaus around the critical point, beyond which higher exergy is approximately offset by reduced mass flow rate. Three types of power cycles were considered: dry steam, flash, and binary, with each cycle corresponding to specific production conditions. Dry steam cycles were found to confer superior exergetic efficiency, but relatively low gross power output because of the characteristically low production density. Flash and binary cycles were found to be a significant improvement on an equal-temperature basis, with the lower exergetic efficiency compensated by a much higher mass flow rate. Single-, double-, and triple-stage cycles were considered for both flash and binary plants, and optimized for exergetic efficiency using gradient ascent algorithms. This yielded heuristics for the optimal design of both cycle types. For binary cycles specifically, pure water was selected as the working fluid of choice on the basis of its superior performance at high temperatures, as compared to the hydrocarbons characteristic of organic Rankine cycles (ORCs). The performances of flash and binary plants were found to be highly similar in the sense of thermal and exergetic efficiency. Diminishing returns were observed in both cycles, with a significant improvement from adding a second stage, and smaller, more localized improvements from a third. The choice between flash and binary may depend more on practical considerations such as geochemistry, reinjection requirements, and capital costs. Altogether, the plants considered herein have the potential to produce about 30 MWe gross per production well with an 8.5 inch minimum inner diameter, up to an order of magnitude more than is typical of current geothermal systems.

1. Introduction

A wide variety of methods have been used to generate electrical power from geothermal heat. Common to all such methods is the drilling of at least one well to produce hot geofluid from a subsurface reservoir, which may be either liquid, vapor, or a two-phase mixture. These wells typically have a minimum inner diameter of $D = 8.5$ inches (IFC/GeothermEx, 2013, p. 22; API 5CT, 2005, p. 185), and are drilled into hydrothermal reservoirs with depths of about 1-3 km (IFC/GeothermEx, 2013, p. 15). Recent global meta-analysis studied the distribution of gross capacity per production well, finding a mode of 3.0 ± 0.5 MWe, with more than 50% of wells between 4.0 ± 2.5 MWe (IFC/GeothermEx, 2013, p. 14).

Research is also underway to enable artificial reservoirs in subsurface rock with minimal pre-existing permeability or fluid content, referred to as enhanced or engineered geothermal systems, or EGS. For generality, this paper considers a geothermal reservoir of arbitrary origin, into which a single production and reinjection well are drilled. The reservoir is assumed to have sufficient pressure to achieve the maximum flow capacity of the production well, as described in the following section.

2. Production Hydraulics

The hydraulic aspect ratio of a production well, as its depth to diameter, is typically on the order of about 10,000, per the figures from the previous section. Drilling to greater depths and temperatures is expected to entail even higher aspect ratios. This extreme slenderness introduces a significant frictional pressure drop between the reservoir and surface. This can be seen from the Darcy-Weisbach equation (Çengel et al., 2012, p. 545):

$$\Delta P = \frac{1}{2} f \frac{L}{D} \rho v^2 \tag{1}$$

Where ΔP is the pressure drop, f is the friction factor, L is the pipe length, D is the pipe diameter, ρ is the fluid density, and v is the average, or superficial, flow velocity. The factor L/D expresses the pipe's aspect ratio, so $\Delta P \propto L/D$, and $\Delta P \to \infty$ as $L/D \to \infty$, all else equal.

Geofluid production can also be expressed in terms of internal flow:

$$\dot{m} = \rho A v \tag{2}$$

Where $\dot{m}$ is the mass flow rate, and A is the cross-sectional flow area. Substituting the expression for v in Eq. (2) into Eq. (1) equation and solving for $\dot{m}$ yields:

$$\dot{m} = \sqrt{\frac{\pi^2 \Delta P D^5 \rho}{8 f L}} \tag{3}$$

For a well with a certain D and L, subject to a certain ΔP between the reservoir and surface:

$$\dot{m} \propto \sqrt{\rho} \tag{4}$$

Neglecting the small dependence of f on the fluid conditions for the sake of approximation. Experiments suggest that the production of high-temperature geothermal systems may be limited

by erosion rather than pressure, even at conventional depths (Ingason et al., 2014). In other words, the production well may be sufficiently pressurized downhole to incur erosion in an open flow scenario. Thereby, safe operation requires controlling the wellhead pressure to limit the production mass flow rate.

The onset and acceptable rate limit of erosion in systems with internal flow are best determined by direct measurement under representative conditions. Without such information, a common empirical standard for two-phase flow states that:

$$v_e = \frac{c}{\sqrt{\rho}} \tag{5}$$

Where v_e is the erosional velocity, and c is an empirical constant, with suggested values of $c =$ 100-250 (ft/s)(lb/ft^3)$^{1/2}$ depending on the duty cycle, presence of solids, and the degree of corrosivity; $c = 100$ (ft/s)(lb/ft^3)$^{1/2}$ is used herein, with appropriate unit conversions (API, 1991, p. 23). The same empirical standard specifies a constant maximum flow velocity of 4.57 m/s [15 ft/sec] for liquid, which is essentially a special case of the two-phase correlation with $x = 0$, where x denotes quality, or dryness fraction. This arises because the density of saturated liquid water is approximately constant with respect to temperature. Vapor flows are more commonly pressure-limited rather than erosion-limited, but the two-phase correlation with $x = 1$ nonetheless provides guidance as to the maximum vapor flow conditions. Supercritical flows are likewise assumed to be limited by the same empirical proportionality, noting that material properties at these higher temperatures require special consideration.

Substituting the expression for v_e in Eq. (5) into Eq. (2) such that $v = v_e$ yields an expression for the maximum mass flow rate of an erosion-limited internal flow:

$$\dot{m} = c\, A \sqrt{\rho} = \frac{\pi}{4}\, c\, D^2 \sqrt{\rho} \tag{6}$$

With respect to fluid properties, this is a restatement of the Darcy-Weisbach equation; namely:

$$\dot{m} \propto \sqrt{\rho} \tag{7}$$

Supposing geofluid production is erosion-limited, with a production pressure no higher than 300 bar per the approximate limitations of current boilers (Çengel et al., 2012, p. 387), the maximum mass flow rate is shown in Figure 1 below.

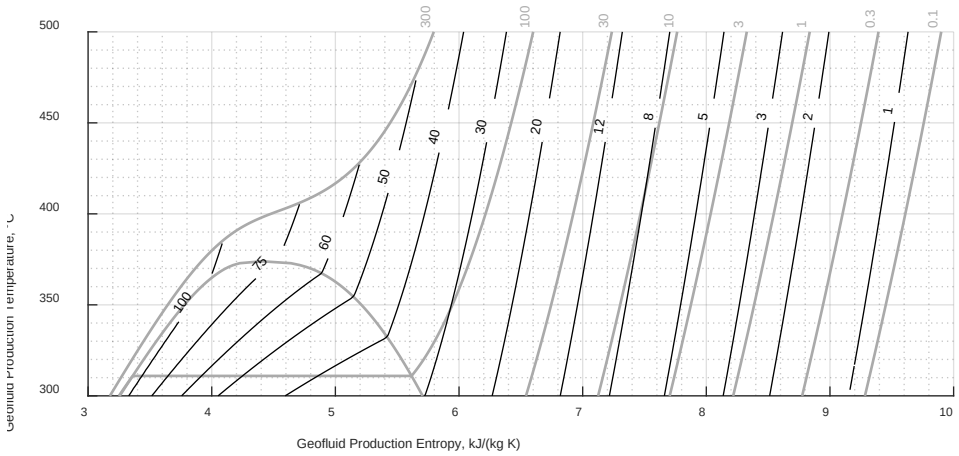

Figure 1: Contours of constant mass flow rate $\dot{m}$ in kg/s (black) for an erosion-limited well with D = 8.5". Overlaid in gray are the phase boundary of water, and a set of isobars labeled in units of bar.

This shows that in the subcritical region, $\dot{m}$ is substantially higher in the liquid phase than the vapor phase, with more than a 3:1 ratio at 300 °C. This disparity decreases to zero as $T \rightarrow T_{crit}$, i.e. as T approaches the critical temperature. In the supercritical region where $T > T_{crit}$, $\dot{m}$ decreases with T on an isobaric basis, because isobaric heat additions strictly decrease density.

3. Exergetic Power

Exergy expresses the maximum amount of work that can be obtained from a substance as it is brought into equilibrium with its surroundings, and can be used to calculate the potential power output of a geofluid flow. Its standard definition in the field of geothermal power is:

$$e = (h - h_o) - T_o\,(s - s_o) \tag{8}$$

Where e is exergy, h is enthalpy, and s is entropy, all of which are specific, or per unit mass; the subscript o refers to the dead state, and T_o is specified in consistent absolute units, e.g. Kelvin (DiPippo, 2016, pp. 295-296). The dead state is commonly taken as saturated liquid, and can thereby be defined by a temperature. The value of $T_o = 50$ °C [323.2 K] is used herein, assuming that heat rejection requires a temperature difference of at least $\Delta T = 10$ °C with respect to a maximum ambient temperature of 40 °C [104 °F] (DiPippo, 2016, p. 128). This represents the anticipated condenser temperature, below which no work can be obtained. Exergetic power, denoted $\dot{E}$, is then given by:

$$\dot{E} = e\,\dot{m} \tag{9}$$

This quantity expresses the maximum power output, e.g. in MWe gross, associated with a geofluid flow, and is shown in Figure 2 below.

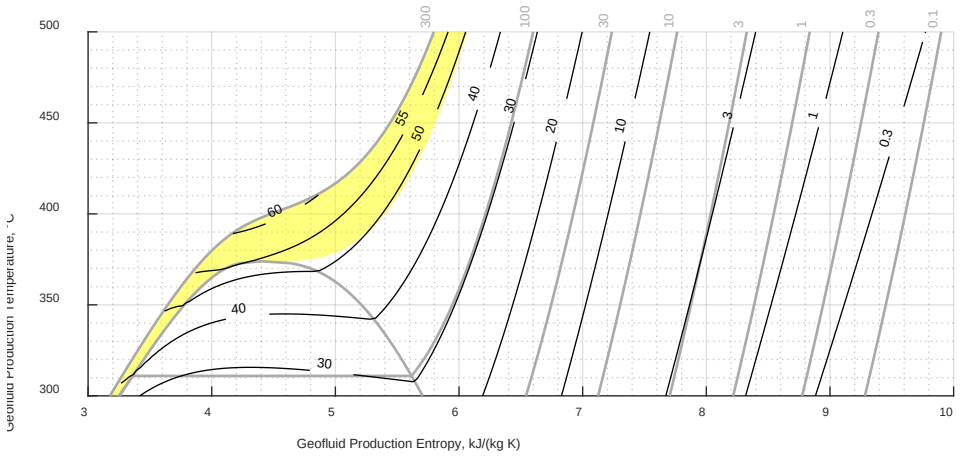

Figure 2: Contours of constant exergetic power $\dot{E}$ in MWe (black) for an erosion-limited well with D = 8.5". Overlaid in gray are the phase boundary of water, and a set of isobars labeled in units of bar. Highlighted in yellow is the region where exergetic power $\dot{E}$ is maximized for a certain production temperature, bounded by $x = 0$ where $T < T_{crit}$, $P = P_{crit}$ where $T > T_{crit}$, and P = 300 bar.

Similar to the earlier plot of $\dot{m}$, this shows in the subcritical region that liquid conveys substantially more exergetic power than vapor. This ratio is about 4:3 at 300 °C, again decreasing to zero at the critical point. In the dry steam and supercritical regions, $\dot{E}$ is approximately constant with respect to T on an isobaric basis, indicating that increases in h and e are offset by decreases in ρ and $\dot{m}$. For a given production temperature, exergetic power $\dot{E}$ is maximized where the production pressure is itself maximized, corresponding to a region spanning both compressed liquid and supercritical fluid. This region is characterized by production pressures of $P >$ 85.9 bar in the subcritical region, and $P >$ 220.6 bar in the supercritical region, per the saturation pressures at 300 °C and the critical pressure, respectively.

Typically, geothermal power plants attain around 25-65% of exergetic power, depending on the type and sophistication of the thermodynamic cycle, which itself is influenced by the geofluid production conditions (DiPippo, 2016, p. 243). This fraction is referred to as exergetic efficiency, or utilization, and is denoted by η_{II}, with the subscript II referring to the Second Law of Thermodynamics on which exergy is based. This is given by:

$$\eta_{II} = \frac{\dot{Q}}{\dot{E}} \tag{10}$$

Where $\dot{Q}$ denotes the gross power output of the plant, itself given by:

$$\dot{Q} = \dot{m}\, w_{net} = \dot{m}\, (q_{in} - q_{out}) \tag{11}$$

Where w_{net} is the net work, q_{in} is the heat input, and q_{out} is the heat rejection. The expression for η_{II} can be simplified to:

$$\eta_{II} = \frac{w_{net}}{e} \tag{12}$$

Note that this neglects parasitic loads from fans, pumps, lights, etc. for simplicity and generality, which are briefly discussed later. This is not to be confused with the more common thermal (or First Law) efficiency η_I, given by:

$$\eta_I = \frac{w_{net}}{q_{in}} = 1 - \frac{q_{out}}{q_{in}} \tag{13}$$

The remainder of this paper seeks to quantify how the value of η_{II} depends on the geofluid production conditions, the type of power cycle, and the cycle's relative sophistication. Thereby, the competing tradeoffs between $\dot{m}$, e, and η_{II} can be balanced, so that local and global optima for $\dot{Q}$ can be found.

4. Cycle Regions

The simplest method of generating power from a geofluid flow is a dry steam power cycle. This entails producing geofluid as a saturated or superheated vapor, then expanding it in a steam turbine, producing work. The basic constraint of this cycle is that the turbine must not have excessive condensation; herein, it is assumed that $x \geq 85\%$ throughout the turbine, based on typical manufacturers' specifications. These cycles also lack reheating, a common feature of non-geothermal plants, because it is not practical to re-flow the geofluid through the reservoir at an intermediate pressure once produced, unlike e.g. with fossil-fired boilers.

After the steam is expanded in the turbine, the residual waste heat is then rejected to ambient conditions by a condenser, as in a Rankine cycle. This imposes an additional constraint that the turbine outlet pressure cannot be lower than about 0.12 bar, the saturation pressure corresponding to 50 °C, the nominal heat rejection temperature.

The performance of the turbine can be described primarily by its dry isentropic, or nominal, efficiency η_{td}, which expresses the ratio of the actual enthalpy change of the steam between the inlet and the outlet, to this same quantity under isentropic conditions without the presence of condensation (Çengel et al., 2012, p. 383). This is taken as 85% herein (DiPippo, 2016, p. 122). Secondarily, the Baumann rule states that turbine efficiency decreases about 1% for each 1% of condensation, in the sense of quality x, according to empirical observations (DiPippo, 2016, p. 122).

Using numerical methods, a turbine process curve can be calculated, representing the set of inlet conditions corresponding to the turbine and condenser specifications described earlier. This curve intersects $x = 1$ at approximately $T = 190$ °C, the approximate maximum saturated vapor temperature for a dry steam power cycle, closely matching actual plants of this type (Calpine Corporation, 2023).

The region in T-s, or temperature-entropy, coordinates to the right of this curve represents the set of acceptable turbine inlet conditions, all of which is superheated vapor. To the left of this curve are regions of superheated vapor (generally, at lower enthalpy), supercritical fluid, saturated vapor, saturated liquid, compressed liquid, and two-phase mixtures. These two regions are denoted as A and B, as shown in Figure 3 below. The boundary between these regions can be approximated by the isentropic curve of $s = 6.236$ kJ/(kg K) over 300-500 °C.

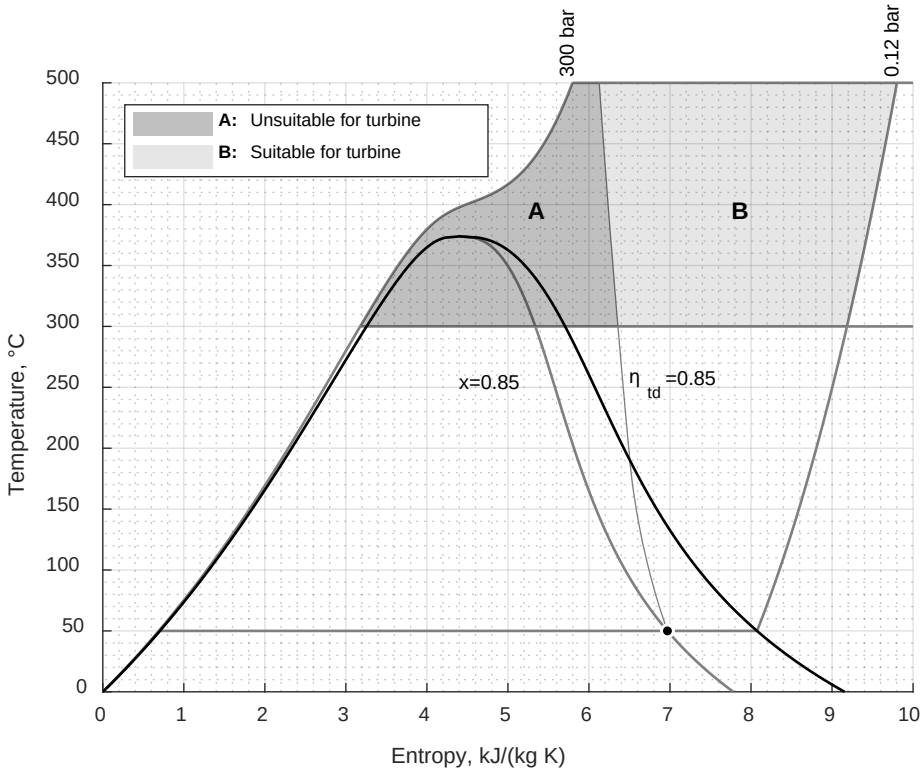

Figure 3: A T-s diagram of water divided into two regions, A and B, based on suitability for supplying typical non-reheat steam turbines.

As will be shown, η_{II} is maximized in dry steam power cycles, because no processing of the geofluid is required to yield vapor suitable for a turbine, which is inherently destructive of exergy. Therefore, this is considered as the most suitable cycle in Region B. In Region A, this type of cycle is not possible, so flash and binary cycles are considered instead. The following three sections describe each of these power cycles in greater detail.

5. Dry Steam Cycles

A dry steam power cycle is essentially a non-reheat Rankine cycle (Çengel et al., 2012, pp. 379-393). The cycle is assumed to be closed by an isobaric heat addition (2-3) for the sake of analysis, so that q_{in}, q_{out}, and w_{net} can be determined. Otherwise, this entails an isobaric rejection of residual heat in a condenser, and an isentropic pumping process. A plant schematic and representative T-s diagram are shown in Figures 4 and 5 below.

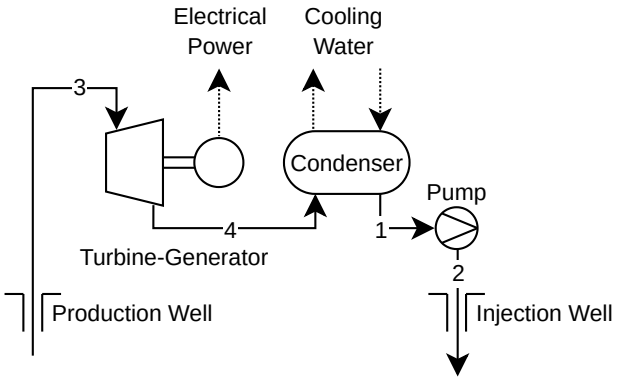

Figure 4: Schematic of a dry steam plant, not to scale.

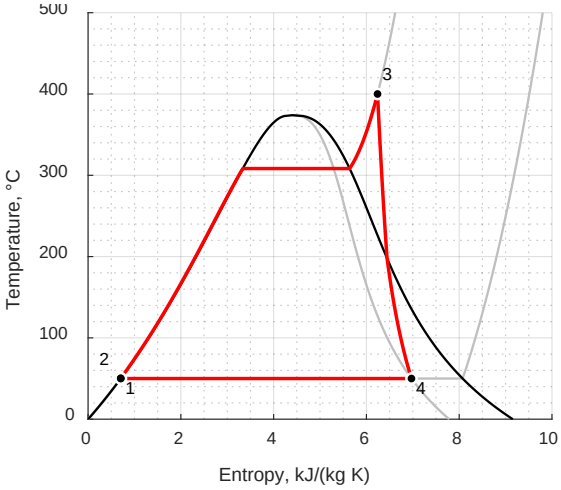

Dry Steam (Non-Reheat Rankine) Cycle

fluid	water	
q_in	2886.0	kJ/kg
q_out	2025.5	kJ/kg
w_net	860.5	kJ/kg
η_I	0.298	~
η_II	0.778	~
x_min	0.850	~

	T	P	h	s	x
1	50.0	0.12	209.6	0.70	0.000
2	50.3	96.45	219.3	0.70	NaN
3	400.0	96.45	3105.3	6.24	NaN
4	50.0	0.12	2235.0	6.97	0.850

Figure 5: T-s diagram of a representative dry steam power cycle with $T = 400$ °C at the turbine inlet, and $x = 0.85$ at the turbine outlet.

Evaluating all cycles in the region of interest, Region B, together with the hydraulic constraints for $\dot{m}$ described earlier, yields the plot shown in Figure 6 below.

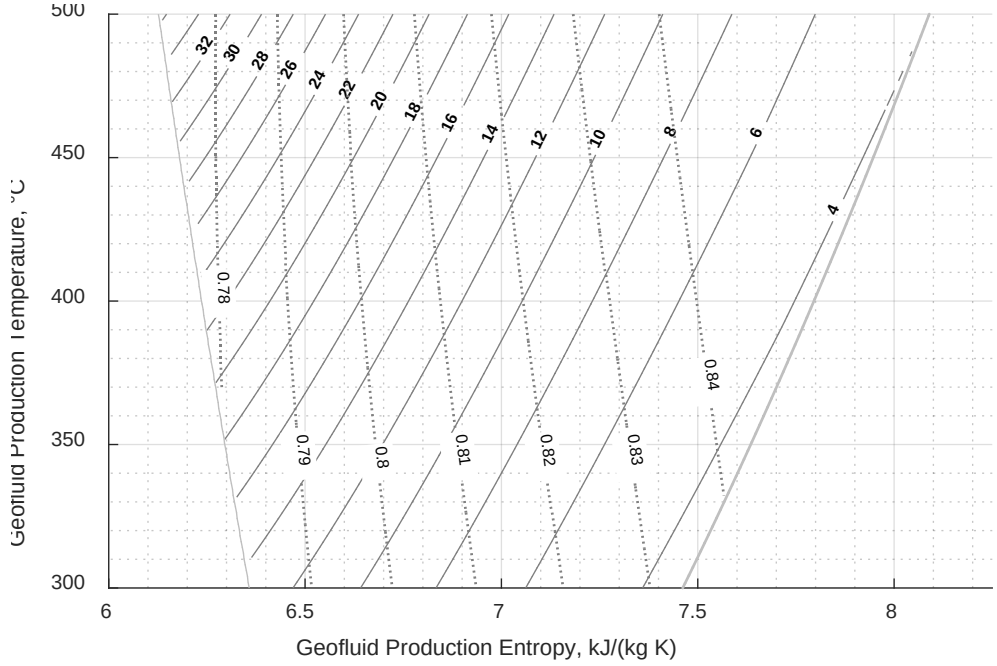

Figure 6: Gross power output in MWe (solid) and exergetic efficiency (dotted) for ideal dry steam cycles. The region of interest is bounded by $\eta_{td} = 0.85$, and $P = 5$ bar.

Although this region shows relatively high exergetic efficiency, this quantity is maximized where ρ and $\dot{m}$ are minimized. The maximum power output $\dot{Q}$ of about 32-34 MWe occurs around 475-500 °C and 150-200 bar, i.e. where the geofluid density ρ is maximized. Per Figure 2, it is anticipated that production in Region A should attain comparable power outputs at significantly lower temperatures, even accounting for the higher exergy in Region B. Thereby, wells producing in Region A could be significantly shallower than in Region B for the same $\dot{Q}$, entailing less capital cost associated with drilling. A further difficulty of producing steam at these extreme conditions is its relatively high compressibility, which typically results in a large frictional pressure drop ΔP between the reservoir and surface. Thereby, sufficiently deep reservoirs may not practically be able to produce at these conditions, because of the characteristic slenderness of the production well.

6. Flash Cycles

Flash cycles work by expanding a liquid-dominated geofluid, separating the resulting saturated vapor, and supplying it to a steam turbine. This is possible because isenthalpic expansion of saturated liquid or two-phase mixtures strictly increases quality x, though it also decreases exergy e. More sophisticated arrangements introduce a second, or less commonly, a third, flash-separation process, yielding higher exergetic efficiency.

Ideal flash cycles are characterized by isenthalpic flash processes, and isobaric separation processes (DiPippo, 2016, pp. 107-163). The separators are assumed to yield separate streams of saturated liquid and saturated vapor. Mixing of fluid streams is assumed to be isobaric, and is governed by conservation of mass and energy. Likewise, the condenser is assumed to be isobaric, and to yield saturated liquid. After leaving the condenser, the geofluid is pumped to the pressure of the final separator and mixed with the residual un-flashed liquid. This yields the final outlet conditions of moderately compressed liquid at an intermediate temperature between that of the condenser and the final separator. A schematic is shown in Figure 7 below.

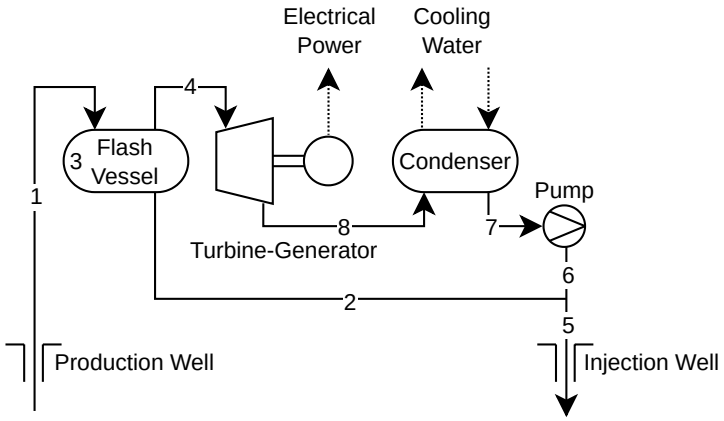

Figure 7: Schematic of a single-flash plant, not to scale.

Conventional geofluid production conditions for flash plants range from about 100-200 °C and $0.1 < x < 0.9$ (Zarrouk and Moon, 2014, pp. 147-148). Because this is generally less than the maximum saturated vapor temperature at the turbine inlet of 190 °C, as derived earlier, geofluid is conventionally separated rather than flashed once produced (DiPippo, 2016, p. 115). However, at the higher temperatures considered herein, the produced geofluid must instead be flashed before it can be separated, to achieve sufficient turbine dryness.

Only a subset of Region A is suitable for flash cycles. Of particular significance is the maximum enthalpy of saturated vapor: where $h >$ 2,800 kJ/kg, isenthalpic expansion generally yields superheated vapor, not a two-phase mixture, as shown in Figure 8 below.

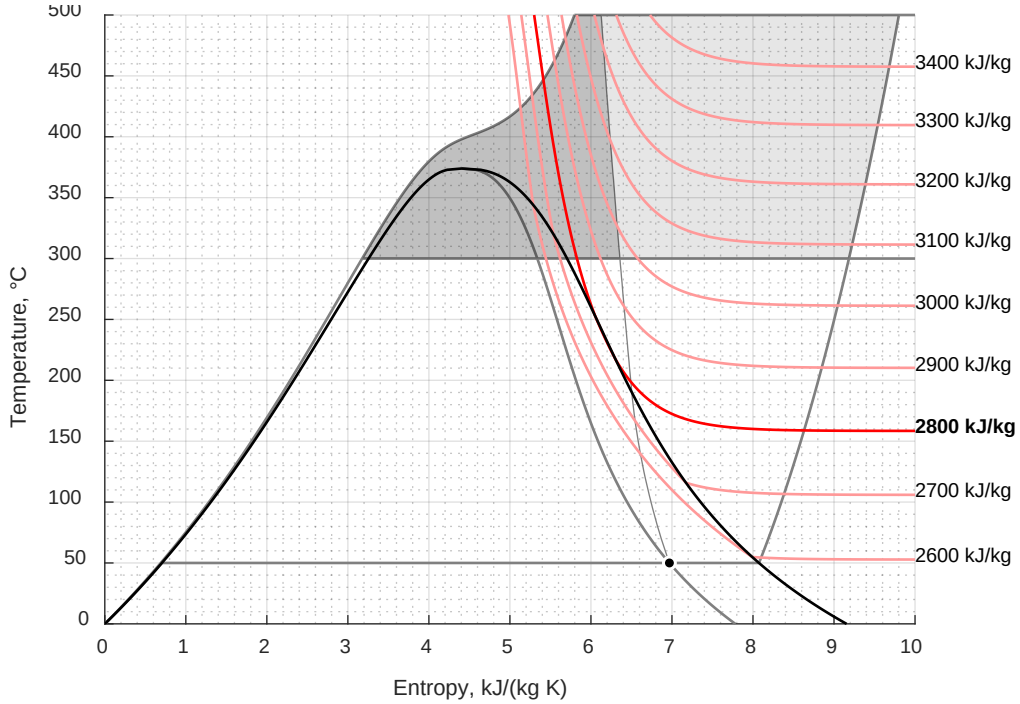

Figure 8: Cycle regions from Figure 3 overlaid with isenthalpic contours in the superheated vapor region. Highlighted is h = 2,800 kJ/kg, the approximate maximum enthalpy of saturated vapor, i.e. $x = 1$.

In the subset of Region A where $h >$ 2,800 kJ/kg, unconventional cycles could nonetheless be developed, for example by expanding the produced geofluid until intersecting the turbine process curve with $\eta_{td} = 0.85$, or by expanding the geofluid in the turbine and separating out the liquid condensate at least once to maintain sufficient dryness, incorporating elements of both dry steam and flash cycles. However, comparing Figures 2 and 8 indicates that the exergetic power $\dot{E}$ in this subset of Region A is relatively low, as compared to where $h <$ 2,800 kJ/kg, on an equal-temperature basis. For this reason, only the subset of Region A where $h <$ 2,800 kJ/kg is considered further in this section.

Given the turbine and condenser specifications described earlier, the main parameters required to define the flash cycle are the quantity of flashes, and the associated separator temperature(s). Conventionally, the optimal separator temperature(s) are well-approximated by the "equal-temperature-split" rule, or ETS, which states that the temperature differences between the inlet, any/all separator(s), and the condenser, are all mutually equal, regardless of the number of flashes (DiPippo, 2016, p. 132).

However, ETS has only limited applicability to high-temperature flash cycles, for two reasons. First, ETS assumes that saturated liquid water has a constant specific heat capacity C_p with respect to temperature. This is accurate to within ±3.6% over 0-200 °C, i.e. over the conventional temperature range for flash plants, but rapidly deteriorates at higher temperatures approaching the critical point, as shown in Figure 9 below. Specific heat at the critical point is effectively undefined, in the sense that $C_p \to \infty$, and $\partial T / \partial h \to 0$, as $T \to T_{crit}$, i.e. heat addition produces no

sensible temperature change, as with vaporization or condensation. Second, it can be shown that ETS generally yields deficient turbine outlet qualities for inlet conditions in Region A.

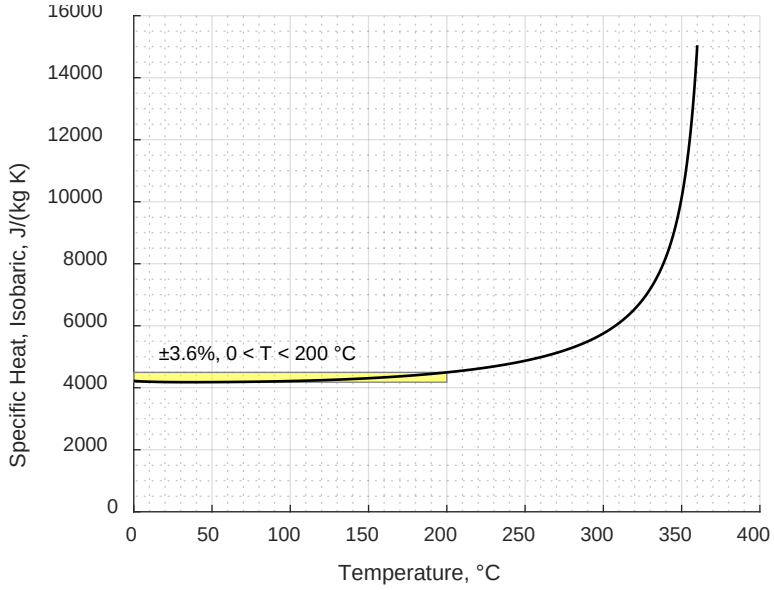

Figure 9: Specific heat capacity of saturated liquid water, showing that relative constancy (highlighted, yellow) breaks down above about 200 °C, as $T \rightarrow T_{crit}$.

Instead, a gradient ascent algorithm is used to determine the optimal separator temperature(s), in the sense of η_{II}, or equivalently w_{net}, with a step size of 1 °C. Although this method is not guaranteed to find global optima because of possible local maxima in w_{net}, its results compared favorably against exhaustive evaluation for select cases. Optimization is constrained such that no separator operates under vacuum, which is generally considered impractical (DiPippo, 2016, p. 155), and sufficient quality is maintained throughout any/all turbine stages.

Figures 10, 11, and 12 on the following pages show single-, double-, and triple-flash cycles, optimized for representative geofluid production at the critical point, where the gross power output is approximately maximized, per Figure 2. The quantity m is introduced to account for the branching and mixing of geofluid flows, expressing the mass flow rate fraction at each state point.

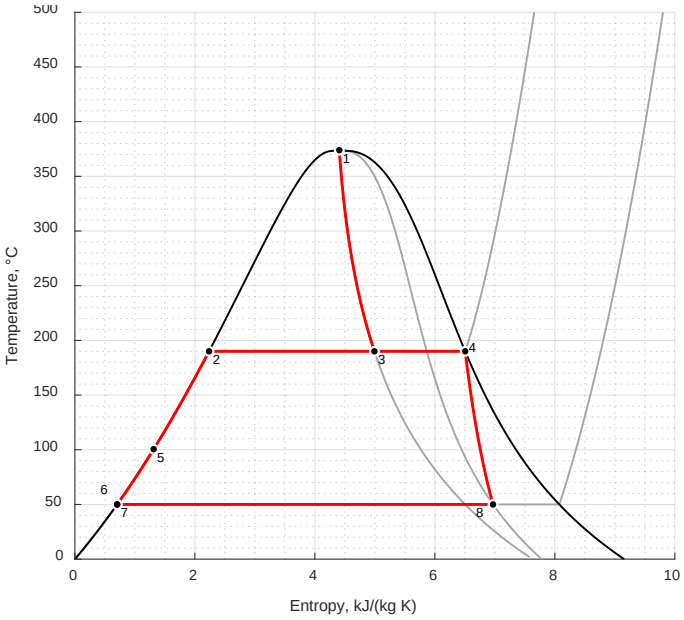

Direct-Use Single-Flash Cycle

q_in	1661.9	kJ/kg
q_out	1307.0	kJ/kg
w_net	354.9	kJ/kg
η_I	0.214	~
η_II	0.523	~
x_min	0.850	~

	T	P	h	s	x	m
1	373.9	220.64	2084.3	4.41	NaN	1.000
2	190.0	12.57	807.7	2.24	0.000	0.354
3	190.0	12.57	2084.3	4.99	0.646	1.000
4	190.0	12.57	2785.3	6.51	1.000	0.646
5	100.5	12.57	422.4	1.31	NaN	1.000
6	50.0	12.57	210.8	0.70	NaN	0.646
7	50.0	0.12	209.6	0.70	0.000	0.646
8	50.0	0.12	2234.2	6.97	0.850	0.646

Figure 10: Single-flash cycle for geofluid production at the critical point.

For a single-flash cycle, optimization generally entails maximizing the turbine inlet temperature, which is limited herein to about 190 °C according to the specifications of the turbine and condenser. Thereby, there is generally no dependence between the geofluid production conditions and the corresponding optimal flash cycle. The geofluid outlet temperature is typically high, at least 100 °C, indicating incomplete utilization of the geofluid.

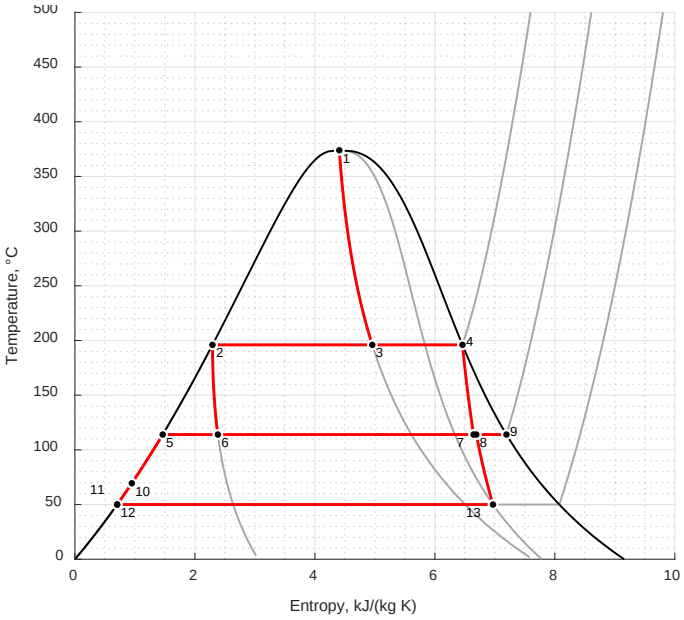

Direct-Use Double-Flash Cycle

q_in	1793.1	kJ/kg
q_out	1411.5	kJ/kg
w_net	381.7	kJ/kg
η_I	0.213	~
η_II	0.563	~
x_min	0.850	~

	T	P	h	s	x	m
1	373.9	220.64	2084.3	4.41	NaN	1.000
2	196.0	14.31	834.5	2.29	0.000	0.361
3	196.0	14.31	2084.3	4.96	0.639	1.000
4	196.0	14.31	2789.5	6.46	1.000	0.639
5	114.0	1.64	478.6	1.46	0.000	0.303
6	114.0	1.64	834.5	2.38	0.160	0.361
7	114.0	1.64	2485.0	6.65	0.904	0.639
8	114.0	1.64	2502.6	6.69	0.912	0.697
9	114.0	1.64	2697.2	7.19	1.000	0.058
10	69.5	1.64	291.1	0.95	NaN	1.000
11	50.0	1.64	209.7	0.70	NaN	0.697
12	50.0	0.12	209.6	0.70	0.000	0.697
13	50.0	0.12	2234.2	6.97	0.850	0.697

Figure 11: Double-flash cycle for geofluid production at the critical point.

Adding a second flash-separation process significantly reduces the geofluid outlet temperature, increasing the exergetic efficiency η_{II}. The small amount of vapor produced in the lower-pressure separator allows the temperature of the first separator to increase slightly, while maintaining the same turbine outlet conditions. The thermal efficiency η_I is essentially unchanged.

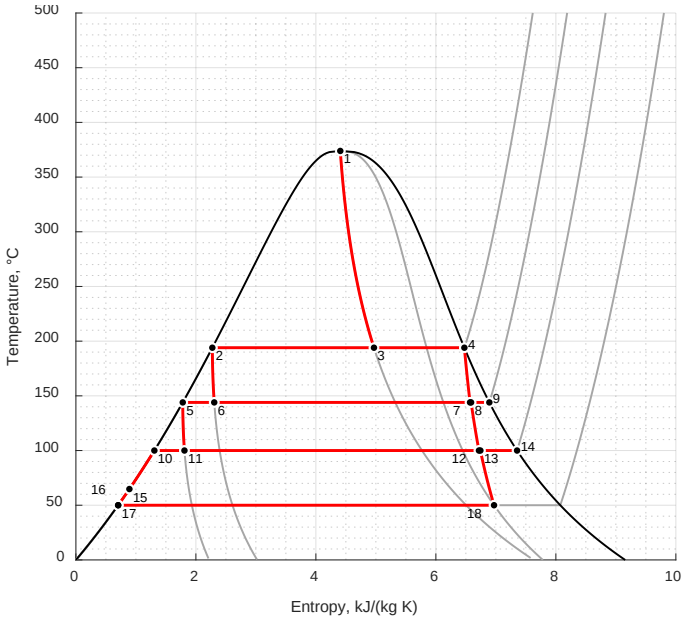

Direct-Use Triple-Flash Cycle

q_in	1812.7	kJ/kg
q_out	1427.3	kJ/kg
w_net	385.4	kJ/kg
η_I	0.213	~
η_II	0.568	~
x_min	0.850	~

	T	P	h	s	x	m
1	373.9	220.64	2084.3	4.41	NaN	1.000
2	194.0	13.71	825.5	2.27	0.000	0.359
3	194.0	13.71	2084.3	4.97	0.641	1.000
4	194.0	13.71	2788.2	6.47	1.000	0.641
5	144.0	4.05	606.6	1.78	0.000	0.322
6	144.0	4.05	825.5	2.31	0.103	0.359
7	144.0	4.05	2604.3	6.57	0.937	0.641
8	144.0	4.05	2611.6	6.59	0.940	0.678
9	144.0	4.05	2738.6	6.89	1.000	0.037
10	100.0	1.02	419.4	1.31	0.000	0.295
11	100.0	1.02	606.6	1.81	0.083	0.322
12	100.0	1.02	2438.4	6.72	0.895	0.678
13	100.0	1.02	2447.4	6.74	0.899	0.705
14	100.0	1.02	2675.6	7.35	1.000	0.027
15	64.8	1.02	271.5	0.89	NaN	1.000
16	50.0	1.02	209.6	0.70	NaN	0.705
17	50.0	0.12	209.6	0.70	0.000	0.705
18	50.0	0.12	2234.4	6.97	0.850	0.705

Figure 12: Triple-flash cycle for geofluid production at the critical point.

By contrast, adding a third flash-separation process yields less than a 1% improvement in η_{II}, and only about a 5 °C reduction in the geofluid outlet temperature. Likewise, there is no improvement in the thermal efficiency η_I. Unlike a more conventional flash cycle, e.g. at 150 °C, introducing a third flash does not significantly increase the vapor fraction at the turbine outlet, which is relatively high because of the large ΔT, ΔP, and Δx of the first flash alone.

Generally, the result of the gradient ascent optimization can be described as a variant of ETS, applied only between the first separator and the condenser, rather than between the inlet and the condenser, such that the first separator temperature is maximized, subject to the constraints of the turbine and condenser. This heuristic method yields a w_{net} that closely approximates the result via gradient ascent.

Figures 13, 14, and 15 on the following pages show the gross power outputs and exergetic efficiencies of single-, double-, and triple-flash plants, for geofluid produced in the subset of Region A where $h < 2{,}800$ kJ/kg.

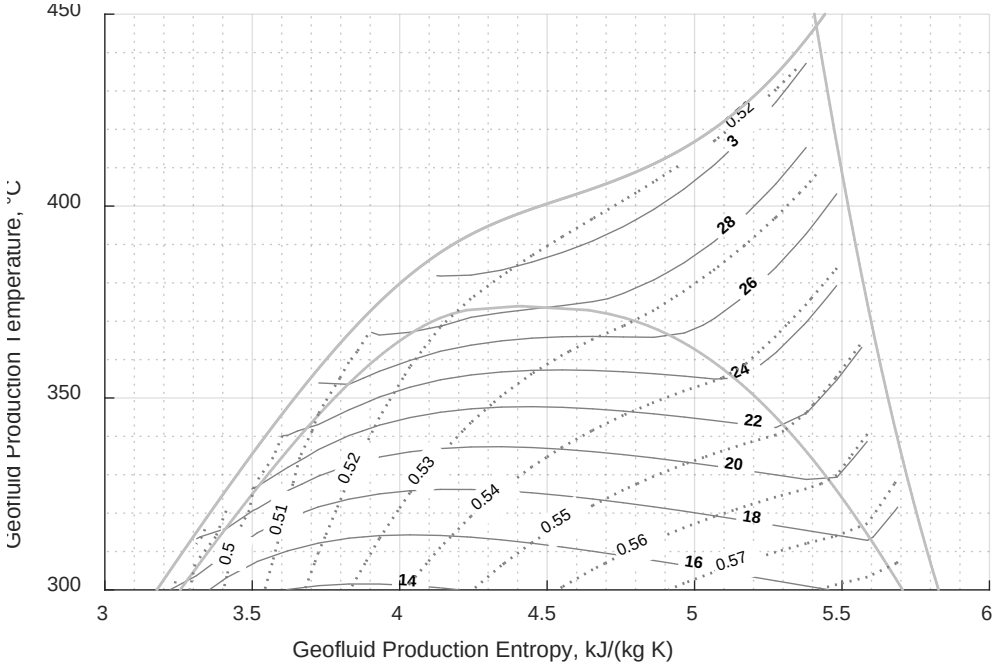

Figure 13: Gross power output in MWe (solid) and exergetic efficiency (dotted) for ideal single-flash cycles.

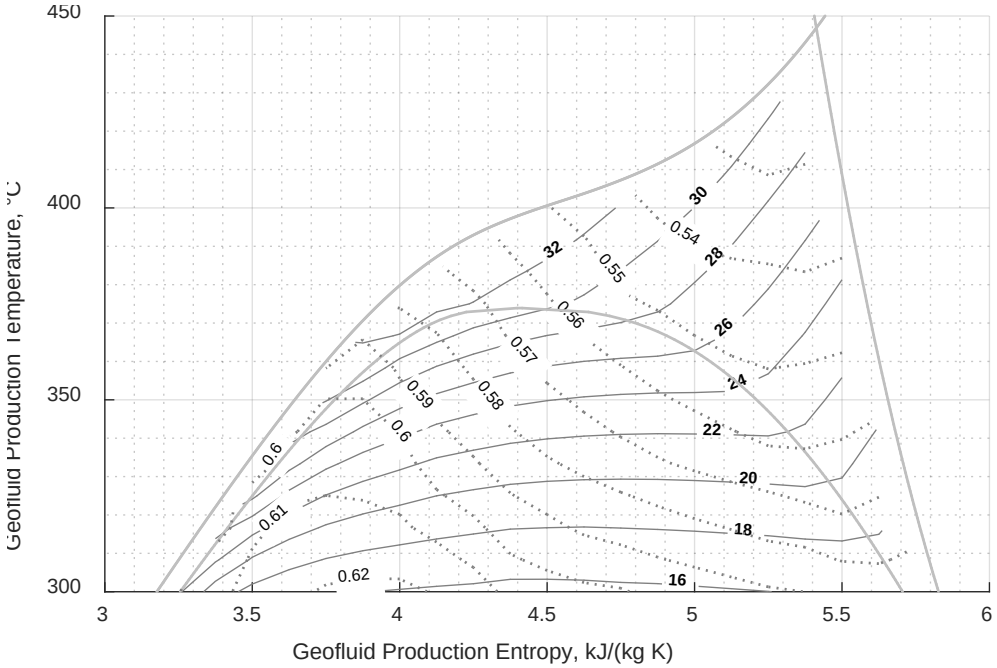

Figure 14: Gross power output in MWe (solid) and exergetic efficiency (dotted) for ideal double-flash cycles.

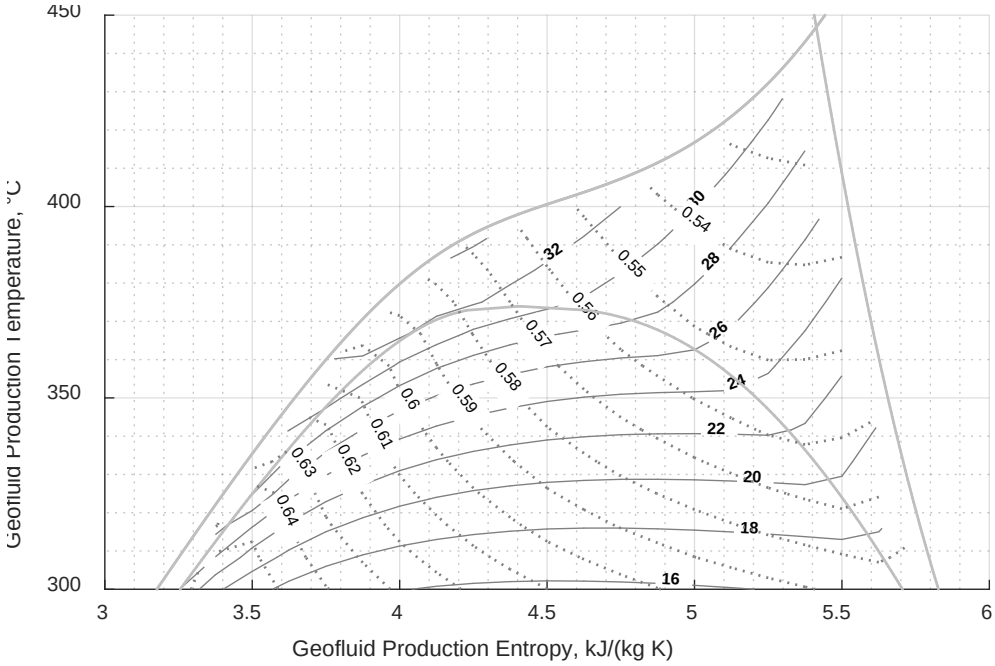

Figure 15: Gross power output in MWe (solid) and exergetic efficiency (dotted) for ideal triple-flash cycles.

These figures show ideal gross power outputs of up to about 30-32 MWe per well. In the subcritical region where $T < T_{crit}$, gross power output $\dot{Q}$ is generally maximized for a given temperature T in the compressed liquid region, confirming the earlier finding on the basis of exergetic power $\dot{E}$. Likewise, in the supercritical region where $T > T_{crit}$, gross power output $\dot{Q}$ increases with pressure P. In the subcritical region, as the quality of the produced geofluid x increases, there is less benefit to incorporating additional flashes, because the first flash alone yields a relatively high fraction of vapor m. The improvement to η_{II} associated with adding a second or third flash depends sensitively on the geofluid production conditions, with generally more improvement towards the liquid-dominated and supercritical regions. Notably, the maximum power attainable is approximately equal between the subcritical and the supercritical regions, indicating that attaining supercriticality is not necessary to maximize the gross power output. Further, the temperature required for maximum power output is significantly lower in the subcritical region.

The main drawbacks associated with flash cycles are their susceptibility to geofluid impurities, and their relatively large pump loads. The flash-separation process concentrates any solid impurities in the residual liquid of the flash vessel(s), which can cause scaling and fouling (DiPippo, 2016, p. 156), while permitting non-condensible gases (NCGs) such as carbon dioxide, methane, and hydrogen sulfide to enter the turbine and condenser, which reduces performance, increases corrosion, and can require specialized treatment (DiPippo, 2016, pp. 660-661). Particularly for subsurface systems requiring high-pressure reinjection, the large amount of geofluid pressure dissipated by the flash cycle increases the plant's parasitic pump load: for example, pressurizing 100 kg/s of water by 100 bar requires at least 1 MWe. Both drawbacks are mitigated by binary cycles, as described in the following section.

7. Binary Cycles

Whereas flash cycles use the produced geofluid directly, binary cycles instead transfer the geofluid's heat to a secondary working fluid in a series of counterflow heat exchangers, producing vapor suitable for a turbine. The main benefit of this approach is that the plant is less exposed to any contaminants that may be present in the produced geofluid, because the geofluid and working fluid do not mix (DiPippo, 2016, pp. 193-234). Because the heat transfer from the geofluid to the working fluid is ideally isobaric, the geofluid may require less pressurization before reinjection as compared to a flash plant, and thereby may incur less parasitic pump load. A schematic is shown in Figure 16 below.

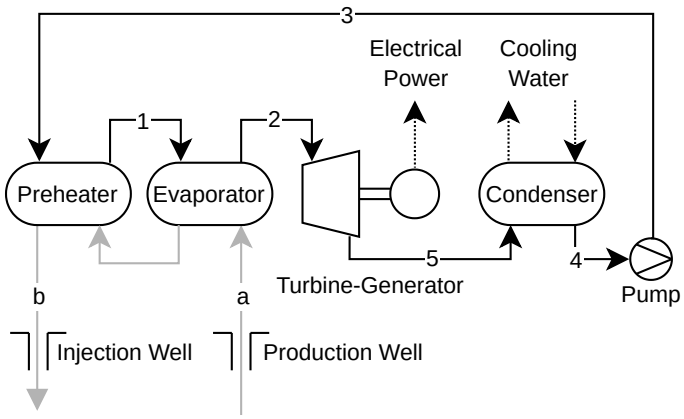

Figure 16: Schematic of a single-pressure binary plant, not to scale. Black arrows denote working fluid, and gray arrows denote geofluid.

The main irreversibility inherent to binary cycles is the heat transfer in the heat exchangers. Because heat can only transfer spontaneously in the direction of decreasing temperature, the working fluid can only approach, but cannot attain, the geofluid's production temperature. Thereby, vaporizing the working fluid inherently destroys some of the geofluid's initial exergy. This loss can be compared to the flash process of flash cycles, which is similarly irreversible and destructive of exergy.

This irreversibility can be mitigated in several ways, the most significant of which is the choice of working fluid. Ideally, the working fluid maintains a constant, small temperature difference ΔT at all points throughout the heat exchanger, as heat is transferred from the geofluid. The degree to which an actual heat transfer approaches this ideal "matched" condition is commonly evaluated using temperature-heat transfer, or T-q, diagrams.

Organic Rankine cycles, or ORCs, are a type of binary cycle that use a hydrocarbon working fluid, most commonly isobutane, butane, isopentane, or pentane, in order of increasing critical temperature. These are well-suited for typical geofluid production temperatures of 100-250 °C (Zarrouk and Moon, 2014, p. 150). This can be understood in terms of the match between the geofluid production temperature and the working fluid critical temperature, the latter of which ranges from 134.6-196.5 °C for the hydrocarbons cited. An additional benefit of an ORC is a relatively compact, dry turbine, because of the high density and retrograde condensation of hydrocarbon vapor, in both senses unlike steam.

However, it is not practical to superheat a hydrocarbon working fluid much beyond its critical temperature. This tends to increase q_{in} approximately as much as q_{out}, such that there is only marginal benefit to w_{net}, η_I, and η_{II}; that is, any superheat added before the turbine must be rejected in approximately equal magnitude by the condenser, as shown in Figure 17 below. This can be attributed to hydrocarbons' retrograde condensation, which causes superheating of the working fluid in the turbine, rather than partial condensation. Secondarily, fluid density decreases sharply after the critical point, progressively inhibiting heat transfer. For these reasons, ORCs do not typically exceed about 200 °C.

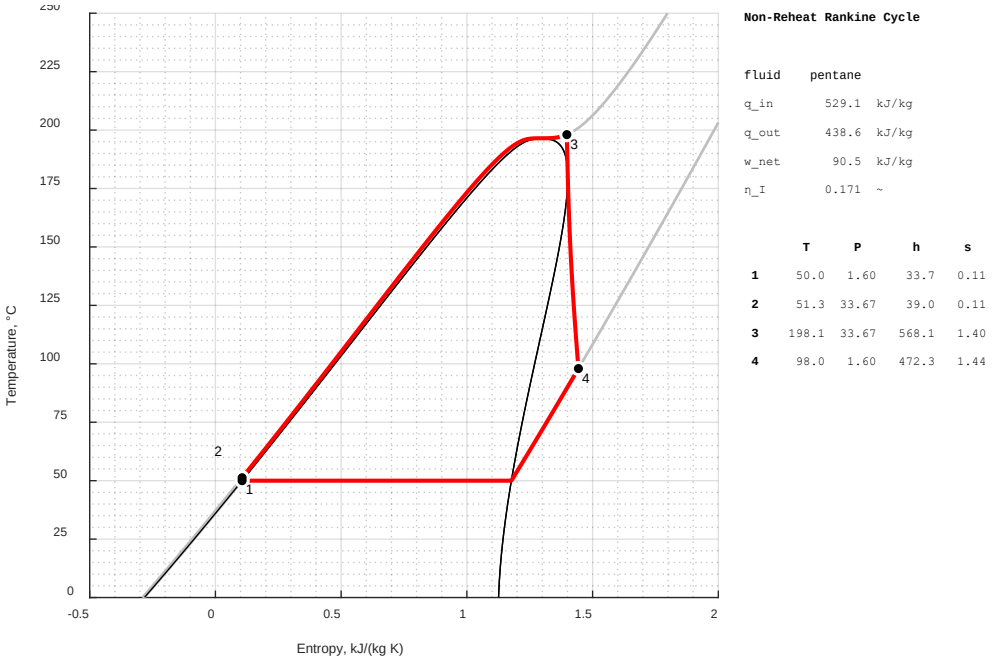

Figure 17: Supercritical pentane cycle, showing that any superheat added before the turbine, 3-4, must be rejected in approximately equal magnitude by the condenser, 4-1.

Because of this limitation, it can be shown using the methods developed later in this section that water outperforms typical ORC hydrocarbons for geofluid production temperatures exceeding about 315 °C, as shown in Figure 18 below. Note that each working fluid's critical temperature T_{crit} correlates to the range of geofluid production temperatures over which it is best suited. It can also be shown that cyclopentane ($T_{crit} = 238.5$ °C) has comparable performance to water over this temperature range, although no such plants are known to exist, and it compares unfavorably in cost, toxicity, and flammability. For these reasons, water is considered as the working fluid of choice for geofluid produced at 300-500 °C.

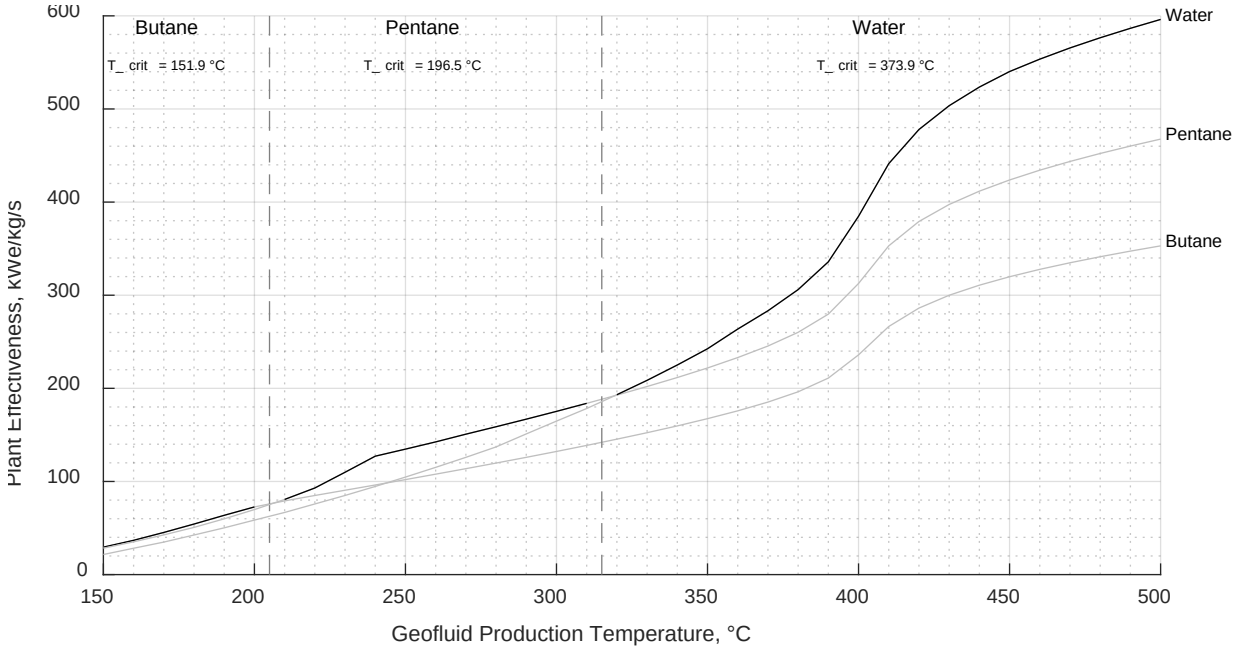

Figure 18: Optimized double-pressure binary plant effectiveness as a function of the working fluid composition and geofluid production temperature, for geofluid produced at 300 bar. Working fluids are emphasized in black over the temperature range for which they are best suited.

The simplest form of a binary cycle consists of two heat exchangers, or sets of heat exchangers, collectively called a preheater, and an evaporator. These produce saturated liquid, then saturated vapor, respectively, which is then supplied to a turbine. This configuration, sometimes referred to as single-pressure, typically has a single pinch point between the preheater and evaporator, where the temperature difference between the two fluids is minimized. The allowable value for this pinch point depends on hardware specifications, but is taken generically as $\Delta T_{pp} = 10$ °C herein. A dual- or double-pressure binary cycle improves on this design by adding an additional pump, preheater, and evaporator at a different pressure, producing vapor at two temperatures simultaneously that eventually mix in the turbine at the appropriate pressure. Typically, two pinch points occur, between both sets of preheaters and evaporators. Triple-pressure cycles are also possible, but are less common because of the diminishing returns associated with additional pressures.

Many of the same assumptions made earlier for ideal flash cycles also apply to ideal binary cycles, specifically: isobaric heat transfers, isentropic pumping, and mixing governed by conservation of mass and energy. Superheating is theoretically possible in binary cycles, but can be shown to confer only marginal benefit, and is less practical because of the decrease in heat transfer efficiency, so is not considered herein. The parameters governing the turbine(s) and condenser are taken as identical to the flash cycles described earlier.

For a given geofluid production scenario and working fluid selection, the remaining parameters required to define a cycle are the quantity of pressure(s), their associated saturation temperature(s), and for multi-pressure cycles specifically, the relative mass flow rate at each pressure. No flow branching occurs in single-pressure cycles, so trivially $m = 1$ throughout these cycles. In double-pressure cycles, m_{HP} implicitly defines m_{LP} by conservation of mass, and likewise with m_{HP}, m_{IP}, and m_{LP} in triple-pressure cycles, where HP, IP, and LP denote the high-, intermediate-, and low-pressure loops. The geofluid's T-q curve, and thereby the q_{out} or Δh of the geofluid, is determined by the bisection method, using the working fluid's T-q curve, and the specified ΔT_{pp}.

Optimization is either one-, three-, or five-dimensional, depending on the choice of a single-, double-, or triple-pressure cycle, respectively. The optimal values of these parameters are again determined using a gradient ascent algorithm, with fixed step sizes of 1 °C for T, and 0.01 (or 1%) for m. The optimization criterion is the exergetic efficiency η_{II} of the coupled geofluid-working fluid system, or equivalently its net work w_{net}. Local minima typically exist in η_{II} for double- and triple-flash cycles, such that converged solutions from the gradient ascent method are not necessarily global optima, but close approximations of it. Optimization is again constrained such that the evaporator(s) do not operate at sub-atmospheric pressure.

The mass flow rate of the working fluid is related to that of the geofluid by conservation of energy; that is, the heat power of the geofluid is ideally equal and opposite to that of the working fluid, neglecting leakage:

$$\dot{m}_g \, \Delta h_g = \dot{m}_w \, \Delta h_w \tag{14}$$

Where the subscripts g and w denote the geofluid and working fluid, respectively. Since $\Delta h_w = q_{in}$, the mass flow rate of the working fluid cycle can be expressed as:

$$\dot{m}_w = \frac{\dot{m}_g \, \Delta h_g}{q_{in}} \tag{15}$$

Figures 19, 20, and 21 on the following pages show T-s and T-q charts for single-, double-, and triple-pressure binary cycles, for representative geofluid production at the critical point.

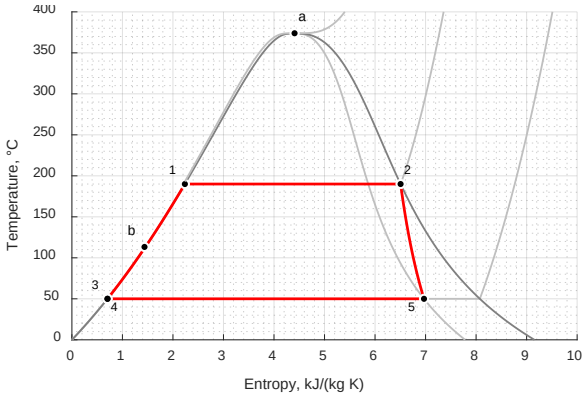

Single-Pressure Binary Cycle

q_in	2574.5	kJ/kg
q_out	2024.7	kJ/kg
w_net	549.8	kJ/kg
η_I	0.214	~
x_min	0.850	~

	T	P	h	s	x	m
1	190.0	12.57	807.7	2.24	0.000	1.000
2	190.0	12.57	2785.3	6.51	1.000	1.000
3	50.0	12.57	210.8	0.70	NaN	1.000
4	50.0	0.12	209.6	0.70	0.000	1.000
5	50.0	0.12	2234.2	6.97	0.850	1.000

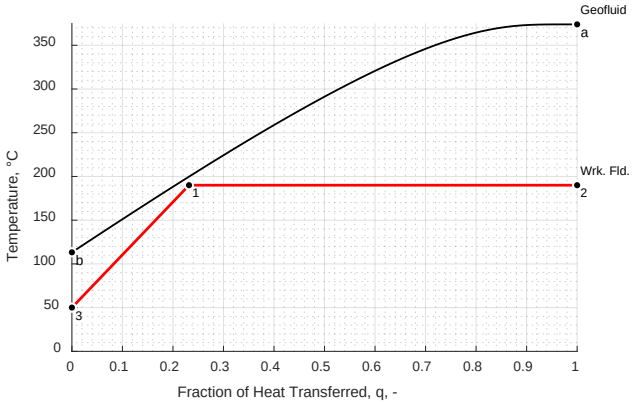

Geofluid

Nominal Pressure	220.6	bar
Inlet Temperature	373.9	°C
Inlet Enthalpy	2084.2	kJ/kg
Outlet Temperature	113.3	°C
Outlet Enthalpy	491.3	kJ/kg
Mass Flow Rate	80.1	kg/s

Plant

Mass Flow Rate (Wrk. Fld.)	49.6	kg/s
Heat Input	127.6	MWt
Condenser Rejection	100.4	MWt
Gross Output	27.3	MWe
Exergetic Efficiency, η_II	0.502	~

Figure 19: Single-pressure binary cycle for geofluid production at the critical point.

The optimal single-pressure working fluid cycle is generally independent of the geofluid production conditions. Maximizing η_{II} entails maximizing the turbine's inlet temperature, which is limited herein to about 190 °C per the constraints of the turbine and condenser. A single pinch point occurs between the preheater and evaporator, at State 1. The geofluid outlet temperature is generally high, at more than 100 °C, except where production is vapor-dominated; in these latter cases, the condensation of the geofluid in the evaporator with $\partial T/\partial q = 0$ increases the geofluid's $\partial T/\partial q$ in the preheater, improving the T-q curve match, and decreasing the geofluid outlet temperature.

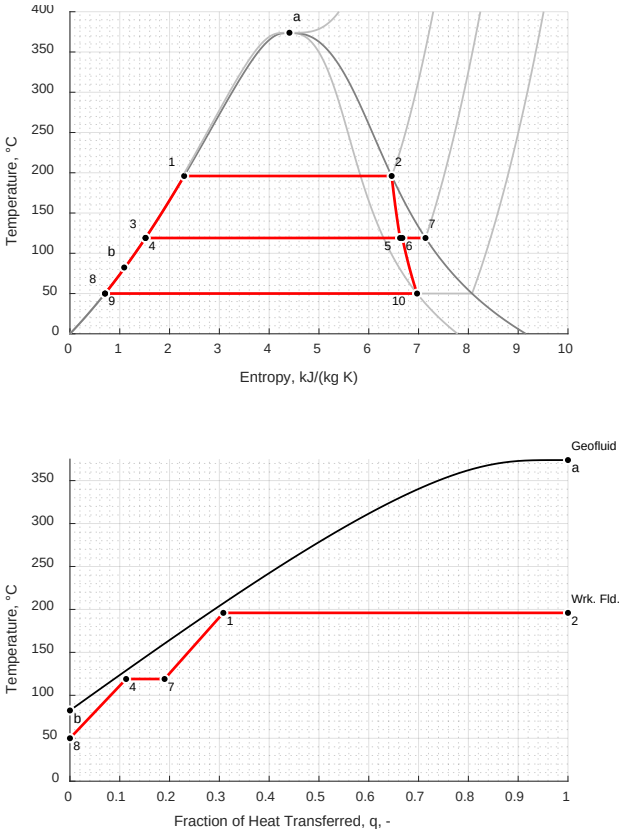

Double-Pressure Binary Cycle

q_in	2570.9	kJ/kg
q_out	2025.0	kJ/kg
w_net	546.0	kJ/kg
η_I	0.212	~
x_min	0.850	~

	T	P	h	s	x	m
1	196.0	14.31	834.5	2.29	0.000	0.910
2	196.0	14.31	2789.5	6.46	1.000	0.910
3	119.1	14.31	501.1	1.52	NaN	0.910
4	119.0	1.93	499.8	1.52	0.000	1.000
5	119.0	1.93	2504.4	6.63	0.909	0.910
6	119.0	1.93	2522.4	6.67	0.917	1.000
7	119.0	1.93	2704.5	7.14	1.000	0.090
8	50.0	1.93	209.7	0.70	NaN	1.000
9	50.0	0.12	209.6	0.70	0.000	1.000
10	50.0	0.12	2234.5	6.97	0.850	1.000

Geofluid

Nominal Pressure	220.6	bar
Inlet Temperature	373.9	°C
Inlet Enthalpy	2084.2	kJ/kg
Outlet Temperature	82.4	°C
Outlet Enthalpy	362.5	kJ/kg
Mass Flow Rate	80.1	kg/s

Plant

Mass Flow Rate (Wrk. Fld.)	53.7	kg/s
Heat Input	138.0	MWt
Condenser Rejection	108.7	MWt
Gross Output	29.3	MWe
Exergetic Efficiency, η_II	0.539	~

Figure 20: Double-pressure binary cycle for geofluid production at the critical point.

Adding a second vaporization pressure enables a better T-q curve match and a lower geofluid outlet temperature, conferring a significant improvement in exergetic efficiency η_{II}, and by extension gross power output $\dot{Q}$. Two pinch points occur between both pairs of preheaters (8-4, 3-1) and evaporators (4-7, 1-2). Optimization equalizes the magnitudes of these two pinch points at States 1 and 4. Most of the working fluid flows through the HP loop, with the small remainder flowing through the LP loop, enabling a slightly higher turbine inlet temperature. The thermal efficiency η_I is essentially unchanged.

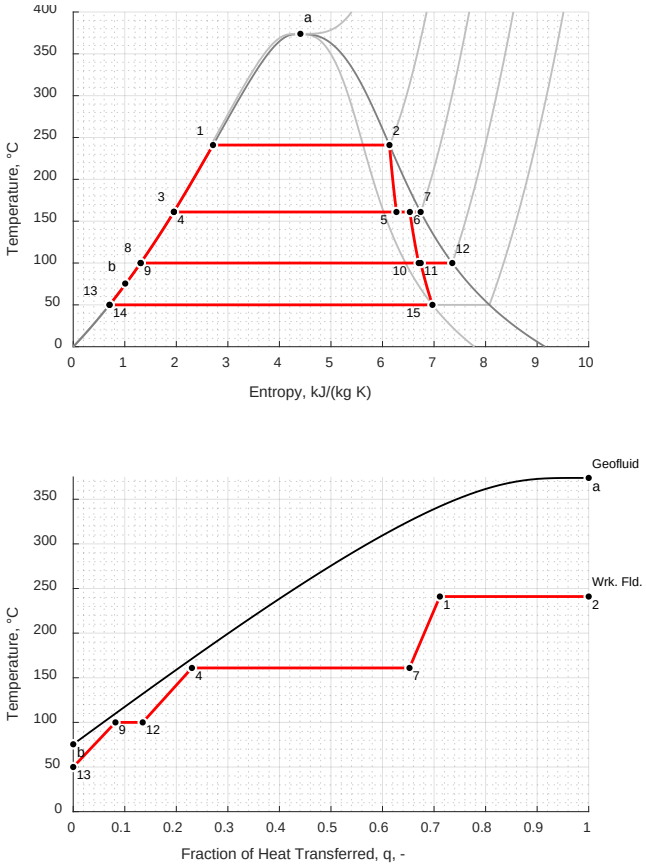

Triple-Pressure Binary Cycle

fluid	water	
q_in	2560.8	kJ/kg
q_out	2024.6	kJ/kg
w_net	536.1	kJ/kg
η_I	0.209	~
x_min	0.850	~

	T	P	h	s	x	m
1	241.0	34.09	1042.6	2.71	0.000	0.420
2	241.0	34.09	2802.8	6.13	1.000	0.420
3	161.3	34.09	683.1	1.95	NaN	0.420
4	161.0	6.35	680.0	1.95	0.000	0.940
5	161.0	6.35	2554.7	6.27	0.902	0.420
6	161.0	6.35	2667.5	6.53	0.956	0.940
7	161.0	6.35	2758.6	6.74	1.000	0.520
8	100.0	6.35	419.9	1.31	NaN	0.940
9	100.0	1.02	419.4	1.31	0.000	1.000
10	100.0	1.02	2432.5	6.70	0.892	0.940
11	100.0	1.02	2447.1	6.74	0.899	1.000
12	100.0	1.02	2675.6	7.35	1.000	0.060
13	50.0	1.02	209.6	0.70	NaN	1.000
14	50.0	0.12	209.6	0.70	0.000	1.000
15	50.0	0.12	2234.2	6.97	0.850	1.000

Geofluid

Nominal Pressure	220.6	bar
Inlet Temperature	373.9	°C
Inlet Enthalpy	2084.2	kJ/kg
Outlet Temperature	75.5	°C
Outlet Enthalpy	334.0	kJ/kg
Mass Flow Rate	80.1	kg/s

Plant

Mass Flow Rate (Wrk. Fld.)	54.8	kg/s
Heat Input	140.3	MWt
Condenser Rejection	110.9	MWt
Gross Output	29.4	MWe
Exergetic Efficiency, η_II	0.540	~

Figure 21: Triple-pressure binary cycle for geofluid production at the critical point.

By contrast, adding a third vaporization pressure does not confer significant benefit to thermal efficiency η_I or exergetic efficiency η_{II}, and thereby does not appear to be economical. This can be seen heuristically from the optimized T-q curves, which show only two significant pinch points at States 4 and 9, one less than the maximum implied by the quantity of vaporization pressures.

Figures 22, 23, and 24 on the following pages show the gross power outputs and exergetic efficiencies of single-, double-, and triple-pressure binary plants for geofluid produced in Region A.

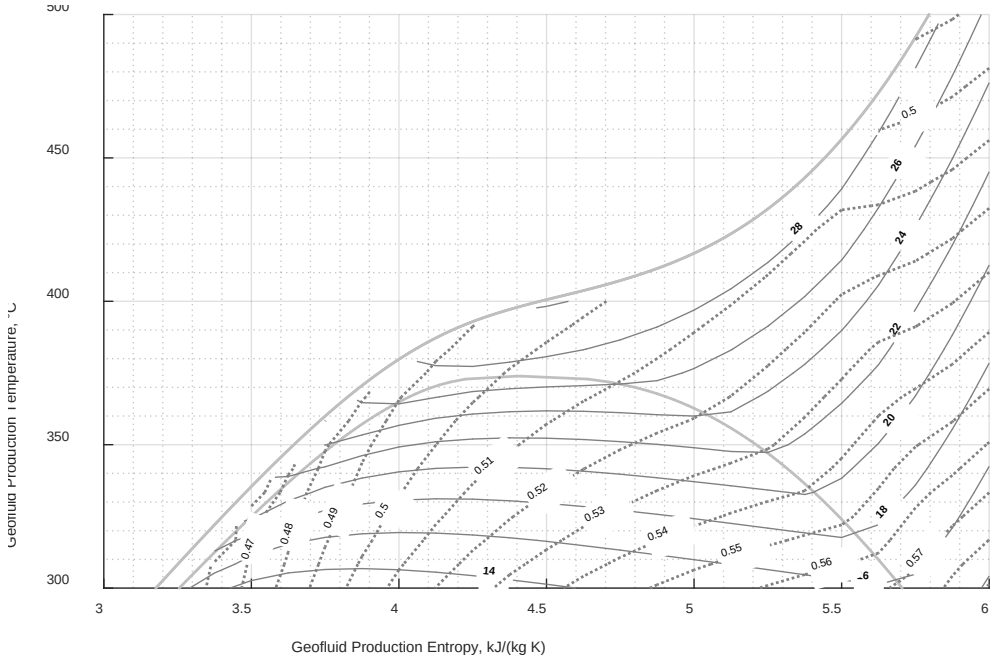

Figure 22: Gross power output in MWe (solid) and exergetic efficiency (dotted) for ideal single-pressure binary cycles.

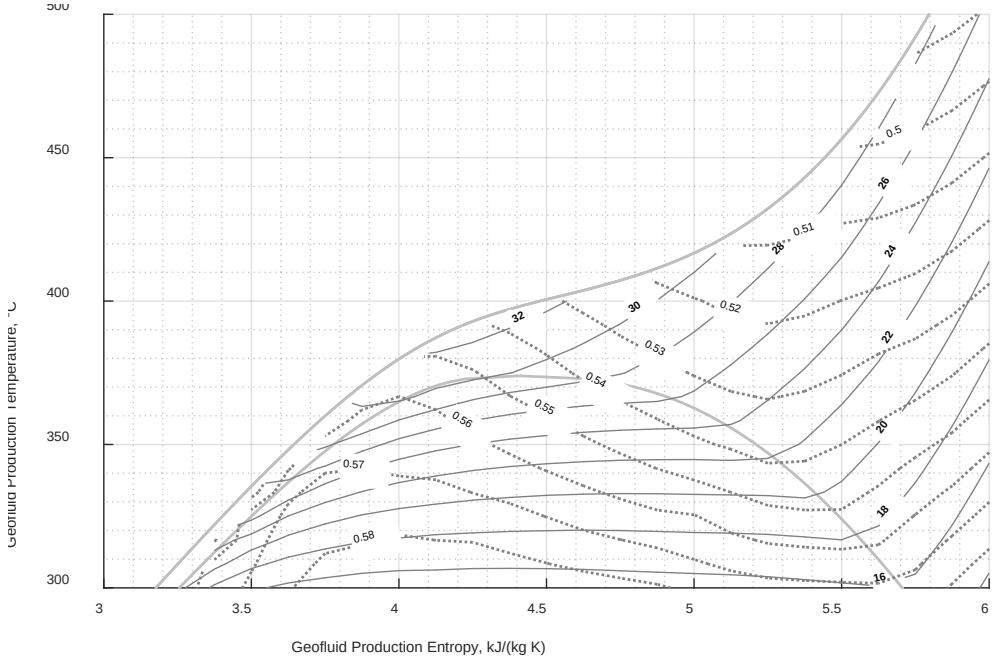

Figure 23: Gross power output in MWe (solid) and exergetic efficiency (dotted) for ideal double-pressure binary cycles.

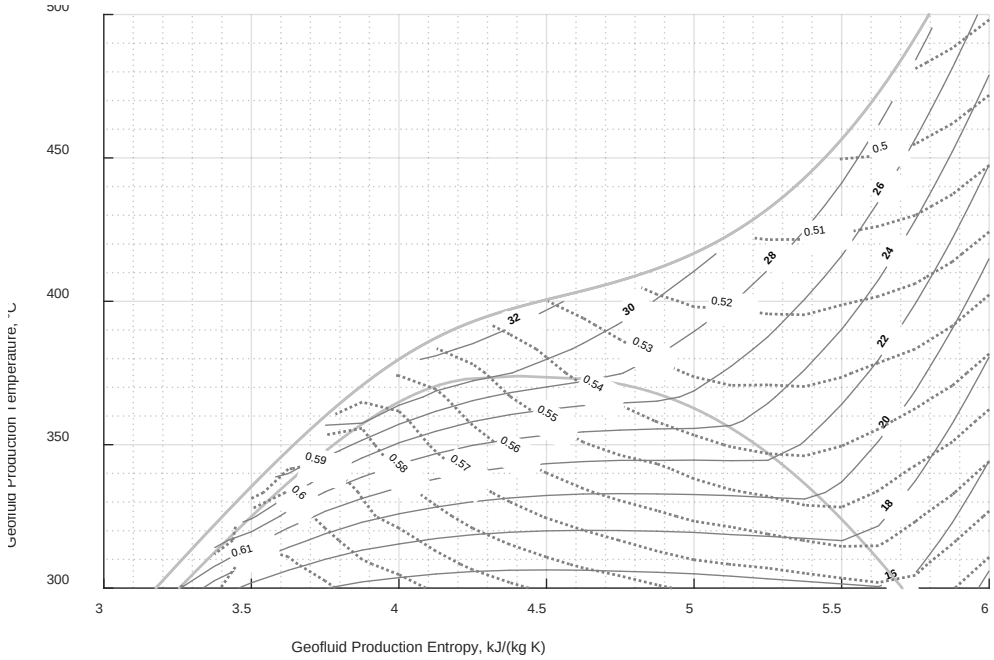

Figure 24: Gross power output in MWe (solid) and exergetic efficiency (dotted) for ideal triple-pressure binary cycles.

These plots show that the characteristics of ideal high-temperature binary plants are highly comparable to those of high-temperature flash plants. The gross power output is increased significantly by introducing a second vaporization pressure, while introducing a third vaporization pressure confers benefit mainly towards the liquid-dominated region. For a given temperature T, the gross power output $\dot{Q}$ is generally maximized where the geofluid production is densest, corresponding to the phase regions of compressed liquid and supercritical fluid. The gross power output increases significantly with temperature in the subcritical region, and less significantly with pressure in the supercritical region.

8. Conclusion

This paper considered the ideal gross output of a generic geothermal power system producing between 300-500 °C. The characteristically high slenderness of the production well imposes significant hydraulic constraints on geofluid production. Accordingly, the maximum mass flow rate of a production well with an 8.5” minimum inner diameter was found to be about 100 kg/s. Combining this hydraulic constraint with the thermodynamic constraint associated with exergy indicated that exergetic power is maximized in the compressed liquid and supercritical regions of water, at about 55-60 MWe, which have characteristic production pressures of $P > 85.9$ bar in the subcritical region, and $P > 220.6$ bar in the supercritical region. Further, it was noted that exergetic power plateaus around the critical point of water, after which gains in exergy are approximately offset by losses in mass flow rate, suggesting that supercriticality is not necessary for maximum performance.

Geofluid production was classified into two regions, A and B, based on suitability for supplying typical non-reheat steam turbines. Region B was defined as being sufficient for a dry steam power cycle, while Region A required a more complex power cycle, i.e. flash or binary, to attain sufficient turbine dryness.

Dry steam power cycles in Region B were found to be superior in terms of exergetic efficiency, ideally around 78-84%, because no processing of the geofluid is required, entailing minimal irreversibility. However, the gross power output is limited by the characteristically low geofluid production density, limiting the production mass flow rate and pressure.

Flash cycles were considered in the subset of Region A where $h < 2{,}800$ kJ/kg, i.e. where isenthalpic expansion generally produces a two-phase mixture. The conventional "equal-temperature-split" (ETS) guideline for flash separator temperatures was shown to break down above about 200 °C, as the temperature approaches the critical point where the specific heat becomes undefined. Instead, a gradient ascent algorithm was used to determine the optimal separator temperatures that maximize the cycle's exergetic efficiency. Single-, double-, and triple-flash cycles were evaluated, showing substantially greater gross power output on an equal-temperature basis, as compared to the earlier dry steam power cycles. Though the exergetic efficiency was lower, at 50-65%, this was more than compensated for by the denser geofluid production, yielding higher mass flow rates. It was noted as a heuristic approximation that ETS applied between the first separator at the highest possible temperature and the condenser yielded a net work that closely matched the result obtained via gradient ascent. Adding a second or third flash was found to be more effective towards the liquid-dominated and supercritical regions. Drawbacks associated with solid and gaseous geofluid impurities, as well as pump loads, were noted.

Binary cycles were also considered in Region A. The choice of working fluid was considered as the primary means of mitigating the irreversibility inherent to this type of cycle. It was shown that the hydrocarbon working fluids characteristic of organic Rankine cycles (ORCs) cannot practically attain temperatures exceeding about 200 °C because of their retrograde condensation. As a result, water was found to outperform these hydrocarbons above a geofluid production temperature of about 315 °C, and was considered as the working fluid of choice. A gradient ascent algorithm was again used to determine the optimal evaporator temperature(s) and mass flow rate fraction(s) to maximize the cycle's exergetic efficiency, accounting for pinch points between the two fluids in T-q coordinates. The thermal efficiencies, exergetic efficiencies, and gross power outputs of these optimized cycles, in single-, double-, and triple-pressure variations, were found to be highly comparable to flash cycles of equal sophistication. This can be attributed to the many properties that are shared between the two cycles, including the working fluid composition, the turbine performance, and the heat rejection scheme. In this sense, binary plants attain performance comparable to flash plants, with significantly less susceptibility to geofluid impurities, and potentially with less parasitic pumping load.

As a whole, this work indicates that geothermal systems may attain their maximum power output with a production temperature as low as 350-375 °C, i.e. near the critical temperature, provided that the production pressure is sufficiently high. For a production well with an 8.5” minimum inner diameter, the ideal power output is about 30-32 MWe gross, using either a double-flash cycle, or a double-pressure binary cycle. This represents the potential of up to an order of magnitude improvement over the typical performance of current geothermal systems.

Nomenclature

The symbols shown in Table 1 below are used throughout this paper. Where applicable, the assumed value is also shown.

Symbol	Definition	Value	Units
C_p	Specific heat capacity, isobaric	-	J/(kg K)
$\dot{E}$	Exergetic power	-	MW, or MWe
$\dot{Q}$	Gross power output	-	MWe
T_{cond}	Condenser temperature	50	°C
T_{crit}	Critical temperature	-	°C
T_o	Temperature, dead state	50	°C
$\dot{m}$	Mass flow rate	-	kg/s
q_{in}	Heat input	-	kJ/kg
q_{out}	Heat output, or rejection	-	kJ/kg
v_e	Erosional velocity	-	m/s
w_{net}	Net work	-	kJ/kg
x_{min}	Turbine minimum quality	0.85	-
η_I	Thermal (First Law) efficiency	-	-
η_{II}	Exergetic (Second Law) efficiency	-	-
η_{td}	Turbine efficiency, dry, isentropic	0.85	-
h	Enthalpy	-	kJ/kg
Δ	Difference, or change	-	-
ΔT_{pp}	Temperature difference at pinch point	10	°C
A	Wellbore minimum cross-sectional flow area	0.0366	m^2
D	Wellbore minimum inner diameter	8.5	in
L	Wellbore length	-	m
P	Pressure	-	bar
T	Temperature	-	°C
c	Erosional constant, empirical, API RP 14E	100	$(ft/s)(lb/ft^3)^{1/2}$
e	Exergy	-	kJ/kg
f	Friction factor	-	-
m	Mass flow rate fraction	-	-
q	Fraction of heat transferred	-	-
s	Entropy	-	kJ/(kg K)
v	Velocity	-	m/s
x	Quality, or dryness fraction	-	-
δ	Partial derivative	-	-
ρ	Density	-	kg/m^3

Table 1: List of symbols used in this paper, and assumed values, where applicable.

REFERENCES

American Petroleum Institute. “API RP 14E: Recommended Practice for Design and Installation of Offshore Production Platform Piping Systems.” 5th ed. (1991, reaffirmed 2013).

American Petroleum Institute. “API Specification 5CT: Specification for Casing and Tubing.” 8th ed. (2005).

Calpine Corporation. “The Geysers Geothermal Field 2022 Statistics.” Mar. 2023, https://geysers.com/The-Geysers/Geysers-By-The-Numbers.

Çengel, Y., et al. “Fundamentals of Thermal-Fluid Sciences”. McGraw-Hill (2012).

DiPippo, R. “Geothermal Power Plants: Principles, Applications, Case Studies and Environmental Impact”. Elsevier/Butterworth-Heinemann (2016).

Ingason, K., et al. “Design and Development of the Discharge System of IDDP-1.” *Geothermics* (2014).

International Finance Corporation (IFC), and GeothermEx, Inc. “Success of Geothermal Wells: A Global Study.” (2013).

Lemmon, E. W., et al. “NIST Standard Reference Database 23: Reference Fluid Thermodynamic and Transport Properties-REFPROP, Version 10.0, National Institute of Standards and Technology.” (2018).

Zarrouk, S., and Moon, H. “Efficiency of Geothermal Power Plants: A Worldwide Review.” *Geothermics* (2014).

Optimizing Energy Production for Large Scale Superhot Rock Geothermal

Jenna Hill[1], Terra Rogers[1], Doug Brown[2], Catherine Roy[2], Jaclyn Urbank[2]

[1]Clean Air Task Force

[2]Jacobs

Keywords

Superhot Rock, Geothermal, Optimization, Power

ABSTRACT

Commercial utilization of superhot rock geothermal energy could significantly contribute to global decarbonization by making high-enthalpy geothermal power available across diverse geographical settings. This paper reviews an assessment of the optimal energy production pathways of superhot rock energy downstream of the geofluid production at the surface. It identifies equipment gaps for dealing with geothermal fluid above 400˚C in a power plant system. The focus is on the need to foster innovation and identify an efficient system that is not currently available off-the-shelf. Setting a benchmark of 500 MW for energy production represents an approach aligned with industry trends in high-temperature, high-pressure, hot dry rock geothermal systems. This benchmark sheds light on critical technological gaps that must be addressed to unlock the full potential of superhot rock energy and facilitate a seamless transition toward sustainable energy sources.

By undertaking this evaluation, the paper provides valuable insights into the current state of superhot rock energy technology and paves the way for future research and demonstration initiatives. Ultimately, the findings of this study are poised to inform strategic decision-making processes, guide investment priorities, and shape the trajectory of superhot rock energy production towards a more sustainable and resilient energy landscape.

1. Introduction

This study assesses the optimal energy production pathway of superhot rock energy after the point of fluid production at the surface. It uses that assessment to define the most efficient production pathway and identify technology gaps that must be tackled for superhot rock energy to enable the energy transition.

The following phases were studied:

Production Pathways and Electricity Demand: Identify and define a high-efficiency electricity production pathway from superhot rock geothermal resources.

Cooling System Analysis: Evaluate various technologies for cooling and/or condensing of the produced fluid.

Component Specifications and Technology Gap Analysis: Further definition of essential characteristics of each significant component based on a final power plant technology.

Cost Estimate: Generate a Class 5 (Association for the Advancement of Cost Engineering, AACE) cost estimate for capital and operating costs.

This study will help to enable policies, further private and public investment, and push continued technological innovation to help commercialize superhot rock geothermal. This study can inform the future research and demonstration needs for the production of superhot rock energy and assess how downstream technologies, such as direct air capture (DAC), hydrolysis, hydrogen production, and more, may be able to benefit from the production of electricity using superhot rock energy.

2. Overview of Relevant Projects (Hill 2022)

Several R&D projects around the world have already drilled into superhot rock and have begun developing methods for operating in these extreme heat and pressure conditions. However, superhot steam has yet to be harnessed for power production.

Iceland Deep Drilling Project: IDDP has been a superhot rock drilling initiative for over a dozen years as a part of the European Union's DEEPEGS program. The first test well, IDDP-1 Krafla, was completed in 2009 after drilling was terminated when it encountered magma. Krafla demonstrated the energy potential of superhot wells with a projected energy flow of 36 MWe. The second IDDP well, IDDP-2 Reykjanes, reached its objective of supercritical (superhot) conditions at 426°C in 2017. IDDP planned to flow test the well in 2021. An inferred casing collapse shortly after completion of the well ultimately rendered it unusable for testing as planned. IDDP is currently planning a third superhot well.

Japan Beyond Brittle Project: The Japan Beyond Brittle project (JBBP) was initiated to investigate the feasibility of creating enhanced geothermal systems in the brittle–ductile transition zone. This study grew out of the initial deep drilling work conducted at the Kakkonda geothermal area in Japan. Anticipated advantages of such a system include a potentially very large geothermal energy resource that could result in economic energy extraction, simpler reservoir design and control, reduced parasitic fluid losses, and reduced induced seismicity.

Hotter and Deeper: The Hotter and Deeper Exploration Science (HADES) project in New Zealand has been exploring superhot resources in the Taupo Volcanic Zone since 2009 and has been planning a scientific drilling project into New Zealand's deep-seated superhot rock. Like JBBP, the project hopes to investigate potential reservoir systems in the superhot plastic brittle-ductile transition zone at about 7 km where geophysics suggests there is little seismic activity. This is another EU supported project.

DESCRAMBLE: Italy's Larderello geothermal field has been a heat resource for over a century, with electric power production since 1913, and was the site of an intensive EU collaborative effort from 2015-18 (known by the acronym DESCRAMBLE) to drill into superhot rock (also as a part of the EU DEEPEGS program). Superhot conditions were initially encountered in the early 1980s in Larderello's San Pompeo-2 well. Larderello's Venelle-2 is the hottest geothermal well on record, registering 514°C at a depth of 2.9 km (1.8 mi).

3. Design Basis

The study site location assumed for this high-level analysis exercise was in the general vicinity of San Luis Obispo, CA, as representative of a location without temperature extremes. The well pads are assumed to be located 500 m from the plant with 5 well pairs per well pad. Each well pair consists of one injection and one supply wellhead as shown in Figure 1.

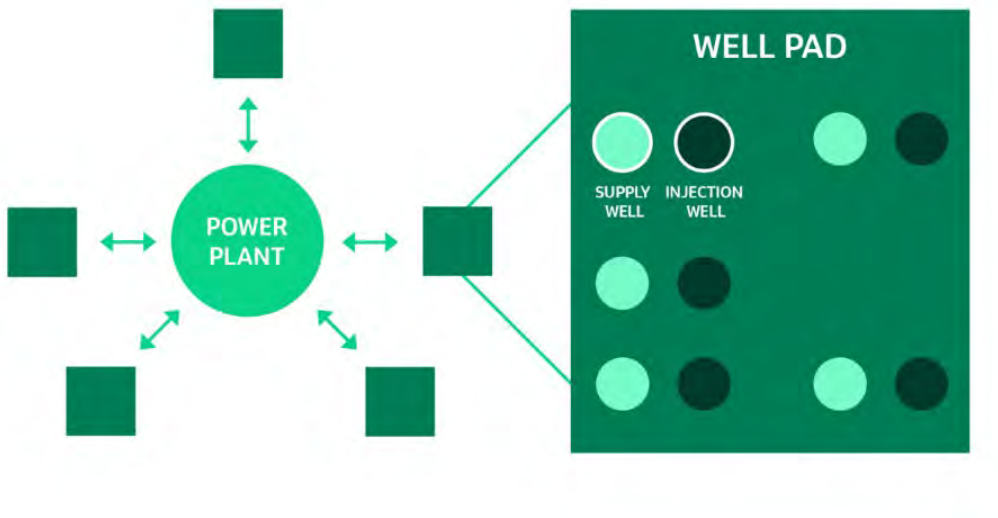

Figure 1: Visual schematic of wells and power plant

The assumptions that form the basis of this study are outlined in Table 1.

Table 1: Design basis assumptions

Parameter	Units	Value
Superheated Steam Supply Pressure (at production wellhead)	bar	140
Superheated Steam Supply Temperature (at production wellhead)	°C	400
Superheated Steam Flow Rate (per production well)	kg/s	33.8
Injection Pressure (at plant boundary)	Bar	155
Injection Flow Rate (at plant boundary)	Kg/s	33.8
Plant Output	MW	500
Water Loss in Downhole Superhot Rock System	%	5
Wet Bulb Temperature	°C	21

Plant inlet conditions were assumed to be 130-135 bar and 390°C to allow for losses in the gathering system. A plant size of 500 MW gross was selected to represent a range for the superhot rock industry to strive for to balance the costs of the wells and the expected revenue generation from electricity production.

For the purpose of evaluating the most efficient energy production pathway, geochemistry of the superhot rock geofluid was considered at a high level. There are considerations in design that would need to be addressed depending on the resource. Traditionally, hydrothermal resources have contaminants that come up with the geofluid, including silica, sodium, chlorides, etc., that, in addition to the fluid pH, can cause a variety of issues, including pipe corrosion and damage to the steam turbine. To remove the contaminants, operators often "wash" the steam with a condensate spray to bring the incoming steam slightly below saturation. The contaminants will become entrained in the condensate that is then separated prior to the steam entering the turbine.

4. Production Pathways for Electricity Demand

Three different plant configurations were evaluated for power production. For evaluating plant output and steam usage, a wet cooling tower was used as a condensing heat sink. With the plant size set to 500 MW gross, the total geofluid required to meet that demand was calculated based on the assumed well capacity. This dictated the number of wells required for the plant and has a significant impact on the overall cost of the facility.

The following plant designs were evaluated:

1. **Dry Steam Plants**
    a. **Direct steam use**. The superheated steam is used directly in the steam turbine as received from the wells.
    b. **Washed steam.** Washing the superheated steam to remove contaminants, resulting in clean but saturated steam fed to the steam turbine.
2. **Binary Cycle Plant:** use the geofluid in a heat exchanger to boil water in a typical closed loop steam cycle.

4.1 Dry Steam Plant Model

Figure 2 displays the dry steam plant model that was developed using a combination of the modeling software packages AspenTech HYSYS and Thermoflow.

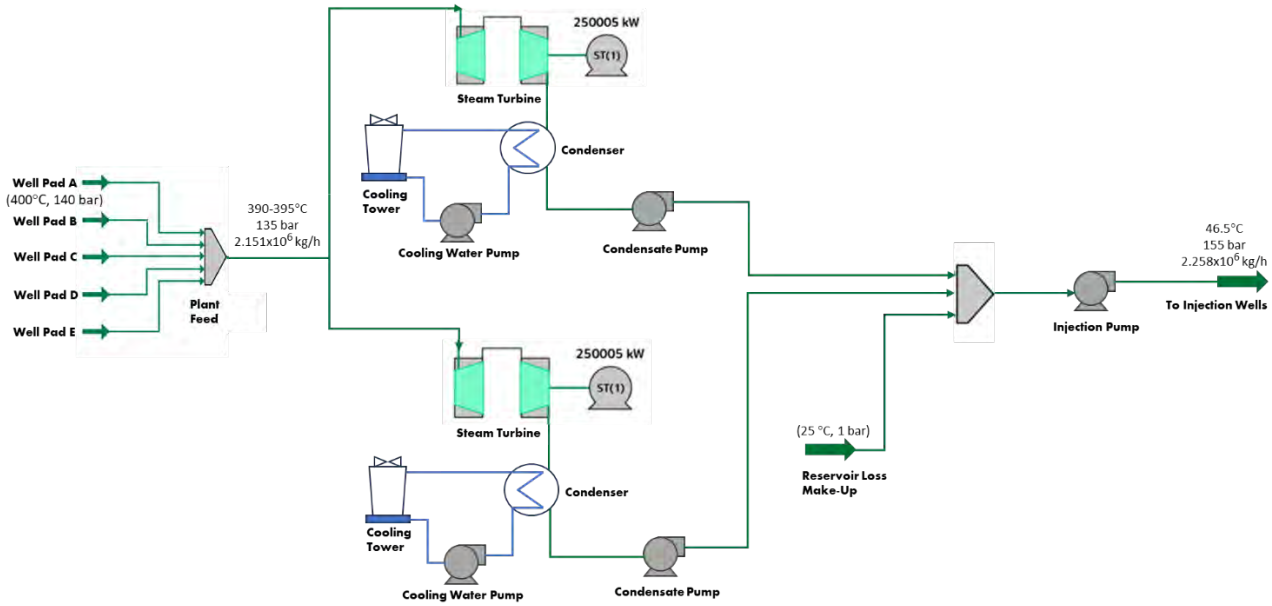

Figure 2: Dry Steam Plant Configuration

The steam is collected from the wellfield and combined into a supply header at the plant boundary. The steam is split into 2 x 250 MW condensing steam turbines to represent the current industry standard for steam turbine sizing. Larger steam turbines are possible but are considered a bespoke product. The cooling tower provides cooling water to condense the turbine exhaust efficiently under vacuum in a surface condenser. The condensate and injection pumps provide the pressure to recirculate the fluid through the downhole superhot rock system. The noncondensable gas (NCG) removal system that would be used to extract the NCGs from the condenser is not shown.

For the washed steam case, water will be sprayed into the incoming steam sufficient to desuperheat and slightly cool the steam. A separator between the wash water spray and the turbine inlet will remove the resulting condensate, which contains a large portion of the steam contaminants that could cause corrosion or deposits in the steam turbine.

4.2 Binary Model

The intent of using a binary cycle to extract energy from a superhot rock resource is to avoid using the potentially contaminated resource directly in a turbine and instead put it through an intermediate heat exchanger. This would eliminate the need for specialized turbine materials, significantly reducing mitigation costs. In Figure 3, the superhot rock resource is used in a heat exchanger where the heat is transferred to a closed water/steam loop. The cooled geofluid is then sent back to injection. Depending on the geofluid process conditions and pressure drops from the wells or in the system,, there may be NCG breakout which would require an NCG removal system (not shown). The closed loop cycle was modeled using water that would be heated and vaporized in the heat exchanger and sent through a similar 2 x 250 MW steam turbine system. A wet cooling tower supplies cooling water to a surface condenser, which condenses the turbine exhaust.

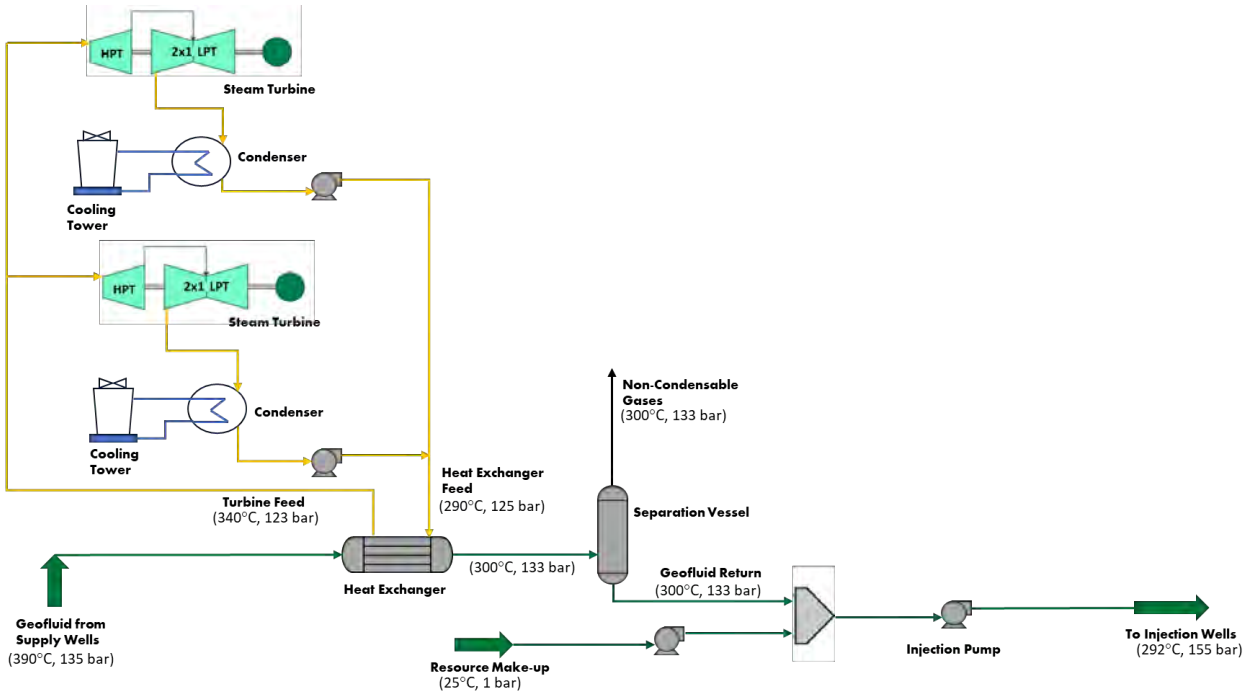

Figure 3: Binary Cycle Plant Configuration

Performance in the binary loop as modeled is limited by temperature approaches in the heat exchanger between the incoming geofluid and the closed water loop. This limits the geofluid exit temperature from the heat exchanger. To improve the efficiency of this type of plant, the geofluid leaving the heat exchanger ("geofluid cold" in the diagram) could become the hot side of a second heat exchanger that generates steam in a closed loop at a lower pressure, which would be fed to the steam turbine at the appropriate pressure location. It is possible that a third (low pressure) steam generation loop could be created, effectively creating a three-pressure steam cycle.

4.3 Results and Conclusions

Table 2 presents a relative comparison of the modelling results and the key performance indicators for the direct use, washed steam, and binary cycle models using the direct use cycle as a basis.

Table 2: Relative Comparison of Values

Relative Comparison	Direct Use	Washed Steam	Binary Cycle
Geofluid Required	1.0	1.16	1.44
Parasitic Load	1.0	1.16	1.39
Geofluid per MW	1.0	1.25	1.51
Production wells	17	20	25

The washed steam and binary cycles require more geofluid, have a higher parasitic load, and require more geofluid per MW of power produced compared to the direct use case. From a performance standpoint, the direct use configuration is the most efficient.

This study focuses on the needs for innovation in a more efficient power plant system that is not yet readily available off-the-shelf. The remainder of this study was based on the direct use configuration for the power plant to address equipment requirements and cost.

5. Water Use Analysis

With the direct use cycle configuration established, different cooling methods were evaluated using the following designs:

- Forced Draft Cooling Tower (CT)
- Natural Draft Cooling Tower (CT)
- Air-Cooled Condenser (ACC)

Table 3 summarizes the water usage for each technology.

Table 3: Water Use Requirements

	Units	Natural Draft CT	Forced Draft CT	ACC
Total Water Required	kg/hr	2,067,840	2,115,216	109,080
Annual Water Use	$x10^6$ kg	18,114	18,529	956
Water Usage	kg/kWh	4.14	4.23	0.22

The total water required for the natural and forced draft cooling towers is similar. There is no water required for air cooling, therefore the only water required for a plant with an ACC system is makeup water due to the loss within the formation. The comparison found that water requirements for a wet cooling system are approximately 20 times that of a plant using dry cooling. Strictly based on water consumption, the ACC would be the best cooling system choice for the plant design. However, there are parasitic power penalties associated with the ACC compared to the wet cooling systems.

Developers may opt to locate plants near large bodies of water and use cooling systems similar to nuclear and Natural Gas Combined Cycle (NGCC) plants as a method to minimize water costs. However, the dry cooling (ACC) option for the final version of the model for this study was selected to represent a plant that could be located anywhere and not limited to sites with access to makeup water.

6. Technology Gap Analysis

The objective of this phase of the study was to develop a major equipment list for the representative power plant model selected: direct use with dry cooling. Ultimately, equipment and material selections will also be dependent on the conditions of the geofluid and the specific site location.

Technology Readiness Levels (TRLs) were originally developed by NASA in the 1970s for space exploration technologies and are used to assess the maturity level of a technology throughout its research, development and deployment phase progression. TRLs are based on a scale from 1 to 9, with 9 being the most mature technology as shown in Table 4.

Table 4: Technology Readiness Level Definitions

TRL Level	Description
1	Basic Principals Observed
2	Technology Concept Formulated
3	Experimental Proof of Concept
4	Technology Validated in Lab
5	Technology Validated in Relevant Environment
6	Technology Demonstrated in Relevant Environment
7	System Prototype demonstrated in Operational Environment
8	System Complete and Qualified
9	Actual System Proven in Operational Environment

The information provided in Table 5 includes potential vendors for each item listed and an assessment of the Technology Readiness Level (TRL) of the various items.

Table 5: Technology Gap List

System	Equipment	TRL
Steam Gathering System	1. Wellhead Unit/Valves (typical geothermal design but rated for 140+ barg) 2. Test Unit 3. Carbon steel piping with large corrosion allowance.	1. TRL 8 2. TRL 9 3. TRL 9
Injection System	316 stainless steel piping	TRL 9
Warm-Up separator/ Atmospheric Flash Tank	Carbon steel with 2205 duplex stainless steel internal cladding and internals	TRL 9
HP Separator	Carbon steel with 3/16" 625 Inconel thermomechanical internal cladding, Inconel 625 internals	TRL 9
Steam Turbine Generator	2x250MW (gross) STG	TRL 5-6
Condenser	Surface condenser: AL2003 Lean Duplex shell & tube	TRL 9

System	Equipment	TRL
Condensate Storage Tank	Carbon steel with corrosion-resistant internal coating	TRL 9
Gas Removal System	1. Steam Jet Ejectors (SJE): 316L stainless steel 2. Liquid ring vacuum pump (LRVP): 316 cast stainless steel, 316L separator tank 3. Intercondensers: 316L stainless steel	TRL 9
Cooling/Condensing System	Air-cooled Condenser	TRL 9
Blowdown tank	Carbon Steel	TRL 9
Drains Tank	Carbon Steel	TRL 9
Brine/wastewater pond	Impervious pond lining	TRL 9
Make-Up water system	Wells, pumps, gathering system, storage tank	TRL 9
Rock Muffler	Standard Rock muffler is a concrete structure	TRL 9
Diesel Genset	Standard 500kW – 1MW size	TRL 9
Fire protection system	1. Diesel, Electric and Jockey pumps 2. Firewater storage tank	TRL 9
Pumps	1. Condensate: 316 SS wetted parts 2. Cooling water: 316 SS wetted parts 3. Injection: Super Duplex SS wetted parts 4. Brine/wastewater pond: 316 SS wetted parts	TRL 9
H_2S Abatement System	(Excluded from this scope, specific needs to be determined by local environmental regulations) Potential technologies in current use: • Liquid redox (Lo-Cat, Lo-Cat II, Stretford)	TRL 9

System	Equipment	TRL
	• Recuperative thermal oxidizer (RTO) • BIOX • Upstream caustic washing • Burner-and-scrubber	

The materials chosen for major equipment are intended to resist corrosion from either short-term exposure to concentrated hydrochloric or sulfuric acid or long-term exposure to dilute solutions of the same. Equipment that does not list any materials does not need any special consideration, e.g., the fire protection system.

Most of the equipment outlined in Table 4 required for the surface facilities has a TRL between 7 (system prototype demonstrated in operational environment) and 9 (system proven in operational environment). The specific design of a steam turbine for the environments considered in this study should currently be considered to exist at a TRL of 5-6 (technology validated or demonstrated in a relevant environment) due to various details of the turbine design need to be adapted to the specific composition of the geofluid.

6.1 Geothermal Superheated Steam Turbine Design Considerations

Various aspects of the turbine design will need to be adapted to the considerations of the geofluid conditions. These are known technologies that are used where needed in a particular turbine application. For example, one manufacturer identified the design of the turbine internals for a particular geothermal application that included special materials specifications for the rotor and certain stage blades, special design of blades in specific stages, special design of blades for vibration control, special design of stage condensate removal components, and specific blade coatings for various stages. All these considerations are within the turbine supplier's knowledge base and have been incorporated either in production turbines or in test units in field conditions. Without requesting a quotation from a specific vendor for a particular geofluid resource, it cannot be determined exactly what design considerations might be used by that vendor for this application. Also, different vendors may address the design requirements using different technologies.

The chloride and hydrogen sulfide (H_2S) contaminants pose a threat of high corrosion in the turbine stages where steam condensation starts to occur, as the condensate droplets will have high concentrations of hydrochloric or sulfuric acid, respectively. The H_2S partitioning into the condensate from the steam is also affected by the ammonia gas (NH_3) content in the steam. The presence of these contaminants in the high pressure/high-temperature environment not normally seen in geothermal steam turbines also affects the consideration of issues such as Stress Corrosion Cracking (SCC) and creep strength. These factors will require evaluation of metallurgies such as ferritic stainless steel, duplex stainless steel, and high nickel alloys in the turbine design, in addition to currently used treatments such as stellite coatings on blade edges.

6.2 Recommendations for Further Study

Certain high-cost materials used in this design, such as duplex stainless steel or Inconel, could be replaced with next-generation materials or coatings. The geothermal environment presents significant challenges for materials, so any new materials should undergo extensive in situ testing before being used as a substitute for current materials.

7. Cost Estimate

The final phase of the study was to develop an American Association of Cost Estimators (AACE) Class 5 (rough order of magnitude, accuracy within -30% to +50%) cost estimate for the construction and operation of the representative SHR geothermal power plant (excluding the wells and gathering system costs) to determine the order of magnitude capital and operating costs. The unique requirements for the turbine increase the equipment cost and consequently increase the plant's overall cost. However, the remaining major equipment has a TRL of 9, so the cost of that equipment should not exceed that of a traditional geothermal plant. As the turbine vendors work to improve materials and bring down costs of the bespoke superheated geothermal steam turbine, the goal would be to bring overall inside the plant costs to ~$2,000 USD/kW.

8. Conclusions

The purpose of this study was to understand the remaining equipment technology gaps for developing superhot rock power plants with focus on the surface infrastructure. After modeling, analysis, and conversations with vendors, it was concluded that most pieces needed for a superhot rock plant already exist, either in power plant designs or in other industries. However, because a SHR test facility has yet to be constructed and commissioned, the TRL is 5 for the system as a whole.

Future research and development for superhot rock power production should focus on achieving cost reductions and moving from specialized equipment to off-the-shelf materials. Future research must focus on this equipment's cost reductions, but most technology gaps for superhot rock remain outside of the power plant system. A superhot rock power plant can be envisioned as a hybrid model between a traditional fossil fuel or nuclear power plant, which deals with high steam temperatures, pressures, and power output, and a geothermal power plant, which deals with the specific needs of accessing subsurface heat.

Investing in research and development for superhot rock energy holds significant promise, not only for providing the heat necessary for industrial processes but also for contributing substantial power to the grid, offering a sustainable and efficient solution to meet energy demands.

REFERENCES

Brown, D., Roy, C., Urbank, J. "Bridging the Gaps: A Survey of Methods, Challenges, and Pathways Forward for Superhot Rock Power Production." Clean Air Task Force, Boston, MA, 2024.

Hill, B. "Superhot Rock Energy: A Vision for Firm, Global Zero-Carbon Energy." Clean Air Task Force, Boston, MA, 2022.

Reinsch, T., Dobson, P., Asanuma, H., Huenges, E., Poletto, F., Sanjuan, B. “Utilizing supercritical geothermal systems: a review of past ventures and ongoing research activities.” Geothermal Energy Journal, Potsdam, Germany, 2017.

Increased Structural Integrity of Casings of High-Temperature Geothermal Wells using Novel Technologies

Gunnar Skúlason Kaldal[1], Steinþór Níelsson[1], Þorri Jökull Þorsteinsson[1]

[1]ÍSOR – Iceland GeoSurvey

Keywords

Geothermal, High-Temperature Geothermal Wells, Casings, Flexible Couplings, Stress Mitigation, Thermal Expansion

ABSTRACT

Well casings in geothermal wells that are used to produce from high-temperature fields are prone to fail due to a combination of factors, e.g. the quality of the cemented annulus and the degree of temperature change, that can result in structural overload. The main failure modes have been identified as collapse and tensile rupture of the casing. Casing collapse is an effect of annular pressure buildup in the cemented annuls primarily due to excess water and/or closed off water in the cement sheath that expands as the well warms up for the first time after drilling. Whereas tensile failure is an effect of permanent deformation in compressive (hot) state where the yield strength is surpassed generating plastic strain in the material that in tensile (cold) state results in tensile failure. Such casing failures can cause significant production problems, both in terms of wellbore flow restrictions and operational safety. Additionally, current lessons learned from drilling and producing from superheated/supercritical deep geothermal wells brings forward the conclusion that the metal casings are a bottleneck for reliable structure and/or a successful project. These challenges need to be solved to continue the pursuit of deep drilling into superhot conditions. Two technological advancements have been in development within ÍSOR, (i) Flexible Couplings are intended to solve the axial thermal expansion problem by allowing displacement of every casing joint into the connection and (ii) Casing Collapse Protection, a pressure relief system to relief temporary overpressure within a cemented annulus that is intended to prevent casing collapse. These two solutions work together in increasing the structural integrity of the casing throughout its lifetime. The patented Flexible Couplings have been developed within ÍSOR from the year 2015 within several research projects (EU Horizon 2020 supported GeoWell and DEEPEGS, and GEOTHERMICA project GeConnect) and the annular pressure relief system is being developed in the EU Horizon Europe supported project COMPASS.

1. Introduction

Design, drilling and operation of high-temperature geothermal wells has improved substantially over the years since utilization of high-temperature fields for electricity power production and combined heat and power utilization was initiated over a half a century ago. Materials and methods have improved and been adapted to conditions that can be quite different between fields as well as within fields. In most cases, the near steady state conditions during production are less demanding than transitional periods, such as conditions that form during warmup of wells and shut-in periods where the chemical attack can increase substantially, e.g. due to condensate and local cooling of the wells. While wells warm up, thermal expansion generates mechanical loads on the constrained casings where compressive stresses build up and lead to permanent (plastic) strains that are non-recoverable. This deformation of the casing material can lead to subsequent tensile failures if the casing is allowed to cool down again. Such tensile failures are oftentimes found around another failure mode of the casing, casing collapse. Such failures can occur if water is trapped in the annulus between casings or if excess water in the cement is high enough to generate annular pressure while the well warms up. During the first flow test of a well, the temperature can increase rapidly in the relatively cool shallow section of the well that is above the geothermal reservoir. This can result in a rapidly forming annular pressure that can result in a casing collapse. The combination of the rate and level of the temperature increase, well geometry, enclosed casing-to-casing annulus, casing material quality, etc. are the leading factors for risk of casing failures occurring. Well design aims to increase reliability of the structure and reduce the likelihood of casing failures by following the guidelines in standards, e.g. the New Zealand code of practice for deep geothermal wells NZS 2403:2015. However, there are limits in e.g. temperature or unforeseen conditions that can form. The two, tensile failure and casing collapse, have been identified as the main casing failures found in high-temperature geothermal wells.

To solve these issues, two technological solutions have been developed. The former is the Flexible Coupling (FC), that has been in development at ÍSOR since the year 2015, is designed to allow the production casing to intermediately thermally expand into the couplings that connect the casing joints together limiting the compressive stress to the elastic regime. FCs have gone through multiple R&D cycles of iterative design, full-scale prototype builds and testing for function and structural loads. Most of the R&D work was done within the EU Horizon 2020 supported research projects GeoWell (no. 654497) and DEEPEGS (no. 690771). The FCs have also been tested in a relevant environment at well conditions of 260°C @ 60 bar-g within the GEOTHERMICA research project GeConnect (no. 731117) where the connection was cemented into a full joint length into a casing-to-casing experimental setup and function tested with repeated thermal cycles. The experiment showed that the inner 9-5/8” casing adapted with a Flexible Coupling expanded and moved in the cement sheath closing the thermal gap inside the coupling, confirming the function and keeping the stress level in the casing below the yield point of the K55 casing material. Flexible Couplings are due to be run in hole for field testing in ON Power a subsidiary to Reykjavik Energy geothermal field Nesjavellir in SW-Iceland in the fall of 2024. The Flexible Couplings will be run in a full production string, replacing the conventional couplings. The casing integrity will be monitored with downhole caliper- and video logs before thermal recovery of the well and the closure of the connections after well heat-up will be monitored with a high-temperature caliper logging tool. Since the closure gap within the connections is only 15 mm, this may become tricky, therefore it is important to log the initial position of the casing before cold injection is stopped and the well is allowed to warm up. The latter developed technology is the annular pressure relief

technology with a working title “Casing Collapse Protection” that has been in development at ÍSOR within the EU Horizon Europe supported project COMPASS (no. 101084623) that is coordinated by ON Power a subsidiary of Reykjavik Energy. The annular pressure relief Casing Collapse Protection is being developed to prevent casing collapse of thermally expanding annular fluids. A patent application has been filed for the novel technology. Combined, the patented “Flexible Couplings” and the patent pending annular pressure relief system the “Casing Collapse Protection”, aim to prevent the most common casing failures and by that increase the structural integrity of the production casing in high-temperature geothermal wells.

2. Structural Integrity

Drilling into high-temperature geothermal areas requires the use of cemented steel casings that enable well control during drilling of the next stage. The last casing, the production casing, that typically reaches up to the surface is the permanent conduit of the geothermal fluid and steam to the surface. Drilled with constant circulation of drilling fluid, the casing is relatively cool when cement locks it into place. Thermal recovery results in thermal expansion of the downhole structure, made of several steel casing strings and cemented annuli. The casings are constrained in the cement, a permanent plastic strain is produced as they thermally expand. Furthermore, if fluids are present in the confined casing-to-casing annulus it can also expand and develop high annular pressure.

A previous study has shown that load history and sequence of loading is important to understand formation of stress and strain that lead to various failure mechanisms (Kaldal G. S., Jonsson, Pálsson, Karlsdóttir, & Thorbjornsson, 2011). The level of permanent (plastic) strain that is developed in the casing is governed by temperature difference and if thermal cycling occurs the strain produced depends highly on the material properties of the casing material. Casing expansion at elevated temperatures, where stresses surpass yield and permanent strain is produced, has called for strain-based mechanical design (Miller & Dall'Acqua, 2023). A diagram shown in Figure 1 describes the problem where if the temperature is high enough the casing material will pass the yield point and deform and if the well cools down again for example for workovers or cleaning, the casing contracts and high residual tensile forces are generated that can lead to tensile failure. An example of such failure is shown in Figure 2.

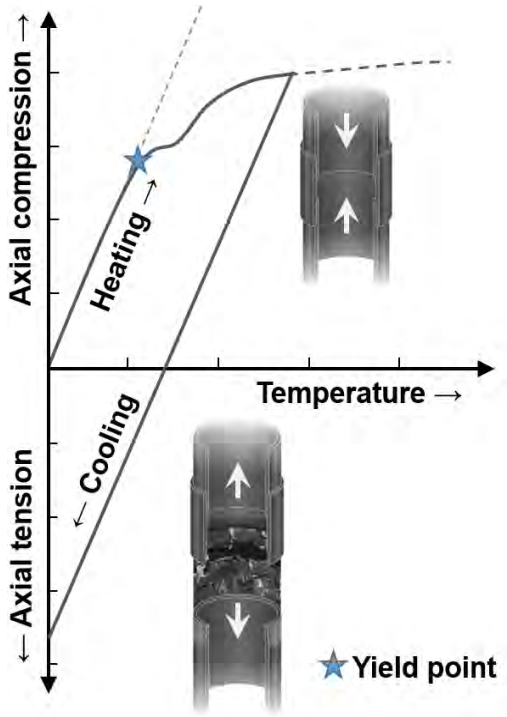

Figure 1: Concept diagram for the failure mechanism where axial tension is generated subsequent to strain that formed in compression, adopted from a diagram by Rahman & Chilingarian (Rahman & Chilingarian, 1995) (Kaldal & Thorbjornsson, Thermal expansion of casings in geothermal wells and possible mitigation of resultant axial strain, 2016).

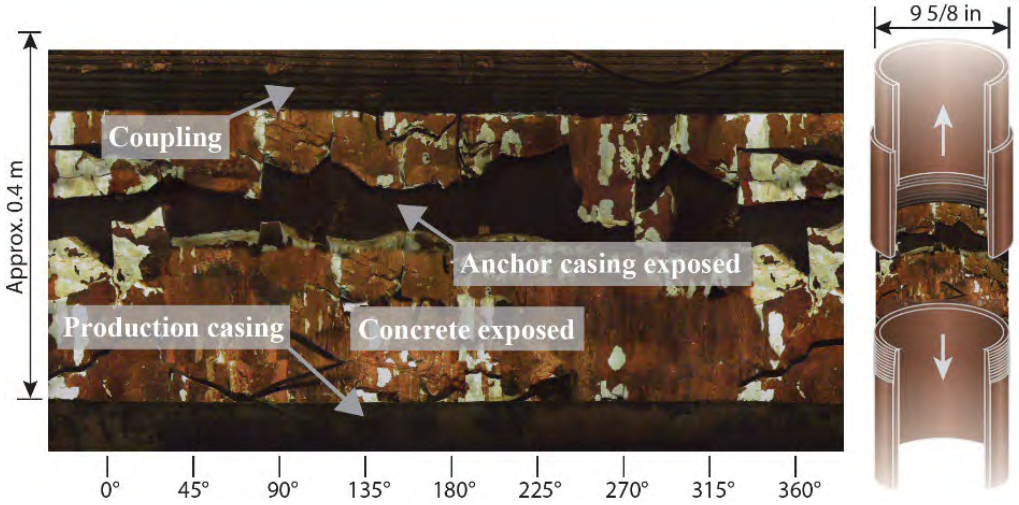

Figure 2: Coupling failure due to casing thermal contraction in the production casing of the IDDP-1 well. The failure occurred while the 450°C hot well was killed with cold water (Kaldal G. S., Jonsson, Palsson, & Karlsdottir, 2016).

Annular pressure buildup (APB) has been extensively studied in uncemented casing-to-casing annulus in oil and gas wells (Jandhyala & Chiney, 2014). Collapse due to annular pressure buildup (APB) in casing pipes of deepwater oil and gas wells in the Gulf of Mexico led to shutdown of the oil field. Control measures for trapped annular pressure (TAP) have been evaluated and reviewed, including increasing casing strengths, eliminating trapped annular pressure, releasing trapped pressure at surface or by using rupture disks, balancing the expansion volume and blocking heat transfer (Dong & Chen, 2017). Suryanarayana et al. 2020 evaluate casing collapse due to APB of trapped fluid pockets in cement between casings and present quantitative basis of design such that the outer string bursts and relieves APB before the inner string collapses. They note that the design basis in NZS 2403 of maintaining ratio of 1.2 between API collapse rating and API burst rating is not adequate basis of design as the burst rating is not representative of the rupture limit of the outer casing. Instead, they propose to use a probabilistic design, however, noting that it may sometimes lead to infeasible choices for the outer or inner string, where the recourse is to ensure good cementing (Suryanarayana, Bowling, Sathuvalli, & Krishnamurthy, 2020). Results from finite-element model analyses of casings have shown that casings supported by cement have higher resistance to collapse, and that non-uniform geometry and/or loads can severely impact the structural stability and cause premature collapse (Figure 3). An example of casing collapse caused by APB is shown in Figure 4. The collapse was punched out leaving the anchor casing exposed to the wellbore fluids.

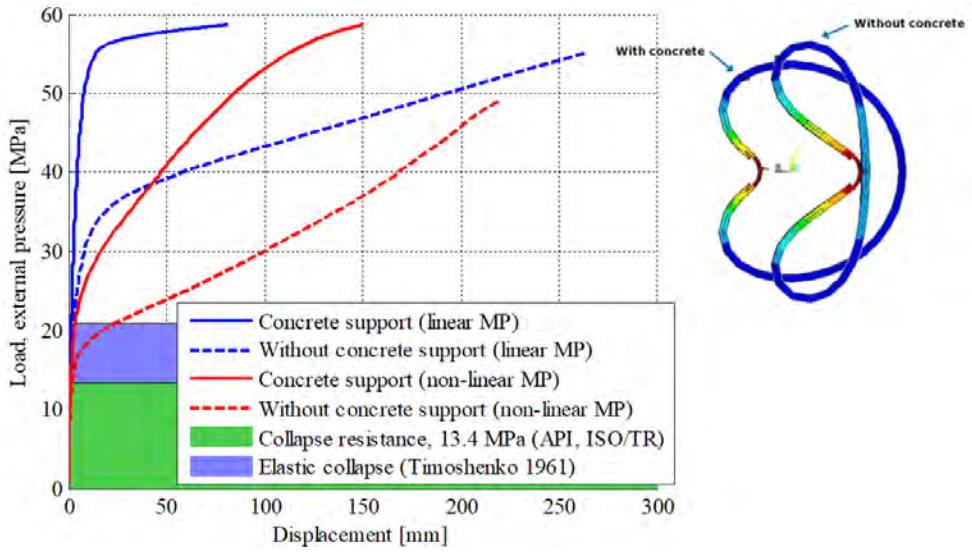

Figure 3. The effect of concrete structural support to the casing. Load-displacement collapse and post-collapse curves of a cement supported casing versus a non-cemented casing showing that cement support increases the collapse resistance of the casing substantially (Kaldal et al. 2013).

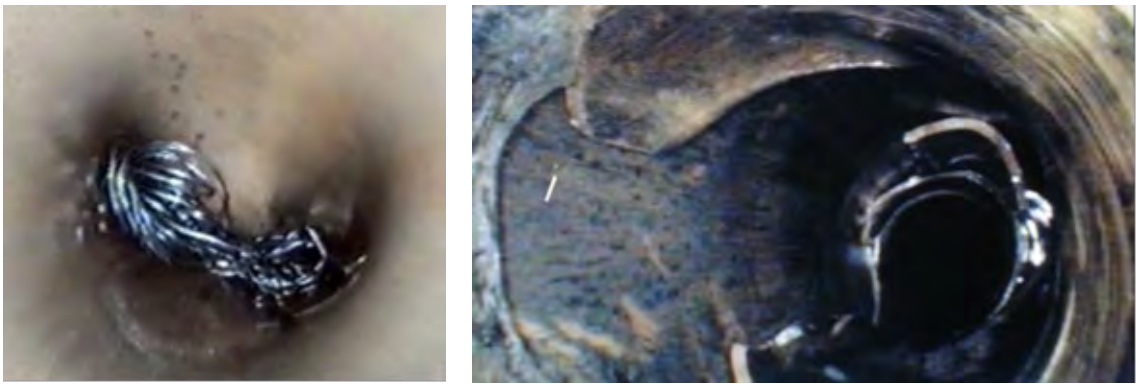

Figure 4. Example of a casing collapse of a 9-5/8“ production casing in a high-temperature geothermal well with remains of slick line from a stuck logging tool (left). The collapse was later punched out leaving the anchor casing exposed to the wellbore fluids (right), by courtesy of Reykjavik Energy and ON Power.

If excess water is high enough or if a water pocket exists, pressure in a cemented casing-to-casing annulus will be generated as the well warms up after being drilled with circulation of cold drilling fluids. In a casing-to-formation cemented annulus the evolution of the pressure can be much less severe than in a casing-to-casing annulus as the rock formation is likely to take excess pressures. The most severe pressure raise is shown in the diagram in Figure 5 where an isochoric process is assumed for a water pocket at initial conditions at point A follows the path to point B. However, the pressure buildup is likely to be less severe due to slight volume change and relief of pressure through the cemented annulus shown in a potential path from A to C. The collapse resistance of two typical production casings (at RT) is shown for reference.

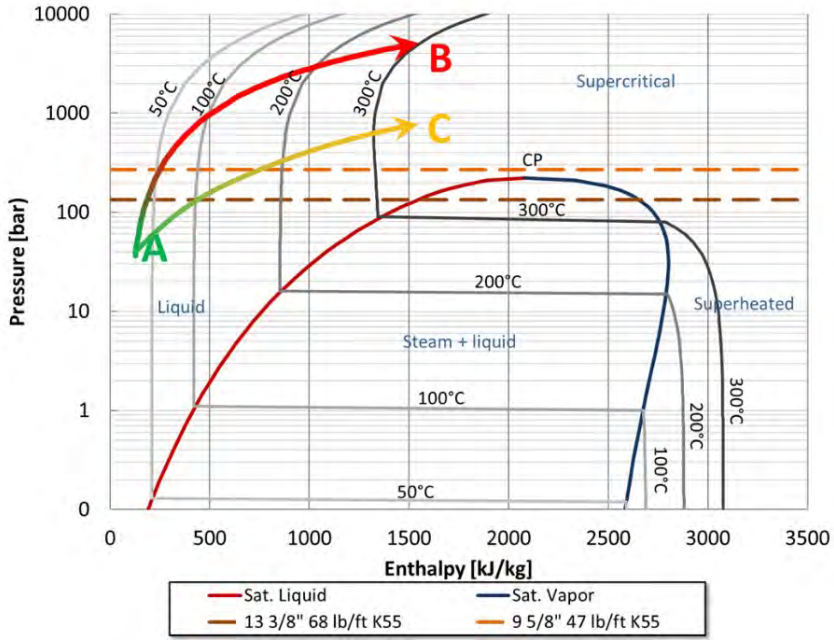

Figure 5. Annular pressure build-up in a casing-to-casing fixed volume is shown in the path A to B, however the pressure buildup is likely to be less severe due to slight volume change and relief of pressure through the cemented annulus and to the rock formation shown in a potential path from A to C. The collapse resistance of two typical production casings (at room temperature) is shown for reference.

Figure 6 shows results from a study conducted at ÍSOR, where out of 136 high-temperature production wells 75 wells have noted incidents whereof 13.3% are confirmed tensile failures and 6.7% are casing collapses (bulge) (Sveinbjörnsson, Kaldal, & Thorbjörnsson, 2015) (Lohne, et al., 2017) (Thorbjornsson, Kaldal, & Ragnarsson, 2019). These problems have been observed during downhole logging and some have been video logged. However, well failures can go unnoticed if no obstruction is observed during downhole logging. Therefore, it can be concluded that the number of failures is likely higher.

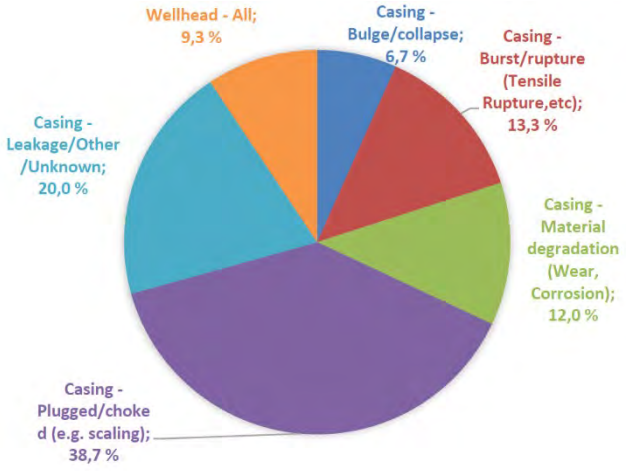

Figure 6. Downhole well problems that have been found in downhole logging. Problems, e.g. casing collapse, casing tensile failure and plugged casing or scaling, were identified in 75 wells out of a set of 136 high-temperature production wells (Sveinbjörnsson, Kaldal, & Thorbjörnsson, 2015) (Lohne, et al., 2017).

3. Mitigation of Casing Failures

The severe casing failures discussed above have called for improved reliability of the downhole structure. The nature of the harsh chemistry of geothermal wells limit material selection for casings. Materials are selected for resistance to H_2S attack to minimize the possibility of failure due to hydrogen embrittlement and sulfide stress corrosion. The New Zealand code of practice for deep geothermal wells states that materials should conform to ANSI/NACE MT 0175/ISO 15156; e.g. K55, L80 type 1, C90 and T95. This constrains the selection and increasing the yield strength unfortunately can produce such negative effects as hydrogen embrittlement that in turn can lead to premature failures.

Flexible Couplings were designed for mitigation of casing failures caused by constrained thermal expansion. The novel connection has been developed for two common sizes for production casing sizes 9 5/8” (244.5 mm) and 13 3/8” (339.7 mm). A prototype that was built within the GeoWell project and a drawing showing the sliding mechanism are displayed in Figure 7. The development and testing of the Flexible Coupling has been thoroughly described in previous conference papers (Kaldal & Thorbjornsson, Thermal expansion of casings in geothermal wells and possible mitigation of resultant axial strain, 2016) (Thorbjörnsson I. Ö., Kaldal, Gunnarsson, & Ragnarsson, 2017) (Thorbjornsson, Kaldal, & Ragnarsson, 2019) (Thorbjörnsson & Kaldal, 2020) (Kaldal & Thorbjornsson, Improved Integrity of the Production Casing in Moderate- to Ultra-High-Temperature Geothermal Wells using Flexible Couplings, 2022) (Kaldal, et al., 2022).

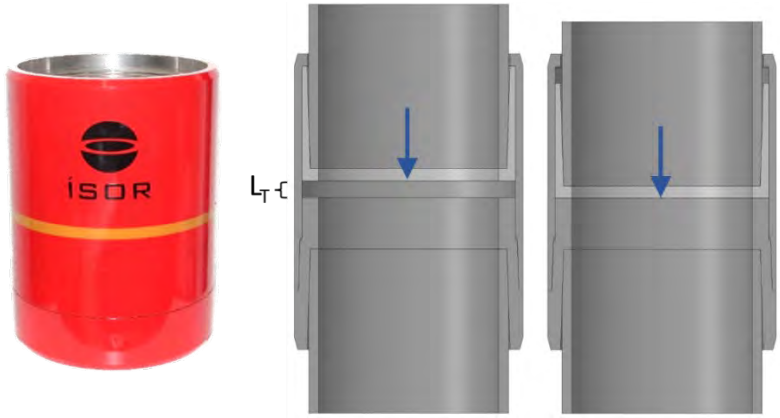

Figure 7: Flexible Coupling prototype – 9 5/8" (left). Sliding principle of FC enabling expansion of cemented-in casings (right).

Flexible couplings have been considered as a solution for thermal strain problems for wells drilling into superhot conditions in the Iceland Deep Drilling Project (IDDP) (Gunnarsson, Pálsdóttir, Ragnarsdóttir, & Friðriksson, 2024) and wells that will be drilled with the objective of in situ magma observatory in the Krafla Magma Testbed (KMT) project (Hólmgeirsson, et al., 2018). The casings of the first two wells of the Iceland Deep Drilling Project, IDDP-1 drilled for Landsvirkjun in Krafla 2008-2009 and IDDP-2 drilled for HS Orka in Reykjanes in 2015-2016, failed due to thermal cycling of the casing and or casing collapse due to expanding annular fluids. The third well is planned to be drilled in the Hengill geothermal system, either Nesjavellir, Hellisheiði or Hverahlíð, for ON Power a subsidiary of Reykjavik Energy. Since both former cases showed that the casing structural integrity is one of the most critical factors to successfully drill and operate the well, different aspects of the well structure is being investigated for improvement in the COMPASS project, e.g. mitigating thermal loading on the casing, collapse prevention, corrosion prevention and increased flexibility and lighter cement for cementing long casing strings. The objective is to improve the well integrity and increase its flexibility in terms of structural loading and chemical attack with cost-effective solutions. It should be noted that mitigation of casing failures also goes hand in hand with selection of good quality casings and cement for the production casing, e.g. selection of round casings (high collapse grades), low free water content in cement and most importantly, careful operations of the well by the operator, e.g. by limiting thermal cycling of wells.

As discussed above, two of these challenges that need to be tackled are casing collapse and tensile ruptures that both are an effect of thermal expansion of materials. Annular Pressure Buildup Relief (APBR) element has been designed to relieve annular pressure in cemented annulus. A patent application has been filed (Icelandic Patent application no. 050685). The invention works on the principle that the pressure propagates through the micro annulus that is formed between the production casing and the cement sheath and into the element that is placed in the casing wall (Figure 8). If high enough, the pressure will activate the element and pressure will be temporarily relieved into the wellbore. This will likely only occur once in the lifetime of the well as it warms up to operation temperature during thermal recovery after drilling. When the annular pressure has been reduced to a level that is acceptable the pre-set element shuts off and seals again. The APBR casing collapse prevention "patent pending" technology shown in Figure 9 is in development within ÍSOR to mitigate annular pressure development in a cemented annulus in high-temperature geothermal wells. Prototypes have been built and are being tested for operational loads and

function. Operational testing within a cemented annulus will be performed in a full-scale test setup within the COMPASS project where questions regarding pressure relief through cemented annulus and through the collapse prevention system that is placed in the innermost casing will be answered.

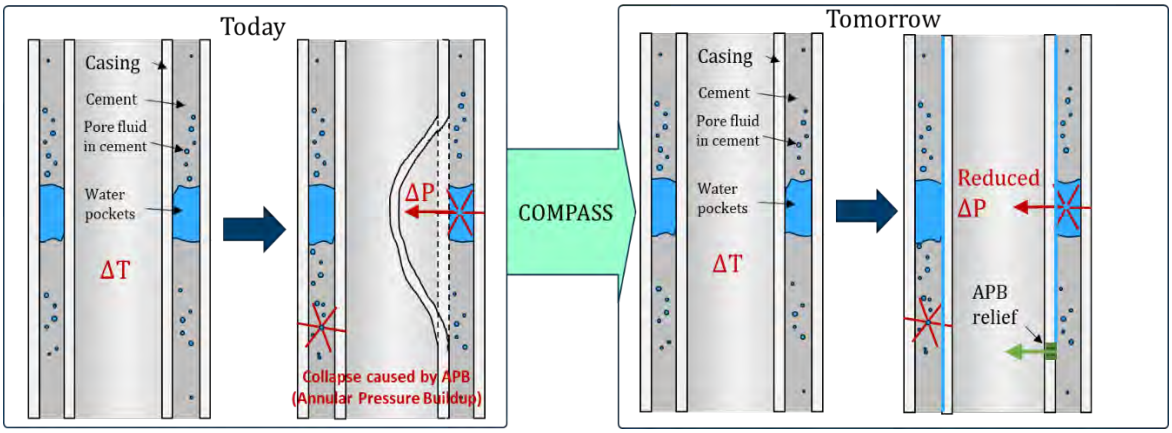

Figure 8. Illustration of the principle of the APBR pressure relief concept for collapse prevention developed within the COMPASS project. Left: casing collapse form annular pressure buildup due to thermal expansion of entrapped annular water. Right: Temporary pressure relief through the Casing Collapse Protection leaving the casing intact.

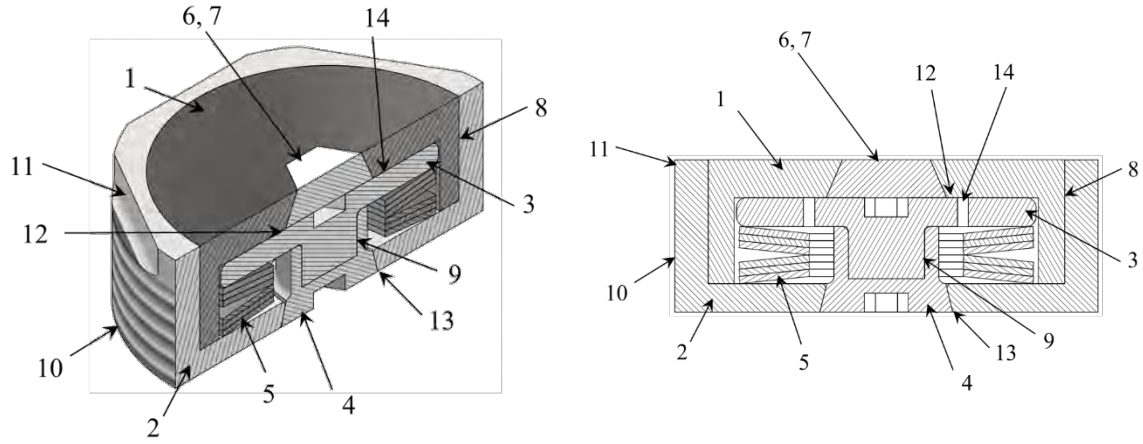

Figure 9. The patent pending Casing Collapse Protection technology for Annular Pressure Buildup Relief (APBR) intended for High-Temperature Geothermal Wells to mitigate casing collapse of the production casing that can occur if enclosed or excess water exists in a cemented casing-to-casing annulus.

Conclusions

Two novel technologies were presented in this paper. Namely, the Flexible Coupling that has been developed for mitigation of casing failures caused by constrained thermal expansion and will be field tested in a new high-temperature geothermal well in the Nesjavellir field that is operated by ON Power this year, and the not yet as well-advanced Casing Collapse Protection technology that

is currently being developed and will be tested in a field condition experiment next year. Both technologies are not yet commercially available but aim to advance the integrity of high-temperature geothermal wells as well as to enable the drilling and operation of future superhot wells, e.g. IDDP and KMT wells.

Acknowledgement

The work presented here has been supported by EU Horizon Europe through project COMPASS (no. 101084623). Previous work on development of the Flexible Coupling was supported by GeoWell (no. 654497) and DEEPEGS (no. 690771), and the GeConnect (no. 731117) project funded through the ERANET co-fund GEOTHERMICA, from the European Commission, Technology Development Fund (Iceland), Bundesministerium für Wirtschaft und Energie aufgrund eines Beschlusses des Deutschen Bundestages (Germany) and Ministerie van Economische Zaken (The Netherlands). We would like to kindly thank our project partners for their valuable contributions to the previously mentioned projects.

REFERENCES

Dong, G., & Chen, P. (2017). A review of the evaluation methods and control technologies for trapped annular pressure in deepwater oil and gas wells. *Journal of Natural Gas Science and Engineering*, 85-105.

Gunnarsson, G., Pálsdóttir, A., Ragnarsdóttir, K. R., & Friðriksson, Þ. (2024). Towards Utilization of Superhot Geothermal Resources ◎ the IDDP Project and Beyond. *PROCEEDINGS, 49th Workshop on Geothermal Reservoir Engineering.* Stanford: Stanford Geothermal Workshop.

Hólmgeirsson, S., Ingólfsson, H. P., Eichelberger, J., Pye, S., Normann, R., Kaldal, G. S., . . . Lavallee, Y. (2018). Krafla Magma Testbed: Engineering challenges of drilling into magma and etracting its energy. Reno: GRC Transactions, Vol. 42, 2018.

Jandhyala, S. R., & Chiney, A. (2014). Finite Element Approach to Predict the Effect of Annular Pressure Buildup on Wellbore Materials. *Offshore Technology Conference Asia.* Kuala Lumpur: Offshore Technology Conference.

Kaldal, G. S., & Thorbjornsson, I. (2016). Thermal expansion of casings in geothermal wells and possible mitigation of resultant axial strain. *European Geothermal Congress, Strasbourg, France, 19-24 Sept 2016.*

Kaldal, G. S., & Thorbjornsson, I. (2022). Improved Integrity of the Production Casing in Moderate- to Ultra-High-Temperature Geothermal Wells using Flexible Couplings. *GRC.* Reno, NV: Geothermal Rising.

Kaldal, G. S., Jonsson, M. T., Palsson, H., & Karlsdottir, S. N. (2016). Structural modeling of the casings in the IDDP-1 well: Load history analysis. *Geothermics*, 1-11.

Kaldal, G. S., Jonsson, M., Pálsson, H., Karlsdóttir, S. N., & Thorbjornsson, I. (2011). Load History and Buckling of the Production Casing in a High Temperature Geothermal Well. Stanford: Stanford University, PROCEEDINGS, Thirty-Sixth Workshop on Geothermal Reservoir Engineering.

Kaldal, G. S., Lipus, M., Jónasson, H., Guðmundsson, L., Gunnarsson, B. S., Thorbjornsson, I., & Einarsson, G. M. (2022). *Experimental Results of Surface Demonstration.* Reykjavik: ÍSOR - Iceland GeoSurvey.

Lohne, H. P., Ford, E. P., Majoumerd, M. M., Randeberg, E., Aldaz, S., Reinsch, T., . . . Brunner, L. G. (2017). *Barrier definitions and risk assessment tools for geothermal wells.* Stavanger: IRIS.

Miller, S. M., & Dall'Acqua, D. (2023). Geothermal Applicability of Strain-Based Casing Design Guidelines from Extreme Temperature Oil and Gas Wells. *SPE Annual Technical Conference and Exhibition.* San Antonio: Society of Petroleum Engineers.

Rahman, S. S., & Chilingarian, G. V. (1995). *Casing design theory and practice.* Amsterdam - Lausanne - New York - Oxford - Shannon - Tokyo: Elsevier.

Standards New Zealand. (2015). *NZS 2403:2015 - Code of practice for deep geothermal wells.* Wellington: Standards New Zealand.

Suryanarayana, P. V., Bowling, J., Sathuvalli, U. B., & Krishnamurthy, R. M. (2020). A Design Basis for Geothermal Well Tubulars Subjected to Annular Pressure Buildup from Fluids Trapped in Cement. *Workshop on Geothermal Reservoir Engineering.* Stanford: SGW 2020.

Sveinbjörnsson, B. M., Kaldal, G. S., & Thorbjörnsson, I. (2015). *Failure modes in Icelandic High Temperature Geothermal Wells (unpublished work).*

Thorbjörnsson, I. Ö., Kaldal, G. S., Gunnarsson, B. S., & Ragnarsson, Á. (2017). A new approach to mitigate casing failures in high-temperature geothermal wells. Salt Lake City: Geothermal Resources Counsil.

Thorbjörnsson, I., & Kaldal, G. S. (2020). Flexible Couplings for Improved Casing Design in high-temperature Geothermal Wells (in proceedings). Reykjavík: World Geothermal Congress.

Thorbjornsson, I., Kaldal, G. S., & Ragnarsson, Á. (2019). Testing Flexible Couplings for Geothermal Wells. *GRC Transactions, Vol. 43.* Palm Springs: Geothermal Resources Counsil.

Superhot Geothermal - Experience and Outlook in Iceland

Bjarni Pálsson[1)]

[1)]Landsvirkjun, the national power company of Iceland

Keywords

Krafla, Theistareykir, Superhot Geothermal, Magma, Coring, IDDP, KMT

ABSTRACT

For half a century Landsvirkjun, the national power company of Iceland, has been exploring and utilizing some of world's hottest geothermal resources. Wells drilled into superheated resources believed to be around or above 360°C have proven to be very powerful but hard to operate due to various challenges including corrosion, particle erosion, silica scaling potential, thermal expansion etc. The most significant effort to date was well IDDP-1 drilled into 950°C hot magmatic body in the Krafla Geothermal Field in 2009. The well was flowtested in 2010-2012 where various tests were carried out providing valuable learning for future projects. The well was flowtested with various wellhead pressure but enthalpy was constant around 3150 kJ/kg and superheat of 160°C (above boiling temperature). Landsvirkjun is currently considering next steps towards utilisation of superhot geothermal in near-magma environment.

This paper presents a brief overview of the experience, challenges and learning from drilling and operating superhot geothermal wells in Iceland and outlines the outlook for further efforts in the near future, including the Krafla Magma Testbed project, KMT, planned in 2025-2029.

THE KRAFLA STORY

In the early hours of May 17th 1724, 300 years ago, a big blast echoed over North Iceland. Inhabitants of the town of Akureyri woke up and thought someone had blasted a cannon in town. The following day, some 65 km away, a few men from the village of Reykjahlíð hiked the 10 km distance to the central volcano Krafla to see what had happened and witnessed an erupting explosion crater, now called Víti, meaning Hell. Víti only erupted 1-2 days but over the next 7 years, several volcanic eruptions occurred in the nearby Mt. Leirhnjúkur, producing lava flows that extended some 10 km south towards the lake Mývatn and village Reykjahlíð. This episode period was named *Mývatn Fires*. Since the end of Mývatn Fires in 1731, the Krafla volcanic system when quiet for 240 years.

In the early 1970's, increasing oil prices caused increased demand for electricity in Northern Iceland. When a protest caused the dam of a hydroelectric power plant close to lake Mývatn to be lowered, resulting in the power outcome to be only quarter of the originally planned capacity, the government started to explore the geothermal field in Krafla. Following surface measurements since the early 1970's the Icelandic parliament decided in 1974 to establish a parliamentary committee, "Kröflunefnd", to build the Krafla Geothermal Power Station. The committee drilled two approximately 1200 m deep exploration wells in 1974 and bought two 30 MW Mitsubishi turbine units, dual pressure, double flow, designed for medium enthalpy. Drilling continued in the summer of 1975, first well K-3, down to 1200 m and then the first deep well, well K-4 in Vítismór, on the plateau at the end of the Hlíðardalur valley, between the Víti crater to the east and Mt. Leirhnjúkur to the west.

August 1975 proved eventful for Krafla. That month, construction of the powerhouse for Krafla Power Plant started. Later that month, drilling of the first well exceeding 1300 m, well K-4 concluded at 2003 m depth after having intersected a powerful feed zone at 1940 m, that started flowing up into an upper feed zone at 700 m. This caused wellhead pressure exceeding pressure rating of the mastervalve, and drillers postphoned completing the well until new wellhead valve had been replaced. In January 1976, steam started leaking between wellhead flange and mastervalve, cutting the bolts and the wellhead blew off, resulting in uncontrollable blowout of steam and highly acidic liquid for several months until the well eventually collapsed. Well K-4 was the first superhot well to be countered in Krafla and possibly also in Iceland.

In December 1975, Mt Leirhnjúkur, some 2 km Northwest from the power station started volcanic eruption, and over the next 9 years, until 1984, in total 9 volcanic eruptions and 18 underground eruptions occurred in the Krafla system. None of the event had direct impact on the Krafla project but CO_2 increase significantly in several wells, magma did enter wells in both Krafla and in Bjarnarflag, 10 km south of Krafla and land elevation changes were 2-3 meters. It was soon decided to only complete installation of turbine unit 1 due to difficulty of getting usable steam. The first trial operation of Krafla was in autumn 1977 and the plant was officially commissioned in February 1978. Only 7 MW of usable steam was available at the beginning. Part of that steam was from a superheated well K-3 and as the wells were equipped with wellhead separators, there was no water phase to scrub the steam and first to turbine rotors were severely damaged during the first year by particle erosion, before a decision was made to install a central separation station to mix wet steam with dry to improve scrubbing.

Drilling efforts were moved further away from the erupting Mt. Leirhnjúkur, to east towards the southern slopes of Mt. Krafla, and to the south to the Hvíthólar area. The Hveragil canyon appeared to divide the Krafla reservoir, west of the canyon, the field followed almost constant temperature of 180-220°C down to 1200-1600 m depth (upper reservoir) and below that temperature followed boiling point curve (lower reservoir). East of the canyon, the field followed boiling curve from 800 m.

The Krafla power station finally reached full capacity of 30 MW in 1984. By then, in total of 23 wells had been drilled, thereof 15 had been connected to the steam gathering system. Around the same time, Landsvirkjun, the national power company of Iceland, bought Krafla and the nearby Bjarnarflag, its first geothermal power stations.

In 1996, Landsvirkjun reached the conclusion that the geothermal reservoir had recovered sufficiently from the Krafla fires to allow installation of unit 2, followed by drilling of wells K-27 to K-34. Many of the deeper wells, exceeding 1800 m true vertical depth, started quite powerful but declined rapidly in power as an obstacle was discovered around 1200-1500 m depth, or around the intersection between the hot and dry lower and wet upper reservoirs. Initially, these obstacles were believed to be caused by silicate scaling, but later analysis suggested heavy corrosion did also play a role. The 2002 m deep vertical well K-34, just east of Víti, was an exception, delivering steam equivalent of 20 MW for several years, before starting to cough black fluid at start of flowtests and declining to 4-5 MW. Highly corroded bits of liner pipes and connections have been discovered in the separator that have been traced to well K-34. This unknown phenomenon in the wells was called “black death”. To date, wells that are known or suspected to suffer from “black death” symptoms are: K-4, K-8, K-10, K-25, K-26, K-29, K-34, K-35, K-36, K-38, K-39 and IDDP-1 (Einarsson, 2010).

Well K-39 was drilled in autumn of 2008. The well is in total 2865 m long, directionally drilled with 30° angle under the southern slopes of Mt. Krafla. After drilling through rather hard rock, as common in the southern slopes, rock suddenly became rather soft at around 2810 m depth and the section from 2830-2845, the rock was very soft, almost no resistance, before the rock became harder again. After two further drill pipe lengths, drilling was stopped at 2865 m depth. Soon after, while circulating, the drill string got stuck around 2848 m depth. After several days of attempts to free the string, where circulation was lost several times but regained after significant pressure before giving up. At one point, temperature log inside the drill string at 2815 m depth (bottom of drill string) showed 386°C at over 220 bar pressure, indicating supercritical conditions, while pumping 47 l/sec through the string (Olafsson, 2010).

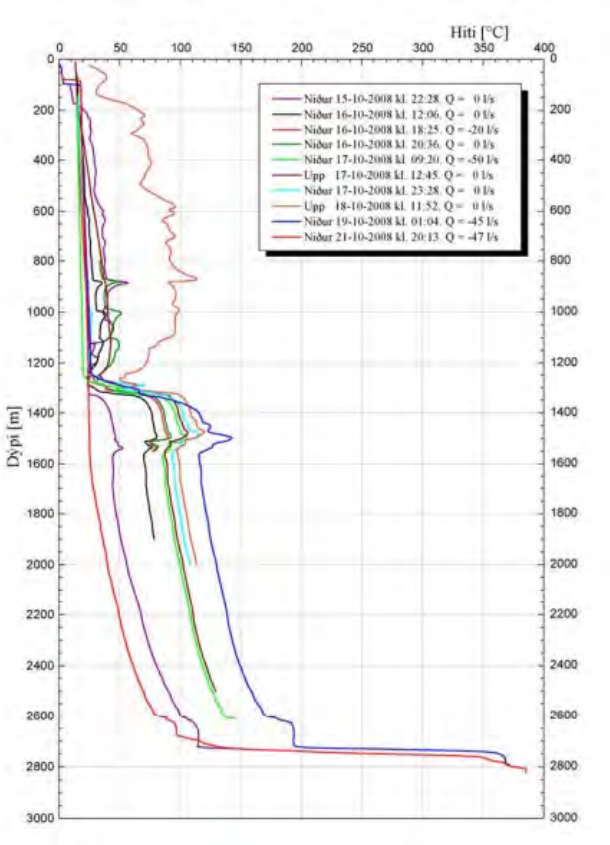

Figure 1: Temperature vs. depth log in well K-39 during attempts to free drillstring (Olafsson, 2010).

A charge was applied to help unscrew the drill string at the 2740 m depth. However, a collar at 2808 was unscrewed, providing longer section of the drill string to be free. When at surface, the bottom three collars were packed with a mix of drill cuttings a fresh quenched silicic glass (Mortensen, 2010). As the wellhead rating of ANSI Class 900 was not considered sufficient to allow the well to flow with the anticipated pressure, the bottom 250 m were cemented before completing the well and opening for flow test. The flow test was carefully monitored and fluid chemistry indicated downhole corrosion due to hydrochloric acid. After three week of flow test, the well was closed and the slotted liner was pulled to surface to analyze its condition. Several sections of the liner proved to be severely corroded, whereas in between were pipes that did not show indication of corrosion. The liner broke apart at around 1500 m depth when half out of the well and the bottom part fell to the bottom of the well. The last pipes to surface showed the greatest signs of corrosion.

Figure 2: Aereal view of the Krafla geothermal field. In front the Víti explosion crater (1724), to the right the lava flow from the 1725-1729 fires to lake Mývatn. In the center, the Krafla geothermal power station. The green field in the center is the drill pad for well IDDP-1. Photo: Mr. Hreinn Hjartarson, project manager at Landsvirkjun.

THE THEISTAREYKIR STORY

The Theistareykir geothermal field is approximately 20 km Northwest of Krafla, named after the Theistareykir shield volcano. The main surface activity is in the Eastern part of the rift valley between the shield volcano and mountain ridge Lambafjöll, under the Mt. Bæjarfjall and Mt. Ketilfjall. The area is large, characterized by faults, fractures and active geothermal surface activity.

Following surface exploration over several decades, first exploration drilling program started in 2002 and to date 20 deep wells have been drilled in the area. In total 12 wells are connection to the 90 MW power plant and further 3-4 wells will be connected when further steam is required. The Theistareykir geothermal power plant was commissioned in 2017 and 2018 and Landsvirkjun is currently preparing a 70 MW expansion.

The first well, ÞG-1, hit overpressure at 190 m depth, causing crossflow and blowout before the well was managed with several cementing attempts. Overpressure and blowout was also experienced in wells ÞG-3, ÞG-4, ÞG-6, ÞG-7, ÞG-9 and finally in well ÞG-10 where blowout could not be controlled until the well was filled with cement and drill string was left in hole. The following wells were drilled with barite which has helped with well control during drilling. Almost all the wells exceed 300°C at 2000 m true depth and average enthalpy is 2100 kJ/kg with several wells completely dry. Several wells have shut-in pressure exceeding 100 bar. The fluid is characterized by low levels of geothermal gasses and minerals, but the high enthalpy wells have

high levels of silica in the separation water, exceeding 1000 mg/kg in two wells, causing significant silica scaling risk. As a precaution, the high enthalpy wells are operated at wellhead pressure of 20-30 bar to minimize risk of downhole precipitation (Hauksson, 2021).

Highest bottom hole temperature was logged in the 2659 m deep vertical well ÞG-3, 380°C. The well is superheated with temperature around 20° above boiling temperature blow approximately 2200 m depth. The well pulsed significantly during the first few years with the up to 30 MW pulses 2-3 times a day. Next well logging after end of pulsing indicated the well was plugged below approximately 1500 m depth or just below the uppermost feed zone.

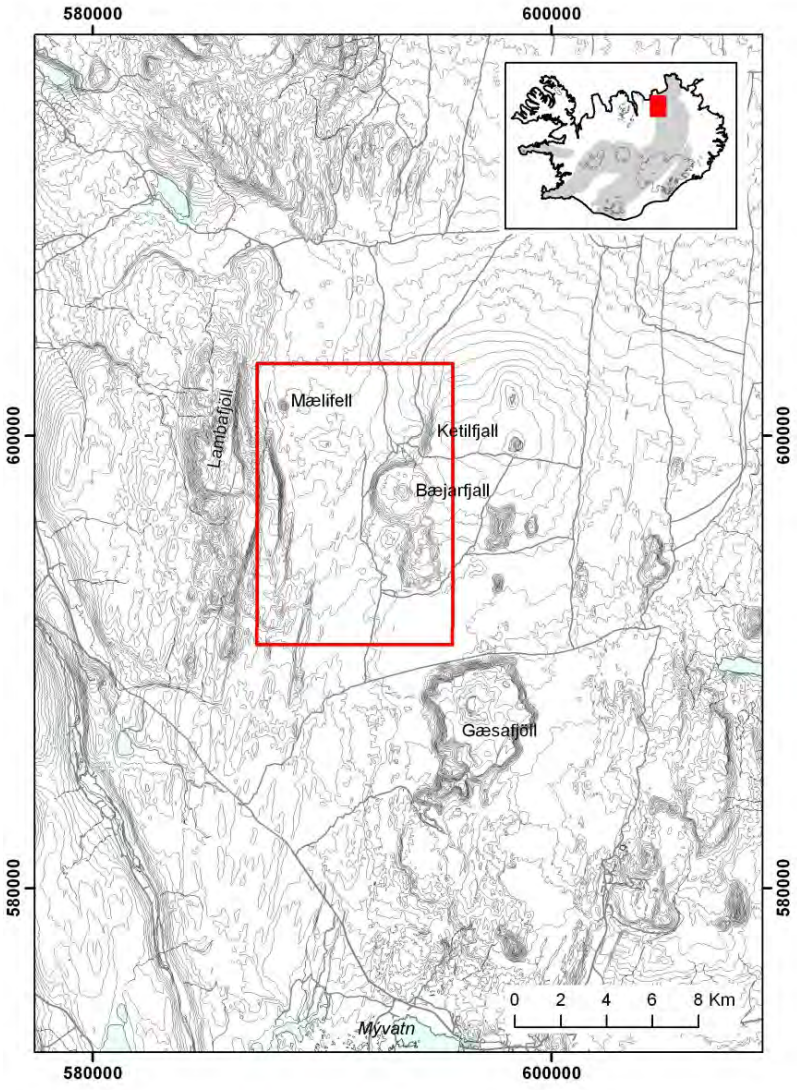

Figure 3: Overview map of the Theistareykir geothermal field (Gautason, 2010)

The high well temperature and enthalpy at Theistareykir is a very strong indicator of the potential for superhot geothermal resource at relatively shallow depth.

ICELAND DEEP DRILLING PROJECT, IDDP

The Iceland Deep Drilling Project, IDDP, has been excessively covered in the literature and various news and documentaries, but understandably as it is the most ambitious geothermal exploration project in recent years. The initial idea behind the IDDP project was to look back at several well that had been drilled in Iceland and had hit resource with such a high pressure and temperature that they could not be handled, such as wells K-4 and K-25 in Krafla, reported above, and well 11 at Nesjavellir geothermal field, drilled in 1985, where over 380°C temperatures was measured around a feed zone at 2200 m depth that caused an underground eruption to a feed zone at 1100 m depth that could only be managed by cementing.

The main objective of the IDDP project is to study the feasibility of extracting geothermal fluid from a resource closer to the roots of the geothermal system, at supercritical conditions, temperature >374°C and pressure >220 bar for benign water but higher temperature and pressure for saline water. The fluid would reduce in pressure as it flows to surface and be handled as superheated fluid. To allow commercialization of the IDDP methodology, the properties of the supercritical have to studied, drilling technology has to be advanced and new fluid handling and evaluation systems need to be designed and applied.

The IDDP consortium was established by three leading energy companies in Iceland, Landsvirkjun, Reykjavik Energy, HS Orka as well as the government through the National Energy Authority (Orkustofnun) in 2000. Later, Equinor (previously Statoil) and Alcoa joined the project.

The first well of three proposed by the Iceland Deep Drilling Project (IDDP) was drilled in the Krafla Geothermal Field in 2008–2009 by Landsvirkjun. The well was designed to reach supercritical conditions at 4500 m, temperatures above 374 °C and pressures above 22 MPa. Drilling progress was as planned down to around 2000 m when drilling became quite challenging, including becoming stuck at 2094 and 2095 m depth, followed by twist offs and subsequent side tracking. Finally, drilling came to an end at 2096 m depth in the third leg when cuttings of fresh glass indicated the presence of a magma body at the bottom. As the well had such a rigorous well design, the steering committee of the IDDP decided to complete and flow test the well, rather than abandoning it. The well was flow tested from 2010-2012 with several different setups. The flow was superheated by 120°C above boiling temperature and wellhead temperature followed wellhead pressure but enthalpy was constant around 3150-3200 kJ/kg (Markusson, 2013). When flow was limited to 17 kg/sec with a small orifice, wellhead flowing pressure was 145 bar and wellhead flowing temperature was 450°C.

IDDP hit several challenges. The key drilling challenges were to drill with a wider diameter than normally done to various different depths to add additional casing strings, wellbore integrity while drilling superhot rock with relatively cold drilling fluid, cementing long casing strings in hot rock environment and finally, avoiding getting stuck when drilling into magma. When flowing the well, the fluid proved to be highly corrosive, flow velocity of the dry steam was very high causing erosion by corrosion particles, cuttings and other particles in the steam. Thermal expansion of casing, surface flowlines and all equipment in contact with the superhot steam, including valves, was also a big challenge. The high flow velocity of the superhot and dry steam did also cause fine vibration that caused extra strain on surface equipment and loud noise. Eventually, the well had to be shut in when a leakage was discovered on flanges and both TIX master valves failed to shut-in. When the well was quenched by pumping 20°C cold water slowly (5 l/sec) on the well, the Tenaris

563 casing connections failed in at least four different locations. When in an attempt to clean the well with a drill rig, metal debris at the bottom of the well prevented full workover and when the well got completely plugged, the only option was to fill it up with cement and gravel.

The well was very powerful and the project proved to be a valuable experience for drilling supercritical wells in the future and what happens when magma is encountered. Most importantly, it proved that it is possible to drill and complete a well in a very hot zone and produce fluid from an environment near a magma body. If sustained long term production proves possible, the drilling of well IDDP-1 will mark a new era in power production in Krafla.

Well IDDP-2 was drilled in 2016-2017 in the saline Reykjanes geothermal field in SW Iceland. An existing 2.5 km deep production well, RN-15, was deepened and cased to almost 3 km depth, and then drilled to 4,650 m slant depth, corresponding to about 4.5 km vertical depth from surface. Supercritical conditions (426°C at 340 bars) were measured during drilling at approximately 4,550 m depth. The well was deepened by additional 100 m, a liner inserted, and a 6” pilot hole and 3 successive drill cores retrieved from the very bottom of the well. Coring was attempted 13 times below 3 km depth, altogether returning some 27 m of drill cores. As the well was drilled with total circulation losses most of the time these core samples comprise almost the only rock samples from the well below 2.5 km depth. Petrological studies, on mineral assemblages, chemistry and fluid inclusions from the drill cores, show absolutely a unique data set from a sheeted dike complex currently at temperatures up to 600°C near the bottom of the well (Fridleifsson, 2021).

The company Reykjavik Energy is currently planning well IDDP-3 at the Hengill area, SE of the capital of Reykjavik in the next coming years. Exact location and well configuration has not yet been fully decided on (Gunnarsson, 2024).

KRAFLA MAGMA TESTBED, KMT

Well IDDP-1 did not only prove to be a great success with regard to providing information about the challenges and potential for superhot geothermal energy production, it also proved unique information about the physics of magma and geological, geophysical and geochemical properties of near-magma formations. Following up from the experience from IDDP a group of leading volcanologists from several different countries teamed up with Landsvirkjun to found the Krafla Magma Testbed project. Landsvirkjun is providing access to the unique conditions at Krafla, with not only unique geological settings but also excessive experience and research data that has been gathered in the field for half a century.

The aim of the project is to improve the knowledge about:

- Volcano monitoring, aiming at better forecasting for future volcanic eruptions
- Geothermal potential in near magma formations
- Geoscience, understanding magma chamber dynamics
- Innovation and technology for superhot and corrosive conditions that could i.e. benefit space industry etc.

The KMT consortium, lead by the geothermal research cluster GEORG, officially founded the KMT Non-Profit Organization, KMT NPO, last year, and Mr. Björn Þór Guðmundsson, a

geologist specialized in Krafla, with vast financial background, was hired as the CEO. Preparation for drilling two exploration wells and setting up a world class volcanological testbed is now completed and the new organization is currently in funding phase. The aim is to drill a monitoring well towards the magma in 2027 and place sensors preferably into the magma body. Two years later, the plan is to drill a "manipulation well" that can be applied to do various tests and studies, i.e. for energy generation in near magma environment.

It is the long term aim of KMT project that the site becomes a long term observatory for magma chamber below to test methods to explore and predict volcanoes and magma energy resources. It is also the long term aim of Landsvirkjun to team up with the energy industry to drill a commercial magma energy well in Krafla and hopefully also in other volcanic geothermal fields.

SUPERHOT GEOTHERMAL IN ICELAND

Superhot geothermal energy is in high demand in the world to power the energy transition needed. Iceland is in the lead for its recent developments and Iceland is open for cooperations with likeminded ambitious international technical companies and science institutions.

It is quite clear that sites with such shallow depth to the roots of geothermal systems, open minded power companies and supportive society are hard to find. Societies like New Zealand, Japan, USA and in particular Hawaii, and others, should consider superhot geothermal as an alternative for future generation of green power and they should consider developing this resource with Iceland.

Acknowledgement

The author would like to than all the numerous participants in the various research and development projects that have been adding to the knowledge of superhot geothermal in recent decades, including but not limited to the participants and sponsors of the Iceland Deep Drilling Project (abovementioned in addition to ICDP and NSF), Deep Roots of Geothermal Systems (The Icelandic Centre for Research), DeepEGS (EU), Image (EU), Improve (EU) and KMT (The Icelandic Centre for Research, NERC, ICDP, Government of Iceland, GEORG).

REFERENCES

Eichelberger, J. et al. "Magma-Sourced Geothermal Energy and Plans for Krafla Magma Testbed, Iceland." Proceedings World Geothermal Congress 2020+1, Reykjavik, Iceland (2021).

Einarsson, K. et al. "Acid Wells in the Krafla Geothermal Field". Proceedings World Geothermal Congress, Bali, Indonesia (2010).

Friðleifsson, G.Ó. et al. " The IDDP success story – Highlights". Proceedings World Geothermal Congress 2020+1, Reykjavik, Iceland (2021).

Gautason, B. et al. "Exploration Drilling in the Theistareykir High-Temperature Field, NE-Iceland: Stratigraphy, Alteration and Its Relationship to Temperature Structure." Proceedings World Geothermal Congress, Bali, Indonesia (2010).

Gunnarsson, G. et al. “Towards Utilization of Superhot Geothermal Resources – the IDDP Project and Beyond.” Proceedings of the 49th Workshop on Geothermal Reservoir Engineering, Stanford University, Stanford, California (2024).

Hauksson, T. ”Theistareykir, Krafla and Bjarnarflag. Flow capacity and chemical content of water and steam phases from wells and in the power cycle in year 2021.” Internal report for Landsvirkjun (2021).

Mortensen, A. et al. “Quenched Silicic Glass from Well KJ-39 in Krafla, North-Eastern Iceland.” Proceedings World Geothermal Congress, Bali, Indonesia (2010).

Olafsson, M. et al. “Krafla – Leirbotnar. Well KJ-39. 3rd section. Drilling Chronology.” Internal Report LV-2009/128 for Landsvirkjun. ÍSOR (2010).

Transition from Oil & Gas

Modeling a Hybrid Renewable Energy System for Bowman County, North Dakota: Assessing the Feasibility of Transitioning from Coal to Wind, Solar, and Geothermal Power

Moones Alamooti[1, 2], Olusegun Stanley Tomomewo[2]

[1]Harold Hamm School of Geology & Geological Engineering, University of North Dakota, Grand Forks 58202, USA

[2]Institute of Energy Studies, University of North Dakota, Grand Forks 58202, USA

Keywords

Hybrid Renewable Energy System, MATLAB Simulation, Bowman County, Wind Energy, Solar Energy, Geothermal Energy, Sustainability, Levelized Cost of Electricity (LCOE), Greenhouse Gas Emissions Reduction

ABSTRACT

Bowman County, North Dakota, currently relies heavily on coal power, accounting for over half of its electricity generation and leading to substantial greenhouse gas emissions. This study utilizes advanced MATLAB modeling to evaluate the potential of transitioning the county to a renewable energy system comprising wind, solar photovoltaics (PV), geothermal, and energy storage. The proposed hybrid system is tailored to Bowman County's growing electricity demand, with nameplate capacities of 85.7 MW for wind, 24.4 MW for solar PV, 2.03 MW for geothermal, and 195 MWh for storage. Simulations verify that by 2040, this custom-designed system could supply over 90% of the county's projected daily loads, with an estimated levelized cost of $105.226/MWh over 15 years that is cost-competitive with conventional power. Implementing this plan would reduce Bowman County's daily carbon dioxide output by approximately 97% relative to continued coal usage. More broadly, this hybrid model serves as a versatile template for other communities striving toward clean, locally focused energy self-sufficiency. It provides a sustainable and adaptable roadmap to support the renewable transition while meeting regional electricity needs, demonstrating one pathway toward a greener future.

1. Introduction

1.1 Background on the Global Energy System

The global energy landscape has been predominantly shaped by the utilization of fossil fuels, which, despite their abundance and historical ease of extraction, have led to significant environmental and climatic challenges. According to the BP Statistical Review of World Energy (2021), fossil fuels account for over 80% of the world's primary energy consumption. This heavy

reliance has resulted in elevated levels of greenhouse gases (GHGs) in the atmosphere, contributing to global warming and climate change (Intergovernmental Panel on Climate Change [IPCC], 2021).

The International Energy Agency (IEA) (2021) reports that global energy demand has been increasing at an annual rate of approximately 1.3%, driven by population growth and industrialization. This surge in demand exacerbates the environmental impact, highlighting the urgent need to transition to more sustainable energy sources. Renewable energy, including solar photovoltaics (PV), wind turbines, hydropower plants, and geothermal heat, presents a promising solution to these challenges. These sources of energy are abundant, sustainable, and have a significantly lower environmental footprint compared to fossil fuels (Chen, Wu, & Wang, 2022).

1.2 Inefficiency of Traditional Energy Systems

Traditional energy systems, particularly those based on coal and natural gas, are inherently inefficient. The energy conversion processes in these systems result in substantial losses. For instance, the average efficiency of coal-fired power plants is around 33%, meaning that two-thirds of the energy content of the coal is lost as waste heat (Patil, Kulkarni, & Kshirsagar, 2018; US Energy Information Administration [EIA], 2020). This inefficiency is compounded by transmission and distribution losses, which further reduce the net energy delivered to end-users.

On the other hand, tri-generation systems offer a more efficient alternative by simultaneously producing electricity, heating, and cooling from the same energy source. These systems can achieve overall efficiencies exceeding 80%, making them significantly more effective in utilizing fuel (Wu & Wang, 2006). By capturing and using waste heat, tri-generation systems improve energy efficiency and reduce greenhouse gas emissions, contributing to environmental sustainability.

1.3 Addressing the Need for Sustainable Energy Solutions in North Dakota

With its vast renewable energy resources, North Dakota is well-positioned to lead the transition to a more sustainable energy system. The state is endowed with significant wind and geothermal resources, which, if harnessed effectively, can provide a substantial portion of its energy needs. Despite this potential, over 70% of North Dakota's electricity generation currently comes from coal-fired power plants characterized by high carbon dioxide emissions and other environmental pollutants (US EIA, 2020b; Zygarlicke et al., 2006).

The heavy reliance on coal has significant environmental and public health implications. Coal combustion releases carbon dioxide, sulfur dioxide, nitrogen oxides, and particulate matter, which contribute to air pollution and associated health problems (Parker, 1979). Transitioning to a hybrid renewable energy system in Bowman County can mitigate these issues by leveraging the region's renewable resources, including wind, solar, and geothermal. This study explores the feasibility of such a transition, providing a comprehensive analysis of the technical, economic, and environmental benefits of a hybrid renewable energy system.

This research evaluates the feasibility of implementing a hybridized tri-generation energy system that combines geothermal, wind, and solar resources to meet the electricity needs of Bowman County, North Dakota. While studies have explored integrating complementary technologies like wind and solar photovoltaics, few have comprehensively analyzed the combination of these three

renewable sources into a unified system. This study contributes an original feasibility assessment tailored to North Dakota's specific renewable energy potential.

The significance lies in exploring a sustainable energy pathway that could reduce greenhouse gas emissions and air pollution by displacing fossil fuels, creating environmental and public health benefits. The proposed tri-generation system presents an opportunity to enhance energy security, drive economic development, and contribute to climate change mitigation efforts. This research offers valuable insights to policymakers and industry stakeholders regarding the viability of investing in innovative renewable energy infrastructure.

Through an interdisciplinary approach, the study synthesizes data and modeling techniques from engineering, geosciences, economics, and environmental science to deliver a robust analysis. The methodology encompasses simulations of energy output, economic cost-benefit evaluations, and quantification of environmental impacts associated with the proposed system. By holistically assessing the technical, economic, and environmental dimensions, this research aims to provide a comprehensive feasibility evaluation.

The integrated tri-generation system leveraging North Dakota's abundant renewable resources could serve as a model for other regions pursuing sustainable energy initiatives. This study's findings may guide policymakers and industry in implementing hybridized renewable solutions that provide consistent and reliable energy.

2. Energy Portfolio of North Dakota

2.1 North Dakota's Wind Energy Potential

North Dakota possesses immense wind energy resources, ranking among the top US states. The state's high wind speeds, flat and expansive lands, low population density, and abundant rural areas provide ideal conditions for large-scale wind projects (Zhang et al., 2014). North Dakota's installed wind capacity has grown exponentially from just 25 megawatts (MW) in 2000 to over 3,000 MW today, currently supplying approximately 26% of the state's total electricity (American Clean Power Association, 2021).

North Dakota's wind resource ranks 5^{th} in the nation, with average wind speeds of 9.9-11.0 m/s at 80-meter hub heights across much of the state (Lopez et al., 2012). The strongest winds are most abundant in the central and north-central regions. The National Renewable Energy Lab has confirmed that North Dakota has some of the best wind resources in the US, with capacity factors exceeding 50% (Figure 1). Higher capacity factors result in greater energy production per turbine.

The state's topography and low surface roughness due to sparse human development allow unobstructed wind flow. Cold winters and warm summers create seasonal wind patterns that are conducive to wind generation. Wind output is typically highest in winter when heating demand is most significant (Raupach & Finnigan, 1997). North Dakota's wind resources can support a significant expansion of wind power.

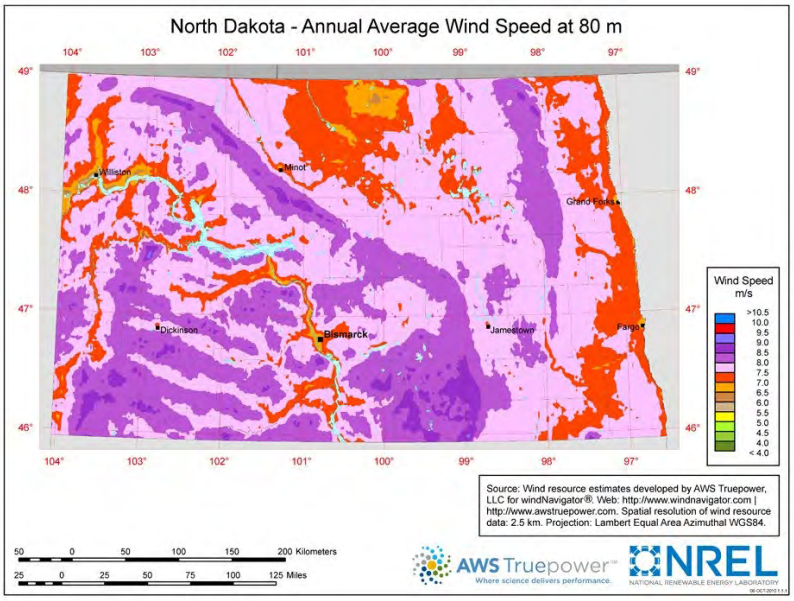

Figure 1. North Dakota's annual average wind speed at 80 m height (NREL, 2021).

North Dakota's first utility-scale wind farm, the 25 MW Lyonsdale project, was built in 1998. Wind growth accelerated after 2000 as technology improved and policy incentives were enacted. As of 2021, North Dakota has over 40 wind power projects in service, comprising 3,065 MW of capacity (American Clean Power Association, 2021). The most significant developments are concentrated in the central and south-central regions with strong winds. Some of the important existing projects are (Wind Energy Database, 2023):

- Baldwin Wind Farm (102 MW), Williams County
- Ashtabula (196.5 MW), Barnes County
- Thunder Spirit Wind Farm (115 MW), Adams County
- Rugby Wind Farm (149.1 MW), Pierce County
- PrairieWinds (115.5 MW), Ward County

Wind accounted for 26.5% of North Dakota's total electricity generation in 2020 (EIA, 2021). The top counties for wind capacity include Ward, Williams, and Barnes in central North Dakota. Wind power has become an essential contributor to the state's electricity portfolio.

Wind project development in North Dakota has yielded substantial economic benefits through investment, tax revenue, income generation, and job creation. Land lease payments provide direct income to farmers and ranchers hosting turbines. Counties also gain property tax revenue from installed projects. From 2000 to 2020, North Dakota wind projects attracted over $5.7 billion in private investment into the state (American Clean Power Association, 2021). Project owners pay property taxes to local governments, providing critical funding for schools, infrastructure, and services. The first ten years of a wind project's operation are estimated to generate $1 million per year in local property tax revenue and $4 million annually over the entire 20-30-year lifespan (Shoeib et al., 2021).

Wind energy supports local jobs in manufacturing, construction, operations, maintenance, consulting, and support services. According to Wiser et al. (2023), a 250 MW wind project requires 1,079 full-time workers over the development and construction period. After that, approximately 24 full-time local workers are needed for operations. Wind projects thus create economic diversity, growth, and revitalization for rural communities in North Dakota. Farmers gain a stable income source while retaining lands for agriculture. Wind contributes to the tax base, infrastructure, schools, and services. Taylor et al. (2019) determined that just five counties in North Dakota realized $59 million in cumulative wind project investments through 2008, corresponding to $21 million in income to farmers and nearly $15 million in local and state income taxes. Unlocking more of North Dakota's extensive wind potential can provide even greater economic benefits statewide.

North Dakota aims to continue expanding its wind energy portfolio to promote economic growth and meet renewable energy targets. In 2020, the state set a goal to generate 1,000 MW from solar and wind by 2030 (Willis, 2021). With only 89 MW of current solar capacity (EIA, 2021), most new renewable generation will likely come from wind. The National Renewable Energy Lab estimates North Dakota has the potential for 907,522 MW of land-based wind energy capacity (Lopez et al., 2012). Less than 1% of this has been utilized so far.

Further wind energy development can bring additional economic activity to North Dakota communities. Key regions with high potential include the Missouri Coteau, Turtle Mountains, and Valley City area (Figure 2). Substantial untapped resources remain across the state. Accessing more wind energy would support continued rural economic development.

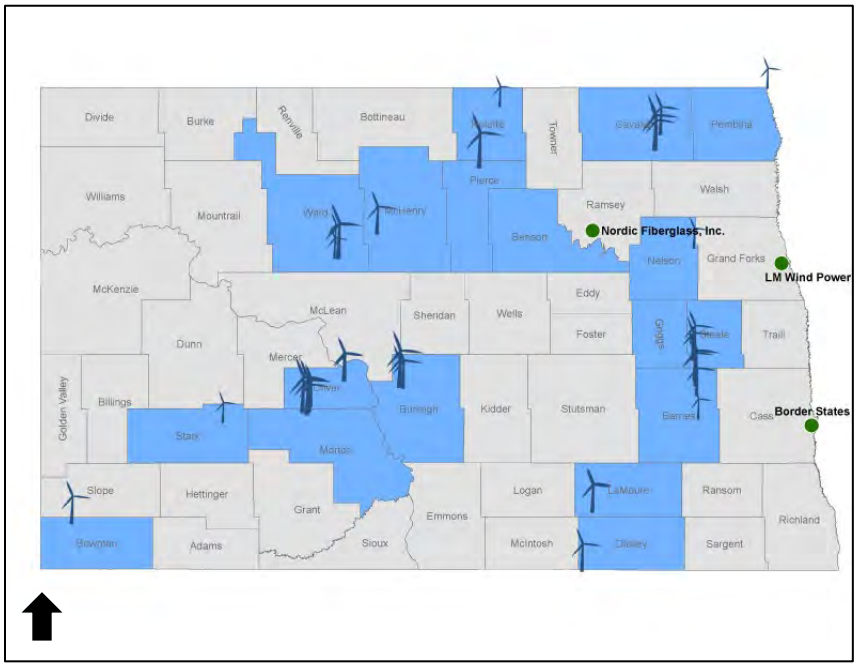

Figure 2. Map of North Dakota wind projects and manufacturing facilities (American Wind Energy Association).

Wind energy expansion faces some challenges. Transmission capacity needs strengthening to deliver remote wind power to population centers. Cold winters pose icing issues for turbines. There is also competition from fossil fuels - North Dakota produces more oil than any state besides Texas

(US EIA, 2022). Still, declining costs, energy diversification, and environmental benefits motivate us to further harness North Dakota's bountiful wind resources. North Dakota can realize its tremendous wind power potential with supportive policies and infrastructure.

2.2 North Dakota's Solar Energy Potential

Despite solar energy's immense potential as a sustainable power source, North Dakota has been slow to adopt it compared to leading states. With only about 12 megawatts (MW) of installed solar photovoltaic capacity, North Dakota ranks 36th nationally for solar development (SEIA, 2023). The state's current solar power capacity can power approximately 1,600 typical homes (Figure 3). In contrast, neighboring Minnesota boasts over 800 MW of solar capacity, more than 60 times that of North Dakota. Germany, a global solar energy leader, has an impressive 45,000 MW of total installed solar capacity (Vaidyanathan, 2013). Most of North Dakota's existing solar arrays are relatively small, with capacities under 2 MW. However, as solar costs continue to decline, some electric utilities are starting to develop larger, utility-scale solar farms in the state. The North Dakota Public Service Commission has implemented policies such as net metering to encourage solar growth, which provides credits to homeowners and businesses for the excess solar power they generate. Despite these efforts, North Dakota has significant potential for further development in its solar energy market.

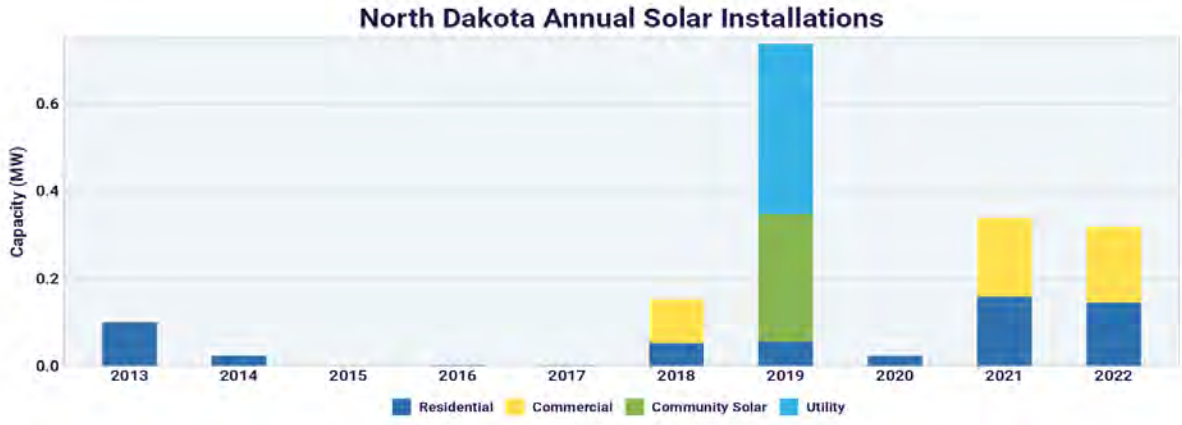

Figure 3. The annual solar installation in North Dakota (North Dakota Solar | SEIA, 2022).

Several factors suggest North Dakota has strong potential for substantially expanding its solar energy capacity. Firstly, the state has reasonably good solar resources, receiving an average of 4 to 5 kWh/m^2/day of solar radiation (Figure 4), which is comparable to Germany's solar resources (NREL, 2020). Even the colder northern regions of North Dakota receive usable levels of sunlight. Secondly, as solar panel manufacturing has scaled up and technology has advanced, costs have decreased significantly, making solar power more economically viable and competitive. Thirdly, federal tax credits and state incentives in North Dakota help reduce the cost of new solar installations, stimulating market growth.

Furthermore, North Dakota has vast rural land areas that could accommodate large, utility-scale solar farms. The declining cost of battery storage technology also complements solar growth by helping to address the intermittent nature of solar power. While solar energy peaks during the day, batteries can store excess power for use at night or on cloudy days. More robust policy mechanisms from state governments, such as renewable portfolio standards, could further incentivize solar

adoption. Given its solar resource potential and available space, North Dakota has the opportunity to significantly increase its solar power generation with the help of continued cost declines.

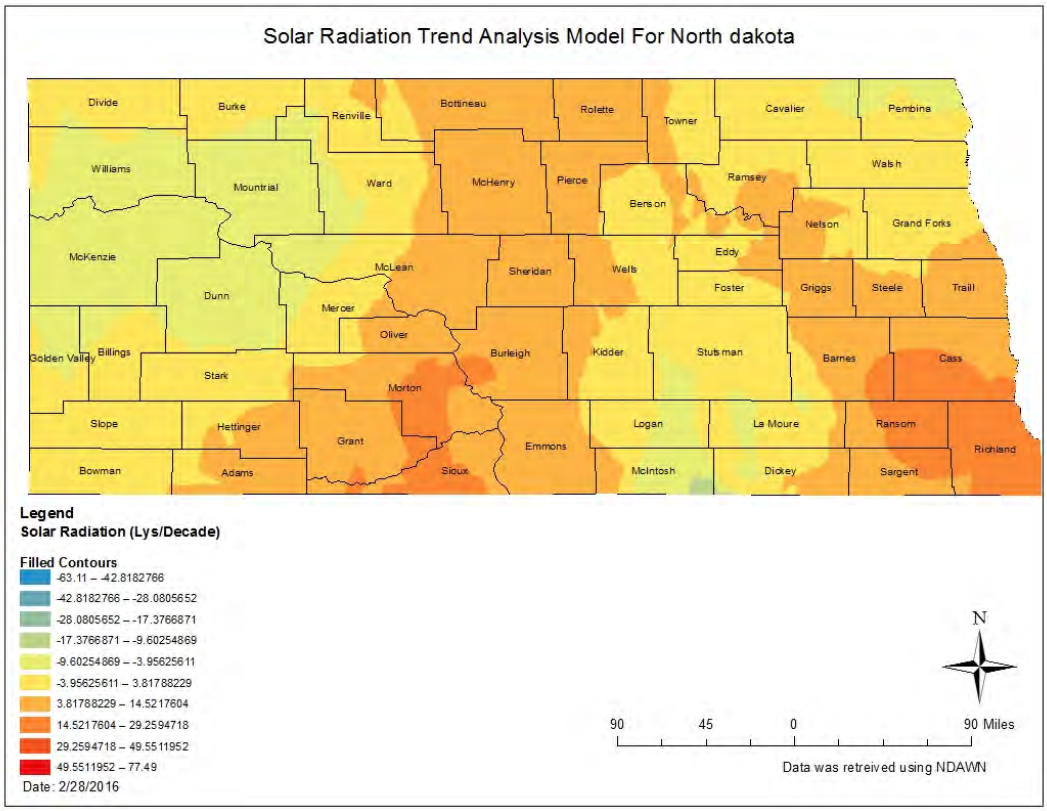

Figure 4. Solar Radiation Trend in North Dakota (Change in Solar Radiation North Dakota, 2016).

However, North Dakota still faces obstacles to substantial solar expansion. The state's cold northern climate reduces solar panel productivity compared to warmer regions like Arizona and Florida (Kim et al., 2017). Additionally, North Dakota's electricity prices have remained relatively low due to abundant local coal and hydraulic fracturing natural gas resources, making alternative sources like solar less competitive. In conclusion, while North Dakota appears well-positioned for growth in solar energy generation, further policy support and cost declines are necessary to enable large-scale solar development in the state.

2.3 North Dakota's Geothermal Energy Potential

Geothermal energy utilizes heat from the Earth's interior to generate electricity and provide direct-use applications such as district heating and heating and cooling of buildings via geothermal networks. North Dakota's geothermal resources, particularly in the Williston Basin, offer significant potential for integration into a hybrid renewable energy system (Matek, 2015). Geothermal energy provides a reliable baseload power source, which is essential for balancing the intermittent nature of wind and solar energy.

Studies have demonstrated the economic and environmental benefits of geothermal energy. Blanco and Faaij (2018) highlight the low greenhouse gas emissions associated with geothermal power, which are typically less than 5% of those from coal-fired power plants. The high capacity factors

of geothermal plants, which can exceed 90%, make them a dependable source of continuous power, complementing wind and solar energy variability.

The subsurface of North Dakota contains high temperatures associated with hot sedimentary aquifers in the Williston Basin. Temperatures above 150-200°C (Figure 5) have been encountered by oil and gas drilling at depths between 3-5 km (Gosnold, 1991). The Williston Basin features many attractive characteristics for geothermal energy development, including deep circulation of saline waters, regional heat flow, thermal gradients, and basement fault systems providing heat transmission (Gosnold, 1984).

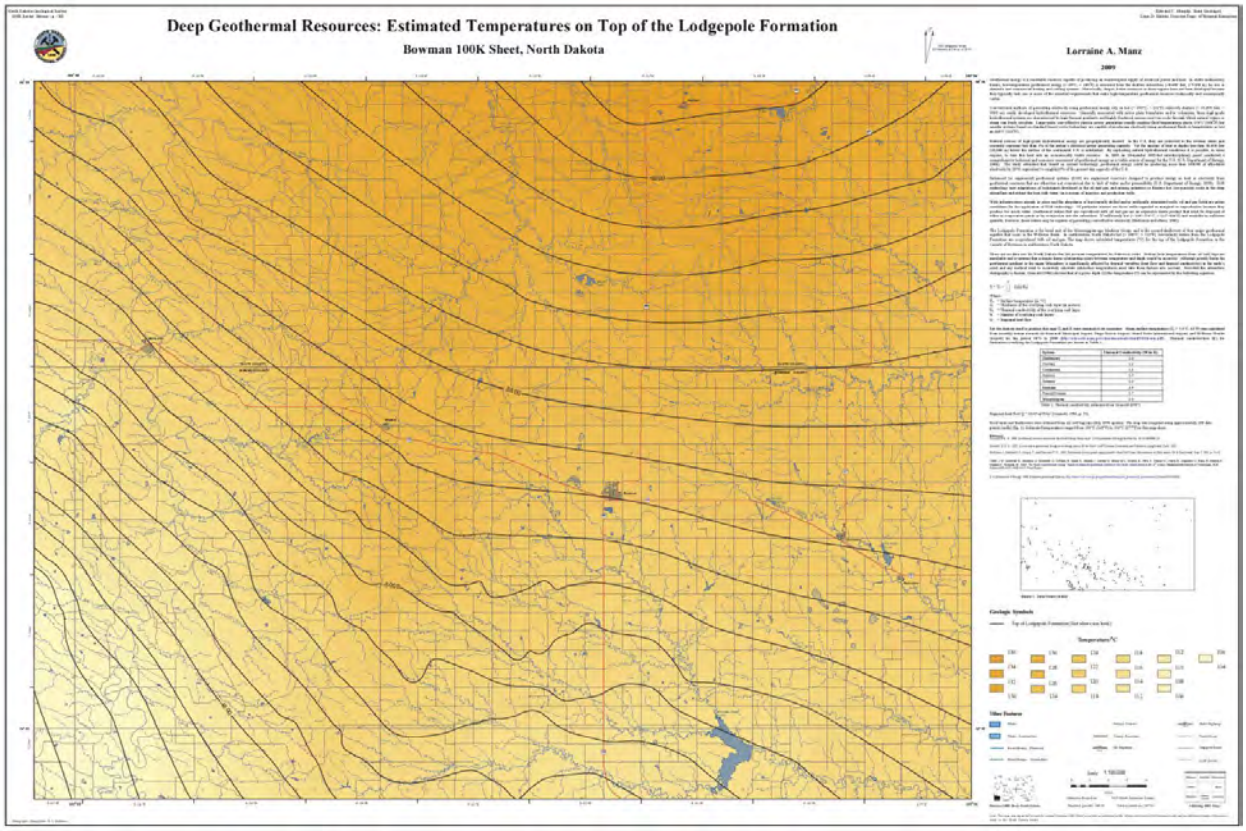

Figure 5. Estimated Temperature on Top of the Lodgepole Formation (Manz, 2008).

The technically accessible geothermal resource base beneath North Dakota has been estimated at 120 MW (Van Brummen et al., 2022). This possible resource excludes even higher temperature resources likely available deeper than current drilling (Williams et al., 2008). While no geothermal power facilities currently operate, promising hot aquifers widespread across the state could support various direct-use applications even at temperatures as low as 50°C.

Developing North Dakota's geothermal resources could deliver significant energy, economic, and environmental benefits. The baseload power potential alone represents over 100 times the state's current electricity consumption. Geothermal heat could be used for district heating systems and industrial applications across North Dakota. Tapping this consistent indigenous resource would provide energy security and price stability. Constructing geothermal power plants and distribution networks would create jobs and revenue in rural areas with energy production and related industries.

Compared to fossil fuels, geothermal energy results in negligible CO_2 and local pollutant emissions when utilized (Fridleifsson et al., 2008). Geothermal could allow North Dakota to continue diversifying its energy mix with homegrown renewable sources like wind and biofuels. Even moderate growth could make geothermal heat and power a significant component of the state's energy portfolio. Further geological surveys, technology improvements, policy incentives, and public-private partnerships can help access this vast clean energy resource.

2.4 Hybrid Systems

Hybrid energy systems combine multiple renewable energy technologies to improve overall system reliability and efficiency. Hybrid systems can provide a stable and continuous energy supply by integrating wind, solar, and geothermal energy with storage solutions. Previous research demonstrates the advantages of hybrid systems in achieving sustainable energy solutions, reducing greenhouse gas emissions, and enhancing energy security (Chen et al., 2022).

Hybrid systems offer the flexibility to optimize energy generation and consumption, ensuring that energy supply matches demand more effectively. This study builds on existing literature to develop a MATLAB-based simulation model for a hybrid renewable energy system tailored to the specific conditions of Bowman County. The hybrid approach also allows for integrating advanced storage technologies, which are crucial for managing the intermittency of renewable energy sources.

3. Methodology

This study employs a comprehensive MATLAB-based simulation to model the proposed hybrid energy system. The research methodology (Figure 6) involves a systematic data collection, system design, simulation, and analysis approach. The key steps in the research methodology include:

3.1 Data Collection

Gathering historical weather data, energy consumption patterns, and renewable resource assessments for Bowman County. This involves obtaining detailed wind speed, solar irradiance, geothermal gradient data, and electricity consumption profiles from various sources, including the National Renewable Energy Laboratory (NREL) and the US Geological Survey (USGS).

3.2 System Design

Defining the capacities of wind turbines, solar PV panels, geothermal energy sources, and storage systems based on the collected data. This step includes selecting appropriate technologies and determining optimal configurations to maximize efficiency and reliability. The design process considers factors such as resource availability, system efficiency, and energy demand patterns.

The system (Figure 7) includes wind turbines, solar PV panels, geothermal energy sources, and storage capacities. The MATLAB model simulates energy production, storage, and consumption based on real-time data and predictive algorithms. The hybrid system is designed to optimize energy production from each renewable source while ensuring a continuous and reliable energy supply.

- *Wind Energy Modeling*: The wind energy component of the model uses historical wind speed data and turbine performance curves to simulate energy production. The model accounts for factors such as wind speed variability, turbine efficiency, and capacity factors.

The performance of different turbine models is evaluated to select the most suitable option for the site.

- *Solar Energy Modeling:* The solar energy component utilizes solar irradiance data and PV module characteristics to estimate energy production. The model includes factors such as panel orientation, tilt angle, shading effects, and temperature coefficients. Different PV technologies are compared to determine the optimal choice for the hybrid system.
- *Geothermal Energy Modeling:* The geothermal energy component simulates heat extraction from the Earth's subsurface and its conversion into electricity. The model incorporates geothermal gradient data, well characteristics, and conversion efficiencies. The potential for direct use applications, such as district heating, is also evaluated.
- *Storage System Modeling:* The storage system is designed to balance supply and demand, ensuring a continuous energy supply. The model simulates the charging and discharging cycles of the storage system based on energy production and consumption patterns. Different storage technologies, including batteries and thermal storage, are analyzed to determine the most effective solution.

3.3 Simulation

In this study, we use MATLAB to model and simulate the hybrid system's energy production, storage, and grid integration. The simulation incorporates various scenarios to assess system performance under different conditions. Key parameters, including capacity factors, energy conversion efficiencies, and storage capacities, are integrated into the model to ensure accurate simulations.

3.4 Analysis

This research evaluates the proposed system's technical feasibility, economic viability, and environmental impact. This analysis includes calculating the levelized cost of electricity (LCOE), assessing greenhouse gas emissions reductions, and conducting sensitivity analyses to determine the impact of different variables on system performance. The analysis comprehensively assesses the hybrid system's potential benefits and challenges.

The economic analysis involves calculating the levelized cost of electricity (LCOE) for the hybrid system. This analysis includes capital, operation, maintenance, and financing costs. The LCOE is compared to traditional coal-based energy systems to assess the economic viability of the hybrid system. The analysis also considers potential cost savings from policy incentives and technological advancements.

The environmental analysis assesses the reductions in greenhouse gas emissions achieved by the hybrid system, which involves comparing the lifecycle emissions of each hybrid system component to a baseline scenario of coal-based energy production. The analysis includes the emissions associated with the system's manufacturing, installation, operation, and decommissioning.

The sensitivity analysis models various scenarios to assess the impact of different variables on the system's economic and environmental performance, which includes changes in capital costs, energy prices, policy incentives, and technological advancements. The sensitivity analysis helps

to identify the most critical factors influencing the viability of the hybrid system and provides insights into potential risks and opportunities.

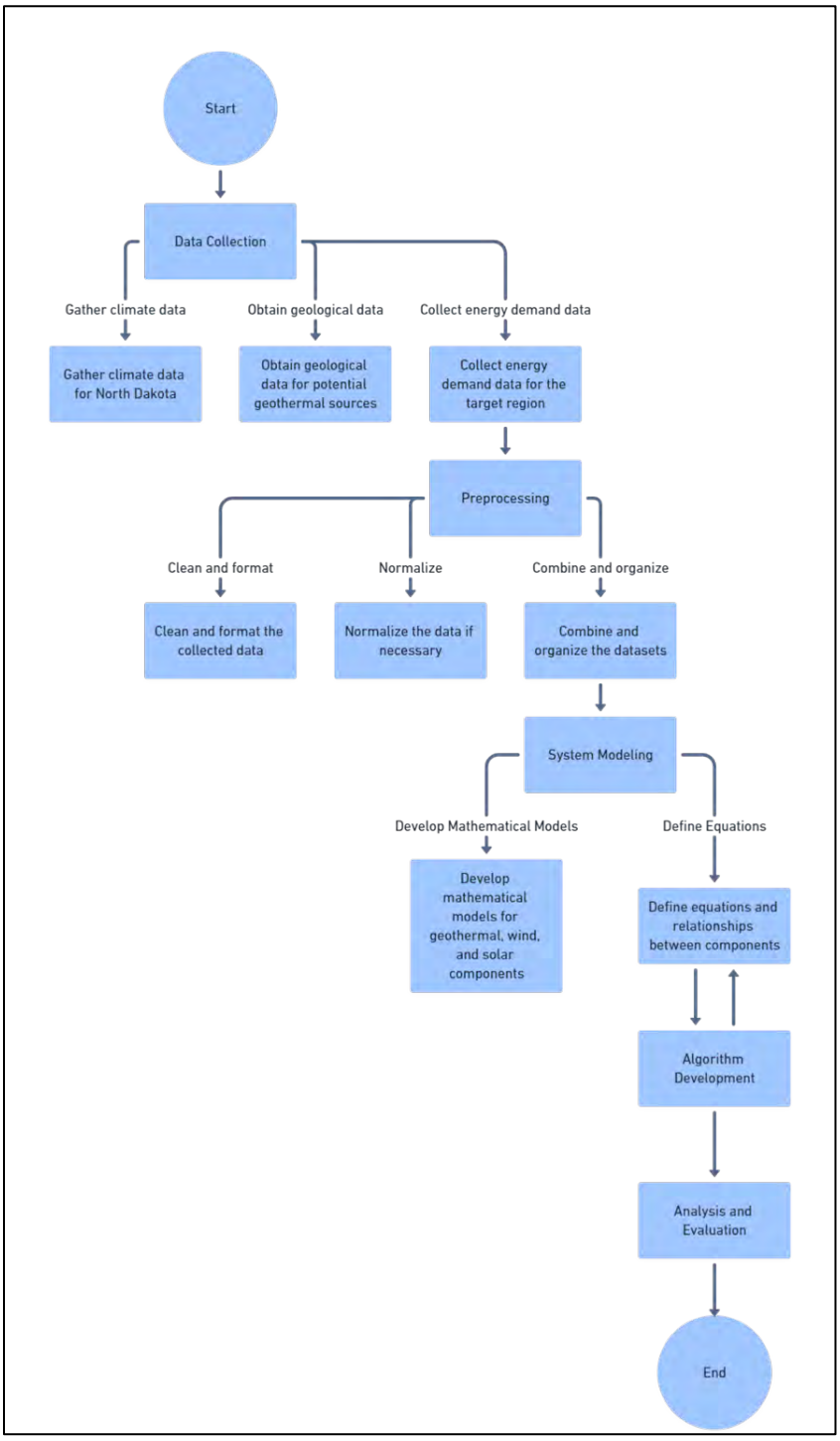

Figure 6. Flow chart for System Modeling and Simulation.

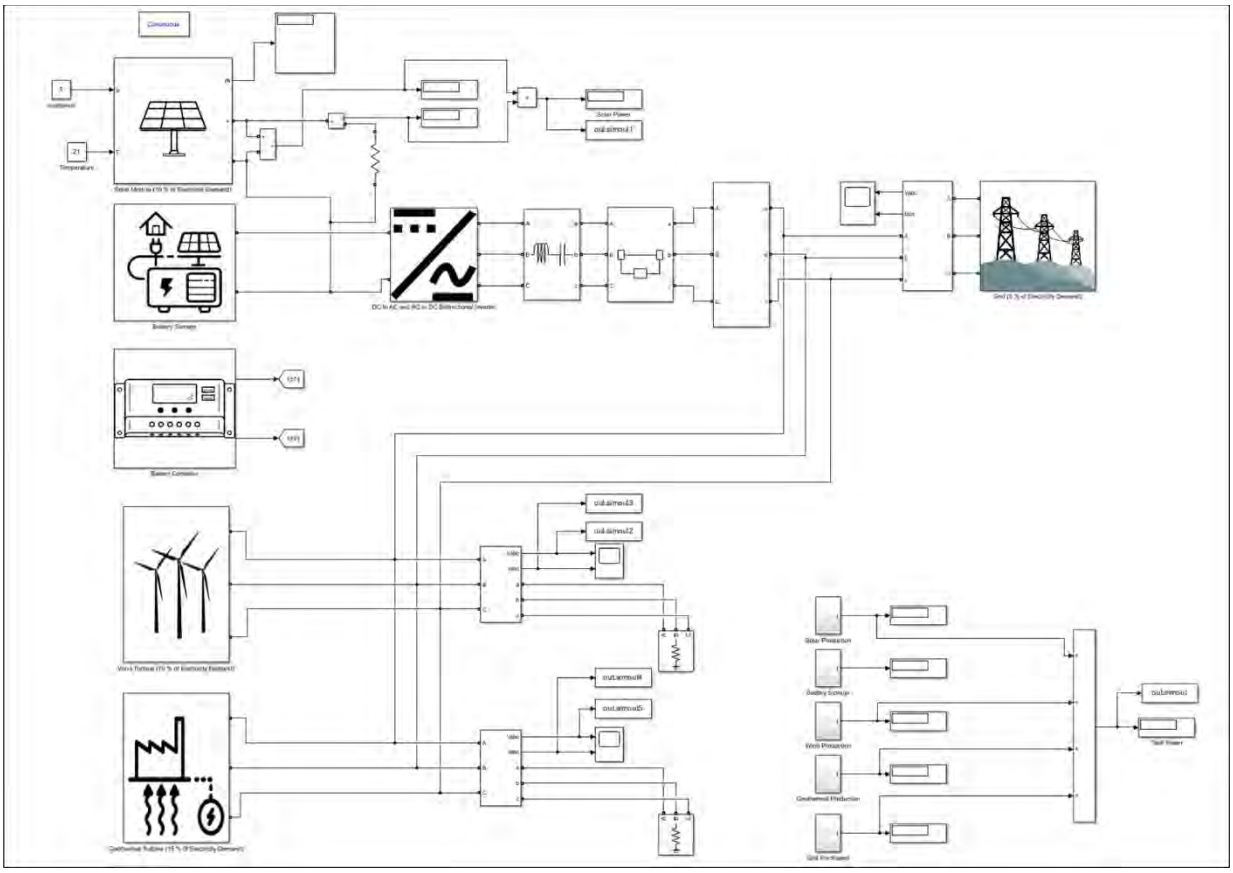

Figure 7. The hybrid system was designed for Bowman County, ND, using Simulink, MATLAB, 2023.

4. Results and Discussions

4.1 Feasibility of the Hybrid System

A proposed hybrid renewable energy system for North Dakota combines wind, solar, geothermal, storage, and grid purchases to meet an assumed local annual electricity demand of 106,865 MWh (Table 1). The system is designed to supply 70% of the total demand from wind, 10% from solar, and 15% from geothermal, with the surplus coming from storage and 5% from grid purchases.

- The wind component of the hybrid system has a capacity of 85.4 MW, with an estimated capital cost of $107,347,800 and an annual operation and maintenance (O&M) cost of $3,561,180. The wind turbines are expected to generate 74,805 MWh of electricity annually.
- The solar PV component has a capacity of 24.4 MW, with an estimated capital cost of $26,181,200 and an annual O&M cost of $458,720. The solar panels are expected to generate 10,688 MWh of electricity annually.
- The geothermal component has a capacity of 2.03 MW, with an estimated capital cost of $13,010,270 and an annual O&M cost of $212,338. The geothermal plant is expected to generate 16,029 MWh of electricity annually.

- The solar storage component has a capacity of 194 MWh, with an estimated capital cost of $243,605.8 and an annual O&M cost of $6,072.2. The storage system will store surplus energy generated by the solar panels for use during periods of low solar output.
- To supplement the renewable energy sources, the system will also purchase 5,343.25 MWh of electricity annually from the grid at an O&M cost of $5,343,250.

Table 1. Monthly production of the hybrid system, Bowman County, North Dakota, by 2040.

Month	Wind (MWh)	Solar (MWh)	Geothermal (MWh)	Grid (MWh)	Total (MWh)
Jan	9,000	500	1,600	300	11,400
Feb	8,500	600	1,600	250	10,950
Mar	9,500	800	1,600	100	12,000
Apr	8,000	900	1,600	150	10,650
May	6,500	1,100	1,600	250	9,450
Jun	5,000	1,300	1,600	350	8,250
Jul	4,500	1,500	1,600	400	8,000
Aug	5,000	1,300	1,600	350	8,250
Sep	6,500	1,100	1,600	250	9,450
Oct	8,000	900	1,600	150	10,650
Nov	9,000	700	1,600	200	11,500
Dec	9,500	600	1,600	100	11,800

The total annual electricity generation from these combined sources is estimated to be 112,210 MWh, which exceeds the assumed local demand of 106,865 MWh. This hybrid renewable energy portfolio is designed to provide a reliable and sustainable source of electricity for North Dakota while minimizing reliance on fossil fuels and reducing greenhouse gas emissions. Simulations indicate that the proposed hybrid system can meet over 90% of Bowman County's daily energy demands by 2040 (Figure 8). The wind and solar components produce the bulk of energy, while the geothermal component offers a stable baseload power source. The storage system effectively balances supply and demand, ensuring a continuous energy supply. The results demonstrate the technical feasibility of integrating multiple renewable energy sources to create a reliable and efficient hybrid system.

This significant expansion leverages complementary resources and storage to surmount intermittency barriers that would constrain further growth of standalone wind or solar. The findings demonstrate hybrid configurations technically enable the vast majority of local load from Indigenous variable generation to be fulfilled via holistic design and control.

However, the geothermal plant specification requires confirmation of sufficient hot aquifer temperatures and flows at depth. Additional geological surveys and test wells would reduce uncertainties. The modeled grid purchases will likely underestimate the need for firming without complete backup. Transmission capacity limits could also constrain renewable penetration. More

granular demand data would improve simulations. Nonetheless, the analysis substantiates that hybrid renewable systems can achieve high penetrations with careful planning.

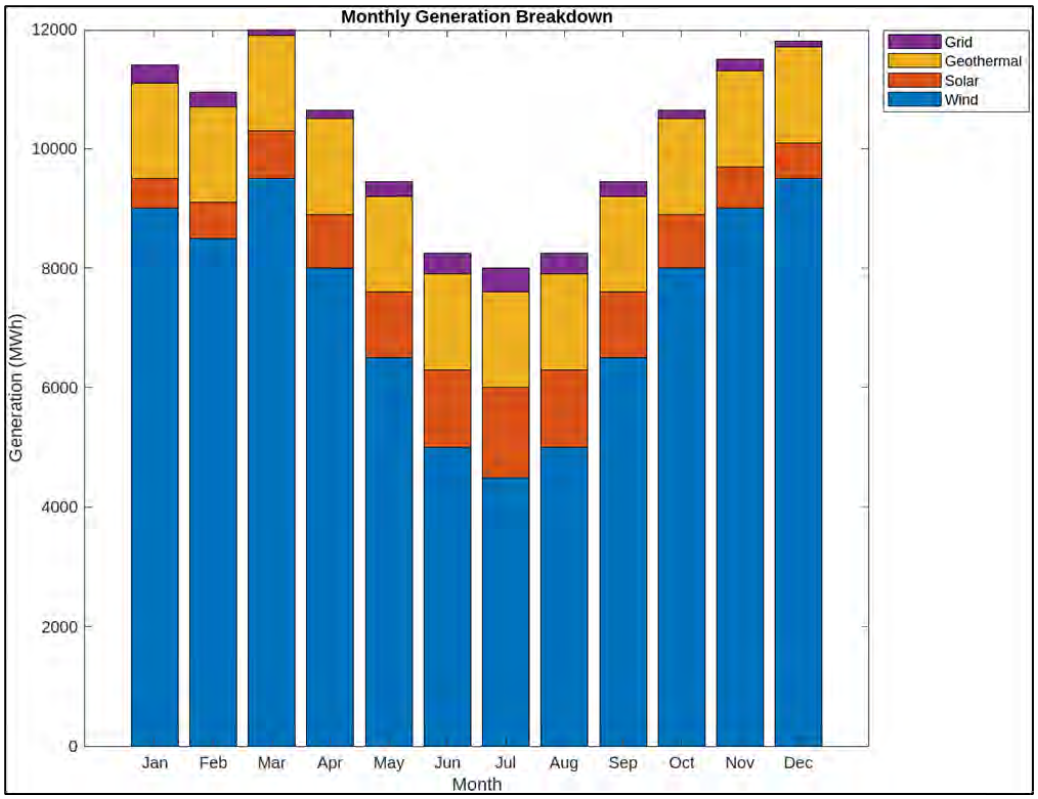

Figure 8 . Monthly electricity generation from the hybrid system by 2040.

4.2 Economic Assessment

The proposed hybrid renewable energy system for Bowman County, North Dakota, demonstrates economic solid viability, with a projected Levelized Cost of Electricity (LCOE) of $105.226/MWh over a 15-year period (Figure 9). This cost is comparable to or lower than traditional coal-based energy systems, making the hybrid system an attractive alternative from a financial perspective. Sensitivity analyses conducted as part of the economic assessment reveal that the hybrid system remains economically viable under various scenarios, including fluctuations in capital costs, energy prices, and policy incentives. Integrating multiple renewable energy sources enhances the system's resilience and reduces dependency on a single energy source, further improving economic stability. The study also highlights the potential for cost savings through policy incentives and technological advancements, which can further improve the hybrid system's economic performance. These findings provide valuable insights for policymakers and investors considering the transition to renewable energy systems. Overall, the economic assessment emphasizes the financial benefits of adopting a hybrid renewable energy system in Bowman County, demonstrating the potential for cost-effective, stable, and environmentally friendly energy production.

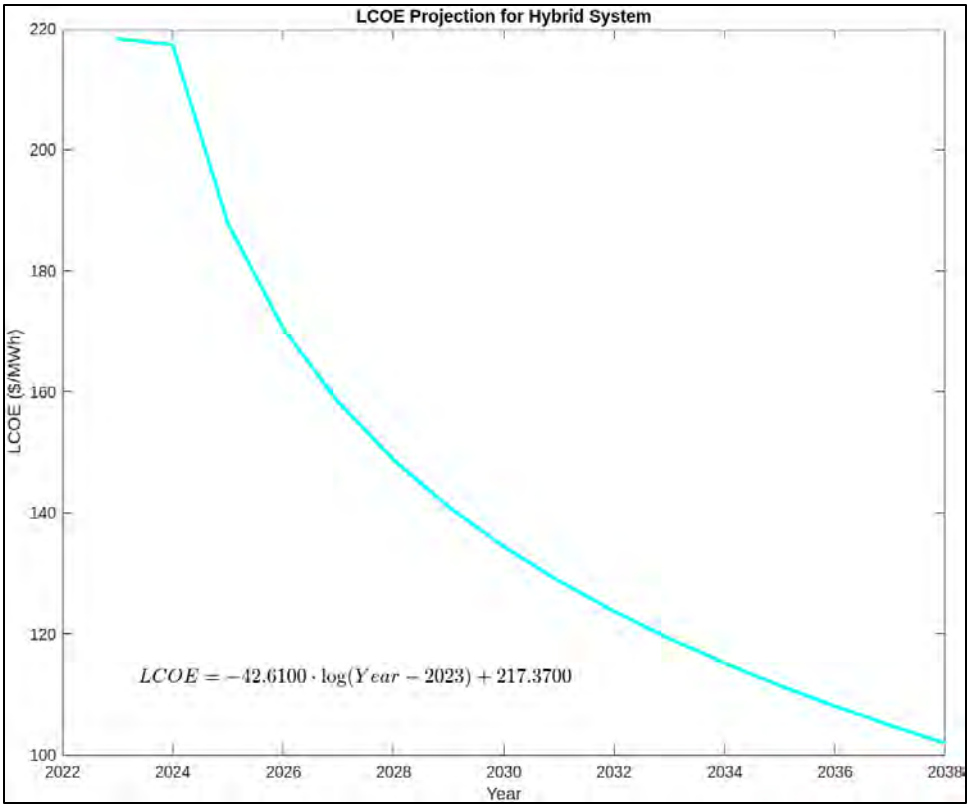

Figure 9. Levelized Cost of Electricity Projection for Hybrid System.

4.3 Environmental Impact

The proposed hybrid renewable energy system for Bowman County, North Dakota, offers significant environmental benefits by reducing daily CO_2 emissions by 97% compared to coal-based energy systems (Figure 10). This substantial reduction in greenhouse gas emissions aligns with global sustainability goals and contributes to the mitigation of climate change (Blanco & Faaij, 2018). The displacement of coal-based energy with clean, renewable energy sources is the primary driver behind the reduction in emissions. By harnessing wind, solar, and geothermal resources, the hybrid system minimizes the environmental impact of energy production and helps improve air quality in the local community. The environmental impact assessment underscores the wide-ranging benefits of reducing greenhouse gas emissions and other pollutants. In addition to combating climate change, the hybrid system can enhance public health by reducing the incidence of respiratory illnesses and other health problems associated with air pollution. Furthermore, the study highlights the potential for renewable energy systems to provide long-term environmental sustainability. Bowman County can contribute to global efforts to create a more sustainable and resilient energy future by transitioning to a hybrid renewable energy system.

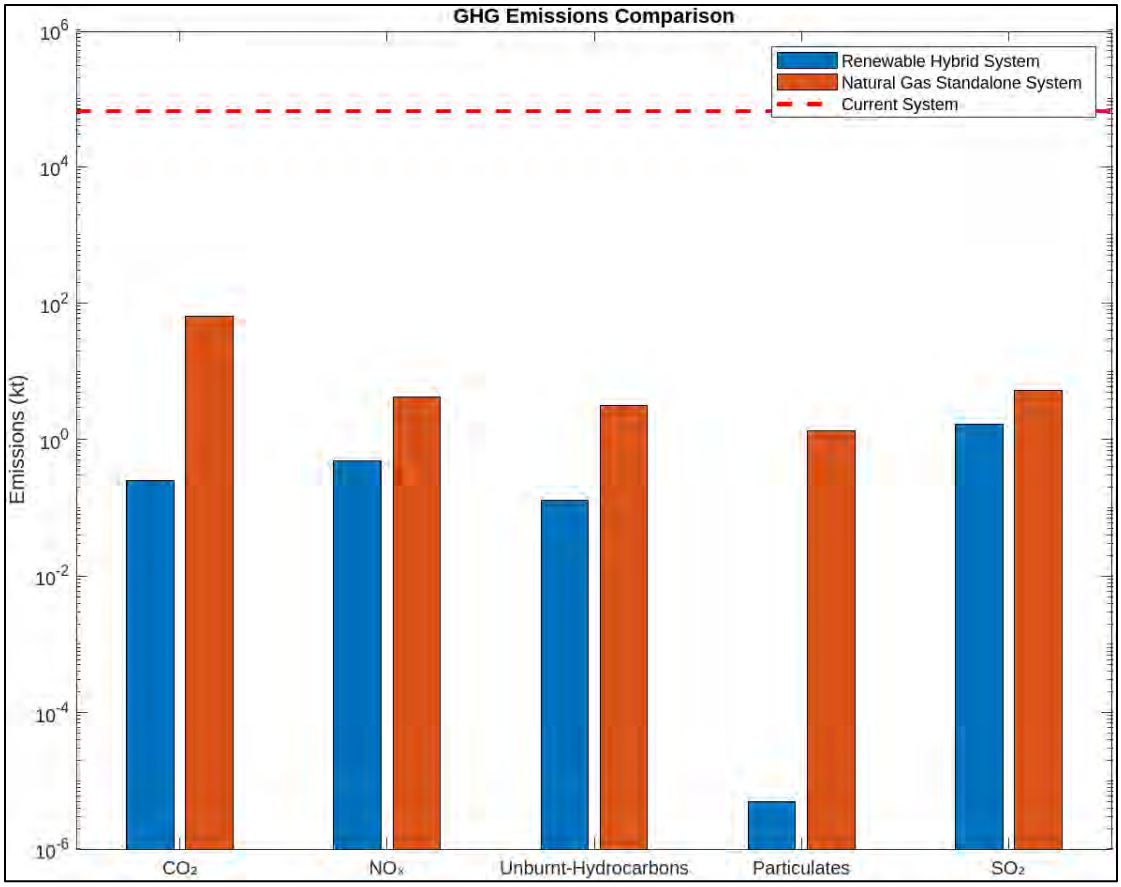

Figure 10. Greenhouse Gas Emission (GHG) Comparison: Hybrid Wind-Solar-Geothermal-Storage System vs. Natural Gas.

5. Conclusions

5.1 Overview of the Study

This study provides a comprehensive analysis of a hybrid renewable energy system tailored to the specific needs of Bowman County, North Dakota. By integrating wind, solar, geothermal energy, and storage technologies, the proposed system aims to meet the growing energy demands while significantly reducing greenhouse gas emissions. The study employs advanced MATLAB-based simulations to model and evaluate the system's performance under various scenarios, ensuring a robust and reliable analysis.

5.2 Key Findings

The simulations and analyses conducted in this study yield several key findings:

- *Technical Feasibility:* With its diverse mix of renewable energy sources, the hybrid system is technically feasible for Bowman County. The integration of wind, solar, and geothermal energy ensures a stable and reliable energy supply that meets over 90% of the county's projected daily energy demands by 2040. Including a storage system effectively balances supply and demand, addressing the intermittency issues associated with wind and solar energy.

- *Economic Viability:* The levelized cost of electricity (LCOE) for the hybrid system is projected to be $105.226/MWh over 15 years, making it competitive with traditional coal-based energy systems. The economic analysis demonstrates that the hybrid system is financially viable, with the potential for cost savings through policy incentives and technological advancements. Sensitivity analyses confirm the system's economic robustness under various scenarios, highlighting its resilience to changes in capital costs, energy prices, and policy environments.
- *Environmental Benefits:* The hybrid system significantly reduces greenhouse gas emissions, with a projected 97% reduction in daily CO_2 emissions compared to coal. This substantial decrease in emissions aligns with global sustainability goals and contributes to mitigating climate change. The environmental analysis also highlights the additional benefits of improved air quality and public health, underscoring the importance of transitioning to renewable energy.

5.3 Implications for Bowman County

The successful implementation of the proposed hybrid renewable energy system has profound implications for Bowman County. It offers a pathway to achieving energy independence and sustainability, reducing reliance on fossil fuels and enhancing energy security. The system's economic viability and environmental benefits make it an attractive option for local policymakers, investors, and the community.

- *Energy Independence:* Bowman County can reduce its dependency on imported fossil fuels by leveraging local renewable resources, which enhances energy security and resilience and protects the community from the volatility of global energy markets and potential supply disruptions.
- *Economic Development:* Developing and deploying renewable energy technologies can stimulate local economic growth. It creates job opportunities in constructing, operating, and maintaining renewable energy facilities, contributing to the local economy. The potential for cost savings and revenue generation from excess energy production further enhances economic benefits.
- *Environmental Stewardship:* Transitioning to a hybrid renewable energy system positions Bowman County as a leader in environmental stewardship. It demonstrates a commitment to sustainability and climate action, serving as a model for other communities. The environmental benefits, including reduced emissions and improved air quality, contribute to the overall well-being of the local population.

5.4 Broader Implications and Future Research

The findings of this study have broader implications beyond Bowman County, providing valuable insights for other communities and regions seeking to transition to renewable energy. The hybrid model serves as a versatile template that can be adapted to different geographic and climatic conditions, offering a scalable solution for sustainable energy development.

- *Scalability and Adaptability:* The hybrid system model can be adapted to various scales, from small communities to larger urban areas. It is flexible enough to incorporate additional renewable energy sources and advanced storage technologies, enhancing its

applicability across different contexts. The model's adaptability makes it a valuable tool for planning and designing renewable energy systems worldwide.

- *Policy and Investment:* The study underscores the importance of supportive policy frameworks and investment in renewable energy. Policy incentives, such as subsidies, tax credits, and feed-in tariffs, play a crucial role in enhancing the economic viability of renewable energy projects. Investment in research and development is also essential to drive technological advancements and cost reductions in renewable energy technologies.
- *Further Research:* While this study provides a comprehensive analysis, further research is needed to explore additional aspects of renewable energy integration. Future research should focus on optimizing system configurations, incorporating emerging technologies, and assessing the long-term sustainability of hybrid systems. Studies on renewable energy transitions' social and cultural impacts are also critical to ensure community acceptance and engagement.

In conclusion, the proposed hybrid renewable energy system offers a viable and sustainable solution for Bowman County, North Dakota. It effectively meets the growing energy demands while significantly reducing greenhouse gas emissions, contributing to environmental sustainability and climate action. The study demonstrates the hybrid system's technical, economic, and environmental feasibility, providing a comprehensive roadmap for its implementation. The findings underscore the potential for renewable energy systems to drive the transition to a sustainable and resilient energy future, offering valuable insights and a model for other communities seeking to achieve clean, locally focused energy independence.

REFERENCES

American Clean Power Association. "North Dakota Wind Energy." 2021. https://cleanpower.org/facts/state-fact-sheets/.

Blanco, H., and A. Faaij. "A Review at the Role of Storage in Energy Systems with a Focus on Power to Gas and Long-Term Storage." Renewable & Sustainable Energy Reviews 81 (2018): 1049–.

BP. "BP Statistical Review of World Energy." 2021. https://www.bp.com/content/dam/bp/business-sites/en/global/corporate/pdfs/energy-economics/statistical-review/bp-stats-review-2021-full-report.pdf.

Chen, C., H. Liu, Y. Xiao, F. Zhu, L. Ding, and F. Yang. "Power Generation Scheduling for a Hydro-Wind-Solar Hybrid System: A Systematic Survey and Prospect." Energies 15, no. 22 (2022): 8747. https://doi.org/10.3390/en15228747.

EIA. "Electric Power Monthly." US Energy Information Administration, 2021. https://www.eia.gov/electricity/monthly/.

Fridleifsson, I. B., R. Bertani, E. Huenges, J. W. Lund, A. Ragnarsson, and L. Rybach. "The Possible Role and Contribution of Geothermal Energy to the Mitigation of Climate Change." In IPCC Scoping Meeting on Renewable Energy Sources, Proceedings, Vol. 20, No. 2, p. 59. Luebeck, Germany: International Panel on Climate Change, 2008.

Gosnold, W. "Stratabound Geothermal Resources in North Dakota and South Dakota." Natural Resources Research 8 (1991): 177-192. https://doi.org/10.2172/6176983.

Gosnold, W. D., Jr. "Geothermal Resource Assessment for North Dakota. Final Report." University of North Dakota, 1984. https://digital.library.unt.edu/ark:/67531/metadc873339/.

Intergovernmental Panel on Climate Change. "IPCC Special Report on Renewable Energy Sources and Climate Change Mitigation." 2011. https://www.ipcc.ch/report/renewable-energy-sources-and-climate-change-mitigation/.

Intergovernmental Panel on Climate Change. "Climate Change 2021: The Physical Science Basis." 2021. https://www.ipcc.ch/report/ar6/wg1/.

International Energy Agency. "Renewables Information: Overview." 2021. https://www.iea.org/reports/renewables-information-overview.

Kim, J., J. Kug, S. Jeong, D. Huntzinger, A. Michalak, C. Schwalm, Y. Wei, and K. Schaefer. "Reduced North American Terrestrial Primary Productivity Linked to Anomalous Arctic Warming." Nature Geoscience 10 (2017): 572-576. https://doi.org/10.1038/NGEO2986.

Lopez, A., B. Roberts, D. Heimiller, N. Blair, and G. Porro. "US Renewable Energy Technical Potentials: A GIS-Based Analysis." 2012. https://doi.org/10.2172/1047328.

Matek, B. "Flexible Opportunities with Geothermal Technology: Barriers and Opportunities." The Electricity Journal 28, no. 9 (2015): 45–51. https://doi.org/10.1016/j.tej.2015.09.020.

NREL. "Wind Maps." National Renewable Energy Lab, 2021. https://www.nrel.gov/gis/wind.html.

Parker, F. "Thermal Pollution Consequences of the Implementation of the President's Energy Message on Increased Coal Utilization." Environmental Health Perspectives 33 (1979): 303–314. https://doi.org/10.1289/ehp.7933303.

Patil, D. S., R. R. Arakerimath, and P. V. Walke. "Thermoelectric Materials and Heat Exchangers for Power Generation – A Review." Renewable & Sustainable Energy Reviews 95 (2018): 1–22. https://doi.org/10.1016/j.rser.2018.07.003.

Raupach, M., and J. Finnigan. "The Influence of Topography on Meteorogical Variables and Surface-Atmosphere Interactions." Journal of Hydrology 190 (1997): 182-213. https://doi.org/10.1016/S0022-1694(96)03127-7.

Shoeib, E., E. H. Infield, and H. Renski. "Measuring the Impacts of Wind Energy Projects on US Rural Counties' Community Services and Cost of Living." Energy Policy 153 (2021): 112279. https://doi.org/10.1016/j.enpol.2021.112279.

Taylor, D., M. Layurova, D. Vogel, and A. Slocum. "Black into Green: A BIG Opportunity for North Dakota's Oil and Gas Producers." Applied Energy (2019). https://doi.org/10.1016/J.APENERGY.2019.03.158.

US Energy Information Administration. "How Much Electricity Is Lost in Electricity Transmission and Distribution in the United States?" 2020. https://www.eia.gov/tools/faqs/faq.php?id=105&t=3.

US Energy Information Administration. "Electric Power Annual." 2020. https://www.eia.gov/electricity/annual/.

SEIA. "US Solar Market Insight." 2023. https://www.seia.org/us-solar-market-insight.

US EIA. "North Dakota State Profile and Energy Estimates." 2022. https://www.eia.gov/state/?sid=ND#tabs-4.

Vaidyanathan, M. "Capturing Inherent Variability in Solar PV Energy through Realistic Estimates: A Case Study for the State of Minnesota." Distributed Generation & Alternative Energy Journal (2013). https://doi.org/10.1080/21563306.2013.10596279.

Van Brummen, A. C., B. M. Adams, R. Wu, J. D. Ogland-Hand, and M. O. Saar. "Using CO2-Plume Geothermal (CPG) Energy Technologies to Support Wind and Solar Power in Renewable-Heavy Electricity Systems." Renewable and Sustainable Energy Transition 2 (2022): 100026. https://doi.org/10.1016/j.rset.2022.100026.

Williams, C. F., M. J. Reed, R. Mariner, J. DeAngelo, and S. Galanis. "Assessment of Moderate- and High-Temperature Geothermal Resources of the United States." Fact Sheet (2008). https://doi.org/10.3133/fs20083082.

Willis, A. "Gov. Burgum Wants to Get North Dakota Carbon Neutral by 2030. It's a Tall Task." InForum, July 12, 2021. https://www.inforum.com/news/gov-burgum-wants-to-get-north-dakota-carbon-neutral-by-2030-its-a-tall-task.

"Wind Energy Database." 2023. https://www.thewindpower.net/.

Zhang, J., S. Chowdhury, and A. Messac. "A Comprehensive Measure of the Energy Resource: Wind Power Potential (WPP)." Energy Conversion and Management 86 (2014): 388-398. https://doi.org/10.1016/J.ENCONMAN.2014.04.083.

Zygarlicke, C. J., A. L. Stomberg, B. C. Folkedahl, and J. R. Strege. "Alkali Influences on Sulfur Capture for North Dakota Lignite Combustion." Fuel Processing Technology 87, no. 10 (2006): 855–861. https://doi.org/10.1016/j.fuproc.2006.03.002.

Optimizing Design and Operation of Closed Loop Geothermal Wells with Integrated Asset Simulation

Stian Engebretsen, Taha Taha and Mohammed Abd-Allah

Aspen Technologies

Keywords

Integrated Asset Modeling, Closed Loop, Coaxial Borehole Heat Exchanger, Organic Rankine Cycle, Hot Dry Rock, Bayesian Optimization

ABSTRACT

Geothermal energy production is attractive since it is dispatchable, has low emissions, and low environmental impact. In the advent of scalable next generation geothermal systems, repurposing of depleted oil and gas wells can be a contributor to the energy transition. Wells can be repurposed for closed loop borehole heat exchange (BHE) for direct geothermal use or electricity production in areas with sufficiently high geothermal gradient. Repurposing old wells for BHE cuts capital expenditure on drilling and has little reservoir uncertainty compared to conventional open loop geothermal. In this paper we look at design and operational parameters for wells circulating water injected in the annulus space and the core tube feeding hot water to an organic Rankine cycle for energy production. An integrated asset model consisting of a multiphase flow simulator and a process simulator is used to optimize the produced electrical power. The aim is to show how commercial oil and gas simulators, and methodology can generate techno-economic studies that lead to successful geothermal project design and operation.

1. Introduction

Among the thousands of oil and gas wells drilled globally, a certain subset has been drilled in regions with geothermal gradients above the average. These hot wells can become geothermal energy resources, by repurposing them to borehole heat exchangers extracting heat by closed loop circulation of a fluid such as water. Old wells, not producing oil and gas anymore can aid the energy transition and provide a segue for oil and gas companies into a sustainable and environmentally friendly industry. Conventional geothermal operators drill wells that for various reasons will never be operated but can be hot candidates for BHE. Figure 1 shows regions where higher geothermal gradient can occur, and where conventional power plants are located, this indicates where there could be potential for BHE in old wells.

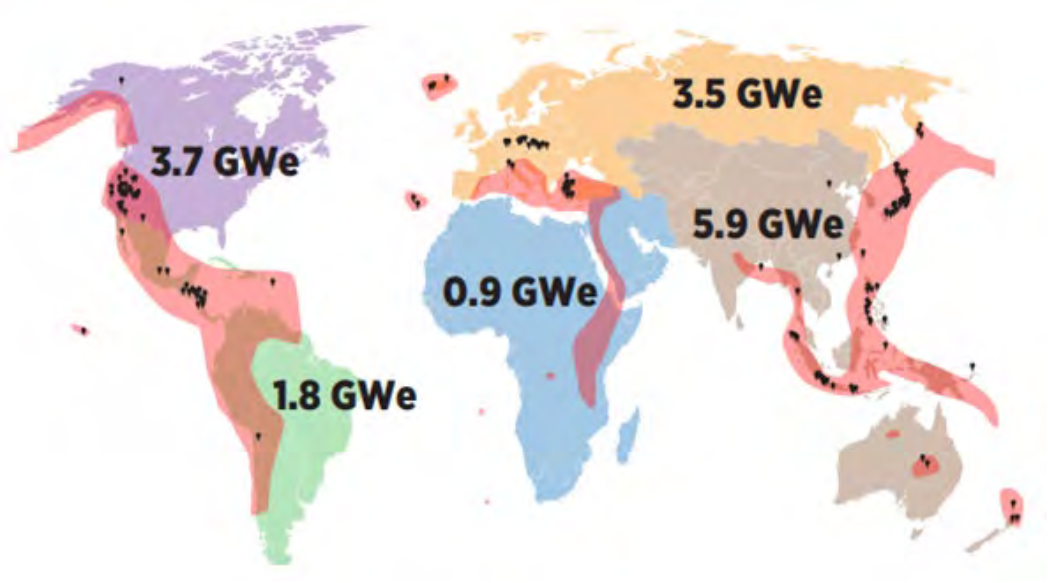

Figure 1: Installed electrical capacity from geothermal plants in 2021. Each black dot is a plant while the red zones indicate high-temperature geothermal zones. Data from IRENA and IGA (2023).

Many factors such as location, depth and number of wells and the available temperatures will determine whether the resource is best applied for direct use of the heat and/or electricity production. Direct use of the heat has a high efficiency and can cut emissions on industrial applications or district heating. For wells with sufficiently high temperatures, borehole diameter, and measured depths, electricity production may be feasible using a steam turbine. Geothermal energy is a firm power source and has a big advantage over other intermittent renewables such as wind and solar. Big capital expenditure is a drawback for geothermal energy, that is why proper tools and workflows to find the optimal design is key for any project.

Previous work by Chaves et al. (2023) showed how a multiphase flow simulator has been adapted and can be used to model well design and operational aspects for closed loop borehole heat exchangers. Expanding on this work, it shows how to apply integrated asset simulation to optimize design and operation of a geothermal plant. A well and network simulator is tightly integrated with a process simulator which is again orchestrated using a Bayesian optimizer. Running multiple simulation scenarios, the workflow will converge toward optimal design and operating conditions that maximizes the net power generation of the plant.

2. Method

In this section the domain specific technical foundation regarding reservoir model, well model, process model and orchestrator software is outlined. The simulators used are Aspen METTE, Aspen HYSYS and Aspen Tempest, and will respectively be referred to as well simulator, process simulator and simulation orchestrator.

2.1 Well and Reservoir Model

A BHE transfers heat by circulating fluids inside a hot well. The fluid used is water in this case. Figure 2 shows the heat transfer effects in the well as the water is heated in the annulus and maintained through the core tubing. Mass is conserved, as there is no mass transfer with the sub-

surface, which also means there is little to no risk of inducing seismicity. The well used in this work has a measured depth of 2000 meters and is nearly vertical. The annulus diameter is 8,5 inches, and it is assumed this can be used as is without drilling a new well. The core tubing diameter and insulation are the main design variables considered for recompleting the well in addition to deciding the circulation rate which is an operating variable. Figure 2 indicates a big temperature difference between the fluid in the annulus and the tubing near the top. Using a vacuum insulated tubing (VIT) near the wellhead will mitigate the temperature loss from the core tubing.

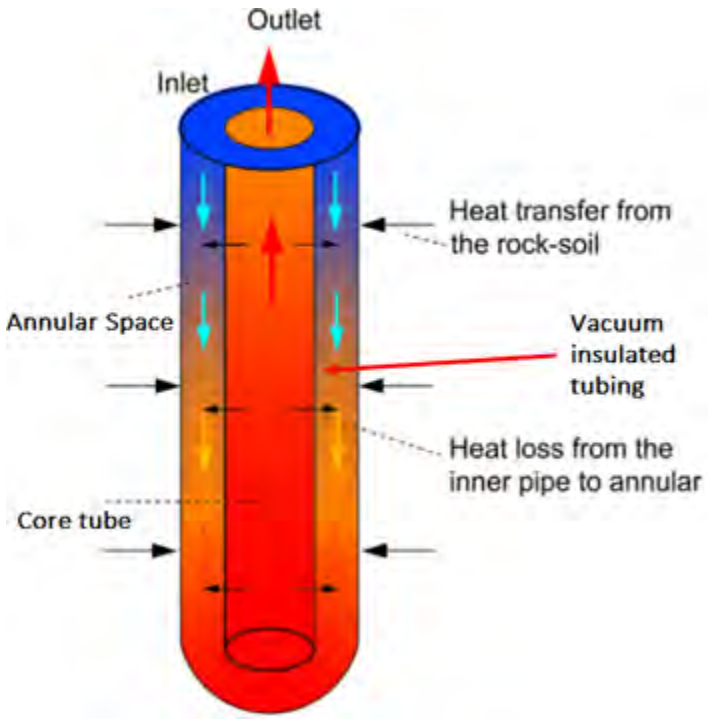

Figure 2: A schematic illustrating heat transfer for the borehole heat exchanger (BHE). Cold fluid (water) is injected into the annulus and gets heated via conduction from the hot casing and rocks surrounding the well. In the bottomhole, the heated fluids transfer into the core tubing, bringing it back to the surface. Using a vacuum insulated tubing helps to maintain the temperature on the return. The figure is taken from Chaves et al. (2023).

The well model has a geothermal gradient as shown in Figure 3, going from 20 °C at the surface to 250 °C at 1800 m TVD. The well simulator is used to model the thermal convection and conduction effects in wellbore material and fluid as well as the rocks/reservoir surrounding the wellbore. The simulator uses a proprietary drift-flux flow model for the pressure loss, and a transient radial model for the heat transfer into the rocks. No reservoir simulator is used in this case, as it is a hot dry rock example with conduction, and no convection effects modeled in the rocks. The model is explained in more detail in Chaves et al. (2023) for reference. Figure 4 shows how the well model is discretized for a cross section of the well. Convection of heat is modelled in the water for the annulus (in grey) and the core (in red) in the center of the well. Between them, where it says “vacuum”, conduction of heat is modeled. The outer layers indicate a discretized model into the rocks or “Formation” which is 10 meters in radius with conduction modeled until an ambient temperature boundary at the outmost circle. The well model has a choke valve and a pump available to meet its target flow rate. At lower flow rates the thermosiphon effect is enough keep the well circulating, and the choke valve is used to balance pressure. At higher flow rates, the

additional frictional loss will become greater than the delta pressure from the density difference between the annulus and the core, at which point the pump can be used to add more head to circulate the wanted rate.

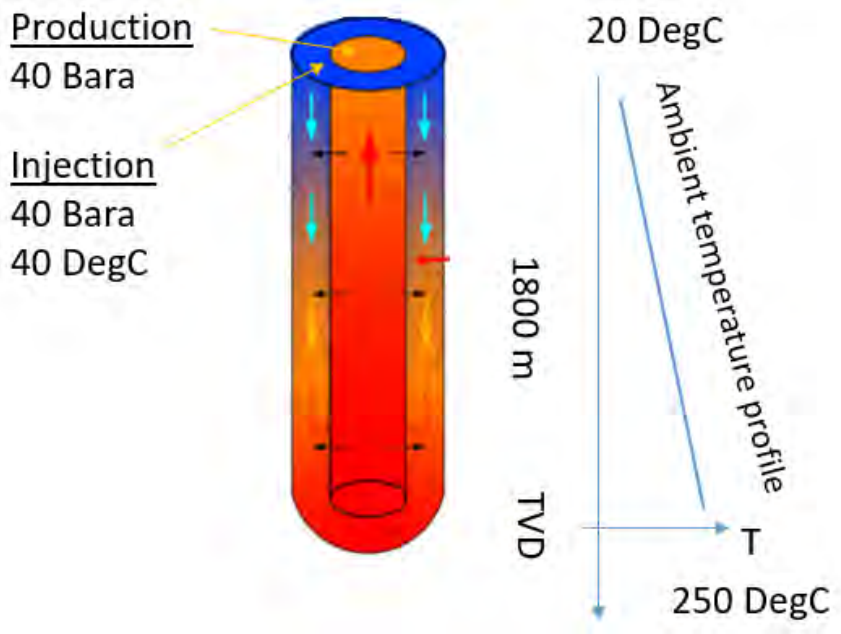

Figure 3: The constant boundary conditions for the model are shown. The model is run from a cold start initial condition at ambient temperature. Flow rates and other parameters are variables in the simulations.

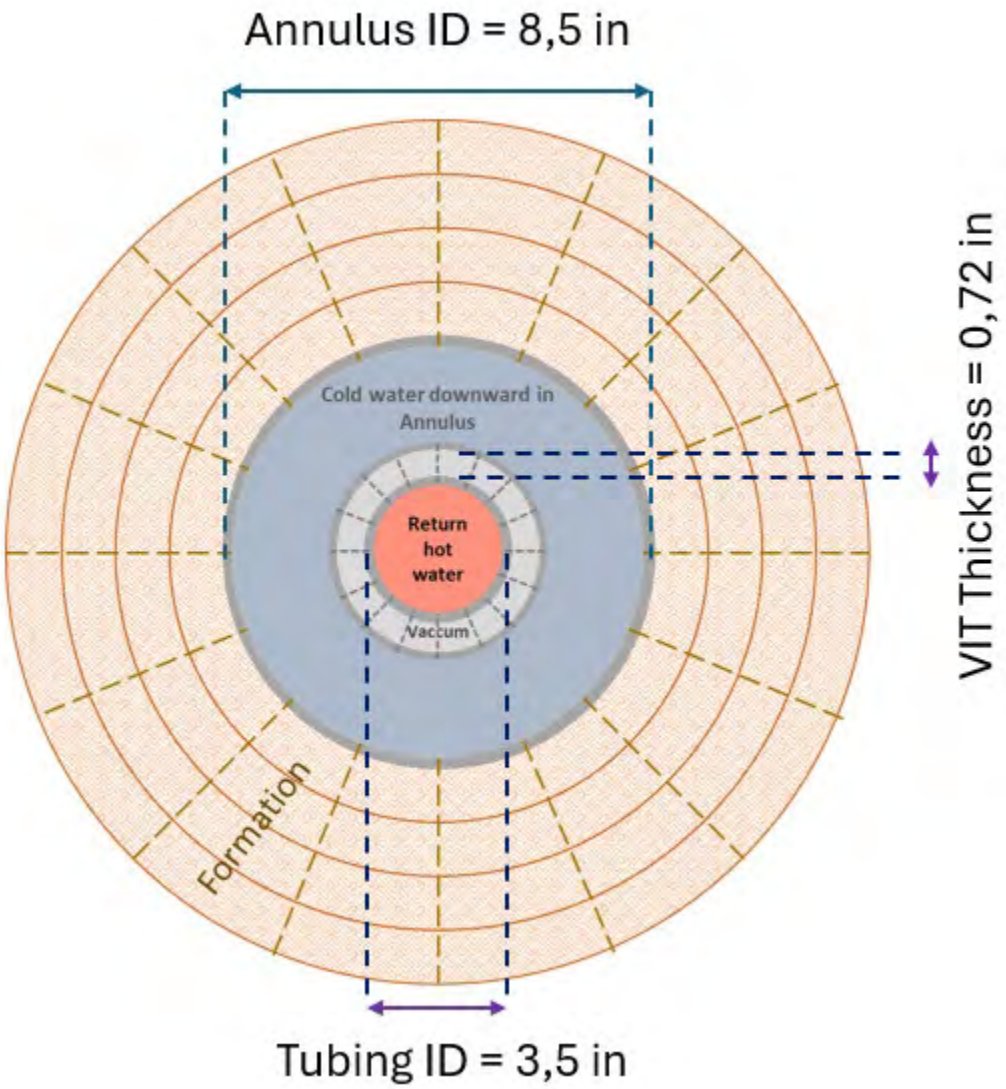

Figure 4: Simplified cross-sectional view of the simulation domain in the well and surrounding rock formation. The annulus inner diameter (ID) is fixed in this work, but the tubing ID is a control parameter for the optimization study. The figure is based on Chaves et al. (2023).

2.2 Process Model

The integrated model consists of an ORC built in the process simulator which has an extension to interface the well simulator, see Figure 5. The integrated model has a consistent handling of pressure, PVT properties, mass and energy balances between the simulators. Each simulation scenario is run for five days with the well simulator giving transient temperatures into the process simulator. For the techno-economic results, a simulation is run for a longer period. The ORC model is inspired by the work of Beckers et al. (2022). Since we only have one well with a realistic model, we multiply the flow coming from this well to account for additional wells feeding into the plant. In Figure 5, two set blocks SET-TEMP and SET-FLOW are used to set the boundary conditions for the MAKEUP stream based on the GF_IN stream from the well simulator. The total number

of wells is set to 10. It is assumed the wells are far enough apart to avoid considerable thermal influence.

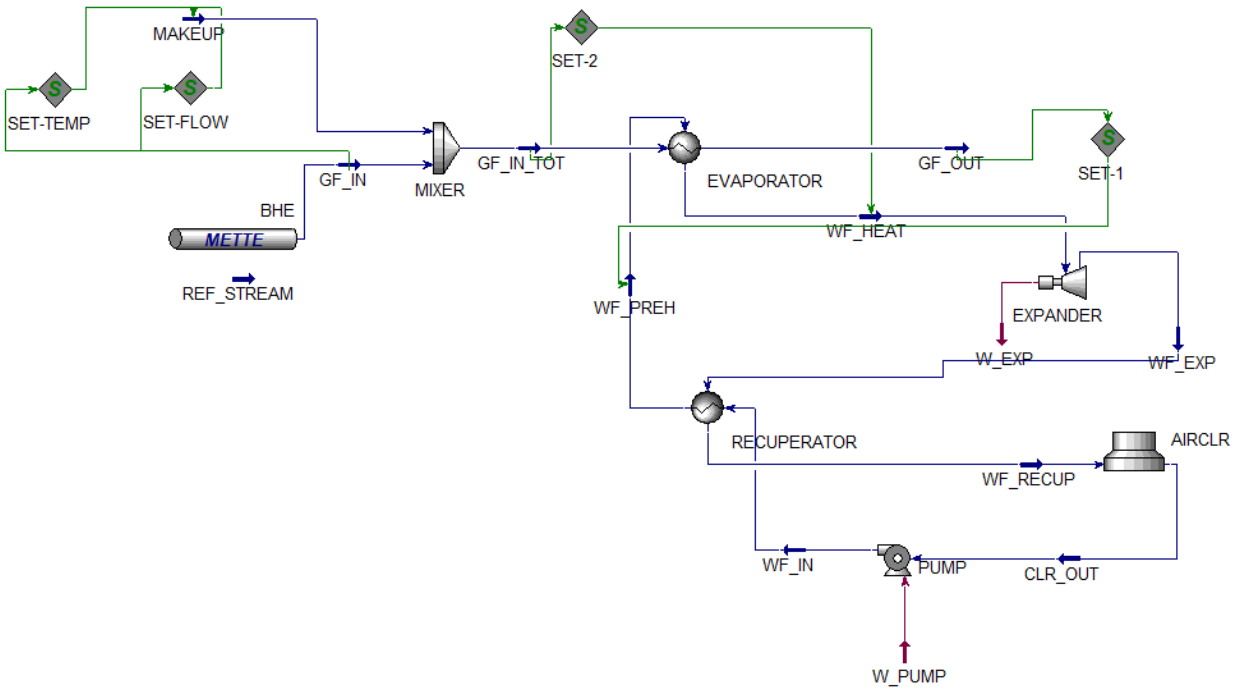

Figure 5: The integrated process model of an ORC with butane as working fluid and water as BHE fluid.

2.3 Orchestrator and Optimizer

The simulation orchestrator is a Bayesian optimization framework described in Bordas et al. (2020) and Taha et al. (2024). The Bayesian approach is effective when optimizing functions that are costly to evaluate. The orchestrator starts an initial set of simulations, called Scoping Runs, which are used as training data to fit an emulator function for the objective function. In this case, the objective function is the net power generation of the ORC plant. Additional batches of simulations, called Refinement Runs, are then run to fine-tune the control parameter values while the emulator function is continuously updated. The orchestrator will explore the solution space and converge towards an optimal solution with an increasing precision as more runs are executed. Relevant control parameters for the optimization are shown in Table 1 with reference to streams in Figure 5. The control parameters are key operating boundary conditions for the ORC and the BHE.

2.3.1 Table 1: Control Parameters for the Optimization with Ranges

Name [control parameter name]	**Description []**	**Value Range [min, max]**
Rate GF_IN.	Well flow rate from the BHE	1– 4 kg/s
Pressure at WF_EXP	Pressure of the working fluid downstream the expander	2 – 5 Bara
Pressure at WF_IN	Pressure of the working fluid downstream the pump	10 – 40 Bara
Temperature at WF_PREH	Temperature of the working fluid into the evaporator	20-50 C°
Depth of VIT	Depth where VIT stops and normal tubing is used for the remaining depths	Six discrete alternatives used: [1,2,3,4,5,6] representing [450 m, 850 m, 1055 m, 1720 m, 1800 m] TVD
Diameter BHE Tubing	Inner diameter of the core tubing in the BHE	0.07 – 0.135 m

2.3.1 Levelized Cost of Electricity

The levelized cost of electricity (LCOE) is calculated for the investment of a new ORC plant including the workover of 10 wells by installing new tubing. The estimated costs of various activities and commodities are tabulated in Table 2 below and are used to calculate the LCOE. ORC cost is taken from Beckers et al. (2022), and well activities are inspired by Lowry et al. (2017). The plant is assumed operable after three years, and the total period is 30 years.

2.3.2 Table 2: Cost Assumptions

Description	**Cost**
ORC Capital Cost	$2500/kWe
Vacuum insulated tubing	$400/m
Normal tubing price	$100/m
Discount rate	7 %
Well logging	$180 000/well
Workover	$30 000/well
O&M Cost	$320 000 k/kWe
O&M Cost Yearly Increase	2%
Parasitic Electricity Cost	$0.3/kWe

3. Results

3.1 Well Simulations

A simple simulation varying the flow rate in the well as seen in Figure 6. The well simulator is efficient for screening design, and well operation but does not model the ORC process rigorously to estimate plant electrical output.

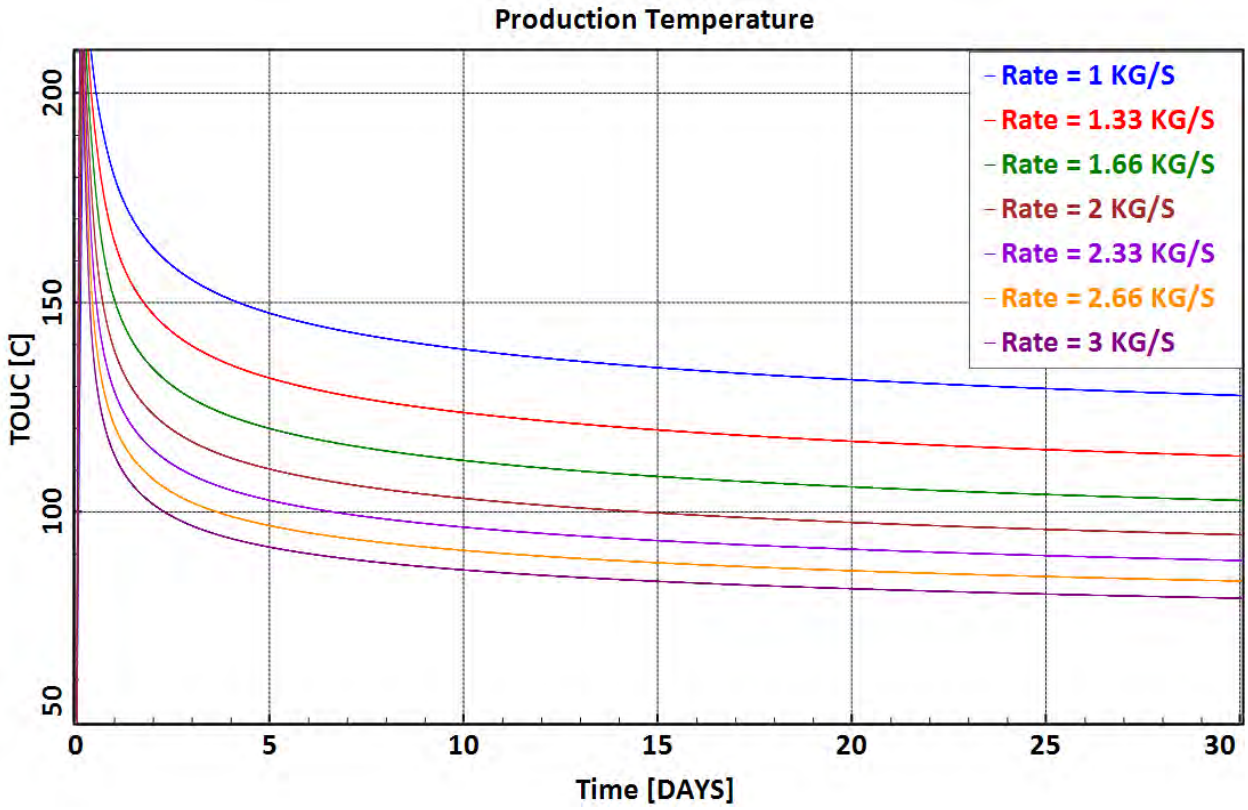

Figure 6: Flow rate sensitivity in the well simulator stand alone. Low rates yield a high outlet temperature, but less thermal energy. The process model is needed to estimate the generated power, and the integrated model is required to estimate the optimal design and operation.

3.2 Optimizing Power Generation

Results are shown where the net power generated is maximized. Figure 7 shows the solution space and maps the combination of control parameters to the wanted net power output. The optimal runs produce more than 950 kWe. As the optimizer explored the solution space it found local optima characterized by different rate and diameter configurations. The best solutions are found when selecting the minimum tubing size paired with a quite low flow rate. Flow rate and tubing diameter are tightly linked, as a lower diameter results in higher velocity through the tubing, with the cost of increased pressure loss. When selecting a lower tubing diameter, the annulus space becomes bigger, resulting in lower velocity through the annulus and higher temperature as the fluid has more time to be in contact with the hot casing and rocks. The low flow rates yield high temperatures and thermal efficiency, but the total power becomes restricted by the amount of mass

transferred. The optimal runs also select the lowest temperatures feeding into the evaporator. A slightly lower solution is found by selecting a higher flow rate and a medium size tubing, as seen in the dark blue distribution. More mass is circulated and the dependency on the downhole pump can be eliminated, but the temperature becomes lower and with it the efficiency drops. The light blue solutions all select the lowest flow rate. The depth of the VIT is consistently giving the best results for a fully insulated tubing, as seen by the fact that most runs converge to this configuration. The pressure at WF_IN is dependent on the temperature from the BHE, as it will result in liquid in the expander, if it is too high. The three distribution tops of this pressure are due to the three distributions of temperatures resulting from the rate and diameter changes. The best runs find a pressure around 25 Bara.

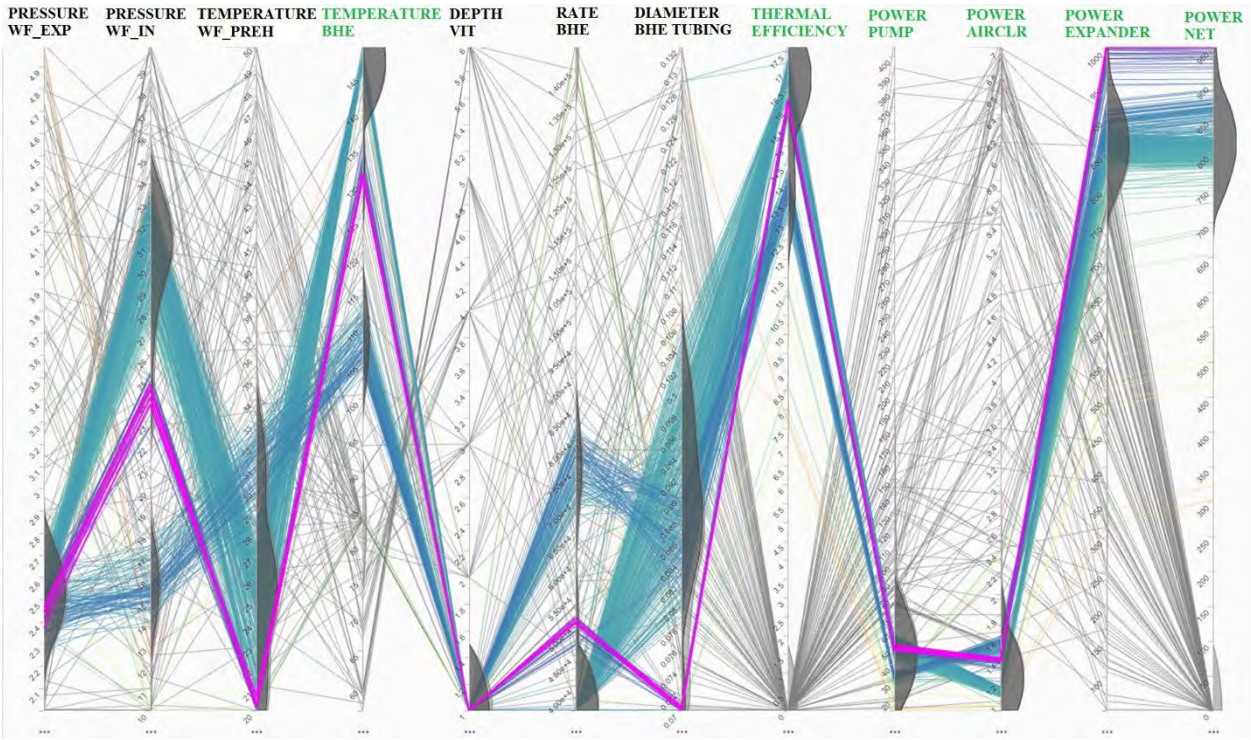

Figure 7: Parallel coordinate plot mapping key asset design and operational variables to the net power generation on the far-right column. Each line represents an integrated simulation run. The black headers notify control parameters while the green headers are dependent variables of interest. The purple lines represent the best scenarios, while blue lines indicate valid scenarios yielding the high power, and the gray lines represent runs that result in non-physical boundary conditions, or the net power generation is zero.

In Figure 8, the evolution of the simulation runs is shown from start to finish. The runs show different local optima before finding the best result as discussed in the above paragraph.

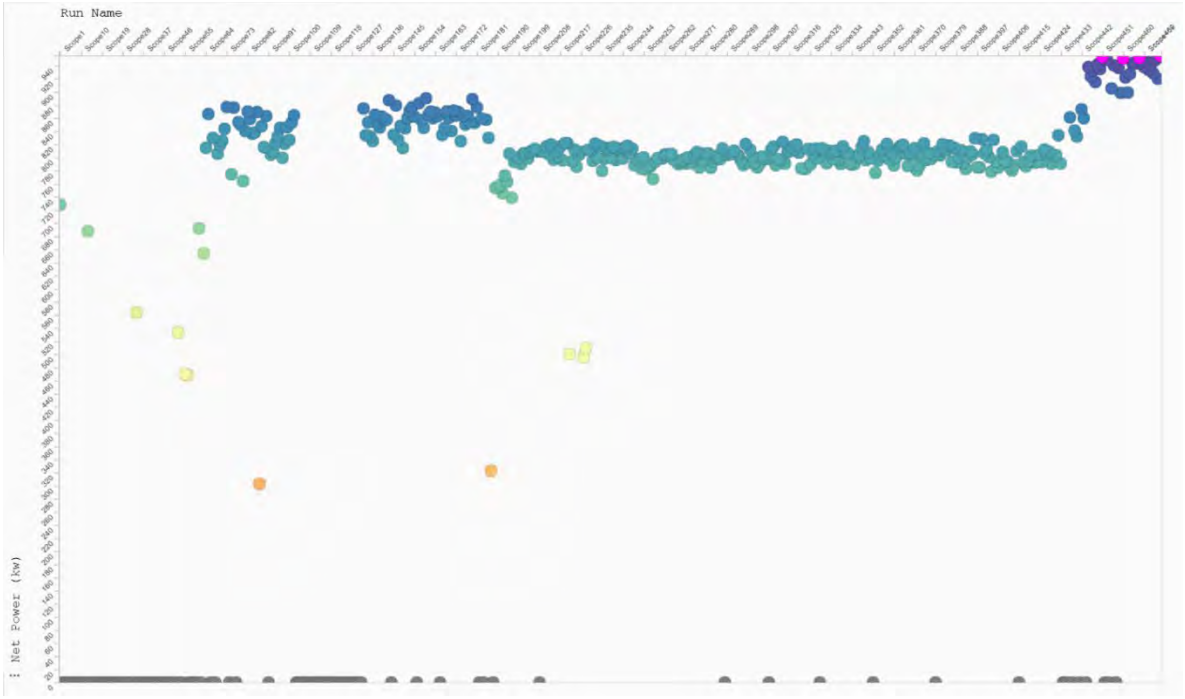

Figure 8: The objective function is plotted vs simulation runs, each dot represents the net power produced for each optimizer run as it progress from start to end. The initial Scoping Runs to the left shows varying results as the optimizer is exploring. On the far-right, the optimal solution is found.

The optimizer is also increasing the thermal efficiency by adjusting the ORC boundary conditions. In Figure 9, a collection of simulation runs is shown together with the best run (yellow) and worst run (green). The best run is obtaining a thermal efficiency just above 16 %.

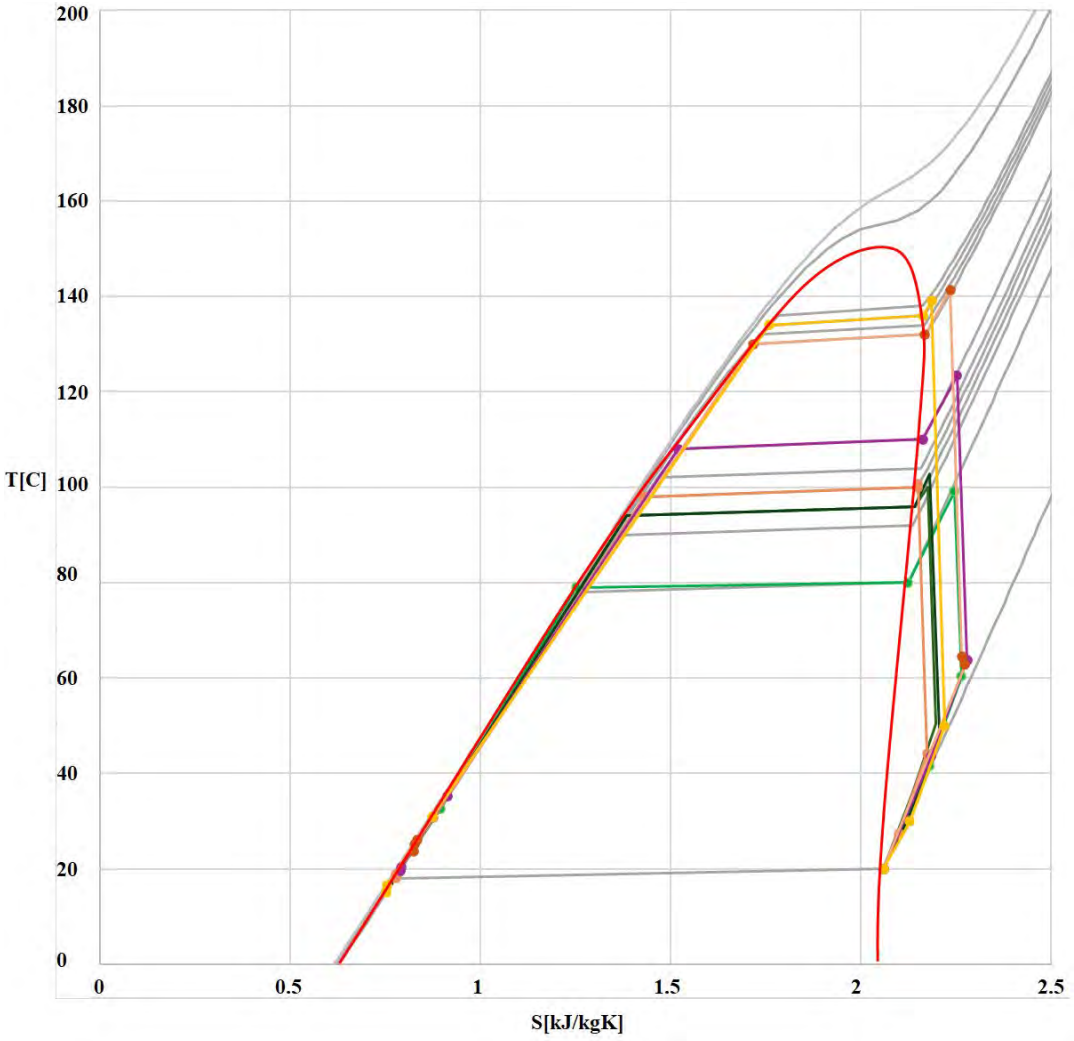

Figure 9: The temperature vs. entropy diagram for butane with a selection of runs from the optimizer. The worst run follows the green curves, and the optimal run follows the yellow line. The other colors represent some arbitrary runs.

3.3 Final Simulation Run and Calculating Levelized Cost of Electricity

A simulation inspired by the optimal runs in Figure 7 has been run standalone to estimate the power generation for 27 years to generate a LCOE estimate for 30 years. The yearly average temperature and power is shown in Figure 10. After 3.5 years of simulation the gradient in temperature starts to drop off at which the temperature for the remainder of the 30 years is extrapolated. The temperature and power generation are averaged over each year and used for yearly input to the LCOE calculation. The average power generation in the first year is 625.7 kWe, and after 3 years it stabilizes at roughly 500 kWe. A downhole pump was not needed, as a choke valve with a DP of 3.5 Bara was needed to balance the pressure, indicating a big enough thermosiphon effect in this case. The LCOE calculation for this scenario is 0.393 $/kWh with the well VIT being the biggest investment.

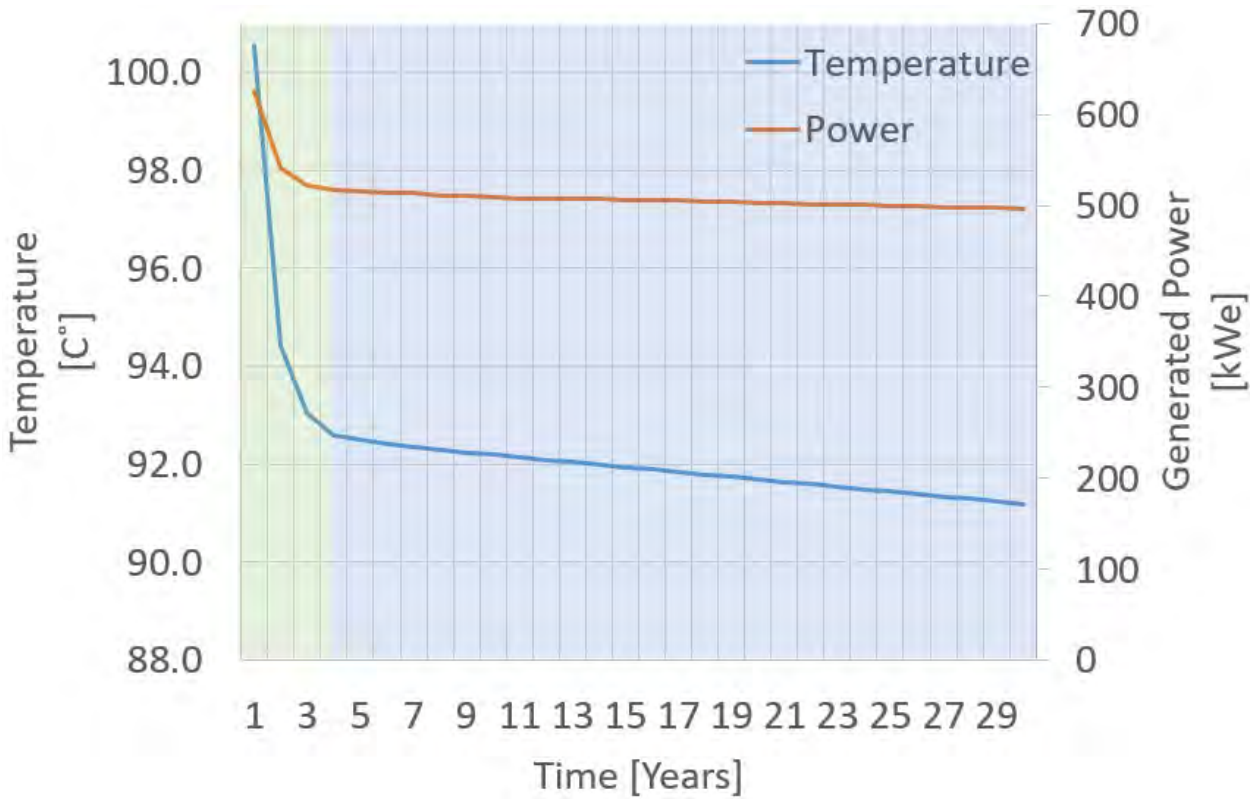

Figure 10: The yearly averaged temperatures and expander power generation used to calculate LCOE for the investment. The simulation is based on the best boundary conditions found in the integrated optimization from Figure 7. The green part is 3.5 years of simulation, and the blue part is extrapolated after the temperature gradient became less than 0.3 degrees per year.

4. Conclusion

A geothermal plant relies on many design parameters that will affect the final power output. This work highlights how integrated modeling with automatic orchestration can aid project teams during the important design phase of a plant. A techno-economic study was performed to assess the feasibility of repurposing old wells for closed loop geothermal power. The optimizer efficiently explores the space of solutions and can aid engineers by considering multiple alternatives. For a 30-year period the LCOE is calculated to 0.393 $/kWh, producing stable power around 500 kWe from hot dry rock. There are many benefits of a closed loop system and an ORC, as mentioned in the paragraph below, which is not factored into the LCOE.

4.1 Benefits of Closed Loop BHE and ORC

While a low LCOE is important for project feasibility, it does not factor in some of the unique political, social and environmental benefits of geothermal power. Closed loop BHE does not require big amounts of water which is good for the economy of the project and the environment, as water can be a restrictive resource in many regions of the world. Corrosion is less of a problem for BHE since clean water can be used, rather than corrosive brine, which may extend the potential life of the asset. Using an ORC and a closed loop BHE in hot dry rock can cut nearly all emission,

since the process is fully closed from the atmosphere. The benefits of geothermal energy which separates it from other energy sources have not been quantified here. Emissions, land usage and loss of nature do have a cost, but it is hard to quantify in an economic study.

4.2 Future Work

A study with LCOE as the objective function for minimization would be interesting to compare with the net power maximization. Another improvement is to run each simulation run for a longer period during the optimization, to provide more realistic results. Geothermal projects have big CAPEX, and optimization under uncertainty of additional parameters is another scenario of interest. In Chaves et al. (2023) the sensitivities of reservoir/rock properties are shown to not be as important, but it would add to the confidence of a thorough techno-economic study.

Abbreviations

Abbreviation/Term	Description
BHE	Borehole Heat Exchanger
CAPEX	Capital Expenditure
DP	Delta Pressure
HDR	Hot Dry Rock
ID	Inner Diameter
VIT	Vacum Insulated Tubing
ORC	Organic Rankine Cycle
LCOE	Levelized Cost of Electricity
kWe	Kilo Watt Electrical
kWh	Kilo Watt Hour
O&M	Operation and Maintenance
PVT	Pressure, Volume and Temperature, referring to fluid properties at different conditions.
TVD	True Vertical Depth

REFERENCES

Chaves, G., Engebretsen, S., Shabani, M., Šarić, M., Jančiković, B. “Applying a multiphase flow simulator for energy transition: Assess the energy potential and operational aspects of repurposing end-of-life oil wells for geothermal energy applications.” *MPT* (2023)

Uihlein, A. “JRC Geothermal Power Plant Dataset. European Commission.” *Joint Research Centre (JRC) (2018)*

IRENA and IGA, “Global geothermal market and technology assessment”, International Renewable Energy Agency, Abu Dhabi; International Geothermal Association, The Hague (2023)

Beckers, K., Johnston, H. “Techno-Economic Performance of Eavor Loop 2.0” *Proceedings, 47th Workshop on Geothermal Reservoir Engineering Stanford University,* Stanford, California, February 7-9, SGP-TR-223 (2022)

Lowry, T., Finger, J., Carrigan, C., Foris, A., Kennedy, M., Corbet, T., Doughty, C., Pye, S., Sonnenthal, E. “GeoVision Analysis Supporting Task Force Report: Reservoir Maintenance and Development” *SAND2017-9977*, (2017)

Bordas, R., Heritage, J. R., Javed, M. A., Peacock, G., Taha, T., Ward, P., Vernon., Hammersley, R. P. “A Bayesian Optimisation Workflow for Field Development Planning Under Geological Uncertainty.” *17th European Conference on the Mathematics of Oil Recovery (ECMOR XVII)* (2020)

Taha, T., Abdallah, M., Shabani, M., Gringarten, E. “A Bayesian Optimization Workflow for Integrated Asset Management Under Uncertainty.” *International Petroleum Technology Conference and Exhibition (IPTC), IPTC 23952.* (2024)

Astolfi, M., Romano, C., M., Bombarda, P., Macchi, E. “Binary ORC (organic Rankine cycles) power plants for the exploitation of medium–low temperature geothermal sources – Part A: Thermodynamic optimization” *Proceedings of the ICE – Energy 66.* (2014)

Geothermal Reservoir Simulation Analysis in Support of Electricity Co-Production Feasibility Study at the Blackburn Oil Field, Nevada

Kagan Kutun, Abra Gold*, and Koenraad Beckers***

***National Renewable Energy Laboratory (NREL), **Colorado School of Mines (work performed at NREL)**

Keywords

Resource characterization, Reservoir Simulation, Co-production, Wells of opportunity, Blackburn Nevada, Organic Rankine cycle

ABSTRACT

Geothermal electricity co-production is a viable option for oil reservoirs producing large water cuts with elevated wellhead temperatures. Repurposing existing oil wells significantly reduces initial investment costs historically associated with geothermal resource utilization. The National Renewable Energy Laboratory (NREL), partnering with Gradient Geothermal, Inc. (formerly known as Transitional Energy) and Grant Canyon Oil and Gas, has been tasked to evaluate the feasibility of geothermal electricity co-production at the Blackburn Oil Field with Organic Rankine Cycle (ORC) generators. The Devonian steady-state reservoir has historically been producing high water cuts of 240°F (115.6°C) observed at the wellhead without documented pressure drawdown or thermal breakthrough. An estimated initial reservoir temperature of approx. 260°F (126.7°C) has been observed in the field and history-matched in a wellbore production analysis and reservoir simulation. Our objective was to develop a conceptual geological model of the subsurface, simulate a natural-state reservoir, model production scenarios, and complete a technical feasibility analysis to accomplish this task. Through extensive modeling and the use of available proprietary and public data, it was possible simulate three scenarios that indicated minimal thermal decline over the duration of a simulated ten-year production and re-injection scheme.

1. Introduction

The Wells of Opportunity: Nevada (WOO Nevada) initiative aims to generate electricity at the Blackburn Field using the co-produced waters associated with the field's oil production. Blackburn Field is an oil field situated in Sections 7 and 8 of Township 27N Range 52E in northern Eureka County, Nevada. The field is in Pine Valley, approximately 45 miles ESE of Elko, NV.

Historical production records (NDOM 2023) indicate that from 1982 to 2022, Blackburn Field yielded 4.3 million barrels of oil and 43.5 million barrels of water. This resulted in an overall cumulative water-to-oil ratio of 91%. In 2022, the annual water cut was 98.98% (Kutun et al., 2023). The reservoir is a naturally fractured reservoir with a strong hydraulic drive, where water naturally recharges the reservoir. Wells historically drilled into the fractured Nevada dolomite

This report is available at no cost from the National Renewable Energy Laboratory (NREL) at www.nrel.gov/publications.

reservoir were typically completed at the shallowest (upper) depths to mitigate water encroachment from below.

An overview of the Blackburn Field wells is presented in Figure 1. Blackburn No. 12, 20, and 21 are three candidate injectors; Blackburn No. 4, 16, 18, 19, and 22 are candidate producers for the WOO Nevada project. Bucy No. 1 is also a candidate injection well located NNW of Blackburn No. 12.

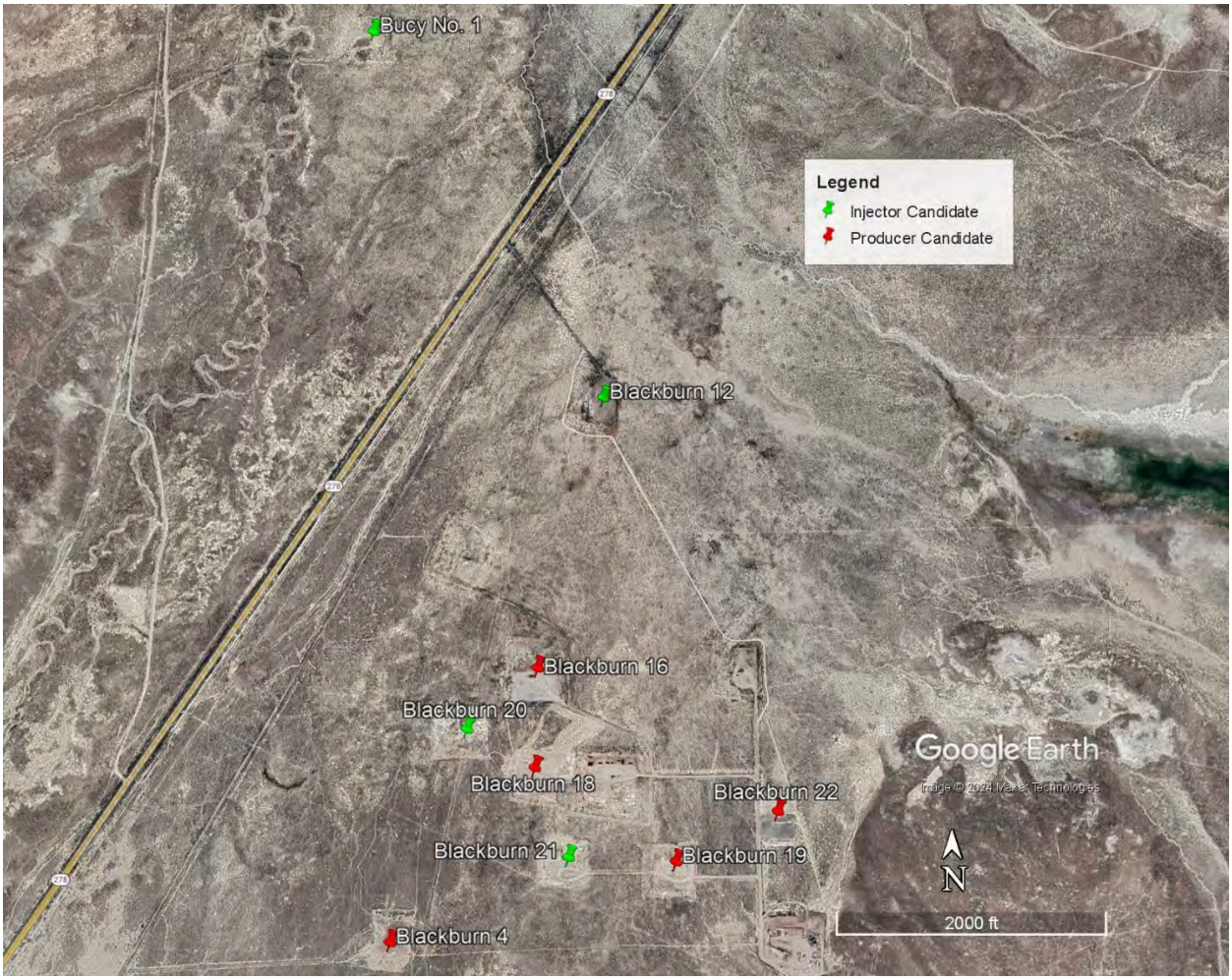

Figure 1: Map showing the locations of the Blackburn project co-production candidate wells.

2. Geological Modeling

The lithologies in the Blackburn field are, in stratigraphic order: the target reservoir Devonian Nevada dolomite, the reservoir-overlying Chainman shale capping layer (deposited post-Antler orogeny), the late Cretaceous quartz monzonite pluton that intruded during a 300 Ma unconformity, the Oligocene Indian Wells tuff, the Oligocene-Miocene lacustrine and conglomerate Humboldt, the Miocene basalt sill, the post-Miocene Hay Ranch (valley fill), and overlying alluvium (Flanigan 1994; Hulen et al. 1990; Scott & Chamberlain 1988). The quartz

This report is available at no cost from the National Renewable Energy Laboratory (NREL) at www.nrel.gov/publications.

monzonite pluton is referred to as the basement because it is the first metamorphic formation underlying the target Devonian reservoir.

A stratigraphic column with associated lithological descriptions is provided below in Figure 2. Formation tops from well completion reports and logs (hosted online by NBMG 2023), Taverna (2019), and our own interpretation (where no data were available), were honored as our primary data source in the creation of this conceptual model.

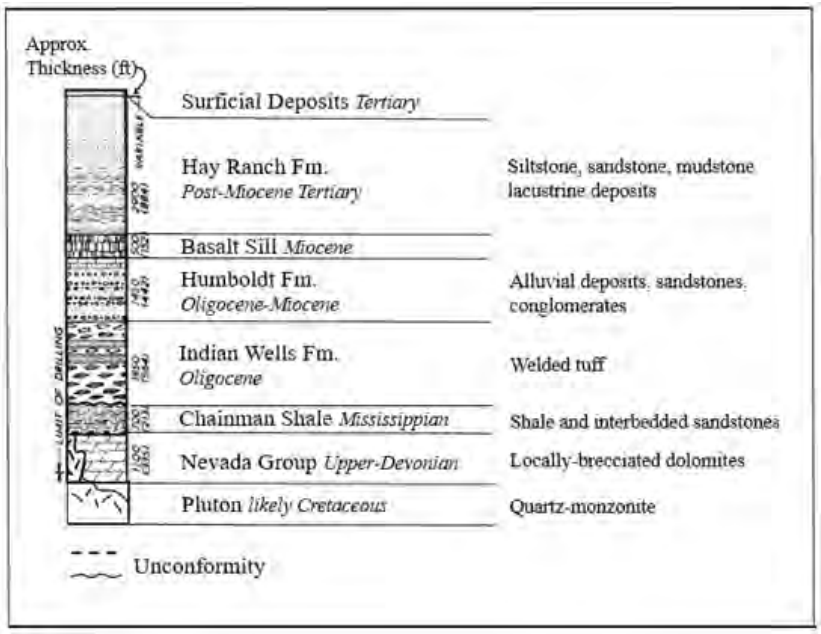

Figure 2: Stratigraphic column and description of formations in the Blackburn Field subsurface, adapted from Hulen et al. 1990.

The crust in this depositional basin is thinner than in other regions of the United States. This phenomenon is attributed to extensional plate tectonics. Extension causes fault dilation, allowing for fluid to flow in larger volumes along intricate fracture and fault pathways. An elevated thermal gradient is observed through the subsurface at the Blackburn Oil Field. It is likely that the heat source for the resource is deep-seated (Hulen et al. 1990). Geothermal fluids rise from depth along fault intersections. Dilated faults also facilitate secondary permeability. Many of the dilated faults in the Blackburn Field subsurface may have been infilled with sedimentary overburden. Future tracer research will offer further insight regarding fault permeability.

In the development of a 3D conceptual geological model, the cross-sections from Hulen et al. (1990) were utilized because they offered NNE and ENE views of the subsurface, whereas other publications did not offer as in-depth an interpretation. Determination of the quartz monzonite pluton contact is variable throughout the publications, because only two wells within the model area struck the pluton: Blackburn No. 1 and No. 6. The basement map from Scott & Chamberlain (1988) showing the quartz monzonite and Devonian surfaces was utilized in addition. As more data became available, the model evolved (Gold et al. 2024).

The next available data source utilized to influence model construction was a time-evolved structural fault map interpreted from a legacy seismic survey that was acquired in previous years (Flanigan, with modifications by the Blackburn field operator). This map was compared to

This report is available at no cost from the National Renewable Energy Laboratory (NREL) at www.nrel.gov/publications.

observed surface structures to provide a level of certainty in fault locations at depth (Gold et al. 2024). For numerical modeling purposes, faults were not extended beyond the top contact of the capping shale layer. All data sources were combined, with more confidence placed in the time-interpreted structural fault map, in the final version of the conceptual geological model and target reservoir contour surface (Figure 3 and Figure 4). The model boundaries were extended to the north and west to facilitate numerical simulation.

As formation tops data became sparse toward the outer boundaries of the model, the contacts were interpreted. Trends in the data were extrapolated from formation top data-dense clusters outward toward the less populated areas in the model.

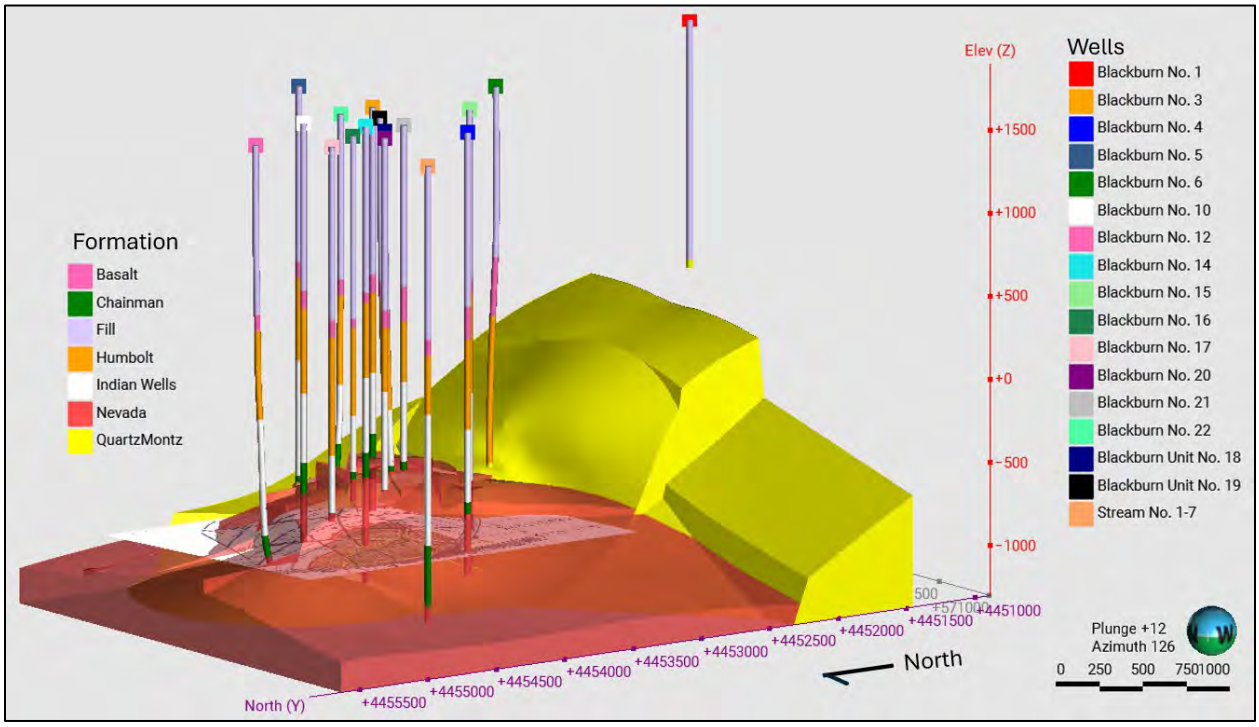

Figure 3: 3D conceptual geological model of the Blackburn Oil Field Nevada dolomite (red) reservoir and underlying quartz monzonite (yellow), with boundaries extended laterally to the north and east.

This report is available at no cost from the National Renewable Energy Laboratory (NREL) at www.nrel.gov/publications.

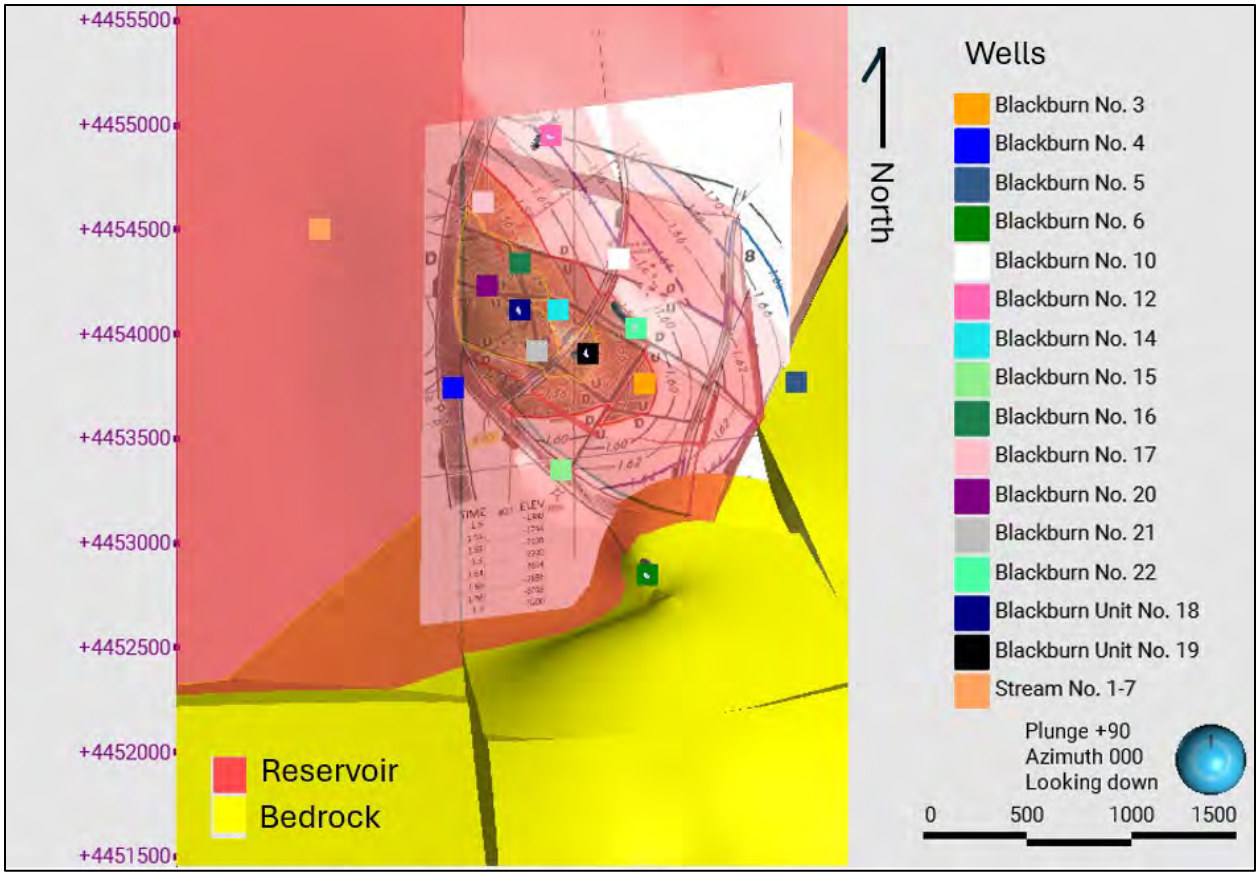

Figure 4: Well locations at depth imposed on the geological model of the reservoir and the basement, underlaid by structural illustration data. The model extents have been edited to exclude Blackburn No. 1 because of reservoir termination prior to the well.

3. Reservoir Modeling

To numerically model the reservoir, the reservoir simulator VOLSUNG Brynhild was utilized. The simulator grid was populated with rock thermophysical properties, flow properties, and boundary conditions to reflect the Blackburn Field subsurface conditions.

The reservoir modeling study consisted of two parts. In the first part, a static reservoir model was created to match the temperature observations obtained from various sources. The purpose of the static modeling was to calibrate the numerically modeled reservoir domain to capture the natural state found in the system. In the second part, the calibrated model was subjected to different production scenarios to estimate the production temperatures for a ten-year project lifetime.

3.1 Reservoir Model Input Parameters

3.1.1 Thermophysical Properties

The thermal conductivity data, λ (W m^{-1} K^{-1}), are mainly from lab analyses of rock types and formation samples obtained from the state of Nevada excepting basalt, the Humboldt, and the Hay Ranch (fill), for which no data points were found (UNR 2021; Blackwell & Steele 1989; Sass et

This report is available at no cost from the National Renewable Energy Laboratory (NREL) at www.nrel.gov/publications.

al. 1988). Specific formation data, if available, were used instead of averaging the range of rock type data measured from associated rocks obtained in the state of Nevada.

Measurements for formation heat capacities, cp (kJ kg^{-1} K^{-1}), and formation densities, ρ (kg m^{-3}), from rock samples collected in the state of Nevada were not available. In this case, averages of ranges of general rock type-specific properties were utilized (Zhu et al. 2022; Schön, 2015, 2011; Waples 2004; Manger 1963). The thermophysical rock properties used in the model are presented in Table 1.

Table 1: Thermophysical properties of formations in the Blackburn Oil Field. Properties were utilized for numerical modeling purposes.

Formation	Designation	*Thermal Conductivity*	*Heat Capacity*	*Density*
		W m^{-1} K^{-1}	**kJ kg^{-1} K^{-1}**	**kg m^{-3}**
Quartz monzonite	Basement	3.05	0.879	2,640
Nevada Group	Reservoir	4.90	0.950	2,712
Chainman	Capping Layer	1.50	1.180	2,585
Indian Wells	Overlying Layer	1.74	0.943	2,416
Humboldt	Overlying Layer	1.82	1.109	2,525
Basalt	Overlying Layer	1.82	0.880	2,800
Hay Ranch & tertiary deposits (fill)	Overlying Layer	1.72	1.089	2,547

3.1.2 Flow Properties

The numerical model considered the flow of water only, i.e., no oil flow was modeled. The oil to water ratio (i.e. approximately 98% to 2%) was low, so excluding oil from the simulation did not influence the results significantly. This decision was determined in consideration of i) model software limitations (lack of water and oil equation of state), ii) relative permeability data unavailability, and iii) the observed 98% (or higher) water cut in the Devonian Nevada dolomite penetrating wells.

The layers above the Nevada Group were modeled as impermeable to fluid flow. The permeability of the Nevada dolomite and the quartz monzonite were chosen as 322 millidarcy based on the Drill Stem Test (DST) results reported for Blackburn well No. 18, October 12–13, 1992 (NBMG, 2023). The Nevada dolomite was set to have homogenous and isotropic permeability. The quartz monzonite basement was set to have homogenous permeability in the vertical direction only, i.e., the formation was incorporated as impermeable in horizontal directions.

Both the Nevada dolomite and the quartz monzonite basement were represented in the model as single porosity because no conclusive data was available to characterize the natural fracture and matrix permeability separately. The porosity of the two permeable formations were set as 5%. Pore compressibility values were set to 7.25×10^{-10} Pa^{-1}. Thermal pore expansivity was not modeled.

The faults modeled in the geological modeling section of this work were not implemented in the numerical grid as no-flow barriers because no conclusive data was available. If these faults are in

This report is available at no cost from the National Renewable Energy Laboratory (NREL) at www.nrel.gov/publications.

fact no-flow barriers, omission of the faults in the numerical model will provide a worst-case scenario for thermal breakthrough concerns. Furthermore, the Blackburn field operator estimated that the faults are non-sealing at depth.

3.1.3 Boundary Conditions

Numerical boundary conditions were applied to the model on the grid top and grid bottom. The top boundary was set as a constant temperature at 55°F. This temperature was estimated from the spatially closest soil temperatures, which are values collected over 4 years at an elevation of 6,000 ft ASL approximately 80 mi away from the Blackburn Field (NRCS 2023).

The bottom boundary was constant temperature (at 273°F) and pressure (at 4,225 psi). Both the top and the bottom boundary conditions span the entire top and bottom surfaces of the grid, respectively. The side faces of the model were set as a no-flow boundary considering heat and fluid flow.

The temperature and pressure combination at the boundary conditions were chosen to impose a match in the reservoir model to multiple parameters. The observed Blackburn No. 18 well flowing field temperature data at the bottom of the wellbore, the overall temperature trends observed in the historical well log and DST temperature data, and the reservoir pressure estimation provided by Gradient Geothermal, Inc. were target parameters to be matched.

3.1.4. Grid Geometry

The grid layer spacing chosen is given in Table 2. The vertical layer spacing was chosen to provide higher resolution at the modeled reservoir layer and near the model's top and bottom boundaries, while staying within the limits of our resources' computational capabilities. Figure 5 presents a N-S cross-section of the grid.

Table 2: Grid layer spacing used in this study. X and Y layers expand with given thicknesses in easterly and northerly directions, respectively. Z layers extend from the model's top surface (5295 ft ASL) to the model's bottom surface (-4300 ft ASL); i.e., layer 1 spanned from 5295 ft ASL to 5290 ft ASL, layer 86 spanned from -4100 ft ASL to -4300 ft ASL.

Extents	Layer Thickness, ft	Layers	Total Extent, ft	Total Layers
X	200	52	10538	53
	138	1		
Y	400	34	13714	35
	114	1		
Z	5	1	9595	86
	122.5	4		
	250	2		
	400	6		
	200	16		
	50	56		
	200	1		

This report is available at no cost from the National Renewable Energy Laboratory (NREL) at www.nrel.gov/publications.

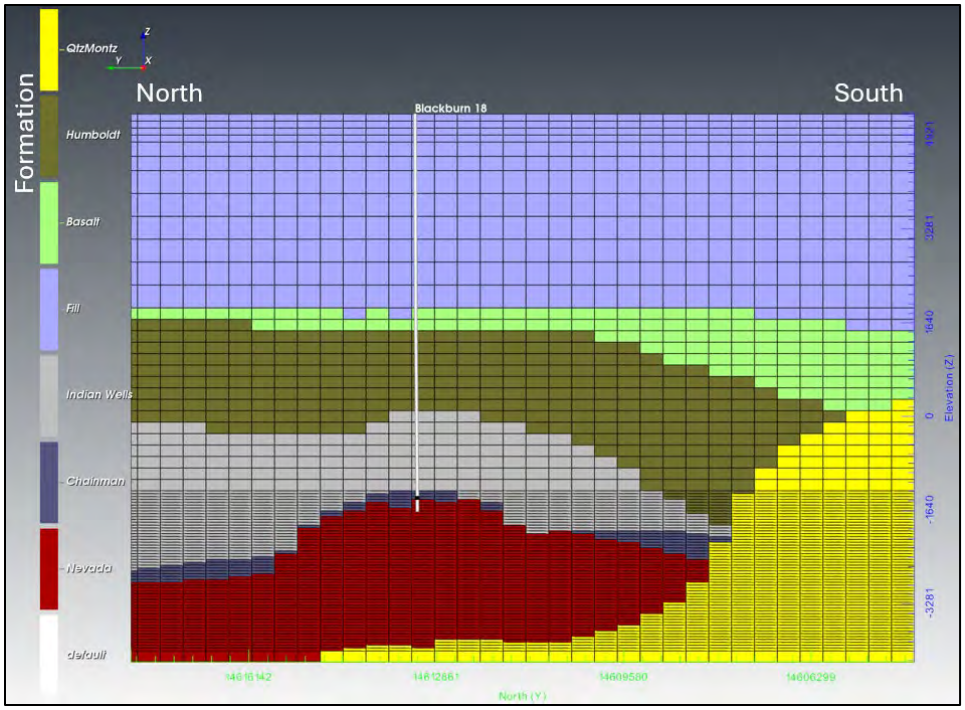

Figure 5: North-south cross section of the constructed grid showing the lithology designation. The axis of the grid coincides with the location of Blackburn No. 18.

3.2 Natural State Modeling

The objective of the static simulation was to calibrate the pressure and the temperature state of the model domain for dynamic production simulations. The static simulation was initialized with a temperature gradient of 0.030°F/ft and a pressure gradient of 0.44 psi/ft. Following the initialization, the simulation was run for 10,000 years, allowing the temperature and the pressure states to stabilize under the influence of the top and bottom boundary conditions. The relative temperature and pressure changes at the last time step of the simulation were 2.3×10^{-8} s^{-1} and 3.3×10^{-12} s^{-1}, respectively. These values indicated a reasonable numerical stabilization of the temperature and pressure distribution in the model domain.

The first targeted parameter match was to the temperature and pressure information obtained from the well flowing test conducted by the Blackburn field operator in August of 2023. In this test, the well flowing temperature and pressure profiles in the tubing were measured during stabilized flow. The observed well flowing temperature inside the tubing at 6,750 ft was 261.9°F; this temperature value was the target for the temperature match.

The observed well flowing pressure at the bottom of Blackburn No. 18 tubing (6,750' MD) was 3,040 psi. The test did not report a static reservoir pressure measurement. A static reservoir pressure estimate, which was based on the flow test, was provided by Gradient Geothermal, Inc., as 3,100 psi at the bottom-hole of Blackburn No. 18. This pressure estimate was the target pressure match for the static simulation run.

Figure 6 presents a N-S cross section of the temperature distribution, and Figure 7 presents a close-up screenshot of the temperature and pressure values obtained at the bottom of Blackburn 18 after

This report is available at no cost from the National Renewable Energy Laboratory (NREL) at www.nrel.gov/publications.

the static simulation was run. The average temperature of the four grid layers below the bottom of the tubing was observed as 261.7°F (in contrast to the 261.9°F observed in the flowing well test).

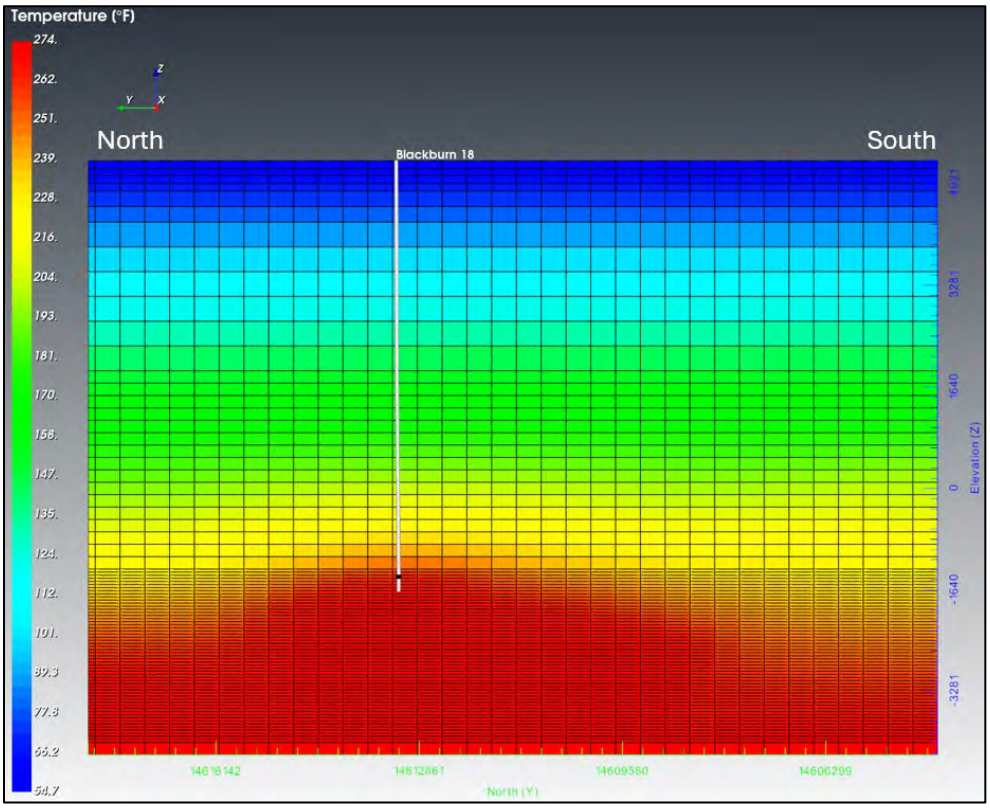

Figure 6: N-S cross section of the stabilized natural state reservoir model. The cross-section line passes through the surface location of Blackburn 18. This well was not actively flowing during the stabilization of the natural-state model.

This report is available at no cost from the National Renewable Energy Laboratory (NREL) at www.nrel.gov/publications.

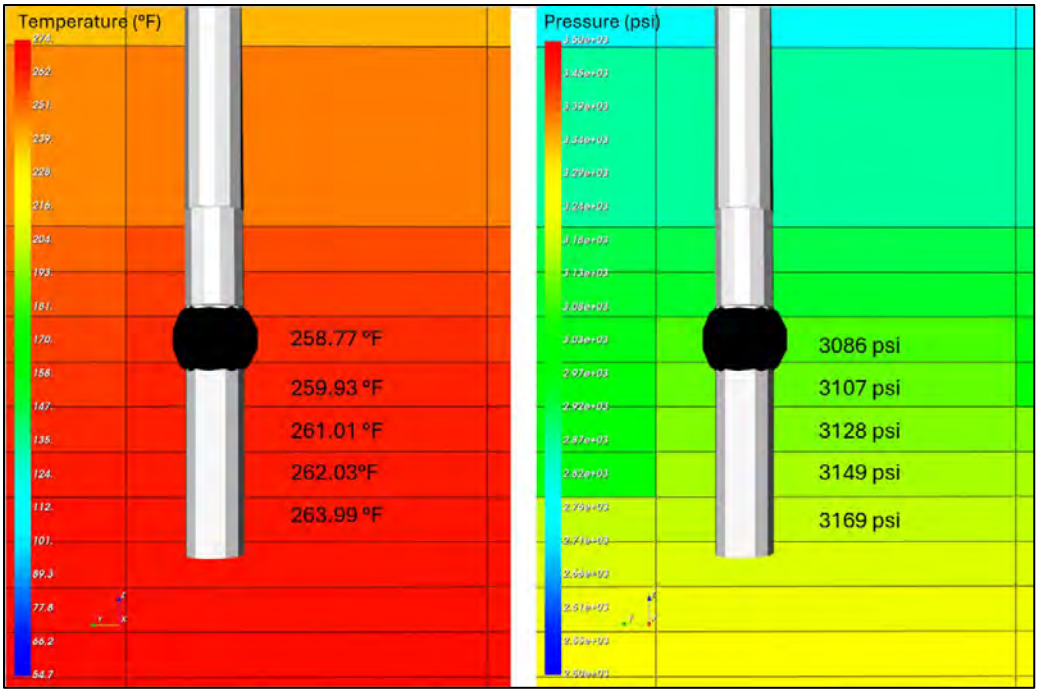

Figure 7: (Left) Modeled temperatures at the center of each grid cell along the Blackburn No. 18 wellbore. (Right) Modeled pressures at the center of each grid cell along the Blackburn No. 18 wellbore. The black ellipsoid denotes the bottom of the tubing at 6,750 ft MD.

Modeled temperature profiles for Blackburn No. 3, 4, 6, and 10 are compared to historic well log temperature profiles in Figure 8. The first Blackburn No. 3 log was taken on March 23, 1982, one week after drilling stopped on March 16, 1982. The second Blackburn No. 3 log was taken July 1, 1982, an estimated 3 months after the well was completed and in production. All other logs were taken within days of completion or drilling: Blackburn No. 4 was taken 3 days after completion, No. 6 was taken 3 days after completion, and No. 10 was taken the day after total depth was reached.

The temperatures from these logs are likely not reflective of the actual subsurface thermal gradient because of post-drilling mud circulation: i.e., the top of the wellbore heats up when mud is circulated from deeper depths to the surface, and the bottom of the wellbore cools as mud is circulated from the surface to deeper depths. The second log of Blackburn No. 3 was suspected of being affected by production-related heating. Model profiles for Blackburn No. 3, 4, 6, and 10 were generated from selecting the temperatures in the center of each calibrated reservoir grid cell along the respective well tracks. The modeled profiles show agreement with historic DST data collected for Blackburn No. 3, 18, 19 Log Header, and 21.

This report is available at no cost from the National Renewable Energy Laboratory (NREL) at www.nrel.gov/publications.

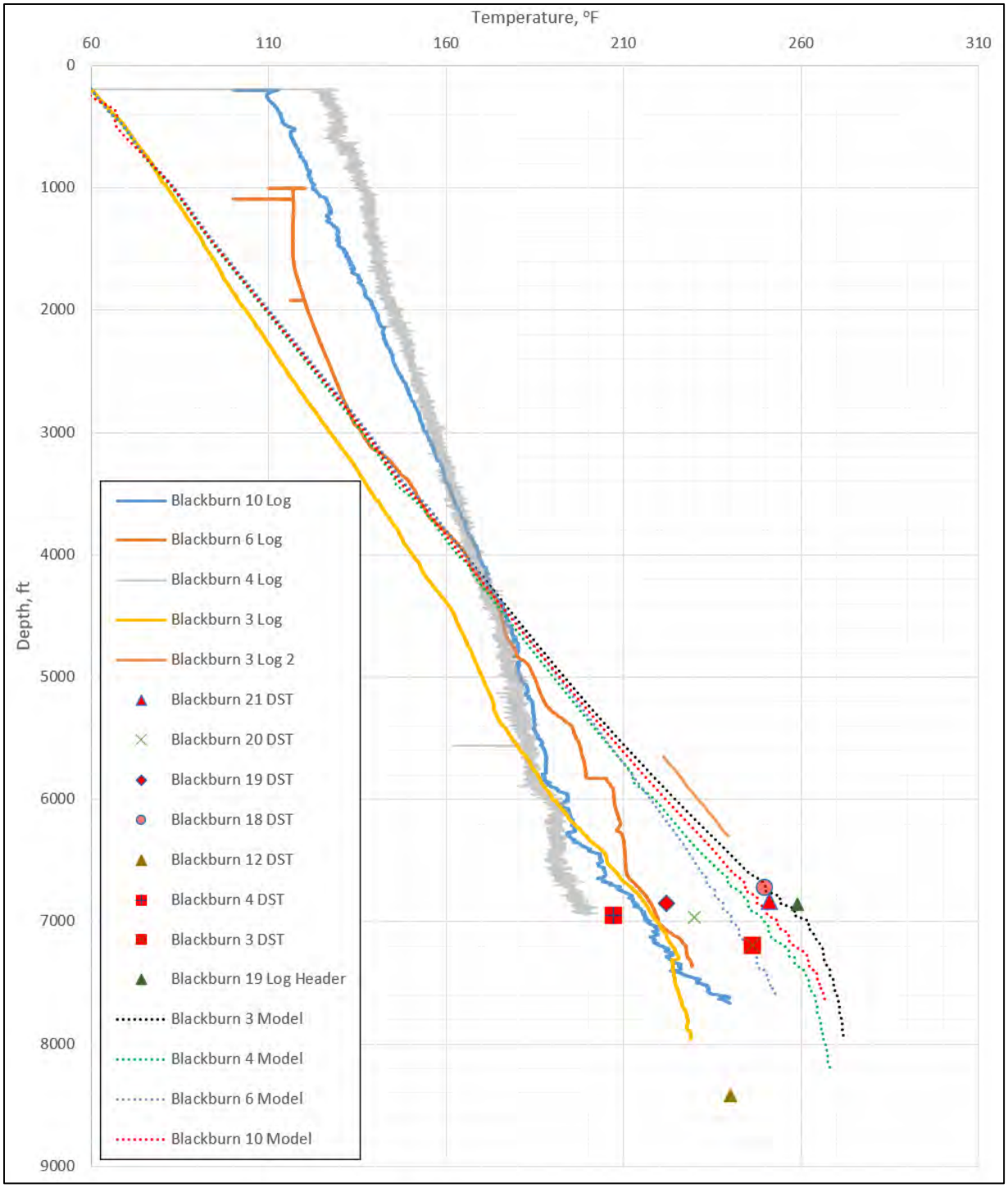

Figure 8: Stabilized temperature profiles modeled by the static reservoir simulation for Blackburn No. 3, 4, 6, and 10 shown alongside historic well log and DST data.

3.3 Production Modeling

The objective of the dynamic reservoir modeling was to simulate production/injection scenarios being considered for field deployment. The focus of this part of the study was to determine whether

This report is available at no cost from the National Renewable Energy Laboratory (NREL) at www.nrel.gov/publications.

detrimental thermal breakthrough or pressure depletion would be present during the lifetime of the project.

Three dynamic production scenarios were selected to simulate production and injection well schemes. These scenarios were chosen mainly to determine the co-production water rate that the Blackburn field can support while considering operational constraints associated with the ongoing oil production. A summary of the scenario details is shown in Table 3. An overview of the well locations with respect to the reservoir is shown in Figure 9. All scenario flow rate inputs were converted from volumetric rate to mass rate using a density of 947.7 kg/m^3; this value represents the density of pure water at 260°F and 3,000 psi.

Table 3: Summary of dynamic production scenarios. All wells denoted with numbers alone are Blackburn Field wells.

Scenario	Producing Wells	Injecting Wells	Total Production	Total Injection
			BPD	BPD
1	16, 18, 19	12, 21	14,200	14,200
2	16, 18, 19, 22	12, 21	24,200	24,200
3	4, 16, 18, 19, 22	12, 20, 21; Bucy No. 1	34,200	34,200

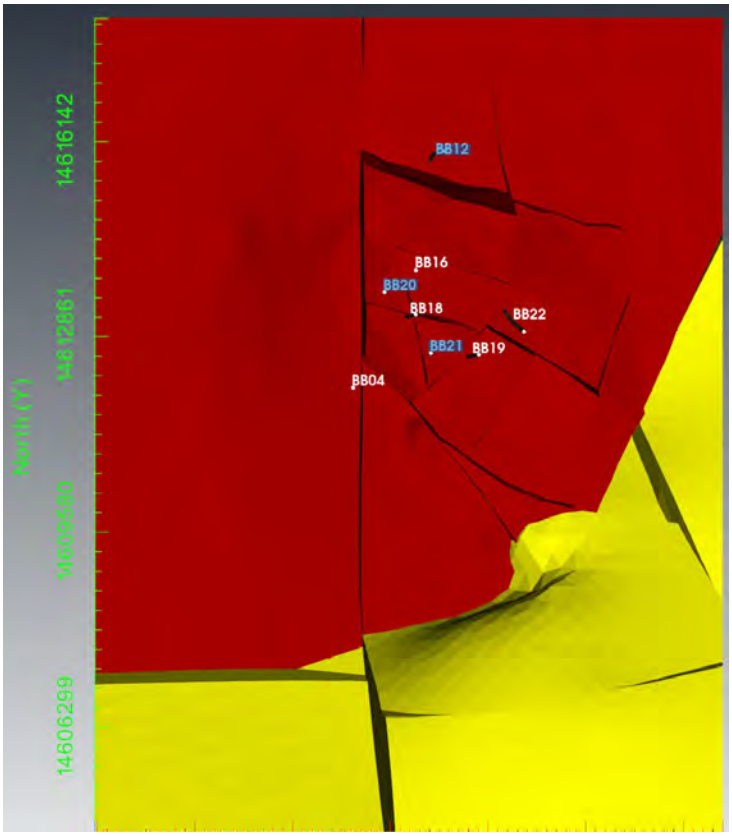

Figure 9: Scenario wells imposed on the geological model. Rock formations depicted in red and yellow colors represent the Nevada and the quartz monzonite formations, respectively. Injector well names are highlighted with blue.

This report is available at no cost from the National Renewable Energy Laboratory (NREL) at www.nrel.gov/publications.

Injection temperatures for scenarios depended on the surface operations and losses encountered at the surface. We assumed a fixed reinjection temperature of 179°F for all scenarios based on ORC performance analysis done by Gradient Geothermal, Inc. We did not incorporate Bucy No. 1's injection into the model because it is located outside the model domain.

The production wells were fully implemented into the numerical simulator to calculate the pressure and temperature changes along the wells. The injection wells were abstracted in the reservoir model by implementing mass sources located in the numerical grid, coinciding with the bottom-hole locations of the injection wells.

To develop wellbore geometry (hole and tubular dimensions), we used our best estimation from well completion reports and reports from the Blackburn field operator (publicly hosted by NBMG, 2023). Well completion reports were most heavily relied upon, because they offered the most comprehensive understanding of the well geometries. Regarding work not included in the well completion reports, specifically deepening of wells, the information obtained from Gradient Geothermal, Inc. and the operator was relied on.

3.3.1 Scenario 1

The details of this co-production scenario were as follows:

- The total production is 14,200 BPD.
- The total injection is 14,200 BPD.
- The combined production target temperature is 250°F.

Table 4: Summary of Scenario 1 dynamic production scheme. All wells denoted with numbers alone are Blackburn Field wells.

Scenario	Producing Wells	Injecting Wells	Target Flow Rate BPD
1	16	-	10,000
	18	-	2,100
	19	-	2,100
	-	12	10,000
	-	21	4,200

The flow rates stated above were incorporated into the respective production wells and injection mass sources in the Brynhild reservoir simulator. Figure 10 presents the temperature behavior of the produced fluids in respective scenario wells. A volumetric rate-weighted combined average temperature was also calculated.

In this scenario, the combined production temperature was 262.4°F at the end of four years, and the average of the combined production temperature was 262.5°F during this period. At the end of the ten-year production period, the combined production temperature was 261.8°F. No significant thermal decline was observed. The design target temperature of 250°F was met. The reservoir pressure support was sufficient to sustain flow naturally at the production wells within the simulated timeframe.

This report is available at no cost from the National Renewable Energy Laboratory (NREL) at www.nrel.gov/publications.

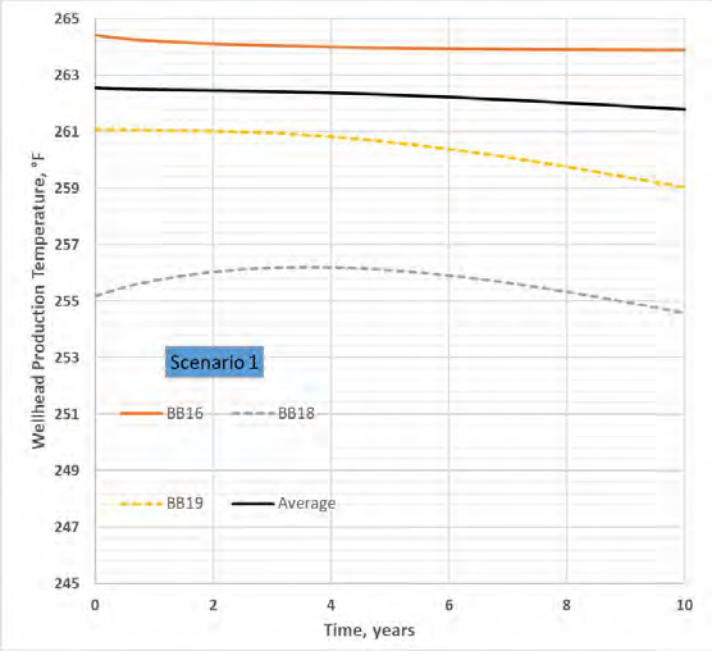

Figure 10: Wellhead production temperatures associated with Scenario 1. The black line represents the volumetric weighted average production temperature. BB denotes Blackburn wells.

3.3.2 Scenario 2

The details of this co-production scenario were as follows:

- The total production is 24,200 BPD.
- The total injection is 24,200 BPD.
- The combined production target temperature is 260°F.

Table 5: Summary of Scenario 2 dynamic production scheme. All wells denoted with numbers alone are Blackburn Field wells.

Scenario	Producing Wells	Injecting Wells	Target Flow Rate
			BPD
2	16	-	10,000
	18	-	2,100
	19	-	2,100
	22	-	10,000
	-	12	12,100
	-	21	12,100

The flow rates stated above were incorporated into the respective production wells and injection mass sources in the Brynhild reservoir simulator. Figure 11 presents the temperature behavior of the produced fluids in respective scenario wells. In this scenario, the combined production temperature was 262.7°F at the end of four years, and the average of the combined production temperature was 263.0°F during this period. At the end of the ten-year production period, the combined production temperature was 260.8°F. The design target temperature of 260°F was met.

This report is available at no cost from the National Renewable Energy Laboratory (NREL) at www.nrel.gov/publications.

The reservoir pressure support was sufficient to sustain flow naturally at the production wells within the simulated timeframe.

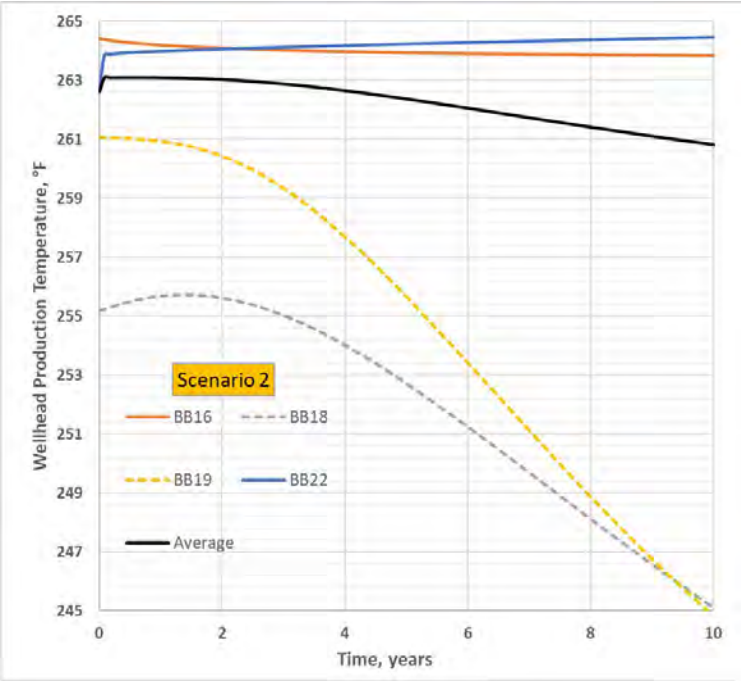

Figure 11: Wellhead production temperatures associated with Scenario 2. The black line represents the volumetric weighted average production temperature. BB denotes Blackburn wells.

3.3.3 Scenario 3

The details of this co-production scenario were as follows:

- The total production is 34,200 BPD.
- The total injection is 34,200 BPD.
- The combined production target temperature is 270°F.

Table 6: Summary of Scenario 3 dynamic production scheme. All wells denoted with numbers alone are Blackburn Field wells.

Scenario	Producing Wells	Injecting Wells	Target Flow Rate
			BPD
3	4	-	10,000
	16	-	10,000
	18	-	2,100
	19	-	2,100
	22	-	10,000
	-	12	8,550
	-	20	8,550
	-	21	8,550
	-	Bucy No. 1	8,550

This report is available at no cost from the National Renewable Energy Laboratory (NREL) at www.nrel.gov/publications.

The flow rates stated above, except Bucy No. 1, were incorporated into the respective production wells and injection mass sources in the Brynhild reservoir simulator. Bucy No. 1 is located 0.6 mi NNW of Blackburn No. 12 and hence is located outside the constructed geological (and hence the reservoir) model. Our model analysis showed that Blackburn No. 12's reinjection did not affect the production wells in all scenarios. The fluids injected at this location predominantly sank down to the constant pressure boundary condition because of the density contrast of the injected fluid. We concluded that, similar to Blackburn 12, injection at Bucy No. 1 would not induce a significant temperature drop at the modeled production wells because of its location.

Figure 12 presents the temperature behavior of the produced fluids in respective scenario wells. In this scenario, the combined production temperature was 262.0°F at the end of four years, and the average of the combined production temperature was 262.1°F during this period. At the end of the ten-year production period, the combined production temperature was 259.5°F. The target production temperature of 270°F was not met. The reservoir pressure support was sufficient to sustain flow naturally at the production wells within the simulated timeframe. Compared to Scenario 2, there is less thermal decline in Blackburn 18 and 19; however, cooling was also observed at Blackburn 16 because of the injection at Blackburn 20, which was only active in this scenario.

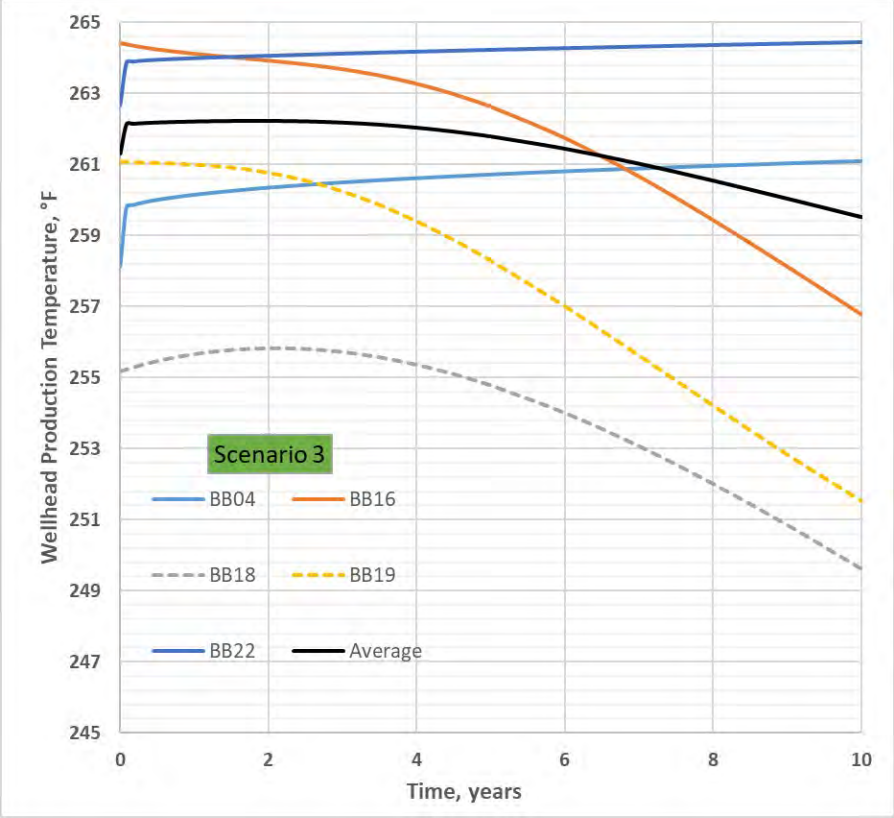

Figure 12: Wellhead production temperatures associated with Scenario 3. The black line represents the volumetric weighted average production temperature. BB denotes Blackburn wells.

This report is available at no cost from the National Renewable Energy Laboratory (NREL) at www.nrel.gov/publications.

3.3.4 Scenario Summary

Presented below are tabulated and graphical summaries of the combined temperatures associated with the three design scenarios, for quick reference.

Table 7: Combined production temperature values associated with three design scenarios.

Scenario	Combined Production Temperature Statistics			
	4-Year Term		10-Year Term	
	End of Term, °F	Term Average, °F	End of Term, °F	Term Average, °F
1	262.4	262.5	261.8	262.4
2	262.7	263.0	260.8	262.7
3	262.0	262.1	259.5	261.9

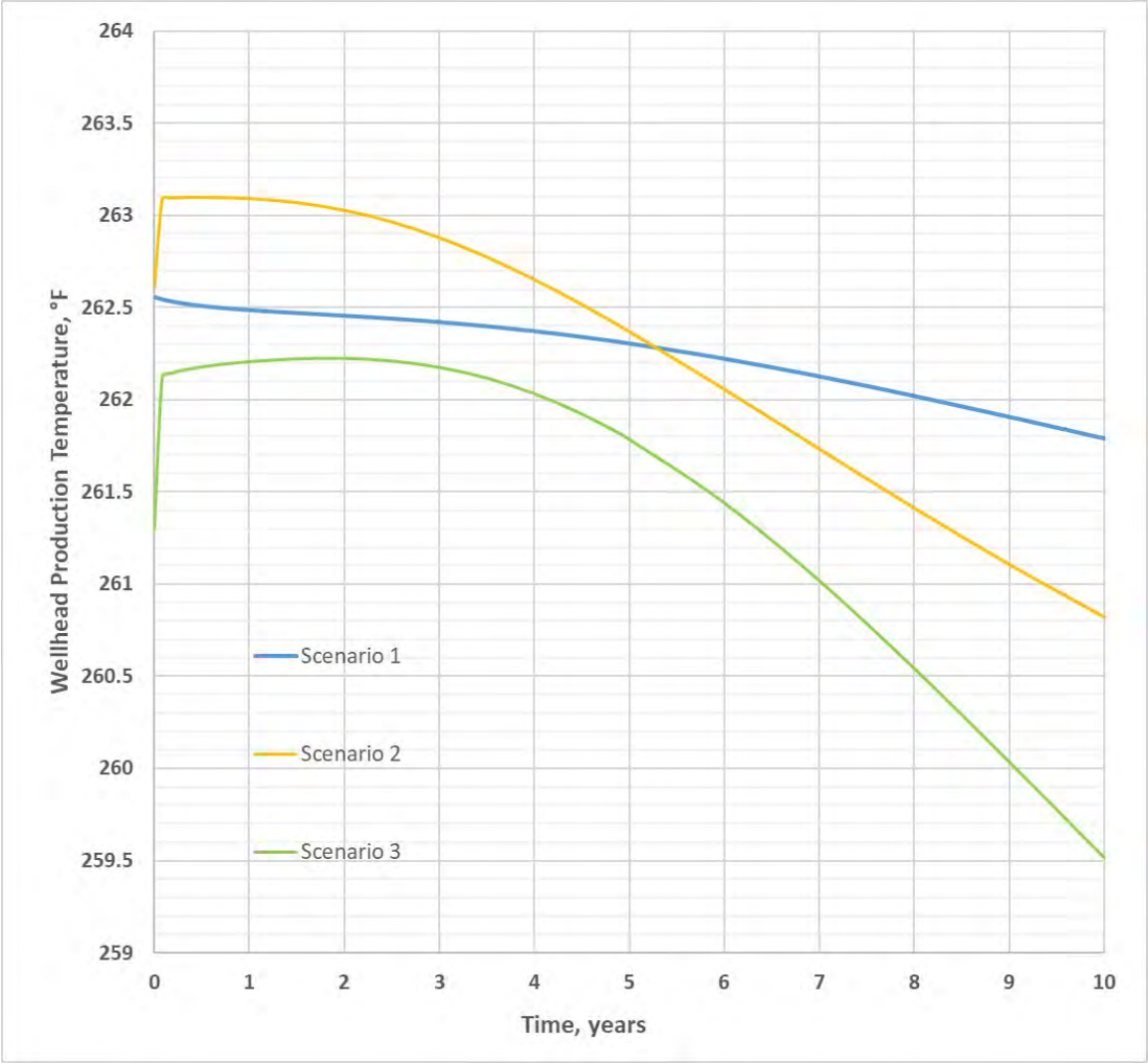

Figure 13: Combined production temperatures associated with three simulated design scenarios.

This report is available at no cost from the National Renewable Energy Laboratory (NREL) at www.nrel.gov/publications.

4. Conclusions

This study presents the results of geological and reservoir modeling work done to support the feasibility analysis study of geothermal co-production at the Blackburn Oil Field. We simulated three production scenarios in the numerical reservoir model. The three scenarios indicate negligible to minimal thermal decline over the duration of a simulated 10-year production and re-injection scheme. The first and second scenarios matched respective production temperature targets. Simulations for the third scenario showed that a target combined production temperature of 270°F cannot be achieved. The first production scenario is the likely deployment candidate for the second phase of the WOO Nevada project. Planned future work for the second phase includes technical design support and data collection from field tests.

Acknowledgement

This work was authored by the National Renewable Energy Laboratory, operated by Alliance for Sustainable Energy, LLC, for the U.S. Department of Energy (DOE) under Contract No. DE-AC36-08GO28308. Funding was provided by the U.S. Department of Energy Office of Energy Efficiency and Renewable Energy Geothermal Technologies Office. The views expressed herein do not necessarily represent the views of the DOE or the U.S. Government. The U.S. Government retains, and the publisher, by accepting the article for publication, acknowledges that the U.S. Government retains a nonexclusive, paid-up, irrevocable, worldwide license to publish or reproduce the published form of this work, or allow others to do so, for U.S. Government purposes. We would like to thank our collaborators at Transitional Energy (now Gradient Geothermal) for their continued support and dedication to this project.

REFERENCES

Blackwell, D. D., & Steele, J. L. (1989). Thermal Conductivity of Sedimentary Rocks: Measurement and Significance. In N. D. Naeser & T. H. McCulloh (Eds.), Thermal History of Sedimentary Basins, pp. 13–36. Springer New York. https://doi.org/10.1007/978-1-4612-3492-0_2

Faulds, J. E., Hinz, N. H., Dering, G. M., & Siler, D. L. (2013). The Hybrid Model—The Most Accommodating Structural Setting for Geothermal Power Generation in the Great Basin, Western USA. Geothermal Resources Council Transactions 37:3-10.

Faulds, J. E., Coolbaugh, M. F., Vice, G. S., & Edwards, M. L. (2006). Characterizing structural controls of geothermal fields in the northwestern Great Basin: A progress report. 30, pp. 69–76. Geothermal Resources Council Transactions.

Fetoui, I. (2017, October 18). Tubing Specifications. Production Technology. https://production-technology.org/tubing-specifications/

Flanigan, T.E., 1994. The Blackburn Oil Field: Oil, above a low-angle detachment fault in Eureka County, Nevada. In Schalla, R.A., and Johnson, E.H. (eds.), Oil fields of the Great Basin, Nevada Petroleum Society, p. 380.

This report is available at no cost from the National Renewable Energy Laboratory (NREL) at www.nrel.gov/publications.

Garside, L.J., Hess, R.H., Fleming, ICL., and Weimer, B.S. (1988). Oil and gas developments in Nevada. Nevada Bureau of Mines and Geology, Bulletin 104, p. 136.

Hulen, J. B., Bereskin, R. S., & Bortz, L. C. (1990). High-Temperature Hydrothermal Origin for Fractured Carbonate Reservoirs in the Blackburn Oil Field, Nevada. The American Association of Petroleum Geologists, 74(2), p. 1262–1272.

Kutun, K., Gold, A., & Beckers, K. (2023). Resource Characterization to Estimate Potential for Electricity Co-Production at Blackburn Oil Field, Nevada. 2498-2514. Paper presented at 2023 Geothermal Rising Conference, Reno, Nevada.

Manger, G. E. (1963). Porosity and bulk density of sedimentary rocks (No. 1144-E). USGPO.

Nevada Division of Minerals (2023). Nevada Division of Minerals Open Data Site. https://data-ndom.opendata.arcgis.com/

Nevada Bureau of Mines and Geology (NBMG). (2023). Oil and Gas Well Log Files. (Database). Nevada Bureau of Mines and Geology. https://nbmg.unr.edu/oil&gas/WellSearch.html

NRCS NWCC Report Generator—Ruby (2229) Nevada SCAN Site—6000 ft (NRCS). (12 Mar. 2024). National Resources Conservation Service. wcc.sc.egov.usda.gov/reportGenerator/

Sass, J. H., Lachenbruch, A. H., Dudley, W. W., Priest, S. S., & Munroe, R. J. (1988). Temperature, thermal conductivity, and heat flow near Yucca Mountain, Nevada: Some tectonic and hydrologic implications. (Open File). 87–649, p. 26). United States Department of the Interior Geological Survey.

Schön, J.H. (Ed.) (2015) Physical Properties of Rocks: Fundamentals and Principles of Petrophysics. Developments in Petroleum Science, 65. Elsevier.

Schön, J.H. (2011). Physical Properties of Rocks: A Workbook (Handbook of Petroleum Exploration and Production). Elsevier.

Scott, C., & Chamberlain, A. K. (1988). The Blackburn Oil Field, Nevada: A Case History. Rocky Mountain Association of Geologists Guidebook, p.241-250. Denver, Colorado.

Takacs, G. (2015). Chapter 2—A Review of Production Engineering Fundamentals. In G. Takacs (Ed.), Sucker-Rod Pumping Handbook. p. 13–56. Gulf Professional Publishing. https://doi.org/10.1016/B978-0-12-417204-3.00002-9

Taverna, Nicole. (2019). Sedimentary Geothermal Feasibility in Eastern Nevada and Millard County, Utah Well Databases. (Database). https://dx.doi.org/10.15121/1637461

U. S. Environmental Protection Agency (2016). National Elevation Dataset (30 m). (Dataset). https://archive.epa.gov/esd/archive-nerl-esd1/web/html/nvgeo_gis3_dem.html#map

University of Nevada, Reno (UNR). (2021). INGENIOUS Thermal Conductivity Measurement Source Categorization. (Data set). Retrieved from https://dx.doi.org/10.15121/1874222.

Waples, D. W., & Waples, J. S. (2004). A Review and Evaluation of Specific Heat Capacities of Rocks, Minerals, and Subsurface Fluids. Part 1: Minerals and Nonporous Rocks. Natural Resources Research, 13(2), p. 97–122. doi.org/10.1023/B:NARR.0000032647.41046.e7

Zhu, X., Gao, Z., Chen, T., Wang, W., Lu, C., & Zhang, Q. (2022). Study on the Thermophysical Properties and Influencing Factors of Regional Surface Shallow Rock and Soil in China. Frontiers in Earth Science, 10, p. 1–13.

This report is available at no cost from the National Renewable Energy Laboratory (NREL) at www.nrel.gov/publications.

Geothermal Prospecting in Existing Oil and Gas Basins

Alfred Lacazette[1], Stephen P. Cumella[2], Veit J. Matt[1], Mark G. Cottrell[3], Saman Karimi[1,4], Bruce D. Marsh[1,4], William R. Chmela[1]

[1]Geothermal Technologies, Inc.

[2]C2 Consulting

[3]WSP UK Ltd.

[4]Johns Hopkins University

Keywords

Geothermal, hot, sedimentary, aquifer, prospecting, oil, gas, basins, thermal groundwater flow modeling

ABSTRACT

Existing oil and gas fields are much more widespread than conventional (hydrothermal) geothermal fields. Many oil fields are desirable places to exploit Hot Sedimentary Aquifers (HSAs) for geothermal electricity generation and/or direct use, for these, and other, reasons:

- High temperatures are required to mature hydrocarbons, so subsurface temperatures of oil and gas fields are often (but not always) warmer than those of surrounding regions. Also, hydrocarbon-bearing intervals are good insulators that trap heat below them.
- HSAs have higher energy density than equivalent temperature hot dry rocks due to the higher heat capacity of brine compared to dry rocks. This brine is produced directly and does not require inefficient conductive heat transfer.
- The petroleum industry routinely collects large amounts of high-quality data, much of which is publicly available. Such large, detailed data sets include well and seismic reflection data, geophysical logs, stratigraphy, structure, fluid chemistry, flow and pressure, stress, core, rock mechanics data, and other data types. Such data sets enable rapid, economical exploration and are not always available for conventional geothermal exploration.
- Sedimentary basins that host petroleum typically have porous, permeable strata. Such strata host petroleum deposits in traps, and porous, brine filled strata are often present. Consequently, the same rocks that host oil and/or gas commonly host even larger amounts

of brine in multiple strata that can be exploited for geothermal electricity generation and/or direct use.
- HSAs are much more widespread than traditional hydrothermal targets.
- HSA geothermal wells rely on porous, permeable strata that may not need expensive stimulation to produce large volumes of brine, which represents a substantial cost savings over stimulated wells. Non-stimulated wells have a reduced risk of stimulation-induced seismicity.
- The large volumes of water available in HSAs, coupled with new proprietary methods of high-rate extraction and modern Organic Rankine Cycle generating systems (ORCs), results in long well lives due to the stable temperature of the produced fluid, and hence favorable economics, even though HSAs are cooler than hydrothermal geothermal fields because high temperatures over geologic time promote cementation which destroys porosity.

We describe a workflow for HSA exploration and reservoir simulation that resulted in the first deep geothermal well permits granted by the State of Colorado. The project is in the "hot spot" of the prolific Wattenberg oil field in the Denver-Julesburg (DJ) Basin and targets the Permian-age Lyons Sandstone. Geothermal brine will be extracted from beneath existing oil and gas production.

A single producer-injector well pair was simulated with multiple production/injection rates, well spacings, and lateral lengths using both the COMSOL™ and FracMan™ software packages to determine prospective drilling targets. COMSOL was used to build simple, rapid, uniform porosity-permeability models. FracMan simulations were based on a detailed, 3D static model developed from representative density-porosity logs from the area and was used for well design and optimization (Cottrell et al, 2023). Both simulation efforts showed that the produced water temperature is stable for more than 20 years. The similarity between the two models likely results from the high porosity and permeability of the formation and the thickness of the Lyons (~40m) relative to the modeled well spacings (600m and 800m).

1. Introduction

Conventional (hydrothermal) geothermal electricity generation is clearly economic. The first commercial hydrothermal plant commenced operation in Tuscany, Italy in 1913. Since then, commercial hydrothermal fields have been developed in many countries around the world. Unfortunately, suitable hydrothermal fields require a unique set of geologic conditions and hence are rare – suitable conditions occur over only 2% - 3% of the earth's surface. Figure 1 shows the locations of existing hydrothermal power plants in the U.S.

Thermal energy is present in rocks and fluids beneath the 97%-98% of the earth's land surface that is not suitable for conventional geothermal plants. Efficiently extracting the heat from these other areas is a challenge. Geothermal resources sufficient for electric power generation are found both in "hot dry" rocks and in Hot Sedimentary Aquifers (HSAs). Currently, there is a strong industry focus on heat extraction from Hot Dry Rocks (HDR) while extraction of thermal energy from HSAs has been mostly ignored because of their more moderate temperatures (typically <150°C). However, recent technological developments allow electrical power generation at much lower temperatures than in the past, but only if coupled with high flow rates (~100L/s). Interest in HSA geothermal electricity generation is growing, e.g. Stautberg and Sonnenberg (2023).

Figure 2 shows both locations with identified hydrothermal potential and areas favorable for Enhanced Geothermal Systems (EGS) or Closed Loop Geothermal Systems (CLGS) in hot dry rock. Hydrothermal sites are limited to the western U.S., most often in areas with recent volcanic activity, and are very localized.

Figure 1: Energy Information Agency map of hydrothermal electricity plants in the US and Mexico.

In theory, EGS and closed-loop geothermal systems can be built anywhere on Earth if either the geothermal gradient is high enough or the wells are drilled deep enough to reach sufficiently high temperatures, providing that the combination of geothermal gradient, drilling depth, and number of wells required is economically favorable. However, both EGS and closed-loop geothermal systems depend on the conduction of heat through rock over substantial distances and hence suffer from a fundamental challenge: rock is a serious insulator and thus conduction of heat is notoriously slow, commonly taking ~1 month to go 1 m.

Figure 2 indicates that Enhanced Geothermal System (EGS) potential is widespread, however EGS has yet to be proven at commercial scale despite a recent experiment (Norbeck and Latimer, 2024). The term “Enhanced” in “EGS” denotes stimulation by hydraulic fracturing. In an EGS system, geothermal waters flow through artificial and natural fractures from an injector well to a producer well. Fluid flow in the fractures heats the fluid but cools the fracture surfaces leaving heat stranded in the interior of rock masses between fractures so that the production temperature declines quickly with time (e.g., Figure 4, Norbeck and Latimer, 2024). Also, experiments to date show that EGS systems in dry rock lose water into the natural fracture network at a rate of 15% or more per day (~7,000 barrels) so that they consume water (e.g. Norbeck and Latimer, 2024). Water consumption is potentially problematic everywhere, but especially in arid to semi-arid regions such as the western U.S.

In closed-loop systems, a working fluid flows through a deep network of sealed wellbores so that heat is transferred to the working fluid through only the wellbore wall. Over time, this results in a cool, insulating volume of rock around the wellbore(s) that conducts heat to the working fluid

only slowly. Moreover, at the industry standard flow rate of 100 kg/s (0.1 m^3/s) necessary to produce ~4 MWe, the fluid in the pipe spends only ~5 minutes at depth, absorbing almost no heat. For significant heating the fluid must spend an hour or more at depth, which reduces the flow rate to 5 kg/s, eliminating this system as a potential provider of electrical power. Consequently, closed-loop geothermal systems suffer from limited power output and high construction costs (Beckers et al, 2022; White et al, 2024). Closed-loop systems do not consume water, but may be suitable for direct-use.

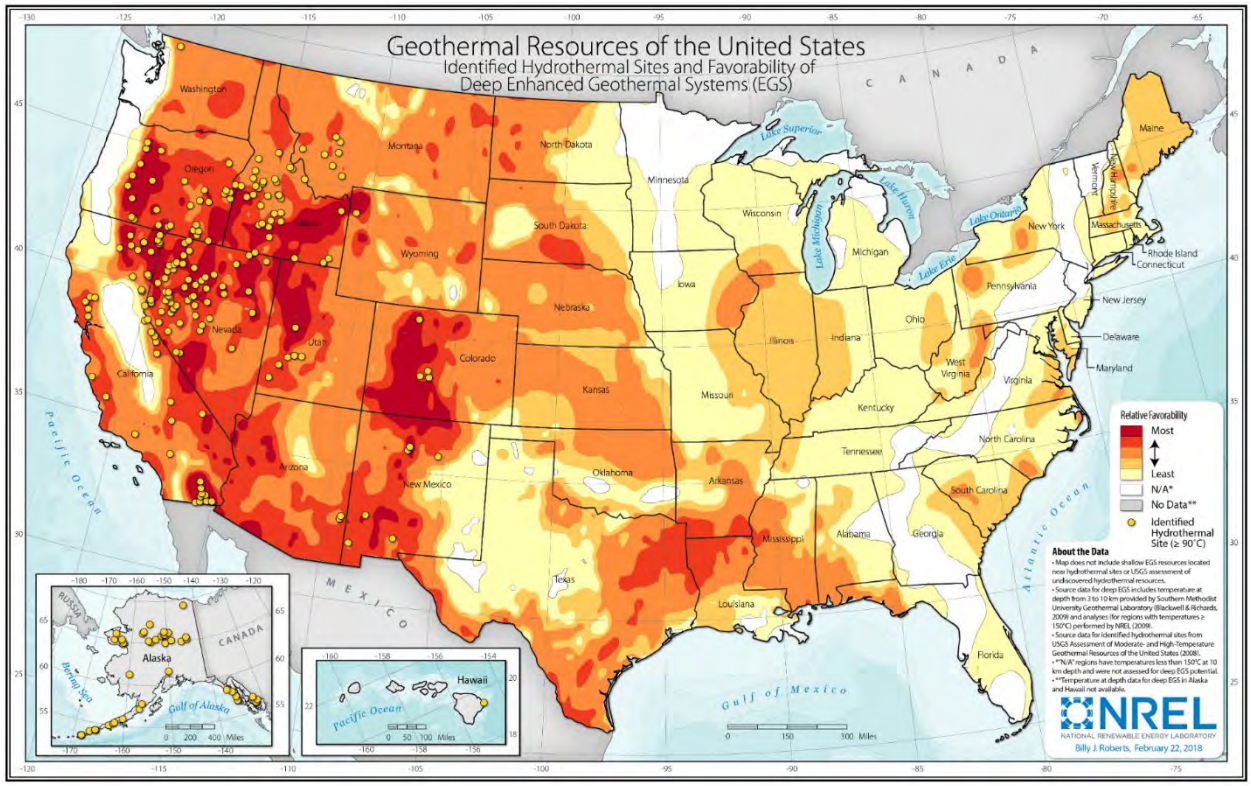

Figure 2: National Renewable Energy Laboratory (NREL) map showing identified hydrothermal sites (yellow dots) and locations that are favorable for Enhanced Geothermal Systems (shading).

In contrast:

- Any sedimentary basin is potentially prospective for HSA geothermal. Figure 3 shows the distribution of oil and gas wells in the United States, which outlines sedimentary basins. Oil and gas wells occur in sedimentary basins, all of which have abundant available data both from the oil and gas wells and additional data sets such as reflection seismic and other geophysical data (e.g., gravity and magnetics).
- HSA geothermal systems flow water through the pore space of the producing strata so that heat is efficiently extracted from the rock mass by the cooled, produced water after injection because conduction occurs essentially instantaneously over grain-scale distances. Heat transfer at the grain scale is much more efficient than conductive heat flow to fractures or closed loop boreholes.
- HSAs have higher energy density than equivalent temperature hot dry rocks due to the higher heat capacity of brine compared to dry rocks. The heat in the in-situ brine is

produced directly from a vast volume of the reservoir with no long distance downhole conductive heat transfer required.

- HSA systems do not consume water because they exploit saturated aquifers and all water extracted from the well is reinjected into the reservoir.

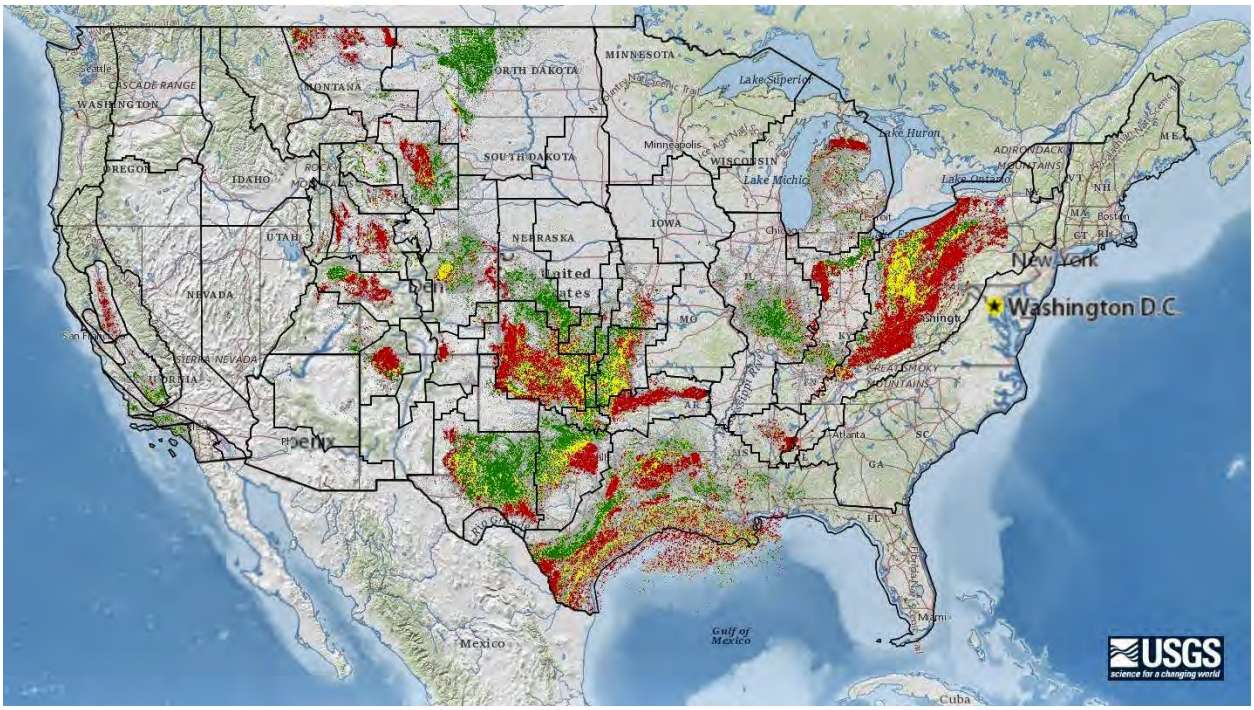

Figure 3: U.S. Geological Survey map of oil and gas wells in the United States.

This paper describes how to use the abundant data collected by the oil and gas industry to explore for Hot Sedimentary Aquifers in oil and gas basins and expands on work of Cottrell et al (2023) and Lacazette et al (2024) which provide additional detail on modeling procedures and location of a specific prospect. However, those papers are focused on a specific prospect while this paper describes exploration on a larger scale.

2. Using Data from Oil and/or Gas Wells

Critical data sets from oil and/or gas wells include bottom-hole temperatures, rock properties from logs, core data, fluid pressure, and fluid chemistry. Reflection seismic and potential fields data (gravity, magnetics) are also commonly collected by the oil and gas industry. This contribution focuses on well and potential fields data. Geothermal Technologies, Inc. is currently developing a geothermal electricity generation project in the Denver-Julesburg (DJ) Basin of Colorado that provides examples of how oil and gas data is used for HSA exploration. Figure 4 is a location map of the study area in the DJ Basin.

2.1 Temperature data

The first, and one of the most important tasks, for geothermal exploration is mapping geothermal gradients. Bottom-hole-temperature data is a standard measurement collected in all oil and gas wells. These measurements must be corrected for cooling by the drilling mud to provide an estimate of the undisturbed reservoir temperature. Cased-hole temperature logs are commonly

collected well after a well has been drilled and cased, so that the temperature log accurately reflects the undisturbed reservoir temperature.

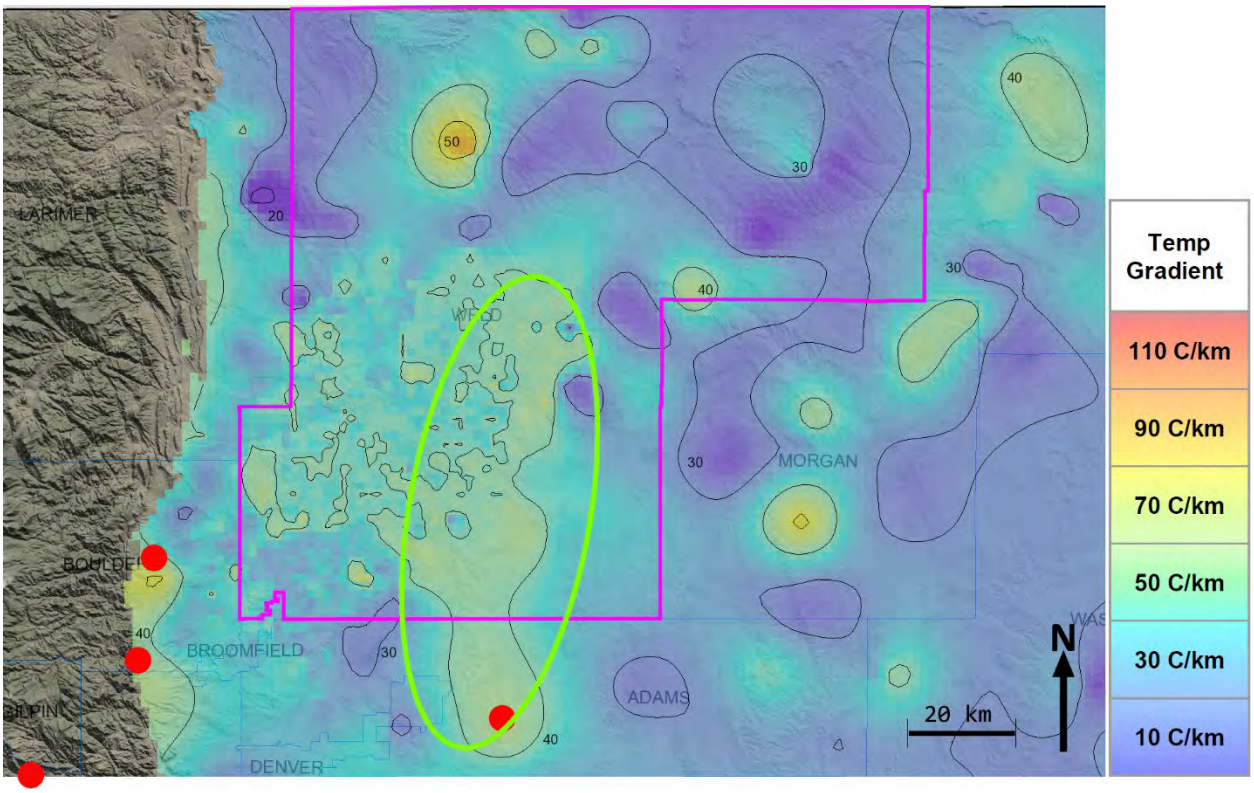

Figure 4: Location map of the study area after Colorado Geological Survey interactive online GIS map. Magenta outline: Weld County, Colorado, U.S.A. Green oval: Indicates the general location of the Wattenberg hot spot. Shading and contours east of the mountain front: Geothermal gradient between the Cretaceous-age Mancos and Dakota Formations. Red dots: Hot springs.

This study tested several temperature correction methods, and found that the correction of Corrigan and Bergman (1996) and Corrigan (2003) provided the best fit to cased-hole temperature logs (Figure 5). The geothermal gradient was computed by first using log data to estimate the thermal properties of the rocks to build a model, then using the corrected bottomhole temperature and a surface temperature map to extrapolate the gradient upwards.

Oil and gas are produced when organic-rich source rocks undergo thermal maturation hence temperature data is of great interest to the oil and gas industry. Correcting bottom-hole-temperature data is subject to errors and the measurements themselves are often of questionable accuracy. Predicting the occurrence of oil and gas depends on the temperature history of an area, not necessarily the present-day temperatures; and the temperature changes of a rock volume over geologic time cannot be measured directly. Consequently, the oil and gas industry uses proxy data (measures of organic matter maturity, e.g. virinite reflectance) to estimate the thermal maturity and maximum formation temperature of an area. Such proxies are sometimes used as guides to the present-day temperature but are not suitable for geothermal exploration, as we show here.

One of the standard and most accurate guides to the cumulative temperature-time history of an area is the reflectance of vitrinite particles in rock samples. Figures 6 and 7 compare the vitrinite reflectance data of Coskey and Cumella (2015) from the Dakota Fm. to the present-day geothermal

gradients of the Wattenberg hot spot and the GOR (ratio of gas to oil in the first 6 months of production of oil and gas wells). The GOR is sometimes taken as a maturity indicator because higher ratios indicate a greater source rock maturity due to higher maximum formation temperatures and time-temperature history. However, GOR also reflects the composition of organic source rocks, the insulating effect of overlying oil/gas deposits and organic-rich beds (Coskey and Cumella, 2015), and other causes. As Figure 6 shows, the GOR is a poor predictor of the cumulative time-temperature history indicated by the vitrinite reflectance data.

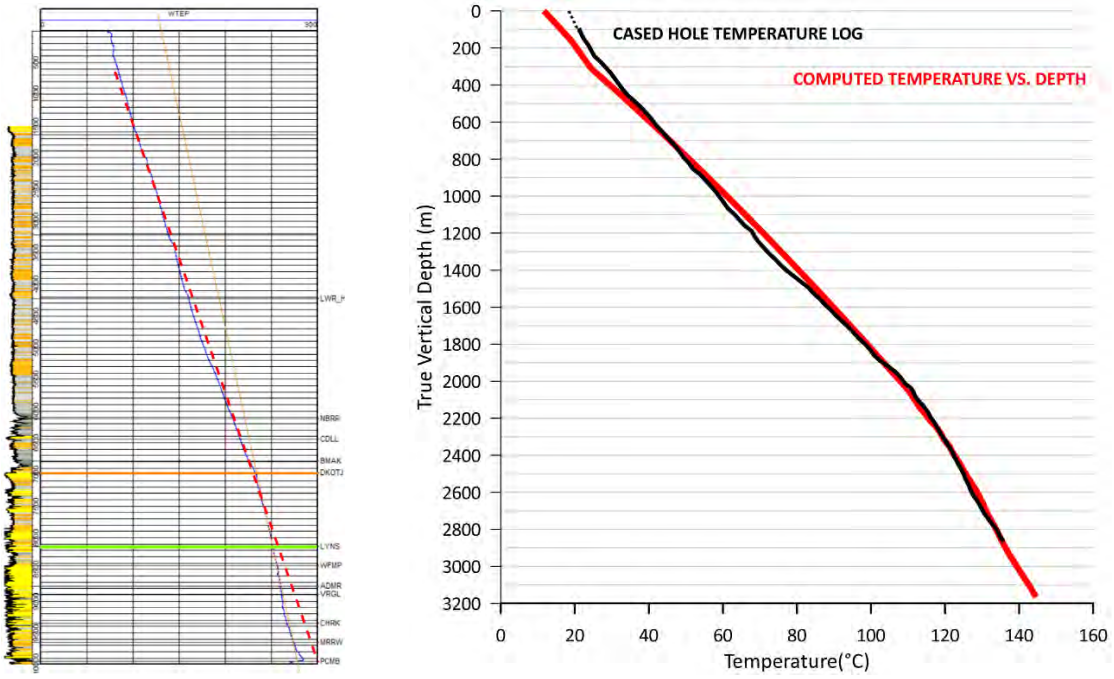

Figure 5: Cased hole temperature log from an oilfield and a one-dimensional thermal model used to validate the temperature correction. LEFT – Temperatures in °F, depths in ft. Blue line-cased hole temperature log. Yellow line – trend of the deep section. Dashed red line – trend of the shallow section. Green line – Lyons top. Orange line – Dakota top. RIGHT – Comparison between a cased-hole temperature log and a one-dimensional thermal model.

The vitrinite reflectance data reflects broadly the geothermal gradient data (Figure 7) but lacks detail compared to the geothermal gradient map for several reasons:

- The geothermal gradient map appears complex, but most of the bull's eyes on the map are supported by several measurements, so that they cannot be attributed to the often-poor quality of bottom-hole temperature data.
- The vitrinite data is sparse compared to the temperature data.
- More importantly, the vitrinite data shows the cumulative effects of temperature over geologic time so that present-day temperatures and spatial temperature variations through time are not captured.

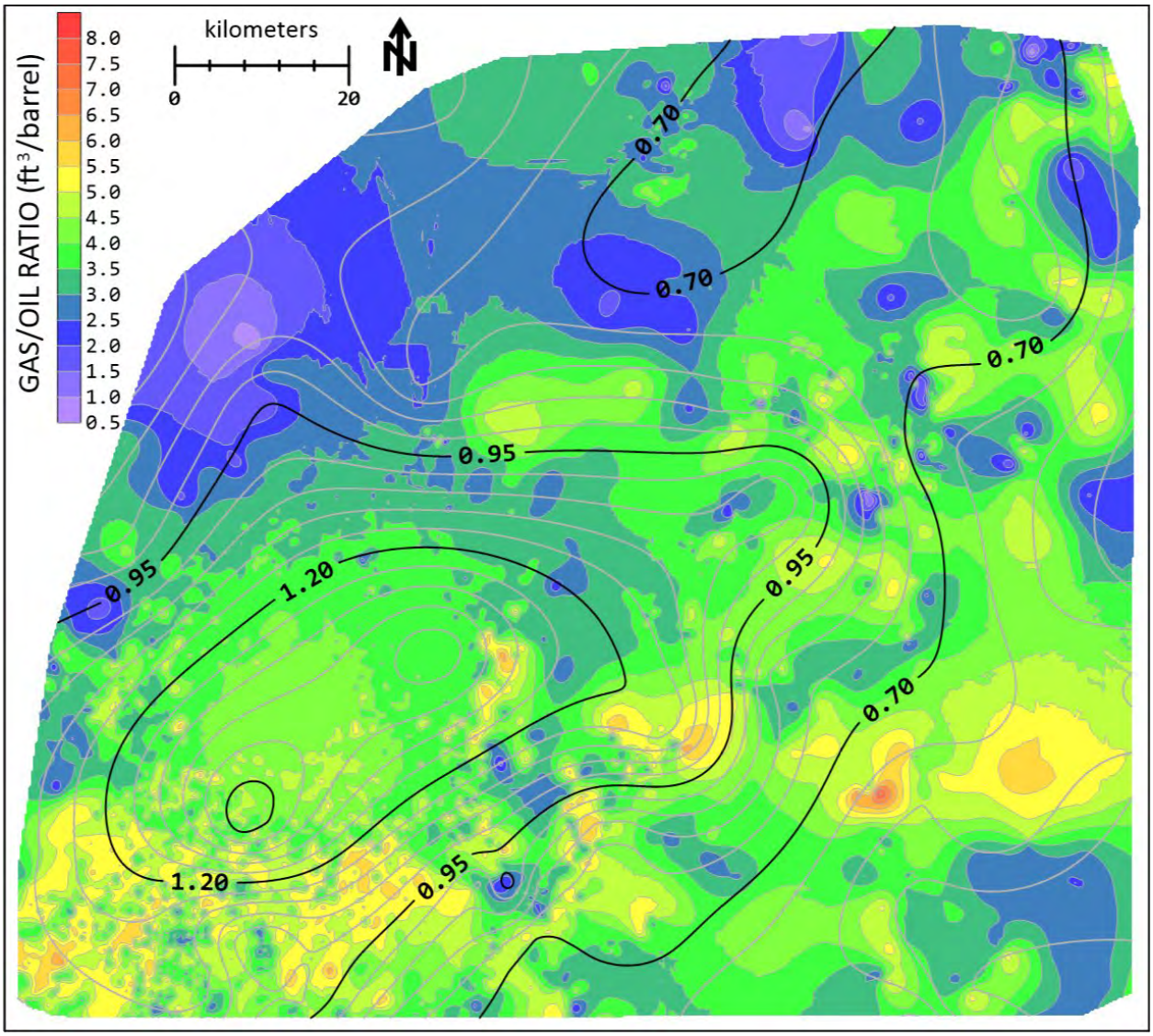

Figure 6: Map of the "hot spot" in the Wattenberg Field and some of the surrounding area. Color shading shows the GOR (gas/oil ratio in the first 6 months of production) from 798 wells in the Niobrara and Codell Fms. Heavy contours are the Dakota Fm. vitrinite reflectance contours of Coskey and Cumella (2015) in %VR_o.

The variability of the present-day geothermal gradients is likely due to hydrothermal fluid movements associated with deep igneous intrusions. Although direct evidence of intrusions has not been published, geologists working the basin have long suspected that intrusions are present at depth. Wattenberg and Redtail fields lie along the trend of the Colorado Mineral Belt (CMB) (see summary by Eaton, 2024) and Eaton (2024) shows that the Lyons Fm. has been altered by mineralizing hydrothermal fluids spatially associated with faulting and temporally associated with CMB intrusions.

Siting an HSA geothermal plant requires specific, local knowledge of present-day temperatures at the scale of typical horizontal well lengths (1-2 km). We conclude that proxy measurements of hydrocarbon maturity are not adequate for siting a plant so that temperature measurements are

required. Petroleum industry vitrinite reflectance maps may be suitable for locating broad regions of interest.

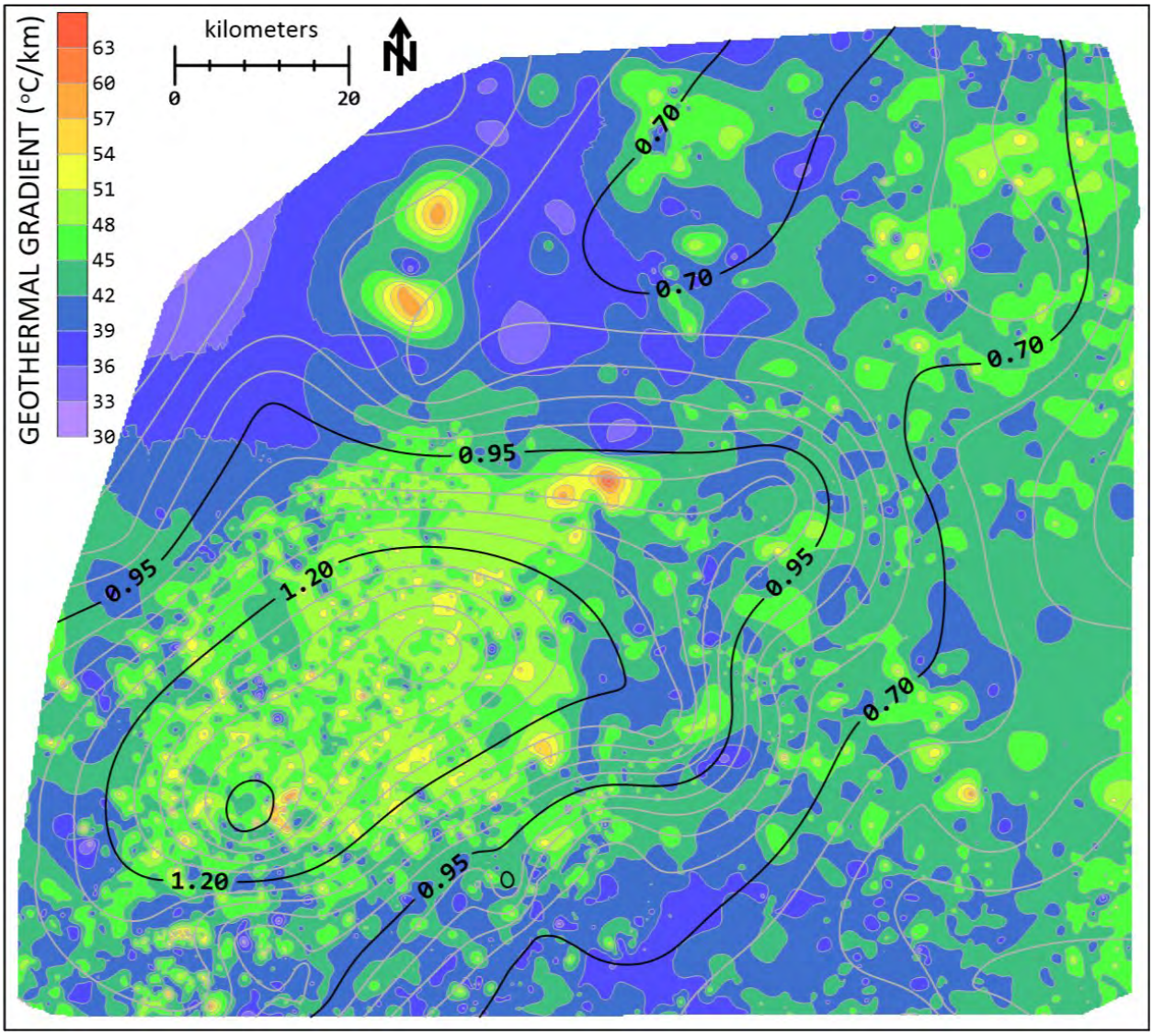

Figure 7: Map of the "hot spot" in the Wattenberg Field and some of the surrounding area. Color shading shows the geothermal gradient determined from 6,181 corrected bottom-hole temperature measurements. Heavy contours are the Dakota Fm. vitrinite reflectance contours of Coskey and Cumella (2015) in %VR_o.

3. Potential Fields Data

Figures 8 and 9 compare gravity and magnetic data (Oshetski and Kucks, 2000) to the present-day geothermal gradients. The gravity map tracks the long-wavelength pattern of the hotspot, but that is not obvious at the scale of figure 8.

In the hot spot, two magnetic anomalies, a low and a high, are centered on geothermal highs while the hot spot occupies a low.

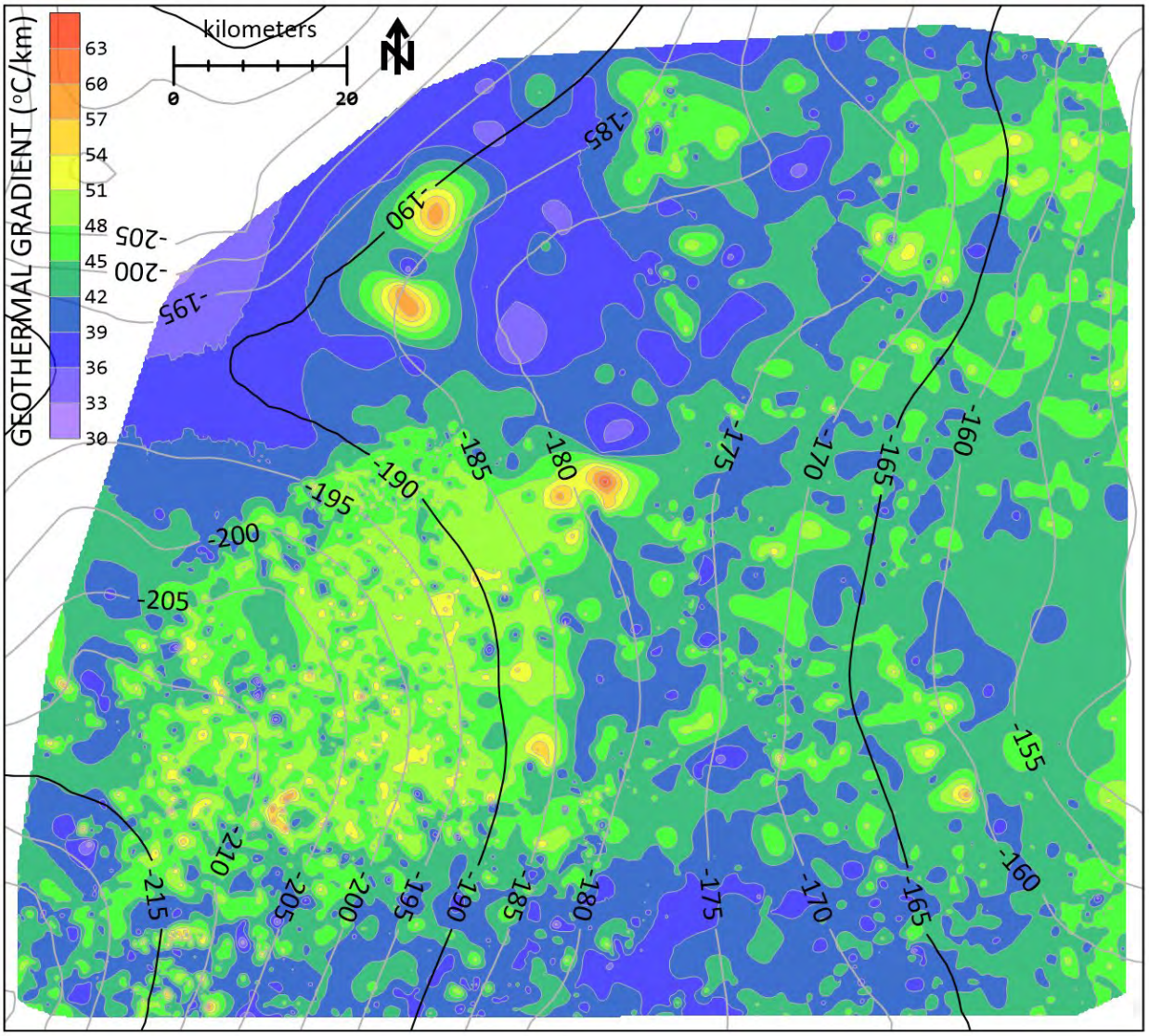

Figure 8: Bouger gravity contours over geothermal gradients.

4. Rock Properties

Unlike hydrothermal production, HSA production depends both on harvesting the existing heated fluids and harvesting the heat in the solid rock matrix via flow through the pore space of producing strata. Therefore, exploration programs rely on knowledge of matrix porosity and permeability of target strata. Existing oil and gas fields have abundant geophysical well logs that provide porosity, and in some cases permeability data, from core measurements. The log data is available from state agencies such as geological surveys and from commercial data providers.

Knowing the volume of the existing hot brine available for power generation is essential. Figures 10 and 11 provide examples of porosity and permeability mapping of the Lyons Sandstone Fm., a Permian age eolian sandstone in the area shown in Figures 6 and 7. Figure 10 shows the porosity-thickness (termed phi*h), which is calculated by multiplying the fractional porosity measurements of a porosity log (density-porosity in this case) by the log sampling interval for all measurements

in the formation of interest and then summing the values for the formation. The result is therefore in length units and represents the thickness of the brine layer that would result if the rock was compacted to eliminate all porosity. For further discussion see Lacazette et al (2024). A phi*h map therefore shows the distribution of water available for power generation.

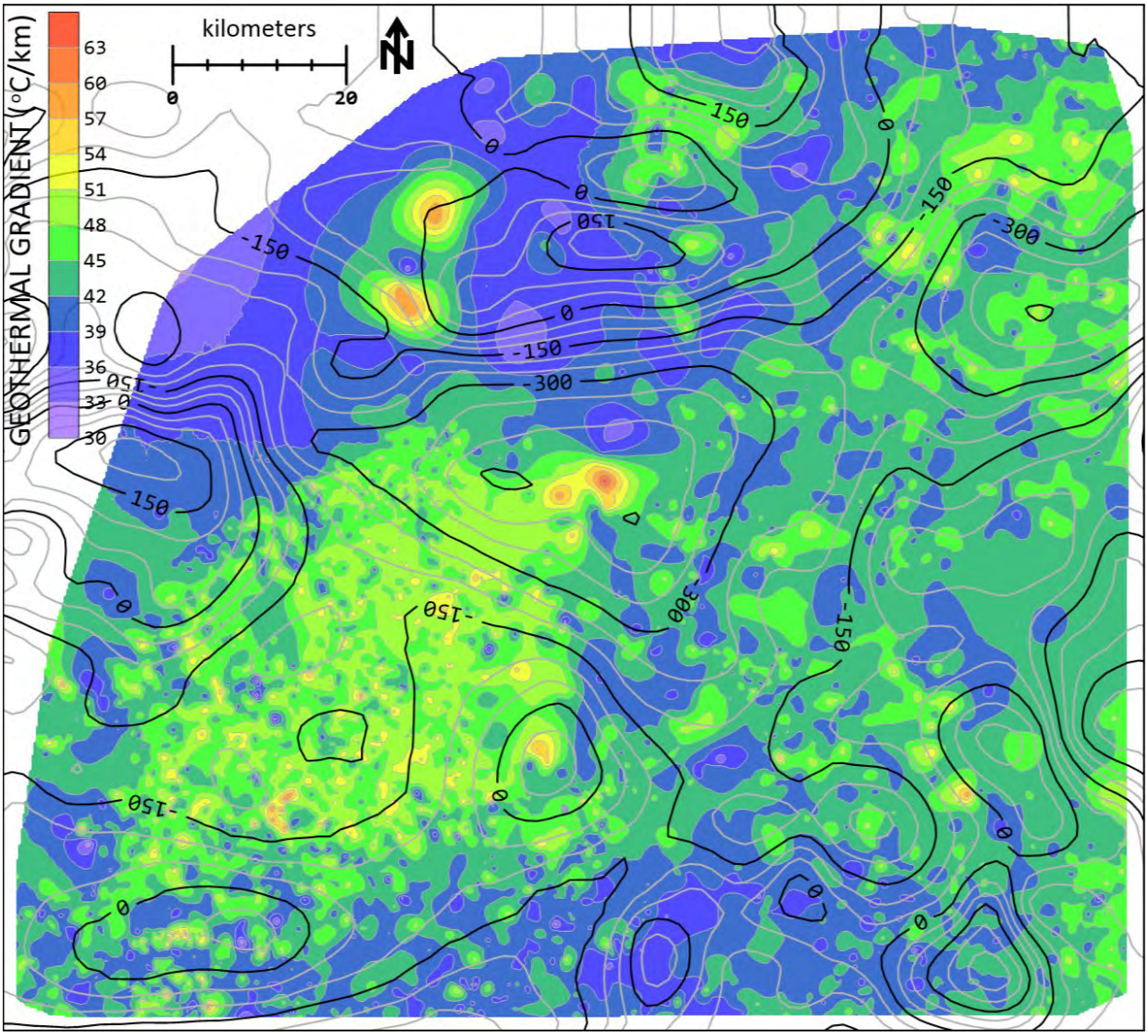

Figure 9: Magnetic anomaly contours over geothermal gradients.

Bulk reservoir permeability is important for determining optimum well spacing and lateral lengths. Permeability can be mapped using the porosity logs if a core-derived porosity-permeability transform is available. Figure 11 is a map of the flow-capacity, which is computed by using a porosity-permeability transform to compute permeability from porosity. Similarly to phi*h, each permeability (i.e. transformed porosity) is multiplied by the log sampling interval and the values are summed for the formation of interest. Figure 11 was computed using the horizontal permeability transform described in Lacazette et al (2024). Again, the Lyons Fm. is an eolian sandstone so that the porosity-permeability data in Lacazette et al (2024) is from those lithologies. Figures 10 and 11 differ because the porosity-permeability transform is non-linear. Reservoir

simulations using the COMSOL™ and FracMan™ software packages indicate that including anisotropic vertical and horizontal permeability yield very similar results to simulations using only the horizontal permeability.

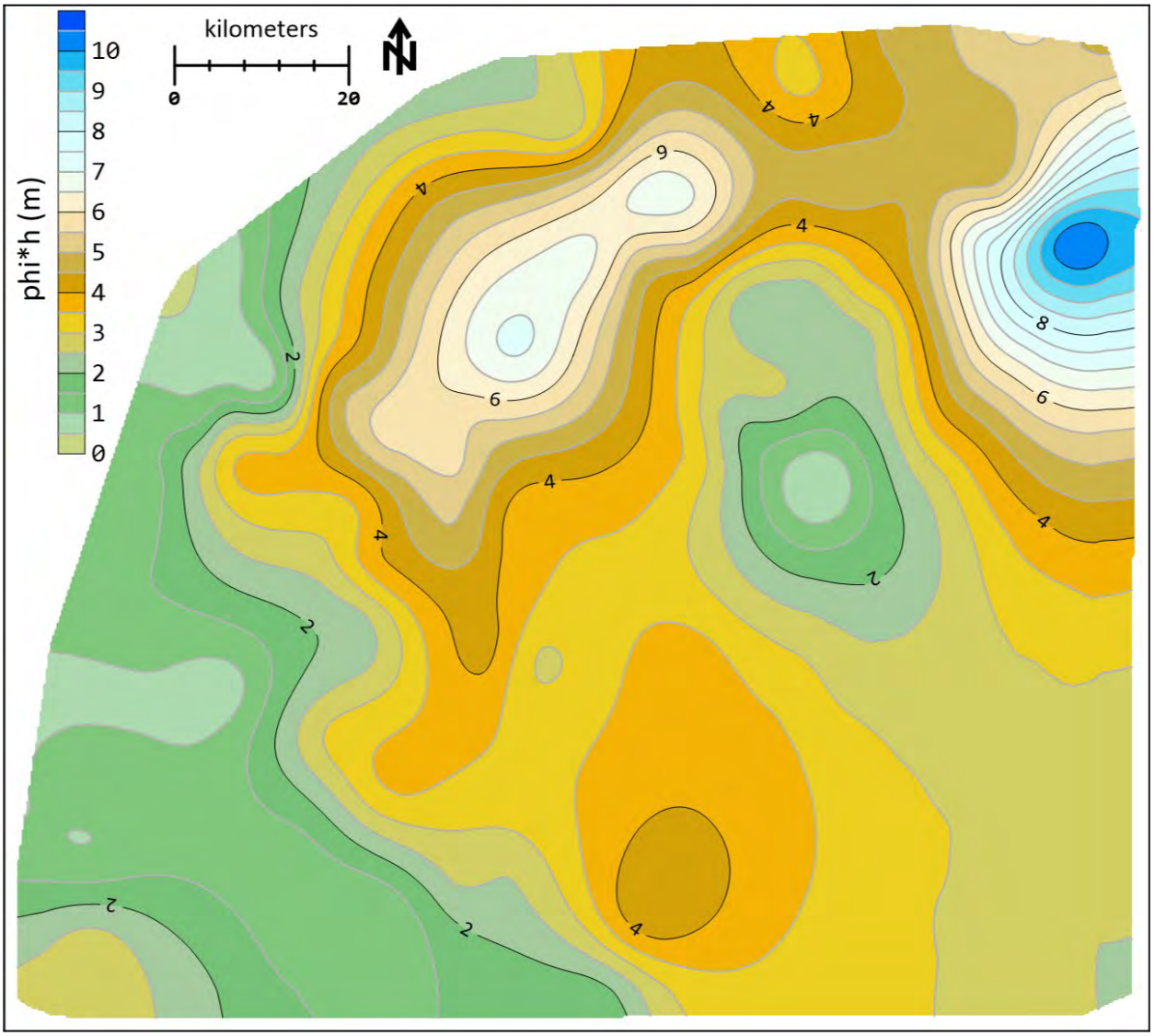

Figure 10: Porosity-thickness (phi*h) map of the Lyons Sandstone.

The heat available for power generation is given by:

$Q = \text{mass } C_p \Delta T$

Where Q is the heat, Cp is the heat capacity, ΔT is the temperature drop in the heat exchanger of an Organic Rankine Cycle generator (ORC). Figure 12 is a map of the available heat from all brine in the Lyons Fm. Such maps can be computed for the heat in the mobile brine, the heat in the solid portion of the rock, and other quantities (Lacazette et al, 2024). Maps such as those in Figures 6 and 10 through 12 are used to identify prospective areas. Suitable sets of conditions are defined by reservoir simulations.

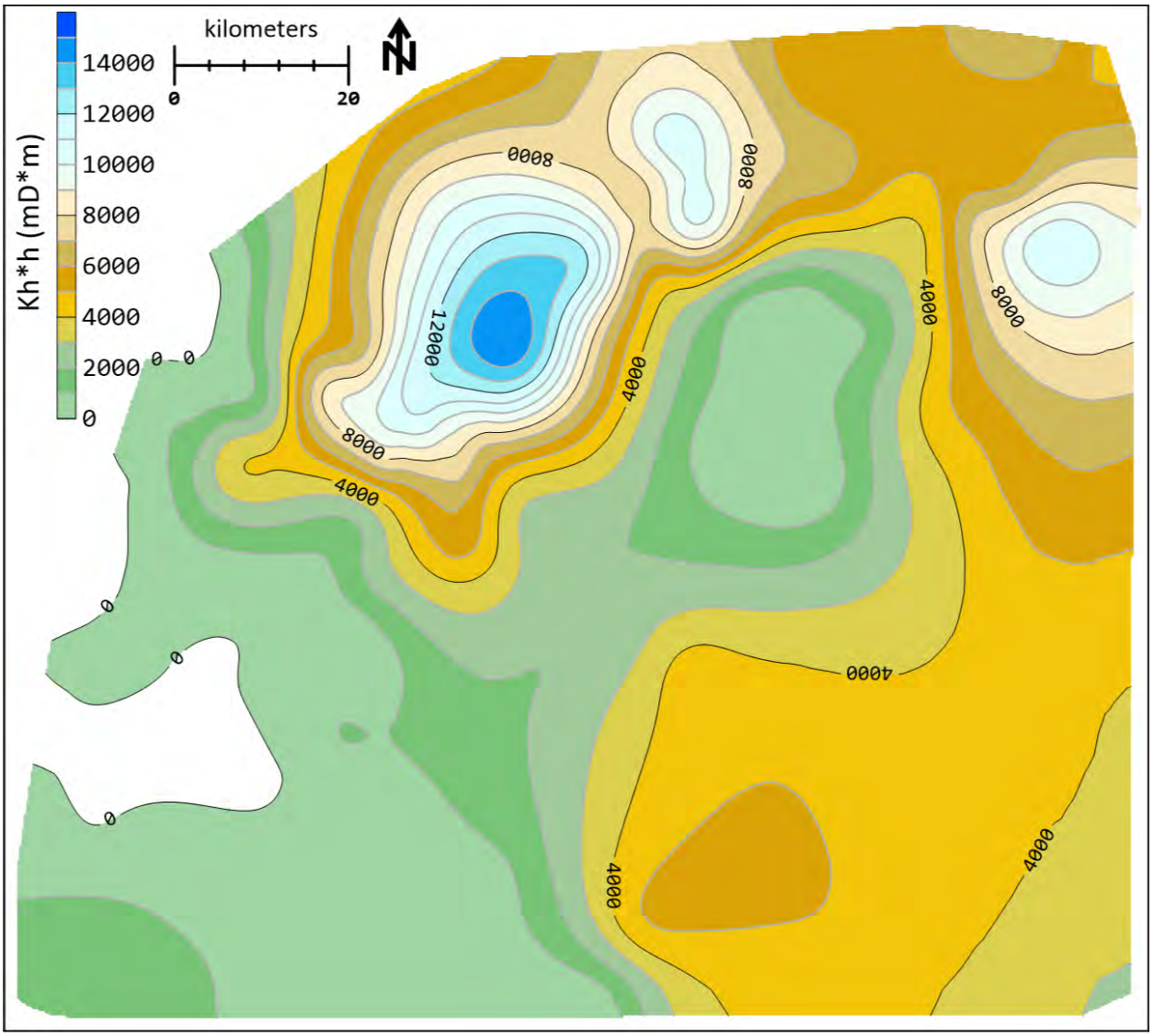

Figure 11: Flow-capacity (Kh*h) map of the Lyons Sandstone.

5. Simulation

Reservoir simulation (flow modeling of the geothermal waters) is required to determine the sets of conditions suitable for power generation. We undertook two simulation efforts: 1) rapid simulations with uniform porosity and permeability in the COMSOL numerical package to determine suitable sets of conditions for power generation at map scale and 2) detailed simulations based on a detailed static reservoir model of the reservoir in a targeted area using the FracMan software package (Lacazette et al, 2024). The methodology of the detailed simulations are described in Cottrell et al (2023).

Once promising areas are identified, the reservoir models are built with the rock properties estimated from regional mapping. Producing an HSA requires returning all of the produced water to the reservoir to maintain the reservoir pressure. Figure 13 shows a depth slice of a COMSOL reservoir simulation at the depth of two parallel horizontal wells. The wells set up a dipole pressure

field stimulating a vast convection cell, as shown in Figure 13. The areal footprint between the wells is about 125 acres and the stimulated recharge zone is about 3,500 acres, which represents a vast supply of hot fluid for over 20 years before significantly cold injected water reaches the production well.

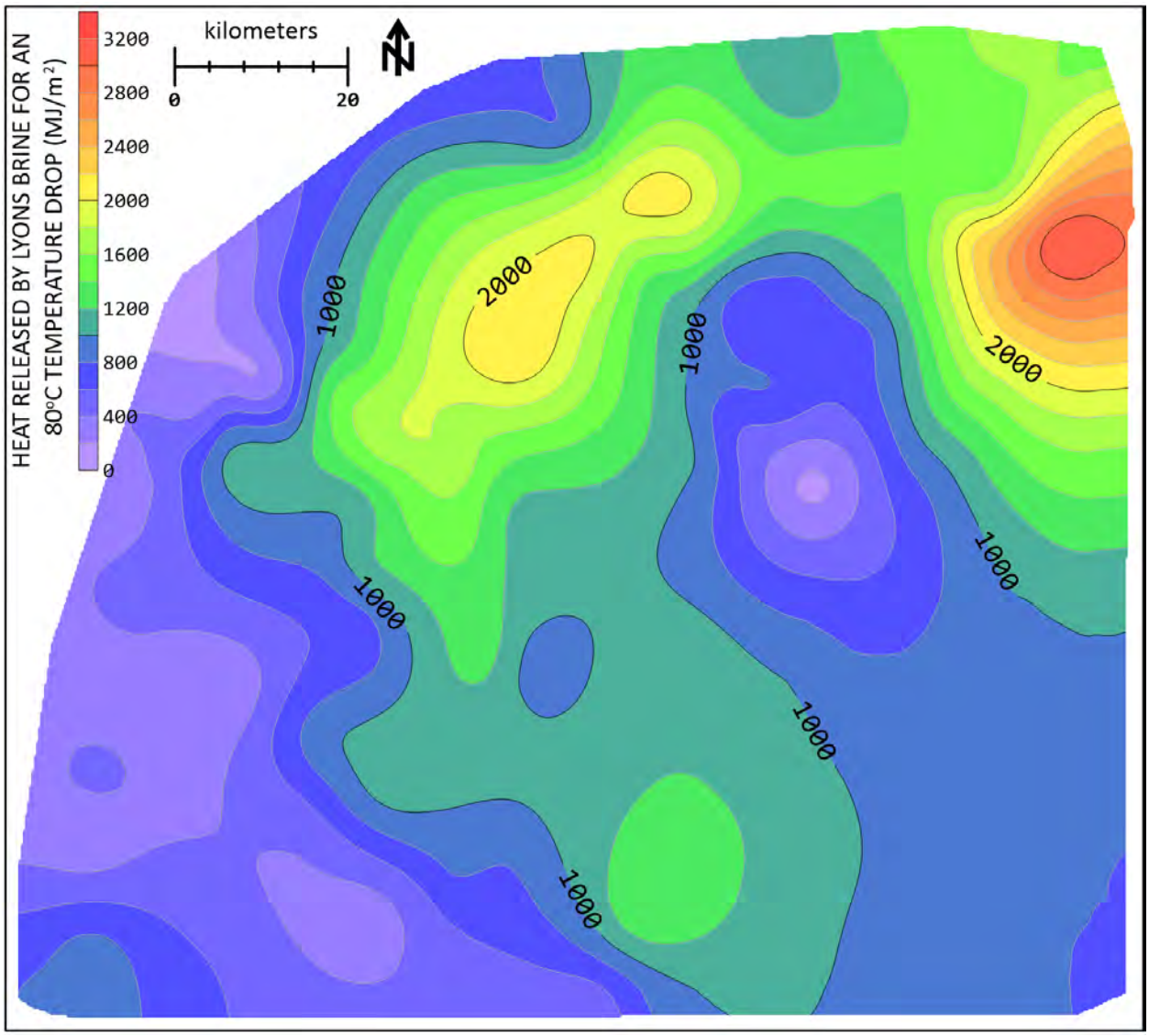

Figure 12: The heat yield for an 80°C temperature drop for all brine in the pore space of the Lyons Fm per square meter of formation.

Figures 14 and 15 show the performance of our planned pilot system over 20 years. Both simulations show that the temperature of the produced water remains economical for at least 20 years. The uniform porosity and permeability model shows less temperature drop than the simulation of the detailed static reservoir model because of thermal breakthrough through a high permeability sandstone streak. Such short-cutting can be managed with downhole flow controllers (Lacazette et al, 2024), which were not used in the simulations.

The long well life from constant production temperature results from two causes:

- Produced water flows through the pore space of the rock completely extracting the heat, from the solid rock matrix.
- Convective circulation continuously brings additional virgin reservoir water to the producing well (Figure 13). GTI's GenaSys™ system for geothermal heat harvesting incorporates these effects and other proprietary GTI technologies.

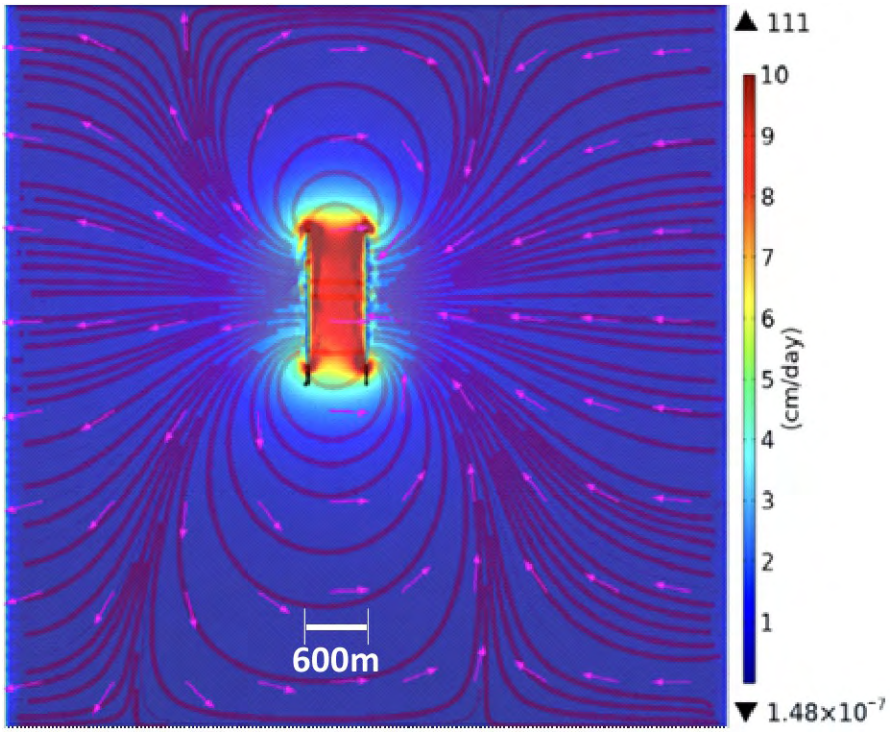

Figure 13: Horizontal slice of a COMSOL reservoir simulation at the depth of the production and injection wells after 20 years of production. Colors show fluid flow velocity in cm/day. Arrows show flow direction.

6. Summary

We provide an example workflow for geothermal exploration in oil and gas basins using existing data collected by the oil and gas industry. Geothermal gradients must be determined with local temperature data because measurements of hydrocarbon maturity that are sometimes used as proxies for temperature are insufficiently precise for siting a geothermal plant. Rock properties measurements such as porosity are available from well logs. Core-derived porosity-permeability transforms allow conversion of porosity data to permeability. Combinations of temperature and rock properties suitable for electricity generation are determined by reservoir simulation. Example reservoir simulations for a planned project show that HSA geothermal wells have long wells life, and this overall system is easily scalable and suitable globally.

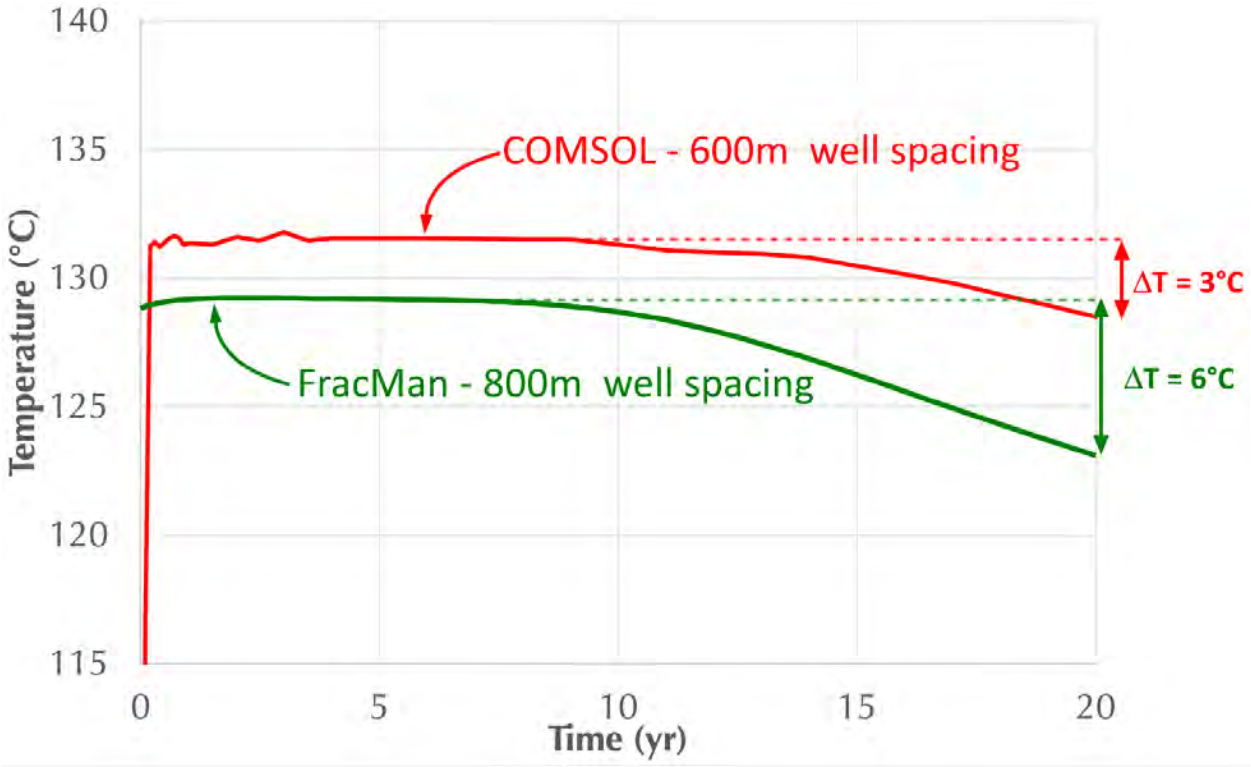

Figure 14: Produced water temperature over 20 years. The two models have different starting temperatures. Although the temperature declines slightly it remains adequate for commercial electricity generation in both cases. The produced water temperature is only slightly below the temperature of the reservoir compared to published EGS and CLGS produced water temperatures, which are a fraction of the reservoir temperature. The heat extraction efficiency potential of HSAs makes them extremely attractive for power generation.

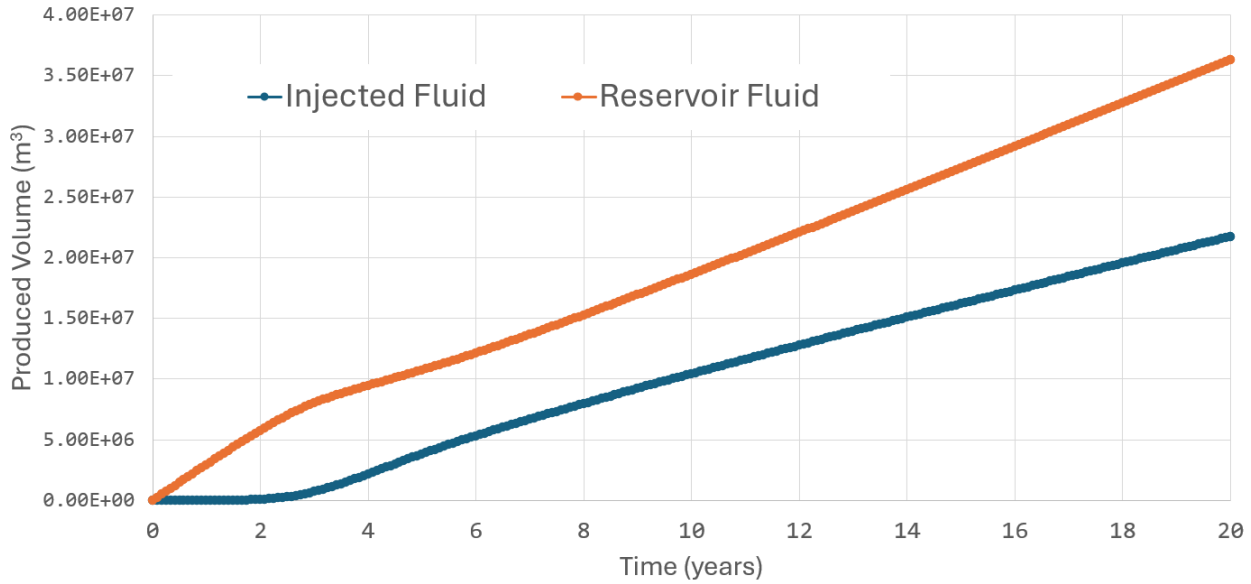

Figure 15: Plot of produced fluids volume from a FracMan reservoir model. The plot shows the volumes of reservoir fluid and injected fluid produced over 20 years.

Acknowledgement

We thank and acknowledge White Eagle Exploration and Chevron for sharing data, the staff of the Colorado Energy and Carbon Management Commission (formerly named the Colorado Oil and Gas Conservation Commission) for helping resolve access problems to publicly available data, and the staff of the Denver U.S.G.S. for access to their cores and thin sections. We thank GTI and WSP for permission to publish. The interpretations presented here are entirely our own.

REFERENCES

Beckers, K.F., Rangel-Jurado, N., Chandrasekar, H., Hawkins, A.J., Fulton, P.M., Tester, J.W., "Techno-Economic Performance of Closed-Loop Geothermal Systems for Heat Production and Electricity Generation." *Geothermics*, 100, (2022), 21p.

Corrigan, J. and Bergman, S.: Thermal modeling and interpretation of thermal indicator data, *AAPG Convention and Exhibition, San Diego, CA* (1996).

Corrigan, J.: ZetaWare utilities – BHT correction homepage, correcting bottom hole temperature data, ZetaWare, Inc, http://www.zetaware.com/utilities/bht/default.html (2003, accessed 2021).

Coskey, R.J. and Cumella, S. "Thermal Conductivity of Organic Shales and Coals – How Their Presence and Persistence Effect Thermal Maturity" *American Association of Petroleum Geologists Search and Discovery Article #41672* (2015).

Cottrell, M., Lacazette, A., Chmela, B., Karimia, S., Marsh, B.D. "Evaluating The Geothermal Potential of Hot Sedimentary Aquifers Using a Hybrid Approach" *American Rock Mechanics Association*, 23-0422, (2023) 11p.

Eaton, M.M. "Cause of Geothermal Temperature Anomalies in Wattenberg Field: Unraveling the Impact of Hydrothermal Fluid Movement in the Lyons Formation" *M.S. Thesis, Colorado School of Mines* (2024) 144p.

Lacazette, A., Cumella, S.P., Matt, V.J., Cottrell, M.G., Karimi, S., Marsh, B.D., Chmela, W.R. "Using Petroleum Industry Data to Locate, Characterize, and Simulate a Hot Sedimentary Aquifer Geothermal Prospect" *Proceedings, 49th Workshop on Geothermal Reservoir Engineering Stanford University, Stanford, California*, February 12-14 (2024), 12p.

Norbeck, J.H, and Latimer, T., "Commercial-Scale Demonstration of a First-of-a-Kind Enhanced Geothermal System." preprint submitted to *EarthArXiv*, downloaded from *fervoenergy.com*, (2024), 16p.

Oshetski, K.C., Kucks, R.P. "Colorado Aeromagnetic and Gravity Maps and Data: A Web Site for Distribution of Data (on-line version)" U.S. Geological Survey Open-File Report 00-0042 (2000).

Stautberg, E., Sonnenberg, S.A., "Sedimentary Geothermal Play Types of the Texas Gulf Coast: Applications to Electrical Power Generation" GRC Transactions, Vol. 47 (2023), p.1587-1602.

White, M., Vasyliv, Y., Beckers, K., Martinez, M., Balestra, P., Parisi, C., Augustine, C., Bran-Anleu, G., Horner, R., Pauley, L., Betting, G., Marshall, T., Bernat, A. "Numerical

investigation of closed-loop geothermal systems in deep geothermal reservoirs” *Geothermics*, 116, (2024), 18p.

Impact of Geothermal District Heating System on Flexibility of Microgrid in Tuttle, Oklahoma

Hyunjun Oh[1], Jonathan Ho[1], Isaias Marroquin[1], Eric Bonnema[1], Zeming Hu[2], Saeed Salehi[2,3], and Runar Nygaard[2]

[1]National Renewable Energy Laboratory, Golden, CO, USA

[2]University of Oklahoma, Norman, OK, USA

[3]Texas A&M International University

Keywords

Grid flexibility, microgrid, geothermal district heating, heating demand, EnergyPlus, Cambium

ABSTRACT

Flexibility is the capability of the power grid to maintain a balance between electricity generation and variable demand. This study presents preliminary results evaluating the impact of geothermal district heating systems on the flexibility of microgrid in Tuttle, Oklahoma. Heating demand profiles were modeled using EnergyPlus for the district that includes two schools and 250 single-family houses. Then, geothermal energy production was modeled using GEOPHIRES to estimate how much heating demand in the district can be supplied by five different geothermal system scenarios. The results indicated that geothermal energy production varied depending on the resource temperature at different depths, system configurations, and flow rates. For the grid flexibility analysis, electricity consumptions in the five geothermal systems were estimated for pump operations to circulate water from the wells to radiators, while electricity consumption by air-source heat pump in the base case was estimated to supply the same heating load. Electricity consumption in the geothermal systems was significantly lower than those in base cases. The electricity saved by the geothermal system was then incorporated into the microgrid electrical load profiles where variable renewable electricity generation is significantly high. The results visually showed that geothermal district heating system can improve grid flexibility as a baseload during the winter season. The results also highlighted potential opportunities to save energy costs that will be further analyzed in future study.

1. Introduction

An electrical grid is defined as an interconnected network where electricity generated from power stations is delivered to end users and varies in size from microgrid to wide area synchronous grid,

or super grid that is trans-continental or interconnected throughout several countries. The microgrid represents a local grid that can be connected or disconnected from the grid, while conventional grid is a large-scale synchronous grid. The power stations connected to microgrids and/or grids in the United States consist of a wide variety of power sources including renewable energy sources particularly wind and solar energy where the resource availability may vary significantly depending on the geographical and environmental conditions. The variable renewable electricity generations increase an uncertainty of the net load met by conventional generators in the grid (i.e., non-renewable electricity generations). The grid thus needs to have a sufficient amount of flexibility to maintain a balance between power supply and variable demand and reliably supply electricity to end users especially if the grid incorporates variable renewable power generations at a high penetration. Grid flexibility describes the system capability to respond to the variability and maintain a balance between demand and supply.

The grid flexibility has been extensively studied by previous researchers, especially for the impact of variable electricity generation from wind and solar energy systems. Denholm and Hand (2011) evaluated the flexibility of an isolated region where the grid is significantly dependent on variable wind and solar power generation (up to 80% of the electric demand) and concluded that the grid requires a variety of enabling technologies including load shifting, thermal storage, or electricity storage to accommodate variable renewable electricity generation at 80% penetration and to avoid excessive curtailment. Similarly, Deetjen et al. (2017) reported growing wind and solar capacity in the electric grid shows only minor impact on the grid flexibility even though growing solar capacity improves the grid flexibility requirements at the early stages. Specifically, solar power generation of 14.5 GW increased maximum 1-h ramp rates by 135%, 3-h ramp rates by 30%, ramp factors by 140%, 1-h volatility by 100%, and 1-day volatility by 30%.

To mitigate the net load ramping and optimize the grid flexibility with variable wind energy, Fang et al. (2020) designed flexible ramping products from wind power using a probabilistic wind power ramp forecasting method. Their results demonstrated that the system operating and ramping cost can be reduced with the flexible ramping products especially when wind power provides flexible ramping products in the day-ahead market. Analogously, although geothermal electricity systems have been traditionally incorporated into a power grid for baseload, the power supply using geothermal energy can improve grid flexibility when flexibly operated. Millstein et al. (2021) reported that simple curtailment of geothermal power system operations during negative pricing episodes could increase the energy value by $1 to $2/MWh on average (up to $4/MWh depending on the amount and type of curtailment and enhancement) resulting in an increase in power production during limited peak rate hours. Moreover, the flexibility can be further optimized with in-reservoir energy storage system (Ricks et al. 2022, Ricks et al. 2024).

In addition to the flexible operations of geothermal power systems, geothermal resources have great potential to improve grid flexibility particularly using geothermal district heating system where thermal energy is supplied from the subsurface to a group of buildings through a distribution network (i.e., large-scale heating system). For example, pumps may be the only component where electricity is consumed in the geothermal system to circulate water from wells to heat exchangers or radiators for heating, while electric boilers and furnace in non-geothermal heating system may consume more electricity for the same heating load. However, there are very limited studies to analyze how much electricity could be saved with the geothermal district heating and how the geothermal district heating can contribute to grid flexibility. This study evaluated the impact of

geothermal district heating system that has five different production scenarios on the flexibility of a conceptual microgrid in Tuttle, Oklahoma. Electricity consumed for circulating pumps in the geothermal system was estimated for the five production scenarios and then incorporated into Cambium data sets, which contain modeled hourly emissions, costs, and operational metrics in Southwest Power Pool (SPP) south region where the study area is located (p50). The results were also compared with a base case where the same heating load is supplied by air-source heat pump (ASHP).

2. Geothermal District Heating System in Tuttle, Oklahoma

The study area includes one primary school, one secondary school, 250 single-family homes, and four inactive oil and gas wells, approximately 1.5 km away from the district (Figure 1). As demonstrated by Oh et al. (2024), this study assumed that geothermal energy is reliably and continuously produced from the four oil and gas wells for space heating using radiators.

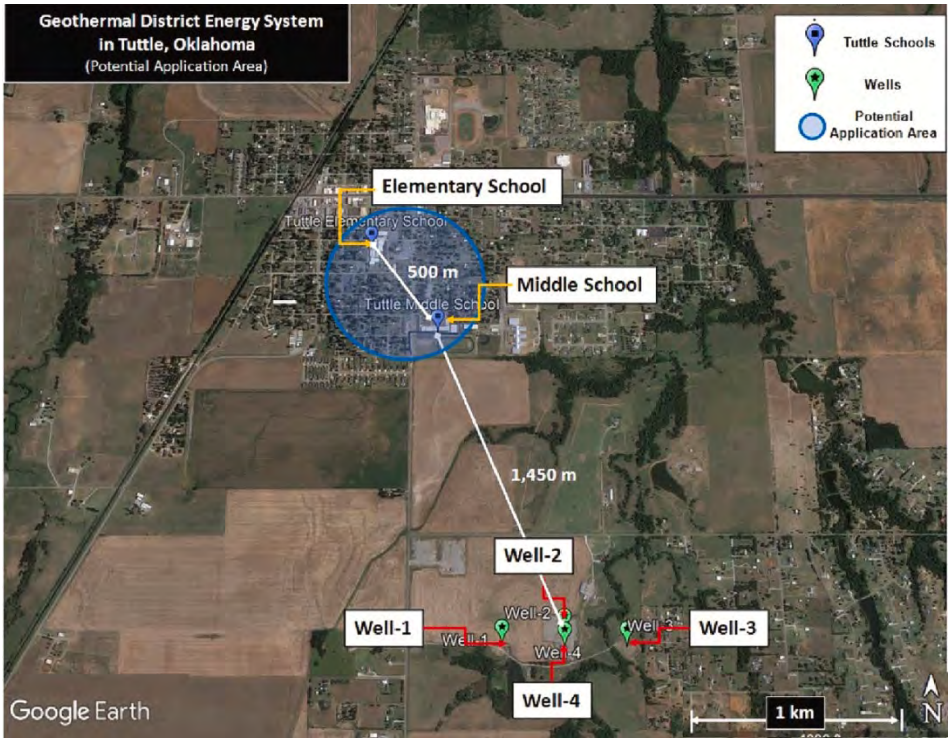

Figure 1. Geothermal district heating system in Tuttle, Oklahoma (Oh et al. 2024).

This study leveraged the reservoir and building energy modeling results in Oh et al. (2024). For geothermal energy production, there were five scenarios that have different well configurations, depths, and flow rates (Table 1). Regional geothermal gradient in the study area was estimated as 25.3 °C/km, and the production temperature, power ($MW_{thermal}$), and energy ($MWh_{thermal}$) varied depending on the configurations and flow rates. Figure 2 shows the variable geothermal energy production with five scenarios. As discussed in Oh et al. (2024), none of the five scenarios fully supply the district heating demand when the system size underwent techno-economically optimization. Peak loads required supply of natural gas to fire boilers during peaking periods (see red bars in Figure 2). The analysis in this study did not consider heating demand supplied by the natural gas boiler but compared power consumptions for each of the same load profiles in the five

scenarios by ASHP (i.e., base case) and by circulating pumps, following the logic: 1) how much geothermal energy can be produced in each scenario, 2) how much electricity is consumed by circulating pumps to produce the energy in each scenario, and 3) how much electricity is consumed by ASHP to supply the same loads.

Table 1. Geothermal district heating system with five production scenarios

Models	Scenario 1	Scenario 2	Scenario 3	Scenario 4	Scenario 5
Number of Production Wells	1	3	1	3	1
Number of Injection Wells	1				
Well Depth (m)	2,100				3,300
Geothermal Gradient (°C/km)	25.3				
Flow Rate per Production Well (kg/s)	9.3	3.1	6.2	6.2	9.3
Initial Reservoir Temp. (°C)	68.1	68.1	68.1	68.1	98.5
Max. Production Temp. (°C)	63.7	55.1	61.8	59.9	87.9
Avg. Production Temp. (°C)	61.3	53	61.3	45.8	87.1
Avg. Heat Production (MW_{th})	0.71	0.39	0.43	0.35	1.42
Avg. Annual Heat Production (GWh_{th}/yr)	1.92	1.33	1.43	1.12	2.49

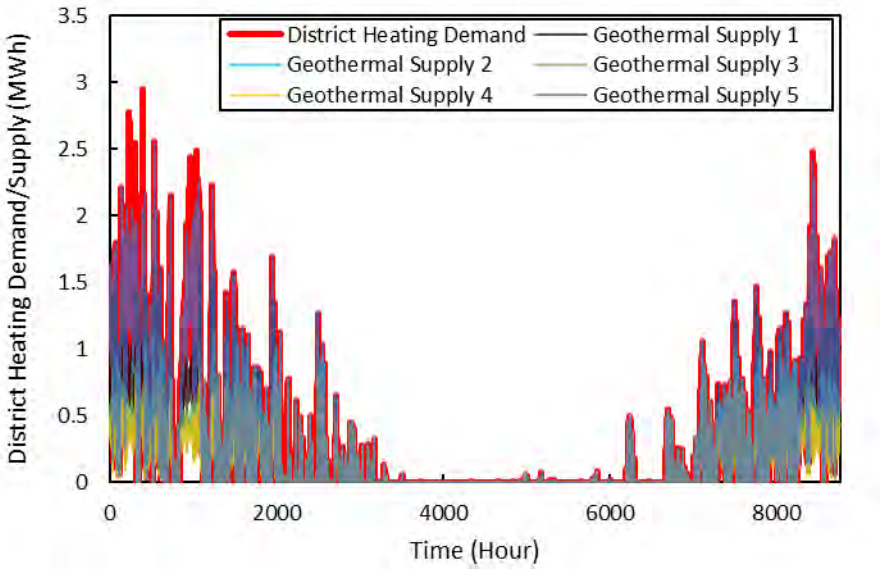

Figure 2. District heating demand and thermal energy supplied by the geothermal system using five production scenarios.

3. Estimating Electricity Consumption in a Base Case and the Five Geothermal Systems

As mentioned, the ASHP was assumed in the base case (i.e., non-geothermal heating system) as a heating equipment to supply the district heating demand and assumed to have a constant coefficient of performance (COP) of 2 (i.e., the ratio of thermal energy generated from the ASHP to electricity consumed in the ASHP is always 2 throughout the year). Solid lines in Figure 3 represent the district heating demand in example days ($MWh_{thermal}$), and the dashed lines demonstrate electricity consumption by the ASHP to supply the demand ($MWh_{electric}$).

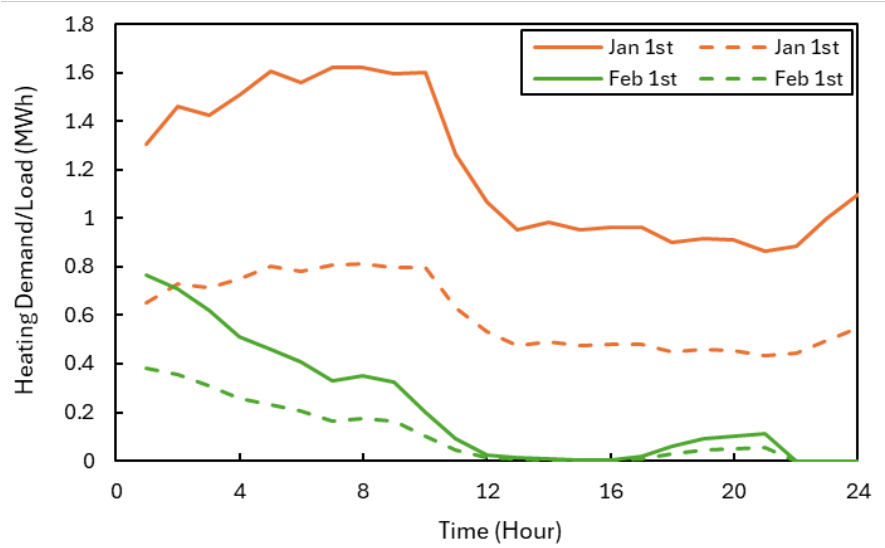

Figure 3. Heating and electrical load profiles in example days. Note that heating demand profiles ($MWh_{thermal}$) are represented as solid lines and dashed lines represent electrical loads by air-source heat pumps for the district heating demand ($MWh_{electric}$).

While electricity consumption in the base case was calculated with the demand profile and COP assuming the ASHP is the only component where electricity is consumed to generate thermal energy for space heating, this study assumed that the geothermal district heating system supplies the heating demand by circulating water throughout the geothermal wells using circulation pumps implying that there is no other energy consumption for generating thermal energy. The pumping power was estimated using Eqn. (1).

$$P = Q \cdot \Delta P / \eta \tag{1}$$

where P = pump power (W), Q = volumetric flow rate (m^3/s), ΔP = pressure drop (Pa), η = pump efficiency, which was assumed as 80% in this study. ΔP was calculated using Darcy-Weisbach equation (i.e., pressure drop caused by friction):

$$\Delta P = \frac{f L V^2 \rho}{2 D} \tag{2}$$

where f = Darcy's friction factor, L = length (m), V = flow velocity (m/s), ρ = fluid density (kg/m^3), D = diameter (m), which was 2.5 in. The calculated pumping powers in the five scenarios were 84.91 kW, 14.29 kW, 26.71 kW, 102.08 kW, and 130.45 kW, respectively. The calculated pumping powers were considered as maximum (i.e., the highest flow rate, such as 9.3 kg/s for Scenario 1 in Table 1) and then reallocated in hourly electrical load profiles in terms of percentage of geothermal system operations (from zero to peak). Figure 4(a) compares electrical load profiles

of the base and geothermal cases in Scenario 1. As the geothermal system does not require power consumption for thermal energy, electrical load in the geothermal system was significantly lower than that in the base case (about 10 times), particularly in Scenario 5 where the heating load supplied by geothermal system was the highest among the five scenarios (Figure 4(b)).

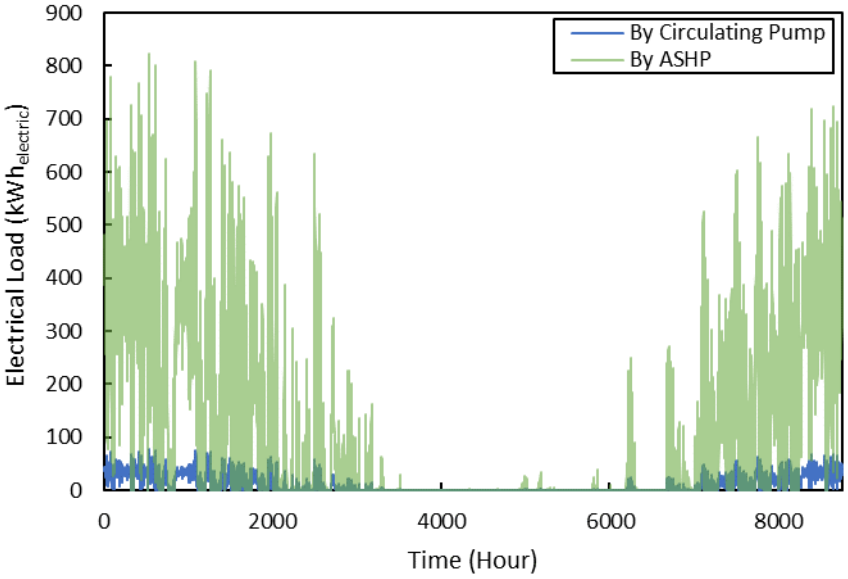

(a)

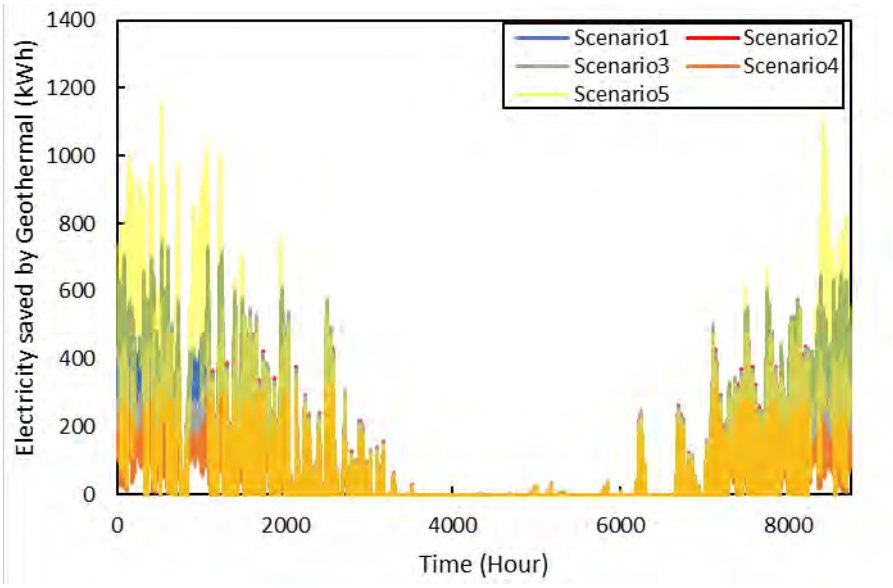

(b)

Figure 4. (a) Electrical load profiles in Scenario 1. Blue bars represent electricity consumed by circulating pump in the geothermal system and green bars represent electricity consumed by ASHP in the base case to supply the same district heating demand. (b) electricity saved by the geothermal district heating system in the five scenarios.

4. Impact of the Geothermal District Heating System on the Microgrid Electrical Load

In addition to the comparison of electricity consumption by circulating pump in the geothermal system and by ASHP in the base case to supply the same heating load, the benefit of geothermal district heating system on the microgrid was evaluated with Cambium, which is a dataset annually released by the National Renewable Energy Laboratory for simulated hourly emissions, cost and operational data of the U.S. electric sector (Gagnon et al. 2024). Balancing area is the smallest geographic resolution for which Cambium data are reported (i.e., model nodes, not perfectly aligned with balancing authority defined by the North American Electric Reliability Corporation). Figure 5(a) shows that the study area is in p50 in Southwest Power Pool (SPP) south region. For the analysis in this study, the Cambium data for p50 was further scaled down to the study area in terms of the populations. Figure 5(b) represents electrical load, imports (into the microgrid through interregional transmission lines), and variable renewable electricity (VRE) and non-variable electricity generations in the microgrid. As an example, electricity saved by the geothermal system scenario 5 was also added in the graph to visualize how the geothermal district heating system may improve the grid flexibility. For example, electrical load in the microgrid was significantly supplied by VRE sources (represented as green bars), particularly including wind and solar energy that may not be always available, while the graph shows that certain amount of electricity can be saved with the geothermal district heating system. In future study, this ongoing effort will be extended more quantitatively.

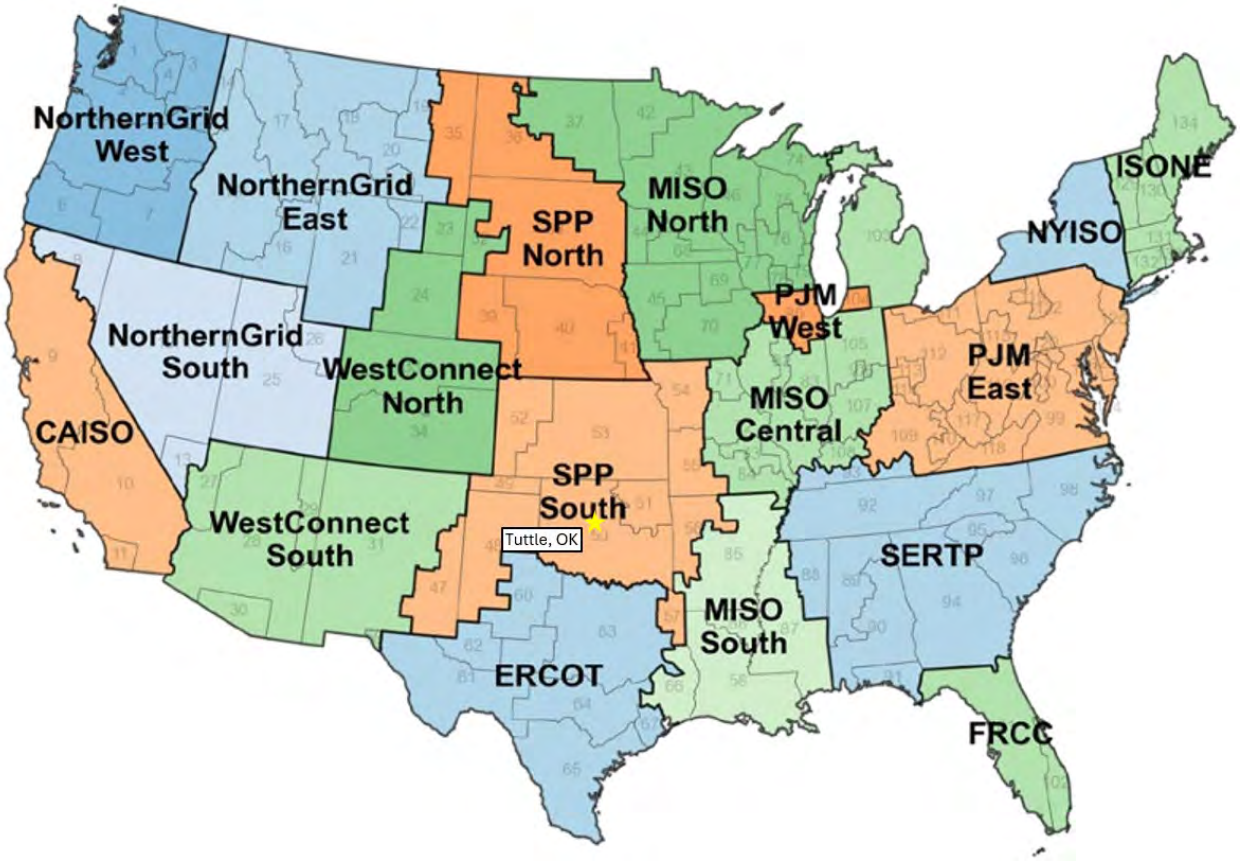

(a)

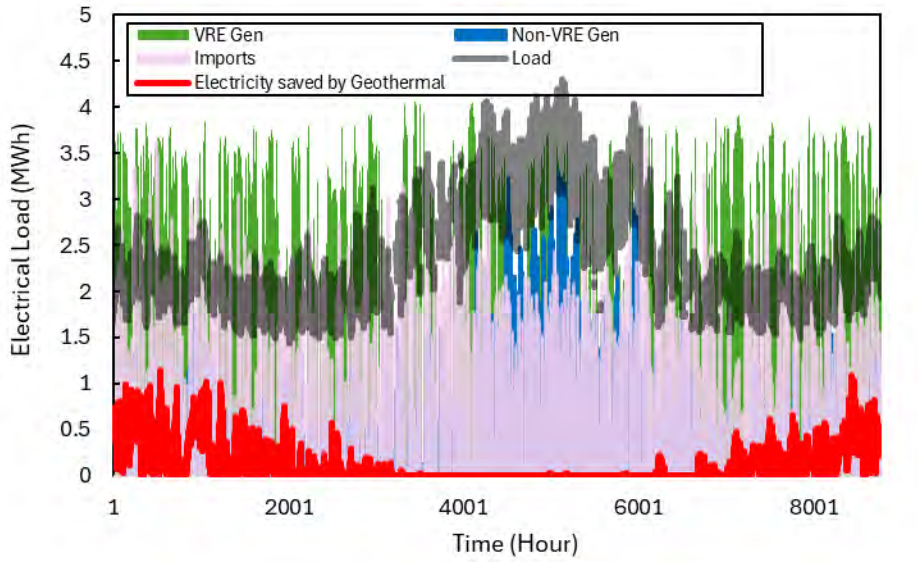

(b)

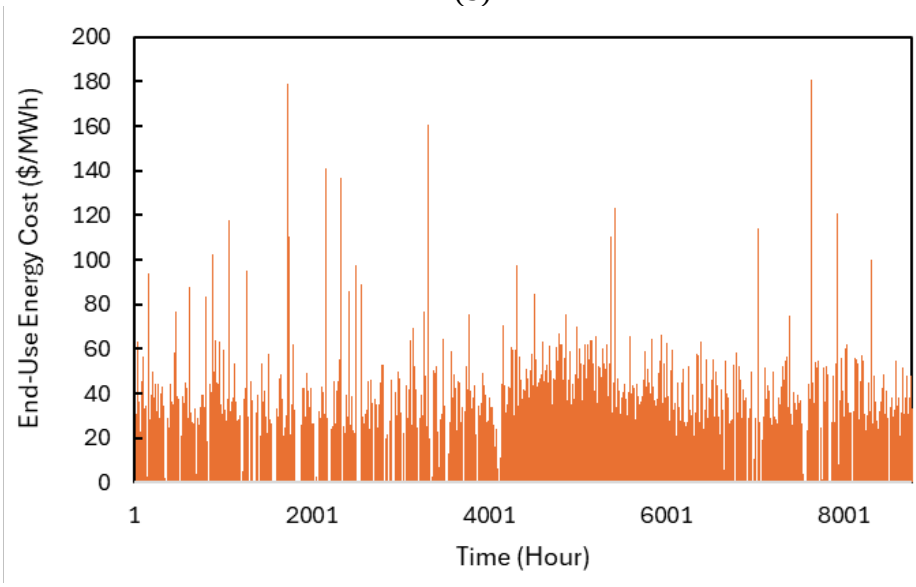

(c)

Figure 5. Cambium dataset used for grid flexibility analysis: (a) the U.S. map for generation and emissions assessment regions. The study area is represented with yellow star sign in p50 in SPP South (Gagnon et al. 2024). (b) electrical load profiles in the microgrid. (c) marginal costs induced by an increase in demand, or costs avoided from a decreased demand, for energy and capacity end uses in p50.

Figure 5(c) shows end-use marginal costs induced by increased demand or costs avoided from a decreased demand in p50. The end-use energy cost represents short-term marginal costs to provide the energy for a marginal increase in load including short-run costs that vary as a function of load, inter-balancing area transmission losses, and inter-balancing area transmission congestion, while other operational costs are not reflected in the energy cost (Gagnon et al. 2024). This is another ongoing effort of this study to quantitatively evaluate the impact of geothermal district heating system on energy cost in the microgrid.

5. Summary and Conclusion

The impact of geothermal district heating system on flexibility of microgrid in Tuttle, Oklahoma was discussed in this study. The annual heating demand profile in the microgrid was modeled using EnergyPlus and geothermal energy production was modeled with five different scenarios to estimate how much the heating load can be supplied by the geothermal systems. Then, electricity consumption by pumps to circulate water from the wells to radiators was estimated for the five scenarios, while electricity consumption by ASHP in base case was estimated to supply the same heating load. Electricity consumptions in the geothermal systems were significantly lower than those in base cases (about 10 times), and electricity saved by the geothermal systems was then calculated. Scenario 5, where the production depth was 3.3 km, showed the greatest geothermal energy production and electricity saving. The electricity saving from the geothermal scenario 5 was incorporated into the electrical load profiles in the microgrid showing potential improvements in grid flexibility especially during the winter season. The analysis will be further extended in future study to quantify the flexibility improvements and energy cost savings.

Acknowledgement

This work was authored by the National Renewable Energy Laboratory, managed and operated by Alliance for Sustainable Energy, LLC for the U.S. Department of Energy (DOE) under Contract No. DE-AC36-08GO28308. Funding provided by the U.S. Department of Energy Geothermal Technologies Office under Contract No. DE-EE0009962. The views expressed in the article do not necessarily represent the views of the DOE or the U.S. Government. The U.S. Government retains and the publisher, by accepting the article for publication, acknowledges that the U.S. Government retains a nonexclusive, paid-up, irrevocable, worldwide license to publish or reproduce the published form of this work, or allow others to do so, for U.S. Government purposes. The authors appreciate Jennifer Kurtz, Craig Turchi, and Deanna Cook, at the National Renewable Energy Laboratory for reviewing the manuscript.

REFERENCES

Deetjen, T. A., Rhodes, J. D., and Webber, M. E. “The impacts of wind and solar on grid flexibility requirements in the Electric Reliability Council of Texas.” *Energy*, 123, (2017), 637-654.

Denholm, P. and Hand, M. “Grid flexibility and storage required to achieve very high penetration of variable renewable electricity.” *Energy Policy*, 39, (2011), 1817-1830.

Fang, X., Sedzro, K., Hodge, B., Zhang, J., Li, B., and Cui, M. “Providing ramping service with wind to enhance power system operational flexibility.” Technical Report, NREL/TP-5D00-73643, National Renewable Energy Laboratory, Golden, CO.

Gagnon, P., Sánchez Pérez, P. A., Obika, K., Schwarz, M., Morris, J., Gu, J., and Eisenman, J. “Cambium 2023 scenario descriptions and documentation.” Technical Report, NREL/TP-6A40-88507, National Renewable Energy Laboratory, Golden, CO.

Joshi, M., Palchak, D., Rehman, S., Soonee, S. K., Saxena, S. C., and Narasimhan, S. R. “Ramping up the ramping capability.” Technical Report, National Renewable Energy Laboratory, Golden, CO.

Kawajiri, K., Kondo, Y., Aki, H., and Murata, A. “Simplified method to estimate grid flexibility: Application to Japanese electrical grids.” *Energy*, 167, (2019), 26-34.

Oh, H., Akar, S., Beckers, K., Bonnema, E., Vivas, C., and Salehi, S. “Techno-economic feasibility of geothermal energy production using inactive oil and gas wells for district heating and cooling systems in Tuttle, Oklahoma.” *Energy Conversion and Management*, 308, (2024), 118390.

Ricks, W., Norbeck, J., and Jenkins, J. “The value of in-reservoir energy storage for flexible dispatch of geothermal power.” *Applied Energy*, 313, (2022), 118807.

Ricks, W., Voller, K., Galban, G., Norbeck, J., and Jenkins, J. “The role of flexible geothermal power in decarbonized electricity systems.” *Nature Energy*, (2024).

Millstein, D., Dobson, P., and Jeong, S. “The potential to improve the value of U.S. geothermal electricity generation through flexible operations.” *Journal of Energy Resources Technology, 143*(1), (2021), 010905.

DeepStor - District Heating From High-Temperature Heat Storage In A Depleted Hydrocarbon Reservoir In The Upper Rhine Graben

Eva Schill[1,2], Florian Bauer[1], Yingqi Zhang[2], Jonny Rutqvist[2], Patrick Dobson[2], Trevor Atkinson[3], Wencheng Jin[3]

[1]Karlsruhe Institute of Technology, Karlsruhe, Germany

[2]Lawrence Berkeley National Laboratory, Berkeley, CA

[3]Idaho National Laboratory, Idaho Falls, ID

Keywords

District heating, heat storage, numerical modelling

ABSTRACT

DeepStor envisions the demonstration of a geologic thermal energy storage system with a return flow temperature of 110°C. The connected district heating network at the North Campus of the Karlsruhe Institute of Technology runs with a base load of 2.1 MWth and reaches up to 50 MWth at peak load.

The subsurface of the campus comprises a series of sandstone horizons with a thickness of a few meters between 800 and 1,300 m depth, which connect to the depleted oil reservoirs of the former Leopoldshafen field. These sandstone layers are embedded in the marly Niederrödern and Froidefontaine formations and have numerically proven contain most of the heat in the reservoir layers when operated as a aquifer thermal energy storage (Stricker et al., 2020). The reservoir temperatures are between 60 and 90°C. At an injection temperature of 140°C and production and injections rates of 2 L/s that were extrapolated from the former oil production, the necessary return temperature is reached after 6 years during the entire production period.

This study investigates what proportion of renewable geothermal heat can be achieved in the district heating network of this campus by adding stored heat from the respective sandstone layers during the six cold months (October to March). In the summer months, the storage system is fed by the excess heat from the deep and fractured reservoir, which is operated in continuous mode.

1. Introduction

Moderate climatic conditions often require the provision of considerable amounts of thermal energy for heating purposes in the winter months, which leads to a seasonal imbalance between heat supply and demand when supply is constant, as it is the case with base load-capable geothermal heat. This discrepancy requires thermal storage systems with a large capacity.

The Upper Rhine Graben exhibits elevated geothermal gradients, which can locally reach up to > 100°C km^{-1} and offer favorable geothermal conditions (e.g., Baillieux et al., 2013; Vidal and Genter, 2018). Currently, 16 geothermal wells are in operation for production and reinjection of thermal brine from Tertiary Formations (2 wells), Muschelkalk Formation (2 wells), Muschelkalk Formation to the Variscian basement rock (2 wells), Buntsandstein Formation to the Variscian basement rock (6 wells), and only Variscian basement rock (4 wells, Frey et al., 2022). The causal close connection between hydrocarbon and geothermal reservoirs is indicated by the spatial proximity of temperature anomalies below hydrocarbon reservoirs and the coexistence of geothermal fluids and hydrocarbons in fractured Mesozoic reservoirs (e.g., Böcker, 2017). The numerous depleted oil fields in the Upper Rhine Graben are proven reservoirs that are well characterized in terms of their depth, geometry and reservoir properties. Moreover, seismicity and environmental impacts have been minimal during hydrocarbon production and have been minimized during reservoir engineering and operation in the deep geothermal systems (e.g., Schill et al., 2017; Genter et al., 2012).

At present, there are numerous storage applications in near-surface underground systems, ranging from gravel pits to aquifer thermal energy storage (ATES). The state of the art is in borehole thermal energy storage, in which the heat pump cycle is reversed to store excess heat. Worldwide, > 2,800 ATES systems are in operation, mainly in the Netherlands, providing more than 2.5 TWh a^{-1} for heating and cooling purposes (Fleuchhaus et al., 2018). The operating temperatures of ATES are generally < 50 °C and cover low-temperature heat applications. There are only a few plants worldwide that operate at higher temperatures. Holstenkamp et al. (2017) describe the conditions and experiences of the two German plants in Berlin and Neubrandenburg. High-temperature heat storage for industrial applications or district heating supply, for which temperatures of up to >110 °C are required, have not yet been developed on a commercial scale.

Assuming a doublet system with seasonal injection and production cycles, a numerical potential study for the injection of 140 °C water into a typical 70°C reservoir shows an annual storage capacity of up to 12 GWh per well and significant recovery efficiencies increasing up to 82 % after ten years of operation (Stricker et al., 2020). Around 90 % of the reservoirs investigated in the Upper Rhine Graben can be converted into such high-temperature ATES (HT-ATES). In summary, this indicates a total storage capacity in depleted oil reservoirs of about 10 TWh a^{-1}, which represents a considerable part of the thermal energy demand in this area.

In the Very-High-Temperature Heat Aquifer Storage (VESTA) project, we numerically investigate the heat extraction from a deep fractured reservoir at the DeepStor site (www.geoenergiecampus.kit.edu) in combination with the seasonal storage of heat at the edge of the depleted Leopoldshafen oil field. One motivation for this study is our concept to mitigate the induced seismicity during operation of the deep fractured reservoir through stable and moderate flow rates (Schill et al., 2017; Genter 2012). To keep the flow rates in the deep fractured reservoir stable, although the heat demand in summer is significantly lower, we propose heat storage in a

porous reservoir with comparatively low potential for induced seismicity (Stricker et al., subm.). This concept has the positive side effect of automatically reducing the flow rates required to cover the heat demand in winter in the deep, fractured reservoir, which has a higher potential for induced seismicity. Compared to conversion into electrical energy, heat storage makes it possible to provide a higher proportion of carbon-neutral heat, which is a major challenge in Germany.

2. Geothermal Setting At The DeepStor Site

The DeepStor site is located in the central segment of the NNE trending, essentially non-volcanic Upper Rhine Graben, formed approximately 47 Ma between Germany, France and Switzerland (Figure 1). 3D seismic data from the northern part of the central Upper Rhine Graben segment show deep-rooted NNE-striking faults controlling early, syn-rift 1, extensional basin evolution from about 47 Ma to 27 Ma (Bauer et al., subm.). The change in stress field at about 27 Ma and subsequent reactivation of these deep-rooted faults resulted in a new set of shallow-rooted en-echelon faults. On a larger scale this change in stress field was accompanied by a shift of regional depocenters and the onset of regionally distributed, minor alkaline volcanic activity. The shallow-rooted en-echelon faults nucleated in 32-28 Ma old strata and are linked by conjugated relay ramps that control the development of latest Oligocene to early Miocene syn-rift 2 basins trending N-NNW.

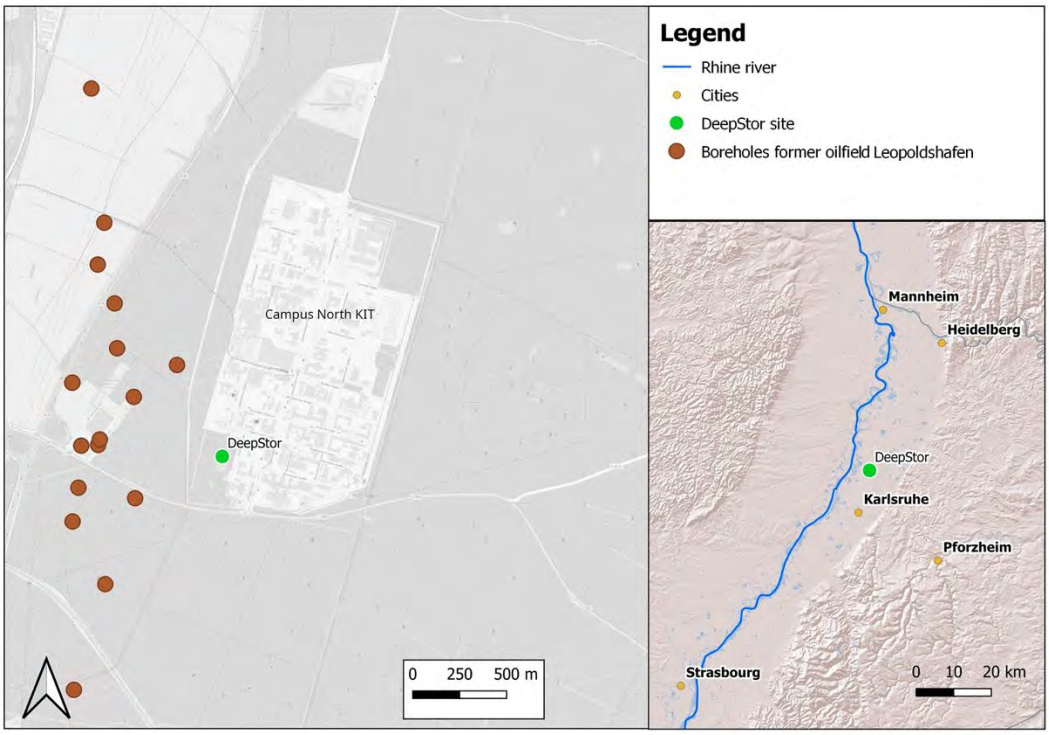

Figure 1: Location of the DeepStor site in the central segment of the NNE trending Upper Rhine Graben between Germany, France and Switzerland.

DeepStor is located in the hanging wall of the Main Eastern Boundary Fault. In the central graben, the Cenozoic sediments reach a thickness of up to 3,500 m (Geyer et al., 2011) and are subdivided into Pliocene to Holocene fluviatil siliciclastics that unconformably overlie late Eocene (Lutetian)

to early Miocene (Burdigalian) syn-rift sequences. These sequences were deposited in a generally low-energy environment under alternating marine, brackish, fluvial and lacustrine conditions and contain deposits of carbonates, sands, silts, clays, marls and locally intercalated evaporites.

The DeepStor site is adjacent to the eastern edge of the depleted Leopoldshafen oil field in the footwall of the Leopoldshafen fault. This NNE-striking normal fault (Wirth, 1962) is part of the Main Eastern Boundary Fault and exhibits a syndepositional normal faulting from the Oligocene to the early Miocene, with the synrift layers dipping shallowly to the NE (Schad, 1964). A total of around 188,000 tons of oil were extracted from several, a few meters thick, fine-grained, mica-rich calcareous sandstones, which are intercalated with hundreds of meters thick, mostly marly Meletta and Bunte Niederrödener layers (Wirth, 1962; Böcker, 2015). The Meletta layers are part of the Froidefontaine Formation and were deposited under marine conditions during a regressive phase. They show coarsening upward trends in the late Rupelian (ca. 29 Ma), followed by a transgressive phase in which the finer upward trends in the upper part of the Meletta strata merge into the marly, still marine to brackish Cyrena strata. These strata show a further phase of regression and further development into the fluvio-lacustrine Niederrödern Formation (Schad, 1962; 1964; Grimm et al., 2011; Pirkenseer et al., 2011; 2013).

The Leopoldshafen oil field was explored by around 20 boreholes to a depth of approximately 3,000 m. The corrected temperature data (Sauer et al., 1981), which yield about 100 °C at a depth of 2,000 m, include measurements in the Meletta and Bunte Niederrödern sandstone layers. Maximum temperatures of 170 °C at a depth of about 3,000 m are reported from the Leopoldshafen-20 borehole.

3. Numerical Modelling Of Heat Cycling

The numerical modeling of optimized heat cycling between the deep fractured reservoir and the porous reservoir at intermediate depth through the surface is based on two individual 3D geological models (Schill et al., 2024). For the two sub-models, the flow and heat transport were calculated for various management scenarios using COMSOL Multiphysics® Finite Element software, version 6.0. The two models are numerically connected via a single node that represents the heat exchanger and connects to the district heating (Zwickel et al., 2022).

For the heat transport model, a Dirichlet boundary condition with a constant mean annual surface temperature of 10 °C is applied at the surface. At the lower boundary of the models a Neumann boundary condition of constant heat flux of 60 mW m^{-2} are used. The flow model simulates hydrostatic conditions with Dirichlet boundary conditions at the base and the ground surface.

3.1. Heat Extraction from the Deep Fractured Reservoir

The drilling target of the deep fractured reservoir is the Mesozoic branch faults in the hanging wall of the main normal faults. They are rooted in the crystalline basement, reach the base of the Tertiary units and show displacements of up to 100 m. Permeabilities are assumed to be elevated in the hanging wall due to the presence of a damage zone of up to 200 m. Comparable to the Soultz-sous-Forêts EGS project (Kohl et al., 2000), a mean permeability of the damage zone was estimated to be $1 \cdot 10^{-13}$ m^2 based on the temperature distribution in the Leopoldshafen-20 well. The full set of parameters used in the modelling are provided in Tables 1 and 2.

The calibration of the model is based on bottom-hole temperature measurements. Temperature adjustment was achieved by varying thermal conductivities, heat production rates in the basement, and basal heat flux.

3.2. Heat Storage in Porous Reservoir at Intermediate Depth

Following Stricker et al. 2020, the heat storage reservoir of the Meletta layers is accessed by horizontal injection and production wells at a depth of around 1,300 meters. The faults crossing these Tertiary formations are assumed to be sealed and thus limit the lateral extent of the reservoir. The low permeability and thermal conductivity of the cap rock insulate the sandstone reservoir.

Given the significant influence of permeability on the effectiveness of the reservoir, one variant was calculated with a reservoir permeability of $2.5 \cdot 10^{-14}$ m^2 (mean permeability of a well close to the modelled production well), where 5 L/s were injected and produced. The second scenario includes a permeability of about $7 \cdot 10^{-14}$ m^2 (Stricker et al., 2020), allowing extraction/injection rates of 10 L/s. The production/injection rates are defined via a maximum drawdown of < 400 m. Injection and production modeling was performed over a period of 10 years heating up the underground storage system to a plateau of performance according to Stricker et al., 2020.

Table 1: Hydraulic parameters used for the thermo-hydraulic modelling of the individual units of the two models, the deep fractured reservoir, and the porous reservoir for heat storage.

Unit	Permeability (m^2)	Porosity (%)
Tertiary marls	$1 \cdot 10^{-18}$	15
Tertiary sandstones	$2.5 \cdot 10^{-14} – 6.6 \cdot 10^{-14}$	15
Jurassic/Keuper (claystones)	$1 \cdot 10^{-18}$	15
Muschelkalk (limestone)	$5.9 \cdot 10^{-15}$	2.7
Buntsandstein (sandstone)	$1 \cdot 10^{-15}$	3
Permian (conglomerates/sandstones)	$1 \cdot 10^{-16}$	5
Basement (granite/metamorphic units)	$5 \cdot 10^{-16}$	5
Damage zone of faults	$1 \cdot 10^{-13}$	15

Table 2: Thermal parameters used for the thermo-hydraulic modelling of the individual units of the two models, the deep fractured reservoir, and the porous reservoir for heat storage.

Unit	Heat conductivity ($W\ m^{-1}K^{-1}$)	Heat capacity ($MJ\ kg^{-1}K^{-1}$)	Heat production rate (μWm^{-3})
Tertiary marls	1.4	2.4	0.0
Tertiary sandstones	2.5	3.2	0.0
Jurassic/Keuper (claystones)	1.4	2.4	0.0
Muschelkalk (limestone)	3.2	2.2	0.0
Buntsandstein (sandstone)	3.3	2.2	0.3
Permian (conglomerates/sandstones)	3.3	2.2	0.9
Basement (granite/metamorphic units)	3.25	2.2	0.9-2.13
Damage zone of faults	3.25	2.2	0.9-2.13

4. Results

Figure 2 shows the undisturbed formation temperatures down to a depth of 8,000 m resulting from a temperature model that accounts for heat conduction, heat production and advection along the higher permeable fault zones.

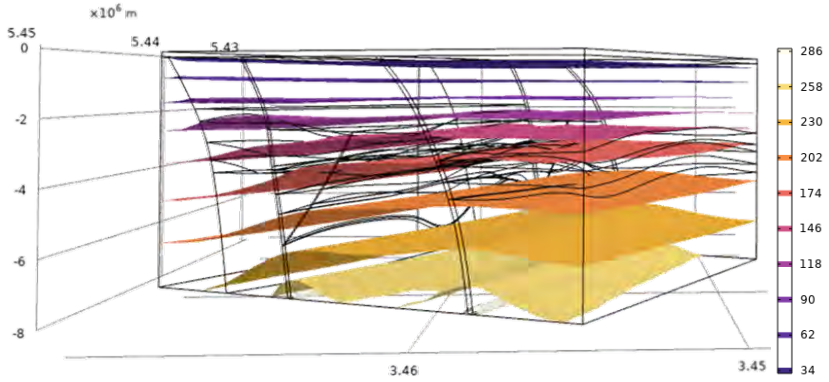

Figure 2: Isotherms in deep underground of the DeepStor site. Black lines outline the sedimentary layers and major faults.

The simulation of a geothermal doublet with a 1,000 m long open hole section in the Muschelkalk, Buntsandstein and Upper Permian Formations and a production rate of 25 L/s that the differential pressure on the main faults remains below 2 MPa. The production temperature at the well head is

approximately 180 °C. About 9 MW thermal output was calculated by the modeling including a buffer for uncertainties and heat losses. In the following section, we model how the expected excess heat can be stored at intermediate depth. Figure 3 shows the pressure and temperature development in the Meletta reservoir for flow rates of 10 L/s and a pressure limit of < 2 MPa at the major faults. After 4 years of operation the target recovery temperature of 110 °C is fully reached.

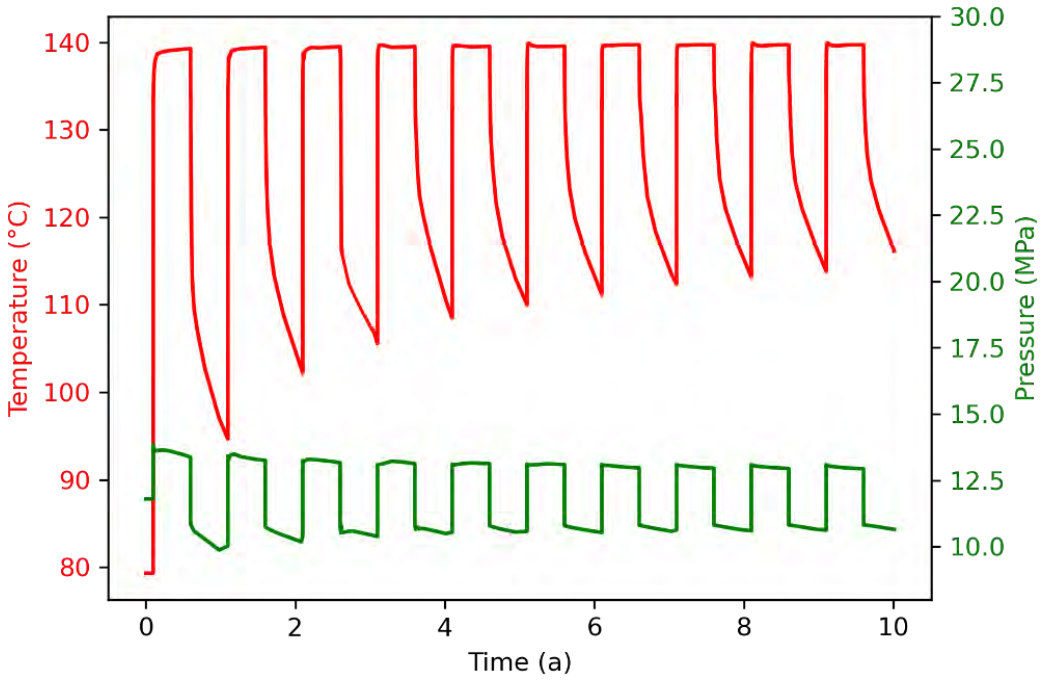

Figure 3: Temperature and pressure evolution during 10 years of operation of the DeepStor reservoir.

5. Conclusion

The storage scenarios are based on a continuous (8000 h) and low-risk (at 25 L/s) heat extraction from the deep fractured reservoir at a thermal load of 9 MW_{th}, which results in an available thermal energy of 72 GWh_{th}. Compared to the total demand of 80 GWh_{th}, which is mainly required during the heating period, this means an overproduction of 21 GWh_{th} during the summer period, which is to be stored in the porous reservoir at intermediate depth. At this point, it appears that approximately 65% of the heat demand can be covered by the deep fractured geothermal system.

With the aim of technically increasing the climate-neutral heat supply in the district heating network, two scenarios of high-temperature heat storage with different capacities are compared in Table 3. Scenarios 1 and 2 assume a low and high permeability of $2.5 \cdot 10^{-14}$ m^2 and $6.6 \cdot 10^{-14}$ m^2, respectively and work with flow rates of 5 and 10 L/s, respectively. When considering one storage doublet, the capacity of the storage system can reach approximately 4.5 GWht at a pumping rate

of 5 L/s and 9 GWht at 10 L/s. With two storage doublets, an 8-20 % of the heat demand can be added to the 65% expected from the deep fractured system.

These results show that the proportion of carbon-neutral geothermal energy at KIT Campus North can be increased from 25 % in a scenario that only takes base load heat into account to around 85 % by storing the excess heat. Assuming realistic costs for the realization of such a plant, (i.e., about $45 million USD or € for access to the deep fractured system and an additional $8 or $15 million USD for one or two doublets in the porous reservoir at medium depth and operating costs of $1 million USD per year), we have calculated heat costs of 3 cents per kWh, which is in the range of heat from natural gas today.

Table 3: Thermal parameters used for the thermo-hydraulic modelling of the individual units of the two models, the deep fractured reservoir and the porous reservoir for heat storage.

	Scenario LOW storage capacity (25 mD, 5 L/s)		Scenario HIGH storage capacity (70 mD, 10 L/s)	
	GWh per yr	% of the total heat demand	GWh per yr	% of the total heat demand
Heat demand at KIT-Campus North	80		80	
Available energy from the deep fractured system at 25 L/s	72		72	
Direct use	51	64	51	64
Storage doublet 1	4.5 (186 days)	5.6	9.1 (186 days)	11.3
Storage doublet 2	2.5 (186 days)	3.1	7.3 (130 days)	9

Acknowledgement

We like to thank the Department of Energy (DOE) of the United States and the German Federal Ministry of Education and Research (BMBF) for funding this study in the framework of the VESTA project. Funding was provided by the U.S. Department of Energy, Office of Energy Efficiency and Renewable Energy, Geothermal Technologies Office to Lawrence Berkeley National Laboratory under Award Number DE-AC02-05CH11231 and Idaho National Laboratory under Award Number DE-AC07-05ID14517.

REFERENCES

Baillieux, P., Schill, E., Edel, J.P., Mauri, G. "Localization of temperature anomalies in the Upper Rhine Graben: insights from geophysics and neotectonic activity." *International Geology Review*, 55, (2013), 1744-1762.

Bauer, F., Grimmer, J. C., Houpt, L., Hertweck, T., Schill, E. " Development of intra-rift basins during stress field change in the central Upper Rhine Graben (SW Germany).", *Basin Research*, (subm.).

Böcker, J., Littke, R., Forster, A. "An overview on source rocks and the petroleum system of the central Upper Rhine Graben." *International Journal of Earth Sciences*, 106, (2017), 707–742.

Choi, J. H., Edwards, P., Ko, K., Kim, Y. S. "Definition and classification of fault damage zones: A review and a new methodological approach." *Earth Science Reviews*, 152, (2016), 70-87.

Fleuchaus, P., Godschalk, B., Stober, I., Blum, P. "Worldwide application of aquifer thermal energy storage—A review." *Renewable and Sustainable Energy Reviews*, 94, (2018), 861–876.

Frey, M., Bär, K., Stober, I., Reinecker, J., van der Vaart, J., Sass, I. "Assessment of deep geothermal research and development in the Upper Rhine Graben." *Geothermal Energy*, 10, (2022), 18.

Genter, A., Cuenot, N., Goerke, X., Bernd, M., Sanjuan, B., Scheiber, J. "Status of the Soultz geothermal project during exploitation between 2010 and 2012." *Proceedings: 37th Workshop on Geothermal Reservoir Engineering*, Stanford University, Stanford, CA (2012).

Geyer, M.; Nitsch, E.; Simon, T. "Geologie von Baden-Württemberg." *5th Edition*, Stuttgart – Mainz, Schweizerbart, (2011).

Grimm, M. C., Wielandt-Schuster, U., Hottenrott, M., Grimm, K. I., Radtke, G., Berger, J.-P., Ellwanger, D., Harms, F.-J., Hoselmann, C., Picot, L., Weidenfeller, M. "Regionalgeologische Darstellungen, Oberrheingraben. *Deutsche Stratigraphische Kommission (ed)*, Stratigraphie von Deutschland IX. Tertiär, 1, (2011), 57-132.

Holstenkamp, L., Meisel, M., Neidig, P., Opel, O., Steffahn, J., Strodel, N., Lauer, J.J., Vogel, M., Degenhart, H., Michalzik, D., Schomerus, T., Schönebeck, J., Növig, T. "Interdisciplinary Review of Medium-deep Aquifer Thermal Energy Storage in North Germany." *Energy Procedia*, 135, (2017), 327–336.

Kohl, T., Bächler, D., Rybach, L. "Steps towards a comprehensive thermo-hydraulic analysis of the HDR test site Soultz-sous-Forets." *Proceedings: World Geothermal Congress*, Kyushu-Tohoku, Japan (2000).

Pirkenseer, C., Spezzaferri, S., Berger, J.-P. "Reworked microfossils as a paleogeographic tool." *Geology*, 39, (2011), 843–846.

Pirkenseer, C., Berger, J.-P., Reichenbacher, B. "The position of the Rupelian/Chattian boundary in the southern Upper Rhine Graben based on new records of microfossils." *Swiss Journal of Geosciences*, 106, (2013), 291–301.

Sauer, K., Nägele, R., Tietze, R. "Geothermische Synthese des Oberrheingrabens zwischen Karlsruhe und Mannheim (Anteil Baden-Württemberg). " *Geologisches Landesamt Baden-Württemberg*, Freiburg im Breisgau, (1981).

Schill, E., Genter, A., Kohl, T., Cuenot, N. "Enhancement of productivity in the Soultz EGS site by 20 hydraulic and chemical stimulation experiments and long-term circulation." *Geothermics*, 70, (2017), 110-124.

Schill, E., Knauthe, R., Garipi, X., Bauer, F. "DeepStor - Heat Cycling in the Deep and Medium-Deep Subsurface." *Proceedings: 49th Workshop on Geothermal Reservoir Engineering*, Stanford University, Stanford, CA (2024).

Stricker, K., Egert, R., Schill, E., Kohl, T. "Risk of surface movements and reservoir deformation for high-temperature aquifer thermal energy storage (HT-ATES)." *Geothermal Energy*, 12, (2020), 19.

Stricker, K., Fokker, P., van Wees, J.-D., Schill, E., Kohl, T. "Risk assessment of fault reactivation and induced seismicity for high-temperature heat storage (HT-ATES) at the DeepStor demonstrator in the Upper Rhine Graben." *Geothermics*, (subm.).

Vidal, J., and Genter, A. "Overview of naturally permeable fractured reservoirs in the central and southern Upper Rhine Graben: Insights from geothermal wells." *Geothermics*, 74, (2018), 57-73.

USGS "USGS EROS Archive - Digital Elevation - Global 30 Arc-Second Elevation (GTOPO30)." (2018).

Wirth, E. "Die Erdöllagerstätten Badens." *Geologische Abhandlung Landesamt Baden-Württemberg*, 4, (1962), 63-80.

Zwickel, P., Bauer, F., Schätzler, K., Steiner, U., Waczowicz, S., Hagenmeyer, V., Schill, E. "Integrated concept of local heat transition using geothermal heat production, aquifer storage and optimization of distribution network." *Proceedings: European Geothermal Congress*, Berlin, Germany (2022).

Tribal Communities

Indigenous Participation in Geothermal Projects: Learnings from Aotearoa New Zealand

A. Blair[1], M. Climo[1], A. Campbell[1], L. Lovell[2]

[1]Upflow Ltd, [2]Lovell & Associates

Keywords

indigenous, New Zealand, stakeholder engagement, business strategies, investment, geothermal

ABSTRACT

Māori, Aotearoa New Zealand's indigenous people, have a recognized and powerful constitutional role in New Zealand society, and a critical and increasing role in the national economy. Since the early 1900s, access to Māori owned land and the geothermal resource beneath, has been sought for power generation. Māori and their organizations have participated in a range of ways in such developments, from landlords to equity owners, providing substantial returns for Māori whanau (family groups) with commercial interests in these projects.

But Māori-owned businesses are not only motivated by financial outcomes; they are also driven by the tikanga (philosophies and principles) inherent in Māori belief systems. Financial goals must be balanced with social, environmental and cultural aspirations. Creating wealth is not seen as an end in itself. Māori are driven to invest in projects that provide intergenerational prosperity, and to care for the sustainability and health of the resources and environment they are responsible for. This core principle of 'kaitiakitanga' (guardianship) strongly aligns with geothermal reservoir management necessary for long-term (30+ years) sustainable commercial operation, the decarbonization of manufacturing, and catalyzing economic development and employment opportunities. The social benefits of these projects (including electricity security) then extend more broadly to the local communities and the region within which they reside.

This paper provides an actionable guide for indigenous groups on how to participate in geothermal projects, beginning with critical internal pre-work before engaging with developers. It is also for developers to grow their knowledge and capacity to effectively and appropriately engage with indigenous groups.

1. Tīmatanga kōrero | Introduction

E tū ki te kei o te waka, kia pakia koe e ngā ngaru o te wā

Stand at the stern of the canoe and feel the spray of the future biting at your face

Māori have a domestic resident population of 978,246 ca. 19.6% of the general population (Statistics NZ, 2024). Demographically, the Māori population is relatively young, with 70% aged less than 40 years compared to 50% for non-Māori. Importantly, the Māori population is growing at approximately more than triple the rate of non-Māori (Statistics NZ, 2024).

The Treaty of Waitangi is New Zealand's founding document. Signed on the 6th February 1840, the Treaty is an agreement made between the British Crown[1] and Māori rangatira (chiefs) to found a nation state and build a government in New Zealand.

Referenced in Acts of Parliament, and acknowledged as a part of New Zealand's common law, the Treaty reflects the partnership contemplated between Māori and Crown. Set up by the Treaty of Waitangi Act 1975, the Waitangi Tribunal is a permanent commission of enquiry that makes recommendations on claims brought by Māori relating to Crown actions that breach the promises made in the Treaty of Waitangi.

Traditional Māori social structures consist of Iwi (tribes), Hapū (sub-tribes) and whānau (extended families). They are held together by kinship with each other and a shared common ancestor.

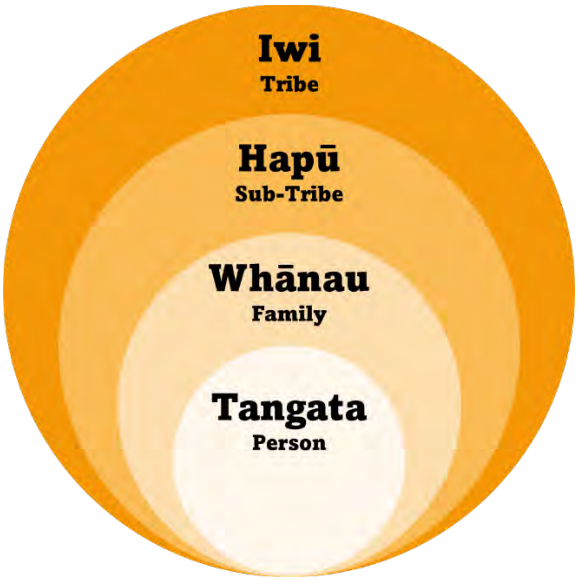

Figure 1. Māori social structures.

Māori-owned businesses are not only motivated by financial outcomes, they are also driven by philosophies and principles inherent in Māori belief systems i.e. they need to balance financial goals with social and cultural aspirations. Creating wealth is not seen as an end in itself (Blair *et al.*, 2018).

A core tikanga is the principle of 'kaitiakitanga'; the exercise of guardianship, of natural resources such as the land, sea and waterways, as well as flora and fauna and of people. Kaitiakitanga requires that sustainability and environmental protection is valued and prioritized. As kaitiaki (guardians of natural resources), those in leadership roles are responsible for protecting (and/or growing) resources for future generations. Kaitiakitanga reinforces why Māori are less likely to sell land, especially where they are mana whenua, that is, where they have customary authority.

[1] The meaning of "the Crown" varies according to the context in which it is used. The premise is that it was the Crown, through Queen Victoria, that signed the Treaty of Waitangi with Iwi Māori. This notion of an ongoing pact derived from that partnership of Māori and Crown has remained with the reference "Crown" transferred to subsequent New Zealand Governments as executive and their administrative arms (e.g. public Service Agencies and Departments).

'*Māori land is not simply a commodity*' (Savage, 2013). Shares in Māori freehold land are rarely transferred, they are usually succeeded to through inheritance.

Reflecting their tikanga, Māori invest in projects that promise intergenerational prosperity, prioritizing sustainability and the well-being of their resources and environment. This perspective and philosophy aligns with geothermal resource development. Their investment strategies focus on long-term returns rather than short-term cash flow, which complements the extended operational lifespan of geothermal power plants (>30 years) and geothermal reservoirs (>100 years).

For international readers, Section 2 below provides a brief overview of how geothermal resources are managed in New Zealand, the constitutional rights of Māori, and how Māori land and assets are managed. For a more detailed review on these topics, readers are directed to Eru and Lovell, 2020.

Section 3 outlines pathways that Māori have taken to be partners in geothermal projects and operations in Aotearoa New Zealand.

Sections 4 and 5 provide advice for other indigenous groups and share lessons and learnings arising from Māori participation in geothermal projects and operations, beginning with critical internal pre-work before doing due diligence on the geothermal landscape and its players.

2. New Zealand Context

2.1 A brief summary of rights to geothermal resources in Aotearoa

No-one can 'own' geothermal resources, but the government can manage them

'Ownership' of natural resources is a highly contentious area, and legal frameworks are ever in flux. The concept of geothermal resources being a sub-surface energy resource arose mid-twentieth century due to the development of engineering technology becoming available to access and harness the energy. Prior to this, any legal regimes in New Zealand were related to the geothermal surface features and tourism; the Thermal Springs District Act 1881 and Scenery Preservation Act 1903 effectively ensured that the Crown (i.e. NZ Government) controlled geothermal areas. The Geothermal Energy Act 1953 created the resource 'ownership' approach still in use today.

Within New Zealand it is generally accepted that water (including geothermal water) is not "owned". The Crown however sets the method and manner by which geothermal resources are *managed,* effectively bypassing the question of who owns the resource. Currently, therefore, geothermal resource use is managed at a regional government level through the Resource Management Act (RMA, 1991) (Kissick, *et al.*, 2021).

Geothermal projects are 'water take' not 'mining'

While geothermal resources are not owned per se, the discharged fluid can be (by the consent holder; Barton, 2015). Likewise, built plant and the underground and surface infrastructure (e.g. wells, piping, other examples, etc.) are owned. Geothermal resources are treated similarly to natural water (rather than petroleum and minerals which are owned by the Crown) whereby volume

takes (t/day) are consented, and thus, there is no present royalty payment charge to the government for the extracted geothermal energy.

Landowners determine access to geothermal resources

While landowners do not own geothermal resources, permission from the landowner is required to access geothermal resources beneath their land. The landowner can defend their rights against an unauthorized intrusion (i.e. trespass). There is no depth at which an intrusion ceases to be trespass, including through the use of directional drilling. There is no rule that restricts the depth to which the owner of land can assert his or her rights to the land (Barton, 2015; Kissick *et al.*, 2021).

Kaitiakitanga is acknowledged in the regulation of geothermal utilization

Successive pieces of New Zealand legislation and governments have attempted to extinguish Māori customary title to geothermal resources. This has been argued in the Waitangi Tribunal and remains a matter of contention between Iwi / Hapū and the Crown.

Under the Resource Management Act, consent holders must have regard to the relationship between Māori, as kaitiaki, and the land. Statutory Acknowledgements (Kissick, *et al*., 2021) are the instrument within Treaty Settlements[2] used to acknowledge particular cultural, spiritual, and traditional associations of Iwi / Hapū with a site of significance, including geothermal fields, or resources identified as a statutory area. In practice, Iwi / Hapū whose traditional lands are located above geothermal reservoirs, and irrespective of whether or not they are the current owners of that land, may be included in resource consent (permit) consultation and decisions regarding utilization of geothermal resources.

2.2 A brief summary of Māori land in Aotearoa

Distinct from land owned by Iwi or Hapū through Treaty Settlements or other means, the land subject to Māori Land Court oversight and held under individual Māori ownership still constitutes a very small proportion of New Zealand's total land area. However, in the central North Island and at Ngawha in Northland, approximately 17 high temperature geothermal systems reside under Māori land and therefore the collective ownership of Māori landowners.

New Zealand's history of colonization resulted in a systematic process of sale, confiscation and fragmentation of Māori land. In pre-European times, Māori land was communally owned, based on traditional Māori custom. In this shared ownership model, there were no specific, identifiable share parcels or interests. After the signing of the Treaty of Waitangi in 1840 the Crown quickly obtained Māori land through acquisition or confiscation, utilizing a purpose-built Native Land Court, which subsequently became the current Māori Land Court. Eventually there was little land remaining in Māori ownership. From the 1950's various reforms attempted to improve the situation by giving the Māori Land Court a stronger focus on protecting Māori land, but this was

[2] Treaty Settlements settle Iwi (tribal) and Hapū (sub tribal) claims of breach by the Crown of the Treaty of Waitangi, which have been considered and accepted by the Waitangi Tribunal.

not without issues; legislation intended to protect remaining lands also created barriers to development.

Te Ture Whenua Māori Act 1993 (TTWMA) remains the Māori Land Court's guiding legislation. It seeks to balance competing objectives of retaining Māori land in Māori ownership with land development. However, Māori land generally has multiple owners and over time as owners decease, their descendants succeed to their interests. Thus, the number of owners of a single piece of Māori land increases significantly and fragmentation of Māori land ownership remains an issue. With this in mind, over time the emphasis of both the Māori Land Court and landowners has been to identify and use appropriate entities to enable collective management of and decision making over Māori land.

Under TTWMA, there are a range of models for individual landowners to hold their interests collectively (e.g. Table 2). For example, utilizing the trust model, trustees are the legal owners of the trust property, which they hold on behalf of the Māori beneficial owners. Where Māori landowners have sought a more commercial model, the TTWMA has provided for a Māori Incorporation structure, with a Committee of Management acting as governors on behalf of its Māori shareholders. See Section 2.3 for further discussion of structures.

Notwithstanding the structures however, there have been barriers to development of Māori land. Common problems encountered by Māori wishing to develop or use their land is described in Table 1.

Table 1. Six barriers to the development of Māori land (MLC, 2024)

BARRIER	SPECIFIC PROBLEM
Multiple ownership	This can lead to problems with obtaining agreement about land use and development, and also reduces the economic return to individual owners.
Governance and management issues	While appropriate management structures for the administration of Māori land may exist, there is a lack of expertise to plan and make decisions about administration.
Access to information	Data on the current use of Māori land is not comprehensive, and it is costly to obtain information on potential use of Māori land.
Access to finance	Multiple ownership of land makes it difficult to use land as security when seeking finance for land development.
Access to land	A large proportion of Māori land is landlocked, reducing the options available for its use and/or reducing the options to lease the land.
Rating of Māori land	Some local authorities are more determined than others to collect rates on Māori land. In cases of arrears, some local authorities have tried to sell the land or place charging orders on the land to recover outstanding rates.

2.3 Māori Organizations

As discussed above, there are governance options available to administer Māori land (Lovett & Eru, 2020). The most commonly used in geothermal developments are Māori Incorporations and

Ahu Whenua Trusts (or 'Māori Trusts' as they are often called). Some different examples of Māori organizations used in geothermal operations are noted in Table 2.

Table 2. Types of legal business entities with investment, shareholding or ownership in industrial scale geothermal development (Source: Climo *et al.*, 2022).

Type	Descriptor	Example
Ahu whenua trust	A common land trust, established under the Te Ture Whenua Māori Act 1993, designed to promote the use and administration of one or more Māori land blocks or general land owned by Māori on behalf of its owners.	Tauhara North No.2 Trust
Community Trust	A community trust, as outlined in their trust deed, with the trust able to hold shares in a Company on behalf of the Consumers and distribute to the Consumers in their capacity as owners, the benefits of ownership of the shares in the Company.	Top Energy Consumer Trust
Joint Venture (JV)	An alliance between two or more parties working to accomplish a specific task or project. Each partner retains their independence while contributing towards mutually shared goals. An incorporated joint venture is a limited liability company. Being a separate entity, the incorporated JV company owns the assets of the venture, enters into contracts, incurs obligations and liabilities, and makes profits or losses.	Unincorporated: Nga Awa Purua Joint Venture (Tauhara North No. 2 Trust & Mercury NZ Ltd) Incorporated: Rotokawa Joint Venture Ltd (Tauhara North No. 2 Trust & Mercury NZ Ltd)
Māori Incorporation	Māori incorporations are constituted by the Māori Land Court over one or more blocks of Māori freehold land provided that at least one of the blocks has more than two owners. They have the powers of a limited liability company and become the legal owner of any lands or assets vested in it.	Taheke 8C Inc.
Mixed Ownership Model Company	A company where the Crown owns at least 51% of the shares and no one other person owns more than 10% of the shares. These partly state owned are monitored by Treasury but are not state enterprises.	Mercury NZ Ltd
NZ Limited (Liability) Company	A separate legal entity liable for all legal and financial obligations. The liability of shareholders is limited.	Ngāwha Generation Ltd
Partnership	A partnership is when two or more people or organisations form a business. Partners set out in a partnership agreement how they share profits, debts and work. Partners are personally liable for all business losses.	Te Ahi O Maui Ltd Partnership (Eastland Group Ltd & Kawerau A8D Ahu Whenua Trust)
Private Company	A firm held under private ownership. Private companies may issue stock and have shareholders, but their shares do not trade on public exchanges, and they have no obligation to release a financial report every financial year.	Tuaropaki Power Company Ltd
Publicly Listed Company	Shares can be bought and sold, and the Company is required by law to annually publish a financial statement.	Contact Energy Ltd

3. Pathways to Participation

Meaningful active participation is a true partnership, which is mutually beneficial. It's not just about being informed or consulted. As described in Figure 2, social license and project acceptance increases when the community is playing a real role in the project.

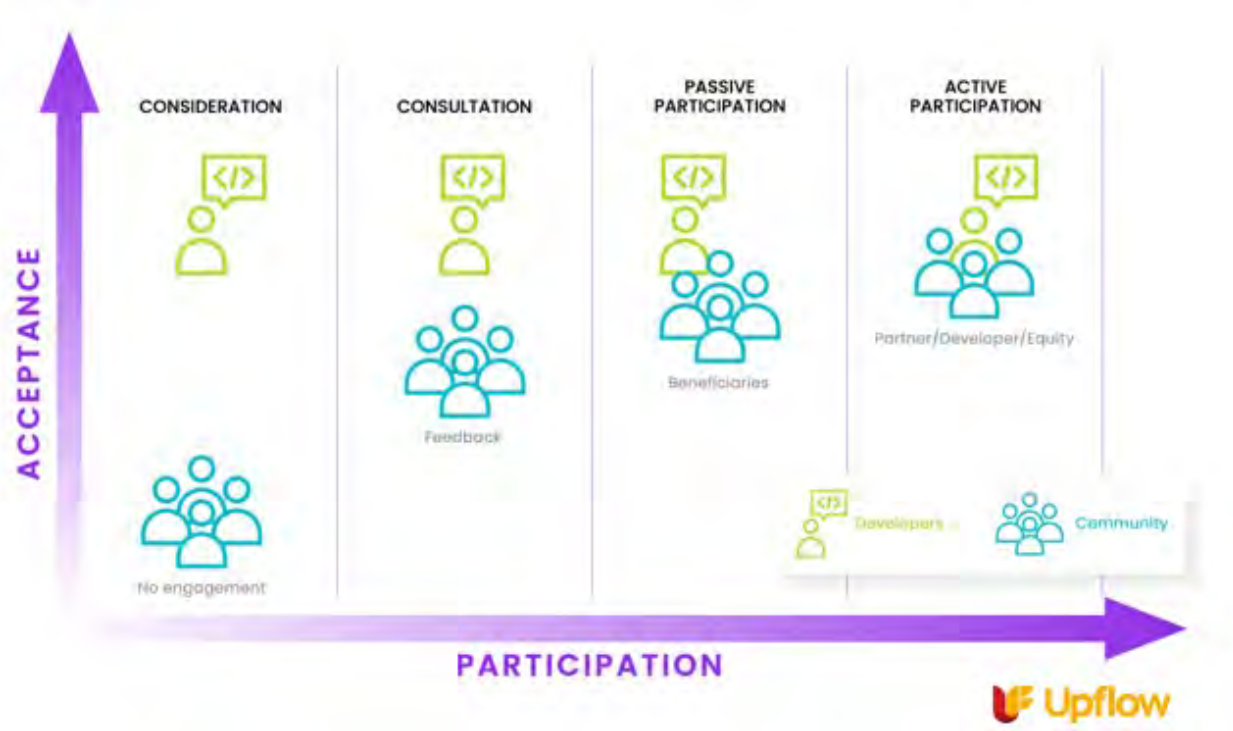

Figure 2. Relationship between participation and acceptance.

There are a variety of bespoke arrangements between private companies, public companies, community trusts and Māori organizations that own and operate large geothermal power stations and industrial scale direct use facilities in Aotearoa New Zealand (Climo *et al.*, 2022). Examples of ways in which Māori have been able to participate in geothermal developments, which varies by project, are outlined below.

3.1 Transfer of government geothermal assets to corporate entities

Geothermal assets (e.g. wells and infrastructure) developed by the Crown on Māori land through to the late 1980's were subsequently transferred out of Government ownership and into Māori ownership via a process of corporatization and deregulation of the New Zealand electricity sector in the 1990's.

Example: Kawerau & Ngāti Tuwharetoa Geothermal Assets

> The Kawerau Crown-owned steam-field assets were transferred to Mighty River Power through an agreement with the Crown in 2005 (Beehive, 2005) with the assets immediately on-sold as part of a commercial acquisition to Ngāti Tūwharetoa Geothermal Assets Ltd (NTGA). This was a commercial arrangement and not as redress under a settlement with the Crown (McClintock *et al.*, 2021).

NTGA supply steam and water to the TOPP power plant and supplementary steam to the Mercury KGL power plant, as well as supplying geothermal energy for processes including wood products processing, timber drying (Sequal Lumber, Carter Holt Harvey), fibre production (Oji), tissue paper manufacture (Essity) and dairy processing (Waiū) (McClintock *et al.*, 2020).

Figure 3. Kawerau Industrial Complex and businesses utilizing geothermal energy (McClintock *et al.*, 2021).

3.2 Equity for landowners

Some geothermal operations have brought together landowners with access to geothermal resources and experienced geothermal operators as development partners for electricity generation.

Example: Rotokawa & Tauhara North No2 Trust

Tauhara North No.2 Trust (TN2T) are an Ahu Whenua Trust within the rohe (region) of Ngāti Tahu – Ngāti Whaoa. They have 11,000 owners and beneficiaries and own 326 hectares of land in Rotokawa, Taupō. The Trust and people are kaitiaki of the whenua, Rotokawa geothermal reservoir, and the surrounding natural resources. At Rotokawa, the Trust landowners retain ownership of the land on which the two power stations were built (McLoughlin *et al.*, 2010).

In seeking to secure a long-term revenue stream for the benefit of their people, TN2T established a joint venture arrangement with generation company Mighty River Power (now Mercury). This structure has provided the Trust with the opportunity, from a low capital base, to raise their own finance for buying into the project to agreed levels. It also provided Mighty River Power with the ability to develop and operate the project in partnership with the Trust as resource owner who, through joint ownership, has closely aligned commercial objectives from the power project (McLoughlin *et al.*, 2010).

Separate agreements relate to the fluid supply and generation units (power stations):

- Fluid Supply: TN2T is an equal joint venture partner (50:50) with Mercury in the Rotokawa Joint Venture (JV). This JV owns the steam-field assets that supply geothermal fluid on agreed rate to three geothermal power stations: Rotokawa Power Station, Ngatamariki Power Station, and Nga Awa Purua Power Station.
- Power Generation: The Nga Awa Purua Power Station is owned by Mercury (65%), and TN2T (35%). The Rotokawa and Ngatamariki power stations are owned by Mercury.

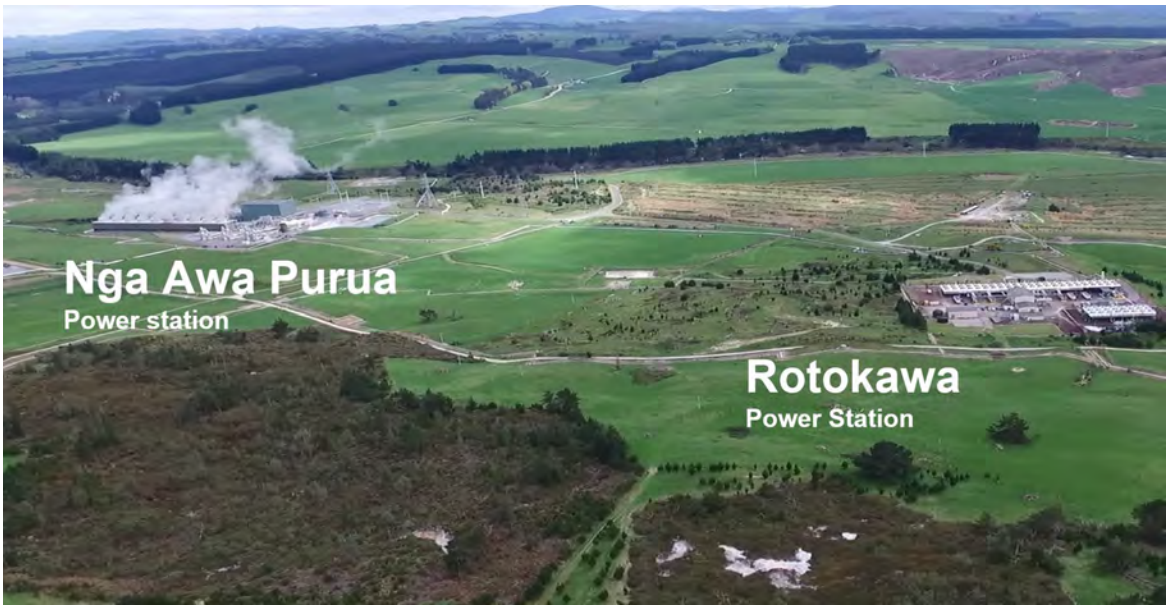

Figure 4. Nga Awa Purua and Rotokawa power stations at the Rotokawa Geothermal Field. Photo credit: Tauhara North No.2 Trust.

3.3 Partnering for direct use

Partnerships also occur with Māori landowners in the direct use of geothermal heat.

Example: Mokai and Tuaropaki Power Company

Since acquiring the Mokai geothermal investigation wells from the Government in 1996 (Menzies *et al*., 2001), Tuaropaki Power Company (Tuaropaki) has been an equity partner with Mercury in the Mokai Power Station (75:25).

Additionally, Tuaropaki are partners in, and supply heat to, a milk processing plant (Miraka), geothermally heated glasshouses (Mokai Gourmet), and the world's first green hydrogen plant (Halcyon Power, 1.25 MW). There are mutually beneficial relationships between the individual operations, for example:

1. The geothermal operation provides heat to the Miraka milk drying facility.
2. The biological residues from the milk drying process are sent to a worm farm, transforming this sludge into a highly valued fertilizer and soil conditioner known as vermicast, for use in agriculture, horticulture, nurseries, and recreation areas.

3. The vermicast is used in a native plant nursery, where plants are grown for riparian planting in the neighboring dairy farm operation for improved environmental performance.

Figure 5. Related operations at the Mokai Geothermal Field. (Photo Credit: MBC, 2024)

4. Internal Pre-work: Get your own house in order first

The first step towards participation in geothermal projects is not to engage with developers. There is a lot of internal pre-work that needs to be done before an indigenous group can have a meaningful conversation with a developer about participation in a geothermal project. Establishing leadership, decision-making processes, authority, legal structures and mandate to make decisions on behalf of the group needs to occur prior to any 'deal' or negotiation being discussed. It is critical to do this early and deeply to establish the 'right' foundation to provide a pathway forward – it is possible to change things later, but it's a lot harder to 'fix' something than to spend time early in the process to build a strong foundation for success.

4.1 Strategy

What is your group's vision and strategic plan for the future?

There must be a mandate from beneficiaries/owners to participate in geothermal development, and that mandate has to be sustained long term (as these projects can take decades to eventuate). This requires an indigenous group to know what they want and how they intend to operate. Identify up front what the priorities are and have a strong sense of who you are. This includes tikanga (protocols), but also the appetite for risk, priorities for investment, expectations about returns, when they might come and how they will be dispensed and managed.

Do we know what is important to us? What are our non-negotiables, for example the non-securitization of the land? What are we prepared to give up? Do our values align with geothermal projects? Is this really helping the future generations and succession planning?

Who do we want to work with and why? And, just as importantly, who do we not want to work with? This refers not just to developers, but also technical, financial, legal and governance expertise and advisers.

4.2 Leadership

Who are the champions? What kind of leader do you need?

The direction of ambitious future projects will differ depending on who is in charge, if they hold the vision and whether or not they are prepared to make, at times, decisions that will be challenged. These leaders may respond to a calling, or be volunteered, but it is critical that their personal vision and values align with the goals of the entity (e.g. trust, business) first and with the implementation of the project. Implementation must be in accord with the entity's, and its leaders', expectations because leadership is a long-term commitment and requires bravery.

In Māori culture, woman are often the leaders who bring people with them. This is why we see many women in critical enabling and influential roles in Te Ao Māori. Whilst they may not always have official titles, they certainly have strong influence upon outcomes.

Collective asset ownership will never reach a consensus so strong leadership is essential. Visionary leaders are required to manage the complexity of negotiating with family – because the people involved are tied to the same place and each other for the long-term. Conflict must be managed – it can't be avoided. This requires time and ongoing honest conversations where the participants keep pushing (peel the layers back) to get to the core issues.

Good leaders will see the multiple views and drivers of others, understand their positives and negatives, and put a plan in place to ensure (notwithstanding differing perspectives) that everyone can choose to join the journey. Leadership will often come with adversity, dealing with different perspectives on strategic direction, backlash on decisions, and critique on, for example, where/when to spend money now versus saving funds for future generations. Geothermal projects require significant investment in capital costs and expertise, but this is necessary for successful outcomes. Whilst the need for financial rigor is paramount, so too is the confidence needed to spend these large sums of money for the future good.

Everyone knows the disruptors within their own organizations. To avoid hostile takeovers, do your homework and hold yourself and these individuals to account. Understand the legal frameworks you and your Māori entity operate within and the limits – get good advisors and advice.

Some projects may require the same leadership to stay in place for longer than usual rotations to maintain continuity and achieve the early development goals. For example, TN2T had the same leadership (i.e. no elections) between 1994-2008 while the geothermal developments occurred at Rotokawa. Then, once the power station was operational, elections resumed. This was achieved by changing the trust order (deed) on two occasions (Note: this is not always legally possible).

During the different stages of geothermal projects, different thinking may be required i.e. in the early exploration phase, leaders need to be comfortable with managing significant risk and the unknown, whereas during power production and (the more predictable) operational phases, a different leader may be more appropriate. Understanding the leadership potential within beneficiaries/shareholders and building capacity and succession are also essential components of leadership within Māori, always thinking to what will be needed in the future.

4.3 Internal Legacy Issues

Does your organization have the legal power to engage in a development?

Indigenous land ownership, as noted in the sections above, differs from private ownership. Typically, mainstream lawyers and financial institutions don't understand indigenous systems and are risk adverse to what is seen as unusual, so you have to know your legal position well from the start and be able to confidently discuss and explain it to others.

Understand your legal rights, laws and legislation. Understand how this works in the regulatory space. Also, if you know how you want to participate in a geothermal development (e.g. equity, lease, royalties), are you legally/structurally ready for each of those approaches? Is your ship in order? Are your land titles appropriately in place? Is your shareholding or beneficiary register up to date? Do you have your systems in place for communicating with your whānau?

Sort out structural legal legacy issues. Where are the gaps? Can the organization actually do what it wants to structurally and legally within existing trust/entity powers and constitution/deeds etc? Internal legacy issues can hold up the future, because everyone is so busy looking at development they forget to resolve internal issues. This is very common and could delay projects for years.

Example

> A Māori organization interested in a geothermal project had a constitution that did not include the powers to establish geothermal activities on its land. Powers were limited to traditional agricultural activities, such as forestry and farming. This meant the Committee of Management did not have a mandate for geothermal development. In the absence of that power, the Committee could not enter into commercial geothermal arrangements and risked Māori Land Court review if shareholders sought a decision for deviation from the Incorporation's constitution. The Constitution was, therefore, subsequently amended. However, this took 12 months and caused delays to development aspirations.

Māori Trusts (more so than Māori Incorporations which are more commercially focused) are broadly risk adverse – they are holding assets for future generations to benefit from. In recent times, these trusts have been more likely to seek to separate risk to their assets by setting up subsidiary investment companies or entering limited partnership arrangements with developers. This however raises a number of questions such as: how do you ensure the appropriate people are appointed to those companies? How does the Trust ensure that the relationship between company or general partner (developer) and Trust (asset owner) is maintained, that delegations are clear, and reporting and oversight is robust?

Review the internal health of the organization to make sure that internal systems support the vision and can't be 'misused' to stall or disrupt advancement. Do you understand your own internal systems policies and culture? How can you use them? How could they be used against you?

Many Māori trusts and incorporations in New Zealand's Bay of Plenty also have had a legacy of external accounting firms holding custodial governance roles or positions of influence whereby they made the decisions and the Māori governors were treated as figureheads. Colonial / patriarchal structures such as these are being slowly dismantled so that Māori entities can manage their own assets. However, there must be a high level of commercial competency at the decision-making

table. If the required skills are not present amongst existing board/trustees, regardless if they are indigenous or not, well-governed organizations will need to bring in external and independent board members and technical advisors where required. The key is to balance self-determination with reliance on external expertise – you need both to be successful.

4.4 He Tangata (people)

The advantage of being connected to the whenua (land) is that, unlike corporate organizations, Māori will always retain their inherent connection to their traditional lands (whether they are legal owners of that land or not). This means institutional knowledge and capabilities can be maintained, succession appropriately planned, and longer-term outcomes are acceptable (i.e. significant benefits from projects may be realized long past the lifetime of those that negotiated agreements). And this outcome may be regarded as success – a strength that indigenous intergenerational philosophies can bring to a negotiating table for long-term projects.

Who are your people? What is your plan for engaging your people, especially the next generation, in the development activities?

The skills required will change during course of the project, and the organization will have to adapt and evolve. This provides long term employment and personal / professional development opportunities to grow capability.

Māori women are good at identifying future leaders and succession. Elders will often tell the younger generation what skills are going to be needed in the future (e.g. legal, technical, resource management) and encourage them to pursue these areas.

4.5 Know the resource

What do you know about your geothermal resource?

Find out everything you can about your geothermal system. What are your traditional stories and long held beliefs relating to the geothermal resource? Look in public repositories for data and publications. Ask and understand. Build and maintain your own information repository – don't rely on others to hold your knowledge.

4.6 Know your neighbors

Can you work with your neighbors?

Geothermal operators look for access to reservoir (depending on the consenting framework), but the boundaries of sub-surface geothermal reservoirs don't match the fence/trust boundaries on the surface. This means that partnering with your neighbors is a likely prospect in order to have a strong landowner voice when negotiating with developers and operators.

It is really difficult to determine a split for benefit sharing when the exact split of the geothermal resource is unknown. The benefit sharing does not have to be equal, but no-one should get something for nothing. Fringe/minority elements shouldn't have unrealistic power/expectations. Those with the most to put in have the most to lose. You should coordinate with your neighbors and organize a structure in which to operate prior to any engagement with a developer.

Be aware of the impact developers can have and what they have done in the past. They can sour relations between neighbors (perhaps by only engaging with one landowner to the exclusion of others) or may even avoid prospects where the landowner relations are too fraught (because they haven't sorted it out between themselves).

5. External Pre-work: Engage with developers

Once you've done all the activities in the Section 4, you are ready to do the pre-work to engage with developers.

5.1 Trusted Advisors

Who do you trust? What skills or insights are missing from the leadership table?

Good advisors are critical. It's important to identify current and future gaps in knowledge, context, insights and capability. It's not only essential to find people and organizations that can supply this expertise, but also to have aligned ethics and values so you can build strong trusting relationships that can withstand being tested over time.

Geothermal utilization is deeply complex and ongoing management of successful operations requires the ability to make decisions in uncertainty. Unlike predictable factory environments, geothermal subsurface and surface operations require constant and agile decision-making frameworks to optimize outputs. Reservoir, steam-field and power production assets and operational decisions constantly interfere with the performance of each other – to manage these projects requires highly trained specialist teams. Therefore, Māori groups must have access to technical insights to provide context for decision making. This may be achieved by internal hiring, contracting external consultants/advisors, or through an independent board role. Either way, all trustees/governors should increase their geothermal literacy prior to and during geothermal developments.

5.2 Due Diligence: Geothermal Operator/Partner

Understanding the organization(s) you plan to engage with is a first step to understanding their purposes, powers and capacity to work with you. Are they willing to learn what's important to you? Who are the people that are leading the organization?

Study their track record. Do they have history you should know about? Do they have a good record in their dealings with other indigenous or community groups? Talk to those who have partnered with them. Some developers/operators can have both good and bad track record. This is subjective – it must align with your values. Have they changed recently? What is their future commitment?

Some geothermal resources have changed hands, and operators often change names and legal structures. Look into these changes and understand the 'real' story. Past behavior may leave both positive and negative impressions. Is this history remembered? Trace back the full history of organizational behavior to ensure you are comfortable with partnering.

There are many examples of 'land banking' whereby organizations secure land and rights to geothermal resources and then do not develop them. This can be for a variety of reasons and sometimes over long periods of time. Having a good agreement (see Section 5.4) that stipulates

investment requirements and timeframes for when activity must occur is important to avoid these situations.

Characteristics of a good geothermal development partner include:

- **True partnership** – respect means treating the indigenous group as a serious commercial entity, important to the success of the project.
- **Understands indigenous frameworks** – good partners don't expect you to teach them about Māori concepts. They recognize that values and barriers are not the same.
- **Respect the taonga (treasure)** - tikanga and the geothermal reservoir is the key concern for Māori groups. This is the resource they have to care for as kaitiaki – the power station on the surface will come and go but the resource will remain (if well managed).[3]
- **Meaningful participation is recognized** through a variety of equity and benefit options in agreements. Land and resource access are acknowledged as having real and tangible value. Provide opportunities for the indigenous group to participate in the project at a level that they want. Options are the rights to increase equity (%) position to a max level at certain times over the power plants life, based on fair market value, with rules around timing and excising.
- **Sustainability is core practice** – evidence of well managed resources for sustainability, good environmental track record, good internal policies and procedures and culture. Any agreement must talk to the health of the reservoir at the end of a power station project.
- **Staff are well regarded**, and they have worked for the company over a long period of time. The geothermal industry is a small industry, and individuals are well known.
- **High transparency** – the developer is open with challenges, issues and opportunities, shares information, and provides greater insight when asked.
- **Good communicators** are developers who have regular engagement with the indigenous group. This can be informal or formal channels, including structured regular meetings, informal chats, briefings on key upcoming investment decisions, etc.

Most importantly, indigenous groups don't want to spend the next 30 years convincing a geothermal development partner of their value. If the developer can demonstrate behaviors and real-life examples of the above thinking and actions, and put pen to paper on this basis, you may actually end up with an arrangement that meets both indigenous values and respects the structures you need for long term partnership.

[3] Examples of splitting access and utilization of the resource via separate fluid supply agreements and power station ownership has in some instances ensured that the Māori landowners interest in the reservoir are maintained. See the TN2T example in Section 3.2. Equally, other Māori entities have sought other arrangements to ensure their taonga is protected.

5.3 Funding Structures & Systems

Systems can be used to accelerate or stop development, to provide protection or to undermine authority of Māori landowners. We see this in the use of the RMA, the Māori Land Court, as well as through relationship structures.

Understand what legal structures are possible. Because of the high costs of development for a power station, parties focus heavily on the negotiation of building and operating power stations. This includes funders, i.e. banks, investors etc. However, the geothermal reservoir will last longer than the surface assets. Explore the structures that best suit a long-term vision and your values. Mainstream does not always mean best.

A point of change in New Zealand landscape that recognized a legal structure with more than one owner and the equity in the resource occurred during Tuaropaki Power Company's initial project to build the Mokai 1 geothermal power station. This was 100% debt financed by Westpac Bank (McLoughlin *et al.,* 2010; Menzies *et al.,* 2001), the first financial arrangement of its kind in New Zealand. Existing wells drilled by the Crown proved the resource and provided sufficient steam for the project's technical and economic feasibility to be demonstrated without further equity injection, and state-owned generation company Mighty River Power (now Mercury) held the power offtake agreement (McLoughlin *et al.,* 2010).

5.4 Good Agreements vs Bad Agreements

There isn't one perfect, 'right' legal agreement for participating in a geothermal development. But there are Good Agreements and Bad Agreements.

Good agreements are fair and equitable, acknowledging the respective values of the parties, and they will have a level of future proofing (and thus respond favorably to changing future scenarios).

Developers and operators may utilize changing entities and structures, based upon commercial expediency, and where projects no longer fit within their values or ethos they may dispose of those interests. In contrast, Māori landowners cannot leave the land or the geothermal resource; both are "taonga tuku iho" – eternal treasures.

Māori landowners are constant. This consistency, and therefore inability to implement the standard business solution to a failed relationship or partnership of sale, requires careful consideration and differing legal solutions when documenting developer/Māori entity partnership arrangements. A good analogy is sharing a house! Indigenous groups can't leave the house, so we need to ensure it is comfortable and we have to have the ability to review our tenancy agreements with the flat-mate/spouse and to ultimately divorce if need.

Examples of bad agreements are those which:

i. don't value your contribution or knowledge,
ii. sit on the asset without implementation (land banking) or
iii. fail to future proof the relationship.

They may lock in for long timeframes, often without meaningful financial or other recompense, and then don't allow an exit when you want/need to.

Contracting is about hoping for best but expecting/preparing for the worst. You have the most leverage and power at the beginning of the contract negotiations (assuming your legislative and constitution rights are supportive), so use this time to build strong legal arrangements that reflect not only the relationship at the start, but also the evolving relationship over the long term and ultimately, should the need occur, at termination. You can't easily change things later. Get it right the first time so you (or more likely your children or grandchildren) are not regretting your decisions later.

5.5 Time is an asset

Use time horizons to your advantage. Māori will utilize their land and resources for the benefit of future generations, so must diversify on site to increase benefits and reduce risk. This means being innovators, including, for example, not only direct use but in indirect use of geothermal heat. NTGA and Tuaropaki lead the way in large scale direct and indirect use in New Zealand and are focused on more than electricity production.

Operators come and go. Consents expire. But the resource and the tangata whenua (people of the land) are forever. Operators are focused on short-term returns for their shareholders, so commercial frameworks tend to be short-sighted.

This means that Māori can structure arrangements differently, because investment now doesn't have to be realized in the short term. Māori can outlast some industries. This might look like an option to take on the geothermal plant / operation at the end of an agreed term. So long as there are legal mechanisms in place to ensure the developer doesn't over exploit the resource or not maintain the plant, Māori groups can inherit assets in the long term which will generate many more years of revenue. Note that geothermal assets can become a burden at the end of their lives, so it's imperative to understand the true cost to maintain and utilize these assets prior to any agreement.

Longevity in location also means that Māori can also outlast market trends/cycles. When the interest in geothermal is high there are more opportunities and choice for selecting partners. Use time as leverage to get what you need for your people. You have more time leverage than most.

There is a constant tension within indigenous groups between spending revenues now to make the lives of current owners and beneficiaries better and investing/saving for future generations to ensure wealth and prosperity. Whilst there are tools to help consider this, it really comes down to the values and vision of the group.

5.6 Demand Respect

Be intolerant of bad partners, notwithstanding if you are the minority in the financial and equity relationship. The land and the resource are in your control and a developer can do nothing without both, and therefore you. It takes bravery to sit at the table – demand the space and then grow into it.

Your mana (authority and status) should be meaningfully acknowledged by a development partner and they should be willing to support you, and to have the structures and processes in place to ensure that you and your entity can participate. Meetings should be board chair to board chair, despite different size organizations.

Remember: Big opportunities can be turned down if they don't fit your values and vision. You have time and it's better to wait than to participate in unhealthy relationships. Geothermal projects are 30+ year relationships, choose wisely.

6. Whakamutunga | Conclusion

Te tū, ki te hoe,

Puritia, kia mau ki tō ngakau.

Whāia ngā whetū,

ki ngā hau

ki ngā au o te moana,

hoea whakamua.

Tihei mauri ora.

Seize the paddle,

hold it firmly to your heart.

Follow the stars,

with the winds,

with the currents of the ocean,

paddle forward.

Kuputaka | Glossary

Te Reo Māori Terms used in this paper.

Term	Description
Hapū	A group of a Māori people or community connected by whakapapa (genealogy). Hapū sometimes are sub-sets of Iwi (tribes) and in other instances they are self-determining groups in their own right.
Iwi	An extended kinship group, tribe, often refers to a large group of people descended from a common ancestor and associated with a distinct territory.
Kaitiaki, kaitiakitanga	Guardian of natural resources and the act of guardianship; principle of intergenerational sustainability and the practices to achieve it
Mana	Prestige, authority, status
Mana whenua	Customary authority; territorial rights
Māori	The Indigenous peoples of Aotearoa New Zealand
Mātauranga Māori	Knowledge, culture, values, and world view held by Māori
Rangahau	Research; to seek, search out, pursue, research, investigate.
Rangitira	Chief
Reo	Language
Rohe	Region
Tangata whenua	People of the land
Taonga	Treasure, property, asset
Te Ao Māori	Māori world views
Tikanga	Correct procedure, custom, practice, protocol - this customary system of values and practices has developed over time and are deeply embedded in the social context
Whanau	Family group
Whenua	Land

Ngā mihi | Acknowledgements

We would like to acknowledge Dr Saddiq Zarrouk and Dr Eylem Kaya from the University of Auckland for their leadership and encouragement of this work and ensure it is a valued aspect of the wider research project “Reversing Carbon Emissions in the Geothermal Energy Industry: Template for Emission-Intensive Industries” (UOAX2211). We would also wish to thank the NZ Ministry of Business, Innovation and Employment for funding this project

Ngā tohutoro | References

Barton, B. *Legal Rights to Minerals in Geothermal Fluids.* Research Report: University of Waikato Research, ISBN 978-0-473-31290-9. (2015)

Beehive. Crown agrees to Kawerau geothermal assets deal (2005) https://www.beehive.govt.nz/node/23671

Blair, A., Siratovich, P., Campbell, *A. Geothermal Fuels Prosperity: How geothermal projects in New Zealand are catalyzing significant socio-economic benefits for Māori.* 2018. Proceedings of the 25th Annual Mexican Geothermal Congress, Morelia, Mexico.

Climo, M., Blair, A., Campbell, A., Carey, B. *Commercial Arrangements Underpinning Aotearoa New Zealand's Industrial Scale Geothermal Operations*. Proceedings 44th New Zealand Geothermal Workshop 23 - 25 November, 2022 (2022). 6p

Eru, S. & Lovell, L. Indigenous Developments: *Looking back to move forward*. Proceedings World Geothermal Congress 2020, Reykjavik, Iceland, April 27 – May 1, 2020 (2020). 16p.

Kissick, D., Carey, B., Climo, M. *An overview of New Zealand's Geothermal Planning and Regulatory Framework.* Traverse Environmental Ltd. ISBN 978-0-773-59132-8. (2021)

MB Century, 2024. https://www.mbcentury.com/projects/h2-project

McClintock, S., Watt, R., Quinao, J. *Lookahead from Kawerau, New Zealand: the Largest Geothermal Industrial Direct Use Complex in the World.* Proceedings World Geothermal Congress 2020+1, Reykjavik, Iceland, April - October 2021.

McLoughlin, K., Campbell, A., Ussher, G. *The Nga Awa Purua Geothermal Project, Rotokawa, New Zealand*. Proceedings World Geothermal Congress (2010)

Menzies, A.J., Brown, P., Searle, J., King, R. *The Mokai Geothermal Power Plant, New Zealand: Analysis of Performance During first Year of Operation*. Geothermal Resources Council Transactions, Vol 25. (2001)

MLC (Māori Land Court) www.Māorilandcourt.govt.nz & https://oag.parliament.nz/2004/maori-land-court/part2.htm (accessed June 2024)

Savage, P.J. 2013. Reflections after nearly 20 years as a Māori Land Court. https://maorilandcourt.govt.nz/assets/Documents/Publications/MLC-2013-Nov-Judges-Corner-Savage-J.pdf

Statistics New Zealand. 2024. 2023 Census population counts (by ethnic group, age, and Māori descent) and dwelling counts. https://www.stats.govt.nz/information-releases/2023-census-population-counts-by-ethnic-group-age-and-maori-descent-and-dwelling-counts/

Further Reading

The following list is a selection of papers that contain more information about Māori participation in geothermal development and resource management in New Zealand. These papers are downloadable from the International Geothermal Association conference database or the link provided.

Adlam, B., King, S. *Connection of Ngati Tuwharetoa (Bay of Plenty) With the Kawerau Geothermal Field, New Zealand*. Proceedings World Geothermal Congress 2015 Melbourne, Australia, 19-25 April 2015 (2015).

Morgan, K., McMillan, O.W., Taute, D.N., Fa'aui, T.N. *Empowering Indigenous Epistemologies in Geothermal Development*. Proceedings 43rd New Zealand Geothermal Workshop 23-25 November 2021, Wellington, New Zealand (2021)

Mutu, T. & Doorman, P. *Incorporating Māori world views in the Rotorua geothermal system management plan*. Proceedings 45th New Zealand Geothermal Workshop, 15-17 November, 2023, Auckland, New Zealand (2023)

Porter, S. Mihinui, R., Hall, H., Naera, R., Clubb, F., Kereopa, L., George, K., Conroy, E., *Cultural views, perspectives and observations of the health and wellbeing of the Rotorua Geothermal System*. Proceedings 42nd New Zealand Geothermal Workshop, 24-26 November 2020, Waitangi, New Zealand. (2020)

Severne, C., Leaf, G., Wairākei Charitable Trust. He puna i rawaka, he puna whakatōto. Proceedings 42nd New Zealand Geothermal Workshop, 24-26 November 2020, Waitangi, New Zealand (2020)

Severne, C. *Traditional use of geothermal resources by New Zealand Māori.* Proceedings World Geothermal Congress Florence, Italy, 18-31 May 1995 (1995)

Stokes, E. 2000. *The Legacy of Ngatoroirangi; Māori Customary Use of Geothermal Resources* https://www.boprc.govt.nz/media/509127/the-legacy-of-ngatoroirangi-Māori-customary-use-of-geothermal-resources.pdf

Stokes, E. *Ohaaki - A Power Station on Māori land*. University of Waikato. (2003) https://hdl.handle.net/10289/6092

Taute, D., Morgan, K., Ingham, J., Archer, R., Fa'aui, T. *An holistic approach to impact assessment: revitalising the presence of Māori values for cultural sustainability in geothermal development*. Proceedings 41st New Zealand Geothermal Workshop, 25-27 November 2019, Auckland, New Zealand (2019)

Tutua-Nathan, T. *Māori issues relating to the geothermal resource*. Proceedings of the 10th New Zealand Geothermal Workshop (1988)

White, B., Morris, G., Lumb, T. *New Zealand geothermal resource ownership – cultural and historical perspective*. Proceedings World Geothermal Congress Florence, Italy, 18-31 May 1995 (1995)

Wilson, A., Nicholson, T., Bignall, G., Bradshaw, D. *Kaitiakitanga future geothermal innovation and direct use*. Proceedings 39th New Zealand Geothermal Workshop 22 - 24 November 2017, Rotorua, New Zealand (2017)

Wilson, A., Nicholson, T., Bignall, G., Bradshaw, D. *Kaitiakitanga and the next 10,000 megawatts*. Proceedings World Geothermal Congress 2015 Melbourne, Australia, 19-25 April 2015 (2015).

The Waiwhatu Project: Developing Shared Language (English-Te Reo Māori) for Communicating Geothermal Scientific Terms

A. Blair[1], A. Campbell[1], M. Climo[1], P. Siratovich[1], U. Fairhall[2], C. Ruha[3]

[1]Upflow Ltd, [2]Tarapō, [3]Mountain to Tide Ltd

Keywords

shared language, linguistics, translation, communication, Aotearoa New Zealand, mātauranga Māori, geothermal, Te Reo Māori, indigenous knowledge

ABSTRACT

In the Waiwhatu Project, we created five new kupu (words) in Te Reo (language) Māori (Indigenous peoples of Aotearoa New Zealand) relating to geothermal. This search for shared understanding was born out of difficulties experienced when trying to source meaningful relevant words in Te Reo Māori to define scientific terms used in geothermal research and development.

This pilot project created an opportunity to understand the practice of others. We listened to scientists explain useful technical concepts, relevant to earth sciences, geothermal and volcanology, and then interpreted these through a Māori lens into a shared language, bringing Mātauranga Māori (indigenous knowledge) and western science into one space. One of the new kupu is *waiwhatu* for geothermal, which means fluid from the core (heart of the Earth), not fresh water, but fluid woven through the inside of the Earth to the surface.

We share the process for developing, testing and sharing the new kupu. Seven learnings from using the Waiwhatu model were:

i. Embrace multiple world views
ii. Don’t rush
iii. Choose the right people
iv. Everyone must be a learner
v. No one owns the words
vi. Value outcomes, not outputs
vii. Be the leader you wish to see in the world

The true test going forward will be in the uptake and use of the words and concepts outside of our project team—that is when language truly exists in the world.

TUHINGA WHAKARĀPOPOTO

I te Whaimahi Waiwhatu nei, hanga ai mātou i ngā kupu hou, i ngā kupu e hāngai ana ki Te Ahi Tupua, arā, ko ngā mea ngāwhā. I ahu ake te whāinga nei i te uaua o te rapu atu i ngā kupu e tika ana mō ngā kupu pūtaiao no te ao o te rangahau me te whakawhanake i aua mea ngāwhā.

Ko tā te whaimahi tōmua nei ko te whakatuhera i te māramatanga ki ngā mahi a tangata kē. I whakarongo mātou ki ngā mātanga pūtaiao e whakamārama ana i ngā āria matua e pā ana ki ngā tikanga pūtaiao ā-nuku, ki te mātai ngāwhā, ki te mātai puia, kātahi ka whakamāori i aua āria me ngā kupu e hāngai ana ki tā tērā tuku, ki tā tērā tuku, e tūtakitaki ai te mātauranga Māori me te pūtaiao o te rātō, e kiia nei, ki te marae kotahi. Ko tētahi o aua kupu ko 'waiwhatu' – *geothermal liquid* – e mea nei ko te wai no te whatu o te ao, ehara kē i te wai māori, engari ko te wai e rangā ake nei i te whatu o Papatūānuku ki te mata o te whenua.

Ko tā mātou ko te whākī i ngā tikanga o te whakawhanake, o te whakamātautau, o te tohatoha i aua kupu hou. E whitu ngā akoranga matua i puta ake i te tauira Waiwhatu nei:

i. Kia tuhera ki ngā tirohanga rere kē o te ao
ii. Kei whakateretere
iii. Whirihia ngā tāngata e tika ana
iv. Me huri ngā tāngata katoa hei ākonga
v. Ehara nō tētahi te mana o ngā kupu, engari no te kupu ake
vi. Uaratia atu ngā putanga i ngā whakaputanga
vii. Kia rite te tangata ki te kaiārahi e tika ana mo te ao

Ko te tino putanga mō ngā tau e whai nei, ko te mau me te kōrero i aua kupu nei me ngā āria e hāngai ana i waho atu o tō mātou kapa—kātahi ka tūturu te noho o te reo i tēnei ao.

1. Tīmatanga kōrero | Introduction

Whaowhia te kete o te mātauranga
Fill the basket of knowledge

1.1 Māori and geothermal resources in New Zealand

Geothermal activity is found all over the world, and each culture has responded to it in their own ways. Aotearoa's central North Island hosts more than twenty world-class high temperature geothermal systems, making it one of the globally rare places where widespread geothermal development is economically viable and technically feasible. Geothermal energy is a critical component of New Zealand's future renewable energy portfolio as it transitions to a low-carbon economy.

Māori, have a recognized and powerful constitutional role in New Zealand society, and a critical and increasing role in the national economy, including future geothermal development (Blair et al., 2018; 2024; Climo et al., 2022). As landowners, investors and kaitiaki (guardians of natural resources), Māori will determine the use of geothermal resources and make influential decisions in how they are developed. The long-term nature of such projects requires a multigenerational approach to resource management, which aligns with Māori values and worldview.

In New Zealand, geothermal use is regulated through the Resource Management Act (1991) and is considered primarily as a water take (i.e. volume of fluid per day), unlike many other countries that provide for geothermal exploration, development and production under mining permits (Blair et al., 2018). Developers in New Zealand can seek and obtain geothermal consents for fluid take; however, to obtain land access, and access to geothermal resources beneath the land, developers must have permission of the landowner(s). This permitting framework provides for landowners to negotiate commercially beneficial agreements (Blair et al., 2018). Most geothermal fields have a commercial arrangement with a Māori-owned entity in the form of, (for example), ownership, fuel supply agreements, royalties and lease agreements (Climo et al., 2022).

Yet, geothermal research still has low representation of, and participation by, Māori. One of the barriers is an inadequate understanding of Mātauranga Māori within the broader geothermal science community; it is our hope that this paper will add to the growing understanding and discussion in this area. A glossary of Māori terms is included at the end of the paper.

1.2 Embracing different knowledge systems make for better science

Western science systems have a strongly defined structure and methodology for excellence. Whilst the focus is increased knowledge, in practice, alternative knowledge systems are often deemed inferior. This is demonstrated by the need for validation of indigenous knowledge using Western scientific knowledge or criteria, assumed to be the gold standard (de Beer, 2022). We should *"not … try to validate indigenous knowledge utilizing the processes of science, but rather to enhance appreciation and respect for the richness of indigenous knowledge and its merit."* (de Beer, 2022)

Therefore, work that seeks to grow indigenous knowledge, whilst not actively discouraged, often fails to be prioritized when funds are limited. And in research, funds are always limited.

However, if the true nature of science excellence is the pursuit of understanding, and that an idea or concept becomes accepted when it is challenged over time and still maintains, the ability to apply an indigenous knowledge lens to Western scientific thinking will surely increase the robustness of scientific ideas, concepts and understanding. *"Challenges to our general knowledge of the world around us are equally challenges to our scientific knowledge."* (McCain, 2016)

1.3 Māori language and geothermal research

Improved connection between Te Ao Māori ki te ao rangahau (the world of Māori to the world of research) was actively sought out in the *Geothermal: The Next Generation* (GNG; Chambefort et al., 2019; GNS Science, 2020) program. This New Zealand Government-funded research program (2019-2024) was established to explore and understand Aotearoa's supercritical geothermal resources, by going hotter and deeper into the Earth than drilled before (>4 km, >400°C).

GNG had an extensive technical workplan, encompassing geophysical, geological, geochemical investigations as well as numerical modelling. In tandem with the geoscience, the program also aimed to reduce non-technical barriers to the adoption of geothermal technologies, including overcoming regulatory hurdles and formation of an engaged stakeholder community. A specific goal was to facilitate more culturally responsive, inclusive and effective approaches for undertaking geothermal research and resource development.

Three key elements in its engagement approach (Climo et al., 2023) were:

i. Māori-first Engagement: interweaving knowledge systems and a multigenerational approach to resource management;

ii. Strategic Partnering: involving others to expand the impact for, and beyond, the science activities; and

iii. Authentic Communication: curating information and being open and honest about the unknowns.

Due to the long lead in times for the development and adoption of technologies and utilization of supercritical resources, and the increasing influence of Māori for legal and social license to operate with respect to natural resource management, Māori were a key stakeholder of this research program. The goal was to engage with Māori in a manner that provides future leaders and decision makers with the relevant insights to enable informed decision making for these projects.

External ‘push’ of scientific information in ways more palatable for Māori wasn’t the focus; often scientists look to educate others to understand their scientific concepts and views. Instead, focus was on broadening and growing the GNG science team’s thinking through exposure to a knowledge system different from their own.

1.4 The need for new language in geothermal

Science is often hard to relate to for non-scientists, as scientists use discipline-specific language, and concepts aren’t easily aligned to the natural knowledge systems of mātauranga (knowledge). Similarly, scientists find it hard to understand and relate to Māori concepts and thinking.

A search for shared understanding was born out of difficulties experienced when trying to source meaningful relevant words in Te Reo Māori to define scientific terms used in geothermal research. While there are traditional Māori terms relating to geothermal systems, the development of geothermal science has resulted in the borrowing or coinage of vocabulary internationally to keep pace. This needs to be matched in Te Reo Māori.

Many geothermal terms used are from specific languages, such as lahar from Javanese, pāhoehoe and a'ā from Hawai'ian, geyser from Icelandic 'geysir' and lava from Italian. Using English words as the basis for translation is also difficult – words driven by English often make no sense in Te Reo Māori. Instead, words and concepts are often cobbled together with literal translations for parts of words. For example, ngawha means hot spring, but is commonly used to replace the word geothermal.

Language is a fundamental tool to share knowledge, and a key barrier limiting effective engagement with Māori. Thus, the ‘Waiwhatu Project’ was developed to improve communication. It is important to note that our goal was to create new language for expression and use within Aotearoa New Zealand, not overseas. There is no expectation that the Māori words created will replace existing global terms for key scientific concepts.

2. The Waiwhatu Project

I orea te tuatara ka patu ki waho
A problem is solved by continuing to find solutions

The Waiwhatu model was developed through a pilot project, designed to take people on the journey of mutual understanding and collaboration through the development of shared language tools.

2.1 Project Goals

The project had two objectives:

1. Create five terms and basic concepts in Te Reo Māori that were meaningful and relevant.
2. Spread and use the new terms in the wider Aotearoa New Zealand geothermal community.

2.2 Team

The project team balanced a range of ages, genders, skills and experience:

1. Uenuku Fairhall (Ngāti Rangiwewehi, Waitaha): An expert Te Reo Māori linguist and fluent speaker who holds the underlying concepts of Te Ao Māori, including whakapapa, mātauranga, noa and tapu.
2. Aroha Campbell (Ngāti Tahu): A kaitiaki consultant who has deep experience navigating geothermal developments and Te Ao Māori.
3. Corey Rehua (Te Arawa, Tainui, Mātaatua): An early career Māori researcher and engineer, with a broad range of interests, who is on a reo journey.
4. Paul Siratovich: A senior scientist (geologist) who understands core geothermal concepts and terminology who is on a Te Ao Māori journey.
5. Andy Blair: A strong communicator, with a background in science and is comfortable in Te Ao Māori, who can help translate the concepts.

2.3 Methods

Selection of concepts/terms

A longlist of ideas was shortened by selecting five of the most common science words used when speaking about and describing geothermal energy and earth processes. These would be the ‘anchor’ words in sentences that other terms relate to.

The shortlist of terms selected were: geothermal fluid, magma, lava, reservoir, and enthalpy.

We deliberately chose common words (more likely to be used) but some are also hard to understand. For example, reservoir and enthalpy are hard concepts to grasp but are used a lot in geothermal research and industry.

Developing shared language

For each selected concept/term the following process was undertaken:

1. Scientific Concept

Scientists explained the technical concept, relevant to earth sciences, geothermal and volcanology. This included the genesis of the word/concept i.e., where it came from and why (including for example, the Latin basis for components of each word).

2. Word Use

The use of each term/concept was discussed. Examples of questions asked included:

- How is/will the word be applied in sentences?
- Does it have negative or positive connotations?
- When should (and shouldn't) the word be used?
- Who uses it?
- How does it work with other words?
- How is the word used within the science/geothermal community?
- How is the word commonly used in a lay context? e.g. the general public would call a geothermal surface feature a 'hot spring'.

3. Interpretation through a Māori Lens

The team discussed the concepts and interpreted them through a Māori lens, i.e. how the natural process of formation (e.g. reservoir, lava, etc) is thought about in Te Ao Māori. Examples of questions asked included:

- How is a reservoir made?
- What are the components?
- How do they behave and interact with the surroundings?

4. Kupu hou (new words)

A few Te Reo Māori kupu were proposed and the spelling and pronunciation clarified. These were tested against other words currently in use.

- How does the word sound? Is it pleasing to say? Does it sound good?
- Does the word flow in a sentence - spoken in Te Reo Māori and in English?
- Can it be used interchangeably in both English and Te Reo Māori sentences with ease?
- Is there an emotive response, and if so, what does it emote and is that consistent with the kupu?

Both the English and Te Reo Māori versions were defined and put into example sentences and the team practiced using the different sentences. The kupu were also informally tested on the Waiwhatu Project team's contacts.

3. Ngā Kupu Hou | New Words

Whāia te mātauranga hei oranga mō koutou
Seek after learning for the sake of your wellbeing

Table 1: The new kupu and their definitions.

Magma: Tokarewa [toh-car-reh-wah]	
Definition	Magma – Extremely hot molten or semi-molten rock that exists exclusively underground. **toka** - rock; **rewa** - to melt, to become liquid.
Example sentence	A surprise **tokarewa** pocket was found in Iceland during deep drilling project. He mea ohorere te kite iho i te pūkoro **tokarewa** i Tiorangi i te wiringa iho ki raro rawa.
Lava: Rangitoto [rung-ee-taw-taw]	
Definition	Lava – Molten rock that has been erupted at the surface of the earth, magma that has now become lava. **Rangitoto** - black lava, scoria; said to be the blood from Tamatekapua's nose.
Example sentence	Scientists use the term **tokarewa** for molten rock that is underground and **rangitoto** for molten rock that breaks through the Earth's surface. Whakamahi ai ngā mātanga pūtaiao i te kupu tokarewa hei tohu i ngā toka kua rewa i raro i te whenua, ā, ko te kupu **'rangitoto'** ina pākaru ake te **tokarewa** ki runga i te mata o te whenua.
Geothermal fluid: Waiwhatu [why-fuh-too]	
Definition	Geothermal fluid - The liquid present inside a geothermal reservoir that can flow to the surface naturally or through wells. Geothermal fluid is the energy carrier that allows the extraction and utilization of heat from the core of the earth. **Wai** - liquid, oil, etc; **whatu** - stone, core.
Example sentence	**Waiwhatu** is a hot and concentrated saline solution, having circulated through the very hot rocks of geothermal areas and are enriched with minerals. He mehanga kurutai kukū wera te **waiwhatu**, na te rērere haere i waenga i ngā toka wera rawa o ngā wāhi ahitupua, ā, nā reira hoki i kīkī ai i ngā kohuke.
Reservoir: Māpuna [mah-poo-nah]	
Definition	Reservoir - The section of a geothermal field below ground that is so hot and permeable that fluid can be economically extracted for the production of fluid and heat. This contains: (1) an aquifer or fracture network containing hot fluid, (2) a path through which cold water can flow to recharge the system or an input of magmatic fluid and (3) a source of heat. **Māpuna** - to well up, to form a pool.
Example sentence	The resource is not the power station on the surface but the **māpuna** in the subsurface. They are a treasure. Ehara te wharehiko i te rawa no runga i te mata o te whenua, engari ko te **māpuna** waiwhatu kē o raro iho. He tāonga ērā.
Enthalpy: Ngaohū [ng-ow-who]	
Definition	Enthalpy - the sum of the internal energy and the product of the pressure and volume of a thermodynamic system **Ngao** - strength, energy; **hū** - still, at rest
Example sentence	The specific **ngaohū** of geothermal liquid depends primarily on temperature. Hāngai ai te **ngaohū** ake o te waiwhatu ki te paemahana.

4. Kōkiritia ngā kupu hou | Sharing the new words

Mā mua ka kite a muri, mā muri ka ora a mua
Those who lead give sight to those who follow, those who follow give life to those who lead

Early Testing

July 2022 — A group of Māori postgraduate students, all ancestrally connected to the Central North Island of Aotearoa New Zealand, attended Reykjavik University's Iceland School of Energy for a 3-week Summer School course on Sustainability and Energy Systems. This was an opportunity for the group to test the kupu, as they were constantly being spoken to about geothermal, they had good Te Reo fluency and they were in a foreign country so could think about how others used the terms. Their overall assessment was:

"In the end, we all collectively agreed that these kupu do effectively support bridging the gap between science and Te Ao Māori."

Launch

November 2022 — Delivery of project report to GNG program team.

February 2023 — Corey Ruha, a member of the Waiwhatu Project team and Ngā Tauira o Rūaumoko, presented the project and shared the new kupu at the IAVCEI (International Association of Volcanology and Chemistry of the Earth's Interior) Scientific Assembly (Ko Rūaumoko e Ngunguru Nei) in Rotorua, New Zealand.

March 2023 — The kupu were shared using the GNG website and social media channels. This included the words, definitions, sentence examples, and accompanying audio files.

April 2023 — The New Zealand Geothermal Association shared the kupu and the Waiwhatu Project information (via a link to the GNG website) to their members through their monthly newsletter.

June 2023 — Engagement with GNS Science to share the kupu (GNS Science is a research institute with geothermal as one of its focus areas and was the lead organization for the GNG program).

July 2023 — To coincide with Geothermal Week, GNS Science posted one kupu per day to their social media channels. This was shared by other groups and was picked up by New Zealand news media.

5. Ngā Whakaaro | Lessons & Learnings

He waka eke noa
A canoe which we are all in with no exception
[we're all in this together]

This endeavor to develop shared language is not unique, and it may be a suitable test case and example for other areas and undertakings. As such, below are seven learnings gained from using the Waiwhatu model.

5.1 Embrace multiple world views

Learning a language is also learning a new culture and discovering new ways of seeing the world. Developing shared language is not the place to contest the relative validity of Western Science and Indigenous Knowledge systems, rather, it is an opportunity to build relationships, seek personal growth, to share understanding, and for innovation.

Whilst English is impacting the evolvement of the Māori language, it was important to be conscious of the need to protect, but not stifle, the scientific understanding as well as the linguistic integrity of either language. For example, English and Te Reo have different language structures – how a word is used in a sentence is different.

The process of looking at scientific concepts through a different lens helped us to know the concepts better, to be more thoughtful than just using the existing terms. For example, a question about how geothermal reservoir formed sparked a discussion about the parallels with a pregnant belly. We moved from a 2D/3D understanding of geothermal terms and levelled up our understanding, bringing in richness through adding time, values and beliefs.

We did not seek to rationalize nor to justify geothermal development in developing the new kupu. It was important that the new kupu did not reinforce a positive or negative association. There is no 'right' and 'wrong'. There is no universal truth – the team did not have to all come to one agreed position. This meant the team had to overcome their own biases, embrace the emotive response to the concepts, and explore the philosophical relationship between humans and the natural environment.

5.2 Don't rush

Learning a language, and developing shared language, is not just having an intellectual discussion about the translation. It's about becoming part of another culture. Don't try to translate. Instead, seek the essence of the relevant scientific terminology by discussing concepts and their deeper meanings.

It's better to focus on taking time to develop less words/concepts in depth, than rushing through many words lightly. We took time to explore, discuss and iterate. We didn't settle for the first 'close-enough' word. Proposed kupu were left alone to percolate and be tested by the group over weeks and months before coming back together to share thoughts and feedback.

5.3 Choose the right people

Ensure the team is diverse. Having a range of ages, genders and experience meant richer conversations and perspectives influenced the development of shared language.

Deduce who the best candidates are to model the language and improve exposure. For example, those who understand the geothermal science, communicate well, and have influence.

It was important to select team members that were predisposed to embracing new ways of working. They had to be willing to try to understand the science. They had to be willing to try to understand indigenous knowledge. Many people may say they're interested, and be genuinely interested, but when selecting team members, look for evidence of interest i.e. judge them on their actions and behavior. What have they done to lean into those interests already? For example, are they scientists who are taking language lessons, and trying to use the second language in their daily lives? Curiosity and commitment are key.

5.4 Everyone must be a learner

Learning a language is an act of bravery and vulnerability. It is important to create a safe space where team members can say something 'wrong' and make mistakes – a prerequisite part of learning a language! No-one can be defensive or protective; ego and pride must be put aside. There should be no hierarchy in the team, with everyone's mana (authority) mutually respected. Everyone in the team is both teacher and student, gaining new knowledge.

This high-trust environment allows team members to challenge each other on definitions, explanations and deeper meanings. Having non-specialist team members is critical – it pushes the 'experts' for a better explanation of something they intrinsically understand. The discourse discussion is more important than the words. The team iterates and optimizes until the shared meaning is reached. This will include open questions, and lots of seeking clarification. Many times, our team built an ideological visual picture of each concept, and then much of the discussion was spent clarifying with each other if they saw the same thing.

Consider colonization and personal histories in the relationships being formed within the team. This is not an academic exercise. If necessary, spend time recording the rules of engagement or how to deal with each other, at the start.

5.5 No one owns the words

It was important to choose Māori kupu that were not already in use or already associated with a particular region, dialect or place. The new words need to be usable across Aotearoa New Zealand without any perceived prior 'ownership' or expectation on their use.

Likewise, the new words are not 'owned' by the creators. Language is common to all who use it, and is a social, not individual act. Te Reo Māori is an ever-evolving language, and the true test of these kupu will be how widely they are used by others outside the test group. If the new words are not adopted, don't be afraid to go back and change them, or to adopt what becomes common use.

5.6 Value outcomes, not outputs

The true value of this work is not the new words – these are outputs, and short-term thinking. Some, especially those who are driven by financial measures of success, may perceive that creating five new words is not good value for money (i.e. because time (money) is required to do this well).

The value in this work is in the long-term outcomes: A proven process that works. Opening lines of communication and inviting diverse perspectives. The start of acceptance within New Zealand's geothermal research and industry that there is another way to view geothermal resources. Supporting Māori stakeholders to feel more included in the geothermal industry. It can be useful to start by asking the questions: *What is this worth to you? What is it worth to the wider industry and community at large?*

5.7 Be the leader you want to see in the world

Individuals are on a personal journey, and many people are not ready for work that decolonizes research and welcomes indigenous voices into 'science' discussions. It challenges the infrastructures that they have built their careers and thinking frameworks on. This means some people can't appreciate the problems and are unable to see the vision. We had this experience.

In order to realize the project, we had to put significant effort into convincing others that this work was important, including self-funding some of the time required. However, once the kupu were developed and shared (and a tangible product was available), many questioners (sceptics) became supporters and the work is now being extended. Adoption of the kupu brings credibility, and credibility converts the sceptics.

If you think developing shared language is important, then you are the right person to move it forward. Leading this work isn't about expertise, rank, titles or your role within an organization. Don't wait. Believe in yourselves and the project. You don't need permission.

6. Ā Mua | Next Steps

Ka mua, ka muri
Walking backwards into the future
[look to the past to inform the future]

This project has been extended and continues under the leadership of the Māori Strategy team at GNS Science, under a new name: Waiwhatu-Arawhata. Arawhata means "bridge", recognizing that the next stage of this journey is transitional. Their goal is to use and refine the Waiwhatu methodology in a workflow that sees more development of shared language.

Through their efforts, in June 2024 the Waiwhatu kupu was officially accepted in Te Aka (Māori dictionary) through a submission to Te Taura Whiri i Te Reo Māori (the Māori Language Commission).

Planned future initiatives (2024-2026) include:

- Promotion of the existing kupu at Geothermal Week 2024
- Develop ten more kupu, and launching them by mid 2025

- Presentations at conferences and workshops
- Delivery of an outreach event to socialise the new terms with Māori geothermal communities

7. Whakamutunga | Conclusion

Whāia e koe te iti kahurangi, ki te tūohu koe, me he maunga teitei
Pursue excellence – should you stumble, let it be to a lofty mountain

The Waiwhatu model was successful in demonstrating an effective methodology for developing shared language and the pilot project produced five new kupu. This approach is a reproducible and not limited to use in Aotearoa New Zealand.

Developing shared language is an opportunity to build relationships, seek personal growth, to share understanding, and for innovation. The discourse and discussion are more important than the words.

Our hope is that the geothermal community becomes a welcoming place for indigenous peoples to meaningfully engage, participate and lead discussions, debate and direction for future research and industrial developments.

Ngā mihi | Acknowledgements

Ehara taku toa i te toa takitahi, engari kē he toa takitini
My success should not be bestowed onto me alone,
it was not individual success but the success of a collective

The authors acknowledge input from many people in challenging our thinking, exposing our biases and assumptions, and teaching us. We are thankful to benefit from your insights and revision of this paper. Thank you to all who shared their experience and mātauranga with us.

We are grateful for the leadership and support from Dr Isabelle Chambefort, Program Leader *Geothermal: The Next Generation*, who gave us the opportunity to do this work. We offer the Māori Strategy team at GNS Science, who are leading the Arawhata Project, our thanks for their interest and continuing effort in this space.

Funding for this project was provided by New Zealand's Ministry of Business, Innovation and Employment (MBIE, contract C05X1904) for the "*Geothermal: The Next Generation*" research programme.

Ngā Tohutoro | References

Blair, A., Climo, M., Campbell, A., Lovell, L. "Indigenous participation in geothermal projects: learnings from Aotearoa New Zealand." *GRC Transactions*, Vol. 48, (2024)

Blair, A., Siratovich, P., Campbell, A. "Geothermal Fuels Prosperity: How geothermal projects in New Zealand are catalyzing significant socio-economic benefits for Māori". *Proceedings:*

Mexican Geothermal Association Annual General Meeting, 19-20th April 2018, Morelia, Michoacán, México (2018)

Chambefort, I., Mountain, B., Blair, A., Bignall, G. "Geothermal: The Next Generation". *Proceedings: 41st New Zealand Geothermal Workshop,* 25-27 November 2019, Auckland, New Zealand (2019)

Climo, M., Blair, A., Campbell, A., Carey, B. "Commercial Arrangements Underpinning Aotearoa New Zealand's Industrial Scale Geothermal Operations". *Proceedings: Proceedings 44th New Zealand Geothermal Workshop*, 23 - 25 November 2022. Auckland, New Zealand (2022)

Climo, M., Blair, A., Campbell, A., Chambefort, I., Fairhall, U. "Stakeholder Engagement: A Supercritical Geothermal Example". *Proceedings: World Geothermal Congress 2023*, Beijing, China, April 17 – 21, 2023. (2023)

de Beer, J.,van Wyk Ben-Erik. "Indigenous Knowledge Systems and Western Science: The Conundrum of Validation." *Indilinga African Journal of Indigenous Knowledge Systems*. Vol. 20, No. 2. 31st January 2022. (2022)

GNS Science. "Geothermal: The Next Generation" (2020) www.geothermalnextgeneration.com

McCain, K. "The Importance of Understanding the Nature of Scientific Knowledge". In: *The Nature of Scientific Knowledge*. Springer Undergraduate Texts in Philosophy. Springer, Cham. (2016) https://doi.org/10.1007/978-3-319-33405-9_1

Te Aka; www.māoridictionary.co.nz

Kuputaka | Glossary

Te Reo Māori Terms used in this paper.

Term	**Description**
Kaitiaki, kaitiakitanga	Guardian of natural resources and the act of guardianship; principle of intergenerational sustainability and the practices to achieve it
Kupu	Word
Māori	The Indigenous peoples of Aotearoa New Zealand
Mātauranga Māori	Knowledge, culture, values, and world view held by Māori
Noa	Ordinary, unrestricted (free from the extensions of tapu)
Tangata whenua	People of the land
Rangahau	Research; to seek, search out, pursue, research, investigate.
Reo	Language
Tauira	Student
Tapu	Sacred, prohibited
Te Ao Māori	Māori world views
Te Reo Māori	Māori language

Why Does Geothermal Matter for Tribal Land? The Geothermal Journey of the Pawnee Nation

Alex Hessinger1, Lyle MacVey1, Jordan Kanuho[2], Alex McSheridan[3], Jorge Andres Alvarez Escobar[3], Catalin Teodoriu[3]

[1] Tribuquent Corp.; [2] VP Pawnee Nation; [3] The University of Oklahoma

Keywords

Tribal Land, Renewables, Geothermal, Oil wells, Sustainability

ABSTRACT

Native American tribes have a profound cultural and spiritual connection to the land, viewing it as a sacred entity rather than a commodity for profit. This perspective has historically created tensions with industries exploiting fossil fuels. The Pawnee Nation's Rural Energy Pilot Program (REPP), initiated in January 2024 and funded by a $2.6 million USDA grant, aims to transition the community towards sustainable energy.

REPP focuses on converting decommissioned oil wells into geothermal energy sources, integrating smart sensors for energy efficiency, promoting solar gardens, and encouraging electric vehicle adoption. This initiative addresses the environmental impact of abandoned oil wells while leveraging renewable resources to support community needs. The program emphasizes community engagement through education and workshops, ensuring an inclusive transition to sustainable energy and addressing environmental justice by targeting the ecological burdens faced by marginalized communities.

The project highlights the underutilized renewable energy potential of tribal lands, aiming to rectify energy inequalities and foster community resilience. Strategic partnerships and innovative models for integrating renewable energy with existing infrastructure underscore the collaborative nature of REPP, setting a precedent for sustainable land use and energy production on tribal lands. This paper presents the Pawnee Nation's Rural Energy Pilot Program that started in January 2024.

1. Introduction

In January 2023, Pawnee Nation was awarded the Rural Energy Pilot Program also known as REPP. The Rural Energy Pilot Program, supported by the United States Department of Agriculture (USDA), represents a transformative initiative focusing on sustainable energy and community empowerment. The Rural Energy Pilot Program is a 2.6-million-dollar grant from the USDA to help transform the energy landscape of Pawnee Nation for a cleaner, more sustainable future. Pawnee Nation is partnering with Pawnee Nation College, Pawnee Nation Housing Authority, Pawnee Public Schools, Indian Electric Cooperative, University of Oklahoma, and Tribuquent Corporation. Central to the program is the conversion of oil wells into sources of renewable energy, coupled with the integrating smart sensors in homes for energy efficiency. This three-year expedition also emphasizes solar gardens, electric vehicle adoption, and community engagement through education and workshops, ensuring an equitable transition to a sustainable future. Moreover, the Pawnee Nation's project stands as a testament to environmental justice, targeting the disproportionate ecological burdens faced by marginalized communities. By emphasizing the underutilized renewable energy potential of tribal lands, which encompass a significant portion of the nation's renewable resources, the initiative aims to rectify energy inequalities and foster community resilience. The formation of the Pawnee Nation Center for Rural Innovation and Strategy (PNCRIS) represents a collaborative endeavor, comprising a Housing Authority, a Tribal College, the Tribal Nation itself, an Electric Cooperative, a State University, and a Non-profit organization. This consortium is ever-evolving, consistently broadening its network to encompass additional local partners. Figure 1 shows the main partners of the project.

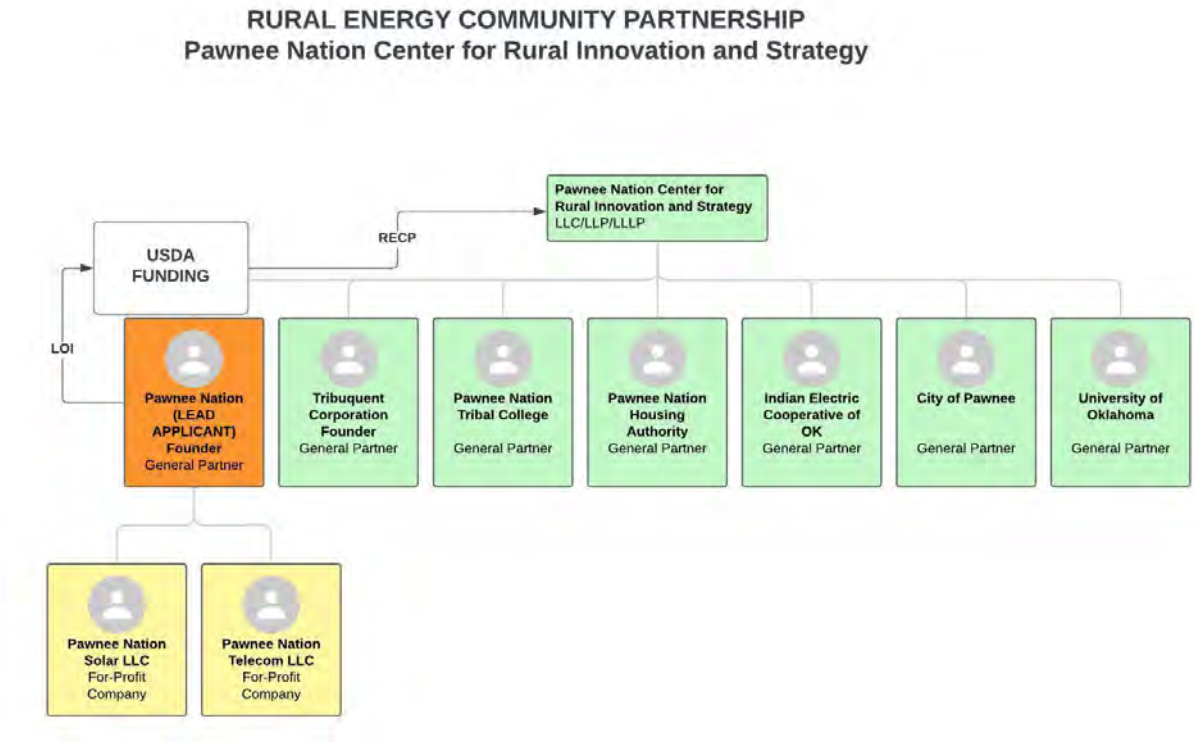

Figure 1. REPP partners' organizational diagram

2. The Significance of Land to Oklahoma Tribes

2.1. Cultural Importance

For Oklahoma tribes, the land holds profound cultural significance, intertwined with their identity, heritage, and spirituality. Tribes view the land not merely as a resource but as a sacred entity, a living relative to be respected and protected. This deep connection to the land is rooted in traditions, oral histories, and spiritual beliefs, where the landscape, flora, and fauna are integral to cultural practices and ceremonies. The Pawnee Nation, for instance, has historically revered specific sites as sacred, conducting rituals and ceremonies that honor their ancestors and the natural world. This relationship fosters a sense of stewardship, where the protection of the land is paramount, ensuring its health and vitality for future generations.

2.2. Economic Importance

Rural areas are also economically vital for tribes. These regions often encompass vast tracts of land rich in natural resources, including agricultural lands, forests, and mineral deposits. For the Pawnee Nation and many other tribes, these resources have historically provided sustenance, economic opportunities, and means of self-sufficiency. Agriculture, hunting, and fishing have been traditional livelihoods, and in recent years, there has been a shift towards exploring renewable energy resources. By harnessing the potential of geothermal energy, as proposed in the Pawnee Nation’s Rural Energy Pilot Program, tribes can diversify their economies, reduce reliance on external energy sources, and create jobs within their communities.

2.3. Environmental Importance

Environmental sustainability is a core principle for many tribes, who have long recognized the importance of maintaining ecological balance. Rural areas offer an opportunity to implement sustainable practices that align with traditional ecological knowledge. The Pawnee Nation's initiative to convert old oil wells into geothermal energy sources exemplifies this commitment. This project not only mitigates the environmental impact of abandoned oil wells but also leverages renewable energy to support community needs. The integration of smart sensors in homes for energy efficiency further illustrates a holistic approach to environmental stewardship, reducing carbon footprints and promoting sustainable living.

2.4. Pawnee National Rural Energy Pilot Project

Central to the REPP is the innovative conversion of decommissioned oil wells into sources of geothermal energy coupled with solar thermal collectors. This process not only addresses environmental concerns associated with abandoned wells but also taps into a renewable resource that aligns with the tribe’s commitment to sustainability. Complementing this initiative, the project involves the installation of smart sensors in homes to enhance energy efficiency, the development of solar gardens, and the promotion of electric vehicle adoption. These efforts collectively aim to reduce energy costs, lower greenhouse gas emissions, and create a more resilient energy infrastructure. The REPP is built on 6 Phases that will enable to validate and prove the concept, see Figure 2.

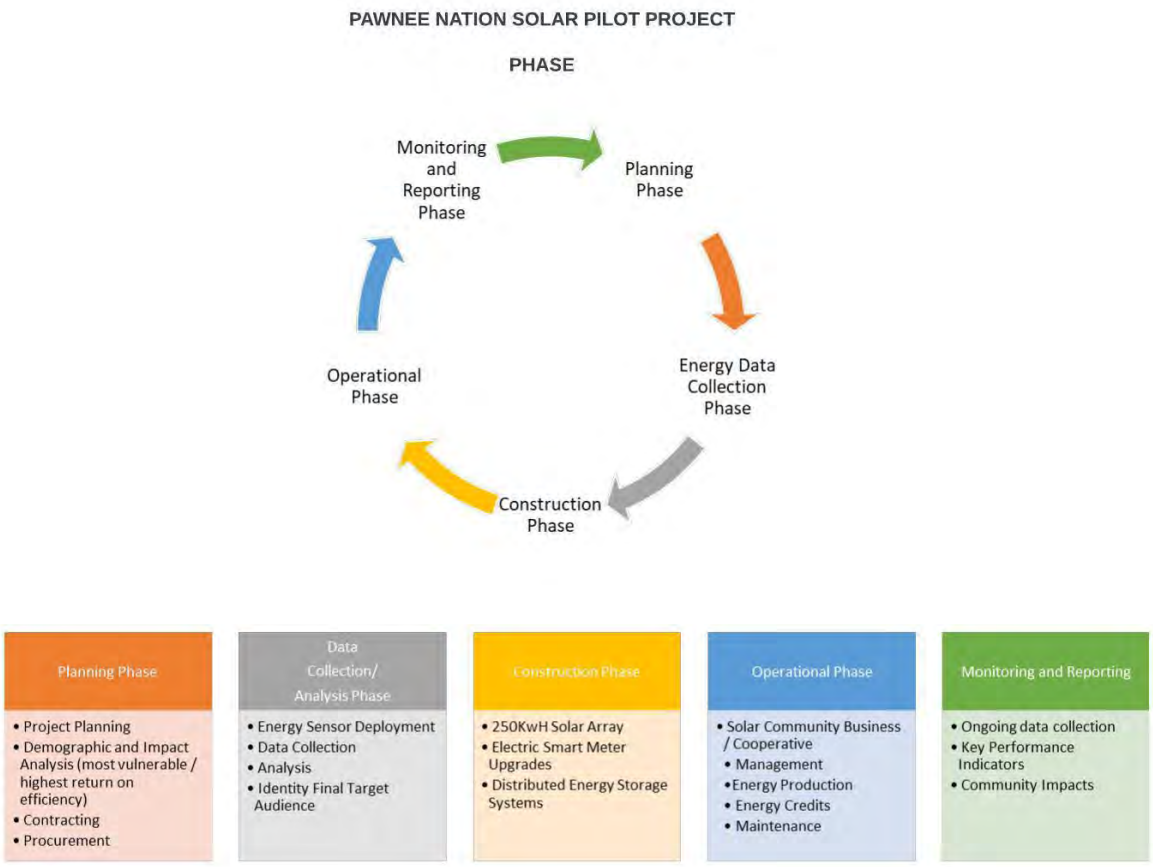

Figure 2. REPP Phases

The project also prioritizes community engagement through education and workshops, ensuring that the transition to renewable energy is equitable and inclusive. By fostering a collaborative environment, the REPP seeks to empower community members with the knowledge and skills necessary to participate in and benefit from the sustainable energy transition.

The Pawnee Nation's approach to geothermal energy is inspired by groundbreaking research into the potential synergy between heavy oil reservoirs and renewable energy sources. By adopting Enhanced Oil Recovery (EOR) techniques for eco-friendly purposes, the project pioneers the use of deep-well geothermal storage, tapping into the latent thermal energy of abandoned oil fields. This innovative approach goes beyond mere repurposing; it transforms dormant geological assets into vital resources for thermal heating, crucially supporting both residential and commercial needs and significantly advancing the Nation's food security through enhanced hydroponic greenhouse operations.

The integration of Solar Thermal Collector technologies with geothermal storage is a testament to the project's commitment to sustainability, providing a consistent energy supply and paving the way for a method that local and global communities can adopt. This harmonious blend of accumulated geothermal heat and solar innovation encapsulates the project's broader ambition toward a resilient and enduring energy transition. Figure 3 shows the main REPP components:

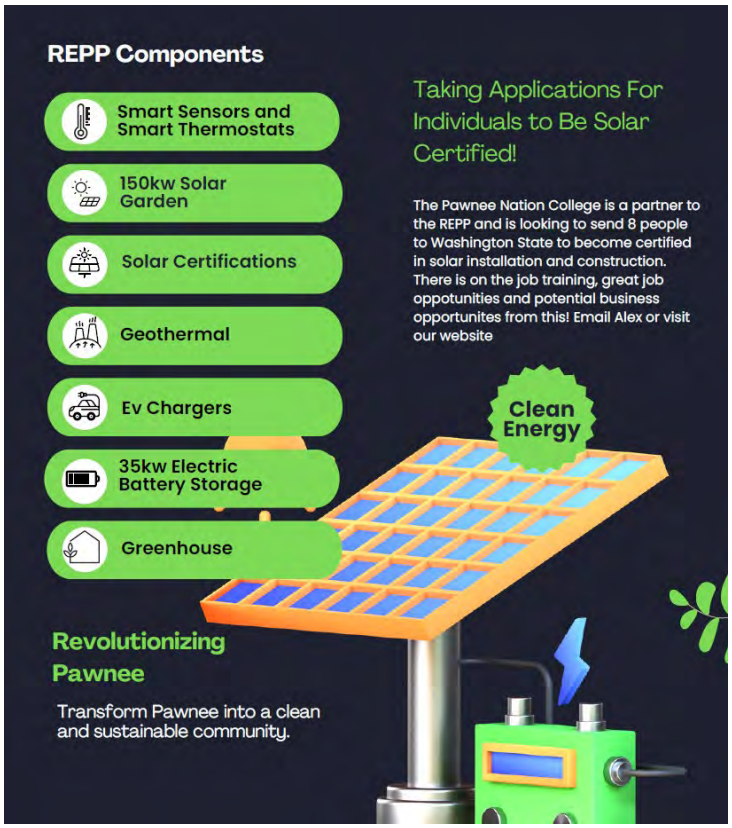

Figure 3. REPP main components

The Pawnee Nation's efforts underscore the untapped renewable energy potential lying dormant within tribal lands, representing a significant share of the nation's resources. The project seeks to correct the imbalances and inequalities in energy access, fostering a sense of resilience and empowerment within the community. Central to this endeavor is the collaborative spirit embodied by PNCRIS, which includes diverse entities such as the Housing Authority, Tribal College, Tribal Nation, Electric Cooperative, State University, and Non-profit organization. This evolving alliance ensures local governance and merges traditional wisdom with modern technological solutions.

Strategic partnerships with the Bureau of Indian Affairs (BIA) and the Bureau of Land Management (BLM) aim to develop a hybrid lease model for geothermal and oil well infrastructure. This innovative model integrates geothermal energy projects with existing oil and gas infrastructure, allowing for a seamless transition from fossil fuels to renewable energy sources on tribal lands. By re-purposing and co-managing oil well sites for geothermal energy production, this model underscores a commitment to sustainable land use and energy production. This collaboration sets a precedent that could redefine the use of tribal lands for renewable energy projects across the United States, respecting tribal sovereignty while fostering economic development and environmental stewardship.

3. The Solar to Geothermal Synergy

Oklahoma is considered to have a poor geothermal gradient to develop electrical power production. However, the thousands of wells drilled on Oklahoma lands shows consistently the availability of low-temperature sources ranging from 30 to 60°C. These sources are beneficial for heat use, especially when existing oil wells are available. While Oklahoma benefits largely of high solar intensity, our project is focusing on combining the solar heat generation with the wellbore heat storage and delivery, to provide a 24-hour constant heat output that can be used for heating and industrial heat purposes.

Some researchers (WEA, 2004) suggest that excess solar power can be stored during the day and utilized at night. As illustrated in Figure 1, part of the energy recovered at night comes from heat storage, with the remainder generated from other "backup" fossil energy sources, as proposed by Teodoriu et al. (2007) and later by Limpasurat et al. (2011). It has been demonstrated (WEA, 2004) that solar-to-thermal energy conversion technologies have an advantage over other technologies due to their unique ability to integrate with conventional heat generators in any energy-producing system, such as power plants. Figure 2 presents an example of combining a solar-to-thermal heater with thermal storage and/or a fossil fuel backup heater to produce electricity without causing stochastic perturbations in the electric grid. However, the innovative concept proposed for the REPP focuses on utilizing wellbore-stored heat for heating purposes. The proposed solar array will generate heat for immediate use during the day, while the excess heat will be injected into selected oil wells for storage.

Although the REPP does not currently focus on the potential for oil recovery, this may remain a future option if oil is still needed during the energy transition to secure national energy demands.

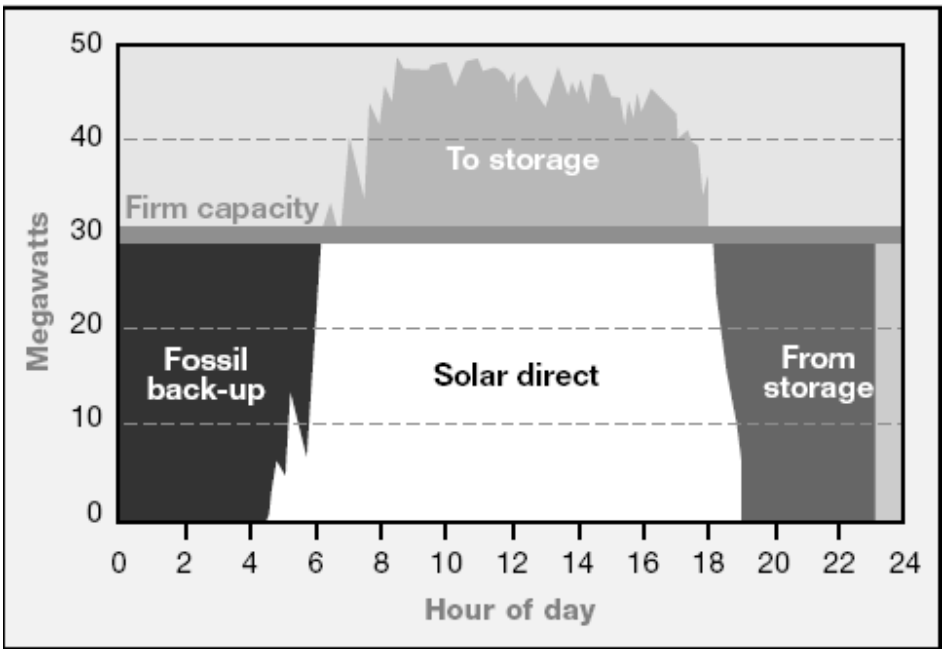

Fig. 4. Solar energy available in 24 hours (WEA, 2004)

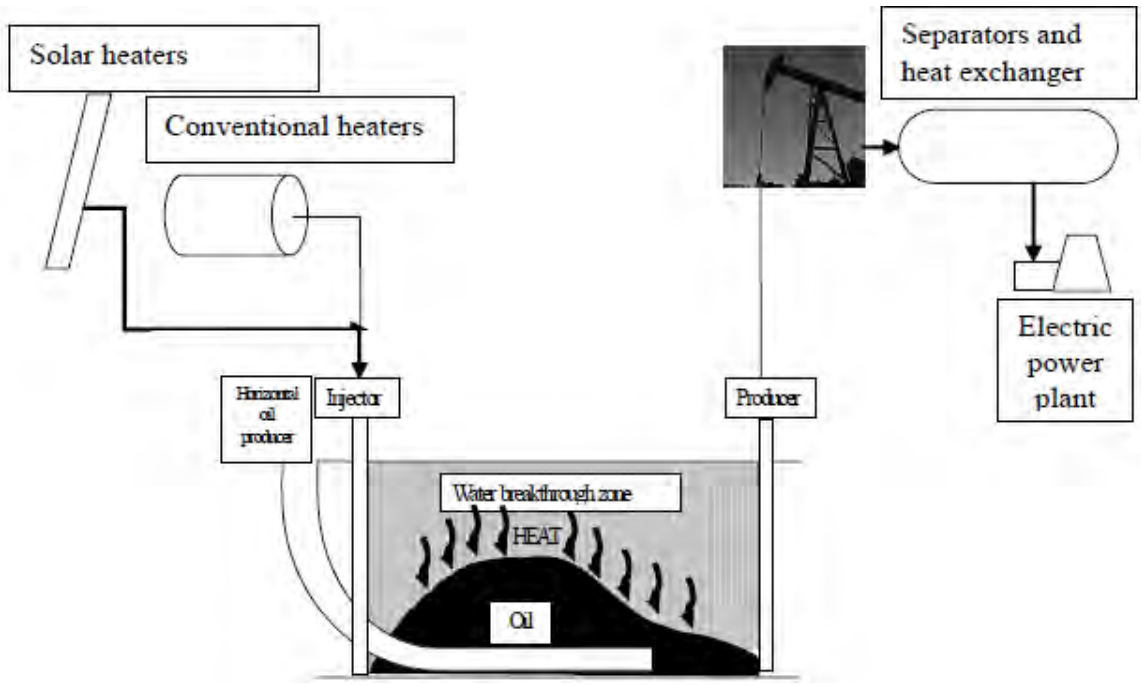

Fig. 5. Schematic of the EOR with electric power-producing process

Why does using old wells matter?

Through the REPP we will be changing the energy landscape of Pawnee in multiple ways. One of these ways is by converting old oil and gas wells into geothermal wells, giving new life to idle and orphaned wells.

Typically, the life cycle of the oil and gas well starts with drilling and ends when the well is deemed to be no longer economically viable. Initially, the well is drilled and cased. The drilling process creates a hole to the targeted formation, and then the casing is run to protect freshwater zones and achieve zonal isolation. Some formations need to be stimulated as well, or other tools need to be used in the well, this is called completing the well. Once you have access to the hydrocarbons, the well is then put on production, and you can begin producing the fluids and gases in the reservoir. Once you have recovered all the oil and gas possible and re-stimulating won't produce enough hydrocarbons to make financial sense, the well is then idled for future use, plugged and abandoned (P&A), or if the operator goes out of business and doesn't have the means to P&A the well, and the well has no known operator, orphaned. Sometimes wells are kept suspended, meaning they are not producing but also not set yet for P&A. Our current project is focusing on the latter.

Instead of permanently abandoning these wells, we can give them a new lease on life by converting them to geothermal wells. Pawnee has 3 idled wells near their greenhouse and administrative buildings that would be great candidates to heat these buildings during the winter by storing heat in the formation during the summer and extracting it during winter. Our goal at REPP is to bring

a cleaner and more sustainable future to Pawnee Nation and the surrounding areas, and with geothermal heating and other energy sources we are bringing to the table, our goal will be achieved.

As part of the community commitment, a team of students from the University of Oklahoma has taken the opportunity to investigate possible solutions for wellbore completion under various scenarios and costs associated with it. Figure 6 shows the final proposed well completion for the selected wellbore. The main task here was to investigate if a single well could provide an adequate flow rate and temperature for the project. The small production casing size and wellbore limitations have shown that the proposed solution using 2 7/8" tuning for production and annulus for injection may be the bottleneck to achieving higher flow rates, especially for phase two of the current REPP when the solar-thermal array and surface hot water pipeline network may be expanded. Currently, the team is also considering the option of using several adjacent wells to expand the geothermal flow rate potential. This new solution will allow us to expand our geothermal storage similarly as shown in Figure 5, but without electricity production, since we aim for direct heat use. As mentioned, the oil recovery from the reservoir may remain as an alternative to quickly recover the investment costs and once oil is depleted the system will remain a true geothermal heat storage solution for the long term.

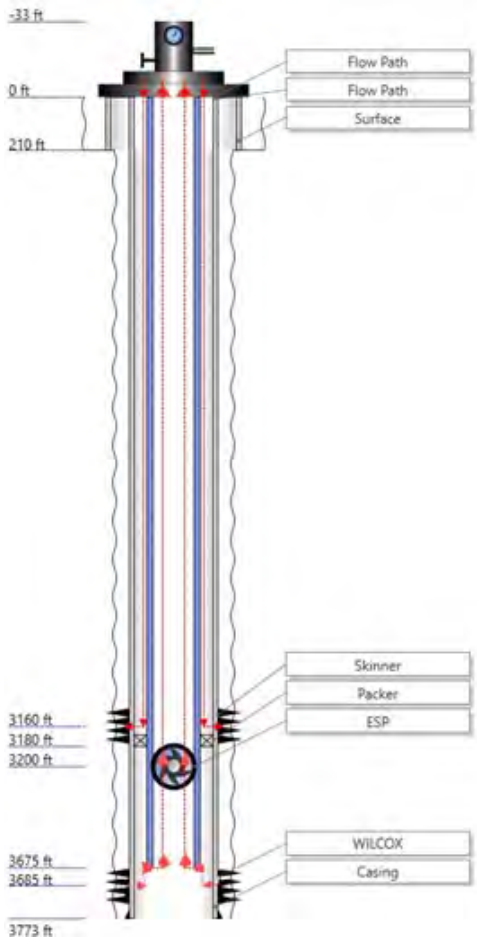

Figure. 6. Selected wellbore completion as an oil-to-geothermal single well concept

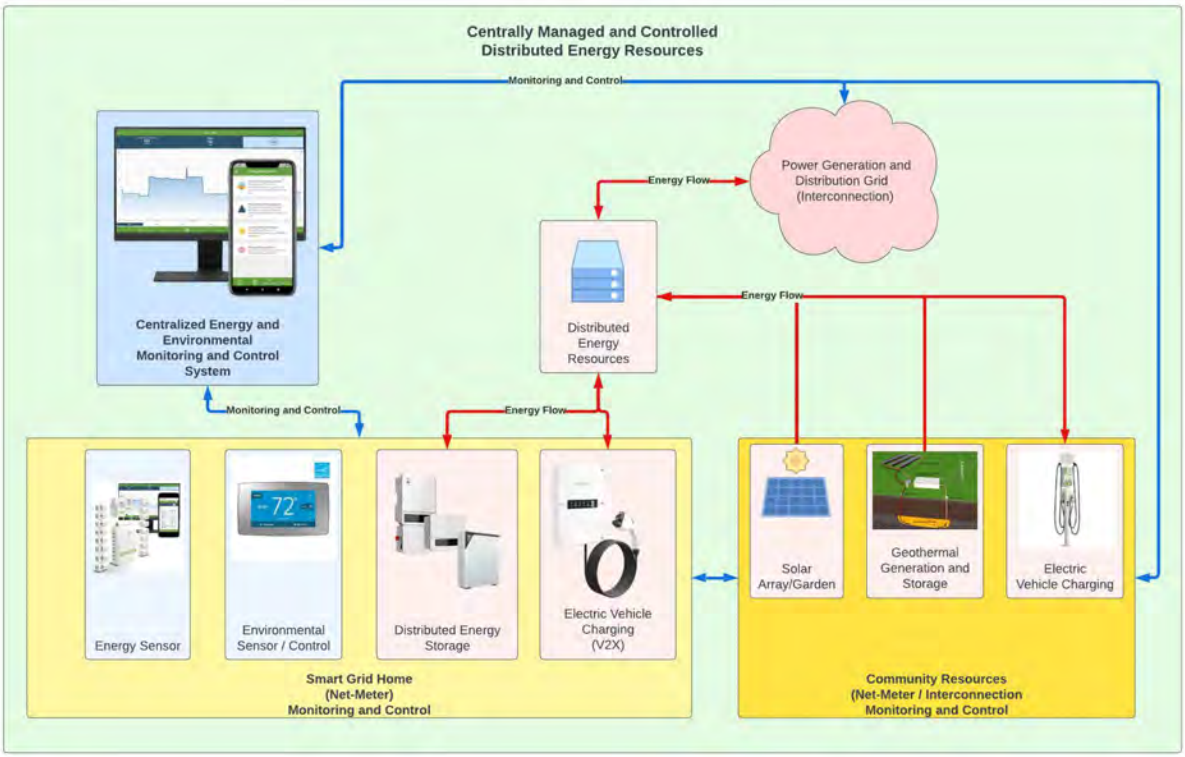

Figure. 8. REPP concept and implementation

4. Conclusions

This project, although small in scale, demonstrates that the most important element of success is the early involvement of the locals in the project phases. Community engagement and workshops were the key to understanding the priorities and needs of rural communities.

We also demonstrated that when geothermal potential is low, a synergy between solar thermal array and geothermal can improve economics and provide continuous heat.

The project also shows the complexity of implementing renewables in rural areas, hence only through prioritization the success of these projects can be achieved. Although we are the beginning of the project, we hope to further improve renewables adoption by emphasizing the need of energy efficiency and efficient use of electricity through smart sensors and usage monitoring.

Acknowledgment

We also acknowledge the generous support from the United States Department of Agriculture (USDA), whose $2.6 million grant made this transformative initiative possible. The guidance and expertise provided by the Bureau of Indian Affairs (BIA) and the Bureau of Land Management

(BLM) have been invaluable in developing the hybrid lease model for geothermal and oil well infrastructure.

The authors would like to extend their deepest gratitude to the Pawnee Nation for their visionary leadership and unwavering commitment to sustainable development, which has been instrumental in the success of the Pawnee Nation's Rural Energy Pilot Program. Special thanks to the Pawnee Nation College, Pawnee Nation Housing Authority, Pawnee Public Schools, Indian Electric Cooperative, and Tribuquent Corporation for their collaborative efforts and partnership.

Our heartfelt appreciation goes to the University of Oklahoma for its substantial contributions, particularly in the research and technical support that have shaped the geothermal energy solutions presented in this project. We are also grateful to the Well Integrity Laboratory at the University of Oklahoma for providing access to their unique cement repository and database, which has been crucial for the project's wellbore completion studies. The dedication and hard work of the students from the University of Oklahoma in investigating and developing wellbore completion solutions under various scenarios are deeply appreciated.

Finally, we extend our gratitude to the community members of the Pawnee Nation for their active participation and support in the project's educational and engagement initiatives. This project is a testament to the power of collaboration, traditional wisdom, and modern technology working hand-in-hand to create a sustainable future.

REFERENCES

Teodoriu, C.; Falcone, G.; Espinel, A. Letting off steam and getting into hot water-harnessing the geothermal energy potential of heavy oil reservoirs, 2007.

Limpasurat, A.; Falcone, G.; Teodoriu, C.; Barrufet, M. A.; Bello, O. Artificial geothermal energy potential of steam-flooded heavy oil reservoirs. Int. J. Oil Gas Coal Technol 2011, 4, 31−46.

World Energy Assessment (2004), Energy and the challenge of sustainability, 2004.

Empowering the Lānaʻi Island Community with Groundwater and Geothermal Resources

Alice Kim, Nicole C. Lautze, and Donald M. Thomas

Hawaiʻi Groundwater and Geothermal Resources Center, University of Hawaiʻi at Mānoa

Keywords

Geothermal, Groundwater, Lānaʻi Island, Pālāwai Basin, Play Fairway Analysis, Hawaiʻi

ABSTRACT

The Hawaiʻi Groundwater and Geothermal Resources Center (HGGRC) engaged with the Lānaʻi Island's community and land management company, Pūlama Lānaʻi, when conducting geothermal and groundwater research. Lānaʻi Island holds blind geothermal resources–the geothermal resources are deep below the surface. Lānaʻi Island will likely undergo substantial development in the near future, which will place additional demands on its freshwater supply and renewable energy resources. More knowledge of Lānaʻi's water supply, source, and quality will be needed. For the Hawaiʻi Play Fairway project, HGGRC deepened an existing water well on Lānaʻi, collected data, and engaged with the Lānaʻi community and Pūlama Lānaʻi. This drilling project is the first deep-drill geothermal research project in the Hawaiian Islands outside of Hawaiʻi Island. HGGRC shared its research with community members in three community meetings and gave them a tour of the drilling site. HGGRC coordinated its geophysical surveys with Pūlama Lānaʻi's archeology division. Local high schoolers contributed to the research as paid interns. HGGRC disseminated its research through peer-reviewed publications, presentations, datasets and a blog with drilling updates. HGGRC's research benefited the Lānaʻi community: the research increased the knowledge of Lānaʻi's water supply and enabled the community to consider geothermal as a renewable energy source. HGGRC aimed to empower the Lānaʻi community, so it can contribute to and benefit from the research and can effectively manage the island's groundwater and geothermal resources for continued sustainable livelihood and development.

1. Introduction

Even with Hawaiʻi's volcanic origins, much of Hawaiʻi's geothermal resources remains unknown (Lautze, 2022). The State of Hawaiʻi is producing geothermal electric power from only one geothermal system: the Kīlauea East Rift Zone (KERZ) on Hawaiʻi Island (Lautze et al., 2017a). Beyond KERZ, Hawaiʻi's geothermal resources are blind–their manifestations, such as hot springs

and steam vents, do not appear on the ground surface because the heated water flows far below (Lautze, 2022). Historically, not a lot of research has been done on the blind resources in the rest of the state; very few deep (~2 km) wells were made for Hawai‘i’s geothermal exploration (Lautze, 2022).

As the State’s leader in earth sciences research, the University of Hawai‘i (UH) conducted the State’s comprehensive statewide geothermal resource assessments and determined that all of the major Hawaiian Islands likely hold geothermal resources. For Hawai‘i’s second assessment, a UH research unit, the Hawai‘i Groundwater and Geothermal Resources Center (HGGRC), produced the Hawai‘i Play Fairway project. From 2014 to 2021, this $2.3 million project accomplished many firsts for Hawai‘i geothermal:

- Hawai‘i’s first comprehensive statewide geothermal resource assessment in over three decades (Lautze et al., 2017a)
- First mathematical application to Hawai‘i’s geothermal resource probability (Ito et al., 2017)
- First deep-drill geothermal research project in the Hawaiian Islands outside of Hawai‘i Island–on Lāna‘i Island (Lautze et al., 2024)

Because of Hawai‘i’s abundance of geothermal resources and the need for more affordable firm renewable energy, HGGRC encourages the State of Hawai‘i to expand geothermal energy use beyond Hawai‘i Island and to other major Hawaiian Islands. Any resource found on Hawai‘i’s older volcanoes will hold temperatures more compatible with binary power generation rather than flash-steam generation. Binary power generation will have significantly less impacts and lower visibility in the community.

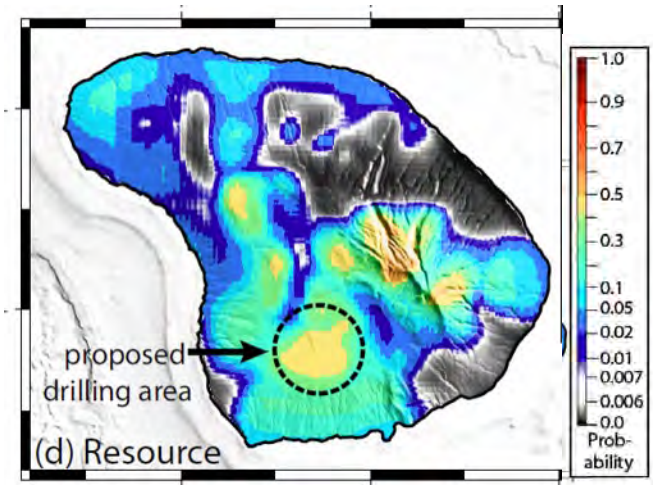

Figure 1: A map of the Lāna‘i Island with the areas colored by local probabilities of a geothermal resource. The color bar on the right shows how the geothermal probabilities are mapped on Lāna‘i. The circle of short dashed lines delineates the proposed drilling area (Lautze et al., 2020).

Throughout the Play Fairway project, HGGRC collected data (Lautze et al., 2017a), developed new simulations for subsurface heat across the Hawaiian Islands (Ito et al., 2017), ranked areas for exploration (Lautze et al., 2017b), and performed on-the-ground experiments (Lautze et al., 2020). HGGRC analyzed data for gravity, resistivity, and groundwater temperature to determine which locations held resources at an accessible depth and considered the costs and logistics for drilling

at each location (Lautze et al., 2020). Ultimately, for deep-drilling geothermal exploration, the project chose Pālāwai Basin, Lānaʻi Island–geologically the caldera region of Lānaʻi volcano (Lautze et al., 2024). Because research should benefit the community, HGGRC incorporated community engagement throughout the entire drilling project on Lānaʻi.

2. Understanding the Lānaʻi Island

Basaltic lava flows from a single shield volcano formed a dome-shaped island–the Lānaʻi Island (Stearns et al., 1940). A three-and-a-half-mile caldera–the Pālāwai Basin–formed during a collapse of the southwest and northwest rift zones and a subsidence at their intersection (Stearns et al., 1940).

Lānaʻi is one of the more arid of the Hawaiian Islands. In the rain-shadow of Maui, Lānaʻi receives very limited rainfall–only 400 to 800 mm of rainfall annually on average (Giambelluca et al., 2013). As a result, most of Lānaʻi's nearshore areas hold very limited basal freshwater aquifers.

During the 1920s, pineapples covered the Pālāwai Basin as part of the world's largest single pineapple plantation. Under James Dole's Hawaiian Pineapple Company, pineapple cultivation became Lānaʻi's main industry, and Lānaʻi earned the nickname the "Pineapple Island" (County of Maui, 2016). For decades afterwards, the pineapple served as Hawaiʻi's major cash crop and a symbol of Hawaiʻi (Hawkins, 2011; County of Maui, 2016).

Today, pineapple is no longer commercially grown on Lānaʻi, and wild grass now covers the Pālāwai Basin (County of Maui, 2016). Lānaʻi's economy now focuses on tourism (County of Maui, 2016). Entrepreneur Larry Ellison owns about 98% of Lānaʻi; the State, County of Maui, and other private landowners own the remaining 2% (County of Maui, 2016). Lānaʻi City operates as Lānaʻi's commercial center and home to 99 percent of the island's population (County of Maui, 2016). Lānaʻi Island will likely undergo substantial development in the near future (Maui County, 2016), which will place additional demands on its water supply.

3. HGGRC's Research on Lānaʻi Island

The current model for groundwater in Hawaiʻi is generalized and not specific to the individual island systems–including Lānaʻi's (Lautze, 2018). A lot about Lānaʻi's groundwater system is unknown–including the groundwater's storage and transport throughout the island (Lautze, 2018). At present, Lānaʻi Island has had minimal efforts to characterize the relationship between its geologic history and structure and its water resources–the U.S. Geological Survey still lists the 1940 work of Stearns as Lānaʻi's primary study of water resources there (Lautze, 2018; Stearns et al., 1940).

HGGRC's research explores the geologic structures in Hawaiian volcanoes and how those structures influence groundwater storage and flow. On the Lānaʻi Island, Pālāwai Basin holds high-level brackish water, a unique feature in the Hawaiian islands (Lautze, 2018). The water's origin remains unknown (Lautze, 2018). As Pālāwai Basin is a remnant caldera, geologically similar locations exist around the state (Lautze, 2018). Hence, this research will inform groundwater management across the state (Lautze, 2018).

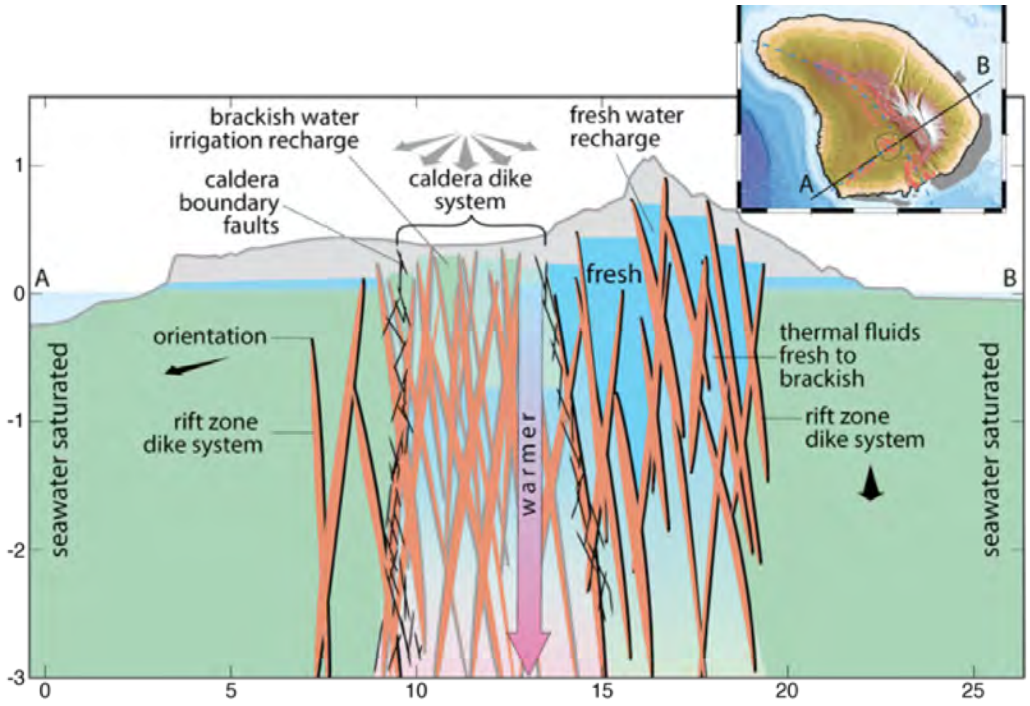

Figure 2: Conceptual model of Lāna‘i’s hydrology along cross-section AB (inset top right). Red hatches are relatively impermeable dikes; black hatches are caldera boundary faults. We theorized the presence of three aquifers: a thin basal low-level aquifer at the coast; a warm brackish high-level aquifer within the Pālāwai Basin; and a cold, fresh higher-level aquifer within the rift zone. The temperature data from Lāna‘i Well 10 indicate that the water within the Pālāwai Basin likely will get warmer and fresher with depth (Lautze et al., 2024).

Figure 3: A panorama of the drill site in Pālāwai Basin. At the work site are shipping containers, a work station for core processing, and a drilling rig, which deepened an existing water well from a depth of ~427 to ~1,057 meters (1,400 to 3,467 feet). The island's highest ridge rises in the background.

By drilling a 4-inch-diameter hole into Pālāwai Basin, HGGRC conducted “slim hole” drilling, using bits less than 7 inches wide, to descend more than a kilometer down. During the drilling, HGGRC collected a drill core–a continuous sample of rock collected from the ground. Currently, HGGRC is analyzing the drill core, which is hundreds of feet long and several inches thick. Analyzing the core will yield information on how minerals and water are distributed underground–

including the brackish water found at elevation in Pālāwai Basin–and Lāna‘i’s hydrologic and volcanic history and geologic structures (Lautze, 2018).

Outside of Kīlauea’s summit and East Rift Zone, Hawai‘i’s geothermal resources are blind. That is, their manifestations, such as hot springs and steam vents, do not appear on the ground surface because the heated water flows far below. Historically, little work had gone into exploring blind resources over the rest of the state. By drilling on Lāna‘i, HGGRC conducted the first deep-drill geothermal research project in the Hawaiian Islands outside of Hawai‘i Island (Lautze et al., 2024).

4. Planning with Pūlama Lāna‘i

The land management company of Lāna‘i, Pūlama Lāna‘i, has supported developing Lāna‘i’s groundwater and geothermal resources. HGGRC provided reports and information to Pūlama Lāna‘i and discussed Lāna‘i’s groundwater management and fresh water resource assessment. Before the drilling, Dr. Lautze gave a talk on Lāna‘i Island’s hydrology to Pūlama Lāna‘i. Furthermore, Pūlama Lāna‘i assisted HGGRC when it produced an Environmental Assessment for the Hawai‘i State Office of Environmental Quality Control (Lautze, 2018).

Prior environmental work and land use of the drilling location reduced the drilling project’s regulatory requirements (Lautze, 2018). According to a regulatory review, Pūlama Lāna‘i already did extensive environmental, cultural, and land use documentation for much of the island (Lautze, 2018). Furthermore, because a pineapple plantation operated in the area for several decades, the area poses little likelihood of hosting threatened or endangered plants or animals (Lautze, 2018).

Pūlama Lāna‘i offered two deep wells for HGGRC to deepen from ~305 m (>1000'). After conducting video and deviation logging of the wells, HGGRC determined that it could deepen Lāna‘i Wells 9 and 10. HGGRC chose Lāna‘i Well 10 because of reports of unconsolidated material at the bottom of Well 9, its proximity to residential areas of Lāna‘i City, and its location closer to the dominant source of cold rainfall recharge.

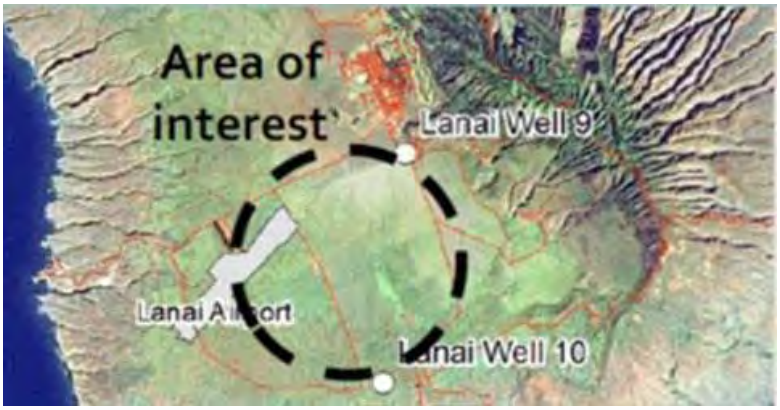

Figure 4: A satellite image of the Pālāwai Basin. The circle of dashed lines delineates the area of interest for research. On the edges of the circle: Lāna‘i Airport on the left, Lāna‘i Well 9 on the top right (just below Lāna‘i City), and Lāna‘i Well 10–the well that the project deepened–on the bottom right.

5. Community Meetings

Throughout the course of the drilling project, HGGRC shared updates with the Lāna‘i community in three community meetings organized by Pūlama Lāna‘i:

Before drilling–September 10, 2018: Senior researchers Nicole Lautze and Don Thomas introduced the Lāna‘i community to the drilling project. Lāna‘i’s newspaper, Lāna‘i Today, published an article about the meeting. In the article, “Straight from the Source,” Lāna‘i Today said, “Although the presentation was technical, it was also fascinating!”

Middle of the drilling, Open House of drilling site–June 29, 2019: HGGRC invited the community to tour the Well 10 drilling site. Walking on the rocky red dirt of Pālāwai Basin, community members viewed the drilling rig, shipping containers, and drill cores. Senior researchers Nicole Lautze, Don Thomas, and Eric Haskins explained the drilling process and drill cores on display and answered questions.

Figure 5: HGGRC invited the community to the drilling open house, and Pūlama Lāna‘i produced the announcement (left image). At the drilling open house, Lāna‘i residents visited the active drill site, and researchers discussed drilling and showed the rock core and drilling fluids. Lāna‘i Today published an article about the open house (right image; Lāna‘i Today, 2019).

After self-potential survey (electrical survey) and end of project–February 27, 2023: The presentation included the following speakers and their topics:

- Nicole Lautze: Updates
- Donald Thomas: Collecting rock cores, research results, and technical information
- Eric Haskins: Collecting and processing rock cores
- Mattox Telwar: Field experience and working with Lāna‘i students

After the meeting, a community member emailed Nicole, thanking her for the presentation:

> Just wanted to thank you for coming back to us. It was very informative and helpful. I hope you all get the chance (and thus the funds!) to come back …

6. Internships

During geophysical surveys with Pūlama Lāna‘i’s archeology division, HGGRC coordinated paid internships for three students from Lāna‘i High and Elementary School. During March 2022, they measured groundwater movement below the surface. For this self-potential survey, an electrical survey of the groundwater, they coupled sensors to the ground and attached them with wire to measure the electrical current between them. The data showed whether water moved up or down and illustrated a high degree of complexity in water movement within the Pālāwai Basin. Bolós et al. (in review) incorporated the data into their research. To support this endeavor, Pūlama Lāna‘i funded this fieldwork and a postdoctoral fellowship and provided housing and a vehicle at no cost (Bolós et al., in review).

Figure 6: Three students from Lāna‘i High and Elementary School contributed to the self-potential survey. In the left image, the interns apply a wire onto the ground. In the right image, a student inserts a sensor into the ground. The collected data illustrated complex water movement within the Pālāwai Basin.

7. Sharing Knowledge

To share the gained knowledge, HGGRC produced the following:

- Lāna‘i Island Project Updates: a blog with updates on the drilling by Rock and Data Manager Eric Haskins on the HGGRC website
- Peer-reviewed publications and presentations: 9 journal articles, 2 theses, 9 conference papers, 19 conference presentations
- Shared datasets: core log photos and report, noble gas data, resistivity and density 3D models, and daily drilling reports.

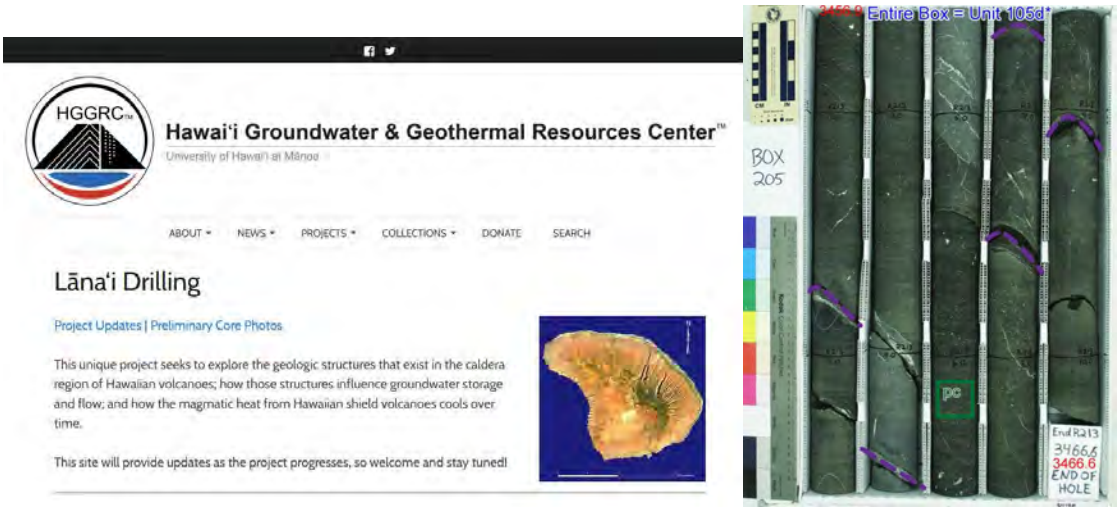

Figure 7: HGGRC's webpage for the Lāna'i drilling project (left) and the last box of cores from Rock Core Log Report: Well 10, Lāna'i Drilling Project (right, deepest cores in the well at a depth of 3,466 feet) .

8. Benefiting the Lāna'i Community

The Lāna'i community's future livelihood, self-sustainability, and development will require additional use of groundwater resources and renewable energy:

Additional water resources – Lāna'i's current water supply is restricted to Lāna'i's single aquifer (Maui County, 2016). As stated earlier, as one of the more arid of the Hawaiian Islands, Lāna'i receives very limited rainfall, and most of Lāna'i's nearshore areas hold very limited basal freshwater aquifers. Therefore, the Lāna'i community will need more knowledge of its water supply, source, and quality. Currently, HGGRC believes that as many as three aquifers store the Lāna'i Island's groundwater (Lautze et al., 2024). By informing the community, HGGRC's research will empower it to efficiently and sustainably manage Lāna'i's groundwater.

Renewable energy sources – By state law, all of the energy that Hawai'i consumes must come from renewable sources by 2045, and the Lāna'i community is still developing its renewable energy sources (Dobbyn, 2022). Two years ago, the Hawaiian Electric Industries initiated Lāna'i's largest utility-scale renewable energy project (DeJournett, 2022). Hawaiian Electric, the state's largest electricity supplier, has contracted with DG Development & Acquisition to build and maintain a solar and battery storage energy storage system (DeJournett, 2022). However, Hawaiian Electric recently paused this project because Pūlama Lāna'i planned to remove the island's two resorts off of Hawaiian Electric's grid and build a microgrid to power them by 2027 (Dobbyn, 2022). Pūlama Lāna'i planned to use solar and battery energy storage systems (Dobbyn, 2022). Because Four Seasons Lāna'i and Sensei Lāna'i currently expend 40 percent of Lāna'i's power, these plans will likely increase electricity rates for the Lāna'i community beyond the two resorts (Dobbyn, 2022).

As a potential solution, geothermal energy can serve as a cost-effective baseload renewable energy source for Lāna'i, and the results from HGGRC's drilling project indicated a potential geothermal resource on Lāna'i (Lautze et al., 2024). In Pālāwai Basin, when HGGRC drilled to a depth of ~427 to ~1,057 meters (1,400 to 3,467 feet), it measured medium-high temperature: a maximum bottom hole temperature of 66°C (151°F) and a gradient of 42°C/km (Lautze et al., 2024). In fact,

this gradient lands within a range of gradients measured in this depth range for exploration wells in the volcanically active East Rift Zone of Kīlauea Volcano (Lautze et al., 2024).

According to HGGRC's analysis, the geophysical datasets–self-potential, magnetotellurics, and gravity data–indicate a probable concealed hydrothermal system and potential magmatic plumbing reservoir beneath the Pālāwai caldera (Bolós et al., in review). As the analysis indicates, a hydrothermal upflow circulates from deep magma reservoirs beneath the central and southern Pālāwai caldera at a depth of ~2 km (Bolós et al., in review). The analysis recommends further research to confirm the geothermal resource's presence (Bolós et al., in review).

9. Conclusion

The drilling project on Lāna‘i serves as a historic milestone for Hawai‘i's geothermal research as the first deep-drill geothermal research project in the Hawaiian Islands outside of Hawai‘i Island (Lautze et al., 2024). The resulting deep-thermal information may serve as the first data on the long-term rates of cooling of the cores of Hawai‘i's volcanoes (Lautze et al., 2020). So far, the initial data analyses indicate that the Lāna‘i Island does indeed hold blind geothermal resources (Lautze et al., 2024; Bolós et al., in review). As information on blind geothermal resources in the main Hawaiian Islands is scarce, project results could direct Hawai‘i's future statewide geothermal development strategy (Lautze et al., 2024).

HGGRC's research on Lāna‘i's will inform groundwater management not only on Lāna‘i but also across the state (Lautze, 2018). The research provides new insights into Lāna‘i's hydrological cycle and will contribute to the island's future planning and siting of water supply wells (Lautze et al., 2024). Furthermore, Pālāwai Basin exemplifies a remnant caldera in the Hawaiian Islands and is similar to other remnant calderas in the Hawaiian Islands (Lautze et al., 2024; Lautze, 2018).

In the near future, the Lāna‘i community will require additional use of groundwater resources and renewable energy to ensure sustainable livelihood and development. Through its research and sharing of knowledge, HGGRC is empowering the community to better understand and manage these resources.

Acknowledgement

We thank the U.S. Department of Energy's Geothermal Technologies Office for funding and managing this project under award number DE-EE0006729 and Pūlama Lāna‘i for its generous financial and logistical support. Warm mahalo to the Lāna‘i community for welcoming us.

REFERENCES

Bolós, X., Lautze, N.C., Boijseauneau, M., and Telwar, M. Unraveling deep hydrothermal activity in Lāna'i (Hawaiian Islands) and its hydrogeological effects. (in review).

County of Maui. Lāna‘i Community Plan 2016: Ordinance No. 4343, Bill No. 67. (2016), 198 p.

DeJournett, T. “Hawaiian Electric selects new developer for Lanai solar project.” Hawaii News Now (2022, July 26), https://www.hawaiinewsnow.com/2022/07/26/hawaiian-electric-selects-new-developer-lanai-solar-project/.

Dobbyn, P. “Larry Ellison Wants Off Lanai’s Electric Grid. That Could Be A Problem For Everyone Else.” Honolulu Civil Beat (2022, Oct. 22), https://www.civilbeat.org/2022/10/larry-ellison-wants-off-lanais-electric-grid-that-could-be-a-problem-for-everyone-else/.

Hawkins, R.A. A Pacific Industry: The History of Pineapple Canning in Hawaii. (2011), I.B. Tauris.

Ito, G., Frazer, N., Lautze, N.C., Thomas, D.M., Hinz, N., Waller, D., Whittier, R., and Wallin, E. “Play Fairway Analysis of Geothermal Resources across the State of Hawaii: 2. Resource Probability Mapping.” Geothermics, 70, (2017), 393-405, doi: 10.1016/j.geothermics.2016.11.004.

Giambelluca, T.W., Chen, Q., Frazier, A.G., Price, J.P., Chen, Y.-L., Chu, P.-S., Eischeid, J.K., and Delparte, D.M. “Online Rainfall Atlas of Hawai‘i:” Bull. Amer. Meteor. Soc., 94, (2013), 313-316, doi: 10.1175/BAMS-D-11-00228.1.

Lāna‘i Today. “Investigating Lanai’s geology.” (2019, July 15), 3.

Lāna‘i Today. “Straight from the Source.” (2018, Oct. 18), 6.

Lautze, N.C. “Hydrogeochemical Assessment of the Pālāwai Basin, Lāna‘i.” University of Hawai‘i at Mānoa, (2018), https://files.hawaii.gov/dbedt/erp/EA_EIS_Library/2018-10-08-LA-DEA-Hydrogeological-Assessment-of-Lanai.pdf.

Lautze, N.C. “Hawai‘i Play Fairway: Final Report.” (2022).

Lautze, N.C., Ito, G., Thomas, D.M., Frazer, N., Martel, S. Hinz, N., Tachera, D.K. Hill, G. Pierce, H.A., Wannamaker, P.E., and Martin, T. “Play Fairway Analysis of geothermal resources across the State of Hawai‘i: 4. Updates with new groundwater chemistry, subsurface stress analysis, and focused geophysical surveys.” Geothermics, 86, (2020), doi: 10.1016/j.geothermics.2019.101798.

Lautze, N.C., Thomas, D.M., and Haskins, E. “Play Fairway Analysis of geothermal resources across the State of Hawai‘i: 5. Slim hole drilling on Lāna‘i island.” Geothermics, 124, (2024), doi: 10.1016/j.geothermics.2024.103147.

Lautze, N.C., Thomas, D.M., Hinz, N., Ito, G., Frazer, N., and Waller, D. “Play Fairway Analysis of Geothermal Resources across the State of Hawaii: 1. Geological, geophysical, and geochemical datasets.” Geothermics, 70, (2017a), 376-392, doi: 10.1016/j.geothermics.2017.02.001.

Lautze, N.C., Thomas, D.M., Waller, D., Hinz, N., Frazer, N., and Ito, G. “Play Fairway Analysis of Geothermal Resources across the State of Hawaii: 3. Use of Development Viability as one criteria to prioritize future exploration activities.” Geothermics, 70, (2017b), 406-413, doi: 10.1016/j.geothermics.2017.07.005.

Stearns, H.T., Macdonald, G.A., and Swartz, J.H. Geology and ground-water resources of the islands of Lanai and Kahoolawe, Hawaii. 6, (1940), Advertiser Publishing Company, Limited.

Geothermal Direct-Use Application for Greenhouse Heating: Case Study of Osage Tribal Nation

Vagif Mammadzada[1], Gurban Hasanov[1], Jose Aramendiz[1], Nabe Konate[1], Cesar Vivas[1], Orkhan Khankishiyev[1], Zeming Hu[1], Saeed Salehi[2]

[1]Well Construction Technology Center, The University of Oklahoma, Norman, Oklahoma

[2]Mechanical Engineering, Southern Methodist University, Dallas, Texas

Keywords

Geothermal Energy, Direct-Use Application, Greenhouse Heating, Osage Tribal Nation, Sustainable Development

ABSTRACT

Geothermal energy stands at the forefront of sustainable solutions, offering a renewable and environmentally friendly alternative to traditional energy sources. The Osage Tribal Nation, like many communities worldwide, recognizes the immense potential of geothermal resources in addressing energy needs while minimizing environmental impact. Utilizing geothermal energy for direct-use applications holds promise for revolutionizing agricultural practices and enhancing community resilience.

This study delves into the transformative potential of geothermal direct-use technology, focusing on its application in greenhouse heating within the Osage Tribal Nation. The greenhouse serves not only as a vital source of fresh produce but also as a symbol of cultural heritage and community sustenance. However, the challenge of providing consistent heating to sustain agricultural operations underscores the need for innovative and sustainable energy solutions.

Against this backdrop, our research endeavors to explore the geothermal landscape of the Osage Nation, employing advanced geological modeling, reservoir simulation, well planning, and economic analysis techniques. By investigating the feasibility of drilling new wells near the greenhouse and harnessing geothermal heat flow, we seek to establish a robust framework for integrating geothermal energy into the tribe's energy portfolio.

The Osage Tribal Nation's commitment to sustainable energy practices aligns with the broader goal of fostering environmental stewardship and self-sufficiency within indigenous communities. This case study serves as a blueprint for leveraging geothermal resources to address food security challenges and promote sustainable development initiatives.

1. Introduction

1.1 Overview

Geothermal energy is a growing renewable energy source that can be used worldwide. Geothermal energy is the energy harnessed from the Earth's natural heat reservoirs. Despite the recent increase in geothermal applications, geothermal energy still has one of the lowest energy usages among all renewable energy sources, accounting for less than 1% of the total utility-scale energy generation. Low geothermal energy usage can be attributed to many factors, such as a lack of awareness and acceptance of geothermal energy, low investment, and low infrastructure. Geothermal energy has multiple applications ranging from electricity generation to direct use. Direct geothermal use provides a range of possibilities, ranging from aquaculture, farming, greenhouse gas, and building heating and cooling. The significance of energy sustainability and self-reliance is deeply engrained in tribal communities around the United States. [] Through its direct-use applications, geothermal energy holds immense promise in ensuring that tribal communities are self-sufficient and have long-term sustainable energy. Direct geothermal energy applications, which encompass various aspects of one's daily life, from heating and cooling buildings to greenhouse heating and beyond, offer a valid path toward energy independence, economic development, and cultural preservation for tribal communities. This project will investigate the techno-economic feasibility of providing direct heat to a greenhouse during winter to support tribe's effort for food sovereignty.

1.2 Motivation

Many tribal communities face economic and energy challenges that affect their daily lives. The Osage Nation tribal community is one of the largest tribal communities in Oklahoma. The Osage Nation tribal community, like many other tribal communities, resides in remote and rural areas with unique energy requirements and challenges. In 2020, during the COVID-19 pandemic, the Osage Nation tribal community experienced a major breakdown in their food system. As a result, a 40,000-square-foot greenhouse was built to increase their food production capacity and increase food sovereignty in the tribal nation. However, the greenhouse is faced with a major challenge during winter, where lack of sufficient heat limits the growth of the crops. This creates a need to provide heat to the greenhouse during winter to facilitate its proper operation. Geothermal wells, through their direct-use application, are a suitable heat source for addressing the issue. The project will investigate the feasibility of drilling two geothermal wells around the greenhouse to provide direct heat during winter.

2. Study Area

2.1 Overview

Within the scope of our collaborative project focused on harnessing geothermal heat for greenhouse and building heating, this section of the report delves into the potential scenarios and challenges associated with implementing geothermal heating systems. This project will explore two scenarios where geothermal heat could be employed as a primary heating source for greenhouses and other structures if need be while also examining the challenges that may emerge during the planning, installation, and operation of such systems. By identifying and addressing these hurdles, we aim to provide valuable insights that inform the decision-making process and promote the sustainable utilization of geothermal energy for heating purposes in our chosen settings. The study area for this project will be the Osage Nation, as shown in Figure 1**.** The Osage

Nation's petrophysical, geologic, and temperature data was obtained from drilled active and inactive wells. The Osage Nation consists of 40,086 drilled wells, which include 2,495 active wells and 34,064 inactive wells. The inactive wells in the study area account for more than 84% of the total wells in the region. The inactive wells in the region provide a good data source for understanding well conditions, formations, and drilling concerns in the area. Two scenarios are investigated in this project for feasibility studies. The study area was narrowed down to a greenhouse located in the Harvest Land Farm of the Osage Nation. The Greenhouse needs heat and cooling during winter and summer respectively, leading to the decision to implement the project in that area to contribute to the community effort toward food sovereignty.

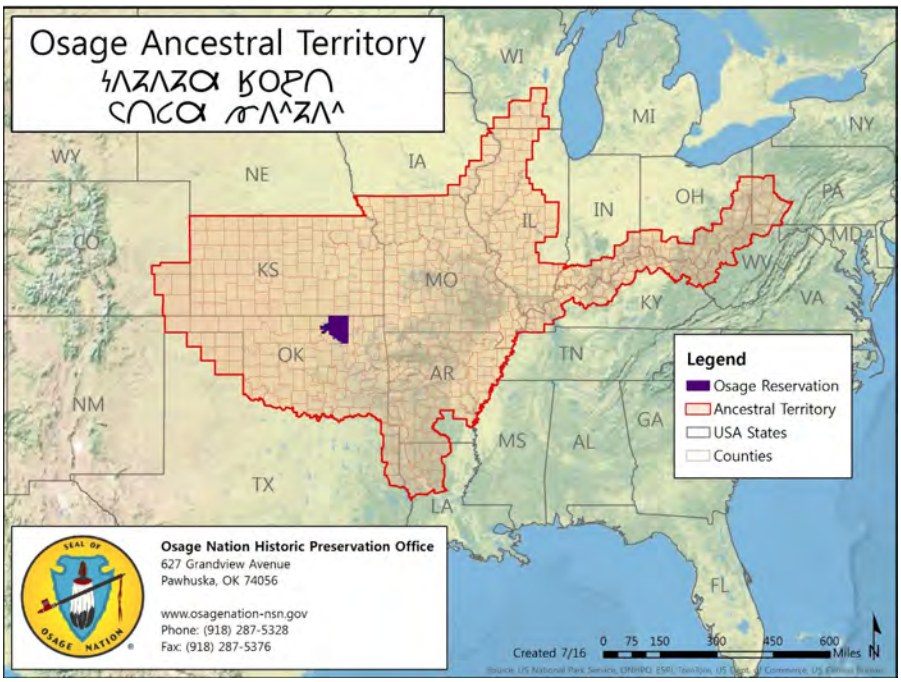

Figure 1: Osage Nation tribal community in Oklahoma (Nation)

3. Scenarios Analysis

3.1 Scenario 1: Repurposing Existing Wells for Geothermal Heat

One of the scenarios under consideration in our project involves repurposing existing wells in the vicinity to extract geothermal heat. This approach holds significant promise, particularly from a cost-effectiveness perspective, as it eliminates the need to undertake the costly and resource-intensive process of drilling new wells. By leveraging these pre-existing wells, we can tap into an established infrastructure, potentially accelerating the implementation of our geothermal heating system. Figure 2 shows a visual of a potential layout consisting of three wells that the team analyzed during a trip to the site in 2023. Figure 3 also shows some relevant information about the wells located in the greenhouse neighborhood.

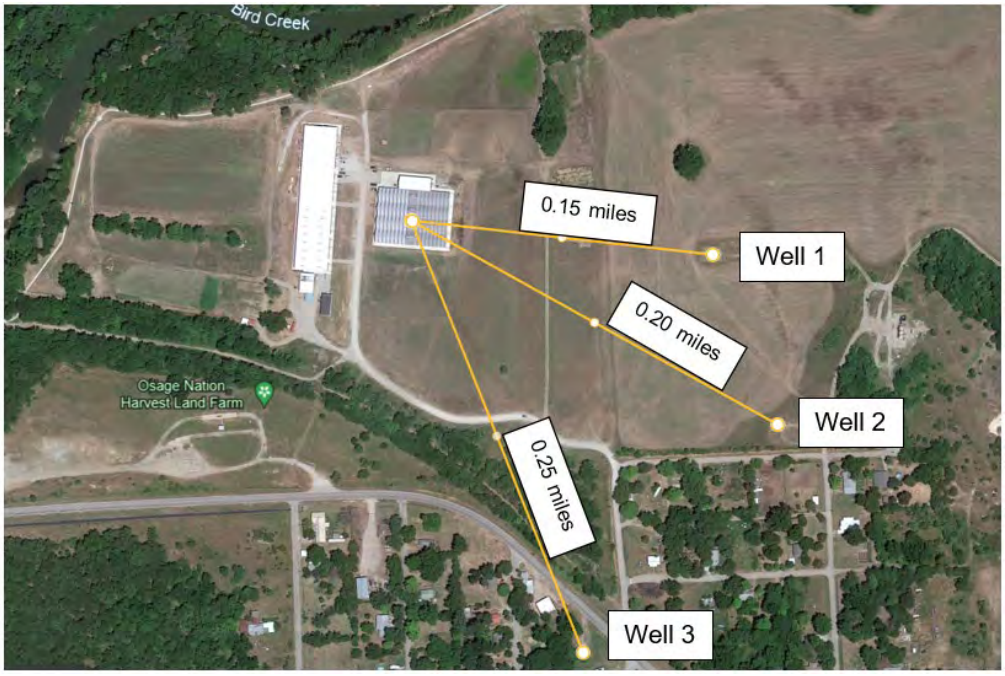

Figure 2: Visual representation of the wells around the area of study

WELL CARD

API: 3511319460 Opr: GARNET OIL CO Name: OSAGE 1 Well #: 1

Well Header

Curr Status:	INACTIVE	Abstract:		Range:	09E
Compl Type:	UNKNOWN	Field:		Quarter-Quarter:	NE
GL:	802 ft	Survey:		Spud Date:	06-21-1920
County:	OSAGE (OK)	Block:		First Completion Date:	07-25-1920
Surface Lat:	36.6595857	Section:	10	Last Completion Date:	07-25-1920
Surface Lon:	-96.3175309	Township:	25N	Wellbore Count:	1

PERMITS | WELLBORES | WELL DESIGN | WELL LOGS | COMPLETION | FORMATIONS | WELL TESTS | PRODUCTION | HISTORY | FILINGS

Casing

API	Casing Type	Casing Size (in)	Top Depth (ft)	Bottom Depth (ft)	Hole Size (in)	Casing Weight (lb/ft)	Casing Grade	Slurry Volume (cu ft)	Cement Amount (sacks)	Cement Class	Cement Top (ft)
35113194600000	CASING	10		585		40					
35113194600000	CASING	8.25		1,091		28					
35113194600000	CASING	6.625		1,976		20					
35113194600000	CASING	2		2,043		4.5					

Liner

No liner data available for this well.

Tubing

API	Tubing Size (in)	Tubing Depth (ft)
35113194600000	2	2,043

Figure 3: Information on Well 2 design

While the location of wells with respect to the site is good, this scenario also presents a unique set of challenges that demand careful consideration. Notably, the wells in question date back to the years between 1900 and 1940, introducing potential well integrity issues. (Khankishiyev, Salehi et al.) These older wells' structural integrity and depth may not be suitable for geothermal applications, necessitating refurbishment, and potential reinforcement to meet modern standards. (Hu, Vivas et al. 2024)

Moreover, geological factors and the thermal characteristics of the existing wells need to be evaluated to ensure their suitability for geothermal heat extraction. Variability in the temperature and flow rate of the geothermal resource can impact the system's efficiency and overall performance. We must also account for potential environmental and regulatory concerns while repurposing these aged wells.

In this scenario, assessing and mitigating these challenges, including those associated with the age and integrity of the wells, will be essential in realizing the cost-effective potential of repurposing existing wells for geothermal heating, making it a worthwhile avenue to explore in our project.

3.2 Scenario 2: Drilling New Geothermal Wells

In our second scenario for geothermal heating implementation, we contemplate the construction of entirely new geothermal wells. This approach offers distinct advantages, notably the assurance of wellbore integrity and the ability to control drilling depth for optimal temperature utilization. By drilling new wells, we can ensure that the well structures are modern, robust, and designed specifically for geothermal applications. This minimizes the risk of structural issues and potential leaks often associated with older or repurposed wells. Furthermore, the flexibility to control well depth enables us to target zones with higher temperature gradients, enhancing the efficiency of our geothermal heating system. It also presents the potential to explore lower depths for geothermal cooling, offering a dual-purpose solution that caters to both heating and cooling needs.

However, this scenario also presents its share of challenges. Notably, the primary challenge concerns the substantial cost implications of drilling new geothermal wells. These expenses encompass drilling equipment, materials, labor, and the depth to be drilled, making it a potentially significant investment. A comprehensive cost-benefit analysis will be imperative to evaluate this option's financial feasibility and sustainability. Additionally, a critical concern is the presence of an aquifer beneath Osage County that provides the nation with drinkable water. If we opt for this scenario, we must design and implement robust isolation methods to ensure that our drilling activities do not interfere with or contaminate the aquifer.

Protecting this vital resource is of utmost importance and will require stringent design and monitoring protocols to mitigate any potential risks and safeguard the nation's drinking water supply. In summary, while drilling new geothermal wells offers precise control over wellbore integrity and drilling depth for optimized geothermal heating and cooling, it must be carefully evaluated in the context of the significant cost implications and the imperative need to protect the underlying aquifer, making it a scenario that requires thorough assessment and planning.

4. Geological Setting

4.1 Geological Deposition

The Osage Reservation is located in the Mid-Continent Cherokee Shelf of NE Oklahoma. The county is underlain by the strata of the Oklahoma platform that lies between two uplifts, the Ozark Dome and the Nemaha Ridge (Figure 4), that were deposited during the late Paleozoic (Cole, 1969). The near-surface bedrock in Osage County consists of a series of north-northeast striking outcrop bands of Upper Pennsylvanian to Lower Permian sedimentary sequences of interbedded shale, sandstone, and limestone, as reported by Hudson et al. (2016). The shale, sandstone, and limestone units were deposited on Mississippian to Cambrian age strata that overlie basement rock

and have a thickness of up to ~1,500 m (~5,000 ft). The subsurface beds of the Pennsylvanian age, which underlie the whole county, are similar in character to those found at the surface; they consist of alternating sandstone, shale, and limestone beds with a thicker shale section. The sedimentary strata in Osage County are shallow, resulting in shallower wells being drilled in the formation. (Cole 1970)

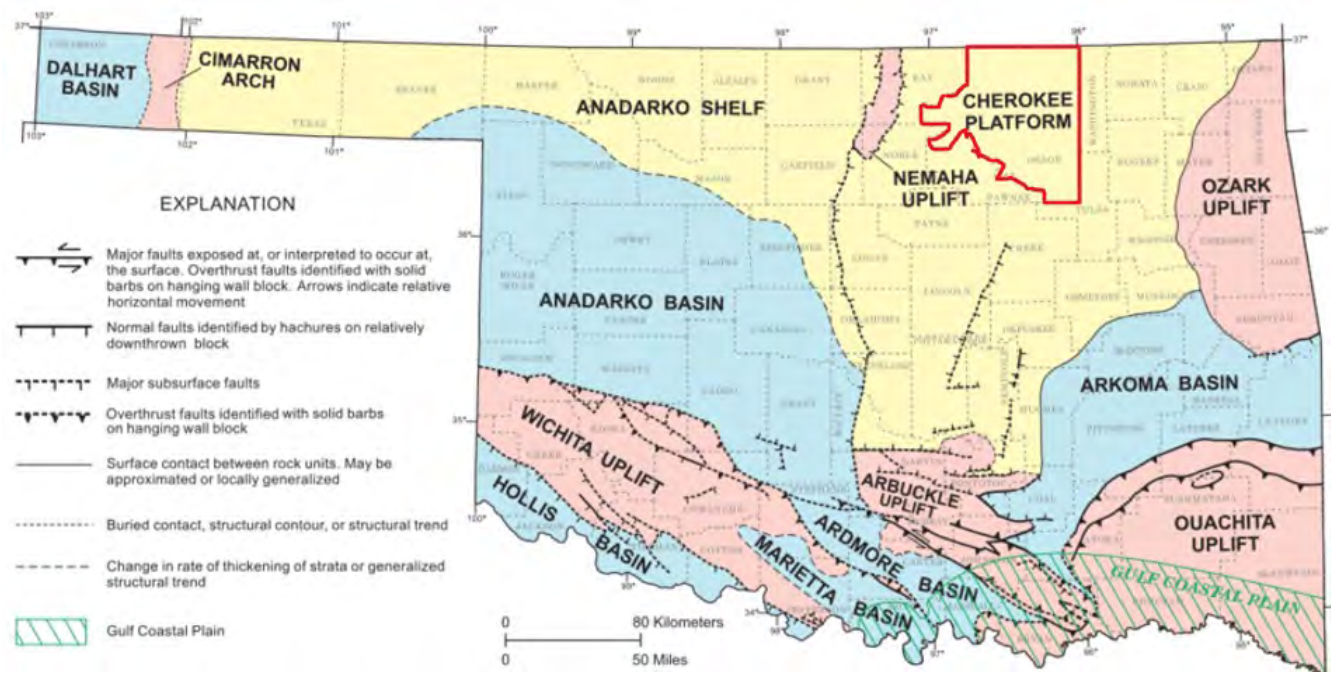

Figure 4: Geologic provinces of Oklahoma (Johnson, 2008; modified from Norhcutt and Campbell, 1995) Osage County outlined in red.

4.2 Stratigraphy

The stratigraphy of Osage County is convoluted due to the use of an informal naming system in various areas during early hydrocarbon exploration. However, the transitional sedimentary facies between the regions of central Oklahoma and southeastern Kansas are well-documented and can indicate the sedimentary facies of Osage County, as reported by Hudson et al. (2016). Despite the variation in the naming system, the rock types and their position to one another are well-documented in the region. The sedimentary rock units at the surface or shallow subsurface of Osage County are mostly interbedded sandstone, shale, and limestone sequences. Figure 5 shows the stratigraphic column for Osage County. The stratigraphic cross-section of Osage County modeled from various wells drilled in the region highlights that the primary formation in the region include Big lime, Oswego lime, Verdigris lime, Pink lime, Mississippian, Woodford shale, Simpson granite, and Arbuckle granite as shown in Figure 6. The most common reservoirs that were penetrated by these wells were all sandstone-dominated. (Vivas, Hu et al. 2023)

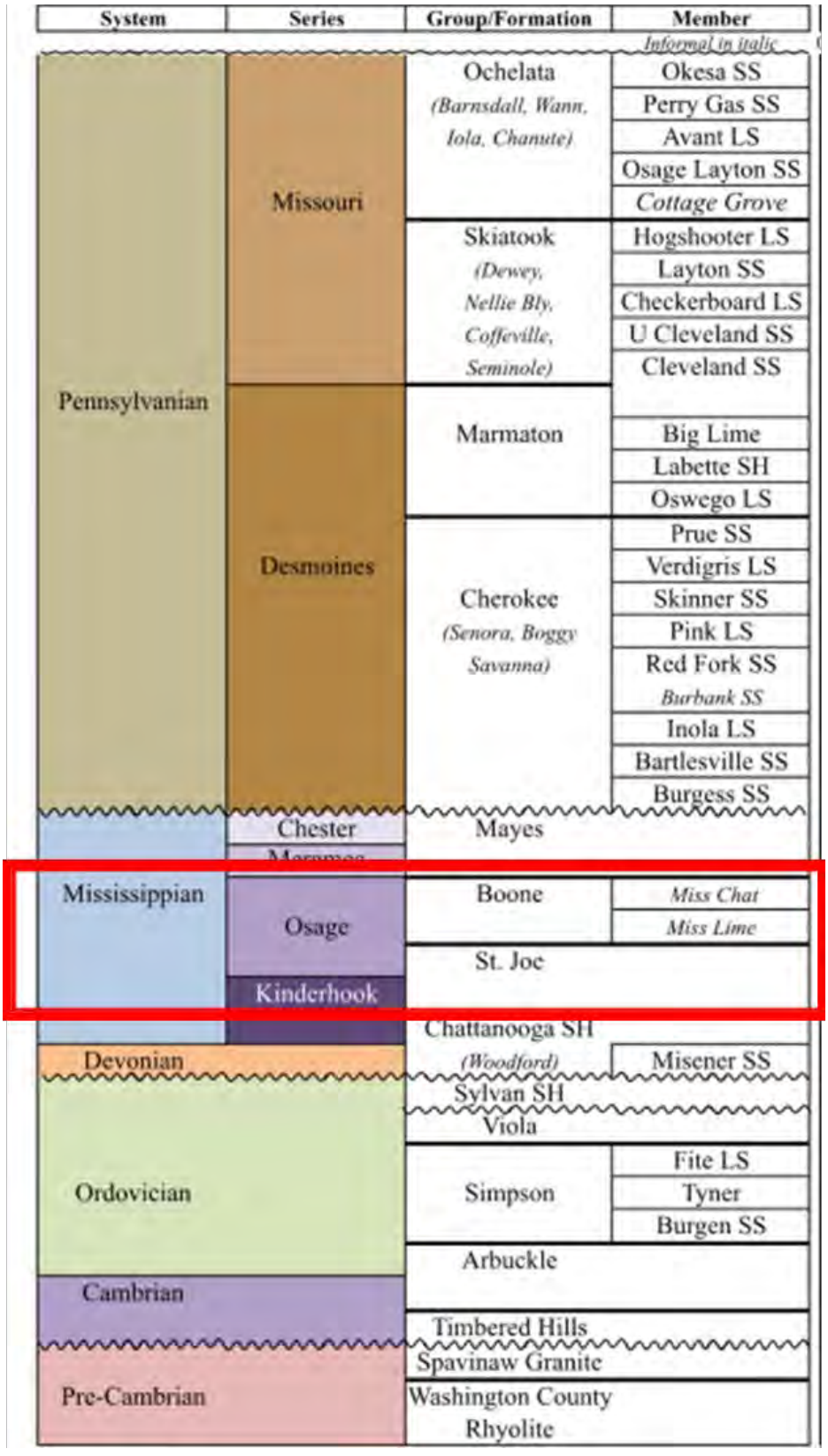

Figure 5: Stratigraphic column for Osage County

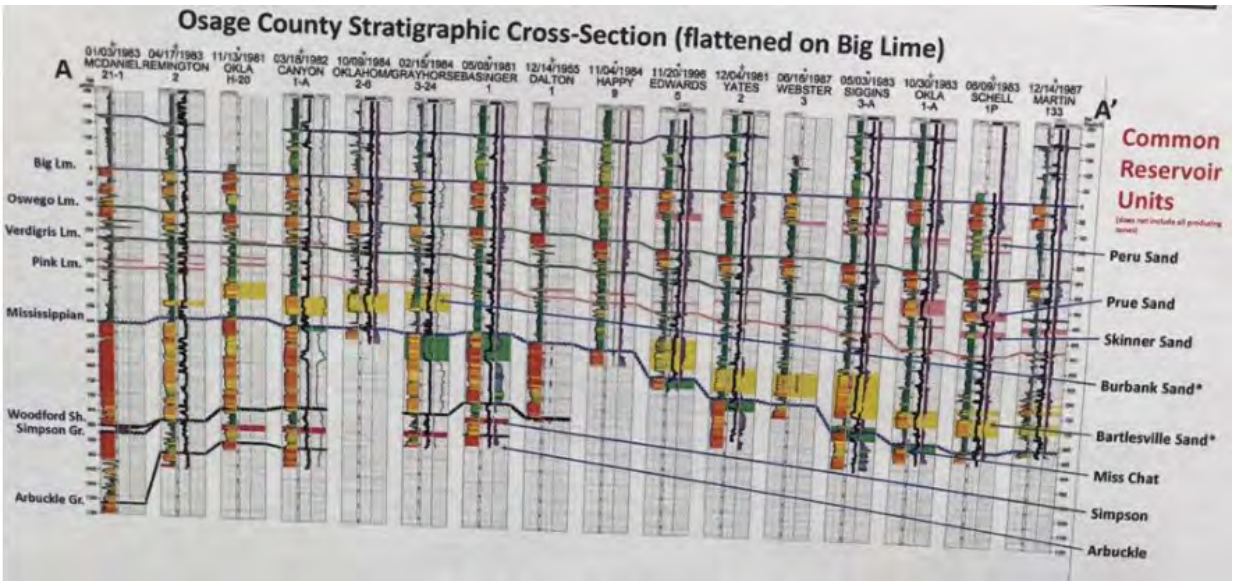

Figure 6: Osage County stratigraphic cross-section of a few wells drilled in the region. (Council)

4.3 Geological and Subsurface Modeling

Reservoir characterization and modeling encompass a comprehensive grasp of petrophysical and thermal characteristics alongside an in-depth understanding of reservoir fluids and the geothermal gradient. Beyond geological insights that aid in comprehending optimal formation facies and properties, understanding how the working fluid will flow through porous media emerges as a crucial factor in assessing the viability of geothermal applications. While geological attributes notably influence energy extraction and well stability, a profound understanding of the subsurface becomes imperative to project evaluation.

The initial phase of subsurface modeling involved digitizing raster logs obtained from the Osage Mineral Council via Petra software by S&P Global. Various logs, including gamma ray, resistivity, neutron porosity, and density porosity, were accessible from 9 wells of Briggs 1A, Briggs 2A, Briggs 3A, Edwards 5-22, Edwards 1-22, Jones 14, Jones 15. Digitizing these logs facilitated the construction of lithology models and the computation of porosity and permeability.

Following this, the Petrel model necessitated the placement of well heads. As crucial data was lacking in the raster logs, the Enverus platform and the Osage Mineral Council website were referenced to determine longitude and latitude coordinates.

Subsequently, three cross sections were generated, and corresponding correlations established. The outcomes of these processes are presented below.

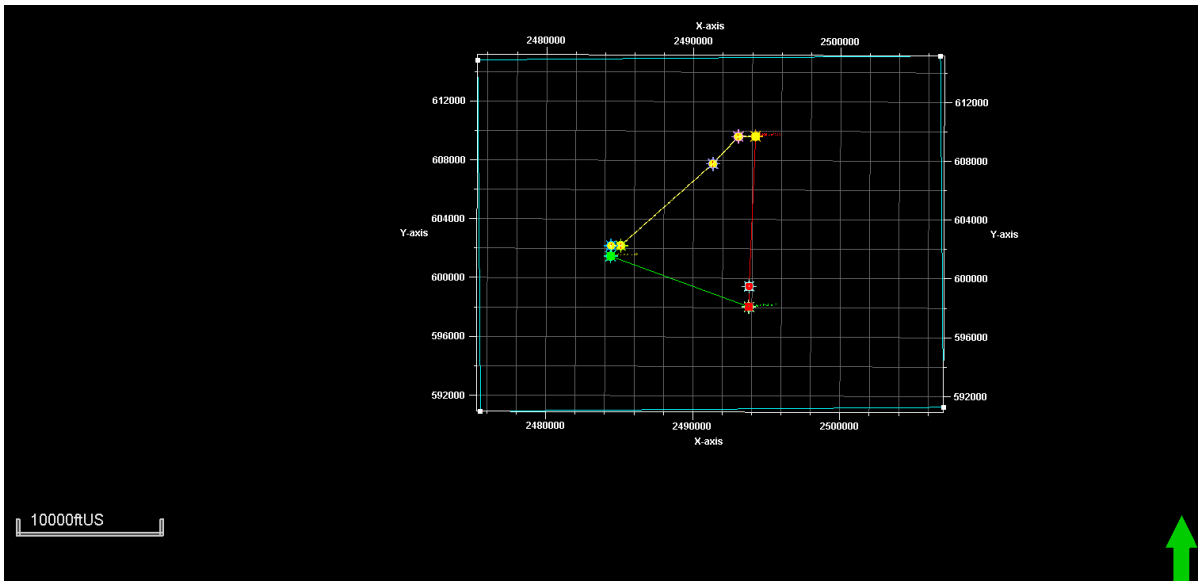

Figure 7: 2D view of cross-sections

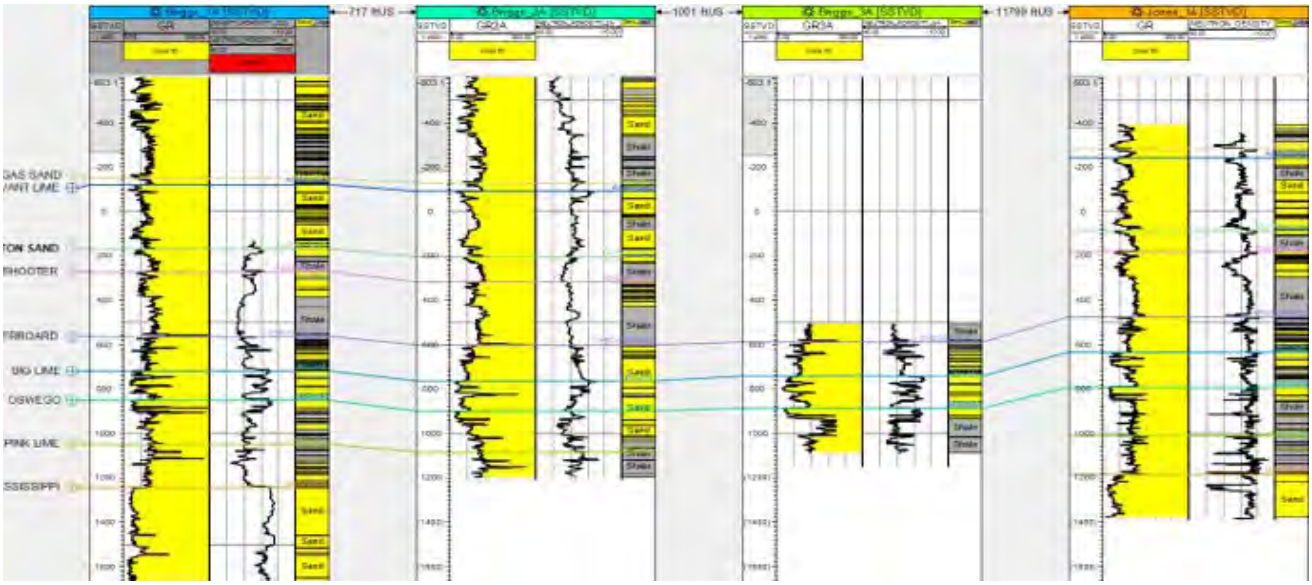

Figure 8: Well top correlations of the formation.

7 formation tops – Layton Sand, Hogshooer, Heckerboard, Big Lime, Oswego, Pink Lime, and Mississippi- were found through Enverus platform and correlated in each cross-section. Then, surfaces, horizons, and zones were created in Petrel, and the resultant 3D model is shown below.

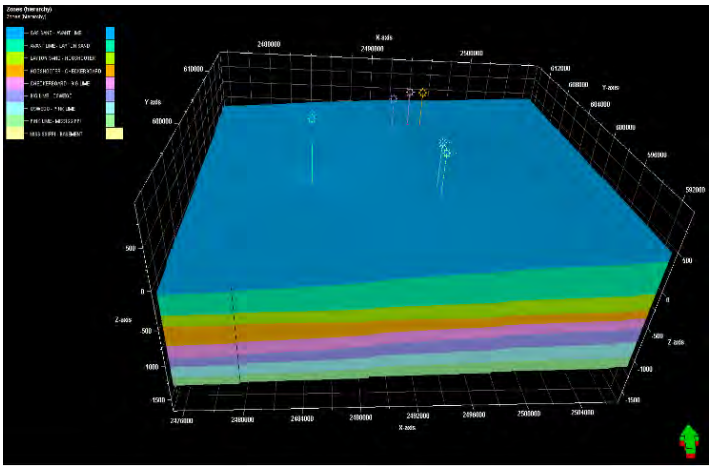

Figure 9: 3D reservoir model with all layers.

The 3D reservoir model was built using a grid that covers an area of 769,747,000 ft^2 .The thickness of the grid varies from ~1,200 ft to ~1,600 ft. A proportional layering of 20 ft was used for the model, and 100 ft x 100 ft cells were assigned to account for 12.3 million cells in the model.

For petrophysical models, the neutron-porosity raster log was readily available for 5 wells Briggs 1A, Briggs 2A, Briggs 3A, Edwards 5-22, Jones 14, and Jones 15, respectively. The Techlog software was utilized to generate porosity values from those wells. It can also be calculated from the density porosity log by the following formula:

$$PHIT = \frac{\rho_{matix} - \rho_{bulk\ volume}}{\rho_{matrix} - \rho_{fluid}} \quad (1)$$

where PHIT is the total porosity with ρ being the density of respective material.

Porosity values were upscaled, and then a 3D petrophysical porosity model was created in Petrel. Sequential Gaussian Simulation modeling was the method used. Porosity values range from 0.0010 to 0.4989, with a mean of 0.247. Too high porosity values may result from the fact that formations are shallow and there is not enough compaction and the resultant overburden stress. (Mahdaviara, Rostami et al. 2021)

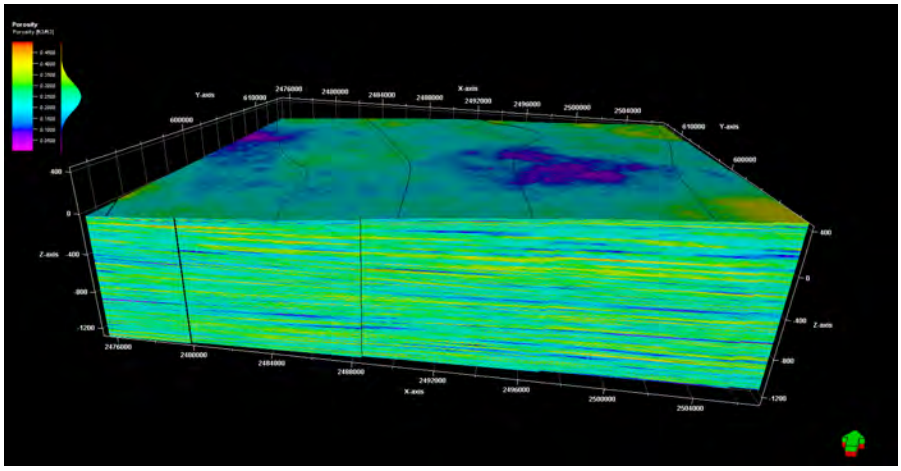

Figure 9: 3D porosity model.

Techlog used the Wyllie-Rose equation to make the correlation between porosity and permeability. Wyllie and Rose proposed a permeability correlation in an attempt to quantitatively evaluate the physical properties of reservoir rock by employing information achieved by electrical logs. They considered two independent variables of porosity and irreducible water saturation as the inputs as follows: (Sciencedirect , Sciencedirect)

$$k = \left(a \frac{\varphi^b}{S_{wirr}}\right)^c \quad (2)$$

Where a, b, c are constants, S_{wirr} is irreducible water saturation, and φ is porosity. Below is an example of how permeability values are created from porosity values. It can be seen that sandy formations' porosity and permeability values are higher than other lithologies.

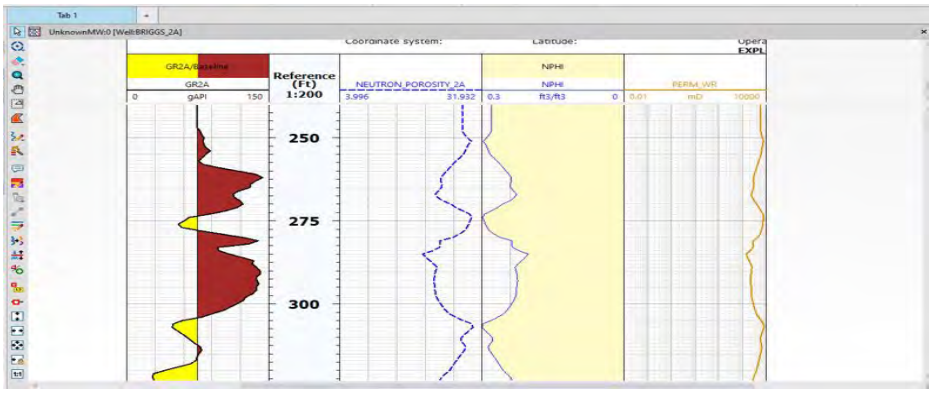

Figure 10: Techlog view of generated logs.

The model for permeability was established utilizing the permeability logs generated through Techlog software. Elevated porosity values corresponded to increased permeability values, as depicted in the permeability model. This characteristic proves advantageous for the working fluid due to its facilitated movement. However, optimizing the flow rate becomes crucial to avoid inefficient heat extraction resulting from overly swift fluid movement.

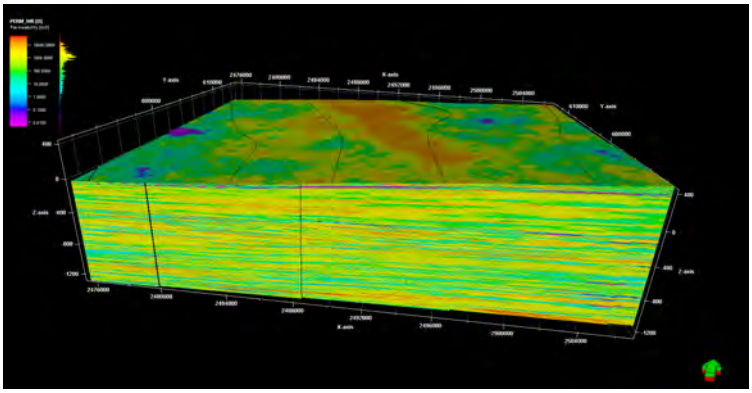

Figure 11: 3D permeability model.

Because of the model's extensive size and lengthy simulation periods, we found it necessary to limit each zone within the reservoir of interest to 10-foot layers. This adjustment significantly reduced the grid size to 7.6 million, optimizing computational efficiency. In response to the CMG model's requirements, we introduced a new zone encompassing the Mississippi-Basement zone to encompass the entirety of the reservoir. This addition was necessitated by the absence of this information in previous well logs, which is crucial because deeper regions contribute to our heat extraction. During the inclusion of this zone, we made an assumption regarding the stratigraphic continuity of permeability and porosity for seamless integration within the model's framework. This step was essential to ensure comprehensive coverage of the reservoir's subsurface characteristics and its deeper heat sources. The resultant 3D grid, porosity, and permeability models after changing layering and adding new zones are given below:

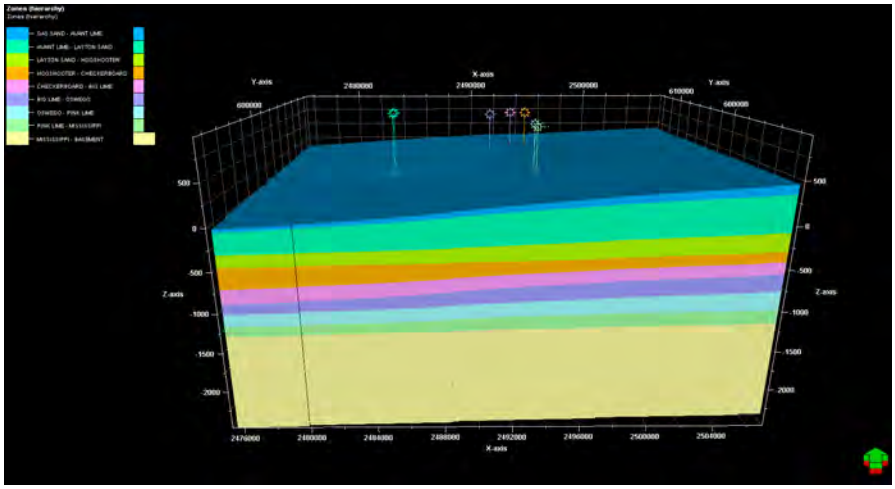

Figure 12: Final 3D reservoir model with all layers.

The final 3D reservoir model was constructed using a grid covering an area of approximately 769,747,000 square feet. The grid's thickness varies between approximately 2,456 feet and 2,800 feet. The model employed a uniform layering of 10 feet, incorporating cells measuring 100 feet by 100 feet, totaling 7.6 million cells within the model.

Permeability values, depicted in Figure 13, range from 0.0118 millidarcies to 10,000 millidarcies, with an average value of 1,660 millidarcies. Porosity values, shown in Figure 14, span from 0.0010 to 0.5, with an average of 0.25.

Visualizing petrophysical properties is valuable for evaluating and identifying the most promising oil and gas well sites within the specified area. For instance, warmer tones in the visualization highlight regions with the most favorable reservoir attributes.

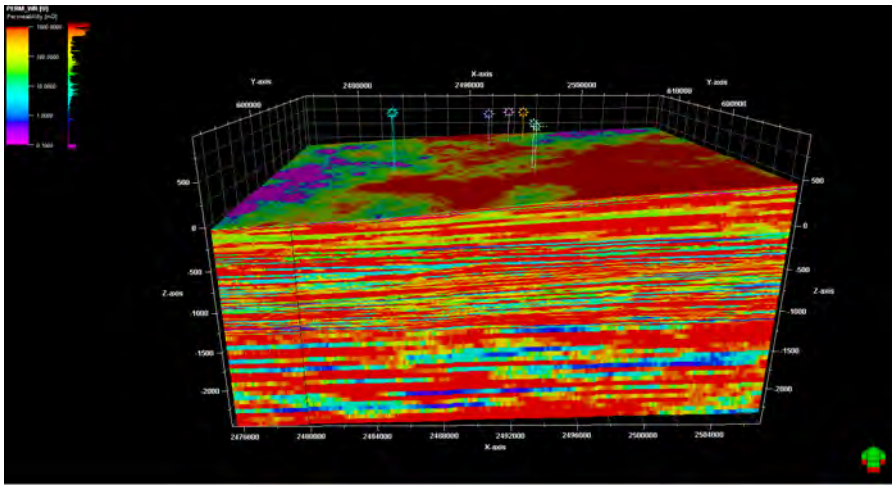

Figure 13: Final 3D permeability model.

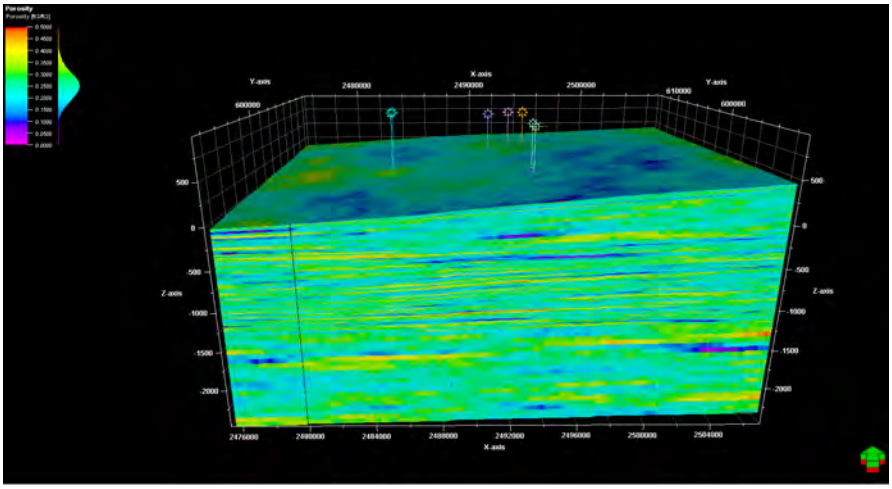

Figure 14: Final 3D porosity model.

5. Modeling

5.1 Temperature Modeling

Temperature survey logs obtained from wells drilled in the neighborhood of the greenhouse were analyzed to characterize the study area's geothermal gradient. A geothermal gradient of 0.0205 °F/ft or 37.36 ℃/km. The estimated geothermal gradient is used to model the heat potential around the greenhouse. The CMG modeling software built the temperature model, where equation 1 was applied.

$$T = 0.0205 * D + 78 \quad (3)$$

Where T represents the temperature, and D is the depth of interest.

Figure 15 shows the temperature model for a total depth of 2,020 ft. A total temperature of 118 °F can be generated from a well drilled at a depth of 2,020 ft. According to the GeoVision report of 2019, a minimum temperature of 110 °F is required for greenhouse and food processing. Therefore,

to maintain the greenhouse in the Osage Nation heated during winter, wells with a minimum depth of 2,000 ft must be drilled to produce the required heat.

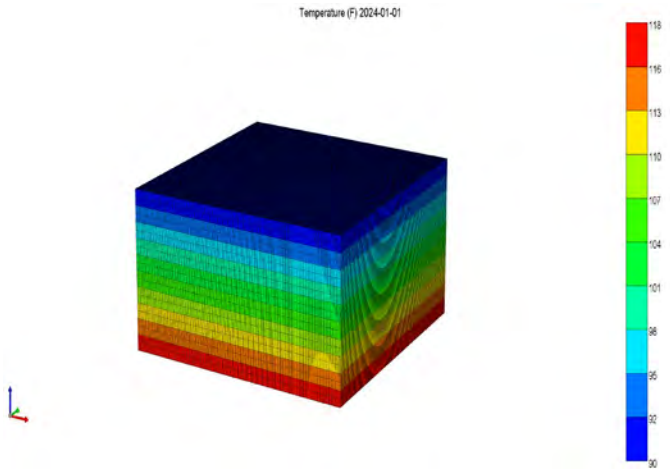

Figure 15: Temperature modeling based on the temperature surveys obtained from wells drilled in the neighborhood of the area of interest.

5.2 Reservoir Modeling and Enthalpy Production

A combination of geological and petrophysical models obtained from Petrel was exported in CMG using STARS to simulate the system's potential enthalpy production over a 20-year lifespan. Due to the excessively long computational time of the simulation, the exported model from Petrel was cropped to the study area to optimize the computational time. The simulated model included two (2) producing wells and one (1) injection well. All three (3) wells used in the simulation were drilled at a depth of 3,000 ft. As the temperature model reports, a minimum depth of 2,000 ft is enough to generate sufficient temperature to sustain a greenhouse. Figure 16 shows the simulated grid. The resources assessment was conducted for various injection rates ranging from 1,000 bbl/d to 5,000 bbl/d. The injection rate on the injection well was varied to estimate the overall enthalpy production at each rate.

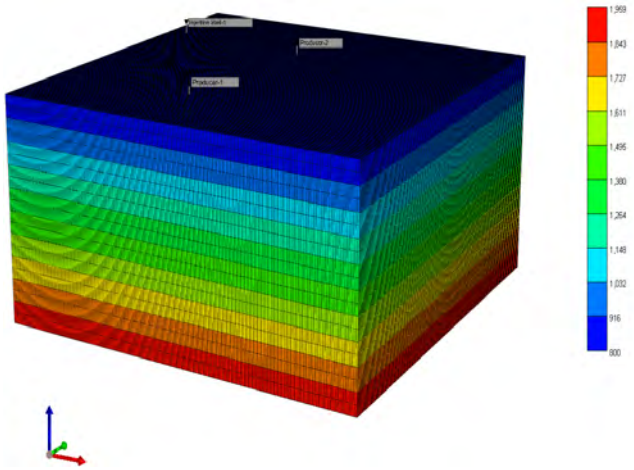

Figure 16: Reservoir model displaying the two (2) producing wells and one (1) injection well.

The cumulative enthalpy production from the producing wells is obtained for all injection rates to estimate the optimum injection rate for generating the required enthalpy needed to fulfill the heat demand for heating the greenhouse. The results of the simulation indicated that the enthalpy production range from 20 MMBTU/day for the injection rate of 1,000 bbl/d to 40 MMBTU/day for the injection rate of 5,000 bbl/d. Figure 17 shows the enthalpy production rate for all injection rates. Based on the results, an injection rate of 2,000 bbl/d is sufficient to produce the heat required for the greenhouse with a total enthalpy production of over 20 MMBTU/d. However, an injection rate of 3,000 bbl/d is chosen so that the extra energy produced can be distributed to the research laboratory and the fish farming buildings near the greenhouse, therefore optimizing the project and making it more economically attractive and beneficial to tribal communities in their pursuit for food sovereignty.

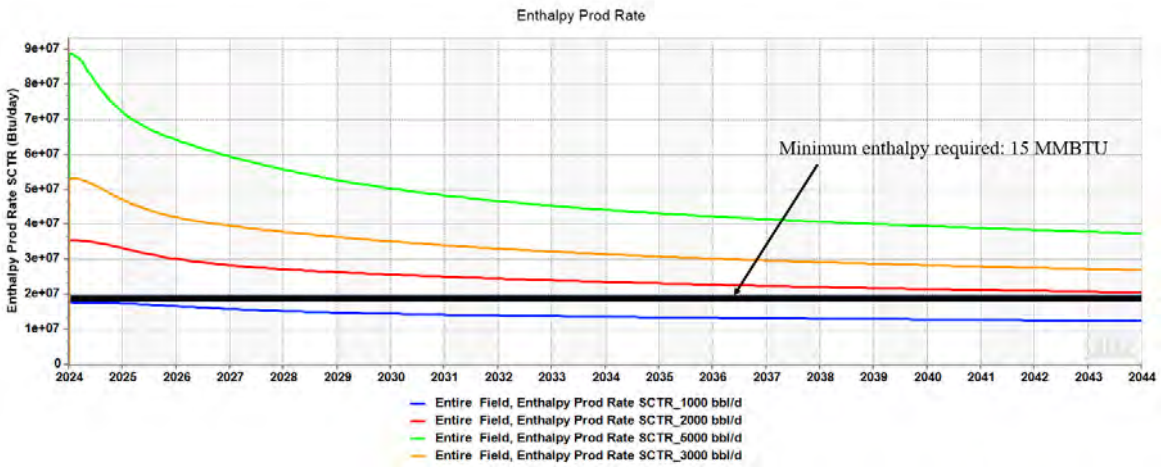

Figure 17: Enthalpy production rate for all four injections rate

Although a very detailed model comprises all the formations in the area, the reservoir model dimensions limit or inhibit the capacity to perform simulations in later stages using CMG. Therefore, it is recommended that the model be simplified without losing the details in the formation of interest. The well models can be optimized to maximize the enthalpy production and investigate the use of secondary production recovery mechanisms to maximize the enthalpy.

The temperature is one of the driving forces behind the energy production from the wells used in this project. A temperature drop analysis revealed that the entire field, which includes the two producing wells, does not exhibit major temperature loss over the 20-year lifespan of the project. A faster temperature decline is obtained when water is injected at a rate of 5,000 bbl/d. This is due to the reservoir cooling down at a faster rate since a larger volume of cooler fluid is injected into it. Figure 18 shows the temperature drop profile for four (4) injection rates over 20 years.

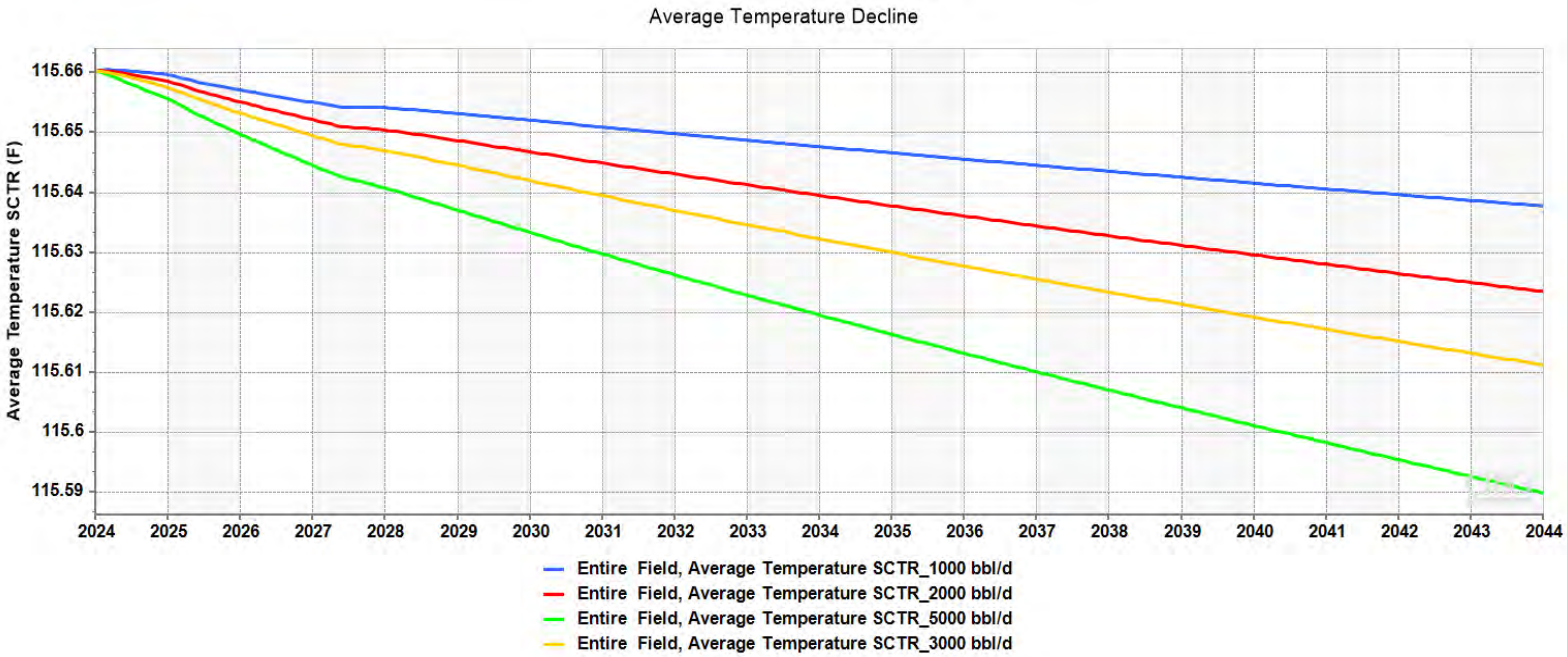

Figure 18: Temperature drop profile for the entire field over 20 years.

5.2 Pipesim Modeling

A geothermal well is modeled in Pipesim to investigate its performance in terms of pressure drop and water flowing rate in the well. The well was designed to a depth of 3,000 ft. The completion includes a surface casing set at a depth of 500 ft to seal the freshwater aquifer in the study area. The intermediate casing was set at a depth of 1,600 ft; finally, the production casing was set at a depth of 3,000 ft. A nodal analysis of the created well was conducted to estimate the well performance. Figure 19 shows the well design and the water flowing rate as a function of temperature. The water flowing rate is shown to be increasing with temperature, indicating the potential for higher steam water production at larger downhole temperatures.

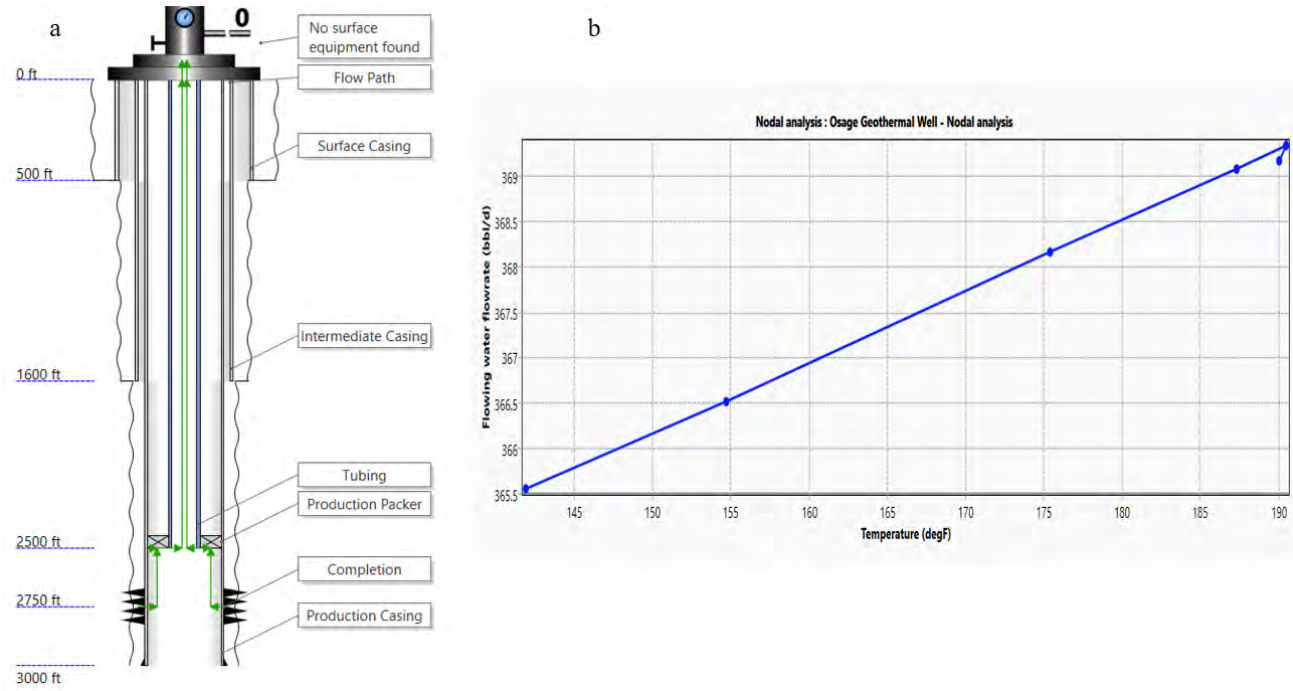

Figure 19: (a) Well design and (b) the water flowing rate as a function of temperature.

The Pipesim model was used to investigate the potential for artificial lift in the different production wells. The implementation of artificial lift will help in optimizing energy production.

6. Economic Analysis

6.1 Energy Consumption of the Greenhouse

The electricity bills for the greenhouse serve as a crucial indicator of its energy consumption trends, and a notable pattern emerges when examining the correlation between energy usage and the seasonal calendar. Figure 20 vividly illustrates a substantial surge in energy demand during the cold months, spanning from December through the beginning of March. This significant uptick in electricity consumption can be attributed to the imperative need for climate control within the greenhouse environment during winter. Maintaining an optimal and consistent climate inside becomes paramount for cultivating plants as temperatures plummet outside. Heaters, ventilation systems, and other climate control mechanisms operate at heightened capacities during these colder months, contributing to a pronounced spike in energy consumption. Consequently, the observed increase in electricity usage during this period underscores energy's critical role in sustaining a conducive environment for greenhouse cultivation when external conditions are less favorable.

Additionally, noteworthy energy consumption spikes are evident during June and July, albeit not as pronounced as during winter. These summer peaks are associated with the cooling requirements of the greenhouse, as the rising external temperatures necessitate active measures to prevent overheating. While the energy demand during these warmer months is not as steep as in winter, it underscores the dynamic nature of the greenhouse's energy needs throughout the year. These insights into seasonal energy consumption patterns lay the groundwork for evaluating how the

Osage County Geothermal Energy Project can effectively address both heating and cooling demands, providing a comprehensive understanding for the subsequent economic analysis.

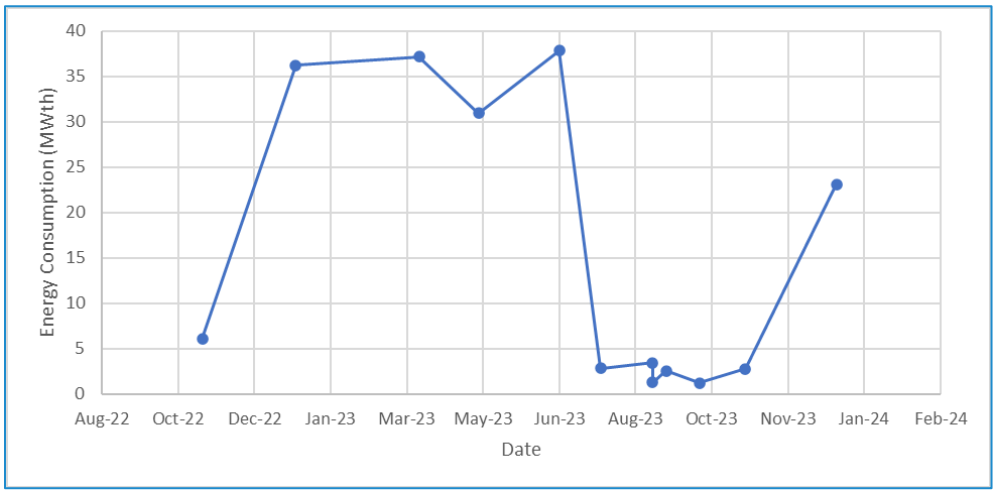

Figure 20: Energy Consumption of the Greenhouse

6.2 Levelized Cost of Energy in Oklahoma, USA

The graph depicting the price of natural gas in $/thousand cubic feet ($/Mcf) in Oklahoma, sourced from the US Energy Information Administration (2023) and covering the period from January 2021 to September 2023, unfolds a dynamic narrative of fluctuation. This variability in natural gas prices directly impacts the overall energy landscape, influencing the levelized cost of electricity (LCOE). Notably, the LCOE experiences discernible spikes, especially during the cold months, reflecting the heightened demand for heating in various sectors, including greenhouse operations.

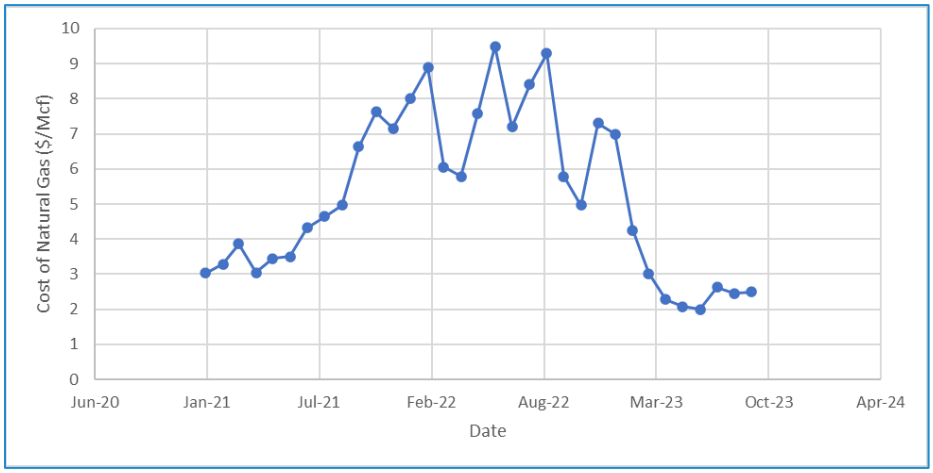

Figure 21: Natural Gas Price, eia (2023)

The reliance on natural gas as a primary driver for electricity generation introduces an element of unpredictability into the cost equation. The sporadic spikes in natural gas prices, particularly evident during colder months, pose a notable challenge when attempting to predict expenditures for the greenhouse. These fluctuations can significantly impact overall electricity costs for the greenhouse, creating an intricate environment for precise budgetary forecasts. As we navigate

through the economic analysis of the project, it becomes imperative to recognize and strategize around the inherent unpredictability in natural gas prices to establish a resilient financial foundation.

6.3 Economical Feasibility Analysis

The foundation of our economic feasibility analysis for the project rests upon the robust capabilities of GEOPHIRES v2, an open-source software by National Renewable Energy Laboratory (NREL). This advanced tool plays a pivotal role in unraveling the intricacies of the project's financial landscape, calculating a comprehensive array of techno-economic values crucial to its success. GEOPHIRES v2 goes beyond conventional analyses, encompassing key metrics such as the Levelized Cost of Heat (LCOH), Capital Expenditures (CAPEX), Operational Expenditures (OPEX), and the simulation of net heat over a specified timeframe. Furthermore, it navigates the nuanced details of reservoir pressure, temperature drop-down, and pressure losses during production, providing a holistic understanding of the geothermal system's behavior.

The utilization of GEOPHIRES v2 for our economic feasibility analysis introduces a versatile suite of calculation methods and accommodates a multitude of inputs to enhance precision. Notable among these inputs are user-provided reservoir output temperature data, with a specific focus on Direct Use as the chosen end-use of geothermal energy, as discussed in preceding chapters. The Standard Levelized Cost Model is the economic model employed for calculating the Levelized Cost of Energy.

In the meticulous breakdown of Capital Expenditures (CAPEX), the calculation encompasses Well Drilling and Completion Capital Cost and surface Plant Capital Cost, while Operational Expenditures (OPEX) amalgamate Wellfield O&M Cost, Surface Plant O&M Cost, Make-Up Water O&M Cost, and Average annual pumping costs. The analysis delves into multiple scenarios, with a standout case featuring well depths set between 3,000 to 4,000 ft. Despite slight variations in drilling and completion costs within this depth range, the resulting values for the Levelized Cost of Heat (LCOH) and net heat prove notably similar.(Clark, Harto et al. 2010)

Key parameters defining the geothermal system include a maximum reservoir temperature set at 120 F, aligning with temperature log readings. The optimal configuration for maximizing net heat at the lowest LCOH involves drilling two producing wells and one injection well, each with a production casing diameter of 7.75 inches. The injection temperature of the working fluid is set at 80 F. Furthermore, the plant's lifetime is conservatively set at 30 years to simulate changes in net heat over time. This nuanced approach ensures a comprehensive evaluation of the Osage County Geothermal Energy Project, considering various factors to enhance the accuracy and reliability of our economic projections.

6.4 CAPEX and OPEX Insights

The detailed economic breakdown provided by GEOPHIRES v2 sheds light on the comprehensive costs associated with the geothermal heat initiative. The Wellfield Cost, covering the drilling and completion of three wells, is quantified at 4.85 million dollars. Complementing this is the Surface Plant Cost, which is estimated at 9.78 million dollars. When combined, these elements contribute to a total Capital Expenditure (CAPEX) of 14.63 million dollars.

Regarding operational expenditures, the annual costs for efficient Wellfield Operation and management amount to 0.29 million dollars. Simultaneously, Surface Plant Operation & Management incurs an annual cost of 0.88 million dollars. The Make-Up Water Operation & Management Cost also contributes an annual expenditure of 0.12 million dollars. This meticulous breakdown of operating costs provides a clear understanding of the ongoing financial commitments necessary for the sustained and effective operation of the geothermal plant.

These detailed CAPEX and OPEX figures offer a comprehensive financial snapshot, essential for evaluating the economic feasibility and sustainability of the geothermal energy initiative. The meticulous accounting of costs ensures a transparent foundation for further economic analyses and decision-making processes.

6.5 LCOH and Market Competitiveness

The simulation results from GEOPHIRES v2 yield a compelling economic assessment for the direct use of geothermal resources in Osage County. The levelized cost of heat (LCOH) calculation stands impressively low at 3.7 $/MMBTU. This figure signifies the economic viability of harnessing geothermal energy for direct use and positions it as an exceptionally cost-effective alternative.

In comparison to the historical natural gas prices over the past three years, the LCOH of 3.7 $/MMBTU represents an average cost reduction of approximately 65%. This substantial cost advantage underscores the economic competitiveness of the geothermal solution, positioning it favorably within the energy landscape. This significant cost differential holds promising implications for the project's sustainability and economic success, reaffirming geothermal energy's potential as a cost-effective and environmentally friendly energy source.

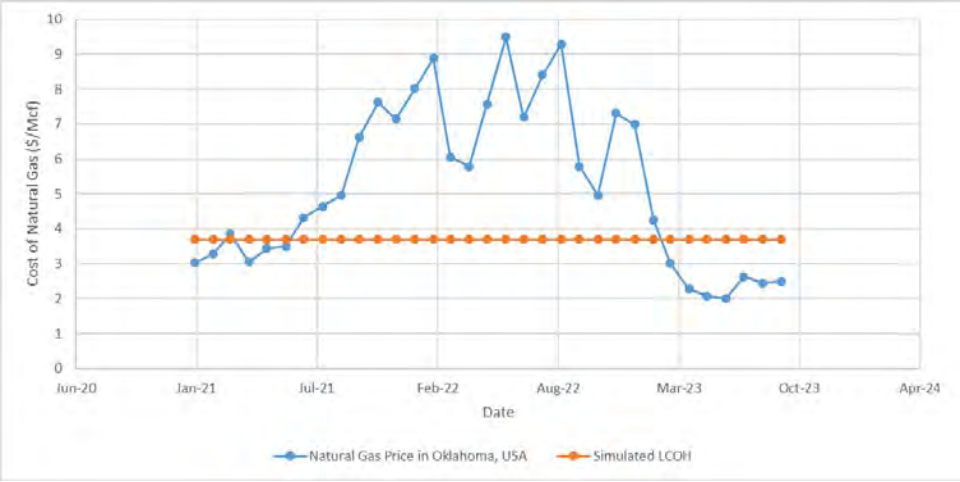

Figure 22: Calculated LCOH vs Gas Prices

6.6 Net Heat's Reliability and Adaptability

The net heat extraction from the geothermal field, as determined by the simulation using GEOPHIRES v2, reveals a robust and consistent performance. The average net heat obtained

stands at an impressive 35.20 MWth. Throughout the comprehensive 30-year simulation period, the net heat production displays a commendable range, spanning from a Minimum Net Heat Production of 32.36 MWth to a Maximum Net Heat Production of 37.97 MWth.

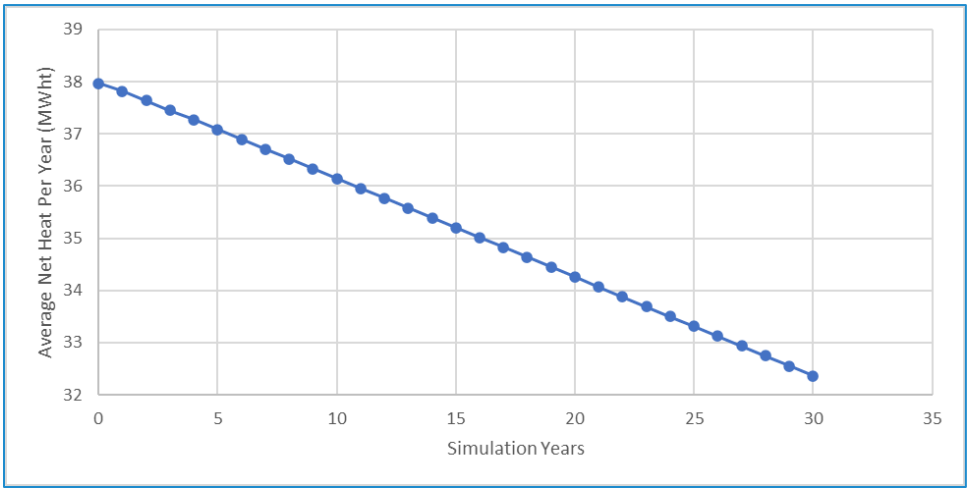

Figure 23: Simulated Net Heat Over 30 Years

The consistently obtained net heat from the geothermal plant, with its commendable average of 35.20 MWth, is sufficient for meeting thermal requirements throughout the majority of the year. This reliability underscores the robust performance and sustained output of the geothermal system. The minor setback noted during periods of massive consumption spikes suggests the plant's capacity to handle varying demands, with occasional adjustments needed during peak consumption intervals.

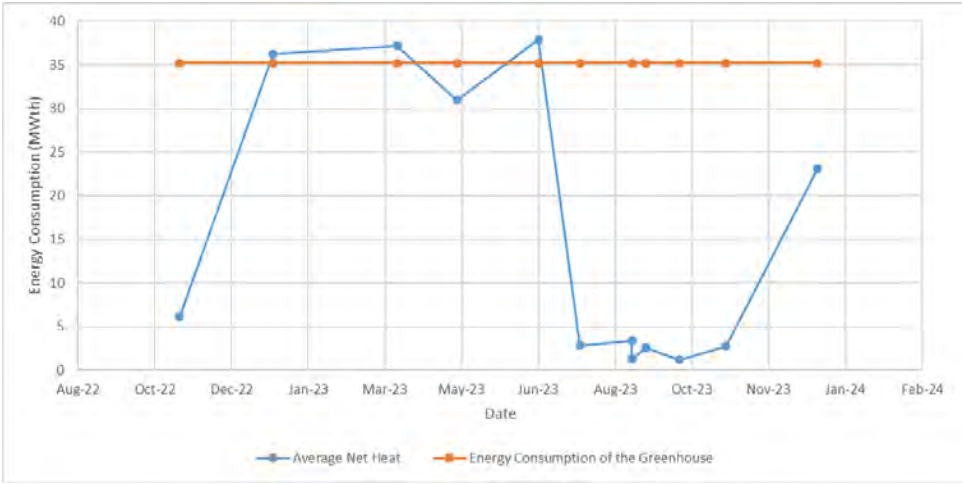

Figure 24: Simulated Net Heat vs Energy Consumption of the Greenhouse

7. Conclusion

The geothermal project within the Osage Nation represents a significant advancement in sustainable energy development, symbolizing the Osage tribe's journey toward energy sovereignty and self-sufficiency. The project's multifaceted benefits include economic stability, environmental

responsibility, and community development, establishing a standard for responsible resource utilization and renewable energy practices within Indigenous communities. This initiative serves as a testament to the Osage tribe's dedication to creating a resilient and sustainable future, showcasing the transformative power of community-driven, environmentally conscious energy projects. Specifically, an injection rate of 3000 barrels per day proved effective for heating and cooling the greenhouse. Additionally, the project achieved a levelized cost of heat of $3.7 per MMBTU, which represents a 65% reduction compared to the average energy costs in the surrounding area.

8. Recommendation

Looking ahead to the future development of the Geothermal Project in the Osage Nation, several key strategies have been outlined to enhance its effectiveness and sustainability. First, there is a push to enhance data integration by incorporating additional well logs and seismic data. This will provide a more comprehensive understanding of subsurface formations, which is crucial for refining reservoir models and improving predictive accuracy.

Secondly, there will be an ongoing effort to continuously refine these reservoir models, utilizing newly acquired data. This iterative process is designed to ensure more accurate predictions and to optimize production strategies, keeping the project efficient and effective over time.

Community engagement is also a priority. Plans are in place to establish educational programs that will inform and engage the local community about the project’s benefits and its commitment to sustainability. These initiatives aim to foster partnerships and maintain transparent communication with community members.

Moreover, thorough environmental impact assessments will be conducted regularly to mitigate any potential adverse effects on local ecosystems. Integrating sustainable practices into all project operations will be a cornerstone of these assessments, ensuring that environmental health is preserved.

Finally, there is a commitment to technological innovation. Investment in research for advancements specific to geothermal energy extraction is planned, which will include fostering collaborations for the development of novel drilling and heat extraction methods. This focus on innovation will help push the boundaries of what is currently possible in geothermal energy, making the project a leader in sustainable energy technology.

9. Acknowledgement

We would like to express our deepest gratitude to Osage Nation members, Osage Mineral Council, greenhouse staff, and our advisor for their invaluable guidance, encouragement, extensive communication, and support throughout this research. Their insights and expertise were instrumental in shaping the direction and quality of this work. We are also grateful to the University of Oklahoma for providing the resources and the DOE Collegiate team for creating this opportunity to formulate and present the project to the vast.

References

Clark, C. E., et al. (2010). Water use in the development and operation of geothermal power plants.

Cole, J. G. (1970). Cherokee Group East Flank of the Nemaha Ridge: North-Central Oklahoma (Part 2).

Council, O. M. "Osage Mineral Council. Osage BIA Wells:." from https://data-osageminerals.hub.arcgis.com/datasets/f3e2c94e54d44b5bab8f591a02168c16_0/explore?location=36.349136%2C-96.245822%2C12.08.

Hu, Z., et al. (2024). "The Application Framework for Geothermal Re-Circulation Proposed for Converting Hydrocarbon Wells Into Geothermal Wells in Oklahoma." Day 1 Wed, June 26, 2024.

Khankishiyev, O., et al. Identification of Undesirable Events in Geothermal Fluid/Steam Production using Machine Learning.

Mahdaviara, M., et al. (2021). "Accurate determination of permeability in carbonate reservoirs using Gaussian Process Regression." Journal of Petroleum Science and Engineering **196**: 107807.

Nation, O. "Osage Nation Map." from https://www.osageculture.com/culture/news-events-activities/news/osage-nation-selects-date-sesquicentennial-celebration.

Sciencedirect. "Accurate determination of permeability in carbonate reservoirs using Gaussian Process Regression." from https://www.sciencedirect.com/science/article/pii/S0920410520308688#bib60.

Sciencedirect. "Irreducible Water Saturation." from https://www.sciencedirect.com/topics/engineering/irreducible-water-saturation.

Vivas, C., et al. (2023). "Texture-Dependent Thermal Properties of Sandstone Rocks Examined by Scanning Electron Microscopy for Thermal Energy Storage Applications." ASME Open Journal of Engineering.

Well Construction & Completion

Zonal Isolation Concept for FORGE Geothermal Wells

Jorge Andres Alvarez Escobar, Alberto Toledo Velazco, Khizar Abid, Yosafat Esquitin, Ricardo Reves Vasques, Leonardo Rocha de Queiroz and Catalin Teodoriu

Keywords

Geothermal, downhole tools, full-scale testing, Utah FORGE

ABSTRACT

The current demand for energy, in addition to the efforts to reduce greenhouse emissions in the United States, has increased the importance of sustainable energy than ever before. In this respect, geothermal energy has become one of the most attractive solutions due to the huge amount of untapped resources that are present in many parts of the world. It is the only source of renewable energy that is not dependent upon climate conditions and remains in operation mode 98% of the time. However, extracting geothermal energy is challenging, as most conventional downhole tools fail under high-temperature, high-pressure (HPHT) conditions. Moreover, if these tools fail during the completion or production phase, it can compromise the well integrity and jeopardize project success. Therefore, this paper provides a summary of downhole tools, such as zonal isolation tool and flow valves developed under FORGE 1 project used for geothermal purposes, that can work under HPHT conditions. In addition, schematics of completions and working procedures will be presented to show how these tools would be installed and operated in the geothermal wells. These downhole tools have been tested at HPHT conditions and will be installed in one of the FORGE (Frontier Observatory for Research in Geothermal Energy) wells.

1. Introduction

The increase in the population around the globe has led to an increment in the energy demand. Dudley (2017) estimates that by 2035, the earth's population will be around 8.8 billion. To meet the rising demand of energy, some challenges need to be addressed, such as the greenhouse effects produced by fossil fuels, which are the primary source of energy at present. Fossil flues have played an essential role during the past years; however, CO_2 emitted by burning these fossil fuels has become an accelerator for global warming. According to Crippa et al. (2022), in 2012 the CO_2 emission per person was about 4.8t.

For this reason, green alternatives such as geothermal have become more attractive, not only because they help with the reduction of the greenhouse effect but also due to the vast amount of untapped resources, availability in different parts of the world, and wide range of applications (Lund, 2000). The possible applications for geothermal energy go from small scales, like heating buildings, to larger scales, such as electric power generation (Abid et al., 2022).

One of the challenges in geothermal engineering is related to the high pressure and high temperature (HPHT) conditions in which they are found. It is estimated that most geothermal systems currently exist in a temperature range between 150 – 300 ºC (Velasquez et al., 2024, as cited by Renisch et al., 2017 and Abid et al., 2022). DiPippo (2016) mentions that approximately 50% of the geothermal budget goes towards drilling and completion due to the extreme conditions of the subsurface. Moreover, the downhole equipment must withstand extreme HPHT conditions of the geothermal wells.

For this reason, and as part of the Utah FORGE project, Welltec Inc. has designed some downhole tools capable of withstanding the extreme HPHT conditions encountered in geothermal projects. In that respect, Welltec Inc. has developed a zonal isolation tool and downhole valve for use in the Utah FORGE Field, where the downhole temperature is 175 to 225°C (Moore, 2020). These tools were tested at HPHT conditions at the University of Oklahoma. The testing temperature ranged between 240 and 320°C, whereas the pressure was about 6,000 psi. The purpose of testing the tool at temperatures higher than those encountered downhole in the Utah FORGE wells is to ensure its reliability and robustness under extreme conditions. By subjecting the tool to these elevated temperatures, we can confirm that it will perform effectively and withstand the maximum temperatures it may encounter in the wells, thereby enhancing its security and operational safety. This paper will present the results of these tests and provide a schematic of how the tools will be deployed in the Utha FORGE wells.

2. Tools description

In this section, a full description of the zonal isolation tool and flow valve will be presented to better understand the functionality of these new tools designed by Welltec.

2.1 Zonal isolation tool

The design and the cross-sectional view of the zonal isolation tool are illustrated in Figure 1. Whereas, Figure 2 shows a picture of the toll before being exposed to the HPHT test.

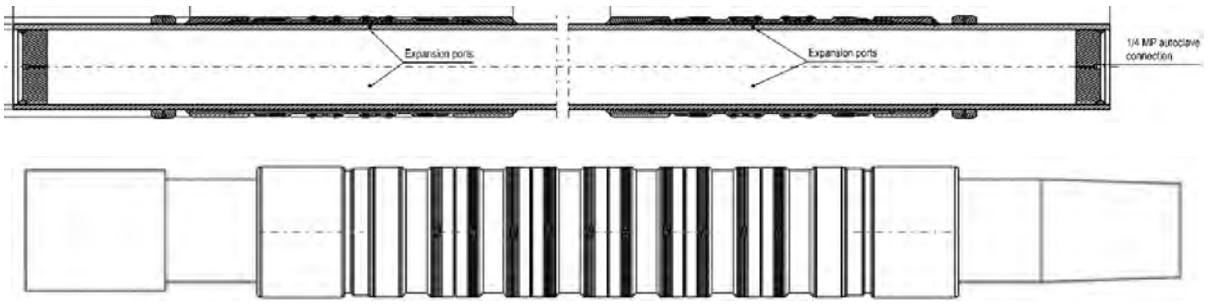

Figure 1: Design and cross-sectional view of the zonal isolation tool

Figure 2: Zonal isolation tool designed by Welltec

The zonal isolation tool is designed to expand and set at 6,000 psi (differential pressure) with the maximum run in hole ID 8.42". It has the capacity to operate at the temperature range of 60 to 260°C.

2.2 Flow Valve

The flow valve is designed to withstand 6,000 psi for burst and collapse conditions, and its operating temperature is 260 ºC. The unloading cycle is closed – open – closed, and to be able to open or close the valve, 1,500 psi of force is necessary, and the valve has to be shifted. The schematic of the flow valve is shown in Figure 3.

Figure 3: Flow valve schematic

3. HPHT test before installation

Before installing the tools in the Utha FORGE well (Well 58-32), they were tested at HPHT conditions in the facilities of the University of Oklahoma at the Well Construction Technology Center (WCTC). Both tools were tested in separate facilities but with same HPHT conditions (6,000 psi and 225 ºC).

3.1 Zonal isolation tool HPHT test

This tool was tested for three cycles (One cycle = heating to 225 ºC and cooling down). However, this paper will focus on one of the HPHT tests performed during cycle #2. Figure 5 shows the schematic of the testing setup, whereas Figure 6 shows thermometers placed in different spots of the setup to monitor the system's temperature.

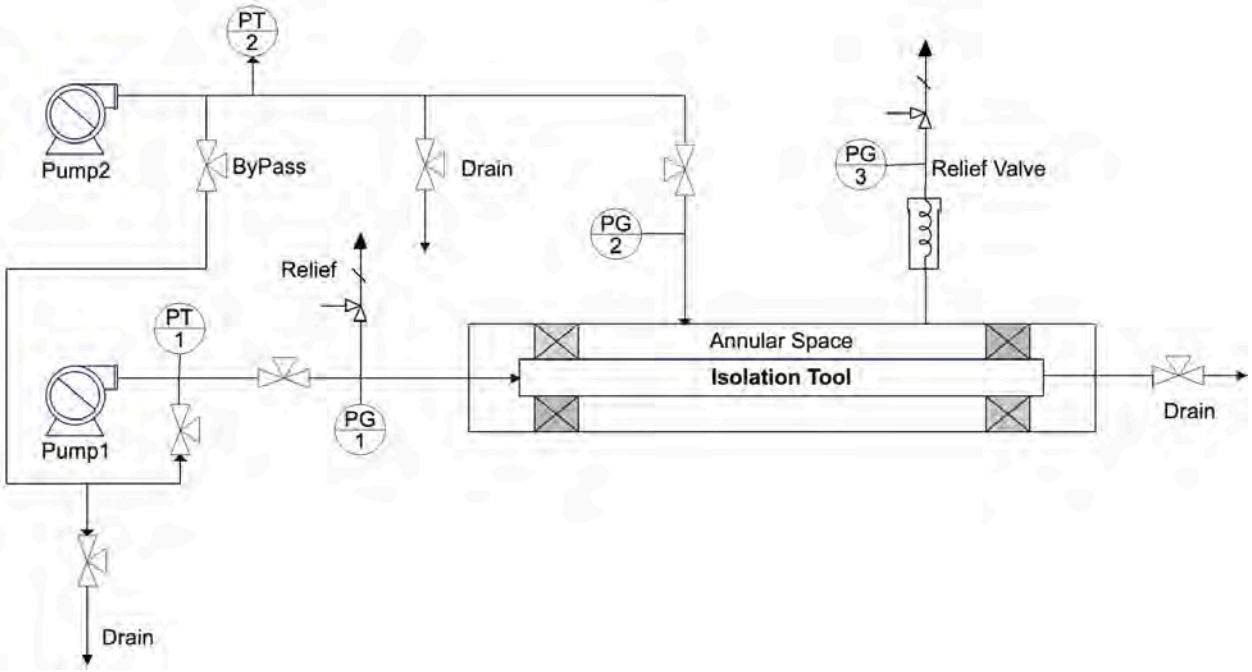

Figure 4: Schematic diagram of the long-scale testing setup

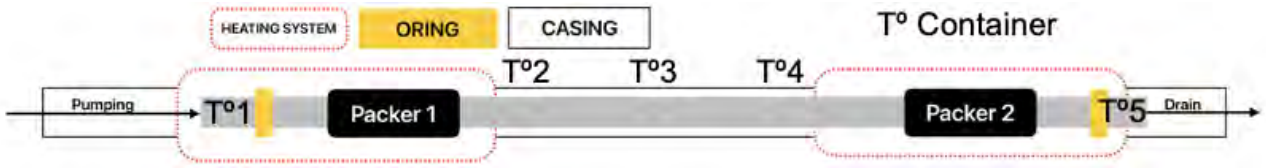

Figure 5: Thermometer placement in the system

The tool was tested for 14 days straight in cycle #2, where the temperature was kept over 225ºC during the whole cycle. Meanwhile, the pressure in the annular section and inside the tool was kept at 3,000 psi and increased to 6,000 psi three times for 1 hour to test the tool at its extreme conditions. Figure 6 presents the temperature and pressure conditions during this cycle.

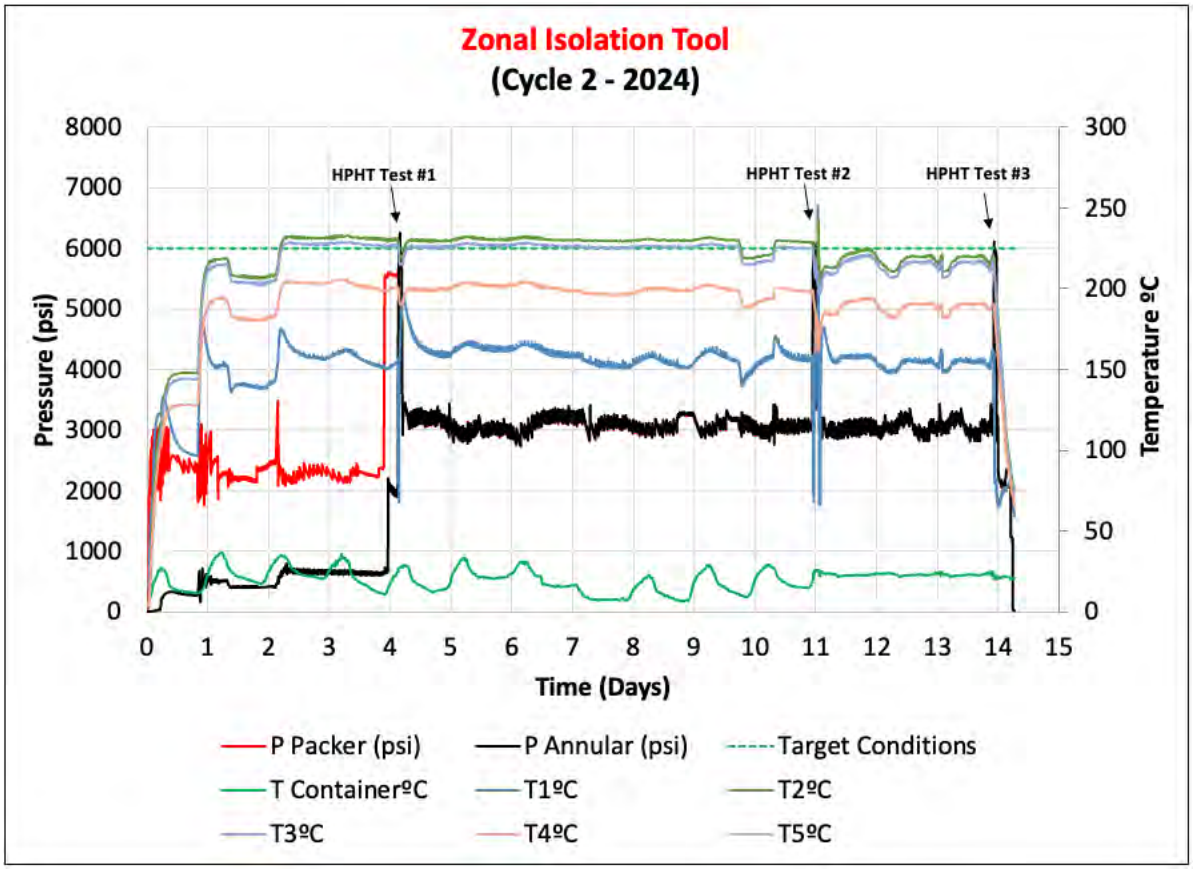

Figure 6: Cycle # 2 performed on zonal isolation tool

In Figure 7, the first HPHT performed on the zonal isolation tool is shown, where it can be seen that the pressure was able to be kept at over 6,000 psi for 1 hour, with an average leak lower than 0.2 GPM.

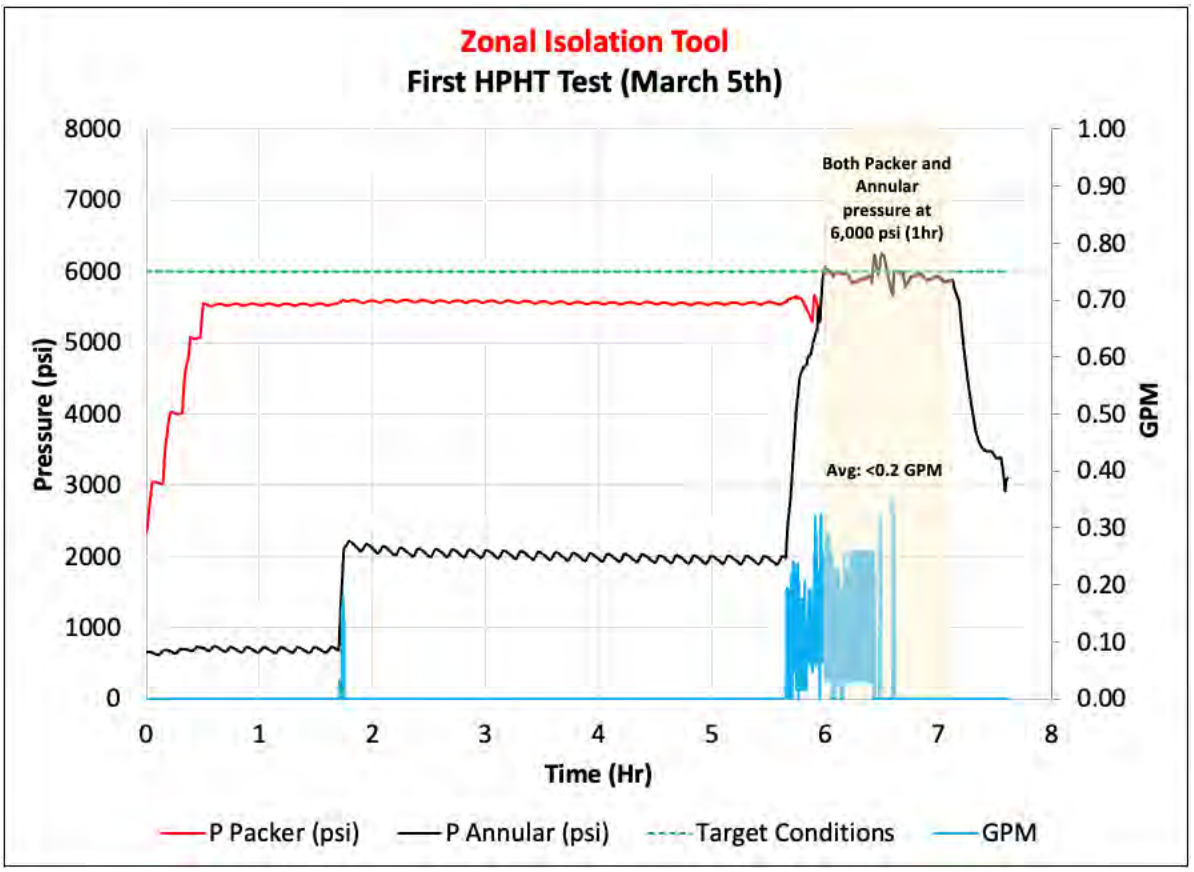

Figure 7: First HPHT test

3.2 Flow valve HPHT test

The flow valve was tested at 6,000 psi and 260 ºC for 30 minutes. Figure 8 illustrates the setup schematic, whereas Figure 9 shows the pressure and temperature behavior during the test. (Velasquez et al., 2024)

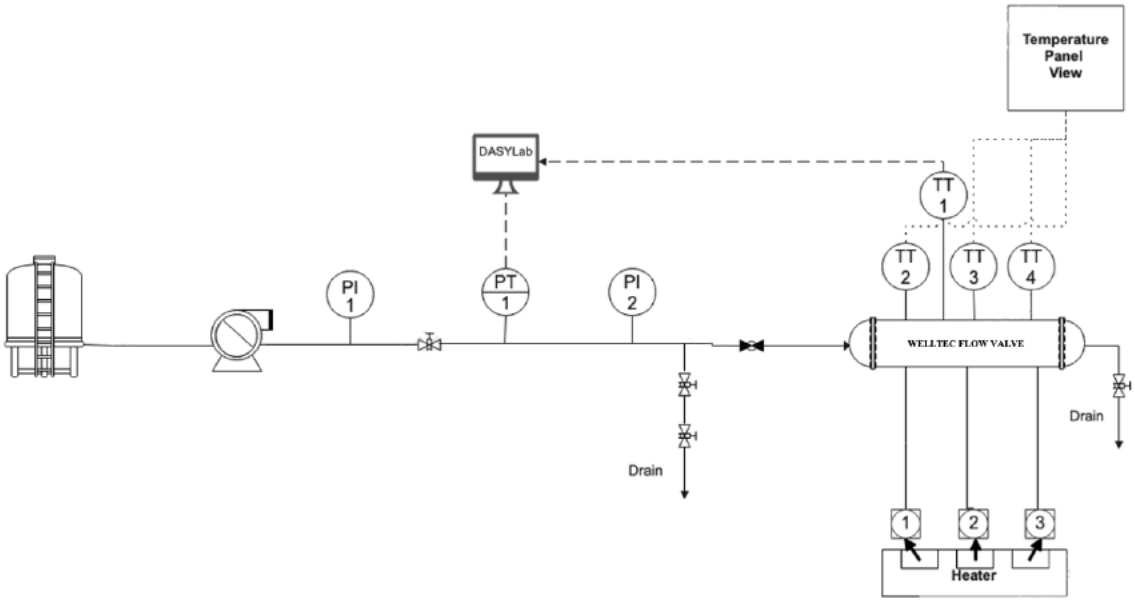

Figure 8: Flow valve testing setup (Velasquez et al., 2024)

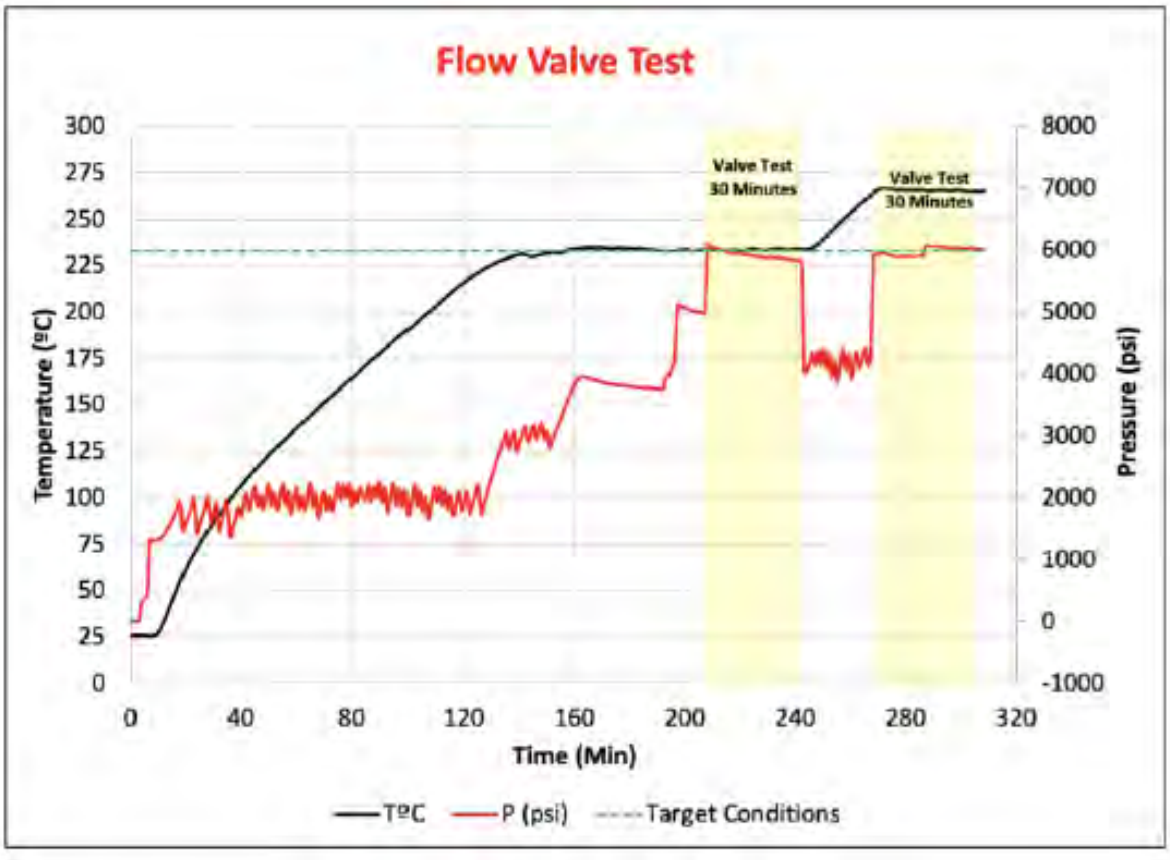

Figure 9: Flow valve HPHT test

4. Tool Installation

4.1 Well selected for installation

The tools are planned to be installed in the Well 16B(78)-32, which is one of the UTAH Forge wells. Figure 10 shows the UTAH Forge project distribution of the wells.

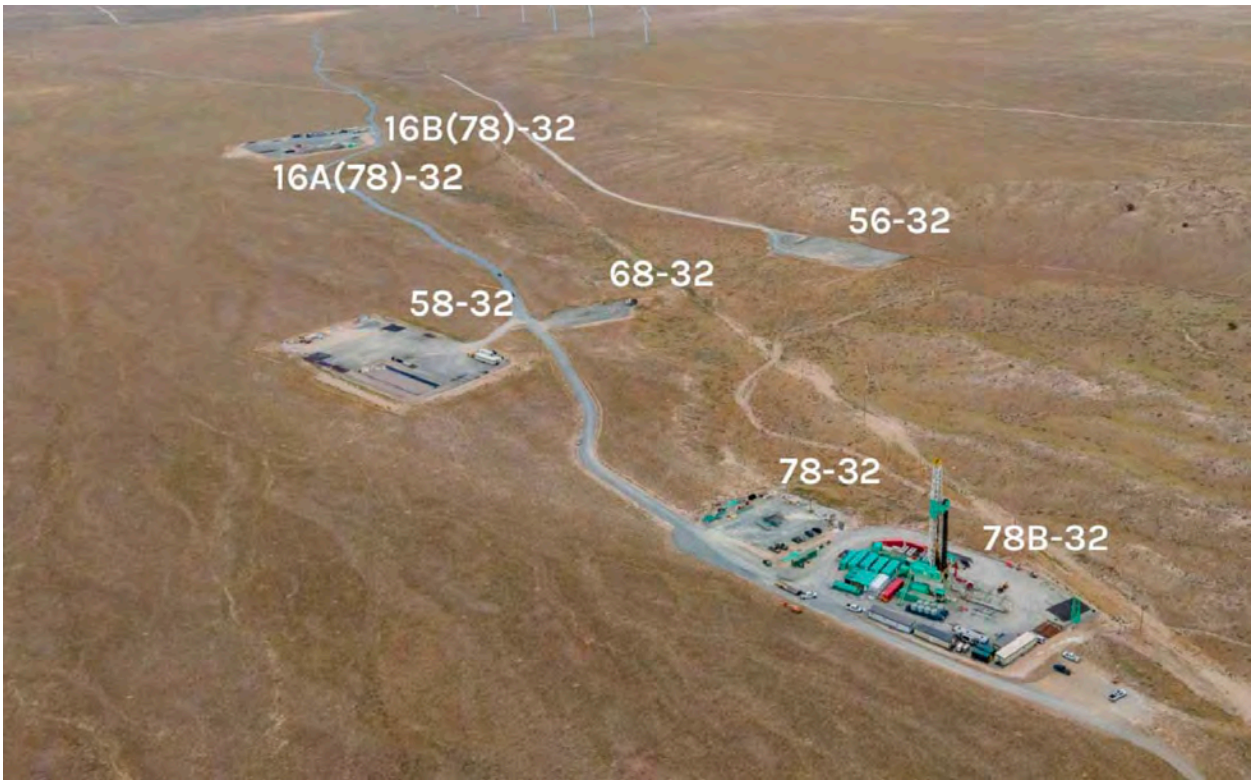

Figure 10: UTAH Forge Wells recovered from Data Dashboard by Utah FORGE (2024)

Following is the list of the wells and their description:

- Well 16B(78)-32: Production well with 10,947 ft MD
- Well 16A(78)-32: Injection well with 10,987 ft MD
- Well 58-32: Pilot well with 7,536 ft MD
- Well 68-32: Seismic monitoring well with 1,000 ft MD
- Well 56-32: Seismic monitoring well with 9,145 ft MD
- Well 78-32: Seismic monitoring well with 3,280 ft MD
- Well 78B-32: Seismic monitoring well with 9,500 ft MD

4.1.1. Well 16B(78)-32 (Production Well)

Table 1 shows the information of well 16B(78)-32, whereas Figure 11 shows a general schematic of the Well.

Table 1: Well 16B(78)-32 information (England et al., 2023)

Northing of Wellhead	13987765.96 ft (UTM 4263471.065)
Easting of Wellhead	1097907.09 ft (UTM 334642.081)
KB Elevation	5447.65 ft (confirm)
GL Elevation	5415.65 ft
Kick-off Depth	5,600 ft KB
Azimuth of Tangent	105°
Build Rate	5.5° /100 ft
TD Northing	UTM 4263110.666 LL: 38.501242, -112.882661
TD Easting	UTM 335832.0477 LL: 38.501242, -112.882661
Total Measured Depth	10,700.97 ft
True Vertical Depth at Toe	8,262.48 ft
Horizontal Offset	4,079.22 ft

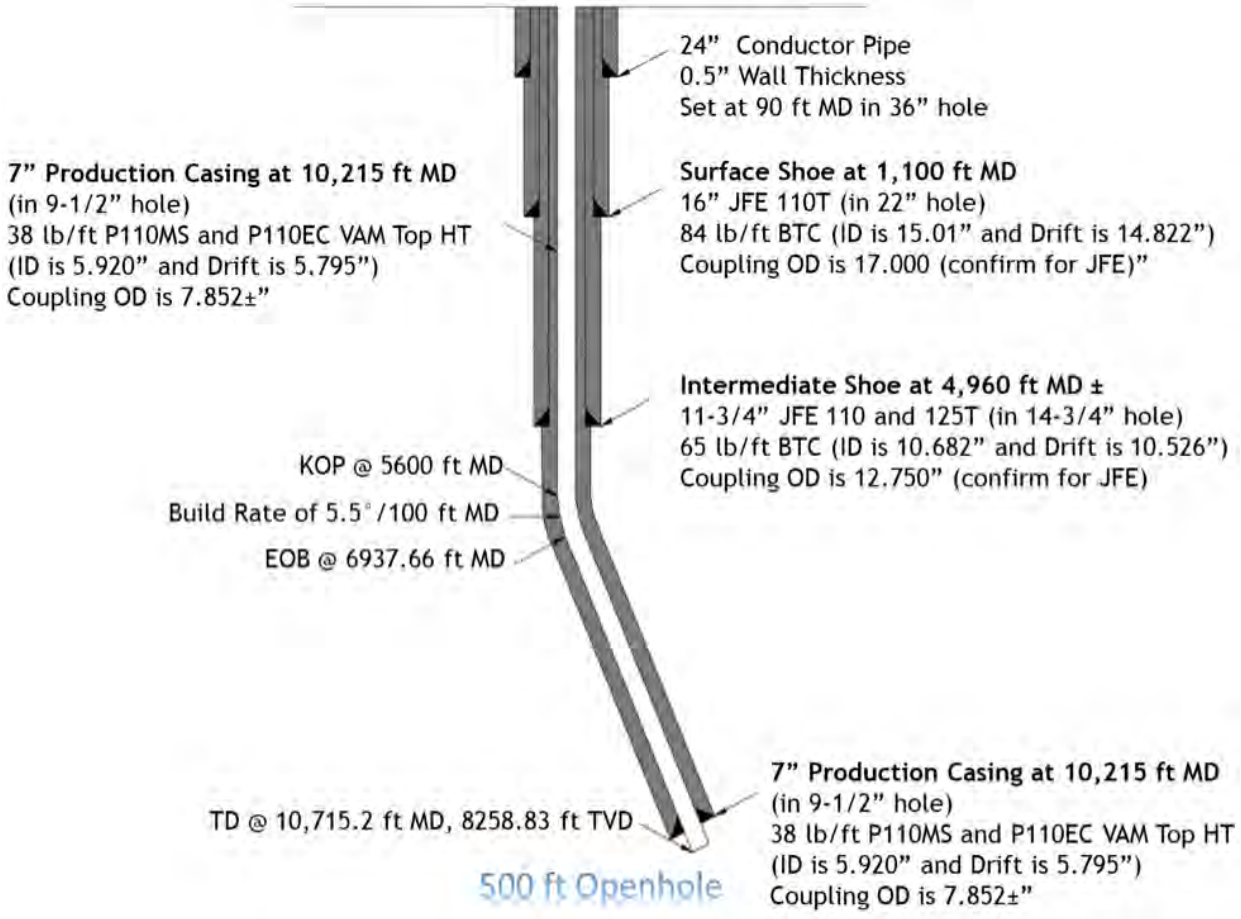

Figure 11: Schematic of Well 16B(78)-32 (Energy and Geoscience Institute, 2023)

The drilling operations for well 16B(78)-32 finished on June 20th, 2023. The main objectives, according to England et al. (2023) of this Well were:

- Develop a companion well, designated as 16B(78)-32, to align with Well 16A(78)-32, which follows a trajectory of roughly 105° with an inclination of 65° to the vertical. The primary aim is to establish a connection with Well 16A(78)-32, utilizing hydraulic fractures created in April 2022. Implement a build angle of 5.5° per 100 feet measured depth (MD) to ensure that Well 16B(78)-32 is vertically displaced from Well 16A(78)-32 by 300 feet true vertical depth (TVD).
- Drill and complete Well 16B(78)-32 to accommodate fiber optics for research programs at the University of Texas and Rice University.
- Keep the section from the 11-3/4-inch casing shoe at 4,837 feet MD to total depth at 10,947 feet MD uncased for a maximum of ten days to allow for potential open-hole stress measurements as part of the Battelle research program.
- Core the toe section of Well 16B(78)-32, specifically the final 500 feet before TD, in strategic intervals to investigate fractures, tracers, and other diagnostic materials introduced during hydraulic fracturing at the toe of Well 16A(78)-32. Allocate core sampling for geologic characterization, mechanical properties analysis, and other research and development (R&D) activities. Begin with an 8-3/4-inch core bit size and subsequently ream it out to 9-1/2-inch.
- Additionally, acquire core samples from a vertical section of the Well in granite formation for geologic characterization and mechanical properties assessments. Initially, it was planned at a depth of 4,970 to 5,030 feet MD, whereas actual coring occurred from 4,855 to 4,878 feet MD.
- Obtain multiple open hole and cased hole logs, including ultrasonic and resistivity imaging runs, a quad combo log at TD, and cement evaluation runs. Monitor for tracers and micro proppant from the stimulations at the toe of Well 16A(78)-32. Plan for production logging (PLT) suites or high-resolution temperature measurements to identify fractures communicating with Well 16A(78)-32.

4.2 Installation of tools in Utah FORGE well

Once the tools are tested individually in the University of Oklahoma's testing facilities, they will be installed in the Well 16B(78)-32 in the Utah FORGE project. The packer should seal a zone where fracturing will be performed through the flow valve. After fracturing, the same flow valve will be utilized for the production. Figure 12 shows how the isolation tool and the flow valve are installed together; it is essential to mention that multiple sets of isolation tools + flow valves will be installed in the Well. Figure 13 shows how three sets of tools (Isolation tool + flow valve) could be installed in the open-hole section of the production well. It is important to mention that at the bottom hole (8,500 ft TVD), the maximum expected temperature is 430ºF (221ºC), lower than the temperature at which the tools were tested.

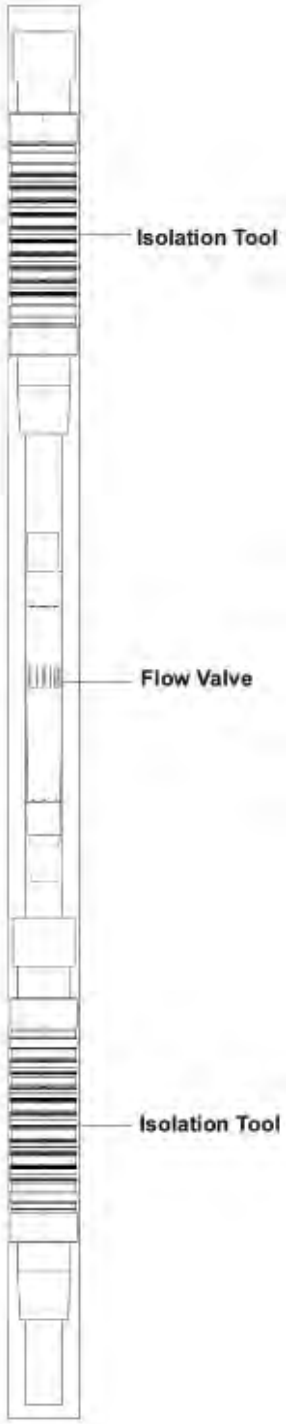

Figure 12: Isolation tool and flow valve

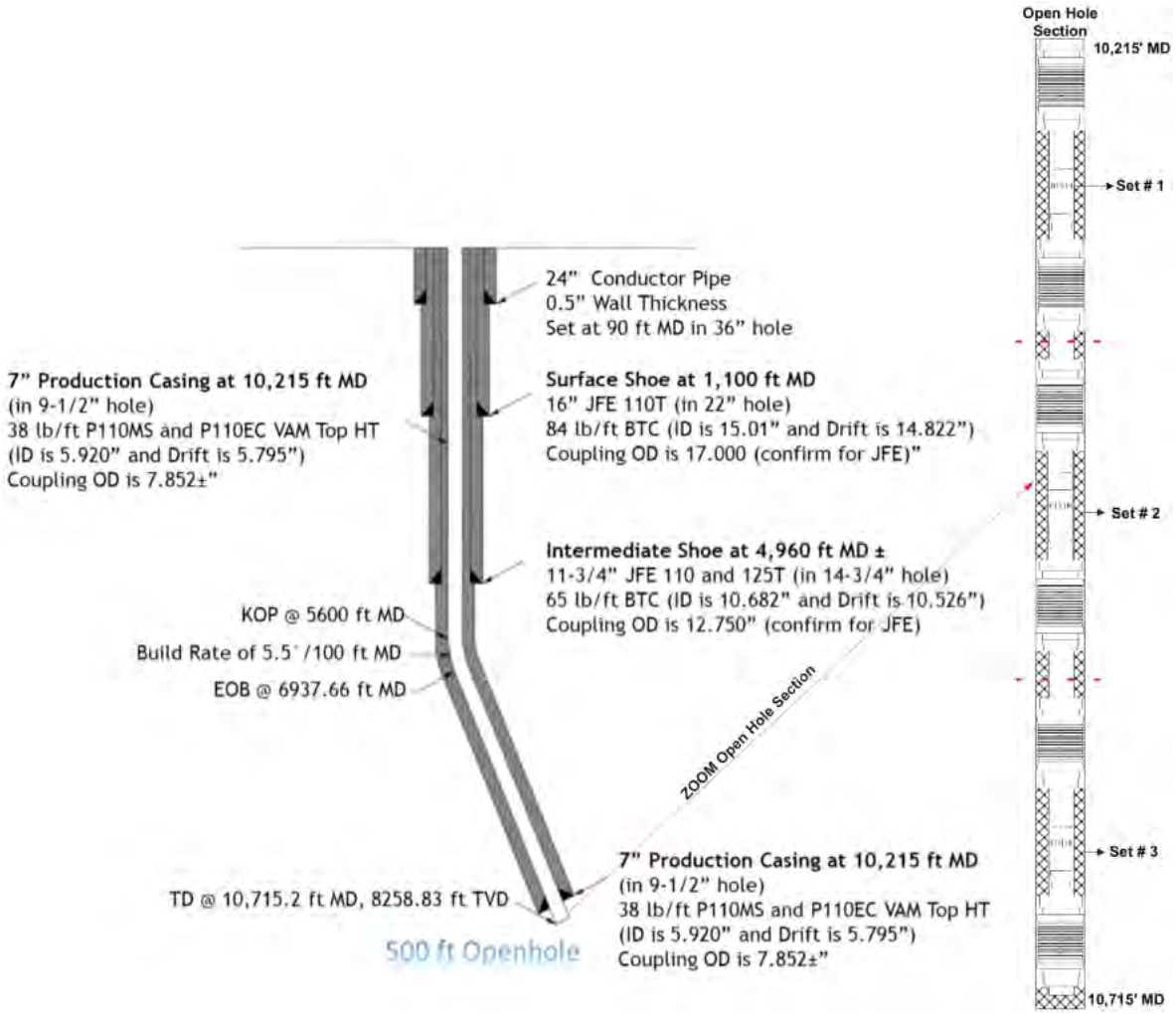

Figure 13: Set of zonal isolation tools and flow valve installed in open hole section (modified from Energy and Geoscience Institute, 2023)

5. Conclusions

From this paper, it can be concluded that the isolation tool and flow valve designed as part of the FORGE project performed satisfactorily during the HPHT tests performed at the University of Oklahoma's facilities. Therefore, these tools are ready to be installed and used in the Well 16B(78)-32 or any other available well. In addition, schematics of the deployment of the tools in this well have been presented in this paper to better understand how the tool would operate in the project. This would help to achieve the objectives set for the Utah FORGE project.

Acknowledgment

The authors of this paper would like to thank Welltec Inc., the manufacturers of the downhole tools, for the help provided in the elaboration of this paper. Additionally, the authors would like to

thank The University of Oklahoma for the facilities provided at the Well Construction Technology Center to conduct the experiments.

REFERENCES

Abid, K., Sharma, A., Ahmed, S., Srivastava, S., Toledo Velazco, A., & Teodoriu, C. (2022). A review on geothermal energy and HPHT packers for geothermal applications. Energies, 15(19), 7357.

Crippa, M., Guizzardi, D., Banja, M., Solazzo, E., Muntean, M., Schaaf, E., ... & Vignati, E. (2022). CO2 emissions of all world countries. JRC Science for Policy Report, European Commission, EUR, 31182

Data Dashboard. (2024, April 4). Utah FORGE. https://utahforge.com/project-data-dashboard/

DiPippo, R. (Ed.). (2016). Geothermal power generation: Developments and innovation. Woodhead Publishing

Dudley, B., & Dale, S. (2017). BP energy outlook-2017 edition. J. Ekon. Malaysia, 51(2), 1-103.

England, K., Swearingen, L., McLennan, J. (2023). End of Well Report Utah FORGE 16B(78)-32. Recovered from: https://gdr.openei.org/files/1516/End%20of%20Well%20Report-16B78-32-May_2024.pdf.

Energy & Geoscience Institute (EGI) (2023). Drilling Program Well 16B(78)-32 – Drilling Well on Paper. Recovered from: https://gdr.openei.org/files/1481/DWOP%20March%202.pdf

Lund, J. W. (2000). World status of geothermal energy use overview 1995-1999.

Moore, J., McLennan, J., Pankow, K., Simmons, S., Podgorney, R., Wannamaker, P., ... & Xing, P. (2020, February). The Utah Frontier Observatory for Research in Geothermal Energy (FORGE): A Laboratory for characterizing, creating, and sustaining enhanced geothermal systems. In Proceedings of the 45th Workshop on Geothermal Reservoir Engineering. Stanford University.

Reinsch, T., Dobson, P., Asanuma, H., Huenges, E., Poletto, F., & Sanjuan, B. (2017). Utilizing supercritical geothermal systems: a review of past ventures and ongoing research activities. Geothermal Energy, 5(1), 1-25.

Velásquez, A. F. B., Velazco, A. T., Escobar, J. A. Á., Abid, K., Esquitin, Y., Vasques, R. R., ... & Teodoriu, C. (2024). Design and Experimental Validation of a Unique Geothermal Downhole Valve for FORGE Project. *In 49th Workshop on Geothermal Reservoir Engineering. Stanford: Stanford University.*

A Summary of the FORGE Project for the Development of Multi-Stage Fracturing System and Wellbore Tractor to Enable Zonal Isolation During Stimulation and EGS Operations in Horizontal Wellbores

Alfred Eustes, William Fleckenstein, Hossein Kazemi, Jennifer Miskimins, Dias Abdimaulen, Balnur Mindygaliyeva, Ozan Uzun, Kaveh Amini

Colorado School of Mines

Thomas Hill, Jason Mailand, Robert Henschel

Tejas Research and Engineering

George King, Santos Ortiz

KSWC Engineering and Mechanical

Cullen Keyes

Defiant Exploration

Keywords

Enhanced Geothermal Systems, UtahFORGE, Casing Port Sleeve, Wellbore Tractors

ABSTRACT

A major technical hurdle for an economically successful Enhanced Geothermal Systems is properly balanced flow conformance to ensure equal heat harvesting from each fracture. Without flow conformance providing a near equal flow from injection to production wells, the system could "short circuit" creating a rapid cooling of produced fluid and subsequent electrical generation decline. The goal of this project is to build the tools necessary to construct and provide for a uniformly distributed flow through Enhanced Geothermal System fractures to maximize heat extraction. This research and development project is referred to as the GeoThermOPTIMAL.

This project is funded by a grant from the DOE Geothermal Technology Office through the Utah FORGE project and consists of Colorado School of Mines with partners Tejas Research & Engineering and KSWC Engineering and Mechanical with Defiant Exploration. The research team is developing two innovative devices. The first device is a casing port sleeve which will be cemented in place for multi-stage fracture stimulation and conformance control. It will be tested at geothermal conditions in experimental facilities. The second device is a downhole tractor optimized for horizontal geothermal well deployment. It will be tested at geothermal conditions in surface facilities. Both devices will be deployed and demonstrated at Utah FORGE or other geothermal sites. Finally, we are conducting mathematical modeling pertaining to the Utah FORGE rock formation flow characteristics and the near-wellbore rock breakdown processes. This paper is a summary of the project thus far.

The cemented casing port sleeves will have a port for a hydraulic fracturing stage and then controlled using the tractor to selectively close the sleeve. Any specific sleeve can be actuated for stimulation with the same size frac ball, regardless of the number of stages for fracture stimulation. Then, afterwards, the injection profile can be optimized at individual casing port sleeves to force injection fluid to move where needed to minimize thermal decline of the produced fluid. To close the casing port sleeves, the wireline wellbore tractor with flow sensors would be deployed to first detect the fluid short circuit and then engage with the sleeve and close it, removing the short circuit.

In addition to device building, mathematical analyses of recent laboratory and field data are being done. These models indicate that the current two-well, injection-production configuration (Utah FORGE and Fervo Energy's Nevada Pilot test), connected with multiple hydraulic fractures, is the most promising, practical method for extracting heat from enhanced geothermal systems. For additional heat recovery, modeling shows the current two-well system could be expanded to a three-well system consisting of one injection well and two symmetric producing wells connected with the same hydraulic fractures that emanate from the injection well. In addition, to enhance the understanding of how the casing port sleeves will behave in-situ, various levels of modeling have also been incorporated in the project to assess how the casing port sleeves enhance the Enhanced Geothermal System process. Near-wellbore breakdown processes have been modeled to determine failure behaviors as the hydraulic fractures initiate from the well.

1. Introduction

Given the success of horizontally drilled and multi-staged fractured wellbores in petroleum operations, there has been a strong interest in applying this technology for horizontally drilled and multi-stage fractured Enhanced Geothermal Systems.

The use of "perf and plug" completions has been the standard means of achieving multi-stage hydraulic fracturing. This method uses a pumped down wireline conveyed perforating gun/composite bridge plug system to a given point within the wellbore. The composite bridge plug is set inside the production casing to isolate the wellbore below the setting point in the wellbore. Then the perforating gun is withdrawn up the wellbore to a desired interval. At that point, the casing is perforated. The fracture stimulation subsequently takes place through those perforations. When a given fracturing stimulation stage is completed, another wireline conveyed perforation gun/composite bridge plug system is pumped down hole to isolate the previous frac stage; and the process starts anew. Getting perforating guns and composite bridge plugs to handle high temperatures and especially be able to be removed for production can be problematic.

There is another means of horizontally drilled and multi-staged fractured wellbore completion which is called the frac sleeve system or "port and packer". Initially casing port sleeves with closed ports are incorporated into the casing string and run into the hole with the production casing. The casing typically had external packers on the outside of the casing between the ports which would eventually expand to fill the open annulus isolating each port from each other. The use of external packers has replaced by completely cemented casing which would be more suited to geothermal operations given the heat related casing design issues. To open the port for fracture stimulation, a "frac" ball is pumped down the hole to engage the port. However, each sequential port requires larger and larger diameter tripping balls the closer to the vertical section of the hole. Depending upon the number of stages, one could run out of tripping ball sizes. In the past, after all

the stages were fracture stimulated, it was necessary to grind out each ball in each port. Today, dissolvable balls are available which eventually dissolve, opening all the stages to flow.

There has also long been a concern with horizontal and fractured Enhanced Geothermal Systems that unequal flow between the injector and producer may be a problem. This is due to varying fracture conductivities between and within each fracture stage. Conformance control is critical for the long-term success of Enhanced Geothermal System. With recent projects coming online, this issue has been shown to be indeed a problem.

This research and development project, called GeoThermOPTIMAL, was initiated to mitigate multiple frac port opening and conformance control. This project is supported by the US Department of Energy Geothermal Technology Office through the University of Utah's FORGE project. The team developing the system consists of the Colorado School of Mines, Tejas Engineering and Research, and KSWC Engineering and Mechanical with the support of Defiant Exploration.

The project consists of the development, construction, testing, and deployment of a casing sleeve port system, a wellbore tractor for sleeve manipulation, and modelling of flow and temperatures both near and far from the wellbore. Tejas Engineering and Research is responsible for the casing sleeve port system, using a patented frac sleeve developed by the Colorado School of Mines. KSWC Engineering and Mechanical along with Defiant Exploration is responsible for the wellbore tractor system. The Colorado School of Mines is responsible for the reservoir modeling as well as overall management of the project. The Principal Investigator is Dr. William Fleckenstein.

The goals of the project are to design, build, test, and demonstrate a low-cost, rapid multistage fracture stimulation device using cemented casing port sleeves. The same device can then be used for injection flow control. And second, to design, build, test, and demonstrate a geothermally suited wellbore tractor to effectively detect and manipulate the casing port sleeve to control the flow from the injector to the production well to improve heat recovery.

2. Problem with Enhanced Geothermal Systems

Enhanced Geothermal Systems are predicated on the assumption that the fluid flow from an injection well flows evenly to the production well, harvesting the heat uniformly. Augustine (2016), using original work by Gringarten et al. (1975), showed that if this doesn't happen, the Enhanced Geothermal System electrical generation capability might prematurely end due to excessive cooling. Fleckenstein et al. (2023) ran a stochastic economic analysis of an Enhanced Geothermal System and found an economically strong sensitivity to thermal decline as well as the size of the system, which drives the maximum fluid circulation rates. As shown in Figure 1, uniform spacing shows the lowest thermal decline rate whereas with variable spacing as well as variable fracture apertures, show much faster temperature declines.

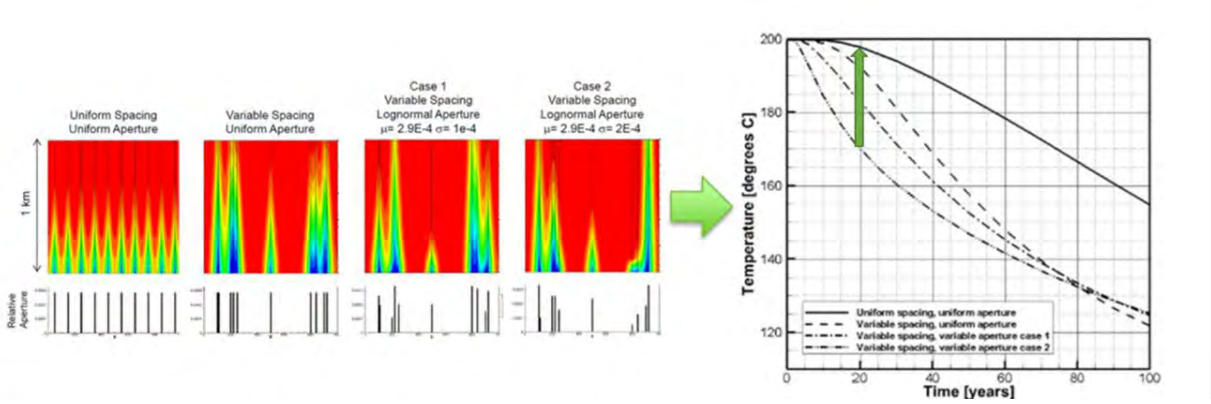

Figure 1: Augustine's (2016) Models Showing the Effect of Non-uniform Flow from the Injector to the Producer

Fleckenstein et al. (2023) shows that this thermal decline significantly impacts the return on investment.

Several key variables in addition to thermal decline impact the economics of Enhanced Geothermal System. The impacts of these variables were evaluated stochastically to determine their impacts on the economics of Enhanced Geothermal System. The three independent variables were determined to be (1) thermal decline, (2) flow rate per well, and (3) Power Purchase Agreement pricing. The thermal decline and flow rates per well are dependent on conformance control to regulate the fluid flow in system and overcome the lack of symmetry in nature. This provides uniform heat recovery and minimizes the system thermal decline.

What is needed to minimize this decline is a means to allow for any number of fracture stimulation initiation points as well to control fluid flow into the various fracture points after stimulation. The DOE, through the Utah FORGE Project, tasked the Mines/Tejas/KWSC Team to develop a casing port sleeve and wellbore tractor to accomplish these tasks. The casing port sleeve is designed to selectively open for stimulation with single sized, large diameter dissolvable balls, regardless of the number of frac stages. The wellbore tractor allows for the detection of abnormally high fluid injection rates in the wellbore and for the casing port sleeve to be closed by the tractor through manipulation of the sleeve at any time and at high bottom hole temperatures.

The casing port sleeves and tractor being developed and tested are envisioned to be demonstrated at the Utah-FORGE site but may be demonstrated at a well of opportunity depending on the funding and rig scheduling.

3. Casing Port Sleeve

The casing port sleeves are designed to catch the same size frac balls and either actuate the sleeve to open position for stimulation or release the frac ball for a downstream casing port sleeve. The catching or releasing of a frac ball depends upon the pumping flow rate. Each frac ball dropped will engage with a collet located at the far end of the casing port sleeve. However, if the flowrate is 12 barrels per minute (1.9 m^3/min) or more, the ball “pops” through the collet, creating a pressure surge that is noted at the surface and continues to travel toward the next port sleeve. When the number of pressure surges detected at the surface equals the number of casing port sleeves to be bypassed, the flowrate is dropped to about 8 barrels per minute (1.3 m^3/min). When the frac ball

catches in the collet this time, because of the slower flow rate, the pressure needed to "pop" through the collet is too low. The frac ball and collet now have enough time to travel far enough to open and lock the sliding sleeve ports and lock the ball into the collet. This is not unlike the process that a hydraulic jar uses with a metering port. Once the casing sleeve port opens, the flow diverts through the casing sleeve port with the ball acting as a sealing plug, isolating the previous frac stages from further flow. The frac balls will eventually dissolve in the heat and wellbore fluid, opening all the frac stages for injection, with no further wellbore intervention.

The casing port sleeves as shown in Figure 2 are designed for use in 7-inch (178 mm) 39 pound for foot (570 N/m) casing in a 9-1/2-inch (24.1 cm) borehole at a bottom hole temperature of 225°C (437°F). The overall length of the sleeve is 146-inches (3.7 m). The casing port sleeves have a total outside diameter of 8-3/4-inches (22.2 cm) which gives a wellbore clearance of 3/8-inch (1 cm) when centered in the borehole. This is a typical clearance for oil field casing port sleeves and has been shown effective for cementing. The casing port sleeves also have an internal clearance at the end housing or 5.95-inches (15.1 cm) which is 0.03-inches (0.76 mm) larger than the 39 pound for foot (570 N/m) casing inside diameter. A cross section of the sleeve is shown in Figure 3. The shifting sleeve itself has an internal diameter of 6.08-inches (15.4 cm). This difference in inside diameters allows for the sleeve ports to be shifted. The port flow area when open is 38 inches^2 (245 cm^2) which is a larger flow area than the casing at 27 inches^2 (174 cm^2). The collets are designed to handle a 5-3/4-inch (14.6 cm) dissolvable frac ball. A magnified drawing of the ports and shifting sleeve is shown in Figure 4.

The casing port sleeves have been designed to minimize any cement being pumped to foul the casing port sleeve mechanism. There is also a spring mechanism that engages upon opening the port. To close the casing port sleeves later, they have a specific profile that allow the wellbore tractor to be able to engage the sleeve. The tractor will "click" into the sleeve, allowing the port to be closed using the stored energy of the spring and a tug of the tractor.

Figure 2: Isometric Model of the GeoThermOPTIMAL Casing Sleeve

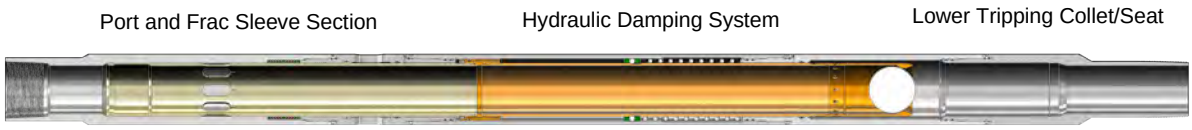

Figure 3: Cross Section of the Casing Sleeve. Note the Ball Sealer Caught in the Collet.

A prototype casing port sleeve has been built and tested for critical components/subassemblies and actuation. The collet has been tested with frac balls and has successfully passed or caught frac balls depending on flowrate. No significant wear has been noted on the collet even after multiple frac ball passage. The seals on the port shifting sleeve have been tested for seal drag friction. After various iterations, the seal drag at room and geothermal temperature regimes have been minimized around 500 pounds force (2.2 kN) for actuation.

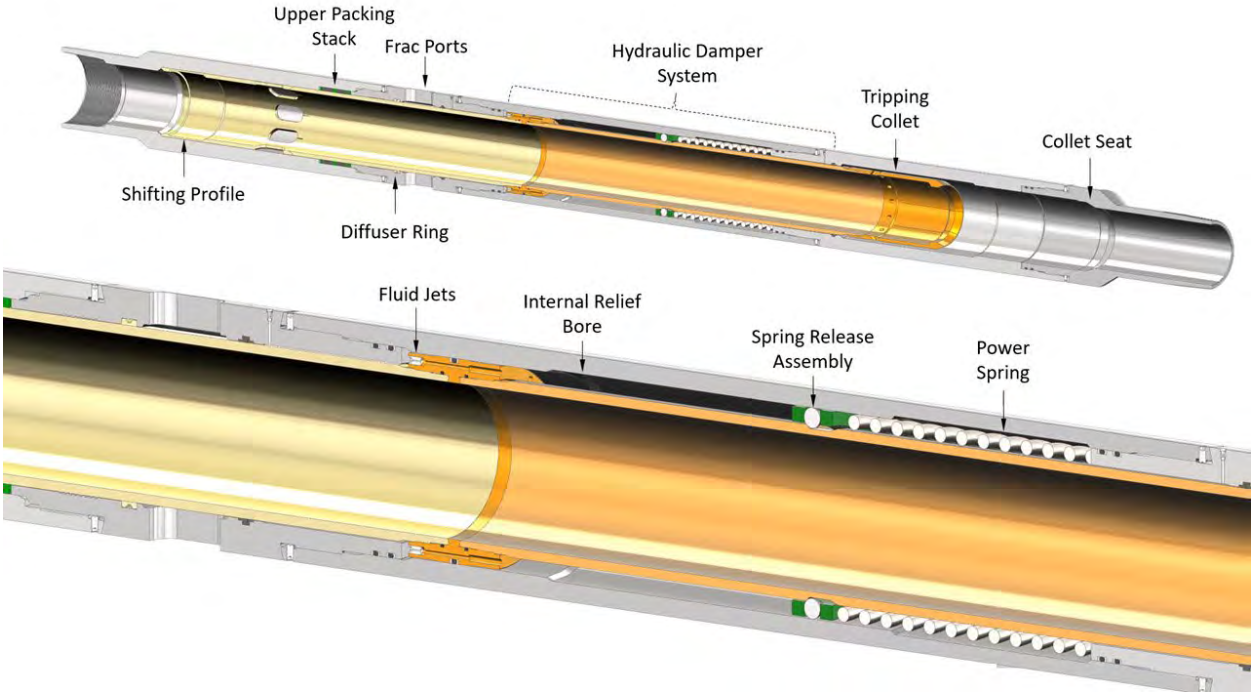

Figure 4: Magnification of Casing Sleeve Ports and Shifting Sleeve

4. High Temperature Tractor

The tractor being developed is based on an oil and gas wireline deployed wellbore tractor modified for higher geothermal temperatures. The tractor has been used for over 30 years. It will be deployed using a high temperature rated monocable. The tractor has a high temperature rated cable

head, swivel joint, a casing collar locator, high resolution temperature and pressure real time sensor package, an electromechanical wheeled tractor, and the hydraulically driven casing port sleeve control device. These are all currently being used in oil and gas operations up to 500°F (260°C). A drawing of the 44-3/4 foot (13.6 m) long tractor is shown in Figure 5**.**

The tractor has the capability to measure fluid flow around the device while injection is ongoing. Once it is determined that a given casing sleeve port is taking "too much fluid", the tractor can engage the casing port sleeve and lock it closed. This is a permanent closure with this casing port sleeve design. This shifts the fluid flow to other more productive ports.

Figure 5: Overall Drawing of the Wellbore Tractor

To protect the electronic and drive sections, these sections are encased in an insulating flask. The electronics section has 350°F (175°C) PC boards rated for continuous operation. The flask is designed to house this equipment at 440°F (225°C) for a duty cycle of 12 hours. This would be enough time to operate various casing port sleeves downhole.

The tractor drive components are modified from current oil and gas industry wellbore tractor hardware. The drive wheels engage the casing inside diameter to propel the unit up and down the casing regardless of the casing orientation. When a casing port sleeve is located, the tractor will anchor itself into the casing (Figure 6), the sleeve engagement latching mechanism (Figure 7) will make contact with the sleeve port, and a hydraulic piston (Figure 8) will latch into the sleeve and pull the port sleeve to the closed position. The position of the sleeve can be monitored from changes in hydraulic pressure. This process can be repeated for any number of casing port sleeves if the time is within the temperature duty cycle.

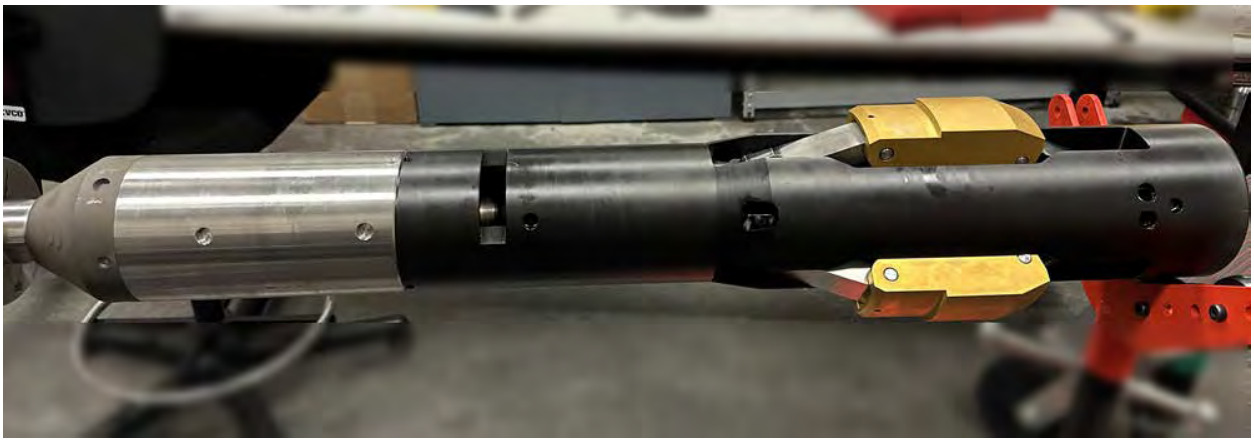

Figure 6: Wellbore Tractor Anchor Module

Figure 7: Wellbore Tractor Latching Tool

Figure 8: Wellbore Tractor Hydraulic Piston

The tractor has been design has been completed. Critical components/subassemblies for the prototype tractor system have also been tested at the component and subassembly stages, including actuation. The final system assembly and test of the tractor remains with further integration testing of the casing port sleeves and tractor at room and geothermal temperatures and pressure conditions in the surface test facility. Upon successful final assembly and integration testing at the laboratory, the system will be deployed to a field location for field trials and testing.

5. Modeling

As part of the GeoThermOPTIMAL team's integrated design efforts, multiple formation modeling efforts have been and continue to be developed. There is a system modeling effort for determining the fluid flow patterns and effectiveness over long distances. There is also a near wellbore

modeling effort to understand the fracture stimulation initiation and flow through the port and cement and into a formation. The mathematical modeling is to support device design and implementation based on assessment of the impact of reservoir stimulation results in the FORGE geothermal reservoir site in Utah as well as the reservoir stimulation and circulation effects at Fervo Energy's Project Red in Nevada. And the modeling will assist in evaluating well stimulation efficacy, effective stimulated formation permeability, and determining formation heat transfer. Furthermore, the modeling will predict induced fracture initiation and reactivation in the near fracture region. The reservoir characterization components of these mathematical models are similar to the models used in assessing unconventional oil and gas reservoirs.

The mathematical modeling includes several components and activities:

- Develop a wellbore heat transfer model to determine the temperature profile for cooling during the fracture stimulation
- Determine the needed duty cycle for the tractor electronics based on temperature thresholds of components under a variety of pumping and temperature scenarios.
- Develop a reservoir heat exchange model to determine the efficacy of heat extraction from the reservoir hot formation rock and reservoir fluid to deliver the heated water in the Enhanced Geothermal System to the power plant.
- Assess viability of the discrete fracture network and its value in quantifying formation stimulation and heat extraction from a formation
- Evaluate past tracer concentration response and diagnostic fracture injection test pressure response from field and conceptual model data to recommend future tests to quantify the efficacy of the fracture network resulting from well stimulation

1. Far-Wellbore Modeling

Earlier this year, the results of the modeling efforts was presented (Mindygaliyeva et al. 2024) pertaining to the effectiveness of fracture stimulation from two recent field test projects—the Utah FORGE field research (Figure 9) and the Blue Mountain commercial filed pilot test (Figure 10). The modeling effort began with laboratory experiments conducted on several core samples from Utah FORGE geothermal reservoir (Figure 11). These experiments were aimed to measure the key

formation parameters such matrix and fracture permeabilities and porosities.

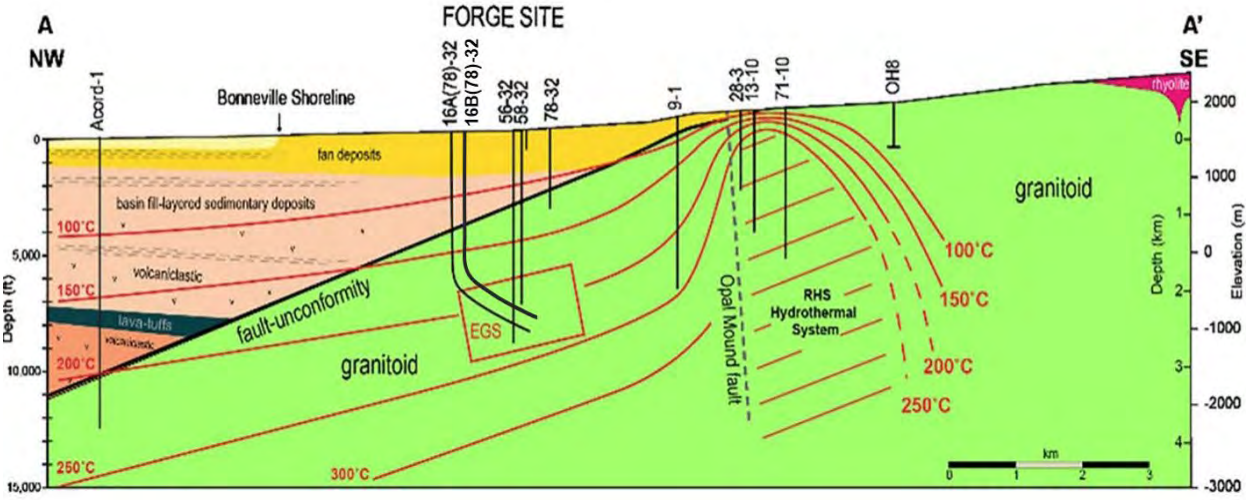

Figure 9: A cross-section of Utah FORGE site highlighting stratigraphy, structure, and thermal regimes—Enhanced Geothermal System on the left and hydrothermal on the right (Adopted from Kirby et al., 2018)

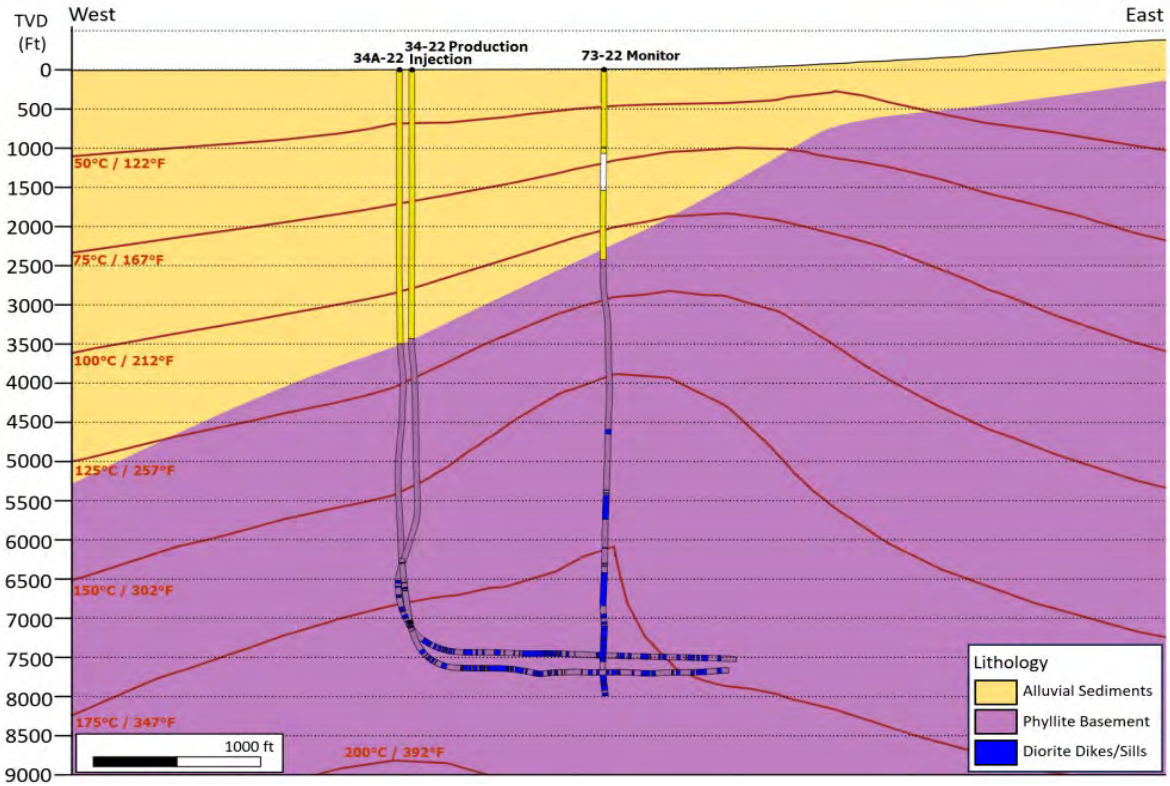

Figure 10: Project Red, the horizontal doublet, and vertical monitoring well in Blue Mountain Enhanced Geothermal System project (Norbeck and Latimer, 2023)

This data served as input for analytical and numerical modeling pertaining to the effectiveness of fracture stimulation.

The experimental results of Utah FORGE rock samples indicate that the rock matrix permeability is around 10^{-3} mD (10^{-18} m^2) and matrix porosity is approximately 1%. The analysis of artificially fractured core measurements yielded an effective fracture permeability of 1 mD (10^{-15} m^2) and the induced micro-fracture & macro-fracture porosity of 0.01%. This data served as guides for the input of analytical and numerical solutions to match field pressure falloff behavior from hydraulic fracture stages 1, 2, and 3 in FORGE (see Figures 12 and 13 for stage 1). While the team did not have any core samples from the Blue Mountain Enhanced Geothermal System wells, the team successfully applied the Utah FORGE analysis approach to some of fracture stages using the Blue Mountain pressure falloff data. This gave similar results as in Utah FORGE. At the time of this paper, the Team is in the process of analyzing the pressure falloff data from the newly implemented stages 4 through 10 of the Utah FORGE and the restimulation data from stages 1, 2, 3 of Utah FORGE.

The pressure falloff analysis technique utilizes the following equation:

$$p_{wf}\left(t_{inj}+\Delta t\right)\Big|_{x=0}-p_{ws}\left(\Delta t\right)\Big|_{x=0}=\frac{4.064\,qB\mu}{\sqrt{k_{f,eff}}\left(h\,L_f\right)}\left(\frac{1}{\left(\phi c_t\right)_{f+m}\mu}\right)^{1/2}\left(\sqrt{t_{inj}+\Delta t}-\sqrt{\Delta t}\right) \tag{1}$$

The Team used the above equation to determine formation effective permeability near the hydraulic fractures. The calculated effective permeability represents the enhanced formation permeability resulting from the hydraulic fracture placement. This permeability is calculated from the slope of:

$$p_{wf}\left(t_{inj}+\Delta t\right)\Big|_{x=0}-p_{ws}\left(\Delta t\right)\Big|_{x=0}\ \text{ vs. }\left(\sqrt{t_{inj}+\Delta t}-\sqrt{\Delta t}\right). \tag{2}$$

In addition to pressure falloff analysis, the Team developed a heat transfer and a stress calculation model to determine the efficacy of heat extraction from Enhanced Geothermal System reservoirs.

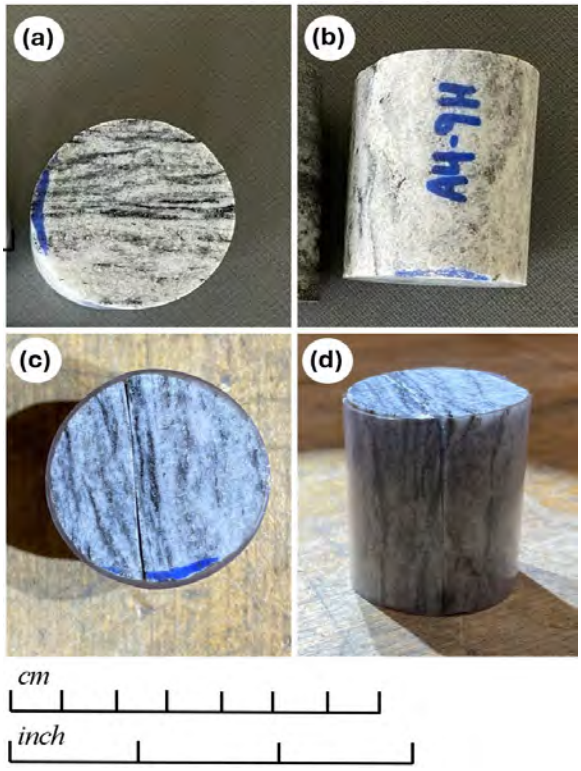

Figure 11: Horizontal core A4-9H from Utah FORGE depicted in (a) top view and (b) side view before fracturing (image scales on the bottom); (c) top view and (d) side view of core with induced fracture, wrapped with PVC tape to maintain core integrity.

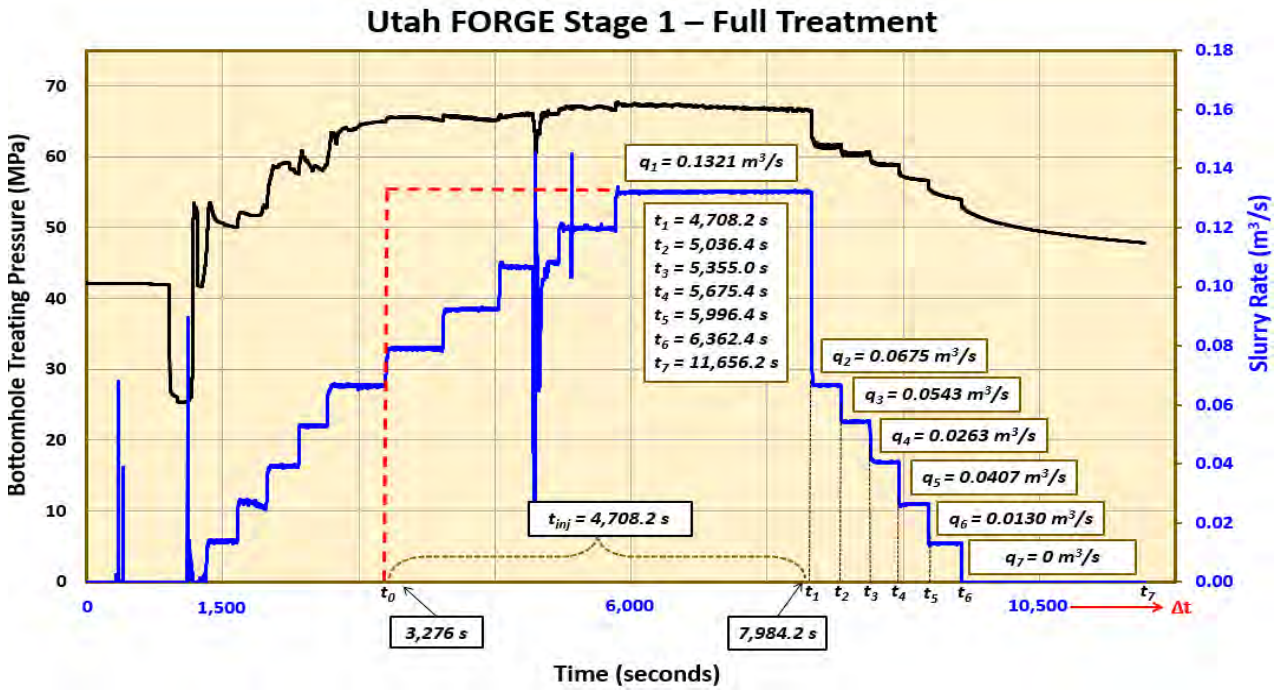

Figure 12: Stage 1 treatment data from Utah FORGE 16A(78)-32. The bottomhole treating pressure is indicated in black (MPa), while the slickwater rate is illustrated in blue (m3/s). Slickwater was pumped into a 200 ft (60.96 m) open-hole section.

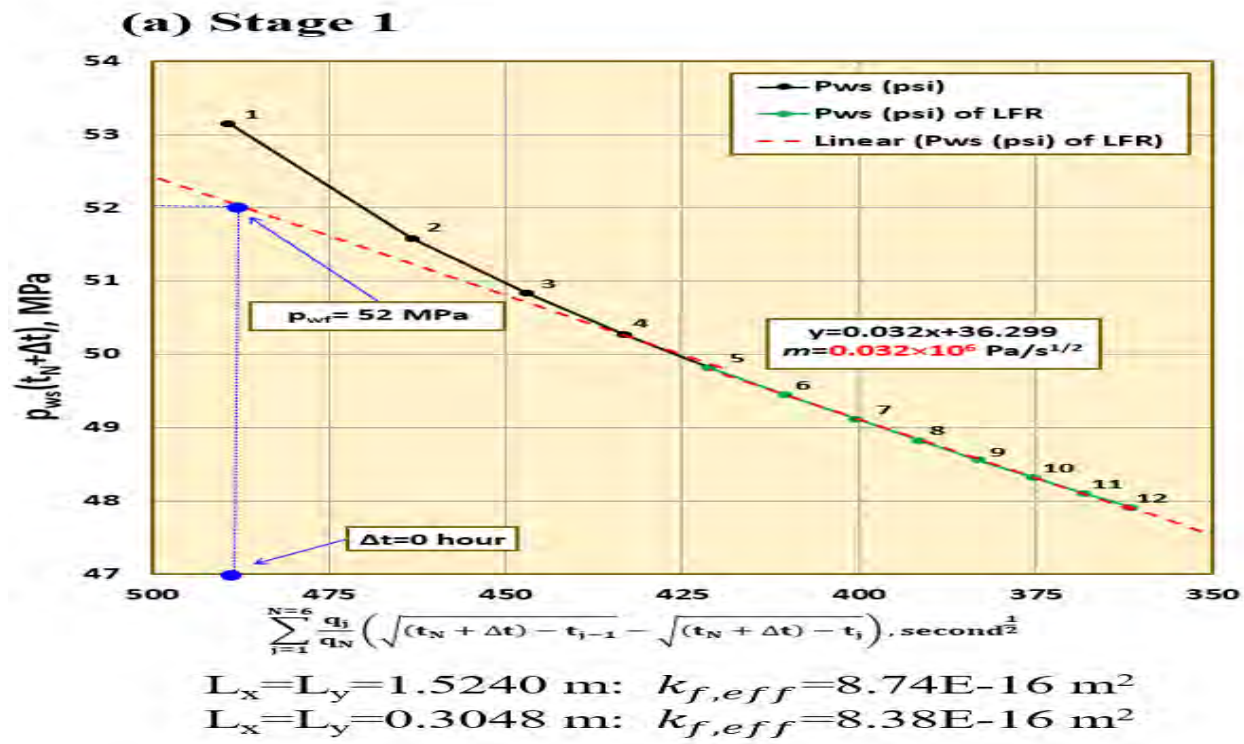

Figure 13: Shut-in bottomhole versus time for field pressure data for Utah FORGE 16A(78)-32, illustrating analytical pressure transient analysis method. The analysis of the line slope yielded the effective formation permeability ($k_{f,eff}$) for two matrix block sizes: 5 × 5 × 20 foot (1.5 × 1.5 × 6.1 m) and 1 × 1× 20 foot (0.31 × 0.31 × 6.1 m). Included are 12 data points recorded every 180 seconds.

2. Near-Wellbore Modeling

The near-wellbore model simulates fracture initiation and propagation through the casing port sleeve and into the immediate vicinity of the wellbore. The results demonstrate different fracture initiation pressures and propagation pathways depends upon the cement initial stresses, eccentricity of the cement sheath, and the location and geometry of existing fractures on the granitoid wellbore surface.

The numerical model employs the extended finite element method approach in a commercial finite element modeling software package. This allows for a detailed simulation of fracture dynamics. This approach explicitly represents the cement sheath and existing natural fractures in granite formation. The software has fully coupled pressure/deformation extended finite element elements are used to model fracture propagation and the fracturing fluid flow. Simultaneously, the deformation of the porous medium and the pore-fluid flow are modeled using coupled 'pore-pressure/deformation' continuum finite elements.

Two numerical models are being employed: a quasi-static model for cement failure and a dynamic model for hydraulic fracture propagation. The first model investigates cement sheath failure during hydraulic fracture initiation through the casing port sleeve. Several cases are being considered including fully concentric cylinders with a uniform cement thickness ring and cases of casing/wellbore eccentricity. The thinnest section of the cement ring was set at the low side of the horizontal wellbore. Additionally, three different initial stress conditions in the cement sheath are considered: zero initial stresses, intermediate compressive stresses, and hydrostatic stresses.

The second model examines hydraulic fracture initiation and propagation in the presence of pre-existing fractures, whether drilling induced or natural. Hydraulic fracturing fluid pressure is exerted through the micro-annulus formed at the casing/cement and cement/granite interfaces. In-situ stress conditions are set to match those at the Utah FORGE site, with the minimum horizontal stress aligned with the wellbore axis. The fluid injection rate in the simulation is 5 bpm (0.013 m^3/s), and the far-field boundaries are fixed.

Simulations are being conducted to study the role of initial stresses in the cement sheath and its eccentricity relative to the wellbore before hydraulic fracturing stimulation. Figure 14 illustrates the modeling results for two scenarios: one with 50% eccentricity and initially unloaded cement, and the other with a uniform cement ring and initial intermediate compressive stresses. At a depth of 8,500 feet (2,591 m), the cement cracks under the hydrostatic pressure exerted by the slick water inside the casing as soon as the casing port sleeve is opened. In the scenario with 50% eccentricity and initial compressive stresses, the pumping surface pressure needs to reach approximately 14,500 psia (100 MPa) to fracture the cement. The geometry of the fracture in both cases is radial (longitudinal).

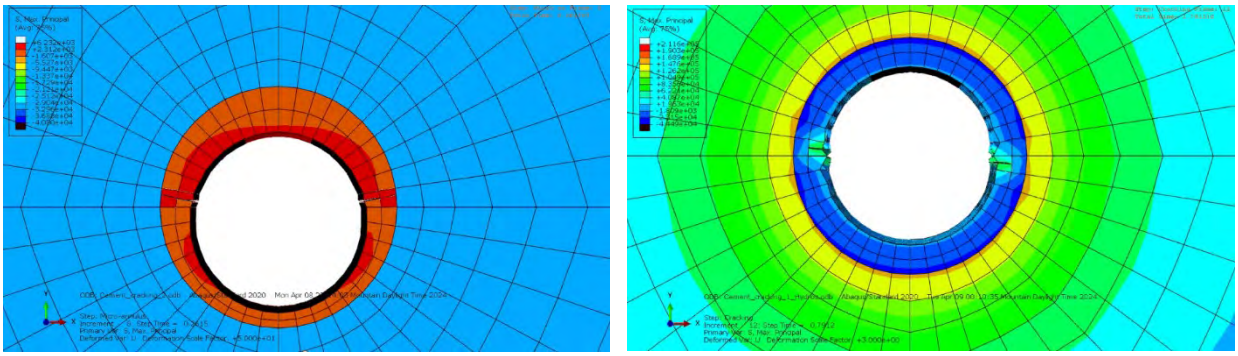

Figure 13: Left: 50% Eccentricity with Zero Initial Stresses in a Cement Sheath. Right: Concentric Cylinders with Intermediate Compressive Initial Stresses in Cement

The second fracture initiation model shown in Figure 15 examines two cases: transverse pre-existing fracture propagation and longitudinal fracture propagation. In the first case, there was a single pre-existing fracture on the side of the wellbore perpendicular to the minimum horizontal in-situ stress. Notably, the fracture grew both circumferentially and away from the wellbore in the direction of the initial crack, forming a penny-shaped, circular, planar fracture. In the case of the longitudinal fracture, it continued to grow along the wellbore axis. Simulations were run for 100 seconds at 5 bpm (0.013 m^3/s) to investigate fracture width, length, fluid pressure, and fluid leak-off into the rock. Future investigations will focus on the impact of varying injection rates and durations to understand fracture behavior under different pumping regimes and fluid properties.

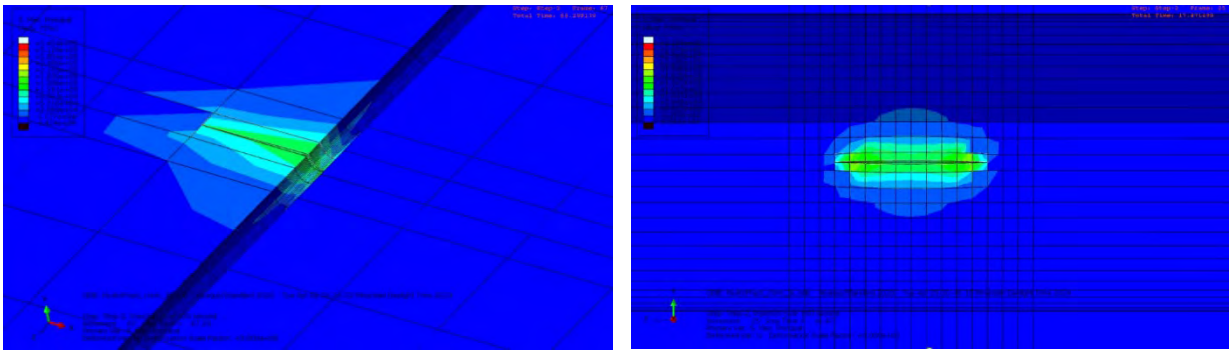

Figure 14: Left: Transverse pre-existing fracture; Right: Longitudinal pre-existing fracture

II. CONCLUSIONS AND FUTURE WORK

A casing sleeve has been designed, built and successfully tested for frac ball passage and sleeve closing at room and expected geothermal temperature and pressure conditions.

The wellbore tractor has been designed and subassemblies built. It will be fully assembled within a few months of this paper's publication and tested at room and expected geothermal temperature and pressure conditions

.

Two finite element models have been successfully developed and conducted pertaining to the Utah FORGE rock formation flow characteristics and near-wellbore rock breakdown processes. They have been used to determine the design parameters of the casing sleeve and tractor.

Finite element modeling performed on the near wellbore fracture initiation indicates that under the Utah FORGE stress and well conditions, fracture initiation occurs immediately upon port opening. This behavior occurred under a variety of sensitivities including eccentricity of the wellbore and varying cement sheath thicknesses (casing-wellbore offset).

The far finite element model was used to successfully assess the flow data from the Utah FORGE project and Fervo's 2023 Project Red pilot test.

Successful completion of this project will provide the devices needed for Enhanced Geothermal System construction using low-cost, rapid multistage fracture stimulation with cemented casing port sleeves. These same cemented casing port sleeves would then be used in conjunction with a geothermally rated wellbore tractor to control the flow of heat-carrier fluid to improve heat recovery.

Future work is being done to determine a means for throttling the injection flow rate, rather than cutting flow off in highly conductive fractures, with a goal of uniform injection in the entire reservoir.

Acknowledgement

This material is based upon work supported by the Department of Energy, Office of Energy Efficiency and Renewable Energy, under Award Number DE-EE0007080. This report was prepared as an account of work sponsored by an agency of the United States Government. Neither the United States Government nor any agency thereof, nor any of their employees, makes any warranty, express or implied, or assumes any legal liability or responsibility for the accuracy, completeness, or usefulness of any information, apparatus, product, or process disclosed, or represents that its use would not infringe privately owned rights. Reference herein to any specific commercial product, process, or service by trade name, trademark, manufacturer, or otherwise does not necessarily constitute or imply its endorsement, recommendation, or favoring by the United States Government or any agency thereof. The views and opinions of authors expressed herein do not necessarily state or reflect those of the United States Government or any agency thereof.

References

Augustine, C., “A Methodology for Calculating Enhanced Geothermal System Electricity Generation Potential Based on the Gringarten Model for Heat Extraction From Fractured Rock”, GRC Transactions, Vol. 40, 2016.

Grinenstein, W., Kazemi, H., Miskimins, J., Eustes, A., Abdimaulen, D., Mindygaliyeva, B., Uzun, O., Amini, K., Hill, T., Mailand, J., Henschel, R., King, G., Ortiz, S., Keyes, C., “Development of Multi-Stage Fracturing System and Wellbore Tractor to Enable Zonal Isolation During Stimulation and Enhanced Geothermal System Operations in Horizontal Wellbores – First Year Progress”, SPE-215107-MS, SPE Annual Technical Conference and Exhibition, October 16-18, 2023

Fleckenstein, W., Kazemi, H., Royer, C., Loff, G., and Zimmermann, J., “A Stochastic Economic Analysis of An Enhanced Geothermal System”, GRC Transactions, Vol. 47, 2023.

Fleckenstein, W., Miskimins, J., Eustes, A., Kazemi, H., Hill, T., Mailand, J., King, G., and Ortiz, S., “Development of Multi-Stage Fracturing System and Wellbore Tractor to Enable Zonal Isolation During Stimulation and Enhanced Geothermal System Operations in Horizontal Wellbores”, Geothermal Rising Conference, San Diego, CA, Oct 3 to 6, 2021.

Fleckenstein, W., Miskimins, J., Kazemi, H., Eustes, A., Abdimaulen, D., Mindygaliyeva, B., Uzun, O., Amini, K., Hill, T., Mailand, J., Henschel, R., King, G., Ortiz, S., Keyes, C., “Development of Multi-Stage Fracturing System and Wellbore Tractor to Enable Zonal Isolation During Stimulation and Enhanced Geothermal System Operations in Horizontal Wellbores”, SPE-210210-MS, SPE Annual Technical Conference and Exhibition, October 3–5, 2022

Gringarten, A., Witherspoon, P., Ohnishi, Y., “Theory of Heat Extraction From Fractured Hot Dry Rock”, Journal of Geophysical Research, Vol. 80, No. 8, March 10, 1975.

Kirby, S.M., Knudsen, T., Kleber, E., Hiscock, A., 2018. Geologic Setting of the Utah FORGE Site, Based on New and Revised Geologic Mapping. GRC Transactions, Vol. 42, 2018.

Mindygaliyeva, B., Uzun, O., Amini, K., Kazemi, H., Fleckenstein, W., 2024. Assessment of two recent hot dry rock thermal energy production projects. Geothermics 122, 103051. https://doi.org/https://doi.org/10.1016/j.geothermics.2024.103051

Norbeck, J.H., Latimer, T.M., 2023. Commercial-Scale Demonstration of a First-of-a-Kind Enhanced Geothermal System. (Preprint). https://doi.org/10.31223/X52X0B.

Development and Qualification of an Elastomer Based Retrievable Packer for Effective Annular Isolation in Enhanced Geothermal Systems

Neil Glover[1], Geoffrey Garrison[2], Steve Glidewell[3]

[1] Swell X Limited

[2] Hotrock Energy Research Association

[3] Techwell Technologies LLC

Keywords

Zonal isolation, well integrity, cementless completions, well construction

ABSTRACT

The potential for geothermal power is significant however the reality of delivering that potential in an economic way remains extremely challenging. This is especially true with regards to well completion technologies and methodologies due to the limitations in the performance of existing equipment in well conditions up to 300°C. A critical requirement for the successful stimulation of geothermal wells is effective well isolation technology.

This paper presents the research and development of a high temperature, elastomer based isolation system, with the potential to be retrievable, that will enable controlled stimulation of an EGS reservoir. It details the test equipment design, test results and the engineering process for the development, testing and qualification of the elastomers chosen for the production packer. Focusing on reduced complexity with minimal moving parts this isolation system draws on experience gained in the oil and gas industry adapted to operate effectively at temperatures up to 300°C.

The paper will also discuss the development of the polymers and packer design to provide sufficient diametrical expansion to provide a seal and further to deliver the differential pressure performance of 6000psi required for these wells. It will also outline the qualification program to API 19OH and the results to date of a successful packer test at 225°C.

1. Introduction

Well stimulation has been used extensively in the oil and gas industry to increase production, hydrocarbon flow, from reservoir rocks. In combination with horizontal drilling to optimize reservoir contact this technique provides higher production rates and higher overall recovery. This is especially true in what have been characterized as unconventional oil and gas wells.

A key enabling technology for these wells has been the use of annular isolation systems to provide wellbore segmentation along the long horizontal well sections. These devices provide a mechanism for efficient stimulation of, now distinct, zones and also allow the possibility to shut-in zones in the event of water or gas breakthrough over the life of the well.

One of the most successful forms of annular isolation system has been the swellable packer. Due to simplicity of design and its ability to swell and seal into microvariations in the wellbore it provides a robust seal even in open hole conditions.

Enhanced Geothermal Systems (EGS) are looking to employ techniques of wellbore stimulation by hydraulic fracturing in the wells to improve overall production and to access further resources. The plan is to use annular seals to isolate sections of the wellbore so that high pressure stimulation above the fracture pressure of the reservoir formation can take place. This hydraulic fracturing creates a highly conductive flow path between the reservoir and the wellbore.

The challenge for these geothermal wells is that existing technology simply cannot perform at these extremely high temperatures. Swell rates are typically too fast to be practical and the elastomers are either too soft to hold pressure or quickly embrittle resulting in failure.

This paper will outline the development and testing of a high temperature swellable packer and critically the polymer to be used for the packer element for use in geothermal applications.

2. Design Concept

The scope of the work is to develop a temporary, wellbore packer system that will allow controlled stimulation of an EGS reservoir at temperatures from 150°C to greater than 225°C and which can hold a differential pressure of at least 6000 psi.

2.1. Specification

The full target technical specification for the system is outlined in the table below:

Table 1: Design specification

Design Temperature	Minimum temperature – 150°C (302°F) Qualification target temperature - 225°C (437°F) Push target temperature - 300°C (572°F)
Required Pressure Rating	6000 psi
Sealing Diameter & tool geometry	Hole Diameter - 12.25”

	Mandrel OD – 9.625” Element OD – 11.75 Hole Diameter – 8.5” Mandrel OD – 7” Element OD – 8.125
Swell Fluid	Brine or Fresh Water
Run in hole time	Typically complete in 6 hours
Design time to contact	12-24 hours (6 hours in and 6 hours safety to POOH)
Time to Pressure hold	As soon after 48 hours as possible
Duration of pressure hold (frac duration)	7-14 days
Subsequent degradation time to retrieval	14 days
Wellbore/swelling fluids	Fresh water – Likely injection fluid 3.5% NaCl – Alternate injection fluid salinity (Seawater) 10% NaCl – (Typical produced water salinity)

The approximate operational performance required from the system was outlined in the guidelines below:

Sequence of Events		**Time**
Run In Hole	-	0-6 Hours
Swell to contact	-	0-12 Hours
Packer set	-	12-48 Hours
Hydraulic Fracturing (packer holds 6000psi)	-	Day 2 to Day 14
Packer degrades	-	Day 15 to 28
Pull Out Of Hole	-	Day 29

The major success criteria for this design were broken down into four phases which lead to the definition of stage gates for the development.

- Controlled expansion of the elastomer within the high temperature window to achieve a realistic running diameter and run in hole time but still be able to expand to contact the wellbore.
- The ability of the elastomer to withstand temperatures between 150°C and 300°C.
- Pressure performance – The system must be able to hold a 6000psi differential pressure across it.
- The system should then be able to reduce in diameter to allow it to be retrieved from the well.

Figure 2: Swellable packer assembly

3. High Temperature Elastomer Development and Testing

A large number of different compounds and compound families were assessed in an initial review phase to find polymers that had previously shown some performance at higher temperatures. From these a short list of three elastomers was selected from three different elastomer families to ascertain their performance at the target temperatures.

Swell testing was carried out in autoclaves, as shown in Figure 3, placed inside ovens, shown in Figure 4, in order to apply a consistent heat to the entire fixture. Test pieces were manufactured as 2” x 2” x 0.5” molded test pieces bonded to a metal plate. Experience has shown that this is a reliable and accurate way to observe swell for the large number of samples required for an R&D program.

Figure 3: Flanged autoclave for high temperature plate testing

Figure 4: Oven containing autoclave for improved temperature control

3.1 Test Results and Analysis

3.1.1 Swell testing at 150°C

Detailed coupon and plate testing was carried out at 150°C and 225°C using 3 compounds from different swellable elastomer families in 3 different salinities. The compounds were designated -

42, -117 and ,155. The different fluids would give further insight into the swell performance and fluid compatibility of the elastomers.

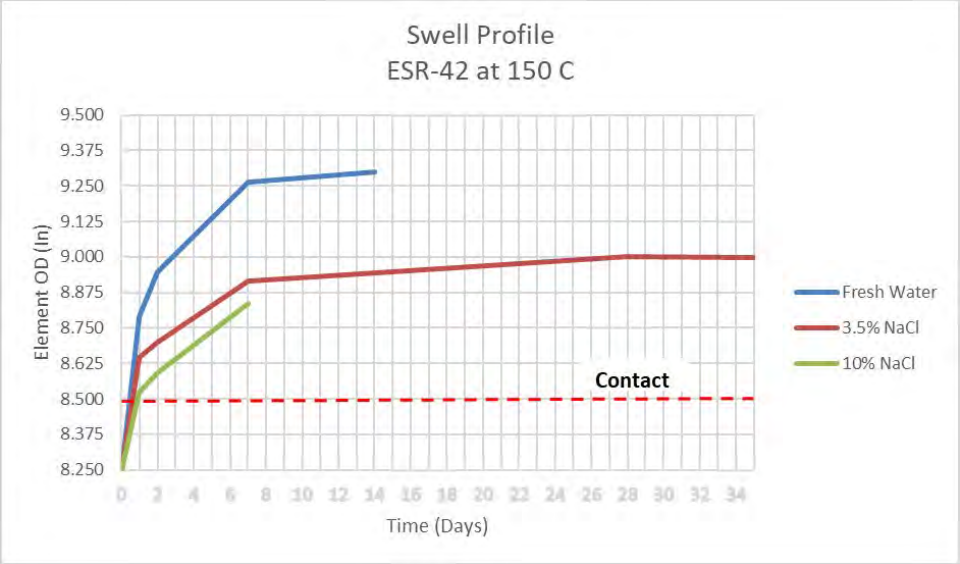

Figure 5: Swell profile of -42 at 150°C

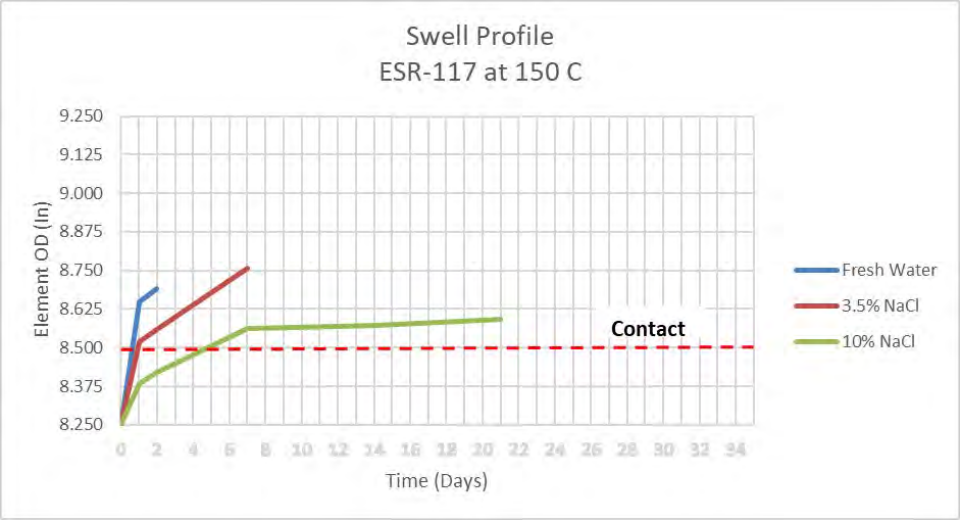

Figure 6: Swell profile of -117 at 150°C

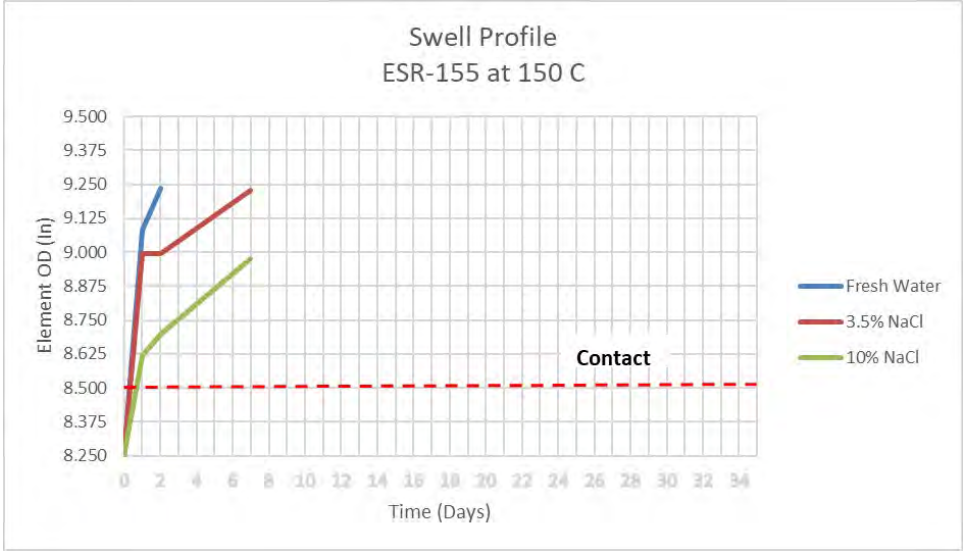

Figure 7: Swell profile of -155 at 150°C

In these graphs if the line has stopped it is because the compound swelled off the plate making further results ineffectual as the sample is no longer constrained. This is also an indication that the compound has begun to breakdown to a significant degree.

3.1.2 Analysis

It is clear from the 3 graphs that the impact of the fluid has a significant effect on the swell rate of the compounds. This is clearly shown in Figure 8:

Figure 8: Plate samples at Day 1 in Fresh water - Pictured L to R: ESR-155, ESR-42, ESR-117

The higher the salinity of the fluid the slower the rate of swell and in some respects the more controlled the swell is also.

The 3 compounds behave differently in terms of rate of swell and ultimate swell but all 3 swell to contact and beyond.

3.1.3 Swell testing at 225°C

The following graphs show the performance of the 3 original compounds in different fluids at 225°C.

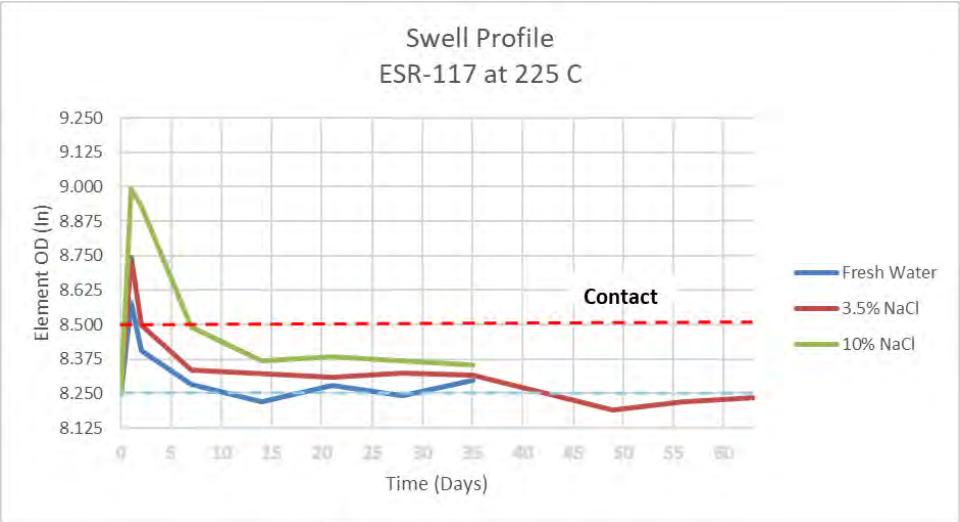

Figure 9: Swell Profile – ESR-117 at 225°C

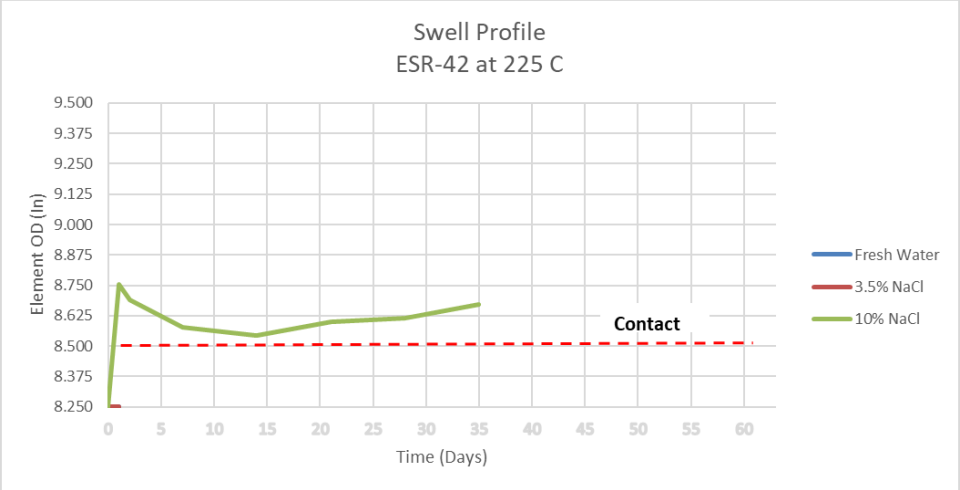

Figure 10: Swell Profile – ESR-42 at 225°C

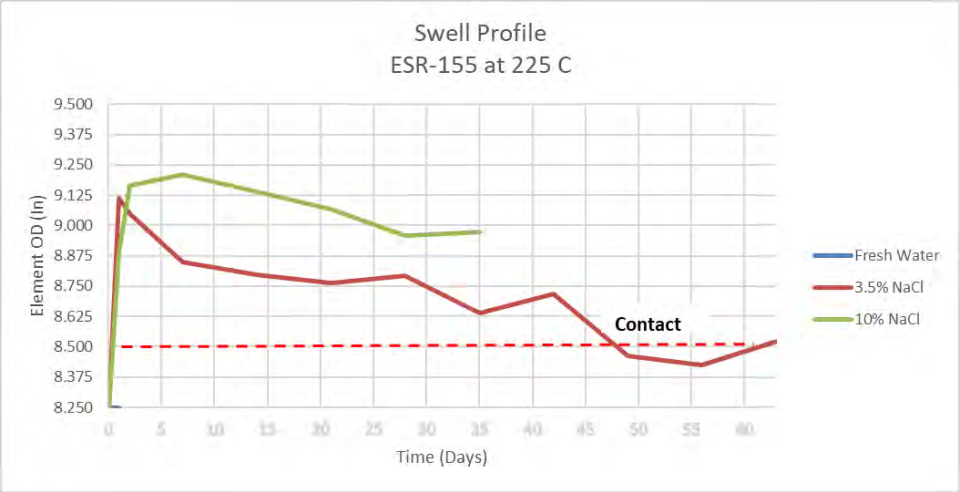

Figure 11: Swell Profile – ESR-155 at 225°C

Further variables were examined, examples of which are shown in Figures 12 and 13 below.

Figure 12: Weight loss over time - ESR-42 at 225°C

Figure 13: Change in hardness over time - ESR-42 at 225°C

3.1.4 Analysis of results at 225°C

The 10% fluid test once again shows the impact of increasing the salinity of the activation fluid. Increasing salinity slows the rate of swell. The -117 shown in Figure 9 clearly shows a very rapid swell and de-swell though definite breakdown of the compound can be observed. This is also demonstrated even more strikingly in -42 as it swelled so rapidly in freshwater and 3.5% salinity that it swelled off the plate within 24 hours. Figures 12 and 13 demonstrate an observable characteristic that the -42 compound does harden over time due to the increased temperature but rather than maintain its volume/weight this reduces over the same period.

Finally Figure 11 shows that -155 performs significantly better at this higher temperature however while the de-swell is much more controlled the swell rate, even in 10% fluid, may be too fast to be practical.

3.1.5 Conclusion and outcome of swell testing

As a result of these tests it was clear that the best performing of these compounds at the higher temperatures was -155. A decision was made to adapt this compound to provide even more controlled swelling and eventually -158 was developed. This compound was subsequently tested at 225°C in 3.5% NaCl and the results are shown in figure 14 below.

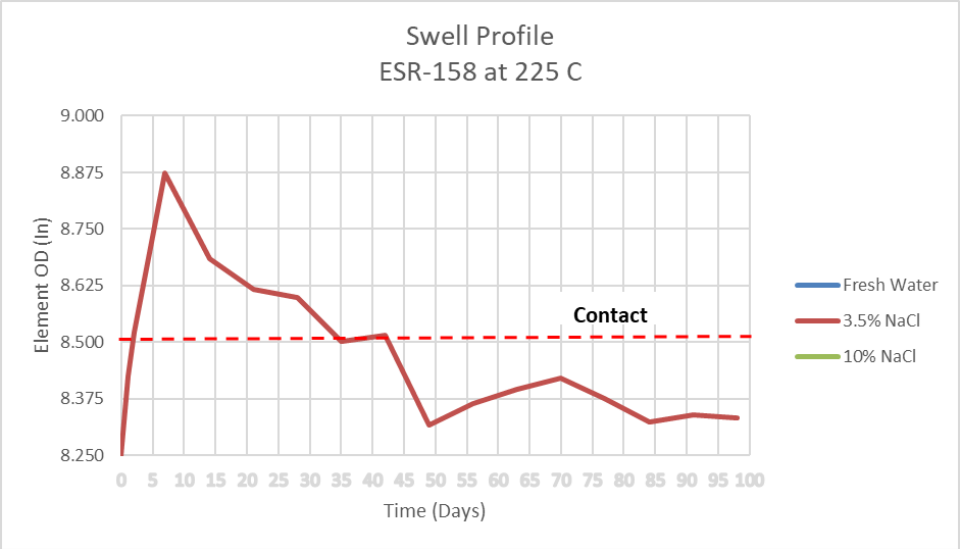

Figure 14: Swell Profile – ESR-158 at 225°C

The key points to note are:

- There is a significantly more controlled swell at this high temperature and salinity compared to previous compounds
- The compound has maintained its elasticity even after nearly 100 days at temperature
- The compound has reduced in diameter to the point it no longer contacts the target wellbore diameter.

3.1.6 Swell performance at 300°C

On the strength of this performance a decision was made to try both versions in this family of compounds at the upper project target temperature of 300°C. The graph below, figure 15, shows the performance of these two compounds at 300°C in 10% salinity.

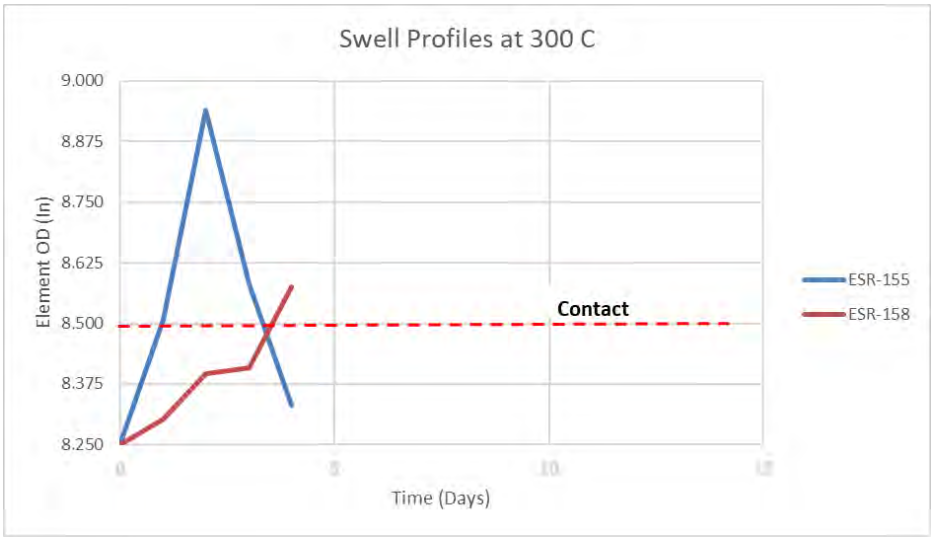

Figure 15: Plate Testing at 300°C

3.1.7 Analysis

It can be observed that ESR-155 swelled and deswelled almost back to its initial size in just 4 days. It had also hardened considerably. This temperature therefore appears to be too high for this compound to perform effectively. On the other hand, ESR-158 was continuing to swell and was still flexible. However, the extreme temperature has now caused another issue in that the rubber sample has swelled off the plate at day 4 due to failure of the bonding agent and primer. This can be seen as a crackled layer in figure 16.

Figure 16: Bonding failure during plate test at 300°C

While this result is disappointing it clearly shows the upward potential of these materials and further work will be carried out.

3.2 High temperature polymer development

The main finding regarding the polymer design for these extreme high temperature conditions has been the observation that while some of the compounds are embrittling as expected they are not remaining at their initial swell volume and are in fact shrinking back.

This can be explained by the following. Typically, in the presence of increased temperature and oxygen rubber will react one of two ways. One way is termed “chain hardening” and the other “chain scission”. Both reactions lead to a reduction in physical properties. The polymer types we are utilizing fall into the “chain hardening” category.

This condition occurs when the environment is one of increased heat and the presence of oxygen will accentuate this condition. Rubber compounds have additives called vulcanizers and accelerators that essentially form bridges between the multiple polymer chains of the raw polymer. These bridges are referred to as cross-links. This is the characteristic that contributes to the properties that the compound will have after it is cured. When exposed to increased heat “free radicals” are formed that create additional cross-links. If you can imagine, each additional cross-link pulls the polymer chains tighter as they are added. As they are pulled tighter properties

change. The material gets harder, elongation goes down, tensile may increase to a point before embrittlement. We believe these processes are responsible for the results observed in these experiments.

4. Pressure Testing

The pressure test was carried in accordance with API specification 19OH. The test was performed in the horizontal condition, which is a worst-case scenario for the element, inside a 6” bore. The test packer used was designed to utilize existing pressure test fixtures at this stage of the project while still replicating the expected rubber thickness and required radial swell as closely as possible. The 5ft element is required to hold a minimum of 2500 psi to meet the performance target. This correlates to 6000psi over the planned 12ft length of the production packer element.

4.1 Test Equipment

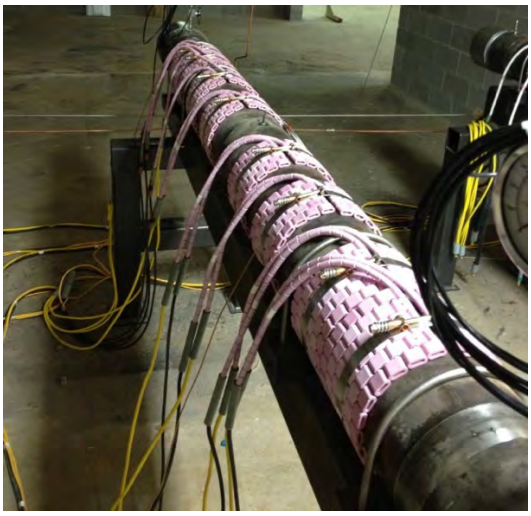

Figure 17: Pressure test fixture with heating blanket

Figure 18: Pressure test fixture with heating blanket – alternate view

4.2 Pressure Test Results

4.2.1 Pressure test at 347°F (175°C)

The graph below shows the overall performance of the packer with the build from 0psi differential all the way up to an eventual pressure hold above 3500 psi. This is in accordance with API 19OH.

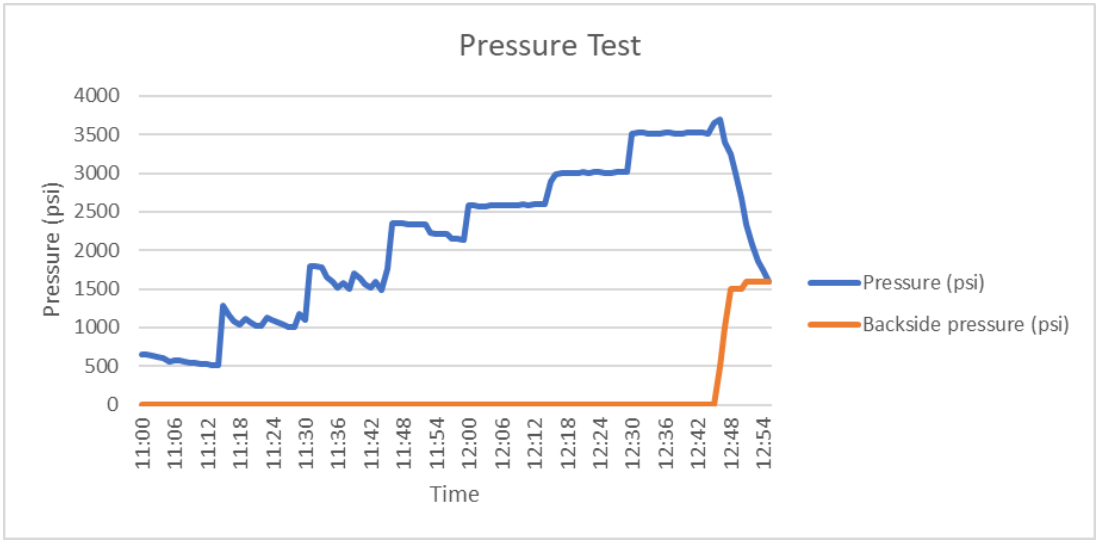

Figure 19: Differential pressure performance of 5ft packer at 347°F (175°C)

At around 3700psi pressure was observed on the back side indicating a leak. The pressure was subsequently bled off and after cooling the packer was removed from the fixture. Figure 5 below shows the packer in situ in the test fixture after the test and shows that there was little to no extrusion of the element past the end rings.

Figure 20: End view of the packer in the test fixture – no visible rubber extrusion

When viewing the full packer outside of the fixture the packer is in good condition, with surface marks from being forced out of the pipe bore in the swelled condition. There is a short section, less than 18”long, of rubber that has broken away down to an OD equivalent to the end ring diameter at the low pressure end. This is typical of observed swellable packer failures at standard oil and gas operating temperatures.

Figure 21: Packer after removal from the test fixture showing typical damage at the low pressure end.

4.2.1 Pressure test at 437°F (225°C)

The graph below shows the overall performance of the packer with the build from 0psi differential all the way up to an eventual pressure hold above 2500 psi. This is in accordance with API Spec 19OH.

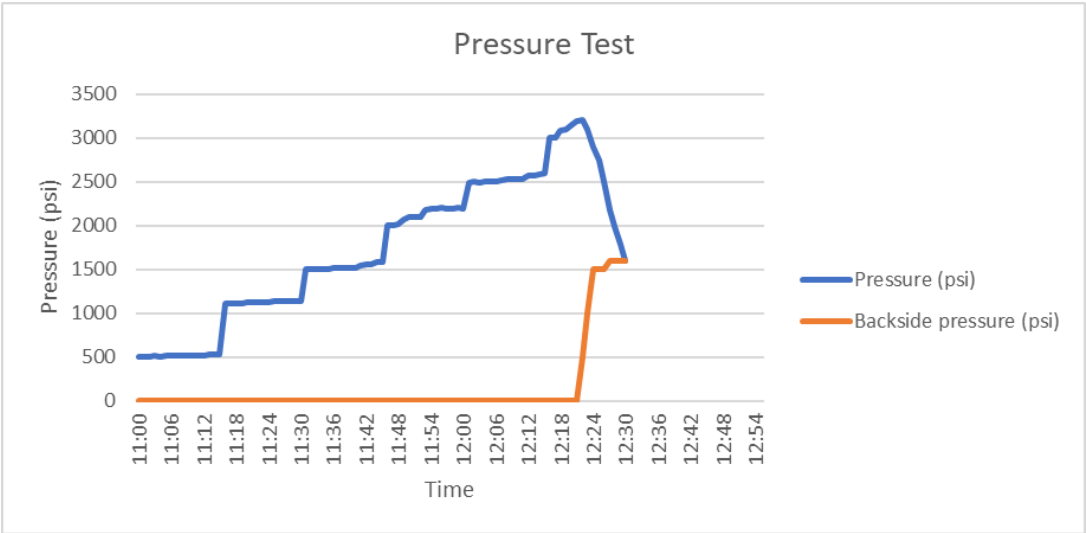

Figure 22: Differential pressure performance of 5ft packer at 437°F (225°C)

At around 3200psi pressure was observed on the back side indicating a leak. The pressure was subsequently bled off and after cooling the packer was removed from the fixture. It was observed that there was little to no extrusion of the element past the end rings.

5. Conclusion

The development work completed on the elastomer compounds has yielded an elastomer that can swell in a controlled manner at temperatures in excess of 225°C. Furthermore, it remains pliable and fit for purpose long after it's design life.

The packers performed well, demonstrating high pressure performance of 3500psi over a 5ft element at 175°C and then above 2500psi at 225°C. Despite some damage to the low pressure end of the element, overall it looked in good condition and would still continue to hold pressure albeit at a lower value. The rubber compound itself was also in good condition with no signs of hardening.

Overall these results provide evidence that this high temperature swellable isolation tool will provide effective annular isolation in geothermal wells.

Acknowledgement

This material is based upon work supported by the U.S. Department of Energy's Office of Energy Efficiency and Renewable Energy, under the Geothermal Technologies Office, under Award Number DE-EE0008487.0000.

Integration Well Construction, Value to Reduce Overall West Java Geothermal Development Cost

Gatra Kusuma, Doddy Darmawan, Ridha Budi Nugraha, Komang Wisnu, Hargi, Timora

Star Energy Geothermal-SLB

Keywords

geothermal drilling, optimization, cost reduction, performance drilling, cost, drilling

ABSTRACT

Geothermal drilling presents unique challenges which including harsh environments, fractured formations, and dynamic operations. These challenges are imperative to address as global interest in green energy escalates. Consequently, the development of geothermal assets remains aggressive and necessitating innovative solutions to overcome drilling complexities.

The demanding drilling conditions require substantial effort, energy, and strategic thinking. Slow penetration rates, short bit life, and equipment damage are the common issues. Understanding and mitigating these technical challenges are essential to minimize risks and enhance economic viability.

Experience and knowledge from the oil and gas industry as a common are invaluable in navigating drilling challenges. While some strategies may prove effective but others lead to inflated costs. Tailoring drilling methodologies and systems for the unique geothermal environment is paramount to optimizing drilling projects and controlling expenses.

Addressing uncertainty, mitigating risks, and enhancing efficiency are primary objectives in geothermal drilling. A structured approach across planning, execution, and post-drilling phases is crucial. By integrating workflows and methodologies, leveraging drilling expertise, and fostering continuous improvement so operational costs can be reduced significantly.

This paper underscores the value of integrated management and drilling advisory in improving performance and reducing costs. Over three years Geothermal Project in West Java, Indonesia, 70-75% reduction in well cost per meter resulted in multimillion-dollar savings through knowledge management and accelerated learning.

1. Introduction

There has been a steep increased in drilling activity over the past years in search of geothermal energy. As the search for new energy, the operators will increasingly start drilling campaign with more challenging trajectories to achieve their goals. Drilling in this environment will present an additional risks, technical challenges and huge economic impact. In fact, geothermal drilling is a

unique operation where drilling in reservoir section under loss circulation can cause bad hole cleaning meanwhile is a good sign of the potential reservoir in the other side. Historical data on previous campaigns shows significant portion of time while handling stuck pipe event and the remedial work process thus become the sources of downtime and cost. New approaches need to be introduced to this industrial climate to pursue efficient and effective geothermal drilling operations.

The new approach starts with integrate the existing resources. The integration come up with the main goal to improve service quality. The idea is to improve process by having all service requirement, increase response time to potential problems before they occur and finally cost reduction. Facing a challenging environment requires integration of every interrelated element. Real-time monitoring program able to provide timely intervention, catch various adverse possibilities and provide solution assistance. The proposed solution is to define operational workflows that utilize data and information integration to make improvements in each phase: planning, implementation, evaluation phase. Discussion of the operational framework and background and the role of technology to support operational performance will be described in this paper.

2. Problem and Challenge

The risk of geothermal drilling will turn into a problem and become non-productive time (NPT) which can extend drilling time if not prevented and mitigated properly. Increasing the drilling process will directly increase well costs due to additional material, mud, drill bits, and other geological obstacles in reaching the target reservoir depth.

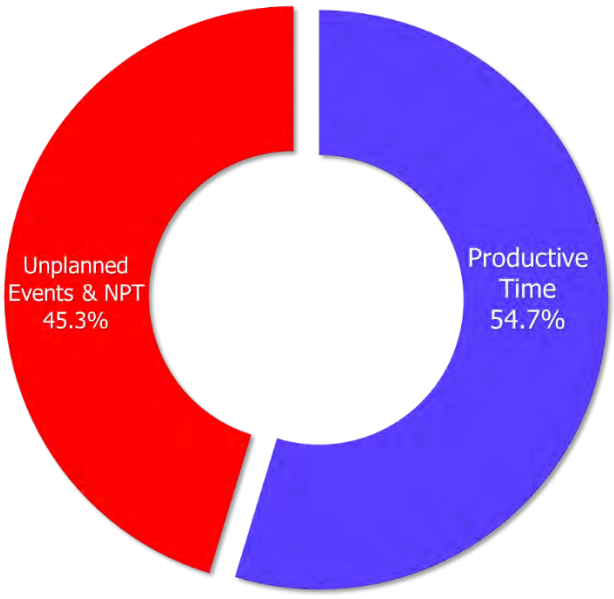

Figure 1: Drilling Time Distribution on Previous Campaign

As can be seen in Figure 1 Drilling Time Distribution, Unplanned events and Non-Productive Time (NPT) during drilling process takes 45.3% of the total time in the whole process. The large

portion of NPT is a result of uncertain drilling conditions being categorized as unplanned event. The uncertain changes in the drilling environment make the decision-making process very dynamic due to frequent changes to the initial plan. Making fast and precise decisions in this dynamic process certainly requires good and valid information from the field to the stakeholder or decision makers.

The time used during the drilling process is analyzed and broken down on each process such as drilling, tripping, casing, cementing, logging and others to see how much time is spent. Knowing which processes take up the largest portion of time, so ineffective on this process will result in significant additional costs. These problems can be derived from potential risks such as Low ROP, Stuck Pipe, Loss Circulation and Flat time issue. These four things are factors that cause company losses that need to be addressed.

The main idea of this research is the need to improve operation model and overcome the negative impact. The modeling system start to interrupt or stop the NPT as quickly as possible and reduce the potential risk and make the right decision to make the process more effective.

2.1 Hard and Abrasive Formation

The hardness and abrasiveness of geothermal formations exert a significant influence on numerous factors. Issues such as slow instantaneous penetration rate (ROP) and equipment damage commonly arise due to the characteristics of geothermal rocks. The decrease in penetration rate will give an impact on both the time and well costs. Equipment damage can halt the drilling process, necessitating equipment replacement. Junk in hole could be happen if damaged equipment was left in the hole and for sure can lead to further complications, prolonging the process and consuming additional resources, including money, time, and energy required for remedial actions.

Figure 2: Drilling Bit Condition, Left: Pre-Run and Right: Post-Run

As depicted in Figure 2 Drilling Bit Condition, the differences of actual drilling bit before-after use are clearly visible. Bit/tool failure causes a decrease in ROP and ultimately stop drilling

operation to POOH for checking and/or changing BHA. Overcoming these challenges has proven to be very challenging, especially in geothermal drilling environments where such conditions exist. Although many efforts have been made to mitigate this problem, the expected results are still not optimal. Therefore, further evaluation is essential, which includes mathematical modeling through simulation results and empirical research based on historical data.

2.2 Stuck pipe and Hole Problems

Many challenges encountered during the drilling process hampered the operator's ability to effectively achieve its objectives. This is shown in Figure 3, Previous Campaign Drilling Curves, where the various patterns appear in drilling performance, both in terms of inclination and final depth results. Highlighting the various issues encountered during drilling, the differences in the time and depth across several wells depicted in the curves are evidence of inconsistent performance.

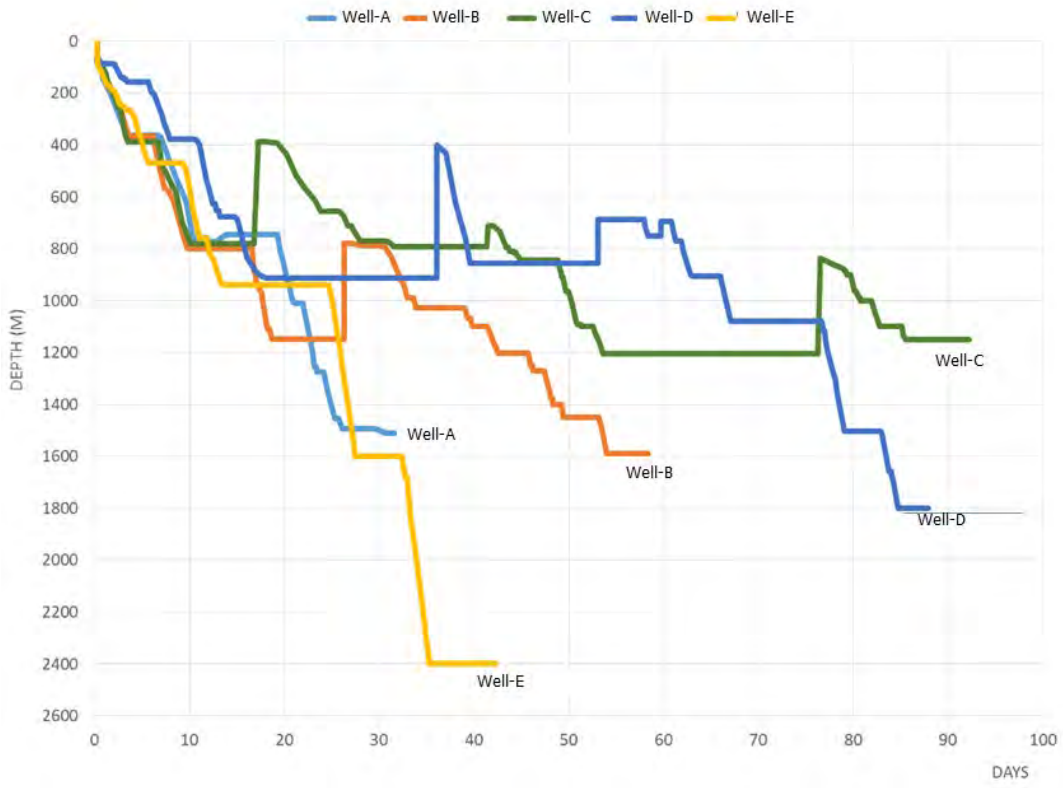

Figure 3: Previous Campaign Drilling Curve

As explained earlier, the significant prevalence of issues arising from uncertain drilling conditions resulted in long time consumption and Non-Productive Time (NPT) during the drilling process, which was classified as unplanned event. For example, the orange curve representing Well-E displays the most prominent and deepest curve among all wells, indicating an obvious deviation from the performance of other wells. None of the wells achieved the inclination and depth as Well-

E did, misalignment between objective and actual achievement. This distinction underscores the need to explore the factors that contribute to the phenomenon and form the basis for designing a strategy.

2.3 Drilling in Total Lost Circulation

Loss circulation is one of the other critical risks which is associated with geothermal drilling. The formation characteristics consist of fracture propagation which is subsequent to lost circulation. It results in significant mud loss and extremely challenging to cure the losses by using stop loss materials (LCM) or even cement plug job. This challenge is further compounded maintaining wellbore stability in formations with micro-network fractures poses considerable challenges during drilling. The drilling fluid penetrate into fractures, fails to equilibrate the pore pressure with the mud pressure and leads the fluid level to drop. Therefore, cuttings-induced pack-off over the Bottom Hole Assembly (BHA) can be happen during making up new connection due to insufficient annular pressure when the pumps is off. This scenario has been observed repeatedly when drilling fluid fails to suspend cuttings, ultimately culminating in a stuck pipe event.

2.4 Prolonged Flat Time

Essentially, well construction encompasses two main phases which are drilling activity(on bottom) and activity where no advancement occurs in hole depth (flat time). As previously mentioned, flat time activities encompass various operations which significantly contributing to the overall time allocation such as pipe tripping, casing and liner installations, cementing, BOP job, wellhead handling, pressure testing, and completions. The failure on these activities will impact to time and cost directly.

Another critical aspect of well construction which occurs during flat times is characterized by substantial the “unseen" loss time. As evidenced in the previous discussion by the Drilling Curves in Figure 3, some wells exhibit long flat periods, depicted by horizontal lines indicating no increase in depth over time. Consequently, any issues arising during these activities can prolong the average time required to condition the well. Rig performance, meticulous planning, comprehensive preparation, and clarity in low-level instructions are paramount in optimizing flat time activities.

3. Solution

The implementation of a comprehensive strategy and extensive consultation with technical experts from service providers to optimize resources, technology and workforce in the last 4 years has had a very significant impact on the drilling process across the system. The primary objective is to tackle drilling challenges, address issues with loss circulation and implement best practices to ensure geothermal drilling process are safe, efficient, and cost-effective. Therefore, this solution enables drilling operations to run smoothly without any obstacles and effectively solves existing problems.

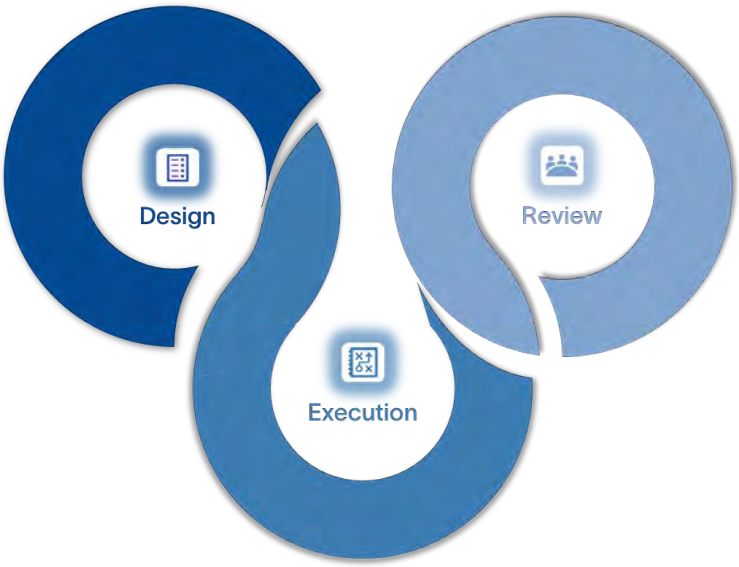

Figure 4: Improvement Cycle

The improvement initiatives encompass three fundamental phases: design, execution, and review, detailed in Figure 4. Each phase yields substantial information and data crucial for developing strategies and bridging operational gaps. In the design stage, the process begins with establishing a Risk Register to proactively identify potential issues. Subsequently, potential problem scenarios are modeled for the subject well using data from offset and similar wells in term of geological prognosis, accompanied by comprehensive solutions and lessons learned. Further analysis will refine initial best practices to uncover opportunities for enhancement and improvement.

Once the strategy and program are finalized in the designing stage, real-time monitoring of all operations will ensure the program adherence and support advisory/remedial plan for any deviations caused by unforeseen challenges. Specifically, the proposed solutions for mitigating loss circulation, hole instability issues led to stuck pipe and optimizing drilling processes empower operators to minimize risks, enhance performance, and achieve safer operation.

4. Managing the Challenges

The implementation of technology solutions and integration strategies has been proven to provide increased cognitive capabilities in improvement cycle and provide significant progress in drilling operations.

Figure 5: Managing the Challenges

The achievement is underpinned by five core pillars: Key Performance Indicators (KPIs), Historical Performance analysis, Performance Improvement plans, Implementation Strategy, and Performance Lookback as shown in Figure5. This discussion will elucidate how optimizing each of these critical components has contributed to this remarkable progress.

4.1 Key Performance Index

To improve the overall efficiency of asset investment, the focus is on assessing and achieving well productivity. This involves strategically selecting the existing locations with tiny space, optimizing resource usage and concerning environmental impact. Collaboration among function plays a crucial role in enhancing collective capabilities for achieving more economical drilling costs in geothermal operations. Integrating resources and expertise, operators can leverage knowledge and technology to streamline processes and reduce operational expenses.

Table 1 Drilling Well Objectives

Objectives	Information
Value Based Well Objective (VBWO)	Maintain well control at all times.
	Meet or exceed P50 initial expected steam rate at commercial wellhead pressure
	Meet or exceed project economic of positive NPV
	Complete well hook-up one month after flow test and put the well on-line right after well hook-up commissioning.
	Complete the well within AFE days and budget.
	Characterize the well as per plan i.e. completion test, flow test, geological data
	Flow test within five days on availability of SIMOPS permission otherwise after rig move
Health, Safety, & Environment (HSE)	No LTI'S (lost time injuries).
	No environmental incidents, spills and minimum environment impact.
	No major or catastrophic service quality incident.
	Incident and injury free operation (IIFO) .

The core of this collaborative approach is the Effort to improve drilling efficiency and minimize environmental impacts. As depicted in Table 1, Key Performance Index are translated into specific objectives for each well drilling activity. Through collaborative initiatives, operators can explore innovative drilling techniques and technologies that enhance operational efficiency while prioritizing sustainability. This collective effort not only facilitates cost-effective geothermal resource development, but also promotes responsible natural resource management. Aligning strategies and leveraging collaborative strengths, operators can pave the way for continued growth in geothermal energy production, while driving economic benefits and environmental sustainability.

4.2 Historical Performance and Performance Lookback

In the domain of drilling operations, data derived from offset wells plays a pivotal role as a foundational reference throughout the stages of design and implementation. This dataset offers critical insights into a spectrum of parameters that influence over drilling conditions. These insights play a critical role in early identification of potential challenges, such as the risk of loss of circulation or drilling damage, which can significantly impact operational efficiency and safety. Moreover, the data helps in developing effective responses to unforeseen issues that may arise during operations, such as managing cuttings during pipe landing and casing operations, and

addressing downtime for repairs, such as the installation of Blowout Preventer (BOP) connections and reaming activities.

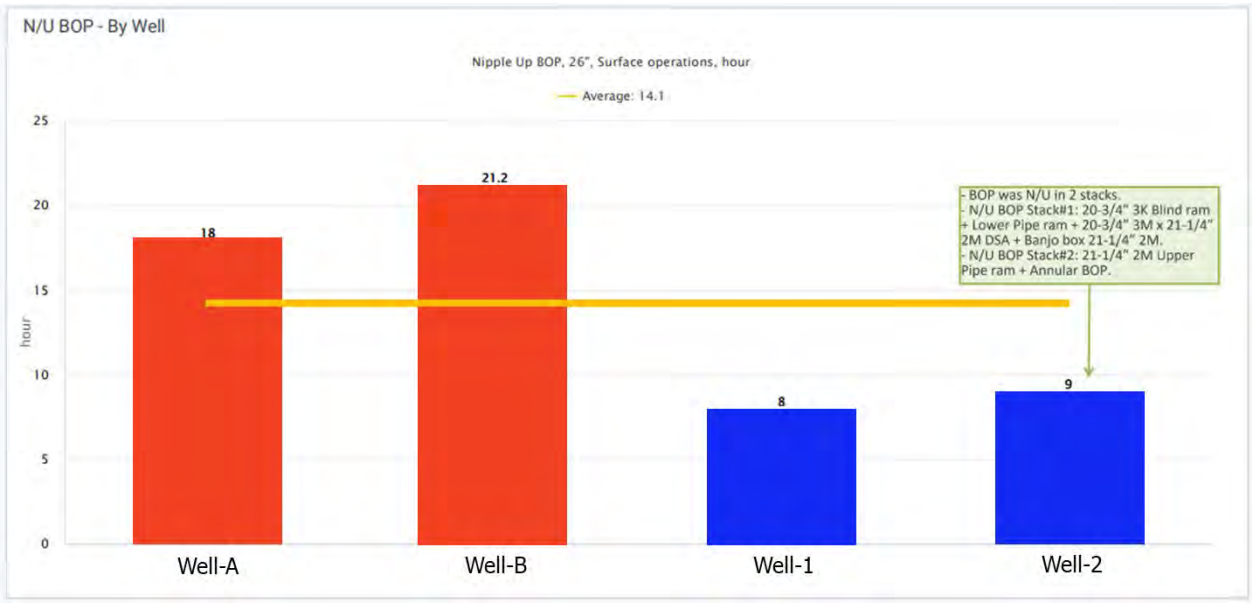

Figure 6: Improvement of N/U BOP

Leveraging the offset well data allows drilling engineers to proactively anticipate issue and develop solutions that mitigate risks while optimizing operational outcomes, as illustrated in Figure 6 which highlights improvements in process efficiency. Through effective utilization of historical data, engineering decision-making processes, streamline operations, and enforcing safety protocols. This proactive approach ensures that drilling activities proceed smoothly, minimizing disruptions and maximizing productivity. Ultimately, integrating comprehensive data analysis from offset wells plays a crucial role in achieving operational excellence and resilience in the dynamic field of drilling operations.

4.3 Performance Improvement Plan and Implementation

Engineering and operational integration initiate strategic interventions using precise principles and methodologies by following the thorough completing comprehensive identification and measurement processes outlined earlier. These actions are addressing inefficiencies and unlocking opportunities for enhancing performance. In response to identified operational shortcomings and instances of downtime, comprehensive strategies have been meticulously formulated to bolster drilling performance across all operational domains. Then these initiatives encompass a comprehensive approach that integrates process improvement, technology integration, and procedure optimization. Thus, the holistic strategy aims to maximize operational efficiency and minimize disruption, addressing both immediate and intermediate time frames.

4.3.1 Immediate Within 6 Month

In the realm of drilling operations, the data from offset wells serves as invaluable reference throughout both the design and execution stages. These datasets provide crucial insights into various parameters that influence drilling conditions. By analyzing how these parameters behaved in past operations, engineers gain a clearer understanding of expected outcomes and potential challenges. This historical data is particularly critical during monitoring phase, where real-time data is consistently benchmarked against established standards from offset wells. This comparison enables Real-time Decision Center (RTDC) engineers to promptly identify and evaluate any deviations or anomalies occurring at depth, as depicted in Figure 7 which illustrates deviations in well trajectory. Through continuous comparison and real-time monitoring, early detection of deviations allows for swift decision-making regarding necessary solutions. These insights facilitate proactive adjustments, ensuring operational continuity and minimizing risks associated with unforeseen drilling conditions.

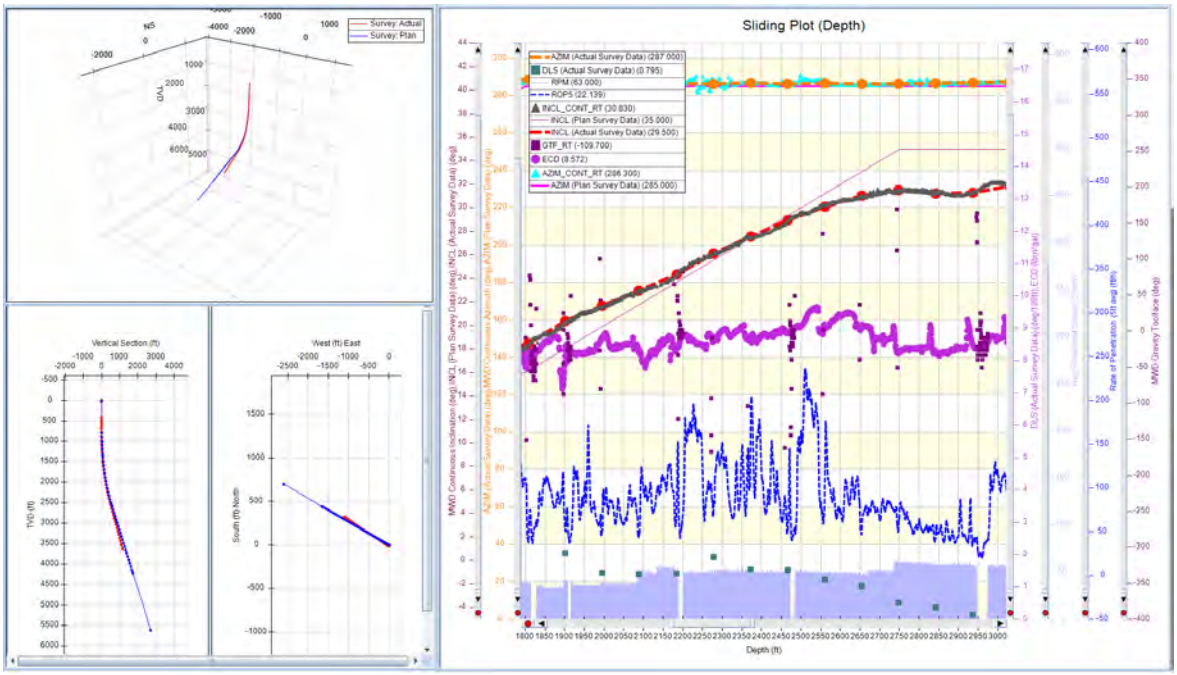

Figure 7: Real-Time Trajectory Monitoring

This visual representation not only facilitates rapid identification of anomalies but also enhances the precision of decision-making processes. Engineers can promptly correlate the parameter trends, diagnose any discrepancies and take appropriate corrective measures. This proactive approach not only enhances operational efficiency but also reduces potential downtime and optimizes resource utilization. The monitoring plot derived from real-time data as shown in Figure 7 provides a clear visualization of trajectory adjustments and their feasibility. Assessing the likelihood of achieving desired trajectories and identifying potential challenges could expedite decision-making throughout drilling operations. Leveraging insights from offset well data empowers engineers to effectively navigate complexities and uphold stringent standards of safety, efficiency, and performance in geothermal operations. This integrated approach ensures that operational objectives are met with precision while minimizing risks and maximizing operational success.

4.3.2 Intermediate 1 – 2 Years

The development of the improvement strategy are introduced to stakeholders and higher-level management, ensuring the alignment with organizational objectives and project goals. This involves comprehensive communication and detailed presentations that methodically outline the potential impact and benefits strategies. This collaborative effort aims to cultivate a shared understanding and commitment among all stakeholders, setting the stage for seamless execution by the project implementation team. Translating these strategies into actionable steps, the teams are well-positioned to implement effective solutions that not only address current inefficiencies but also establish a pathway towards sustained operational excellence in drilling operations.

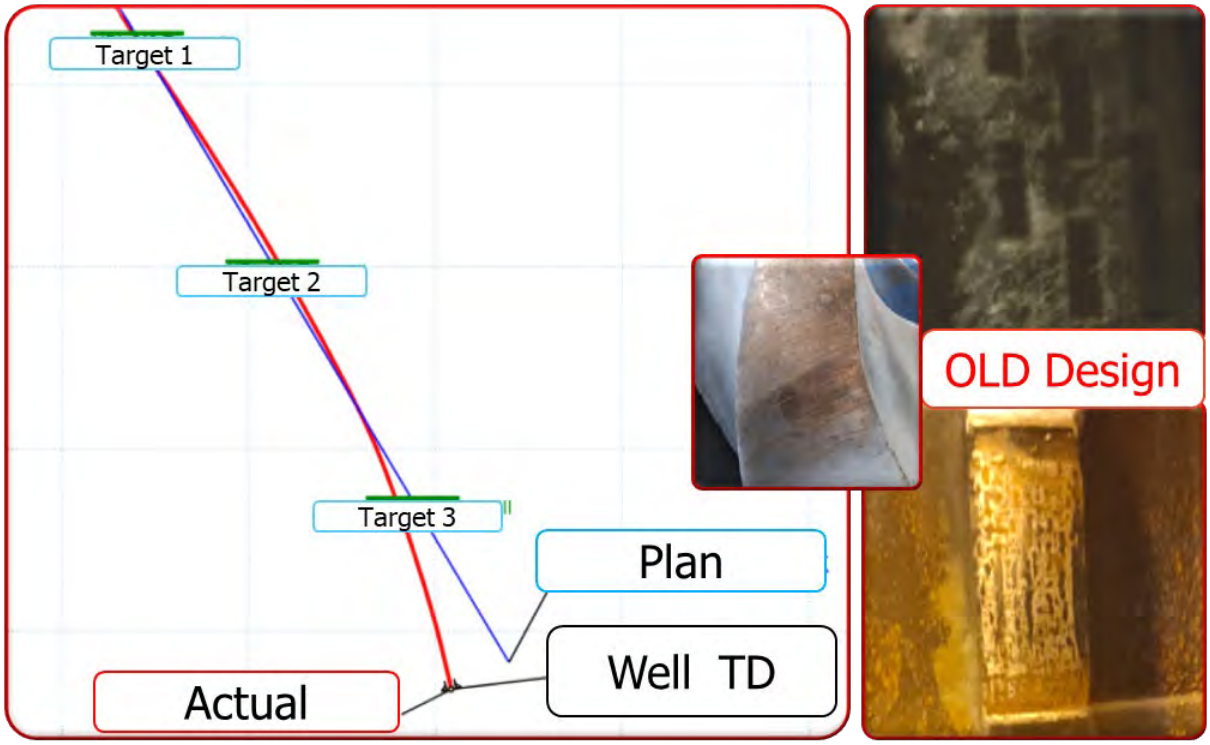

Figure 8: Equipment Deformation and Consequence

Several important factors are taken into account to optimize performance and reduce risk when designing a well. Anticipating subsurface hazards is critical and time consuming as it involves a thorough geological and geophysical assessment to identify potential challenges such as unbalanced formation pressure, lost circulation, or hard and abrasive formations. The impact of subsurface issues can be seen in figure 8 as a result of a worn stabilizer causing a near-miss incident to miss the target.

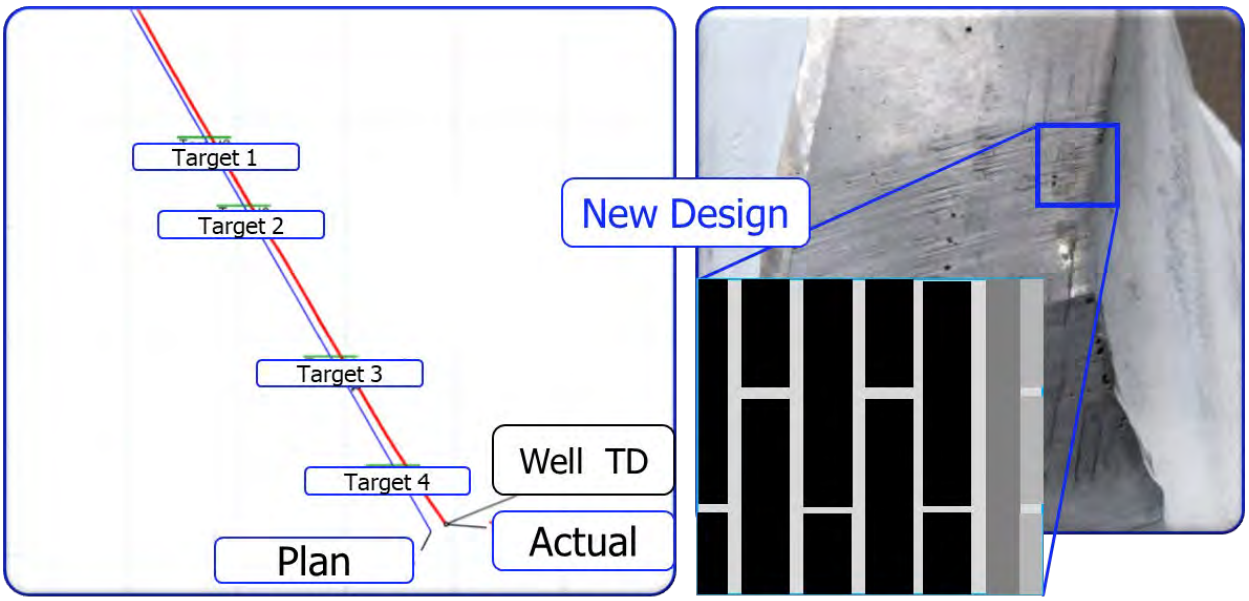

Figure 9: Quality Assurance through Innovative Design

Improvements have been made with studies on depth, formation hardness, and well trajectory requirements to ensure quality service assurance. Increasing drilling efficiency involves adapting equipment protection designs for abrasive formations and implementing advanced drilling techniques, which contribute to increasing penetration rates and guaranteeing the quality of services provided as shown in Figure 9. Additionally, selecting appropriate drilling equipment protection plays a vital role in preventing drilling problems, ensuring robust equipment no drop tendency is shown and all targets are hit without any exception in term of efficient drilling operations.

In conclusion, integrating these advanced strategies and technologies into drilling operations not only improves immediate efficiency but also lays the groundwork for long-term success. By focusing on meticulous planning, stakeholder alignment, and leveraging cutting-edge technologies, drilling teams can navigate challenges effectively, achieve operational excellence, and uphold high standards of safety and performance in geothermal and other drilling operations.

5. Result

Building up a strong organizational capability is crucial for achieving continuous improvement in drilling operations. This entails leveraging advanced technologies such as real-time monitoring systems and enhancing cognitive skills. Efforts are also focused on enhancing overall asset investment efficiency through the assessment and drilling of complex wells aimed at increasing productivity.

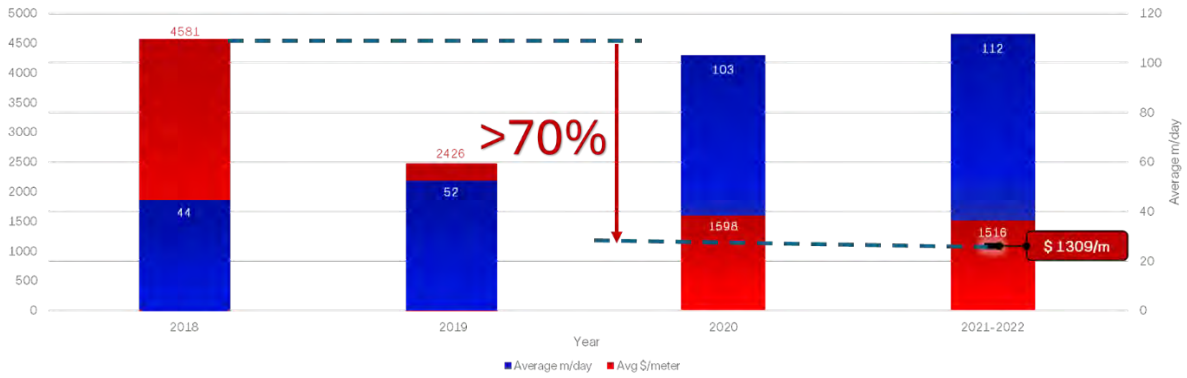

Figure 10: Reduction in Well Cost per Meter

These initiatives embody a holistic approach to optimizing operational efficiency, reducing expenses, and ensuring long-term sustainability in geothermal drilling practices. This is exemplified by the fastest and most cost-effective drilling of geothermal wells in Indonesia over the past five years, as depicted in Figure 10. The learning curve and improvements achieved in this campaign are clearly shown, with drilling costs per meter decreasing by 70-75% and drilling speed increasing. Collaborative efforts among operators further enhance capabilities, aiming to achieve more cost-effective drilling operations in future geothermal developments.

Acknowledgement

This successful implementation of systems, technology, and integration by Star Energy Geothermal demonstrates that Integrated Well Construction is a viable solution for the entire geothermal industry. The author extends sincere gratitude to Star Energy Geothermal for their invaluable support of this research. We are grateful for their permission to publish this paper and commend their dedication to advancing sustainable geothermal drilling. Special thanks are also due to the field and office personnel, including SEG and SLB crews, wellsite supervisors, and workshop personnel, whose contributions were instrumental in achieving this success.

REFERENCES

"DOX Single Point Analysis -Torque and Drag BasicConcept in Correlation with API RP 7G" (Content ID6042882).

Fridleifsson, Ingvar B. The possible role and contribution of geothermal energy to the mitigation of climate change. IPCC Geothermal. 2008

Lavrov, A. Lost circulation: mechanisms and solutions. Gulf Professional Publishing. 2016

M. Radov et al. Enhancing Production from High-Enthalpy Geothermal Wells with New Electric Submersible Pump Technology. Electric Submersible Pumps Symposium held in The Woodlands, Texas, USA, 2–6 October. 2023

N.C Meany. Method and apparatus for determining potential interfacial severity for a formation.

Nahun Vega, “Drilling Efficiency Through MSE” IPM Project

Optimization, and Decision Making

P.A.Curry. New Method Of Representing Rock Properties Over Entire Bit Run Improves Computer Generated Bit Recommendations. SPE/IADC Drilling Conf. Dallas. 2004

R Pessier. Quantifying common drilling problems with mechanical specific energy and a bit-specific coefficient of sliding friction. SPE paper no. 24584. Washington DC. 1992

Rehm, B. Circulating fluid losses during drilling operations. In SPE/IADC Drilling Conference and Exhibition. Society of Petroleum Engineers. 2009

SPE-110563-PP. Improving the Value of Real-Time Drilling Data To Aid Collaboration, Drilling

SPE-172740. The Implementation Of Real Time Data Drilling Decision Centre (RTTDC) in Kuwait

Alkali-Activated Gibbsite Cement for Use in CO_2-rich Geothermal Wells

Tatiana Pyatina, Toshifumi Sugama

Brookhaven National Laboratory

Keywords

Geothermal wells, carbon storage, cementitious materials for supercritical wells, carbonation resistant materials, ductile well cement

ABSTRACT

In this study calcium-free (and nearly Ca-free), aluminum-based cement was hydrothermally synthesized from sodium metasilicate (SMS) alkali-activated gibbsite, characterized, and evaluated for applications in supercritical and high-temperature (HT) CO_2-rich geothermal wells. Hydrous ZrO_2, silica flour, calcium aluminate cement (CAC), and microcarbon fibers (MCF) were used for matrix reinforcement. The hydrothermal synthesis was performed by autoclaving SMS-activated gibbsite at 300^{o}C for 24 hours followed by exposures for 30 days in supercritical water (scH_2O) at 400^{o}C or 9 months in deep geothermal Newberry well at 325-350^{o}C. Changes in thermal stability, porosity, mechanical properties caused by changes in phase compositions and phase transitions were evaluated. The absence of calcium in its composition allowed this cement to avoid carbonation under the HT geothermal well conditions and to preserve its mechanical properties, including high ductility. Differences in phase compositions observed under laboratory supercritical and well conditions are discussed.

1. Introduction

Deep and hot geothermal wells can provide several advantages, including an increased power output and a possibility of critical minerals recovery (Asanuma et al., 2012, 2015; Bonneville et al., 2018; Garrison et al., 2020; Muraoka et al., 2014; Petty et al., 2021; Reinsch et al., 2017). However, requirements for materials used for construction and operation of such wells are very stringent. While the life span of some materials used in well construction is limited by days and months, cements that provide zonal isolation, casing corrosion protection, well structure support, preventing annual pressure buildup, are expected to survive for many years for the well to support operations of a power plant. These functions of cementitious materials must be fulfilled under the environments that are difficult for them to withstand (H_2S and/or CO_2 rich with high Total Dissolved Solids hydrothermal environments). Moreover, with the high well temperatures all the

degradation reactions accelerate dramatically. The decalcification of Ordinary Portland Cement (OPC) under acidic conditions has been known for a long time (Biczok, 1967). Decalcification under high temperatures may cause OPC-based formulations to lose their mechanical properties in CO_2-rich environments in a short time. Previous tests of cement samples exposure in HT Newberry well showed that commonly used OPC/silica HT cement formulation lost its mechanical properties in 9 months when exposed to the well environment (Pyatina et al., 2024). Severe samples carbonation was believed to lead to the loss of its performance. On the other hand, the strength of calcium-aluminate-based cement samples increased, while their porosity decreased during the 9-month period of their exposure in Newberry well. The extent of carbonation of these samples correlated with the calcium content, where higher carbonation was seen for samples with higher calcium (Pyatina et al., 2023, 2024; Pyatina & Sugama, 2024). The persistence and even improvement of the properties for these formulations was linked to the presence of aluminum that did not show formation of carbonated minerals under the high -CO_2 well conditions.

In this paper we report the results of well exposure tests for aluminum-based, calcium-free cementitious materials (or materials with low-calcium content), alkali-activated gibbsite cement (AGC). The materials were originally tested under laboratory supercritical conditions (Pyatina & Sugama, 2023; Sugama & Pyatina, 2022) and later exposed in Newberry well. The aluminum-based material is interesting as a standalone cementitious system that meets cement requirements for geothermal wells (specifically, strength of above 1000 psi) while being highly flexible, but also as a part of other possible formulations with mineral compositions including aluminum, which are stable under HT geothermal well conditions. Most of the geological phases that survive in such environments are aluminum-rich and calcium poor, which is very different from the currently used cementing solutions historically created for above the ground constructions. Investigation of aluminum-based cementitious composite lays a groundwork for design of new geothermal materials.

2. Materials and methods

2.1 Materials

Aluminum hydroxide, an EMPLURA® hydragillite powder with a bulk density of ~90 g/100 mL and particle size < 150 μm for 90% of the material, was obtained from Sigma Aldrich. Zirconium (IV) hydroxide as hydrous zirconium oxide, $ZrO_2.nH_2O$ (Zr), was also obtained from Sigma Aldrich.

Calcium–aluminate cement (CAC), Secar #80, was used in this study. It was supplied by Imerys. The X-ray powder diffraction (XRD) data showed that the crystalline compounds of #80 CAC were the following three principal phases: calcium monoaluminate ($CaO{\cdot}Al_2O_3$, CA), calcium dialuminate ($CaO{\cdot}2Al_2O_3$, CA_2), and corundum (α-Al_2O_3).

SMS (Na_2SiO_3), an alkali-activator powder of 93% purity with particle sizes of 0.23 to 0.85 mm, trade named “MetsoBeads 2048,” was supplied by the PQ Corporation. It had a 50.5/46.6 Na_2O/SiO_2 weight ratio.

Some formulations were modified with 10% by weight of dry blend carbon microfibers (MCF, AGM-94) derived from a polyacrylonitrile precursor supplied by Asbury Graphite Mills, Inc. They were 7–9 microns in diameter and 100–200 microns in length. These fibers are stable at

temperatures up to 600°C. Earlier application of these fibers was shown to improve the ductility and cement–carbon steel bond of HT cement samples, which commonly decrease with longer HT curing times in laboratory tests (Pyatina & Sugama, 2015). They were used to improve the mechanical properties of the tested composites and to evaluate fibers' long-term chemical and thermal stability in field tests.

2.2 Cement Formulations and Samples Preparation

The compositions (in mass percent) of cement samples discussed in this paper are given in Table 1. Cement slurries were prepared by dry-blending all components, hand-mixing them with water amount that allowed to obtain comparable self-leveling properties and poring them into glass tubes (18 × 150 mm). The glass tubes were left at room temperature for 12 h. Then samples were exposed to an 85°C environment with a relative humidity of 99.9% for another 12 h. Finally, they were autoclaved at 300°C for 12 more hours in a non-stirred Parr Reactor 4622. After the 300°C autoclaving, each tube was cut into 3 cylinders of ~40 mm each, and the solidified cement samples were removed from the glass before their shipment to the wellsite for well-exposure tests or conducting mechanical properties tests.

Table 1. Compositions of AGC samples exposed in Newberry well in mass percent. The concentrations of SMS, MCF, and Zr are given in mass percent by the total mass of ($Al(OH)_3$, CAC#80, and SiO_2).

Sample name	$Al(OH)_3$	CAC#80	SiO_2	SMS	MCF	Zr	Water
AGC/MCF	60	-	40	5	10	-	51.6
AGC/Zr/MCF	60	-	40	5	10	10	51.6
AGC/CAC#80	50	10	40	5	-	-	44
AGC/CAC#80/MCF	50	10	40	5	10	-	51.6

2.3 Exposure Tools and Exposure Conditions

Detailed information on exposure tools and well conditions can be found elsewhere (Pyatina et al., 2023, 2024). The Exposure tools were fabricated from stainless steel to host cylindrical samples. They had open slots for sample exposure to the well environment and side plates for centralized placement in the well.

According to earlier well service data, the bottom hole temperature of the well where the sample baskets were released was ~325-350°C (communications with AltaRock). Information on the pressure at the bottom of the well was not available; the pressure at the depth of about 1.6 km was nearly 14 MPa. If a constant pressure gradient is assumed between 1.6 and 3.0 km, the bottom hole pressure can be estimated to be ~26 MPa.

Geochemical analysis from flow testing of this well by Geologica performed in 2008 showed that a non-condensable gas, identified as being >99% CO_2, was coming from a geological source (hydrothermal or magmatic).

2.4 Sample Analyses

The percent of water-fillable porosity of the well-exposed samples was determined using the following formula: $(W_{wet} - W_{dry})/V \times 100$, where W_{wet} is the weight of water-saturated samples and W_{dry} is the weight of a sample dried for at least 4 days in a vacuum oven at 60 °C until the weight of the sample was constant, and V is the volume of the sample.

JEOL 7600 F (Pleasanton, CA, USA) scanning electron microscope image analysis coupled with energy dispersive X-ray (EDX) elemental composition measurements on freshly broken surfaces was employed for morphological analyses and phase identifications.

TGA/DTA (heating rate of 20°C/min in a N_2 flow, ~10 mg sample weight, model Q50, TA Instruments) and X-ray diffraction measurements (40 kV, 40 mA copper anode X-ray tube, Rigaku Smartlab) were used for sample characterization. The PDF-4/Minerals 2023 database of the International Center for Diffraction Data (ICDD) was used for the analysis of XRD patterns. The background was subtracted from all the XRD patterns before their analyses.

The uniaxial compressive strength, Young's modulus, and compressive toughness were determined using the Electromechanical Instron System Model 5967. The measurements were performed on unconfined, dry samples after the water-fillable porosity determinations. The instrument had a 30 kN load capacity, and the measurements were performed at a 1.25 cm/min loading rate. The measurements were used to obtain the comparative performance of different formulations without focusing on absolute values. The mechanical properties and percent of water-fillable porosity of the reference samples after the 300°C autoclaving were measured in the same manner. The compressive toughness was computed from the area under the compressive stress–strain curve.

3. Results

3.1 Unconfined Mechanical Properties and Water-Fillable Porosity

Compressive strength and Youngs modulus of 300°C-autoclaved and 9-month well exposed samples are shown in Figure 1. All the samples survived the 9-month exposure tests with only minor changes in strength and modulus. The strength slightly decreased for AGC/MCF samples with and without Zr (~12% strength decreased), persisted for the AGC/CAC sample and increased for AGC/CAC/MCF sample (~40% increase). The changes in the modulus mirrored those of the compressive strength with the modulus after the exposure remaining in the desirable moderate range around 1000 MPa (145 kpsi) for all the formulations except the AGC/Zr/MCF one where the value of the modulus declined to 600 MPa (87 kpsi). Such moderate values of the modulus even after the long well exposure are uncommon for cementitious composites and indicate that ductility of the systems can persist in an HT well.

Interestingly the toughness of all the tested formulations noticeably improved after the exposure. Toughness is a combination of strength and ductility and is a very desirable property for geothermal cements. Because of the high ductility of these formulations their average toughness was relatively high even before the exposure tests despite their moderate strength (0.29 $N*mm/mm^3$). It further increased by stunning ~240% after the exposure reaching 0.97 $N*mm/mm^3$ (Figure 2).

The high ductility of these formulations is partially due to their relatively high porosity of about 50%. Porosity of the samples after exposure decreased by nearly 6% with the largest decrease experienced by the AGC/CAC/MCF sample. The porosity of that formulation dropped to ~48%.

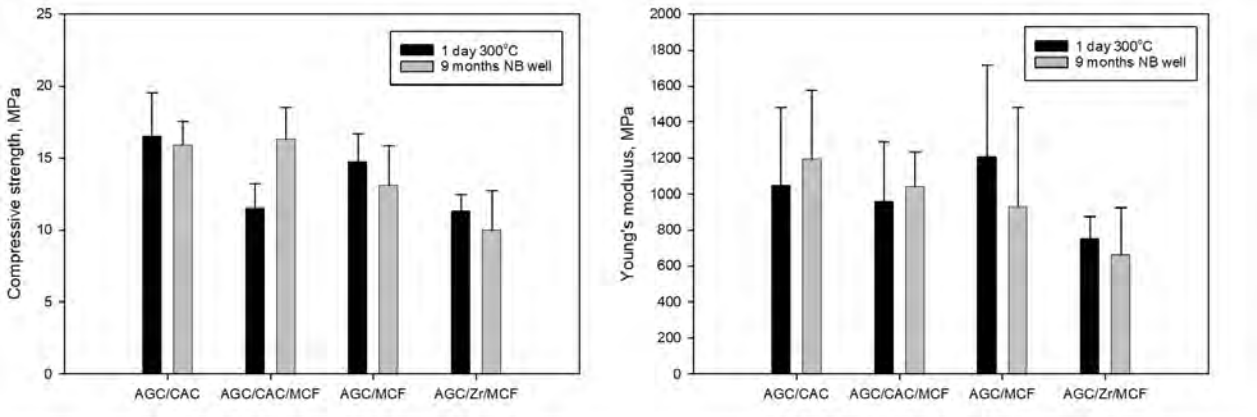

Figure 1: Compressive strength and Youngs's modulus of 300ºC autoclaved and 9-month well exposed samples.

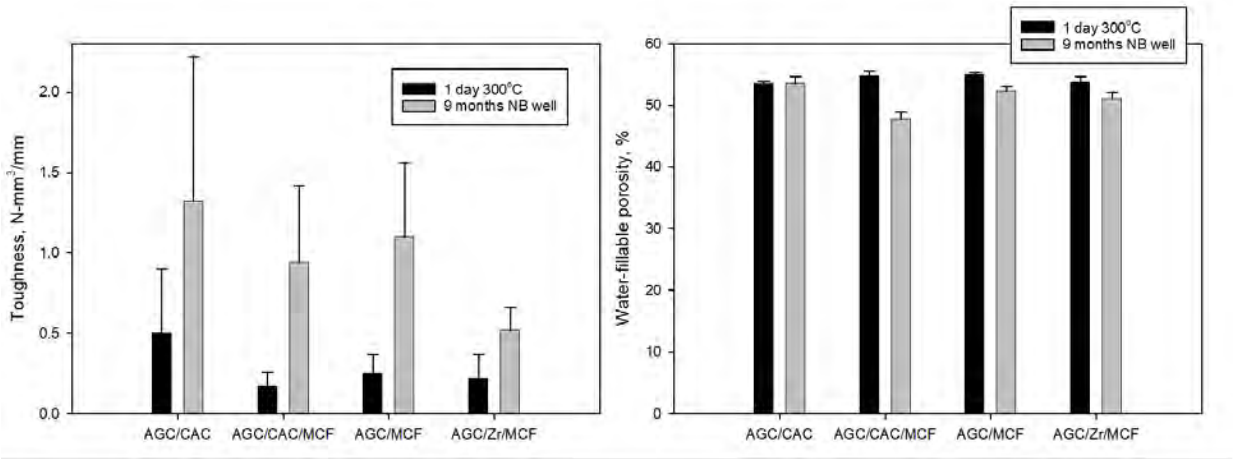

Figure 2: Compressive toughness and water-fillable porosity of 300ºC autoclaved and 9-month well exposed samples.

Noticeably, increase in compressive strength and porosity decrease after the 9-month exposure did not compromise high ductility of these formulations.

AGC and AGC/Zr formulations were tested under supercritical conditions earlier (Pyatina & Sugama, 2023). They both showed decreased strength (~20% decrease) and increased porosity (~10%) after 30 days under supercritical water. These performance differences could be partially attributed to the difference in exposure times (months of supercritical conditions were not feasible in the laboratory tests). It could also be the effect of the well fluid environment, which was not pure water as in the laboratory tests. CMF used in the case of the field-exposed samples and absent in the laboratory supercritical tests are chemically inert and could not change samples' compositions. To better understand mechanical behavior of these formulations phase analyses were undertaken to elucidate compositional changes in the well-exposed samples.

3.2 Phase Compositions

3.2.1 Crystalline phase compositions

The crystalline phase compositions of the tested samples are shown in Figure 3. There is no difference between the patterns of the samples with and without MCF and Zr. In fact, albite was the major phase in all three samples. In the case of AGC with CAC albite/anorthite formed (ICDD number 04-024-2151). Most of the other high-intensity peaks were attributed to paragonite and halloysite (ICDD numbers 04-014-7680 and 00-058-2031). Since the patterns of these two phases strongly overlap it is difficult to conclude whether both or only one of them was present in the samples. All samples showed some silica peaks and the samples with CAC also had small peaks of HT zeolite analcime commonly reported in the alkali-activated formulations with CAC. It was also observed in another alkali-activated formulation of CAC after the 9-month Newberry well exposure (Pyatina et al., 2024). In nature albite can undergo metasomatic replacement by sodium-rich nepheline and sodalite (Drüppel & Wirth, 2018). Some nepheline was also discovered in the samples after the 9-month exposure (ICDD number 00-019-1176). Paragonite is generally stable at these temperatures and if it breaks, it forms albite and corundum (Chatterjee, 1970). Thus, the formation of albite, nepheline, and paragonite was consistent with the samples' compositions and the expected formation of HT minerals under the well conditions. The sample modified with Zr, contained vlasovite mineral (ICDD number 04-016-5105) suggesting some reactivity of added Zr over the exposure period.

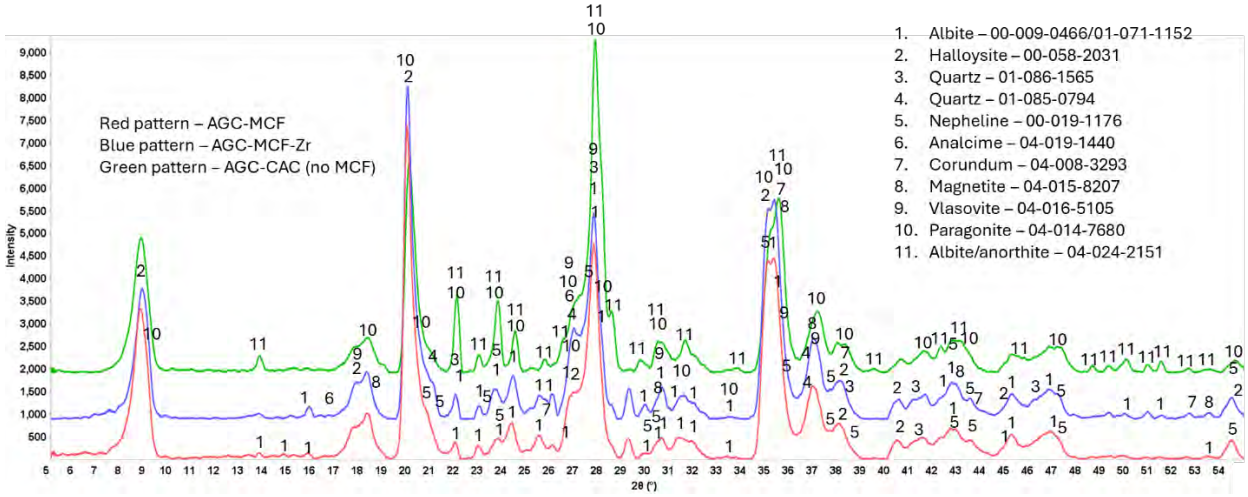

Figure 3: Crystalline phase compositions of the three tested AGC formulations after the exposure in Newberry well for 9 months.

Interestingly, crystalline boehmite was not detected in any of the samples. Aluminum was reacting with silicon with formation of albite and paragonite in these samples with a silica source. Likewise, the initially formed boehmite disappeared in other highly alkaline formulations after the 9 months in the well (Pyatina et al., 2024). The only formulation where boehmite persisted had noticeably lower pH of the slurries (calcium phosphate cement). Boehmite transition to gamma aluminum hydroxide during thermal shock tests was observed in our previous work with alkaline-activated calcium-aluminate/fly ash F blend (Sugama & Pyatina, 2018).Boehmite is not necessarily the most desirable binding phase, it is compressible due to its layered structure with hydrogen bonds. But it is carbonation resistant and provides high material ductility. Nevertheless, although crystalline

boehmite was not detected in the AGC samples, all the phases present in them resisted the carbonation that compromised OPC/silica formulation mechanical properties. This was reflected in the absence of crystalline carbonate peaks in the XRD patterns.

For the samples cured under supercritical conditions for 30 days boehmite, paragonite, as well as small amounts of analcime were detected. On the other hand, the end member of the feldspar mineral series, albite, or its decomposition product nepheline were not detected. These differences in the compositions suggest that mechanical properties of the samples can be explained by shorter curing time under supercritical conditions, so that the expected final phase compositions of the samples with boehmite transforming into albite in reactions with silicon were not reached.

3.2.2 Thermogravimetric analysis

The results of thermogravimetric and differential thermogravimetric analyses for AGC/CAC and AGC/MCF samples are shown in Figure 4. The major weight loss event for both samples occurred between ~450 and 650°C (3.9 and 3.6% respectively for AGC/CAC and AGC/MCF). This range corresponds to the decomposition of boehmite or its polymorph diaspore. However, XRD patterns did not contain peaks of crystalline boehmite. So, the likely contributors to that weight loss are halloysite, which dehydroxylates to metahalloysite ~530-590°C and albite that decomposes at ~650°C (Feng et al., 2012). The AGC/CAC sample also had a small weight loss between ~270°C and 500°C (a shoulder). Zeolite, analcime, decomposes in that temperature range (Cruciani, 2006).

The weight loss above ~700°C corresponds to the decomposition of CMF. It was also observed in the AGC/CAC/MCF sample, the decomposition pattern of which was otherwise identical to that of AGC/CAC sample. The decomposition pattern of AGC/MCF/Zr sample was identical to that of AGC/MCF.

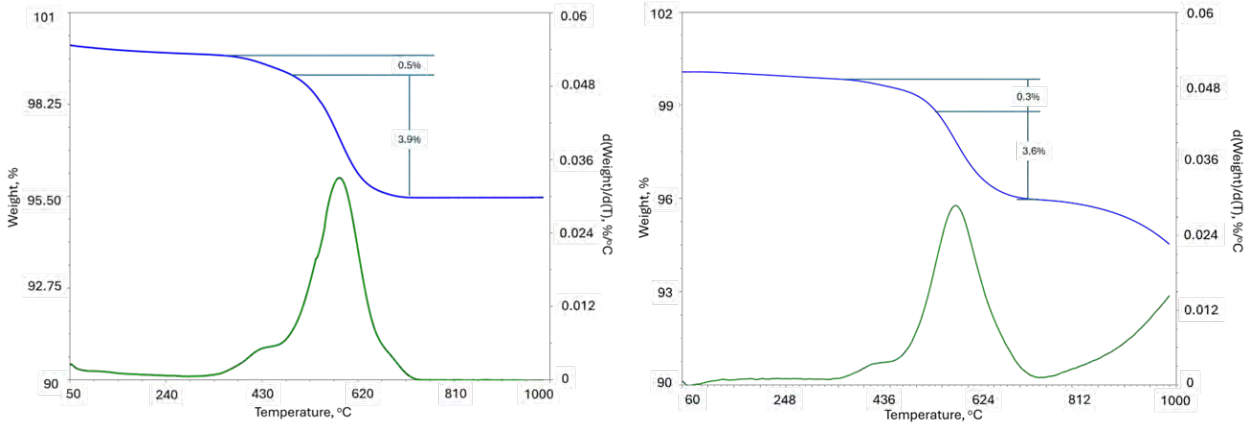

Figure 4: Thermogravimetric and differential thermogravimetric analyses of the AGC/CAC (left) and AGC/MCF (right) 9-month well exposed samples.

3.2.3 Morphologies of the exposed samples

Figure 5 shows photomicrographs and elemental compositions of typical sites of AGC/CAC samples exposed for 9 months in Newberry well. A flaky crystals morphology and elemental

compositions of sodium deficient paragonite can be seen in locations 1 and 3. Smaller denser crystals with the typical albite/anorthite composition are seen in location 2.

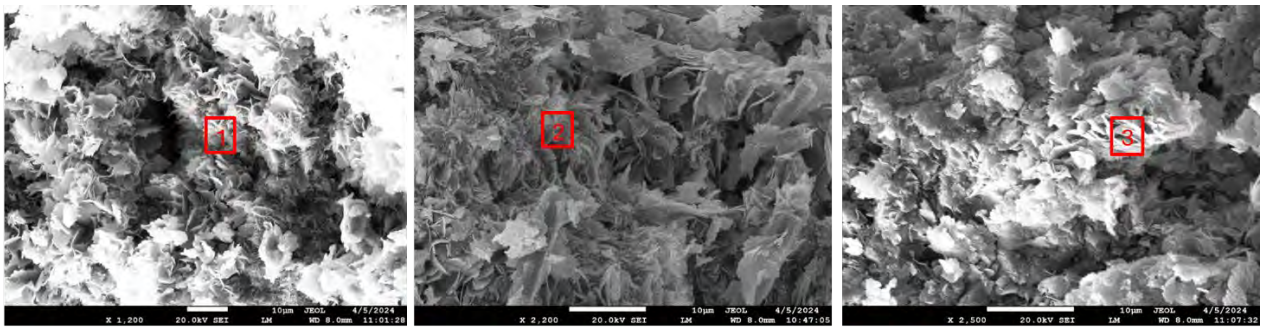

Spectrum 1

Element	Wt%	Wt% Sigma	Atomic %
O	37.08	0.67	51.01
Na	2.33	0.21	2.23
Al	24.81	0.38	20.23
Si	29.08	0.44	22.79
K	4.93	0.31	2.78
Ca	1.76	0.20	0.97

Spectrum 2

Element	Wt%	Wt% Sigma	Atomic %
O	37.17	0.88	50.66
Na	5.28	0.32	5.01
Al	15.79	0.41	12.76
Si	37.98	0.67	29.48
K	2.63	0.48	1.46
Ca	1.15	0.28	0.63

Spectrum 3

Element	Wt%	Wt% Sigma	Atomic %
O	36.40	1.03	50.30
Na	2.03	0.32	1.95
Al	24.09	0.57	19.74
Si	30.84	0.69	24.28
K	4.59	0.61	2.60
Ca	2.05	0.36	1.13

Figure 5: Photomicrographs and elemental compositions of AGC/CAC 9-month well exposed sample.

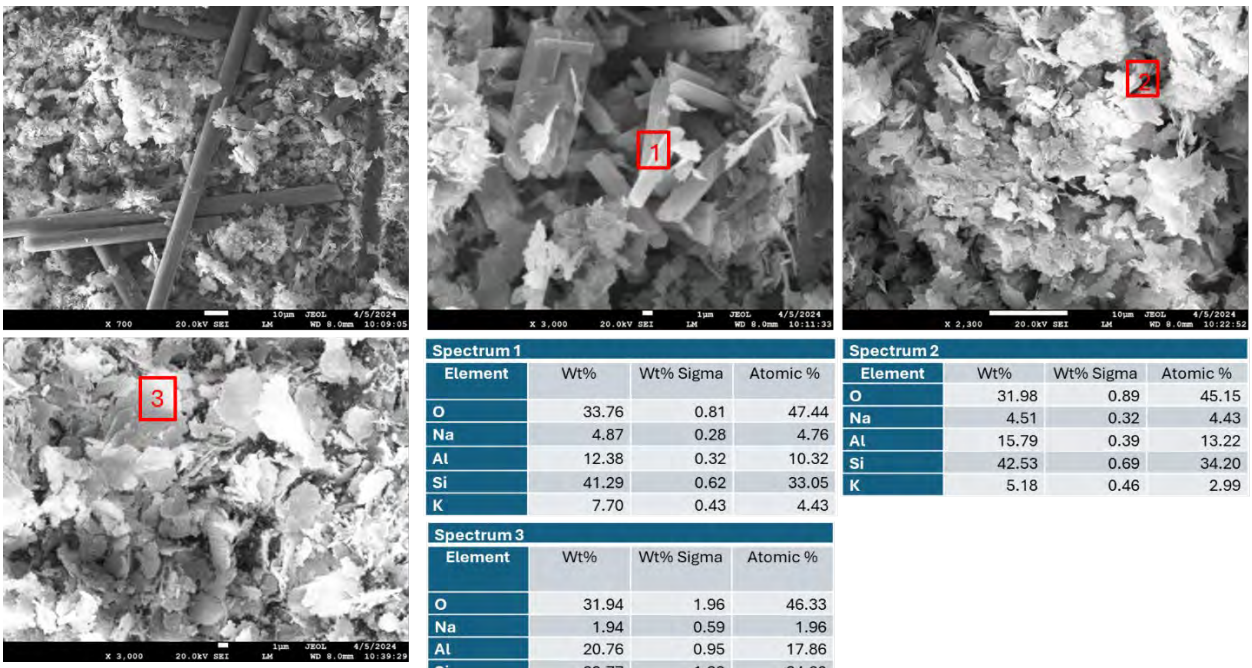

Spectrum 1

Element	Wt%	Wt% Sigma	Atomic %
O	33.76	0.81	47.44
Na	4.87	0.28	4.76
Al	12.38	0.32	10.32
Si	41.29	0.62	33.05
K	7.70	0.43	4.43

Spectrum 2

Element	Wt%	Wt% Sigma	Atomic %
O	31.98	0.89	45.15
Na	4.51	0.32	4.43
Al	15.79	0.39	13.22
Si	42.53	0.69	34.20
K	5.18	0.46	2.99

Spectrum 3

Element	Wt%	Wt% Sigma	Atomic %
O	31.94	1.96	46.33
Na	1.94	0.59	1.96
Al	20.76	0.95	17.86
Si	29.77	1.22	24.60
K	15.60	1.53	9.26

Figure 6: Photomicrographs and elemental compositions of AGC/MCF 9-month well exposed sample.

Figure 6 shows photomicrographs and elemental compositions of typical sites of AGC/MCF well-exposed samples. Intact MCF can be seen in the lower magnification photomicrograph on the left. The fibers survived the 9-month exposure without any visible damage. The tubular crystals have a composition of halloysite, however, albite that has similar elemental composition can also

crystallize as tubulars or flat and bladed crystals (site 2) (Christidis, 2011). Crystals in site 3 have flake-like morphology and elemental composition of paragonite.

The morphological features of the other 2 tested formulations were like the ones shown for AGC/CAC/MCF and AGC/MCF/Zr samples, with intact MCF, and crystals of paragonite and albite dominating samples' morphologies.

In summary, the morphological data agreed with the XRD results confirming presence of albite, paragonite and, possibly, halloysite. Also, in agreement with the XRD results boehmite crystals were not detected in the samples.

4. Discussion

Alkali-activated gibbsite based cementitious blends that are of interest as standalone systems or parts of other cementitious materials have some very attractive properties for EGS, including low or no calcium, providing its high carbonation resistance, and very high ductility, essential for applications in wells with frequent thermo-mechanical stresses. Their relatively high porosity can accommodate internal interstitial water expansion during the rapid well heating by the HT geothermal fluids. Tested under supercritical conditions (up to 30 days) and Newberry well (up to 9 months) they showed somewhat different changes of properties, with the strength decrease and porosity increase in the first case and varied strength response that depended on the formulation but without any significant strength decrease and porosity mostly decreasing in Newberry tests. Importantly, unlike most of the cementitious composites that experienced stiffening after longer exposures to high-temperature conditions gibbsite cement increased its toughness on average by 240% after the 9-month exposure to 325-350^{o}C Newberry well environments without any significant increase in stiffness. High cement ductility ensures a large safety operational envelope of cements decreasing the probability of cement failure under the thermal shock conditions typical for geothermal wells (Meng et al., 2024). The fact that gibbsite cement does not stiffen after 9 months of HT exposure is remarkable. Currently, the general strive for well integrity is to increase ductility or/and allow some casing movement during the stresses of the systems exposed to supercritical conditions (Thorbjornsson & Kaldal, 2021). The flexibility of the casing allows avoiding metal breakage under large thermal stresses. However, movements of the cemented casing will necessarily break the cement sheath if cement ductility and the magnitude of the casing movements are mismatched. Cement ductility can be increased by foaming it or adding fibers. However, for the large thermal stresses foam may not be appropriate, since gas expansion during heating will damage foam cement that is generally noticeably weaker than regular cement formulations and is unlikely to be able to withstand large gas expansion. For these reasons, AGC's remarkable ductility is very attractive for wells under large thermal stresses. This property of AGC can be seen in Figure 7 that compares stress-strain curves of phosphate-based cement, OPC/silica formulation and AGC after a day of 300^{o}C curing. While currently used OPC- and phosphate-based formulations reach high stress before the fracture, their abrupt fracture is typical for brittle materials. The AGC formulation, on the other hand, exhibits very ductile behavior with a long displacement tail under compression.

Under elevated temperatures AGC formulations undergo some phase transitions that take time. Incomplete phase transitions under the shorter period of supercritical exposures can account for the difference in mechanical properties of the samples cured at 400^{o}C and those exposed in Newberry well. Longer curing times causing boehmite decomposition, aluminum reactions with

silica with formation of paragonite and albite were observed in the field exposed samples. Small nepheline peaks in these samples suggest a possibility of further albite transition into nepheline or nepheline formation from aluminum from decomposing boehmite. Clay minerals, formed as the decomposition products of feldspars by water saturated with carbon dioxide in nature, and found in the AGC after the well exposure tests, including paragonite and halloysite, ensure consistent performance of this blend and its carbonation resistance. The tubular and flaky morphologies of the samples can explain their high toughness and low stiffness.

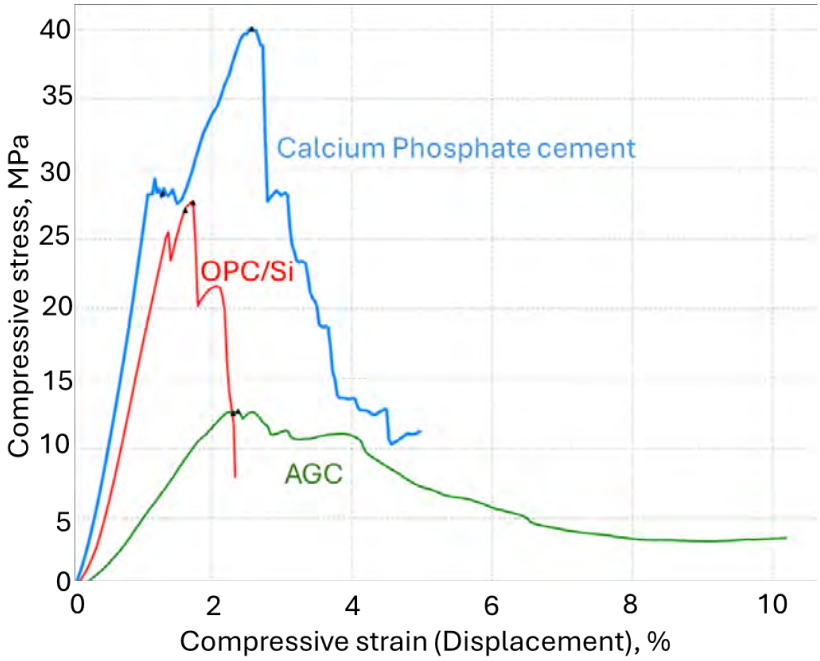

Figure 7: Comparison of typical stress-strain compressive curves for OPC/silica, phosphate cement, and AGC formulations after a day of curing at 300°C.

Nevertheless, whether AGC with its high porosity and very low stiffness can withstand large thermal shocks and provide good corrosion protection of the metal casing remains to be seen. Good metal-cement bond and low cement permeability are necessary in addition to the resistance to acidic environments for the metal protection in EGS. Higher porosity cements that are great to accommodate thermal shock conditions (e.g. foam cements) are generally less favorable for metal corrosion protection.

5. Conclusions

AGC is an attractive material for EGS applications due to its high toughness and great carbonation resistance. The results of supercritical and field exposure tests showed that AGC meets geothermal well strength criteria, with the mechanical properties and cement ductility persisting after long-term (9-month) exposure to high-temperature, high-carbonate concentration conditions in a geothermal well. The phase transitions taking place in the cement over long periods at high temperature result in boehmite reactions with silica forming paragonite, halloysite, albite, nepheline mineral phases. Boehmite persisted during shorter (30-day) exposures to supercritical conditions in laboratory experiments. Further AGC modifications may be needed to decrease its porosity, currently nearing 50%, and to ensure its ability to provide good steel corrosion protection.

Acknowledgement

This work was supported by the Geothermal Technologies Office in the US Department of Energy (DOE) Office of Energy Efficiency and Renewable Energy (EERE), under the auspices of the US DOE, Washington, DC, USA, under contract No. DE-AC02-98CH 10886.

The material is based upon work supported by the U.S. Department of Energy, Office of Science Energy Earthshot Initiative as part of the C^4M at BNL under contract # 2026-BNL-IS012-FUND.

This project has been partially subsidized through the Cofund GEOTHERMICA by DoE (the USA), RVO NL (the Netherlands), and the Research Council of Norway. Contributions from our partners Equinor (Norway), EBN (The Netherlands), Imerys (France), and CURISTEC (France) are greatly acknowledged.

Research was carried out in part at the Center for Functional Nanomaterials, Brookhaven National Laboratory, which is supported by the US Department of Energy, Office of Basic Energy Sciences, under contract No. DE-SC0012704.

REFERENCES

Asanuma, H., Muraoka, H., Tsuchiya, N., & Ito, H. (2012). The concept of the Japan Beyond-Brittle project (JBBP) to develop EGS reservoirs in ductile zones. *GRC Transactions, Vol 36*.

Asanuma, H., Soma, N., Tsuchiya, N., Kajiwara, T., & Yamada, S. (2015). Concept of development of supercritical geothermal resources in Japan. *International Conference on Geothermal Energy in Taiwan*.

Biczok, I. (1967). *Concrete Corrosion-Concrete Protection*. Chemical Publishing Co., Inc.

Bonneville, A., Cladouhos, T., Petty, S., Schults, A., & Sorlie, C. (2018). Toward Super Hot EGS: The Newberry Deep Drilling Project. *GRC Transactions, Vol. 42*.

Chatterjee, N. D. (1970). Synthesis and Upper Stability of Paragonite*. In *Contr. Mineral. and Petrol* (Vol. 27).

Christidis, G. E. (2011). Industrial clays. In *European Mineralogical Union Notes in Mineralogy* (Vol. 9, Issue 1, pp. 341–414). Universitat Jena - Mineralogie. https://doi.org/10.1180/EMU-notes.9.9

Cruciani, G. (2006). Zeolites upon heating: Factors governing their thermal stability and structural changes. *Journal of Physics and Chemistry of Solids*, *67*(9–10), 1973–1994. https://doi.org/10.1016/j.jpcs.2006.05.057

Drüppel, K., & Wirth, R. (2018). Metasomatic replacement of albite in nature and experiments. *Minerals*, *8*(5). https://doi.org/10.3390/min8050214

Feng, D., Provis, J. L., & Van Deventer, J. S. J. (2012). Thermal activation of albite for the synthesis of one-part mix geopolymers. *Journal of the American Ceramic Society*, *95*(2), 565–572. https://doi.org/10.1111/j.1551-2916.2011.04925.x

Garrison, G., Uddenberg, M., Petty, S., Watz, J., & Hill, L. B. (2020). Resource Potential of SuperHot Rock. *GRC Transactions, Vol 44*.

Meng, M., Pyatina, T., Frash, L., Bijay, K., Madenova, Y., Uwaila, I., & Zhang, W. (2024). Mechanical Performance of One Latex Cement System for Thermal Storage Wells. *ARMA 24-248, 58th US Rock Mechanics/Geomechanics Symposium*.

Muraoka, H., Asanuma, H., Tsuchiya, N., Ito, T, Mogi, T., & Ito, H. (2014). The Japan Beyond-Brittle project. *Sci. Drill*, *17*(51–59). https://doi.org/10.5194/sd-17-51-2014.

Petty, S., Watz, J., Uddenberg, M., & Garrison, G. (2021). Technology Development for SuperHot Geothermal Energy. *GRC Transactions, Vol 45*.

Pyatina, T., & Sugama, T. (2015). Use of carbon microfibers for reinforcement of calcium aluminate-class F fly ash cement activated with sodium meta-silicate at up to 300°C. *Transactions - Geothermal Resources Council*, *39*.

Pyatina, T., & Sugama, T. (2023). Cements for Supercritical Geothermal Wells at 400oC. *GRC Transactions, Vol. 47*, 447–467.

Pyatina, T., & Sugama, T. (2024). Aluminum-Rich Cements for High Temperature Geothermal Wells. *49th Workshop Geothermal Reservoir Engineering*, 145–153.

Pyatina, T., Sugama, T., Garrison, G., Bour, D., & Petty, S. (2023). Results of High-Temperature Cement Blends Exposure in Newberry Well, Oregon. *GRC Transaction, Vo. 47*, 468–488.

Pyatina, T., Sugama, T., Moghadam, A., Naumann, M., Skorpa, R., Feneuil, B., Soustelle, V., & Godøy, R. (2024). Assessment of Cementitious Composites for High-Temperature Geothermal Wells. *Materials*, *17*(6). https://doi.org/10.3390/ma17061320

Reinsch, T., Dobson, P., Asanuma, H., Huenges, E., Poletto, F., & Sanjuan, B. (2017). Utilizing supercritical geothermal systems : a review of past ventures and ongoing research activities. *Geothermal Energy*, 1–25. https://doi.org/10.1186/s40517-017-0075-y

Sugama, T., & Pyatina, T. (2018). *Alkali-activated cement composites for high temperature geothermal wells*. Scientific Research Books.

Sugama, T., & Pyatina, T. (2022, February 7). Cement Formulations for Super-Critical Geothermal Wells. *47th Workshop on Geothermal Reservoir Engineering*.

Thorbjornsson, I., & Kaldal, G. (2021). *Flexible Couplings for Improved Casing Design in High-Temperature Geothermal Wells*.

Comparative Analysis of Casing-Cement Interfacial Bonding Shear Strength Using Class G and Class H Cement at Room and Elevated Temperatures

Kayode Sanni, Jorge Andres Alvarez Escobar, Khizar Abid, Catalin Teodoriu

University of Oklahoma

Keywords

Interfacial Bonding Shear Strength, Unconfined Compressive Strength, Geothermal well, Elevated Temperature Curing

ABSTRACT

Geothermal energy is an important sustainable energy source and demands uncompromising well integrity for environmental protection and operational efficiency. Central to this integrity is the cement sheath that provides critical zonal isolation throughout a well's lifecycle. However, the integrity of wellbores is often compromised by debonding at the casing-cement and cement-formation interfaces, leading to potential fluid leakage and environmental hazards. Therefore, this study aims to elucidate the impact of cement class (Class G and H) on the interfacial bonding shear strength (IBSS) of casing-cement at both room and elevated temperatures (75°C). To simulate the field condition, the cement slurry was poured in the annulus space of cylindrical pipes that were placed one inside the other. Then the cement was cured in the room and elevated temperature for 1 and 3 days. After this, the shear stress analysis was conducted on the inner casing with the help of a hydraulic press. Moreover, the unconfined compressive strength (UCS) test was conducted on the Class G and H cement cubes to obtain additional information on mechanical strength. The findings underscore the significance of curing duration and temperature on cement's mechanical properties. Class H cement demonstrated an average IBSS of 339psi at room temperature and 218psi at elevated temperatures after 3 days of curing, with UCS measurements of 27 and 45MPa, respectively. In contrast, Class G cement performed better, with 3 days room temperature cured sample having the IBSS values of 310psi and 268psi at elevated temperatures, alongside UCS values of 22MPa and 46MPa, respectively. The study also revealed that 1-day cured samples had lower values of IBSS and UCS across all settings, highlighting the critical nature of the curing process. Notably, the research indicates a general trend: as temperatures increase, IBSS decreases, whereas UCS tends to rise, suggesting a complex interplay between thermal exposure and cement matrix integrity.

1. Introduction

With the increasing energy demand and the global push towards renewable energy, the pursuit of clean and unconventional energy sources has become highly desirable (Okoroafor et al., 2022).

Geothermal energy, in particular, plays a crucial role as a sustainable and clean energy source (Srivastava & Teodoriu, 2018). Its versatility enables its application in various sectors, including agriculture, heating, and electricity generation, making it invaluable for many countries. One of the primary advantages of geothermal energy over other renewable sources is its independence from meteorological conditions, allowing it to be utilized in any location with a suitable geothermal gradient (Abid et al., 2022; Vargas et al., 2022). At present, the United States is a leader in geothermal power generation. In 2020, the US produced nearly 17 billion kWh of electricity from geothermal resources, accounting for approximately 0.4% of the nation's total electricity consumption (Administration, 2022).

In geothermal wells, cement plays a crucial role by providing zonal isolation, sealing unwanted formations, plugging thief zones, supporting casing, protecting it from corrosion, and plugging wells (Rincon et al., 2022). Loss of zonal isolation can cause the leakage of the subsurface fluid to the surface, which can lead to sustained casing pressure (SCP) that can compromise the integrity of the well (Celia et al., 2005). One common leakage pathway for formation/reservoir fluids is along the interfaces within the well, such as the cement-casing interface or the cement-formation interface. The bonding of cement to these interfaces is typically measured in terms of shear bond strength or hydraulic strength. Shear bond strength is defined as the force needed to initiate casing movement within the cement sheath or displacement of the cement from the wellbore. Hydraulic strength refers to the bond between the casing and cement, or the cement and formation, that prevents fluid flow. Although shear bond strength and hydraulic bond strength are distinct measures, their values often fall within the same order of magnitude. Studies by (Carter & Evans, 1964; Evans & Carter, 1962) found a correlation between compressive strength and shear bond strength, but no correlation between compressive strength and hydraulic bond strength is present. Current official guidelines and field practices use cement's bulk compressive or tensile strength as the target value to determine if the cement will effectively seal the annulus. While the bulk properties can be suitable for predicting leakage through the cement matrix, they do not necessarily indicate sufficient bonding to different phases.

Among the various properties of cement, the Unconfined Compressive Strength (UCS) is identified as the most critical parameter for annular sealants exposed to high-pressure high-temperature (HPHT) conditions (Bosma et al., 1999). Throughout the well's lifecycle, the cement sheath endures varying pressures and loads from formation pore pressure, casing hydrostatic pressure due to drilling mud, thermal loads from temperature fluctuations of the fluids, and periodic loads from operations such as workovers, well tests, stimulations, and hydrocarbon production (Abid et al., 2022). The compressive strength of the cement is influenced by the homogeneity of the cement matrix, its composition, loading rate, and the geometry of the tested sample (Gul, 2016). The cement composition is tailored to specific downhole conditions, while matrix homogeneity depends on the mixing strategy and slurry design. Additionally, variations in loading rate, as well as the shape and size of the specimen, can lead to different results from the same batch of mixed cement samples.

Oil well cement is classified into eight types (Class A to H) based on factors such as depth, temperature, pressure, and sulfate resistance (Abid et al., 2023). Various additives can be

incorporated into the cement to modify its properties according to the specific downhole conditions. The most commonly used cements in geothermal wells are Class G and H (Abid et al., 2015). Cement is manufactured from argillaceous and calcareous rocks, which are dried, broken into pieces, and mixed in precise proportions. This mixture is then subjected to pyroprocessing in a kiln at temperatures ranging from 1426 to 1540 °C. The resulting clinker is ground and blended with gypsum to produce Portland cement (Ichim et al., 2018).

Cementing operation in geothermal, oil, and gas wells is critical for ensuring well integrity. Many geothermal wells feature open-hole completions, yet they also include sections where the casing is cemented to the formation. With the increasing demand for geothermal energy, deeper wells necessitate a high-quality cementing job. Cement integrity in these extreme environments, where temperatures can reach up to 400 °C, relies on its physical, chemical, thermal, and mechanical properties. A study by (Davies et al., 2014) revealed that nearly 380,000 wells in the US, UK, Norway, China, Holland, and Canada experienced well integrity issues due to cement failure. Thermal loading on the cement sheath between the casing and formation can lead to shrinkage and expansion, resulting in stress redistribution and jeopardizing well integrity (Therond et al., 2016; Zhang & Wang, 2017).

This research focues on the bond strength between two types of cement (Class G and H) and different steel casing materials. The shear bond is measured to study the maximum force that the pipe can exert before the bonding fails. In addition, the mechanical properties of the cement are studied by unconfined compressive strength (UCS) testing.

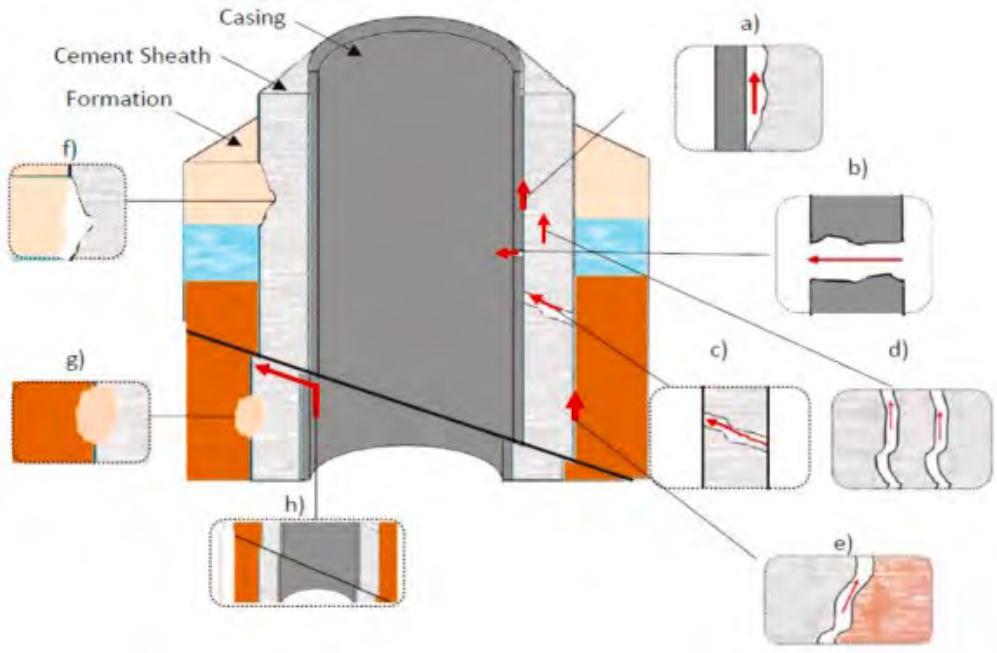

Figure 1: Possible leakage pathways in a cased wellbore (Wu et al., 2020)

2. Experimental Procedure

2.1 Materials

Two different class of well cement were used for testing: API Class G and H. The Class G Well Cement—Grade MSR (Moderate Sulfate Resistant) was obtained from Mountain Cement Company, and the Class H Well Cement was obtained from Central Plains Cement Company. Table 1 provides the chemical and physical analysis of both cement classes. Deionized water was used for the mixing of the cement. Table 2 tabulated the mix design of cement slurries.

Table 1A: Chemical and Physical Analysis of Class G Cement

CHEMICAL ANALYSIS		**Test Result**
Item	**Specification Limit**	**Class G**
MgO (%)	6.0 max	1.0
SO_3 (%)	3.0 max	3.0
Loss on ignition (%)	3.0 max	1.5
Insoluble Residue	0.75 max	0.41
C_3S (%)	48 min – 58 max	58
C_3A (%)	8 max	6
PHYSICAL ANALYSIS		
Free Fluid Content (%)	5.9 max	4.2
Compressive Strength (PSI)		
8hr @ 38°C	300 min	1360
8hr @ 60°C	1500 min	2710
Thickening Time (minutes)		
API Schedule 5: mins to 100bc	90 min – 120 max	95

Table 1B: Chemical and Physical Analysis of Class H Cement

CHEMICAL ANALYSIS		**Test Result**
Item	**Specification Limit**	**Class H**
SiO_2 (%)	--	20.7
Al_2O_3 (%)	--	3.2
Fe_2O_3 (%)	--	5.5
CaO (%)	--	62.8
MgO (%)	6.0 max	2.0
SO_3 (%)	3.0 max	2.6
Loss on ignition (%)	3.0 max	1.2
NaEq (%)	0.75 max	0.47
Insoluble Residue	0.75 max	0.39
Free Lime		1.3
C_3S (%)	48 min – 65 max	61
C_3A (%)	3 max	-1
C4AF + 2’C_3A	24 max	15
PHYSICAL ANALYSIS		
Blaine Fineness (m^2/kg) (C 204)	--	273

Free Fluid Content (%)	5.9 max	5.2
Compressive Strength (PSI)		
8hr @ 100°F	300 min	480
8hr @ 140°F	1500 min	2010
Thickening Time (minutes)		
API Schedule 5: mins to 100bc	90 min – 120 max	112

Table 2: Mix designs of slurries used in our experiments.

Cement Type	Mass of Cement (grams)	Mass of Water (grams)	Water to cement ratio (by weight)
Class G	792.72	348.53	0.44
Class H	860.26	326.90	0.38

Three steel pipes were used in the bond strength measurements for each cement formulation and temperature. Table 3 shows the pipe dimensions used for the experiment. All the pipe samples were washed and cleaned with acetone.

Table 3: Pipe types and their dimension

Sample ID	Pipe OD (mm)	Pipe Thickness (mm)	Pipe Roughness (μ-in)
TSO16	73.82	5.63	36.92
TSO17	73.94	5.65	35.52
TSO18	73.89	5.61	37.17

2.2 Testing and analysis methods

For each sample, which includes the inner pipe and the outer casing, 900 ml of cement was prepared. Right after mixing, the cement was poured into one cube mold to assess unconfined compressive strength (UCS) and conduct ultrasonic pulse velocity (UPV) measurements. The remaining cement was then slowly poured into the annular space between the inner and outer pipe, and distilled water was added to the remaining annular space, after which the samples were placed in a water bath, as shown in Figure 2.

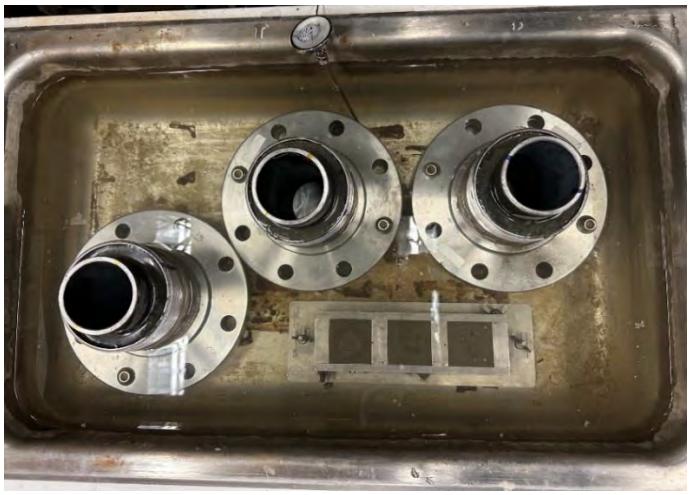

Figure 2: Experimental set up in water bath

To prepare the cement slurries, the Cement Constant Speed Blender manufactured by OFITE Testing Equipment, Inc. was used. This blender is a bottom-driven, blade-type mixer designed in accordance with API RP 10B-2 standards.

The mixing of cement and water was done in accordance with API standard 10-B (API). In this practice, cement is added to water in 15 seconds while the mixer's motor is at 4,000 rpm. Then, mixing is continued for 35 seconds at 12,000 rpm.

2.3 Interfacial Bonding Shear Strength

A shear bond is defined as the bond that mechanically supports a pipe in the hole. It is determined by measuring the force required to initiate pipe movement in a cement sheath. This force, when divided by the cement-casing contact surface area, yields the shear bond in psi (Carter & Evans, 1964).

A 2 7/8” OD steel casing pipe was placed in a 4-inch ID Casing pipe. The 4-inch ID was used to simulate the wellbore. Figure 3 shows the setup schematic used to create the bonding between casing and cement for shear bond strength measurements. Figure 4 shows the actual mold assembly used for the shear debonding test. The slurry is poured through the annulus between the outer casing and the inner casing, and on top of the slurry, free water is spread. For the elevated temperature tests, the water bath was set to 75°C and ambient pressure for curing duration of 1 and 3 days. The temperature was diligently maintained within a range of ±2°C, except briefly when fresh water was introduced into the bath, causing a temporary drop in temperature of 5-8°C. It is noteworthy that all tests adhered to the same procedural standards. After curing, it is necessary to gradually drop the temperature to avoid introducing thermal stresses to the system.

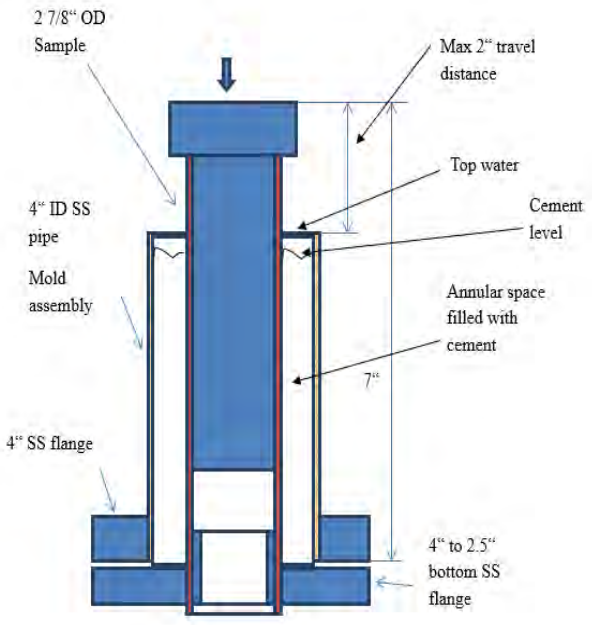

Figure 3: Schematic of the Mold assembly for the shear bond testing.

Figure 4: Mold assembly for the shear bond testing

A hydraulic press machine (Figure 5) was used to apply force on the inner casing until the point where debonding occurred. The loading rate of the machine was 1000psi/min. Using DasyLab Software, the displacement of the inner casing and the corresponding force in attaining the displacement were recorded every 0.1 seconds. After the debonding occurred, which is notable with a loud sound, the inner casing was further pushed through the cement sheath by an extra 40mm to ascertain that the debonding had occurred. After this, the entire cement sheath and the inner casing were pushed out with the help of the hydraulic press. The interfacial Bonding Shear Strength was calculated by knowing the volume of the cement in the annulus. For the shear bond strength calculation, the peak in the corresponding Force-distance plots was used to measure the force required to break the bond and move the casing sample. Combined with the known interface between the cement and casing, the shear bond strength was calculated by dividing the force by the interfacial area.

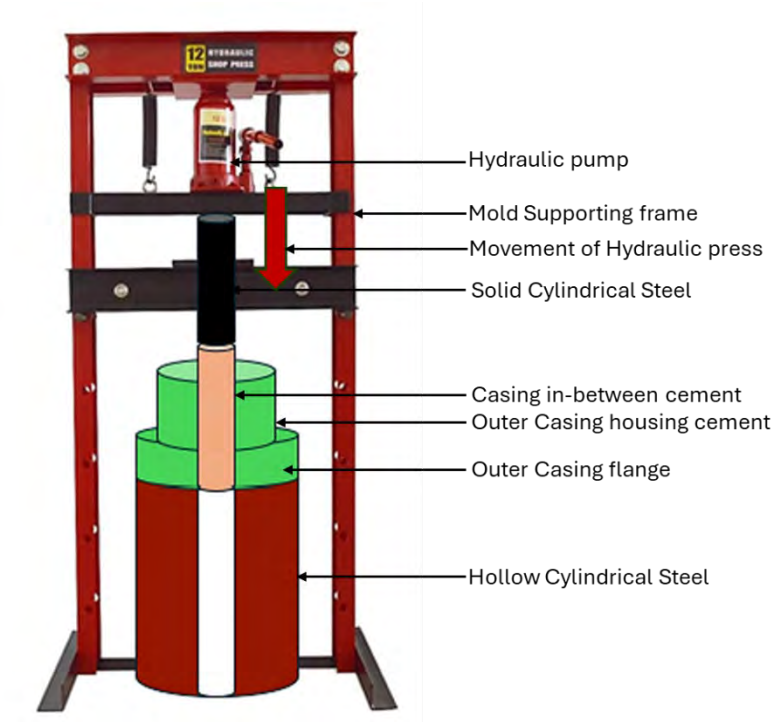

Figure 5: Hydraulic Bond Shear Testing Machine Frame

2.4 Unconfined Compressive Strength

In this study, two-inch cube molds, as shown in Figure 6, was used for the UCS test as directed by the API standards. As per the recommendations outlined in API RP 10B-2, these molds must be watertight, and the contact surfaces must be coated with a release agent, such as grease. The blended cement slurry was carefully poured into the molds until the slurry filled up the mold's depth.

Figure 6. Two-Inch Cube Molds

Prior to completely filling each sample mold, a puddling rod was employed to prevent the formation of air bubbles within the cement cubes. Subsequently, the molds were positioned in a curing bath. The samples underwent curing at atmospheric pressure, with the water bath temperature maintained at approximately 24°C (74°F). The cement samples remained in this water

bath until the testing phase. In terms of room temperature, there was a minor variation of about ±2°C.

API RP 10B-2 prescribes the testing of cubes with an edge length of 50.8 mm (2 inches). Following the removal of the cured cement cubes from the molds, the specimen dimensions were assessed using a digital calibrated caliper. The length and width of the cubes were measured at specific points, as depicted in Figure 7. This meticulous measurement process ensured strict compliance with the recommended dimensions and allowed for calculating the area required to determine compressive strength. It is worth noting that the edge length of the tested cubes consistently remained within 5% of the API recommended value, demonstrating adherence to the specified standards.

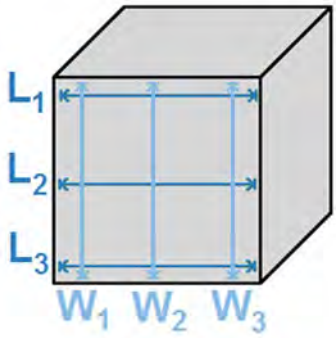

Figure 7: Cement Cube and Measurement Sites (L – length, W – width)

In contemporary practice, compressive strength can be assessed using two methods: a destructive approach (crush test) and a non-destructive approach (ultrasonic pulse velocity). Both techniques were employed to facilitate a comparison of their accuracy and the results they yield.

For the measurement of the UCS through destructive testing, the CM-2500 compression testing machine (depicted in Figure 8) manufactured by Test Mark Industries was utilized. This machine has an accuracy of ±0.5% (Test Mark Industries, 2015). The device applies a uniaxial load to the cement cube, measuring the force required to induce a permanent deformation in the cube. Subsequently, the compressive strength is automatically calculated by dividing the load by the measured surface area.

Figure 8:. Crush Test Device (Test Mark Industries, 2015)

The non-destructive method employed for determining compressive strength is ultrasonic pulse velocity (UPV) testing. These non-destructive measurements were conducted using the Pundit Lab+ device manufactured by Proceq SA (as shown in Figure 9). The process involved calibrating the measurement device using a special calibration rod. After the calibration, the transducers are placed on two opposite ends of the cement cube. To enhance the contact between the transducer and the cement cubes and ensure accurate results, a couplant was applied to the two ultrasonic pulse transducers (proceq, 2017).

This method measures the time required for the ultrasonic pulse to travel from the transmitter to the receiver. The velocity is automatically calculated using the cube's known edge length. For this particular study, the pulse was transmitted at 250 kHz. The testing device has an accuracy of ±0.1µs (PCTE, 2017).

Figure 9. UPV Measurement Device (proceq, 2017)

3. Result and Discussions

3.1 Interfacial Bonding Shear Strength

The bar chart in Figure 10 displays the Interfacial Bonding Shear Strength (IBSS) of Class G cement composites measured in psi under two different conditions: Room Temperature and Elevated Temperature (75°C), at two different time intervals (1 day and 3 days). The IBSS is higher at Elevated Temperature compared to Room Temperature after 1 day, indicating that the bonding strength of the cement composites improves with higher temperatures over this short duration. After 3 days, the IBSS at Room Temperature is higher than at Elevated Temperature. This suggests that over a longer period, the bonding strength of the cement composites improves more at Room Temperature than at Elevated Temperature. Moreover, as the hydration of the cement is accelerated at elevated temperatures and the cement matrix consolidates faster, sufficient time is not provided for the cement to get properly bonded with the casing interface (Teodoriu et al., 2019) due to which a decrease in the IBSS at elevated temperatures was noted. As noted by Teodoriu et al. (2019) the magnitude of IBSS for class H cements is lower than Class G, which is also visible in this paper. The results indicate a shift in the performance of Class G cement composites over time, with room temperature conditions becoming more favorable for bonding strength as time progresses.

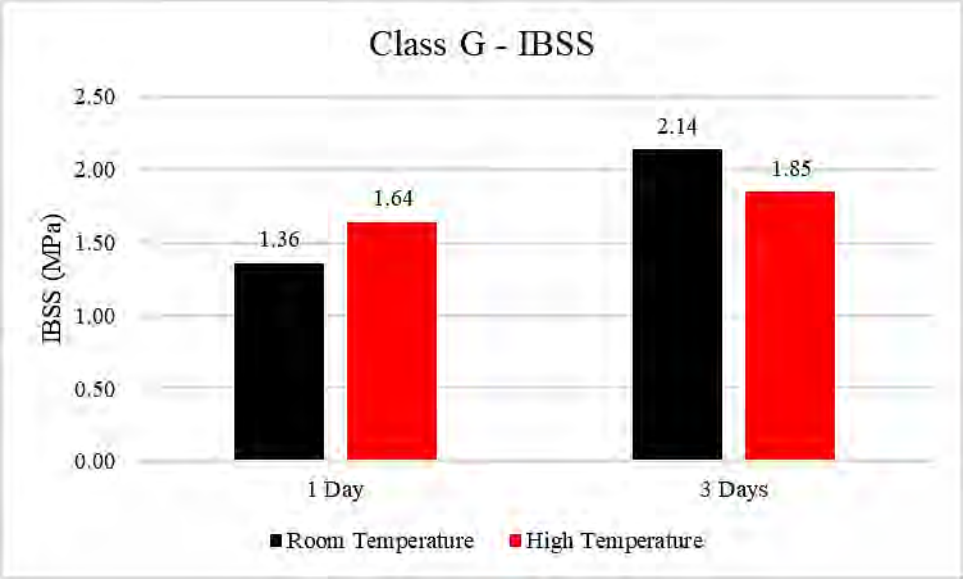

Figure 10: Interfacial Bonding Shear Strength of Class G at room and high temperatures.

The bar chart in Figure 11 illustrates the Interfacial Bonding Shear Strength (IBSS) of Class H cement composites at 1 and 3 days of curing at room and elevated temperature. The IBSS at Room Temperature is much higher than at Elevated Temperature after 1 day, indicating that the bonding strength of Class H cement composites is better at Room Temperature initially. After 3 days, the IBSS at Room Temperature remains higher than at Elevated Temperature. Although the bonding strength at High Temperature improves over time, it does not reach the level observed at Room Temperature. These results indicate that Class H cement composites perform better in terms of bonding strength at Room Temperature both initially and over time compared to Elevated Temperature.

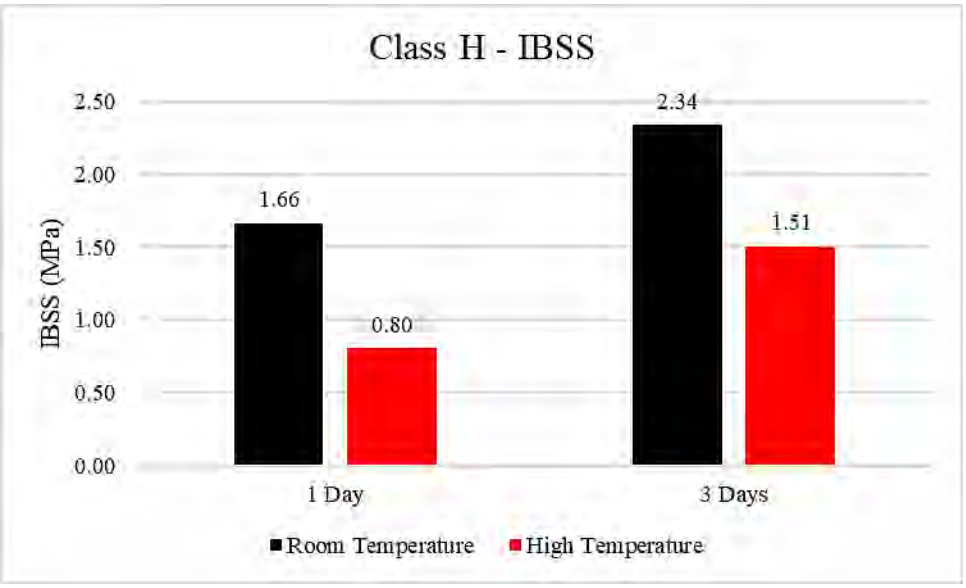

Figure 11: Interfacial Bonding Shear Strength of Class H at room and high temperatures.

From the above, it can be observed that for a one-day curing duration, Class G cement performs better at high temperatures compared to Class H, while Class H cement has a higher bonding strength at room temperature than Class G. After three days, both Class G and H cement show improved IBSS at room temperature over time. Class G performs better than Class H at high temperatures initially but not for three days of curing.

3.2 Unconfined Compressive Strength

The bar chart in Figure 12 displays the Unconfined Compressive Strength (UCS) of Class G cement composites measured in MPa under two different conditions: Room and Elevated Temperature, at two different time intervals (1 day and 3 days). The UCS at Elevated Temperature is substantially greater than at Room Temperature after 1 day, indicating that the compressive strength of Class G cement composites improves significantly when subjected to high temperatures in the short term. After 3 days, the UCS continues to be higher at Elevated Temperature compared to Room Temperature. The UCS of the sample cured at Room Temperature at day three was almost double the UCS of day one. Meanwhile, a slight increase in UCS was recorded for the elevated temperature sample on day 3. While there is an increase in compressive strength at both temperatures over time, the strength at High Temperature remains markedly higher.

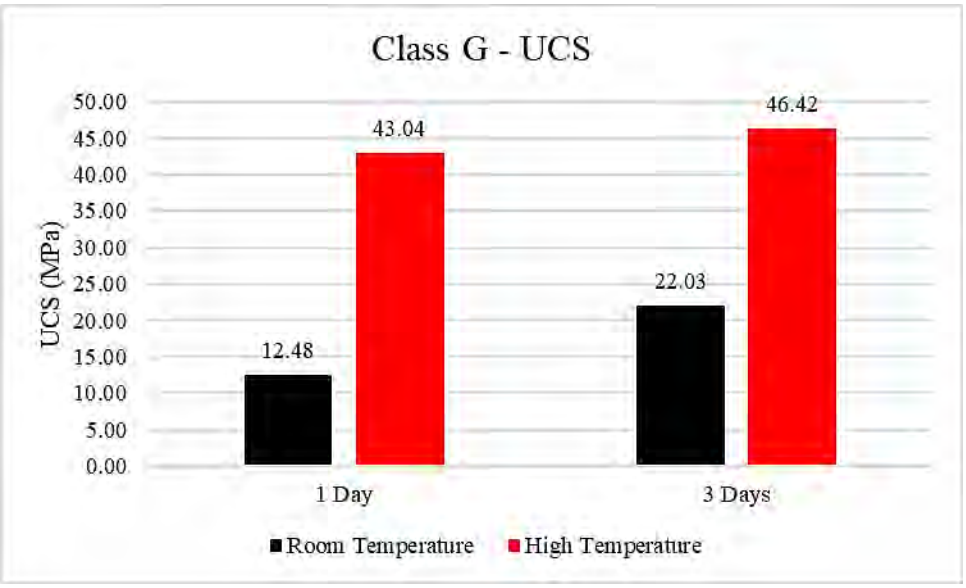

Figure 12: Unconfined Compressive Strength of Class G at room and high temperatures.

Figure 13 shows the Unconfined Compressive Strength (UCS) of Class H cement composites, measured in MPa, under Room Temperature and Elevated Temperature conditions, at 1-day and 3-day intervals. The UCS values at Elevated Temperature are markedly higher than those at Room Temperature after just 1 day, demonstrating a significant short-term enhancement in compressive strength for Class H cement composites when exposed to high temperatures. After 3 days, the UCS continues to be higher at High Temperature compared to Room Temperature. Although compressive strength increases over time at both temperatures, the strength at Elevated Temperature consistently remains significantly higher.

As seen from the above figures, the UCS of Class G and H samples at elevated temperatures, irrespective of the curing days, was higher than that of the Room Temperature samples but an expected behavior. This is because the rate of hydration accelerates at high temperatures, so the matrix of the cement solidifies faster and gains higher UCS strength.

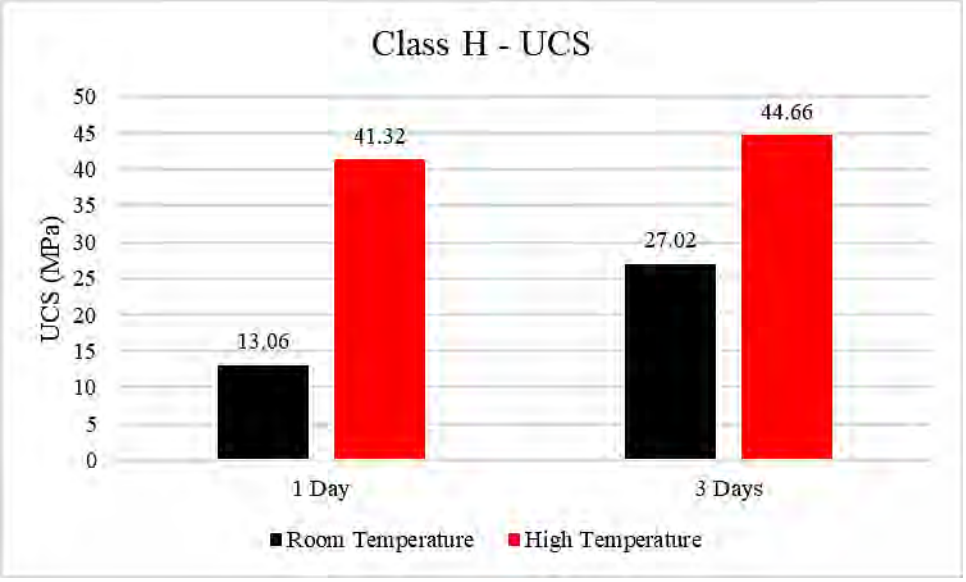

Figure 13: Unconfined Compressive Strength of Class G at room and high temperatures.

4. Conclusions

For geothermal applications where high temperatures are expected, Class G Cement might be the better choice due to its superior initial bonding strength at high temperatures. It ensures a strong initial set, which is critical for geothermal well integrity. Although the performance decreases slightly over time, it remains robust.

However, if the environment involves fluctuating temperatures and extended periods at lower temperatures, Class H Cement might be advantageous due to its superior long-term bonding strength at room temperature. Class H Cement could be considered at the well's surface and intermediate casing section.

The performance at elevated temperatures and over time is crucial for geothermal applications where high temperatures are prevalent. Class G Cement demonstrates a marginally higher initial UCS at high temperatures and maintains this strength over time, making it a good choice for environments where immediate high strength is essential. Class H Cement, while slightly lower in initial high-temperature UCS compared to Class G, still provides strong performance and better long-term UCS at room temperature, suggesting versatility in varying temperature conditions.

Considering these factors, Class G Cement is likely the better choice for geothermal applications focusing on high UCS and IBSS at elevated temperatures.

Acknowledgement

We would like to thank TENARIS for their financial and technical support. Our heartfelt appreciation goes to the University of Oklahoma for its substantial contributions, particularly in the research and technical support that is presented in this paper. We are also grateful to the Well Integrity Laboratory at the University of Oklahoma for providing access to their unique cement repository and database. The dedication and hard work of the students from the University of Oklahoma in investigating and developing the cement repository are deeply appreciated.

REFERENCES

Abid, K., Gholami, R., Choate, P., & Nagaratnam, B. H. (2015). A review on cement degradation under CO2-rich environment of sequestration projects. *Journal of Natural Gas Science and Engineering*, *27*, 1149-1157.

Abid, K., Sharma, A., Ahmed, S., Srivastava, S., Toledo Velazco, A., & Teodoriu, C. (2022). A review on geothermal energy and HPHT packers for geothermal applications. *Energies*, *15*(19), 7357.

Abid, K., Srivastava, S., Tellez, M. L. R., Amani, M., & Teodoriu, C. (2023). Experimental and machine learning study of thermal conductivity of cement composites for geothermal wells. *Geothermics*, *110*, 102659.

Administration, U. E. I. (2022). *Geothermal explained Where geothermal energy is found*. Retrieved February 15, 2022 from

API, R. 10B-2, Recommended practice for testing well cements, second. In: Washington, DC: API.

Bosma, M., Ravi, K., Driel, W. v., & Schreppers, G. J. (1999). Design approach to sealant selection for the life of the well. SPE Annual Technical Conference and Exhibition?,

Carter, L. G., & Evans, G. W. (1964). A Study of Cement-Pipe Bonding. *Journal of Petroleum Technology*, *16*(02), 157-160. https://doi.org/10.2118/764-pa

Celia, M. A., Bachu, S., Nordbotten, J. M., Gasda, S. E., & Dahle, H. K. (2005). Quantitative estimation of CO2 leakage from geological storage: Analytical models, numerical models, and data needs. In *Greenhouse Gas Control Technologies 7* (pp. 663-671). Elsevier.

Davies, R. J., Almond, S., Ward, R. S., Jackson, R. B., Adams, C., Worrall, F., Herringshaw, L. G., Gluyas, J. G., & Whitehead, M. A. (2014). Oil and gas wells and their integrity: Implications for shale and unconventional resource exploitation. *Marine and Petroleum Geology*, *56*, 239-254.

Evans, G. W., & Carter, L. G. (1962). Bounding studies of cementing compositions to pipe and formations. Drilling and production Practice,

Gul, M. (2016). Effect of cube size on the compressive strength of concrete. *Int. J. Eng. Dev. Res*, *4*(4), 956-959.

Ichim, A., Teodoriu, C., & Falcone, G. (2018). Estimation of cement thermal properties through the three-phase model with application to geothermal wells. *Energies*, *11*(10), 2839.

Okoroafor, E. R., Smith, C. M., Ochie, K. I., Nwosu, C. J., Gudmundsdottir, H., & Aljubran, M. J. (2022). Machine learning in subsurface geothermal energy: Two decades in review. *Geothermics*, *102*, 102401.

PCTE. (2017). *Pundit Lab - Ultrasonic Pulse Velocity Tester*.

proceq. (2017). *Pundit Lab Operating Instructions*. proceq. https://www.screeningeagle.com/en/sales-flyers/SF-pundit-lab

Rincon, F., Abid, K., Arbad, N., & Teodoriu, C. (2022). A comprehensive analysis of class H cement Unconfined Compressive Strength using cubical and cylindrical samples. *Journal of Petroleum Science and Engineering*, *215*, 110692.

Srivastava, S., & Teodoriu, C. (2018). Gas Well Conversion To Geothermal: A Case Study For Oklahoma. Proceedings of 43rd Annual Stanford Geothermal Workshop,

Teodoriu, C., Yi, M. C., & Salehi, S. (2019). A novel experimental investigation of cement mechanical properties with application to geothermal wells. *Energies*, *12*(18), 3426.

Test Mark Industries, I. (2015). *iD Operators Manual CM-2500 iD*. Test Mark Industries.

Therond, E., Bois, A.-P., Whaley, K., & Murillo, R. (2016). Large scale testing & modelling for cement zonal isolation of water injection wells. SPE Annual Technical Conference and Exhibition?,

Vargas, C. A., Caracciolo, L., & Ball, P. J. (2022). Geothermal energy as a means to decarbonize the energy mix of megacities. *Communications Earth & Environment*, *3*(1), 66.

Wu, B., Arjomand, E., Tian, W., Dan, B., & Yan, S. (2020). Sealant technologies for remediating cement-related oil and gas well leakage. *CSIRO*.

Zhang, Z., & Wang, H. (2017). Effect of thermal expansion annulus pressure on cement sheath mechanical integrity in HPHT gas wells. *Applied Thermal Engineering*, *118*, 600-611.